**The EUChemSoc Societies have taken the significant step into the future by merging their traditional journals, to form two leading chemistry journals, the *European Journal of Inorganic Chemistry* and the *European Journal of Organic Chemistry.* Three further EUChemSoc Societies (Austria, Czech Republic and Sweden) are Associates of the two journals.**

## COVER PICTURE

**The cover picture shows** the role played by synthetic metalloenzyme analogues in uncovering the relationship between metalloenzyme active site structure, properties, and function at the molecular level. Details are presented in the Microreview by L. M. Brines and J. A. Kovacs on p. 29 ff.

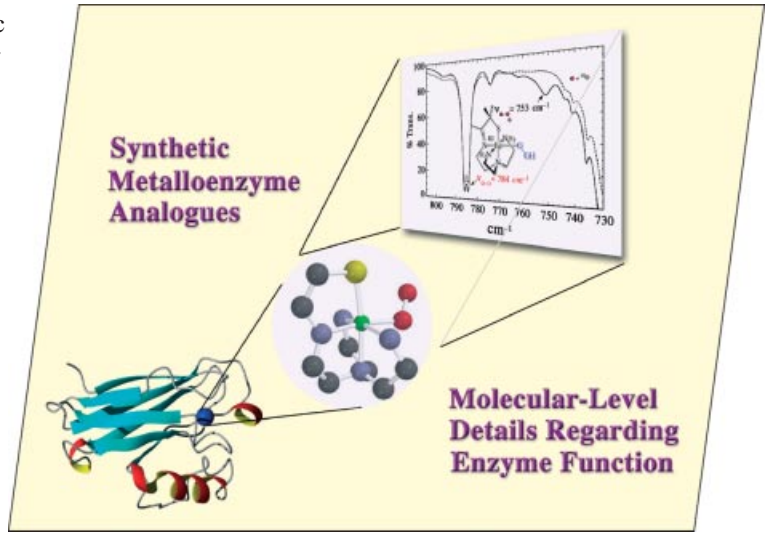


 © 2007 Wiley-VCH Verlag GmbH & Co. KGaA, Weinheim 

# Jubilees and Anniversaries

**Karen Hindson**
**Editor, EurJIC**

When 13 societies are co-owners of a journal, it must be quite likely that important milestones in their history overlap. This year several important anniversaries, not only of EurJIC's owner societies but also of the publisher John Wiley & Sons, Inc. and of the journal itself, coincide. EurJIC congratulates the Hungarian Chemical Society (MKE) on 100 years and the French Chemical Society (SFC) on 150 years of service to chemists and chemistry in their countries. The SFC is the oldest society associated with EurJIC, but the countries in Europe awoke to the importance of chemistry within a short spate of time. In the nineteenth and early twentieth centuries, farsighted chemists formed these associations to advance chemistry and promote exchange of knowledge, not only within their countries but across the boundaries. Table 1 lists the dates of foundation of our partner societies, but here I would like to mention the German Chemical Society, which set down its roots 140 years ago; one of the Belgian Societies, La Société Royale de Chemie (SRC), which is 20 years younger; the Czech Society, which is heading into its 15th decade; and the Austrian Chemical Society, which was established in 1897. EurJIC and the other members of the family of European journals bear witness to the success of the societies in one of their goals − the dissemination of knowledge across the world.

The printed word has been the business of John Wiley & Sons for 200 years (see the pages following this editorial). My contact with the company started with my first year at university − it is my pleasure to work for the publisher that probably had the most impact on my career in chemistry. Its excellence in publishing facilitated my studies through comprehensive textbooks and the outstanding journals that are now part of its program.

Finally, the latest anniversary is that of EurJIC itself. Although the journal in this form is only ten years old in 2007, one of the predecessor journals was founded before any of the societies. Yet you can read the first papers electronically in the Chemical Society Backfile Collection and jump to the reference rapidly through CrossRef. One of our projects underway at the moment is to provide electronic access to all the predecessor journals as quickly as possible. All will have the same convenient CrossRef feature.

What else is new in this auspicious tenth year?

Günter Schmid (Essen, Germany) and Ivano Bertini (Sesto Fiorentino, Italy), who since the first issue have worked hard to create this Inorganic Chemistry society journal,

Table 1. The European chemical societies that co-own EurJIC.

| Country | Society | Founded | Web address |
|---|---|---|---|
| Austria | Gesellschaft Österreichischer Chemiker (GÖCh) | 1897 | http://www.goech.at/ |
| Belgium | La Société Royale de Chimie (SRC) | 1887 | http://www.ulb.ac.be/assoc/src/ |
| Belgium | Koninklijke Vlaamse Chemische Vereniging (KVCV) | 1939 | http://www.kvcv.be/ |
| Czech Republic | Česká společnost chemická (ČSCh) | 1866 | http://www.csch.cz/ |
| France | Société Française de Chimie (SFC) | 1857 | http://www.sfc.fr/ |
| Germany | Gesellschaft Deutscher Chemiker (GDCh) | 1867 | http://www.gdch.de/ |
| Greece | Association of Greek Chemists (AGC) | 1924 | http://www.eex.gr/ |
| Hungary | Magyar Kémikusok Egyesülete (MKE) (Hungarian Chemical Society) | 1907 | http://www.mke.org.hu/ |
| | Magyar Tudományos Akadémia (Hungarian Academy of Sciences) | 1825 | http://www.mta.hu/ |
| Italy | Società Chimica Italiana (SCI) | 1909 | http://www.soc.it/ |
| The Netherlands | Koninklijke Nederlandse Chemische Vereniging (KNCV) | 1903 | http://www.kncv.nl/ |
| Portugal | Sociedade Portuguesa de Química (SPQ) | 1911 | http://www.spq.pt/ |
| Spain | Real Sociedad Española de Química (RSEQ) | 1903 | http://www.rseq.org/ |
| Sweden | Svenska Kemistsamfundet | 1883 | http://www.chemsoc.se/ |

 © 2007 Wiley-VCH Verlag GmbH & Co. KGaA, Weinheim 

have retired from the Editorial Board. Ivano in addition served as Chairman for eight years. My sincere thanks go to them for their advice and support. In these days of rapid publishing, it was essential that I could rely on their quick reply for any critical decision. Taking over as Chairman is Jan Reedijk (Leiden, the Netherlands). He brings long experience in publishing and a thorough knowledge of the journal and the Societies' standards to this position. The new members are Maurizio Peruzzini (Sesto Fiorentino), who adds expertise in the core inorganic chemistry areas of coordination chemistry and catalysis, and Ulrich Simon (Aachen, Germany), who has a broad background in inorganic chemistry including the topical nanoscience fields. On behalf of all members of the Board I welcome them and look forward to our closer collaboration in EurJIC.

New Board Members

My thanks are also due to the retiring members of the International Advisory Board. Three, Cornelis Elsevier (Amsterdam, the Netherlands), Bernt Krebs (Münster, Germany) and José González-Calbet (Madrid, Spain), also worked from the start to ensure the successful integration of their societies' journals into the new European Journal and two (Alejandro Vila, Argentina and Kazuko Matsumoto, Japan) joined this Board when, after the successful unification, members were invited from outside Europe. All have worked for EurJIC for many years and we appreciate their support. Their successors are Mauro Botta (Alessandria, Italy), Susumu Kitagawa (Kyoto, Japan), Nils Metzler-Nolte (Bochum, Germany), Barbara Milani (Trieste, Italy) and Joost Reek (Amsterdam).

You probably have already noticed that the Table of Contents has a new look. Our aims were to assist fast browsing of the contents by highlighting the individual papers optimally. A survey on the use of the Table of Contents revealed that although the graphics are useful, an additional short text helps in rapid orientation in the latest issue. The use of colour will make the selection of the graphic much easier in some fields of inorganic chemistry. The two templates available for authors on the homepage (www.eurjic.org) are a guide to the length and style required. Again to enable inorganic chemists to discover the latest developments in their field fast, in 2007 EurJIC will publish 36 issues. The rapid expansion of EurJIC at the beginning of the decade led to a long list of papers in each issue. A shorter Table of Contents, in particular with the key topic flag, ensures that important papers are less likely to be overlooked. *Chemistry – A European Journal* made this change in 2006. Its success persuaded EurJIC and its sister journal EurJOC to follow suit.

Easier To Browse Table of Contents

The Table of Contents of EurJIC – like those of any other journal available on Wiley InterScience – can now be accessed as RSS feeds. An RSS feed delivers updates of text content on web pages, determined by the user, to a computer or even a mobile phone. Once the news reader software program is installed and the Webpage selected, the feeds are automatic. Again, for more information, just visit the homepage of EurJIC and click on the orange RSS icon next to the cover picture. Authors and peer reviewers can also expect changes to simplify their collaboration with the journal. Many authors used our first templates ten years ago for the manuscripts they submitted. The state of the art has, however, changed since then: with peer review by PDF, the need to reduce the number of pages for review has become increasingly important, and graphics placed where they are intended facilitate the assessment. In addition, authors prefer to see how their article is likely to look in print. Soon EurJIC templates that mimic the print version will be available for all article types amongst the tools "for authors" on the journal homepage.

RSS Feeds Available

Templates Help Authors and Reviewers

In honour of the 10th anniversary of EurJIC, the journal will sponsor a poster prize at the 9th FIGIPAS meeting in Vienna from July 4–7, 2007 (http://figipas.tuwien.ac.at/). This European conference was selected, because, like the journal, it covers the full spectrum of Inorganic Chemistry. A special issue is planned to coincide with the conference.

Finally, at the start of this New Year in which Inorganic Chemistry will continue to search for new, improved materials or production protocols for a modern world, as well as for both an understanding of – and solutions for – the problems that exist, I wish all our authors and readers peace and prosperity in all continents of the world and fulfilment as your research contributes to these goals.

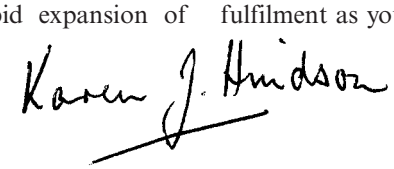

 © 2007 Wiley-VCH Verlag GmbH & Co. KGaA, Weinheim 

# A Passion for Publishing

*History of John Wiley & Sons, Inc.*

***Figure 1.*** Charles Wiley.

### *The Early Years*

**1807** Charles Wiley (Figure 1) opens small printing shop in Manhattan, New York City.

**1814** Wiley becomes a publisher and within five years begins to produce works by New York City's literary set, notably Fitz-Greene Halleck, Washington Irving, and James Fenimore Cooper.

**1826** John Wiley heads family business following his father's death, launching a 65-year career in publishing.

**1836** George Palmer Putman becomes junior partner, a relationship that leads to the publication of outstanding contemporary writers on both sides of the Atlantic. Together they achieve prominence publishing such works as Herman Melville's *Typee: A Peep at Polynesian Life*, Edgar Allan Poe's *The Raven*, and Nathaniel Hawthorne's *Mosses from an Old Manse*. They published the works of European writers such as Hans Christian Andersen, Victor Hugo, Charles Dickens, and Elizabeth Barrett Browning.

### *Changing Course*

**1848** Wiley & Putnam end their association. John Wiley broadens the company's publishing to include works on art, religion, architecture, agriculture, science, and technology.

**1849** Wiley publishes the first volume by art critic John Ruskin.

**1865** John's son Charles joins the firm to form John Wiley & Son.

**1876** William Halsted Wiley, another son of John, enters the business, creating John Wiley & Sons.

**1880** The handbook *Field Engineering* by Williams Searles is published, evidence of William Halsted Wiley's enthusiasm for engineering, railroads, and construction, marking a shift away from general-interest books and the marketing policies of his father. Wiley continues to expand into new fields, including electrical, civil and mechanical engineering, architecture, construction, agriculture, and chemistry (Figure 2).

**1890** William O. Wiley, eldest son of Charles joins the company as Secretary. He is the first member of the fourth generation to work at Wiley.

**1891** John Wiley dies at age 82. William Halsted Wiley becomes the new head of the company.

**1914** Edward Hamilton, nephew of William H. and Charles, joins the company.

**1925** William O. Wiley, eldest son of Charles, succeeds to the presidency after the death of William Halsted Wiley.

**1929** Sales top $1 million. Meanwhile, William O. Wiley begins to emphasize fields other than engineering and science. Wiley branches out into social sciences and business management publishing.

**1932** W. Bradford Wiley becomes the fifth generation to work at Wiley.

**1941** Edward P. Hamilton, a nephew of William Halstead Wiley and Charles Wiley, succeeds William O. Wiley as President. Staff numbers about ninety, including a dozen travellers, a precursor of Sales Representatives today. Travellers canvassed colleges and universities in search of course adoptions for existing titles and manuscript submissions. Sales pass $2 million mark, a new record.

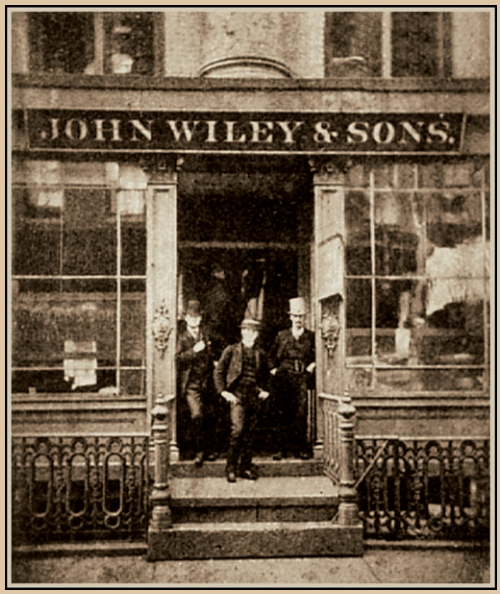


***Figure 2.*** Photo of John Wiley & Sons entrance (1880).

## *Building a Modern Corporation*

**1956** W. Bradford Wiley, age 46, succeeds Hamilton as President.

**1957** Wiley marks 150th anniversary.

**1960** Wiley opens its first international subsidiary in London.

**1962** First public sale of company stock.

**1963** Wiley opens Wiley Australasia in Sydney.

**1965** Sales top $20 million and three years later reach $30 million as operations expand to Mexico, South America, Australia, and Japan.

**1968** W. Bradford Wiley's daughter, Deborah, the sixth generation involved in the family business, joins the company. Wiley opens Canadian office in Toronto.

**1971** Andrew H. Neilly becomes President and Chief Operating Officer of John Wiley & Sons. W. Bradford Wiley becomes Chairman, continuing as Chief Executive Officer.

**1978** Publishing activities are realigned into four major groups: professional, educational, international, and medical.

**1979** Andrew Neilly's responsibilities increase as he becomes Chief Executive Officer, continuing as Chief Operating Officer. Bradford Wiley II, son of W. Bradford, joins the company's Board of Directors.

**1982** Wiley celebrates 175 years of publishing and expanded beyond its traditional businesses into the area of business education and training with the acquisition of Wilson Learning Corporation.

**1984** Peter Booth Wiley, son of W. Bradford Wiley joins the company's Board of Directors.

**1985** The Business, Law, and General book division (later renamed the Professional/Trade publishing division, as it is known today) is founded.

**1988** Ruth McMullin succeeds Andrew Neilly as President and Chief Executive Officer.

**1989** Wiley significantly expands its scientific, technical, and medical publishing program with the acquisition of Alan R. Liss, Inc., a leading publisher of journals and books in the life sciences.

**1990** Charles R. Ellis succeeds Ruth McMullin as President and Chief Executive Officer.

**1993** Brad Wiley II succeeds his father as Chairman of the Board.

## *Planning, Expansion, and Property*

**1995** Wiley first establishes http://www.wiley.com/ the company's Web site. It continues to evolve providing access to Wiley products and services, such as Wiley InterScience.

**1996** Wiley acquires a 90% interest in VCH, an important scientific, technical, and professional publisher based in Weinheim (Figure 3). VCH, founded in 1921, is one of the leading technical publishers in Germany with an emphasis on science. For several years, technical and specialist information in print and electronic form, for professionals and experts, has been a major focus. VCH has a longstanding publishing partnership with the German Chemical Society, and the acquisition of the VCH Group, which now includes Ernst & Sohn, Verlag Helvetica Chimica Acta, and GIT Verlag, further strengthens Wiley's leadership in these markets.

***Figure 3.*** Photo of Wiley-VCH entrance.

**1997** Wiley acquires Van Nostrand Reinhold (VNR), an eminent publishing imprint of books and electronic products for professionals in architecture/design, environmental/industrial science, culinary arts/hospitality, and business technology.

**1998** William J. Pesce (Figure 4) is named President and Chief Executive Officer, becoming the tenth leader of the company. Pesce contributes significantly to the growth and profitability of the company's global publishing program. Wiley is selected as one of the "most respected companies" with "a strong and well thought out strategy," by the *Financial Times* in a global survey of Chief Executive Officers.

**1999** Wiley commercially launches Wiley InterScience (http://www.interscience.wiley.com/) which provides online access to journals, major reference works, and books, as well as such key resources as the Cochrane Library of evidence-based medicine databases. Later Wiley will undertake an initiative to digitize all its journal backfile holdings. When completed Wiley InterScience will be one of the largest archives of its kind with content dating back to 1799, and over 1.6 million articles of scholarly and scientific research.

**1999** Wiley acquires Pearson Education's college textbooks and instructional packages in biology/anatomy and physiology; engineering; mathematics; economics/finance; and teacher education; the San Francisco-based Jossey-Bass, a publisher of books and journals for professionals and executives in business, psychology, education, and health management; and the J. K. Lasser tax and financial guides to enhance its already strong presence in the financial planning market.

**2001** Wiley acquires Hungry Minds, Inc., the largest acquisition in the company's history to date. Through it, a portfolio of high profile brands came under the umbrella, including the *For Dummies* series, the *Webster's New World*™ dictionaries and *CliffsNotes*™ study guides, the *Frommer's*™ travel guides, and the *Betty Crocker*® and *Weight Watchers*® cookbooks.

**2002** Peter Booth Wiley (Figure 4) installed as Chairman, succeeding Brad, who continues to serve as a Board member. Wiley relocates its global headquarters from New York City to a new building on the waterfront in Hoboken, New Jersey.

**2003** *Working Mother* magazine lists Wiley as one of the "100 Best Companies for Working Mothers". The company also receives the Enterprise Award from the New Jersey Business & Industry Association in recognition of the contribution to the state's economic growth.

**2005** FORTUNE magazine names Wiley one of the "100 Best Companies to Work For." Wiley receives this distinction for the second consecutive year in 2006.

**2006** Wiley acquires outstanding shares of Wiley Dreamtech (India) Private Ltd., and renames it, Wiley India Private Ltd. The acquisition enables Wiley to strengthen its presence in India. Wiley Canada is named to Canadian Business magazine's 2006 list of "100 Best Workplaces in Canada," and Wiley Australia receives the Australian governments's "Employer of Choice for Women" citation as it has every year since its inception in 2001. Wiley reaches a significant milestone in fiscal year 2006 and reports revenue of $1 billion. Wiley acquires Blackwell Publishing (Holdings) Ltd., one of the world's foremost academic and professional publishers. The combined Wiley and Blackwell business will publish approximately 1,250 scholarly peer-reviewed journals as well as an extensive collection of books with global appeal.

**2007** Wiley celebrates 200 years of publishing.

***Figure 4.*** William J. Pesce, William H. Wiley (picture), and Peter Booth Wiley.

EurJIC European Journal of Inorganic Chemistry

# MICROREVIEW

Synthetic models of the iron enzyme superoxide reductase (SOR) are described that, in combination with biochemical studies, are beginning to generate a clearer picture of the biological mechanism of superoxide reduction. Iron−peroxo species, trapped at low temperatures, are shown to be viable SOR intermediates, and provide key spectroscopic parameters for their identification.

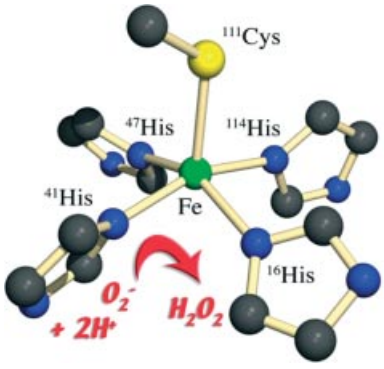


**Functional Metalloenzyme Models**

**L. M. Brines, J. A. Kovacs* ..... 29−38**

Understanding the Mechanism of Superoxide Reductase Promoted Reduction of Superoxide

**Keywords:** Bioinorganic chemistry / Metalloenzymes / Thiolate-ligated nonheme iron / Superoxide

# SHORT COMMUNICATIONS

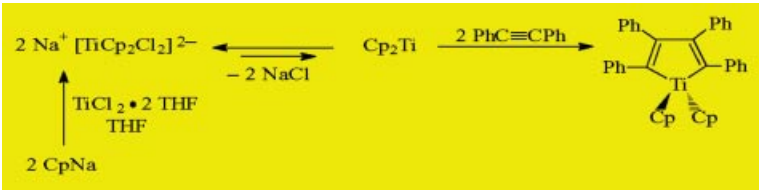


Titanocene(II) has been directly synthesized by the interaction of THF-soluble titanium(II) chloride with two equivalents of cyclopentadienylsodium in THF solution at 0°C. Because of the instability of titanocene(II), it was trapped in high yield as 1,1-bis(cyclopentadienyl)-2,3,4,5-tetraphenyltitanacyclopentadiene with diphenylacetylene.

**Carbenoid Character of Titanocene(II)**

**J. J. Eisch,* A. A. Adeosun, J. M. Birmingham ..... 39−43**

The Transient Titanocene(II): Direct Synthesis from Solvated Titanium(II) Chloride and Cyclopentadienylsodium and Ensuing Interception with Diphenylacetylene as 1,1-Bis-(cyclopentadienyl)-2,3,4,5-tetraphenyltitanacyclopentadiene

**Keywords:** Titanocene / Wilkinson metallocene synthesis / Epititanation

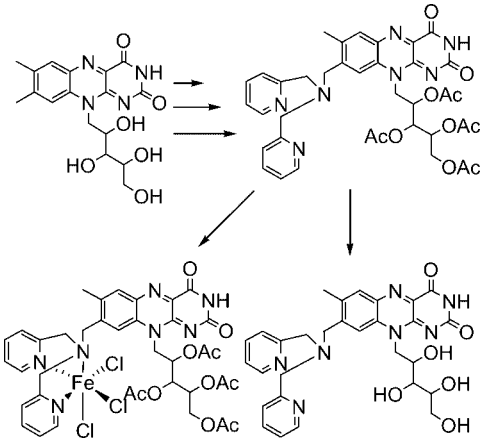


The preparation of the 8α-[bis(2-pyridylmethyl)amine]-*N*-Ac$_4$riboflavin ligand is reported. The trichloroferric complex has been prepared, and together with the low potential reduction wave of the flavin moiety, the presence of a reversible $Fe^{III}$/$Fe^{II}$ couple at a higher potential is observed. The deacetylated ligand 8α-[bis-(2-pyridylmethyl)amine]-*N*-riboflavin can easily be obtained.

**Chelates Linked to Vitamin B2**

**N. K. Thallaj, D. Mandon,* K. A. White ..... 44−47**

The Design of Metal Chelates with a Biologically Related Redox-Active Part: Conjugation of Riboflavin to Bis(2-pyridylmethyl)amine Ligand and Preparation of a Ferric Complex

**Keywords:** N ligands / Iron complexes / Riboflavin / Electrochemistry / Electron mediators

 © 2007 Wiley-VCH Verlag GmbH & Co. KGaA, Weinheim 

# CONTENTS


### Resonance Raman Overtones

**R. Beaulac, A. B. P. Lever,* C. Reber* ..... 48–52**

Resonance Raman Spectroscopy with Overtones Involving Metal-Ligand and Ligand-Centered Modes in (*o*-Benzoquinonediimine)ruthenium(II) Complexes

**Keywords:** Raman spectroscopy / Ruthenium complexes / Charge transfer / Density functional calculations / Luminescence

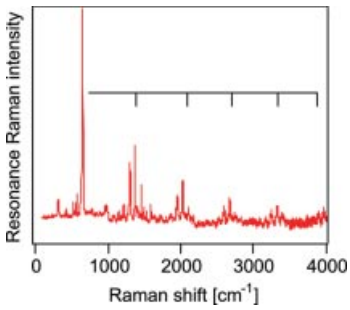


Resonance Raman spectra with visible excitation wavelengths show distinct resonance enhancements and intense overtone and combination bands resulting from charge-transfer excitations. Assignments of fundamental bands are based on theoretical spectra obtained from DFT calculations.


## FULL PAPERS


### Phosphorylcarborane Complexes

**J. M. Dou,* D. P. Zhang, D. C. Li, D. Q. Wang ..... 53–59**

Synthesis and Crystal Structure of Three Carborane Complexes, [M{7,8-(OPPh$_2$)$_2$-7,8-$C_2B_9H_{10}$}$_2$] (M = Cu, Zn) and [Ni(thf)-{7,8-(OPPh$_2$)$_2$-7,8-$C_2B_9H_{10}$}$_2$]·thf, and Two Carborane Compounds, 1-(OPPh$_2$)-2-(PPh$_2$)-1,2-$C_2B_{10}H_{10}$ and H[7,8-(OPPh$_2$)$_2$-7,8-$C_2B_9H_{10}$]·0.25$C_2H_5OH$

**Keywords:** Cu complexes / Zn complexes / Ni complexes / Carborane complexes / Oxidation / Degradation

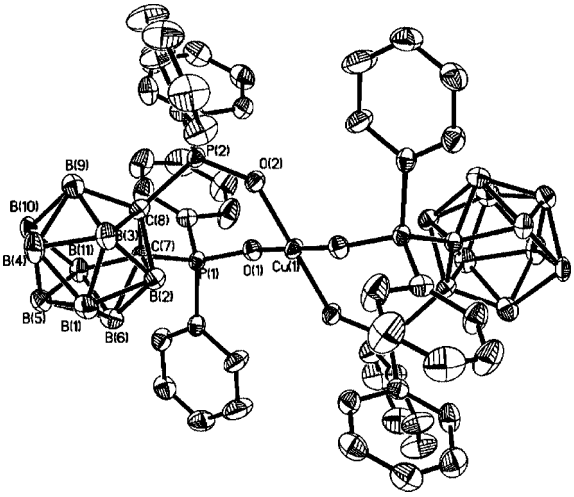


Three new carborane complexes containing a phosphoryl-*nido*-carborane ligand were synthesized by the reactions of 1,2-(PPh$_2$)$_2$-1,2-$C_2B_{10}H_{10}$ with three inorgnic compounds in ethanol in air. Two other phosphoryl compounds were also obtained through the oxidation of the *closo* ligand in air.

### Supported Membranes

**M. Arnold,* P. Kortunov, D. J. Jones, Y. Nedellec, J. Kärger, J. Caro ..... 60–64**

Oriented Crystallisation on Supports and Anisotropic Mass Transport of the Metal-Organic Framework Manganese Formate

**Keywords:** Organic–inorganic hybrid composites / Membranes / Anisotropic mass transport / Oriented crystallisation / Manganese

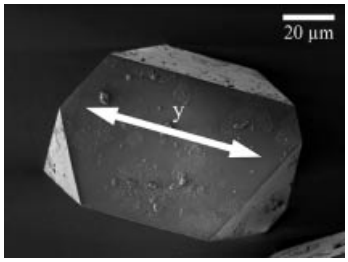


The MOF manganese formate was examined regarding its ability to be applied in supported gas-separating membranes. For this purpose, the anisotropic mass transport of methanol in the MOF has been investigated by IFM, proving a 1D channel system. Additionally, the oriented crystallisation of the manganese formate on different supports has been investigated by XRD and SEM.


 © 2007 Wiley-VCH Verlag GmbH & Co. KGaA, Weinheim 

## O−O Bond Cleavage

Density functional theory reveals two distinct pathways for the decomposition of an $LFe^{II}(H_2O_2)$ complex to $LFe^{IV}(O)$ and water. One pathway involves initial O−O bond homolysis followed by hydrogen-atom transfer while in the other proton transfer precedes O−O bond heterolysis. The barriers to the two processes are rather similar, suggesting that subtle changes in the identity of L or in the reaction conditions may cause a complete change in mechanism.

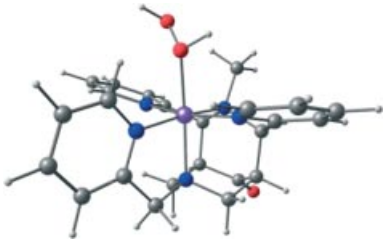

**A. E. Anastasi, A. Lienke, P. Comba, H. Rohwer, J. E. McGrady* ..... 65−73**

Competing Radical and Non-Radical Pathways for the Decomposition of $LFe^{II}(H_2O_2)$ Complexes: a Density Functional Study

**Keywords:** Density functional calculations / Oxido ligands / O−O activation / Electronic structure / Transition states

## Copper-Iron Chalcogenide Clusters

Reactions of mixtures of copper and iron salts with $PhSeSiMe_3$ led in the prescence of phosphanes or ammonium salts to the formation of mixed copper-iron selenolate cluster molecules. Heating of the clusters results in the formation of mixtures of binary $Cu_2Se$ and ternary $CuFeSe_2$.

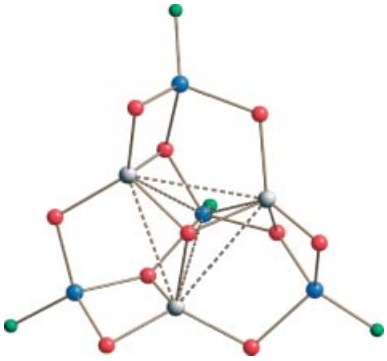

**A. Eichhöfer,* D. Fenske, J. Olkowska-Oetzel ..... 74−79**

Synthesis and Structure of $[n\mathrm{Pr_3N(CH_2)_6N}n\mathrm{Pr_3}][CuFe_3Br_3(SePh)_6]$, $[Cu_5Fe(SePh)_7(PPh_3)_4]$ and $[Cu_4Fe_3(SePh)_{10}(PPh_3)_4]$

**Keywords:** Iron / Copper / Selenium / Cluster compounds

## Bimetallic Ion Pairs

Complexes of the type [Cp*MCl(N−N)][X] (M = Rh and Ir) have been synthesised, where N−N is a series of bidentate ligands with $sp^2$ N-donors and X = $[Cp^*MCl_3]^-$, $Cl^-$ or $BF_4^-$.

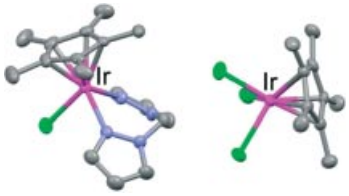


**D. F. Kennedy, B. A. Messerle,* M. K. Smith ..... 80−89**

Synthesis of Cp* Iridium and Rhodium Complexes Containing Bidentate $sp^2$-N-Donor Ligands and Counter-Anions $[Cp^*MCl_3]^-$

**Keywords:** Iridium(III) / Rhodium(III) / N-donor ligands / Cyclopentadienyl ligands

## Ligand Conformation

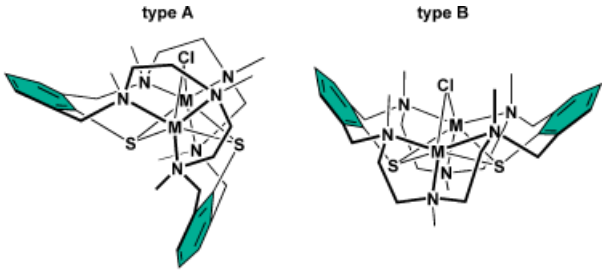


**M. Gressenbuch, B. Kersting* ..... 90−102**

Synthesis and Characterisation of Dinuclear Nickel(II) and Cadmium(II) Complexes of *N*-Alkylated Derivatives of Hexaazadithiophenolate Macrocycles

**Keywords:** Macrocyclic ligands / N ligands / S ligands / Nickel / Cadmium

The effect of *N*-alkylation on the coordination properties of macrocyclic $N_6S_2$ ligands has been examined. The ligand conformation adopted depends on the type of the coligand, the metal ion radius, and the *N*-alkylation grade.

 © 2007 Wiley-VCH Verlag GmbH & Co. KGaA, Weinheim 

# CONTENTS


## (Sulfinylamino)ferrocenes

**B. Wrackmeyer,* E. V. Klimkina, W. Milius, M. Siebenbürger, O. L. Tok, M. Herberhold ..... 103–109**

Ferrocenes Bearing Sulfinylamino Groups

**Keywords:** Ferrocenes / Sulfinylamine pendant groups / Electronic structure

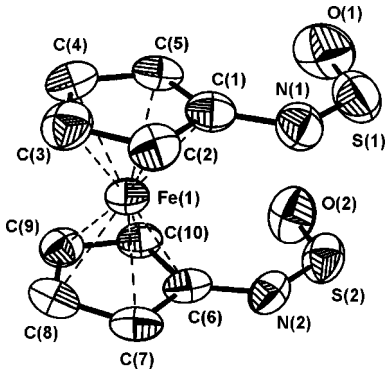


Three new (sulfinylamino)ferrocenes [1,1'-bis(sulfinylamino)ferrocene, 6-amino-1-sulfinylaminoferrocene, 1-sulfinylamino-6-(trimethylsilylamino)ferrocene] were prepared and characterised by X-ray structural analysis in the solid state, and by $^{1}H$, $^{13}C$, $^{14}N$, $^{15}N$, $^{29}Si$ and $^{57}Fe$ NMR spectroscopy in solution.

## Structure–Back Bonding Correlation

**C. Makedonas, C. A. Mitsopoulou* ..... 110–119**

$W(CO)_4$(diimine) Structure Revised – Correlating Structure to π* Back-Bonding

**Keywords:** Tungsten / Pi interactions / N ligands / Carbonyls / Ligand effects

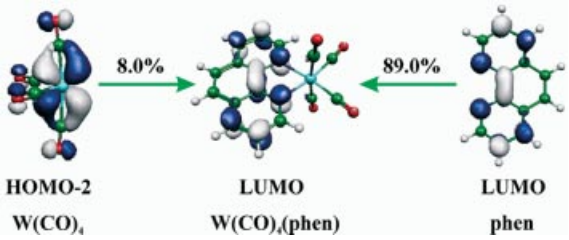


DFT calculations carried out on a series of $W(CO)_4$(diimine) compounds reveal that the best indices for the extent of back donation are both the deviation of C–W–C and O–C–W angles from orthogonality and linearity, respectively. This is quantitatively described by a structure–properties relation.

## Conformation and Electronic Structure

**C. Makedonas, I. Veroni, C. A. Mitsopoulou* ..... 120–131**

Pentacarbonyl[2-(2′-pyridyl)quinoxaline-κ$N^4$]tungsten: A Combined Study of Its Conformational and Electronic Structure Based on Experimental and DFT-TDDFT Data

**Keywords:** Pentacarbonyl complexes / Monodantatepyridyl)quinoxaline / Tungsten / TD-DFT calculations / Pi stacking

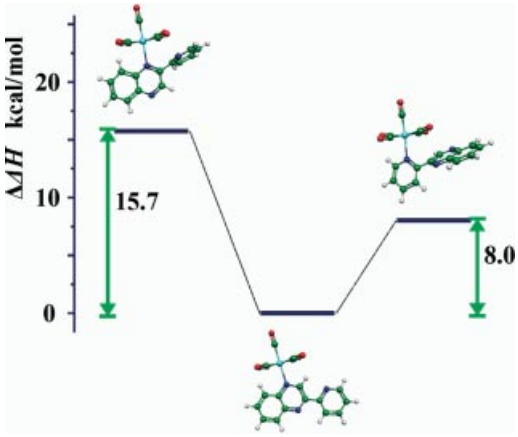


The title compound is isolated en route to photolytic $W(CO)_4$pq chelate ring closure and it is the first example where the pq ligand is coordinated in a monodentate fashion. The preference of the coordinated nitrogen atom is elucidated both experimentally by spectroscopic and crystallographic methods and theoretically by means of DFT and TDDFT calculations.


 © 2007 Wiley-VCH Verlag GmbH & Co. KGaA, Weinheim 

## Pd/Imidazolines in Allylic Alkylations

**A. Bastero, A. F. Bella, F. Fernández, S. Jansat, C. Claver,* M. Gómez,* G. Muller, A. Ruiz, M. Font-Bardía, X. Solans ..... 132–139**

First Allylpalladium Systems Containing Chiral Imidazolylpyridine Ligands – Structural Studies and Catalytic Behaviour

**Keywords:** Palladium / Chiral imidazolines / Catalysis / Allylic alkylation / Intermediates / Heterocycles

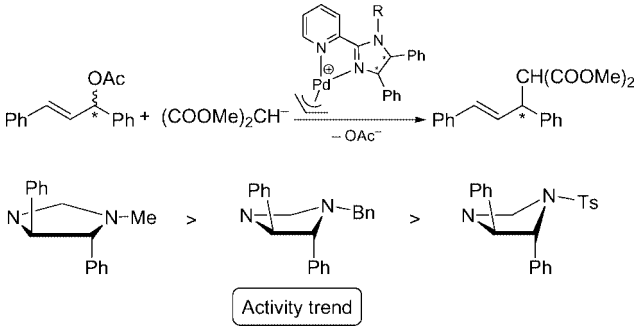


Palladium/chiral imidazolylpyridines systems were tested in allylic alkylation of *rac*-3-acetoxy-1,3-diphenyl-1-propene and 3-acetoxy-1-phenyl-1-propene, paying particular attention to the influence of the amine nitrogen hybridisation on their catalytic behaviour. Allylpalladium intermediates containing phenylallyl groups were synthesised and fully characterised both in solution (NMR) and the solid state (single-crystal X-ray diffraction).

## Hemilabile Clusters

**E. V. Grachova, G. Linti, H.-G. Stammler, B. Neumann, S. P. Tunik,* H. Wadepohl ..... 140–146**

Reactions of GaCp* with a Hemilabile Derivative of $Rh_6(CO)_{16}$ – Synthesis and Structural Characterization of Two Novel Heterometallic Clusters: $Rh_6(CO)_{13}(\mu,\kappa^3\text{-}Ph_2PC_2H_3)(\mu_3\text{-}GaCp^*)$ and $Rh_6(CO)_{13}(\kappa^1\text{-}Ph_2PC_2H_3)(\mu_3\text{-}GaCp^*)_2$

**Keywords:** Cluster compounds / Heterometallic complexes / Phosphane ligands

Reaction of the $Rh_6(CO)_{14}(Ph_2PCH{=}CH_2)$ cluster containing hemilabile diphenylvinylphosphane with GaCp* (Cp* = $C_5Me_5$) affords two novel heterometallic clusters, $Rh_6(CO)_{13}(\mu,\kappa^3\text{-}Ph_2PC_2H_3)(\mu_3\text{-}GaCp^*)$ and $Rh_6(CO)_{13}(\kappa^1\text{-}Ph_2PC_2H_3)(\mu_3\text{-}GaCp^*)_2$.

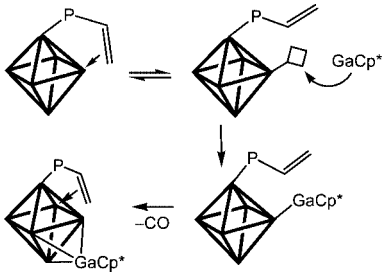


## Ti Complexes in Polymerisation

**M. González-Maupoey, T. Cuenca,* L. M. Frutos, O. Castaño, E. Herdtweck, B. Rieger ..... 147–161**

Alkylmono(cyclopentadienyl)titanium Complexes Containing the 2,2′-Methylenebis(6-*tert*-butyl-4-methylphenoxido) Ligand – Studies on the Nature of the Catalytic Species Present in α-Olefin Polymerisation Processes

**Keywords:** Titanium / Chelates / Olefin polymerisation / Density functional calculations

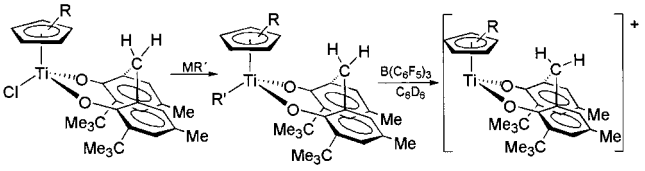


The synthesis of 2,2′-methylenebis(6-*tert*-butyl-4-methylphenoxido)titanium complexes is described. Structural data are derived from DFT methods and X-ray diffraction studies. The complexes polymerise α-olefins when activated with MAO or $[Ph_3C][B(C_6F_5)_4]$, while they are inactive in the presence of $B(C_6F_5)_3$. Stoichiometric reactions with Lewis acids were studied by NMR spectroscopy.

 © 2007 Wiley-VCH Verlag GmbH & Co. KGaA, Weinheim 

# CONTENTS


## Iron Complexes with Tridentate Ligands

**P. Pelagatti,* A. Bacchi, M. Balordi, A. Caneschi, M. Giannetto, C. Pelizzi, L. Gonsalvi, M. Peruzzini, F. Ugozzoli ..... 162–171**

A Ligand-Driven Geometry Switch in Octahedral and Trigonal-Bipyramidal Iron Complexes Containing (H)PNO and PNN Ligands

**Keywords:** Iron / N,P ligands / Ligand effects

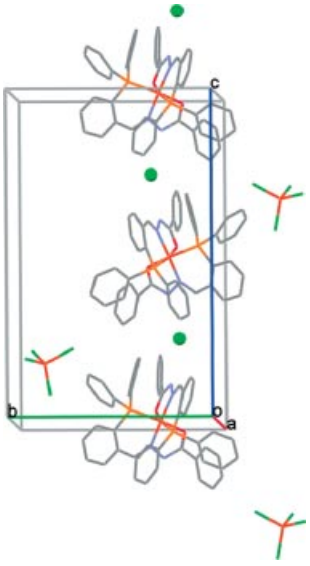


Complexation reactions of $Fe^{II}$ and $Fe^{III}$ salts with the tridentate ligands (H)PNO and PNN are reported. (H)PNO leads to the formation of the octahedral cation *fac*-$[Fe\{\kappa^3\text{-(H)PNO}\}_2]^{n+}$ ($n$ = 2 or 3), while PNN leads to the formation of the trigonal-bipyramidal complex [*mer*-Fe($\kappa^3$-PNN)$Cl_2$].

## Tetraazamacrocyclic Complexes

**A. Rybka, R. Koliński, J. Kowalski, R. Szmigielski, S. Domagała, K. Woźniak,* A. Więckowska, R. Bilewicz,* B. Korybut-Daszkiewicz* ..... 172–185**

Tuning the Properties of Neutral Tetraazamacrocyclic Complexes of Copper(II) and Nickel(II) for Use as Host–Guest Compounds with Bismacrocyclic Transition Metal Cations

**Keywords:** Macrocyclic ligands / Copper / Nickel / Cyclic voltammetry / Template synthesis

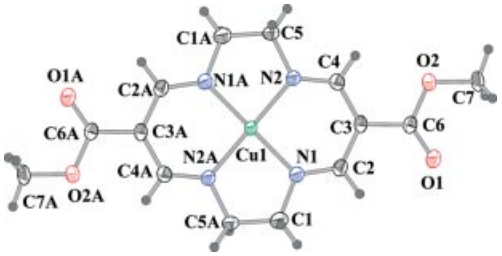


Deviations from planarity increase with increasing size of the tetraazamacrocyclic ligands and their neutral and protonated 14-, 15-, and 16-membered complexes of $Cu^{II}$ and $Ni^{II}$. As a consequence, the donor properties are weaker, the redox potential is shifted towards more positive values, and contribution of chemical reactions can also be observed. The formation of host–guest complexes between the strongest metal-containing donors and transition-metal-containing bismacrocyclic acceptors of suitable size is proved in solution and the gas phase by voltammetric and ESI MS methods. The transition metal building blocks described in this contribution could be applied in the synthesis of new redox-active rotaxane and catenane systems.

## Coordination Polymers

**S. Benmansour, F. Setifi, S. Triki,* J.-Y. Salaün, F. Vandevelde, J. Sala-Pala, C. J. Gómez-García,* T. Roisnel 186–194**

New Multidimensional Coordination Polymers with $\mu_2$- and $\mu_3$-dcno Cyano Carbanion Ligand {dcno$^-$ = $[(NC)_2CC(O)O(CH_2)_2OH]^-$}

**Keywords:** Cyano carbanions / Bridging ligands / Coordination polymers / Multidimensional networks / Magnetic properties

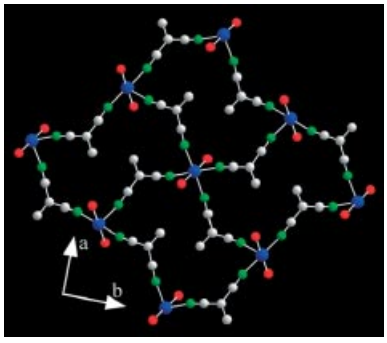


This study involves the design of multidimensional transition metal compounds with the cyano carbanion dcno$^-$ acting as $\mu_2$- and $\mu_3$-bridging ligand. The bonding affinity and flexibility of the cyano carbanion ligand towards transition metal ions are clearly illustrated.


**If not otherwise indicated in the article, papers in issue 24 were published online on December 6, 2006**

 © 2007 Wiley-VCH Verlag GmbH & Co. KGaA, Weinheim

## 1.General Information

The *European Journal of Inorganic Chemistry (EurJIC)* publishes 36 issues per year.

**Manuscripts should be submitted online** using our online submission service at http://www.manuscriptXpress.org. You should prepare a **single file containing all tables, graphics, supporting information (where appropriate) etc.** Acceptable file formats are **Microsoft Word, Rich Text Format, Postscript and PDF**. Avoid the use of page breaks even between the title page and the introduction. If graphics are included at the end of the manuscript, try to fit as many as possible onto a single page. The file should have margins of 2 cm and be 1.5-line spaced.

Authors can follow the progress of their manuscript on their **personal homepage**, which is created automatically upon initial registration. This homepage is the same for the family of Wiley-VCH European journals and can be used to **store the latest version of a submitted paper** and to **upload the document file after acceptance**. Your referee reports for the family of Wiley-VCH European journals are also archived here.

**No paper copies of the manuscript are required when using this system.**

- EurJIC does not publish manuscripts that have already appeared in print or electronically. **The author must inform the editor of manuscripts submitted, soon to be submitted, or in press at other journals that have a bearing on the manuscript being submitted.** If a manuscript is, in fact, a revised/extended version of a manuscript previously rejected by EurJIC, **the author must inform the editor about the previous submission in the cover letter and explain in detail which changes have been made**. The *Ethical Guidelines for Publication in Journals and Reviews* issued by the European Association for Chemical and Molecular Sciences (EuCheMS) are followed and applied by the editors of EurJIC. **Authors should reveal all sources of funding for the work presented in the manuscript and should declare any conflict of interest.**
- Manuscripts containing **animal experiments** must include a statement in the Experimental Section to state that permission was obtained from the relevant national or local authorities. The institutional committees that have approved the experiments must be identified and the accreditation number of the laboratory or of the investigator given where applicable. If no such rules or permissions are in place in the country where the experiments were performed, then this must also be clearly stated. Manuscripts with experiments with **human subjects** or **tissue samples** from human subjects must contain a disclaimer in the Experimental Section to state that informed signed consent was obtained either from the patient or from next of kin.
- The correspondence author of a Microreview will receive a complimentary copy of the journal along with a PDF file of his/her paper restricted to 50 printouts; the correspondence author of other articles will receive a PDF file restricted to 25 printouts. Colour figures can be reproduced. Unless the editor deems colour to be essential for the understanding of a paper, authors will be requested to make a contribution towards the costs of colour reproduction. Details will be provided after acceptance of the manuscript.
- We encourage authors to submit pictures for the cover page. A template of our cover page, **eurjiccover.pdf**, can be reached by clicking the link "For Authors" on our journal homepage (http://www.eurjic.org), to help you visualize the final effect of your design.

**IMPORTANT:** Any manuscript already available on personal/group web pages will be considered by the editors as already published and will not be accepted.

On behalf of our authors who are also US National Institutes of Health (NIH) grantees, Wiley-VCH will deposit the peer-reviewed version of the manuscript in PubMed Central (PMC). PMC may display the material 12 months after Wiley-VCH has published the article. By assuming this responsibility, we will ensure that our authors are in compliance with the NIH request and make certain that the appropriate version of the manuscript is deposited. We await the release by PMC of the protocols regarding manuscript submission. We reserve the right to change or rescind this policy.

## 2. Types of Contributions

**EurJIC publishes articles on inorganic, organometallic, bioinorganic, physical inorganic and solid-state chemistry. EurJIC is a fully peer-reviewed journal. An author may appeal against the decision on his/her manuscript, in writing. Three types of contributions are accepted for publication:**

- **Full Papers** are articles with an Experimental Section that describe a significant contribution to the development of an area of research of importance. There are no restrictions placed on the length of a Full Paper.
- **Short Communications** are brief reports on results of high significance and urgency. Generally, they are no longer than 8–10

 © 2007 Wiley-VCH Verlag GmbH & Co. KGaA, Weinheim 

1.5-line-spaced pages or 3–4 typeset pages. An Experimental Section (as a separate paragraph or as part of the references) is desirable; if it is not included in the paper, the experimental data should be submitted as Supporting Information for refereeing purposes, and marked as such. A justification for urgent publication should accompany submission.

- **A Microreview** is a highly focused overview of a selected topic. In general it includes a concise overview of the author's own research; reference to all appropriate work by others is essential, but the Experimental Sections of the original papers should not be repeated. As a rule, Microreviews are written on invitation, although unsolicited articles are also welcome. It is recommended, however, to contact the editor before submitting an unsolicited Microreview. The content should balance scope with depth in 25–30 1.5-line-spaced pages or 10–12 typeset pages. Microreviews will undergo peer review.

## 3. Manuscript Preparation

### 3.1 General

The whole of the manuscript should be 1.5-line spaced and in a large script (Times New Roman, 12 pt). We recommend that you prepare your text with **Microsoft Word (PC or Macintosh versions)** (see Section 3.2). Page numbers are essential: use the automatic pagination function incorporated in your word processing software. Leave a 2-cm margin around the perimeter of each page. **The figures, schemes and graphical abstract in the accepted version should be camera-ready**. Consult a current issue of the journal for an overview of the format. A manuscript should comprise: ✧ Title Page ✧ Keywords ✧ Abstract ✧ Main Text including Introduction, Results and Discussion etc. ✧ Experimental Section ✧ Acknowledgments (optional) ✧ Captions ✧ Tables ✧ References ✧ Schemes and Figures ✧ Graphical Abstract including a short text (max. 350 characters) and a graphical element (use of free colour is strongly recommended). Refer to the homepage Table of Contents template (http://www3.interscience.wiley.com/cgi-bin/jabout/27721/2005_guidelines.html). ✧ For Microreviews only: Biographical sketches and a portrait-quality photograph of all authors (when several authors from one institution are involved, group photographs are preferred).

### 3.2 Text

The text should be typed with carriage returns (hard returns) only at the end of a paragraph, title, heading and similar features. Avoid end-of-line word divisions.

**Abbreviations and acronyms** should be used sparingly and consistently. Where they first appear in the text, the complete term – apart from the most common ones such as NMR, IR, thf, *t*Bu etc. – should also be given.

**In the Experimental Section**, quantities of reactants, solvents etc. should be included in parentheses [e.g. A solution of triphenylphosphane (500 mg, 1.91 mmol) in dichloromethane (15 mL) was added to...].

**NMR spectroscopic data** should be quoted as in the following example: $^1$H NMR (300 MHz, $C_6D_6$, 25 °C): $\delta$ = 1.3 (s, 18 H, $SiMe_3$), 0.9 (d, $^3J_{H,H}$ = 5.7 Hz, 2 H, 2-H) ppm. For each chemical shift, additional information should be given in the order: multiplicity, coupling constant, number of protons, assignment.

**The purity of all new compounds** should be verified by elemental analysis to an accuracy within ±0.4%. In special cases, for instance when the compound is unstable or not available in sufficient quantities for complete analysis, the exact relative molecular mass obtained from a high-resolution mass spectrum and a clean $^{13}$C NMR spectrum (as additional material for inspection by the referees) should be supplied.

**Symbols of physical quantities**, but not their units (e.g. *T* for temperature, *J*, $\lambda$), stereochemical information (*cis*, *trans*, *Z*, *R*), locants (*N*-methyl), symmetry and space groups ($P2_1/c$), and prefixes in formulas (*t*Bu) or compound names (*tert*-butyl) **must be in italics**. Latin phrases, such as "in situ", should not.

**Stereochemical descriptors**, such as D- and L-, and molar (M) or normal (N) should be in **small capitals**. Use character formatting for italic and bold characters. Avoid any *special style sheets* to format these features. Write *capital letters* using the keyboard (shift + letter key), **not** the format "Capital letter" in Word.

**Use only characters from the Symbol and Normal Text character sets**, especially when inserting Greek letters and characters with umlauts, accents, tildes, etc.: α, ä, à, ã, Å.

There are three types of hyphens: normal dashes (-), en dashes (–), and em dashes (—). Use these as illustrated — spacing is important too — in the following examples:

| | |
|---|---|
| well-known reaction | C–H bond |
| six-membered ring | Tables 2–4 |
| 3-position of the ring | carbon–oxygen bond |
| signal-to-noise ratio | C–N stretch |
| Mo-$K_\alpha$ | Diels–Alder reaction |
| 1,2-dicyanobutane | structure–activity relationship |
| *p*-*tert*-butylphenol | 80–100 mg |
| (–)-tartaric acid | carried out at –10 °C |
| [$M^+$ – CH3] | $cm^{-1}$ |

Use the symbol × where appropriate, rather than the letter x:

... washed with water (2 × 150 mL) ...

Use the double quotation marks "..." rather than „...“, "..." or «...».

**Graphics (including structural formulas, schemes, figures, equations and small graphical items that appear in captions) must be submitted camera-ready on separate pages after acceptance of the manuscript (see Section 3.5).**

**Lines** or **arcs**, for example to indicate ring compounds, cannot be used within the text. Another method for indicating such compounds must be devised. Please contact the Editorial Office if any help is needed.

If practical, authors should use a systematic name (IUPAC or Chemical Abstracts) for each title compound in the Experimental Section. Please avoid complicated, multi-line names if a simpler version (e.g. alcohol **4**, ketone **5**, compound **6**) could be used instead. EurJIC follows the IUPAC rules of nomenclature as updated by the latest recommendations and revisions.

According to a recent recommendation [N. G. Connelly, T. Damhus, R. M. Hartshorn, A. T. Hutton (Eds.), *Nomenclature of Inorganic Chemistry IUPAC Recommendations 2005*, RSC Publishing, Cambridge, UK, **2005**]:

 © 2007 Wiley-VCH Verlag GmbH & Co. KGaA, Weinheim 

- "Names of anionic ligands, whether inorganic or organic, are modified to end in 'o'. In general, if the anion name ends in 'ide', 'ite' or 'ate', the final 'e' is replaced by 'o', giving 'ido', 'ito' and 'ato', respectively. It follows that halide ligands are named fluorido, chlorido, bromido and iodido, and coordinated cyanide is named cyanido. In its complexes, except for those of molecular hydrogen, hydrogen is always treated as anionic, and therefore 'hydrido' is used for hydrogen coordinating to all elements including boron."
- "In the formulae for coordination entities, ligands are now ordered alphabetically according to first symbol of the abbreviation or formula used for the ligand, *as written*, irrespective of the charge."
- "No numerical subscript should follow the square bracket used to enclose a whole coordination entity of a neutral (formal) coordination compound."

For further details, please see the "Frequently Asked Questions" section (http://www3.interscience.wiley.com/cgi-bin/jabout/27721/2005_faq.html) at the journal website and IUPAC publications and websites.

### 3.3 Tables

Use the Insert Table command from the Table menu or use the Insert Table button on the Standard toolbar for creating tables, and use tabs ONLY to move between cells.

### 3.4 References

We strongly recommend the use of the Endnotes feature of Word. If you prefer not to use this function, references should be indicated by numbers in square brackets as superscripts and, if applicable, after punctuation (example: text.[1]). Use the Format Font menu.

Journal titles should be abbreviated according to the Chemical Abstracts Service Source Index (CASSI).

The Author is responsible for correct citations. The *European Journal of Inorganic Chemistry* is a member of Cross Ref. (http://www.crossref.org), a service which links reference citations to the online content that those references cite. This can only function if the citations are accurate. Please ensure that a composite reference is subdivided into parts a), b) etc. For example:

[1] a) A. Einstein, A. N. Other, *Eur. J. Inorg. Chem.* **2003**, 1–15; b) R. Schoenfeld, *The Chemist's English*, 3rd ed., VCH, Weinheim, **1990**, p. 111.

If a paper has been published online but has not appeared in print yet, it is cited by listing the author names and then the abbreviated title of the journal followed by the DOI number, e.g.:

[1] J. J. Schneider, J. Engstler, *Eur. J. Inorg. Chem.*, DOI: 10.1002/ejic.200501145.

### 3.5 Graphics

Graphics are schemes, figures, equations and small graphical items that appear in captions. Graphics differ fundamentally from the text portion of your manuscript in that they must be scanned or electronically processed. Schemes should be self-explanatory: reaction conditions should therefore be given above the arrows rather than in the caption.

In the revised version please submit **each graphic in its own file** within a graphic folder. For good reproduction, the following formats are preferred: *.cdr, *.cdx, *.tif, *.pdf, *.psd, *.ai, *.fh, *.qxd, *.pct, *.eps. The resolution should be a minimum of 300 dpi and 600 dpi for bitmap graphics.

Consult the following table for the appropriate size of lettering. Lettering smaller than 3.0 mm will reproduce poorly. Please use only one size of lettering per graphic and the same letter font for all graphics.

Table 1. Guide for preparing graphics

| | | Maximum Graphic Width[a] | |
|---|---|---|---|
| **Letter Size** | **Font** | **1-Column Format** | **2-Column Format** |
| | Times New Roman | | |
| 3.0 mm | 12 | 13 cm | 26 cm |
| **3.5 mm** | **14** | **15 cm**[b] | – |
| **4.0 mm** | **16** | **17 cm**[b] | – |
| 4.5 mm | 18 | 19 cm | – |

[a] Most graphics are in 1-column format. [b] We prefer lettering of 3.5 or 4.0 mm with maximum graphic widths of 15 or 17 cm, respectively.

The settings for one-column graphics constructed with Chem Draw are: Print Setup: Orientation Portrait. Caption and Label Settings: Font Times New Roman, Font Style Standard, Size 12. These settings help ensure the correct letter-size-to-graphic-width ratio for best reproduction.

Use abbreviations such as $R^1$, $R^2$ (not $R_2$), R′, R′′, Ph, Me, Et, *i*Pr, *t*Bu, Ph, Bn (benzyl), Bz (benzoyl), Hal, L, M (metal), X (heteroatom).

## 4. Crystallographic Data

Authors must deposit the data of X-ray structure analyses in a crystallographic database before submitting their manuscript, so that referees can access the information electronically. The two databases, the Cambridge Crystallographic Data Centre (CCDC) and the Fachinformationszentrum Karlsruhe (FIZ) have the same procedure for the deposition of data and both will be pleased to provide help. In general, you will receive a depository number from the database two working days after electronic deposition. Send your data to the appropriate address below and quote the standard text, including the depository number, in your manuscript.

- **For all compounds without C–H bonds**

Fachinformationszentrum Karlsruhe (FIZ)
76344 Eggenstein-Leopoldshafen, Germany
Phone: +49-(0)7247/808-205
Fax: +49-(0)7247/808-666
E-mail: crysdata@fiz-karlsruhe.de
FTP: ftp.fiz-karlsruhe.de (under path /pub/csd)
WWW: http://www.fiz-karlsruhe.de (under "Products and Services")
Further details of the crystal-structure investigation(s) may be obtained from the Fachinformationszentrum Karlsruhe, 76344 Eggenstein-Leopoldshafen, Germany, on quoting the depository number(s) CSD-....

 © 2007 Wiley-VCH Verlag GmbH & Co. KGaA, Weinheim 

- **For all compounds with at least one C–H bond:**

Cambridge Crystallographic Data Centre (CCDC)
12 Union Road, Cambridge CB2 1EZ, UK
Phone: +44-(0)1223/336-408
Fax: +44-(0)1223/336-033
E-mail: deposit@ccdc.cam.ac.uk
WWW: http://www.ccdc.cam.ac.uk
CCDC-****** contains the supplementary crystallographic data for this paper. These data can be obtained free of charge from The Cambridge Crystallographic Data Centre via www.ccdc.cam.ac.uk/data_request/cif.

**NOTE:** Please use the free online **Checkcif** service provided by the International Union of Crystallography and submit the Checkcif report along with your manuscript: http://journals.iucr.org/services/cif/checkcif.html.

Finally, before you return your revised manuscript, please update your database entry if necessary.

## 5. Electronic Supporting Information

A manuscript may include Electronic Supporting Information which will be accessible only on the WWW. Authors must keep a copy to make available to readers who do not have access to the internet. As this material [text, tables, schemes, figures **but not crystallographic (CIF) data**, which must be submitted to either the FIZ or the CCDC] undergoes the peer review process, it must be included, clearly marked as "Supporting Information to be published electronically", when the paper is submitted. The following file formats are accepted: MS Winword or ASCII (*.doc, *.txt), MS Excel (*.xls), Encapsulated Postscript (*.eps), Portable Document Format (*.pdf), graphics embedded in MS Winword; if you wish to submit other formats, please consult the Editorial Office. When preparing such material, authors should keep in mind that − once accepted − it will be made available as provided by the author and not edited. Material accepted for electronic publication will be available mostly as PDF files (Adobe Acrobat Reader required) by following the Table of Contents link of EurJIC's WWW home page. A standard text will be added on the first page of the article in the printed version:

- Supporting information for this article is available on the WWW under http://www.eurjic.org or from the author.

The supporting information file must start with the title of the paper, the authors and the CASSI abbreviation of the journal to which it was submitted (e.g. *Eur. J. Inorg. Chem.*).

## 6. Basic Keyword List

To increase the relevance of articles found by search engines of Wiley InterScience, we have compiled a keyword catalogue common to our chemistry journals that is printed here and is also available online (http://www.eurjic.org).

To assist you in finding keywords they are listed according to categories. You may choose keywords from any category. As with all such records, a few guidelines facilitate the catalogue's use, and these are briefly explained below:

1. As many as possible, but at least two, of the maximum of five keywords assigned to an article must come from this list.

2. Named reactions will be incorporated only in exceptional cases. Generally the reaction type is selected instead. For example, Diels–Alder reactions will be found under "Cycloadditions" and Claisen rearrangements under "Rearrangements".

3. Heteroanalogues of compounds are mainly classified under the C variants, for example, (hetero)cumulenes, (hetero)dienes. A few aza and phospha derivatives are exceptions.

4. Compounds with inorganic components that are central to the article are listed under the element, for instance, iron complexes under "Iron". Some group names like "Alkali metals" exist alongside the names of important members of the group like "Lithium". In such cases the group name is used for these members only when comparative studies are described. The members not appearing separately are also categorized under the group name.

5. A keyword in the form "N ligand" is only chosen if a considerable portion of the paper deals with the coordination of any ligand ligating through the atom concerned.

6. Spectroscopic methods are assigned as keywords only if the article is about the method itself, or if the spectroscopic technique has made an important contribution to the problem under investigation.

7. "Structure elucidation" is intended only if the crux of the paper is a structural elucidation or if a combination of several spectroscopic techniques were needed for conclusive solution of the structure.

8. An attempt has been made to avoid synonyms and to select more general concepts rather than specialized terms. Thus, the term "Double-decker complexes" is excluded in favour of "Sandwich complexes".

This list will be a "living" catalogue to be flexible enough to absorb the new developments in chemistry. We therefore welcome all suggestions from our authors that might improve its user-friendliness.

 © 2007 Wiley-VCH Verlag GmbH & Co. KGaA, Weinheim 

**Analytical Chemistry and Spectroscopic Methods**

Analytical methods
Circular dichroism
Cyclic voltammetry
Electron diffraction
Electron microscopy
Electrophoresis
ENDOR spectroscopy
EPR spectroscopy
EXAFS spectroscopy
Fluorescence spectroscopy
Gas chromatography
High-throughput screening
Ion chromatography
Ion exchange
IR spectroscopy
Isotopic labeling
Laser spectroscopy
Liquid chromatography
Luminescence
Mass spectrometry
Moessbauer spectroscopy
Neutron diffraction
NMR spectroscopy
Photoelectron spectroscopy
Plasma chemistry
Raman spectroscopy
Rotational spectroscopy
Scanning probe microscopy
Sensors
Surface analysis
Surface plasmon resonance
Trace analysis
UV/Vis spectroscopy
Vibrational spectroscopy
Water chemistry
X-ray absorption spectroscopy
X-ray diffraction
ZEKE spectroscopy

**Biological Chemistry and Chemical Biology (including Biochemistry, Bioinorganic Chemistry, Bioorganic Chemistry, Medicinal Chemistry and Molecular Cell Biology)**

Allosterism
Amino acids
Angiogenesis
Antibiotics
Antibodies
Antifungal agents
Antigens
Antisense agents
Antitumor agents
Antiviral agents
Azapeptides
Azasugars
Bioinformatics
Bioinorganic chemistry
Biological activity
Biomimetic synthesis
Bioorganic chemistry
Biophysics
Biosensors
Biosynthesis
Biotransformations
C-Glycosides
Carbohydrates
Carbon dioxide fixation
Carotenoids
Cell adhesion
Cell recognition
Cerebrosides
Chaperone proteins
Cobalamines
Cofactors
Combinatorial chemistry
Cyclitols
Cyclodextrins
Cytokines
DNA
DNA cleavage
DNA damage
DNA methylation
DNA recognition
DNA replication
DNA structures
Dopamines
Drug delivery
Drug design
Electron transport
Enzyme models
Enzymes
Fibrous proteins
Fluorescent probes
Gene expression
Gene sequencing
Gene technology
Genomics
Glycoconjugates
Glycolipids
Glycopeptides
Glycoproteins
Glycosides
Glycosylation
Growth factors
Helical structures
Heme proteins
Hormones
Hydrolases
Immobilization
Immunoassays
Immunochemistry
Immunology
Inhibitors
Ion channels
Ionophores
Isomerases
Ligases
Lipids
Lipophilicity
Lipoproteins
Liposomes
Lyases
Medicinal chemistry
Membrane proteins
Membranes
Metabolism
Metalloenzymes
Metalloproteins
Micelles
Molecular evolution
mRNA
Mutagenesis
Natural products
Neurochemistry
Neurotransmitters
Nitrogen fixation
Nitrogenases
Nucleic acids
Nucleobases
Nucleosides
Nucleotides
Oligonucleotides
Oligosaccharides
Oxidoreductases
Peptide nucleic acids
Peptides
Peptidomimetics
Pheromones
Phospholipids
Photoaffinity labeling
Photosynthesis
Phytochemistry
Polyketides
Polymerase chain reaction
Prodrugs
Prostaglandins
Protein design
Protein engineering
Protein folding
Protein models
Protein modifications
Protein structures
Proteins
Proteomics
Proton transport
Radiopharmaceuticals
Receptors
Redox chemistry
Ribonucleosides
Ribozymes
RNA
RNA recognition
RNA structures
Sensitizers
Sequence determination
Sialic acids
Siderophores
Signal transduction
Sphingolipids
Steroids
Structure–activity relationships
Terpenoids
Toxicology
Transferases
tRNA
Vesicles
Vitamins

**Catalysis**

Asymmetric catalysis
Autocatalysis
Biphasic catalysis
Catalytic antibodies
Enzyme catalysis
Heterogeneous catalysis
Homogeneous catalysis
Phase-transfer catalysis
Supported catalysts

 © 2007 Wiley-VCH Verlag GmbH & Co. KGaA, Weinheim 

# GUIDELINES FOR AUTHORS

**Coordination Chemistry: Compound Classes**

Cage compounds
Chelates
Clathrates
Cluster compounds
Cuprates
Dendrimers
Heterometallic complexes
Metallacycles
Metallocenes
Nitrogen oxides
Polyoxometalates
Sandwich complexes
Ylides

**Coordination Chemistry: Ligand Classes**

Alkene ligands
Alkyne ligands
Allyl ligands
Arene ligands
As ligands
Bridging ligands
Carbene ligands
Carbonyl ligands
Carboxylate ligands
Carbyne ligands
Cyclopentadienyl ligands
Diene ligands
Dioxygen ligands
Fluorinated ligands
Hydride ligands
Isocyanide ligands
Macrocyclic ligands
N ligands
N,O ligands
N,P ligands
O ligands
Oxo ligands
Peroxo ligands
Phosphane ligands
P ligands
S ligands
Si ligands
Tridentate ligands
Tripodal ligands
Vinylidene ligands

**Coordination Chemistry: Methodology and Reactions**

Carbon dioxide fixation
Chemical vapor deposition
Chiral resolution
Crystal engineering
Ligand design
Matrix isolation
Metathesis
Neighboring-group effects
Nitrogen fixation
O–O activation
Oxidation
Radical reactions
Reduction
Ring-opening polymerization
Solvent effects
Solvolysis
Substituent effects
Template synthesis

**Coordination Chemistry: Structure**

Agostic interactions
Aurophilicity
Charge transfer
Cooperative effects
Coordination modes
Donor–acceptor systems
Electron-deficient compounds
Electronic structure
Electrostatic interactions
Fluxionality
Helical structures
Host–guest systems
Hydrogen bonds
Inclusion compounds
Isolobal relationship
Jahn–Teller distortion
Ligand effects
Metal–metal interactions
Multiple bonds
Noncovalent interactions
Pi interactions
Stacking interactions
Structure elucidation
Through-bond interactions
Through-space interactions

**Elements and Element Groups**

Actinides
Alkali metals
Alkaline earth metals
Aluminum
Antimony
Argon
Arsenic
Barium
Beryllium
Bismuth
Boron
Bromine
Cadmium
Calcium
Carbon
Cerium
Cesium
Chalcogens
Chlorine
Chromium
Cobalt
Copper
Deuterium
Fluorine
Gallium
Germanium
Gold
Group 13 elements
Group 14 elements
Hafnium
Halogens
Helium
Hydrogen
Indium
Iodine
Iridium
Iron
Krypton
Lanthanides
Lanthanum
Lead
Lithium
Magnesium
Manganese
Mercury
Molybdenum
Neon
Nickel
Niobium
Nitrogen
Noble gases
Osmium
Oxygen
Palladium
Phosphorus
Platinum
Pnicogens
Potassium
Rare earths
Rhenium
Rhodium
Rubidium
Ruthenium
Samarium
Scandium
Selenium
Silicon
Silver
Sodium
Strontium
Sulfur
Tantalum

 © 2007 Wiley-VCH Verlag GmbH & Co. KGaA, Weinheim 

Technetium
Tellurium
Thallium
Tin
Titanium
Tungsten
Uranium
Vanadium
Xenon
Ytterbium
Yttrium
Zinc
Zirconium

**Environmental and Atmospheric Chemistry**

Anions
Atmospheric chemistry
Cations
Chlorine
Computer chemistry
Crop protection agents
Cycloaddition
Denitrification
Desulfurization
Environmental chemistry
Fluorine
Gas-phase reactions
Green chemistry
Halogenation
Kinetics
Molecular dynamics
Molecular modeling
Nitrogen oxides
Oxidation
Ozone
Peroxides
Photochemistry
Photolysis
Photooxidation
Radical ions
Radical reactions
Radicals
Reaction mechanisms
Reactive intermediates
Sensors
Toxicology
Trace analysis
Waste prevention
Water chemistry

**Inorganic Chemistry**

Alanes
Allotropy
Alloys
Aluminosilicates
Amalgams
Amorphous materials
Anions
Automerization
Autoxidation
Azides
Bond theory
Boranes
Borates
Carbene homologues
Carbides
Carboranes
Cations
Chain structures
Chromates
Clathrates
Cluster compounds
Cyanides
Electron-deficient compounds
Fluorides
Halides
High-pressure chemistry
Host–guest systems
Hydrates
Hydrides
Hydrothermal synthesis
Hypervalent compounds
Inclusion compounds
Intercalations
Intermetallic phases
Isoelectronic analogues
Isomers
Layered compounds
Lewis acids
Lewis bases
Main group elements
Metal–metal interactions
Mixed-valent compounds
Nitrides
Nonstoichiometric compounds
Organic–inorganic hybrid composites
Perovskite phases
Peroxides
Phosphaalkenes
Phosphaalkynes
Phosphanes
Phosphazenes
Platinates
Pnictides
Polyanions
Polycations
Polychalcogenides
Polyhalides
Polymorphism
Polyoxometalates
Radical ions
Radicals
Silanes
Silicates
Sol–gel processes
Solid-phase synthesis
Solid-state reactions
Solid-state structures
Spinel phases
Stannanes
Subvalent compounds
Synthesis design
Titanates
Topochemistry
Transition metals
Transuranium elements
Valence isomerization
Vanadates
Zeolite analogues
Zeolites
Zincates
Zintl anions
Zintl phases

**Materials Science: General**

Alloys
Amorphous materials
Automerization
Block copolymers
Ceramics
Charge-carrier injection
Chemical vapor deposition
Chemical vapor transport
Clays
Cluster compounds
Colloids
Conducting materials
Copolymerization
Crystal engineering
Crystal growth
Cyclooligomerization
Cyclotrimerization
Dendrimers
Doping
Energy conversion
Fullerenes
Gels
Glasses
Holography
Imprinting
Intercalations
Interfaces
Intermetallic phases
Ladder polymers
Layered compounds
Liquid crystals
Materials science
Mechanical properties
Membranes
Mesophases
Mesoporous materials
Metal–metal interactions
Metallomesogens
Micelles
Microporous materials
Monolayers
Nanostructures
Nanotechnology
Nanotubes
Nonlinear optics
Polymerization
Polymers
Ring-opening polymerization
Scanning probe microscopy
Semiconductors
Sensitizers
Sensors
Superconductors
Surface chemistry
Thin films
Vesicles
Zeolite analogues
Zeolites

 © 2007 Wiley-VCH Verlag GmbH & Co. KGaA, Weinheim 

# GUIDELINES FOR AUTHORS

**Miscellaneous**

History of science

**Organic Chemistry: Compound Classes**

Alcohols
Aldehydes
Alkaloids
Alkanes
Alkenes
Alkynes
Allenes
Allylic compounds
Amides
Amines
Amino acids
Amino alcohols
Amino aldehydes
Amphiphiles
Anhydrides
Anions
Annulenes
Arenes
Arynes
Azides
Azo compounds
Azomethine ylides
Betaines
Biaryls
Calixarenes
Carbanions
Carbenes
Carbenoids
Carbocations
Carbocycles
Carbohydrates
Carboxylic acids
Carotenoids
Catenanes
Cations
Cavitands
Crown compounds
Cryptands
Cumulenes
Cyanides
Cyanines
Cyclodextrins
Cyclophanes
Dendrimers
Diazo compounds
Dyes/Pigments
Enols
Enones
Enynes
Fatty acids
Fragrances
Fullerenes
Fused-ring systems
Heterocycles
Hydrazones
Hydrides
Hydrocarbons
Ketones
Lactams
Lactones
Ladder polymers
Macrocycles
Mannich bases
Medium-ring compounds
Metallacycles
Natural products
Nitrogen heterocycles
Oxygen heterocycles
Peroxides
Pheromones
Phosphorus heterocycles
Phthalocyanines
Polycycles
Polymethines
Porphyrinoids
Quinodimethanes
Quinones
Radical ions
Radicals
Rotaxanes
Schiff bases
Small ring systems
Spiro compounds
Steroids
Sulfonamides
Sulfur heterocycles
Surfactants
Terpenoids
Ylides
Zwitterions

**Organic Chemistry: Methodology and Reactions**

Acylation
Aldol reactions
Alkylation
Allylation
Amination
Annulation
Aromatic substitution
Aromaticity
Asymmetric amplification
Asymmetric catalysis
Asymmetric synthesis
Automerization
Autoxidation
Biomimetic synthesis
C–C activation
C–C coupling
C–H activation
C1 building blocks
Carbonylation
Carboxylation
Chiral auxiliaries
Chiral pool
Cleavage reactions
Combinatorial chemistry
Cracking
Cross-coupling
Cyclization
Cycloaddition
Cyclotrimerization
Dehydrogenation
Dihydroxylation
Dimerization
Domino reactions
Electrocyclic reactions
Electrophilic addition
Electrophilic substitution
Elimination
Ene reaction
Epoxidation
Flash pyrolysis
Glycosylation
Grignard reaction
Halogenation
Heck reaction
High-pressure chemistry
Hydroamination
Hydroboration
Hydroformylation
Hydrogen transfer
Hydrogenation
Hydrolysis
Hydrosilylation
Hydrostannation
Hydroxylation
Immobilization
Insertion
Ionic liquids
Isomerization
Lithiation
Metalation
Michael addition
Molecular diversity
Multicomponent reactions
Nucleophilic addition
Nucleophilic substitution
Olefination
Oligomerization
Oxidation
Oxygenation
Ozonolysis
Perfluorinated solvents
Pericyclic reaction
Phosphorylation
Photooxidation
Polymerization
Protecting groups
Protonation
Radical reactions
Rearrangement
Reduction
Retro reactions
Ring contraction
Ring expansion
Sigmatropic rearrangement
Solid-phase synthesis
Solvent effects
Solvolysis
Steric hindrance
Substituent effects
Synthesis design
Synthetic methods
Template synthesis
Topochemistry
Total synthesis
Transesterification
Umpolung
Wittig reactions

**Organic Chemistry: Stereochemistry and Structures**

Atropisomerism
Chemoselectivity
Chiral resolution
Chirality
Configuration determination
Conformation analysis
Conjugation
Diastereoselectivity
Enantioselectivity
Hyperconjugation
Kinetic resolution
Regioselectivity
Strained molecules
Structure elucidation
Tautomerism
Valence isomerization

 © 2007 Wiley-VCH Verlag GmbH & Co. KGaA, Weinheim 

**Physical Chemistry and Chemical Physics (including Electrochemistry, Kinetics, Photochemistry, Radiochemistry, Thermodynamics and Theoretical Chemistry)**

Ab initio calculations
Absorption
Acidity
Adsorption
Basicity
Biophysics
Bond energy
Bond theory
Calorimetry
CARS (Coherent Anti-Stokes Raman Scattering)
Charge-carrier injection
Charge transfer
Chemisorption
Chromophores
Colloids
Computer chemistry
Conducting materials
Conical intersections
Crystal engineering
Crystal growth
Cyclic voltammetry
Density functional calculations
Donor–acceptor systems
Doping
Electrochemistry
Electron microscopy
Electron transfer
ELF (Electron Localization Function)
Energy conversion
Exchange interactions
Femtochemistry
Fluorescence
Fluorescent probes
Fractals
FRET (Fluorescence Resonance Energy Transfer)
Gas-phase reactions
Gels
Glasses
Group theory
Heats of formation
High-pressure chemistry
High-temperature chemistry
Hot-atom chemistry
Hydrophobic effect
Imaging agents
Ion pairs
Ion–molecule reactions
Ionization potentials
Isotope effects
Isotopes
Kinetics
Langmuir–Blodgett films
Laser chemistry
Lewis acids
Lewis bases
Linear free energy relationships
Liquid crystals
Liquids
Low-temperature studies
Magnetic properties
Matrix isolation
Mesophases
Metallomesogens
Metastable compounds
Microreactors
Molecular dynamics
Molecular electronics
Molecular modeling
Monolayers
Nanotechnology
Neighboring-group effects
Nonequilibrium processes
Phase diagrams
Phase transitions
Photochemistry
Photochromism
Photolysis
Physisorption
Plasma chemistry
Polarized spectroscopy
Quantum chemistry
Radiochemistry
Radiopharmaceuticals
Reaction mechanisms
Reactive intermediates
Redox chemistry
Salt effect
Semiempirical calculations
Single-molecule studies
Singlet oxygen
Sol–gel processes
Solvatochromism
Spin crossover
Statistical mechanics
Statistical thermodynamics
Structure–activity relationships
Superacidic systems
Supercritical fluids
Thermochemistry
Thermodynamics
Time-resolved spectroscopy
Transition states
Viruses
Voltammetry

**Supramolecular Chemistry**

Aggregation
Host–guest systems
Molecular devices
Molecular evolution
Molecular recognition
Nanostructures
Pi interactions
Receptors
Self-assembly
Supramolecular chemistry

 © 2007 Wiley-VCH Verlag GmbH & Co. KGaA, Weinheim 

DOI: 10.1002/ejic.200600461

# Understanding the Mechanism of Superoxide Reductase Promoted Reduction of Superoxide

**Lisa M. Brines[a] and Julie A. Kovacs*[a]**

**Keywords:** Bioinorganic chemistry / Metalloenzymes / Thiolate-ligated nonheme iron / Superoxide

Superoxide reductases (SORs) are nonheme, iron-containing enzymes which reduce superoxide ($O_2^-$) to hydrogen peroxide ($H_2O_2$) in anaerobic organisms. In contrast to the classical superoxide dismutases (SODs), SORs selectively reduce, rather than disproportionate, superoxide at an unusual [Fe(NHis)$_4$SCys] catalytic site. Studies of the native enzyme and mutants have suggested the formation of a transient ferric-(hydro)peroxide intermediate in SOR's catalytic cycle, with subsequent protonation to yield hydrogen peroxide and a glutamate-bound ferric resting state. With the synthesis of small molecular model compounds of the enzyme's active site, analogous intermediates can be more thoroughly investigated in order to understand how the structure at the nonheme iron active site affects its function. Specific goals include the understanding of the role of the *trans* cysteinate in the promotion of SOR chemistry, as well as the role of the protons in the mechanism of the reaction. Because hydrogen peroxide formation requires two protons, investigation of the proton-dependence of the formation of ferric-(hydro)peroxo model complexes, as well as their subsequent reactivity with proton donors, yields important information about possible mechanisms. As new biochemical data on SORs become available, synthetic modeling, biophysical characterization, and DFT calculations continue to be important tools in the identification of viable mechanistic pathways.

(© Wiley-VCH Verlag GmbH & Co. KGaA, 69451 Weinheim, Germany, 2007)

## 1. Introduction

Organisms exposed to molecular oxygen inevitably encounter reactive oxygen species that are formed by the adventitious reduction of $O_2$ by redox-active enzymes.[1] These species include superoxide, $O_2^-$, the one-electron-reduced product of dioxygen. Elevated superoxide levels have been implicated in a number of diseases including diabetes[2] and the cell death and tissue damage that occurs following a stroke or heart attack.[3] Severe neurological disorders such as Parkinson's[4,5] and Alzheimer's[6,7] diseases may also be related to nerve cell damage caused by $O_2^-$. Additionally, some types of cancer are thought to arise from mutations induced by $O_2^-$ damage to DNA.[8,9] Organisms have evolved two known defenses for the detoxification of superoxide. In particular, two classes of enzymes have been identified whose function is the reduction and/or oxidation of superoxide: the superoxide dismutases (SODs) and the superoxide reductases (SORs).[10–16] The classical SODs disproportionate superoxide to hydrogen peroxide and dioxygen. In contrast, SORs selectively reduce superoxide to hydrogen peroxide in anaerobic organisms without the formation of dioxygen as a byproduct. How SORs are able to selectively reduce $O_2^-$ and avoid SOD activity is still not well understood. The active site's redox potential and access to protons are key parameters that govern this reactivity (vide infra).

[a] Department of Chemistry, University of Washington,
Box 351700, Seattle, WA 98195, USA
Fax: +1-206-685-8665
E-mail: kovacs@chem.washington.edu

$$O_2^{\bullet-} + 2H^+ + e^- \xrightarrow{SOR} H_2O_2$$

$$2O_2^{\bullet-} + 2H^+ \xrightarrow{SOD} O_2 + H_2O_2$$

*Julie Kovacs (left) received her Ph.D. from Harvard in 1986, and was a President's Postdoctoral Fellow at U. C. Berkeley from 1986–88. She has been on the faculty at the University of Washington, in Seattle, since 1988, where she is currently a full Professor of Chemistry. Her interest in metalloenzymes developed while at Harvard. Her research focuses on the synthesis of thiolate-ligated transition-metal complexes and on the comprehension of how sulfur ligands influence function in cysteinate-ligated nonheme iron enzymes.*

*Lisa M. Brines (right) was born in Spokane, Washington, USA. She received a Bachelor of Science degree in Chemistry from Seattle University in 2002 and later that year joined the Department of Chemistry at the University of Washington as a graduate student. She works in Professor Kovacs' group and studies the active sites of metalloenzymes with the use of synthetic modeling techniques.*

 © 2007 Wiley-VCH Verlag GmbH & Co. KGaA, Weinheim 

In order to confirm the viability of the proposed intermediates in the mechanism of enzymatic superoxide reduction, synthetic models have proven useful in the establishment of spectroscopic parameters with which the biochemical data can be compared. Interpretation of the protein structure in relation to its function can be complicated by a lack of resolution of the spectra or the inability to trap intermediates because of solvent constraints. Small molecules are often used to trap and characterize key intermediates that may not be observable in the enzyme. In combination, biochemical and synthetic modeling data have begun to generate a clearer picture of the mechanism of superoxide reduction. These data include information on the role of the *trans* thiolate in the nonheme iron active site and the effect of spin-state on the reactivity of the proposed peroxo-bound ferric intermediates. Furthermore, exploration of the reactivity of synthetic peroxide intermediates with proton donors in a controlled fashion may help elucidate the identity and role of proton donors in the SOR-catalyzed reduction of $O_2^-$ to $H_2O_2$.

## 2. Superoxide Reductases (SORs)

Five crystal structures of SOR have been reported from four different bacterial sources: *Pyrococcus furiosus*,[17] *Desulfovibrio desulfuricans*,[18] *Treponema palladium*,[19] and *Desulfoarculus baarsii*.[20] In the catalytically active reduced state, SORs contain a high-spin ($S$ = 2) $Fe^{II}$ center (center II) ligated by four equatorial histidine units and one apical cysteinate residue *trans* to an open site (Figure 1). Additionally, a number of SORs also contain a second rubredoxin-like [$Fe(SCys)_4$] center (center I) and are sometimes termed 2Fe-SORs to indicate the presence of a second iron site.[16] The C13S mutant of *D. vulgaris* 2Fe-SOR leads to the loss of center I, but does not prevent SOR activity.[21] Thus, center I is not believed to participate in the catalytic cycle. In the oxidized resting state, the active site is high-spin ($S$ = 5/2) and contains a glutamate moiety coordinated to the sixth axial site. This glutamate ($Glu^{14}$ or $Glu^{47}$, depending on the organism) is attached to a solvent-exposed flexible loop region of the protein and moves to a distance of 7.1 Å away from the metal ion upon reduction to the $Fe^{II}$ state.[17] This flexible loop region also contains a conserved lysine ($Lys^{47}$ or $Lys^{48}$) unit that has been proposed to play an essential role in the promotion of the catalytic activity of SOR by the attraction of the anionic superoxide ion to the enzyme's active site via coulombic forces.[22,23] The ammonium group of this lysine unit lies 6–12 Å away from the iron center. Because two protons are necessary to form $H_2O_2$, protonation of (Fe–$\eta^2$-$O_2$) or (Fe–$\eta^1$-OOH) intermediates plays an important role in the overall mechanism of superoxide reduction by SOR. The identity of the two proton sources is currently under investigation in the wild-type (WT) and mutant enzymes and through the study of synthetic enzyme active site models.

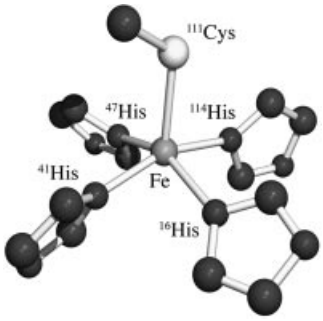


Figure 1. Active site of the reduced catalytically active form of the nonheme iron enzyme superoxide reductase (SOR).

### 2.1 SOD versus SOR

SODs disproportionate $O_2^-$ into hydrogen peroxide and dioxgen in aerobic organisms.[13,14,24] In contrast, SORs selectively reduce $O_2^-$ to hydrogen peroxide; this avoids the formation of dioxygen, which would otherwise be toxic to the anaerobic organisms that contain them.[10,12,25] Bacterial SODs typically contain either nonheme iron or manganese at the active site (FeSOD or MnSOD) although copper–zinc (Cu, ZnSOD) and nickel (NiSOD) enzymes are also known.[26,27] Reduced FeSODs contain a nonheme iron active site ligated by three histidine units, an aspartate group, and a $H_2O/OH^-$ ligand ($pK_a$ = 8.5) supported by a conserved H-bonding network. The azide-inhibited oxidized form has been crystallographically characterized and possesses the structure shown in Figure 2. A coordination environment with a 2His-1-carboxylate motif is common among nonheme iron enzymes.[28] In contrast, SOR is part of a new class of nonheme iron enzymes that contain a thiolate moiety in the coordination sphere.[29] Recent reviews describe the superoxide dismutase (SOD) mechanism and biophysical properties in more detail.[13,14,26]

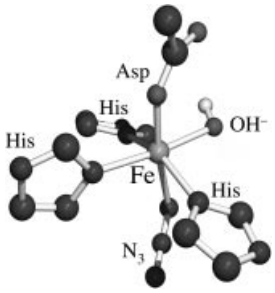


Figure 2. Active site of the oxidized azide-inhibited form of iron superoxide dismutase (Fe-SOD).

FeSODs and MnSODs are homologous and catalyze the disproportionation of superoxide through a cyclic (ping-pong) mechanism that involves $O_2^-$ oxidation at $M^{3+}$ followed by proton-induced $O_2^-$ reduction at $M^{2+}$.[13,14,24] By poising the SOD redox potential half-way between the potentials at which superoxide is oxidized and reduced, the redox active metal center of SOD is able to both oxidize and reduce superoxide depending on the protonation states of the nearby residues and the oxidation state of the metal. In contrast to SOR, the SOD catalytic cycle does not re-

 © 2007 Wiley-VCH Verlag GmbH & Co. KGaA, Weinheim 

quire an external source of electrons. The redox potential of the SOD $Fe^{2+}/Fe^{3+}$ couple is pH-dependent, and falls in the range from +0.03 to –0.31 V versus SCE.[14,30,31] The redox potential of the SOR $Fe^{2+}/Fe^{3+}$ couple (reported range: 0.00 to –0.15 V versus SCE[29]) is similar to that of SOD, which indicates that the redox potential alone cannot be responsible for the two distinct reactions that are catalyzed. Differences in the protein structure might be responsible. Because the active site of SOR is close to the surface of the protein, a constant source of protons is available from the solvent.[17] In contrast, the active site of SOD is buried within the protein, which makes it easier to control proton delivery. The amount of protons available is perhaps limited when the metal ion is in its 3+ oxidation state so as to favor superoxide oxidation. The redox potential of superoxide ($O_2^-$) is highly dependent on the pH of the system and it is significantly easier to reduce under acidic conditions. At pH = 0, superoxide is reduced at a potential of +1.27 V versus SCE, whereas at pH = 7.5 and pH = 14, it is reduced at +0.83 and –0.041 V, respectively. Protons are probably used to raise the redox potential of superoxide and to drive its reduction by SOR. Given that superoxide reduction by SOR has been shown to occur via an inner sphere mechanism (vide infra), redox potentials are somewhat less important. However, they can influence the reaction pathway in a more indirect manner by determining the energy of the frontier (LUMO) orbitals.

Another barrier to SOD activity in SOR may involve the reorganizational energy that is required to convert from a six- to a five-coordinate structure.[10] In SOD, the ferric state is five-coordinate which would be amenable to rereduction by superoxide via an inner sphere mechanism. In contrast, the resting state of SOR is a six-coordinate ferric site, and the low levels of superoxide present may not be able to effectively compete with the solvent (or the glutamate moiety) and bind to the metal ion.[10]

### 2.2 Enzymatic SOR Data

Superoxide has been shown to bind to the reduced $Fe^{II}$ state of SOR at diffusion controlled rates ($> 10^9$ $M^{-1}s^{-1}$). The transfer of an electron from the metal ion to the bound substrate via an inner sphere pathway is then proposed to afford one or two $Fe^{III}$-peroxide intermediates, depending on the organism. These intermediates have been observed in pulse radiolysis experiments by electron absorption spectroscopy.[32,33] Consistent with an inner sphere pathway, exogenous ligands such as azide, nitric oxide, and cyanide have also been shown to bind to the iron site of SOR.[34–36] The putative peroxide intermediate displays a charge-transfer band at 600 ($\sim 3500$ $M^{-1}cm^{-1}$) nm and releases $H_2O_2$ at a rate of 40–50 $s^{-1}$.[32,33,37] The intense low-energy charge-transfer (CT) band was originally assigned as a combination peroxide/sulfur-to-metal charge-transfer transition,[32] but more recently it was suggested that this band is too low in energy for the peroxide to be involved.[38] This comes as somewhat of a surprise given that a number of $Fe^{III}$–OOR (R = alkyl, H) model complexes have been synthesized which display a peroxide-to-metal CT band in the range 500–600 nm, at least when the iron is low-spin.[39] High-spin $Fe^{III}$–OOH species are extremely rare so there is less known about their spectroscopic properties. Upon the release of hydrogen peroxide from SOR, a nearby glutamate ($Glu^{14}$ or $Glu^{47}$) coordinates to the iron center to afford the six-coordinate $Fe^{III}$-oxidized resting state.[17,23]

When the $Glu^{47}$ residue is replaced with an alanine group (in an E47A SOR mutant of *D. baarsii*), a transient species is observed by resonance Raman spectroscopy upon the addition of hydrogen peroxide.[40] Stretches are observed for the O–O and Fe–O bonds at 850 and 438 $cm^{-1}$, respectively, which shift to 802 and 415 $cm^{-1}$ in the $^{18}O$-labeled spectrum.[40] Stretching frequencies in this range are consistent with a metal–peroxide species. Mössbauer parameters for this E47A intermediate enriched in $^{57}Fe$ include an isomeric shift of $\delta = 0.54(1)$ mm/s, with $\Delta E_Q = -0.80(5)$ mm/s, and an asymmetry parameter $\eta = 0.60(5)$ mm/s.[41] These data are consistent with the assignment of the $H_2O_2$-generated mutant species as a monomeric, high-spin ($S = 5/2$) ferric–peroxo. EPR, resonance Raman, and pulse radiolysis experiments have also been reported for the SOR isolated from *Treponema pallidum*.[42] Data consistent with the formation of an $Fe^{III}$–peroxo species was also observed upon treatment of the ferric or ferrous E48A mutant of *Treponema pallidum* SOR with $H_2O_2$. The same $Fe^{III}$–peroxo species could also be trapped in the corresponding wild-type, *D. baarsii* and *T. pallidum*, upon the addition of $H_2O_2$ but with much lower yields.[42] Mononuclear $Fe^{III}$–peroxide species have also been proposed, or identified, in the catalytic cycles of the antitumor drug bleomycin,[43] heme oxygenase,[44] cytochrome P450,[45–48] and Rieske dioxygenases.[49–51] DFT calculations comparing the stabilities of possible SOR intermediates suggest that a side-on peroxide would be much less stable than an end-on peroxide.[38]

Because two protons are needed to form $H_2O_2$, the active site's access to proton donors is a key consideration in the mechanism of SOR. In an attempt to identify potential proton donors, the pH-dependence of the spectroscopic and redox properties of WT and mutant (E47A and K48I) *D. baarsii* SOR has been recently examined.[52] With an increase in the pH, the S→$Fe^{III}$ absorption band of center II exhibited an 84 nm shift from 644 to 560 nm in both the WT and the mutants. However, this shift occurred at a higher pH for the WT enzyme than for the mutants. This observation is consistent with the presence of an additional base other than $Lys^{48}$ or $Glu^{47}$ ($Glu^{14}$ in *D. baarsii*), whose $pK_a$ is influenced by the presence of these residues. The nearby Lys and Glu residues are highly conserved among SORs; however, only the Lys unit has been shown to noticeably influence the catalytic activity of the enzyme.[21,22] The Glu residue is proposed to play an important role in the structural reorganization that accompanies iron oxidation, whereas the positively charged Lys residue is believed to provide an electrostatic driving force that guides superoxide toward the reduced iron.[53] Resonance Raman spectroscopic data for $K_2IrCl_6$-oxidized WT and mutant *D. baarsii*

 © 2007 Wiley-VCH Verlag GmbH & Co. KGaA, Weinheim 

SOR, collected at various pHs, revealed a pH-dependent stretch that is consistent with the formation of a previously unidentified $Fe^{III}$–OH species.[54] Resonance Raman spectroscopy revealed that the stretches observed for these species (in the range $\nu$ = 466–471 $cm^{-1}$) were sensitive to isotopic labeling with $H_2{}^{18}O$ or $^2H_2O$ buffer. This indicates that an oxygen atom that is derived from the solvent that contains an exchangeable proton is coordinated to the ferric site. This $Fe^{III}$–OH species (Figure 3) is proposed to be the previously observed base responsible for the pH-dependence of the SOR electronic absorption spectrum.[52] The protonated base (i.e. solvent = $H_2O$) is then presumed to be the second proton donor needed for $H_2O_2$ formation. This would allow the release of $H_2O_2$ with concomitant formation of the $Fe^{III}$–OH species (Figure 3).[54] Currently, the involvement of a solvent water molecule is proposed to only affect the second protonation step because $Fe^{III}$–OH formation cannot occur until $H_2O_2$ is released. The mechanism of $H_2O_2$ release, whether by an associative or dissociative process, however, is still unclear. The rate constant of $H_2O_2$ release by *D. baarsii* is estimated to be slow ($< 5\ s^{-1}$) but has not been directly measured.[52] Furthermore, the dependence of this second protonation step on pH still requires further study.

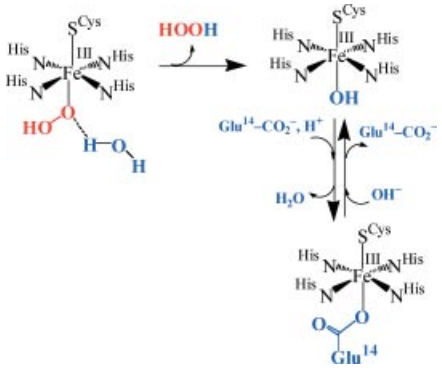


Figure 3. Proposed mechanism (see ref.[54]) for the solvent-induced $H_2O_2$ release from the putative $Fe^{III}$–OOH SOR intermediate, to initially afford a hydroxide-bound $Fe^{III}$–OH species, which converts to the glutamate-bound resting state $Fe^{III}$–OC(O)Glu under acidic conditions.

Nitric oxide (NO), a substrate analogue, has also been shown to bind to the active site of reduced *P. furiosus* SOR.[35] Reaction of ascorbate-reduced SOR with NO results in the reversible formation of a stable six-coordinate derivative with NO bound *trans* to the cysteinate ligand. EPR spectroscopy of the NO adduct shows a near-axial $S$ = 3/2 ground state with $E/D$ = 0.06 and $D = (12 \pm 2)\ cm^{-1}$.[35] Resonance Raman studies indicate that the NO ligand is most likely in a bent conformation *trans* to the cysteinate ligand, with $\nu$(N≡O) = 1721 $cm^{-1}$, $\nu$(Fe–NO) = 475 $cm^{-1}$, and $\nu$(Fe–S) = 291 $cm^{-1}$, confirmed by $^{15}NO$ and $^{34}S$ isotopic labeling.[35] The best electronic description of the $S$ = 3/2 $\{FeNO\}^7$ unit is that of a high-spin ($S$ = 5/2) $Fe^{III}$ center, antiferromagnetically coupled to an ($S$ = 1) $NO^-$ anion, which indicates that NO oxidatively adds to the $Fe^{II}$ center. These observations are consistent with the first step of the SOR mechanism that involves oxidative addition of superoxide to form the proposed ferric peroxide intermediate.

To regenerate the $Fe^{II}$-active state, rubredoxin has been proposed to serve as an electron donor on the basis of genetic and biochemical evidence.[55] Rubredoxin is a small (ca. 6 kDa) iron-containing protein which contains a single [$Fe(SCys)_4$] site. These proteins are found in many anaerobic bacteria and archaea where they serve as one-electron carriers involved in numerous electron transfer chains. *D. vulgaris* rubredoxin has been found to efficiently catalyze the reduction of *D. vulgaris* 2Fe-SOD.[55] Rubredoxin has also been shown to act as an electron donor for neelaredoxin (a 1Fe-SOR) in vitro.[56] Additionally, rubredoxins have been shown to be reduced in vivo by NAD(P)H:rubredoxin oxidoreductase (NROR), and this reduction pathway was recently reconstituted in vitro with the use of recombinant proteins.[57]

### 2.3 Biomimetic Models of SOR

The spectroscopic characterization and isolation of $Fe^{III}$–peroxo complexes is extremely challenging because of their high reactivity, thermal instability, and photolability.[29,58] Que[39] (Figure 4) and Girerd[59] have reported the most extensively characterized set of synthetic nonheme iron peroxides. Both groups have shown that when ligated by nitrogen ligands, a side-on ferric peroxide [$Fe^{III}(\eta^2\text{-}O_2)$] will convert to an end-on ferric hydroperoxide species [$Fe^{III}(\eta^1\text{-}OOH)$] upon protonation.[60–63] In the published examples, the side-on peroxides are high-spin ($S$ = 5/2), and the end-on hydroperoxides are low-spin ($S$ = 1/2). The $\nu_{O-O}$ stretching frequencies of these side-on peroxides appear at higher energies than those of the corresponding end-on hydroperoxides. The $\nu_{Fe-O}$ stretch shifts to higher energies upon protonation, a spin-state change from $S$ = 5/2 to $S$ = 1/2 occurs, and, as predicted by Solomon,[64,65] the O–O bond weakens. Because protons are needed for SOR catalysis, any side-on peroxide that is possibly formed in wild-type SOR probably converts to an end-on hydroperoxide prior to the release of $H_2O_2$.

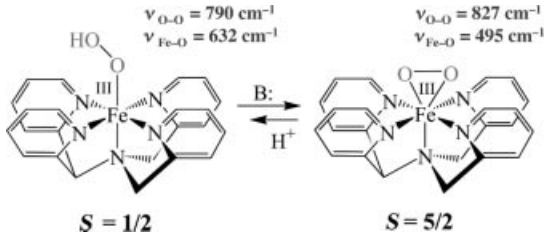


Figure 4. Que's synthetic end-on and side-on peroxide complexes, $[(N_4Py)Fe^{III}(\eta^2\text{-}O_2)]^+$ and $[(N_4Py)Fe^{III}(\eta^1\text{-}OOH)]^{2+}$, and their respective vibrational data and spin-states.

None of the synthetic complexes described above contain thiolate ligands. An obvious question related to SOR concerns how a thiolate sulfur would affect $H_2O_2$ formation and release. The *trans* positioning of the thiolate moiety in SOR has been suggested to provide a pathway for electron delivery to the iron site. Additionally, the *trans*-effect of the

 © 2007 Wiley-VCH Verlag GmbH & Co. KGaA, Weinheim 

thiolate ligand would cause the Fe–O bond to become labile, which favors peroxide release.[34] As established for porphyrin-containing systems,[66–68] a thiolate would be expected to perturb the spectroscopic and magnetic properties of $Fe^{III}$-peroxide species and their preferred reaction pathways relative to those not containing a thiolate ligand. The correlation between the peroxide binding mode, spin-state, and vibrational parameters, established for nitrogen-ligated nonheme iron systems,[39] would not necessarily hold true for thiolate ligated systems. For example, the π-donor sulfur ligand may favor a high-spin $Fe^{III}$–OOH species with a weaker Fe–O bond, which would then favor peroxide release (vide infra). In order to confirm these hypotheses, thiolate-ligated $Fe^{III}$–OOH complexes are needed. Thiolate-ligated $Fe^{III}$–OOH species are, however, difficult synthetic targets because thiolates tend to reduce $Fe^{III}$, are easily oxidized by peroxides, and form μ-SR bridged dimers.[29]

Halfen and coworkers have successfully modeled the square pyramidal structure of reduced SOR with a pyridyl appended diazacyclooctane ligand (Figure 5).[69] Aromatic thiolate groups coordinate to the apical position of the reduced, high-spin ($S = 2$) complex *trans* to an open coordination site, which affords a fairly accurate structural model of the reduced form of SOR ($SOR_{red}$), $[L_8py_2Fe(SC_6H_4\text{-}m\text{-}CH_3)]^+$ (**1**). Although **1** is stereochemically very similar to $SOR_{red}$, its electronic structure is notably different.[70] Electronic absorption, magnetic circular dichroism (MCD), and variable-temperature variable-field MCD (VTVH-MCD) spectroscopy, in conjunction with density functional theory (DFT) and semiemperical INDO/S-CI calculations, showed that the π-acceptor pyridine ligands stabilize the reduced state of **1** relative to that of SOR. This, coupled with the poor sigma-donor properties of the aromatic thiolate compared with those of alkyl thiolate cysteinates, causes a blue-shift in the $S\rightarrow Fe^{II}$ CT manifold of **1** by 9,000 $cm^{-1}$ relative to that of the enzyme. Initially, the oxidation of **1** was found to be irreversible, which resulted in the formation of disulfides.[69] No reaction was reported with superoxide. More recently, *t*BuOOH was shown to react with **1** to afford a high-spin ($S = 5/2$) ferric alkylperoxide complex, $[L_8py_2Fe(SC_6H_4\text{-}m\text{-}CH_3)(OOR)]^+$ (**2**).[71] The resonance Raman spectrum of **2** shows vibrations that are consistent with an end-on $Fe^{III}$–OOR species.[71]

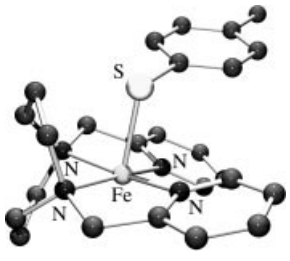


Figure 5. Halfen's thiolate-ligated, pyridyl-appended diazacyclooctane iron complex $[L_8py_2Fe(SC_6H_4\text{-}m\text{-}CH_3)]^+$ (**1**, see ref.[69]).

In 2001, Shearer and Kovacs showed that when the thiolate sulfur is incorporated into a multidentate ligand, biomimetic SOR reactivity is observed.[72,73] This occurs even though the thiolate moiety is coordinated *cis* to the open site and not *trans* to the open site as in the enzyme. In the model, five-coordinate thiolate-ligated $[Fe^{II}\{S^{Me2}N_4(tren)\}]^+$ (**3**, Figure 6) reacts with superoxide (solubilized as an 18-crown-6-$K^+$ salt in THF) to afford $H_2O_2$ and solvent-ligated $[Fe^{III}\{S^{Me2}N_4(tren)\}(solv)]^{2+}$ (solv = $MeO^-$ or MeCN). The reaction requires a proton source (such as MeOH or a trace amount of water from MeCN) and does not occur in rigorously dried THF. At low temperatures (≤ –78 °C), a transient hydroperoxide intermediate, $[Fe^{III}\{S^{Me2}N_4(tren)(OOH)\}]^+$ (**4**, Figure 7), is observed that has been characterized by electronic absorption, EPR, IR, and XAS spectroscopies.[73] The orange peroxide intermediate displays a charge-transfer band at 452 (2780 $M^{-1}cm^{-1}$) nm and is low-spin ($S = 1/2$; $g_{\|} = 2.14$, $g_{\perp} = 1.97$). Peroxide bound **4** displays a Fermi doublet in the IR spectrum at 788 and 781 $cm^{-1}$ which collapses to a singlet at 784 $cm^{-1}$ upon deuteration with $D_2O$.[73] A new $\nu_{O\text{–}O}$ stretch is observed at 752 $cm^{-1}$ when $^{18}O$-labeled superoxide is used, which confirms the $\nu_{O\text{–}O}$ assignment. This 31 $cm^{-1}$ shift is close to that predicted (44 $cm^{-1}$) for a diatomic oxygen species. Fits to the EXAFS data of **4** required the addition of a new short Fe–O bond at 1.86(3) Å that is not present in either the $Fe^{II}$ precursor (**3**) or the $MeO^-$-bound product.[73] The XANES spectrum is consistent with a six-coordinate oxidized $Fe^{III}$ intermediate. Addition of an outer sphere oxygen at 2.79(6) Å improved the EXAFS fits slightly. The small Debye-Waller factor that is associated with this outer sphere oxygen suggests that it is highly ordered, possibly due to H-bonding between the hydroperoxide and the *cis* thiolate sulfur. This hydrogen bonding may also help explain the shift in the $S\rightarrow Fe^{III}$ charge-transfer band to higher energies in the absorption spectrum relative to that of the enzyme (452 nm versus 600 nm). More likely, notable differences that distinguish **4** from the enzyme intermediate are responsible. These differences include the low-spin state and the *cis* positioning of the thiolate group relative to the peroxide of **4** compared with the high-spin state and the *trans* positioning of the thiolate group in the enzyme intermediate. Hydrogen peroxide is released from **4** at a rate of 65(1) $s^{-1}$ (at 298 K), which is comparable to the rate of $H_2O_2$ release in the SOR enzyme, and a stable solvent-bound species $[Fe^{III}\{S^{Me2}N_4(tren)(solv)\}]^{2+}$ is afforded. Together, these data are consistent with a mechanism that involves the inner sphere oxidative addition of superoxide to $[Fe^{II}\{S^{Me2}N_4(tren)\}]^+$ to form an end-on $Fe^{III}(\eta^1\text{-OOH})$ intermediate, $[Fe^{III}\{S^{Me2}N_4(tren)(OOH)\}]^+$. This represents the first example of a thiolate-ligated peroxide species.

The role of protons in the formation of $Fe^{III}$–peroxide model complex **4** has been examined in more detail in order to help identify viable proton donors in the SOR mechanism.[74] The source of the first proton in SOR is unclear and is dependent on the local pH. Under acidic conditions, $^{14}Glu\text{-}CO_2H$ has been proposed to serve as the proton donor. The solvent was shown to be capable of providing protons in *D. baarsii* SOR.[52] A highly conserved $Lys\text{-}NH_3^+$ residue ($^{15}Lys$ or $^{48}Lys$), essential for the catalytic activity of the enzyme, has been shown to affect rates

 © 2007 Wiley-VCH Verlag GmbH & Co. KGaA, Weinheim 

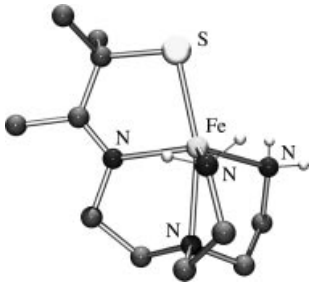


Figure 6. Kovacs' reactive *cis*-thiolate-ligated iron complex $[Fe^{II}\{S^{Me2}N_4(tren)\}]^+$ (**3**), which has been shown to convert superoxide to $H_2O_2$ via a $Fe^{III}$–OOH intermediate in a proton-dependent mechanism (see refs.[73,74]).

Figure 7. The hydroperoxide-bound intermediate $[Fe^{III}\{S^{Me2}N_4(tren)(OOH)\}]^+$ (**4**) shown to be involved in superoxide reduction by reduced **3** (see ref.[73]).

of $H_2O_2$ formation, which implies its involvement in the mechanism.[12,23] In order to explore this, the rate of formation of the synthetic peroxide intermediate $[Fe^{III}\{S^{Me2}N_4(tren)(OOH)\}]^+$ (**4**) was examined in dry THF with a variety of proton donors including HOAc and $NH_4^+$ as analogs for glutamic acid and lysine.[74] No reaction occurs between pre-purified **3** and superoxide in rigorously dried solvents, which rules out a mechanism that involves $H^+$ or H-atom abstraction from the ligand. The rates of formation of **4** are also dependent on the p$K_a$ of the proton donor: for the reaction to occur at comparable rates, the concentration of EtOH must be ca. 500 times higher than that of $NH_4^+$.[74] Although the p$K_a$'s (both relative and absolute) of these proton donors are likely to differ dramatically in THF (versus $H_2O$), and at low temperatures, the observation that EtOH will serve as a proton source to afford **4** suggests that the initial protonation site is rather basic. Additionally, superoxide is quite basic in aprotic solvents [p$K_a(HO_2)$ = 25.3 in DMF],[75] which indicates that these observations do not rule out a mechanism that involves the initial protonation of the superoxide anion prior to its oxidative addition to the metal ion. Protonated superoxide, $HO_2$, is a more potent oxidant than $O_2^-$, and the kinetic experiments needed to distinguish between these mechanisms are ongoing.

Subsequent addition of a second proton to **4** results in the release of hydrogen peroxide to afford the solvent-bound complex $[Fe^{III}\{S^{Me2}N_4(tren)(solv)\}]^{2+}$.[74] The second protonation step requires strong acids such as HOAc, $HBF_4$, or $HClO_4$ (Figure 8). Weaker acids (e.g. $NH_4^+$, a lysine analogue, and MeOH) do not release $H_2O_2$ from **4** in MeOH at reasonable rates at –78 °C. Noncoordinating acids ($HBF_4$, $HClO_4$) cleanly afford a common purple intermediate, $[Fe^{III}\{S^{Me2}N_4(tren)(MeOH)\}]^{2+}$ (**5**). Acetic acid also reacts with **4** to form **5** (Figure 8), which then converts to acetate-bound $[Fe^{III}\{S^{Me2}N_4(tren)(OAc)\}]^+$ at ambient temperature. Reaction rates are dependent on the p$K_a$ of the proton donor and are complete in seconds with strong acids ($HBF_4$, $HClO_4$) versus hours with HOAc. Glutamic acid-promoted $H_2O_2$ release by SOR could occur via a similar mechanism involving a solvent-bound intermediate. The common MeOH-bound intermediate **5** observed in all three reactions suggests that $H_2O_2$ release occurs via a proton-induced dissociative mechanism. An associative mechanism that involves nucleophilic displacement is ruled out because $NH_4^+OAc^-$ does not release $H_2O_2$ from **4**.

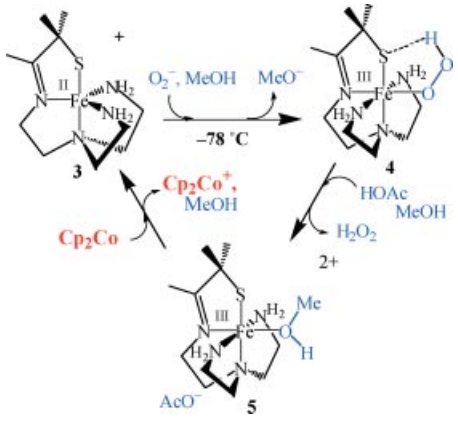


Figure 8. The catalytic cycle involving $[Fe^{II}\{S^{Me2}N_4(tren)\}]^+$ (**3**) promoted reduction of superoxide, which involves sequential protonation and $Cp_2Co$ promoted reduction to afford $H_2O_2$.

To mimic the reduction of the oxidized $Fe^{III}$ state of SOR, and to complete the catalytic cycle, cobaltacene was added as a source of electrons to oxidized solvent-bound **5**. This resulted in the regeneration of reduced $[Fe^{II}\{S^{Me2}N_4(tren)\}]^+$ (**3**), which subsequently reacts with additional superoxide to regenerate the peroxide intermediate (Figure 8). Eight turnovers have been achieved in this stepwise manner.[74] The catalytic activity is believed to be limited because of the decomposition of the catalyst by $H_2O_2$. Conditions are currently being optimized to remove the $H_2O_2$ that is formed in situ, in hopes of increasing the lifetime of the catalyst.

Cyanide, azide, and acetate all bind to oxidized solvent-bound $[Fe^{III}\{S^{Me2}N_4(tren)(MeCN)\}]^{2+}$ to afford models for the $CN^-$-inhibited, $N_3^-$-bound, and Glu-bound resting state of SOR.[76] Cyanide and azide do not bind to reduced **3**, and do not prevent **3** from stoichiometrically reducing superoxide. Azide- and acetate-coordinated $[Fe^{III}\{S^{Me2}N_4(tren)(N_3)\}]^+$ (**6**) and $[Fe^{III}\{S^{Me2}N_4(tren)(OAc)\}]^+$ (**7**) each have an $S$ = 1/2 ground state with a thermally accessible higher spin state. Cyanide-bound $[Fe^{III}\{S^{Me2}N_4(tren)(CN)\}]^+$ (**8**), on the other hand, is $S$ = 1/2 over a wide temperature range (2–300 K). Cyanide also dramatically alters the magnetic properties of SOR: CN-SOR is low-spin ($S$ =

 © 2007 Wiley-VCH Verlag GmbH & Co. KGaA, Weinheim 

1/2), whereas $N_3$-SOR and Glu-SOR are high-spin ($S$ = 5/2). These differences in spin-state do not come as a surprise given the differences in ligand field strengths of $N_3^-$ versus $RCO_2^-$ versus $CN^-$. The redox properties of these model complexes show a similar trend. Azide- and OAc-ligated **6** and **7** are reduced at comparable potentials of –410 and –335 mV (versus. SCE), respectively, whereas CN-ligated **8** is reduced at a much more anodic potential of –805 mV versus SCE.[76] If cyanide were to cause an anodic shift in the redox potential of SOR by approximately the same amount ($|\Delta E| \geq 470$ mV), then the reduction potential of the catalytic iron center would fall well-below those of its biological reductants (center I, –236 mV versus SCE; rubredoxin, reported range –191 to –291 versus SCE). Thus, cyanide by preventing the enzyme from turning over because it prevents the regeneration of the reduced, catalytically active $Fe^{2+}$ state of SOR. There is no data to support such a mechanism with the SOR enzyme; however, cyanide has been shown to inhibit superoxide dismutase in this manner.[77] Given that electron transfer plays a prominent role in SOR chemistry, inhibition may occur if these redox processes are interfered with.

With the use of a rigid macrocyclic ligand with tertiary amines and an appended alkyl thiolate, Halfen was more recently able to synthesize a high-spin ($S$ = 2) $SOR_{red}$ model, $[Fe^{II}(Me_3\text{-cyclam-EtS})]^+$ (**9**, Figure 9), which displays an absorption spectrum similar to that reported for the reduced SOR enzyme ($SOR_{red}$). This suggests that this model accurately mimics key elements of the electronic structure of the enzyme's active site, specifically its highly covalent Fe–S π- and σ-bonding interactions.[70] The geometry of **9** is distorted from the square pyramidal architecture, which results in a shift of the redox active orbital from the equatorial $N_4$ plane, as it occurs in SOR, to an axial ($d_{yz}$) position. Although **9** does not appear to react with superoxide, it reacts with either $H_2O_2$ in MeOH or *m*-chloroperbenzoic acid (*m*CPBA) in the presence of a base at –60 °C to afford a high-valent $Fe^{IV}$=O species, $[(Me_3\text{-cyclam-EtS})Fe^{IV}(O)]^+$ (**10**).[78] The Mössbauer parameters associated with $^{57}$Fe-enriched **10** ($\delta$ = 0.19 mm/s; $\Delta E_Q$ = 0.22 mm/s) are consistent with related $Fe^{IV}$=O cyclam-ligated complexes {i.e. $[(Me_4\text{-cyclam})Fe^{IV}(O)(MeCN)]^{2+}$} that have been crystallographically characterized,[79] but which do not contain a thiolate sulfur in the coordination sphere. Bond lengths of **10**, as determined by EXAFS and DFT methods, include a short Fe–O bond of 1.70(2) Å, 3 Fe–N/O bonds of 2.09(2) Å, and one Fe–S bond of 2.33(2) Å. The formation of **10** presumably occurs via the cleavage of the O–O bond of a transient peroxide species. Thus, the reactivity of **9** appears to better mimic that of the heme enzyme cytochrome P450[45] rather than SOR. The tertiary amines possibly contribute to this (vide infra).

If secondary amines are incorporated into **9** in place of the tertiary amines and an extra methylene is inserted into the apical arm, the resulting thiolate-ligated complex $[Fe^{II}(cyclam)\text{-PrS}]^+$ (**11**, Figure 10) reacts with superoxide (solubilized as an 18-crown-6 salt in THF) in $CH_2Cl_2$ to form a metastable burgundy-colored peroxide species

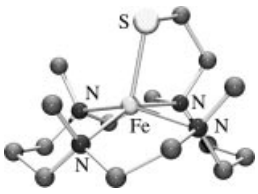


Figure 9. Halfen's $SOR_{red}$ model, $[Fe^{II}(Me_3\text{-cyclam-EtS})]^+$ (**9**), which has been shown[70,78] to react with *m*CPBA to afford a high-valent $Fe^{IV}$=O species, $[(Me_3\text{-cyclam-EtS})Fe^{IV}(O)]^+$ (**10**).

[$\lambda_{max}$ = 530(1350) nm], $[Fe^{III}(cyclam\text{-PrS})(OO(H))]^+$ (**12**), upon the addition of a proton donor (e.g. MeOH).[80] This intermediate is high-spin ($g$ = 7.72, 5.40, 4.15), and displays $\nu_{O-O}$, $\nu_{Fe-O}$, and $\nu_{Fe-S}$ stretches in the resonance Raman spectrum at 891 $cm^{-1}$ (a Fermi doublet), 419 $cm^{-1}$, and 352 $cm^{-1}$, respectively.[80] The $\nu_{O-O}$ and $\nu_{Fe-O}$ peaks shift to 856 $cm^{-1}$ and 400 $cm^{-1}$, respectively, upon the introduction of an isotopic label derived from $K^{18}O_2$ (50% enriched). The $\nu_{Fe-O}$ stretch of **12** (419 $cm^{-1}$) is unusually low, and the $\nu_{O-O}$ stretch (891 $cm^{-1}$) is unusually high, compared with other reported synthetic nonheme iron peroxo species (reported range: 450–639 $cm^{-1}$ for $\nu_{Fe-O}$ and 820–860 $cm^{-1}$ for $\nu_{O-O}$),[39] but compares well with that of the only reported SOR peroxide species ($\nu_{Fe-O}$ = 438 $cm^{-1}$ and $\nu_{O-O}$ = 850 $cm^{-1}$).[40] These vibrational data, along with the calculated force constant ($k_{Fe-O}$ = 1.20 mdynes $cm^{-2}$), indicate that *the Fe–O(peroxide) bond is significantly weakened upon the introduction of a trans thiolate into the coordination sphere*. An increased lability of the Fe–O bond supports this conclusion. Peroxide-ligated **12** releases $H_2O_2$ much more rapidly (on the order of minutes) than does *cis* thiolate ligated $[Fe^{III}\{S^{Me2}N_4(tren)(OOH)\}]^+$ (**4**, $t_{1/2}$ = 69 h), and represents the first example of a *trans* thiolate-ligated $Fe^{III}$-peroxo.[80] The more rapid rate of $H_2O_2$ release from **12** versus that of **4** suggests that the *trans* positioning of the thiolate in **12** (as well as in the SOR enzyme) plays an important functional role in the promotion of the rapid release of $H_2O_2$ and perhaps explains why this stereochemical arrangement is utilized by the enzyme.

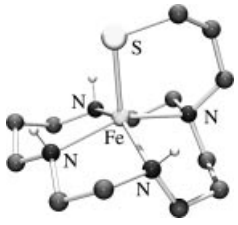


Figure 10. Kovacs' secondary amine-ligated $SOR_{red}$ model, $[Fe^{II}(cyclam)\text{-PrS}]^+$ (**11**), which was recently shown[80] to react with superoxide to afford $H_2O_2$ via the peroxo intermediate $[Fe^{III}(cyclam\text{-PrS})(OO(H))]^+$ (**12**).

### 2.4 SOR versus Cytochrome P450

Cytochrome P450 is a heme (i.e. porphyrin-containing) iron enzyme involved in the metabolism of drugs and xenobiotics, the biosynthesis of key steroid hormones, and the

 © 2007 Wiley-VCH Verlag GmbH & Co. KGaA, Weinheim 

conversion of polyunsaturated fatty acids to biologically active molecules.[45] Like SOR, the P450 catalytic cycle proceeds via an end-on hydroperoxide intermediate (Figure 11).[45] However, the subsequent reactivity of the hydroperoxide is different in each case and has been shown to be dependent on the site of protonation as well as the spin-state of the molecule.[64,81–83] In SOR, $Fe^{III}$–OOH is presumably protonated at the proximal oxygen (the oxygen bound to the metal ion) to weaken the Fe–O bond, release hydrogen peroxide, and generate the oxidized $Fe^{III}$ state. In P450, protonation occurs at the distal oxygen, which polarizes the O–O bond, liberates $H_2O$, and affords a high-valent $Fe^{IV}$=O π cation radical.[45] Initially, this difference in reactivity was ascribed to the presence of a porphyrin ring in cytochrome P450.[48,84] The highly conjugated, negatively charged porphyrin is able to delocalize excess positive charge, which allows for the formation of high-valent "$Fe^{V}$=O" in this environment. However, Que et al. have observed $Fe^{IV}$=O outside of a porphyrin environment and have definitive X-ray crystallographic evidence for examples of these species.[79] Another explanation for the differences in reactivity of SOR versus P450 may involve differences in the spin-state of the hydroperoxide intermediate.[29] The low-spin Fe–OOH of P450 and synthetic analogues have been shown to favor a reaction pathway that involves cleavage of the O–O bond.[64,82,85] In contrast, a high-spin Fe-peroxide ($S$ = 5/2) would favor a reaction pathway that involves cleavage of the Fe–O bond because it would possess populated antibonding σ*(Fe–O) orbitals. The peroxide species formed upon the reaction of the E47A SOR mutant with $H_2O_2$ is high-spin ($S$ = 5/2); however, this may not be true for the native enzyme intermediate. Recent calculations suggest that the peroxide-bound SOR intermediate is low-spin ($S$ = 1/2);[38] however, there is no experimental evidence to confirm this. There is no evidence for oxygenase activity with SOR, which suggests that O–O bond cleavage does not occur, and reduced $Fe^{II}$-SOR is believed to be unreactive towards $O_2$.

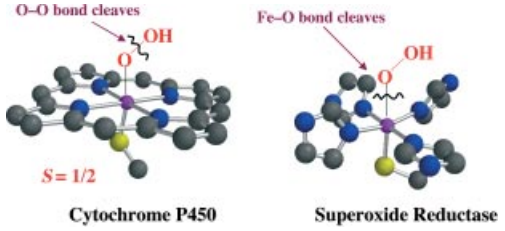


Figure 11. The hydroperoxide intermediates formed during catalysis by the heme iron oxygenase enzyme cytochrome P450 and non-heme iron enzyme SOR, which shows how their reaction pathways (i.e. O–O versus Fe–O bond cleavage) differ.

## 3. Perspective

The accumulation of biochemical and modeling data has begun to generate a clearer picture of the mechanism of superoxide reduction by SOR, but some questions still remain. How SOR is able to selectively reduce superoxide rather than disproportionate $O_2^-$ to $O_2$ and $H_2O_2$ (i.e. SOD activity) is not completely understood. Furthermore, how O–O bond cleavage is avoided in SOR remains unclear. The spin-state of the intermediate peroxide seems to play an important role in determining whether the Fe–O or O–O bond cleaves. It is still unknown whether the peroxide intermediate that is observed during catalysis of wild-type SOR is high- or low-spin. If such an intermediate can be detected in wild-type SOR, then resonance Raman experiments of the peroxide should be carried out with doubly-labeled superoxide, $^{16}O^{18}O^-$, in order to conclusively determine whether this intermediate contains an end-on or a side-on peroxide.

The position of the thiolate (*trans* versus *cis* to the peroxide) does not appear to be critical for the reduction of superoxide given that a five-coordinate $Fe^{II}N_4S$ SOR model complex with the thiolate positioned *cis* to the open site has been shown to reduce superoxide. However, the mechanism of superoxide reduction, and the rate of superoxide binding and hydrogen peroxide release, is likely to be affected by the position of the sulfur moiety. When a *trans* thiolate sulfur is incorporated into a macrocyclic five-coordinate $Fe^{II}N_4S$ SOR model complex, the $Fe^{III}$–OOH intermediate is high-spin and hydrogen peroxide is released more rapidly. The $\nu_{Fe-O}$ is also lower than any iron peroxide, with the exception of the SOR-peroxide. This suggests that the *trans* thiolate weakens the Fe–O bond and favors $H_2O_2$ release. However, one other *trans* thiolate-ligated five-coordinate non-heme $Fe^{II}N_4S$ model complex has been reported that does not reduce superoxide, yet reacts with $H_2O_2$ to afford a high-valent $Fe^{IV}$=O species via cleavage of the O–O bond analogous to that observed in P450. Clearly, more than just the stereochemical relationship between the thiolate and the peroxide is important in the determination of the favored reaction pathway. A more thorough investigation that involves a series of structurally-related compounds is needed to correlate Fe–O (versus O–O) bond-cleaving properties with the spin-state of the molecule, the positioning of the thiolate sulfur (*cis* versus *trans* to the peroxide), redox properties, as well as proximal peroxide oxygen basicity.

## Acknowledgments

The NIH is gratefully acknowledged for its support of the work carried out in the Kovacs laboratory (GM 45881-15).

[1] J. A. Imlay, *J. Biol. Inorg. Chem.* **2002**, *7*, 659–663.
[2] A. C. Maritim, R. A. Sanders, J. B. Watkins III, *J. Biochem. Mol. Toxicol.* **2003**, *17*, 24–38.
[3] G. Fortunato, A. Pastinese, M. Intrieri, M. M. Lofrano, G. Gaeta, M. B. Censi, A. Boccalatte, F. Salvatore, L. Sacchetti, *Clin. Biochem.* **1997**, *30*, 569–571.
[4] P. A. Kocaturk, M. C. Akbostanci, F. Tan, G. O. Kavas, *Pathophysiology* **2000**, *7*, 63–67.
[5] Y. Ihara, M. Chuda, S. Kuroda, T. Hayabara, *J. Neurol. Sci.* **1999**, *170*, 90–95.
[6] M. E. De Leo, S. Borrello, M. Passantino, B. Palazzotti, A. Mordente, A. Daniele, V. Filippini, T. Galeotti, C. Masullo, *Neurosci. Lett.* **1998**, *250*, 173–176.

 © 2007 Wiley-VCH Verlag GmbH & Co. KGaA, Weinheim 

[7] S. L. Marklund, R. Adolfsson, C. G. Gottfries, B. Winblad, *J. Neurol. Sci.* **1985**, *67*, 319–325.
[8] Y. Toh, S. Kuninaka, M. Mori, T. Oshiro, Y. Ikeda, H. Nakashima, H. Baba, S. Kohnoe, T. Okamura, K. Sugimachi, *Oncology* **2000**, *59*, 223–228.
[9] R. H. Burdon, *Free Rad. Biol. Med.* **1995**, *18*, 775–794.
[10] D. M. Kurtz Jr, *Acc. Chem. Res.* **2004**, *37*, 902–908.
[11] V. Nivière, M. Fontecave, *J. Biol. Inorg. Chem.* **2004**, *9*, 119–123.
[12] D. M. Kurtz Jr, *J. Inorg. Biochem.* **2006**, *100*, 679–693.
[13] A.-F. Miller, *Curr. Op. Chem. Biol.* **2004**, *8*, 162–168.
[14] T. A. Jackson, T. C. Brunold, *Acc. Chem. Res.* **2004**, *37*, 461–470.
[15] F. Auchere, F. Rusnak, *J. Biol. Inorg. Chem.* **2002**, *7*, 664–667.
[16] M. W. W. Adams, F. E. Jenney Jr, M. D. Clay, M. K. Johnson, *J. Biol. Inorg. Chem.* **2002**, *7*, 647–652.
[17] A. P. Yeh, Y. Hu, F. E. Jenney Jr, M. W. W. Adams, D. C. Rees, *Biochemistry* **2000**, *39*, 2499–2508.
[18] A. V. Coelho, P. Matias, V. Fulop, A. Thompson, A. Gonzalez, M. A. Carrondo, *J. Biol. Inorg. Chem.* **1997**, *2*, 680–689.
[19] T. Santos-Silva, J. Trincao, A. L. Carvalho, C. Bonifacio, F. Auchere, P. Raleiras, I. Moura, J. J. G. Moura, M. J. Romao, *J. Biol. Inorg. Chem.* **2006**, *11*, 548–558.
[20] V. Adam, A. Royant, V. Niviere, F. P. Molina-Heredia, D. Bourgeois, *Structure* **2004**, *12*, 1729–1740.
[21] J. P. Emerson, D. E. Cabelli, D. M. Kurtz Jr, *Proc. Natl. Acad. Sci. USA* **2003**, *100*, 3802–3807.
[22] J. P. Emerson, E. D. Coulter, D. E. Cabelli, R. S. Phillips, D. M. Kurtz Jr, *Biochemistry* **2002**, *41*, 4348–4357.
[23] M. Lombard, C. Houee-Levin, D. Touati, M. Fontecave, V. Niviere, *Biochemistry* **2001**, *40*, 5032–5040.
[24] Fridovich, *Acc. Chem. Res.* **1972**, *5*, 321–326.
[25] F. E. Jenney Jr, M. F. J. M. Verhagen, X. Cui, M. W. W. Adams, *Science* **1999**, *286*, 306–309.
[26] A.-F. Miller in *Handbook of Metalloproteins* (Eds.: A. Messerschmidt, R. M. T. Poulos, K. Wieghardt), Wiley, New York, **2001**, vol. 1, pp. 668–682.
[27] J. Wuerges, J.-W. Lee, Y.-I. Yim, H.-S. Yim, S.-O. Kang, K. D. Carugo, *Proc. Natl. Acad. Sci. USA* **2004**, *101*, 8569–8574.
[28] E. L. Hegg, L. Que Jr, *Eur. J. Biochem.* **1997**, *250*, 625–629.
[29] J. A. Kovacs, *Chem. Rev.* **2004**, *104*, 825–848.
[30] C. K. Vance, A.-F. Miller, *Biochemistry* **2001**, *40*, 13079–13087.
[31] C. K. Vance, A.-F. Miller, *J. Am. Chem. Soc.* **1998**, *120*, 461–467.
[32] E. D. Coulter, J. P. Emerson, D. M. Kurtz Jr, D. E. Cabelli, *J. Am. Chem. Soc.* **2000**, *122*, 11555–11556.
[33] V. Nivière, M. Lombard, M. Fontecave, C. Houee-Levin, *FEBS Lett.* **2001**, *497*, 171–173.
[34] M. D. Clay, F. E. Jenney Jr, P. L. Hagedoorn, G. N. George, M. W. W. Adams, M. K. Johnson, *J. Am. Chem. Soc.* **2002**, *124*, 788–805.
[35] M. Clay, C. A. Cosper, F. E. Jenney Jr, M. W. W. Adams, M. K. Johnson, *Proc. Natl. Acad. Sci. USA* **2003**, *100*, 3796–3801.
[36] M. D. Clay, T.-C. Yang, F. E. Jenney Jr, I. Y. Kung, C. A. Cosper, R. Krishnan, D. M. Kurtz Jr, M. W. W. Adams, B. M. Hoffman, M. K. Johnson, *Biochemistry* **2006**, *45*, 427–438.
[37] D. M. Kurtz, E. D. Coulter, *J. Biol. Inorg. Chem.* **2002**, *7*, 653–658.
[38] R. Silaghi-Dumitrescu, I. Silaghi-Dumitrescu, E. D. Coulter, D. M. Kurtz Jr, *Inorg. Chem.* **2003**, *42*, 446–456.
[39] G. Roelfes, V. Vrajmasu, K. Chen, R. Y. N. Ho, J.-U. Rohde, C. Zondervan, R. M. Crois, E. P. Schudde, M. Lutz, A. L. Spek, R. Hage, B. L. Feringa, E. Munck, L. Que Jr, *Inorg. Chem.* **2003**, *42*, 2639–2653.
[40] C. Mathe, T. A. Mattioli, O. Horner, M. Lombard, M. J. Latour, M. Fontecave, V. Niviere, *J. Am. Chem. Soc.* **2002**, *124*, 4966–4967.
[41] O. Horner, J.-M. Mouesca, J.-L. Oddou, C. Jeandy, V. Niviere, T. A. Mattioli, C. Mathe, M. Fontecave, P. Maldivi, P. Bonville, J. A. Halfen, J.-M. Latour, *Biochemistry* **2004**, *43*, 8815–8825.
[42] C. Mathé, V. Nivière, C. Houée-Levin, T. A. Mattioli, *Biophys. Chem.* **2006**, *119*, 38–48.
[43] R. M. Burger, *Struct. Bonding* **2000**, *97*, 287–303.
[44] P. R. Ortiz de Montellano, *Acc. Chem. Res.* **1998**, *31*, 543–549.
[45] I. G. Denisov, T. M. Makris, S. G. Sligar, I. Schlichting, *Chem. Rev.* **2005**, *105*, 2253–2277.
[46] I. Schlichting, J. Berendzen, K. Chu, A. M. Stock, S. A. Maves, D. E. Benson, R. M. Sweet, D. Ringe, G. A. Petsko, S. G. Sligar, *Science* **2000**, *287*, 1615–1622.
[47] G. H. Loew, D. L. Harris, *Chem. Rev.* **2000**, *100*, 407–419.
[48] M. Sono, M. P. Roach, E. D. Coulter, J. H. Dawson, *Chem. Rev.* **1996**, *96*, 2841–2887.
[49] M. D. Wolfe, J. V. Parales, D. T. Gibson, J. D. Lipscomb, *J. Biol. Chem.* **2001**, *276*, 1945–1953.
[50] A. Karlsson, J. V. Parales, R. E. Parales, D. T. Gibson, H. Eklund, S. Ramaswamy, *Science* **2003**, *299*, 1039–1042.
[51] L. Que Jr, R. Y. N. Ho, *Chem. Rev.* **1996**, *96*, 2607–2624.
[52] V. Nivière, M. Asso, C. O. Weill, M. Lombard, B. Guigliarelli, V. Favaudon, C. Houée-Levin, *Biochemistry* **2004**, *43*, 808–818.
[53] C. Berthomieu, F. Dupeyrat, M. Fontecave, A. Verméglio, V. Nivière, *Biochemistry* **2002**, *41*, 10360–10368.
[54] C. Mathé, V. Nivière, T. A. Mattioli, *J. Am. Chem. Soc.* **2005**, *127*, 16436–16441.
[55] E. D. Coulter, D. M. Kurtz, *Arch. Biochem. Biophys.* **2001**, *394*, 76–86.
[56] J. V. Rodrigues, I. A. Abreu, L. M. Saraiva, M. Teixeira, *Biochem. Biophys. Res. Commun.* **2005**, *329*, 1300–1305.
[57] A. M. Grunden, F. E. Jenney Jr, K. Ma, M. Ji, M. V. Weinberg, M. W. W. Adams, *Appl. Environ. Microbiol.* **2005**, *71*, 1522–1530.
[58] M. Costas, M. P. Mehn, M. P. Jensen, L. Que Jr, *Chem. Rev.* **2004**, *104*, 939–986.
[59] J.-J. Girerd, F. Banse, A. J. Simaan, *Struct. Bonding* **2000**, *97*, 145–177.
[60] G. Roelfes, M. Lubben, K. Chen, R. Y. N. Ho, A. Mettsma, S. Genseberger, R. M. Hermant, R. Hage, S. K. Mandal, V. G. Young Jr, Y. Zang, H. Kooijman, A. L. Spek, L. Que Jr, B. L. Feringa, *Inorg. Chem.* **1999**, *38*, 1929–1936.
[61] A. J. Simaan, F. Banse, P. Mialane, A. Boussac, S. Un, T. Karger-Grisel, G. Bouchoux, J.-J. Girerd, *Eur. J. Inorg. Chem.* **1999**, 993–996.
[62] R. Y. N. Ho, G. Roelfes, B. L. Feringa, L. Que Jr, *J. Am. Chem. Soc.* **1999**, *121*, 264–265.
[63] A. J. Simaan, F. Banse, J.-J. Girerd, K. Wieghardt, E. Bill, *Inorg. Chem.* **2001**, *40*, 6538–6540.
[64] N. Lehnert, R. Y. N. Ho, L. Que Jr, E. I. Solomon, *J. Am. Chem. Soc.* **2001**, *123*, 12802–12816.
[65] N. Lehnert, R. Y. N. Ho, L. Que Jr, E. I. Solomon, *J. Am. Chem. Soc.* **2001**, *123*, 8271–8290.
[66] S.-I. Adachi, S. Nagano, K. Ishimori, Y. Watanabe, I. Morishima, T. Egawa, T. Kitagawa, R. Makino, *Biochemistry* **1993**, *32*, 241–252.
[67] J. T. Groves, Y. Watanabe, *J. Am. Chem. Soc.* **1988**, *110*, 8443–8452.
[68] K. Yamaguchi, Y. Watanabe, I. Morishima, *J. Am. Chem. Soc.* **1993**, *115*, 4058–4065.
[69] J. A. Halfen, H. L. Moore, D. C. Fox, *Inorg. Chem.* **2002**, *41*, 3935–3943.
[70] A. T. Fiedler, H. L. Halfen, J. A. Halfen, T. C. Brunold, *J. Am. Chem. Soc.* **2005**, *127*, 1675–1689.
[71] M. R. Bukowski, H. L. Halfen, T. A. van der Berg, J. A. Halfen, L. Que Jr, *Angew. Chem. Int. Ed.* **2005**, *44*, 584–587.
[72] J. Shearer, J. Nehring, W. Kaminsky, J. A. Kovacs, *Inorg. Chem.* **2001**, *40*, 5483–5484.
[73] J. Shearer, R. C. Scarrow, J. A. Kovacs, *J. Am. Chem. Soc.* **2002**, *124*, 11709–11717.
[74] R. M. Theisen, J. A. Kovacs, *Inorg. Chem.* **2005**, *44*, 1169–1171.
[75] D. T. Sawyer, J. S. Valentine, *Acc. Chem. Res.* **1981**, *14*, 393–400.


 © 2007 Wiley-VCH Verlag GmbH & Co. KGaA, Weinheim 

[76] J. Shearer, S. B. Fitch, W. Kaminsky, J. Benedict, R. C. Scarrow, J. A. Kovacs, *Proc. Natl. Acad. Sci. USA* **2003**, *100*, 3671–3676.
[77] S. Ozaki, J. Kirose, Y. Kidani, *Inorg. Chem.* **1988**, *27*, 3746–3751.
[78] M. R. Bukowski, K. D. Koehntop, A. Stubna, E. L. Bominaar, J. A. Halfen, E. Münck, W. Nam, L. Que Jr, *Science* **2005**, *310*, 1000–1002.
[79] J.-U. Rohde, J.-H. In, M. H. Lim, W. W. Brennessel, M. R. Bukowski, A. Stubna, E. Munck, W. Nam, L. Que Jr, *Science* **2003**, *299*, 1037–1039.
[80] T. Kitagawa, A. Dey, P. Lugo-Mas, J. Benedict, W. Kaminsky, E. I. Solomon, J. A. Kovacs, **2006**, submitted.
[81] D. L. Harris, G. H. Loew, *J. Am. Chem. Soc.* **1998**, *120*, 8941–8948.
[82] A. Decker, E. I. Solomon, *Curr. Op. Chem. Biol.* **2005**, *9*, 152–163.
[83] E. I. Solomon, A. Decker, N. Lehnert, *Proc. Natl. Acad. Sci. USA* **2003**, *100*, 3589–3594.
[84] S. Ferguson-Miller, G. T. Babcock, *Chem. Rev.* **1996**, *96*, 2889–2907.
[85] N. Lehnert, F. Neese, R. Y. Ho, L. Que Jr, E. I. Solomon, *J. Am. Chem. Soc.* **2002**, *124*, 10810–10822.

Received: May 18, 2006
Published Online: October 2, 2006

 © 2007 Wiley-VCH Verlag GmbH & Co. KGaA, Weinheim 

DOI: 10.1002/ejic.200600766

# The Transient Titanocene(II): Direct Synthesis from Solvated Titanium(II) Chloride and Cyclopentadienylsodium and Ensuing Interception with Diphenylacetylene as 1,1-Bis(cyclopentadienyl)-2,3,4,5-tetraphenyltitanacyclopentadiene[‡]

**John J. Eisch,*[a] Adetenu A. Adeosun,[a] and John M. Birmingham[b]**

**Keywords:** Titanocene(II) / Wilkinson metallocene synthesis / Epititanation / 1,1-Bis(cyclopentadienyl)titanacyclopropenes / 1,1-Bis(cyclopentadienyl)titanacyclopentadienes

For the first time the unstable titanocene(II) has been directly synthesized by the Wilkinson metallocene approach, namely the interaction of a THF-soluble form of titanium(II) chloride with two equivalents of cyclopentadienylsodium in THF solution at 0°–25 °C. Because of the transient existence of the titanocene(II) thereby obtained, it could only be chemically trapped in high yield as 1,1-bis(cyclopentadienyl)-2,3,4,5-tetraphenyltitanacyclopentadiene by two equivalents of diphenylacetylene, if the acetylene was added at 25 °C, *without* removal of the by-product LiCl and NaCl. If the addition of the acetylene was delayed, in order to filter off the LiCl and NaCl from the reaction mixture, then no trace of the titanacyclopentadiene derivative was found upon hydrolytic workup. Instead, a significant portion of the acetylene was found to have undergone hydrotitanation. This finding is clear evidence that the titanocene(II) had undergone a precedented rearrangement to a known dimer having the structure of a titanocene(III) hydride with a fulvalene bridge between the titanium centers. We suggest that the LiCl and NaCl present in the unfiltered reaction mixture form a dichloro complex with titanocene(II) and thereby retard its dimerizing rearrangement to the titanocene(III) hydride.
(© Wiley-VCH Verlag GmbH & Co. KGaA, 69451 Weinheim, Germany, 2007)

## Introduction

Shortly after the serendipitous synthesis and discovery of ferrocene through the independent routes of Pauson and Kealy[2] and of Miller and co-workers[3] the systematic synthesis of analogous cyclopentadienyl derivatives of transition metals was undertaken with great success by both the Wilkinson and the Fischer research groups.[4] From group 4 tetrahalides the bis(cyclopentadienyl)metal(IV) dihalides were the most readily formed and isolated. Although the preparation of bis(cyclopentadienyl)titanium(III) halides was achieved by the activated metal reduction of $Cp_2TiX_2$ in donor, nonprotic solvents,[5,6] the preparation of bis(cyclopentadienyl)titanium(II) or titanocene(II) (**2**) has received the attention of many researchers during the period of 1956–1976 with an overall indecisive outcome.[7]

The attempted preparations of titanocene(II) (**2**) have involved either the direct reaction of polymeric $TiCl_2$ (**1a**) in ethereal suspension with two equiv. of bis(cyclopentadienyl)-sodium (**3**)[8a,8b] or the α-elimination of the two groups G from $Cp_2TiG_2$ (**4**) (G = Cl, or $CH_3$) by an active metal for G = Cl,[9] dihydrogen,[10] heat,[11] or light[12] for G = $CH_3$ (Scheme 1). None of the socalled "titanocene" products thus generated could be isolated in a crystalline form suitable for single-crystal X-ray structure analysis.

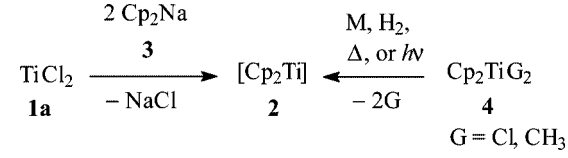


Scheme 1.

A range of different "titanocene" products have been accordingly isolated, varying in color (green, brown, violet or black) and in spectroscopic as well as magnetic properties. It is generally agreed that none of these products is titanocene (**2**) itself, which should be very reactive due to its carbenoid nature.[13,14] Therefore, in order to take into account the anticipated high reactivity of authentic titanocene (**2**), provision was made to capture **2** as it was purportedly formed by the reduction of $Cp_2TiCl_2$ with the sodium–naphthalene adduct in THF.[9a] When diphenylacetylene (**5**) was included as the trapping agent in the reaction, the titanacyclopentadiene **6** was isolated in low yield. This finding was taken as convincing evidence that titanocene (**2**) had

[‡] Organic Chemistry of Subvalent Transition Metal Complexes, 39. Part 38: Ref.[1]

[a] State University of New York at Binghamton, Department of Chemistry,
P. O. Box 6000, Binghamton, NY 13902-6000, USA
Fax: +1-607-777-4865
E-mail: jjeisch@binghamton.edu
[b] The Boulder Scientific Company,
Mead, CO, USA

 © 2007 Wiley-VCH Verlag GmbH & Co. KGaA, Weinheim 

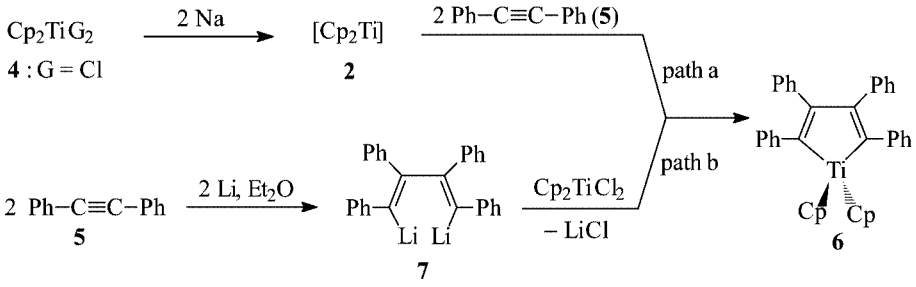


Scheme 2.

been generated [**4** (G = Cl)→**2**] and had been captured by diphenylacetylene (**5**) (path a, Scheme 1, **2**→**6**).[15] However, the conclusion that titanocene (**2**) has been captured in this experiment is ambiguous and thus inconclusive. It has long been recognized that alkali metals in general and lithium metal in particular can effect the reductive dimerization of diphenylacetylene in ethers (**5**→**7**, Scheme 2).[16,17] The 1,4-dilithiobutadiene of proven (*E*,*E*)-configuration has been successfully employed for the synthesis of **6** and several other metallacyclopentadienes.[18,19] Thus the titanocycle **6** isolated from the reaction of $Cp_2TiCl_2$ and diphenylacetylene with sodium could equally as well have been formed from path b in Scheme 2 (**5**→**7**→**6**) and would *not* have required the presence of free titanocene (**2**), as in path a.

## Results and Discussion

In the present research the direct reaction of titanium(II) chloride with bis(cyclopentadienyl)sodium (**3**) was again investigated but with one significant difference. Instead of employing the insoluble, polymeric form, $[TiCl_2]_x$ (**1a**), obtainable by the high-temperature disproportionation of titanium(III) chloride, a newly discovered, THF-soluble form of titanium(II) chloride (**1b**), $[TiCl_2{\cdot}THF]_n$, generated by the alkylative reduction of titanium(IV) chloride,[20] has been used to great advantage [Equations (1) and (2)]. The degree of aggregation (*n*) of **1b** is not yet known with certainty but the existence of the paramagnetic open-chain, trimeric biradical, $[Ti(OiPr)_2]_3$, supports the proposal that the diamagnetic **1b** may form a cyclic trimer in which a core of 3 titanium atoms is bonded as a triangular structure.[1]

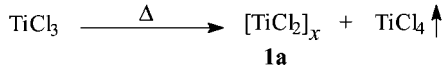


(1)

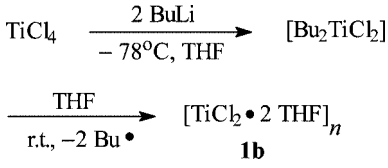


(2)

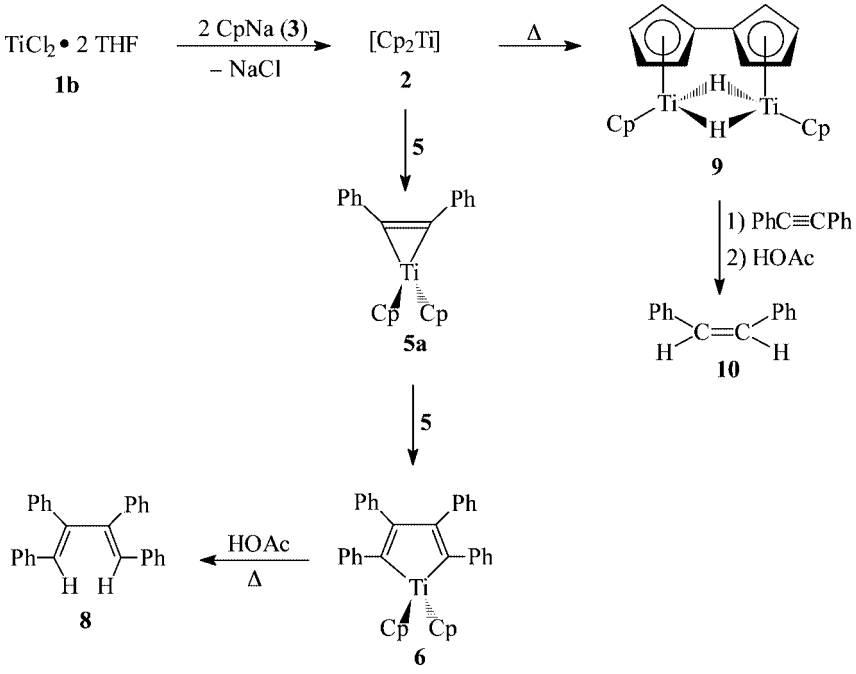


Scheme 3.

 © 2007 Wiley-VCH Verlag GmbH & Co. KGaA, Weinheim 

A THF solution of 0.10 mmol of freshly prepared **1b**, still containing the LiCl by-product, was treated at 0 °C with 0.22 mmol of bis(cyclopentadienyl)sodium (**3**). The black reaction mixture, presumably containing titanocene(II) (**2**), was brought to 25 °C and the LiCl and NaCl solids filtered off. Treating the filtrate with diphenylacetylene (**5**), however, produced no trace of 1,1-bis(cyclopentadieny)-l-2,3,4,5-tetraphenyltitanacyclopentadiene (**6**). This conclusion was reached after protolysis of the reaction mixture with acetic acid was shown to produce no (*E*,*E*)-1,2,3,4-tetraphenyl-1,3-butadiene (**8**) (Scheme 3), the expected protolysis product that would have arisen from **6**, which would have formed by the trapping of **2** by diphenylacetylene (**5**) (path a, Scheme 2). That on the other hand *cis*-stilbene (**10**) was isolated as the sole protolysis product is consistent with the view that any **2** formed from **1b** and **3** had undergone the known rearrangement to **9** before it could be intercepted by **5**.[7b] The resultant **9** could then have hydrotitanated acetylene **5** and hence have generated *cis*-olefin **10**, upon protolysis.

In our further attempt to intercept any titanocene(II) (**2**) formed from **1b** and **2**, we repeated the reaction between **1b** and **2** at 0 °C, brought the reaction mixture to 25 °C, but this time immediately added the diphenylacetylene (**5**) *without attempting to filter off the suspended LiCl and NaCl*. A nonhydrolytic workup involving removal of any solids from the hexane extracts of the final reaction mixture led, via epititanation to titanacyclopropene **5a**,[14] to the isolation of **6** in 83% yield. Its identity was confirmed by $^1$H NMR and IR spectral comparisons with an authentic sample of **6** prepared according to a previously outlined method,[21] whose details are published here for the first time [Equation (3)]. Furthermore, the sample of **6** isolated from **1b** and **2** was smoothly protolyzed to yield solely **8** in high yield (Scheme 3).

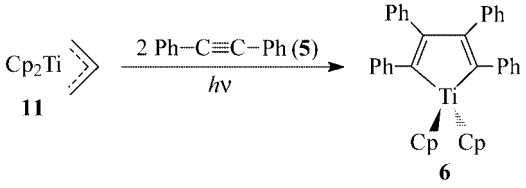


(3)

The success of this present procedure for generating **2** from **1b** and **3** and in trapping titanocene(II) (**2**) before it could rearrange to **9** we ascribe to two factors: 1) the shorter time the THF solution of **2** stood at 25 °C before acetylene **5** was introduced; and 2) the presence of LiCl and NaCl, which furnish an ample source of Lewis basic chloride ions, capable of coordinating with monomeric $Cp_2Ti$ and thereby retarding its rearrangement to **7** [Equation (4)]. A relevant precedent is the complex **12** formed from **1a** and NaCl as shown in Equation (5).[22]

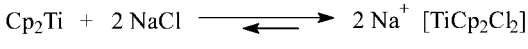


(4)

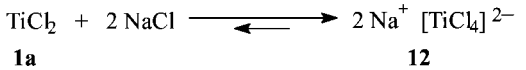


(5)

## Conclusions

From the foregoing experiments we have now shown that the transient titanocene(II) can also be prepared by the classic method introduced by the Wilkinson group some 50 years ago. Its existence, although short, has been firmly established by its chemical trapping with diphenylacetylene as the titanacyclopentadiene **6**.[23]

## Experimental Section

**Starting Materials, Reaction Conditions and Instrumentation:** The starting $TiCl_4$ employed was of at least 98% purity as commercially available and the *n*-butyllithium used was as a 1.60 M solution in hexane. The cyclopentadiene was obtained from the thermolysis of commercial dicyclopentadiene under argon and collected in an ice bath. The sample for the preparation of cyclopentadienylsodium resulted from a redistillation of the monomer just before use.[24] The titanium(II) chloride in THF, containing 2 equiv. of the by-product, LiCl, was obtained from the treatment of $TiCl_4$ in THF with 2 equiv. of *n*-butyllithium at low temperatures according to the published procedure.[20] In the same reference are given experimental details for removing LiCl from the product and obtaining analytically pure $TiCl_2$·THF.[20] However, for its reaction here with cyclopentadienylsodium, the titanium(II) chloride/lithium chloride mixture was used directly. Finally, the diphenylacetylene used in trapping reactions was 99% pure and was shown by TLC and $^1$H NMR spectroscopy to be free of *cis*- or *trans*-stilbene. All reactions, transfers and separations were carried out under a positive pressure of anhydrous, oxygen-free argon.[25] All solvents employed, mainly tetrahydrofuran, heptane and toluene, with these air- and moisture-sensitive reagents were dried and distilled from a sodium metal benzophenone ketyl mixture prior to use.[25]

The $^1$H and $^{13}$C NMR spectra were recorded with a Bruker spectrometer, model AM-360, with tetramethylsilane ($Me_4Si$) as the internal standard. The chemical shifts reported are expressed on the $\delta$-scale in parts per million (ppm) from the $Me_4Si$ reference signal.

**1,1-Bis(cyclopentadienyl)-2,3,4,5-tetraphenyltitanacyclopentadiene (6):** Although an authentic sample of this known compound can be prepared by a number of previous published methods,[12,15] a method developed in our laboratory proved most convenient,[21] because its starting material, **11** is available through a verified experimental procedure.[26,27] A 100-mL quartz phototube, having ground-glass joints at the upper end for attachment to the argon source and for a rubber septum, respectively, was repeatedly evacuated and filled with argon gas. Then a solution of $\eta^3$-allylbis(cyclopentadienyl)titanium(III) (365 mg, 1.67 mmol) prepared under argon in anhydrous, deoxygenated cyclohexane (25 mL) was introduced into the tube through the septum, after which a similarly prepared solution of diphenylacetylene (594 mg, 3.34 mmol) in 10 mL of purified cyclohexane was introduced. The reaction solution was irradiated for 48 h in a Rayonet photochemical reactor, model 100, equipped with a cylindrical array of phototubes emitting radiation at 254 nm. The cylindrical cavity of the lamp bank had a diameter of 24 cm. During this time the initial purple color of the reaction mixture became greenish-yellow. The cyclohexane

 © 2007 Wiley-VCH Verlag GmbH & Co. KGaA, Weinheim 

was removed from the photolysate under reduced pressure and the dark green residue was extracted under argon with 3 × 10-mL portions of hexane. Such combined extracts were filtered and then concentrated. Storage of the hexane solution at 0 °C led to the deposition of between 339 mg to 491 mg of dark green **6** (38–55%) in two different runs; m.p. (capillary under argon) 148.5–150 °C [lit. 150 °C];[17] $^1$H NMR ($C_6D_6$): $\delta$ = 6.06(s, 10 H), 6.4–6.9 (m, 20 H) ppm. IR (KBr): $\tilde{\nu}$ = 697 cm$^{-1}$ (vs), 725 (m), 750 (m), 770 (s), 780 (m), 800 (vs), 807 (vs), 830 (sh), 840 (w), 905 (vw), 945 (vw), 1015 (s), 1075 (s), 1095 (sh), 1145 (sh), 1155 (w), 1180 (w), 1245 (w), 1260 (w), 1362 (w), 1370 (sh), 1440 (s), 1480 (s), 1590 (s), 3040 (w), 3060 (w), 3080 (w) cm$^{-1}$.

**Interaction of Bis(cyclopentadienyl)sodium (3) with Titanium(II) Chloride–Bis(tetrahydrofuran) (1b) in Tetrahydrofuran**

**1) Reaction at 0 °C, Removal of Alkali Metal Salts by Filtration and Reaction of the Titanocene Filtrate with Diphenylacetylene (5):** A solution of titanium(IV) chloride (1.90 g, 10 mmol) in toluene (10 mL) was added to dry THF (60 mL) and the mixture cooled to –78 °C to yield a yellow suspension. Then *n*-butyllithium (20 mmol) in hexane (2.50 M) was introduced into the yellow slurry dropwise. Allowing this reaction mixture to come to 25 °C over 1 h produced a black slurry of $TiCl_2$·THF (**1b**) in solution with suspended LiCl by-product, as has been established by a published procedure.[22] Then an orange solution of the cyclopentadienylsodium **3** (22 mmol), previously prepared from sodium metal dispersion (0.51 g, 22 mmol) and freshly distilled cyclopentadiene (1.50 g, 23 mmol) in THF (50 mL) was added rapidly to the solution of **1b** maintained at 0 °C. The resulting reaction mixture was allowed to stand at 25 °C for 2 h before the suspended salts (LiCl and NaCl) were filtered off on a glass frit under argon. The filtration step required about 90 min. The green-black filtrate was then treated with a solution of diphenylacetylene (**5**) (3.56 g, 20 mmol) in THF (40 mL). This final mixture was allowed to stand at room temp. for 10 h and then heated at reflux for 6 h. Treatment of an aliquot of the reaction mixture with glacial acetic acid and usual hydrolytic workup of the dried organic extract showed that 35% of the diphenylacetylene initially introduced had been converted into *cis*-stilbene (**10**) (7.0 mmol.). Equally noteworthy was the absence of any (*E*,*E*)-1,2,3,4-tetraphenyl-1,3-butadiene (**8**), the protolysis product expected to arise if any **6** had been formed from the reaction of the titanocene(II) **2** with the added diphenylacetylene.

**2) Reaction at 25 °C, Followed by the Immediate Addition of Diphenylacetylene (5) without the Removal of Alkali Metal Salts:** Parallel to the foregoing procedure, a freshly prepared black slurry of $TiCl_2$·THF (**1b**, 10 mmol) and LiCl (20 mmol) in THF (60 mL) was treated dropwise at 0 °C with **3** (22 mmol) in THF (50 mL). The resulting mixture was allowed to stand for 2 h at 20–25 °C, after which time a solution of diphenylacetylene (**5**) (3.56 g, 20 mmol) in THF (40 mL) was added rapidly. The final reaction mixture was kept at room temp. for 10 h and then heated at reflux for 6 h. After removal of all volatiles under reduced pressure the residue was extracted with 4 × 15-mL portions of warm hexane, the combined extracts filtered and the filtrate concentrated to about half its volume. Storage of the hexane solution at 0 °C deposited 4.27 g (83%) of dark green crystals of **6**, m.p. 148–150 °C, whose $^1$H NMR ($C_6D_6$) and IR (KBr) spectra were identical with those of the authentic sample. Treatment of a sample of such a product with hot glacial acetic acid, followed by the usual hydrolytic workup, afforded pure (*E*,*E*)-1,2,34-tetraphenyl-1,3-butadiene (**8**), m.p. 181–183 °C, as the only nonvolatile organic product. $^1$H NMR ($CDCl_3$): $\delta$ = 6.40 (s, 2 H), 6.98–7.38 (m, 20). When the protolysis of **6** was repeated with glacial *O*-deuterioacetic acid (99%), the resulting **8** lacked the $^1$H NMR singlet at $\delta$ = 6.40 ppm, showing that this sample of **8** was deuteriated at the $C^1$ and $C^4$ sites.

## Acknowledgments

The authors are grateful to the Boulder Scientific Company, Mead, Colorado, for the generous support of their research with transition-metal metallocenes and to the Alexander von Humboldt Foundationfor a Senior Scientist Award to the first-cited author, renewed in 2005 for studies in the laboratory of Professor W. A. Herrmann, Institute of Inorganic Chemistry, Technische Universität München, Germany.

[1] J. J. Eisch, J. N. Gitua, D. C. Doetschman, *Eur. J. Inorg. Chem.* **2006**, 1968–1975.
[2] T. J. Kealy, P. L. Pauson, *Nature* **1951**, *168*, 1039–1040.
[3] S. A. Miller, J. A. Tebboth, J. F. Tremaine, *J. Chem. Soc.* **1952**, 632–635.
[4] A comprehensive survey of the various syntheses of cyclopentadienyl-metal compounds reported in the scientific and patent literature prior to 1963 has appeared: J. M. Birmingham, *Adv. Organomet. Chem.* **1964**, *2*, 365.
[5] J. M. Birmingham, A. K. Fischer, G. Wilkinson, *Naturwissenschaften* **1955**, *42*, 96.
[6] P. C. Wailes, R. S. P. Coutts, H. Weigold, *Organometallic Chemistry of Titanium, Zirconium, and Hafnium*, Academic Press, New York, **1981**, pp. 98–100.
[7] A detailed recounting of the "Titanocene Saga" has appeared in two reviews: a) An empirical summary of the several experimental efforts: P. C. Wailes, R. S. P. Coutts, H. Weigold, *Organometallic Chemistry of Titanium, Zirconium, and Hafnium*, Academic Press, New York, **1974**, pp. 228–239; b) A more recent review of experimental observations with considerable structure interpretation: M. Bottrill, P. D. Gavens, J. McMeeking, in: *Comprehensive Organometallic Chemistry* (Eds.: G. Wilkinson, F. G. A. Stone, E. W. Abel), Pergamon Press, Oxford, **1982**, pp. 314–320.
[8] a) A. K. Fischer, G. Wilkinson, *J. Inorg. Nucl. Chem.* **1956**, *2*, 149–152; b) J. M. Birmingham, Doctoral Thesis, Harvard University, **1955**.
[9] a) G. W. Watt, L. J. Baye, F. O. Drummond Jr., *J. Am. Chem. Soc.* **1966**, *88*, 1138–1140 (sodium naphthalenide); b) J. J. Salzmann, P. Mosimann, *Helv. Chim. Acta* **1967**, *50*, 1831–1836 (sodium dispersion); c) G. P. Pez, *J. Am. Chem. Soc.* **1976**, *98*, 8072–8074 (potassium naphthalenide to give by XRD a structure, CpTi-TiCp$_2$ unit, whose Ti centers have a $C_5H_4$ bridging ring π-bonded to the Ti on the left and σ-bonded to the Ti on the right).
[10] K. Clauss, H. Bestian, *Justus Liebigs Ann. Chem.* **1962**, *654*, 8–19.
[11] G. A. Razuvaev, V. N. Latyaeva, L. I. Vishinskaya, A. M. Rabinovitch, *J. Organomet. Chem.* **1973**, *49*, 441–444.
[12] H. Alt, M. D. Rausch, *J. Am. Chem. Soc.* **1974**, *96*, 5936–5937.
[13] H. H. Brintzinger, L. S. Bartell, *J. Am. Chem. Soc.* **1970**, *92*, 1105–1107.
[14] J. J. Eisch, *J. Organomet. Chem.* **2001**, *617–618*, 148–157.
[15] G. W. Watt, F. O. Drummond Jr., *J. Am. Chem. Soc.* **1970**, *92*, 826–828.
[16] L. I. Smith, H. H. Hoehn, *J. Am. Chem. Soc.* **1941**, *63*, 1184–1187.
[17] J. J. Eisch, *Organometallic Syntheses*, vol. 2, Academic Press, New York, **1981**, pp. 98–100.
[18] F. C. Leavitt, T. A. Manuel, F. Johnson, L. U. Matternas, D. S. Lehman, *J. Am. Chem. Soc.* **1960**, *82*, 5099–5102.
[19] E. H. Braye, W. Hübel, I. Caplier, *J. Am. Chem. Soc.* **1961**, *83*, 4406–4413.

 © 2007 Wiley-VCH Verlag GmbH & Co. KGaA, Weinheim 

[20] J. J. Eisch, X. Shi, J. Lasota, *Z. Naturforsch., Teil B* **1995**, *50*, 342–350.
[21] J. J. Eisch, S. I. Pombrik, X. Shi, S. C. Wu, *Macromol. Symp.* **1995**, *89*, 221–229.
[22] G. W. A. Fowles, T. E. Lester, R. A. Walton, *J. Chem. Soc. A* **1968**, 1081–1085.
[23] For a leading reference to other recent chemical trapping methods for intercepting assumed titanocene(II) as an intermediate in other reactions of titanocene(IV) derivatives: N. Mézailles, N. Avarvari, D. Bourissou, F. Mathey, P. LeFloch, *Organometallics* **1998**, *17*, 2677–2679.
[24] R. B. King, in: *Organometallic Syntheses* (Eds.: J. J. Eisch, R. B. King), vol. 1, Academic Press, New York, **1965**, pp. 64–66.
[25] J. J. Eisch, in: *Organometallic Syntheses* (Eds.: J. J. Eisch, R. B. King), vol. 2, Academic Press, New York, **1981**, pp. 3–37.
[26] H. A. Martin, F. Jellinek, *J. Organomet. Chem.* **1967**, *8*, 115–118.
[27] M. P. Boleslawski, J. J. Eisch, *Organometallic Syntheses* (Eds.: R. B. King, J. J. Eisch), vol. 3, Elsevier, Amsterdam, **1986**, pp. 19–21.

Received: August 17, 2006
Published Online: November 17, 2006

 © 2007 Wiley-VCH Verlag GmbH & Co. KGaA, Weinheim 

DOI: 10.1002/ejic.200600789

# The Design of Metal Chelates with a Biologically Related Redox-Active Part: Conjugation of Riboflavin to Bis(2-pyridylmethyl)amine Ligand and Preparation of a Ferric Complex

**Nasser K. Thallaj,[a] Dominique Mandon,*[a] and Kristen A. White[a]**

**Keywords:** N ligands / Iron complexes / Riboflavin / Electrochemistry / Electron mediators

Reaction of a twofold molar excess of bis(2-pyridylmethyl)-amine DPA with 8α-bromoAc4riboflavin in dry DMF over 24 h affords the 8α-[bis(2-pyridylmethyl)amine]-*N*-$Ac_4$riboflavin ligand. This compound can be described as a tweezer in which the flavin moiety acts as a potential electron mediator. The trichloroferric complex has been prepared, and together with the low potential reduction wave of the flavin moiety, the presence of a reversible $Fe^{III}/Fe^{II}$ couple at a higher potential is observed. The deacetylated ligand 8α-[bis(2-pyridylmethyl)amine]-*N*-riboflavin can easily be obtained.

(© Wiley-VCH Verlag GmbH & Co. KGaA, 69451 Weinheim, Germany, 2007)

## Introduction

One of the most fascinating aspects of chemical sciences is the way chemists can affect Nature's legacy by modification of biological material, especially when going as far as to design artificial proteins or enzymes that lead to new and sometimes unexpected reactivities.[1–4]

Flavin analogues are well-known as versatile catalysts and are involved in various reactions such as oxidation of tertiary amines, sulfides and ketones, generally with the use of $H_2O_2$ as the oxidant;[5–7] some cases of oxidation by molecular oxygen have also reported.[8] The idea of linking flavin derivatives to biological compounds in order to access artificial proteins is not new: early examples in which flavins were covalently linked to small proteins like papain for instance encountered some success in the oxidation of dihydronicotinamides.[4] In that case, the flavin fragment acted as the site where the reaction took place. Flavins and derivatives, however, are also known as major electron mediators in biological oxidation processes. It is therefore tempting to associate these derivatives with systems that require electron delivery. First attempts to link flavin derivatives with hemes were reported a long time ago, with an example of a semisynthetic hydroxylase that displayed P-450 activity without a reductase.[9] More recently, covalent binding between a riboflavin and protoporphyrin IX allowed reductive activation of dioxygen by an artificial myoglobin.[10] In these examples, the porphyrin/flavin binds the protein through the porphyrin side. Flavin derivatives, however, can bind proteins by themselves. The ability of riboflavin to bind low potential electron carriers, such as flavoproteins for instance, to produce stable complexes is now well-documented.[11–13] The fact that the flavin/flavodoxin complex can function as a one-electron carrier at a potential close to that of the hydrogen electrode[13] makes the design of flavin appended ligands that can accommodate a redox-active metal highly desirable in order to carry out further redox-assisted chemistry.

For several years now, we have been studying dichloroferrous complexes of pyridylmethyl-amine containing ligands, and we have reported cases of fast biomimetic reactions of dioxygen with the metal centre.[14–16] The end product recovered after oxygenation of the ferrous complex can sometimes be reduced back to ferrous, which prefigures the metal centre for further redox chemistry. It was thus tempting to prepare a system in which a pyridylmethylamine-containing ligand would be covalently attached to a riboflavin derivative, the latter acting here as a redox mediator. Examples of substituted DPA ligands with electron mediators can be found in the literature.[17,18] However, those mediators are synthetic compounds and, to the best of our knowledge, there is currently no example of conjugation with a universal and biologically relevant mediator such as riboflavin. We thus report in this communication the first example of synthesis and characterization of such a ligand, 8α-[bis(2-pyridylmethyl)amine]-*N*-riboflavin, as well as the preparation of an air-stable trichloroferric complex of the acetylated precursor. In addition to standard analytical methods used in synthesis, both acetylated precursor and complex have been characterized by cyclic voltammetry. As a result,

[a] Laboratoire de Chimie Biomimétique des Métaux de Transition, Institut de Chimie, UMR CNRS no. 7177, Université Louis Pasteur,
4 rue Blaise Pascal, B. P. 1032, 67070 Strasbourg cedex France
Fax: +33-390-245-001
E-mail: mandon@chimie.u-strasbg.fr


© 2007 Wiley-VCH Verlag GmbH & Co. KGaA, Weinheim

riboflavin can indeed be considered as a redox active mediator in future artificial constructions built around such compounds.

## Results and Discussion

As depicted in Scheme 1, ligand $L^1$ 8α-[bis(2-pyridylmethyl)amine]-*N*-$Ac_4$riboflavin was prepared by reaction of a twofold molar excess of bis(2-pyridylmethyl)amine DPA[19] with 8α-Bromo$Ac_4$riboflavin[20] in dry DMF over 24 h, by adaptation of the procedure published for the preparation of 8α-*N*-imidazolylriboflavin.[21] The brownish–orange solid obtained upon crystallization from a $CH_2Cl_2$/$Et_2O$ solution is a stable compound and was obtained in a 60% yield. Deprotection of the acetyl groups was performed by conventional methods with $K_2CO_3$ in dry EtOH at room temperature within 48 h. The solution was then neutralized with Amberlite IR–120 exchange resin and afforded, upon concentration, $L^2$ as a brownish solid moderately soluble in most organic solvents.

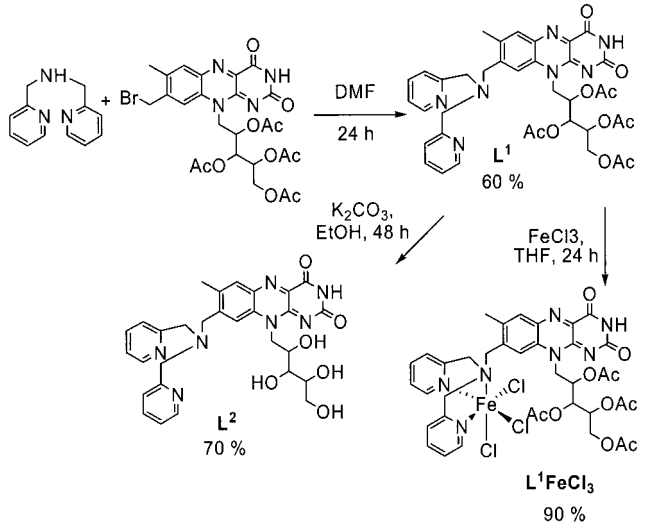


Scheme 1. Access to the DPA-riboflavin derivatives $L^1$, $L^2$ and ferric complex $L^1FeCl_3$.

$L^1$ and $L^2$ were characterized by mass spectroscopy, elemental analysis and $^1$H- and $^{13}$C NMR spectroscopy. Complex $L^1FeCl_3$ was prepared by stirring ligand $L^1$ with an equimolar amount of anhydrous $FeCl_3$ under an inert atmosphere in dry THF (although $L^1FeCl_3$ is air stable). Following a standard workup,[22] a brownish–yellow solid was obtained in 90% yield. In the $^1$H NMR spectrum, $L^1FeCl_3$ displayed extremely broad resonances at $\delta$ = 108 and 93 ppm (mid-intensity peak width, 1800 and 1500 Hz, respectively – signals accounting for the DPA moiety[22]), which is in line with a high-spin state for the metal. The flavin part lies further away from the paramagnetic metal than the DPA moiety and related signals appear as broadened resonances between 12 and 3 ppm. The complex was also characterized by mass spectroscopy, elemental analysis, and UV/Vis spectroscopy. The second absorption at $\lambda$ = 327 nm exhibited a molecular extinction coefficient ($\varepsilon$ = $11.31 \cdot 10^3$ $mmol^{-1} \cdot cm^2$) significantly higher than that of the free organic compounds ($\varepsilon$ = 7.72 and $5.83 \cdot 10^3$ $mmol^{-1} \cdot cm^2$ for $L^1$ and $L^2$, respectively), which indicates the presence of an extra LMCT component due to coordination of the ferric ion.[22]

The cyclic voltammogram ($CH_3CN$, $TBAPF_6$ 0.1 M, SCE as reference electrode, 100 mV/s – all traces displayed in Figure 1) of $L^1$ exhibited one reversible reduction wave at $E_{1/2}$ = –0.726 V ($\Delta_E$ = 130 mV) and is assigned to the reduction of the acetylated riboflavin moiety [the $Ac_4$riboflavin recorded as a blank underwent reversible reduction at $E_{1/2}$ = –0.770 V ($\Delta_E$ = 50 mV) under the same conditions]. In oxidation, an irreversible anodic signal was found at 1.183 V, which corresponds to the oxidation of the aliphatic amine of the DPA moiety. Upon metallation, this latter signal completely disappeared and a new reversible wave, which accounts for the $L^1Fe^{III}/L^1Fe^{II}$ couple, was observed at $E_{1/2}$ = 0.002 V ($\Delta_E$ = 85 mV). For comparison, a reversible couple has already been reported for $DPAFeCl_3$ at $E_{1/2}$ = –0.019 V.[23]

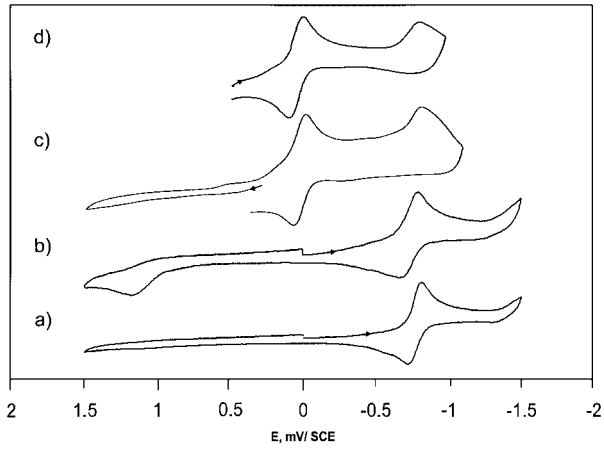


Figure 1. Cyclic voltammograms ($CH_3CN$, $TBAPF_6$ 0.1 M, SCE as reference electrode, 100 mV/s) of: a) tetraacetyl riboflavin; b) ligand $L^1$; c) complex $L^1FeCl_3$; d) detail of $L^1FeCl_3$ at 200 mV/s.

The reduction of the acetylated riboflavin fragment was found at $E_c$ = –0.838 V, with a signal pattern strongly suggestive of aggregation of the reduced compound at the electrode. Scanning up to 1000 mV/s allowed improvement of the reversibility pattern; however, it remained slightly different from what was expected for an ideally reversible couple. From Figure 1d, the potential is estimated to $E_{1/2}$ = –0.804 V ($\Delta_E$ = 68 mV), that is cathodically shifted by 78 mV with respect to $L^1$. This difference may reflect the presence of a ferrous centre close to the flavin side.

To summarize, a ligand system in which a ubiquitous redox mediator – riboflavin, that is vitamin B2 – is covalently linked to a tridentate nitrogen chelate is now available. A trichloroferric complex with a reversible $Fe^{III}/Fe^{II}$ redox couple can easily be obtained. All compounds reported are stable and easy to handle. We thus believe that the syntheses reported in this communication represent a significant step towards the preparation of functional artificial systems with

 © 2007 Wiley-VCH Verlag GmbH & Co. KGaA, Weinheim 

DPA-based complexes in which the active metal-containing site is linked through the flavin part to proteins. This approach is currently under investigation in our laboratory.

## Experimental Section

$^1$H- and $^{13}$C NMR spectroscopic data were recorded with a Bruker AC 300 spectrometer and chemical shifts are standardized to the residual signal of the solvent as a reference. UV/Vis spectra were recorded with a Varian Cary 05 E UV/Vis NIR spectrophotometer. Cyclic voltammetry measurements were obtained with a EG&G PAR 173A potentiostat in a 0.1 M acetonitrile solution of $TBAPF_6$ (supporting electrolyte), with platinum electrodes and saturated calomel electrode as reference. Traces are given in the text. Elemental analyses were carried out by the Service Central d'Analyses du CNRS in Vernaison, France. Mass spectroscopy was carried out with a MicroTOF instrument in the positive mode.

**Preparation and Characterization of 8α-[Bis(2-pyridylmethyl)amine]-*N*-Ac$_4$riboflavin (L$^1$):** Bis(2-pyridylmethyl)amine (5 g, 25.2 mmol) in a solution of DMF (10 mL) was added to a solution of 8α-BromoAc$_4$riboflavin (8 g, 12.8 mmol) in DMF (100 mL). The mixture was stirred for 24 h at ambient temperature. DMF was then removed in vacuo, and the resulting oil was dissolved in $CH_2Cl_2$ (50 mL). This phase was washed twice with distilled water. The organic phase was dried with magnesium sulfate, reduced to 15 mL and a brownish–yellow compound was obtained as a solid by the addition of cold diethyl ether (100 mL). Upon drying, compound L$^1$ was obtained (5.75 g, 60%). Further recrystallization yielded a compound for which the elemental analysis was satisfactory. L$^1$·2H$_2$O: $C_{37}H_{43}N_7O_{12}$ (777.30): calcd. C 57.14, H 5.53, N 12.61; found C 56.83, H 5.11, N 12.57. $^1$H NMR (300 MHz, $CDCl_3$): $\delta$ = 8.69 (d, $J$ = 4.0 Hz, 2 H, DPA α), 8.53 (s, 1 H, NH), 7.92 (s, 1H Ar), 7.71 (t, $J$ = 7.6 Hz, 2 H, DPA γ), 7.56 (s, 1 H, Ar), 7.46 (d, $J$ = 7.6 Hz, 2 H, DPA β′), 7.23–7.19 (m, 2 H, DPA β), 5.59 (d, 1 H, ribityl CH), 5.46 (m, 2 H, ribityl $CH_2$), 5.3–5.1 (m, 2 H, N-$CH_2$), 4.44–4.39 (dd, $J$ = 2.2–1.8 Hz, 1 H, aliphatic), 4.31–4.23 (m, 1 H, aliphatic), 4.11–3.98 (dd, $J$ = 14.0–13.9 Hz, 4 H, $CH_2$-DPA), 3.82 (s, 2 H, $CH_2$-ribofl.), 2.55 (s, 3 H, methyl), 2.42 (s, 3 H, acetyl), 2.32 (s, 3 H, acetyl), 2.26 (s, 3 H, acetyl), 2.19 (s, 3 H, acetyl) ppm. $^{13}$C NMR (75 MHz, $CDCl_3$): $\delta$ = 170.6–169.4 (4 acetyl C=O), 159.4 (flavin C=O), 157.8 (2 $C_{quat}$), 154.7 (flavin C=O), 150.6 ($C_{quat}$), 149.4 (2 $CH_{pyridyl}$), 148.0 ($C_{quat}$), 136.5 (2$CH_{pyridyl}$), 134.5 (2 $C_{quat}$), 132.9 (2$CH_{pyridyl}$), 123.5 ($CH_{pyridyl}$), 122.6 ($CH_{pyridyl}$), 115.5 (2 $CH_{Ar}$), 70.4, 69.4, 69.1 (3 CH), 61.9 ($CH_2$ ribofl.), 59.7 (2 $CH_{2pyridyl}$), 55.1 ($CH_2$), 45.0 ($CH_2$), 21.4, 21.1, 21.0, 20.8, 20.7 ($CH_3$) ppm. UV/Vis: $\lambda$ ($\varepsilon$, $10^3$ mmol·cm$^2$) = 443.6 (9.47), 342.0 (7.72), 268.8 (24.94) nm. MS ( ES$^+$, $CH_3CN$ + 0.1% formic acid): $m/z$ = 742.32 [M + H]$^+$.

**Preparation and Characterization of Complex L$^1$FeCl$_3$:** The procedure outlined in ref.[22] was followed. To a solution of 8α-[bis(2-pyridylmethyl)amine]-*N*-Ac$_4$riboflavin (L$^1$; 100 mg, 0.135 mmol) in dry THF (30 mL), was added a solution of anhydrous $FeCl_3$ (22 mg, 0.135 mmol) in dry THF (20 mL). Although the compounds are air stable, the reaction was carried out by using Schlenk tubes and cannula. The mixture was stirred for 24 h, and the solvent was then evaporated. The brownish solid was dissolved in $CH_3CN$, filtered and the solution was concentrated (rotary evaporator). Addition of dry diethyl ether allowed precipitation of L$^1$FeCl$_3$, as a brown, air-stable solid. After washing with diethyl ether and drying, the product was obtained (110 mg, 90%). The compound was recrystallized from acetonitrile/diethyl ether several times. L$^1$FeCl$_3$·4H$_2$O: $C_{37}H_{47}N_7O_{14}FeCl_3$ (974.16): calcd. C 45.51, H 4.81, N 10.04; found C 45.17, H 4.47, N 10.12. $^1$H NMR (300 MHz, $CD_3CN$): $\delta$ = presence of two very broad signals at 108 and 93 ppm (mid-intensity peak width 1800 and 1500 Hz, respectively). Weak signal at $\delta$ = 52 ppm with mid-intensity peak width of 600 Hz. Presence of moderately broadened signals between 3 and 12 ppm. UV/Vis: $\lambda$ ($\varepsilon$, $10^3$ mmol·cm$^2$) = 445.3 (8.57); 326.9 (11.31); 267.0 (26.78) nm. MS (ES$^+$, $CH_3CN$ = 0.1% formic acid) $m/z$ = 927.07 [M + Na]$^+$, 890.13 [M + Na – Cl]$^+$.

**Preparation and Characterization of 8α-[Bis(2-pyridylmethyl)amine]-*N*-riboflavin (L$^2$):** To a solution of potassium carbonate (3 g, 21.3 mmol) in absolute ethanol (150 mL), 8α-[bis(2-pyridylmethyl) amine]-*N*-Ac$_4$riboflavin (L$^1$; 3 g, 4.3 mmol) was added. The mixture was stirred for 48 h at ambient temperature. After neutralization with AMBERLITE IR-20 resin, the solution was filtered and concentrated in vacuo until a brownish solid precipitated. The solution was washed several times with ether and dried in vacuo. The compound was dissolved in DMF and precipitated by the addition of diethyl ether. The solid was dried in vacuo to afford the product (1.75 g, 70%). Microcrystals of this compound could be obtained from an ethanolic solution by slow evaporation of the solvent. These were kept for elemental analysis and NMR spectroscopy. The $^1$H NMR spectrum is poorly defined, especially in the aliphatic area. This might be due to agitation of the ribityl moiety and interaction with residual water of the DMSO. $^1$H NMR (300 MHz, [D$_6$]DMSO): $\delta$ = 11.6–11.3 (4 H, OH), 10.32 [OH (EtOH)], 8.73 (d, $J$ = 4.4 Hz, 2 H, DPA α), 8.31 (s, 1 H, NH), 8.04 (m, 2 H, DPA β), 7.91 (s, 1 H, Ar), 7.85 (s, 1 H, Ar), 7.72 (d, $J$ = 6.2 Hz, 2 H, DPA β′), 7.56 (m, 2 H, DPA γ), 5.20–4.10 (broad signal, ribityl protons and residual water of the DMSO), 4.19 (broad, 2 H, $CH_2$), 3.65 (broad, 4 H, DPA $CH_2$), 3.44 [q, $J$ = 7.1 Hz, $CH_2$ (EtOH)], 2.47 (s, 3 H, $CH_3$), 1.05 [t, $J$ = 7.1 Hz, $CH_3$ (EtOH)] ppm. $^{13}$C NMR (75 MHz, [D$_6$]DMSO) $\delta$ = 159.4 (flavin C=O), 157.8 (2 $C_{quat}$), 154.7 (flavin C=O), 150.6 ($C_{quat}$), 149.4 (2 $CH_{pyridyl}$), 148.0 ($C_{quat}$), 136.5 (2 $CH_{pyridyl}$), 134.5 (2 $C_{quat}$), 132.9 (2 $CH_{pyridyl}$), 123.5 ($CH_{pyridyl}$), 122.6 ($CH_{pyridyl}$), 115.5 (2 $CH_{Ar}$), 74.0, 73.2, 69.1 (3 CH), 63.8 ($CH_2$), 63.7 (2 $CH_{2pyridine}$), 58.2 (4 $CH_{2EtOH}$), 56.4 ($CH_2$), 50.1 ($CH_2$), 21.2 ($CH_3$), 19.2 (4 $CH_{3EtOH}$). UV/Vis: $\lambda$ ($\varepsilon$, $10^3$ mmol·cm$^2$) = 447.0 (6.85), 344.7 (5.83), 269.5 (19.03). MS (ES$^+$, $CH_3CN/H_2O$ + 0.1% formic acid): $m/z$ = 574.24 [M + H]$^+$. L$^2$·4EtOH: $C_{37}H_{55}N_7O_{10}$ (757.40): calcd. C 58.65, H 7.26, N 12.94; found C 58.37, H 7.60, N 12.30.

## Acknowledgments

The authors thank Dr Remy Louis, for constant encouragements and support. The Institut de Chimie, CNRS and ULP; are gratefully acknowledged for financial support.

[1] C.-H. Wong, G. M. Whitesides, *Enzymes in Synthetic Organic Chemistry*, Tetrahedron Organic Chemistry Series, Pergamon, Oxford, **1994**.
[2] K. Drauz, H. Waldmann (Eds.), *Enzyme Catalysis in Organic Synthesis*, VCH, Weinheim, **1995**.
[3] R. Breslow (Ed.), *Artificial Enzymes*, Wiley-VCH, Weinheim, **2005**.
[4] D. Qi, C.-H. Tann, D. Haring, M. D. Distefano, *Chem. Rev.* **2001**, *101*, 3081–3111.
[5] K. Bergstad, S. Y. Jonsson, J. E. Bäckvall, *J. Am. Chem. Soc.* **1999**, *121*, 10424–10425.
[6] A. B. E. Minidis, J. E. Bäckvall, *Chem. Eur. J.* **2001**, *7*, 297–302.
[7] C. Mazzinin, J. Lebreton, R. Furstoss, *J. Org. Chem.* **1996**, *61*, 8–9.

 © 2007 Wiley-VCH Verlag GmbH & Co. KGaA, Weinheim 

[8] Y. Imada, H. Ida, S. Ono, S.-I. Murahashi, *J. Am. Chem. Soc.* **2003**, *125*, 2868–2869.
[9] J. Kuriyan, R. J. Simon, T. Kobuko, E. T. Kaiser, *J. Am. Chem. Soc.* **1988**, *110*, 6261–6263.
[10] T. Matsuo, T. Hayashi, Y. Hisaeda, *J. Am. Chem. Soc.* **2002**, *124*, 11234–11235.
[11] S. G. Mayhew, G. Tollin "General Properties of Flavodoxins" in *Chemistry and Biochemistry of Flavoenzymes* (Ed.: F. Müller), CRC Press, Boca Raton, **1992**, vol. 3, pp. 389–426, .
[12] J. J. Pueyo, G. P. Curley, S. G. Mayhew, *Biochem. J.* **1996**, *313*, 855–861.
[13] G. P. Curley, M. C. Carr, S. G. Mayhew, G. Voordouw, *Eur. J. Biochem.* **1991**, *202*, 1091–1100.
[14] D. Mandon, A. Machkour, S. Goetz, R. Welter, *Inorg. Chem.* **2002**, *41*, 5364–5372.
[15] A. Machkour, D. Mandon, M. Lachkar, R. Welter, *Inorg. Chem.* **2004**, *43*, 1545–1550.
[16] A. Machkour, D. Mandon, M. Lachkar, R. Welter, *Eur. J. Inorg. Chem.* **2005**, 158–161.
[17] A. J. Evans, S. E. Watkins, D. C. Craig, S. B. Colbran, *J. Chem. Soc., Dalton Trans.* **2000**, 983–994.
[18] Y. Xu, G. Eilres, M. Borgström, J. Pan, M. Abrahamsson, A. Magnuson, R. Lomoth, J. Bergquist, T. Polivka, L. Sun, V. Sundström, S. Styring, L. Hammarström, B. Akermark, *Chem. Eur. J.* **2005**, *11*, 7305–7314.
[19] M. S. Nelson, J. Rodgers, *J. Chem. Soc. A* **1968**, 272–276.
[20] W. H. Walker, T. P. Singer, S. Ghisla, P. Hemmerich, *Eur. J. Biochem.* **1972**, *26*, 279–289.
[21] E. D. Edmonson, R. De Francesco in *Chemistry and Biochemistry of Flavoenzymes* (Ed.: F. Müller),CRC Press, Boca Raton, **1991**, vol. 1, pp. 73–103.
[22] D. Mandon, A. Nopper, T. Litrol, S. Goetz, *Inorg. Chem.* **2001**, *40*, 4803–4806.
[23] M. C. Rodrigez, F. Lambert, I. Morgenstern-Badarau, M. Cesario, J. Guilhem, B. B. Keita, L. Nadjo, *Inorg. Chem.* **1997**, *36*, 3525–3531.

Received: August 25, 2006
Published Online: November 17, 2006

 © 2007 Wiley-VCH Verlag GmbH & Co. KGaA, Weinheim 

DOI: 10.1002/ejic.200600925

# Resonance Raman Spectroscopy with Overtones Involving Metal-Ligand and Ligand-Centered Modes in (*o*-Benzoquinonediimine)ruthenium(II) Complexes

**Rémi Beaulac,[a] A. B. P. Lever,*[b] and Christian Reber*[a]**

**Keywords:** Raman spectroscopy / Ruthenium complexes / *o*-Benzoquinonediimine / Electronic structure / Covalency / π-Back donation / Charge transfer / Density functional calculations / Overtones / Combination bands / Luminescence / Absorption

Resonance Raman spectra of (*o*-benzoquinonediimine)ruthenium(II) complexes measured with visible excitation wavelengths show distinct resonance enhancements and intense overtone and combination bands. Assignments of the most prominent fundamental bands are made on the basis of comparisons with theoretical spectra obtained from DFT calculations. Excited state distortions are determined from the resonance Raman intensities and lead to calculated luminescence and absorption spectra in good agreement with experiment.

(© Wiley-VCH Verlag GmbH & Co. KGaA, 69451 Weinheim, Germany, 2007)

## Introduction

Resonance Raman spectroscopy can be used as a powerful technique to study excited-state structure, in particular for systems with broad, unresolved absorption transitions that do not provide detailed information through resolved vibronic structure.[1–5] Charge-transfer processes in transition-metal complexes, in particular those of ruthenium(II), are of particular interest for spectroscopic investigations, as detailed spectra combined with theoretical models provide quantitative insight on the structural and dynamics aspects of these important excited states.[6,7] In the vast majority of reported resonance Raman studies on ruthenium(II) complexes only fundamental bands are observed.[7–10,11]

The ligand *o*-benzoquinonediimine (BQDI) and its derivatives are of interest because of the extensive delocalization of Ru 4d electron density over the BQDI ligand.[12–18] This delocalization has been discussed in terms of metal–ligand orbital mixing or donor–acceptor electronic coupling. The covalent interactions between the metal and the ligand can be separated into ligand-to-metal donation and metal-to-ligand back-donation.[12–18] Complexes with these ligands, in particular [Ru(BQDI)(acac)$_2$] and [Ru(BQDI)(NH$_3$)$_2$Cl$_2$], show resonance Raman spectra with exceptionally rich patterns involving harmonics and combination bands. We present and analyze these spectra in the following report.

## Results and Discussion

Resonance Raman spectra of [Ru(BQDI)(acac)$_2$] and [Ru(BQDI)(NH$_3$)$_2$Cl$_2$] were measured with excitation wavelengths near the lowest-energy intense absorption maximum at ca. 20000 cm$^{-1}$, and are shown in Figure 1. Strong resonance enhancements are accompanied by an exceptionally detailed series of overtones and combination bands (identified by the labels I, II, III), which provide relevant information on excited-state distortions in the title complexes. Raman spectra measured with off-resonance excitation at 12700 cm$^{-1}$ are compared to the resonance Raman spectra in Figure 2. It is likely that each peak observed in the off-resonance Raman spectra corresponds to a fundamental transition, as overtones and combination bands are too weak to be observed in the absence of resonance enhancements; we can identify on the order of 16–18 experimental vibrational frequencies as listed in Table 1. The comparison of resonance and off-resonance spectra shows very clearly

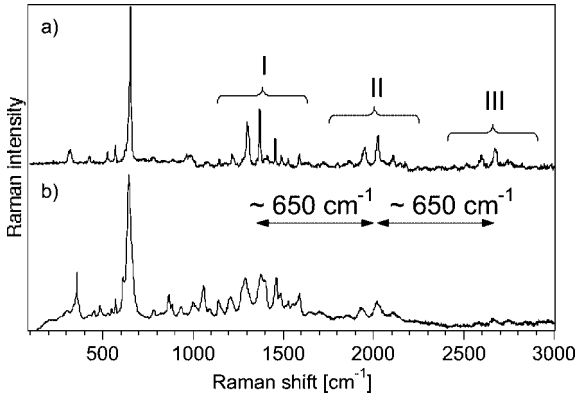


Figure 1. Comparison of resonance Raman spectra (solid samples, 77 K) of a) [Ru(BQDI)(NH$_3$)$_2$Cl$_2$] ($\lambda_{exc}$ = 488 nm) and of b) [Ru(BQDI)(acac)$_2$] ($\lambda_{exc}$ = 514 nm). The baseline was corrected to remove the luminescence onset and the total integrated intensity of each spectrum was normalized.

[a] Département de chimie, Université de Montréal, Montréal QC H3C 3J7, Canada
[b] Department of Chemistry, York University, CB124, 4700 Keele Street, Toronto, ON M3J 1P3, Canada


© 2007 Wiley-VCH Verlag GmbH & Co. KGaA, Weinheim

that all peaks observed at frequencies between 1700 $cm^{-1}$ and 3000 $cm^{-1}$ correspond to resonance-enhanced overtones or combination bands. Calculated Raman spectra obtained from DFT are in good agreement with the experimental spectra, as shown by the dotted traces in Figure 2. In particular, the calculated spectra do not show any bands where overtones and combination bands are observed, and they indicate a larger number of bands in the 1200 to 1500 $cm^{-1}$ region for [Ru(BQDI)(acac)$_2$] than for [Ru(BQDI)(NH$_3$)$_2$Cl$_2$], providing a qualitative rationale for the large, poorly resolved feature observed for the former complex in this wavenumber range. The Raman peaks in the off-resonance spectrum of [Ru(BQDI)(acac)$_2$] are weak and broad, especially in the 1200 to 1500 $cm^{-1}$ region, complicating the identification of fundamental bands. Only the peaks that can clearly be assigned as fundamentals involved in the resonance Raman spectrum were labeled as such in Figure 2 and in Table 1.

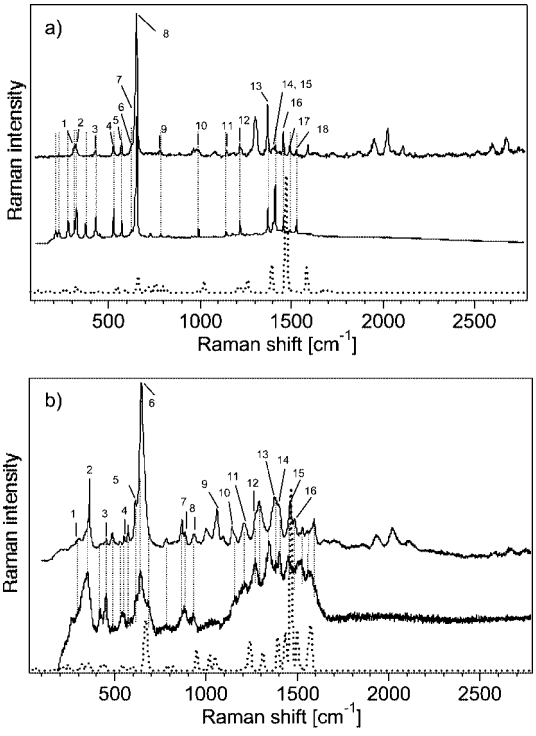


Figure 2. Comparison of resonance Raman (top spectrum) and off-resonance Raman (middle spectrum) in solid phase at 77 K and (lower) DFT calculated spectrum. a) [Ru(BQDI)(NH$_3$)$_2$Cl$_2$], top: $\lambda_{exc}$ = 488 nm, middle: $\lambda_{exc}$ = 788 nm. b) [Ru(BQDI)(acac)$_2$], top: $\lambda_{exc}$ = 514 nm, middle: $\lambda_{exc}$ = 788 nm. The number labels refer to Table 1.

All peaks observed in the resonance Raman spectra not corresponding to fundamental frequencies are assigned as harmonics or combination bands built on one or several of the fundamental frequencies listed in Table 1. The analysis of the Raman spectra of [Ru(BQDI)(NH$_3$)$_2$Cl$_2$] is more straightforward because the identification of the fundamental frequencies in the off-resonance Raman spectrum is obvious. In both systems, it appears clearly that the peaks labeled II and III in Figure 1 observed at Raman shifts of approximately 2000 $cm^{-1}$ and 2600 $cm^{-1}$ are not fundamentals, and their spacing of approximately 650 $cm^{-1}$ corresponds to the Raman shift of the most intense peak in each resonance Raman spectrum, observed at 655 and 646 $cm^{-1}$ in [Ru(BQDI)(NH$_3$)$_2$Cl$_2$] and [Ru(BQDI)(acac)$_2$], respectively. The high relative intensities of the transitions at 655 and 646 $cm^{-1}$ show directly that the largest distortions between the ground-state and the excited-state structures probed here occur along the normal coordinates of these modes and that the peaks in regions II and III are combination bands involving these modes. The peaks in region I are not as easily identified, as both fundamental bands and the first overtone of the most intense fundamental occur at the Raman shifts of approximately 1300 $cm^{-1}$ corresponding to this region and calculated spectra have to be used to identify individual transitions.

Table 1. Observed vibrational frequencies $\omega_k$ [$cm^{-1}$] and calculated excited-state distortions $\Delta_k$ [dimensionless] of the modes observed in the resonance Raman spectra of [Ru(BQDI)(NH$_3$)$_2$Cl$_2$] and [Ru(BQDI)(acac)$_2$]. The index $k$ refers to the numerical labels shown in Figure 2 and numbers the normal coordinates in Equation (3); the parameters $E_{00}$ and $\Gamma$ refer to Equation (2).

| | [Ru(BQDI)(NH$_3$)$_2$Cl$_2$] | | [Ru(BQDI)(acac)$_2$] | |
|---|---|---|---|---|
| $k$ | $\omega_k$ | $\Delta_k$ | $\omega_k$ | $\Delta_k$ |
| 1 | 314 | 1.0 | 306 | 1.0 |
| 2 | 324 | 1.0 | 355 | 1.2 |
| 3 | 427 | 0.5 | 454 | 0.5 |
| 4 | 527 | 0.6 | 550 | 0.7 |
| 5 | 572 | 0.9 | 613 | 1.0 |
| 6 | 624 | 0.6 | 646 | 2.0 |
| 7 | 645 | 1.3 | 886 | 0.5 |
| 8 | 655 | 2.0 | 934 | 0.4 |
| 9 | 782 | 0.3 | 1058 | 0.6 |
| 10 | 992 | 0.3 | 1142 | 0.4 |
| 11 | 1145 | 0.2 | 1208 | 0.4 |
| 12 | 1218 | 0.3 | 1270 | 0.5 |
| 13 | 1370 | 0.8 | 1378 | 0.6 |
| 14 | 1398 | 0.2 | 1400 | 0.5 |
| 15 | 1413 | 0.2 | 1460 | 0.5 |
| 16 | 1456 | 0.5 | 1484 | 0.4 |
| 17 | 1491 | 0.2 | | |
| 18 | 1528 | 0.2 | | |
| Total distortion $\sum_k \Delta_k$ | | 11.1 | | 11.2 |
| $E_{00}$ [$cm^{-1}$] | | 17250 | | 16830 |
| $\Gamma$ [$cm^{-1}$] | | 150 | | 400 |

The DFT calculations are used to assign the most prominent observed Raman transitions. Calculated at 665 $cm^{-1}$ and 662 $cm^{-1}$ are the Ru–NH(BQDI) stretching modes for [Ru(BQDI)(NH$_3$)$_2$Cl$_2$] and [Ru(BQDI)(acac)$_2$], respectively, which involve fairly large breathing motion in the BQDI ring for both complexes. These frequencies are higher by 10 and 16 $cm^{-1}$ than the experimental values, illustrating the excellent quantitative agreement. The 1394 and 1392 $cm^{-1}$ peaks correspond to the C=NH vibration coupled strongly to the CH bonds localized on the BQDI ligand. The calculated frequencies are higher than the experimental values by 24 and 14 $cm^{-1}$ for [Ru(BQDI)(NH$_3$)$_2$Cl$_2$] and [Ru(BQDI)(acac)$_2$], respectively. The calculated vibrational frequencies tend to be slightly higher than the experimental values,

 © 2007 Wiley-VCH Verlag GmbH & Co. KGaA, Weinheim 

possibly due to the B3LYP functional slightly over-emphasizing the covalent contribution to the Ru–N bonds,[19] but overall the agreement between calculated and observed frequencies is excellent.

A quantitative analysis of the resonance Raman intensities leads to a more precise picture of excited-state distortions and allows us to identify similarities and differences between the two compounds studied here. The resonance Raman intensities can be calculated very efficiently using the time-dependent approach described previously by Heller, Zink and associates.[1,3,4,20–22] The simplest approach, used here, is based on a single electronic excited state and the Raman intensity $I_{i\rightarrow f}$ at frequency $\omega_s$ is given by Equation (1):

$$I_{i\rightarrow f} \propto \omega_I \omega_S{}^3 \left[\alpha_{fi}\right]^* \left[\alpha_{fi}\right] \quad (1)$$

with Equation (2):

$$\left[\alpha_{fi}\right] = \frac{i}{\hbar}\int_0^\infty \left\langle \phi_f \middle| \phi(t)\right\rangle \cdot exp\left(-iE_{00}t - \Gamma t\right) \cdot \exp\left(i\left(\omega_i + \omega_I\right)t\right)dt \quad (2)$$

where $\Gamma$ is a constant damping factor (in $cm^{-1}$), $\hbar\omega_i$ is the zero-point energy of the ground electronic potential energy surface and $\hbar\omega_I$ is the energy of the incident radiation. $\langle\phi_f|\phi(t)\rangle$ is the autocorrelation function, which takes a simple analytical form if it is assumed that (a) the force constants are the same in both ground and excited states, (b) the potential energy surfaces are harmonic, (c) the transition dipole moment is independent of the normal coordinates and (d) the normal coordinates are not coupled, see Equation (3).

$\omega_k$ and $\Delta_k$ denote the wavenumber (in $cm^{-1}$) and the difference between potential-energy minima of the ground and excited states along the $k$th normal coordinate, respectively, and $n_k$ is the vibrational quantum number of the $k$th normal mode in the ground electronic state. As an example, the combination band ($2\nu_1 + \nu_2$) in a three-mode case would have $n_1 = 2$, $n_2 = 1$ and $n_3 = 0$. Equation (1) can be used to calculate the excitation profile for each fundamental, harmonic and combination band involved in the resonance Raman spectrum. The experimental spectra in Figure 1 and Figure 2 do not provide full excitation profiles, but an analysis is still possible. The approach consists of adjusting the ratio of intensities between calculated profiles for different modes by fitting the displacements $\Delta_k{}^{n_k}$ in Equation (3) until the ratios of calculated intensities are in agreement with the experiment. Adjusting as many parameters as there are in Table 1 can be tedious, but the task is somewhat facilitated by using Savin's approximation to estimate the relative displacements between two modes $k$ and k' in the resonance Raman spectrum [Equation (4)].[4]

$$\frac{I_k}{I_{k'}} = \left(\frac{\Delta_k \omega_k}{\Delta_{k'} \omega_{k'}}\right)^2 \quad (4)$$

The best parameter values obtained in this way are given in Table 1 for both complexes; the calculated intensities are compared to the experimental resonance Raman spectra in Figure 3 and Figure 4 for $[Ru(BQDI)(NH_3)_2Cl_2]$ and $[Ru(BQDI)(acac)_2]$, respectively. These calculations involve all modes identified as fundamentals in the experimental Raman spectra, in contrast to the simplified analysis for $[Ru(BQDI)(NH_3)_2Cl_2]$,[18] where only five modes were considered. Figure 3 and Figure 4 illustrate the very good agreement between calculated and experimental intensities of the resonance Raman spectra. An additional criterion to compare model calculations and experimental spectra is provided by the intensities of overtones and combination bands, which are also reproduced well, as shown for the first overtone of the 650 $cm^{-1}$ mode in Figure 3 and Fig-

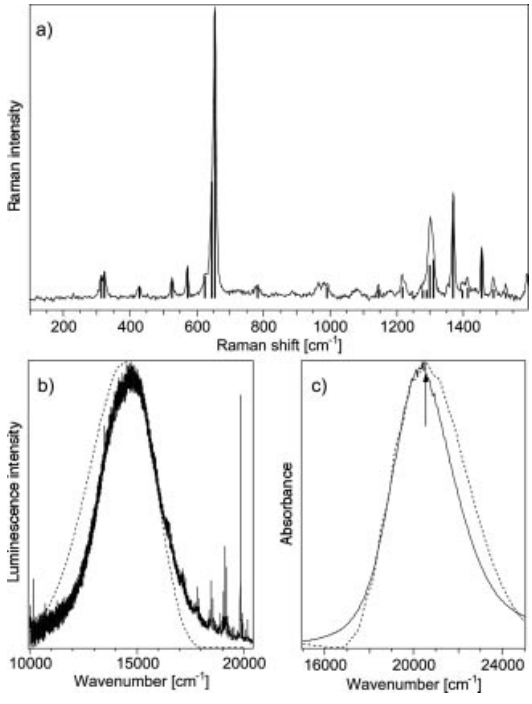


Figure 3. Comparison of calculated and experimental spectra for $[Ru(BQDI)(NH_3)_2Cl_2]$. a) Resonance Raman, b) 77 K solid-state luminescence and c) room-temperature absorption in dimethylformamide solution. The calculated spectra in b) and c) are given as dotted lines. The vertical arrow in c) indicates the resonance Raman excitation wavelength (488 nm).

$$\left\langle \phi_f \middle| \phi(t)\right\rangle = \prod_k \left\{ \exp\left[-\frac{\Delta_k^2}{2}\left(1-\exp\left(-i\omega_k t\right)\right) - \frac{i\omega_k t}{2}\right] \times \left(1-\exp\left(-i\omega_k t\right)\right)^{n_k} \times \frac{\left(-1\right)^{n_k}\Delta_k^{n_k}}{\left(2^{n_k} n_k!\right)^{1/2}} \right\} \quad (3)$$

 © 2007 Wiley-VCH Verlag GmbH & Co. KGaA, Weinheim 

ure 4. Identical total distortions are obtained for both complexes, further corroborating the consistency of our analysis. The luminescence and absorption spectra for both complexes studied here can be calculated from the parameters in Table 1 and are shown for comparison in Figure 3 and Figure 4. These spectra are calculated without any adjustable parameters and the good agreement further illustrates that the parameters in Table 1 are physically meaningful.

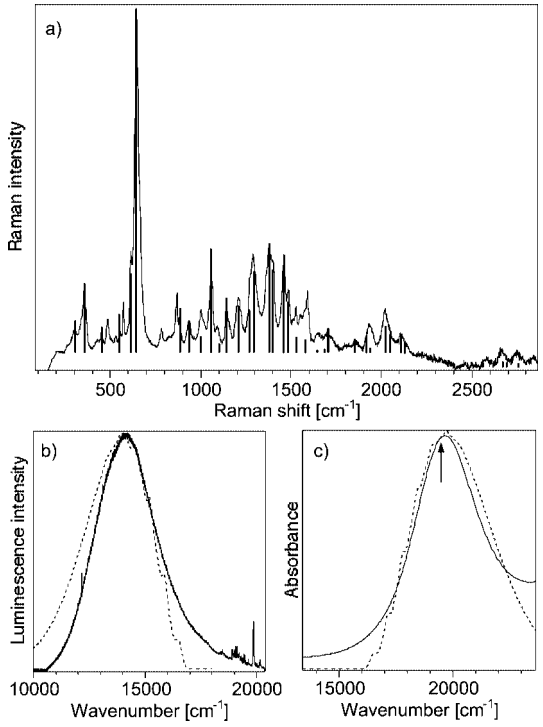


Figure 4. Comparison of calculated and experimental spectra for [Ru(BQDI)(acac)$_2$]. a) Resonance Raman, b) 77 K solid-state luminescence and c) room-temperature absorption in dimethylformamide solution. The calculated spectra in b) and c) are given as dotted lines. The vertical arrow in c) denotes the resonance Raman excitation wavelength (514 nm).

The calculations show that the largest excited state distortion occurs along the coordinate associated to the mode with a frequency of approximately 650 cm$^{-1}$, in agreement with the qualitative observation made before, and distortions of identical magnitude are obtained for both complexes. The quantitative analysis allows more general observations to be made. We can separate the excited-state distortions into two groups, one containing modes whose frequencies are between 300 and 650 cm$^{-1}$ and whose displacements are relatively high, and another group containing modes with higher frequencies between 1000 and 1500 cm$^{-1}$ and lower displacements. The latter group can be assigned to ligand-centered modes, whereas the former is clearly related to metal-ligand modes. This observation is in agreement with the proposed MLCT character of the transition, and shows that both complexes are quite similar, despite the minor differences discussed previously. This suggests that the BQDI ligand plays a major role in the electronic transition, as acceptor of charge, and that the auxiliary ligands modify the electronic structure of the entire complex in a slightly different manner for the two complexes studied here, as shown by the resonance Raman intensities and the analysis based on time-dependent theory. Much larger effects of auxiliary ligands on a variety of chemical properties of this category of complexes are discussed elsewhere.[18] However, it is critical to note that the primary changes in geometry in the excited MLCT states occur within the Ru–N$^a$H=C–C=N$^b$H(*Ru–N$^b$*) metallacycle, which is quasi aromatic (6-electron ring) with much less distortion within the six membered benzene ring of BQDI. Indeed one might describe the transitions as mainly π–π* within the quasi aromatic metallocycle ring system. Our results show that the excited-state distortions in the title complexes can be explored by resonance Raman spectroscopy in unprecedented detail not accessible for other charge-transfer excited states in ruthenium(II) complexes.

## Experimental Section

The species [Ru(BQDI)(NH$_3$)$_2$Cl$_2$] and [Ru(BQDI)(acac)$_2$] were prepared by literature methods.[18,23] Raman spectra were measured with a Renishaw 3000 Raman imaging microscope at 488, 514 and 788 nm excitation laser wavelengths. The microscope was used to focus the light onto a spot of approximately 1 μm in diameter and to collect the scattered light. The backscattered Raman light was detected with a Peltier cooled CCD detector. This instrument was also used to measure luminescence spectra. Absorption spectra were measured with a Varian Cary 5E spectrometer.

Density functional theory (DFT) spin-restricted calculations were performed using the Gaussian 03 program (Revision C.01 and C.02).[24] Optimized geometries were calculated by using the B3LYP exchange-correlation functional[25,26] with the LanL2DZ basis set.[27–30] The SWIZARD program[31] was used to extract the calculated Raman spectra from the Gaussian output files with a line width of 15 cm$^{-1}$.

## Acknowledgments

We thank the Natural Sciences and Engineering Research Council of Canada for financial support and Harini Kaluarachchi and Daria Kalinina for laboratory assistance.

[1] J. I. Zink, *Coord. Chem. Rev.* **2001**, *211*, 69.
[2] J. L. Wootton, J. I. Zink, *J. Am. Chem. Soc.* **1997**, *119*, 1895.
[3] K.-S. K. Shin, J. I. Zink, *J. Am. Chem. Soc.* **1990**, *112*, 7148.
[4] K.-S. K. Shin, J. I. Zink, *Inorg. Chem.* **1989**, *28*, 4358.
[5] L. Tutt, J. I. Zink, *J. Am. Chem. Soc.* **1986**, *108*, 5830.
[6] Y.-J. Chen, P. Xie, J. F. Endicott, O. S. Odongo, *J. Phys. Chem. A* **2006**, *110*, 7970.
[7] J. T. Hupp, R. D. Williams, *Acc. Chem. Res.* **2001**, *34*, 808.
[8] G. D. Danzer, J. R. Kincaid, *J. Raman Spectrosc.* **1992**, *23*, 681.
[9] S. K. Doorn, J. T. Hupp, *J. Am. Chem. Soc.* **1989**, *111*, 4704.
[10] L. C. T. Shoute, G. R. Loppnow, *J. Am. Chem. Soc.* **2003**, *125*, 15636.
[11] J. Streiff, J. L. McHale, *J. Chem. Phys.* **2000**, *112*, 841.
[12] C. J. Da Cunha, S. S. Fielder, D. V. Stynes, H. Masui, P. R. Auburn, A. B. P. Lever, *Inorg. Chim. Acta* **1996**, *242*, 293.
[13] S. I. Gorelsky, E. S. Dodsworth, A. B. P. Lever, A. A. Vlcek, *Coord. Chem. Rev.* **1998**, *174*, 469.
[14] A. B. P. Lever, S. I. Gorelsky, *Coord. Chem. Rev.* **2000**, *208*, 153.
[15] H. Masui, A. B. P. Lever, E. S. Dodsworth, *Inorg. Chem.* **1993**, *32*, 258.

 © 2007 Wiley-VCH Verlag GmbH & Co. KGaA, Weinheim 

[16] R. A. Metcalfe, E. S. Dodsworth, S. S. Fielder, D. J. Stufkens, A. B. P. Lever, W. J. Pietro, *Inorg. Chem.* **1996**, *35*, 7741.
[17] R. A. Metcalfe, A. B. P. Lever, *Inorg. Chem.* **1997**, *36*, 4762.
[18] J. Rusanova, E. Rusanov, S. I. Gorelsky, D. Christendat, R. Popescu, A. A. Farah, R. Beaulac, C. Reber, A. B. P. Lever, *Inorg. Chem.* **2006**, *45*, 6246.
[19] E. I. Solomon, *Inorg. Chem.* **2006**, *45*, 8012.
[20] E. J. Heller, *Acc. Chem. Res.* **1981**, *14*, 368.
[21] E. J. Heller, R. L. Sundberg, D. Tannor, *J. Phys. Chem.* **1982**, *86*, 1822.
[22] S.-Y. Lee, E. J. Heller, *J. Chem. Phys.* **1979**, *71*, 4777.
[23] K. N. Mitra, S. Choudhury, A. Castińeiras, S. Goswami, *J. Chem. Soc., Dalton Trans.* **1998**, 2901.
[24] M. J. Frisch, G. W. Trucks, H. B. Schlegel, G. E. Scuseria, M. A. Robb, J. R. Cheeseman, J. J. A. Montgomery, T. Vreven, K. N. Kudin, J. C. Burant, J. M. Millam, S. S. Iyengar, J. Tomasi, V. Barone, B. Mennucci, M. Cossi, G. Scalmani, N. Rega, G. A. Petersson, H. Nakatsuji, M. Hada, M. Ehara, K. Toyota, R. Fukuda, J. Hasegawa, M. Ishida, T. Nakajima, Y. Honda, O. Kitao, H. Nakai, M. Klene, X. Li, J. E. Knox, H. P. Hratchian, J. B. Cross, V. Bakken, C. Adamo, J. Jaramillo, R. Gomperts, R. E. Stratmann, O. Yazyev, A. J. Austin, R. Cammi, C. Pomelli, J. W. Ochterski, P. Y. Ayala, K. Morokuma, G. A. Voth, P. Salvador, J. J. Dannenberg, V. G. Zakrzewski, S. Dapprich, A. D. Daniels, M. C. Strain, O. Farkas, D. K. Malick, A. D. Rabuck, K. Raghavachari, J. B. Foresman, J. V. Ortiz, Q. Cui, A. G. Baboul, S. Clifford, J. Cioslowski, B. B. Stefanov, G. Liu, A. Liashenko, P. Piskorz, I. Komaromi, R. L. Martin, D. J. Fox, T. Keith, M. A. Al-Laham, C. Y. Peng, A. Nanayakkara, M. Challacombe, P. M. W. Gill, B. Johnson, W. Chen, M. W. Wong, C. Gonzalez J. A. Pople, in Gaussian 03, C02., Gaussian, Inc., **2004**.
[25] A. D. Becke, *J. Chem. Phys.* **1993**, *98*, 5648.
[26] C. Lee, W. Yang, R. G. Parr, *Phys. Rev. B* **1988**, *37*, 785.
[27] J. T. H. Dunning, P. J. Hay, in *Modern Theoretical Chemistry*, vol. 3 (Ed.: I. H. F. Schaefer), Plenum, New York, **1976**, p. 1.
[28] P. J. Hay, W. R. Wadt, *J. Chem. Phys.* **1985**, *82*, 270.
[29] P. J. Hay, W. R. Wadt, *J. Chem. Phys.* **1985**, *82*, 284.
[30] P. J. Hay, W. R. Wadt, *J. Chem. Phys.* **1985**, *82*, 299.
[31] S. I. Gorelsky, SWizard program, revision 4.2, http://www.sgchem.net/swizard/.

Received: October 1, 2006
Published Online: November 17, 2006

 © 2007 Wiley-VCH Verlag GmbH & Co. KGaA, Weinheim 

DOI: 10.1002/ejic.200600679

# Synthesis and Crystal Structure of Three Carborane Complexes, [M{7,8-(OPPh$_2$)$_2$-7,8-C$_2$B$_9$H$_{10}$}$_2$] (M = Cu, Zn) and [Ni(thf){7,8-(OPPh$_2$)$_2$-7,8-C$_2$B$_9$H$_{10}$}$_2$]·thf, and Two Carborane Compounds, 1-(OPPh$_2$)-2-(PPh$_2$)-1,2-C$_2$B$_{10}$H$_{10}$ and H[7,8-(OPPh$_2$)$_2$-7,8-C$_2$B$_9$H$_{10}$]·0.25C$_2$H$_5$OH

**Jianmin Dou,*[a] Daopeng Zhang,[a] Dacheng Li,[a] and Daqi Wang[a]**

**Keywords:** Cu complexes / Zn complexes / Ni complexes / Carborane complexes / Oxidation / Degradation

Three new carborane complexes containing the bis(phosphoryl)-*nido*-carborane ligand, [Cu{7,8-(OPPh$_2$)$_2$-7,8-C$_2$B$_9$H$_{10}$}$_2$] (**1**), [Zn{7,8-(OPPh$_2$)$_2$-7,8-C$_2$B$_9$H$_{10}$}$_2$] (**2**), and [Ni(thf){7,8-(OPPh$_2$)$_2$-7,8-C$_2$B$_9$H$_{10}$}$_2$]·thf (**3**), were synthesized by the reactions of 1,2-(PPh$_2$)$_2$-1,2-C$_2$B$_{10}$H$_{10}$ with CuCl$_2$·2H$_2$O, ZnCl$_2$, and NiCl$_2$·6H$_2$O, respectively, in ethanol in air. Two other compounds, 1-(OPPh$_2$)-2-(PPh$_2$)-1,2-C$_2$B$_{10}$H$_{10}$ (**4**) and H[7,8-(OPPh$_2$)$_2$-7,8-C$_2$B$_9$H$_{10}$]·0.25C$_2$H$_5$OH (**5**), were also obtained through the oxidation of the *closo* ligand in air. All new compounds were characterized by elemental analysis, FT-IR, $^1$H and $^{13}$C NMR spectroscopy, and single-crystal X-ray diffraction. In complexes **1** and **2**, the metal atoms are coordinated to the four oxygen atoms of the two bidentate bis(phosphoryl) ligands [7,8-(OPPh$_2$)$_2$-7,8-C$_2$B$_9$H$_{10}$]$^-$ and adopt a square-planar geometry. For complex **3**, the molecular structure reveals that the geometry at the nickel atom is square-pyramidal, with four oxygen atoms from the four OPPh$_2$ groups and one additional one from a thf molecule.
(© Wiley-VCH Verlag GmbH & Co. KGaA, 69451 Weinheim, Germany, 2007)

## Introduction

The synthesis and properties of dicarba-*closo*-dodecaborane, 1,2-C$_2$B$_{10}$H$_{12}$, and the -*nido*-species, [7,8-C$_2$B$_9$H$_{12}$]$^-$, were first reported in the early 1960s.[1–4] Since then, both *closo*- and *nido*-carboranes have proven to be excellent bulky and stable building blocks that allow for the synthesis of a wide range of carborane derivatives and have shown a lot of potential in various applications, including medicinal chemistry, especially Boron Neutron Capture Therapy (BNCT) of tumors, solvent extraction, materials science, catalysis, host–guest chemistry, and coordination chemistry,[5–18] which made carborane chemistry all along an interesting growth area.

In recent years, the 1,2-bis(phosphanyl) derivative of *o*-carborane, 1,2-(PPh$_2$)$_2$-1,2-C$_2$B$_{10}$H$_{10}$, and its partially degraded anion, *nido*-[7,8-(PPh$_2$)$_2$-7,8-C$_2$B$_9$H$_{10}$]$^-$, have attracted much attention because of the coordinating capabilities of the two phosphorus atoms. Up to now, complexes containing the 1,2-(PPh$_2$)$_2$-1,2-C$_2$B$_{10}$H$_{10}$ and *nido*-[7,8-(PPh$_2$)$_2$-7,8-C$_2$B$_9$H$_{10}$]$^-$ ligands and Cu$^{I}$,[19] Ru$^{II}$,[20] Ag$^{I}$,[21,22] Au$^{I}$,[23–29] Pd$^{II}$,[30–33] and Rh[34] have been reported and characterized by single-crystal X-ray diffraction. We are also interested in these kinds of complexes and have reported on the synthesis and crystal structures of Cu$^{I}$,[35] Au$^{I}$,[36] Ni$^{II}$, Pd$^{II}$, and Pt$^{II}$ complexes,[37] and we investigated the effect of different reaction conditions on the products. When the reaction of 1,2-(PPh$_2$)$_2$-1,2-C$_2$B$_{10}$H$_{10}$ with NiCl$_2$·6H$_2$O was carried out in air, a new complex containing one bis(phosphanyl)-*nido*-carborane ligand and one unsymmetrical semi-oxidized (phosphoryl)(phosphanyl) ligand with the formula [Ni{7-(OPPh$_2$)-8-(PPh$_2$)-7,8-C$_2$B$_9$H$_{10}$}{7,8-(PPh$_2$)$_2$-7,8-C$_2$B$_9$H$_{10}$}] were obtained.[38]

This result indicates that the environment has an obvious influence on the reaction. To continue with the reactions of the bis(phosphanyl)-*closo*-carborane ligand with different metal ions without the protection of inert gases, we investigated three reactions of the bis(phosphanyl)-*closo*-carborane ligand with CuCl$_2$·2H$_2$O, ZnCl$_2$, and NiCl$_2$·6H$_2$O in air and obtained three new carborane complexes containing the *nido*-[7,8-(OPPh$_2$)$_2$-7,8-C$_2$B$_9$H$_{10}$]$^-$ anion, [Cu{7,8-(OPPh$_2$)$_2$-7,8-C$_2$B$_9$H$_{10}$}$_2$] (**1**), [Zn{7,8-(OPPh$_2$)$_2$-7,8-C$_2$B$_9$H$_{10}$}$_2$] (**2**), and [Ni(thf){7,8-(OPPh$_2$)$_2$-7,8-C$_2$B$_9$H$_{10}$}$_2$]·thf (**3**). To the best of our knowledge, there has been no report on the metal ion complex of the bis(phosphoryl)carborane ligand [7,8-(OPPh$_2$)$_2$-7,8-C$_2$B$_9$H$_{10}$]$^-$, which has been reported by Teixidor's group.[39] In addition, the oxidation and degradation process of the free bis(phosphanyl)-*closo*-carborane ligand, 1,2-(PPh$_2$)$_2$-1,2-C$_2$B$_{10}$H$_{10}$, in air was studied for the first time.

## Results and Discussion

### Synthesis and Spectral Characterization

In our recent work[38] we found that, with or without the protection of N$_2$, results of the reactions of the bis(phos-

[a] Department of Chemistry, Liaocheng University, Liaocheng 252059, P. R. China
E-mail: jmdou@lcu.edu.cn

 © 2007 Wiley-VCH Verlag GmbH & Co. KGaA, Weinheim 

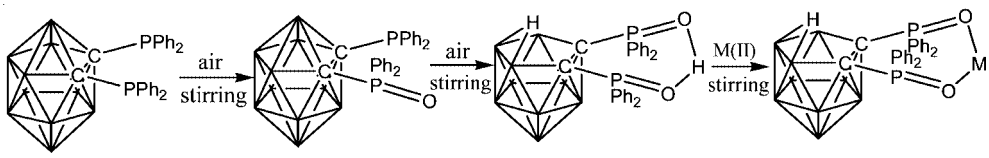


Scheme 1. The rational reaction process for the preparation of the complexes **1** to **3** [M = Cu(**1**), Zn(**2**), Ni(**3**)].

phanyl)-*closo*-carborane ligand 1,2-$(PPh_2)_2$-1,2-$C_2B_{10}H_{10}$ with some $Ni^{II}$ compounds were very different, indicating that the reaction environment could play an important role during the reaction process. By stirring the mixture of $NiCl_2{\cdot}6H_2O$ and the *closo* ligand for 6 h in ethanol at room temperature, we obtained the complex [Ni{7-$(OPPh_2)$-8-$(PPh_2)$-7,8-$C_2B_9H_{10}$}{7,8-$(PPh_2)_2$-7,8-$C_2B_9H_{10}$}]. However, when the stirring time was increased to 12 h in air, both P atoms of the initial bis(phosphanyl)-*closo*-carborane ligand were oxidized, and a new complex containing the bis(phosphoryl)-*nido*-carborane ligand [7,8-$(OPPh_2)_2$-7,8-$C_2B_9H_{10}$]$^-$ was obtained. This result showed that both of the P atoms could be oxidized, but the oxidation of the two P atoms did not take place at the same time. Subsequently, the reactions between $CuCl_2{\cdot}2H_2O$, $ZnCl_2$, and the bis(phosphanyl)-*closo*-carborane ligand in a molar ratio of 1:1 in ethanol were carried out. After the stirring process was continued for 6 h in air at room temperature, two complexes with the formula [Cu{7,8-$(OPPh_2)_2$-7,8-$C_2B_9H_{10}$}$_2$] and [Zn{7,8-$(OPPh_2)_2$-7,8-$C_2B_9H_{10}$}$_2$] were obtained. As indicated by their similar crystal data, listed in Table 2, these two complexes are isostructural. The difference in the reaction times of the above three reactions implied that the metal atom itself could also affect the reaction process. The rational reaction process for the preparation of these three complexes is shown in Scheme 1.

With an aim to find out whether the phosphorus atom of the *closo* ligand could be oxidized and the carborane skeleton could be converted from *closo* to *nido* by oxygen without the presence of the metal ion, we studied another experiment. The free *closo* ligand 1,2-$(PPh_2)_2$-1,2-$C_2B_{10}H_{10}$ was suspended in ethanol, and the mixture was stirred for 8 h, while air was continually and slowly bubbled into the reaction mixture. Contrary to our expectation, a compound containing the *closo*-carborane skeleton, but not the *nido* form, with the formula 1-$(OPPh_2)$-2-$(PPh_2)$-1,2-$C_2B_{10}H_{10}$ (**4**), was obtained, in which also only one phosphorus atom was oxidized. A marked difference from the complex [Ni{7-$(OPPh_2)$-8-$(PPh_2)$-7,8-$C_2B_9H_{10}$}{7,8-$(PPh_2)_2$-7,8-$C_2B_9H_{10}$}] was that the *closo*-carborane skeleton in this compound was maintained. Following the procedure for the synthesis of compound **4**, the mixture was stirred for 18 h, and a compound with the formula H[7,8-$(OPPh_2)_2$-7,8-$C_2B_9H_{10}$]$\cdot$ $0.25C_2H_5OH$ (**5**) was obtained. This compound is very similar to another neutral compound H[7,8-$(OPPh_2)_2$-7,8-$C_2B_9H_{10}$], which has been obtained with very high yield (94–97%) by oxidation of 1,2-$(PPh_2)_2$-1,2-$C_2B_{10}H_{10}$ with $H_2O_2$ in thf at 0 °C.[39] The aim of oxidizing another phosphorus atom of the semi-oxidized (phosphoryl)(phosphanyl)-*closo*-carborane ligand was fulfilled, but the *closo*-carborane skeleton degraded. The proposed mechanism for the partial degradation of the semi-oxidized (phosphoryl)(phosphanyl)-*closo*-carborane ligand, which is similar to the degradation of 1-SR-2-$PPh_2$-1,2-$C_2B_{10}H_{10}$,[40] is shown in Scheme 2.

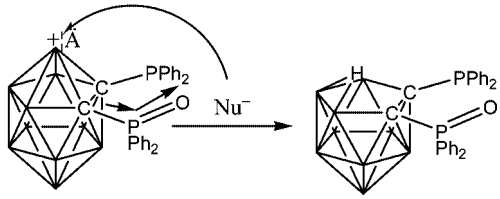


Scheme 2. Proposed mechanism for the partial degradation of compound **4**.

The $C_{cage}$–P=O group pulls electron density off the cage, and its electron-withdrawing capacity favors the removal of the B(3) atom (the boron atom adjacent to the carbon atom), especially under the attack of the nucleophilic solvent. According to these results, we think that compound **4** is an intermediate formed during the oxidation and degradation process of the *closo* ligand. This process may be accomplished in three steps which occur in the following order: (1) the oxidation of one phosphorus atom, (2) the degradation of the *closo*-carborane skeleton, and (3) the oxidation of another phosphorus atom.

All the three carborane complexes and two bis(phosphoryl)carborane compounds were characterized by FT-IR, $^1H$ and $^{13}C$ NMR spectroscopy. The IR spectra of compounds **1**–**5** are very similar to each other and exhibit absorptions characteristic of terminal B–H vibrations at 2510–2550 $cm^{-1}$, which fall in the normal range of B–H vibration from 2450 to 2625 $cm^{-1}$.[41] The absorption at about 3100 $cm^{-1}$ may be attributed to the $\nu_{C-H}$ stretching vibration of the benzene rings. Several peaks are found between 1689 and 1400 $cm^{-1}$, which may be assigned to the $\nu_{C=C}$ stretching vibration. The peak at ca. 1400 $cm^{-1}$ is the in-plane deformation mode of the benzene ring, and the peak at ca. 1100 $cm^{-1}$ is the absorption of $\nu_{C(aryl)-P}$, which is a little shifted, in keeping with phosphorus coordination to the carborane moiety. The strong absorption at about 1250–1260 $cm^{-1}$ in all the compounds may be attributed to the P=O bond. The absorption at 700–750 $cm^{-1}$ shows the existence of the deformation cage. The $^1H$ NMR spectra (400.15 MHz) of these carborane compounds display a common resonance pattern at about 7.1–7.6 ppm, which can be attributed to the aryl-H of the $PPh_2$ groups. The resonance at ca. –2.2 ppm is the bridging H atom of B–H–B in the three complexes.[19] In the $^{13}C$ NMR spectra (100.63 MHz), the resonance at about 132–139 ppm can be

 © 2007 Wiley-VCH Verlag GmbH & Co. KGaA, Weinheim 

assigned to the benzene-ring C atoms, and that at ca. $\delta = 77$ can be attributed to the carbon atom of carborane cage.[42]

### X-ray Crystallographic Study

The molecular structures of the new compounds **1**–**5** are shown in Figure 1, Figure 2, Figure 3, Figure 4, and Figure 5 respectively, and the selected bond lengths and angles of the three carborane complexes are listed in Table 1. A common feature of the complexes **1**–**3** is that they all contain the same bis(phosphoryl)-*nido*-carborane ligand [7,8-$(OPPh_2)_2$-7,8-$C_2B_9H_{10}]^-$. The average P–$C_{cage}$ distances in the three metal complexes are 1.804, 1.809, 1.816 Å, respectively, which are slightly shorter than the mean value 1.87 Å in $[NH_4][7,8\text{-}(PPh_2)_2\text{-}7,8\text{-}C_2B_9H_{10}]$,[43] indicating that in these *nido* species the oxidation of the P atom has an influence on the P–$C_{cage}$ bond length. This conclusion could also be proved by the corresponding bond lengths in $[Ni\{7\text{-}(OPPh_2)\text{-}8\text{-}(PPh_2)\text{-}7,8\text{-}C_2B_9H_{10}\}\{7,8\text{-}(PPh_2)_2\text{-}7,8\text{-}C_2B_9H_{10}\}]$[38] [P–C(7): 1.769(7), P–C(8): 1.867(7) Å]. The C(7)–C(8) bond lengths, ranging from 1.593(7) to 1.606(8) Å in **1**–**3** are in good agreement with the corresponding distance 1.61(2) Å in $[NH_4][7,8\text{-}(PPh_2)_2\text{-}7,8\text{-}C_2B_9H_{10}]$,[43] but obviously shorter than 1.697(4) Å in the *closo* ligand 1,2-$(PPh_2)_2$-1,2-$C_2B_{10}H_{10}$.[44] The angles P(1)–C(7)–C(8) and P(2)–C(8)–C(7) in complexes **1**–**3** [120.4(3)–

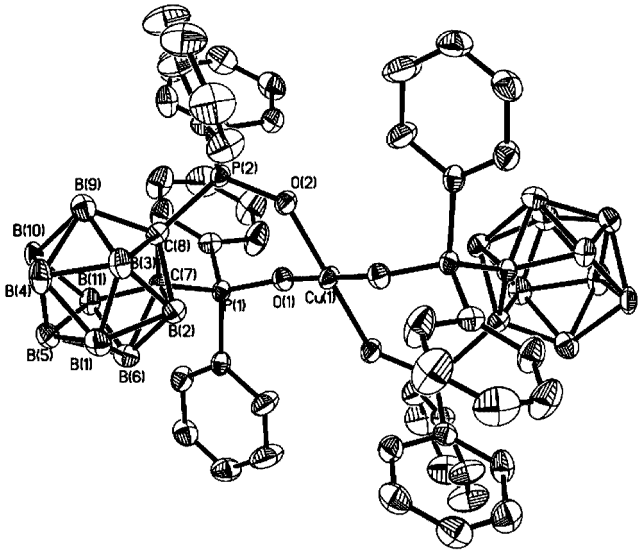


Figure 1. The crystal structure of complex **1**. The H atoms were omitted for clarity.

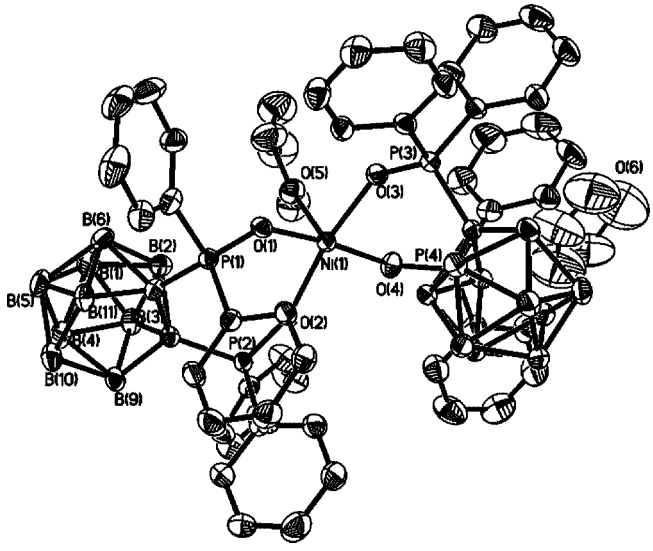


Figure 3. The crystal structure of complex **3**. The H atoms were omitted for clarity.

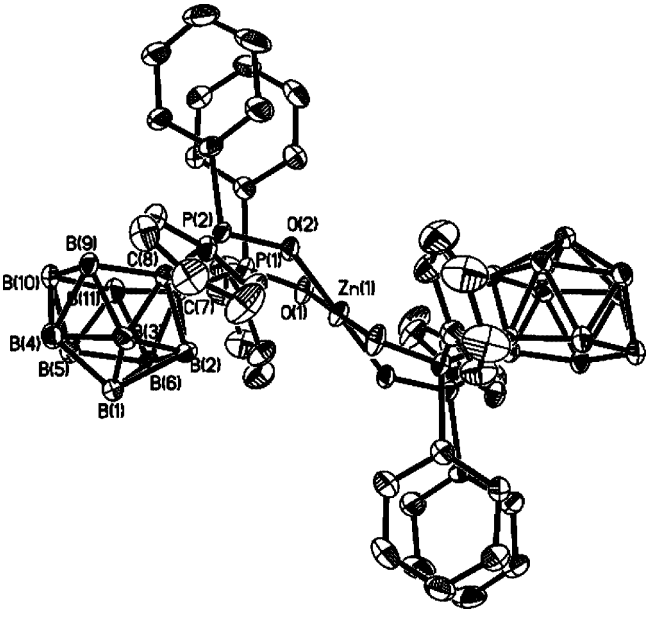


Figure 2. The crystal structure of complex **2**. The H atoms were omitted for clarity.

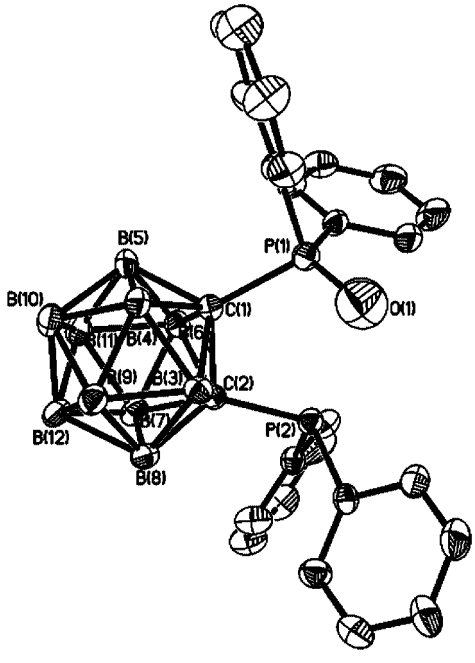


Figure 4. The crystal structure of compound **4**. The H atoms were omitted for clarity.

 © 2007 Wiley-VCH Verlag GmbH & Co. KGaA, Weinheim 

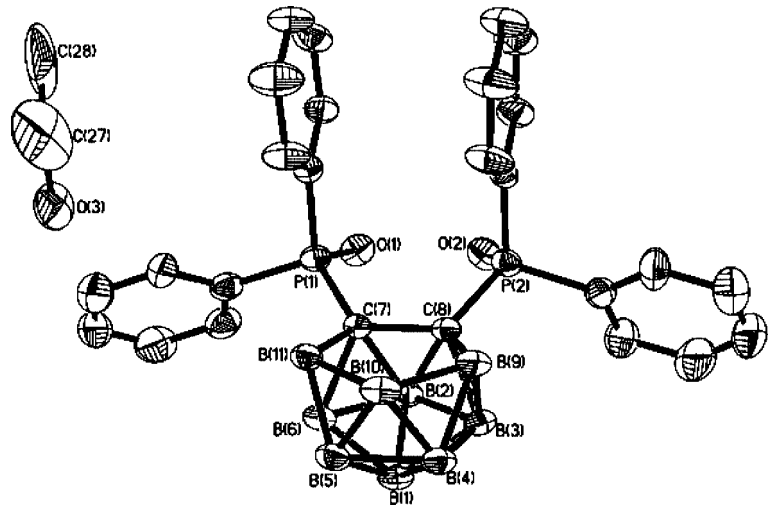


Figure 5. The crystal structure of compound **5**. The H atoms were omitted for clarity.

Table 1. Selected bond lengths [Å] and angles [°] for complexes **1**, **2**, and **3**.[a]

| **1** | | **2** | | **3** | |
|---|---|---|---|---|---|
| Cu(1)–O(1) | 1.913(4) | Zn(1)–O(1) | 1.904(4) | Ni(1)–O(1) | 2.011(4) |
| Cu(1)–O(2) | 1.900(4) | Zn(1)–O(2) | 1.931(3) | Ni(1)–O(2) | 1.987(4) |
| P(1)–O(1) | 1.525(4) | P(1)–O(1) | 1.495(4) | P(1)–O(1) | 1.501(4) |
| P(2)–O(2) | 1.505(4) | P(2)–O(2) | 1.506(4) | P(2)–O(2) | 1.493(4) |
| P(1)–C(7) | 1.804(6) | P(1)–C(7) | 1.822(5) | P(1)–C(7) | 1.801(6) |
| P(2)–C(8) | 1.814(7) | P(2)–C(8) | 1.810(6) | P(2)–C(8) | 1.813(5) |
| C(7)–C(8) | 1.606(8) | C(7)–C(8) | 1.594(7) | C(7)–C(8) | 1.608(8) |
| C(7)–B(11) | 1.663(9) | C(7)–B(11) | 1.654(8) | C(7)–B(11) | 1.646(9) |
| C(8)–B(9) | 1.652(10) | C(8)–B(9) | 1.634(8) | C(8)–B(9) | 1.631(9) |
| C(7)–B(2) | 1.759(9) | C(7)–B(2) | 1.720(8) | C(7)–B(2) | 1.753(9) |
| C(8)–B(3) | 1.742(2) | C(8)–B(3) | 1.740(8) | C(8)–B(3) | 1.738(8) |
| O(1)–Cu(1)–O(2) | 90.03(19) | O(1)–Zn(1)–O(2) | 90.63(16) | O(1)–Ni(1)–O(2) | 86.28(16) |
| O(1)–Cu(1)–O(1)#1 | 180.0(1) | O(1)–Zn(1)–O(1)#1 | 180.0(1) | O(1)–Ni(1)–O(4) | 170.68(15) |
| P(1)–O(1)–Cu(1) | 143.0(3) | P(1)–O(1)–Zn(1) | 137.1(2) | P(1)–O(1)–Ni(1) | 141.1(2) |
| P(2)–O(2)–Cu(1) | 136.9(3) | P(2)–O(2)–Zn(1) | 141.6(2) | P(2)–O(2)–Ni(1) | 161.6(2) |
| O(1)–P(1)–C(7) | 112.8(3) | O(1)–P(1)–C(7) | 115.6(2) | O(1)–P(1)–C(7) | 117.1(2) |
| O(2)–P(2)–C(8) | 115.7(3) | O(2)–P(2)–C(8) | 113.5(2) | O(2)–P(2)–C(8) | 113.3(2) |
| C(7)–C(8)–P(2) | 122.8(4) | C(7)–C(8)–P(2) | 122.3(4) | C(7)–C(8)–P(2) | 120.4(4) |
| C(8)–C(7)–P(1) | 122.4(4) | C(8)–C(7)–P(1) | 122.8(4) | C(8)–C(7)–P(1) | 124.6(4) |

[a] Symmetry transformations used to generate equivalent atoms: complex **1**: $-x+1, -y+1, -z$; complex **2**: $-x+1, -y+1, -z+2$.

124.6(3)°] are slightly larger than the corresponding angles [113.4(9) and 116.5(9)°] in $[NH_4][7,8\text{-}(PPh_2)_2\text{-}7,8\text{-}C_2B_9H_{10}]$. The P=O bond lengths are within a narrow range from 1.488(4) to 1.525(4) Å, which is basically consistent with the average values 1.528 Å in $H[7,8\text{-}(OPPh_2)_2\text{-}7,8\text{-}C_2B_9H_{10}]$, 1.483(5) Å in $[Ni\{7\text{-}(OPPh_2)\text{-}8\text{-}(PPh_2)\text{-}7,8\text{-}C_2B_9H_{10}\}\{7,8\text{-}(PPh_2)_2\text{-}7,8\text{-}C_2B_9H_{10}\}]$, and 1.486(6) Å in $1\text{-}(OPPh_2)\text{-}2\text{-}(PPh_2)\text{-}1,2\text{-}C_2B_{10}H_{10}$.

The structures of complexes **1** and **2** are symmetrical, with the $M^{II}$ (M = Cu, Zn) atom as the symmetry center. Symmetry transformations used to generate equivalent atoms are $-x+1, -y+1, -z$ for **1** and $-x+1, -y+1, -z+2$ for **2**. The bis(phosphoryl) ligand $[7,8\text{-}(OPPh_2)_2\text{-}7,8\text{-}C_2B_9H_{10}]^-$ is coordinated in a bidentate fashion through the O atoms to the $M^{II}$ ion. The $M^{II}$ and four oxygen atoms can form a perfect plane in complexes **1** and **2**, and the O(1), M, O(1)# and O(2), M, O(2)# (# denotes the equivalent atom generated by symmetry) are in an ideal line. The two bis(phosphoryl)carborane moieties are located at two opposite sides of this plane with a *trans* conformation. The average M–O distances are 1.907 and 1.919 Å in complexes **1** and **2**, respectively, which are slightly shorter than the corresponding values of 2.113 Å in $[Cu(dppf)(odppf)]^{+}$[45] and 1.968 Å in $ZnBr_2(OPPh_3)_2$.[46] The O–M–O angles in these two complexes are almost equal to each other with a value of about 90°. As M, C(7), and C(8) are all out of the plane O(1) P(1)P(2)O(2) in the same orientation, a boat conformation between the seven atoms of the chelating ring between the ligand and the metal is formed, in which the O(1)P(1)P(2) O(2) plane can be used as the bottom of the boat.

As shown in Figure 3, the crystal structure of the complex **3** is a little different from the above two complexes. Although the two bis(phosphoryl) ligands are still coordinated in a bidentate fashion to the Ni atom, and a plane is also formed by the four oxygen atoms, the coordination sphere of the Ni atom has been changed by one tetra-

 © 2007 Wiley-VCH Verlag GmbH & Co. KGaA, Weinheim 

hydrofuran molecule whose oxygen atom is coordinated to the $Ni^{II}$ atom. The Ni atom is therefore out of the plane by 0.1884 Å, positioned towards the fifth Ni–O bond. Therefore, the coordination sphere of the metal atom should be characterized as a square pyramid, different from the square-planar coordination mode in complexes **1** and **2**. Another difference is the P–O–M angles in the seven-membered ring formed by two P, two O, two $C_{cage}$ atoms and the Ni atom. These two angles in complex **3** are 141.4(2) and 161.7(2)°, respectively, whereas there is no noticeable difference between these two angles in complexes **1** and **2**. In complex **3**, the five Ni–O bond lengths are almost equal to each other within a narrow range 1.992(4)–2.011(3) Å, which is obviously shorter than the average value of 2.112 Å in $[Ni\{CH_2(OPPh_2)_2\}_3(ClO_4)_2]\cdot CH_3OH$.[47]

## Conclusions

In this work, we reported two free compounds with a *closo*- or *nido*-carborane skeleton and three new metal–carborane complexes containing the bis(phosphoryl)-*nido*-carborane ligand, which were obtained by the reactions of the *closo* ligand 1,2-$(PPh_2)_2$-1,2-$C_2B_{10}H_{10}$ with some inorganic metal compounds in air. The obtainment of the two free bis(phosphoryl)carborane compounds could give us some information for understanding the oxidation and degradation of the *closo* ligand in air. The results obtained from this paper and our recent work[38] indicated that the oxidation process occurs before the partial degradation, and that the oxidation of the two phosphorus atoms is not synchronous.

## Experimental Section

**Materials and Measurements:** All reactions and subsequent manipulations were carried out in air. 1,2-bis(diphenylphosphanyl)-1,2-dicarba-*closo*-dodecaborane(10) was prepared according to the literature procedure.[48] All chemicals were purchased and used as received. Infrared spectra were recorded in the range 400–4000 $cm^{-1}$ from KBr pellets with a Nicolet-460 FT-IR spectrophotometer. Elemental analysis (C, H) was carried out with a Perkin–Elmer 2400 II elemental analyzer. The $^1H$ and $^{13}C$-NMR were recorded with a Varian Mercury 400 spectrometer in $CDCl_3$ solution, with tetramethylsilane (TMS) as the internal standard, at 400.15 and 100.63 MHz, respectively. The $^{13}C$ spectra are broadband proton decoupled. The chemical shifts are reported in parts per million with respect to the references and are stated relative to external TMS for $^1H$ and $^{13}C$ NMR spectroscopy.

### Synthetic Procedures

**Synthesis of [Cu{7,8-$(OPPh_2)_2$-7,8-$C_2B_9H_{10}$}$_2$] (1):** To a suspension of 1,2-$(PPh_2)_2$-1,2-$C_2B_{10}H_{10}$ (51.2 mg, 0.10 mmol) in ethanol (10 mL, 95%) was added $CuCl_2\cdot 2H_2O$ (17.1 mg, 0.10 mmol). The mixture was stirred for about 6 h in air at room temperature. The blue solid formed was filtered off and dried in vacuo (20.9 mg, 36.96%). M.p. 215–216 °C. A suitable crystal for X-ray diffraction was grown from a dichloromethane/*n*-hexane solution. FT-IR: $\tilde{\nu}_{KBr}$ = 3090 (m), 2550 (m), 1670 (s), 1400 (m), 1255 (s), 1100 (m), 756 (m), 660 (s), 530 (m) $cm^{-1}$. $^1H$ NMR (400.15 MHz, $CDCl_3$): $\delta$ = 7.128–7.400 (40 H, Aryl-H); –2.312 (2 H, B–H–B) ppm. $^{13}C$ NMR (100.63 MHz, $CDCl_3$): $\delta$ = 25.212–135.856 (48 C, Aryl-C), 77.101 (4 C, $C_{cage}$) ppm. $C_{52}H_{60}B_{18}CuO_4P_4$ (1131.00): calcd. C 55.22, H 5.35; found C 55.30, H 5.38.

**Synthesis of [Zn{7,8-$(OPPh_2)_2$-7,8-$C_2B_9H_{10}$}$_2$] (2):** $ZnCl_2$ (13.6 mg, 0.10 mmol) and 1,2-$(PPh_2)_2$-1,2-$C_2B_{10}H_{10}$ (51.2 mg, 0.10 mmol) were mixed in ethanol (10 mL, 95%). The stirring process was continued for about 6 h in air at room temperature. The white solid was filtered off and dried in vacuo (19.7 mg, 34.78%). M.p. > 300 °C (dec.). A suitable crystal for X-ray diffraction was obtained from a dichloromethane solution after partial evaporation of the solvent. FT-IR: $\tilde{\nu}_{KBr}$ = 3100 (m), 2557 (m), 1625 (s), 1454 (m), 1263 (s), 1120 (m), 735 (m), 690 (s), 510 (m) $cm^{-1}$. $^1H$ NMR (400.15 MHz, $CDCl_3$): $\delta$ = 7.284–7.563 (40 H, Aryl-H), –2.301 (2 H, B–H–B) ppm. $^{13}C$ NMR (100.63 MHz, $CDCl_3$): $\delta$ = 23.421–136.000 (48 C, Aryl-C), 76.863 (4 C, $C_{cage}$) ppm. $C_{52}H_{60}B_{18}O_4P_4Zn$ (1132.83): calcd. C 55.13, H 5.34; found C 55.10, H 5.30.

**Synthesis of [Ni{7-$(OPPh_2)$-8-$(PPh_2)$-7,8-$C_2B_9H_{10}$}{7,8-$(PPh_2)_2$-7,8-$C_2B_9H_{10}$}]:** $NiCl_2\cdot 6H_2O$ (23.8 mg, 0.10 mmol) and 1,2-$(PPh_2)_2$-1,2-$C_2B_{10}H_{10}$ (51.2 mg, 0.10 mmol) were mixed in ethanol (10 mL, 95%). The stirring process was continued for about 6 h at room temperature in air, and then the yellow solid was filtered off, washed with ethanol, and dried in vacuo (27.5 mg, 51.01%). M.p. 207–208 °C. A single crystal for X-ray diffraction was grown from a dichloromethane/*n*-hexane solution. FT-IR: $\tilde{\nu}_{KBr}$ = 3000 (m), 2545 (m), 1475 (m), 1250 (s), 730 (m) $cm^{-1}$. $^1H$ NMR (400.15 MHz, $CDCl_3$): $\delta$ = 7.20–7.58 (40 H, Aryl-H); –2.24 (2 H, B–H–B) ppm. $^{13}C$ NMR (100.63 MHz, $CDCl_3$): $\delta$ = 125.913–134.942 (48 C, Aryl-C); 76.198 (4 C, $C_{cage}$) ppm. $C_{52}H_{60}B_{18}NiOP_4$ (1078.17): calcd. C 57.92, H 5.61; found C 57.85, H 5.55.

**Synthesis of [Ni(thf){7,8-$(OPPh_2)_2$-7,8-$C_2B_9H_{10}$}$_2$]·thf (3):** $NiCl_2\cdot 6H_2O$ (23.8 mg, 0.10 mmol) was added to a suspension of 1,2-$(PPh_2)_2$-1,2-$C_2B_{10}H_{10}$ (51.2 mg, 0.10 mmol) in ethanol (10 mL, 95%). After the mixture was stirred for 12 h in air at room temperature, the yellow solid was filtered off, washed with ethanol, and dried in vacuo (18.4 mg, 32.68%). M.p. 198–199 °C. A single crystal suitable for X-ray analysis was obtained from a tetrahydrofuran solution after partial evaporation of the solvent. FT-IR: $\tilde{\nu}_{KBr}$ = 3120 m, 2540 (m), 1689 (s), 1425 (m), 1260 (s), 1078 (m), 725 (m), 680 (s), 490 (m) $cm^{-1}$. $^1H$ NMR (400.15 MHz, $CDCl_3$): $\delta$ = 7.187–7.594 (40 H, Aryl-H), –2.222 (2 H, B–H–B) ppm. $^{13}C$ NMR (100.63 MHz, $CDCl_3$): $\delta$ = 26.334–139.114 (48 C, Aryl-C), 77.007 (4 C, $C_{cage}$) ppm. $C_{60}H_{76}B_{18}NiO_6P_4$ (1270.38): calcd. C 56.72, H 6.03; found C 56.67, H 5.98.

**Synthesis of [1-$(OPPh_2)$-2-$(PPh_2)$-1,2-$C_2B_{10}H_{10}$] (4):** 1,2-$(PPh_2)_2$-1,2-$C_2B_{10}H_{10}$ (51.2 mg, 0.10 mmol) was added to ethanol (10 mL, 95%). The suspension was stirred for 8 h; air was continuously and slowly bubbled into the mixture at room temperature. The white solid was filtered off and dried in vacuo (36.5 mg, 69.06%). M.p. 232–233 °C. A single crystal suitable for X-ray analysis was obtained from a dichloromethane/*n*-hexane solution. FT-IR: $\tilde{\nu}_{KBr}$ = 3045 (m), 2510 (m), 1669 (s), 1415 (m), 1250 (s), 1083 (m), 707 (m), 672 (s), 510 (m) $cm^{-1}$. $^1H$ NMR (400.15 MHz, $CDCl_3$): $\delta$ = 7.057–7.784 (20 H, Aryl-H) ppm. $^{13}C$ NMR (100.63 MHz, $CDCl_3$): $\delta$ = 25.886–137.553 (24 C, Aryl-C), 76.825 (2 C, $C_{cage}$) ppm. $C_{26}H_{30}B_{10}OP_2$ (528.54): calcd. C 59.08, H 5.72; found C 59.11, H 5.80.

**Synthesis of H[7,8-$(OPPh_2)_2$-7,8-$C_2B_9H_{10}$]·0.25$C_2H_5OH$ (5):** In a manner similar to the procedure for the preparation of compound **4**, the mixture was stirred for 18 h. The white solid was filtered off and dried in vacuo (46.4 mg, 84.94%). M.p. 208–209 °C. A suitable crystal for X-ray diffraction was grown from a dichloromethane solution layered with *n*-hexane. FT-IR: $\tilde{\nu}_{KBr}$ = 3050 (m), 2520 (m),

 © 2007 Wiley-VCH Verlag GmbH & Co. KGaA, Weinheim 

Table 2. Details of the crystal parameters, data collections and refinements for **1**–**5**.

| Crystal data | **1** | **2** | **3** | **4** | **5** |
|---|---|---|---|---|---|
| Empirical formula | $C_{52}H_{60}B_{18}CuO_4P_4$ | $C_{52}H_{60}B_{18}O_4P_4Zn$ | $C_{60}H_{76}B_{18}O_6P_4Ni$ | $C_{26}H_{30}B_{10}OP_2$ | $C_{26.5}H_{32.5}B_9O_{2.25}P_2$ |
| Formula weight | 1131.00 | 1132.83 | 1270.38 | 528.54 | 546.26 |
| Temperature [K] | 298(2) | 298(2) | 298(2) | 298(2) | 298(2) |
| Wavelength [Å] | 0.71073 | 0.71073 | 0.71073 | 0.71073 | 0.71073 |
| Crystal system | triclinic | triclinic | triclinic | monoclinic | triclinic |
| Space group | $P\bar{1}$ | $P\bar{1}$ | $P\bar{1}$ | *P21/n* | $P\bar{1}$ |
| *a* [Å] | 11.576(4) | 11.568(4) | 13.990(3) | 16.438(4) | 11.424(3) |
| *b* [Å] | 12.774(4) | 12.748(4) | 15.389(3) | 10.423(2) | 11.714(3) |
| *c* [Å] | 13.332(4) | 13.318(4) | 20.441(4) | 17.739(4) | 13.559(4) |
| *α* [°] | 101.423(5) | 101.203(5) | 93.069(3) | 90 | 95.401(5) |
| *β* [°] | 109.229(5) | 109.358(5) | 96.878(3) | 111.868(3) | 108.386(4) |
| *V* [Å$^3$] | 1670.1(9) | 1661.4(9) | 3884.2(12) | 2820.6(11) | 1597.1(8) |
| *Z* | 1 | 1 | 2 | 4 | 2 |
| Absorption coefficient [mm$^{-1}$] | 0.461 | 0.505 | 0.374 | 0.175 | 0.160 |
| *D* [Mg·m$^{-3}$] | 1.125 | 1.132 | 1.086 | 1.245 | 1.136 |
| *F*(000) | 583 | 584 | 1324 | 1096 | 1206 |
| Crystal size [mm] | 0.35 × 0.32 × 0.29 | 0.23 × 0.21 × 0.19 | 0.46 × 0.40 × 0.20 | 0.55 × 0.50 × 0.48 | 0.35 × 0.31 × 0.29 |
| Theta range [°] | 2.09 to 25.01 | 2.04 to 25.01 | 1.97 to 25.01 | 2.37 to 25.01 | 2.92 to 25.01 |
| Limiting indices | $-13 \le h \le 13$ | $-9 \le h \le 13$ | $-16 \le h \le 14$ | $-19 \le h \le 15$ | $-13 \le h \le 13$ |
| | $-15 \le k \le 15$ | $-15 \le k \le 15$ | $-18 \le k \le 18$ | $-9 \le k \le 12$ | $-13 \le k \le 13$ |
| | $-8 \le l \le 15$ | $-15 \le l \le 15$ | $-19 \le l \le 24$ | $-21 \le l \le 20$ | $-10 \le l \le 16$ |
| Independent reflection | 5663 | 5573 | 13040 | 4921 | 5492 |
| Max. and min. transmission | 0.8778 and 0.8552 | 0.9102 and 0.8928 | 0.9290 and 0.8468 | 0.9206 and 0.9097 | 0.9551 and 0.9461 |
| Goodness-of-fit on $F^2$ | 1.009 | 1.003 | 1.002 | 1.007 | 1.010 |
| *R* [$I > 2\sigma(I)$] | $R_1 = 0.0790$ | $R_1 = 0.0715$ | $R_1 = 0.0781$ | $R_1 = 0.0616$ | $R_1 = 0.0762$ |
| | $wR_2 = 0.1825$ | $wR_2 = 0.1755$ | $wR_2 = 0.1894$ | $wR_2 = 0.1678$ | $wR_2 = 0.1777$ |
| *R* (all data) | $R_1 = 0.1616$ | $R_1 = 0.1375$ | $R_1 = 0.1588$ | $R_1 = 0.0917$ | $R_1 = 0.1492$ |
| | $wR_2 = 0.2264$ | $wR_2 = 0.2237$ | $wR_2 = 0.2482$ | $wR_2 = 0.2093$ | $wR_2 = 0.2193$ |
| Largest diff. peak and hole ($\times 10^2$ electrons Å$^{-3}$) | 1.067 and –0.514 | 1.356 and –0.406 | 1.135 and –0.423 | 0.894 and –1.186 | 0.584 and –0.287 |

1669 (s), 1400 (m), 1260 (s), 1085 (m), 700 (m), 660 (s), 510 (m) cm$^{-1}$. $^1$H NMR (400.15 MHz, $CDCl_3$): $\delta$ = 7.206–7.598 (20 H, Aryl-H); –2.105 (1 H, B–H–B) ppm. $^{13}$C NMR (100.63 MHz, $CDCl_3$): $\delta$ = 22.300–135.198 (24 C, Aryl-C), 76.887 (2 C, $C_{cage}$) ppm. $C_{26.5}H_{32.5}B_9O_{2.25}P_2$ (546.26): calcd. C 58.26, H 5.99; found C 58.31, H 5.96.

### X-ray Structure Determination

The collections of the crystallographic data for the three carborane complexes and two carborane compounds were carried out with a Bruker Smart-1000 CCD diffractometer, by using graphite-monochromatized Mo-$K_\alpha$ ($\lambda$ = 0.71073 Å) at 298(2) K. The structures were solved by direct methods and expanded by using Fourier difference techniques with the SHELXTL-97 program package.[49] The solvent content in compound **5** is disordered. Partially occupied atoms of the solvent molecule were refined with isotropic displacement parameters, but the rest of the non-hydrogen atoms were refined anisotropically by full-matrix least-squares calculations on $F^2$. All the H atoms were located in a difference Fourier map and thereafter refined isotropically, except the H atoms of the solvent $C_2H_5OH$ of compound **5**. The bridging H atoms of the *nido* carborane skeleton were refined isotropically with fixed *U*. Details of the crystal parameters, data collection, and refinement are summarized in Table 2.

CCDC-602225 (for **1**), -602226 (for **2**), -602227 (for **3**), -607283 (for **4**), and -609307 (for **5**) contain the supplementary crystallographic data for this paper. These data can be obtained free of charge from The Cambridge Crystallographic Data Centre via www.ccdc.cam.ac.uk/data_request/cif.

## Acknowledgments

This work was supported by the National Natural Science Foundation of the P. R. China (project no. 20371025) and Open Research Fund Program of the Key Laboratory of Marine Drugs (Ocean University of China), Ministry of Education [project no. KLMD (OUC) 2004].

[1] T. L. Heying, J. W. Ager Jr, S. L. Clark, D. J. Mangold, H. L. Goldstein, M. Hillman, R. J. Polak, J. W. Szymanski, *Inorg. Chem.* **1963**, *2*, 1089–1092.
[2] M. M. Fein, J. Bobinski, N. Mayes, N. Schwartz, M. S. Cohen, *Inorg. Chem.* **1963**, *2*, 1111–1115.
[3] R. A. Wiesboeck, M. F. Hawthorne, *J. Am. Chem. Soc.* **1964**, *86*, 1642–1643.
[4] M. F. Hawthorne, D. C. Young, P. M. Garrett, D. A. Owen, S. G. Schwerin, F. N. Tebbe, P. A. Wegner, *J. Am. Chem. Soc.* **1968**, *90*, 862–868.
[5] J. F. Valliant, K. J. Guenther, A. S. King, P. Morel, P. Schaffer, O. O. Sogbein, K. A. Stephenson, *Coord. Chem. Rev.* **2002**, *232*, 173–230.
[6] M. F. Hawthorne, *Angew. Chem. Int. Ed. Engl.* **1993**, *32*, 950–984.
[7] J. Plesek, *Chem. Rev.* **1992**, *92*, 269–278.
[8] R. N. Grimes, *J. Chem. Educ.* **2004**, *81*, 657–672.
[9] M. F. Hawthorne, X. G. Yang, Z. Zheng, *Pure Appl. Chem.* **1994**, *66*, 245–254.
[10] M. F. Hawthorne, Z. Zheng, *Acc. Chem. Res.* **1997**, *30*, 267–276.
[11] M. J. Hardie, C. L. Raston, *Angew. Chem. Int. Ed.* **2000**, *39*, 3835.
[12] M. J. Hardie, C. L. Raston, *Chem. Commun.* **2001**, 905–906.

 © 2007 Wiley-VCH Verlag GmbH & Co. KGaA, Weinheim 

[13] N. Malic, P. J. Nichols, C. L. Raston, *Chem. Commun.* **2002**, 16–17.
[14] A. K. Saxena, N. S. Hosmane, *Chem. Rev.* **1993**, *93*, 1081–1124.
[15] A. K. Saxena, J. A. Maguire, N. S. Hosmane, *Chem. Rev.* **1997**, *97*, 2421–2462.
[16] Z. Xie, *Coord. Chem. Rev.* **2002**, *231*, 23–46.
[17] G. X. Jin, *Coord. Chem. Rev.* **2004**, *248*, 587–602.
[18] Z. Xie, *Coord. Chem. Rev.* **2006**, *250*, 259–272.
[19] F. Teixidor, C. Viñas, M. M. Abad, M. Lopez, J. Casabó, *Organometallics* **1993**, *12*, 3766–3768.
[20] R. Nuñez, C. Viñas, F. Teixidor, M. M. Abad, *Appl. Organomet. Chem.* **2003**, *17*, 509–517.
[21] E. Bembenek, O. Crespo, M. C. Gimeno, P. G. Jones, A. Laguna, *Chem. Ber.* **1994**, *127*, 835–840.
[22] O. Crespo, M. C. Gimeno, P. G. Jones, A. Laguna, *J. Chem. Soc., Dalton Trans.* **1996**, 4583–4588.
[23] F. Teixidor, C. Viñas, M. M. Abad, R. Kivekäs, R. Sillanpää, *J. Organomet. Chem.* **1996**, *509*, 139–150.
[24] O. Crespo, M. C. Gimeno, A. Laguna, P. G. Jones, *J. Chem. Soc., Dalton Trans.* **1992**, 1601–1605.
[25] O. Crespo, M. C. Gimeno, P. G. Jones, A. Laguna, *J. Chem. Soc., Chem. Commun.* **1993**, 1696–1697.
[26] O. Crespo, M. C. Gimeno, P. G. Jones, A. Laguna, *Inorg. Chem.* **1994**, *33*, 6128–6131.
[27] O. Crespo, M. C. Gimeno, P. G. Jones, A. Laguna, *Inorg. Chem.* **1996**, *35*, 1361–1366.
[28] M. J. Calhorda, O. Crespo, M. C. Gimeno, P. G. Jones, A. Laguna, J. M. López-de-Luzuriaga, J. L. Perez, M. A. Ramón, L. F. Veiros, *Inorg. Chem.* **2000**, *39*, 4280–4285.
[29] O. Crespo, M. C. Gimeno, P. G. Jones, A. Laguna, M. D. Villacampa, *Angew. Chem. Int. Ed. Engl.* **1997**, *36*, 993–995.
[30] C. Viñas, M. M. Abad, F. Teixidor, R. Sillanpaa, R. Kivekas, *J. Organomet. Chem.* **1998**, *555*, 17–23.
[31] S. Paavola, R. Kivekäs, F. Teixidor, C. Viñas, *J. Organomet. Chem.* **2000**, *606*, 183–187.
[32] S. Paavola, F. Teixidor, C. Viñas, R. Kivekäs, *J. Organomet. Chem.* **2002**, *645*, 39–45.
[33] S. Paavola, F. Teixidor, C. Viñas, R. Kivekäs, *J. Organomet. Chem.* **2002**, *657*, 187–193.
[34] F. Teixidor, C. Viñas, M. M. Abad, C. Whitaker, J. Rius, *Organometallics* **1996**, *15*, 3154–3160.
[35] D. P. Zhang, J. M. Dou, D. C. Li, D. Q. Wang, *Appl. Organomet. Chem.* **2006**, *20*, 632–637.
[36] D. P. Zhang, J. M. Dou, D. C. Li, D. Q. Wang, *J. Coord. Chem.*, in press.
[37] D. P. Zhang, J. M. Dou, D. C. Li, D. Q. Wang, *Inorg. Chim. Acta* **2006**, *359*, 4243–4249.
[38] J. M. Dou, D. P. Zhang, D. C. Li, D. Q. Wang, *J. Organomet. Chem.*, in press.
[39] C. Viñas, R. Nuñez, I. Rojo, F. Teixidor, R. Kivekäs, R. Sillanpää, *Inorg. Chem.* **2001**, *40*, 3259–3260.
[40] F. Teixidor, R. Benakki, C. Viñas, R. Kivekäs, R. Sillanpää, *Inorg. Chem.* **1999**, *38*, 5916–5919.
[41] J. E. Crook, N. N. Greenwood, J. D. Kennedy, *J. Chem. Soc., Dalton Trans.* **1972**, 171–175.
[42] V. P. Balema, M. Pink, J. Sieler, E. Hey-Hawkins, L. Hennig, *Polyhedron* **1998**, *17*, 2087–2093.
[43] F. Teixidor, C. Viñas, M. M. Abad, R. Nuñez, R. Kivekäs, R. Sillanpää, *J. Organomet. Chem.* **1995**, *503*, 193–203.
[44] D. P. Zhang, J. M. Dou, D. C. Li, D. Q. Wang, *Acta Crystallogr., Sect. E* **2006**, *62*, 418–419.
[45] G. Pilloni, B. Corain, M. Degano, B. Longato, G. Zanotti, *J. Chem. Soc., Dalton Trans.* **1993**, 1777–1778.
[46] C. A. Kosky, J. Gayda, J. F. Gibson, S. F. Jones, *Inorg. Chem.* **1982**, *21*, 3173–3179.
[47] E. Bermejo, A. Castineiras, R. Dominguez, C. Schule, *J. Coord. Chem.* **1994**, *33*, 353–357.
[48] R. P. Alexander, H. Schroeder, *Inorg. Chem.* **1963**, *2*, 1107–1110.
[49] G. M. Sheldrick, *SHELXTL 5.10 for Windows NT: Structure Determination Software Programs*, Bruker Analytical X-ray Systems, Madison, WI, **1997**.

Received: July 20, 2006
Published Online: November 17, 2006

 © 2007 Wiley-VCH Verlag GmbH & Co. KGaA, Weinheim 

DOI: 10.1002/ejic.200600698

# Oriented Crystallisation on Supports and Anisotropic Mass Transport of the Metal-Organic Framework Manganese Formate

Mirko Arnold,*[a] Pavel Kortunov,[b] Deborah J. Jones,[c] Yannig Nedellec,[c] Jörg Kärger,[b] and Jürgen Caro[a]

**Keywords:** Organic–inorganic hybrid composites / Membranes / Anisotropic mass transport / Oriented crystallisation / Manganese

The oriented in situ crystallisation of microporous manganese(II) formate [$Mn(HCO_2)_2$] on different porous supports (e.g. porous alumina and graphite) has been investigated. The anisotropic growth of $Mn(HCO_2)_2$ was examined by X-ray diffraction (XRD) and scanning electron microscopy (SEM). The intracrystalline diffusion of methanol in $Mn(HCO_2)_2$ was studied by observation of the sorption kinetics by interference microscopy (IFM). It was found that untreated discs of porous alumina and graphite supports exhibit poor densities of $Mn(HCO_2)_2$ crystals per supported area. Even lower crystal densities are found for activated supports such as for alumina after basic treatment and for oxidized graphite supports. Improved results have been achieved by replacing formic acid by sodium formate in the synthesis route. Crystal growth on graphite gives results superior to those on alumina with respect to the crystal density as well as the relative orientation of the 1D channel network to the support surface. Methanol uptake from the vapour phase is similar at 25 and 40 °C and gives an adsorption capacity of about 95 $mL\,g^{-1}$. The BET surface area was found to be 280 $m^2\,g^{-1}$. IFM indicates that diffusion occurs only along one crystallographic axis, thus proving the presence of a 1D channel system. Diffusion coefficients of about $10^{-12}$ $m^2\,s^{-1}$ for methanol in microporous $Mn(HCO_2)_2$ were found. These results can be used to prepare supported metal–organic framework (MOF) membranes for molecular sieving.
(© Wiley-VCH Verlag GmbH & Co. KGaA, 69451 Weinheim, Germany, 2007)

## Introduction

Commonly used porous materials for gas-separating membranes are zeolites and metal oxides such as $Al_2O_3$, $TiO_2$ and $SiO_2$. These materials offer high thermal stability and permanent porosity. Furthermore, zeolites present well-defined channels and cavities, which allow them to be used as molecular sieving membranes.[1]

Despite these outstanding properties, the demand for novel microporous materials remains high because the rational design of zeolites and other inorganic materials with pore diameters less than about 0.4 nm is still difficult and the separation of small molecules (e.g. $H_2$, $N_2$, $O_2$, $CH_4$) by molecular sieving membranes has not yet been achieved successfully. Metal–organic frameworks (MOFs), which are a new class of porous materials, are novel candidates for molecular sieving membranes. MOFs represent an interface between organic and inorganic compounds since they consist of metal ions linked by organic molecules (ligands). MOFs comprise ionic organic–inorganic hybrid materials,[2] such as the manganese formate[3,4] studied in this paper, as well as coordination polymers based on di- to tetravalent carboxylic acids.[5–8] This novel approach for preparing porous materials exhibits a rational and even more flexible design of the network compared to the already known inorganic materials. In addition to these advanced properties, access to the entire pore volume, as well as variable nanoscale pore sizes, indicates that MOFs are clearly an attractive new class of porous materials.

As might be expected, the first reports of MOFs in prospective industrial processes have already been published.[9] Possible applications for MOFs are catalysis,[10] gas purification and gas storage, which needs information on the molecular transport in MOFs.[11] The employment of MOFs as heterogeneous catalysts might be a promising field in view of their great structural and compositional variety and possible accessibility of the metal ion sites in the structure.[9] Recently, Chen reported the application of MOFs in GC columns in order to segregate alkane isomer mixtures with good separation capabilities.[12] In spite of the considerable attention given to these promising materials, only a handful MOFs with permanent porosity have been reported so far, in part because framework stability after template removal in these materials has emerged as a serious problem. Studies on functional aspects, especially the application in mem-

[a] University of Hanover,
Callinstr. 3A, 30167 Hanover, Germany
[b] University of Leipzig,
Linnéstr. 5, 04103 Leipzig, Germany
[c] Laboratoire des Agrégats Moléculaires et Matériaux Inorganiques, UMR CNRS 5072, Université Montpellier
2, Place E. Bataillon, 34095 Montpellier CEDEX 5, France
Supporting information for this article is available on the WWW under http://www.eurjic.org or from the author.


© 2007 Wiley-VCH Verlag GmbH & Co. KGaA, Weinheim

branes, accumulate rather slowly, and thus only one example using MOFs in a gas-separating membrane is known. In a unique approach, Won et al.[13] embedded a $Cu^{II}$ complex in a polymer matrix to yield membranes with high $H_2$ selectivities and remarkable permeabilities. In the work presented here, the novel porous manganese formate, first reported by Dybtsev et al. and at around the same time by Wang et al.,[3,4] was chosen due to its high thermal stability, selective, high $H_2$ adsorption rates and facile preparation route. Synthesis follows a solvothermal route using formic acid, manganese(II) chloride and 1,4-dioxane as the structure-directing agent. After removal of 1,4-dioxane, the framework becomes a porous structure with a 1D channel system, where each $Mn^{II}$ cation is coordinated by six formate ligands to give a network of corner- and edge-shared $MnO_6$ octahedra, as shown in Figure 1. The porous network exhibits thermal stability up to 300 °C, as indicated by XRD and TG/DTA studies (see Supporting Information). In order to use microporous materials (e.g. zeolites, porous $SiO_2$) as gas-separating materials in membrane technology they need to be grown on porous substrates. Commonly, zeolite crystals are grown on substrates like porous alumina and titania, which offer high thermal and mechanical stability, in order to obtain composite membranes and thus to be able to use them as gas-separating membranes. Due to the similarity between zeolites and MOFs, in this work the oriented growth of microporous manganese formate on different substrates is investigated.

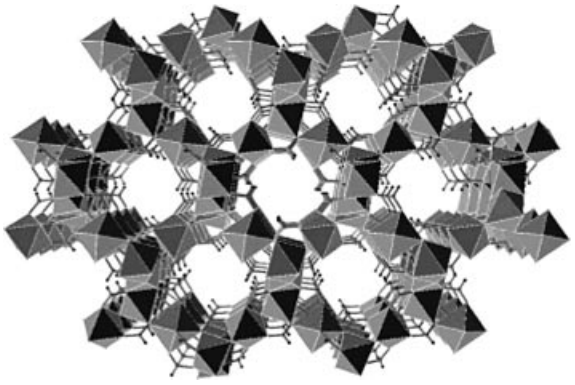

Figure 1. Schematic drawing of the guest-free framework along the *b* axis. Corner- and edge-shared $MnO_6$ octahedra as well as the formate ligands are shown, according to Dybtsev et al.[3]

## Results and Discussion

Significant uptake of methanol from the vapour phase was observed, the total amount adsorbed being similar at 25 and 40 °C. The sorption isotherms obtained in gravimetric experiments have a shape characteristic of a microporous solid, as shown in Figure 2.

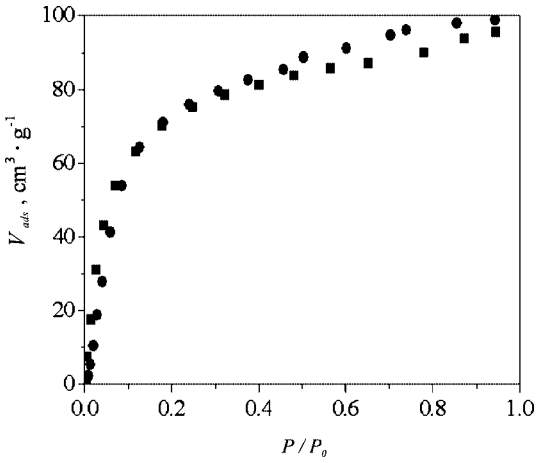


Figure 2. Adsorption isotherms of methanol in $Mn(HCO_2)_2$ at 25 °C (■) and 40 °C (●). $V_{ads}$ represents the STP volume of the adsorbed amount of methanol.

Volumetric experiments were also performed (not shown), and a small hysteresis was observed between adsorption and desorption branches. The BET surface area was calculated to be 278 $m^2 g^{-1}$, which is in excellent agreement with that obtained from previously reported $H_2$ (240 $m^2 g^{-1}$) or $CO_2$ (297 $m^2 g^{-1}$) sorption isotherms.[3]

IFM studies were performed to gain more information about the diffusion kinetics as well as to demonstrate the presence of a 1D channel system. Figures 3b and c show the time-dependent intracrystalline concentration profiles of methanol (0–10 mbar) in an $Mn(HCO_2)_2$ single crystal (Figure 3a). Uptake was found only along the *y* axis, with no significant transport along the *z* and *x* axes. This result confirms the existence of a 1D channel system along the crystallographic *b* axis in Figure 1. Furthermore, no evidence for an intergrowth structure was observed, and methanol was found to be distributed homogeneously throughout the whole crystal. The molecular diffusivity evaluated in the middle part of the chosen crystal from Fick's Second Law does not depend on the methanol concentration, and its average value ($9.15 \times 10^{-13}$ $m^2 s^{-1}$) is in good agreement with data obtained from the uptake rate ($1.05 \times 10^{-12}$ $m^2 s^{-1}$) using the $t^{1/2}$ approach. However, the sorption uptake concentration profiles cannot be described exclusively by intracrystalline diffusion. The sorption uptake is determined to a minor extent by surface permeability, which, most remarkably, is found to depend on the methanol concentration. Values for the surface permeability of $2 \times 10^{-1}$ $m s^{-1}$ for 0.2 of the final loading and $3 \times 10^{-1}$ $m s^{-1}$ for 0.9 of the final methanol loading (95 mL $g^{-1}$) are estimated.

Initial attempts to prepare a composite membrane of $Mn(HCO_2)_2$ grown on alumina and graphite were carried out without any treatment of the support surfaces. The growth of $Mn(HCO_2)_2$ crystals on alumina discs resulted in only poor densities (10 crystals/mm$^2$). In situ crystallisation on graphite shows, in general, a more distinct growth of $Mn(HCO_2)_2$ crystals on support surfaces (80 crystals/mm$^2$).

 © 2007 Wiley-VCH Verlag GmbH & Co. KGaA, Weinheim 

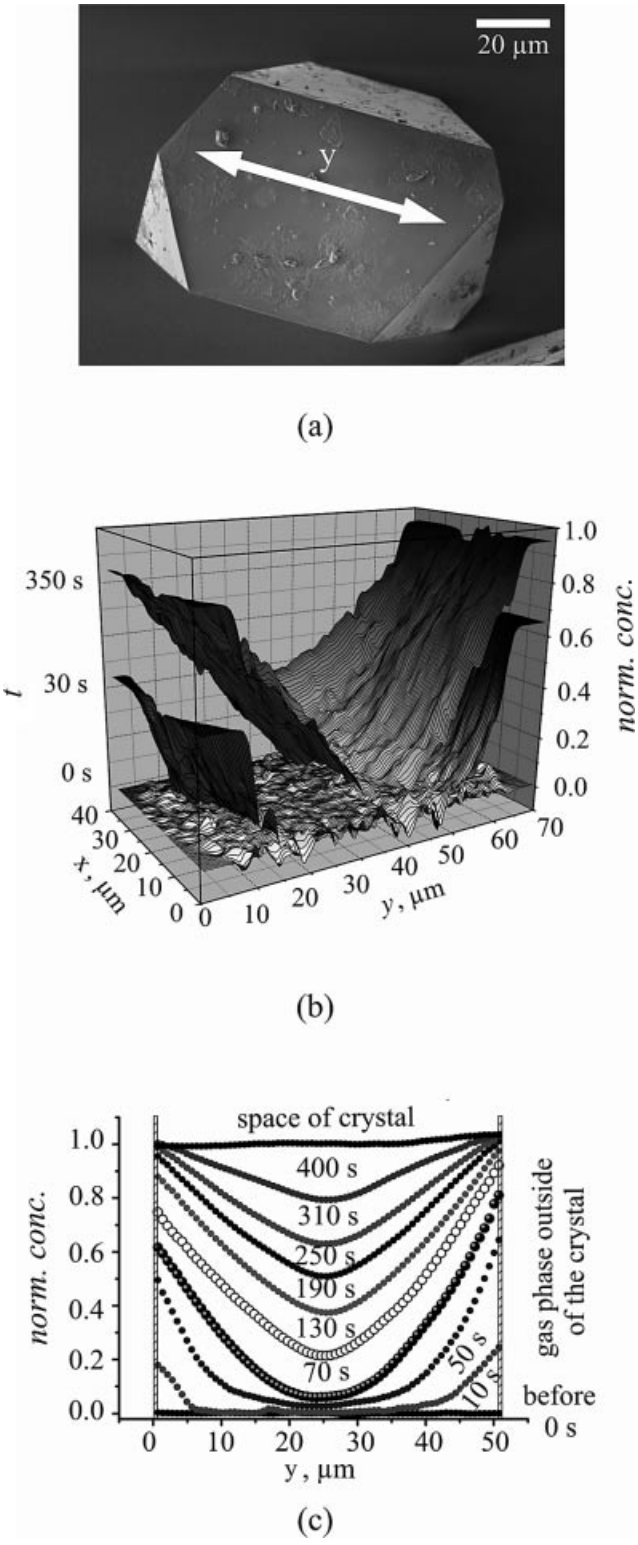


Figure 3. SEM micrograph of an $Mn(HCO_2)_2$ crystal used for IFM (a). Arrows indicate the 1D channel system along the *b* axis. 2D intracrystalline concentration profiles for methanol sorption by an $Mn(HCO_2)_2$ single crystal in the same orientation as shown in (a), obtained by IFM at room temperature (b), and the corresponding 1D intracrystalline concentration profiles (c).

To increase the crystal density, different methods for support activation were evaluated.

In order to increase the crystal growth on alumina, the supports were treated with sodium hydroxide. Alumina surfaces treated with sodium hydroxide are even less suitable for $Mn(HCO_2)_2$ crystal growth as virtually no crystals were observed after in situ crystallisation on those supports

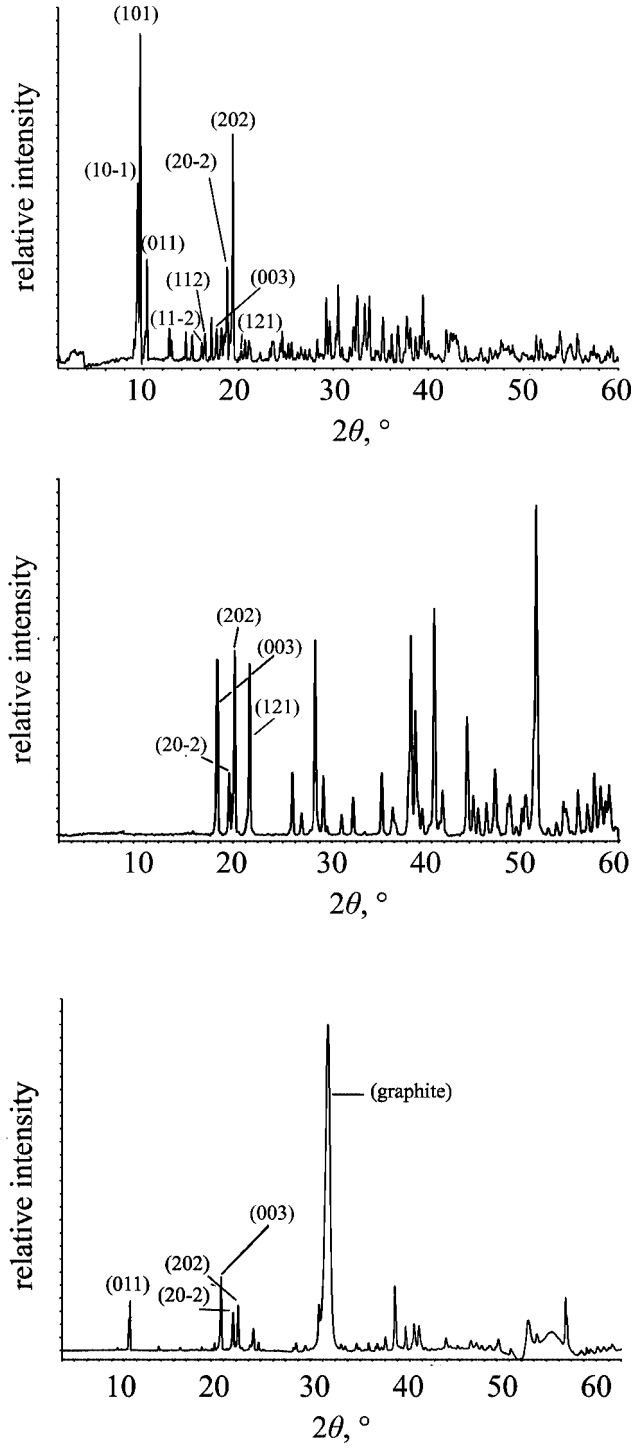


Figure 4. Powder XRD pattern of as-synthesised $Mn(HCO_2)_2$ (a), $Mn(HCO_2)_2$ grown on alumina support discs showing the peaks for the (202), (20$\bar{2}$) and (003) planes are dominant (b) and $Mn(HCO_2)_2$ grown on graphite supports by the "formate" route showing an additional dominant peak for the (011) plane (c).

 © 2007 Wiley-VCH Verlag GmbH & Co. KGaA, Weinheim 

(1 crystal/mm$^2$). The commonly used seeding method resulted in an increase in the crystal density to 150 crystals/mm$^2$. It must be stressed, however, that despite an improved density of $Mn(HCO_2)_2$ crystals on the surface, the orientation of the 1D channel system was undesirable. This was concluded by comparing the XRD pattern of $Mn(HCO_2)_2$ grown on the alumina support (see Figures 4a and b). This indicates that the 1D channel system lies parallel to the support surface. With this orientation, no mass transfer would occur through membranes prepared with this method. Oxidised graphite supports show a trend similar to the alumina supports treated with sodium hydroxide, since crystal growth on these supports exhibits a lower crystal density than the untreated ones (40 crystals/mm$^2$).

The crystal density achieved by this method underlines the influence of electrostatic interactions during the growth of $Mn(HCO_2)_2$ on these supports. As activated supports – treatment with sodium hydroxide in the case of alumina and oxidation in the case of graphite – lead to poor crystal densities, a different synthesis method using sodium formate rather than formic acid was developed. This is based on the assumption that positively charged surfaces could inhibit the formation of crystals on the surface because of electrostatic repulsion. $Mn(HCO_2)_2$ crystals grown on oxidized carbon supports by the formate route are characterised by advanced crystal densities (see Figure 5a) as well as a reasonable tilt angle of 34° of the 1D channel system to the support surface (see Figures 4a and c). Additionally, it was found that $Mn(HCO_2)_2$ crystals were grown into the porous graphite to a certain extent, which suggests a proper connection to the support (see Figure 5b).

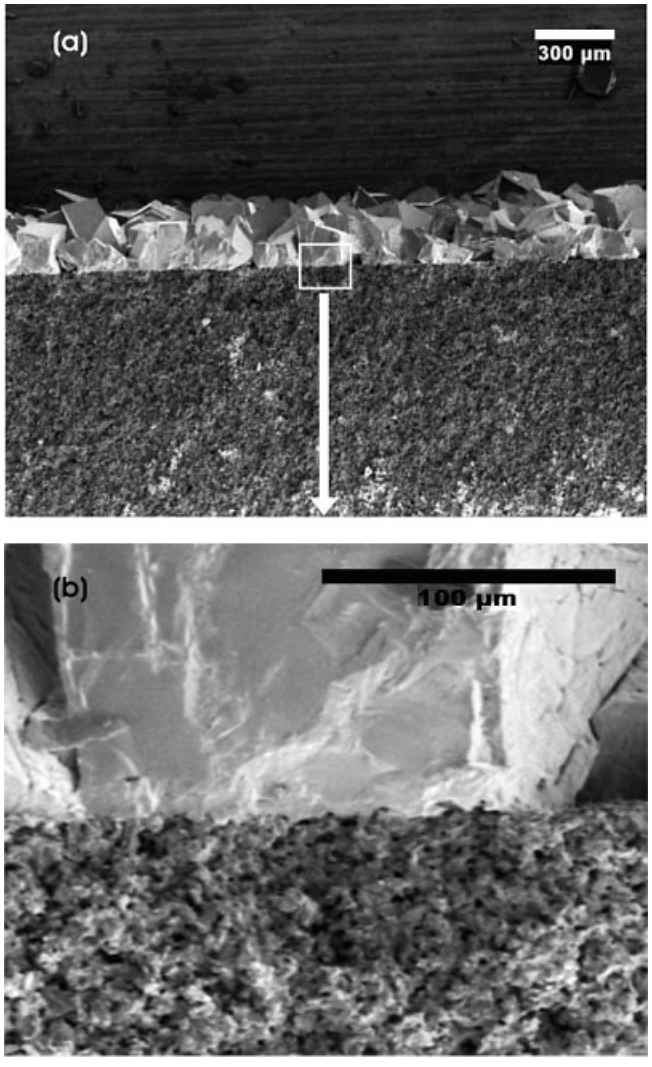


Figure 5. Profile of $Mn(HCO_2)_2$ crystals grown on a graphite support disc after two in situ crystallisations by the "formate" route (a). The magnified image shows intergrowth between the carbon support and $Mn(CO_2)_2$ (b).

## Conclusions

It has been shown that the synthesis of supported MOF composite membranes based on manganese(II) formate [$Mn(HCO_2)_2$] is possible in principle. The amount of crystals grown on the supports and the orientation of the 1D channel system on the surface depends strongly on the selected support as well as on the synthesis route. While membrane-quality coatings have still not been achieved, this study has identified factors that are important for the production of continuous layered $Mn(HCO_2)_2$ membranes. Future work should focus on a detailed examination of the surface charges during synthesis, and the obtained results can be applied in a direct modification of in situ synthesis and/or surface treatment in order to increase the amount of crystals on the supports. Additionally, in situ crystallisation of other promising MOFs for new composite molecular sieving membranes seems to be reasonable. For instance, Pan et al. have published the synthesis of a porous, lanthanum-containing MOF with stability up to 450 °C and high and selective $H_2$ adsorption rates.[14]

## Experimental Section

Porous $Mn(HCO_2)_2$ was synthesised according to Dybtsev et al.[3] in a steel autoclave with Teflon-lined insert ("formic acid" route). $MnCl_2 \cdot 2H_2O$ (2.5 g, 12.5 mmol) and $HCO_2H$ (0.94 mL, 25 mmol) were dissolved in 1,4-dioxane (25 mL) and 50 mL of *N*,*N*-diethylformamide (50 mL). The solution was then autoclaved at 115 °C for 48 h. The obtained crystals were filtered and washed with acetone. In order to remove the 1,4-dioxane template molecules, the crystals were heated to 150 °C for 24 h under reduced pressure. All employed chemicals were used as delivered without any purification.

In order to maintain the advantage of the high thermal stability of $Mn(HCO_2)_2$, the in situ crystallisation was performed on supporting discs of porous $\alpha$-$Al_2O_3$ (Inocermic GmbH, Germany) and porous graphite (Poco Graphite Inc., USA) with a diameter of 18 mm and a thickness of 1 mm to form composite membranes in the same manner as zeolite membranes. Before in situ crystallisation, supports were cleaned with deionised water and acetone to remove impurities from the surface. Finally, they were dried at 80 °C for 1 h.

To improve the crystal growth on the support, they were treated differently before in situ crystallisation: $\alpha$-$Al_2O_3$ supports were au-

 © 2007 Wiley-VCH Verlag GmbH & Co. KGaA, Weinheim 

toclaved at 150 °C for 4 h with a solution of 50% NaOH to increase the concentration of free OH groups, which are possible connecting nodes for $Mn(HCO_2)_2$. Another approach for increasing the crystal growth on alumina supports consists of placing seed crystals on the surface. For this purpose, ground $Mn(HCO_2)_2$ was simply rubbed onto the alumina surface.

The activity of graphite supports was increased by heating in air at 300 °C for 12 h to increase the concentration of several different functional groups, especially carbonyl, carboxyl and hydroxy groups, on the carbon surface.[15] Since a positively charged surface might reduce the crystal growth, an alternative synthesis method that replaces formic acid with sodium formate was also developed ("formate route").

The adsorption–desorption isotherms of methanol in microporous $Mn(HCO_2)_2$ were measured by monitoring the mass uptake of the sample, recorded with a Sartorius S3D-V microbalance, following successive injections of known amounts of methanol in the vapour phase. To monitor the equilibrium pressure and to calculate the amount of injected vapour, two pressure gauges (Edwards) were used, with ranges from $10^{-5}$ to 1 Torr and from 10 to 1000 Torr. Secondary vacuum was achieved with a Varian Turbomolecular drag pump coupled to a dry primary pump. Prior to each experiment, the sample was introduced into a specially designed glass cell and weighed. The cell was then fixed to the suspending rod of the microbalance, and equilibrated with a reference cell. After a short time to allow the balance to stabilize, the sample was heated in situ at 150 °C, and out-gassed under vacuum for 24 h.

To confirm the structure of $Mn(HCO_2)_2$ crystals and to determine the orientation of the crystals on supports, X-ray diffraction data were obtained with a Philips X′PERT diffractometer and evaluated using the software WinXPOW. Reflections were collected in the range from $2\theta = 5$ to 90° (step width: 0.01°; time per step: 10 s) at a voltage of 40 kV and a current of 40 mA. In order to confirm the structure of the obtained $Mn(HCO_2)_2$ crystals, powder XRD data were collected from ground samples. The obtained data were used to determine the preferred orientation of crystal growth on the applied supports. The dominant planes in the XRD pattern obtained from $Mn(HCO_2)_2$ on the employed supports were taken to be perpendicular to the surface. The tilt angle between the 1D channel system and the support surface could then be determined by calculating the angle between the 1D channel system and the vertical to the support plane of $Mn(HCO_2)_2$.

Both the crystal morphologies and the quantitative growth of $Mn(HCO_2)_2$ on different supports were evaluated with a field-emission scanning electron microscope (JEOL JSM 6700F). In view of the metal–organic nature of the $Mn(HCO_2)_2$ only low accelerating voltages (1 kV) were applied in order to avoid decomposition of the structure and charging of the sample surface.

Interference microscopy (IFM) measurements allow in situ observation of the sorption uptake of gaseous species in porous media with a spatial resolution of 0.5 μm.[16,17] Methanol sorption was studied with a pressure step from 0 to 10 mbar at room temperature. For these measurements, the calcined MOF sample was introduced into an optical cell and prior activated under reduced pressure at 150 °C for 24 h. The IFM setup consists of a vacuum system, a Carl Zeiss Jenapol interference microscope and a Mach-Zehnder type interferometer. Interference patterns were recorded with a CCD camera (XC-77CE, Sony).

**Supporting Information** (see footnote on the first page of this article): Figure S1 shows the TG/DTA analysis of as-synthesised $Mn(HCO_2)_2$ still containing 1,4-dioxane template molecules. The first weight loss (140–280 °C, 16.5%) is clearly related to the selective removal of the template molecules. The XRD patterns before (a) and after template removal (b) (Figure S2) show that even after template removal the framework remains stable.

[1] J. Caro, M. Noack, P. Kölsch, R. Schäfer, *Microporous Mesoporous Mater.* **2000**, *38*, 3.
[2] N. Stock, T. Bein, *Angew. Chem.* **2004**, *116*, 767; *Angew. Chem. Int. Ed.* **2004**, *43*, 749.
[3] D. N. Dybtsev, H. Chun, S. H. Yoon, D. Kim, K. Kim, *J. Am. Chem. Soc.* **2004**, *126*, 32.
[4] Z. Wang, B. Zhang, H. Fujiwara, H. Kobayashi, M. Kurmoo, *Chem. Commun.* **2004**, 416.
[5] H. Li, M. Eddaoudi, M. O'Keeffe, O. M. Yaghi, *Nature* **1999**, *402*, 276.
[6] O. M. Yaghi, M. O'Keeffe, N. W. Oekwig, H. K. Chae, M. Eddaoudi, J. Kim, *Nature* **2003**, *423*, 705.
[7] B. Moulton, M. J. Zaworotko, *Chem. Rev.* **2001**, *101*, 1629.
[8] C. J. Janiak, *Dalton Trans.* **2003**, 2781.
[9] U. Müller, M. Schubert, F. Teich, H. Puetter, K. Schierle-Arndt, J. Pastré, *J. Mater. Chem.* **2006**, *16*, 626.
[10] K. Schlichte, T. Kratzke, S. Kaskel, *Microporous Mesoporous Mater.* **2004**, *73*, 81.
[11] F. Stallmach, S. Gröger, V. Künzel, J. Kärger, O. M. Yaghi, M. Hesse, U. Müller, *Angew. Chem.* **2006**, *118*, 2177; *Angew. Chem. Int. Ed.* **2006**, *45*, 2123.
[12] B. Chen, C. Liang, J. Yang, D. S. Contreras, Y. L. Clancy, E. B. Lobkovsky, O. M. Yaghi, S. Dai, *Angew. Chem.* **2006**, *118*, 1418; *Angew. Chem. Int. Ed.* **2006**, *45*, 1390.
[13] J. Won, J. S. Seo, J. H. Kim, H. S. Kim, Y. S. Kang, S. J. Kim, Y. Kim, J. Jegal, *Adv. Mater.* **2005**, *17*, 81.
[14] L. Pan, K. M. Adams, H. E. Hernandez, X. Wang, C. Zheng, Y. Hattori, K. Kaneko, *J. Am. Chem. Soc.* **2003**, *125*, 3062.
[15] J. Garciá-Martinez, D. Cazorla-Amorós, A. Linares-Solano, Y. S. Lin, *Microporous Mesoporous Mater.* **2001**, *42*, 255.
[16] P. Kortunov, C. Chmelik, J. Kärger, *Adsorption* **2005**, *11*, 235.
[17] O. Geier, S. Vasenkov, E. Lehmann, J. Kärger, R. A. Rakoczy, J. Weitkamp, *J. Phys. Chem. B* **2001**, *105*, 10217.

Received: July 26, 2006
Published Online: November 17, 2006

 © 2007 Wiley-VCH Verlag GmbH & Co. KGaA, Weinheim 

DOI: 10.1002/ejic.200600786

# Competing Radical and Non-Radical Pathways for the Decomposition of $LFe^{II}(H_2O_2)$ Complexes: a Density Functional Study

**Anna E. Anastasi,[a] Achim Lienke,[b] Peter Comba,[c] Heidi Rohwer,[c] and John E. McGrady*[d]**

**Keywords:** Density functional calculations / Oxido ligands / O–O activation / Electronic structure / Transition states

Density functional theory has been used to explore the mechanism of hydrogen peroxide decomposition when coordinated to a bispidone iron(II) complex. Two quite distinct pathways are identified, one involving O–O bond homolysis followed by a "rebound" hydrogen atom abstraction, the other involving proton transfer followed by O–O bond heterolysis. A water molecule in the second coordination sphere plays a key role in both pathways.
(© Wiley-VCH Verlag GmbH & Co. KGaA, 69451 Weinheim, Germany, 2007)

## Introduction

Mononuclear non-heme iron enzymes are involved in many different types of biological oxidation reactions, including hydroxylation and hydroperoxidation of C–H bonds, cleavage of aromatic rings and oxidative ring closure.[1–3] As a result, there has been a great deal of interest in synthesising model complexes that mimic aspects of the structure and reactivity of these enzymes. The chemistry of model complexes with multidentate nitrogen-donor ligands such as N4Py,[4] trispicene[5] and the pentadentate $N_2Py_3$ bispidones,[6] $L^1$ and $L^2$ (Scheme 1) is particularly well developed. The $Fe^{II}$ complexes are known to be potent bleaching catalysts,[7] reacting with excess $H_2O_2$ to form hydroperoxide species, $LFe^{III}(OOH)$,[4–6,8] which then generate $LFe^{IV}(O)$ by homolytic cleavage of the O–O bond.[9] Whilst the mechanism of decomposition of the $LFe^{III}(OOH)$ species has been extensively explored by both experiment and theory, the initial formation of the $Fe^{III}$ species has received comparatively little attention. There are, however, obvious parallels with classic Fenton chemistry, where $H_2O_2$ is used to oxidise aqueous solutions of $Fe^{II}$, eventually yielding $Fe^{III}$ if no substrate is present.[10] Although the Fenton reagent has been used extensively in organic chemistry for over a century, the precise identity of the active intermediate remains a topic of debate.[11] The Haber–Weiss mechanism,[12,13] first proposed in 1934, identifies OH radicals as the active oxidant, a suggestion that has been substantiated by radical trapping experiments and also kinetic comparisons with radiolytically generated radicals. Alternatively, the reactive species may be a high-valent iron complex such as $Fe^{IV}(O)$ as first suggested by Bray and Gorin in 1932.[14] The participation of high-valent oxido–iron species has been supported by a detailed kinetic analysis by Kremer,[15] which suggested that the $Fe^{III}$ products were formed by comproportionation of an intermediate $Fe^{IV}(O)$ species with excess $Fe^{II}$.

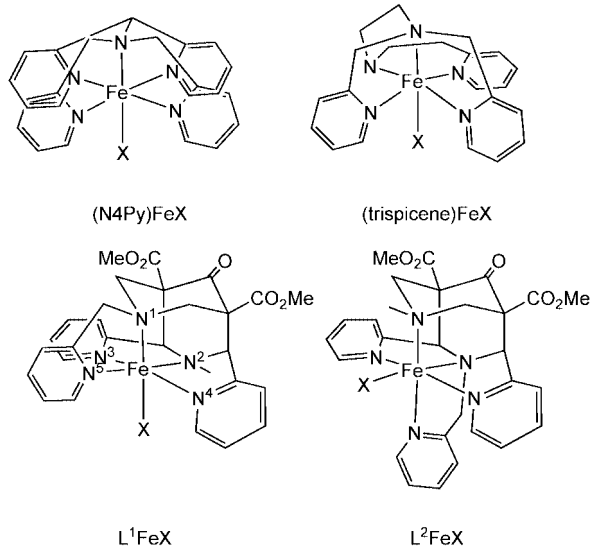


Scheme 1. Structure of complexes of pentadentate ligands, N4Py, trispicene and the bispidones $L^1$ and $L^2$.

[a] Department of Chemistry, University of York, Heslington, York, YO10 5DD, United Kingdom
Fax: +44-1904-432516
E-mail: aa155@york.ac.uk
[b] Unilever Research and Development, Olivier van Noortlaan 120, 3133AT Vlaadingen, The Netherlands
Fax: +31-10-460-5166
E-mail: achim.lienke@unilever.com
[c] Universität Heidelberg, Anorganisch-Chemisches Institut, Im Neuenheimer Feld 270, 69120 Heidelberg, Germany
Fax: +49-6226-546617
E-mail: comba@aci.uni-heidelberg.de
[d] WestCHEM, Department of Chemistry, University of Glasgow, Glasgow, G12 8QQ, United Kingdom
Fax: +44-141-3304888
E-mail: j.mcgrady@chem.gla.ac.uk

 © 2007 Wiley-VCH Verlag GmbH & Co. KGaA, Weinheim 

Buda et al. have recently used density functional theory to explore the energetics of the reaction between aqueous $Fe^{II}$ and $H_2O_2$.[16,17] The first step in their proposed reaction pathway (Scheme 2) involves a ligand-substitution reaction where $H_2O_2$ replaces a molecule of water in the first coordination sphere of $[Fe(H_2O)_6]^{2+}$, giving $[(H_2O)_5Fe^{II}(H_2O_2)]^{2+}$. Meyerstein and co-workers have argued that coordination of the $H_2O_2$ is a necessary precursor to bond cleavage, as the alternative, outer-sphere electron transfer, is energetically unfavourable.[11d,18] Homolytic cleavage of the O–O bond then leads directly to an $Fe^{IV}$ species, $[(H_2O)_4Fe^{IV}(OH)_2]^{2+}$, which subsequently rearranges by proton-transfer to the product, $[Fe^{IV}(H_2O)_5(O)]^{2+}$. A critical feature of the pathway is that as the O–O bond elongates, the developing OH radical abstracts a hydrogen atom from a neighbouring water ligand, and so is effectively trapped in the first coordination sphere. Thus, although the O–O bond cleavage is homolytic, no free radicals are released into solution. The putative $Fe^{IV}(O)$ intermediate in Scheme 2, $[(H_2O)_5Fe^{IV}(O)]^{2+}$, has recently been obtained by oxidation of aqueous $Fe^{II}$ with ozone, and characterised using a combination of Mössbauer and X-ray absorption spectroscopy.[19] Consistent with Kremer's scheme, this species does indeed comproportionate with excess $[Fe^{II}(H_2O)_6]^{2+}$ to form an $Fe^{III}$ dimer $[(H_2O)_4Fe^{III}(OH)_2Fe^{III}(H_2O)_4]^{4+}$. The latter is *not*, however, observed when $H_2O_2$ is used in place of $O_3$, suggesting that $[(H_2O)_5Fe^{IV}(O)]^{2+}$ is not the active Fenton intermediate, at least in aqueous solution.

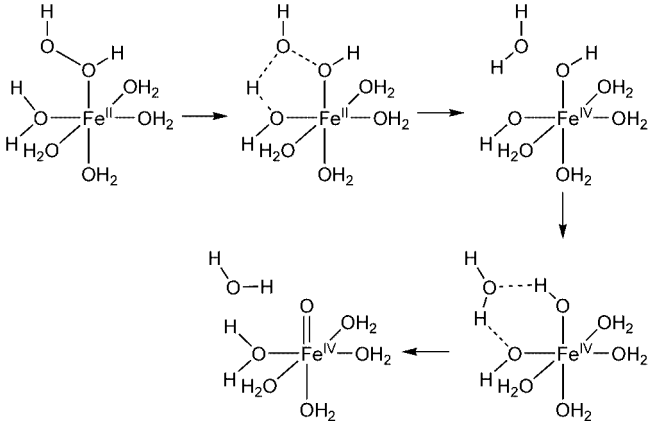

Scheme 2. Mechanism for the decomposition of $[Fe^{II}(H_2O)_5(H_2O_2)]^{2+}$ proposed by Buda et al.[16]

The presence of chelating nitrogen-donor ligands such as the bispidones, $L^1$ and $L^2$, will clearly alter the electron density at the metal centre relative to the aqua complex. Perhaps more significantly, the pentadentate nature of the ligand means that the coordination of additional water molecules is blocked in the putative intermediates, $[LFe^{II}(H_2O_2)]^{2+}$, and the all-important trapping of the developing OH radical in the first coordination sphere (Scheme 2) is therefore not possible. Nevertheless, Que and co-workers have shown that, in the case of $[(N4Py)Fe^{II}(CH_3CN)]^{2+}$, the addition of precisely 0.5 equiv. of $H_2O_2$ still gives quantitative oxidation to $Fe^{III}$ {present as a mixture of $[(N4Py)Fe^{III}(OH)]^{2+}$ and the oxido-bridged dimer, $[(N4Py)Fe^{III}(O)Fe^{III}(N4Py)]^{4+}$} with no evidence of ligand oxidation.[4] Girerd and co-workers have observed similar behaviour in the reaction of $Fe^{II}$ complexes of the trispicene ligand with $H_2O_2$, where the intermediate was tentatively assigned as $[LFe^{III}Cl]^{2+}$.[5c] From a mechanistic perspective, the clean oxidation of $Fe^{II}$ to $Fe^{III}$ with 0.5 equiv. of $H_2O_2$ seems inconsistent with the generation of free OH radicals, which would cause ligand degradation and therefore reduce the yield of $Fe^{III}$. The direct formation of transient $Fe^{IV}(O)$, followed by comproportionation with excess $Fe^{II}$, as proposed by Kremer, seems more consistent with this observation. Very recently, Comba and co-workers have studied the formation of $[L^2Fe^{IV}(O)]^{2+}$ from a mixture of the bispidone complex $[L^2Fe^{II}(BF_4)_2]$ and $H_2O_2$.[6c] The presence of clear isosbestic points in the UV/Vis spectrum, along with second-order kinetics and a large negative entropy of activation support a mechanism where binding of $H_2O_2$ to the $Fe^{II}$ centre is followed by direct conversion to $Fe^{IV}(O)$ by O–O bond heterolysis. This pathway is quite different from the O–O bond *homolysis* proposed for the aqua complex,[16] and poses a number of intriguing questions regarding the precise role of the pentadentate ligand in the reaction.

In this paper, we use density functional theory to explore possible pathways that can lead to a high-valent $[LFe^{IV}(O)]^{2+}$ species from $[LFe^{II}(H_2O_2)]^{2+}$, where L is a member of the bispidone family. Specifically, we focus on the bispidone ligand $L^1$ shown in Scheme 1 above – a comparison of the properties of complexes of $L^1$ and $L^2$ will form the basis of a subsequent communication. In all cases, the ester groups on the ligand backbone have been replaced by hydrogen atoms to simplify the computational model. We identify two distinct mechanisms for decomposition of the hydrogen peroxide. The first is qualitatively similar to the homolytic fission pathway proposed for the aqua complex,[16] except in this case the developing OH radical is trapped in the vicinity of the metal centre only by non-covalent interactions. The second pathway, in contrast, involves proton transfer, mediated by a water molecule in the second coordination sphere, followed by heterolysis of the O–O bond, and so is very similar to the mechanism proposed in ref.[6b] The barriers to the two processes prove to be comparable, suggesting that subtle changes in ligand structure and/or reaction conditions could shift the balance from one to the other.

## Results and Discussion

In the initial section, we present a detailed description of the electronic structure of the aqua complex, $[L^1Fe^{II}(H_2O)]^{2+}$, which we take as the starting point for these calculations, along with the various metal-based species that may play a role in the decomposition of $H_2O_2$: viz. the hydrogen peroxide adduct, $[L^1Fe^{II}(H_2O_2)]^{2+}$, the $Fe^{III}$ intermediate, $[L^1Fe^{III}(OH)]^{2+}$ and the product $[L^1Fe^{IV}(O)]^{2+}$. We subsequently consider mechanisms for their interconversion, paying particular attention to the possible role of solvent.

 © 2007 Wiley-VCH Verlag GmbH & Co. KGaA, Weinheim 

### Electronic Structure of $[L^1Fe^{II}(H_2O)]^{2+}$, $[L^1Fe^{II}(H_2O_2)]^{2+}$, $[L^1Fe^{III}(OH)]^{2+}$ and $[L^1Fe^{IV}(O)]^{2+}$

The optimised structures of the most stable spin states of $[L^1Fe^{II}(H_2O)]^{2+}$, $[L^1Fe^{II}(H_2O_2)]^{2+}$, $[L^1Fe^{III}(OH)]^{2+}$ and $[L^1Fe^{IV}(O)]^{2+}$ are shown in Figure 1, and the structural parameters for all accessible spin states are collected in Table 1. For both the aqua and hydrogen peroxide complexes, the optimised $S = 0$ and $S = 2$ structures show the typical features of low-spin/high-spin $Fe^{II}$ species, with the metal–ligand bonds approximately 0.2 Å longer in the latter. A strong Jahn–Teller distortion is present in the triplet state, resulting in very long bonds to the $H_2O$ and $H_2O_2$ ligands. The O–O bond in the hydrogen peroxide ligand is relatively insensitive to spin state, although the marginal elongation in the singlet can be ascribed to the better back-donating ability of low-spin $Fe^{II}$. The quintet is the most stable spin state in both systems, with relatively large gas-phase separations of ca. 35 kJ mol$^{-1}$ to the singlet and ca. 45 kJ mol$^{-1}$ to the intermediate spin[20] ($S = 1$) state. The inclusion of solvation through the PCM approach stabilises the $S = 0$ and, to a lesser extent, $S = 1$ states relative to the $S = 2$ ground state. The solvation energy in these systems is dominated by electrostatic interactions between the solvent continuum and the +2 charge on the solute, and its magnitude is therefore largely determined by the size of the solute cavity. The preferential stabilisation of states of lower multiplicity is therefore a general observation in these systems, and simply reflects the shorter Fe–N and Fe–O bonds, which lead in turn to a smaller solute cavity, and hence to stronger electrostatic interactions.

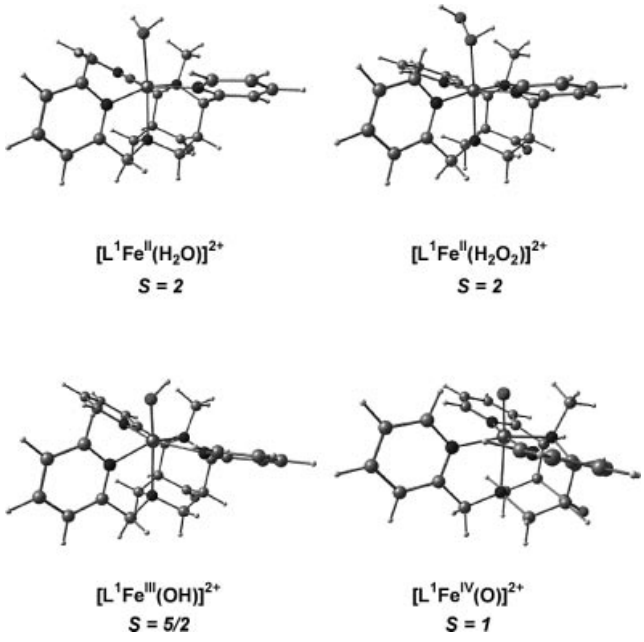


Figure 1. Optimised structures of the ground states of $[L^1Fe^{II}(H_2O)]^{2+}$, $[L^1Fe^{II}(H_2O_2)]^{2+}$, $[L^1Fe^{III}(OH)]^{2+}$ and $[L^1Fe^{IV}(O)]^{2+}$.

For the $Fe^{III}$ intermediate, $[L^1Fe^{III}(OH)]^{2+}$, we have located distinct minima for $S = 1/2$, 3/2 and 5/2 spin states. The structures show the usual trend towards longer bonds in the higher multiplicity states, most obviously in the comparison of the equatorial Fe–N distances in the $S = 1/2$ and S = 5/2 states. In the gas phase, the sextet (shown in Figure 1c) is the most stable, but the doublet is only 8 kJ mol$^{-1}$ higher in energy. We have noted above the tendency of solvation to stabilise lower spin states, and in this case it leads to a reversal of the order, with $S = 1/2$ lying 10 kJ mol$^{-1}$ *below* $S = 5/2$. There has been considerable debate over the ability of density functional theory to accurately model spin-state splittings, and the case of $Fe^{III}$ seems to be particularly problematic.[21] This uncertainty, along with the approximate nature of the PCM solvation model, precludes a definitive conclusion on the multiplicity of the ground state of $[L^1Fe^{III}(OH)]^{2+}$. Neither $[L^1Fe^{III}(OH)]^{2+}$ nor $[L^1Fe^{III}(Cl)]^{2+}$ has been isolated experimentally, although the hydroperoxide complex, $[L^1Fe^{III}(OOH)]^{2+}$, is known to have a doublet ground state.

The $d^4$ configuration of the $[L^1Fe^{IV}(O)]^{2+}$ species leads to $S = 0$, 1 and 2 spin states. Of these, the ground state (Figure 1, d) is clearly the triplet (gas phase and in solution), a situation typical of $d^4$ metal–oxido species, where two of the three $t_{2g}$-based orbitals are strongly destabilised by M–O π*-interactions. The open-shell singlet state ($<S^2> = 1.03$) has almost identical bond lengths and angles, and lies 38 kJ mol$^{-1}$ higher in energy. High-spin states of $Fe^{IV}(O)$ have attracted considerable attention since the identification of such a species in the active site of the enzyme tauD,[3] but in this case the quintet lies 20 kJ mol$^{-1}$ above the ground state, sufficient to rule out its participation in the oxidation pathway.

Table 1. Optimised Fe–N and Fe–O bond lengths [Å] and relative energies [kJ mol$^{-1}$] of the various spin states of $[L^1Fe^{II}(H_2O)]^{2+}$, $[L^1Fe^{II}(H_2O_2)]^{2+}$, $[L^1Fe^{III}(OH)]^{2+}$ and $[L^1Fe^{IV}(O)]^{2+}$. Energies are given relative to the most stable spin state for each species.

| | $[L^1Fe^{II}(H_2O)]^{2+}$ | | | $[L^1Fe^{II}(H_2O_2)]^{2+}$ | | | $[L^1Fe^{III}(OH)]^{2+}$ | | | $[L^1Fe^{IV}(O)]^{2+}$ | | |
|---|---|---|---|---|---|---|---|---|---|---|---|---|
| $S$ | 0 | 1 | 2 | 0 | 1 | 2 | 1/2 | 3/2 | 5/2 | 0 | 1 | 2 |
| Fe–O | 2.08 | 2.73 | 2.24 | 2.05 | 3.40 | 2.22 | 1.79 | 1.83 | 1.80 | 1.62 | 1.62 | 1.61 |
| Fe–$N^1$ | 2.10 | 2.33 | 2.29 | 2.11 | 2.19 | 2.32 | 2.16 | 2.52 | 2.41 | 2.24 | 2.24 | 2.22 |
| Fe–$N^2$ | 2.03 | 2.00 | 2.23 | 2.03 | 2.00 | 2.23 | 2.01 | 2.06 | 2.22 | 2.01 | 2.01 | 2.20 |
| Fe–$N^3$ | 1.99 | 2.04 | 2.18 | 1.99 | 2.03 | 2.18 | 1.99 | 1.98 | 2.17 | 2.00 | 2.00 | 2.13 |
| Fe–$N^4$ | 1.99 | 1.98 | 2.14 | 2.00 | 1.96 | 2.16 | 2.00 | 2.09 | 2.12 | 1.99 | 1.99 | 2.06 |
| Fe–$N^5$ | 2.00 | 2.04 | 2.21 | 2.00 | 2.04 | 2.16 | 2.02 | 1.99 | 2.18 | 2.01 | 2.01 | 2.18 |
| O–O | | | | 1.46 | 1.45 | 1.46 | | | | | | |
| $E_{(gas\text{-}phase)}$ | +35 | +50 | 0 | +33 | +40 | 0 | +8 | +55 | 0 | +38 | 0 | +20 |
| $E_{(PCM)}$ | +10 | +38 | 0 | +15 | +33 | 0 | 0 | +50 | +12 | +38 | 0 | +32 |

 © 2007 Wiley-VCH Verlag GmbH & Co. KGaA, Weinheim 

### Thermodynamics of the Decomposition of $[L^1Fe^{II}(H_2O_2)]^{2+}$ into $[L^1Fe^{IV}(O)]^{2+}$

The balanced equation for the decomposition of $[L^1Fe^{II}(H_2O_2)]^{2+}$ to $[L^1Fe^{IV}(O)]^{2+}$ via the putative $[L^1Fe^{III}(OH)]^{2+}$ intermediate is:

$$[L^1Fe^{II}(H_2O_2)]^{2+} \rightarrow [L^1Fe^{III}(OH)]^{2+} + OH \rightarrow [L^1Fe^{IV}(O)]^{2+} + H_2O$$

The first step, the homolytic cleavage of the O–O bond, is strongly endothermic [$\Delta E_{(gas\text{-}phase)} = +34\ kJ\,mol^{-1}$], while the second is highly exothermic [$\Delta E_{(gas\text{-}phase)} = -114\ kJ\,mol^{-1}$], and as a result the decomposition of $[(H_2O)_5Fe^{II}(H_2O_2)]^{2+}$ to $[L^2Fe^{IV}(O)]^{2+} + H_2O$ is strongly favoured [$\Delta E_{(gas\text{-}phase)} = -80\ kJ\,mol^{-1}$]. On purely thermodynamic grounds, therefore, the direct generation of $Fe^{III}$, along with the liberation of free OH radicals, seems rather unlikely. The alternative pathway to $Fe^{III}$, by comproportionation of $Fe^{IV}(O)$ with excess $Fe^{II}$ is, in contrast, exothermic [$\Delta E_{(gas\text{-}phase)} = -62\ kJ\,mol^{-1}$], confirming it as the more likely source of $Fe^{III}$ in this case:

$$[L^1Fe^{II}(H_2O)]^{2+} + [L^1Fe^{IV}(O)]^{2+} \rightarrow 2\,[L^1Fe^{III}(OH)]^{2+}$$

### Influence of Solvent

When considering possible pathways that might link the various species discussed in the previous section, we need to pay careful attention to the motion of hydrogen atoms as well as the cleavage of the O–O bond. Indeed, the role of a water ligand as a hydrogen-atom shuttle has been highlighted previously.[16] We have noted above that water is excluded from the first coordination sphere by the pentadentate bispidone ligand, and so for the exploration of reaction pathways we choose the solvated species $[L^1Fe^{II}(H_2O_2)]^{2+}\cdot H_2O$ as our minimal model, where the second coordination sphere water can, at least in principle, play the same role as the water ligand in $[(H_2O)_5Fe^{II}(H_2O_2)]^{2+}$. The balanced equation for the decomposition of the $H_2O_2$ complex is then:

$$[L^1Fe^{II}(H_2O_2)]^{2+}\cdot H_2O \rightarrow [L^1Fe^{III}(OH)]^{2+}\cdot H_2O\cdot OH \rightarrow [L^1Fe^{IV}(O)]^{2+}\cdot 2H_2O$$

Representative structures of the important hydrated species are shown in Figure 2, and the optimised energies and bond lengths are collected in Table 2. The oxygen and hydrogen atoms on the hydrogen peroxide are labelled as proximal (p) and terminal (t), while those on the water molecule are labelled "w" (see Figure 2, inset, for a schematic diagram of the hydrogen-bonded network). In the hydrogen peroxide complexes ($S = 0$, 1 and 2), the water molecule is aligned such that one lone pair interacts with the more acidic proton on the proximal (coordinated) oxygen centre. A comparison of Table 1 and Table 2 confirms that the additional water molecule has only a marginal impact on the metal–ligand bond lengths and the relative stabilities of the different spin states. The only exception is the highly distorted $S = 1$ state, where the increased basicity of the proximal oxygen atom on the $H_2O_2$ ligand results in a significant contraction of the Fe–O and Fe–$N^2$ bonds.

We have identified minima corresponding to the caged radical species $[L^1Fe^{III}(OH)]^{2+}\cdot H_2O\cdot OH$ in four distinct spin states ($S = 0$, 1, 2 and 3). The optimised structure of the most stable gas-phase species ($S = 2$) is shown in Fig-

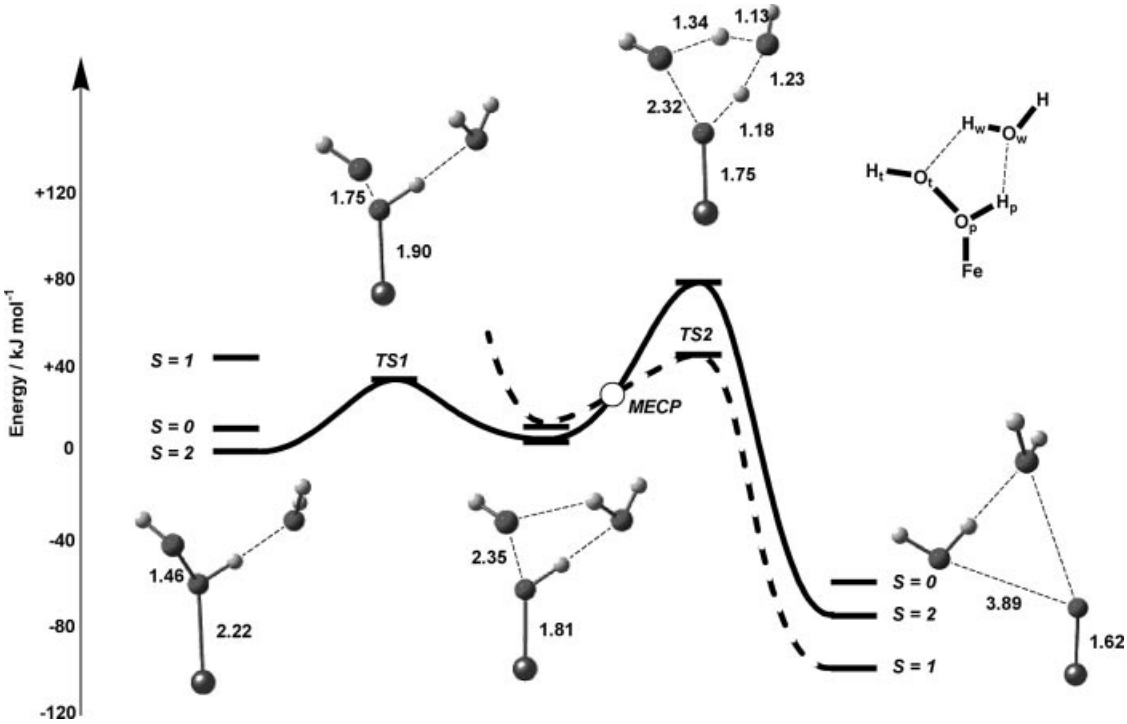


Figure 2. Potential energy surface for the O–O homolysis pathway for decomposition of $[L^1Fe^{II}(H_2O_2)]^{2+}\cdot H_2O$. Energies include the effects of solvation introduced by the PCM model. For clarity, the bispidone ligand is not shown in the structures.

 © 2007 Wiley-VCH Verlag GmbH & Co. KGaA, Weinheim 

Table 2. Optimised Fe–N and Fe–O bond lengths [Å] and relative energies [kJ mol$^{-1}$] for stationary points on the O–O homolysis pathway linking $[L^1Fe^{II}(H_2O_2)]^{2+}\cdot H_2O$ and $[L^1Fe^{IV}(O)]^{2+}\cdot 2H_2O$. Energies of all species are reported relative to the $S$ = 2 ground state of the $[L^1Fe^{II}(H_2O_2)]^{2+}\cdot H_2O$ complex.

| | $[L^1Fe^{II}(H_2O_2)]^{2+}\cdot H_2O$ | | | $[L^1Fe^{III}(OH)]^{2+}\cdot H_2O\cdot OH$ | | | | $[L^1Fe^{IV}(O)]^{2+}\cdot 2H_2O$ | | | **TS1** | MECP | **TS2** | | **TS3** | | |
|---|---|---|---|---|---|---|---|---|---|---|---|---|---|---|---|---|---|
| $S$ | 0 | 1 | 2 | 0 | 1 | 2 | 3 | 0 | 1 | 2 | 2 | 1, 2 | 1 | 2 | 0 | 1 | 2 |
| Fe–O | 2.05 | 2.34 | 2.22 | 1.79 | 1.79 | 1.81 | 1.81 | 1.62 | 1.62 | 1.61 | 1.90 | 1.78 | 1.75 | 1.73 | 1.96 | 2.02 | 1.98 |
| Fe–$N^1$ | 2.11 | 2.37 | 2.32 | 2.18 | 2.18 | 2.43 | 2.45 | 2.25 | 2.25 | 2.22 | 2.37 | 2.19 | 2.20 | 2.20 | 2.13 | 2.47 | 2.37 |
| Fe–$N^2$ | 2.03 | 2.03 | 2.23 | 2.01 | 2.01 | 2.21 | 2.22 | 2.00 | 2.01 | 2.20 | 2.21 | 2.17 | 2.01 | 2.23 | 2.03 | 2.07 | 2.24 |
| Fe–$N^3$ | 1.99 | 1.99 | 2.18 | 2.01 | 2.00 | 2.15 | 2.15 | 2.01 | 2.00 | 2.12 | 2.16 | 2.06 | 1.98 | 2.08 | 2.01 | 1.98 | 2.21 |
| Fe–$N^4$ | 2.00 | 2.04 | 2.16 | 2.01 | 2.00 | 2.13 | 2.13 | 1.99 | 1.99 | 2.06 | 2.14 | 2.11 | 2.01 | 2.11 | 2.00 | 2.09 | 2.17 |
| Fe–$N^5$ | 2.00 | 1.99 | 2.16 | 1.99 | 2.00 | 2.18 | 2.18 | 2.01 | 2.01 | 2.21 | 2.22 | 2.09 | 2.02 | 2.16 | 1.99 | 1.99 | 2.23 |
| $O_p$–$O_t$ | 1.46 | 1.46 | 1.46 | 2.32 | 2.53 | 2.35 | 2.60 | 3.89 | 3.89 | 3.63 | 1.75 | 2.52 | 2.32 | 2.36 | 1.52 | 1.52 | 1.54 |
| $O_p$–$H_p$ | 1.00 | 1.00 | 1.00 | 0.99 | 1.00 | 0.99 | 0.99 | 6.37 | 6.37 | 6.71 | 1.00 | 0.99 | 1.18 | 1.20 | 1.73 | 1.74 | 1.72 |
| $H_p$–$O_w$ | 1.66 | 1.68 | 1.66 | 1.73 | 1.72 | 1.81 | 1.80 | 0.97 | 0.97 | 0.97 | 1.66 | 1.79 | 1.23 | 1.22 | 1.02 | 1.02 | 1.02 |
| $O_w$–$H_w$ | 0.97 | 0.97 | 0.97 | 0.98 | 0.98 | 0.98 | 0.98 | 1.85 | 1.85 | 1.80 | 0.97 | 0.98 | 1.13 | 1.11 | 1.11 | 1.11 | 1.11 |
| $H_w$–$O_t$ | 3.07 | 3.04 | 3.19 | 1.98 | 1.95 | 1.98 | 1.95 | 0.98 | 0.98 | 0.99 | 2.26 | 1.93 | 1.34 | 1.36 | 1.38 | 1.37 | 1.38 |
| $E_{(gas\text{-}phase)}$ | 31 | 50 | 0 | 20 | 27 | 11 | 16 | –61 | –99 | –78 | 40 | 57 | 79 | 104 | 130 | 156 | 101 |
| $E_{(PCM)}$ | 13 | 44 | 0 | 1 | 8 | 3 | 8 | –63 | –101 | –80 | 34 | 23 | 44 | 78 | 101 | 133 | 87 |

ure 2, and bond lengths for all four spin states are collected in Table 2. The complex spin-state manifold in this region of the potential energy surface arises from parallel (ferromagnetic) or antiparallel (antiferromagnetic) alignment of the spins on the $[L^1Fe^{III}(OH)]^{2+}$ ($S$ = 1/2, 3/2, 5/2) and OH radicals ($S$ = 1/2), giving rise to coupled spin states with total $S$ = 0, 1, 2 and 3. The description of the $S$ = 3 spin state is unambiguous – it can only be achieved through parallel alignment of the spin vectors on $S$ = 5/2 $Fe^{III}$ and $S$ = 1/2 OH, and indeed the structural parameters and net spin densities (4.22 on Fe, 0.94 on $O_t$) confirm this to be the case. Likewise, the $S$ = 0 state arises unambiguously from the antiparallel alignment of $S$ = 1/2 $Fe^{III}$ and $S$ = 1/2 OH (net spin densities 0.95 on Fe, –0.93 on $O_t$). In contrast, the $S$ = 1 and $S$ = 2 states could, in principle, contain intermediate spin ($S$ = 3/2) $Fe^{III}$. However, the rather high energy of this spin state in isolated $[L^1Fe^{III}(OH)]^{2+}$ (Table 1) suggests that this is unlikely, and indeed the Fe–N and Fe–O bond lengths in the $S$ = 1 and $S$ = 2 states are almost identical to those in $S$ = 0 and $S$ = 3, confirming the presence of low- and high-spin $Fe^{III}$, respectively. When the alignment of spins is antiparallel ($S$ = 0, 2), the separation between proximal oxygen atom ($O_p$) and the hydroxyl radical ($O_t$) is somewhat smaller than where the alignment is parallel ($S$ = 1, 3), but the rather small energy differences between $S$ = 0 and 1 (7 kJ mol$^{-1}$) and between $S$ = 2 and 3 (5 kJ mol$^{-1}$) are indicative of only weak coupling.

The most stable spin state ($S$ = 2 in the gas phase) lies only 11 kJ mol$^{-1}$ above the reactants, representing a substantial stabilisation relative to the fully separated reactants, $[L^1Fe^{III}(OH)]^{2+}$ and OH ($\Delta E$ = +34 kJ mol$^{-1}$). The much lower energy required to cleave the O–O bond is due to the residual electrostatic attraction between the OH radical and the +2 cation in the "caged radical" species, $[L^1Fe^{III}(OH)]^{2+}\cdot H_2O\cdot OH$, that is absent in the separated species. As was the case for the isolated $[L^1Fe^{III}(OH)]^{2+}$ molecule, solvation (introduced through the PCM model) has a significant impact on the manifold of spin states, selectively stabilising those containing the smaller low-spin $Fe^{III}$ centre ($S$ = 0, 1) relative to those containing high-spin $Fe^{III}$ ($S$ = 2, 3). As a result, the $S$ = 0 state becomes the most stable at this level of theory, and the caged radical is now almost isoenergetic with the hydrogen peroxide complex. At this point, it is useful to contrast the pathway shown in Figure 2 with that described for $[(H_2O)_5Fe(H_2O_2)]^{2+}$.[16] In this aqua complex, the incipient OH radical is "trapped" by abstracting a hydrogen atom from a neighbouring water molecule, and the strength of the resultant Fe–OH bonds stabilises the intermediate, such that it lies over 80 kJ mol$^{-1}$ below the hydrogen peroxide complex. In the case of $[L^1Fe^{II}(H_2O_2)]^{2+}$, the free OH radical is trapped only by electrostatic interactions with the +2 charge on the metal core, along with hydrogen bonding with the solvent cage, and as a result, the O–O homolysis step is less favourable ($\Delta E$ = 11 kJ mol$^{-1}$, in the gas phase and +1 kJ mol$^{-1}$ at the PCM level of theory). In the context of the reaction chemistry, the weak trapping of the radical means that diffusion to neighbouring organic species may be competitive with a "rebound" reaction with the $Fe^{III}(OH)$ unit. Caged radicals such as these have previously been proposed to play a role in oxidation chemistry.[6b,22]

In the $[L^1Fe^{IV}(O)]^{2+}$ complex, the presence of the two additional water molecules has a negligible impact on either the relative energies of the spin states or on the bond lengths in the first coordination sphere. The interaction energy between the complex and the solvent molecules is again dominated by the electrostatic interaction with the +2 charge on the metal core, and so the presence of the additional water molecule stabilises the products by 19 kJ mol$^{-1}$ relative to the hydrogen peroxide complex.

In terms of the overall energetics of the reaction, the picture is largely unaffected when we consider the "supermolecule" $[L^1Fe^{II}(H_2O_2)]^{2+}\cdot H_2O$ rather than the fully separated species The intermediate and products are stabilised by electrostatic interactions between the dicationic core and the OH or $H_2O$ unit that is generated by cleavage of the O–O bond, but this serves only to increase the already substantial thermodynamic driving force for the cleavage of the O–O bond. It is also important to note that the mixture of explicit and continuum models for solvent described above

 © 2007 Wiley-VCH Verlag GmbH & Co. KGaA, Weinheim 

is problematic, particularly where a solvent molecule is involved in the reaction[23] {in our case one molecule of $H_2O$ is formed in the reaction $[L^1Fe^{II}(H_2O_2)]^{2+}\cdot H_2O \rightarrow [L^1Fe^{IV}(O)]^{2+}\cdot 2H_2O$}. In the context of this work, the non-cancellation of errors that arises through the mixture of continuum and explicit solvent models introduces significant uncertainties in the accuracy of the computed energies of the different asymptotes. In the remainder of this paper, we therefore focus on the qualitative mechanistic picture, and do not place undue emphasis on the absolute values of the computed energies.

In the following sections we describe two distinct pathways that lead to the formation of an $Fe^{IV}(O)$ species – the first where O–O bond homolysis is followed by hydrogen-atom abstraction, the second where proton transfer induces O–O bond heterolysis. In both cases, we pay particular attention to the various spin states that are accessible at different points on the potential energy surface. This latter point is critical here because the ground states of the $[L^1Fe^{II}(H_2O_2)]^{2+}$ and $[L^1Fe^{IV}(O)]^{2+}$ species are a quintet and a triplet, respectively. Intersystem crossing from one potential energy surface to the other is therefore an integral component of the reaction coordinate.

### O–O Bond Homolysis Pathway

We have located a transition state, **TS1**, linking the reactant, $[L^1Fe^{II}(H_2O_2)]^{2+}\cdot H_2O$, and the caged radical, $[L^1Fe^{III}(OH)]^{2+}\cdot H_2O\cdot OH$, on the $S = 2$ surface. The O–O bond is significantly elongated at the transition structure (1.75 Å vs. 1.46 Å in the reactants), and the imaginary frequency is clearly associated with the O–O stretching mode. The Fe–O separation is also significantly reduced compared to the reactants, due to the partial oxidation of the metal centre. We have also located transition states (**TS2**) linking the radical intermediates with the $[L^1Fe^{IV}(O)]^{2+}\cdot 2H_2O$ asymptote on both quintet and triplet surfaces. At this point, the $O_p$–$H_p$ distance is significantly elongated while the separation between this hydrogen atom and the OH radical is much reduced, and the imaginary frequency corresponds to an $O_p$–$H_p$ stretch. The net effect is that the solvent water molecule acts as a hydrogen atom shuttle, mediating the abstraction of a hydrogen atom from the coordinated OH ligand by the OH radical. The energy of **TS2** is highly dependent on the spin state – the triplet lies significantly *below* the quintet, reflecting its product-like nature. The shape of the potential energy surfaces also dictates that the crossover between the quintet and triplet surfaces must occur at some point between the radical intermediate ($S = 2$) and **TS2** ($S = 1$). We have located the minimum energy crossing point (MECP1) between these surfaces, and the structural changes leading up to this point are largely associated with the metal–ligand bonds, all of which contract significantly from the intermediate to the MECP. The separation between the metal fragment and the OH radical is, in contrast, essentially unchanged. We therefore conclude that the crossover from the quintet to triplet surfaces involves a localised $S = 5/2 \rightarrow S = 1/2$ transition on the $Fe^{III}$ centre, and the nature of the interaction between the metal centre and the OH radical remains unchanged. In the gas phase, the MECP lies 46 kJ mol$^{-1}$ above the $S = 2$ intermediate, but this is reduced to 31 kJ mol$^{-1}$ when solvation is included, as a result of the contracted metal–ligand bonds in the former. It is important to emphasise, however, that the effects of solvation are only included post-optimisation. We have noted previously that solvation stabilises low-spin states, and indeed the $S = 1$ and $S = 2$ caged radical species are almost isoenergetic when solvation effects are included. If the energies of these two states were, in fact, reversed, then the $S = 2 \rightarrow S = 1$ spin crossover would occur before, rather than just after, the radical intermediate. Given the intrinsic uncertainties in determining accurate spin-state energies with DFT and the approximate nature of the PCM solvation model, we are unable to reach a definitive conclusion on this point. It will not, however, have a major impact on the potential energy surface: the nature of the crossover – viz. a localised high-spin/low-spin transition on the $Fe^{III}$ centre – remains unchanged.

To summarise, the early part of the reaction coordinate shown in Figure 2 lies along the quintet surface, and involves homolysis of the O–O bond. The resulting intermediate contains an $[L^1Fe^{III}(OH)]^{2+}$ species, weakly coupled to an OH radical, the whole unit being held together by electrostatic interactions with the dicationic metal core and hydrogen bonding within the solvent cage. A localised high-spin/low-spin transition on the $Fe^{III}$ centre then causes a crossover to the triplet surface, after which the OH radical abstracts a hydrogen atom from the coordinated OH ligand. Whilst the initial O–O bond homolysis step was marginally endothermic, the hydrogen atom abstraction step is highly exothermic, and the $[L^1Fe^{IV}(O)]^{2+}$ product is 101 kJ mol$^{-1}$ more stable than the reactants. In comparison, a value of 117 kJ mol$^{-1}$ was reported for the aqua complex.[16] Thus, the major difference between the two pathways lies not in the overall exothermicity of the decomposition of the $H_2O_2$ complex, but rather in the details of the intervening potential energy surface. In the aqua complex, the O–O homolysis and hydrogen atom abstraction steps are concerted, while in the case of $[L^1Fe^{II}(H_2O_2)]^{2+}$, the absence of an additional water ligand effectively separates the two processes, leading to an identifiable $Fe^{III}(OH)$ intermediate. The rate-determining step in this reaction clearly depends on the relative energies of the two transition states, **TS1** and **TS2** shown in Figure 2. In the gas phase, **TS2** (79 kJ mol$^{-1}$) lies substantially above **TS1** (40 kJ mol$^{-1}$), suggesting that the OH "rebound" step should be rate-determining. In these circumstances, diffusion of the OH radical into solution should be competitive with formation of the $Fe^{IV}(O)$ species. However, when solvation is included, **TS2** is strongly stabilised relative to **TS1** because the latter contains the smaller low-spin $Fe^{III}$ centre, and the two barriers are now rather similar (34 and 44 kJ mol$^{-1}$, respectively). We return to a discussion of this point in the concluding remarks.

 © 2007 Wiley-VCH Verlag GmbH & Co. KGaA, Weinheim 

### O–O Bond Heterolysis Pathway

In the previous section we identified a pathway linking the two asymptotes, $[L^1Fe^{II}(H_2O_2)]^{2+}\cdot H_2O$ and $[L^1Fe^{IV}(O)]^{2+}\cdot 2H_2O$, via an intermediate containing a weakly trapped OH radical. Comba, Que and co-workers have proposed an alternative pathway involving proton (as distinct from hydrogen atom) transfer, followed by O–O heterolysis, to account for the observed decomposition of $[L^2Fe^{II}(H_2O_2)]^{2+}$.[6c] We have considered this possibility, and identified a further transition state, **TS3**, that directly links the reactants and products for each of the three spin states ($S$ = 0, 1, 2). The structure of the most stable transition state ($S$ = 2) is shown in Figure 3, and key bond lengths for all three are collected in Table 2. The most remarkable feature of the transition structures is the near-identical geometry of the $H_2O_2\cdot H_2O$ unit in each case. The proton initially attached to the proximal oxygen atom of the hydrogen peroxide has been almost completely transferred to the water molecule ($O_p\cdots H_p$ = 1.72–1.74 Å, $H_p$–$O_w$ = 1.02 Å), suggesting that the reaction coordinate leading up to the transition state is a simple proton transfer. The Fe–O bond lengths contract somewhat as a result of the removal of the proximal proton (by 0.24 Å for $S$ = 2), but the equatorial and axial Fe–N distances remain largely unchanged. The marginal elongation of the O–O bond (1.52–1.54 Å, c.f. 1.45–1.46 in the equilibrium structures) also confirms that O–O bond cleavage is not well advanced at the transition state. The imaginary frequency in each spin state corresponds to the transfer of the proton from $H_3O^+$ to the terminal oxygen atom of the hydrogen peroxide, and a small displacement along this mode results in decomposition to the hydrated $[L^1Fe^{IV}(O)]^{2+}\cdot 2H_2O$ species, with no further barrier. Given that the motion along the reaction coordinate prior to the transition state is almost entirely centred on the $H_2O_2\cdot H_2O$ unit, it is unsurprising that the barriers, measured relative to the reactant, are essentially independent of the spin state of the iron centre (87–89 kJ mol$^{-1}$, Figure 3). The lowest energy pathway therefore lies along the quintet surface until well after the transition state. Intersystem crossing between the $S$ = 2 and $S$ = 1 surfaces must again occur at some later stage on the reaction coordinate, and will correspond to a localised high-spin/low-spin transition on the developing $Fe^{IV}(O)$ unit. In summary, although the proton-transfer mechanism leading to O–O bond cleavage is concerted and does not involve any stable intermediates, it is also highly asynchronous. The reaction coordinate prior to the transition state involves deprotonation of the hydrogen peroxide ligand at the proximal oxygen atom, while afterwards transfer of the proton to the terminal oxygen leads to spontaneous cleavage of the O–O bond. This mechanism is qualitatively similar to that proposed by Que and Comba for the decomposition of $[L^2Fe^{IV}(H_2O_2)]^{2+}$, with the subtle difference that it is the proton transfer, rather than the O–O bond heterolysis, that determines the magnitude of the barrier.

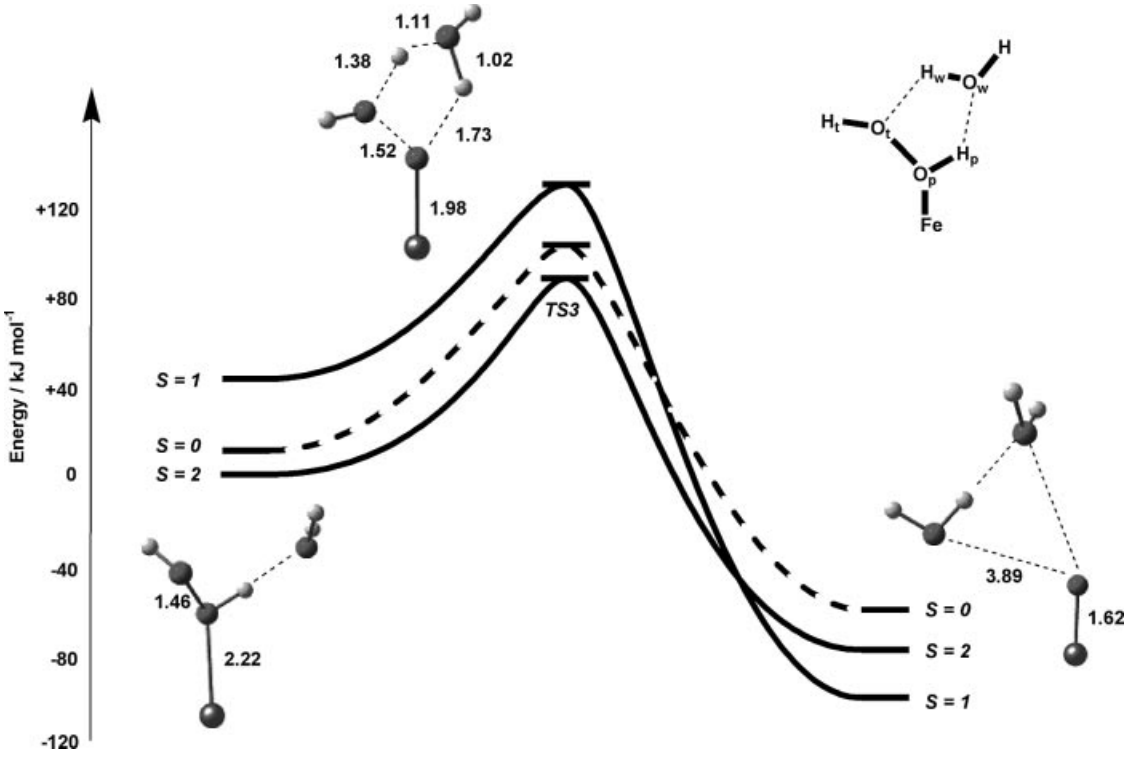


Figure 3. Potential energy surface for the O–O bond heterolysis mechanism for decomposition of $[L^1Fe^{II}(H_2O_2)]^{2+}\cdot H_2O$. Energies include the effects of solvation introduced by the PCM model.

 © 2007 Wiley-VCH Verlag GmbH & Co. KGaA, Weinheim 

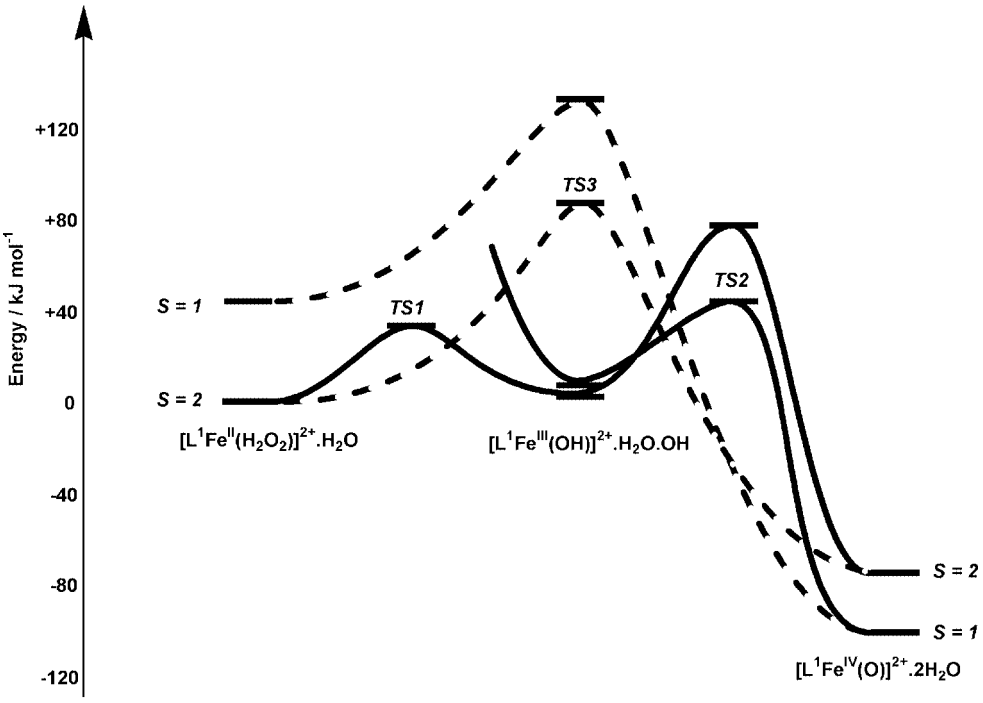


Figure 4. Comparison of the key features of the potential energy surface homolytic and heterolytic (dashed) O–O bond cleavage in $[L^1Fe^{II}(H_2O_2)]^{2+}\cdot H_2O$.

## Conclusions

The key features of the two possible pathways for O–O bond cleavage are compared in Figure 4. Returning to the question of radical (Haber–Weiss) vs. non-radical (Bray–Gorin) mechanisms, we can identify three quite distinct scenarios, depending on the relative energies of the three transition states **TS1**, **TS2** and **TS3**. If **TS3** < **TS1**, the concerted mechanism will dominate, and any $Fe^{III}$ product must be generated by comproportionation of the initially formed $Fe^{IV}(O)$ with excess $Fe^{II}$. If, in contrast, **TS3** > **TS1**, then the homolytic pathway will dominate, and this in turn can lead to two distinct outcomes depending on the energies of **TS1** and **TS2**. If **TS1** > **TS2**, rebound of the transient OH radical will be rapid, leading again to formation of $Fe^{IV}(O)$, but in this case via transient $Fe^{III}(OH)$. In contrast, if **TS2** > **TS1**, the products of the reaction will depend critically on the rate of the rebound step (**TS2**) relative to the rate of diffusion through the solvent. If the latter is rapid, then the OH radicals are likely to escape and oxidise the ligand, solvent or any other accessible substrate. The presence of three distinct scenarios offers a possible explanation for the very complex nature of Fenton chemistry, and in particular for the apparent generation of radicals in some cases but not others.[11] It also provides a framework for understanding the way in which changes in ligand can perturb the reaction pathway.

## Calculation Details

In all cases, the bispidone ligand was simplified by replacing the ester groups with hydrogen atoms. All calculations described in this paper were performed using the Gaussian03 package.[24] The B3LYP[25b,25c] functional was used throughout, in conjunction with the 6-31G* basis set on all atoms. Full geometry optimisations were performed without symmetry constraints, and stationary points were characterised as minima or transition states by vibrational analysis. Minimum energy crossing points (MECPs) were located using the code developed by Harvey and co-workers.[26] Solvation energies were calculated by Tomasi's reaction field method using the polarized continuum model (PCM) with a dielectric constant ($\varepsilon$) of 78.39.

## Acknowledgments

A. A. acknowledges financial support from the EPSRC and Unilever Research.

[1] a) E. I. Solomon, *Inorg. Chem.* **2001**, *40*, 3656; b) E. I. Solomon, T. C. Brunold, M. I. Davis, J. N. Kemsley, S.-K. Lee, N. Lehnert, F. Neese, A. J. Skulan, Y.-S. Yang, J. Zhou, *Chem. Rev.* **2000**, *100*, 235.

[2] a) N. Lehnert, F. Neese, R. Y. N. Ho, L. Que Jr, E. I. Solomon, *J. Am. Chem. Soc.* **2002**, *124*, 10810; b) F. Neese, J. M. Zaleski, K. Loeb Zaleski, E. I. Solomon, *J. Am. Chem. Soc.* **2000**, *122*, 11703.

[3] P. J. Riggs-Gelasco, J. C. Price, R. B. Guyer, J. J. Brehm, E. W. Barr, J. M. Bollinger Jr, C. Krebs, *J. Am. Chem. Soc.* **2004**, *126*, 8108.

[4] a) M. Lubben, A. Meetsma, E. C. Wilkinson, B. L. Feringa, L. Que Jr, *Angew. Chem. Int. Ed. Engl.* **1995**, *34*, 1512; b) G. Roelfes, M. Lubben, K. Chen, R. Y. N. Ho, A. Meetsma, S. Genseberger, R. H. Hermant, R. Hage, S. K. Mandal, V. G. Young Jr, Y. Zang, H. Kooijman, A. L. Spek, L. Que Jr, B. L. Feringa, *Inorg. Chem.* **1999**, *38*, 1929; c) R. Y. N. Ho, G. Roelfes, B. L. Feringa, L. Que Jr, *J. Am. Chem. Soc.* **1994**, *116*, 264; d) G. Roelfes, M. Lubben, R. Hage, L. Que Jr, B. L. Feringa, *Chem. Eur. J.* **2000**, *6*, 2152.

 © 2007 Wiley-VCH Verlag GmbH & Co. KGaA, Weinheim 

[5] a) I. Bernal, I. M. Jensen, K. B. Jensen, C. J. McKenzie, H. Toftlund, J. P. Tuchagues, *J. Chem. Soc., Dalton Trans.* **1995**, 3667; b) V. Balland, F. Banse, E. Anxolabehere-Mallart, M. Ghiladi, T. A. Mattioli, C. Pilouze, G. Blondin, J.-J. Girerd, *Inorg. Chem.* **2003**, *42*, 2470; c) P. Mialane, A. Novorojkine, G. Pratviel, L. Azema, M. Slany, F. Godde, A. J. Simaan, F. Banse, T. Kargar-Grisel, G. Bouchoux, J. Saiton, O. Horner, J. Guilheim, L. Tchertanov, B. Meunier, J.-J. Girerd, *Inorg. Chem.* **1999**, *38*, 1085.

[6] a) M. R. Bukowksi, P. Comba, C. Limberg, M. Merz, L. Que Jr, T. Wistuba, *Angew. Chem. Int. Ed.* **2004**, *43*, 1283; b) M. R. Bukowski, P. Comba, A. Lienke, C. Limberg, C. Lopez de Laorden, R. Mas-Balleste, M. Merz, L. Que Jr, *Angew. Chem. Int. Ed.* **2006**, *45*, 3446; c) J. Bautz, M. R. Bukowski, M. Kerscher, A. Stubna, P. Comba, A. Lienke, E. Muenck, L Que Jr, *Angew. Chem*., in press; d) J. Bautz, P. Comba, L. Que Jr, *Inorg. Chem*., accepted.

[7] R. Hage, A. Lienke, *Angew. Chem. Int. Ed.* **2006**, *45*, 2006.

[8] A. Hazel, C. J. McKenzie, L. P. Nielsen, S. Schindler, M. Weitzer, *J. Chem. Soc., Dalton Trans.* **2002**, 310.

[9] a) N. Lehnert, R. Y. N. Ho, L. Que Jr, E. I. Solomon, *J. Am. Chem. Soc.* **2001**, *123*, 12802; b) A. Decker, M. S. Chow, J. N. Kemsley, N. Lehnert, E. I. Solomon, *J. Am. Chem. Soc.* **2006**, *128*, 4719.

[10] H. J. H. Fenton, *J. Chem. Soc.* **1894**, *65*, 889.

[11] a) D. T. Sawyer, A. Sobkowiak, T. Matsushita, *Acc. Chem. Res.* **1996**, *29*, 409; b) C. Walling, *Acc. Chem. Res.* **1998**, *31*, 155; c) P. H. MacFaul, D. D. M. Wayner, K. W. Ingold, *Acc. Chem. Res.* **1998**, *31*, 159; d) S. Goldstein, D. Meyerstein, *Acc. Chem. Res.* **1999**, *32*, 547.

[12] F. Haber, J. Weiss, *Proc. R. Soc. London* **1934**, *147*, 332.

[13] W. G. Barb, J. H. Baxendale, P. George, K. R. Hargrave, *Trans. Faraday Soc.* **1951**, *47*, 462.

[14] W. C. Bray, M. H. Gorin, *J. Am. Chem. Soc.* **1932**, *54*, 2124.

[15] M. L. Kremer, *Phys. Chem. Chem. Phys.* **1999**, *1*, 3595.

[16] F. Buda, B. Ensing, M. C. M. Gribnau, E. J. Baerends, *Chem. Eur. J.* **2001**, *7*, 2775.

[17] B. Ensing, F. Buda, P. Blöchl, E. J. Baerends, *Angew. Chem. Int. Ed.* **2001**, *113*, 2977.

[18] M. Masarwa, H. Cohen, D. Meyerstein, D. L. Hickman, A. Bakac, J. H. Espenson, *J. Am. Chem. Soc.* **1988**, *110*, 4293.

[19] a) O. Pestovsky, S. Stoian, E. L. Bominaar, X. Shan, E. Münck, L. Que Jr, A. Bakac, *Angew. Chem. Int. Ed.* **2005**, *44*, 6871; b) O. Pestovsky, A. Bakac, *J. Am. Chem. Soc.* **2004**, *126*, 15757.

[20] H. Keutel, I. Kapplinger, E.-G. Jager, M. Grodzicki, V. Schunemann, A. X. Trautwein, *Inorg. Chem.* **1999**, *38*, 2320.

[21] a) A. Ghosh, E. Tangen, H. Ryeng, P. R. Taylor, *Eur. J. Inorg. Chem.* **2004**, 4555; b) A. Ghosh, P. R. Taylor, *Curr. Opin. Chem. Biol.* **2003**, *7*, 113.

[22] Y. Mekmouche, S. Menage, C. Toia-Duboc, M. Fontecave, J.-B. Galey, C. Lebrun, J. Pecaut, *Angew. Chem. Int. Ed.* **2001**, *40*, 949.

[23] X. Fang, M.-H. Baik, *J. Am. Chem. Soc.* **2006**, *128*, 7476.

[24] M. J. Frisch, G. W. Trucks, H. B. Schlegel, G. E. Scuseria, M. A. Robb, J. R. Cheeseman, J. A. Montgomery Jr, T. Vreven, K. N. Kudin, J. C. Burant, J. M. Millam, S. S. Iyengar, J. Tomasi, V. Barone, B. Mennucci, M. Cossi, G. Scalmani, N. Rega, G. A. Petersson, H. Nakatsuji, M. Hada, M. Ehara, K. Toyota, R. Fukuda, J. Hasegawa, M. Ishida, T. Nakajima, Y. Honda, O. Kitao, H. Nakai, M. Klene, X. Li, J. E. Knox, H. P. Hratchian, J. B. Cross, C. Adamo, J. Jaramillo, R. Gomperts, R. E. Stratmann, O. Yazyev, A. J. Austin, R. Cammi, C. Pomelli, J. W. Ochterski, P. Y. Ayala, K. Morokuma, G. A. Voth, P. Salvador, J. J. Dannenberg, V. G. Zakrzewski, S. Dapprich, A. D. Daniels, M. C. Strain, O. Farkas, D. K. Malick, A. D. Rabuck, K. Raghavachari, J. B. Foresman, J. V. Ortiz, Q. Cui, A. G. Baboul, S. Clifford, J. Cioslowski, B. B. Stefanov, G. Liu, A. Liashenko, P. Piskorz, I. Komaromi, R. L. Martin, D. J. Fox, T. Keith, M. A. Al-Laham, C. Y. Peng, A. Nanayakkara, M. Challacombe, P. M. W. Gill, B. Johnson, W. Chen, M. W. Wong, C. Gonzalez, J. A. Pople, *Gaussian 03*, Revision B.03, Gaussian, Inc., Pittsburgh, PA, **2003**.

[25] a) A. D. Becke, *Phys. Rev. A* **1988**, *38*, 3098; b) A. D. Becke, *J. Chem. Phys.* **1993**, *98*, 1372; c) A. D. Becke, *J. Chem. Phys.* **1993**, *98*, 5648; d) S. H. Vosko, L. Wilk, M. Nusair, *Can. J. Phys.* **1980**, *58*, 1200; e) C. Lee, W. Yang, R. G. Parr, *Phys. Rev. B* **1988**, *37*, 785; f) A. D. Becke, *J. Chem. Phys.* **1986**, *84*, 4524; g) J. P. Perdew, *Phys. Rev. B* **1986**, *33*, 8822.

[26] a) J. N. Harvey, M. Aschi, H. Schwarz, W. Koch, *Theor. Chem. Acc.* **1998**, *99*, 95; b) J. N. Harvey, M. Aschi, *Phys. Chem. Chem. Phys.* **1999**, *1*, 5555.

Received: August 25, 2006
Published Online: November 17, 2006

 © 2007 Wiley-VCH Verlag GmbH & Co. KGaA, Weinheim 

DOI: 10.1002/ejic.200600631

# Synthesis and Structure of $[n\mathrm{Pr_3N(CH_2)_6N}n\mathrm{Pr_3}][\mathrm{CuFe_3Br_3(SePh)_6}]$, $[\mathrm{Cu_5Fe(SePh)_7(PPh_3)_4}]$ and $[\mathrm{Cu_4Fe_3(SePh)_{10}(PPh_3)_4}]$

**Andreas Eichhöfer,*[a] Dieter Fenske,[a,b] and Jolanta Olkowska-Oetzel[a]**

*Dedicated to Michael Binnewies on the occasion of his 60th birthday*

**Keywords:** Iron / Copper / Selenium / Cluster compounds

CuBr and $Fe(OOCCH_3)_2$ react with $PhSeSiMe_3$ in acetonitrile in the presence of the diammonium salt $[n\mathrm{Pr_3N(CH_2)_6N}n\mathrm{Pr_3}]\mathrm{Br_2}$ to yield ionic $[n\mathrm{Pr_3N(CH_2)_6N}n\mathrm{Pr_3}][\mathrm{CuFe_3Br_3(SePh)_6}]$. The neutral complexes $[\mathrm{Cu_5Fe(SePh)_7(PPh_3)_4}]$ and $[\mathrm{Cu_4Fe_3(SePh)_{10}(PPh_3)_4}]$ were obtained by similar reactions of different stoichiometric mixtures of $CuOOCCH_3$ and $FeCl_2$ with $PPh_3$ and $PhSeSiMe_3$. The crystal structures of the compounds were determined by single-crystal X-ray analysis to give new structural types of molecular cluster compounds formed by copper, iron and selenium. Thermal treatment of $[\mathrm{Cu_5Fe(SePh)_7(PPh_3)_4}]$ and $[\mathrm{Cu_4Fe_3(SePh)_{10}(PPh_3)_4}]$ results in the formation of mixtures of binary $Cu_2Se$ and ternary $CuFeSe_2$.

(© Wiley-VCH Verlag GmbH & Co. KGaA, 69451 Weinheim, Germany, 2007)

## Introduction

The synthesis of ternary cluster molecules has attracted interest recently. Examples of different compounds include $(PPh_4)[Cu_6In_3(SEt)_{16}]$,[1] $[M^I{}_6M^{III}{}_8Cl_4E_{13}(PPh_3)_6]$ ($M^I$ = Cu, Ag; $M^{III}$ = Ga, In; E = S, Se),[2] $[Cu_{11}In_{15}Se_{16}(SePh)_{24}(PPh_3)_4]$,[3] $[Ag_{26}In_{18}S_{36}Cl_6(dppm)_{10}(thf)_4][InCl_4(thf)]_2$,[4] $[Hg_{15}Cu_{20}S_{25}(Pn\mathrm{Pr_3})_{18}]$,[5,6] $[Cu_4Nb_2Se_6(PMe_3)_8]$,[7] $[Ta_4Cu_{12}Cl_8S_{12}(PMe_3)_{12}]$,[8] $[(N,N'\text{-tmeda})_5Zn_5Cd_{11}Se_{13}(SePh)_6(thf)_2]$,[9] and $[(py)_8Ln_4M_2Se_6(SePh)_4]$ (Ln = Er, Yb, Lu; M = Cd, Hg).[10] Interest in these compounds lies in the characterization of their structures and an investigation of their properties. In this context, Kanatzidis et al. have studied the suitability of mixed copper/indium chalcogenolates as precursor materials for the photovoltaic materials $CuInE_2$ (E = S, Se).[1,11] Corrigan et al. have observed room-temperature fluorescence for the ternary 12-12′-16 cluster (12 = Zn; 12′ = Cd; 16 = Se) $[(N,N'\text{-tmeda})_5Zn_5Cd_{11}Se_{13}(SePh)_6(thf)_2]$,[9] while binary cadmium or zinc selenide clusters show weak luminescence only at temperatures below 50 K.[12,13] Strong infrared fluorescence behavior has been observed to occur in the heterometallic chalcogenido cluster molecules $[(py)_8Ln_4M_2Se_6(SePh)_4]$ (Ln = Er; M = Cd, Hg).[10]

The ternary phase $CuFeS_2$ has been known to be a semiconductor material for a long time and was one of the first compounds to be used for the construction of radio frequency detectors,[14] while information about $CuFeSe_2$ is limited and only a few papers have been devoted to this compound during the last five years.[15] Until now only a limited number of cluster compounds have been synthesized that contain copper, iron and sulfur or selenium; these include $[Fe_3Cu(Si\mathrm{Pr})_6Cl_3]^{2-}$,[16] $[Fe_3Cu(Se\mathrm{Pr})_6Cl_3]^{2-}$, and $[Fe_2Cu_4(Si\mathrm{Pr})_8Cl_3]^{2-}$.[17] Here we report the synthesis and characterization of three new compounds of this type, namely $[n\mathrm{Pr_3N(CH_2)_6N}n\mathrm{Pr_3}][\mathrm{CuFe_3Br_3(SePh)_6}]$, $[\mathrm{Cu_5Fe(SePh)_7(PPh_3)_4}]$ and $[\mathrm{Cu_4Fe_3(SePh)_{10}(PPh_3)_4}]$.

## Results and Discussion

### Synthesis

Reaction of a 1:3 mixture of CuBr and $Fe(OOCCH_3)_2$ with $PhSeSiMe_3$ in acetonitrile in the presence of the diammonium salt $[n\mathrm{Pr_3N(CH_2)_6N}n\mathrm{Pr_3}]\mathrm{Br_2}$ yielded, after layering with diethyl ether, dark red-orange crystals of **1** after a few days (Scheme 1).

The use of the neutral ligand $PPh_3$ instead of the diammonium salt $[n\mathrm{Pr_3N(CH_2)_6N}n\mathrm{Pr_3}]\mathrm{Br_2}$ in reactions of $CuOOCCH_3$ and $FeCl_2$ with $PhSeSiMe_3$ led to the formation of dark-red solutions from which red crystals of **2** (Scheme 2) grew over the course of several days.

A similar reaction with a 1:0.8 ratio of $CuOOCCH_3$ and $FeCl_2$ yielded red-orange crystals of **3** (Scheme 3).

[a] Institut für Nanotechnologie, Forschungszentrum Karlsruhe, Postfach 3640, 76021 Karlsruhe, Germany
Fax: +49-7247-82-6368
E-mail: eichhoefer@int.fzk.de
[b] Institut für Anorganische Chemie der Universität, Engesserstrasse, Geb. 30.45, 76128 Karlsruhe, Germany


InterScience
© 2007 Wiley-VCH Verlag GmbH & Co. KGaA, Weinheim

$$CuBr_2 + 3Fe(OOCCH_3)_2 + [nPr_3N(CH_2)_6NnPr_3]Br_2 \xrightarrow[CH_3CN/Et_2O]{+\ 6\ PhSeSiMe_3} (nPr_3N(CH_2)_6NnPr_3)[CuFe_3Br_3(SePh)_6]\ (\mathbf{1})$$

Scheme 1.

$$CuOOCCH_3 + 0.2\ FeCl_2 + 1.5\ PPh_3 \xrightarrow[DME]{+\ 1.6\ PhSeSiMe_3} [Cu_5Fe(SePh)_7(PPh_3)_4]\ (\mathbf{2})$$

Scheme 2.

$$CuOOCCH_3 + 0.8\ FeCl_2 + 4\ PPh_3 \xrightarrow[dme]{+\ 3\ PhSeSiMe_3} [Cu_4Fe_3(SePh)_{10}(PPh_3)_4]\ (\mathbf{3})$$

Scheme 3.

## Crystal Structures

Ionic **1** crystallizes in the trigonal space group $P\bar{3}$ with three crystallographically independent $[CuFe_3Br_3(SePh)_6]^{2-}$ cluster anions, two of which reside on a threefold and one on a $\bar{3}$ axis (see Experimental Section for further details). Because the structures of the cluster cores, including bond lengths and angles, are quite similar for all three, only one of them is discussed in the following. The cluster anion $[CuFe_3Br_3(SePh)_6]^{2-}$ (Figure 1) consists of a six-membered $Fe_3(SePh)_3$ ring in a chair conformation that is capped by a nearly trigonal-planar $Cu(SePh)_3$ unit [Cu, Se(1), Se(1′), Se(1′′); Se–Cu–Se = 119.96(1)°]. A threefold axis runs through the copper atom and the center of the hexanuclear ring, and the copper atom is slightly shifted by 4.7 pm from the triangular selenium face towards the iron atoms (mean Cu–Fe distance of 339.2 pm). Each of the iron atoms is additionally coordinated by a terminal bromido ligand to give a distorted tetrahedral coordination environment for the iron atoms [Fe–Br = 241.7(2) pm]. The metal–selenium distances are found to be longer for iron [246.7–246.8(2) pm] than for copper [234.2–234.3(1) pm], which is most probably a result of the different coordination modes. This adamantoid cluster core in **1** is therefore similar to the structures of $[CuFe_3Cl_3(EiPr)_6]^{2-}$ (E = Se, S), which have been crystallized previously with singly charged ammonium cations.[16,17]

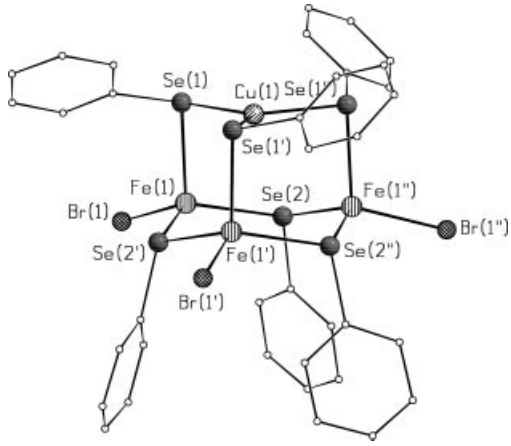


Figure 1. Molecular structure of the cluster anion $[CuFe_3Br_3(SePh)_6]^{2-}$ in $[nPr_3N(CH_2)_6NnPr_3][CuFe_3Br_3(SePh)_6]$ (**1**). C and H atoms omitted for clarity. Selected bond lengths [pm] and angles [°]: Se(1)–Cu(1) 234.2(1), Se(1)–Fe(1) 247.3(2), Se(2)–Fe(1) 246.7(2), Se(2)–Fe(1′) 246.8(2), Cu(1)–Se(1′′) 234.3(1), Cu(1)–Se(1′) 234.3(9), Br(1)–Fe(1) 241.7(2), Fe(1)–Se(2′′) 246.8(2); Fe(1)–Se(2)–Fe(1′) 112.64(6), Se(1)–Cu(1)–Se(1′′) 119.96(1), Se(1)–Cu(1)–Se(1′) 119.96(1), Se(1′′)–Cu(1)–Se(1′) 119.96(1), Br(1)–Fe(1)–Se(2) 109.71(6), Br(1)–Fe(1)–Se(2′′) 115.11(6), Se(2)–Fe(1)–Se(2′′) 118.86(6), Br(1)–Fe(1)–Se(1) 108.00(6), Se(2)–Fe(1)–Se(1) 103.55(6), Se(2′′)–Fe(1)–Se(1) 99.87(6). Symmetry transformations for the generation of equivalent atoms: ′: $1 - y, x - y, z$; ′′: $-x + y + 1, -x + 1, z$.

Cluster **2** crystallizes in the monoclinic space group $P2_1/c$ (Figure 2). The structure comprises a central $Cu_3Fe$ trigonal pyramid formed by Cu(1), Cu(2), Cu(3), and Fe(1) [Cu···Cu = 430.1–451.4(1); Cu···Fe = 403.0–417.2(1) pm] with the six edges bridged by $SePh^-$ ligands [Se(1)–Se(6); Cu–Se = 244.4–270.9(1); Fe(1)–Se = 242.9–249.5(1) pm]. One additional copper atom [Cu(4)] is bonded to this adamantoid cluster cage through the three selenium atoms of the basal six-membered ring [Se(1)–Se(3); Cu–Se = 242.0–249.0(1) pm], which displays only a weak chair conformation [maximum deviation of 66.5 pm for Se(3) from the trigonal plane formed by Cu(1)–Cu(3)]. The coordination environment of Cu(4) is trigonal-planar [sum of Se–Cu(4)–Se angles is 360°]. The copper atoms Cu(1)–Cu(3) which form the basal plane of the $Cu_3Fe$ pyramid are each additionally coordinated by a terminal $PPh_3$ ligand to result in an overall distorted tetrahedral coordination environment for these atoms. Fe(1), at the apex of the $Cu_3Fe$ pyramid, is additionally coordinated by another $SePh^-$ ligand [Se(7)], and a further $CuPPh_3$ unit is attached through this and two other $SePh^-$ ligands [Se(5), Se(6), Se(7)] to the adamantoid cluster cage.

Compound **3** crystallizes in the monoclinic space group $P2_1/c$ (Figure 3). Similar to **1**, the structure contains a central $CuFe_3$ trigonal pyramid formed by Fe(1), Fe(2), Fe(3), and Cu(4) [Fe···Cu = 393.1–420.5(2); Fe···Fe = 402.1–410.2 pm]. Thus, three iron atoms define the vertices of the basal triangular plane, which is bridged by a $\mu_3$-$SePh^-$ ligand [Fe–Se(10) = 250.1–251.2(2) pm], while the apex of the pyramid is occupied by a $CuPPh_3$ unit [Cu(4)–P(4) =

 © 2007 Wiley-VCH Verlag GmbH & Co. KGaA, Weinheim 

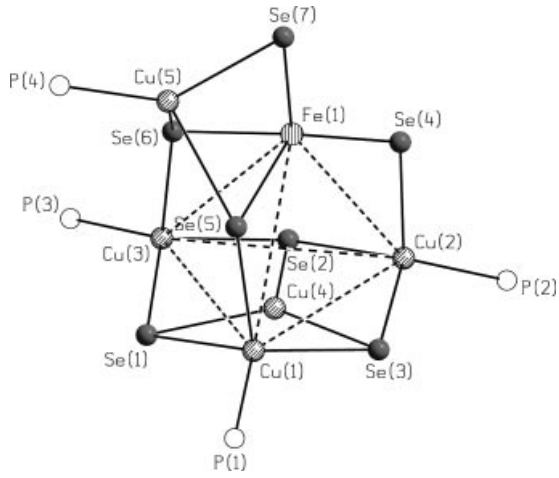


Figure 2. Molecular structure of $[Cu_5Fe(SePh)_7(PPh_3)_4]$ (**2**). C and H atoms omitted for clarity. Selected bond lengths [pm]: Fe(1)–Se(4) 2.4294(12), Fe(1)–Se(7) 247.7(1), Fe(1)–Se(5) 248.9(1), Fe(1)–Se(6) 249.5(1), Se(1)–Cu(4) 249.0(1), Se(1)–Cu(3) 249.5(1), Se(1)–Cu(1) 256.3(1), Se(2)–Cu(4) 243.7(1), Se(2)–Cu(2) 249.5(1), Se(2)–Cu(3) 254.1(1), Se(3)–Cu(4) 242.0(1), Se(3)–Cu(1) 252.1(1), Se(3)–Cu(2) 270.8(1), Se(4)–Cu(2) 244.4(1), Se(5)–Cu(1) 247.8(1), Se(5)–Cu(5) 261.5(1), Se(6)–Cu(3) 254.3(1), Se(6)–Cu(5) 258.0(1), Se(7)–Cu(5) 244.4(1), Cu(1)–P(1) 223.7(2), Cu(2)–P(2) 226.4(2), Cu(3)–P(3) 225.4(2), Cu(5)–P(4) 221.1(2); nonbonding metal–metal distances: Cu(1)–Cu(4) 254.6(1), Cu(2)–Cu(4) 263.6(1), Cu(3)–Cu(4) 261.4(1), Cu(5)–Fe(1) 266.2(1) (not drawn), Cu(1)–Cu(2) 451.4, Cu(1)–Cu(3) 430.1, Cu(2)–Cu(3) 442.0, Cu(1)–Fe(1) 403.7, Cu(2)–Fe(1) 403.0, Fe(1)–Cu(3) 417.2 (dashed lines).

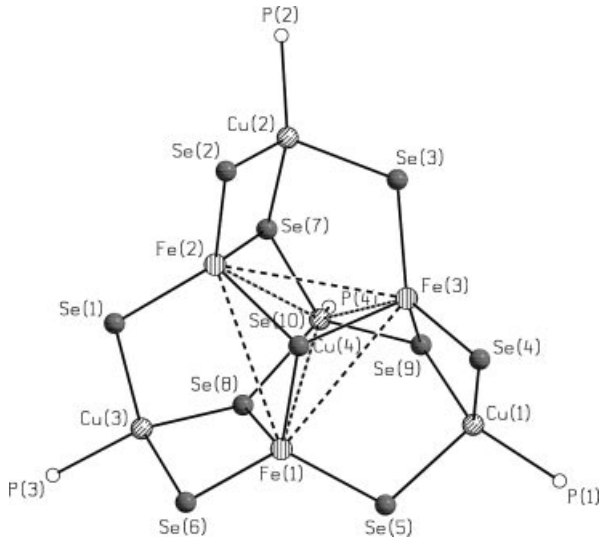


Figure 3. Molecular structure of $[Cu_4Fe_3(SePh)_{10}(PPh_3)_4]$ (**3**). C and H atoms omitted for clarity. Selected bond lengths [pm]: Se(7)–Fe(2) 249.4(2), Se(7)–Cu(4), 251.6(2) Se(7)–Cu(2) 252.1(2), Se(8)–Cu(4) 246.9(2), Se(8)–Fe(1) 247.3(2), Se(8)–Cu(3) 250.6(2), Se(9)–Cu(4) 246.9(2), Se(9)–Fe(3) 247.4(2), Se(9)–Cu(1) 256.9(2), Se(10)–Fe(2) 250.1(2), Se(10)–Fe(1) 250.9(2), Se(10)–Fe(3) 251.2(2), Se(1)–Fe(2) 244.8(2), Se(1)–Cu(3) 247.5(2), Se(2)–Fe(2) 245.5(2), Se(2)–Cu(2) 248.7(2), Se(3)–Fe(3) 246.6(2), Se(3)–Cu(2) 250.6(2), Se(4)–Fe(3) 244.1(2), Se(4)–Cu(1) 247.4(2), Se(5)–Fe(1) 244.0(2), Se(5)–Cu(1) 245.6(2), Se(6)–Fe(1) 243.1(2), Se(6)–Cu(3) 250.3(2), Cu(1)–P(1) 226.1(3), Cu(2)–P(2) 224.7(3), Cu(3)–P(3) 226.1(3), Cu(4)–P(4) 223.7(3); shortest nonbonding metal–metal distances: Cu(1)–Fe(3) 301.6(2), Cu(2)–Fe(2) 306.4(2), Cu(3)–Fe(1) 304.5(2) (not drawn), Cu(4)–Fe(1) 397.1(2), Cu(4)–Fe(2) 420.5(2), Cu(4)–Fe(3) 393.0(2), Fe(1)–Fe(2) 409.7(2), Fe(1)–Fe(3) 410.2(2), Fe(2)–Fe(3) 402.0(2) (dashed lines).

223.7(3) pm]. The other faces of the pyramid are capped by three distorted tetrahedral $PPh_3Cu(SePh)_3$ units in such a way that six $SePh^-$ ligands [Se(1)–Se(6)] adopt a $\mu_2$- and three [Se(8)–Se(9)] a $\mu_3$-bridging mode, which results in an overall distorted tetrahedral coordination of the metal atoms. All copper atoms are surrounded by two $\mu_2$-$SePh^-$ moieties [mean Cu–Se distance of 248.4(2) pm], one $\mu_3$-$SePh^-$ [mean Cu–Se distance of 250.8(2) pm], and a terminal $PPh_3$ ligand [mean Cu–P distance of 252.2(3) pm]. The iron atoms are four-coordinated by two $\mu_2$-$SePh^-$ [mean Fe–Se distance of 244.7(2) pm] and two $\mu_3$-$SePh^-$ ligands [mean Fe–Se distance of 249.5(2) pm]. Obviously, the core of the cluster complex comprises a pseudo-threefold axis running through Se(10), Cu(4), and P(4); however, the organic ligands do not have this symmetry.

### Optical Spectra

The UV/Vis spectra of **1**–**3** measured as a mull in nujol between quartz plates display several absorption features in the region between 600 and 220 nm. The spectrum of **1** displays a very broad shoulder around 370 nm, another one at 275 nm, and a peak at 249 nm. The spectrum of **2** consists of two shoulders around 450 and 290 nm, while that of **3** shows a broad absorption maximum at 440 nm followed by a shoulder at 280 nm (Figure 4). In solution (**1** in $CH_3CN$; **2**, **3** in thf), the ratio of the maxima and shoulders at higher wavelengths to those below 350 nm increases compared to the spectra measured in nujol. Compounds **1** and **3** display a shoulder at 390 ($\varepsilon$ = 7409) and 415 nm ($\varepsilon$ = 6868), respectively, while the corresponding feature of **2** is most probably obscured by the tail of the following intense band with a maximum at 272 nm ($\varepsilon = 8.87 \times 10^4$ $M^{-1}cm^{-1}$). This band is followed by a very weak shoulder at 252 nm ($\varepsilon = 8.756 \times 10^4$ $M^{-1}cm^{-1}$). Two similar features are observed for **3** at 270 ($\varepsilon = 1.092 \times 10^5$) and 255 nm ($\varepsilon = 1.142 \times 10^5$ $M^{-1}cm^{-1}$), while **1** displays only one broad additional absorption maximum at 250 nm ($\varepsilon = 6.802 \times 10^4$ $M^{-1}cm^{-1}$). A detailed assignment of the bands is complicated as there are several possible absorption processes for the compounds. However, due to their relatively low extinction coefficients of about 7000 $M^{-1}cm^{-1}$, it is possible that the broad bands at higher wavelengths originate from spin-allowed d–d transitions in tetrahedrally coordinated $Fe^{2+}$ while the intense bands at lower wavelengths correspond to either Se→Cu or Se→Fe charge-transfer bands partially overlapped by π–π* transitions of the $SePh^-$ and/or $PPh_3$ ligands.

 © 2007 Wiley-VCH Verlag GmbH & Co. KGaA, Weinheim 

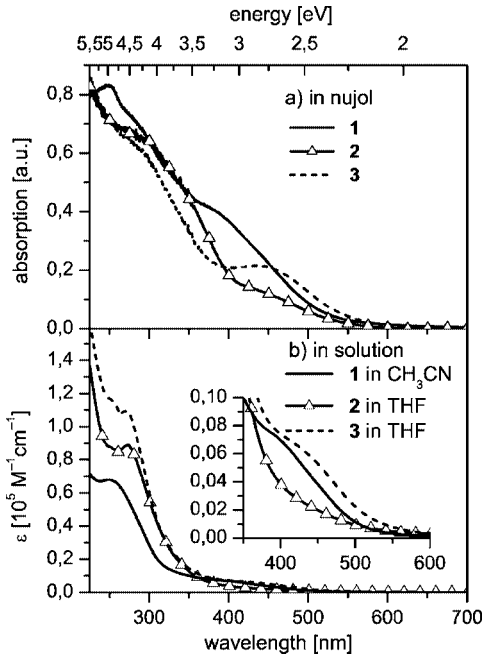


Figure 4. UV/Vis spectra of $(n\text{Pr}_3\text{N}(\text{CH}_2)_6\text{N}n\text{Pr}_3)[\text{CuFe}_3\text{Br}_3(\text{SePh})_6]$ (**1**), $[\text{Cu}_5\text{Fe}(\text{SePh})_7(\text{PPh}_3)_4]$ (**2**), and $[\text{Cu}_4\text{Fe}_3(\text{SePh})_{10}(\text{PPh}_3)_4]$ (**3**) as mulls in nujol (a) and in solution (b).

### Thermogravimetric Analysis

The decomposition of **2** and **3** upon heating was monitored by TGA in vacuo (Figure 5). The mass changes of **2** and **3** both display one-step processes due to the cleavage of most of the ligands, although the temperature range of the cleavage is much narrower for **3** (125–275 °C) than for **2** (125–375 °C). The observed mass losses of 76.2% (**2**) and 75.1% (**3**) agree with the calculated values [loss of 3.5 $\text{SePh}_2$ and four $\text{PPh}_3$ molecules for **2** (76%) and five $\text{SePh}_2$ and four $\text{PPh}_3$ molecules for **3** (73.7%)]. The powder diffraction patterns (Figure 6) of the residues indicate the formation of mixtures of the known phases $\text{Cu}_2\text{Se}$[18] and $\text{CuFeSe}_2$.[19] The thermal treatment of **2** should result in a powder with the theoretical composition $\text{Cu}_5\text{FeSe}_{3.5}$. The ratio of the peak intensities of the different patterns reveals a higher amount of $\text{Cu}_2\text{Se}$ in comparison to $\text{CuFeSe}_2$, although two peaks at $2\theta$ = 44.8° and 47.9°, which have been marked with an asterisk, could not be assigned. For **3**, the residue should have the composition $\text{Cu}_4\text{Fe}_3\text{Se}_5$, which is much closer to the formula of the ternary solid-state phase $\text{CuFeSe}_2$ than that of the residue of **2**. In agreement with this, the powder pattern corresponds to a larger fraction of $\text{CuFeSe}_2$ and a smaller fraction of $\text{Cu}_2\text{Se}$.

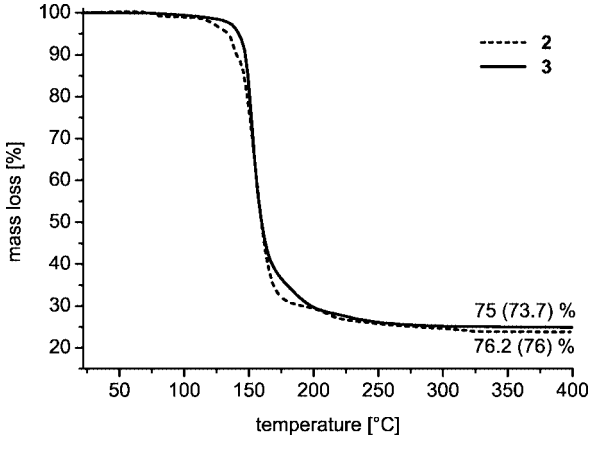


Figure 5. Thermogravimetric analysis of $[\text{Cu}_5\text{Fe}(\text{SePh})_7(\text{PPh}_3)_4]$ (**2**) and $[\text{Cu}_4\text{Fe}_3(\text{SePh})_{10}(\text{PPh}_3)_4]$ (**3**) in vacuo. Theoretical values for the calculated mass loss of 4 $\text{PPh}_3$/3.5 $\text{SePh}_2$ in **2** and 4 $\text{PPh}_3$/5 $\text{SePh}_2$ in **3** are given in parentheses.

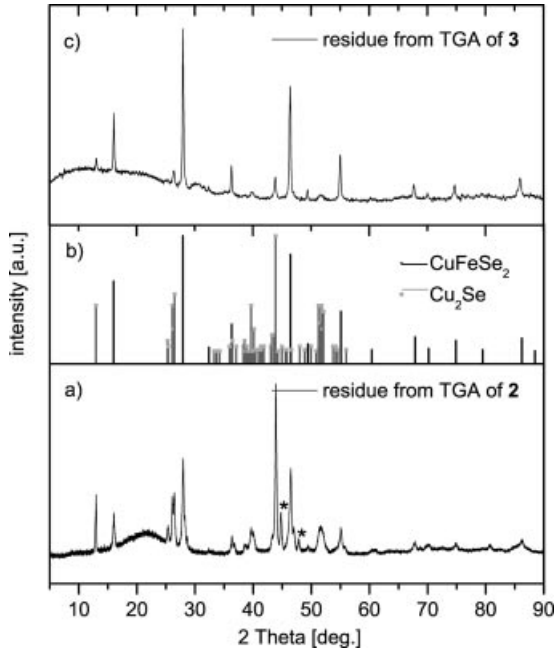


Figure 6. Powder diffraction patterns of a) the residue of the TGA of $[\text{Cu}_5\text{Fe}(\text{SePh})_7(\text{PPh}_3)_4]$ (**2**). Peaks marked by an asterisk cannot be assigned; b) monoclinic α-$\text{Cu}_2\text{Se}$ (grey lines)[18] and tetragonal $\text{CuFeSe}_2$ (black lines);[19] c) residue of the TGA of $[\text{Cu}_4\text{Fe}_3(\text{SePh})_{10}(\text{PPh}_3)_4]$ (**3**).

## Conclusion

The raction of mixtures of copper and iron salts with $\text{PhSeSiMe}_3$ can be used for the synthesis of mixed-metal Cu/Fe/Se cluster molecules. Different structures are formed depending on the kind of ligands and the ratio of the precursor compounds. Thermal cleavage of the organic ligands results in the formation of mixtures of binary $\text{Cu}_2\text{Se}$ and ternary $\text{CuFeSe}_2$, the ratio of which depends on the ratio of the elements in the precursor cluster molecules.

## Experimental Section

**Synthesis:** Standard Schlenk techniques were employed throughout the syntheses using a double-manifold vacuum line ($10^{-3}$ mbar) with high-purity nitrogen (99.9999%). Diethyl ether, and dme were dried with sodium/benzophenone, $\text{CH}_3\text{CN}$ with $\text{CaH}_2$, and all were distilled under nitrogen. CuCl was washed with HCl, $\text{CH}_3\text{OH}$, and diethyl ether to remove traces of $\text{CuCl}_2$, and then dried under vac-

 © 2007 Wiley-VCH Verlag GmbH & Co. KGaA, Weinheim 

uum. $CuOOCCH_3$[20] and $PhSeSiMe_3$[21] were prepared according to literature procedures.

**Physical Measurements:** UV/Vis absorption spectra of cluster molecules in solution were measured with a Varian Cary 500 spectrophotometer in quartz cuvettes. Solid-state UV/Vis spectra were measured as a mull in nujol between quartz plates with a Labsphere integrating sphere. Thermogravimetric analyses were run with a thermobalance STA 409 from Netzsch in vacuo (heating rate 2 K min$^{-1}$).

**[*n*Pr$_3$N(CH$_2$)$_6$N*n*Pr$_3$]Br$_2$:** 1,6-Diaminohexane (8.3 mL, 0.07 mol), *n*-propyl bromide (39.4 mL, 0.43 mol) and $NaHCO_3$ (28 g, 0.33 mol) were added to 120 mL of a 1:1 mixture of $H_2O$ and $CH_3CN$. Two liquid phases and one solid phase were formed. The mixture was then heated under reflux and the formation of $CO_2$ indicated the reaction progress. After 2 d, once the solid phase had disappeared, the organic phase was separated and the solvent evaporated to dryness. The residue was then treated with 100 mL of $CHCl_3$ to precipitate NaBr. Removal of this solid by filtration and renewed evaporation of the solvent yielded [*n*Pr$_3$N(CH$_2$)$_6$N*n*Pr$_3$]Br$_2$ as a pale-yellow precipitate. Yield: 8.56 g (23%). $C_{24}H_{54}Br_2N_2$ (531.61): calcd. C 54.38, H 10.26, N 5.28, found C 53.13, H 10.82, N 5.06.

**[*n*Pr$_3$N(CH$_2$)$_6$N*n*Pr$_3$][CuFe$_3$Br$_3$(SePh)$_6$] (1):** CuBr (50 mg, 0.35 mmol), Fe(OOCCH$_3$)$_2$ (183 mg, 1.05 mmol), and [*n*Pr$_3$N(CH$_2$)$_6$N*n*Pr$_3$]Br$_2$ (185 mg, 0.35 mmol) were suspended in 40 mL of $CH_3CN$. After 1 d of stirring, $PhSeSiMe_3$ (0.44 mL, 2.1 mmol) was added at 0 °C and the mixture warmed to room temperature which led to the formation of red-orange crystals of **1**. Yield: 530 mg (73%). $C_{60}H_{84}Br_3CuFe_3N_2Se_6$ (1644.6): calcd. C 40.5, H 4.8, N 1.6; found C 40.9, H 4.9, N 1.8.

**[Cu$_5$Fe(SePh)$_7$(PPh$_3$)$_4$] (2):** $CuOOCCH_3$ (100 mg, 0.82 mmol), $FeCl_2$ (21 mg, 0.16 mmol), and $PPh_3$ (0.32 g, 1.2 mmol) were suspended in 30 mL of dme. After 1 d of stirring, $PhSeSiMe_3$ (0.32 mL, 1.39 mmol) was added at –30 °C and the mixture warmed to room temperature to give a clear red solution. After 1 d, the reaction solution was layered with 50 mL of pentane by autothermal condensation. Red, needle-like crystals of **2** grew over several days. Yield: 308 mg (75%). $C_{114}H_{95}Cu_5FeP_4Se_7$ (2515.1): calcd. C 54.4, H 3.81; found C 54.5, H 4.10.

**[Cu$_4$Fe$_3$(SePh)$_{10}$(PPh$_3$)$_4$] (3):** $CuOOCCH_3$ (100 mg, 0.82 mmol), $FeCl_2$ (86 mg, 0.68 mmol), and $PPh_3$ (0.86 g, 3.3 mmol) were suspended in 100 mL of dme. After 1 d of stirring, $PhSeSiMe_3$ (0.57 mL, 2.46 mmol) was added to give a red solution. After another day, approximately 1/3 of the solvent was removed by condensation, which resulted in the immediate crystallization of orange, plate-like needles of **3**. Yield: 460 mg (74%). $C_{132}H_{110}Cu_4Fe_3P_4Se_{10}$ (3031.5): calcd. C 52.3, H 3.7; found C 52.6, H 4.0.

**Crystallography:** Crystals suitable for single-crystal X-ray diffraction were taken directly from the reaction solution of the compound and then selected in perfluoroalkyl ether oil. Single-crystal X-ray diffraction data of **1** and **2** were collected using graphite-monochromatized Mo-$K_\alpha$ radiation ($\lambda$ = 0.71073 Å) with a STOE IPDS II (Imaging Plate Diffraction System) equipped with a Schneider rotating anode. Single-crystal X-ray diffraction data of **3** were collected using synchrotron radiation ($\lambda$ = 0.80 Å) with a STOE IPDS II (Imaging Plate Diffraction System) at the ANKA synchrotron source in Karlsruhe. Further details are given in Table 1. The structures were solved with the direct-methods program SHELXS[22] of the SHELXTL PC program suite, and were refined with the use of the full-matrix least-squares program SHELXL.[22] Molecular diagrams were prepared using SCHAKAL 97.[23] All Cu, Fe, Se, Br, P, Cl, and C atoms of the cluster molecules were refined with anisotropic displacement parameters with the exception of **3**, whose C atoms were refined isotropically. In addition, split positions with isotropic displacement parameters were calculated in **1** for the C atoms of the phenyl rings C11, C12, C20, C21, and C22 as well as of the *n*-propyl groups of the ammonium salt C43, C44, C45, and C57. N and C atoms of the solvent molecules were refined isotropically. H atoms were calculated in fixed positions for **2** and **3**. CCDC-612653 (**1**), -612654 (**2**) and -612655 (**3**) contain the supplementary crystallographic data for this paper. These data can be obtained free of charge from The Cambridge Crystallographic Data Center via www.ccdc.cam.ac.uk/data_request/cif. X-ray powder diffraction patterns were recorded with a STOE STADI P diffractometer (Cu-$K_{\alpha1}$ radiation, germanium monochromator, Debye–Scherrer geometry) in sealed glass capillaries.

Table 1. Crystallographic data for [*n*Pr$_3$N(CH$_2$)$_6$N*n*Pr$_3$][CuFe$_3$Br$_3$(SePh)$_6$] (**1**), [Cu$_5$Fe(SePh)$_7$(PPh$_3$)$_4$] (**2**), and [Cu$_4$Fe$_3$(SePh)$_{10}$(PPh$_3$)$_4$] (**3**).

| | **1**·0.5CH$_3$CN | **2** | **3**·dme |
|---|---|---|---|
| Formula mass [g mol$^{-1}$] | 1798.4 | 2515.1 | 3121.5 |
| Crystal system | trigonal | monoclinic | monoclinic |
| Space group | $P\bar{3}$ | $P2_1/n$ | $P2_1/c$ |
| *a* [pm] | 2315.1(3) | 1471.2(3) | 1660.5(3) |
| *b* [pm] | 2315.1(3) | 2768.4(6) | 5227.9(11) |
| *c* [pm] | 2304.6(5) | 2663.5(5) | 1540.6(3) |
| $\beta$ [°] | | 92.60(3) | 113.44(3) |
| *V* [10$^9$ pm$^3$] | 10697(3) | 10837(4) | 12270(4) |
| *Z* | 6 | 4 | 4 |
| *T* [K] | 190 | 180 | 150 |
| $D_c$ [g cm$^{-3}$] | 1.675 | 1.541 | 1.690 |
| $\mu(\lambda)$ [mm$^{-1}$] | 5.671 (Mo-$K_\alpha$) | 3.550 (Mo-$K_\alpha$) | 5.552 (0.80 Å) |
| *F*(000) | 5310 | 4992 | 6184 |
| $2\theta_{max}$ [°] | 50 | 50 | 46 |
| Measd. reflns. | 33328 | 46983 | 25256 |
| Unique reflns. | 11964 | 18081 | 9924 |
| $R_{int}$ | 0.0556 | 0.0421 | 0.1056 |
| Reflns. with $I > 2\sigma(I)$ | 7086 | 14080 | 8261 |
| Refined parameters | 680 | 1180 | 754 |
| $R_1$ [$I > 2\sigma(I)$][a] | 0.0592 | 0.0519 | 0.0480 |
| $wR_2$ (all data)[b] | 0.1771 | 0.1547 | 0.1465 |

[a] $R_1 = \Sigma||F_o| - |F_c||/\Sigma|F_o|$. [b] $wR_2 = \{\Sigma[w(F_o^2 - F_c^2)^2]/\Sigma[w(F_o^2)^2]\}^{1/2}$.

## Acknowledgments

This work was supported by the Deutsch–Israelisches Programm (DIP) and the Deutsche Forschungsgemeinschaft (Center for Functional Nanostructures CFN). The authors are grateful to Dr. S. Chitsaz for performing the TGA experiments.

[1] W. Hirpo, S. Dhingra, M. Kanatzidis, *J. Chem. Soc., Chem. Commun.* **1992**, 557–559.
[2] J. Olkowska-Oetzel, D. Fenske, P. Scheer, A. Eichhöfer, *Z. Anorg. Allg. Chem.* **2003**, *629*, 415–420.
[3] A. Eichhöfer, D. Fenske, *J. Chem. Soc., Dalton Trans.* **2000**, 941–944.
[4] R. Ahlrichs, A. Eichhöfer, D. Fenske, O. Hampe, M. M. Kappes, P. Nava, J. Olkowska-Oetzel, *Angew. Chem.* **2004**, *116*, 3911–3915; *Angew. Chem. Int. Ed.* **2004**, *43*, 3823–3827.
[5] D. T. T. Tran, L. M. C. Beltran, C. M. Kowalchuk, N. R. Trefiak, N. J. Taylor, J. F. Corrigan, *Inorg. Chem.* **2002**, *41*, 5693–5698.

 © 2007 Wiley-VCH Verlag GmbH & Co. KGaA, Weinheim 

[6] D. T. T. Tran, N. J. Taylor, J. F. Corrigan, *Angew. Chem.* **2000**, *112*, 965–967; *Angew. Chem. Int. Ed.* **2000**, *39*, 935–937.
[7] A. Lorenz, D. Fenske, *Angew. Chem.* **2001**, *113*, 4537–4541; *Angew. Chem. Int. Ed.* **2001**, *40*, 4402; A. Lorenz, D. Fenske, *Z. Anorg. Allg. Chem.* **2001**, *627*, 2232–2248.
[8] R. Pätow, D. Fenske, *Z. Anorg. Allg. Chem.* **2002**, *628*, 1279–1288.
[9] M. W. DeGroot, N. J. Taylor, J. F. Corrigan, *J. Am. Chem. Soc.* **2003**, *125*, 864–865.
[10] A. Kornienko, S. Banerjee, G. A. Kumar, R. E. Riman, T. J. Emge, J. G. Brennan, *J. Am. Chem. Soc.* **2005**, *127*, 14008–14014.
[11] W. Hirpo, S. Dhingra, A. C. Sutorik, M. Kanatzidis, *J. Am. Chem. Soc.* **1993**, *115*, 1597–1599.
[12] V. Soloviev, A. Eichhöfer, D. Fenske, U. Banin, *J. Am. Chem. Soc.* **2000**, *122*, 2673–2674.
[13] V. Soloviev, A. Eichhöfer, D. Fenske, U. Banin, *J. Am. Chem. Soc.* **2001**, *123*, 2354–2364.
[14] J. Lazewski, H. Neumann, H. Parlinski, *Phys. Rev. B* **2004**, *70*, 195206.
[15] N. Hamdadou, M. Morsli, A. Khelil, J. C. Bernède, *J. Phys. D: Appl. Phys.* **2006**, *39*, 1042–1049.
[16] H.-O. Stephan, G. Henkel, M. G. Kanatzidis, *Chem. Commun.* **1997**, 67–68.
[17] J. Lackmann, R. Hauptmann, S. Weißgräber, G. Henkel, *Chem. Commun.* **1999**, 1995–1996.
[18] In Powder Diffraction File PDF-2 Database Sets 1–85, **1993**, International Center for Diffraction Data, Newtown Square USA, file number 27-1131; A. L. N. Stevels, *Philips Res. Rep. Suppl.* **1969**, *9*, 39–44.
[19] In Powder Diffraction File PDF-2 Database Sets 1–85, **1993**, International Center for Diffraction Data, Newtown Square USA, file number 44-1305; J. Henao, J. Delgado, M. Quintero, *Powder Diff.* **1994**, *9*, 108.
[20] D. A. Edwards, R. Richards, *J. Chem. Soc., Dalton Trans.* **1973**, 2463–2468.
[21] N. Miyoshi, H. Ishii, K. Kondo, S. Mui, N. Sonoda, *Synthesis* **1979**, 301–304.
[22] G. M. Sheldrick, *SHELXTL, An Integrated System for Solving, Refining, and Displaying Crystal Structures from Diffraction Data*, PC version 5.1, Bruker Analytical X-ray Systems, Karlsruhe, **2000**.
[23] E. Keller, *SCHAKAL 97, A Computer Program for the Graphic Representation of Molecular and Crystallographic Models*, University of Freiburg, **1997**.

Received: July 4, 2006
Published Online: November 17, 2006

 © 2007 Wiley-VCH Verlag GmbH & Co. KGaA, Weinheim 

DOI: 10.1002/ejic.200600735

# Synthesis of Cp* Iridium and Rhodium Complexes Containing Bidentate $sp^2$-N-Donor Ligands and Counter-Anions $[Cp^*MCl_3]^-$

**Danielle F. Kennedy,[a] Barbara A. Messerle,*[a] and Matthew K. Smith[b]**

**Keywords:** Iridium(III) / Rhodium(III) / N-donor ligands / Cyclopentadienyl ligands

Complexes of the type $[Cp^*MCl(N–N)][X]$ (M = Rh and Ir) have been synthesised, where N–N is a series of bidentate ligands with $sp^2$ N-donors: bis(pyrazol-1-yl)methane (bpm), bis(1-methylimidazol-2-yl)methane (bim), bis(3,5-dimethylpyrazol-1-yl)methane (dmbpm), bis(1-methylimidazol-2-yl) ketone (bik), bis(2,4,6-trimethylphenylimino)acenapthene (mesBIAN), 2,4,6-trimethylphenylimino-(1-methyl-2-imidazolyl)methane (mesim–mim), and X = $Cl^-$, $BF_4^-$ and the unusual anion $[Cp^*MCl_3]^-$. All of these complexes were synthesised by treatment of $[Cp^*MCl_2]_2$ with 2 equivalents of ligand and were isolated as air stable solids. The solid-state structures of $[Cp^*MCl(bpm)][Cp^*MCl_3]$ (M = Rh and Ir) and $[Cp^*IrCl(bim)][Cp^*IrCl_3]$ have been determined by single-crystal X-ray diffraction analysis. All of the structures of the bimetallic species displayed a "piano stool" configuration about the both the anionic and cationic metal centre. The solid-state structures of the monometallic iridium species $[Cp^*IrCl(N–N)][BF_4]$, where N–N = bim, mesBIAN, and mesim-mim, were also determined using single-crystal X-ray diffraction analysis.
(© Wiley-VCH Verlag GmbH & Co. KGaA, 69451 Weinheim, Germany, 2007)

## Introduction

Complexes containing rhodium(I) and iridium(I) metal centres have found wide application in homogeneous catalysis. Reactions catalysed by these complexes include the hydrosilylation of imines,[1,2] the hydroamination and hydroalkoxylation of alkynes,[3–9] the hydroamination and hydroaminomethylation of olefins,[10,11] and the Pauson–Khand reaction.[12,13] Increasingly, metal complexes containing $Ir^{III}$ and $Rh^{III}$ metal centres are being investigated as catalysts for a variety of transformations. Unlike $Ir^I$ and $Rh^I$ catalysts, $Ir^{III}$ and $Rh^{III}$ complexes can not promote reactions which require the initial oxidative addition of a substrate. However, $Ir^{III}$ and $Rh^{III}$ metal centres are reactive and have the potential to catalyse a range of other transformations not reliant on oxidative addition. Work by Bergmann et al. with the complexes $Cp^*(PMe_3)Ir(CH_3)(OTf)$, and $Tp^{Me2}(PMe_3)Ir(CH_3)(OTf)$ illustrated the ability of $Ir^{III}$ complexes to effect C–H activation.[14,15] Recent work by Crabtree et al. has utilised an $Ir^{III}$ hydride complex to catalyse the intramolecular hydroamination and hydroalkoxylation of alkynes.[16] $[Cp^*IrCl_2]_2$ is effective as a catalyst for the hydroborylation of styryl sulfonamides,[17] the *N*-alkylation of amines with alcohols[18] and also the transfer hydrogenation of ketones[19] and quinolines.[20] $Rh^{III}$ complexes are known to be effective in catalysing carbon–carbon bond formation,[21] and $[Cp^*RhCl_2]_2$ has been shown to effect transfer dehydrochlorination of aryl chlorides.[22]

1,2,3,4,5-Pentamethylcyclopentadienyl (Cp*) is ubiquitous as a ligand in organometallic complexes. Many complexes incorporating this ligand are important as active catalysts, largely due to the electron-rich nature of the Cp* group and also the ability of Cp* to completely block one face of the complex, imparting steric bulk and structural rigidity. $Ir^{III}$ and $Rh^{III}$ complexes incorporating both the Cp* ligand and bidentate $sp^2$-nitrogen donor ligands have been synthesised previously.[23–31] In particular, the complex $[Cp^*Ir(bipy)(H_2O)]SO_4$ (bipy = 2,2′-bipyridine) was found to be active as a catalyst for the hydration of phenylacetylene in water,[32] and the complex $[Cp^*Rh(i\text{Pr-pymox})]^{2+}$ (pymox = pyridyloxazoline) was found to promote the enantioselective Diels–Alder reaction of methacrolein with cyclopentadiene.[27]

In the course of the study of both $Ir^{III}$ and $Rh^{III}$ complexes as potential catalysts we have synthesised a series of 1,2,3,4,5-pentamethylcyclopentadienyl complexes incorporating bidentate N donor ligands. Here, we report the synthesis and characterisation of $Rh/Ir^{III}$ complexes of the type $[Cp^*MCl(N–N)][X]$ (M = Rh and Ir), where N–N is a series of bidentate ligands with $sp^2$ N-donors: bis(pyrazol-1-yl)-methane (bpm), bis(1-methylimidazol-2-yl)methane (bim), bis(3,5-dimethylpyrazol-1-yl)methane (dmbpm), bis(1-methylimidazol-2-yl) ketone (bik), bis(2,4,6-trimethylphenylimino)acenapthene (mesBIAN), 2,4,6-trimethylphenylimino-(1-methyl-2-imidazolyl)methane (mesim–mim), and X = $Cl^-$, $BF_4^-$ and the unusual anion $[Cp^*MCl_3]^-$ (Fig-

[a] School of Chemistry, University of New South Wales, Sydney, NSW 2052, Australia
Fax: +61-2-9385-6141
E-mail: b.messerle@unsw.edu.au
[b] Research School of Chemistry, Australian National University, Canberra, Australia


© 2007 Wiley-VCH Verlag GmbH & Co. KGaA, Weinheim

ure 1). The solid-state structures of the complexes **1c**, **2b**, **2c**, **3c**, **7b** and **8b** have been determined by single-crystal X-ray diffraction analysis. The complexes **1c**, **2c** incorporate the novel anion $[Cp^*IrCl_3]^-$, and complex **3c** incorporates the rare anion $[Cp^*RhCl_3]^-$.

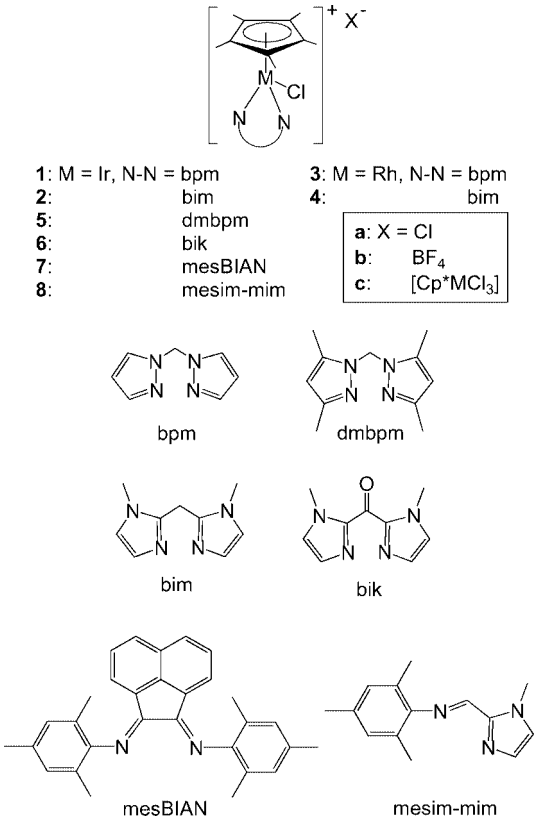


Figure 1. The general structure of complexes **1a**–**8b** and **1a**–**3c** where N–N = bpm = bis(pyrazol-1-yl)methane; bim = bis(1-methylimidazol-2-yl)methane; dmbpm = bis(3,5-dimethylpyrazol-1-yl)-methane; bik = bis(1-methylimidazol-2-yl) ketone; mesBIAN = bis(2,4,6-trimethylphenylimino)acenapthene; mesim–mim = (2,4,6-trimethylphenyl)imino-(1-methylimidazol-2-yl)methane.

## Results and Discussion

### Synthesis of Complexes [Cp*MCl(N–N)][Cp*MCl$_3$] 1c, 2c, and 3c

Toluene suspensions of the metal precursors $[Cp^*IrCl_2]_2$ and $[Cp^*RhCl_2]_2$ were treated with two molar equivalents of the bidentate nitrogen donor ligands bpm and bim (Scheme 1) to generate the ion pairs $[Cp^*IrCl(bpm)][Cp^*IrCl_3]$ (**1c**), $[Cp^*IrCl(bim)][Cp^*IrCl_3]$ (**2c**), and $[Cp^*RhCl(bpm)][Cp^*RhCl_3]$ (**3c**) (Scheme 1). Using the same approach, **2c** was obtained in low yield as the minor product, with $[Cp^*IrCl(bim)]Cl$ (**2a**) being formed as the major product. Complexes **1c**, **2c**, and **3c** were thermally and air stable over extended periods. The sterically hindered ligand mesBIAN failed to bind to $[IrCp^*Cl_2]_2$.

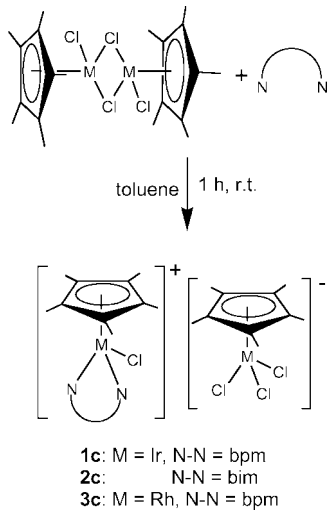


Scheme 1.

The $^1H$ NMR spectra of complexes **1c**–**3c** showed the presence of two molar equivalents of bound Cp* per mol of ligand. $^1H$ NOESY NMR spectrum confirmed that for each of the complexes **1c**–**3c** the sharper singlet occurring slightly downfield at $\delta$ = 1.66, 1.61 and 1.69 ppm, respectively, was due to the $CH_3$ protons of the Cp* moiety bound to the cationic fragment (Table 1). The $^1H$ NMR spectra also show that the two bridging methylene backbone protons of the N–N ligands, $H_a$ and $H_b$, are in magnetically distinct environments for each of the complexes **1c**, **2c** and **3c**. For all of the complexes, the resonances due to $H_a$ and $H_b$ occur as doublets. The assignment of these resonances was established using $^1H$ NOESY NMR, and the resonances due to $H_a$ were consistently shifted significantly downfield relative to the resonances due to $H_b$ (Table 1).

Table 1. Selected chemical shifts for complexes **1c**–**3c**.

| Compound | $\delta$ (ppm) | | | |
|---|---|---|---|---|
| | $H_a$ | $H_b$ | Cp* in cation | Cp* in anion |
| $[Cp^*Ir(bpm)Cl][Cp^*IrCl_3]$ (**1c**) | 8.35 | 5.67 | 1.66 (s) | 1.58 (br. s) |
| $[Cp^*Ir(bim)Cl][Cp^*IrCl_3]$ (**2c**) | 5.01 | 4.73 | 1.61 (s) | 1.54 (br. s) |
| $[Cp^*Rh(bpm)Cl][Cp^*RhCl_3]$ (**3c**) | 8.07 | 5.84 | 1.69 (s) | 1.61 (br. s) |

The complexes **1c** and **2c** contain the novel anion $[Cp^*IrCl_3]^-$. Complex **3c** contains the analogous anion $[Cp^*RhCl_3]^-$ which has been reported recently by Severin et al.[33] as the anion in the ruthenium complex $[Cp^*Ru(C_6H_6)][Cp^*RhCl_3]$.[33] The $[Cp^*RhCl_3]^-$ anion has also been observed in equilibrium in solution with the hydrazine-bridged dimer $[(Cp^*RhCl_2)_2(\mu\text{-}NH_2NHMe)]$ by Maitlis et al.[34]

The relative binding strengths of the N-donor ligands correlates to the nature of the products formed on reaction with the dimeric Ir/Rh starting materials. The strongly coordinating bim ligand brings about the complete dissociation of the metal precursor dimer ($[Cp^*IrCl_2]_2$) and primarily formation of the product monomer, [Cp*IrCl-

 © 2007 Wiley-VCH Verlag GmbH & Co. KGaA, Weinheim 

(bim)]$^+$Cl, **2a**. The more weakly coordinating bpm ligand leads to the formation of bimetallic ion pairs, [Cp*MCl(bpm)][Cp*$MCl_3$] **1c** and **3c**. The mesBIAN ligand is unable to bind to Ir with sufficient strength to split the iridium precursor dimer, due to both the weaker binding ability of the imine N-donors and the large steric bulk imparted by the mesityl groups. The complexes **1c**–**3c**, which contain bimetallic pairs, are of interest from the perspective of coordination chemistry. For the purposes of catalysis, the fact that molecules **1c**–**3c** contain two metal centres makes them inefficient in terms of the proportion of metal involved, as only the cationic fragment of the metal complex is catalytically active. To increase the efficiency of the synthesis with respect to the quantity of metal used, the complexes incorporating the alternate counterion $BF_4^-$ were synthesised.

### Solid-State Structures of 1c, 2c and 3c

The solid-state structures of **1c**, **2c** and **3c** with thermal ellipsoids at the 50% probability level are shown in Figure 2. Selected bond lengths and angles for **1c**, **2c** and **3c** are presented in Table 2 and crystal structure and refinement data are given in Table 5.

The cationic fragments of **1c**, **2c** and **3c** have very similar structures. The metal centres of **1c**, **2c** and **3c** exist in the piano-stool conformation with the six-membered metallocycle formed by coordination of the bidentate ligands to the metal centres in each case existing in the boat configuration. The N–M–N angles for **1c**, **2c** and **3c** are between 83.8(2)° and 85.25(9)°, which is significantly larger than the values for related [IrCp*Cl(N–N)][X] complexes reported in the literature, where the N–N ligand defines a five-membered metallocycle (values of between 75.6 and 77.5° have been reported previously).[32,23,27,31] The N–M–N bite angles are, however, similar to those reported for other Ir complexes containing the bim and bpm ligand (values of 85.9° and 86.8°).[35,36] N–M–Cl angles of between 85.06(15)° and 88.56(7)° for **1c**, **2c** and **3c** are consistent with literature values of between 83.1° and 91.9° for similar complexes.[32,23,27] The M–N distances in each of the complexes are also comparable to those previously reported in the literature with M–N(pyrazole) distances of 2.107(4) and 2.114(2) Å for **1c** and **3c** respectively and a slightly shorter Ir–N(imidazole) distance of 2.089(5) Å for **2c**. Literature values range from 2.028 and 2.230 Å depending on the nature of the N-donor ligand.[15,23,24,26]

In all of the solid-state structures for **1c**–**3c**, the anions [Cp*$MCl_3$]$^-$ have the same piano-stool geometry described by the three chloride atoms and the $\eta^5$-Cp* ligand around the iridium(III) or rhodium(III) metal centres. The piano-stool geometry is frequently reported for Cp* iridium(III) or rhodium(III) complexes.[24,26,37] The equivalent conformation was also previously observed for the anion of the complex [Cp*Ru($C_6H_6$)][Cp*$RhCl_3$].[33] The M–Cl bond lengths reported for this complex were between 2.409 and 2.434 Å, which are comparable to the M–Cl bond lengths of between 2.4100(16) and 2.4335(7) Å for the anions of complexes **1c**–**3c**.

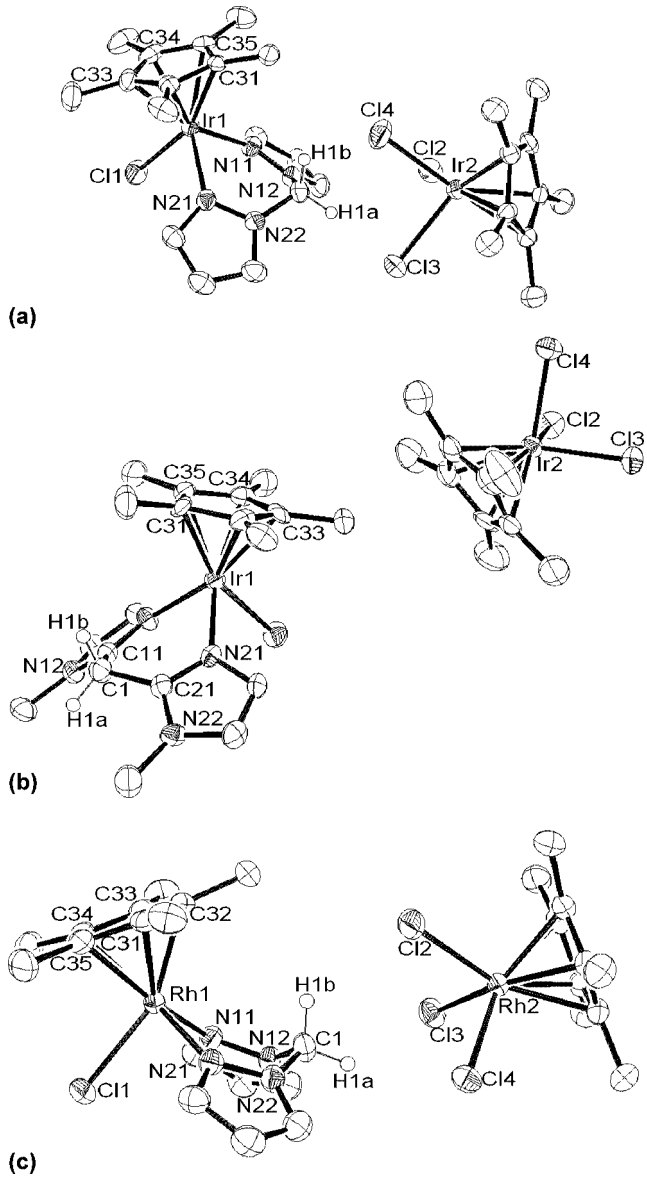


Figure 2. ORTEP depiction of (a) [Cp*IrCl(bpm)][Cp*$IrCl_3$] (**1c**); (b) [Cp*IrCl(bim)][Cp*$IrCl_3$] (**2c**); and (c) [Cp*RhCl(bpm)]-[Cp*$RhCl_3$] (**3c**) at 50% thermal ellipsoids for the non-hydrogen atoms.

### Synthesis of Complexes [Cp*MCl(N–N)][$BF_4$] 1b, 2b, 3b, 4b, 5b, 6b, 7b and 8b

Treatment of toluene suspensions of [$MCp^*Cl_2$]$_2$ with two molar equivalents of a bidentate nitrogen donor ligand (N–N) and two molar equivalents of $NaBF_4$ in MeOH at room temperature resulted in the formation of the complexes [Cp*IrCl(N–N)]$BF_4$, [N–N = bpm (**1b**), bim (**2b**) and dmbpm (**5b**), bik (**6b**), mesBIAN (**7b**) and mesim-mim (**8b**)] and [Cp*RhCl(N–N)]$BF_4$, [N–N = bpm (**3b**), bim (**4b**)] in good to moderate yields (Scheme 2). Selected $^1$H NMR

 © 2007 Wiley-VCH Verlag GmbH & Co. KGaA, Weinheim 

Table 2. Selected bond lengths [Å] and bond angles [°][a] for the inner coordination sphere of **1c**, **2c** and **3c**.

| **1c** | | **2c** | | **3c** | |
|---|---|---|---|---|---|
| Atomic distance [Å] | | | | | |
| Ir(1)–N(11) | 2.107(4) | Ir(1)–N(11) | 2.089(5) | Rh(1)–N(11) | 2.114(2) |
| Ir(1)–N(21) | 2.105(4) | Ir(1)–N(21) | 2.090(5) | Rh(1)–N(21) | 2.113(2) |
| Ir(1)–Cl(1) | 2.4076(16) | Ir(1)–Cl(1) | 2.4012(18) | Rh(1)–Cl(1) | 2.4174(8) |
| Ir(1)–C(31) | 2.170(5) | Ir(1)–C(31) | 2.143(6) | Rh(1)–C(31) | 2.170(3) |
| Ir(1)–C(32) | 2.176(4) | Ir(1)–C(32) | 2.158(6) | Rh(1)–C(32) | 2.161(3) |
| Ir(1)–C(33) | 2.144(5) | Ir(1)–C(33) | 2.149(6) | Rh(1)–C(33) | 2.170(3) |
| Ir(1)–C(34) | 2.152(5) | Ir(1)–C(34) | 2.156(6) | Rh(1)–C(34) | 2.147(3) |
| Ir(1)–C(35) | 2.169(5) | Ir(1)–C(35) | 2.160(6) | Rh(1)–C(35) | 2.142(3) |
| Ir(2)–Cl(2) | 2.4130(13) | Ir(2)–Cl(2) | 2.4163(19) | Rh(2)–Cl(2) | 2.4090(8) |
| Ir(2)–Cl(3) | 2.4322(13) | Ir(2)–Cl(3) | 2.4100(16) | Rh(2)–Cl(3) | 2.4126(7) |
| Ir(2)–Cl(4) | 2.4111(17) | Ir(2)–Cl(4) | 2.4158(18) | Rh(2)–Cl(4) | 2.4335(7) |
| Bond angle [°] | | | | | |
| N(21)–Ir(1)–N(11) | 83.95(17) | N(11)–Ir(1)–N(21) | 83.8(2) | N(21)–Rh(1)–N(11) | 85.25(9) |
| N(11)–Ir(1)–Cl(1) | 87.09(12) | N(11)–Ir(1)–Cl(1) | 85.06(15) | N(11)–Rh(1)–Cl(1) | 88.56(7) |
| N(21)–Ir(1)–Cl(1) | 86.77(12) | N(21)–Ir(1)–Cl(1) | 85.67(15) | N(21)–Rh(1)–Cl(1) | 88.41(7) |
| N(22)–C(1)–N(12) | 109.5(4) | C(11)–C(1)–C(21) | 109.6(6) | N(22)–C(1)–N(12) | 109.8(2) |
| N(11)–N(12)–C(1) | 119.8(4) | N(11)–C(11)–C(1) | 125.0(5) | N(11)–N(12)–C(1) | 120.1(2) |
| N(21)–N(22)–C(1) | 120.5(4) | N(12)–C(11)–C(1) | 125.6(6) | N(21)–N(22)–C(1) | 120.5(2) |
| N(12)–N(11)–Ir(1) | 123.7(3) | C(11)–N(11)–Ir(1) | 124.9(4) | N(12)–N(11)–Rh(1) | 122.88(17) |
| N(22)–N(21)–Ir(1) | 123.3(3) | C(21)–N(21)–Ir(1) | 125.3(4) | N(22)–N(21)–Rh(1) | 122.87(17) |

[a] Estimated standard deviation in the least significant figure are given in parentheses.

chemical shifts for these complexes are presented in Table 3. As already observed for the complexes **1c**–**3c**, the two methylene protons ($H_a$ and $H_b$) of the bridging carbon atoms of the bidentate ligands of the complexes **1b**–**5b** exist in very different magnetic environments, with the $^1H$ NMR chemical shifts for $H_a$ protons being significantly deshielded. The $^1H$ chemical shift of the resonance due to the -$CH_3$ groups of the Cp* ligand of complex **7b** (at $\delta$ = 1.27 ppm) is shifted significantly relative to that of the corresponding resonances of the other iridium complexes in this series (complexes **1b**–**5b**), which lie between 1.53 and 1.59 ppm, most likely a result of ring current effects due to the mesityl substituents on the mesim-mim ligand.

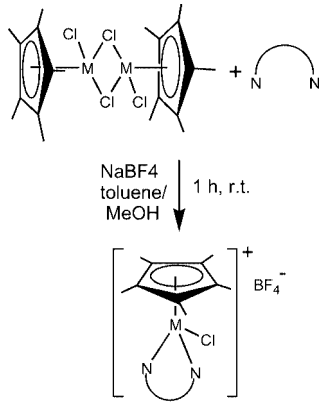


**1b**: M = Ir, N-N = bpm
**2b**: bim
**5b**: dmbpm
**6b**: bik
**7b**: mesBIAN
**8b**: mesim-im
**3b**: M = Rh, N-N = bpm
**4b**: bim

Scheme 2.

Table 3. Selected chemical shifts for complexes **1b**–**8b**.

| Compound | $\delta$ (ppm) $H_a$ | $H_b$ | Cp* |
|---|---|---|---|
| [Cp*Ir(bpm)Cl]$BF_4$ (**1b**) | 7.03 | 5.68 | 1.56 (br. s) |
| [Cp*Ir(bim)Cl]$BF_4$ (**2b**) | 4.52 | 4.14 | 1.59 (s) |
| [Cp*Rh(bpm)Cl]$BF_4$ (**3b**) | 7.28 | 6.00 | 1.71 (br. s) |
| [Cp*Rh(bim)Cl]$BF_4$ (**4b**) | 4.47 | 4.16 | 1.60 (s) |
| [Cp*Ir(dmbpm)Cl]$BF_4$ (**5b**) | 6.48 | 5.67 | 1.56 (s) |
| [Cp*Ir(bik)Cl]$BF_4$ (**6b**) | – | – | 1.53 (s) |
| [Cp*Ir(mesBIAN)Cl]$BF_4$ (**7b**) | – | – | 1.27 (s) |
| [Cp*Ir(mesim-mim)Cl]$BF_4$ (**8b**) | – | – | 1.49 (s) |

The [Cp*IrCl(N–N)]$BF_4$ complex **7b** (N–N = mesBIAN) was made in good yield, however, the synthesis of the corresponding rhodium complex was unsuccessful. This was attributed to the steric bulk of the mesityl groups on this ligand, which may hinder binding of the ligand to the rhodium metal centre.

The interconversion of the bimetallic ion pair **1c** to **1b**, the analogous $BF_4^-$ salt, was investigated. A toluene solution of **1c**, 1 equivalent of bpm and 1 equivalent of $NaBF_4$ with a small amount of MeOH was stirred at room temperature. **1b** was isolated from the reaction mixture as the only product and its identity was confirmed using $^1H$ and $^{13}C$ NMR spectroscopy. The addition of MeOH to the reaction is necessary for the conversion of $[IrCp^*Cl_3]^-$ and anion exchange to occur as both $BF_4^-$ and $Cl^-$ are poorly solubilised by toluene.

 © 2007 Wiley-VCH Verlag GmbH & Co. KGaA, Weinheim 

**Solid-State Structures of 2b, 7b and 8b**

Crystals suitable for X-ray structure determination were obtained for **2b**, **7b** and **8b** and ORTEP depictions of their solid-state structures are depicted in Figure 3. Selected bond lengths and angles for **2b**, **7b** and **8b** are presented in Table 4, and crystal structure and refinement data are given in Table 6.

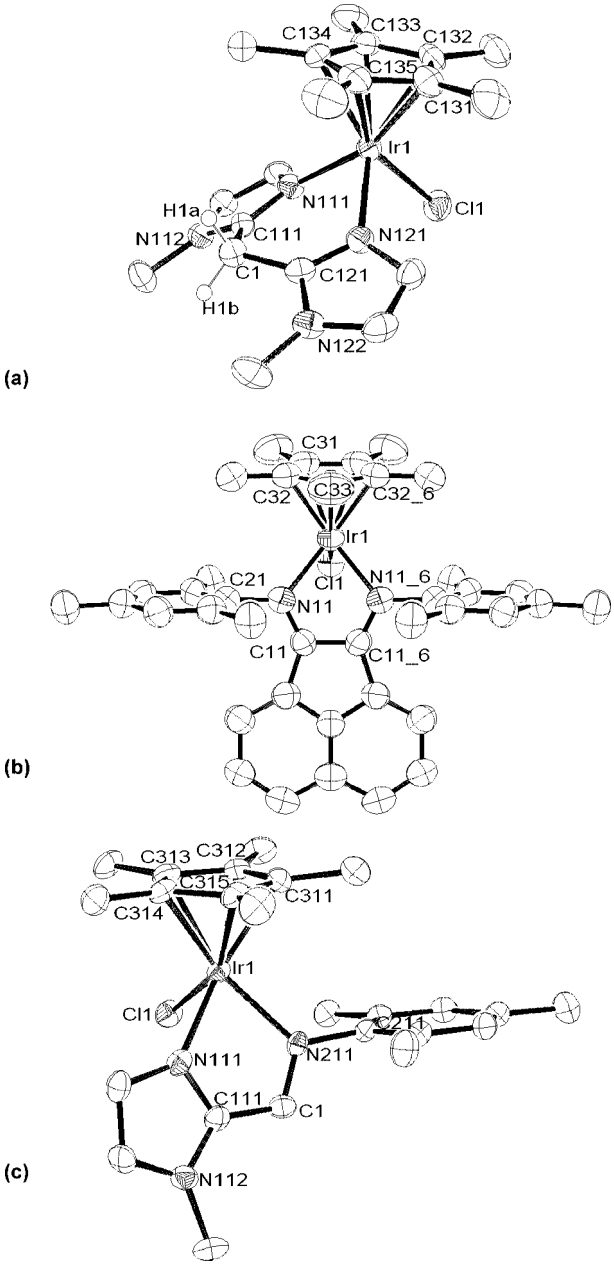


Figure 3. ORTEP depiction of (a) $[Cp^*IrCl(bim)]^+$ (**2b**); (b) $[Cp^*IrCl(mesBIAN)]^+$ (**7b**) and (c) $[Cp^*IrCl(mesim\text{-}mim)]^+$ (**8b**) at 50% thermal ellipsoids for the non-hydrogen atoms.

The solid-state structure of **2b** is very similar to that of **2c** with comparable N–Ir–N bite angles of 83.51(11)° and 83.8(2)°, respectively, and Ir–N bond lengths of 2.095(3) and 2.101(3) Å for **2b** and 2.089(5) and 2.090(5) Å for **2c**. The two Ir–N bond lengths of **7b** are 2.122(5) Å. The Ir–N bond lengths for complex **8b** are 2.100(5) and 2.121(4) Å for the Ir–N(imidazole) and Ir–N(imine) bonds, respectively. These are comparable to the Ir–N(imidazole) and Ir–N(imine) bond lengths in complexes **2b** and **7b**, respectively. All of the Ir–N bond lengths are comparable to the distances found in the literature for similar complexes (values between 2.076 and 2.128 Å).[23,24,26]

The length of the Ir–Cp* bond was dependent on the nature of the cation as well as the nature of the ligand. The Cp*–Ir bond lengths are slightly larger on average for the $BF_4^-$ salt **2b** (2.144–2.181 Å), compared with the equivalent bond lengths in the bimetallic ion pair **2c** (2.143–2.160 Å). The Cp*–Ir bond length in the solid-state structure of **7b** is significantly longer than in **2b** and **2c** (2.171–2.193 Å) due to the high degree of steric hindrance caused by the bulky mesBIAN ligand. The Cp*–Ir bond lengths for complex **8b** (2.158–2.189 Å) containing the hybrid mesitylimine-imidazole ligand are midway between those of complexes **2b** containing the imidazolium ligand, and **7b** which contains the bulky mesBIAN ligand. The Cp*–Ir bond lengths for all of these complexes are within the range previously described in the literature (2.110–2.195 Å).[23,24]

## Conclusions

Complexes of the type [Cp*MCl(N–N)][X] were synthesised (M = $Rh/Ir^{III}$), with a series of bidentate N-donor ligands. Where N–N was bpm or bim and there was no alternate counterion present, bimetallic complexes formed containing the counterion X = $[Cp^*MCl_3]^-$. In the case of the sterically hindered N-donor ligands, these bimetallic complexes did not form. In the presence of the counterion $BF_4^-$, the complexes where X = $BF_4^-$ were synthesised successfully.

The three dimensional solid-state structures of the cationic fragments of the bimetallic complexes **1c**, **2c** and **3c** were all very similar. Changing the counterion from the $[Cp^*MCl_3]^-$ fragment to the smaller $BF_4^-$ anion, did not significantly change the structure of the cationic fragment. The chemical shift of the resonance due to the -$CH_3$ protons of the Cp* of the Ir complex containing the mesBIAN ligand $[Cp^*IrCl(mesBIAN)]BF_4$ (**7b**) was significantly shifted upfield relative to the same resonance of the remaining Ir complexes, and this was attributed to the presence of the aromatic rings of the mesBIAN ligand.

The catalytic activity of the complexes reported in this paper is currently under investigation and will be reported in a future paper.

## Experimental Section

**General Procedures:** All manipulations of metal complexes and air-sensitive reagents were carried out using standard Schlenk techniques or in a nitrogen- or argon-filled drybox. All solvents were distilled under argon. *n*-Hexane, *n*-pentane and toluene were distilled from sodium benzophenone ketyl. Dichloromethane was dis-

 © 2007 Wiley-VCH Verlag GmbH & Co. KGaA, Weinheim 

Table 4. Selected bond lengths [Å] and bond angles [°][a] for the inner coordination sphere of **2b**, **7b** and **8b**.

| **2b** Atomic distance [Å] | | **7b** | | **8b** | |
|---|---|---|---|---|---|
| Ir(1)–N(111) | 2.095(3) | Ir(1)–N(11) | 2.122(5) | Ir(1)–N(111) | 2.100(5) |
| Ir(1)–N(121) | 2.101(3) | Ir(1)–N(11)#1 | 2.122(5) | Ir(1)–N(211) | 2.121(4) |
| Ir(1)–C(131) | 2.166(4) | Ir(1)–C(31) | 2.171(6) | Ir(1)–C(311) | 2.178(5) |
| Ir(1)–C(132) | 2.181(3) | Ir(1)–C(31)#1 | 2.171(6) | Ir(1)–C(312) | 2.158(6) |
| Ir(1)–C(133) | 2.155(4) | Ir(1)–C(32) | 2.193(7) | Ir(1)–C(313) | 2.175(5) |
| Ir(1)–C(134) | 2.144(4) | Ir(1)–C(32)#1 | 2.193(7) | Ir(1)–C(314) | 2.189(5) |
| Ir(1)–C(135) | 2.155(4) | Ir(1)–C(33) | 2.187(9) | Ir(1)–C(315) | 2.176(6) |
| Ir(1)–Cl(1) | 2.4025(10) | Ir(1)–Cl(1) | 2.377(2) | Ir(1)–Cl(1) | 2.4009(17) |
| Bond angle [°] | | | | | |
| N(111)–Ir(1)–N(121) | 83.51(11) | N(11)–Ir(1)–N(11)#1 | 76.5(3) | N(111)–Ir(1)–N(211) | 75.80(18) |
| N(111)–Ir(1)–Cl(1) | 85.63(9) | N(11)–Ir(1)–Cl(1) | 85.51(13) | N(111)–Ir(1)–Cl(1) | 84.05(13) |
| N(121)–Ir(1)–Cl(1) | 87.71(9) | N(11)#1–Ir(1)–Cl(1) | 85.51(13) | –Ir(1)–Cl(1) | 87.58(13) |
| –N(111)–Ir(1) | 124.6(2) | C(11)–N(11)–Ir(1) | 113.4(4) | –N(111)–Ir(1) | 114.0(4) |
| C(112)–N(111)–Ir(1) | 127.6(2) | C(21)–N(11)–Ir(1) | 128.5(4) | –N(211)–Ir(1) | 127.5(3) |
| –C(111)–C(1) | 126.9(3) | N(11)–C(11)–C(11)#1 | 116.9(3) | N(111)–C(111)–C(1) | 117.4(5) |
| N(112)–C(111)–C(1) | 123.9(3) | C(11)–N(11)–Ir(1) | 113.4(4) | N(211)–C(1)–C(111) | 115.7(5) |
| –C(1)–C(111) | 112.0(3) | | | | |

[a] Estimated standard deviation in the least significant figure are given in parentheses.

tilled from calcium hydride. $CD_2Cl_2$ was dried with calcium hydride and vacuum-distilled before use. 1,2,3,4,5-Pentamethylcyclopentadiene was purchased from Lancaster and used without further purification. Iridium(III) chloride hydrate and rhodium(III) chloride hydrate were obtained from Precious Metals Online (PMO) and were used without further purification. $[IrCp^*Cl_2]_2$, $[RhCp^*Cl_2]_2$,[37] bis(1-pyrazolyl)methane,[38] bis(1-methylimidazol-2-yl)methane,[39] bis(1-methylimidazol-2-yl) ketone,[40] bis(2,4,6-trimethylphenylimino)acenapthene[41,42] and 2-formyl-1-methylimidazole[43] were prepared following literature methods.

$^1H$, $^{13}C$ and $^{19}F$ NMR spectra were recorded with Bruker DPX300 and DMX500 spectrometers. All spectra were recorded at 298 K unless otherwise specified. $^1H$ NMR and $^{13}C$ NMR chemical shifts were referenced internally to residual solvent resonances. $^{19}F$ NMR was referenced externally using α,α,α-trifluorotoluene in $CDCl_3$. Melting points were recorded using a Mel-Temp apparatus and are uncorrected. IR spectra were recorded using an ATI Mattson Genesis Series FT-IR spectrometer. Electrospray mass spectra were performed by the Biomedical Mass Spectrometry Facility (BMSF) at the University of New South Wales, Sydney, Australia. Elemental analyses were performed by the Campbell Microanalytical Laboratory at the University of Otago, New Zealand. Single-crystal X-ray structure analyses were obtained at the Research School of Chemistry at the Australian National University, Canberra, Australia.

**Synthesis of [Cp*IrCl(bpm)][Cp*IrCl$_3$] (1c):** A toluene suspension (25 mL) of $[IrCp^*Cl_2]_2$ (90 mg, 0.11 mmol) was stirred for 30 min and a toluene solution (10 mL) of bis(pyrazolyl)methane, bpm (38 mg, 0.25 mmol) was added dropwise. On addition of the ligand, the suspension immediately changed colour from orange–red to yellow. The mixture was stirred for a further 45 min. The yellow solid was collected by filtration, washed with toluene (2 × 5 mL) and dried in vacuo to give the compound as a yellow air stable solid. The solid was recrystallised by slow diffusion of pentane into a $CH_2Cl_2$ solution of the complex to give **1c** as small orange crystals which were suitable for X-ray analysis. Yield: 31% (32 mg). M.p. > 230 °C. $C_{27}H_{38}Cl_4Ir_2N_4$ (944.9): calcd. C 34.32, H 4.05, N 5.93; found C 34.23, H 4.14 N 5.30. IR (KBr): ṽ = 3475 (br), 3111 (m), 2962 (w), 2915 (m), 2341 (w), 1635 (w), 1558 (w), 1421 (vs), 1273 (vs), 1096 (m), 1067 (m), 1031 (m), 772 (m), 754 (m) cm$^{-1}$. MS (ES$^+$, $CH_2Cl_2$): *m*/*z* (%) = 511 (10) [Cp*IrCl(bpm)]$^+$, 363 (100) [Cp*IrCl]$^+$. $^1H$ NMR ($CD_2Cl_2$, 300 MHz): $\delta$ = 8.79 (d, $^3J_{H5\text{-}H4}$ = 2.3 Hz, 2 H, H5), 8.35 (d, $^2J_{Ha\text{-}Hb}$ = 15.1 Hz, 1 H, Ha), 7.60 (d, $^3J_{H3\text{-}H4}$ = 2.3 Hz, 2 H, H3), 6.44 (m, 2 H, H4), 5.67 (d, $^2J_{Ha\text{-}Hb}$ = 15.1 Hz, 1 H, Hb), 1.66 [s, 15 H, $CH_3(Cp^*)_{cation}$], 1.58 [s, 15 H, $CH_3(Cp^*)_{anion}$] ppm. $^{13}C\{^1H\}$ NMR ($CD_2Cl_2$, 75 MHz): $\delta$ = 143 (C5), 136 (C3), 107 (C4), 88 (Cp*), 84 ($CH_2$), 8.8 [$CH_3$(Cp*)], 8.6 [$CH_3$(Cp*)] ppm.

**Synthesis of [Cp*IrCl(bim)][Cp*IrCl$_3$] (2c) and [Cp*IrCl(bim)]Cl (2a):** A toluene suspension (25 mL) of $[IrCp^*Cl_2]_2$ (99 mg, 0.11 mmol) was stirred for 30 min. A toluene solution (10 mL) of bis(1-methylimidazol-2-yl)methane, bim, (43 mg, 0.24 mmol) was then added dropwise and the mixture was stirred for 45 min. The yellow solid was collected by filtration, washed with toluene (2 × 5 mL) and recrystallised from dichloromethane and pentane. A yellow powder was isolated by filtration and dried in vacuo. This crude compound was a mixture of [Cp*IrCl(bim)]Cl and [Cp*IrCl(bim)][Cp*IrCl$_3$] and was recrystallised by slow diffusion of petroleum into a $CH_2Cl_2$ solution of the complex. Two sets of analytically pure crystals were obtained; microcrystalline yellow [Cp*IrCl(bim)]Cl Yield: 28% (40 mg) and large red cubic crystals of [Cp*IrCl(bim)][Cp*IrCl$_3$]$_3$. Yield: 17% (16 mg). The crystals of **2a** and **2c** were separated physically. The red cubic crystals of **2c** were suitable for X-ray crystal structure analysis.

**[Cp*IrCl(bim)]Cl (2a):** M.p. 225–228 °C. IR (KBr disc): ṽ 3427 (br), 3118 (m), 2918 (m), 1637 (w), 1508 (m), 1450 (m), 1412 (m), 1381 (w), 1279 (w), 1261 (w), 1150 (m), 1096 (m), 1032 (vs), 796 (m) 7,61 (m) cm$^{-1}$. MS (ES$^+$, $CH_2Cl_2$): *m*/*z* (%)= 539 (100) [M$^+$], 540 (90), 537 (80), 541 (70), 503 (50). $^1H$ NMR ($CD_2Cl_2$, 300 MHz): $\delta$ = 7.00 (s, 4 H, H4 and H5), 5.36 (d, $^2J_{Hb\text{-}Ha}$ = 18.8 Hz, 1 H, Ha), 4.52 (d, $^2J_{Ha\text{-}Hb}$ = 19.2 Hz, 1 H, Hb), 4.10 (s, 6 H, N–$CH_3$), 1.62 [s, 15 H, $CH_3$(Cp*)] ppm. $^{13}C\{^1H\}$ NMR ($CD_2Cl_2$, 75 MHz): $\delta$ = 141.3 (C2), 128.7 (C4), 122.7 (C5), 86.9 (Cp*), 35.4 (N–$CH_3$), 26.1 ($CH_2$), 8.7 [$CH_3$(Cp*)] ppm.

**[Cp*IrCl(bim)][Cp*IrCl$_3$] (2c):** M.p. 270–275 °C. $C_{29}H_{42}Cl_4Ir_2N_4 \cdot CH_2Cl_2$ (1057.9): calcd. C 34.06, H 4.19, N 5.30; found C 33.76, H 4.17, N 5.03. IR (KBr disc): ṽ = 3466 (br), 3143 (m), 3117 (m), 2977 (w), 2910 (m), 1635 (m), 1551 (w), 1514 (vs), 1452 (s), 1377 (m), 1292 (w), 1178 (w), 1144 (w), 1081 (w), 1035 (s), 758 (s) cm$^{-1}$. MS (ES$^+$, $CH_2Cl_2$): *m*/*z* (%) = 539 (10) [Cp*IrCl(bim)]$^+$), 503 (100). $^1H$ NMR ($CD_2Cl_2$, 300 MHz): $\delta$ = 6.95 (s, 4 H, H4 and H5), 5.01

 © 2007 Wiley-VCH Verlag GmbH & Co. KGaA, Weinheim 

(d, $^2J_{Hb-Ha}$ = 19.2 Hz, 1 H, Ha), 4.73 (d, $^2J_{Ha-Hb}$ = 19.2 Hz, 1 H, Hb), 4.04 (s, 6 H, N–$CH_3$), 1.61 [s, 15 H, $CH_3(Cp^*)_{cation}$], 1.54 [s, 15 H, $CH_3(Cp^*)_{anion}$] ppm. $^{13}C\{^1H\}$ NMR ($CD_2Cl_2$, 75 MHz): $\delta$ = 141.8 (C2), 128.1 (C4), 122.5 (C5), 86.9 (Cp), 35.9 (N–$CH_3$), 25.2 ($CH_2$), 8.8 [$CH_3(Cp^*)$] ppm.

**Synthesis of [Cp*RhCl(bpm)][Cp*RhCl$_3$] (3c):** $[RhCp^*Cl_2]_2$ (215 mg, 0.35 mmol) and bpm (383 mg, 2.5 mmol) were suspended in toluene and stirred for 3 h. The orange-brown solid which formed was collected by filtration and was recrystallised by layering a $CH_2Cl_2$ solution of the compound with pentane. The product crystallised both as large red plates and small orange crystals. Both crystal forms were found to be analytically pure [Cp*RhCl(bpm)][Cp*RhCl$_3$]. The red plates of [Cp*RhCl(bpm)][Cp*RhCl$_3$] were suitable for X-ray crystal structure analysis. Yield: 32% (105 mg). M.p. > 310 °C. IR (KBr disc): $\tilde{\nu}$ = 3409 (br), 3120 (w), 2965 (w), 1635 (m), 1522 (m), 1489 (m), 1458 (m), 1403 (s), 1375 (m), 1288 (s), 1264 (m), 1096 (s), 1058 (s), 1017 (s), 799 (s), 168 (s) cm$^{-1}$. $^1H$ NMR ($CD_2Cl_2$, 300 MHz): $\delta$ = 8.76 (d, $^3J_{H5-H4}$ = 2.5 Hz, 2 H, H5), 8.07 (d, $^2J_{Hb-Ha}$ = 15.1 Hz, 1 H, Ha), 7.60 (d, $^3J_{H3-H4}$ = 2.3 Hz, 2 H, H3), 6.39 (m, 2 H, H4), 5.84 (d, $^2J_{Ha-Hb}$ = 15.1 Hz, 1 H, Hb), 1.69 [s, 15 H, $CH_3(Cp^*)_{cation}$], 1.61 [br. s, 15 H, $CH_3(Cp^*)_{anion}$] ppm. $^{13}C\{^1H\}$ NMR ($CD_2Cl_2$, 75 MHz): $\delta$ = 145.0 (C5), 137.5 (C3), 108.3 (C4), 97.3 (d, $^1J_{Rh-Cp^*}$ = 8.7 Hz, Cp), 64.3 ($CH_2$), 9.8 (Cp–$CH_3$), 9.6 [$CH_3(Cp^*)$] ppm.

**Synthesis of [Cp*IrCl(bpm)]BF$_4$ (1b):** $[IrCp^*Cl_2]_2$ (53 mg, 0.067 mmol) was suspended in toluene (10 mL) and stirred for 10 min. A toluene (5 mL) solution of bpm (23 mg, 0.16 mmol) was added and the mixture was stirred for 30 min before a methanol solution (5 mL) of $NaBF_4$ (14 mg, 0.127 mmol) was added. The solid dissolved to generate a yellow solution which was allowed to stir overnight. The solvent volume was reduced to ca. 5 mL, filtered and layered with pentane (10 mL). The resulting precipitate was collected by filtration, washed with pentane (5 mL) and dried in vacuo to give [Cp*IrCl(bpm)]BF$_4$ as a yellow solid. Yield: 53% (42 mg). M.p. 275–285 °C. $C_{17}H_{23}Cl_1BF_4Ir_1N_1$ (597.2): calcd. C 34.15, H 3.88, N 9.37; found C 34.18, H 3.91, N 9.14. IR (KBr disc): $\tilde{\nu}$ = 3649 (w), 3427 (br), 3119 (m), 3081 (m), 2984 (w), 2913 (w), 1636 (m), 1489 (w), 1456 (m), 1418 (s), 1288 (s), 1277 (m), 1084 (vs), 989 (vs), 764 (m) cm$^{-1}$. MS (ES$^+$, $CH_2Cl_2$): *m/z* (%) = 511 (100) [Cp*IrCl(bpm)]$^+$), 509 (80), 513 (80). $^1H$ NMR ($CD_2Cl_2$, 300 MHz): $\delta$ = 8.07 (d, $^3J_{H5-H4}$ = 2.7 Hz, 2 H, H5), 7.58 (d, $^3J_{H3-H4}$ = 2.5 Hz, 2 H, H3), 7.03 (d, $^2J_{Hb-Ha}$ = 14.5 Hz, 1 H, Ha), 6.43 (dd, $^3J_{H5-H4}$ = 2.7 Hz, $^3J_{H5-H4}$ = 2.5 Hz, 2 H, H4), 5.68 (d, $^2J_{Ha-Hb}$ = 14.5 Hz, 1 H, Hb), 1.56 [br. s, 15 H, $CH_3(Cp^*)$] ppm. $^{13}C\{^1H\}$ NMR ($CD_2Cl_2$, 75 MHz): $\delta$ = 144.8 (C3), 135.0 (C5), 108.7 (C4), 88.8 (Cp*), 62.7 ($CH_2$), 8.7 [$CH_3(Cp^*)$] ppm. $^{19}F$ NMR ($CD_2Cl_2$, 282.41 MHz): $\delta$ = –151.4 ppm.

**Synthesis of [Cp*IrCl(bim)]BF$_4$ (2b):** $[IrCp^*Cl_2]_2$ (58.8 mg, 0.073 mmol), bim (27.2 mg, 0.154 mmol) and $NaBF_4$ (19.2 mg, 0.175 mmol) were dissolved in toluene (10 mL) and MeOH (5 mL) and stirred for 2 h. The solution was reduced in volume, filtered and layered with pentane. The product was allowed to precipitate overnight, collected by filtration, washed with pentane and dried in vacuo to isolate [Cp*IrCl(bim)]BF$_4$ as a yellow powder. Yield: 73% (67.3 mg). Yellow crystals of [Cp*IrCl(bim)]BF$_4$ obtained by layering a $CH_2Cl_2$ solution of **2b** with petroleum in air were suitable for X-ray crystal structure analysis. M.p. 273–278 °C. $C_{19}H_{27}ClBF_4IrN_4{\cdot}H_2O$ (625.9): calcd. C 35.44, H 4.54, N 8.70; found C 35.81, H 4.37, N 8.73%. IR (KBr disc): $\tilde{\nu}$ = 3432 (br), 3108 (m), 1716 (w), 1699 (w), 1652 (m), 1655 (m), 1557 (w), 1514 (m), 1456 (w), 1413 (w), 1290 (w), 1084 (br. s), 1032 (vs), 820 (w), 758 (m) cm$^{-1}$. MS (ES$^+$, $CH_2Cl_2$): *m/z* (%) = 539 (100) [Cp*IrCl(bim)]$^+$, 537 (30). $^1H$ NMR ($CD_2Cl_2$, 300 MHz): $\delta$ = 7.02 (d, $^3J_{H4-H5}$ = 1.8 Hz, 2 H, H4 or H5), 6.99 (d, $^3J_{H4-H5}$ = 1.8 Hz, 2 H, H4 or H5), 4.52 (d, $^2J_{Hb-Ha}$ = 19.0 Hz, 1 H, Ha), 4.14 (d, $^2J_{Ha-Hb}$ = 19.0 Hz, 1 H, Hb), 3.86 (s, 6 H, N-$CH_3$), 1.59 [s, 15 H, $CH_3(Cp^*)$] ppm. $^{13}C$ NMR ($CD_2Cl_2$, 75 MHz): $\delta$ = 141.1 (C2), 129.3 (C4), 123.7 (C5), 86.9 (Cp*), 35.9 (N–$CH_3$), 25.2 ($CH_2$), 8.8 [$CH_3(Cp^*)$] ppm. $^{19}F$ NMR ($CD_2Cl_2$, 282.41 MHz): $\delta$ = –154.1 ppm.

**Synthesis of [Cp*IrCl(dmbpm)]BF$_4$ (5b):** A toluene (10 mL) suspension of $[IrCp^*Cl_2]_2$ (52.4 mg, 0.066 mmol) was stirred for 10 min prior to the addition of a toluene solution (5 mL) of bis(3,5-dimethylpyrazolyl)methane, dmbpm (24.1 mg, 0.139 mmol). The suspension was stirred for 45 min before addition of a methanol solution of $NaBF_4$ (24.2 mg, 0.221 mmol). The orange solid dissolved producing a yellow solution which was stirred overnight. The volume of the solution was reduced in vacuo, filtered and was layered with pentane. The precipitate was collected, washed with pentane and dried to give [Cp*IrCl(dmbpm)]BF$_4$ as a yellow solid. Yield: 50% (42.5 mg). $C_{21}H_{31}BClF_4IrN_4$ (654.0): calcd. C 38.57, H 4.78, N 8.57; found C 38.30, H 4.78., N 8.40%. IR (KBr disc): $\tilde{\nu}$ = 3448 (br), 3136 (w), 2986 (w), 1699 (w), 1652 (w), 1561 (s), 1490 (m), 1472 (s), 1426 (s), 1396 (s), 1288 (vs), 1156 (vs), 843 (m), 806 (m), 705 (w), 686 (m), 658 (w), 624 (w), 520 (m), 456 (m) cm$^{-1}$. MS (ES$^+$, $CH_2Cl_2$): *m/z* (%) = 568 (100) [Cp*IrCl(dmbpm)]$^+$), 567 (90), 569 (80), 565 (60). $^1H$ NMR ($CD_2Cl_2$, 300 MHz): $\delta$ = 6.48 (d, $^2J_{Hb-Ha}$ = 15.9 Hz, 1 H, Ha), 6.14 (s, 2 H, H4), 5.67 (d, $^2J_{Hb-Ha}$ = 15.9 Hz, 1 H, Hb), 2.54 (s, 6 H, $CH_3$), 2.42 (s, 6 H, $CH_3$), 1.56 [s, 15 H, $CH_3(Cp^*)$] ppm. $^{13}C\{^1H\}$ NMR ($CD_2Cl_2$, 75 MHz): $\delta$ = 155.1 (C3 or 5), 144.04 (C3 or 5), 109.51 (C4), 89.35 (Cp*), 58.4 ($CH_2$), 15.2 (Me), 11.6 (Me), 9.7 [$CH_3(Cp^*)$] ppm. $^{19}F$ NMR ($CD_2Cl_2$, 282.41 MHz): $\delta$ = –152.5 ppm.

**Synthesis of [Cp*IrCl(bik)]BF$_4$ (6b):** A toluene (10 mL) suspension of $[IrCp^*Cl_2]_2$ (46.3 mg, 0.058 mmol) was stirred for 30 min prior to the addition of a MeOH solution (5 mL) of bis(1-methylimidazol-2-yl) ketone, bik, (44.1 mg, 0.231 mmol). The suspension was stirred for 30 min before addition of a MeOH solution (5 mL) of $NaBF_4$ (24.2 mg, 0.221 mmol). The yellow solution was stirred for 2 h before the volume of the solution was reduced, filtered and was layered with pentane. The yellow solid obtained was collected, washed with pentane and dried in vacuo to give [Cp*IrCl(bik)]BF$_4$. Yield: 31% (23 mg). M.p. 301–305 °C. $C_{19}H_{25}BClF_4IrN_4O$ (639.9): calcd. C 35.66, H 3.94, N 8.76; found C 35.44, H 4.13, N 8.47. IR (KBr disc): $\tilde{\nu}$ = 3522 (br), 3442 (br), 3374 (br), 3153 (w), 3128 (w), 1634 (vs), 1558 (w), 1481 (w), 1421 (vs), 1386 (m), 1293 (m), 1189 (m), 1083 (m), 1032 (m), 904 (vs) cm$^{-1}$. MS (ES$^+$, $CH_2Cl_2$): *m/z* (%) = 554 (100), 552 (95), 555 (92), 553 (90) [Cp*IrCl(bik)]$^+$), 551 (50). $^1H$ NMR ($CD_2Cl_2$, 300 MHz): $\delta$ = 7.52 (d, $^3J_{H5-H4}$ = 1.10 Hz, 2 H, H4 or H5), 7.36 (d, $^3J_{H5-H4}$ = 1.10 Hz, 2 H, H4 or H5), 4.23 (s, 6 H, N–Me) 1.53 [s, 15 H, $CH_3(Cp^*)$] ppm. $^{13}C\{^1H\}$ NMR ($CD_2Cl_2$, 75 MHz): $\delta$ = 172.7 (C=O), 132.7 (C2), 129.9 (C4), 128.0 (C5), 88.5 (Cp*), 38.2 (N–Me), 8.3 [$CH_3(Cp^*)$] ppm. $^{19}F$ NMR ($CD_2Cl_2$, 282.41 MHz): $\delta$ = –153.9 ppm

**Synthesis of [Cp*IrCl(mesBIAN)]BF$_4$ (7b):** A toluene (20 mL) suspension of $[IrCp^*Cl_2]_2$ (110.5 mg, 0.139 mmol) was stirred for 30 min prior to the addition of a toluene solution (5 mL) of 1,2-bis(2,4,6-trimethylphenylimino)acenapthene, mesBIAN, (129.2 mg, 0.310 mmol). The suspension was stirred for 30 min before drop wise addition of a MeOH/toluene solution (5 mL, 1: 4) of $NaBF_4$ (34.1 mg, 0.310 mmol). The dark brown solution was stirred overnight; the solvent was removed in vacuo to give a brown solid. The solid was recrystallised from $CH_2Cl_2$, by slow diffusion of pentane. Dark brown crystals of [Cp*IrCl(mesBIAN)]BF$_4$ were collected,

 © 2007 Wiley-VCH Verlag GmbH & Co. KGaA, Weinheim 

washed with pentane (2 5 mL) and dried. Yield: 54% (129 mg). The dark brown crystals of **6b** obtained were suitable for X-ray crystal structure analysis. M.p. > 230 °C. $C_{40}H_{43}BClF_4IrN_2{\cdot}H_2O{\cdot}CH_2Cl_2{\cdot}CH_3OH$[44] (1001.3): calcd. C 50.38, H 5.13, N 2.80; found C 50.07, H 4.75, N 2.80%. IR (KBr disc): $\tilde{\nu}$ = 3629 (w), 3588 (w), 3433 (br), 2917 (w), 2361 (w), 1624 (w), 1064 (m),1473 (m) 1436 (m), 1417 (m), 1382 (m), 1302 (m), 1058 (vs), 1031 (vs), 778 (m) $cm^{-1}$. MS ($ES^+$, $CH_2Cl_2$): *m*/*z* (%) = 782 (100) [Cp*IrCl(mesBIAN)]$^+$), 783 (60), 784 (10), 743 (10). $^1H$ NMR ($CD_2Cl_2$, 300 MHz): $\delta$ = 8.19 (d, $^3J_{H5\text{-}H4}$ = 8.4 Hz, 2 H, H5), 7.55 (m, 2 H, H4), 7.23 (s, 2 H, H10), 7.10 (s, 2 H, H12), 6.89 (d, $^3J_{H3\text{-}H4}$ = 7.3 Hz, 2 H, H3), 2.48 (s, 6 H, *o*-Me), 2.46 (p, 6 H, *p*-Me), 1.92 (s, 6 H, *o*′-Me), 1.27 [s, 15 H, $CH_3$(Cp*)] ppm. $^{13}C\{^1H\}$ NMR ($CD_2Cl_2$, 75 MHz): $\delta$ = 178.7 (C1), 145.0 (C7), 142.1 (C8), 139.9 (C11), 133.2 (C5), 132.0 (C6), 131.7 (C9), 131.5 (C10), 130.6 (C12), 130.0 (C4), 129.2 (C13), 126.8 (C2), 125.5 (C3), 93.5 (Cp*), 21.3 (*p*-Me), 20.5 (*o*-Me), 18.6 (*o*′-Me), 8.6 [$CH_3$(Cp*)] ppm. $^{19}F$ NMR ($CD_2Cl_2$, 282.41 MHz): $\delta$ = –154.0 (br. s, $BF_4$) ppm.

**Synthesis of [(2,4,6-Trimethylphenyl)imino](1-methyl-2-imidazolyl)-methane:** 2-Formyl-1-methylimidazole (1.38 g, 12.5 mmol) and 2,4,6-trimethylaniline (4 mL, 26.5 mmol) were dissolved in ethanol (12 mL) and heated to reflux for 3 h. The solvent was removed in vacuo to give a brown oil which was purified by kugelrohr distillation. The product [(2,4,6-trimethylphenyl)imino](1-methyl-2-imidazolyl)methane was obtained as a viscous yellow oil. Yield: 25% (878 mg). $C_{14}H_{17}N_3$ (227.3): calcd. C 73.98, H 7.54, N 18.49; found C 73.49, H 7.88, N 17.73. MS (GC-EI, $CH_2Cl_2$): *m*/*z* (%) = 120 (100), 135 (90) [$M^+$]. $^1H$ NMR ([$D_6$]acetone, 300 MHz): $\delta$ = 8.18 (s, 1 H, N=CH), 7.27 (s, 1 H, H5), 7.12 (s, 1 H, H4), 6.87 (s, 2 H, *m*-H), 4.14 (s, 3 H, N–Me), 2.23 (s, 3 H, *p*-Me), 2.11 (s, 6 H, *o*-Me) ppm. $^{13}C\{^1H\}$ NMR ([$D_6$]acetone, 75 MHz): $\delta$ = 154.8 (N=CH), 148.4 (C7), 142.9 (C1), 129.4 (C4), 128.6 (*p*), 128.5 (*o*), 126.5 (*o*), 126.0 (C5), 35.0 (N–Me), 19.9 (*p*-Me), 17.6 (*o*-Me) ppm.

**Synthesis of [Cp*IrCl(mesim-mim)]$BF_4$ (8b):** $[IrCp^*Cl_2]_2$ (75.6 mg, 0.095 mmol) and 2,4,6-trimethylphenylimino-(1-methyl-2-imidazolyl)methane (**7**) (86.3 mg, 0.400 mmol) were dissolved in toluene (10 mL) and stirred for 30 min prior to the addition of a methanol solution (5 mL) of $NaBF_4$ (24.2 mg, 0.221 mmol). The dark orange solution was stirred for 2 h before the volume was reduced, filtered and the solution was layered with pentane (10 mL). Orange crystals of [Cp*IrCl(mesim-mim)]$BF_4$ were collected in air and dried. Yield: 38% (49.1 mg) M.p. 283–288 °C. $C_{24}H_{32}BClF_4IrN_3$ (677.0): calcd. C 42.58, H 4.76, N 6.21; found C 42.44, H 4.74, N 6.09. IR (KBr disc): $\tilde{\nu}$ = 3853 (w), 3736 (w), 3394 (br), 3153 (w), 2190 (m), 1584 (m), 1488 (m), 1424 (s), 1386 (m), 1309 (m), 1298 (m), 1142 (m), 1061 (vs), 989 (m), 853 (m), 782 (m) $cm^{-1}$.

MS ($ES^+$, $CH_2Cl_2$): *m*/*z* (%) = 590 (100) [Cp*IrCl(mesim-mim)]$^+$) 588 (80), 592 (50). $^1H$ NMR ($CD_2Cl_2$, 300 MHz): $\delta$ = 8.57 (s, 1 H, H6), 7.42 (d, $^3J_{H5\text{-}H4}$ = 1.51 Hz, 1 H, H5) 7.32 (d, $^3J_{H4\text{-}H5}$ = 1.51 Hz, 1 H, H4), 6.96 (s, 1 H, H10), 6.93 (s, 1 H, H12), 3.99 (s, 3 H, N–Me), 2.26 (s, 3 H, *p*-Me), 2.20 (s, 3 H, *o*′-Me), 2.00 (s, 3 H, *o*-Me), 1.49 [s, 15 H, $CH_3$(Cp*)] ppm. $^{13}C\{^1H\}$ NMR ($CD_2Cl_2$, 75 MHz): $\delta$ = 156.6 (C6), 149.8 (C2), 144.7 (C8), 138.5 (C11), 131.9 (C13), 130.0 (C12), 129.9 (C9), 128.6 (C4), 128.3 (C5), 89.7

Table 5. Crystal structure and refinement data for **1c**, **2c** and **3c**.

| Compound | **1c** | **2c** | **3c** |
|---|---|---|---|
| Empirical formula | $C_{27}H_{38}Cl_4Ir_2N_4$ | $C_{31}H_{46}C_{18}Ir_2N_4$ | $C_{27}H_{38}Cl_4N_4Rh_2$ |
| Formula weight | 944.81 | 1142.72 | 766.23 |
| Temperature [K] | 200(2) | 200(2) | 200(2) |
| Wavelength [Å] | 0.71073 | 0.71073 | 0.71073 |
| Crystal system | monoclinic | orthorhombic | monoclinic |
| Space group | *P*21/*a* | *P*212121 | *P*21/*a* |
| Crystal size [mm] | 0.19 × 0.12 × 0.11 | 0.34 × 0.31 × 0.28 | 0.51 × 0.43 × 0.12 |
| *a* [Å] | 14.626(3) | 12.001(2) | 14.596(2) |
| *b* [Å] | 14.413(3) | 15.082(3) | 14.436(2) |
| *c* [Å] | 14.918(3) | 21.807(4) | 14.876(2) |
| *α* [°] | 90 | 90 | 90 |
| *β* [°] | 103.20(3) | 90 | 103.1620(10) |
| *γ* [°] | 90 | 90 | 90 |
| *V* [Å$^3$] | 3061.7(11) | 3947.0(14) | 3052.0(7) |
| *Z* | 4 | 4 | 4 |
| $D_{calcd.}$ [Mg/m$^3$] | 2.05 | 1.923 | 1.668 |
| *μ* [mm$^{-1}$] | 9.057 | 7.305 | 1.455 |
| *F*(000) | 1800 | 2200 | 1544 |
| *θ* Range for data collection [°] | 3.14–27.50 | 3.11–27.49 | 3.15–27.49 |
| Limiting indices | $-18 \le h \le 18$, $-17 \le k \le 18$, $-19 \le l \le 19$ | $-15 \le h \le 12$, $-19 \le k \le 19$, $-28 \le l \le 28$ | $-18 \le h \le 18$, $-18 \le k \le 17$, $-19 \le l \le 18$ |
| Reflections collected | 63766 | 55293 | 63992 |
| Independent reflections | 7009 [$R_{int}$ = 0.0820] | 9054 [$R_{int}$ = 0.1317] | 6976 [$R_{int}$ = 0.0685] |
| Completeness to theta | 27.50°, 99.8% | 27.49°, 99.8% | 27.49°, 99.6% |
| Max. and min. transmission | 0.451 and 0.285 | 0.356 and 0.161 | 0.921 and 0.719 |
| Refinement method | full-matrix least squares on $F^2$ | full-matrix least squares on $F^2$ | full-matrix least squares on $F^2$ |
| Data/restraints/parameters | 7009/0/345 | 9054/0/418 | 6976/0/344 |
| Goodness-of-fit on $F^2$ | 1.022 | 1.01 | 1.009 |
| Final *R* indices [$I > 2\sigma(I)$] | $R_1$ = 0.0334, $wR_2$ = 0.0757 | $R_1$ = 0.0346, $wR_2$ = 0.0752 | $R_1$ = 0.0324, $wR_2$ = 0.0855 |
| *R* indices (all data) | $R_1$ = 0.0530, $wR_2$ = 0.0846 | $R_1$ = 0.0464, $wR_2$ = 0.0796 | $R_1$ = 0.0401, $wR_2$ = 0.0914 |
| Extinction coefficient | 0.00088(6) | –0.014(7) | |
| Largest diff. peak and hole [e·Å$^{-3}$] | 1.385 and –2.072 | 0.936 and –1.096 | 1.521 and –0.932 |

 © 2007 Wiley-VCH Verlag GmbH & Co. KGaA, Weinheim 

Table 6. Crystal structure and refinement data for **2b**, **7b** and **8b**.

| Compound | **2b** | **7b** | **8b** |
|---|---|---|---|
| Empirical formula | $C_{19}H_{27}BClF_4IrN_4$ | $C_{42}H_{51}BCl_5F_4IrN_2O_2$ | $C_{25}H_{34}BCl_3F_4IrN_3$ |
| Formula weight | 625.91 | 1072.11 | 761.91 |
| Temperature [K] | 200(2) | 200(2) | 200(2) |
| Wavelength [Å] | 0.71073 | 0.71073 | 0.71073 |
| Crystal system | orthorhombic | orthorhombic | triclinic |
| Space group | *Pcab* | *Pbnm* | $P\bar{1}$ |
| Crystal size [mm] | $0.19 \times 0.17 \times 0.12$ | $0.20 \times 0.18 \times 0.18$ | $0.25 \times 0.10 \times 0.05$ |
| $a$ [Å] | 15.2650(10) | 15.265(3) | 9.5200(19) |
| $b$ [Å] | 16.6330(10) | 16.509(4) | 12.287(3) |
| $c$ [Å] | 17.4210(10) | 17.182(3) | 13.418(3) |
| $\alpha$ [°] | 90 | 90 | 68.51(3) |
| $\beta$ [°] | 90 | 90 | 85.49(3) |
| $\gamma$ [°] | 90 | 90 | 77.04(3) |
| $V$ [Å$^3$] | 4423.2(5) | 4330.0(15) | 1423.2(5) |
| $Z$ | 8 | 4 | 2 |
| $D_{calcd.}$ [Mg/m$^3$] | 1.88 | 1.645 | 1.778 |
| $\mu$ [mm$^{-1}$] | 6.204 | 3.448 | 5.019 |
| $F(000)$ | 2432 | 2144 | 748 |
| $\theta$ Range for data collection [°] | 2.91–27.49 | 2.94–27.47 | 3.11–25.04 |
| Limiting indices | $-19 \le h \le 19$, $-21 \le k \le 21$, $-22 \le l \le 22$ | $-19 \le h \le 19$, $-21 \le k \le 21$, $-22 \le l \le 22$ | $-11 \le h \le 10$, $-14 \le k \le 14$, $-15 \le l \le 15$ |
| Reflections collected | 65229 | 81934 | 16560 |
| Independent reflections | 5070 [$R_{int}$ = 0.0948] | 5091 [$R_{int}$ = 0.1034] | 5027 [$R_{int}$ = 0.0709] |
| Completeness to theta | 27.49°, 99.9% | 27.50°, 99.3% | 25.04°, 99.7% |
| Max. and min. transmission | 0.512 and 0.336 | 0.712 and 0.557 | 0.805 and 0.478 |
| Refinement method | full-matrix least squares on $F^2$ | full-matrix least squares on $F^2$ | full-matrix least squares on $F^2$ |
| Data/restraints/parameters | 5070/0/278 | 5091/47/308 | 5027/0/343 |
| Goodness-of-fit on $F^2$ | 1.006 | 1.007 | 1.019 |
| Final $R$ indices [$I > 2\sigma(I)$] | $R_1$ = 0.0306, $wR_2$ = 0.0716 | $R_1$ = 0.0514, $wR_2$ = 0.1398 | $R_1$ = 0.0343, $wR_2$ = 0.0783 |
| $R$ indices (all data) | $R_1$ = 0.0456, $wR_2$ = 0.0797 | $R_1$ = 0.0680, $wR_2$ = 0.1520 | $R_1$ = 0.0439, $wR_2$ = 0.0827 |
| Largest diff. peak and hole [e·Å$^{-3}$] | 0.898 and –1.747 | 0.765 and –0.640 | 1.193 and –1.008 |

($^1J_{Rh\text{-}Cp}$ = 8.7 Hz, Cp*), 35.5 (N–Me), 20.4 (*p*-Me), 19.6 (*o*′-Me), 18.6 (*o*-Me), 8.3 [$CH_3$(Cp*)] ppm. $^{19}$F NMR ($CD_2Cl_2$, 282.41 MHz): $\delta$ = 153.7 ppm.

**Synthesis of [Cp*RhCl(bpm)]BF$_4$ (3b):** [RhCp*Cl$_2$]$_2$ (99 mg, 0.16 mmol), bpm (86 mg, 0.58 mmol) and $NaBF_4$ (67 mg, 0.61 mmol) were suspended in toluene and stirred for 12 h at room temp. The yellow-orange solid was collected in air by filtration and was recrystallised from a $CH_2Cl_2$/hexane (1:1) mix. [Cp*RhCl(bpm)]$BF_4$ was obtained as an orange powder. Yield: 47% (77 mg). MP > 230 °C dec. $C_{17}H_{23}BClF_4N_4Rh$ (508.55): calcd. C 40.15, H 4.56, N 11.02; found C 39.97, H 4.77, N 10.94. IR (KBr disc): $\tilde{\nu}$ = 3144 (m), 3117 (w), 3081 (w), 2959 (w), 2922 (w), 1493 (m), 1457 (m), 1430 (m), 1403 (s), 1288 (vs), 1278 (s), 1098 (vs), 1038 (vs), 986 (m), 767 (s) cm$^{-1}$. $^1$H NMR ($CD_2Cl_2$, 300 MHz): $\delta$ = 8.27 (d, $^3J_{H5\text{-}H4}$ = 2.64 Hz, 2 H, H5), 7.73 (d, $^3J_{H3\text{-}H4}$ = 2.26 Hz, 2 H, H3), 7.28 (d, $^2J_{Hb\text{-}Ha}$ = 14.7 Hz, 1 H, Ha), 6.50 (dd, $^3J_{H5\text{-}H4}$ = 2.64 Hz, $^3J_{H3\text{-}H4}$ = 2.26 Hz, 2 H, H4), 6.00 (d, $^2J_{Ha\text{-}Hb}$ = 14.7 Hz, 1 H, Hb), 1.71 [br. s, 15 H, $CH_3$(Cp*)] ppm. $^{13}$C{$^1$H} NMR ($CD_2Cl_2$, 75 MHz): $\delta$ = 144.8 (C3), 135.0 (C5), 108.7 (C4), 88.8 (Cp*), 62.7 ($CH_2$), 8.7 [$CH_3$(Cp*)] ppm. $^{19}$F NMR ($CD_2Cl_2$, 282.41 MHz): $\delta$ = –151.6 ppm.

**Synthesis of [Cp*RhCl(bim)]BF$_4$ (4b):** [RhCp*Cl$_2$]$_2$ (104 mg, 0.17 mmol), bim (115 mg, 0.65 mmol) and $NaBF_4$ were suspended in toluene and stirred for 12 h at room temp. The orange solid was collected via filtration and recrystallised from $CH_2Cl_2$: pentane. Red cubic crystals of [Cp*RhCl(bim)]$BF_4$ were obtained. Yield: 63% (115 mg). M.p. 290 °C (dec.). $C_{19}H_{27}BClF_4N_4Rh$ (536.6): calcd. C 42.53, H 5.07, N 10.44; found C 42.56, H 5.20, N 10.50. IR (KBr disc): $\tilde{\nu}$ = 3129 (m), 2961 (w), 1621 (w), 1547 (m), 1515 (s), 1456 (m), 1417 (s), 1378 (m), 1288 (m), 1171 (w), 1143 (m), 1057 (br. s), 819 (w), 762 (s), 618 (m), 521 (m), 436 (m), 409 (m) cm$^{-1}$. MS (ES$^+$, $CH_2Cl_2$) *m*/*z*: 449 (M$^+$, 100%), 451 (80%), 413 (70%). $^1$H NMR ($CD_2Cl_2$, 300 MHz): $\delta$ = 7.03 (d, 4 H, H4 and H5), 4.47 (d, $^2J_{Hb\text{-}Ha}$ = 19.0 Hz, 1 H, Ha), 4.16 (d, $^2J_{Ha\text{-}Hb}$ = 19.0 Hz, 1 H, Hb), 3.83 (s, 6 H, N–$CH_3$), 1.60 [s, 15 H, $CH_3$(Cp*)] ppm. $^{13}$C NMR [$CD_2Cl_2$, 75 MHz]: $\delta$ = 142.0 (C2), 129.1 (C4 or 5), 123.8 (C5 or 4), 96.0 ($^1J_{Rh\text{-}Cp}$ = 8.0 Hz, Cp*), 34.9 (N–$CH_3$), 22.8 ($CH_2$), 9.4 [$CH_3$(Cp*)] ppm. $^{19}$F NMR ($CD_2Cl_2$, 282.41 MHz): $\delta$ = –152.2 ppm.

### X-ray Crystallography

Details of the crystals and their refinements are given in Table 5 and Table 6. CCDC- 291178, -291179, -291180, -291478, -609638 and -609639 contain the supplementary crystallographic information for **1c**, **7b**, **2c**, **3c**, **8b** and **2b**, respectively. These data can be obtained free of charge from The Cambridge Crystallographic Data Centre via www.ccdc.cam.ac.uk/data_request/cif.

## Acknowledgments

We gratefully acknowledge financial support from The University of New South Wales, The Australian Research Council and the Australian government for an Australian Postgraduate Award (D.F.K.). We acknowledge Bradley Man for assistance.

 © 2007 Wiley-VCH Verlag GmbH & Co. KGaA, Weinheim 

[1] L. D. Field, B. A. Messerle, S. L. Rumble, *Eur. J. Org. Chem.* **2005**, 2881–2883.
[2] I. Takei, Y. Nishibayashi, Y. Arikawa, S. Uemura, M. Hidai, *Organometallics* **1999**, *18*, 2271–2274.
[3] L. D. Field, B. A. Messerle, S. L. Wren, *Organometallics* **2003**, *22*, 4393–4395.
[4] S. Burling, L. D. Field, B. A. Messerle, P. Turner, *Organometallics* **2004**, *23*, 1714–1721.
[5] L. D. Field, B. A. Messerle, K. Q. Vuong, P. Turner, *Organometallics* **2005**, *24*, 4241–4250.
[6] C. G. Hartung, A. Tillack, H. Trauthwein, M. Beller, *J. Org. Chem.* **2001**, *66*, 6339–6343.
[7] B. M. Trost, Y. H. Rhee, *J. Am. Chem. Soc.* **2003**, *125*, 7482–7483.
[8] S. Elgafi, L. D. Field, B. A. Messerle, *J. Organomet. Chem.* **2000**, *607*, 97–104.
[9] E. Mas-Marzá, M. Sanaú, E. Peris, *Inorg. Chem.* **2005**, *44*, 9961–9967.
[10] M. Utsunimiya, K. Ryoichi, M. Kawatsura, J. F. Hartwig, *J. Am. Chem. Soc.* **2003**, *125*, 5608–5609.
[11] A. M. Seayad, K. Selvauma, M. Ahmed, M. Beller, *Tetrahedron Lett.* **2003**, *44*, 1679–1683.
[12] T. Kobayashi, Y. Koga, K. Narasaka, *J. Organomet. Chem.* **2001**, *614–640*, 73–87.
[13] P. A. Wender, N. M. Deschamps, T. J. Williams, *Angew. Chem. Int. Ed.* **2004**, *43*, 3076–3079.
[14] P. Burger, R. G. Bergmann, *J. Am. Chem. Soc.* **1993**, *115*, 10463–10463.
[15] D. M. Tellers, R. G. Bergmann, *Organometallics* **2001**, *20*, 4819–4832.
[16] X. Li, A. R. Chianese, T. Vogel, R. H. Crabtree, *Org. Lett.* **2005**, *24*, 5437–5440.
[17] N. A. Wynberg, L. J. Leger, M. L. Contad, C. M. Vogels, A. Decken, S. J. Duffy, S. A. Wescott, *Can. J. Chem. Eng.* **2005**, *83*, 666–667.
[18] K.-I. Fujita, Z. Li, N. Ozeki, R. Yamaguchi, *Tetrahedron Lett.* **2003**, *44*, 2687–2690.
[19] M. Furegati, A. J. Rippert, *Tetrahedron: Asymmetery* **2005**, 3947–3950.
[20] K.-I. Fujita, C. Kitasuji, S. Furukawa, R. Yamagushi, *Tetrahedron Lett.* **2004**, *45*, 3215–3217.
[21] For a recent review of rhodium-catalysed C–C bond formation; K. Fagnou, M. Lautens, *Chem. Rev.* **2003**, *103*, 169–196.
[22] K.-I. Fujita, M. Owaki, R. Yamaguchi, *Chem. Commun.* **2002**, 2964–2965.
[23] M.-T. Youinou, R. Ziessel, *J. Organomet. Chem.* **1989**, *363*, 197–208.
[24] S. Greulicj, A. Klein, A. Knödler, W. Kaim, *Organometallics* **2002**, *21*, 765–769.
[25] Y. Himeda, N. Onozawa-Komatsuaki, H. Sugihara, H. Arakawa, K. Kasuga, *Organometallics* **2004**, *23*, 1480–1483.
[26] P. Govindaswamy, Y. A. Mozharivskyj, M. R. Kollipara, *Polyhedron* **2005**, *24*, 1710–1716.
[27] D. L. Davies, J. Fawcett, S. A. Garrat, D. R. Russel, *Dalton Trans.* **2004**, 3629–3634.
[28] B. J. Wik, C. Rømming, M. Tilset, *J. Mol. Catal. A* **2002**, 23–32.
[29] E. Carmona, A. Cingolani, F. Marcheti, C. Pettinari, R. Pettinari, B. W. Skelton, A. H. White, *Organometallics* **2003**, *22*, 2820–2826.
[30] P. Govindaswamy, M. Kollipara, *J. Coord. Chem.* **2006**, *59*, 663–669.
[31] S. Berger, F. Baumann, T. Scheiring, W. Kaim, *Z. Anorg. Allg. Chem.* **2001**, *627*, 620–630.
[32] S. Ogo, K. Uehara, T. Abura, Y. Watanabe, S. Fukuzumi, *J. Am. Chem. Soc.* **2004**, *126*, 16520–16527.
[33] L. Quebatte, R. Scopelliti, K. Severin, *Eur. J. Inorg. Chem.* **2006**, 231–236.
[34] W. Rigby, J. A. McCleverty, P. M. Maitlis, *J. Chem. Soc., Dalton Trans.* **1979**, 382–386.
[35] S. Burling, L. D. Field, B. A. Messerle, P. Turner, *Organometallics* **2004**, *23*, 1714–1721.
[36] L. D. Field, B. A. Messerle, M. Rehr, L. P. Soler, T. W. Hambley, *Organometallics* **2003**, *22*, 2387–2395.
[37] C. White, A. Yates, P. M. Maitlis, *Inorg. Synth.* **1992**, *29*, 228.
[38] S. Juliá, J. M. Mazo, L. Avila, *Organic Preparations and Procedures Int.* **1984**, *16*, 299–307.
[39] S. Elgafi, L. D. Field, B. A. Messerle, T. W. Hambley, P. Turner, *J. Chem. Soc., Dalton Trans.* **1997**, 2341.
[40] P. K. Byers, A. J. Canty, *Organometallics* **1990**, *9*, 210.
[41] R. van Asselt, C. J. Elsevier, W. J. J. Smeets, A. L. Spek, R. Benedix, *Recl. Trav. Chim. Pays-Bas* **1994**, *113*, 88–98.
[42] M. Gasperini, F. Ragaini, S. Cenini, *Organometallics* **2002**, *21*, 2950–2957.
[43] F. J. LaRonde, M. A. Brook, *Inorg. Chim. Acta* **1999**, *296*, 208–221.
[44] This solvent inclusion is evidenced in the crystal structure for this compound.

Received: August 7, 2006
Published Online: November 14, 2006

 © 2007 Wiley-VCH Verlag GmbH & Co. KGaA, Weinheim 

DOI: 10.1002/ejic.200600318

# Synthesis and Characterisation of Dinuclear Nickel(II) and Cadmium(II) Complexes of *N*-Alkylated Derivatives of Hexaazadithiophenolate Macrocycles

**Mathias Gressenbuch[a] and Berthold Kersting*[a]**

**Keywords:** Macrocyclic ligands / N ligands / S ligands / Nickel / Cadmium

The effect of *N*-alkylation on the ligating properties of the Robson-type 24-membered hexaazadithiophenolate macrocycle $H_2L^1$ [13,27-bis(*tert*-butyl)-3,6,9,17,20,23-hexaazatricyclo[23.3.1$^{11,15}$]triaconta-1(28),11,13,15(30),25,26-hexaene-29,30-dithiol] has been examined. Two new derivatives ($H_2L^3$ and $H_2L^4$) of $H_2L^1$ have been prepared. $H_2L^3$ is a dimethylated derivative of $H_2L^1$ and $H_2L^4$ is a tetraethylated derivative of $H_2L^3$. A series of complexes of the type $[(L^R)M^{II}_2(\mu\text{-}Cl)]^+$ [R = 1, M = Cd (**10**), R = 3, M = Ni (**8**), M = Cd (**12**), R = 4, M = Ni (**9**), M = Cd (**13**)] have been prepared and structurally characterised. The X-ray crystal structure determination of these dioctahedral complexes with an $N_3M(S)_2(\mu\text{-}Cl)MN_3$ core structure has revealed two conformations of the supporting ligands. In **8**, **9**, **10** and **12** the ligands adopt a folded $C_s$-symmetric conformation of type A whereas in the cadmium complex **13** the alternative $C_{2v}$-symmetric "bowl-shaped" conformation (type B) is present. A structural comparison has allowed us to determine the factors that determine the ligand conformations. It has been established that the ligand conformations adopted depend not only on the co-ligand but also on the metal ion radius and the *N*-alkylation grade.

(© Wiley-VCH Verlag GmbH & Co. KGaA, 69451 Weinheim, Germany, 2007)

## Introduction

Macrocyclic ligands containing 14 or more ring atoms are known to have a rather flexible structure, and it is often observed that such ligands can adopt several different conformations.[1,2] Typical examples are the $N_4$ macrocycle cyclam and its countless *N*-alkylated derivatives,[3] which can have planar (*trans*) or folded (*cis*) conformations in octahedral complexes.[4–6] It is well-known that the physical and chemical properties of macrocyclic complexes are highly dependent on the conformations of the supporting ligands. This is of importance for a number of applications, since often only one of several possible conformational isomers exhibits the desired property.[7] Thus, in macrocyclic chemistry it is of importance to establish the factors that are responsible for the stabilisation/destabilisation of the various structural forms.

We recently reported the synthesis of the hexaazadithiophenolate macrocycle $H_2L^1$ and its permethylated derivative

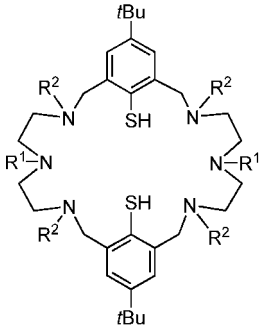


$H_2L^1$ ($R^1 = R^2 = H$)
$H_2L^2$ ($R^1 = R^2 = CH_3$)
$H_2L^3$ ($R^1 = CH_3$, $R^2 = H$)
$H_2L^4$ ($R^1 = CH_3$, $R^2 = CH_2CH_3$)

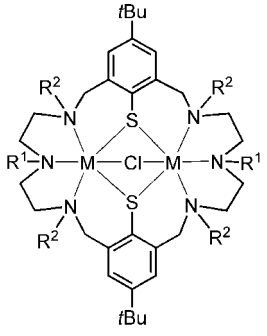


**6**, $[(L^1)Ni_2(\mu\text{-}Cl)]^+$ **10**, $[(L^1)Cd_2(\mu\text{-}Cl)]^+$
**7**, $[(L^2)Ni_2(\mu\text{-}Cl)]^+$ **11**, $[(L^2)Cd_2(\mu\text{-}Cl)]^+$
**8**, $[(L^3)Ni_2(\mu\text{-}Cl)]^+$ **12**, $[(L^3)Cd_2(\mu\text{-}Cl)]^+$
**9**, $[(L^4)Ni_2(\mu\text{-}Cl)]^+$ **13**, $[(L^4)Cd_2(\mu\text{-}Cl)]^+$

Scheme 1. Ligands and complexes studied in this work.

[a] Institut für Anorganische Chemie, Universität Leipzig, Johannisallee 29, 04103 Leipzig, Germany
Fax: +49-341-973-6199
E-mail: b.kersting@uni-leipzig.de

$H_2L^2$ (Scheme 1)[8] and their use in the preparation of dinuclear transition metal complexes for regioselective substrate transformations.[9,10]


© 2007 Wiley-VCH Verlag GmbH & Co. KGaA, Weinheim

Examination of the structures of the chlorido-bridged $[(L^R)M^{II}_2(\mu\text{-Cl})]^+$ complexes has revealed that the octadentate ligands most often adopt a folded $C_s$-symmetric conformation of type A (e.g. complexes **6** and **7**, see Scheme 2).[11,12] Very recently, however, the alternative $C_{2v}$-symmetric "bowl-shaped" conformation of type B was detected for the chlorido-bridged cadmium complex **11**.[13] These findings encouraged us to look for the factors that determine these ligand conformations.

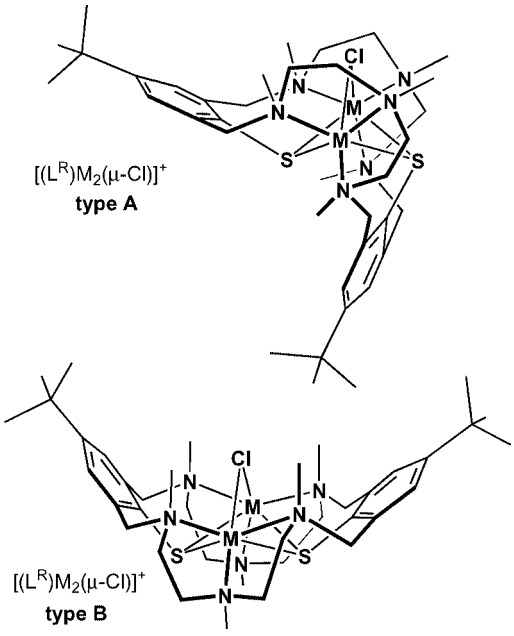


Scheme 2. Schematic representation of the two ligand conformations of the octadentate macrocycles $(L^R)^{2-}$ observed in the chlorido-bridged $[(L^R)M_2(\mu\text{-Cl})]^+$ complexes **6**, **7** and **11**.[11,13]

In this study we describe the synthesis and characterisation of a series of chlorido-bridged Ni and Cd complexes of the type $[(L^R)M_2(\mu\text{-Cl})]^+$ supported by 24-membered hexaazadithiophenolate ligands $(L^R)^{2-}$ with different *N*-alkylation grades and patterns (see Scheme 1 for ligand abbreviations). We have obtained single crystals of the complexes **8**, **9**, **10**, **12** and **13** suitable for X-ray structure determinations, which has allowed us to study the ligating properties of the supporting ligands as a function of the *N*-alkylation grade. The solution-state structures of the cadmium complexes **10**–**13** derived from NMR studies and the solid-state structure of one proligand are also presented.

## Results and Discussion

### Ligand Synthesis

The synthetic route to the new ligands $H_2L^3$ and $H_2L^4$ is outlined in Scheme 3. The bicyclic macrocycle **3** was prepared by a [2 + 1] condensation reaction between tetraaldehyde **1**[14] and bis(aminoethyl)methylamine (**2**) in an etha-

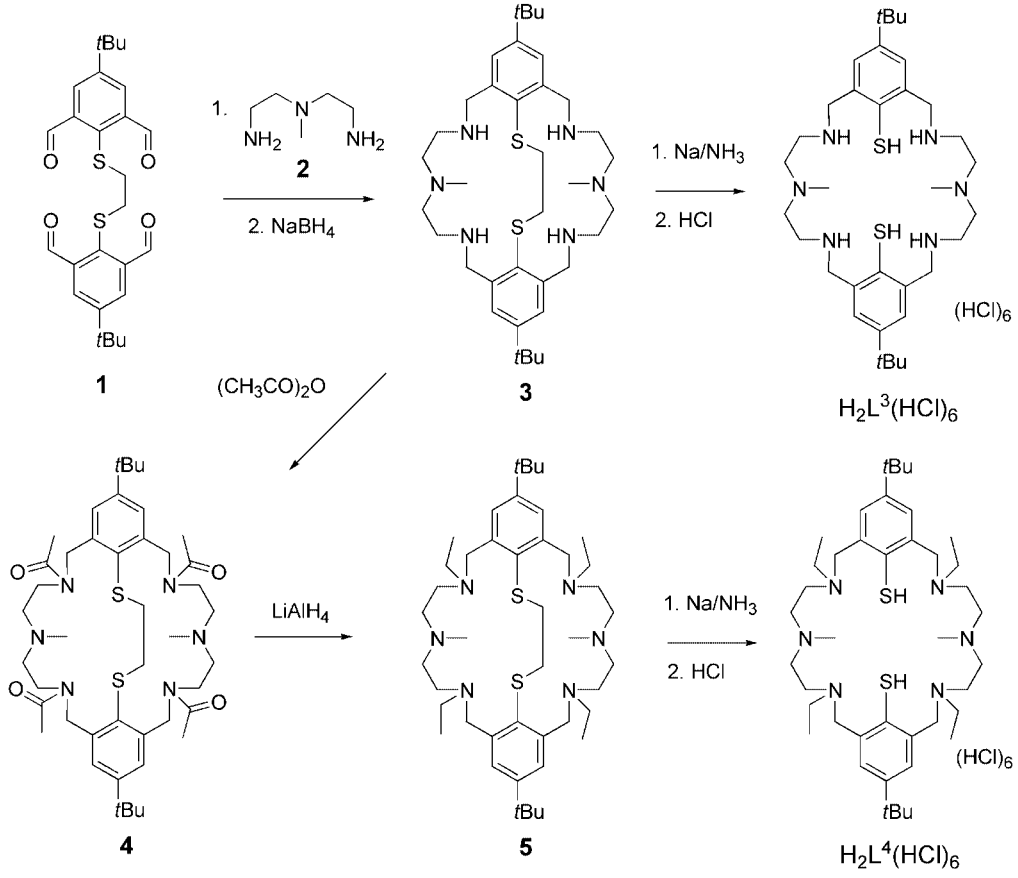


Scheme 3. Synthesis of the ligands $H_2L^3$ and $H_2L^4$.

 © 2007 Wiley-VCH Verlag GmbH & Co. KGaA, Weinheim 

nol/dichloromethane mixed solvent system, followed by reduction of the intermediate imine functions with $NaBH_4$. To prevent the formation of higher condensation products the cyclisation reaction was performed under high dilution conditions. Thus, proligand **3** was obtained in nearly quantitative yield upon workup. Subsequent deprotection of the thioether functions was achieved in the usual way,[14] with sodium in liquid ammonia followed by acidic workup. The second ligand system was prepared according to a protocol used for the alkylation of triazacyclononane[15] and cyclam.[16] Acylation of the four benzylic nitrogen donors of **3** was accomplished with acetic anhydride. The subsequent $LiAlH_4$ reduction of the resulting tetraamide **4** furnished the tetraethylated macrobicycle **5** in good yield. The final deprotection of the masked thiophenolate functions with sodium in liquid ammonia followed by acidic workup gave $H_2L^4$ as its hexahydrochloride salt. These new ligands were obtained in good overall yields without the need for metal templates. All new compounds were characterised by elemental analysis, IR, $^1H$ and $^{13}C$ NMR spectroscopy (see Exp. Sect.), and compound **5** also by X-ray crystallography. The hydrochloride salts of the ligands $H_2L^3$ and $H_2L^4$ could not be obtained in analytically pure form. Nevertheless, they were of sufficient purity for metal complex syntheses.

### Synthesis of Complexes

A series of chlorido-bridged nickel(II) and cadmium(II) complexes of the type $[(L^R)M_2(\mu\text{-}Cl)]^+$ were prepared in order to systematically investigate the effect of *N*-alkylation on metal ion complexation and metal complex structures. The synthesised complexes and their labels are collected in Scheme 1. Of these, $[(L^1)Ni_2(\mu\text{-}Cl)]^+$ (**6**),[11] $[(L^2)Ni_2(\mu\text{-}Cl)]^+$ (**7**)[17] and $[(L^2)Cd_2(\mu\text{-}Cl)]^+$ (**11**)[13] have been reported previously. The complexation reactions of the macrocycles with $NiCl_2{\cdot}6H_2O$ (or $CdCl_2{\cdot}H_2O$) in the presence of triethylamine proceeded smoothly and yielded yellow or colourless solutions of the respective $[(L^R)M_2(\mu\text{-}Cl)]^+$ monocations, which could be readily isolated as their crystalline perchlorate or tetraphenylborate salts. The new compounds gave satisfactory elemental analyses and were characterised by spectroscopic methods (IR, UV/Vis, $^1H$ and $^{13}C$ NMR spectroscopy) and compounds **8**$[BPh_4]$, **9**$[BPh_4]$, **10**$[BPh_4]$, **12**$[BPh_4]$ and **13**$[BPh_4]$ also by X-ray structure analysis.

### Spectroscopic Characterisation: IR and UV/Vis Spectroscopy

The infrared spectra of all compounds display the bands expected for the macrocyclic ligands and counterions, but are not informative with respect to the conformations of the supporting ligands. The electronic absorption spectra of the nickel complexes were recorded in the range 300–1600 nm in acetonitrile solution. Selected spectroscopic data are reported in Table 1. The data for complexes **6** and **7** have been reported previously and are included for comparative purposes.[11] The spectra of the nickel complexes are similar but not identical. Each compound displays three weak absorption bands above 500 nm. The absorption band in the range 620–670 nm can be attributed to the $\nu_2$ transition $[^3A_{2g}(F) \rightarrow {}^3T_{1g}(F)]$ of an octahedral nickel(II) ($d^8$) ion. The bands between 900 and 1100 nm can be assigned to the $\nu_1$ transition $[^3A_{2g}(F) \rightarrow {}^3T_{2g}(F)]$, which is split presumably due to lower symmetry. The slight differences in the positions of the d–d transitions indicate that each complex retains its integrity in solution. This is also supported by the NMR spectroscopic data for the cadmium complexes **10**, **12** and **13** described below.

Table 1. Synthesised complexes, their labels, structure type and selected UV/Vis data.

| Complex | Structure type | $\lambda_{max}$ [nm] ($\varepsilon$ [$M^{-1}\,cm^{-1}$])[a] | Ref. |
|---|---|---|---|
| **6** $[(L^1)Ni_2(\mu\text{-}Cl)]^+$ | A | 625 (58), 894 (54), 941 (56) | [11] |
| **7** $[(L^2)Ni_2(\mu\text{-}Cl)]^+$ | A | 658 (41), 920 (59), 1002 (80) | [11] |
| **8** $[(L^3)Ni_2(\mu\text{-}Cl)]^+$ | A | 623 (76), 902 (63), 960 (68) | this work |
| **9** $[(L^4)Ni_2(\mu\text{-}Cl)]^+$ | A | 675 (31), 928 (62), 1013 (82) | this work |
| **10** $[(L^1)Cd_2(\mu\text{-}Cl)]^+$ | A | | this work |
| **11** $[(L^2)Cd_2(\mu\text{-}Cl)]^+$ | B | | [13] |
| **12** $[(L^3)Cd_2(\mu\text{-}Cl)]^+$ | A | | this work |
| **13** $[(L^4)Cd_2(\mu\text{-}Cl)]^+$ | B | | this work |

[a] The UV/Vis spectra were recorded for the perchlorate salts. Spectra were recorded in $CH_3CN$ solution at 295 K for solutions with a concentration of about $1.0\times10^{-3}$ M for **6** and **7** and $1.9\times10^{-3}$ M for complex **8**.

### NMR Spectroscopy

Selected $^1H$ and $^{13}C$ NMR spectroscopic data for the cadmium complexes **10**, **12** and **13** are presented in Table 2. The data for complex **11** have been reported previously and are included for comparative purposes.[13] The $^1H$ NMR spectra of the dicadmium complexes **10** and **12** are different from those of **11** and **13**. For example, the signals for the aromatic protons and the *tert*-butyl protons are split into two singlets. Similarly, the $^{13}C$ NMR spectra of **10** and **12** display eight signals for the aromatic carbon atoms labelled $C^{11}$–$C^{18}$, whereas only four signals are seen for the respective atoms in **11** and **13**. These data are indicative of a ligand conformation of type A for **10** and **12** and of type B for **11** and **13**. Thus, in contrast to the nickel complexes above, the ligand conformations in the $[(L^R)Cd_2(\mu\text{-}Cl)]^+$ complexes clearly depend on the *N*-alkylation grade. This conclusion is also borne out by the single-crystal X-ray structure determinations of **10**, **12** and **13** described below.

### X-ray Crystallography

The X-ray crystal structures of the proligand **5** and the complexes **8**$[BPh_4]{\cdot}3EtOH$, **9**$[BPh_4]{\cdot}5MeCN$, **10**$[BPh_4]{\cdot}5MeOH$, **12**$[BPh_4]{\cdot}2MeCN$ and $\{$**13**$[BPh_4]{\cdot}3.5MeCN\}_2$ were determined in order to establish the geometries about the metal ions and the bonding modes of the supporting ligands.

 © 2007 Wiley-VCH Verlag GmbH & Co. KGaA, Weinheim 

Table 2. Selected $^1H$ and $^{13}C$ NMR spectroscopic data for complexes **10**–**13**.[a]

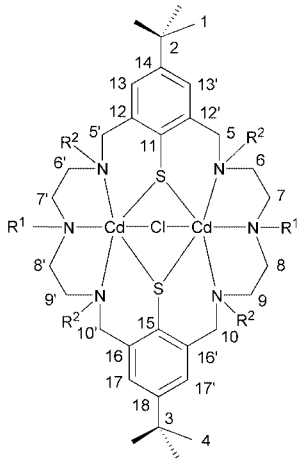


$(L^1)^{2-}$, $R^1$ = H, $R^2$ = H
$(L^2)^{2-}$, $R^1$ = $CH_3$, $R^2$ = $CH_3$
$(L^3)^{2-}$, $R^1$ = $CH_3$, $R^2$ = H
$(L^4)^{2-}$, $R^1$ = $CH_3$, $R^2$ = Et

| | **10**[$ClO_4$] | **11**[$ClO_4$] | **12**[$ClO_4$] | **13**[$ClO_4$] |
|---|---|---|---|---|
| $^1H$ NMR[a] | | | | |
| $C^{13,13',17,17'}H$ | 7.34 s | 7.20 s | 7.17 s | 7.28 s |
| | 7.16 s | | 7.32 s | |
| $R^1$ | – | 2.84 s ($CH_3$) | 2.65 s ($CH_3$) | 2.83 s ($CH_3$) |
| $R^2$ | – | 2.33 s ($CH_3$) | – | 1.12 t ($CH_2CH_3$)[b] |
| $C^1H_3$, $C^4H_3$ | 1.26 | 1.26 s | 1.25 s | 1.27 s |
| | 1.32 | | 1.29 s | |
| $^{13}C$ NMR[c] | | | | |
| $C^{14,18}$ | 145.1 | 147.1 | 148.21 | 146.78 |
| | 145.0 | | 147.96 | |
| $C^{11,15}$ | 139.1 | 141.8 | 140.24 | 142.13 |
| | 138.2 | | 138.45 | |
| $C^{12,12',16,16'}$ | 137.4 | 135.8 | 139.46 | 136.29 |
| | 137.3 | | 138.95 | |
| $C^{13,13',17,17'}$ | 127.8 | 131.0 | 129.01 | 130.18 |
| | 127.5 | | 129.28 | |
| $C^{5-10,5'-10'}$ | 56.0, 55.2 | 63.8 | 60.37, 58.17 | 58.13 |
| | 54.2, 49.2 | 60.8 | 58.06, 56.20 | 56.65 |
| | 48.9, 47.4 | 58.0 | 55.19, 50.68 | 55.74 |
| $R^1$ | – | 50.1 ($CH_3$) | 49.48 ($CH_3$) | 50.30 ($CH_3$) |
| $R^2$ | – | 46.0 ($CH_3$) | – | 6.63 ($CH_2$), 50.00 ($CH_3$) |
| $C^{2,3}$ | 33.8 | 34.7 | 34.84 | 34.70 |
| | 33.7 | | 34.93 | |
| $C^{1,4}$ | 31.3 | 31.6 | 31.61 | 31.50 |
| | 31.2 | | 31.74 | |

[a] Spectra were recorded in $CD_3CN$ (**11**–**13**) or $CD_3OD$ (**10**) solution at 295 K. [b] The resonances for the methylene protons of the ethyl substituents are obscured by the resonances of the ethylene groups. [c] Spectra were recorded in $CD_3CN$ (**11**–**13**) or [$D_6$]DMSO (**10**) solution at 295 K.

### *Compound 5*

The molecular structure of the proligand **5** is shown in Figure 1. The thioether adopts a highly folded conformation that is typical for such large macrocycles.[18] The two phenyl rings are not really coplanar to each other, the dihedral angle being 30.9°. The ethyl substituents bonded to N(3) and N(3′) point into the central cavity, partly filling the void between the phenyl rings. The distance between their centroids amounts to 6.216 Å. There are no unusual features as far as bond lengths and angles are concerned. The C–S sulfur bond lengths involving the $sp^2$-hybridized carbon atoms (C1, C1′) [1.786(2) Å] are shorter than the ones involving the $sp^3$-hybridized carbon atoms [1.820 Å] C22 and C22′. Virtually the same distances are seen in the permethylated derivative.[19]

### *[($L^3$)$Ni^{II}_2$(μ-Cl)][$BPh_4$]·3EtOH (8[$BPh_4$]·3EtOH) and [($L^4$)$Ni^{II}_2$(μ-Cl)][$BPh_4$]·5MeCN (9[$BPh_4$]·5MeCN)*

The crystal-structure determinations of the two title compounds reveal the presence of dioctahedral complex

 © 2007 Wiley-VCH Verlag GmbH & Co. KGaA, Weinheim 

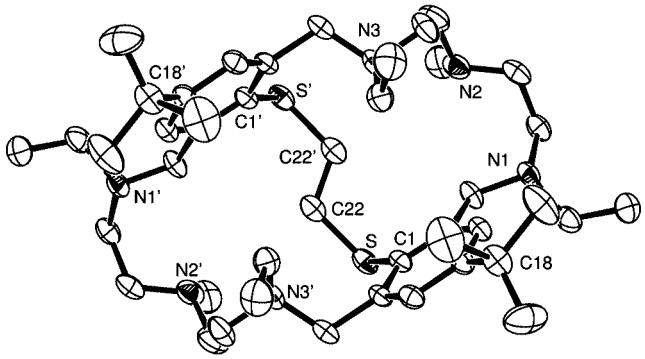


Figure 1. Molecular structure of compound **5** with atomic numbering for key atoms. Hydrogen atoms have been omitted for clarity. Symmetry codes used to generate equivalent atoms: $-x$, $+y$, $0.5 - z$ ($'$).

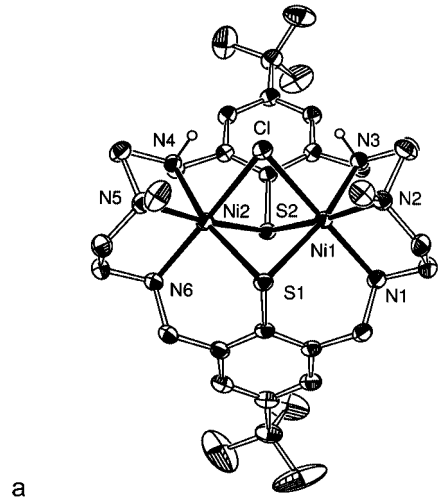


a

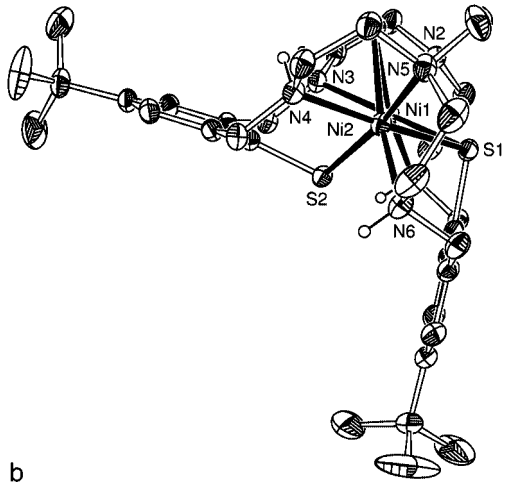


b

Figure 2. Two perspective views of the molecular structure of **8** with atomic numbering for key atoms (30% probability thermal ellipsoids). Hydrogen atoms (except those bonded to N atoms) have been omitted for clarity.

cations, tetraphenylborate anions and ethanol or acetonitrile molecules of solvent of crystallisation. ORTEP plots of **8** and **9** are displayed in Figures 2 and 3, respectively. The atomic numbering scheme for the central $N_3Ni(\mu\text{-}S)_2(\mu\text{-}Cl)NiN_3$ core in **8** is used throughout to facilitate structural comparisons. Selected bond lengths and angles are listed in Tables 3 and 4. The corresponding values for $[(L^1)Ni_2(\mu\text{-}Cl)]^+$ (**6**) and $[(L^2)Ni_2(\mu\text{-}Cl)]^+$ (**7**) are included for comparative purposes.

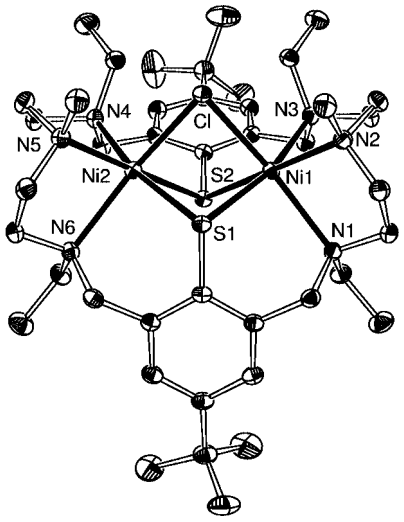


Figure 3. Molecular structure of **9** with atomic numbering for key atoms (30% probability thermal ellipsoids). Hydrogen atoms have been omitted for clarity.

The structures of the chlorido-bridged dinickel(II) complexes **8** and **9** are very similar and, with the exception of the *N*-alkyl substituents, almost superimposable with those of **6** and **7**.[11] The structure of **8** is representative for all complexes. As can be seen from Figure 2, the supporting ligand adopts a saddle-shaped, $C_s$-symmetric conformation that is reminiscent of the "partial-cone" conformation of calixarenes.[20] The metal ions are in a strongly distorted octahedral $N_3S_2Cl$ environment, being coordinated by two sulfur and three facially oriented nitrogen atoms of the macrocycle and a symmetrically bridging chloride ion to give an $N_3Ni^{II}(\mu\text{-}SR)_2(\mu\text{-}Cl)Ni^{II}N_3$ core. The distortions from the ideal octahedral geometry are manifested in the *cis* and *trans* L–M–L bond angles, which deviate by as much as 18.2° from their ideal values (see Table 4). The diethylenetriamine units coordinate facially with one larger and two smaller N–M–N bond angles. This is commonly observed in complexes with this tridentate unit.[21]

As can be seen in Table 3, the metal–ligand bond lengths in **6**–**9** clearly depend on the type of nitrogen donor atoms. Thus, upon conversion of the six secondary amines in **6** to tertiary amine functions in **9**, the average M–N bond length increases by about 0.15 Å. This, in turn, results in a large decrease in the M–Cl bond lengths by about 0.25 Å. In other words, the larger the number of tertiary amine donors the shorter the distance between the metal ions and the co-ligand. Similar effects have been reported for nickel complexes of other azamacrocycles and their peralkylated deriv-

 © 2007 Wiley-VCH Verlag GmbH & Co. KGaA, Weinheim 

Table 3. Selected bond lengths [Å] in complexes **6**–**13**.

| | **6** | **7**[b] | **8** | **9** | **10** | **11** | **12** | **13**[b] |
|---|---|---|---|---|---|---|---|---|
| M(1)–Cl | 2.639(2) | 2.433(2) [2.516(2)] | 2.512(1) | 2.4870(4) | 2.728(2) | 2.682(1) | 2.747(3) | 2.676(1) [2.703(1)] |
| M(1)–N(1) | 2.078(6) | 2.352(5) [2.349(5)] | 2.129(3) | 2.383(1) | 2.411(5) | 2.453(3) | 2.351(6) | 2.456(4) [2.410(3)] |
| M(1)–N(2) | 2.103(7) | 2.173(5) [2.173(5)] | 2.167(3) | 2.163(1) | 2.354(5) | 2.424(3) | 2.460(7) | 2.399(3) [2.395(3)] |
| M(1)–N(3) | 2.085(6) | 2.181(5) [2.167(5)] | 2.083(3) | 2.232(1) | 2.386(5) | 2.410(4) | 2.388(7) | 2.444(3) [2.508(3)] |
| M(1)–S(1) | 2.418(2) | 2.471(2) [2.475(2)] | 2.453(1) | 2.4843(4) | 2.699(2) | 2.653(1) | 2.660(2) | 2.709(1) [2.685(1)] |
| M(1)–S(2) | 2.419(2) | 2.405(2) [2.407(2)] | 2.420(1) | 2.3750(4) | 2.637(2) | 2.699(2) | 2.656(2) | 2.653(1) [2.693(1)] |
| M(2)–Cl | 2.602(2) | 2.450(2) [2.455(2)] | 2.535(1) | 2.4885(4) | 2.674(3) | 2.723(1) | 2.793(3) | 2.645(2) [2.648(1)] |
| M(2)–N(4) | 2.099(7) | 2.171(5) [2.222(5)] | 2.081(3) | 2.188(1) | 2.368(5) | 2.441(3) | 2.353(6) | 2.442(3) [2.464(3)] |
| M(2)–N(5) | 2.141(7) | 2.175(6) [2.172(5)] | 2.161(3) | 2.165(1) | 2.372(6) | 2.388(3) | 2.440(7) | 2.399(3) [2.399(3)] |
| M(2)–N(6) | 2.134(7) | 2.380(6) [2.357(5)] | 2.141(3) | 2.411(1) | 2.447(6) | 2.409(3) | 2.401(8) | 2.474(3) [2.473(3)] |
| M(2)–S(1) | 2.423(2) | 2.498(2) [2.483(2)] | 2.458(1) | 2.4968(4) | 2.682(2) | 2.696(1) | 2.611(2) | 2.663(1) [2.656(1)] |
| M(2)–S(2) | 2.405(2) | 2.423(2) [2.371(2)] | 2.423(1) | 2.3940(4) | 2.664(2) | 2.659(1) | 2.662(2) | 2.698(1) [2.713(1)] |
| M–N[a] | 2.107(7) | 2.239(6) [2.240(5)] | 2.127(3) | 2.257(1) | 2.390(5) | 2.421(4) | 2.399(7) | 2.436(4) [2.442(3)] |
| M–Cl[a] | 2.621(2) | 2.442(2) [2.486(2)] | 2.524(1) | 2.4878(4) | 2.701(3) | 2.703(1) | 2.770(3) | 2.661(1) [2.676(1)] |
| M–S[a] | 2.416(2) | 2.449(2) [2.434(2)] | 2.439(1) | 2.4375(4) | 2.671(2) | 2.677(1) | 2.647(2) | 2.681(1) [2.687(1)] |
| M···M | 3.098(2) | 3.184(2) [3.217(2)] | 3.074(1) | 3.2400(4) | 3.2666(17) | 3.3584(9) | 3.267(1) | 3.3550(8) [3.3387(8)] |

[a] Average values. [b] There are two crystallographically independent molecules A and B in the asymmetric unit. Values in square brackets refer to molecule B.

Table 4. Selected bond angles [°] in complexes **6**–**13**.

| | **6** | **7**[c] | **8** | **9** | **10** | **12** | | **11** | **13**[c] |
|---|---|---|---|---|---|---|---|---|---|
| N(1)–M(1)–N(2) | 82.7(3) | 78.9(2) [78.6(2)] | 83.17(12) | 78.55(5) | 75.9(2) | 76.3(3) | N(1)–M(1)–N(2) | 75.2(1) | 75.4(1) [76.0(1)] |
| N(1)–M(1)–N(3) | 101.6(3) | 100.2(2) [100.6(2)] | 97.97(12) | 102.09(5) | 100.0(2) | 89.0(2) | N(1)–M(1)–N(3) | 99.4(1) | 102.8(1) [102.1(1)] |
| N(2)–M(1)–N(3) | 82.4(3) | 83.2(2) [82.6(2)] | 83.07(11) | 82.94(5) | 76.2(2) | 73.5(3) | N(2)–M(1)–N(3) | 76.5(1) | 76.4(1) [75.1(1)] |
| N(4)–M(2)–N(5) | 81.6(3) | 82.4(2) [82.5(2)] | 83.21(11) | 82.92(5) | 76.1(2) | 73.5(2) | N(4)–M(2)–N(5) | 76.0(1) | 75.5(1) [76.1(1)] |
| N(4)–M(2)–N(6) | 101.7(3) | 101.8(2) [100.7(2)] | 98.83(12) | 100.97(5) | 99.9(2) | 107.9(2) | N(4)–M(2)–N(6) | 99.8(1) | 103.6(1) [101.4(1)] |
| N(5)–M(2)–N(6) | 82.7(3) | 79.5(2) [78.4(2)] | 82.40(12) | 78.77(5) | 75.4(2) | 75.6(3) | N(5)–M(2)–N(6) | 76.8(1) | 75.2(1) [76.0(1)] |
| *N–M–N*[a] | *88.8(3)* | *87.7(2) [87.2(2)]* | *88.11(12)* | *87.6(5)* | *83.9(2)* | *82.6(3)* | | *84.0(1)* | *84.8(1) [84.5(1)]* |
| *Dev*[b] | *8.9(3)* | *9.7(2) [9.9(2)]* | *7.49(12)* | *9.99(5)* | *12.7(2)* | *13.37(3)* | | *12.5(1)* | *14.0(1) [14.3]* |
| N(1)–M(1)–S(1) | 95.0(2) | 90.8(1) [90.4(1)] | 91.80(9) | 89.95(3) | 87.0(1) | 87.2(2) | N(1)–M(1)–S(1) | 87.52(9) | 86.29(9) [87.24(8)] |
| N(2)–M(1)–S(1) | 105.8(2) | 105.2(1) [107.2(1)] | 104.45(9) | 107.57(4) | 111.9(2) | 109.5(2) | N(2)–M(1)–S(1) | 102.53(9) | 103.29(9) [98.70(8)] |
| N(1)–M(1)–S(2) | 96.2(2) | 99.9(1) [101.1(1)] | 98.13(9) | 100.94(4) | 97.9(1) | 113.2(2) | N(2)–M(1)–S(2) | 100.59(9) | 102.1(1) [104.67(9)] |
| N(3)–M(1)–S(2) | 88.2(2) | 91.4(1) [91.4(1)] | 89.39(8) | 90.52(4) | 86.4(1) | 85.0(2) | N(3)–M(1)–S(2) | 87.81(9) | 86.99(9) [86.11(8)] |
| N(4)–M(2)–S(2) | 87.7(2) | 91.0(1) [91.9(2)] | 88.83(8) | 90.69(4) | 86.1(1) | 87.1(2) | N(4)–M(2)–S(2) | 88.12(9) | 85.16(8) [87.73(8)] |
| N(5)–M(2)–S(1) | 106.4(2) | 106.9(2) [106.8(2)] | 104.92(9) | 107.82(4) | 112.4(1) | 107.1(2) | N(5)–M(2)–S(1) | 101.04(9) | 102.45(9) [99.78(8)] |
| N(6)–M(2)–S(1) | 92.8(2) | 88.7(2) [90.5(1)] | 92.59(9) | 89.53(4) | 87.2(1) | 87.3(2) | N(6)–M(2)–S(1) | 87.12(9) | 86.99(8) [85.66(8)] |
| N(6)–M(2)–S(2) | 98.6(2) | 101.7(2) [98.7(1)] | 99.53(9) | 101.69(3) | 100.1(2) | 103.8(2) | N(5)–M(2)–S(2) | 104.0(1) | 100.46(9) [99.58(9)] |
| *N–M–S*[a] | *96.3(2)* | *97.0(2) [97.3(2)]* | *96.21(9)* | *97.34(4)* | *96.1(1)* | *97.5(2)* | | *94.84(9)* | *94.22(9) [93.68(8)]* |
| *Dev*[b] | *7.4(2)* | *7.3(2) [7.3(2)]* | *6.65(9)* | *7.47(4)* | *6.95(1)* | *10.9(2)* | | *7.20(9)* | *7.86(9) [7.00(9)]* |
| Cl–M(1)–N(2) | 92.6(2) | 94.2(1) [95.7(2)] | 91.03(9) | 95.20(4) | 99.2(2) | 90.1(2) | Cl–M(1)–N(1) | 99.97(9) | 98.3(1) [95.52(8)] |
| Cl–M(1)–N(3) | 83.6(2) | 92.0(1) [93.8(2)] | 85.82(9) | 92.99(4) | 93.2(1) | 104.7(2) | Cl–M(1)–N(3) | 96.2(1) | 97.25(8) [102.03(8)] |
| Cl–M(2)–N(4) | 85.7(2) | 93.6(2) [92.5(2)] | 84.91(9) | 94.95(4) | 92.2(1) | 84.1(2) | Cl–M(2)–N(4) | 100.4(1) | 97.34(9) [97.21(8)] |
| Cl–M(2)–N(5) | 89.6(2) | 93.2(2) [95.9(2)] | 91.01(9) | 94.70(4) | 96.7(1) | 100.1(2) | Cl–M(2)–N(6) | 94.41(9) | 100.4(1) [100.64(9)] |

 © 2007 Wiley-VCH Verlag GmbH & Co. KGaA, Weinheim 

Table 4. *(continued)*.

| | 6 | 7[c] | 8 | 9 | 10 | 12 | | 11 | 13[c] |
|---|---|---|---|---|---|---|---|---|---|
| *Cl–M–N*[a] | *87.9(2)* | *93.3(2) [94.5(2)]* | *88.19(9)* | *94.46(4)* | *95.3(1)* | *94.8(2)* | | *97.8(1)* | *98.3(1) [98.85(8)]* |
| *Dev*[b] | *3.4(2)* | *3.3(2) [4.5(2)]* | *2.83(9)* | *4.46(4)* | *5.3(1)* | *7.7(2)* | | *7.8(1)* | *8.3(1) [8.85(8)]* |
| Cl–M(1)–S(1) | 80.39(7) | 78.26(6) [76.53(6)] | 85.20(4) | 76.48(1) | 80.97(6) | 80.21(8) | Cl–M(1)–S(1) | 85.54(4) | 84.41(4) [85.91(4)] |
| Cl–M(1)–S(2) | 89.45(7) | 88.29(6) [86.32(6)] | 88.22(5) | 87.16(2) | 91.50(6) | 86.49(7) | Cl–M(1)–S(2) | 85.46(5) | 85.71(4) [84.49(3)] |
| Cl–M(2)–S(1) | 81.05(8) | 77.42(7) [77.52(6)] | 84.60(4) | 76.23(1) | 82.26(6) | 80.21(8) | Cl–M(2)–S(1) | 83.90(5) | 85.93(4) [87.62(4)] |
| Cl–M(2)–S(2) | 90.64(7) | 87.47(6) [88.51(6)] | 87.63(4) | 86.71(1) | 92.11(6) | 85.45(7) | Cl–M(2)–S(2) | 85.43(5) | 85.43(4) [85.17(3)] |
| *Cl–M–S*[a] | *85.38(7)* | *82.94(6) [82.22(6)]* | *86.41(4)* | *81.65(1)* | *86.71(6)* | *83.09(8)* | | *85.08(5)* | *85.37(4) [85.79(4)]* |
| *Dev*[b] | *4.94(7)* | *7.14(6) [7.78(6)]* | *3.59(4)* | *8.36(1)* | *5.10(6)* | *6.91(8)* | | *4.92(5)* | *4.67(4) [4.21(4)]* |
| S(1)–M(1)–S(2) | 84.03(8) | 80.48(6) [79.01(6)] | 82.96(4) | 79.23(1) | 86.30(7) | 92.67(7) | S(1)–M(1)–S(2) | 84.97(4) | 83.67(4) [84.39(5)] |
| S(1)–M(2)–S(2) | 84.22(8) | 79.58(6) [79.54(6)] | 82.79(4) | 78.63(1) | 86.09(5) | 93.68(7) | S(1)–M(2)–S(2) | 84.90(5) | 83.69(4) [84.55(5)] |
| *S–M–S*[a] | *84.13(8)* | *80.03(6) [79.29(6)]* | *82.88(4)* | *78.93(1)* | *86.19(6)* | *93.18(7)* | | *84.94(5)* | *83.68(4) [84.47(5)]* |
| *Dev*[b] | *5.87(8)* | *9.97(6) [10.73]* | *7.12(4)* | *11.07(1)* | *3.81(6)* | *3.18(7)* | | *5.06(5)* | *6.32(4) [5.53(5)]* |
| Cl–M(1)–N(1) | 172.4(2) | 165.2(1) [163.6(1)] | 172.61(9) | 162.72(4) | 164.2(1) | 157.2(2) | Cl–M(1)–N(2) | 170.23(9) | 169.5(1) [170.04(9)] |
| N(2)–M(1)–S(2) | 170.1(2) | 174.2(1) [173.8(1)] | 172.47(8) | 173.14(4) | 160.0(2) | 156.7(2) | N(1)–M(1)–S(2) | 170.37(9) | 168.79(9) [171.61(8)] |
| N(3)–M(1)–S(1) | 162.3(2) | 167.4(1) [166.7(1)] | 168.37(8) | 165.55(4) | 170.5(1) | 174.4(2) | N(3)–M(1)–S(1) | 172.41(9) | 170.37(8) [166.98(8)] |
| Cl–M(2)–N(6) | 168.4(2) | 161.8(2) [164.7(2)] | 171.94(9) | 161.83(4) | 163.3(2) | 165.0(2) | Cl–M(2)–N(5) | 169.60(9) | 170.17(9) [171.52(9)] |
| N(4)–M(2)–S(1) | 164.4(2) | 167.2(2) [166.9(2)] | 166.83(8) | 166.40(4) | 170.2(1) | 164.1(2) | N(4)–M(2)–S(1) | 171.51(9) | 168.09(8) [170.53(7)] |
| N(5)–M(2)–S(2) | 169.3(2) | 173.5(2) [173.0(2)] | 172.01(8) | 173.55(4) | 160.4(1) | 159.1(2) | N(6)–M(2)–S(2) | 172.00(8) | 168.65(8) [168.40(8)] |
| *X–M–Y*[a] | *167.8(2)* | *168.2(2) [168.1(2)]* | *170.71(9)* | *167.20(4)* | *164.8(1)* | *162.8(2)* | | *171.02(9)* | *169.26(9) [169.85(9)]* |
| *Dev*[b] | *12.2(2)* | *11.8(2) [11.9(2)]* | *9.29(9)* | *12.80(4)* | *15.2(1)* | *17.2(2)* | | *8.98(9)* | *10.74(9) [10.15(9)]* |
| M(1)–S(1)–M(2) | 79.55(7) | 79.70(6) [80.90(6)] | 77.50(4) | 81.16(1) | 74.75(5) | 76.60(6) | M(1)–S(1)–M(2) | 77.78(4) | 77.29(4) [77.37(4)] |
| M(1)–S(2)–M(2) | 79.90(7) | 82.51(6) [84.63(6)] | 78.78(4) | 85.60(1) | 76.07(5) | 75.81(6) | M(1)–S(2)–M(2) | 77.63(4) | 77.66(3) [76.28(4)] |
| *M–S–M*[a] | *79.73(7)* | *81.11(6) [82.77(6)]* | *78.14(4)* | *83.38(1)* | *75.41(5)* | *76.21(6)* | | *77.71(4)* | *77.48(4) [76.83(4)]* |
| *Dev*[b] | *10.27(7)* | *8.89(6) [7.23(6)]* | *11.86(4)* | *6.62(1)* | *14.59(5)* | *13.79(6)* | | *12.29(4)* | *12.52(4) [13.17(4)]* |
| M(1)–Cl–M(2) | 72.46(6) | 81.38(6) [80.66(6)] | 75.03(4) | 81.27(1) | 74.41(5) | 72.27(6) | M(1)–Cl–M(2) | 76.83(4) | 78.18(4) [77.20(3)] |

[a] *Average values.* [b] *Average deviations* from the ideal 90° or 180° L–M–L bond angles of a perfect octahedron. [c] There are two crystallogrphically independent molecules in the asymmetric unit. Values in square brackets refer to molecule B.

atives.[22] The dependence of the bond angles on the type of N donors is not so pronounced. The most visible changes across the series include the M–Cl–M bond angles, which increase by around 10° upon going from **6** to **9**. In summary, all $N_6S_2$ macrocycles support the formation of dinuclear nickel complexes of type A. As we will show below, a completely different situation is seen in the case of the cadmium complexes **10**–**13**.

### *Description of the Crystal Structures of [(L¹)Cd$^{II}_2$(μ-Cl)][BPh$_4$]·5MeOH (10[BPh$_4$]·5MeOH) and [(L³)-Cd$^{II}_2$(μ-Cl)][BPh$_4$]·2MeCN (12[BPh$_4$]·2MeCN)*

The crystal structure determinations of the two title compounds revealed the presence of dioctahedral complex cations, tetraphenylborate anions and methanol or acetonitrile molecules of solvent of crystallisation. ORTEP plots of **10**

 © 2007 Wiley-VCH Verlag GmbH & Co. KGaA, Weinheim 

and **12** are displayed in Figures 4 and 5, respectively. Selected bond lengths and angles are collected in Tables 3 and 4. The structure of the $[(L^2)Cd_2^{II}(\mu\text{-}Cl)]^+$ complex **11** has been reported previously,[13] and its metrical parameters are also given for comparison. The conformation adopted by the supporting ligands in **10** and **12** is that of type A. For reasons that are still unclear, however, the configuration at N(3) in **12** is opposite to that found in **10** and in the nickel complexes above. Each cadmium atom is coordinated by two S and three N atoms from the supporting ligand and a bridging chloride in a severely distorted octahedral fashion. The distortions from the ideal octahedral geometry are somewhat more pronounced than in the nickel complexes above and in the cadmium complexes of type B described below, which is probably a consequence of the larger ionic radius of cadmium(II) (Cd$^{II}$: 1.06 Å; Ni$^{II}$: 0.83 Å).[23] The average Cd–N bond lengths of 2.390(5) (**10**) and 2.399(7) Å (**12**) are normal for six-coordinate cadmium complexes with amine donors.[24,25] The same holds for the average Cd–S [2.671(2) and 2.647(2) Å][26] and Cd–Cl distances [2.701(3) and 2.770(1) Å].[27–29] As expected, the Cd–N(secondary amine) distances in **10** and **12** are shorter (by about 0.04 Å) than the corresponding Cd–N(tertiary amine) bonds in **11** and **13**. The same trend was observed in the series of nickel complexes above.

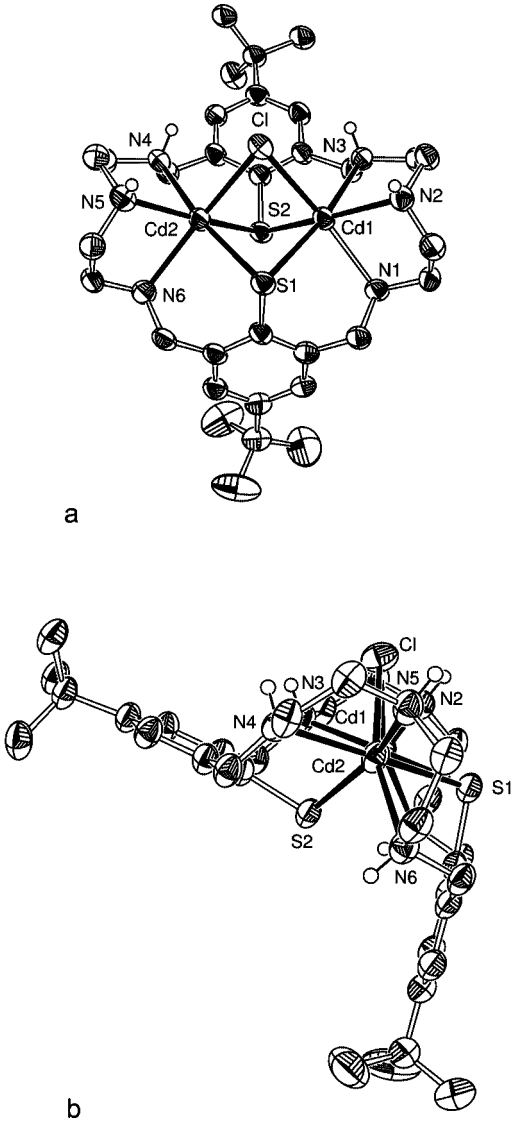


Figure 4. Two perspective views of the molecular structure of **10** with atomic numbering for key atoms (30% probability thermal ellipsoids). Hydrogen atoms (except those bonded to N atoms) have been omitted for clarity.

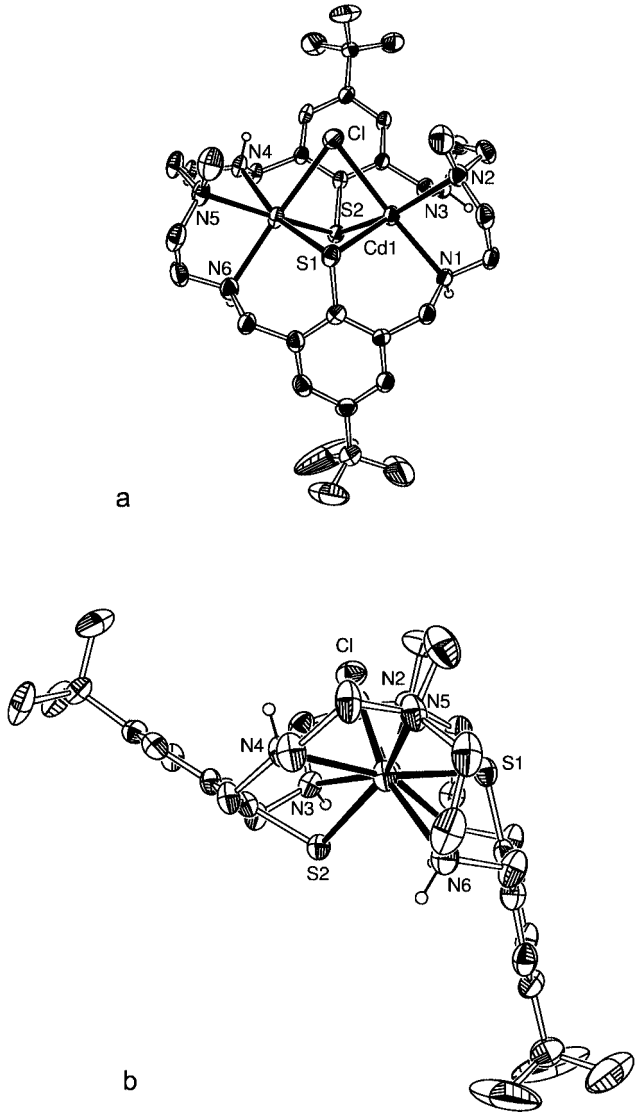


Figure 5. Two perspective views of the molecular structure of **12** with atomic numbering for key atoms (30% probability thermal ellipsoids). Hydrogen atoms (except those bonded to N atoms) have been omitted for clarity.

### *Description of the Crystal Structure of {[(L$^4$)Cd$^{II}_2$(μ-Cl)][BPh$_4$]·3.5MeCN}$_2$ {13[BPh$_4$]·3.5MeCN}$_2$*

Crystals of the title complex grown from a mixed acetonitrile/ethanol solution are monoclinic with space group $P2_1/n$. The asymmetric unit contains two crystallographically independent molecules. A perspective view of the structure of molecule A is displayed in Figure 6. The structure of molecule B is identical to that of molecule A and is

 © 2007 Wiley-VCH Verlag GmbH & Co. KGaA, Weinheim 

not considered further. The $[(L^4)Cd_2(\mu\text{-}Cl)]^+$ complex **13** is isostructural with the $[(L^2)Cd_2(\mu\text{-}Cl)]^+$ cation **11**, with the macrocycle having a type-B conformation. There are no unusual features as far as bond lengths and angles are concerned. The average Cd–(μ-Cl) [2.661(1) Å], Cd–N [2.436(4) Å] and Cd–S [2.681(1) Å] bond lengths are very similar to the corresponding values in **11**. As in **11**, the two metal ions are coordinated in a distorted octahedral fashion by the two *fac*-$N_3(\mu\text{-}S)_2$ donor sets of the doubly deprotonated macrocycle and the bridging chloride. The diethylene triamine units are facially coordinated, with one larger and two smaller N–M–N bond angles. The same situation is observed in **11** and other complexes with this tridentate unit.[21] Likewise, the M–N bond lengths involving the four benzylic nitrogen donors are invariably longer (by around 0.1 Å) than the ones comprising the central nitrogen atoms of the linking diethylenetriamine units. This is also normal for complexes of this ligand system. The most salient feature of the structure of **13** is that $(L^4)^{2-}$ adopts a bowl-shaped, $C_{2v}$-symmetric conformation, an effect that may be traced to the more optimal L–Cd–L bond angles. In fact, it can be readily seen from Table 4 that there is a consistent decrease in the deviations of the *cis*- and *trans*-L–Cd–L bond angles upon going from **12** to **13** (or from **10** to **11**). Thus, for the present $[(L^R)M_2(\mu\text{-}Cl)]^+$ complexes the conformation adopted depends not only on the *N*-alkylation grade but also on the metal ion radius.

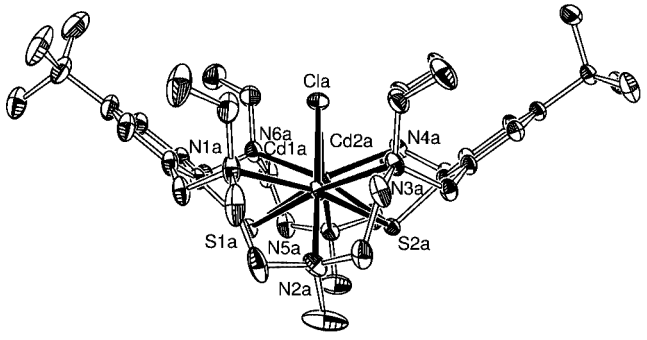


Figure 6. Molecular structure of **13** with atomic numbering for key atoms (30% probability thermal ellipsoids). Hydrogen atoms have been omitted for clarity.

## Conclusions

The main findings of this investigation are as follows: a) *N*-alkylated variants of $H_2L^1$ with different *N*-alkylation grades and patterns can be readily prepared by a [2 + 1] condensation reaction of tetraaldehyde **1** with bis(aminoethyl)methylamine followed by acylation and reduction of the resultant hexaamine dithioether compound **3**. b) All ligand systems are effective dinucleating ligands that support the formation of dioctahedral $[(L^R)M_2(\mu\text{-}Cl)]^+$ cations (M = $Ni^{II}$ and $Cd^{II}$). c) The macrocycles adopt either a saddle-shaped (type A) or a bowl-shaped (type B) conformation. d) The actual conformation adopted depends not only on the type of co-ligand,[30] but also on the metal ion radius and the *N*-alkylation grade. Two trends are apparent for the present $[(L^R)M_2(\mu\text{-}Cl)]^+$ cations. In the case of small metal ions such as $Ni^{II}$, the conformation is always that of type A, irrespective of the *N*-alkylation grade, whereas for the larger $Cd^{II}$ ion a clear correlation exists between the *N*-alkylation grade and the macrocycle conformation. Here, the higher the *N*-alkylation grade the more preferred the conformation of type B. e) Finally, it has also been demonstrated that the complexes exist as single isomers in solution. Computational studies are underway to determine the energy differences between the two complex conformations.

## Experimental Section

**Materials and Methods:** Compounds **1** and $H_2L^1$ were prepared as described in the literature.[14] The syntheses of the metal complexes were carried out under a protective atmosphere of argon. Melting points were determined in open glass capillaries and are uncorrected. NMR spectra were recorded with a Bruker Avance DPX-200 spectrometer or a Bruker Avance DRX 400 spectrometer at 298 K. Chemical shifts are referred to solvent signals. Infrared spectra were recorded with a Bruker Vector 22 FT-IR spectrometer and electronic absorption spectra with a Jasco V-570 UV/VIS/NIR spectrometer. Elemental analyses were recorded with a VARIO EL-elemental analyzer. ESI-FTICR mass spectra were recorded with a Bruker Apex II instrument using dilute $CH_2Cl_2$/MeOH solutions.

***CAUTION!*** *Perchlorate salts are potentially explosive and should therefore be prepared only in small quantities and handled with appropriate care.*

**Preparation of Compound 3:** Solutions of 1,2-bis(4-*tert*-butyl-2,6-diformylphenylthio)ethane (**1**; 3.00 g, 6.37 mmol) in dichloromethane (100 mL) and bis(aminoethyl)methylamine (**2**; 1.51 g, 12.9 mmol) in ethanol (100 mL) were added simultaneously over a period of 3 h to a mixture of dichloromethane (300 mL) and ethanol (300 mL). After complete addition, the reaction mixture was stirred at room temperature for 18 h. The dichloromethane was removed under reduced pressure and a solution of sodium borohydride (1.21 g, 32.0 mmol) in ethanol (50 mL) was added. After stirring at room temperature for 2 h, the reaction mixture was acidified to pH 1 with conc. hydrochloric acid and the resulting colourless suspension was evaporated to dryness. The residue was taken up in aqueous potassium hydroxide (3 M, 80 mL) and extracted with dichloromethane (4 × 100 mL). The combined organic fractions were dried with magnesium sulfate. Evaporation of the solvent gave **3** (3.96 g, 97%) as a colourless, foamy solid. M.p. 84 °C. $^1$H NMR (400 MHz, $CDCl_3$): $\delta$ = 1.29 [s, 18 H, ArC($CH_3$)$_3$], 2.31 (s, 6 H, N$CH_3$), 2.69 (m, 8 H, N$CH_2$ $CH_2$N), 2.93 (m, 8 H, N$CH_2CH_2$N), 3.07 [s, 4 H, (ArS$CH_2$)$_2$], 3.99 (s, 8 H, Ar$CH_2$N), 7.49 ppm (s, 4 H, Ar*H*). $^{13}$C{$^1$H}NMR (50 MHz, $CDCl_3$): $\delta$ = 30.2 [C($CH_3$)$_3$], 33.6 [*C*($CH_3$)$_3$], 34.9 (S$CH_2$), 40.7 (N$CH_3$), 46.6 (Ar$CH_2$N), 52.7 (N$CH_2CH_2$N), 56.7 (N$CH_2CH_2$N), 125.7 ($C^{Ar}$H), 127.9 ($C^{Ar}$S), 143.2 ($C^{Ar}CH_2$N), 150.9 ppm ($C^{Ar}t$Bu). IR (KBr): $\tilde{\nu}$ = 3425 (w), 3307 (w), 3049 (vw), 2952 (vs), 2902 (s), 2867 (s), 2801 (s), 2370 (w), 2273 (vw), 1641 (vw), 1630 (vw), 1596 (w), 1564 (vw), 1554 (vw), 1534 (vw), 1512 (vw), 1459 (s), 1393 (w), 1362 (m), 1330 (w), 1293 (w), 1262 (m), 1223 (m), 1203 (m), 1119 (s), 1045 (s), 926 (vw), 884 (w), 800 (m), 744 (w), 653 (vw), 631 cm$^{-1}$ (vw). $C_{36}H_{60}N_6S_2{\cdot}H_2O$ (641.03 + 18.02): calcd. C 65.61, H 9.48, N 12.75, S 9.73; found C 65.40, H 9.28, N 12.39, S 10.52.

**Preparation of Compound 4:** A solution of **3** (3.40 g, 5.30 mmol) in acetic anhydride (150 mL) was stirred at 50 °C for 6 h. After re-

 © 2007 Wiley-VCH Verlag GmbH & Co. KGaA, Weinheim 

moval of the solvent under reduced pressure, the residue was taken up in aqueous potassium hydroxide solution (3 M, 100 mL) and extracted with dichloromethane (3 × 100 mL). The combined organic phases were dried with magnesium sulfate and the solvents evaporated to dryness. The residue was taken up in methanol and purified by flash chromatography on silica gel using a methanol/water (9:1) mixture as eluting solvent. Drying in vacuo gave **4** (3.56 g, 83%) as a colourless solid. M.p. 116 °C. $^1$H NMR (300 MHz, [D$_6$]-DMSO, 373 K): $\delta$ = 1.21 [s, 18 H, C(C*H*$_3$)$_3$], 2.31 (s, 6 H, NC*H*$_3$), 2.49–2.65 (m, 8 H, NC*H*$_2$CH$_2$N), 2.91 (s, 4 H, ArSC*H*$_2$), 3.03 (s, 12 H, COC*H*$_3$), 3.34 [m, 8 H, CH$_3$N(CH$_2$C*H*$_2$N)$_2$], 4.73 (s, 8 H, ArC*H*$_2$N), 6.99 ppm (s, 4 H, Ar*H*). IR (KBr): $\tilde{\nu}$ = 3442 (w), 2963 (s), 2868 (w), 2796 (w), 1649 [vs, $\nu$(CO)], 1559 (vw), 1467 (s), 1413 (s), 1362 (m), 1298 (w), 1261 (m), 1231 (m), 1149 (m), 1083 (w), 1024 (m), 976 (w), 940 (w), 873 (vw), 801 (w), 730 (w), 698 (vw), 660 (vw), 602 (w), 572 (vw), 535 (vw), 463 cm$^{-1}$ (vw). $C_{44}H_{68}N_6O_4S_2$·$H_2O$ (809.18 + 18.02): calcd. C 63.89, H 8.53, N 10.16, S 7.75; found C 63.77, H 8.28, N 9.88, S 7.52.

**Preparation of Compound 5:** A solution of **4** (620 mg, 0.766 mmol) in tetrahydrofuran (40 mL) was added dropwise to a suspension of lithium aluminium hydride (429 mg, 11.3 mmol) in tetrahydrofuran (40 mL). After refluxing the reaction mixture for 12 h, the oil bath was removed. Water (5 mL) was carefully added to the hot reaction mixture in small portions followed by 3 M potassium hydroxide solution (20 mL). The reaction mixture was stirred for an additional hour without heating. The organic layer was decanted off from a white residue, which was rinsed with boiling tetrahydrofuran (2 × 50 mL). The solvent was removed by distillation under reduced pressure. The residue was treated with 3 M potassium hydroxide solution (50 mL) and the resulting mixture was extracted with dichloromethane (3 × 50 mL). The combined organic layers were dried with potassium carbonate. Evaporation of the solvent gave the product as a colourless, foamy solid (568 mg, 98%). The crude material was purified by recrystallisation from a dichloromethane/ethanol (1:1) mixed solvent system. M.p. 146 °C. $^1$H NMR (200 MHz, CDCl$_3$): $\delta$ = 0.87 (t, $^3J$ = 7 Hz, 12 H, NCH$_2$C*H*$_3$), 1.22 [s, 18 H, C(C*H*$_3$)$_3$], 2.19 (s, 6 H, NC*H*$_3$), 2.30 (q, $^3J$ = 7 Hz, 8 H, NC*H*$_2$CH$_3$), 2.42–2.52 (m, 16 H, NC*H*$_2$C*H*$_2$N), 2.83 (s, 4 H, ArSC*H*$_2$), 3.66 (s, 8 H, ArC*H*$_2$N), 7.36 ppm (s, 4 H, Ar*H*). $^{13}$C{$^1$H}NMR (50 MHz, CDCl$_3$): $\delta$ = 11.9 (NCH$_2$*C*H$_3$), 31.3 [C(*C*H$_3$)$_3$], 34.6 [*C*(CH$_3$)$_3$], 36.5 (S*C*H$_2$), 43.6 (N*C*H$_3$), 47.6 (N*C*H$_2$CH$_3$), 51.4 (N*C*H$_2$CH$_2$N), 55.2 (Ar*C*H$_2$), 57.8 (NCH$_2$*C*H$_2$N), 125.2 (C$^{Ar}$H), 128.7 (C$^{Ar}$S), 144.2 (*C*$^{Ar}$CH$_2$N), 150.8 ppm (C$^{Ar}$*t*Bu). IR (KBr): $\tilde{\nu}$ = 3425 (vw), 2965 (vs), 2868 (s), 2798 (vs), 1595 (w), 1559 (vw), 1461 (w), 1407 (w), 1384 (m), 1366 (s), 1335 (w), 1312 (m), 1296 (w), 1274 (m), 1260 (m), 1217 (w), 1187 (m), 1163 (w), 1123 (s), 1100 (m), 1081 (m), 1039 (s), 1002 (w), 979 (w), 950 (w), 936 (w), 915 (w), 898 (w), 882 (w), 791 (w), 770 (w), 730 (vw), 683 (w), 653 (w), 607 (vw), 575 (vw), 555 (vw), 529 (vw), 475 cm$^{-1}$ (vw). $C_{44}H_{76}N_6S_2$·$H_2O$ (753.24 + 18.02): calcd. C 68.52, H 10.19, N 10.90, S 8.31; found C 68.35, H 10.16, N 10.57, S 7.92. This compound was additionally characterised by X-ray crystallography.

**Preparation of $H_2L^3$·6HCl:** A solution of **3** (3.80 g, 5.93 mmol) in tetrahydrofuran (50 mL) was added dropwise to a solution of sodium (2.0 g, 87 mmol) in liquid ammonia (150 mL). The resulting blue reaction mixture was stirred for a further 3 h at –76 °C. Solid ammonium chloride was then added to destroy the excess reducing agent. The resulting colourless suspension was warmed to room temperature. After 12 h, the remaining solvent was distilled off under reduced pressure. The residue was taken up in water (20 mL) and the solution was acidified to pH 1 with conc. hydrochloric acid. To remove sodium chloride and ammonium chloride from the product, the residue was triturated with methanol (3 × 50 mL) and filtered. The crude product was further purified by recrystallisation from a mixed methanol/ethanol (1:1) solvent system. This material (3.55 g, 72%) was used without further purification. M.p. 259 °C. $^1$H NMR (400 MHz, CD$_3$OD): $\delta$ = 1.34 [s, 18 H, C(C*H*$_3$)$_3$], 3.00 (s, 6 H, NCH$_3$), 3.67 (m, 16 H, NC*H*$_2$C*H*$_2$N), 4.64 (s, 8 H, ArC*H*$_2$N), 7.80 ppm (s, 4 H, Ar*H*) ppm. $^{13}$C{$^1$H} NMR (100 MHz, CD$_3$OD): $\delta$ = 31.5 [C(*C*H$_3$)$_3$], 35.9 [*C*(CH$_3$)$_3$], 42.1 (NCH$_3$), 43.4 (N*C*H$_2$), 52.2 (N*C*H$_2$), 53.6 (N*C*H$_2$), 130.4 (C$^{Ar}$H), 132.1 (C$^{Ar}$S), 135.8 (*C*$^{Ar}$CH$_2$N), 153.8 ppm (C$^{Ar}$*t*Bu). IR (KBr): $\tilde{\nu}$ = 3425 (vs), 2961 (vs), 2869 (s), 2640 (s), 1724 (vw), 1629 (w), 1601 (w), 1512 (vw), 1462 (s), 1366 (w), 1231 (w), 1161 (vw), 1019 (vw), 993 (vw), 895 (vw), 786 (vw), 753 (vw), 663 (vw), 557 cm$^{-1}$ (vw). $C_{34}H_{64}Cl_6N_6S_2$·1.5EtOH (830.28 + 69.04): calcd. C 49.22, H 8.15, Cl 23.56, N 9.31, S 7.10; found C 48.8, H 8.38, Cl 23.53, N 9.13, S 7.55.

**Preparation of $H_2L^4$·6HCl:** The preparation of this ligand was analogous to that of $H_2L^3$·6HCl except that compound **5** was used instead of **3**. Yield: 672 mg (71%). The hexahydrochloride salt could not be obtained in analytically pure form, but it was pure enough for the preparation of the metal complexes. $^1$H NMR (200 MHz, CD$_3$OD): $\delta$ = 1.24–1.70 [m, 30 H, C(C*H*$_3$)$_3$ and NCH$_2$C*H*$_3$], 2.67–3.05 (m, 6 H, NC*H*$_3$), 3.17–3.99 (m, 24 H, NC*H*$_2$), 7.42–8.15 ppm (m, 4 H, Ar*H*). $^{13}$C{$^1$H}NMR (100 MHz, CD$_3$OD): $\delta$ = 9.04 (NCH$_2$*C*H$_3$), 31.6 [C(*C*H$_3$)$_3$], 35.2 [*C*(CH$_3$)$_3$], 41.3 (N*C*H$_3$), 47.7 (N*C*H$_2$CH$_3$), 50.1 (Ar*C*H$_2$N), 52.5 (N*C*H$_2$CH$_2$N), 59.5 (NCH$_2$*C*H$_2$N), 132.2 (C$^{Ar}$H), 132.6 (C$^{Ar}$S), 135.4 (*C*$^{Ar}$CH$_2$N), 148.9 ppm (C$^{Ar}$*t*Bu). IR (KBr): $\tilde{\nu}$ = 3404 (vs), 2964 (vs), 2870 (s), 2604 (vs), 1633 (w), 1602 (w), 1467 (vs), 1414 (s), 1398 (s), 1366 (m), 1232 (w), 1202 (vw), 1164 (w), 1081 (w), 1046 (m), 992 (vw), 959 (vw), 897 (vw), 795 (w), 737 cm$^{-1}$ (vw).

**Preparation of [(L$^3$)Ni$_2$(Cl)][ClO$_4$] (8[ClO$_4$]) and [(L$^3$)Ni$_2$(Cl)][BPh$_4$] (8[BPh$_4$]):** A solution of NiCl$_2$·6H$_2$O (261 mg, 1.10 mmol) in methanol (2 mL) was added to a suspension of $H_2L^3$·6HCl (460 mg, 0.552 mmol) in methanol (15 mL). A solution of NEt$_3$ (448 mg, 4.43 mmol) in methanol (3 mL) was then added dropwise to give a dark red solution. The solution was stirred for a further 2 d at room to give a yellow solution. Solid LiClO$_4$·3H$_2$O (882 mg, 5.50 mmol) was added and half of the solvent was removed in vacuo. The resulting yellow precipitate was filtered off, recrystallised once from a few millilitres of acetonitrile, and dried in vacuo. Yield: 416 mg (87%). M.p. 299 °C (decomp.). IR (KBr): $\tilde{\nu}$ = 3430 (m), 3286 (w), 3256 (w), 3095 (vw), 2955 (m), 2870 (m), 2023 (vw), 1629 (w), 1461 (m), 1393 (w), 1363 (w), 1333 (vw), 1307 (vw), 1258 (w), 1229 (w), 1156 (m), 1094 [vs, $\nu$(ClO$_4^-$)], 1000 (w), 975 (w), 957 (vw), 930 (w), 894 (vw), 871 (w), 854 (w), 806 (vw), 750 (w), 623 (m), 568 (vw), 546 (vw), 472 cm$^{-1}$ (vw). UV/Vis (CH$_3$CN): $\lambda_{max}$ ($\varepsilon$) = 623(76), 902 (63), 960 nm (68 M$^{-1}$ cm$^{-1}$). $C_{34}H_{56}Cl_2N_6Ni_2O_4S_2$ (865.27): calcd. C 47.20, H 6.52, N 9.71, S 7.41; found C 47.20, H 6.29, N 9.32, S 7.10. The tetraphenylborate salt **8**[BPh$_4$] was prepared by adding NaBPh$_4$ (342 mg, 1.00 mmol) to a solution of **8**[ClO$_4$] (86.5 mg, 0.100 mmol) in methanol (40 mL). The yellow microcrystalline solid was isolated by filtration, washed with ethanol, and dried in air. Yield: 96.2 mg (89%). M.p. 249 °C (decomp). IR (KBr): $\tilde{\nu}$ = 3440 (w), 3275 (m), 3055 (w), 2963 (m), 2872 (m), 1948 (vw), 1658 (w), 1578 (vs), 1479 (m), 1457 (s), 1426 (s), 1392 (w), 1362 (w), 1311 (w), 1260 (w), 1229 (w), 1151 (w), 1081 (m), 1057 (w), 1032 (w), 984 (w), 930 (w), 877 (w), 849 (w), 733 [m, $\nu$(BPh$_4^-$)], 705 [s, $\nu$(BPh$_4^-$)], 612 (m), 545 (vw), 464 (vw) cm$^{-1}$. $C_{58}H_{76}BClN_6Ni_2S_2$ (1085.05): calcd. C 64.20, H 7.06, N 7.75, S 5.91; found C 63.81, H 7.14, N 7.44, S 5.64. The tetraphenylborate salt was additionally characterised by X-ray crystallography.

 © 2007 Wiley-VCH Verlag GmbH & Co. KGaA, Weinheim 

**Preparation of [($L^4$)$Ni_2$(Cl)][$ClO_4$] (9[$ClO_4$]) and [($L^4$)$Ni_2$(Cl)][$BPh_4$] (9[$BPh_4$]):** A solution of $NiCl_2·6H_2O$ (59.4 mg, 0.250 mmol) in methanol (2 mL) was added to a suspension of $H_2L^4·6HCl$ (118 mg, 0.125 mmol) in methanol (15 mL). A solution of $NEt_3$ (101 mg, 1.00 mmol) in methanol (3 mL) was then added to give a dark red solution. The solution was stirred for a further 2 d at room temp. to give a yellow solution. Solid $LiClO_4·3H_2O$ (200 mg, 1.25 mmol) was added and half of the solvent was removed in vacuo. The resulting yellow precipitate was filtered off, recrystallised once from a few millilitres of acetonitrile, and dried in vacuo. Yield: 78 mg (64%). M.p. 296 °C (decomp.). IR (KBr): $\tilde{\nu}$ = 3438 (m), 2963 (s), 2891 (s), 2018 (vw), 1629 (w), 1460 (s), 1377 (m), 1363 (m), 1314 (w), 1259 (w), 1232 (w), 1201 (vw), 1158 (m), 1098 (vs, $\nu ClO_4^-$), 1058 (m), 1023 (m), 988 (vw), 968 (vw), 955 (vw), 925 (vw), 907 (w), 883 (w), 809 (vw), 778 (m), 732 (w), 673 (vw), 624 (m) $cm^{-1}$. UV/Vis ($CH_3CN$): $\lambda_{max}$ ($\varepsilon$) = 675 (31), 928 (62), 1013 (82 $M^{-1}cm^{-1}$). $C_{42}H_{72}Cl_2N_6Ni_2O_4S_2·H_2O$ (977.48 + 18.02): calcd. C 50.67, H 7.49, N 8.44, S 6.44; found C 50.5, H 7.51, N 8.09, S 6.56. The tetraphenylborate salt **9**[$BPh_4$] was prepared by adding $NaBPh_4$ (342 mg, 1.00 mmol) to a solution of **9**[$ClO_4$] (100 mg, 0.100 mmol) in methanol (40 mL). The yellow microcrystalline solid was filtered, recrystallised from a few millilitres of acetonitrile, and dried in air. Yield: 113 mg (94%). M.p. 205 °C (decomp). IR (KBr): $\tilde{\nu}$ = 3427 (m), 3055 (m), 3033 (m), 2963 (vs), 2894 (s), 2866 (s), 1816 (vw), 1615 (w), 1579 (w), 1478 (vs), 1461 (vs), 1429 (m), 1379 (m), 1362 (m), 1343 (w), 1312 (w), 1262 (w), 1233 (w), 1201 (vw), 1184 (vw), 1157 (w), 1096 (vs), 1058 (s), 1032 (s), 988 (w), 954 (w), 907 (w), 884 (w), 844 (w), 807 (w), 777 (m), 732 [vs, $\nu(BPh_4^-)$], 704 [vs, $\nu(BPh_4^-)$], 630 (w) 612 (m) $cm^{-1}$. UV/Vis ($CH_3CN$): $\lambda_{max}$ ($\varepsilon$) = 658 (25), 928 (48), 1018 nm (63 $M^{-1}cm^{-1}$). $C_{66}H_{92}BClN_6Ni_2S_2·3H_2O·CH_3CN$ (1197.26 + 95.10): calcd. C 63.20, H 7.88, N 7.59, S 4.96; found C 62.90, H 7.64, N 7.73, S 5.36. The tetraphenylborate salt was additionally characterised by X-ray crystal structure analysis.

**Preparation of [($L^1$)$Cd_2$(Cl)][$ClO_4$] (10[$ClO_4$]):** A solution of $CdCl_2·H_2O$ (402 mg, 2.00 mmol) in MeOH (10 mL) was added to a suspension of $H_2L^1·6HCl$ (806 mg, 1.00 mmol) in MeOH (30 mL). A solution of triethylamine (809 mg, 8.08 mmol) in MeOH (3 mL) was then added. After stirring at ambient temperature for 2 d, solid $LiClO_4·3H_2O$ (1.60 g, 10.0 mmol) was added. The precipitate was filtered and purified by recrystallisation from MeCN. Yield: 432 mg (46%). IR (KBr): $\tilde{\nu}$ = 3445 (m), 3229 [s, $\nu$(NH)], 2953 (s), 2902 (s), 2855 (s), 1623 (m), 1456 (m), 1395 (w), 1363 (m), 1344 (w), 1297 (w), 1268 (vw), 1227 (m), 1151 (m), 1100 (s), 1078 (m), 1024 (m), 942 (m), 910 (m), 873 (m), 850 (m), 812 (w), 780 (w), 747 (vw), 627 (m) $cm^{-1}$. $^1H$ NMR (400 MHz, $CD_3OD$, for atom labels see inset of Table 2): $\delta$ = 1.26 (s, 9 H, $C^1H_3$ or $C^4H_3$), 1.32 (s, 9 H, $C^1H_3$ or $C^4H_3$), 2.40–3.70 (m, 20 H, $C^{6-9,6'-9'}H_2$ + $C^{5,5',10,10'}H$*H*), 4.30–4.40 (m, 4 H, $C^{5,5',10,10'}H$H), 7.16 (s, 2 H, $C^{13,13'}H$ or $C^{17,17'}H$), 7.34 ppm (s, 2 H, $C^{13,13'}H$ or $C^{17,17'}H$). $^{13}C\{^1H\}$NMR (100 MHz, [$D_6$]DMSO): $\delta$ = 31.2 ($C^1$ or $C^4$), 31.3 ($C^1$ or $C^4$), 33.7 ($C^2$ or $C^3$), 33.8 ($C^2$ or $C^3$), 47.4, 48.9, 49.2, 54.2, 55.2, 56.0 ($C^{5-10,5'-10'}$), 127.5, 127.8 ($C^{13,13',17,17'}$), 137.3, 137.4 ($C^{12,12',16,16'}$), 138.2, 139.1 ($C^{11,15}$), 145.0, 145.1 ($C^{14,18}$) ppm. ESI-MS: *m*/*z* 905.3 (100%) [($L^1$)$Cd_2$(Cl)]$^+$. The tetraphenylborate salt **10**[$BPh_4$] was prepared by adding $NaBPh_4$ (674 mg, 1.97 mmol) to a solution of **10**[$ClO_4$] (186 mg, 0.197 mmol) in methanol (50 mL). The resulting colourless microcrystalline solid was isolated by filtration, washed with ethanol, and dried in air. Yield: 172 mg (74%). IR (KBr): $\tilde{\nu}$ = 3445 [m, $\nu$(OH)], 3279 [s, $\nu$(NH)], 3054 [m, $\nu$(Ar)], [2962 (vs), 2864 (s)] [$\nu$(CH)], 1616 (w), 1580 (w), 1477 (s), 1455 (s), 1394 (w), 1365 (w), 1300 (w), 1253 (w), 1227 (w), 1202 (vw), 1152 (w), 1098 (w), 1072 (w), 1033 (w), 909 (m), 849 (m), 735 (vs), 707 (vs), 612 (m) $cm^{-1}$. $^1H$ NMR (400 MHz, $CD_3OD$): $\delta$ = 1.26 (s, 9 H, $C^1H_3$ or $C^4H_3$), 1.32 (s, 9 H, $C^1H_3$ or $C^4H_3$), 2.50–3.75 (m, 20 H, $C^{6-9,6'-9'}H_2$ + $C^{5,5',10,10'}H$*H*), 4.35–4.41 (m, 4 H, $C^{5,5',10,10'}H$H), 6.82 (t, *J* = 8 Hz, 4 H, $BPh_4^-$), 6.96 (t, *J* = 8 Hz, 8 H, $BPh_4^-$), 7.16 (s, 2 H, $C^{13,13'}H$ or $C^{17,17'}H$), 7.29 (m, 8 H, $BPh_4^-$), 7.33 ppm (s, 2 H, $C^{13,13'}H$ or $C^{17,17'}H$). $^{13}C\{^1H\}$NMR (100 MHz, [$D_6$]DMSO): $\delta$ = 31.1 ($C^1$ or $C^4$), 31.2 ($C^1$ or $C^4$), 33.7 ($C^2$ or $C^3$), 33.8 ($C^2$ or $C^3$), 47.4, 48.6, 49.1, 49.3, 54.2, 55.2 ($C^{5-10,5'-10'}$), 127.5, 127.8 ($C^{13,13',17,17'}$), 138.0, 138.2 ($C^{12,12',16,16'}$), 139.0, 139.9 ($C^{11,15}$), 140.0, 145.8 ($C^{14,18}$), 121.5 ($BPh_4^-$), 125.3 ($BPh_4^-$), 135.5 ($BPh_4^-$), 164.0 ppm ($BPh_4^-$). This salt was additionally characterised by X-ray crystallography.

**Preparation of [($L^3$)$Cd_2$(Cl)][$ClO_4$] (12[$ClO_4$]) and [($L^3$)-$Cd_2$(Cl)][$BPh_4$] (12[$BPh_4$]):** A solution of $CdCl_2·H_2O$ (223 mg, 1.10 mmol) in MeOH (2 mL) was added to a suspension of $H_2L^3·6HCl$ (460 mg, 0.552 mmol) in MeOH (15 mL). A solution of triethylamine (445 mg, 4.40 mol) in MeOH (3 mL) was then added to give a colourless solution. After stirring at ambient temperature for 4 d, solid $LiClO_4·3H_2O$ (118 mg, 0.735 mmol) was added to give the perchlorate salt **12**[$ClO_4$] as a white microcrystalline solid. The precipitate was filtered and purified by recrystallisation from MeCN. Yield: 432 mg (80%). M.p. 332 °C (decomp.). $^1H$ NMR (200 MHz, $CD_3CN$, for atom labels see inset of Table 2): $\delta$ = 1.25 (s, 9 H, $C^1H_3$ or $C^4H_3$), 1.29 (s, 9 H, $C^1H_3$ or $C^4H_3$), 2.65 [s, 6 H, $CH_3(R^1)$], 2.70–3.60 (m, 20 H, $C^{6-9,6'-9'}H_2$ + $C^{5,5',10,10'}H$), 4.25–4.43 (m, 4 H, $C^{5,5',10,10'}H$), 7.17 (s, 2 H, $C^{13,13'}H$ or $C^{17,17'}H$), 7.32 ppm (s, 2 H, $C^{13,13'}H$ or $C^{17,17'}H$). $^{13}C\{^1H\}$NMR (75 MHz, $CD_3CN$): $\delta$ = 31.61 ($C^1$ or $C^4$), 31.74 ($C^1$ or $C^4$), 34.84 ($C^2$ or $C^3$), 34.93 ($C^2$ or $C^3$), 49.48 ($CH_3$, $R^1$), 50.68, 55.19, 56.20, 58.06, 58.17, 60.37 ($C^{5-10,5'-10'}$), 129.01, 129.28 ($C^{13,13',17,17'}$), 138.95, 139.46 ($C^{12,12',16,16'}$), 138.45, 140.24 ($C^{11,15}$), 147.96, 148.21 ppm ($C^{14,18}$). IR (KBr): $\tilde{\nu}$ = 3453 (m), 3283 (m), 2953 (m), 2864 (m), 1629 (w), 1462 (m), 1363 (w), 1300 (vw), 1266 (vw), 1229 (w), 1202 (vw), 1154 (w), 1097 [vs, $\nu(ClO_4^-)$], 989 (w), 931 (w), 860 (w), 751 (vs), 624 (m) $cm^{-1}$. $C_{34}H_{56}Cd_2Cl_2N_6O_4S_2·2H_2O$ (972.70 + 36.03): calcd. C 40.48, H 6.00, N 8.33, S 6.36; found C 40.20, H 5.88, N 7.61, S 6.11. The tetraphenylborate salt **12**[$BPh_4$] was prepared by adding $NaBPh_4$ (342 mg, 1.00 mmol) to a solution of **12**[$ClO_4$] (97 mg, 0.100 mmol) in methanol (40 mL). The colourless microcrystalline solid was isolated by filtration, washed with ethanol, and dried in air. Yield: 82 mg (69%). $^1H$ NMR (200 MHz, $CD_3CN$, for atom labels see inset Table 2): $\delta$ = 1.25 (s, 9 H, $C^1H_3$ or $C^4H_3$), 1.29 (s, 9 H, $C^1H_3$ or $C^4H_3$), 2.65 [s, 6 H, $CH_3(R^1)$] 2.65–3.60 (m, 20 H, $C^{6-9,6'-9'}H_2$ + $C^{5,5',10,10'}H$H), 4.20–4.45 (m, 4 H, $C^{5,5',10,10'}H$*H*), 6.83 (m, 4 H, $BPh_4^-$), 6.99 (m, 8 H, $BPh_4^-$), 7.17 (s, 2 H, $C^{13,13'}H$ or $C^{17,17'}H$), 7.28 (m, 8 H, $BPh_4^-$), 7.32 ppm (s, 2 H, $C^{13,13'}H$ or $C^{17,17'}H$). $^{13}C\{^1H\}$NMR (75 MHz, $CD_3CN$): $\delta$ = 31.49 ($C^1$ or $C^4$), 31.61 ($C^1$ or $C^4$), 34.9 ($C^2$ or $C^3$), 35.0 ($C^2$ or $C^3$), 49.3 [$CH_3(R^1)$], 49.4, 50.6, 55.0, 56.1, 58.0, 60.2 ($C^{5-10,5'-10'}$), 128.9, 129.1 ($C^{13,13',17,17'}$), 138.5, 140.1 ($C^{12,12',16,16'}$), 139.0, 139.5 ($C^{11,15}$), 147.1, 147.8 ($C^{14,18}$); 122.7 ($BPh_4^-$), 126.5 ($BPh_4^-$), 136.7 ($BPh_4^-$), 165.04 ($BPh_4^-$) ppm. IR (KBr): $\tilde{\nu}$ = 3426 (m), 3275 (s), 3054 (m), 2965 (vs), 2867 (s), 2250 (vw), 1618 (vw), 1579 (w), 1479 (s), 1463 (s), 1427 (m), 1391 (w), 1363 (m), 1296 (w), 1267 (w), 1229 (w), 1201 (w), 1153 (m), 1086 (s), 1047 (s), 982 (w), 929 (w), 904 (w), 884 (w), 862 (m), 816 (vw), 749 (m), 735 [vs. $\nu(BPh_4^-)$], 706 [vs. $\nu(BPh_4^-)$], 680 (vw), 625 (w), 612 (m), 543 (vw), 469 (vw) $cm^{-1}$. $C_{58}H_{76}BCd_2ClNS_2·H_2O$ (1192.48 + 18.02): calcd. C 57.55, H 6.49, N 6.94, S 5.30; found C 57.20, H 7.13, N 7.54, S 5.56. The tetraphenylborate salt was additionally characterised by X-ray crystal structure analysis.

**Preparation of [($L^4$)$Cd_2$(Cl)][$ClO_4$] (13[$ClO_4$]) and [($L^4$)-$Cd_2$(Cl)][$BPh_4$] (13[$BPh_4$]):** A solution of $CdCl_2·H_2O$ (43.2 mg,

 © 2007 Wiley-VCH Verlag GmbH & Co. KGaA, Weinheim 

0.215 mmol) in MeOH (2 mL) was added to a suspension of $H_2L^4$·6HCl (101 mg, 0.107 mmol) in MeOH (20 mL). A solution of triethylamine (86.7 mg, 0.857 mmol) in MeOH (3 mL) was then added to give a colourless solution. After stirring at ambient temperature for 2 d, solid $LiClO_4$·$3H_2O$ (171 mg, 1.07 mmol) was added to give the perchlorate salt **13**[$ClO_4$] as a white microcrystalline solid. The precipitate was filtered and purified by recrystallisation from a mixed EtOH/MeCN (1:1) solvent system. Yield: 102 mg (88%). M.p. 328 °C (decomp.). $^1$H NMR (200 MHz, $CD_3CN$, for atom labels see inset Table 2): $\delta$ = 1.12 [t, $J$ = 14 Hz, 12 H, $NCH_2CH_3(R^2)$], 1.27 (s, 18 H, $C^1H_3$ + $C^4H_3$), 2.36–4.52 (m, 38 H, $NCH_2$), 2.83 [s, 6 H, $CH_3(R^1)$], 7.28 (s, 4 H, $C^{13,13',17,17'}H$) ppm. $^{13}C\{^1H\}$NMR (75 MHz, $CD_3CN$): $\delta$ = 6.63 [$CH_2CH_3(R^2)$], 31.5 ($C^{1,4}$), 34.7 ($C^{2,3}$), 50.00 [$CH_2CH_3(R^2)$], 50.30 [$CH_3(R^1)$], 55.74, 56.55, 58.13 ($C^{5-10,5'-10'}$), 130.18 ($C^{13,13',17,17'}$), 136.29 ($C^{12,12',16,16'}$), 142.13 ($C^{11,15}$), 146.78 ($C^{14,18}$) ppm. IR (KBr): $\tilde{\nu}$ = 3440 (m), 2961 (s), 2867 (m), 1628 (w), 1465 (s), 1383 (m), 1367 (m), 1313 (w), 1268 (w), 1231 (w), 1203 (vw), 1100 (vs, $\nu ClO_4^-$), 1052 (s), 985 (w), 948 (vw), 926 (vw), 887 (w), 778 (m), 624 (m) cm$^{-1}$. $C_{42}H_{72}Cd_2Cl_2N_6O_4S_2$·$7H_2O$ (1084.92 + 126.11): calcd. C 41.65, H 7.16, N 6.94, S 5.30; found C 42.1, H 7.01, N 7.09, S 5.54. The tetraphenylborate salt **13**[$BPh_4$] was prepared by adding $NaBPh_4$ (342 mg, 1.00 mmol) to a solution of **13**[$ClO_4$] (108 mg, 0.100 mmol) in methanol (40 mL). The colourless microcrystalline solid was isolated by filtration, washed with ethanol, and dried in air. Yield: 119 mg (91%). M.p. 231 °C (decomp.). $^1$H NMR (400 MHz, $CD_3CN$, for atom labels see inset Table 2): $\delta$ = 1.16 [m, 12 H, $CH_2CH_3(R^2)$], 1.28 (s, 18 H, $C^1H_3$ + $C^4H_3$), 2.86 [s, 6 H, $CH_3(R^1)$], 2.70–4.47 (m, 38 H, $NCH_2$), 6.85 (m, 4 H, $BPh_4^-$), 7.00 (m, 8 H, $BPh_4^-$), 7.23 ppm (m, 4 H + 8 H, $C^{13,13',17,17'}H$ + $BPh_4^-$). $^{13}C\{^1H\}$NMR (75 MHz, $CD_3CN$): $\delta$ = 6.56 [$CH_2CH_3(R^2)$], 31.5 ($C^{1,4}$), 34.65 ($C^{2,3}$), 49.91 [$CH_2CH_3(R^2)$], 50.21 [$CH_3(R^1)$], 55.64,

Table 5. Crystallographic data for **5**, **8**[$BPh_4$]·3EtOH, **9**[$BPh_4$]·5MeCN, **10**[$BPh_4$]·5MeOH, **12**[$BPh_4$]·2MeCN and {**13**[$BPh_4$]·3.5MeCN}$_2$.

| | **5** | **8**[$BPh_4$]·3EtOH | **9**[$BPh_4$]·5MeCN |
|---|---|---|---|
| Formula | $C_{44}H_{76}N_6S_2$ | $C_{64}H_{94}BClN_6Ni_2O_3S_2$ | $C_{76}H_{107}BClN_{11}Ni_2S_2$ |
| $M_r$ [g mol$^{-1}$] | 753.23 | 1223.25 | 1402.53 |
| Space group | $C2/c$ | $P\bar{1}$ | $P\bar{1}$ |
| $a$ [Å] | 24.437(4) | 14.872(3) | 13.3420(5) |
| $b$ [Å] | 9.734(3) | 14.949(3) | 14.7530(5) |
| $c$ [Å] | 19.004(4) | 16.132(3) | 19.0750(7) |
| $\alpha$ [°] | 90.00 | 71.14(3) | 85.653(3) |
| $\beta$ [°] | 90.52(2) | 78.41(3) | 88.787(3) |
| $\gamma$ [°] | 90.00 | 71.92(3) | 84.854(3) |
| $V$ [Å$^3$] | 4520.0(18) | 3206.1(11) | 3728.3(2) |
| $Z$ | 4 | 2 | 2 |
| $D_{calcd.}$ [g cm$^{-3}$] | 1.107 | 1.267 | 1.249 |
| $\mu$(Mo-$K_\alpha$) [mm$^{-1}$] | 0.154 | 0.742 | 0.646 |
| $\theta$ limits [°] | 1.67–28.86 | 1.34–28.82 | 3.26-31.99 |
| Measured refl. | 19600 | 29072 | 34637 |
| Independent refl. | 5472 | 14990 | 25571 |
| Observed refl.[a] | 2602 | 7750 | 17381 |
| parameters | 263 | 682 | 763 |
| $R1$[b] ($R1$ all data) | 0.0585 (0.1281) | 0.0511 (0.1144) | 0.0403 (0.0627) |
| $wR2$[c] ($wR2$ all data) | 0.1579 (0.1908) | 0.1197 (0.1461) | 0.0999 (0.1054) |
| Max., min. peaks [e/Å$^3$] | 0.443/–0.207 | 0.885/–0.532 | 1.226/–0.729 |
| CCDC | 600010 | 600011 | 600012 |
| | **10**[$BPh_4$]·5MeOH | **12**[$BPh_4$]·2MeCN | {**13**[$BPh_4$]·3.5MeCN}$_2$ |
| Formula | $C_{61}H_{92}BCd_2ClN_6O_5S_2$ | $C_{62}H_{82}BCd_2ClN_8S_2$ | $C_{146}H_{205}B_2Cd_4Cl_2N_{19}S_4$ |
| $M_r$ [g mol$^{-1}$] | 1324.59 | 1274.54 | 2896.65 |
| Space group | $P\bar{1}$ | $P2_1/c$ | $P\bar{1}$ |
| $a$ [Å] | 14.202(3) | 15.283(3) | 18.984(4) |
| $b$ [Å] | 17.019(3) | 28.264(6) | 20.143(4) |
| $c$ [Å] | 17.928(4) | 16.995(3) | 22.112(4) |
| $\alpha$ [°] | 109.77(3) | 90.00 | 98.55(3) |
| $\beta$ [°] | 105.85(3) | 107.28(3) | 115.29(3) |
| $\gamma$ [°] | 113.66(3) | 90.00 | 95.67(3) |
| $V$ [Å$^3$] | 3288.1(11) | 7010(2) | 7434(3) |
| $Z$ | 2 | 4 | 2 |
| $D_{calcd.}$ [g cm$^{-3}$] | 1.338 | 1.208 | 1.294 |
| $\mu$(Mo-$K_\alpha$) [mm$^{-1}$] | 0.800 | 0.744 | 0.710 |
| $\theta$ limits [°] | 5.10–31.97 | 1.44–29.03 | 3.21–28.01 |
| Measured refl. | 49433 | 44336 | 137595 |
| Independent refl. | 22415 | 16567 | 34637 |
| Observed refl.[a] | 11546 | 5816 | 26501 |
| parameters | 741 | 655 | 1489 |
| $R1$[b] ($R1$ all data) | 0.0922 (0.1596) | 0.0720 (0.1981) | 0.0478 (0.0647) |
| $wR2$[c] ($wR2$ all data) | 0.2259 (0.2670) | 0.2013 (0.2551) | 0.1313 (0.1447) |
| Max., min. peaks [e/Å$^3$] | 2.841/–2.582 | 1.310/–0.829 | 1.331/–1.155 |
| CCDC | 622729 | 600013 | 600014 |

[a] Observation criterion: $I > 2\sigma(I)$. [b] $R1 = \Sigma||F_o| - |F_c||/\Sigma|F_o|$. [c] $wR2 = \{\Sigma[w(F_o^2 - F_c^2)^2]/\Sigma[w(F_o^2)^2]\}^{1/2}$.

 © 2007 Wiley-VCH Verlag GmbH & Co. KGaA, Weinheim 

56.46, 59.02 ($C^{5–10,5'–10'}$), 130.10 ($C^{13,13',17,17'}$), 136.20 ($C^{12,12',16,16'}$), 142.06 ($C^{11,15}$), 146.67 ($C^{14,18}$); 122.79 ($BPh_4^-$), 126.58 ($BPh_4^-$), 136.77 ($BPh_4^-$), 164.82 ($BPh_4^-$) ppm. IR (KBr): $\tilde{\nu}$ = 3441 (w), 3034 (m), 3054 (m), 2964 (vs), 2863 (s), 1748 (vw), 1616 (vw), 1580 (w), 1464 (vs), 1383 (m), 1367 (m), 1311 (w), 1267 (w), 1232 (w), 1185 (vw), 1159 (w), 1100 (m), 1053 (vs), 986 (vw), 949 (vw), 925 (vw), 886 (w), 845 (vw), 777 (m), 734 (s), 705 [vs. $\nu(BPh_4^-)$], 613 (m) $cm^{-1}$. $C_{66}H_{92}BCd_2ClN_6S_2$ (1304.69): calcd. C 60.76, H 7.11, N 6.44, S 4.92; found C 60.94, H 6.85, N 6.37, S 5.42. The tetraphenylborate salt was additionally characterised by X-ray crystal structure analysis.

**Crystal Structure Determinations:** Large single crystals of **5** were obtained by slow evaporation of a $CH_2Cl_2/CH_3OH$ solution. Crystals of **8**[$BPh_4$]·3EtOH, **9**[$BPh_4$]·5MeCN, **12**[$BPh_4$]·2MeCN and {**13**[$BPh_4$]·3.5MeCN}$_2$ were obtained by slow evaporation from a mixed MeCN/EtOH (1:1) solvent system. Crystals of **10**[$BPh_4$]·5MeOH were grown by recrystallisation from MeOH. The diffraction experiments were carried out with Bruker CCD (for **5**, **8** and **12**) or STOE IPDS-2T X-ray diffractometers (for **9**, **10** and **13**). The intensity data were processed with the programs SAINT (**5**, **8**, **12**) or STOE X-AREA (**9**, **10**, **13**). Structures were solved by direct methods and refined by full-matrix least-squares on the basis of all data against $F^2$ using SHELXL-97.[31] PLATON was used to search for higher symmetry.[32] H atoms were placed in calculated positions and treated isotropically using the 1.2-fold $U_{iso}$ value of the parent atom, except for methyl protons, which were assigned the 1.5-fold $U_{iso}$ value of the parent C atoms. Unless otherwise noted, all non-hydrogen atoms were refined anisotropically. ORTEP-3 was used for the artwork of the structures.[33] Experimental crystallographic data are summarised in Table 5. Further data are available in the Supporting Information.

In the crystal structure of **5** and **10**[$BPh_4$]·5MeOH a *tert*-butyl group is disordered over two positions. Two split positions were successfully refined to give the following site occupancies: C(19a)-C20(a)C(21a)/C(19b)C20(b)C(21b) = 0.60(1)/0.40(1) (for **5**), C(26a)C(27a)C(28a)/C(26b)C(27b)C(28b) = 0.60(2)/0.40(2) (for **10**[$BPh_4$]·5MeOH). The C, N, and O atoms of the solvates in **8**[$BPh_4$]·3EtOH, **9**[$BPh_4$]·5MeCN and {**13**[$BPh_4$]·3.5MeCN}$_2$ were refined isotropically.

CCDC-600010 to -600014 and -622729 (see Table 5 for assignments) contain the supplementary crystallographic data for this paper. These data can be obtained free of charge from The Cambridge Crystallographic Data Centre via www.ccdc.cam.ac.uk/data_request/cif.

## Acknowledgments

We are particularly grateful to Prof. Dr. H. Vahrenkamp, Prof. Dr. E. Hey-Hawkins and Prof. Dr. H. Krautscheid for providing facilities for NMR and X-ray crystallographic measurements. This work was supported by the Deutsche Forschungsgemeinschaft (priority programme "Sekundäre Wechselwirkungen", KE 585/3-3).

[1] a) L. F. Lindoy, *The Chemistry of Macrocyclic Complexes*, Cambridge University Press, **1989**; b) E. C. Constable, *Metals and Ligand Reactivity*, VCH, Weinheim, **1995**.
[2] P. Comba, B. Martin, *Macrocyclic Chemistry – Current Trends and Future Perspectives* (Ed.: K. Gloe), Springer, Dordrecht, **2005**.
[3] M. Meyer, V. Dahaoui-Gindrey, C. Lecomte, R. Guilard, *Coord. Chem. Rev.* **1998**, *178–180*, 1313–1405.
[4] B. Bosnich, C. K. Poon, M. L. Tobe, *Inorg. Chem.* **1965**, *4*, 1102–1108.
[5] F. Wagner, E. K. Barefield, *Inorg. Chem.* **1976**, *15*, 408–417.
[6] M. A. Donnelly, M. Zimmer, *Inorg. Chem.* **1999**, *38*, 1650–1656.
[7] X. Liang, J. A. Parkinson, S. Parsons, M. Weishäupl, P. J. Sadler, *Inorg. Chem.* **2002**, *41*, 4539–4547.
[8] B. Kersting, *Z. Anorg. Allg. Chem.* **2004**, *630*, 765–780.
[9] G. Steinfeld, V. Lozan, B. Kersting, *Angew. Chem.* **2003**, *115*, 2363–2365; *Angew. Chem. Int. Ed.* **2003**, *42*, 2261–2263.
[10] S. Käss, T. Gregor, B. Kersting, *Angew. Chem.* **2006**, *118*, 107–110; *Angew. Chem. Int. Ed.* **2006**, *45*, 101–104.
[11] B. Kersting, G. Steinfeld, *Chem. Commun.* **2001**, 1376–1377.
[12] B. Kersting, G. Steinfeld, *Inorg. Chem.* **2002**, *41*, 1140–1150.
[13] V. Lozan, B. Kersting, *Eur. J. Inorg. Chem.* **2005**, 504–512.
[14] a) M. H. Klingele, G. Steinfeld, B. Kersting, *Z. Naturforsch., Teil B* **2001**, *56*, 901–907; b) G. Siedle, B. Kersting, *Z. Anorg. Allg. Chem.* **2003**, *629*, 2083–2090.
[15] K. Wieghardt, P. Chaudhuri, B. Nuber, J. Weiss, *Inorg. Chem.* **1982**, *21*, 3086–3090.
[16] N. W. Alcock, A. C. Benniston, S. J. Grant, H. A. A. Omar, P. Moore, *J. Chem. Soc., Chem. Commun.* **1991**, 1573–1575.
[17] B. Kersting, *Angew. Chem.* **2001**, *113*, 4110–4112; *Angew. Chem. Int. Ed.* **2001**, *40*, 3988–3990.
[18] A. J. Atkins, D. Black, A. J. Blake, A. Marin-Becerra, S. Parsons, L. Ruiz-Ramirez, M. Schröder, *Chem. Commun.* **1996**, 457–464.
[19] G. Siedle, B. Kersting, *Z. Anorg. Allg. Chem.* **2003**, *629*, 2083–2090.
[20] C. D. Gutsche, *Calixarenes*, Royal Society of Chemistry, Cambridge, UK, **1989**.
[21] D. A. House, in *Comprehensive Coordination Chemistry* (Eds.: G. Wilkinson, R. D. Gillard, J. A. McCleverty), **1996**, vol. 2, pp. 23–72.
[22] a) E. K. Barefield, G. M. Freeman, D. G. Van Derveer, *Inorg. Chem.* **1986**, *25*, 552–558; b) P. Chaudhuri, K. Wieghardt, *Prog. Inorg. Chem.* **1986**, *35*, 329–436.
[23] a) R. D. Shannon, C. T. Prewitt, *Acta Crystallogr., Sect. B* **1969**, *25*, 925–946; b) R. D. Shannon, *Acta Crystallogr., Sect. A* **1976**, *32*, 751–767.
[24] O. Schlager, K. Wieghardt, H. Grondey, A. Rufinska, B. Nuber, *Inorg. Chem.* **1995**, *34*, 6440–6448.
[25] P. V. Bernhardt, P. Comba, T. W. Hambley, G. A. Lawrance, K. Varnagy, *J. Chem. Soc., Dalton Trans.* **1992**, 355–359.
[26] H. Strasdeit, A.-K. Duhme, M. Weber, S. Pohl, *Acta Crystallogr., Sect. C* **1992**, *48*, 437–440.
[27] B. Krebs, G. Henkel, *Angew. Chem.* **1991**, *103*, 785–804; *Angew. Chem. Int. Ed. Engl.* **1991**, *30*, 769–788.
[28] M. G. B. Drew, O. W. Howarth, G. G. Morgan, J. Nelson, *J. Chem. Soc., Dalton Trans.* **1994**, 3149–3158.
[29] S. S. Tandon, S. Chander, L. K. Thompson, J. N. Bridson, V. McKee, *Inorg. Chim. Acta* **1994**, *219*, 55–65.
[30] J. Hausmann, M. H. Klingele, V. Lozan, G. Steinfeld, D. Siebert, Y. Journaux, J. J. Girerd, B. Kersting, *Chem. Eur. J.* **2004**, *10*, 1716–1728.
[31] Sheldrick, G. M. *SHELXL-97*, *Computer program for crystal structure refinement*, University of Göttingen, Germany, **1997**.
[32] A. L. Spek, *PLATON – A Multipurpose Crystallographic Tool*, Utrecht University, Utrecht, The Netherlands, **2000**.
[33] L. J. Farrugia, *J. Appl. Crystallogr.* **1997**, *30*, 565–568.

Received: April 6, 2006
Published Online: November 21, 2006

 © 2007 Wiley-VCH Verlag GmbH & Co. KGaA, Weinheim 

DOI: 10.1002/ejic.200600326

# Ferrocenes Bearing Sulfinylamino Groups

**Bernd Wrackmeyer,*[a] Elena V. Klimkina,[a] Wolfgang Milius,[a] Miriam Siebenbürger,[a] Oleg L. Tok,[a] and Max Herberhold[a]**

*Dedicated to Professor Dr. Walter Siebert on the occasion of his 70th birthday*

**Keywords:** 1,1′-Diaminoferrocene / 1,1′-Bis(trimethylsilylamino)ferrocene / Thionyl chloride / Sulfinylamines

1,1′-Diaminoferrocene (**2**) and 1,1′-bis(trimethylsilylamino)-ferrocene (**3**) have been converted into sulfinylamines by treatment with thionyl chloride in the presence of triethylamine. In the case of **2** the 1:2 reaction affords 1,1′-bis(sulfinylamino)ferrocene (**5**) and the 1:1 reaction gives 6-amino-1-sulfinylaminoferrocene (**6**). Bis(trimethylsilylamino)ferrocene reacts with thionyl chloride in a 1:1 molar ratio to give 1-sulfinylamino-6-(trimethylsilylamino)ferrocene (**8**). In contrast, the reaction of *N*,*N*′-dilithiobis(trimethylsilylamino)ferrocene (**4**) with thionyl chloride gives the [3]ferrocenophane **9**, which contains an N–S(O)–N bridge, rather than sulfinylamines or a sulfur diimide. The molecular structures of **5** and **8** were determined by X-ray analysis. The $^{57}$Fe NMR chemical shift ($\delta$ = +2597.0 ppm) for **5** indicates the strong π-acceptor properties of the NSO groups. Dynamic $^{1}$H and $^{13}$C NMR spectra prove the hindered rotation of the NSO group about the C–N bonds in **5**, **6** and **8**.

(© Wiley-VCH Verlag GmbH & Co. KGaA, 69451 Weinheim, Germany, 2007)

## Introduction

The combination of the rich chemistry of ferrocenes[1] with that of sulfinylamines[2] is an attractive target. Convenient routes for the synthesis of sulfinylamines (R-NSO) start either from the corresponding primary amines ($RNH_2$) or from *N*-trimethylsilylamines [RN(H)-$SiMe_3$].[2] The latter approach has been successful in the case of ferrocenylsufinylamine (Fc-NSO, **1**), which has been structurally characterised in the solid state.[3] The structure of **1** in solution has been established by various physical methods, including routine NMR spectroscopy[3] and also $^{57}$Fe NMR spectroscopy.[4] The synthesis of 1,1′-diaminoferrocene [fc$(NH_2)_2$, **2**][5] has recently been improved,[6] therefore access to *N*,*N*′-disubstituted derivatives of 1,1′-diaminoferrocene, such as 1,1′-bis(trimethylsilylamino)ferrocene (**3**)[6] or its dilithiated derivative **4**,[7] has become more feasible. This is mirrored by advances in the synthesis of numerous [*n*]ferrocenophanes, for example with *n* = 3, with various elements between the nitrogen atoms.[7–12] In the present work, we describe attempts to convert the ferrocenes **2**–**4** into sulfinylamines, aiming particularly for NMR spectroscopic studies in solution and structural characterisation in the solid state.

[a] Laboratorium für Anorganische Chemie, Universität Bayreuth, 95440 Bayreuth, Germany
Fax: +49-921-552157
E-mail: b.wrack@uni-bayreuth.de

## Results and Discussion

The reaction of **2** with thionyl chloride in the presence of an excess of triethylamine leads to the ferrocenes **5** or **6**, depending on the ratio of the starting compounds (Scheme 1). The complete conversion of **2** into 1,1′-bis(sulfinylamino)ferrocene (**5**) requires two equivalents of thionyl chloride. Complex **5** was isolated as a violet-blue, air- and moisture-sensitive solid, which gave violet crystals after recrystallisation. The 1:1 reaction affords 6-amino-1-sulfinylaminoferrocene (**6**), which, however, is contaminated with **2** and **5**. Purification by repeated crystallisation gave pure **6** as a blue powder. The availability of **5** calls for an attempt to prepare the sulfur diimide **7**. However, the reaction of **5** with KO*t*Bu in DMF[2,3] gave only **6**, most likely as the result of partial hydrolysis of **5**.

Another route to sulfinylaminoferrocenes is conceivable from the reaction of 1,1′-bis(trimethylsilylamino)ferrocene (**3**) with thionyl chloride in the presence of triethylamine (Scheme 2). The product of the 1:1 reaction, 1-sulfinylamino-6-(trimethylsilylamino)ferrocene (**8**), is formed along with a small amount of **5**, and **8** was isolated after recrystallisation as a blue crystalline solid.

*N*,*N*′-Dilithiation of **3** gives **4**, and its 1:1 reaction with thionyl chloride leads to the [3]ferrocenophane **9** (Scheme 3). The formation of **9** is accompanied by decomposition leading mainly to **3**. The elimination of hexamethyldisiloxane [$O(SiMe_3)_2$] from **9** to give the sulfur diimide **7** was not observed.

 © 2007 Wiley-VCH Verlag GmbH & Co. KGaA, Weinheim 

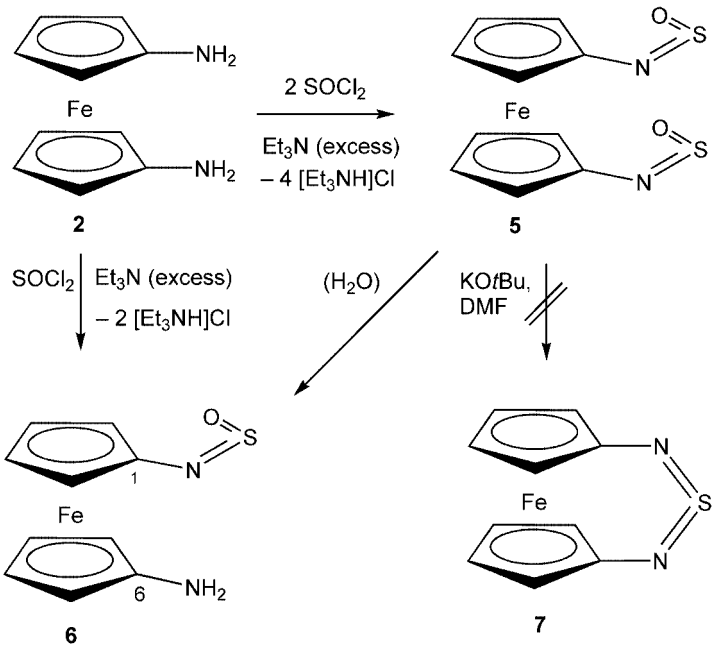


Scheme 1. Reaction of 1,1′-diaminoferrocene (**2**) with thionyl chloride and attempted synthesis of the sulfur diimide **7**.

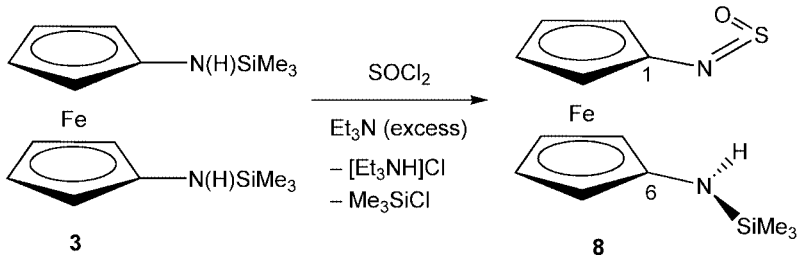


Scheme 2. Reaction of 1,1′-bis(trimethylsilylamino)ferrocene (**3**) with thionyl chloride .

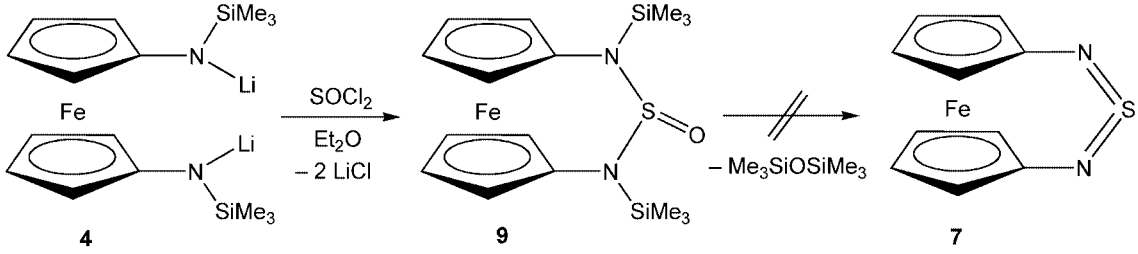


Scheme 3. Reaction of *N*,*N*′-dilithio-1,1′-bis(trimethylsilylamino)ferrocene (**4**) with thionyl chloride — another failure to obtain the sulfur diimide **7**.

### NMR Spectroscopic Studies in Solution

Relevant NMR spectroscopic data for the ferrocenes **1** (for comparison), **5**, **6**, **8** and **9** are given in Table 1 and in the Experimental Section ($^1$H NMR). The cyclopentadienyl groups are clearly identified by the $^1$H and $^{13}$C NMR spectroscopic data measured at room temperature. The presence of the NSO group is evident both from characteristic $^{14}$N NMR signals at high frequencies[13] and the symmetric and antisymmetric NSO stretching vibrations[2] in the IR spectra. The $^{15}$N NMR spectra ($^1$H coupled) prove the existence of the $NH_2$ and $N(H)SiMe_3$ groups in **6** and **8**, respectively. The $^{29}$Si NMR signal of **8** is notably different from that of the [3]ferrocenophane **9**, and $^{29}$Si nuclear deshielding is rather typical for the ring closure in **9**.[9–12]

Owing to the low NMR receptivity of $^{57}$Fe nuclei, $^{57}$Fe NMR spectra have rarely been reported.[14] However, careful setting of experimental parameters allows the measurement of meaningful spectra within a reasonable time.[4,15,16] The $^{57}$Fe nuclear shielding in ferrocene derivatives is sensi-

 © 2007 Wiley-VCH Verlag GmbH & Co. KGaA, Weinheim 

Table 1. $^{13}C$, $^{14}N$, $^{15}N$, $^{29}Si$ and $^{57}Fe$ NMR spectroscopic data[a] of compounds **1**, **5**, **6**, **8** and **9**.

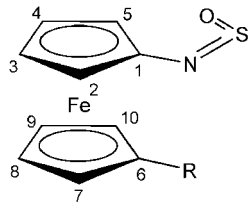

**1**, **5**, **6**, **8**

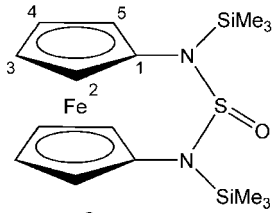

**9**

| Compound | **1**[3] | **5** | **6** | | **8** | | **9** |
|---|---|---|---|---|---|---|---|
| | R = H | R = NSO | R = $NH_2$ | | R = N(H)$SiMe_3$ | | |
| *T* [K] | 298 K | 298 K | 298 K | 198 K | 298 K | 203 K | 298 K |
| $\delta^{13}C$ (fc-$C^1$) | 71.2 | 97.3 | 97.4 | 97.8 | 97.8 | 97.7 | 105.7 |
| $\delta^{13}C$ (fc-$C^{2,5}$) | 69.2 | 70.7[b] | 70.3 | 68.1, 71.0 | 70.1 | 66.9, 71.0 | 63.3, 65.1[b] 68.4, 72.3[b] |
| $\delta^{13}C$ (fc-$C^{3,4}$) | 70.1 | 72.4[b] | 71.4 | 70.2, 72.3 | 71.4 | 69.5, 72.1 | |
| $\delta^{13}C$ (fc-$C^6$) | 71.2 | 97.3 | 105.7 | 101.3 | 108.6 | 105.7 | |
| $\delta^{13}C$ (fc-$C^{7,10}$) | | 70.7 | 59.5 | 57.3, 59.0 | 59.5 | 56.8, 58.6 | |
| $\delta^{13}C$ (fc-$C^{8,9}$) | | 72.4 | 66.5 | 65.5, 67.4 | 66.4 | 64.7, 66.8 | |
| $\delta^{13}C$ ($Me_3Si$) | | | | | –0.2 (57.1) | –1.7 (57.3) | 0.3 (57.4) |
| $\delta^{14}N$ (NSO) | –67 | –62 | –57 | | –57 | | |
| $\delta^{15}N$ | | | –356.4 | | –345.6 | | n.o. |
| $^1J(^{15}N,^1H)$ (Hz) | | | 78.8 | | 76.5 | | |
| $\delta^{29}Si$ | | | | | 6.0 (57.1) | 6.5 | 12.0 (57.4) |
| $\delta^{57}Fe$ | 1966.3 | 2597.0 | | | 2131.0 | | |

[a] Measured in $CDCl_3$ (**1**) or $CD_2Cl_2$ (**5**, **6**, **8** and **9**); $^1J(^{29}Si,^{13}C)$ coupling constants (±0.5 Hz) are given in parentheses; n.o. = not observed. [b] Assignment might be reversed.

tive to π-acceptor substituents, and deshielding is usually observed if the ferrocene structural geometry remains fairly undistorted.[4,16] According to the $\delta^{57}Fe$ value of **1**, the NSO group is a strong π-acceptor; this is also supported by the molecular structure of **1**, where the planes of the NSO group and the substituted cyclopentadienyl rings almost coincide.[3] Frequently, the contributions to $^{57}Fe$ nuclear shielding in ferrocenes are approximately additive for any substituents in 1,1′-positions.[17] Thus, the rather extreme $^{57}Fe$ nuclear deshielding observed for **5** ($\delta^{57}Fe$ =

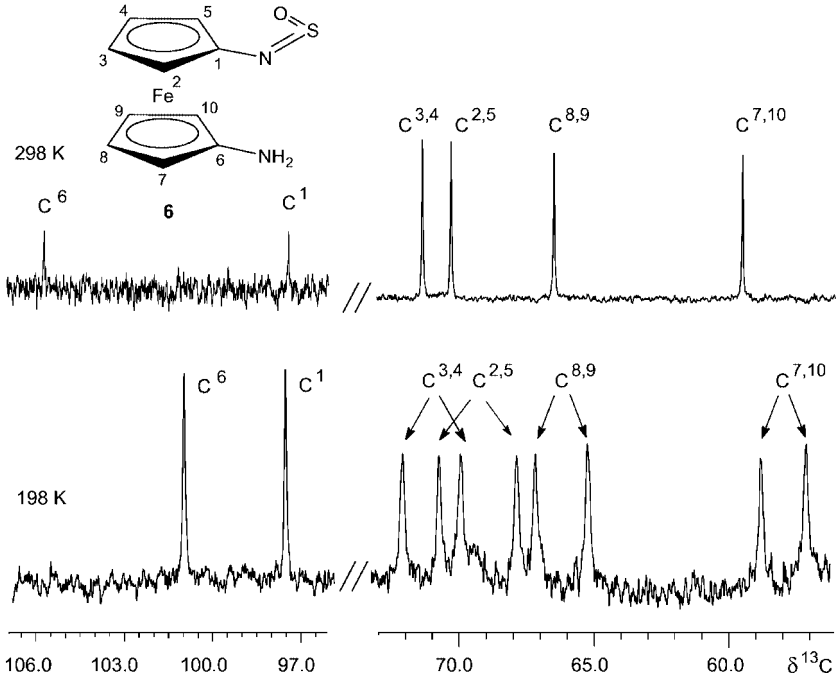


Figure 1. 62.9 MHz $^{13}C\{^1H\}$ NMR spectra of **6** at 298 K (upper trace) and 198 K (lower trace).

 © 2007 Wiley-VCH Verlag GmbH & Co. KGaA, Weinheim 

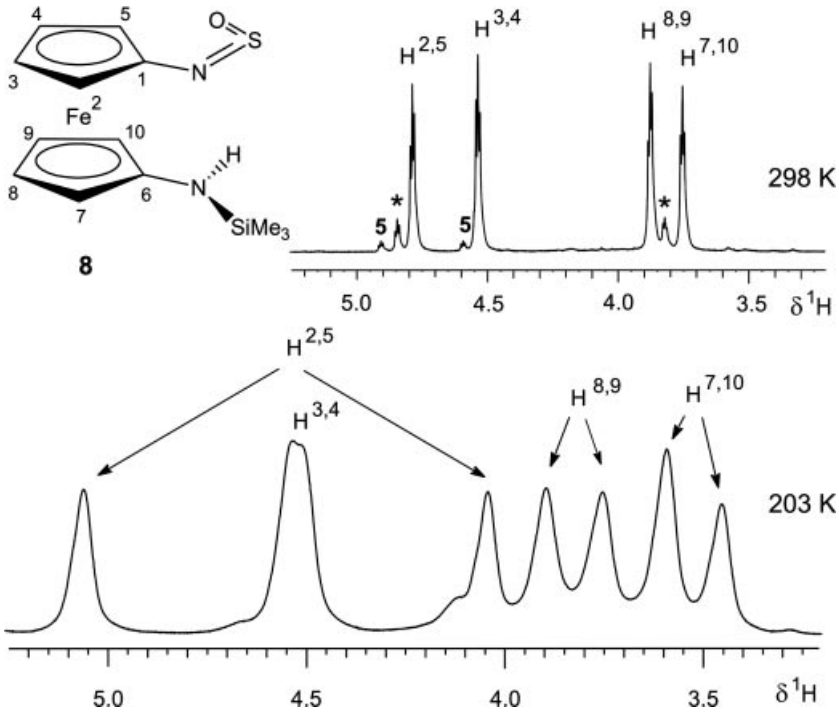


Figure 2. Parts of the 250.1 MHz $^1$H NMR spectra of the ferrocene **8** at 298 K (upper trace) and 203 K (lower trace). Signals of a side product are marked with asterisks.

+2597.0 ppm), when compared with ferrocene itself ($\delta^{57}$Fe = +1538.4 ppm[15]), is expected; the $\delta^{57}$Fe value for **8** ($\delta^{57}$Fe = +2131.0 ppm) is close to that of **1** ($\delta^{57}$Fe = +1966.3 ppm).

The π-acceptor properties of the NSO group should be reflected by restricted rotation about the C$^1$–N or C$^{1'}$-N bonds. Indeed, this is evident from the low-temperature $^1$H and $^{13}$C NMR spectra (Table 1, Figure 1 and Figure 2). In the case of **5**, the $^1$H and $^{13}$C NMR signals become broad at low temperature just before the complex crystallises, and in the cases of **6** and **8**, splitting of the C$^{2,5}$-H and C$^{3,4}$-H NMR signals into two signals each is observed (Figure 1 and Figure 2). In the cases of **6** and **8**, the barrier to rotation about the C$^1$–N(SO) bond can be estimated[18] as 43.0 ± 1 kJ mol$^{-1}$ at –65 °C (coalescence) from both $^1$H and $^{13}$C NMR spectra. The preferred orientation of the NSO group at low temperature is also indicated by the changes in the positions of the $^{13}$C$^6$ NMR signals in **6** and **8**.

### X-ray Structural Studies of the Sulfinylaminoferrocenes 5 and 8

The molecular structures of **5** and **8** are shown in Figures 3 and 4, respectively, and selected structural param-

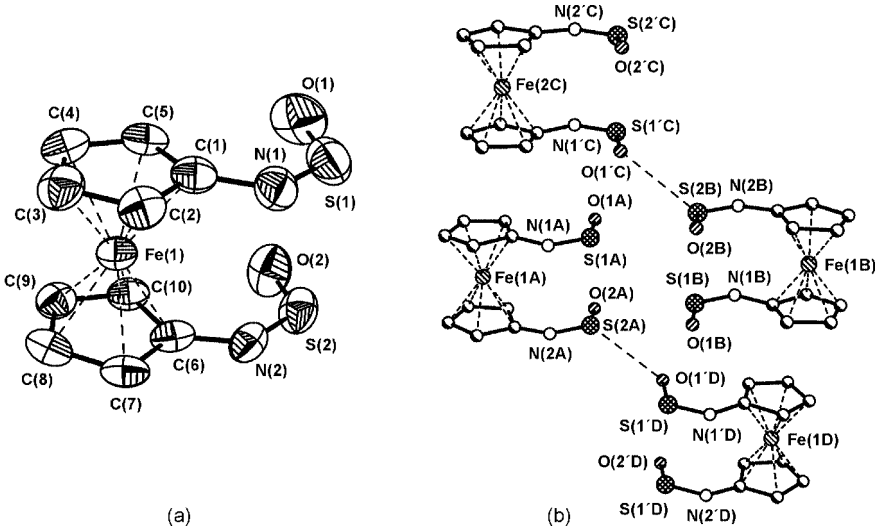


Figure 3. (a) Molecular structure of **5** (ORTEP plot, 50% probability; hydrogen atoms are omitted for clarity). S(1A)···S(2A) = 328.4, S(1′C)···S(2′C) 325.9 pm. For other selected distances and angles see Table 2. (b) Positions of the molecules of **5** in the lattice showing close intermolecular contacts: S(2A)···O(1′D) = 327.0, S(2B)···O(1′C) = 327.0 pm.

 © 2007 Wiley-VCH Verlag GmbH & Co. KGaA, Weinheim 

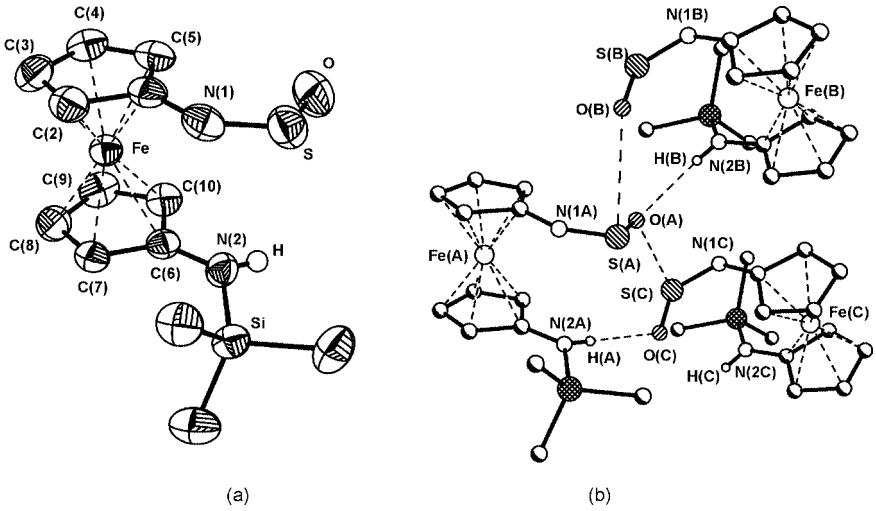


Figure 4. (a) Molecular structure of **8** (ORTEP plot, 50% probability; hydrogen atoms are omitted for clarity). For selected distances and angles see Table 2. (b) Positions of the molecules of **8** in the lattice showing close intermolecular contacts: O···H–N = 229.1, S···O = 328.9 pm.

eters are given in Table 2. In both cases, intermolecular interactions have to be considered, namely S···O contacts in **5** (Figure 3, b) and N–H···O bridges in **8** (Figure 4, b). It is tempting to trace the identical orientations of both NSO groups in **5** primarily to intermolecular interactions. However, there may also be important intramolecular contacts between the NSO groups, as indicated, for example, by the S···S contact (328.4 pm). The C–N vectors are slightly bent toward the iron atom ($\beta$ = 4.1° and 5.7°[19]), and the $C_5$ rings are almost exactly in eclipsed positions ($\tau$ = 0.1° and 0.4°[19]). The bond lengths and angles of **5** are in the usual range and compare favourably with those found for **1**.[3]

In the case of **8**, the C–N(SO) vector points toward iron (5.0°), whereas the C–N(Si) vector points away from iron

Table 2. Selected bond lengths [pm] and angles [°][a] of the ferrocenes **1**,[b] **5** (Figure 3) and **8** (Figure 4).

| **1**[c] | | **5** | | **8** | |
|---|---|---|---|---|---|
| C(1)–N(1) | 140.02(2) | C(1)–N(1) | 139.2(8) | C(1)–N(1) | 139.0(4) |
| C(11)–N(2) | 139.4(2) | C(1′)–N(1′) | 138.0(8) | | |
| – | | C(6)–N(2) | 138.8(8) | C(6)–N(2) | 137.9(4) |
| | | C(6′)–N(2′) | 140.0(9) | | |
| N(1)–S(1) | 152.0(1) | N(1)–S(1) | 152.8(6) | N(1)–S | 151.2(3) |
| N(2)–S(2) | 152.1(1) | N(1′)–S(1′) | 152.3(6) | | |
| – | | N(2)–S(2) | 151.9(6) | N(2)–Si | 174.2(2) |
| | | N(2′)–S(2′) | 152.4(6) | | |
| S(1)–O(1) | 145.7(2) | S(1)–O(1) | 144.4(6) | S–O | 146.6(3) |
| S(2)–O(2) | 146.6(2) | S(1′)–O(1′) | 145.2(5) | | |
| | | S(2)–O(2) | 144.6(6) | – | |
| | | S(2′)–O(2′) | 144.5(5) | | |
| | | H(5)···O(1) | 256.8 | H(5)···O | 256.7 |
| | | H(5′)···O(1′) | 249.4 | | |
| | | H(10)···O(2) | 253.7 | – | |
| | | H(10′)···O(2′) | 247.6 | | |
| Fe(1)$C_5$(1) | 164.5 | Fe(1)$C_5$(1) | 166.4 | Fe$C_5$(1) | 164.9 |
| Fe(2)$C_5$(1′) | 164.6 | Fe(2)$C_5$(1′) | 165.9 | | |
| Fe(1)$C_5$(2) | 165.4 | Fe(1)$C_5$(2) | 165.9 | Fe$C_5$(2) | 166.6 |
| Fe(2)$C_5$(2′) | 165.6 | Fe(2)$C_5$(2′) | 166.2 | | |
| $C_5$/$C_5$ ($\alpha$) | 1.6 | $C_5$/$C_5$ ($\alpha$) | 3.4 | $C_5$/$C_5$ ($\alpha$) | 2.0 |
| $C_5$/$C_5$ ($\alpha'$) | 2.0 | $C_5$/$C_5$ ($\alpha'$) | 2.6 | | |
| $C_5$/N(1) ($\beta_1$) | < 1 | $C_5$/N(1) ($\beta_1$) | 4.7 (towards Fe) | $C_5$/N(1) ($\beta_1$) | 5.0 |
| $C_5$/N(1′) ($\beta_1$) | < 1 | $C_5$/N(1′) ($\beta_1$) | 5.3 (towards Fe) | | (towards Fe) |
| | | $C_5$/N(2) ($\beta_2$) | 5.0 (towards Fe) | $C_5$/N(2) ($\beta_2$) | 2.9 (away from Fe) |
| | | $C_5$/N(2′) ($\beta_2$) | 3.9 (towards Fe) | | |
| $C_5$–Fe(1)–$C_5$ ($\gamma$) | 179.3 | $C_5$–Fe(1)–$C_5$ ($\gamma$) | 176.4 | $C_5$–Fe–$C_5$ ($\gamma$) | 178.8 |
| $C_5$–Fe(2)–$C_5$ ($\gamma'$) | 178.1 | $C_5$–Fe(2)–$C_5$ ($\gamma'$) | 176.8 | | |
| $C_5$/$C_5$ (twist) ($\tau$) | 2.0 | $C_5$/$C_5$ (twist) ($\tau$) | 0.1 | $C_5$/$C_5$(twist) ($\tau$) | 2.2 |
| $C_5$/$C_5$ (twist) ($\tau'$) | 2.5 | $C_5$/$C_5$ (twist) ($\tau'$) | 0.4 | | |

[a] See ref.[19] for the definition of the angles $\alpha$, $\beta$, $\gamma$ and $\tau$. [b] Taken from ref.[3]. [c] Data for two different molecules in the unit cell, as given in ref.[3]

 © 2007 Wiley-VCH Verlag GmbH & Co. KGaA, Weinheim 

(2.9°). The deviation from the eclipsed position of the cyclopentadienyl rings is again small ($\tau$ = 2.2°). Otherwise, the positions of the SO and the $SiMe_3$ groups are ideal for minimising steric interactions. The surroundings of the amino nitrogen atoms are close to trigonal planar.

## Experimental Section

**General:** All syntheses and the handling of the samples were carried out observing necessary precautions to exclude traces of air and moisture. Carefully dried solvents and oven-dried glassware were used throughout. The deuterated solvents $CD_2Cl_2$ and $CDCl_3$ were distilled from $CaH_2$ under argon. All other solvents were distilled from Na metal in an atmosphere of argon. The starting materials 1,1′-diaminoferrocene (**2**),[6] 1,1′-bis(trimethylsilylamino)ferrocene (**3**)[6] and *N*,*N*′-dilithio-1,1′-bis(trimethylsilylamino)ferrocene (**4**) and $[fc(NSiMe_3)_2Li_2]$[7] were prepared as described in the literature. Triethylamine was distilled from Na prior to use. DMF was purchased from Aldrich and distilled from KOH. Other starting materials were purchased from Aldrich [butyllithium (1.6 M in hexane)] or Acros ($SOCl_2$, KO*t*Bu), and used without further purification. NMR measurements: Bruker ARX 250: $^1H$, $^{13}C$, $^{14}N$, $^{15}N$ and $^{29}Si$ NMR (refocused INEPT[20] based on $^2J_{^{29}Si,^1H}$ = 7 Hz); Bruker DRX 500: $^{57}Fe$ NMR; Varian INOVA 400: $^1H$, $^{13}C$ NMR; chemical shifts are given with respect to $Me_4Si$ [$\delta^1H$ ($CHDCl_2$) = 5.33 ppm; $\delta^{13}C$ ($CD_2Cl_2$) = 53.5 ppm; $\delta^{29}Si$ = 0 ppm for $\Xi(^{29}Si)$ = 19.867184 MHz]; $\delta^{14}N$ = 0 ppm [external neat $MeNO_2$ with $\Xi(^{14}N)$ = 7.226324 MHz], $\delta^{15}N$ = 0 ppm [external neat $MeNO_2$ with $\Xi(^{15}N)$ = 10.136767 MHz]; $\delta^{57}Fe$ = 0 ppm [external neat $Fe(CO)_5$ with $\Xi(^{57}Fe)$ = 3.237798 MHz]. IR spectra: Perkin–Elmer Spectrum 2000 FTIR. EI-mass spectra: Finnigan MAT 8500 spectrometer (ionisation energy 70eV) with direct inlet; the *m*/*z* data refer to the isotopes $^1H$, $^{12}C$, $^{14}N$, $^{16}O$, $^{32}S$, $^{28}Si$, and $^{56}Fe$. The melting points (uncorrected) were determined using a Büchi 510 melting point apparatus.

**1,1′-Bis(sulfinylamino)ferrocene (5):** A suspension of 1,1′-diaminoferrocene (**2**; 295 mg, 1.37 mmol) in $Et_2O$ (20 mL) and triethylamine (0.91 mL, 6.52 mmol) was prepared. The suspension was cooled to –78 °C and $SOCl_2$ (326 mg, 0.20 mL, 2.74 mmol) dissolved in $Et_2O$ (3 mL) was injected slowly with a syringe. The reaction mixture was stirred at –78 °C for 1 h; then it was allowed to reach ambient temperature and kept stirring for 1.5 h. Insoluble materials were filtered off, washed with $Et_2O$ (20 mL), and volatile materials were removed from the filtrate in vacuo. The remaining violet-blue solid was dissolved in $Et_2O$ (30 mL) and the violet solution was filtered. After removal of the solvent in vacuo the product **5** (220 mg; 52%) was left as a violet-blue solid. Crystallisation from $CD_2Cl_2$, after 2 weeks at –20 °C, gave violet crystals of **5** (m.p. 149–151 °C). $^1H$ NMR (250.1 MHz, $CD_2Cl_2$, 298 K): $\delta$ = 4.60 (m, 4 H, $H^{3,4,3',4'}$), 4.90 ppm (m, 4 H, $H^{2,5,2',5'}$). $^1H$ NMR (250.1 MHz, $CD_2Cl_2$, 203 K): $\delta$ = 4.63 (m, 4 H, $H^{3,4,3',4'}$), 4.55 ppm (br. m, 4 H, $H^{2,5,2',5'}$). EI-MS (70 eV) for $C_{10}H_8FeN_2O_2S_2$ (308.15): *m*/*z* (%) = 308 (100) [$M^+$], 244 (6) [$M^+ - SO_2$], 212 (85) [$M^+ - 2SO$], 182 (12), 166 (7), 134 (40), 116 (16), 108 (14), 82 (16), 56 [$Fe^+$] (74). IR (toluene) $\tilde{\nu}$ = 1261 $cm^{-1}$ ($\nu_{as}$), 1093 ($\nu_s$) (NSO).

**6-Amino-1-(sulfinylamino)ferrocene (6). Method A:** The same procedure was employed as for **5**, except that an equimolar amount of $SOCl_2$ (175 mg, 1.48 mmol) in $Et_2O$ (4 mL) was used and the reaction mixture was kept stirring for 20 h. A mixture was obtained (72 mg) which, according to NMR spectra, contained **6** (ca. 35%) and **5** (ca. 15%), together with a lot of **2** (ca. 50%), as a violet-blue solid. This solid was dissolved in hexane (20 mL) and the blue solution was filtered. After removing the solvent in vacuo **6** was left as blue solid which still contained some **5** (5%). Crystallisation from hexane at –30 °C, gave a blue powder of **6** (m.p. 79–81 °C).

**Method B:** Freshly distilled DMF (20 mL) was added to a mixture of **5** (38 mg; 0.12 mmol) and KO*t*Bu (15 mg; 0.13 mmol). The colour of the violet solution changed to blue. The reaction mixture was stirred for 1 h, and volatile materials were removed in vacuo. The remaining blue solid was dissolved in $Et_2O$ (20 mL) and the blue solution was filtered. After removing the solvent in vacuo **6** (28 mg; 88%) was left as a blue solid. $^1H$ NMR (250.1 MHz, $CD_2Cl_2$, 298 K): $\delta$ = 2.75 (br. s, 2 H, NH), 3.82 (m, 2 H, $H^{7,10}$), 3.87 (m, 2 H, $H^{8,9}$), 4.54 (m, 2 H, $H^{3,4}$), 4.84 ppm (m, 2 H, $H^{2,5}$). $^1H$ NMR (250.1 MHz, $CD_2Cl_2$, 198 K): $\delta$ = 2.95 (br. s, 2 H, NH), 3.58 (m, 2 H, $H^{7,10}$), 3.78, 3.87 (m, m, 1 H, 1 H, $H^{8,9}$), 4.10, 5.03 (m, m, 1 H, 1 H, $H^{2,5}$), 4.51 ppm (m, 2 H, $H^{3,4}$). EI-MS (70 eV) for $C_{10}H_{10}FeN_2OS$ (262.11): *m*/*z* (%) = 262 (100) [$M^+$], 214 (12) [$M^+ - SO$], 198 (12) [$M^+ - SO - NH_2$], 197 (11), 187 (12), 185 (6), 152 (6), 137 (13), 135 (16), 133 (18), 108 (6), 80 [$CpNH_2^+$] (56), 56 [$Fe^+$] (31). IR (toluene) $\tilde{\nu}$ = 1261 $cm^{-1}$ ($\nu_{as}$), 1097 ($\nu_s$) (NSO).

**1-(Sulfinylamino)-6-(trimethylsilylamino)ferrocene (8):** A solution of 1,1′-bis(trimethylsilylamino)ferrocene (**3**; 240 mg, 0.67 mmol) in $Et_2O$ (20 mL) and triethylamine (0.19 mL, 1.36 mmol) was prepared. The solution was cooled to –78 °C, and $SOCl_2$ (79 mg, 0.049 mL, 0.67 mmol) dissolved in $Et_2O$ (4 mL) was injected slowly with a syringe. The reaction mixture was stirred at –78 °C for 1 h, then it was allowed to reach ambient temperature and kept stirring for 20 h. Insoluble materials were filtered off, and volatiles were removed from the filtrate in vacuo to give 185 mg of a mixture containing **8** (ca. 90%) and **5** (ca. 10%) as a blue solid. This solid was dissolved in hexane (20 mL) and the blue solution was filtered. After removing the solvent in vacuo **8** was left as a blue solid. Crystallisation from hexane/$CH_2Cl_2$ (1:1), after 2 weeks at –30 °C, gave blue crystals of **8** (m.p. 89–91 °C). $^1H$ NMR (250.1 MHz, $CD_2Cl_2$, 298 K): $\delta$ = 0.20 (s, 9 H, $Me_3Si$), 2.30 (br. s, 1 H, NH), 3.75 (m, 2 H, $H^{7,10}$), 3.88 (m, 2 H, $H^{8,9}$), 4.53 (m, 2 H, $H^{3,4}$), 4.79 ppm (m, 2 H, $H^{2,5}$). $^1H$ NMR (250.1 MHz, $CD_2Cl_2$, 203 K): $\delta$ = 0.08 (s, 9 H, $Me_3Si$), 2.60 (br. s, 1 H, NH), 3.45, 3.59 (m, m, 1 H, 1 H, $H^{7,10}$), 3.75, 3.89 (m, m, 1 H, 1 H, $H^{8,9}$), 4.04, 5.06 (m, m, 1 H, 1 H, $H^{2,5}$), 4.51, 4.53 ppm (m, m, 1 H, 1 H, $H^{3,4}$). EI-MS (70 eV) for $C_{13}H_{18}FeN_2OSSi$ (334.29): *m*/*z* (%) = 334 (100) [$M^+$], 286 (6) [$M^+ - SO$], 271 (10) [$M^+ - CH_3SO$], 234 (9), 205 (13), 182 (7) [$FeCpNSO^+$], 178 (6), 152 (20) [$CpN(H)SiMe_3^+$], 134 (22) [$FeCpN^+$], 108 (6), 73 [$SiMe_3^+$] (71), 56 [$Fe^+$] (13). IR (toluene) $\tilde{\nu}$ = 1261 $cm^{-1}$ ($\nu_{as}$), 1096 ($\nu_s$) (NSO).

**1,3-Bis(trimethylsilyl)-2-oxo-1,3,2-diazathia-[3]ferrocenophane (9):** Freshly prepared $fc(NSiMe_3)_2Li_2$ (**4**; 300 mg, 0.83 mmol) was dissolved in $Et_2O$ (20 mL), the solution was cooled to –78 °C, and $SOCl_2$ (55 mg, 0.034 mL, 0.46 mmol) dissolved in $Et_2O$ (4 mL) was injected slowly with a syringe. The reaction mixture was stirred at –78 °C for 0.5 h, then it was allowed to reach ambient temperature and kept stirring for 20 h. Volatile materials were removed in vacuo, and the resulting oil was dissolved in hexane (20 mL). Insoluble materials were separated by centrifugation, and the clear liquid was collected. The solvent was removed in vacuo to give 204 mg of a mixture containing **9** (ca. 25%) and **3** (ca. 75%) as a green oil. $^1H$ NMR (250.1 MHz, $CD_2Cl_2$, 298 K): $\delta$ = 0.26 (s, 18 H, $Me_3Si$), 3.82, 3.86 (m, m, 2 H, 2 H, $H^{2,3,2',3'}$), 4.13, 4.19 (m, m, 2 H, 2 H, $H^{4,5,4',5'}$).

**Crystal Structure Determinations of the Ferrocenes 5 and 8:** Details pertinent to the crystal structure determinations are listed in

 © 2007 Wiley-VCH Verlag GmbH & Co. KGaA, Weinheim 

Table 3. Crystallographic data for the ferrocenes **5** and **8**.

| | **5** | **8** |
|---|---|---|
| Formula | $C_{10}H_8FeN_2O_2S_2$ | $C_{13}H_{18}FeN_2OSSi$ |
| Crystal | violet prism | blue needle |
| Dimensions [mm] | $0.20 \times 0.18 \times 0.16$ | $0.28 \times 0.18 \times 0.16$ |
| Crystal system | triclinic | monoclinic |
| Space group | $P\bar{1}$ | $P2_1/n$ |
| Lattice parameters (pm [°]) | $a$ = 1041.8(2) | $a$ = 878.21(18) |
| | $b$ = 1091.9(2) | $b$ = 697.96(14) |
| | $c$ = 1113.6(2) | $c$ = 2455.6(5) |
| | $\alpha$ = 63.68(3) | |
| | $\beta$ = 86.44(3) | $\beta$ = 92.75(3) |
| | $\gamma$ = 79.73(3) | |
| $Z$ | 2 | 4 |
| Absorption coefficient $\mu$ [$mm^{-1}$] | 1.711 | 1.214 |
| Diffractometer | STOE IPDS I (Mo-$K_\alpha$, $\lambda$ = 71.073 pm), graphite monochromator | |
| Measuring range ($\vartheta$ [°]) | 2.0–26 | 2.4–25.9 |
| Reflections collected | 7630 | 2743 |
| Independent reflections [$I > 2\sigma[I]$] | 3998 | 2743 |
| Absorption correction[a] | none | numerical |
| Refined parameters | 307 | 175 |
| $wR_2/R_1$ [$I > 2\sigma[I]$] | 0.122/0.054 | 0.085/0.036 |
| Max./min. residual electron density ($10^{-6}$ e $pm^{-3}$) | 0.597/–0.375 | 0.626/–0.210 |

[a] Absorption corrections did not improve the parameter set.

Table 3. Crystals of appropriate size were sealed under argon in a Lindemann capillary, and the data collections were carried out at 20 °C.[21]

## Acknowledgments

This work was supported by the Deutsche Forschungsgemeinschaft.

[1] a) *Ferrocenes. Homogeneous Catalysis, Organic Synthesis Materials Science* (Eds.: A. Togni, T. Hayashi), VCH, Weinheim, **1995**; b) T. J. Peckham, P. Gómez-Elipe, I. Manners, in *Metallocenes –Synthesis, Reactivity, Applications* (Eds.: A. Togni, R. L. Haltermann), vol. 2, Wiley-VCH, Weinheim, **1998**, chapter 12, pp. 723–771; c) P. Nguyen, P. Gómez-Elipe, I. Manners, *Chem. Rev.* **1999**, *99*, 1515–1548.

[2] a) R. Bussas, G. Kresze, H. Münsterer, A. Schwöbel, *Sulfur Rep.* **1983**, *2*, 215–377; b) G. Kresze, W. Wucherpfennig, *Angew. Chem.* **1967**, *79*, 109–127; *Angew. Chem. Int. Ed. Engl.* **1967**, *6*, 149–167.

[3] M. Herberhold, B. Distler, H. E. Maisel, W. Milius, B. Wrackmeyer, P. Zanello, *Z. Anorg. Allg. Chem.* **1996**, *622*, 1515–1523.

[4] B. Wrackmeyer, O. L. Tok, A. Ayazi, H. E. Maisel, M. Herberhold, *Magn. Reson. Chem.* **2004**, *42*, 827–830.

[5] a) G. R. Knox, *Proc. Chem. Soc. London* **1959**, 56–57; b) J. M. Osgerby, P. L. Pauson, *J. Chem. Soc.* **1961**, 4615–4618; c) A. N. Nesmeyanov, V. N. Drozd, V. A. Sazonova, *Dokl. Akad. Nauk SSSR* **1963**, *150*, 321–324.

[6] A. Shafir, M. P. Power, G. D. Whitener, J. Arnold, *Organometallics* **2000**, *19*, 3978–3982.

[7] A. Shafir, M. P. Power, G. D. Whitener, J. Arnold, *Organometallics* **2001**, *20*, 1365–1369.

[8] A. Shafir, J. Arnold, *J. Am. Chem. Soc.* **2001**, *123*, 9212–9213.

[9] a) B. Wrackmeyer, E. V. Klimkina, H. E. Maisel, W. Milius, M. Herberhold, *Inorg. Chim. Acta* **2004**, *357*, 1703–1710; b) B. Wrackmeyer, W. Milius, H. E. Maisel, H. Vollrath, M. Herberhold, *Z. Anorg. Allg. Chem.* **2003**, *629*, 1169–1174; c) B. Wrackmeyer, H. E. Maisel, W. Milius, M. Herberhold, *J. Organomet. Chem.* **2003**, *680*, 271–280.

[10] a) B. Wrackmeyer, E. V. Klimkina, W. Milius, *Struct. Chem.* **2004**, *15*, 333–337; b) B. Wrackmeyer, E. V. Klimkina, W. Milius, *Inorg. Chem. Commun.* **2004**, *7*, 412–416.

[11] B. Wrackmeyer, E. V. Klimkina, W. Milius, *Inorg. Chem. Commun.* **2004**, *7*, 884–888.

[12] B. Wrackmeyer, E. V. Klimkina, W. Milius, O. L. Tok, M. Herberhold, *Inorg. Chim. Acta* **2005**, *358*, 1420–1428.

[13] W. Sicinska, L. Stefaniak, M. Witanowski, G. A. Webb, *Org. Magn. Reson.* **1981**, *15*, 241–243.

[14] For a review on $^{57}$Fe NMR spectroscopy, see R. Benn, in *Transition Metal NMR* (Ed.: P. S. Pregosin), Elsevier, Amsterdam, **1991**, pp. 103–142.

[15] B. Wrackmeyer, O. L. Tok, M. Herberhold, *Organometallics* **2001**, *20*, 5774–5776.

[16] B. Wrackmeyer, O. L. Tok, A. A. Koridze, *Magn. Reson. Chem.* **2004**, *42*, 750–755.

[17] a) E. Haslinger, W. Robien, K. Schlögl, W. Weissensteiner, *J. Organomet. Chem.* **1981**, *218*, C11–C14; b) E. Haslinger, K. Koci, W. Robien, K. Schlögl, *Monatsh. Chem.* **1983**, *114*, 495–499.

[18] J. Sandström, *Dynamic NMR Spectroscopy*, Academic Press, London, **1982**, pp. 93–123.

[19] M. Herberhold, *Angew. Chem.* **1995**, *107*, 1985; *Angew. Chem. Int. Ed. Engl.* **1995**, *34*, 1837.

[20] a) G. A. Morris, R. Freeman, *J. Am. Chem. Soc.* **1979**, *101*, 760–762; b) G. A. Morris, *J. Am. Chem. Soc.* **1980**, *102*, 428–429; c) D. P. Burum, R. R. Ernst, *J. Magn. Reson.* **1980**, *39*, 163–168.

[21] CCDC-600889 (for **5**) and -600888 (for **8**) contain the supplementary crystallographic data for this paper. These data can be obtained free of charge from The Cambridge Crystallographic Data Centre via www.ccdc.cam.ac.uk/data_request/cif.

Received: April 10, 2006
Published Online: August 3, 2006

 © 2007 Wiley-VCH Verlag GmbH & Co. KGaA, Weinheim 

DOI: 10.1002/ejic.200600670

# $W(CO)_4$(diimine) Structure Revised – Correlating Structure to π* Back-Bonding

**Christodoulos Makedonas[a] and Christiana A. Mitsopoulou*[a]**

**Keywords:** Tungsten / Pi interactions / N ligands / Carbonyls / Ligand effects

The bending of axial and equatorial carbonyls, one of the main structural features of the $M(CO)_4$(diimine) compounds (M = Cr, Mo, and W), is elucidated in terms of the π* back-bonding theory by a frontier molecular orbital analysis. Employing $W(CO)_4$(phen) (phen = 1,10-phenanthroline) as a reference compound has proved that the deviation from orthogonality stabilizes the structure by a total amount of 2.95 kJ/mol. Moreover, by an extended comparison of several $W(CO)_4$(diimine) structures, the importance of the magnitude of the binding angle in determining the bonding in these complexes in comparison to the traditional approach of the W–C and C–O bond lengths is underlined. As a result, it is proposed that the correct indices of the extent of back-donation are the deviations of the C–W–C angles from orthogonality and the O–C–W angles from linearity. It is indicated for the first time that the larger the existing deviation the stronger the back-donation. Moreover, a structure-to-properties relation is provided that correlates the bending of the carbonyls to the extent of back-donation. Back-donation is expected to be correlated to the electronic properties of the compounds, such as the extent of solvatochromism.

(© Wiley-VCH Verlag GmbH & Co. KGaA, 69451 Weinheim, Germany, 2007)

## 1. Introduction

The complexes of the type $M(CO)_4$(diimine) (M = Cr, Mo, and W) play an important role in our understanding of the spectroscopic, photophysical, and photochemical behavior of chromophores with low-lying metal-to-ligand (MLCT) charge-transfer excited states.[1–3] These compounds combine an electron-rich, low-valent, typically $d^6$ metal atom, which is stabilized by the presence of four carbonyl groups along with the good π*-accepting *a*-diimine ligand. The observed lowest lying MLCT state is responsible for several interesting features, such as the negative solvatochromism and the solution luminescence, while it is associated with large, second-order molecular hyperpolarizabilities. This state arises from the transition between a metal/CO localized HOMO–2 and a diimine LUMO (both of $b_1$ symmetry in the case of the $C_{2v}$ point group).[4,5] Thus the electronic properties of $M(CO)_4$(diimine) make their use quite essential in areas such as the investigation of polymerization processes,[2] the labeling of biomolecules,[6] and the exploitation of solar energy.[7]

All the structures of tetracarbonyl diimine compounds, which are either crystallographically elucidated or theoretically predicted, share two common features. Both of these features are related to the nonorthogonality of the $W(CO)_4$ fragment. More specifically, according to all published structures, the axial carbonyls bend away from the diimine moiety. Moreover, in the majority of the known structures, the two equatorial carbonyl groups bend away from each other. In both cases the linearity of the two CO units is no longer valid.[4–5,8–9] It is also worth mentioning that the M–C–O angle often changes upon electronic excitation.[4] These above-mentioned two features have been observed several times in the past, but they have never been explained in the literature. Herein, these structural characteristics are studied by means of DFT calculations, and our approach is divided into two parts. Firstly, by employing the highly symmetric $W(CO)_4$(phen) complex (phen = 1,10-phenanthroline) we attempted to investigate and discuss their structure from an electronic point of view in terms of the π* back-bonding theory. To proceed with our analysis, we performed a fragments' molecular orbital analysis (FMO) using DFT electron density calculations. Recently, this procedure was successfully used in the case of a related tungsten compound.[5] Secondly, we discussed the same characteristics as they evolved through a series of bidentate N-donor ligands. In the latter case, we succeeded in extracting the structure-to-properties relation (SPR) that governs these compounds.

[a] Inorganic Chemistry Laboratory, Department of Chemistry, National and Kapodistrian University of Athens, Panepistimiopolis, Zografou 15771, Greece
Fax: +30-210-8322828
E-mail: cmitsop@chem.uoa.gr

Supporting information for this article is available on the WWW under http://www.eurjic.org or from the author.

## 2. Results and Discussion

### 2.1. Evolution of Back-Donation in $W(CO)_4$(phen)

We started our analysis with $W(CO)_4$(phen) (**1**). Despite this complex being one of the most extensively studied

 © 2007 Wiley-VCH Verlag GmbH & Co. KGaA, Weinheim 

among compounds of this type it was only recently that Vlček et al. described its electronic ground state and elucidated its emission behavior.[4c,4d] Apart from being easily produced[12] and having an interesting photochemistry it is usually employed for its high symmetry. It belongs to the $C_{2v}$ point group and this makes its structure elucidation, through spectra, significantly easier. Theoretical calculations are also favored for the same reason. In such a molecule, bending of the CO ligands should be clear and free from the difficult to describe nonorthogonal dihedral angles, as in the case of W(CO)$_4$(pq) [pq = 2-(2′-pyridyl)-quinoxaline] where the calculated dihedral angle for $N_{py}$–$N_{qn}$–W–$C_{ax}$ is –92.6°.[5]

In the literature, three crystal structures exist as reported in ref.[10a,10c,11] In our case, ground-state calculations have been performed with the aid of Gaussian 98 packages, employing the well-known B3LYP functional, under $C_{2v}$ molecular symmetry. The final structure, obtained by full geometry optimization, is essentially equivalent to the ones that have been previously reported.[4] Nevertheless, there are some differences arising from the comparison with the crystal structure reported in the work of Xiong et al.[11] Specifically, the bending of the two axial carbonyl groups is not identical in the solid phase. This is also depicted by the observed differences in the dihedral angles (78.2 and 151.9° as compared to –103.4 and –177.2° for the dihedral angles $O_{ax}$–$C_{ax}$–W–$N^1$ and $O_{ax}$–$C_{ax}$–W–$N^2$, respectively). These differences are due to the extended hydrogen bonding developed between the oxygen atom of the CO group and a diimine hydrogen atom present in the crystal. Some of the ground-state structural features of the complex that were theoretically derived and experimentally extracted are presented in Table 1. For uniformity purposes the structure under study is the one derived from the calculation.

Table 1. Comparison of selected calculated bond lengths [Å] and angles [°] for **1** with experimental values from X-ray analysis.

| C.I.[a] | Exp.[10] | Exp.[11] | Calcd. |
|---|---|---|---|
| W–N | 2.239 | 2.245 | 2.226 |
| W–$C_{ax}$ | 2.011 | 2.007 | 2.033 |
| W–$C_{eq}$ | 1.968 | 1.945 | 1.976 |
| C–$O_{ax}$ | 1.140 | 1.172 | 1.187 |
| C–$O_{eq}$ | 1.147 | 1.189 | 1.197 |
| C=N | 1.348 | 1.401 | 1.384 |
| C=$C^{diim.}$ | 1.435 | 1.365 | 1.433 |
| N–W–N | 73.7 | 73.5 | 74.2 |
| $C_{ax}$–W–$C_{ax}$ | 172.4 | 166.2 | 173.5 |
| $C_{eq}$–W–$C_{eq}$ | 88.7 | 93.9 | 92.7 |

[a] The average value of symmetry related distances or angles is provided.

In order to accomplish the aforementioned task of structure elucidation in terms of back-donation we decided to design a theoretical model. We introduced four theoretical nonexisting structures for the system under study, which represent steps that are equal in number towards orthogonality. Thus, in **1a** the bending of axial oxygen atoms towards one another no longer exists and the W–C–O moiety is linear, while in **1b** the CO groups take up a position along the *x*-axis of the molecule. In **1c**, starting from structure **1**, equatorial oxygen atoms are placed in such a way that the angle W–C–O becomes 180°. Finally, all the above changes are incorporated into structure **1d**. We should underline that all the encountered distances are kept constant. Another constraint, in terms of the selected strategy, is the fixed position of the W–diimine part. By keeping the W–diimine part constant we succeed in revealing the developed electronic forces. Otherwise the system would relax in several directions, leaving the comparison worthless. The above analysis is depicted in Figure 1. The small structural changes that we introduced induce a relative change in the electronic structure of the complex. These changes, along with several electronic characteristics of the five structures, are depicted in Table 2. Frontier molecular orbitals for all the cases are summarized in Table 3.

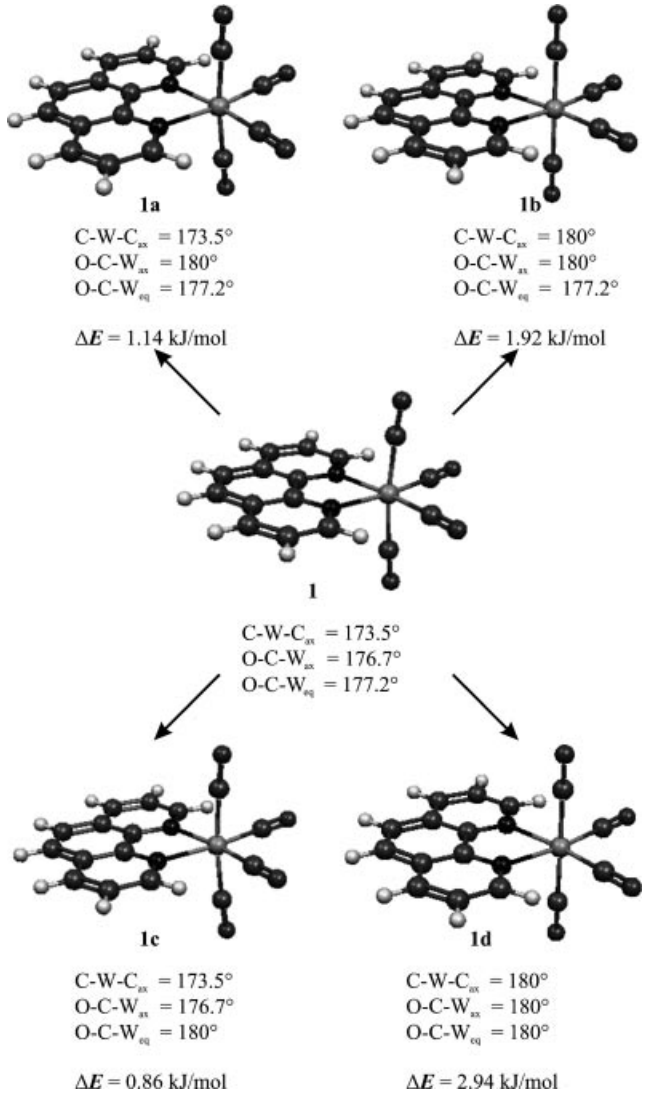


Figure 1. Fragment molecular orbital analysis for **1**.

Before we proceed with our results it is essential to analyze the concepts of donation and back-donation in W(CO)$_4$(diimine) complexes. Bonding in carbonyl compounds is synergic. A carbon σ orbital in CO (the slightly antibonding HOMO) donates electron density to an empty

 © 2007 Wiley-VCH Verlag GmbH & Co. KGaA, Weinheim 

Table 2. Comparison of selected calculated angles [°] for the ground-state structure of **1** and the hypothetical structures **1a**–**1d**, along with calculated data on electron density donation between the $W(CO)_4$ and the diimine fragments. Data in italics represent the induced changes in **1a**–**1d**.

| C.I. | **1** | **1a** | **1b** | **1c** | **1d** |
|---|---|---|---|---|---|
| $C_{ax}$–W–$C_{ax}$ | 173.5 | 173.5 | *180* | 173.5 | *180* |
| $O_{ax}$–W–$O_{ax}$ | 171.1 | *173.5* | *180* | 171.1 | *180* |
| $C_{eq}$–W–$C_{eq}$ | 92.7 | 92.7 | 92.7 | 92.7 | 92.7 |
| $O_{eq}$–W–$O_{eq}$ | 94.8 | 94.8 | 94.8 | *92.7* | *92.7* |
| $O_{ax}$–$C_{ax}$–W | 176.7 | *0* | *0* | 176.7 | *0* |
| $O_{eq}$–$C_{eq}$–W | 177.2 | 177.2 | 177.2 | *180* | *180* |
| Diim. → W[a] | 0.385 | 0.394 | 0.398 | 0.385 | 0.398 |
| El. repulsion[a] | –0.514 | –0.521 | –0.522 | –0.513 | –0.521 |
| H-2 to L[b] | 8.0 | 8.2 | 7.5 | 8.1 | 7.6 |
| $b_1$ to H-2[c] | 6.5[d] | 6.7[d] | 6.1[d] | 6.6[d] | 6.2[d] |
| $\Delta E$[e] | 2.36 | 2.39 | 2.29 | 2.35 | 2.28 |
| $\Delta E$[f] | 0 | 1.14 | 1.92 | 0.86 | 2.95 |
| $\mu_z$[g] | 12.86 | 12.66 | 12.76 | 12.93 | 12.85 |

[a] Total charge donation and electron repulsion between $W(CO)_4$ and phen fragments. [b] Contribution of the $b_1$/HOMO–2 (HOMO–1 for **1c**) of the $W(CO)_4$ fragment to the LUMO of the complex. [c] Contribution of the $b_1$/LUMO of the phen fragment to the HOMO–2 of the complex. [d] In each case there is an additional 1.8% (1.9% for **1a**) contribution from the LUMO+2 of the diimine (also $b_1$ in symmetry). [e] HOMO–LUMO energy difference in eV. [f] Energy difference between structures, as compared to **1**, in kJ/mol. HOMO–LUMO energy difference in eV. [g] Calculated dipole moment in Debye.

metal orbital of proper symmetry, whereas a filled metal π orbital forms a second dative overlap with an empty CO π orbital. Up to a point, the π-bonding formation strengthens the σ bond and vice versa.

Back-donation also occurs in the case of other π*-accepting ligands, such as 1,10-phenanthroline. On the basis of group theory concepts back-bonding can occur through an overlap with the $d_{xz}$, $d_{xy}$ and $d_{x^2-y^2}$ metal orbitals, with the latter being more realistically envisioned as a linear combination of $d_{z^2}$. Under the framework of the above discussion the diimines in the complexes under study certainly act competitively (*trans* influence) with the equatorial carbonyls. Furthermore, the molecules develop their conformation in space in a way that diminishes steric hindrance and electronic repulsion. This electronic repulsion is formed from several interactions among occupied fragment orbitals. $W(CO)_4$(diimine) compounds have a first coordination sphere of octahedral geometry and consequently steric hindrance does not play a significant role in the observed structure. As a result, the interesting structural features that we described seem to arise from a compromise between back-bonding and other electronic repulsions.

According to data presented in Table 3, the three highest occupied molecular orbitals are very close in energy, with the major contributions coming from the d orbitals of the metal and the π* character of the carbonyl group. The high diimine contribution to the HOMO–2 describes the W → diimine π* back-bonding. This energetic similarity holds for all the other complexes of the same type[1] indicating that HOMO–2 is spectroscopically the most important of the

Table 3. Contribution of different fragments to the valence orbitals of the complexes. The HOMO and LUMO are shown in bold.

| MO | *E* [eV] | W | phen | $CO_{ax}$ | $CO_{eq}$ |
|---|---|---|---|---|---|
| **1** | | | | | |
| $37a_1$ | –1.20 | 16.2 | –2.1 | 85.8 | 0.1 |
| $28b_2$ | –1.46 | 20.3 | –0.1 | 70.6 | 9.2 |
| $15b_1$ | –1.57 | 0.7 | 97.2 | 0.8 | 1.4 |
| $7a_2$ | –2.86 | 0.2 | 99.1 | 0.2 | 0.5 |
| **$14b_1$** | **–2.93** | **3.8** | **89.8** | **3.1** | **3.4** |
| **$36a_1$** | **–5.30** | **64.0** | **0.7** | **0.7** | **34.5** |
| $6a_2$ | –5.58 | 58.3 | 3.7 | 22.8 | 15.1 |
| $13b_1$ | –5.60 | 54.6 | 13.7 | 21.6 | 10.1 |
| $12b_1$ | –7.69 | 1.5 | 97.6 | 0.7 | 0.2 |
| $5a_2$ | –8.00 | 0.3 | 99.5 | 0.1 | 0.0 |
| $27b_2$ | –9.35 | 0.4 | 80.0 | 1.8 | 17.7 |
| **1a** | | | | | |
| $37a_1$ | –1.19 | 15.7 | –2.3 | 86.4 | 0.1 |
| $28b_2$ | –1.47 | 20.4 | 0.0 | 70.7 | 9.0 |
| $15b_1$ | –1.56 | 0.7 | 97.1 | 0.7 | 1.4 |
| $7a_2$ | –2.85 | 0.2 | 99.1 | 0.2 | 0.5 |
| **$14b_1$** | **–2.92** | **3.9** | **89.6** | **3.1** | **3.4** |
| **$36a_1$** | **–5.31** | **64.0** | **0.7** | **0.8** | **34.5** |
| $13b_1$ | –5.59 | 54.4 | 14.1 | 21.7 | 9.9 |
| $6a_2$ | –5.59 | 58.2 | 3.7 | 22.8 | 15.2 |
| $12b_1$ | –7.68 | 1.5 | 97.6 | 0.7 | 0.2 |
| $5a_2$ | –7.98 | 0.3 | 99.5 | 0.1 | 0.0 |
| $27b_2$ | –9.35 | 0.4 | 80.4 | 1.8 | 17.3 |
| **1b** | | | | | |
| $37a_1$ | –1.27 | 16.3 | –2.3 | 86.3 | –0.3 |
| $28b_2$ | –1.51 | 20.2 | –0.1 | 72.1 | 7.8 |
| $15b_1$ | –1.58 | 0.9 | 97.2 | 0.4 | 1.5 |
| $7a_2$ | –2.86 | 0.3 | 99.0 | 0.2 | 0.5 |
| **$14b_1$** | **–2.94** | **3.9** | **90.4** | **2.4** | **3.3** |
| **$36a_1$** | **–5.24** | **64.0** | **0.8** | **0.3** | **34.8** |
| $6a_2$ | –5.56 | 58.8 | 4.0 | 22.9 | 14.3 |
| $13b_1$ | –5.62 | 55.4 | 13.1 | 20.5 | 11.0 |
| $12b_1$ | –7.69 | 1.3 | 97.6 | 0.9 | 0.2 |
| $5a_2$ | –8.00 | 0.3 | 99.5 | 0.2 | 0.0 |
| $27b_2$ | –9.35 | 0.5 | 79.2 | 1.8 | 18.4 |
| **1c** | | | | | |
| $37a_1$ | –1.20 | 16.4 | –2.1 | 85.7 | 0.1 |
| $28b_2$ | –1.46 | 20.9 | 0.0 | 69.3 | 9.8 |
| $15b_1$ | –1.57 | 0.7 | 97.2 | 0.8 | 1.3 |
| $7a_2$ | –2.86 | 0.2 | 99.1 | 0.2 | 0.5 |
| **$14b_1$** | **–2.94** | **3.8** | **89.7** | **3.1** | **3.3** |
| **$36a_1$** | **–5.29** | **64.1** | **0.7** | **0.8** | **34.3** |
| $6a_2$ | –5.59 | 58.4 | 3.8 | 22.8 | 15.1 |
| $13b_1$ | –5.59 | 54.5 | 13.8 | 21.6 | 10.0 |
| $12b_1$ | –7.69 | 1.4 | 97.7 | 0.7 | 0.2 |
| $5a_2$ | –8.00 | 0.3 | 99.5 | 0.1 | 0.0 |
| $27b_2$ | –9.36 | 0.4 | 80.3 | 1.8 | 17.4 |
| **1d** | | | | | |
| $37a_1$ | –1.27 | 16.4 | –2.3 | 86.2 | –0.3 |
| $28b_2$ | –1.52 | 20.8 | 0.0 | 70.8 | 8.4 |
| $15b_1$ | –1.58 | 0.9 | 97.2 | 0.4 | 1.5 |
| $7a_2$ | –2.87 | 0.3 | 99.0 | 0.2 | 0.5 |
| **$14b_1$** | **–2.95** | **3.9** | **90.3** | **2.4** | **3.3** |
| **$36a_1$** | **–5.23** | **64.1** | **0.9** | **0.3** | **34.7** |
| $6a_2$ | –5.56 | 58.8 | 4.0 | 22.9 | 14.3 |
| $13b_1$ | –5.62 | 55.3 | 13.2 | 20.6 | 11.0 |
| $12b_1$ | –7.69 | 1.3 | 97.6 | 0.9 | 0.2 |
| $5a_2$ | –8.01 | 0.3 | 99.5 | 0.2 | 0.0 |
| $27b_2$ | –9.36 | 0.5 | 79.4 | 1.8 | 18.2 |

 © 2007 Wiley-VCH Verlag GmbH & Co. KGaA, Weinheim 

higher occupied orbitals. The main difference between the HOMO and both the HOMO–1 and HOMO–2 is that the character of the carbonyl group is not the same. The HOMO is mainly dominated by the equatorial COs, while HOMO–1 and HOMO–2 are dominated by the axial ones. These three orbitals are related to the $t_{2g}$ orbital set in W(CO)$_6$[13] concerning their π*-back-bonding character. We have to keep in mind that a splitting to $a_1$, $a_2$, and $b_1$ is caused by the $C_{2v}$ symmetry. On the other hand, HOMO–3 to HOMO–5 are localized on the diimine moiety, as well as LUMO, LUMO+1, and LUMO+2, with the first being very close in energy. LUMO+3 and LUMO+4 arise mainly from the axial carbonyls.

The metal $d_{xz}$ contribution to the LUMO and the W/diimine mixing in the HOMO–2 (it contains bonding interactions between the d orbital of the metal and the π* orbitals of the carbonyl groups) are consistent with the π-back-bonding theory. To gain more insight into the bonding scheme of **1** we envisioned the molecule as consisting of two fragments, namely W(CO)$_4$ and phen, acting as a donor and acceptor of electron density, respectively.[14] The derived picture of this fragment orbital analysis is demonstrated in Figure 2 for the HOMO–2 to LUMO. The FMOs of the central unit W(CO)$_4$ are presented on the left side of the diagram, whereas those of the diimine are on the right side. As indicated, the HOMO and HOMO–1 are predominantly localized on the W(CO)$_4$ fragment, with the LUMO being a combination of the LUMO from the diimine and the HOMO–2 from the metal–carbonyls. Of course we have to keep in mind that an increased back-donation of the metal to the heteroligand (N ligand) results in a decreased back-donation to the carbonyl ligands. The aforementioned combination along with the localization of HOMO–2 are indicative of the back-donation procedure. To be more precise, the HOMO–2 of the complex is a mixture of 86.2% of the HOMO–2 of W(CO)$_4$ and 6.5% of the LUMO of phen. This reveals the back-donation path of the electron density from the main core back to the diimine, for a total amount of 0.022 e$^-$, as computed by the Frenking et al.[14] charge decomposition method.

Recently, an analogous treatment of the W(CO)$_4$(pq) complex yielded an amount of 0.054 e$^-$, revealing a more effective back-bonding pathway.[5] At this point we should emphasize that mixing of frontier orbitals is an important parameter of the system and is connected to the negative solvatochromism and the existence of NLO properties for these types of compounds.

According to the aforementioned scheme we could expect the back-donation to the CO groups to be more effective if **1** had not adopted its existing bent geometry. Even if we adopt the atomic angular overlap model it is clear that more electron density is necessary to keep the W(CO)$_4$ fragment together when the structure deviates from orthogonality.

In the current analysis, we examine the bending of the axial carbonyl as a two-step procedure, **1b**→**1a**→**1**. Stated otherwise, we keep the bend of the equatorial CO units towards each other constant and monitor the axial ones

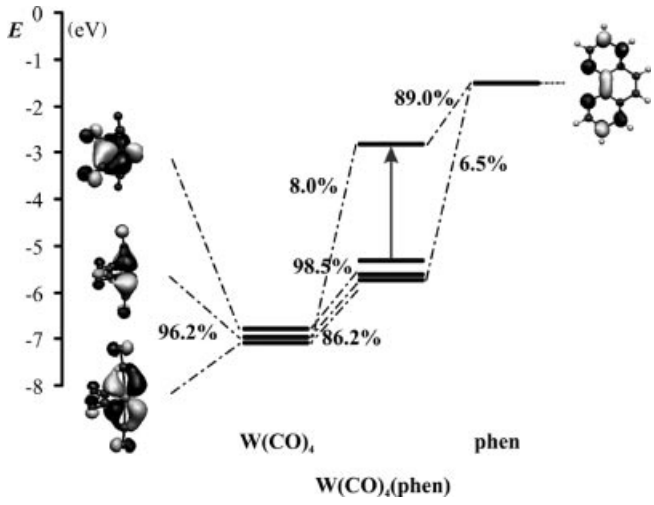


Figure 2. Schematic energy diagram of the induced structural changes in **1**.

deviating from orthogonality. From a frontier orbital point of view, the first step induces major changes, as is expected by the relative geometrical ones. Metal and equatorial carbonyl orbitals are significantly stabilized, while axial carbonyl orbitals seem to become destabilized as well. Diimine orbitals are less destabilised. This finding justifies the inverse order of HOMO–2 (the main, spectroscopically relevant orbital in **1**) and HOMO–1 in **1a**. These trends have an immediate effect on the HOMO–LUMO gap, which according to our calculations increases from 2.30 eV to 2.39 eV in the first step, while it is minimized to 2.37 eV in the second step. This second step is connected to the slight diimine orbital stabilization, whereas the rest of the molecule is destabilized to the same extent. Both steps offer a total 1.92 kJ/mol stabilization to the system. From a partial charges point of view, as calculated by Mulliken's population analysis (provided as Supporting Information), we ascertain that, along the series, the metal and diimine gain electron density at the expense of the carbonyls.

Considering all the aforementioned data, from the back-bonding concept we conclude that the diimine ligation is very crucial. As soon as phenanthroline binds, it demands, as a π acceptor, more electron density. The latter is moved from the carbonyls to phenanthroline. We will try to clarify this concept in terms of a fragment orbital analysis. First of all, starting from **1b**, we confirm that the σ donation of the diimine to the system reduces as we move towards **1**. This is also clearly demonstrated by the contributions of the W(CO)$_4$ empty orbitals to the formation of $27b_2$ (HOMO–5) and $35a_1$ (HOMO–8) orbitals (3.9% and 4.9% for **1b**, 3.8% and 4.6% for **1a** and **1**). The total donation is reduced from 0.398 to 0.394 and 0.385 e$^-$, respectively. On the other hand, back-donation to *o*-phenanthroline is increased when going from **1b** to **1a**, as expected. Back-bonding occurs through the transfer of electron density from the HOMO–2 of W(CO)$_4$ to the $5b_1$ and $6b_1$ of the diimine, forming the $13b_1$ and $14b_1$ orbitals of the complex. Thus,

 © 2007 Wiley-VCH Verlag GmbH & Co. KGaA, Weinheim 

the contribution of the empty orbitals of the diimine to the formation of $13b_1$ increases from 7.9% to 8.6%, while the contribution of the $W(CO)_4$ fragment to $5b_1$ of the diimine increases from 7.5% to 8.2%. Back-donation reduces slightly when going from **1a** to **1** and this is where the electron repulsion concept is applied. $W(CO)_4$ and phenanthroline filled orbitals repulse each other and the oxygen atoms bend in order for these forces to reach equilibrium. But this is rather the result than the cause (vide infra).

Up to this point we determined the nature of the driving forces that bend the system from **1b** to **1**, through **1a**. In summary, the major effect comes from the existence of phenanthroline. The system adopts the geometry that minimizes the electron repulsion for all the present ligands. This is further enhanced by the need for diminishing the electron repulsion of the fragment. If the system has a perfect octahedral geometry before these changes started to occur then another feature must also be explained. The bend of the axial carbonyls is sensitive to the back-bonding of the equatorial diimine ligands. Thus, the axial COs deviate from linearity by 3.25°, while the related differentiation in the case of the equatorial COs is only 1.35°. This means that the axial ligands are the most sensitive to the coordination diimines on the metal atom. The aforementioned conclusion is rather peculiar if the *trans* influence is kept in mind, along with the fact that the bite angle of the equatorial COs certainly has to be enlarged in order for the phenanthroline σ bonding to be effective. A natural arising question is why that happens. To provide a satisfactory answer we should examine the way back-donation evolves in space. As we have already mentioned back-bonding to phenanthroline is set through the $5d_{xz}$ orbital ($b_1$ in symmetry) of the metal and consequently the carbonyls that compete with the diimine are the axial and not the equatorial ones.

To proceed with our analysis, the bending of oxygen atoms should be further explained. As we have already mentioned, in the axial sites the carbonyls bend towards the "inside", while in the equatorial ones they bend towards the "outside". According to a frontier orbitals point of view, bending in the latter case causes stabilization of the orbitals centered on both carbonyls and the metal, whereas it destabilizes the diimine orbitals in a complete inverse way as compared to **1a**→**1**. Thus **1c**→**1** offers 0.86 kJ/mol to the system. This is slightly less than the 1.14 kJ/mol for **1a**→**1**. The induced stabilization, as an absolute value, is in both cases rather small. On the other hand, if compared to the relative value for **1b**→**1a**, which arises from changes in back-donation, it is considered relatively high and this finding becomes more valuable if we take into account the significantly smaller geometric change in this case.

Going from **1c** to **1** the back-donation to the carbonyls increases (0.3% rise in the carbonyl LUMO contribution to $36a_1$). This happens because carbonyls have a better overlap with the $5d_{x^2-y^2}$ of the metal, which is the most suitable d orbital for back-donation, because of its orthogonal arrangement to the *yz* plane. Furthermore, a linear combination of $d_{z^2}$ and $d_{x^2-y^2}$ is also present. This situation leads us to reevaluate the C to O σ donation. In order to reevaluate this process we used the concept of natural hybrid orbitals, which are derived by a natural bond orbital analysis.[15] Before we proceed we have to clarify that although the absolute values, which are extracted from the NBO analysis, are different from those extracted through the Mulliken population analysis applied in the rest of this report, the following results and described trends are in total accordance. Indeed, σ bonding through the equatorial W–C–O unit is also favored. Calculated deviations between the geometrical direction of the bond and the related direction of the hybrid orbital are reduced by up to 1.9° for W–C and 4.7° for C–O. This is a direct consequence of the diimine ligation to the system.

The case of **1a**→**1** seems to be analogous. It is clear that axial carbonyls accept electron density from the metal $d_{xy}$ orbital. Unfortunately, in each case changes in fragment contributions and relative energy are below the method precision. The hybrid orbitals of the complex seem to slightly change their conformation due to a best alignment of the carbon atoms to the π-orbital of the tungsten, at the expense of carbon–oxygen overlap and σ bonding.

Trying to summarize the above facts, we must emphasize that the suitable orbitals for back-donation are the $d_{xz}$, $d_{xy}$, and $d_{x^2-y^2}/d_{z^2}$ metal orbitals, which offer electron density to the diimine and also the axial and equatorial carbonyls. The bending of the C–O bonds is, in each case, the result of the tendency of the system to adopt a configuration in space that minimizes the electron repulsions between the bonds involved in the complex formation. The whole situation is best described by **1d**, which contains all the aforementioned changes. As demonstrated in Table 2 this structure shows the greatest destabilization, giving a final value of 2.95 kJ/mol. Despite the fact that this value is relatively low it is indicative of the energy stabilization that is offered to the system from the arrangement of the ligand in space, in such a way that is convenient from an electronic point of view.

### 2.2. Relation Between Structure, Back-Bonding, and Electron Properties

At the second level of our approach, we tried to discover the trends that govern the structural features of the complexes under study, such as the bending of axial carbonyls in terms of the ability of the ligand to partake in back-donation. As already mentioned (vide supra), these features are anticipated to be correlated to the electronic properties of the compound. This is an essential hypothesis, which we try to test in this report.

There are three important factors that govern the electronic structure of $W(CO)_4$(diimine) complexes. First of all, the σ-donating ability of the coordinating nitrogen atoms, followed by the existence of π*-orbitals of proper energy and symmetry, which are suitable for the evolution of back-donation, and thirdly the magnitude of the binding N–W–N angle. Taking all these factors into consideration we properly selected eight ligands in order to demonstrate probable induced differences in compound structure and

 © 2007 Wiley-VCH Verlag GmbH & Co. KGaA, Weinheim 

electronic behavior. First of all, we employed 1,10-phenanthroline (phen – compound **1**) and 2,2′-bipyridine (bpy – compound **2**), which are two of the most widely used aromatic ligands in synthesis. In order to test the influence of symmetry and binding angle we also employed two pyridine moieties (2py – compound **3**), in a sense that they would create an aromatic, but not a chelated first coordination sphere, around the metal. Consequently, we selected 1,4-diazabutadiene (DAB – compound **4**), *N*,*N*′-bis-methyl-1,4-diazabutadiene (Me-DAB – compound **5**) and *N*,*N*′-bis-isopropyl-1,4-diazabutadiene (*iPr*-DAB – compound **6**). These are highly symmetric aliphatic diimines and their properties will be compared to those of the aromatic ones. Finally, we introduced 1,2-ethylenediamine (en – compound **7**), since it is a bidentate diamine without any orbitals suitable for back-bonding and two ammonia ligands (2 $NH_3$ compound **8**) with almost the same σ-donating ability to the en, but without any steric constraints present.

Structural characteristics of compounds **2**–**8** are depicted in Table 4. Relative data for **1**, extracted from Table 1 and Table 2 (vide supra) are also reported for uniformity purposes. All data presented are extracted at the G98-B3LYP level of theory and show satisfactory agreement with other reported computational results and crystal structures.[4,9,11] To the best of our knowledge, compound **8** has not yet been prepared, but is included in our analysis for comparison purposes.

All of the complexes under study adopt a distorted pseudo-octahedral geometry. We started our analysis with the approximation described in all standard textbooks.[16] Within the framework of π* back-bonding different structures are compared based on the magnitude of the W–L and C–O bond lengths. In our case, the axial W–C bonds are significantly longer than the relative equatorial ones. The length of the W–N bond is increased in the order **4** < **5** ≈ **6** ≈ **2** < **1** < **3** < **8** < **7**. Thus, bonding of the N ligand seems to be stronger in the case of the DAB ligands as compared to the aromatic ones, while the amine complexes demonstrate weaker bonding along the series. This series is also indicative of the nitrogen hybridization where $sp^3$ hybridization (present in the amines) affords longer W–N bonds. The relative series, regarding the W–$C_{eq}$, W–$C_{ax}$, C–$O_{eq}$, and C–$O_{ax}$ bonds, is **8** < **3** ≈ **1** ≈ **2** < **7** < **4** < **6** ≈ **5**, **8** ≈ **3** < **1** ≈ **2** < **4** ≈ **7** < **6** ≈ **5**, **5** < **6** < **7** < **4** < **3** ≈ **1** ≈ **2** ≈ **8**, and **5** ≈ **6** < **7** < **4** < **1** ≈ **2** < **3** ≈ **8**, respectively. According to the above bonding scheme we conclude that diazabutadiene ligands are better π* acids than *a*-diimines and amines, a finding that definitely make sense. Nevertheless, there are some points in the above series that certainly deserve to be further explained. First of all, within the R-DAB ligands it seems that the series of π* acidity that holds is H- < Me- < *iPr*-. In other words, the increase of the electron-releasing character of the substituents on the nitrogen atoms in the R-DAB ligands increases the electron-donating character of the σ bond and in consequence it increases the π-acceptor character. The observed trend is certainly not normally expected. Secondly, the first coordination sphere of **7** seems to resemble that of the R-DAB ligands, while several similarities exist between **3** and **8**. This trend should be further explained on the basis of important differences in nature between these organic substances.

To proceed with our analysis we examined, at first, a structural feature that is certainly underestimated in the existing literature in the field. This is the binding and bending angles of the carbonyl moieties. In Figure 3 and Figure 4 these features are schematically depicted. Thus, we observe that the N–W–N bite angle increases in the series **5** ≈ **4** ≈ **6** < **2** < **7** ≈ **1** < **3** ≈ **8**, while the relative series in the case of $C_{eq}$–W–$C_{eq}$/$O_{eq}$–W–$O_{eq}$ ($\varphi_1$/$\varphi_2$) and $C_{ax}$–W–$C_{ax}$/$O_{ax}$–W–$O_{ax}$ ($\varphi_3$/$\varphi_4$) is **8** < **3** ≈ **7** < **2** ≈ **1** < **6** < **5** < **4** and **4** < **6** <

Table 4. Comparison of selected calculated bond lengths [Å] and angles [°] for the ground-state structure of complexes **1**–**8** along with calculated data on electron density donation between the W(CO)$_4$ and the diimine fragments.

| C | **1** | **2** | **3** | **4** | **5** | **6** | **7** | **8** |
|---|---|---|---|---|---|---|---|---|
| W–N | 2.226 | 2.219 | 2.274 | 2.134 | 2.215 | 2.216 | 2.365 | 2.349 |
| W–$C_{ax}$ | 2.033 | 2.033 | 2.023 | 2.042 | 2.068 | 2.064 | 2.049 | 2.023 |
| W–$C_{eq}$ | 1.976 | 1.977 | 1.975 | 2.002 | 2.016 | 2.011 | 1.985 | 1.965 |
| C–$O_{ax}$ | 1.187 | 1.187 | 1.191 | 1.183 | 1.158 | 1.162 | 1.169 | 1.192 |
| C–$O_{eq}$ | 1.197 | 1.197 | 1.196 | 1.19 | 1.165 | 1.17 | 1.174 | 1.198 |
| C=N | 1.384 | 1.378 | 1.368 | 1.338 | 1.308 | 1.312 | 1.487 | – |
| N–W–N | 74.2 | 73.2 | 84.7 | 72.1 | 72 | 72.5 | 73.9 | 84.7 |
| $C_{ax}$–W–$C_{ax}$ | 173.5 | 173.2 | 174.9 | 162.1 | 169.4 | 166.1 | 174.9 | 176.4 |
| $O_{ax}$–W–$O_{ax}$ | 171.1 | 170.7 | 172.6 | 158.9 | 167 | 162.7 | 172.5 | 174.4 |
| $C_{eq}$–W–$C_{eq}$ | 92.7 | 92.3 | 90.9 | 99.6 | 95.1 | 94.8 | 91.1 | 90.3 |
| $O_{eq}$–W–$O_{eq}$ | 94.8 | 94.6 | 91.8 | 102.2 | 97.0 | 96.8 | 92.4 | 90.9 |
| $\Delta E$[a] | 2.36 | 2.33 | 2.92 | 2.43 | 2.36 | 2.40 | 3.51 | 3.48 |
| b[b] | 0.385 | 0.391 | 0.460 | 0.427 | 0.464 | 0.574 | 0.472 | 0.477 |
| bd[b] | 0.022 | 0.021 | 0.021 | 0.121 | 0.111 | 0.091 | 0 | –0.02 |
| $r$[b] | –0.514 | –0.536 | –0.084 | –0.517 | –0.434 | –0.46 | –0.338 | –0.41 |
| Total π*(N) to H-2[c] | 8.3[d] | 8.8[e] | 4.1[f] | 30.3[g] | 20.4 | 20.5 | 0 | 0 |

[a] HOMO–LUMO energy differece in eV. [b] Total charge donation, back-donation, and electron repulsion between W(CO)$_4$ and diimine fragments. [c] Mainly the HOMO–2 [W(CO)$_4$ – $b_1$ in symmetry] to $b_1$*-LUMO (N ligand) type. [d] It contains a 1.8% contribution from the LUMO+2 of the phen. [e] It contains a 2.8% contribution from the LUMO+1 of the bpy. [f] An interaction between the orbitals of a symmetry. [g] Contains 1.0% contribution from the LUMO+1 of DAB.

 © 2007 Wiley-VCH Verlag GmbH & Co. KGaA, Weinheim 

**5** < **2** ≈ **1** < **7** ≈ **3** < **8**, respectively. All the complexes under study share the same structural features, described earlier (vide supra). The $W(CO)_4$ fragment deviates from orthogonality with the axial carbonyls bending away, while the equatorial ones bend towards the N ligand. In both cases, the bending of the oxygen atoms is larger. Moreover, several other features deserve attention. First of all, both axial and equatorial carbonyls deviate from orthogonality in an analogous way and the following relations, Equation (1) and (2), are extracted.

$$\varphi_1 = -0.5935\ \varphi_3 + 195.03\ (r = 0.97) \quad (1)$$

$$\varphi_2 = -0.6372\ \varphi_4 + 202.59\ (r = 0.95) \quad (2)$$

$\varphi_1$ and $\varphi_2$ are the angles $C_{eq}$–W–$C_{eq}$ and $O_{eq}$–W–$O_{eq}$ and $\varphi_3$ and $\varphi_4$ the angles $C_{ax}$–W–$C_{ax}$ and $O_{ax}$–W–$O_{ax}$, respectively.

Moreover, as it is depicted in Figure 3 and Figure 4 in both cases the deviation from linearity observed in the carbonyl moiety is enhanced, in general terms, with the deviation of the whole group from orthogonality. Thus, in the case of the axial carbonyls, the largest deviation is observed for **6** and **4** and the smallest for **8** and **9**, whereas for the equatorial carbonyls the largest deviation is observed in **4** and the smallest are also in **8** and **9**. Last but not least, the trend followed within the $W(CO)_4$ moiety is reversed in the case of the W–heteroligand bite angle. Nevertheless, we

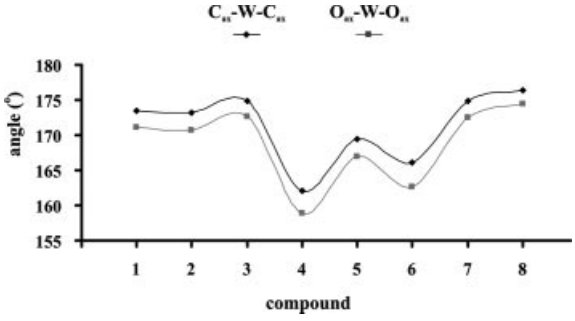


Figure 3. Schematic diagram of the $C_{ax}$–W–$C_{ax}$ and $O_{ax}$–W–$O_{ax}$ angles for compounds **1**–**8**.

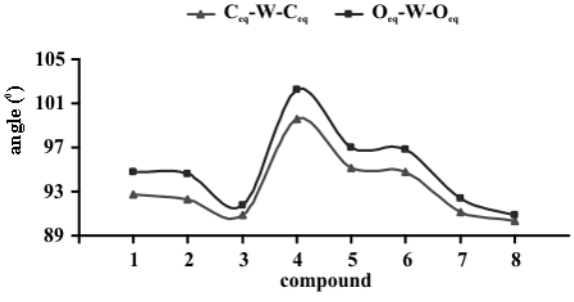


Figure 4. Schematic diagram of the $C_{eq}$–W–$C_{eq}$ and $O_{eq}$–W–$O_{eq}$ for compounds **1**–**8**.

should emphasize the fact that the two compounds without a bidentate ligand, namely **3** and **8**, show the same N–W–N angle, despite the different nature of the nitrogen ligands.

Proceeding with our discussion in electronic terms the contribution of different fragments to the frontier orbitals of the complexes is depicted in Table 5. Complex **2** has a framework of frontier orbitals analogous to the aforementioned one for **1** (vide supra), with the expected changes that arise from the fact that they have different aromatic diimine groups. For example, the first unoccupied diimine based $a_2$ orbital lies at a lower energy in **1** as compared to **2**. On the contrary in compounds **4**–**6** a different pattern is observed. The LUMO+3/+4 in **2** are stabilized and become the LUMO+1/+2 in **3**. These are predominantly axial carbonyl in character. The HOMO manifold for these compounds remains localized, mainly on the metal giving a relevant bonding scheme.

Complex **3** contains two pyridine moieties and not a bidentate ligand. The relaxed structure, in which the two pyridines are twisted from the planar disposition in order to minimize the hindrance that appears between the pyridine *ortho*-H atoms, destabilizes the frontier orbitals and affects the back-donation pathway. As a result back-bonding is no longer evolved through an orbital of b symmetry. In the case of pyridine ligands a metal $d_{x^2-y^2}/d_{z^2}$ ($a_1$ in $C_{2v}$ first coordination sphere) linear combination interacts with a pyridine-based a* orbital (Figure 5).

Finally, in the case of the diamine and bis-amine complexes the bonding scheme, apart from the three highest occupied orbitals, is different. Most of the unoccupied orbitals are carbonyl localized, with the contribution of the heteroligand being of low to only moderate importance (e.g. LUMO+3 in **7** and LUMO+2 in **8**). Moreover, an unoccupied orbital with a predominant d(σ*) character was not found in any of the above compounds. In cases where this sort of contribution existed it corresponded to only a part of a highly delocalized orbital. Thus, low-lying LF states contradict the arguments of the traditional ligand field theory. This fact is consistent with previous work done by Vlček et al.[4]

In terms of back-donation to the N ligand the main pathway followed for all cases (apart from **3**) is the out-of-phase interaction between an orbital of $d_{xz}$ tungsten/π*-axial carbonyl character and a π* heteroligand. This is best demonstrated by the HOMO–2 and LUMO (vide supra). Through an FMO analysis, analogous to that described in the previous paragraph, we concluded the following series of increasing back-donation, **8** ≈ **7** < **3** < **1** < **2** < **5** ≈ **6** < **4**, with the diamine and bis-amine compounds showing trivial back-bonding and **4**, which contains the DAB ligand, having the maximum back-bonding in the series. The comparison was based on the interaction of the HOMO–2 of the $W(CO)_4$ fragment (HOMO in the case of **3**) with the π* orbitals of the heteroligand (LUMO to LUMO+2 of proper symmetry), as demonstrated in Table 4. The same series in terms of the ligands is $NH_3$ ≈ en < py < bpy < phen < Me-DAB ≈ *iPr*-DAB < DAB. Thus, aliphatic diimines interact stronger with the metal fragment than aromatic ones,

 © 2007 Wiley-VCH Verlag GmbH & Co. KGaA, Weinheim 

Table 5. Contribution of different fragments to the valence orbitals of complexes **2**–**8**. The HOMO and LUMO are shown in bold.

| MO | *E* [eV] | W | diimine | $CO_{ax}$ | $CO_{eq}$ |
|---|---|---|---|---|---|
| **2** | | | | | |
| $34a_1$ | –1.22 | 16.0 | –2.2 | 86.0 | 0.2 |
| $26b_2$ | –1.49 | 20.2 | –0.2 | 70.8 | 9.1 |
| $7a_2$ | –1.97 | 0.1 | 97.8 | 0.5 | 1.6 |
| $14b_1$ | –2.12 | 1.0 | 96.8 | 1.0 | 1.2 |
| **$13b_1$** | **–3.00** | **3.7** | **90.1** | **3.0** | **3.2** |
| **$33a_1$** | **–5.33** | **63.8** | **0.8** | **0.8** | **34.6** |
| $6a_2$ | –5.61 | 58.3 | 3.8 | 22.8 | 15.1 |
| $12b_1$ | –5.64 | 54.7 | 13.6 | 21.6 | 10.1 |
| $5a_2$ | –7.83 | 0.1 | 99.9 | 0.0 | 0.0 |
| $11b_1$ | –9.19 | 1.2 | 95.3 | 3.0 | 0.5 |
| $4a_2$ | –9.20 | 1.4 | 97.5 | 0.8 | 0.3 |
| **3** | | | | | |
| 41b | –1.30 | 11.4 | 46.4 | 36.2 | 6.0 |
| 40b | –1.57 | 5.8 | 54.5 | 39.3 | 0.5 |
| 41a | –1.72 | 3.6 | 77.0 | 19.6 | –0.2 |
| 40a | –2.18 | 2.6 | 89.8 | 2.8 | 4.8 |
| **39b** | **–2.21** | **1.4** | **94.5** | **2.3** | **1.9** |
| **39a** | **–5.13** | **61.2** | **7.2** | **0.3** | **31.3** |
| 38b | –5.56 | 60.1 | 3.1 | 25.0 | 11.8 |
| 38a | –5.58 | 60.2 | 1.3 | 23.9 | 14.5 |
| 37b | –8.28 | 0.1 | 99.8 | 0.1 | 0.0 |
| 37a | –8.39 | 0.2 | 99.5 | 0.1 | 0.2 |
| 36b | –8.99 | 0.8 | 95.3 | 1.9 | 2.1 |
| **4** | | | | | |
| $12b_1$ | –0.51 | 13.2 | 2.7 | 11.6 | 72.6 |
| $16b_2$ | –1.02 | 3.4 | 0.5 | 20.6 | 75.5 |
| $23a_1$ | –1.58 | 12.1 | –0.6 | 85.7 | 2.9 |
| $15b_2$ | –1.93 | 16.9 | 0.7 | 70.1 | 12.3 |
| **$11b_1$** | **–3.48** | **12.6** | **62.6** | **15.3** | **9.4** |
| **$22a_1$** | **–5.92** | **63.2** | **1.7** | **3.4** | **31.7** |
| $4a_2$ | –6.22 | 54.7 | 6.8 | 21.8 | 16.7 |
| $10b_1$ | –6.35 | 43.0 | 34.1 | 18.7 | 4.2 |
| $3a_2$ | –9.47 | 4.6 | 92.8 | 1.9 | 0.8 |
| $14b_2$ | –10.13 | 3.0 | 70.3 | 2.4 | 24.3 |
| $21a_1$ | –10.28 | 4.8 | 74.2 | 1.9 | 19.1 |
| **5** | | | | | |
| $13b_1$ | –0.12 | 17.3 | 1.8 | 13.9 | 67.0 |
| $19b_2$ | –0.37 | 3.5 | 1.0 | 17.4 | 78.1 |
| $26a_1$ | –1.27 | 13.0 | –0.4 | 86.7 | 0.7 |
| $18b_2$ | –1.59 | 17.8 | 1.3 | 72.1 | 8.7 |
| **$12b_1$** | **–3.07** | **10.0** | **74.5** | **8.5** | **7.0** |
| **$25a_1$** | **–5.43** | **65.5** | **1.1** | **1.5** | **31.9** |
| $5a_2$ | –5.76 | 59.3 | 4.0 | 21.9 | 14.8 |
| $11b_1$ | –5.91 | 51.4 | 23.2 | 18.9 | 6.5 |
| $4a_2$ | –8.65 | 2.3 | 96.7 | 0.8 | 0.2 |
| $17b_2$ | –9.36 | 3.0 | 81.7 | 1.1 | 14.3 |
| $24a_1$ | –9.68 | 5.1 | 80.1 | 1.2 | 13.5 |
| **6** | | | | | |
| $17b_1$ | –0.04 | 16.2 | 2.9 | 13.2 | 67.7 |
| $23b_2$ | –0.39 | 3.7 | 1.1 | 19.4 | 75.8 |
| $30a_1$ | –1.18 | 12.4 | –0.5 | 87.0 | 1.1 |
| $22b_2$ | –1.51 | 17.4 | 1.3 | 71.1 | 10.2 |
| **$16b_1$** | **–3.01** | **9.3** | **73.5** | **9.5** | **7.8** |
| **$29a_1$** | **–5.42** | **64.7** | **1.5** | **1.9** | **31.9** |
| $9a_2$ | –5.70 | 57.5 | 5.5 | 21.7 | 15.4 |
| $15b_1$ | –5.84 | 50.4 | 23.5 | 19.8 | 6.2 |
| $8a_2$ | –8.42 | 3.2 | 95.2 | 1.2 | 0.4 |
| $21b_2$ | –8.77 | 1.5 | 88.5 | 1.0 | 9.0 |
| $28a_1$ | –9.13 | 4.1 | 89.0 | 0.7 | 6.1 |
| **7** | | | | | |
| 29b | 0.35 | 33.2 | 16.2 | 0.3 | 50.4 |
| 28b | 0.17 | 34.3 | 4.5 | 16.9 | 44.3 |
| 29a | 0.09 | 62.8 | 24.0 | 16.5 | –3.2 |
| 27b | 0.01 | 37.9 | 8.9 | 28.7 | 24.5 |
| 28a | –1.31 | 20.8 | 8.2 | 71.1 | –0.2 |
| **26b** | **–1.52** | **25.8** | **6.8** | **60.9** | **6.5** |
| **27a** | **–5.03** | **65.3** | **0.8** | **0.5** | **33.4** |
| 26a | –5.40 | 61.7 | 0.2 | 24.2 | 13.9 |
| 25b | –5.41 | 63.3 | 0.7 | 24.7 | 11.3 |
| 24b | –9.39 | 2.3 | 78.4 | 1.7 | 17.7 |
| 25a | –9.43 | 3.9 | 81.0 | 1.4 | 13.7 |
| 23b | –10.22 | 4.6 | 0.5 | 71.4 | 23.5 |
| **8** | | | | | |
| 50 | –0.06 | 18.3 | 0.0 | 21.8 | 60.0 |
| 49 | –0.29 | 30.3 | 7.5 | 25.4 | 36.8 |
| 48 | –0.58 | 56.3 | 22.5 | 25.2 | –4.0 |
| 47 | –1.75 | 29.8 | 9.7 | 60.8 | –0.2 |
| **46** | **–1.80** | **24.9** | **5.1** | **63.9** | **6.1** |
| **45** | **–5.28** | **64.6** | **0.6** | **0.2** | **34.7** |
| 44 | –5.70 | 61.2 | 0.2 | 25.3 | 13.3 |
| 43 | –5.72 | 61.4 | 0.4 | 24.8 | 13.4 |
| 42 | –9.83 | 2.7 | 63.6 | 2.8 | 30.9 |
| 41 | –10.09 | 3.5 | 60.4 | 4.1 | 31.9 |
| 40 | –10.25 | 4.0 | 0.4 | 63.8 | 31.8 |

with the amines not showing back-donation at all. This conclusion certainly makes sense and it certainly reflects the nitrogen hybridization changing from $sp^3$ for $NH_3$ to $sp^2$ for DAB.

Taking the aforementioned findings into consideration we verified that the bond lengths do not demonstrate the correct behavior according to the induced back-donation. On the contrary, the C–W–C deviation from orthogonality and C–O deviation from linearity follow the back-donation trends! In other words, the stronger the back-donation the larger the deviations. This observation is originally presented in this report. Indeed, C–W–C and O–W–O angles correlate effectively with the observed back-donation magnitude (bd), as proven from the following relations [bd can also be provided as a function of the angles $\varphi_1$ and $\varphi_2$, through Equations (1) and (2) since the deviation of the equatorial ligands are a consequence of the bending of the axial ones]. In these relations bd is the total percentage of contribution of unoccupied π*-type heteroligand orbitals in the back-donation pathway.

From the above Equation (3) and (4) we verify that the bite angles of the CO groups are not only indicative of π* back-donation but they are also correlated to back-donation in a linear fashion. In other words, it is proved that the structural indices that best describe back-donation in symmetric compounds of the type W(CO)$_4$(NN) or W(CO)$_4$N$_2$, are the deviations of the C–W–C angles from orthogonality and O–C–W angles from linearity. The larger the existing deviation the stronger the back-donation. This contradicts the traditional concept of bond lengths, which does not always lead to correct results. This conclusion

 © 2007 Wiley-VCH Verlag GmbH & Co. KGaA, Weinheim 

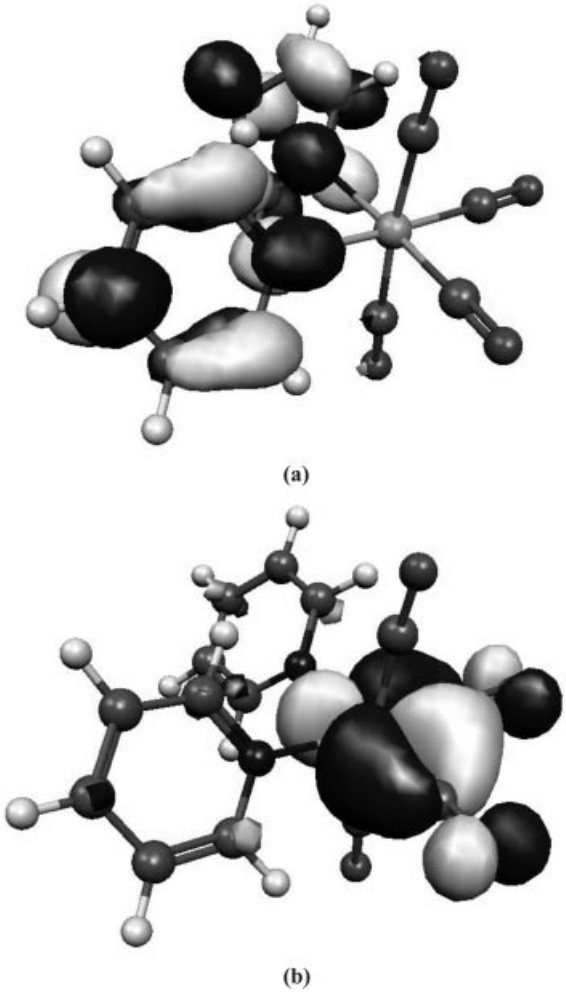


Figure 5. Contour plots of the HOMO (a) and LUMO (b) for compound **3**.

should also apply to the symmetric carbonyl compounds with other types of ligands, such as phosphanes and phosphites.

$$bd = -2.1238\ \varphi_3 + 375.51\ (r = 0.97) \quad (3)$$

$$bd = -1.9562\ \varphi_4 + 341.63\ (r = 0.97) \quad (4)$$

## 3. Concluding Remarks

In the present report, we tried to study the structures of $W(CO)_4(NN)$ and $W(CO)_4N_2$ compounds in terms of π* back-donation. Our approach was divided into two parts. Firstly, we proved, for the first time, that the observed structural deviations from orthogonality, regarding C–W–C bite angles and deviations from the linearity of the O–C–W angles present in complexes of this type, have their origin in the evolution of the necessary back-donation pathways. The energy difference between the two structures (the bent and the totally orthogonal one) is computed to be 2.95 kJ/mol.

Secondly, we analyzed the back-donation pathways of a series of compounds having different types of ligands. We proved that this is achieved through a $d_{xz} \rightarrow$ N-ligand electron donation, except in the case of the $W(CO)_4(py)_2$ compound. Moreover, we showed that back-donation is correlated to the above-mentioned structural features in a linear manner.

Keeping this scheme in mind, along with the fact that among all the ligands studied in our series DAB is involved in the maximum back-bonding and $NH_3$ the minimum, we can develop a new structure-to-properties type scale regarding back-donation. From a multiple regression analysis of the aforementioned data (Figure 6) we developed the following relation (details for the linear regression are supplied in the Supporting Information) which implies that the magnitude of back-donation is a linear combination of the four angles of the CO groups (since $\varphi_1$ and $\varphi_2$ are dependant on $\varphi_3$ and $\varphi_4$, respectively), see Equation (5).

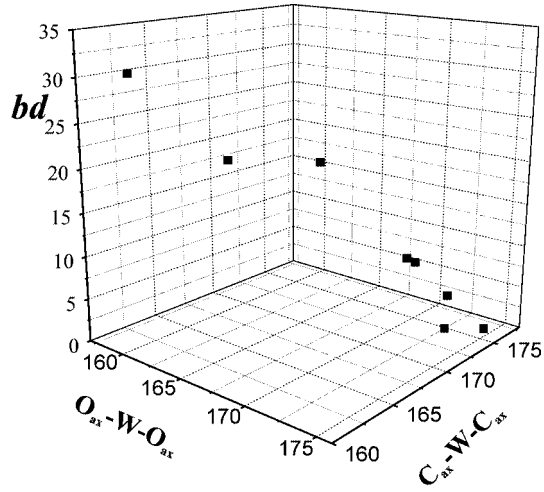


Figure 6. Scatter plot of bd = $f(\varphi_3, \varphi_4)$. $R^2 = 0.98$ (from multiple regression analysis).

$$bd = 510.15 - 10.58\ \varphi_3 + 7.79\ \varphi_4 \quad (5)$$

The standard deviation is 2.34.

Moreover, if we define the π* acidity related to the DAB (100% π* acid) and ammonia molecules (0% π* acid) we get Equation (6).

$$bd' = 3.00\ bd \quad (6)$$

On the basis of Equation (6) we can attribute a 29% of π*-accepting ability to bpy compared with DAB.

The extent of back-donation and thus the bending of the $W(CO)_4$ group should be correlated to other properties of the system such as the slope of solvatochromic plots.[8] It is well known that the complexes under study exhibit a large negative solvatochromism, which refers to the blue shift of the low energy MLCT transition of the complex, with a simultaneous increase in the polarity of the solvent. This phenomenon is directly related to a difference between the ground- and excited-state dipole moment. The ground-state dipole moment is certainly determined by the geometry of the compounds and this geometry has its origin in the extent of back-donation as we have already proved (vide infra). As a result the extent of solvatochromism should be correlated to the extent of back-donation.

 © 2007 Wiley-VCH Verlag GmbH & Co. KGaA, Weinheim 

## 4. Computational Details

Ground-state electronic structure calculations of all complexes under study have been performed using density functional theory (DFT)[17] methods by employing the Gaussian 98 software package.[18] The functional that was used throughout this study is the B3LYP, consisting of a hybrid exchange functional, as defined by Becke's three-parameter equation[19] and the Lee–Yang–Par correlation functional.[20] The ground-state geometries were obtained in the gas phase by full geometry optimization and the optimum structures, located as stationary points on the potential energy surfaces, were verified by the absence of imaginary frequencies. Moreover, the derived wave functions were free from internal instabilities. Structures were regularized in order to satisfy the $C_{2v}$ geometry in **1**–**2** and **4**–**6**. Complex **3** was optimized under no symmetry constraint. The optimum structure obtained a practically $C_2$ symmetry and the optimization was repeated in this point group. Complex **7** was optimized also under the $C_2$ symmetry, whereas complex **8** was optimized without any symmetry constraint. The basis set used throughout this study is the full double-ζ LANL2DZ basis function, together with the corresponding effective core potential for tungsten.[21] Percentage compositions of molecular orbitals from the four contributing fragments (the metal, the N ligand, the axial and equatorial carbonyls) were calculated and analyzed using the AOMix and AOMix-CDA programs, with the latter being extensively used for the fragment molecular orbital (FMO) analysis.[22] The graphics presented here were drawn with the aid of Molekel.[23] An NBO population analysis has been performed with the NBO 3.1 program as implemented in Gaussian.[15b] Finally, a multiple regression analysis was carried out using the commercial Origin 6.0 software package.

**Supporting Information** (see also the footnote on the first page of this article): Mulliken charges for compounds **1** and **1a**–**1d** (Table S1), details for the linear regression provided for Equation (5) and calculated atomic coordinates (S2–S9) for all compounds under study.

## Acknowledgments

The project was cofunded by the European Social Fund (EPEAEK II)and National Resources (PYTHAGORAS).

[1] A. Vlček Jr., *Coord. Chem. Rev.* **2002**, *230*, 225–242.
[2] A. J. Lees, *Coord. Chem. Rev.* **1998**, *177*, 3–35.
[3] D. J. Stufkens, *Coord. Chem. Rev.* **1990**, *104*, 39–112.
[4] a) S. Záliš, M. Busby, T. Kotrba, P. Matousek, M. Towrie, A. Vlček Jr., *Inorg. Chem.* **2004**, *43*, 1723–1734; b) S. Záliš, I. R. Farrel, A. Vlček Jr., *J. Am. Chem. Soc.* **2003**, *125*, 4580–4592; c) I. R. Farrel, J. van Slageren, S. Záliš, A. Vlček Jr., *Inorg. Chim. Acta* **2001**, *315*, 44–52; d) I. R. Farrel, H. František, S. Záliš, T. Mahabiersing, A. Vlček Jr., *J. Chem. Soc., Dalton Trans.* **2000**, 4323–4331; e) S. Záliš, C. Daniel, A. Vlček Jr., *J. Chem. Soc., Dalton Trans.* **1999**, 3081–3086; f) S. Záliš, A. Vlček Jr., C. Daniel, *Collect. Czech. Chem. Commun.* **2003**, *68*, 89–104; g) Z. Hu, R. J. Boyd, H. Nakatsuji, *J. Am. Chem. Soc.* **2002**, *124*, 2664–2671.
[5] I. Veroni, C. Makedonas, A. Rontoyanni, C. A. Mitsopoulou, *J. Organomet. Chem.* **2006**, *691*, 267–281.
[6] a) D. R. Van Staveren, N. Metzler-Nolte, *Chem. Commun.* **2002**, 1406–1407; b) N. Metzler-Nolte, *Angew. Chem. Int. Ed.* **2001**, *40*, 1040–1043.
[7] V. Balzani, A. Juris, M. Venturi, S. Campagna, S. Serroni, *Chem. Rev.* **1996**, *96*, 759–833.
[8] I. Veroni, A. Rontoyanni, C. A. Mitsopoulou, *Dalton Trans.* **2003**, 255–260.
[9] a) H. J. B. Slot, N. W. Murral, A. Welch, *Acta Crystallogr., Sect. C* **1985**, *41*, 1309–1312; b) P. N. W. Baxter, J. A. Connor, J. D. Wallis, D. C. Povey, *J. Organomet. Chem.* **1992**, *426*, 187–194; c) M. A. Bakar, H.-K. Fun, K. Chinnakali, S.-G. Teoh, O. B. Shawkataly, F. M. Lopez, *Acta Crystallogr., Sect. C* **1993**, *49*, 582–584; d) E. C. Alyea, G. Ferguson, V. K. Jain, *Acta Crystallogr., Sect. C* **1994**, *50*, 854–857; e) R. S. Herrick, K. L. Houde, J. S. McDowell, L. P. Kiczek, G. Bonavia, *J. Organomet. Chem.* **1999**, *589*, 29–37; f) R. S. Herrick, C. J. Ziegler, H. Bohan, M. Corey, M. Eskander, J. Giguere, N. McMicken, I. E. Wrona, *J. Organomet. Chem.* **2003**, *687*, 178–184; g) H. tom Dieck, T. Mack, K. Peters, H.-G. von Schnering, *Z. Naturforsch., Teil B* **1983**, *38*, 568–579; h) J. Powell, A. Lough, M. Raso, *J. Chem. Soc., Dalton Trans.* **1994**, 1571–1576.
[10] a) H. Jinshuan, C. Qingrong, W. Manfrag, L. Shimei, *Chin. J. Struct. Chem.* **1985**, *4*, 69–71; b) H. Jinshuan, C. Qingrong, W. Manfrag, H. Meiyun, *Chin. J. Struct. Chem.* **1985**, *4*, 66; c) N. S. Magomedova, G. K.-I. Magomedov, *Metalloorg. Khim.* **1990**, *3*, 129–134.
[11] Q. Ye, Q. Wu, H. Zhao, Y.-M. Song, X. Xue, R.-G. Xiong, S.-M. Pang, G.-H. Lee, *J. Organomet. Chem.* **2005**, *690*, 286–290.
[12] M. H. B. Stiddard, *J. Chem. Soc.* **1962**, 4712–4715.
[13] A. Rosa, E. J. Baerends, S. J. A. van Gisbergen, E. van Lenthe, J. A. Goeneveld, J. G. Snijders, *J. Am. Chem. Soc.* **1999**, *121*, 10356–10365.
[14] a) S. Dapprich, G. Frenking, *J. Chem. Phys.* **1995**, *99*, 9352–9362; b) G. Frenking, N. Fröhlich, *Chem. Rev.* **2000**, *100*, 717–774.
[15] a) A. E. Reed, L. A. Curtiss, F. Weinhold, *Chem. Rev.* **1988**, *88*, 899–926; b) E. D. Glendening, A. E. Reed, J. E. Carpenter, F. Weinhold, *NBO Version 3.1*.
[16] F. A. Cotton, G. Wilkinson, *Advanced Inorganic Chemistry*, 5th ed., John Wiley & Sons, New York, **1988**.
[17] R. G. Parr, W. Yang, *Density Functional Theory of Atoms and Molecules*; Oxford University Press: Oxford, **1989**.
[18] , M. J. Frisch, G. W. Trucks, H. B. Schlegel, G. E. Scuseria, M. A. Robb, J. R. Cheeseman, V. G. Zakrzewski, J. A. Montgomery Jr., R. E. Stratmann, J. C. Burant, S. Dapprich, J. M. Millam, A. D. Daniels, K. N. Kudin, M. C. Strain, O. Farkas, J. Tomasi, V. Barone, M. Cossi, R. Cammi, B. Mennucci, C. Pomelli, C. Adamo, S. Clifford, J. Ochterski, G. A. Petersson, P. Y. Ayala, Q. Cui, K. Morokuma, D. K. Malick, A. D. Rabuck, K. Raghavachari, J. B. Foresman, J. Cioslowski, J. V. Ortiz, A. G. Baboul, B. B. Stefanov, G. Liu, A. Liashenko, P. Piskorz, I. Komaromi, R. Gomperts, R. L. Martin, D. J. Fox, T. Keith, M. A. Al-Laham, C. Y. Peng, A. Nanayakkara, M. Challacombe, P. M. W. Gill, B. Johnson, W. Chen, M. W. Wong, J. L. Andres, C. Gonzalez, M. Head-Gordon, E. S. Replogle, and J. A. Pople, *Gaussian 98, Revision A.9*, Gaussian, Inc., Pittsburgh PA, **1998**.
[19] A. D. Becke, *J. Chem. Phys.* **1993**, *98*, 5648–5652.
[20] C. Lee, W. Yang, R. G. Parr, *Phys. Rev. B* **1988**, *37*, 785–789.
[21] a) T. H. Dunning Jr., P. J. Hay, in: *Modern Theoretical Chemistry* (Ed.: H. F.Schaefer III); Plenum Press: New York, **1976**, vol. 3; b) P. J. Hay, W. R. Wadt, *J. Chem. Phys.* **1985**, *82*, 270–283.
[22] a) S. I. Gorelsky, *AOMix Progam, Revision 5.95 and AOMix-CDA, Revision 1.7*, http://www.sg-chem.net/; b) S. I. Gorelsky, A. B. P. Lever, *J. Organomet. Chem.* **2001**, *635*, 187–196.
[23] P. Flükiger, H. P. Lüthi, S. Portman, J. Weber, *MOLEKEL Version 4.3*, Swiss Center for Scientific Computing, Manno, Switzerland, **2000**–**2002**.

Received: July 18, 2006
Published Online: November 6, 2006

 © 2007 Wiley-VCH Verlag GmbH & Co. KGaA, Weinheim 

DOI: 10.1002/ejic.200600677

# Pentacarbonyl[2-(2′-pyridyl)quinoxaline-κ$N^4$]tungsten: A Combined Study of Its Conformational and Electronic Structure Based on Experimental and DFT-TDDFT Data

**Christodoulos Makedonas,[a] Irene Veroni,[a] and Christiana A. Mitsopoulou*[a]**

**Keywords:** Pentacarbonyl complexes / 2-(2-Pyridyl)quinoxaline / Tungsten / DFT calculations / TD-DFT calculations / Pi stacking

Photolysis of $W(CO)_6$ in the presence of 2-(2′-pyridyl)quinoxaline (pq) results in the formation of $W(CO)_4$(pq) via an intermediate product $W(CO)_5(N^4$-pq) (**1**). In **1** the pq ligand that has three nitrogen atoms – two pyridine and one quinoxaline type – is coordinated in a monodentate fashion. This is the first example, where the pq ligand is coordinated in a monodentate fashion and especially from a quinoxaline nitrogen atom ($N^4$). Complex **1** has been fully characterized and its crystal structure has unambiguously demonstrated that pq is preferably coordinated through $N^4$ rather than the $N^1$ and $N^{1'}$ atoms, while its packing is governed by π–π interactions and hydrogen bonds. The almost perfect "face-to-face" alignment of the condensed quinoxaline rings is attributed to the existence of the electron-withdrawing groups, namely $W(CO)_5$ and the pyridine ring. The aforementioned preference for $N^4$ atoms has been elucidated by thermodynamic means and explained in terms of the frontier orbitals. Time-dependent density functional theory has been used for the investigation of the excited states of **1**. The calculated vertical excitation energies are consistent with the experimental data showing that the low-lying solvatochromic band of **1** in the UV/Vis spectra is best described by the term MLCT/LLCT.

(© Wiley-VCH Verlag GmbH & Co. KGaA, 69451 Weinheim, Germany, 2007)

## 1. Introduction

Both the photochemical substitution of complexes such as $M(CO)_6$ and the organometallic complexes between transition-metal carbonyls and N-containing heterocycles continues to be the subject of intense interest.[1] The photochemical and electronic properties, along with the potential of these complexes in industrial applications, have led to many studies for use as photosensitizers, catalysts, and conducting coordinating polymers.[2–4] Photolysis of the group VI metal hexacarbonyl compounds in the presence of potentially bidentate diimine-type ligands N–N [2,2′-bipyridines, 1,4-diazabutadienes, or 2-(2′-pyridyl)quinoxaline] ultimately results in the formation of the respective $M(CO)_4$(N–N) chelate complexes.[1,5–6] This process reportedly involves the initial photosubstitution of one CO group, leading to an intermediate product of type $M(CO)_5$(N–N) in which the N–N ligand is coordinated in a monodentate fashion. The importance of asymmetrical transition-metal complexes, namely $M(CO)_5L$ where M = Cr, W and L = π-conjugated ligand, in the field of second-order NLO materials is now very well documented.[7]

Among the aforementioned bidentate N–N ligands our attention has been attracted by 2-(2′-pyridyl)quinoxaline (pq), which combines the bridging properties of quinoxalines along with the chelating efficiency of 2,2′-bipyridine. The former can be explained by the discovery that polypyridyl ligands, which own low-lying LUMOs and contain more than one nucleophilic center, play an important role in the synthesis of metallo–organic compounds with various applications in material chemistry. Besides, the quinoxaline structure is widely recognized as an important component of a great number of natural compounds with applications in areas as diverse as antibacterial, antiviral, anticancer, antifungal, antihelmintic, insecticidal agents,[8] electron-withdrawing groups in p-conjugated polymer chemistry,[9] fluorescent dyes,[10,11] and optical-based sensors for anions in organic media.[12] While the vast majority of these materials are based on organic molecules there has been a growing interest in developing metal–containing compounds over the last few years. The central motivation behind this effort has been to combine the unique properties of transition-metal complexes (e.g. color, redox behavior) with those associated with the existence of the two nitrogen atoms in suitable bridging *para* positions, which can easily be functionalized allowing one to tailor their properties.[13]

[a] Inorganic Chemistry Laboratory, Department of Chemistry, National and Kapodistrian University of Athens, Panepistimiopolis, Zografou 15771, Greece
Fax: +30-210-8322828
E-mail: cmitsop@chem.uoa.gr

 WILEY InterScience DISCOVER SOMETHING GREAT © 2007 Wiley-VCH Verlag GmbH & Co. KGaA, Weinheim 

Up until now, a plethora of metal complexes have been reported where pq is bicoordinated through the $N^1$ and $N^{1'}$ atoms,[5,6,14,15] but there has never been any undoubted proof for coordination of a metal at a $N^4$ atom. In spite of this semi-empirical calculations have shown that the HOMO of pq is mostly a "lone" electron pair on $N^1$ and $N^4$,[16] thus these two nitrogen atoms should share almost the same propensity for coordination. The thermodynamic stability that offers the chelation of pq after its coordination at $N^1$ should be the major reason for the above experimental observation.

During the photolysis of $W(CO)_6$ in THF in the presence of pq we surprisingly discovered that the photogenarated ring closure reaction of $W(CO)_4$(pq) goes through $W(CO)_5$($N^4$-pq) (**1**);[17] the latter has been isolated and fully characterized. In order to explain the preference of the $N^4$ atom over the $N^1$ and $N^{1'}$ atom upon ligation (Scheme 1), and explain the electronic spectra of **1**, we have undertaken a DFT and TDDFT study and combined the data with the experimental results.

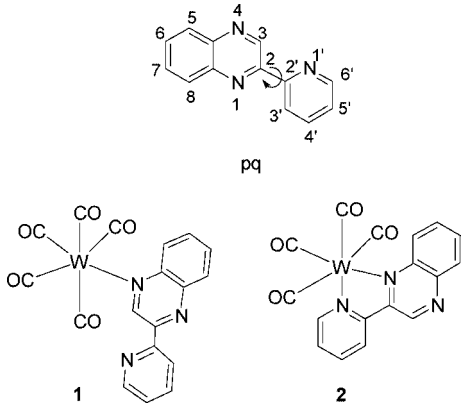


Scheme 1.

The main part of this report is organized as follows: in Section 2.1 a discussion of experimental data such as 2D NMR spectra indicating the coordinating nitrogen atom and crystal packing of **1** on the basis of the developed intermolecular forces is given. The theoretical results are critically analyzed and compared with experimental data in Section 2.2. This section is subdivided into two subsections. In the first subsection the ground state of **1** along with the structure of the other two possible isomers are discussed in terms of DFT data compared with the experimental structures. In the second part the predominant conformation structure is given in thermodynamic terms. Finally, in the last section, the UV/Vis spectrum is fully characterized by TD-DFT means.

## 2. Results and Discussion

### 2.1. NMR Spectroscopic Data and Crystal Packing

The complex $W(CO)_5$(pq) (**1**) is an intermediate product from the photolysis of $W(CO)_6$ in THF in the presence of pq leading to the photogenerated ring closure reaction $W(CO)_4$(pq). Surprisingly, the coordinated nitrogen atom is $N^4$ and not the usually referenced $N^1$. Of course, **1** is not the only intermediate product but it is the main one (yield 70%). The $W(CO)_5$($N^4$-pq) (**1**) complex was isolated photochemically by a two-stage reaction (Scheme 2).

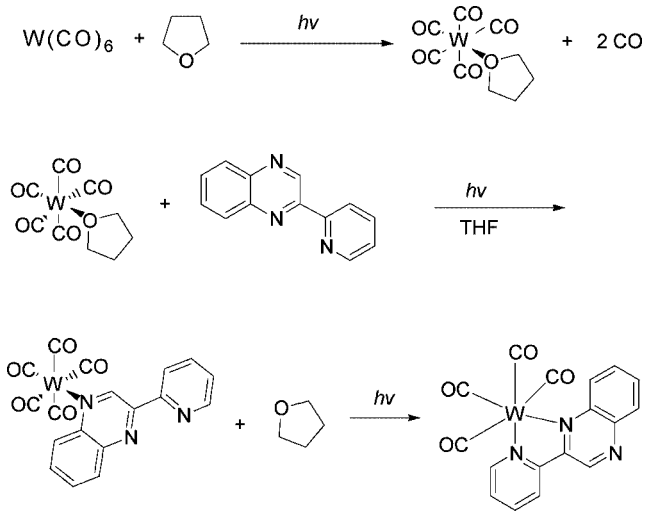


Scheme 2.

On the basis of a method by Strohmeier and Müller[18] the photolysis of $W(CO)_6$ in THF yields the mononuclear THF adduct $W(CO)_5$(THF), which on further photochemical reaction with an excess of pq after a short irradiation time (about 10 min) gives **1** as an orange solid in good yield; further irradiation yields **2**.

A first indication of the coordination site is provided by both $^1$H NMR and HMBC $^1$H-$^{15}$N NMR spectra of **1**. The HMBC $^1$H-$^{15}$N NMR spectrum of pq in $CDCl_3$ (Figure 1) was considered as a first probe for the partial charges on the nitrogen atoms of the free ligand that could be extrapolated so as to provide us with the necessary evidences for the coordinated nitrogen atom in **1**. The aforementioned spectrum contains three independent *J* networks, where each nitrogen atom couples across two or three bonds with the adjacent protons. The nitrogen atoms are of the pyridine type, that is, they provide only one 2p electron to the involved π-electron system and they have their lone pairs in the plane of the conjugated system, in this way keeping their basicity. This is illustrated by the positions of the $^{15}$N NMR chemical shifts that are characteristic of $sp^2$ hybridized nitrogen atoms.[19] Unfortunately, $N^1$ and $N^4$ cannot be assigned unequivocally as the long-range connectivity of both $N^1$ and $N^4$ with $H^3$ and correspondingly with $H^8$ and $H^5$ are not particularly enlightening since $H^8$ and $H^5$ are NMR equivalent. Nevertheless, it has been reported that the chemical shift of $N^4$ is relatively insensitive to the different heteroaromatic substituents at the 2-position of the quinoxaline ring,[20] while the $^{15}$N NMR chemical shift of $N^1$ is found to be strongly dependent on these substituents. On this basis, the most downfield shifted nitrogen atom is $N^4$ ($\delta$ = 331 ppm), followed by $N^1$ ($\delta$ = 319 ppm) and $N^{1'}$ ($\delta$ = 311 ppm), this is in accordance with the semi-empirically calculated partial charges on the nitrogen atom

 © 2007 Wiley-VCH Verlag GmbH & Co. KGaA, Weinheim 

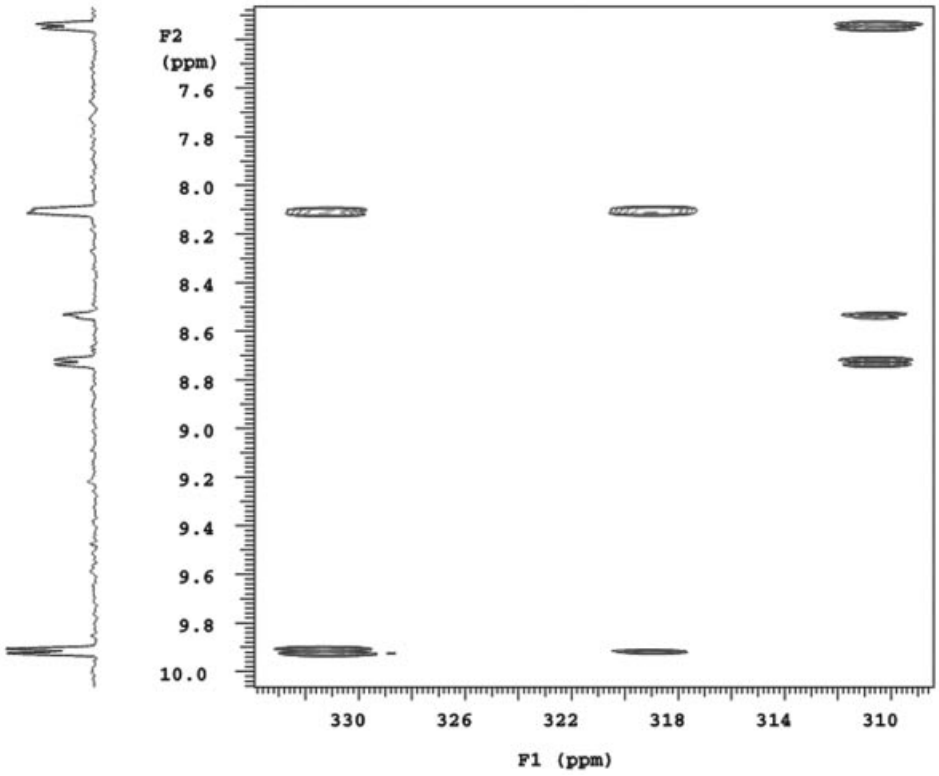


Figure 1. HMBC $^{1}H$-$^{15}N$ NMR spectra of **1**.

of pq.[19] The planarity of pq should establish an inter-annular conjugation between its quinoxaline and pyridyl moiety that allows the π-deficient quinoxaline moiety to accept π electron density from the pyridyl ring. This is illustrated by the downfield shift (deshielding) of the pyridine N in pq, in comparison to the $^{15}N$ NMR chemical shift in the (2-methyl)pyridine molecule.[19]

The ligation of pq to the $W(CO)_5$ moiety through the $N^4$ atom has been proven unambiguously by the elucidation of its structure by single-crystal X-ray diffraction methods.[17] Complex **1** crystallizes in the $P2_1/c$ space group. It is stacked in two different columns in a V-type assembly. In Figure 2, the crystal packing of the complex is depicted along the a axis. In each column the individual molecules are stacked in a "face-to-face" arrangement creating couples (Figure 3). The intermolecular distance of the N-ligand atoms (or planes) involved in this couple is 3.37 Å, suggesting π stacking with strong π–π interactions. Moreover, an almost perfect "face-to-face" alignment of the quinoxaline rings is observed, which is extremely rare.[21] This might be

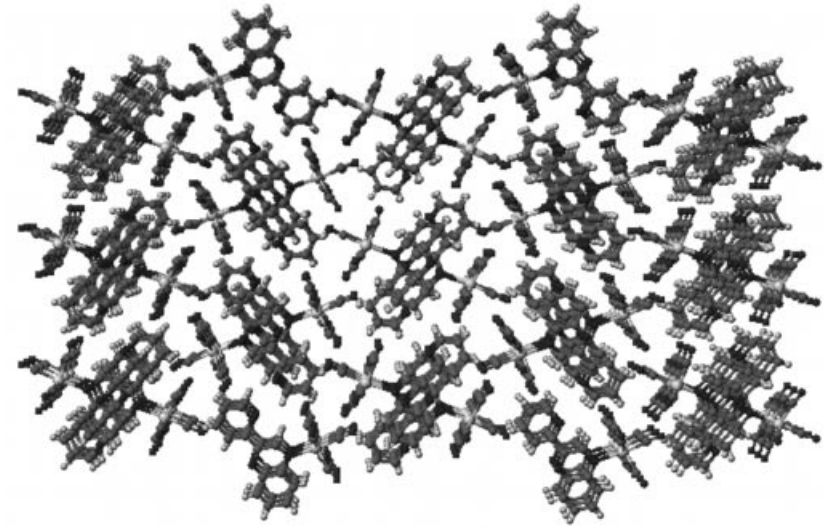

Figure 2. Crystal packing of **1** as it is viewed along the a axis.

 © 2007 Wiley-VCH Verlag GmbH & Co. KGaA, Weinheim 

because of the existence of the two electron-withdrawing groups present on the same quinoxaline ring, namely the $W(CO)_5$ fragment and the pyridine moiety, which cause a decrease in π-electron density on the parent ring and consequently the π–π repulsion. The aforementioned observations are of fundamental importance for the further development of inorganic supramolecular chemistry and the tuning and prediction of crystal structures. Moreover, an interesting feature observed in the crystal structure of **1** is the existence of two internal hydrogen bonds $H^{3'}$–$N^2$ [2.548 (0.060) Å and C–H···N = 101.59 (4.10)°] and $H^3$–$N^1$ [2.453 (0.54) Å and C–H···N = 103.37 (4.90)°] and two intermolecular hydrogen bonds between H atoms of the pq ligand and CO groups [$H^5$–$O_{tr}$ 2.382(0.054) Å and 132.12 (4.63)° and $H^8$–$O^4$ 2.514 (0.060) Å and 164.01 (5.18)°], which probably reflects their stacking.

Figure 3. π–π Interactions in complex **1**. A "face-to-face" alignment of quinoxaline rings that overlap with their nitrogen–carbon atoms.

### 2.2. Ground-State Structure

2-(2′-Pyridyl)quinoxaline with its three nitrogen atoms can adopt three different conformations when acting as a monodentate ligand to the $W(CO)_5$ fragment. The first conformation arises from ligation through the pyridine $N^1$, giving structure **N1**, the second arises from ligation through the $N^{1'}$ atom of the first quinoxaline, giving structure **N2**, whereas the third conformation leads to complex **1**, through ligation to **N4**, as pictorially depicted in Figure 4. During the photolytic procedure the parent compound $W(CO)_6$ reacts with the ligand in order to first afford the title complex. In the following sections, its ground-state and electronic behavior are studied by means of DFT calculations.

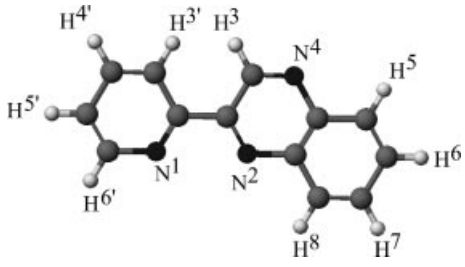


Figure 4. The three different coordination sites of the 2-(2′-pyridyl)quinoxaline ligand along with the numbering system of the H atoms.

#### 2.2.1. Calculation of the Ground-State Structure

In $W(CO)_5$(pq) the tungsten has a distorted octahedral coordination sphere, as is expected, with the diimine ligand to adopt an *anti* conformation. DFT calculations were performed on complex **1** in the gas phase starting from crystallographic data. The main structural features that were taken from both the crystal structure **1** and the calculation **N4** are summarized in Table 1. In the same table structural characteristics of the other two possible isomers are also depicted (vide infra). All theoretical structures under study are viewed in a manner such that the coordinated nitrogen ligand (e.g. the quinoxaline in **N4**) bisects the $W(CO)_4$ fragment, while the noncoordinating nitrogen (e.g. the pyridine in **N4**) lies at the back side of the molecule. In this scheme the numbering of the equatorial carbonyls starts from the front right site of the molecule and continues clockwise. According to data presented in Table 1 the overall agreement between the theoretical (**N4**) and experimental (**1**) structures is generally satisfactory. Nevertheless, the geometrical features (distances and angles) associated with carbonyls 1 and 2 do not follow the general trend. The difference in W–C–O angles, along with the followed numbering scheme, is depicted in Figure 5.

Optimization of the molecule has been performed without any symmetry constraints. This, along with the successful application of the same combination of functional/core potential/basis set in the completely relevant case of the $W(CO)_4$(pq) complex[6] where the 2-(2′-pyridyl)quinoxaline acts as a bidentate ligand through $N^1$ and $N^2$, lead us to hypothesize that electronic effects on their own are not enough to cause carbonyls 1 and 2 to bend by at least 5° more than that of the carbonyls 3 and 4. In order to clarify this difference an inspection of the crystal structure of **1** is essential.

As we have already mentioned the packing of **1** in the solid state is governed by π–π interactions and hydrogen bonding. In Table 2 all the observed C–H···O short contacts are depicted. The entries printed in **bold** refer to the hydrogen bonds that we already mentioned (vide supra), two more entries shown printed in regular font type represent strong interactions, while six short contacts are also given in *italics*.

Both π-stacking and hydrogen bonding stabilize couples of molecules within the same column. Moreover, hydrogen bonds determine the final conformation of **1** within the $P2_1/c$ space group. We believe that the existence of these hydrogen bonds reflects the aforementioned structural differences between **1** and **N4**. In the case where the bonding scheme of $CO^1$ was exactly the same as that of $CO^4$ (88.6° for the N–W–C angle and 176.9° for the W–C–O angle) a decrease in the $CO^1$–$H^{4'}$ interaction (from 2.63 Å and 130.4° to 2.16 Å and 118.8°) and consequently the strengthening of the second short contact ($CO^1$–$H^{3'}$, from 3.03 Å and 130.4° to 2.46 Å and 106.2°) will occur. As a result the parent molecule will take a new position closest to the neighboring one and this could destabilize the packing. Taking into consideration the fact that, for electronic

 © 2007 Wiley-VCH Verlag GmbH & Co. KGaA, Weinheim 

Table 1. A comparison of the calculated selected bond lengths [Å] and angles [°] for the three different structural isomers with the experimental values **1** from the X-ray analysis.

| C.I. | $W(CO)_5(pq)$ | | | |
|---|---|---|---|---|
| **M** | **1** | **N4** | **N1** | **N2** |
| W–N | 2.311(4) | 2.321 | 2.360 | 2.408 |
| $W–C_{trans}$ | 1.959(5) | 1.987 | 1.984 | 1.977 |
| W–C1 | 2.049(5) | 2.037 | 2.041 | 2.037 |
| W–C2 | 2.048(5) | 2.037 | 2.032 | 2.033 |
| W–C3 | 2.047(5) | 2.040 | 2.038 | 2.037 |
| W–C4 | 2.043(5) | 2.040 | 2.041 | 2.056 |
| $C–O_{trans}$ | 1.156(6) | 1.188 | 1.188 | 1.189 |
| C–O1 | 1.138(6) | 1.183 | 1.182 | 1.185 |
| C–O2 | 1.146(6) | 1.183 | 1.186 | 1.184 |
| C–O3 | 1.136(6) | 1.182 | 1.182 | 1.184 |
| C–O4 | 1.140(6) | 1.182 | 1.183 | 1.179 |
| $N–W–C_{tr}$ | 175.62(19) | 177.5 | 176.1 | 176.6 |
| N–W–C1 | 98.90(17) | 93.5 | 85.9 | 95.5 |
| N–W–C2 | 96.98(17) | 93.5 | 92.2 | 88.5 |
| N–W–C3 | 89.72(18) | 89.4 | 93.5 | 93.2 |
| N–W–C4 | 88.61(17) | 89.4 | 96.0 | 95.6 |
| $W–C–O_{tr}$ | 178.6(5) | 180.0 | 179.8 | 179.5 |
| W–C–O1 | 171.3(4) | 176.9 | 179.0 | 174.3 |
| W–C–O2 | 172.3(5) | 176.9 | 175.7 | 176.9 |
| W–C–O3 | 176.3(5) | 177.7 | 177.9 | 173.2 |
| W–C–O4 | 176.9(4) | 177.7 | 173.8 | 171.7 |

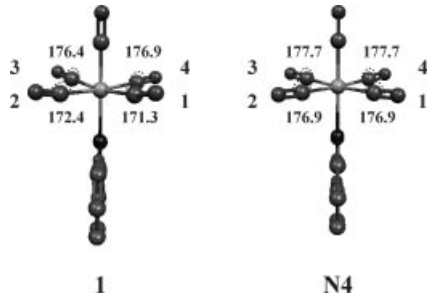


Figure 5. Differences in W–C–O angles between the theoretical (**N4**) and experimental (**1**) data.

Table 2. C–H···O short contacts in the crystal. *d* is the O···H distance in Å, $\varphi$ is the C–H···O angle in °, X is the hydrogen nucleus and P the molecular column where it belongs to; S the same, N neighboring, V neighboring with a V conformation.

| CO | *d* | $\varphi$ | X | P |
|---|---|---|---|---|
| ***trans*** | **2.371** | **132.4** | **H5** | **V** |
| | *2.837* | *115.2* | *H6* | *V* |
| **1** | 2.626 | 130.4 | H4′ | S |
| | *3.029* | *112.1* | *H3′* | *S* |
| **2** | *2.774* | *148.1* | *H3′* | *S* |
| **3** | *2.882* | *150.7* | *H6* | *N* |
| | *3.036* | *122.5* | *H8* | *S* |
| | *3.172* | *122.2* | *H7* | *S* |
| **4** | **2.517** | **164.1** | **H8** | **S** |
| | 2.591 | 131.0 | H5′ | N |

reasons, carbonyl coordination must be equal in couples (1–2 and 3–4) we conclude that the difference in binding angles arises in order for the stacking to be energetically more favorable.

On the basis of both experimental and theoretical results there are some points that certainly deserve to be further analyzed. Firstly, as it has already been mentioned (vide supra), tungsten has a distorted octahedral coordination sphere, and both the bonds W–N and $W–C_{tr}$ are almost equal to the relative bond lengths W–N(qn) and W–C11 (*trans* to the coordinated nitrogen atom) in $W(CO)_4(pq)$.[6] This implies a similar bonding behavior of the quinoxaline part of the ligand whatever the coordinated nitrogen atom. The induced *trans* influence from the N-donor is postulated by the W–C and C–O distances on the equatiorial plane. The $W–C_{tr}$ bond length is shorter than the relative distances in the equatorial plane, whereas the $C–O_{tr}$ bond is elongated. Secondly, the characteristic bending of carbonyls observed in several other carbonyl compounds is also present here.

To further discuss the aforementioned trend the orbital energies along with the contributions from the different ligands and the metal are given in Table 3. According to data presented in Table 3 the three highest occupied molecular orbitals of **N4** are close in energy and predominantly consist of metal d orbitals [$d_{xz}$ in HOMO, $d_{yz}$ in HOMO–1 and $d_{z^2}$ (as a linear combination with $d_{x^2-y^2}$) in HOMO–2] with a significant contribution from the carbonyl π* orbitals.

These three orbitals are related to the $t_{2g}$ orbital set in $W(CO)_6$[6,22] regarding their π*-back-bonding character. They are mainly dominated by π-type W–C bonding and C–O antibonding interactions and are indicative of the W→CO π* back-bonding. In the HOMO–2 these interactions are mainly localized on the equatorial plane, while in HOMO and HOMO–1 the contribution of the axial carbonyl group is ca. 12.8%. On the other hand, the orbitals HOMO–3 to HOMO–5 are localized on the quinoxaline moiety of the organic ligand; more precisely, HOMO–3 is

 © 2007 Wiley-VCH Verlag GmbH & Co. KGaA, Weinheim 

Table 3. Selected orbital energies and orbital compositions for the three conformations **N1**, **N2**, and **N4**. The HOMO and LUMO are shown in bold.

| MO | *E* [eV] | W | $CO^1$ | $CO^2$ | $CO^3$ | $CO^4$ | $CO_{tr}$ | qn | py |
|---|---|---|---|---|---|---|---|---|---|
| **N1** | | | | | | | | | |
| 101 | –1.78 | 8.6 | 30.1 | 12.7 | 29.5 | 12.9 | 0.4 | 0.7 | 5.1 |
| 100 | –1.93 | 1.5 | 1.3 | 5.5 | 1.8 | 4.7 | 0.2 | 30.4 | 54.7 |
| 99 | –2.14 | 9.1 | 14.3 | 6.5 | 10.1 | 7.8 | 0.5 | 23.5 | 28.2 |
| 98 | –2.44 | 12.1 | 9.7 | 11.7 | 12.4 | 9.2 | –0.3 | 8.1 | 37.2 |
| **97** | **–2.91** | **1.6** | **0.6** | **1.4** | **0.1** | **1.4** | **0.9** | **67.4** | **26.6** |
| **96** | **–6.22** | **60.8** | **6.5** | **4.8** | **6.8** | **4.4** | **13.0** | **2.1** | **1.5** |
| 95 | –6.25 | 60.3 | 3.8 | 8.3 | 4.5 | 7.5 | 12.6 | 0.4 | 2.6 |
| 94 | –6.66 | 60.5 | 9.6 | 9.9 | 9.3 | 9.2 | 0.0 | 1.1 | 0.4 |
| 93 | –7.19 | 0.3 | 0.0 | 0.0 | 0.1 | 0.1 | 0.1 | 97.0 | 2.3 |
| 92 | –7.26 | 0.1 | 0.0 | 0.0 | 0.0 | 0.1 | 0.0 | 97.1 | 2.7 |
| 91 | –7.72 | 1.5 | 0.1 | 0.1 | 0.3 | 0.9 | 0.1 | 82.7 | 14.2 |
| **N2** | | | | | | | | | |
| 101 | –1.65 | 4.5 | 14.9 | 2.2 | 14.8 | 2.2 | 0.8 | 15.1 | 45.6 |
| 100 | –1.78 | 6.9 | 23.3 | 18.1 | 18.5 | 18.1 | 0.0 | 10.6 | 4.4 |
| 99 | –2.03 | 6.1 | 1.8 | 12.8 | 1.4 | 11.8 | –0.6 | 38.6 | 28.1 |
| 98 | –2.23 | 13.8 | 20.0 | 8.4 | 22.0 | 7.2 | –0.9 | 11.8 | 17.7 |
| **97** | **–3.30** | **1.0** | **0.4** | **0.3** | **0.1** | **0.4** | **1.0** | **89.9** | **6.9** |
| **96** | **–6.09** | **61.1** | **3.1** | **8.5** | **3.8** | **6.8** | **13.9** | **1.0** | **2.0** |
| 95 | –6.21 | 59.1 | 9.7 | 3.2 | 8.7 | 2.9 | 12.4 | 3.6 | 0.3 |
| 94 | –6.53 | 60.7 | 9.7 | 10.2 | 9.6 | 8.2 | 0.1 | 0.6 | 1.0 |
| 93 | –7.61 | 0.5 | 0.1 | 0.1 | 0.0 | 1.0 | 0.1 | 55.7 | 42.5 |
| 92 | –7.68 | 1.8 | 0.1 | 0.1 | 0.1 | 2.0 | 0.2 | 49.4 | 46.3 |
| 91 | –7.85 | 0.6 | 0.1 | 0.1 | 0.4 | 0.1 | 0.2 | 60.1 | 38.7 |
| **N4** | | | | | | | | | |
| 101 | –1.73 | 11.1 | 21.2 | 21.3 | 22.2 | 22.3 | 1.3 | 0.6 | 0.0 |
| 100 | –1.80 | 9.0 | 22.9 | 22.9 | 21.1 | 21.1 | 0.5 | 2.1 | 0.5 |
| 99 | –2.31 | 20.8 | 19.6 | 19.6 | 20.3 | 20.3 | –1.5 | 1.0 | 0.1 |
| 98 | –2.33 | 0.6 | 0.8 | 0.8 | 1.8 | 1.8 | 0.1 | 61.0 | 33.1 |
| **97** | **–3.34** | **0.9** | **0.4** | **0.4** | **0.3** | **0.3** | **1.1** | **86.7** | **10.0** |
| **96** | **–6.24** | **59.3** | **5.6** | **6.1** | **5.2** | **5.3** | **12.4** | **5.7** | **0.0** |
| 95 | –6.25 | 63.0 | 5.8 | 5.7 | 5.8 | 5.7 | 13.2 | 0.8 | 0.1 |
| 94 | –6.67 | 61.1 | 9.8 | 9.8 | 9.5 | 9.5 | 0.0 | 0.4 | 0.1 |
| 93 | –7.37 | 0.6 | 0.0 | 0.0 | 0.0 | 0.0 | 0.1 | 57.5 | 41.6 |
| 92 | –7.55 | 0.8 | 0.1 | 0.1 | 0.0 | 0.0 | 0.2 | 19.0 | 79.8 |
| 91 | –7.86 | 0.7 | 0.0 | 0.0 | 0.2 | 0.2 | 0.1 | 87.8 | 11.0 |

delocalized over the three rings of the ligand, whereas HOMO–4 and HOMO–5 are localized mainly on the pyridine and quinoxaline moiety, respectively. The LUMO and LUMO+1 are dominated by quinoxaline π* orbitals of the ligand, whereas LUMO+2 to LUMO+4, also of π* character, arise mainly from the equatorial carbonyls. The HOMO and LUMO of **N4** are depicted in Figure 6.

An unoccupied orbital with a predominant d(σ*) character was not found among the spectroscopically important orbitals. In cases where this sort of contribution exists it corresponds to only a part of a highly delocalized orbital. Thus, low lying LF states, contradictory to the arguments of the traditional ligand field theory, are not expected. This is consistent with previous work done by Vlček et al.[23–27]

### *2.2.2. Conformational Analysis*

Complex **1** can adopt three conformations in space as has already been mentioned. These conformations are depicted in Figure 7 and their structural characteristics are presented in Table 1.

The plane formed by the binding organic ring lies in an *anti* conformation to the $W(CO)_4$ fragment in **N4** with a $C^3$–N–W–$C_{(CO^3)}$ dihedral angle of 45.3°. This is more or less the same case for **N2** with a dihedral angle of 34.4°. On the contrary, in **N1** a *gauche* conformation is adopted, since the dihedral angle is 83.0°. The aforementioned difference for **N1** has a great impact on the structure, since the orthogonality holds only for the first coordination sphere around the central metal. Thus, the pyridine ligand bends away from the $CO^3$ moeity and the observed $C^{6'}$–N–W–$C_{tr}$ dihedral angle is 45.7°. In other words, the structure is folded. But the most important structural difference between **N4** and **N1** and **N2** is that all the three aromatic rings of the ligand adopt a coplanar conformation in **N4**, but not in **N1** and **N2**. More specifically, a $N^1$–$C^{2'}$–$C^2$–$N^2$ dihedral angle of 127.5° and 64.4° is observed in **N1** and **N2**, respectively, in accordance with the one observed in the free ligand. This twisting around the single bond $C^2$–$C^{2'}$ is necessary for the system, otherwise if a coplanar arrangement was adopted there would be strong intramolecular interactions between

 © 2007 Wiley-VCH Verlag GmbH & Co. KGaA, Weinheim 

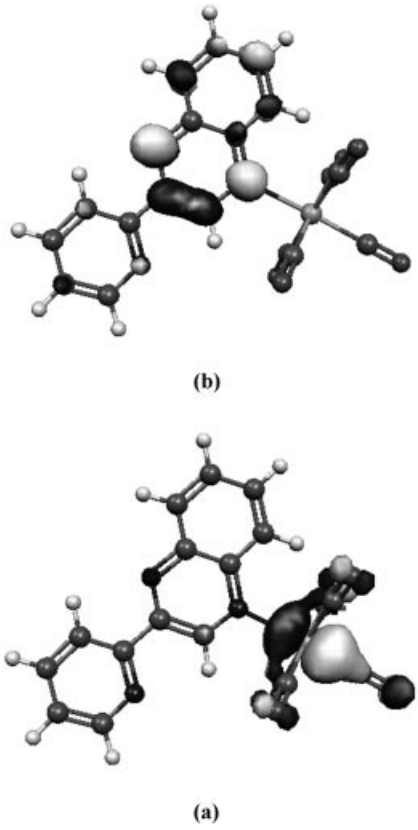


Figure 6. 0.05 a.u. contour plots of the HOMO (a) and LUMO (b) of complex **N4**.

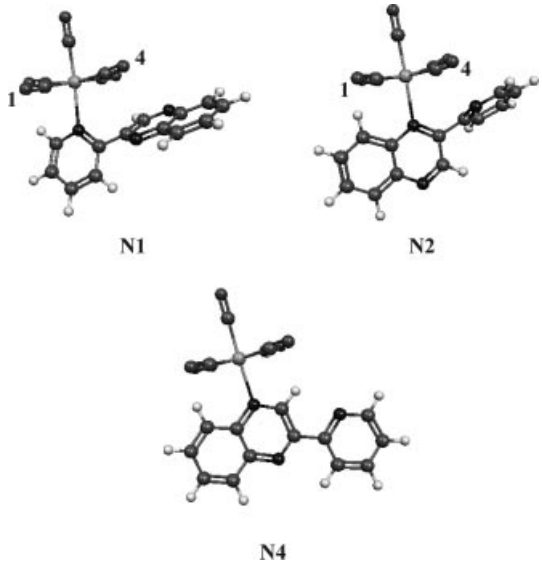


Figure 7. The three different conformations of the $W(CO)_4$(pq) complex. In the case of **N1** and **N2** the numbering of the carbonyls in front is also presented.

the noncoordinating organic ring and carbonyls 3 and 4. The W–N–C angles, as presented in Table 1, are indicative of these interactions. Thus, the values of the W–N–$C_{(CO^3)}$ [and W–N–$C_{(CO^4)}$] are larger than the relative values for W–N–$C_{(CO^1)}$ [and W–N–$C_{(CO^2)}$].

During the photolytic route to the $W(CO)_4$pq chelate ring closure, complex **1**, having the conformation **N4**, is the main intermediate product. In order to better understand this result, we performed a conformational analysis of the three isomers under study. Our results are summarized in Figure 8.

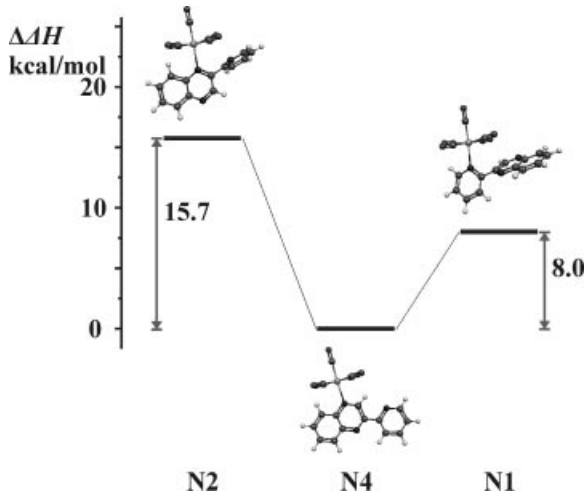


Figure 8. Energy differences among the conformations under study.

According to data presented in Figure 8, we concluded that the isomer **N4** has the most stable structure among the three conformational isomers. It is more stable by 8.0 kcal/mol than **N1** and by 15.7 kcal/mol than **N2**. The latter seems to be the less favorable isomer to be formed in the reaction process. The calculated difference in the stability of the isomers is attributed to electronic and steric repulsions between carbonyls 3 and 4 and the noncoordinating organic ring. In Figure 9, the three isomers are depicted using the space-filling model. The destabilization of the conformations **N1** and **N2** may attribute to the intramolecular $O_{(CO^4)}$–N interaction; the latter is not present in **N4**. More specifically, the $O_{(CO^4)}$–$N^1$ distance is 3.04 Å in **N2**, while in **N1** the $O_{(CO^4)}$–N2 and $O_{(CO^4)}$–$N^4$ distances are 3.38 Å and 3.53 Å, respectively.

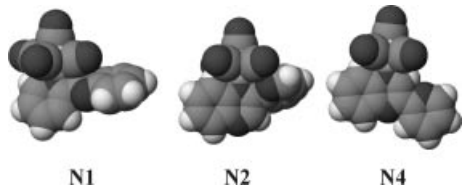


Figure 9. The structure of the three isomers with the space-filling model.

From an orbital point of view (Table 3 and Figure 10), we observe that the HOMO to HOMO–2, having a significant $d_\pi$-metal character, are destabilized in **N2** as compared with **N1** and **N4**. Moreover, an orbital inversion occurs. The HOMO of **N4**, mainly of a $d_{xz}/\pi^*$(CO) character of **N4** becomes HOMO–1 in the other two isomers. This inversion

 © 2007 Wiley-VCH Verlag GmbH & Co. KGaA, Weinheim 

happens since the HOMO–1 in **N4**, which contains a large contribution from the metal $d_{yz}$ orbital, is destabilized from the presence of the twisted organic ring and becomes HOMO in **N1** and **N2**. Taking into consideration that tungsten-centered $d_{xz}$ and $d_{xy}$ orbitals in **1** are nearly degenerate the geometrical changes predicted in conformations **N1** to **N4** can cause intercrossing of the HOMO and HOMO–1. A nonextensive delocalization of electron cloud on the carbonyls in the HOMO and HOMO–1 has its origin in the presence of the twisted rings in **N1** and **N2** conformations. Thus, in **N4** the electron cloud is equipartitioned on the equatorial carbonyls; the situation is different in the case of the isomers **N1** and **N2**, with the asymmetry being more obvious in **N2**. This is another reason for the increase in the HOMO energy in the latter case. Moreover, in **N4** the diimine accepts more electron density from the $W(CO)_5$ core, through back-donation, as compared with **N1** and **N2**. This is postulated by the contributions of the coordinated organic ring to the HOMO in **N4** and to the HOMO–1 in the other two isomers. Finally, there is a substantial difference in the LUMO of the three isomers. In both **N2** and **N4** the LUMO is mainly localized on the coordinating ring of the ligand. On the contrary, in **N1** the contribution of the orbitals of the noncoordinated quinoxaline moiety to the LUMO is double that of the contribution of the coordinated pyridine ring. This reflects a significant increase in the energy of the **N1** LUMO, which becomes less stable. The HOMO and LUMO of conformations **N1** and **N2** are depicted in Figure 11 and Figure 12, respectively.

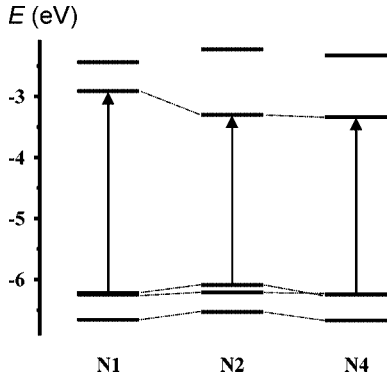


Figure 10. Energy diagram of the frontier orbitals of the three conformations under study.

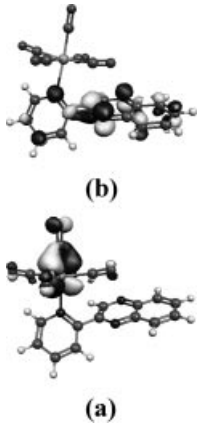


Figure 11. 0.05 a.u. contour plots of the HOMO (a) and LUMO (b) of complex **N1**.

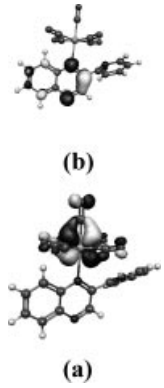


Figure 12. 0.05 a.u. contour plots of the HOMO (a) and LUMO (b) of complex **N2**.

### 2.3. Electronic Transitions and Excited States

The electronic absorption spectra of **1** in two solvents are indicated in Figure 13 and the corresponding data are included in Table 4. As a whole the spectra consist of three main bands: a broad and structured high-energy band extending from 309 to 380 nm, a shoulder at 398 nm, and a broad low-energy band. The change of the solvent mainly affects the low-energy band that is blue-shifted as the polarity of the solvent increases (negative solvatochromism).

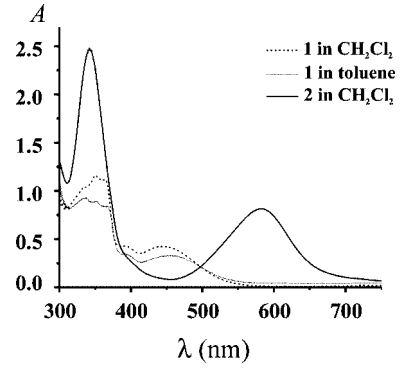


Figure 13. UV/Vis spectra of **1** and **2** in toluene and dichloromethane.

The shape along with the position and the solvent dependence of the low-energy band denote its (W)$d_\pi \rightarrow \pi^*$(L) charge-transfer (MLCT) character, which agrees with previous interpretations of many mononuclear metal pentacarbonyl complexes.[28] In order to investigate the lowest-lying singlet states of **1**, TDDFT calculations have been performed. Selected calculated low-lying singlet states along

 © 2007 Wiley-VCH Verlag GmbH & Co. KGaA, Weinheim 

Table 4. Position of the low-energy MLCT band of **1** in various solvents.

| Solvents | $\lambda_{max}$ [nm] |
|---|---|
| $CCl_4$ | 483 |
| $CH_2Cl_2$ | 446 |
| $CHCl_3$ | 455 |
| $(CH_3CH_2)_2O$ | 449 |
| $C_6H_{14}$ | 486 |
| Toluene | 459 |
| THF | 424 |

with their vertical excitation energies and oscillator strengths are displayed in Table 5. The transitions under study fulfill the criteria posed by Casida.[29]

The lowest in energy, highly solvatochromic transition of **1** can be assigned predominantly to the HOMO→LUMO ($n \rightarrow \pi^*$) transition since the contributions from several other transitions to the final state are minor. It is observed at 483 nm in $CCl_4$ and 455 nm in $CHCl_3$ and has W/CO → pq character. The fact that ca. 40% of the HOMO electron density is localized on parts of the molecule other than the metal (Table 3) contradicts the widely accepted MLCT notation for this transition; it could be characterized as an oversimplification. Therefore, we adopted the term MLCT/LLCT, suggested by Vlček and coworkers,[30] and employed it for the characterization of excited states of the relevant compound $W(CO)_4$(pq).[6] In the literature two other relative notations exist and can also be employed in our case. These are metal-ligand-to-ligand charge transfers (MLLCT)[31] and mixed-metal-ligand-to-ligand charge transfers (MMLL′CT).[32] The aforementioned transition arises from orbitals in total accordance with the case of the complex $W(CO)_5$(pyCN) described by Vlček and coworkers.[23] The shoulder of the main band on the high energy side, computed around 405 nm, is attributed to a superposition of several transitions with close energies and mainly to two MLCT($CO_{eq}$) transitions of W/CO→$CO_{eq}$ character. Finally, the higher-intensity broad band centered at 351 nm presenting a triple splitting and computed around 344 nm is mainly attributed to a double π–π*(pq) transition of the HOMO–3/HOMO–5 → LUMO character and a transition of MLCT/LLCT character. The MO picture given here is totally inconsistent with the traditional view that contains low-lying LF transitions. All calculated valence orbitals that contain metal contribution are highly delocalized. Thus no orbital of net $d_{\sigma^*}$ character has been found with relatively low energy. So transitions with a predominant d–d charac-

Table 5. Selected TDDFT calculated energies and compositions of the lowest-lying singlet energy states together with oscillator strengths of **1**.[a] Only transitions with *f* greater than 0.001 are presented.

| State | Composition[b] | $\Delta E$[c] | *f*[d] | Character |
|---|---|---|---|---|
| **3** | **HOMO→LUMO**, ***92%*** | **2.39** | **0.1049** | **W/CO→qn/py (MLCT/LLCT)** |
| 5 | HOMO–1→LUMO+2, *81%*<br>HOMO–2→LUMO+4, *13%* | 3.05 | 0.0080 | W/CO→$CO_{eq}$ (MLCT/LLCT) |
| 6 | HOMO→LUMO+2, *80%*<br>HOMO–2→LUMO+3, *13%* | 3.06 | 0.0104 | W/CO→$CO_{eq}$ (MLCT) |
| 9 | HOMO→LUMO+1, *69%*<br>HOMO–2→LUMO+2, *18%*<br>HOMO→LUMO+3, *6%* | 3.28 | 0.0031 | W/CO→qn/py (MLCT/LLCT) |
| 12 | HOMO→LUMO+3, *48%*<br>HOMO–1→LUMO+4, *23%*<br>HOMO→LUMO+1, *14%*<br>HOMO–2→LUMO+2, *13%* | 3.38 | 0.0036 | W/CO→$CO_{eq}$ (MLCT)<br>W/CO→$CO_{eq}$ (MLCT)<br>W/CO→qn/py (MLCT/LLCT)<br>W/$CO_{eq}$→qn/py (MLCT/LLCT) |
| 14 | HOMO–1→LUMO+4, *67%*<br>HOMO→LUMO+3, *31%* | 3.50 | 0.0070 | W/CO→$CO_{eq}$ (MLCT) |
| 15 | HOMO-3→LUMO, *81%* | 3.61 | 0.1338 | π–π*(pq) |
| 19 | HOMO→LUMO+6, *32%*<br>HOMO→LUMO+5, *25%*<br>HOMO–2→LUMO+4, *25%*<br>HOMO–5→LUMO, *14%* | 3.83 | 0.0046 | W/$CO_{eq}$→qn/py (MLCT/LLCT) |
| 20 | HOMO–5→LUMO, *67%*<br>HOMO–3→LUMO+1, *7%*<br>HOMO–2→LUMO+4, *6%*<br>HOMO→LUMO+5, *5%* | 3.90 | 0.0460 | π–π*(pq) |

[a] The principal singlet transition responsible for the main absorption band in the visible region is shown in **bold**. [b] Compositions of electronic transitions are expressed in terms of contributing excitations between ground-state Kohn–Sham molecular orbitals. [c] Transition energy from the $a^1S$ ground state in eV. [d] Oscillator strength.

 © 2007 Wiley-VCH Verlag GmbH & Co. KGaA, Weinheim 

ter are not expected to be observed in the UV/Vis spectra of **1**. In Figure 13, the UV/Vis spectrum of $W(CO)_4(pq)$[6] (**2**) in $CH_2Cl_2$ is also presented. Bidentate coordination of the pq ligand, with the simultaneous abstraction of the CO moiety, induces several optical effects. The most important is that the main solvatochromic W/CO → qn/py transition exhibits a strong red shift (≈0.66 eV), because of the destabilization of the orbitals localized on carbonyl ligands. The latter is a consequence of the chelation of pq that results in a less efficient back-donation from the metal to the carbonyls. Thus, the optically active HOMO in **1**, which also reflects the back-donation to the N-ligand becomes HOMO–2 in **2** ($\Delta E$ = 0.34 eV). Moreover, if we consider that $CO_{tr}$ of **1** is analogous to $CO_{eq}$ of **2** then HOMO–1 and HOMO–2 in **1** become HOMO ($\Delta E$ = 0.74 eV) and HOMO–1 ($\Delta E$ = 0.91 eV) in **2**, respectively. On the other hand, the LUMO and LUMO+1, localized on pq, are stabilized in **2** as the pq contribution is increased from 10% in **1** to 25% in **2**. On the other hand, the ligand based π–π* transitions are kept almost constant in both complexes as depicted in Figure 13. Finally, comparing the molar absorptivities of both complexes (1600 $M^{-1}cm^{-1}$ for **1** and 3600 $M^{-1}cm^{-1}$ for **2**) we observe that they are in total accordance with the oscillator strengths, where *f* is 0.1049 (Table 5) and 0.1158[5] for **1** and **2**, respectively. The larger oscillator strength of **2** can be related to a better overlap between the contributed orbitals of the transition. In other words, a better overlap among the orbitals of pq and the $W(CO)_4$ fragment is obtained when the pq is coordinated in a bidentate fashion as in **2** compared with a monodentate one as in **1**.

## 3. Conclusions

The isolation of the monodentate intermediate $W(CO)_5$-($N^4$-pq) (**1**), en route to photolytic $W(CO)_4$(pq) chelate ring closure has been achieved. This is the first example where the ligand pq is coordinated in a monodentate fashion. Complex **1** has been fully characterized and its crystal structure has unambiguously demonstrated that pq is preferably coordinated through $N^4$ rather than the $N^1$ and $N^2$ atoms, while its packing is governed by π–π interactions and hydrogen bonds. The face-to-face alignment of condensed quinoxaline rings is attributed to the existence of the electron-withdrawing groups, namely $W(CO)_5$ and the pyridine ring.

The aforementioned preference for the $N^4$ atom has been elucidated both by theoretical (structural and thermodynamic) means and in terms of the frontier orbitals. The theoretical calculations reveal that the coplanarity of the pq ligand, which exists in the **N4** conformation in accordance with the experimental results, no longer exists in the **N1** and **N2** conformations. Actually, the coordinated pyridine moiety of the ligand to the $W(CO)_5$ fragment in **N1**, keeping a *gauche* conformation, causes a twist and fold of the whole pq molecule; whereas the same ring in **N2**, which is noncoordinated, is twisted along the $C^2$–$C^{2'}$ bond. This results in a destabilization of the electronic distribution as is indicated by the energies of the frontier orbitals and leads to new intramolecular interactions. This situation is best described by DFT thermodynamic calculations. Thus, it is predicted that the **N4** conformation should be more stable than the other two conformations (8.0 kcal/mol vs. **N1** and 15.7 kcal/mol vs. **N2**).

Moreover, the ground state of **1** has been fully elucidated by DFT means. Thus, the HOMO and HOMO–1 of **1** are nearly degenerate and predominantly consist of tungsten 5d orbitals with near equal contributions from quinoxaline and carbonyl ligands. The LUMO is energetically well separated and is practically a pure π* orbital localized on the quinoxaline moiety of the ligand. Finally, the electronic transitions of **1** have been fully characterized by TD-DFT calculations, indicating that its low lying solvatochromic band is best ascribed as a HOMO to LUMO transition. Since it has a W/CO → pq character the term MLCT/LLCT is adopted.

## Experimental Section

**Materials and Equipment:** The ligand 2,2′-pq was synthesized as described previously.[5,6] The complex $W(CO)_6$ along with THF, which was used in the syntheses, were obtained from Aldrich Chemicals and used after being dried. The solvents used in UV/Visible spectroscopic studies were purified to spectroscopic quality by standard methods.[33] The deuterated solvents, which were utilized in the NMR spectroscopic experiments were purchased from Aldrich and were of 99.99% purity.

The photolysis experiment was carried out with a 1000 W Xenon lamp with an Oriel, model 68820, Universal Arc. Lamp source selected with an appropriate interference filter (Corning). FT-IR spectra in solution and with KBr pellets were recorded with a Nicolet Magna IR 560 spectrophotometer with a 1.0 $cm^{-1}$ resolution. Electronic absorption spectra were recorded with a Varian Cary 300 spectrometer with a circulating thermostat. The solute concentration was about $10^{-5}$ M and the samples were prepared just before the measurements were taken. The $^1H$-$^{15}N$ HMBC NMR spectra were recorded with a Varian INOVA 500-MHz NMR spectrometer using $NH_3$ as the external standard. Microanalyses were performed with a Euro Vector EA 3000 analyzer

**Synthesis of the $W(CO)_5(N^4$-pq) Complex 1:** A tetrahydrofuran solution (50 mL) of the parent hexacarbonyltungsten (0.351 g, 1 mmol) was deoxygenated by continuous nitrogen purging and then irradiated with a 1000 W Xenon lamp at 25 °C for 20 min. An excess amount of pq (0.269 g, approximately 30%) was then added to the reaction vessel and the irradiation was continued for 10 more minutes. The tetrahydrofuran was slowly evaporated under atmospheric pressure and the residue was passed through a silica gel column using hexane as the eluent. After slow evaporation of the hexane, complex **1** was obtained as an orange solid in 70% (0.372 g) yield. $C_{18}H_9N_3O_5W$ (531.12): calcd. C 40.60, H 1.72, N 7.91, O, 15.12, W 34.81; found C 40.70, H 1.71, N 7.89, O 15.00. IR (in DCM): $\tilde{\nu}_{CO}$ = 2073 (w), 1932 (st), 1904 (m) $cm^{-1}$.

**Computational Details:** Ground-state electronic structure calculations of all compounds under investigation have been performed using density functional theory (DFT)[34] methods employing the GAUSSIAN 2003 software package.[35] The functional that was used throughout this study is the B3LYP, consisting of a hybrid exchange functional as defined by Becke's three-parameter equa-

 © 2007 Wiley-VCH Verlag GmbH & Co. KGaA, Weinheim 

tion[36] and the Lee–Yang–Parr correlation functional.[37] The ground-state geometries were obtained in the gas phase by full geometry optimization starting from structural data. The optimum structures located as stationary points on the potential energy surfaces were verified by the absence of imaginary frequencies. The derived wave functions were found free from internal instabilities. The basis set used throughout this study is the full double-ζ LANL2DZ basis functions along with the corresponding effective core potential for tungsten.[38] The thermodynamic data given in this report include zero-point energy (ZPE) and thermal corrections, without the introduction of scaling factors. Percentage compositions of molecular orbitals from the contributing fragments (the central metal, the diimine, and the axial and equatorial carbonyls) were calculated and analyzed using the AOMix and AOMix-S progams.[39] The first 21 singlet excited states of the closed shell complex were calculated within the TDDFT formalism.[40] The percentage of different transitions contributing to a state and the simulations of calculated IR spectra, when needed, were calculated with the aid of SWizard.[41] The graphics presented in the report have been prepared with the aid of the Molekel[42] and CAChe[43] programs.

## Acknowledgments

The project was cofunded by the European Social Fund (EPEAEK II)and National Resources (PYTHAGORAS). We also thank the Special Research Account of NKUA.

[1] D. J. Stufkens, *Coord. Chem. Rev.* **1990**, *104*, 39–112.
[2] C. A. Hunter, *Angew. Chem. Int. Ed. Engl.* **1995**, *34*, 1079–1081.
[3] P. J. Stang, D. H. Cao, S. Saito, A. M. Arif, *J. Am. Chem. Soc.* **1995**, *117*, 6273–6283 and references cited therein.
[4] I. Y. Wu, J. T. Lin, J. Luo, S. S. Sun, C. S. Li, K. J. Lin, C. Tsai, C. C. Hsu, J. L. Lin, *Organometallics* **1997**, *16*, 2038–2048.
[5] I. Veroni, A. Rontoyianni, C. A. Mitsopoulou, *Dalton Trans.* **2003**, 255–260.
[6] I. Veroni, C. Makedonas, A. Rontoyianni, C. A. Mitsopoulou, *J. Organomet. Chem.* **2006**, *691*, 267–281.
[7] M. Bruschi, P. Fantucci, M. Pizzotti, *J. Phys. Chem. A* **2005**, *109*, 9637–9645.
[8] B. Zarranz, A. Jaso, I. Aldana, A. Monge, *Bioorg. Med. Chem.* **2004**, *12*, 3711–3721.
[9] M. X. Chen, E. Perzon, N. Robisson, S. K. M. Jönsson, M. R. Andersson, M. Fahlman, M. Berggren, *Synth. Met.* **2004**, *146*, 233–236.
[10] D. W. Rangnekar, N. D. Sonawane, *Dyes Pigm.* **2000**, *45*, 87–96.
[11] A. Katoh, T. Yoshida, J. Ohkanda, *Heterocycles* **2000**, *52*, 911–920.
[12] S. V. Shevchuk, V. M. Lynch, J. L. Sessler, *Tetrahedron* **2004**, *60*, 11283–11291 and references cited therein.
[13] W. Kaim, *Angew. Chem. Int. Ed. Engl.* **1983**, *22*, 171–190.
[14] C.-X. Shao, W.-H. Sun, Z.-L. Li, Y.-L. Hu, L.-Q. Han, *Catal. Commun.* **2002**, *3*, 405–410.
[15] A. Garoufis, A. Koutsodimou, N. Katsaros, C. A. Mitsopoulou, N. Hadjiliadis, *Polyhedron* **1999**, *18*, 361–369.
[16] E. G. Bakalbassis, J. Mrozinski, S. P. Perlepes, N. Hadjiliadis, F. Lianza, A. Albinati, *Polyhedron* **1994**, *13*, 3209–3218.
[17] I. Veroni, C. A. Mitsopoulou, F. J. Lahoz, *J. Organomet. Chem.* **2006**, submitted.
[18] W. Strohmeier, F. J. Müller, *Chem. Ber.* **1969**, *102*, 3608–3612.
[19] M. Witanowski, L. Stefaniak, G. A. Webb, *Nitrogen NMR Spectroscopy*, Annual Reports on NMR Spectroscopy, Academic Press, London, **1986**, *18*, p. 1.
[20] L. Hilfert, G. Sarodnick, G. Kempter, E. Kleinpeter, *J. Mol. Struct.* **1998**, *444*, 199–211.
[21] C. Janiak, *J. Chem. Soc., Dalton Trans.* **2000**, 3885–3896.
[22] A. Rosa, E. J. Baerends, S. J. A. van Gisbergen, E. van Lenthe, J. A. Goeneveld, J. G. Snijders, *J. Am. Chem. Soc.* **1999**, *121*, 10356–10365.
[23] S. Záliš, M. Busby, T. Kotrba, P. Matousek, M. Towrie, A. Vlček Jr., *Inorg. Chem.* **2004**, *43*, 1723–1734 and references cited therein.
[24] S. Záliš, I. R. Farrel, A. Vlček Jr., *J. Am. Chem. Soc.* **2003**, *125*, 4580–4592.
[25] I. R. Farrel, H. František, S. Záliš, T. Mahabiersing, A. Vlček Jr., *J. Chem. Soc., Dalton Trans.* **2000**, 4323–4331.
[26] I. R. Farrel, J. van Slageren, S. Záliš, A. Vlček Jr., *Inorg. Chim. Acta* **2001**, *315*, 44–52.
[27] S. Záliš, A. Vlček Jr., C. Daniel, *Collect. Czech. Chem. Commun.* **2003**, *68*, 89–104.
[28] A. Hameed, A. Rybarczyk-Pirek, J. Zakrzewski, *J. Organomet. Chem.* **2002**, *656*, 102–107.
[29] M. E. Casida, C. Jamorski, K. C. Casida, D. R. Salahub, *J. Chem. Phys.* **1998**, *108*, 4439–4449.
[30] I. R. Farrel, A. Vlček Jr., *Coord. Chem. Rev.* **2000**, *208*, 87–101.
[31] a) A. B. Tamayo, S. Garon, T. Sajoto, P. I. Djurovich, I. M. Tsyba, R. Bau, M. E. Thompson, *Inorg. Chem.* **2005**, *44*, 8723–8732; b) J. M. Villegas, S. R. Stoyanov, W. Huang, D. P. Rillema, *Inorg. Chem.* **2005**, *44*, 2297–2309; c) J. M. Villegas, S. R. Stoyanov, J. H. Reibensies, D. P. Rillema, *Organometallics* **2005**, *24*, 395–404; d) S. R. Stoyanov, J. M. Villegas, A. J. Cruz, L. L. Lockyear, J. H. Reibensies, D. P. Rillema, *J. Chem. Theory Comput.* **2005**, *1*, 95–106; e) J. M. Villegas, S. R. Stoyanov, W. Huang, L. L. Lockyear, J. H. Reibensies, D. P. Rillema, *Inorg. Chem.* **2004**, *43*, 6383–6396; f) S. Kar, B. Sarkar, S. Ghumaan, D. Roy, F. A. Urbanos, J. Fiedler, R. B. Sunoj, R. Jimenez-Aparicio, W. Kaim, G. K. Lahiri, *Inorg. Chem.* **2005**, *44*, 8715–8722.
[32] a) C. Makedonas, C. A. Mitsopoulou, *Eur. J. Inorg. Chem.* **2006**, 2460–2468; b) C. Makedonas, C. A. Mitsopoulou, *Eur. J. Inorg. Chem.* **2006**, 590–598; c) C. Makedonas, C. A. Mitsopoulou, *Spectrochim. Acta Part A* **2006**, *64*, 918–930; d) C. Makedonas, C. A. Mitsopoulou, F. J. Lahoz, A. I. Balana, *Inorg. Chem.* **2003**, *43*, 8853–8865.
[33] D. D. Perrin, W. L. F. Armarego, *Purification of Laboratory Chemicals*, Pergamon Press, 3rd ed., **1988**.
[34] R. G. Parr, W. Yang, *Density Functional Theory of Atoms and Molecules*, Oxford University Press, Oxford, **1989**.
[35] M. J. Frisch, G. W. Trucks, H. B. Schlegel, G. E. Scuseria, M. A. Robb, J. R. Cheeseman, J. A. Montgomery Jr., T. Vreven, K. N. Kudin, J. C. Burant, J. M. Millam, S. S. Iyengar, J. Tomasi, V. Barone, B. Mennucci, M. Cossi, G. Scalmani, N. Rega, G. A. Petersson, H. Nakatsuji, M. Hada, M. Ehara, K. Toyota, R. Fukuda, J. Hasegawa, M. Ishida, T. Nakajima, Y. Honda, O. Kitao, H. Nakai, M. Klene, X. Li, J. E. Knox, H. P. Hratchian, J. B. Cross, C. Adamo, J. Jaramillo, R. Gomperts, R. E. Stratmann, O. Yazyev, A. J. Austin, R. Cammi, C. Pomelli, J. W. Ochterski, P. Y. Ayala, K. Morokuma, G. A. Voth, P. Salvador, J. J. Dannenberg, V. G. Zakrzewski, S. Dapprich, A. D. Daniels, M. C. Strain, O. Farkas, D. K. Malick, A. D. Rabuck, K. Raghavachari, J. B. Foresman, J. V. Ortiz, Q. Cui, A. G. Baboul, S. Clifford, J. Cioslowski, B. B. Stefanov, G. Liu, A. Liashenko, P. Piskorz, I. Komaromi, R. L. Martin, D. J. Fox, T. Keith, M. A. Al-Laham, C. Y. Peng, A. Nanayakkara, M. Challacombe, P. M. W. Gill, B. Johnson, W. Chen, M. W. Wong, C. Gonzalez, J. A. Pople, *Gaussian 03, Revision B.1*, Gaussian, Inc., Pittsburgh PA, **2003**.
[36] A. D. Becke, *J. Chem. Phys.* **1993**, *98*, 5648–5652.
[37] C. Lee, W. Yang, R. G. Parr, *Phys. Rev. B* **1988**, *37*, 785–789.
[38] a) T. H. Dunning Jr., P. J. Hay, in: *Modern Theoretical Chemistry* (Ed.: H. F. Schaefer III), Plenum Press, New York, **1976**, vol. 3; b) P. J. Hay, W. R. Wadt, *J. Chem. Phys.* **1985**, *82*, 270–283.

 © 2007 Wiley-VCH Verlag GmbH & Co. KGaA, Weinheim 

[39] a) S. I. Gorelsky, *AOMix and AOMix-S progam, revision 6.11*, http://www.sg-chem.net/; b) S. I. Gorelsky, A. B. P. Lever, *J. Organomet. Chem.* **2001**, *635*, 187–196.
[40] R. Stratmann, G. Scuseria, M. Frisch, *J. Chem. Phys.* **1998**, *109*, 8218–8224.
[41] S. I. Gorelsky, *SWizard progam*, http://www.sg-chem.net/.
[42] P. Flükiger, H. P. Lüthi, S. Portman, J. Weber, *MOLEKEL Version 4.3*, Swiss Center for Scientific Computing, Manno, Switzerland, **2000–2002**.
[43] CAChe Worksystem 4.4, Fujitsu Ltd., **2000**.

Received: July 19, 2006
Published Online: November 6, 2006

 © 2007 Wiley-VCH Verlag GmbH & Co. KGaA, Weinheim 

DOI: 10.1002/ejic.200600682

# First Allylpalladium Systems Containing Chiral Imidazolylpyridine Ligands – Structural Studies and Catalytic Behaviour

**Amaia Bastero,[a] Antonio F. Bella,[a] Fernando Fernández,[b] Susanna Jansat,[b] Carmen Claver,*[a] Montserrat Gómez,*[b,c] Guillermo Muller,[b] Aurora Ruiz,[a] Mercè Font-Bardía,[d] and Xavier Solans[d]**

**Keywords:** Palladium / Chiral imidazolines / Catalysis / Allylic alkylation / Intermediates / Heterocycles

Palladium/chiral imidazolylpyridine systems were tested in allylic alkylation of *rac*-3-acetoxy-1,3-diphenyl-1-propene (*rac*-**I**) and 3-acetoxy-1-phenyl-1-propene (**II**), paying particular attention to the influence of the amine nitrogen hybridisation on their catalytic behaviour. Allylpalladium complexes **9**–**11** containing optically pure imidazolines were synthesised and fully characterised both in solution (NMR) and the solid state (single-crystal X-ray diffraction). NMR studies showed four species in solution for complex **9** containing the unsymmetrical 1-phenylallyl group, while for **10** and **11**, involving the symmetrical 1,3-diphenylallyl moiety, two species, *endo* and *exo*, were identified. In the solid state, only *endo* isomers crystallised for each complex.

(© Wiley-VCH Verlag GmbH & Co. KGaA, 69451 Weinheim, Germany, 2007)

## Introduction

In comparison with ligands containing oxazoline groups,[1] chiral imidazolines have been used less in catalysis, despite the structural analogy between the two heterocycles.[2] For imidazolines, the additional nitrogen atom in place of oxygen provides a further point for tuning the ligand basicity by changing the nature of the $R^3$ group, and consequently a new modifiable region to be considered in selective catalytic processes (Figure 1).

Figure 1. Oxazoline and imidazoline heterocycles.

The first enantioselective catalytic application of chiral imidazolines appeared in 1997 when Achiwa and co-workers published their research about Pd-catalysed allylic alkylation using chiral thioimidazoline ligands, obtaining moderate activities but excellent enantioselectivities (up to 96% *ee*),[3] comparable to those obtained with thioether–oxazolines.[4] Later, chiral phosphanylimidazolines were tested in Ir-catalysed enantioselective hydrogenation,[5,6] giving in some cases better asymmetric inductions than those involving analogous phosphanyloxazolines.[5] This kind of ligand has also been used in Pd-catalysed asymmetric Heck reactions, yielding better enantioselectivities than BINAP and phosphanyloxazolines.[7] Besides mono(imidazolines), bis(imidazolines) have also been used in catalysis. Therefore, chiral tridentate 2,6-bis(imidazolinyl)pyridines, structurally analogous to pybox ligands,[8] have been tested in Ru-catalysed asymmetric epoxidation reactions.[9] In addition, $C_2$-symmetric bis(imidazolines) have also been prepared and successfully used in Pd-catalysed allylic alkylation,[10,11] giving asymmetric inductions comparable to those obtained with analogous bis(oxazolines).[1d]

Concerning imidazolylpyridines, our investigation on Pd-catalysed copolymerisation of carbon monoxide and styrene, which represents the first catalytic work involving this type of ligand,[12] showed that the electronic nature of the $R^3$ substituent (Figure 1) could somehow control the stereoregularity of the polyketones obtained,[13,14] in contrast to the comparable oxazolylpyridine systems, affording invariably highly syndiotactic polymers.[15] At the same time, Davies et al. reported the use of chiral imidazolylpyridines in Ru-catalysed Diels–Alder reactions and the synthesis and full characterisation of the first complex containing a chiral imidazoline group.[16]

[a] Departament de Química Física i Inorgànica, Universitat Rovira i Virgili,
Marcel.lí Domingo s/n, 43007 Tarragona, Spain
Fax: +34-977559563
E-mail: carmen.claver@urv.net
[b] Departament de Química Inorgànica, Universitat de Barcelona, Martí i Franquès 1-11, 08028 Barcelona, Spain
[c] Laboratoire Hétérochimie Fondamentale et Appliquée, UMR CNRS 5069, Université Paul Sabatier,
118 route de Narbonne, 31120 Toulouse cedex 9, France
Fax: +33-5-61558204
E-mail: gomez@chimie.ups-tlse.fr
[d] Departament de Cristal.lografia, Mineralogia i Dipòsits Minerals, Universitat de Barcelona,
Martí i Franquès s/n, 08028 Barcelona, Spain


© 2007 Wiley-VCH Verlag GmbH & Co. KGaA, Weinheim

With regard to structural studies, few metal complexes containing chiral imidazoline moieties have been fully characterised.[17] Only our palladium complexes of type [PdClR(κ²-*N*,*N*′-L*)] (R = Cl, Me),[13,14] rhodium compounds, [Rh(cod)(κ²-*N*,*N*′-L*)]$BF_4$,[14] and Davies' ruthenium complexes, [RuCl(1,3,5-trimethylbenzene)(κ²-*N*,*N*′-L*)]$SbF_6$,[16] have been published involving chiral imidazolylpyridines.

Following our research in allylic alkylation,[18] we have carried out a catalytic and structural study with imidazolylpyridines (Figure 1) to compare their behaviour with those containing analogous oxazoline derivatives (like ligands **7** and **8**, see Table 4).[19,20] For this purpose, we have chosen a short family of imidazolylpyridines coming from 1,2-diphenylethylenediamine, by varying the substituent nature on the amine nitrogen atom (R = H, Me, Bn, Ts, Figure 2). The influence of heterocycle stereochemistry on catalysis has also been considered [(*R*,*R*)-**1**, (*S*,*S*)-**2** and *rac*-(*R*,*S*)-**3**, Figure 1]. Allylpalladium intermediates have been synthesised and fully characterised in order to show a relationship with the catalytic behaviour observed.

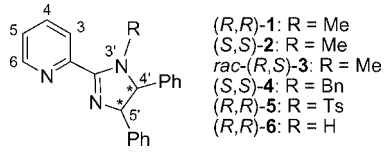


Figure 2. 2-(4′,5′-Diphenyl-3′-R-imidazolyl)pyridines **1**–**6** with numbering scheme.

## Results and Discussion

### Palladium Complexes

Ionic palladium complexes **9**–**11** containing 1-phenyl- (**9**) and 1,3-diphenylallyl groups (**10** and **11**) were prepared from the corresponding palladium precursor and the appropriate chiral imidazolylpyridine ligand, (*R*,*R*)-**1** for **9**, (*S*,*S*)-**2** for **10** and (*S*,*S*)-**4** for **11**, in the presence of ammonium hexafluorophosphate (Scheme 1), according to the methodology previously described.[19,21]

These compounds were obtained as monometallic complexes of general formula [Pd(η³-1-Ph-3-R-$C_3H_n$)(L)]$PF_6$ [**9**: R = H, *n* = 4, L = (*R*,*R*)-**1**; **10**: R = Ph, *n* = 3, L = (*S*,*S*)-**2**; **11**: R = Ph, *n* = 3, L = (*S*,*S*)-**4**], where L acts as a κ²-*N*,*N*′-bidentate ligand affording a five-membered palladacycle. Complexes **9**–**11** were fully characterised by the usual techniques. IR spectra showed strong signals at 1559–1549 $cm^{-1}$ corresponding to the C=$N_{imine}$ moiety and at about 835 $cm^{-1}$ assigned to P–F stretching of the $PF_6$ anion. Mass spectra exhibited a peak corresponding to the [Pd(η³-1-Ph-3-R-$C_3H_n$)(L)]⁺ fragment.

Suitable monocrystals of **9**, **10** and **11** for X-ray diffraction measurements were obtained from dichloromethane solutions of the corresponding complexes by slow diffusion of hexane.

In these structures (Figure 3), the palladium atom shows a distorted square-planar coordination, bonded to two nitrogen (N7 and N1) and two terminal allylic carbon atoms (Table 1), which are nearly coplanar (N1–C12–C14–N7 is about 4.8° for **9** and **10**, and 1.9° for **11**). These complexes crystallised as *endo* isomers, meaning that the central allylic carbon atom and the phenyl substituent at 5′-position on the imidazoline ring point in opposite directions.

In a previous study based in neutral and cationic Pd complexes involving this kind of ligand, it was found that the C–N bond lengths were sensitive to the R substituents at 3′-position, providing information about the electronic delocalisation through the amidine fragment.[14] Therefore, in order to analyse the electronic density involved in the C–N bonds, $N_{amine}$ (N4) and $N_{imine}$ (N1) with their common bonded C atom (C5), we have compared the bond length difference between C5–N4 and C5–N1. For **9** and **10**, the difference is slightly smaller than for **11** [Δ(N1–C5 – N4–C5) = 0.051 Å for **9**; Δ(N1–C5 – N4–C5) = 0.054 Å for **10**; Δ(N1–C5 – N4–C5) = 0.069 Å for **11** (Table 1)]. Comparing these figures with those of related compounds, [PdClMe(*R*,*R*-**2**)] (Δ = 0.037 Å) and [PdClMe(*R*,*R*-**5**)] (Δ = 0.139 Å),[14] we can state that complexes containing ligands (*R*,*R*)-**1** and (*S*,*S*)-**2** {complexes **9**, **10** and [PdClMe(*R*,*R*-**1**)]} have C–N bonds of a similar nature, with bond lengths intermediate between those for single and double bonds; while for **11**, containing (*S*,*S*-**4**), both single and double bonds are present. In addition, IR spectra for **9**–**11** exhibit C=N stretching absorptions (1559–1549 $cm^{-1}$, see Experimental Section) at lower frequency than those observed for allylpalladium complexes containing bis(oxazolines) (1650–1670 $cm^{-1}$)[22,18a] or oxazolinylpyridines (1630–1660 $cm^{-1}$);[19] consequently, weaker C=$N_{imine}$ bonds for imidazoline than for oxazoline derivatives are observed. These structural data point out an electronic delocalisation between the two nitrogen atoms of the imidazoline heterocycle, mainly when the substituent on the $N_{amine}$ atom is a methyl group [ligands (*R*,*R*)-**1** and (*S*,*S*-**2**)].

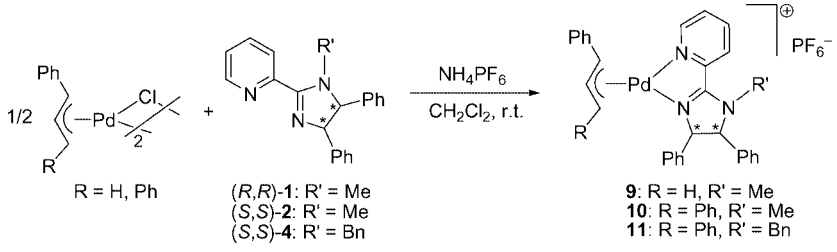


Scheme 1. Allylpalladium complexes **9**–**11** containing chiral ligands (*R*,*R*)-**1**, (*S*,*S*)-**2** and (*S*,*S*)-**4**.

 © 2007 Wiley-VCH Verlag GmbH & Co. KGaA, Weinheim 

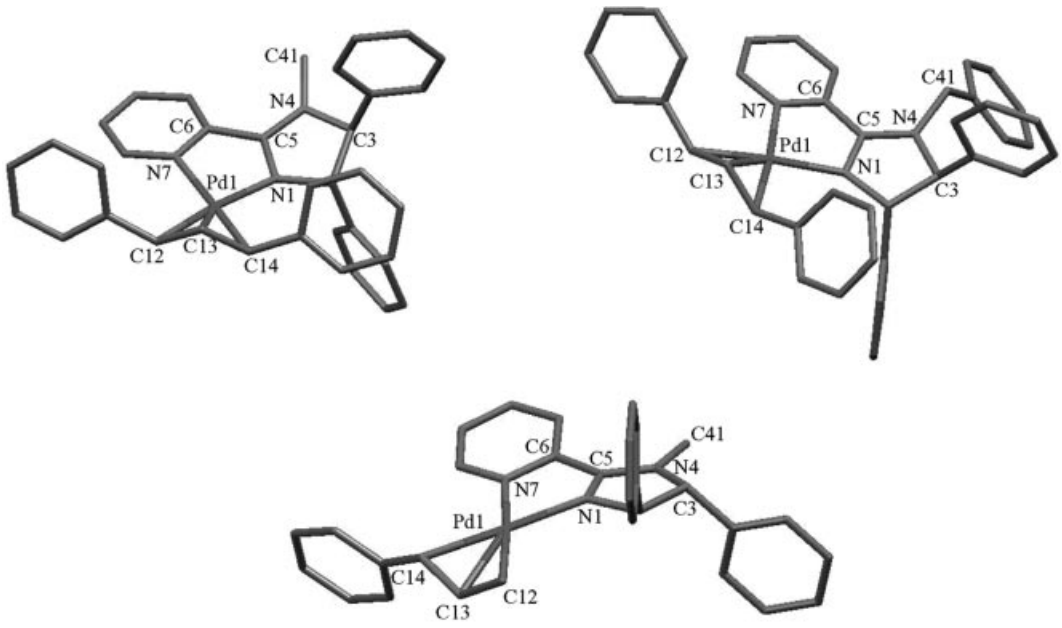


Figure 3. View of the molecular structures of complexes **9** (bottom), **10** (top left) and **11** (top right). Hydrogen atoms and hexafluorophosphate anion are omitted for clarity.

Table 1. Selected bond lengths [Å] and bond angles [°] for **9**, **10** and **11** (with esds in parentheses).

| | **9** | **10** | **11** |
|---|---|---|---|
| Pd1–N1 | 2.053(4) | 2.096(4) | 2.109(3) |
| Pd1–N7 | 2.124(4) | 2.147(5) | 2.137(3) |
| Pd1–C12 | 2.168(5) | 2.173(5) | 2.173(4) |
| Pd1–C13 | 2.087(5) | 2.122(5) | 2.145(4) |
| Pd1–C14 | 2.107(5) | 2.137(5) | 2.163(4) |
| N1–C5 | 1.289(6) | 1.304(6) | 1.291(5) |
| N4–C5 | 1.340(6) | 1.358(6) | 1.360(5) |
| N1–Pd1–N7 | 77.24(15) | 77.64(15) | 76.53(12) |
| C12–Pd1–C14 | 67.9(2) | 67.77(18) | 68.11(15) |

Concerning the planarity around $N_{amine}$, the angle between the two planes around this atom has been considered. The C5–C41–C3–N4 angle is less than 7° for **9** (2.4°) and **10** (6.9°), and 10.2° for **11**. Comparing with two other related complexes, the corresponding angles are 0.6° for [PdClMe(*R*,*R*-**1**)] and 21.6° for [PdClMe(*R*,*R*-**5**)].[14] Likewise, the distance of C41 to N1–C5–N4 is 0.025, 0.133 and 0.365 Å for **9**, **10** and **11**, respectively. Then a quasi-$sp^2$ hybridisation for [PdClMe(*R*,*R*-**1**)], **9** and **10** can be inferred, in contrast to an $N_{amine}$ $sp^3$ hybridisation for [PdClMe(*R*,*R*-**5**)]; for **11**, containing the (*S*,*S*)-**4** ligand, a significant planarity deviation is observed. This prominent feature about the $sp^2$ character for nitrogen atoms of the imidazoline ring has been recently stated from the X-ray structural analysis of a bis(imidazolinyl)pyridine ligand.[23]

The Pd–C distances in *trans* position to both nitrogen atoms, Pd1–C12 versus Pd1–C14, point to a higher *trans* influence for $N_{imine}$ than for $N_{pyridine}$. Therefore, the differences in the distance between palladium and both terminal allylic carbon atoms [Δ(Pd1–C12 – Pd1–C14)] are 0.036 and 0.010 Å for **10** and **11** respectively. However, the electronic effect of the R substituent on $N_{amine}$ is not reflected in the Pd–C distances in *trans* position to $N_{imine}$, as they are the same (Pd1–C12 = 2.173 Å for **10** and **11**). But the small increase observed in the Pd–C distances in *cis* position to $N_{imine}$ (Pd1–C14), 2.137 versus 2.163 Å for **10** and **11**, respectively, is probably due to the electronic and also steric effect of the substituent on $N_{amine}$.

$^1$H NMR spectroscopy allowed the determination of the structure of these complexes in solution.[19,24] For complex **9**, four isomers were observed in deuterated chloroform solution at room temperature, with a relative ratio 46:31:15:8 for **9a**/**9b**/**9c**/**9d**. Only for the two major isomers, **9a** and **9b**, were all carbon and proton atoms assigned. The isomers detected are formed because of (i) the relative position of the central allylic carbon atom and the phenyl substituent at the 5′-position on the imidazoline ring (giving *exo* and *endo* isomers, see above) and (ii) the substitution on the allyl moiety. 2D NOESY experiments exhibited interconversion between **9a** and **9d** and between **9b** and **9c**, but no π-σ-π allyl isomerisation was observed.

Concerning relative chemical shifts, the signals of the terminal allyl protons ($H^3$ and $H^4$, Table 2) for the two major isomers (δ = 2.19–3.33 ppm for **9a** and **9b**) are upfield-shielded relative to those of the other two isomers (δ = 3.51–4.25 ppm for **9c** and **9d**), a fact that can be attributed to the spatial proximity of the phenyl group at the heterocycle 5′-position; similarly, the signal of the $H^2$ proton of **9c** is also upfield-shifted with respect to **9a** and **9b** [δ = 3.96 (**9c**) vs. 4.52 and 4.53 ppm for **9a** and **9b**, respectively, Table 2]; $H^5$ is also sensitive to the allyl group and for **9c** its signal is more than 1 ppm upfield-shifted because of the close allylphenyl group [δ = 3.86 (**9c**) vs. 4.84 and 5.00 ppm for **9a** and **9b**, respectively]. Consequently, the two major isomers could be attributed to *exo* and *endo* isomers where the phenylallyl group is located in *cis* position relative to

 © 2007 Wiley-VCH Verlag GmbH & Co. KGaA, Weinheim 

the pyridine nitrogen atom, while **9c** corresponds to one of the minor isomers where the phenylallyl group is located in *trans* position relative to the pyridine nitrogen atom. These data lead us to propose the structures shown in Figure 4.

Table 2. Selected $^1$H NMR ($CDCl_3$, 400 MHz, 298 K) chemical shifts for **9** (signal multiplicity in parentheses).[a]

| | **9a** | **9b** | **9c** | **9d**[b] |
|---|---|---|---|---|
| $H^1$ (central) | 5.76 (td) | 5.69 (td) | 5.87–5.95 (m) | n.d. |
| $H^2$ (*anti*-Ph) | 4.52 (d) | 4.53 (d) | 3.96 (d) | n.d. |
| $H^3$ (*anti*) | 2.19 (ddd) | 2.72 (d) | 3.51 (d) | n.d. |
| $H^4$ (*syn*) | 3.33 (dd) | 2.79 (dd) | 4.25 (d) | 4.14 (d) |
| $H^5$ | 4.84 (d) | 5.00 (d) | 3.86 (d) | n.d. |
| $H^6$ | 4.90 (d) | 4.86 (d) | 4.41 (d) | n.d. |
| $H^{7–9}$ ($CH_3$) | 3.31 (s) | 3.29 (s) | 3.21 (s) | n.d. |

[a] Proton labels: 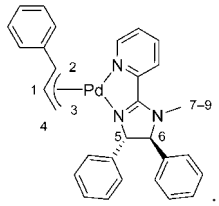 [b] n.d. means not distinguished.

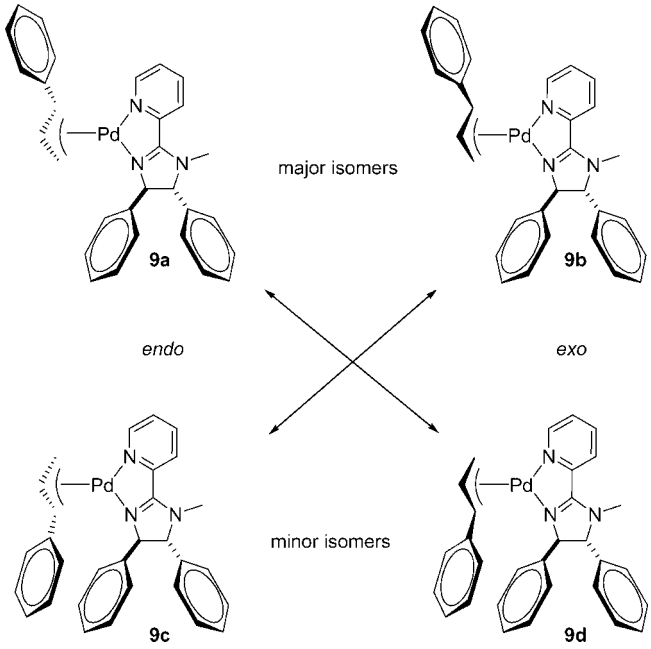


Figure 4. Proposed structures for the four isomers of **9** observed in solution (arrows indicate the isomer interconversion observed by 2D NOESY, between **9a** and **9d**, and **9b** and **9c**).

For complexes **10** and **11**, only two isomers were observed in deuterated chloroform solution, with a relative ratio of about 6:1. Most of the resonances for minor isomers are overlapped by signals corresponding to those of major species. 2D NOESY experiments exhibited, in both cases, interconversion between both isomers and no π-σ-π allyl isomerisation was detected. Because of the steric hindrance between both phenyl groups, from the imidazoline ring and allyl group, the major species for each complex could be assigned to the *endo* isomer.

## Pd-Catalysed Allylic Alkylation

Asymmetric allylic alkylation of the racemic substrate *rac*-3-acetoxy-1,3-diphenyl-1-propene (*rac*-**I**) and 3-acetoxy-1-phenyl-1-propene (**III**) with dimethyl malonate under basic Trost conditions[25] was carried out using a Pd catalytic systems containing 2-(4′,5′-diphenyl-5′-substituted-imidazolyl)pyridines **1**–**6** (Scheme 2). The results are summarised in Table 3. Catalytic precursors were generated in situ from $[PdCl(C_3H_5)]_2$ and the appropriated ligand (Pd/L = 1:1.25).

For the allylic alkylation of *rac*-**I**, we observed that the most active palladium systems were those containing a methyl group in the 5′-position of the imidazolyl ring, ligands (*R*,*R*)-**1**, (*S*,*S*)-**2** and *rac*-(*R*,*S*)-**3** (Entries 2, 4 and 5, Table 3). Benzyl and tosyl derivatives [ligands (*S*,*S*)-**4** and (*R*,*R*)-**5**, respectively] led to less active catalysts (Entries 7 and 9, Table 3), especially the Pd/(*R*,*R*)-**5** system, which showed a very low conversion [36% after 48 h of reaction (Entry 9, Table 3)].

The activity trend shown by these Pd/**L*** systems correlates quite well with the $N_{amine}$ hybridisation character. Actually, methyl derivatives containing $sp^2$-hybridised $N_{amine}$ (ligands **1**, **2** and **3**) are more active than benzyl [(*S*,*S*)-**4**], whose $N_{amine}$ atom exhibits a significant $sp^3$ character and is clearly more active than the tosyl derivative, which contains an $sp^3$-hybridised $N_{amine}$ atom (Entries 2, 4, 5, 7 and 9, Table 3).

Concerning the enantioselectivity, only the Pd/(*S*,*S*)-**4** system gave a significant asymmetric induction, up to 19% *ee* (Entry 7, Table 3). The low enantioselectivity observed is probably due to the higher *trans* influence of $N_{imine}$ than that of $N_{pyridine}$ (see above), directing the nucleophile attack towards the terminal allylic carbon atom *trans* to the imine nitrogen atom. In that position no steric hindrance coming

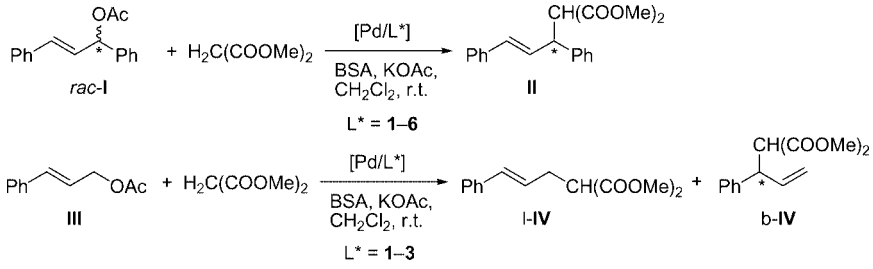


Scheme 2. Allylic alkylation of *rac*-**I** and **III** catalysed by Pd/**L*** systems (**L*** = **1**–**6**).

 © 2007 Wiley-VCH Verlag GmbH & Co. KGaA, Weinheim 

Table 3. Allylic alkylation of *rac*-**I** and **III** catalysed by palladium systems containing imidazolylpyridines, Pd/**L*** (**L*** = **1**–**6**).[a]

| Entry | L* | Substrate | Time [h] | Conversion [%][b] | *ee* of **II** [%][b] | l-**IV**/b-**IV**[b] |
|---|---|---|---|---|---|---|
| 1 | **1** | **I** | 5 | 41 | 0 | – |
| 2 | **1** | **I** | 24 | 97 | 0 | – |
| 3 | **2** | **I** | 5 | 34 | 0 | – |
| 4 | **2** | **I** | 24 | 100 | 0 | – |
| 5 | **3** | **I** | 24 | 81 | 0 | – |
| 6 | **4** | **I** | 5 | 0 | – | – |
| 7 | **4** | **I** | 24 | 46 | 19 (*S*) | – |
| 8 | **4** | **I** | 48 | 99 | 15 (*S*) | – |
| 9 | **5** | **I** | 48 | 36 | 0 | – |
| 10 | **5** | **I** | 96 | 94 | 0 | – |
| 11 | **1** | **III** | 24 | 100 | – | 13:1 |
| 12 | **2** | **III** | 24 | 100 | – | 13:1 |

[a] Results from duplicated experiments. Pd/**L***/substrate = 1:1.25:50. See Scheme 2. [b] Conversions based on substrate **I** or **III** determined by $^1$H NMR spectroscopy; enantiomeric excesses (absolute configuration in parentheses) determined by HPLC and l(inear)/b(ranched) ratio, by GC.

from the 6-position of the pyridine group exists to discriminate this attack between both *endo* and *exo* isomers. In addition, the electronic effect due to the $N_{amine}$ substituent can contribute to this lack of enantioselectivity. An increase of pyramidal arrangement around the $N_{amine}$ atom means a decrease of π-electron delocalisation between the amine and imine nitrogen atom (see above) and consequently $N_{imine}$ becomes a better donor Lewis centre, favouring the stability of cationic intermediate catalytic species responsible for the enantioselectivity control. The lack of enantioselectivity for (*R*,*R*)-**5** (Entries 9 and 10, Table 3) could be due to electronic factors.

The Pd/(*R*,*R*)-**6** system was not active, doubtless because of the NH deprotonation of the imidazoline group under the basic catalytic conditions used. In this case, the plausible palladium intermediate containing the anionic imidazolylpyridine ligand could induce a less electrophilic character on the allyl moiety than cationic allylic intermediates involving bidentate neutral ligands.

The most active catalytic systems [Pd/(*R*,*R*)-**1** and Pd/(*S*,*S*)-**2**] were used in the allylic alkylation of 3-acetoxy-1-phenyl-1-propene (**III**), under the same conditions described above for *rac*-**I**, showing a high regioselectivity towards the linear isomer, l-**IV**/b-**IV** ratio = 13:1 (Entries 11 and 12, Table 3).

From a structural point of view, the imidazoline ring is close to the oxazoline heterocycle. When we compare the catalytic results obtained for *rac*-**I** alkylation with (5′-phenyl-oxazolinyl)pyridine and (4′,5′-disubstituted)oxazolinylpyridine ligands **7** and **8**, respectively (Table 4), we observe that Pd/**7** and Pd/**8** catalysts are more active and selective than the most active and selective imidazoline derivatives [ligands (*R*,*R*)-**1**, (*S*,*S*)-**2** and (*S*,*S*)-**4**, respectively; Entries 4 and 5 vs. 1, 2 and 3, Table 4].

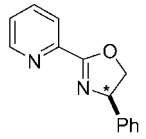


**7**

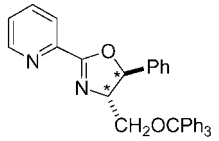


**8**

Table 4. Allylic alkylation of *rac*-**I** catalysed by palladium systems containing imidazolyl- [(*R*,*R*)-**1**, (*S*,*S*)-**2**, (*S*,*S*)-**4**] and oxazolinylpyridines (**7**, **8**).

| Entry | L* | Time [h] | Conversion [%][a] | *ee* of **II** [%][a] | Reference |
|---|---|---|---|---|---|
| 1 | **1** | 5 | 41 | 0 | this work |
| 2 | **2** | 5 | 34 | 0 | this work |
| 3 | **4** | 24 | 46 | 19 (*S*) | this work |
| 4 | **7** | 2.5 | 86 | 55 (*R*)[b] | [20] |
| 5 | **8** | 2 | 84 | 25 (*S*) | [19] |

[a] Conversions based on substrate **I** determined by $^1$H NMR spectroscopy; enantiomeric excesses (absolute configuration in parentheses) determined by HPLC. [b] Determined by $^1$H NMR spectroscopy using Eu(hfc)$_3$ as the chiral shift reagent.

The higher electronegativity of oxygen with respect to nitrogen avoids any π-delocalisation between oxygen and nitrogen atoms in the oxazoline heterocycle. Then the Lewis base character of the $N_{imine}$ atom in oxazolines is more important than that for analogous imidazolines, especially for those containing an sp$^2$-hybridised amine nitrogen atom. Therefore, this behaviour becomes crucial to understand the activity and selectivity diminution of imidazolylpyridines compared to related oxazolines.

## Conclusion

We have found the fine-tuning effect of the remote $N_{amine}$ centre on the Pd-catalysed allylic alkylation reaction. The delocalisation of the nonbonding electron pair of $N_{amine}$ causes a basicity diminution in $N_{imine}$, which is directly bonded to the metal atom. This effect seems to be directly related with the activity and asymmetric induction of Pd/imidazolylpyridine catalytic systems.

## Experimental Section

**General Remarks:** All compounds were prepared under purified nitrogen using standard Schlenk and vacuum-line techniques. The solvents were purified by standard procedures and distilled under nitrogen.[26] [Pd(η$^3$-1-phenylallyl)(μ-Cl)][27] and ligands (*R*,*R*)-**1**,[14]

 © 2007 Wiley-VCH Verlag GmbH & Co. KGaA, Weinheim 

(*S*,*S*)-**2**,[16] (*R*,*R*)-**5**[14] and (*R*,*R*)-**6**[14] were prepared as described previously. NMR spectra were recorded with Varian XL-500 ($^1$H, standard $SiMe_4$), Varian Gemini ($^1$H, 200 MHz; $^{13}$C, 50 MHz; standard $SiMe_4$), Bruker DRX 250 ($^{13}$C, 62.9 MHz, standard $SiMe_4$) and Varian Mercury 400 ($^1$H, 400 MHz; $^{13}$C, 100 MHz, standard $SiMe_4$) spectrometers, using $CDCl_3$ as solvent, unless stated otherwise. Chemical shifts were reported downfield from standards. IR spectra were recorded with FTIR Nicolet 520 and Nicolet 5700 spectrometers. Electron-spray mass spectra were obtained with a Mass ZQ Micromass instrument. High-resolution mass spectra were obtained with a Waters LCT Premier spectrometer operated in ESI mode. The GC analyses were performed with a Hewlett-Packard 6890-Network GC system gas chromatograph [30 m HP5 (5% phenyl)methylpolysiloxane column] with an FID detector. Enantiomeric excesses were determined by HPLC on a Chiralcel OD column. Elemental analyses were carried out by the Serveis Cientifico-Tècnics de la Universitat de Barcelona with an Eager 1108 microanalyser. Optical rotations were measured with a JASCO P-1030 polarimeter.

**(4′*R*,5′*S*)-2-(3′-Methyl-4′,5′-diphenyl-2′-imidazolyl)pyridine [*rac*-(*R*,*S*)-3]:** (4′*R*,5′*S*)-2-(4′,5′-Diphenyl-2′-imidazolyl)pyridine[12] (0.100 g, 0.33 mmol) was dissolved in THF (3 mL) and treated with NaH (9.5 mg, 0.4 mmol) for 1 h. MeI (22.4 μL, 0.36 mmol) was then added dropwise at room temperature. After 7 h, the solvent was removed under reduced pressure, giving a paste, which was purified by column chromatography yielding a white solid (77.8 mg, 75%). $^1$H NMR (200 MHz, $CDCl_3$, 298 K): $\delta$ = 8.72–7.26 (m, 14 H, aromatic), 4.99 (d, 1 H, $J$ = 10.4 Hz), 4.36 (d, 1 H, $J$ = 10.4 Hz), 2.99 (s, 3 H) ppm. $^{13}$C NMR (100.6 MHz, $CDCl_3$, 298 K): $\delta$ = 164.6 (C=N), 149.2 (CH), 137.1 (CH), 129.2–127.11 (CH), 125.3 (CH), 124.9 (CH), 79.0 (CH), 77.4 (CH), 34.4 ($CH_3$) ppm. HRMS-ESI: *m*/*z* calcd. for $C_{21}H_{20}N_3$ 314.1657; found 314.1647 $[M + H]^+$.

**(4′*S*,5′*S*)-2-(3′-Benzyl-4′,5′-diphenyl-2′-imidazolyl)pyridine [(*S*,*S*)-4]:** (4′*S*,5′*S*)-2-(4′,5′-Diphenyl-2′-imidazolyl)pyridine[16] (0.100 g, 0.33 mmol) was dissolved in THF (3 mL) and treated with NaH (9.5 mg, 0.4 mmol) for 1 h. Benzyl bromide (42.5 μL, 0.36 mmol) was then added dropwise at room temperature. After 5 h, the solvent was removed under reduced pressure, giving a brown paste, which was purified by column chromatography yielding a white solid (96.6 mg, 75%). $^1$H NMR (400 MHz, $CDCl_3$, 298 K): $\delta$ = 8.73–6.97 (m, 19 H, aromatic), 5.67 (d, 1 H, $J$ = 15.6 Hz), 5.03 (d, 1 H, $J$ = 9.2 Hz), 4.45 (d, 1 H, $J$ = 9.2 Hz), 3.96 (d, 1 H, $J$ = 15.6 Hz) ppm. $^{13}$C NMR (100.6 MHz, $CDCl_3$, 298 K): $\delta$ = 162.8 (C=N), 148.5 (CH), 136.9 (CH), 128.8–126.9 (CH), 125.6 (CH), 122.6 (CH), 77.4 (CH), 73.6 (CH), 49.1 ($CH_2$) ppm. HRMS-ESI: *m*/*z* calcd. for $C_{27}H_{24}N_3$ 390.1970; found 390.1980 $[M + H]^+$. $[\alpha]_D^{20}$ –4.90 (*c* = 0.88, $CHCl_3$).

**($\eta^3$-1-Phenylallyl)[(4′*R*,5′*R*)-2-(3′-methyl-4′,5′-diphenyl-2′-imidazolyl)pyridine-*N*,*N*]palladium(II) Hexafluorophosphate (9):** Ligand (*R*,*R*)-**1** (0.050 g, 0.160 mmol) and $[Pd(\mu\text{-}Cl)(\eta^3\text{-}1\text{-}Ph\text{-}C_3H_4)]_2$ (0.043 g, 0.083 mmol) were dissolved in dichloromethane (25 mL) at room temperature under nitrogen overnight. $NH_4PF_6$ (0.156 g, 0.960 mmol) was then added and the mixture was stirred for 3 h. Then the mixture was washed with water (6 × 20 mL). The aqueous phase was extracted with dichloromethane (3 × 10 mL). All the organic extracts were dried with $Na_2SO_4$, filtered off and the solvent was then evaporated to afford a yellow solid. The product was recrystallised from a mixture of dichloromethane and hexane (0.061 g, 56% yield). IR (KBr): $\tilde{\nu}$ = 1559 (C=N), 838 ($PF_6$) cm$^{-1}$. $C_{30}H_{28}F_6N_3PPd$ (681.94): calcd. C 52.84, H 4.14, N 6.16; found C 53.28, H 4.26, N 6.02. ESI$^+$ MS: *m*/*z* = 536.1 $[M - PF_6]^+$ (calcd. 536.975 for $C_{30}H_{28}N_3Pd^+$). $^1$H NMR (400 MHz, 298 K): **Isomer a** (46%): $\delta$ = 2.19 (ddd, 1 H, $J$ = 12.4, 1.6, 1.2 Hz), 3.31 (s, 3 H), 3.33 (dd, 1 H, $J$ = 7.0, 1.6 Hz), 4.52 (d, 1 H, $J$ = 11.6 Hz), 4.84 (d, 1 H, $J$ = 10.8 Hz), 4.90 (d, 1 H, $J$ = 10.8 Hz), 5.76 (td, 1 H, $J$ = 12.1, 7.0 Hz), 6.80–8.35 (aromatic protons, 19 H); **Isomer b** (31%): $\delta$ = 2.72 (d, 1 H, $J$ = 12.0 Hz), 2.79 (dd, 1 H, $J$ = 7.2, 1.2 Hz), 3.29 (s, 3 H), 4.53 (d, 1 H, $J$ = 11.6 Hz), 4.86 (d, 1 H, $J$ = 10.8 Hz), 5.00 (d, 1 H, $J$ = 11.2 Hz), 5.69 (td, 1 H, $J$ = 12.0, 6.8 Hz), 6.80–8.35 (aromatic protons, 19 H); **Isomer c** (15%): $\delta$ = 3.21 (s, 3 H), 3.51 (d, 1 H, $J$ = 12.8 Hz), 3.86 (d, 1 H, $J$ = 8.4 Hz), 3.96 (d, 1 H, $J$ = 11.2 Hz), 4.25 (d, 1 H, $J$ = 7.2 Hz), 4.41 (d, 1 H, $J$ = 8.0 Hz), 5.90 (m, 1 H), 6.80–8.35 (aromatic protons, 19 H) ppm. $^{13}$C{$^1$H} NMR (100.6 MHz): **Isomer a** (46%): $\delta$ = 35.0 ($CH_3$), 55.5 ($CH_2$), 76.9 (CH), 80.2 (CH), 80.3 (CH), 109.4 (CH), 126.0 (CH), 127.0 (CH), 127.8 (CH), 127.9 (CH), 128.3 (CH), 128.8 (CH), 129.1 (CH), 129.2 (CH), 129.5 (CH), 130.0 (CH), 136.4 (C), 137.9 (C), 140.9 (C), 140.9 (CH), 146.6 (C), 149.4 (CH), 165.8 (C=N); **Isomer b** (31%): $\delta$ = 34.8 ($CH_3$), 55.0 ($CH_2$), 77.0 (CH), 80.2 (CH), 80.9 (CH), 110.2 (CH), 126.1 (CH), 127.2 (CH), 127.7 (CH), 128.0 (CH), 128.4 (CH), 128.8 (CH), 129.0 (CH), 129.1 (CH), 129.5 (CH), 130.0 (CH), 136.2 (C), 137.7 (C), 140.7 (C), 140.9 (CH), 146.5 (C), 149.6 (CH), 165.9 (C=N) ppm.

**($\eta^3$-1,3-Diphenylallyl)[(4′*S*,5′*S*)-2-(3′-methyl-4′,5′-diphenyl-2′-imidazolyl)pyridine-*N*,*N*]palladium(II) Hexafluorophosphate (10):** Ligand (*S*,*S*)-**2** (0.075 g, 0.240 mmol) and $[Pd(\mu\text{-}Cl)(\eta^3\text{-}1,3\text{-}Ph\text{-}C_3H_3)]_2$ (0.084 g, 0.13 mmol) were dissolved in dichloromethane (20 mL) at room temperature under nitrogen overnight. $NH_4PF_6$ (0.123 g, 0.760 mmol) was then added and the mixture was stirred for 24 h. Then the mixture was washed with water (6 × 15 mL). The aqueous phase was extracted with dichloromethane (3 × 10 mL). All the organic extracts were dried with $Na_2SO_4$, filtered and the solvent was then evaporated to afford a yellow oil. The product was recrystallised from a mixture of dichloromethane and hexane (0.095 g, 52% yield). IR (KBr): $\tilde{\nu}$ = 1556 (C=N), 838 ($PF_6$) cm$^{-1}$. $C_{36}H_{32}F_6N_3PPd{\cdot}0.2C_4H_{10}O{\cdot}0.5CH_2Cl_2$ (815.29): calcd. C 54.95, H 4.33, N 5.15; found C 55.09, H 4.02, N 5.07. FAB$^+$ MS: *m*/*z* = 613.8 $[M - PF_6]^+$ (calcd. 613.077 for $C_{36}H_{32}N_3Pd^+$). $^1$H NMR (400 MHz, 298 K): **Isomer a** (88%): $\delta$ = 3.18 (s, 3 H), 3.83 (d, $J$ = 8.4 Hz, 1 H), 4.11 (d, $J$ = 11.2 Hz, 1 H), 4.41 (d, $J$ = 8.4 Hz, 1 H), 4.81 (d, $J$ = 11.6 Hz, 1 H), 6.23 (t, $J$ = 11.6 Hz, 1 H), 6.86–8.29 (aromatic protons, 24 H) ppm. $^{13}$C{$^1$H} NMR (100.6 MHz): **Isomer a** (88%): $\delta$ = 34.6 ($CH_3$), 72.4 (CH), 74.6 (CH), 79.2 (CH), 79.4 (CH), 107.6 (CH), 126.0 (CH), 126.0 (CH), 126.8 (CH), 127.7 (CH), 128.0 (CH), 128.1 (CH), 128.2 (CH), 128.4 (CH), 128.9 (CH), 129.1 (CH), 129.3 (CH), 129.4 (CH), 130.2 (CH), 136.4 (C), 137.4 (C), 138.4 (C), 141.0 (C), 141.1 (CH), 145.9 (C), 149.6 (CH), 165.2 (C=N) ppm.

**($\eta^3$-1,3-Diphenylallyl)[(4′*S*,5′*S*)-2-(3′-benzyl-4′,5′-diphenyl-2′-imidazolyl)pyridine-*N*,*N*]palladium(II) Hexafluorophosphate (11):** Ligand (*S*,*S*)-**4** (0.029 g, 0.075 mmol) and $[Pd(\mu\text{-}Cl)(\eta^3\text{-}1,3\text{-}Ph\text{-}C_3H_3)]_2$ (0.025 g, 0.037 mmol) were dissolved in dichloromethane (10 mL) at room temperature under nitrogen overnight. $NH_4PF_6$ (0.037 g, 0.220 mmol) was then added and the mixture was stirred for 72 h. Then the mixture was washed with water (6 × 15 mL). The aqueous phase was extracted with dichloromethane (2 × 10 mL). All the organic extracts were dried with $Na_2SO_4$, filtered and the solvent was then evaporated to afford a yellow gum. The product was recrystallised from a mixture of dichloromethane and hexane (0.021 g, 33% yield). IR (KBr): $\tilde{\nu}$ = 1549 (C=N), 832 (P–F) cm$^{-1}$. $C_{42}H_{36}F_6N_3PPd$ (833.01): calcd. C 60.48, H 4.35, N 5.04; found 60.90, H 4.95, N 5.16. ESI MS: *m*/*z* = 688.1 $[M - PF_6]^+$ (calcd. 688.194 for $C_{42}H_{36}N_3Pd^+$). $^1$H NMR (500 MHz, 298 K): **Isomer a** (86%): $\delta$ = 3.90 (d, $J$ = 6.0 Hz, H), 4.15 (d, $J$ =

 © 2007 Wiley-VCH Verlag GmbH & Co. KGaA, Weinheim 

Table 5. Crystal data for **9**, **10** and **11**.

| | **9** | **10** | **11** |
|---|---|---|---|
| Empirical formula | $C_{31}H_{30}Cl_2F_6N_3PPd$ | $C_{37}H_{34}Cl_2F_6N_3PPd$ | $C_{42}H_{36}F_6N_3OPPd{\cdot}H_2O$ |
| Formula mass | 766.85 | 842.94 | 852.12 |
| Crystal size [mm] | $0.30\times0.27\times0.05$ | $0.2\times0.18\times0.02$ | $0.2\times0.1\times0.1$ |
| Temperature [K] | 120(2) | 120(2) | 293(2) |
| Crystal system | monoclinic | monoclinic | monoclinic |
| Space group | *P*21/*c* | *C*2/*c* | *P*21/*c* |
| *a* [Å] | 18.781(5) | 39.157(8) | 10.113(6) |
| *b* [Å] | 9.728(3) | 10.708(2) | 26.731(11) |
| *c* [Å] | 17.523(5) | 17.471(4) | 15.026(6) |
| *β* [°] | 92.297(4) | 103.537(4) | 107.46(2) |
| Volume [Å$^3$] | 3199.0(16) | 7122(3) | 3875(3) |
| *Z* | 4 | 8 | 4 |
| Density (calculated) [Mg/m$^3$] | 1.592 | 1.572 | 1.461 |
| Absorption coefficient [mm$^{-1}$] | 0.859 | 0.780 | 0.586 |
| *θ* range for data collection [°] | 2.17–26.02 | 1.98–26.73 | 2.60–30.00 |
| Reflections collected [$I \geq 2\sigma(I)$] | 6272 | 7569 | 8370 |
| Independent reflections | 6272 [*R*(int) = 0.0000] | 7569 [*R*(int) = 0.0000] | 8489 [*R*(int) = 0.0000] |
| Final *R* indices [$I > 2\sigma(I)$][a] | $R_1 = 0.0492$, $wR_2 = 0.1332$ | $R_1 = 0.0530$, $wR_2 = 0.1237$ | $R_1 = 0.0608$, $wR_2 = 0.1043$ |
| *R* indices (all data)[a] | $R_1 = 0.0791$, $wR_2 = 0.1480$ | $R_1 = 0.0928$, $wR_2 = 0.1370$ | $R_1 = 0.0612$, $wR_2 = 0.1044$ |
| Gof on $F^2$ | 1.120 | 1.051 | 1.423 |
| Largest diff. peak/hole [e/Å$^3$] | 1.308/–0.696 | 0.762/–1.401 | 0.424/–0.382 |

[a] $R_1 = \Sigma||F_o| - |F_c||/\Sigma|F_o|$ and $wR_2 = \{\Sigma[w(F_o^2 - F_c^2)^2]/\Sigma[w(F_o^2)^2]\}^{1/2}$.

8.8 Hz, H), 4.41 (d, *J* = 14.4 Hz, H), 4.50 (d, *J* = 6.4 Hz, H), 4.83 (d, *J* = 9.6 Hz, H), 5.05 (d, *J* = 14.4 Hz, H), 6.31 (t, *J* = 9.2 Hz, H), 6.87–7.97 (aromatic protons, 29 H) ppm. $^{13}C\{^1H\}$ NMR (100.6 MHz): **Isomer a** (86%): $\delta$ = 49.6 ($CH_2$), 72.3 (CH), 74.4 (CH), 76.9 (CH), 79.6 (CH), 107.8 (CH), 126.0 (CH), 126.0 (CH), 126.8 (CH), 127.7 (CH), 128.0 (CH), 128.1 (CH), 128.2 (CH), 128.4 (CH), 128.9 (CH), 129.1 (CH), 129.3 (CH), 129.4 (CH), 130.2 (CH), 136.4 (C), 137.4 (C), 138.4 (C), 141.0 (C), 141.1 (CH), 145.9 (C), 149.6 (CH), 165.6 (C=N) ppm.

**Palladium-Catalysed Allylic Alkylation of *rac*-3-Acetoxy-1,3-diphenyl-1-propene (I):** The catalytic precursor was generated in situ from $[Pd(\eta^3\text{-}C_3H_5)(\mu\text{-}Cl)]_2$ and the appropriate ligand (0.02 mmol of Pd source and 0.025 mmol of chiral ligand) in $CH_2Cl_2$ (2 mL) for 30 min before adding the substrate. *rac*-3-Acetoxy-1,3-diphenyl-1-propene (0.252 g, 1 mmol), dissolved in $CH_2Cl_2$ (2 mL), was added followed by dimethyl malonate (0.396 g, 3 mmol), BSA (0.610 mg, 3 mmol) and a catalytic amount of KOAc. The mixture was stirred at room temperature until total conversion of the substrate (monitored by TLC, unless stated otherwise). The solution was then diluted with diethyl ether, filtered through Celite, and washed with saturated ammonium chloride solution ($4\times10$ mL) and water ($4\times10$ mL). The organic phase was dried with anhydrous $Na_2SO_4$, filtered and the solvent was removed under reduced pressure. The product was purified by column chromatography ($SiO_2$; ethyl acetate). The enantiomeric excesses were determined by HPLC on a Chiralcel OD column, using hexane/2-propanol, 99:1, as eluent in a flow of 0.3 mL/min.

**Palladium-Catalysed Allylic Alkylation of (*E*)-3-Acetoxy-1-phenyl-1-propene (III):** The procedure was analogous to the one described for *rac*-3-acetoxy-1,3-diphenyl-1-propene (**I**). The product was purified by column chromatography ($SiO_2$; ethyl acetate). Regioselectivity was determined by GC.

**X-ray Crystallographic Study:** Yellow crystals of **9**, **10** and **11** were selected and mounted on a Bruker SMART-CCD-1000 area detector single crystal diffractometer with graphite-monochromated Mo-$K_\alpha$ radiation ($\lambda$ = 0.71073 Å). Crystal data are summarised in Table 5. Preliminary unit cell constants were calculated with a set of 45 narrow-frame (0.3° in $\omega$) scans. Data were collected using the φ-ω scan method. Absorption corrections were applied using the SADABS program.[28] The structures were solved by direct methods using the SHELXS-97 computer program[29] for crystal structure determination and refined by full-matrix least-squares method on $F^2$, with the SHELXL-97 computer program.[30] The weighting schemes employed were $w = 1/[\sigma^2\{F_o^2 + (0.08259P)\}^2 + 0.0000P]$ for **9**, $w = 1/[\sigma^2\{F_o^2 + (0.0678P)\}^2 + 0.0000P]$ for **10** and $w = 1/[\sigma^2\{F_o^2 + (0.0079P)\}^2 + 4.7017P]$ for **11**, where $P = (|F_o|^2 + 2|F_c|^2)/3$. Hydrogen atoms were included in calculated positions and refined in riding mode. CCDC-291543 (for **9**), -614143 (for **10**) and -613925 (for **11**) contain the supplementary crystallographic data for this paper. These data can be obtained free of charge from The Cambridge Crystallographic Data Centre via www.ccdc.cam.ac.uk/data_request/cif.

## Acknowledgments

The authors wish to thank the Ministerio de Educación y Ciencia (CTQ2004-01546/BQU) and the Generalitat de Catalunya for financial support. The authors also thank the Unidade de RaiosX of the Universidade de Santiago de Compostela for their X-ray crystallographic contribution.

[1] General references about oxazolines and their catalytic applications: a) I. Ojima (Ed.), *Catalytic Asymmetric Synth*esis, 2nd ed., Wiley, New York, **2000**; b) G. Helmchen, A. Pfaltz, *Acc. Chem. Res.* **2000**, *33*, 336–345; c) P. G. Cozzi, N. Zimmermann, R. Hilgraf, S. Schaffner, A. Pfaltz, *Adv. Synth. Catal.* **2001**, *343*, 450–454; d) A. Ghosh, P. Mathivanan, J. Cappiello, *Tetrahedron: Asymmetry* **1998**, *9*, 1–45; e) M. Gómez, G. Muller, M. Rocamora, *Coord. Chem. Rev.* **1999**, *193–195*, 769–835.

[2] P. J. Guiry, C. P. Saunders, *Adv. Synth. Catal.* **2004**, *346*, 497–537.

[3] T. Morimoto, K. Tachibana, K. Achiwa, *Synlett* **1997**, 783–785.

[4] J. V. Allen, G. J. Dawson, C. G. Frost, I. M. J. Williams, *Tetrahedron* **1994**, *50*, 799–808.

[5] F. Menges, M. Neuburger, A. Pfaltz, *Org. Lett.* **2002**, *4*, 4713–4716.

 © 2007 Wiley-VCH Verlag GmbH & Co. KGaA, Weinheim 

[6] E. Guiu, C. Claver, J. Benet-Buchholz, S. Castillón, *Tetrahedron: Asymmetry* **2004**, *15*, 3365–3373.
[7] a) C. A. Busacca, D. Grossbach, R. C. So, E. M. O'Brien, E. M. Spinelli, *Org. Lett.* **2003**, *5*, 595–598; b) C. A. Busacca, D. Grossbach, S. J. Campbell, Y. Dong, M. C. Ericsson, R. E. Harris, P.-J. Jones, J.-Y. Kim, J. C. Lorenz, K. B. McKellop, E. M. O'Brien, F. Qiu, R. D. Simpson, L. Smith, R. C. So, E. M. Spinelli, J. Vitous, C. Zavattaro, *J. Org. Chem.* **2004**, *69*, 5187–5195.
[8] H. Nishiyama, *Adv. Catal. Processes* **1997**, *2*, 153–188.
[9] S. Bhor, G. Anilkumar, M. K. Tse, M. Klawonn, C. Döbler, B. Bitterlich, A. Grotevendt, M. Beller, *Org. Lett.* **2005**, *7*, 3393–3396.
[10] N. A. Boland, M. Casey, S. J. Hynes, J. W. Matthews, H. Müller-Bunz, P. Wilkes, *Org. Biomol. Chem.* **2004**, *2*, 1995–2002.
[11] J. Dupont, G. Ebeling, M. R. Delgado, C. S. Consorte, R. Burrow, D. H. Farrar, A. J. Lough, *Inorg. Chem. Commun.* **2001**, *4*, 471–474.
[12] A. Bastero, A. Ruiz, C. Claver, S. Castillón, *Eur. J. Inorg. Chem.* **2001**, 3009–3011.
[13] A. Bastero, A. Ruiz, C. Claver, B. Milani, E. Zangrando, *Organometallics* **2002**, *21*, 5820–5829.
[14] A. Bastero, C. Claver, A. Ruiz, S. Castillón, E. Daura, C. Bo, E. Zangrando, *Chem. Eur. J.* **2004**, *10*, 3747–3760.
[15] M. Brookhart, M. I. Wagner, G. G. A. Balavoine, H. A. Haddou, *J. Am. Chem. Soc.* **1994**, *116*, 3641–3642.
[16] A. J. Davenport, D. L. Davies, J. Fawcett, D. R. Russell, *J. Chem. Soc., Perkin Trans. 1* **2001**, 1500–1503.
[17] For complexes containing chiral imidazolylphosphane ligands, see refs.[6,7b]; for a palladium complex containing a chiral bis(imidazoline)ligand, see ref.[11]
[18] For recent contributions, see: a) M. Gómez, S. Jansat, G. Muller, M. A. Maestro, J. Mahia, *Organometallics* **2002**, *21*, 1077–1087; b) M. A. Pericàs, C. Puigjaner, A. Riera, A. Vidal-Ferran, M. Gómez, F. Jiménez, G. Muller, M. Rocamora, *Chem. Eur. J.* **2002**, *8*, 4164–4178; c) D. Franco, M. Gómez, F. Jiménez, G. Muller, M. Rocamora, M. A. Maestro, J. Mahía, *Organometallics* **2004**, *23*, 3197–3209.
[19] J. M. Canal, M. Gómez, F. Jiménez, M. Rocamora, G. Muller, E. Dunach, D. Franco, A. Jiménez, F. H. Cano, *Organometallics* **2000**, *19*, 966–978.
[20] G. Chelucci, S. Medici, A. Saba, *Tetrahedron: Asymmetry* **1997**, *8*, 3183–3184.
[21] P. von Matt, G. C. Lloyd-Jones, A. B. E. Minidis, A. Pfaltz, L. Macko, M. Neuburger, M. Zehnder, H. Rüegger, P. S. Pregosin, *Helv. Chim. Acta* **1995**, *78*, 265–284.
[22] M. Gómez, S. Jansat, G. Muller, M. A. Maestro, J. Mahia, M. Font-Bardia, X. Solans, *J. Chem. Soc., Dalton Trans.* **2001**, 1432–1439.
[23] K. Ma, L. Cheng, H. Mou Gau, J. You, *Acta Crystallogr., Sect. E: Struct. Rep. Online* **2006**, *62*, o1595–o1597.
[24] a) P. S. Pregosin, H. Rüegger, R. Salzmann, A. Albinati, F. Lianza, R. W. Kunz, *Organometallics* **1994**, *13*, 83–90; b) P. S. Pregosin, R. Salzmann, *Coord. Chem. Rev.* **1996**, *155*, 35–68.
[25] B. M. Trost, D. J. Murphy, *Organometallics* **1985**, *4*, 1143–1145.
[26] W. L. F. Armarego, D. D. Perrin, *Purification of Laboratory Chemicals*, 4th ed., Butterworth-Heinemann, Oxford, UK, **1996**.
[27] Y. Tatsuno, T. Yoshida, S. Otsuka, *Inorg. Synth.* **1990**, *28*, 342.
[28] G. M. Sheldrick, *SADABS, A Program for Empirical Absorption Correction of Area Detector Data*, University of Göttingen, Germany, **1996**. Based on the method of Robert Blessing: R. H. Blessing, *Acta Crystallogr., Sect. A: Found. Crystallogr.* **1995**, *51*, 33.
[29] G. M. Sheldrick, *SHELXS 97, a computer program for crystal structure determination*, University of Göttingen, **1997**.
[30] G. M. Sheldrick, *SHELXL 97, a computer program for crystal structure refinement*, University of Göttingen, **1997**.

Received: July 21, 2006
Published Online: November 14, 2006

 © 2007 Wiley-VCH Verlag GmbH & Co. KGaA, Weinheim 

DOI: 10.1002/ejic.200600705

# Reactions of GaCp* with a Hemilabile Derivative of $Rh_6(CO)_{16}$ – Synthesis and Structural Characterization of Two Novel Heterometallic Clusters: $Rh_6(CO)_{13}$-($\mu,\kappa^3$-$Ph_2PC_2H_3$)($\mu_3$-GaCp*) and $Rh_6(CO)_{13}$($\kappa^1$-$Ph_2PC_2H_3$)($\mu_3$-GaCp*)$_2$

**Elena V. Grachova,[a] Gerald Linti,[b] Hans-Georg Stammler,[c] Beate Neumann,[c] Sergey P. Tunik,*[a] and Hubert Wadepohl[b]**

**Keywords:** Cluster compounds / Heterometallic complexes / Phosphane ligands

The reaction of $Rh_6(CO)_{14}(Ph_2PCH{=}CH_2)$ with a twofold excess of GaCp* (Cp* = $C_5Me_5$) affords two novel heterometallic clusters $Rh_6(CO)_{13}(\mu,\kappa^3\text{-}Ph_2PC_2H_3)(\mu_3\text{-}GaCp^*)$ (**1**) and $Rh_6(CO)_{13}(\kappa^1\text{-}Ph_2PC_2H_3)(\mu_3\text{-}GaCp^*)_2$ (**2**) in a moderate yield. The hemilabile behavior of coordinated diphenylvinylphosphane in the starting cluster allows the easy insertion of GaCp* into the cluster coordination sphere, which eventually gives the cluster **1** with face-bridging coordination of the gallium fragment and the phosphane ligand recoordinated in an edge-bridging position. The further substitution of the vinyl function in **1** for the second GaCp* ligand affords cluster **2**, where recoordination of the double bond is blocked by steric hindrance from adjacent GaCp* fragments. Both clusters were structurally characterized by X-ray crystallography in the solid state and by IR and NMR spectroscopy in solution. Hemilability of diphenylvinylphosphane in **1** was independently confirmed by the cluster reaction with CO, which gives the $Rh_6(CO)_{14}(\kappa^1\text{-}Ph_2PC_2H_3)(GaCp^*)$ adduct (**3**) with the phosphane ligand only coordinated through the phosphorus atom.
(© Wiley-VCH Verlag GmbH & Co. KGaA, 69451 Weinheim, Germany, 2007)

## Introduction

Syntheses of heterometallic complexes with a direct bond between transition and nontransition metals has attracted considerable attention because of their unusual physico–chemical properties and their potential application in material science.[1–3] In this area the chemistry of gallium containing compounds has been significantly developed over the last years owing to the use of GaCp* as a ligand in the coordination chemistry of mono-[4–8] and polynuclear[9–12] complexes. Recently we reported the synthesis and structural characterization[13,14] of a series of "very-mixed-metal" clusters containing GaCp* fragments in $\mu_3$- and $\mu_2$-bridging positions over the $Rh_6$ and $Ru_6(C)$ metal frameworks. An extension of these studies in our laboratory was aimed at the modification of the cluster properties through further substitution of CO for such typically modifying ligands as the phosphanes. However, neither of the straightforward approaches, reactions of the phosphane substituted derivatives with GaCp* or treatment of the gallium containing clusters with phosphanes, gave positive results. To explore this chemistry further we attempted to prepare analogous heterometallic complexes using a hemilabile phosphanyl-alkenyl derivative of the $Rh_6(CO)_{16}$ cluster.[15] In general, the hemilabile ligands in cluster compounds facilitate substitution reactions and make it possible to direct the coordination of an incoming ligand to the position initially occupied by the labile function that determines the stereochemistry of the substituted product and mode of transformation of the coordinated substrate.[16–18] This approach proved to be successful and in this paper we report on the synthesis, structural characterization, and reactivity of three novel clusters: $Rh_6(CO)_{13}(\mu,\kappa^3\text{-}Ph_2PC_2H_3)(\mu_3\text{-}GaCp^*)$ (**1**), $Rh_6(CO)_{13}(\kappa^1\text{-}Ph_2PC_2H_3)(\mu_3\text{-}GaCp^*)_2$ (**2**), and $Rh_6(CO)_{14}(\kappa^1\text{-}Ph_2PC_2H_3)(GaCp^*)$ (**3**).

## Results and Discussion

The low temperature reaction of the starting $Rh_6(CO)_{14}(\mu,\kappa^3\text{-}Ph_2PC_2H_3)$ cluster with a twofold excess of GaCp* gives a mixture of the $Rh_6(CO)_{13}(\mu,\kappa^3\text{-}Ph_2PC_2H_3)(\mu_3\text{-}GaCp^*)$ (**1**) and $Rh_6(CO)_{13}(\kappa^1\text{-}Ph_2PC_2H_3)(\mu_3\text{-}GaCp^*)_2$ (**2**) clusters together with $Rh_6(CO)_{16-x}(GaCp^*)_x$ derivatives, and the latter were identified by their characteristic IR spectra.[13,14] Solid-state structures of **1** and **2** were established by X-ray crystallographic analysis. Selected structural pa-

[a] Department of Chemistry, St. Petersburg State University, Universitetskii pr. 26, 198504 St. Petersburg, Russia
Fax: +7-812-428-6939
E-mail: stunik@chem.spbu.ru
[b] Anorganisch-Chemisches Institut, Ruprecht-Karls-Universität Heidelberg,
Im Neuenheimer Feld 270, 69120 Heidelberg, Germany
[c] Fakultät für Chemie, Universität Bielefeld,
Universitätsstraße 25, 33615 Bielefeld, Germany
Supporting information for this article is available on the WWW under http://www.eurjic.org or from the author.

 © 2007 Wiley-VCH Verlag GmbH & Co. KGaA, Weinheim 

rameters of these molecules are given in Table 1, ORTEP views of **1** and **2** are shown in Figures 1 and 3, respectively.

The crystal structure of the cluster **1** appears disordered because of the presence of two isomers (approximate ratio 7:3), which differ in the orientation of the "$PhPCH{=}CH_2$" moiety with respect to the $Rh_3$ triangle it is coordinated to. The remaining part of the molecule is essentially identical for both isomers. The molecule of **1** consists of a $Rh_6$ octahedron with a face-bridging GaCp* and an edge-bridging $\mu,\kappa^3$-diphenylvinylphosphane coordinated over opposite faces of the octahedron. The ligand shell of the metal cluster is completed by three face-bridging and ten terminal CO

Table 1. Selected bond lengths [Å] and angles [°] for **1** and **2**.

| | **$Rh_6(CO)_{13}(Ph_2PC_2H_3)(GaCp^*)$, 1** | | | | **$Rh_6(CO)_{13}(Ph_2PC_2H_3)(GaCp^*)_2$, 2** | |
|---|---|---|---|---|---|---|
| Rh Rh triangles capped by GaCp* | Rh(1) Rh(2) | 2.8746(4) | | | Rh(1) Rh(2) | 2.8317(3) |
| | Rh(1) Rh(3) | 2.8123(4) | | | Rh(1) Rh(3) | 2.7920(3) |
| | Rh(2) Rh(3) | 2.8021(4) | | | Rh(1) Rh(4) | 2.8431(3) |
| | | | | | Rh(1) Rh(5) | 2.8508(3) |
| | | | | | Rh(2) Rh(3) | 2.8418(3) |
| | | | | | Rh(4) Rh(5) | 2.7859(3) |
| **Average**[a] | | **2.8297(0.0320)** | | | | **2.8242(0.0256)** |
| Rh Rh bonds remote to GaCp* | Rh(1) Rh(4) | 2.7380(3) | Rh(1) Rh(6) | 2.7428(3) | Rh(2) Rh(5) | 2.7526(3) |
| | Rh(2) Rh(4) | 2.7495(3) | Rh(2) Rh(5) | 2.7587(3) | Rh(2) Rh(6) | 2.7556(3) |
| | Rh(3) Rh(5) | 2.7810(3) | Rh(3) Rh(6) | 2.8016(3) | Rh(3) Rh(4) | 2.7815(3) |
| | Rh(4) Rh(5) | 2.7814(4) | Rh(4) Rh(6) | 2.7821(4) | Rh(3) Rh(6) | 2.7698(3) |
| | Rh(5) Rh(6) | 2.7065(3) | | | Rh(4) Rh(6) | 2.7933(3) |
| | | | | | Rh(5) Rh(6) | 2.8459(3) |
| **Average**[a] | | | | **2.7602(0.0276)** | | **2.7831(0.0314)** |
| Rh–($\mu_3$-CO) bond length | C(21) Rh(2) | 2.305(3) | C(22) Rh(1) | 2.192(3) | C(25) Rh(2) | 2.244(3) |
| | C(21) Rh(4) | 2.203(3) | C(22) Rh(4) | 2.204(3) | C(25) Rh(5) | 2.161(3) |
| | C(21) Rh(5) | 2.102(3) | C(22) Rh(6) | 2.130(3) | C(25) Rh(6) | 2.117(3) |
| | C(23) Rh(3) | 2.100(3) | | | C(28) Rh(3) | 2.206(3) |
| | C(23) Rh(5) | 2.153(3) | | | C(28) Rh(4) | 2.182(3) |
| | C(23) Rh(6) | 2.282(3) | | | C(28) Rh(6) | 2.155(3) |
| | **Major isomer** | | **Minor isomer** | | | |
| Bond lengths and angles in the $Ph_2PC_2H_3$ ligand | Rh(5) P(1a) | 2.260(5) | Rh(5) P(1b) | 2.351(11) | Rh(6) P(1) | 2.3416(8) |
| | Rh(6) C(25a) | 2.267(4) | Rh(6) C(25b) | 2.193(9) | P(1) C(34) | 1.809(3) |
| | Rh(6) C(24a) | 2.231(4) | Rh(6) C(24b) | 2.225(9) | C(34) C(35) | 1.314(5) |
| | P(1a) C(25a) | 1.812(6) | P(1b) C(25b) | 1.807(16) | Rh(6) P(1) C(34) | 115.51(10) |
| | C(24a) C(25a) | 1.384(7) | C(24b) C(25b) | 1.338(16) | P(1) C(34) C(35) | 124.8(3) |
| | Rh(5) P(1a) C(25a) | 101.6(2) | Rh(5) P(1b) C(25b) | 103.4(6) | | |
| | P(1a) C(25a) C(24a) | 125.7(4) | P(1b) C(25b) C(24b) | 125.3(11) | | |
| Non-bonding contacts of the $Ph_2PC_2H_3$ ligand and $\mu_3$-CO | C(22) H(24a) | 2.656 | C(22) H(26b) | 2.885 | | |
| | C(23) C(25a) | 2.834 | C(23) H(24b) | 2.750 | | |
| | C(23) H(26a) | 2.717 | O(23) H(24b) | 2.635 | | |
| | O(23) H(26a) | 2.646 | | | | |
| | **$Rh_6(CO)_{13}(Ph_2PC_2H_3)(GaCp^*)$, 1** | | **$Rh_6(CO)_{13}(Ph_2PC_2H_3)(GaCp^*)_2$, 2** | | | |
| Ga–Rh bond lengths | Ga(1) Rh(1) | 2.5800(4) | Ga(1) Rh(1) | 2.5835(4) | Ga(2) Rh(1) | 2.5214(4) |
| | Ga(1) Rh(2) | 2.5508(4) | Ga(1) Rh(2) | 2.5441(4) | Ga(2) Rh(4) | 2.5886(4) |
| | Ga(1) Rh(3) | 2.5789(4) | Ga(1) Rh(3) | 2.5703(4) | Ga(2) Rh(5) | 2.5822(4) |
| Ga $C_{centroid}$ | Ga(1) $C_{centroid}$ | 1.978 | Ga(1) $C_{centroid}$ | 1.994 | Ga(2) $C_{centroid}$ | 2.041 |
| Ga $Rh_{triangle}$ | Ga(1) $Rh_{triangle}$ | 1.984 | Ga(1) $Rh_{triangle}$ | 1.982 | Ga(2) $Rh_{triangle}$ | 1.978 |
| $C_{centroid}$ Ga $Rh_{triangle}$ | $C_{centroid}$ Ga(1) $Rh_{triangle}$ | 177.98 | $C_{centroid}$ Ga(1) $Rh_{triangle}$ | 177.35 | | |
| | | | $C_{centroid}$ Ga(2) $Rh_{triangle}$ | 171.75 | | |

[a] Values of standard deviations are given in brackets.

 © 2007 Wiley-VCH Verlag GmbH & Co. KGaA, Weinheim 

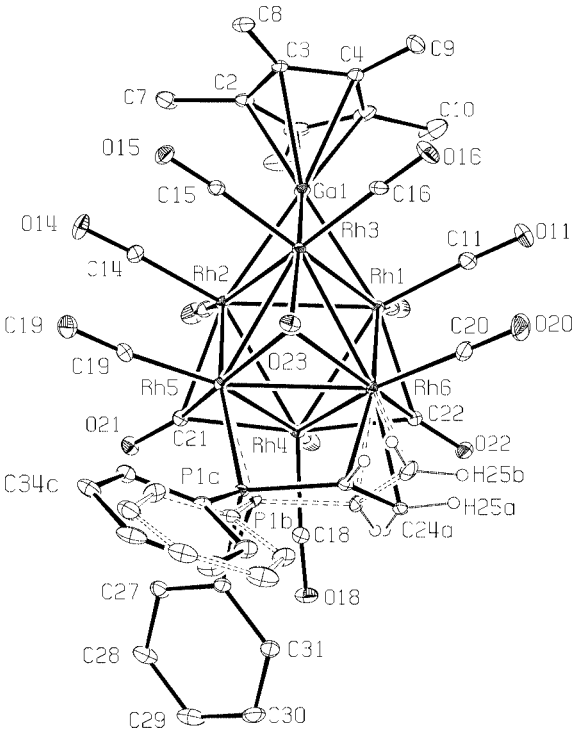


Figure 1. The ORTEP view of the $Rh_6(CO)_{13}(\mu,\kappa^3\text{-}Ph_2PC_2H_3)(\mu_3\text{-}GaCp^*)$ (**1**). Thermal ellipsoids are drawn at the 50% level.

ligands. The stoichiometry of **1** results in 86 valence electrons, which is consistent with the *closo* octahedral structure of the metal framework[19,20] as in the parent $Rh_6(CO)_{16}$[21] and its substituted derivatives.[15,21–24] The general structural motif of **1** is closely analogous to that of $[Rh_6(CO)_{14}(\mu,\kappa^3\text{-}Ph_2PC_2H_3)]$[15] apart from the presence of the GaCp* fragment in **1** instead of a face-bridging CO.

The effects of both substituting ligands ($Ph_2PC_2H_3$ and GaCp*) are nearly independent and their influence is observed in the vicinity of the substitution sites, see Table 1. Coordination of the short-bite vinylphosphane moiety results in contraction of the Rh–Rh edge spanned by the phosphane ligand. This bond is the shortest [2.7065(3) Å] metal–metal distance in the molecule. Very similar to the monosubstituted $Rh_6(CO)_{15}GaCp^*$ cluster[13] the metal–metal bonds in the rhodium triangle capped by the gallium ligand are considerably elongated. This is a typical electronic effect of the weak π acceptor and was found earlier in the clusters $Rh_6(CO)_{16-x}(GaCp^*)_x$[13] and $Ru_6(C)(CO)_{17-x}(GaCp^*)_x$.[14] The Ga–Rh distances fall into quite a narrow range (2.551–2.580 Å), which indicates an essentially symmetric coordination of the GaCp* moiety to the rhodium triangle.

The two isomers of **1** differ in the orientation of the P–C=C fragment of the vinylphosphane ligand relative to the Rh(4)Rh(5)Rh(6) triangle, Figure 2. In the major isomer the Rh–P distance [2.260(5) Å] is considerably shorter [cf. 2.351(11) Å in the minor species], which is indicative of a stronger metal-to-phosphorus bonding. A comparison of the angular parameters that characterize the P–Rh(5) interaction also points to a less strained bonding mode of the phosphorus atom to the octahedral framework in the major isomer. The Rh(4)–Rh(5)–P and Rh(6)–Rh(5)–P angles are equal to 96.8° and 78.0° (major isomer), and 88.3° and 73.8° (minor isomer), whereas the *cis* Rh–Rh–C(O) angles in the parent (unstrained) $Rh_6(CO)_{16}$ are equal to ca. 97°.[21] On the contrary, distances from the carbon atoms of the coordinated vinyl moiety to Rh(6) are somewhat longer in the major species (Table 1), which is evidently a geometrical consequence of the strong phosphorus-to-rhodium bond mentioned above. Similar to the $Rh_6(CO)_{14}(\mu,\kappa^3\text{-}Ph_2PC_2H_3)$ cluster[15] both isomers display short (<2.9 Å) nonbonding contacts between atoms of the vinyl fragment and adjacent face-bridging C(22)O and C(23)O ligands. This steric hindrance results in the shift of the C(23)O group from the substituted Rh(5) and Rh(6) centers to Rh(3), opposite to the regular shift caused by the electronic effect of a heteroligand.[15,21,22,25] It is worth noting that the present crystallographic study, which revealed two conformations of the P–C=C fragment in the solid-state structure of **1**, independently confirmed the structural models of the $Rh_6(CO)_{14}(\mu,\kappa^3\text{-}Ph_2PC_2H_3)$ isomers suggested in our earlier work, which was solely based on NMR spectroscopic data.[15] The disposition of the vinyl moiety over the metal triangle in the minor conformer of the parent $Rh_6(CO)_{14}(\mu,\kappa^3\text{-}Ph_2PC_2H_3)$ cluster[15] matches well the structural pattern shown in part b of Figure 2.

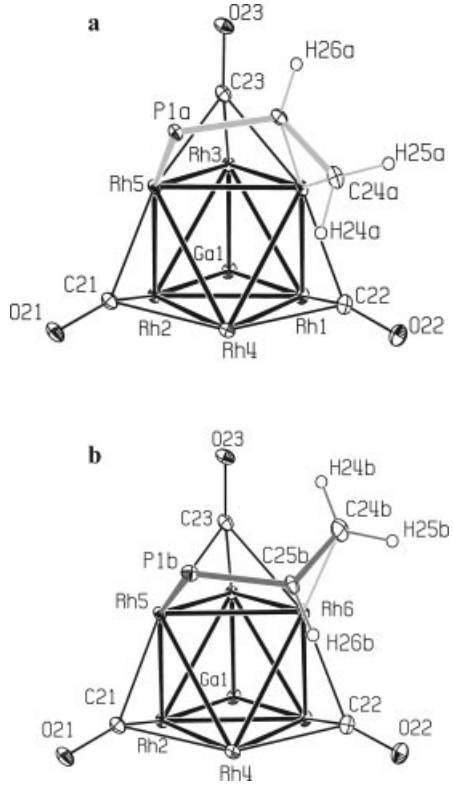


Figure 2. Two isomers of the **1** cluster; (a) major isomer, (b) minor isomer. For the sake of simplicity terminal CO ligands are omitted.

The $^1H$ and $^{31}P$ NMR spectroscopic study of **1** showed that in solution this cluster exists as a mixture of two isomers, the structures of which obviously match those found

 © 2007 Wiley-VCH Verlag GmbH & Co. KGaA, Weinheim 

in the solid state. The chemical shifts and coupling constants of the signals observed in the $^1H$ spectrum are completely consistent with the data obtained earlier for the conformers of $Rh_6(CO)_{14}(\mu,\kappa^3\text{-}Ph_2PC_2H_3)$.[15] It is also worth noting that the Rh–P coupling constants of the isomers of **1** are in agreement with the Rh–P bond lengths in these species. The stronger Rh–P bond in the major isomer gives rise to a higher value of the corresponding coupling constant. These two forms of the vinyl fragment coordination easily convert into each other; the rate of the dynamic process is slow at 273 K and gives the low-temperature-limiting spectrum shown in Figure S1 (S denotes data in Supporting Information file). The resonances from the minor isomer broaden on heating and eventually disappear into the baseline at 313 K. This behavior is very similar to the dynamics observed in $Rh_6(CO)_{14}(\mu,\kappa^3\text{-}Ph_2PC_2H_3)$,[15] however, the exchange rate in the latter case is slightly higher.

The $Rh_6(CO)_{13}(\kappa^1\text{-}Ph_2PC_2H_3)(\mu_3\text{-}GaCp^*)_2$ cluster (**2**) is evidently a result of the hemilabile vinyl function substitution for GaCp* followed by the rearrangement of the ligand sphere to give the face-bridging coordination of the GaCp* moiety (Figure 3). The substitution does not change the electron count for **2**, which is in agreement with the *closo* octahedral structure of the cluster framework. In contrast to **1** the phosphane ligand is only coordinated through the phosphorus atom, occupying a terminal position at the Rh(6) center. Possible coordination of the vinyl double bond to either Rh(4) or Rh(5) is obviously prevented by steric hindrance from the Ga(2)Cp* ligand. Local changes of the cluster geometry in **2** are in line with the regular effects of face-bridging GaCp*[13,14] and terminal phosphane ligands.[21] Metal–metal distances inside the rhodium triangles capped by GaCp* are significantly elongated ($d^{av}$ = 2.824 Å) compared with the bond lengths of the rest of the octahedron ($d^{av}$ = 2.783 Å). In the latter group the two bonds *cis* to the phosphane ligand are the longest (see Table 1), which is consistent with the general trend observed in the substituted $Rh_6(CO)_{16}$ derivatives.[21] The NMR spectroscopic data of **2** indicate that the structure found in the solid state remains unchanged in solution. The $^1H$ NMR spectrum of this cluster displays a broad multiplet of phenyl rings centered at 7.5 ppm, two singlets of slightly inequivalent Cp* methyl groups (2.17 and 2.19 ppm), and three resonances of the vinyl protons {$\delta$ =5.02 ppm [H(34)], 5.83 ppm [H(35b)], and 6.61 ppm [H(35a)]}, which are considerably low-field shifted compared with the spectrum of the coordinated vinyl fragment in **1** (see Experimental Section) and in $Rh_6(CO)_{14}(\mu,\kappa^3\text{-}Ph_2PCH{=}CH_2)$,[15] and demonstrate a very good agreement with the proton NMR spectrum of free diphenylvinylphosphane (see Figure S2). This observation clearly indicates that in solution the vinyl functionality remains uncoordinated as found in the solid state.

The $^{13}C$ NMR spectrum (see Experimental Section and Figure S3 in Supporting Information file) also fits well the structure found in the solid state. The spectrum displays resonances of two phenyl rings and the signals of inequivalent GaCp* ligands. The spectroscopic pattern observed in the carbonyl region of the spectrum displays three doublets and two dd resonances of terminal CO groups together with a quartet of the face bridging ligand that is in agreement with the presence of the symmetry plane through the Rh(1), Rh(6), C(33), and P(1) atoms. Additional phosphorus–car-

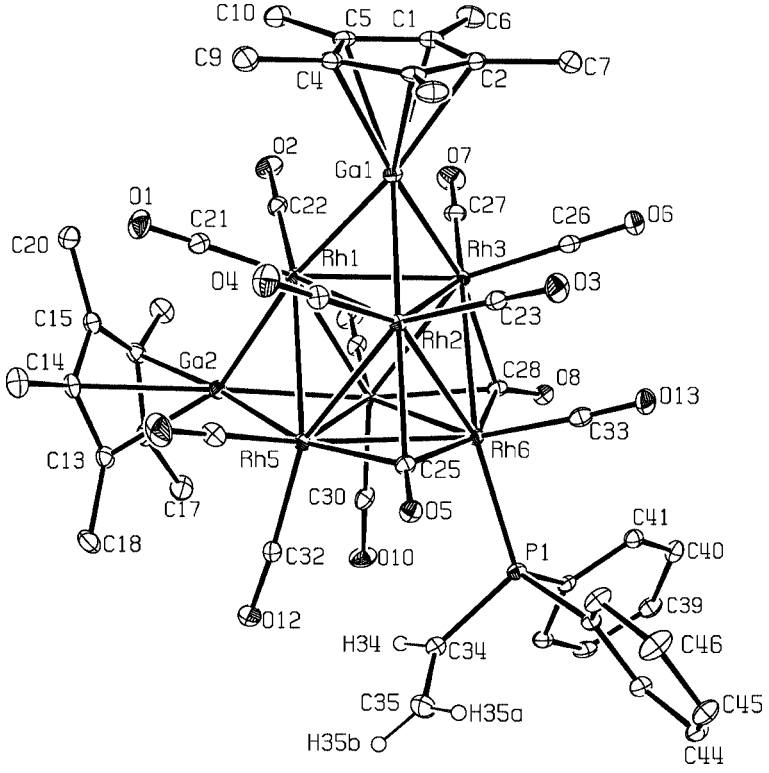


Figure 3. The ORTEP view of the $Rh_6(CO)_{13}(\mu,\kappa^1\text{-}Ph_2PC_2H_3)(\mu_3\text{-}GaCp^*)_2$ (**2**). Thermal ellipsoids are drawn at the 50% level.

 © 2007 Wiley-VCH Verlag GmbH & Co. KGaA, Weinheim 

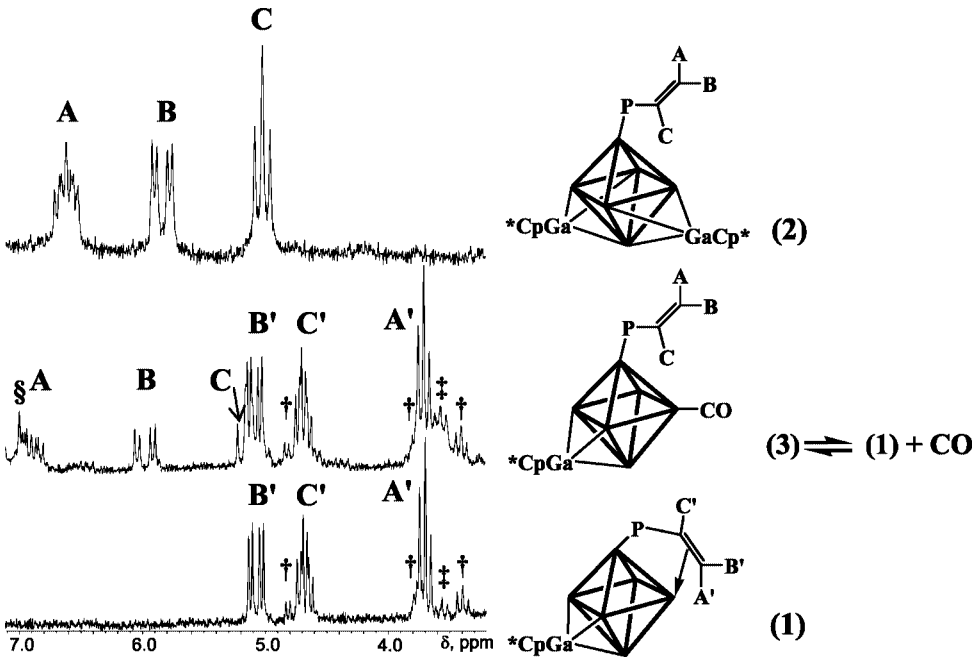


Figure 4. $^1$H NMR spectra of **1**, **2**, and **3**; $CDCl_3$, 25 °C. The structures of the corresponding molecules are schematically shown on the right side of the figure. The admixture of the $Rh_6(CO)_{14}(\mu,\kappa^3\text{-}Ph_2PC_2H_3)$ starting cluster is marked by ‡. The signals of minor isomer **1** are marked by †. A signal of an unidentified impurity is marked by §.

bon couplings $^2J_{P–C(33)}$ and $^3J_{P–C(24,27)}$ are completely consistent with the stereochemistry of the intervening nuclei. It is interesting to note that this molecule is stereochemically rigid at room temperature in contrast with the $Rh_6(CO)_{15}PR_3$ derivatives that display low-temperature exchange between terminal and face-bridging CO groups bonded to the phosphane substituted rhodium atoms.[25] A similar C(33)O ↔ C(28)O, C(25)O exchange is still mechanistically possible in **2** but the electronic effect of the $\mu_3$-GaCp* ligands in some way enlarges the barrier of these dynamics.

It has to be noted that the closest analogs of the starting cluster $[Rh_6(CO)_{14}(\mu\text{-dppm})]$ and $Rh_6(CO)_{14}(\mu,\kappa^2\text{-}Ph_2PPy)$, which contain non-hemilabile bridging phosphanes,[15,22] do not react with GaCp*, neither in the presence of $Me_3NO$ nor under heating up to 50 °C. These observations stress a crucial role of the vinyl function hemilability in the chemistry under study. Initial coordination of the gallium ligand is at the terminal vacancy and this is followed by its migration into the thermodynamically stable face-bridging position. At the first stage this migration is accompanied by the recoordination of the vinyl function to keep it apart from the GaCp* moiety as shown in Figure 4. In the case of the cluster **2** the recoordination is sterically hindered because all available edge-bridging (with respect to phosphorus) positions are adjacent to $\mu_3$-GaCp* ligands. This keeps the vinyl function in **2** uncoordinated.

Hemilabile behavior of the vinylphosphane in **1** was confirmed by the reaction of this cluster with gaseous CO. Saturation of the $CDCl_3$ solution of **1** with CO followed by the proton (Figure 4) and $^{31}$P NMR (Figure S4) spectroscopic measurements showed that under these conditions **1** exists in equilibrium with the CO adduct **3**. Three multiplets of the vinyl protons in the adduct are very similar in location to those of cluster **2**, as are the spin-spin couplings (see Experimental Section), which clearly points to decoordination of the vinyl moiety. The $^{31}$P NMR spectrum of the CO saturated solution of **1** is also very similar to that of $Rh_6(CO)_{14}(\mu,\kappa^3\text{-}Ph_2PCH{=}CH_2)$ under similar conditions (Figure S4). It was shown earlier[15] that the latter cluster easily substitutes the vinyl functionality with CO and similar spectroscopic characteristics of CO saturated solutions of these clusters implies a similarity in the chemistry that has occurred. A relative amount of the adduct **3** is ca 10–15% and purging of the reaction mixture with argon easily converts **3** into **1**.

In conclusion, this study has shown that hemilabile ligands in cluster complexes may provide easy access to various substituted products including those that contain such unusual substituents as GaCp* moieties. The presence of additional phosphane ligands in the coordination sphere of the starting cluster determines the stoichiometry of the products and their stereochemistry because of the mutual influence of the phosphane and incoming ligands.

## Experimental Section

**General Comments:** All operations were carried out under an atmosphere of dry argon using standard Schlenk techniques. All solvents were distilled under an inert atmosphere over the appropriate drying agents prior to use. Commercial grade $Ph_2PC_2H_3$ (Aldrich) was used without additional purification. The starting $Rh_6(CO)_{14}(Ph_2PC_2H_3)$[15] cluster and the GaCp*[26] complex were synthesized according to literature procedures. Infrared spectra were recorded using a Specord M80 spectrometer. $^1$H, $^{13}$C{$^1$H}, and $^{31}$P{$^1$H}

 © 2007 Wiley-VCH Verlag GmbH & Co. KGaA, Weinheim 

NMR spectra were recorded in $C_6D_6$ and $CDCl_3$ at room temperature using a Bruker DPX-300 instrument. The chemical shifts were referenced to residual solvent resonances for the $^1H$ and $^{13}C$ NMR spectra and external 85% $H_3PO_4$ for the $^{31}P$ NMR spectra. Microanalyses were carried out in the Microanalytical Laboratory of St. Petersburg State University. FAB mass spectra were obtained with a VG Autospec instrument (Institute of Organic Chemistry, University of Heidelberg). The observed isotopic distribution patterns completely fit the calculated ones. The products were purified by column chromatography on silica, 5–40 mesh, Merck Kieselgel 60.

**Synthesis of 1 and 2:** $Rh_6(CO)_{14}(Ph_2PC_2H_3)$ (50 mg, 0.041 mmol) was dissolved in THF (20 mL) and frozen in a Schlenk vessel by liquid nitrogen. A glass capillary tube with GaCp* (20 mg, 0.097 mmol) was placed into the vessel. The reaction mixture was warmed to room temperature under vigorous stirring, which broke the capillary tube immediately. After an hour all volatile components of the reaction mixture were removed in vacuo to leave a brown-greenish precipitate, which was washed with *n*-hexane (10 mL) and dried once more in vacuo. The residue was redissolved in $CH_2Cl_2$ (10 mL) and diluted with *n*-hexane (30 mL). The solution was transferred onto a chromatographic column (3 × 10 cm). Elution with *n*-hexane/$CH_2Cl_2$ (3:1 v/v) gave the following bands in the order of elution: $Rh_6(CO)_{12}(GaCp^*)_4$, $Rh_6(CO)_{13}(GaCp^*)_3$, $Rh_6(CO)_{13}(Ph_2PC_2H_3)(GaCp^*)_2$ (**2**, 23 mg), $Rh_6(CO)_{15}(GaCp^*)$, and $Rh_6(CO)_{13}(Ph_2PC_2H_3)(GaCp^*)$ (**1**, 14 mg). Removal of the solvents from the third and fifth bands gave brown and green-brown crystalline materials, respectively. The other components of the reaction mixture were identified by comparison of their IR spectroscopic characteristics with the literature data.[13]

**1:** IR ($CH_2Cl_2$): $\tilde{\nu}_{max}$(CO) = 2076 (w), 2052 (s), 2040 (s), 2016 (m), 1780 (m br), 1768 (m br) $cm^{-1}$. $^1H$ NMR (300 MHz, $CDCl_3$): **Major isomer:** $\delta$ = 2.24 (s, 15 H, $C_5Me_5$), 3.67 [ddd, $^2J_{H(24a)-H(25a)}$ = 2.0, $^3J_{H(24a)-H(26a)}$ = 14.0, $^3J_{H(24a)-P(1a)}$ = 14.0, 1 H, *H*(24a)], 4.68 [ddd, $^3J_{H(26a)-H(24a)}$ = 14.0, $^2J_{H(26a)-P(1a)}$= 14.0, $^3J_{H(26a)-H(25a)}$ = 10.0, 1 H, *H*(26a)], 5.07 [ddd, $^3J_{H(26a)-H(25a)}$ = 10.0, $^2J_{H(25a)-H(24a)}$ = 2.0, $^3J_{H(25a)-P(1a)}$ = 26.0, 1 H, *H*(25a)], 7.36–8.14 (m, 10 H, *phenyl rings*) ppm. **Minor isomer:** $\delta$ = 2.25 (s, 15 H, $C_5Me_5$), 3.40 [dd, $^3J_{H(24b)-H(26b)}$ = 14.0, $^3J_{H(24b)-P(1b)}$ = 14.0, 1 H, *H*(24b)], 3.74 [ddd, $^3J_{H(26b)-H(25b)}$ = 10.0, $^2J_{H(26b)-P(1b)}$ = 14.0, $^3J_{H(26b)-H(24b)}$ = 10.0, 1 H, *H*(26b)], 4.77 [dd, $^3J_{H(25b)-H(26b)}$ = 10.0, $^3J_{H(25b)-P(1b)}$ = 26.0, 1 H, *H*(25b)], 7.36–8.14 (m, 10 H, *phenyl rings*) ppm. $^{31}P\{^1H\}$ NMR (121 MHz, $CDCl_3$) **Major isomer:** $\delta$ = 17.0 [dd, $^1J_{Rh(5)-P(1a)}$ = 130, $^2J_{Rh(2)-P(1a)}$ = 7, 1 P, *P*(1a)] ppm. **Minor isomer:** $\delta$ = 27.0 [d, $^1J_{Rh(5)-P(1b)}$ = 122, 1 P, *P*(1b)] ppm. $C_{37}H_{28}GaO_{13}PRh_6$: calcd. C 31.77, H 2.02; found C 31.98, H 2.47. MS FAB$^+$: 1397 ($M^+$), 1369 ($M^+$ – 1 CO), 1285 ($M^+$ – 4 CO), 1257 ($M^+$ – 5 CO), 1229 ($M^+$ – 6 CO), 1201 ($M^+$ – 7 CO), 1173 ($M^+$ – 8 CO). Single crystals of **1** suitable for X-ray studies were obtained by gas-phase diffusion of *n*-hexane into $CH_2Cl_2$ solution under a nitrogen atmosphere.

**2:** IR ($CH_2Cl_2$): $\tilde{\nu}_{max}$(CO) = 2040 (vs), 2024 (s), 2000 (m), 1772 (m br), 1756 (m br) $cm^{-1}$. $^1H$ NMR (300 MHz, $CDCl_3$): $\delta$ = 2.17 (s, 15 H, $C_5Me_5$), 2.19 (s, 15 H, $C_5Me_5$), 5.02 [dd, $^3J_{H(34)-H(35a)}$ = 17.0, $^2J_{H(34)-P}$ = 20.0, 1 H, *H*(34)], 5.83 [dd, $^3J_{H(35b)-P}$ = 36.0, $^2J_{H(35b)-H(35a)}$ = 12.0, 1 H, *H*(35b)], 6.61 [ddd, $^3J_{H(34)-H(35a)}$ = 17.0, $^2J_{H(35b)-H(35a)}$ = 12.0, $^2J_{H(35a)-P}$ = 28.0, 1 H, *H*(35a)], 7.38–7.68 (m, 10 H, *phenyl rings*) ppm. $^{31}C\{^1H\}$ NMR (125 MHz, $CDCl_3$, ambient temperature): $\delta$ = 11.03 (s, $C_5Me_5$), 11.15 (s, $C_5Me_5$), 119.19 (s, $C_5Me_5$), 119.38 (s, $C_5Me_5$), 128.80 (d, $^1J_{C-P}$ = 10, 4 C, $C_{ortho/meta}$), 131.15 (s, 2 C, $C_{para}$), 134.14 (d, $^1J_{C-P}$ = 10, 4 C, $C_{meta/ortho}$), 184.27 (d, $^1J_{C-Rh}$ = 64, 2 CO, *t*-*CO*), 184.73 (d, $^1J_{C-Rh}$ = 64, 2 CO, *t*-*CO*), 185.84 (dd, $^1J_{C-Rh}$ = 70, $^2J_{C-P}$ = 13, 1CO, *t*-*C*(33)*O*), 186.53 [dd, $^1J_{C-Rh}$ = 68, $^3J_{C-P}$ = 19, 2 CO, *t*-*C*(24)*O* and *t*-*C*(27)*O*], 187.23 (d, $^1J_{C-Rh}$ = 62, 2 CO, *t*-*CO*), 188.08 (d, $^1J_{C-Rh}$ = 65, 2 CO, *t*-*CO*), 253.93 (ddd, $^1J_{C-Rh}$ = 21, $^1J_{C-Rh}$ = 28, $^1J_{C-Rh}$ = 32, 2 CO, $\mu_3$-*CO*) ppm. $^{31}P\{^1H\}$ NMR (121 MHz, $CDCl_3$, ambient temperature): $\delta$ = 21.0 [d, $^1J_{Rh-P}$ = 131, *P*(1)] ppm. $C_{47}H_{43}Ga_2O_{13}PRh_6$ + $C_6H_{14}$: calcd. C 37.67, H 3.40; found C 36.99, H 3.77. MS FAB$^+$: 1604 ($M^+$), 1549 ($M^+$ – 2 CO), 1436 ($M^+$ – 6 CO), 1408 ($M^+$ – 7 CO), 1380 ($M^+$ – 8 CO), 1352 ($M^+$ – 9 CO), 1324 ($M^+$ – 10 CO). Single crystals of **2** suitable for X-ray studies were obtained by gas-phase diffusion of *n*-hexane into $CH_2Cl_2$ solution under a nitrogen atmosphere.

**Reaction of 1 with Gaseous CO:** A solution of the $Rh_6(CO)_{13}(Ph_2PC_2H_3)(GaCp^*)$ in $CDCl_3$ (0.5 $cm^3$) in a standard NMR tube (5 mm) was saturated with gaseous CO at room temperature. $^1H$ and $^{31}P$ NMR spectra showed the formation of a new $Rh_6(CO)_{14}(\kappa^1\text{-}Ph_2PC_2H_3)(GaCp^*)$ (**3**) complex, which was characterized by $^1H$ and $^{31}P\{^1H\}$ NMR spectroscopy. Under these conditions the

Table 2. Crystallographic data for **1** and **2**.

| | | |
|---|---|---|
| Empirical formula | $C_{37}H_{28}Ga_1O_{13}PRh_6$ (**1**) | $C_{47}H_{43}Ga_2O_{13}PRh_6 \cdot CH_2Cl_2$ (**2**) |
| Formula mass [g mol$^{-1}$] | 1398.74 | 1688.61 |
| Temperature [K] | 100(2) | 100 |
| Wavelength [Å] | 0.71073 | 0.71073 |
| Space group | $P2_1/c$ | $P2_1/c$ |
| *a* [Å] | 20.4099(16) | 20.0500(2) |
| *b* [Å] | 10.8774(9) | 14.85500(10) |
| *c* [Å] | 21.9594(14) | 18.6900(2) |
| $\beta$ [°] | 122.238(5) | 102.6100(5) |
| *V* [Å$^3$] | 4123.6(5) | 5432.40(9) |
| *Z* | 4 | 4 |
| Calculated density [g cm$^{-3}$] | 2.253 | 2.065 |
| *F*(000) | 2680 | 3272 |
| Crystal size [mm] | 0.15 × 0.15 × 0.10 | 0.30 × 0.30 × 0.05 |
| $\theta$ range for data collection [°] | 1.85 to 32.02 | 2.9 to 27.5 |
| Index ranges | $-30 \le h \le 27$, $-16 \le k \le 0$, $-32 \le l \le 26$ | $-26 \le h \le 25$, $-19 \le k \le 19$, $-24 \le l \le 24$ |
| Reflections collected/unique | 73119/14142 [*R*(int) = 0.0440] | 130198/12404 [*R*(int) = 0.050] |
| Completeness to: | $\theta$ = 32.02° 98.5% | $\theta$ = 27.5° 99.7% |
| Data/restraints/parameters | 14142/0/574 | 12404/0/659 |
| Goodness-of-fit on $F^2$ | 1.076 | 1.062 |
| Final *R* indices [$I > 2(I)$] | $R_1$ = 0.0303, $wR_2$ = 0.0656 | $R_1$ = 0.0262, $wR_2$ = 0.0595 |
| *R* indices (all data) | $R_1$ = 0.0445, $wR_2$ = 0.0703 | $R_1$ = 0.0339, $wR_2$ = 0.0620 |
| Largest diff. peak [e Å$^{-3}$] | 0.151, 1.111 | 1.119 |

 © 2007 Wiley-VCH Verlag GmbH & Co. KGaA, Weinheim 

ratio **1/3** equals 7:1. The cluster **3** is unstable and readily converts back to **1** after purging the CO saturated solution with argon.

**3:** $^1$H NMR (300 MHz, $CDCl_3$, ambient temperature): $\delta$ = 2.21 (s, 15 H, $C_5Me_5$), 5.15 {dd, $^3J_{H(26)-H(24)}$ 18.5, $^2J_{H(26)-P(1)}$ 20.0, 1 H, *H*(26)], 5.97 [dd, $^3J_{H(25)-P(1)}$ 37.2, $^2J_{H(25)-H(24)}$ 12.2, 1 H, *H*(25)], 6.89 [ddd, $^3J_{H(26)-H(24)}$ 18.5, $^2J_{H(25)-H(24)}$ 12.2, $^2J_{H(24)-P(1)}$ 29.0, 1 H, *H*(24)], 7.36–8.14 (m, 10 H, *phenyl rings*) ppm. $^{31}P\{^1H\}$ NMR (121 MHz, $CDCl_3$, ambient temperature): $\delta$ = 20.0 [d, $^1J_{Rh(5)-P}$ = 131, *P*(1)] ppm. A resolution enhancement procedure was used to obtain spin-spin coupling constants in the $^1$H spectrum of **3**.

**X-ray Crystal Structure Determinations**

**Complex 1:** Intensity data were collected at low temperature with a Bruker AXS Smart1000 CCD diffractometer, and corrected for absorption and other effects.[27] The structure was solved by the Patterson method and refined by full-matrix least-squares based on $F^2$. All non-hydrogen atoms were given anisotropic displacement parameters. Hydrogen atoms were inserted in calculated positions. The calculations were performed using the programs DIRDIF[27] and SHELXL.[28]

**Complex 2:** Single crystals of **2** (dimensions $0.30 \times 0.30 \times 0.05$ mm) were used for data collection at 100 K with a Bruker-Nonius KappaCCD diffractometer with graphite-monochromated Mo-$K_\alpha$ radiation ($\lambda$ = 0.71073 Å). The structure was solved by direct methods. The program package used was SHELXL 97.[28] Full-matrix least-squares refinement on $F^2$ was carried out anisotropically for the non-hydrogen atoms. Hydrogen atoms were included at calculated positions using a riding model.

The crystallographic data are summarized in Table 2. Selected bond lengths and angles for **1** and **2** are shown in Table 1.

**Supporting Information** (see also the footnote on the first page of this article): VT $^1$H NMR spectra of **1**, $^1$H NMR spectrum of free diphenylvinylphosphane, $^{13}$C NMR spectrum of **2**, $^{31}$P NMR spectra of **1**, **2** and **3**.

## Acknowledgments

Financial support from the Alexander von Humboldt Foundation (for E. V. G.) and RFBR (Grant 05-03-33266) is gratefully acknowledged.

[1] C. Gemel, T. Steinke, M. Cokoja, A. Kempter, R. A. Fischer, *Eur. J. Inorg. Chem.* **2004**, 4161–4176.
[2] G. Linti, H. Schnöckel, *Coord. Chem. Rev.* **2000**, *206–207*, 285–319.
[3] G. Linti, W. Kostler, *Chem. Eur. J.* **1998**, *4*, 942–949.
[4] P. Jutzi, B. Neumann, G. Reumann, H.-G. Stammler, *Organometallics* **1998**, *17*, 1305–1314.
[5] P. Jutzi, B. Neumann, L. O. Schebaum, A. Stammler, H.-G. Stammler, *Organometallics* **2000**, *19*, 1445–1447.
[6] P. Jutzi, B. Neumann, L. O. Schebaum, A. Stammler, H.-G. Stammler, *Organometallics* **1999**, *18*, 4462–4464.
[7] D. Weiss, T. Steinke, M. Winter, R. A. Fischer, N. Frohlich, J. Uddin, G. Frenking, *Organometallics* **2000**, *19*, 4583–4588.
[8] H. Folsing, O. Segnitz, U. Bossek, K. Merz, M. Winter, R. A. Fischer, *J. Organomet. Chem.* **2000**, *606*, 132–140.
[9] P. Jutzi, N. Lenze, B. Neumann, H.-G. Stammler, *Angew. Chem. Int. Ed.* **2001**, *40*, 1424–1427.
[10] D. Weiss, M. Winter, R. A. Fischer, C. Yu, K. Wichmann, G. Frenking, *Chem. Commun.* **2000**, 2495–2496.
[11] M. Cokoja, T. Steinke, C. Gemel, T. Welzel, M. Winter, K. Merz, R. A. Fischer, *J. Organomet. Chem.* **2003**, *684*, 277–286.
[12] C. Gemel, T. Steinke, D. Weiss, M. Cokoja, M. Winter, R. A. Fischer, *Organometallics* **2003**, *22*, 2705–2710.
[13] E. V. Grachova, P. Jutzi, B. Neumann, L. O. Schebaum, H.-G. Stammler, S. P. Tunik, *J. Chem. Soc., Dalton Trans.* **2002**, 302–304.
[14] E. V. Grachova, P. Jutzi, B. Neumann, H.-G. Stammler, *Dalton Trans.* **2005**, 3614–3616.
[15] E. V. Grachova, M. Haukka, B. T. Heaton, E. Nordlander, T. A. Pakkanen, I. S. Podkorytov, S. P. Tunik, *Dalton Trans.* **2003**, 2468–2473.
[16] N. Lugan, F. Laurent, G. Lavigne, T. P. Newcomb, E. W. Liimatta, J. J. Bonnet, *Organometallics* **1992**, *11*, 1351–1363.
[17] E. Rosenberg, L. Milone, R. Gobetto, D. Osella, K. Hardcastle, S. Hajela, K. Moizeau, M. Day, E. Wolf, D. Espitia, *Organometallics* **1997**, *16*, 2665–2673.
[18] J. A. Cabeza, *Eur. J. Inorg. Chem.* **2002**, 1559–1570.
[19] M. McPartlin, D. M. P. Mingos, *Polyhedron* **1984**, *3*, 1321–1328.
[20] M. S. Owen, *Polyhedron* **1988**, *7*, 253.
[21] D. H. Farrar, E. V. Grachova, A. Lough, C. Patirana, A. J. Poe, S. P. Tunik, *J. Chem. Soc., Dalton Trans.* **2001**, 2015–2019.
[22] D. H. Farrar, E. V. Grachova, M. Haukka, B. T. Heaton, J. A. Iggo, T. A. Pakkanen, I. S. Podkorytov, S. P. Tunik, *Inorg. Chim. Acta* **2003**, *354*, 11–20.
[23] S. P. Tunik, I. O. Koshevoy, A. J. Poe, D. H. Farrar, E. Nordlander, M. Haukka, T. A. Pakkanen, *Dalton Trans.* **2003**, 2457–2467.
[24] D. V. Krupenya, S. I. Selivanov, S. P. Tunik, M. Haukka, T. A. Pakkanen, *Dalton Trans.* **2004**, 2541–2549.
[25] E. V. Grachova, B. T. Heaton, J. A. Iggo, I. S. Podkorytov, D. J. Smawfield, S. P. Tunik, R. Whyman, *J. Chem. Soc., Dalton Trans.* **2001**, 3303–3311.
[26] P. Jutzi, L. O. Schebaum, *J. Organomet. Chem.* **2002**, *654*, 176–179.
[27] P. T. Beurskens, G. Beurskens, R. de Gelder, S. Garcia-Granda, R. O. Gould, R. Israel, J. M. M. Smits, in: *The DIRDIF-99 program system*, The Netherlands, **1999**.
[28] G. M. Sheldrick, in: *SHELXL97, Program for Crystal Structure Refinement*, **1997**.

Received: July 28, 2006
Published Online: November 9, 2006

 © 2007 Wiley-VCH Verlag GmbH & Co. KGaA, Weinheim 

DOI: 10.1002/ejic.200600710

# Alkylmono(cyclopentadienyl)titanium Complexes Containing the 2,2′-Methylenebis(6-*tert*-butyl-4-methylphenoxido) Ligand – Studies on the Nature of the Catalytic Species Present in α-Olefin Polymerisation Processes

**Marta González-Maupoey,[a] Tomás Cuenca,*[a] Luis Manuel Frutos,[b] Obis Castaño,[b] Eberhardt Herdtweck,[c] and Bernhard Rieger[d]**

**Keywords:** Titanium / Chelates / Olefin polymerisation / Density functional calculations

The mono(alkyl)bis(phenoxido)titanium complexes [TiR′($\eta^5$-$C_5R_5$)($\eta^2$-mbmp)] [R = H, R′ = Me (**4**), $CH_2Ph$ (**5**), Ph (**6**), $CH_2SiMe_3$ (**7**); R = Me, R′ = Me (**8**), $CH_2Ph$ (**9**), $CH_2SiMe_3$ (**10**); $\eta^2$-mbmp = 2,2′-methylenebis(6-*tert*-butyl-4-methylphenoxido)] have been prepared in good yields by reaction of the appropriate alkylating reagent with the corresponding chlorido(cyclopentadienyl)bis(phenoxido)titanium derivative. Compound **6** reacts in toluene with traces of water to afford the μ-oxidotitanium complex {Ti($\eta^5$-$C_5H_5$)($\eta^2$-mbmp)}$_2$(μ-O) (**11**). Compounds **8**, **9** and **11** have been characterised by single-crystal X-ray crystallography, and density functional calculations have been performed in order to elucidate the energetic and structural properties of these compounds. The activity of these complexes in the presence of methylaluminoxane (MAO), $B(C_6F_5)_3$ or $[Ph_3C][B(C_6F_5)_4]$ as co-catalysts in the polymerisation of propylene and styrene has been studied. In an effort to model the nature of the catalytic species generated from these precursors, the reactions of the mono(cyclopentadienyl)bis(phenoxido)chlorido- and -alkyltitanium derivatives with Lewis acids were examined. $B(C_6F_5)_3$ reacts with the neutral complexes [TiR′($\eta^5$-$C_5R_5$)($\eta^2$-mbmp)] by abstraction of the alkyl group R′ to give the highly stable species [Ti($\eta^5$-$C_5H_5$)($\eta^2$-mbmp)][$MeB(C_6F_5)_3$] (**12**), [Ti($\eta^5$-$C_5H_5$)($\eta^2$-mbmp)][$(PhCH_2)B(C_6F_5)_3$] (**13**), [Ti($\eta^5$-$C_5Me_5$)($\eta^2$-mbmp)][$MeB(C_6F_5)_3$] (**14**) and [Ti($\eta^5$-$C_5Me_5$)($\eta^2$-mbmp)][$(PhCH_2)B(C_6F_5)_3$] (**15**), which are inactive in propylene and styrene polymerisation. In contrast, the reaction between the neutral alkyl derivatives and $[CPh_3][B(C_6F_5)_4]$ affords species that are active in α-olefin polymerisation. Treatment of the mono(chlorido) compound [TiCl($\eta^5$-$C_5H_5$)($\eta^2$-mbmp)] with 1 equiv. of $AlMe_3$ affords the methyl derivative **4** as essentially the only reaction product. When an excess of $AlMe_3$ is used, transmetallation reactions of the bis(phenoxido) ligand from titanium to aluminium are observed. Reactions of the bis(phenol) $mbmpH_2$ with $AlMe_3$ or $AlClMe_2$ yield $[AlMe(mbmp)]_2$ (**16**) and $[AlCl(mbmp)]_2$ (**17**).
(© Wiley-VCH Verlag GmbH & Co. KGaA, 69451 Weinheim, Germany, 2007)

## Introduction

Alkoxido derivatives of transition metals are used as catalysts in a wide range of homogeneous reactions, and early transition metal elements are strongly stabilized in high oxidation states by alkoxido (or phenoxido) ligands.[1–3] Alkoxidotitanium and -zirconium compounds combined with a co-catalyst (MAO) are highly active catalysts in α-olefin polymerisation.[4–9] The synthesis of dialkyl(alkoxido) derivatives of group 4 elements is very difficult as they are sensitive to atmospheric moisture and to light. The reaction of $[MR_{4-x}(OAr)_x]$ complexes with the Lewis acid $B(C_6F_5)_3$ has been reported to give the zwitterionic species $[M(CH_2Ph)(OAr)_2][B(\eta^6\text{-}C_6H_5CH_2)(C_6F_5)_3]$ for the benzyl derivatives and a mixture of $[Ti(C_6F_5)Me(OAr)_2]$ and $BMe(C_6F_5)_2$ for the methyl complexes.[10]

In a previous paper we reported the synthesis and characterisation of the mono(cyclopentadienyl)titanium complexes [TiClCp′($\eta^2$-mbmp)] [Cp′ = $\eta^5$-$C_5H_5$ (**1**), $\eta^5$-$C_5Me_5$ (**2**), $\eta^5$-$C_5H_4SiMe_2Cl$ (**3**)] containing the bis(phenoxido) bidentate dianionic ligand 2,2′-methylenebis(6-*tert*-butyl-4-methylphenoxido) ($\eta^2$-mbmp). Density functional calculations developed for these complexes provide remarkable conclusions about their structural behaviour, which were subsequently confirmed by X-ray diffraction studies in the solid state. After activation with MAO, these mono(cyclopentadienyl)titanium derivatives are suitable catalysts for olefin (propylene, styrene and isoprene) polymerisation.[11]

To elucidate the influence of the co-catalyst used in these studies on the activity of the catalyst, as well as on the poly-

[a] Departamento de Química Inorgánica, Universidad de Alcalá, Campus Universitario,
28871 Alcalá de Henares, Spain
Fax: +34-91-885-4683
E-mail: tomas.cuenca@uah.es
[b] Departamento de Química Física, Universidad de Alcalá, Campus Universitario,
28871 Alcalá de Henares, Spain
[c] Anorganisch-chemisches Institut, Technische Universität München,
Lichtenberstrasse 4, 85747 Garching bei München, Germany
[d] Abteilung Anorganische Chemie II, Universität Ulm,
Albert-Einstein-Allee 11, 89069 Ulm, Germany
Supporting information for this article is available on the WWW under http://www.eurjic.org or from the author.

 © 2007 Wiley-VCH Verlag GmbH & Co. KGaA, Weinheim 

merisation mechanism, we have synthesised new alkylmono(cyclopentadienyl)titanium systems containing the mbmp ligand. Here we report the synthesis of [TiR′($\eta^5$-$C_5R_5$)($\eta^2$-mbmp)] (R = H, Me; R′ = Me, $CH_2Ph$, Ph, $CH_2SiMe_3$) derivatives, their reactions with Lewis acids {$AlMe_3$, $B(C_6F_5)_3$ and $[CPh_3][B(C_6F_5)_4]$} as well as their catalytic application in α-olefin polymerisation, in which different co-catalysts and temperature conditions were employed. The synthesis of a dinuclear μ-oxidotitanium derivative [{Ti($\eta^5$-$C_5H_5$)($\eta^2$-mbmp)}$_2$(μ-O)] and dinuclear aluminium compounds [AlX(mbmp)]$_2$ (X = Cl, Me) with a μ-$\eta^1$,$\eta^2$ disposition of the mbmp ligand are also reported. The X-ray molecular structures of [TiR′($\eta^5$-$C_5Me_5$)($\eta^2$-mbmp)] (R′ = Me, $CH_2Ph$) and [{Ti($\eta^5$-$C_5R_5$)($\eta^2$-mbmp)}$_2$(μ-O)] complexes were determined by diffraction methods and density functional calculations performed for [TiR′($\eta^5$-$C_5H_5$)($\eta^2$-mbmp)] (R′ = Me, $CH_2Ph$, Ph).

## Results and Discussion

### Synthesis of Complexes

The reaction of the chlorido derivatives [TiCl($\eta^5$-$C_5R_5$)($\eta^2$-mbmp)] [R = H (**1**), Me (**2**); $\eta^2$-mbmp = 2,2′-$CH_2$-bis(6-*t*Bu-4-$CH_3C_6H_2$-1-O)],[11] with 1.2 equiv. of MR′ (M = Li, R′ = Me, $CH_2Ph$, Ph, $CH_2SiMe_3$; M = Mg, R′ = $ClCH_2$, $ClCH_2Ph$), in hexane at –78 °C, affords the alkylmono(cyclopentadienyl) complexes [TiR′($\eta^5$-$C_5R_5$)($\eta^2$-mbmp)] [R = H, R′ = Me (**4**), $CH_2Ph$ (**5**), Ph (**6**), $CH_2SiMe_3$ (**7**); R = Me, R′ = Me (**8**), $CH_2Ph$ (**9**), $CH_2SiMe_3$ (**10**)] containing a bidentate bis(phenoxido) ligand (Scheme 1). The compounds were isolated as yellow-orange solids in 60–80% yield.

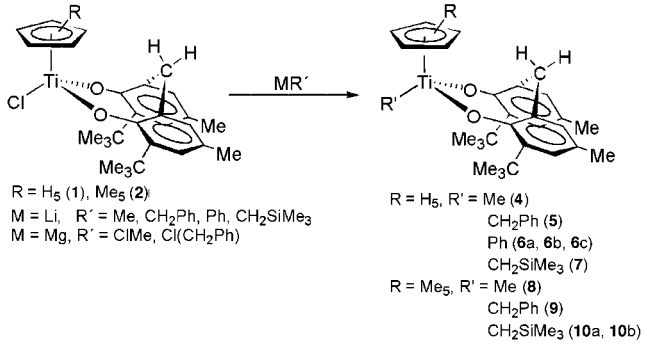


Scheme 1.

When compound **6** reacts in toluene with traces of water at room temperature crystals of a dimetallic complex with an oxygen atom bridging two titanium atoms and identified as [{Ti($\eta^5$-$C_5H_5$)($\eta^2$-mbmp)}$_2$(μ-O)] (**11**) were obtained (Scheme 2).

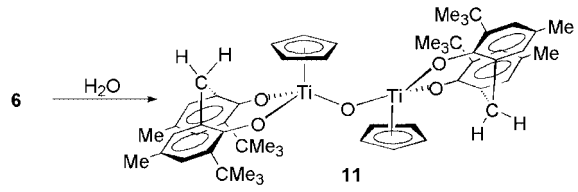


Scheme 2.

Compounds **4**–**10** are soluble in chlorinated solvents (chloroform and dichloromethane) and aromatic (benzene, toluene) and aliphatic hydrocarbons (pentane and hexane), while complex **11** only presents low solubility in toluene and chlorinated solvents (chloroform and dichloromethane). They can be stored under an inert gas in solution for months and are stable for some weeks in the solid state without decomposition. They were characterised by elemental analysis and NMR spectroscopy. The elemental analysis values found for **5** were inaccurate due to the presence of small amounts of impurities which could not be removed, although this compound has been characterised by spectroscopic methods. The analytical composition fits the proposed formulation exactly. The molecular structures of **8**, **9** and **11** have been determined by X-ray diffraction.

The NMR spectra ($C_6D_6$ and $CDCl_3$, room temperature) of complexes **4**–**10** show patterns for the mbmp fragment similar to those described for compounds containing the same bis(phenoxido) ligand.[11] The two $CH_2$ protons appear in the $^1$H NMR spectra as a pair of doublets; the value of the chemical shift difference ($\Delta\delta$, $C_6D_6$) between their chemical shifts varies between 2.13 and 0.28 ppm. This difference seems to be due to changes in the configuration of the metallacyclic ring in solution.[11] Both equivalent *tert*-butyl groups and the two methyl substituents on the phenyl rings appear as singlets between $\delta$ = 1.49–1.20 and 2.18–2.07 ppm in $C_6D_6$, respectively. The protons at the 3- and 5-positions on the phenyl ring give two doublets, corresponding to AA′ spin systems, with a $^4J_{H,H}$ coupling constant of 1.83 Hz. Singlets are observed for the cyclopentadienyl and the methylcyclopentadienyl ring protons in the expected region of the spectra. For all of these compounds, structural features similar to those determined by $^1$H NMR spectroscopy can be deduced from the $^{13}C\{^1H\}$ NMR spectra ($C_6D_6$, room temperature). These spectroscopic data are consistent with $C_s$-symmetrical molecules. In the $^1$H NMR spectra, the alkyl substituents at the titanium centre show the expected behaviour for this kind of group in $C_s$ molecules, namely one singlet for the methyl group, two singlets that integrate for two and nine protons for the $CH_2SiMe_3$ substituent, one singlet and signals of aromatic protons for the $CH_2Ph$ group and resonances of aromatic protons for the phenyl group, with the corresponding resonances in the $^{13}C\{^1H\}$ NMR spectra.

The $^1$H NMR spectrum of **11** shows two doublets for the methylene protons with a chemical shift difference between them of 1.00 ppm ($C_6D_6$). The *tert*-butyl and methyl groups of each bis(phenoxido) ligand are not equivalent and appear as two singlets. The protons in the 3- and 5-positions

 © 2007 Wiley-VCH Verlag GmbH & Co. KGaA, Weinheim 

on the phenyl rings are also not equivalent and appear as four doublets. However, the molecule is symmetric as a result of the presence of a $C_2$ axis through the bridging oxygen atom that runs perpendicular to the titanium–oxygen bonds. As a consequence, each fragment of the phenoxido ligand of one titanium centre is equivalent to the opposite fragment of the phenoxido ligand of the other titanium centre, as shown in Scheme 2. The molecular structure determined by X-ray diffraction confirms this proposed arrangement, thus indicating that the solid-state structure is maintained in solution.

The $^1$H NMR spectra of analytically pure samples of **4**, **5** and **7** show only one pattern for the signals discussed. The study of the phenyl derivative **6** showed the presence of three different isomers (**6a**, **6b** and **6c**). Isomers **6a** and **6b** can be separated as pure samples by repeated recrystallisation from toluene because of their different solubility. A solution of **6b** in deuterated benzene evolves to a 1:1 molar ratio mixture of **6b** and **6c** at room temperature in 3 h, while a solution of **6a** under the same conditions remains unaltered for a long time. The formation of a single compound was observed spectroscopically for the pentamethylcyclopentadienyl derivatives **8** and **9**, while the $^1$H NMR spectrum of **10** shows two sets of signals, thus indicating that this complex is obtained in solution as a mixture of two isomers (**10a/10b**) in a 10:1 molar ratio. Theoretical studies (see below) permitted us to understand this behaviour.

### Study of the Molecular Structure – Theoretical and Conformational Studies and Crystal Structure of [TiMe($\eta^5$-$C_5Me_5$)($\eta^2$-mbmp)] (8), [Ti($CH_2Ph$)($\eta^5$-$C_5Me_5$)($\eta^2$-mbmp)] (9) and [{Ti($\eta^5$-$C_5H_5$)($\eta^2$-mbmp)}$_2$(μ-O)] (11)

For the [TiR′Cp($\eta^2$-mbmp)] type of compounds the existence of four possible conformers related by two different conformational change processes, i.e., by ring inversion and boat/chair interconversion (Scheme 3) can be proposed.[11]

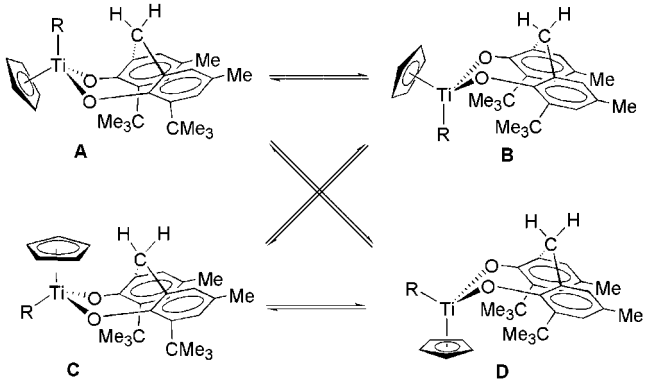


Scheme 3.

The HF method with B3LYP hybrid exchange-correlation energy functional[12] implemented in the Gaussian suite of programs[13] using a 3-21g* basis set was employed in order to explore the potential energy surface (PES) and to locate the minima involved in the related processes. All the structures were optimised at this level of theory. To study the character of the stationary points found, an analysis of the approximate Hessian was made, which confirmed all these points as minima on the PES. In our search, three different conformers (**I**, **II**, and **III**) were found (Figure 1).

The equilibrium Ti–O bond length, the relative electronic energies and the relative population based on Boltzmann's equilibrium distribution at 298 K of these three conformers for compounds **4**–**6** and previously reported **1**[11] are listed in Table 1.

For almost all of the complexes studied, the most stable conformer (**I**) has a geometry intermediate between a boat and a chair conformation (intermediate between **C** and **B** in Scheme 3, although slightly closer to the boat than to the chair), with the Cp ligand close to the methylene bridge between the phenyl groups and short Ti–O bond lengths (1.78–1.807 Å).

The second calculated conformer (**II** in Figure 1, corresponding to a disposition similar to **A** in Scheme 3 but intermediate between **A** and **D**) has a similar arrangement to conformer **I**, with the Cp and alkyl ligands interchanged. The Ti–O bond lengths are analogous (1.79–1.803 Å) to those found for conformer **I**. These calculations suggest a clear degree of multiple bonding in the Ti–O link close to sp hybridisation for both conformers. For complex **6**, we can see how the high planarity of the C–O–Ti–O–C fragment makes isomers **I** and **II** very close in energy.

The third conformer (**III** in Figure 1, corresponding to a disposition close to **D** in Scheme 3) exhibits different behaviour to **I** and **II** as a result of its geometrical structure. It presents a closer $sp^2$ oxygen angle and a larger Ti–O bond length (1.81–1.814 Å).

As a result of the calculations, two boat conformers (**I** and **II**) related through a ring-inversion process could be expected. Conformer **III**, in which the oxygen atoms move toward $sp^2$ hybridisation, is the most unstable due to Ti–O bond weakening, which raises the energy by around 13 kcal mol$^{-1}$ with respect to the most stable conformer for compounds **1** and **4**. The stability of each conformer is reflected in the Ti–O bond order in such a way that the shorter the bond the greater the stability. The preference to adopt conformation **I** or **II** depends on the steric impediment exerted by the cyclopentadienyl ring and the alkyl substituent at the titanium centre.

As shown in Table 1, **I** is the most stable conformer for compounds **1**, **4** and **6**, in which the Cp ligand is located towards the methylene bridge. A small difference in stability between **I** and **II** is predicted for compound **6**, while for compounds **1** and **4** higher differences in the related energies are deduced; only for complex **5** is conformation **II** more stable than **I** due to the high steric hindrance produced between the *t*Bu groups of the bis(phenoxido) ligand and the ring of the benzyl substituent. The high relative energies of conformations **I** and **III** for complex **5** are comparable as a result of this steric hindrance, which in **III** is due to the steric hindrance between the cyclopentadienyl

 © 2007 Wiley-VCH Verlag GmbH & Co. KGaA, Weinheim 

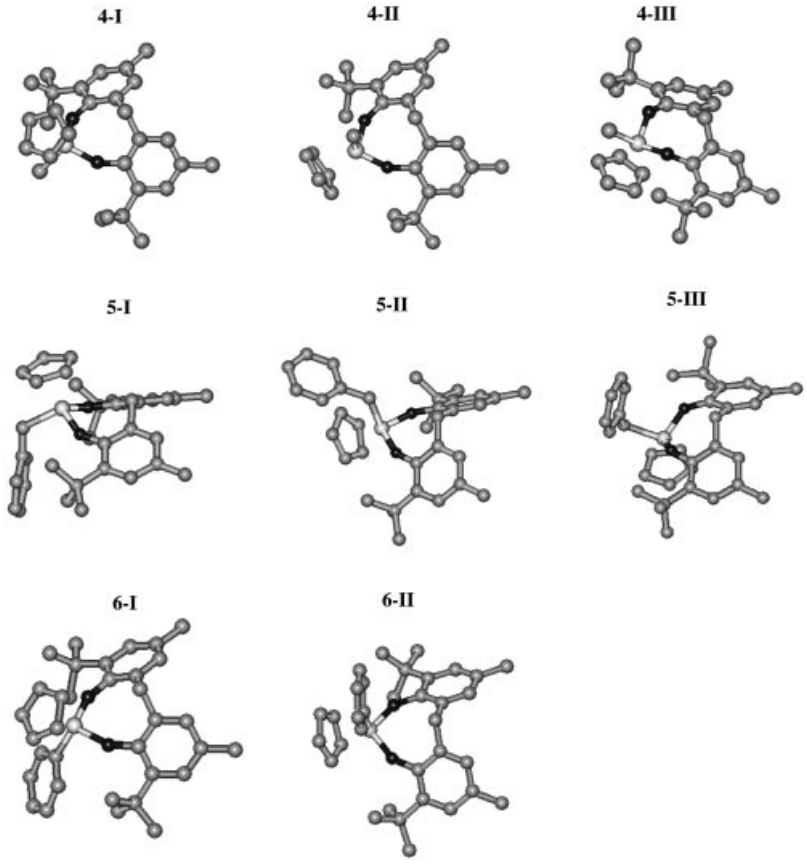


Figure 1. Optimised structures for [TiR′Cp($\eta^2$-mbmp)] [R′ = Me (**4**), $CH_2Ph$ (**5**), Ph (**6**)] complexes.

Table 1. Ti–O distances, energetics and Boltzmann populations for the calculated isomers.

| | Ti–O distance [Å] | | | | Relative energy[a] [kcal mol$^{-1}$] | | | | Boltzmann equilibrium population[b] | | | |
|---|---|---|---|---|---|---|---|---|---|---|---|---|
| | **1** | **4** | **5** | **6** | **1** | **4** | **5** | **6** | **1** | **4** | **5** | **6** |
| **I** | 1.78 | 1.797 | 1.807 | 1.799 | 0.0 | 0.0 | 5.02 | 0.0 | 98.5 | 99.9 | ca. 0.0 | 81.3 |
| **II** | 1.79 | 1.801 | 1.801 | 1.803 | 2.5 | 4.30 | 0.0 | 0.86 | 1.5 | 0.1 | <99.9 | 18.7 |
| **III** | 1.81 | 1.814 | 1.813 | – | 12.1 | 13.68 | 6.06 | – | 0.0 | 0.0 | 0.0 | – |

[a] Energy relative to the most stable conformer. [b] Percent populations of the different conformers at 298 K following a distribution of the energies according to Boltzman's distribution law.

ligand and the *t*Bu groups. These theoretical results are in agreement with the NMR experimental data. Although complexes **1**, **4** and **5** could exist in three different conformations, the high stability of disposition **I** for **1** and **4** (or **II** for **5**) is enough to make these the only preferred conformations, which leads to the formation of one unique isomer, as observed spectroscopically.

For complex **6**, the theoretical studies predict the possibility of two boat conformations (**I** and **II**) with similar energies and therefore both species can coexist in solution at room temperature. These theoretical studies explain the presence of two of the three patterns of signals found in the NMR spectra. In contrast, the value of the chemical shift difference for the two methylene protons of the bis(phenoxido) ligand in the $^1$H NMR spectrum is initially an excellent probe for the detection of the metallacycle conformation.[11] Taking into account the relationship between this value and the conformation found in the X-ray structures elucidated for this type of complex (see below and ref.[11]), a $\Delta\delta_{CH_2}$ value of around or below 1.00 ppm points to a boat conformation. In this sense, conformations **I** and **II** would correspond to isomers **6a** and **6b**. The third pattern (**6c**) could correspond to conformer **III**, which, although it is not found by the theoretical calculations, is experimentally plausible and would explain why a pure solution of **6b** interconverts at room temperature to an equimolecular mixture of **6b** and **6c**.

To establish and to confirm the structural details of the molecular geometry in the solid state for this type of compound, X-ray crystal structure analyses of **8**, **9** and **11** were carried out. Single crystals of **8** obtained by slow recrystallisation from hexane solution were of good enough quality to be analysed by X-ray diffraction. The crystal structure of **8** is shown in Figure 2. Crystals of **9** were also obtained

 © 2007 Wiley-VCH Verlag GmbH & Co. KGaA, Weinheim 

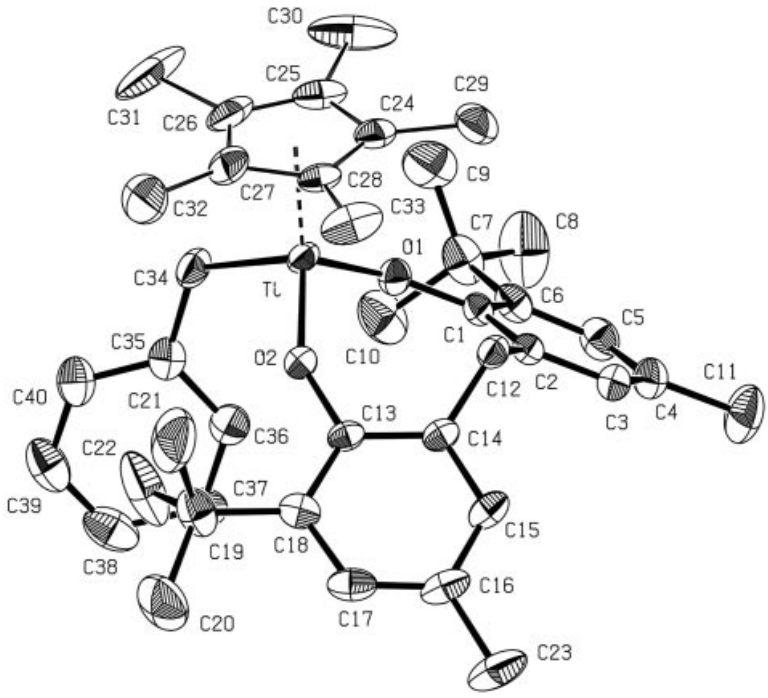


Figure 2. ORTEP plot of compound **8** in the solid state. Thermal ellipsoids are drawn at the 50% probability level. Hydrogen atoms are omitted for clarity.

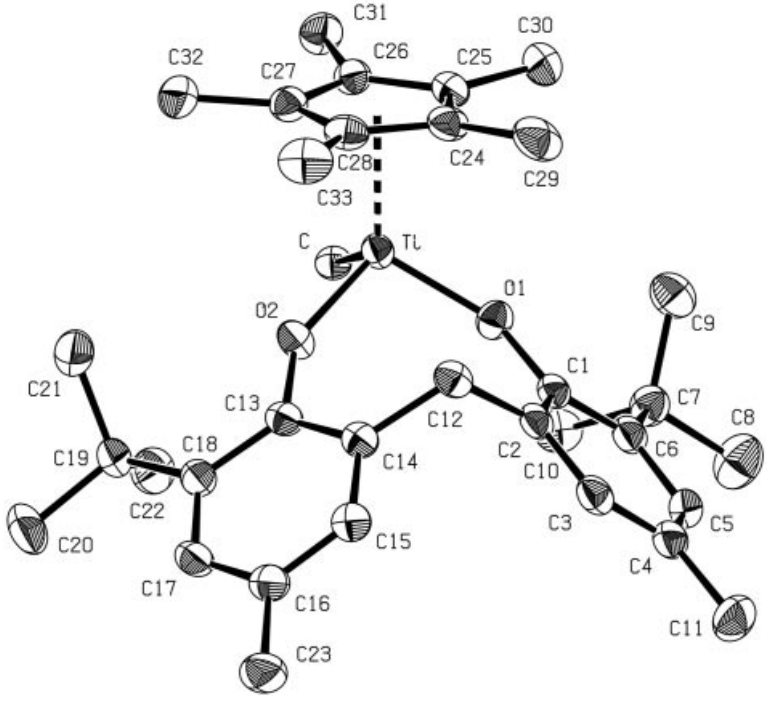


Figure 3. ORTEP plot of compound **9** in the solid state. The major part (82.1%) of the disordered Cp ligand is shown. Thermal ellipsoids are drawn at the 50% probability level. Hydrogen atoms are omitted for clarity.

from hexane solution at –20 °C but were not good enough for X-ray crystallography. However, it was possible to determine its molecular structure, which is depicted in Figure 3. Table 2 summarises selected bond lengths and angles.

The mbmp ligand adopts a puckered chelate disposition with the typical boat conformation in the solid state with the methylene bridge pointing toward the cyclopentadienyl ring.[9,14,15] The observed structural parameters correlate

 © 2007 Wiley-VCH Verlag GmbH & Co. KGaA, Weinheim 

Table 2. Selected bond lengths [Å] and bond angles [°] for **8** and **9**.

| | **8** | **9** |
|---|---|---|
| Ti–O1 | 1.840(1) | 1.828(2) |
| Ti–O2 | 1.834(1) | 1.833(2) |
| Ti–C–C34 | 1.993(2) | 2.154(2) |
| O1–C1 | 1.364(2) | 1.365(2) |
| O2–C13 | 1.372(2) | 1.362(3) |
| Ti–C24 | 2.370(2) | 2.373(3)[a] |
| Ti–C25 | 2.404(2) | 2.430(3)[a] |
| Ti–C26 | 2.436(2) | 2.425(3)[a] |
| Ti–C27 | 2.403(2) | 2.364(3)[a] |
| Ti–C28 | 2.373(2) | 2.341(3)[a] |
| Ti···Cg[b] | 2.071 | 2.064[a] |
| O1–Ti–O2 | 101.63(6) | 102.96(7) |
| O1–Ti–C/C34 | 101.39(6) | 97.15(7) |
| O1–Ti···Cg[b] | 119.62 | 120.45[a] |
| O2–Ti–C/C34 | 101.07(7) | 105.37(8) |
| O2–Ti···Cg[b] | 119.37 | 118.11[a] |
| C–C34–Ti···Cg[b] | 110.84 | 109.98[a] |
| Ti–O1–C1 | 148.9(1) | 151.3(1) |
| Ti–O2–C13 | 149.1(1) | 148.0(1) |
| C2–C12–C14 | 113.2(1) | 117.2(2) |

[a] Distances and angles to the major part (82.1%) of the disordered Cp ligand. [b] Cg denotes the cyclopentadienyl ring centroid.

well with those calculated for the most stable conformer determined by density functional calculations. This confirms that the preferred structure for these complexes in the solid state is the boat conformation, in agreement with the theoretical results, from which a similar boat conformation is predicted for the analogous complexes bearing an $\eta^5$-$C_5H_5$ ligand.

The coordination geometry around the titanium atom is a pseudo-three-legged piano stool, as expected for complexes of the type $TiCpL_3$.[16] The metal–oxygen bond lengths in **8** (av. 1.8367 Å) and **9** (av. 1.8300 Å) are in the expected range for titanium complexes with a linked bis(phenoxido) ligand with ($\sigma + \pi$) donor oxygen atoms.[3,17] Compared with the related structure of the chlorido derivative **2**,[11] the presence of a less electronegative alkyl group increases the electronic density at the metal centre, which leads to longer average Ti–O bonds and a more open O1–Ti–O2 angle.

The geometry adopted for these complexes is a compromise situation where the least steric hindrance between the pentamethylcyclopentadienyl ring and the methylene bridge is produced and the methyl substituent is located far away from the *tert*-butyl groups of the bis(phenoxido) ligand.

Crystals of compound **9** diffracted poorly, as indicated by the weak diffraction patterns, the high thermal parameters and the high *R* values. The pentamethylcyclopentadienyl ring is disordered but the refinement shows undoubtedly that complex **9** is present as described. As can be seen in Figure 3, complex **9** presents a boat conformation with the methylene bridge pointing toward the pentamethylcyclopentadienyl ring, in a similar manner to conformation **I** obtained in the theoretical study. This study for the analogous benzylmono(cyclopentadienyl) complex **5** predicted a boat conformation of type **II**, with the benzyl substituent far away from the *tert*-butyl groups of the bis(phenoxido) ligand. Nevertheless, the difference in steric relaxation between the benzyl group and the pentamethylcyclopentadienyl ring near the *tert*-butyl groups should not be significant for compound **9**, which prefers to adopt the most stable type-**I** conformation, which is the preferred conformation for the chlorido-, methyl- and phenyl(cyclopentadienyl) derivatives deduced from the theoretical study.

The structure of compound **11** was confirmed by X-ray diffraction analysis. A view of the molecular structure is given in Figure 4 and selected bond lengths and angles are listed in Table 3.

The coordination sphere around the metal centre is a four-legged piano stool. The bite angles of the bis(phenoxido) ligands [O(1)–Ti(1)–O(2) = 103.23(6)° and O(3)–Ti(2)–O(4) = 103.97(6)°] are larger than 90° and in the same range

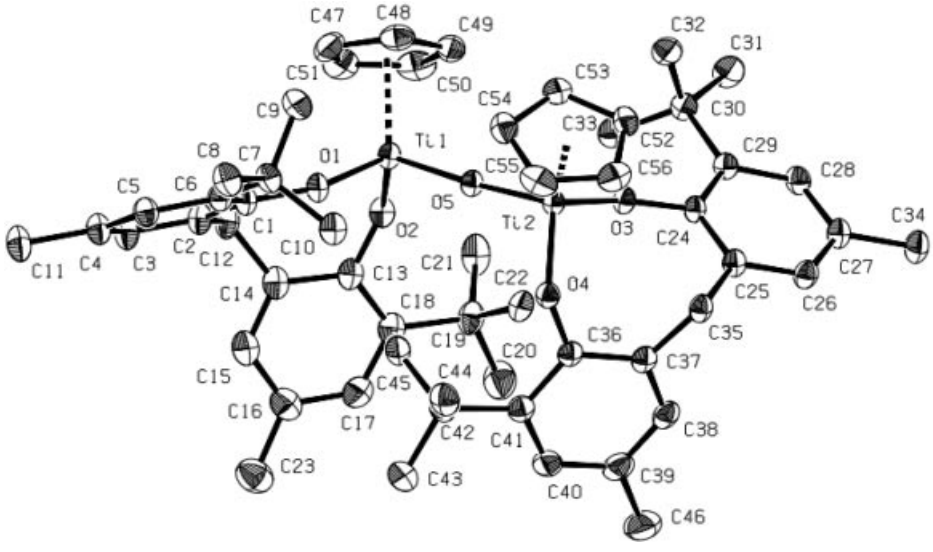


Figure 4. ORTEP plot of compound **11** in the solid state. Thermal ellipsoids are drawn at the 40% probability level. Hydrogen atoms are omitted for clarity.

 © 2007 Wiley-VCH Verlag GmbH & Co. KGaA, Weinheim 

Table 3. Selected bond lengths [Å] and bond angles [°] for **11**·0.75$C_6H_{14}$.

| Bond lengths [Å] | | Bond angles [°] | |
|---|---|---|---|
| Ti1–O1 | 1.808(2) | O1–Ti1–O2 | 103.23(6) |
| Ti1–O2 | 1.843(2) | O1–Ti1···Cg1[a] | 117.85 |
| Ti2–O3 | 1.809(2) | O2–Ti1···Cg1[a] | 111.56 |
| Ti2–O4 | 1.857(2) | O5–Ti1···Cg1[a] | 114.87 |
| Ti1–O5 | 1.826(1) | O1–Ti1–O5 | 102.13(6) |
| Ti2–O5 | 1.816(1) | O2–Ti1–O5 | 105.80(6) |
| Ti1···Cg1[a] | 2.069 | O3–Ti2–O4 | 103.97(6) |
| Ti2···Cg2[a] | 2.066 | O3–Ti2···Cg2[a] | 116.88 |
| O1–C1 | 1.367(3) | O4–Ti2···Cg2[a] | 111.83 |
| O2–C13 | 1.352(3) | O5–Ti2···Cg2[a] | 114.12 |
| O3–C24 | 1.363(2) | O3–Ti2–O5 | 102.13(6) |
| O4–C36 | 1.360(3) | O4–Ti2–O5 | 106.76(6) |
| | | Ti1–O5–Ti2 | 174.30(8) |
| | | C14–C12–C2 | 115.9(2) |
| | | C25–C35–C37 | 115.5(2) |
| | | Ti1–O1–C1 | 152.9(1) |
| | | Ti1–O2–C13 | 134.5(1) |
| | | Ti2–O3–C24 | 152.3(1) |
| | | Ti2–O4–C36 | 132.0(1) |

[a] Cg denotes the cyclopentadienyl ring centroid.

as those obtained for complexes containing the mbmp ligand, such as [Ti(mbmp)$_2$] [106.24(7)° and 107.28(8)°],[3] [$TiCl_2$(mbmp)] [106.5(2)°],[18] [$TiMe_2$(mbmp)] [112.7(2)°],[18] [Ti(mbmp)($BH_4$)$_2$] [103.9(2)°],[19] and the mono(cyclopentadienyl)bis(phenoxido)titanium complexes [CpTiX($OC_6H_3$-*i*$Pr_2$)$_2$] [X = Cl, *t*Bu and Me; 103.0(3)°, 107.7(9)° and 109.0(5)°, respectively].[20] The dihedral angles between both phenyl rings are 115.92(19)° and 115.52(18)°, more open than those found for analogous ligands with different bridging units {S in tmbp and Te in tebp [tmbp = 2,2′-thiobis(6-*tert*-butyl-4-methylphenoxido), tebp = 2,2′-tellurobis(6-*tert*-butyl-4-methylphenoxido)]; [Ti(mbmp)($BH_4$)$_2$] = 64.1(2)°,[19] [$TiCl_2$(mbmp)(thf)] = 113.4(3)°,[21] [$TiCl_2$(tmbp)]$_2$ = 102.9(3)°,[5] [CpTiCl(tmbp)] = 107.3(1)°[9] and [$TiCl_2$(tebp)]$_2$ = 96.0(2)°}.[15]

The mbmp ligand adopts a typical boat conformation in the solid state, with one of the methylene bridge protons pointing towards the metal centre and the other away from it and with both in the proximity of the cyclopentadienyl ring.[9,15] The metal–oxygen bond lengths [Ti(1)–O(1) = 1.808(2), Ti(1)–O(2) = 1.843(2), Ti(2)–O(3) = 1.809(2) and Ti(2)–O(4) = 1.857(2) Å] are short but in the expected range for titanium complexes with a linked bis(phenoxido) ligand with (σ + π) donor oxygen atoms, such as [Ti(mbmp)$_2$] [av. 1.802(6) Å],[3] [$TiCl_2$(mbmp)(thf)] [av. 1.791(2) Å],[21] [$TiCl_2$(tmbp)]$_2$ [av. 1.818(4) Å],[5] [$TiCl_2$(tebp)]$_2$ [av. 1.801(9) Å],[15] [CpTiCl(tmbp)] [av. 1.827(2) Å][9] and [Ti($CH_2Ph$)$_2${2,2′-(4-MeO-6-*t*Bu$C_6H_2O$)$_2$}] [av. 1.810(7) Å],[7] and slightly larger than those found in analogous compounds such as [$TiCl_2$(mbmp)] [av. 1.751(4) Å][18] and [$TiBr_2$(ebmp)] [ethylene-bridged analogue; av. 1.750(9) Å].[17] Similar results were found in titanium complexes with non-linked phenoxido ligands, such as [CpTiX($OC_6H_3$*i*$Pr_2$)$_2$] [X = Cl, *t*Bu, Me; av. 1.801(5), 1.79(2) and 1.817(9) Å, respectively], due to the presence of a cyclopentadienyl ligand, which decreases the π-donation from the oxygen atoms to the metal centre.[20] Finally, the angle at the oxygen bridge atom is crystallographically restricted to 174.30(8)° and the metal–bridging oxygen bond lengths of 1.826(1) and 1.816(1) Å are typical for bridged titanium oxides.[22]

## Olefin Polymerisation

Using MAO in excess or $B(C_6F_5)_3$ or [$CPh_3$][$B(C_6F_5)_4$] [1:1 molar ratio with respect to the precursor in the presence of triisobutylaluminium (TIBA) as scavenger] as co-catalysts, complexes **4**, **5**, **8** and **9** were studied as α-olefin polymerisation catalysts under various conditions.

Propylene polymerisation was investigated by using 27 μmol of catalyst in 150 mL total volume of toluene with a 1000:1 Al(MAO)/Ti or 250:1:1 Al(TIBA)/Ti/[$CPh_3$][$B(C_6F_5)_4$] molar ratio at different temperatures and monomer pressures (conditions and results are summarised in Tables 4 and 5). Only traces of polymer or no polymerisation was found when the reaction was carried out at 30 °C with 5 atm of monomer and MAO as co-catalyst (runs 1, 4, 7 and 10). However, polymer was found at 0 °C using liquid propylene and MAO as co-catalyst for complexes **4** and **5** (runs 2 and 5), while compounds **8** and **9** (runs 8 and 11) showed poor activity. Decomposition of the catalyst system in the presence of the monomer at high temperatures could be a possible explanation for this behaviour. The activity [7.4 kg PP (mol Ti)$^{-1}$ h$^{-1}$] at 0 °C for the chlorido(cyclopentadienyl) system **1**/MAO[11] is markedly higher than that found for the corresponding alkyl derivatives **4** and **5**. Polymerisation runs at 0 °C resulted in the formation of PP with a molecular weight ($M_w$) of around $10^5$ for the pentamethylcyclopentadienyl derivatives **8** and **9** (2.5–$5.6 \times 10^5$), one order of magnitude higher than the corresponding non-substituted alkyl(cyclopentadienyl) derivatives **4** and **5**, probably due to the more electron-donating capability of the $\eta^5$-$C_5Me_5$ ligand, which prevents β-elimination processes.

When the salt [$CPh_3$][$B(C_6F_5)_4$] was used as co-catalyst, complexes **4** and **5** exhibited analogous activity (runs 3 and 6), but the activity was greatly increased for compounds **8** and **9** (runs 9 and 12), producing around 20–40 kg PP (mol Ti)$^{-1}$ h$^{-1}$. A similar behaviour is observed with the molecular weight of the polymer synthesised, and the high value found with systems **8**/[$CPh_3$][$B(C_6F_5)_4$] and **9**/[$CPh_3$][$B(C_6F_5)_4$] is worthy of mention, with each reaching values of $2–3 \times 10^6$, with similar polydispersity values to those reported in the literature.[7,15,20,23] For these samples, values of $T_g$, $T_m$ and $\Delta H$ similar to those found with the **1**/MAO system[11] are observed.

The use of the borane salt produces a decrease in the stereoselectivity of the process, as shown in Table 5 from an analysis of the degree of isotacticity in the samples by $^{13}C$ NMR spectroscopy. The activation of the precursors with MAO at 0 °C gives isotactic PP with an isotacticity (mmmm) of 24–30% (runs 2 and 5) for the cyclopentadienyl complexes **4** and **5**. However, activation with

 © 2007 Wiley-VCH Verlag GmbH & Co. KGaA, Weinheim 

Table 4. Polymerisation of propylene with [TiR′(η$^5$-$C_5R_5$)(η$^2$-mbmp)] compounds.

| Run | Catalyst[a] | Time [min] | Yield [mg] | Activity [kg PP (mol Ti)$^{-1}$ h$^{-1}$] | $10^{-4}$ $M_w$ | $M_w/M_n$ | $T_g$ [°C] | $T_m$ [°C] | $\Delta H$ [J g$^{-1}$] |
|---|---|---|---|---|---|---|---|---|---|
| 1 | 4[b] | 120 | traces | – | – | – | – | – | – |
| 2 | 4[c] | 120 | 189 | 3.5 | 3.8 | 1.86 | –9.8 | 101 | 5.2 |
| 3 | 4[d] | 120 | 158 | 3.0 | – | – | – | – | – |
| 4 | 5[b] | 120 | traces | – | – | – | – | – | – |
| 5 | 5[c] | 120 | 256 | 4.7 | 2.7 | 1.78 | –9.0 | 80 | 5.4 |
| 6 | 5[d] | 120 | 298 | 5.5 | 53 | 3.54 | – | – | – |
| 7 | 8[b] | 120 | 79 | 1.5 | 25 | 3.57 | – | – | – |
| 8 | 8[c] | 120 | 63 | 1.2 | 56 | 2.42 | – | – | – |
| 9 | 8[d] | 120 | 2067 | 38.1 | 217 | 47.5 | – | – | – |
| 10 | 9[b] | 120 | traces | – | – | – | – | – | – |
| 11 | 9[c] | 120 | 141 | 2.6 | 25 | 1.86 | – | – | – |
| 12 | 9[d] | 120 | 1159 | 21.5 | 301 | 37.0 | – | – | – |

[a] 27 μmol of catalyst. [b] Propylene gas (5 atm), 30 °C, co-catalyst: MAO. [c] Propylene liquid (40 mL), 0 °C, co-catalyst: MAO. [d] Propylene liquid (40 mL), 0 °C, co-catalyst: $[CPh_3][B(C_6F_5)_4]$.

Table 5. Pentand distributions obtained for PP.

| Run | Catalyst | % mmmm[a] | Run | Catalyst | % mmmm[a] |
|---|---|---|---|---|---|
| 1 | **4** | – | 7 | **8** | – |
| 2 | **4** | 24.1 | 8 | **8** | 12.5 |
| 3 | **4** | 8.2 | 9 | **8** | insoluble |
| 4 | **5** | – | 10 | **9** | – |
| 5 | **5** | 30.2 | 11 | **9** | 17.9 |
| 6 | **5** | 5.0 | 12 | **9** | insoluble |

[a] From $^{13}$C NMR spectra.

$[CPh_3][B(C_6F_5)_4]$ produces atactic PP (runs 3 and 6). The pentamethylcyclopentadienyl complexes **8** and **9** activated with either MAO or $[CPh_3][B(C_6F_5)_4]$ afford atactic PP. The high molecular weights of the samples obtained in runs 9 and 12 impeded the detection of their degree of isotacticity due to their lack of solubility in the deuterated solvents used for the spectroscopic analysis.

The results obtained at different temperatures and the microstructures of the polymers synthesised with MAO as co-catalyst are similar to those found with the **1**/MAO system[11] and resemble those reported by Ewen[24] for PP obtained with the achiral metallocene $[TiCp_2Ph_2]$, which is very unusual for monocyclopentadienyl compounds. This analysis permits us to conclude that the polymer obtained at low temperature with precursors **4** and **5** activated with MAO contains large isotactic stereoblocks produced by a chain-end control mechanism with a certain atactic character due to 2,1-enchainments. Nevertheless, it is noteworthy that the activation of precursors **8** and **9** with $[CPh_3][B(C_6F_5)_4]$ co-catalyst produces atactic PP with a high molecular weight of $10^6$.

Styrene polymerisation was studied using 40 mL total volume of reaction and 5 mL of monomer (conditions and results are summarised in Table 6). When the precursors are activated with MAO (runs 3, 7, 11 and 15), the activity of the cyclopentadienyl complexes **4** and **5** is higher (7–$8 \times 10^5$) than the activity found for the pentamethylcyclopentadienyl compounds **8** and **9** (2–$3 \times 10^5$), in all cases leading to syndiotactic PS (>95% syndiotacticity). Increased activity can be achieved with donor substituents in

Table 6. Polymerisation of styrene with [TiR′(η$^5$-$C_5R_5$)(η$^2$-mbmp)] compounds.

| Run | | Catalyst | $T$ [°C] | Time [min] | Al/Ti | Yield [g] | Activity [kg PS (mol Ti)$^{-1}$ h$^{-1}$] | Tacticity | $10^{-4}$ $M_w$ | $M_w/M_n$ |
|---|---|---|---|---|---|---|---|---|---|---|
| 13 | 1 | 4[a] | 50 | 45 | – | 2.82 | 190 | atactic | 0.4 | 1.89 |
| 14 | 2 | 4[b] | 50 | 45 | 20 | 0.02 | 1.6 | atactic | [c] | [c] |
| 15 | 3 | 4[d] | 50 | 12 | 1000 | 3.36 | 840 | syndiotactic | 3.2 | 2.19 |
| 16 | 4 | 4[e] | 50 | 30 | – | – | – | – | – | – |
| 17 | 5 | 5[a] | 50 | 45 | – | 3.28 | 220 | atactic | 0.4 | 1.95 |
| 18 | 6 | 5[b] | 50 | 45 | 20 | 0.03 | 2.3 | atactic | [c] | [c] |
| 19 | 7 | 5[d] | 50 | 20 | 1000 | 4.58 | 700 | syndiotactic | 2.7 | 3.68 |
| 20 | 8 | 5[e] | 50 | 30 | – | – | – | – | – | – |
| 21 | 9 | 8[a] | 50 | 45 | – | 3.37 | 220 | atactic | 0.5 | 1.85 |
| 22 | 10 | 8[b] | 50 | 45 | 20 | 0.15 | 9.5 | atactic | 0.9 | 1.70 |
| 23 | 11 | 8[f] | 50 | 15 | 1000 | 2.00 | 160 | syndiotactic | 9.8 | 2.15 |
| 24 | 12 | 8[e] | 50 | 30 | – | – | – | – | – | – |
| 25 | 13 | 9[a] | 50 | 45 | – | 2.77 | 180 | atactic | 0.6 | 1.91 |
| 26 | 14 | 9[b] | 50 | 45 | 20 | 0.05 | 3.0 | atactic | [c] | [c] |
| 27 | 15 | 9[f] | 50 | 10 | 1000 | 2.57 | 308 | syndiotactic | 12.4 | 1.98 |
| 28 | 16 | 9[e] | 50 | 30 | – | – | – | – | – | – |

[a] 20 μmol of catalyst; co-catalyst: $[CPh_3][B(C_6F_5)_4]$. [b] 20 μmol of catalyst; co-catalyst: $[CPh_3][B(C_6F_5)_4]$/TIBA; Al/Ti molar ratio: 20:1. [c] Not enough sample for analysis. [d] 20 μmol of catalyst; co-catalyst: MAO; Al/Ti molar ratio: 1000:1. [e] 20 μmol of catalyst; co-catalyst: $B(C_6F_5)_3$. [f] 50 μmol of catalyst; co-catalyst: MAO; Al/Ti molar ratio: 1000:1.

 © 2007 Wiley-VCH Verlag GmbH & Co. KGaA, Weinheim 

the cyclopentadienyl ring, while the presence of bulky substituents results in a decrease in activity. The bulky substituents would inhibit 2,1-insertion through steric effects and simultaneously inhibit the generation of the active species.

When $[CPh_3][B(C_6F_5)_4]$ is used as co-catalyst (runs 1, 5, 9 and 13) the activity is of the same order of magnitude as that obtained with MAO as co-catalyst. However, and in agreement with the results obtained in the propylene polymerisation, activation with the borane salt affords atactic PS (>92% of atactic microstructure). The similarity in the activity values found for the four alkyl complexes studied when the borane salt is used as co-catalyst is noteworthy and shows that the nature of the cyclopentadienyl ring has no influence on the activity. The addition of TIBA as scavenger in the precursor/$[CPh_3][B(C_6F_5)_4]$ systems (runs 2, 6, 10 and 14) dramatically decreased the activity. No polymerisation was found for the precursor/$[B(C_6F_5)_3]$ system (runs 4, 8, 12 and 16). The molecular weight of the PS obtained with the precursor/$[CPh_3][B(C_6F_5)_4]$ systems is very low but increases when MAO is used as co-catalyst, reaching an order of magnitude of $10^5$ with the pentamethylcyclopentadienyl compounds **8** and **9**.

### Reaction with Lewis Acids

In order to gain a better knowledge of the nature of the active species and the chemical behaviour of the mono(alkyl)bis(phenoxido) precatalyst systems in the α-olefin polymerisation processes, the reactions of the methyl and benzyl derivatives **4**, **5**, **8** and **9** with Lewis acids such as $B(C_6F_5)_3$ and $[CPh_3][B(C_6F_5)_4]$ were studied using a stoichiometric 1:1 Ti/B ratio and monitored by $^1H$ NMR spectroscopy. Likewise, the reaction of the chloromono(cyclopentadienyl) derivative **1** with trimethylaluminium was examined. All the procedures were carried out in NMR tubes fitted with Teflon valves to prevent water and oxygen entry and with $C_6D_6$ as reaction solvent at room temperature.

After addition of $C_6D_6$ to a mixture of $B(C_6F_5)_3$ and the corresponding neutral derivative **4**, **5**, **8** or **9** at room temperature in an NMR tube in a glovebox, the samples were quickly introduced into the spectrometer and the spectra recorded at 25 °C over a period of time. The reaction produces an appreciable change in the solution's colour from yellow for the methyl derivatives or orange for the benzyl compounds to dark red. After 1 h at room temperature, formation of the ionic species $[Ti(\eta^5\text{-}C_5H_5)(\eta^2\text{-}mbmp)][MeB(C_6F_5)_3]$ (**12**) and $[Ti(\eta^5\text{-}C_5H_5)(\eta^2\text{-}mbmp)][(PhCH_2)B(C_6F_5)_3]$ (**13**; Scheme 4) was detected. For the $\eta^5\text{-}C_5Me_5$ derivatives it was necessary to heat the reaction mixtures at 100 °C for 24 h to complete the reaction and to obtain the ionic compounds $[Ti(\eta^5\text{-}C_5Me_5)(\eta^2\text{-}mbmp)][MeB(C_6F_5)_3]$ (**14**) and $[Ti(\eta^5\text{-}C_5Me_5)(\eta^2\text{-}mbmp)][(PhCH_2)B(C_6F_5)_3]$ (**15**; Scheme 4). However, the reaction of **4** with an equimolecular amount of $[CPh_3][B(C_6F_5)_4]$ at room temperature in $C_6D_6$ gave an intractable mixture of unidentified products.

Complexes **12**–**15** are partially soluble in $C_6D_6$ and are stable in solution at room temperature over long periods of time (days). The $^1H$ NMR spectra ($C_6D_6$, 25 °C) show signals of equivalent *t*Bu and Me groups and two resonances for the phenyl protons of the bis(phenoxido) ligand, consistent with a $C_s$ symmetry. The resonances of the cyclopentadienyl protons are shifted to low field with respect to the neutral precursors, as expected. The methyl group of the $[MeB(C_6F_5)_4]^-$ fragment gives signals at $\delta$ = 0.84 and 0.91 ppm for derivatives **12** and **14**, respectively, suggesting a certain interaction between the anionic and the cationic centres.[25–29] The signals of the methylene protons of the benzylborate anion $[(PhCH_2)B(C_6F_5)_4]^-$ appear at $\delta$ = 3.14 and 2.90 ppm for derivatives **13** and **15**, respectively. It is not easy to establish a limit to determine the coordination or non-coordination of the anionic and cationic centres by analysing the methylene benzylborate anion resonances. Generally, values of $\delta_{CH_2B} < 3.0$ ppm seem to indicate the existence of an anion–cation interaction for the $[(PhCH_2)B(C_6F_5)_4]^-$ anion,[10,25,30,31] although exceptions to this rule have been found.[8,32] The resonance of the $C_{ipso}$ phenyl ring of the benzylborate anion is a good probe to determine the type of interaction with the metal centre. The $^{13}C$ NMR spectra ($C_6D_6$, 25 °C) for derivatives **13** and **15** show signals at $\delta$ = 152.5 and 160.3 ppm assignable to the $C_{ipso}$ phenyl ring carbon atom. This indicates a certain degree of $\eta^6$-coordination of the phenyl ring of the benzylborate anion to the cationic metal centre ($\delta$ = 148.6 ppm in the free anion).[33,34] The $^{19}F$ NMR spectra of the cationic species **12**–**15** give $\Delta\delta(p,m\text{-F})$ values of 3.52, 3.40, 3.41 and 5.10 ppm, respectively, indicating the existence of interactions between the ion pairs that are particularly strong for the pentamethylcyclopentadienyl ionic species **15** with the benzylborate anion.[25,35]

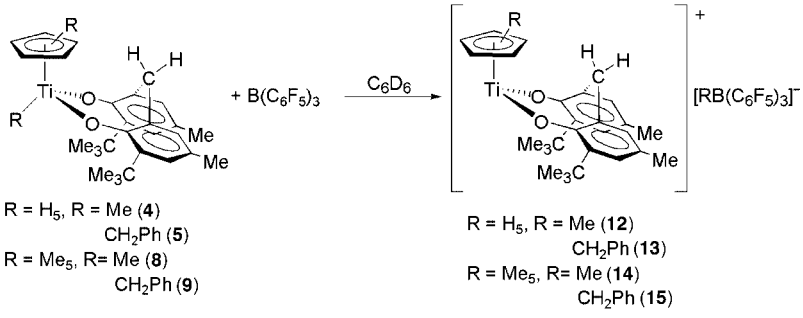


Scheme 4.

 © 2007 Wiley-VCH Verlag GmbH & Co. KGaA, Weinheim 

These results permit us to conclude that the Lewis acid $B(C_6F_5)_3$ reacts with the neutral complexes [TiR′($\eta^5$-$C_5R_5$)($\eta^2$-mbmp)] by abstraction of the alkyl group R′ to give the highly stable cationic species [Ti($\eta^5$-$C_5R_5$)($\eta^2$-mbmp)]$^+$, which retains the Ti–O bonds and the bidentate bis(phenoxido) ligand bonded to the titanium centre. Formation of such a stable species exhibiting strong interactions with the anionic unit prevents coordination of the olefin and, as a consequence, these systems are inactive in propylene and styrene polymerisation. With $[CPh_3][B(C_6F_5)_4]$ we could initially assume a similar reactivity. However, the $[B(C_6F_5)_4]^-$ unit is a less coordinating anion than $[RB(C_6F_5)_4]^-$ to afford [Ti($\eta^5$-$C_5R_5$)($\eta^2$-mbmp)][$B(C_6F_5)_4$], which is active in styrene polymerisation. In the absence of olefin, these $[B(C_6F_5)_4]^-$ systems show a lack of stability, with fast and immediate decomposition observed in solution.

A new family of compounds containing only one metal–alkyl bond that are active in olefin polymerisation has been reported recently. Mechanistic pathways to explain the efficient α-olefin polymerisation of these compounds activated with boron reagents have been proposed.[36–39] In the absence of TIBA, the olefin polymerisation activity observed for complexes **4**, **5**, **8** and **9** with $[CPh_3][B(C_6F_5)_4]$ as co-catalyst can be explained by these mechanistic pathways.

Aluminium compounds are normally used as co-catalysts (MAO) to generate the active species or as scavenger reagents (TIBA) during olefin polymerisation. The former occurs by replacement of the halo groups in the precursor with alkyl groups and then abstraction of one of these alkyl groups to give cationic alkyl species, which are considered to be the active species in the process. As our neutral species with general formula [TiCl($\eta^5$-$C_5R_5$)($\eta^2$-mbmp)] [$\eta^5$-$C_5R_5$ = $\eta^5$-$C_5H_5$ (**1**), $\eta^5$-$C_5Me_5$ (**2**), $\eta^5$-$C_5H_4SiMe_2Cl$ (**3**)][11] only possess one chlorido group at the metal centre, we were motivated to investigate the reactivity of compound **1** with $AlMe_3$. Thus, a solution of the mono(chlorido) compound [Ti($\eta^5$-$C_5H_5$)($\eta^2$-mbmp)Cl] (**1**) was treated with 1 equiv. of $AlMe_3$ in toluene at –78 °C (Scheme 5). $^1$H NMR spectroscopic analysis revealed complex **4** to be essentially the only reaction product, thereby indicating alkylation of the Ti–Cl bond and selective formation of the methyl derivative. The NMR spectra also show the presence of traces of signals assignable to secondary products containing the bis(phenoxido) ligand. The intensity of these signals increases when an excess of $AlMe_3$ is used as reagent, along with the disappearance of the signals assignable to compound **4**. Transmetallation reactions of the bis(phenoxido) ligand from titanium to aluminium could explain the formation of these secondary products.[20,40]

In an attempt to identify the nature of these secondary products, we performed the reaction of the bis(phenol) $mbmpH_2$ with $AlMe_3$ or $AlClMe_2$ in a 1:1 molar ratio in toluene at –78 °C. White solids were obtained in both cases, which were characterised by elemental analysis and NMR spectroscopy as the compounds $[AlMe(mbmp)]_2$ (**16**) and $[AlCl(mbmp)]_2$ (**17**; Scheme 6). The thf adduct monomer species [AlCl(mbmp)(thf)] obtained by reaction of $mbmpH_2$ with $AlClEt_2$ in thf has been described previously, although the dimeric species was not characterised.[41]

Complexes **16** and **17** are insoluble in aliphatic hydrocarbons (hexane, pentane), scarcely soluble in aromatic solvents and highly water-sensitive. They can be stored for months under an inert gas without decomposition. The $^1$H NMR spectra ($C_6D_6$ and $CDCl_3$, 25 °C) show AB spin systems for the methylene protons, indicating coordination of the bis(phenoxido) ligand. The *tert*-butyl and methyl groups are not equivalent, with each appearing as two singlets. A

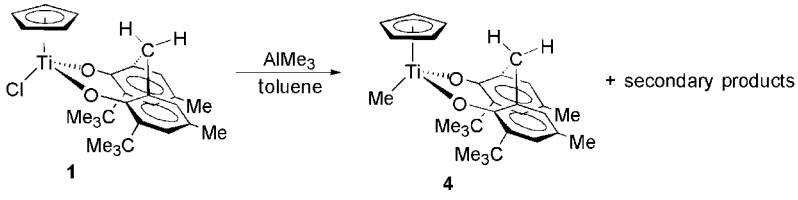


Scheme 5.

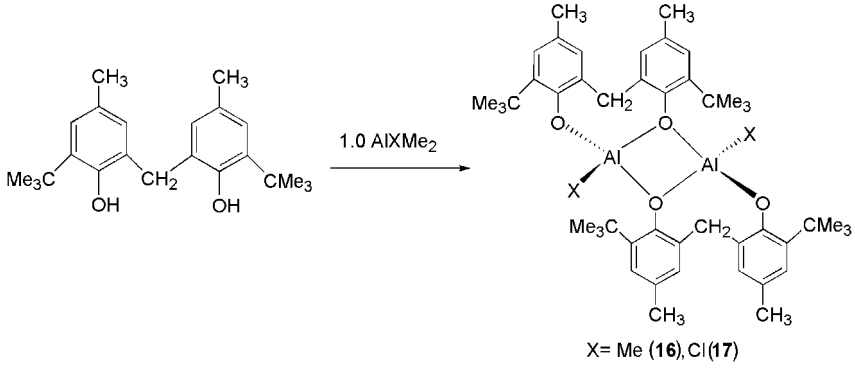


Scheme 6.

 © 2007 Wiley-VCH Verlag GmbH & Co. KGaA, Weinheim 

high-field-shifted signal assignable to equivalent Al–Me groups is also observed for complex **16**. The $^{13}C\{^1H\}$ NMR spectra show twelve signals for the phenyl rings and a pair of signals for the *tert*-butyl and methyl groups. These spectroscopic data agree with the structure proposed in Scheme 6.

Comparison of the spectroscopic data rules out the presence of complexes **16** and **17** in the final products obtained in the reaction of **1** with $AlMe_3$, although transmetallation reactions of the bis(phenoxido) ligand from titanium to aluminium could produce bis(phenoxido)aluminium derivatives of different composition.

The complexes $[TiR'(\eta^5\text{-}C_5R_5)(\eta^2\text{-mbmp})]$ have only one alkyl ligand coordinated to the metal centre. We therefore assume that in these polymerisation reactions the aluminium reagents (MAO used as co-catalyst or TIBA used as scavenger) react with these precursors through transmetallation processes of the bis(phenoxido) ligand from titanium to aluminium to generate active cationic alkyltitanium species in a Ziegler–Natta-type olefin polymerisation.

## Concluding Remarks

We have described the synthesis and characterisation of mono(alkyl)mono(cyclopentadienyl)titanium complexes $[TiR'(\eta^5\text{-}C_5R_5)(\eta^2\text{-mbmp})]$ containing the bis(phenoxido) bidentate dianionic ligand 2,2′-methylenebis(6-*tert*-butyl-4-methylphenoxido) ($\eta^2$-mbmp). The μ-oxido compound $[\{Ti(\eta^5\text{-}C_5H_5)(\eta^2\text{-mbmp})\}_2(\mu\text{-O})]$ is also obtained by reaction of $[TiPh(\eta^5\text{-}C_5H_5)(\eta^2\text{-mbmp})]$ with traces of water in toluene. Density functional calculations for these complexes have provided remarkable conclusions about their structural behaviour, which have been confirmed by X-ray diffraction studies in the solid state. After activation with MAO or $[CPh_3][B(C_6F_5)_4]$, these alkylmono(cyclopentadienyl)titanium derivatives are suitable for olefin (propylene and styrene) polymerisation, while reaction with $B(C_6F_5)_3$ produces inactive species. Polypropylene containing large isotactic stereoblocks obtained by a chain-end control mechanism is produced at low temperature. The nature of the active species in the olefin polymerisation processes has been examined spectroscopically.

## Experimental Section

**General Considerations:** All manipulations were performed under argon using Schlenk and vacuum-line techniques or in a glovebox (model HE-63). The solvents were purified by distillation under argon before use in the presence of the appropriate drying/deoxygenating agent. Deuterated solvents were stored under an inert gas over activated molecular sieves (4 Å) and degassed by several freeze-pump-thaw cycles. LiMe, MgClBz, LiPh, $mbmpH_2$ [2,2′-$CH_2$-bis(6-*t*Bu-4-$CH_3C_6H_2$-1-OH)], $AlMe_3$ (2.0 M hexane solution), $AlClMe_2$ (1.0 M hexane solution) were purchased (Aldrich) and used without further purification. $Li_2mbmp$,[3] $[B(C_6F_5)_3]$,[42] $[CPh_3][B(C_6F_5)_4]$[43] and $LiCH_2SiMe_3$[44] were prepared by known procedures. Polymerisation-grade propylene from Aldrich was purified by passage through two columns packed with activated alumina and molecular sieves (4 Å). Styrene was distilled at reduced pressure from calcium hydride and stored in the refrigerator. Methylaluminoxane (MAO, 10% solution in toluene) was purchased from WITCO GmbH. C, H and N microanalyses were performed with a Perkin–Elmer 240B and/or Heraeus CHN-O-Rapid microanalyzer. Polymer melt endotherms were determined with a Perkin–Elmer DSC-4 differential scanning calorimeter. NMR spectra, measured at 25 °C, were recorded with Varian Unity FT-300 ($^1H$ NMR at 300 MHz, $^{13}C$ NMR at 75 MHz) or Unity-Plus FT-500 ($^1H$ NMR at 500 MHz, $^{13}C$ NMR at 125 MHz) spectrometers, and chemical shifts ($\delta$, ppm) are referenced to $SiMe_4$ relative to the carbon resonances ($^{13}C$) and the residual protons ($^1H$) of the solvent. $^{19}F$ NMR spectra were recorded with a Varian Unity FT-500 and chemical shifts ($\delta$, ppm) are referenced to $CFCl_3$.

**$[TiMe(\eta^5\text{-}C_5H_5)(\eta^2\text{-mbmp})]$ (4):** A 1.5 M solution of LiMe in diethyl ether (0.30 mL, 0.45 mmol) was added at –78 °C to a solution of **1** (0.22 g, 0.45 mmol) in hexane (50 mL). The reaction mixture was slowly warmed to room temperature and stirred overnight. The solvent was completely removed and after extraction with hexane and concentration of the combined extracts, a bright yellow solid was obtained which was recrystallised from cold hexane and characterised as **4** (0.16 g, 75% yield). $C_{29}H_{38}O_2Ti$ (466.50): calcd. C 74.70, H 8.16; found C 74.57, H 8.19. $^1H$ NMR (300 MHz, $C_6D_6$, 25 °C): $\delta$ = 7.13, 7.00 (AA′ spin system, 2 × 2 H, Ph), 6.13 (s, 5 H, $C_5H_5$), 3.83, 3.43 (AB spin system, $\Delta\delta$ = 0.40 ppm, $^2J_{H,H}$ = 13.5 Hz, 2 × 1 H, $CH_2$), 2.17 (s, 6 H, $CH_3$Ph), 1.38 [s, 18 H, $C(CH_3)_3$], 1.31 (s, 3 H, $TiCH_3$) ppm. $^1H$ NMR (300 MHz, $CDCl_3$, 25 °C): $\delta$ = 7.07, 6.89 (AA′ spin system, 2 × 2 H, Ph), 6.53 (s, 5 H, $C_5H_5$), 3.76, 3.40 (AB spin system, 2 × 1 H, $CH_2$), 2.25 (s, 6 H, $CH_3$Ph), 1.28 [s, 18 H, $C(CH_3)_3$], 1.14 (s, 3 H, $TiCH_3$) ppm. $^{13}C$ NMR (125 MHz, $C_6D_6$, 25 °C): $\delta$ = 161.6, 137.3, 136.5, 130.2, 129.3, 126.2 (all Ph), 114.98 ($C_5H_5$), 52.8 ($TiCH_3$), 36.0 ($CH_2$), 35.5 [$C(CH_3)_3$], 30.9 [$C(CH_3)_3$], 21.4 ($CH_3$-Ph) ppm.

**$[Ti(CH_2Ph)(\eta^5\text{-}C_5H_5)(\eta^2\text{-mbmp})]$ (5):** A 2.0 M solution of MgClBz in thf (0.30 mL, 0.62 mmol) was added at –78 °C to a solution of **1** (0.30 g, 0.62 mmol) in hexane (50 mL). The reaction mixture was slowly warmed to room temperature and stirred overnight and the solvent was then completely removed under vacuum. Recrystallisation from hexane gave a light orange solid which was characterised as **5** (0.23 g, 70% yield). Correct elemental analysis data could not be obtained, although satisfactory spectroscopic data were obtained. $^1H$ NMR (300 MHz, $C_6D_6$, 25 °C): $\delta$ = 7.28 (m, 5 H, $CH_2Ph$), 7.11, 7.01 (AA′ spin system, 2 × 2 H, Ph), 6.01 (s, 5 H, $C_5H_5$), 3.84, 3.36 (AB spin system, $\Delta\delta$ = 0.48 ppm, $^2J_{H,H}$ = 13.7 Hz, 2 × 1 H, $CH_2$), 3.24 (s, 2 H, $TiCH_2$Ph), 2.18 (s, 6 H, $CH_3$Ph), 1.47 [s, 18 H, $C(CH_3)_3$] ppm. $^1H$ NMR (300 MHz, $CDCl_3$, 25 °C): $\delta$ = 7.07, 6.92 (AA′ spin system, 2 × 2 H, Ph), 7.30 (t, $J_{H,H}$ = 8.0 Hz, 2 H, *m*-$CH_2Ph$), 7.17 (d, $J_{H,H}$ = 7.9 Hz, 2 H, *o*-$CH_2Ph$), 7.01 (t, $J_{H,H}$ = 8.1 Hz, 1 H, *p*-$CH_2Ph$), 6.27 (s, 5 H, $C_5H_5$), 3.83, 3.38 (AB spin system, 2 × 1 H, $CH_2$), 2.99 (s, 2 H, $TiCH_2$Ph), 2.25 (s, 6 H, $CH_3$Ph), 1.41 [s, 18 H, $C(CH_3)_3$] ppm. $^{13}C$ NMR (125 MHz, $C_6D_6$, 25 °C): $\delta$ = 161.8, 137.1, 137.0, 130.0, 129.3, 126.4 (all Ph), 152.0 (*ipso*-$CH_2Ph$), 128.6 (*p*-$CH_2Ph$), 126.0 (*m*-$CH_2Ph$), 123.4 (*o*-$CH_2Ph$), 117.0 ($C_5H_5$), 77.2 ($TiCH_2$Ph), 36.1 ($CH_2$), 35.4 [$C(CH_3)_3$], 30.8 [$C(CH_3)_3$], 21.0 ($CH_3$-Ph) ppm.

**$[TiPh(\eta^5\text{-}C_5H_5)(\eta^2\text{-mbmp})]$ (6a, 6b, 6c):** A 1.8 M solution of LiPh in diethyl ether (0.35 mL, 0.62 mmol) was added at –78 °C to a solution of **1** (0.30 g, 0.62 mmol) in hexane (50 mL). The reaction mixture was slowly warmed to room temperature and stirred for 12 h. The resulting solution was concentrated under vacuum and a brown oily solid was obtained; spectroscopic analysis revealed a mixture of three isomers **6a**, **6b** and **6c**. Two isomers were obtained

 © 2007 Wiley-VCH Verlag GmbH & Co. KGaA, Weinheim 

as analytically pure samples after repeated recrystallisation from toluene. $C_{34}H_{40}O_2Ti$ (528.56): calcd. C 77.29, H 7.58; found C 77.12, H 7.74. $^1$H NMR (300 MHz, $C_6D_6$, 25 °C): **6a**: $\delta$ = 7.08, 7.00 (AA′ spin system, 2×2 H, Ph), 7.45, 7.02 (d, $J_{H,H}$ = 8.0 Hz, and m, 2 H + 3 H, Ph), 6.26 (s, 5 H, $C_5H_5$), 4.51, 3.36 (AB spin system, $\Delta\delta$ = 1.15 ppm, $^2J_{H,H}$ = 13.2 Hz, 2×1 H, $CH_2$), 2.18 (s, 6 H, $CH_3$Ph), 1.43 [s, 18 H, C($CH_3$)$_3$] ppm; **6b**: $\delta$ = 7.19, 7.04 (AA′ spin system, 2×2 H, Ph), 7.61, 6.92 (d, $J_{H,H}$ = 8.0 Hz, and m, 2 H + 3 H, Ph), 6.42 (s, 5 H, $C_5H_5$), 3.95, 3.49 (AB spin system, 2×1 H, $\Delta\delta$ = 0.46 ppm, $^2J_{H,H}$ = 13.7 Hz, $CH_2$), 2.18 (s, 6 H, $CH_3$Ph), 1.20 [s, 18 H, C($CH_3$)$_3$] ppm; **6c**: $\delta$ = 7.06, 6.95 (AA′ spin system, 2×2 H, Ph), 7.35, 7.09 (d, $J_{H,H}$ = 8.0 Hz, and m, 2 H + 3 H, Ph), 6.55 (s, 5 H, $C_5H_5$), 5.15, 3.02 (AB spin system, $\Delta\delta$ = 2.13 ppm, $^2J_{H,H}$ = 13.7 Hz, 2×1 H, $CH_2$), 2.07 (s, 6 H, $CH_3$Ph), 1.45 [s, 18 H, C($CH_3$)$_3$] ppm. $^{13}$C NMR (125 MHz, $C_6D_6$, 25 °C): **6a**: $\delta$ = 162.6, 136.9, 136.7, 133.9, 128.9, 125.6 (all Ph), 129.2 (*p*-*Ph*), 129.0 (*m*-*Ph*), 127.4 (*o*-*Ph*), 115.6 ($C_5H_5$), 35.1 ($CH_2$), 35.2 [*C*($CH_3$)$_3$], 30.8 [C(*C*$H_3$)$_3$], 21.1 (*C*$H_3$-Ph) ppm; **6b**, $\delta$ = 161.7, 137.0, 135.6, 129.2, 128.0, 126.8 (all Ph), 134.8 (*p*-*Ph*), 130.3 (*m*-*Ph*), 126.3 (*o*-*Ph*), 116.1 ($C_5H_5$), 35.4 ($CH_2$), 35.2 [*C*($CH_3$)$_3$], 31.0 [C(*C*$H_3$)$_3$], 21.1 (*C*$H_3$-Ph ppm); **6c**: $\delta$ = 161.7, 140.6, 134.8, 131.1, 126.4, 125.4 (all Ph), 134.3 (*p*-$CH_2$*Ph*), 129.7 (*m*-$CH_2$*Ph*), 127.6 (*o*-$CH_2$*Ph*), 116.5 ($C_5H_5$), 35.2 ($CH_2$), 35.1 [*C*($CH_3$)$_3$], 29.9 [C(*C*$H_3$)$_3$], 21.0 (*C*$H_3$-Ph) ppm.

**[Ti($CH_2SiMe_3$)($\eta^5$-$C_5H_5$)($\eta^2$-mbmp)] (7):** A red solution of **1** (0.30 g, 0.62 mmol) in 40 mL of hexane was treated with a solution of $LiCH_2SiMe_3$ (0.06 g, 0.62 mmol) in diethyl ether (20 mL), at –78 °C. The reaction mixture was slowly warmed to room temperature, stirred for 12 h and the solvent completely removed. After extraction with hexane and concentration of the combined extracts, an orange microcrystalline solid was obtained, which was recrystallised from a cold mixture of toluene and hexane and characterised as **7** (0.25 g, 73% yield). $C_{32}H_{46}O_2SiTi$ (538.67): calcd. C 71.38, H 8.55; found C 71.23, H 8.34. $^1$H NMR (300 MHz, $C_6D_6$, 25 °C): $\delta$ = 7.11, 6.98 (AA′ spin system, 2×2 H, Ph), 6.32 (s, 5 H, $C_5H_5$), 4.02, 3.34 (AB spin system, $\Delta\delta$ = 0.68 ppm, $^2J_{H,H}$ = 13.5 Hz, 2×1 H, $CH_2$), 2.17 (s, 6 H, $CH_3$Ph), 1.80 (s, 2 H, Ti$CH_2$Si$Me_3$), 1.38 [s, 18 H, C($CH_3$)$_3$], 0.29 (s, 9 H, TiCH$_2$Si$Me_3$) ppm. $^1$H NMR (300 MHz, $CDCl_3$, 25 °C): $\delta$ = 7.04, 6.87 (AA′ spin system, 2×2 H, Ph), 6.57 (s, 5 H, $C_5H_5$), 3.98, 3.34 (AB spin system, 2×1 H, $CH_2$), 2.24 (s, 6 H, $CH_3$Ph), 1.58 (s, 2 H, Ti$CH_2$Si$Me_3$), 1.29 [s, 18 H, C($CH_3$)$_3$], 0.16 (s, 9 H, TiCH$_2$Si$Me_3$) ppm. $^{13}$C NMR (125 MHz, $C_6D_6$, 25 °C): $\delta$ = 161.9, 136.9, 136.5, 129.8, 129.1, 125.8 (all Ph), 114.5 ($C_5H_5$), 72.5 (Ti*C*H$_2$SiMe$_3$), 35.7 ($CH_2$), 35.3 [*C*($CH_3$)$_3$], 30.7 [C(*C*$H_3$)$_3$], 21.0 (*C*$H_3$-Ph), 3.2 (TiCH$_2$Si$Me_3$) ppm.

**[TiMe($\eta^5$-$C_5Me_5$)($\eta^2$-mbmp)] (8):** A 1.5 M solution of LiMe in diethyl ether (0.36 mL, 0.54 mmol) was added to a solution of **2** (0.30 g, 0.54 mmol) in hexane (60 mL) at –78 °C. The reaction mixture was slowly warmed to room temperature and stirred for 6 h. After filtration, the resulting bright yellow solution was concentrated to dryness. A bright yellow solid was obtained, which was recrystallised from cold hexane and characterised as **8** (0.22 g, 77% yield). $C_{34}H_{48}TiO_2$ (536.63): calcd. C 76.14, H 8.96; found C 76.07, H 8.91. $^1$H NMR (300 MHz, $C_6D_6$, 25 °C): $\delta$ = 7.13, 7.00 (AA′ spin system, 2×2 H, Ph), 3.88, 3.47 (AB spin system, $\Delta\delta$ = 0.41 ppm, $^2J_{H,H}$ = 13.4 Hz, 2×1 H, $CH_2$), 2.16 (s, 6 H, $CH_3$Ph), 1.92 (s, 15 H, $C_5Me_5$), 1.39 [s, 18 H, C($CH_3$)$_3$], 1.10 (s, 3 H, TiCH$_3$) ppm. $^{13}$C NMR (125 MHz, $C_6D_6$, 25 °C): $\delta$ = 160.1, 137.1, 134.9, 129.2, 128.7, 123.6 (all Ph), 126.2 ($C_5Me_5$), 54.8 (TiCH$_3$), 35.1 ($CH_2$), 35.0 [*C*($CH_3$)$_3$], 30.8 [C(*C*$H_3$)$_3$], 21.0 (*C*$H_3$-Ph), 11.9 ($C_5Me_5$) ppm.

**[Ti($CH_2$Ph)($\eta^5$-$C_5Me_5$)($\eta^2$-mbmp)] (9):** A 2.0 M solution of MgClBz in thf (0.50 mL, 1.00 mmol) was added to a solution of **2** (0.56 g, 1.00 mmol) in hexane (60 mL) at –78 °C. The reaction mixture was slowly warmed to room temperature and stirred overnight. After filtration, the solvent was completely removed from the resulting orange solution. Recrystallisation from hexane gave a light orange solid, which was again recrystallised from cold hexane and characterised as **9** (0.39 g, 63% yield). $C_{40}H_{52}O_2Ti$ (612.72): calcd. C 78.43, H 8.50; found C 78.31, H 8.77. $^1$H NMR (300 MHz, $C_6D_6$, 25 °C): $\delta$ = 7.02, 7.00 (AA′ spin system, 2×2 H, Ph), 7.00 (m, 5 H, $CH_2$*Ph*), 3.75, 3.44 (AB spin system, $\Delta\delta$ = 0.31 ppm, $^2J_{H,H}$ = 13.7 Hz, 2×1 H, $CH_2$), 2.91 (s, 2 H, Ti$CH_2$Ph), 2.17 (s, 6 H, $CH_3$Ph), 1.89 (s, 15 H, $C_5Me_5$), 1.34 [s, 18 H, C($CH_3$)$_3$] ppm. $^1$H NMR (300 MHz, $CDCl_3$, 25 °C): $\delta$ = 7.03–6.95 (m, 4 H and 5 H, Ph and $CH_2$*Ph*), 3.64, 3.39 (AB spin system, 2×1 H, $CH_2$), 2.77 (s, 2 H, Ti$CH_2$Ph), 2.24 (s, 6 H, $CH_3$Ph), 1.97 (s, 15 H, $C_5Me_5$), 1.24 [s, 18 H, C($CH_3$)$_3$] ppm. $^{13}$C NMR (125 MHz, $C_6D_6$, 25 °C): $\delta$ = 160.4, 137.1, 135.1, 129.5, 128.9, 126.6 (all Ph), 148.4 (*ipso*-$CH_2$*Ph*), 129.4 (*p*-$CH_2$*Ph*), 124.7 (*m*-$CH_2$*Ph*), 123.6 (*o*-$CH_2$*Ph*), 127.8 ($C_5Me_5$), 76.7 (Ti*C*H$_2$Ph), 35.4 ($CH_2$), 35.3 [*C*($CH_3$)$_3$], 31.3 [C(*C*$H_3$)$_3$], 21.0 (*C*$H_3$-Ph), 12.0 ($C_5Me_5$) ppm.

**[Ti($CH_2SiMe_3$)($\eta^5$-$C_5Me_5$)($\eta^2$-mbmp)] (10a, 10b):** A red solution of **2** (0.52 g, 0.93 mmol) in 50 mL of hexane was treated, at –78 °C, with a solution of $LiCH_2SiMe_3$ (0.09 g, 0.95 mmol) in 20 mL of diethyl ether. The reaction mixture was warmed to room temperature, stirred for 12 h and the solvent was completely removed. After extraction with hexane and concentration of the combined extracts, an orange microcrystalline solid was obtained, which was recrystallised from cold hexane and characterised as **10a** (0.34 g, 60%) containing a small amount of isomer **10b**. $C_{37}H_{56}O_2SiTi$ (608.81): calcd. C 73.03, H 9.21; found C 72.91, H 9.16. $^1$H NMR (300 MHz, $C_6D_6$, 25 °C): **10a**: $\delta$ = 7.11, 7.04 (AA′ spin system, 2×2 H, Ph), 3.66, 3.38 (AB spin system, $\Delta\delta$ = 0.28 ppm, $^2J_{H,H}$ = 13.4 Hz, 2×1 H, $CH_2$), 2.17 (s, 6 H, $CH_3$Ph), 1.93 (s, 15 H, $C_5Me_5$), 1.49 [s, 18 H, C($CH_3$)$_3$], 1.16 (s, 2 H, Ti$CH_2$SiMe$_3$), 0.18 (s, 9 H, TiCH$_2$Si$Me_3$) ppm; **10b**: $\delta$ = 7.04, 6.96 (AA′ spin system, 2×2 H, Ph), 4.08, 3.40 (AB spin system, $\Delta\delta$ = 0.68 ppm, $^2J_{H,H}$ = 13.4 Hz, 2×1 H, $CH_2$), 2.11 (s, 6 H, $CH_3$Ph), 2.02 (s, 15 H, $C_5Me_5$), 1.47 (s, 2 H, Ti$CH_2$SiMe$_3$), 1.44 [s, 18 H, C($CH_3$)$_3$], –0.007 (s, 9 H, TiCH$_2$Si$Me_3$) ppm. $^{13}$C NMR (125 MHz, $C_6D_6$, 25 °C): **10a**: $\delta$ = 160.8, 136.6, 134.8, 129.0, 128.3, 124.2 (all Ph), 126.6 ($C_5Me_5$), 67.9 (Ti*C*H$_2$SiMe$_3$), 35.4 ($CH_2$), 35.7 [*C*($CH_3$)$_3$], 32.3 [C(*C*$H_3$)$_3$], 21.1 (*C*$H_3$-Ph), 12.5 ($C_5Me_5$), 4.4 (TiCH$_2$Si$Me_3$) ppm. The small amount of **10b** in the sample did not allow its $^{13}$C NMR signals to be assigned accurately.

**[{Ti($\eta^5$-$C_5H_5$)($\eta^2$-mbmp)}$_2$(μ-O)] (11):** Distilled water (6.8 μL, 0.38 mmol) was added at room temperature to a solution of **6** (0.20 g, 0.38 mmol) in toluene (20 mL). The solvent was completely removed to give a red solid, which was recrystallised from diethyl ether to afford **11** as a crystalline solid. $C_{56}H_{70}O_5Ti_2$ (918.91): calcd. C 73.22, H 7.67; found C 73.20, H 7.49. $^1$H NMR (300 MHz, $C_6D_6$, 25 °C): $\delta$ = 7.10, 7.02, 6.83 (two AA′ spin systems, 1 H, 2×1 H, 1 H, Ph), 6.56 (s, 10 H, $C_5H_5$), 4.24, 3.24 (AB spin system, $\Delta\delta$ = 1.00 ppm, $^2J_{H,H}$ = 13.6 Hz, 2×2 H, $CH_2$), 2.21, 2.18 (s, 2×6 H, $CH_3$Ph), 1.69, 0.94 [s, 2×18 H, C($CH_3$)$_3$] ppm. $^{13}$C NMR (125 MHz, $C_6D_6$, 25 °C): $\delta$ = 164.1, 163.3, 136.9, 136.6, 136.4, 133.0, 130.6, 129.8, 128.9, 128.5, 125.7, 125.2 (all Ph), 116.4 ($C_5H_5$), 34.8 ($CH_2$), 35.3, 35.1 [2×*C*($CH_3$)$_3$], 31.9, 30.0 [2×C-(*C*$H_3$)$_3$], 21.1, 21.0 (2×*C*$H_3$-Ph) ppm.

**[Ti($\eta^5$-$C_5H_5$)($\eta^2$-mbmp)][MeB($C_6F_5$)$_3$] (12):** $C_6D_6$ was added to a mixture of **4** (0.018 g, 0.04 mmol) and B($C_6F_5$)$_3$ (0.019 g, 0.04 mmol) at room temperature in an NMR tube fitted with a Teflon valve inside a glovebox. The NMR tube was quickly introduced into the NMR equipment and the spectra were recorded at room temperature. The formation of **12** was deduced spectroscopi-

 © 2007 Wiley-VCH Verlag GmbH & Co. KGaA, Weinheim 

cally. $^1$H NMR (300 MHz, $C_6D_6$, 25 °C): $\delta$ = 7.03, 6.94 (AA′ spin system, 2×2 H, Ph), 6.33 (s, 5 H, $C_5H_5$), 4.05, 3,36 (AB spin system, 2×1 H, $\Delta\delta$ = 0.69 ppm, $CH_2$), 2.12 (s, 6 H, *CH*$_3$Ph), 1.43 [s, 18 H, $C(CH_3)_3$], 0.84 (br. s, 3 H, $BCH_3$) ppm. $^{13}$C NMR (125 MHz, $C_6D_6$, 25 °C): $\delta$ = 163.6, 137.4, 136.6, 131.2, 129.1, 126.2 (all Ph), 149.8, 147.8, 138.2, 136.5 (all $C_6F_5$), 118.2 ($C_5H_5$), 35.5 ($CH_2$), 35.4 [*C*$(CH_3)_3$], 31.2 [C(*C*$H_3)_3$], 21.1 (*C*$H_3$-Ph), 10.5 ($BCH_3$) ppm. $^{19}$F NMR (300 MHz, $C_6D_6$, 25 °C): $\delta$ = –136.5, –160.0, –163.5 ppm.

**[Ti(η$^5$-$C_5H_5$)(η$^2$-mbmp)][($CH_2$Ph)B($C_6F_5$)$_3$] (13):** The same procedure described for **12**, using a mixture of **5** (0.020 g, 0.04 mmol) and B($C_6F_5$)$_3$ (0.019 g, 0.04 mmol), resulted in the formation of **13**. $^1$H NMR (300 MHz, $C_6D_6$, 25 °C): $\delta$ = 7.03, 6.94 (AA′ spin system, 2×2 H, Ph), 6.50, 6.41, 6.26 (o, m, *p*-$CH_2$*Ph*), 6.33 (s, 5 H, $C_5H_5$), 4.05, 3.36 (AB spin system, 2×1 H, $\Delta\delta$ = 0.69 ppm, $CH_2$), 2.12 (s, 6 H, *CH*$_3$Ph), 1.43 [s, 18 H, $C(CH_3)_3$], 3.14 (br. s, 2 H, B*CH*$_2$Ph) ppm. $^{13}$C NMR (125 MHz, $C_6D_6$, 25 °C): $\delta$ = 163.6, 137.4, 136.6, 131.2, 129.1, 126.2 (all Ph), 149.8, 147.8, 138.6, 136.4 (all $C_6F_5$), 152.5 ($C_{ipso}$-$CH_2$*Ph*), 129.4, 127.4, 122.3 (*o*-, *m*-, *p*-$CH_2$*Ph*), 118.2 ($C_5H_5$), 38.2 (B*C*H$_2$Ph), 35.5 ($CH_2$), 35.4 [*C*$(CH_3)_3$], 31.2 [C(*C*$H_3)_3$], 21.1 (*C*$H_3$-Ph) ppm. $^{19}$F NMR (300 MHz, $C_6D_6$, 25 °C): $\delta$ = –132.7, –161.1, –164.5 ppm.

**[Ti(η$^5$-$C_5Me_5$)(η$^2$-mbmp)][MeB($C_6F_5$)$_3$] (14):** The same procedure described for **12**, using a mixture of **8** (0.021 g, 0.04 mmol) and B($C_6F_5$)$_3$ (0.019 g, 0.04 mmol), resulted in the formation of **14**. $^1$H NMR (300 MHz, $C_6D_6$, 25 °C): $\delta$ = 7.04, 6.96 (AA′ spin system, 2×2 H, Ph), 3.98, 3.40 (AB spin system, 2×1 H, $\Delta\delta$ = 0.58 ppm, $CH_2$), 2.11 (s, 6 H, *CH*$_3$Ph), 2.02 (s, 15 H, $C_5Me_5$), 1.45 [s, 18 H, $C(CH_3)_3$], 0.91 (br. s, 3 H, $BCH_3$) ppm. $^{13}$C NMR (125 MHz, $C_6D_6$, 25 °C): $\delta$ = 161.4, 137.6, 134.8, 130.4, 129.4, 126.6 (all Ph), 149.6, 147.8, 138.6, 136.5 (all $C_6F_5$), 128.3 (*C*$_5$Me$_5$), 35.1 ($CH_2$), 35.4 [*C*$(CH_3)_3$], 31.5 [C(*C*$H_3)_3$], 21.1 (*C*$H_3$-Ph), 13.1 ($C_5$*Me*$_5$), 10.5 ($BCH_3$) ppm. $^{19}$F NMR (300 MHz, $C_6D_6$, 25 °C): $\delta$ = –136.1, –160.5, –163.9 ppm.

**[Ti(η$^5$-$C_5Me_5$)(η$^2$-mbmp)][($CH_2$Ph)B($C_6F_5$)$_3$] (15):** The same procedure described for **12**, using a mixture of **9** (0.024 g, 0.04 mmol) and B($C_6F_5$)$_3$ (0.019 g, 0.04 mmol), resulted in the formation of **15**. $^1$H NMR (300 MHz, $C_6D_6$, 25 °C): $\delta$ = 7.04, 6.96 (AA′ spin system, 2×2 H, Ph), 7.10–6.70 (*o*-, *m*-, *p*-$CH_2$*Ph*), 3.96, 3.40 (AB spin system, 2×1 H, $\Delta\delta$ = 0.56 ppm, $CH_2$), 2.10 (s, 6 H, *CH*$_3$Ph), 2.02 (s, 15 H, $C_5Me_5$), 1.45 [s, 18 H, $C(CH_3)_3$], 2.90 (br. s, 2 H, B*CH*$_2$Ph) ppm. $^{13}$C NMR (125 MHz, $C_6D_6$, 25 °C): $\delta$ = 161.5, 137.6, 134.8, 130.5, 129.5, 126.6 (all Ph), 150.4, 147.2, 139.0, 135.6 (all $C_6F_5$), 160.3 ($C_{ipso}$-$CH_2$*Ph*), 128.6 (*C*$_5$Me$_5$), 37.3 (B*C*H$_2$Ph), 35.1 ($CH_2$), 35.4 [*C*$(CH_3)_3$], 31.5 [C(*C*$H_3)_3$], 21.1 (*C*$H_3$-Ph), 13.1 ($C_5$*Me*$_5$) ppm; signals of *o*-, *m*-, *p*-$CH_2$*Ph* not found. $^{19}$F NMR (300 MHz, $C_6D_6$, 25 °C): $\delta$ = –135.0, –159.5, –164.6 ppm.

**[AlMe(mbmp)]$_2$ (16):** $AlMe_3$ (0.3 mL of a 2.0 M solution in hexane, 0.59 mmol) was added to a solution of mbmp$H_2$ (0.2 g, 0.59 mmol) in 25 mL of toluene at room temperature. After a few minutes, a white solid appeared and the reaction mixture was stirred for 5 h. The solution was filtered and the white solid was washed twice with hexane and characterised as **16** (0.29 g, 65% yield). $C_{48}H_{66}Al_2O_4$ (761.02): calcd. C 75.80, H 8.68; found C 75.67, H 8.90. $^1$H NMR (300 MHz, $C_6D_6$, 25 °C): $\delta$ = 7.41, 7.21, 7.04, 6.88 (AA′ spin systems, 4×2 H, Ph), 4.70, 3.69 (AB spin system, 2×2 H, $\Delta\delta$ = 1.01 ppm, $CH_2$), 2.32, 1.83 (s, 2×6 H, *CH*$_3$Ph), 1.40, 1.37 [s, 2×18 H, $C(CH_3)_3$], 0.15 (s, 6 H, $AlCH_3$) ppm. $^1$H NMR (300 MHz, $CDCl_3$, 25 °C): $\delta$ = 7.07, 7.03, 6.98, 6.95 (AA′ spin systems, 4×2 H, Ph), 4.33, 3.53 (AB spin system, $\Delta\delta$ = 0.80 ppm, $^2J_{H,H}$ = 13.7 Hz, 2×2 H, $CH_2$), 2.30, 2.22 (s, 2×6 H, *CH*$_3$Ph), 1.36, 1.21 [s, 2×18 H, $C(CH_3)_3$], –0.33 (s, 6 H, $AlCH_3$) ppm. $^{13}$C NMR (125 MHz, $CDCl_3$, 25 °C): $\delta$ = 151.2, 144.3, 140.9, 137.7, 134.4, 132.7, 130.6, 130.5, 127.8, 127.4, 127.1, 126.3 (all Ph), 35.0 ($CH_2$), 36.1, 34.5 [*C*$(CH_3)_3$], 31.8, 29.7 [C(*C*$H_3)_3$], 21.1, 21.0 (*C*$H_3$-Ph), 14.2 ($AlCH_3$) ppm.

**[AlCl(mbmp)]$_2$ (17):** $AlClMe_2$ (0.9 mL of a 1.0 M solution in hexane, 0.88 mmol) was added to a solution of mbmp$H_2$ (0.3 g, 0.88 mmol) in 25 mL of toluene at room temperature. After a few minutes, a white solid appeared and the reaction mixture was stirred for 3 h. The solution was filtered and the white solid was washed twice with hexane and toluene and characterised as **17** (0.37 g, 53% yield). $C_{46}H_{60}Al_2Cl_2O_4$ (801.85): calcd. C 68.90, H 7.54; found C 68.83, H 7.49. $^1$H NMR (300 MHz, $C_6D_6$, 25 °C): $\delta$ = 7.41, 7.18, 7.05, 6.88 (AA′ spin systems, 4×2 H, Ph), 4.83, 3.90 (AB spin system, 2×2 H, $\Delta\delta$ = 0.93 ppm, $CH_2$), 2.27, 1.79 (s, 2×6 H, *CH*$_3$Ph), 1.44, 1.43 [s, 2×18 H, $C(CH_3)_3$] ppm. $^1$H NMR (300 MHz, $CDCl_3$, 25 °C): $\delta$ = 7.09, 7.05, 7.02, 6.97 (AA′ spin systems, 4×2 H, Ph), 4.35, 3.68 (AB sin systems, $\Delta\delta$ = 0.67 ppm, $^2J_{H,H}$ = 14.6 Hz, 2×2 H, $CH_2$), 2.31, 2.22 (s, 2×6 H, *CH*$_3$Ph), 1.40, 1.23 [s, 2×18 H, $C(CH_3)_3$] ppm. $^{13}$C NMR (125 MHz, $CDCl_3$, 25 °C): $\delta$ = 149.9, 140.8, 138.5, 135.9, 132.8, 131.0, 130.2, 129.1, 128.9, 128.2, 128.0, 126.7 (all Ph), 35.2 ($CH_2$), 36.1, 34.5 [*C*$(CH_3)_3$], 32.3, 29.8 [C(*C*$H_3)_3$], 21.1, 21.0 (*C*$H_3$-Ph) ppm.

**Polymerisation of Propylene:** A 250-mL Büchi reactor equipped with a mechanical stirrer was first evacuated and then charged with dried scavenger (MAO) and toluene (150 mL). A 10-mL pressure tube was charged with the titanium complex solution in toluene (4 mL). The reactor was purged three times with the monomer by pressurizing and venting. The monomer was then equilibrated with the toluene in the reactor for 30 min at the polymerisation temperature and pressure (kept constant at 1 atm over the run) with constant stirring. In the runs in which liquid propylene was used, the reactor was first equilibrated at 0 °C with constant stirring and then fed with the monomer. The reaction was initiated by injecting the solution containing the catalytic system under argon pressure. After the desired reaction time, the reactor was vented and the polymer was precipitated into 10% HCl in methanol, washed with clean methanol and dried in a vacuum oven at 60 °C to constant weight.

**Polymerisation of Styrene:** A 100-mL glass pressure bottle with magnetic stirrer was vented and charged with toluene, MAO and 5 mL of the monomer. The mixture was then equilibrated at the polymerisation temperature with constant stirring and the reaction was initiated by injecting the solution of the catalyst in toluene (4 mL). After the desired reaction time, the reactor was vented and the polymer was precipitated into 10% HCl in methanol, washed with clean methanol and dried in a vacuum oven at 40 °C to constant weight. The polymer was extracted with refluxing thf for 5 h and dried again to constant weight in order to determine the sPS portion of the polymer obtained.

**Polymer Analyses:** Molecular weights were determined by high-temperature gel permeation chromatography using propylene and polystyrene as GPC calibration standards and 1,2,4-trichlorobenzene as eluent. The glass transition temperature and melting temperature were determined at a heating rate of 20 °C min$^{-1}$. $^1$H and $^{13}$C NMR measurements were performed at 363 K in [$D_2$]1,1,2,2-tetrachloroethane and referenced using the solvent peaks. The areas of the nine peaks in the methyl region determined from spectral integrations in polypropylene samples were used to characterise the sample microstructure. Analyses of the polymer properties were performed at the University of Ulm (Germany), Inorganic Chemistry II Department.

**Single-Crystal X-ray Structure Determination of Compounds 8, 9 and 11·0.75$C_6H_{14}$:** Crystal data and details of the structure deter-

 © 2007 Wiley-VCH Verlag GmbH & Co. KGaA, Weinheim 

Table 7. Crystallographic data for compounds **8**, **9** and **11**·0.75 $C_6H_{14}$.

| | **8** | **9** | **11**·0.75 $C_6H_{14}$ |
|---|---|---|---|
| Empirical formula | $C_{34}H_{48}O_2Ti$ | $C_{40}H_{52}O_2Ti$ | $C_{121}H_{161}O_{10}Ti_4$ |
| Formula mass | 536.59 | 612.69 | 1967.10 |
| Colour/habit | orange/fragment | orange/fragment | orange/fragment |
| Crystal dimensions [mm] | 0.20 × 0.36 × 0.61 | 0.15 × 0.33 × 0.64 | 0.23 × 0.36 × 0.56 |
| Crystal system | monoclinic | monoclinic | triclinic |
| Space group | $P2_1/n$ (no. 14) | $P2_1/c$ (no. 14) | $P\bar{1}$ (no. 2) |
| $a$ [Å] | 11.0192(1) | 11.2375(1) | 11.5443(1) |
| $b$ [Å] | 16.2903(1) | 17.6831(1) | 14.4543(1) |
| $c$ [Å] | 18.7555(2) | 17.9601(1) | 18.1492(2) |
| $\alpha$ [°] | 90 | 90 | 98.6156(3) |
| $\beta$ [°] | 90.1907(4) | 105.4970(4) | 106.9058(4) |
| $\gamma$ [°] | 90 | 90 | 91.9242(4) |
| $V$ [Å$^3$] | 3366.71(5) | 3439.17(4) | 2855.35(5) |
| $Z$ | 4 | 4 | 1 |
| $T$ [K] | 153 | 173 | 123 |
| $D_{calcd.}$ [g cm$^{-3}$] | 1.059 | 1.183 | 1.144 |
| $\mu$ [mm$^{-1}$] | 0.279 | 0.281 | 0.324 |
| $F$(000) | 1160 | 1320 | 1055 |
| $\theta$ range [°] | 2.48–25.35 | 1.65–25.32 | 1.85–25.38 |
| Index ranges ($h$, $k$, $l$) | ±13, ±19, ±22 | ±13, ±21, ±21 | ±13, ±17, ±21 |
| No. of refections collected | 80030 | 62663 | 59488 |
| No. of independent reflections/$R_{int}$ | 6157/0.044 | 6249/0.034 | 10449/0.042 |
| No. of obsd reflections [$I > 2\sigma(I)$] | 4990 | 5495 | 8948 |
| No. of data/restraints/parameters | 6157/0/348 | 6249/0/405 | 10449/0/920 |
| $R1$/$wR2$ [$I > 2\sigma(I)$][a] | 0.0400/0.1202 | 0.0458/0.1258 | 0.0431/0.1129 |
| $R1$/$wR2$ (all data)[a] | 0.0510/0.1248 | 0.0521/0.1307 | 0.0522/0.1205 |
| $GOF$ (on $F^2$)[a] | 1.118 | 1.032 | 1.027 |
| Largest difference peak/hole [e Å$^{-3}$] | +0.43/–0.36 | +0.44/–0.35 | +0.52/–0.57 |

[a] $R1 = \Sigma(||F_o| - |F_c||)/\Sigma|F_o|$; $wR2 = \{\Sigma[w(F_o^2 - F_c^2)^2]/\Sigma[w(F_o^2)^2]\}^{1/2}$; $GOF = \{\Sigma[w(F_o^2 - F_c^2)^2]/(n - p)\}^{1/2}$.

mination are presented in Table 7. Suitable single crystals for the X-ray diffraction study were grown from hexane in all cases. A clear orange fragment was stored under perfluorinated ether, transferred into a Lindemann capillary, fixed, and sealed. Preliminary examination and data collection were carried out with an area detecting system (Nonius, MACH3, κ-CCD) at the window of a rotating anode (Nonius, FR591) with graphite-monochromated Mo-$K_\alpha$ radiation ($\lambda$ = 0.71073 Å). The unit-cell parameters were obtained by full-matrix least-squares refinement of 6411 (6477, 10431) reflections. Data collection was performed at 153 (173, 123) K (Oxford Cryosystems) in the range 2.48°< $\theta$ < 25.35° (1.65°< $\theta$ < 25.32°, 1.85°< $\theta$ < 25.38°) for a total of nine (nine, seven) data sets in rotation scan mode with $\Delta\varphi/\Delta\omega$ = 1.0° (1.0°, 1.0°). A total of 80030 (62663, 59488) intensities were integrated. Raw data were corrected for Lorentz, polarisation, and, arising from the scaling procedure, latent decay and absorption effects. After merging [$R_{int}$ = 0.044 (0.034, 0.042)] a total of 6157 (6249, 10449) (all data) and 4990 (5495, 8948) [$I > 2\sigma(I)$] reflections remained and all these data were used in the subsequent refinement. The structures were solved by a combination of direct methods and difference Fourier syntheses. All non-hydrogen atoms were refined with anisotropic displacement parameters. For **8** and **9**, all hydrogen atoms were placed in ideal positions (riding model). For **11**·0.75 $C_6H_{14}$, all hydrogen atoms located at the titanium complex were found in the difference map calculated from the model containing all non-hydrogen atoms. The hydrogen positions were refined with individual isotropic displacement parameters. All hydrogen positions located at the disordered hexane solvent molecule were placed in calculated positions (riding model). Full-matrix least-squares refinements with 348 (405, 920) parameters were carried out by minimizing $\Sigma w(F_o^2 - F_c^2)^2$ with the SHELXL-97 weighting scheme and stopped at shift/err < 0.001 (0.001, 0.001). The final residual electron density maps showed no remarkable features. Neutral atom scattering factors for all atoms and anomalous dispersion corrections for the non-hydrogen atoms were taken from the International Tables for Crystallography. All calculations were performed with an Intel Pentium II PC, with the STRUX-V system, including the programs PLATON, SIR92 and SHELXL-97.[45–50] In **8**, a problem with an unresolvable solvent molecule was resolved with the PLATON[49] *Calc Squeeze* procedure. For **9**, a disorder [0.821(4):0.179(4)] of the cyclopentadienyl ring was clearly resolved. For **11**·0.75 $C_6H_{14}$, the solvent molecule appeared to be disordered over three positions (3:2:1) with an overall occupancy factor of 0.75. CCDC-631035 (**8**), -631036 (**9**) and -631037 (**11**·0.75 $C_6H_{14}$) contain the supplementary crystallographic data for this paper. These data can be obtained free of charge from The Cambridge Crystallographic Data Centre via www.ccdc.cam.ac.uk/data_request/cif.

**Supporting Information** (see footnote on the first page of this article): $^{13}C$ NMR spectra for the PP sample obtained in run 2 and run 6 (Table 5).

## Acknowledgments

Financial support for this research by DGICYT (project MAT2004-02614), CAM (project S-0505-PPQ/0328-02) and the European Commission (contract no. HPRN-CT2000-00004) is gratefully acknowledged. M. G.-M. acknowledges the Comunidad de Madrid (CAM) for the award of a Fellowship.

[1] D. C. Bradley, R. C. Mehrotra, D. P. Gaur, *Metal Alkoxides*, Academic Press, New York, **1978**.
[2] D. C. Bradley, R. C. Mehrotra, J. P. Rothwell, A. Singh, *Alkoxo and Aryloxo Derivatives of Metals*, Academic Press, San Diego, **2001**.

 © 2007 Wiley-VCH Verlag GmbH & Co. KGaA, Weinheim 

[3] M. H. Chisholm, J. H. Huang, J. C. Huffman, W. E. Streib, D. Tiedtke, *Polyhedron* **1997**, *16*, 2941–2949.
[4] F. G. Sernetz, R. Mülhaupt, S. Fokken, J. Okuda, *Macromolecules* **1997**, *30*, 1562–1569.
[5] T. Miyatake, K. Mizunuma, Y. Seki, M. Kakugo, *Makromol. Chem. Rapid Commun.* **1989**, *10*, 349–352.
[6] T. Miyatake, K. Mizunuma, M. Kakugo, *Makromol. Chem. Macromol. Symposia* **1993**, *66*, 203–214.
[7] A. Vanderlinden, C. J. Schaverien, N. Meijboom, C. Ganter, A. G. Orpen, *J. Am. Chem. Soc.* **1995**, *117*, 3008–3021.
[8] Y. X. Chen, P. F. Fu, C. L. Stern, T. J. Marks, *Organometallics* **1997**, *16*, 5958–5963.
[9] F. Amor, S. Fokken, T. Kleinhenn, T. P. Spaniol, J. Okuda, *J. Organomet. Chem.* **2001**, *621*, 3–9.
[10] M. G. Thorn, Z. C. Etheridge, P. E. Fanwick, I. P. Rothwell, *J. Organomet. Chem.* **1999**, *591*, 148–162.
[11] M. González-Maupoey, T. Cuenca, L. M. Frutos, O. Castaño, E. Herdtweck, *Organometallics* **2003**, *22*, 2694–2704.
[12] A. D. Becke, *J. Chem. Phys.* **1993**, *98*, 5648–5652.
[13] M. J. Frisch, G. W. Trucks, H. B. Schlegel, G. E. Scuseria, M. A. Robb, J. R. Cheeseman, V. G. Zakrzewski, J. A. J. Montgomery, R. E. Stratman, J. C. Burant, S. Dapprich, J. M. Millam, A. D. Daniels, K. N. Kudin, M. C. Strain, O. Farkas, J. Tomasi, V. Barone, M. Cossi, R. Cammi, B. Menucci, C. Pomelli, C. Adamo, S. Clifford, J. Ochterski, G. A. Petersson, P. Y. Ayala, Q. Cui, K. Morokuma, D. K. Malick, A. D. Rabuck, K. Raghavachari, J. B. Foresman, J. Cioslowski, J. V. Ortiz, B. B. Stefanov, G. Liu, A. Liashenko, P. Piskorz, I. Komaromi, R. Gomperts, R. L. Martin, D. J. Fox, T. Keith, M. A. Al-Laham, C. Y. Peng, A. Nanayakkara, C. Gonzalez, M. Challacombe, P. M. W. Gill, B. G. Johnson, W. Chen, M. W. Wong, J. L. Andres, C. Gonzalez, M. Head-Gordon, E. S. Replogle, J. A. Pople, *Gaussian 98*, revision A.7, Gaussian, Inc., Pittsburgh, PA, **1998**.
[14] S. Fokken, T. P. Spaniol, H. C. Kang, W. Massa, J. Okuda, *Organometallics* **1996**, *15*, 5069–5072.
[15] Y. Nakayama, K. Watanabe, N. Ueyama, A. Nakamura, A. Harada, J. Okuda, *Organometallics* **2000**, *19*, 2498–2503.
[16] R. D. Rogers, M. M. Benning, L. K. Kurihara, K. J. Moriarty, M. D. Rausch, *J. Organomet. Chem.* **1985**, *293*, 51–60.
[17] S. Fokken, T. P. Spaniol, J. Okuda, F. G. Sernetz, R. Mulhaupt, *Organometallics* **1997**, *16*, 4240–4242.
[18] C. Floriani, F. Corazza, W. Lesueur, A. Chiesi-Villa, C. Guastini, *Angew. Chem. Int. Ed. Engl.* **1989**, *28*, 66–67.
[19] F. Corazza, C. Floriani, A. Chiesi-Villa, C. Guastini, *Inorg. Chem.* **1991**, *30*, 145–148.
[20] A. V. Firth, J. C. Stewart, A. J. Hoskin, D. W. Stephan, *J. Organomet. Chem.* **1999**, *591*, 185–193.
[21] J. Okuda, S. Fokken, H. C. Kang, W. Massa, *Chem. Ber.* **1995**, *128*, 221–227.
[22] A. V. Firth, D. W. Stephan, *Inorg. Chem.* **1998**, *37*, 4726–4731.
[23] K. Nomura, N. Naga, M. Miki, K. Yanagi, A. Imai, *Organometallics* **1998**, *17*, 2152–2154.
[24] J. A. Ewen, *J. Am. Chem. Soc.* **1984**, *106*, 6355–6364.
[25] A. D. Horton, J. de With, A. J. van der Linden, H. van der Weg, *Organometallics* **1996**, *15*, 2672–2674.
[26] D. J. Gillis, R. Quyoum, M. J. Tudoret, Q. Y. Wang, D. Jeremic, A. W. Roszak, M. C. Baird, *Organometallics* **1996**, *15*, 3600–3605.
[27] Q. Y. Wang, D. J. Gillis, R. Quyoum, D. Jeremic, M. J. Tudoret, M. C. Baird, *J. Organomet. Chem.* **1997**, *527*, 7–14.
[28] J. I. Amor, T. Cuenca, M. Galakhov, P. Gómez-Sal, A. Manzanero, P. Royo, *J. Organomet. Chem.* **1997**, *535*, 155–168.
[29] T. Cuenca, M. Galakhov, G. Jiménez, E. Royo, P. Royo, M. Bochmann, *J. Organomet. Chem.* **1997**, *543*, 209–215.
[30] C. Pellecchia, A. Immirzi, A. Grassi, A. Zambelli, *Organometallics* **1993**, *12*, 4473–4478.
[31] M. G. Thorn, Z. C. Etheridge, P. E. Fanwick, I. P. Rothwell, *Organometallics* **1998**, *17*, 3636–3638.
[32] M. Bochmann, S. J. Lancaster, M. B. Hursthouse, K. M. Abdul Malik, *Organometallics* **1994**, *13*, 2235–2243.
[33] A. D. Horton, J. de With, *Chem. Commun.* **1996**, 1375–1376.
[34] E. E. E. C. G. Gielens, J. Y. Tiesnitsch, B. Hessen, J. H. Teuben, *Organometallics* **1998**, *17*, 1652–1654.
[35] J. M. Wright, C. R. Landis, M. A. M. P. Ros, A. D. Horton, *Organometallics* **1998**, *17*, 5031–5040.
[36] M. C. Baird, *Chem. Rev.* **2000**, *100*, 1471–1478.
[37] J. Cano, P. Royo, M. Lanfranchi, M. A. Pellinghelli, A. Tiripicchio, *Angew. Chem. Int. Ed.* **2001**, *40*, 2495–2497.
[38] J. Z. Jin, D. R. Wilson, E. Y. X. Chen, *Chem. Commun.* **2002**, 708–709.
[39] G. Natta, G. Mazzanti, *Tetrahedron* **1960**, *8*, 86–100.
[40] E. A. Ison, K. A. Abboud, I. Ghiviriga, J. M. Boncella, *Organometallics* **2004**, *23*, 929–931.
[41] B. Antelmann, M. H. Chisholm, S. S. Iyer, J. C. Huffman, D. Navarro-Llobet, M. Pagel, W. J. Simonsick, W. Q. Zhong, *Macromolecules* **2001**, *34*, 3159–3175.
[42] A. G. Massey, A. J. Park, *J. Organomet. Chem.* **1964**, *2*, 245–250.
[43] J. C. W. Chien, W. M. Tsai, M. D. Rausch, *J. Am. Chem. Soc.* **1991**, *113*, 8570–8571.
[44] M. Wedler, F. Knosel, F. T. Edelmann, U. Behrens, *Chem. Ber.* **1992**, *125*, 1313–1318.
[45] *Data Collection Software for Nonius k-CCD devices*, Delft, The Netherlands, **2001**.
[46] Z. Otwinowski, W. Minor, *Methods Enzymol.* **1997**, *276*, 307ff.
[47] *SIR92*: A. Altomare, G. Cascarano, C. Giacovazzo, A. Guagliardi, M. C. Burla, G. Polidori, M. Camalli, *J. Appl. Crystallogr.* **1994**, *27*, 435–436.
[48] *International Tables for Crystallography*, vol. C, Tables 6.1.1.4, 4.2.6.8, and 4.2.4.2, Kluwer Academic Publishers, Dordrecht, The Netherlands, **1992**.
[49] A. L. Spek, *PLATON, A Multipurpose Crystallographic Tool*, Utrecht University, Utrecht, The Netherlands, **2001**.
[50] G. M. Sheldrick, *SHELXL-97*, University of Göttingen, Germany, **1998**.

Received: July 31, 2006
Published Online: November 9, 2006

 © 2007 Wiley-VCH Verlag GmbH & Co. KGaA, Weinheim 

DOI: 10.1002/ejic.200600731

# A Ligand-Driven Geometry Switch in Octahedral and Trigonal-Bipyramidal Iron Complexes Containing (H)PNO and PNN Ligands

**Paolo Pelagatti,*[a] Alessia Bacchi,[a] Marcella Balordi,[a] Andrea Caneschi,[c] Marco Giannetto,[a] Corrado Pelizzi,[a] Luca Gonsalvi,[b] Maurizio Peruzzini,[b] and Franco Ugozzoli[a]**

**Keywords:** Iron / N,P ligands / Ligand effects

Complexation reactions of $Fe^{II}$ and $Fe^{III}$ salts with the tridentate ligands 2-(diphenylphosphanyl)benzaldehyde benzoylhydrazone [(H)PNO] and *N*-[2-(diphenylphosphanyl)benzylidene]-2-(2-pyridyl)ethanamine (PNN) was carried out. For (H)PNO, reaction of a stoichiometric amount of anhydrous $FeCl_2$ in the presence of a primary alcohol such as MeOH, EtOH or *n*BuOH gave the mixed-valence $Fe^{II}/Fe^{III}$ paramagnetic complex $[Fe\{\kappa^3\text{-}(H)PNO\}_2]Cl[FeCl_4]$, whereas the reaction between $FeCl_2$ and a twofold excess of (H)PNO in the presence of AgOTf (OTf = triflate, $OSO_2CF_3$) led to the isolation of the bis-chelate paramagnetic ferrous complex $[Fe\{\kappa^3\text{-}(H)PNO\}_2][OTf]_2$. A diamagnetic bis-chelate ferrous complex $[Fe\{\kappa^3\text{-}(PNO)_2\}]$ was instead obtained from the reaction of $FeCl_2$ with a twofold excess of (H)PNO in the presence of NaOMe. In the case of the PNN ligand, the 1:1 reaction with $FeCl_2$ gave the neutral paramagnetic trigonal-bipyramidal complex $[Fe(\kappa^3\text{-PNN})Cl_2]$. The X-ray structures of $[Fe\{\kappa^3\text{-}(H)PNO\}_2]Cl[FeCl_4]$, $[Fe_2\{\kappa^3\text{-}(H)PNO\}_2Cl_6]$ and $[Fe(\kappa^3\text{-PNN})Cl_2]$ are reported, together with CV and magnetic susceptibility measurements and an ab initio study aimed at rationalizing the different stoichiometries and structures observed with the two tridentate ligands.
(© Wiley-VCH Verlag GmbH & Co. KGaA, 69451 Weinheim, Germany, 2007)

## Introduction

The interest in five-coordinate iron(II) complexes with tridentate ligands stems mainly from their high catalytic activity in olefin polymerisation. The most active and studied systems are those containing the 2,6-bis(arylimino)-pyridyl moiety (NNN ligands),[1] although examples with ONN[2] and PNP[3] ligands have also been reported. Recently, cobalt complexes containing tridentate ligands have also been combined with iron to create mixed-valence and heterometallic [2 × 2] grid-like arrays,[4] spin-crossover complexes,[5] models of enzyme active sites such as catechol dioxygenases[6] and nitrile hydratase,[7] and asymmetric sulfide oxidation catalysts.[8] Some of us have been involved in the study of the coordinating behaviour of asymmetric tridentate ligands towards transition metals for several years.[9] The most thoroughly investigated ligand, 2-(diphenylphosphanyl)benzaldehyde benzoylhydrazone [(H)-PNO, Scheme 1], has been used to synthesise $Pd^{II}$ and $Ru^{II}$ complexes that are active catalysts in alkene hydrogenation[10] and addition of benzoic acid to terminal alkynes,[11] respectively. The importance of the iron complexes containing the Fe(LLL) moiety (LLL = tridentate ligand) prompted us to investigate the coordinating behaviour of (H)PNO towards $FeCl_2$. This study was subsequently extended to another tridentate ligand, namely *N*-[2-(diphenylphosphanyl)benzylidene]-2-(2-pyridyl)ethanamine (PNN),[12] which bears a 2-(2-aminoethyl)pyridine function

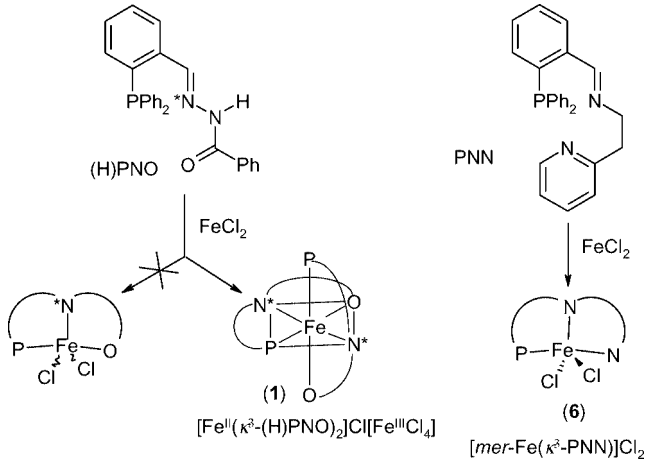


Scheme 1. The anions of complex **1** have been omitted.

[a] Dipartimento di Chimica Generale ed Inorganica, Chimica Analitica, Chimica Fisica, Università degli Studi di Parma, Viale G.P. Usberti 17/A, 43100 Parma, Italy
E-mail: paolo.pelagatti@unipr.it
[b] Istituto di Chimica dei Composti OrganoMetallici, Consiglio Nazionale delle Ricerche (I.C.C.O.M.), Via Madonna del Piano 10, 50019 Sesto Fiorentino, Firenze, Italy
[c] Dipartimento di Chimica & UdR INSTM, Università degli Studi di Firenze, Via della Lastruccia 3, Polo Scientifico, 50019 Sesto Fiorentino, Firenze, Italy

 © 2007 Wiley-VCH Verlag GmbH & Co. KGaA, Weinheim 

instead of an (H)NC(O)Ph arm (Scheme 1). The ligand PNN differs from HPNO as it is aprotic and forms two six-membered chelate rings instead of a six- and a five-membered chelation ring as for (H)PNO upon complexation.

In this paper we describe the synthesis and full characterisation of a series of iron complexes obtained by reaction between (H)PNO and anhydrous $FeCl_2$ or hydrated $FeCl_3$ and PNN and anhydrous $FeCl_2$. The X-ray structures of $[Fe\{\kappa^3\text{-(H)PNO}\}_2]Cl[FeCl_4]$ (**1**), $[Fe_2\{\kappa^3\text{-(H)PNO}\}_2Cl_6]$ (**2**) and *mer*-$[Fe(\kappa^3\text{-PNN})Cl_2]$ (**6**) are also reported. A rationalisation of the different stoichiometries and geometries observed for the iron complexes with the two tridentate ligands is also provided on the basis of ab initio calculations.

## Results and Discussion

### Complexes Containing HPNO

Tridentate aroyl hydrazones easily form iron complexes containing the octahedral entity $[FeL_2]^{n+}$ (L = tridentate aroyl hydrazone, $n$ = 0, 2 or 3), where the charge depends on the anionic or neutral character of the ligands as well as on the oxidation state of the metal. These complexes, which are usually synthesised by employing an L:Fe molar ratio of 2:1, are generally very stable, and aroyl hydrazones are in fact being studied as sequestrating agents for the treatment of iron overload diseases.[13] As octahedral bis-chelate complexes are usually considered to be ineffective in catalysis, our first aim was to isolate five-coordinate iron(II) species of the type *mer*-$[Fe\{\kappa^3\text{-(H)PNO}\}Cl_2]$ (Scheme 1) with a trigonal-bipyramidal or square-pyramidal geometry. Therefore, we initially treated a dichloromethane solution of (H)PNO with a stoichiometric amount of anhydrous $FeCl_2$ dissolved in *n*-butanol[14] at room temperature. The reaction gave a purple solid of formula *mer*-$[Fe\{\kappa^3\text{-(H)PNO}\}_2]Cl[FeCl_4]$ (**1**) in good yield. The same product could also be isolated by carrying out the reaction at reflux in other alcohols such as MeOH or EtOH, by reverting the sequence of addition of the reagents, or by adding the ligand-containing solution dropwise to the alcoholic solution of the iron salt. The use of neat thf as solvent as well as an (H)PNO:$FeCl_2$ molar ratio of 1:5 did not change the reaction course either. Complex **1** contains the ferrous cationic fragment $[Fe\{\kappa^3\text{-(H)PNO}\}_2]^{2+}$, the tetrahedral tetrachloroferrate anion $[FeCl_4]^-$ and a free chloride ion (Scheme 1).

Two ligands bind to the iron(II) ion in a neutral tridentate fashion through the phosphorus, the imine nitrogen and the amide oxygen in the octahedral cation. The neutral character of the (H)PNO ligands is indicated by a weak IR stretching band at 3255 $cm^{-1}$ for the N–H groups, while a single band at 1607 $cm^{-1}$ indicates that both C=O groups are involved in the coordination.[9a,9g] The FAB(+) spectrum shows the presence of the fragment $m/z$ = 1070 belonging to the cation $[\{Fe(HPNO)_2\}\{FeCl_4\}]^+$. Another intense cluster signal is centred at $m/z$ = 871 belonging to the fragment $[Fe\{(H)PNO\}(PNO)]^+$, while a signal at $m/z$ = 463 accounts for the fragment $[Fe(PNO)]^+$. In the ESI(+) spectrum of a methanol solution of **1**, the signal generated by the loss of the $Cl^-$ is absent, while the cluster at $m/z$ = 871 is well visible. Importantly, the ESI(–) spectrum shows a signal at $m/z$ = 198 due to the $[FeCl_4]^-$ anion.

The electronic spectrum of an acetonitrile solution ($10^{-7}$ M) of **1** shows the following bands in the region 250–1000 nm: 261 ($\varepsilon$ = 55483 $M^{-1}cm^{-1}$), 306 (39774), 357 (29000) and a broad absorption band at 518 nm (7081). The bands at 261, 306 and 518 nm are typical of bis-chelate $Fe^{II}$ complexes containing tridentate benzoylhydrazones, and are attributed to LMCT processes.[15] The absorption peak at 357 nm can be tentatively assigned to the $[FeCl_4]^-$ anion.[16] The alternative formula $[Fe^{III}\{\kappa^3\text{-(H)PNO}\}_2]Cl[Fe^{II}Cl_4]$ for complex **1** is unlikely because of the sensitivity of the $[FeCl_4]^{2-}$ anion to air[16a] and because of the soft character of the (H)PNO ligand (due to the phosphane moiety), which is expected to stabilize $Fe^{II}$. A further confirmation comes from the voltammetric measurements. Figure 1 shows the cyclic voltammogram of compound **1** (third of three scans) recorded in acetonitrile solution: the anodic signal at about +0.0025 V and the cathodic wave at about –0.2 V can be assigned, respectively, to the oxidation of the complexed $Fe^{II}$ to $Fe^{III}$ and the corresponding reduction back to $Fe^{II}$. The weak signal at about 0.75 V is ascribable to the ligand, which was also characterised by means of the same technique. The potential values observed for the $Fe^{II}$/$Fe^{III}$ couple are, in fact, unusual for uncomplexed iron, such as $FeCl_4^-$ counterions. Moreover, cyclic voltammetric measurements carried out on a freshly prepared solution of anhydrous $FeCl_3$ in acetonitrile, under the same experimental conditions employed for the studied complex, show a system of anodic and cathodic signals at potential values above +0.250 V.

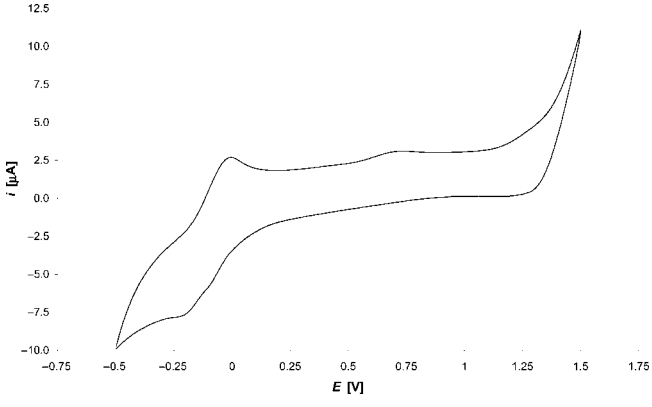


Figure 1. Cyclic voltammogram of compound **1** (third of three scans) recorded in acetonitrile solution. Scan rate: 0.1 $V s^{-1}$.

The $^1H$ NMR spectrum of **1** shows very broad signals in the 300–233 K temperature range owing to the presence of the paramagnetic $[FeCl_4]^-$ anion. However, the $^{31}P\{^1H\}$ NMR spectrum recorded at 300 K shows a singlet at $\delta$ = 63.4 ppm, as expected for two magnetically equivalent phosphorus nuclei in the complex cation. The paramagnetic character of **1** is evidenced by its magnetic behaviour. $\chi T$ vs. $T$ data were recorded in the range 50–300 K with an applied field of 1 T, where the zero-field splitting contri-

 © 2007 Wiley-VCH Verlag GmbH & Co. KGaA, Weinheim 

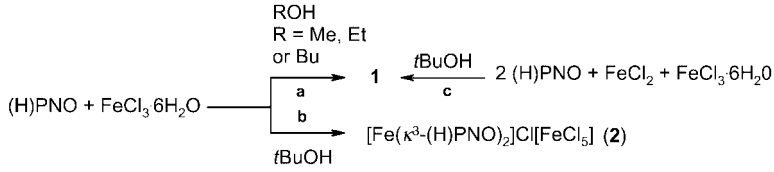


Scheme 2.

bution is not attended and saturation effects should not be yet present. These data show a Curie behaviour of around 4.2 emu mol $K^{-1}$ in the whole temperature range, quite close to the expected $S = 5/2$ value for an isolated spin with $g = 2.0$ (4.375 emu mol $K^{-1}$).

Complex **1** was also obtained by treating (H)PNO with $FeCl_3 \cdot 6H_2O$ in methanol or ethanol at 80 °C, as confirmed by X-ray diffraction analysis on a single crystal isolated from the mother liquor and by IR and UV spectroscopy and elemental analysis (Scheme 2, pathway a). The X-ray structure of **1** is shown in Figure 2, where the $Cl^-$ and $[FeCl_4]^-$ anions have been omitted for clarity.

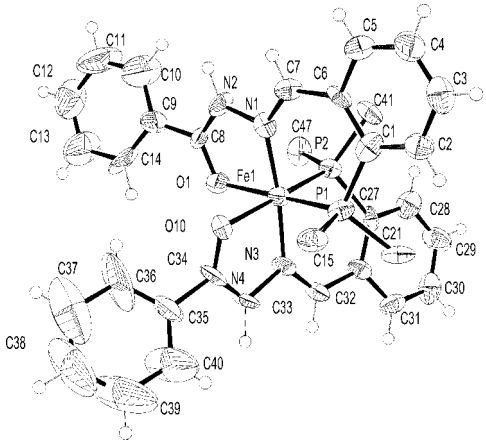


Figure 2. Perspective view and labelling scheme of *mer*-[Fe{κ$^3$-(H)-PNO}$_2$]$^{2+}$ in **1**. Thermal ellipsoids are shown at the 50% probability level. Phenyl groups C16–C20 (at C15), C22–C26 (at C21), C42–C46 (at C41), C48–C52 (at C47) have been omitted for clarity. A $Cl^-$ and a $FeCl_4^-$ complete the structure.

Table 1 lists the main bond lengths and angles for **1**. The conformation of the two ligands is almost identical, and the complex shows a non-crystallographic symmetry around a twofold axis bisecting the O1–Fe1–O10 and the P1–Fe1–P2 angles. The PNO coordination forms a five-membered and a six-membered chelation ring for each ligand. In both cases the former is planar within 0.06 Å, while in the latter the P atom deviates significantly (0.5 Å) from the average plane defined by the remaining five atoms; this deformation is characteristic of most instances of coordinated 2-(diphenylphosphanyl)benzaldehyde hydrazones.[9g] However, even taking into account the out-of-plane deformation involving the P atoms, the overall conformation of the ligand backbone is planar within 0.30 Å. This feature will be a matter for comparison with complex **6**. The steric crowding of the diphenylphosphanyl groups belonging to the two ligands in the bis-chelate coordination induces intramolecular parallel stacking (3.5 Å) between the benzaldehyde aromatic ring of each ligand and one free phenyl of the other ligand. The complex cations are bridged by $Cl^-$ anions through the hydrogen bonds N4–H···Cl5 [N···Cl = 3.04(1) Å; N–H···Cl = 160(10)°] N2–H···Cl5($x$, 0.5 – $y$, 0.5 + $z$) [N···Cl = 3.10(5) Å; N–H···Cl = 154(6)°] to form a chain motif (Figure 3, left).

Table 1. Bond lengths [Å] and angles [°] for **1** and **6**.

| **1** | | **6** | |
|---|---|---|---|
| Fe1–N3 | 1.88(1) | Fe–N2 | 2.1083(3) |
| Fe1–N1 | 1.90(1) | Fe–N1 | 2.241(3) |
| Fe1–O10 | 1.971(9) | Fe–Cl1 | 2.294(1) |
| Fe1–O1 | 1.979(9) | Fe–Cl2 | 2.329(1) |
| Fe1–P2 | 2.232(4) | Fe–P | 2.541(1) |
| Fe1–P1 | 2.249(4) | | |
| N3–Fe1–N1 | 173.4(5) | N2–Fe–N1 | 86.7(1) |
| N3–Fe1–O10 | 82.3(5) | N2–Fe–Cl1 | 119.79(9) |
| N1–Fe1–O10 | 92.7(5) | N1–Fe–Cl1 | 91.80(9) |
| N3–Fe1–O1 | 92.7(5) | N2–Fe–Cl2 | 113.78(8) |
| N1–Fe1–O1 | 82.1(5) | N1–Fe–Cl2 | 91.35(8) |
| O10–Fe1–O1 | 80.0(4) | Cl1–Fe–Cl2 | 126.43(5) |
| N3–Fe1–P2 | 92.2(4) | N2–Fe–P | 80.96(8) |
| N1–Fe1–P2 | 91.9(3) | N1–Fe–P | 167.33(8) |
| O10–Fe1–P2 | 168.6(3) | Cl1–Fe–P | 96.82(4) |
| O1–Fe1–P2 | 90.4(3) | Cl2–Fe–P | 90.97(3) |
| N3–Fe1–P1 | 92.2(3) | | |
| N1–Fe1–P1 | 92.1(4) | | |
| O10–Fe1–P1 | 90.0(3) | | |
| O1–Fe1–P1 | 168.1(3) | | |
| P2–Fe1–P1 | 100.2(2) | | |

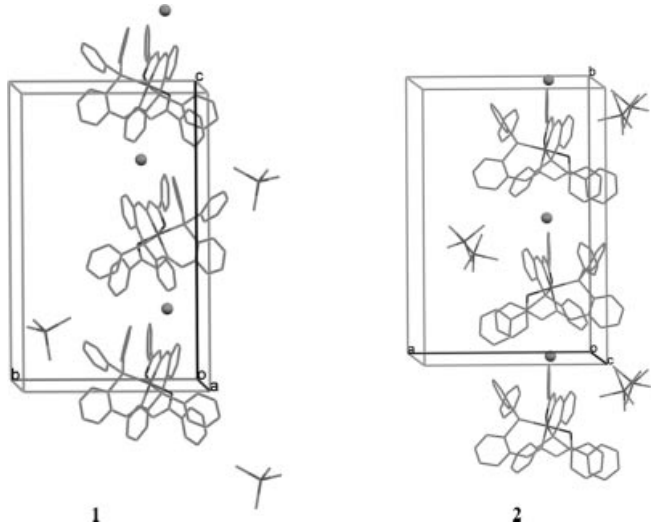


Figure 3. Comparison of the packing arrangements of **1** (left) and **2** (right), oriented so that axes of similar lengths correspond. The 60:40 disorder of $FeCl_4^{2-}$ and $FeCl_5^{2-}$ anions is shown in **2**.

 © 2007 Wiley-VCH Verlag GmbH & Co. KGaA, Weinheim 

The formation of **1** from the ferric salt clearly requires the presence of a reductant; since no traces of oxidized ligand were detected or isolated [two possible oxidative processes could involve the (H)PNO ligand: oxidation of the phosphane moiety to the corresponding phosphane oxide or oxidation of the aroyl hydrazone to diacyl hydrazine[13a]], the oxidation of the primary alcohols to the corresponding aldehyde must be invoked. The oxidation of primary alcohols promoted by $Fe^{III}$ species is a rather uncommon process which, to the best of our knowledge, has been reported only rarely.[16a,17] Regrettably, repeated attempts to detect the expected aldehydes failed. However, the in situ iron(III) → iron(II) reduction was proved by treating (H)PNO with $FeCl_3·6H_2O$ and $FeCl_2$ in a 2:1:1 molar ratio in a *t*BuOH/$CH_2Cl_2$ mixture heated at reflux. The reaction gave complex **1** in high yield and purity, as demonstrated by the IR, UV and FAB mass spectra and microanalysis. Moreover, when the reaction between (H)PNO and $FeCl_3·6H_2O$ was repeated under reflux in a tertiary alcohol, such as *t*BuOH, which cannot undergo oxidative processes, a complex containing two $Fe^{III}$ nuclei of stoichiometry $[Fe_2\{\kappa^3\text{-}(H)PNO\}_2Cl_6]$ (**2**) formed, as evidenced by elemental analysis (Scheme 2, pathway b).

Unfortunately, the mass (FAB and ESI) and IR spectra are not informative as they are identical to those of **1**. Cyclic voltammograms of complex **2** show a pattern comparable to **1**. This behaviour can be explained by considering that $Fe^{III}$ is initially reduced to $Fe^{II}$ in the first stage of the scan, starting from –0.5 V. The tendency to undergo reduction shown by the octahedral $Fe^{III}$ centre in **2** explains the similarity of the mass spectra of complexes **1** and **2**, since redox processes can occur during such analysis.[18]

Crystals of **2** suitable for X-ray diffraction analysis were collected from the mother liquor. Compound **2**, with stoichiometry $[Fe_2\{\kappa^3\text{-}(H)PNO\}_2Cl_6]$, contains the $[Fe\{\kappa^3\text{-}(H)PNO\}_2]^{3+}$ cation, one chloride anion, and an apparent mixture of $[FeCl_4]^{2-}$ and $[FeCl_5]^{2-}$ anions disordered over two sites 3.7 Å apart (Figure 3, right).

The Fourier map of the region occupied by the complex anions was interpreted in terms of a substitutional disorder where some $[FeCl_4]^{2-}$ replaces the $[FeCl_5]^{2-}$ anions in a 60:40 proportion, even though this would imply a reduction of $[FeCl_5]^{2-}$, whose oxidized products have not been detected. The same disorder pattern was found when repeating the structure determination on crystals grown from different batches. Due to structural disorder and to the consequent poor quality of the refinement, the geometry of the trivalent bis-chelate cation is not significantly different from the divalent one crystallised with pure $[FeCl_4]^-$ in **1** and therefore does not allow us to assign unequivocally the oxidation state of the Fe atom based uniquely on the comparison of the Fe–P distances. The structure is based on chains of cations bridged by chloride anions via N–H···Cl hydrogen bonds; in both cases these chains are aligned along the 21 Å axis, which, however, has different symmetry properties in the two crystals (Table 3). These result in an array of heterochiral complexes generated by a *c* glide in **1** and in a homochiral chain generated by a $2_1$ screw axis in **2**. In fact, the presence of a relevant amount of $[FeCl_5]^{2-}$ causes a remarkable rearrangement of the symmetry elements between the two compounds accompanied by a repositioning of the complex anions, which occupy different sites along the chains in the two cases (Figure 3).

When a methanol solution of anhydrous $FeCl_2$ was treated with a twofold excess of (H)PNO dissolved in dichloromethane at reflux, a purple solid of formula $[Fe\{\kappa^3\text{-}(H)PNO\}_2]Cl_2$ (**3**) was obtained (Scheme 3).

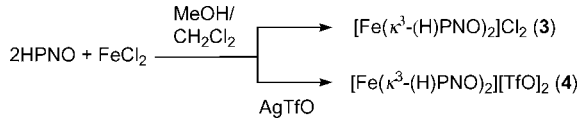


Scheme 3.

The ESI(+) mass spectrum of **3** shows a unique cluster centred at *m*/*z* = 871 due to the octahedral unit $[Fe\{(H)PNO\}(PNO)]^+$. The electronic spectrum does not show the band at 357 nm while the charge-transfer absorptions at 261, 306 and 507 nm are well visible. The IR spectrum shows a weak stretching band at 3220 $cm^{-1}$, which is indicative of the protic character of the ligands, whereas a band at 1603 $cm^{-1}$ confirms that the C=O groups of the two PNO ligands are both involved in the coordination. Broad and uninformative bands are present in the $^1H$ NMR spectrum recorded at 300 K, while the $^{31}P\{^1H\}$ NMR spectrum shows a singlet at $\delta$ = 64.4 ppm that is compatible with the presence of the octahedral cation $[Fe\{\kappa^3\text{-}(H)PNO\}_2]^{2+}$; a small singlet at $\delta$ = 36.8 ppm is also visible, probably due to the partial oxidation of the phosphane P-atom of the (H)PNO ligand. On lowering the temperature to 233 K, the $^1H$ NMR signals do not sharpen. Careful inspection of the solid showed a substantial heterogeneity, as evidenced by the presence of differently coloured agglomerates (from red to deep purple). Regrettably, repeated recrystallisations did not improve the analytical quality of the product leading, in some cases, to decomposition and, in general, to irreproducible elemental analyses. On the basis of magnetic susceptibility measurements, the paramagnetic character of **3** seems imputable to traces of iron(III) species, probably due to aerobic oxidation. A rough evaluation of the $\chi T$ versus $T$ value in the temperature range 50–300 K with an applied field of 1 T for compound **3** gives a coarse percentage of about 10% of noninteracting iron(III) versus diamagnetic iron(II).

A clearer picture was obtained by treating (H)PNO with $FeCl_2$ in the presence of silver triflate; the removal of the chlorides led to the smooth formation of the bis-chelate complex $[Fe\{\kappa^3\text{-}(H)PNO\}_2][OTf]_2$ (**4**; Scheme 3). The reaction occurred with precipitation of silver chloride, which was separated by filtration to leave a red solution, from which a red powder was isolated. In this case, the elemental analysis is in agreement with the expected stoichiometry. The ESI(+) mass spectrum of a dichloromethane solution of **4** shows a cluster centred at *m*/*z* = 1021, corresponding to the loss of a triflate anion, and a second cluster centred at *m*/*z* = 871, corresponding to the fragment $[Fe\{(H)$

 © 2007 Wiley-VCH Verlag GmbH & Co. KGaA, Weinheim 

PNO}(PNO)]$^+$. The UV spectrum does not show the band at 357 nm, as expected due to the absence of the $[FeCl_4]^-$ anion. The IR spectrum agrees with the presence of two neutral (H)PNO ligands bound to the metal, as indicated by the stretching bands of the N–H and C=O groups at 3198 and 1605 cm$^{-1}$, respectively. The presence of the triflate anion is testified by intense IR bands at 1027 cm$^{-1}$ [$\nu_s(SO_3)$], 1157 cm$^{-1}$ [$\nu_{as}(CF_3)$], 1238 cm$^{-1}$ [$\nu_s(CF_3)$] and 1296 cm$^{-1}$ [$\nu_{as}(SO_3)$].[19] The $^1$H NMR spectrum indicates a paramagnetic character of the complex, as inferred by the broad bands observed even at 233 K, while the $^{31}P\{^1H\}$ NMR spectrum shows a unique sharp signal at $\delta$ = 62 ppm, even at room temperature, as expected for two magnetically equivalent P nuclei. The cyclic voltammograms of complex **4** show a quite different behaviour with respect to complex **1** as these complexes contain different counterions. The presence of the triflate anion shifts both the anodic and cathodic peaks to potential values above +0.75 V. A higher value of $\Delta E_p$ (difference between anodic peak potential and cathodic peak potential) is also detected. These phenomena could be interpreted by considering the possibility that, in complex **1**, the metallic centre contained in the $[FeCl_4]^-$ counterion is actively involved in the electron-transfer mechanism of the coordinated iron.[20]

It is well known that a reinforced ligand–metal interaction favours a high crystal-field separation and leads preferentially to low-spin complexes that, in the case of d$^6$ metals in an octahedral environment, are diamagnetic. With the aim of isolating a neutral diamagnetic octahedral complex of the type [Fe($\kappa^3$-PNO)$_2$] (**5**), a dichloromethane solution of (H)PNO was at first treated with a stoichiometric amount of NaOMe dissolved in methanol and the NaPNO salt thus formed was treated with a methanol solution of anhydrous $FeCl_2$ (ligand/metal = 2:1; Scheme 4).

$$2(H)PNO + FeCl_2 \xrightarrow[NaOMe]{MeOH/CH_2Cl_2} [Fe(\kappa^3\text{-}PNO)_2]\ (\mathbf{5})$$

Scheme 4.

The elemental analysis of the isolated purple solid agrees with the expected stoichiometry and the CI mass spectrum shows an intense cluster at $m/z$ = 871 corresponding to [**5**+H]$^+$. The absence of the IR stretching bands of the N–H and C=O groups indicates that the two deprotonated ligands bind iron in an anionic PNO tridentate fashion. Measurements of the magnetic susceptibility at an applied magnetic field of 1 T suggest that the complex is diamagnetic in the temperature range 10–300 K. However, the $^1$H NMR spectrum of a $CDCl_3$ solution of **5** recorded at 300 K contains very broad signals, which sharpen on lowering the temperature to 233 K. At this temperature the C(H)=N proton resonates at $\delta$ = 9.42 ppm as a singlet, while a doublet is observed at $\delta$ = 7.71 ppm ($^3J_{H,H}$ = 7.05 Hz) due to the two phenyl protons adjacent to the C=O group of the benzoyl function. The $^{31}P\{^1H\}$ NMR spectrum recorded at 233 K shows a singlet at $\delta$ = 69.2 ppm and a small singlet at around $\delta$ = –17 ppm. The first signal corresponds to the two magnetically equivalent P nuclei of the two coordinated (H)PNO ligands, while the more shielded singlet is indicative of a partial decoordination of a phosphorus. Because complex **5** is diamagnetic at 300 K, the broadening of the $^1$H NMR lines at this temperature must be caused by molecular motions in solutions, which are absent at 233 K. Because the broadening involves the entire $^1$H NMR spectrum, the fluxionality seems to be due to the decoordination and subsequent re-entering of the P (as further indicated by $^{31}P\{^1H\}$ NMR spectroscopy) and N-imine donors in the coordination sphere. This can reasonably be imputed to the isomerisation between the two $\Delta$ and $\Lambda$ isomers that are expected to coexist in solution.

### A Complex Containing the PNN Ligand

Substitution of the (H)NC(O)Ph arm with the 2-(2-aminoethyl)pyridine function certainly makes the ligand PNN more flexible than (H)PNO. This allows for different coordination modes, such as *mer*-$\kappa^3$-PNN with Pd$^{II}$[12,21] and Rh$^{I–III}$,[22] *fac*-$\kappa^3$-PNN or $\kappa^2$-PN with Cr, Mo and W,[23] $\mu$-$\kappa^3$-PNN and even $\mu$-$\kappa^4$-PNCN with Os clusters.[24] The reaction between equimolar amounts of anhydrous $FeCl_2$ and PNN in a $MeOH/CH_2Cl_2$ mixture at room temperature led to the isolation of the trigonal bipyramidal complex [*mer*-Fe(PNN)Cl$_2$]·1/2$CH_2Cl_2$ (**6**; Scheme 1) in good yield. The complex is a paramagnetic orange crystalline solid. The IR spectrum shows a shift of the IR stretching band of the C(H)=N moiety with respect to the free ligand, from 1653 to 1629 cm$^{-1}$, which is indicative of a Fe–N(imine) coordination. The FAB(+) mass spectrum shows a high degree of fragmentation of the analyte, which does not allow any simple interpretation. However, after amplification of the signal a small cluster at $m/z$ = 63, corresponding to **6**, becomes visible. The structure of complex **6** was confirmed by single-crystal X-ray analysis. The tridentate PNN ligand in **6** occupies two apical and one equatorial sites of a trigonal bipyramidal coordination, which is completed by two Cl$^-$ ligands at the remaining equatorial sites (Figure 4). Table 1 lists the main bond lengths and angles for **6**. The tridentate coordination of PNN to the metal generates two six-membered chelation rings whose conformation is highly puckered, in contrast to the almost planar geometry observed for the coordination of (H)PNO in **1**. The ring formed by chelation of N1 and N2 is best described as a half-chair with the vector N2–C8 twisted relative to the ring plane (Cremer and Pople[25] puckering coordinates: $Q_T$ = 0.56 Å, $\phi$2 = –91°, $\theta$2 = 44°), while the ring defined by chelation of N2 and P1 is intermediate between half-boat and a twisted chair, with a major displacement of P and Fe from the average ring plane (puckering coordinates: $Q_T$ = 0.95 Å, $\phi$2 = 149°, $\theta$2 = 117°). The dramatic distortion from planarity observed in **6** is a consequence of the enlargement of the chelate ring by replacement of the hydrazonic arm of (H)PNO with a $CH_2CH_2N$ system in PNN. The insertion of the ethyl segment in the chelate ring is necessarily accompanied by a deviation of C9 out of the local plane de-

 © 2007 Wiley-VCH Verlag GmbH & Co. KGaA, Weinheim 

fined by C6, C7, N2 and C8 around the iminic double bond. Consequently, the pyridine attached to C9 is rotated relative to the iminic plane (P–Fe–N2–C7 = 43°), and the phosphane group on the other side of the molecule is constrained to follow this rotation in order to maintain the *trans* geometry for the P–Fe–N1 angle. The overall molecular deformation of **6** relative to the planar tridentate chelation observed in **1** can be viewed as a rotation of the apical axis P–Fe–N1 of the coordination polyhedron around the hinge represented by the Fe–N2 vector. A similar deformation, with P–M–N=C torsion angles ranging between 17° and 44°, has been observed in the four other occurrences of complexes containing the PNN ligand[12,23a,26] characterised in the solid state.

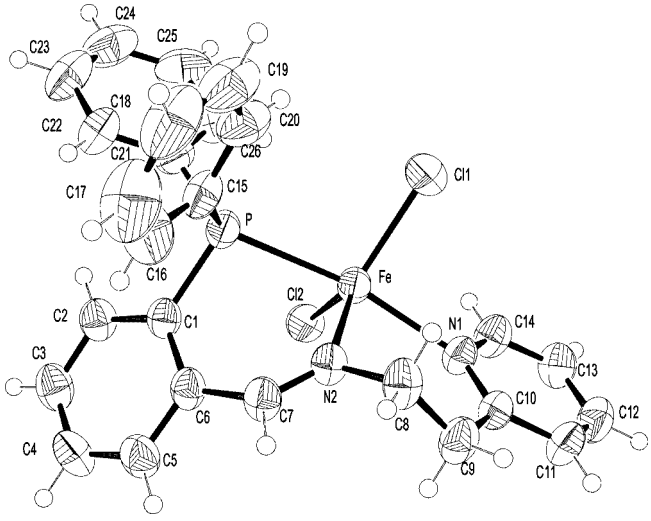


Figure 4. Perspective view and labelling scheme of *mer*-[Fe($\kappa^3$-PNN)$Cl_2$] in **6**. Thermal ellipsoids are shown at the 50% probability level.

## Modelling

To clarify the reasons for the formation of the octahedral cation $[Fe\{\kappa^3\text{-}(H)PNO\}_2]^{2+}$ rather than the analogous cation $[Fe(\kappa^3\text{-}PNN)_2]^{2+}$, we have undertaken theoretical calculations to predict and then to investigate their molecular structures.

The optimised geometries of the two ions were obtained by ab initio calculations using the semi-empirical PM3 method[27] in the Spartan 04 program[28] and are illustrated in Figure 5. The calculated bond lengths and angles in the five- and six-membered chelate rings are collected in Table 2. The results of the calculations indicate that the distances are consistent with the values reported in the literature. However, although the Fe–P distance in the $[Fe\{\kappa^3\text{-}(H)PNO\}_2]^{2+}$ ion (2.264 Å) falls just in the middle of the range observed from a perusal of the data available in the CSD (from 2.2 to 2.3 Å), the analogous distance calculated from the $[Fe(\kappa^3\text{-}PNN)_2]^{2+}$ ion (2.413 Å) is significantly longer and, to the best of our knowledge, is unprecedented in the solid-state structures reported in the CSD file.

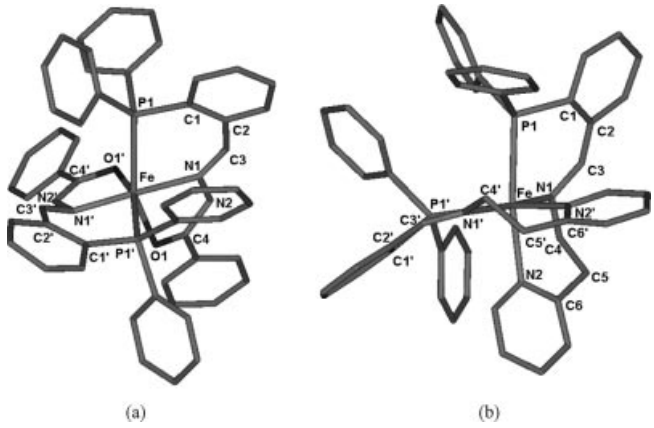


Figure 5. Optimised geometries obtained for the two cationic fragments $[Fe\{\kappa^3\text{-}(H)PNO\}_2]^{2+}$ (a) and $[Fe(\kappa^3\text{-}PNN)_2]^{2+}$ (b). Hydrogen atoms have been omitted for clarity.

This suggests that the increase of the Fe–P bond lengths in $[Fe(\kappa^3\text{-}PNN)_2]^{2+}$ compared to that in $[Fe\{\kappa^3\text{-}(H)PNO\}_2]^{2+}$ may be the reason why formation of the former cationic fragment is not observed. To further investigate this aspect we have studied in detail the electron density distribution along the Fe–P bond in the two cations. This was done by comparing the molecular isodensity surfaces in the two fragments at the same electron density value (for a large series of electron density values). We observed that the elec-

Table 2. Bond lengths and angles in the optimised geometries of the $[Fe\{\kappa^3\text{-}(H)PNO\}_2]^{2+}$ and $[Fe(\kappa^3\text{-}PNN)_2]^{2+}$ complexes obtained with the semi-empirical PM3 method. The distances between primed atoms are identical to those between unprimed ones (see Figure 5).

| $[Fe\{\kappa^3\text{-}(H)PNO\}_2]^{2+}$ | | | | $[Fe(\kappa^3\text{-}PNN)_2]^{2+}$ | | | |
|---|---|---|---|---|---|---|---|
| Bond lengths [Å] | | Bond angles [°] | | Bond lengths [Å] | | Bond angles [°] | |
| Fe–P1 | 2.264 | P1–Fe–O1 | 156.1 | Fe–P1 | 2.413 | P1–Fe–N4 | 171.8 |
| Fe–N1 | 1.9 | N1–Fe–P1 | 81.9 | Fe–N1 | 1.941 | N1–Fe–P1 | 83.5 |
| Fe–O1 | 1.976 | O1–Fe–N1 | 75.3 | Fe–N2 | 1.944 | N4–Fe–N1 | 92.7 |
| P1–C1 | 1.828 | Fe–P1–C1 | 107.7 | P1–C1 | 1.845 | Fe–P1–C1 | 105.3 |
| C1–C2 | 1.4 | P1–C1–C2 | 121.3 | C1–C2 | 1.396 | P1–C1–C2 | 116.8 |
| C2–C3 | 1.461 | C1–C2–C3 | 127.8 | C2–C3 | 1.460 | C1–C2–C3 | 128.6 |
| C3–N1 | 1.307 | C2–C3–N1 | 128.6 | C3–N1 | 1.311 | C2–C3–N1 | 132.6 |
| N1–N2 | 1.463 | C3–N1–Fe | 137.7 | N1–C4 | 1.485 | C3–N1–Fe | 133.2 |
| N2–C4 | 1.401 | | | C4–C5 | 1.517 | | |
| C4–O1 | 1.261 | | | C5–C6 | 1.489 | | |
| | | | | C6–N2 | 1.377 | | |

 © 2007 Wiley-VCH Verlag GmbH & Co. KGaA, Weinheim 

tron density along the Fe–P bond is much larger in $[Fe\{\kappa^3\text{-}(H)PNO\}_2]^{2+}$ than in $[Fe(\kappa^3\text{-}PNN)_2]^{2+}$. Figure 6 shows, as an example, that two voids in the electron density along the two Fe–P bonds in $[Fe(\kappa^3\text{-}PNN)_2]^{2+}$ are evident in the molecular isodensity surfaces calculated at 0.1 e Å$^{-3}$ obtained by PM3 calculations for the two ions.

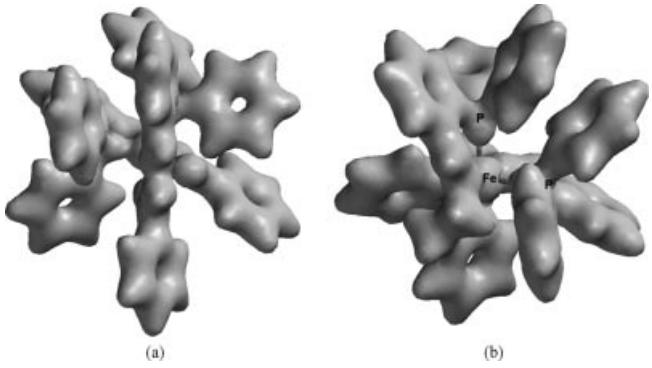


Figure 6. Molecular isodensity surfaces (obtained from the PM3 calculations) drawn at 0.1 e Å$^{-3}$ for $[Fe\{\kappa^3\text{-}(H)PNO\}_2]^{2+}$ (a) and $[Fe(\kappa^3\text{-}PNN)_2]^{2+}$ (b).

Although the choice of the 0.1-e Å$^{-3}$ value is arbitrary, it is noteworthy that the molecular surface of $[Fe\{\kappa^3\text{-}(H)PNO\}_2]^{2+}$ drawn at the same isodensity value does not show analogous voids. This fact seems to suggest that the higher stability of $[Fe\{\kappa^3\text{-}(H)PNO\}_2]^{2+}$ with respect to that of $[Fe(\kappa^3\text{-}PNN)_2]^{2+}$ could be attributed to the different stability (length) of the Fe–P bond in the two fragments, thus explaining the impossibility of forming the bis-chelate octahedral species containing the PNN ligand.

## Conclusions

This work has described the synthesis and full characterisation of a new series of iron complexes containing two different tridentate ligands, namely (H)PNO and PNN. Both molecules behave as *mer*-tridentate ligands towards $Fe^{II}$, but while the benzoyl hydrazone (H)PNO forms the bis-chelate octahedral cation $[Fe\{\kappa^3\text{-}(H)PNO\}_2]^{n+}$ ($n$ = 2, 3), the Schiff base PNN forms exclusively the neutral trigonal-bipyramidal complex $[Fe(\kappa^3\text{-}PNN)Cl_2]$. The formation of complex **1** from hydrate $FeCl_3$ in primary alcohols is worthy of note. The reduction from $Fe^{III}$ to $Fe^{II}$ occurs with oxidation of the alcohol to the corresponding aldehydes, as demonstrated by treating $FeCl_2$, $FeCl_3$ and (H)PNO in *t*BuOH. The different stoichiometries and geometries originated by the two ligands have been investigated by ab initio calculations in order to compare the relative stability of the structurally characterised cationic fragment $[Fe\{\kappa^3\text{-}(H)PNO\}_2]^{2+}$ and the simulated $[Fe(\kappa^3\text{-}PNN)_2]^{2+}$. The results indicate that the $[Fe(\kappa^3\text{-}PNN)_2]^{2+}$ cation is less stable because, due to the long Fe–P distances, the electron density along these bonds is not enough to stabilize the complex. Thus, although the planarity of the aroyl hydrazone (H)PNO makes the embedding of two ligand molecules to form an octahedral entity possible, the high puckering of the chelation rings generated by PNN does not allow the construction of the same coordination geometry.

## Experimental Section

All reactions were performed under an atmosphere of dry nitrogen, unless otherwise stated, employing standard Schlenk techniques. Solvents were dried prior to use and stored under an atmosphere of nitrogen. Elemental analyses (C, H, N, S) were performed with a Carlo Erba Mod. EA 1108 apparatus. IR spectra were recorded with a Nicolet 5PCFT-IR spectrophotometer in the 4000–400 cm$^{-1}$ range from KBr disks. Electronic spectra were recorded in the range 250–1000 nm with a Perkin–Elmer Lambda 25 spectrophotometer, employing quartz cuvettes ($d$ = 1 cm). The concentration of the solutions in acetonitrile was $10^{-7}$ M. $^1$H NMR spectra were obtained at 300 K with a Bruker 300 FT spectrometer by using $SiMe_4$ as an internal standard. Low-temperature $^1$H NMR spectra were recorded with a Bruker AC200 spectrometer operating at 200.13 MHz. Peak positions are quoted relative to tetramethylsilane and were calibrated against the residual solvent resonance. $^{31}P\{^1H\}$ NMR spectra were recorded on the same instrument operating at 81.01 MHz. Chemical shifts were measured relative to external 85% $H_3PO_4$, with downfield shifts considered positive. CI mass spectra (methane) were collected with a Finnigan SSQ 710, FAB mass spectra with a EVG Autospec M, and ESI mass spectra with a Quattro LC triple quadrupole instrument (Micromass, Manchester, UK) equipped with an electrospray interface and Masslynx v. 3.4 software (Micromass). The nebulizing gas (nitrogen, 99.999% purity) and the desolvation gas (nitrogen, 99.998% purity) were delivered at a flow rate of 80 and 500 L h$^{-1}$, respectively. ESI mass analyses were performed by operating the mass spectrometer in positive-ion (PI) mode, acquiring mass spectra over the scan range $m/z$ = 100–1300 with a step size of 0.1 Da and a scan time of 1.2 s. The operating parameters of the interface were as follows: source temperature: 70 °C; desolvation temperature: 70 °C; ES(+) voltage: 3.0 kV; cone voltage: 30 and 50 V; rf lens: 0.3 V.

All the magnetic susceptibility measurements were performed with a Cryogenic Ltd. S600 SQUID magnetometer. Measurements were always performed on powder samples contained in a thin Teflon film. Data were corrected for the magnetism of the sample holder, which was independently determined at the same temperature range and field. The underlying diamagnetism of the samples was estimated from Pascal's constants.

The cyclic voltammetry experiments were carried out with a computerized potentiostat (PGSTAT 20, Ecochemie) controlled by customized software (GPES 4.8). All measurements were conducted in dry acetonitrile solutions of the studied compound ($10^{-3}$ M) and tetrabutylammonium hexafluorophosphate ($10^{-1}$ M) as supporting electrolyte. Voltammetric characterisations were conducted in oxygen-free solutions that had been previously purged with $N_2$ for 5 min. Voltammograms were recorded with a scan rate of 0.1 V s$^{-1}$. A Pt disk electrode with a surface of 7 mm$^2$ and a Pt rod electrode were used as working and counter electrodes, respectively. Ag/AgCl/3 M KCl was employed as reference electrode.

The ligands (H)PNO[29] and PNN[12] were synthesised according to literature methods. Anhydrous $FeCl_2$, $FeCl_3{\cdot}6H_2O$ and AgOTf (OTf = triflate) were purchased from Aldrich and used as received.

**$[Fe\{\kappa^3\text{-}(H)PNO\}_2]Cl[FeCl_4]$ (1) – Method 1:** (H)PNO (150 mg, 0.368 mmol) was dissolved in 20 mL of dichloromethane and added dropwise to an ethanol solution (15 mL) containing $FeCl_2$

 © 2007 Wiley-VCH Verlag GmbH & Co. KGaA, Weinheim 

(50 mg, 0.394 mmol). The resulting red solution was stirred at room temperature for 3 h, concentrated under vacuum and, after the addition of 20 mL of *n*-hexane, cooled to –18 °C overnight. The deep-red solid thus formed was filtered off, washed with *n*-hexane and dried under vacuum. Crystal data and structure refinement for **1** are shown in Table 3. Yield: 130 mg (50%). M.p. 191 °C (dec.). $^{31}P\{^{1}H\}$ NMR ($CDCl_3$, 233 K): $\delta$ = 63.4 ppm (s). IR: $\tilde{\nu}$ = 3255 $cm^{-1}$ (w) (N–H), 1607 (m) (C=O). MS (FAB+): *m*/*z* = 1070 $\{[Fe\{(H)PNO\}_2][FeCl_4]\}^+$, 871 $[Fe\{(H)PNO\}(PNO)]^+$, 463 $[Fe(PNO)]^+$. MS (ESI+): *m*/*z* = 871, 463, 409 $[(H)PNO + H^+]^+$. MS (ESI–): *m*/*z* = 198 $[FeCl_4]^-$. $C_{52}H_{42}Cl_5Fe_2N_4O_2P_2 \cdot 2CH_2Cl_2$ (1275.7): calcd. C 50.82, H 3.61, N 4.39; found C 50.74, H 3.58, N 4.19.

**Method 2:** $FeCl_3 \cdot 6H_2O$ (90 mg, 0.333 mmol) was dissolved in 15 mL of ethanol and the solution was thermostated at 80 °C. (H)PNO (140 mg, 0.343 mmol) was dissolved in 20 mL of ethanol and added dropwise to the iron-containing solution. The resulting red solution was stirred for 48 h, then the volume was reduced under vacuum. After the addition of 20 mL of *n*-hexane and refrigeration at –18 °C prismatic red crystals suitable for X-ray analysis formed. Yield: 270 mg (73%). M.p. 195 °C (dec.). $C_{52}H_{42}Cl_5Fe_2N_4O_2P_2 \cdot 1/2CH_2Cl_2$ (1148.3): calcd. C 54.90, H 3.74, N 4.88; found C 54.53, H 3.75, N 4.35.

**Method 3:** $FeCl_2$ (16 mg, 0.130 mmol) and $FeCl_3 \cdot 6H_2O$ (35 mg, 0.130 mmol) were dissolved in 10 mL of methanol. (H)PNO (110 mg, 0.270 mmol) was dissolved in 20 mL of dichloromethane and the two solutions were mixed and stirred at room temperature for 5 h to give a deep-red solution. The solvent was then removed under vacuum and the solid residue redissolved in dichloromethane. After the addition of *n*-hexane and refrigeration at –18 °C, a purple solid was collected. Yield: 140 mg (71%). M.p. 192 °C (dec.). $C_{52}H_{42}Cl_5Fe_2N_4O_2P_2 \cdot CH_2Cl_2$ (1190.78): calcd. C 53.43, H 3.70, N 4.70; found C 53.44, H 3.51, N 4.74.

**$[Fe_2\{\kappa^3\text{-}(H)PNO\}_2Cl_6]$ (2):** (H)PNO (140 mg, 0.343 mmol) was dissolved in dichloromethane (20 mL) and added dropwise to a *t*BuOH solution (15 mL) of $FeCl_3 \cdot 6H_2O$ (90 mg, 0.343 mmol). The resulting red solution was heated at reflux overnight and the microcrystalline red solid formed was filtered off, washed with *n*-hexane and vacuum dried. Crystal data and structure refinement for **2** are shown in Table 3.Yield: 290 mg (88%). M.p. 214–216 °C. ESI(+) MS: *m*/*z* = 872 $[Fe\{(H)PNO\}(PNO)]^+$. MS (ESI–): *m*/*z* = 198 $[FeCl_4]^-$. $C_{52}H_{42}Cl_6Fe_2N_4O_2P_2$ (1141.29): calcd. C 54.74, H 3.71, N 4.91; found C 55.01, H 3.74, N 4.96.

**$[Fe\{\kappa^3\text{-}(H)PNO\}_2]Cl_2$ (3):** $FeCl_2$ (40 mg, 0.315 mmol) was dissolved in methanol (15 mL) and the solution was heated at 80 °C. (H)-PNO (280 mg, 0.686 mmol) dissolved in 20 mL of dichloromethane was added, and the resulting red solution stirred for 7 h. The solution was then reduced in volume under vacuum and refrigerated at –18 °C overnight. A microcrystalline red solid was filtered off and washed with *n*-hexane. Yield: 220 mg (74%). M.p. 166–173 °C. Owing to oxidation, irreproducible microanalyses were obtained. IR: $\tilde{\nu}$ = 3220 (w) (NH), 1608 (s) (C=O) $cm^{-1}$. MS (ESI+): *m*/*z* = 871 $[Fe\{(H)PNO\}(PNO)]^+$.

**$[Fe\{\kappa^3\text{-}(H)PNO\}_2][TfO]_2$ (4):** $FeCl_2$ (20 mg, 0.157 mmol) was dissolved in 15 mL of methanol, and (H)PNO (100 mg, 0.245 mmol) dissolved in 20 mL of dichloromethane was added. The resulting red solution was stirred at room temperature for a few minutes and then AgOTf (70 mg, 0.273 mmol) was added. After 1 h the precipitated AgCl was filtered off and the remaining red solution stirred overnight. The solvent was then removed under vacuum to give a red solid. Yield: 200 mg (70%). M.p. 167–171 °C. $^{31}P\{^{1}H\}$ NMR ($CDCl_3$, 233 K): $\delta$ = 62 ppm (s). IR: $\tilde{\nu}$ = 3441 (w) (N–H), 1605 (s) (C=O), 1296 (s) $(SO_3)_{as}$, 1238 (s) $(CF_3)_s$, 1157 (s) $(CF_3)_{as}$, 1027 (s) $(S=O)_s$ $cm^{-1}$. MS (ESI+): *m*/*z* = 1022 $\{[Fe\{(H)PNO\}_2][TfO]\}^+$, 871 $[Fe\{(H)PNO\}(PNO)]^+$. $C_{54}H_{42}F_6FeN_4O_8P_2S_2 \cdot CH_2Cl_2$ (1255.79): calcd. C 55.38, H 3.59, N 4.79, S 5.47; found C 55.65, H 3.57, N 4.97, S 5.00.

**$[Fe(\kappa^3\text{-}PNO)_2]$ (5):** NaOMe (30 mg, 0.564 mmol) was dissolved in the minimum amount of methanol and (H)PNO (230 mg, 0.563 mmol) dissolved in 15 mL of dichloromethane was added. $FeCl_2$ (35 mg, 0.282 mmol) was then added and the deep-red solution thus obtained was stirred at room temperature for 48 h. After partial removal of the solvent under vacuum, a red solid was filtered off and washed with *n*-hexane. Yield: 200 mg (80%). M.p. 193–196 °C. $^{1}H$ NMR ($CDCl_3$, 233 K): $\delta$ = 9.60 (s, 1 H, CH=N), 7.68–6.80 (m, 19 H, Ph) ppm. $^{31}P\{^{1}H\}$ NMR ($CDCl_3$, 233 K): $\delta$ = 69.2 (s) ppm. MS (CI+): *m*/*z* = 871 $[\mathbf{5} + H^+]^+$.

Table 3. Crystal data and structure refinement for **1**, **2** and **6**.

| | **1** | **2** | **6** |
|---|---|---|---|
| Empirical formula | $C_{52}H_{42}Cl_5Fe_2N_4O_2P_2$ | $C_{52}H_{42}Cl_{5.4}Fe_2N_4O_2P_2$ | $C_{26.5}H_{24}Cl_3FeN_2P$ |
| Formula weight | 1105.79 | 1119.97 | 563.65 |
| Wavelength [Å] | 0.71073 | 0.71073 | 0.71073 |
| Crystal system | monoclinic | monoclinic | monoclinic |
| Space group | $P2_1/c$ | $P2_1/n$ | $C2/c$ |
| *a* [Å] | 17.541(3) | 14.0974(8) | 38.884(3) |
| *b* [Å] | 13.665(3) | 21.446(1) | 18.1301(5) |
| *c* [Å] | 21.882(4) | 18.440(1) | 16.890(1) |
| $\beta$ [°] | 96.431(3) | 93.081(1) | 101.153(1) |
| Volume [$Å^3$] | 5212.1(17) | 5567.0(5) | 5238.6(6) |
| *Z* | 4 | 4 | 8 |
| Density (calculated) [$Mg\,m^{-3}$] | 1.409 | 1.336 | 1.429 |
| Absorption coefficient [$mm^{-1}$] | 0.918 | 0.879 | 0.961 |
| *F*(000) | 2260 | 2287 | 2312 |
| $\theta$ range for data collection [°] | 1.76–18.86 | 1.46–24.73 | 1.07–26.38 |
| Independent reflections | 4052 [*R*(int) = 0.1019] | 9511 [*R*(int) = 0.0353] | 5361 [*R*(int) = 0.0235] |
| Data/restraints/parameters | 4052/9/540 | 9511/1/667 | 5361/3/305 |
| Goodness-of-fit on $F^2$ | 1.262 | 1.443 | 1.086 |
| Final *R* indices [$I > 2\sigma(I)$] ($R_1$, $wR_2$) | 0.0946, 0.1775 | 0.1039, 0.3185 | 0.0545, 0.1806 |
| *R* indices (all data) ($R_1$, $wR_2$) | 0.1317, 0.1985 | 0.1299, 0.3518 | 0.0657, 0.1910 |
| Final $\Delta F$ max./min. [$e\,Å^{-3}$] | 0.436/–0.425 | 2.577/–0.532 | 1.616/–0.854 |

 © 2007 Wiley-VCH Verlag GmbH & Co. KGaA, Weinheim 

$C_{52}H_{42}FeN_4O_2P_2 \cdot 2CH_3OH$ (936.81): calcd. C 69.23, H 5.34, N 5.98; found C 69.47, H 4.88, N 5.46.

**[Fe(κ³-PNN)Cl₂] (6):** $FeCl_2$ (40 mg, 0.331 mmol) was dissolved in methanol (15 mL) and a dichloromethane solution (20 mL) of PNN (130 mg, 0.330 mmol) was added dropwise at room temperature. After 24 h of stirring the orange solid formed was removed by filtration while the remaining solution was dried under vacuum to give a light red solid. This solid was dissolved in dichloromethane (10 mL) and the clear solution was added to *n*-hexane (10 mL) and then cooled overnight at –18 °C. Orange crystals suitable for X-ray analysis were collected. Crystal data and structure refinement for **6** are shown in Table 3.Yield: 120 mg (70%). M.p. 86–90 °C. IR: $\tilde{\nu}$ = 1629 (s) (C=N) $cm^{-1}$. MS (FAB+): *m/z* = 563 $[\mathbf{6}]^+$. $C_{26}H_{23}Cl_2FeN_2P \cdot 1/2CH_2Cl_2$ (563.68): calcd. C 56.47, H 4.29, N 4.97; found C 56.94, H 4.26, N 4.60.

**X-ray Analysis:** Mo-*Kα* radiation (λ = 0.71073 Å), *T* = 293 K for all compounds (SMART AXS 1000 CCD diffractometer). Lorentz, polarization, and absorption corrections were applied.[30] Structures solved by direct methods by using SIR97[31] and refined by full-matrix least-squares on all $F^2$ by using SHELXL97[32] implemented in the WingX package.[33] Hydrogen atoms partly located on Fourier difference maps and refined isotropically and partly introduced in calculated positions. Anisotropic displacement parameters refined for all non-hydrogen atoms. In **6** a partially occupied (50%) $CH_2Cl_2$ molecule is found in the asymmetric unit, with traces of residual electron density around the central carbon in the final map. Compound **2**, with stoichiometry $[Fe_2\{\kappa^3\text{-}(H)\text{-}PNO\}_2Cl_6]$, shows substitutional disorder which has been modelled as a replacement between $[FeCl_5]^2$- and $[FeCl_4]^2$- anions; the poor quality of diffraction data, however, did not allow for the establishment of an accurate description of the disordered entities, and quite high electron density residuals were present in the final maps in the disordered region. Molecular and crystal geometries have been analyzed with SHELXL97[32] and PARST97[34], and extensive use was made of the Cambridge Crystallographic Data Centre packages[35]. Table 3 summarizes crystal data and structure determination results. CCDC-616781 (for **1**), -616782 (for **2**) and -616783 (for **3**) contain the supplementary crystallographic data for this paper. These data can be obtained free of charge from The Cambridge Crystallographic Data Centre via www.ccdc.cam.ac.uk/data_request/cif.

## Acknowledgments

Prof. Maria Carmen Rodriguez Argüelles (University of Vigo, Spain) is thanked for the FAB-MS analyses, while Dr. Elisa Elviri (University of Parma) is thanked for the ESI-MS analyses. The authors wish to thank the C.I.M. (Centro Interfacoltà di Misure G. Casnati) of the University of Parma for the instrument facilities.

[1] a) V. C. Gibson, S. K. Spitzmesser, *Chem. Rev.* **2003**, *103*, 283–315; b) S. D. Ittel, L. K. Johnson, M. Brookhart, *Chem. Rev.* **2000**, *100*, 1169–1203.
[2] R. K. O'Reilly, V. C. Gibson, A. J. P. White, D. J. Williams, *J. Am. Chem. Soc.* **2003**, *125*, 8450–8451.
[3] G. Müller, M. Klinga, B. Rieger, *Z. Anorg. Allg. Chem.* **2002**, *628*, 2839–2846.
[4] L. H. Uppadine, J. M. Lehn, *Angew. Chem. Int. Ed.* **2004**, *43*, 240–243.
[5] H. Torigoe, H. Hagiwara, S. Arata, M. Yamada, N. Matsumoto, *Chem. Lett.* **2005**, *34*, 956–957.
[6] M. Velusamy, R. Mayilmurugan, M. Palaniandavar, *J. Inorg. Biochem.* **2005**, *99*, 1032–1042.
[7] T. C. Harrop, M. M. Olmstead, P. K. Mascharak, *Inorg. Chem.* **2005**, *44*, 9527–9533.
[8] J. Legros, C. Bolm, *Chem. Eur. J.* **2005**, *11*, 1086–1092.
[9] a) P. Pelagatti, A. Bacchi, C. Bobbio, M. Carcelli, M. Costa, C. Pelizzi, C. Vivorio, *Organometallics* **2000**, *19*, 5440–5446; b) A. Bacchi, M. Carcelli, M. Costa, A. Fochi, C. Monici, P. Pelagatti, C. Pelizzi, G. Pelizzi, L. M. Sanjuan Roca, *J. Organomet. Chem.* **2000**, *593–594*, 180–191; c) P. Pelagatti, M. Carcelli, F. Franchi, C. Pelizzi, A. Bacchi, A. Fochi, H.-W. Frühauf, K. Goubitz, K. Vrieze, *Eur. J. Inorg. Chem.* **2000**, 463–475; d) P. Pelagatti, A. Bacchi, C. Bobbio, M. Carcelli, M. Costa, A. Fochi, C. Pelizzi, *J. Chem. Soc., Dalton Trans.* **2002**, 1820–1825; e) P. Pelagatti, A. Vergnani, M. Carcelli, M. Costa, D. Rogolino, A. Bacchi, C. Pelizzi, *Inorg. Chim. Acta* **2003**, *351*, 235–241; f) P. Pelagatti, A. Bacchi, M. Carcelli, M. Costa, H.-W. Frühauf, K. Goubitz, C. Pelizzi, M. Triclistri, K. Vrieze, *Eur. J. Inorg. Chem.* **2002**, 139–446; g) A. Bacchi, M. Carcelli, C. Pelizzi, G. Pelizzi, P. Pelagatti, S. Ugolotti, *Eur. J. Inorg. Chem.* **2002**, 2179–2187.
[10] a) P. Pelagatti, A. Venturini, A. Leporati, M. Carcelli, M. Costa, A. Bacchi, G. Pelizzi, C. Pelizzi, *J. Chem. Soc., Dalton Trans.* **1998**, 2715–2721; b) P. Pelagatti, A. Bacchi, M. Carcelli, M. Costa, A. Fochi, P. Ghidini, E. Leporati, M. Masi, C. Pelizzi, G. Pelizzi, *J. Organomet. Chem.* **1999**, *583*, 94–105; c) M. Costa, P. Pelagatti, C. Pelizzi, D. Rogolino, *J. Mol. Catal. A* **2002**, *178*, 21–26.
[11] P. Pelagatti, A. Bacchi, M. Balordi, S. Bolaño, F. Calbiani, L. Elviri, L. Gonsalvi, C. Pelizzi, M. Peruzzini, D. Rogolino, *Eur. J. Inorg. Chem.* **2006**, 2422–2436.
[12] R. E. Rülke, V. E. Kaasjager, P. Wehman, C. J. Elsevier, P. W. N. M. van Leeuwen, K. Vrieze, J. Fraanje, K. Goubitz, A. L. Spek, *Organometallics* **1996**, *15*, 3022–3031.
[13] a) P. V. Bernhardt, P. Chin, D. R. Richardson, *J. Biol. Inorg. Chem.* **2001**, *6*, 801–809; b) C. M. Armstrong, P. V. Bernhardt, P. Chin, D. S. Richardson, *Eur. J. Inorg. Chem.* **2003**, 1145–1156; c) P. V. Bernhardt, L. M. Caldwell, T. B. Chaston, P. Chin, D. R. Richardson, *J. Biol. Inorg. Chem.* **2003**, *8*, 866–880.
[14] G. J. P. Britovsek, V. C. Gobson, B. S. Kimberley, S. Mastroianni, C. Redshaw, G. A. Solan, A. J. P. White, D. J. Williams, *J. Chem. Soc., Dalton Trans.* **2001**, 1639–1644.
[15] J. E. Dubois, H. Fakhrayan, J.-P. Doucet, J.-M. El H. Chahine, *Inorg. Chem.* **1992**, *31*, 853–859.
[16] a) M. Di Vaira, F. Mani, P. Stoppioni, *J. Chem. Soc., Dalton Trans.* **1997**, 1375–1379; b) C. A. Clausen, M. L. Good, *Inorg. Chem.* **1970**, *9*, 220–223.
[17] a) D. Onggo, A. D. Rae, H. A. Goodwin, *Inorg. Chim. Acta* **1990**, *178*, 151–163; b) S. E. Livingstone, J. D. Nolan, *J. Chem. Soc., Dalton Trans.* **1972**, 218–223.
[18] a) O. Schramel, B. Michalke, A. Kettrup, *J. Chromatogr. A* **1998**, *819*, 231–242; b) G. Weber, N. von Wirén, H. Hayen, *Rapid Commun. Mass Spectrom.* **2006**, *20*, 973–980.
[19] D. H. Johnston, D. F. Shriver, *Inorg. Chem.* **1993**, *32*, 1045–1047.
[20] J. Wang, F. R. Keene, *Electrochim. Acta* **1996**, *41*, 2563–2569, and references cited therein.
[21] a) F. Benvenuti, C. Carlini, M. Marchionna, R. Patrini, A. M. Raspolli Galletti, G. Sbrana, *J. Mol. Catal. A* **1999**, *140*, 139–155; b) L. Canovese, F. Visentin, G. Chessa, A. Niero, P. Uguagliati, *Inorg. Chim. Acta* **1999**, *293*, 44–52.
[22] J.-P. Masson, A. A. Bahsoun, M.-T. Youinou, J. A. Osborn, *C. R. Chim.* **2002**, *5*, 303–308.
[23] a) C.-C. Yang, W.-Y. Yeh, G.-H. Lee, S.-M. Peng, *J. Organomet. Chem.* **2000**, *598*, 353–358; b) M. E. Bluhm, O. Walter, M. Döring, *J. Organomet. Chem.* **2005**, *690*, 713–721.
[24] W.-Y. Yeh, C.-C. Yang, S.-M. Peng, G.-H. Lee, *J. Chem. Soc., Dalton Trans.* **2000**, 1649–1654.
[25] D. Cremer, J. A. Pople, *J. Am. Chem. Soc.* **1975**, *97*, 1354–1358.

 © 2007 Wiley-VCH Verlag GmbH & Co. KGaA, Weinheim 

[26] P. Wehman, R. E. Rülke, V. E. Kaasjager, P. C. J. Kamer, H. Kooijman, A. L. Spek, C. J. Elsevier, K. Vrieze, P. W. N. M. van Leeuwen, *J. Chem. Soc., Chem. Commun.* **1995**, 331–332.
[27] a) J. J. P. Stewart, *J. Comput. Chem.* **1989**, *10*, 209; b) J. J. P. Stewart, *J. Comput. Chem.* **1989**, *10*, 221.
[28] Spartan 04, Release 1.01, **2004**, Wavefunction, Inc., 18401 Von Karman Avenue, Suite 370, Irvine, Ca 92612 USA (http://www.wavefun.com).
[29] A. Bacchi, M. Carcelli, M. Costa, P. Pelagatti, C. Pelizzi, G. Pelizzi, *Gazz. Chim. Ital.* **1994**, *124*, 429–435.
[30] a) SAINT: SAX, Area Detector Integration, Siemens Analytical instruments Inc., Madison, Wisconsin, USA; b) G. Sheldrick, *SADABS: Siemens Area Detector Absorption Correction Software*, **1996**, University of Göttingen, Germany.
[31] A. Altomare, M. C. Burla, M. Cavalli, G. Cascarano, C., Giacovazzo, A. Gagliardi, A. G. Moliterni, G. Polidori, R. Spagna, *Sir97: A New Program for Solving and Refining Crystal Structures* **1997**, Istituto di Ricerca per lo Sviluppo di Metodologie Cristallografiche CNR, Bari.
[32] G. Sheldrick, *SHELXL97: Program for Structure Refinement*, University of Göttingen, Germany, **1997**.
[33] L. J. Farrugia, *J. Appl. Crystallogr.* **1999**, *32*, 837–838.
[34] M. Nardelli, *J. Appl. Crystallogr.* **1995**, *28*, 659.
[35] a) F. H. Allen, O. Kennard, R. Taylor, *Acc. Chem. Res.* **1983**, *16*, 146–153; b) I. J. Bruno, J. C. Cole, P. R. Edgington, M. Kessler, C. F. Macrae, P. McCabe, J. Pearson, R. Taylor, *Acta Crystallogr. Sect. B* **2002**, *58*, 389–397.

Received: August 4, 2006
Published Online: November 27, 2006

 © 2007 Wiley-VCH Verlag GmbH & Co. KGaA, Weinheim 

DOI: 10.1002/ejic.200600744

# Tuning the Properties of Neutral Tetraazamacrocyclic Complexes of Copper(II) and Nickel(II) for Use as Host–Guest Compounds with Bismacrocyclic Transition Metal Cations

**Anita Rybka,[a,b] Ryszard Koliński,[b] Jarosław Kowalski,[c] Rafał Szmigielski,[c] Sławomir Domagała,[d] Krzysztof Woźniak,*[d] Agnieszka Więckowska,[d] Renata Bilewicz,*[d] and Bohdan Korybut-Daszkiewicz*[a,c]**

**Keywords:** Macrocyclic ligands / Copper / Nickel / Cyclic voltammetry / Template synthesis

The synthesis and structural properties of tetraazamacrocyclic ligands and their neutral and protonated 14-, 15- and 16-membered complexes of $Cu^{II}$ and $Ni^{II}$ are described. Molecules of the free 14-membered ligands have a nonplanar, step-like structure of the central molecular fragments. Conformational changes are introduced upon protonation, with the protons pointing above and below the macrocycle plane. This prevents the formation of intramolecular N–H···N hydrogen bonds. On insertion of the transition metal ions a planar structure of the macrocycle is obtained, which has consequences for the electrochemical behaviour of the complexes. The deviations from planarity increase with increasing macrocycle size. As a consequence the donor properties are weaker, the redox potential is shifted towards more positive values and the contribution of chemical reactions can be observed. The formation of host–guest complexes between the strongest metal-containing donors and transition-metal-containing bismacrocyclic acceptors of suitable size is proved in solution and the gas phase by voltammetric and ESI MS methods. The transition metal building blocks described in this contribution can be applied in the synthesis of new redox-active rotaxane and catenane systems.
(© Wiley-VCH Verlag GmbH & Co. KGaA, 69451 Weinheim, Germany, 2007)

## Introduction

The well-known ability of azamacrocyclic ligands to stabilize unusual oxidation states of coordinated transition metal ions makes them a promising tool for the construction of molecular devices. Recently, we have reported the self-assembly of [2]catenanes built from an electron-rich component (dibenzo-24-crown-8) and an electron-deficient unsaturated bis-macrocyclic [14]cyclidene complex that coordinates two metal ions [either the same[1] or different (copper and nickel) [2]]. The electron-rich benzene rings of the interlocked crown ether in these compounds adopt a conformation that maximizes the donor–acceptor interactions with the bismacrocyclic subunit. By applying appropriate potentials, the coordinated metal ions can be oxidized selectively to the higher oxidation state (+3), which favours the interaction of these centres with the π-electron-rich aromatic rings of the crown unit. As a consequence, the relocation of the crown towards the oxidized metal centre takes place.

[a] Cardinal Stefan Wyszyński University, College of Science, Department of Mathematics & Natural Science, 01-815 Warszawa, Poland
[b] Institute of Physical Chemistry, Polish Academy of Sciences, Kasprzaka 44/52, 01-224 Warszawa, Poland
[c] Institute of Organic Chemistry Polish Academy of Sciences, Kasprzaka 44/52, 01-224 Warszawa, Poland
[d] Department of Chemistry, Warsaw University, Pasteura 1, 02-093 Warszawa, Poland
Fax: +48-22-8222892
E-mail: kwozniak@chem.uw.edu.pl

The introduction of an additional transition metal centre into similar supramolecular systems would enhance the prospects for the control of their properties. Therefore, the aim of this work is to synthesise some neutral macrocyclic complexes of the transition metals which could be used as π-electron-rich building blocks for the self-assembly of intertwined molecules. We have focused on dianionic tetraimine macrocyclic ligands substituted in the *meso* positions with some reactive groups. These groups could then be used for the extension of the ligand superstructure. The synthesis of the 14-membered tetraimine **4** (see Scheme 1) was recently reported by Takamura,[3a] although the 15- (**5**) and 16-membered (**6**) analogues were not accessible by this procedure. We have synthesised the 15- and 16-membered derivatives following a template Jäger synthetic strategy[4,5] from 2-formyl-3-hydroxypropenoic methyl ester and the appropriate diamines.

In this paper, we describe the synthesis of a series of neutral azamacrocyclic complexes of Cu and Ni and characterise their structures and redox properties. We also demonstrate their unique complexing abilities, which can be tuned simply by changing the size of the macrocycles in the host and guest molecules. The latter property is of special importance since the macrocyclic complexes may be considered as building blocks for new rotaxane-like meccano-molecular devices, which are one of the long-term goals of our project.

 © 2007 Wiley-VCH Verlag GmbH & Co. KGaA, Weinheim 

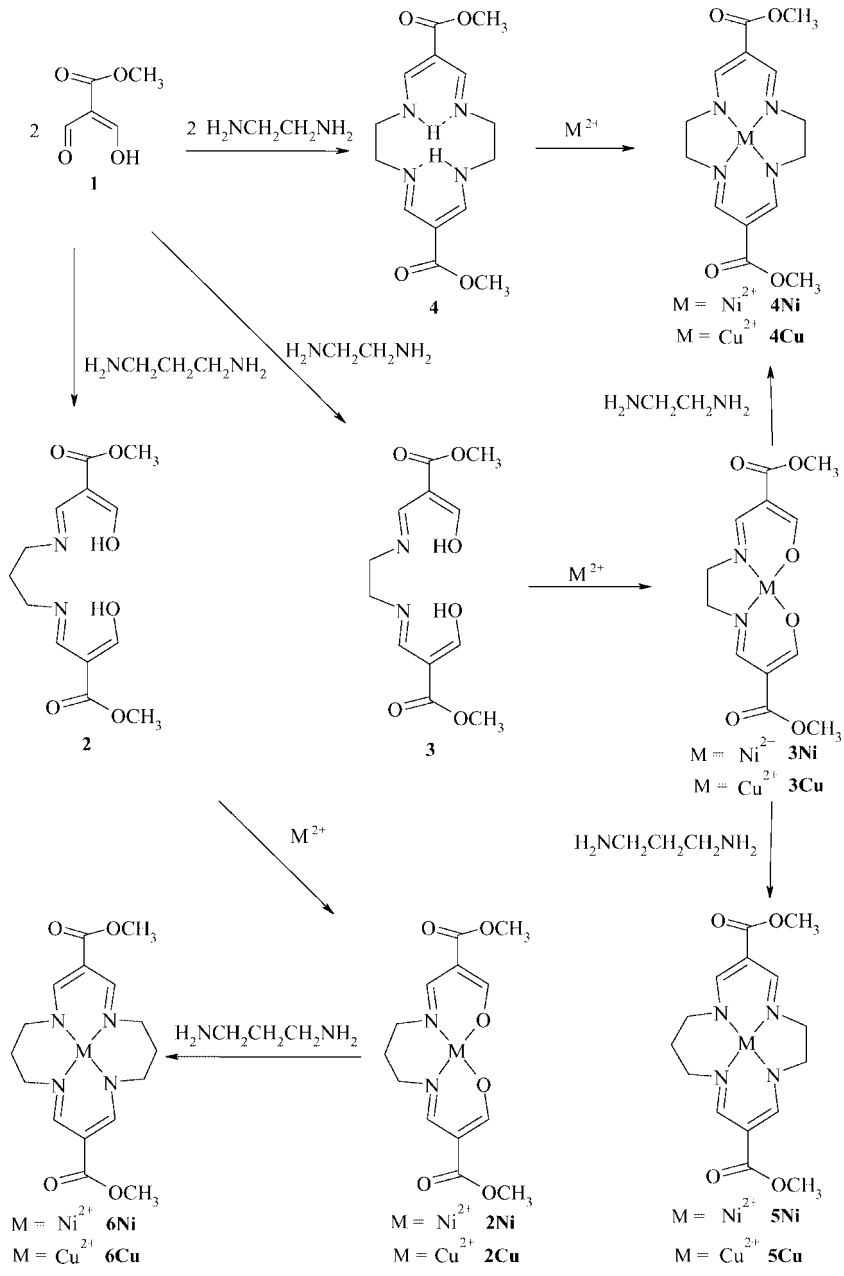


Scheme 1. Synthesis of neutral macrocyclic complexes of $Ni^{II}$ and $Cu^{II}$.

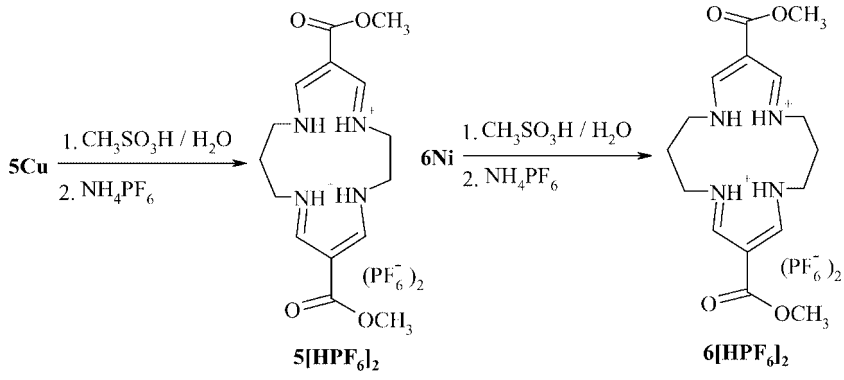


Scheme 2. Demetallation of complexes **5Cu** and **6Ni**.

 © 2007 Wiley-VCH Verlag GmbH & Co. KGaA, Weinheim 

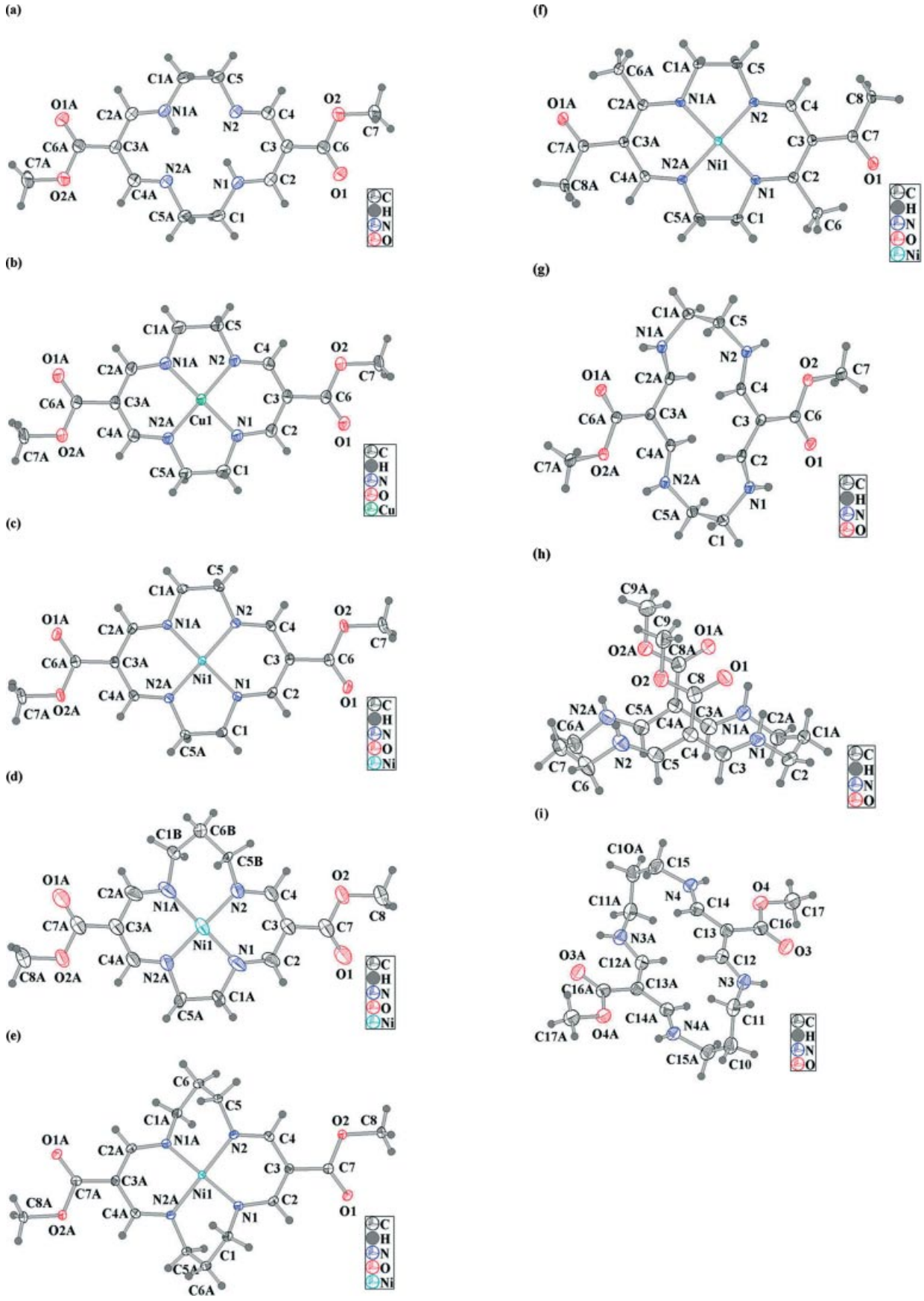


Figure 1. Thermal ellipsoids and atom numbering schemes in **4** (a), **4Cu** (b), **4Ni** (c), **5Ni** (d), **6Ni** (e), **10Ni** (f), **4[HCl]$_2$** (g) and the first (h) and second (i) molecules of **6[HPF$_6$]$_2$**. The atoms related by symmetry are labelled with the letter "A".

 © 2007 Wiley-VCH Verlag GmbH & Co. KGaA, Weinheim 

## Results and Discussion

### Synthesis

The synthesis of the nickel(II) and copper(II) complexes **4Ni**, **4Cu**, **5Ni**, **5Cu**, **6Ni** and **6Cu** is summarised in Scheme 1. The 14-membered ligand **4** was obtained by direct condensation of an equimolar mixture of 2-formyl-3-hydroxypropenoic methyl ester[3b] and ethylenediamine.[3a] Refluxing the ligand **4** with nickel(II) or copper(II) acetate in methanol solution gave the neutral complexes **4Ni** and **4Cu**, respectively. The reaction of 2-formyl-3-hydroxypropenoic methyl ester with diamines in a 2:1 ratio followed by complexation with nickel or copper acetate gave the complexes **2Ni** or **3Ni** and **2Cu** or **3Cu**, respectively.[6] The template reaction with a second diamine molecule afforded the 15- and 16-membered complexes. However, the reaction of the chelates **2Ni** and **2Cu** with an excess of ethylenediamine produced mainly the 14-membered complexes **4Ni** and **4Cu**, respectively.

The decomplexation of **5Cu** and **6Ni** by treatment with an excess of methanesulfonic acid in aqueous solution, followed by precipitation with $NH_4PF_6$, afforded the free ligands as their diprotonated hexafluorophosphates **5[HPF$_6$]$_2$** and **6[HPF$_6$]$_2$**, respectively (Scheme 2).

### Structural Properties

Figure 1 shows thermal ellipsoid representation of atoms with atomic labels for the series of neutral and protonated macrocyclic compounds studied and their complexes with $Ni^{II}$ or $Cu^{II}$ ions. All compounds crystallise in centrosymmetric space groups with molecules located at special positions (inversion centre or mirror plane). Therefore, only half of all atoms constituting a given molecule and corresponding solvent molecules, or counterions, are independent in all cases (see the Experimental Section for crystallographic details).

All the compounds described are composed of tetraazamacrocyclic rings with different numbers of atoms (14, 15 or 16). The electron density of the 16-membered rings is delocalised over the chelate rings and the functional groups. As a result, a bond-length alternation is present in those parts of the molecules. In the case of **4Cu**, **4Ni**, **5Ni**, **6Ni** and **10Ni**[4,5,7] the $Cu^{II}$ or $Ni^{II}$ ions are coordinated by the nitrogen atoms from the macrocyclic ligands to form square-planar complexes. In the free ligands (**4[HCl]$_2$** and **6[HPF$_6$]$_2$**), all of the nitrogen atoms are protonated and the conformation of the molecule is completely different. In all cases, except for **10Ni**, the macrocyclic ring is functionalised with two methoxycarbonyl groups, which can adopt either *trans* or *cis* conformations (see Figure 1, parts h and i). The 14-membered ring of **10Ni** has two types of substituents, namely two acyl and two methyl groups located *trans* to each other, thus confirming the structural results of Alcock et al.[7] and contrary to earlier reports.[4,5] The 14-membered macrocyclic ring in the structure of the free ligand **4** is not coplanar. Due to the coordination of Cu and Ni by the nitrogen atoms of the ring, the structures of the complexes formed (**4Cu**, **4Ni**, **5Ni**, **6Ni** and **10Ni**) are more planar than those of the free ligands. The RMS deviation of the fitted atoms to the least-square plane $L^1$ varies from 0.04 to 0.09 Å for the 14-membered complexes, whereas for the free ligands it is equal to 0.23 Å. Some smaller values of the angles between the previously defined plane and the plane fitted to the atoms of the ethylene bridges $L^2$ for Ni and Cu complexes indicate the more planar nature of the complexes (see Table 1 and Figure 2).

Table 1. Values of the RMS deviation [Å] of all the fitted atoms and angles [°] between the least-squares planes $L^1$ and $L^2$. $L^1$ is defined by the following sequence of atoms: M1, N1, N2, C2, C3, C4, N1#1, N2#1, C2#1, C3#1, C4#1, where M is a metal ion, and $L^2$ is based on the ethylene or propylene (**5Ni** and **6Ni**) groups: C1, C5, C1#1, C5#1 or C1A C5A, C1B, C5B and C6B for **5Ni**.[a]

| Least-squares plane | **4** | **4Cu** | **4Ni** | **10Ni** | **5Ni** | **6Ni** |
|---|---|---|---|---|---|---|
| $L^1$ | 0.2291 | 0.0400 | 0.0696 | 0.0910 | 0.1413 | 0.2189 |
| $L^1$–$L^2$ angle | 36.4(1) | 22.4(2) | 26.9(1) | 26.6(1) | 41.4(3) | 46.65(4) |

[a] Symmetry transformations used to generate equivalent atoms: #1 1 – *x*, 1 – *y*, 1 – *z*.

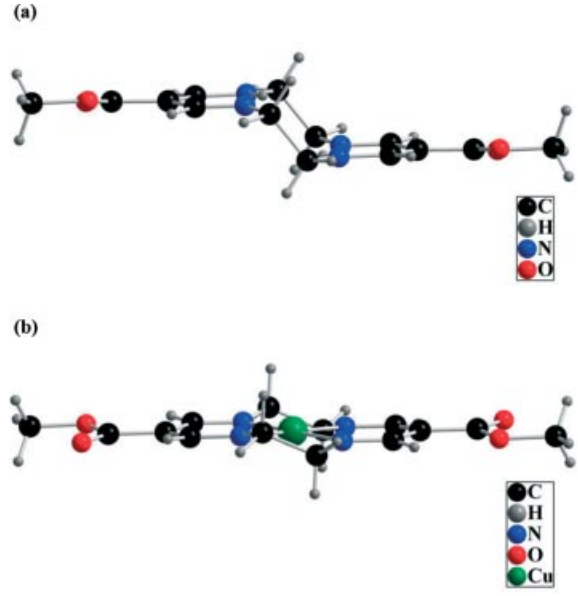


Figure 2. The structure of **4** (a) and **4Cu** (b).

The Ni–N and Cu–N distances vary within the ranges 1.836–1.890 and 1.912–1.922 Å and are typical for Ni and Cu complexes (see Table 2). The Ni–N distance increases with increasing size of the main macrocyclic ring (**4Ni**, **5Ni**, **6Ni**).

The compounds **4[HCl]$_2$** and **6[HPF$_6$]$_2$** have totally different structures. As a result of demetallation of the corresponding complexes, both imine nitrogen atoms in these compounds are protonated to form ammonium groups. Due to some steric hindrance coming from the interactions between the closely located hydrogen atoms, a change of the

 © 2007 Wiley-VCH Verlag GmbH & Co. KGaA, Weinheim 

Table 2. Selected bond lengths and distances [Å]. $L^1$: least-squares plane defined by the following sequence of atoms: M1, N1, N2, C2, C3, C4, N1#1, N2#1, C2#1, C3#1, C4#1, where M is a metal ion; $X_1$: centroid of the N1, N2, N1#1 and N2#1 atoms.

| Parameter[a] | **4Ni** | **4Cu** | **4** | **10Ni** | **5Ni** | **6Ni** | **4**$[HCl]_2$ | **6**$[HPF_6]_2$[b] |
|---|---|---|---|---|---|---|---|---|
| M1···M1#2 | 6.3188(5) | 6.322(1) | | 4.7792(4) | 6.714(1) | 7.6007(5) | | |
| $L^1$···M1#2 | 3.303(1) | 3.333(3) | | 3.617(2) | 3.287(5) | 3.062(2) | | |
| $L^1$···$X_1$#2 | | | 4.269 | | | | | |
| M1–N1 | 1.856(1) | 1.912(2) | | 1.882(1) | 1.871(4) | 1.892(1) | | |
| M1–N2 | 1.851(1) | 1.922(2) | | 1.836(1) | 1.865(3) | 1.890(1) | | |
| O1–C6 | 1.216(2) | 1.213(3) | 1.220(3) | | | | 1.228(2) | |
| O1–C7 | | | | 1.244(2) | 1.199(5) | 1.221(2) | | |
| O1–C8 | | | | | | | | 1.207(5) |
| O2–C6 | 1.363(2) | 1.360(3) | 1.362(3) | | | | 1.346(2) | |
| O2–C7 | 1.439(2) | 1.446(3) | 1.443(3) | | 1.357(5) | 1.365(2) | 1.460(2) | |
| O2–C8 | | | | | 1.443(5) | 1.444(2) | | 1.339(4) |
| N1–C1 | 1.474(2) | 1.473(4) | 1.450(3) | 1.482(2) | | 1.481(2) | 1.469(2) | |
| N1–C1A | | | | | 1.449(9) | | | |
| N1–C1B#1 | | | | | 1.556(9) | | | |
| N1–C2 | 1.306(2) | 1.308(3) | 1.316(3) | 1.316(2) | 1.304(6) | 1.310(2) | 1.317(2) | 1.476(5) |
| N1–C3 | | | | | | | | 1.302(5) |
| N2–C4 | 1.307(2) | 1.300(3) | 1.288(3) | 1.303(2) | 1.295(5) | 1.309(2) | 1.310(2) | |
| N2–C5 | 1.473(2) | 1.480(3) | 1.463(3) | 1.464(2) | | 1.473(2) | 1.475(2) | 1.295(5) |
| N2–C5A#1 | | | | | 1.47(1) | | | |
| N2–C5B | | | | | 1.54(1) | | | |
| C1–C5#1 | 1.518(2) | 1.506(5) | 1.527(3) | 1.511(2) | | | 1.540(2) | |
| C1A–C5A | | | | | 1.50(2) | | | |
| C1–C6#1 | | | | | | 1.533(2) | | |
| C1B–C6B | | | | | 1.54(1) | | | |
| C5–C6 | | | | | | 1.521(2) | | |
| C5B–C6B | | | | | 1.55(1) | | | |
| C2–C3 | 1.408(2) | 1.417(4) | 1.395(3) | 1.448(2) | 1.410(6) | 1.415(2) | 1.412(2) | |
| C2–C6 | | | | 1.512(2) | | | | |
| C3–C4 | 1.413(2) | 1.412(4) | 1.442(3) | 1.411(2) | 1.404(6) | 1.406(2) | 1.420(2) | 1.411(5) |
| C3–C6 | 1.456(2) | 1.465(4) | 1.451(3) | | | | 1.471(2) | |
| C3–C7 | | | | 1.453(2) | 1.461(6) | 1.453(2) | | |

[a] Symmetry transformations: #1: 1 – *x*, 1 – *y*, 1 – *z*; #2: 1 + *x*, *y*, *z* (**4Ni**, **5Ni**, **6Ni**, **10Ni**); *x*, 1 + *y*, *z* (**4Cu**). [b] Additionally for **6**$[HPF_6]_2$: O2–C9 1.442(5), O3–C16 1.212(5), O4–C16 1.332(4), O4–C17 1.459(4), N2–C6 1.464(5), N3–C11 1.468(5), N3–C12 1.312(5), N4–C14 1.300(5), N4–C15 1.482(5), C1–C2 1.517(5), C4–C5 1.405(5), C4–C8 1.467(5), C6–C7 1.516(5), C10–C11 1.509(6), C10–C15#3 1.511(6), C12–C13 1.389(5), C13–C14 1.395(5), C13–C16 1.480(5) Å (#3: 1/2 – *x*, 1/2 – *y*, 1/2 – *z*).

Table 3. Geometry of the hydrogen bonds [Å and °] in the compounds studied.

| D–H···A | Symmetry | *d*(D–H) | *d*(H···A) | *d*(D···A) | <(DHA) |
|---|---|---|---|---|---|
| **4** | | | | | |
| N1–H1N···N2 | *x*, *y*, *z* | 0.88(3) | 1.93(3) | 2.656(3) | 138(2) |
| **10Ni** | | | | | |
| O1W–H1W1···O1 | *x*, *y*, *z* | 0.77(2) | 2.06(2) | 2.826(2) | 172(2) |
| O1W–H2W1···O1W | –*x*, –*y*, –*z* | 0.69(4) | 2.13(4) | 2.815(3) | 172(5) |
| O1W–H3W1···O1W | 1 – *x*, –*y*, –*z* | 0.76(4) | 2.07(4) | 2.810(3) | 163(4) |
| **4**$[HCl]_2$ | | | | | |
| N1–H1N···O1 | *x*, *y*, *z* | 0.82(2) | 2.12(2) | 2.731(2) | 131(1) |
| N2–H2N···O2 | *x*, *y*, *z* | 0.89(2) | 2.14(2) | 2.719(2) | 122(1) |
| N2–H2N···O1W | *x*, *y*, *z* | 0.89(2) | 2.04(2) | 2.823(2) | 147(1) |
| O1W–H1W···Cl1 | 1 + *x*, *y*, *z* | 0.82(2) | 2.36(2) | 3.177(2) | 176(2) |
| O1W–H2W···Cl1 | 1 – *x*, 2 – *y*, 1 – *z* | 0.87(3) | 2.30(3) | 3.168(2) | 177(2) |
| **6**$[HPF_6]_2$ | | | | | |
| N1–H1N···O1 | *x*, *y*, *z* | 0.96(4) | 1.99(4) | 2.678(4) | 127(3) |
| N2–H2N···O2 | *x*, *y*, *z* | 0.68(4) | 2.31(4) | 2.738(5) | 123(4) |
| N3–H3N···O3 | *x*, *y*, *z* | 0.88(4) | 2.14(4) | 2.751(4) | 127(3) |
| N4–H4N···O4 | *x*, *y*, *z* | 0.80(5) | 2.25(5) | 2.781(4) | 125(4) |
| N1–H1N···F11 | *x*, *y*, *z* | 0.96(4) | 2.49(4) | 3.088(5) | 120(3) |
| N2–H2N···F15A | 1 – *y*, *x*, *z* | 0.68(4) | 2.50(4) | 3.140(7) | 158(4) |
| N3–H3N···F8 | *x*, *y*, *z* | 0.88(4) | 2.48(4) | 3.042(4) | 122(3) |
| N4–H4N···F6 | *y*, –*x*, *z* | 0.80(5) | 2.32(5) | 3.013(4) | 145(4) |

 © 2007 Wiley-VCH Verlag GmbH & Co. KGaA, Weinheim 

conformation of the whole moiety takes place. The CHNH groups are rotated about the C–N bond, thus the N–H bonds are oriented outside of the ring whereas the C–H bonds are directed inside. Therefore, the distance between the ethylene bridges is elongated whereas the separation between the methoxycarbonyl groups decreases. Such a conformation is stabilized by numerous intramolecular hydrogen bonds formed between the nitrogen and oxygen atoms from the ester groups (see Table 3 and Figure 3).

In neutral compounds, hydrogen bonds are formed between the macrocycles and some solvent molecules (**10Ni**) or between the nitrogen atoms in the main macrocyclic ring (**4**).

The crystal packing of the compounds is shown in Figure 4. The molecules of the neutral compounds create parallel and slightly shifted stacks in the crystal lattice. The distances between the neighbouring macrocyclic rings in the crystal lattice vary from 3.062 to 3.617 Å and are given in Table 2.

In the structures of **4Ni** and **5Ni**, disordered solvent (toluene) molecules are located at special positions and form layers of molecules sandwiched between layers of the macrocyclic moieties. The toluene molecules are oriented so as to maximize the C–H···π interaction between the electron-rich benzene rings and the hydrogen atoms from the ethylene bridges. These compounds crystallise in the $P\bar{1}$ space group, whereas the protonated compounds crystallise in different space groups. The voids between neighbouring molecules in the structures are filled with counterions in the case of protonated ligand salts or solvent molecules.

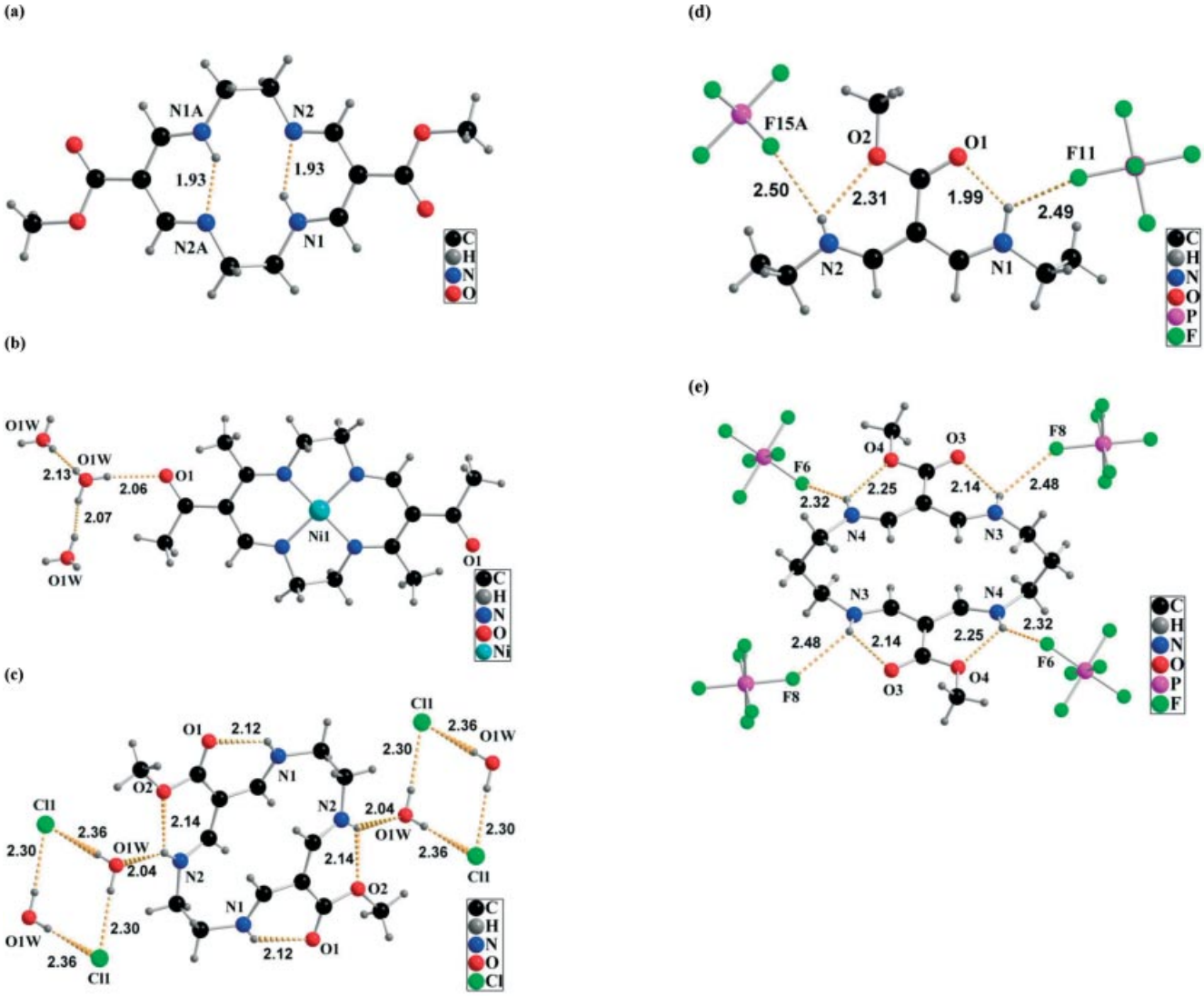


Figure 3. Hydrogen bonds formed by molecules of **4** (a), **10Ni** (b), **4[HCl]$_2$** (c) and the first (d) and second (e) molecules of **6[HPF$_6$]$_2$**.

 © 2007 Wiley-VCH Verlag GmbH & Co. KGaA, Weinheim 

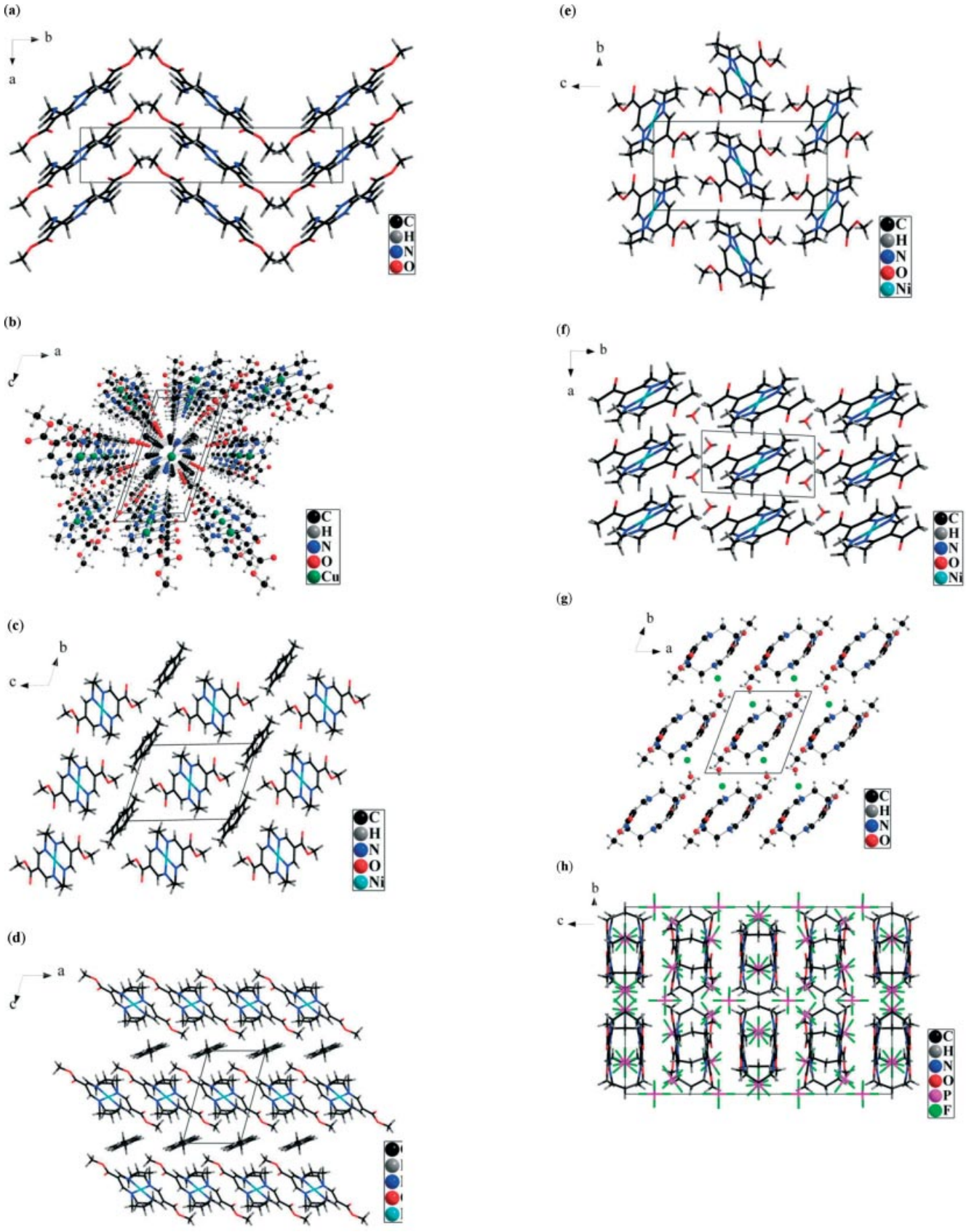


Figure 4. Selected perspective views of the crystal packing in **4** (a), **4Cu** (b), **4Ni** (c), **5Ni** (d), **6Ni** (e), **10Ni** (f), **4[HCl]$_2$** (g) and **6[HPF$_6$]$_2$** (h).

 © 2007 Wiley-VCH Verlag GmbH & Co. KGaA, Weinheim 

### Voltammetry

The linear-scan, differential and normal-pulse voltammograms recorded for **4Cu**, **5Cu** and **6Cu** indicate a striking difference in the formal potentials with no major deviations from reversibility (see Figure 5). Upon increasing the macrocycle size, the donor abilities of the $Cu^{II}$ complex become weaker — the mid-potential $(E_{p_c} + E_{p_a})/2$ is shifted towards more positive potentials by as much as 330 mV. The peak current is also smaller, although the complex is soluble in the supporting electrolyte solution. This shift is not seen for the corresponding $Ni^{II}$ complexes (Figure 6) and reveals that the smaller ring in **4Cu** has a more planar coordination environment of the copper centre, which allows reversible oxidation to the $Cu^{III}$ complex. We have noted a similar dependence on the macrocycle size for other tetraazamacrocyclic complexes of copper.[8] In these compounds a decrease of the $Cu^{III}$ reduction current was observed together with a shift to more positive potentials. This indicates that the electron-transfer reaction is followed by a chemical reaction.

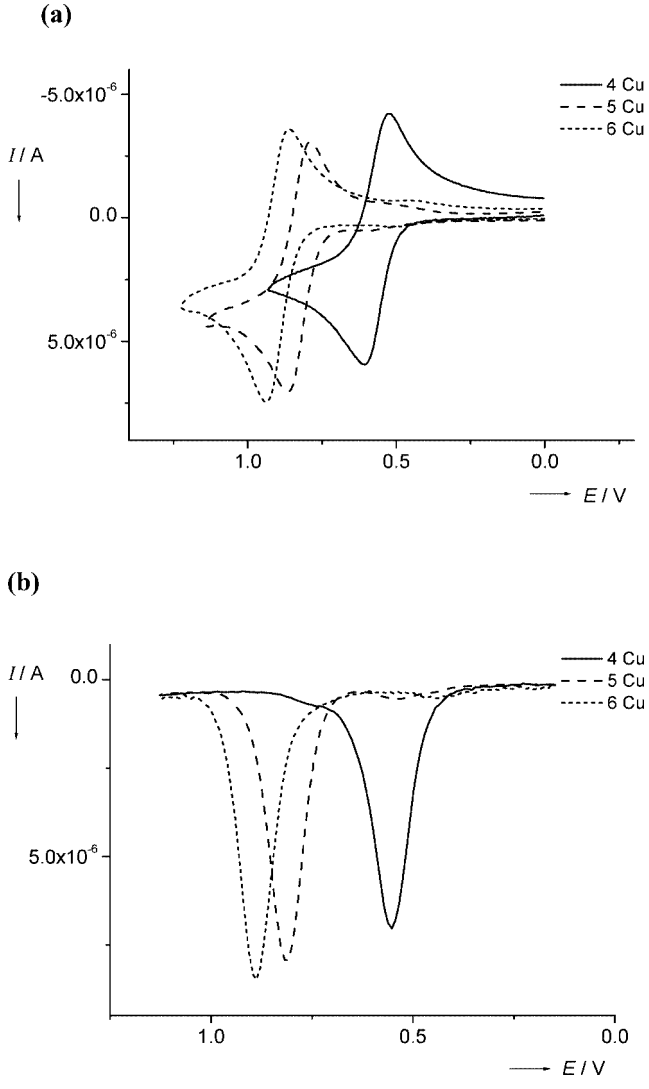


Figure 5. Cyclic voltammograms (a) and differential pulse voltammograms (b) for 0.5 mM **4Cu**, **5Cu** and **6Cu** complexes recorded using a GCE in 0.1 M tetrabutylammonium hexafluorophosphate (TBAHFP)/acetonitrile (AN) solution.

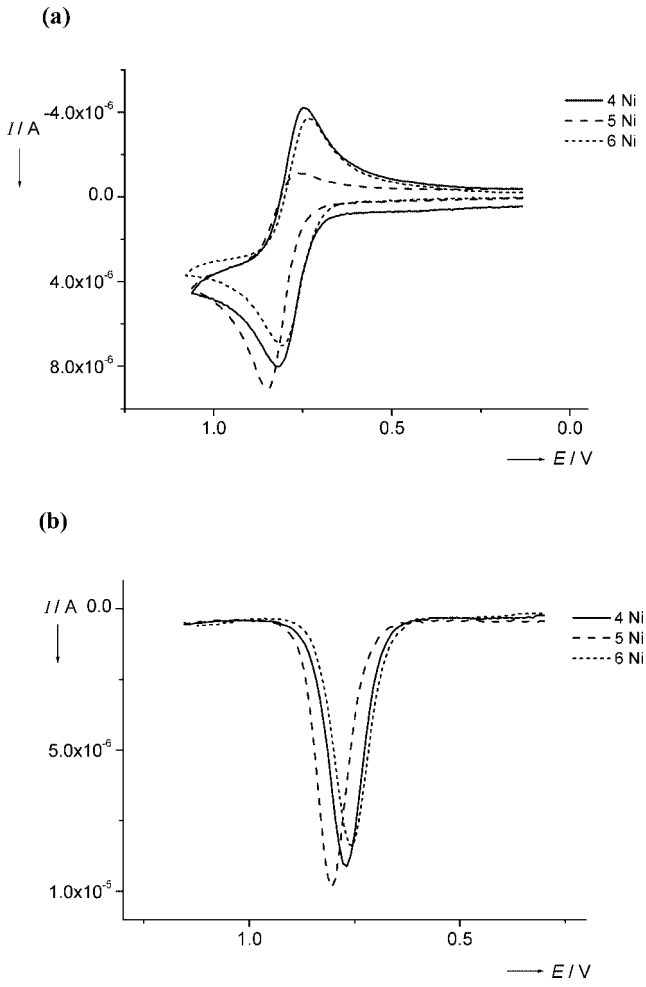


Figure 6. Cyclic voltammograms (a) and differential pulse voltammograms (b) for 0.5 mM **4Ni**, **5Ni** and **6Ni** recorded using a GCE in 0.1 M TBAHFP/AN solution.

In the compounds presented in this contribution, the electrode processes of all copper complexes clearly remain close to reversible and no chemical reactions are involved. The changes in the redox potential with increasing macrocycle size can be explained by assuming increased non-planarity of the complex. The structures of the larger systems[7,8] show deviations from planarity. On the other hand, in the case of **5Ni** a diminished cathodic peak reveals an instability of $Ni^{III}$ and involvement of further chemical reactions. The redox properties and diffusion coefficient values, based on the voltammetry peaks or limiting currents, are collected in Table 4.

 © 2007 Wiley-VCH Verlag GmbH & Co. KGaA, Weinheim 

Table 4. Redox properties and diffusion coefficients of the $Cu^{II}$ and $Ni^{II}$ complexes studied.

| | CV | | | DPV | NPV | D |
|---|---|---|---|---|---|---|
| | $E_{pa}$ [V] | $E_{pc}$ [V] | $E^{o\prime}$ [V] | $E_p$ [V] | $E_{1/2}$ [V] | $10^{-5}$ [$cm^2 s^{-1}$] |
| **4Ni** | 0.817 | 0.749 | 0.783 | 0.768 | 0.783 | 1.15 |
| **5Ni** | 0.852 | 0.759 | 0.806 | 0.804 | 0.819 | 1.72 |
| **6Ni** | 0.811 | 0.738 | 0.775 | 0.755 | 0.769 | 1.02 |
| **4Cu** | 0.605 | 0.527 | 0.566 | 0.552 | 0.565 | 0.70 |
| **5Cu** | 0.862 | 0.788 | 0.825 | 0.809 | 0.827 | 0.95 |
| **6Cu** | 0.940 | 0.862 | 0.901 | 0.887 | 0.989 | 1.12 |

## Host–Guest Interactions

The bis-macrocyclic receptors shown in Scheme 3[9,10] have been shown to form host–guest complexes with π-electron-rich aromatic guests.[11] Their structures are based on donor–acceptor interactions between the π-electron-rich aromatic rings and π-electron-deficient cyclidene units. The same type of interactions should result in the affinity of such receptors towards the planar, neutral complexes **4Cu** and **4Ni**.

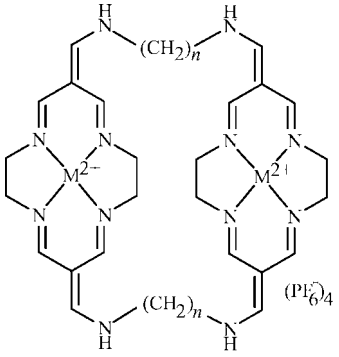

$n = 5$, M = Ni **7NiNi**
$n = 7$, M = Ni **8NiNi**
$n = 7$, M = Cu **8CuCu**
$n = 9$, M = Ni **9NiNi**
$n = 9$, M = Cu **9CuCu**

Scheme 3. Structures of the host complexes.

The changes of the cyclic voltammogram for **4Cu** alone, and after mixing with bis-macrocyclic receptor **8NiNi**, are shown in Figure 7. The midpoint potential $E^{o\prime} = (E_{pa} + E_{pc})/2$ is shifted by 20 mV towards less positive potentials upon mixing with the excess of bis-macrocycle, thereby indicating the stronger donor properties of the complex. These stronger donor properties may be interpreted as an indication of the associative properties of the bis-macrocyclic complex towards the **4Cu** moiety. Thus, **8NiNi** may be acting as a receptor molecule towards the guest planar **4Cu** complex. These unique complexing properties were probed by electrospray mass spectrometry (ESI-MS).

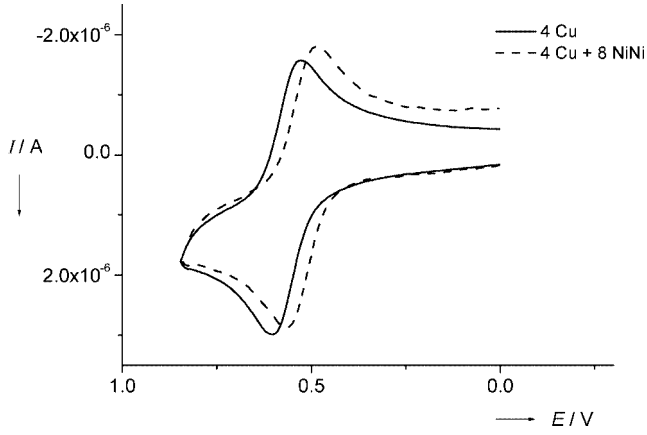


Figure 7. Cyclic voltammograms for $1 \times 10^{-4}$ M **4Cu** and its 1:10 mixture with **8NiNi** after 5 d. Scan rate: 0.1 $V s^{-1}$. GCE in 0.1 M TBAHFP/AN solution.

Despite the fact that ESI-MS might not reflect the solution binding affinities accurately, it provides important information on host–guest complexes and the nature of their interactions.[12] The ESI mass spectra of an equimolar mixture ($10^{-3}$ M) of neutral complexes **4Cu** or **4Ni** and bis-macrocyclic receptors **8NiNi** or **8CuCu** in dichloromethane/acetonitrile (1:3) solution confirmed the formation of the host–guest complexes. New peaks at *m*/*z* 437.2, 438.9, 440.5, 442.2 corresponding to the formation of the 1:1 adducts **8NiNi+4Ni**, **8NiNi+4Cu**, **8CuCu+4Ni** and **8CuCu+4Cu**, respectively, with a +4 charge, were observed in the spectra of their mixtures. In order to compare the affinities of bis-macrocyclic receptors towards neutral guests, the ESI mass spectra of equimolar mixtures of **7NiNi**, **8NiNi** and **9NiNi** with **4Cu** were measured (Figure 8, a). The spectra show that the cavity size in **7NiNi**, which contains $(CH_2)_5$ linkers, is too small to accommodate the guest molecules and no common peaks were recorded. On the other hand, the cavity size in **9NiNi**, which contains $(CH_2)_9$ linkers, is too large to enable simultaneous and equally strong interactions of guest molecules with both sides of the receptor cation, therefore the intensity of the common peak (*m*/*z* 457.5) is very low in comparison with the peak of the **8NiNi+4Cu** associate (*m*/*z* 438.9). A comparison of the dinickel (**8NiNi**) and dicopper (**8CuCu**) receptors (Figure 8, b) shows their similar affinities towards the **4Cu** guest. On the other hand, the neutral **4Cu** complex forms a more stable associate with **8NiNi** than its nickel(II) analogue **4Ni** (see Figure 8, c).

 © 2007 Wiley-VCH Verlag GmbH & Co. KGaA, Weinheim 

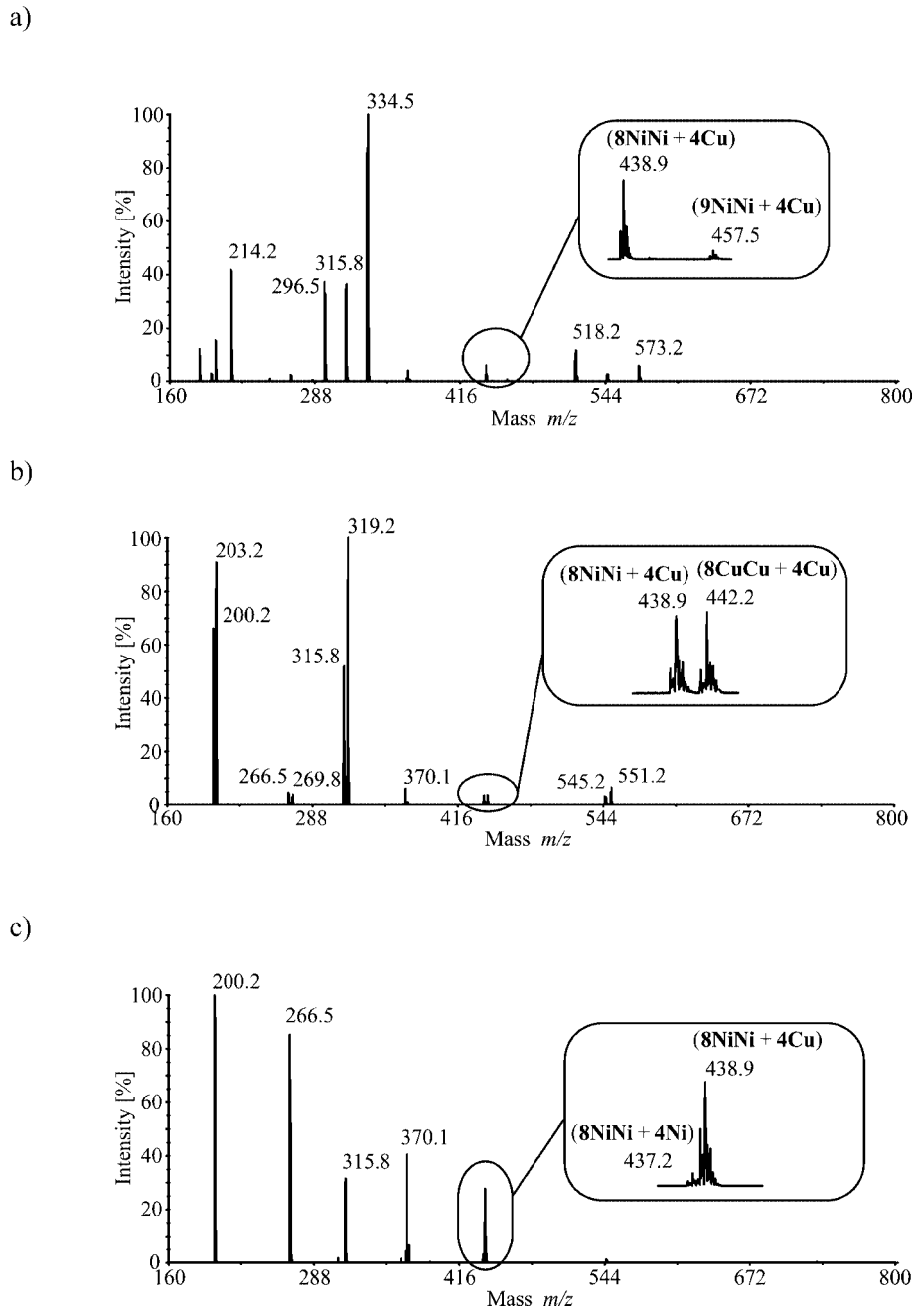


Figure 8. ESI mass spectra of equimolar mixtures of **7NiNi**, **8NiNi** and **9NiNi** with **4Cu** (a), **8NiNi** and **8CuCu** with **4Cu** (b) and (c) **4Ni** and **4Cu** with **8NiNi**.

## Conclusions

In this work we have presented the synthesis and structural properties of ligands and their neutral 14-, 15- and 16-membered complexes with $Cu^{II}$ and $Ni^{II}$. It appears that molecules of the free 14-membered ligands have a non-planar, step-like structure of the ethylene bridges. Significant changes in the geometry of the central macrocyclic fragments are observed on protonation as the protons no longer occupy the central positions of the ring but point above and below the macrocycle plane. This prevents the formation of intramolecular N–H···N hydrogen bonds. The insertion of transition metal ions is accompanied by an increased planarity of the structures of the complexes, which has consequences for the electrochemical reversibility and redox potentials of the complexes. The deviations from planarity increase with increasing macrocycle size and, as a consequence, the redox potential is shifted towards more positive values. In the case of the $Ni^{II}$ complexes, a contribution of chemical reactions is detected by the decrease of the reduction peak.

 © 2007 Wiley-VCH Verlag GmbH & Co. KGaA, Weinheim 

The formation of host–guest complexes with bis-macrocyclic cations can be achieved by appropriate tuning of the properties of the macrocyclic complexes, as demonstrated for planar, neutral macrocyclic guests associating with the bis-macrocyclic **8NiNi** (or **8CuCu**) cation receptors. This type of interaction, which leads to a new transition-ion complex structure, is of special interest in the design of new rotaxane-like systems for mechano-molecular devices, and work in this direction is currently underway in our laboratories.

## Experimental Section

**Synthesis:** 6,13-Bis(methoxycarbonyl)-1,4,8,11-tetraazacyclotetradeca-4,6,11,13-tetraene (**4**),[3] ligands **2** and **3** as well as their nickel(II) [(**2Ni**)$_2$·Ni(CH$_3$COO)$_2$·2CH$_3$OH and **3Ni**] and copper(II) complexes (**2Cu** and **3Cu**)[6] were obtained according to procedures described elsewhere. Crystals of the neutral nickel(II) complex **10Ni**[4,5] were obtained by slow evaporation of its solution in a 1:1 dichloromethane/methanol mixture.

**Spectroscopic Measurements:** The NMR spectra were obtained with Varian Mercury 400 and Varian Gemini 2000BB spectrometers. Signals are reported in ppm relative to the residual solvent signal. IR spectra (paraffin oil mulls) were recorded with a Perkin–Elmer Spectrum 2000 FT-IR spectrometer. UV/Vis absorption spectra were recorded with a Shimadzu UV-3100 spectrometer. ESI mass spectra were measured with a Mariner Perseptive Biosystem mass spectrometer.

**Voltametry:** Linear-scan, differential-pulse and normal-pulse voltammetry experiments were performed with an Autolab potentiostat (ECO Chemie, Netherlands) in a three-electrode arrangement with silver/silver chloride (Ag/AgCl) as the reference electrode, platinum foil as the counter electrode and a glassy carbon electrode (GCE, BAS, 3 mm diameter) as the working electrode. The reference electrode was separated from the working solution by an electrolytic bridge filled with 0.1 M TBAHFP/AN solution. The reference electrode potential was calibrated by using ferrocene oxidation process in the same TBAHFP/AN solution. AN containing 0.1 M TBAHFP was used as the supporting electrolyte solution. Argon was used to deaerate the solution and an argon blanket was maintained over the solution during the experiments.

**6,13-Bis(methoxycarbonyl)-1,4,8,11-tetraazacyclotetradeca-4,6,11,13-tetraenato(2–)-κ$^4$N$^{1,4,8,11}$nickel(II) (4Ni). (a) From Ligand 4:** Macrocyclic ligand **4** (0.62 g, 0.002 mol) and nickel acetate tetrahydrate (0.55 g, 0.0022 mol) were refluxed in methanol (200 mL) for 1 h. The reaction mixture was cooled down and left in a refrigerator for crystallisation. The resulting orange precipitate was filtered off and recrystallised from a dichloromethane/methanol mixture (1:5, 300 mL). Yield: 0.64 g (88%).

**(b) From Complex 3Ni:** Complex **3Ni** (0.341 g, 0.001 mol) was dissolved in ethylenediamine (2.5 mL). The mixture was refluxed for 1 h, cooled and diluted with 25 mL of water. The resulting orange precipitate was filtered off and purified by chromatography on neutral alumina (Merck) with chloroform/methanol (99:1) as eluent. The eluate was evaporated to dryness and the residue recrystallised from dichloromethane/methanol (1:5). Yield: 0.275 g (77%); m.p. 284 °C. Slow evaporation of a solution of **4Ni** in dichloromethane/toluene (1:1) gave crystals suitable for X-ray data collection. $C_{14}H_{20}N_4NiO_4$ (365.0): calcd. C 46.1, H 5.0, N 15.3; found C 46.2, H 5.1, N 15.3. ESI MS: *m/z* 365.3 [$C_{14}H_{20}N_4O_4Ni$ + H]$^+$, 387.3 [$C_{14}H_{20}N_4O_4Ni$ + Na]$^+$. $^1$H NMR (400 MHz, $CDCl_3$): $\delta$ = 7.81 (s, 4 H, =CH-N), 3.73 (s, 6 H, $CH_3$), 3.38 (s, 8 H, N-$CH_2$) ppm. $^{13}$C NMR (100 MHz, $CDCl_3$): $\delta$ = 154.9 (=CH-N), 168.2 (O-C=O), 98,2 (-C=), 51.2 ($CH_3$), 58.7 (N-$CH_2$) ppm. UV/Vis (methanol): $\lambda_{max}$ ($\varepsilon$) = 201 nm (25020 M$^{-1}$ cm$^{-1}$), 229 (30220), 316 (40640), 374 (5310), 497 (275). IR (nujol): $\tilde{\nu}$ = 1677 vs. (C=O), 1598 vs. (C=N), 1539 m (C=C) cm$^{-1}$.

**6,13-Bis(methoxycarbonyl)-1,4,8,11-tetraazacyclotetradeca-4,6,11,13-tetraenato(2–)-κ$^4$N$^{1,4,8,11}$copper(II) (4Cu):** This complex was obtained following the same procedures: (a) from ligand **4** with copper(II) acetate instead of nickel(II) acetate. Yield: 77%; (b) condensation of **3Cu** with ethylenediamine. Yield: 51%, m.p. 295 °C. $C_{14}H_{20}CuN_4O_4$ (369.9): calcd. C 45.5, H 4.9, N 15.2; found C 45.4, H 5.1, N 15.0. ESI MS: *m/z* 370.2 [$C_{14}H_{20}N_4O_4Cu$ + H]$^+$, 392.2 [$C_{14}H_{20}N_4O_4Cu$ + Na]$^+$. UV/Vis (methanol): $\lambda_{max}$ ($\varepsilon$) = 205 nm (24540 M$^{-1}$ cm$^{-1}$), 238 (11730), 286 (64380), 318 (20670), 550 (140). IR (nujol): $\tilde{\nu}$ = 1678 vs. (C=O), 1596 vs. (C=N), 1547 m (C=C) cm$^{-1}$.

**6,14-Bis(methoxycarbonyl)-1,4,8,12-tetraazacyclopentadeca-4,6,12,14-tetraenato(2–)-κ$^4$N$^{1,4,8,12}$nickel(II) (5Ni):** Complex **3Ni** (0.341 g, 0.001 mol) was dissolved in 1,3-propylenediamine (2.5 mL). The mixture was refluxed for 2 h, cooled and diluted with 25 mL of water. The resulting red precipitate was filtered off and purified by chromatography on neutral alumina (Merck) with chloroform methanol (99:1) as eluent. The eluate was evaporated to dryness and the residue recrystallised from dichloromethane/methanol (1:5). Yield: 0.370 g (91%); m.p. 231 °C. Crystals of **5Ni** used for X-ray data collection were obtained by slow evaporation of a dichloromethane/toluene solution. $C_{15}H_{20}N_4NiO_4$ (379.1): calcd. C 47.5, H 5.3, N 14.8; found C 47.6, H 5.4, N 14.4. ESI MS: *m/z* 379.3 [$C_{15}H_{20}N_4O_4Ni$ + H]$^+$, 401.2 [$C_{15}H_{20}N_4O_4Ni$ + Na]$^+$. $^1$H NMR (400 MHz, $CDCl_3$): $\delta$ = 7.61 (s, 2 H) and 7.60 (s, 2 H, =CH-N), 3.72 (s, 6 H, $CH_3$), 3.36 (t, *J* = 6.7 Hz, 4 H, N-$CH_2$), 3.18 (s, 4 H, N-$CH_2$), 1.87 (quint, *J* = 6.7 Hz, 2 H, $CH_2$) ppm. $^{13}$C NMR (100 MHz, $CDCl_3$): $\delta$ = 154.9 and 157.9 (=CH-N), 168.2 (O-C=O), 97.3 (-C=), 50.7 ($CH_3$), 58.7 and 58.7 (N-$CH_2$), 28.0 ($CH_2$) ppm. UV/Vis (methanol): $\lambda_{max}$ ($\varepsilon$) = 238 nm (28995 M$^{-1}$ cm$^{-1}$), 299 (39510), 370 (5230), 539 (170). IR (nujol): $\tilde{\nu}$ = 1674 m (C=O), 1604 vs. (C=N), 1539 m (C=C) cm$^{-1}$.

**6,14-Bis(methoxycarbonyl)-1,4,8,12-tetraazacyclopentadeca-4,6,12,14-tetraenato(2–)-κ$^4$N$^{1,4,8,12}$copper(II) (5Cu):** This complex was obtained from **3Cu** following the same procedure as for **5Ni**. Yield: 33%, m.p. 238 °C. $C_{15}H_{20}CuN_4O_4$·0.5$H_2O$ (392.9): calcd. C 45.9, H 5.4, N 14.3; found C 45.7, H 5.1, N 14.4. ESI MS: *m/z* 384.1 [$C_{15}H_{20}N_4O_4Cu$ + H]$^+$, 406.1 [$C_{15}H_{20}N_4O_4Cu$ + Na]$^+$. UV/Vis (methanol): $\lambda_{max}$ ($\varepsilon$) = 203 nm (20700 M$^{-1}$ cm$^{-1}$), 281 (66080), 314 (21250), 510 (12910), 662 (130). IR (nujol): $\tilde{\nu}$ = 1682 m (C=O), 1613 vs. (C=N), 1549 m (C=C) cm$^{-1}$.

**3,11-Bis(methoxycarbonyl)-1,5,9,13-tetraazacyclohexadeca-1,3,9,11-tetraenato(2–)-κ$^4$N$^{1,5,9,13}$nickel(II) (6Ni):** This complex was obtained from **2Ni** and 1,3-propylenediamine following the same procedure as for **5Ni**. Yield: 23%, m.p. 198 °C. $C_{16}H_{22}N_4NiO_4$ (393.1): calcd. C 48.9, H 5.6, N 14.3; found C 49.1, H 5.9, N 14.0. ESI MS: *m/z* 393.2 [$C_{16}H_{22}N_4O_4Ni$ + H]$^+$, 415.3 [$C_{16}H_{22}N_4O_4Ni$ + Na]$^+$. $^1$H NMR (400 MHz, $CDCl_3$): $\delta$ = 7.36 (s, 4 H, =CH-N), 3.72 (s, 6 H, $CH_3$), 3.36 (t, *J* = 6.4 Hz, 8 H, N-$CH_2$), 1.84 (quint, *J* = 6.4 Hz, 4 H, $CH_2$) ppm. $^{13}$C NMR (100 MHz, $CDCl_3$): $\delta$ = 157.3 (=CH-N), 168.3 (O-C=O), 98.2 (-C=), 50.6 ($CH_3$), 54.3 (N-$CH_2$), 27.9 ($CH_2$) ppm. UV/Vis (methanol): $\lambda_{max}$ ($\varepsilon$) = 250 nm (21660 M$^{-1}$ cm$^{-1}$), 295 (33430), 343 (4820), 493 (140). IR (nujol): $\tilde{\nu}$ = 1665 m (C=O), 1605 vs. (C=N), 1532 vs. (C=C) cm$^{-1}$.

 © 2007 Wiley-VCH Verlag GmbH & Co. KGaA, Weinheim 

**3,11-Bis(methoxycarbonyl)-1,5,9,13-tetraazacyclohexadeca-1,3,9,11-tetraenato(2–)-κ$^4$N$^{1,5,9,13}$copper(II) (6Cu):** This complex was obtained from **2Cu** and 1,3-propylenediamine following the same procedure as for **5Ni**. Yield: 13%, m.p. 227 °C. $C_{16}H_{22}CuN_4O_4$ (397.9): calcd. C 48.3, H 5.6, N 14.1; found C 48.1, H 5.4, N 14.1. ESI MS: *m*/*z* 398.1 $[C_{16}H_{22}N_4O_4Cu + H]^+$, 420.1 $[C_{16}H_{22}N_4O_4Cu + Na]^+$. UV/Vis (methanol): $\lambda_{max}$ ($\varepsilon$) = 201 nm (21620 $M^{-1}cm^{-1}$), 277 (64355), 318 (16245), 531 (240), 754 (220). IR (nujol): $\tilde{\nu}$ = 1677 m (C=O), 1610 vs. (C=N), 1536 m (C=C) $cm^{-1}$.

**6,14-Bis(methoxycarbonyl)-1,4,8,12-tetraazacyclopentadeca-4,6,12,14-tetraene Di(hydrogen hexafluorophosphate) {5[HPF$_6$]$_2$}:** Complex **5Cu** (0.767 g. 0.002 mol) was stirred in an aqueous solution of methanesulfonic acid (9 mL, 0.02 mol) at room temperature. After 24 h, when all starting complex had dissolved, an excess of solid $NH_4PF_6$ (1 g) was added and the colourless solid that precipitated filtered off, washed with water and dried under reduced pressure. Yield: 0.687 g (56%), m.p. 245 °C. $C_{15}H_{24}N_4O_4{\cdot}2(PF_6){\cdot}H_2O$ (632.3): calcd. C 28.5, H 4.1, N 8.9; found C 28.4, H 4.5, N 8.8. ESI MS: *m*/*z* 162.1 $[C_{15}H_{24}N_4O_4]^{2+}$, 323.2 $[C_{15}H_{24}N_4O_4 - H]^+$. $^1$H NMR (400 MHz, $CD_3CN$): $\delta$ = 9.54 (br. m, 2 H, N-H), 9.41 (br. m, 2 H, N-H), 7.43 (d, *J* = 15.4 Hz, 2 H, =CH-N), 7.21 (d, *J* = 15.7 Hz, 2 H, =CH-N), 3.92 (s, 6 H, $CH_3$), 3.40 (br. m, 4 H, N-$CH_2$), 3.97 (br. s, 4 H, N-$CH_2$), 2.20 (quint, 2 H, $CH_2$) ppm. $^{13}$C NMR (100 MHz, $CD_3CN$): $\delta$ = 167.0 and 167.8 (=CH-N), 166.3 (O-C=O), 96.7 (-C=), 53.1 $CH_3$, 50.1 and 51.4 (N-$CH_2$), 24.9 ($CH_2$) ppm. UV/Vis (methanol): $\lambda_{max}$ ($\varepsilon$) = 235 nm (27190 $M^{-1}cm^{-1}$), 303 (26345). IR (nujol): $\tilde{\nu}$ = 3345 vs. and 3255 (O–H and N–H), 1715 m (C=O), 1664 w and 1625 vs. (C=N and C=C), 845 vs. and 560 m ($PF_6$) $cm^{-1}$.

**3,11-Bis(methoxycarbonyl)-1,5,9,13-tetraazacyclopentadeca-1,3,9,11-tetraene Di(hydrogen hexafluorophosphate) {6[HPF$_6$]$_2$}:** This complex was obtained from **6Ni** following the same procedure. Yield: 56%, m.p. 261 °C. $C_{16}H_{26}N_4O_4{\cdot}2(PF_6){\cdot}H_2O$ (646.4): calcd. C 29.7, H 4.4, N 8.7; found C 30.5, H 4.6, N 8.7. ESI MS: *m*/*z* 169.1 $[C_{16}H_{26}N_4O_4]^{2+}$, 337.2 $[C_{16}H_{24}N_4O_4 - H]^+$. $^1$H NMR (400 MHz, $CD_3CN$): $\delta$ = 9.66 (br. m, 4 H, N-H), 7.85 (d, *J* = 15.0 Hz, 4 H, =CH-N), 4.00 (s, 6 H, $CH_3$), 3.70 (br. m, 8 H, N-$CH_2$), 2.17 (quint, 4 H, $CH_2$) ppm. $^{13}$C NMR (100 MHz, $CD_3CN$): $\delta$ = 176.4 (=CH-N), 165.9 (O-C=O), 101.4 (-C=), 52.3 ($CH_3$), 48.3 (N-$CH_2$), 30.1 ($CH_2$) ppm. UV/Vis [methanol/acetonitrile (9:1)]: $\lambda_{max}$ ($\varepsilon$) = 252 nm (10630 $M^{-1}cm^{-1}$), 289 (17360). IR (nujol): $\tilde{\nu}$ = 3326 vs. and 3240 (O–H and N–H), 1703 m (C=O), 1672 w and 1637 vs. (C=N and C=C), 851 vs. and 558 m ($PF_6$) $cm^{-1}$.

**(3,13,17,20,24,34,38,41,44,47,50,53-Dodecaazatricyclo[34.6.6.6$^{15,22}$]-tetrapentaconta-1,14,16,20,22,35,37,41,43,47,49,53-dodecaene-κ$^8$N)-dinickel(II) Hexafluorophosphate (9NiNi):** 6,13-Bis(methoxymethylidene)-1,4,8,11-tetraazacyclotetradeca-4,7,11,14-tetraenato(2-)-nickel(II) dihexafluorophosphate[1] (0.625 g, 1 mmol) and 1,9-nonanediamine (0.158 mL, 1 mmol) were separately dissolved in 25 mL of dry acetonitrile and added dropwise to 100 mL of acetonitrile with a peristaltic pump at a rate of 15 mL $h^{-1}$. The mixture was then left for 3 h at room temperature and partly evaporated. The remaining 20 mL of solution was diluted with 20 mL of water and applied to a silica gel column (Merck 60 silanized, 25 × 2.5 cm). The column was washed with $CH_3CN/H_2O$ (5:4) and eluted with $CH_3CN/H_2O$ (3:2) with addition of $NH_4PF_6$ (3 g per 100 mL). The first major band was collected and slowly evaporated to give yellow crystals. Yield: 0.277 g (19.2%). $C_{42}H_{68}F_{24}N_{12}Ni_2P_4$ (1438.3): calcd. C 35.1, H 4.8, N 11.7; found C 34.6, H 4.5, N 11.5. IR (nujol): $\tilde{\nu}$ = 1615 v s, 834 v s, 557 s $cm^{-1}$. MS (ESI, $CH_3CN$): *m*/*z* 214.1 $[C_{42}H_{68}N_{12}Ni_2]^{4+}$, 285.2 $[C_{42}H_{67}N_{12}Ni_2]^{3+}$, 334.5 $[(C_{42}H_{68}N_{12}Ni_2)^{4+} + PF_6^-]$, 427.2 $[C_{42}H_{66}N_{12}Ni_2]^{2+}$, 573.2 $[(C_{42}H_{68}N_{12}Ni_2)^{4+} + 2PF_6^-]$. $^1$H NMR ($CD_3CN$, 400 MHz): $\delta$ = 1.31 (br. s, 20 H, γ-, δ- and ε-$CH_2$), 1.62 (br. s, 8 H, β-$CH_2$), 3.46–3.57 (m, 24 H, α-$CH_2$ and ring $CH_2CH_2$), 7.65 (s, 4 H, =CH-N), 7.50, 7.97 (br. s, 2 × 4 H, N=C-H), 8.06 (br. s, 4 H, N-H) ppm. $^{13}$C NMR ($CD_3CN$, 100 MHz): $\delta$ = 26.5, 29.5, 29.9, 30.1 (β-, γ-, δ- and ε-$CH_2$), 51.7 (α-$CH_2$), 59.5, 60.2 (br., ring $CH_2CH_2$), 104.1 (ring =C), 155.1 (br.) and 160.7 (br., HC=N, 164.0 (=CH-N) ppm.

**(3,13,17,20,24,34,38,41,44,47,50,53-Dodecaazatricyclo[34.6.6.6$^{15,22}$]-tetrapentaconta-1,14,16,20,22,35,37,41,43,47,49,53-dodecaene-κ$^8$N)-dicopper(II) Hexafluorophosphate (9CuCu):** 6,13-Bis(methoxymethylidene)-1,4,8,11-tetraazacyclotetradeca-4,7,11,14-tetraenato(2-)-copper(II) dihexafluorophosphate[1] (0.364 g, 0.58 mmol) and 1,9-nonanediamine (0.092 mg, 0.58 mmol) were dissolved in 50 mL of dry acetonitrile. After six hours of continuous stirring the mixture was evaporated and dissolved in 20 mL of $CH_3CN/H_2O$ (5:4). The mixture was applied to a silica gel 60 silanized column (20 × 2 cm, Merck), washed with $CH_3CN/H_2O$ (5:4) and eluted with $CH_3CN/H_2O$ (6:4) with addition of $NH_4PF_6$ (3 g per 100 mL). Red crystals were obtained upon slow evaporation of the solvent. Yield: 0.115 g (13.7%). $C_{42}H_{68}Cu_2F_{24}N_{12}P_4$ (1448.0): calcd. C 34.8, H 4.7, N 11.6; found C 34.6, H 4.6, N 11.4. IR (nujol): $\tilde{\nu}$ = 1617 vs, 840 vs, 557 s $cm^{-1}$. MS (ESI, $CH_3CN$): *m*/*z* 217.1 $[C_{42}H_{68}N_{12}Cu_2]^{4+}$, 289.2 $[C_{42}H_{67}N_{12}Cu_2]^{3+}$, 337.8 $[(C_{42}H_{68}N_{12}Cu_2)^{4+} + PF_6^-]$, 433.2 $[C_{42}H_{66}N_{12}Cu_2]^{2+}$, 579.2 $[(C_{42}H_{68}N_{12}Cu_2)^{4+} + 2PF_6^-]$.

**Single Crystal X-ray Diffraction:** Single crystal X-ray measurements of **10Ni**, **4Cu**, **4Ni**, **5Ni**, **6Ni**, **4**, **4[HCl]$_2$** and **6[HPF$_6$]$_2$** were performed on a Kuma KM4CCD κ-axis diffractometer with graphite-monochromated Mo-$K_\alpha$ radiation at 100 K (**4Ni**, **5Ni**, **6Ni**, **4[HCl]$_2$**, **6[HPF$_6$]$_2$**) or at 120 K (**10Ni**, **4Cu**, **4**). The single crystal was positioned at a distance of 65 mm from the KM4CCD camera. A total of 1150 (**6Ni**), 1204 (**10Ni**, **4Cu**, **4Ni**, **5Ni**, **4**, **4**[HCl]$_2$) and 1332 (**6**[HPF$_6$]$_2$) frames were measured at 1.0° (**10Ni**, **4Cu**, **4Ni**, **5Ni**, **6Ni**, **4**, **4**[HCl]$_2$) and at 0.9° (**6**[HPF$_6$]$_2$) intervals with a counting time of 15 s (**4Cu**, **4**), 20 s (**6**[HPF$_6$]$_2$), 22 s (**5Ni**), 25 s (**10Ni**, **4Ni**), and 30 s (**6Ni** and **4**[HCl]$_2$). The data were corrected for Lorentz and polarisation effects, and a numerical absorption correction was applied for **4Cu** and **6Ni**). Data collection, cell refinement and data reduction were carried out with the Kuma Diffraction programs: CrysAlis CCD and CrysAlis RED.[13]

The structures were solved by direct methods[14] and refined using SHELXL.[15] The refinements were based on $F^2$ for all reflections except those with very negative $F^2$ values. Weighted *R* factors (*wR*) and all goodness-of-fit ($\sigma$) values are based on $F^2$. Conventional *R* factors are based on *F* with *F* set to zero for negative $F^2$. The $F_o^2 > 2\sigma(F_o^2)$ criterion was used only for calculating *R* factors and is not relevant to the choice of reflections for the refinement. The *R* factors based on $F^2$ are about twice as large as those based on *F*. Most of the hydrogen atoms were located from a differential map and refined isotropically. All remaining hydrogen atoms were located in idealised averaged geometrical positions and allowed to ride on the heavy atoms. The disorder of the toluene molecules located at special positions was resolved (**4Ni** and **5Ni**). Some of the atoms of the counterions were refined isotropically (**6[HPF$_6$]$_2$**). Scattering factors were taken from Tables 6.1.1.4 and 4.2.4.2 in ref.[16]

**10Ni:** $C_{16}H_{26}N_4NiO_4$, *fw* = 397.12; *T* = 120 K; $\lambda$ = 0.71073 Å; triclinic; space group, $P\bar{1}$; unit cell dimensions: *a* = 4.7792(4), *b* = 9.6841(8), *c* = 10.475(1) Å, $\alpha$ = 64.510(9)°, $\beta$ = 81.876(8)°, $\gamma$ = 84.052(7)°; *V* = 432.74(7) Å$^3$; *Z* = 1; $D_{calcd}$ = 1.524 Mg m$^{-3}$; absorption coefficient: 1.150 mm$^{-1}$; *F*(000) = 210; crystal size: 0.61 × 0.18 × 0.11 mm$^3$; $\theta$ range for data collection: 3.80–25.00°; index ranges: $-5 \le h \le 5$, $-11 \le k \le 11$, $-12 \le l \le 12$; reflections

 © 2007 Wiley-VCH Verlag GmbH & Co. KGaA, Weinheim 

collected: 6458; independent reflections: 1530 ($R_{int}$ = 0.0340); refinement method, full-matrix least-squares on $F^2$; data/restraints/parameters: 1530/0/171; goodness-of-fit on $F^2$ = 1.096; final $R$ indices [$I > 2\sigma(I)$]: $R1$ = 0.0201, $wR2$ = 0.0479; $R$ indices (all data): $R1$ = 0.0213, $wR2$ = 0.0485; weight: $1/[\sigma^2(F_o^2) + (0.0258P)^2 + 0.0779P]$ where $P = [\mathrm{Max}(F_o^2, 0) + 2F_c^2]/3$; largest diffraction peak and hole: 0.323 and –0.281 e Å$^{-3}$.

**4Cu:** $C_{14}H_{18}CuN_4O_4$, $fw$ = 369.86; $T$ = 120 K; $\lambda$ = 0.71073 Å; monoclinic; space group, $P2_1/c$; unit cell dimensions: $a$ = 8.220(2), $b$ = 6.322(1), $c$ = 15.546(3) Å, $\alpha$ = 90°, $\beta$ = 108.41(3)°, $\gamma$ = 90°; $V$ = 766.5(3) Å$^3$; $Z$ = 2; $D_{calcd}$ = 1.602 Mg m$^{-3}$; absorption coefficient: 1.451 mm$^{-1}$; $F$(000) = 382; crystal size: 0.53 × 0.11 × 0.11 mm$^3$; $\theta$ range for data collection: 3.51–24.99°; index ranges: $-9 \le h \le 9$, $-7 \le k \le 7$, $-18 \le l \le 18$; reflections collected: 11278; independent reflections: 1351 ($R_{int}$ = 0.0485); absorption correction: numerical; max. and min. transmission: 0.89822 and 0.58548; refinement method, full-matrix least-squares on $F^2$; data/restraints/parameters: 1351/0/115; goodness-of-fit on $F^2$ = 1.075; final $R$ indices [$I > 2\sigma(I)$]: $R1$ = 0.0398, $wR2$ = 0.1064; $R$ indices (all data): $R1$ = 0.0454, $wR2$ = 0.1114; weight: $1/[\sigma^2(F_o^2) + (0.0840P)^2 + 0.0107P]$ where $P = [\mathrm{Max}(F_o^2, 0) + 2F_c^2]/3$; largest diffraction peak and hole: 0.923 and –0.528 e Å$^{-3}$.

**4Ni:** $C_{21}H_{26}N_4NiO_4$, $fw$ = 457.17; $T$ = 100 K; $\lambda$ = 0.71073 Å; triclinic; space group, $P\bar{1}$; unit cell dimensions: $a$ = 6.3188(5), $b$ = 7.7913(6), $c$ = 11.1511(9) Å, $\alpha$ = 107.429(7)°, $\beta$ = 98.737(7)°, $\gamma$ = 95.131(7)°; $V$ = 512.38(7) Å$^3$; $Z$ = 1; $D_{calcd}$ = 1.482 Mg m$^{-3}$; absorption coefficient: 0.983 mm$^{-1}$; $F$(000) = 240; crystal size: 0.79 × 0.32 × 0.21 mm$^3$; $\theta$ range for data collection: 3.86–25.00°; index ranges: $-7 \le h \le 7$, $-9 \le k \le 9$, $-13 \le l \le 13$; reflections collected: 7602; independent reflections: 1809 ($R_{int}$ = 0.0456); refinement method, full-matrix least-squares on $F^2$; data/restraints/parameters: 1809/0/218; goodness-of-fit on $F^2$ = 1.116; final $R$ indices [$I > 2\sigma(I)$]: $R1$ = 0.0208, $wR2$ = 0.0532; $R$ indices (all data): $R1$ = 0.0214, $wR2$ = 0.0541; extinction coefficient: 0.045(4); weight: $1/[\sigma^2(F_o^2) + (0.0248P)^2 + 0.2216P]$ where $P = [\mathrm{Max}(F_o^2, 0) + 2F_c^2]/3$; largest diffraction peak and hole: 0.318 and –0.251 e Å$^{-3}$.

**5Ni:** $C_{22}H_{28}N_4NiO_4$, $fw$ = 471.19; $T$ = 100 K; $\lambda$ = 0.71073 Å; triclinic; space group, $P\bar{1}$; unit cell dimensions: $a$ = 6.714(1), $b$ = 7.550(1), $c$ = 11.307(2) Å, $\alpha$ = 102.94(1)°, $\beta$ = 104.11(1)°, $\gamma$ = 94.03(1)°; $V$ = 537.0(2) Å$^3$; $Z$ = 1; $D_{calcd}$ = 1.457 Mg m$^{-3}$; absorption coefficient: 0.940 mm$^{-1}$; $F$(000) = 248; crystal size: 0.51 × 0.39 × 0.26 mm$^3$; $\theta$ range for data collection: 3.76–24.99°; index ranges: $-7 \le h \le 7$, $-8 \le k \le 8$, $-13 \le l \le 13$; reflections collected: 7848; independent reflections: 1885 ($R_{int}$ = 0.0867); refinement method, full-matrix least-squares on $F^2$; data/restraints/parameters: 1885/79/208; goodness-of-fit on $F^2$ = 1.094; final $R$ indices [$I > 2\sigma(I)$]: $R1$ = 0.0650, $wR2$ = 0.1749; $R$ indices (all data): $R1$ = 0.0685, $wR2$ = 0.1833; weight: $1/[\sigma^2(F_o^2) + (0.1318P)^2 + 0.3394P]$ where $P = [\mathrm{Max}(F_o^2, 0) + 2F_c^2]/3$; largest diffraction peak and hole: 0.869 and –0.804 e Å$^{-3}$.

**6Ni:** $C_{16}H_{22}N_4NiO_4$, $fw$ = 393.09; $T$ = 100 K; $\lambda$ = 0.71073 Å; monoclinic; space group, $P2_1/c$; unit cell dimensions: $a$ = 7.6007(5), $b$ = 7.4494(4), $c$ = 15.3716(9) Å, $\alpha$ = 90°, $\beta$ = 107.166(5)°, $\gamma$ = 90°; $V$ = 831.58(9) Å$^3$; $Z$ = 2; $D_{calcd}$ = 1.570 Mg m$^{-3}$; absorption coefficient: 1.197 mm$^{-1}$; $F$(000) = 412; crystal size: 0.44 × 0.39 × 0.16 mm$^3$; $\theta$ range for data collection: 3.31–24.99°; index ranges: $-9 \le h \le 9$, $-8 \le k \le 8$, $-18 \le l \le 18$; reflections collected: 11670; independent reflections: 1455 ($R_{int}$ = 0.0195); Absorption correction: numerical; max. and min. transmission: 0.82771 and 0.63239; refinement method, full-matrix least-squares on $F^2$; data/restraints/parameters: 1455/0/160; goodness-of-fit on $F^2$ = 1.072; final $R$ indices [$I > 2\sigma(I)$]: $R1$ = 0.0207, $wR2$ = 0.0499; $R$ indices (all data): $R1$ = 0.0232, $wR2$ = 0.0510; extinction coefficient: 0.01(2); weight: $1/[\sigma^2(F_o^2) + (0.0261P)^2 + 0.5008P]$ where $P = [\mathrm{Max}(F_o^2, 0) + 2F_c^2]/3$; largest diffraction peak and hole: 0.322 and –0.239 e Å$^{-3}$.

**4:** $C_{14}H_{20}N_4O_4$, $fw$ = 308.34; $T$ = 120 K; $\lambda$ = 0.71073 Å; monoclinic; space group, $P2_1/c$; unit cell dimensions: $a$ = 4.2689(9), $b$ = 19.479(4), $c$ = 9.630(2) Å, $\alpha$ = 90°, $\beta$ = 109.89(3)°, $\gamma$ = 90°; $V$ = 753.0(3) Å$^3$; $Z$ = 2; $D_{calcd}$ = 1.360 Mg m$^{-3}$; absorption coefficient: 0.101 mm$^{-1}$; $F$(000) = 328; crystal size: 0.70 × 0.12 × 0.11 mm$^3$; $\theta$ range for data collection: 3.86–25.00°; index ranges: $-5 \le h \le 5$, $-23 \le k \le 23$, $-11 \le l \le 11$; reflections collected: 11347; independent reflections: 1315 ($R_{int}$ = 0.0807); refinement method, full-matrix least-squares on $F^2$; data/restraints/parameters: 1315/0/140; goodness-of-fit on $F^2$ = 1.016; final $R$ indices [$I > 2\sigma(I)$]: $R1$ = 0.0489, $wR2$ = 0.1111; $R$ indices (all data): $R1$ = 0.0776, $wR2$ = 0.1261; weight: $1/[\sigma^2(F_o^2) + (0.0672P)^2]$ where $P = [\mathrm{Max}(F_o^2, 0) + 2F_c^2]/3$; largest diffraction peak and hole: 0.250 and –0.242 e Å$^{-3}$.

**4[HCl]$_2$:** $C_{14}H_{26}Cl_2N_4O_6$, $fw$ = 417.29; $T$ = 100 K; $\lambda$ = 0.71073 Å; triclinic; space group, $P\bar{1}$; unit cell dimensions: $a$ = 7.676(1), $b$ = 8.3605(9), $c$ = 8.545(1) Å, $\alpha$ = 83.504(9)°, $\beta$ = 71.69(1)°, $\gamma$ = 68.56(1)°; $V$ = 484.6(1) Å$^3$; $Z$ = 1; $D_{calcd}$ = 1.430 Mg m$^{-3}$; absorption coefficient: 0.373 mm$^{-1}$; $F$(000) = 220; crystal size = 0.14 × 0.12 × 0.08 mm$^3$; $\theta$ range for data collection: 3.49–24.99°; index ranges: $-9 \le h \le 9$, $-9 \le k \le 9$, $-10 \le l \le 10$; reflections collected: 7509; independent reflections: 1704 ($R_{int}$ = 0.0332); refinement method, full-matrix least-squares on $F^2$; data/restraints/parameters: 1704/0/170; goodness-of-fit on $F^2$: 1.002; final $R$ indices [$I > 2\sigma(I)$]: $R1$ = 0.0278, $wR2$ = 0.0593; $R$ indices (all data): $R1$ = 0.0400, $wR2$ = 0.0627; weight: $1/[\sigma^2(F_o^2) + (0.0337P)^2]$ where $P = [\mathrm{Max}(F_o^2, 0) + 2F_c^2]/3$; largest diffraction peak and hole: 0.185 and –0.186 e Å$^{-3}$.

**6[HPF$_6$]$_2$:** $C_{16}H_{26}F_{12}N_4O_4P_2$, $fw$ = 628.35; $T$ = 100 K; $\lambda$ = 0.71073 Å; tetragonal; space group, $I4/m$; unit cell dimensions: $a$ = 19.025(3), $b$ = 19.025(3), $c$ = 27.271(6) Å, $\alpha$ = 90°, $\beta$ = 90°, $\gamma$ = 90°; $V$ = 9871(3) Å$^3$; $Z$ = 16; $D_{calcd}$ = 1.691 Mg m$^{-3}$; absorption coefficient: 0.299 mm$^{-1}$; $F$(000) = 5120; crystal size: 0.56 × 0.28 × 0.28 mm$^3$; $\theta$ range for data collection: 3.38–25.00°; index ranges: $-22 \le h \le 22$, $-22 \le k \le 22$, $-32 \le l \le 32$; reflections collected: 72505; independent reflections: 4439 ($R_{int}$ = 0.0441); refinement method, full-matrix least-squares on $F^2$; data/restraints/parameters: 4439/133/449; goodness-of-fit on $F^2$ = 1.108; final $R$ indices [$I > 2\sigma(I)$]: $R1$ = 0.0731, $wR2$ = 0.2067; $R$ indices (all data): $R1$ = 0.0805, $wR2$ = 0.2158; weight: $1/[\sigma^2(F_o^2) + (0.1317P)^2 + 34.2860P]$ where $P = [\mathrm{Max}(F_o^2, 0) + 2F_c^2]/3$; largest diffraction peak and hole: 1.179 and –1.605 e Å$^{-3}$.

CCDC-606234 to -606241 (for **4**, **4Cu**, **4Ni**, **5Ni**, **6Ni**, **10Ni**, **4[HCl]$_2$** and **6[HPF$_6$]$_2$**, respectively) contain the supplementary crystallographic data for this paper. These data can be obtained free of charge from The Cambridge Crystallographic Data Centre via www.ccdc.cam.ac.uk/data_request/cif.

## Acknowledgments

This work was financially supported by the State Committee for Scientific Research (MEiN: project 4 T09A 048 23). The X-ray measurements were undertaken in the Crystallographic Unit of the Physical Chemistry Laboratory at the Chemistry Department of the University of Warsaw. S. D. and K. W. are very grateful to the Polish State Committee for Scientific Research (MEiN) for financial support within the project 3 T09A 018 28 and A. W. within the project 120-501/68-BW-1681/18/05.

 © 2007 Wiley-VCH Verlag GmbH & Co. KGaA, Weinheim 

[1] B. Korybut-Daszkiewicz, A. Więckowska, R. Bilewicz, S. Domagała, K. Woźniak, *J. Am. Chem. Soc.* **2001**, *123*, 9356–9366.
[2] B. Korybut-Daszkiewicz, A. Więckowska, R. Bilewicz, S. Domagała, K. Woźniak, *Angew. Chem. Int. Ed.* **2004**, *43*, 1700–1704.
[3] a) S. Takamura, T. Yoshimiya, S. Kameyama, A. Nishida, H. Yamamoto, M. Noguchi, *Synthesis* **2000**, 637–664; b) M. Nakane, H. Gollhan, C. R. Hutchinson, P. L. Knutson, *J. Org. Chem.* **1980**, *45*, 2536–2538.
[4] E.-G. Jäger, *Z. Chem.* **1968**, *8*, 392.
[5] D. P. Riley, D. H. Busch, *Inorg. Synth.* **1978**, *18*, 36.
[6] A. Rybka, R. A. Koliński, S. Domagała, J. Kłak, J. Mroziński, K. Woźniak, B. Korybut-Daszkiewicz, *Inorg. Chim. Acta* **2006**, *359*, 4526–4534.
[7] N. Alcock, W.-K. Lin, A. Jircitano, J. D. Mokren, P. V. W. R. Corfield, G. Johnson, G. Novotnak, C. Cairns, D. H. Busch, *Inorg. Chem.* **1987**, *26*, 440–452.
[8] W. Grochala, A. Jagielska, K. Woźniak, A. Więckowska, R. Bilewicz, B. Korybut-Daszkiewicz, J. Bukowska, L. Piela, *J. Phys. Org. Chem.* **2001**, *14*, 63–73.
[9] R. Bilewicz, A. Więckowska, B. Korybut-Daszkiewicz, A. Olszewska, N. Feeder, K. Woźniak, *J. Phys. Chem. B* **2000**, *104*, 11430–11434.
[10] A. Wieckowska, R. Bilewicz, S. Domagala, K. Wozniak, B. Korybut-Daszkiewicz, A. Tomkiewicz, J. Mrozinski, *Inorg. Chem.* **2003**, *42*, 5513–5522.
[11] S. Domagała, A. Więckowska, J. Kowalski, A. Rogowska, J. Szydłowska, B. Korybut-Daszkiewicz, R. Bilewicz, K. Woźniak, *Chem. Eur. J.* **2006**, *12*, 2967–2981.
[12] M. Vincenti, *J. Mass Spectrom.* **1995**, *30*, 925–939.
[13] Oxford Diffraction (**2001**). *CrysAlis CCD* and *CrysAlis RED*. Oxford Diffraction Poland, Wrocław, Poland.
[14] G. M. Sheldrick, *Acta Crystallogr. Sect. A* **1990**, *46*, 467–473.
[15] G. M. Sheldrick, *SHELXL93*. *Program for the Refinement of Crystal Structures*, University of Göttingen, Germany.
[16] *International Tables for Crystallography* (Ed.: A. J. C. Wilson), Kluwer, Dordrecht, **1992**, vol. C.

Received: May 3, 2006
Published Online: November 27, 2006

 © 2007 Wiley-VCH Verlag GmbH & Co. KGaA, Weinheim 

DOI: 10.1002/ejic.200600449

# New Multidimensional Coordination Polymers with $\mu_2$- and $\mu_3$-dcno Cyano Carbanion Ligand {dcno$^-$ = $[(NC)_2CC(O)O(CH_2)_2OH]^-$}

**Samia Benmansour,[a,b] Fatima Setifi,[a][‡] Smail Triki,*[a] Jean-Yves Salaün,[a] Fanny Vandevelde,[a] Jean Sala-Pala,[a] Carlos J. Gómez-García,*[b] and Thierry Roisnel[c]**

**Keywords:** Cyano carbanions / Bridging ligands / Coordination polymers / Multidimensional networks / Magnetic properties

New polymeric materials $[M(dcno)_2(H_2O)_2]$ [M = $Fe^{II}$ (**1**), $Co^{II}$ (**2**)] and $[M(dcno)_2]$ [M = $Cu^{II}$ (**3**), $Mn^{II}$ (**4**)] with dcno$^-$ = $[(NC)_2CC(O)O(CH_2)_2OH]^-$ = 2,2-dicyano-1-(2-hydroxyethoxy)ethenolate anion have been synthesised and characterised by IR spectroscopy, X-ray crystallography and magnetic measurements. In compounds **1** and **2**, each organic ligand acts in a bridging mode with its two nitrogen atoms bound to two different metal ions, while in compounds **3** and **4**, each organic anion acts as a $\mu_3$-bridging ligand through its two nitrogen atoms and the oxygen atom of the OH group. Each metal ion has a pseudo-octahedral *trans*-$MN_4O_2$ environment with four nitrogen atoms from four different organic ligands and two oxygen atoms from two water molecules in compounds **1** and **2** and from the OH group of the cyanocarbanion ligand in compounds **3** and **4**. These coordination modes give rise to 1D, 2D and 3D arrangements for compounds **1**, **2** and **3**–**4**, respectively. Magnetic measurements show weak antiferromagnetic coupling between metal centres in the four compounds.

(© Wiley-VCH Verlag GmbH & Co. KGaA, 69451 Weinheim, Germany, 2007)

## Introduction

Cyano carbanions and cyano azacarbanions are interesting ligands for the preparation of a large variety of discrete and extended molecular structures due to the fact that their cyano groups are disposed in such a way that they cannot coordinate to the same metal ion and that association of the π-electronic system of the nitrile groups with the π-system of the central fragment induces an electronic delocalisation that facilitates transmission of electronic effects between the metal centres (Scheme 1).[1,2]

Thus, reaction of such anions with d-block transition-metal ions leads to the isolation of a variety of new compounds displaying rich structural topological features and unusual magnetic properties;[3–16] most of them concern those involving the simplest anions such as the dicyanamide and the tricyanomethanide anions (dca$^-$ and tcm$^-$, respectively).[3–9] In this regard, binary (dca)metal and (tcm)metal complexes, $M(dca)_2$ and $M(tcm)_2$ (M = $Cr^{II}$, $Mn^{II}$, $Fe^{II}$, $Co^{II}$, $Ni^{II}$ and $Cu^{II}$), built from tricoordinate dca and tcm ligands exhibit 3D rutile-like architectures and some of them show long-range magnetic ordering, hard magnetic behaviour or spin-canted antiferromagnetism.[4,5] In addition to these binary dca and tcm compounds, a few binary examples involving sophisticated cyano carbanions and cyano azacarbanions have been reported by others and us.[11–15] Obviously, in these compounds, structural and physical properties are greatly affected by the number of donor groups and by the nature of the central fragment of the anionic ligand; we therefore find it interesting to study new ligands involving two cyano groups, as in the dca ligand, as well as one oxygen atom able to act as a donor or to participate in hydrogen bonds. Thus, using the 2,2-dicyano-1-ethoxyethenolate anion (dcne$^-$) and its methyl analogue (dcnm$^-$) (Scheme 1) led us and Kremer et al. to new compounds whose structures are built from monodimensional chains of 12-membered dimetallacycles.[11,12] These studies showed that the terminal oxygen atom does not enter in the coordination sphere of the metal ion, as the negative charge of the $[(NC)_2CC(O)OR]^-$ anion is not mainly located on this terminal oxygen atom. In an effort to increase the dimensionality of the structural arrangements as observed in the dicyanamide binary systems having a rutile-like structure, we have prepared the dcno$^-$ anion, where an $-O(CH_2)_2OH$ group replaces the –OEt group of the dcne$^-$ anion. This can affect the electronic delocalisation of the whole ligand and modify the role of the terminal oxygen atoms of the organic ligand and, therefore, its coordination mode around the metal ion. Herein, we report the syntheses, structural characterisation and magnetic properties of new polymeric compounds of formula $[M(dcno)_2(H_2O)_2]$

[a] UMR 6521 CNRS – Université de Bretagne Occidentale, B. P. 809, 29285 Brest Cedex, France
E-mail: triki@univ-brest.fr
[b] ICMol, Universidad de Valencia, Edificio Institutos de Paterna, P. O. Box 22085, 46071 Valencia, Spain
[c] UMR 6226 CNRS – Université de Rennes 1 Ave du Gal Leclerc, 35042 Rennes Cedex, France
[‡] Permanent address: Département de Chimie, Faculté des Sciences, Université Ferhat-Abbas, Sétif 19000, Algeria

 © 2007 Wiley-VCH Verlag GmbH & Co. KGaA, Weinheim 

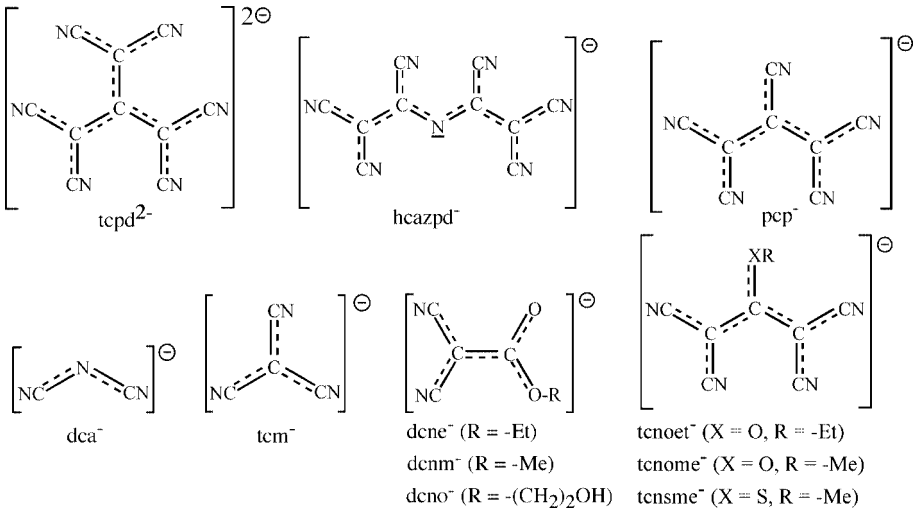


Scheme 1.

[M = $Fe^{II}$ (**1**), $Co^{II}$ (**2**)] and [M(dcno)$_2$] [M = $Cu^{II}$ (**3**), $Mn^{II}$ (**4**)] containing the bridging 2,2-dicyano-1-(2-hydroxyethoxy)ethenolate anion {dcno$^-$ = [(NC)$_2$CC(O)O(CH$_2$)$_2$-OH]$^-$}.

## Results and Discussion

### Syntheses and Characterisation

Silver 2,2-dicyano-1-(2-hydroxyethoxy)ethenolate [Ag(dcno)] was prepared by smooth hydrolysis of 2-(1,3-dioxolan-2-ylidene)malononitrile in the presence of an excess of silver nitrate; the pH of the aqueous solution (initial value: 6.5) decreased to 1.0 after boiling the solution for a few minutes in agreement with the reaction in Scheme 2. The tetraethylammonium salt was obtained as a white powder by reaction with 1 equiv. of [(C$_2$H$_5$)$_4$N]Cl. Its $^{13}$C NMR spectrum (see Experimental Section) is in good agreement with the proposed structure. However, it is worth noting the presence of a single signal for the two nonequivalent C≡N groups. This observation suggests a fast rotation, compared to the NMR detection around the central "C=C" bond resulting from an efficient electron delocalisation along the molecule induced by the presence of the two electron-withdrawing C≡N groups. Treatment of a saturated solution of Ag(dcno) with a saturated aqueous solution of the corresponding metal salt ($MCl_2 \cdot nH_2O$) in a dcno$^-$/$M^{II}$ ratio of 2 gave, after slow concentration, the new compounds [M(dcno)$_2$(H$_2$O)$_2$] [M = $Fe^{II}$ (**1**), $Co^{II}$ (**2**)] and [M(dcno)$_2$] [M = $Cu^{II}$ (**3**), $Mn^{II}$ (**4**)]. All compounds can also be prepared in the same way as the silver salt by direct reaction in aqueous solution of 2-(1,3-dioxolan-2-ylidene)-malononitrile with the corresponding transition-metal salt (Scheme 2).

The IR spectra of compounds **1**–**4** show similar patterns with two strong absorption bands assigned to $\nu_{CN}$. In agreement with the coordination of the organic ligand through its nitrile groups, these bands are slightly shifted to higher wavenumbers (2190–2260 cm$^{-1}$) than those of the corresponding tetraethylammonium salt containing the uncoordinated dcno$^-$ moiety (2169–2197 cm$^{-1}$).

### Crystal Structures

The two compounds of formula [M(dcno)$_2$(H$_2$O)$_2$] [M = $Fe^{II}$ (**1**), $Co^{II}$ (**2**)] display two different structures although generated by similar asymmetric units consisting of a metal ion and a water molecule, both on special positions [(0,–*y*,3/4) and (0,0,0) for **1** and **2**, respectively], and one dcno$^-$ organic ligand located on a general position. Each metal ion is linked to four nitrogen atoms from four organic ligands and to two symmetrically equivalent water molecules in a *trans* configuration.

In compound **1**, the coordination sphere of the metal atom can be described as a noncentrosymmetric *trans*-$FeN_4O_2$ pseudo-octahedron formed by an $FeN_4$ plane, arising from four nitrogen atoms (N1$^{(b)}$, N1$^{(c)}$, N2, N2$^{(a)}$), and two water molecules (O4 and O4$^{(a)}$) in axial positions (Figure 1). The six bond lengths are almost equivalent [ranging from 2.137(3) to 2.141(4) Å]. The structure involves 12-membered [Fe(NCCCN)$_2$Fe] dimetallacycles, as two bridging dcno$^-$ ligands connect two $Fe^{II}$ ions (Figure 1). These

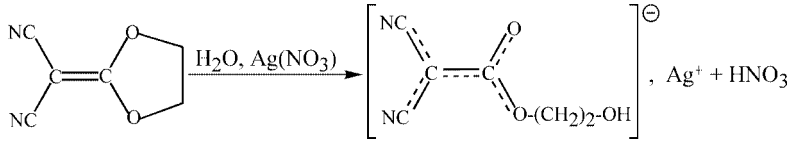


Scheme 2.

 © 2007 Wiley-VCH Verlag GmbH & Co. KGaA, Weinheim 

almost planar rings (larger deviation from the corresponding mean plane of 0.04 Å) share metal ions to give a chain of dimetallacycles running along the [010] direction (Figure 1).

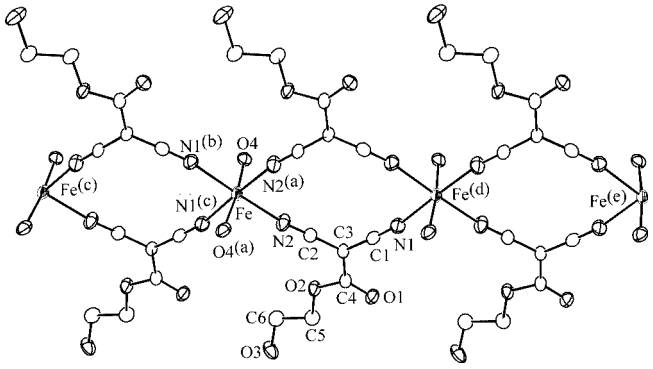


Figure 1. ORTEP perspective view of **1** (50% probability ellipsoid) showing the atom-labelling scheme, the $Fe^{II}$ environment and the 1D structure generated by the $\mu_2$-dcno ligand. Codes of equivalent positions: (a) 1 – *x*, *y*, 3/2 – *z*; (b) 1 – *x*, –1 + *y*, 3/2 – *z*; (c) *x*, –1 + *y*, *z*; (d) *x*, 1 + *y*, *z*; (e) *x*, 2 + *y*, *z*.

The intrachain Fe···Fe distance [7.450(1) Å], slightly shorter than the shortest interchain one [7.8660(6) Å], is close to that observed in the iron–dicyanamide compounds $[Fe(dca)_2(CH_3OH)_2]$[4d] and $\{[Fe(4,4'\text{-bpy})(dca)_2]\cdot bt\}$[16] (bt = 2,2′-bithiazoline) involving similar chains [7.392(1) and 7.418(1) Å, respectively].

In compound **2** each metal ion has a *trans*-$CoN_4O_2$ octahedral environment formed by four nitrogen atoms from four organic ligands (N1, $N1^{(a)}$, $N2^{(b)}$ and $N2^{(c)}$) and two equivalent water molecules (O4 and $O4^{(a)}$) (Figure 2a); this environment, essentially similar to that observed in compound **1**, is centrosymmetric here. As in **1**, the organic ligand acts in a bridging mode, with its two nitrogen atoms, N1 and N2, bound to two different cobalt ions (Figure 2a); but here the coordination mode leads to a two-dimensional structure, as the four organic ligands of one $[Co(dcno)_4]$ fragment are linked to four different $Co^{II}$ ions (Figure 2b). Thus, the two structures **1** and **2**, despite their essentially equivalent asymmetric units, display two very different molecular arrangements.

As shown in Figure 2b, the 2D layers of **2** can be described as formed by a succession of nonplanar [Co(NCCCN)Co(NCCCN)Co(NCCCN)Co(NCCCN)] cycles; these 24-membered tetrametallacycles are of course clearly different from the essentially planar 12-membered dimetallacycles described above for compound **1**. The shortest intramolecular Co···Co distance [7.929(1) Å] is shorter than that observed between the adjacent layers [8.421(1) Å]. This relatively long interlayer distance can be explained by the steric effects due to the nonplanar metallacycles, as clearly shown in Figure 2c. Careful examination of the interlayer distances reveals the presence of hydrogen bonds between the coordinated water molecule (O4) and the oxygen atom of the $-(CH_2)_2OH$ group of the $dcno^-$ ligand (O3) [O3···O4 2.81(1) Å]. This gives rise to the overall 3D structure depicted in Figure 2c.

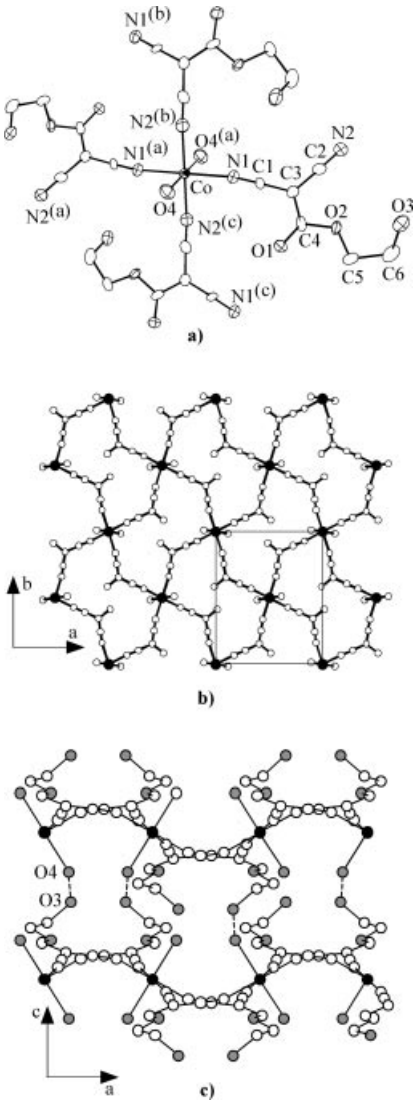


Figure 2. Structure of **2**. a) ORTEP perspective view (50% probability ellipsoid) showing the atom-labelling scheme and the $Co^{II}$ environment. Codes of equivalent positions: (a) –*x*, –*y*, –*z*; (b) –1/2 – *x*, 1/2 + *y*, *z*; and (c) 1/2 + *x*, –1/2 – *y*, –*z*. b) Two-dimensional structure in the *ab* plane; noncoordinated groups [–O and $-OCH_2CH_2OH$] omitted for clarity. c) Projection of two adjacent 2D layers in the *ac* plane showing hydrogen bonds in **2** [O3···O4 2.81(1) Å]. Shortest interlayer Co···Co distance: 8.421(1) Å.

Compounds **3** and **4** are isostructural. In both cases, the asymmetric unit contains a metal ion located on a special position (0,0,0) and a $dcno^-$ ligand on a general position (Figure 3). Each metal ion has a centrosymmetric *trans*-$MN_4O_2$ distorted octahedral environment formed by an $MN_4$ plane arising from four nitrogen atoms (N1, $N1^{(a)}$, $N2^{(c)}$ and $N2^{(e)}$) of four organic ligands, and two oxygen atoms from OH groups ($O3^{(b)}$ and $O3^{(d)}$) of two other $dcno^-$ ligands (Figure 3). Thus, in contrast to compounds **1** and **2**, here the metal ions are linked to six organic ligands.

Examination of the crystallographic data depicted in Table 1 reveals that the $Cu^{II}$ octahedral environment of compound **3** is much more distorted than that of the $Mn^{II}$

 © 2007 Wiley-VCH Verlag GmbH & Co. KGaA, Weinheim 

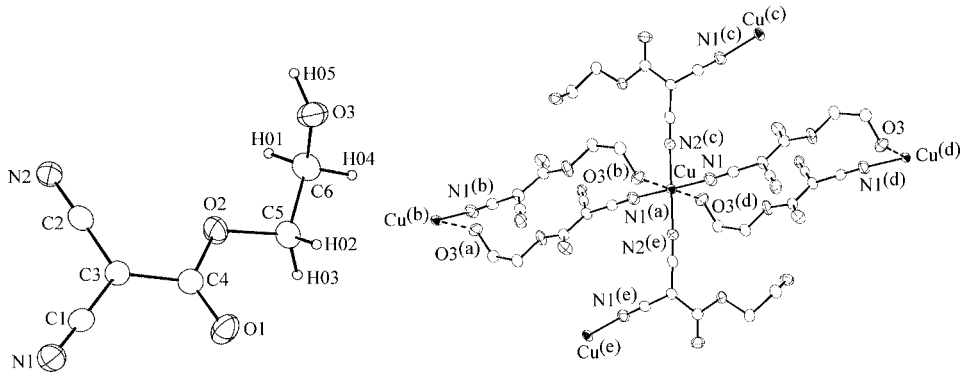


Figure 3. Structure of **3** and **4**. ORTEP view of **3** (50% probability ellipsoid) showing the atom-labelling scheme and the $Cu^{II}$ environment. M···M distances [Å] in **3**: Cu···Cu$^{(c)}$ 7.5648(4), Cu···Cu$^{(b)}$ 10.1242(4); in **4**: Mn···Mn$^{(c)}$ 7.740(5), Mn···Mn$^{(b)}$ 10.264(5). Codes of equivalent positions: (a) $-x, -y, -z$; (b) $x, y, -1 + z$; (c) $1/2 - x, -1/2 + y, 1/2 - z$; (d) $-x, -y, 1 - z$; (e) $-1/2 + x, 1/2 - y, -1/2 + z$.

ion in **4**, as the six metal–ligand bond lengths in **4** are almost equivalent [from 2.197(2) to 2.230(2) Å], while in the Cu compound **3**, the $CuN_4$ equatorial plane involves four essentially equivalent Cu–N bond lengths [1.995(2) and 1.998(2) Å], which are significantly shorter than the two axial Cu–O ones [2.359(2) Å]. These bond lengths clearly show the presence of Jahn–Teller distortions, as usually observed in octahedral $Cu^{II}$ complexes. The coordination mode of the dcno$^-$ ligand is different from that observed for compounds **1** and **2**, as, here, this ligand acts as a $\mu_3$-bridging ligand through its two nitrogen atoms (N1 and N2) and its oxygen atom (O3) of the OH group (Figure 3), leading to the overall three-dimensional structure depicted in Figure 4b.

Table 1. Selected bond lengths [Å] and bond angles [°] in compounds **1**–**4**.

| | **1** | **2** | **3** | **4** |
|---|---|---|---|---|
| M–N1 | 2.141(4) | 2.104(7) | 1.998(2) | 2.230(2) |
| M–N2 | 2.137(3) | 2.083(8) | 1.995(2) | 2.197(2) |
| M–O4 | 2.141(3) | 2.144(5) | | |
| M–O3 | | | 2.359(2) | 2.197(2) |
| N1–C1 | 1.153(5) | 1.15(1) | 1.141(3) | 1.144(2) |
| N2–C2 | 1.143(5) | 1.17(1) | 1.145(3) | 1.145(2) |
| C1–C3 | 1.393(6) | 1.39(1) | 1.408(4) | 1.409(2) |
| C2–C3 | 1.408(6) | 1.40(1) | 1.396(4) | 1.399(2) |
| C3–C4 | 1.434(6) | 1.43(1) | 1.442(4) | 1.433(2) |
| C4–O1 | 1.221(5) | 1.23(1) | 1.220(3) | 1.222(2) |
| C4–O2 | 1.345(5) | 1.345(9) | 1.334(3) | 1.346(2) |
| C5–C6 | 1.485(7) | 1.50(1) | 1.494(4) | 1.498(2) |
| C5–O2 | 1.441(5) | 1.45(1) | 1.463(3) | 1.448(2) |
| C6–O3 | 1.422(5) | 1.45(1) | 1.430(4) | 1.435(2) |
| N1–C1–C3 | 177.2(4) | 178.0(9) | 179.2(3) | 177.3(2) |
| N2–C2–C3 | 178.2(4) | 177.3(9) | 178.4(3) | 179.2(2) |
| C1–C3–C2 | 118.5(4) | 118.5(7) | 118.3(2) | 118.0(1) |
| C1–C3–C4 | 121.0(4) | 122.7(7) | 120.1(2) | 120.5(1) |
| C2–C3–C4 | 120.4(4) | 118.8(8) | 121.6(2) | 121.5(1) |
| C3–C4–O1 | 125.2(4) | 126.9(7) | 124.4(2) | 125.8(1) |
| C3–C4–O2 | 111.3(3) | 111.1(8) | 111.0(2) | 110.8(1) |
| O1–C4–O2 | 123.6(4) | 122.0(7) | 124.6(2) | 123.5(1) |
| C4–O2–C5 | 118.6(3) | 118.5(6) | 117.4(2) | 117.6(1) |
| O2–C5–C6 | 105.7(3) | 106.4(7) | 106.9(2) | 106.6(1) |
| C5–C6–O3 | 108.4(4) | 111.6(6) | 110.2(2) | 110.5(1) |
| N1–M–N1 | 88.2(1) | 180.00 | 180.00 | 180.00 |
| N1–M–N2 | 93.3(1) | 90.0(3) | 92.17(9) | 93.77(4) |
| N1–M–N2 | 177.7(1) | 90.0(3) | 87.83(9) | 86.23(4) |
| N2–M–N2 | 85.4(1) | 180.00 | 180.00 | 180.00 |
| N1–M–O4 | 87.1(1) | 88.9(3) | | |
| N1–M–O4 | 89.0(1) | 91.1(3) | | |
| N1–M–O3 | | | 90.53(9) | 90.70(5) |
| N1–M–O3 | | | 89.47(9) | 89.30(5) |
| N2–M–O4 | 94.7(1) | 90.9(3) | | |
| N2–M–O4 | 89.3(1) | 88.9(3) | | |
| N2–M–O3 | | | 90.49(8) | 91.06(4) |
| N2–M–O3 | | | 89.51(8) | 88.94(4) |
| O4–M–O4 | 174.6(1) | 180.00 | | |
| O3–M–O3 | | | 180.00 | 180.00 |

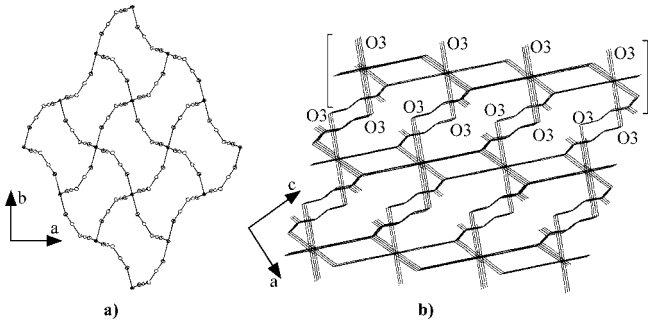


Figure 4. Sophisticated three-dimensional structure of **3** and **4**. a) 2D motif generated by the $C(CN)_2$ fragment in **3**; –C(O)($OCH_2$-$CH_2OH$) group of the dcno$^-$ ligand omitted for clarity. b) 3D structure of **3** showing the 2D motifs linked through the OH group (O3 atom) of the dcno$^-$ ligand.

The shortest $M^{II}$···$M^{II}$ distance through the dcno$^-$ ligand corresponds to that observed between two metal ions linked by the $C(CN)_2$ fragment [Cu···Cu$^{(c)}$ 7.5648(4) Å; Mn···Mn$^{(c)}$ 7.740(5) Å]; whereas the $M^{II}$···$M^{II}$ distance observed through the $NCCCO(CH_2)_2OH$ fragment (see Figure 3) is significantly longer [Cu···Cu$^{(b)}$ 10.1242(4) Å; Mn···Mn$^{(b)}$ 10.264(5) Å] (Figure 4b). It is worth noting that the best way to describe this complicated 3D molecular arrangement is to consider the 2D elemental unit generated by the $\mu_2$-$C(CN)_2$ fragment as shown in Figure 4a. These layers are connected to each other through the $M^{II}$–O3 bridges leading to the 3D structure of **3** and **4**.

Examination of bond lengths and bond angles clearly shows that the crystallographic parameters of the dcno$^-$ ligand are not significantly different in compounds **1**–**4** (Table 1 and Figure 3). With the exception of the

 © 2007 Wiley-VCH Verlag GmbH & Co. KGaA, Weinheim 

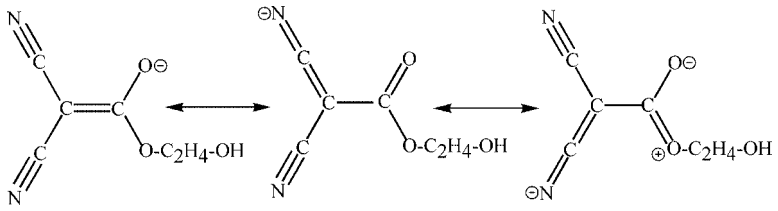

Scheme 3.

"–$CH_2CH_2OH$" group, the organic ligand is essentially planar within a maximum deviation of 0.06 Å from the corresponding mean plane. This is in agreement with an $sp^2$ hybridisation of the two central carbon atoms (C3 and C4), also shown by the bond angles around these atoms in each compound (sums of bond angles around C3 and C4 range from 359.9 to 360.1°), associated with an sp hybridisation of the carbon atoms of the cyano groups. Crystallographic data depicted in Table 1 for these compounds clearly show that the cyanocarbanion ligand includes a highly delocalised conjugated system. The electronic delocalisation is clearly shown by (i) a rather short terminal C4–O1 bond (1.22–1.23 Å) that strongly deviates from a normal C–O single bond (1.50 Å); (ii) a central C3–C4 bond (1.43–1.44 Å) longer than a normal C=C double bond (1.34 Å) [this low double-bond character is in good agreement with the $^{13}C$ NMR spectrum, as only a single signal was observed for the two C≡N groups of the free dcno$^-$ anion (see Experimental Section)]; and (iii) two C–CN bonds (1.39–1.41 Å) and a C4–O2 bond (1.33–1.35 Å), all presenting some multiple character. These observations indicate that the bonding in the dcno$^-$ ligand cannot be explained by a simple Lewis structure; this organic ligand must be considered as a resonance hybrid of different canonical structures (Scheme 3).

These canonical forms, and their symmetrical ones (not shown in Scheme 3), give rise to the mean electronic structure of Scheme 4, in agreement with the planarity of the $[(NC)_2CC(O)O]$ group and with the structural data (Table 1). Thus, it is clear that in this ligand the negative charge is not mainly located on the terminal oxygen atom and therefore, as also observed in the dcne$^-$ anion (Scheme 1),[11] it is not surprising that this atom does not enter in the coordination sphere of the metal ion.

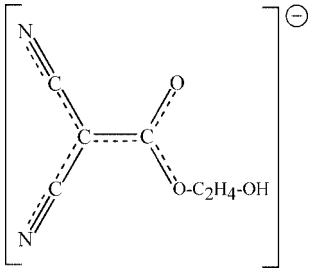

Scheme 4.

## Magnetic Properties

The thermal variation of the product of the molar susceptibility times the temperature ($\chi_M T$) for compound **1** shows a room-temperature value of 3.2 emu K mol$^{-1}$. When cooling down, $\chi_M T$ remains constant to about 30 K, where a progressive decrease is observed, to reach a value of about 0.6 emu K mol$^{-1}$ at 2 K (Figure 5).

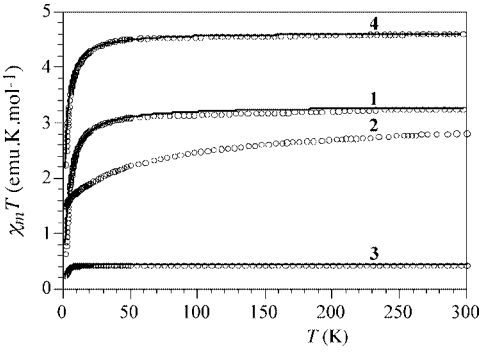


Figure 5. Thermal variation of $\chi_M T$ for compounds **1**–**4**. Solid lines represent the best fit to the models (see text).

Compound **2** shows a room-temperature $\chi_M T$ value of 2.8 emu K mol$^{-1}$ and a continuous decrease when the temperature is lowered, reaching a value of about 1.5 emu K mol$^{-1}$ at 2 K (Figure 5).

Finally, compounds **3** and **4** show a similar behaviour to that of compound **1**: they present room-temperature $\chi_M T$ values of 0.4 and 4.6 emu K mol$^{-1}$, respectively, which remain constant down to about 15 K (for **3**) and about 50 K (for **4**), where a progressive decrease is observed in both compounds, reaching values at 2 K of 0.2 and 2.2 emu K mol$^{-1}$, respectively. In compounds **1**, **3** and **4** the room-temperature $\chi_M T$ values are very close to the expected ones for high-spin $Fe^{II}$ ($S$ = 2), $Cu^{II}$ ($S$ = 1/2) and $Mn^{II}$ ($S$ = 5/2) ions with spin-only contribution (3.0, 0.375 and 4.375 emu K mol$^{-1}$, respectively). In compound **2**, the $\chi_M T$ value (2.8 emu K mol$^{-1}$) is in the range of the observed values for high-spin octahedral monomeric $Co^{II}$ ions (2.7–3.4 emu K mol$^{-1}$), where a significant orbital contribution is expected due to its orbitally degenerated $^4T_{1g}$ ground state.[17] The decrease observed at high temperatures in compound **2** is due to the presence of spin-orbit coupling, as expected for paramagnetic $Co^{II}$ compounds.[18] In compounds **1**, **3** and **4**, the decrease observed in $\chi_M T$ at low temperatures can be attributed to the presence of weak, although noticeable, antiferromagnetic interactions. Note that for compounds **1** and **4** we cannot exclude the presence of a zero-field splitting (ZFS), which may also account for the decrease observed in $\chi_M T$ at low temperatures. Note also that the decrease observed in compound **3** (where no ZFS is to be expected) and the structural similarities in all

 © 2007 Wiley-VCH Verlag GmbH & Co. KGaA, Weinheim 

compounds (same kind of –NC–C–CN– bridges between metal centres) indicate that the ZFS cannot be the only reason for the decrease in $\chi_M T$ at low temperatures and, therefore, that there must be a weak antiferromagnetic coupling in all cases. Furthermore, although the attempts to fit the $\chi_M T$ product for compounds **1** and **4** to isolated monomers with ZFS satisfactorily reproduce the magnetic properties in the whole temperature range, the $|D|$ values obtained are unrealistically high (above 16 and 10 K for **1** and **4**, respectively), confirming the presence of a weak, although not negligible, antiferromagnetic coupling.

From the structural data that show the presence of a chain of dimetallacycles in compound **1**, we have reproduced the magnetic behaviour of **1** with the model derived by Fisher for a regular antiferromagnetic chain (with $S$ = 2 in compound **1**);[19] $N$ is the Avogadro number, $k$ is the Boltzmann constant and $\beta$ is the Bohr magneton.

$$\chi_M = \frac{Ng^2\beta^2 S(S+1)}{3kT}\left[\frac{1+u}{1-u}\right], \text{ where } u = \coth\left[\frac{JS(S+1)}{kT}\right] - \left[\frac{kT}{JS(S+1)}\right]$$

This model very satisfactorily reproduces the magnetic behaviour of compound **1** in the whole temperature range (solid line in Figure 5) with $g$ = 2.094(3) and $J$ = –0.78(1) K = –0.54(1) cm$^{-1}$ (the Hamiltonian is written as $H = -J\,\Sigma S_i S_{i+1}$).

In compounds **3** and **4** the structure shows the presence of a 2D lattice with identical exchange pathways (NC–C–CN) in the two directions and an extra connection through a very long NCCC(O)$(CH_2)_2$OH bridge. In a first approximation we can consider that the magnetic exchange is mainly due to the shorter NC–C–CN bridges and, accordingly, we have used the antiferromagnetic square 2D model (Quadratic Layer Antiferromagnet) proposed by Lines[20] to reproduce the magnetic data of these compounds:

$$\chi_M = \frac{Ng^2\beta^2}{J}\left(3\theta + \sum_n \frac{C_n}{\theta^{n-1}}\right)^{-1}, \text{ where } \theta = \frac{kT}{JS(S+1)}$$

The six first $C_n$ coefficients are: 4.0, 2.667, 1.185, 0.149, –0.191 and 0.001 for $S$ = 1/2 (compound **3**) and 4.0, 1.448, 0.228, 0.262, 0.119 and 0.017 for $S$ = 5/2 (compound **4**). This model very satisfactorily reproduces the magnetic behaviour of compounds **3** and **4** in the whole temperature range (solid lines in Figure 5) with $g$ = 2.195(3) and $J$ = –0.92(3) K = –0.64(2) cm$^{-1}$ for **3** and $g$ = 2.054(1) and $J$ = –0.128(1) K = –0.089(1) cm$^{-1}$ for **4** (the Hamiltonian is written as $H = -J\,\Sigma S_i S_j$).

These results indicate that the antiferromagnetic coupling is very weak in the three compounds, as expected from the presence of identical M–NC–C–CN–M bridges, and that the long bridges present in the structures of compounds **3** and **4** do not play an important role in the magnetic interactions. Furthermore, the $J$ values are very similar to those obtained in the related family of compounds $[M(dcne)_2(H_2O)_2]$ and $[Cu(dcne)_2(H_2O)]$, where similar NC–C–CN bridges are present.[11] An additional confirmation of the weak antiferromagnetic interactions in the four compounds is provided by the isothermal magnetisation measurements at 2 K. These measurements show in each case a behaviour close to that expected for isolated magnetic centres and can be well reproduced with the Brillouin function but with lower $g$ values due to the non-negligible population of the $S$ = 0 ground state, confirming the presence of antiferromagnetic exchange interactions in all compounds.

## Conclusions

This study involves the design of multidimensional transition-metal compounds with dcno$^-$ cyano carbanion acting as $\mu_2$- and $\mu_3$-bridging ligand. Previous work showed that reactions of the $[(NC)_2CC(O)(OR)]^-$ ligands (dcnm$^-$ for R = Me and dcne$^-$ for R = Et) with transition-metal ions afford 1D coordination polymers resulting from coordination of both ligands by their two nitrile groups.[11,12] A slight modification of the alkyl group leads us to the dnco$^-$ anion, for which the coordination modes in its metal ion binary systems strongly differ from those observed in the corresponding (dcnm)M and (dcne)M systems. However, as observed in the dcne$^-$ coordination polymers,[11] the highly conjugated $[(NC)_2CC(O)O]$ group of the organic ligand precludes any localisation of the negative charge on the terminal oxygen atom and, therefore, its coordination to the metal centres. Thus, in the compounds $[M(dcno)_2(H_2O)_2]$ [M = Fe$^{II}$ (**1**), Co$^{II}$ (**2**)], this anion acts as a $\mu_2$ ligand, leading to 1D and 2D molecular arrangements respectively, while in the binary systems $[M(dcno)_2]$ [M = Cu$^{II}$ (**3**), Mn$^{II}$ (**4**)] with the 3D networks, this anion acts as a $\mu_3$ bridging ligand. This clearly illustrates the bonding affinity and flexibility of the cyanocarbanion ligand towards transition-metal ions. These unexpected structural differences can be partially explained by the less restricting coordination preferences of Cu$^{II}$ (due to Jahn–Teller distortions) and Mn$^{II}$ (due to its larger ionic radius). In contrast, in compounds **1** and **2** the dcno$^-$ ligand is not flexible enough to link the Fe$^{II}$ and the Co$^{II}$ ions through its terminal OH group (O3) as the metal–oxygen bonds should be shorter than the corresponding ones observed (and expected) for the Mn$^{II}$ and Cu$^{II}$ compounds [M–O distances observed in **1**–**4**: 2.141(3), 2.144(5), 2.359(2) and 2.197(2) Å, respectively]. This lack of flexibility induces the presence of water molecules in axial positions, leading to materials with low dimensionalities. In an effort to facilitate formation of 3D systems, syntheses of new parent cyanocarbanion ligands involving more flexible groups such as –O$(CH_2)_n$OH ($n$ = 3, 4, …) are in progress.

## Experimental Section

**General:** All reactions were performed under aerobic conditions. The reagents $AgNO_3$, $MnCl_2{\cdot}4H_2O$, $FeCl_2{\cdot}4H_2O$, $CoCl_2{\cdot}6H_2O$ and $CuCl_2{\cdot}2H_2O$ were purchased from commercial sources and used as received. 2-(1,3-Dioxolan-2-ylidene)malononitrile was prepared according to ref.[1g] IR spectra were recorded in the range 4000–200 cm$^{-1}$ as KBr pellets with an FTIR NEXUS NICOLET Spectrometer. NMR spectra were recorded with a Bruker AMX 400 MHz instrument. Elemental analyses were obtained from the Service de microanalyses, CNRS, Gif sur Yvette, France. The mag-

 © 2007 Wiley-VCH Verlag GmbH & Co. KGaA, Weinheim 

netic studies were carried out on powder samples enclosed in medical caps. The magnetic susceptibility measurements were performed at 0.1 T, in the temperature range 2–300 K, with a SQUID magnetometer MPMS-XL-5 from Quantum Design. The molar susceptibility was corrected from the sample holder and diamagnetic contributions of all atoms (Pascal's tables).

**Synthesis of the Silver Salt of 2,2-Dicyano-1-(2-hydroxyethoxy)-ethenolate [Ag(dcno)]:** Silver 2,2-dicyano-1-(2-hydroxyethoxy)-ethenolate [Ag(dcno)] was prepared by smooth hydrolysis of 2-(1,3-dioxolan-2-ylidene)malononitrile in the presence of an excess of silver nitrate; the pH of the aqueous solution (initial value: 6.5) decreased to 1.0 after boiling the solution for a few minutes. An excess of $AgNO_3$ (4.077 g, 24 mmol) was added to a hot aqueous solution (30 mL) of 2-(1,3-dioxolan-2-ylidene)malononitrile (1.633 g, 12 mmol). The solution was stirred and heated until the solid dissolved. Slow concentration of the resulting solution at room temperature gave crystals of silver 2,2-dicyano-1-(2-hydroxyethoxy)-ethenolate as white needles (58% yield). $C_6H_5AgN_2O_3$ (260.99): calcd. C 27.6, H 1.9, Ag 41.3, N 10.7; found C 27.9, H 1.9, Ag 40.9, N 10.6. IR (KBr): $\tilde{\nu}$ = 3451 br, 2963 m, 2204 s, 2177 s, 1803 s, 1777 s, 1642 s, 1480 w, 1385 s, 1319 s, 1181 m, 1134 s, 1079 s, 975 m, 901 m, 824 m, 777 m, 755 m, 719 m, 553 m $cm^{-1}$. Because of the low solubility of this salt in most organic solvents, we prepared, by metathesis, its tetraethylammonium homologue by reaction of [Ag(dcno)] with 1 equiv. of $[(C_2H_5)_4N]Cl$ in $CH_3CN$ in order to record the NMR spectrum and perform the IR study of the noncoordinated $dcno^-$ anion. IR (KBr): $\tilde{\nu}$ = 3456 br, 2988 s, 2952 m, 2396 w, 2197 s, 2169 s, 1802 s, 1776 s, 1649 s, 1396 br, 1173 s, 1125 s, 1076 s, 1033 w, 1002 s, 974 w, 894 m, 825 m, 787 s, 756 m, 717 w, 555 m $cm^{-1}$. $^{13}C$ NMR ([D$_6$]acetone): $\delta$ = 170 [C(O)O], 123.7 (CN), 72.9 ($CH_2$), 65.4 ($CH_2$), 46.7 [$C(CN)_2$; 52.6, 7.4 $(C_2H_5)_4N$] ppm.

**Syntheses of $[M(dcno)_2(H_2O)_2]$ [M = $Fe^{II}$ (1), $Co^{II}$ (2)] and $[M(dcno)_2]$ [M = $Cu^{II}$ (3), $Mn^{II}$ (4)]:** The four compounds were prepared in the same way by treating aqueous solutions (10 mL) of the corresponding metal chloride (1 mmol) with aqueous solutions (15 mL) of silver 2,2-dicyano-1-(2-hydroxyethoxy)ethenolate (2 mmol, 0.384 g). The samples were stirred at room temperature for about 30 min and left to stand. Slow concentration of the resulting solutions at room temperature gave prismatic crystals for compounds **1**–**4** that were filtered and air-dried. All compounds were satisfactory analysed for C, H and N. All compounds can also be prepared in the same way as the silver salts by direct reaction in aqueous solution of 2-(1,3-dioxolan-2-ylidene)malononitrile with the corresponding transition-metal salt, but this procedure does not allow the isolation of the pure $dcno^-$ anion as the starting ligand and yields less pure compounds **1**–**4**, as the hydrolysis of the precursor is not complete.

**1:** Yield: 0.219 g (55%). $C_{12}H_{14}FeN_4O_8$ (398.11): calcd. C 36.2, H 3.5, N 14.1; found C 35.9, H 3.7, N 14.3. IR (KBr): $\tilde{\nu}$ = 3411 br, 3075 br, 2231 s, 2191 s, 1656 s, 1487 w, 1383 s, 1359 m, 1334 m, 1310 s, 1280 m, 1158 s, 1070 m, 1043 s, 986 w, 849 m, 815 m, 749 s, 585 w, 563 m $cm^{-1}$.

**2:** Yield: 0.233 g (58%). $C_{12}H_{14}CoN_4O_8$ (401.20): calcd. C 35.9, H 3.5, N 14.0; found C 35.6, H 3.6, N 14.3. IR (KBr): $\tilde{\nu}$ = 3411 br, 2250 s, 2215 s, 1623 s, 1457 w, 1437 w, 1392 m, 1326 s, 1284 m, 1265 w, 1171 s, 1075 m, 1013 w, 900 w, 758 w, 668 w, 553 w $cm^{-1}$.

**3:** Yield: 0.288 g (78%). $C_{12}H_{10}CuN_4O_6$ (369.78): calcd. C 39.0, H 2.7, N 15.2; found C 38.6, H 2.8, N 15.5. IR (KBr): $\tilde{\nu}$ = 3315 br, 2252 s, 2199 s, 1646 s, 1478 m, 1406 m, 1374 s, 1328 s, 1282 s, 1145 s, 1022 m, 810 w, 754 s, 556 s, 493 w, 431 m, 386 m $cm^{-1}$.

**4:** Yield: 0.173 g (48%). $C_{12}H_{10}MnN_4O_6$ (361.18): calcd. C 39.9, H 2.8, N 15.5; found C 40.3, H 2.6, N 15.2. IR (KBr): $\tilde{\nu}$ = 3401 br, 2232 s, 2196 s, 1650 s, 1615 s, 1460 m, 1400 s, 1383 m, 1285 w, 1229 w, 1160 s, 1087 m, 1070 m, 1020 w, 902 m, 758 m, 640 w, 558 m $cm^{-1}$.

**X-ray Crystallography:** Data for compounds **1**–**3** were collected with an Xcalibur 2 diffractometer (Oxford Diffraction) at room temperature (294 K for **1** and **2** and 288 K for **3**). The three structures were solved by direct methods and successive Fourier difference syntheses, and were refined, on *F*, by weighted anisotropic full-matrix least-squares methods.[21] The hydrogen atoms were located by difference Fourier map, except those of the "$CH_2$–$CH_2$" group of the $dcno^-$ ligand in **1** and **2**, which were calculated [*d*(C–H) = 0.95 Å]; the thermal parameters were taken as $U_{iso} = 1.3U_{equ}(C)$ and therefore included as isotropic fixed contributors to $F_c$. Note

Table 2. Crystallographic data and structural refinement parameters for compounds **1**–**4**.

| | **1** | **2** | **3** | **4** |
|---|---|---|---|---|
| Empirical formula[a] | $C_{12}H_{14}FeN_4O_8$ | $C_{12}H_{14}CoN_4O_8$ | $C_{12}H_{10}CuN_4O_6$ | $C_{12}H_{10}MnN_4O_6$ |
| Formula mass[a] | 398.11 | 401.20 | 369.78 | 361.18 |
| $T$ [K] | 294(2) | 294(2) | 288(2) | 293(2) |
| Crystal system | monoclinic | orthorhombic | monoclinic | monoclinic |
| Space group | *C*2/*c* | *Pbca* | $P2_1/n$ | $P2_1/n$ |
| $a$ [Å] | 13.856(1) | 9.952(1) | 8.0521(3) | 7.917(1) |
| $b$ [Å] | 7.450(1) | 12.346(1) | 8.9499(3) | 9.114(2) |
| $c$ [Å] | 16.054(1) | 13.587(1) | 10.1242(4) | 10.264(2) |
| $\beta$ [°] | 93.9(1) | | 96.5(1) | 94.05(1) |
| $V$ [Å$^3$] | 1653.5 | 1669.3 | 724.9 | 738.8 |
| $D_{calcd.}$ [g cm$^{-3}$] | 1.60 | 1.60 | 1.69 | 1.62 |
| $Z$[a] | 4 | 4 | 2 | 2 |
| $\mu$ [cm$^{-1}$] | 9.57 | 10.71 | 15.44 | 9.31 |
| Unique reflections/$R_{int}$ | 1745/0.052 | 1315/0.081 | 1995/0.03 | 14908 |
| Reflections [$I > n\sigma(I)$] | 909 ($n$ = 2) | 532 ($n$ = 1.2) | 1166 ($n$ = 3) | 14908 ($n$ = 2) |
| $N_v$ | 126 | 115 | 106 | 127 |
| $R$[b] | 0.045 | 0.052 | 0.033 | 0.051 |
| $R_w$[c] | 0.048 ($F_o$) | 0.056 ($F_o$) | 0.037 ($F_o$) | 0.152 ($F_o^2$) |
| Gof[d] | 0.995 | 0.989 | 1.007 | 1.129 |
| $\Delta\rho_{max}/\Delta\rho_{min}$ [e Å$^{-3}$] | +0.130/–0.239 | +0.611/–0.513 | +0.295/–0.600 | +0.380/–0.287 |

[a] For all compounds the asymmetric unit contains 0.5 of the empirical formula. [b] $R = \Sigma||F_o| - |F_c||/\Sigma|F_o|$. [c] $R_w(F_o) = \{\Sigma[w(F_o - F_c)^2]/\Sigma[w(F_o)^2]\}^{1/2}$; $R_w(F_o) = wR_2 = \{\Sigma[w(F_o^2 - F_c^2)^2]/\Sigma[w(F_o^2)^2]\}^{1/2}$. [d] Gof = $S = \{\Sigma[w(F_o^2 - F_c^2)^2]/(N_{obs} - N_{var})\}^{1/2}$.

 © 2007 Wiley-VCH Verlag GmbH & Co. KGaA, Weinheim 

that the hydrogen atoms of the water molecule and of the terminal "OH" group of the dcno⁻ ligand in **2** were not calculated. It is noteworthy that it was difficult to collect correct X-ray data for compounds **1** and **2** because of their low diffracting power, essentially because of the low dimensions of the single crystals. However, the corresponding bond lengths and bond angles (see Table 1) are relatively correct, as they are in the normal range when compared to their corresponding values observed in the parent compounds **3** and **4**. For **4**, no pure single crystal was found. φ-χ scans performed on the KCCD diffractometer at 288 K and combined with the use of DIRAX program[22,23] revealed the existence of two misaligned crystal components with identical unit-cell parameters. Finally, the collected frames were integrated using the EVAL program considering both orientation matrices.[24] An HKLF5 file for the SHELX refinement program was created with a list of integrated intensities for the two observed contributors. For all integrated reflections, a reflection index specifying the quality of the reflection (pure #1, pure #2 or common reflection) was given. The structure was then solved by direct methods and successive Fourier difference syntheses, and was refined, on $F^2$, by weighted anisotropic full-matrix least-squares methods.[25] All the hydrogen atoms were located by difference Fourier map and were refined isotropically. In the least-square refinement procedure, a supplementary parameter defining the fractional contribution of the second component was refined. Note that because of the bicrystalline character of the studied object, the $R_{int}$ parameter has no significance and so is not calculated by the refinement program. Scattering factors and corrections for anomalous dispersion were taken from the International Tables for X-ray Crystallography.[26] The thermal ellipsoid drawings were created with the ORTEP program.[27] Selected bond lengths and bond angles are listed in Table 1. Pertinent crystal data are mentioned in Table 2. CCDC-604823 to -604826 (for **1**–**4**, respectively) contain the supplementary crystallographic data for this paper. These data can be obtained free of charge from the Cambridge Crystallographic Data Centre via www.ccdc.cam.ac.uk/data_request/cif.

## Acknowledgments

The authors gratefully acknowledge the Centre National de la Recherche Scientifique (CNRS) and the framework of a French–Spanish Integrated Action (PICASSO 2005/No. 07137XK and HF2003-258) for financial support. F. S. thanks the "Agence Universitaire pour la Francophonie" for a postdoctoral grant.

[1] a) O. W. Webster, W. Mahler, R. E. Benson, *J. Am. Chem. Soc.* **1962**, *84*, 3678–3684; b) L. R. Melby, R. J. Harder, W. R. Hertler, W. Mahler, R. E. Benson, W. E. Mochel, *J. Am. Chem. Soc.* **1962**, *84*, 3374–3387; c) T. L. Cairns, B. C. McKusick, *Angew. Chem.* **1961**, *73*, 520–525; d) W. J. Middleton, E. L. Little, D. D. Coffman, V. A. Engelhardt, *J. Am. Chem. Soc.* **1958**, *80*, 2775–2778; e) R. E. Merrifield, W. D. Phillips, *J. Am. Chem. Soc.* **1958**, *80*, 2778–2782; f) W. J. Middleton, R. E. Heckert, E. L. Little, C. G. Krespan, *J. Am. Chem. Soc.* **1958**, *80*, 2783–2788; g) W. J. Middleton, V. A. Engelhardt, *J. Am. Chem. Soc.* **1958**, *80*, 2788–2795; h) W. J. Middleton, E. L. Little, D. D. Coffman, V. A. Engelhardt, *J. Am. Chem. Soc.* **1958**, *80*, 2795–2809.

[2] a) K. R. Dunbar, *Angew. Chem.* **1996**, *108*, 1769–1771; *Angew. Chem. Int. Ed. Engl.* **1996**, *35*, 1659–1671; b) W. Kaim, M. Moscherosch, *Coord. Chem. Rev.* **1994**, *129*, 157–173; c) J. M. Manriquez, T. Y. Gordon, R. S. McLean, A. J. Epstein, J. S. Miller, *Science* **1991**, *252*, 1415–1417; d) R. Kato, H. Kobayashi, A. Kobayashi, *J. Am. Chem. Soc.* **1989**, *111*, 5224–5232; e) J. S. Miller, A. J. Epstein, W. M. Reiff, *Chem. Rev.* **1988**, *88*, 201–220.

[3] S. R. Batten, K. S. Murray, *Coord. Chem. Rev.* **2003**, *246*, 103–130 and references cited therein.

[4] a) M. R. Pederson, A. Y. Liu, T. Baruah, E. Z. Kurmaev, A. Moewes, S. Chiuzbaian, M. Neumann, C. R. Kmety, K. L. Stevenson, D. Ederer, *Phys. Rev. C: Nucl. Phys.* **2002**, *66*, 014446/1–014446/8; b) J. L. Manson, C. R. Kmety, F. Palacio, A. J. Epstein, J. S. Miller, *Chem. Mater.* **2001**, *13*, 1068–1073; c) C. R. Kmety, Q.-Z. Huang, J. W. Lynn, R. W. Erwin, J. L. Manson, S. McCall, J. E. Crow, K. L. Stevenson, J. S. Miller, A. J. Epstein, *Phys. Rev. B: Condens. Matter* **2000**, *62*, 5576–5588; d) S. R. Batten, P. Jensen, C. J. Kepert, M. Kurmoo, B. Moubaraki, K. S. Murray, D. J. Price, *J. Chem. Soc., Dalton Trans.* **1999**, 2987–2997; e) P. Jensen, S. R. Batten, G. D. Fallon, B. Moubaraki, K. S. Murray, D. J. Price, *Chem. Commun.* **1999**, 177–178; f) J. L. Manson, C. R. Kmety, A. J. Epstein, J. S. Miller, *Inorg. Chem.* **1999**, *38*, 2552–2553; g) S. R. Batten, P. Jensen, B. Moubaraki, K. S. Murray, R. Robson, *Chem. Commun.* **1998**, 439–440; h) M. Kurmoo, C. J. Kepert, *New J. Chem.* **1998**, *22*, 1515–1524; i) J. L. Manson, C. R. Kmety, Q. Z. Huang, J. W. Lynn, G. M. Bendele, S. Pagola, P. W. Stephens, L. M. Liable-Sands, A. L. Rheingold, A. J. Epstein, J. S. Miller, *Chem. Mater.* **1998**, *10*, 2552–2560.

[5] a) R. Feyerherm, A. Loose, J. L. Manson, *J. Phys.: Condens. Matter* **2003**, *15*, 663–673; b) J. L. Manson, E. Ressouche, J. S. Miller, *Inorg. Chem.* **2000**, *39*, 1135–1141; c) S. R. Batten, B. F. Hoskins, B. Moubaraki, K. S. Murray, R. Robson, *J. Chem. Soc., Dalton Trans.* **1999**, 2977–2986; d) H. Oshino, K. Iida, T. Kawamoto, T. Mori, *Inorg. Chem.* **1999**, *38*, 4229–4232; e) J. L. Manson, C. Campana, J. S. Miller, *Chem. Commun.* **1998**, 251–252; f) S. R. Batten, B. F. Hoskins, R. Robson, *New J. Chem.* **1998**, *22*, 173–175.

[6] P. Jensen, D. J. Price, S. R. Batten, B. Moubaraki, K. S. Murray, *Chem. Eur. J.* **2000**, *6*, 3186–3195.

[7] a) J. A. Schlueter, J. L. Manson, K. A. Hyzer, U. Geiser, *Inorg. Chem.* **2004**, *43*, 4100–4102; b) P. M. van der Werff, S. R. Batten, P. Jensen, B. Moubaraki, K. S. Murray, E. H. K. Tan, *Polyhedron* **2001**, *20*, 1129–1138; c) J. W. Raebiger, J. L. Manson, R. D. Sommer, U. Geiser, A. L. Rheingold, J. S. Miller, *Inorg. Chem.* **2001**, *40*, 2578–2581; d) P. M. van der Werff, S. R. Batten, P. Jensen, B. Moubaraki, K. S. Murray, *Inorg. Chem.* **2001**, *40*, 1718–1722; e) S. R. Batten, P. Jensen, B. Moubaraki, K. S. Murray, *Chem. Commun.* **2000**, 2331–2332.

[8] a) S. C. Manna, A. K. Ghosh, J. Ribas, M. G. B. Drew, C.-N. Lin, E. Zangrando, N. R. Chaudhuri, *Inorg. Chim. Acta* **2006**, *359*, 1395–1403; b) L. F. Jones, L. O'Dea, D. A. Offermann, P. Jensen, B. Moubaraki, K. S. Murray, *Polyhedron* **2006**, *25*, 360–372; c) J. Luo, Z.-H. Shao, E.-Q. Gao, C.-F. Wang, R.-F. Cai, X.-G. Zhou, *Inorg. Chem. Commun.* **2006**, *9*, 196–200; d) G.-Y. Hsu, C.-W. Chen, S.-C. Cheng, S.-H. Lin, H.-H. Wei, C.-J. Lee, *Polyhedron* **2005**, *24*, 487–494; e) C.-F. Hsu, S.-H. Lin, H.-H. Wie, *Inorg. Chem. Commun.* **2005**, *7*, 1128–1132; f) J. Luo, X.-G. Zhou, S. Gao, L.-H. Weng, Z.-H. Shao, C.-M. Zhang, Y.-R. Li, J. Zhang, R.-F. Cai, *Inorg. Chem. Commun.* **2004**, *7*, 669–672; g) J. L. Manson, J. A. Schlueter, *Inorg. Chim. Acta* **2004**, *357*, 3975–3979; h) J. L. Manson, J. A. Schlueter, H.-J. Koo, M.-H. Whangbo, *Inorg. Chem.* **2004**, *43*, 4007–4011.

[9] a) E. Colacio, I. Ben Mimoun, F. Lloret, J. Suárez-Varela, *Inorg. Chem.* **2005**, *44*, 3771–3773; b) O. V. Nesterova, S. R. Petrusenko, V. N. Kokozay, B. W. Skelton, W. Linert, *Inorg. Chem. Commun.* **2004**, *7*, 450–454; c) Z. M. Wang, B.-W. Sun, J. Luo, S. Gao, C.-S. Liao, C.-H. Yan, Y. Li, *Inorg. Chim. Acta* **2002**, *332*, 127–134.

[10] a) S. Triki, F. Thétiot, F. Vandevelde, J. Sala-Pala, C. J. Gómez-García, *Inorg. Chem.* **2005**, *44*, 4086–4093; b) F. Thétiot, S. Triki, J. Sala-Pala, S. Golhen, *Inorg. Chim. Acta* **2005**, *358*, 3277–3282; c) F. Thétiot, S. Triki, J. Sala-Pala, J. R. Galán-Mascarós, J. M. Martínez-Agudo, K. R. Dunbar, *Eur. J. Inorg.*

 © 2007 Wiley-VCH Verlag GmbH & Co. KGaA, Weinheim 

*Chem.* **2004**, 3783–3791; d) F. Thétiot, S. Triki, J. Sala-Pala, S. Golhen, *Inorg. Chim. Acta* **2003**, *350*, 314–320.
[11] F. Thétiot, S. Triki, J. Sala-Pala, C. J. Gómez-García, *J. Chem. Soc., Dalton Trans.* **2002**, 1687–1693.
[12] C. Kremer, C. Melián, J. Torres, M. P. Juanicó, C. Lamas, H. Pezaroglo, E. Manta, H. Schumann, J. Pickardt, F. Girgsdies, O. N. Ventura, F. Lloret, *Inorg. Chim. Acta* **2001**, *314*, 83–90.
[13] F. Thétiot, S. Triki, J. Sala-Pala, *Polyhedron* **2003**, *22*, 1837–1843.
[14] a) S. Triki, J. Sala-Pala, M. Decoster, P. Molinié, L. Toupet, *Angew. Chem.* **1999**, *111*, 155–158; *Angew. Chem. Int. Ed.* **1999**, *38*, 113–115; b) S. Triki, J. Sala-Pala, A. Riou, P. Molinié, *Synth. Met.* **1999**, *102*, 1472–1473.
[15] M. Decoster, J. E. Guerchais, Y. Le Mest, J. Sala-Pala, S. Triki, L. Toupet, *Polyhedron* **1996**, *15*, 195–202.
[16] A. B. Gaspar, M. C. Munoz, J. A. Real, *Inorg. Chem. Commun.* **2004**, *7*, 815–817.
[17] See, for example: R. March, W. Clegg, R. A. Coxall, L. Cucurull-Sánchez, L. Lezama, T. Rojo, P. González-Duarte, *Inorg. Chim. Acta* **2003**, *353*, 129.
[18] O. Kahn, *Molecular Magnetism*, VCH Publishers, New York, **1993**.
[19] M. E. Fisher, *Am. J. Phys.* **1964**, *32*, 343.
[20] M. E. Lines, *J. Phys. Chem. Solids* **1970**, *31*, 101.
[21] C. K. Fair, *MolEN, An Interactive Intelligent System for Crystal Structure Analysis*, User Manual, Enraf-Nonius, Delft, The Netherlands, **1985**.
[22] A. J. M. Duisenberg, R. W. W. Hooft, A. M. M. Schreurs, J. Kroon, *J. Appl. Crystallogr.* **2000**, *33*, 893–898.
[23] A. J. M. Duisenberg, *J. Appl. Crystallogr.* **1992**, *25*, 92–96.
[24] A. J. M. Duisenberg, L. M. J. Kroon-Batenburg, A. M. M. Schreurs, *J. Appl. Crystallogr.* **2003**, *36*, 220–229.
[25] G. M. Sheldrick, *SHELX97, Programs for Crystal Structure Analysis*, University of Göttingen, Göttingen, Germany, **1997**.
[26] *International Tables for X-ray Crystallography*, Kynoch Press, Birmingham, **1975**, vol. 4.
[27] C. K. Johnson, *ORTEP*, Rep. ONL-3794, Delft, The Netherlands, **1985**.

Received: May 13, 2006
Published Online: November 21, 2006

 © 2007 Wiley-VCH Verlag GmbH & Co. KGaA, Weinheim

**The EUChemSoc Societies have taken the significant step into the future by merging their traditional journals, to form two leading chemistry journals, the *European Journal of Inorganic Chemistry* and the *European Journal of Organic Chemistry.* Three further EUChemSoc Societies (Austria, Czech Republic and Sweden) are Associates of the two journals.**

## COVER PICTURE

**The cover picture shows** a water pipe (wire-frame representation in blue), constructed solely from solvent water molecules that are present in the crystal lattice of an organic–inorganic hybrid compound $[Cu_2(phen)_2(CH_3COO)(CH_3COOH)(H_2O)_2][Al(OH)_6Mo_6O_{18}]\cdot 28H_2O$. The supramolecular interactions of the water pipe with its surrounding (that includes a heteropolyanion, $[Al(OH)_6Mo_6O_{18}]^{3-}$, shown as red polyhedra and a copper dimeric complex, shown as magenta ball-and-stick models) stabilise the compound so that it can be observed crystallographically. The background depicts the unit-cell packing of the water pipes in the relevant crystal. Details are described in the Short Communication by S. K. Das et al. on p. 231ff. The artwork was designed by Ms. Sabbani Supriya.

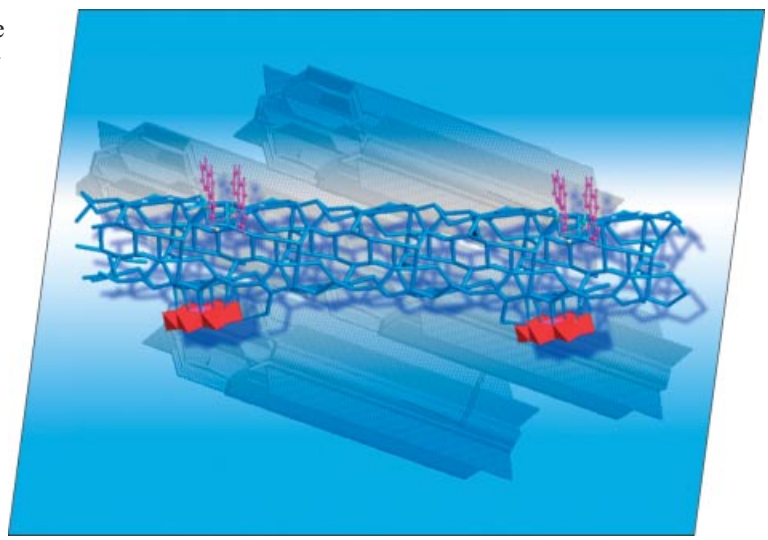

 © 2007 Wiley-VCH Verlag GmbH & Co. KGaA, Weinheim 

# CONTENTS

## MICROREVIEW


### Radical Organometallic Chemistry

**B. de Bruin,***
**D. G. H. Hetterscheid ..... 211–230**

Paramagnetic (Alkene)Rh and (Alkene)Ir Complexes: Metal or Ligand Radicals?

**Keywords:** Rhodium / Iridium / Alkene ligands / Metallo-radicals / Ligand radicals

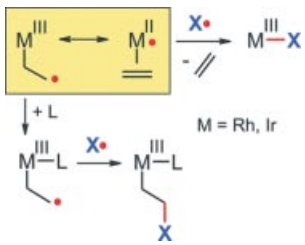


Paramagnetic alkene rhodium and iridium complexes reveal features of both metallo-radicals and ligand radicals. This dual-mode behavior is reflected by their high and diverse reactivity, as discussed in this review.


## SHORT COMMUNICATIONS


### Water Pipe in Inorganic Matrix

**V. Shivaiah, T. Chatterjee, K. Srinivasu, S. K. Das* ..... 231–234**

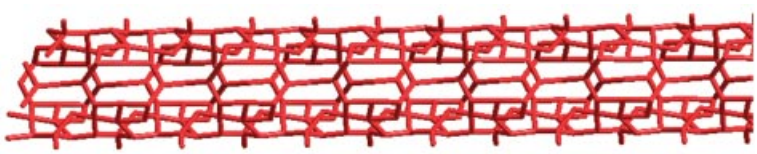

A Water Pipe Held Up by a Polyoxometalate Supported Transition Metal Complex: Synthesis and Characterization of $[Cu_2(phen)_2(CH_3COO)\text{-}(CH_3COOH)(H_2O)_2][Al(OH)_6Mo_6O_{18}]\cdot 28H_2O$

**Keywords:** Heteropolyanion / Copper acetate dimer / Crystal structure / Lattice waters / Hydrogen bonds / Supramolecular chemistry

A water pipe, shown in wire-frame representation, is constructed by hydrogen-bonding interactions solely from solvent water molecules that are present in the crystal lattice of an inorganic–organic hybrid compound, $[Cu_2(phen)_2(CH_3COO)(CH_3COOH)(H_2O)_2]\text{-}[Al(OH)_6Mo_6O_{18}]\cdot 28H_2O$. This is a unique example of a water tube, observed crystallographically in a polyoxometalate-based hybrid material.

### Linear Metal Clusters

**K. Mashima,* Y. Shimoyama, Y. Kusumi, A. Fukumoto, T. Yamagata, M. Ohashi ..... 235–238**

Formation of a Dative Bond Between $Pt^0$ and $Mo^{II}$ in Linear $Pt^0–Mo^{II}–Mo^{II}–Pt^0$ Complexes, $Mo^{II}_2Pt^0_2(pyphos)_4(PR_3)_2$, and Unique 1,4-Oxidative Addition Reaction of Diaryl Disulfides Giving $Mo^{II}_2Pt^{I}_2(pyphos)_4(SAr)_2$ (pyphos = 6-Diphenylphosphanyl-2-pyridonato)

**Keywords:** Linear clusters / Dative bonds / Oxidative addition / Thiolates / Platinum / Molybdenum

The addition of diaryl disulfides to the $Pt^0\cdots Mo^{II}$ datively bonded $Pt^0–Mo^{II}–Mo^{II}–Pt^0$ complex **4a** afforded dithiolate $Pt^I$ complexes $Mo_2Pt_2(SAr)_2(pyphos)_4$ (**5**) by 1,4-oxidative addition.


 © 2007 Wiley-VCH Verlag GmbH & Co. KGaA, Weinheim 

# FULL PAPERS

## Tetraselenide Oxidative Coupling

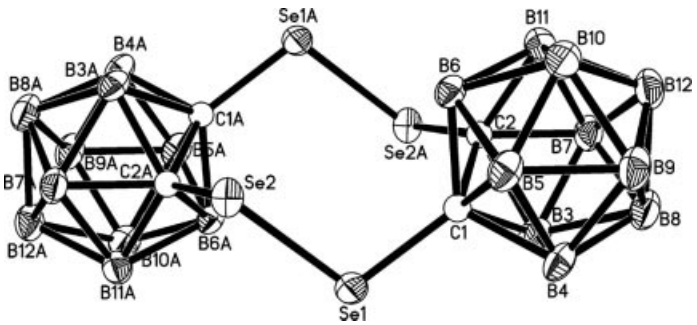


**B. Wrackmeyer,* Z. Garćia Hernández, R. Kempe, M. Herberhold ..... 239–246**

Novel 1,2-Dicarba-*closo*-dodecaborane(12) Derivatives of Selenium

**Keywords:** Carboranes / Selenium / Platinum / Oxidative addition / NMR spectroscopy

Oxidative coupling of the 1,2-diselenolato-1,2-dicarba-*closo*-dodecaborane(12) dianion gives the cyclic eight-membered bis(diselane) with annellated carborane moieties. This tetraselenide reacts with ethenebis(triphenylphosphane)platinum(0) by oxidative addition to give the platinum(II) complex, which contains the chelating 1,2-diselenolato-1,2-dicarba-*closo*-dodecaborane(12) ligand. The molecular structures of the tetraselenide and the $Pt^{II}$ complex were determined by X-ray analysis, and by $^{1}H$, $^{13}C$, $^{31}P$, $^{77}Se$ and $^{195}Pt$ NMR spectroscopy in solution.

## Multimetallic Systems

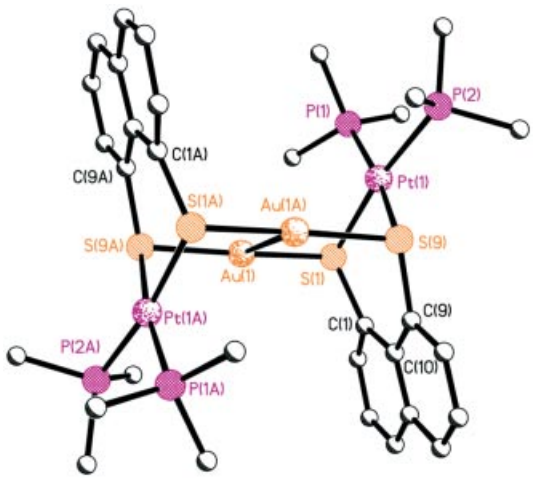


**S. D. Robertson, A. M. Z. Slawin, J. D. Woollins ..... 247–253**

Constructing Multimetallic Systems with the Naphthalene-1,8-bis(thiolato) Ligand

**Keywords:** Sulfur ligand / Multimetallic systems / Gold / Bridging ligands / X-ray structure

The construction of multimetallic systems from sulfur donor ligands can be achieved by using a simple building-block approach.

## Dissociation of P=C Ylidec Bonds

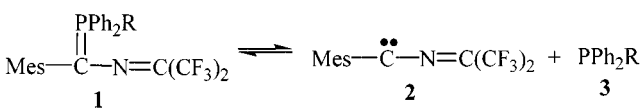


**I. Shevchenko,* A. Rogalyov, A. B. Rozhenko, G.-V. Röschenthaler ..... 254–258**

Dissociation of the P=C Ylidic Bond

**Keywords:** Ylides / Carbenes / Phosphanes / Density functional calculations

Phosphorus ylides **1** [R = Ph, $Ph_2P(O)CH_2$] in solutution undergo reversible dissociation of the P=C ylidic bond to give carbene **2** and phosphanes **3**. Carbene **2** can be trapped as carbene or as mesomeric nitrile ylide.

 © 2007 Wiley-VCH Verlag GmbH & Co. KGaA, Weinheim 

# CONTENTS


## Decomposition of Zwitterions

**I. Shevchenko,* V. Andrushko, E. Lork, G.-V. Röschenthaler* ..... 259–262**

Oxidation of Phosphanes with Orthoquinones: An Unusual Decomposition of an Unexpectedly Stable Zwitterion

**Keywords:** Ylides / Phosphanes / Zwitterions / Carbodiphosphorane

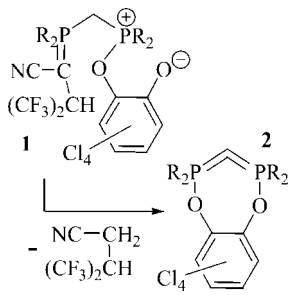


Oxidation of the appropriate phosphane with tetrachlororthobenzoquinone gives unexpectedly stable zwitterion **1** which undergoes an unusual decomposition into symmetrical carbodiphosphorane **2** and hexafluoroisovaleronitrile.

## Sarcophagines

**J. M. Harrowfield, G. A. Koutsantonis,* H.-B. Kraatz, G. L. Nealon, G. A. Orlowski, B. W. Skelton, A. H. White ..... 263–278**

Cages on Surfaces: Thiol Functionalisation of $Co^{III}$ Sarcophagine Complexes

**Keywords:** Sarcophagine / Amino acids / Disulfides / Cobalt / Self-assembled monolayers / Electrodeposition

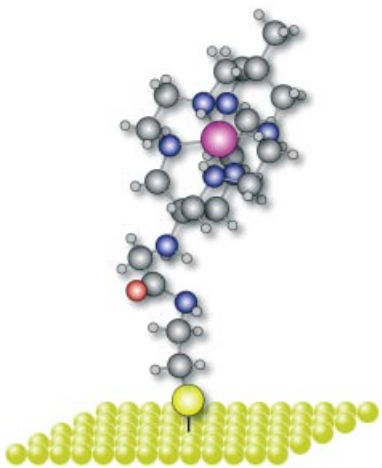

New cage cobalt complexes with oligopeptide tethers have been immobilised on Au surfaces via terminal mercaptoethylamide units. Their electrochemistry on the surface and of the untethered complexes in solution have been investigated.

## Ionic Liquids

**D. Zhao, Z. Fei, W. H. Ang, R. Scopelliti, P. J. Dyson* ..... 279–284**

Thiocyanate Functionalised Ionic Liquids: Synthesis, Characterisation and Reactivity

**Keywords:** Ionic liquids / Thiocyanate / Palladium complexes / Imidazolium salts

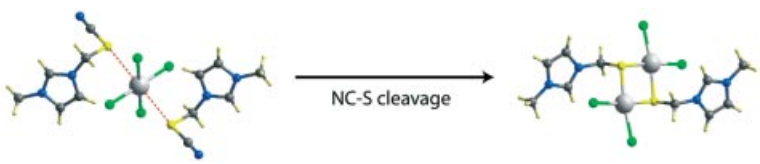


A series of novel thiocyanate functionalised ionic liquids based on the 1-thiocyanomethyl-3-methylimidazolium cation was prepared. Their solid-state structures were investigated, including their reactivity with palladium(II) chloride under acidic conditions.

## Lithium Rare Earth Polyphosphates

**J. Zhu, W.-D. Cheng,* D.-S. Wu, H. Zhang, Y.-J. Gong, H.-N. Tong, D. Zhao ..... 285–290**

A Series of Lithium Rare Earth Polyphosphates [$LiLn(PO_3)_4$] (Ln = La, Eu, Gd) and Their Structural, Optical, and Electronic Properties

**Keywords:** Density functional calculations / UV/Vis spectroscopy / Rare earths / Phosphates

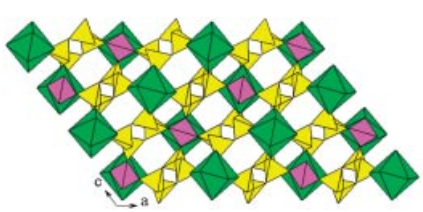

A series of lithium rare earth polyphosphates $LiLn(PO_3)_4$ (Ln = La, Eu, Gd) crystallizes in the monoclinic space group *C*2/*c* with $Z = 4$. Their unit-cell parameters decrease as the ionic radius of $Ln^{3+}$ decreases ($La^{3+} > Eu^{3+} > Gd^{3+}$). In the structure, both $(PO_4)^{3-}$ zig-zag chains and infinite chains formed by the alternative connection of $LnO_8$ polyhedra and $LiO_4$ tetrahedra run parallel to the *b*-axis.


 © 2007 Wiley-VCH Verlag GmbH & Co. KGaA, Weinheim 

## Luminescent Lanthanoid Materials

The synthesis and structural and spectroscopic charaterisation of some lanthanoid *p*-aminobenzoates and their bipyridine, 1,10-phenanthroline or terpyridine adducts are presented. Incorporation of the lanthanoid *p*-aminibenzoates into polyurethane composites and the luminescence properties of these materials are also reported.

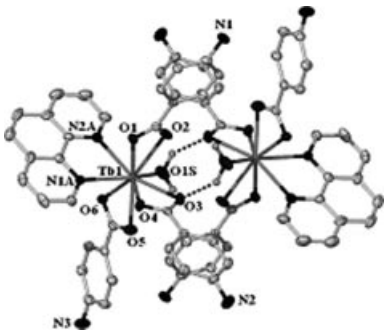


**T. Fiedler, M. Hilder, P. C. Junk,***
**U. H. Kynast, M. M. Lezhnina,***
**M. Warzala ..... 291–301**

Synthesis, Structural and Spectroscopic Studies on the Lanthanoid *p*-Aminobenzoates and Derived Optically Functional Polyurethane Composites

**Keywords:** Luminescence / Lanthanoids / Polyurethane composites / Carboxylates

## Near-Infrared Emitters

Water-soluble, stable and easily synthesizable 1:4 complexes of rare-earth ions with 8-hydroxy-5-nitroquinolinate ligands have been prepared. These complexes can be sensitized by visible light with wavelengths up to 480 nm and show near-infrared emission in aqueous solution.

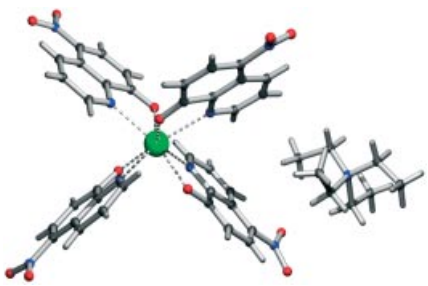

**R. Van Deun,* P. Fias, P. Nockemann,**
**K. Van Hecke, L. Van Meervelt,**
**K. Binnemans ..... 302–305**

Rare-Earth Nitroquinolinates: Visible-Light-Sensitizable Near-Infrared Emitters in Aqueous Solution

**Keywords:** Rare earth metals / Luminescence / Chelates / N,O ligands / Sensing

## Tungsten Chemistry

Phosphane oxide complexes of dioxidotungsten(VI), $[WO_2X_2(OPR_3)_2]$ (X = Cl or Br), have been prepared under anhydrous conditions from $WX_6$ and $(Me_3Si)_2O$ in $CH_2Cl_2$, followed by addition of $OPR_3$. The difluorido-dioxido complexes $[MO_2F_2(OPR_3)_2]$ (M = Mo or W) have been prepared by fluorination of the corresponding chlorido complexes with $Me_3SnF$ in $CH_2Cl_2$.

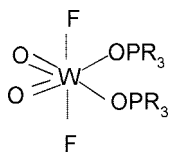


**M. F. Davis, W. Levason,* R. Ratnani,***
**G. Reid,* T. Rose, M. Webster .. 306–313**

Synthesis and Characterisation of $W^{VI}$ Complexes of Phosphane Oxide Ligands, $[WO_2X_2(OPR_3)_2]$ (X = F, Cl or Br; R = Me or Ph), and of the $[MoO_2F_2(OPR_3)_2]$

**Keywords:** Tungsten / Molybdenum / Phosphane oxide / Crystal structures / Fluoride

## Valence-State Distributions

DFT-supported experimental results suggest that the valence formulation of $[Ru(trpy)(Cl)(L^{1/2})]^+$ ($\mathbf{1}^+/\mathbf{2}^+$) can be best interpreted as spin-coupled $Ru^{III}-L_{Sq}$ with a minority contribution from the diamagnetic $Ru^{II}-L_Q$ state and the involvement of d(Ru)- and (L)-based frontier orbitals, respectively, in the successive oxidation processes and preferential involvement of Ru-based orbitals in the first reduction step.

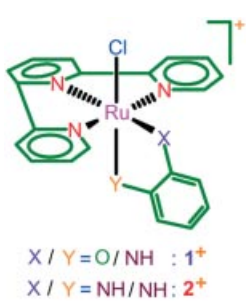


**S. Maji, S. Patra, S. Chakraborty,**
**D. Janardanan, S. M. Mobin, R. B. Sunoj,***
**G. K. Lahiri* ..... 314–323**

Valence-State Distribution in the Ruthenium *o*-Quinonoid Systems $[Ru(trpy)(Cl)(L^1)]^+$ and $[Ru(trpy)(Cl)(L^2)]^+$ ($L^1$ = *o*-Iminobenzoquinone, $L^2$ = *o*-Diiminobenzoquinone; trpy = 2,2′:6′,2′′-Terpyridine)

**Keywords:** Ruthenium / Quinonoid ligands / Valence-state distributions / Density functional calculations / Spectroelectrochemistry

 © 2007 Wiley-VCH Verlag GmbH & Co. KGaA, Weinheim 

# CONTENTS


## Chiral Discrimination

**O. Picazo, I. Alkorta,* J. Elguero, M. R. Sundberg,* J. Valo ..... 324–332**

Bonding Properties Related with Chiral Discrimination in Dinuclear Metal Complexes of Group 10

**Keywords:** Ab initio calculations / Coordination chemistry / Chiral discrimination / Bonding properties / *trans* influence

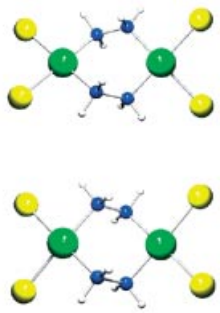

Homo- and heterochiral complexes formed by hydrazine, a metal atom of group 10, and halogen atoms have been studied by means of DFT, NBO and QTAIM methods.

## Bis(phosphonate) Complexes

**V. Kubíček,* J. Kotek, P. Hermann, I. Lukeš ..... 333–344**

Aminoalkylbis(phosphonates): Their Complexation Properties in Solution and in the Solid State

**Keywords:** Phosphonates / Complexation / Stability constants / Potentiometry

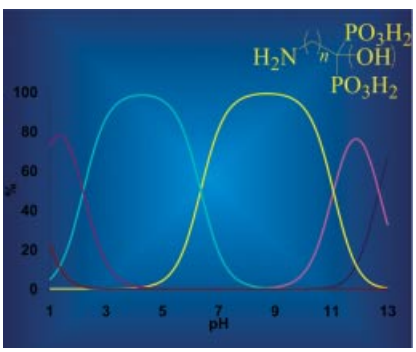


Acid–base and complexation properties of (aminoalkyl)bis(phosphonates) were studied by potentiometry. The crystal structures of the ligands, determined by X-ray diffraction analysis, show a different degree of protonation. Dimeric units of the $Cu^{2+}$ complex of pamidronate in the solid state form a coordination polymer with a short metal–metal distance.

## Functional Coordination

**Y.-P. Tian,* Y.-M. Zhu, H.-P. Zhou,* P. Wang, J.-Y. Wu, X.-T. Tao, M.-H. Jiang ..... 345–351**

Three Novel Functional $Cd^{II}$ Dicarboxylates with Nanometer Channels: Hydrothermal Synthesis, Crystal Structures, and Luminescence Properties

**Keywords:** Carboxylate / Supramolecular chemistry / Fluorescence / Coordination modes

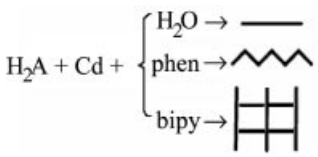


Three novel functional cadmium(II) dicarboxylates were obtained by the skilful combination of carboxylate, the other coligands and cadmium nitrate. Their luminescent properties were also changed by the coordination modes.


**If not otherwise indicated in the article, papers in issue 1 were published online on December 22, 2006**

 © 2007 Wiley-VCH Verlag GmbH & Co. KGaA, Weinheim

**The EUChemSoc Societies have taken the significant step into the future by merging their traditional journals, to form two leading chemistry journals, the *European Journal of Inorganic Chemistry* and the *European Journal of Organic Chemistry.* Three further EUChemSoc Societies (Austria, Czech Republic and Sweden) are Associates of the two journals.**

## COVER PICTURE

**The cover picture shows** a water pipe (wire-frame representation in blue), constructed solely from solvent water molecules that are present in the crystal lattice of an organic–inorganic hybrid compound $[Cu_2(phen)_2(CH_3COO)(CH_3COOH)(H_2O)_2][Al(OH)_6Mo_6O_{18}]\cdot 28H_2O$. The supramolecular interactions of the water pipe with its surrounding (that includes a heteropolyanion, $[Al(OH)_6Mo_6O_{18}]^{3-}$, shown as red polyhedra and a copper dimeric complex, shown as magenta ball-and-stick models) stabilise the compound so that it can be observed crystallographically. The background depicts the unit-cell packing of the water pipes in the relevant crystal. Details are described in the Short Communication by S. K. Das et al. on p. 231ff. The artwork was designed by Ms. Sabbani Supriya.

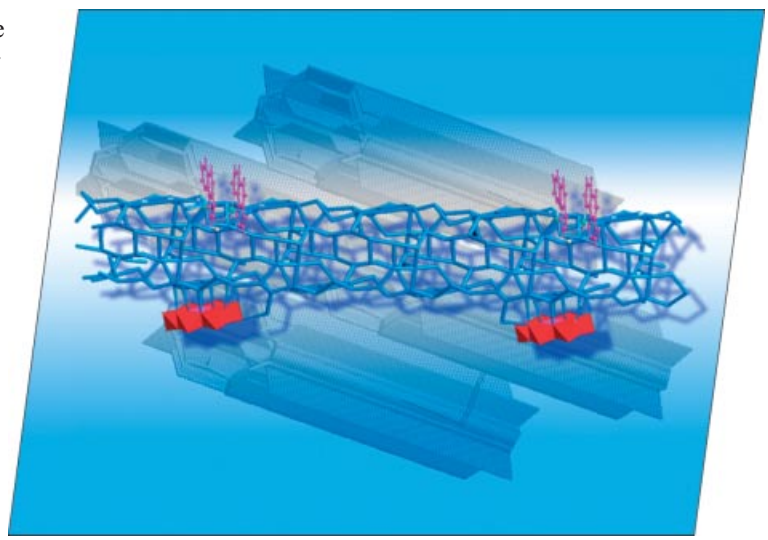

 © 2007 Wiley-VCH Verlag GmbH & Co. KGaA, Weinheim 

DOI: 10.1002/ejic.200600923

# Paramagnetic (Alkene)Rh and (Alkene)Ir Complexes: Metal or Ligand Radicals?

**Bas de Bruin*[a] and Dennis G. H. Hetterscheid[b]**

*Dedicated to Professor Karl Wieghardt on occasion of his 65th birthday*

**Keywords:** Rhodium / Iridium / Alkene ligands / Metallo-radicals / Ligand radicals

In this review a detailed overview is given of the (electronic) structure and reactivity of open-shell (paramagnetic) alkene rhodium and iridium complexes $M^x$(alkene) (M = Rh, Ir; $x$ = 0, +II). In most cases these species are highly reactive, but some notable exceptions of stable species for which not much reactivity has been described are also included (section 2). Understanding the electronic structure of the reactive nitrogen-ligand-based [$M^{II}$(por)(alkene)] and [$M^{II}$(alkene)(N-ligand)]$^{2+}$ species (section 3) is complicated by a substantial spin distribution over the metal and the alkene ligand. This dual-mode metallo-radical and ligand radical behavior is reflected by their high and diverse reactivity. Metallo-radical character is demonstrated by a variety of metal-to-radical coupling reactions with a series of other radicals, as well as metal-based allylic hydrogen atom abstractions from $M^{II}$(α-alkene) species. On the other hand, (donor induced) ligand radical character is crucial in a variety of M–C and C–C radical coupling reactions, C–O bond formation by oxygenation of $M^{II}$(alkene) species and alkene "insertions" into (por)M–H bonds. The review concludes with some speculations about possible roles of paramagnetic M(olefin) (M = Rh, Ir) species in catalytic olefin oxygenation and carbene transfer reactions.

(© Wiley-VCH Verlag GmbH & Co. KGaA, 69451 Weinheim, Germany, 2007)

## 1. Introduction

Our understanding of Rh and Ir organometallic chemistry is mainly based on studies of diamagnetic complexes in homogeneous solutions. Much less is known of the structure, reactivity and physical properties of their *paramagnetic* analogs. Interest in the properties and reactivity of such open-shell organometallic species is however rising.[1] This is triggered by the idea that such species might reveal special reactivity patterns, perhaps even as crucial intermediates in some catalytic reactions.[2]

[a] University of Amsterdam, Van't Hoff Institute for Molecular Chemistry (HIMS), Department of Homogeneous and Supramolecular Catalysis,
Nieuwe Achtergracht 166, 1018 WV Amsterdam, The Netherlands
Fax: +31-20-525-6422
E-mail: bdebruin@science.uva.nl
[b] Radboud University Nijmegen, Institute for Molecules and Materials (IMM),
Toernooiveld 1, 6525 ED Nijmegen, The Netherlands

*Bas de Bruin obtained his PhD in 1999 from the Radboud University Nijmegen (the Netherlands). In the same year he joined the group of Prof. Karl Wieghardt at the Max-Planck Institute for Bio-Inorganic Chemistry in Mülheim/Ruhr (Germany) as an Alexander-von-Humboldt fellow. A year later he returned to the Metal-Organic Chemistry group of Prof. Anton W. Gal in Nijmegen as an assistant professor (UD). In 2005 he received a national NWO-VIDI grant to start up an independent research-line. November 2005 he moved to the University of Amsterdam (UvA) to join the Homogeneous and Supramolecular Catalysis group.*

*Dennis Hetterscheid obtained his master's degree in Chemistry in 2002 at the Radboud University Nijmegen (the Netherlands). Currently he is finishing his PhD at the same university (under supervision of Bas de Bruin), dealing with the synthesis, characterization and reactivity of mononucleair $Rh^{II}$ and $Ir^{II}$ complexes. July 2006 he obtained a national NWO-Rubicon grant for a two-year postdoc abroad, which he will carry out at the Massachusetts Institute of Technology in the group of Prof. Richard R. Schrock.*

 © 2007 Wiley-VCH Verlag GmbH & Co. KGaA, Weinheim 

Paramagnetic Rh and Ir species are frequently more reactive than their closed-shell counterparts, and reveal a very different reactivity. Most of these metallo-radicals are low-spin 17- or 19-VE (valence electron) species with the unpaired spin-density located *at the metal*. Consequently, most of these species reveal metal-centered radical-type reactivity like halogen-atom abstraction, hydrogen abstraction and capture of other radicals by the metal (which includes dimerization with formation of metal–metal bonds).[3] Even more reactive $Rh^{II}$ porphyrin species are capable of breaking C–H bonds of rather inert substrates such as methane and methanol.[4] The reactivity of these "metallo-radicals" thus closely resembles that of an organic radical.

With increasing number of papers reporting about paramagnetic mononuclear Rh and Ir species,[5] their alkene adducts are still quite rare. This is not surprising, because these species tend to be very reactive and reveal a remarkable diversity of different radical-type reactions, both at the metal and at the alkene fragment.

Interestingly, the π-accepting alkene fragment is a potentially "redox non-innocent"[6] ligand (Figure 1), and "metallo-radical" and "alkene radical" descriptions both contribute to the electronic structure of a paramagnetic $M^x$(alkene) complex (M = Rh, Ir; $x$ = 0, +II). Species with an increased "alkene radical" contribution generally have a stronger tendency to undergo ligand-centered radical-type reactions. Such reactions are potentially useful as new alkene functionalization reactions, very different from those in traditional organometallic chemistry. Such species might participate in (new or existing) catalytic alkene transformation reactions, such as oxygenation, cyclopropanation and other alkene functionalization reactions.

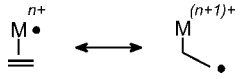


Figure 1. Ligand "redox non-innocence" in open-shell alkene transition-metal complexes.

In most cases the "metallo-radical" and "alkene radical" descriptions are limiting resonance structures of the real electronic structure, and frequently the "metallo-radical" description prevails (Figure 1). But the other extreme, in which the alkene accepts most of the spin density, can also play an important role. For example, "alkene radicals" of the type $Ir^{III}$–$CH_2$–$CH_2^{\cdot}$ are plausible intermediates in a series of radical-type reactions triggered by coordination of an additional ligand to otherwise stable $Ir^{II}$(ethene) species.[7,8]

In this review we provide an up-to-date overview of the unusual chemistry of paramagnetic $M^x$(alkene) species (M = Rh, Ir; $x$ = 0, +II). We start with a short description of species for which not much reactivity has been reported; i.e. sterically protected species and species where spin delocalization over other parts of the molecule deprives much of the radical character of the M(alkene) fragment. This review however focuses at the intriguing reactivity of paramagnetic M(alkene) species, underlining their dual-mode "metallo-radical" and "alkene-radical" behavior.

## 2. M(Alkene) Species Deprived of Metal- and Alkene-Radical Behavior

In this section we summarize the properties of a few rather inert paramagnetic M(alkene) radicals (M = Rh, Ir) for which not much reactivity has been reported. This includes sterically protected species and a series of species in which the unpaired spin is highly delocalized and/or located at another part of the molecule, thus depriving much of the radical character of the M(alkene) fragment.

### 2.1 Highly Delocalized Radicals and Paramagnetic M(Alkene) Species Bearing the Spin Density at Other Parts of the Molecule

Compared to alkenes, some well-known other "redox non-innocent" ligands are even more inclined to accept unpaired electrons from the metal to form ligand radicals. Paramagnetic M(alkene) species containing other "redox non-inocent" ligands are less inclined to undergo metal- or alkene-centered radical reactions. The radical is usually substantially stabilized when the spin density is spread out over an extended π system of the "redox non-innocent" ligand. Delocalization of unpaired spin density over multiple metal atoms of multinuclear species and clusters is another way to stabilize open-shell M(alkene) species (M = Rh, Ir). Such examples are summarized in this section.

#### *Spin Delocalization over Multiple Metal Atoms*

Several paramagnetic organometallic clusters, multinuclear wires and dinuclear species involving platinum, palladium, rhodium and iridium have been reported, among them a number of alkene complexes. The unpaired electron of such species is usually strongly delocalized over multiple metal centers, and consequently they do not behave like reactive M(alkene) radicals. It is not our intention to give a full comprehensive overview of all paramagnetic multinuclear species here. We will restrict ourselves to a very concise description of some of these species, and then proceed with a focus on the radical-type chemistry of mononuclear M(alkene) species.

Most multinuclear paramagnetic clusters and wires are connected by metal–metal bonds, often supported by bridging ligands. Examples are the wire-like tri- and tetranuclear Rh and Ir compounds of the type $[Rh_3(\mu_3\text{-}L)_2(CO)_2(\eta_4\text{-}cod)_2]^{2+}$,[9] $[Rh_2Ir(\mu_3\text{-}OMe_2napy)_2(CO)_2(cod)_2]^{2+}$,[10] and $[M_4(\mu\text{-}PyS_2)_2(bis\text{-}alkene)_4]^{+}$ (M = Rh, Ir).[11] These "molecular wires" have the unpaired electron delocalized over multiple metal centers, suggestive of potential conducting properties of such wires. The delocalization of the unpaired spin density contributes to the relative stability of these species. Several mixed-valent dinuclear rhodium and iridium complexes of the type $[M_2]^{3+}$ and $[M_2]^{5+}$ have been reported (M = Rh, Ir). These species are formally $M^{II}$ species bound to

 © 2007 Wiley-VCH Verlag GmbH & Co. KGaA, Weinheim 

closed-shell $M^{I}$ or $M^{III}$ ions by metal–metal interactions. However, the actual electronic configuration of the $[Rh_2]^{5+}$ species is highly dependent on the type and number of ligands bound to the axial sites.[12–15] For example, in the complexes $[Rh(\eta^4\text{-cod})(\mu\text{-RNNNR})_2Ir(CO)_2]^+$ and $[Ir(\eta^4\text{-cod})(\mu\text{-RNNNR})_2Rh(CO)_2]^+$, the M(cod) fragment contains most of the unpaired electron density (80% and 75%, respectively).[16] This is even more drastic in case of $[I_2Rh(\mu\text{-RNNNR})_2Pd(\eta^3\text{-}C_3H_5)]^-$, which has 90% of the unpaired electron spin density located at the rhodium atom, with only 10% at palladium.[17] The steric bulk of these species likely protects these cod species from decomposing via allylic C–H activation (vide infra).

### *Semiquinone-Type Ligands*

Catecholate/quinone-type ligands are nowadays well-known "redox non-innocent" ligands.[18] The metal quinone, $M^{I}(Q)$, metal semi-quinone, $M^{II}(SQ^{\cdot-})$, and metal catecholate, $M^{III}(Cat^{2-})$, are description of either one electronic ground state (mesomeric form) or are distinct electronic states which are in equilibrium (redox isomerism) (Figure 2).

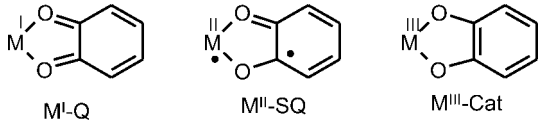


Figure 2. "Redox non-innocence" of catecholate/quinone-type ligands.

In 1992, when the "redox non-innocent" behavior of such ligands was not as well established as it is by now, formation of a paramagnetic $Ir^{IV}$(cod) species containing two 3,6-di-*tert*-butylcatecholate (3,6-DBCat) ligands was claimed.[19] A broad EPR resonance (200 G, $g$ = 1.986) was observed in solution. In frozen solution, the signal splits to give a rhombic spectrum with components $g_{11}$ = 1.948, $g_{22}$ = 1.942 and $g_{33}$ = 2.006, indicative of a mainly ligand-centered radical. Considering the meanwhile well-known "redox non-innocence" of catecholate/quinone-type ligands, the $[Ir^{III}$(3,6-DBCat)(3,6-DBSQ)(cod)] might thus be a better description of the electronic structure of this stable species.

### *Pyridine-2,6-diimine Complexes*

Pyridine-2,6-diimine ligands are meanwhile also well-known to be "redox non-innocent".[20] This also seems to play a role in their Rh chemistry. Reaction of alkyl pyridine-2,6-diimine rhodium(I) complexes with dihydrogen (Figure 3) leads to the formation of a paramagnetic $[Rh^{III}(H)_2(L^{-1})]$ or $[Rh^{I}(L^{-1})(X)]$ species (X = arene solvent, dinitrogen or dihydrogen).[21] The EPR spectrum of this species in frozen toluene shows an axial signal indicative of an $S = {}^1/_2$ species [$g_{\parallel}$ = 1.9775, $g_{\perp}$ = 2.0169, $A_{\parallel}$(N) = 40 MHz] with the unpaired electron being mainly located in one of the π* orbitals of the 2,6-pyridine-diimine ligand.[21,22] The mechanism by which these species are generated is not entirely clear.

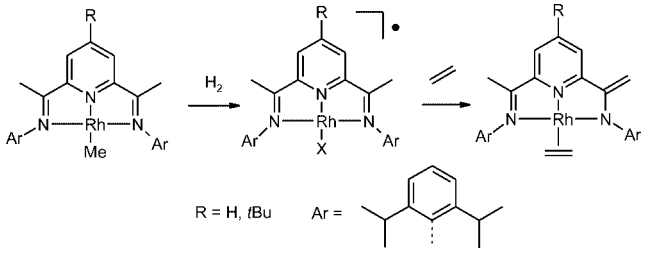


Figure 3. Chemistry of pyridine-diimine-supported alkyl rhodium(I) compounds involving open-shell intermediates.

Treatment of this species with an excess of alkenes eventually yields diamagnetic $[Rh^{I}(L_{-H})$(alkene)] species. The paramagnetic intermediate seems to be a hydrogenation catalyst of primary and secondary alkenes in the presence of $H_2$. The unpaired spin density in the π system of the pyridine-2,6-diimine ligand apparently has little influence on the intrinsic reactivity of Rh, as hydrogenation activity is most commonly observed for closed-shell Rh species.[21,22]

### *Aminyl Radical Complexes and Related Species Based on Trop-Type Ligands*

The Grützmacher group has extensively used tropylidene (trop) type ligands to stabilize a series of paramagnetic rhodium and iridium complexes (Figure 4, Figure 5). Remarkably, these complexes all appear to be "ligand radicals" and/or highly delocalized radicals.

For example, trop-type ligands allow isolation of $Rh^{I}$-coordinated aminyl radicals. Deprotonation of cationic $[Rh^{I}(trop_2NH)(bpy)]^+$ species generates a stable (under inert atmosphere) neutral amido complex $[Rh^{I}(trop_2N^{-})(bpy)]$. Remarkably, one-electron oxidation of the latter with $[Fc]^+$ does not result in the expected $Rh^{II}$ species, but yields an aminyl radical complex $[Rh^{I}(trop_2N^{\cdot})(bpy)]^+$ (see Figure 4). This is the first example of a stable aminyl radical coordinated to a transition metal ever reported.[23] Both detailed EPR spectroscopic investigations ($g_{11}$ = 2.0822, $g_{22}$ = 2.0467, $g_{33}$ = 2.0247, $A^{N}_{iso}$ = 45 MHz), and DFT calculations revealed that the unpaired electron is delocalized over the $R_2N$ (ca. 57%) fragment and Rh (ca. 30%), but with a clear preference for the N atom (Figure 4, top).

The nitrogen-centered radical is stable in organic solvents for days, and even when samples are brought in contact with air or water the EPR signals persist for hours. The aminyl radical fragment nevertheless behaves as a nucleophilic radical, capable of hydrogen atom abstraction reactions from $Bu_3Sn$–H or RSH (R = Ph, *t*Bu, $CH_2COOMe$), thus regenerating the $[Rh^{I}(trop_2NH)(bpy)]^+$ starting compound and $Bu_3Sn$–$SnBu_3$ or RS–SR coupled products. Despite a still significant spin density at the metal, metal-centered radical reactions were not observed. In later studies

 © 2007 Wiley-VCH Verlag GmbH & Co. KGaA, Weinheim 

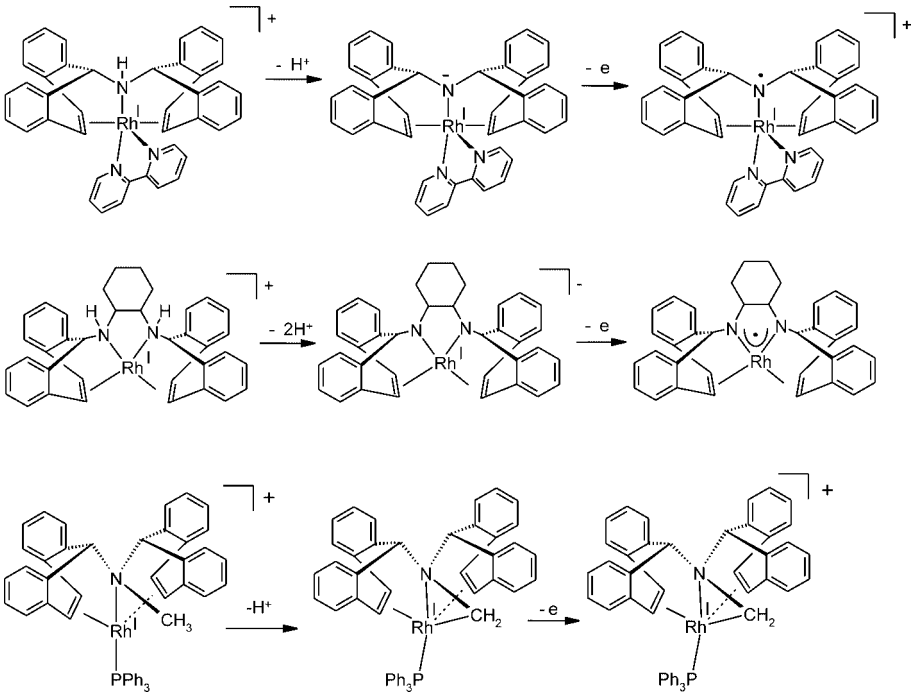

Figure 4. Top: Formation of a stable aminyl-$Rh^{I}$ radical complex by one-electron oxidation of a amido-$Rh^{I}$ complex. Middle: Formation of a trop-based N–M–N delocalized radical. Bottom: Formation of a highly delocalized rhoda-aza-cyclopropane radical from $trop_2N$-Me ligands.

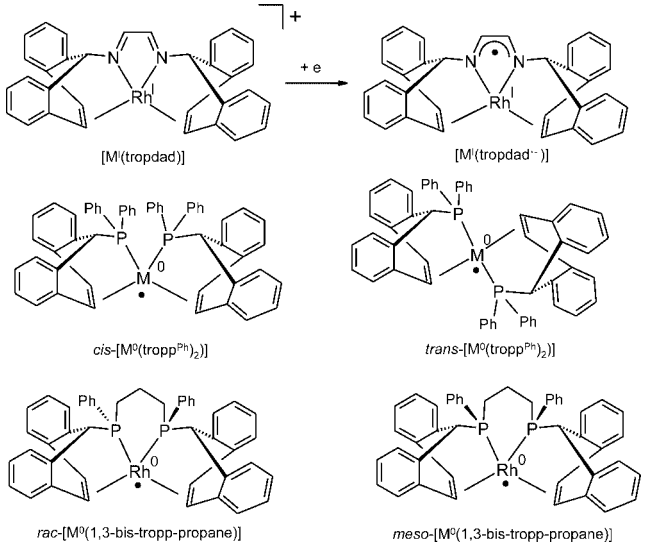

Figure 5."Low-valent" species based on the trop-type ligands.

the group also demonstrated the synthesis of a square-planar analog, in which the radical is substantially delocalized over Rh (ca. 41%) and the N atoms of two $NR_2$ fragments (ca. 24–28% each), see Figure 4.[24] The species still behaves as a nucleophilic *N*-centered radical, abstracting a hydrogen atom from $Bu_3Si$–H, despite a reduced spin localization per N atom.

Similar experiments were performed with a rhodium complex of the methyl-substituted $trop_2N$–Me ligand (Figure 4, middle). Deprotonation of $[Rh^{I}(trop_2N–Me)(PPh_3)]^+$ occurs at the methyl moiety of the $trop_2N$–Me ligand, resulting in formation of a rhoda-aza-cyclopropane ring structure.[25] The $[Rh^{I}(trop_2N–CH_2–)(PPh_3)]$ complex reveals a reversible oxidation wave in the cyclic voltammogram at a remarkably low potential (–0.51 V vs. $Fc/Fc^+$). Preparative one-electron oxidation of this species yields a stable cationic radical analog. The EPR data ($g_{11}$ = 2.121, $g_{22}$ = 2.014, $g_{33}$ = 2.016) reveal hyperfine couplings to Rh, N, the aza-cyclopropane methylene carbon and hydrogen atoms, and the trop olefinic carbon and hydrogen atoms. DFT calculations reveal that the unpaired electron is strongly delocalized over rhodium (47%), the methylene (14%), and the four olefinic carbon atoms (15%, 15%, 3% and 3%). This species is perhaps best described as a highly delocalized radical.

### *"Low-Valent" Species*

Tropylidene (trop) type ligands have also been used to stabilize a series of "low-valent" species. Electrochemical reduction of $[M^{I}(tropdad)]$ complexes, containing a "redox non-innocent" α-diimine fragment (Figure 5, top), leads to species in which the unpaired electron is located in the α-diimine π system.[26] Consistent with this formulation, the axial EPR spectra (M = Rh: $g_{\|}$ = 2.0113, $g_{\perp}$ = 1.9977, M = Ir: $g_{\|}$ = 2.0332, $g_{\perp}$ = 1.9870) have small deviations of the *g* values from $g_e$, and reveal small hyperfine couplings with Rh (no Ir hyperfine couplings were observed), and comparably stronger superhyperfine couplings with two equivalent N nuclei and two equivalent protons.

A further series of "low-valent" M(alkene) complexes were supported by tropylidene-phosphane (tropp) ligands (Figure 5). These species were also prepared by one-electron

 © 2007 Wiley-VCH Verlag GmbH & Co. KGaA, Weinheim 

reduction of their $M^I$ precursors (requiring strong reducing agents, such as metallic Li, Na or K). With the bidentate tropp$^{Ph}$ ligands, mixtures of *cis* and *trans* isomers of [$M^0$(tropp$^{Ph}$)$_2$] (M = Rh, Ir) were obtained. The EPR spectra reveal axial *g* tensors (*cis*-[(Rh$^0$(tropp$^{Ph}$)$_2$]: $g_\parallel$ = 2.030, $g_\perp$ = 2.014; *trans*-[(Rh$^0$(tropp$^{Ph}$)$_2$]: $g_\parallel$ = 2.050, $g_\perp$ = 2.030; *cis*-[(Ir$^0$(tropp$^{Ph}$)$_2$]: $g_\parallel$ = 2.030, $g_\perp$ = 2.060; *trans*-[(Ir$^0$-(tropp$^{Ph}$)$_2$]: $g_\parallel$ = 1.980, $g_\perp$ = 2.150. Detailed EPR characterization of these species reveal (super)hyperfine couplings with Rh (16–23 MHz) and the two equivalent P atoms of the tropp ligand (40–80 MHz). Remarkably, Ir hyperfine couplings were not observed, and Rh hyperfine couplings are quite small. The [(Rh$^0$(1,3-bis-tropp-propane)] analog (Figure 5) was prepared as a mixture of the *rac* and *meso* forms, but also in a pure *rac* form. The solution EPR spectrum of the *rac* form ($g_{iso}$ = 2.021) reveals superhyperfine coupling with two equivalent P nuclei (84 MHz). The *meso* form ($g_{iso}$ = 2.014) reveals superhyperfine coupling with two non-equivalent P nuclei (82 MHz and 51 MHz), likely caused by a distortion along one of the P–Rh bonds.

The *g* values of these "zero-valent" M(alkene) complexes are quite close to $g = g_e$. Their small *g* anisotropy and quite weak metal hyperfine couplings suggest that these species might not be real $d^9$ metal-centered radicals, but are perhaps better described as highly delocalized systems in which the unpaired spin density is substantially spread out over the metal and the trop ligand fragments. This is, however, not very clear and theoretical investigations are probably required to understand the electronic structure of these species. Spin delocalization to π-accepting CO and olefin ligands seems to be more general, and other Rh$^0$ complexes also reveal small deviations from $g = g_e$ (with weak metal hyperfine couplings), e.g. [Rh$^0$(cod)$_2$]: $g_{iso}$ = 2.030 ($A^{Rh}_{iso}$ not resolved);[27] [Rh$^0$(CO)$_4$]: $g_{iso}$ = 2.006 ($A^{Rh}_{iso}$ = 21 MHz).[28] The same holds for a series of Rh$^0$ complexes with π-accepting P ligands, which reveal larger phosphorus superhyperfine couplings than metal hyperfine couplings.[29] DFT calculations are in progress, and will hopefully lead to a more detailed understanding of the electronic structure of these Rh$^0$ species in the near future.[30] Notably, Rh$^0$ complexes of phosphinine-ring (P-analogs of pyridines, $R_5C_5P$) containing macrocyclic ligands (known to accommodate electrons) reveal similar EPR parameters ($g_{iso}$ = 2.0016, $A^P_{iso}$ = 49, $A^{Rh}_{iso}$ not resolved; $g_{iso}$ = 2.0180, $A^P_{iso}$ = 271 MHz, $A^{Rh}_{iso}$ = 27 MHz). According to DFT calculations (supported by EPR property calculations) these latter species are best described as ligand radicals.[31]

## 2.2 Sterically Protected Species

### *Sterically Protected M$^0$(alkene) Species*

Rh$^0$(cot) complexes (cot = cyclooctatetraene) with the very bulky $CpPh_5^-$ ligand have been prepared electrochemically.

Electrochemical reduction of [Rh$^I$(CpPh$_5$)(1,5-η$^4$-cot)] (cot = cyclooctatetraene) initially leads to the 1,5-COT Rh$^0$ analog, but this species quickly converts to the more stable 1,3-cot Rh$^0$ isomer (Figure 6). As a consequence, reoxidation of the Rh$^0$(1,3-cot) species occurs at a less negative potential (–1.37 V vs. Fc/Fc$^+$, Fc/Fc$^+$ = ferrocene/ferrocenium) than reduction of the Rh$^I$(1,5-cot) species (ca. –2.7 V vs. Fc/Fc$^+$). The EPR spectrum of [Rh$^0$(CpPh$_5$)(1,3-η$^4$-cot)] reveals a rhombic spectrum with $g_1$ = 2.064, $g_2$ = 2.014 and $g_3$ = 1.893. The $g_2$ line reveals a resolved Rh hyperfine coupling (ca. 20 MHz). No further reactivity has been reported.

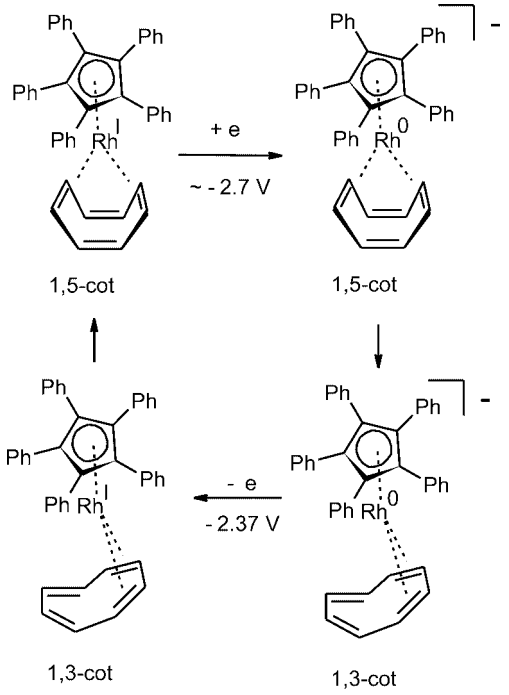


Figure 6. Formation of [Rh$^0$(CpPh$_5$)(1,3-η$^4$-cot)] upon one-electron reduction of [Rh$^I$(CpPh$_5$)(1,5-η$^4$-cot)].

Not much is known about the intrinsic reactivity of "zero-valent" M(alkene) species. Metal or alkene reactivity has not been reported for any of the above species, but this might be because these species are protected by steric bulk and/or substantial delocalization of their spin density. The situation might be different for species which are less delocalized and better accessible. This seems to be the case for [Rh$^0$(cod)$_2$], the only "zero-valent" species for which metal and alkene radical reactivity has been reported (to our best knowledge). [Rh$^0$(cod)$_2$] was prepared by electrochemical reduction of the [Rh$^I$(cod)$_2$]$^+$ precursor (cod = *Z,Z*-1,5-cyclooctadiene).[32] At low temperatures, the 17 VE (VE = valence electron) species is sufficiently long-lived for EPR measurements, revealing rhombic *g* values $g_1$ = 2.056, $g_2$ = 2.019 and $g_3$ = 2.016. Poorly resolved Rh hyperfine couplings (ca. 40–60 MHz) were observed. In chlorinated solvents such as $CH_2Cl_2$, the species abstracts a Cl atom from the solvent to form [{Rh$^I$(μ$_2$-Cl)(cod)}$_2$]. In acetone, the fate of [Rh$^0$(cod)$_2$] is less clear, but NMR spectroscopic data point to formation of diamagnetic species containing π-allylic moieties derived from cod, as is also observed for $M^{II}$(cod) species with an accessible metal center (see section 3.3).

 © 2007 Wiley-VCH Verlag GmbH & Co. KGaA, Weinheim 

### *Sterically Protected $M^{II}$(alkene) Species*

Most divalent $M^{II}$(alkene) complexes are based on hard multidentate N-donor ligands (see section 3). Exceptions are a couple of stable $M^{II}$-cod complexes (cod = cyclooctadiene) stabilized by very bulky σ-aryl $C_6Cl_5^-$ and pentaphenylcyclopentadienyl ($\eta^5$-$CpPh_5^-$) type ligands, namely $[Ir^{II}(C_6Cl_5)_2(cod)]$,[33] $[Rh^{II}(C_6Cl_5)_2(cod)]$,[34] $[Rh^{II}(\eta^5$-$C_5Ph_5)(1,5\text{-cod})]^+$,[35] and $[Rh^{II}(\eta^5$-$C_5Ph_5)(1,3\text{-cod})]^+$,[35] see Figure 7. Steric shielding of the metal by the bulky ligands apparently results in stable species, and these complexes can be kept in solution for many hours without decomposition.

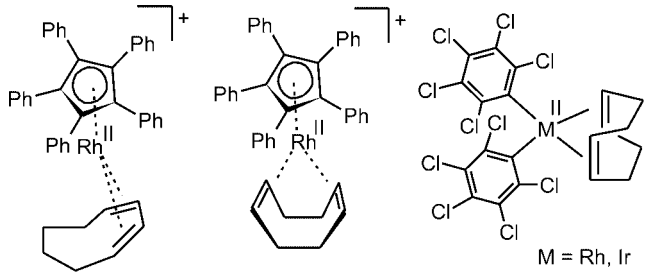


Figure 7. Stable $M^{II}$(alkene) complexes stabilized by $\eta^5$-$CpPh_5$ and σ-aryl-type ligands.

Rhombic EPR spectra have been observed for $[Ir^{II}(C_6Cl_5)_2(cod)]$ ($g_{11}$ = 3.00, $g_{22}$ = 2.79, $g_{33}$ = 1.85) and $[Rh^{II}(C_6Cl_5)_2(cod)]$ ($g_{11}$ = 2.55, $g_{22}$ = 2.45, $g_{33}$ = 1.99). The large *g* anisotropies are consistent with the proposed electronic structures, with the unpaired electron mainly residing in a $d_{xy}$ or $d_{z^2}$ orbital (with the *z* axis perpendicular to the coordination plane of rhodium). Substantially larger spin–orbit couplings are observed for the Ir compound ($g_{av}$ = 2.55) than for the Rh compound ($g_{av}$ = 2.32) which is usual for third row-compared to second-row transition metals. As expected, the $[Rh^{II}(\eta^5$-$C_5Ph_5)(1,3\text{-cod})]^+$ radical also gives rise to a rhombic EPR spectrum ($g_{11}$ = 2.329, $g_{22}$ = 2.120, $g_{33}$ = 2.003). The 1,5 isomer $[Rh^{II}(\eta^5$-$C_5Ph_5)(1,5\text{-cod})]^+$ reveals an axial EPR spectrum ($g_{\|}$ = 2.181, $g_{\perp}$ = 1.997) indicative of an approximate $C_{2v}$ symmetry. Neither of the species reveals resolved hyperfine couplings with the $^{103}$Rh nucleus, preventing assignments of the orbital composition of the SOMO.

Electrochemically reversible oxidation has been reported for the related complex $[Rh^{I}(Cp)(ethene)_2]$. Coulometrically generated samples revealed a broad spectrum around *g* = 1.9855 without a resolved hyperfine structure in dimethoxyethane solution at –70 °C (frozen solutions at 20–100 K would have probably resulted in more informative spectra).[36,37] A detailed characterization of this radical cation, which is only stable at low temperatures, is lacking so far. Clearly such $Cp^-$ complexes are much less stable than the above sterically protected $CpPh_5^-$ species.

More information about the intrinsic reactivity of $M^{II}$(alkene) species has been gathered using N-ligands. This is described in section 3.

## 3. Reactive $M^{II}$(alkene)(N-ligand) Species. Metal or Alkene Radicals?

Apart from the above exceptions, all other $M^{II}$(alkene) complexes (M = Rh, Ir), and reactions of $M^{II}$ radicals with alkenes, have been studied using mononuclear complexes with multidenate N-donor ligands. Neutral-type complexes of the $[M^{II}(por)]$-type based on dianionic porphyrinato ($por^{2-}$) ligands and dicationic complexes of the type $M^{II}(N_4\text{-ligand})]^{2+}$ and $[M^{II}(N_3\text{-ligand})]^{2+}$ based on neutral, podal $N\{CH_2Py\}_n$ (*n* = 2, 3) type ligands have so far dominated these studies (Figure 8).

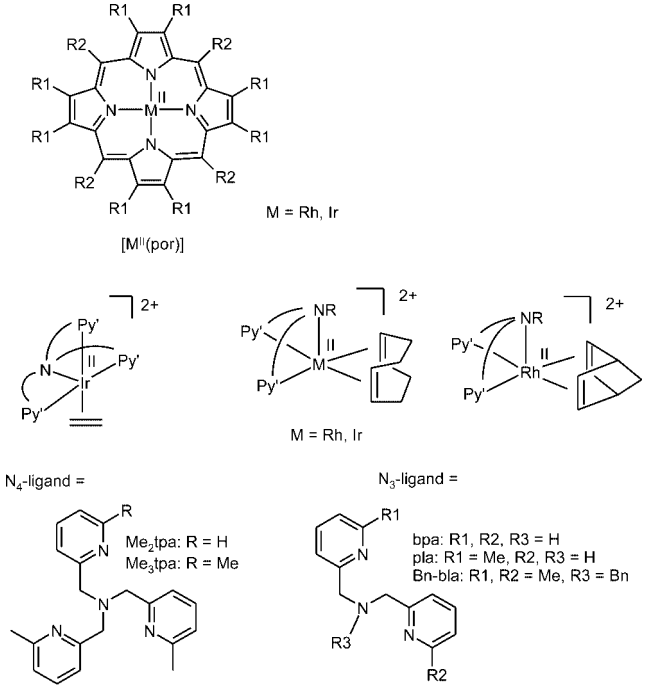


Figure 8. Structure of neutral $[M^{II}(por)]$ and dicationic $[Ir^{II}(N_4\text{-ligand})(ethene)]^{2+}$, $[Rh^{II}(N_3\text{-ligand})(nbd)]^{2+}$ and $[M^{II}(N_3\text{-ligand})(cod)]^{2+}$ species.

### 3.1 Geometries and Electronic Structures

Before we continue with a more detailed description of the geometry and electronic structures of complexes of the type $[M^{II}(por)]$ and $[M^{II}(N\{CH_2Py\}_n)]^{2+}$ (*n* = 2, 3) (section 3.1.2 and 3.1.3), let us first consider the most important differences between these types of species which are most relevant for their reactivity.

#### *3.1.1 Metal or Ligand Radicals?*

First of all, the porphyrinato complexes have *trans* vacant sites, and although perhaps not entirely impossible, *cis* reactivity patterns of alkenes and other substrates are not very likely for $[M^{II}(por)(alkene)]$ species. This should not be a problem for the dicationic $[M^{II}(alkene)(N_4\text{-ligand})]^{2+}$ and $[M^{II}(bis\text{-alkene})(N_3\text{-ligand})]^{2+}$ species, having a "vacant site" *cis* to the alkene (half occupied by the unpaired electron). Alkenes have a low affinity for $[M^{II}(por)]$ radicals, and once formed such alkene adducts tend to be very reac-

 © 2007 Wiley-VCH Verlag GmbH & Co. KGaA, Weinheim 

tive. As a result, alkene adducts of $[M^{II}(por)]$ radicals cannot be isolated, although they do reveal interesting reactions towards alkenes (section 3.2.1–3.3). Alkenes bind much stronger to dicationic $[M^{II}(N_4\text{-ligand})]^{2+}$- and $[M^{II}(N_3\text{-ligand})]^{2+}$-type complexes, allowing isolation and detailed characterization of the alkene adducts (section 3.1.2).

For the neutral $[M^{II}(por)]$ species, alkene→metal σ bonding is expected to be weaker than the dicationic $[M^{II}(N_4\text{-ligand})]^{2+}$ and $[M^{II}(N_3\text{-ligand})]^{2+}$ complexes (Figure 8). On the other hand, metal→alkene π(back)bonding, which contributes substantially to the metal–alkene interaction (Chatt–Dewar–Duncanson model), is expected to be stronger for the neutral $[M^{II}(por)]$ species. Therefore, one cannot ascribe the different alkene affinities *only* to the charge differences.

Another important difference between these types of complexes is the orbital symmetry. The $[M^{II}(N_4\text{-ligand})]^{2+}$ and $[M^{II}(N_3\text{-ligand})]^{2+}$ complexes have an empty $d_{x^2-y^2}$ and an empty p orbital available for alkene→metal σ bonding. The planar $[M^{II}(por)]$ species, however, have the *half-filled* $d_{z^2}$ orbital and the higher lying empty p orbital available for alkene→metal σ bonding, further weakening this interaction (Figure 9). A consequence of the $d_{z^2}$ orbital being involved in binding of the alkene in 17-VE $[M^{II}(por)(alkene)]$ species is that the alkene ligand will always bear a significant part of the unpaired spin density, thus making the alkene fragment sensitive to radical reactions. This is clearly reflected by the reactivity of $[M^{II}(por)(alkene)]$ species (see sections 3.2–3.3).

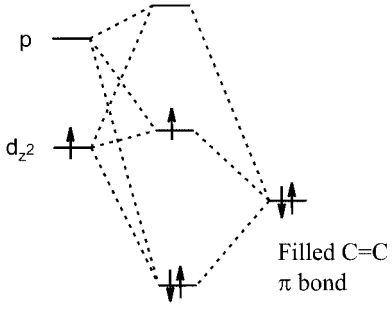


Figure 9. Alkene→metal σ bonding in $[M^{II}(por)(alkene)]$ species.

The alkene ligands of the 17-VE dicationic $[M^{II}(alkene)(N_4\text{-ligand})]^{2+}$ and $[M^{II}(di\text{-alkene})(N_3\text{-ligand})]^{2+}$ complexes do not bear much spin density (< 5%). The $d_{z^2}$ orbital, in which the unpaired electron is located, predominantly interacts with $N_{amine}$ donors, leaving the alkene ligands virtually unaffected.

### *Donor-Induced Metal to Ligand Radical Transformations in "19-VE" Species*

Binding of a 6th ligand to 17-VE five-coordinate $M^{II}$-(alkene) species substantially influences the reactivity of these species. Binding of an additional σ-donor ligand without loss of the alkene should be more easy for the dicationic $[M^{II}(alkene)(N_4\text{-ligand})]^{2+}$ and $[M^{II}(bis\text{-alkene})(N_3\text{-ligand})]^{2+}$ complexes compared to the neutral $[M^{II}(por)(alkene)]$ species. Indeed, indications for formation of such 19-VE intermediates have thus far only been obtained for $[Ir^{II}(ethene)(Me_ntpa)]^{2+}$ ($n$ = 2, 3) complexes.

Although the PyMe groups shield the "vacant site" of $[Ir^{II}(Me_ntpa)(ethene)]^{2+}$ species ($n$ = 2, 3) from attack by bulky reagents, MeCN is small enough to coordinate to iridium *trans* to the amine (Figure 10). Obviously, this is most easy for the least hindered $Me_2tpa$ species ($n$ = 2). Binding of MeCN (or other small ligands) causes these otherwise inert species to undergo alkene radical reactions (see sections 3.2.1 and 4).

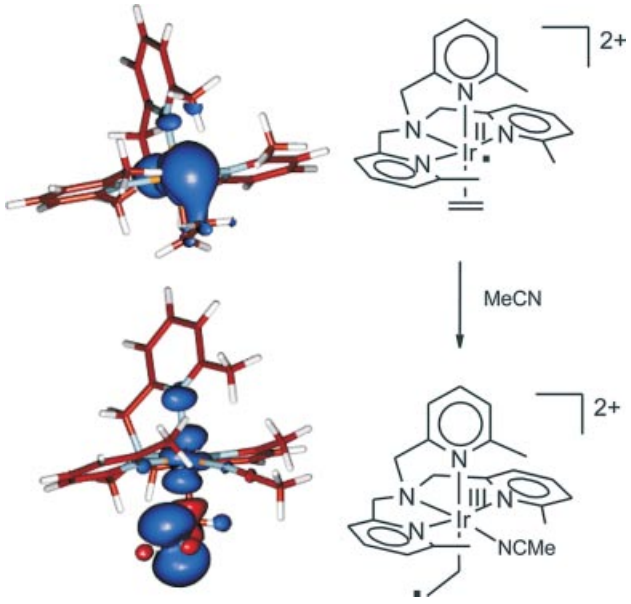


Figure 10. Spin density plots of $[Ir^{II}(Me_3tpa)(CH_2{=}CH_2)]^{2+}$ (above) and $[Ir^{III}(\text{-}CH_2\text{-}CH_2^{\cdot})(Me_3tpa)(NCMe)]^{2+}$ (below).

According to DFT calculations, these MeCN adducts have the ethene fragment coordinated in a "slipped" way. Whereas the α-carbon of the "slipped alkene" fragment seems to be tetrahedral and $sp^3$-hybridized, the β-carbon atom is planar and $sp^2$-hydridized. A spin-density plot (Figure 10) reveals that these species are not real 19 VE species, but are intermediate between a 19 VE "slipped alkene" description $Ir^{II}\text{–}CH_2\text{–}CH_2^+$ and an 18 VE ethyl radical description $Ir^{III}\text{–}CH_2\text{–}CH_2^{\cdot}$, but the 18 VE ethyl radical description prevails.[7] Thus, MeCN binding apparently leads to a donor induced shift of the spin density from the metal to the alkene with formation of $Ir^{III}\text{–}CH_2\text{–}CH_2^{\cdot}$ radicals. This substantially influences the reactivity of these species (see sections 3.2.1 and 4), and constitutes a new approach to tuning the reactivity of open-shell metal-alkene complexes.

### *3.1.2 (Electronic) Structure of Dicationic 17-VE $M^{II}$(alkene)(N{$CH_2Py$}$_n$) Radicals*

Species of the type $[Ir^{II}(N_4\text{-ligand})(ethene)]^{2+}$,[7,38,39] $[Rh^{II}(N_3\text{-ligand})(nbd)]^{2+}$[40] (nbd = norbornadiene) and $[M^{II}(N_3\text{-ligand})(cod)]^{2+}$[41,42] have been obtained from their

 © 2007 Wiley-VCH Verlag GmbH & Co. KGaA, Weinheim 

$M^I$ precursors by one-electron oxidation using either $[Fc]^+$ or $Ag^+$ as an oxidant (Figure 8).

Cyclic voltammograms of these complexes revealed reversible waves for the $M^I/M^{II}$ couple in all cases, except for some of the less bulky cyclooctadiene complexes. The $M^{II}/M^{III}$ couple was not observed at potentials below oxidation of the solvent. Direct electron-transfer (ET) disproportionation of the dicationic $M^{II}$ species to monocationic $M^I$ and tricationic $M^{III}$ species is substantially endergonic (> 92–125 kJ mol$^{-1}$ in both acetone and $CH_2Cl_2$), and thus an unlikely decomposition pathway of these species.

The X-ray structures of $[Ir^{II}(Me_3tpa)(ethene)]^{2+}$[7,38] and $[Rh^{II}(Bn\text{-}bla)(cod)]^{2+}$[42] as well as their $M^I$ precursors have been reported. The $M^I$ species adopt a trigonal-bipyramidal geometry. Upon oxidation the geometry changes to a square pyramid with the amine at the apical position and the alkene(s) and the pyridines coordinating in the basal plane. The pyridylmethyl groups shield the "vacant position" *trans* to the amine (Figure 11). On going from $M^I$ to $M^{II}$, the M→alkene π backbonding becomes weaker, resulting in longer M–C and shorter C=C bonds. The M–N interactions become stronger. The structures elucidated by X-ray diffraction are consistent with DFT calculations and EPR data.

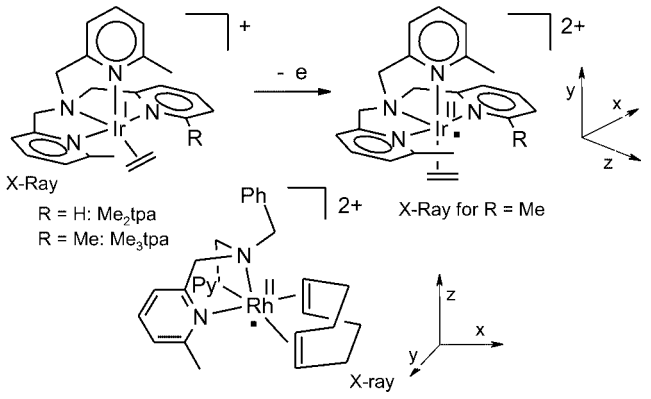


Figure 11. Sterically protected $[Ir^{II}(Me_ntpa)(ethene)]^{2+}$ and $[Rh^{II}(Bn\text{-}bla)(cod)]^{2+}$ species.

$[Rh^{II}(N_3\text{-ligand})(nbd)]^{2+}$ and $[Rh^{II}(N_3\text{-ligand})(cod)]^{2+}$ show EPR spectra with $g_x$, $g_y > 2$ and $g_z \approx 2$, with $g_z$ revealing a strong (super)hyperfine coupling with both the metal and the apical $N_{amine}$ donor.[40–42] These data suggest that the unpaired electron resides in the $d_{z^2}$ orbital, in good agreement with results from DFT calculations. For all analogous Ir compounds the $g_z$ value is notably lower than $g_e$, pointing to some mixing of the $d_{z^2}$ orbital with a $d_{x^2-y^2}$ orbital ($d_{xy}$ for the cod complexes) in the SOMO.

The EPR parameters calculated with DFT are in satisfactory agreement with the experimentally derived parameters. Experimental ENDOR measurements, as well as DFT spin density plots reveal that the spin density is substantially delocalized over the $N_{amine}$ donor (15–18%) and the metal (73–78%).[42] Delocalization of the unpaired electron over the metal and the amine might contribute to the relative stability of these species.

### *3.1.3 (Electronic) Structure of Neutral 17-VE $M^{II}$(alkene)(por) Radicals*

Radical-type chemistry of neutral square-planar $N_4$-ligand $Rh^{II}$ species has been mainly studied with porphyrinato ($por^{2-}$) ligands, but similar chemistry for the dianionic planar coordinating $N_4$-ligands TMTAA,[43] OETAP,[44] and DBPB[45] (Figure 12) has been reported.

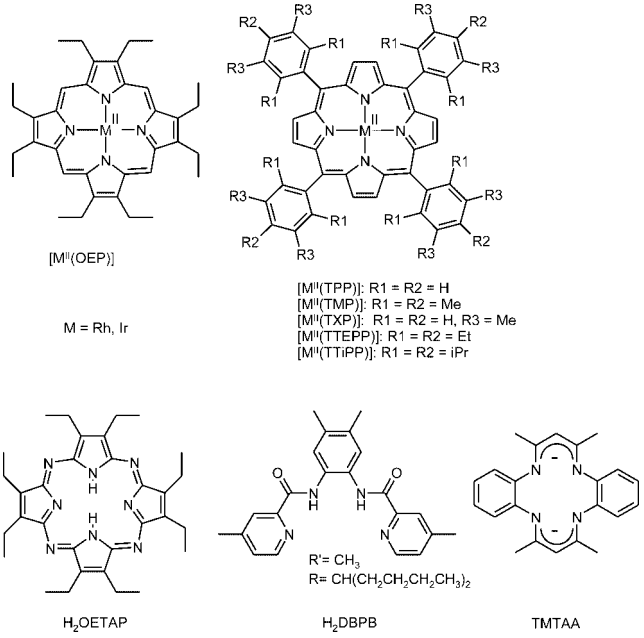


Figure 12. Porphyrinato $Rh^{II}$ and $Ir^{II}$ complexes and related N-ligands used in the organometallic chemistry of planar $Rh^{II}$ metallo-radicals.

Generally, mononuclear $[M^{II}(por)]$ species (Figure 12) are prepared by thermally or photo-chemically induced homolytic M–M, M–H or M–C bond splitting of their corresponding M–M, $M^{III}$–Me or $M^{III}$–H precursors.[46] Occasionally, also (electro)chemical reduction or oxidation has been applied.[47–49]

In all cases the mononuclear square planar $d^7$ complexes are very reactive. As a result, the least hindered complexes containing the porphyrins OEP (octaethylporphyrinato), TPP tetraphenylporphyrinato, TTP (tetratolylporphyrinato) and TXP [tetrakis(3,5-dimethylphenyl)porphyrinato] easily dimerize (Figure 13) to form diamagnetic metal–metal-bonded dinuclear species (in which a description as $M^I$–$M^{III}$ is indistinguishable from a antiferromagnetically coupled $M^{II}$–$M^{II}$ system). The Rh–Rh bond is, however, rather weak and allows thermal homolytic Rh–Rh bond splitting to study the reactivity of the mononuclear species. To promote dissociation of the dinuclear Rh–Rh species in mononuclear square planar $d^7$ species, porphyrin ligands have been supplied with bulky groups at their periphery. The steric bulk of the porphyrin dianion decreases in the order TTiPP > TTEPP > TMP > TXP > TTP > TPP > OEP

 © 2007 Wiley-VCH Verlag GmbH & Co. KGaA, Weinheim 

(see Figure 12). More bulky porphyrins result in weaker Rh–Rh bonds (Rh–Rh bond dissociation enthalpies: OEP: 69 kJ mol$^{-1}$; TXP: about 50 kJ mol$^{-1}$; TMP: about 0 kJ mol$^{-1}$) and consequently more reactive systems.[50–52]

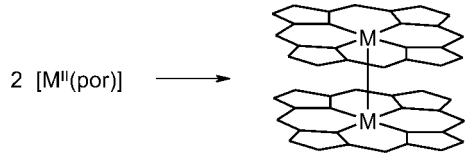


Figure 13. Formation of dinuclear M–M bonded species from [M$^{II}$(por)] species (M = Rh, Ir).

The complexes [Rh$^{II}$(TMP)], [Rh$^{II}$(TTEPP)], [Rh$^{II}$-(TTiPP)], [Ir$^{II}$(TTEPP)] and [Ir$^{II}$(TTiPP)] are sufficiently bulky to completely prevent dimerization [TMP = tetramesitylporphyrinato; TTEPP = tetra(2,4,6-triethylphenyl)porphyrinato TTiPP = tetra(2,4,6-triisopropylphenyl)porphyrinato]. EPR spectroscopy, $^1$H NMR paramagnetic shifts and line broadening studies have proven useful to study the (electronic) structure of these paramagnetic complexes (and their adducts with ethene, see below).[52–54] EPR parameters of the rhodium complexes [Rh$^{II}$(TMP)] and [Rh$^{II}$-(TTiPP)] are consistent with a prevalent $d_{z^2}$ SOMO associated with a $(d_{xy})^2(d_{xz,yz})^4(d_{z^2})^1$ ground state. Remarkably, the iridium complex [Ir$^{II}$(TTiPP)] does not reveal an observable EPR spectrum, which was explained by the presence of one or more excited states with energies close to the ground state, causing rapid electron-spin relaxation.[55] This was further confirmed by the thermal behavior of the pyrrole chemical shifts. While a linear dependence of the paramagnetic shift of [Rh$^{II}$(TTiPP)] against 1/T (inverse of the temperature) indicates a simple Curie paramagnetic behavior associated with a single contributing state [$(d_{z^2})^1$], the curvature of the plot for [Ir$^{II}$(TTiPP)] suggests that several states are thermally populated. The upfield chemical shifts of the pyrrole hydrogen atoms ($\delta_{pyr}$ = –20.9 ppm) compared to the downfield chemical shift of [Rh$^{II}$(TTiPP)] ($\delta_{pyr}$ = +17.5 ppm) was taken as evidence for spin population of the porphyrin π*-orbitals in case of iridium. This can be explained by assuming an $(d_{xy})^2(d_{z^2})^2(d_{xz,yz})^3$ground state, in contrast to the $(d_{xy})^2(d_{xz,yz})^4(d_{z^2})^1$ ground state observed for the rhodium analog.

### 3.2 Reactivity of M$^{II}$(alkene)(N-ligand) Species without Allylic Hydrogen Atoms

#### *3.2.1 M–C and C–C Coupling Reactions*

A variety of alkenes react with [Rh$^{II}$(OEP)] (Figure 12) to form binuclear alkyl-bridged [Rh$^{III}$(OEP)(μ-CH$_2$CHR-)-Rh$^{III}$(OEP)] complexes (Figure 14). The reaction of [Rh$^{II}$-(OEP)] with styrene was claimed to proceed by a radical chain mechanism.[56] In the absence of [Rh$^{III}$(OEP)(H)], the initially formed [Rh$^{II}$(OEP)(CH$_2$=CHPh)] intermediate reacts with another [Rh$^{II}$(OEP)]$_2$ complex abstracting a [Rh$^{II}$(por)] radical, thus yielding the alkyl-bridged species [Rh$^{III}$(OEP)(μ$_2$-CH$_2$CHPh-)Rh$^{III}$(OEP)]. In the presence of [Rh$^{III}$(OEP)(H)], the intermediate [Rh$^{II}$(OEP)(CH$_2$=CHPh)] abstracts a hydrogen atom from [Rh$^{III}$(OEP)(H)] to form a mononuclear alkyl complex [Rh$^{III}$(OEP)(CH$_2$CH$_2$Ph)] (Figure 14).

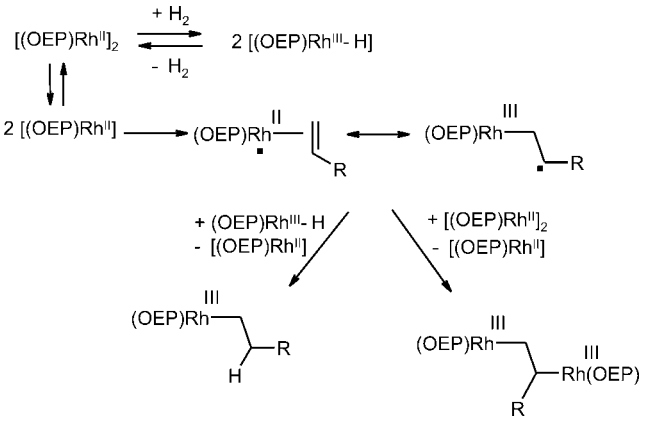


Figure 14. Reactivity of [Rh$^{II}$(por)] and [Rh$^{III}$(por)(H)] towards alkenes without allylic hydrogen atoms.

Other alkenes like acrylates[57] give similar alkyl-bridged species [Rh$^{III}$(OEP)(μ$_2$-CH$_2$CHR-)Rh$^{III}$(OEP)], and acetylenes give the corresponding μ$_2$-CH=CR-bridged species [Rh$^{III}$(OEP)(μ$_2$-CH=CHR-)Rh$^{III}$(OEP)].[58]

A series of more hindered [Rh$^{II}$(por)] complexes with por = TMP, TTEPP and TTiPP provide further insight in the behavior of the [Rh$^{II}$(por)(alkene)] intermediates. Like [Rh$^{II}$(OEP)], the least hindered [Rh$^{II}$(TMP)] reacts with ethene to form the diamagnetic ethylene-bridged species [Rh$^{III}$(TMP)(μ$_2$-C$_2$H$_4$-)Rh$^{III}$(TMP)] by a bimolecular M–C coupling reaction.[59] Increasing the steric bulk by using TTEPP prevents direct M–C coupling, and [Rh$^{II}$(TTEPP)] reacts with ethene via a bimolecular C–C coupling between two rhodium–ethene radicals to form the butylene-bridged species [Rh$^{III}$(TTEPP){μ$_2$-CH$_2$CH$_2$–CH$_2$CH$_2$–Rh$^{III}$-

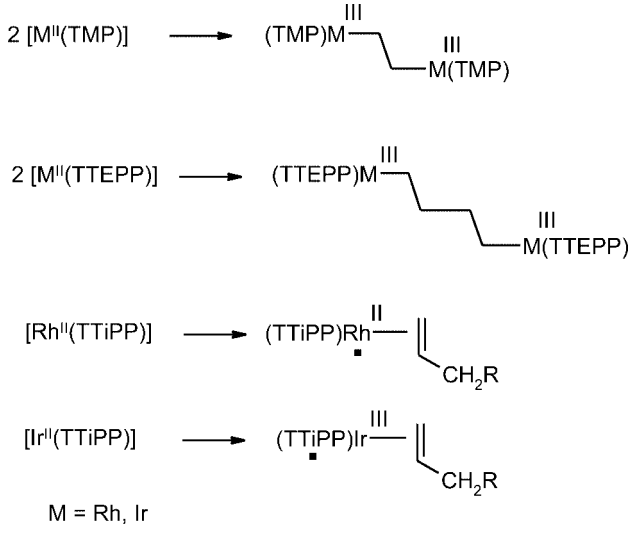


Figure 15. The reactivity of [M$^{II}$(por)] species changes from M–C to C–C coupling to no coupling at all upon increasing the steric bulk.

 © 2007 Wiley-VCH Verlag GmbH & Co. KGaA, Weinheim 

(TTEPP)}], see Figure 15.[60] A similar intermolecular $C_{alkene}$–$C_{alkene}$ bond formation involving two cot ligands was observed following oxidation of [$Rh^{I}$(Cp)(cot)].[61]

Neither for [$Rh^{II}$(TMP)] nor for [$Rh^{II}$(TTEPP)] any intermediates were observed with EPR spectroscopy. However, a further increase of the steric bulk by using [$Rh^{II}$(TTiPP)] gives rise to a reasonably stable paramagnetic ethene adduct [$Rh^{II}$(TTiPP)($CH_2$=$CH_2$)]$^{\cdot}$, revealing a rhombic EPR spectrum at 90 K ($g$ values: $g_1$ = 2.323, $g_2$ = 2.222 and $g_3$ = 1.982). A substantial spin population at ethene (ca. 0.29) was derived from the $^{13}$C hyperfine couplings of [$Rh^{II}$(TTiPP)($^{13}CH_2$=$^{13}CH_2$)] ($A_{zz}$: 38 MHz, $A_{xx}$ = $A_{yy}$ ≈ 5 MHz).[60,62] The spin population at rhodium was estimated at about 0.67. The equivalence of the two $^{13}$C atoms in the EPR spectrum reveals a symmetrically bound ethene π complex, and the delocalization of the unpaired electron to the ethene fragment (29%) occurs almost entirely by the $C_{2p}$ orbitals. At temperatures > 200 K [$Rh^{II}$(TTiPP)(ethene)] loses the ethene fragment to form [$Rh^{II}$(TTiPP)].[63]

Reactions of the iridium complexes [$Ir^{II}$(TMP)] and [$Ir^{II}$(TTEPP)] with ethene proceed analogously to the above described rhodium analogs (Figure 16).[64] Like its rhodium analog, reaction of [$Ir^{II}$(TTiPP)] with ethene does not result in M–C or C–C coupling, and formation of the ethene adduct is witnessed by NMR, UV/Vis ($\lambda_{max}$ = 444 nm and 730 nm) and EPR spectroscopy [$<g>$ = 1.987 (290 K); $g_{\|}$ = 1.96, $g_{\perp}$ = 1.998 (90 K)]. However, these spectroscopic data are indicative of a donor-induced intramolecular electron transfer from the $Ir^{II}$ center to the porphyrin ligand π* orbital to yield a $Ir^{III}$(por$^{\cdot 3-}$) species. This contrasts the results obtained by ethene binding to [$Rh^{II}$(TTiPP)], where the unpaired electron remains in the $d_{z^2}$ orbital.

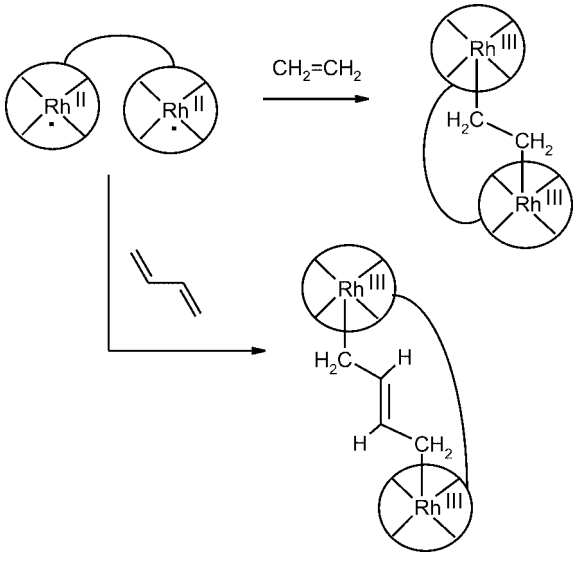


Figure 16. Reaction of alkenes with tethered (por)$Rh^{II}$ complexes.

Selective binding of ethene and butadiene between the two rhodium sites of a tethered bimolecular bis(por)Rh species with steric demands comparable to TMP, results in selective intramolecular coupling (Figure 16).[65] This gives further support to the idea that formation of alkyl-bridged species from alkenes and [$M^{II}$(por)] requires a concerted action of two metallo-radical sites.[60]

The reactions of [$Rh^{II}$(por)] with alkenes reveal that the [$Rh^{II}$(por)(alkene)] intermediates have a substantial spin density at the alkene fragment. This prompted the Wayland group to investigate attempts to initiate radical polymerization of acrylates with these species.[57] Although photo-promoted radical initiation (involving homolytic Rh–C bond splitting) was achieved, direct radical initiation with [$Rh^{II}$(OEP)] or [$Rh^{II}$(TMP)] proved not possible.

On the basis of an estimated Rh–$CH_2$R bond dissociation enthalpy (BDE) of ca. 209 kJ mol$^{-1}$, the energy associated with alkene binding to [$Rh^{II}$(por)] estimated at 0–33 kJ mol$^{-1}$,[57,63] and the energy required to convert ethene into its diradical $^{\cdot}CH_2$–$CH_2^{\cdot}$ (268 kJ mol$^{-1}$), formation of an intermediate [$Rh^{III}$(por)($CH_2$–$CH_2^{\cdot}$)] species with 100% spin population at the β-carbon atom requires about 59 kJ mol$^{-1}$. Relaxation of this species to the more stable π complex [$Rh^{II}$(por)($CH_2$=$CH_2$)] should be exothermic by about 59–92 kJ mol$^{-1}$.[57] On the basis of these arguments (and the above EPR results), the authors argued that [$Rh^{II}$(por)(alkene)] complexes are not authentic alkyl radicals and therefore cannot initiate alkene polymerization reactions (Figure 17).

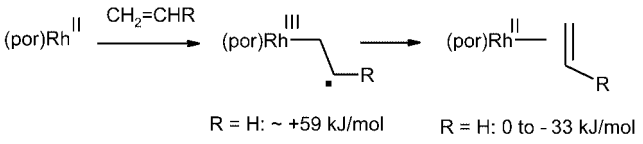


Figure 17. [$Rh^{II}$(por)(alkenes)]; metal- or carbon-centered radicals?

These arguments also imply that formation of "slipped olefin"/ethyl radical species [$M^{II}$(por)($CH_2$–$CH_2^{\cdot}$)] could be rather unfavorable for these complexes. On the other hand, coupling of two [$M^{II}$(por)(alkene)] species with C–C bond formation to yield $M^{III}$–$CH_2CH_2$–$CH_2CH_2$–$M^{III}$ are most likely to proceed via species having at least some [$Rh^{III}$(por)($CH_2$–$CH_2^{\cdot}$)] contribution to their electronic structure. Furthermore, substituents known to stabilize radicals should favor the [$Rh^{III}$(por)($CH_2$–$CHR^{\cdot}$)] contribution [e.g. R = Ph, C(O)R, CN, alkyls in Figure 17].

Binding of an additional σ-donor ligand to neutral 17-VE [$M^{II}$(por)(alkene)] species might not be very easy, but might nevertheless facilitate formation of such bent [$Rh^{III}$(por)($CH_2$–$CH_2^{\cdot}$)] intermediates. This is inspired by recent investigations concerning the reactivity of [$Ir^{II}$($Me_3$tpa)(ethene)]$^{2+}$ with a variation of substrates in MeCN as a solvent. Unlike the [$M^{II}$(por)(alkene)] species, these [$Ir^{II}$($Me_3$tpa)(ethene)]$^{2+}$ complexes do not spontaneously form butylene or ethylene-bridged dinuclear $M^{III}$–$CH_2$-$CH_2CH_2CH_2$–$M^{III}$ or $M^{III}$–$CH_2CH_2$–$M^{III}$ species. In the presence of MeCN, however, such reactivity is triggered (Figure 18). These reactions likely proceed via the $Ir^{III}$–$CH_2$–$CH_2^{\cdot}$-type radicals shown in Figure 10 (see section 3.1.1). A stronger M–C bond of Ir compared to Rh is per-

 © 2007 Wiley-VCH Verlag GmbH & Co. KGaA, Weinheim 

haps a further contributing factor to stabilization of the bent alkene structure in $[Ir^{III}(Me_3tpa)(MeCN)(CH_2–CH_2^{\cdot})]^{2+}$ compared to $[Rh^{II}(por)(alkene)]$.

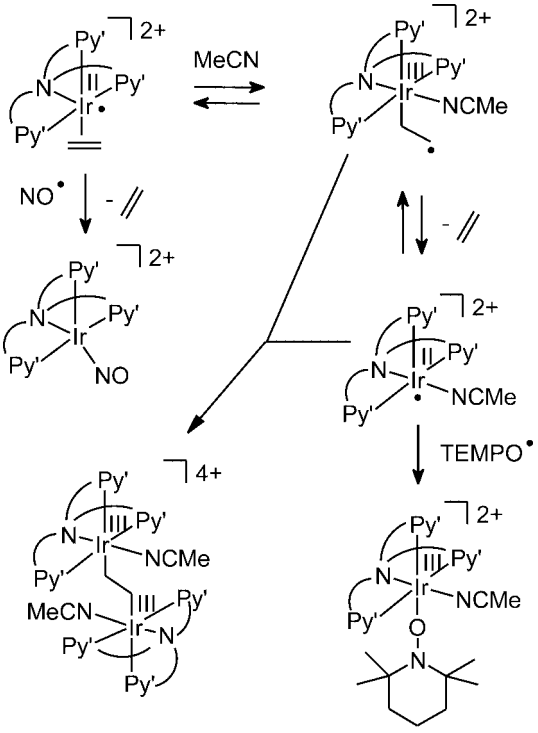


Figure 18. Formation of $Ir^{III}–CH_2CH_2–Ir^{III}$ and $Ir^{III}$-TEMPO via $Ir^{III}(CH_2CH_2^{\cdot})$(NCMe) and $Ir^{II}$(NCMe) species.

Dissociation of ethene from $[Ir^{III}(CH_2CH_2^{\cdot})(Me_3tpa)(NCMe)]^{2+}$ leads to the reactive metallo-radical $[Ir^{II}(Me_3tpa)(NCMe)]^{2+}$. This species contains only N-donor ligands and has its unpaired electron located in an orbital which is not sterically shielded by the ligand bulk. Although there is no spectroscopic evidence for formation of $[Ir^{III}(CH_2CH_2^{\cdot})(Me_3tpa)(NCMe)]^{2+}$ nor $[Ir^{II}(Me_3tpa)(NCMe)]^{2+}$, their existence can be rationalized from the reaction products of the $Ir^{II}$(ethene) species in acetonitrile. In the presence of the stable radical TEMPO, radical coupling of the metallo-radical $[Ir^{II}(Me_3tpa)(NCMe)]^{2+}$ with TEMPO takes place, leading to the formation of $[Ir^{III}(TEMPO^{-})(Me_3tpa)(NCMe)]^{2+}$. In the absence of TEMPO, $[Ir^{II}(Me_3tpa)(NCMe)]^{2+}$ couples with $[Ir^{II}(Me_3tpa)(CH_2CH_2)]^{2+}$, or perhaps more likely $[Ir^{III}(CH_2CH_2^{\cdot})(Me_3tpa)(MeCN)]^{2+}$ to form an ethylene-bridged species (Figure 18).[7,39] The increased reactivity on going from $Me_3tpa$ to the less bulky $Me_2tpa$ complex in formation of the ethylene-bridged species, is in good agreement with the proposed associative addition of acetonitrile to $[Ir^{II}(Me_ntpa)(ethene)]^{2+}$ being the first step of the dimerization process.

In contrast to reactions of $[M^{II}(por)]$ with alkenes, no butylene-bridged species were formed. Apparently, the concentration of $[Ir^{III}(CH_2CH_2^{\cdot})(N_4\text{-ligand})(MeCN)]^{2+}$ is too low for carbon–carbon coupling reactions to take place, and metal–carbon couplings with $[Ir^{II}(N_4\text{-ligand})(NCMe)]^{2+}$ species prevail.

The formation of the similar products $[\{Ir^{III}(Me_3tpa)(NCMe)\}_2(\mu_2\text{-}CH_2CH_2)]^{4+}$, $[\{Ir^{III}(Me_3tpa)(NCPh)\}_2(\mu_2\text{-}CH_2CH_2)]^{4+}$ and $[\{Ir^{III}(Cl)(Me_3tpa)\}_2(\mu_2\text{-}CH_2CH_2)]^{2+}$ indicate that this chemistry is not restricted to acetonitrile and expands to other σ-donors (nitrils, $Cl^{-}$, $H_2O$).[7,8]

### *3.2.2 [$Rh^{II}$(por)(alkene)] Intermediates in Alkene Insertions into Rh–H Bonds*

Insertion reactions of alkenes into the Rh–H bonds of the less hindered porphyrinato complexes $[Rh^{III}(OEP)(H)]$ and $[Rh^{III}(TPP)(H)]$ are strongly related to the above described reactivity of $[M^{II}(por)]$ radicals with alkenes. Because $[Rh^{III}(por)(H)]$ species lack any *cis* vacant sites, these insertion reactions are quite remarkable and do not likely proceed via a common (migratory) insertion requiring coordination of the olefinic substrates *cis* to the Rh–H bond. In fact the insertion reactions are reported to proceed through radical mechanisms. The hydride species are in equilibrium with the $[Rh^{II}(por)]_2$ dimeric species (Figure 14) through bimolecular reductive elimination of $H_2$ (a process not accessible for the more hindered TMP or TTiPP complexes).[66] Then, thermal homolytic bond splitting of the Rh–Rh bond allows formation of a reactive mononuclear $Rh^{II}$(alkene) adduct, which subsequently reacts with $H_2$ or $[Rh^{III}(por)(H)]$ to abstract a hydrogen atom to give the "insertion" product $[Rh^{III}(por)(CH_2CH_2R)]$. Similar "insertions" of alkenes into the Rh–H bond of $[Rh^{III}(TPP)(H)]$ (via similar radical pathways) have been used to obtain $Rh^{III}–CH_2–$(alkyl)–Nu*H* species (Nu*H* = OH, NH) using alkenes functionalized with end-on -OH and -NH functionalities. Under basic conditions, intramolecular $S_N2$-type attack of the Nu at the α-carbon atom of $Rh^{III}–CH_2–$(alkyl)–Nu yields $[Rh^{I}(TPP)]^{-}$ and cyclic organic products [–$CH_2$–(alkyl)–Nu–], see Figure 19. Protonation of $[Rh^{I}(TPP)]^{-}$ then allows regeneration of $[Rh^{III}(TPP)(H)]$. The combination of these reactions constitutes a new method for selective intramolecular anti-Markovnikov hydrofunctionalization of alkenes with O–H and N–H functionalities.[67] In this way three- and five-membered ring compounds (epoxides, furan deriv-

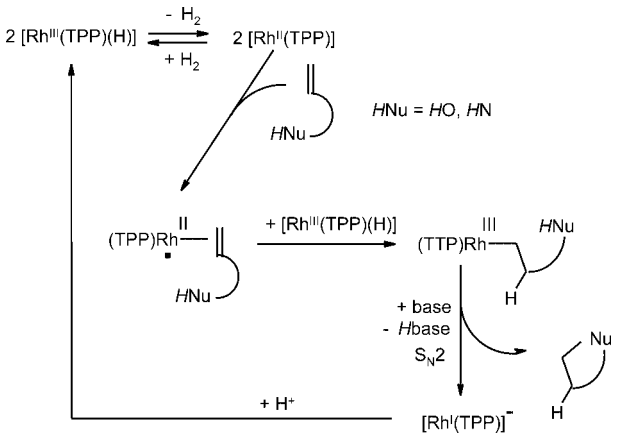


Figure 19. Selective intramolecular anti-Markovnikov hydrofunctionalization of alkenes with O–H and N–H functionalities via radical insertion of alkenes in the Rh–H bond.

 © 2007 Wiley-VCH Verlag GmbH & Co. KGaA, Weinheim 

atives, pyrrolidine derivatives) were readily obtained. Formation of four- or six-membered rings proved not possible, and lead to regeneration of the starting alkenes instead (by a net β-hydrogen elimination).

The (TPP)Rh system efficiently mediates all steps, but the system is not capable of mediating the anti-Markovnikov hydro-functionalization reactions in a one-pot catalytic reaction. So far, the reaction conditions required for the different reaction steps proved incompatible.

### *3.2.3. [M$^{II}$(por)(alkene)] Intermediates in Reactions of [M$^{III}$(por)(alkyl)] Species with Nitroxyl Radicals*

[M$^{II}$(por)(alkene)] species (M = Rh, Ir) also seem to be important intermediates in reactions of [M$^{III}$(por)(alkyl)] species with TEMPO and related nitroxyl radicals (M = Rh, Ir, por = TTP, TMP and some less common OMP, BTPP and BOCP porphyrinato ligands shown in Figure 20).

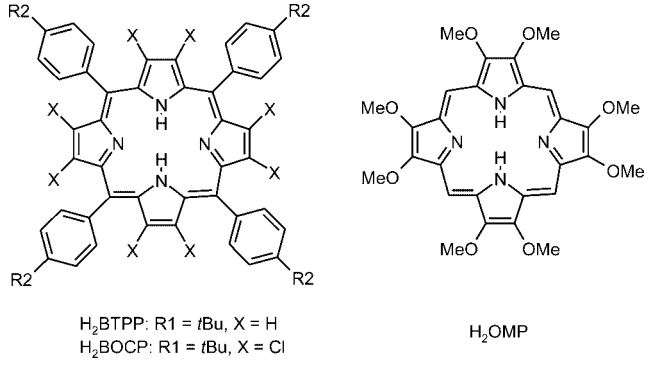


Figure 20. Ligand coding of the porphyrins BTPP, BOCP and OMP.

The [M$^{III}$(por)(alkyl)] complexes lacking β-hydrogen atoms do not react with nitroxyl radicals, but (por)Rh–alkyl species with β-hydrogen atoms eliminate alkene fragments upon heating in the presence of TEMPO.[68,69] For R = –CH$_2$–CH$_2$–Ph, formation of styrene was confirmed with NMR (Figure 21).

Abstraction of β-hydrogen atoms from alkyl species [M$^{III}$(por)(–CH$_2$CH$_2$R)] yields alkyl radical species [M$^{III}$(por)(–CH$_2$CHR$^{\cdot}$)], which are in fact the same activated β-alkyl radicals resulting from increasing the M–C–C angle of [M$^{II}$(por)(CH$_2$=CHR)] species. These [M$^{III}$(por)(–CH$_2$CHR$^{\cdot}$)] species should thus easily relax to the more stable alkene complexes [M$^{II}$(por)(CH$_2$=CHR)]. Because [Rh$^{II}$(por)] species have only a weak affinity for alkenes,[63] [M$^{II}$(por)(CH$_2$=CHR)] should readily lose the alkene (Figure 21). The resulting 15 VE [Rh$^{II}$(por)] species subsequently react with TEMPO to form [Rh$^{III}$(por)(CH$_3$)] by a C–C bond activation reaction with net abstraction of a methyl radical from TEMPO. Formation of [Rh$^{II}$(TMP)(R)] species by a net abstraction of an alkyl radical R$^{\cdot}$ from a nitroxyl radical (R′R$_2$C)$_2$NO$^{\cdot}$ has also been observed for isolated [Rh$^{II}$(TMP)] species in the presence of nitroxyl radicals (see Figure 21).[70] The mechanisms of the latter reactions are not very clear yet.

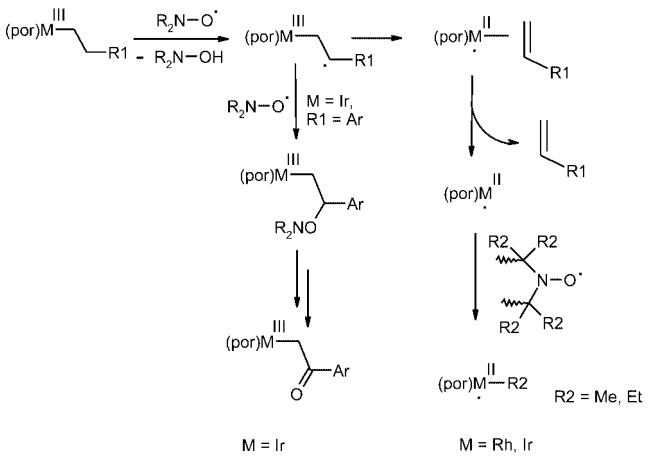


Figure 21. Reaction of TEMPO and related nitroxyl radicals with [M$^{III}$(por)(alkyl)] species (M = Rh, Ir) via [M$^{II}$(por)(alkene)] intermediates.

For the analogous iridium complexes [Ir$^{III}$(TTP)(R)], similar results were obtained upon reaction with TEMPO. Complexes lacking β-hydrogen atoms did not react, and non-aromatic alkyl complexes eliminate alkenes allowing formation of [Ir$^{III}$(TTP)(CH$_3$)] by C–C activation of TEMPO by [Ir$^{II}$(TTP)]. Arylethyl complexes [Ir$^{III}$(TTP)(–CH$_2$CH$_2$Ar)], however, reveal different products, which further support the proposed radical abstraction mechanism.[71] Under N$_2$, TEMPO oxidizes the [Ir$^{III}$(TTP)(–CH$_2$CH$_2$Ar)] species selectively at the β position to yield [Ir$^{III}$(TTP){–CH$_2$C(O)Ar}] (Figure 21). The mechanism proposed for this reaction involves abstraction of a β-hydrogen atom from [Ir$^{III}$(TTP)(–CH$_2$CH$_2$Ar)] by TEMPO to give [Ir$^{III}$(TTP)(–CH$_2$CH$^{\cdot}$Ar)] and TEMPO*H*. Apparently, due to stabilization of the β-carbon radical by the aromatic group and a substantially stronger Ir–C bond compared to a Rh–C bond, this species is sufficiently long-lived to react with a second TEMPO moiety. Coupling of the [Ir$^{III}$(TTP)(–CH$_2$CH$^{\cdot}$Ar)] radical with the TEMPO radical was proposed to yield a [Ir$^{III}$(TTP)(–CH$_2$CHAr–O–NR$_2$)] intermediate. The latter could then decompose to the observed [Ir$^{III}$(TTP){–CH$_2$C(O)Ar}] species, either directly through a hydrogen shift (with elimination of R$_2$NH) or by abstraction of the remaining β-hydrogen by an additional TEMPO moiety.

### 3.3 Reactivity of M$^{II}$(alkene)(N-ligand) Species Bearing Allylic Hydrogen Atoms

Reaction of [Rh$^{II}$(OEP)] with alkenes (CH$_2$=CHR) containing allylic hydrogen atoms such as allylbenzene (R = CH$_2$Ph), allyl cyanide (R = CH$_2$CN) and 1-hexene (R = CH$_2$C$_3$H$_8$) results in formation of σ-allyl complexes [Rh$^{III}$(OEP)(CH$_2$CH=CHR)] in about 50% yield (Figure 22).[58] A more detailed study concerning the behavior of [Rh$^{II}$(OEP)] towards propene was reported.[72] Propene initially forms the alkyl-bridged species [Rh$^{III}$(OEP){μ$_2$-CH$_2$CH(Me)-}Rh$^{III}$(OEP)]. This species reveals an interest-

 © 2007 Wiley-VCH Verlag GmbH & Co. KGaA, Weinheim 

ing 1,2-exchange of the two metal sites, reflecting the lability of the Rh–C bond. The species is not stable and converts over the course of some days to a 1:1 mixture of the σ-allyl species [$Rh^{III}$(OEP)($CH_2CH{=}CH_2$)] and the propyl species [$Rh^{III}$(OEP)($CH_2CH_2CH_2$)], which likely involves a net transfer of an allylic hydrogen atom from [$Rh^{II}$(OEP)-(propene)] to another [$Rh^{II}$(OEP)(propene)] species (obtained from [$Rh^{III}$(OEP)($\mu_2$-$CH_2CH$(Me)-)$Rh^{III}$(OEP)] by Rh–C homolysis), see Figure 22.

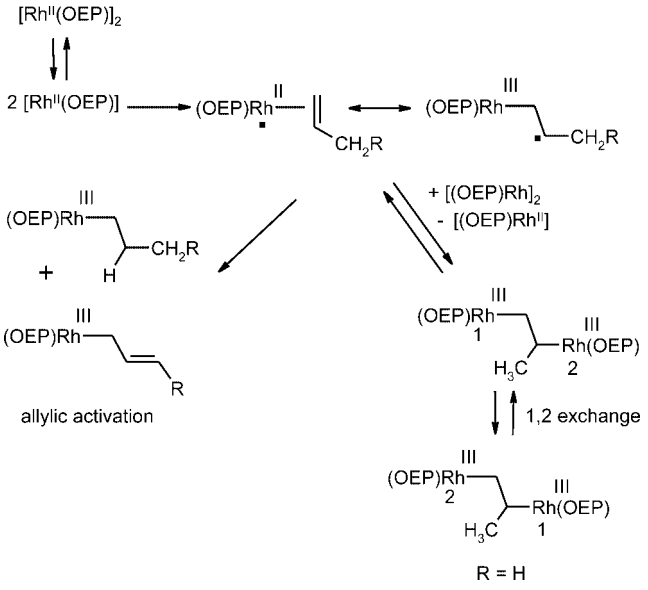


Figure 22. Reactivity of [$Rh^{II}$(por)] species towards alkenes containing allylic hydrogen atoms.

A comparable allylic activation of methyl methacrylate [$CH_2$=C(Me)(COOMe)] was reported to give a 1:1 mixture of [$Rh^{III}$(OEP){$CH_2C$(COOMe)=$CH_2$}] and [$Rh^{III}$(OEP)-{$CH_2CH$(Me)(COOMe)}]. Reaction of the sterically more hindered [$Rh^{II}$(TMP)] with methyl metacrylate yields a 1:1 mixture of [$Rh^{III}$(TMP){$CH_2C$(COOMe)=$CH_2$}] and [$Rh^{III}$(TMP)(H)]. The reactions were proposed to proceed by abstraction of an allylic hydrogen atom from the metallo-radical alkene complex [$Rh^{II}$(por){$CH_2$=C-(Me)(COOMe)}] by the metallo-radical [$Rh^{II}$(por)] to yield directly the σ-allyl complex [$Rh^{III}$(por){$CH_2C$-(COOMe)=$CH_2$}] and the hydride species [$Rh^{III}$(por)(H)]. As described above, the OEP complexes allow "insertion" reactions into the Rh–H bond, which for methyl methacrylate yields [$Rh^{III}$(OEP){$CH_2CH$(Me)(COOMe)}]. Alkene "insertion" into the Rh–H bond of the TMP complexes does not occur, presumably for steric reasons.

Further evidence for allylic C–H activation of $M^{II}$(α-alkene) species proceeding via bimolecular abstraction of an allylic hydrogen by another $M^{II}$ species was gathered by studying the decomposition of dicationic [$M^{II}$(cod)($N_3$-ligand)]$^{2+}$ species. Although the [$M^{II}$(cod)($N_3$-ligand)]$^{2+}$ species can be isolated as pure compounds, in solution they decompose through an allylic C–H activation process. The [$M^{II}$($N_3$-ligand)(cod)]$^{2+}$ complexes invariably decompose to 1:1 mixtures of [$M^{III}$($N_3$-ligand)(cyclooctadienyl)]$^{2+}$ and species that could be described as "protonated $M^{I}$(cod)" species. For the "protonated $M^{I}$(cod)" species the position of the proton depends on the nature of the metal. The proton ends-up at the metal for iridium, forming [$Ir^{III}$(H)($N_3$-ligand)(cod)]$^{2+}$, and at the $N_3$-ligand Py moiety for rhodium, forming [$Rh^{I}$($N_3$-ligand*H*)(cod)]$^{2+}$ (Figure 23).[41,42] The reaction rates decrease upon increasing the steric bulk of the $N_3$-ligand.

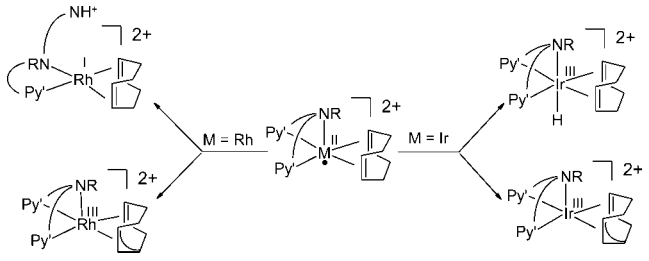


Figure 23. Selective conversion of the [$M^{II}$($N_3$-ligand)(cod)]$^{2+}$ complexes to allyl species [$M^{III}$(cyclooctadienyl)($N_3$-ligand)]$^{2+}$ (M = Rh, Ir) and equimolar amounts of [$Rh^{I}$($N_3$-ligandH)(cod)]$^{2+}$ (for M = Rh) or [$Ir^{III}$(H)($N_3$-ligand)(cod)]$^{2+}$ (for M = Ir).

The product ratio can be explained by a hydrogen-atom transfer from one $M^{II}$(cod) species to another $M^{II}$(cod) species. An electron-transfer (ET) disproportionation reaction between two $M^{II}$(cod) species to give $M^{I}$(cod) and $M^{III}$-(cod) followed by a proton transfer from an allylic position of $M^{III}$(cod) to $M^{I}$(cod) was ruled out.[41,42] A direct hydrogen-atom abstraction (at least in case of the more hindered Bn-dla ligands) of an allylic hydrogen atom of $M^{II}$(cod) by another $M^{II}$ species also seems unlikely, because the metal is rather shielded by the $N_3$-ligand PyMe bulk. The kinetic rate expression $v = k_{obsd.}$ [$M^{II}$]$^2$ in acetone, with $k_{obsd.} = k$[$H^+$][S] and [S] being the concentration of additional coordinating reagents (MeCN), is in agreement with a solvent-assisted dissociation of one of the pyridine donors.[42] Pyridine dissociation results in formation of more open, reactive species. Protonation of the non-coordinating pyridine increases the concentration of this species, and thus [$H^+$] appears in the kinetic rate expression. Both the rate expression and the kinetic activation parameters ($\Delta H^{\#}$ = 50 ± 8 kJ mol$^{-1}$, $\Delta S^{\#}$ = –113 ± 42 J K$^{-1}$ mol$^{-1}$ and $\Delta G_{289K}{}^{\#}$ = 84 ± 21 kJ mol$^{-1}$) are in agreement with a subsequent bimolecular hydrogen-atom transfer from an allylic $M^{II}$(cod) position to another $M^{II}$ species (Figure 24).

Formation of $M^{III}$(allyl) species from $M^{II}$(alkene) species (M = Rh, Ir) bearing allylic hydrogen atoms seems to be a more general decomposition pathway of such species. As described above, it has been observed as a decomposition pathway of [$M^{II}$(cod)($N_3$-ligand)]$^{2+}$ compounds, and in reactions of α-alkenes with [$Rh^{II}$(por)] species. Formation of [$Rh^{III}$($R_3$-Cp)(allyl)]$^+$ (allyl) species was also reported for in situ generated [$Rh^{II}$($R_3$-Cp)(cod)]$^+$.[73] Furthermore, one-electron oxidation of [$Ir^{I}$($Me_2$tpa)(propene)]$^+$ with [Ag]$PF_6$ in acetonitrile afforded the $Ir^{III}$(allyl) species [$Ir^{III}$($\eta^3$-propenyl)($Me_2$tpa)]$^{2+}$ in about 50% yield ($Me_2$-tpa = *N*-(2-pyridylmethyl)-*N*,*N*-bis[(6-methyl-2-pyridyl)methyl]amine), see Figure 25.[42]

 © 2007 Wiley-VCH Verlag GmbH & Co. KGaA, Weinheim 

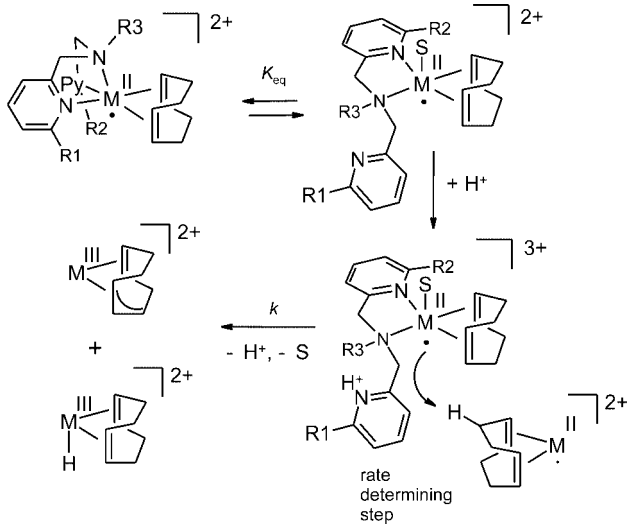


Figure 24. Proposed mechanism for the hydrogen-atom transfer between two $M^{II}$(cod) species.

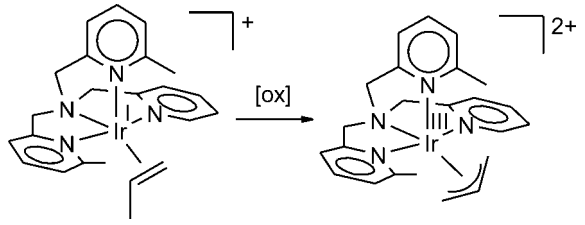


Figure 25. Formation of an $Ir^{III}$(allyl) species by oxidation of $[Ir^{I}(propene)(Me_2tpa)]^+$.

Notable exceptions to the general tendency of $M^{II}$(α-alkene) species (M = Rh, Ir) decomposing to $M^{III}$(allyl) species are the complexes $[M^{II}(C_6Cl_5)_2(1,5\text{-cod})]$ (M = Rh, Ir), $[Rh^{II}(\eta^5\text{-}C_5Ph_5)(1,5\text{-cod})]^+$ and $[Rh^{II}(\eta^5\text{-}C_5Ph_5)(1,3\text{-cod})]^+$, which are stable at room temp.[33–35] These species are sterically rather shielded around the metal, which might explain their relative stability. This can be taken as a further indication that such decomposition pathways proceed through bimolecular allylic H-atom abstraction by metal-centered radicals.

## 4. $M^{II}$(alkene) Species as Intermediates in Rh- and Ir-Catalyzed Alkene Oxygenation?

Though less well-known than Pd, both Rh and Ir are able to catalyze oxidation of alkenes with $O_2$ and $H_2O_2$,[74] Rh generally being more effective than Ir. Oxidation of terminal alkenes almost invariably results in formation of methyl ketones. Oxidation of internal alkenes leads to epoxides, allylic alcohols, ethers or ketones. The mechanistic picture of rhodium-catalyzed oxidations is complex with several mechanisms being proposed for various catalysts under different conditions: Wacker-type reactivity, reaction of a metal peroxide with the alkene to a peroxymetallacycle, formation of an intermediate hydroperoxo or alkylperoxo complex which reacts with the alkene, and some early work on alkene oxidation with peroxo Rh and Ir complexes was shown to proceed through free-radical pathways. In attempts to collect mechanistic information about rhodium- and iridium-catalyzed oxygenation of alkenes, stoichiometric oxygenation of N-ligand $Rh^{I}$- and $Ir^{I}$-alkene complexes by $O_2$ has been investigated in detail over the past years.[74,75] Oxygenation products strongly vary with the N-ligand, the alkene (ethene, propene, 1,5-cyclooctadiene and other dienes) and the central metal (Rh, Ir), see Figure 26.

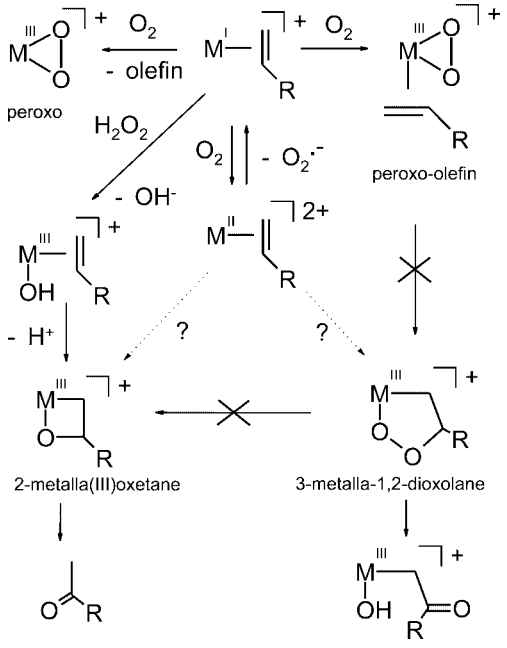


Figure 26. Oxygenation products from reaction of $[M^{I}(alkene)(N\text{-ligand})]^+$ species with $O_2$.

The reactivity of N-ligand $Rh^{I}$ and $Ir^{I}$-alkene fragments towards dioxygen varies between alkene displacement, formation of mixed $O_2$-alkene complexes, C–O bond formation (giving a 3-metalla-1,2-dioxolane), and combined O–O bond breaking/C–O bond making (giving a 2-metallaoxetane). Isolated peroxo complexes showed no further reactivity towards alkenes or alkene complexes, and isolated peroxo–ethene complexes did not contract to the corresponding peroxo-metallacycles (Figure 26). Isolated 3-metalla-1,2-dioxolanes, which were proposed as key-intermediates in the catalytic reactions, do not eliminate methyl ketones at all, but instead convert to formylmethyl-hydroxido complexes (Figure 26). The isolated 2-metalla(III)oxetanes, despite not being proposed in the catalytic reactions previously, proved actually much more likely candidates to be such key-intermediates. These species readily eliminate methyl ketones (acetaldehyde in case of the ethene precursor); the exact same products as obtained in the catalytic reactions. Formation of methyl ketones could not be demonstrated for any of the peroxo, peroxo–alkene or metal-dioxolane species. An important unanswered question is the mechanism of 2-metalla(III)oxetane formation in these reactions. Formation of 2-metalla(III)oxetanes from $M^{I}$-(alkene) and $H_2O_2$ seems straightforward (a net $OH^+$ transfer to the metal, followed by alkene insertion into the $M^{III}$–OH fragment,[74] see Figure 26), but the essential C–O

 © 2007 Wiley-VCH Verlag GmbH & Co. KGaA, Weinheim 

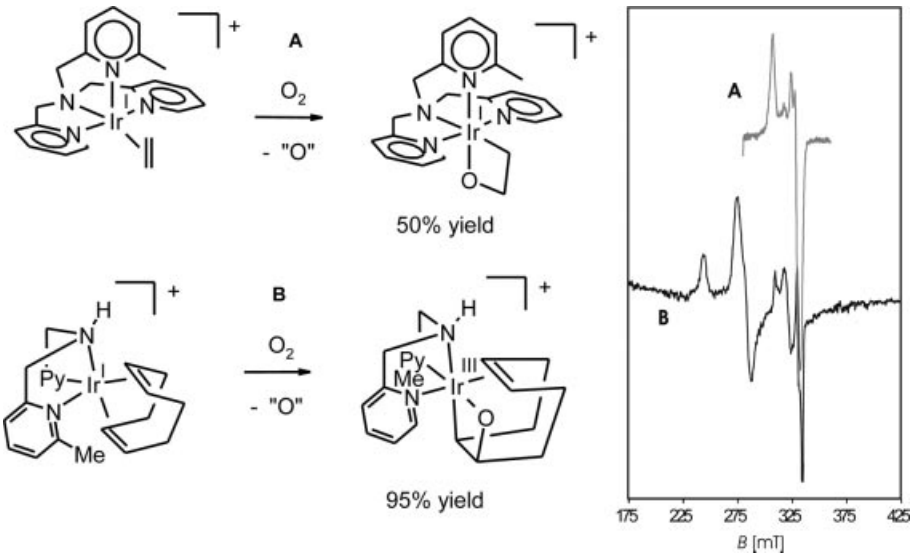


Figure 27. Formation of metallaoxetanes from reaction of $Ir^{I}$-alkene fragments with $O_2$ and the detection of possible $Ir^{II}$ and $Ir–O_2^{\cdot-}$ intermediates.

bond making step in oxygenation reactions of $M^{I}$(alkene) species with $O_2$ remains rather unclear.

Notably, for some of the more interesting reactions in Figure 26 leading to C–O bond formation with $O_2$, paramagnetic species were detected accompanying product formation. For example, reaction of $[Ir^{I}$(ethene)(Metpa)$]^+$ and $[Ir^{I}$(cod)(bpaMe)$]^+$ with $O_2$ in $CH_2Cl_2$ leads to formation of the corresponding 2-metallaoxetanes (Figure 27) in about 50% and 95% yield, respectively. These reactions consume only one O atom of $O_2$ per metal complex. The fate of the other O atom is not known.[76,77] Interestingly, during the course of these reactions, weak EPR signals were observed pointing to formation of paramagnetic Ir species, which are either intermediates or side products.[78,79]

To shed some light on the possible role of paramagnetic $M^{II}$(alkene) complexes in the essential C–O bond formation steps of these reactions, the reactivity of isolated $[M^{II}$-(alkene)(N-ligand)$]^{2+}$ species towards $O_2$ has been investigated in detail.

Treatment of $[Ir^{II}(Me_3tpa)(ethene)]^{2+}$ and $[M^{II}$(dpa)-(cod)$]^{2+}$ with dioxygen leads to formation of new EPR spectra.[8,38,41,42] A substantial decrease in the *g* anisotropy indicates a shift of the spin density from the metal to dioxygen. The observed spectra are consistent with formation of the superoxide complexes $[Ir^{III}(O_2^{\cdot})(Me_3tpa)(ethene)]^{2+}$ and $[M^{III}(O_2^{\cdot})$(dpa)(cod)$]^{2+}$. Formation of superoxide complexes from $[M^{II}(N_3$-ligand)(cod)$]^{2+}$ and $O_2$ appears to be reversible. Increasing the N-ligand steric bulk decreases the oxygen affinities. Reaction of $[Rh^{II}$(pla)(cod)$]^{2+}$ with $O_2$ only leads to small concentrations of $[Ir^{III}(O_2^{\cdot})$(pla)(cod)$]^{2+}$. The $[Rh^{II}$(R-bla)(cod)$]^{2+}$ (R = H, Bn) and $[Rh^{II}$(pla)-(nbd)$]^{2+}$ complexes proved to be air stable as a result of shielding by the bulky Py–Me groups.

No C–O bond-formation reactions were observed for any of the $[M^{III}(O_2^{\cdot})(N_3$-ligand)(cod)$]^{2+}$ complexes. These species decompose to the same mixture of compounds as observed for $[M^{II}(N_3$-ligand)(cod)$]^{2+}$ in absence of $O_2$ (see above).[41,42] Thus, unless these species play a role as co-catalysts, it seems unlikely that $M^{II}$(cod) species are intermediates in formation of 2-metalla-oxetanes from $M^{I}$(cod) complexes and $O_2$. For ethene complexes the situation might be different. $[Ir^{II}(Me_2tpa)(ethene)]^{2+}$ reacts rapidly with $O_2$, but not selectively (all solvents). The fate of the more hindered analog $[Ir^{III}(O_2^{\cdot})(Me_3tpa)(ethene)]^{2+}$ depends on the solvent. The reaction in acetone leads to yet unidentified products. The reaction in MeCN takes a different course (as described hereafter). To shed some light on these reactions, $[Ir^{III}(O_2^{\cdot})$(ethene) $(Me_3tpa)]^{2+}$ was trapped with DMPO.[8] This led to dissociation of ethene and formation of a C–O bond between the superoxide and DMPO (Figure 28). The peroxide-bridged species likely rearranges to a species with an acetal group, thus explaining the absence of proton hyperfine couplings in EPR. The unusual large N hyperfine coupling ($A^{N}_{average}$ = 74 MHz) compared to trapped organic radicals ($A^{N}$ = 42 MHz) indicates that the unpaired electron resides mainly at the nitrogen part of the nitroxyl group.[80] Therefore, DMPO appears to be coordinated to the iridium center. This is confirmed by the unusually large *g* anisotropy ($g_{11}$ = 2.036, $g_{22}$ = 2.014, $g_{33}$ = 1.986) for a DMPO-trapped radical (Figure 28). At room temperature this species converts to a diamagnetic species with a coordinated oxygenated DMPO fragment. This likely involves hydrogen abstraction from the solvent and elimination of $H_2O$ (Figure 28). Remarkably, such obtained solvent radicals were trapped by $Ir^{II}$ species, rather than the spin-trap DMPO. ESI-MS indicated clear formation of $[Ir^{III}(CH_2CN)(Me_3tpa)]^{2+}$ in acetonitrile and $[Ir^{III}(CH_2COCH_3)(Me_3tpa)]^{2+}$ in acetone.

The reactions of $[Ir^{III}$(ethene)$(N_4$-ligand)$]^{2+}$ species with dioxygen in the presence of MeCN result in formation of $Ir^{III}–CH_2C(O)H$ species. These reactions likely proceed via $[Ir^{III}(CH_2CH_2^{\cdot})(N_4$-ligand)(MeCN)$]^{2+}$ intermediates, which are easily formed upon contact with MeCN as described in section 3.1.1 (Figure 10). Quite likely, the triplet biradical

 © 2007 Wiley-VCH Verlag GmbH & Co. KGaA, Weinheim 

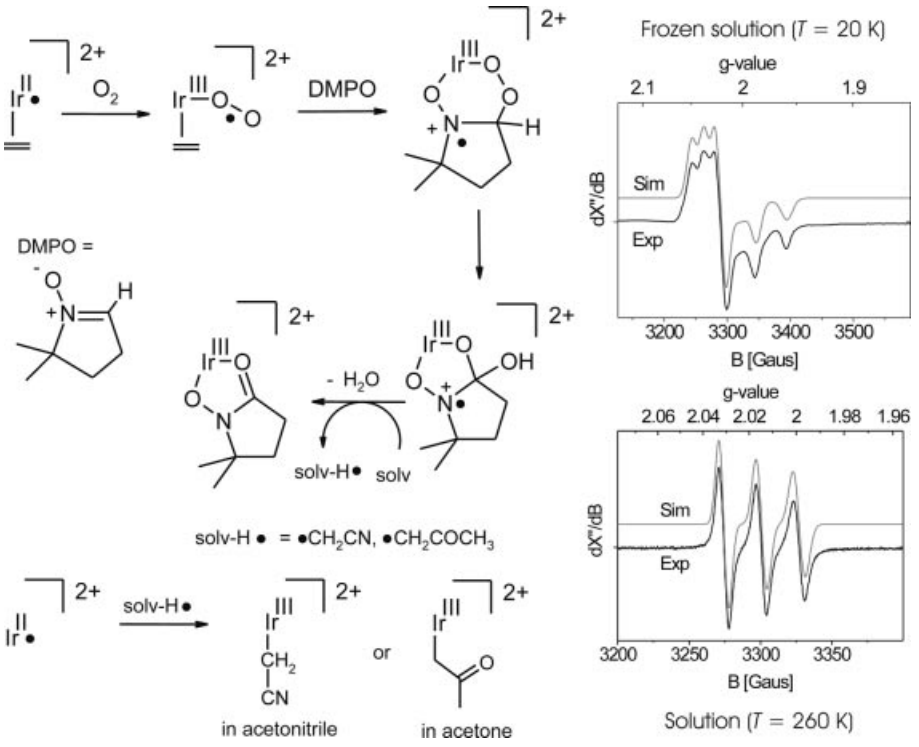


Figure 28. Proposed mechanism for the oxygenation of DMPO at $Ir^{II}$ and the EPR spectra belonging to the paramagnetic Ir–$O_2$–DMPO intermediate.

dioxygen reacts directly with the β-carbon-centered radical of $[Ir^{III}(CH_2CH_2^{\cdot})(N_4\text{-ligand})(MeCN)]^{2+}$ to give $Ir^{III}$–$CH_2CH_2OO^{\cdot}$ species. The latter alkylperoxo radical species then abstracts a hydrogen atom from acetonitrile, leading to a hydroperoxo intermediate $Ir^{III}$–$CH_2CH_2OOH$, which eliminates water to give the observed $Ir^{III}$–$CH_2C(O)H$ species (Figure 29).[8,38] Also in this case, the remaining solvent radical is trapped by the $Ir^{II}$ starting material. An alternative mechanism via $[Ir^{III}(O_2^{\cdot})(N_4\text{-ligand})(ethene)]^{2+}$ species cannot be ruled out completely though.

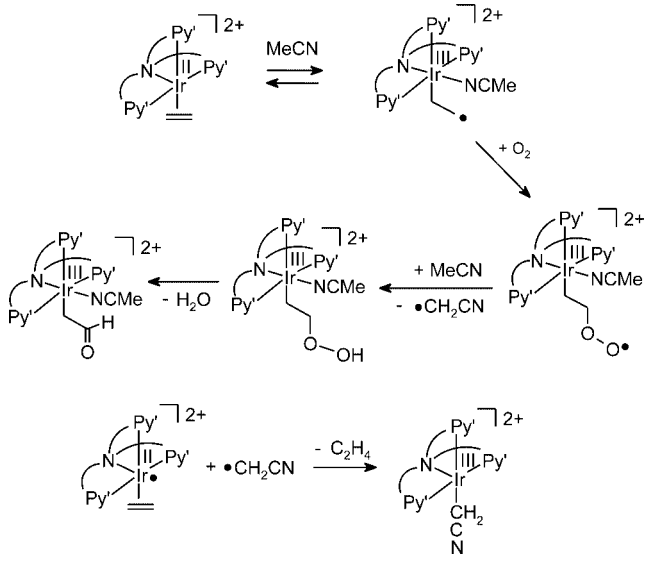


Figure 29. Proposed mechanism for the mono-oxygenation of $[Ir^{II}(Me_3tpa)(ethene)]^{2+}$ in acetonitrile.

With the exception of $M^{II}$(ethene) species, $M^{II}$(α-alkene) species are not very likely to be directly involved in the C–O bond-making processes of rhodium- and iridium-catalyzed alkene oxygenation reactions described by Mimoun, Read, Drago and others.[74] It seems that even in the presence of $O_2$, allylic C–H activation is the preferred kinetic decomposition pathway of such α-alkene complexes. Generally, such obtained (kinetically inert) $M^{III}$(allyl) species are not reactive towards $O_2$. $M^{II}$ species without a coordinated alkene might be involved though, perhaps facilitating formation of peroxides from $O_2$ and a sacrificial reductant (often an alcohol in the catalytic reactions). Such peroxides easily react with $M^{I}$(α-alkene) species to yield methyl ketones [via 2-metalla(III)oxetanes as intermediates, as described above, see Figure 26].

Somewhat related to this topic, $M^{II}$(nbd) species are potential Wacker-type catalysts for oxidation of norbornadiene to norbornenone. Dicationic $[M^{II}(bis\text{-alkene})(N_3\text{-ligand})]^{2+}$ species are stable towards ET disproportionation. The situation, however, changes in the presence of chloride anions, which trigger ET disproportionation. Formation of dicationic $[M^{III}(Cl)]$ products is probably less unfavorable than formation of tricationic $M^{III}$ species. Interestingly, $Cl^-$ triggered disproportionation of $[Rh^{II}(pla)(nbd)]^{2+}$ in the presence of water or alcohols led to formation of $[Rh^{I}(pla)(nbd)]^{+}$ and $[\{Rh^{III}(Cl)(nbd\text{-}OR)(pla)\}_2]^{2+}$ (Figure 30). The latter species likely result from a Wacker-type attack of water/alcohols to the $[Rh^{III}(Cl)(pla)(nbd)]^{2+}$ intermediate.

 © 2007 Wiley-VCH Verlag GmbH & Co. KGaA, Weinheim 

Heating $[\{Rh^{III}(Cl)(nbd\text{-}OH)(pla)\}_2]^{2+}$ in the presence of an excess of the oxidant $FeCl_3$ led to catalytic formation of norbornenone, albeit with only low total turnover numbers.[40] These reactions are nevertheless noteworthy, because no Wacker oxidation catalysts for norbornadiene have been reported and oxidation of other bis-alkenes also gives poor results or diketones.[81] The main problem with palladium-mediated Wacker oxidation of bis-alkenes is that attack of $OH^-$ or $H_2O$ to the $Pd^{II}$(bis-alkene) complex usually yields a $\eta^3$-3-hydroxy-enyl σ–π complex, in which coordination of the second double bond prevents easy β elimination.[82]

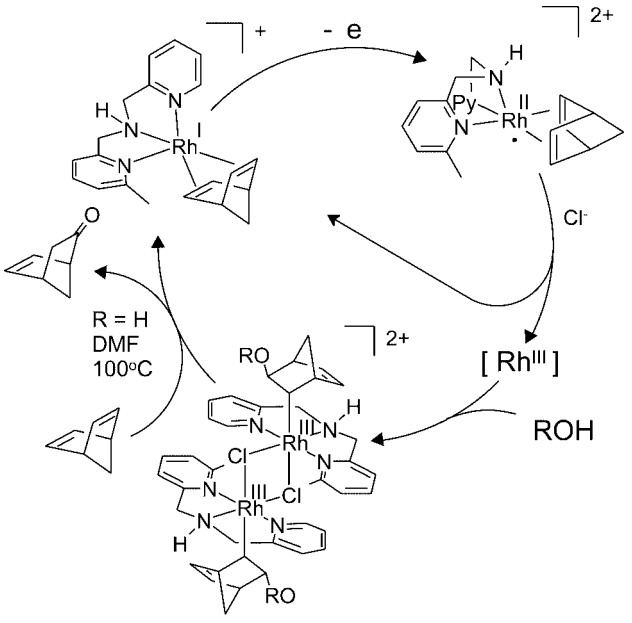


Figure 30. Catalytic formation of norbornenone through chloride-triggered disproportionation of $[Rh^{II}(pla)(nbd)]^{2+}$.

## 5. $Rh^{II}$-Alkene Species as Intermediates in Catalytic Carbene Transfer Reactions?

Diamagnetic dinuclear carboxylate-bridged $Rh^{II}$–$Rh^{II}$ species have been extensively studied as a catalysts for carbene-transfer reactions.[83] It has always been assumed that the $Rh^{II}$–$Rh^{II}$ species stay intact during catalysis, but this was never really proven. A study by Bergman clearly reveals that mononuclear $Rh^{II}$ species can also be active catalysts for carbene-transfer reactions. $[Rh^{II}(Cl)(Tf)(bisoxozaline)]$ ($Tf^-$ = triflate) is an active alkene cyclopropanation catalyst. Although the catalytic precursor does not contain Rh-alkene fragment, the carbene-transfer reaction is highly likely to involve such species as intermediates.

The catalytic activity is enhanced by addition of $NaBAr_F$, yielding $[Rh^{II}(bisoxozaline)(Cl)(CH_2Cl_2)]^+$ {$BAr_F^-$ = tetrakis[3,5-bis(trifluoromethyl)phenyl]borate}.[84] The active species is believed to be a low-valent 15 VE species with two (bis)oxozaline nitrogen atoms in mutual *trans* positions and a chlorido ligand occupying a third position. Two sites of the rhodium center are sterically hindered by the (bis)-oxozaline methyl groups and the bridging arene. In the *trans* position to the chloro ligand, a labile triflate anion or dichloromethane ligand is bound allowing easy formation of a vacant site. In the presence of diazoacetates, dimerization to fumarates and maleates takes place, indicative of carbene-transfer reactions.[84] Also selective cyclopropanation (Figure 31) of alkenes and formation of aziridines from imines is catalyzed by these complexes. With these results, one might consider open-shell species to play an active role in other carbene-transfer reactions as well.

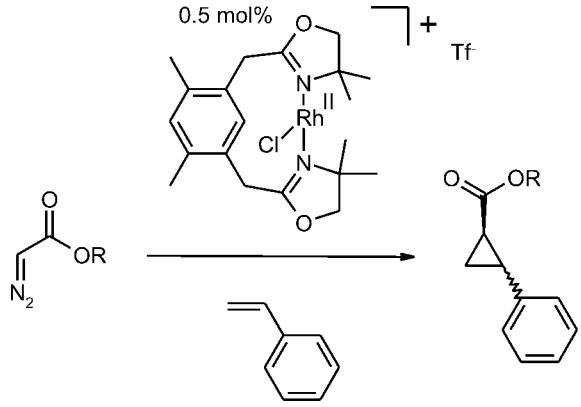


Figure 31. Cyclopropanation of styrene-mediated by a mononuclear $[Rh^{II}(Cl)_2(benbox)]^+$ complex.

For example, in the recently discovered Rh-mediated stereoselective polymerization of carbenes from diazoacetates, $Rh^{II}$(alkene) radicals might well be important (Figure 32).[85] It was shown that $[Rh^{I}$(prolinate)(cod)] is a catalyst precursor for polymerization of carbenes from diazoacetates, leading to formation of new, stereoregular (most likely syndiotactic) ester-functionalized polymethylenes. This new family of polymers contain a functional side group at each carbon of the polymer backbone. Polymers with molecular weights up to 190000 ($M_w$) were obtained as solid materials with interesting material properties. Notably, only about 1% of the Rh material becomes active in the polymerization reaction. Therefore, it is interesting to note that EPR measurements have indicated formation of (very) low concentrations of radical species during the reaction.[78] Whereas these radicals are just side products, or are involved as intermediates in the polymerization reaction needs to be established in future studies.

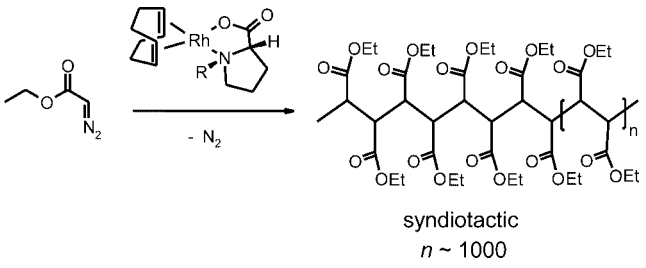


Figure 32. Are radical species involved in the recently discovered stereoselective Rh-mediated polymerization of "carbenes"?

 © 2007 Wiley-VCH Verlag GmbH & Co. KGaA, Weinheim 

## 6. Conclusions

Paramagnetic rhodium and iridium alkene species, especially the nitrogen-ligand-based $[M^{II}(por)(alkene)]$ and $[M^{II}(alkene)(N\text{-ligand})]^{2+}$ species, reveal a remarkable variety of radical-type reactions. The five-coordinate $[M^{II}(por)(alkene)]$ species, for which mixing of the $d_{z^2}$ and alkene orbitals ensures that part of the unpaired electron density is located at the olefinic ligand, are especially reactive. These alkene adducts cannot be isolated due to fast M–C and C–C radical couplings leading to alkylene-bridged species. Attempts to sterically prevent these reactions leads to alkene adducts which easily lose the alkene. Alkenes bind stronger to dicationic five-coordinate $[M^{II}(N_4\text{-ligand})]$ and $[M^{II}(N_3\text{-ligand})]$ complexes containing neutral tetradentate or tridentate podal $N\{CH_2Py\}_n$ ($n$ = 2,3) type ligands. The orbital arrangement of these species is different, so that the $d_{z^2}$ orbital containing the unpaired electron interacts with a $N_{amine}$ donor instead of the alkene. Consequently, the alkene fragments do not reveal much radical-type reactivity without activation. The situation changes upon binding of a strong coordinating solvent (e.g. MeCN), resulting in a donor-induced shift of the spin-density from the metal to the π* orbitals of the alkene. Most of the spin density of the resulting $M^{III}(NCMe)(CH_2CH_2^{\cdot})$ species is located at the β-carbon of the "slipped" alkene, thus triggering radical-type reactivity at the alkene/ethyl radical fragment. This donor-induced shift of the spin density from the metal to the alkene constitutes a new approach to tuning the reactivity of open-shell metal-alkene species.

Stable examples of $M^{II}$(α-alkene) complexes, containing reactive allylic hydrogen atoms, all have their metal center sterically protected. All other examples tend to decompose with formation of $M^{III}$(allyl) and $M^{III}$(H) species. The presence of unpaired spin density at the alkene is of less concern for these decomposition pathways, as they proceed through a dinuclear pathway in which an allylic hydrogen atom of one $M^{II}$(alkene) species is abstracted by another $M^{II}$(alkene) radical *at the metal*.

Although limited in number, there are a few examples in which experimental evidence for the involvement of paramagnetic rhodium and iridium species in catalytic reactions is quite strong. For example, paramagnetic intermediates might play a role in the catalytic alkene oxygenation reactions described in the 1970s and early 1980s by Mimoun, Drago, Read and others.[74,75] Whether or not this concerns paramagnetic alkene species remains a question. $M^{II}$(α-alkene) species perhaps too easily undergo allylic C–H activation, making them less attractive candidates to be intermediates in the C–O bond formation processes. C–O bond formation through oxidation of diamagnetic $M^{I}$(alkene) species (by peroxides for example) to 2-metalla(III)oxetane intermediates seems a more likely pathway. Paramagnetic $M^{II}$ species might nevertheless be important in these reactions, e.g. by facilitating peroxide formation from $O_2$ and a sacrificial reductant (e.g. an alcohol). On the other hand, the situation may strongly depend on the olefinic substrate. Model reactions of $[Ir^{II}(ethene)(N_4\text{-ligand})]^{2+}$ species with $O_2$ have revealed that with these ethene species, lacking reactive allylic hydrogens, facile C–O bond formation is certainly possible. This reaction likely proceeds via external attack of the "alkene radical" species $M^{III}(NCMe)(CH_2CH_2^{\cdot})$ by $O_2$. This demonstrates the potential of donor induced generation of "alkene radicals" from $M^{II}$(alkene) species as a new approach to steer the reactivity of open-shell M(alkene) species.

Catalytic cyclopropanation of alkenes with ethyl diazoacetate mediated by well defined $Rh^{II}$(alkene) species has been demonstrated,[84] and it is well possible that open-shell $M^{II}$(alkene) species are also active in other carbene-transfer reactions. Wacker-type oxidation of norbornadiene to norbornenone is another reaction which definitely proceeds via discrete $Rh^{II}$(alkene) species.[40]

The rich chemistry displayed by paramagnetic M(alkene) species is fascinating. Whether or nor these species will turn out to be important in new or existing catalytic reactions remains a question to be answered in the future.

## Acknowledgments

This work was supported by the Netherlands Organization for Scientific Research (NWO-CW), the Radboud University Nijmegen and the University of Amsterdam.

[1] a) D. Astruc, Electron-Transfer and Radical Processes, in: *Transition-Metal Chemistry*, VCH, New York, **1995**; b) M. C. Baird, *Chem. Rev.* **1988**, *88*, 1217–1227; c) W. C. Trogler (Ed.), Organometallic Radical Processes, *Journal of Organometallic Chemistry Library*, vol. 22, Elsevier, Amsterdam, **1990**; d) N. G. Connelly, *Chem. Soc. Rev.* **1989**, *18*, 153–185; e) M. Channon, M. Julliard, J. C. Poite (Eds.), Paramagnetic Organometallic Species, in: *Activation/Selectivity, Catalysis*, NATO ASI series, Kluwer Academic, Dordrecht, **1987**; f) L. A. MacAdams, G. P. Buffone, C. D. Incarvito, J. A. Golen, A. L. Rheingold, K. H. Theopold, *Chem. Commun.* **2003**, *10*, 1164–1165; g) C. Pariya, K. H. Theopold, *Curr. Sci.* **2000**, *78*, 1345–1351; h) J. D. Jewson, L. M. Liable-Sands, G. P. A. Yap, A. L. Rheingold, K. H. Theopold, *Organometallics* **1999**, *18*, 300–305; i) R. Poli, *Chem. Rev.* **1996**, *96*, 2135–2204; j) C. Limberg, *Angew. Chem. Int. Ed.* **2003**, *42*, 5932–5954; *Angew. Chem.* **2003**, *115*, 6112–6136.

[2] $Rh^{II}$(alkene) intermediates were considered as possible intermediates the catalytic isomerization of 1-nonene to 2-nonene, hydrogenation of ketones and alkenes and iridium-catalyzed carbonylation of alcohols to carboxylic acids has been claimed to involve $Ir^{II}$ species; a) G. Strukul, M. Bonivento, M. Graziani, E. Cerna, N. Palladino, *Inorg. Chim. Acta* **1975**, *12*, 15–21; b) L. D. Tyutchenkova, V. G. Vinogradova, Z. K. Maizus, *Izv. Akad. Nauk SSSR, Ser. Khim.* **1978**, *4*, 773–777; c) S. Padhye, R. Yerande, R. P. Patil, A. A. Kelkar, R. V. Chaudhari, *Inorg. Chim. Acta* **1989**, *156*, 23–25.

[3] K. E. Toracca, L. McElwee-White, *Coord. Chem. Rev.* **2000**, *206–207*, 469–491.

[4] a) B. B. Wayland, S. Ba, A. E. Sherry, *J. Am. Chem. Soc.* **1991**, *113*, 5305–5311; b) A. E. Sherry, B. B. Wayland, *J. Am. Chem. Soc.* **1990**, *112*, 1259–1261; c) B. B. Wayland, S. Ba, A. E. Sherry, *Inorg. Chem.* **1992**, *31*, 148–150; d) X.-X. Zhang, B. B. Wayland, *Inorg. Chem.* **2000**, *39*, 5318–5325; e) X. X. Zhang, B. B. Wayland, *J. Am. Chem. Soc.* **1994**, *116*, 7897–7898; f) W. H. Cui, X. P. Zhang, B. B. Wayland, *J. Am. Chem. Soc.* **2003**, *125*, 4994–4995; g) W. H. Cui, B. B. Wayland, *J. Am. Chem. Soc.* **2004**, *126*, 8266–8274.

 © 2007 Wiley-VCH Verlag GmbH & Co. KGaA, Weinheim 

[5] a) K. K. Pandey, *Coord. Chem. Rev.* **1991**, *121*, 1–42; b) D. G. DeWitt, *Coord. Chem. Rev.* **1996**, *147*, 209–246; c) D. G.H Hetterscheid, A. J. J. Koekkoek, H. Grüzmacher, B. de Bruin, *Progress in Inorganic Chemistry*, accepted.

[6] C. K. Jørgensen, *Oxidation numbers and oxidation states*, Springer, Berlin, Germany, **1969**.

[7] D. G. H. Hetterscheid, J. Kaiser, E. Reijerse, T. P. J. Peters, S. Thewissen, A. N. J. Blok, J. M. M. Smits, R. de Gelder, B. de Bruin, *J. Am. Chem. Soc.* **2005**, *127*, 1895–1905.

[8] D. G. H. Hetterscheid, M. Bens, B. de Bruin, *Dalton Trans.* **2005**, 979–984.

[9] N. G. Connelly, A. C. Loyns, M. A. Ciriano, M. J. Fernandez, L. A. Oro, B. E. Villarroya, *J. Chem. Soc., Dalton Trans.* **1989**, 689–691.

[10] B. E. Villarroya, L. A. Oro, F. J. Lahoz, A. J. Edwards, M. A. Ciriano, P. J. Alonso, A. Tiripicchio, M. T. Camellini, *Inorg. Chim. Acta* **1996**, *250*, 241–264.

[11] M. A. Casado, J. J. Pérez-Torrente, J. A. López, M. A. Ciriano, P. J. Alonso, F. J. Lahoz, L. A. Oro, *Inorg. Chem.* **2001**, *40*, 4785–4792.

[12] D. C. Boyd, N. G. Connelly, G. G. Herbosa, M. G. Hill, K. R. Mann, C. Mealli, A. G. Orpen, K. E. Richardson, P. H. Rieger, *Inorg. Chem.* **1994**, *33*, 960–971 and references cited therein.

[13] N. Kanematsu, M. Ebihara, T. Kawamura, *Inorg. Chim. Acta* **2001**, *323*, 96–104.

[14] J. M. Poblet, M. Bernard, *Inorg. Chem.* **1988**, *27*, 2935–2941.

[15] K. M. Kadish, T. D. Phan, L. Giribabu, E. Van Caemelbecke, J. L. Bear, *Inorg. Chem.* **2003**, *42*, 8663–8673.

[16] N. G. Connelly, O. D. Hayward, P. Klangsinsirikul, A. G. Orpen, P. H. Rieger, *Chem. Commun.* **2000**, 963–964.

[17] C. J. Adams, R. A. Baber, N. G. Connelly, P. Harding, O. D. Hayward, M. Kandiah, A. G. Orpen, *Dalton Trans.* **2006**, 1749–1757.

[18] a) C. G. Pierpont, C. W. Lange, *Prog. Inorg. Chem.* **1994**, *41*, 331–442; b) C. G. Pierpont, A. S. Attia, *Collect. Czech. Chem. Commun.* **2001**, *66*, 33–51; c) H. Chun, C. N. Verani, P. Chaudhuri, E. Bothe, E. Bill, T. Weyhermuller, K. Wieghardt, *Inorg. Chem.* **2001**, *40*, 4157–4166; d) P. Chaudhuri, C. N. Verani, E. Bill, E. Bothe, T. Weyhermuller, K. Wieghardt, *J. Am. Chem. Soc.* **2001**, *123*, 2213–2223; e) D. Herebian, P. Ghosh, H. Chun, E. Bothe, T. Weyhermuller, K. Wieghardt, *Eur. J. Inorg. Chem.* **2002**, 1957–1967; f) D. N. Hendrickson, C. G. Pierpont, *Top. Curr. Chem.* **2004**, *234*, 63–95.

[19] C. W. Lange, C. G. Pierpont, *J. Am. Chem. Soc.* **1992**, *114*, 6582–6583.

[20] a) B. de Bruin, E. Bill, E. Bothe, T. Weyhermüller, K. Wieghardt, *Inorg. Chem.* **2000**, *39*, 2936; b) P. H. M. Budzelaar, B. de Bruin, A. W. Gal, K. Wieghardt, J. H. van Lenthe, *Inorg. Chem.* **2001**, *40*, 4649–4655; c) D. Enright, S. Gambarotta, G. P. A. Yap, P. H. M. Budzelaar, *Angew. Chem. Int. Ed.* **2002**, *41*, 3873–3876; *Angew. Chem.* **2002**, *20*, 4029–4032; d) I. Sugiyama, I. Korobkov, S. Gambarotta, A. Mueller, P. H. M. Budzelaar, *Inorg. Chem.* **2004**, *43*, 5771–5779; e) J. Scott, S. Gambarotta, I. Korobkov, Q. Knijnenburg, B. de Bruin, P. H. M. Budzelaar, *J. Am. Chem. Soc.* **2005**, *127*, 17204–17206.

[21] T. M. Kooistra, D. G. H. Hetterscheid, E. Schwartz, Q. Knijnenburg, P. H. M. Budzelaar, A. W. Gal, *Inorg. Chim. Acta* **2004**, *357*, 2945–2952.

[22] Q. Knijnenburg, A. D. Horton, H. van der Heijden, T. M. Kooistra, D. G. H. Hetterscheid, J. M. M. Smits, B. de Bruin, P. H. M. Budzelaar, A. W. Gal, *J. Mol. Catal. A* **2005**, *232*, 151–159.

[23] T. Büttner, J. Geier, G. Frison, J. Harmer, C. Calle, A. Schweiger, H. Schönberg, H. Grützmacher, *Science* **2005**, *307*, 235–238.

[24] P. Maire, M. Königsmann, A. Sreekanth, J. Harmer, A. Schweiger, H. Grützmacher, *J. Am. Chem. Soc.* **2006**, *128*, 6578–6580.

[25] P. Maire, A. Sreekanth, T. Büttner, J. Harmer, I. Gromov, H. Rüegger, F. Breher, A. Schweiger, H. Grützmacher, *Angew. Chem. Int. Ed.* **2006**, *45*, 3265–3269; *Angew. Chem.* **2006**, *118*, 3343–3347.

[26] F. Breher, C. Böhler, G. Frison, J. Harmer, L. Liesum, A. Schweiger, H. Grützmacher, *Chem. Eur. J.* **2003**, *9*, 3859–3866.

[27] a) E. Makrtik, J. Hanzlik, A. Camus, *J. Org. Chem.* **1977**, *142*, 95; b) J. Orsini, W. E. Geiger, *J. Electroanal. Chem.* **1995**, *380*, 83; c) J. Orsini, W. E. Geiger, *Organometallics* **1999**, *18*, 1854.

[28] J. H. B. Chenier, M. Histed, J. A. Howard, H. A. Jolly, H. Morris, B. Mile, *Inorg. Chem.* **1989**, *28*, 4114.

[29] a) A. J. Kunin, E. J. Nanni, R. Eisenberg, *Inorg. Chem.* **1985**, *24*, 1852; b) G. C. Johnston, M. C. Baird, *J. Organomet. Chem.* **1986**, *314*, C51; c) B. Bogdanovic, W. Leitner, C. Six, U. Wilczok, K. Wittmann, *Angew. Chem. Int. Ed. Engl.* **1997**, *36*, 502; d) K. T. Mueller, A. J. Kunin, S. Greiner, T. Henderson, R. W. Kreilick, R. Eisenberg, *J. Am. Chem. Soc.* **1987**, *109*, 6313.

[30] B. de Bruin, J. C. Russcher, H. Grützmacher, work in progress.

[31] L. Cataldo, S. Choua, T. Berclaz, M. Geoffroy, N. Mézailles, N. Avarvari, F. Matthey, P. Le Floch, *J. Phys. Chem. A* **2002**, *106*, 3017–3022.

[32] a) E. Makrtik, J. Hanzlik, A. Camus, *J. Organomet. Chem.* **1977**, *142*, 95–103; b) J. Orsini, W. E. Geiger, *J. Electroanal. Chem.* **1995**, *380*, 83–90.

[33] M. P. García, M. V. Jiménez, L. A. Oro, F. J. Lahoz, P. J. Alonso, *Angew. Chem. Int. Ed. Engl.* **1992**, *31*, 1527–1529; *Angew. Chem.* **1992**, *104*, 1513–1514.

[34] M. P. García, M. V. Jiménez, L. A. Oro, F. J. Lahoz, J. M. Casas, P. J. Alonso, *Organometallics* **1993**, *12*, 3257–3263.

[35] a) M. J. Shaw, W. E. Geiger, J. Hyde, C. White, *Organometallics* **1998**, *17*, 5486–5491; b) M. J. Shaw, J. Hyde, C. White, W. E. Geiger, *Organometallics* **2004**, *23*, 2205–2208.

[36] R. E. Dessy, R. B. King, M. Waldrop, *J. Am. Chem. Soc.* **1966**, *88*, 471–476.

[37] R. E. Dessy, R. B. King, M. Waldrop, *J. Am. Chem. Soc.* **1966**, *88*, 5112–5117.

[38] B. de Bruin, T. P. J. Peters, S. Thewissen, A. N. J. Blok, J. B. M. Wilting, R. de Gelder, J. M. M. Smits, A. W. Gal, *Angew. Chem. Int. Ed.* **2002**, *41*, 2135–2138; *Angew. Chem.* **2002**, *114*, 2239–2242.

[39] B. de Bruin, S. Thewissen, T.-W. Yuen, T. P. J. Peters, J. M. M. Smits, A. W. Gal, *Organometallics* **2002**, *21*, 4312–4314.

[40] D. G. H. Hetterscheid, J. M. M. Smits, B. de Bruin, *Organometallics* **2004**, *23*, 4236–4246.

[41] D. G. H. Hetterscheid, B. de Bruin, J. M. M. Smits, A. W. Gal, *Organometallics* **2003**, *22*, 3022–3024.

[42] D. G. H. Hetterscheid, M. Klop, R. J. N. A. M. Kicken, J. M. M. Smits, E. J. Reijerse, B. de Bruin, *Chem. Eur. J.*, manuscript accepted.

[43] S. L. van Voorhees, B. B. Wayland, *Organometallics* **1987**, *6*, 204–206.

[44] Y. Ni, J. P. Fitzgerald, P. Carrol, B. B. Wayland, *Inorg. Chem.* **1994**, *33*, 2029–2035.

[45] M. Wei, B. B. Wayland, *Organometallics* **1996**, *15*, 4681–4683.

[46] D. G. DeWitt, *Coord. Chem. Rev.* **1996**, *147*, 209–246.

[47] J. E. Anderson, C.-L. Yao, K. M. Kadish, *Inorg. Chem.* **1986**, *25*, 718–719.

[48] J. E. Anderson, C.-L. Yao, K. M. Kadish, *Organometallics* **1987**, *6*, 706–711.

[49] J. E. Anderson, C.-L. Yao, K. M. Kadish, *J. Am. Chem. Soc.* **1987**, *109*, 1106–1111.

[50] B. B. Wayland, *Polyhedron* **1988**, *16*/*17*, 1545–1555.

[51] B. B. Wayland, S. Ba, A. E. Sherry, *J. Am. Chem. Soc.* **1991**, *119*, 5305–5311.

[52] B. B. Wayland, V. L. K. Coffin, M. D. Farnos, *Inorg. Chem.* **1988**, *27*, 2745–2747.

[53] B. B. Wayland, A. E. Sherry, A. G. Bunn, *J. Am. Chem. Soc.* **1993**, *115*, 7675–7684.

[54] L. Basickes, A. W. Bunn, B. B. Wayland, *Can. J. Chem.* **2001**, *79*, 854–856.

[55] H. Zhai, A. Bunn, B. B. Wayland, *Chem. Commun.* **2001**, 1294–1295.


 © 2007 Wiley-VCH Verlag GmbH & Co. KGaA, Weinheim 

[56] R. S. Paonessa, N. C. Thomas, J. Halpern, *J. Am. Chem. Soc.* **1985**, *107*, 4333–4335.
[57] B. B. Wayland, G. Poszmik, M. Fryd, *Organometallics* **1992**, *11*, 3534–3542.
[58] H. Ogoshi, J. Setsunu, Z. Yoshida, *J. Am. Chem. Soc.* **1977**, *99:11*, 3869–3870.
[59] B. B. Wayland, A. E. Sherry, G. Pozmik, A. G. Bunn, *J. Am. Chem. Soc.* **1992**, *114*, 1673–1681.
[60] A. G. Bunn, B. B. Wayland, *J. Am. Chem. Soc.* **1992**, *114*, 6917–6919.
[61] L. Brammer, N. G. Connelly, J. Edwin, W. E. Geiger, A. G. Orpen, J. B. Sheridan, *Organometallics* **1988**, *7*, 1259–1265.
[62] B. B. Wayland, A. E. Sherry, A. G. Bunn, *J. Am. Chem. Soc.* **1993**, *115*, 7675–7684.
[63] L. Basickes, A. W. Bunn, B. B. Wayland, *Can. J. Chem.* **2001**, *79*, 854–856.
[64] H. Zhai, A. Bunn, B. B. Wayland, *Chem. Commun.* **2001**, 1294–1295.
[65] X.-X. Zhang, G. F. Parks, B. B. Wayland, *J. Am. Chem. Soc.* **1997**, *119*, 7938–7944.
[66] B. B. Wayland, K. J. Del Rossi, *J. Organomet. Chem.* **1984**, *276*, C27–C30.
[67] M. S. Sanford, J. T. Groves, *Angew. Chem. Int. Ed.* **2004**, *43*, 588–590; *Angew. Chem.* **2004**, *116*/*5*, 598–600.
[68] M. Feng, K. S. Chan, *J. Organomet. Chem.* **1999**, *584*, 235–239.
[69] K. W. Mak, S. K. Yeung, K. S. Chan, *Organometallics* **2002**, *21*, 2362–2364.
[70] M. K. Tse, K. S. Chan, *J. Chem. Soc., Dalton Trans.* **2001**, 510–511.
[71] S. K. Yeung, K. S. Chan, *Organometallics* **2005**, *24*, 6426–6430.
[72] B. B. Wayland, Y. Feng, S. Ba, *Organometallics* **1989**, *8*, 1438–1441.
[73] A. D. Burrows, M. Green, J. C. Jeffery, J. M. Lynam, M. F. Mahon, *Angew. Chem. Int. Ed.* **1999**, *38*, 3043–3045; *Angew. Chem.* **1999**, *111*, 3228–3230.
[74] B. de Bruin, P. H. M. Budzelaar, A. W. Gal, *Angew. Chem. Int. Ed.* **2004**, *43*/*32*, 4142–4157; *Angew. Chem.* **2004**, *116*, 4236–4251, and references therein.
[75] C. Tejel, M. A. Cireano, *Top. Organomet. Chem.*, accepted.
[76] R. J. N. A. M. Kicken, PhD Thesis, University of Nijmegen, **2001**.
[77] B. de Bruin, J. A. Brands, J. J. J. M. Donners, M. P. J. Donners, R. de Gelder, J. M. M. Smits, A. W. Gal, *Chem. Eur. J.* **1999**, *5*, 2921.
[78] B. de Bruin, unpublished results.
[79] D. G. H. Hetterscheid, B. de Bruin, *J. Mol. Catal. A* **2006**, *251*, 291–296.
[80] For examples see the NIEST spin-trap database, which can be found at: https://dir-apps.niehs.nih.gov/stdb/index.cfm. Supporting references are provided therein.
[81] a) L. Carlton, G. Read, M. Urgelles, *J. Chem. Soc., Chem. Commun.* **1983**, 586; b) J. M. Takacs, X.-T. Jiang, *Curr. Org. Chem.* **2003**, *7*, 369.
[82] a) E. Donato, F. C. Priolo, *J. Organomet. Chem.* **1983**, *251*, 273; b) D. A. White, *J. Chem. Soc. A* **1971**, 145; c) J. K. Stille, D. E. James, *J. Am. Chem. Soc.* **1975**, *97*, 674.
[83] See for example: H. M. L. Davies, R. E. J. Beckwith, *Chem. Rev.* **2003**, *103*, 2861–2903 and references cited therein.
[84] J. R. Krumper, M. Gerisch, J. M. Suh, R. G. Bergman, T. D. Tilley, *J. Org. Chem.* **2003**, *68*, 9705–9710.
[85] D. G. H. Hetterscheid, C. Hendriksen, W. I. Dzik, J. M. M. Smits, E. R. H. van Eck, A. E. Rowan, V. Busico, M. Vacatello, V. Van Axel Castelli, A. Segre, E. Jellema, T. G. Bloemberg, B. de Bruin, *J. Am. Chem. Soc.* **2006**, *128*, 9746–9752.

Received: September 29, 2006
Published Online: December 11, 2006

 © 2007 Wiley-VCH Verlag GmbH & Co. KGaA, Weinheim 

DOI: 10.1002/ejic.200600751

# A Water Pipe Held Up by a Polyoxometalate Supported Transition Metal Complex: Synthesis and Characterization of $[Cu_2(phen)_2(CH_3COO)(CH_3COOH)(H_2O)_2][Al(OH)_6Mo_6O_{18}]\cdot 28H_2O$

**Vaddypally Shivaiah,[a] Tanmay Chatterjee,[a] Khandregula Srinivasu,[a] and Samar K. Das*[a]**

**Keywords:** Heteropolyanion / Copper acetate dimer / Crystal structure / Lattice waters / Hydrogen bonds / Supramolecular chemistry

A water pipe, formed exclusively from lattice water molecules, is stabilized in an organic–inorganic hybrid material $Cu_2(phen)_2(CH_3COO)(CH_3COOH)(H_2O)_2][Al(OH)_6Mo_6O_{18}]\cdot 28H_2O$ (**1**). Compound **1** consists of an Anderson-type heteropolyanion, a copper acetate dimer, and 28 lattice water molecules. Once the relevant crystal is removed from the mother liquor it loses water molecules, which results in the demolition of the water pipe.
(© Wiley-VCH Verlag GmbH & Co. KGaA, 69451 Weinheim, Germany, 2007)

Water is a major constituent of our planet earth and it plays an important role in many natural systems, but it is not a fully understood liquid. There has been extensive investigation of water structures in recent years in which helical protein matrixes act as a stabilizing host[1] because water aggregations are prevalent in many biological systems. Studies on small water clusters and their noncovalent interactions are significant because these stabilize the supramolecular systems both in solution and in the solid state and there is a clear need to understand how such aggregates influences the overall structures of their surroundings.[2] It has been demonstrated that a giant icosahedral metaloxide-based spherical polyoxometalate (POM) cluster can encapsulate an icosahedral $(H_2O)_{100}$ cluster.[3] Other POM clusters are also found to stabilize small water clusters.[4] There are reports on several types of water polymers that have been crystallographically identified; these include chains,[5] tapes/layers,[6] and helices[7] etc. Infantes and Motherwell have described the patterns of water clusters within the Cambridge Structural Database (CSD), and they have classified them as discrete rings and chains, infinite chains and tapes, and layer structures.[8] According to their CSD search, a water pipe/tube was not known until 2002. There are two reports of water tubes in recent time: both are stabilized with inorganic coordination compounds.[9] Very recently, Mascal et al. have written a popular article on water oligomers in crystalline hydrates by choosing 17 random recent publications that describe unprecedented assemblies of water molecules and compared these structures against those already in the CSD.[10] However, the context of a water pipe/tube is not discussed in this essay. We describe here the crystallographic observation of a new type of water pipe that was identified in supramolecular channels and formed in a polyoxometalate-based inorganic–organic hybrid compound, $[Cu_2(phen)_2(CH_3COO)(CH_3COOH)(H_2O)_2][Al(OH)_6Mo_6O_{18}]\cdot 28H_2O$ (**1**).

Compound **1** was synthesized in an organo–aqueous medium containing copper nitrate, sodium molybdate, aluminum chloride, acetic acid, acetonitrile, and sodium acetate. The blue crystals of **1** with block morphology were separated on standing at room temperature in 28% yield (based on Mo). These crystals are unstable when they are removed from the mother liquor, loss of crystallinity was registered. Thus, the data collection was performed on a single-crystal of **1** suspended in a capillary that contained frozen mother liquor (at liquid nitrogen temperature).

Compound **1** consists of an Anderson anion, $[Al(OH)_6Mo_6O_{18}]^{3-}$, a dimeric copper complex cation $[Cu_2(phen)_2(CH_3COO)(CH_3COOH)(H_2O)_2]^{3+}$ and 28 lattice water molecules. Thus, the asymmetric unit in the crystal of compound **1** is composed of half of a dimeric complex cation, half of the Anderson heteropolyanion, and 14 solvent water molecules as shown in Figure 1. An Anderson anion $[Al(OH)_6Mo_6O_{18}]^{3-}$ consists of seven edge-shared octahedra, six of which are molybdenum octahedra arranged hexagonally surrounding the aluminum octahedra (see Figure S4 in Supporting information). In compound **1**, copper dimer $[Cu_2(phen)_2(CH_3COO)(CH_3COOH)(H_2O)]^{3+}$ acts as a cation that compensates for the anionic charge of the Anderson anion resulting in the formation of the title compound. The copper ion adopts a square pyramidal geome-

[a] School of Chemistry, University of Hyderabad, Hyderabad 500046, India
Fax: +91-40-2301-2460
E-mail: skdsc@uohyd.ernet.in
Supporting information for this article is available on the WWW under http://www.eurjic.org or from the author.

 © 2007 Wiley-VCH Verlag GmbH & Co. KGaA, Weinheim 

try, whereby the basal sites are occupied by two phenanthroline nitrogen atoms and two acetate oxygen atoms (Cu–N = 2.01 Å; Cu–O = 1.956 Å), and the axial position is occupied by water oxygen atoms. The axial Cu–O distance is 2.154 Å, which is relatively longer than those in the basal plane. Intradimer Cu···Cu separation of 2.988 Å has been observed, which is comparable to the Cu···Cu separation of 3.05 Å in the similar dimer reported in the literature.[11] The phenanthroline ligands of the copper dimer are almost parallel to each other and they are also ring-to-ring stacked, which reveals intramolecular π-π interactions [$C_t$–$C_t$ = 3.632 (2) Å; MPS = 3.355 Å].

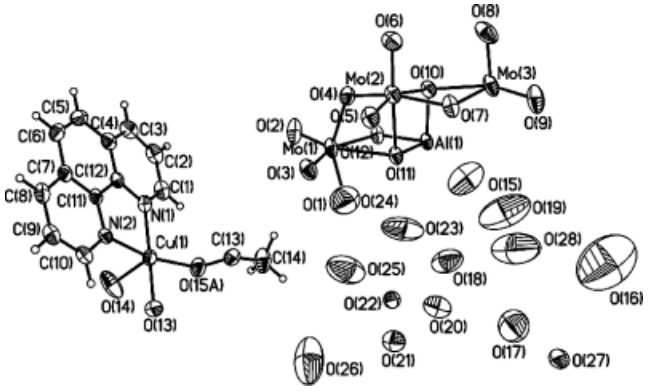


Figure 1. Thermal ellipsoidal plot (at 50% probability) of the asymmetric unit in compound **1**, which consists of half of the dimeric copper complex cation, half of the Anderson heteropolyanion and 14 solvent water molecules.

The most fascinating aspect of this work is the formation of a water pipe that is formed exclusively from lattice water molecules present in the crystal of **1**. There are 14 lattice water molecules in the asymmetric unit in the crystal structure of **1** (see Figure 1). These are O(15) through O(28). Out of these 14 lattice water molecules, 13 are involved in the formation of a $(H_2O)_{13}$ cluster [the O(24) water is not involved in hydrogen bonding interactions] as shown in Figure 2. The growing and repetitive arrangement of the $(H_2O)_{13}$ cluster leads to the construction of a new type of water pipe as shown in Figure 3. The relevant O···O hydrogen bond lengths are given in Table 1. Water hydrogen atoms could not be located in the crystal structure. Among the 13 lattice water molecules that are involved in the construction of the water pipe, two water molecules [O(22) and O(26)] are disordered. Each of these is disordered over two positions [O(22), O(22A) and O(26), O(26A), respectively].

The dimensions of the inner diameter of the water tube are found to be $8.527 \times 8.061$ Å$^2$. The packing of the water pipes in the unit cell is shown in Figure 4. The existence of such an unstable pipe (vide supra) has been made possible by the interactions with its surroundings that include an Anderson heteropolyanion and a dimeric copper complex cation. There are extensive hydrogen bonding interactions between surface oxygens of the Anderson anion (terminal, bridging, and $\mu_3$-O oxygens), crystal waters (water tube), and copper coordinated waters as shown in Figure 5a (see also Figures S10–S12 in Supporting information for detailed interactions between the water pipe and its surrounding). The packing of the Anderson heteropolyanions and the dimeric copper complex cations in the crystal forms a grid-type supramolecular framework having channels (when viewed looking down the crystallographic *c* axis). These channels accommodate the water pipes that run along the crystallographic *c* axis too (see Figure 5b).

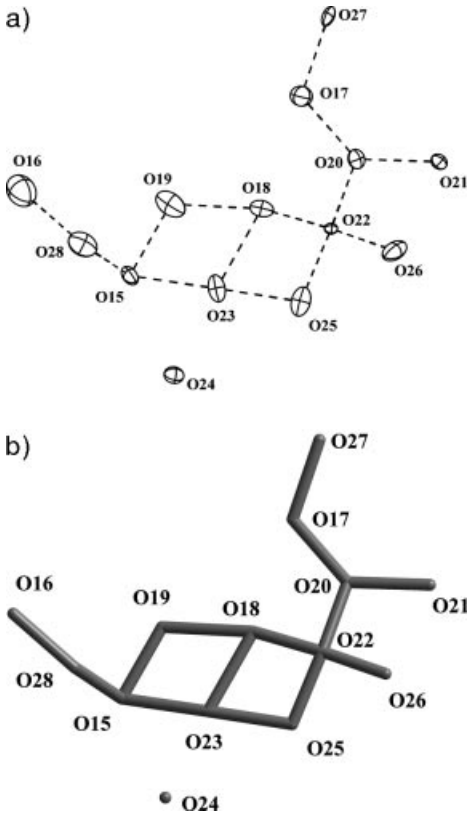


Figure 2. Hydrogen bonding interactions among lattice water molecules O(15) through O(28), which results in the formation of a $(H_2O)_{13}$ cluster. O(24) water remains non-hydrogen bonded in the crystal. (a) thermal ellipsoidal and (b) wire-frame representations. The disordered part of O(22) and O(26) are not shown.

Figure 3. The generation of a water pipe formed by the repetition of $(H_2O)_{13}$ cluster (as shown in Figure 2).

Table 1. O···O hydrogen bond lengths [Å] in water tube (see Figure 2).

| | | | |
|---|---|---|---|
| O15···O19 | 2.736(11) | O15···O23 | 3.051(9) |
| O15···O28 | 3.137(12) | O16···O28 | 2.750(15) |
| O17···O27 | 2.801(10) | O17···O20 | 2.834(10) |
| O18···O22 | 2.579(10) | O18···O23 | 3.050(10) |
| O18···O19 | 3.152(14) | O20···O22 | 2.549(9) |
| O20···O21 | 2.819(7) | O22···O25 | 2.613(13) |
| O22···O26 | 2.379(19) | O23···O25 | 2.922(10) |

 © 2007 Wiley-VCH Verlag GmbH & Co. KGaA, Weinheim 

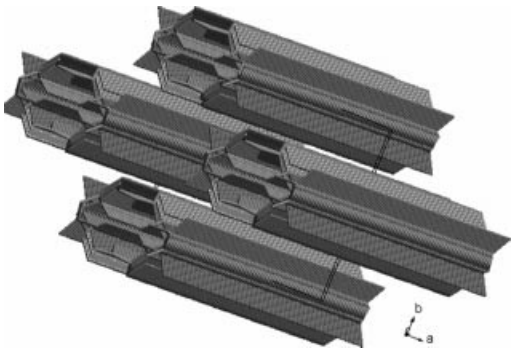

Figure 4. The packing of the water tubes in the unit cell excluding the Anderson anions and dimeric copper complex cations.

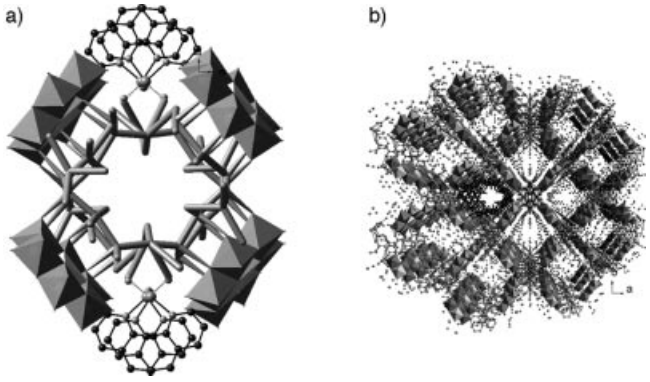


Figure 5. (a) Front view of the water pipe, supported by its surroundings that include dimeric copper complex cations and Anderson heteropolyanions through noncovalent interactions. Anderson anion is shown in polyhedral representation and water tube in sticks representation. Acetate carbons and hydrogens are not shown for clarity. (b) The perspective view of the water tubes in the square-grid channels ($3 \times 3$ cell). Only one water tube is shown for clarity. The view is along the crystallographic *c* axis.

In the present study, we could not determine the precise number of water molecules forming the water pipe by thermogravimetric (TG) studies because once the relevant crystals are removed from the mother liquor (synthesis), they lose their single crystallinity and form a powdery material. TG studies were performed on the powdery compound. The TG curve shows the first weight loss starts at around 100 °C with the loss of 13.50%. This corresponds to the loss of ca.16 crystal water molecules. The molecules lost at this stage were identified as water molecules from the corresponding mass spectrum (TGA-Mass). This clearly tells us that the relevant crystal already looses 12 water molecules at room temperature before its TG measurements start. This is consistent with the X-ray powder diffraction studies and the visual observation (single-crystals convert to powder) during the process of removing the crystals from the mother liquor.

In conclusion, we have described here the crystallographic observation of a supramolecular water pipe that is exclusively constructed from solvent/lattice water molecules. We believe that the heteropolyanion and the copper dimeric complex play an important role in the stabilization of such an unusual and unstable water tube. Conversely, the water pipe acts as a support to hold the host chemical entities (grid-framework) as evidenced by the loss of crystallinity that occurs when lattice water molecules are lost during the drying process of the relevant crystal at room temperature. To the best of our knowledge, this is the first crystallographically characterized water tube in a POM-based hybrid material.

## Experimental Section

**General:** Infrared spectra were recorded with a JASCO-5300 FTIR spectrophotometer. Powder X-ray diffraction data were collected with a Phillips PW 3710 diffractometer. EDAX analyses were performed with Philips XL 30 SEM equipment.

**Synthesis of $[Cu_2(phen)_2(CH_3COO)(CH_3COOH)(H_2O)_2][Al(OH)_6Mo_6O_{18}]\cdot 28H_2O$ (1):** To a stirred aqueous (50 mL) solution of aluminum chloride (1.5 g, 6.21 mmol), a solution of sodium molybdate (3.5 g, 14.46 mmol) in water (100 mL) was mixed followed by the addition of an aqueous methanolic solution (100 mL; water/MeOH, 1:1) of 1,10-phenanthroline (0.2 g, 1 mmol) and copper acetate (1 g, 5 mmol). To this reaction mixture, sodium acetate (3 g, 22.04 mmol) was added. Finally, the whole reaction mixture was acidified with glacial acetic acid until the pH reached 3.4. The mixture was then stirred for 10 min and filtered in a 250 mL conical flask. Blue crystals of **1** were obtained after one week from the filtrate. Yield: 1.5 g (28% based on molybdenum).

**Note:** Crystals of **1** lose single crystallinity when they are removed from the mother liquor. The single-crystals lose a considerable amount of solvent/lattice water molecules (as is evidenced by TGA studies, vide infra) immediately after they are separated from the mother liquid and convert to a powdery form.

**X-ray Crystallographic Study:** One single crystal of dimensions $0.45 \times 0.22 \times 0.10\ mm^3$ was placed in a capillary tube with its mother liquor and cooled to liquid nitrogen temperature with immediate effect (for details see Supporting Information). CCDC-613002 contains the supplementary crystallographic data for this paper. These data can be obtained free of charge from The Cambridge Crystallographic Data Center via www.ccdc.cam.ac.uk/data_request/cif.

**Supporting Information** (see footnote on the first page of this article): Synthesis, X-ray powder diffraction studies, TGA studies, structure refinement data, structural description and interactions of compound **1**

## Acknowledgments

We thank Department of Science and Technology, Government of India, for financial support. The National X-ray Diffractometer facility at University of Hyderabad by the Department of Science and Technology, Government of India, is gratefully acknowledged. Special thanks are due to Professor Samudranil Pal, School of Chemistry, University of Hyderabad, for his helpful suggestions. We are grateful to UGC, New Delhi, for providing infrastructure facility at University of Hyderabad under UPE grant. V. S. and T. C. thank CSIR, New Delhi, for their fellowships.

[1] L. E. Cheruzel, M. S. Pomentum, M. R. Cecil, M. S. Mashuta, R. J. Wittebort, R. M. Buchanan, *Angew. Chem. Int. Ed.* **2003**, *42*, 5452–5455; R. Ludwig, *Angew. Chem. Int. Ed.* **2001**, *40*, 1808–1827.

 © 2007 Wiley-VCH Verlag GmbH & Co. KGaA, Weinheim 

[2] S. D. Colson, T. H. Dunning, *Science* **1994**, *265*, 43–44; K. Liu, J. D. Cruzan, R. S. Saykally, *Science* **1996**, *271*, 929–933.
[3] A. Müller, E. Krickemeyer, M. Schmidtmann, B. Botar, M. O. Talismanova, *Angew. Chem. Int. Ed.* **2003**, *42*, 2085–2090.
[4] R. J. Doedens, E. Yohannes, M. I. Khan, *Chem. Commun.* **2002**, 62–63; S. Manikumari, V. Shivaiah, S. K. Das, *Inorg. Chem.* **2002**, *41*, 6953–6955.
[5] S. Pal, N. B. Sankaran, A. Samanta, *Angew. Chem. Int. Ed.* **2003**, *42*, 1741–1743; Q.-Y. Liu, L. Xu, *CrystEngComm* **2005**, *7*, 87–89.
[6] B.-Q. Ma, H.-Ling, S. Gao, *Angew. Chem. Int. Ed.* **2004**, *43*, 1374–1376; R. Custelcean, C. Afloroaei, M. Vlassa, M. Polverejan, *Angew. Chem. Int. Ed.* **2000**, *39*, 3094–3096; J. P. Naskar, M. G. B. Drew, A. Hulme, D. A. Tocher, D. Datta, *CrystEngComm* **2005**, *7*, 67–70.
[7] A. Wakahara, T. Ishida, *Chem. Lett.* **2004**, *33*, 354–355; A. Mukherjee, M. K. Saha, M. Nethaji, A. R. Chakravarty, *Chem. Commun.* **2004**, 716–717.
[8] L. Infantes, S. Motherwell, *CrystEngComm* **2002**, *4*, 454–461.
[9] B. Zhao, P. Cheng, X. Chen, C. Cheng, W. Shi, D. Liao, S. Yan, Z. Jiang, *J. Am. Chem. Soc.* **2004**, *126*, 3012–3013; M. Tadokoro, S. Fukui, T. Kitajima, Y. Nagao, S. Ishimaru, H. Kitagawa, K. Isobe, K. Nakasuji, *Chem. Commun.* **2006**, 1274–1275.
[10] M. Mascal, L. Infantes, J. Chisholm, *Angew. Chem. Int. Ed.* **2006**, *45*, 32–36.
[11] S. Reinoso, P. Vitoria, L. S. Felices, L. Lezama, J. M. Zorilla, *Chem. Eur. J.* **2005**, *11*, 1538–1548; S. Reinoso, P. Vitoria, L. S. Felices, L. Lezama, J. M. Zorilla, *Inorg. Chem.* **2006**, *45*, 108–118; E. Dubler, U. K. Haring, K. H. Scheller, P. Baltzer, H. Sigel, *Inorg. Chem.* **1984**, *23*, 3785–3792.

Received: August 11, 2006
Published Online: November 9, 2006

 © 2007 Wiley-VCH Verlag GmbH & Co. KGaA, Weinheim 

DOI: 10.1002/ejic.200601018

# Formation of a Dative Bond Between $Pt^0$ and $Mo^{II}$ in Linear $Pt^0$–$Mo^{II}$–$Mo^{II}$–$Pt^0$ Complexes, $Mo^{II}_2Pt^0_2(pyphos)_4(PR_3)_2$, and Unique 1,4-Oxidative Addition Reaction of Diaryl Disulfides Giving $Mo^{II}_2Pt^I_2(pyphos)_4(SAr)_2$ (pyphos = 6-Diphenylphosphanyl-2-pyridonato)

**Kazushi Mashima,*[a] Yuuji Shimoyama,[a] Yoshitaka Kusumi,[a] Atsushi Fukumoto,[a] Tsuneaki Yamagata,[a] and Masato Ohashi[a]**

**Keywords:** Linear clusters / Dative bonds / Oxidative addition / Thiolates / Platinum / Molybdenum

The $Pt^0\cdots Mo^{II}$ dative bond of linear tetrametal $Pt^0$–$Mo^{II}$–$Mo^{II}$–$Pt^0$ complexes, $Mo_2Pt_2(pyphos)_4(L)_2$ [**4a**: $L$ = $PPh_3$; **4b**: $L$ = $PMe_3$; **4c**: $L$ = $PMe_2Ph$; **4d**: $L$ = $PMePh_2$; **4e**: $L$ = $P(OMe)_3$], was characterized by means of spectroscopic analysis and X-ray crystallographic studies. Complex **4a** reacted with diaryl disulfides to give dithiolate $Pt^I$ complexes, $Mo_2Pt_2(SAr)_2(pyphos)_4$ [**5a**: Ar = $C_6H_4Me$-4; **5b**: $C_6H_4OMe$-4; **5c**: $C_6H_3Me_2$-2,6; **5d**: $C_6H_5$], which are unique 1,4-oxidative addition products.

(© Wiley-VCH Verlag GmbH & Co. KGaA, 69451 Weinheim, Germany, 2007)

## Introduction

Low-dimensional multimetallic molecules have attracted much interest in view of their fundamental bonding nature as well as their potential as magnetic, electronic, and optical materials.[1] They are mainly constructed by assembling dinuclear metal units[1,2] by using appropriate multidentate ligands,[3–9] or by electrochemical methods.[10–15] We previously reported the preparation of *linear heterometallic clusters* with the use of a quadruply bonded dimolybdenum(II) complex, $Mo_2(pyphos)_4$ (**1**) (pyphos = 6-diphenylphosphanyl-2-pyridonato), as a core part of metal strings, and their unique reactivity arising from the electronic anisotropy involving dative metal–metal bonds:[16] the oxidative reaction of 2 equiv. of dichloromethane to a $Pd^0$ cluster, $Mo_2Pd_2(pyphos)_4$ (**2**), which has two $Pd^0\cdots Mo^{II}$ dative bonds, proceeded under mild conditions to give a $Pd^{II}$ cluster, $Mo_2Pd_2Cl_2(CH_2Cl)_2(pyphos)_4$ (**3**).[16d] Thus, the presence of the $Pd^0\cdots Mo$ dative bond of **2** enhances its reactivity toward oxidants,[16d] which is relevant to the fact that some dinuclear metal complexes with a bonding interaction between $d^{10}$ metal centers exhibit higher reactivity compared with the corresponding mononuclear complexes.[17] In this contribution, we report the structural and spectral characterization of the $Pt^0\cdots Mo^{II}$ dative bond of linear tetrametal complexes, $Mo_2Pt_2(pyphos)_4(PR_3)_2$ (**4**), whose reactivity was assessed by an unprecedented 1,4-oxidative addition reaction of diaryl disulfides, which gives dithiolate $Pt^I$ complexes, $Mo_2Pt_2(SAr)_2(pyphos)_4$ (**5**).

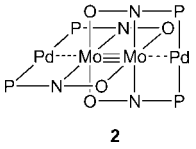

**2**

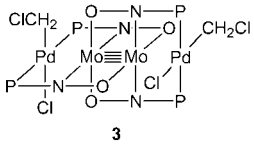

**3**

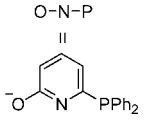

Treatment of $Mo_2(pyphos)_4$ (**1**) with 2 equiv. of $Pt(PPh_3)_4$ in THF afforded a tetrametal cluster, $Mo_2Pt_2(pyphos)_4(PPh_3)_2$ (**4a**), with a $Pt^0$–$Mo^{II}$–$Mo^{II}$–$Pt^0$ array in 85% yield. The triphenylphosphane bound to each platinum(0) atom was labile[18] and readily replaced by adding excess $PMe_3$, $PMe_2Ph$, $PMePh_2$, and $P(OMe)_3$ in THF to give the corresponding complexes $Mo_2Pt_2(pyphos)_4(L)_2$ [**4b**: $L$ = $PMe_3$; **4c**: $L$ = $PMe_2Ph$; **4d**: $L$ = $PMePh_2$; **4e**: $L$ = $P(OMe)_3$] (Scheme 1). All complexes **4a**–**e** were unequivocally characterized by spectroscopic data and combustion analysis. The $^{31}P\{^1H\}$ NMR spectra of **4a**–**e** provided two peaks with a coupling constant $J_{P\text{-}P}$ = 140–192 Hz, the value of which was comparable to the coupling constant ($J_{P\text{-}P}$ = 110 Hz) reported for a dinuclear trigonal planar complex, $Pt_2(\mu\text{-dppm})_3$.[19] This clearly indicates that complexes **4a**–**e** adopt a trigonal planar geometry at each Pt center, and this was further confirmed by X-ray analysis of **4e** (Figure 1).[20] Each platinum atom in **4e** is coordinated by two phosphorus atoms of the pyphos ligands and $P(OMe)_3$, which forms a trigonal planar geometry with P–Pt–P angles of 123.95(4), 116.98(4), and 118.96(4)° for Pt1, with a sum = 359.89°, and 124.95(4), 117.87(4), and

[a] Department of Chemistry, Graduate School of Engineering Science
Osaka University, Toyonaka, Osaka 560-8531, Japan

Supporting information for this article is available on the WWW under http://www.eurjic.org or from the author.

 © 2007 Wiley-VCH Verlag GmbH & Co. KGaA, Weinheim 

117.15(5)° for Pt2, with a sum = 359.97°, respectively. Notably, the trigonally coordinated $d^{10}$ center, such as $Pt^0$ and $Au^I$, interacts by attracting heavier $s^2$ metals such as $Tl^I$ and $Pb^{II}$.[21] Similar angles [114.9(2)–123.1(2)°] are reported for trigonal planar complexes such as $Pt(PPh_3)_3$[22] and $Pt_2(\mu\text{-dppm})_3$.[19,23] Each platinum atom of **4e** was slightly out of reach of the $Mo_2$ vector [Pt1–Mo1–Mo2 = 170.66(2)°; Pt2–Mo2–Mo1 = 167.94(2)°]. Although the distances of Pt1–Mo1 [2.9082(4) Å] and Pt2–Mo2 [2.9276(4) Å] are long, the distance of Mo1–Mo2 [2.1198(5) Å] is longer than that of quadruply-bonded $Mo^{II}_2$ complexes such as **1** [2.098(2) Å],[16a,16b] a $Pt^{II}$ complex, $Mo_2Pt_2Cl_4(pyphos)_4$ [2.101(2) Å],[16b] $Mo_2(O_2CCH_3)_4$ [2.0934(8) Å],[24] and $Mo_2(mhp)_4$ [2.065(1) Å, mhp = 6-methylpyridonate],[25] and slightly shorter than that of the triple bond of the $Pt^I$ complex $Mo_2Pt_2Cl_2(pyphos)_4$ [2.134(1) Å],[16b] which indicates that each platinum atom interacts by attracting the $Mo_2$ part to form a dative bond.[26] This is further supported by the Raman active ν(Mo–Mo) frequencies (382–388 $cm^{-1}$) observed for complexes **4a**–**e**, whose values are comparable to that of the triple bonded $Mo_2$ in $Mo_2Pt_2Cl_2(pyphos)_4$ (381 $cm^{-1}$) and its palladium derivative $Mo_2Pd_2Cl_2(pyphos)_4$ (386 $cm^{-1}$), but lower than that of the quadruply bonded $Mo_2$ in **1** (394 $cm^{-1}$) and $Mo_2Pt_2Cl_4(pyphos)_4$ (403 $cm^{-1}$).

Complex **4a** showed unique reactivity toward diaryl disulfides. The addition of excess ArSSAr (Ar = $C_6H_4Me$-4, $C_6H_4OMe$-4, $C_6H_3Me_2$-2,6, $C_6H_5$) to a solution of **4a** in THF yielded the corresponding 1,4-bis(thiolate) tetrametal complexes $Mo_2Pt_2(SAr)_2(pyphos)_4$ [**5a**: Ar = $C_6H_4Me$-4; **5b**: $C_6H_4OMe$-4; **5c**: $C_6H_3Me_2$-2,6; **5d**: $C_6H_5$] [Equation (1)], whose formulation was confirmed by NMR spectroscopic data and combustion analysis together with X-ray analysis of **5c**. A 1,4-addition of disulfides to the tetrametal skeleton of **4a** resulted in the formation of two $Pt^I$–$Mo^{II}$ single bonds as a consequence of one-electron oxidation of each platinum.

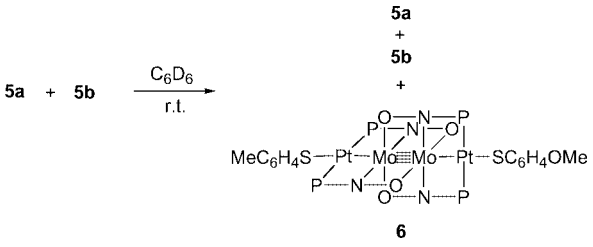


(1)

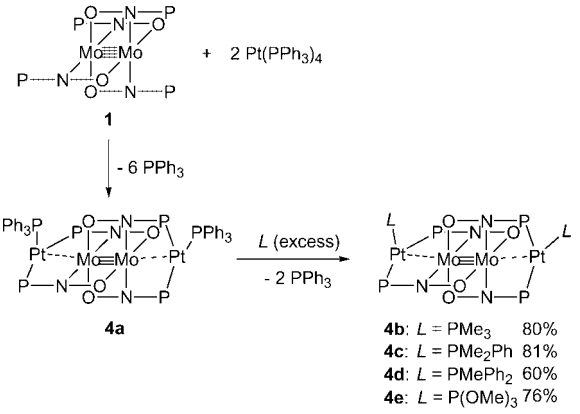


Scheme 1. Synthesis of complexes **4a**–**e**. O–N–P = 6-diphenylphosphanyl-2-pyridonato.

X-ray analysis of **5c** (Figure 2)[27] revealed that the two $Pt^I$ centers adopt a square-planar geometry where two phosphorus atoms of the pyphos ligands occupy *trans* positions and the sulfur atom and the molybdenum atom are placed at the opposing corners of the square planar, which results in the formation of a linear tetrametal $Pt^I$–$Mo^{II}$–$Mo^{II}$–$Pt^I$ skeleton with the angles of Pt1–Mo1–Mo2 [174.92(3)°] and Pt2–Mo2–Mo1 [173.37(3)°]. The bond lengths of Pt–Mo [2.6916(5) and 2.7306(5) Å] are short enough to have a single bond, which is comparable with that of $(CO)_3Mo(\mu\text{-}PPh_2)_2Pt(PEt_3)$ [2.766(1) Å].[28] The significantly longer Mo–Mo bond length [2.1413(8) Å] than that of **1** [2.098(2) Å][16a,16b] and **4e** [2.1196(5) Å] led us to conclude that the Mo–Mo bond had a bond order of three. The lower-shift of the ν(Mo–Mo) frequency (379 $cm^{-1}$) for **5c** also supported the elongated Mo–Mo bond.

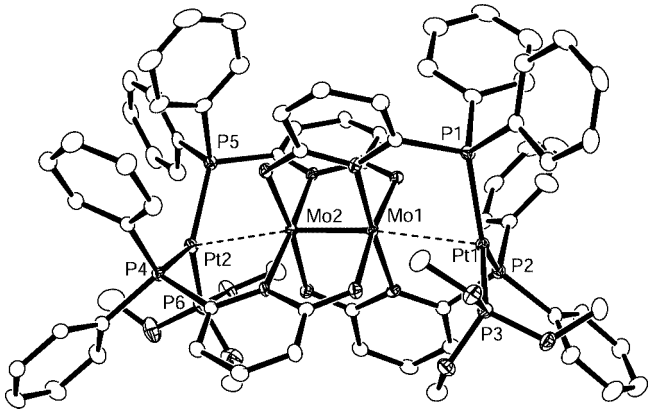


Figure 1. Molecular structure of complex **4e** with the numbering scheme. Hydrogen atoms and solvent molecules are omitted for clarity.

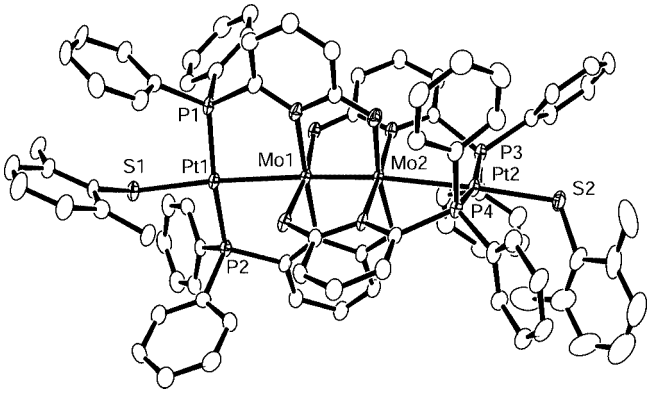


Figure 2. Molecular structure of complex **5c** with the numbering scheme. Hydrogen atoms and solvent molecules are omitted for clarity.

 © 2007 Wiley-VCH Verlag GmbH & Co. KGaA, Weinheim 

By mixing isolated thiolate complexes **5a** and **5b** in $C_6D_6$, a new mixed thiolate complex, $Mo_2Pt_2(SC_6H_4Me\text{-}4)(SC_6H_4OMe\text{-}4)(pyphos)_4$ (**6**), was generated whose $^{31}P\{^1H\}$ NMR spectrum showed new singlet signals at $\delta$ = 30.8 and 30.9 ppm [Equation (2)]. Additionally, the reaction of **5a** with 1 equiv. of bis(4-methoxyphenyl) disulfide produced complex **6** together with **5b**. In contrast, dark conditions suppressed these reactions as judged by $^{31}P\{^1H\}$ NMR spectroscopy. In a reverse reaction, the addition of 10 equiv. of $PPh_3$ to **5c** in $C_6D_6$ resulted in the slow formation of the corresponding disulfide $(XylS)_2$ (18%) together with the precipitation of **4a** after 12 h at room temperature, as monitored by $^1H$ NMR spectroscopy. Thus, these experimental observations suggested that the formation and cleavage of the Pt–SAr bond proceeded through a radical process.

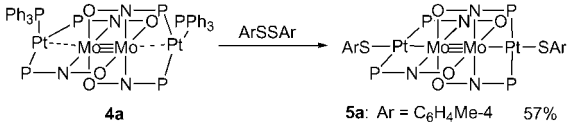


(2)

In conclusion, we successfully prepared tetranuclear $Pt^0$–$Mo^{II}$–$Mo^{II}$–$Pt^0$ clusters supported by four pyphos and two phosphane or phosphite ligands, and we provided clear structural and spectral evidence for the dative bond between two $Pt^0$ atoms and the $Mo_2$ core. The 1,4-oxidative addition of diaryldisulfides to the two platinum(0) centers linked by an $Mo_2$ core gave unique tetranuclear complexes with a linear ArS–$Pt^I$–$Mo^{II}$–$Mo^{II}$–$Pt^I$–SAr skeleton. Further investigation on the propensity of such a dative bond in the cluster system is in progress.

**Supporting Information** (see footnote on the first page of this article): Preparation of $Mo_2Pt_2(pyphos)_4(PPh_3)_2$ (**4a**–**e**), oxidative addition of bis(4-methoxyphenyl) disulfide to **4a**, view of $[Mo_2Pt_2Cl_2(C_{17}H_{13}NOP)_4(C_3H_9O_3P)_2]\cdot 1.5(hexane)$, and PLUTO view of $[Mo_2Pt_2(C_{17}H_{13}NOP)_4(2,6\text{-}Me_2C_6H_4S)_2]\cdot 4(C_4H_8O)$.

## Acknowledgments

We are grateful for financial support from the Ministry of Education, Culture, Sports, Science, and Technology. This work is in part financially supported by Mitsubishi Foundation and JST (CREST).

[1] F. A. Cotton, R. A. Walton, *Multiple Bonds Between Metal Atoms*, 2nd ed., Clarendon Press, Oxford, **1993**; F. A. Cotton, *Inorg. Chem.* **1998**, *37*, 5710; F. A. Cotton, C. Lin, C. A. Murillo, *Acc. Chem. Res.* **2001**, *34*, 759.

[2] J. K. Bera, K. R. Dunbar, *Angew. Chem. Int. Ed.* **2002**, *41*, 4453; J. K. Bera, P. Angaridis, F. A. Cotton, M. A. Petrukhina, P. E. Fanwick, R. A. Walton, *J. Am. Chem. Soc.* **2001**, *123*, 1515.

[3] Some references of clusters with pyridylamino ligands: E.-C. Yang, M.-C. Cheng, M.-S. Tsai, S.-M. Peng, *J. Chem. Soc., Chem. Commun.* **1994**, 2377; J.-T. Sheu, C.-C. Lin, I. Chao, C.-C. Wang, S.-M. Peng, *Chem. Commun.* **1996**, 315; F. A. Cotton, L. M. Daniels, C. A. Murillo, I. Pascual, *J. Am. Chem. Soc.* **1997**, *119*, 10223; F. A. Cotton, L. M. Daniels, G. T. Jordan IV, C. A. Murillo, *J. Am. Chem. Soc.* **1997**, *119*, 10377; S.-J. Shieh, C.-C. Chou, G.-H. Lee, C.-C. Wang, S.-M. Peng, *Angew. Chem. Int. Ed. Engl.* **1997**, *36*, 56; F. A. Cotton, L. M. Daniels, C. A. Murillo, X. Wang, *Chem. Commun.* **1998**, 39; C.-C. Wang, W.-C. Lo, C.-C. Chou, G.-H. Lee, J.-M. Chen, S.-M. Peng, *Inorg. Chem.* **1998**, *37*, 4059; M.-M. Rohmer, M. Bénard, *J. Am. Chem. Soc.* **1998**, *120*, 9372; F. A. Cotton, C. A. Murillo, X. Wang, *J. Chem. Soc., Dalton Trans.* **1999**, 3327; Y.-H. Chen, C.-C. Lee, C.-C. Wang, G.-H. Lee, S.-Y. Lai, F.-Y. Li, C.-Y. Mou, S.-M. Peng, *Chem. Commun.* **1999**, 1667; H.-C. Chang, J.-T. Li, C.-C. Wang, T.-W. Lin, H.-C. Lee, G.-H. Lee, G.-H. Lee, S.-M. Peng, *Eur. J. Inorg. Chem.* **1999**, 1243; S.-Y. Lai, T.-W. Lin, Y.-H. Chen, C.-C. Wang, G.-H. Lee, M.-H. Yang, M.-K. Leung, S.-M. Peng, *J. Am. Chem. Soc.* **1999**, *121*, 250; R. Clérac, F. A. Cotton, K. R. Dunbar, C. A. Murillo, I. Pascual, X. Wang, *Inorg. Chem.* **1999**, *38*, 2655; R. Clérac, F. A. Cotton, L. M. Daniels, K. R. Dunbar, K. Kirschbaum, C. A. Murillo, A. A. Pinkerton, A. J. Schultz, X. Wang, *J. Am. Chem. Soc.* **2000**, *122*, 6226; R. Clérac, F. A. Cotton, L. M. Daniels, K. R. Dunbar, C. A. Murillo, I. Pascual, *Inorg. Chem.* **2000**, *39*, 748; R. Clérac, F. A. Cotton, L. M. Daniels, K. R. Dunbar, C. A. Murillo, I. Pascual, *Inorg. Chem.* **2000**, *39*, 752; R. Clérac, F. A. Cotton, L. M. Daniels, K. R. Dunbar, C. A. Murillo, X. Wang, *Inorg. Chem.* **2001**, *40*, 1256; J. F. Berry, F. A. Cotton, L. M. Daniels, C. A. Murillo, *J. Am. Chem. Soc.* **2002**, *124*, 3212; C.-Y. Yeh, C.-H. Chou, K.-C. Pan, C.-C. Wang, G.-H. Lee, Y. O. Su, S.-M. Peng, *J. Chem. Soc., Dalton Trans.* **2002**, 2670; T.-B. Tsao, G.-H. Lee, C.-Y. Yeh, S.-M. Peng, *Dalton Trans.* **2003**, 1465; H. Li, G.-H. Lee, S.-M. Peng, *Inorg. Chem. Commun.* **2003**, *6*, 1; J. F. Berry, F. A. Cotton, T. Lu, C. A. Murillo, B. K. Roberts, X. Wang, *J. Am. Chem. Soc.* **2004**, *126*, 7082; J. F. Berry, F. A. Cotton, C. A. Murillo, *Organometallics* **2004**, *23*, 2503; J. F. Berry, F. A. Cotton, C. S. Fewox, T. Lu, C. A. Murillo, X. Wang, *Dalton Trans.* **2004**, 2297; J. F. Berry, F. A. Cotton, C. A. Murillo, *Inorg. Chim. Acta* **2004**, *357*, 3847; H. Li, G.-H. Lee, S.-M. Peng, *J. Mol. Struct.* **2004**, *707*, 179; M. Bénard, J. F. Berry, F. A. Cotton, C. Gaudin, X. López, C. A. Murillo, M.-M. Rohmer, *Inorg. Chem.* **2006**, *45*, 3932.

[4] T. Murahashi, E. Mochizuki, Y. Kai, H. Kurosawa, *J. Am. Chem. Soc.* **1999**, *121*, 10660; T. Murahashi, Y. Higuchi, T. Katoh, H. Kurosawa, *J. Am. Chem. Soc.* **2002**, *124*, 14288; T. Murahashi, T. Uemura, H. Kurosawa, *J. Am. Chem. Soc.* **2003**, *125*, 8436; T. Murahashi, H. Nakashima, T. Nagai, Y. Mino, T. Okuno, M. Abdul Jalil, H. Kurosawa, *J. Am. Chem. Soc.* **2006**, *128*, 4377.

[5] M.-M. Rohmer, M. Bénard, *J. Am. Chem. Soc.* **1998**, *120*, 9372.

[6] B. Oskui, W. S. Sheldrick, *Eur. J. Inorg. Chem.* **1999**, 1325.

[7] T. Zhang, M. Drouin, P. D. Harvey, *Inorg. Chem.* **1999**, *38*, 957; T. Zhang, M. Drouin, P. D. Harvey, *Inorg. Chem.* **1999**, *38*, 1305.

[8] R. Clérac, F. A. Cotton, L. M. Daniels, K. R. Dunbar, C. A. Murillo, I. Pascual, *Inorg. Chem.* **2000**, *39*, 3414; F. A. Cotton, L. M. Daniels, P. Lei, C. A. Murillo, X. Wang, *Inorg. Chem.* **2001**, *40*, 2778; F. A. Cotton, P. Lei, C. A. Murillo, L.-S. Wang, *Inorg. Chim. Acta* **2003**, *349*, 165; F. A. Cotton, P. Lei, C. A. Murillo, *Inorg. Chim. Acta* **2003**, *351*, 183; F. A. Cotton, P. Lei, C. A. Murillo, *Inorg. Chim. Acta* **2003**, *349*, 173.

[9] C.-C. Chien, J.-C. Chang, C.-Y. Yeh, G.-H. Lee, J.-M. Fang, S.-M. Peng, *Dalton Trans.* **2006**, 2106.

[10] G. M. Finniss, E. Canadell, C. Campana, K. R. Dunbar, *Angew. Chem. Int. Ed. Engl.* **1996**, *35*, 2772; M. E. Prater, L. E. Pence, R. Clérac, G. M. Finniss, C. Campana, P. Auban-Senzier, D. Jérome, E. Canadell, K. R. Dunbar, *J. Am. Chem. Soc.* **1999**, *121*, 8005.

[11] K. Sakai, Y. Tanaka, Y. Tsuchiya, K. Hirata, T. Tsubomura, S. Iijima, A. Bhattacharjee, *J. Am. Chem. Soc.* **1998**, *120*, 8366; K. Sakai, M. Takeshita, Y. Tanaka, T. Ue, M. Yanagisawa, M. Kosaka, T. Tsubomura, M. Ato, T. Nakano, *J. Am. Chem. Soc.*

 © 2007 Wiley-VCH Verlag GmbH & Co. KGaA, Weinheim 

**1998**, *120*, 11353; K. Sakai, E. Ishigami, Y. Konno, T. Kajiwara, T. Ito, *J. Am. Chem. Soc.* **2002**, *124*, 12088.

[12] T. Tanase, E. Goto, R. A. Begum, M. Hamaguchi, S. Zhan, M. Iida, K. Sakai, *Organometallics* **2004**, *23*, 5975.

[13] C. Tejel, M. A. Ciriano, L. A. Oro, *Angew. Chem. Int. Ed. Engl.* **1998**, *37*, 1542; C. Tejel, M. A. Ciriano, L. A. Oro, *Chem. Eur. J.* **1999**, *5*, 1131.

[14] A. Laguna, L. M. J. Jiménez, F. J. Lahoz, E. Olmos, *Organometallics* **1994**, *13*, 253.

[15] S.-S. Chern, G.-H. Lee, S.-M. Peng, *J. Chem. Soc., Chem. Commun.* **1994**, 1645.

[16] a) K. Mashima, H. Nakano, A. Nakamura, *J. Am. Chem. Soc.* **1993**, *115*, 11632; b) K. Mashima, H. Nakano, A. Nakamura, *J. Am. Chem. Soc.* **1996**, *118*, 9083; c) K. Mashima, M. Tanaka, K. Tani, A. Nakamura, W. Mori, S. Takeda, K. Yamaguchi, *J. Am. Chem. Soc.* **1997**, *119*, 4307; d) K. Mashima, A. Fukumoto, H. Nakano, Y. Kaneda, K. Tani, A. Nakamura, *J. Am. Chem. Soc.* **1998**, *120*, 12151; e) T. Rüffer, M. Ohashi, A. Shima, H. Mizomoto, Y. Kaneda, K. Mashima, *J. Am. Chem. Soc.* **2004**, *126*, 12244.

[17] T. Yoshida, T. Yamagata, T. H. Tulip, J. A. Ibers, S. Otuka, *J. Am. Chem. Soc.* **1978**, *100*, 2063; A. L. Balch, C. T. Hunt, C.-L. Lee, M. M. Olmstead, J. P. Farr, *J. Am. Chem. Soc.* **1981**, *103*, 3764; S. Schreiner, T. N. Gallaher, *Organometallics* **1993**, *12*, 4201; Y. Pan, J. T. Mague, M. J. Fink, *J. Am. Chem. Soc.* **1993**, *115*, 3842.

[18] Complex **4a** in [D$_8$]THF exhibited temperature-dependent $^1$H NMR spectroscopy due to a process of dissociation and recoordination of $PPh_3$, which gives thermodynamic parameters of $\Delta G^{\ddagger}(298)$ = 15(2) kcal/mol, $\Delta H^{\ddagger}$ = 11.8(9) kcal/mol, $\Delta S^{\ddagger}$ = –12(3) eu.

[19] L. Manojlovic-Muir, K. W. Muir, M. C. Grossel, M. P. Brown, C. D. Nelson, A. Yavari, E. Kallas, R. P. Moulding, K. R. Seddon, *J. Chem. Soc., Dalton Trans.* **1986**, 1955.

[20] Crystal data for **4e**·1.5hexane: $Fw$ = 2072.48 (0.27 × 0.20 × 0.10 mm), space group $P\bar{1}$ (#2), $a$ = 14.35524(17), $b$ = 16.24695(7), $c$ = 19.5725(3) Å, $\alpha$ = 108.9657(8), $\beta$ = 97.8677(6), $\gamma$ = 106.1829(6)°, $V$ = 4013.86(8) Å$^3$, $Z$ = 2, calculated density = 1.715 Mg/m$^3$. Data were collected with Rigaku RAXIS RAPID imaging plate area detector with graphite monochromated Mo-$K_\alpha$ radiation at a temperature of 100(2) K to a maximum 2$\theta$ value of 63.0°. A total of 240 oscillation images were collected. Of the 99273 reflections that were collected, 26544 were unique ($R_{int}$ = 0.0920); equivalent reflections were merged. The linear absorption coefficient, $\mu$, for Mo-$K_\alpha$ radiation of 3.960 mm$^{-1}$ was applied, which resulted in transmission factors ranging from 0.4898 to 0.6740. The data were corrected for Lorentz and polarization effects. The structure was solved by direct methods (SHELXL-97) and refined on $F^2$ by full-matrix least-squares methods by using SHELXL-97.[29] Final $R$ factors, $R1$ and $wR2$ are 0.0507 and 0.0825 for 20546 reflections with $I > 2.0\sigma(I)$, respectively. $R1$ and $wR2$ for all data are 0.0771 and 0.0891 for 26544 reflections. The number of parameters was 964. GOF values are 1.045 for $I > 2.0\sigma(I)$ and 1.045 for all data, respectively.

[21] V. J. Catalano, B. L. Bennett, H. M. Kar, *J. Am. Chem. Soc.* **1999**, *121*, 10235; V. J. Catalano, B. L. Bennett, S. Muratidis, B. C. Noll, *J. Am. Chem. Soc.* **2001**, *123*, 173; V. J. Catalano, B. L. Bennett, B. C. Noll, *Chem. Commun.* **2000**, 1413; V. J. Catalano, B. L. Bennett, R. L. Yson, B. C. Noll, *J. Am. Chem. Soc.* **2000**, *122*, 10056; V. J. Catalano, M. A. Malwitz, *J. Am. Chem. Soc.* **2004**, *126*, 6560.

[22] V. Alabano, P. L. Bellon, V. Scatturin, *Chem. Commun. (London)* **1966**, 507.

[23] L. Manojlovi-Muir, K. W. Muir, *J. Chem. Soc., Chem. Commun.* **1982**, 1155.

[24] F. A. Cotton, Z. C. Mester, T. R. Webb, *Acta Crystallogr., Sect. B* **1974**, *30*, 2768.

[25] F. A. Cotton, P. E. Fanwick, R. H. Niswander, J. C. Sekutowski, *J. Am. Chem. Soc.* **1978**, *100*, 4725.

[26] Some references of heterometal molecules with dative bond: T. Tanase, H. Toda, K. Kobayashi, Y. Yamamoto, *Organometallics* **1996**, *15*, 5272; T. Yamaguchi, F. Yamazaki, T. Ito, *J. Am. Chem. Soc.* **1999**, *121*, 7405; T. Yamaguchi, F. Yamazaki, T. Ito, *J. Am. Chem. Soc.* **2001**, *123*, 743; N. Oberbeckmann-Winter, X. Morise, P. Braunstein, R. Welter, *Inorg. Chem.* **2005**, *44*, 1391; D. E. Janzen, J. F. Mehne, D. G. VanDerveer, G. J. Grant, *Inorg. Chem.* **2005**, *44*, 8182.

[27] Crystal data for **5c**·4C$_4$H$_8$O: $Fw$ = 2257.92 (0.33 × 0.17 × 0.10 mm), triclinic, space group $P\bar{1}$ (#2), $a$ = 14.5331(4), $b$ = 17.0949(6), $c$ = 21.0655(6) Å, $\alpha$ = 70.6216(8), $\beta$ = 70.4231(10), $\gamma$ = 72.5510(10)°, $V$ = 4545.7(2) Å$^3$, $Z$ = 2, calculated density = 1.650 Mg/m$^3$. Data were collected with Rigaku RAXIS RAPID imaging plate area detector with graphite monochromated Mo-$K_\alpha$ radiation at a temperature of 100(2) K to a maximum 2$\theta$ value of 61.0°. A total of 270 oscillation images were collected. Of the 80453 reflections that were collected, 27259 were unique ($R_{int}$ = 0.1024); equivalent reflections were merged. The linear absorption coefficient, $\mu$, for Mo-$K_\alpha$ radiation of 3.514 mm$^{-1}$ was applied, which resulted in transmission factors ranging from 0.4844 to 0.7049. The data were corrected for Lorentz and polarization effects. The structure was solved by Patterson methods (DIRDIF-99, PATTY)[30] and refined on $F^2$ by full-matrix least-squares methods by using SHELXL-97.[29] Final $R$ factors, $R1$ and $wR2$ are 0.0645 and 0.1456 for 20608 reflections with $I > 2.0\sigma(I)$, respectively. $R1$ and $wR2$ for all data are 0.0926 and 0.1585 for 27259 reflections. The number of parameters was 964. GOF values are 1.028 for $I > 2.0\sigma(I)$ and 1.028 for all data, respectively. CCDC-620212 and 620213 contain the supplementary crystallographic data for this paper. These data can be obtained free of charge from The Cambridge Crystallographic Data Centre via www.ccdc.cam.ac.uk/data_request/cif.

[28] J. Powell, C. Couture, M. R. Gregg, J. F. Sawyer, *Inorg. Chem.* **1989**, *28*, 3437.

[29] G. M., Sheldrick, *SHELXL-97: Programs for Crystal Structure Analysis* (Release 97–2), University of Göttingen, Germany, **1997**.

[30] P. T. Beurskens, G. Beurskens, R. de Gelder, S. Garcia-Granda, R. O. Gould, R. Israel, J. M. M. Smits, *The DIRDIF-99 Program System* (version 99.2), Crystallography Laboratory, University of Nijmegen, The Netherlands, **1999**. P. T. Beurskens, G. Admiraal, H. Behm, G. Beurskens, J. M. M. Smits, C. Smykalla, *Program PATTY, Z. Kristallogr.*, **1991**, Suppl. 4, p. 99.

Received: September 11, 2006
Published Online: November 29, 2006

 © 2007 Wiley-VCH Verlag GmbH & Co. KGaA, Weinheim 

DOI: 10.1002/ejic.200600701

# Novel 1,2-Dicarba-*closo*-dodecaborane(12) Derivatives of Selenium

**Bernd Wrackmeyer,*[a] Zureima García Hernández,[a] Rhett Kempe,[a] and Max Herberhold[a]**

**Keywords:** Carboranes / Selenium / Platinum / Oxidative addition / NMR spectroscopy

Lithiation of 1,2-dicarba-*closo*-dodecaborane(12) (**1**) followed by insertion of selenium into both C–Li bonds leads to the 1,2-diselenolato-1,2-dicarba-*closo*-dodecaborane(12) dianion (**3**), which is converted by oxidative coupling into the cyclic eight-membered bis(diselane) **4** with annellated carborane moieties. Oxidative addition of **4** to ethenebis(triphenylphosphane)platinum(0) gives the bis(triphenylphosphane)platinum(II) complex **7**, which contains a chelating 1,2-diselenolato-1,2-dicarba-*closo*-dodecaborane(12) ligand, by symmetric cleavage of the eight-membered ring in **4** and displacement of ethene. The molecular structures of **4** and **7** were determined by X-ray analysis. The solution-state structures of the new compounds are supported by multinuclear NMR data ($^{1}H$, $^{11}B$, $^{13}C$, $^{29}Si$, $^{31}P$, $^{77}Se$, $^{195}Pt$).
(© Wiley-VCH Verlag GmbH & Co. KGaA, 69451 Weinheim, Germany, 2007)

## Introduction

An important aspect of the rich chemistry of 1,2-dicarba-*closo*-dodecaborane(12) (**1**) ("*ortho*-carborane") is the variation of substituents at the carbon atoms in the 1,2-positions.[1,2] Most conveniently, this chemistry starts with metallation at the carbon atom(s), for example to form the dilithiated carborane 1,2-$Li_2$-1,2-$C_2B_{10}H_{10}$ (**2**), followed by further transformations.[1,2] We and others became interested in the 1,2-dichalcogenolato-1,2-dicarba-*closo*-dodecaborane(12) anions $[1,2\text{-}(1,2\text{-}C_2B_{10}H_{10})E_2]^{2-}$ (E = S, Se, Te) as chelating ligands,[3–10] and this chemistry has been further developed into various areas.[11–15] Tellurium derivatives are rarely studied since clean access to the anion $[1,2\text{-}(1,2\text{-}C_2B_{10}H_{10})Te_2]^{2-}$ appears to be difficult.[16,17] However, the corresponding anions with sulfur or selenium are more readily accessible, and the anion containing selenium $[1,2\text{-}(1,2\text{-}C_2B_{10}H_{10})Se_2]^{2-}$ (**3**) is particularly attractive considering the useful NMR properties of $^{77}Se$[18] ($I$ = 1/2; natural abundance 7.58%; about three times more sensitive in NMR experiments than $^{13}C$). In the present work, we report on observations of oxidative coupling of **3**, or derivatives of **3**, and cleavage of the resulting Se–Se bonds by oxidative addition to $[Pt(PPh_3)_2(CH_2{=}CH_2)]$.

## Results and Discussion

Formation of the anion $[1,2\text{-}(1,2\text{-}C_2B_{10}H_{10})Se_2]^{2-}$ (**3**) and its conversion into the cyclic bis(diselane) **4** are shown in Scheme 1. The reaction of **3** with an excess of $Me_3SiCl$ gave the disilylated derivative **5** in high yield along with a small amount of 1-$Me_3SiSe$-1,2-$C_2B_{10}H_{11}$ (**6**) and unreacted carborane **1**, thus indicating the preferred conversion of **1** into **2**, followed by double insertion of selenium into the C–Li bonds to give **3**. In context with the chemistry of heterosubstituted tropylium derivatives we have attempted to prepare a 1,2-bis(tropyliumseleno)-1,2-dicarba-*closo*-docecaborane(12) by cleavage of the Se–Si bonds. Surprisingly, the reaction of **5** with two equivalents of tropylium bromide, $C_7H_7Br$, gave **4** as the final product of a complex redox reaction together with the expected $Me_3SiBr$ and various organic compounds. The oxidative coupling of **3** with iodine led directly to **4**, as expected. Attempts to prepare a spirosilane from the reaction of **3** with $SiCl_4$ again gave **4** together with unidentified materials. The bis(diselane) **4** could be isolated as yellow crystals from benzene or toluene solutions and its molecular structure was determined by X-ray analysis (vide infra).

Diselanes are known as reagents for oxidative addition reactions.[19] Thus, the reaction of $[Pt(PPh_3)_2(CH_2{=}CH_2)]$ with **4** was studied (Scheme 2). Monitoring of the reaction by $^{31}P$ NMR spectroscopy showed that the eight-membered ring in **4** was cleaved symmetrically to give the platinum(II) complex **7** in essentially quantitative yield. Orange crystals of **7** were isolated and studied by X-ray analysis (vide infra). Complexes of type **7** or their palladium analogues are potential catalysts of the *cis*-addition of the Se–Se bond to the C≡C bond in alkynes.[19c,19d]

Addition of an excess of methyl iodide to a solution of **7** in dichloromethane led to cleavage of the Pt–Se bonds to give a mixture containing in the beginning *cis*-$[PtI_2(PPh_3)_2]$, and the anionic complexes $[PtI_3(PPh_3)]^-$ and

[a] Anorganische Chemie II, Universität Bayreuth, 95440 Bayreuth, Germany
Fax: +49-921-552-157
E-mail: b.wrack@uni-bayreuth.de

 © 2007 Wiley-VCH Verlag GmbH & Co. KGaA, Weinheim 

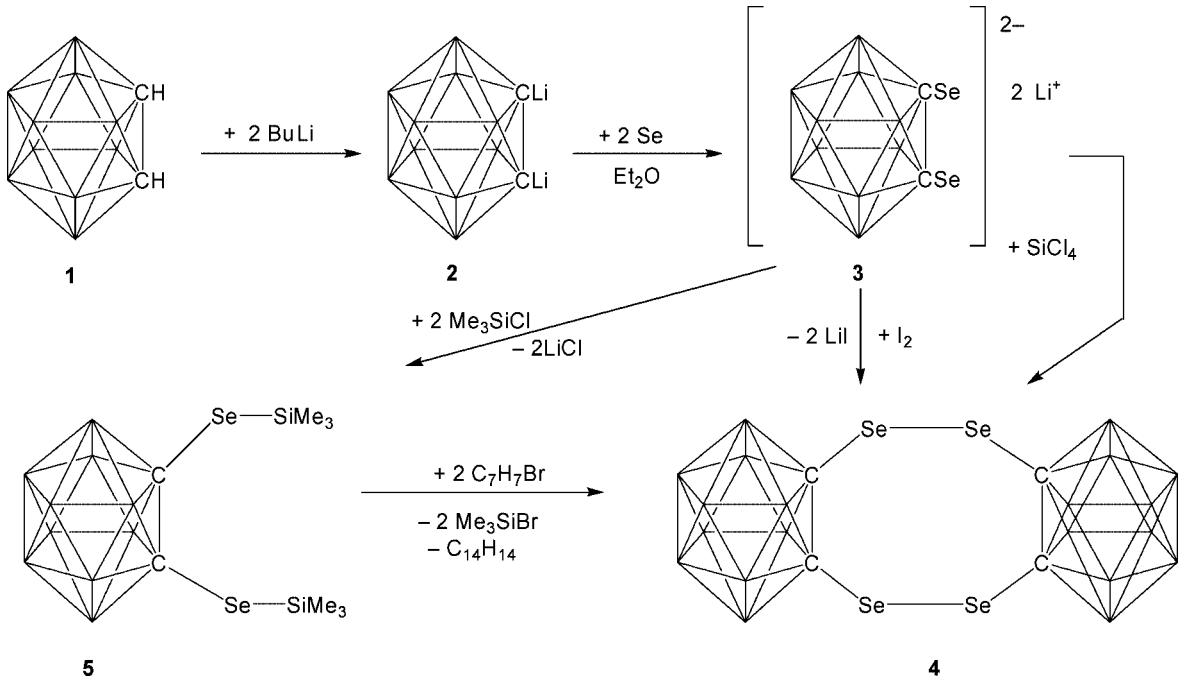


Scheme 1. Oxidative coupling: three routes to the bis(diselane) **4**.

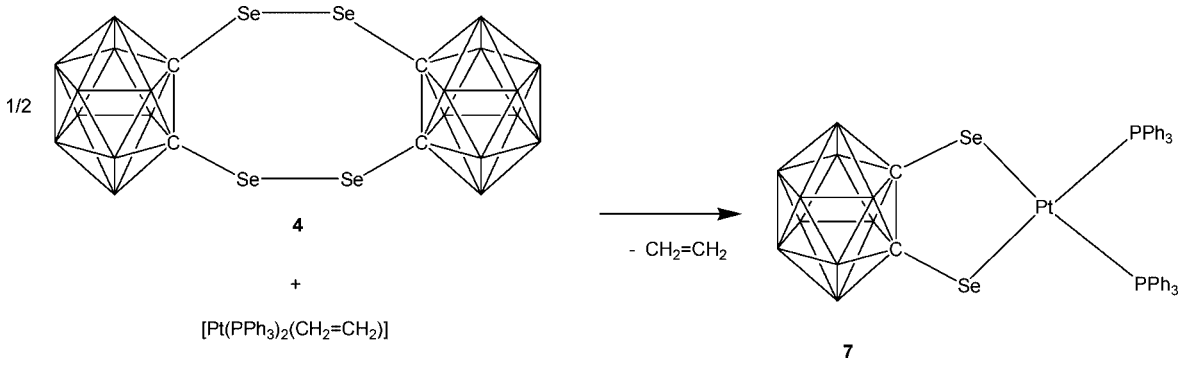


Scheme 2. Oxidative addition of the bis(diselane) **4** to give the platinum(II) complex **7**.

$[PtI_4]^{2-}$ with $[P(Me)Ph_3]^+$ as the counterion. The complex *cis*-$[PtI_2(PPh_3)_2]$ slowly rearranges into the more stable *trans*-isomer.

## NMR Spectroscopic Studies in Solution

The proposed structures of the new compounds are fully supported by the solution-state NMR spectroscopic data (see Table 1 and Experimental Section). The $^{13}C$(carborane) NMR signals are frequently not reported in the literature since they tend to be weak and broad.[1a,20] However, careful setting of the experimental conditions enables the measurement of these signals readily, and further information is provided by observation of $^{77}Se$ satellite signals, as shown in the case of **5** (Figure 1). The $^1J_{^{77}Se,^{13}C}$ and $^2J_{^{77}Se,^{13}C}$ coupling constants measured here are the first examples for this type of carbon atom. The magnitude of $^1J_{^{77}Se,^{13}C}$ in **5** (158.9 Hz) is markedly increased when compared with phenylselenium derivatives[18a,21,22] (e.g. in $Ph_2Se$: $^1J_{^{77}Se,^{13}C}$ = 103.1 Hz[21]).

$^{29}Si$ NMR spectra helped us to monitor the reaction of **5** with tropylium bromide (Scheme 1), and they also established the formation of the monosubstituted species **6** as a side product (Figure 2). The presence of the $^{77}Se$ satellite signals corresponding to $^1J_{^{77}Se,^{29}Si}$ indicates the presence of an Si–Se bond; the magnitude of $^1J_{^{77}Se,^{29}Si}$ is similar in **5** and **6** and also to data reported for other silylselanes.[23,24]

The formation of complex **7** is best monitored by $^{31}P$ NMR spectroscopy. The $^{31}P$ NMR signal of **7** is accompanied by $^{195}Pt$ and $^{77}Se$ satellites. The magnitude of the coupling constant $^1J_{^{195}Pt,^{31}P}$ is in the usual range for this type of complex.[25] The situation is somewhat more complex for the $^2J_{^{77}Se,^{31}P}$ data. In the literature, the *cis* and *trans* coupling pathway for comparable complexes has not been clearly distinguished.[19a,26a,26b] In the case of a platinum(II) diselenolene complex containing the ligand tri(1-cyclohepta-2,4,6-trienyl)phosphane, this discrimination was

 © 2007 Wiley-VCH Verlag GmbH & Co. KGaA, Weinheim 

Table 1. $^{13}C$, $^{29}Si$, $^{31}P$, $^{77}Se$ and $^{195}Pt$ NMR spectroscopic data[a] of the 1,2-dicarba-*closo*-dodecaborane(12) derivatives **4**–**7**.

| | $[(B_{10}H_{10})C_2]_2Se_4$ (**4**) | $(B_{10}H_{10})C_2(SeSiMe_3)_2$ (**5**) | $(B_{10}H_{10})CHCSeSiMe_3$ (**6**) | $(B_{10}H_{10}C_2)Se_2Pt(PPh_3)_2$ (**7**)[b] |
|---|---|---|---|---|
| $\delta_{^{77}Se}$ | 733.8 (s) | 308.6 (s) | 338.7 (s) | 573.0 (t)<br>313.7 ($^1J_{^{195}Pt,^{77}Se}$)<br>ca. 51 ($^2J_{^{77}Se,^{31}P}$)[c] |
| $\delta_{^{13}C}$ | | | | |
| $C^1$, $C^2$ | 69.1 (s) | 69.5 (s) | 70.1 (s, C–Se) | 71.8 (t) |
| | – | 158.9 ($^1J_{^{77}Se,^{13}C}$) | 66.4 (s, C–H) | 16 ($^3J_{^{31}P,^{13}C}$)[c] |
| $SiMe_3$ | – | 2.0 (s)<br>53.4 ($^1J_{^{29}Si,^{13}C}$) | 1.3 (s)<br>53.5 ($^1J_{^{29}Si,^{13}C}$) | – |
| $\delta_{^{29}Si}$ | – | 20.9 (s)<br>112.6 ($^1J_{^{77}Se,^{29}Si}$)<br>53.4 ($^1J_{^{29}Si,^{13}C}$) | 21.0 (s)<br>109.9 ($^1J_{^{77}Se,^{29}Si}$)<br>53.5 ($^1J_{^{29}Si,^{13}C}$) | – |
| $\delta_{^{31}P}$ | – | – | – | 15.7 (s)<br>2972.5 ($^1J_{^{195}Pt,^{31}P}$)<br>ca. 51 ($^2J_{^{77}Se,^{31}P}$)[d] |
| $\delta_{^{195}Pt}$ | – | – | – | –89.1 (t)<br>2972.5 ($^1J_{^{195}Pt,^{31}P}$)<br>313.7 ($^1J_{^{195}Pt,^{77}Se}$) |

[a] NMR measurements in $CD_2Cl_2$ at 23 °C, coupling constants $J$ are given in Hz. [b] $\delta^{13}C$(phenyl) ($^nJ_{^{31}P,^{13}C}$): 138.1 (45) $C^{ipso}$, 134.9 (11) $C^{ortho}$, 128.3 (11) $C^{meta}$, 131.5 $C^{para}$. [c] The signal appears as a multiplet, typical of an AA′X spin system, for which $\Sigma(^3J_{^{31}P,Pt,Se,^{13}C}\,cis + {}^3J^3{}_{^{31}P,Pt,Se,^{13}C}\,trans) = 16$ Hz can be determined from the spectrum. Simulation suggests that $^3J_{^{31}P,Pt,Se,^{13}C}$ values are around 20 and 4 Hz, with opposite signs, and that $|^2J_{^{31}P,^{31}P}| = 15$ Hz. [d] Coupling appears to be similar for *cis* and *trans* coupling pathway.

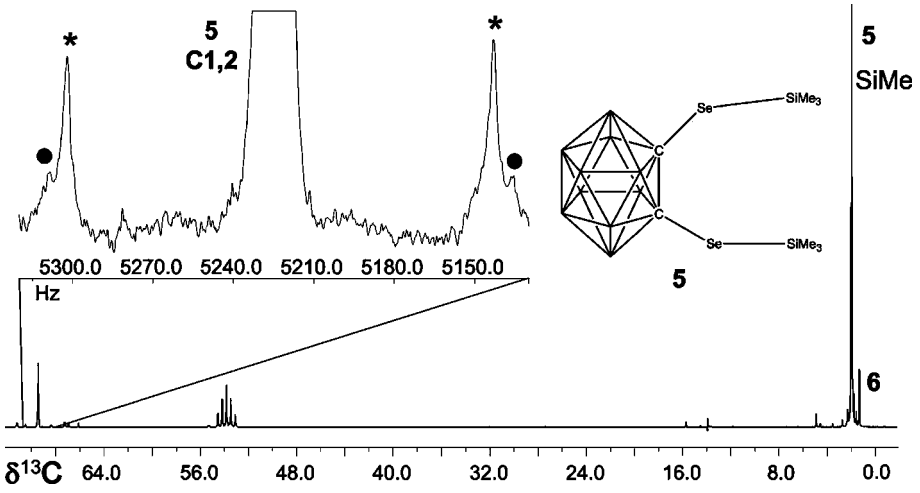


Figure 1. $^{13}C\{^1H\}$ NMR spectrum (75.4 MHz) of a mixture of [1,2-$(Me_3SiSe)_2$-1,2-$C_2B_{10}H_{10}$] (**5**) together with a small amount of [1-$Me_3SiSe$-1,2-$C_2B_{10}H_{11}$] (**6**; in $CD_2Cl_2$ at 23 °C). The $^{77}Se$ satellites marked by asterisks due to $^1J_{^{77}Se,^{13}C} = 158.9$ Hz are clearly visible in the expanded spectral region. The weak outer lines (marked by full circles) arise from the isotopomer containing one $^{13}C$ and two $^{77}Se$ nuclei and correspond to the transitions of an AA′X spin system, separated by $\Sigma(^1J_{^{77}Se,^{13}C} + {}^2J_{^{77}Se,^{13}C}) = 172.8$ Hz, from which the magnitude of $^2J_{^{77}Se,^{13}C}$ (13.9 Hz) can be deduced. Both the one- and two-bond coupling constants possess the same sign (<0). Simulation suggests that $|^3J_{^{77}Se,^{77}Se}|$ is between 20 and 40 Hz.

straightforward and a positive sign of $^2J_{^{77}Se,^{31}P}\,cis,trans$ was determined [$^2J_{^{77}Se,^{31}P}\,cis$ = 35.1 Hz and $^2J_{^{77}Se,^{31}P}\,trans$ = 88.7 Hz].[26c] The observation of only one pair of satellites with approximately correct intensities in the case of **7** (Figure 3) indicates that the magnitude of these two-bond coupling constants is similar. Simulation of the spectrum as an AA′X spin system for the $^{77}Se$ and two $^{31}P$ nuclei suggests that $^2J_{^{31}P,^{31}P}\,cis$ is of the order of 15–20 Hz (vide infra) and of either sign, and that the values for $^2J_{^{77}Se,^{31}P}\,cis,trans$ can range between about 45 and 60 Hz, but are more likely to be close to 50 Hz for both coupling constants. The simulation suggests that their signs should be alike. The $^{13}C$(carborane) signals of **7** reveal a pattern corresponding to an AA′X spin system, and reasonable agreement between simulated and experimental spectra is observed if the signs of $^3J_{^{31}P,Pt,Se,^{13}C}$ are opposite and $^2J_{^{31}P,^{31}P} \approx 15$ Hz.

The evidence from the $^{31}P$ NMR spectra is supported by the $^{77}Se$ NMR spectrum (Figure 4), which reveals an apparently simple triplet accompanied by $^{195}Pt$ satellites ($^1J_{^{195}Pt,^{77}Se}$ = 313.7 Hz). The value of this coupling is similar to that reported for a platinum(II) diselenolene complex[26c] ($^1J_{^{195}Pt,^{77}Se}$ = –327.6 Hz), where the $^{31}P$ nucleus is *trans* with

 © 2007 Wiley-VCH Verlag GmbH & Co. KGaA, Weinheim 

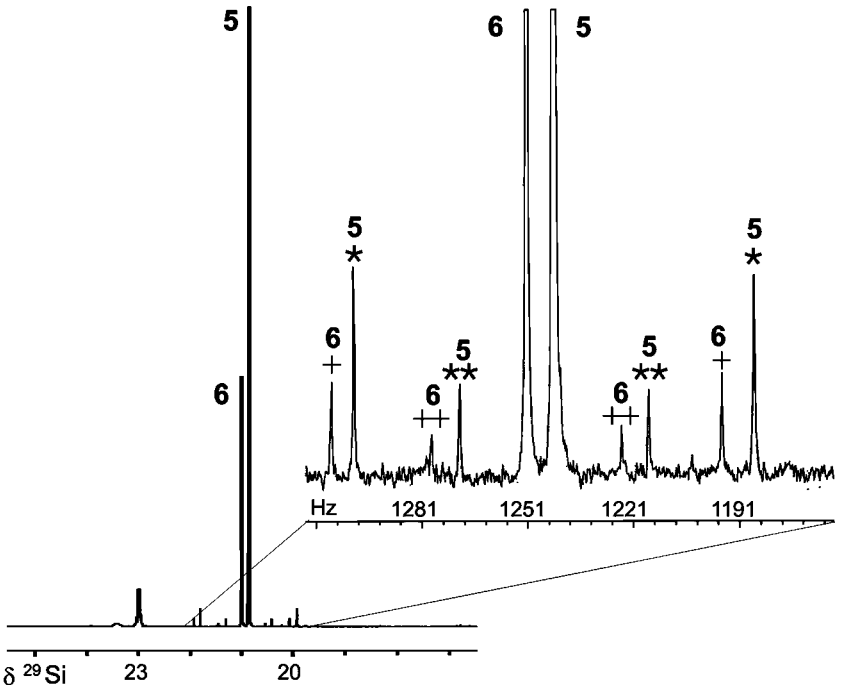


Figure 2. $^{29}Si\{^1H\}$ NMR spectrum (59.6 MHz; INEPT, refocused[32]) of an unpurified reaction mixture containing mainly [1,2-$(Me_3SiSe)_2$-1,2-$C_2B_{10}H_{10}$] (**5**) together with [1-$Me_3SiSe$-1,2-$C_2B_{10}H_{11}$] (**6**; in $CD_2Cl_2$ at 25 °C). The $^{77}Se$ and $^{13}C$ satellites are marked for the coupling constants (* and +) $^1J_{^{77}Se,^{29}Si}$ = 112.6 Hz (**5**) and 109.9 Hz (**6**); (** and ++) $^1J_{^{29}Si,^{13}C}$ = 53.4 (**5**) and 53.5 Hz (**6**).

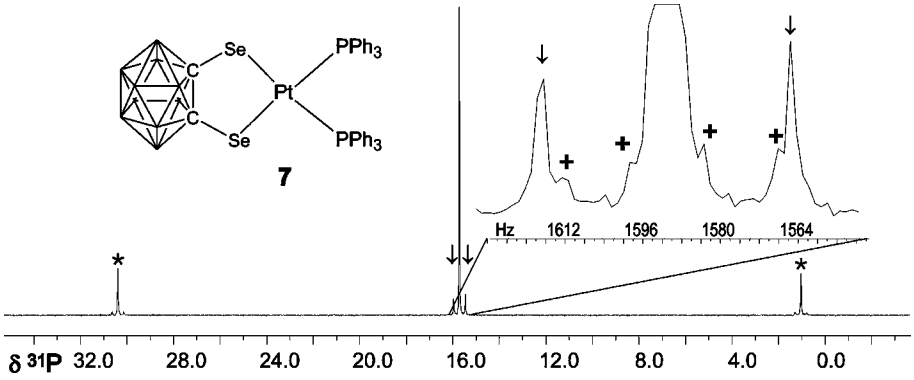


Figure 3. $^{31}P\{^1H\}$ NMR spectrum (121.4 MHz) of the complex [$Pt(PPh_3)_2$(1,2-$Se_2$-1,2-$C_2B_{10}H_{10}$)] (**7**; in $CD_2Cl_2$ at 25 °C). The $^{31}P$ NMR signal is accompanied by $^{195}Pt$ (asterisks) and $^{77}Se$ satellites (arrows) due to $^1J_{^{195}Pt,^{31}P}$ (2972.5 Hz) and $^2J_{^{77}Se,^{31}P}$ (ca. 51 Hz). The signals marked by (+) are some of the $^{13}C$ satellites.

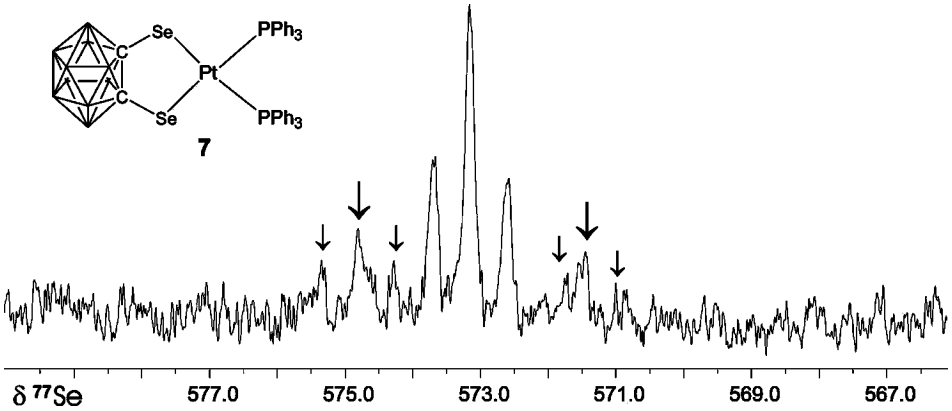


Figure 4. $^{77}Se\{^1H\}$ NMR spectrum (57.2 MHz; FT with LB = 2.5 Hz) of the complex [$Pt(PPh_3)_2$(1,2-$Se_2$-1,2-$C_2B_{10}H_{10}$)] (**7**; in $CD_2Cl_2$ at 25 °C) showing the splitting due to $^1J_{^{195}Pt,^{77}Se}$ (313.7 Hz, arrows) and $^2J_{^{77}Se,^{31}P}$ (ca. 51 Hz).

 © 2007 Wiley-VCH Verlag GmbH & Co. KGaA, Weinheim 

respect to selenium. The $^{195}Pt$ NMR spectrum shows a triplet accompanied by $^{77}Se$ satellites with the same splitting as in the $^{31}P$ and $^{77}Se$ NMR spectra, respectively.

### X-ray Structural Studies of the Bis(diselane) 4 and the Platinum(II) Complex 7

The molecular structures of the bis(diselane) **4** and of the platinum(II) complex **7** are shown in Figures 5 and 6, respectively. Selected structural data are listed in Table 2, together with some data for the tellurium analogue of **4**.[17]

The geometry of the carborane moiety[1] in molecules **4** and **7** is scarcely affected by the various substituents at carbon. The C–C bond lengths appear to be slightly elongated when compared with the *ortho*-carborane itself, although it is difficult to relate these data owing to different experimental conditions. The Se–Se bond lengths are found in the usual range for diselanes (2.28–2.39 Å).[27] A comparison between the crystal systems of **4** and its tellurium analogue[17] is meaningless since the former crystallises with benzene.

The cycle Pt–Se–C–C–Se is close to planar within the experimental error. The Pt–Se bond lengths in **7** [2.4372(6) and 2.4371(6) Å] tend to be slightly shorter than in *cis*-$[Pt(PPh_3)_2(SePh)_2]$[26a] [2.4885(3) and 2.4506(3) Å]. The Pt–Se distance for the selenium *trans* to phosphorus in the platinum(II) diselenolene complex is also fairly short [2.4310(8) Å], and the one for selenium *trans* to the $\eta^2$-C=C bond is even shorter [2.3698(9) Å]. However, the data reported here for **7** compare well with other Pt–Se bond lengths given in the literature.[28] The Pt–P bond lengths in $Pt^{II}$ complexes (2.22–2.32 Å) depend on the polarizing ability of the other ligands, mainly on the *trans* ligand.[29] Thus, the Pt–P distances found here are typical of selenium in a

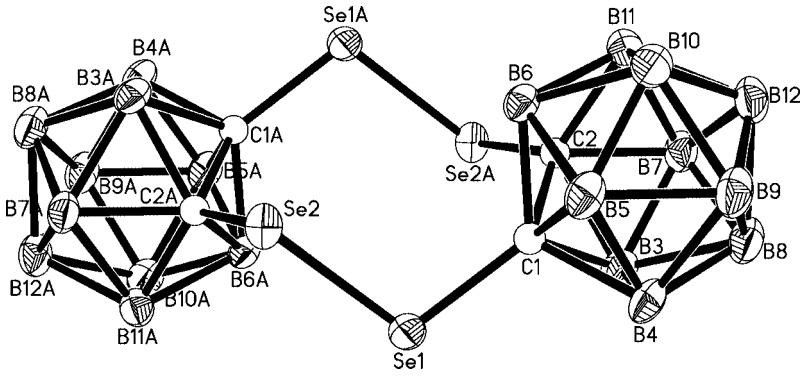


Figure 5. ORTEP plot (50% probability) of the molecular structure of the bis(diselane) **4**; hydrogen atoms have been omitted for clarity. See Table 2 for selected structural parameters.

Table 2. Selected bond lengths [Å] and angles [°] for $[(B_{10}H_{10})C_2]_2Se_4$ (**4**), $[(B_{10}H_{10})C_2]_2Te_4$ for comparison[17] and $[(B_{10}H_{10})C_2Se_2]Pt(PPh_3)_2$ (**7**).

| | $[(B_{10}H_{10})C_2]_2Te_4$ | $[(B_{10}H_{10})C_2]_2Se_4 \cdot C_6H_6$ (**4**) | $[(B_{10}H_{10})C_2Se_2]Pt(PPh_3)_2 \cdot CH_2Cl_2$ (**7**) |
|---|---|---|---|
| C–C | 1.70(3) | 1.691(6), 1.689(6) | 1.625(8) |
| C–E | 2.15(3), 2.17(2) | 1.944(4), 1.940(4) 1.935(4) | 1.938(5), 1.939(6) |
| C–C–E | 123.9(15), 123.2(17) | 121.5(3), 120.9(3) 123.5(3), 123.3(3) | 119.2(4) |
| E–C–C–E | 4.204, –4.205 | 0.41, –1.23 | 2.23 |
| E···E | 4.048, 4.900, 4.885 | 3.822, 3.703 4.408, 4.412 | 3.49 |
| E–E | 2.676(3) | 2.302(7) | – |
| C–E–E | 104.0(7), 102.7(8) | 103.85(13), 103.81(13) 104.12(13), 104.78(13) | – |
| C–E–E–C | 112.8 | 113.7, –112.5 | – |
| E–E···E | 89.9, 90.2 | 88.4, 91.5 | – |
| $Pt(PPh_3)_2$ in **7** | | | |
| Se–Pt | 2.4372(6), 2.4371(6) | Se–Pt–Se | 91.45(2) |
| P–Pt | 2.2958(15), 2.2770(15) | P–Pt–P | 96.22(5) |
| Pt–Se–C | 103.94(17), 103.73(17) | C–C–Se–Pt | 10.9, –14.1 |
| Se–Pt–P | 86.47(4), 86.58(4), 173.22(4), 173.18(4) | C–Se–Pt–P | 56.7, 89.3, –157.2, 171.2 |
| | | SePtSe/PPtP | 8.7 |

 © 2007 Wiley-VCH Verlag GmbH & Co. KGaA, Weinheim 

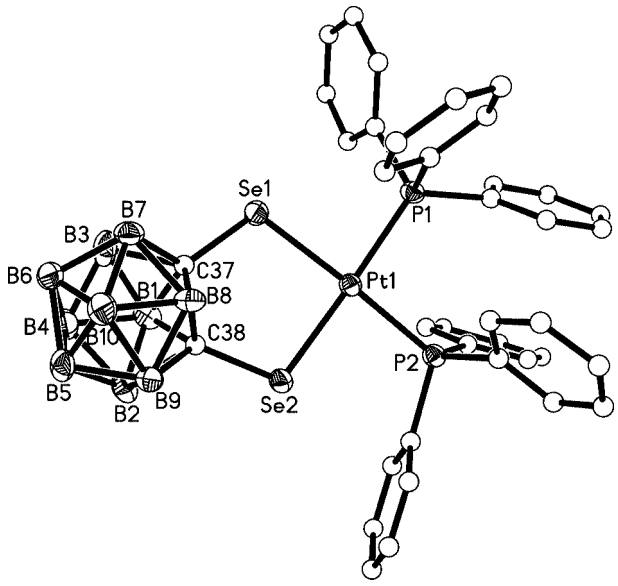


Figure 6. ORTEP plot (50% probability) of the molecular structure of the platinum(II) complex **7** ; hydrogen atoms have been omitted for clarity. See Table 2 for selected structural parameters.

*trans* position, as evident, for example, by comparison with the data for *cis*-$[Pt(PPh_3)_2(SePh)_2]$[26a] [2.2900(6) and 2.2937(6) Å].

## Experimental Section

**General:** All syntheses and the handling of the samples were carried out in the absence of air and moisture. Carefully dried solvents and oven-dried glassware were used throughout. The complex $[Pt(PPh_3)_2(C_2H_4)]$,[30] 1,2-dicarba-*closo*-dodecaborane-1,2-diselenolate[16] and tropylium bromide[31] were prepared according to established procedures; the *ortho*-carborane 1,2-$C_2B_{10}H_{12}$ (Katchem), BuLi (1.6 M in hexane), iodomethane and selenium (Aldrich) were commercially available. NMR measurements: Bruker ARX 250, Varian Inova 300 and Varian Inova 400 NMR spectrometers; chemical shifts are given relative to $SiMe_4$ [$CD_2Cl_2$: $\delta_{^1H}$ = 5.33; $\delta_{^{13}C}$ = 53.8; $\delta_{^{29}Si}$ = 0 ppm for $\Xi(^{29}Si)$ = 19.867184 MHz], external $Et_2O{\cdot}BF_3$ [$\delta_{^{11}B}$ = 0 ppm for $\Xi(^{11}B)$ = 32.083971 MHz], external 85% aqueous $H_3PO_4$ [$\delta_{^{31}P}$ = 0 ppm for $\Xi(^{31}P)$ = 40.480747 MHz], external $Me_2Se$ [$\delta_{^{77}Se}$ = 0 for $\Xi(^{77}Se)$ = 19.071523 MHz]. $\Xi(^{195}Pt)$ = 21.4 MHz for $\delta_{^{195}Pt}$ = 0 ppm. Except for the $^{29}Si$ NMR spectra (refocused INEPT[32]) all other NMR spectra were recorded by single pulse methods. The melting points (uncorrected) were determined using a Büchi 510 melting point apparatus.

**1,2-Bis(trimethysilylseleno)-1,2-dicarba-*closo*-dodecaborane(12) [1,2-$(Me_3SiSe)_2$-1,2-$C_2B_{10}H_{10}$] (5):** Butyllithium (2.94 mL of a 1.6 M solution in hexane 4.7 mmol) was added to a solution of *ortho*-carborane **1** (0.34 g, 2.35 mmol) in diethyl ether (100 mL) at room temperature. A white suspension was obtained and stirred for 2 h. Addition of selenium (0.37 g; 4.7 mmol) gave, after 24 h, a yellow solution containing **3**, which was cooled to –78 °C and added to a cold (–78 °C) solution of chlorotrimethylsilane (1.2 mL, 9.40 mmol) in diethyl ether (50 mL). A white precipitate was formed; the mixture was stirred overnight, concentrated, insoluble materials were filtered off and washed with 30 mL of pentane. Volatile materials were then removed in vacuum, and compound **5** was obtained as the main product in a mixture. The NMR analysis showed the presence of the monoselenosilylated derivative **6** along with unreacted carborane as minor products.

**5:** $^1H$ NMR (300 MHz, $CD_2Cl_2$): $\delta$ = 0.59 ppm (s, 18 H, $SiMe_3$). $^{11}B\{^1H\}$ NMR (96.2 MHz, $CD_2Cl_2$): $\delta$ = –4 (2 B), –8 ppm (8 B).

**6:** $^1H$ NMR (300 MHz, $CD_2Cl_2$): $\delta$ = 0.11 (s, 9 H, $SiMe_3$), 2.25 ppm (s, 1 H, CH). $^{11}B\{^1H\}$ NMR (96.2 MHz, $CD_2Cl_2$): $\delta$ = –2 (s, 2 B), –8 (s, 2 B), –9 (s, 2 B), –14 ppm (s, 4 B).

**3,4,7,8-Bis(1,2-dicarba-*closo*-dodecaborano[1,2])-1,2,5,6-tetraselenacyclooctane, [1,2-(1,2-$C_2B_{10}H_{10}$)-Se-Se-]$_2$ (4). Method A:** In an NMR tube, tropylium bromide (0.15 g, 0.88 mmol) was added to a solution of compound **5** (0.1 g, 0.224 mmol) in deuterated toluene (1.0 mL). A yellow solution was observed and analysed by NMR spectroscopy. The NMR analysis showed the mixture consisted of $[(B_{10}H_{10})C_2]_2Se_4$ (**4**) and organic compounds, e.g. $(C_7H_7)_2$ and bromotrimethylsilane. After one month, the formation of yellow crystals was observed on the walls of the NMR tube; the crystals (yield: 12%; 0.012 g; 0.02 mmol; m.p. 170 °C decomp.) were isolated and analysed by NMR and X-ray diffraction.

**Method B:** Addition of an ethereal solution of iodine (0.22 g, 0.9 mmol) to a solution of **3** (starting from 0.9 mmol of *ortho*-carborane) in diethyl ether (100 mL) gave the instantaneous formation of an orange-red suspension, which was stirred overnight at room temperature. The precipitate was filtered off, washed three times with pentane and diethyl ether, dried under high vacuum, and identified as **4** (yield: 150 mg, 30%).

**Method C:** A solution of **3** (0.89 mmol) in $Et_2O$ (100 mL) was added to a solution of $SiCl_4$ (0.075 g, 0.44 mmol) in pentane (100 mL) at –78 °C. After 24 h of stirring at room temperature, the mixture was concentrated, and insoluble materials were separated. After removal of the solvents under vacuum, a yellow solid was obtained and analysed by NMR spectroscopy. It contained mainly **4** (yield 0.19 g, 72%) along with a small amount of unidentified compounds.

**4:** $^1H\{^{11}B\}$ NMR (250 MHz, $CD_2Cl_2$): $\delta$ = 1.56 (br., 1 H), 2.25 (br., 1 H), 2.44 (br., 2 H), 2.53 (br., 2 H), 2.72 (br., 3 H), 3.27 ppm (br., 1 H). $^{11}B\{^1H\}$ NMR (80.2 MHz, $CD_2Cl_2$): $\delta$ = –1.0 (2 B), –7.0 (4 B), –8.0 (2 B), –11.0 ppm (2 B).

**1,2-Diselenolato-1,2-dicarba-*closo*-dodecaboranebis(triphenylphosphane)platinum [$Pt(PPh_3)_2$(1,2-$Se_2$-1,2-$C_2B_{10}H_{10}$)] (7):** A solution of bis(*ortho*-carboran-1,2-diyl)tetraselenide (**4**; 0.0125 g, 0.017 mmol) in $CD_2Cl_2$ (0.5 mL) was added to a solution of ethenebis(triphenylphosphane)platinum(0) (0.02 g, 0.033 mmol) in $CD_2Cl_2$ (0.5 mL) at room temperature. A yellow-orange solution was obtained. After one day the formation of orange crystals was observed, which were isolated in essentially quantitative yield (m.p. 344 °C, decomp.) and characterised as complex **7** by NMR and X-ray diffraction. $^1H$ NMR (300 MHz, $CD_2Cl_2$): $\delta$ = 1.0–3.5 (br., m, 10 H, $B_{10}H_{10}$), 7.35 ppm (m, 30 H, $PPh_3$). $^{11}B\{^1H\}$ NMR (96.2 MHz, $CD_2Cl_2$): $\delta$ = –1.0 (2 B), –7.0 (2 B), –8.0 (4 B), –12.0 ppm (2 B).

**Reaction of [$Pt(PPh_3)_2$(1,2-$Se_2$-1,2-$C_2B_{10}H_{10}$)] (7) with Methyl Iodide:** An excess of methyl iodide (0.46 g, 3.2 mmol) was added to a solution of complex **7** (0.005 g, 0.005 mmol) in $CD_2Cl_2$ (0.5 mL). A yellow solution was obtained, and the reaction mixture was analysed by $^{31}P$ NMR spectroscopy. The spectrum of the equilibrated mixture showed the formation of *cis*-$[PtI_2(PPh_3)_2]$ ($\delta_{^{31}P}$ = 12.5 ppm, $^1J_{^{195}Pt,^{31}P}$ = 3454 Hz; decreasing signal), *trans*-$[PtI_2(PPh_3)_2]$ ($\delta_{^{31}P}$ = 13.0 ppm, $^1J_{^{195}Pt,^{31}P}$ = 2486 Hz; increasing signal), $[MePh_3P]^+$ ($\delta_{^{31}P}$ = 22.5 ppm; the cation was also evident from the $^{13}C\{^1H\}$ NMR spectrum) and $[PtI_3(PPh_3)]^-$ {$\delta_{^{31}P}$ = 12.0 ppm, $^1J_{^{195}Pt,^{31}P}$ = 3633 Hz}; one weak signal at $\delta_{^{31}P}$ = 12.3 ppm ($^1J_{^{195}Pt,^{31}P}$ = 3472 Hz) could

 © 2007 Wiley-VCH Verlag GmbH & Co. KGaA, Weinheim 

not be assigned. The assigned data are similar to those reported previously.[25b,25c]

**Crystal Structure Determinations of the Bis(diselane) 4 and the Platinum Complex 7:** Details pertinent to the crystal structure determinations are listed in Table 3. The X-ray crystal structural analyses were carried out for single crystals using a STOE IPDS II system equipped with an Oxford Cryostream low-temperature unit. Crystals of appropriate size were selected in perfluorinated oil at room temperature, and the data collections were carried out at 193(2) K (for **4**) and 191(2) K (for **7**). Structure solution and refinement were accomplished using SIR97,[33] SHELXL-97,[34] and WinGX.[35]

Table 3. Details of the X-ray crystal structure analyses of **4** and **7**.

| | **4**·$C_6H_6$ | **7**·$CH_2Cl_2$ |
|---|---|---|
| Crystal system | triclinic | triclinic |
| Space group | $P\bar{1}$ | $P\bar{1}$ |
| $a$ [Å] | 7.3750(7) | 11.1600(10) |
| $b$ [Å] | 10.5270(10) | 15.1370(14) |
| $c$ [Å] | 11.0290(11) | 15.5910(15) |
| $\alpha$ [°] | 100.050(7) | 62.034(7) |
| $\beta$ [°] | 103.862(7) | 83.856(7) |
| $\gamma$ [°] | 96.740(7) | 69.006(7) |
| $V$ [Å$^3$] | 807.13(14) | 2165.8(3) |
| $Z$ | 2 | 2 |
| Crystal size [mm] | $0.9 \times 0.32 \times 0.24$ | $0.38 \times 0.28 \times 0.23$ |
| $\rho_{calcd.}$ [g cm$^{-3}$] | 1.614 | 1.691 |
| $\mu_{calcd.}$ [mm$^{-1}$] (Mo-$K_\alpha$) | 0.71069 | 0.71069 |
| $T$ [K] | 193(2) | 191(2) |
| $\theta$ range [°] | 1.95–25.72 | 1.96–25.11 |
| Reflections collected | 3034 | 7127 |
| Independent reflections | 3034 | 7127 |
| $F$(000) | 380 | 1068 |
| $R_1$ | 0.0338 | 0.0355 |
| $wR_2$ (all data) | 0.1190 | 0.0956 |
| No. of parameters | 190 | 505 |

CCDC-613551 (for **4**) and -613552 (for **7**) contain the supplementary crystallographic data for this paper. These data can be obtained free of charge from The Cambridge Crystallographic Data Centre via www.ccdc.cam.ac.uk/data_request/cif.

## Acknowledgments

This work was supported by the Deutsche Forschungsgemeinschaft.

[1] a) V. I. Bregadze, *Chem. Rev.* **1992**, *92*, 209–223; b) R. N. Grimes, *Carboranes*, Academic Press, New York, **1970**.
[2] a) A. Laromaine, F. Teixidor, R. Kivekäs, R. Sillanpää, R. Benakki, B. Grüner, C. Viñas, *Dalton Trans.* **2005**, 1785–1795; b) S. Paavola, F. Teixidor, C. Viñas, R. Kivekäs, *Acta Crystallogr., Sect. C* **2002**, *58*, 237–239; c) H. Beall, in *Boron Hydride Chemistry* (Ed.: E. L. Muetterties), Academic Press, London, **1975**, p. 316 and references cited therein.
[3] J. D. McKinney, H. Chen, T. A. Hamor, K. Paxton, C. T. Jones, *J. Chem. Soc., Dalton Trans.* **1998**, 2163–2168.
[4] K. Base, M. W. Grinstaff, *Inorg. Chem.* **1998**, *37*, 1432–1433.
[5] O. Crespo, M. C. Gimeno, P. G. Jones, A. Laguna, *J. Organomet. Chem.* **1999**, *547*, 89–95.
[6] a) D.-H. Kim, J. Ko, K. Park, S. Cho, S. O. Kang, *Organometallics* **1999**, *18*, 2738–2740; b) J.-Y. Bae, Y.-I. Park, J. Ko, K.-I. Park, S.-I. Cho, S. O. Kang, *Inorg. Chim. Acta* **1999**, *289*, 141–148; c) J.-Y. Bae, Y.-J. Lee, S.-J. Kim, J. Ko, S. Cho, S. O. Kang, *Organometallics* **2000**, *19*, 1514–1521.
[7] a) J.-Q. Wang, C.-X. Ren, G.-X. Jin, *Chem. Commun.* **2005**, 4738–4740; b) M. Herberhold, H. Yan, W. Milius, *J. Organomet. Chem.* **2000**, *598*, 142–149.
[8] a) M. Herberhold, H. Yan, W. Milius, B. Wrackmeyer, *Angew. Chem.* **1999**, *111*, 3888–3890; *Angew. Chem. Int. Ed.* **1999**, *38*, 3689–3691; b) M. Herberhold, H. Yan, W. Milius, B. Wrackmeyer, *Chem. Eur. J.* **2000**, *6*, 3026–3032.
[9] a) M. Herberhold, H. Yan, W. Milius, B. Wrackmeyer, *Organometallics* **2000**, *19*, 4289–4294; b) M. Herberhold, H. Yan, W. Milius, B. Wrackmeyer, *J. Organomet. Chem.* **2000**, *604*, 170–177; and M. Herberhold, H. Yan, W. Milius, B. Wrackmeyer, *J. Organomet. Chem.* **2001**, *623*, 149–152; c) M. Herberhold, H. Yan, W. Milius, B. Wrackmeyer, *J. Chem. Soc., Dalton Trans.* **2001**, 1782–1789; d) M. Herberhold, H. Yan, W. Milius, B. Wrackmeyer, *Chem. Eur. J.* **2002**, *8*, 388–395; e) M. Herberhold, H. Yan, W. Milius, B. Wrackmeyer, *Russ. Chem. Bull. Int. Ed.* **2001**, *50*, 1518–1524; f) M. Herberhold, G.-X. Jin, H. Yan, W. Milius, B. Wrackmeyer, *Eur. J. Inorg. Chem.* **1999**, 873–875; g) M. Herberhold, H. Yan, W. Milius, B. Wrackmeyer, *Z. Anorg. Allg. Chem.* **2000**, *626*, 1627–1633.
[10] a) X.-Y. Yu, G.-X. Jin, N.-H. Hu, L.-H. Weng, *Organometallics* **2002**, *21*, 5540–5548; b) W. Li, L.-H. Weng, G.-X. Jin, *Inorg. Chem. Commun.* **2004**, *7*, 1174–1177; c) X.-F. Hou, X.-Ch. Wang, J.-Q. Wang, G.-X. Jin, *J. Organomet. Chem.* **2004**, *689*, 2228–2235; d) X.-Y. Yu, S.-X. Lu, G.-X. Jin, L.-H. Weng, *Inorg. Chim. Acta* **2004**, *357*, 361–366.
[11] G.-X. Jin, *Coord. Chem. Rev.* **2004**, *248*, 587–602.
[12] a) S. Lu, G.-X. Jin, St. Eibl, M. Herberhold, Y. Xin, *Organometallics* **2002**, *21*, 2533–2535; b) J.-Q. Wang, S. Cai, G.-X. Jin, L.-H. Weng, M. Herberhold, *Chem. Eur. J.* **2005**, *11*, 7342–7350; c) G.-X. Jin, J.-Q. Wang, C. Zhang, L.-H. Weng, M. Herberhold, *Angew. Chem.* **2005**, *117*, 264–267; *Angew. Chem. Int. Ed.* **2005**, *44*, 259–262.
[13] a) J.-Q. Wang, L.-H. Weng, G.-X. Jin, *J. Organomet. Chem.* **2005**, *690*, 249–252; b) J.-Q. Wang, L.-H. Weng, G.-X. Jin, *Rev. Inorg. Chem.* **2005**, *27*, 55–66.
[14] a) S. Cai, X. Hou, L.-H. Weng, G.-X. Jin, *J. Organomet. Chem.* **2005**, *690*, 910–915; b) J.-Q. Wang, X. Hou, L.-H. Weng, G.-X. Jin, *Organometallics* **2005**, *24*, 826–830.
[15] a) S. Cai, J.-Q. Wang, G.-X. Jin, *Organometallics* **2005**, *24*, 4226–4231; b) S. Cai, G.-X. Jin, *Organometallics* **2005**, *24*, 5280–5286; c) S. Liu, X. Wang, G.-X. Jin, *J. Organomet. Chem.* **2006**, *691*, 261–265; d) G.-X. Jin, J.-Q. Wang, *Dalton Trans.* **2006**, 86–90; e) S. Cai, Y. Lin, G.-X. Jin, *Dalton Trans.* **2006**, 912–918.
[16] M. Herberhold, G.-X. Jin, H. Yan, W. Milius, B. Wrackmeyer, *J. Organomet. Chem.* **1999**, *587*, 252–257.
[17] M. Herberhold, W. Milius, G.-X. Jin, W. Kremnitz, B. Wrackmeyer, *Z. Anorg. Allg. Chem.* **2006**, *632*, 2031–2036.
[18] a) T. Klapötke, M. Broschag, *Compilation of Reported $^{77}$Se NMR Chemical Shifts*, Wiley, Chichester, **1996**; b) H. Duddeck, *Prog. Nucl. Magn. Reson. Spectrosc.* **1995**, *27*, 1–323; c) H. Duddeck, *Annu. Rep. NMR Spectrosc.* **2004**, *52*, 105–166.
[19] a) V. W. Day, D. A. Lesch, T. B. Rauchfuss, *J. Am. Chem. Soc.* **1982**, *104*, 1290–1295; b) R. Oilunkaniemi, R. S. Laitinen, M. Ahlgren, *J. Organomet. Chem.* **1999**, *587*, 200–206; c) H. Kuniyasu, A. Ogawa, S.-I. Miyazaki, I. Ryu, N. Kambe, N. Sonoda, *J. Am. Chem. Soc.* **1991**, *113*, 9796–9803; d) V. P. Ananikov, I. P. Beletskaya, G. G. Aleksandrov, I. L. Eremenko, *Organometallics* **2003**, *22*, 1414–1421.
[20] B. Wrackmeyer, *Prog. Nucl. Magn. Reson. Spectrosc.* **1979**, *12*, 227–259.
[21] B. Wrackmeyer, E. V. Klimikina, W. Milius, *Z. Anorg. Allg. Chem.* **2006**, in press.
[22] M. Herberhold, M. Keller, W. Kremnitz, T. Daniel, W. Milius, B. Wrackmeyer, H. Nöth, *Z. Anorg. Allg. Chem.* **1998**, *624*, 1324–1328.
[23] a) H. G. Horn, *J. Prakt. Chem./Chem.-Ztg.* **1992**, *334*, 201–213; b) U. Herzog, *Prakt. Chem.* **2000**, *342*, 379–388; c) U. Herzog, H. Borrmann, *J. Organomet. Chem.* **2003**, *675*, 42–47; d) U.

 © 2007 Wiley-VCH Verlag GmbH & Co. KGaA, Weinheim 

Herzog, H. Borrmann, *J. Organomet. Chem.* **2004**, *689*, 564–574; e) R. Köster, G. Seidel, R. Boese, B. Wrackmeyer, *Chem. Ber.* **1988**, *121*, 1955–1966; f) B. Wrackmeyer, G. Kehr, K. Bauer, U. Dörfler, *Main Group Met. Chem.* **1995**, *18*, 1–7.

[24] a) U. Herzog, U. Böhme, *Silicon Chem.* **2003**, *2*, 77–92; b) U. Herzog, H. Borrmann, *J. Organomet. Chem.* **2003**, *681*, 5–11; c) U. Herzog, *Main Group Met. Chem.* **2001**, *24*, 31–38.

[25] a) P. S. Pregosin, R. W. Kunz, in *$^{31}P$ and $^{13}C$ NMR of Transition Metal Phosphine Complexes. NMR – Basic Principles and Progress*, vol. 16 (Eds.: P. Diehl, E. Fluck, R. Kosfeld), Springer, Berlin, **1979**; b) E. Farkas, L. Kollár, M. Moret, A. Sironi, *Organometallics* **1996**, *15*, 1345–1350; c) O. F. Wendt, L. I. Elding, *J. Chem. Soc., Dalton Trans.* **1997**, 4725–4731.

[26] a) R. Oilunkaniemi, R. S. Laitinen, M. Ahlgen, *Z. Naturforsch., B: Chem. Sci.* **2000**, *55*, 361–368; b) W.-H. Pan, J. P. Fackler Jr, W. H. Chen, *Inorg. Chem.* **1981**, *20*, 856–863; c) M. Herberhold, T. Schmalz, W. Milius, B. Wrackmeyer, *Z. Naturforsch., Teil B* **2002**, *57*, 53–60.

[27] a) H. U. Hummel, T. Fischer, D. Gruss, A. Franke, W. Dietzsch, *J. Chem. Soc., Dalton Trans.* **1992**, 2781–2785; b) S. Kumar, S. K. Tripathi, H. B. Singh, G. Wolmershaeuser, *J. Organomet. Chem.* **2004**, *689*, 3046–3055; c) S. S. Zade, S. Panda, H. B. Singh, R. B. Sunoj, R. J. Butcher, *J. Org. Chem.* **2005**, *70*, 3693–3704.

[28] a) M. R. Lewtas, C. P. Morley, M. Di Vaira, *Polyhedron* **2000**, *19*, 751–756; b) V. K. Jain, S. Kannan, R. J. Butcher, J. P. Jasinski, *J. Chem. Soc., Dalton Trans.* **1993**, 1509–1513.

[29] G. G. Mather, A. Pidcock, G. J. N. Rapsey, *J. Chem. Soc., Dalton Trans.* **1973**, 2095–2099.

[30] U. Nagel, *Chem. Ber.* **1982**, *115*, 1998–1999.

[31] W. Doering, L. H. Knox, *J. Am. Chem. Soc.* **1957**, *79*, 352–356.

[32] a) G. A. Morris, R. Freeman, *J. Am. Chem. Soc.* **1979**, *101*, 760–762; b) G. A. Morris, *J. Am. Chem. Soc.* **1980**, *102*, 428–429; c) D. P. Burum, R. R. Ernst, *J. Magn. Reson.* **1980**, *39*, 163–168.

[33] A. Altomare, M. C. Burla, M. Camalli, G. L. Cascarano, C. Giacovazzo, A. Guagliardi, A. G. G. Moliterni, G. Polidori, R. Spagna, *J. Appl. Crystallogr.* **1999**, *32*, 115–119.

[34] G. M. Sheldrick, *SHELX-97*, *Program for Crystal Structure Analysis* (release 97-2), University of Göttingen, Germany, **1998**.

[35] L. J. Farrugia, *J. Appl. Crystallogr.* **1999**, *32*, 837–838.

Received: July 27, 2006
Published Online: October 27, 2006

 © 2007 Wiley-VCH Verlag GmbH & Co. KGaA, Weinheim 

DOI: 10.1002/ejic.200600788

# Constructing Multimetallic Systems with the Naphthalene-1,8-bis(thiolato) Ligand

**Stuart D. Robertson,[a] Alexandra M. Z. Slawin,[a] and J. Derek Woollins*[a]**

**Keywords:** Sulfur ligand / Multimetallic systems / Gold / Bridging ligands / X-ray structure

Addition of 1 equiv. $(Ph_3P)Au(ClO_4)$ (formed by ion exchange of $Ph_3PAuCl$ with $AgClO_4$) to [naphthalene-1,8-bis(thiolato)]-bis(triphenylphosphane)platinum results in the formation of a novel dimetallic cationic complex with a (triphenylphosphane)gold moiety attached to the sulfur of the naphthalene-1,8-bis(thiolato) ligand. NMR spectroscopic evidence suggests that this gold-containing fragment is fluxional in its bonding and X-ray crystallography confirms the asymmetric complex, which shows this gold atom attached to one of these sulfur atoms. Addition of more than 1 equiv. $(Ph_3P)Au(ClO_4)$ results in the formation of a tetrametallic sandwich complex with two bridging gold atoms between the sulfur atoms of the two $PtS_2C_3$ rings. Tri- and tetrametallic silver-containing complexes can be prepared by addition of 0.5 and 1 equiv. $AgClO_4$ to $(Ph_3P)_2Pt(S_2C_{10}H_6)$, respectively.

(© Wiley-VCH Verlag GmbH & Co. KGaA, 69451 Weinheim, Germany, 2007)

## Introduction

Heterometallic complexes formed by reaction of sulfur-containing platinum(II) complexes with a group 11 complex have been well documented recently and are of great interest as they have a variety of possibilities for coordination of the group 11 metal to the platinum complex. This can partly be attributed to the presence of sulfur in the platinum complex because gold and silver have a great affinity for sulfur. Any heterometallic complex formed by bonding of an Au or Ag complex to sulfur may or may not contain a Pt–M bond, depending on the geometry of the two metals around the sulfur centre. One of the most common starting materials is the highly nucleophilic complex $[\{Pt(PPh_3)_2(\mu\text{-}S)\}_2]$.[1] For example, the $AuPPh_3$ unit is inserted between the two sulfur atoms to give a trigonal-planar structure with no Pt···Au interaction.[2] Similarly, the analogous silver complex has also been obtained,[3] again with no interaction between the two metal atoms.

A number of complexes containing a gold(III) atom bridging the two sulfur atoms in a square-planar configuration have also been described recently.[4,5] These are formed by reaction of the platinum starting material with a gold(III) dichloride such as $Au(pap)Cl_2$ [pap = $\eta^2$ ligand, 2-(2-pyridylamino)phenyl]. The reaction of 2 equiv. $[Ag(PR_3)_2]^+$ with $[Pt(mnt)_2]^{2-}$ (mnt = maleonitriledithiolate, a bidentate S,S-bound ligand) also results in the insertion of silver between two sulfur atoms.[6] In this case, one Ag unit lies above the plane of the $PtS_4$ unit bound to two *cis* sulfur atoms, while the other lies between the other two sulfur atoms but below the plane.

Gold-containing species have also been treated with $[\{Pt(PPh_3)_2(\mu\text{-}S)\}_2]$ to give products where the gold fragment ($Au\text{–}PPh_3$) is bound to only one sulfur atom but not to the other so that it is not bridging.[7,8] Silver has also been seen bound to one or two sulfur atoms of ethylenedithiolato complexes in the form of $Ag(PPh_3)_2$.[9] This work has been extended so that both sulfur atoms bind to a different metal with no bridges between the two sulfur atoms, both in the gold[8,10] and silver complexes.[10,11]

While in all these examples the group 11 atom is in a configuration without Au/Ag···platinum interactions, examples are also known where an $MPPh_3$ fragment is bound to only one of the two platinum-bound sulfur atoms in a configuration with a Pt···M interaction.[12] In this case, the platinum starting material is not the butterfly-core-containing $[\{Pt(PPh_3)_2(\mu\text{-}S)\}_2]$ but is cyclometallated $[Pt\{CH_2C_6H_4P(C_6H_4Me\text{-}o)_2\}(S_2CNMe_2)]$.

While the previously mentioned examples have included complexes where one gold or silver atom is bridging between the two platinum-bound sulfur atoms, it is also possible for this bridge to contain two gold or silver atoms. For example, the hexametallic compound $[Au_2\{Pt_2(PPh_3)_4(\mu_3\text{-}S)_2\}_2]Cl_2$ is formed by reaction of 1 equiv. $[\{Pt(PPh_3)_2(\mu\text{-}S)\}_2]$ with 1 equiv. $AuCl(SMe_2)$.[10] This complex has a hexanuclear $\{Au_2Pt_4\}$ cage-framework comprising two hinged $\{Pt_2S_2\}$ groups anchored across an Au–Au bond as shown in Figure 1.

[a] School of Chemistry, University of St. Andrews, Fife, Scotland, KY16 9ST, UK
Fax: +44-1334-463384
E-mail: jdw3@st-and.ac.uk

 © 2007 Wiley-VCH Verlag GmbH & Co. KGaA, Weinheim 

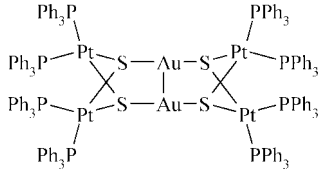

Figure 1. Structure of the dication of $[Au_2\{Pt_2(PPh_3)_4(\mu_3\text{-}S)_2\}_2]Cl_2$; the two anions are omitted for clarity.

Silver examples of this structure are also known, formed from $[\{Pt(PPh_3)_2(\mu\text{-}S)\}_2]$ and $AgBF_4$,[13] $AgNO_3$[13] and $AgClPPh_3$.[11] A similar complex exists where the two sulfur atoms share only a single platinum atom rather than two platinum atoms.[9] In each case, X-ray crystallographic data suggests that the two silver atoms are within bonding distance.

Examples are also known where two gold atoms attached to either sulfur atom are weakly bound or not bound to each other, but are connected through a larger phosphorus-containing backbone.[7] In this case, the starting materials are $[\{Pt(PPh_3)_2(\mu\text{-}S)\}_2]$ and either $Au_2Cl_2$(dppm) or $Au_2Cl_2$(dppf) [dppm = (diphenylphosphanyl)methane, dppf = (diphenylphosphanyl)ferrocene]. When the backbone is dppm, the two gold atoms are in close proximity (approximately 2.9 Å) such that a considerable aurophilic interaction can be considered to exist. In the case of dppf, the Au–Au distance is much larger [3.759(3) Å] and can be considered non-bonding.

We have a longstanding interest in the coordination and bridging effects of sulfur donor ligands.[14a,14b] Here, we report gold and silver complexes of $(Ph_3P_2)PtS_2C_{10}H_6$ where the sulfur atoms of one molecule of this complex are bridged to another molecule by either one or two group 11 atoms.

## Results and Discussion

The anionic exchange of the gold complex $Ph_3PAuCl$ with $AgClO_4$ proceeds smoothly in a mixture of dichloromethane and acetonitrile at room temperature. The product is freed of AgCl by removing all solvent and re-dissolving the desired product in dichloromethane before filtering. The resultant gold complex reacts with $(Ph_3P)_2Pt(S_2C_{10}H_6)$ to give the cationic complex $[(Ph_3P)_2Pt(S_2C_{10}H_6)(AuPPh_3)]^+$-$ClO_4^-$ (**1**).

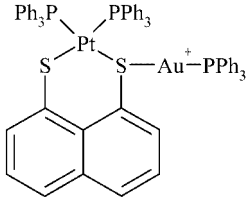

**1**

The $^{31}P$ NMR spectrum of **1** shows a peak at $\delta$ = 32.7 ppm corresponding to the triphenylphosphane group attached to the gold atom and a peak at $\delta$ = 17.6 ppm corresponding to the two triphenylphosphane groups bonded to the central platinum atom. The expected platinum satellites are also evident, with a coupling constant of 3080 Hz, [over 100 Hz higher in magnitude than that of the starting material].[13] The asymmetry of complex **1** caused by the gold-containing fragment bonded to one sulfur atom suggests that the two platinum-bound phosphorus atoms should be non-equivalent and therefore should display an AB spin system. However, fluxionality of this gold fragment from one sulfur atom to the other, as seen in Scheme 1, causes these two Pt-coordinated phosphane groups to appear equivalent down to temperatures as low as –80 °C, suggesting that this flipping from one sulfur atom to the other is relatively facile in solution.

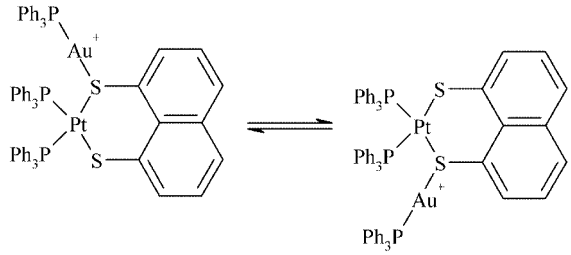

Scheme 1. The equilibrium in complex **1**. Perchlorate anion is omitted for clarity.

The $^{195}Pt$ NMR spectrum displays the expected peak at –4674 ppm with the corresponding phosphorus coupling. The mass spectrum ($ES^+$) of complex **1** shows the parent ion at *m*/*z* 1367–1370 in the predicted pattern with the primary peak at 1368. The identity of the counteranion is proved by the $ES^-$ mass spectrum, which shows two peaks at 99 and 101 in the correct ratio.

Complex **2** is formed by the reaction of more than one equilavent of $Ph_3PAu^+ClO_4^-$ with $(Ph_3P)_2Pt(S_2C_{10}H_6)$ in dichloromethane. This tetrametallic dication is charge-balanced with two perchlorate ions.

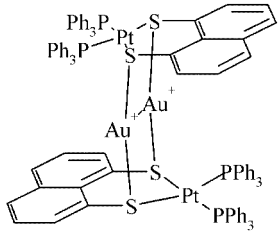

**2**

Complexes **3** and **4** are formed by addition of a solution containing 0.5 and 1 equiv. $AgClO_4$ (in acetronitile) to $(Ph_3P)_2Pt(S_2C_{10}H_6)$ (in tetrahydrofuran), respectively. It is somewhat surprising that we could not obtain a simple gold analogue of **3** [especially considering the lability of the Au–P bond in the formation of **2**], and this may reflect the very strong preference for linear geometry in $Au^I$; we did attempt to prepare gold complexes from $HAuCl_4$ but obtained intractable mixtures.

 © 2007 Wiley-VCH Verlag GmbH & Co. KGaA, Weinheim 

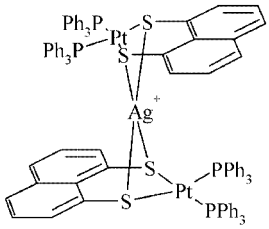

**3**

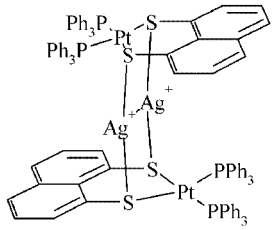

**4**

Isolation of the final complexes was achieved by removing the mixed solvent in vacuo, redissolving in a minimum volume of dichloromethane and precipitating by slow addition of diethyl ether while stirring. The final products are obtained as an orange and a yellow powder, respectively.

The $^{31}P$ NMR spectra of complexes **3** and **4** show a peak at $\delta$ = 6.8 and 18.3 ppm, respectively, with platinum satellites. The coupling constants for these sets of peaks are 2989 Hz (complex **3**) and 3122 Hz (complex **4**). This value for complex **4** is close to that of the digold analogue **2**. The $^{195}Pt$ NMR spectrum of **3** displays a triplet at –4698 ppm. Unfortunately, no peak was observed in the $^{195}Pt$ NMR spectrum of **4**, possibly because the sample was not sufficiently concentrated. The mass spectrum ($ES^+$) of complex **3** is excellent, displaying the parent ion at 1927–1932 in the predicted pattern with the primary peak at 1929. The mass spectrum of **4** displays the expected peaks in the region 1016–1019, half the mass of the complex, which is expected since this complex carries a 2+ charge. The identity of the counteranion in both cases is again proved by the $ES^-$ mass spectrum, which shows two peaks at 99 and 101 in the correct ratio.

## X-ray Crystallography

The crystal structures of complexes **1**–**4** are shown in Figures 3–7, and selected bond lengths and angles are in Table 1 and Table 2. The crystal structure of $(Me_3P)_2Pt(S_2C_{10}H_6)$[15] is also shown (Figure 2 as this complex is closely related to the starting material $(Ph_3P)_2Pt(S_2C_{10}H_6)$, which has never been crystallographically characterised, and is useful for comparison with the complexes **1**–**4**. The X-ray analysis of complex **1** (see Figure 3 and Table 1) shows that the $AuPPh_3$ unit is attached to only one of the sulfur atoms, S(1)–Au(1) = 2.3614(12) and S(9)–Au(1) = 2.979(1) Å. These values, along with the virtually linear S(1)–Au(1)–P(3) angle [174.71(4)°] are similar to those of other disulfur complexes containing a Au–$PPh_3$ arm on one of the sulfur atoms[7,8] and longer than, for example, the Au–S distances in linear $[RS–Au–SR]^-$ containing anionic S donors.[15] The Au(1)–P(3) bond length is also similar to those seen previously. The addition of the Au–$PPh_3$ arm also changes the geometry around S(1) so that it is now in a distorted trigonal-planar structure. This distortion is proven since the largest of the three angles around this sulfur atom is only 104°, a significant deviation from perfect trigonal planarity (120°). This suggests that the geometry around this sulfur atom can possibly be considered as trigonal pyramidal. This new gold fragment considerably reduces the Pt–S(1)–C(1) angle by almost 10°. This forces the naphthalene backbone to realign slightly, which results in the dihedral angle [deviation form planarity between the Pt(1)–S(1)–S(9) and C(10)–S(1)–S(9) planes] being markedly reduced from 136° in $(Me_3P)_2Pt(S_2C_{10}H_6)$ to only 121°. The effect of the gold-containing arm on the geometry around the Pt atom is only slight, a 3° tightening of the S–Pt–S angle is noticed, which in turn is compensated for by a 4° widening of the P–Pt–P angle, resulting in a more distorted square-planar arrangement around the platinum centre with respect to the square-planar platinum complex $(Me_3P)_2Pt(S_2C_{10}H_6)$. This tightening of the S–Pt–S bond also results in a smaller splay angle (18.6°) in complex **1**, as expected. The changes in bond lengths relative to those in $(Me_3P)_2Pt(S_2C_{10}H_6)$ are negligible.

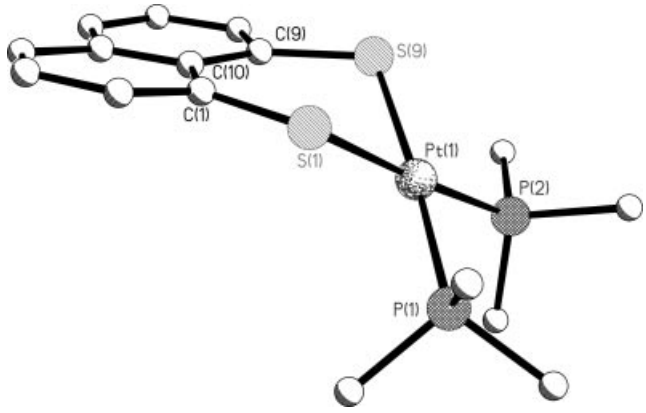


Figure 2. Crystal structure of $(Me_3P)_2Pt(S_2C_{10}H_6)$.[15] This complex is closely related to the starting material $(Ph_3P)_2Pt(S_2C_{10}H_6)$, which has never been crystallographically characterised, and is useful for a comparison with the complexes **1**–**4**.

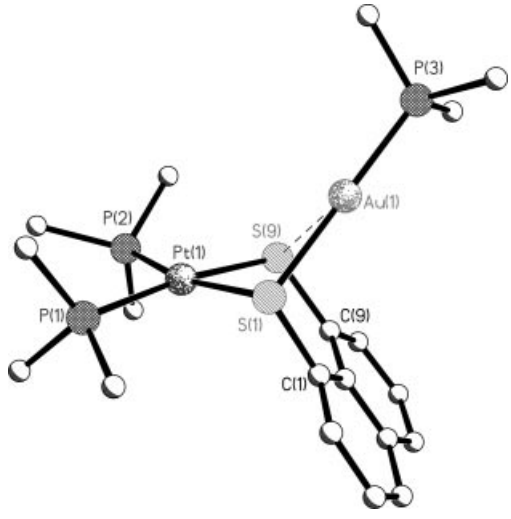


Figure 3. Crystal structure of $[(Ph_3P)_2Pt(S_2C_{10}H_6)(AuPPh_3)]^+ClO_4^-$ (**1**); $ClO_4^-$ anion is omitted for clarity.

We found no intermolecular packing effects in the solid-state structure of **1**, which would account for the longer Pt–S(9) distance.

 © 2007 Wiley-VCH Verlag GmbH & Co. KGaA, Weinheim 

Table 1. Bond lengths [Å] and angles [°] for platinum starting material and complexes **1** and **3**, where M = Au (**1**) and Ag (**3**).

| | $(Me_3P)_2Pt(S_2C_{10}H_6)$[15] | **1** | **3** |
|---|---|---|---|
| Pt(1)–S(1) | 2.320(1) | 2.3492(12) | 2.352(4) |
| Pt(1)–S(9) | 2.326(1) | 2.3504(12) | 2.362(4) |
| Pt(1)–P(1) | 2.284(1) | 2.3121(12) | 2.319(4) |
| Pt(1)–P(2) | 2.273(1) | 2.2985(13) | 2.307(4) |
| S(1)–C(1) | 1.754(4) | 1.787(5) | 1.788(16) |
| S(9)–C(9) | 1.760(4) | 1.775(5) | 1.773(17) |
| S(1)–S(9) | 3.22(9) | 3.151(2) | 3.184(5) |
| S(1)–M(1) | – | 2.3614(12) | 2.622(4) |
| S(9)–M(1) | – | 2.979(1) | 2.580(4) |
| M(1)–P(3) | – | 2.2553(13) | – |
| Pt(2)–S(51) | – | – | 2.363(4) |
| Pt(2)–S(59) | – | – | 2.352(4) |
| Pt(2)–P(3) | – | – | 2.303(4) |
| Pt(2)–P(4) | – | – | 2.297(4) |
| S(51)–C(51) | – | – | 1.792(16) |
| S(59)–C(59) | – | – | 1.790(15) |
| S(51)–S(59) | – | – | 3.192(5) |
| S(51)–M(1) | – | – | 2.537(4) |
| S(59)–M(1) | – | – | 2.690(4) |
| M(1)-Pt(1) | – | – | 3.0739(13) |
| M(1)-Pt(2) | – | – | 3.2044(13) |
| S(1)–Pt(1)–S(9) | 87.62(4) | 84.20(4) | 84.99(13) |
| P(1)–Pt(1)–P(2) | 96.55(4) | 101.03(4) | 100.03(14) |
| P(1)–Pt(1)–S(1) | 85.88(4) | 92.53(4) | 90.14(13) |
| P(2)–Pt(1)–S(9) | 89.97(4) | 82.78(4) | 85.86(14) |
| P(1)–Pt(1)–S(9) | 173.45(4) | 172.60(4) | 170.07(14) |
| P(2)–Pt(1)–S(1) | 176.83(4) | 165.88(4) | 168.04(14) |
| Pt(1)–S(1)–C(1) | 113.24(14) | 103.85(16) | 107.7(5) |
| Pt(1)–S(1)–M(1) | – | 98.10(4) | 76.13(12) |
| C(1)–S(1)–M(1) | – | 104.04(16) | 112.7(5) |
| C(9)–S(9)–Pt(1) | 110.28(14) | 107.01(16) | 105.8(5) |
| Pt(1)–S(9)–M(1) | – | 82.87(3) | 76.79(11) |
| C(9)–S(9)–M(1) | – | – | 111.3(6) |
| S(1)–C(1)–C(10) | 128.4(3) | 124.9(4) | 124.8(11) |
| C(10)–C(9)–S(9) | 127.1(3) | 127.7(4) | 128.8(12) |
| C(1)–C(10)–C(9) | 125.8(3) | 126.0(5) | 126.3(14) |
| S(51)–Pt(2)–S(59) | – | – | 85.20(13) |
| P(3)–Pt(2)–P(4) | – | – | 99.21(13) |
| P(3)–Pt(2)–S(51) | – | – | 84.06(13) |
| P(4)–Pt(2)–S(59) | – | – | 91.53(13) |
| P(3)–Pt(2)–S(59) | – | – | 168.23(13) |
| P(4)–Pt(2)–S(51) | – | – | 176.73(14) |
| Pt(2)–S(51)–C(51) | – | – | 103.4(5) |
| Pt(2)–S(51)–M(1) | – | – | 81.60(11) |
| C(51)–S(51)–M(1) | – | – | 109.5(5) |
| C(59)–S(59)–Pt(2) | – | – | 106.4(5) |
| Pt(2)–S(59)–M(1) | – | – | 78.60(11) |
| C(59)–S(59)–M(1) | – | – | 107.7(5) |
| S(51)–C(51)–C(60) | – | – | 129.6(12) |
| C(60)–C(59)–S(59) | – | – | 126.8(15) |
| C(51)–C(60)–C(59) | – | – | 124.7(15) |
| S(1)–M(1)–P(3) | – | 174.71(4) | – |
| S(9)–M(1)–P(3) | – | 113.97(4) | – |
| S(1)–M(1)–S(9) | – | 71.26(4) | 75.49(12) |
| S(51)–M(1)–S(59) | – | – | 75.20(11) |
| S(1)–M(1)–S(51) | – | – | 148.85(13) |
| S(9)–M(1)–S(59) | – | – | 139.22(13) |
| S(1)–M(1)–S(59) | – | – | 94.31(12) |
| S(9)–M(1)–S(51) | – | – | 131.00(12) |
| Splay angle | 21.3 | 18.6 | 19.9, 21.1 |
| Dihedral angle | 136 | 121 | 124, 122 |

Complex **3** consists of two $[P_2PtS_2]$ units connected by a single bridging silver atom connected to all four sulfur atoms (see Figure 4. Both $[P_2PtS_2]$ units are similarly affected by the introduction of a silver atom between the two sulfur atoms. It is notable that the Ag–S distance is longer in **3** than in **4** (vide infra) and other $Pt_2Ag_2$ systems.[9] The silver atom pulls the two sulfur atoms closer together, as shown by the tighter S–Pt–S and Pt–S–C angles and the reduced splay angles on the naphthalene-1,8-bis(thiolato) backbone. With regard to the geometry around platinum, the reduced S–Pt–S angle is again compensated for by an increase in the P–Pt–P angle, and the configuration around the platinum atom deviates from square planarity. Similarly to complex **1**, the effect of the silver atom is such that the geometry around all the sulfur atoms changes to distorted trigonal pyramidal, with the largest angle around sulfur [C(1)–S(1)–Ag(1) = 112.7(5)°] displaying that there is considerable deviation from trigonal planarity. The presence of the silver atom has also forced the naphthalene backbone and the triphenylphosphane groups closer together, as proven by the reduced dihedral angles in complex **3**. The silver atom can be considered four coordinate and can probably best be described as having a heavily distorted tetrahedral geometry. The metal–sulfur bonds are in the range 2.537(4)–2.690(4) Å. The S(1)–Ag–S(9) and S(51)–Ag–S(59) bond angles are approximately 75°, but the other S–Ag–S angles (i.e. those involving two sulfur atoms from opposite molecules) have a large range, which displays the deviation away from a tetrahedral geometry. The smallest of these angles is only 94.31(12)°, while the largest is 148.85(13)°.

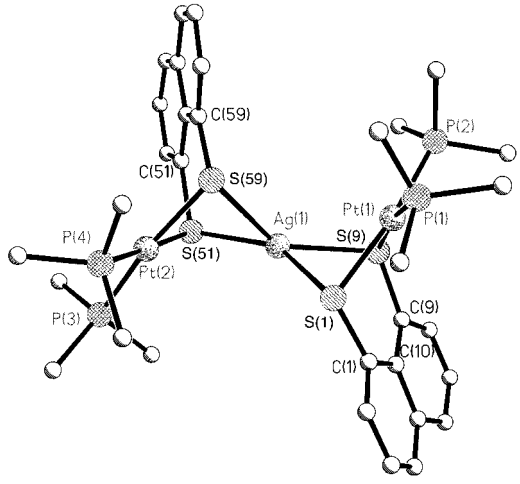


Figure 4. Crystal structure $Ag[(Ph_3P)_2Pt(S_2C_{10}H_6)]_2^+ClO_4^-$ (**3**); $ClO_4^-$ anion is omitted for clarity.

Complex **2** was found to crystallise in two different unit cells, one monoclinic (Figure 5) and one triclinic (Figure 6). In each case, however, the bond lengths and angles are very similar (Table 2). Complex **4** gave a triclinic unit cell (Figure 7), and the structure is again similar to those obtained for **2**. In these structures, the two $[P_2PtS_2]$ units are linked to each other by two metal atoms as opposed to one metal atom in complex **3** such that there are two S–M–S bridges. The Au–S distances are shorter than the Ag–S distances as a consequence of the difference in the covalent radii of the metals. The distances reported here are comparable with those in ethylenethiolato $Pt_2M_2$ complexes, which also dis-

 © 2007 Wiley-VCH Verlag GmbH & Co. KGaA, Weinheim 

play similar $Pt_2M_2S_2$ six-membered chair conformation rings.[9] The bridging has a great effect on the geometry of the original platinum structures, although bond angles have changed by a negligible and unremarkable amount. While **3** was found to contain a six-membered $MS_2C_3$ ring, **2** and **4** contain seven-membered $M_2S_2C_3$ rings. This has had a converse affect as the insertion of the two new metal atoms actually increases the sulfur–sulfur distances and also the splay angles with respect to $(Me_3P)_2Pt(S_2C_{10}H_6)$. This results in the S–Pt–S angles widening slightly to almost exactly 90°. The P–Pt–P angles also increase slightly, but in this case, not as much as in complex **3**. This allows us to consider the platinum centre to be in a less distorted square-planar configuration than in $(Me_3P)_2Pt(S_2C_{10}H_6)$.

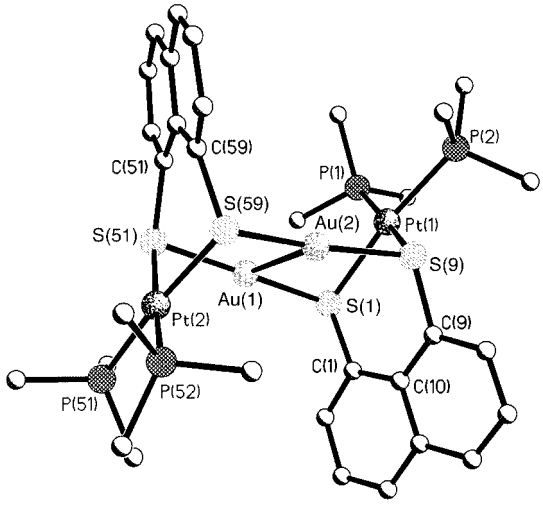


Figure 5. Crystal structure of $[Au(Ph_3P)_2Pt(S_2C_{10}H_6)]_2^{2+}2ClO_4^-$ (**2**); $ClO_4^-$ anions are omitted for clarity.

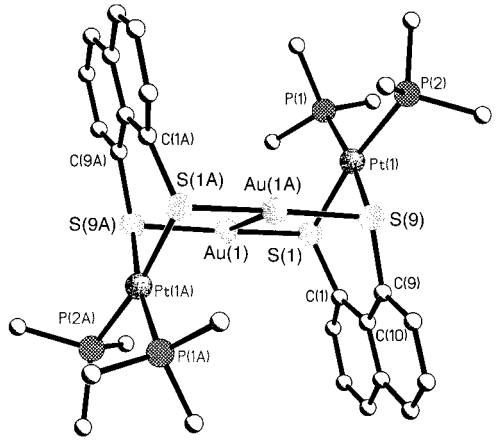


Figure 6. Crystal structure of $[Au(Ph_3P)_2Pt(S_2C_{10}H_6)]_2^{2+}2ClO_4^-$ (**2′**); $ClO_4^-$ anions are omitted for clarity.

Again, the geometry around the sulfur atoms is trigonal pyramidal, but it is slightly closer to a trigonal planar geometry than that in **3** since the presence of the other metal atom pushes the metal atom closer to the plane of the S, C and Pt atoms. This is evidenced by a general increase in the bond angles around the sulfur atoms, moving towards 120°.

Table 2. Bond lengths [Å] and angles [°] for complexes **2** and **4**, where M = Au (**2**) and Ag (**4**).

| | **2** | **2′** | **4** |
|---|---|---|---|
| Pt(1)–S(1) | 2.3320(16) | 2.318(4) | 2.353(4) |
| Pt(1)–S(9) | 2.3547(16) | 2.344(4) | 2.330(4) |
| Pt(1)–P(1) | 2.2951(16) | 2.299(4) | 2.319(4) |
| Pt(1)–P(2) | 2.3059(17) | 2.297(4) | 2.306(4) |
| S(1)–C(1) | 1.801(6) | 1.752(16) | 1.774(16) |
| S(9)–C(9) | 1.777(7) | 1.783(14) | 1.790(16) |
| S(1)–S(9) | 3.315(2) | 3.312(5) | 3.356(7) |
| S(1)–M(1) | 2.2943(16) | 2.317(4) | 2.426(5) |
| S(9)–M(1A) | – | 2.327(4) | 2.389(5) |
| S(9)–M(2) | 2.3202(16) | – | – |
| M(1)–M(1A) | – | 3.0042(14) | 3.069(4) |
| Pt(2)–S(51) | 2.3406(16) | – | – |
| Pt(2)–S(59) | 2.3435(16) | – | – |
| Pt(2)–P(51) | 2.3066(17) | – | – |
| Pt(2)–P(52) | 2.2996(17) | – | – |
| S(51)–C(51) | 1.810(7) | – | – |
| S(59)–C(59) | 1.797(7) | – | – |
| S(51)–S(59) | 3.336(2) | – | – |
| S(51)–M(1) | 2.3069(16) | – | – |
| S(59)–M(2) | 2.3174(16) | – | – |
| M(1)–M(2) | 2.9801(4) | – | – |
| S(1)–Pt(1)–S(9) | 90.02(6) | 90.55(13) | 91.54(15) |
| P(1)–Pt(1)–P(2) | 96.39(6) | 99.12(13) | 98.88(15) |
| P(1)–Pt(1)–S(1) | 90.08(6) | 87.79(13) | 83.15(15) |
| P(2)–Pt(1)–S(9) | 84.04(6) | 83.27(13) | 87.13(15) |
| P(1)–Pt(1)–S(9) | 174.24(6) | 172.16(12) | 171.53(14) |
| P(2)–Pt(1)–S(1) | 171.88(6) | 171.44(14) | 173.46(14) |
| Pt(1)–S(1)–C(1) | 115.0(2) | 114.6(5) | 118.7(6) |
| Pt(1)–S(1)–M(1) | 98.25(6) | 98.26(14) | 89.84(15) |
| C(1)–S(1)–M(1) | 106.3(2) | 108.7(5) | 109.4(5) |
| C(9)–S(9)–Pt(1) | 110.1(2) | 117.0(5) | 114.1(6) |
| Pt(1)–S(9)–M(1A) | – | 94.36(14) | 95.98(17) |
| C(9)–S(9)–M(1A) | – | 105.5(5) | 112.0(5) |
| Pt(1)–S(9)–M(2) | 100.84(6) | – | – |
| C(9)–S(9)–M(2) | 108.4(2) | – | – |
| S(1)–C(1)–C(10) | 129.0(5) | 130.6(12) | 126.2(13) |
| C(10)–C(9)–S(9) | 126.6(5) | 128.7(11) | 129.6(13) |
| C(1)–C(10)–C(9) | 126.8(6) | 124.7(13) | 126.9(15) |
| S(1)–M(1)–M(1A) | – | 92.45(10) | 94.47(14) |
| S(9A)–M(1)–M(1A) | – | 95.10(10) | 92.12(14) |
| S(1)–M(1)–S(9A) | – | 171.92(14) | 171.28(16) |
| S(1)–M(1)–M(2) | 90.77(4) | – | – |
| S(51)–M(1)–M(2) | 93.56(4) | – | – |
| S(1)–M(1)–S(51) | 175.56(6) | – | – |
| S(51)–Pt(2)–S(59) | 90.84(6) | – | – |
| P(51)–Pt(2)–P(52) | 98.15(6) | – | – |
| P(51)–Pt(2)–S(51) | 88.78(6) | – | – |
| P(52)–Pt(2)–S(59) | 82.50(6) | – | – |
| P(51)–Pt(2)–S(59) | 173.80(6) | – | – |
| P(52)–Pt(2)–S(51) | 172.74(6) | – | – |
| Pt(2)–S(51)–C(51) | 115.9(2) | – | – |
| Pt(2)–S(51)–M(1) | 94.29(6) | – | – |
| C(51)–S(51)–M(1) | 104.0(2) | – | – |
| C(59)–S(59)–Pt(2) | 111.0(2) | – | – |
| Pt(2)–S(59)–M(2) | 100.46(6) | – | – |
| C(59)–S(59)–M(2) | 108.6(2) | – | – |
| S(51)–C(51)–C(60) | 128.4(5) | – | – |
| C(60)–C(59)–S(59) | 127.5(5) | – | – |
| C(51)–C(60)–C(59) | 126.7(6) | – | – |
| S(9)–M(2)–M(1) | 96.65(4) | – | – |
| S(59)–M(2)–M(1) | 94.46(4) | – | – |
| S(9)–M(2)–S(59) | 168.81(6) | – | – |
| Splay angle | 22.4, 22.6 | 24.0 | 22.7 |
| Dihedral angle | 142, 146 | 149 | 150 |

 © 2007 Wiley-VCH Verlag GmbH & Co. KGaA, Weinheim 

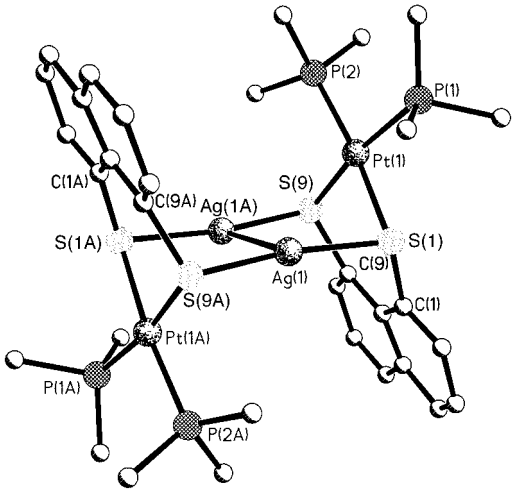


Figure 7. Crystal structure of $[Ag(Ph_3P)_2Pt(S_2C_{10}H_6)]_2^{2+}2ClO_4^-$ (**4**); $ClO_4^-$ anions are omitted for clarity.

The metal–metal bond lengths [2.9801(4), 3.0042(14) and 3.069(4) Å] are larger than those seen in similar sulfur–platinum complexes containing a gold–gold[10] or silver–silver[13] bond, but are still short enough to confirm a metal–metal interaction. Metal–sulfur bond lengths are similar and unremarkable. The M–M–S angles are in the range 90.77(4)–95.10(10)°, and the S–M–S angles are in the range 171.28(16)–175.56(6)°. This signifies that the metal atoms are in only slightly distorted T-shaped environments. Again, these values are close to those of previously studied examples.[10,13] One major point worth mentioning is that the presence of two metal atoms in the bridge actually pushes the sulfur atoms more into the plane of the Pt and C(10) atoms, giving these structures a greater dihedral angle than in $(Me_3P)_2Pt(S_2C_{10}H_6)$, as opposed to a smaller dihedral angle in the case of complex **3**. These values now lie in the range 142–150° compared with 136° in $(Me_3P)_2Pt(S_2C_{10}H_6)$ and 121–124° in complexes **1** and **3**.

## Conclusions

This paper illustrates the ability of sulfur-donor atoms to bridge metal centres. It is apparent that the planar naphthalene backbone used here is sterically undemanding with respect to. bridging systems, and thus these ligands may be capable of supporting many different multimetallic systems.

## Experimental Section

**General:** Manipulations were performed under anoxygen-free nitrogen atmosphere using standard Schlenk techniques and glassware. Solvents were dried, purified and stored according to common procedures.[16] [Naphthalene-1,8-bis(thiolato)]bis(triphenylphenylphosphane)platinum was prepared according to literature procedures.[14] $^{31}P\{^1H\}$ (109.4 MHz) and $^{195}Pt$ (58.1 MHz) NMR spectra were recorded with a Jeol DELTA GSX270 spectrometer with $\delta(^{31}P)$ referenced to external 85% $H_3PO_4$ and $\delta(^{195}Pt)$ to external $H_2PtCl_6$. $ES^+$ mass spectra were carried out by the University of St Andrews Mass Spectrometry Service.

**$[(Ph_3P)_2Pt(S_2C_{10}H_6)(AuPPh_3)][ClO_4]$ (1):** $Ph_3PAuCl$ (0.049 g, 0.1 mmol) was dissolved in dichloromethane (5 $cm^3$), and $AgClO_4$ (0.021 g, 0.1 mmol) in acetonitrile (1 $cm^3$) was added. The mixture was stirred in the dark for 2 h. A white solid precipitated, which was then dried in vacuo, redissolved in dichloromethane (10 $cm^3$) and filtered to remove insoluble AgCl. Solid $(Ph_3P)_2Pt(S_2C_{10}H_6)$ (0.091 g, 0.1 mmol) was added in one portion, and the mixture was allowed to stir overnight. The resulting solution was filtered through celite and washed with dichloromethane (20 $cm^3$). The solution was reduced in volume to approximately 1 $cm^3$, and the final product was precipitated by slow addition of diethyl ether (15 $cm^3$). The final product was filtered off and dried in vacuo as a yellow powder. Yield 0.079 g, 58%. $^{31}P$ NMR ($CD_2Cl_2$): $\delta$ = 17.6 [$^1J(P_A,Pt)$ = 3080 Hz, Pt–*P* ], 32.69 (Au–*P*) ppm. $^{195}Pt$ NMR ($CD_2Cl_2$): $\delta$ = –4674 ppm. $ES^+$ MS: *m*/*z* = 1368 $[M]^+$. $ES^-$ MS: *m*/*z* = 99 $[ClO_4]^-$.

**$[Au(Ph_3P)_2Pt(S_2C_{10}H_6)]_2[ClO4]_2$ (2):** $Ph_3PAuCl$ (0.098 g, 0.2 mmol) was dissolved in dichloromethane (5 $cm^3$), and $AgClO_4$ (0.042 g, 0.2 mmol) in acetonitrile (1 $cm^3$) was added. The mixture was stirred in the dark for 2 h. A white solid precipitated, which was then dried in vacuo, redissolved in dichloromethane (10 $cm^3$) and filtered to remove insoluble AgCl. Solid $(Ph_3P)_2Pt(S_2C_{10}H_6)$ (0.091 g, 0.1 mmol) was added in one portion, and the mixture was allowed to stir overnight. The resulting solution was filtered through celite and washed with dichloromethane (20 $cm^3$). The solution was reduced in volume to approximately 1 $cm^3$, and the final product was precipitated by slow addition of diethyl ether (15 $cm^3$). The final product was filtered off and dried in vacuo as a yellow powder. Yield 0.074 g, 67%. $^{31}P$ NMR ($CD_2Cl_2$): $\delta$ = 14.4 [$^1J(P_A,Pt)$ = 3134 Hz] ppm. $^{195}Pt$ NMR ($CD_2Cl_2$): $\delta$ = –4563 ppm. $ES^+$ MS: *m*/*z*= 1107 $[1/2\ M]^+$. $ES^-$ MS: *m*/*z* = 99 $[ClO_4]^-$.

**$Ag[(Ph_3P)_2Pt(S_2C_{10}H_6)]_2[ClO_4]$ (3):** $(Ph_3P)_2Pt(S_2C_{10}H_6)$ (0.150 g, 0.165 mmol) was dissolved in tetrahydrofuran (15 $cm^3$), and a solution of $AgClO_4$ (0.017 g, 0.0825 mmol) in acetonitrile (10 $cm^3$) was slowly added. The mixture was stirred for 3 h. The resulting solution was dried in vacuo, redissolved in a minimum volume of dichloromethane, and the final product was precipitated by slow addition of diethyl ether (20 $cm^3$). The final product was filtered off and dried in vacuo as an orange powder. Yield 0.081 g, 51%. $^{31}P$ NMR ($CD_2Cl_2$): $\delta$ = 6.83 [$^1J(P_A,Pt)$ = 2989 Hz] ppm. $^{195}Pt$ NMR ($CD_2Cl_2$): $\delta$ = –4698 ppm. $ES^+$ MS: *m*/*z* = 1928 $[M]^+$. $ES^-$ MS: *m*/*z* = 99 $[ClO_4]^-$.

**$[Ag(Ph_3P)_2Pt(S_2C_{10}H_6)]_2[ClO_4]_2$ (4):** $(Ph_3P)_2Pt(S_2C_{10}H_6)$ (0.150 g, 0.165 mmol) was dissolved in tetrahydrofuran (15 $cm^3$), and a solution of $AgClO_4$ (0.034 g, 0.165 mmol) in acetonitrile (10 $cm^3$) was slowly added. The mixture was stirred for 3 h. The resulting solution was dried in vacuo, redissolved in a minimum volume of dichloromethane, and the final product was precipitated by slow addition of diethyl ether (20 $cm^3$). The final product was filtered off and dried in vacuo as a yellow powder. Yield 0.101 g, 60%. $^{31}P$ NMR ($CD_2Cl_2$): $\delta$ = 18.29 [$^1J(P_A,Pt)$ = 3122 Hz] ppm. $ES^+$ MS: *m*/*z* = 1928 $[M]^+$. $ES^-$ MS: *m*/*z* = 99 $[ClO_4]^-$.

**Crystal-Structure Analysis:** Table 3 lists the details of data collections and refinements. Intensities were corrected for Lorentz-polarisation and for absorption. For **1**, **2** and **2′**, data were collected at 93 K by using Mo-$K_\alpha$ radiation from a high brilliance Rigaku MM007 generator and a Rigaku Mercury ccd detector, and for **3** and **4**, at 93 K using a Rigaku Saturn70 ccd detector. The structures were solved by the heavy-atom method or by direct methods. The positions of the hydrogen atoms were idealised. Refinements were performed by full-matrix least-squares based on $F^2$ with SHELXTL.[17] CCDC-614032–614036 for **1**–**4** contain the supple-

 © 2007 Wiley-VCH Verlag GmbH & Co. KGaA, Weinheim 

Table 3. Crystallographic data for complexes **1**–**4**.

| | **1** | **2** | **2′** | **3** | **4** |
|---|---|---|---|---|---|
| Empirical formula | $C_{64}H_{51}AuClO_4P_3PtS_2$ | $C_{95}H_{78}Au_2Cl_8O_8P_4Pt_2S_4$ | $C_{96}H_{80}Au_2Cl_{10}O_8P_4Pt_2S_4$ | $C_{92}H_{72}AgClO_4P_4Pt_2S_4$ | $C_{96}H_{96}Ag_2Cl_{10}O_{16}P_4Pt_2S_4$ |
| $M$ | 1468.58 | 2667.41 | 2752.33 | 2027.12 | 2718.27 |
| Crystal system | orthorhombic | monoclinic | triclinic | monoclinic | triclinic |
| Space group | *Pbca* | *P21/n* | $P\bar{1}$ | *P*21/*c* | $P\bar{1}$ |
| $a$ [Å] | 24.0844(19) | 17.8905(16) | 12.022(2) | 22.7346(15) | 12.181(8) |
| $b$ [Å] | 18.3113(11) | 14.8263(13) | 13.401(3) | 14.6105(9) | 15.192(9) |
| $c$ [Å] | 25.076(2) | 34.810(3) | 16.917(3) | 26.0999(18) | 16.788(10) |
| $\alpha$ [°] | 90 | 90 | 84.158(11) | 90 | 66.82(6) |
| $\beta$ [°] | 90 | 95.180(2) | 69.678(8) | 114.872(3) | 69.11(6) |
| $\gamma$ [°] | 90 | 90 | 67.000(8) | 90 | 69.45(5) |
| $U$ [Å$^3$] | 11059.1(14) | 9195.5(15) | 2350.8(8) | 7865.3(9) | 2587(3) |
| $Z$ | 8 | 4 | 1 | 4 | 1 |
| $\rho_{calcd.}$ [g cm$^{-3}$] | 1.764 | 1.927 | 1.944 | 1.712 | 1.745 |
| $\mu$ [mm$^{-1}$] | 5.438 | 6.664 | 6.575 | 4.070 | 3.532 |
| Reflections measured | 69772 | 55134 | 12800 | 51011 | 15497 |
| Independent reflections | 9994 | 16234 | 7453 | 13973 | 8069 |
| Final $R_1$, $wR_2$ [$I>2\sigma(I)$] | 0.0329, 0.0630 | 0.0372, 0.0771 | 0.0722, 0.1583 | 0.0827, 0.1852 | 0.1324, 0.3528 |

mentary crystallographic data for this paper. These data can be obtained free of charge from The Cambridge Crystallographic Data Centre via www.ccdc.cam.ac.uk/data_request/cif.


[1] R. Ugo, G. La Monica, S. Cenini, A. Segre, F. Conti, *J. Chem. Soc. A* **1971**, 522–528.

[2] B. H. Aw, K. K. Looh, H. S. O. Chan, K. L. Tan, T. S. A. Hor, *J. Chem. Soc., Dalton Trans.* **1994**, 3177–3182.

[3] H. Liu, A. L. Tan, K. F. Mok, T. C. W. Mak, A. S. Batsanov, J. A. K. Howard, T. S. A. Hor, *J. Am. Chem. Soc.* **1997**, *119*, 11006–11011.

[4] S.-W. A. Fong, J. J. Vittal, W. Henderson, T. S. A. Hor, A. G. Oliver, C. E. F. Rickard, *Chem. Commun.* **2001**, 421–422.

[5] S.-W. A. Fong, W. T. Yap, J. J. Vittal, T. S. A. Hor, W. Henderson, A. G. Oliver, C. E. F. Rickard, *J. Chem. Soc., Dalton Trans.* **2001**, 1986–2002.

[6] M. Ebihara, M. Tsuchiya, M. Yamada, K. Tokoro, T. Kawamura, *Inorg. Chim. Acta* **1995**, *231*, 35–43.

[7] Z. Li, Z.-H. Loh, K. F. Mok, T. S. A. Hor, *Inorg. Chem.* **2000**, *39*, 5299–5305.

[8] W. Bos, J. J. Bour, P. P. J. Schlebos, P. Hageman, W. P. Bosman, J. M. M. Smits, J. A. C. Van Wietmarschen, P. T. Beurskens, *Inorg. Chim. Acta* **1986**, *119*, 141–148.

[9] J. Vicente, M. T. Chicote, S. Huertas, D. Bautista, P. G. Jones, A. K. Fischer, *Inorg. Chem.* **2001**, *40*, 2051–2057; J. Vicente, M. T. Chicote, S. Huertas, P. G. Jones, *Inorg. Chem.* **2001**, *40*, 6193–6200; J. Vicente, M. T. Chicote, S. Huertas, P. G. Jones, *Inorg. Chem.* **2003**, *42*, 4268–4274; Y. D. Len, L. Y. Zhang, L. X. Shi, Z. N. Chen, *Inorg. Chem.* **2004**,*43*, 7493–7501.

[10] Z. Li, K. F. Mok, T. S. A. Hor, *J. Organomet. Chem.* **2003**, *682*, 73–78.

[11] H. Liu, A. L. Tan, C. R. Cheng, K. F. Mok, T. S. A. Hor, *Inorg. Chem.* **1997**, *36*, 2916–2918.

[12] J. Fornies, A. Martin, R. Navarro, V. Sicilia, P. Villarroya, A. G. Orpen, *J. Chem. Soc., Dalton Trans.* **1998**, 3721–3726.

[13] C. E. Bryant, T. S. A. Hor, N. D. Howells, D. M. P. Mingos, *J. Organomet. Chem.* **1983**, *256*, C15–C18.

[14] a) S. M. Aucott, H. L. Milton, S. D. Robertson, A. M. Z. Slawin, G. D. Walker, J. D. Woollins, *Chem. Eur. J.* **2004**, *10*, 1666–1676; S. M. Aucott, H. L. Milton, S. D. Robertson, A. M. Z. Slawin, J. D. Woollins, *Dalton Trans.* **2004**, 3347–3352; S. M. Aucott, P. Kilian, H. L. Milton, S. D. Robertson, A. M. Z. Slawin, J. D. Woollins, *Inorg. Chem.* **2005**, *44*, 2710–2718; S. D. Robertson, A. M. Z. Slawin, J. D. Woollins, *Polyhedron* **2006**,*25*, 823–826; b) C. J. Burchell, S. M. Aucott, H. L. Milton, A. M. Z. Slawin, J. D. Woollins, *Dalton Trans.* **2004**, 369–374; R. Jones, P. F. Kelly, D. J. Williams, J. D. Woollins, *J. Chem. Soc. Chem. Soc. Chem. Commun.* **1985**, 1325–1326; R. Jones, D. J. Williams, P. T. Wood, J. D. Woollins, *Polyhedron* **1987**, *6*, 539–542; R. Jones, P. F. Kelly, D. J. Williams, J. D. Woollins, *J. Chem. Soc., Dalton Trans.* **1988**, 803–807; J. R. Phillips, A. M. Z. Slawin, A. J. P. White, D. J. Williams, J. D. Woollins, *J. Chem. Soc., Dalton Trans.* **1995**, 2467–2468; R. Cea-Olivares, V. García-Montalvo, J. Novosad, J. D. Woollins, R. A. Toscanoa, G. Espinosa-Pérez, *Chem. Ber.* **1996**,*129*, 919–923; U. Abram, E. Schulz Lang, S. Abram, J. Wegmann, J. R. Dilworth, R. Kirmse, J. D. Woollins, *J. Chem. Soc., Dalton Trans.* **1997**, 623–630; A. M. Z. Slawin, M. B. Smith, J. D. Woollins, *J. Chem. Soc., Dalton Trans.* **1996**, 3659–3665; R. Jones, D. J. Williams, P. T. Wood, J. D. Woollins, *Polyhedron* **1989**, *8*, 91–96.

[15] J. Vicente, M. T. Chicote, P. Gonzalez-Herrero, P. G. Jones, *J. Chem. Soc., Dalton Trans.* **1994**, 3183–3187.

[16] D. D. Perrin, W. L. F. Armarego, *Purification of Laboratory Chemicals*, 3rd ed., Pergamon Press, Oxford, **1988**.

[17] *SHELXTL 6.10*, Bruker AXS, Madison.


Received: August 25, 2006
Published Online: November 13, 2006

 © 2007 Wiley-VCH Verlag GmbH & Co. KGaA, Weinheim 

DOI: 10.1002/ejic.200600577

# Dissociation of the P=C Ylidic Bond

**Igor Shevchenko,*[a] Alexey Rogalyov,[a] Alexander B. Rozhenko,[b] and Gerd-Volker Röschenthaler[c]**

*Dedicated to Professor Edgar Niecke*

**Keywords:** Ylides / Carbenes / Phosphanes / Density functional calculations

The phosphorus ylides $RPh_2P{=}C(Mes)N{=}C(CF_3)_2$ [R = Ph, $Ph_2P(O)CH_2$] in solution undergo reversible dissociation of the P=C ylidic bond to give phosphanes $RPh_2P$ and the carbene $MesC(:)N{=}C(CF_3)_2$. The latter can be trapped as its mesomeric nitrile ylide by treatment with cyclohexene or phenyl isocyanate to give cyclic addition products.
(© Wiley-VCH Verlag GmbH & Co. KGaA, 69451 Weinheim, Germany, 2007)

## Introduction

The formation of phosphorus ylides by the reaction of trivalent phosphorus compounds with unstable carbenes generated in situ is well established (Scheme 1).[1]

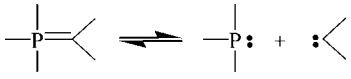

Scheme 1.

The use of stable carbenes[2] in reactions with phosphanes, however, is almost unknown.[3] Although the chemistry of phosphorus ylides is rather well studied[4] and a large number of unstable ylides have been synthesised, the reverse process, namely decomposition of phosphorus ylides to give carbenes and phosphanes, has not been known up to now. We have reported previously that diylide **1**, which contains bulky diethylamino groups at phosphorus[5a] rather than dimethylamino groups,[5b] is not stable and undergoes an unusual decomposition reaction to give ylide **2** and triene **3** almost quantitatively. The most probable route for formation of the symmetric triene **3** is the dimerisation of the appropriate carbene, whose appearance in the reaction mixture can be explained in terms of cleavage of the ylidic bond to phosphorus (Scheme 2).

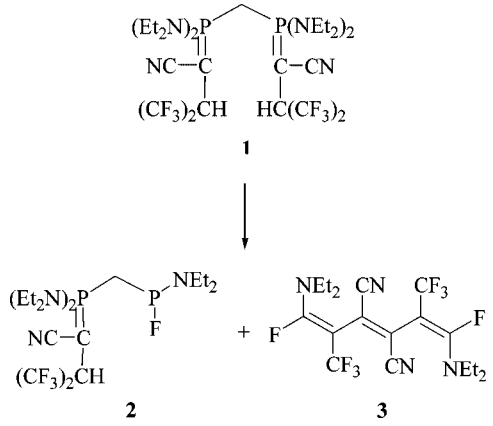

Scheme 2.

Whilst this paper was being prepared for publication a report was published on the cleavage of a phosphorus ylidic bond forming part of a strained four-membered ring to give a stable carbene.[6] We now have evidence to show that acyclic non strained ylides can also undergo such a decomposition.

## Results and Discussion

We have found that ylides **4** and **7** are capable of reversible cleavage of the P=C bond in solution with the formation of carbene (nitrile ylide) **6** and phosphanes **5** and **8**, respectively. The equilibrium is shifted to the ylidic side. The amounts of phosphane and carbene in the reaction solution are too low for NMR spectroscopic observation,

[a] Institute of Bioorganic Chemistry and Petrochemistry, Murmanskaya Street 1, 02094 Kiev, Ukraine
Fax: +380-44-573-2552
E-mail: igorshevchenko@yahoo.com
[b] Institute of Organic Chemistry, Murmanskaya Street 5, 02094 Kiev, Ukraine
E-mail: rozhenko@bpci.kiev.ua
[c] Institute of Inorganic and Physical Chemistry, University of Bremen, NW2 C2350, Leobener Strasse, 28334 Bremen, Germany
Fax: +49-421-218-4267
E-mail: gvr@chemie.uni-bremen.de
Supporting information for this article is available on the WWW under http://www.eurjic.org or from the author.

 © 2007 Wiley-VCH Verlag GmbH & Co. KGaA, Weinheim 

even upon heating to 50 °C. Although nitrile ylide **6** contains the bulky mesityl group it is not stable at 50–70 °C.[7] Because of the different thermodynamic stabilities of the starting ylides **4** and **7** their decomposition rates are also different. For example, ylide **7** decomposes completely in solution after 3–4 h at 70 °C whereas 80% of ylide **4** remains unchanged under the same conditions after 24 h. The $^{31}P$ NMR spectra of the reaction mixtures only display signals for the appropriate phosphanes **5** or **8** after completion of the decomposition.

The reversible character of the P=C ylidic bond cleavage as well as the presence of carbene **6** (or the mesomeric nitrile ylide) in the reaction mixture is in agreement with the fact that the rate of decomposition of the starting ylides becomes drastically shorter in the presence of trapping agents. For example, compound **6** reacts as a nitrile ylide with cyclohexene or phenyl isocyanate to give stable cyclic products **9** or **10** and **11** (Scheme 3). Other phosphanes that form more thermodynamically stable P=C bonds with **6** than the starting ylide can also be used as trapping agents. For example, heating of a solution of ylide **7** with triphenylphosphane (**5**) gave ylide **4** and compound **8** quickly and almost quantitatively.

The formation of carbene **6** and the appropriate phosphane is due to the dissociation of the $P^+$–$C^-$ ylidic bond and can be considered as a self-reduction reaction of the phosphorus ylides **4** and **7**. One could assume that the $P^+$–$C^-$ bond in these compounds should be longer than the normal ylidic bond. Indeed, our DFT calculations (RI-BP86/TZVP, see Experimental Section) show that the P–C1 bond length in compound **4** (Figure 1, a) is 1.81 Å, which is about 0.15 Å longer than the standard ylidic bond and comparable with the value of a phosphorus–carbon single bond.[8] This could be due to steric repulsion between the mesityl group at the carbon atom and the $PPh_3$ moiety. The decomposition of analogous ylides in which the mesityl group is replaced by the less bulky phenyl group proceeds in the same way but requires more time and a higher temperature. At first sight, this is in line with the suggestion made above. However, calculations carried out for the analogous compound with the Ph group (**4a**; Figure 1, b) indicate almost the same P=C bond length (1.80 Å). There is only one structural difference which can be related to the steric properties of the two aromatic moieties: the dihedral angle between the phenyl ring and the C1–N2–C3 plane in **4a** is about 66° whereas the Mes substituent in **4** is orthogonal ($C^{ortho}$–C4–C1–N2 angles are 99.2° and –86.5° and $C^{ortho}$–C4–C1–P5 angles are 86.8° and –87.5°). Additionally, similar C1–N2–C3 bond angles (ca. 137°) are found for both structures. This supports a significant contribution of the mesomeric structures **B** and **C**, where negative charge is formally localised on the terminal imino carbon and is additionally delocalised on the electron-withdrawing $CF_3$ substituents. This means that positive charge is localised simultaneously on phosphorus and at least partially on nitrogen due to the contribution of the form **C**. This latter formal positive charge on nitrogen is sufficiently counterbalanced by the polarisation of the C–N σ- and π-bonds towards nitrogen due to its higher electronegativity. Thus, the elongation of the P–C ylidic bond in **4** to 1.81 Å (compared with the classical polarised ylidic bond) is accounted for by the contribution of mesomeric structures **B** and **C**. The large Ar–C–N bond angle (approximately 131°) and the short C–N distances (1.31 and 1.32 Å for the central and terminal C–N bonds, respectively) are also in agreement with the contribution of form **C** (Scheme 4). This mesomeric form literally predetermines the P–C bond dissociation. The reaction product, nitrile ylide **6**, keeps

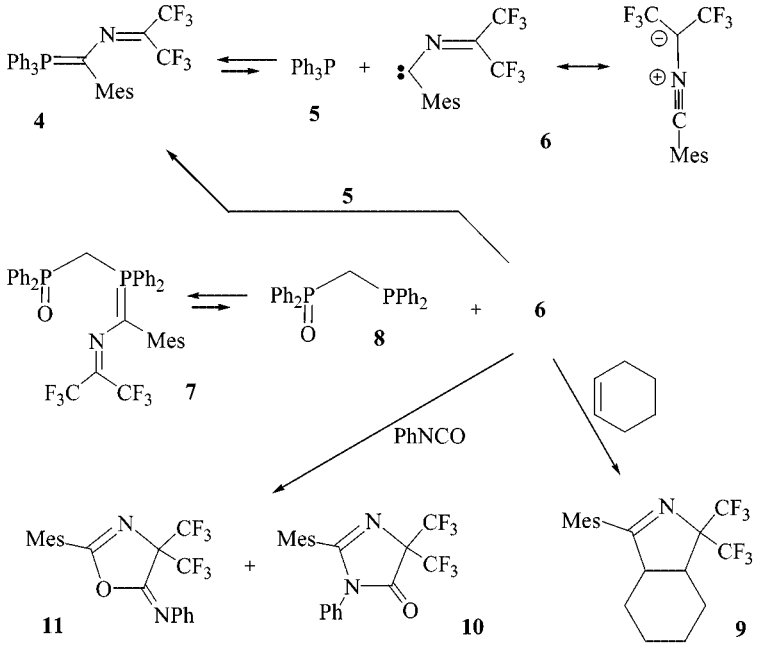


Scheme 3.

 © 2007 Wiley-VCH Verlag GmbH & Co. KGaA, Weinheim 

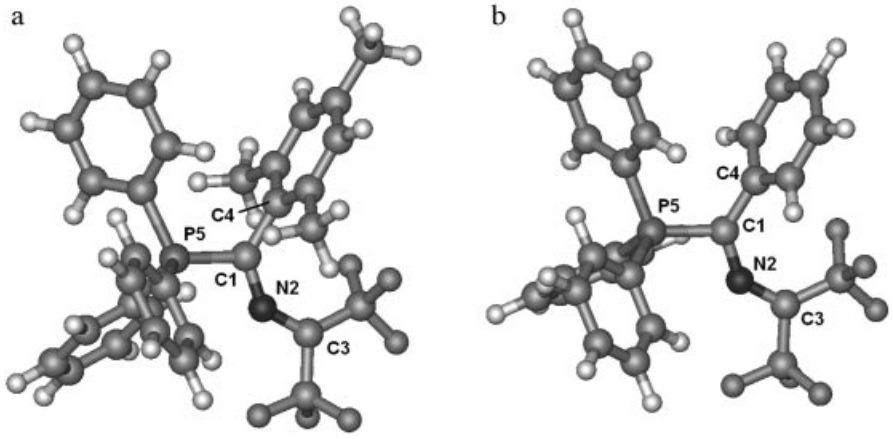


Figure 1. The equilibrium (RI-BP86/TZVP) structures of **4** (a) and **4a** (b). The most important bond lengths [Å] and bond angles [°] for **4** and **4a**, respectively, are: C1–N2 1.324, 1.327; N2–C3 1.312, 1.310; C1–C4 1.497, 1.493; C1–P5 1.808, 1.803; C1–N2–C3 137.0, 137.2; N2–C1–C4 131.2, 131.3; N2–C1–P5 107.6, 108.6; C4–C1–P5 120.4, 119.8.

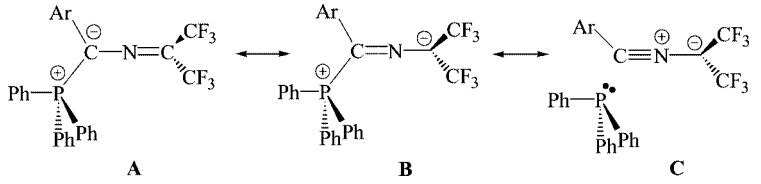


Scheme 4.

many structural features inherent to this fragment as part of the starting ylide (Figure 2).

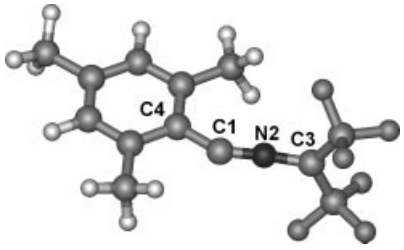


Figure 2. The equilibrium (RI-BP86/TZVP) structure of **6**. The most important bond lengths [Å] and bond angles [°] are: C1–N2 1.198, N2–C3 1.310, C1–C4 1.424; C1–N2–C3 173.7, N2–C1–C4 147.2.

Ylides **4** and **7** were synthesised by the reaction of triphenylphosphane (**5**) or bis(diphenylphosphanyl)methane (**14**) with the acylimine **12** of hexafluoroacetone. These reactions are quite interesting because they occur with complete cleavage of the C=O double bond. The formation of new bonds by the interaction of an electrophilic carbonyl group with trivalent phosphorus usually proceeds with the cleavage of only one bond of the carbonyl function. For this reason the formation of cyclic products is frequently observed. For example, the reaction of acylimines of hexafluoroacetone with phosphites has been shown to give $\Delta^4$-1,4,2$\lambda^5$-oxazaphospholines.[9]

In solution, compound **7** exists in equilibrium with its structural isomer **7a** because of prototropic migration (Scheme 5). The isomers differ from each other in the positions of the ylidic bond and one of the protons. The distribution between the isomers depends on the polarity of the solvent used. In dichloromethane, for example, the equilibrium is shifted to isomer **7** whereas in hexane it is shifted to isomer **7a**. The isomers are readily distinguishable in the $^{19}$F NMR spectrum by the signals of the non-equivalent $CF_3$ groups (compound **7**) and equivalent $CF_3$ groups (compound **7a**) bonded to $sp^2$ and $sp^3$ carbon atoms, respectively. The ylide **7a** contains a stabilizing diphenylphosphane oxide group at the ylidic bond and does not decompose on heating, isomerizing into the other isomer **7** as it disintegrates to form phosphane **8** and carbene **6**. No products that could result from the decomposition of isomer **7a** were found after the thermolysis either in the presence of trapping agents or without them.

Taking into account the reversible character of the formation of carbene **6** from ylides **4** and **7**, one can conclude that the formation of these ylides also includes the reaction of the same carbene with appropriate phosphanes. This conclusion is in agreement with our calculations. As the ArC–N bond angle of **6** was found to be 147.2°, this compound can display carbene-like properties. The intermediate formation of unstable carbenes has been indirectly confirmed in another deoxygenation reaction of a carbonyl group by phosphanes.[10]

In general, there are only a few examples known of the behaviour of nitrile ylides as imine-substituted carbenes, all of which are devoted to their dimerisation.[11] For example, the imine-stabilized carbene **16**, which results from the thermolysis or photolysis of 4,5-dihydro-1,2,3$\lambda^5$-dioxaphosphole (**15**), has been postulated as one of the intermediates in the formation of compound **19** (Scheme 6).[12]

 © 2007 Wiley-VCH Verlag GmbH & Co. KGaA, Weinheim 

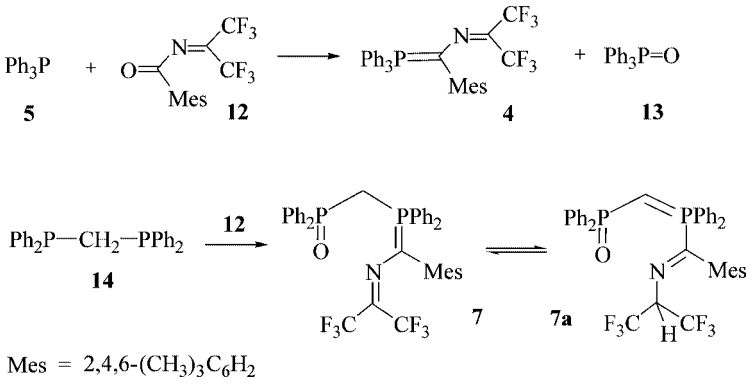


Scheme 5.

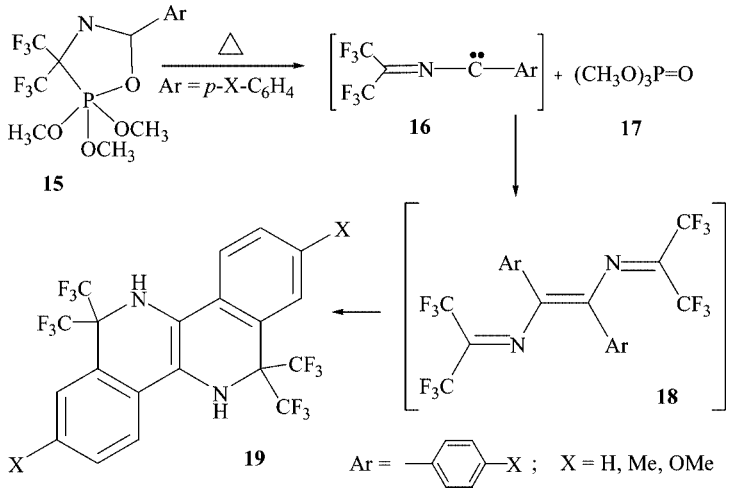


Scheme 6.

In summary, our results show that nitrile ylides can display their carbene-like properties not only in dimerisation reactions but also in their reaction with phosphanes.

## Experimental Section

**General Remarks:** All operations were performed under nitrogen in a dry box. The solvents were dried by the usual procedures. The NMR spectra were recorded with Varian Gemini 400 MHz and JEOL FX-90Q spectrometers. The mass spectrum of compound **9** was recorded with an Agilent 1100 LC/MSD spectrometer. The $^{1}H$ and $^{13}C$ chemical shifts are referenced to tetramethylsilane (TMS) and $^{19}F$ to $CFCl_3$. The $^{31}P$ chemical shifts were measured using 85% aqueous $H_3PO_4$ as an external standard.

**Compound 4:** Acylimine **12** (26 mg, 0.083 mmol) in thf (0.4 mL) was added to a solution of triphenylphosphane (**5**; 52 mg, 0.198 mmol) in thf (0.4 mL) at room temperature. After 24 h the NMR spectra of the light-yellow reaction mixture showed quantitative formation of ylide **4** and triphenylphosphane oxide (**13**). This mixture was used for the decomposition of **4** without further purification. $^{1}H$ NMR ($CDCl_3$): $\delta$ = 2.19 (s, 3 H, Me), 2.35 (s, 6 H, Me), 6.6–8.1 (m, 17 H, Ar) ppm. $^{19}F$ NMR ($CDCl_3$): $\delta$ = –56.83 (q, $^{4}J_{F,F}$ = 8.5 Hz, 3 F), 59.25 (qd, $^{4}J_{F,F}$ = 8.5, $J_{P,F}$ = 3.4 Hz, 3 F) ppm. $^{31}P$ NMR ($CDCl_3$): $\delta$ = 4.28 (s) ppm.

**Compounds 7 and 7a:** A solution of methylenebis(diphenylphosphane) (50 mg, 0.13 mmol) in $CDCl_3$ (0.4 mL) was added, whilst stirring, to a solution of acylimine **12** (50 mg, 0.16 mmol) in $CDCl_3$ (0.6 mL) over 2 min at 20 °C. After 10 min the NMR spectra showed almost quantitative formation of the isomers **7** and **7a**. This mixture was used for further reactions without purification.

**7:** $^{1}H$ NMR ($CDCl_3$): $\delta$ = 2.13 (s, 3 H, Me), 2.28 (s, 6 H, Me), 4.16 (dd, $^{2}J_{P,H}$ = 10.7, $^{2}J_{P,H}$ = 15.1 Hz, 2 H, P-C$H_2$-P), 6.57–8.05 (m, 22 H, Ar) ppm. $^{13}C$ NMR ($CDCl_3$): $\delta$ = 10.78 (dm, $J_{P,C}$ = 180.0 Hz, 1 C, P*C*CN), 26.22 (dd, $^{1}J_{P,C}$ = 25.4 Hz, $^{1}J_{P,C}$ = 85.8 Hz, P*C*P), 36.60 (d, $^{2}J_{P,C}$ = 2.9 Hz, 2 C, $NMe_2$), 36.76 (d, $^{2}J_{P,C}$ = 3.9 Hz, 2 C, $NMe_2$), 40.40 (d, $^{2}J_{P,C}$ = 15.6 Hz, 4 C, $NMe_2$), 45.62 [sept dd, $^{2}J_{P,C}$ = 16.6 Hz, $J_{P,C}$ = 5.9 Hz, $^{2}J_{F,C}$ = 29.3 Hz, 1 C, *C*H($CF_3$)$_2$], 124.20 (q, $^{1}J_{F,C}$ = 282.9 Hz, 2 C, *C*$F_3$), 125.02 (d, $^{2}J_{P,C}$ = 10.8 Hz, *C*N) ppm. $^{19}F$ NMR ($CDCl_3$): $\delta$ = –56.6 (qd, $^{4}J_{F,F}$ = 8.5 Hz, $J_{P,F}$ = 2.5 Hz, 3 F), –58.5 (qd, $^{4}J_{F,F}$ = 8.5 Hz, $J_{P,F}$ = 3.4 Hz, 3 F) ppm. $^{31}P$ NMR ($CDCl_3$): $\delta$ = 6.3 (br. d, $^{2}J_{P,P}$ = 14.0 Hz), 23.7 (d, $^{2}J_{P,P}$ = 14.0 Hz) ppm.

**7a:** $^{1}H$ NMR ($CDCl_3$): $\delta$ = 1.33 (s, 1 H, P-C*H*-P), 1.82 (s, 3 H, Me), 1.97 (s, 6 H, Me), 4.27 (sept., $^{3}J_{F,H}$ = 5.9 Hz, 1 H, $CF_3$-C*H*-$CF_3$), 6.57–8.05 (m, 22 H, Ar) ppm. $^{19}F$ NMR ($CDCl_3$): $\delta$ = –68.48 (d, $^{3}J_{H,F}$ = 5.9 Hz, 6 F) ppm. $^{31}P$ NMR ($CDCl_3$): $\delta$ = 20.8 (d, $^{2}J_{P,P}$ = 20.3 Hz), 27.5 (d, $^{2}J_{P,P}$ = 20.3 Hz) ppm.

**Compound 9:** Ylide **7** (550 mg) was obtained in chloroform as described above. The solvent was removed in vacuo and the residue was dissolved in cyclohexene (1600 mg). The mixture was heated at 75 °C for 2 h. The excess of cyclohexene was removed and the residue was extracted twice with hexane (2 × 5 mL). Column chromatography on silica gel (hexane/toluene, 3:1) of the solid re-

 © 2007 Wiley-VCH Verlag GmbH & Co. KGaA, Weinheim 

maining after evaporation of hexane afforded 50 mg of a white product. M.p. 164–165 °C. $^1$H NMR ($CDCl_3$): $\delta$ = 1.3–1.9 (m, 8 H), 2.20 (s, 6 H, Me), 2.28 (s, 3 H, Me), 2.90 (m, 1 H),, 3.38 (m, 1 H), 6.87 (br. s, 2 H, Ar) ppm. $^{13}$C NMR ($CDCl_3$): $\delta$ = 20.03 (br. s), 20.35 (s), 20.51 (s), 20.67 (s), 21.47 (s), 39.90 (s), 52.93 (s), 85.25 (m), 123.63 (q, $^1J_{F,C}$ = 284 Hz, $CF_3$), 124.50 (q, $^1J_{F,C}$ = 284 Hz, $CF_3$), 128.76 (s), 128.85 (s), 130.79 (s), 134.34 (br. s), 135.80 (br. s), 138.71 (s), 190.64 (s) ppm. $^{19}$F NMR ($CDCl_3$): $\delta$ = –67.56 (q, $^4J_{F,F}$ = 10.2 Hz, 3 F), –73.80 (q, $^4J_{F,F}$ = 10.2 Hz, 3 F) ppm. MS (APCI): *m*/*z* 378 $[M + H]^+$.

The same product was obtained when ylide **4**, obtained as described above (together with $Ph_3PO$), was heated in cyclohexene at 75 °C for 6 h.

**Compounds 10 and 11:** PhNCO (0.8 mL) was added to a reaction solution of ylide **4** obtained from acylimine **12** (50 mg) and triphenylphosphane (100 mg) in thf (0.8 mL) as described above and the mixture was heated at 60 °C for 10 h. The $^{19}$F NMR spectrum showed almost quantitative formation of the isomers **10** and **11** ($\delta$ = –72.7 and –74.0 ppm, respectively; both 6 F), which were isolated chromatographically as described previously.[13]

When a solution of ylide **7** in $CDCl_3$ was heated at 55 °C in the presence of PhNCO the yield of compounds **10** and **11** was substantially lower (about 20%). The main process in this case is an addition reaction between PhNCO and ylide **4**. This product will be described in a subsequent paper.

**Computational Details:** All of the structures were fully optimised without symmetry constraints. The BP86 functional[14,15] with an approximate treatment of the electronic Coulomb interaction [resolution of identity (RI)[16] algorithm] and the triple-zeta valence (TZV) quality basis sets[17] implemented in the TURBOMOLE program set[18] was used for the geometry optimisation. One set of polarisation functions was added for all atoms (the standard TZVP basis sets included in the TURBOMOLE packet). An SCF convergence criterion SCFConv = $1.0 \times 10^{-8}$ Hartree and the finest grid value (grid = 5) was used in the optimisation. All the structures were proved to be local minima in energy; the vibration analyses were performed by computing analytical first- and second-order derivatives.[19] A full account of the optimised geometries is given in the Supporting Information. The VMD program packet[20] was used for the graphical presentation of the calculated structures.

## Acknowledgments

We thank Professor W. W. Schoeller at the University of Bielefeld for access to the TURBOMOLE program set. Financial support by the Deutsche Forschungsgemeinschaft (DFG) (436 UKR 113/58/0-1) is gratefully acknowledged (I. S.)

[1] H. J. Bestmann, R. Zimmermann, in *Organic Phosphorus Compounds* (Eds.: G. M. Kosolapoff, L. Maier), Wiley-Interscience, New York, **1976**, vol. 3, chapter 5a.
[2] D. Bourissou, O. Guerret, F. P. Gabbai, G. Bertrand, *Chem. Rev.* **2000**, *100*, 39–91.
[3] N. Kuhn, J. Fahl, D. Blaser, R. Boese, *Z. Anorg. Allg. Chem.* **1999**, *625*, 729.
[4] O. I. Kolodiazhnyi, *Phosphorus Ylides*, Wiley-VCH, Weinheim, New York, Chichester, Brisbane, Singapore, Toronto, **1999**.
[5] a) I. Shevchenko, V. Andrushko, E. Lork, G.-V. Röschenthaler, *Eur. J. Inorg. Chem.* **2003**, 54–56; b) I. Shevchenko, V. Andrushko, E. Lork, G.-V. Röschenthaler, *Eur. J. Inorg. Chem.* **2002**, 2985–2990.
[6] Y. Canac, S. Conejero, M. Soleilhavoup, B. Donnadieu, G. Bertrand, *J. Am. Chem. Soc.* **2006**, *128*, 459–464.
[7] Only a nitrile ylide substituted with an adamantyl group is known to be stable in crystalline form at room temperature: E. P. Janulis, S. R. Willson, A. J. Arduengo III, *Tetrahedron Lett.* **1984**, *25*, 405.
[8] D. G. Gilheany, in *The Chemistry of Organophosphorus Compounds*, vol. 3 (Ed.: F. R. Hartley), John Wiley & Sons, Chichester, UK, **1994**, p. 1–44.
[9] J. Albanbauer, K. Burger, E. Burgis, D. Marquarding, L. Schabl, I. Ugi, *Justus Liebigs Ann. Chem.* **1976**, 36–53.
[10] D. V. Griffiths, J. C. Tebby, *J. Chem. Soc., Chem. Commun.* **1986**, 871–872.
[11] S. Fergus, S. J. Eustace, A. F. Hegarty, *J. Org. Chem.* **2004**, *69*, 4663–4669.
[12] K. Burger, K. Einhellig, G. Süss, A. Gieren, *Angew. Chem. Int. Ed. Engl.* **1973**, *12*, 156–157.
[13] K. Burger, H. Goth, W. Höhenberger, *Chem. Ztg.* **1977**, *101*, 453–454.
[14] A. D. Becke, *Phys. Rev. A* **1988**, *38*, 3098–3100.
[15] J. P. Perdew, *Phys. Rev. B* **1986**, *33*, 8822–8824.
[16] a) B. I. Dunlap, J. W. Conolly, J. R. Sabin, *J. Chem. Phys.* **1979**, *71*, 3396–3402; b) O. Vahtras, J. Almlöf, M. W. Feyereisen, *Chem. Phys. Lett.* **1993**, *213*, 514–518; K. Eichkorn, O. Treutler, H. Öhm, M. Häser, R. Ahlrichs, *Chem. Phys. Lett.* **1995**, *240*, 283–289.
[17] A. Schaefer, C. Huber, R. Ahlrichs, *J. Chem. Phys.* **1994**, *100*, 5829–5835.
[18] R. Ahlrichs, M. Bär, M. Häser, H. Horn, C. Kölmel, *Chem. Phys. Lett.* **1989**, *162*, 165–169; R. Ahlrichs, M. v. Arnim, in *Methods and Techniques in Computational Chemistry* METECC-95 (Eds.: E. Clementi, G. Corongiu), STEF, Cagliari, **1995**, p. 509 ff; see also http://www.cosmologic.de/QuantumChemistry/main_turbomole.html.
[19] P. Deglmann, F. Furche, R. Ahlrichs, *Chem. Phys. Lett.* **2002**, *362*, 511–518; P. Deglmann, F. Furche, *J. Chem. Phys.* **2002**, *117*, 9535–9538.
[20] VMD for WIN-32, Version 1.8.2 (December 4, 2003): W. Humphrey, A. Dalke, K. Schulten, *J. Mol. Graphics* **1996**, *14*, 33–38.

Received: June 20, 2006
Published Online: October 27, 2006

 © 2007 Wiley-VCH Verlag GmbH & Co. KGaA, Weinheim 

DOI: 10.1002/ejic.200600579

# Oxidation of Phosphanes with Orthoquinones: An Unusual Decomposition of an Unexpectedly Stable Zwitterion

**Igor Shevchenko,*[a] Vasyl Andrushko,[a] Enno Lork,[b] and Gerd-Volker Röschenthaler*[b]**

**Keywords:** Ylides / Phosphanes / Zwitterions / Carbodiphosphorane

Oxidation of the ylide $(Et_2N)_2P[=C(CN)CH(CF_3)_2]CH_2P(NEt_2)_2$ (**3**) with tetrachloroorthobenzoquinone (TOB) does not give the expected 1,3,2-dioxaphospholane but stops at the formation of the unusually stable intermediate zwitterion **6**. The molecular structure of **6** was established by X-ray analysis. In solution at temperatures above 15 °C zwitterion **6** undergoes an unusual decomposition into symmetrical carbodiphosphorane **7** and hexafluoroisovaleronitrile **8**.
(© Wiley-VCH Verlag GmbH & Co. KGaA, 69451 Weinheim, Germany, 2007)

## Introduction

Previously we have described the addition of 4,4,4-trifluoro-3-(trifluoromethyl)-2-butenenitrile (**2**) to bis[bis(dimethylamino)phosphanyl]methane (**1**) to give the monoylide **3**. The reaction of **3** with a second equivalent of **2** does not give the expected symmetrical diylide but leads unexpectedly to the almost quantitative formation of the fluorinated triene **4**.[1,2] The second product of this reaction was identified as the fluorine-substituted ylide **5**. These two reactions can be combined in one and triene **4** can be easily prepared by adding two equivalents of **2** to the starting methylenediphosphane **1**.

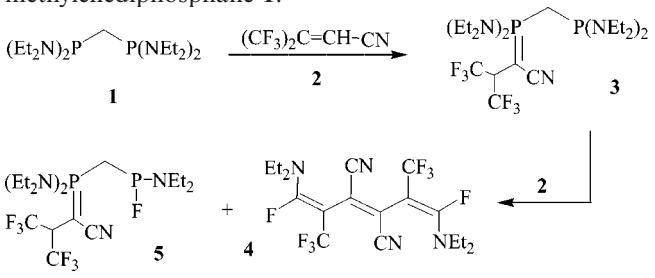

The most probable route for formation of the symmetric molecule of triene **4** is the dimerization of the appropriate carbene, and the only possible way for this to form is by dissociation of the ylidic P=C bond. We reasoned that if this is not a particular case, then an analogous cleavage may also be observed if the trivalent phosphorus atom of **3** were to react with other electrophilic reagents.

Here we wish to report on the rather unusual reaction of mono ylide **3** with tetrachloro-orthobenzoquinone (TOB). The oxidation of phosphanes with orthobenzoquinones normally leads to the formation of five-coordinate phosphoranes in which two oxygen atoms are connected to phosphorus to form 1,3,2-dioxophospholane **B**. Such reactions proceed in two steps via intermediate zwitterionic compounds **A**, which are very unstable and can only be detected by NMR spectroscopy at low temperatures.[3] The increase of steric hindrance stabilizes the zwitterionic intermediate. For example, the use of the more bulky phenanthrenequinone instead of benzoquinone in the reaction with triphenylphosphane gave the appropriate intermediate of type **A**, which is stable at room temperature.[4] Unfortunately, X-ray investigation of this compound could not be performed.

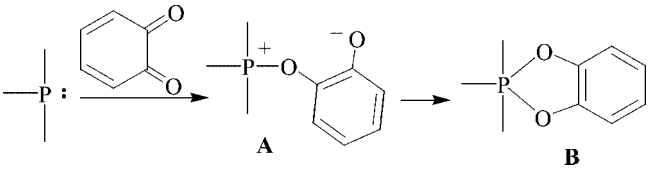

We have found that the reaction of compound **3** with TOB does not lead to the expected phosphorane structure, but stops at the formation of zwitterionic intermediate **6**. This compound crystallizes easily from the reaction mixture in diethyl ether in 65% yield as colorless crystals that turned out to be unusually stable. The detailed molecular structure of **6** (Figure 1) was established by X-ray analysis.

The bonding situation around phosphorus P(2) does not correspond to the trigonal-bipyramidal coordination geometry typical of a $\lambda^5P^5$ configuration but displays the tetrahedral geometry of the phosphonium structure $\lambda^4P^5$. The appearance of a positive charge at phosphorus P(2) causes some shortening of the P(2)–C(1) bond in comparison with

[a] Institute of Bioorganic Chemistry,
Murmanskaya Street 1, 02094 Kiev, Ukraine
Fax: +38-044-573-2552
E-mail: ishev@bpci.kiev.ua
[b] Institute of Inorganic and Physical Chemistry, University of Bremen,
NW2, C2350, Leobener Str, 28334 Bremen, Germany
Fax: +49-421-218-4267
E-mail: gvr@chemie.uni-bremen.de
Supporting information for this article is available on the WWW under http://www.eurjic.org or from the author.

 © 2007 Wiley-VCH Verlag GmbH & Co. KGaA, Weinheim 

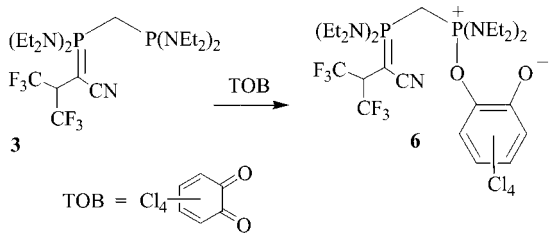


the starting compound **3** (179.5 and 187.6 pm, respectively). The negatively charged oxygen O(2) is situated between the two positively charged phosphorus atoms. The P(1)–O(2) and P(2)–O(2) distances (415.9 and 320.1 pm, respectively) are substantially longer than the P(2)–O(1) bond [157.93(19)], which excludes bonding between the atoms. The structure around the ylidic phosphorus P(1) does not differ substantially from that of the starting compound **3**. The two adjacent nitrogen atoms N(1) and N(2) have slightly different configuration. The N(1) atom is almost flat, whereas the N(2) atom has a more pronounced tetrahedral geometry [the sums of angles are 358.5(6)° and 348.0(1)°, respectively]. In solution, however, both diethylamino groups are equivalent and display common signals in the $^1$H NMR spectrum.

The ylidic carbon C(10) has an ideal flat conformation accounting for the delocalization of the negative charge on the nitrile group. That is why the P(1)–C(10) bond (171.4 pm) is somewhat longer than a normal ylidic bond (168 pm),[5] whereas the C(1)–C(2) distance is considerably shorter (139.7 pm) than the average single C–C bond. These data are consistent with the structure of the other nitrile-substituted phosphorus ylides.[6–8]

Considering that the ylidic P(1)–C(10) bond is highly polarized, the molecule contains two positively charged phosphorus atoms and negatively charged oxygen and carbon atoms. The $^{31}$P NMR spectrum of **6** displays two doublets at $\delta$ = 44.51 and 57.20 ppm ($^2J_{P,P}$ = 11.2 Hz). These values are typical for ylidic and positively charged tetracoordinate phosphonium structures, respectively. If phosphorus P(2) were connected to the second oxygen O(2) it would have a five-coordinate phosphorane structure and a chemical shift of about $\delta$ = –50 ppm. The methylene group between the two electron-withdrawing phosphonium centers displays a doublet of doublets at $\delta$ = 4.74 ppm in the $^1$H NMR spectrum. This value suggests that the acidity of the $CH_2$ protons is comparable with that of $CH_2Cl_2$. In the presence of the adjacent anionic centers in the molecule this may lead to the appearance of other prototropic forms. Indeed, the $^1$H NMR spectrum of compound **6** in chloroform displays a temperature-dependent equilibrium between zwitterionic form **6** and other possible forms **6a**,**b** resulting from the migration of one of the protons to the negatively charged oxygen O(2).

At +15 °C the position of the equilibrium is completely shifted to the zwitterionic form **6** and the P–$CH_2$–P methylene protons display a broad doublet of doublets at $\delta$ = 4.74 ppm. At 0 °C two additional very broad signals at $\delta$ = 9.46 and 2.46 ppm appear in the spectrum. The low-field signal belongs to the OH proton and the chemical shift value of the second one is more in agreement with the P=CH–P proton of isomer **6a**. This proton is connected to the negatively charged ylidic carbon atom and is thus shifted to higher field than that of structure **6b**. The intensity of the signals of the OH-containing isomers increases upon lowering the temperature. The contribution of structure **6b** probably increases at low temperature because the broad signal of the CH proton shifts gradually to lower field ($\delta_H$ = 2.94 ppm at –40 °C). The ratio between isomers **6** and **6a**,**b** at this temperature reaches 40:60. We did not find signals for the fourth possible prototropic form **6c** in the $^1$H NMR spectrum.

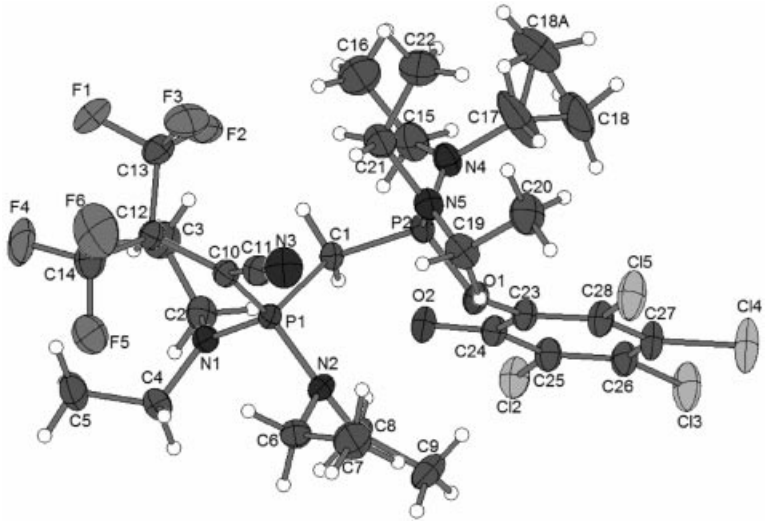


Figure 1. Perspective view and labeling scheme for **6**. Selected interatomic distances [pm] and bond angles [°]: P(1)–C(10) 171.4(3), P(1)–C(1) 183.0(3), C(1)–P(2) 179.5(2), P(1)–N(1) 165.3(2), P(1)–N(2) 165.5(2), P(2)–N(4) 161.2(2), P(2)–N(5) 162.3(2), C(10)–C(11) 139.7(4), C(11)–N(3) 116.1(4), C(10)–C(12) 151.3(3), P(2)–O(1) 157.93(19), O(2)–P(1) 415.9, O(2)–P(2) 320.1; C(10)–P(1)–C(1) 115.05(12), P(2)–C(1)–P(1) 122.90(14), C(11)–C(10)–C(12) 118.6(2), C(11)–C(10)–P(1) 122.0(2), C(12)–C(10)–P(1) 119.37(19), N(3)–C(11)–C(10) 178.8(3), O(1)–P(2)–C(1) 107.57(11), N(4)–P(2)–C(1) 106.08(12).

 © 2007 Wiley-VCH Verlag GmbH & Co. KGaA, Weinheim 

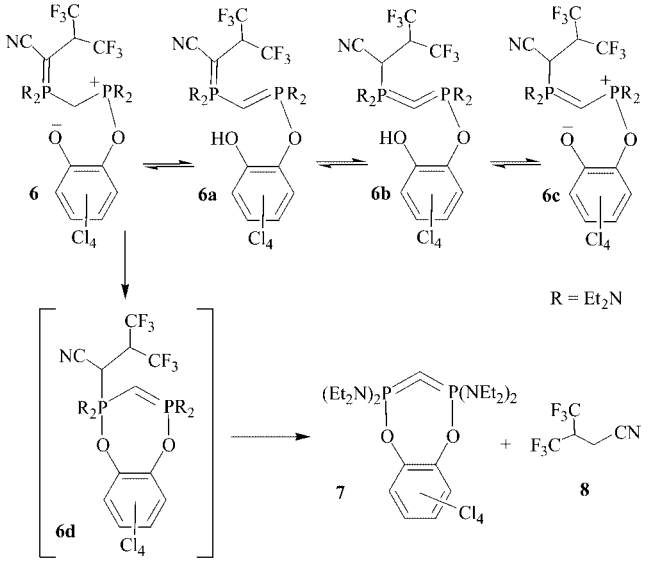


It is interesting that the $^{31}P$ NMR spectrum does not reflect all these changes of the molecule and shows two well-resolved doublets with constant chemical shifts at all temperatures below 20 °C.

In crystalline form zwitterion **6** is stable at room temperature under an inert atmosphere. For example, after 12 h we did not find additional signals in the NMR spectra. In chloroform solution compound **6** is stable up to 15 °C, and at 20 °C irreversible decomposition begins. The two doublets of **6** in the $^{31}P$ NMR spectrum become broad and unresolved and a new, sharp singlet appears at $\delta$ = 56.8 ppm. After about 25–30 h the spectrum contains only traces of the starting material. The conversion of two doublets due to the two inequivalent phosphorus nuclei into one singlet, and its chemical shift value, indicate that compound **6** rearranges into the symmetrical carbodiphosphorane **7**, which contains magnetically equivalent phosphorus nuclei. In the $^{19}F$ NMR spectrum the decomposition of **6** is shown by the disappearance of the doublet at $\delta$ = –66.42 ppm ($^3J_{H,F}$ = 8 Hz) and the growth of a new doublet at $\delta$ = –68.04 ppm ($^3J_{H,F}$ = 6.5 Hz), which belongs to six equivalent fluorine atoms of the second decomposition product [hexafluoroisovaleronitrile (**8**)]. This compound is a colorless, volatile liquid that can be easily distilled from the reaction mixture together with the solvent (chloroform). Its structure was confirmed by NMR spectroscopy and mass spectrometry. The decomposition rate depends on the properties of the solvent used. In chlorobenzene it is twice as fast as in chloroform.

Unlike other known unstable zwitterions of this type, the negatively charged oxygen atom O(2) of the former orthoquinone unit does not form the expected 1,3,2-dioxaphospholane cycle with phosphorus P(2), but attacks the other positively charged phosphorus P(1). The mechanism of the decomposition should include the dissociation of the P(1)–C(10) ylidic bond and the elimination of two hydrogen atoms from the methylene unit. There is no clue as to whether these processes proceed consecutively or are concerted. Taking into account our previous results,[1,2] as well as the recently reported P=C bond dissociation of strained four-membered cyclic ylides,[9] the homolytic cleavage of the P(1)–C(10) ylidic bond of **6** with the intermediate formation of the reactive carbene in this reaction cannot be excluded. Another possible mechanism of the decomposition of **6** may include, for example, an intermediate formation of compound **6d** which, because of steric hindrance around phosphorus P(1), may eliminate **8** to give carbodiphosphorane **7**.

In the early stages of the decomposition of zwitterion **6** carbodiphosphorane **7** is the only product and no other signals except for those of the starting material and the product are observed in the $^{31}P$ and $^{19}F$ NMR spectra. However, after completion of the process the content of numerous byproducts in the $^{31}P$ NMR spectrum reaches 30–40%. Carbodiphosphorane **7** is rather stable in the reaction solution and its signal decreases only gradually on heating to 70 °C during 10 h. However, our attempts to isolate the product in crystalline form failed. The structure of **7** was confirmed by its reaction with water. This process includes the formation of several intermediate compounds which finally give the product **9**. Unlike carbodiphosphorane **7**, this compound is not symmetrical and contains two magnetically inequivalent phosphorus atoms that appear as two doublets of an AB spin system at $\delta$ = 18.00 and 30.72 ppm ($^2J_{P,P}$ = 5.5 Hz) in the $^{31}P$ NMR spectrum. The signal at $\delta$ = 18 ppm, when recorded without proton decoupling, appears as a characteristic doublet of triplets. It belongs to the phosphorus atom of the 1,3,2-dioxaphospholane system because of the interaction with only two P–$CH_2$–P protons. Compound **9** was isolated as colorless crystals and its structure was additionally confirmed by $^1H$ NMR and HR mass spectrometry.

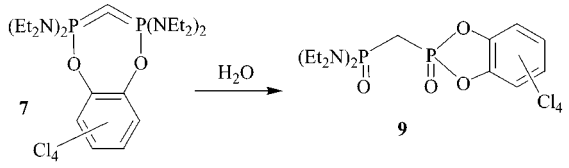


## Experimental Section

**General Remarks:** All operations were performed under nitrogen in a dry box. The solvents were dried by the usual procedures. The NMR spectra were recorded with Varian Gemini-400 and JEOL FX-90Q spectrometers. The $^1H$ and $^{13}C$ chemical shifts were referenced to tetramethylsilane (TMS). The $^{19}F$ and $^{31}P$ chemical shifts were measured using $CFCl_3$ and 85% aqueous $H_3PO_4$ as standards, respectively. The digital resolutions were 0.25, 0.5, 1.0, and 1.25 Hz for $^1H$, $^{13}C$, $^{19}F$, and $^{31}P$ NMR spectra, respectively.

**Zwitterionic Compound 6:** A solution of tetrachlororthobenzoquinone (37 mg, 0.150 mmol) in 2 mL of dry diethyl ether was added in portions of 5–8 drops to a solution of compound **3** (85 mg, 0.153 mmol) in 3 mL of diethyl ether at –10 °C. Each portion of TOB was added at an interval of 2–3 min. The reaction solution was left for 12 h at –10 °C and then for 48 h at –30 °C. The colorless crystals of **6** formed over this time were separated from the

 © 2007 Wiley-VCH Verlag GmbH & Co. KGaA, Weinheim 

mother liquor, washed with cold diethyl ether, and dried in vacuo (0.05 Torr). Yield: 73 mg (59%). $^1$H NMR ($CDCl_3$, 15 °C): $\delta$ = 1.12 (t, $^3J_{H,H}$ = 7.1 Hz, 12 H, $NCH_2CH_3$), 1.13 (t, $^3J_{H,H}$ = 7.1 Hz, 12 H, $NCH_2CH_3$), 2.62 (dd, $^2J_{P,H}$ = 16.5, $^2J_{P,H}$ = 21.1 Hz, 1 H, P–C*H*–P), 3.02–3.29 (m, 16 H, $NCH_2CH_3$), 3.47 [sept, $^3J_{F,H}$ = 6.9 Hz 1 H, $CH(CF_3)_2$], 4.74 (br. dd, $^2J_{P,H}$ = 18.4, $^2J_{P,H}$ = 21.8 Hz, 1 H, P–$CH_2$–P) ppm. $^{19}$F NMR ($CDCl_3$): $\delta$ = –66.4 ppm (d, $^3J_{H,F}$ = 7.5 Hz, 6 F). $^{31}$P NMR ($CDCl_3$): $\delta$ = 44.5 (d, $^2J_{P,P}$ = 11.2 Hz), 57.0 ppm (d, $^2J_{P,P}$ = 11.2 Hz).

**Decomposition of 6:** A solution of freshly crystallized zwitterionic compound **6** in $CDCl_3$ was left at 20 °C for 24 h.

**Carbodiphosphorane 7:** $^{31}$P NMR ($CDCl_3$): $\delta$ = 56.8 ppm (s).

**Hexafluoroisovaleronitrile 8:** $^1$H NMR ($CDCl_3$): $\delta$ = 2.93 (d, $^3J_{H,H}$ = 6.5 Hz, 2 H, $CH_2CN$), 3.37 ppm [m, $^3J_{H,H}$ = 6.5, $^3J_{F,H}$ = 7.0 Hz, 1 H, $(CF_3)_2CH$]. $^{19}$F NMR ($CDCl_3$): $\delta$ = –68.0 ppm (d, $^3J_{H,F}$ = 7.0 Hz, 6 F). MS (EI, 70 eV, 250 °C): *m*/*z* (%) 191 (2) [$M^+$], 172 (36) [M – F]$^+$, 122 (100) [M – $CF_3$]$^+$. HRMS [M – F]: calcd. 172.01857; found 172.01787 (–4.0 ppm, –0.7 mmu).

**Compound 9:** A solution of **6** (100 mg, 0.18 mmol) in $CH_2Cl_2$ (2 mL) was left at 20 °C for 24 h, then water (50 mg) was added and the mixture was stirred for 48 h at 20 °C. The solvent was evaporated, the residue was dried in vacuo (0.05 Torr), washed with diethyl ether and crystallized from toluene/hexane (at –20 °C) to give 15 mg of a colorless solid. $^1$H NMR ($CDCl_3$): $\delta$ = 1.09 (t, $^3J_{H,H}$ = 7.3 Hz, 12 H, $NCH_2CH_3$), 2.40 (dd, $^2J_{P,H}$ = 16.5, $^2J_{P,H}$ = 20.8 Hz, 2 H, P–$CH_2$–P), 3.04 (m, 8 H, $NCH_2CH_3$) ppm. $^{31}$P NMR ($CDCl_3$): $\delta$ = 18.0 (d, $^2J_{P,P}$ = 5.6 Hz), 30.7 (d, $^2J_{P,P}$ = 5.6 Hz) ppm. MS (CI, negative, $NH_3$, 200 °C): *m*/*z* (%) 496 (90) [M]; (EI, 70 eV, 207 °C): *m*/*z* (%) 496 (10) [$M^+$], 424 , (35) [M – $Et_2N$]$^+$. HRMS [$M^+$]: calcd. 495.98090; found 495.97677 (–8.3 ppm, –4.1 mmu); calcd. for [M – $Et_2N$]: 423.89957; found 423.89897 (–1.4 ppm, –0.6 mmu).

**X-ray Crystallographic Study:** The single-crystal X-ray structure determination was performed at 173(2) K on a Siemens P4 diffractometer using graphite-monochromated Mo-$K_\alpha$ radiation ($\lambda$ = 71.073 pm) and an LT2 low temperature device. The structure was solved by direct methods and refined by full-matrix least-squares on $F^2$ using the SHELX-97 program system.[10]

Crystal data for **6** ($C_{28}H_{43}Cl_4F_6N_5O_2P_2$): $M_w$ = 799.46, triclinic, space group $P\bar{1}$, $a$ = 1199.2(2), $b$ = 1279.93(15), $c$ = 1428.87(17) pm, $\alpha$ = 82.875(8)°, $\beta$ = 89.202(12)°, $\gamma$ = 85.148(11)°, $V$ = 2.1685(6) nm$^3$, $Z$ = 2, $D_c$ = 1.484 Mg m$^{-3}$, $\mu$ = 0.654 mm$^{-1}$; 11563 reflections collected, 256 parameters refined using 9956 unique reflections ($R_{int}$ = 0.0334) to final indices $R_1$ [$I > 2\sigma(I)$] = 0.0745 and $wR_2$ (all data) = 0.1465 {$w = 1/[\sigma^2(F_o^2) + (0.0698\,P)^2 + P]$}, where $P = (2F_c^2 + F_o^2)/3$. All non-hydrogen atoms were refined anisotropically and the position of the hydrogen atoms was calculated as a riding model. The final residual Fourier positive and negative peaks were equal to 1.024 and –1.034 e Å$^{-3}$. One ethyl group of one $NEt_2$ moiety is disordered. The terminal C(18) atom is split over two positions with an occupancy of 70% for C(18) and 30% for C(18a). The distances C(17)–C(18) and C(17)–C(18a) were set to be equal. The Cl atoms of one solvent molecule are disordered over two positions (50% occupancy). The distances C(30)–Cl(8), C(30)–Cl(9), C(30)–Cl(8a) and C(30)–Cl(9a) were set to be equal.

CCDC-610625 contains the supplementary crystallographic data for this paper. These data can be obtained free of charge from The Cambridge Crystallographic Data Center via www.ccdc.cam.ac.uk/data_request/cif.

## Acknowledgments

We thank the Deutsche Forschungsgemeinschaft (DFG, 436 UKR 113/58/0-1) for financial support. We are grateful to Dr. Thomas Duelks and Dr. Dorit Kaempke for mass spectrometric measurements.

[1] I. Shevchenko, V. Andruschko, E. Lork, G.-V. Röschenthaler, *Eur. J. Inorg. Chem.* **2003**, 54–56.
[2] I. Shevchenko, V. Andruschko, E. Lork, G.-V. Röschenthaler, *Eur. J. Inorg. Chem.* **2002**, 2985–2990.
[3] N. Dubau-Assibat, A. Baceiredo, G. Bertrand, *J. Am. Chem. Soc.* **1996**, *118*, 5216–5220.
[4] F. Ramirez, A. S. Gulati, C. P. Smith, *J. Am. Chem. Soc.* **1967**, *89*, 6276–6282.
[5] O. I. Kolodiazhnyi, in *Phosphorus Ylides*, Wiley-VCH, Weinheim, New York, Chichester, Brisbane, Singapore, Toronto, **1999**.
[6] I. Kawamoto, T. Hata, Y. Kishida, C. Tamura, *Tetrahedron Lett.* **1971**, *12*, 2417.
[7] H. J. Hecht, G. Ruban, *Cryst. Struct. Commun.* **1981**, 495.
[8] H. Grützmacher, H. Pritzkow, *Chem. Ber.* **1989**, *122*, 1411–1416.
[9] Y. Canac, S. Conejero, M. Soleilhavoup, B. Donnadieu, G. Bertrand, *J. Am. Chem. Soc.* **2006**, *128*, 459–464.
[10] G. M. Sheldrick, *SHELX-97*, University of Göttingen, Germany, **1997**.

Received: June 20, 2006
Published Online: November 17, 2006

 © 2007 Wiley-VCH Verlag GmbH & Co. KGaA, Weinheim 

DOI: 10.1002/ejic.200600626

# Cages on Surfaces: Thiol Functionalisation of $Co^{III}$ Sarcophagine Complexes

**Jack M. Harrowfield,[a,b] George A. Koutsantonis,*[b] Heinz-Bernhard Kraatz,[c] Gareth L. Nealon,[b] Grzegorz A. Orlowski,[c] Brian W. Skelton,[b] and Allan H. White[b]**

**Keywords:** Sarcophagine / Amino acids / Disulfides / Cobalt / Self-assembled monolayers / Electrodeposition

A number of new (sarcophagine)cobalt compounds containing oligopeptide substituents terminated by a mercaptoethylamide unit, $[Co(R)(R')sar]_2^{6+}$ (R = $NH_2$, $CH_3$; R′ = NHpeptide-$CONHCH_2CH_2S$–), have been prepared utilising the carboxymethyl complexes $[Co(R)\{N(CH_2CO_2H)\}sar]^{3+}$ (R = $NH_2$, $CH_3$), and subsequently characterised. The amino acid residues, terminating with cystamine groups, were introduced into the carboxymethyl complexes using standard peptide coupling chemistry. The solid-state structures of $[Co(CH_3)\{N(CH_2CO_2H)\}sar]Cl_4\cdot H_2O$, $[Co(CH_3)\{N(CH_2CO_2H)_2\}sar]Cl_3\cdot 2H_2O$ and $[Co(CH_3)\{N(CH_2CO_2)_2\}sar]Cl\cdot 6.5H_2O$ were determined by single-crystal X-ray diffraction experiments, the first two forming lattices containing homochiral sheets of cations in planes parallel to [0,0,1]. In the structure of $[Co(CH_3)\{N(CH_2CO_2H)\}sar]Cl_4\cdot H_2O$, the cations are of the same absolute configuration, but this alternates from one sheet to the next. In the dihydrate, $[Co(CH_3)\{N(CH_2CO_2H)_2\}sar]Cl_3\cdot 2H_2O$, the structure appears to be very similar. The sheet alternation is different from the structure of the monohydrate, $[Co(CH_3)\{N(CH_2CO_2H)\}sar]Cl_4\cdot H_2O$. The deprotonated imidodiacetate complex, $[Co(CH_3)\{N(CH_2CO_2)_2\}sar]Cl\cdot 6.5H_2O$, was prepared in an unrelated reaction; the structure displays hydogen-bonding interactions involving the carboxylate groups and coordinated NH units. The solution electrochemistry of these compounds has been investigated using both cyclic voltammetry and differential pulse voltammetry. The compounds exhibited pH-dependent, quasi-reversible redox behaviour. A monolayer was prepared by the interaction of $[Co(R)sar(GlyNHCH_2CH_2S–)]_2^{6+}$ and a gold microelectrode using both conventional "self assembly" (SAM) and electrodeposition (EDM) techniques. Surface cyclic voltammograms were measured, which, after a period of induction associated with surface reorganisation, were typical of an ordered monolayer. The monolayer was characterised by XPS, showing peaks assigned to the presence of S, Co, N, O and C. Ellipsometry gave a film thickness of $7 \pm 1$ Å, consistent with the formation of a mono- rather than a multi-layer.

(© Wiley-VCH Verlag GmbH & Co. KGaA, 69451 Weinheim, Germany, 2007)

## Introduction

Reagent immobilisation on surfaces is a sophisticated pathway to materials with a wide range of applications,[1,2] heterogeneous catalysis being one obvious application, such applications depending on the functionality introduced with the bound reagent, as well as upon the ease and convenience of the immobilisation procedure and the stability of the final product. Given the remarkable stability and varied electronic, magnetic and redox properties of metal complexes of the macrobicyclic polyamines known as "sarcophagines" (Figure 1),[3] these are species of particular appeal as entities for attachment to surfaces and for various related applications.[4] Reduction potentials for readily accessible species span a range of 2 V,[5] subject to modification in an interfacial environment,[6] and outer-sphere redox processes involving Co complexes are, for example, known to be rapid steps in reactions leading to photoinduced hydrogen production[7–10] and the reduction of oxygen to hydrogen peroxide.[11] Of practical importance in relation to immobilisation of such complexes is the facile synthesis of the ligand in forms with reactive "external" functional groups R (Figure 1).[12]

[a] Institut de Science et d'Ingénierie Supramoléculaires, Université Louis Pasteur,
8, allée Gaspard Monge, 67083 Strasbourg, France
Fax: +33-3-90245140
E-mail: harrowfield@isis.u-strasbg.fr
[b] Chemistry, M313, School of Biomedical, Biomolecular and Chemical Sciences, University of Western Australia,
Crawley 6009, Australia
Fax: +61-8-64887247
E-mail: gak@chem.uwa.edu.au
[c] Department of Chemistry, University of Saskatchewan,
110 Science Place, Saskatoon, S7N 5C9, Canada
Fax: +1-306-966-4730
E-mail: kraatz@skyway.usask.ca

Supporting information for this article is available on the WWW under http://www.eurjic.org or from the author.

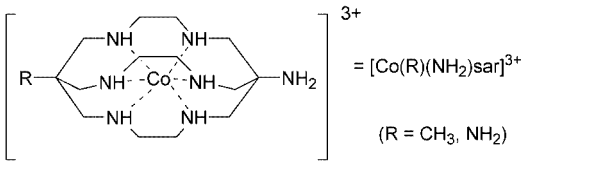


Cage = sarcophagine = "sar" = 3,6,10,13,16,19-hexaazabicyclo[6.6.6]icosane

Figure 1. Trivial nomenclature used throughout this work.

 © 2007 Wiley-VCH Verlag GmbH & Co. KGaA, Weinheim 

Limited earlier work on surface-bound cage complexes has involved modification of electrodes by impregnation of thin Nafion films on graphite with simple cage complexes,[5] electropolymerisation of a thiophenylmethylamino cage complex on Pt,[12] and carbodiimide coupling of carboxyl groups on partially oxidised graphite to a diamino cage complex.[13] Amphiphilic cages[14,15] have also proved to have interesting biological properties, probably associated with their ability to be bound within membranes.[15] As a simple approach to the immobilisation of cage complexes on surfaces, we are currently exploring the use of the well-established surface chemistry of disulfides[1] to form monolayers of (sarcophagine)cobalt complexes on gold. This is based on the introduction of peptide substituents associated with cystamine units onto the cage, a facile synthesis when starting from readily synthesised glycylated derivatives.[16] The use of peptide-based tethering groups is advantageous as the length of the spacer between the surface and the cage moiety can be increased incrementally with relative ease, using common peptide synthetic techniques,[17] and tightly packed monolayers can be formed, presumably by hydrogen bonding between the amide groups.[18] A similar approach has been applied to the synthesis of ferrocene-decorated peptides as probes for elucidation of the mechanism(s) of electron transfer in proteins.[19]

Our immediate aim in the present work was to synthesise a series of disulfides bearing peptido cage complex substituents, evaluate their solution electrochemical characteristics, and determine a suitable method for their immobilisation onto gold electrodes. Because only a single disulfide substituent is required for surface tethering, our focus has been on obtaining derivatives of the monosubstituted cage complex $[Co(CH_3)(NH_2)sar]^{3+}$, though the more complicated syntheses of monofunctionalised derivatives of $[Co(NH_2)_2sar]^{3+}$ have also been investigated. These $Co^{III}$ complexes exist in stable enantiomeric forms and thus the formation of diastereomeric forms of their oligopeptide derivatives was anticipated, though prior work suggested that differences between such diastereomers should be small.[12]

## Results and Discussion

### Synthesis

The primary amine group on a cage complex such as $[Co(NH_2)_2sar]^{3+}$ is a relatively poor nucleophile,[16] the proximity of the cationic metal centre diminishing this property, and, in cases where it is not convenient to use either the amine or an attacking electrophile in large excess, the cage complex is not an appropriate reagent for efficient synthesis, despite the fact that reactions of this type can be conducted.[13,20] Logically, it is more appropriate to use an electrophilic centre attached to the cage, because this property should be enhanced by the adjacent charge and indeed it is known that carboxymethyl derivatives of $[Co(NH_2)_2sar]^{3+}$ can be used efficiently in amide and peptide formation reactions.[21] Acceptably efficient carboxymethylation of $[Co(CH_3)(NH_2)sar]^{3+}$ (**1**) can be achieved under conditions involving reaction with a large excess of chloroacetate, which are similar to those used to obtain carboxymethyl derivatives of $[Co(NH_2)_2sar]^{3+}$.[16] Thus, the complexes $[Co(CH_3)(NHCH_2CO_2H)sar]^{3+}$ and $[Co(CH_3)\{N(CH_2CO_2H)_2\}sar]^{3+}$ were obtained as outlined in Scheme 1. These complexes, along with $[Co(NH_2)(NHCH_2CO_2H)sar]^{3+}$,[16] provided reactants to which standard peptide coupling methodologies could be applied to obtain derivatives incorporating cystamine residues as disulfide units linking two cages (Scheme 2).

In one reaction unrelated to peptide elaboration, crystals of the deprotonated diacid, $[Co(CH_3)\{N(CH_2CO_2)_2\}sar]^{+}$, were obtained (as the chloride) from an aqueous solution containing complex **3** held at a pH of approximately eight. We include below a discussion of the structure of this compound.

The syntheses produced mixtures that were readily separated by ion-exchange chromatography on Sephadex SP (using sodium citrate elution) due to the fact that the bis(cage) product has a charge of 6+ in neutral to basic solution, enabling facile discrimination between it and the less highly charged mono(cage) intermediate and any unreacted starting material.

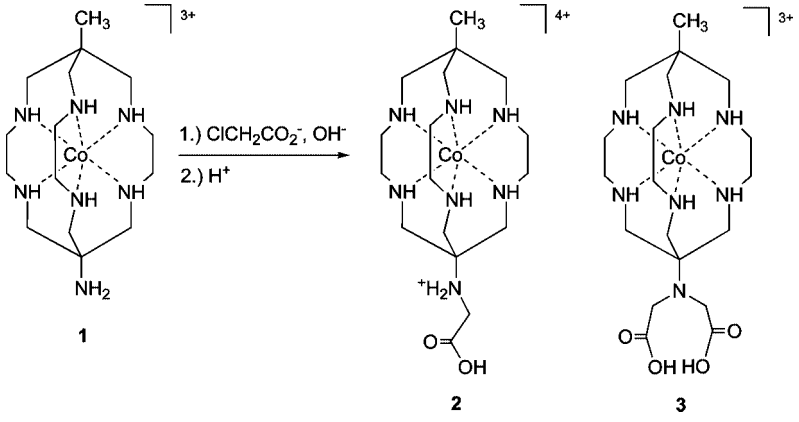


Scheme 1. Synthesis of carboxymethylated starting materials $[Co(CH_3)(NH_2CH_2CO_2H)sar]^{4+}$ (**2**) and $[Co(CH_3)\{N(CH_2CO_2H)_2\}sar]^{3+}$ (**3**).

 © 2007 Wiley-VCH Verlag GmbH & Co. KGaA, Weinheim 

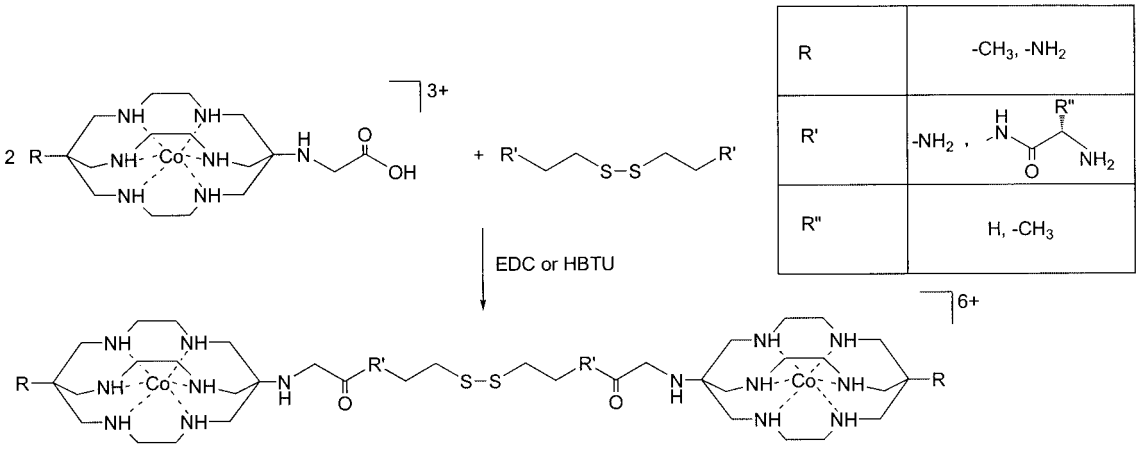


Scheme 2. Synthetic methodology used for the preparation of the disulfide complexes.

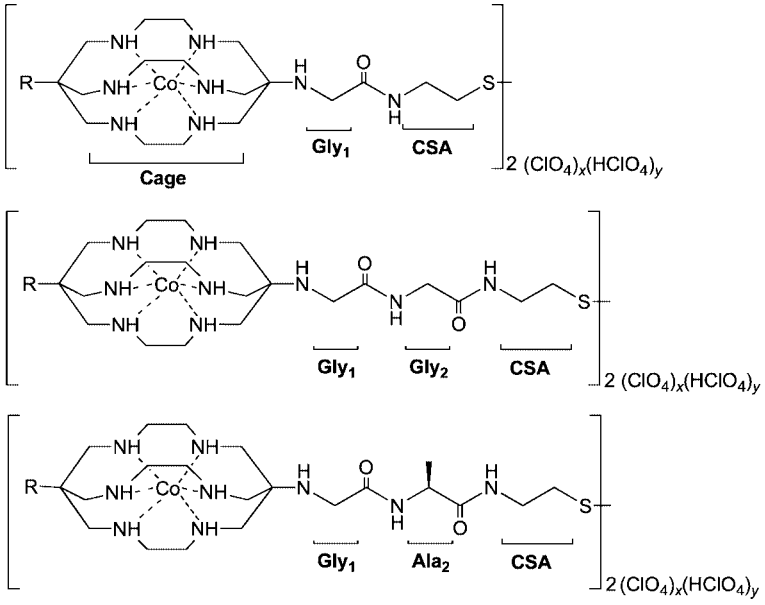


The method commonly employed to isolate $Co^{III}$ complexes of the present type from Sephadex SP column eluates, including absorbing them on Dowex 50W strong acid resin, re-eluting with HCl and then concentrating to dryness,[16] proved to lead here to some hydrolysis of the peptides. Fortunately, the complexes could be readily isolated from the citrate eluates by precipitation as their very insoluble picrates. These could readily be converted into the perchlorates, preferred to the chlorides for electrochemical studies involving gold electrodes. It is worth noting that, despite the modest isolated yields reported for the compounds, the major band in the ion-exchange chromatography was always the disubstituted disulfide, indicating a relatively efficient reaction to give the desired product.

## NMR Spectroscopy

All compounds synthesised (Table 1) exhibited NMR spectra consistent with their proposed structures. Evidence for the introduction of the carboxymethyl substituent to give the compounds **2** and **3** was observed with peaks between $\delta \approx 3.6$ and 3.7 ppm in their $^1$H NMR and two peaks at $\delta = 43.6$, 52.5 ($-CH_2-$) and $\delta = 172.5$, 176.8 (C=O) ppm in their $^{13}$C NMR spectra. The compounds **4**, **7** and **8** displayed a single amide –NH– peak ($\delta = 7.9$–8.0 ppm) in their $^1$H NMR and a single C=O peak ($\delta \approx 170$ ppm) in their $^{13}$C NMR spectra due to their CSA moieties. The compounds **5**, **6**, **9** and **10** displayed two peaks in both their $^1$H NMR ($\delta = 7.8$–8.2 ppm) and $^{13}$C NMR ($\delta = 168.7$–172.2 ppm) spectra, corresponding to the inequivalent NH and carbonyl centres of the amino acid (Gly or Ala) and CSA. The complex multiplets observed in the $^1$H NMR spectra in the region between $\delta \approx 2$ and 3.5 ppm due to the methylene group resonances of the $[Co(CH_3)(NH_2)sar]^{3+}$ and $[Co(NH_2)_2sar]^{3+}$ moieties sometimes obscured other peaks corresponding to the $Gly_1$ $-CH_2-$ group and/or the $-CH_2-N$ group of CSA. The presence and position of the obscured peaks was deduced from the overall integration of the protons in this region, as well as cross-peaks observed in the 2D NMR experiments. $^{13}$C NMR spectra reflected

 © 2007 Wiley-VCH Verlag GmbH & Co. KGaA, Weinheim 

the complete asymmetry of the compounds, except for the compounds **8**, **9** and **10** in which two cage methylene signals were coincident. This was determined from the high intensity of the composite peak relative to the other cage methylene signals and by 2D NMR experiments. It is presumed that the use of racemic $[Co(CH_3)(NHCH_2CO_2H)sar]^{3+}$ as a reactant leads to the production of a mixture of *meso* and *rac* forms of the bis(cage) peptides but only in the case of compound **6** was any spectroscopic evidence for the presence of such a mixture obtained. The $^{13}C$ NMR spectrum of this complex shows some doubling of signals, similar to that observed in a dipeptide derivative of racemic $[Co(NH_2)(NHCH_2CO_2H)sar]^{3+}$.[21] This could reflect some racemisation of the amino acid during the synthesis but the product presently obtained by reaction of Δ-$[Co(NH_2)(NHCH_2CO_2H)sar]^{3+}$ with (L-Ala)$_2$CSA shows only sharp singlets in its $^{13}C$ NMR spectrum, indicating that this is not the case.

Table 1. List of compounds synthesised.

| Compound | R | Cage | R′ |
|---|---|---|---|
| **2** | $-CH_3$ | racemic | –Gly-OH |
| **3** | $-CH_3$ | racemic | $-N(CH_2CO_2H)_2$ |
| **4** | $-CH_3$ | racemic | –Gly-CSA- |
| **5** | $-CH_3$ | racemic | –Gly-Gly-CSA- |
| **6** | $-CH_3$ | racemic | –Gly-Ala-CSA- |
| **7** | $-NH_2$ | racemic | –Gly-CSA- |
| **8** | $-NH_2$ | Δ-enantiomer | –Gly-CSA- |
| **9** | $-NH_2$ | Δ-enantiomer | –Gly-Gly-CSA- |
| **10** | $-NH_2$ | Δ-enantiomer | –Gly-Ala-CSA- |

## Mass Spectrometry

Electrospray mass spectrometry (ESMS) has been recognised as a valuable method for obtaining molecular weights of cage complexes with little to no fragmentation.[22] ESMS spectra of compounds **2** and **3** display peaks consistent with the molecular ions corresponding to a loss of $H^+$ from the cation, and some peaks consistent with an additional association of chloride anions. ESMS spectra of compounds **4**–**10** in several cases display multiple peaks, corresponding to the molecular ion in charge states of 2+, 3+ and 4+, which are assigned as successive losses of $H^+$ from the parent ion, sometimes accompanied by association of a perchlorate anion. Loss of $H^+$ from a coordinated –NH– group of the cage is known and the resolution of the measurements here are sufficient to distinguish this possibility from that of $Co^{III}$ reduction to $Co^{II}$ in the mass spectrometer, as has also been observed.[22] There also appears to be no cleavage of the disulfide link during volatilisation.

## Structure Determinations of Salts of Cations 2 and 3

The crystal structure determinations, modelled as $[Co(CH_3)(NH_2CH_2CO_2H)sar]Cl_4{\cdot}H_2O$, [**2**]$Cl_4{\cdot}H_2O$, $[Co(CH_3)\{N(CH_2CO_2H)_2\}sar]Cl_3{\cdot}2H_2O$, [**3**]$Cl_3{\cdot}2H_2O$, and $[Co(CH_3)\{N(CH_2CO_2)_2\}sar]Cl{\cdot}6.5H_2O$, [**3**–2H]$Cl{\cdot}6.5H_2O$ confirm the nature of the functionalisation (indicated by the given formulae) of the original cage complex $[Co(CH_3)(NH_2)sar]^{3+}$ expected on the basis of the method of synthesis and spectroscopic measurements; in the first two complexes, one, in the latter, two, formula units, devoid of crystallographic symmetry, comprise the asymmetric unit of the structure. The experimental details and refinement details are collected in Table 2, while structural representations showing the atom numbering schemes of the cations are given in Figure 2. Table 3 collects pertinent hydrogen-bonding data for the complexes. In [**2**]$Cl_4{\cdot}H_2O$, the O- and N-sites of the glycyl functional are both protonated, whereas in [**3**]$Cl_3{\cdot}2H_2O$, although a zwitterionic form is possible, the two carboxyl groups appear to retain their pro-

Table 2. Crystal data, details of data collection and structure refinement for the complexes.

| Complex | [**2**]$Cl_4{\cdot}H_2O$ | [**3**]$Cl_3{\cdot}2H_2O$ | [**3**–2H]$Cl{\cdot}6.5H_2O$ |
|---|---|---|---|
| Empirical formula | $C_{17}H_{40}Cl_4CoN_7O_3$ | $C_{19}H_{43}Cl_3CoN_7O_6$ | $C_{19}H_{50}ClCoN_7O_{10.5}$ |
| $M$ | 591.3 | 639.9 | 639.0 |
| Crystal system | triclinic | monoclinic | monoclinic |
| Space group | $P\bar{1}$ | $P2_1/c$ | $P2_1/c$ |
| $a$ [Å] | 9.1450(7) | 9.9703(5) | 16.918(1) |
| $b$ [Å] | 11.4703(9) | 9.9864(5) | 14.243(1) |
| $c$ [Å] | 12.521(9) | 27.8730(10) | 25.024(2) |
| $\alpha$ [°] | 83.594(1) | 90 | 90 |
| $\beta$ [°] | 87.671(1) | 93.379(1) | 103.099(5) |
| $\gamma$ [°] | 79.557(1) | 90 | 90 |
| $V$ [Å$^3$] | 1283.30(9) | 2770.4(2) | 5872.9(7) |
| $D_{calcd.}$ [g cm$^{-3}$] | 1.53 | 1.51 | 1.445 |
| $Z$ | 2 | 4 | 8 |
| Size [mm] | $0.45\times0.37\times0.28$ | $0.43\times0.43\times0.18$ | $0.65\times0.40\times0.22$ |
| $\mu_o$ [mm$^{-1}$] | 1.12 | 0.96 | 0.74 |
| Trans. (min./max.) | 0.87 | 0.81 | 0.88 |
| $2\Theta_{max.}$ [°] | 64 | 70 | 63 |
| $N_t$ | 17618 | 55294 | 154432 |
| $N$ ($R_{int.}$) | 8747 (0.022) | 11863 (0.37) | 19162 (0.035) |
| $N_o$ | 7177 | 8958 | 15820 |
| $R$ | 0.034 | 0.050 | 0.055 |
| $R_w$ ($n_w$) | 0.073 (3.2) | 0.095 (7) | 0.102 (28) |
| $T$ [K] | 170 | 298 | 100 |

 © 2007 Wiley-VCH Verlag GmbH & Co. KGaA, Weinheim 

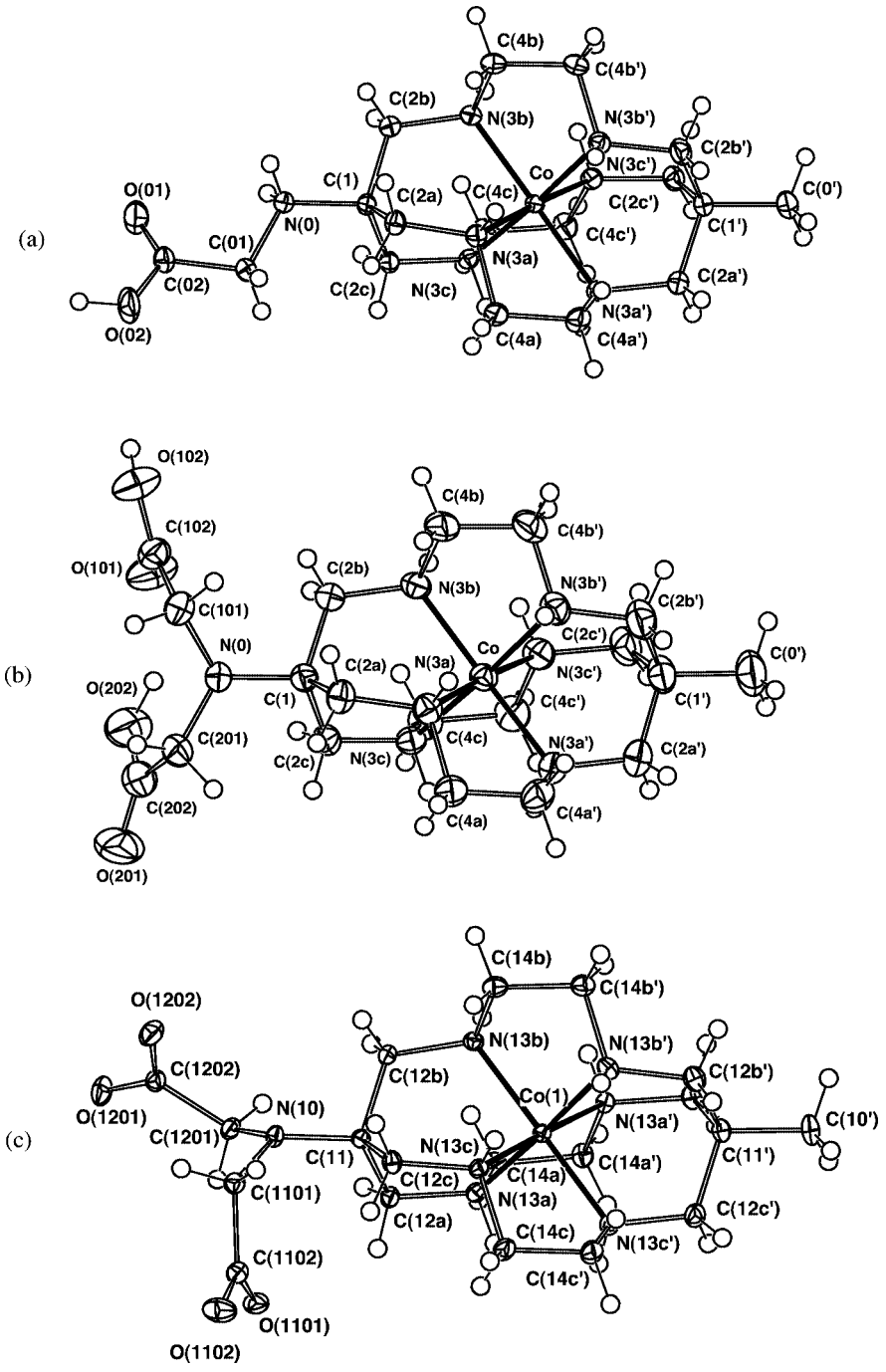


Figure 2. Structural representation of the cations in complexes (a) $[Co(CH_3)(NH_2CH_2CO_2H)sar]Cl_4{\cdot}H_2O$ [**2**]$Cl_4{\cdot}H_2O$, (b) $[Co(CH_3)\{N(CH_2CO_2H)_2\}sar]Cl_3{\cdot}2H_2O$, [**3**]$Cl_3{\cdot}2H_2O$ and (c) one of the two cations in $[Co(CH_3)\{N(CH_2CO_2)_2\}sar]Cl{\cdot}6.5H_2O$, [**3**–2H]$Cl{\cdot}6.5H_2O$. Probability ellipsoids shown at 50 [(a), (c)] and 20% (b) amplitude.

tons and the N-centre is unprotonated. This is despite the fact that the two complexes were isolated under essentially identical conditions from quite concentrated HCl solutions, though of course it need not be the case that the dominant species in solution are those which crystallise. The carboxylate groups are deprotonated in [**3**–2H]$Cl{\cdot}6.5H_2O$. All cation cores are of $lel_3$ conformation.

A view of the lattice of [**2**]$Cl_4{\cdot}H_2O$ along the *a* axis shows [Figure 3(a)], edge-on, sheets of cations lying in planes parallel to [0,0,1] which appear to form pairs separated by sheets of chloride ions. Within any given sheet, all cations are of the same absolute configuration, which alternates from one sheet to the next, and all adopt the $lel_3$ conformation. As has been discussed in detail elsewhere,[23] this conformation of amine cage complexes of $Co^{III}$ is frequently associated with "hydrogen-bonding chelation" in which two coordinated NH centres on an open octahedral edge bind to the one unit, very commonly a chloride ion, just as is the case here [Figure 3(b)]. Each of the three chloride ions involved in such chelation by every cation has a third con-

 © 2007 Wiley-VCH Verlag GmbH & Co. KGaA, Weinheim 

Table 3. Solution electrochemical data for compounds **2**–**10**. All $E_{1/2}$ values are referenced to the Ag/AgCl reference electrode. Scan rate 100 mV s$^{-1}$. Errors are the standard deviations from five measurements.

| Compound | $E_{1/2}$ [V] | $\Delta E$ [V] | $I_a/I_c$ |
|---|---|---|---|
| **2** | –0.552(2) | 0.074(3) | 1 |
| **3** | –0.607(2) | 0.073(2) | 1 |
| **4** | –0.565(3) | 0.12(1) | 1 |
| **5** | –0.562(5) | 0.09(1) | 1 |
| **6** | –0.563(2) | 0.09(1) | 0.9 |
| **7** | –0.494(6) | 0.118(5) | 0.8 |
| **8** | –0.497(2) | 0.122(2) | 0.8 |
| **9** | –0.497(4) | 0.116(5) | 0.8 |
| **10** | –0.496(5) | 0.15(1) | 0.8 |

tact at a similar or slightly shorter distance to oxygen, in two cases that of water molecules and in the third (the shortest of all contacts), that of a carboxyl group and specifically of its hydroxy unit. [The presence of the proton on the carboxyl group is clearly reflected in the asymmetry of the C–O distances of 1.198(2) and 1.327(3) Å.] The sheets of chloride ions which appear to separate the double sheets of cations contain this last "chelated" chloride ion plus the fourth chloride ion, which has one short contact [2.975(2) Å] to N of the pendent arm plus some rather remote CH contacts. Both can be considered as part of a centrosymmetric unit involving enantiomeric cations. It is also possible to identify centrosymmetric units linking the

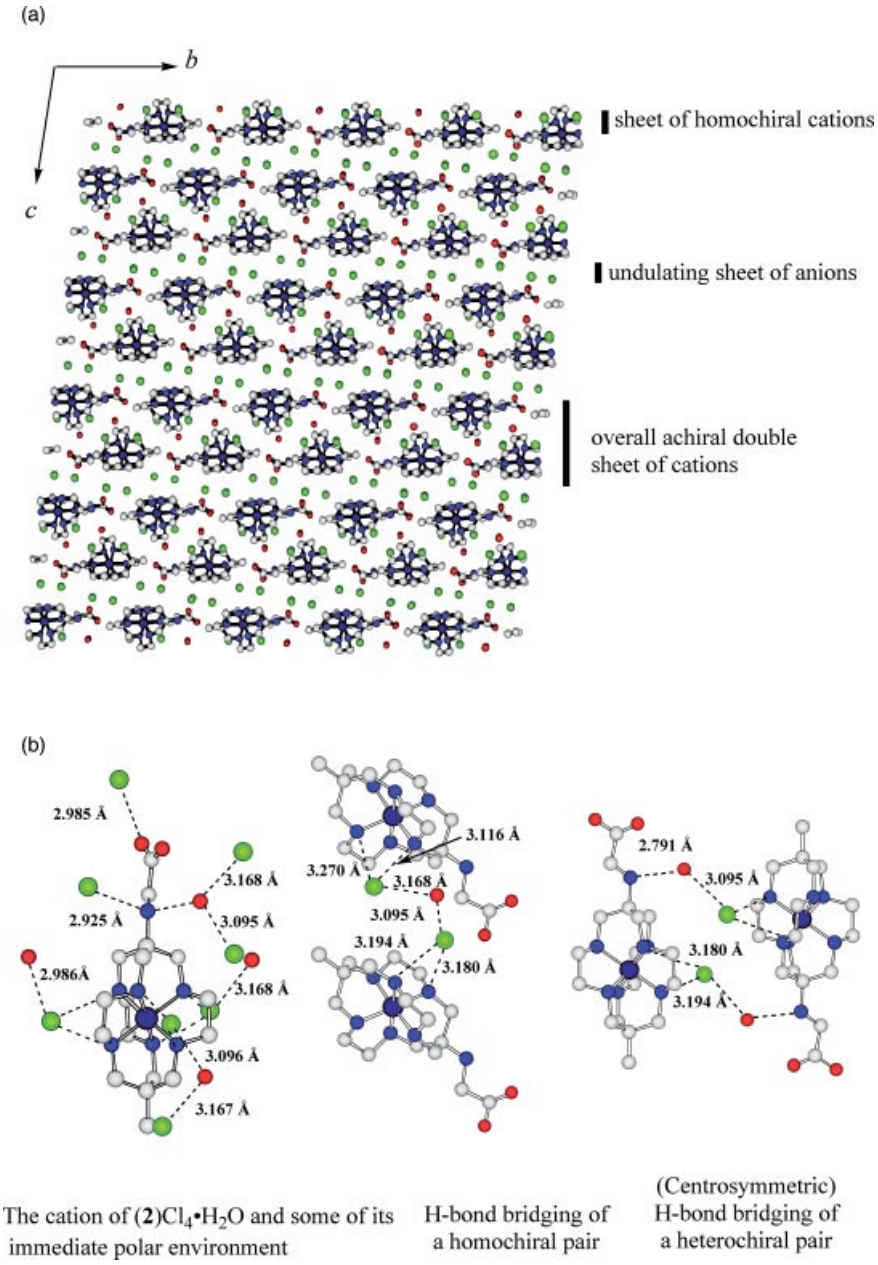


Figure 3. (a) View along the *a*-axis of the lattice of [Co(CH$_3$)(NH$_2$CH$_2$CO$_2$H)sar]Cl$_4$·H$_2$O, [**2**]Cl$_4$·H$_2$O; (b) representations of [Co(CH$_3$)(NH$_2$CH$_2$CO$_2$H)sar]Cl$_4$·H$_2$O, [**2**]Cl$_4$·H$_2$O, showing close contacts.

 © 2007 Wiley-VCH Verlag GmbH & Co. KGaA, Weinheim 

double sheets where the water molecule and one of the chelated chloride ions with which it interacts provide hydrogen-bond bridges between the cations. The water molecule serves further as part of a hydrogen-bond network (involving its second chelated chloride neighbour) that links the homochiral columns of cations running parallel to the *a*-axis within any cation sheet. Hydrogen bonding, presumably to be regarded as "charge-assisted" within the formally ionic lattice, would appear to be the principal force determining the form of the lattice array.

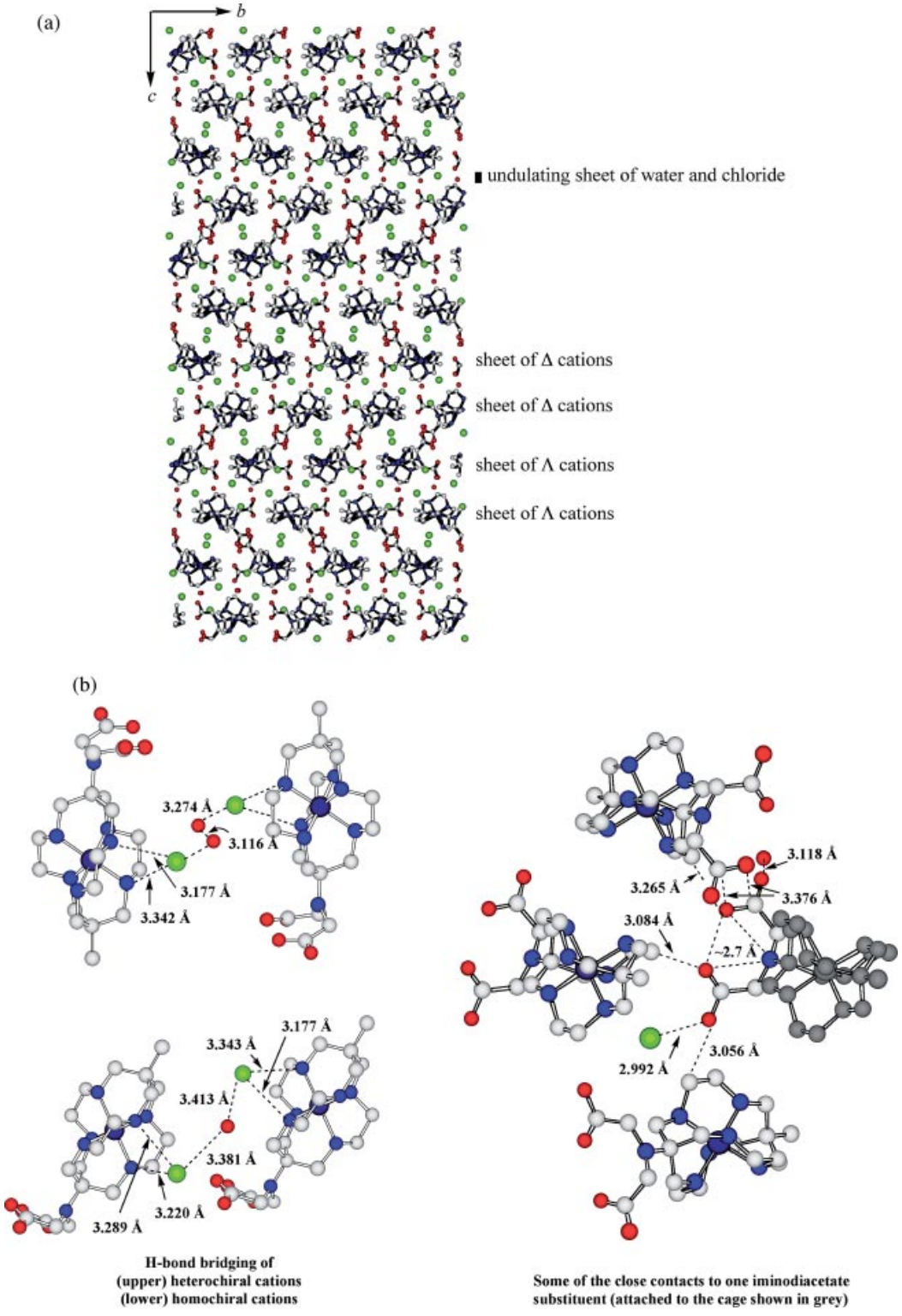


Figure 4. (a) Lattice of $[Co(CH_3)\{N(CH_2CO_2H)_2\}sar]Cl_3{\cdot}2H_2O$, **[3]**$Cl_3{\cdot}2H_2O$, along the *a*-axis; (b). Close contacts for $[Co(CH_3)\{N(CH_2CO_2H)_2\}sar]Cl_3{\cdot}2H_2O$, **[3]**$Cl_3{\cdot}2H_2O$.

 © 2007 Wiley-VCH Verlag GmbH & Co. KGaA, Weinheim 

The lattice of $[Co(CH_3)\{N(CH_2CO_2H)_2\}sar]Cl_3{\cdot}2H_2O$, [**3**]$Cl_3{\cdot}2H_2O$, shows many close similarities to that of [**2**]-$Cl_4{\cdot}H_2O$ [Figure 4(a)]. When viewed again along the *a*-axis, homochiral cation sheets, parallel to [0,0,1], can be discerned edge-on and pairs of such sheets can be considered to be separated by undulating layers of chloride ions and water molecules. Such paired sheets are of opposite chirality, but sheets separated by the chloride/water layer are homochiral, so that the sheet alternation here is ...(Δ Λ)(Λ Δ)(Δ Λ)... and not ...Δ Λ Δ Λ Δ Λ... as in (**2**)$Cl_4{\cdot}H_2O$.

A network of conventional hydrogen bonds involving the NH, chloride and water entities serves to link cations of the same and opposite chirality but there is also more convincing evidence here that CH···O and even stacking interactions may play some role in the lattice construction [Figure 4(b)]. In this regard, the iminodiacetate pendent group in (**3**)$Cl_3{\cdot}2H_2O$ has several interesting features. The protons are clearly associated with O(*n*02), on the basis of difference map and geometrical evidence [C(102)–O(101, 202) 1.201(3), 1.309(3); C(202)–O(201, 202) 1.204(4), 1.314(4) Å]. The N-atom and the two "internal" O-atoms from separate carboxylate units form a nearly equilateral triangle ca. 2.7 Å on edge, indicating that one proton may in fact interact with all three, in a mode similar to that in which iminodiacetate can act as a tridentate ligand towards a metal ion. The external carboxyl hydroxy O-atom of the iminodiacetate entity has a relatively short contact [2.993(2) Å] to a chloride ion but is also within 3.056(3) Å of an ethylene bridge C-atom and within 3.470(4) Å of the methyl group carbon atom of different adjacent cations of the same chirality. The internal carboxyl carbonyl O-atom has, in addition to its N- and O-contacts mentioned above, two relatively short contacts [3.084(3), 3.184(3) Å] to carbon atoms of an ethylene bridge on another cation of the same chirality. The internal carboxyl hydroxy O-atom has a contact of 3.265(3) Å to a cap methylene C-atom, and the carboxyl group of which it is part lies in a plane parallel to that of another carboxyl group such that there are mutual C···O contacts (stacks?) of 3.376(3) Å, both these contacts involving an enantiomorphic cation. The external carboxyl carbonyl O-atom has a contact of 3.328(3) Å to an ethylene bridge C-atom and probably a more significant contact of 3.119(3) Å to a water oxygen atom which is hydrogen-bonded to a symmetry-related water molecule and thus connected to an enantiomorphic cation. The latter contacts, coupled to the stacking just mentioned, give rise to an infinite column parallel to *a*, linking sheets of both chiralities. In view of the nonlocation of the water molecule hydrogen atoms, and the lack of close contacts to other charged or polar components, reflected in (very) high displacement parameters for the residues assigned as oxygen atoms, hydrogen bonding plays a less dominant role in the lattice array seen for (**3**)$Cl_3{\cdot}2H_2O$ although clearly it remains a major influence.

In (**3**–2H)$Cl{\cdot}6.5H_2O$, the pendents are deprotonated, and devoid of any polar NH or OH hydrogen atoms; rather, the pendent groups themselves are now charged and are competitive with the halide ions (now deficient in numbers, there being only one per cation) in their interactions with the core NH sites and the water molecules. In each of the cations, one chloride ion is chelated between one pair of unprimed and primed NH groups from adjacent cage strings, one single carboxylate oxygen atom from the alternate cation of the asymmetric unit between a second, and a carboxylate pair, also from the alternate cation (symmetry-related) between the third. "Chelation" does not appear to impact on the carboxylate geometries in the manner that protonation does, there being no substantial distinction between the geometries of *O*,CO- and *O*,*O*C-chelated carboxylate groups, C–O tightly ranged between 1.252 and 1.265(3) [< > 1.258(4) Å], O–C–O similarly 123.6–124.7(2) [< > 124.1(5)°]. The interactions of each of the chloride ions are again {(chelate-H)$_2$ plus water molecule-H}. The interactions of the carboxylate oxygen atoms are such that

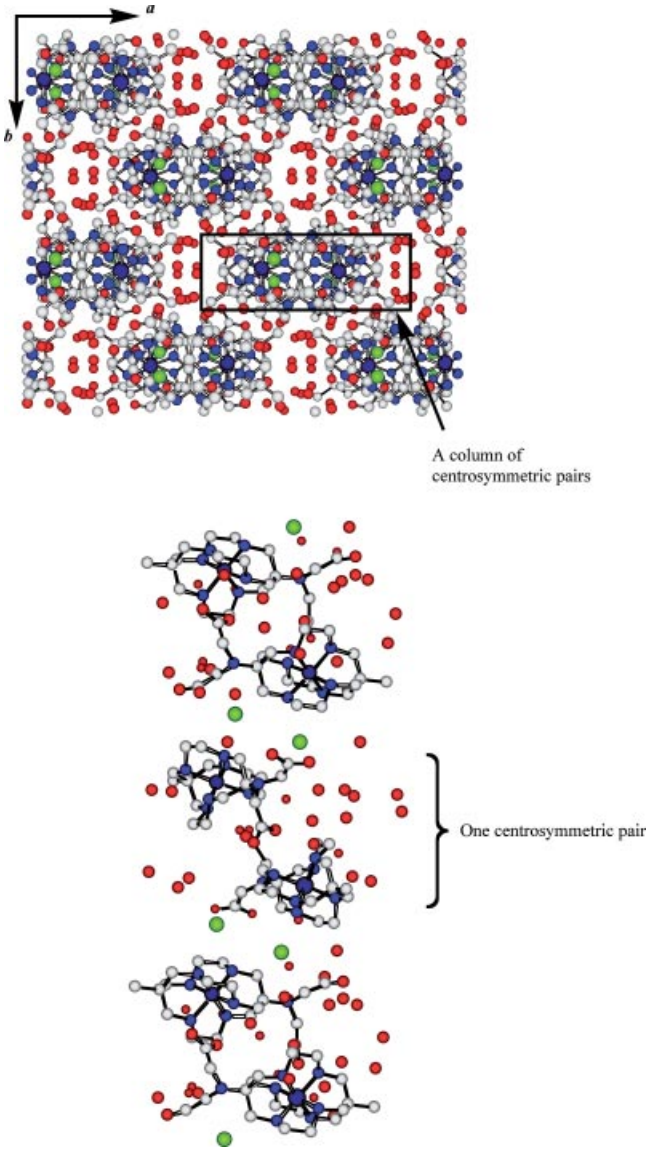


Figure 5. View of the unit cell of [**3**–2H]$Cl{\cdot}6.5H_2O$ along the *c*-axis (top) and perpendicular to one of the columns of the centrosymmetric pairs (bottom).

 © 2007 Wiley-VCH Verlag GmbH & Co. KGaA, Weinheim 

each is associated with two hydrogen atoms: O(1101, 2201) are associated with/chelated by 2× NH, O(1202, 1202, 2102, 2102) are each associated with one NH group and one water molecule hydrogen atom, and O(1102, 2202) each with a pair of water molecule hydrogen atoms, the overall result being the formation of columns of centrosymmetric pairs of complex cations [Co(1)···Co(2) 8.3943(6) Å] along *c*; the pairs sandwich pairs of chloride ions, with associated Co(1)···Co(2) (*x*, 1½ – *y*, *z* – ½) 8.6617(6) Å involving cations of opposite chirality (Figure 5). A number of the water molecules (7, 9, 12, 13) are involved in hydrogen-donor interactions only to other water molecules, none forming aggregates in isolation, but, rather, linking the columns together.

## Solution Electrochemistry

The solution electrochemistry of compounds **2**–**10** was investigated by cyclic voltammetry (CV) and differential pulse voltammetry (DPV) performed in aqueous solution using $NaClO_4$ as the supporting electrolyte, and selected data are presented in Table 3. Figure 6 depicts typical CV and DPV data for two of the complexes, **4** and **7**. The electrochemical behaviour of the compounds was found to be pH-sensitive and was often complicated by adsorption effects, particularly at Au or Pt working electrodes, which is consistent with previous work performed on the parent cages.[24] Adsorption behaviour at an Au electrode was confirmed by quartz crystal microbalance (QCM) measurements, whereby an increase in mass at the working electrode was observed at the potential corresponding to the pre-wave attributed to an adsorption phenomenon. In order to obtain reproducible results, the electrochemistry was performed in aqueous $NaClO_4$ adjusted to pH = 7.3 utilising a tris(hydroxymethyl)aminomethane (TRIS)/$HClO_4$ buffer. As the data in Table 3 show, the compounds display quasi-reversible redox behaviour, as determined from the $\Delta E$ values ($> 0.059$ V) and the peak current ratio $I_a/I_c$ being lower than unity for most of the compounds. It is known that the $E_{1/2}$ values for the cages are sensitive to the nature of the apical substituents[24] and this is evident for the compounds synthesised here. The $E_{1/2}$ for compound **2** with one glycyl substituent is shifted by 55 mV to a more positive potential than that for compound **3**, which is terminated with an iminodiacetate moiety. The nature of the terminal group in compounds **4**–**10** also affects the $E_{1/2}$ value in that there is a significant shift (ca. 60–70 mV) to more positive potentials when the methyl group at the apex of the cage is replaced by an amino group. It is worth noting, however, that the $E_{1/2}$ value does not change when moving from the Gly-CSA to Gly-Gly-CSA and Gly-Ala-CSA derivatives if the group (–$CH_3$ or –$NH_2$) at the apex is held constant. This implies that changing the nature of the substituent beyond the initial –Gly- group does not affect the electronic environment about the Co centre and therefore explains the absence of any significant differences between diastereomers. The lack of an effect on the resulting $E_{1/2}$ value is important when considering the possible use of the complexes as electrocatalysts.

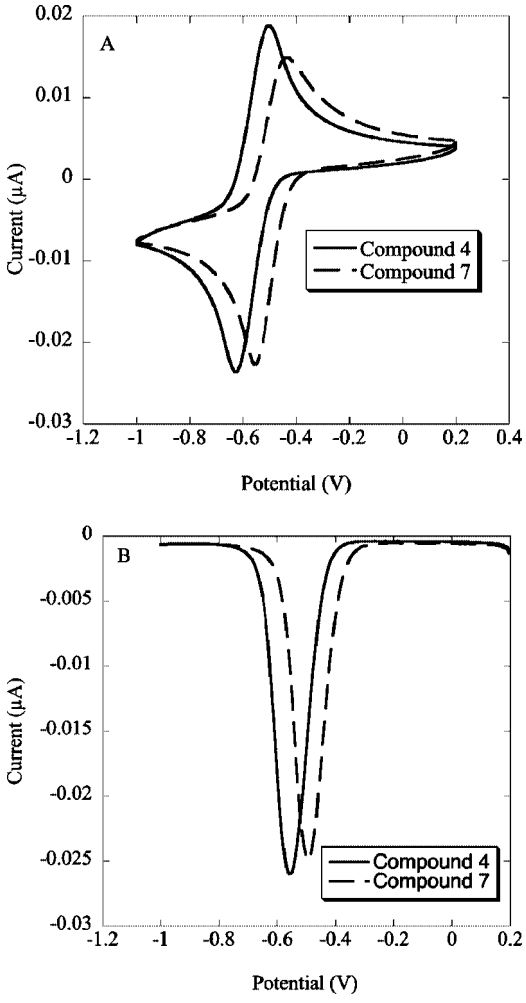


Figure 6. (a) Solution CVs of compounds **4** and **7** with GC working electrode at pH = 7.3, vs. Ag/AgCl (100 mV $s^{-1}$, 0.1 M $NaClO_4$). (b) DPVs of the reduction processes (scan rate 20 mV $s^{-1}$, pulse amplitude 50 mV).

## Surface Electrochemistry

Preparation of gold microelectrodes modified by a film of one of the cage disulfides was achieved using both conventional "self-assembly" (SAM) by soaking the electrodes in aqueous solutions of the disulfides for 5 d, and by electrodeposition (EDM).[18] All surface cyclic voltammograms (CVs) were carried out in $H_2O$ and in the presence of 2 M $NaClO_4$ as the supporting electrolyte in order to minimise the *iR* drop. Determination of the surface concentration of the cage was achieved by integration of the Faradaic peak currents of the cyclic voltammograms. Some of the characteristics of the film are shown in Table 4.

During repeated experiments it became clear that the films that formed immediately after the electrodeposition and washing steps displayed some unusual characteristics. CVs performed on the fresh films often displayed very small

 © 2007 Wiley-VCH Verlag GmbH & Co. KGaA, Weinheim 

Table 4. Comparison of electrochemical data and surface coverage using ED and SA films for compound **4**. $E_{fwhm}$ values reported for reduction waves. Values in parentheses indicate standard deviations from five measurements.

| Technique | $E°$ [mV] | $\Delta E$ [mV] | $I_a/I_c$ | $E_{fwhm}$ [mV] | Specific area [Å$^2$] | $\Gamma$ [mol cm$^{-2}$] |
|---|---|---|---|---|---|---|
| ED | –619(4) | 56(8) | 0.94(8) | 195(12) | 150(30) | $1.1(2) \times 10^{-10}$ |
| SA | –602(20) | 66(6) | 0.84(4) | 193(15) | 150(40) | $1.2(3) \times 10^{-10}$ |

or unobservable current peaks corresponding to the cage species, and if they were present, the $E_{1/2}$ values were shifted to more negative potentials than the normal "equilibrium" potentials. It was found that repeated cycling of the potential, at scan rates from 0.1 to 10 V s$^{-1}$, for periods of up to and above 30 min produced CVs that displayed sharper and more intense peak currents, with a reduction in charging current (Figure 7). This effect could be explained by a random distribution of molecules on the surface at the start of the electrochemical experiment, which gradually changes to give a more ordered film. It is worth pointing out that the electrostatic repulsion between the cationic Co conjugates is likely to induce an initial disorder in the film as the Co headgroups maximise their physical separation. Electrochemical cycling might allow greater penetration of the anions into the film, and the enhanced charge neutrality would promote better packing within the film. As the film becomes more ordered, the Co centres become more thermodynamically homogeneous, which helps explain the reduction in peak half-widths during the experiment. A more ordered film would also help to explain the lower charging current observed with time, as a more effective "blocking layer" is formed. A similar effect has been observed in films produced from immobilised $Ni^{II/III}$ redox species[25] whereby a reduction in capacitive current and sharper Faradaic current peaks were observed with longer exposure times of the modified electrode to the disulfide solution. To interpret the results, the authors proposed a process whereby an initially random (disordered) film was replaced by a more ordered and compact film by replacement of surface molecules present in defective sites with fresh molecules in solution, whilst the total surface coverage ($\Gamma$) remained constant. Whilst replacement of surface-bound molecules with those in solution is clearly not possible here,

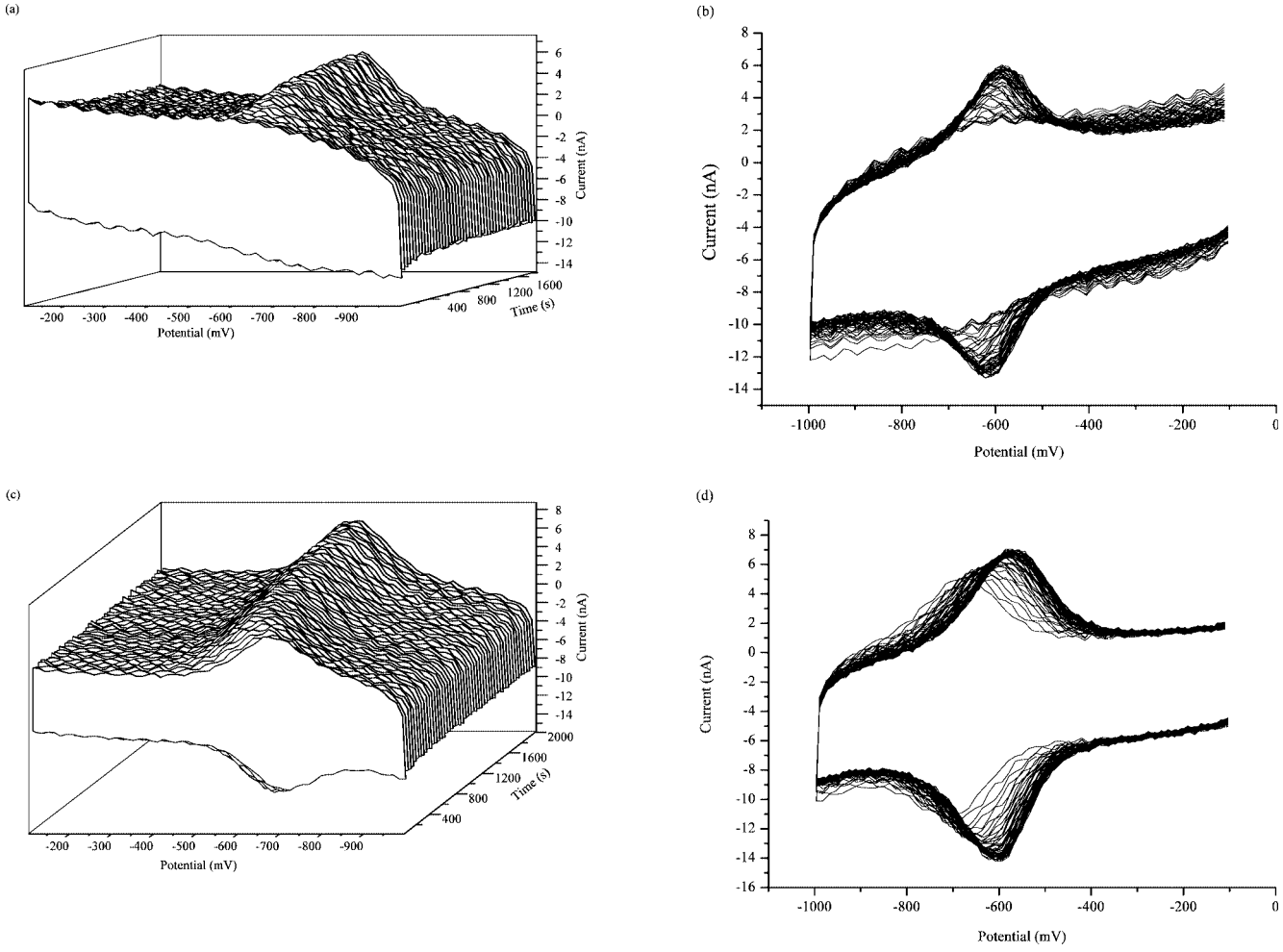


Figure 7. (a) Plot of repeated CVs vs. time for compound **4** immediately after ED and washing (10 V s$^{-1}$) [Note: Potential axis reversed for clarity in (a) and (c)]; (b) plot (a) viewed along the current/potential plane; (c): same as (a) but for SA; (d) plot (c) viewed along the current/potential plane.

 © 2007 Wiley-VCH Verlag GmbH & Co. KGaA, Weinheim 

if a surface reorganisation effect is taking place, for example by surface migration of the gold thiolate molecules[26] or the potentially slow cleavage of the disulfide bond, the results between the two experiments would be almost identical. It is worth noting that this effect was more pronounced for the films produced by ED, when compared to those prepared by SA, and this phenomenon may be explained by the relative rates at which the two films are formed. Rapid film formation during ED might not allow the molecules enough time to orient themselves on the surface, which could be exacerbated by the negative potential "pulling" the cationic cage units to the surface, whereas the long time and lack of applied potential in SA would overcome and obviate these effects (Figure 8). Thus, in order to obtain stable and reproducible CVs, all freshly prepared films were subjected to the above electrochemical treatment before the determination of the electrochemical parameters shown in Table 4.

Plotting the peak current against scan rate for monolayers of compound **4** prepared using both SA and ED shows a linear relationship (Figure 9), which is expected for a surface-adsorbed species.[27] These results indicate the successful immobilisation of compound **4** onto the gold surface using both ED and SA techniques.

The stability of the monolayers was examined by repeated electrochemical cycling, from the open circuit potential (ca. –100 mV) to –1000 mV with a scan rate of 100 $V s^{-1}$ (Figure 10). The signal due to the reduction of the surface-bound $Co^{III}$ conjugate shows virtually no loss in signal in-

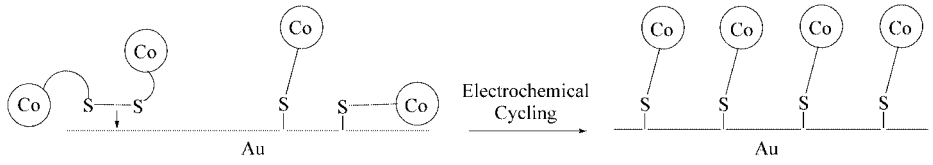


Figure 8. Diagram illustrating the possible reorganisation process leading to the observed increase in peak current and concomitant sharpening of peaks.

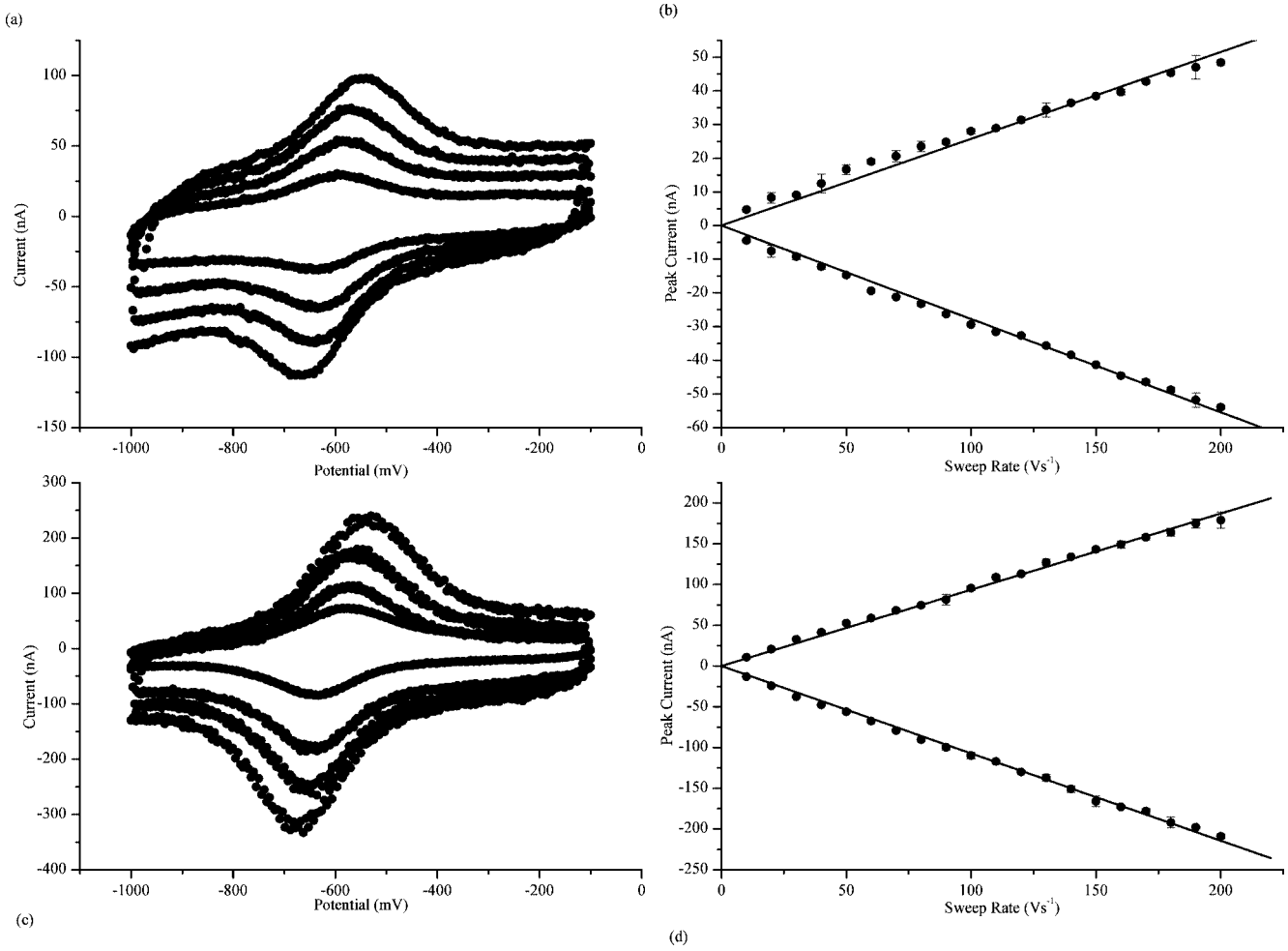


Figure 9. (a) CVs obtained at 50, 100, 150 and 200 $V s^{-1}$ for an EDM of compound **4**; (b) plot of peak current vs. scan rate for monolayer in plot (a); (c): as in plot (a) but for SAM; (d) as in plot (b) but for SAM.

 © 2007 Wiley-VCH Verlag GmbH & Co. KGaA, Weinheim 

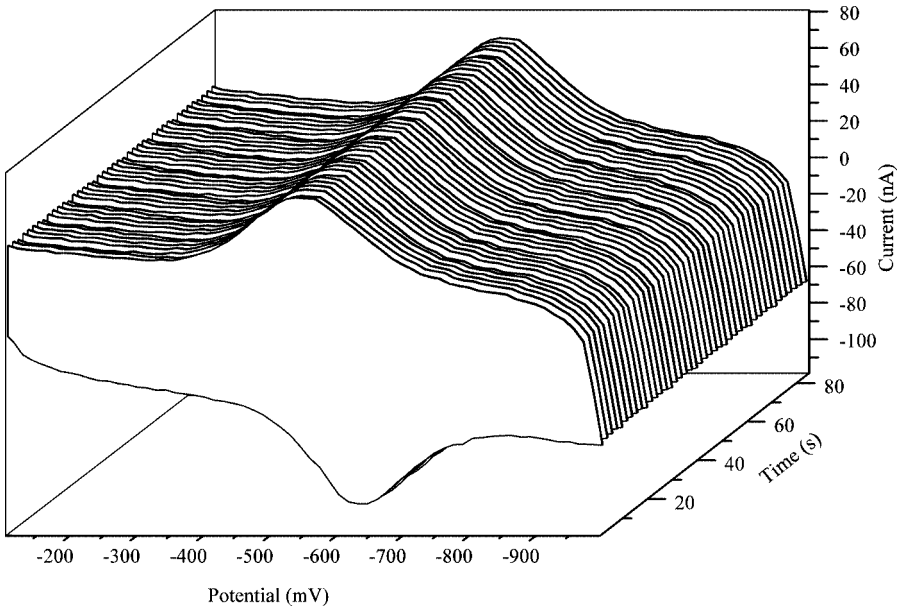


Figure 10. Repeated electrochemical cycling for film of compound **4** (100 $V s^{-1}$). (Note: Potential axis reversed for clarity.).

tensity upon repeated cycling for 100 s, indicating a stable monolayer has been formed.

As the data in Table 4 indicates, the monolayers formed using both the ED and SA techniques display very similar properties. The experimentally determined values for both films are virtually identical. Both films exhibit a reversible reduction of the $Co^{III}$ cage at $E° = –619(4)$ mV vs. Ag/AgCl, which is anodically shifted compared to the solution electrochemistry. The peak separation is nonzero but significantly reduced compared to the solution electrochemistry, indicating potentially an increase in the reversibility of the process on the surface. This also signifies that there is some barrier for electron transfer through the spacer. As would be expected, the molecular footprint is larger than the more compact and neutral ferrocene conjugates.[18,28] This can be rationalised considering the electrostatic repulsion between the positively charged (sarcophagine)$Co^{III}$ conjugates on the surface, and the large $E_{fwhm}$ of ca. 200 mV is consistent with this, as theoretical treatments[29,30] predict a broadening of Faradaic peaks when the film consists of repulsive entities. However, it is important to point out that the footprint and thus the surface concentration for films deposited electrochemically and prepared by self-assembly are identical. All of the experimentally determined values for $E_{1/2}$, and importantly, the surface concentration and the related specific area of the molecule are in agreement between the two techniques. This shows that both methods can be used to generate monolayers of the compounds on a gold electrode.

SAMs of compound **4** on Au-coated silicon wafers were also prepared, displaying contact angles of 57(2)° (advancing) and 26(5)° (receding), indicating the presence of a polar

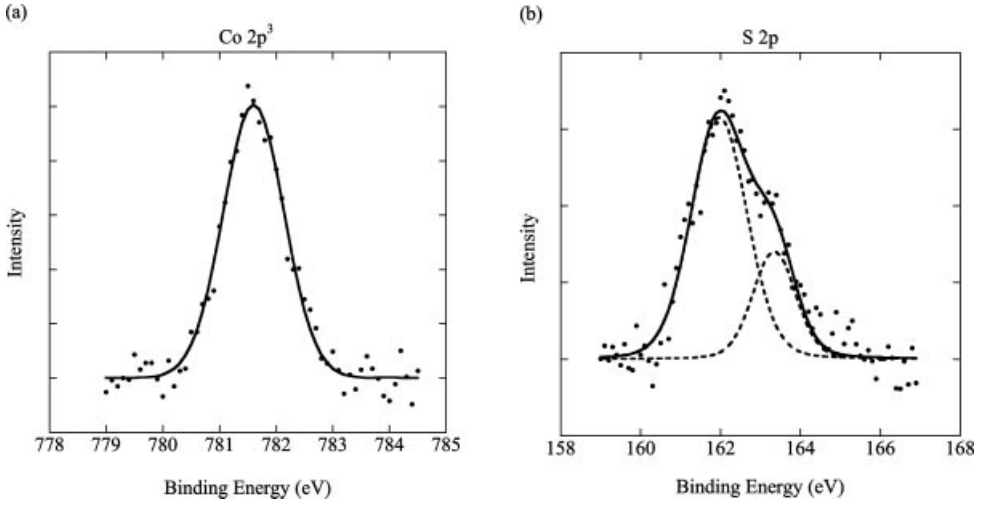


Figure 11. (a) XPS of the Co($2p^3$) region; (b) XPS of the S(2p) region. Closed circles represent experimental spectrum, solid line represents calculated spectrum and dashed lines indicate deconvoluted peaks.

 © 2007 Wiley-VCH Verlag GmbH & Co. KGaA, Weinheim 

species on the surface. Evidence for a monolayer was obtained through the use of ellipsometry, which indicated a film thickness of ($7 \pm 1$ Å) which is lower than the value expected for a fully extended molecule of compound **4** (ca. 15 Å). A low value for the film thickness could be due to the molecules lying at an angle to the surface and/or poor surface coverage, but it does suggest that the surface is modified by a monolayer and not a multilayer.

An XPS analysis of a SAM prepared on an Au-coated silicon substrate of compound **4** was undertaken in order to define the nature of the adsorption of the compound onto the gold surface. Disulfide chemisorption onto gold is generally believed to occur through a process in which the disulfide bond is broken to give two chemically independent molecules on the surface, bound as thiolates.[26] Peaks corresponding to S, Co, N, O and C are observed in the XPS spectrum which demonstrates the presence of compound **4** on the substrate. Figure 11 shows the major peak in the S(2p) region at 162 eV, which is consistent with the formation of an Au–S bond,[31] allowing us to conclude that the compound is bound as a thiolate on the surface. The Co binding energy of 781.5 eV is higher than the reported binding energy of 780.5 eV for the related $[Co(NO_2)_2sar]Cl_3$,[32] but does fall within the range of binding energy values for the $Co^{III}$ $N_6$ complexes $[Co(en)_3]Cl_3$ and $[Co(NH_3)_6]Cl_3$ of 780.2–781.8 eV,[32,33] which indicates the cobalt atom is present as $Co^{III}$.

## Conclusions

In this paper we have described the synthesis and solution electrochemical behaviour of a series of cobalt cage complexes bridged with short disulfide-containing peptides. In this way we have demonstrated the efficacy of this synthetic strategy which will allow us to tune "tail" length in a number of applications. We have also shown that it is possible, at least in one case, to immobilise a complex on a gold substrate utilising the disulfide linkage present. We believe that this undergoes facile cleavage to give initially species which lack ordering and subsequent electrochemical cycling allows them to attain thermodynamically stable surface ordering, although this phenomenon requires further study.

The surface attachment of these peptide-tethered sarcophagine complexes has allowed us to form modified surfaces containing redox-active centres and promise entry to an exciting range of applications.

## Experimental Section

**General:** Nuclear magnetic resonance (NMR) spectra were acquired with a Bruker ARX 300 ($^1H$ at 300 MHz and $^{13}C$ at 75.5 MHz), Bruker AV 500 ($^1H$ at 500.13 MHz and $^{13}C$ at 125.8 MHz), or Bruker AV 600 ($^1H$ at 600.13 MHz and $^{13}C$ at 150.9 MHz). Chemical shifts for samples measured in $D_2O$ are expressed in ppm relative to an internal standard of acetone which was taken as being $\delta = 2.22$ ppm for $^1H$ NMR spectra and $\delta = 30.89$ ppm for $^{13}C$ NMR relative to TMS. Chemical shifts for samples measured in $[D_6]$DMSO were referenced to the residual solvent peak. Assignments were made with the aid of either the DEPT or HSQC techniques. Mass spectra were recorded using the electrospray technique (positive ion trap) with a VG Autospec instrument or QSTAR XL-MS/MS. Microanalyses for carbon, nitrogen and hydrogen were carried out by The Australian National University Microanalytical Service. All samples were thoroughly dried under vacuum at 50 °C for at least 4 h prior to their analysis. Ion exchange chromatography was performed under gravity flow using SP Sephadex C25 ($Na^+$ form, 200–400 mesh) or $H^+$ form Dowex 50Wx2 (200–400 mesh) cation exchange resin. Deionised water was used in all preparations. DMF was predried with molecular sieves (4 Å) prior to use. Dichloromethane was dried by distillation from $CaH_2$ and stored over molecular sieves (3 Å). Trisodium citrate ($Na_3Cit$) (Ajax), chloroacetic acid (Ajax), sodium picrate (BDH), *N*-[3-(dimethylamino)propyl]-*N*′-ethylcarbodiimide hydrochloride (EDC·HCl) (Aldrich), cystamine dihydrochloride (CSA·2HCl) (Aldrich), diisopropylethylamine (DIPEA) (Lancaster), *N*-hydroxysuccinimide (HOSu) (Aldrich), 2-benzotriazole-*N*,*N*,*N*,*N*,-tetramethyluronium hexafluorophosphate (HBTU) (Auspep), trifluoroacetic acid (TFA) (Aldrich), Boc-protected amino acids (Auspep), and trifluoromethanesulfonic (triflic) acid (Lancaster) were used as received. Solution electrochemical experiments were carried out at room temperature ($23 \pm 1$ °C) with a MacLab Potentiostat or CHInstruments potentiostat model 660B or 440 in 0.1 M $NaClO_{4(aq)}$ adjusted to pH = 7.3 with tris(perchlorate) buffer, and an analyte concentration of 1 mM. A three-electrode cell system consisting of glassy carbon (BAS, 3.0 mm diameter) as the working electrode, Pt wire as the counter electrode and Ag/AgCl (3.0 M KCl) as the reference electrode was employed. The carbon electrodes were cleaned by polishing with a micro-cloth pad with $Al_2O_3$ slurry (0.05 μm) and washed thoroughly with water before use. For the cyclic voltametric (CV) studies the scan rate was 100 mV $s^{-1}$ and for the DPV experiments a scan rate of 20 mV $s^{-1}$ and pulse amplitude of 50 mV was used. Cyclic voltammograms (CVs) were scanned in the potential range of 0.2 to –1.0 V vs. Ag/AgCl. $[Co(CH_3)(NH_2)sar]Cl_3·HCl·0.5H_2O$,[34] *rac*- and Δ-$[Co(NH_2)(NH_2CH_2CO_2H)sar]Cl_3·2HCl$,[16] [Boc-Gly-CSA]$_2$ and [Boc-Ala-CSA]$_2$[35] were all synthesised as reported previously.

**Structure Determinations:** Full spheres of CCD area-detector diffractometer data were measured ($\omega$-scans; monochromatic Mo-$K_\alpha$ radiation, $\lambda = 0.7107_3$ Å). $N_{t(otal)}$ reflections were obtained, these merging to $N$ unique ($R_{int}$ cited) after "empirical"/multiscan absorption correction (proprietary software), $N_o$ with $F > 4\sigma(F)$ considered "observed" and used in the full-matrix least-squares refinements on $F^2$, refining anisotropic displacement parameter forms, $(x,y,z,U_{iso})_H$ being included constrained at estimates. Conventional residuals $R$, $R_w$ {weights: $[\sigma^2(F^2) + n_wF^2]^{-1}$} are cited at convergence. Neutral atom complex scattering factors were employed within the context of the Xtal 3.7 program system.[36] Pertinent results are given above and in Tables 2 and 3 and Figure 2. In (**3**)$Cl_4·2H_2O$, a pair of substantial difference map residues were assigned as water molecule oxygen atoms, site occupancies unity after trial refinement, albeit with high displacement parameters, associated hydrogen atoms not being located. CCDC-605503 to -605505 contain the supplementary crystallographic data for this paper. These data can be obtained free of charge from The Cambridge Crystallographic Data Centre via www.ccdc.cam.ac.uk/data_request/cif.

**Electrodeposition:** All electrodeposition experiments were performed using a three-electrode cell system consisting of Au (25 μm diameter) as the working electrode, Pt wire as the counter electrode and Ag wire as the reference electrode. Electrodeposition was ac-

 © 2007 Wiley-VCH Verlag GmbH & Co. KGaA, Weinheim 

complished by placing a freshly oxidised microelectrode (electrochemical cycling from –0.4 to +1.2 V vs. Pt wire in 0.5 M $H_2SO_4$) into a 1 mM solution of the analyte in 0.1 M $NaClO_{4(aq)}$ and applying –1.5 V for 30 min. After this period, the electrode was washed with water, then suspended in a vigorously stirred beaker of water for 10 min, and then 2 M $NaClO_{4(aq)}$ for 30 s. All electrochemical measurements were performed using a custom-built potentiostat in 2 M $NaClO_{4(aq)}$ using a three-electrode cell system consisting of Au (25 μm diameter) as the working electrode, Pt wire as the counter electrode and Ag/AgCl as the reference electrode, which was placed in a separate cell and connected to the analyte cell with a salt bridge ($KNO_3$). The electrochemical cell was enclosed in a grounded Faraday cage, and all electrolytes were degassed with a flow of $N_{2(g)}$ prior to the experiments, and an $N_{2(g)}$ blanket maintained throughout the course of the measurements. All electrochemical measurements were performed on at least five different microelectrodes to ensure reproducibility.

**Self-Assembly:** Monolayers were formed by soaking a freshly cleaned electrode (electrochemical cycling from –0.4 to +1.2 V vs. Pt wire in 0.5 M $H_2SO_4$) in a 1 mM aqueous solution of the complex for 5 d. After this period, the electrodes were treated exactly as above for the electrodeposited materials.

**X-ray Photoelectron Spectroscopy:** XPS measurements were performed using an Axis-165 X-ray Photoelectron Spectrometer (Kratos Analytical) with a monochromatic Al-$K_a$ X-ray source (1486.7 eV). Survey spectra (0–1100 eV) were taken at constant analyser pass energy of 160 eV and high-resolution spectra of Au4f, C1s, N1s, O1s, S2p and Co2p, were acquired with a pass energy of 20 eV and a down time of 200 ms. The take-off angle measured as the angle between the film surface and the photoelectron energy analyser was 90°. The typical operating pressure in the analysing chamber was ca. $5 \cdot 10^{-10}$ Torr. Number of scans for high resolution required obtaining high signal/noise ratio varied from 4 for Au to 40 for Co, and 60 for S. The binding energies were referenced to Au4f7/2 at 84.0 eV.

**[Co(CH$_3$)(NH$_2$CH$_2$CO$_2$H)sar]Cl$_4$·H$_2$O (2)Cl$_4$·H$_2$O and [Co(CH$_3$)-{N(CH$_2$CO$_2$H)$_2$}sar]Cl$_3$·2H$_2$O (3)Cl$_3$·2H$_2$O:** [Co(CH$_3$)(NH$_2$)sar]-$Cl_3$·HCl·0.5$H_2O$ (2.10 g, 4.0 mmol) was dissolved in $H_2O$ (ca. 20 mL) in a three-necked round-bottomed flask, and the pH adjusted to ca. 10 by the addition of NaOH(aq). A solution of Na-$CO_2CH_2Cl$ (25 g, 0.21 mol) in water (ca. 100 mL) was then added, and the pH again adjusted to ca. 10 by addition of more NaOH(aq). The solution was then heated at 80 °C under Ar(g) for 7 d, and the pH maintained at ca. 9–10 by dropwise addition of NaOH(aq). The reaction was monitored on micro-columns of $Na^+$ form SP C25 Sephadex by elution with 0.1 M $Na_3Cit$. More Na-$CO_2CH_2Cl$ was added after 3 d (25 g, 0.21 mmol) and 5 d (10 g, 0.09 mmol), and after 7 d, the reaction mixture was acidified with acetic acid (pH < 5), diluted to 2 L in water, and applied to a column of $H^+$ form Dowex 50Wx2 cation exchange resin. The column was washed with water (500 mL), 1 M HCl (500 mL, to remove $Na^+$) and finally the products eluted with 3 M HCl. The fraction containing the products was then dried in the rotary evaporator, and the solid thus obtained dissolved into water (1 L) and applied to a column of $Na^+$ form Sephadex cation exchange resin. Elution with 0.05 M $Na_3Cit$ produced three bands, the first being a minor yellow band, the second the major orange band, and the third a minor orange band. The three bands were applied to $H^+$ form Dowex 50Wx2 cation exchange resin separately, and treated with water (500 mL), 1 M HCl (500 mL) and eluted with 3 M HCl. The product from Band 1 was dried in a rotary evaporator, dissolved in hot water and precipitated by the addition of EtOH and finally $Et_2O$ and cooling in the freezer. The product was collected by suction filtration, washed with a little cold EtOH, then finally $Et_2O$, and dried under vacuum to give (**3**)$Cl_3$·2$H_2O$ (0.22 g, 0.35 mmol) as orange crystals. $^1$H NMR (300 MHz, $D_2O$): $\delta$ = 0.9 (s, 3 H, –$CH_3$), 2.4–3.5 (m, 24 H, cage –$CH_2$–), 3.6 (s, 4 H, 2 iminodiacetate –$CH_2$–). $^{13}$C NMR (75.5 MHz, $D_2O$): $\delta$ = 20.1 (–$CH_3$), 42.3 (C of methyl cage cap), 52.1 (cage –$CH_2$–), 52.5 (iminodiacetate –$CH_2$–), 54.4, 54.7, 55.2 (cage –$CH_2$–), 64.5 (C of amino cage cap), 176.8 (C=O). ES-MS: *m*/*z* = 243.64 [$C_{19}H_{39}CoN_7O_4$ – $H^+$]$^{2+}$, 486.21 [$C_{19}H_{39}CoN_7O_4$ – 2 $H^+$]$^+$, 522.22 [$C_{19}H_{39}CoN_7O_4$ – $H^+$ + $Cl^–$]$^+$. $C_{19}H_{43}Cl_3CoN_7O_6$ [(**3**)$Cl_3$·2$H_2O$, 630.88]: calcd. C 36.17, H 6.87, N 15.54; found C 36.49, H 6.52, N 15.70. Crystals of (**3**)$Cl_3$·2$H_2O$ suitable for an X-ray structure determination were grown by slow concentration of a 2 M $HCl_{(aq)}$ solution of the complex. The product from Band 2 was treated as above for Band 1 to give (**2**)$Cl_4$·$H_2O$ (1.26 g, 2.13 mmol) as orange crystals. $^1$H NMR (500 MHz, $D_2O$): $\delta$ = 0.93 (s, 3 H, –$CH_3$), 2.4–3.5 (m, 24 H, cage –$CH_2$–), 3.69 (AB q, 2 H, Gly –$CH_2$–). $^{13}$C NMR (126 MHz, $D_2O$): $\delta$ = 19.9 (–$CH_3$), 42.8 (C of methyl cage cap), 43.6 (Gly –$CH_2$–), 52.0, 55.1, 55.2, 55.3 (cage –$CH_2$–), 60.8 (C of amino cage cap), 172.5 (C=O). ES-MS: *m*/*z* = 464.21 [$C_{17}H_{37}CoN_7O_2$ – $H^+$ + $Cl^–$]$^+$, 428.23 [$C_{17}H_{37}CoN_7O_2$ – 2 $H^+$]$^+$, 500.16 [$C_{17}H_{37}CoN_7O_2$ + 2 $Cl^–$]$^+$. $C_{17}H_{40}Cl_4CoN_7O_3$ [(**2**)$Cl_4$·$H_2O$, 591.29]: calcd. C 34.53, H 6.82, N 16.58; found C 34.58, H 6.72, N 16.62. Crystals of (**2**)$Cl_4$·$H_2O$ suitable for an X-ray structure determination were grown by slow concentration of a 2 M $HCl_{(aq)}$ solution of the complex. The triflate of [Co(CH$_3$)(NHCH$_2$CO$_2$H)sar]$^{3+}$ was obtained by dissolution of the chloride in neat triflic acid at ca. 50 °C whilst a constant stream of $N_2$ was bubbled though the solution for at least 1 h. The orange solution thus obtained was then cooled on ice and $Et_2O$ added slowly with stirring to precipitate the triflate as a yellow-orange powder, which was collected by suction filtration and washed with copious quantities of $Et_2O$. The product from Band 3 was determined from $^1$H NMR spectroscopy to be the starting material (0.35 g, 0.67 mmol).

**[Co(CH$_3$)(Gly-NHCH$_2$CH$_2$S-)sar]$_2$(ClO$_4$)$_6$·HClO$_4$ (4)(ClO$_4$)$_6$·HClO$_4$:** [Co(CH$_3$)(NH$_2$CH$_2$CO$_2$H)sar](CF$_3$SO$_3$)$_4$ (0.60 g, 0.58 mmol) was dissolved in DMF (30 mL), and *N*-hydroxysuccinimide (0.067 g, 0.58 mmol) was added to the orange solution, followed by DIPEA (0.4 mL, 2.3 mmol) and EDC·HCl (1.0 g, 5.2 mmol) and the orange mixture was stirred for 10 min. Cystamine dihydrochloride (CSA·2HCl) (0.063 g, 0.28 mmol) was then added, causing a precipitate to form immediately, which redissolved after ca. 10 min to give an almost clear solution. The mixture was stirred for 24 h, during which time a white precipitate had formed. The reaction mixture was then diluted into water (500 mL) and applied to a column of $Na^+$ form SP Sephadex SP 25 resin, which was washed with water (500 mL), then elution was commenced with 0.05–0.2 M $Na_3Cit$, which began to remove four bands, the fourth by far the major component. Band 4 was treated with a concentrated aqueous solution of sodium picrate (NaPic), until the precipitation of a very fine bright yellow solid ceased. The precipitate was collected on a sintered glass frit, at first by gravity, and then suction filtration. This material was washed well with water, and the moist yellow solid obtained was then suspended in water (ca. 100 mL) containing ca. 3 mL of concd. $HClO_{4(aq)}$, and to this was added EtOAc and the mixture stirred vigorously. Stirring was stopped periodically and the top layer of EtOAc decanted off and replaced with fresh solvent, until all of the solid had dissolved, leaving an orange aqueous phase, which was subsequently transferred to a separating funnel and extracted with EtOAc until the organic phase was colourless. The aqueous phase was then concentrated in a rotary evaporator until precipitation of an orange solid

 © 2007 Wiley-VCH Verlag GmbH & Co. KGaA, Weinheim 

commenced, then placed on ice to complete the precipitation. The orange precipitate was collected on a sintered glass frit and washed with EtOH and then $Et_2O$ and air-dried to give (**4**)$(ClO_4)_6$·$HClO_4$ (0.32 g, 0.19 mmol). The sample was recrystallised from warm $H_2O$/EtOH by the addition of $Et_2O$. $^1H$ NMR 600 MHz, [$D_6$]-DMSO): $\delta$ = 0.8 (s, 6 H, 2 $–CH_3$), 2.20–2.48 and 2.85–3.15 (m, 48 H, 2 cage $–CH_2–$), 2.53 (t, ca. 2 H, 2 cage pendent –NH–), 2.79 (t, 4 H, 2 $–CH_2–$S), 3.18 (m, 4 H, 2 $Gly_1$ $–CH_2–$), 3.39 (q, 4 H, 2 CSA $–CH_2–$N), 6.5 (br., 12 H, cage –NH–), 7.95 (t, 2 H, 2 CSA amide NH). $^{13}C$ NMR (151 MHz, [$D_6$]DMSO): $\delta$ = 19.5 ($–CH_3$), 37.0 (CSA $–CH_2–$S), 37.8 (CSA $–CH_2–$N), 42.1 (C of methyl cage cap), 44.3 ($Gly_1$ $–CH_2–$), 52.0, 53.5, 54.0, 54.2 (cage $–CH_2–$), 60.3 (C of amino cage cap), 171.0 (C=O). ES-MS: *m/z* = 486.22 [$C_{38}H_{82}Co_2N_{16}O_2S_2$ – 4 $H^+$]$^{2+}$. $C_{38}H_{83}Cl_7Co_2N_{16}O_{30}S_2$ [(**4**)$(ClO_4)_6$·$HClO_4$, 1674.32]: calcd. C 27.26, H 5.00, N 13.38; found C 27.43, H 5.38, N 13.31.

**[Co($CH_3$)(Gly-Gly-$NHCH_2CH_2S$-)sar]$_2(ClO_4)_6$·$HClO_4$·0.5$H_2O$ (5)-$(ClO_4)_6$·$HClO_4$·0.5$H_2O$:** [Co($CH_3$)($NH_2CH_2CO_2H$)sar]$(CF_3SO_3)_4$ (0.80 g, 0.78 mmol) was dissolved in DMF (20 mL), and DIPEA (0.14 mL, 0.80 mmol) added, followed by *N*-hydroxysuccinimide (0.138 g, 1.20 mmol), followed by HBTU (0.445 g, 1.17 mmol) and the orange solution was stirred for 20 min. In a separate round-bottomed flask, Boc-Gly-CSA (0.177 g, 0.380 mmol) was dissolved in $CH_2Cl_2$ (3 mL) containing TFA (1.5 mL) and the solution stirred for 1 h, during which time, an oily material separated from the mixture. The solvents were removed under reduced pressure, and the oily residue redissolved in DMF (6 mL) containing an excess of DIPEA (0.36 mL), and then added to the orange cage solution, which was then stirred at room temp. for 18 h. The workup procedure was identical to that of compound **4** above, to give (**5**)-$(ClO_4)_6$·$HClO_4$·0.5$H_2O$ as an orange solid (0.43 g, 0.24 mmol). The sample was recrystallised from warm $H_2O$ by the addition of EtOH, to give an orange oil which solidified upon standing at room temp. for several hours. $^1H$ NMR (600 MHz, [$D_6$]DMSO): $\delta$ = 0.80 (s, 6 H, 2 $–CH_3$), 2.20–2.50 and 2.85–3.15 (m, 48 H, 2 cage $–CH_2–$), 2.60 (t, 2 H, 2 cage pendent –NH–), 2.76 (t, 4 H, 2 $–CH_2–$S), 3.21 (dq, 4 H, 2 $Gly_1$ $–CH_2–$), 3.36 (m, 4 H, 2 CSA $–CH_2–$N), 3.73 (d, 4 H, 2 $Gly_2$ $–CH_2–$), 6.51 (br. s, 6 H, 2 cage NH), 6.56 (br. s, 6 H, 2 cage NH), 8.00 (t, 2 H, 2 $Gly_2$ amide NH), 8.08 (t, 2 H, 2 CSA amide NH). $^{13}C$ NMR (151 MHz, [$D_6$]DMSO): $\delta$ = 19.5 ($–CH_3$), 36.9 (CSA $–CH_2–$S), 38.0 (CSA $–CH_2–$N), 41.5 ($Gly_2$ $–CH_2–$), 42.1 (C of methyl cage cap), 44.3 ($Gly_1$ $–CH_2–$), 52.1, 53.6, 54.0, 54.1 (cage $–CH_2–$), 60.3 (C of amino cage cap), 168.9, 171.2 (C=O). ES-MS: *m/z* = 362.51 [$C_{42}H_{88}Co_2N_{18}O_4S_2$ – 3 $H^+$]$^{3+}$, 395.83 [$C_{42}H_{88}Co_2N_{18}O_4S_2$ – 2 $H^+$ + $ClO_4^-$]$^{3+}$, 272.13 [$C_{42}H_{88}Co_2N_{18}O_4S_2$ – 2 $H^+$]$^{4+}$, 543.25 [$C_{42}H_{88}Co_2N_{18}O_4S_2$ – 4 $H^+$]$^{2+}$. $C_{42}H_{90}Cl_7Co_2N_{18}O_{32.5}S_2$ [(**5**)$(ClO_4)_6$·$HClO_4$·0.5$H_2O$, 1797.43]: calcd. C 28.06, H 5.05, N 14.03; found C 28.14, H 5.43, N 13.99.

**[Co($CH_3$)(Gly-Ala-$NHCH_2CH_2S$-)sar]$_2(ClO_4)_6$·$HClO_4$·$H_2O$ (6)-$(ClO_4)_6$·$HClO_4$·$H_2O$:** The procedure used was the same as that for compound **5** above. From [Co($CH_3$)($NH_2CH_2CO_2H$)sar]-$(CF_3SO_3)_4$ (0.86 g, 0.84 mmol), DMF (15 mL), DIPEA (0.15 mL, 0.86 mmol + 0.5 mL, 3 mmol), *N*-hydroxysuccinimide (0.11 g, 0.96 mmol), HBTU (0.35 g, 0.92 mmol), Boc-Ala-CSA (0.20 g, 0.40 mmol), was obtained (**6**)$(ClO_4)_6$·$HClO_4$·$H_2O$ (0.36 g, 0.20 mmol). The sample was recrystallised from warm $H_2O$ by the addition of EtOH. $^1H$ NMR (600 MHz, [$D_6$]DMSO): $\delta$ = 0.79 (s, 6 H, 2 cage $–CH_3$), 1.22 (d, 6 H, 2 Ala $–CH_3$), 2.20–2.50 and 2.85–3.15 (m, 48 H, 2 cage $–CH_2–$), 2.56 (AB q, 2 H, 2 cage pendent –NH–), 2.76 (m, 4 H, 2 $–CH_2–$S), 3.17 (m, 4 H, 2 $Gly_1$ $–CH_2–$), 3.25–3.50 (m, 4 H, 2 CSA $–CH_2–$N), 4.28 [sext, 2 H, $Ala_2$ –CHα–), 6.51 (br. s, 6 H, 2 cage –NH–), 6.56 (br. s, 6 H, 2 cage –NH–), 7.85 (d, 2 H, 2 $Ala_2$ amide NH), 8.16 (t, 2 H, 2 CSA amide NH). $^{13}C$ NMR (151 MHz, [$D_6$]DMSO): $\delta$ = 18.9 (Ala $–CH_3$), 19.5 (cage $–CH_3$), 36.9 (CSA $–CH_2–$S), 37.9 (CSA $–CH_2–$N), 42.0 (C of methyl cage cap), 44.4 ($Gly_1$ $–CH_2–$), 47.7 ($Ala_2$ –CHα–), 52.2, 53.6, 53.9, 54.0 (cage $–CH_2–$), 60.2 (C of amino cage cap), 170.1, 172.1 (C=O). Note: Some peaks were doubled due to the presence of *meso* and *rac* compounds but these doubled peaks are reported with a single chemical shift in order to simplify the analysis of the spectra. ES-MS: *m/z* = 371.85 [$C_{44}H_{92}Co_2N_{18}O_4S_2$ – 3 $H^+$]$^{3+}$, 557.27 [$C_{44}H_{92}Co_2N_{18}O_4S_2$ – 4 $H^+$]$^{2+}$. $C_{44}H_{95}Cl_7Co_2N_{18}O_{33}S_2$ [(**6**)$(ClO_4)_6$·$HClO_4$·$H_2O$, 1834.49]: calcd. C 28.81, H 5.22, N 13.74; found C 28.82, H 5.41, N 13.69.

**[Co($NH_2$)(Gly-$NHCH_2CH_2S$-)sar]$_2(ClO_4)_6$·$HClO_4$·2$H_2O$ (7)-$(ClO_4)_6$·$HClO_4$·2$H_2O$:** The procedure used was the same as that for compound **4** above. From [Co($NH_3$)($NH_2CH_2CO_2H$)-sar]$(CF_3SO_3)_5$ (2.55 g, 2.16 mmol), DMF (15 mL), DIPEA (0.76 mL, 4.4 mmol + 0.5 mL, 3 mmol), *N*-hydroxysuccinimide (1.01 g, 8.8 mmol), EDC·HCl (1.7 g, 8.9 mmol), CSA·2HCl (0.22 g, 1.0 mmol), was obtained (**7**)$(ClO_4)_6$·$HClO_4$·2$H_2O$ (0.45 g, 0.26 mmol). The sample was recrystallised from warm $H_2O$ by the addition of EtOH. $^1H$ NMR (600 MHz, [$D_6$]DMSO): $\delta$ = 1.72 (br., 4 H, 2 $–NH_2$), 2.25–2.50 and 2.75–3.20 (m, 48 H, 2 cage $–CH_2–$), 2.53 (t, 1 H, 2 $Gly_1$ –NH–), 2.79 (t, 4 H, 2 $–CH_2–$S), 3.16 (m, 4 H, 2 $Gly_1$ $–CH_2–$), 3.39 (q, 4 H, 2 CSA $–CH_2–$N), 6.53 (br. s, 6 H, 2 cage NH), 6.59 (br. s, 6 H, 2 cage NH), 7.95 (t, 2 H, 2 CSA amide NH). $^{13}C$ NMR (151 MHz, [$D_6$]DMSO): $\delta$ = 37.0 ($–CH_2–$S), 37.7 (CSA $–CH_2–$N), 44.3 ($Gly_1$ $–CH_2–$), 52.1, 54.0, 54.1, 54.5 (cage $–CH_2–$), 56.9, 60.3 (cage C), 170.9 ($Gly_1$ C=O). ES-MS: *m/z* = 325.15 [$C_{36}H_{80}Co_2N_{18}O_2S_2$ – 3 $H^+$]$^{3+}$, 244.12 [$C_{36}H_{80}Co_2N_{18}O_2S_2$ – 2 $H^+$]$^{4+}$, 487.22 [$C_{36}H_{80}Co_2N_{18}O_2S_2$ – 4 $H^+$]$^{2+}$, 358.47 [$C_{36}H_{80}Co_2N_{18}O_2S_2$ – 2 $H^+$ + $ClO_4^-$]$^{3+}$. $C_{36}H_{85}Cl_7Co_2N_{18}O_{32}S_2$ [(**7**)$(ClO_4)_6$·$HClO_4$·2$H_2O$, 1712.33]: calcd. C 25.25, H 5.00, N 14.72; found C 25.44, H 4.87, N 14.57.

**Δ-[Co($NH_2$)(Gly-$NHCH_2CH_2S$-)sar]$_2(ClO_4)_6$·$HClO_4$·2$H_2O$ (8)-$(ClO_4)_6$·$HClO_4$·2$H_2O$:** The procedure used was the same as that for compound **4** above. From [Co($NH_3$)($NH_2CH_2CO_2H$)sar]$Cl_5$·3$H_2O$ (0.50 g, 0.75 mmol), DMF (15 mL), DIPEA (0.26 mL, 1.5 mmol + 0.5 mL, 3 mmol), *N*-hydroxysuccinimide (0.17 g, 1.5 mmol), EDC·HCl (0.29 g, 1.5 mmol), CSA·2HCl (0.084 g, 0.37 mmol), was obtained (**8**)$(ClO_4)_6$·$HClO_4$·2$H_2O$ (0.42 g, 0.24 mmol). The sample was recrystallised from warm $H_2O$ by the addition of EtOH. $^1H$ NMR (600 MHz, [$D_6$]DMSO): $\delta$ = 2.40–2.65 and 2.90–3.35 (m, 48 H, 2 cage $–CH_2–$), 2.79 (t, 4 H, 2 $–CH_2–$S), 3.17 (m, 4 H, 2 $Gly_1$ $–CH_2–$), 3.41 (q, 4 H, 2 CSA $–CH_2–$N), 6.57 (br. s, 6 H, 2 cage –NH–), 6.84 (br. s, 6 H, 2 cage –NH–), 7.97 (t, 2 H, 2 CSA amide NH), 8.36 (br. s, 4 H, 2 free $–NH_2$). $^{13}C$ NMR (151 MHz, [$D_6$]-DMSO): $\delta$ = 36.9 (CSA $–CH_2–$S), 37.8 (CSA $–CH_2–$N), 44.3 ($Gly_1$ $–CH_2–$), 50.9, 52.1, 53.6 (2 C) (cage $–CH_2–$), 55.6, 60.5 (C), 170.2 (C=O). ES-MS: *m/z* = 244.16 [$C_{36}H_{80}Co_2N_{18}O_2S_2$ – 2 $H^+$]$^{3+}$, 358.51 [$C_{36}H_{80}Co_2N_{18}O_2S_2$ – 2 $H^+$ + $ClO_4^-$]$^{3+}$. $C_{36}H_{85}Cl_7Co_2N_{18}O_{32}S_2$ [(**8**)$(ClO_4)_6$·$HClO_4$·2$H_2O$, 1712.33]: calcd. C 25.25, H 5.00, N 14.72; found C 24.99, H 5.02, N 14.35.

**Δ-[Co($NH_2$)(Gly-Gly-$NHCH_2CH_2S$-)sar]$_2(ClO_4)_6$·4$HClO_4$ (9)-$(ClO_4)_6$·4$HClO_4$:** The procedure used was the same as that for compound **5** above. From [Co($NH_3$)($NH_2CH_2CO_2H$)sar]$Cl_5$·3$H_2O$ (0.50 g, 0.75 mmol), DMF (15 mL), DIPEA (0.26 mL, 1.5 mmol + 0.5 mL, 3 mmol), *N*-hydroxysuccinimide (0.17 g, 1.5 mmol), EDC·HCl (0.29 g, 1.5 mmol), Boc-Gly-CSA (0.17 g, 0.36 mmol), was obtained (**9**)$(ClO_4)_6$·4$HClO_4$ (0.21 g, 0.10 mmol). The sample was recrystallised from warm $H_2O$ by the addition of EtOH. $^1H$ NMR (600 MHz, [$D_6$]DMSO): $\delta$ = 2.40–2.70 and 2.90–3.35 (m, 48 H, 2 cage $–CH_2–$), 2.76 (t, 4 H, 2 $–CH_2–$S), 3.24 (s, 4 H, 2 $Gly_1$ $–CH_2–$), 3.36 (q, 4 H, 2 CSA $–CH_2–$N), 3.74 (d, 4 H, 2 $Gly_2$

 © 2007 Wiley-VCH Verlag GmbH & Co. KGaA, Weinheim 

–$CH_2$–), 6.59 (br. s, 6 H, 2 cage –NH–), 6.85 (br. s, 6 H, 2 cage –NH–), 8.01 (s, 2 H, 2 $Gly_2$ amide NH), 8.11 (t, 2 H, 2 CSA amide NH), 8.41 (br. s, 4 H, 2 free $–NH_2$). $^{13}C$ NMR (151 MHz, [$D_6$]DMSO): $\delta$ = 36.9 (CSA $–CH_2–S$), 37.9 (CSA $–CH_2–N$), 41.6 ($Gly_2$ $–CH_2–$), 44.3 ($Gly_1$ $–CH_2–$), 50.9, 52.1, 53.4 (2 C) (cage $–CH_2–$), 55.5, 60.4 (C), 168.7, 170.6 (C=O). ES-MS: *m*/*z* = 544.24 $[C_{40}H_{86}Co_2N_{20}O_4S_2 – 4\ H^+]^{2+}$. $C_{40}H_{90}Cl_{10}Co_2N_{20}O_{44}S_2$ [(**9**)$(ClO_4)_6$·4$HClO_4$, 2091.78]: calcd. C 22.97, H 4.34, N 13.39; found C 23.20, H 4.47, N 13.38.

**Δ-[Co($NH_2$)(Gly-Ala-NH$CH_2CH_2$S-)sar]$_2$($ClO_4$)$_6$·2$HClO_4$·$H_2O$ (10)($ClO_4$)$_6$·2$HClO_4$·$H_2O$:** The procedure used was the same as that for compound **5** above. From [Co($NH_3$)($NH_2CH_2CO_2H$)-sar]($CF_3SO_3$)$_5$ (1.00 g, 0.85 mmol), DMF (15 mL), DIPEA (0.30 mL, 1.7 mmol + 0.50 mL, 3 mmol), *N*-hydroxysuccinimide (0.11 g, 0.96 mmol), HBTU (0.35 g, 0.92 mmol), Boc-Ala-CSA (0.20 g, 0.40 mmol), was obtained (**10**)$(ClO_4)_6$·2$HClO_4$·$H_2O$ (0.42 g, 0.22 mmol). The sample was recrystallised from warm $H_2O$ by the addition of EtOH. $^1H$ NMR (600 MHz, [$D_6$]DMSO): $\delta$ = 1.22 (d, 6 H, 2 Ala $–CH_3$), 2.40–2.70 and 2.85–3.40 (m, 48 H, 2 cage $–CH_2–$), 2.76 (m, 4 H, 2 $–CH_2–S$), 3.17 (AB q, 4 H, 2 $Gly_1$ $–CH_2–$), 3.25–3.45 (m, 4 H, 2 CSA $–CH_2–N$), 4.30 (quint, 2 H, 2 $Ala_2$ –CHα–), 6.54 (br. s, 6 H, 2 cage –NH), 6.80 (br. s, 6 H, 2 cage –NH), 7.85 (d, 2 H, 2 $Ala_2$ amide NH), 8.20 (t, 2 H, 2 CSA amide NH), 8.41 (br. s, 4 H, 2 free $–NH_2$). $^{13}C$ NMR (151 MHz, [$D_6$]DMSO): $\delta$ = 19.00 ($Ala_2$ $–CH_3$), 36.92 (CSA $–CH_2–S$), 37.87 (CSA $–CH_2–N$), 44.47 ($Gly_1$ $–CH_2–$), 47.73 ($Ala_2$ –CHα–), 51.20, 52.32, 53.28 (cage $–CH_2–$), 55.62, 60.34 (cage C), 169.90, 172.12 (C=O). ES-MS: *m*/*z* = 372.51 $[C_{42}H_{90}Co_2N_{20}O_4S_2 – 3\ H^+]^{3+}$, 279.64 $[C_{42}H_{90}Co_2N_{20}O_4S_2 – 2\ H^+]^{4+}$. $C_{42}H_{94}Cl_8Co_2N_{20}O_{37}S_2$ [(**10**)$(ClO_4)_6$·2$HClO_4$·$H_2O$, 1936.93]: calcd. C 26.04, H 4.89, N 14.46; found C 26.24, H 5.01, N 14.28.

## Acknowledgments

We thank the University of Western Australia for partial funding of this research and NSERC for financial support. H.-B. K. is the Canadian Research Chair in Biomaterials. G. L. N. was the holder of an Australian Postgraduate Award. We also thank Dr. Dimitre Karpuzov, University of Alberta, for the XPS measurements.

[1] J. C. Love, L. A. Estroff, J. K. Kriebel, R. G. Nuzzo, G. M. Whitesides, *Chem. Rev.* **2005**, *105*, 1103.
[2] M.-C. Daniel, D. Astruc, *Chem. Rev.* **2004**, *104*, 293.
[3] A. M. Sargeson, *Pure Appl. Chem.* **1986**, *58*, 1511.
[4] A. M. Sargeson, *Coord. Chem. Rev.* **1996**, *151*, 89.
[5] M. H. Jensen, P. Osvath, A. M. Sargeson, J. Ulstrup, *J. Electroanal. Chem.* **1994**, *377*, 131.
[6] J. T. Hupp, H. Y. Liu, P. A. Lay, W. H. F. Petri, A. M. Sargeson, M. J. Weaver, *J. Electroanal. Chem. Interfacial Electrochem.* **1984**, *163*, 371.
[7] I. I. Creaser, A. Hammershoei, A. Launikonis, A. W. H. Mau, A. M. Sargeson, W. H. F. Sasse, *Photochem. Photobiol.* **1989**, *49*, 19.
[8] C. Konigstein, A. W. H. Mau, P. Osvath, A. M. Sargeson, *Chem. Commun.* **1997**, 423.
[9] A. Launikonis, P. A. Lay, A. W. H. Mau, A. M. Sargeson, W. H. F. Sasse, *Sci. Pap. Inst. Phys. Chem. Res. (Jpn.)* **1984**, *78*, 198.
[10] A. W. H. Mau, W. H. F. Sasse, I. I. Creaser, A. M. Sargeson, *Nouv. J. Chim.* **1986**, *10*, 589.
[11] L. R. Gahan, T. W. Hambley, A. M. Sargeson, M. R. Snow, *Inorg. Chem.* **1982**, *21*, 2699.
[12] S. Burnet, M.-H. Choi, P. S. Donnelly, J. M. Harrowfield, I. Ivanova, S.-H. Jeong, Y. Kim, M. Mocerino, B. W. Skelton, A. H. White, C. C. Williams, Z.-L. Zeng, *Eur. J. Inorg. Chem.* **2001**, 1869.
[13] A. S. Paxinos, H. Gunther, D. J. M. Schmedding, H. Simon, *Bioelectrochem. Bioenerg.* **1991**, *25*, 425.
[14] J. M. Harrowfield, G. A. Koutsantonis, G. L. Nealon, B. W. Skelton, A. H. White, *Eur. J. Inorg. Chem.* **2005**, 2384.
[15] G. W. Walker, R. J. Geue, A. M. Sargeson, C. A. Behm, *Dalton Trans.* **2003**, 2992.
[16] P. S. Donnelly, J. M. Harrowfield, B. W. Skelton, A. H. White, *Inorg. Chem.* **2000**, *39*, 5817.
[17] M. Bodanszky, A. Bodanszky, *The Practice of Peptide Synthesis*, 2nd ed., Springer Verlag, Berlin, **1994**.
[18] G. A. Orlowski, S. Chowdhury, Y.-T. Long, T. C. Sutherland, H.-B. Kraatz, *Chem. Commun.* **2005**, 1330.
[19] H.-B. Kraatz, *J. Inorg. Organomet. Polym.* **2005**, *15*, 83.
[20] D. W. Conrad, H. Zhang, D. E. Stewart, R. A. Scott, *J. Am. Chem. Soc.* **1992**, *114*, 9909.
[21] P. S. Donnelly, J. M. Harrowfield, *J. Chem. Soc., Dalton Trans.* **2002**, 906.
[22] S. F. Ralph, M. M. Sheil, L. A. Hick, R. J. Geue, A. M. Sargeson, *J. Chem. Soc., Dalton Trans.* **1996**, 4417.
[23] J. M. Harrowfield, *Supramol. Chem.* **2006**, *18*, 125 and references cited therein.
[24] A. M. Bond, G. A. Lawrance, P. A. Lay, A. M. Sargeson, *Inorg. Chem.* **1983**, *22*, 2010.
[25] K. V. Gobi, T. Okajima, K. Tokuda, T. Ohsaka, *Langmuir* **1998**, *14*, 1108.
[26] A. Ulman, *Chem. Rev.* **1996**, *96*, 1533 and references cited therein.
[27] A. J. Bard, L. R. Faulkner, *Electrochemical Methods*, 2nd ed., John Wiley & Sons, New York, **2001**.
[28] I. Bediako-Amoa, T. C. Sutherland, C.-Z. Li, R. Silerova, H.-B. Kraatz, *J. Phys. Chem. B* **2004**, *108*, 704.
[29] E. Laviron, *J. Electroanal. Chem.* **1979**, *100*, 263.
[30] H. Matsuda, K. Aoki, K. Tokuda, *J. Electroanal. Chem.* **1987**, *217*, 15.
[31] T. Ishida, N. Choi, W. Mizutani, H. Tokumoto, I. Kojima, H. Azehara, H. Hokari, U. Akiba, M. Fujihira, *Langmuir* **1999**, *15*, 6799.
[32] A. A. Achilleos, L. R. Gahan, T. W. Hambley, P. C. Healy, D. M. Weedon, *Inorg. Chim. Acta* **1989**, *157*, 209.
[33] Y. Okamoto, H. Nakano, T. Imanaka, S. Teranishi, *Bull. Chem. Soc. Jpn.* **1975**, *48*, 1163.
[34] R. J. Geue, T. W. Hambley, J. M. Harrowfield, A. M. Sargeson, M. R. Snow, *J. Am. Chem. Soc.* **1984**, *106*, 5478.
[35] S. Chowdhury, G. Schatte, H.-B. Kraatz, *Dalton Trans.* **2004**, 1726.
[36] S. R. Hall, D. J. Du Boulay, R. E. Olthof-Hazekamp, XTAL 3.7, The University of Western Australia, **2001**.

Received: May 3, 2006
Published Online: November 9, 2006

 © 2007 Wiley-VCH Verlag GmbH & Co. KGaA, Weinheim 

DOI: 10.1002/ejic.200600737

# Thiocyanate Functionalised Ionic Liquids: Synthesis, Characterisation and Reactivity

**Dongbin Zhao,[a] Zhaofu Fei,[a] Wee Han Ang,[a] Rosario Scopelliti,[a] and Paul J. Dyson*[a]**

**Keywords:** Ionic liquids / Thiocyanate / Palladium complexes / Imidazolium salts

The reaction of chloromethyl thiocyanate with 1-methylimidazole affords the imidazolium salt, 1-thiocyanomethyl-3-methylimidazolium chloride, [$C_1$SCNmim]Cl (**1a**). Exchange of the chloride anion in **1a** by $[PF_6]^-$, $[BF_4]^-$, $[Tf_2N]^-$ or $[AuCl_4]^-$ affords salts **1b**, **1c**, **1d** and **1e**, respectively. Salts [$C_1$SCNmim][$BF_4$] (**1c**) and [$C_1$SCNmim][$Tf_2N$] (**1d**) melt below 100 °C and can therefore be classified as ionic liquids. The reaction of **1a** with $PdCl_2$ affords [$C_1$SCNmim]$_2$[$PdCl_4$] (**2a**), whereas **1c** reacts with $PdCl_2$ to form the complex [$PdCl_2${$C_1$SCNmim}$_2$][$BF_4$]$_2$ (**2c**). In the presence of $HNO_3$ both **1a** and **1c** react with $PdCl_2$ with the loss of HCN to form a sulfide-bridged palladium dimer [$PdCl_2${$C_1$Smim}]$_2$ (**3**). The structures of **1a**, **1e**, **2a** and **3** have been determined in the solid state by single-crystal X-ray diffraction.
(© Wiley-VCH Verlag GmbH & Co. KGaA, 69451 Weinheim, Germany, 2007)

## Introduction

Ionic liquids incorporating functional groups on the cation and/or anion have started to receive extensive attention as media for a wide range of applications, in particular in homogeneous and heterogeneous catalysis, but also in material science.[1] In certain instances, when a functional group is incorporated into an ionic liquid structure, highly specific properties are imparted to the liquid, and in such cases these functional ionic liquids are often referred to as task-specific ionic liquids.[2] Many different functional groups have already been incorporated onto ionic liquid cations, for example, alkenes,[3–5] alkynes,[6,7] amines,[8] amides,[9] ethers, alcohols,[10] acids,[11] thiols,[12–14] urea and thiourea,[2] fluorous chains,[15] glycidyl chains,[16] phosphoryl,[17] and ferrocenyl groups.[18] In addition, ionic liquids with functional anions have also been reported, for example, with transition metal carbonyl anions,[19,20] perfluoroalkyl-[21] and nitrile-functionalised[22] trifluoroborate anions, as well as numerous others.[23]

We have previously reported the synthesis, characterisation and reactivity of ionic liquids carrying the nitrile functionality based on both imidazolium[24] and pyridinium[25] cations. It was shown that the nitrile-functionalised ionic liquids were excellent solvents for conducting Suzuki and Stille coupling reactions employing $PdCl_2$ as a precatalyst.[26] While the nitrile group was shown to coordinate to the palladium(II) centre following dissolution in the ionic liquids, it was found that under the catalytic conditions palladium nanoparticles formed. Transmission electron microscopy (TEM) revealed the presence of nanoparticles with a typical diameter of 5 nm and the nanoparticles showed superior stability to those isolated from nonfunctionalised ionic liquids. Thus, we thought that it might be interesting to see if related thiocyanate ionic liquids could be prepared and used in a similar fashion and in this paper we describe the synthesis, characterisation and the reactivity of a series of imidazolium ionic liquids incorporating the thiocyanate functionality.

## Results and Discussion

The synthetic route used to prepare the thiocyanate-functionalised imidazolium salts described herein is illustrated in Scheme 1. In the first step chloromethyl thiocyanate and 1-methylimidazole are stirred at 0 °C in acetone to afford the new imidazolium salt, [$C_1$SCNmim]Cl (**1a**). The product precipitates from the reaction and is obtained as a fine colourless microcrystalline material following filtration and washing.

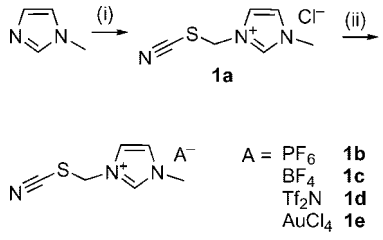


Scheme 1. Synthesis of thiocyanate-functionalised imidazolium salts; Reagents and conditions: (i) $ClCH_2SCN$, acetone, 0 °C; (ii) $HPF_6$, Li[$Tf_2N$] or $HAuCl_4$ in water, $NaBF_4$ in acetone, room temp.

[a] Institut des Sciences et Ingénierie Chimiques, Ecole Polytechnique Fédérale de Lausanne (EPFL),
1015 Lausanne, Switzerland
E-mail: paul.dyson@epfl.ch

 © 2007 Wiley-VCH Verlag GmbH & Co. KGaA, Weinheim 

Single crystals of **1a** suitable for X-ray diffraction analysis were grown by slow diffusion of diethyl ether into a saturated acetonitrile solution of the compound at room temperature. The structure of **1a** that corroborates the spectroscopic data obtained in solution (see below) is shown in Figure 1 with key bond parameters given in the caption. The imidazolium ring is almost perfectly planar, bond angles in the rings range from 106.7(2) to 107.6(2)° and distances from 1.331(3) to 1.379(3) Å. The –S–C≡N moiety is essentially linear with a C–N distance of 1.147(3) Å, which is in the expected range.

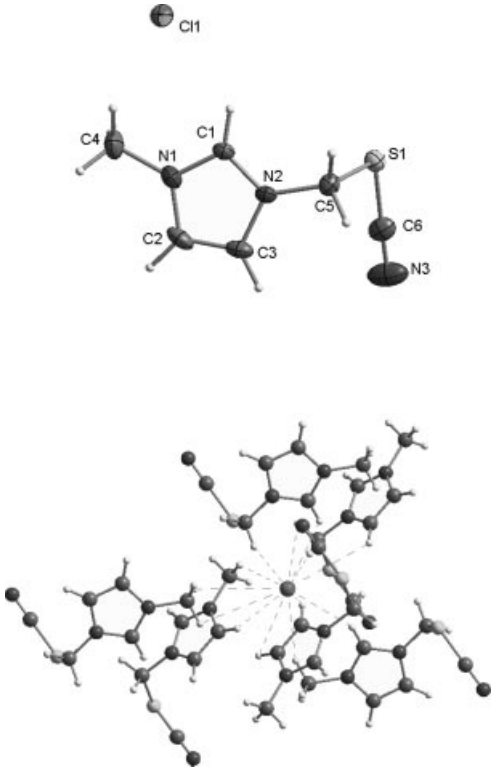


Figure 1. ORTEP representation of **1a** (top) and its packing diagram (bottom) indicating the positions of the imidazolium cations with respect to the chloride anion; atoms are represented by ellipsoids at the 50% probability level. Key bond lengths [Å] and angles [°]: C1–N1, 1.331(3); C1–N2, 1.338(3); N1–C4, 1.468(3); N2–C5, 1.453(3); C5–S1, 1.825(2); S1–C6, 1.704(3); C6–N3, 1.147(3); N1–C1–N2, 107.6(2); C1–N1–C4, 124.8(2); C1–N2–C5, 125.0(2); N2–S1–C6, 113.1(2); C5–S1–C6, 98.4(2); S1–C6–N3, 177.7(2).

The lattice of **1a** is characterised by extensive H bonding between the imidazolium cations and the chloride anion (see Figure 1 for **1a**), resulting in a compact structure held together by short contacts.

Subsequent reaction of **1a** with $HPF_6$, $NaBF_4$, $LiTf_2N$ [$Tf_2N$ = bis(trifluoromethanesulfonyl)imide] or $HAuCl_4$ in water or acetone affords [$C_1$SCNmim][$PF_6$] (**1b**), [$C_1$SCNmim][$BF_4$] (**1c**), [$C_1$SCNmim][$Tf_2N$] (**1d**) and [$C_1$SCNmim][$AuCl_4$] (**1e**), respectively (see Scheme 1). Salts **1b**–**1e** are all solids at room temperature with melting points of 120, 78, 47 and 150 °C, respectively, and thus **1c** and **1d** can be considered as ionic liquids on the basis of the widely accepted definition.[26]

Salts **1a**–**1e** were characterised using electrospray ionisation mass spectrometry (ESI-MS) and IR, $^1$H NMR and $^{13}$C NMR spectroscopy. The positive ion ESI mass spectra of **1a**–**1e** in methanol disclose a parent peak at *m*/*z* = 154 corresponding to the cation [$C_1$SCNmim]$^+$. In the negative ion mode intense peaks corresponding to the anticipated anions in **1a**–**1e** are observed. In keeping with previous observations, aggregates are also observed but dissipate when the spectra are recorded under high dilution conditions.[21]

The main feature in the IR spectra of **1a**–**1e** is the characteristic –S–C≡N vibrations. For **1a**, the stretching vibrations of C–S and C≡N bands are observed at 730 and 2159 cm$^{-1}$, respectively. For **1b**–**1e**, the C–S vibrations are essentially the same, however, the C≡N vibration shifts to higher wavenumbers, ca. 2169 cm$^{-1}$. The $^1$H and $^{13}$C NMR spectra of **1a**–**1e** in $CD_3CN$ or [$D_6$]DMSO are as expected with little change in the spectra as the anion is varied. The proton at the 2-position in the imidazolium ring is observed at 9.05 pm for compound **1a** in $D_2O$ solution. Compounds **1b**, **1c** and **1d** are poorly soluble in $D_2O$, the chemical shifts of the proton at the 2-position are 8.63, 8.72 and 8.78 ppm

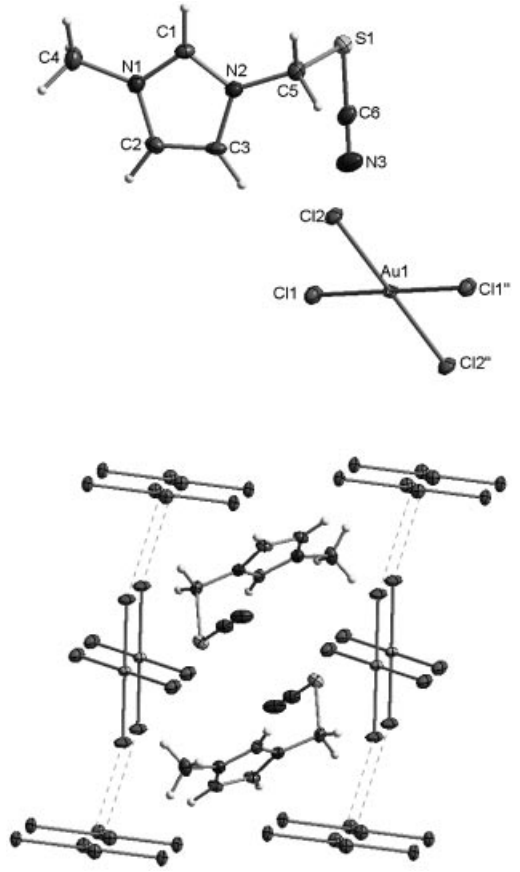


Figure 2. ORTEP representation of **1e** (top) and its packing diagram (bottom); atoms are represented by ellipsoids at the 50% probability level. Key bond lengths [Å] and angles [°]: C1–N1, 1.329(4); C1–N2, 1.334(4); N1–C4, 1.472(4); N2–C5, 1.453(4); C5–S1, 1.840(3); S1–C6, 1.698(3); C6–N3, 1.149(4); Au1–$Cl_{ave}$, 2.290(2); N1–C1–N2, 108.0(3); C1–N1–C4, 125.5(3); C1–N2–C5, 125.0(3); N2–S1–C6, 112.3(2); C5–S1–C6, 96.6(2); S1–C6–N3, 177.9(3).

 © 2007 Wiley-VCH Verlag GmbH & Co. KGaA, Weinheim 

in $CD_3CN$, respectively. The other ring protons have chemical shifts between 7.4 and 7.6 ppm. The $-CH_3$ and $-CH_2-$ protons exhibit peaks at ca. 5.70 and 3.90 ppm, respectively, and these values differ only slightly as the anion varies from **1a** to **1d**.

Single crystals of the $AuCl_4^-$ **1e** compound suitable for X-ray crystallographic analyses were obtained from aqueous solutions by slow evaporation. The structure of **1e** is shown in Figure 2 and key bond parameters are given in the caption. The solid-state structures of the related salts $[C_2mim][AuCl_4]$ and $[C_4mim][AuCl_4]$ have previously been reported[27] and the crystal structure of complex **1e** is very similar to these earlier reported salts, i.e. forming a pseudo-rhombic structure with the imidazolium cation encased within a box composed of the $[AuCl_4]^-$ anions. In addition, the Au–Cl bond lengths within the square planar $[AuCl_4]^-$ anion and the intermolecular $Cl\cdots AuCl_4$ distance [3.445(1) Å] are comparable to those in $[C_2mim][AuCl_4]$ and $[C_4mim][AuCl_4]$ [3.356(3) and 3.452(3) Å, respectively].

### Reactivity of the Thiocyanate-Functionalised Ionic Liquids with Palladium(II) Chloride

A dichloromethane solution of **1a** was treated with 0.5 equiv. $PdCl_2$, affording $[C_1SCNmim]_2[PdCl_4]$ (**2a**) as shown in Scheme 2. The reaction requires several days to reach completion, presumably because of the low solubility of **1a** and $PdCl_2$ in this solvent. Related compounds containing the $[PdCl_4]^{2-}$ with other imidazolium cations have previously been reported.[26,28] In contrast to the chloride salt, the tetrafluoroborate salt (**1c**) reacts with $PdCl_2$ in dichloromethane at room temperature to form $[PdCl_2\{C_1SCNmim\}_2][BF_4]_2$ (**2c**).

Both of the palladium compounds have been characterised by $^1H$ and $^{13}C$ NMR spectroscopy, although this provided only limited information. A comparison of their IR spectra was, however, very informative; the stretching vibration of the C≡N group remains essentially unchanged in **2a**, relative to the imidazolium precursor **1a**, whereas in **2c**, the $\upsilon_{C\equiv N}$ stretching band is observed at a higher wavenumber, 2219 $cm^{-1}$, indicating coordination of the nitrile

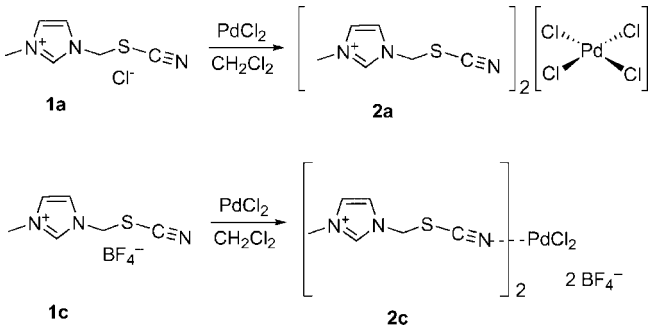


Scheme 2. Synthesis of complexes **2a** and **2c**.

group to the palladium(II) centre. Single crystals of **2a** suitable for X-ray diffraction analysis were grown from aqueous solution by slow evaporation and the structure of **2a** is shown in Figure 3, and key bond parameters are given in the caption. Indeed, the CN moieties do not interact with the Pd centre, instead the S atoms of the thiocyanate moiety are directed towards the Pd centre with a Pd···S distance of 3.513(1) Å. A common feature of square-planar $Pd^{II}$ and $Pt^{II}$ complexes in the solid state is long interactions in the axial positions so as to form pseudo-octahedral structures.[29]

The thiocyanate group is relatively reactive and the cleavage of the carbon–sulfur bond can occur in both acidic and basic media[30] such that the resulting mercaptan anion can potentially coordinate to a metal centre. Accordingly, the reaction of **1a** or **1c** with $PdCl_2$ in 20% $HNO_3$ solution slowly affords orange-red crystals, which were characterised as $[PdCl_2\{C_1Smim\}]_2$ (**3**) by X-ray crystallographic analysis. The structure of **3** is shown in Figure 4, with key bond parameters given in the caption, and contains a mercaptoimidazolium zwitterion as a ligand. In keeping with other related $Pd^{II}$ complexes[31] the geometry around the Pd centres is distorted square planar with the mercapto-S atoms functioning as a bidentate-bridging ligand. The dimer complex contains numerous intramolecular H-bonding interactions between the chloro atoms and the H atoms on the imidazolium moiety.

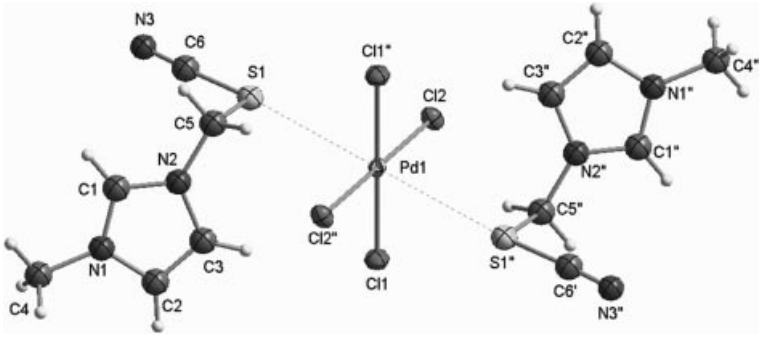


Figure 3. ORTEP representation of **2a**; atoms are represented by ellipsoids at the 50% probability level. The dotted lines (for visual purposes only) show the alignment of the thiocynate bonds towards Pd1. Key bond lengths [Å] and angles [°]: C1–N1, 1.319(4); C1–N2, 1.345(4); N1–C4, 1.464(14); N2–C5, 1.453(4); C5–S1, 1.818(3); S1–C6, 1.699(4); C6–N3, 1.141(4); Pd1–$Cl_{ave}$, 2.31; N1–C1–N2, 108.6(3); C1–N1–C4, 125.7(3); C1–N2–C5, 125.1(3); N2–S1–C6, 113.9(2); C5–S1–C6, 98.3(2); S1–C6–N3, 177.3(3).

 © 2007 Wiley-VCH Verlag GmbH & Co. KGaA, Weinheim 

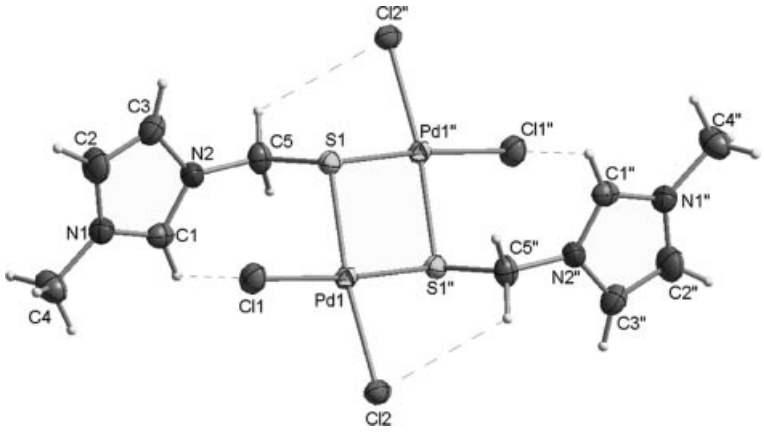


Figure 4. ORTEP representation of **3**; atoms are represented by ellipsoids at the 50% probability level. Key bond lengths [Å] and angles [°]: C1–N1, 1.331(14); C1–N2, 1.334(14); N1–C4, 1.474(14); N2–C5, 1.471(13); C5–S1, 1.828(11); Pd1–$Cl_{ave}$, 2.346(3); N1–C1–N2, 107.7(9); C1–N1–C4, 123.6(9); C1–N2–C5, 126.0(9); N2–S1–C6, 113.7(7).

## Concluding Remarks

In the present study, a series of thiocyanate-functionalised imidazolium salts were prepared, two of which can be classified as ionic liquids. According to the nature of the anion, viz. coordinating or noncoordinating, the salts react differently with palladium(II) chloride. However, in the presence of nitric acid cleavage of the C–S bond is induced and the same palladium dimer is formed irrespective of the type of anion present. Since none of the thiocyanate-functionalised imidazolium salts are liquid at room temperature, and the C–S bond is susceptible to cleavage, it was decided not to use them for palladium-catalysed reactions.

## Experimental Section

1-Methylimidazole, 1-chloromethyl thiocyanate, $HPF_6$, $NaBF_4$, $LiTf_2N$ and $HAuCl_4$ were obtained commercially and used as received. The synthesis of **1a** was performed under an inert atmosphere of dry nitrogen using standard Schlenk techniques in solvents dried using the appropriate reagents and distilled prior to use. All other compounds were made without precautions to exclude air or moisture. IR spectra were recorded with a Perkin–Elmer FT-IR 2000 system. NMR spectra were measured with a Bruker DMX 400, using $SiMe_4$ as the external standard for the $^1H$ NMR spectra at 20 °C. Electrospray ionization mass spectra (ESI-MS) were recorded with a ThermoFinnigan LCQ™ Deca XP Plus quadrupole ion trap instrument on samples diluted in solvents (methanol, water or DMSO). Samples were infused directly into the source at 5 μL min$^{-1}$ using a syringe pump and the spray voltage was set at 5 kV and the capillary temperature at 50 °C.[32] Elemental analysis was carried out at the Institute of Chemical Science and Engineering at the EPFL.

**Synthesis of [$C_1$SCNmim]Cl (1a):** A solution of 1-methylimidazole (8.21 g, 0.10 mol) and $ClCH_2SCN$ (12.9 g, 0.12 mol) in acetone (20 mL) was stirred at room temp. for 1 h during which time a white precipitate formed. The precipitate was washed with THF (3 × 30 mL) and dried under vacuum for 24 h. Yield: 18.6 g, 98%. M.p. 145 °C. Crystals suitable for X-ray diffraction were obtained by slow diffusion of diethyl ether into a saturated acetonitrile solution of the compound at room temp. ESI-MS ($H_2O$) (*m*/*z*) positive ion: 154 [$C_1$SCNmim], negative ion: 35 [Cl]. $^1H$ NMR ($D_2O$): $\delta$ = 9.05 (s, 1 H), 7.69 (s, 1 H), 7.54 (s, 1 H), 5.85 (s, 2 H), 3.92 (s, 3 H) ppm. $^{13}C$ NMR ($D_2O$): $\delta$ = 136.98, 124.32, 122.60, 111.62, 50.43, 36.36 ppm. IR (neat): $\tilde{\nu}$ = 3134, 3064 ($\upsilon_{C-H}$ aromatic), 2980, 2920, 2848, 2821 ($\upsilon_{C-H}$ aliphatic), 2159 ($\upsilon_{C\equiv N}$), 1731 ($\upsilon_{C=N}$), 730 ($\upsilon_{C-S}$) cm$^{-1}$. $C_6H_8ClN_3S$ (189.66): calcd. C 38.00, H 4.25, N 22.15; found C 37.97, H 4.26, N 22.18.

**Synthesis of [$C_1$SCNmim]$PF_6$ (1b):** $HPF_6$ (8.03 g, 60 wt.-%, 0.033 mol) was added to a solution of **1a** (5.7 g, 0.03 mol) in water (50 mL) at room temp. After 10 min the white solid that had formed was collected by filtration and washed with ice water (3 × 15 mL), and then dried under vacuum. Yield: 8.07 g, 90%. M.p. 120 °C. ESI-MS (methanol) (*m*/*z*) positive ion: 154 [$C_1$SCNmim], negative ion: 145 [$PF_6$]. $^1H$ NMR ($CD_3CN$): $\delta$ = 8.63 (s, 1 H), 7.60 (s, 1 H), 7.47 (s, 1 H), 5.63 (s, 2 H), 3.90 (s, 3 H) ppm. $^{13}C$ NMR ($CD_3CN$): $\delta$ = 136.74, 124.99, 122.28, 109.79, 50.34, 36.55 ppm. IR (neat): $\tilde{\nu}$ = 3167, 3125, 3106 ($\upsilon_{C-H}$ aromatic), 2987, 2938 ($\upsilon_{C-H}$ aliphatic), 2169 ($\upsilon_{C\equiv N}$), 1713 ($\upsilon_{C=N}$), 726 ($\upsilon_{C-S}$) cm$^{-1}$. $C_6H_8PF_6N_3S$ (299.18): calcd. C 24.09, H 2.70, N 14.05; found C 23.97, H 2.65, N 14.08.

**Synthesis of [$C_1$SCNmim]$BF_4$ (1c):** A mixture of **1a** (5.7 g, 0.03 mol) and $NaBF_4$ (3.62 g, 0.033 mol) in acetone (50 mL) was stirred at room temp. for 48 h. After filtration and removal of the solvent the resulting colourless solid was washed with THF and diethyl ether to give the product. Yield: 6.7 g, 93%. M.p. 78 °C. ESI-MS ($H_2O$) (*m*/*z*) positive ion: 154 [$C_1$SCNmim], negative ion: 87 [$BF_4$]. $^1H$ NMR ($CD_3CN$): $\delta$ = 8.78 (s, 1 H), 7.64 (s, 1 H), 7.50 (s, 1 H), 5.70 (s, 2 H), 3.91 (s, 3 H) ppm. $^{13}C$ NMR ($CD_3CN$): $\delta$ = 136.93, 124.98, 122.33, 109.90, 50.33, 36.47 ppm. IR: (neat): $\tilde{\nu}$ = 3156, 3117, 3093 ($\upsilon_{C-H}$ aromatic), 2989, 2901 ($\upsilon_{C-H}$ aliphatic), 2169 ($\upsilon_{C\equiv N}$), 1713 ($\upsilon_{C=N}$), 727 ($\upsilon_{C-S}$) cm$^{-1}$. $C_6H_8BF_4N_3S$ (241.02): calcd. C 29.90, H 3.35, N 17.43; found C 29.93, H 3.32, N 17.38.

**Synthesis of [$C_1$SCNmim][$Tf_2N$] (1d):** $LiTf_2N$ (8.61 g, 0.03 mol) was added to a solution of **1a** (5.7 g, 0.03 mol) in water (50 mL) at room temp. After 10 min the pale yellow liquid that had formed was collected by decantation and washed with ice water (3 × 15 mL) and then dried under vacuum. The liquid slowly crystallised from water at room temp. Yield: 11.60 g, 89%. M.p. 47 °C. ESI-MS (methanol) (*m*/*z*) positive ion: 154 [$C_1$SCNmim], negative ion: 280 [$Tf_2N$]. $^1H$ NMR ($CD_3CN$): $\delta$ = 8.72 (s, 1 H), 7.60 (s, 1 H), 7.48 (s, 1 H), 5.72 (s, 2 H), 3.91 (s, 3 H) ppm. $^{13}C$ NMR ($CD_3CN$): $\delta$ = 136.65, 124.97, 122.29, 109.66, 50.34, 36.49 ppm. IR: (neat): $\tilde{\nu}$ = 3145, 3112, 3091 ($\upsilon_{C-H}$ aromatic), 2988, 2901 ($\upsilon_{C-H}$ aliphatic), 2168 ($\upsilon_{C\equiv N}$), 1718

 © 2007 Wiley-VCH Verlag GmbH & Co. KGaA, Weinheim 

($\upsilon_{C=N}$), 731 ($\upsilon_{C-S}$) $cm^{-1}$. $C_8H_8F_6N_4O_4S_3$ (434.36): calcd. C 22.12, H 1.86, N 12.90, found C 22.15, H 1.87, N 12.87.

**Synthesis of $[C_1SCNmim]AuCl_4$ (1e):** A mixture of $HAuCl_4$ (340 mg, 1.0 mmol) and **1a** (378 mg, 1.00 mmol) in water (10 mL) was stirred at room temp. for 10 min. The resulting suspension was heated to 100 °C to give a clear solution. After cooling to room temp. the resulting orange crystals were collected by filtration and dried under vacuum to give the product. Yield: 335 mg, 68%. M.p. 150 °C. ESI-MS ($H_2O$) (*m*/*z*) positive ion: 154 [$C_1SCNmim$], negative ion: 337 [$AuCl_4$]. $^1H$ NMR ([D$_6$]DMSO): $\delta$ = 9.76 (s, 1 H), 7.93 (s, 1 H), 7.85 (s, 1 H), 6.06 (s, 2 H), 3.94 (s, 3 H) ppm. $^{13}C$ NMR ([D$_6$]DMSO): $\delta$ = 137.70, 125.19, 122.75, 111.82, 50.99, 36.80 ppm. IR: (neat): $\tilde{\nu}$ = 3135, 3111 ($\upsilon_{C-H}$ aromatic), 2977, 2901 ($\upsilon_{C-H}$ aliphatic), 2169 ($\upsilon_{C\equiv N}$), 1714 ($\upsilon_{C=N}$), 729 ($\upsilon_{C-S}$) $cm^{-1}$. $C_6H_8AuCl_4N_3S$ (492.98): calcd. C 14.62, H 1.64, N 8.52; found C 14.64, H 1.68, N 8.57.

**Synthesis of $[C_1SCNmim]_2PdCl_4$ (2a):** A mixture of $PdCl_2$ (177 mg, 1.0 mmol) and **1a** (378 mg, 2.00 mmol) in acetonitrile (5 mL) was stirred at room temp. for 7 d. After removal of the solvent the resulting orange solid was washed with dichloromethane (2 × 2 mL), and dried under vacuum to give the product. Yield: 549 mg, 99%. M.p. 146 °C. ESI-MS (DMSO) (*m*/*z*) positive ion: 154 [$C_1SCNmim$], negative ion: 124, 1/2 $[PdCl_4]^{2-}$. $^1H$ NMR ([D$_6$]-DMSO): $\delta$ = 9.76 (s, 1 H), 7.93 (s, 1 H), 7.85 (s, 1 H), 6.06 (s, 2 H), 3.94 (s, 3 H) ppm. $^{13}C$ NMR ([D$_6$]DMSO): $\delta$ = 137.70, 125.19, 122.75, 111.82, 50.99, 36.80 ppm. IR: (neat): $\tilde{\nu}$ = 3139, 3116, 3088 ($\upsilon_{C-H}$ aromatic), 2989, 2911 ($\upsilon_{C-H}$ aliphatic), 2168 ($\upsilon_{C\equiv N}$), 1718 ($\upsilon_{C=N}$), 734 ($\upsilon_{C-S}$) $cm^{-1}$. $C_{12}H_{16}Cl_4N_6PdS_2$ (556.63): calcd. C 25.89, H 2.90, N 15.10;. found C 25.91, H 2.88, N 15.17.

**Synthesis of $[C_1SCNmim]_2PdCl_2[BF_4]_2$ (2c):** A mixture of $PdCl_2$ (177 mg, 1.0 mmol) and **1c** (482 mg, 2.00 mmol) in dichloromethane (5 mL) was stirred at room temperature for 7 d. After removal of the solvent the resulting orange solid was washed with dichloromethane (2 × 2 mL), and dried under vacuum to give the product. Yield: 652 mg, 99%. M.p. 144 °C. ESI-MS (DMSO) (*m*/*z*) positive ion: 154 [$C_1SCNmim$]. $^1H$ NMR ([D$_6$]DMSO): $\delta$ = 9.25 (s, 1 H), 7.83 (s, 1 H), 7.77 (s, 1 H), 5.91 (s, 2 H), 3.91 (s, 3 H) ppm. $^{13}C$ NMR ([D$_6$]DMSO): $\delta$ = 137.38, 125.20, 122.89, 111.71, 50.71, 36.71 ppm. IR: (neat): $\tilde{\nu}$ = 3144, 3109, 3084 ($\upsilon_{C-H}$ aromatic), 2911 ($\upsilon_{C-H}$ aliphatic), 2219 ($\upsilon_{C\equiv N}$) $cm^{-1}$. $C_{12}H_{16}B_2Cl_2F_8N_6PdS_2$ (659.37): calcd. C 21.86, H 2.45, N 12.75; found C 21.89, H 2.47, N 12.70.

**Synthesis of 3:** **1a** or **1c** (0.2 mmol) was added to an aqueous solution of $PdCl_2$ in 20% $HNO_3$ (20 mmol $L^{-1}$, 10 mL) at room temp. After 5 d red crystals precipitated from the solution, which were collected by filtration. Yield: 11 mg, 9%. M.p. 137 °C. $^1H$ NMR ([D$_6$]DMSO): $\delta$ = 9.76 (s, 1 H), 7.88 (s, 1 H), 7.83 (s, 1 H), 3.94 (s, 3 H) ppm. $^{13}C$ NMR ([D$_6$]DMSO): $\delta$ = 137.81, 122.90, 121.66, 110.81, 35.97 ppm. IR: (neat): $\tilde{\nu}$ = 3158, 3117, 3066 ($\upsilon_{C-H}$ aromatic), 2911 ($\upsilon_{C-H}$ aliphatic), 733 ($\upsilon_{C-S}$) $cm^{-1}$. $C_{10}H_{16}C_{l4}N_4Pd_2S_2$ (610.99): calcd. C 19.66, H 2.64, N 9.17; found C 19.66, H 2.67, N 9.14.

**Structural Characterisation in the Solid State:** Relevant details about the structure refinements are compiled in Table 1 and selected bond lengths and angles are given in the figure captions. For **1a**, **2a** and **3** the data collection was performed with a four-circle Kappa goniometer equipped with an Oxford Diffraction KM4 Sapphire CCD at 140(2) K and data reduction was performed using CrysAlis RED.[33] For **1e** data collection was carried out with a Bruker Nonius APEX II CCD at 100(2) K and data reduction was performed using EVALCCD. Structure solution was carried out using SiR92,[34] and refined by full-matrix least-squares refinement (against $F^2$) using SHELXTL software.[35] All non-hydrogen atoms were refined anisotropically while hydrogen atoms were placed in their geometrically generated positions and refined using the riding model. Empirical absorption corrections were applied for **1a**, **2a** and **3** using DELABS[36] and **1e** using SADABS,[35] and graphical representations of the structures were made with the program Diamond.[37]

Table 1. Crystallographic data.

| Compound | **1a** | **1e** | **2a** | **3** |
|---|---|---|---|---|
| Formula | $C_6H_8ClN_3S$ | $C_6H_8Cl_4AuN_3S$ | $C_{12}H_{16}Cl_4N_6PdS_2$ | $C_{10}H_{16}Cl_4N_4Pd_2S_2$ |
| $M_r$ [g mol$^{-1}$] | 189.66 | 492.98 | 556.63 | 610.99 |
| Crystal system | monoclinic | triclinic | monoclinic | monoclinic |
| Space group | $P2_1/c$ | $P\bar{1}$ | $P2_1/n$ | $P2_1/c$ |
| $a$ [Å] | 8.2923(9) | 7.7347(6) | 9.0699(6) | 11.2276(14) |
| $b$ [Å] | 11.2624(12) | 8.0004(4) | 11.9124(8) | 7.6512(9) |
| $c$ [Å] | 9.9957(11) | 11.2628(7) | 9.5890(6) | 11.5705(10) |
| $\alpha$ [°] | 90 | 101.023(5) | 90 | 90 |
| $\beta$ [°] | 105.032(10) | 91.615(6) | 105.032(10) | 104.606(10) |
| $\gamma$ [°] | 90 | 106.686(5) | 90 | 90 |
| Volume [Å$^3$] | 901.57(17) | 652.72(7) | 101.077(5) | 961.84(18) |
| $Z$ | 4 | 2 | 2 | 2 |
| $D_{calcd}$ [g cm$^{-3}$] | 1.397 | 2.508 | 1.818 | 2.110 |
| $\mu$ [mm$^{-1}$] | 0.596 | 12.219 | 1.653 | 2.641 |
| $F$(000) | 392 | 456 | 552 | 592 |
| Temperature [K] | 140(2) | 100(2) | 140(2) | 140(2) |
| Wavelength [Å] | 0.71073 | 0.71073 | 0.71073 | 0.71073 |
| Measured reflections | 5108 | 12330 | 6001 | 5643 |
| Unique reflns | 1512 | 2964 | 1698 | 1634 |
| Unique reflns [$I > 2\sigma(I)$] | 1191 | 2550 | 1404 | 1196 |
| No. of data / restraints / parameters | 1512 / 0 / 101 | 2964 / 0 / 140 | 1698 / 0 / 116 | 1634 / 0 / 101 |
| $R$[a] [$I > 2\sigma(I)$] | 0.0286 | 0.0171 | 0.0252 | 0.0577 |
| $wR_2$[a] (all data) | 0.0688 | 0.0362 | 0.0555 | 0.1641 |
| GoF[b] | 0.965 | 1.112 | 0.977 | 1.133 |

[a] $R = \Sigma||F_o| - |F_c|| / \Sigma|F_o|$, $wR_2 = \{\Sigma[w(F_o^2 - F_c^2)^2] / \Sigma[w(F_o^2)^2]\}^{1/2}$. [b] GoF = $\{\Sigma[w(F_o^2 - F_c^2)^2] / (n - p)\}^{1/2}$ where $n$ is the number of data and $p$ is the number of parameters refined.

 © 2007 Wiley-VCH Verlag GmbH & Co. KGaA, Weinheim 

## Acknowledgments

We thank Ecole Polytechnique Fédérale de Lausanne (EPFL) and the Swiss National Science Foundation for financial support.

[1] a) J. H. Davis Jr., *Chem. Lett.* **2004**, *33*, 1072; b) S.-G. Lee, *Chem. Commun.* **2006**, 1049; c) Z. Fei, T. J. Geldbach, D. Zhao, P. J. Dyson, *Chem. Eur. J.* **2006**, *12*, 2122; d) H. Xue, R. Verma, J. M. Shreeve, *J. Fluorine Chem.* **2006**, *127*, 159.

[2] A. E. Visser, R. P. Swatloski, W. M. Reichert, R. Mayton, S. Sheff, A. Wierzbicki, J. H. Davis Jr., R. D. Rogers, *Chem. Commun.* **2001**, 135.

[3] B. K. M. Chan, N.-H. Chang, M. R. Grimmett, *Austr. J. Chem.* **1977**, *30*, 2005.

[4] W. Chen, F. Liu, *J. Organomet. Chem.* **2003**, *673*, 5.

[5] M. Sorm, S. Nespurek, *Acta Polym.* **1985**, *36*, 433.

[6] H. Schottenberger, K. Wurst, U. E. I. Horvath, S. Cronje, J. Lukasser, J. Polin, J. M. McKenzie, H. G. Raubenheimer, *Dalton Trans.* **2003**, 4275.

[7] Z. Fei, D. Zhao, R. Scopelliti, P. J. Dyson, *Organometallics* **2004**, *23*, 1622.

[8] W. A. Herrmann, C. Köcher, L. J. Goossen, G. R. J. Artus, *Chem. Eur. J.* **1996**, *2*, 1627.

[9] K.-M. Lee, Y.-T. Lee, I. J. B. Lin, *J. Mater. Chem.* **2003**, *13*, 1079.

[10] a) L. C. Branco, J. N. Rosa, J. J. Moura Ramos, C. A. M. Afonso, *Chem. Eur. J.* **2002**, *8*, 3671; b) A. P. Abbott, G. Capper, D. L. Davies, R. Rasheed, *Inorg. Chem.* **2004**, *43*, 3447.

[11] a) A. C. Cole, J. L. Jensen, I. Ntai, K. L. T. Tran, K. J. Weaver, D. C. Forbes, J. H. Davis Jr., *J. Am. Chem. Soc.* **2002**, *124*, 5962; b) J. D. Holbrey, W. M. Reichert, I. Tkatchenko, E. Bouajila, O. Walter, I. Tommasi, R. D. Rogers, *Chem. Commun.* **2003**, 28; c) N. Brausch, A. Metlen, P. Wasserscheid, *Chem. Commun.* **2004**, 1552; d) Z. Fei, D. Zhao, T. J. Geldbach, R. Scopelliti, P. J. Dyson, *Chem. Eur. J.* **2004**, *10*, 4886; e) D. Li, F. Shi, J. Peng, S. Guo, Y. Deng, *J. Org. Chem.* **2004**, *69*, 3582.

[12] K.-S. Kim, D. Demberelnyamba, H. Lee, *Langmuir* **2004**, *20*, 556.

[13] H. Itoh, K. Naka, Y. Chujo, *J. Am. Chem. Soc.* **2004**, *126*, 3026.

[14] C. Baleizao, B. Gigante, H. Garcia, A. Corma, *Tetrahedron Lett.* **2003**, *44*, 6813.

[15] a) T. L. Merrigan, E. D. Bates, S. C. Dorman, J. H. Davis Jr, *Chem. Commun.* **2000**, 2051; b) Y. R. Mirzaei, H. Xue, J. M. Shreeve, *Inorg. Chem.* **2004**, *43*, 361.

[16] D. Demberelnyamba, S. J. Yoon, H. Lee, *Chem. Lett.* **2004**, *33*, 560.

[17] Z. Mu, W. Liu, S. Zhang, F. Zhou, *Chem. Lett.* **2004**, *33*, 524.

[18] Y. Gao, B. Twamley, J. M. Shreeve, *Inorg. Chem.* **2004**, *43*, 3406.

[19] R. J. C. Brown, P. J. Dyson, D. J. Ellis, T. Welton, *Chem. Commun.* **2001**, 1862.

[20] P. J. Dyson, J. S. McIndoe, D. Zhao, *Chem. Commun.* **2003**, 508.

[21] Z.-B. Zhou, M. Takeda, M. Ue, *J. Flourine Chem.* **2004**, *125*, 471.

[22] D. Zhao, Z. Fei, C. A. Ohlin, G. Laurenczy, P. J. Dyson, *Chem. Commun.* **2004**, 2500.

[23] a) H. S. Kim, Y. J. Kim, J. Y. Bae, S. J. Kim, M. S. Lah, C. S. Chin, *Organometallics* **2003**, *22*, 2498; b) P. Wasserscheid, A. Bösmann, C. Bolm, *Chem. Commun.* **2002**, 200; c) J. Levillain, G. Dubant, I. Abrunhosa, M. Gulea, A.-C. Gaumont, *Chem. Commun.* **2003**, 2914.

[24] D. Zhao, Z. Fei, R. Scopelliti, P. J. Dyson, *Inorg. Chem.* **2004**, *43*, 2197.

[25] a) D. Zhao, Z. Fei, T. J. Geldbach, R. Scopelliti, P. J. Dyson, *J. Am. Chem. Soc.* **2004**, *126*, 15876; b) C. Chiappe, D. Pieraccini, D. Zhao, Z. Fei, P. J. Dyson, *Adv. Synth. Catal.* **2006**, *348*, 68.

[26] P. Wasserscheid, T. Welton (Ed.), *Ionic Liquids in Synthesis*, Wiley-VCH, Weinheim, Germany, **2002**, p. 1.

[27] M. Hasan, I. V. Kozhevnikov, M. R. H. Siddiqui, A. Steiner, N. Winterton, *Inorg. Chem.* **1999**, *28*, 5637.

[28] D. Zhao, Z. Fei, T. J. Geldbach, R. Scopelliti, G. Laurenczy, P. J. Dyson, *Helv. Chim. Acta* **2005**, *88*, 665.

[29] For example see, a) E. C. Alyea, G. Ferguson, S. Kannan, *Chem. Commun.* **1998**, 345; b) P. W. Dyer, P. J. Dyson, S. L. James, P. Suman, J. E. Davies, C. M. Martin, *Chem. Commun.* **1998**, 1375.

[30] D. S. Tarbell, D. P. Harnish, *Chem. Rev.* **1951**, *49*, 1.

[31] a) J. Sola, R. Yanez, *J. Chem. Soc., Dalton Trans.* **1986**, 2021; b) T. Boschi, B. Crociani, L. Toniolo, U. Belluco, *Inorg. Chem.* **1970**, *9*, 532.

[32] P. J. Dyson, J. S. McIndoe, *Inorg. Chim. Acta* **2003**, *354*, 68.

[33] Oxford Diffraction Ltd., Abingdon, Oxfordshire, UK, **2002**.

[34] A. Altomare, M. C. Burla, G. Camalli, G. Cascarano, C. Giacovazzo, A. Gualiardi, G. Polidori, *J. Appl. Crystallogr.* **1994**, *27*, 435.

[35] G. M. Sheldrick, University of Göttingen, Germany, **1997**; Bruker AXS, Inc., Madison, Wisconsin, 53719, USA, **1997**.

[36] DELABS, N. Walker, D. Stuart, *Acta Crystallogr., Sect. A* **1983**, *39*, 158.

[37] *Diamond 3.0a*, Crystal Impact GbR, Bonn, Germany.

Received: August 7, 2006
Published Online: November 17, 2006

 © 2007 Wiley-VCH Verlag GmbH & Co. KGaA, Weinheim 

DOI: 10.1002/ejic.200600764

# A Series of Lithium Rare Earth Polyphosphates [$LiLn(PO_3)_4$] (Ln = La, Eu, Gd) and Their Structural, Optical, and Electronic Properties

**Jing Zhu,[a] Wen-Dan Cheng,*[a] Dong-Sheng Wu,[a] Hao Zhang,[a] Ya-Jing Gong,[a] Hua-Nan Tong,[a] and Dan Zhao[a]**

**Keywords:** Density functional calculations / UV/Vis spectroscopy / Rare earths / Phosphates

The structural, optical, and electronic properties of a series of lithium rare earth polyphosphates [$LiLn(PO_3)_4$] [Ln = La (**1**), Eu (**2**), Gd (**3**)] have been investigated by means of single-crystal X-ray diffraction, elemental analyses, and spectroscopic measurements, as well as calculations of energy-band structures, density of states, and optical response functions by density functional methods. These $LiLn(PO_3)_4$ systems are monoclinic with space group $C2/c$ and $Z = 4$. Their unit-cell parameters decrease as the ionic radius of $Ln^{3+}$ decreases ($La^{3+} > Eu^{3+} > Gd^{3+}$). Both $(PO_4)^{3-}$ zig-zag chains and infinite chains formed by the alternate connection of $LnO_8$ polyhedra and $LiO_4$ tetrahedra run parallel to the *b*-axis in the structure. The energy-band structures, density of states, the chemical bonds, and optical properties have been investigated by density functional methods for some of the title compounds.
(© Wiley-VCH Verlag GmbH & Co. KGaA, 69451 Weinheim, Germany, 2007)

## Introduction

Rare earth phosphate materials have been extensively investigated due to their structural diversity[1–3] and potential properties (magnetism,[4] electricity,[5] and optics[6]). Furthermore, their chemical and thermal stability ensures their utility in industrial applications. The common basic structural unit of these materials is the $PO_4$ group, and the varied condensations of $PO_4$ groups result in several structural families,[7–10] one of which is polyphosphates with the general formula [$MLn(PO_3)_4$] (M = alkali metal, Ln = rare earth metal).[11] Some polyphosphates with interesting optical properties have been reported in this family. For example, Yamada et al. have reported the use of [$LiNd(PO_3)_4$][12,13] as a solid-state laser material whose relatively large Nd–Nd distance gives rise to a lesser degree of fluorescence quenching. Parreu et al. have investigated noncentrosymmetric [$KLn(PO_3)_4$] (Ln = Nd, Gd) crystals[14,15] and explored their second harmonic generation, and Naili et al. have reported the crystal structures of [$MGd(PO_3)_4$] (M = K, Cs).[16,17] Recently, [$NaLa(PO_3)_4$][18] was synthesized in our laboratory. In addition, some phosphates involving lithium, such as [$LiMPO_4$] (M = Fe, Co, Ni),[19] exhibit excellent electrochemical properties with potential applications in lithium ion batteries. Although the lattice parameters of [$LiLn(PO_3)_4$] (Ln = La, Eu) have been reported previously,[20,21] no X-ray crystal structural determinations were able to support these parameters.

Here we will report the structures and optical properties of [$LiLn(PO_3)_4$] [Ln = La (**1**), Eu (**2**), Gd (**3**)]. We will also describe their electronic properties and the results of calculations of the crystal energy bands, density of states (DOS), and optical response functions of **1** and **3** by density functional methods in order to analyze the chemical bonding properties and electronic origins of the optical transitions.

## Results and Discussion

### Crystal Structure Descriptions

Crystals of **1**–**3** are isostructural and crystallize in the monoclinic space group $C2/c$ (see Supporting Information). The asymmetric units of **1**–**3** have the same number of crystallographically distinct atoms. As expected, the unit-cell parameters of **1**–**3** decrease as the ionic radius of $Ln^{3+}$ decreases ($La^{3+} > Eu^{3+} > Gd^{3+}$). Selected bond lengths and angles are given in Table 1. The structure can be simply described as a three-dimensional framework made up from $(PO_4)^{3-}$ zig-zag chains and infinite chains involving $LnO_8$ and $LiO_4$ polyhedra. We will discuss their structural characterization by taking **1** as an example. Figure 1 shows a projection of the structure of **1** along the *b*-axis. The basic structural units are $PO_4$, $LaO_8$, and $LiO_4$ polyhedra. Two crystallographically distinct $P(1)O_4$ and $P(2)O_4$ tetrahedra form $(PO_4)^{3-}$ zig-zag chains by corner-sharing along the *b*-axis. The P(1) atom is connected to O(1), O(2), O(3), and O(4), and the P(2) atom is connected to O(2), O(3), O(5), and O(6). All P–O bond distances vary from 1.483(4) to

[a] State Key Laboratory of Structural Chemistry, Fujian Institute of Research on the Structure of Matter, Chinese Academy of Sciences,
Fuzhou, Fujian 350002, P. R. China
E-mail: cwd@fjirsm.ac.cn
Supporting information for this article is available on the WWW under http://www.eurjic.org or from the author.

 © 2007 Wiley-VCH Verlag GmbH & Co. KGaA, Weinheim 

Table 1. Selected bond lengths [Å] and angles [°] for compounds **1**–**3**.

| | | | | | | | |
|---|---|---|---|---|---|---|---|
| | | | $[LiLa(PO_3)_4]$ (**1**) | | | | |
| La–O6 (×2) | 2.437(3) | P1–O1 | 1.491(4) | O1–P1–O4 | 118.6(2) | O6–P2–O5 | 119.5(2) |
| La–O1 (×2) | 2.482(4) | P1–O4 | 1.500(3) | O1–P1–O2 | 106.4(2) | O6–P2–O3 | 111.8(2) |
| La–O5 (×2) | 2.556(3) | P1–O2 | 1.592(4) | O4–P1–O2 | 111.5(2) | O5–P2–O3 | 106.9(2) |
| La–O4 (×2) | 2.636(4) | P1–O3 | 1.595(3) | O1–P1–O3 | 111.4(2) | O6–P2–O2 | 110.0(2) |
| Li–O5 (×2) | 1.945(8) | P2–O6 | 1.483(4) | O4–P1–O3 | 104.9(2) | O5–P2–O2 | 105.4(2) |
| Li–O4 (×2) | 1.985(8) | P2–O5 | 1.492(3) | O2–P1–O3 | 103.1(2) | O3–P2–O2 | 101.5(2) |
| | | P2–O3 | 1.594(3) | | | | |
| | | P2–O2 | 1.606(4) | | | | |
| | | | $[LiEu(PO_3)_4]$ (**2**) | | | | |
| Eu–O6 (×2) | 2.333(3) | P1–O1 | 1.481(3) | O1–P1–O4 | 118.3(2) | O6–P2–O5 | 119.8(2) |
| Eu–O1 (×2) | 2.388(4) | P1–O4 | 1.497(3) | O1–P1–O2 | 106.7(2) | O6–P2–O3 | 111.9(2) |
| Eu–O5 (×2) | 2.452(3) | P1–O2 | 1.583(3) | O4–P1–O2 | 111.2(2) | O5–P2–O3 | 107.9(2) |
| Eu–O4 (×2) | 2.540(3) | P1–O3 | 1.584(3) | O1–P1–O3 | 111.5(2) | O6–P2–O2 | 109.9(2) |
| Li–O5 (×2) | 1.955(9) | P2–O6 | 1.481(3) | O4–P1–O3 | 105.1(2) | O5–P2–O2 | 104.6(2) |
| Li–O4 (×2) | 1.975(8) | P2–O5 | 1.481(3) | O2–P1–O3 | 103.0(2) | O3–P2–O2 | 101.0(2) |
| | | P2–O3 | 1.583(3) | | | | |
| | | P2–O2 | 1.601(3) | | | | |
| | | | $[LiGd(PO_3)_4]$ (**3**) | | | | |
| Gd–O6 (×2) | 2.321(5) | P1–O1 | 1.485(5) | O1–P1–O4 | 118.5(3) | O6–P2–O5 | 119.7(3) |
| Gd–O1 (×2) | 2.379(5) | P1–O4 | 1.496(5) | O1–P1–O2 | 106.0(3) | O6–P2–O3 | 112.1(3) |
| Gd–O5 (×2) | 2.436(5) | P1–O2 | 1.584(5) | O4–P1–O2 | 111.4(3) | O5–P2–O3 | 107.6(3) |
| Gd–O4 (×2) | 2.533(5) | P1–O3 | 1.595(5) | O1–P1–O3 | 111.7(3) | O6–P2–O2 | 110.0(3) |
| Li–O5 (×2) | 1.97(1) | P2–O6 | 1.486(5) | O4–P1–O3 | 105.3(3) | O5–P2–O2 | 104.6(3) |
| Li–O4 (×2) | 1.98(1) | P2–O5 | 1.490(5) | O2–P1–O3 | 102.9(3) | O3–P2–O2 | 101.1(3) |
| | | P2–O3 | 1.578(5) | | | | |
| | | P2–O2 | 1.610(5) | | | | |

1.606(4) Å, and the O–P–O angles range from 101.5(2)° to 119.5(2)° (Table 1), thus indicating that these $PO_4$ tetrahedra are distorted. The largest distance is the P–O bond in the P–O–P bridge and the shortest one corresponds to that in the nonbridging connections. The $(PO_4)^{3-}$ chains are isolated from each other and surrounded by $LaO_8$ and $LiO_4$ polyhedra. In addition, an alternating arrangement of $LaO_8$ and $LiO_4$ polyhedra forms infinite chains along the *b*-axis by edge-sharing (Figure 2), each of which is surrounded by neighboring $(PO_4)^{3-}$ zig-zag chains. The La atom is coordinated by eight O atoms and the $LaO_8$ polyhedra are distorted, with La–O bond lengths ranging from 2.437(3) to 2.636(4) Å (Table 1). Each $LaO_8$ polyhedron is corner-connected to eight different $PO_4$ tetrahedra and edge-connected to two $LiO_4$ tetrahedra. The isolation of the $LaO_8$ polyhedra gives rise to large La–La distances, the shortest of which is 6.5690(3) Å. The Li atom is four-coordinate, with the Li–O bond distance ranging from 1.945(8) to 1.985(8) Å. Each $LiO_4$ tetrahedron shares all four O atoms with two $LaO_8$ polyhedra and four different $PO_4$ tetrahedra. The edge-sharing of $LaO_8$ and $LiO_4$ polyhedra results in infinite chains along the *b*-axis.

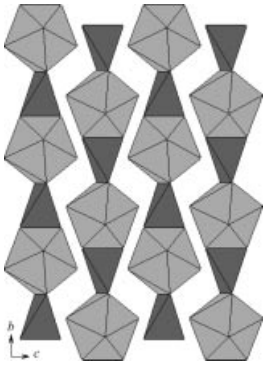

Figure 2. Projection of the structure of **1** along the *a*-axis showing the alternating arrangement of $LaO_8$ polyhedra and $LiO_4$ tetrahedra (the P atoms have been omitted for clarity).

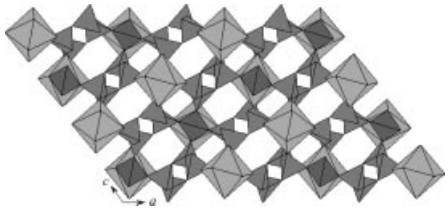

Figure 1. Projection of the structure of **1** along *b*-axis.

### Band Structure, Density of States, and Chemical Bonds

The energy band structures and density of states (DOS) of **1** and **3** were calculated by density functional methods. For **3**, the spin-polarization was properly taken into account by considering the unpaired f-electron effect of the $Gd^{3+}$ ion (α and β represent spin-up and spin-down, respectively). The calculated band structure of **1**, as shown in Fig-

 © 2007 Wiley-VCH Verlag GmbH & Co. KGaA, Weinheim 

ure 3, displays similar features, except for the f-band, to that of **3**, which is given as Supporting Information. In order to assign these bands, the total density of states (TDOS) and partial DOS (PDOS) of **1** and **3** are shown in Figure 4.

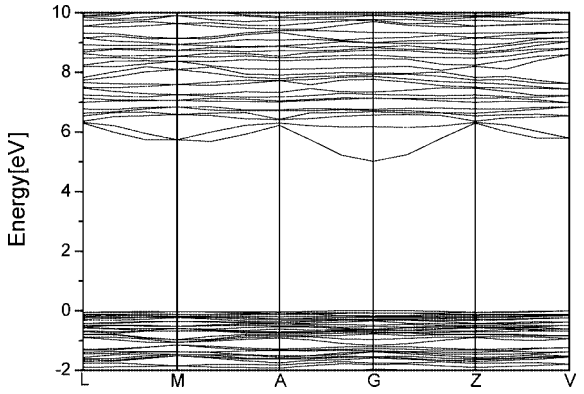


Figure 3. Calculated band structure of **1**.

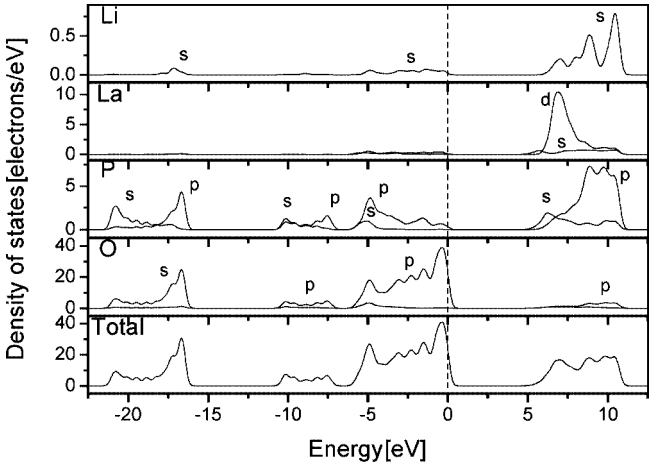


(a)

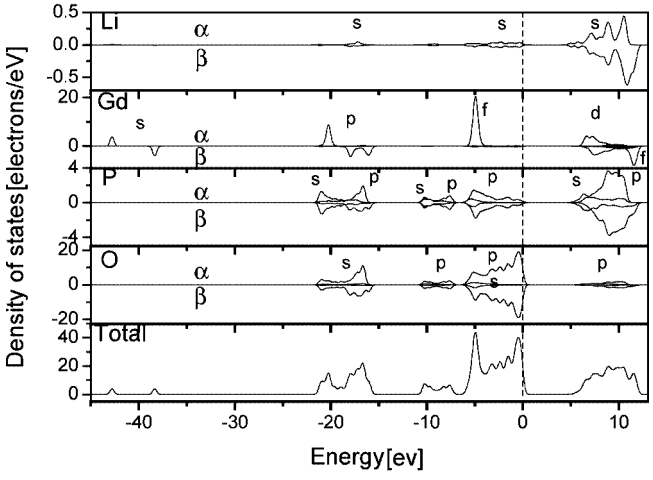


(b)

Figure 4. Total and partial densities of states of **1** (a) and **3** (b).

The calculated band structures of **1** and **3** exhibit similar features. It is observed that the top of the valence bands (VBs) is nearly flat and close to the Fermi level (0.0 eV), and the bottom of the conduction bands (CBs) exhibits obvious dispersion. The lowest energy of the CBs is localized at G (Figure 3), which means that **1** and **3** show an insulator character with a direct bandgap of around 5.02 and 4.99 eV, respectively. According to Figure 4, the O 2p states are the main contributors to the VBs ranging from –10.7 eV to the Fermi level, and the O 2s states form the VBs between –21.5 and –16.0 eV. In addition, the CBs between 5.0 and 11.0 eV are mostly formed by the P 3p states. The La 5d and Gd 5d states also give rise to CBs in **1** and **3**, respectively. Furthermore, for **3**, the VBs near about –40.0, –20.0, and –5.0 eV also result from the Gd 5s, Gd 5p, and Gd 4f states, respectively.

We also elucidated the features of the chemical bonds for **1** and **3** on the basis of the total and angular momentum projected DOS (Figure 4). In the range from –10.7 eV to the Fermi level the O 2p and P 3p states exist simultaneously, although the DOS is much larger for the former, which indicates that some P 3p electrons transform into the VBs and take part in the covalent interactions between P and O atoms and that hybridization between the P 3p and O 2p states takes place. The chemical bonding properties were also confirmed by means of the population analysis. The calculated bond orders of **1** and **3** in the unit cell are 0.45–0.82, 0.20–0.30, and 0.02–0.03 e for P–O, Ln–O, and Li–O bonds, respectively. It is well known that a covalent single-bond order is generally 1.0 e. Accordingly, the covalent character of the P–O bond is larger than that of the Ln–O bond, and the ionic character of the Li–O bond is larger than that of the Ln–O bond.

## Optical Properties

Figure 5 illustrates the absorption and emission spectra of **1**–**3**. The absorption spectra were determined by the diffuse-reflectance technique. $F(R)$ and $R$ are linked by $F(R) = (1 - R)^2/2R$, where $R$ is the reflectance and $F(R)$ is the Kubelka–Munk remission function. The minima in the second-derivative curves of the Kubelka–Munk function are taken as the position of the absorption bands. Their absorption edges are around 320 (3.88), 330 (3.76), and 350 nm (3.55 eV), respectively. A strong absorption peak only appears at around 245 nm (5.07 eV) for **1**, 250 nm (4.97 eV) for **2**, and 260 nm (4.78 eV) for **3**.

In order to assign these experimental spectra, we examined the linear optical response properties of crystals **1** and **3**. We calculate the imaginary part $\varepsilon_2(\omega)$ and the real part $\varepsilon_1(\omega)$ of the frequency-dependent dielectric function without the DFT scissor-operator approximation, as displayed in Figure 6. The $\varepsilon_2(\omega)$ part can be used to describe the real transitions between the occupied and unoccupied electronic states. There are distinct peaks at around 7.50 and 8.50 eV for **1** and **3**, respectively, which correspond to those of the experimental spectra [Figure 5(a)]. According to Figure 4,

 © 2007 Wiley-VCH Verlag GmbH & Co. KGaA, Weinheim 

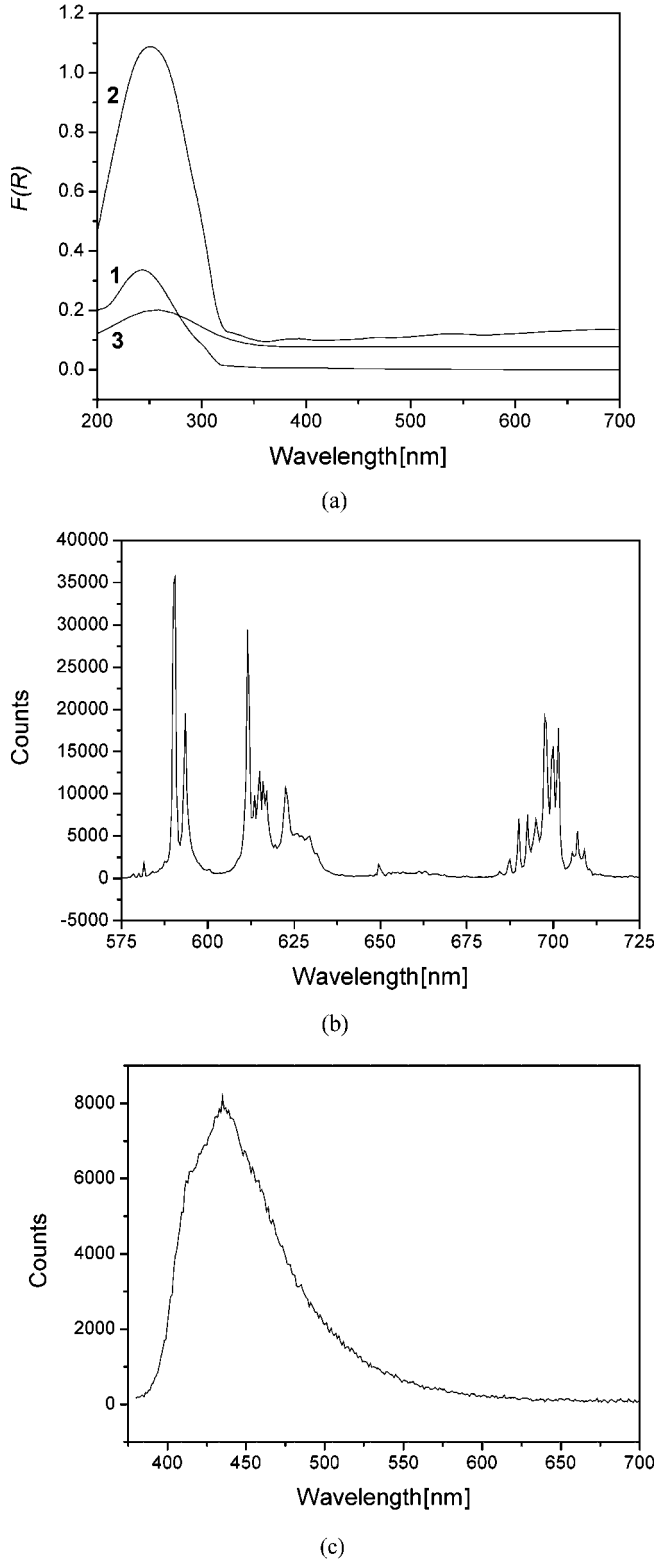


Figure 5. Absorption spectra of **1**–**3** (a); emission spectrum of **2** upon excitation at 295 nm (b); emission spectrum of **3** upon excitation at 365 nm (c).

these peaks are due to the electronic transitions from the O 2p to La 5d states for **1** and from the O 2p to Gd 5d states for **3**. In addition, comparing the calculated UV/Vis absorption edges (about 5.20 eV for **1** and 4.60 eV for **3**) of the crystals with the experimental ones (about 3.88 eV for **1** and 3.55 eV for **3**) of the powder samples shows that the transmission width is larger for the crystals than the powder samples, which indicates that the result of the calculation is reasonable. For **3**, the emission peak is located at 435 nm (2.86 eV) at an excitation wavelength of 365 nm [Figure 5(c)]. The emission energy is less than the experimental absorption edge of 3.55 eV, which means that the emission peak probably originates from defects or excitons. For **2**, the emission spectrum displays the characteristic yellow-red emissions that result from the intraconfigurational electronic $^5D_0$–$^7F_J$ transitions ($J$ = 0–4) of the $Eu^{3+}$ ion[22] in the range from 575 to 725 nm under excitation at 295 nm [Figure 5(b)]. Five emission regions correspond to 582 ($^5D_0$–$^7F_0$), 590–595 ($^5D_0$–$^7F_1$), 610–630 ($^5D_0$–$^7F_2$), 650 ($^5D_0$–$^7F_3$), and 685–710 nm ($^5D_0$–$^7F_4$), respectively. The presence of only one narrow band for the $^5D_0$–$^7F_0$ transition of the $Eu^{3+}$ ion implies that there is only one such

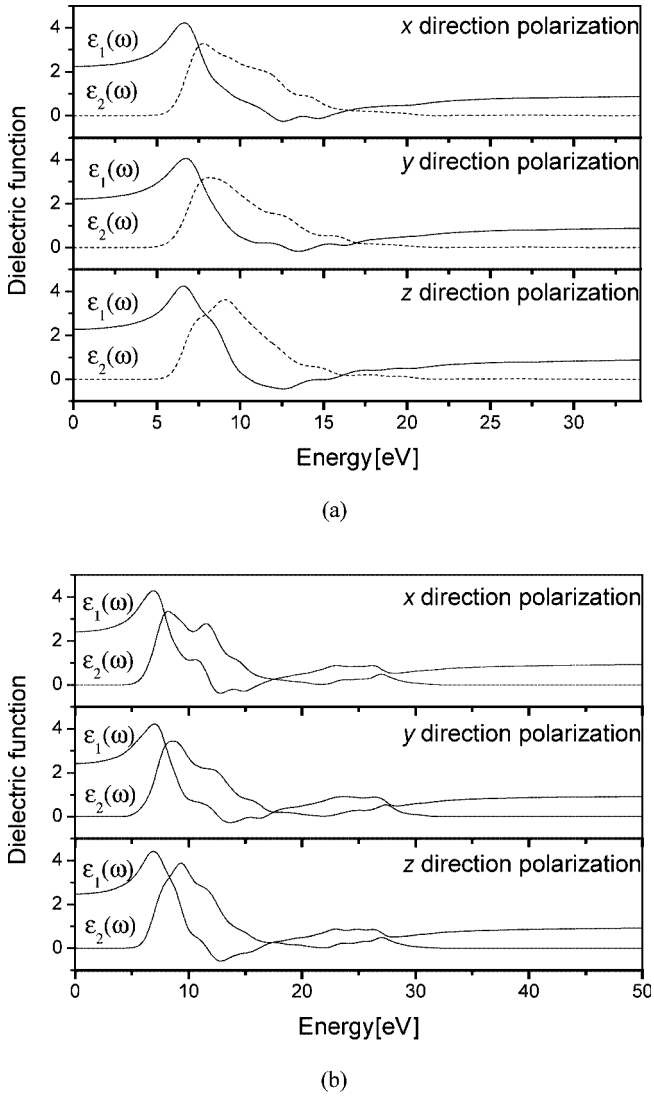


Figure 6. Calculated real and imaginary parts of the dielectric functions in different polarization directions for **1** (a) and **3** (b).

 © 2007 Wiley-VCH Verlag GmbH & Co. KGaA, Weinheim 

coordination environment, which is consistent with the above-mentioned structural data for **2**.

We also investigated the calculated dielectric constants of the static case, $\varepsilon(0)$, and the refractive indices, $n$, of **1** and **3**. The refractive index is linked to the dielectric constant by the relation $n^2(\omega) = \varepsilon(\omega)$. The calculated dielectric constants of the static case in the $x$, $y$, and $z$ directions are 2.2378, 2.2135, and 2.2768 for **1** and 2.4142, 2.4232, and 2.4645 for **3**, respectively. The corresponding refractive indices in the different directions at 1064 nm are 1.5034, 1.4951, and 1.5165 for **1** and 1.5614, 1.5645, and 1.5775 for **3**. It should be noted that the calculated dielectric constants of the static case and refractive indices at 1064 nm are larger for **3** than for **1**. Since the refractive indices of **1** and **3** have not been measured or reported, we compared the calculated results with the observed refractive indices of the other phosphate crystals, which generally range from 1.40 to 1.6;[23] the calculated refractive indices of **1** and **3** are therefore reasonable.

## Conclusions

In summary, a series of isostructural lithium rare earth polyphosphates [LiLn(PO$_3$)$_4$] (Ln = La, Eu, Gd) have been synthesized by a high-temperature solution reaction. Their crystallographic data obtained by single-crystal X-ray diffraction show that their structures belong to the monoclinic space group $C2/c$. The unit-cell parameters of **1**–**3** decrease as the ionic radius of $Ln^{3+}$ decreases ($La^{3+} > Eu^{3+} > Gd^{3+}$). Both $(PO_4)^{3-}$ zig-zag chains and infinite chains with an alternating arrangement of $LaO_8$ and $LiO_4$ polyhedra run along the $b$-axis. The Li–O bond exhibits ionic character, and the P–O bond is more covalent than the Ln–O bond. Spectral measurements and theoretical computations show that **1**–**3** are insulators. [LiEu(PO$_3$)$_4$] displays the characteristic yellow-red emissions that result from the intraconfigurational electronic $^5D_0$–$^7F_J$ transitions ($J$ = 0–4) of the $Eu^{3+}$ ion. In addition, the dielectric constants of the static case, $\varepsilon(0)$, and refractive indices, $n$, of [LiLa(PO$_3$)$_4$] and LiGd(PO$_3$)$_4$ have also been estimated. Further studies aimed at synthesizing new phosphate materials with other alkali and rare earth metals are currently in progress.

## Experimental Section

**Syntheses:** Single crystals of **1**–**3** were prepared by a high-temperature solution reaction from $Li_2CO_3$, $La_2O_3$ (**1**), $Eu_2O_3$ (**2**), or $Gd_2O_3$ (**3**), and $NH_4H_2PO_4$ with an Li/Ln/P molar ratio of 7:1:12. The excess $Li_2CO_3$ and $NH_4H_2PO_4$ formed the flux. The starting mixtures were finely ground in an agate mortar to ensure the best homogeneity and reactivity, then placed in a platinum crucible and heated at 473 K for 4 h. The mixtures were then reground and heated to 1173 K for 24 h. Finally, the mixture was cooled to 773 K at a rate of 2 K h$^{-1}$, followed by air-quenching to room temperature. A few colorless, block-shaped crystals were obtained from the melt of the mixtures.

**Crystal Structure Determinations:** Single crystals of **1**–**3** with dimensions $0.18 \times 0.10 \times 0.03$ (**1**), $0.20 \times 0.04 \times 0.02$ (**2**), and $0.30 \times 0.12 \times 0.08$ mm (**3**) were selected for X-ray diffraction determination. The diffraction data for **1** were collected with a Siemens SMART CCD diffractometer with graphite-monochromated Mo-$K_a$ radiation ($\lambda$ = 0.71073 Å) using the $\omega/2\theta$-scan mode at a temperature of 293 K, and those for **2** and **3** were collected with a Rigaku Mercury CCD diffractometer with graphite-monochromated Mo-$K_a$ radiation ($\lambda$ = 0.71073 Å) using the $\omega$-scan mode at a temperature of 293 K. Lorentz and polarization corrections were applied to all data. The structures were solved by direct methods and refined on $F^2$ by the full-matrix least-squares method with SHELXL97.[24] The positions of the La, Eu, and Gd atoms were refined by direct methods and the remaining atoms were located in successive difference Fourier syntheses. In order to confirm the chemical compositions of the four compounds, the single crystals of **1**–**3** investigated with the diffractometer were analyzed by energy-dispersive X-ray spectroscopy (EDX) using a JSM6700F scanning electron microscope. The obtained results are in good agreement with those obtained by the refinement of the crystal structures. No impurity elements were detected, although the light element Li could not be satisfactorily determined by the EDX measurement. The results of the elemental analyses are given as Supporting Information. Crystal data for **1**: LiLa(PO$_3$)$_4$ (461.73), monoclinic, space group $C2/c$, $T$ = 293(2) K, $a$ = 16.6230(3), $b$ = 7.1198(1), $c$ = 9.905 Å, $\beta$ = 126.43°, $V$ = 943.19(2) Å$^3$, $Z$ = 4, $D_{calcd.}$ = 3.252 g cm$^{-3}$, $F(000)$ = 864, $\mu$(Mo-$K_a$) = 5.272 mm$^{-1}$, 2461 reflections collected, 891 unique ($R_{int}$ = 0.0335), $R_1$ = 0.0282, $wR_2$ = 0.0685 [$I > 2\sigma(I)$], $R_1$ = 0.0284, $wR_2$ = 0.0686 (all data) and final Gof = 1.017. Crystal data for **2**: LiEu(PO$_3$)$_4$ (474.78), monoclinic, space group $C2/c$, $T$ = 293(2) K, $a$ = 16.3300(9), $b$ = 7.0330(4), $c$ = 9.6465(6) Å, $\beta$ = 126.14(3)°, $V$ = 894.7(0) Å$^3$, $Z$ = 4, $D_{calcd.}$ = 3.525 g cm$^{-3}$, $F(000)$ = 888, $\mu$(Mo-$K_a$) = 7.794 mm$^{-1}$, 3389 reflections collected, 1032 unique ($R_{int}$ = 0.0412), $R_1$ = 0.0259, $wR_2$ = 0.0584 [$I > 2\sigma(I)$], $R_1$ = 0.0279, $wR_2$ = 0.0596 (all data) and final Gof = 1.000. Crystal data for **3**: LiGd(PO$_3$)$_4$ (480.07), monoclinic, space group $C2/c$, $T$ = 293(2) K, $a$ = 16.330(1), $b$ = 7.0327(4), $c$ = 9.6450(8) Å, $\beta$ = 126.12(4)°, $V$ = 894.8(1) Å$^3$, $Z$ = 4, $D_{calcd.}$ = 3.564 g cm$^{-3}$, $F(000)$ = 892, $\mu$(Mo-$K_a$) = 8.195 mm$^{-1}$, 3313 reflections collected, 1030 unique ($R_{int}$ = 0.0426), $R_1$ = 0.0319, $wR_2$ = 0.0820 [$I > 2\sigma(I)$], $R_1$ = 0.0323, $wR_2$ = 0.0822 (all data) and final Gof = 1.025. Further details of the crystal-structure investigations may be obtained from the Fachinformationzentrum Karlsruhe, 76344 Eggenstein-Leopoldshafen, Germany, on quoting the depository numbers CSD-416877 to -416879 (for **1**–**3**, respectively).

**Spectral Measurements:** The purity of the polycrystalline samples for spectral measurements of **1**–**3** was confirmed by powder XRD studies using a Rigaku DMAX2500 diffractometer with Cu-$K_a$ radiation (step size of 0.05° and $2\theta$ range of 10–80°). The powder XRD patterns of **1**–**3** are given as Supporting Information. The absorption spectra were recorded with a Lambda-35 UV/Vis spectrophotometer in the wavelength range 200–800 nm. The emission spectra were measured with an FLS920 time-resolved fluorescence spectrometer using an Xe lamp at room temperature.

**Computational Details:** The crystallographic data of **1** and **3** determined by single-crystal X-ray diffraction were used to calculate their electronic band structures. Calculations of electronic band structures were performed at the density functional theory (DFT) level using one of the three nonlocal gradient-corrected exchange-correlation functionals (GGA-PBE) and with the CASTEP code,[25,26] which uses a plane wave basis set for the valence electrons and norm-conserving pseudopotential[27] for the core states. The number of plane waves included in the basis was determined by a cutoff energy, $E_c$, of 550 eV. Pseudoatomic calculations were performed for O ($2s^2 2p^4$), P ($3s^2 3p^3$), Li ($2s^1$), La ($5d^1 6s^2$), and

 © 2007 Wiley-VCH Verlag GmbH & Co. KGaA, Weinheim 

Gd ($4f^7 5s^2 5p^6 5d^1 6s^2$). The calculating parameters and convergent criteria were set by the default values of the CASTEP code.[25] The linear optical properties were also calculated; $\varepsilon_2(\omega)$ can be thought of as detailing the real transitions between occupied and unoccupied electronic states. Since the dielectric constant describes a causal response, the real and imaginary parts are linked by the Kramers–Kronig transformation,[28] where P is the principal value of the integral. This transformation is used to obtain the real part of the dielectric function, $\varepsilon_1(\omega)$.

$$\varepsilon_1(\omega) - 1 = \frac{2}{\pi} \mathrm{P} \int_0^\infty \frac{\omega' \varepsilon_2(\omega') d\omega'}{\omega'^2 - \omega^2} \quad \text{and} \quad \varepsilon_2(\omega) = -\frac{2\omega}{\pi} \mathrm{P} \int_0^\infty \frac{\varepsilon_1(\omega') d\omega'}{\omega'^2 - \omega^2}$$

**Supporting Information** (see footnote on the first page of this article): Full results of elemental analysis for **1**–**3**. Experimental and simulated X-ray powder diffraction patterns of **1**–**3**. The calculated band structure of **3**.

## Acknowledgments

This investigation was supported by the National Basic Research Program of China (grant no. 2004CB720605), the National Natural Science Foundation of China under projects 20373073 and 90201015, the Science Foundation of the Fujian Province (grant no. E0210028), and the Foundation of the State Key Laboratory of Structural Chemistry (grant no. 060007).

[1] L. Campayo, F. Audubert, D. Bermache-Assollant, *Solid State Ionics* **2005**, *176*, 2663–2669.
[2] L. Rghioui, L. E. Ammari, L. Benarafa, J. P. Wignacourt, *Acta Crystallogr., Sect. C* **2002**, *58*, i90–i91.
[3] I. Szczygiel, *Solid State Sci.* **2005**, *7*, 189–194.
[4] J. M. Cole, M. R. Lees, J. A. K. Howard, R. J. Newport, G. A. Saunders, E. Schönherr, *J. Solid State Chem.* **2000**, *150*, 377–382.
[5] M. Ferid, K. Horchani-Naifer, *Solid State Ionics* **2005**, *176*, 1949–1953.
[6] J. J. Gavaldà, I. Parreu, R. Solé, X. Solans, F. Díaz, M. Aguiló, *Chem. Mater.* **2005**, *17*, 6746–6754.
[7] A. Hamady, T. Jouini, *Acta Crystallogr., Sect. C* **1996**, *52*, 2949–2951.
[8] H. Y.-P. Hong, S. R. Chinn, *Mater. Res. Bull.* **1976**, *11*, 421–428.
[9] W. Rekik, H. Naïli, T. Mhiri, *Acta Crystallogr., Sect. C* **2004**, *60*, i50–i52.
[10] I. Szczygiel, *Thermochim. Acta* **2004**, *417*, 75–78.
[11] E. B. Zarkouna, A. Driss, *Acta Crystallogr., Sect. E* **2004**, *60*, i102–i104.
[12] T. Yamada, K. Otsuka, J. Nakano, *J. Appl. Phys.* **1974**, *45*, 5096.
[13] K. Otsuka, T. Yamada, *Appl. Phys. Lett.* **1975**, *26*, 311.
[14] I. Parreu, J. J. Carvajal, X. Solans, F. Díaz, M. Aguiló, *Chem. Mater.* **2006**, *18*, 221–228.
[15] I. Parreu, R. Solé, J. Gavaldà, J. Massons, F. Díaz, M. Aguiló, *Chem. Mater.* **2003**, *15*, 5059–5064.
[16] H. Naïli, T. Mhiri, *Acta Crystallogr., Sect. E* **2005**, *61*, i204–i207.
[17] H. Ettis, H. Naïli, T. Mhiri, *Cryst. Growth Des.* **2003**, *3*, 599–602.
[18] J. Zhu, W. D. Cheng, D. S. Wu, H. Zhang, Y. J. Gong, H. N. Tong, *J. Solid State Chem.* **2006**, *179*, 597–604.
[19] R. Ruffo, R. A. Huggins, C. M. Mari, M. Piana, W. Weppner, *Ionics* **2005**, *11*, 213–219.
[20] N. N. Chudinova, N. V. Vinogradova, *Izv. Akad. Nauk SSSR, Neorg. Mater.* **1979**, *15*, 2171–2175; *Chem. Abstr.* **1980**, *92*, 100210m.
[21] M. F. Moktar, N. Kbir-Ariguib, M. Trabelsi, *J. Solid State Chem.* **1981**, *38*, 130–132.
[22] E. E. S. Teotonio, H. F. Brito, M. C. F. C. Felinto, L. C. Thompson, V. G. Young, O. L. Malta, *J. Mol. Struct.* **2005**, *751*, 85–94.
[23] *Lange's Handbook of Chemistry*, 13th ed. (Ed.: J. A. Deans), McGraw–Hill Book Company, New York, **1985**.
[24] G. M. Sheldrick, *SHELXTL-97, Program for Refining Crystal Structure*, University of Göttingen, Germany, **1997**.
[25] M. Segall, P. Linda, M. Probert, C. Pickard, P. Hasnip, S. Clark, M. Payne, *Materials Studio CASTEP*, version 2.2, **2002**.
[26] M. Segall, P. Linda, M. Probert, C. Pickard, P. Hasnip, S. Clark, M. Payne, *J. Phys.: Condens. Mater.* **2002**, *14*, 2717–2744.
[27] D. R. Hamann, M. Schluter, C. Chiang, *Phys. Rev. Lett.* **1979**, *43*, 1494–1497.
[28] J. R. Macdonald, M. K. Brachman, *Rev. Mod. Phys.* **1956**, *28*, 383.

Received: August 17, 2006
Published Online: November 6, 2006

 © 2007 Wiley-VCH Verlag GmbH & Co. KGaA, Weinheim 

DOI: 10.1002/ejic.200600797

# Synthesis, Structural and Spectroscopic Studies on the Lanthanoid *p*-Aminobenzoates and Derived Optically Functional Polyurethane Composites

**Timothy Fiedler,[a][‡] Matthias Hilder,[b] Peter C. Junk,*[b] Ulrich H. Kynast,[a] Marina M. Lezhnina,*[a][‡‡] and Marek Warzala[a]**

**Keywords:** Luminescence / Lanthanoids / Polyurethane composites / Carboxylates

Aromatic carboxylates of the rare earths are known for highly efficient luminescence, thus holding the promise of applicability in optical devices, but may be problematic to apply as such due to their structure, which is polymeric in nature. Therefore, means of conversion into molecular species or eventually polymer embeddings are sought, while at the same time maintaining their advantageous optical features. For these purposes, co-ligations of rare earth *p*-aminobenzoates with bidentate bipyridine and phenanthroline, tridentate terpyridine and polyurethanes, which may also be perceived as polydentate ligands, have been carried out. The materials were characterised with focus on their structure and optical performance. Brightly luminescing composites were obtained from reactions with aromatic and aliphatic diisocyanates. Prolonged UV-irradiation of the materials proved hexamethylene diisocyanates to be superior with regard to photodegradation. Transparent polyurethane monoliths with emission quantum yields between 40 % and 55 % were eventually prepared from covalent attachement of Tb(*p*-aminobenzoate)$_3$ and its bipyridine co-ligated complexes to a hexamethylene diisocyanate/polyol system.

(© Wiley-VCH Verlag GmbH & Co. KGaA, 69451 Weinheim, Germany, 2007)

## 1. Introduction

Efficiently luminescing complexes of the rare earths are not only spectacular visually, but also of interest in numerous photophysical applications, ranging from sensors over light emitting devices (LEDs, OLEDs) to luminescent immunoassays. Practically, it is frequently desirable to incorporate them into matrices in order to render them applicable, or even appropriately functional in corresponding devices. As such, sol-gel matrices, zeolites and various polymers have been utilised.

Although the principle "local" intramolecular luminescence mechanism of the complexes is understood comparably well, especially in β-diketonates,[1–5] a reliable and comprehensive description of the structural factors influencing the optical performance appears to be lacking, especially with regard to carboxylates.

[a] University of Applied Sciences Muenster, Dep. of Chemical Engineering/Applied Materials Sciences,
Stegerwaldstr. 39, 48565 Steinfurt, Germany
Fax: +49-2551-962-187
E-mail: marina@fh-muenster.de
[b] School of Chemistry, Box 23, Monash University,
Clayton, Vic. 3800, Australia
Fax: +61-03-9905-4597
E-mail: peter.junk@sci.monash.edu.au
[‡] Current address: OSRAM GmbH, Phosphor Development & Applications,
Hellabrunner Straße 1, 81543 München
[‡‡]On leave from: Mari Technical State University Yoshkar-Ola, Institute of Physics,
Lenin-pl. 3, 424000 Yoshkar-Ola, Russia

This lack of understanding is particularly true for the group of aromatic carboxylates imbedded in mentioned hosting matrices, which includes some of the most efficiently luminescing rare earth species. Rare earth aromatic carboxylates generally form coordination-polymeric associates with corresponding short-range interactions rather than isolated molecular entities.[6] Resulting insolubility and low vapour pressure pose a practical shortcoming with regard to matrix incorporation schemes, as the destruction of the original rare earth coordination polymer often quenches or diminishes the luminescence efficiencies. Bipyridines ("bipy") and phenanthrolines ("phen"), acting both as co-chelating and co-sensitizing ligands, can help to circumvent the solubility or volatility problem by forming new molecular coordination complexes. At the same time, they can help to keep the immediate chemical environment of the ion free from water, which is frequently encountered in the pure carboxylates. In addition to these bidentate co-ligands, we have additionally used terpyridine ("terpy") as a co-ligand. Also, some matrices may analogously be understood in terms of co-ligation, in that they may also occupy the rare earth coordination sphere in polydentate fashion as well, e.g. oxygen atoms of silica based matrices or silicones.

In this report, we focus on *p*-aminobenzoic acid ("pabaH"), because we learnt from single crystal structure data that the amino group might be chemically accessible for covalent attachment to a matrix on one hand, and, e.g. Tb(*p*-aminobenzoate)$_3$ ["Tb(paba)$_3$"], show intense luminescence

 © 2007 Wiley-VCH Verlag GmbH & Co. KGaA, Weinheim InterScience 

as the pure coordination polymer on the other hand, which can be enhanced by co-coordination,[7] and even be maintained on incorporation into zeolite matrix.[8] While this research was in progress, some of the crystal structures were confirmed by reports from other groups, or were previously published.[9] We will additionally provide results on the interaction of $Tb(paba)_3$, $Tb(paba)_3$phen and $Tb(paba)_3$bipy with isocyanates and eventually a polyurethane matrix and their behaviour under prolonged UV irradiation.

$$LnCl_3{\cdot}n(H_2O) + 3\ Na(paba) \xrightarrow{H_2O} [Ln(paba)_3H_2O]_n + 3\ NaCl \quad (1)$$

$$TbCl_3{\cdot}n(H_2O) + 3\ Na(paba) \xrightarrow[1,10\text{-phen}]{H_2O} [Tb(paba)_3(H_2O)_2]_2{\cdot}2\ H_2O + 3\ NaCl \quad (2)$$

## 2. Results and Discussion

### 2.1. Coordination Polymers

A $[Ln(paba)_3{\cdot}H_2O]_n$ series with the members [Ln = Eu (**1**), Gd (**2**) and Tb (**3**); pabaH = *p*-aminobenzoic acid], were conveniently synthesised in good yield by treatment of an aqueous solution of the respective lanthanoid chloride with sodium *p*-aminobenzoate [Equation (1)]. We could also obtain a modified phase of the terbium complex, being the dimeric $[Tb(paba)_3(H_2O)_2]_2{\cdot}2H_2O$ (**4**), which was obtained in a similar manner [Equation (2)], but in the presence of 1,10-phenanthroline, in an attempt to prepare phenanthroline co-coordinated complexes of the series. In the case of compound **4**, phenanthroline was not incorporated in the final product, rather a different structural phase (of a previously published structure[9d]) of the terbium *p*-aminobenzoate was isolated. This was therefore not characterised further because it was a previously known compound.

The FTIR spectra of all compounds showed significant changes in the carbonyl stretching frequency compared with the free ligand (see the representative representation of $[Eu(paba)_3H_2O]$, and $[Tb(paba)_3H_2O]$ in comparison with H(paba) in Figure 1). In *p*-aminobenzoic acid, the C=O stretch occurs at 1655 $cm^{-1}$, whereas in the lanthanoid complexes, the band is shifted to significantly lower wave numbers and is split into two distinct bands around 1390 and 1500 $cm^{-1}$. In the compounds **1**–**3** there are increased absorbances in the 3300–3450 $cm^{-1}$ region attributable to water in the metal complexes. The complexes **1**–**3** were pure by $Na_2EDTA$ titration for lanthanoid content and carbon microanalysis for the composition $[Ln(paba)_3H_2O]$ as suggested by the X-ray crystal structures (below).

To ascertain the thermal stability of a representative sample of the $[Ln(paba)_3H_2O]$ series, the Eu analogue was analysed by thermogravimetric analysis. The exothermic release of water (peak maximum at 200 °C), which takes place in the temperature range of 120–220 °C is accompanied by a weight loss of 3% which is identical to the weight loss expected for the stated composition. This reaction can be described by Equation (3).

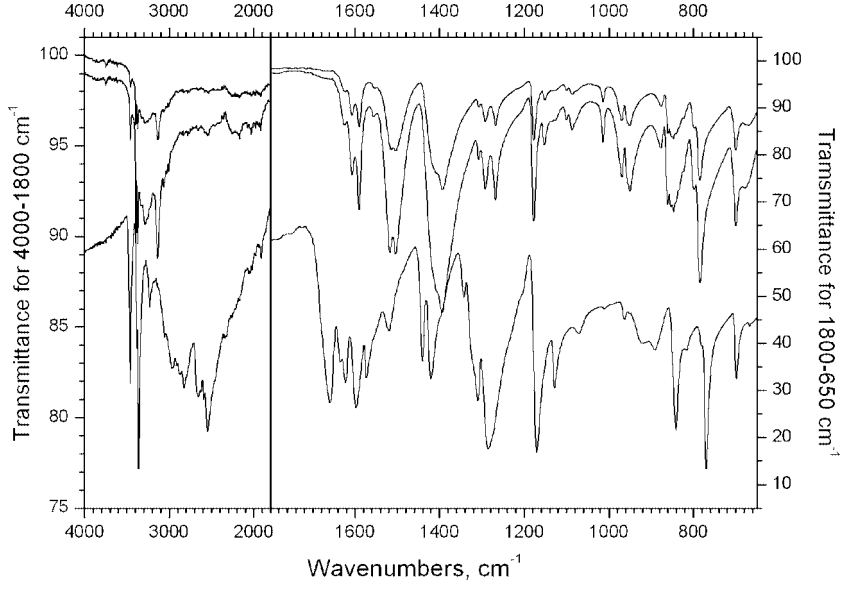


Figure 1. FTIR spectra of H(paba) (bottom), $Tb(paba)_3H_2O$ (middle) and $Eu(paba)_3H_2O$ (top).

 © 2007 Wiley-VCH Verlag GmbH & Co. KGaA, Weinheim 

$$Eu(C_6H_4NH_2COO)_3(H_2O) \rightarrow Eu(C_6H_4NH_2COO)_3 + H_2O \quad (3)$$

The thermal decay starts at 330 °C and continues to 810 °C. It is accompanied by several endothermic events (390, 430, 500, and 740 °C). Although the slope of the TG curve is very steady, there is a slight change in the gradient (330–460 °C) accompanied by a weight loss of 30%. This is the weight loss expected for the formation of the dimeric europium benzoate complex connected by an oxo bridge. A plausible reaction sequence is shown in Equations (4), (5) and (6).

$$Eu(C_6H_4NH_2COO)_3 + 3\ O_2 \rightarrow Eu(C_6H_5COO)_3 + 1.5\ H_2O + 3\ NO \quad (4)$$

$$Eu(C_6H_5COO)_3 + 7.5\ O_2 \rightarrow Eu(C_6H_5COO)_2(OH) + 2\ H_2O + 7\ CO_2 \quad (5)$$

$$2\ Eu(C_6H_5COO)_2(OH) \rightarrow (C_6H_5COO)_2Eu{-}O{-}Eu(C_6H_5COO)_2 + H_2O \quad (6)$$

In the range of 460–810 °C the final oxidation product is formed. The total mass loss of 70% is very close to the expected (69%) as shown in Equation (7).

$$(C_6H_5COO)_2Eu{-}O{-}Eu(C_6H_5COO)_2 + 30.5\ O_2 \rightarrow Eu_2O_3 + 10\ H_2O + 28\ CO_2 \quad (7)$$

Single crystals of compound **2** were grown by slow concentration of aqueous samples and its solid-state structures determined using X-ray crystallography. $[Gd(paba)_3H_2O]_n$ is isomorphous and structurally identical to that previously published for $[Ln(paba)_3H_2O]_n$ Ln = La, Ce, Pr, Nd, Sm, Eu, Tb, Dy, Er,[9] effectively establishing this structural type for the lighter and larger lanthanoids extends to Ln = Er. Compound **2** crystallises in the monoclinic space group $P2_1/n$ with one whole monomeric unit in the asymmetric unit. The lanthanoid metal centre is eight coordinate being bound by one chelating carboxylate, four monodentate carboxylates, one water molecule and perhaps surprisingly, one $N_{(amino)}$ group [Figure 2, a)]. Each of the monodentate carboxylate groups bridge to an adjacent Ln centre, while the chelating carboxylate is solely bound to one Ln centre. The overall structure is thus a three-dimensional polymeric species [Figure 2, b)] which is additionally extended through O–H···O and N–H···O hydrogen bonds. The Ln–O and Ln–N bond lengths (see Figure 2, caption) demonstrates well the lanthanoid contraction when compared with the other lanthanoid analogues,[9] with all internuclear distances about the Ln centres diminishing across the series in line with the reduction in ionic radii of the metal.[10] It is rather surprising that the lanthanoid centre is coordinated by an amine, given the compound was crystallised from water. It may be expected that water would complete the coordination sphere of the oxophilic rare-earth metal and presumably, binding of the amine to the metal, arises from a packing effect. It is worthy to mention the Ln···Ln internuclear distances, particularly with respect to the possibility of Ln···Ln energy transfer (see later). The Ln···Ln distances for this series of compounds are approximately 4.50 to 4.80 Å and for compound **2**, this distance is 4.725(3) Å.

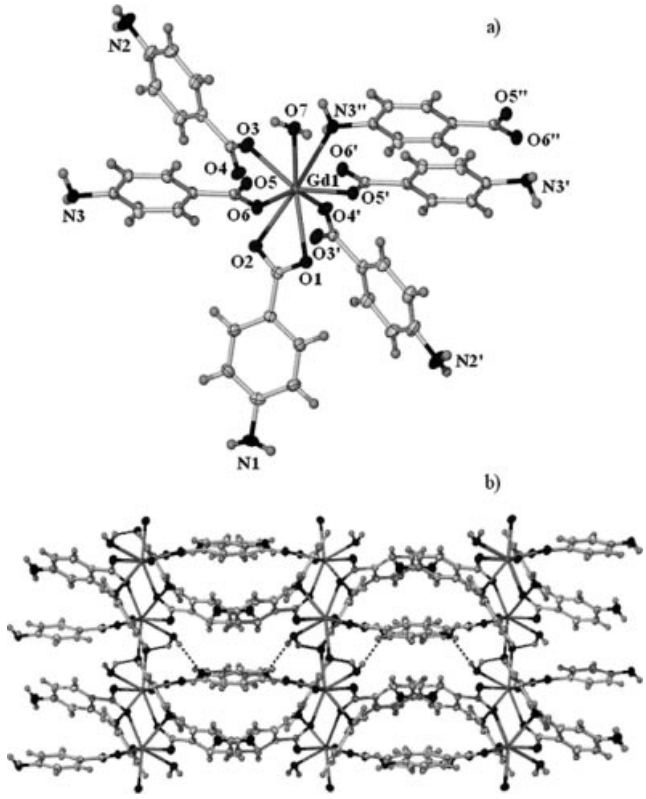


Figure 2. a) X-ray crystal structure of coordination sphere about Gd in polymeric $[Gd(paba)_3]\cdot H_2O$ (**2**). Thermal ellipsoids are at the 50% probability level. Selected bond lengths [Å]: Gd(1)–O(1) 2.461(2), Gd(1)–O(2) 2.455(2), Gd(1)–O(3) 2.336(2), Gd(1)–O(4) 2.304(2), Gd(1)–O(5) 2.342(2), Gd(1)–O(6) 2.349(3), Gd(1)–O(7) 2.513(3), Gd(1)–N(3) 2.668(3). b) X-ray crystal structure of polymeric $[Gd(paba)_3]\cdot H_2O$ (**2**). Thermal ellipsoids are at the 50% probability level.

Single crystals of compound **6** suitable for X-ray diffraction studies were grown from an aqueous solution of $[Tb(paba)_3H_2O]_n$ in the presence of 1,10-phenanthroline. The structure of this phase of the terbium analogue is isomorphous to that established for $[Ln(paba)_3(H_2O)_2]_2\cdot 2H_2O$ (Ln = Tb,[9d] Dy,[11] Ho,[9d] Y,[9d] Yb,[9d,12] Lu[9d]) and thus an example of the heavier structural type for the *p*-aminobenzoates of the lanthanoids and will not be discussed further. Significantly, by crystallisation of the terbium analogue as both structural phases, the structural boundary for the lanthanoid *p*-aminobenzoates existing as a dimer has now been established to start at Tb ranging to Lu, while the polymeric phase extends from La to Er. The reason for the isolation of two different phases presumably lies in the mode of crystallisation. We isolated the dimer phase in the presence of 1,10-phenanthroline and this presumably affects the solubility of the polymeric phase.

X-ray powder diffraction patterns of bulk material of compounds **1** to **3** were compared with patterns calculated from X-ray single crystal experiments and established that the structure of the bulk materials in all cases was identical to that obtained in the single crystals.

 © 2007 Wiley-VCH Verlag GmbH & Co. KGaA, Weinheim 

The $Tb^{3+}$ analogue of this series showed significant and exploitable luminescence in the visible, while $Eu^{3+}$ is quenched by charge-transfer states and MLCT,[13] additionally supported by vibrational quenching.[14] $Gd^{3+}$ is known to promote ligand phosphorescence at 24445 $cm^{-1}$,[15] we observe corresponding broad emission bands in $Gd(paba)_3$ at 420 nm and 478 nm, however, accompanied by a comparably strong emission due to minute $Tb^{3+}$ impurities (see below).

The luminescence of $Tb(paba)_3$ relies on the following successive steps:[16,17] 1. singlet–singlet absorption of the ligand ($^1S_0 \rightarrow {}^1S^*$, $\pi$–$\pi$ in nature), 2. intersystem crossing (ISC, $^1S^* \rightarrow {}^3T$, promoted by the spin-orbit coupling due to the $Tb^{3+}$ ion), 3. (exchange resonance driven) energy transfer Ligand($^3T$)$\rightarrow Tb^{3+}(^5D_4)$. Emission, excitation end reflectance spectra of solid $Tb(paba)_3H_2O$ are given in Figure 3.

As may be seen clearly, excitation can most efficiently be accomplished in this complex at a comparably short wavelength of approximately 310 nm. The quantum yield of the complex amounts to an unexpectedly high value (88%, e.g. $\lambda_{exc}$ = 340 nm), which is very surprising in view of the coordination of both, -$NH_2$ and $OH_2$ as ligands, as they are usually both essential vibrational deactivators of the excited state. However, it should be noted that both the Ln–$OH_2$ distance (261 pm) and the Ln–$NH_2$ distance (276 pm) are fairly long and multiphoton emission may thus be of secondary importance only, which is even more pronounced due to fairly strong hydrogen bonding.

A significant shortcoming for further utilisation of the complexes is that their strong degree of association [see Figure 2, b)] prevents, for example, evaporation without decomposition or dissolution in aprotic organic solvents. We could obtain solutions from $[Tb(paba)_3H_2O]$ only in refluxing DMF, albeit to a high cost in luminescence efficiency.

### 2.2. Co-coordinated Complexes

To explore further the luminescence properties of derivatives of the paba series above, we co-coordinated $[Tb(paba)_3H_2O]$ with the bidentate ligands bipyridine and phenanthroline as well as the tridentate terpyridine. The complexes were accessed by crystallisation from solutions of pabaH and bipy, phen, or terpy, respectively, in ethanol, to which aqueous $TbCl_3$ was added. In order to identify the immediate $Tb^{3+}$ coordination environment in the complexes obtained {$[Tb(paba)_3(bipy)(H_2O)]_2 \cdot 2H_2O$ (**5**), $[Tb(paba)_3(phen)(H_2O)]_2 \cdot 2H_2O$ (**6**), $[Tb(paba)_3(terpy)(H_2O)]_2 \cdot 6.7H_2O$ (**7**)}, single crystals grown from these solutions by slow evaporation were subjected to single-crystal structure analyses. The X-ray crystal structure of $[Tb(paba)_3(bipy)(H_2O)]_2 \cdot 2H_2O$ was previously reported.[18] For comparison, the La and Eu and analogues involving 1,10-phenanthroline were also structurally investigated. It is of importance to understand the structural variation of the rare earth series when investigating their luminescence properties. For example, we have shown that in the coordination polymer $Na[Tb(pic)_4] \cdot 1.5H_2O$ (picH = 2-picolinic acid) one-dimensional energy migration occurs, which can be utilised to transfer energy to $Eu^{3+}$ if the latter is co-doped into the material.[19] However, co-doping is only successful in these compounds, if the structural integrity of the parent compound is not compromised, a factor, which we have observed in the above-mentioned picolinates, if lanthanum was introduced. Therefore, we typically address the structural characteristics of several of the lanthanoid series.

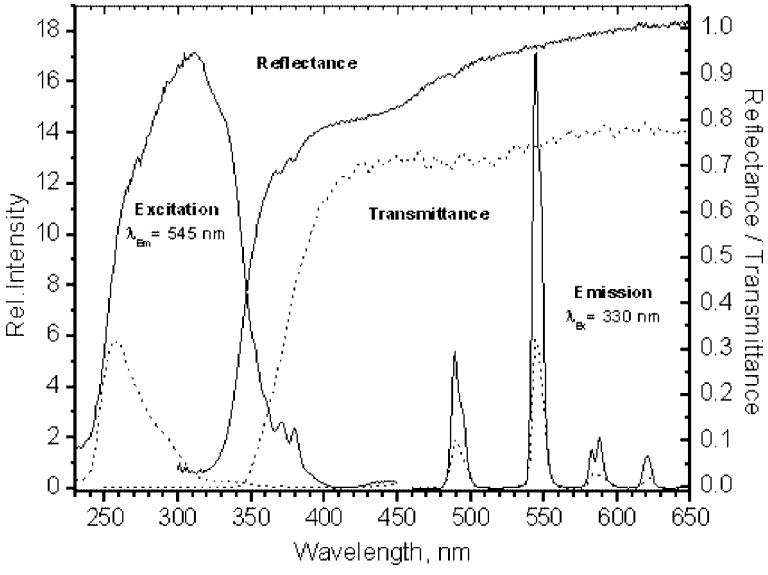


Figure 3. Comparison of optical spectra of the free complex $Tb(paba)_3H_2O$ (powder, solid line) and the polymer composite $Tb(paba)_3$PU (monolith, broken line).

 © 2007 Wiley-VCH Verlag GmbH & Co. KGaA, Weinheim 

Therefore, we also present the X-ray structural characterisation of $[Eu(paba)_3(phen)(H_2O)]_2{\cdot}2H_2O$ (**8**) and $[La(paba)_3(pabaH)(phen)_2]{\cdot}H_2O$ (**9**). Additional support for the significance of detailed structural data will be provided at the end of this paragraph.

In the published structure of $[Tb(paba)_3(bipy)(H_2O)]_2{\cdot}2H_2O$ (**5**) the compound exists as a dimer, with each terbium atom eight-coordinate. Each Tb atom is bound by a bidentate bipy ligand, a monodentate water molecule and three carboxylates, each with different binding modes. One carboxylate is chelating bidentate, the second is a monodentate-bound ligand, while the third bridges to the other Tb atom. There is a water molecule in the lattice and the *p*-amino groups of the paba ligands are not coordinated to the Tb atoms. The Tb···Tb distance in the dimer is 5.554(3) Å, thus allowing energy migration between the ions within the dimer.

$[Tb(paba)_3(phen)(H_2O)]_2{\cdot}2H_2O$ (**6**) crystallises in the triclinic space group $P\bar{1}$ with one whole monomer comprising the asymmetric unit. The compound dimerises through hydrogen bonding from a Tb-bound water molecule to the O atom of a Tb-bound carboxylate group (Figure 4). Each Tb atom is nine-coordinate, being bound by a bidentate 1,10-phenanthroline ligand, three chelating bidentate carboxylate groups and a water molecule. There are also two lattice water molecules per hydrogen-bonded dimer. The Tb···Tb distance in the hydrogen-bonded dimer is 5.884(5) Å. $[Eu(paba)_3(phen)(H_2O)]_2{\cdot}2H_2O$ (**8**) is isomorphous with **6** (Figure 4).

Figure 4. X-ray crystal structure of dimeric, hydrogen-bonded $[Tb(paba)_3(phen)(H_2O)]_2{\cdot}2H_2O$ (**6**); hydrogen atoms on the aromatic groups are omitted for clarity. Thermal ellipsoids are at the 50% probability level. $[Eu(paba)_3(phen)(H_2O)]_2{\cdot}2H_2O$ (**8**) is isostructural.

In compound **8** the Eu···Eu distance is 5.909(5) Å and is slightly longer due to the larger ionic radius of Eu over Tb.[10]

$[Tb(paba)_3(terpy)(H_2O)]_2{\cdot}6.7H_2O$ (**7**) crystallises in the triclinic space group $P\bar{1}$ with one whole $[Tb(paba)_3(terpy)(H_2O)]_2$ dimer and another half dimer (as well as 10 lattice water molecules) comprising the asymmetric unit. Each Tb atom is nine-coordinate, being bound by a tridentate terpy molecule, a monodentate water molecule, a bidentate carboxylate group, a monodentate carboxylate group and a monodentate carboxylate group that bridges to the other Tb atom (Figure 5). The Tb···Tb distance in this dimer is 5.312(8) Å.

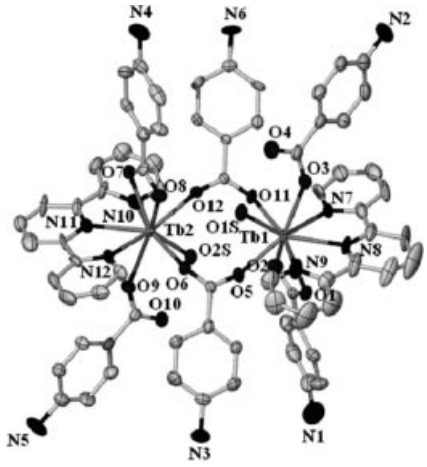


Figure 5. X-ray crystal structure of dimeric, hydrogen-bonded $[Tb(paba)_3(terpy)(H_2O)]_2{\cdot}H_2O$ (**7**); hydrogen atoms on the aromatic groups are omitted for clarity. Thermal ellipsoids are at the 50% probability level.

$[La(paba)_3(pabaH)(phen)_2]{\cdot}H_2O$ (**9**) crystallises in the monoclinic space group $P2_1/c$ with one whole mononuclear unit and one lattice water molecule comprising the asymmetric unit of the structure. The nine-coordinate lanthanum centre is now bound by two bidentate 1,10-phenanthroline ligands, one bidentate carboxylate, two unidentate carboxylate and one unidentate carboxylic acid molecule (Figure 6). It is significant that the lanthanum centre is now bound by a unidentate carboxylic acid molecule rather than by water (or ethanol) molecules, from which the compound was crystallised.

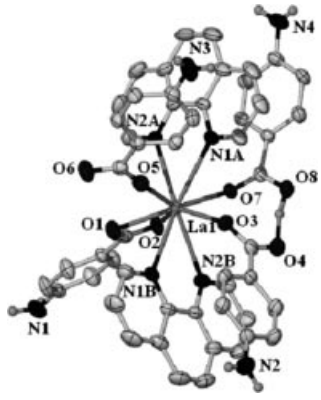


Figure 6. X-ray crystal structure of mononuclear $[La(paba)_3(pabaH)(phen)_2]_2$ (**9**); hydrogen atoms on the aromatic groups are omitted for clarity. Thermal ellipsoids are at the 50% probability level.

The proton on the bound carboxylic acid molecule is involved in hydrogen bonding with one of the O atoms of a unidentate bound carboxylate group. The fact that this compound is a new structural type for this chemistry, and

 © 2007 Wiley-VCH Verlag GmbH & Co. KGaA, Weinheim 

also that it is mononuclear is exciting, because we now intend to expand this chemistry to the Eu and Tb analogues, where luminescence may be enhanced due to decreased possibility of Ln···Ln quenching. The shortest La···La distance in compound **9** is 10.594(2) Å.

In all compounds comprising the bidentate bipy or phen or tridentate terpy, bond lengths are unexceptional between ligands and metal centres. A noteworthy feature of these compounds, when compared with the parent $[Ln(paba)_3(H_2O)]$ compounds, is that the *para*-nitrogen atoms of the paba group are not involved in binding to the lanthanoid centre (cf. above).

The optical properties of $[Tb(paba)_3(bipy)(H_2O)]_2{\cdot}2H_2O$ and $[Tb(paba)_3(phen)(H_2O)]_2{\cdot}2H_2O$ are depicted in Figure 7. In comparison to $[Tb(paba)_3{\cdot}H_2O]_n$ the excitation maximum has been red-shifted by approximately 50 nm on bipy-co-coordination and about 70 nm on phen-co-coordination $[Tb(paba)_3(bipy)(H_2O)]_2{\cdot}2H_2O$.

This redshift is of high applicatory interest; because the excitation now falls in the range of commercially available and ever improving semiconductor LED excitation sources, and may thus be used in a broader range of low-cost devices. Furthermore, the quantum yield of $[Tb(paba)_3(bipy)(H_2O)]_2{\cdot}2H_2O$ now even amounts to 95% under excitation at 350 nm. This somewhat unusual result may, just as argued for $[Tb(paba)_3H_2O]$ above, once more be interpreted in terms of the molecular structure, displaying long Tb–$OH_2$ distances and hydrogen bonding. Unfortunately, that high a quantum efficiency is not maintained in $[Tb(paba)_3(phen)(H_2O)]_2{\cdot}2H_2O$, where a drop to 38% is measured at 380 nm.

It was furthermore striking to us to note that the short Ln···Ln distances of 4.725(3) Å found in $[Gd(paba)_3H_2O]$ have an immediate impact on the luminescence spectra: terbium impurities (sub-percent level, $< 0.01\%$) in the Gd complex lead to a strong $Tb^{3+}$ emission, which had approximately 10 times the intensity of the corresponding ligand phosphorescence. Characteristically, the sensitisation of $Tb^{3+}$ is already 4 times weaker in $[Gd(paba)bipy(H_2O)_2]$ (Ln···Ln ca. 5.5 Å) and is not detectable in $[Gd(paba)phen(H_2O)_2](H_2O)_{1.5}$. (Ln···Ln ca. 5.9 Å). This behaviour signals the importance of detailed structural data in the interpretation of luminescent properties. Unfortunately, suitable crystals of the Gd analogue to $[La(paba)_3(pabaH)(phen)_2](H_2O)$ with a La···La distance 10.594(2) Å could not be obtained as yet, but may in the future be an interesting system to evaluate the details of Ln···Ln energy transfer in rare earth metallo-organic complexes.

### 2.3. Reactions with Isocyanates

The amino group of the paba complexes appeared to be a suitable reaction centre for the attachment of the complexes to polymeric backbones, isocyanates and polyurethanes ("PUs") in particular. As suitable polymer matrices,

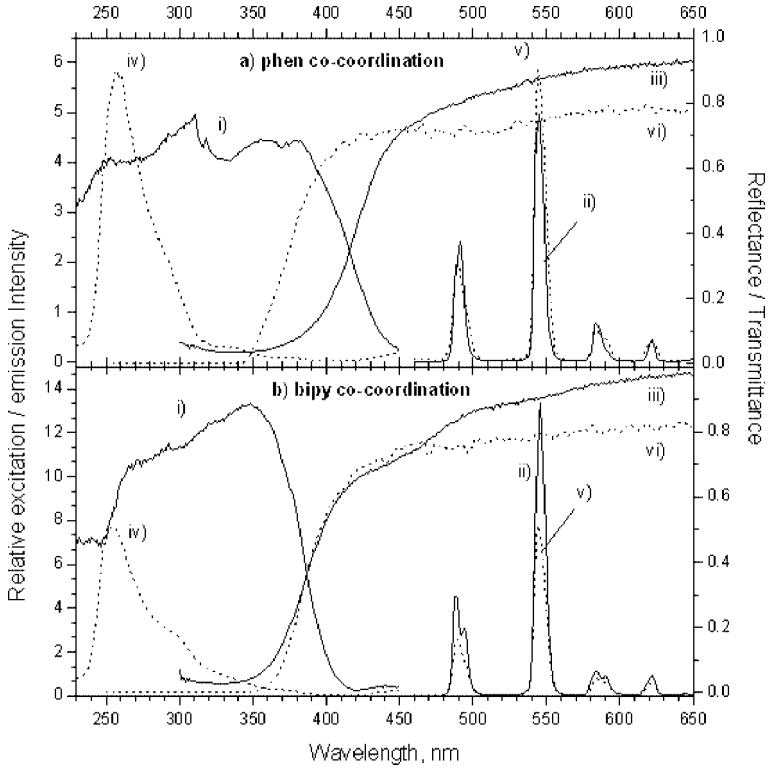


Figure 7. Comparison of free and polymer-imbedded complexes. Top, solid line: $Tb(paba)_3phen$; broken line: $Tb(paba)_3phenPU$. Bottom, solid line: $Tb(paba)_3bipy$; broken line: $Tb(paba)_3bipyPU$. i) excitation, ii) emission ii) reflectance of pure complexes; iv) excitation, v) emission, vi) reflectance of PU composites.

 © 2007 Wiley-VCH Verlag GmbH & Co. KGaA, Weinheim 

hexamethylene diisocyanates [O=C=N–$(CH_2)_6$–N=C=O, "HDIs"] and derived prepolymers were chosen rather than e.g. methylenebis(1,4-phenylene) diisocyanate (O=C=N–$C_6H_4$–$CH_2$–$C_6H_4$–N=C=O, "DPDIs") or 1,4-phenylene diisocyanate (O=C=N–$C_6H_4$–N=C=O, "PDIs"), because their optical transparency still allows optical measurements of the complexes imbedded, which might otherwise be obscured due to the extended π electrons, if DPDIs or PDIs were chosen as the matrix. However, reactions of $Tb(paba)_3$ with pure HDI, PDI and MDI were tested as "concentrated polymers" without further crosslinkers [see reaction schemes Figure 8, Equation (8)]. In the following, "$Tb(paba)_3$HDI", "$Tb(paba)_3$PDI" and "$Tb(paba)_3$DPDI" exclusively designate the reaction products of $Tb(paba)_3$ with HDI, PDI and DPDI, respectively, according to Equation (8), while "$Tb(paba)_3$PU" refers to a complete polyurethane matrix, based on HDI and a polyol, in which doping with $Tb(paba)_3$ substitutes a corresponding amount of the polyol [Equation (9)]. Analogously, $Tb(paba)_3$bipy and $Tb(paba)_3$phen have been reacted with HDI and polyol to give $Tb(paba)_3$bipyPU and $Tb(paba)_3$phenPU. The "concentrated" polymeric $Tb(paba)_3$PDI, $Tb(paba)_3$DPDI and $Tb(paba)_3$HDI are obtained as white powders, which are insoluble in all polar and apolar solvents tested; it was not possible to obtain transparent layers or monoliths from these materials. The excitation spectra of these reaction products are represented in Figure 9 in comparison to $Tb(paba)_3$; the corresponding emission spectra only differ in intensities and are not reproduced. Evidently, PDI linkage leads to a slight increase in intensity accompanied by a redshift of the excitation maximum to approximately 330 nm. Unfortunately, due to cloudiness (i.e. light scat-

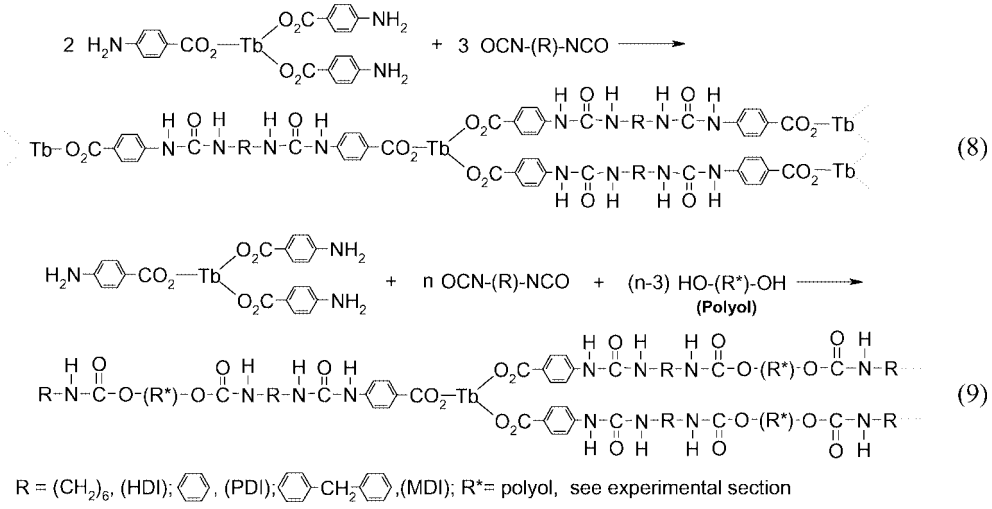


Figure 8. Reaction schemes of $Tb(paba)_3$ and diisocyanates formation of "concentrated" polymeric $Tb(paba)_3$ diisocyanates, Equation (8). Formation of PU-polymer "doped" with $Tb(paba)_3$, Equation (9).

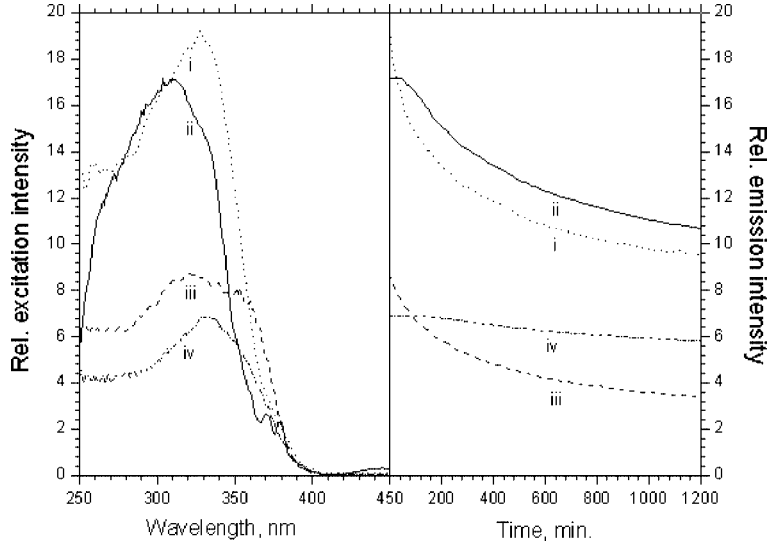


Figure 9. Reaction products of $Tb(paba)_3$ with different diisocyanates. Left: excitation spectra. Right: Photodegradation. i) $Tb(paba)_3$PDI; ii) $Tb(paba)_3$; iii) $Tb(paba)_3$DPDI; iv) $Tb(paba)_3$HDI, see text.

 © 2007 Wiley-VCH Verlag GmbH & Co. KGaA, Weinheim 

tering), shape and morphology of the polymer layers, reliable data on quantum efficiencies could not be determined, however, a crude visual comparison with diluted samples of $Tb(paba)_3$ in PU [$Tb(paba)_3$PU, see following paragraph] suggests comparable efficiencies.

Transparent composite materials, $Tb(paba)_3$PU, could eventually be prepared using DMF solutions of $Tb(paba)_3$ in a polyol (see experimental section), to which HDI was added [Equation (9)] in Figure 8, R = $(CH_2)_6$. As opposed to that, for reasons not obvious to us, the reactions of polyol-dissolved $Tb(paba)_3$ with PDI and DPDI only gave turbid products. The optical spectra of transparent $Tb(paba)_3$-PU are given in Figure 3. The comparison with pure $Tb(paba)_3$ immediately demonstrates the shortcomings of the composite. The onset of absorption is red-shifted to approximately 400 nm due to matrix contributions, which do not produce a noteworthy emissive response down to 320 nm, while the excitation maximum is blueshifted to 260 nm. The overall emission quantum yield is thus reduced by a factor of two to four (42%, $\lambda_{exc}$ = 260 nm; 17%, $\lambda_{exc}$ = 300). However, some error in this value may arise from differing sample and reference shapes (see Exp. Sect.). Correspondingly, the extended conjugation brought about by the –$C_6H_4$–NH–CO–NH– substituents [see Figure 8, Equation (2)] may be held responsible for the redshift of the absorption. At the same time, the coordination numbers of six for the $Tb^{3+}$ ion, as sketched for simplicity in Figure 8, is most unlikely in the polymer. Instead, coordination of N and O atoms of neighbouring fragments may be expected, thus giving rise to radiationless deactivation by high frequency vibrations.

The initial idea of using bipyridine and phenanthroline as co-ligands to increase their solubility in the (pre-)polymers did not lead to the desired results with respect to efficiency. Although bipyridine co-coordinated $Tb(paba)_3$ could eventually be used to form a clear polymer ["$Tb(paba)_3$bipyPU"], if the $Tb(paba)_3$bipy was initially dissolved in excess HDI followed by addition/crosslinking with polyol, its efficiency is again lowered by a factor of two to three (55%, $\lambda_{exc}$ = 260 nm to 28%, $\lambda_{exc}$ = 300 nm) in comparison to pure $Tb(paba)_3$. If $Tb(paba)_3$bipy was dissolved in the polyol prior to HDI addition, bipyridine appeared to be liberated, as indicated by the excitation spectrum, which is then again in resemblance of $Tb(paba)_3$PU, albeit at much lower intensity, at least partly due to the radiation "lost" to bipy absorption. This behaviour is yet more pronounced and evident in $Tb(paba)_3$phen, where a blue emission of phen indicates the presence of the uncoordinated co-ligand. The emission of phen is here seen to a similar extent, regardless of the addition sequence (dissolution in polyol followed by addition of HDI, or dissolution in HDI, followed by polyol admixture). The loss of phen is clearly visible from the spectral agreement of $Tb(paba)_3$PU (broken line in Figure 3) with $Tb(paba)_3$phenPU (broken line in Figure 7, a); the substitution of the bidentate co-ligands by the polydentate polymer fragments may then be interpreted in terms of an entropy increase. Due to the blue ligand emission, we refrained from the determination of quantum yields of $Tb(paba)_3$phenPU, but from the excitation spectra, they may be estimated to amount to > 40% under 260 nm excitation.

For eventual applications of the polymers described, knowledge on further material parameters next to the optical performance will be required, among them the durability and stability of the emission intensity. We have therefore also invested some effort into the characterisation of the emissive properties under prolonged irradiation with UV light. For this purpose, pressed sample polymer disks of approximately uniform thickness of approximately 1 mm to grant complete absorption were irradiated and the depreciation of the $Tb^{3+}$ 545 nm emission line ($^5D_4 \rightarrow {}^7F_5$) was monitored. For comparison, pure $Tb(paba)_3$ was pressed to a powder disk and included in the series. The results of the ageing experiments on $Tb(paba)_3$PDI, $Tb(paba)_3$DPDI and $Tb(paba)_3$HDI and $Tb(paba)_3$ are contained in Figure 9.

The evaluation of the depreciation of $Tb(paba)_3$PDI, which shows the highest initial efficiency, reveals that a maintenance crossover with pure $Tb(paba)_3$ is reached after only a few minutes, indicating that the aromatic polymer backbone of PDI is liable to relatively fast photodegradation. Similarly, $Tb(paba)_3$DPDI shows very similar degradation behaviour, albeit at a lower efficiency level. Remarkably, the aliphatic HDI based polymer is comparably stable, even more so than the pure complex. All curves could be fitted as single exponentials, if the initial degradation delay observed for $Tb(paba)_3$ and $Tb(paba)_3$HDI was taken into account. Based on extrapolation, the maintenance level of $Tb(paba)_3$HDI can accordingly be estimated to amount to almost 80% after 10000 h of operation. Future efforts will thus be directed towards luminescence improvement of aliphatic polyurethanes.

## Conclusions

Stimulated by high luminescence efficiencies of *p*-aminobenzoates of $Tb^{3+}$ (quantum yields > 80%), detailed structural investigations have been performed in order to derive materials from $Tb(paba)_3$, which are applicable in photoluminescenct applications, e.g. luminescent markers, or, eventually electrooptical devices, such as OLEDs. Typically, in the series of rare earth *p*-aminobenzoates coordination polymers are formed, which were broken down to molecular species for further manufacture. Such can in part be accomplished using chelating ligands such as bipyridine, phenanthroline, or terpyridine, although crystal structure determinations reveal that they essentially still exist as dimeric units and disadvantageously contain coordinated water. Nevertheless, on co-coordination of with bipyridine, a slight increase in quantum yield is accomplished (> 90%) in the case of $Tb^{3+}$, while phenanthroline reduces the overall efficiency (36%). The *p*-aminobenzoates of $Tb^{3+}$ were linked to aliphatic and aromatic diisocyanates through the benzoate amino group, yielding brightly green luminescing, insoluble polymer composites. Consecutively, transparent polyurethane monoliths incorporating backbone-linked *p*-

 © 2007 Wiley-VCH Verlag GmbH & Co. KGaA, Weinheim 

aminobenzoates of $Tb^{3+}$ and co-ligated complexes could be fabricated using aliphatic diisocyanates, and polyols as additional components. These "doped" polyurethanes show photoluminescence with quantum yields in the range between 40 and 55%, albeit at lowered excitation wavelengths. In anticipation of potential applications, the photodegradation of some aromatic and aliphatic composites were evaluated. In these experiments, aliphatic polymer backbones proved to be superior, but had lower initial efficiencies. Future work will thus focus on increasing the *p*-aminobenzoate composite efficiencies. Additionally, we are currently testing other benzoic acid derivatives.

## Experimental Section

Lanthanoid salts were purchased from Rhodia, Chempur and Aldrich with specified purity levels of in excess of 99.9%; *p*-aminobenzoic acid was obtained from Aldrich. All starting materials were used without further purification. Deionised water was used in all syntheses. Infrared spectra were recorded on sodium chloride plates as Nujol mulls or pressed into KBr disks (Figure 1) on a Perkin–Elmer Spectrum One FTIR spectrometer. Lanthanoid metal analyses were determined titrimetrically using the $Na_2EDTA$ method. Carbon analyses were carried out using a C-analyser with IR-detection unit (ELTRA, Germany). Melting points were performed in unsealed tubes.

**Synthesis:** The complexes **1**–**3** were synthesised following a similar procedure. Thus, sodium *p*-aminobenzoate (obtained by the reaction of the free *p*-aminocarboxylic acid with sodium hydrogencarbonate) was added to and aqueous solution of lanthanoid chloride. The crystals were obtained from slightly acidic aqueous medium. The samples were evaporated until large crystals of the complexes deposited. Complex **4** was synthesised in a similar manner, except 1,10-phenanthroline was added to the reaction mixture. Details of the properties for each compound follow. Yields reported are for isolated crystalline material. Yields of these reactions can be enhanced by precipitation of the compounds by addition of acetone to a saturated aqueous solution or increasing the pH value to just below 8 with 2 M ammonia.

**$[Eu(paba)_3(H_2O)]$ (1):** $V_{Eu}$: 2.43 $cm^3$ (0.52 $mol/dm^3$) = 1.26 mmol. $m_{H-p-ABA}$: 0.52 g = 3.79 mmol. $m_{product}$: 0.68 g (yield 93.0%). $C_{21}H_{20}EuN_3O_7$: calcd. C 43.6, Eu 26.3; found C 43.4; Eu 26.5. FTIR: see Figure 1. Powder XRD: 7.72 (s), 9.96 (s), 15.56 (m), 18.50 (w), 20.04 (m), 22.38 (w), 23.74 (m), 24.16 (m), 24.98 (w), 27.50 (w), 28.54 (w), 29.48 (w), 30.02 (w), 30.96 (w), 32.52 (w), 33.62 (w), 36.78 (m), 37.08 (m), 38.46 (s), 39.68 (w), 40.64 (w), 42.00 (w), 42.92 (w), 44.04 (w), 44.72 (s), 45.76 (w), 46.70 (w), 47.60 (w), 49.42 (w). DTA: 200 °C (exothermic), 390 °C (endothermic), 430 °C (endothermic), 500 °C (endothermic), 740 °C (endothermic). DTG: 120–220 °C (3% weight loss), 330–460 °C (30%), 460–810 °C (69% weight loss).

**$[Gd(paba)_3(H_2O)]$ (2):** Yield 17%. IR (Nujol): $\tilde{\nu}$ = 3400 m (br), 1660 s, 1595 s, 1567 s, 1399 m, 1347 s, 1306 w, 1297 m, 1260 w, 1240 w, 1163 m, 1149 w, 1093 w, 1051 w, 1013 w, 848 w, 787 m, 760 m, 698 s, 634 m $cm^{-1}$. $C_{21}H_{20}GdN_3O_7$: calcd. C 43.00; found C 43.08.

**$[Tb(paba)_3(H_2O)]$ (3):** $V_{Tb}$: 2.30 $cm^3$ (0.58 $mol/dm^3$) = 1.34 mmol. $m_{H-p-ABA}$: 0.55 g = 4.01 mmol

$m_{product}$: 0.72 g (yield 92.0%). $C_{21}H_{20}N_3O_7Tb$: calcd. C 43.1, Tb 27.3; found C 43.9, Tb 27.2.. FTIR: see Figure 1. Powder XRD: 7.72 (s), 10.00 (s), 14.88 (m), 15.56 (m), 18.38 (w), 18.76 (w), 19.46 (w), 20.04 (m), 21.62 (w), 22.34 (m), 23.74 (m), 24.12 (m), 24.92 (m), 27.44 (w), 28.54 (w), 28.98 (w), 29.52 (w), 30.04 (w), 30.42 (w), 31.06 (w), 32.80 (w), 33.74 (w), 35.48 (w), 36.62 (m), 37.22 (w), 38.56 (w), 39.80 (w), 40.58 (w), 42.10 (m), 44.00 (w), 44.72 (m), 45.70 (w), 47.82 (w).

**$[Tb(paba)_3(H_2O)_2]_2{\cdot}2H_2O$ (4):** From one attempted synthesis of co-crystallising $[Tb(paba)_3(H_2O)]$ with phenanthroline, we obtained crystals of the title compound that were isostructural with the previously reported complex.[9d] Unit cell data for compound **4**: triclinic, space group $P\bar{1}$ (No. 2), $a$ = 10.7819(7), $b$ = 12.0981(8), $c$ = 13.2695(9) Å, $\alpha$ = 72.407(1), $\beta$ = 66.679(1), $\gamma$ = 87.981(1)°, $V$ = 1508.0(2) $Å^3$.

**$[Tb(paba)_3(bipy)(H_2O)]_2{\cdot}2H_2O$ (5) and $[Tb(paba)_3(phen)(H_2O)]_2{\cdot}2H_2O$ (6), $[Tb(paba)_3(terpy)(H_2O)]_2{\cdot}6.7H_2O$ (7), $[Eu(paba)_3(phen)(H_2O)]_2{\cdot}2H_2O$ (8) and $[La(paba)_3(pabaH)(phen)_2].H_2O$ (9), $[Gd(paba)_3(bipy)(H_2O)]_2{\cdot}2H_2O$ (10) $[Gd(paba)_3(phen)(H_2O)]_2{\cdot}2H_2O$ (11):** $[Tb(paba)_3(bipy)(H_2O)]_2{\cdot}2H_2O$ was prepared by adding an aqueous solution of $TbCl_3$ (0.25 g) to an ethanol/water ($C_2H_5OH/H_2O$, 1:1) solution of *p*-aminobenzoic acid (0.2 g) and bipyridine (0.3 g), to give a volume of ca. 30 mL. The colourless crystals were obtained by slowly evaporating the mixture at room temperature for several days.

Analogously, the preparation of $[Ln(paba)_3(phen)(H_2O)]_2{\cdot}2H_2O$, [Ln = Eu, (**8**) Tb (**6**), Gd (**11**)] involved the addition of an aqueous $LnCl_3$ (Eu, Tb, Gd) solution (0.2 g) to an ethanol solution of *p*-aminobenzoic acid (0.3 g) and 1,10 phenanthroline (0.3 g) after two weeks in an open vessel afforded small light yellow crystals suitable for single crystal structure determination.

"Working amounts" of **5**, **6**, **10** and **11** were obtained using H(paba) (3 mmol) and bipy (or phen) (2 mmol), dissolved in of water/ethanol mixture (20 mL, 1: 1), adjustment of the pH to 5 using 2 M ammonia solution. An aqueous solution of $Tb^{3+}$ [1 mmol of from of 0.5 M $TbCl_3$ ($GdCl_3$) stock solution] was then slowly added to the ligand solution under vigorous stirring. Almost complete and immediate precipitation occurs after slowly raising the pH of this solution to just below 8.0. The complexes were filtered and dried at 60 °C. The products deviated in their composition from the material used for crystal structure determination due to the drying procedure (loss of lattice water): $[Gd(paba)_3bipy(H_2O)_2]$: calcd. C 48.95; found 48.96; $[Gd(paba)_3phen(H_2O)_2](H_2O)_{1.5}$: calcd. C 48.83; found C 48.90].

For the synthesis of crystals of $[Tb(paba)_3(terpy)(H_2O)]_2{\cdot}6.7H_2O$ (**7**) terpyridine (0.3 g) and *p*-aminobenzoic acid (0.2 g) were dissolved in 50% ethanol (3 mL). To the resulting clear solution, $TbCl_3$ solution (0.2 g in 3 mL water) was added dropwise. The reaction was stirred for 5 h. A few light-yellow crystals were received on partial evaporation of the solvent.

Single crystals of $[La(paba)_3(pabaH)(phen)_2]{\cdot}H_2O$ (**9**) were prepared as for compounds **6** and **8** except $LaCl_3$ solution was used in place of $LnCl_3$(Ln = Eu, Tb).

**$Tb(paba)_3HDI$, $Tb(paba)_3PDI$ and $Tb(paba)_3DPDI$:** The complex polymer composites were synthesised by adjusting a procedure described in the literature.[20] All operations were carried out providing for the exclusion of water (standard Schlenk techniques). Vacuum dried $Tb(paba)_3$ ($10^{-3}$ mbar, 140 °C, 5 h, 0.010 mol) was dissolved in dry DMF (20 mL). To this solution the pure diisocyanate (0.017 mol) was added dropwise. The reaction was carried out within 14 h at 80 °C under argon. After solvent evaporation, the residue was dried in vacuo and powdered using a mortar and pestle.

 © 2007 Wiley-VCH Verlag GmbH & Co. KGaA, Weinheim 

**$Tb(paba)_3PU$, $Tb(paba)_3bipyPU$ and $Tb(paba)_3phenPU$:** For the preparation of the transparent polyurethanes a commercial system consisting of a hexamethylene diisocyanate prepolymer and a polyol was used (from Lackwerke Peters, 47906 Kempen, Germany, VT 3402 KK). To determine the exact amounts of polyol to be substituted by the corresponding Tb complexes, the NCO content was determined using chlorobenzene as solvent, dibutylamine as reagent and bromothymol blue as the indicator for the HDI, for the OH number of the polyol, pyridine, phthalic anhydride and phenolphthalein were used, according to procedures previously described.[21] Analytically, 5.40 mmol NCO/g diisocyanate and 5.34 mmol OH/g polyol were found.

To obtain dilute samples for efficiency measurements, the complexes (2 mmol) were dissolved in DMF and added to the hexamethylene diisocyanate (1 g, ratio paba: NCO group approximately 1:100), DMF was evaporated in vacuo and the complex solution in diisocyanate thus obtained was mixed with the polyol (1:1 ratio), the mixture was placed in a transparent cuvette of 1 cm path length, air bubbles were removed under vacuum. The polymerisation to give the polyurethane was carried out at 60 °C in a drying chamber. Polymers containing more than $1{\cdot}10^{-2}$ mol complex/L could be prepared in an analogous manner. For such samples, the consumption of HDI by $Tb(paba)_3$ or was accounted for in that a lower amount of polyol was used. However, the emission intensities (not quantum yields) were at a maximum at approximately $1{\cdot}10^{-2}$ mol complex/L.

**Optical Characterisation:** All emission and excitation intensities in the spectra reproduced are scaled against each other, such as to grant direct comparability.

Emission and excitation spectra of the solids were recorded at an angle of incidence of ca. 50° using a praying mantis type of set up to allow horizontal sample positioning without a cover. Reflectance spectra were obtained using an integrating sphere with a diameter of 70 mm and 10 mm port openings vs. commercial white and black references (Labsphere), and $BaSO_4$, respectively. Two Acton 300 Monochromators of 300 mm focal length were thus synchronously scanned. The intensity of the 450 W Xe source was detected with an Acton Photomultiplier tube P2, the gratings had 1200 $gmm^{-1}$. The excitation spectra of $Tb(paba)_3HDI$, $Tb(paba)_3PDI$ and $Tb(paba)_3DPDI$ presented in Figure 9 were corrected for the lamp and spectrometer profiles with $BaMgAl_{10}O_{17}$: Eu ("BAM"). $Tb(paba)_3$, $Tb(paba)_3bipy$, $Tb(paba)_3phen$ were also measured against Lumogen Red doped PMMA powders (doping level 50 ppm), whose quantum yield was taken as a constant 42% in the excitation range between 250 nm and 500 nm. Relative quantum yields of the clear PU composite monoliths [$Tb(paba)_3PU$, $Tb(paba)_3bipyPU$, $Tb(paba)_3phenPU$], prepared in 1 cm cuvettes, were determined relative to a Lumen Red/PMMA disk of 3 mm thickness. Due to the confinement in the reference disk of lower thickness, some loss due to lateral propagation of emitted light within the disk is possible, but could not be accounted for, because neither sample cuvette nor reference disk could be inserted into the integrating sphere. Additionally, we would like to point out that the quantum efficiencies given, while reproducible within our optical setup, may still carry imprecisions, not the least owing to the lack of a suitable green emitting standard with continuous quantum yield in the spectral excitation range between 250 and 500 nm (estimated imprecision margin ±10%). However, the general trends described and discussed will not be affected.

The photochemical degradation data of the samples presented in Figure 9 were collected under irradiation with a 150-W Xe lamp that was shone onto an area of 400 $cm^2$ through a UV band pass filter (from Schott, Germany, UG11, 3 mm). The change of emission was monitored through a green interference filter (from LOT-Oriel, 64293 Darmstadt, Germany, 546FS10-50) and focussed on a CCD camera (from Acton Research, Spectrum MM) through a Nikon® lens at a distance of 25 cm. Light source, filters and detection unit were attached to a housing, which contained the samples at the bottom. A freshly prepared Al mirror (thermal evaporation, 25 $cm^2$) was used to turn the horizontally entering beam onto the samples at the bottom, the camera was aligned on top of the housing. Background radiation was accounted for by subtraction of $BaSO_4$ measurements prior to interpretation.

**Xray Crystallography Studies:** For all compounds X-ray quality crystals were sealed and mounted in thin-walled capillaries, with hemispheres of data collected at room temperature with a Bruker SMART CCD diffractometer (Mo-$K_\alpha$ radiation, $\lambda$ = 0.71073 Å) using the omega scan mode. Data sets were corrected for absorption using the program SADABS.[22] For all structures, the position of the heavy atoms were found using the Patterson method for heavy atoms and refined on $F^2$ using SHELXL97–2[23] with X-SEED as the graphic interface.[24] All non-hydrogen atoms were located and were refined with anisotropic thermal parameters. Hydrogen atoms were placed in calculated positions (riding model) and were not refined. For compounds **2**, **6**, **8** and **9** hydrogen atoms were located on the $NH_2$ groups and on water molecules and were refined isotropically. For compound **7** hydrogen atoms were not located on heteroatoms and were not included in the refinement. Crystal data, and a summary of data collection are listed below.

CCDC-607965 (for **2**), -607966 (for **6**), -607967 (for **7**), -607968 (for **8**) and -607969 (for **9**) contain the supplementary crystallographic data for this paper. These data can be obtained free of charge from The Cambridge Crystallographic Data Centre via www.ccdc.cam.ac.uk/data_request/cif.

**Crystal Data for Compound 2:** $C_{21}H_{20}GdN_3O_7$, $M$ = 583.65, $0.24\times0.18\times0.15$ mm, monoclinic, space group $P2_1/n$ (No. 14), $a$ = 9.7452(9), $b$ = 22.736(2), $c$ = 9.8229(9) Å, $\beta$ = 99.9290(10)°, $V$ = 2143.9(3) $Å^3$, $Z$ = 4, $D_c$ = 1.808 $g/cm^3$, $F(000)$ = 1148, 9744 reflections collected, 3072 unique ($R_{int}$ = 0.0665). Final $GooF$ = 1.045, $R_1$ = 0.0287, $wR_2$ = 0.0691, $R$ indices based on 2639 reflections with $I>2\sigma(I)$ (refinement on $F^2$), 323 parameters, 0 restraints. Lp and absorption corrections applied, $\mu$ = 3.142 $mm^{-1}$.

**Crystal Data for Compound 6:** $C_{33}H_{30}N_5O_8Tb$, $M$ = 783.54, $0.36\times0.35\times0.32$ mm, triclinic, space group $P\bar{1}$ (No. 2), $a$ = 10.4554(8), $b$ = 12.3129(9), $c$ = 14.0035(10) Å, $\alpha$ = 92.8650(10), $\beta$ = 102.8890(10), $\gamma$ = 109.0390(10)°, $V$ = 1646.4(2) $Å^3$, $Z$ = 2, $D_c$ = 1.581 $g/cm^3$, $F(000)$ = 784, 7545 reflections collected, 4665 unique ($R_{int}$ = 0.0461). Final $GooF$ = 1.050, $R_1$ = 0.0466, $wR_2$ = 0.1283, $R$ indices based on 4260 reflections with $I>2\sigma(I)$ (refinement on $F^2$), 466 parameters, 15 restraints. Lp and absorption corrections applied, $\mu$ = 2.206 $mm^{-1}$.

**Crystal Data for Compound 7:** $C_{230}H_{228}N_{38}O_{66}Tb_6$, $M$ = 5534.02, $0.32\times0.30\times0.15$ mm, triclinic, space group $P\bar{1}$ (No. 2), $a$ = 17.460(3), $b$ = 18.615(3), $c$ = 19.377(3) Å, $\alpha$ = 80.199(3), $\beta$ = 72.342(3), $\gamma$ = 73.823(3)°, $V$ = 5738.3(14) $Å^3$, $Z$ = 1, $D_c$ = 1.601 $g/cm^3$, $F(000)$ = 2792, 26873 reflections collected, 16542 unique ($R_{int}$ = 0.0803). Final $GooF$ = 1.011, $R_1$ = 0.0768, $wR_2$ = 0.1882, $R$ indices based on 9943 reflections with $I>2\sigma(I)$ (refinement on $F^2$), 1531 parameters, 0 restraints. Lp and absorption corrections applied, $\mu$ = 1.918 $mm^{-1}$.

**Crystal Data for Compound 8:** $C_{33}H_{30}EuN_5O_8$, $M$ = 776.58, $0.20\times0.20\times0.20$ mm, triclinic, space group $P\bar{1}$ (No. 2), $a$ = 10.4543(11), $b$ = 12.2021(13), $c$ = 14.0607(15) Å, $\alpha$ = 92.904(2), $\beta$

 © 2007 Wiley-VCH Verlag GmbH & Co. KGaA, Weinheim 

= 102.593(2), $\gamma$ = 108.734(2)°, $V$ = 1643.6(3) Å$^3$, $Z$ = 2, $D_c$ = 1.569 g/cm$^3$, $F$(000) = 780, 7553 reflections collected, 4692 unique ($R_{int}$ = 0.0394). Final *GooF* = 1.071, $R_1$ = 0.0537, $wR_2$ = 0.1398, $R$ indices based on 4315 reflections with $I > 2\sigma(I)$ (refinement on $F^2$), 465 parameters, 15 restraints. Lp and absorption corrections applied, $\mu$ = 1.966 mm$^{-1}$.

**Crystal Data for Compound 9:** $C_{52}H_{43}LaN_8O_9$, $M$ = 1062.85, 0.40 × 0.40 × 0.20 mm, monoclinic, space group $P2_1/c$ (No. 14), $a$ = 18.8602(12), $b$ = 19.7204(13), $c$ = 13.1888(9) Å, $\beta$ = 97.1610(10)°, $V$ = 4867.1(6) Å$^3$, $Z$ = 4, $D_c$ = 1.450 g/cm$^3$, $F$(000) = 2160, 22150 reflections collected, 6988 unique ($R_{int}$ = 0.0646). Final *GooF* = 1.003, $R_1$ = 0.0340, $wR_2$ = 0.0648, $R$ indices based on 5324 reflections with $I > 2\sigma(I)$ (refinement on $F^2$), 676 parameters, 0 restraints. Lp and absorption corrections applied, $\mu$ = 0.943 mm$^{-1}$.

## Acknowledgments

We acknowledge the Australian Research Council for continued support. We also acknowledge an IPRS scholarship and Monash Graduate Scholarship (to M.H.) and funding by the Bundesministerium für Bildung und Forschung (BMB+F Grant 17 094 00) to M.W. BAM and Lumogen Red references were generously provided by Philips Research Laboratories (Aachen, Germany) and BASF (Ludwigshafen, Germany), respectively.

[1] S. Sato, S. M. Wada, *Bull. Chem. Soc. Jpn.* **1970**, *43*, 1955.
[2] W. R. Dawson, J. L. Kropp, M. Windsor, *J. Chem. Phys.* **1966**, *45*, 2410.
[3] O. L. Malta, *J. Lumin.* **1997**, *71*, 229.
[4] F. R. G. e Silva, O. L. Malta, *J. Alloys Compd.* **1997**, *250*, 427.
[5] G. F. G. F. de Sá, O. L. Malta, L. de Mello Donegá, A. R. Simas, R. L. Longo, P. A. da Silva Jr., E. F. Santa Cruz, *Coord. Chem. Rev.* **2000**, *196*, 165.
[6] A. Ouchi, Y. Suzuki, Y. Ohki, Y. Koizumi, *Coord. Chem. Rev.* **1998**, *92*, 29.
[7] B. Yan, H. Zhang, *Mater. Res. Bull.* **1998**, *10*, 1517.
[8] D. Sendor, P. C. Junk, U. Kynast, *Solid State Phenomena* **2003**, *90/91*, 521.
[9] a) M. S. Khiyalov, I. R. Amiraslanov, Kh. S. Mamedov, E. M. Movsumov, *Zh. Strukt. Khim. (J. Struct. Chem.)* **1981**, *22*, 113; b) S.-Y. Niu, Y.-L. Zhang, W. Lai, Z.-Z. Yang, G.-D. Yang, L. Ye, *Huaxue Xuebao* **2001**, *59*, 2170; c) S. Y. Niu, G. D. Yang, Y. L. Zhang, J. Jin, L. Ye, Z. Z. Yang, *J. Mol. Struct.* **2002**, *608*, 95; d) H.-L. Sun, C.-H. Ye, X.-Y. Wang, J.-R. Li, S. Gao, K.-B. Yu, *J. Mol. Struct.* **2004**, *702*, 77; e) C.-H. Ye, H.-L. Sun, X.-Y. Wang, J.-R. Li, D.-B. Nie, W.-F. Fu, S. Gao, *J. Solid State Chem.* **2004**, *177*, 3735.
[10] R. D. Shannon, *Acta Crystallogr., Sect. A* **1976**, *32*, 751.
[11] Z. Rzaczynska, V. K. Belskii, *Pol. J. Chem.* **1994**, *68*, 309.
[12] L. Z. Rzaczynska, V. K. Belskii, *Pol. J. Chem.* **1994**, *68*, 309.
[13] S. T. Frey, W. D. Horrocks Jr., *Inorg. Chem.* **1991**, *30*, 1073.
[14] G. Blasse, B. C. Grabmeier, *Luminescent Materials*, Springer, **1994**.
[15] B. Yan, S. B. Wang, J. Z. Ni, *Monatsh. Chem.* **1998**, *129*, 151.
[16] V. L. Ermolaev, V. G. Aleshin, E. A. Saenko, *Dokl. Akad. Nauk* **1965**, *165*, 1048.
[17] M. W. S. Sato, *Bull. Chem. Soc. Jpn.* **1970**, *43*, 1955.
[18] L. Oyang, H.-L. Sun, X.-Y. Wang, J.-R. Li, D.-B. Nie, W.-F. Fu, S. Gao, K.-B. Yu, *J. Mol. Struct.* **2005**, *740*, 175.
[19] D. Sendor, M. Hilder, T. Juestel, P. C. Junk, U. H. Kynast, *New J. Chem.* **2003**, *27*, 1070.
[20] C.-L. Lin, H.-M. Mao, R.-R. Wu, P.-L. Kuo, *Macromolecules* **2002**, *35*, 3083.
[21] Z. Wirpsza, *Poliuretany, Chemia technologia zastosowanie*, WNT Warszawa, **1991**.
[22] R. H. Blessing, *Acta Crystallogr., Sect. A* **1995**, *51*, 33.
[23] G. M. Sheldrick, *University of Göttingen*, **1997**.
[24] L. J. Barbour, *J. Supramol. Chem.* **2001**, *1*, 189.

Received: August 29, 2006
Published Online: November 13, 2006

 © 2007 Wiley-VCH Verlag GmbH & Co. KGaA, Weinheim 

DOI: 10.1002/ejic.200600812

# Rare-Earth Nitroquinolinates: Visible-Light-Sensitizable Near-Infrared Emitters in Aqueous Solution

Rik Van Deun,*[a] Pascal Fias,[a] Peter Nockemann,[a] Kristof Van Hecke,[a] Luc Van Meervelt,[a] and Koen Binnemans[a]

**Keywords:** Rare earth metals / Luminescence / Chelates / N,O ligands / Sensing

Water-soluble, stable, and easily synthesizable 1:4 complexes of rare-earth ions with 8-hydroxy-5-nitroquinolinate ligands have been prepared. These complexes can be sensitized by visible light with wavelengths up to 480 nm and show near-infrared emission in aqueous solution. The incorporation of a nitro group in the quinoline moiety shifts its absorption bands to longer wavelengths and also increases its molar absorptivity by a factor of 2.5, thereby significantly enhancing its light-harvesting power. The presence of the nitro group also increases the solubility of the resulting complexes, making them water-soluble.

(© Wiley-VCH Verlag GmbH & Co. KGaA, 69451 Weinheim, Germany, 2007)

## Introduction

Research towards efficient near-infrared emitting lanthanide systems that are compatible with aqueous media is becoming increasingly popular.[1–6] There are several reasons for this. First of all, in vivo imaging using near-infrared radiation has the advantage of being noninvasive and tissue-friendly because of the longer emission wavelengths used. Secondly, although several rare-earth complexes have been reported to show bright near-infrared emission, most of these systems are soluble in (deuterated) organic solvents only. Moreover, because of the small energy gap between the excited states of the near-infrared emitting lanthanide ion and its lower lying energy levels, the introduction of water into these systems provides a very efficient route for radiationless deactivation, which quenches the luminescence and makes these systems useless for applications.

Lanthanide complexes that exhibit visible emission should preferentially have antenna ligands with triplet levels at rather high energy in order to prevent energy back-transfer from the accepting energy level of the lanthanide ion to the triplet level of the ligand. This usually means that the excitation wavelength of such systems is located in the ultraviolet spectral region, although some visible-light-sensitizable systems have been reported.[7–11] In the case of biosensing applications, it is obvious that excitation with visible light offers the advantage of being less harmful towards living tissue. In lanthanide complexes that emit in the near-infrared, the position of the triplet level can be much lower because of the lower lying emission levels of the lanthanide ion. However, in many cases, excitation of these systems still requires ultraviolet radiation.

Here, we report the visible light sensitization of lanthanide complexes with nitrated 8-hydroxyquinoline ligands. The ligand 8-hydroxy-5-nitroquinoline (Figure 1) forms water-soluble 4:1 complexes with trivalent lanthanide ions that show visible-light-sensitized near-infrared emission in aqueous media. In addition, these complexes can be made in an easy one-step synthetic method.

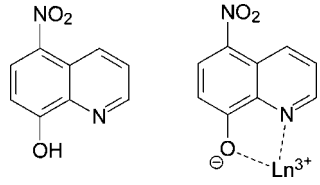


Figure 1. Chemical structure of 8-hydroxy-5-nitroquinoline (left) and its coordination mode to a rare-earth ion (right).

## Results and Discussion

8-Hydroxyquinoline has historically been used as a gravimetric agent for the determination of a large variety of metal ions, so its application was mainly based on its good complexing properties and on the low solubility of the resulting complexes in aqueous media.[12] Recently, we have shown that complexes of 8-hydroxyquinoline and its derivatives with trivalent rare-earth ions possess a rich structural chemistry that results in the formation of hydrated 3:1 tris structures, 4:1 tetrakis structures, and 8:3 trimeric species.[13] Because of the promising near-infrared luminescence properties of the quinolinates of trivalent erbium, ytterbium, and neodymium, interest in these materials has in-

[a] Katholieke Universiteit Leuven, Department of Chemistry, Celestijnenlaan 200F, 3001 Leuven, Belgium
Fax: +32-16-32-79-92
E-mail: rik.vandeun@chem.kuleuven.be

 © 2007 Wiley-VCH Verlag GmbH & Co. KGaA, Weinheim 

creased substantially in the last years, resulting in the appearance of several literature reports.[14–20]

This paper is the first, however, to report on complexes of 8-hydroxy-5-nitroquinoline as near-infrared emitting materials. Introduction of the nitro group in the 5-position of the 8-hydroxyquinoline moiety changes its physical and chemical properties significantly. The resulting complex is soluble in water at ambient temperature, whereas the non-nitrated equivalents are not. The electron-withdrawing properties of the nitro group decrease the basicity of the coordinating oxygen atom, resulting in the preferential formation of 4:1 tetrakis complexes rather than 8:3 trimeric oxygen-bridged species (an electron-poor oxygen atom is less capable of bridging two rare-earth ions, which is needed to form 8:3 trimeric species). Also, the use of excess ligand and of excess cations in the synthetic procedure stimulates the formation of 4:1 tetrakis complexes instead of 8:3 trimers even though no substituents are present in the 7-position of the quinoline ligand (see Experimental Section). The molecular structure of the yttrium(III) complex of 8-hydroxy-5-nitroquinoline with a tetraethylammonium counterion is shown in Figure 2; the crystal structure data are summarized in the Experimental Section.

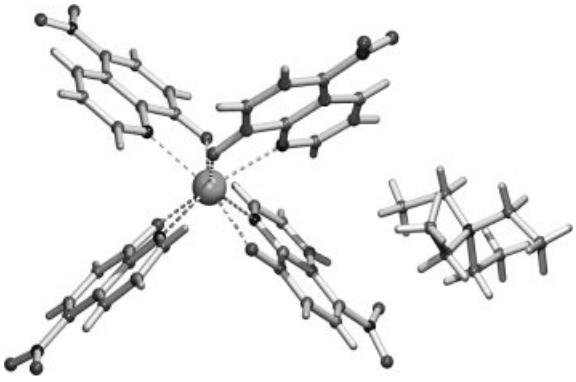

Figure 2. Detail of the molecular structure of the yttrium(III) complex of 8-hydroxy-5-nitroquinoline with a tetraethylammonium counterion.

The structure contains only one tetrakis(nitroquinolinate) complex in the asymmetric unit, together with one tetraethylammonium counter cation. The yttrium(III) ion is surrounded by four nitroquinolinate ligands. The coordination number of the yttrium(III) ion is eight, and the coordination polyhedron can be described as a slightly distorted square antiprism. No solvent molecules are coordinated to the yttrium(III) ion.

Because of the more pronounced electron delocalization in the nitro group, the electronic absorption spectrum of the ligand also differs from that of the non-nitrated equivalents. The absorption spectrum of a nitrated rare-earth quinolinate is shown in Figure 3 along with the luminescence spectra of aqueous solutions of the neodymium(III) and ytterbium(III) complexes of 8-hydroxy-5-nitroquinoline with a tetraethylammonium counterion. The absorption spectrum shows the typical features of deprotonated 8-hydroxyquinolines, namely two absorption bands corresponding to $\pi \rightarrow \pi^*$ transitions. The longer wavelength transition is associated with a shift of electron density from the phenolate oxygen to the $\pi^*$ orbitals of the aromatic ring.[21] It can easily be seen that the longer wavelength transition allows excitation with visible light with wavelengths of up to 480 nm. Another important effect of the incorporation of the nitro substituent is a significant increase in the molar absorptivity of the complex, which results in an enhanced light harvesting power: the $\varepsilon$ value of the neodymium(III) complex of 8-hydroxy-5-nitroquinoline with a tetraethylammonium counterion, measured at the absorption maximum (445 nm), is 36800 $M^{-1}\,cm^{-1}$, whereas the $\varepsilon$ value of the comparable neodymium(III) complex of 5,7-dichloro-8-hydroxyquinoline with a tetraethylammonium counterion measured at the absorption maximum (405 nm) is only 14300 $M^{-1}\,cm^{-1}$.[22]

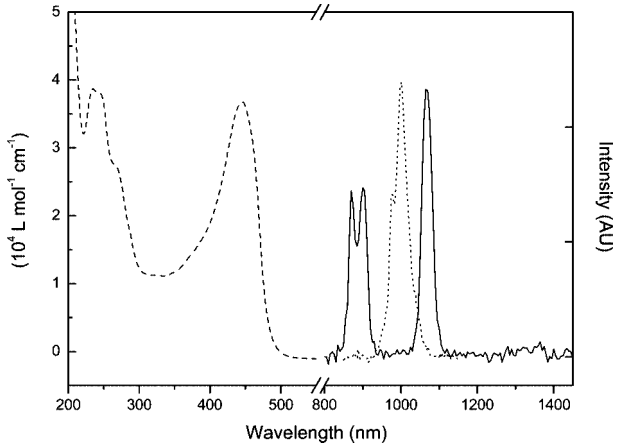


Figure 3. Absorption (dashed line) and emission spectra of the neodymium (solid line) and the ytterbium complexes (dotted line) of 8-hydroxy-5-nitroquinoline with tetraethylammonium counterions in water ($c \approx 10^{-5}$ M; $\lambda_{exc}$ = 445 nm).

The luminescence spectrum of the neodymium(III) complex shows the typical bands of the ion, two of which are very distinct ($^4F_{3/2} \rightarrow {}^4I_{9/2}$ at 902 nm and $^4F_{3/2} \rightarrow {}^4I_{11/2}$ at 1067 nm), whereas the $^4F_{3/2} \rightarrow {}^4I_{13/2}$ transition can be observed at about 1350 nm, albeit very weak, because of the strong light absorption by water in that spectral region. The luminescence spectrum of the ytterbium(III) complex shows only one band, corresponding to the $^2F_{5/2} \rightarrow {}^2F_{7/2}$ transition, centered at 1001 nm. The concentrations of the solutions were between $10^{-6}$ and $10^{-5}$ M. An overview of the luminescence decay times, $\tau$, and the calculated level quantum efficiencies, $\Phi$, of the neodymium(III) and ytterbium(III) complexes of 8-hydroxy-5-nitroquinoline, both in water and in thf, is given in Table 1. Because of the difficulties involved in performing reliable quantum yield measurements, we decided not to measure these values but to calculate approximate values by comparing the luminescence decay time, $\tau$, with the radiative lifetime, $\tau_0$, of the ions, taken from the literature: $\Phi = \tau/\tau_0 \times 100\,\%$. The radiative lifetime, $\tau_0$, of $Nd^{3+}$ was taken to be 0.25 ms, whereas that of $Yb^{3+}$ is 2 ms.[23]

 © 2007 Wiley-VCH Verlag GmbH & Co. KGaA, Weinheim 

Table 1. Luminescence decay times, $\tau$, of the $Nd^{3+}$ ($^4F_{3/2}$) and $Yb^{3+}$ ($^2F_{5/2}$) levels and calculated level quantum efficiencies $\Phi$.[a]

| $Ln^{3+}$ | Solvent | $\tau$ [μs] | $\Phi$ [%] |
|---|---|---|---|
| $Nd^{3+}$ | thf | 0.51 | 0.20 |
| | water | 0.47 | 0.19 |
| $Yb^{3+}$ | thf | 8.3 | 0.41 |
| | water | 1.4 | 0.07 |

[a] Lifetimes measured at room temperature; $\lambda_{exc}$ = 355 nm; $c \approx 10^{-5}$ M.

The luminescence decay times of the neodymium(III) and ytterbium(III) complexes in thf (Table 2) are typical for complexes of these ions in an organic solvent.[24] In water, two striking features become obvious: 1) there is hardly any difference in the efficiency of the neodymium(III) complex in water as compared to thf, and 2) the efficiency of the ytterbium(III) complex in water is much lower than in thf. The first feature can be explained by looking at the crystal structure (Figure 2), from which it is obvious that no solvent molecules are coordinated to the central metal ion. It seems that the four ligands form a very efficient shell around the lanthanide ion.[25,26] These values compare well with those found by Imbert et al.[5] and Comby et al.,[6] who reported luminescence decay times for neodymium(III) complexes of a hydroxyquinoline-containing podand in water of between 0.13 and 0.25 μs. In these reports, however, the efficiencies of the ytterbium(III) complexes are much better than those of the neodymium(III) complexes, which is in line with what one would expect. A possible explanation for the aberrant behavior of the ytterbium(III) complex in our system could be the nitro substituent on the quinoline moiety, although the difference in redox potentials between the neodymium(III) and ytterbium(III) ions is also known to have an influence.[27] We are currently investigating the energy-transfer properties of these nitroquinolinate complexes in more detail.

## Conclusions

In conclusion, we have shown that visible-light-sensitizable near-infrared emission can be obtained from neodymium(III) and ytterbium(III) complexes of 8-hydroxy-5-nitroquinoline in aqueous solution. This is the first report in which this nitrated quinoline has been used as a ligand for near-infrared-emitting lanthanide ions. The incorporation of a nitro group in the quinoline moiety shifts its absorption bands to longer wavelengths and also increases its molar absorptivity by a factor of 2.5, thereby significantly enhancing its light-harvesting power. Furthermore, the resulting 4:1 complexes are water-soluble.

## Experimental Section

**Equipment and Techniques:** Absorption spectra were recorded with a Varian Cary 5000 spectrophotometer. The steady-state near-infrared luminescence spectra and the decay time measurements were recorded on an Edinburgh Instruments FS920P near infrared spectrometer, with a 450-W xenon lamp as the steady-state excitation source, a double excitation monochromator with 1800 lines per millimeter, an emission monochromator with 600 lines per millimeter, and a liquid-nitrogen-cooled Hamamatsu R5509-72 near-infrared photomultiplier tube. For luminescence decay time measurements, the setup includes a Continuum Minilite Nd:YAG laser, equipped with 2nd, 3rd and 4th harmonic crystals, which allows excitation at 1064, 532, 355, and 266 nm. Repetition rate: 10 Hz; pulse width: 3–5 ns. Standard quartz 1-cm fluorescence cuvettes (Hellma type QS-111) were used. CHN elemental analyses were performed with a CE Instruments EA-1110 elemental analyzer.

**Synthesis:** 8-Hydroxy-5-nitroquinoline was purchased from Acros. Sodium hydroxide, sodium chloride, tetraethylammonium hydroxide, tetraethylammonium chloride, yttrium(III) chloride hexahydrate, neodymium(III) chloride hexahydrate, and ytterbium(III) chloride hexahydrate were purchased from Aldrich.

**$NEt_4[Y(Q5N)_4]\cdot 2H_2O$ (HQ5N = 8-hydroxy-5-nitroquinoline):** In a first step, 0.75 mmol of 8-hydroxy-5-nitroquinoline was added to 50 mL of water together with 0.75 mmol of tetraethylammonium hydroxide solution and 3 mmol of tetraethylammonium chloride (to have a large excess of the counterion). The solution was then heated to 60 °C until the ligand had completely dissolved. The pH was checked and, if lower than 7.5, some extra hydroxide base was added. Subsequently, 0.15 mmol of yttrium(III) chloride hexahydrate in 10 mL of water was slowly added and the resulting solution was stirred for an hour. After cooling, the water was removed by evaporation under reduced pressure. The resulting oily product was dissolved in a small amount of methanol (approx. 5 mL). The precipitate formed was washed with small amounts of water and ethanol. Yield: 64 mg (34%). $C_{44}H_{40}N_9O_{12}Y\cdot 2H_2O$ (1011.8): calcd. C 52.23, H 4.38, N 12.46; found C 52.49, H 4.31, N 12.14. $^1$H NMR (400 MHz, [D$_6$]DMSO): $\delta$ = 1.15 [t, 3 H, $N(CH_2CH_3)_4$], 3.17 [q, 2 H, $N(CH_2CH_3)_4$], 6.62 (d, 1 H, H$^7$), 7.74 (dd, 1 H, H$^3$), 8.46 (d, 1 H, H$^4$), 8.96 (d, 1 H, H$^6$), 9.26 (d, 1 H, H$^2$) ppm. MS (ESI$^-$): *m*/*z* 845 $[Y(Q5N)_4]^-$.

**$Na[Nd(Q5N)_4]\cdot H_2O$:** In a first step, 0.75 mmol of 8-hydroxy-5-nitroquinoline was added to 50 mL of water together with 0.75 mmol of sodium hydroxide solution and 3 mmol of sodium chloride (to have a large excess of the counterion). The solution was then heated to 60 °C until the ligand had completely dissolved. The pH was checked and, if lower than 7.5, some extra hydroxide base was added. Subsequently, 0.15 mmol of neodymium(III) chloride hexahydrate in 10 mL of water was slowly added and the resulting solution was stirred for an hour. After cooling, a precipitate formed, which was filtered off and washed with small amounts of water and ethanol. Yield: 102 mg (58%). $C_{36}H_{20}N_8NaNdO_{12}\cdot H_2O$ (941.84): calcd. C 45.91, H 2.35, N 11.90; found C 46.12, H 2.29, N 11.78. The solubility in EtOH/chloroform was too low to obtain good mass spectra.

**$NEt_4[Yb(Q5N)_4]\cdot 3H_2O$:** In a first step, 0.75 mmol of 8-hydroxy-5-nitroquinoline was added to 50 mL of water together with 0.75 mmol of tetraethylammonium hydroxide solution and 3 mmol of tetraethylammonium chloride (to have a large excess of the counterion). The solution was then heated to 60 °C until the ligand had completely dissolved. The pH was checked and, if lower than 7.5, some extra hydroxide base was added. Subsequently, 0.15 mmol of ytterbium(III) chloride hexahydrate in 10 mL of water was slowly added and the resulting solution was stirred for an hour. After cooling, the water was removed by evaporation under reduced pressure. The resulting oily product was dissolved in a small amount of methanol (approx. 5 mL). The precipitate formed was washed with small amounts of water and ethanol. Yield: 84 mg

 © 2007 Wiley-VCH Verlag GmbH & Co. KGaA, Weinheim 

(40%). $C_{44}H_{40}N_9O_{12}Yb{\cdot}3H_2O$ (1113.9): calcd. C 47.44, H 4.16, N 11.32; found C 47.58, H 4.01, N 11.22. MS ($ESI^-$): *m*/*z* 930 $[Yb(Q5N)_4]^-$.

**Crystal Data for the Yttrium(III) Complex of 8-Hydroxy-5-nitroquinoline:** Crystals were obtained by diffusion of diethyl ether into a solution of the compound in dmf. Intensity data were collected on a SMART 6000 diffractometer equipped with a CCD detector using Cu-$K_\alpha$ radiation ($\lambda$ = 1.54178 Å). The images were interpreted and integrated with the program SAINT from Bruker.[28] $[C_8H_{20}N][C_{36}H_{20}N_8O_{12}Y]$, $M$ = 975.76, monoclinic, $P2_1/c$, $a$ = 17.771(2), $b$ = 13.994(1), $c$ = 16.893(2) Å, $\beta$ = 96.063(6)°, $V$ = 4177.7(8) Å$^3$, $T$ = 100 K, $Z$ = 4, $D_c$ = 1.551 g cm$^{-3}$, $\mu$(Cu-$K_\alpha$) = 2.632 mm$^{-1}$, $F$(000) = 2008, crystal size 0.3 × 0.3 × 0.1 mm$^3$, 7338 independent reflections ($R_{int}$ = 0.1359). Final $R$ = 0.0918 for 3940 reflections with $I > 2\sigma(I)$ and $\omega R_2$ = 0.2488 for all data. See Table 2 for further details. The structure was solved by direct methods and refined by full-matrix least-squares on $F^2$ using the SHELXTL program package.[29] Non-hydrogen atoms were refined anisotropically and the hydrogen atoms in the riding mode with isotropic temperature factors fixed at 1.2-times $U$(eq) of the parent atoms (1.5-times for methyl groups). The refinement of the data was difficult due to the low diffraction intensity at higher $2\theta$ angles.

Table 2. Summary of crystal data, intensity measurements, and structure refinement of the yttrium complex.

| | |
|---|---|
| Formula | $C_{44}H_{40}N_9O_{12}Y$ |
| Molecular weight | 975.76 |
| Crystal dimensions [mm] | 0.3 × 0.3 × 0.1 |
| Crystal system | monoclinic |
| Space group | $P2_1/c$ |
| $a$ [Å] | 17.771(2) |
| $b$ [Å] | 13.994(1) |
| $c$ [Å] | 16.893(2) |
| $\alpha$ [°] | 90 |
| $\beta$ [°] | 96.063(6) |
| $\gamma$ [°] | 90 |
| $V$ [Å$^3$] | 4177.7(8) |
| $Z$ | 4 |
| $D_{calcd.}$ [g cm$^{-3}$] | 1.551 |
| $\mu$(Cu-$K_\alpha$) [mm$^{-1}$] | 2.632 |
| Absorption correction | refined from $\Delta F$ |
| $F$(000) | 2008 |
| Measured reflections | 8236 |
| Unique reflections | 7338 |
| Observed reflections [$I_o > 2\sigma(I_o)$] | 3940 |
| Parameters refined | 599 |
| Goodness-of-fit | 1.015 |
| $R_1$ | 0.0918 |
| $\omega R_2$ | 0.2129 |
| $R_1$ (all data) | 0.1719 |
| $\omega R_2$ (all data) | 0.2488 |

CCDC-619338 contains the supplementary crystallographic data for this paper. These data can be obtained free of charge from The Cambridge Crystallographic Data Centre via www.ccdc.cam.ac.uk/data_request/cif.

## Acknowledgments

R. V. D. is a Postdoctoral Fellow of the FWO-Flanders. P. F. is indebted to the IWT for a PhD grant. Financial support by the FWO-Flanders (project G.0117.03), the K. U. Leuven (project GOA 03/03) and the EU CSG Programme (project no. G5RD-CT-2001-00577 OPAMD) is gratefully acknowledged. R. V. D. thanks the FWO-Flanders for a Research Grant from the Fund for Scientific Research – Flanders (FWO; project 1.5.099.06).

[1] M. H. V. Werts, R. H. Woudenberg, P. G. Emmerink, R. van Gassel, J. W. Hofstraat, J. W. Verhoeven, *Angew. Chem. Int. Ed.* **2000**, *39*, 4542–4544.
[2] J.-C. G. Bünzli, C. Piguet, *Chem. Soc. Rev.* **2005**, *34*, 1048–1077.
[3] Y. Korovin, N. Rusakova, *Inorg. Chem. Rev.* **2001**, *21*, 299–329.
[4] J.-C. G. Bünzli, G. R. Choppin, in *Lanthanide Probes in Life, Chemical and Earth Sciences – Theory and Practice*, **1989**, Elsevier, Amsterdam.
[5] D. Imbert, S. Comby, A.-S. Chauvin, J.-C. G. Bünzli, *Chem. Commun.* **2005**, 1432–1434.
[6] S. Comby, D. Imbert, A.-S. Chauvin, J.-C. G. Bünzli, *Inorg. Chem.* **2006**, *45*, 732–743.
[7] M. H. V. Werts, M. A. Duin, J. W. Hofstraat, J. W. Verhoeven, *Chem. Commun.* **1999**, 799–800.
[8] R. Van Deun, P. Nockemann, P. Fias, K. Van Hecke, L. Van Meervelt, K. Binnemans, *Chem. Commun.* **2005**, 590–592.
[9] N. M. Shavaleev, L. P. Moorcraft, S. J. A. Pope, Z. R. Bell, S. Faulkner, M. D. Ward, *Chem. Commun.* **2003**, 1134–1135.
[10] J.-M. Herrera, S. J. A. Pope, H. Adams, S. Faulkner, M. D. Ward, *Inorg. Chem.* **2006**, *45*, 3895–3904.
[11] D. Imbert, M. Cantuel, J.-C. G. Bunzli, G. Bernardinelli, C. Piguet, *J. Am. Chem. Soc.* **2003**, *125*, 15698–15699.
[12] E. R. Birnbaum, J. H. Forsberg, *Gmelin Handbook of Inorganic Chemistry, Sc, Y, La–Lu Rare Earth Elements*, Springer-Verlag, Berlin, **1982**; Part D2, System Nr. 39, p. 5–24 and references cited therein.
[13] R. Van Deun, P. Fias, P. Nockemann, A. Schepers, T. N. Parac-Vogt, K. Van Hecke, L. Van Meervelt, K. Binnemans, *Inorg. Chem.* **2004**, *43*, 8461–8469.
[14] M. Iwamuro, T. Adachi, Y. Wada, T. Kitamura, N. Nakashima, S. Yanagida, *Bull. Chem. Soc. Jpn.* **2000**, *73*, 1359–1363.
[15] W. P. Gillin, R. J. Curry, *Appl. Phys. Lett.* **1999**, *74*, 798–799.
[16] S. W. Magennis, A. J. Ferguson, T. Bryden, T. S. Jones, A. Beeby, I. D. W. Samuel, *Synth. Met.* **2003**, *138*, 463–469.
[17] J. Thompson, R. I. R. Blyth, G. Gigli, R. Cingolani, *Adv. Funct. Mater.* **2004**, *14*, 979–984.
[18] F. Artizzu, P. Deplano, L. Marchio, M. L. Mercuri, L. Pilia, A. Serpe, F. Quochi, R. Orru, F. Cordella, F. Meinardi, R. Tubino, A. Mura, G. Bongiovanni, *Inorg. Chem.* **2005**, *44*, 840–842.
[19] F. Quochi, R. Orru, F. Cordella, A. Mura, G. Bongiovanni, F. Artizzu, P. Deplano, M. L. Mercuri, L. Pilia, A. Serpe, *J. Appl. Phys.* **2006**, *99*, 053520.
[20] S. G. Leary, G. B. Deacon, P. C. Junk, *Z. Anorg. Allg. Chem.* **2005**, *631*, 2647–2650.
[21] H. Kunkely, A. Vogler, *Inorg. Chem. Commun.* **2000**, *3*, 645–647.
[22] P. Fias, PhD Thesis, K. U. Leuven, **2005**.
[23] S. I. Klink, G. A. Hebbink, L. Grave, F. C. J. M. van Veggel, D. N. Reinhoudt, L. H. Slooff, A. Polman, J. W. Hofstraat, *J. Appl. Phys.* **1999**, *86*, 1181–1185.
[24] G. A. Hebbink, L. Grave, L. A. Woldering, D. N. Reinhoudt, F. C. J. M. van Veggel, *J. Phys. Chem. A* **2003**, *107*, 2483–2491.
[25] S. W. Magennis, S. Parsons, Z. Pikramenou, *Chem. Eur. J.* **2002**, *8*, 5761–5771.
[26] A. P. Bassett, R. Van Deun, P. Nockemann, P. B. Glover, B. M. Kariuki, K. Van Hecke, L. Van Meervelt, Z. Pikramenou, *Inorg. Chem.* **2005**, *44*, 6140–6142.
[27] W. D. Horrocks, J. P. Bolender, W. D. Smith, R. M. Supkowski, *J. Am. Chem. Soc.* **1997**, *119*, 5972–5973.
[28] SAINT, Manual Version 5/6.0, Bruker Analytical X-ray Systems Inc., Madison, Wisconsin, **1997**.
[29] SHELXTL-PC, Manual Version 5.1, Bruker Analytical X-ray Systems Inc., Madison, Wisconsin, **1997**.

Received: September 2, 2006
Published Online: November 13, 2006

 © 2007 Wiley-VCH Verlag GmbH & Co. KGaA, Weinheim 

DOI: 10.1002/ejic.200600823

# Synthesis and Characterisation of $W^{VI}$ Complexes of Phosphane Oxide Ligands, $[WO_2X_2(OPR_3)_2]$ (X = F, Cl or Br; R = Me or Ph), and of the $[MoO_2F_2(OPR_3)_2]$

**Martin F. Davis,[a] William Levason,*[a] Raju Ratnani,*[b] Gillian Reid,*[a] Tim Rose,[a] and Michael Webster[a]**

**Keywords:** Tungsten / Molybdenum / Phosphane oxide / Crystal structures / Fluoride

Phosphane oxide complexes of dioxidotungsten$^{VI}$, $[WO_2X_2(OPR_3)_2]$ (X = Cl or Br, M = Ph or Me) have been prepared under anhydrous conditions from the reaction of $WX_6$ with $(Me_3Si)_2O$ in $CH_2Cl_2$, followed by addition of $OPR_3$. Some diphosphane dioxide analogues have been made similarly, viz, $[WO_2X_2(L–L)]$ {L–L = $Ph_2P(O)(CH_2)_nP(O)Ph_2$ ($n$ = 1 or 2), $o$-$C_6H_4[P(O)Ph_2]_2$}. The complexes have been characterised by elemental analysis, IR and NMR ($^1H$ and $^{31}P\{^1H\}$) spectroscopy, and the structures of $[WO_2Br_2(OPPh_3)_2]$ and $[WO_2Cl_2(OPMe_3)_2]$ determined, revealing distorted six-coordinate tungsten centres with *cis*-$WO_2$ and *trans*-$WX_2$ units. The difluorido-dioxido complexes $[MO_2F_2(OPR_3)_2]$ (M = Mo or W) and $[WO_2F_2(L'–L')]$ (L'–L' = 2,2'-bipyridyl, 1,10-phenanthroline) have been prepared by fluorination of the corresponding chlorido complexes with $Me_3SnF$ in $CH_2Cl_2$. These are characterised similarly and by $^{19}F\{^1H\}$ NMR spectroscopy. Attempts to make $[MO_2I_2(OPR_3)_2]$ were unsuccessful. No adduct formation occurs between $CrO_2Cl_2$ and $OPPh_3$ under rigorously anhydrous conditions. Crystal structures of $[Me_3SnCl(OPPh_3)]$ and two forms of $[WO_2Cl_2(1,10\text{-phen})]$ are also reported and discussed.

(© Wiley-VCH Verlag GmbH & Co. KGaA, 69451 Weinheim, Germany, 2007)

## Introduction

The coordination chemistries of $Mo^{VI}$ and $W^{VI}$ continue to attract much research effort, their importance including such diverse areas as metalloenzymes,[1] oxido-transfer reagents, catalyst precursors and epoxidation catalysts.[2–4] Complexes of the $MoO_2X_2$ (X = Cl or Br) with a wide range of O- and N-donor ligands are known and can be obtained by direct reaction of $MoO_2X_2$ [5,6] or $MoO_3$/aqueous HX[7] with the ligands, or more rarely by halogenation of $[Mo(CO)_4(ligand)]$.[8] The $WO_2X_2$ (X = Cl or Br) are insoluble and relatively unreactive and their chemistry has been less thoroughly explored. Some complexes were initially obtained by reaction of $WO_2X_2$ with excess molten ligand,[9] but more recently routes based upon the reaction of $WOCl_4$ with a disiloxane to produce $WO_2Cl_2$ in situ, followed by reaction with the ligand have been developed.[10] Little is known about $WO_2F_2$[11] and the only structurally characterised adduct, $[WO_2F_2(2,2'\text{-bipy})]$, was isolated from the decomposition of $[WOF_4(2,2'\text{-bipy})]$.[12] The dark green $WO_2I_2$[13] is known, but no complexes have been reported. A small number of adducts of $MO_2F_2$ (M = Mo or W) with phosphane oxides have been prepared from $MO_3$/aqueous HF and the ligands,[7,14] and the structure of $[MoO_2F_2(OPPh_2Me)_2]$ determined, although spectroscopic data are limited. The structure of $[MoO_2F_2(thf)_2]$, obtained by hydrolysis of $[MoF_4(NCl)]$, has also been reported.[15] We are interested in developing the chemistry of high-valent, early transition metals with softer donors such as thio- or seleno-ethers, and have reported examples with $MoO_2X_2$ (X = Cl or Br),[16] $TiX_4$, $ZrCl_4$ and $HfCl_4$.[17] Currently we are exploring routes to $W^{VI}$ complexes with these ligands, and because complexes of this type are very moisture sensitive and the ligands prone to oxidation or C–S(Se) bond fission under forcing conditions, many of the routes described above are not suitable. As a prelude to this work, we describe here the synthesis and characterisation of a series of phosphane oxide complexes of $WO_2X_2$ (X = Cl or Br) using anhydrous conditions and a route based upon $WX_6$/$(Me_3Si)_2O$. We also describe the (anhydrous) synthesis of fluorido analogues with both $Mo^{VI}$ and $W^{VI}$ using $Me_3SnF$[18] as fluorinating agent. Attempts to obtain $[MO_2I_2(OPR_3)_2]$ are also briefly discussed.

## Results and Discussion

### $[WO_2X_2(OPR_3)_2]$ (X = Cl or Br) Complexes

As expected, attempts to react commercial $WO_2Cl_2$ directly with $OPR_3$ (R = Me or Ph) in $CH_2Cl_2$ solution were unsuccessful, even after prolonged reflux. In contrast,

[a] School of Chemistry, University of Southampton, Highfield, Southampton SO17 1BJ, UK
[b] Department of Pure and Applied Chemistry, M. D. S. University, Ajmer 305009, India

 © 2007 Wiley-VCH Verlag GmbH & Co. KGaA, Weinheim 

"$WO_2Cl_2$" made in situ from reaction of $WCl_6$ with hexamethyldisiloxane, $(Me_3Si)_2O$, in anhydrous $CH_2Cl_2$, reacted readily with both phosphane oxides to produce [$WO_2Cl_2(OPR_3)_2$] in good yields as white powders, moderately soluble in chlorocarbon solvents. Similar reactions using $WBr_6/(Me_3Si)_2O$ gave the corresponding cream [$WO_2Br_2(OPR_3)_2$]. To obtain pure products it is important to allow the $WX_6/(Me_3Si)_2O$ reaction to go to completion before adding the neutral ligand; similar observations were made by Dreisch et al.[10a] who examined the synthesis of [$WO_2Cl_2$(dme)] (dme = $MeOCH_2CH_2OMe$) from $WOCl_4/(Me_3Si)_2O$ in some detail and observed significant amounts of $W^V$ complexes under some conditions. Gibson et al.[10c] reported that $WO_2Cl_2$ could not be isolated from $CH_2Cl_2$ solution at ambient temperatures by this route, rather off-white tungsten siloxanes were formed. We obtained white materials, which although we did not isolate or characterise them, reacted in situ with $OPR_3$ to give high yields of [$WO_2Cl_2(OPR_3)_2$], and the spectroscopic data showed no -$OSiMe_3$ present in the products. Extension of this route was also successful in affording diphosphane dioxide complexes [$WO_2X_2$(L–L)] {L–L = $Ph_2P(O)CH_2P(O)Ph_2$, $Ph_2P(O)CH_2CH_2P(O)Ph_2$, and *o*-$C_6H_4[P(O)Ph_2]_2$} (Table 1), although these are only slightly soluble in chlorocarbons, and it is necessary to use larger volumes of solvent and longer reaction times, and also to recrystallise the products to obtain pure samples. The spectroscopic data on the [$WO_2X_2(OPR_3)_2$] complexes (Table 1) are consistent with the limited literature data[9] and the geometries were confirmed by crystal structures of two examples (below). In particular two medium intensity features in the IR spectra in the range 900–965 $cm^{-1}$ are the $\upsilon_{sym}$ and $\upsilon_{asym}$ vibrations of the *cis*-$WO_2$ group [for the $OPMe_3$ complexes $\rho(PMe_3)$ modes in the same region complicate the assignments – see Table 1], whilst the *trans*-$WX_2$ units have single bands at ca. 310 $cm^{-1}$ (X = Cl) or ca. 240 $cm^{-1}$ (X = Br). The $\upsilon$(PO) modes occur as broad features typically shifted to low frequency by 40–70 $cm^{-1}$ from the values in the parent $OPR_3$. Trends in the spectroscopic data with changes in halogen and between corresponding Mo and W complexes are discussed further in a later section.

The structures of [$WO_2Br_2(OPPh_3)_2$] and [$WO_2Cl_2(OPMe_3)_2$] are shown in Figure 1 and Figure 2 and selected bond lengths and angles are in Table 2 and Table 3. Both structures show distorted octahedral coordination at tungsten with *trans*-halides and with the phosphane oxide *trans* to W=O and with the X–W–X bent towards the neutral ligands and away from the $WO_2$ groups. The data can be compared with that for [$WO_2Cl_2(OPPh_3)_2$][9b] which has W=O 1.706(8), 1.702(9) Å, W–Cl 2.385(3), 2.366(3) Å, and W–O(P) 2.175(8), 2.163(7) Å, P–O 1.499(8), 1.500(7) Å, O=W=O 102.2(4)° and Cl–W–Cl 163.5(1)°. Thus for [$WO_2X_2(OPPh_3)_2$] (X = Cl or Br), the W=O, W–O(P) and P–O distances are the same within experimental error. The same basic features are present in the structure of [$WO_2Cl_2(OPMe_3)_2$]. The structures are also very similar to those of the molybdenum analogues reported previously.[6,7] As noted before, the M–O–P angle is rather variable. Within each structure, the M–O–P angles at the two phosphane

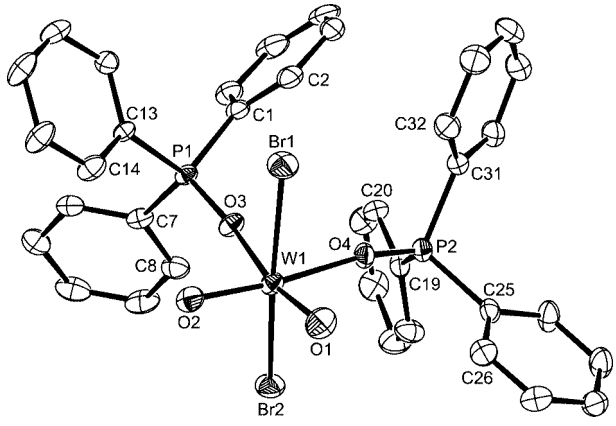


Figure 1. View of the structure of [$WO_2Br_2(OPPh_3)_2$] with numbering scheme adopted. H atoms have been omitted for clarity and the ellipsoids are drawn at the 50% probability level.

Table 1. Selected spectroscopic data.

| Compound | $\delta(^{31}P\{^1H\})$/ppm[a] | $\delta(^{19}F\{^1H\})$/ppm[a] | $\upsilon$(W=O) [$cm^{-1}$][b] | $\upsilon$(P=O) [$cm^{-1}$][b] | $\upsilon$(W–X) [$cm^{-1}$][b] |
|---|---|---|---|---|---|
| [$WO_2F_2(OPMe_3)_2$] | 59.9 | –65.9 ($J$ = 110 Hz) | 956,935,896[c] | 1144, 1097 | 555 |
| [$WO_2Cl_2(OPMe_3)_2$] | 61.9 | – | 957, 937, 894[c] | 1148, 1085 | 305 |
| [$WO_2Br_2(OPMe_3)_2$] | 63.9 | – | 956, 938, 891[c] | 1155, 1100 | 235 |
| [$WO_2F_2(OPPh_3)_2$] | 40.2 | –61.8 ($J$ = 91 Hz) | 963, 918 | 1164, 1096 | 584 |
| [$WO_2Cl_2(OPPh_3)_2$] | 42.1 | – | 959, 911 | 1156, 1140 | 310 |
| [$WO_2Br_2(OPPh_3)_2$] | 43.3 | – | 960, 914 | 1169, 1140 | 238 |
| [$WO_2Cl_2${$Ph_2P(O)CH_2P(O)Ph_2$}] | 40.3 | – | 963, 912 | 1156 | 324, 304 |
| [$WO_2Br_2${$Ph_2P(O)CH_2P(O)Ph_2$}] | 43.7 | – | 961, 910 | 1150 | 239 |
| [$WO_2Cl_2${$Ph_2P(O)(CH_2)_2P(O)Ph_2$}] | 47.1 | – | 957, 909 | 1173, 1145 | 317, 300 |
| [$WO_2Cl_2${*o*-$C_6H_4[P(O)Ph_2]_2$}] | 44.7 | – | 959, 915 | 1174, 1148 | 313 |
| [$WO_2Br_2${*o*-$C_6H_4[P(O)Ph_2]_2$}] | 45.9 | – | 958, 913 | 1169, 1160 | 234 |
| [$MoO_2F_2(OPMe_3)_2$] | 55.4 | –57.2 | 955,943,906,892[c,d] | 1141, 1092 | 566[e] |
| [$MoO_2F_2(OPPh_3)_2$] | 38.5 | –51.1 | 949, 915[d] | 1141, 1083 | 587[e] |
| [$WO_2F_2$(2,2′-bipy)] | – | –69.6 ($J$ = 95 Hz) | 962, 921 | – | 584 |
| [$WO_2F_2$(1,10-phen)] | – | –68.0 ($J$ = 96 Hz) | 961, 926 | – | 585 |

[a] In $CH_2Cl_2$ solution. [b] Nujol mull, $OPMe_3$ has $\upsilon$(PO) = 1161 $cm^{-1}$, $OPPh_3$ has $\upsilon$(PO) = 1195 $cm^{-1}$. [c] $\rho(PMe_3)$ in uncoordinated $OPMe_3$ occurs at 955, 937 and 867 $cm^{-1}$ therefore assignment of $\upsilon$(M=O) uncertain. [d] $\upsilon$(Mo=O). [e] $\upsilon$(Mo–F).

 © 2007 Wiley-VCH Verlag GmbH & Co. KGaA, Weinheim 

oxides vary by 6° (Ph) and 9° (Me) with the mean angle for $OPMe_3$ some 25° smaller than that in the $OPPh_3$ complex.

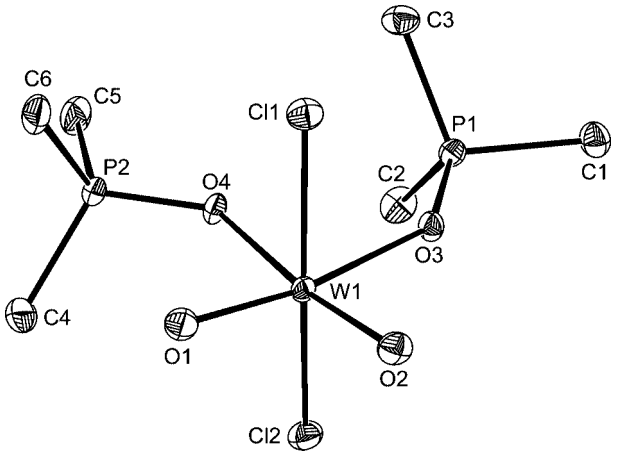


Figure 2. View of the structure of $[WO_2Cl_2(OPMe_3)_2]$ with numbering scheme adopted. H atoms have been omitted for clarity and the ellipsoids are drawn at the 50% probability level.

Table 2. Selected bond lengths [Å] and angles [°] for $[WO_2Br_2(OPPh_3)_2]$.

| | | | |
|---|---|---|---|
| W1–O1 | 1.709(4) | W1–Br1 | 2.5469(7) |
| W1–O2 | 1.708(4) | W1–Br2 | 2.5398(7) |
| W1–O3 | 2.166(3) | P1–O3 | 1.511(4) |
| W1–O4 | 2.161(3) | P2–O4 | 1.508(4) |
| P–C | 1.792(5)–1.809(5) | | |
| O1–W1–O2 | 101.89(19) | O1–W1–O3 | 167.61(17) |
| O1–W1–O4 | 90.70(17) | O2–W1–O3 | 90.34(16) |
| O2–W1–O4 | 167.25(15) | O3–W1–O4 | 77.15(13) |
| Br1–W1–Br2 | 166.14(2) | O–P–C | 108.6(2)–116.5(2) |
| W1–O3–P1 | 159.2(2) | O1/O2–W1–Br | 92.93(13)–96.10(14) |
| W1–O4–P2 | 165.4(2) | O3/O4–W1–Br | 83.65(10)–85.81(10) |

Table 3. Selected bond lengths [Å] and angles [°] for $[WO_2Cl_2(OPMe_3)_2]$.

| | | | |
|---|---|---|---|
| W1–O1 | 1.718(2) | W1–Cl1 | 2.3888(9) |
| W1–O2 | 1.717(2) | W1–Cl2 | 2.3881(9) |
| W1–O3 | 2.125(2) | P1–O3 | 1.518(2) |
| W1–O4 | 2.190(2) | P2–O4 | 1.522(2) |
| P–C | 1.769(4)–1.785(3) | | |
| O1–W1–O2 | 102.66(10) | O1–W1–O3 | 166.53(9) |
| O1–W1–O4 | 88.70(9) | O2–W1–O3 | 90.80(9) |
| O2–W1–O4 | 168.43(9) | O3–W1–O4 | 77.87(8) |
| Cl1–W1–Cl2 | 164.08(3) | O–P–C | 108.48(14)–112.77(14) |
| W1–O3–P1 | 141.87(13) | O1/O2–W1–Cl | 93.58(7)–96.78(8) |
| W1–O4–P2 | 131.01(12) | O3/O4–W1–Cl | 82.23(6)–84.54(6) |

### $[MO_2F_2(OPR_3)_2]$ (M = Mo or W) Complexes

The $[MoO_2Cl_2(OPR_3)_2]$[6] complexes were dissolved in anhydrous $CH_2Cl_2$ and stirred with a 50% excess of powdered $Me_3SnF$ for ca. 24 h, which slowly dissolves as the reaction proceeds, to form $[MoO_2F_2(OPR_3)_2]$ and $Me_3SnCl$. The completion of the reaction is best monitored by checking the $^{31}P\{^1H\}$ NMR spectrum of the reaction mixture for complete loss of the resonance of the $[MoO_2Cl_2(OPR_3)_2]$ starting material, because we found that reaction times were quite variable, ranging from ca. 4–20 h. The polymeric $Me_3SnF$ is insoluble in chlorocarbons and only dissolves as the reaction proceeds, and this solid-solution reaction probably accounts for the highly variable reaction times. It is also important to use sufficient solvent volume to prevent the product complexes from separating out on the suspended $Me_3SnF$. When reaction is complete, unreacted $Me_3SnF$ was removed by filtration, the solvent and most of the $Me_3SnCl$ pumped off in vacuo, and the residue washed thoroughly with *n*-hexane to remove any residual $Me_3SnCl$ ($Me_3SnCl$ is easily detected in the $^1H$ NMR spectra as singlet at $\delta$ = 0.62 ppm with $^{119/117}Sn$ satellites). The corresponding reactions of $[WO_2Cl_2(OPR_3)_2]$ with $Me_3SnF$ were carried out similarly, although the reaction times required are longer, and sometimes insoluble by-products are formed, which contain broad IR bands 850–700 $cm^{-1}$ presumably due to W–O–W bridges. In attempts to overcome these problems we explored the effects of using $[WO_2Cl_2(OPR_3)_2]/Me_3SnF$ ratios of 1:2 (stoichiometric), 1:3 and 1:4, and also adding excess $OPR_3$ (ca. 2 mol. equiv.) to suppress oligomerisation, because it is known that the W=O groups exhibit a *trans* labilising effect.[14] In fact we find that the best route is to use rigorously anhydrous conditions, stoichiometric $[WO_2Cl_2(OPR_3)_2]/Me_3SnF$ ratio (1:2), without added $OPR_3$, and dilute solutions. Excess phosphane oxide forms adducts with the $Me_3SnX$ (see below) making it harder to remove after the reaction is complete. After removing all volatiles in vacuo, the products were washed with anhydrous hexane, and the residue recrystallised from anhydrous $CH_2Cl_2$, discarding any insoluble material. The $^{31}P\{^1H\}$ NMR spectra obtained during the reactions show an additional resonance intermediate in chemical shift between those of the dichlorido- and difluorido-species, almost certainly due to $[WO_2ClF(OPR_3)_2]$ (although no attempt was made to isolate these), indicating that fluorination occurs stepwise. We also made $[WO_2F_2(OPMe_3)_2]$ by adding excess $OPMe_3$ in ethanol to a solution of "tungstic acid" (hydrated $WO_3$) in aqueous HF and allowing the solution to evaporate in air,[14] until very small colourless crystals separated (ca. 3 d). The products from the two routes were spectroscopically identical.

A small number of white crystals were isolated as a by-product from the $[WO_2Cl_2(OPPh_3)_2]/Me_3SnF$ reaction and were identified by a crystal structure determination as $[Me_3SnCl(OPPh_3)]$. The structure (Figure 3, Table 4) reveals a trigonal-bipyramidal tin centre with equatorial methyl groups. The structure of the parent molecule $Me_3SnCl$ is also composed of distorted trigonal-bipyramidal units with axially disposed asymmetric chlorine bridges [Sn–Cl 2.430(2), 3.269(2) Å].[19] The Sn–C bonds are not significantly different between the parent [2.119 Å (av)] and the phosphane oxide adduct [2.120 Å (av)], and in the adduct the $OPPh_3$ simply replaces the longer Sn–Cl bridging interaction. The weak coordination of the phosphane oxide is evident in the long *d*(Sn–O) = 2.375(2) Å and short *d*(P–O) = 1.497(2) Å, which may be compared with values in $[SnX_4(OPPh_3)_2]$, which range from *d*(Sn–O) = 2.050(3) Å (X = F) to 2.13 Å (av) (X = I) and *d*(P–O) range from

 © 2007 Wiley-VCH Verlag GmbH & Co. KGaA, Weinheim 

1.523(3)–1.485 Å.[20] The compound has been reported several times before[21] and the $^1H$ and $^{31}P\{^1H\}$ NMR spectroscopic data in $CH_2Cl_2$ solution are little different from those of the constituents, suggesting only weak interaction in solution.

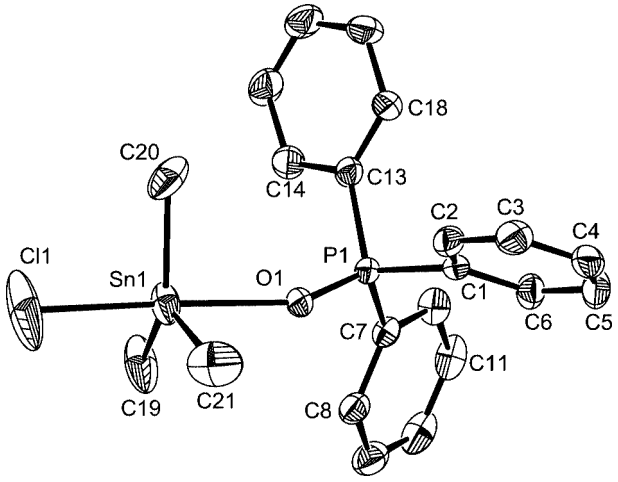


Figure 3. View of the structure of [$Me_3SnCl(OPPh_3)$] with numbering scheme adopted. H atoms have been omitted for clarity and the ellipsoids are drawn at the 50% probability level.

Table 4. Selected bond lengths [Å] and angles [°] for [$Me_3SnCl(OPPh_3)$].

| | | | |
|---|---|---|---|
| Sn1–Cl1 | 2.515(1) | Sn1–O1 | 2.375(2) |
| P1–O1 | 1.497(2) | Sn1–C19 | 2.125(4) |
| Sn1–C20 | 2.116(4) | Sn1–C21 | 2.119(4) |
| O1–Sn1–Cl1 | 177.57(7) | C19–Sn1–Cl1 | 94.71(10) |
| C20–Sn1–Cl1 | 93.39(11) | C21–Sn1–Cl1 | 94.84(12) |
| C19–Sn1–O1 | 85.43(11) | C20–Sn1–O1 | 88.64(11) |
| C21–Sn1–O1 | 83.03(12) | C–Sn1–C | 117.4(2)–121.1(2) |

The spectroscopic data on the four fluorido $Mo^{VI}$ and $W^{VI}$ complexes are given in Table 1. The *trans*-$MF_2$ units exhibit a strong IR vibration ca. 550–590 $cm^{-1}$. The [$MoO_2F_2(OPR_3)_2$] exhibit sharp singlet $^{19}F$ NMR resonances at $\delta$ = –51.7 (R = Ph) or –57.2 (R = Me), and the $^{95}Mo$ resonances appear as broad triplets at $\delta$ = –114 (R = Ph) or –93 (R = Me) with $^1J(^{95}Mo\text{-}^{19}F)$ ca. 115–120 Hz. Literature data on molybdenum fluorides are sparse, and the only closely related species appears to be [$MoO_2F_2$-(acac)]$^-$ which has $\delta(^{19}F)$ = –53.0, $\delta(^{95}Mo)$ = –76.3 (t) $^1J(^{95}Mo\text{-}^{19}F)$ = 114 Hz.[22] The [$WO_2F_2(OPR_3)_2$] complexes exhibit $^{19}F$ NMR resonances in a similar region to the molybdenum analogues (Table 1), with $^{183}W$ satellites $^1J(^{183}W\text{-}^{19}F)$ ca. 90–110 Hz. The $^{19}F$ resonances are significantly to low frequency of those in $WF_6$ or $WOF_4$ adducts.[23]

As a further test of this method, the [$WO_2Cl_2$(L–L)] (L–L = 2,2′-bipy, 1,10-phen), originally obtained from $WO_2Cl_2$ and the molten diimines,[9a] were prepared from $WCl_6$/$(Me_3Si)_2O$ and the appropriate diimine, and then fluorinated with $Me_3SnF$, in these cases under reflux for 48 h, due to the poor solubility of reagents and products. The [$WO_2F_2$(L–L)] are poorly soluble, white powders (Table 1), with the data in good agreement with those reported[12] for [$WO_2F_2$(L–L)] made from [$WOF_4$(2,2′-bipy)] or from [$WOF_2(OEt)_2$]. During this work two different crystalline forms of [$WO_2Cl_2$(1,10-phen)] were obtained, an unsolvated form (the structure of which has been reported previously)[24a] and a 1:1 $CH_2Cl_2$ solvate. The structures of both were determined (see Table 5 and Figure 4 and Figure 5). The distortions from regular octahedal angles at W are similar to those observed above for the phosphane oxides, but with the O=W=O angle ca. 4° larger and the Cl–W–Cl angle ca. 6° smaller in the 1,10-phenanthroline complexes. The tungsten residues in these two structures have very similar bond lengths and angles and they provide good examples of the effect of chemical environment on molecular geometry.[24b] The data on the unsolvated form agree well with that reported.[24a] Comparison of the data show that *d*(W=O) and *d*(W–Cl) differ little from the values in the phosphane oxide adduct, indicating that these are the dominant bonds to tungsten, with the neutral ligands filling the remaining coordination sites.

Table 5. Selected bond lengths [Å] and angles [°] for [$WO_2Cl_2$(1,10-phen)] species. (a) [$WO_2Cl_2$(1,10-phen)]·$CH_2Cl_2$. (b) [$WO_2Cl_2$(1,10-phen)].[a]

| | | | |
|---|---|---|---|
| (a) | | | |
| W1–O1 | 1.717(2) | W1–Cl1 | 2.3623(10) |
| W1–O2 | 1.721(2) | W1–Cl2 | 2.3518(10) |
| W1–N1 | 2.318(3) | W1–N2 | 2.303(3) |
| N–C | 1.321(4)–1.363(4) | | |
| O1–W1–O2 | 106.23(11) | O1–W1–N1 | 92.55(10) |
| O1–W1–N2 | 163.21(10) | O2–W1–N1 | 161.20(10) |
| O2–W1–N2 | 90.56(10) | N1–W1–N2 | 70.67(9) |
| Cl1–W1–Cl2 | 157.93(3) | | |
| O–W1–Cl | 96.23(9)–96.96(8) | N–W1–Cl | 80.29(7)–81.41(7) |
| (b) | | | |
| W1–O1 | 1.718(3) | W1–N1 | 2.298(3) |
| W1–Cl1 | 2.3586(12) | N1–C | 1.340(5), 1.353(5) |
| O1–W1–O1a | 106.7(2) | O1–W1–N1 | 91.27(12) |
| O1–W1–N1a | 162.05(13) | N1–W1–N1a | 70.81(16) |
| Cl1–W1–Cl1a | 157.34(6) | | |
| O1–W1–Cl | 96.31(11), 97.17(10) | N1–W1–Cl | 80.50(8), 81.07(8) |

[a] Symmetry operation: a = 1–*x*, *y*, 1/2–*z*.

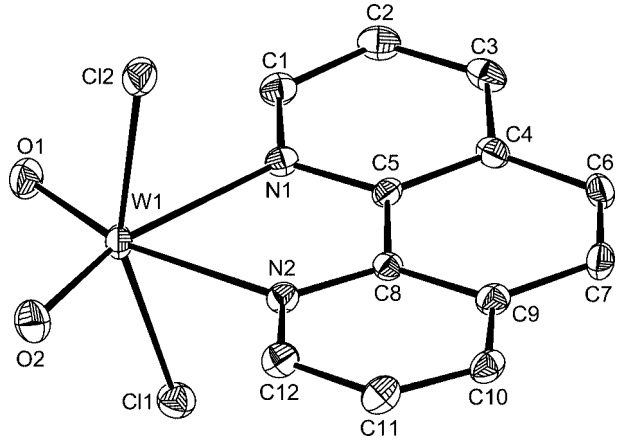


Figure 4. View of the structure of [$WO_2Cl_2$(1,10-phen)]·$CH_2Cl_2$ with numbering scheme adopted. The solvate molecule is not shown, H atoms have been omitted for clarity and the ellipsoids are drawn at the 50% probability level.

 © 2007 Wiley-VCH Verlag GmbH & Co. KGaA, Weinheim 

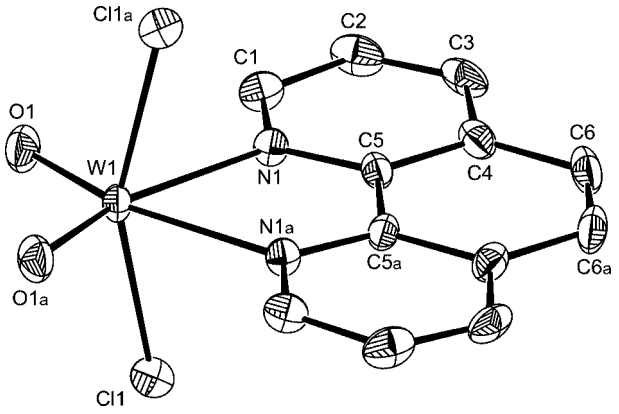


Figure 5. View of the structure of $[WO_2Cl_2(1,10\text{-phen})]$ with numbering scheme adopted. H atoms have been omitted for clarity and the ellipsoids are drawn at the 50% probability level. The molecule has crystallographic twofold symmetry. Symmetry operation: $a = 1-x, y, 1/2-z$.

### Attempted Preparation of $[MO_2I_2(OPR_3)_2]$

A $CH_2Cl_2$ solution of $[MoO_2Cl_2(OPPh_3)_2]$ treated with 2.5 equiv. of $Me_3SnI$, slowly developed a dark green colour. After ca. 24 h an in situ $^{31}P\{^1H\}$ NMR spectrum showed that the $[MoO_2Cl_2(OPPh_3)_2]$ had been completely consumed, and there were no new phosphorus resonances. Evaporation of the solution gave a paramagnetic green-brown solid which showed no evidence of $\upsilon(MoO_2)$ vibrations in the IR spectrum, and the UV/Vis spectrum contained, in addition to intense bands $> 25000\ cm^{-1}$, a broad, weak feature ca. $16000\ cm^{-1}$ assignable as a d–d transition, consistent with the reduction of the molybdenum to a lower oxidation state. The reaction of $[WO_2Cl_2(OPPh_3)_2]$ with $Me_3SnI$ was very slow, but after 7 d a yellow solution formed and a $^{31}P\{^1H\}$ NMR spectrum of this solution showed that all the chlorido complex had reacted. However, neither the IR nor the $^{31}P\{^1H\}$ NMR spectra of the product(s) were consistent with the formation of $[WO_2I_2(OPPh_3)_2]$, and we conclude that the latter is not formed by this route.

### Some Comparisons

The spectroscopic data on the $[MO_2X_2(OPR_3)_2]$ complexes show no systematic variation in $\upsilon(PO)$ or $\upsilon(MO_2)$, for which the broadness of the bands and probably some coupling to other modes are responsible. However, systematic trends are evident in the multinuclear NMR spectroscopic data. The $^{31}P\{^1H\}$ NMR chemical shifts of the coordinated phosphane oxides show high frequency shifts F < Cl < Br (Table 1 and Table 6), the opposite of that expected on electronegativity grounds, and probably reflecting less effective $\pi(X)\rightarrow Mo$ donation as the halogen orbitals become larger. Similarly, the $^{95}Mo$ chemical shifts show an inverse halogen dependence, also seen in $MoO_2X_2$ (X = Cl or Br) complexes with N-donor ligands,[25] although this appears to be the first time data have been available for complexes containing F. (Our attempts to record $^{183}W$ NMR spectroscopic data for that series of compounds were unsuccessful due to the poor solubility of the complexes and the inherent insensitivity of the W nucleus.) The changes between the corresponding Mo and W complexes are also systematic for fixed $OPR_3$ and X, the $^{31}P\{^1H\}$ chemical shift is always slightly to higher frequency for M = W than Mo, whilst the $^{19}F$ chemical shifts in the fluorides are to lower frequency for the tungsten complexes.

Table 6. $^{95}Mo$ and $^{31}P\{^1H\}$ NMR spectroscopic data.[a]

| Compound | $\delta(^{95}Mo)$ [ppm] | | $\delta(^{31}P\{^1H\})$ [ppm] |
|---|---|---|---|
| $[MoO_2F_2(OPMe_3)_2]$ | –95 (t) | $^1J(^{95}Mo\text{-}^{19}F) = 115$ Hz | 55.4 |
| $[MoO_2F_2(OPPh_3)_2]$ | –114 (t) | $^1J(^{95}Mo\text{-}^{19}F) = 120$ Hz | 38.5 |
| $[MoO_2Cl_2(OPMe_3)_2]$[b] | 149 | | 59.1 |
| $[MoO_2Br_2(OPMe_3)_2]$[b] | 179 | | 60.6 |
| $[MoO_2Cl_2(OPPh_3)_2]$[b] | 137 | | 40.6 |
| $[MoO_2Br_2(OPPh_3)_2]$[b] | 171 | | 42.0 |
| $[Et_4N][MoO_2F_2(acac)]$[c] | –73.5 (t) | $^1J(^{95}Mo\text{-}^{19}F) = 114$ Hz | |

[a] In $CH_2Cl_2$ solution. [b] Data from ref.[6] [c] Data from ref.[22]

### Attempted Synthesis of Chromium(VI) Analogues

The extensive data obtained on the series of $Mo^{VI}$ and $W^{VI}$ $[MO_2X_2(OPR_3)_2]$ compounds, prompts the consideration of the 3d analogues containing $Cr^{VI}$. Chromyl fluoride, $CrO_2F_2$, is an orange gas and a powerful fluorinating agent,[26] whilst $CrO_2Br_2$ is very unstable, decomposing rapidly above ca. 210 K,[27] seemingly ruling out any coordination chemistry. However, the commercially available $CrO_2Cl_2$ was briefly examined. The UV/Vis spectrum of a solution of freshly distilled chromyl chloride in anhydrous $CH_2Cl_2$ exhibited a strong broad band at ca. $26000\ cm^{-1}$ and a weak broader feature at ca. $18000\ cm^{-1}$,[28] and these bands were unchanged on addition of dry $OPPh_3$, indicating no adduct formation. Over a few hours the initially deep orange-red solution turns red-brown and new weak features appear at low energy, which we assign to reduction to $d^1$ $Cr^V$. Decomposition is much faster in the presence of moisture or in bright light. The $^{31}P\{^1H\}$ NMR spectrum of a mixture of $CrO_2Cl_2$ and $OPPh_3$ in rigorously anhydrous $CH_2Cl_2$ also shows no reaction, but in the presence of traces of moisture a resonance at $\delta$ ca. +46 ppm appears due to the formation of $Ph_3POH^+$.[29] On a preparative scale, the reaction of $CrO_2Cl_2$ and $OPPh_3$ (1:1 mol. ratio) in anhydrous $CH_2Cl_2$ gave a deep red solution, which on removal of all volatiles in vacuo at 25 °C, left a sticky red-brown, paramagnetic solid. The IR spectrum of the solid showed no uncoordinated $OPPh_3$, but a broad feature at ca. $1140\ cm^{-1}$ was assignable to coordinated phosphane oxide, and features at ca. 970 and $875\ cm^{-1}$ may be $\upsilon(CrO)$ modes. The evidence points to the red-brown solid being a $Cr^V$ species (or mixture of $Cr^V$ compounds), and there is no evidence that $CrO_2Cl_2$ forms adducts with phosphane oxides. This contrasts with the behaviour of $VOCl_3$ which forms $[VOCl_3(OPPh_3)]$ and $[VOCl_3(OPMe_3)_2]$.[30] A few adducts of $CrO_2Cl_2$ with N-heterocycles, amines or amides have been claimed on the basis of analytical and IR spectro-

 © 2007 Wiley-VCH Verlag GmbH & Co. KGaA, Weinheim 

scopic data,[31] but it appears that these are chloridooxidochromate(V) species with protonated N-base cations.[32] A literature search failed to find any clearly established examples of $Cr^{VI}$ compounds with coordination numbers > 4, except in the oxide-fluorides[26] or imido complexes.[33]

## Conclusions

A route to [$WO_2X_2(OPR_3)_2$] (X = Cl or Br) compounds using anhydrous conditions has been developed, and the (also anhydrous) fluorination of these and related complexes achieved using $Me_3SnF$. These routes should allow the synthesis of highly moisture sensitive $WO_2X_2$ (X = F, Cl or Br) complexes of soft ligands containing heavier groups 15 or 16 donors, and work is underway to test this approach in our laboratories.

## Experimental Section

Infrared spectra were recorded as Nujol mulls between CsI plates with a Perkin–Elmer 983G spectrometer over the range 4000–200 $cm^{-1}$. $^1H$ and $^{19}F\{^1H\}$ NMR spectra were recorded with a Bruker AV300 spectrometer and referenced to TMS and $CFCl_3$, respectively. $^{31}P\{^1H\}$ and $^{95}Mo$ NMR spectra were recorded with a Bruker DPX400 spectrometer and are referenced to external 85% $H_3PO_4$ and aqueous $Na_2MoO_4$ at pH = 11, respectively. Microanalyses were undertaken by the University of Strathclyde microanalytical service. Solvents were dried prior to use and all preparations were undertaken using standard Schlenk techniques under $N_2$. $WCl_6$, $OPMe_3$ and $OPPh_3$ were obtained commercially (Alfa or Aldrich), while the other phosphane oxides were obtained by oxidation of the parent phosphane by the literature method.[34] The $OPMe_3$ was freshly sublimed in vacuo before use. $WBr_6$ was obtained by treatment of solid [$W(CO)_6$] with $Br_2$.[35] $Me_3SnF$ was obtained by the literature methods.[36] $CrO_2Cl_2$ (Aldrich) was freshly distilled, and freeze/thaw degassed immediately before use.

**[$WO_2Cl_2(OPMe_3)_2$]:** $WCl_6$ (0.23 g, 0.58 mmol) and $(Me_3Si)_2O$ (0.19 g, 1.7 mmol) were stirred in anhydrous $CH_2Cl_2$ (30 $cm^3$) under $N_2$ when the red solution rapidly turned orange ($WOCl_4$) and then colourless. After 2 h, $OPMe_3$ (0.12 g, 1.3 mmol) in $CH_2Cl_2$ (10 $cm^3$) was added. The solution was stirred for a further ca. 2 h. The resulting colourless solution was filtered and the solvent removed in vacuo. The white solid was washed thoroughly with hexane (100 $cm^3$) and dried in vacuo. Yield 0.26 g, 95%. $C_6H_{18}Cl_2O_4P_2W$ (470.9): calcd. C 15.3, H 3.9; found C 15.2, H 4.1. $^1H$ NMR ($CDCl_3$): $\delta$ = 1.82 (d, $^2J_{PH}$ = 13.2 Hz, Me) ppm.

**[$WO_2Cl_2(OPPh_3)_2$]:** Method as above to give a white solid. Yield 91%. $C_{36}H_{30}Cl_2O_4P_2W{\cdot}CH_2Cl_2$ (928.2): calcd. C 47.9, H 3.5; found C 47.5, H 3.2. $^1H$ NMR ($CDCl_3$): $\delta$ = 7.30–7.75 (m, Ph) ppm.

**[$WO_2Cl_2\{Ph_2P(O)CH_2P(O)Ph_2\}$]:** Method as above to give a white solid. Yield 89%. $C_{25}H_{22}Cl_2O_4P_2W$ (703.2): calcd. C 42.7, H 3.1; found C 42.8, H 3.1. $^1H$ NMR ($CDCl_3$): $\delta$ = 3.86 (t, 2 H, $CH_2$), 7.35–7.90 (m, 20 H, Ph) ppm.

**[$WO_2Cl_2\{Ph_2P(O)CH_2CH_2P(O)Ph_2\}$]:** Method as above to give a white solid contaminated with $WO_2Cl_2$. The [$WO_2Cl_2\{Ph_2P(O)CH_2CH_2P(O)Ph_2\}$] was then re-dissolved in $CH_2Cl_2$ (10 $cm^3$) and filtered (to remove the $WO_2Cl_2$). Addition of $Et_2O$ gave the complex as a white solid. Yield 64%. $C_{26}H_{24}Cl_2O_4P_2W$ (717.8): calcd. C 43.6, H 3.4; found C 44.3, H 3.4. $^1H$ NMR ($CDCl_3$): $\delta$ = 7.50–7.85 (m, 20 H, Ph), 2.67 (d, $^2J_{PH}$ = 10.5 Hz, 4 H, $CH_2$) ppm.

**[$WO_2Cl_2\{o\text{-}C_6H_4[P(O)Ph_2]_2\}$]:** Method as for [$WO_2Cl_2\{Ph_2P(O)CH_2CH_2P(O)Ph_2\}$] above to give a white solid. Yield 60%. $C_{30}H_{24}Cl_2O_4P_2W{\cdot}(C_2H_5)_2O$ (839.3): calcd. C 48.7, H 4.0; found C 49.6, H 4.3. $^1H$ NMR ($CD_2Cl_2$): $\delta$ = 7.30–7.90 (m, aromatic CH) ppm.

**[$WO_2Br_2(OPMe_3)_2$]:** $WBr_6$ (0.17 g, 0.26 mmol) with $(Me_3Si)_2O$ (0.08 g, 0.52 mmol) were stirred in $CH_2Cl_2$ (30 $cm^3$) under $N_2$ for 3 h until a pale cream solution was obtained and then $OPMe_3$ (0.05 g, 0.54 mmol) was added, and the solution was stirred overnight. The resulting solution was filtered and pumped to dryness. The white solid obtained was washed thoroughly with hexane (100 $cm^3$) and dried in vacuo. Yield 0.11 g, 76%. $C_6H_{18}Br_2O_4P_2W$ (559.8): calcd. C 12.9, H, 3.3; found C 13.5, H 4.4. $^1H$ NMR ($CDCl_3$): $\delta$ = 2.02 (d, $^2J_{PH}$ = 13.5 Hz, Me) ppm.

**[$WO_2Br_2(OPPh_3)_2$]:** Method as [$WO_2Br_2(OPMe_3)_2$] to give a white solid. Yield 82%. $C_{36}H_{30}Br_2O_4P_2W$ (932.2): calcd. C 46.4, H 3.2; found C 47.3, H 3.2. $^1H$ NMR ($CDCl_3$): $\delta$ = 7.35–7.80 (m, Ph) ppm.

**[$WO_2Br_2\{Ph_2P(O)CH_2P(O)Ph_2\}$]:** Method as [$WO_2Br_2(OPMe_3)_2$] to give a light yellow solid. Yield 94%. $C_{25}H_{22}Br_2O_4P_2W$ (792.1): calcd. C 37.9, H 2.8; found C 38.0, H 2.9. $^1H$ NMR ($CDCl_3$): $\delta$ = 4.12 (t, 2 H, $CH_2$), 7.40–7.95 (m, 20 H, Ph) ppm.

**[$WO_2Br_2\{o\text{-}C_6H_4[P(O)Ph_2]_2\}$]:** Method as for [$WO_2Cl_2\{Ph_2P(O)CH_2CH_2P(O)Ph_2\}$] above to give a yellow solid. Yield 69%. $C_{30}H_{24}Br_2O_4P_2W{\cdot}(C_2H_5)_2O$ (928.3): calcd. C 43.9, H, 3.7; found C 44.1, H 3.0. $^1H$ NMR ($CDCl_3$): $\delta$ = 7.33–7.85 (m, aromatic CH) ppm.

**[$MoO_2F_2(OPPh_3)_2$]:** [$MoO_2Cl_2(OPPh_3)_2$][6] (0.22 g, 0.29 mmol) was dissolved in dry dichloromethane (10 $cm^3$), powdered anhydrous $Me_3SnF$ (0.158 g, 0.87 mmol) added and the mixture stirred for 24 h. The solution was filtered, and the filtrate treated dropwise with hexane (5 $cm^3$) to precipitate the complex as a white solid. This was filtered off, rinsed with hexane (5 $cm^3$) and dried in vacuo. Yield 0.18 g, 86%. $C_{36}H_{30}F_2MoO_4P_2{\cdot}CH_2Cl_2$ (807.5): calcd. C 55.0, H 4.0; found C 54.9, H 3.9. $^1H$ NMR ($CDCl_3$): $\delta$ = 7.20–7.80 (m, Ph) ppm.

**[$MoO_2F_2(OPMe_3)_2$]:** Was prepared similarly. Yield 91%. $C_6H_{18}F_2MoO_4P_2{\cdot}CH_2Cl_2$ (471.1): calcd. C 19.3, H 4.6; found C 19.2, H 4.7. $^1H$ NMR ($CDCl_3$): $\delta$ = 1.65 (d, $^2J_{PH}$ = 13.0 Hz, Me) ppm.

**[$WO_2F_2(OPPh_3)_2$]:** [$WO_2Cl_2(OPPh_3)_2$] (0.18 g, 0.24 mmol) was dissolved in dry $CH_2Cl_2$ (20 $cm^3$), powdered $Me_3SnF$ (0.088 g, 0.48 mmol) added and the mixture stirred for 24 h. The solution was taken to dryness in vacuo, the residue washed with anhydrous hexane (20 $cm^3$), filtered, and the solid dissolved in anhydrous $CH_2Cl_2$ (50 $cm^3$). Any insoluble material was filtered off and discarded, and the filtrate concentrated to ca. 5 $cm^3$ and treated dropwise with hexane (5 $cm^3$) to precipitate the complex as a white solid. This was filtered off, rinsed with hexane (5 $cm^3$) and dried in vacuo. Yield 0.13 g, 64%. $C_{36}H_{30}F_2O_4P_2W$ (810.4): calcd. C 53.4, H 3.7. (Repeated attempts to obtain carbon analyses on samples of this compound gave values 5–8% low and with poor reproducibility; we believe this is a combustion problem, since the samples appeared identical and spectroscopically pure). $^1H$ NMR ($CDCl_3$): $\delta$ = 7.20–7.80 (m, Ph) ppm.

**[$WO_2F_2(OPMe_3)_2$]. Method 1:** In a Teflon® beaker, tungstic acid ("$H_2WO_4{\cdot}nH_2O$") (0.15 g, ca. 0.5 mmol) was dissolved in a mixture of 40% HF (5 $cm^3$) and water (5 $cm^3$) with gentle warming to give

 © 2007 Wiley-VCH Verlag GmbH & Co. KGaA, Weinheim 

a colourless solution. The solution was cooled, decanted from any solid and a solution of $OPMe_3$ (0.184 g, 2.0 mmol) in ethanol (15 $cm^3$) added. The solution was stirred for 2 h, then allowed to evaporate at room temperature. After 3 d colourless small crystals formed, the mother liquor was decanted off, the crystals rinsed with diethyl ether (5 $cm^3$) and dried in vacuo. Yield 0.12 g 54%.

**Method 2:** $[WO_2Cl_2(OPMe_3)_2]$ (0.11 g, 0.24 mmol) was dissolved in dry $CH_2Cl_2$ (50 $cm^3$), powdered $Me_3SnF$ (0.09 g, 0.50 mmol) and the mixture stirred for 48 h. The solution was taken to dryness in vacuo, the residue stirred with anhydrous hexane (50 $cm^3$) for 3 h, the solid filtered off and dissolved in anhydrous $CH_2Cl_2$ (20 $cm^3$). Any insoluble material was filtered off and discarded, and the filtrate concentrated to ca. 5 $cm^3$ and treated dropwise with hexane (5 $cm^3$) to precipitate the complex as a white solid. This was filtered off and dried in vacuo. Yield 0.06 g, 57% Spectroscopically the two methods gave identical products. $C_6H_{18}F_2O_4P_2W$ (438.0): calcd. C 16.5, H 4.1; found C 16.4, H 3.8. $^1H$ NMR ($CDCl_3$): $\delta$ = 1.65 (d, $^2J_{PH}$ = 13 Hz) ppm.

**$[WO_2Cl_2(1,10\text{-phen})]$:** $WCl_6$ (0.27 g, 0.68 mmol) was suspended in dry $CH_2Cl_2$ (10 $cm^3$) and $(Me_3Si)_2O$ (0.22 g, 1.4 mmol) added, and the mixture stirred for 2 h during which time it turned colourless. A solution of 1,10-phen (0.12 g, 0.68 mmol) in dry $CH_2Cl_2$ (20 $cm^3$) was added and the mixture stirred for 2 h. The solution was filtered, and the product precipitated from the filtrate by slow addition of hexane (100 $cm^3$), filtered off, washed thoroughly with hexane (100 $cm^3$) and dried in vacuo. Yield 0.32 g, 84%. $^1H$ NMR ($CDCl_3$): $\delta$ = 8.06 (m, 4 H), 8.64 (m, 2 H), 9.83 (m, 2 H) ppm. IR (Nujol): $\tilde{\nu}$ = 936, 919 $\upsilon(WO_2)$, 320 $\upsilon(WCl)$ $cm^{-1}$.

**$[WO_2Cl_2(2,2'\text{-bipy})]$:** This was made analogously to the 1,10-phenanthroline complex above. Yield 85%. $^1H$ NMR ($CDCl_3$): $\delta$ = 7.08 (m, 2 H), 8.30 (m, 4 H), 9.60 (m, 2 H) ppm. IR (Nujol): $\tilde{\nu}$ = 952, 915 $\upsilon(WO_2)$, 338 $\upsilon(WCl)$ $cm^{-1}$.

**$[WO_2F_2(1,10\text{-phen})]$:** $[WO_2Cl_2(1,10\text{-phen})]$ (0.16 g, 0.34 mmol) was suspended in anhydrous $CHCl_3$ (80 $cm^3$), powdered anhydrous $Me_3SnF$ (0.18 g, 0.98 mmol) added and the mixture refluxed for 48 h. The mixture was filtered and the filtrate concentrated to ca. 5 $cm^3$, then treated with hexane (5 $cm^3$) to precipitate the product, which was separated and dried in vacuo. Yield 0.10 g, 73%. $^1H$ NMR ($CDCl_3$): $\delta$ = 8.07 (m, 4 H), 8.68 (m, 2 H), 9.85 (m, 2 H) ppm.

**$[WO_2F_2(2,2'\text{-bipy})]$:** Was made similarly to the above. Yield 78%. $^1H$ NMR ($CD_2Cl_2$): $\delta$ = 7.78 (m, 2 H), 8.24 (m, 4 H), 9.43 (m, 2 H) ppm.

**X-ray Crystallography:** Details of the crystallographic data collection and refinement parameters are given in Table 7. Colourless crystals of $[WO_2Cl_2(OPMe_3)_2]$ and light-yellow crystals of $[WO_2Br_2(OPPh_3)_2]$ were obtained by cooling a solution of the appropriate complex in $CH_2Cl_2$. Crystals of $[WO_2Cl_2(1,10\text{-phen})]\cdot CH_2Cl_2$ were obtained by layering *n*-hexane onto a $CH_2Cl_2$ solution of the complex and the non-solvated complex isolated from an attempted synthesis of $[WO_2F_2(1,10\text{-phen})]$. Colourless crystals of $[Me_3SnCl(OPPh_3)]$ were obtained from the reaction mixture used to prepare $[WO_2F_2(OPPh_3)_2]$. Data collections used a Bruker-Nonius Kappa CCD diffractometer fitted with Mo-$K_\alpha$ radiation ($\lambda$ = 0.71073 Å) and either a graphite monochromator or confocal mirrors. The crystals were held at 120 K in a nitrogen gas stream. Structure solution and refinement were routine[37–39] with H atoms introduced into the models in calculated positions. The choice of space group for $[Me_3SnCl(OPPh_3)]$ depended on a few 0*k*0 reflections. The reflections in this group were weaker than other zones and the choice of $P2_1/c$ or *Pc*-$P2/c$ was not as clear cut as one would wish. Both $P2_1/c$ and *Pc* were explored and $P2_1/c$ used on the basis of providing as good a fit to the data with less parameters and avoiding the high correlations found in *Pc* with two molecules in the asymmetric unit. The structure agrees with unpublished work.[40] Selected bond lengths and angles are given in Table 2, Table 3, Table 4 and Table 5.

CCDC-615946 (for W/Br/Ph), -615947 (for W/Cl/Me), -615949 (for W/Cl/N/$CH_2Cl_2$), C-615948 (for W/Cl/N), and -615950 (for Sn/Cl) contain the supplementary crystallographic data for this paper (the atoms in parentheses indicate the species in the compounds). These

Table 7. Crystal data and structure refinement details.[a]

| Compound | $[WO_2Br_2(OPPh_3)_2]$ | $[WO_2Cl_2(OPMe_3)_2]$ | $[WO_2Cl_2(1,10\text{-phen})]\cdot CH_2Cl_2$ | $[WO_2Cl_2(1,10\text{-phen})]$ | $[Me_3SnCl(OPPh_3)]$ |
|---|---|---|---|---|---|
| Formula | $C_{36}H_{30}Br_2O_4P_2W$ | $C_6H_{18}Cl_2O_4P_2W$ | $C_{13}H_{10}Cl_4N_2O_2W$ | $C_{12}H_8Cl_2N_2O_2W$ | $C_{21}H_{24}ClOPSn$ |
| *M* | 932.21 | 470.89 | 551.88 | 466.95 | 477.51 |
| Crystal system | monoclinic | monoclinic | monoclinic | monoclinic | monoclinic |
| Space group | $P2_1/c$ (no. 14) | $P2_1/n$ (no. 14) | $P2_1/c$ (no. 14) | $C2/c$ (no. 15) | $P2_1/c$ (no. 14) |
| *a* [Å] | 18.883(3) | 10.521(2) | 8.9590(10) | 13.718(4) | 12.7036(10) |
| *b* [Å] | 9.9430(15) | 11.485(2) | 13.389(3) | 9.794(3) | 8.5432(10) |
| *c* [Å] | 19.043(3) | 12.256(3) | 13.226(3) | 11.500(4) | 20.293(2) |
| *α* [°] | 90 | 90 | 90 | 90 | 90 |
| *β* [°] | 110.937(7) | 92.338(8) | 95.385(13) | 121.752(15) | 98.892(5) |
| *γ* [°] | 90 | 90 | 90 | 90 | 90 |
| *U* [Å$^3$] | 3339.4(8) | 1479.8(5) | 1579.5(5) | 1313.8(7) | 2175.9(4) |
| Z | 4 | 4 | 4 | 4 | 4 |
| $\mu$ [mm$^{-1}$] | 5.987 | 8.376 | 7.995 | 9.195 | 1.376 |
| *F*(000) | 1808 | 896 | 1040 | 872 | 960 |
| Total no. of observations ($R_{int}$) | 43216 (0.059) | 12465 (0.031) | 21531 (0.038) | 8473 (0.038) | 22531 (0.039) |
| Unique observations | 7650 | 3387 | 3604 | 1497 | 4980 |
| Min., max. transmission | 0.796, 1.000 | 0.723, 1.000 | 0.702, 1.000 | 0.599, 1.000 | 0.768, 1.000 |
| No. of parameters, restraints | 406, 0 | 143, 0 | 199, 0 | 87, 0 | 226, 0 |
| Goodness-of-fit on $F^2$ | 1.04 | 1.07 | 1.05 | 1.02 | 1.04 |
| Residual electron density [e Å$^{-3}$] | –0.99 to +1.15 | –1.31 to +0.57 | –0.68 to +0.65 | –1.54 to +0.71 | –0.82 to +0.92 |
| $R_1$, $wR_2$ [$I > 2\sigma(I)$][b] | 0.039, 0.081 | 0.021, 0.043 | 0.022, 0.044 | 0.024, 0.058 | 0.036, 0.081 |
| $R_1$, $wR_2$ (all data) | 0.062, 0.088 | 0.026, 0.044 | 0.026, 0.046 | 0.028, 0.060 | 0.048, 0.087 |

[a] Common items: temperature = 120 K; wavelength (Mo-$K_\alpha$) = 0.71073 Å; $\theta$(max) = 27.5°. [b] $R_1 = \Sigma||F_o| - |F_c||/\Sigma|F_o|$. $wR_2 = [\Sigma w(F_o^2 - F_c^2)^2/\Sigma w F_o^4]^{1/2}$.

 © 2007 Wiley-VCH Verlag GmbH & Co. KGaA, Weinheim 

data can be obtained free of charge from The Cambridge Crystallographic Data Centre via www.ccdc.cam.ac.uk/data_request/cif.

## Acknowledgments

We thank the Royal Society for an Overseas Network Award and M. D. S. University, Ajmer (India) for granting a leave of absence (R. R.), and the Engineering and Physical Sciences Research Council (EPSRC) for support (M. F. D).

[1] J. M. Tunney, J. McMaster, C. D. Garner, *Comprehensive Coordination Chemistry II* (Eds.: J. A. McCleverty, T. J. Meyer), **2004**, *8*, 459–477, Elsevier, Amsterdam.
[2] R. H. Holm, *Chem. Rev.* **1987**, *87*, 1401–1449.
[3] C. G. Young, *Comprehensive Coordination Chemistry II* (Eds.: J. A. McCleverty, T. J. Meyer), **2004**, *4*, 415–527, Elsevier, Amsterdam.
[4] T. Okamura, N. Ueyama, *Comprehensive Coordination Chemistry II* (Eds.: J. A. McCleverty, T. J. Meyer), **2004**, *4*, 529–573, Elsevier, Amsterdam.
[5] a) K. Dreisch, C. Andersson, C. Stalhandske, *Polyhedron* **1992**, *11*, 2143–2150; b) K. Dreisch, C. Andersson, C. Stalhandske, *Polyhedron* **1993**, *12*, 301–311.
[6] M. B. Hursthouse, W. Levason, R. Ratnani, G. Reid, *Polyhedron* **2004**, *23*, 1915–1921.
[7] a) R. J. Butcher, B. R. Penfold, E. Sinn, *J. Chem. Soc., Dalton Trans.* **1979**, 668–675; b) G. Wang, G. Chen, R. L. Luck, Z. Wang, Z. Mu, D. G. Evans, X. Duan, *Inorg. Chim. Acta* **2004**, *357*, 3223–3229.
[8] C. G. Hull, M. H. B. Stiddard, *J. Chem. Soc. A* **1966**, 1633–1635.
[9] a) B. J. Brisdon, *Inorg. Chem.* **1967**, *6*, 1791–1795; b) J. F. de Wet, M. R. Caira, B. J. Gellatly, *Acta Crystallogr., Sect. B* **1978**, *34*, 762–766.
[10] a) K. Dreisch, C. Andersson, C. Stalhandske, *Polyhedron* **1991**, *10*, 2417–2421; b) H. Arzoumanian, G. Agrifoglio, M. V. Capparelli, R. Atencio, A. Briceno, A. Alvarez-Larena, *Inorg. Chim. Acta* **2006**, *359*, 81–89; c) V. C. Gibson, T. P. Kee, A. Shaw, *Polyhedron* **1990**, *9*, 2293–2298.
[11] a) M. J. Atherton, J. H. Holloway, *J. Chem. Soc., Chem. Commun.* **1978**, 254–255; A. K. Brisdon, J. H. Holloway, E. G. Hope, *J. Fluorine Chem.* **1998**, *89*, 35–37.
[12] a) L. Arnaudet, R. Bougon, B. Ban, P. Charpin, J. Isabey, M. Lance, M. Nierlich, J. Vigner, *Can. J. Chem.* **1990**, *68*, 507–512; b) Yu. A. Buslaev, Yu. V. Kokunov, V. A. Bochkareva, *Russ. J. Inorg. Chem.* **1975**, *20*, 495–498.
[13] a) J. Tillack, P. Eckerlin, J. H. Dettingmeijer, *Angew. Chem. Int. Ed. Engl.* **1966**, *5*, 421; b) J. Tillack, *Inorg. Synth.* **1973**, *14*, 109–122.
[14] a) R. Kergoat, J. E. Guerchais, *Bull. Soc. Chim. Fr.* **1970**, 2932–2937; b) M. Postel, J. G. Riess, J. Y. Calves, J. Guerchais, *Inorg. Chim. Acta* **1979**, *32*, 175–180.
[15] M. Rhiel, S. Wacadlo, W. Massa, K. Dehnicke, *Z. Anorg. Allg. Chem.* **1996**, *622*, 1195–1199.
[16] M. D. Brown, M. B. Hursthouse, W. Levason, R. Ratnani, G. Reid, *Dalton Trans.* **2004**, 2487–2491.
[17] a) R. Hart, W. Levason, B. Patel, G. Reid, *J. Chem. Soc., Dalton Trans.* **2002**, 3153–3159; b) R. Hart, W. Levason, B. Patel, G. Reid, *Eur. J. Inorg. Chem.* **2001**, 2927–2933.
[18] E. F. Murphy, R. Murugavel, H. W. Roesky, *Chem. Rev.* **1997**, *97*, 3425–3468.
[19] J. L. Lefferts, K. C. Molloy, M. B. Hossain, D. van der Helm, J. J. Zuckerman, *J. Organomet. Chem.* **1982**, *240*, 349–361.
[20] a) M. F. Davis, W. Levason, G. Reid, M. Webster, *Polyhedron* **2006**, *25*, 930–936; b) M. F. Davis, M. Clarke, W. Levason, G. Reid, M. Webster, *Eur. J. Inorg. Chem.* **2006**, 2773–2782.
[21] a) M. Zeldin, P. Mehta, W. D. Vernon, *Inorg. Chem.* **1979**, *18*, 463–466; A. C. Sau, L. A. Carpino, R. R. Holmes, *J. Organomet. Chem.* **1980**, *197*, 181–197.
[22] A. Stasch, M. Schormann, J. Prust, H. W. Roesky, H.-G. Schmidt, M. Noltemeyer, *J. Chem. Soc., Dalton Trans.* **2001**, 1945–1947.
[23] a) L. Arnaudet, R. Bougon, B. Ban, P. Charpin, J. Isabey, M. Lance, M. Nierlich, J. Vigner, *Inorg. Chem.* **1989**, *28*, 257–262; b) L. Arnaudet, R. Bougon, B. Ban, M. Lance, M. Nierlich, J. Vigner, *Inorg. Chem.* **1993**, *32*, 1142–1146.
[24] a) S.-O. Oh, S.-J. Mo, *J. Korean Chem. Soc.* **1995**, *39*, 318–322 (CCDC Refcode TOFLEF); b) A. Martín, A. G. Orpen, *J. Am. Chem. Soc.* **1996**, *118*, 1464–1470.
[25] F. E. Kühn, A. D. Lopes, A. M. Santos, E. Herdtweck, J. J. Haider, C. C. Romao, A. G. Santos, *J. Mol. Catal. A* **2000**, *151*, 147–160.
[26] M. Gerken, H. P. A. Mercier, G. J. Schrobilgen, in: *Advanced Inorganic Fluorides* (Eds.: T. Nakajima, B. Zemva, A. Tressaud), Elsevier, NY. **2000**, *5*, 117–174.
[27] E. G. Hope, W. Levason, J. S. Ogden, M. Tajik, *J. Chem. Soc., Dalton Trans.* **1986**, 1587–1591.
[28] P. R. Hammond, W. S. McEwan, *J. Chem. Soc. A* **1971**, 3812–3819.
[29] P. Mehta, M. Zeldin, *Inorg. Chim. Acta* **1977**, *22*, L33–34.
[30] C. D. Beard, R. J. Barrie, J. Evans, W. Levason, G. Reid, M. D. Spicer, *Eur. J. Inorg. Chem*. **2006**, 4391–4398.
[31] a) J. Bernard, M. Camelot, *C. R. Acad. Sci.* **1964**, *258*, 5881–5883; b) R. C. Paul, O. Khosla, R. Dev, *Ind. J. Chem.* **1969**, *7*, 1254–1256; c) M. N. Majumder, R. K. Mukhopadhya, A. K. Saha, *Ind. J. Chem.* **1975**, *13*, 69–71.
[32] E. K. Mooney, K. R. Seddon, *Transition Met. Chem.* **1977**, *2*, 215–216.
[33] a) H.-W. Lam, G. Wilkinson, B. Hussain-Bates, M. B. Hursthouse, *J. Chem. Soc., Dalton Trans.* **1993**, 1477–1482; b) A. A. Danopoulos, G. Wilkinson, T. K. N. Sweet, M. B. Hursthouse, *J. Chem. Soc., Dalton Trans.* **1995**, 2111–2124.
[34] W. Levason, R. Patel, G. Reid, *J. Organomet. Chem.* **2003**, *688*, 280–282.
[35] a) A. K. Brisdon, E. G. Hope, W. Levason, J. S. Ogden, *J. Chem. Soc., Dalton Trans.* **1989**, 313–316; b) P. C. Crouch, G. W. A. Fowles, R. A. Walton, *J. Inorg. Nucl. Chem.* **1970**, *32*, 329–333.
[36] E. Krause, *Ber. Dtsch. Chem. Ges.* **1918**, *51*, 1447–1456.
[37] G. M. Sheldrick, SHELXS-97, *Program for crystal structure solution*, University of Göttingen, Germany, **1997**.
[38] G. M. Sheldrick, SHELXL-97, *Program for crystal structure refinement*, University of Göttingen, Germany, **1997**.
[39] G. M. Sheldrick, SADABS, *Bruker-Nonius area detector scaling and absorption correction* (V2.10), University of Göttingen, Germany, **2003**.
[40] C. Yoder, A. L. Rheingold, M. B. Allen, unpublished work, **1996**. [Cambridge Structural Database, refcode HIGRUK for room temperature structure].

Received: September 5, 2006
Published Online: November 14, 2006

 © 2007 Wiley-VCH Verlag GmbH & Co. KGaA, Weinheim 

DOI: 10.1002/ejic.200600830

# Valence-State Distribution in the Ruthenium *o*-Quinonoid Systems [Ru(trpy)(Cl)($L^1$)]$^+$ and [Ru(trpy)(Cl)($L^2$)]$^+$ ($L^1$ = *o*-Iminobenzoquinone, $L^2$ = *o*-Diiminobenzoquinone; trpy = 2,2′:6′,2′′-Terpyridine)

**Somnath Maji,[a] Srikanta Patra,[a] Saumen Chakraborty,[a] Deepa Janardanan,[a] Shaikh M. Mobin,[a] Raghavan B. Sunoj,*[a] and Goutam Kumar Lahiri*[a]**

**Keywords:** Ruthenium / Quinonoid ligands / Valence-state distributions / Density functional calculations / Spectroelectrochemistry

Valence-state distributions in the ruthenium quinonoid (L) frameworks of [Ru(trpy)(Cl)($L^1$)]$ClO_4$ (**1**-$ClO_4$) and [Ru(trpy)(Cl)($L^2$)]$ClO_4$ (**2**-$ClO_4$) ($L^1$ = *o*-iminobenzoquinone, $L^2$ = *o*-diiminobenzoquinone, and trpy = 2,2′:6′,2′′-terpyridine) have been examined by structural, spectroelectrochemical, and density functional studies. The structural data, in corroboration with the DFT-calculated bond lengths, suggest that the primary valence formulation of $\mathbf{1}^+$ and $\mathbf{2}^+$ is a spin-coupled singlet configuration of [$Ru^{III}$(trpy)(Cl)($L_{Sq}$)]$^+$ with a minority contribution from diamagnetic [$Ru^{II}$(trpy)(Cl)($L_Q$)]$^+$. Consequently, the closely spaced successive two oxidation processes of $\mathbf{1}^+$ and $\mathbf{2}^+$ can be assigned to $Ru^{III} \rightarrow Ru^{IV}$ and $L_{Sq} \rightarrow L_Q$, which involve the HOMO and HOMO–3 levels, respectively. The one-electron-oxidized species $\mathbf{1}^{2+}$ and $\mathbf{2}^{2+}$ display sharp EPR signals with *g* values of 2.011 and 2.014 at 77 K, respectively. The free radical EPR signal ($g \approx 2.0$) of the one-electron-reduced species **1** or **2** signifies the preferential involvement of the ruthenium-based orbitals in the first reduction process to yield [$Ru^{II}$(trpy)(Cl)($L_{Sq}$)], although the LUMO is calculated to be a mixture of dπ(Ru) (≈24 %) and π*(L) (≈ 70 %). The subsequent second ($\mathbf{1}^-/\mathbf{2}^-$) and third ($\mathbf{1}^{2-}/\mathbf{2}^{2-}$) reduction steps in each case are associated simply with the terpyridyl-based orbitals (≥90 %). The lowest energy charge-transfer transitions of $\mathbf{1}^+$ and $\mathbf{2}^+$ at 556 and 509 nm are predicted to be HOMO → LUMO+1 and HOMO–1 → LUMO+1 transitions, respectively. In the successive oxidations $\mathbf{1}^+/\mathbf{2}^+ \rightarrow \mathbf{1}^{2+}/\mathbf{2}^{2+} \rightarrow \mathbf{1}^{3+}/\mathbf{2}^{3+}$ the lowest energy charge-transfer transitions undergo a blue shift with a substantial reduction in intensity. The lowest energy charge-transfer transitions, however, are red shifted with a reduction in intensity on going from ($\mathbf{1}^+/\mathbf{2}^+$) to **1/2**. The origin of the transitions in the $\mathbf{1}^{2+}/\mathbf{2}^{2+}$ and **1/2** systems is predicted by TDDFT analysis.

(© Wiley-VCH Verlag GmbH & Co. KGaA, 69451 Weinheim, Germany, 2007)

## Introduction

The ground-state formulation of a particular mononuclear quinonoid system [(AL)$Ru^n$–$L^{m+}$] ["*n*" and "*m*" are the formal charges associated with the electronic states of the metal and quinonoid ligand (L)] can either be any of the possible valence-localized tautomeric forms, [(AL)$Ru^{II}$–$L°_Q$] ↔ [(AL)$Ru^{III}$–$L^{\cdot-}_{Sq}$] ↔ [(AL)$Ru^{IV}$–$L^{2-}_{Cat}$] or a mixed M(dπ)-L(pπ) delocalized situation depending on the electronic aspects of all the associated entities ($Ru^n$, $L^m$ and AL) in the complex frameworks (Cat = fully reduced dianionic catecholate form; Sq = intermediate monoanionic radical form; Q = fully oxidized quinine form, Scheme 1; AL = ancillary ligands). The remarkable mixing of redox-facile-metal-ion- and ligand-based frontier orbitals in the ruthenium quinonoid (L) frameworks often introduces considerable ambiguities in assigning their precise valence configurations in the native state, as well as preferential involvement of the metal- or ligand-based orbitals in the accessible electron-transfer processes.[1,2] For example, experimental results have convincingly established the $Ru^{III}L_{Sq}$ formulation[3] of [Ru(acac)$_2$(L)] [acac$^-$ = acetylacetonate; L = iminoquinone (X = O, Y = NH) or iminothioquinone (X = S, Y = NH); Scheme 1] but subsequent theoretical studies suggest that the alternate resonance form of $Ru^{II}L_Q$ also contributes in the native state to some extent.[4] Thus, establishing the primary contributing electronic forms of the metal ion and L in such complexes is a formidable challenge. Although a wide variety of mononuclear ruthenium-*o*-quinonoid systems have been scrutinized over the past years, the complexities vary substantially from one molecule to another depending on the nature of X and Y in the quinonoid (L) framework (Scheme 1) and the electronic nature of the ancillary ligands (AL) associated with the complex moieties. For instance, distinct localized {$Ru^{II}L_{Cat}$} and {$Ru^{II}L_{Sq}$} configurations have been stabilized in [(tap)$_2$RuL][5] [tap = 2-(*m*-tolylazo)pyridine] and [($PPh_3$)$_2$$RuL_2$],[6]

[a] Department of Chemistry, Indian Institute of Technology, Bombay,
Powai, Mumbai 400076, India
E-mail: lahiri@chem.iitb.ac.in

Supporting information for this article is available on the WWW under http://www.eurjic.org or from the author.


© 2007 Wiley-VCH Verlag GmbH & Co. KGaA, Weinheim

respectively, although the $[(bpy)_2RuL]^+$ (bpy = 2,2′-bipyridine) and $[(t\text{Bupy})_2RuL_2]$ analogs (L = X = Y = O, Scheme 1) have been described as RuL charge-delocalized systems.[2b,2u] Similarly, the RuL valence-state features in [(Cl/OAc)(trpy)RuL] (L = X = Y = O; trpy = 2,2′:6′,2′′-terpyridine, Scheme 1) have been addressed as a resonance equilibrium between $Ru^{II}L_{Sq}$ and $Ru^{III}L_{Cat}$.[7] This unique electronic characteristic of metal quinonoids justifies their continuous experimental and theoretical explorations with newer molecules.[1,2,8] This indeed is the origin of the present work, which scrutinizes the valence-state distribution profile of {RuL} coordinated to the hitherto relatively less explored terpyridine as ancillary ligand.[7,9]

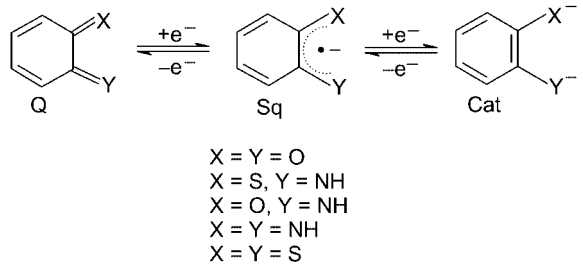


Scheme 1.

This work deals with two such conceptually simple ruthenium *o*-quinonoid species, namely $[Ru(trpy)(Cl)(L^1)]ClO_4$ (**1**-$ClO_4$) and $[Ru(trpy)(Cl)(L^2)]ClO_4$ (**2**-$ClO_4$), where $L^1$ and $L^2$ are *o*-iminobenzoquinone (X = O and Y = NH) and *o*-diiminobenzoquinone (X = Y = NH) respectively (Scheme 1). Unlike many other apparently similar systems, establishment of the {RuL} redox configurations in $\mathbf{1}^+$ and $\mathbf{2}^+$ was not as straightforward as we envisaged (see below),[3,5,6] therefore the primary objectives of the present article are to address the charge-distribution phenomena of $\{Ru^nL^m\}$ in $\mathbf{1}^+$ and $\mathbf{2}^+$ by parallel considerations of experimental results and the theoretically generated information on their optimized geometries.

## Results and Discussion

The diamagnetic complexes $[Ru(trpy)(Cl)(L^1)]ClO_4$ (**1**-$ClO_4$) and $[Ru(trpy)(Cl)(L^2)]ClO_4$ (**2**-$ClO_4$) ($L^1$ = *o*-iminobenzoquinone and $L^2$ = *o*-diiminobenzoquinone; trpy = 2,2′:6′,2′′-terpyridine) were prepared by the reaction of $[RuCl_3(trpy)]$ with *o*-aminophenol and *o*-phenylenediamine, respectively, in the presence of $NEt_3$ as a base, in refluxing ethanol, followed by chromatographic purification on a neutral alumina column.

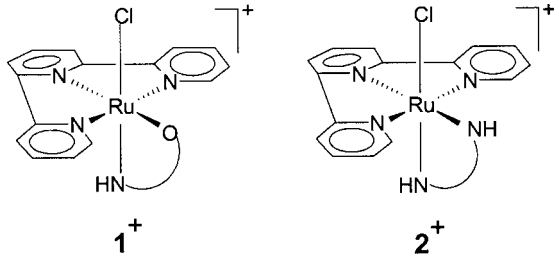


The unsymmetrical $L^1$ in combination with the meridional configuration of trpy in $\mathbf{1}^+$ is expected to give rise to an isomeric mixture of **A** and **B**. However, the preferential crystallization of isomer **B** was confirmed by its crystal structure (see below).

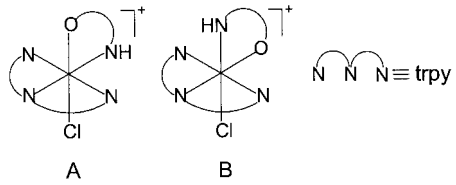


Complexes **1**-$ClO_4$ and **2**-$ClO_4$ are 1:1 conductors in acetonitrile and exhibit satisfactory microanalytical data (see Exp. Sect.). The positive-ion electrospray mass spectra show molecular ion peaks at 476.90 and 475.85 (Figure S1, Supporting Information) for $\mathbf{1}^+$ (calcd.: 477.00) and $\mathbf{2}^+$ (calcd.: 475.92), respectively. The presence of the $ClO_4^-$ counteranion was confirmed by the appearance of characteristic $\nu(ClO_4^-)$ frequencies at 1100 and 630 $cm^{-1}$ in their IR spectra; the NH vibrations appear near 3300 $cm^{-1}$ (see Exp. Sect.). The $^1H$ NMR spectra of $\mathbf{1}^+$ and $\mathbf{2}^+$ exhibit the expected fifteen (eleven from trpy and four from $L^1$ or $L^2$), although partially overlapping, aromatic signals. The $D_2O$ exchangeable one and two NH proton signals of coordinated $L^1$ and $L^2$ in $\mathbf{1}^+$ and $\mathbf{2}^+$, respectively, are observed in the downfield region (Figure S2, Supporting Information; see Exp. Sect.).[10] The synthesis of **2**-$ClO_4$ by a different synthetic route and its electronic spectrum [in $H_2O$; $\lambda_{max}$ ($\varepsilon$) = 506 nm (16000 $M^{-1}cm^{-1}$), 316 (22000), 280 (20000), 274 (21000), 232 (28000)] and metal oxidation potential (0.96 V vs. Ag/AgCl in $CH_3CN$) have been reported earlier.[11]

The structures of **1**-$ClO_4$ and **2**-$ClO_4$ were authenticated by their single-crystal X-ray structures (Figures 1 and 2, respectively, and Table 1). The geometrical constraint that arises due to the usual meridional mode of the tridentate trpy ligand is reflected in the *trans* angles (Table 1).[12,13] The chloride is preferentially *trans* to N1H in $\mathbf{1}^+$ (structural form **B**). As a consequence of the small bite angle involving the coordinated ligand $L^1$ [N1–Ru–O1 78.1(3)°] or $L^2$ [N1–Ru–N5 78.0(3)°], the N1–Ru–Cl *trans* angle is tilted by about 10°. The Ru–Cl and Ru–N(trpy) bond lengths and the associated angles are in good agreement with the data reported for related molecules.[12–14] The Ru–N distances involving $L^1$ [1.942(8) Å] and $L^2$ [1.985(6) and 1.991(7) Å] are appreciably shorter than the corresponding Ru–N(trpy) distances (2.022 Å in $\mathbf{1}^+$ and 2.043 Å in $\mathbf{2}^+$; Table 1), which implies significant mixing of dπ(Ru) and π* of L in the respective LUMOs (see below).[15]

The C1–O1 and C6–N1H bond lengths pertaining to $L^1$ in $\mathbf{1}^+$ are 1.270(11) and 1.312(12) Å, respectively [C–O/C–NH distances to individual localized oxidation states (Sq and Q) are 1.30/1.35 and 1.22/1.31 Å, respectively, based on hundreds of structure of *o*-quinonoid molecules determined since 1985[8b]]. This, together with the two short C–C intraring distances in $L^1$ [C2–C3 1.322(13) and C4–C5 1.377(14) Å], suggests that $\mathbf{1}^+$ is primarily in a $\{Ru^{III}–Sq\}$ state, with a minor contribution from the alternate reso-

 © 2007 Wiley-VCH Verlag GmbH & Co. KGaA, Weinheim 

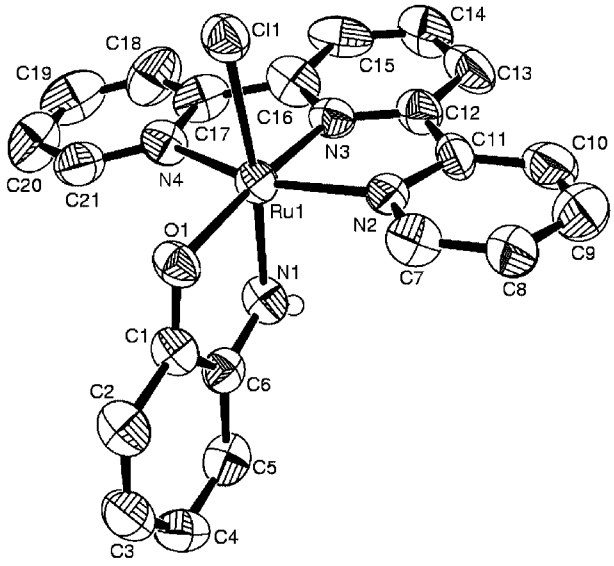


Figure 1. Crystal structure of the cation of **1**-$ClO_4$. Ellipsoids are drawn at the 50% probability.

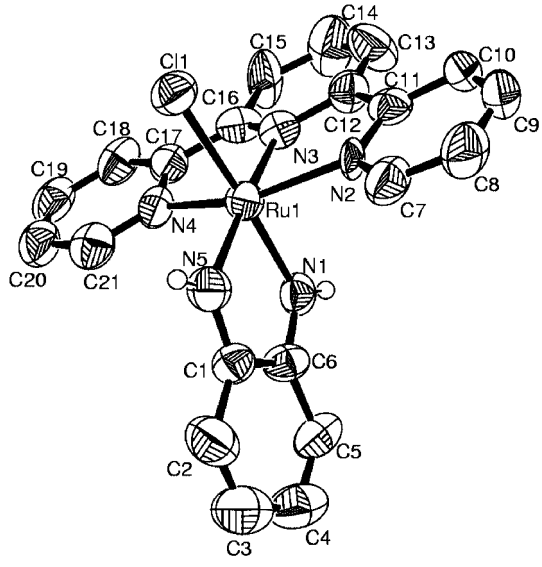


Figure 2. Crystal structure of the cation of **2**-$ClO_4$. Ellipsoids are drawn at the 50% probability.

nance form {$Ru^{II}$–Q}. On the other hand, C1–N5H, C6–N1H and the two short intra-ring bond lengths (C2–C3 and C4–C5) of $L^2$ in $\mathbf{2}^+$ [1.316(9), 1.317(9), 1.310(13) and 1.331(13) Å, respectively] indicate a charge-delocalized resonance form of $Ru^{III}$–Sq ↔ $Ru^{II}$–Q. Thus, the 1:1 conducting behavior and singlet ($S$ = O) ground states of $\mathbf{1}^+$ and $\mathbf{2}^+$ can be addressed in terms of a valence tautomeric formulation of spin-coupled $[Ru^{III}(trpy)(Cl)(L_{Sq})]^+$ and diamagnetic $[Ru^{II}(trpy)(Cl)(L_Q)]^+$, as observed in $[(bpy)_2RuL]^+$ (L = X = Y = O; X = Y = NH; X = O, Y = NH).[2b,2i,7,16] However, the corresponding Ru-trpy-dioxolene derivatives [(Cl/OAc)(trpy)RuL] (L = X = Y = O, Scheme 1) are described as a resonance equilibrium between $Ru^{II}L_{Sq}$ and $Ru^{III}L_{Cat}$.[7] Hence, density functional calculations at the B3LYP level were performed for $\mathbf{1}^+$ and $\mathbf{2}^+$ in order to obtain additional structural insights from the optimized geometries.[17] In addition, geometry optimizations of the oxidized and reduced species were also performed.

The optimized geometries of $\mathbf{1}^+$ and $\mathbf{2}^+$ are shown in Figure 3, and a selected list of calculated geometric parameters is provided in Table 1 (coordinates for $\mathbf{1}^+$ and $\mathbf{2}^+$ are given in Table S1 in the Supporting Information). In general, the computed structural parameters of $\mathbf{1}^+$ and $\mathbf{2}^+$ are in reasonably good agreement with the experimental ones (Table 1). The calculated intra-ligand C–C distances of $L^1$ and $L^2$ in $\mathbf{1}^+$ and $\mathbf{2}^+$, respectively, also show two short distances (C4–

Table 1. Important experimental[a] and computed[b] bond lengths [Å] and angles [°] for **1**-$ClO_4$ and **2**-$ClO_4$.

| Bond lengths | | | | | Bond angles | | | | |
|---|---|---|---|---|---|---|---|---|---|
| | **1**-$ClO_4$ | | **2**-$ClO_4$ | | | **1**-$ClO_4$ | | **2**-$ClO_4$ | |
| | Exp. | Comp. | Exp. | Comp. | | Exp. | Comp. | Exp. | Comp. |
| Ru1–N1 | 1.942(8) | 1.988 | 1.985(6) | 2.034 | N1–Ru1–Cl1 | 170.0(2) | 170.54 | 171.8(2) | 167.87 |
| Ru1–N2 | 2.068(8) | 2.098 | 2.082(5) | 2.102 | N2–Ru1–Cl1 | 89.8(2) | 86.56 | 87.85(17) | 87.66 |
| Ru1–N3 | 1.958(8) | 1.976 | 1.980(6) | 2.014 | N3–Ru1–Cl1 | 91.9(2) | 90.73 | 92.55(18) | 91.29 |
| Ru1–N4 | 2.040(8) | 2.098(0.06) | 2.068(6) | 2.102 | N4–Ru1–Cl1 | 89.1(2) | 86.54 | 90.48(19) | 87.66 |
| Ru1–Cl1 | 2.402(3) | 2.387 | 2.407(2) | 2.400 | O1–Ru1–Cl1 | 91.97(19) | 93.19 | – | – |
| Ru1–O1 | 2.053(6) | 2.104 | – | – | N1–Ru1–N2 | 93.2(3) | 95.18 | 91.6(2) | 94.77 |
| Ru1–N5 | – | – | 1.991(7) | 2.018 | N1–Ru1–N3 | 98.0(3) | 98.73 | 95.4(3) | 100.84 |
| N1–C6 | 1.312(12) | 1.335 | 1.317(9) | 1.329 | N1–Ru1–N4 | 91.5(3) | 95.15 | 93.2(2) | 94.77 |
| C1–O1 | 1.270(11) | 1.280 | – | – | N2–Ru1–N3 | 78.9(3) | 79.27 | 79.8(3) | 78.22 |
| C1–C2 | 1.416(13) | 1.427 | 1.401(11) | 1.432 | N2–Ru1–N4 | 158.8(3) | 157.34 | 157.4(3) | 155.85 |
| C2–C3 | 1.322(13) | 1.372 | 1.310(13) | 1.367 | N3–Ru1–N4 | 80.0(4) | 79.26 | 77.7(3) | 78.22 |
| C3–C4 | 1.446(15) | 1.437 | 1.423(15) | 1.438 | N1–Ru1–O1 | 78.1(3) | 77.05 | – | – |
| C4–C5 | 1.377(14) | 1.369 | 1.331(13) | 1.368 | N2–Ru1–O1 | 99.2(3) | 100.96 | – | – |
| C5–C6 | 1.430(13) | 1.429 | 1.429(11) | 1.431 | N3–Ru1–O1 | 175.7(3) | 175.78 | – | – |
| C1–C6 | 1.433(13) | 1.462 | 1.419(11) | 1.462 | N4–Ru1–O1 | 102.0(3) | 101.00 | – | – |
| C1–N5 | – | – | 1.316(9) | 1.326 | N1–Ru1–N5 | – | – | 78.0(3) | 76.62 |
| | | | | | N2–Ru1–N5 | – | – | 103.3(3) | 101.90 |
| | | | | | N3–Ru1–N5 | – | – | 172.7(3) | 177.46 |
| | | | | | N4–Ru1–N5 | – | – | 99.3(3) | 101.88 |

[a] Taken from the X-ray crystal data. [b] Calculated at the B3LYP level of theory by employing the SDD basis set for Ru and 6-31G* for all other atoms.

 © 2007 Wiley-VCH Verlag GmbH & Co. KGaA, Weinheim 

C5 1.369/1.368 and C2–C3 1.372/1.367 Å; Table 1). More importantly, the C1–O1/C6–N1H and C1–N5H–C6–N1H distances of 1.280/1.335 and 1.326/1.329 Å in $\mathbf{1}^+$ and $\mathbf{2}^+$, respectively, also suggest the charge delocalization situation of $\{Ru^{III}\text{–}Sq\} \longleftrightarrow \{Ru^{II}\text{–}Q\}$.

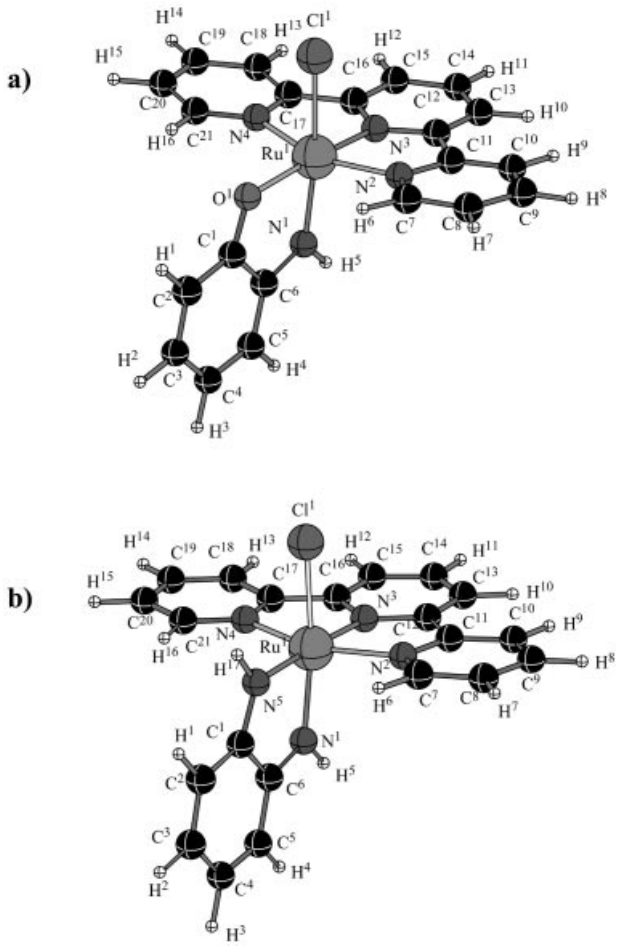


Figure 3. The B3LYP/SDD,6-31G* optimized geometries for the singlet ground state of (a) $\mathbf{1}^+$ and (b) $\mathbf{2}^+$.

Thus, a combination of the experimental and calculated structural data of $\mathbf{1}^+$ and $\mathbf{2}^+$ provide justification for the preferential ground-state formulation of $[Ru^{III}(trpy)(Cl)(L_{Sq})]^+$, with a minority contribution from $[Ru^{II}(trpy)(Cl)(L_Q)]^+$.

Both $\mathbf{1}^+$ and $\mathbf{2}^+$ show two closely spaced successive oxidation (couples I and II) and three reduction processes (couples III–V) in the potential ranges 0.94 to 1.45 and –0.26 to –1.79 V, respectively, vs. SCE (Figure 4, Table 2). The large separations in potentials between the first oxidation (couple I) and reduction (couple III) processes, $\Delta E$ = 1.45 and 1.49 V for $\mathbf{1}^+$ and $\mathbf{2}^+$, respectively, translate to comproportionation constants ($K_c$) of $10^{24.6}$ and $10^{25.2}$ [$RT\ln K_c = nF(\Delta E)$],[18] thereby reflecting the high stability of the native states. The more basic character of the diimine-based ligand ($L^2$) in $\mathbf{2}^+$ makes the first oxidation process (couple I) easier and the first reduction process (couple III) more difficult relative to iminoquinone-based $L^1$ in $\mathbf{1}^+$ (Table 2).[19] Although the separation in potential between couples I and II is greater in $\mathbf{2}^+$ than in $\mathbf{1}^+$, the reverse order is observed for couples III and IV, thus implying the greater and lower stabilities of the intermediate oxidized $\mathbf{2}^{2+}$ and reduced **2**, respectively, relative to the corresponding $\mathbf{1}^{2+}$ and **1**. Moreover, the irreversible profile of couples I and II for $\mathbf{1}^+$ (Figure 4a) also suggests that, unlike $\mathbf{2}^{2+/3+}$, the oxidized species $\mathbf{1}^{2+/3+}$ are not stable even on the cyclic voltammetric timescale. The relatively higher energy HOMO of complex $\mathbf{2}^+$ also points to its easier oxidation than complex $\mathbf{1}^+$ (Figure 5, Table 3). The presence of the semiquinone form of $L^{\cdot-}$ along with the anionic $Cl^-$ in $\mathbf{1}^+$ and $\mathbf{2}^+$ makes the $Ru^{III}$–$Ru^{II}$ potential substantially negative (approx. –0.3 V, see below), which, in turn, facilitates the stabilization of the $Ru^{III}$ state under the atmospheric reaction conditions. Since the $Ru^{III}$ and $L_{Sq}$ states are each susceptible to one-electron oxidation to $Ru^{IV}$ and $L_Q$, respectively, couples I and II can therefore be assigned to ruthenium(III)→ruthenium(IV) and coordinated $L_{Sq}\rightarrow L_Q$ processes, respectively, or vice versa.[20] The correspondence of couples I and II with metal- ($Ru^{III}\rightarrow Ru^{IV}$) and ligand-based ($L_{Sq}\rightarrow L_Q$) processes is supported by the fact that the HOMOs of $\mathbf{1}^+$

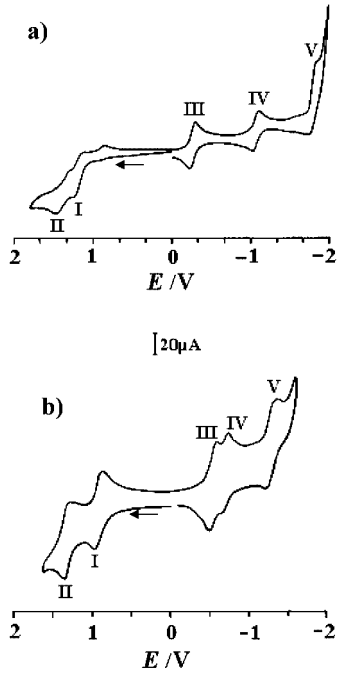


Figure 4. Cyclic voltammograms of a $10^{-3}$ M solution of (a) (**1**-$ClO_4$) and (b) (**2**-$ClO_4$) in $CH_3CN$/0.1 M $Et_4NClO_4$ at 298 K (scan rate: 50 mV $s^{-1}$).

Table 2. Redox potentials[a,b] of the complexes.

| | Couple I | II | III | IV | V |
|---|---|---|---|---|---|
| **1**-$ClO_4$ | 1.26[c] | 1.45[c] | –0.26 (90) | –1.07 (80) | –1.79 (100) |
| **2**-$ClO_4$ | 0.94 (70) | 1.32 (90) | –0.54 (70) | –0.70 (60) | –1.27 (140) |

[a] Potentials $E°_{298}$ [V] ($\Delta E$ [mV]) vs. SCE. [b] In $CH_3CN$/0.1 M $Et_4NClO_4$. [c] $E_{pa}$ is considered due to the irreversible nature of the voltammograms.

 © 2007 Wiley-VCH Verlag GmbH & Co. KGaA, Weinheim 

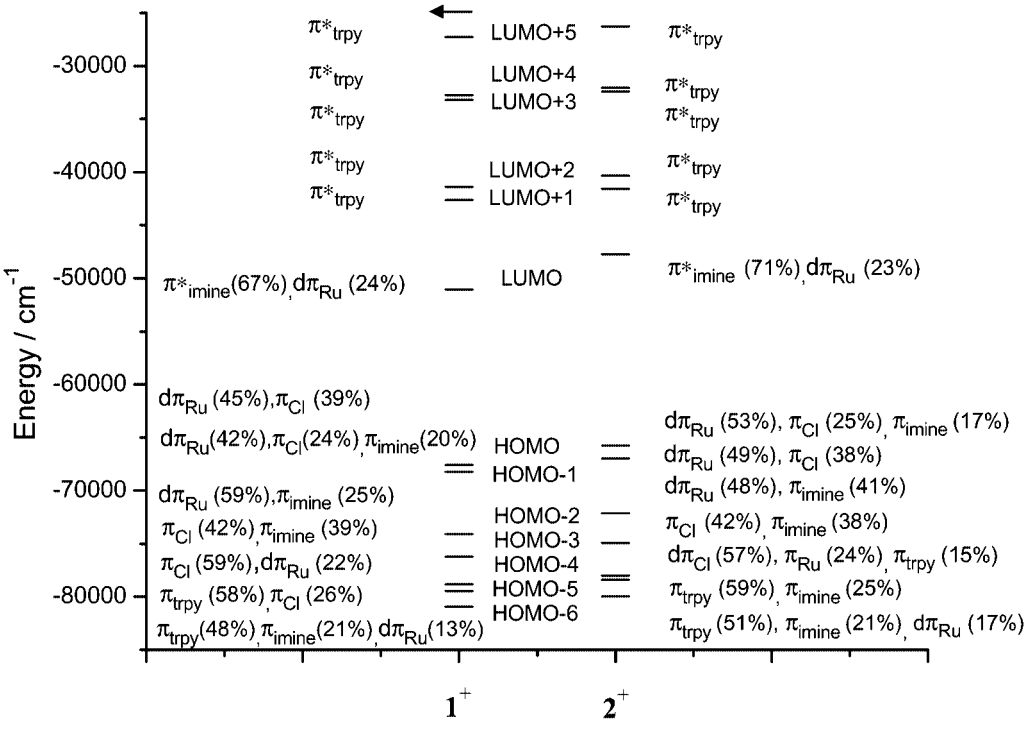


Figure 5. Orbital energy diagrams for $\mathbf{1}^+$ and $\mathbf{2}^+$ computed at the B3LYP/SDD,6-31G* level of theory.

and $\mathbf{2}^+$consist of 45% and 53% of dπ(Ru) with zero and 17% contributions from π($L^1$) and π($L^2$), respectively, and the HOMO–3s are dominated by π($L^1$) (39%) and π($L^2$) (38%), with slight metal contributions of 5.7% and 11% for $\mathbf{1}^+$ and $\mathbf{2}^+$, respectively (Figure 5, Table 3). The electrochemically generated one-electron-oxidized $Ru^{IV}$–$L_{Sq}$ states in $\mathbf{1}^{2+}$ and $\mathbf{2}^{2+}$ exhibit free radical EPR signals in $CH_3CN$ with *g* values of 2.011 (peak-to-peak separation: 18 G) and 2.014 (peak-to-peak separation: 15 G), respectively.

The DFT results also suggest that the mixing of π($L^2$) and dπ(Ru) orbitals at both the HOMO and HOMO–3 levels is more pronounced in $\mathbf{2}^+$.[15,21] It is interesting to note that HOMO and HOMO–3 exhibit a fairly good mixing with chloride π orbitals (39/25% and 42% for $\mathbf{1}^+$ and $\mathbf{2}^+$, respectively), as observed in the analogous isomeric ruthenium terpyridine complexes [Ru(trpy)(Cl){3-amino-6-(3,5-dimethylpyrazol-1-yl)-1,2,4,5-tetrazine}].[13]

The observed Ru- and L-based successive two-step oxidation processes (couples I and II) in $\mathbf{1}^+$ and $\mathbf{2}^+$ also support their primary valence-state composition of $\{Ru^{III}–L_{Sq}\}$ in solution instead of the alternate possible formulation of $\{Ru^{II}–L_Q\}^+$ in which only a ruthenium-based oxidation process is expected due to the fully oxidized nature of $L_Q$. Similarly, the first reduction (couple III) could either be associated with the ruthenium(III) or $L_{Sq}$ center as both are susceptible to one-electron reduction and the resultant reduced species (**1/2**) would then be formulated as $[Ru^{III}(trpy)(Cl)(L_{Sq})]^+$ ($\mathbf{1}^+/\mathbf{2}^+$) + $e^- \rightarrow [Ru^{II}(trpy)(Cl)(L_{Sq})]$ or $[Ru^{III}(trpy)(Cl)(L_{Cat})]$ (**1/2**), leaving the unpaired spin predominantly on the $L_{Sq}$ or $Ru^{III}$. The semiquinone-based free radical EPR signals (*g* = 2.0023 and 2.0051, with peak-to-peak separations of 17 and 20 G for **1** and **2**, respectively;[22] see Figure 6), however, suggest a preferential metal-based reduction process to form $[Ru^{II}(trpy)(Cl)(L_{Sq})]$. The separation in potentials of approximately 1.5 V between the first oxidation (couple I) and reduction (couple III) processes in $\mathbf{1}^+$ and $\mathbf{2}^+$ also matches well with the earlier observed ruthenium-based average potential difference of about 1.5 V between the $Ru^{IV/III}$ and $Ru^{III/II}$ couples.[23]

Table 3. Orbital energies and atomic orbital contribution of frontier molecular orbitals of $\mathbf{1}^+$ and $\mathbf{2}^+$ computed at the B3LYP level of theory by employing the SDD basis set for Ru and 6-31G* for all other atoms.

| MO | Energy (eV) | % Ru | % Cl | % imine ($L^1$/$L^2$) | % trpy |
|---|---|---|---|---|---|
| $\mathbf{1}^+$ | LUMO – HOMO = 2.05 eV (16528 cm$^{-1}$) | | | | |
| LUMO+2 | –5.13 (–41380)[a] | 2.1 | 0.0 | 0.0 | 96.5 |
| LUMO+1 | –5.29 (–42638) | 7.4 | 0.0 | 0.0 | 89.6 |
| LUMO | –6.33 (–51056) | 24.4 | 0.0 | 66.3 | 4.7 |
| HOMO | –8.38 (–67585) | 44.6 | 38.5 | 0.0 | 7.3 |
| HOMO–1 | –8.46 (–68224) | 42.2 | 23.8 | 19.6 | 0.0 |
| HOMO–2 | –9.18 (–74079) | 59.0 | 0.0 | 24.6 | 4.0 |
| HOMO–3 | –9.45 (–76213) | 5.7 | 41.9 | 39.0 | 3.2 |
| $\mathbf{2}^+$ | LUMO – HOMO = 2.24 eV (18028 cm$^{-1}$) | | | | |
| LUMO+2 | –5.00 (–40351) | 2.2 | 0.0 | 0.6 | 97.2 |
| LUMO+1 | –5.16(–41582) | 7.0 | 1.2 | 0.8 | 91.0 |
| LUMO | –5.92 (–47734) | 23.0 | 1.26 | 70.5 | 5.3 |
| HOMO | –8.15 (–65762) | 52.6 | 24.5 | 16.6 | 6.3 |
| HOMO–1 | –8.30 (–66973) | 49.3 | 37.5 | 3.1 | 10.0 |
| HOMO–2 | –8.94 (–72116) | 47.7 | 5.8 | 40.7 | 5.8 |
| HOMO–3 | –9.29 (–74951) | 10.8 | 41.6 | 38.2 | 9.5 |

[a] Values in parentheses are orbital energies [cm$^{-1}$].

While the EPR results are strongly in favor of a metal-based reduction, the participation of Ru orbitals in the

 © 2007 Wiley-VCH Verlag GmbH & Co. KGaA, Weinheim 

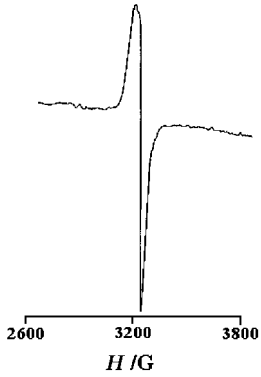


Figure 6. EPR spectrum of **1** in $CH_3CN/Et_4NClO_4$ at 77 K. The expected nitrogen hyperfine lines cannot be resolved at 77 K.

LUMOs is predicted to be lower than that of $L_{Sq}$. The contributions of $Ru/L_{Sq}$ orbitals to the LUMOs are found to be 24/66% and 23/70%, respectively, for $\mathbf{1}^+$ and $\mathbf{2}^+$ (Figure 5, Table 3). Hence, a comparatively lower, but still significant, metal contribution favors the metal-centered reduction process in a mixed Ru(dπ)/L(π*) situation.[21] The subsequent higher energy unoccupied MOs such as LUMO+1 and LUMO+2 are primarily localized on the trpy ligand with a composition of >90% π*(trpy) orbitals along with a slight metal contribution (2–7%), which implies that the second (couple IV) and third (couple V) reductions are trpy-based (Figure 4, Table 2).[24]

In order to get further insights into the reduced species the spin densities[25] for one-electron-reduced species **1** and **2** were computed at the same level of theory. The results are in accordance with the nature of the LUMOs described earlier. The overall spin density of the complexes was found to be distributed over the metal and $L^1/L^2$, thus supporting an "Sq" formalism for the reduced species (Figure S3, Supporting Information). It is also worth mentioning that the contribution of the trpy ligand to the first reduction process is negligible.

Natural population analysis (NPA) for $\mathbf{1}^+$ and $\mathbf{2}^+$ at the B3LYP/SDD,6-31G* level[8c,26] suggest a d-orbital population of 6.98 and 7.03 electrons for $\mathbf{1}^+$ and $\mathbf{2}^+$, respectively (Table 4). The extra population of about $2e^-$ is expected to be an effect of charge transfer from the anionic forms of the ligands ($Cl^-$ is a $2e^-$ donor and $L^{\cdot -}_{Sq}$ a $1e^-$ donor). The d-electron population further indicates a relatively high electron density for $\mathbf{2}^+$, in agreement with its easier oxidation than $\mathbf{1}^+$ (Table 2, Figures 4 and 5).

Table 4. Valence shell electron population of the Ru centers in $\mathbf{1}^+$ and $\mathbf{2}^+$ computed at the B3LYP/SDD, 6-31G* level.

| Complex | Valence shell population | |
|---|---|---|
| | 5s | 4d |
| $\mathbf{1}^+$ | 0.30 | 6.98 |
| $\mathbf{2}^+$ | 0.30 | 7.03 |

Both $\mathbf{1}^+$ and $\mathbf{2}^+$ display multiple charge-transfer transitions in the visible region in addition to intense ligand-based bands in the UV region (Figure 7, see Exp. Sect.). Selected computed vertical excitation energies with the TD-DFT/B3LYP formalism for the B3LYP/SDD,6-31G* geometries of $\mathbf{1}^+$ and $\mathbf{2}^+$ in their singlet ground states are summarized in Table 5 (complete lists are given in Tables S2 and S3 in the Supporting Information).[27] A comparison between the observed and computed transitions was performed by examining the transitions of comparable intensities guided by their respective oscillator strengths and absorptivity values.[28] The nature of the excited states is assigned based on the percent Kohn–Sham orbital contributions of the orbitals involved in the electronic transitions. Based on the predicted values for the oscillator strengths it is found that the most intense long-wavelength transition at 556 nm (calcd.: 522 nm) for $\mathbf{1}^+$ is from the HOMO [dπ(Ru) (45%) and π(Cl) (39%)] to the LUMO+1 [π*(trpy) (90%)] (Figure 8, a). The other two closely spaced higher energy transitions at 483 and 459 nm (calcd.: 482 and 458 nm) are due to HOMO–3→LUMO/HOMO–1→LUMO+2 and HOMO→LUMO+2 transitions, respectively (Table 5, Figure 8, a).

Similarly, the lowest energy charge-transfer band for $\mathbf{2}^+$ appears at 509 nm, which is very much in agreement with

Table 5. Singlet excitation energies computed for $\mathbf{1}^+$ and $\mathbf{2}^+$at the B3LYP level of theory.[a]

| Excitation energy[b] ($10^3$ $cm^{-1}$) | Oscillator strength | $\varepsilon$[c] | $\psi_o$–$\psi_v$ [d] | Type of transition |
|---|---|---|---|---|
| $\mathbf{1}^+$ | | | | |
| 19.167 (521.70) | 0.1172 | 8230.6278 | HOMO→LUMO+1 (0.59)[e] | $d\pi_{Ru}$, $\pi_{Cl}\rightarrow\pi^*_{trpy}$ |
| (exp. 556) | | (exp. 19790) | | |
| 20.751 (481.91) | 0.0966 | 6783.9475 | HOMO–3→LUMO (0.45) | $\pi_{Cl}$, $\pi_{imine}\rightarrow\pi^*_{imine}$, $d\pi_{Ru}$ |
| (exp. 483) | | (exp. 10400) | HOMO–1→LUMO+2 (0.41) | $d\pi_{Ru}$, $\pi_{Cl}$, $\pi_{imine}\rightarrow\pi^*_{trpy}$ |
| 21.838 (457.92) | 0.0611 | 4290.8819 | HOMO→LUMO +2 (0.47) | $d\pi_{Ru}$, $\pi_{Cl}\rightarrow\pi^*_{trpy}$ |
| (exp. 459) | | (exp. 8200) | | |
| $\mathbf{2}^+$ | | | | |
| 20.243 (493.98) | 0.1098 | 7710.9465 | HOMO–1→LUMO+1 (0.47) | $d\pi_{Ru}$, $\pi_{Cl}\rightarrow\pi^*_{trpy}$ |
| (exp.509) | | (exp. 15670) | | |
| 21.828 (458.13) | 0.0364 | 2556.2700 | HOMO–3→LUMO (0.54) | $\pi_{Cl}$, $\pi_{imine}$, $d\pi_{Ru}\rightarrow\pi^*_{imine}$, $d\pi_{Ru}$ |
| 23.557 (424.51) | 0.2341 | 16440.1870 | HOMO–3→LUMO (0.33) | $\pi_{Cl}$, $\pi_{imine}$, $d\pi_{Ru}\rightarrow\pi^*_{imine}$, $d\pi_{Ru}$ |

[a] Calculations were done by employing the SDD basis set for Ru and 6-31G* for all other elements. [b] Singlet excitation energies. Energy values [nm] given in parentheses. [c] $\varepsilon$ [$M^{-1}cm^{-1}$]. [d] Occupied and virtual orbitals. [e] Transition coefficients.

 © 2007 Wiley-VCH Verlag GmbH & Co. KGaA, Weinheim 

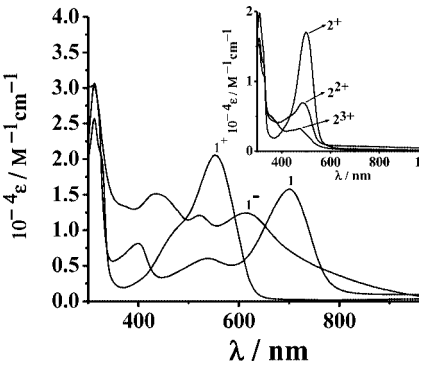


Figure 7. Electronic spectra of $\mathbf{1}^+$, **1**, and $\mathbf{1}^-$ in $CH_3CN/Et_4NClO_4$. The inset shows the electronic spectra of $\mathbf{2}^+$, **2**, and $\mathbf{2}^{2+}$ in $CH_3CN/Et_4NClO_4$.

the calculated value of 494 nm, and is due to a HOMO–1 [dπ(Ru) (49%) and π(Cl) (38%)]→LUMO+1 [π*(trpy) (91%)] transition, which is again a MLLCT transition as in $\mathbf{1}^+$. The other two closely spaced predicted transitions at 458 and 425 nm (HOMO–3→LUMO; Figure 8 (b), Table 5) could not be resolved experimentally.

On electrochemical successive oxidations of $\mathbf{1}^+$ to $\mathbf{1}^{2+}$ and $\mathbf{1}^{3+}$ and $\mathbf{2}^+$ to $\mathbf{2}^{2+}$ and $\mathbf{2}^{3+}$ the lowest energy charge-transfer bands are blue shifted from 556 to 475 and 436 nm and 509 to 487 and 476 nm, respectively, with a substantial reduction in intensity [Figure 7 (inset); see Exp. Sect.], thus indicating a lower degree of delocalization in the oxidized states. The predicted transitions for $\mathbf{1}^{2+}$ and $\mathbf{2}^{2+}$, respectively, are 491 nm [HOMO–3 {π($L^1$), dπ(Ru)}→LUMO+1 {π*($L^1$), dπ(Ru)}] and 465 nm [HOMO–3 {π(Cl), π($L^2$), dπ(Ru)}→LUMO {π*($L^2$)}] (Table S4).

During the one-electron reduction $\mathbf{1}^+ \rightarrow \mathbf{1}$ the lowest energy charge-transfer band undergoes a substantial red shift from 556 to 702 nm with a slight decrease in intensity that suggests a comparable extent of delocalization in both states. However, on further reduction to $\mathbf{1}^-$ the bands are blue shifted and undergo a reasonable intensity reduction, which implies a relatively localized state (Figure 7 and Exp. Sect.). Similar spectral features have also been observed with **2** and $\mathbf{2}^-$ (see Exp. Sect.).[4c,4d] TD-DFT calculations on the reduced species indicate that during the one electron reductions $[\mathbf{1}]^+ \rightarrow \mathbf{1}$ and $[\mathbf{2}]^+ \rightarrow \mathbf{2}$, the lowest energy charge transfer (MLLCT) bands undergo a red shift to 604 and 556 nm, respectively. These bands are predicted to have contributions from intra-ligand transitions as well, namely HOMO–2 [dπ(Ru) (58%), π($L^1$) (32%)]→LUMO [π*($L^1$) (48%), π*(trpy) (44%)] and HOMO–2 [dπ(Ru) (55%), π($L^2$) (32%)]→LUMO [π*($L^2$) (7%), π*(trpy) (91%)], respectively (Table S4). The deviation of the predicted value from the experimental one might be due to the absence of solvent effects in our calculations.

The frontier orbital analysis further indicates that the nature of the HOMOs and LUMOs remains essentially the same after oxidation. For instance, the composition of the HOMO changes only from 45% (Ru) and 39% (Cl) in $\mathbf{1}^+$ to 43% (Ru) and 46% (Cl) in $\mathbf{1}^{2+}$ upon oxidation, whereas the contribution of the ligand orbital to the frontier orbitals

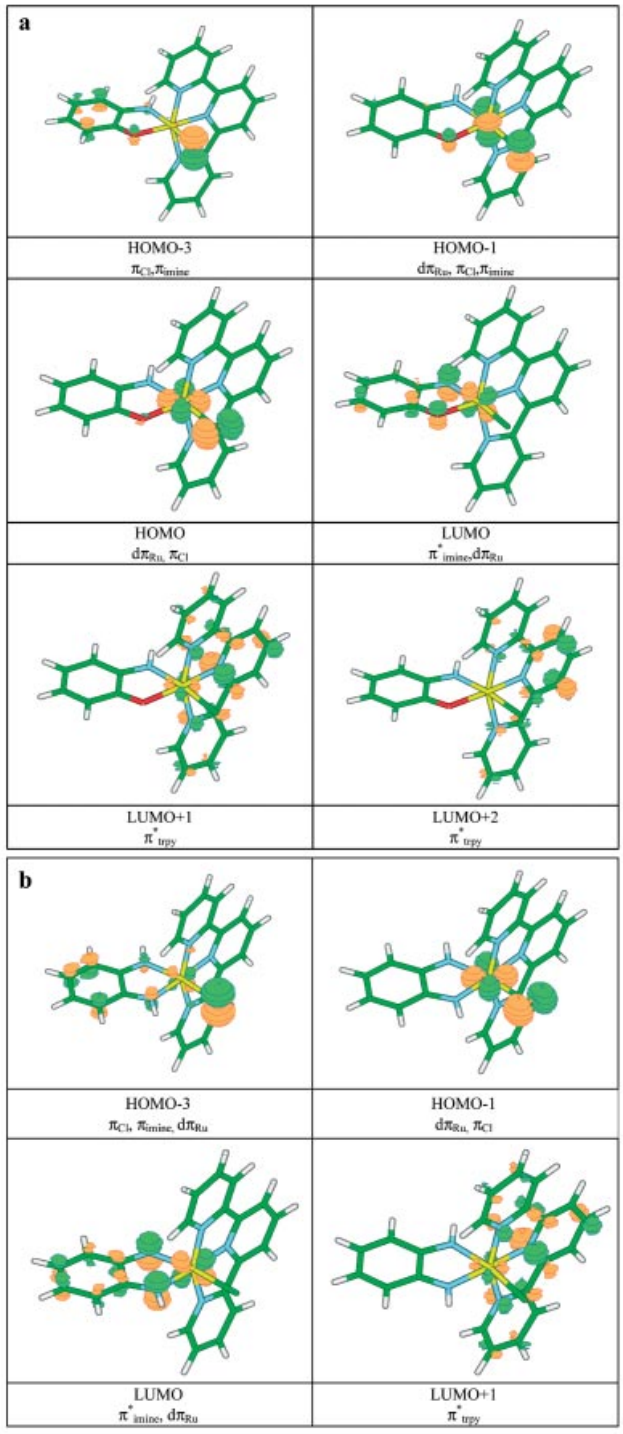


Figure 8. a) Kohn–Sham orbital contours of the frontier MOs of $\mathbf{1}^+$ involved in the intense long-wavelength transitions. b) Kohn–Sham orbital contours of the frontier MOs of $\mathbf{2}^+$ involved in the intense long-wavelength transitions.

increases to a greater extent upon reduction to **1**. The LUMO becomes primarily ligand centered and is composed mainly of $L^1$- (48%) and trpy-based (44%) orbitals along with less than 10% Ru contribution. However, the HOMOs are essentially dominated by L — the Ru/L contributions

 © 2007 Wiley-VCH Verlag GmbH & Co. KGaA, Weinheim 

are 19/74 and 18/77%, respectively, for **1** and **2** (Tables S5 and S6).

It should be noted that the experimental results reported for similar molecules $[Ru^{III}(acac)_2(L_{Sq})]$ ($acac^-$ = acetylacetonate; L corresponds to X = O, Y = NH/X = S, Y = NH, Scheme 1) established the preferential involvement of $L_{Sq}$ in the oxidation and reduction processes, which leaves the unpaired spin on the ruthenium(III) ion.[3] However, the DFT-supported experimental results for the present molecules $\mathbf{1}^+$ and $\mathbf{2}^+$ demonstrate a metal-based first oxidation and first reduction, which leaves the resultant spin on the ligand center (L). Thus, the present study further emphasizes that ruthenium quinonoid systems of apparently similar chemical structures may exhibit substantial variations in their electronic features both in native and accessible redox states, which indeed justifies the need for further critical explorations with the newer molecular frameworks.

In conclusion, a combination of experimental and DFT results suggests the following: (i) the ground-state valence formulation of $[Ru(trpy)(Cl)(L^{1/2})]^+$ ($\mathbf{1}^+/\mathbf{2}^+$) can be best interpreted as spin-coupled $Ru^{III}$–$L_{Sq}$ in combination with a minority contribution from diamagnetic $Ru^{II}$–$L_Q$; (ii) the involvement of dπ(Ru)- and π(L)-based frontier orbitals, respectively, in the successive oxidation processes (couples I and II); (iii) the preferential involvement of Ru-based orbitals in the first reduction step (couple III), although the LUMO is calculated to be a mixture of dπ(Ru) (≈ 24%) and π*(L) (≈ 70%) orbitals; (iv) the primary participation of π*(trpy) orbitals in the subsequent second and third reductions (couples IV and V).

## Experimental Section

**Materials and Instrumentation:** The precursor complex $[Ru(trpy)Cl_3]$ was prepared according to the reported procedure.[29] 2,2′:6′,2′′-Terpyridine (trpy), *o*-aminophenol and *o*-phenylenediamine were procured from Aldrich, USA. Other chemicals and solvents were reagent grade and used as received. HPLC-grade solvents were used for spectroscopic and electrochemical studies.

UV/Vis spectral studies were performed with a Perkin–Elmer Lambda-950 spectrophotometer. FT-IR spectra were recorded with a Nicolet spectrophotometer with samples prepared as KBr pellets. Solution electrical conductivity was checked using a Systronic 305 conductivity bridge. $^1$H NMR spectra were obtained with a 400 MHz Varian FT spectrometer. The EPR measurements were performed with a Varian model 109C E-line X-band spectrometer fitted with a quartz dewar for measurements at 77 K. Cyclic voltammetric, differential pulse voltammetric, and coulometric measurements were carried out using a PAR model 273A electrochemistry system. Platinum wire working and auxiliary electrodes and an aqueous saturated calomel reference electrode (SCE) were used in a three-electrode configuration. The supporting electrolyte was $Et_4NClO_4$ and the solute concentration was around $10^{-3}$ M. The half-wave potential, $E°_{298}$, was set equal to $0.5(E_{pa} + E_{pc})$, where $E_{pa}$ and $E_{pc}$ are the anodic and cathodic cyclic voltammetric peak potentials, respectively. A platinum wire-gauze working electrode was used in coulometric experiments. All measurements were carried out under dinitrogen. The magnetic susceptibility was measured with a Faraday balance (CAHN Instruments Inc.; Serial no. 76240). Electrospray mass spectra were recorded with a Micromass Q-ToF mass spectrometer.

**$[Ru(trpy)(Cl)(L^1)]ClO_4$ (1-$ClO_4$) and $[Ru(trpy)(Cl)(L^2)]ClO_4$ (2-$ClO_4$):** These complexes were prepared by following the same general procedure. $[Ru(trpy)Cl_3]$ (100 mg, 0.226 mmol), *o*-aminophenol (24 mg, 0.220 mmol) or *o*-phenylenediamine (25 mg, 0.226 mmol), and $NEt_3$ (0.4 mL, 2.86 mmol) were taken in 20 mL of ethanol and the mixture was heated at reflux for 5 h under atmospheric conditions. The initial dark brown color changed to purple or red. The solvent of the reaction mixture was evaporated to dryness under reduced pressure. The solid mass thus obtained was dissolved in a minimum volume (5 mL) of $CH_3CN/CH_3OH$ (4:1) and reprecipitated by addition of a saturated aqueous solution of $NaClO_4$. The dark precipitate was filtered off and washed thoroughly with ice-cold water. The product was dried in vacuo over $P_4O_{10}$. It was then purified on an alumina (neutral) column. The purple or red product was eluted with $CH_2Cl_2$/$CH_3CN$ (1:1). Evaporation of the solvent under reduced pressure afforded the pure complexes.

**1-$ClO_4$:** Yield: 55 mg (42%). $C_{21}H_{16}Cl_2N_4O_5Ru$: calcd. C 43.73, H 2.80, N 9.72; found C 43.56, H 2.87, N 9.51. Molar conductivity in acetonitrile: $\Lambda_M$ = 110 $\Omega^{-1}cm^2M^{-1}$. $^1$H NMR [400 MHz, $(CD_3)_2SO$, 298 K]: $\delta$ = 15.31 (s, 1 H, NH), 8.85 (d, $J$ = 7.6 Hz, 2 H), 8.72 (d, $J$ = 7.6 Hz, 2 H), 8.34 (t, $J$ = 8.4, 8.0 Hz, 1 H), 8.16 (m, 3 H), 7.89 (d, $J$ = 9.2 Hz, 1 H), 7.54 (t, $J$ = 6.4, 6.0 Hz, 2 H), 7.43 (d, $J$ = 5.6 Hz, 2 H), 7.27 (d, $J$ = 8.8 Hz, 1 H), 7.02 ppm (t, $J$ = 6.4, 7.2 Hz, 1 H). UV/Vis (acetonitrile): $\lambda_{max}$ ($\varepsilon$) = 556 nm (19790 $M^{-1}cm^{-1}$), 483 (10400), 459 (8200), 311 (24630), 270 (24910), 232 (35280). IR (KBr disk): ν($ClO_4^-$) = 1086/624 $cm^{-1}$; ν(NH) = 3217.

**$\mathbf{1}^{2+}$:** UV/Vis (acetonitrile/0.1 M $Et_4NClO_4$): $\lambda_{max}$ ($\varepsilon$) = 475 nm (3900 $M^{-1}cm^{-1}$), 438 (4500), 324 (17400), 308 (19600), 232 (29400).

**$\mathbf{1}^{3+}$:** UV/Vis (acetonitrile/0.1 M $Et_4NClO_4$): $\lambda_{max}$ ($\varepsilon$) = 436 nm (3100 $M^{-1}cm^{-1}$), 332 (12700), 318 (14600), 285 (19400), 273 (19900).

**1:** UV/Vis (acetonitrile/0.1 M $Et_4NClO_4$): $\lambda_{max}$ ($\varepsilon$) = 702 nm (15380 $M^{-1}cm^{-1}$), 537 (5980), 399 (7920), 311 (29460), 277 (28090), 235 (47020).

**$\mathbf{1}^-$:** UV/Vis (acetonitrile/0.1 M $Et_4NClO_4$): $\lambda_{max}$ ($\varepsilon$) = 615 nm (12020 $M^{-1}cm^{-1}$), 521 (11720), 436 (14650), 311 (29020).

**2-$ClO_4$:** Yield: 40 mg (30%). $C_{21}H_{17}Cl_2N_5O_4Ru$: calcd. C 43.84, H 2.98, N 12.17; found C 44.19, H 2.75, N 11.99. Molar conductivity in acetonitrile: $\Lambda_M$ = 140 $\Omega^{-1}cm^2M^{-1}$. $^1$H NMR [400 MHz, $(CD_3)_2SO$, 298 K]: $\delta$ = 14.36 (s, NH), 11.91 (s, NH), 8.90 (d, $J$ = 8.4 Hz, 2 H), 8.72 (d, $J$ = 8.4 Hz, 2 H), 8.41 (t, $J$ = 8.0 Hz, 1 H), 8.07 (t, $J$ = 6.4, 8.0 Hz, 2 H), 7.76 (d, $J$ = 8.8 Hz, 1 H), 7.44 (t, $J$ = 6.8, 6.4 Hz, 2 H), 7.38 (d, $J$ = 5.6 Hz, 2 H), 7.07 (t, $J$ = 5.2, 6.0 Hz, 1 H), 6.93 ppm (d, $J$ = 5.6 Hz, 2 H). UV/Vis (acetonitrile): $\lambda_{max}$ ($\varepsilon$) = 509 nm (15670 $M^{-1}cm^{-1}$), 311 (17210), 280 (16190), 269 (18330), 234 (22690), 208 (28930). IR (KBr disk): ν($ClO_4^-$) = 1086/625 $cm^{-1}$; ν(NH) = 3317.

**$\mathbf{2}^{2+}$:** UV/Vis (acetonitrile/0.1 M $Et_4NClO_4$): $\lambda_{max}$ ($\varepsilon$) = 487 nm (6630 $M^{-1}cm^{-1}$), 440 (5030), 327 (12070), 308 (15580), 282 (16330), 270 (17750), 232 (26300).

**$\mathbf{2}^{3+}$:** UV/Vis (acetonitrile/0.1 M $Et_4NClO_4$): $\lambda_{max}$ ($\varepsilon$) = 476 nm (3140 $M^{-1}cm^{-1}$), 376 (4190), 327 (10640), 305 (14720), 268 (18600).

**2:** UV/Vis (acetonitrile/0.1 M $Et_4NClO_4$): $\lambda_{max}$ ($\varepsilon$) = 718 nm (2530 $M^{-1}cm^{-1}$), 516 (4580), 477 (5140), 328 (5930), 309 (9020), 243 (20400), 204 (27000).

**$\mathbf{2}^-$:** UV/Vis (acetonitrile/0.1 M $Et_4NClO_4$): $\lambda_{max}$ ($\varepsilon$) = 596 nm (4180 $M^{-1}cm^{-1}$), 523 (5740), 475 (7580), 439 (8840), 325 (11860), 262 (29940).

 © 2007 Wiley-VCH Verlag GmbH & Co. KGaA, Weinheim 

**X-ray Crystallography:** Single crystals of **1**-$ClO_4$ and **2**-$ClO_4$ were grown by slow evaporation of their 1:1 acetonitrile/methanol and 1:1 acetonitrile/toluene solutions, respectively. Diffraction data for **1**-$ClO_4$ and **2**-$ClO_4$ were collected with Enraf–Nonius CAD-4 (MACH-3) and OXFORD XCALIBUR-S CCD single-crystal X-ray diffractometers, respectively. The structures were solved and refined by full-matrix least-squares techniques on $F^2$ using SHELX-97.[30] The absorption corrections for **1**-$ClO_4$ and **2**-$ClO_4$ were done by psi-scans and multi-scans, respectively. All the data were corrected for Lorentz and polarization effects, and the non-hydrogen atoms were refined anisotropically. Hydrogen atoms were included in the refinement process as per the riding model. See Table 6 for further details.

Table 6. Crystallographic data for **1**-$ClO_4$ and **2**-$ClO_4$.

| | (**1**-$ClO_4$) | (**2**-$ClO_4$) |
|---|---|---|
| Formula | $C_{21}H_{16}Cl_2N_4O_5Ru$ | $C_{21}H_{17}Cl_2N_5O_{4.50}Ru$ |
| $M_r$ | 576.35 | 583.37 |
| Crystal system | monoclinic | orthorhombic |
| Space group | *C*2/*c* | *Pbcn* |
| $T$ [K] | 293(2) | 293(2) |
| $\lambda$ [Å] | 0.71073 | 0.71073 |
| $a$ [Å] | 23.269(3) | 21.126(6) |
| $b$ [Å] | 13.354(2) | 13.379(4) |
| $c$ [Å] | 15.3500(12) | 15.837(9) |
| $\beta$ [°] | 113.335(8) | 90 |
| $V$ [Å$^3$] | 4379.6(9) | 4476(3) |
| Crystal size [mm] | $0.20\times0.15\times0.05$ | $0.30\times0.25\times0.20$ |
| $\rho_{calcd.}$ [g cm$^{-3}$] | 1.748 | 1.731 |
| $Z$ | 8 | 8 |
| $\mu$ [mm$^{-1}$] | 1.003 | 0.982 |
| $F$ (000) | 2304 | 2336 |
| $2\theta$ range [°] | 3.60 to 49.94 | 6.28 to 50.00 |
| Reflections collected | 3886 | 31091 |
| Unique reflections ($R_{int}$) | 3790 (0.0338) | 3931 (0.0991) |
| Data/restraints/parameters | 3790/0/298 | 3931/0/303 |
| Goodness-of-fit | 0.968 | 0.884 |
| $R_1$ [$I > 2\sigma(I)$] | 0.0617 | 0.0605 |
| $wR_2$ [all data] | 0.1737 | 0.1598 |
| Largest diff. peak/hole, [e Å$^{-3}$] | 0.943/–0.602 | 1.132/–0.454 |

CCDC-606479 (for **1**-$ClO_4$) and -606480 (for **2**-$ClO_4$) contain the supplementary crystallographic data for this paper. These data can be obtained free of charge from The Cambridge Crystallographic Data Centre via www.ccdc.cam.ac.uk/data_request/cif.

**Computational Details:** Full geometry optimizations of $\mathbf{1}^+$ and $\mathbf{2}^+$ were carried out using the density functional theory method at the (U)B3LYP level.[31a,31b] All elements except ruthenium were assigned the 6-31G* basis set. The SDD basis set with effective core potential was employed for the ruthenium atoms.[31c,31d] Calculations were performed with Gaussian 98 and Gaussian 03.[31e,31f] Vertical electronic excitations based on the B3LYP-optimized geometries were computed using the time-dependent density functional theory (TD-DFT) formalism,[31g] with the B3LYP functional using the above combination of basis sets. Natural population analysis was performed using the NBO 3.1 program package as implemented in Gaussian98.[31h,31i] The spin densities of complexes were computed using the CUBE option as implemented in Gaussian 03. Visual inspection of the key orbitals was done with MOLDEN,[31h] to assign the nature of the various electronic transitions. Molecular orbital compositions were analyzed using the AOMIX program.[31i,31j]

**Supporting Information** (see also the footnote on the first page of this article): Optimized coordinates (Table S1), excitation energies (Tables S2/S3/S4), MO compositions (Tables S5/S6), mass and NMR spectra (Figures S1/S2), spin densities (Figure S3), Kohn–Sham orbitals (Figures S4/S5).

## Acknowledgments

Financial support received from the Department of Science and Technology and Council of Scientific and Industrial Research, New Delhi, India is gratefully acknowledged. X-ray structural studies for **1**-$ClO_4$ and **2**-$ClO_4$ were carried out at the National Single Crystal Diffractometer Facility, Indian Institute of Technology, Bombay. Special acknowledgment is made to the Sophisticated Analytical Instrument Facility (SAIF) and the Computer Center, Indian Institute of Technology, Bombay, respectively, for providing the EPR and computational facilities.

[1] a) C. G. Pierpont, C. W. Lange, *Prog. Inorg. Chem.* **1994**, *41*, 331; b) S. Kar, B. Sarkar, S. Ghumaan, D. Janardanan, J. van Slageren, J. Fiedlar, V. G. Puranik, R. B. Sunoj, W. Kaim, G. K. Lahiri, *Chem. Eur. J.* **2005**, *11*, 4901; c) A. Vlček Jr., *Comments Inorg. Chem.* **1994**, *16*, 207.

[2] a) R. B. Salmonsen, A. Abelleira, M. J. Clarke, *Inorg. Chem.* **1984**, *23*, 387; b) M. Haga, E. S. Dodsworth, A. B. P. Lever, *Inorg. Chem.* **1986**, *25*, 447; c) A. Dei, D. Gatteschi, L. Pardi, *Inorg. Chem.* **1990**, *29*, 1443; d) C. G. Pierpont, A. S. Attia, *Collect. Czech. Chem. Commun.* **2001**, *66*, 33; e) C. G. Pierpont, *Coord. Chem. Rev.* **2001**, *219–221*, 415; f) J. Rall, M. Wanner, M. Albrecht, F. M. Hornung, W. Kaim, *Chem. Eur. J.* **1999**, *5*, 2802; g) G. Speier, A. Whalen, J. Csihony, C. G. Pierpont, *Inorg. Chem.* **1995**, *34*, 1355; h) V. Kasack, W. Kaim, H. Binder, J. Jordanov, E. Roth, *Inorg. Chem.* **1995**, *34*, 1924; i) M. Ebadi, A. B. P. Lever, *Inorg. Chem.* **1999**, *38*, 467; j) C. N. Verani, S. Gallert, E. Bill, T. Weyhermüller, K. Wieghardt, P. Chaudhuri, *Chem. Commun.* **1999**, 1747; k) P. Chaudhuri, C. N. Verani, E. Bill, E. Bothe, T. Weyhermüller, K. Wieghardt, *J. Am. Chem. Soc.* **2001**, *123*, 2213; l) H. Chun, E. Bill, E. Bothe, T. Weyhermüller, K. Wieghardt, *Inorg. Chem.* **2002**, *41*, 5091; m) P. Ghosh, A. Begum, D. Herebian, E. Bothe, K. Hildenbrand, T. Weyhermüller, K. Wieghardt, *Angew. Chem. Int. Ed.* **2003**, *42*, 563; n) K. S. Min, T. Weyhermüller, K. Wieghardt, *Dalton Trans.* **2003**, 1126; o) S. Patra, B. Sarkar, S. Ghumaan, J. Fiedler, S. Zalis, W. Kaim, G. K. Lahiri, *Dalton Trans.* **2004**, 750; p) S. I. Gorelsky, A. B. P. Lever, *J. Organomet. Chem.* **2001**, *635*, 187; q) S. I. Gorelsky, E. S. Dodsworth, A. B. P. Lever, A. A. Vlcek, *Coord. Chem. Rev.* **1998**, *174*, 469; r) A. B. P. Lever, S. I. Gorelsky, *Coord. Chem. Rev.* **2000**, *208*, 153; s) C. J. Cunha, E. S. Dodsworth, M. A. Monteiro, A. B. P. Lever, *Inorg. Chem.* **1999**, *38*, 5399; t) R. A. Metcalfe, A. B. P. Lever, *Inorg. Chem.* **1997**, *36*, 4762; u) S. R. Boone, C. G. Pierpont, *Inorg. Chem.* **1987**, *26*, 1769.

[3] S. Patra, B. Sarkar, S. M. Mobin, W. Kaim, G. K. Lahiri, *Inorg. Chem.* **2003**, *42*, 6469.

[4] C. Remenyi, M. Kaupp, *J. Am. Chem. Soc.* **2005**, *127*, 11399.

[5] N. Bag, A. Pramanik, G. K. Lahiri, A. Chakravorty, *Inorg. Chem.* **1992**, *31*, 40.

[6] N. Bag, G. K. Lahiri, P. Basu, A. Chakravorty, *J. Chem. Soc., Dalton Trans.* **1992**, 113.

[7] a) M. Kurihara, S. Daniele, K. Tsuge, H. Sugimoto, K. Tanaka, *Bull. Chem. Soc. Jpn.* **1998**, *71*, 867; b) S. Bhattacharya, *Polyhedron* **1994**, *13*, 451.

[8] a) K. Ray, A. Begum, T. Weyhermüller, S. Piligkos, J. van Slageren, F. Neese, K. Wieghardt, *J. Am. Chem. Soc.* **2005**, *127*, 4403; b) S. Bhattacharya, P. Gupta, F. Basuli, C. G. Pierpont, *Inorg. Chem.* **2002**, *41*, 5810; c) V. Bachler, G. Olbrich, F. Neese, K. Wieghardt, *Inorg. Chem.* **2002**, *41*, 4179; d) J. Tao, H. Maruyama, O. Sato, *J. Am. Chem. Soc.* **2006**, *128*, 1790.

[9] R. Okamura, T. Wada, K. Aikawa, T. Nagata, K. Tanaka, *Inorg. Chem.* **2004**, *43*, 7210.

 © 2007 Wiley-VCH Verlag GmbH & Co. KGaA, Weinheim 

[10] S. Maji, B. Sarkar, S. Patra, J. Fiedler, S. M. Mobin, V. G. Puranik, W. Kaim, G. K. Lahiri, *Inorg. Chem.* **2006**, *45*, 1316.
[11] N. Gupta, N. Grover, G. A. Neyhart, P. Singh, H. H. Thorp, *Inorg. Chem.* **1993**, *32*, 310.
[12] a) N. Chanda, S. M. Mobin, V. G. Puranik, A. Dutta, M. Niemeyer, G. K. Lahiri, *Inorg. Chem.* **2004**, *43*, 1056; b) B. Mondal, V. G. Puranik, G. K. Lahiri, *Inorg. Chem.* **2002**, *41*, 5831; c) N. Chanda, B. Mondal, V. G. Puranik, G. K. Lahiri, *Polyhedron* **2002**, *21*, 2033; d) B. Mondal, H. Paul, V. G. Puranik, G. K. Lahiri, *J. Chem. Soc., Dalton Trans.* **2001**, 481; e) B. Mondal, M. G. Walawalkar, G. K. Lahiri, *J. Chem. Soc., Dalton Trans.* **2000**, 4209; f) S. Sarkar, B. Sarkar, N. Chanda, S. Kar, S. M. Mobin, J. Fiedler, W. Kaim, G. K. Lahiri, *Inorg. Chem.* **2005**, *44*, 6092; g) N. Chanda, D. Paul, S. Kar, S. M. Mobin, A. Dutta, V. G. Puranik, K. K. Rao, G. K. Lahiri, *Inorg. Chem.* **2005**, *44*, 3499.
[13] S. Patra, B. Sarkar, S. Ghumaan, M. P. Patil, S. M. Mobin, R. B. Sunoj, W. Kaim, G. K. Lahiri, *Dalton Trans.* **2005**, 1188.
[14] a) C. Sans, M. Rodriguez, I. Romero, A. Llobet, *Inorg. Chem.* **2003**, *42*, 8385; b) C. M. Hartshorn, K. A. Maxwell, P. S. White, J. M. DeSimone, T. J. Meyer, *Inorg. Chem.* **2001**, *40*, 601; c) I. Claustro, G. Abate, E. Sanchez, J. H. Acquaye, *Inorg. Chim. Acta* **2003**, *342*, 29; d) R. Ziessel, V. Grosshenny, M. Hissler, C. Stroh, *Inorg. Chem.* **2004**, *43*, 4262; e) K. Kobayashi, H. Ohtsu, T. Wada, T. Kato, K. Tanaka, *J. Am. Chem. Soc.* **2003**, *125*, 6729; f) C. Bonnefous, A. Chouai, R. P. Thummel, *Inorg. Chem.* **2001**, *40*, 5851; g) J. J. Rack, J. R. Winkler, H. B. Gray, *J. Am. Chem. Soc.* **2001**, *123*, 2432; h) H. Hadadzadeh, M. C. DeRosa, G. P. A. Yap, A. R. Rezvani, R. J. Crutchley, *Inorg. Chem.* **2002**, *41*, 6521; i) A. Gerli, J. Reedijk, M. T. Lakin, A. L. Spek, *Inorg. Chem.* **1995**, *34*, 1836.
[15] S. I. Gorelsky, A. B. P. Lever, M. Ebadi, *Coord. Chem. Rev.* **2002**, *230*, 97.
[16] a) A. B. P. Lever, P. R. Auburn, E. S. Dodsworth, M. Haga, W. Liu, M. Melnik, W. A. Nevin, *J. Am. Chem. Soc.* **1988**, *110*, 8076; b) P. R. Auburn, E. S. Dodsworth, M. Haga, W. Liu, W. A. Nevin, A. B. P. Lever, *Inorg. Chem.* **1991**, *30*, 3502; c) H. Masui, P. R. Auburn, A. B. P. Lever, *Inorg. Chem.* **1991**, *30*, 2402; d) A. B. P. Lever, H. Masui, R. A. Metcalfe, D. J. Stufkens, E. S. Dodsworth, P. R. Auburn, *Coord. Chem. Rev.* **1993**, *125*, 317; e) H. Masui, A. B. P. Lever, E. S. Dodsworth, *Inorg. Chem.* **1993**, *32*, 258.
[17] a) R. Bauernschmitt, R. Ahlrichs, *Chem. Phys. Lett.* **1996**, *256*, 454; b) M. Casida, K. C. Jamorski, K. C. Casida, D. R. Salahub, *J. Chem. Phys.* **1998**, *108*, 4439.
[18] M. B. Robin, P. Day, *Adv. Inorg. Chem. Radiochem.* **1967**, *10*, 247.
[19] S. Ghumaan, B. Sarkar, S. Patra, J. van Slageren, J. Fiedler, W. Kaim, G. K. Lahiri, *Inorg. Chem.* **2005**, *45*, 3210.
[20] S. Chakarborty, R. H. Laye, R. L. Paul, R. G. Gonnade, V. G. Puranik, M. D. Ward, G. K. Lahiri, *J. Chem. Soc., Dalton Trans.* **2002**, 1172.
[21] J. Rusanova, E. Rusanova, S. I. Gorelsky, D. Christendat, R. Popescu, A. A. Rarah, R. Beaulac, C. Reber, A. B. P. Lever, *Inorg. Chem.* **2006**, *45*, 6246.
[22] a) N. Chanda, R. H. Laye, S. Chakraborty, R. L. Paul, J. C. Jeffery, M. D. Ward, G. K. Lahiri, *J. Chem. Soc., Dalton Trans.* **2002**, 3496; b) M. D. Ward, *Inorg. Chem.* **1996**, *35*, 1712; c) N. Chanda, B. Sarkar, J. Fiedler, W. Kaim, G. K. Lahiri, *Dalton Trans.* **2003**, 3550; d) S. Patra, B. Sarkar, S. Maji, J. Fiedler, F. A. Urbanos, R. Jimenez-Aparicio, W. Kaim, G. K. Lahiri, *Chem. Eur. J.* **2006**, *12*, 489.
[23] R. Hariram, B. K. Santra, G. K. Lahiri, *J. Organomet. Chem.* **1997**, *540*, 155.
[24] a) B. Mondal, S. Chakraborty, P. Munshi, M. G. Walawalkar, G. K. Lahiri, *J. Chem. Soc., Dalton Trans.* **2000**, 2327; b) T. B. Hedda, H. L. Bozec, *Inorg. Chim. Acta* **1993**, *204*, 103; c) G. B. Deacon, J. M. Patrick, B. W. Skelton, N. C. Thomas, A. H. White, *Aust. J. Chem.* **1984**, *37*, 929.
[25] a) M.-F. Charlot, Y. Pellegrin, A. Quaranta, W. Leibl, A. Aukauloo, *Chem. Eur. J.* **2006**, *12*, 796; b) P. J. O'Malley, *J. Phys. Chem. B* **2001**, *105*, 11290; c) A. Lozsán, P. Nieto, S. Acevedo, V. Mujica, *J. Phys. Chem. A* **2002**, *106*, 10374.
[26] E. J. P. Malar, *Theor. Chem. Acc.* **2005**, *114*, 213.
[27] a) J. M. Villegas, S. R. Stoyanov, W. Huang, L. L. Lockyear, J. H. Reibenspies, D. P. Rillema, *Inorg. Chem.* **2004**, *43*, 6383; b) S. R. Stoyanov, J. M. Villegas, D. P. Rillema, *Inorg. Chem.* **2002**, *41*, 2941; c) S. R. Stoyanov, J. M. Villegas, D. P. Rillema, *Inorg. Chem. Commun.* **2004**, *7*, 838.
[28] Conversion of the calculated oscillator strength to molar absorptivity was done based on the following references: a) R. S. Drago, *Physical Methods for Chemists*, 2nd ed. Saunders College Publishing, Ft. Worth, **1992**; b) J. E. Monat, J. H. Rodriguez, J. K. McCusker, *J. Phys. Chem. A* **2002**, *106*, 7399.
[29] R. A. Leising, S. A. Kubow, M. R. Churchill, L. A. Buttery, J. W. Ziller, K. J. Takeuchi, *Inorg. Chem.* **1990**, *29*, 1306.
[30] G. M. Sheldrick, SHELX-97, Program for Crystal Structure Solution and Refinement; University of Göttingen, Germany, **1997**.
[31] a) A. D. Becke, *Phys. Rev. A* **1988**, *38*, 3098; b) C. Lee, W. Yang, R. G. Parr, *Phys. Rev. B* **1988**, *37*, 785; c) D. Andrae, U. Haeussermann, M. Dolg, H. Stoll, H. Preuss, *Theor. Chim. Acta* **1990**, *77*, 123; d) P. Fuentealba, H. Preuss, H. Stoll, L. V. Szentpaly, *Chem. Phys. Lett.* **1989**, *89*, 418; e) M. J. Frisch, G. W. Trucks, H. B. Schlegel, G. E. Scuseria, M. A. Robb, J. R. Cheeseman, J. A. Montgomery, Jr., T. Vreven, K. N. Kudin, J. C. Burant, J. M. Millam, S. S. Iyengar, J. Tomasi, V. Barone, B. Mennucci, M. Cossi, G. Scalmani, N. Rega, G. A. Petersson, H. Nakatsuji, M. Hada, M. Ehara, K. Toyota, R. Fukuda, J. Hasegawa, M. Ishida, T. Nakajima, Y. Honda, O. Kitao, H. Nakai, M. Klene, X. Li, J. E. Knox, H. P. Hratchian, J. B. Cross, V. Bakken, C. Adamo, J. Jaramillo, R. Gomperts, R. E. Stratmann, O. Yazyev, A. J. Austin, R. Cammi, C. Pomelli, J. W. Ochterski, P. Y. Ayala, K. Morokuma, G. A. Voth, P. Salvador, J. J. Dannenberg, V. G. Zakrzewski, S. Dapprich, A. D. Daniels, M. C. Strain, O. Farkas, D. K. Malick, A. D. Rabuck, K. Raghavachari, J. B. Foresman, J. V. Ortiz, Q. Cui, A. G. Baboul, S. Clifford, J. Cioslowski, B. B. Stefanov, G. Liu, A. Liashenko, P. Piskorz, I. Komaromi, R. L. Martin, D. J. Fox, T. Keith, M. A. Al-Laham, C. Y. Peng, A. Nanayakkara, M. Challacombe, P. M. W. Gill, B. Johnson, W. Chen, M. W. Wong, C. Gonzalez, J. A. Pople, *Gaussian03* (Revision C.02), Gaussian, Inc., Wallingford, CT, **2004**; f) M. J. Frisch, G. W. Trucks, H. B. Schlegel, G. E. Scuseria, M. A. Robb, J. R. Cheeseman, V. G. Zakrzewski, J. A. Montgomery, Jr., R. E. Stratmann, J. C. Burant, S. Dapprich, J. M. Millam, A. D. Daniels, K. N. Kudin, M. C. Strain, O. Farkas, J. Tomasi, V. Barone, M. Cossi, R. Cammi, B. Mennucci, C. Pomelli, C. Adamo, S. Clifford, J. Ochterski, G. A. Petersson, P. Y. Ayala, Q. Cui, K. Morokuma, P. Salvador, J. J. Dannenberg, D. K. Malick, A. D. Rabuck, K. Raghavachari, J. B. Foresman, J. Cioslowski, J. V. Ortiz, A. G. Baboul, B. B. Stefanov, G. Liu, A. Liashenko, P. Piskorz, I. Komaromi, R. Gomperts, R. L. Martin, D. J. Fox, T. Keith, M. A. Al-Laham, C. Y. Peng, A. Nanayakkara, M. Challacombe, P. M. W. Gill, B. Johnson, W. Chen, M. W. Wong, J. L. Andres, C. Gonzalez, M. Head-Gordon, E. S. Replogle, J. A. Pople, *Gaussian98* (Revision A. 11.4.), Gaussian, Inc., Pittsburgh, PA, **2002**; g) M. Casida, in *Recent Advances in Density Functional Methods* (Ed.: D. P. Chong), World Scientific Press, Singapore, **1995**; vol. I, p. 155; h) G. Schaftenaar, J. H. Noordik, *J. Comput. Aided Mol. Des.* **2000**, *14*, 123; i) S. I. Gorelsky, *AOMIX* program, http://www.sg-chem.net; j) S. I. Gorelsky, A. P. B. Lever, *J. Organomet. Chem.* **2001**, *635*, 187.

Received: September 6, 2006
Published Online: November 17, 2006

 © 2007 Wiley-VCH Verlag GmbH & Co. KGaA, Weinheim 

DOI: 10.1002/ejic.200600938

# Bonding Properties Related with Chiral Discrimination in Dinuclear Metal Complexes of Group 10

**Oscar Picazo,[a] Ibon Alkorta,*[a] José Elguero,[a] Markku R. Sundberg,*[b] and Jaana Valo[b]**

**Keywords:** Ab initio calculations / Coordination chemistry / Chiral discrimination / Bonding properties / *trans* influence

A series of neutral dinuclear homo- and heterochiral complexes formed by hydrazine (a molecule with axial chirality), a metal atom of group 10 (Ni, Pd, Pt), and halogen atoms (F, Cl, Br, I) was studied by computational methods including density functional theory. In the optimized structures the heterochiral complexes were always found to be energetically favored. The chiral discrimination depends on the contributions coming from the metal atoms and the halogen anions attached to them. Moreover, the relative energies of the optimized complexes are correlated with the electronegativity of the metals and the halogens as well as with the relative distances of the bond critical points in the metal–nitrogen bonds. Also the smaller deviation of the ligand–metal–ligand angles from the ideal value of 90° corresponds to the heterochiral complexes. An analysis of the bonding properties reveals a complex mechanism for the behavior of the electron lone pairs of the nitrogen and halogen atoms. The electronic properties of the optimized complexes were studied by NBO (Natural Bond Orbital) and QTAIM (Quantum Theory of Atoms in Molecules) methods. An NBO analysis of the energy differences between the stabilizing energies related to the interactions between an electron lone pair of the coordinated nitrogen atom and the opposite M–X antibonding orbital explain the differences of the total energies between the diastereomeric heterochiral and homochiral complexes. The stabilizing energies have systematically more negative values in the heterochiral complexes; this can be interpreteted as a measure of the *trans* influence. Small energy values related to the *cis* influence were found mainly in the nickel complexes. The M–N bonds in the heterochiral complexes are more polar with a higher bond order than that in the homochiral ones, as shown by QTAIM methods.
(© Wiley-VCH Verlag GmbH & Co. KGaA, 69451 Weinheim, Germany, 2007)

## Introduction

In order to understand the chemical properties of a compound it is necessary to know not only the structure, but also the electronic properties and their mutual relationship. Computational methods offer a means to elucidate both aspects. We employ here DFT (Density Functional Theory) calculations to evaluate the structural and electronic characteristics of dinuclear hydrazine complexes formed by group 10 metals displaying chiral discrimination. To understand the correlations between structural and electronic properties in metal complexes it is necessary to consider concepts related with the deformations in the coordination polyhedra.

Chiral recognition is an important concept in many chemical processes, for which nonlinear effects in asymmetric synthesis and stereoselective reactions are some examples.[1] Peroxides and hydrazine present axial chirality with low racemization barriers.[2,3] The presence of different chiral molecules of hydrazine has been used to explain the experimental results of clusters in the gas phase.[4] A topic that has received only a limited experimental interest so far is chiral biodiscrimination based upon axial chirality. As an example, mutations at the putative distal site of cytochrome P450 have been shown to be dependent on axial chirality.[5]

The factors leading to chiral discrimination have been computationally studied only a few times in metal complexes or related systems. The effect of fluoro substitution on the chiral discrimination has been discussed in bis(diphenylborate)s and isoelectronic structures.[6] In addition, 1:1 and 2:1 complexes of chiral bis(5*H*-pyrrole)s and bis(oxazoline)s with the lithium cation have been shown to favor the heterochiral complexes, except for the *tert*-butyl derivatives.[7]

The *trans* influence, also called structural *trans* effect, is one of the key concepts in understanding the structure-bonding relation in metal complexes.[8] The concept involves the idea that a bond *trans* to a donor atom should be longer and weaker than that in a *cis* position. The influence has been evaluated by using statistical methods applied

[a] Instituto de Química Médica (C.S.I.C.)
Juan de la Cierva 3, 28006 Madrid, Spain
Fax: +34-91-564-4853
E-mail: ibon@iqm.csic.es
[b] Laboratory of Inorganic Chemistry, Department of Chemistry, University of Helsinki
P. O. Box 55 (A. I. Virtasen aukio 1), 00014 Helsinki, Finland
Fax: +958-9-19150198
E-mail: markku.sundberg@helsinki.fi
Supporting information for this article is available on the WWW under http://www.eurjic.org or from the author.

 © 2007 Wiley-VCH Verlag GmbH & Co. KGaA, Weinheim 

to existing structural data[9] by using a theoretical approach[10] as well as computational methods.[11–14] Related to the *trans* influence there is also an analogous *cis* influence. Their mutual relative magnitude is obviously dependent on the electron configuration of a central metal atom.[9]

In an earlier study on (phosphane)molybdenum complexes[12] the amount of *trans* influence was found to be dependent on the angular distortion on the coordination sphere and consequently on the overlap between the metal d orbital and the phosphane σ* orbitals. The importance of the electronic occupation on antibonding orbitals was established earlier by Burdett and Albright.[11] A correlation between the *trans* influence and bond order values was found in *cis*-dichloridobis(triphenylstibane)platinum.[15] Interestingly, the *trans* influence has been shown to have an important role in creating new $Pd^{II}$ complexes with nonlinear optical properties.[16]

In general, the geometry around a central metal atom in the complexes is dependent on the electronic properties. Among the concepts to be taken into account are the Jahn–Teller effect, the pseudo-Jahn–Teller effect, and Bent's rule. In our case, only the last concept might be relevant, since the planar complexes of the group 10 metals do not have an electronic configuration involving unpaired electrons.

There have been discussions about the applicability of Bent's rule on transition metal complexes. When applied to the main group elements, Bent's rule states that the more electronegative substituents are related with more central-atom p-orbital character resulting in smaller angles, whereas the less electronegative subsituents obtain more s-orbital character and consequently wider angles.[17] However, the bonding in transition metal complexes involves not only s- but essentially also d-orbitals, and thus the situation is essentially different.[18] Although Bent's rule has been reformulated by Frenking et al.,[19] it seems that Bent's rule will be of limited use for transition metal complexes.[20]

The studied complexes are related to *cis*-platinum and the newly described asymmetric *trans*-platinum(II) complexes, which have shown anticancer activity.[21] In addition, hydrazine in the presence of manganese and copper ions has been evaluated for site-specific DNA damage.[22] On the other hand, both platinum and palladium have the propensity to form dinuclear complexes.[23] The idea surrounding the synthesis of hydrazine-bridged dinuclear platinum complexes is that they should be able to crosslink two adjacent bases of DNA without bending the double helix.[24] Some dinuclear platinum complexes containing N-mediated bridges have been shown to be cytotoxic.[25,26] However, none of these contained two similar bridges. In our preliminary communication we have shown, by computational methods, how the doubly hydrazine-bridged dinuclear complexes formed by halogens and group 10 metal cations display axial discrimination.[27]

In this paper we study the electronic properties of the doubly bridged hydrazine complexes in more detail by using computational methods. The basic question related to our work is whether electronic properties could explain the differences in the energies between the diastereomer homochiral and heterochiral complexes. Special emphasis was placed on the importance of the electron lone pairs of the coordinated atoms and their role in complex formation.

## Results and Discussion

### 1. Energy

The complexes under study are dinuclear with two neutral hydrazine molecules acting as bridges. The planar coordination sphere around each metal atom of group 10 (Ni, Pd, Pt) is formed by two nitrogen atoms of two hydrazine molecules and two halogen atoms (F, Cl, Br, I). The axial chirality (noted as subscript a) of hydrazine results in two diastereomeric complexes, namely homochiral [($R_a$/$R_a$) or ($S_a$/$S_a$)] and heterochiral [($R_a$/$S_a$) or ($S_a$/$R_a$)] complexes. Hereafter, the notifications *RR* and *RS* will be used for the homochiral and heterochiral enantiomers, respectively.

The optimized geometry of the complexes presents $D_2$ and $C_{2h}$ symmetry for all the homochiral and heterochiral cases, respectively. Typical structures are shown in Figure 1.

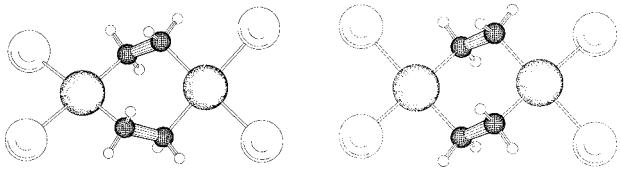

Figure 1. The *RS* (left) and *RR* (right) diasteromers of dinuclear metal complexes formed by hydrazine molecules and halogen atoms.

The energies for the optimized complexes at the B3LYP/LANL2DZ level of theory are shown in Table 1, as well as the relative energies, $E_{rel}$. The relative energy $E_{rel}$ is defined as $E_{rel} = E_{RS} - E_{RR}$.

In all the hydrazine derivatives the heterochiral complexes are favored over the homochiral ones, with energy differences that range between 1.4 and 3.8 kcal/mol. As the size of the metal atom increases the differences also increase; the opposite takes place with the size of the halogen atoms, the largest differences are found for fluorine and the smallest for iodine for a given metal complex. Although the differences are relatively small, it is possible to see some trends by using statistical methods, as shown below.

A Free–Wilson correlation[28] [Equation (1)] was found between the presence/absence of each metal and halogen atom and the relative energy of the homo-/heterochiral pairs. The underlying hypothesis in a Free–Wilson approach is the independence of the effects of halogens and metals. In the equation the coefficient corresponding to the presence of Pt has been arbitrarily fixed to 1 and thus the rest of the contributions can be compared. The coefficient for each variable provides the energy contribution to the chiral selectivity in each pair using as a reference the homochiral system. It must be underlined that the Free–Wilson method gives no direct physicochemical interpretation.

 © 2007 Wiley-VCH Verlag GmbH & Co. KGaA, Weinheim 

Table 1. Total energy [hartree] and relative energy, $E_{rel}$ [kcal/mol; 1 kcal/mol = 4.1868 kJ/mol], of the hydrazine complexes $[MX_2hy]_2$ (M = Ni, Pd, Pt; X = F, Cl, Br, I; hy = hydrazine) calculated at the B3LYP/LAN2DZ computational level. The compounds are identified by their $MX_2$ fragments.

| Fragment | Chirality | Total energy | $E_{rel}$ |
|---|---|---|---|
| $NiF_2$ | *RR* | –961.965473 | 0 |
| $NiF_2$ | *RS* | –961.969945 | –2.805 |
| $NiCl_2$ | *RR* | –622.399674 | 0 |
| $NiCl_2$ | *RS* | –622.402660 | –1.876 |
| $NiBr_2$ | *RR* | –615.266813 | 0 |
| $NiBr_2$ | *RS* | –615.269359 | –1.598 |
| $NiI_2$ | *RR* | –608.133750 | 0 |
| $NiI_2$ | *RS* | –608.135931 | –1.368 |
| $PdF_2$ | *RR* | –876.761868 | 0 |
| $PdF_2$ | *RS* | –876.766906 | –3.161 |
| $PdCl_2$ | *RR* | –537.238303 | 0 |
| $PdCl_2$ | *RS* | –537.241901 | –2.258 |
| $PdBr_2$ | *RR* | –530.122256 | 0 |
| $PdBr_2$ | *RS* | –530.125219 | –1.859 |
| $PdI_2$ | *RR* | –523.008274 | 0 |
| $PdI_2$ | *RS* | –523.010781 | –1.575 |
| $PtF_2$ | *RR* | –861.614577 | 0 |
| $PtF_2$ | *RS* | –861.620643 | –3.806 |
| $PtCl_2$ | *RR* | –522.079012 | 0 |
| $PtCl_2$ | *RS* | –522.083867 | –3.047 |
| $PtBr_2$ | *RR* | –514.960402 | 0 |
| $PtBr_2$ | *RS* | –514.964730 | –2.716 |
| $PtI_2$ | *RR* | –507.847389 | 0 |
| $PtI_2$ | *RS* | –507.851357 | –2.491 |

$$E_{rel}\,[\text{kcal/mol}] = -4.89(\text{F}) - 4.03(\text{Cl}) - 3.69(\text{Br}) - 3.45(\text{I}) + 2.10(\text{Ni}) + 1.80(\text{Pd}) + 1.00(\text{Pt}) \quad (1)$$

The statistical $r^2$ value in Equation (1) is 0.996. The coefficients for the halogens are always negative and for the metals positive. Moreover, the absolute values of the weights for the halogen atoms are larger than those of the metal atoms. The smaller and more electronegative a counter anion is, the larger its negative weight will be. Such a clear relation between the coefficients of Equation (1) and the electronegativity values for the group 10 metal atoms does not exist.

The energy differences are also strongly correlated with the electronegativity values of the participating metals and halogens [Equation (2), where $\chi$ refers to the Pauling electronegativity values recalculated by Allred[29]].

$$E_{rel} = 4.13 - 1.11\chi\text{Hal} - 1.29\chi\text{Met} \quad (2)$$

The $r^2$ value for the correlation is 0.991. According to the original idea of Linus Pauling, electronegativity describes the electron-withdrawing capacity of an atom. It is clear that the electron-withdrawing capacity must be distance-dependent. Therefore, we may assume at this stage that the relative energies should correlate with the M–L bond lengths.

Both of the equations contain parameters that are isotropic. However, we may well assume that the energy differences should be because of the differences in bonding in the complexes. On the other hand, the bonds have a directionality, thus destroying the spherical symmetry. Therefore, the bonds and their properties should be examined.

The parameter connected with the deformation of spherical symmetry is the bond angle. Selected bond angles of the optimized complexes are gathered in Table 2 in which there are two additional parameters displayed. The first one, Σdef, gives the sum of the absolute values of the deformation of the angles from the ideal value of 90°. The second one, ΔΣdef, is the difference between the Σdef values between the heterochiral and homochiral complexes.

Table 2. Selected geometrical parameters of the hydrazine complexes optimized at the B3LYP/LANL2DZ level (bond lengths in Å, bond angles and dihedral angles in °).

| Fragment | Chirality | X–M–X | N–M–N | X–M–N | Σdef | ΔΣdef |
|---|---|---|---|---|---|---|
| $NiF_2$ | *RR* | 99.47 | 99.36 | 80.63 | 28.60 | |
| $NiF_2$ | *RS* | 99.14 | 98.23 | 81.26 | 26.11 | –2.09 |
| $NiCl_2$ | *RR* | 95.91 | 95.24 | 84.42 | 16.73 | |
| $NiCl_2$ | *RS* | 96.32 | 93.41 | 85.01 | 14.72 | –2.01 |
| $NiBr_2$ | *RR* | 95.07 | 94.45 | 85.25 | 14.27 | |
| $NiBr_2$ | *RS* | 95.06 | 92.45 | 86.12 | 11.39 | –2.88 |
| $NiI_2$ | *RR* | 94.30 | 93.61 | 86.22 | 11.69 | |
| $NiI_2$ | *RS* | 94.25 | 91.33 | 87.08 | 8.50 | –3.19 |
| $PdF_2$ | *RR* | 101.6 | 103.6 | 77.42 | 37.8 | |
| $PdF_2$ | *RS* | 101.7 | 102.8 | 77.73 | 35.8 | –2.00 |
| $PdCl_2$ | *RR* | 96.89 | 98.91 | 82.11 | 23.79 | |
| $PdCl_2$ | *RS* | 96.99 | 97.33 | 82.82 | 21.50 | –2.29 |
| $PdBr_2$ | *RR* | 94.51 | 97.55 | 83.98 | 18.08 | |
| $PdBr_2$ | *RS* | 94.77 | 95.87 | 84.66 | 15.98 | –2.10 |
| $PdI_2$ | *RR* | 92.49 | 95.85 | 85.83 | 12.41 | |
| $PdI_2$ | *RS* | 93.00 | 93.94 | 86.50 | 10.44 | –1.97 |
| $PtF_2$ | *RR* | 101.1 | 103.9 | 77.54 | 37.5 | |
| $PtF_2$ | *RS* | 101.2 | 102.9 | 77.91 | 36.2 | –1.30 |
| $PtCl_2$ | *RR* | 97.19 | 99.42 | 81.71 | 24.90 | |
| $PtCl_2$ | *RS* | 97.34 | 97.71 | 82.47 | 22.58 | –2.32 |
| $PtBr_2$ | *RR* | 95.20 | 98.05 | 83.39 | 19.86 | |
| $PtBr_2$ | *RS* | 95.55 | 96.11 | 84.17 | 17.49 | –2.37 |
| $PtI_2$ | *RR* | 93.60 | 96.13 | 85.14 | 14.59 | |
| $PtI_2$ | *RS* | 94.17 | 93.96 | 85.92 | 12.11 | –2.48 |

The ΔΣdef values are always negative (between –1.30 and –3.19°) meaning that the angles are closer to the ideal value of 90° for the heterochiral complexes. It is important to note that for the dications of the group 10 metals the empty d-orbital is the $d_{x^2-y^2}$. This orbital is used in the bond formation between a metal cation and the four ligand atoms. The plausible explanation for the relative stability of the heterochiral complexes is obviously the bigger overlap between the metal $d_{x^2-y^2}$-orbital and the electron lone pairs of the ligand atoms.

There are also some trends in the bond lengths. In the first two families (Ni and Pd) and for each pair of complexes the homochiral metal–halogen bond length is slightly shorter than the heterochiral one. Interestingly, the$M–N bond lengths tend to have larger values in the Pd and Pt complexes, whereas in the nickel complexes no trend can be seen. For all the metals studied here, the shortest M–X distances correspond to X = F, followed by Cl, Br and the longest ones are with I. This ordering is in accordance with the covalent radii of the halogen atoms and electronegativ-

 © 2007 Wiley-VCH Verlag GmbH & Co. KGaA, Weinheim 

ity scale of the X atoms. There is a correlation between the M–X and M–N bond lengths, which is shown in Figure 2.

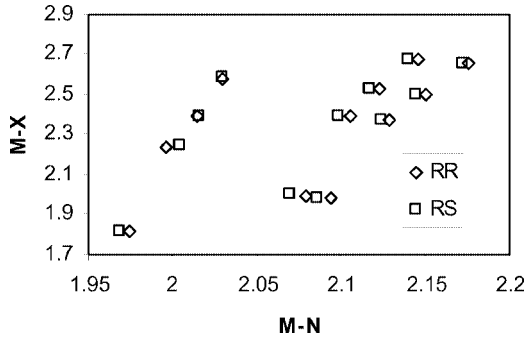


Figure 2. Scatter plot displaying the M–X vs. M–N bond length [Å]. There are six almost linear correlations to be seen, three of them corresponding to the *RS* and three to the *RR* families. From left to right the order is Ni, Pt, and Pd.

If the chirality is not taken into account, the analysis of the metal–halogen vs. metal–nitrogen bond lengths for the analogous complexes show good correlations for every metal family ($r^2$ values of 0.99 and higher).

It was not possible to establish any correlation with the relative energies and the M–L bond lengths, however, although this was expected based on the reasoning related to Equation (2). It is very important to note, however, that in the heterochiral complexes the M–N bond lengths have the propensity to be shorter than in their homochiral analogs. The opposite holds for the M–X bond lengths.

Owing to the different point groups, there are also differences in the torsional angles related to the hydrazine molecules. The homochiral and heterochiral complexes can be divided into two categories based on the torsional angles X–M–N–N and X–M–N–$H_{eq}$. Furthermore, there is a strong linear correlation between the torsional angles, as seen in Figure 3.

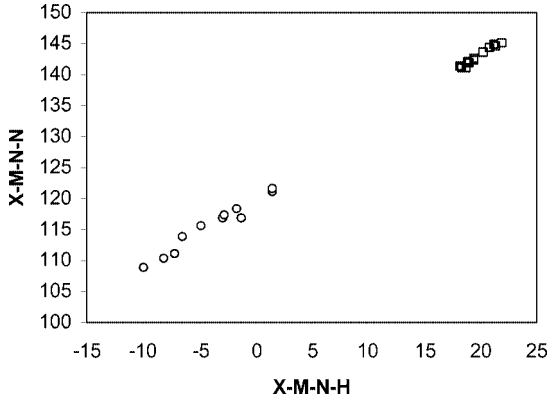


Figure 3. Scatter plot of the X–M–N–N and X–M–N–H torsional angles (in °). The hydrogen atom refers to that in the equatorial position. The spheres refer to the heterochiral complexes and the squares to the homochiral diasteromers.

## 2. Electronic Properties

To explain the differences in energy for the hetero- and homochiral complexes it is necessary to study the influence of the electron lone pairs of the coordinated atoms. To obtain qualitative numerical values to characterize the influence both QTAIM and NBO methods were employed. Since both N–M–N angles and M–N bond lengths are relatively strongly affected by the central metal atom and the halogen atoms, special emphasis was laid on the bonding properties of the M–N bonds.

### *2.1 Topological Analysis of Charge Density*

In QTAIM theory a bond between two atoms is characterized by a line of maximum electron density (i.e. the bond path), which connects the two nuclei and intersects a zero-flux surface in the gradient field at a (3,–1) saddle point (i.e. the bond critical point). There are several descriptive parameters at the bond critical point that can be used to characterize the interaction between two atoms. These are the electron density $\rho(r)$ and its Laplacian $\nabla^2\rho(r)$. The Laplacian of the electronic charge density characterizes the two extreme conditions: either the charge density is locally concentrated [$\nabla^2\rho(r) < 0$] or it is locally depleted [$\nabla^2\rho(r) > 0$]. In the former case the bond has a covalent character, whereas in the latter case the interaction can be understood in terms of a closed-shell interaction. The eigenvalues $\lambda_1$, $\lambda_2$, and $\lambda_3$ of the Hessian describe the curvature of the gradient field at the bond critical point. The ellipticity $\varepsilon$ of a bond is defined as $\varepsilon = \lambda_1/\lambda_2 - 1$. Furthermore, the local electronic energy density $E_d(r)$ is the sum of the local kinetic and potential energy density, $E_d(r) = G(r) + V(r)$. A detailed discussion of the parameters can be found in ref.[27] Descriptive QTAIM parameters related to the bond critical points for the M–N bonds are given in Table 3.

The M–N bonds are all polar bonds, as is the case usually with the coordinate bonds.[31] This is seen in the positive Laplacian [$= \nabla^2\rho(r)$] values, which indicate charge depletion in the bond critical points. The charge depletion is clearly seen in Figure 4 where the negative Laplacian contour plot is given for the heterochiral $[NiF_2(hydrazine)]_2$ compound.

The ratio $|\lambda_1|/\lambda_3$, which is expected to be smaller than 1 in ionic bonds,[30a] shows very small values. As will be shown in the discussion related with the NBO results the coordinated nitrogen atoms carry a significant negative charge. Accordingly, the bonds also have a significant ionic nature. The potential electronic energy density dominates the kinetic electronic energy density at the bond critical points, and thus all $E_d(r)$ values are negative, thus indicating sharing of charge.[30a]

There is also an interesting difference seen in the coordination of fluorine and nitrogen in Figure 4. Both nitrogen atoms have an electron lone pair pointing approximately towards the central nickel atom, whereas the fluorine atoms have an almost isotropic distribution of the Laplacian of the charge density. This phenomenon will be discussed later on in more detail in connection with the NBO analysis.

It has been shown by Matta and Hernandez-Trujillo that there is a linear correlation between bond order and ellipticity.[32] As seen in Table 3, the ellipticity values always have larger values for the M–N bonds in the heterochiral

 © 2007 Wiley-VCH Verlag GmbH & Co. KGaA, Weinheim 

Table 3. Descriptive parameters for the bond critical bonds for the M–N bonds in the $[MX_2hy]_2$ complexes. The distance $D$ [a.u.] is the distance of the bond critical point from the metal atom in an M–N bond.

| Fragment | Chirality | $D$ | $\rho(r)$ [e/ao3] | $\nabla^2\rho(r)$ [e/ao5] | $\lambda_1$ | $\lambda_2$ | $\lambda_3$ | $\varepsilon$ | $\lvert\lambda_1\rvert/\lambda_3$ | $E_d(r)$ [a.u.] |
|---|---|---|---|---|---|---|---|---|---|---|
| $NiF_2$ | *RR* | 1.938 | 0.091 | 0.482 | –0.109 | –0.102 | 0.693 | 0.064 | 0.1573 | –0.0188 |
| $NiF_2$ | *RS* | 1.932 | 0.092 | 0.487 | –0.112 | –0.104 | 0.702 | 0.081 | 0.1595 | –0.0199 |
| $NiCl_2$ | *RR* | 1.987 | 0.081 | 0.439 | –0.095 | –0.090 | 0.624 | 0.054 | 0.1522 | –0.0123 |
| $NiCl_2$ | *RS* | 1.986 | 0.082 | 0.441 | –0.098 | –0.091 | 0.630 | 0.072 | 0.1556 | –0.0129 |
| $NiBr_2$ | *RR* | 1.995 | 0.079 | 0.435 | –0.093 | –0.088 | 0.615 | 0.053 | 0.1512 | –0.0112 |
| $NiBr_2$ | *RS* | 1.997 | 0.080 | 0.434 | –0.094 | –0.088 | 0.617 | 0.070 | 0.1524 | –0.0115 |
| $NiI_2$ | *RR* | 2.010 | 0.077 | 0.426 | –0.089 | –0.085 | 0.600 | 0.052 | 0.1483 | –0.0096 |
| $NiI_2$ | *RS* | 2.012 | 0.078 | 0.426 | –0.091 | –0.085 | 0.602 | 0.070 | 0.1512 | –0.0100 |
| $PdF_2$ | *RR* | 1.953 | 0.092 | 0.388 | –0.093 | –0.091 | 0.572 | 0.028 | 0.1626 | –0.0238 |
| $PdF_2$ | *RS* | 1.944 | 0.094 | 0.395 | –0.096 | –0.093 | 0.583 | 0.035 | 0.1647 | –0.0247 |
| $PdCl_2$ | *RR* | 1.982 | 0.087 | 0.351 | –0.087 | –0.082 | 0.519 | 0.067 | 0.1676 | –0.0227 |
| $PdCl_2$ | *RS* | 1.978 | 0.088 | 0.355 | –0.089 | –0.082 | 0.526 | 0.082 | 0.1692 | –0.0232 |
| $PdBr_2$ | *RR* | 2.000 | 0.083 | 0.336 | –0.083 | –0.078 | 0.497 | 0.069 | 0.1670 | –0.0216 |
| $PdBr_2$ | *RS* | 1.997 | 0.084 | 0.340 | –0.085 | –0.078 | 0.503 | 0.082 | 0.1690 | –0.0220 |
| $PdI_2$ | *RR* | 2.025 | 0.079 | 0.317 | –0.078 | –0.073 | 0.469 | 0.069 | 0.1663 | –0.0201 |
| $PdI_2$ | *RS* | 2.022 | 0.080 | 0.321 | –0.080 | –0.074 | 0.475 | 0.082 | 0.1684 | –0.0205 |
| $PtF_2$ | *RR* | 1.913 | 0.104 | 0.433 | –0.097 | –0.094 | 0.624 | 0.029 | 0.1554 | –0.0257 |
| $PtF_2$ | *RS* | 1.902 | 0.106 | 0.443 | –0.099 | –0.097 | 0.639 | 0.012 | 0.1549 | –0.0268 |
| $PtCl_2$ | *RR* | 1.932 | 0.099 | 0.403 | –0.093 | –0.087 | 0.582 | 0.067 | 0.1598 | –0.0248 |
| $PtCl_2$ | *RS* | 1.926 | 0.101 | 0.410 | –0.094 | –0.087 | 0.592 | 0.081 | 0.1588 | –0.0255 |
| $PtBr_2$ | *RR* | 1.947 | 0.096 | 0.389 | –0.089 | –0.083 | 0.562 | 0.078 | 0.1584 | –0.0237 |
| $PtBr_2$ | *RS* | 1.942 | 0.098 | 0.396 | –0.091 | –0.084 | 0.570 | 0.090 | 0.1596 | –0.0243 |
| $PtI_2$ | *RR* | 1.968 | 0.092 | 0.371 | –0.085 | –0.078 | 0.535 | 0.085 | 0.1589 | –0.0222 |
| $PtI_2$ | *RS* | 1.962 | 0.093 | 0.377 | –0.087 | –0.079 | 0.543 | 0.094 | 0.1602 | –0.0228 |

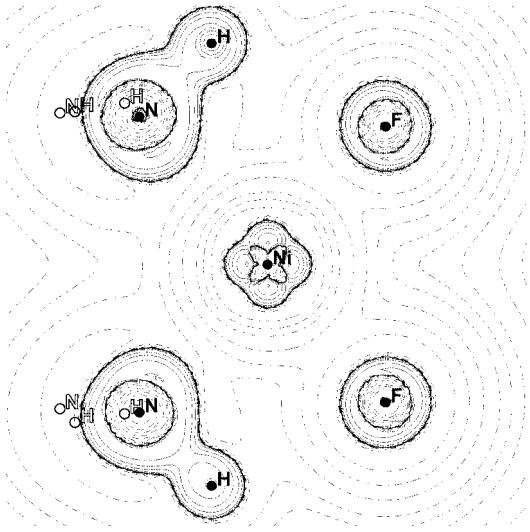


Figure 4. Laplacian contour map for *RS*-$[NiF_2(hydrazine)]_2$ (solid black line refers to positive values and the dotted ones to negative values of the Laplacian).

complexes, thus indicating a higher bond order in these bonds.

The only significant correlation to explain the relative energy $E_{rel}$ with the parameters at the bond critical points was found with the relative distance $D_{rel}$ of a bond critical point from a metal atom ($D_{rel} = D_{RR} - D_{RS}$) in the M–N bonds. The equation of the fitted model is Equation (3).

$$E_{rel} = -2.474 - 2374D_{rel} \quad (3)$$

Since the $P$ value in the ANOVA (Analysis of Variance)[33] result is less than 0.05, there is a statistically significant relationship between $E_{rel}$ and $D_{rel}$ at the 95% confidence level. The $r^2$ statistic indicates that the model as fitted explains 89.3% of the variability in $E_{rel}$. The correlation coefficient equals –0.945, indicating a relatively strong relationship between the variables.

The differences between the positions of the bond critical points are thus correlated with the energy differences. The longer the distance of the bcp from a metal atom in an *RR* complex is with regard to the point in an *RS* analog, the more favored the *RS* complex will be in terms of energy. This is in accordance with the finding that the bond order is higher in the *RS* diastereomers.

### *2.2 NBO Analysis*

To obtain a wider insight into the influence of the halogen ions on the M–N bonds and especially on the relative stabilities of the diastereomers we carried out additional analyses employing NBO methods.

There were no differences in the electronic configurations for the metals between different diastereomers. (The hybridization of the metals varied depending on the counter anion and metal species itself.) Thus, we may say that Bent's rule does not seem to play any significant role in explaining chiral discrimination. NBO charges for the metal, nitrogen, and halogen atoms are shown in Table 4.

The metal atom charges tend to have larger values in the heterochiral complexes than in their homochiral diastereomers. This tendency increases concomitantly with increasing $Z$. The highest absolute values are found for the nickel complexes and the lowest ones for the platinum complexes. The range of the charges goes from 0.3210 to 0.9889. The range for the halogen atom charges is also quite wide, from –0.3254 to –0.6567. The charge is always more negative in a heterochiral complex. The charges of the nitrogen

 © 2007 Wiley-VCH Verlag GmbH & Co. KGaA, Weinheim 

Table 4. NBO charges for the metal, nitrogen, and halogen atoms in the $[MX_2(hydrazine)]_2$ complexes.

| Fragment | Chirality | M charge | N charge | X charge |
|---|---|---|---|---|
| $NiF_2$ | *RR* | 0.9887 | –0.7219 | –0.6539 |
| $NiF_2$ | *RS* | 0.9889 | –0.7187 | –0.6567 |
| $NiCl_2$ | *RR* | 0.7603 | –0.7299 | –0.5254 |
| $NiCl_2$ | *RS* | 0.7614 | –0.7202 | –0.5308 |
| $NiBr_2$ | *RR* | 0.6967 | –0.7376 | –0.4814 |
| $NiBr_2$ | *RS* | 0.6977 | –0.7267 | –0.4877 |
| $NiI_2$ | *RR* | 0.6257 | –0.7487 | –0.4297 |
| $NiI_2$ | *RS* | 0.6260 | –0.7365 | –0.4365 |
| $PdF_2$ | *RR* | 0.8749 | –0.6943 | –0.6271 |
| $PdF_2$ | *RS* | 0.8786 | –0.6930 | –0.6314 |
| $PdCl_2$ | *RR* | 0.6238 | –0.7034 | –0.4837 |
| $PdCl_2$ | *RS* | 0.6274 | –0.6977 | –0.4888 |
| $PdBr_2$ | *RR* | 0.5338 | –0.7109 | –0.4250 |
| $PdBr_2$ | *RS* | 0.5370 | –0.7047 | –0.4307 |
| $PdI_2$ | *RR* | 0.4259 | –0.7205 | –0.3531 |
| $PdI_2$ | *RS* | 0.4282 | –0.7140 | –0.3596 |
| $PtF_2$ | *RR* | 0.8651 | –0.6921 | –0.6321 |
| $PtF_2$ | *RS* | 0.8744 | –0.6931 | –0.6359 |
| $PtCl_2$ | *RR* | 0.5686 | –0.6964 | –0.4759 |
| $PtCl_2$ | *RS* | 0.5756 | –0.6930 | –0.4803 |
| $PtBr_2$ | *RR* | 0.4578 | –0.7027 | –0.4097 |
| $PtBr_2$ | *RS* | 0.4637 | –0.6983 | –0.4148 |
| $PtI_2$ | *RR* | 0.3210 | –0.7116 | –0.3254 |
| $PtI_2$ | *RS* | 0.3254 | –0.7064 | –0.3313 |

Table 5. The main components (>1%) of the electron lone pairs of the nitrogen atoms. Percentage values are given.

| Fragment | Chirality | N [%] | M [%] | X [%] |
|---|---|---|---|---|
| $NiF_2$ | *RR* | 88.463 | 8.688 | 1.704 |
| $NiF_2$ | *RS* | 88.183 | 9.021 | 1.740 |
| $NiCl_2$ | *RR* | 88.774 | 8.059 | 2.329 |
| $NiCl_2$ | *RS* | 88.520 | 8.263 | 2.380 |
| $NiBr_2$ | *RR* | 89.280 | 7.462 | 2.446 |
| $NiBr_2$ | *RS* | 89.040 | 7.635 | 2.504 |
| $NiI_2$ | *RR* | 89.999 | 6.715 | 2.489 |
| $NiI_2$ | *RS* | 89.807 | 6.827 | 2.546 |
| $PdF_2$ | *RR* | 87.090 | 9.604 | 2.228 |
| $PdF_2$ | *RS* | 86.663 | 10.020 | 2.261 |
| $PdCl_2$ | *RR* | 86.065 | 9.522 | 3.525 |
| $PdCl_2$ | *RS* | 85.789 | 9.775 | 3.576 |
| $PdBr_2$ | *RR* | 88.315 | 7.469 | 3.186 |
| $PdBr_2$ | *RS* | 88.059 | 7.663 | 3.246 |
| $PdI_2$ | *RR* | 89.252 | 6.464 | 3.282 |
| $PdI_2$ | *RS* | 89.019 | 6.619 | 3.349 |
| $PtF_2$ | *RR* | 86.127 | 10.569 | 2.439 |
| $PtF_2$ | *RS* | 85.779 | 10.938 | 2.469 |
| $PtCl_2$ | *RR* | 86.065 | 9.522 | 3.525 |
| $PtCl_2$ | *RS* | 85.789 | 9.775 | 3.576 |
| $PtBr_2$ | *RR* | 86.576 | 8.691 | 3.857 |
| $PtBr_2$ | *RS* | 86.315 | 8.915 | 3.916 |
| $PtI_2$ | *RR* | 87.322 | 7.679 | 4.147 |
| $PtI_2$ | *RS* | 87.068 | 7.864 | 4.226 |

atoms vary considerably less, the range being from –0.6921 to –0.7487. Again there is a difference between the heterochiral and homochiral complexes; in the former ones the halogen charges are more negative than in the latter ones. This means that the M–X bonds in the heterochiral complexes have more ionic character than in the homochiral diastereomers.

To study the M–N bonds in more detail, an NLMO analysis was carried out. (A full description of the electron lone pair compositions is given as Supporting Information.) There was a profound difference between the halogen and nitrogen atoms. The nitrogen atoms clearly showed the expected hybridization, but the halogen atoms did not. In the halogen atoms the electron lone pair participating in the coordination to the metal atom always had a clear p-orbital character. The main components of the nitrogen lone pairs are given in Table 5.

According to the results, the electron lone pair of nitrogen in terms of the NLMO consists only partly of the localized electron lone pair of nitrogen but also of the halogen *trans* to the nitrogen and the metal atom. The electron lone pair is systematically more delocalized in the heterochiral complexes. The interpretation of the delocalization can be expressed by two different mechanisms. In the case of the metals, the delocalization can be interpreted simply by covalency of a metal–nitrogen bond, which is higher in the M–N bonds of the heterochiral complexes. As for the halogens, their contribution is opposite to the mechanism of the *trans* influence, where the electron transfer should take place to an antibonding orbital. In our case the stabilizing energy found for this contribution is less than 0.1 kcal/mol. Instead, the contribution can be explained in terms of 3c–4e bonding. The NBO analyses were not able to directly find the M–N or X–M–N bonds because of the pronounced polarity of these bonds, and an illustration (Figure 5) for the formal M–N bonding orbital produced by NBOView corroborates this assumption. Furthermore, the interactions are found in the NLMO listings.

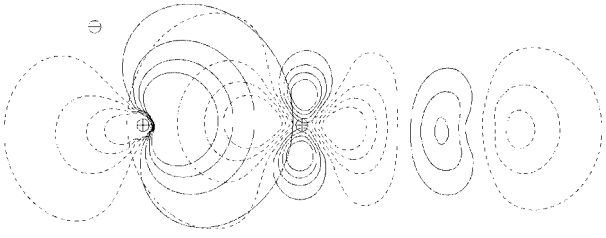

Figure 5. NBO contour plot illustrating the interaction between an electron lone pair of nitrogen with an antibonding Pd–Cl orbital in *R*,*R*-bis[($\mu_2$-hydrazine)$PdCl_2$].

To evaluate the role of the *trans* and *cis* influence, we carried out a second-order perturbation theory analysis of the Fock matrix with the NBO basis set. There are several charge transfers to be taken into account. These involve the charge transfer from the lone pair of nitrogen and a lone pair of halogen. In the former case the charge transfer takes place to an antibonding molecular orbital of the halogen atom *trans* to the nitrogen atom. The NBO delocalization energies were computed based on the deletion of off-diagonal elements between M–X bond orbitals and lone pairs of the nitrogen atom. There are some (mainly nickel) complexes, where there is a small but significant additional charge transfer to an antibonding molecular orbital of the halogen atom *cis* to the nitrogen atom. In the former case the related stabilization energy is defined as $E_{trans}$, and in the latter case $E_{cis}$. Furthermore, we shall use, for compari-

 © 2007 Wiley-VCH Verlag GmbH & Co. KGaA, Weinheim 

son purposes, an additional parameter, $\Delta E_{trans}$, which is the difference between the stabilizing energies of the heterochiral and homochiral pairs. As for the charge transfers involving a lone pair of the halogen, there are two different antibonding orbitals that receive the charge, namely antibonding N–N and N–$H_{equatorial}$ molecular orbitals. In both cases the atoms involved are vicinal to the halogen atom. The related stabilizing energies are given as $E_{XNN}$ and $E_{XNH}$ [kcal/mol]. The values are shown in Table 6. Interestingly, there is no charge transfer from the coordinated electron lone pair to an antibonding M–N molecular orbital *trans* to the halogen atom.

Table 6. Selected results obtained from second-order perturbation theory analysis of the Fock matrix with the NBO basis set. The stabilizing energies are given in kcal/mol.

| Fragment | Chirality | $E_{trans}$ | $\Delta E_{trans}$ | $E_{cis}$ | $E_{XNN}$ | $E_{XNH}$ |
|---|---|---|---|---|---|---|
| $NiF_2$ | *RR* | 74.59 | | 2.91 | 5.97 | 0.29 |
| $NiF_2$ | *RS* | 75.83 | –1.24 | 2.91 | 3.46 | 1.77 |
| $NiCl_2$ | *RR* | 67.66 | | 3.02 | 5.70 | 0.38 |
| $NiCl_2$ | *RS* | 68.11 | –0.45 | 3.19 | 4.42 | 1.78 |
| $NiBr_2$ | *RR* | 61.72 | | 2.42 | 5.36 | 0.38 |
| $NiBr_2$ | *RS* | 62.87 | –1.15 | 2.65 | 4.25 | 1.71 |
| $NiI_2$ | *RR* | 53.42 | | 1.55 | 4.91 | 0.38 |
| $NiI_2$ | *RS* | 53.08 | –0.34 | 0.09 | 3.93 | 1.68 |
| $PdF_2$ | *RR* | 71.65 | | 0.07 | 5.42 | 0.18 |
| $PdF_2$ | *RS* | 73.58 | –1.92 | 0.08 | 3.00 | 1.36 |
| $PdCl_2$ | *RR* | 61.15 | | 0.00 | 4.66 | 0.19 |
| $PdCl_2$ | *RS* | 62.14 | –0.99 | 0.00 | 3.54 | 1.10 |
| $PdBr_2$ | *RR* | 54.40 | | 0.00 | 3.90 | 0.17 |
| $PdBr_2$ | *RS* | 55.16 | –0.76 | 0.00 | 3.13 | 0.97 |
| $PdI_2$ | *RR* | 46.21 | | 0.00 | 3.14 | 0.17 |
| $PdI_2$ | *RS* | 46.82 | –0.61 | 0.00 | 2.78 | 0.85 |
| $PtF_2$ | *RR* | 96.48 | | 0.00 | 3.88 | 0.18 |
| $PtF_2$ | *RS* | 99.51 | –3.03 | 0.00 | 2.29 | 1.22 |
| $PtCl_2$ | *RR* | 88.93 | | 0.00 | 4.50 | 0.17 |
| $PtCl_2$ | *RS* | 91.09 | –2.16 | 0.00 | 3.44 | 0.99 |
| $PtBr_2$ | *RR* | 80.97 | | 0.00 | 4.19 | 0.17 |
| $PtBr_2$ | *RS* | 82.82 | –1.85 | 0.00 | 3.37 | 0.90 |
| $PtI_2$ | *RR* | 71.32 | | 0.00 | 3.84 | 0.17 |
| $PtI_2$ | *RS* | 73.04 | –1.62 | 0.00 | 3.29 | 0.83 |

The results clearly show that there is always a charge transfer from a nitrogen lone pair to an antibonding M–X molecular orbital with a marked stabilization energy involved. Furthermore, the stabilization energy is always larger in the heterochiral complexes. There is also a correlation between the relative stabilization energies $\Delta E_{trans}$ and the relative total energies ($E_{rel}$), as shown in Figure 6. The $r^2$ value for the linear correlation is 0.854.

The $E_{XNN}$ and $E_{XNH}$ stabilization energies are clearly different in heterochiral and homochiral complexes. However, the effects are reversed so that the stabilizing energies $E_{XNN}$ have larger values for homochiral complexes while the opposite holds true for the $E_{XNH}$ values. Furthermore, the values tend to cancel out each other pairwise leaving $E_{trans}$ to act as an explaining factor described in Figure 6.

The differences between the relative stabilization energies are obviously due to the different geometries caused by different orientations of the hydrazine molecules in the homo-

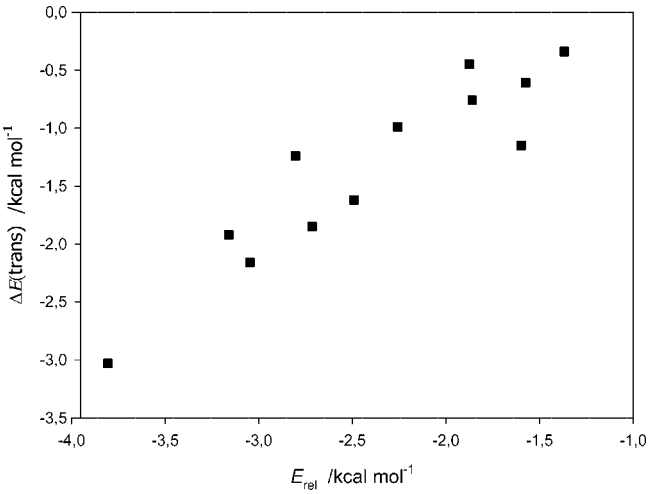


Figure 6. Scatter plot showing the correclation between the relative total energies $E_{rel}$ and the relative stabilization energies indicating the *trans* influence.

and heterochiral complexes. This might also give a plausible explanation for the differences in the bond order and covalency of the M–N bonds. In the heterochiral complexes the values are higher, which might be explained by the smaller charge transfer into antibonding orbitals of the nitrogen atom. Furthermore, the different orientations also result in different L–M–L angles in the coordination spheres. In the heterochiral complexes the deviations are smaller leading to enhanced overlapping of the metal $d_{x^2-y^2}$-orbital and the electron lone pairs of the ligand atoms.

There is also a charge transfer from an electron lone pair of the nitrogen atom to another M–X antibonding molecular orbital. The stabilizing energies related to this *cis* influence are more than ten times smaller than the respective energies related to the *trans* influence in the nickel complexes. In the palladium and platinum complexes no *cis* influence was found, with the exception of the compounds composed of palladium and fluorine. Presumably, the *cis* influence might be correlated with the differences concerning the nickel complexes presented in Figure 3.

To conclude, we have shown that the electron lone pairs of the coordinated ligand atoms have a marked yet complicated role in bonding, and have not been properly considered in some important previous studies concerning bonding to platinum.[34]

## Conclusions

Based upon the optimizations carried out at the B3LYP/LANL2DZ level of theory, the heterochiral complexes are more stable than the homochiral ones. The relative stability is correlated with the nature of both the metals and the anions. Moreover, the relative stability is correlated with the electronegativity values of the metals and the halogens. The QTAIM and NBO results indicated that the M–X bonds have marked ionic character with the halogen atoms show-

 © 2007 Wiley-VCH Verlag GmbH & Co. KGaA, Weinheim 

ing no hybridization. The coordinate M–X bonds are formed by an electron pair resting essentially on a p-type orbital of a halogen. Another profound difference is that the halogen atoms do not show any marked charge transfer to an antibonding M–N molecular orbital related to the *trans* influence. Instead, the contribution is seen in the composition of the electron lone pair of the nitrogen atom *trans* to the halogen atom. In sharp contrast to this, there is always a marked stabilization energy for the charge transition from the electron lone pair of nitrogen to an antibonding M–X orbital *trans* to the nitrogen atom. The M–N bonds formed formally by the electron lone pair of nitrogen also contain a contribution from the metal atom, thus indicating covalency of the bonds. The covalency, as well as the bond order, have a larger contribution in the M–N bonds of the heterochiral complexes. There is also a correlation between the relative distance of the bond critical points in the M–N bonds and the relative energy.

Although there are no experimental structures available, which could corroborate the calculated chiral discrimination, we feel confident that the predicted trends are correct.

## Computational Methods

The geometries of the compounds were optimized by applying DFT methods and using Becke's three-parameter hybrid exchange functional in combination with the gradient-corrected correlation functional of Lee, Yang, and Parr.[35] The basis set applied in every calculation was LANL2DZ to include the relativistic effect.[36] The presence of true energy minima were checked by frequency calculations. No imaginary frequencies were found for the optimized structures. For every nickel complex it was necessary to check the stability of the wave function to see whether any instability existed from unrestricted contributions. We found instability in every case. After the check, the wave function was optimized to remove the contributions. The structures were then reoptimized using the optimized wave functions, their wave function stabilities rechecked, and frequencies recalculated. The calculations were carried out with the Gaussian 03 program suite.[37] The electronic properties were evaluated by QTAIM (Quantum Theory of Atoms in Molecules)[38] and NBO (Natural Bond Orbital) methods.[39] The NBO program used was the version installed in Gaussian 03. The QTAIM-based programs were MORPHY98,[40] AIMPAC,[41] and AIM2000.[42] We verified that similar geometries were obtained for some test cases using the Turbomole[43] program at the B3LYP/TZVP level of theory. Accordingly, the inclusion of polarization does not result in significant changes.

**Supporting Information** (see footnote on the first page of this article): Geometries of the optimized compounds and their respective energies.

## Acknowledgments

This work was carried out with financial support from the Ministerio de Ciencia y Tecnología (Project No. BQU2003-01251). M. R. S. acknowledges the grant given by the Ministerio de Educación y Ciencia de España (SAB2003-0171). Thanks are given to the CTI (CSIC), CESGA, and CSC (Centre of Scientific Computing, Espoo, Finland) for the allocation of computer time.

[1] C. Girard, H. B. Kagan, *Angew. Chem. Int. Ed.* **1998**, *37*, 2922.
[2] I. Alkorta, J. Elguero, *J. Chem. Phys.* **2002**, *117*, 6463.
[3] K. Zborowski, I. Alkorta, J. Elguero, *J. Phys. Chem. A* **2006**, *110*, 7247.
[4] T. A. Beu, U. Buck, *Z. Phys. Chem.* **2000**, *214*, 437.
[5] G. Krainev, T. Shimizu, M. Ishigooka, K. Hiroya, M. Hatano, *Biochemistry* **1993**, *32*, 1951.
[6] I. Alkorta, O. Picazo, J. Elguero, *Tetrahedron Asym.* **2005**, *16*, 755.
[7] I. Alkorta, O. Picazo, J. Elguero, *J. Phys. Chem. A* **2005**, *109*, 9573.
[8] E. Housecroft, A. G. Sharpe, *Inorganic Chemistry*, 2nd ed., Pearson Education Limited, Harlow, **2005**, p. 686–687; B. J. Coe, S. J. Glenwright, *Coord. Chem. Rev.* **2000**, *203*, 5.
[9] M. Anderson, A. G. Orpen, *Chem. Commun.* **2001**, 2682–2683.
[10] K. Burdett, T. A. Albright, *Inorg. Chem.* **1979**, *18*, 2112.
[11] R. J. Deeth, *J. Chem. Soc., Dalton Trans.* **1993**, 781.
[12] P. D. Lyne, D. M. P. Mingos, *J. Organomet. Chem.* **1994**, *478*, 141.
[13] P. D. Lyne, D. M. P. Mingos, *J. Chem. Soc., Dalton Trans.* **1995**, 1635.
[14] N. Kaltsoyannis, P. Mountford, *J. Chem. Soc., Dalton Trans.* **1999**, 781.
[15] R. Salcedo, P. Sharma, A. Cabrera, S. Fomine, *J. Mol. Struct. (THEOCHEM)* **2002**, *579*, 151.
[16] C. Fave, M. Hissler, K. Sénéchal, I. Ledoux, J. Zyss, R. Réau, *Chem. Commun.* **2002**, 1674.
[17] H. Bent, *Chem. Rev.* **1961**, *61*, 275; J. P. Foster, F. Weinhold, *J. Am. Chem. Soc.* **1980**, *102*, 7211.
[18] C. R. Landis, T. K. Firman, D. M. Root, T. Cleveland, *J. Am. Chem. Soc.* **1998**, *120*, 1842.
[19] V. Jonas, C. Boehme, G. Frenking, *Inorg. Chem.* **1996**, *35*, 2097.
[20] M. Kaupp, *Chem. Eur. J.* **1999**, *5*, 3631; M. Kaupp, *Angew. Chem. Int. Ed.* **2001**, *40*, 3535.
[21] S. van Zutphen, E. Pantoja, R. Soriano, C. Soro, D. M. Tooke, A. L. Spek, H. den Dulk, J. Brouwer, J. Reedijk, *Dalton Trans.* **2006**, 1020.
[22] K. Yamamoto, S. Kawanishi, *J. Biol. Chem.* **1991**, *266*, 1509.
[23] K. Vimal, L. Jain, *Coord. Chem. Rev.* **2005**, *249*, 3075.
[24] J. Kozelka, E. Segal, C. Bois, *J. Inorg. Biochem.* **1992**, *47*, 67.
[25] S. Komeda, S. Bombard, S. Perrier, J. Reedijk, J. Kozelka, *J. Inorg. Biochem.* **2003**, *96*, 357.
[26] Y. Montet, J. Kozelka, *Inorg. Chim. Acta* **1999**, *284*, 103.
[27] O. Picazo, I. Alkorta, J. Elguero, M. R. Sundberg, *Inorg. Chem. Commun.* **2006**, *9*, 712.
[28] S. M. Free, J. W. Wilson, *J. Med. Chem.* **1964**, *7*, 395.
[29] L. Allred, *J. Inorg. Nuclear Chem.* **1961**, *17*, 215.
[30] a) R. F. W. Bader, *Atoms in Molecules: A Quantum Theory*, Oxford: Clarendon, **1990**; b) P. Popelier, *Atoms in Molecules – An Introduction*, Prentice Hall, Singapore, **2000**.
[31] a) P. Macchi, A. Sironi, *Coord. Chem. Rev.* **2003**, *238–239*, 383; b) C.-R. Lee, C.-C. Wang, K.-C. Chen, G.-H. Lee, Y. Wang, *J. Phys. Chem. A* **1999**, *103*, 156.
[32] C. Matta, J. Hernandez-Trujillo, *J. Phys. Chem. A* **2003**, *107*, 7496.
[33] R. Carlson, *Design and Optimization in Organic Synthesis*, Elsevier, Amsterdam, **1992**.
[34] H. Baik, R. A. Friesner, S. J. Lippard, *Inorg. Chem.* **2003**, *42*, 8615; D. V. Deubel, *J. Am. Chem. Soc.* **2002**, *124*, 5834.
[35] D. Becke, *J. Chem. Phys.* **1993**, *98*, 5648; C. Lee, W. Yang, R. G. Parr, *Phys. Rev. B* **1988**, *37*, 785.
[36] P. J. Hay, W. R. Wadt, *J. Chem. Phys.* **1985**, *82*, 299.
[37] M. J. Frisch, G. W. Trucks, H. B. Schlegel, G. E. Scuseria, M. A. Robb, J. R. Cheeseman, J. A. Montgomery Jr, T. Vreven, K. N. Kudin, J. C. Burant, J. M. Millam, S. S. Iyengar, J. Tomasi, V. Barone, B. Mennucci, M. Cossi, G. Scalmani, N. Rega, G. A. Petersson, H. Nakatsuji, M. Hada, M. Ehara, K. Toyota, R. Fukuda, J. Hasegawa, M. Ishida, T. Nakajima, Y. Honda, O. Kitao, H. Nakai, M. Klene, X. Li, J. E. Knox, H. P. Hratch-

 © 2007 Wiley-VCH Verlag GmbH & Co. KGaA, Weinheim 

ian, J. B. Cross, C. Adamo, J. Jaramillo, R. Gomperts, R. E. Stratmann, O. Yazyev, A. J. Austin, R. Cammi, C. Pomelli, J. W. Ochterski, P. Y. Ayala, K. Morokuma, G. A. Voth, P. Salvador, J. J. Dannenberg, V. G. Zakrzewski, S. Dapprich, A. D. Daniels, M. C. Strain, O. Farkas, D. K. Malick, A. D. Rabuck, K. Raghavachari, J. B. Foresman, J. V. Ortiz, Q. Cui, A. G. Baboul, S. Clifford, J. Cioslowski, B. B. Stefanov, G. Liu, A. Liashenko, P. Piskorz, I. Komaromi, R. L. Martin, D. J. Fox, T. Keith, M. A. Al-Laham, C. Y. Peng, A. Nanayakkara, M. Challacombe, P. M. W. Gill, B. Johnson, W. Chen, M. W. Wong, C. Gonzalez, J. A. Pople, *Gaussian 03*, Gaussian, Inc., Pittsburgh, PA, **2003**.

[38] a) R. F. W. Bader, *Atoms in Molecules: A Quantum Theory*, Clarendon, Oxford, **1990**; b) P. Popelier, *Atoms in Molecules – An Introduction*, Prentice Hall, Singapore, **2000**.

[39] a) E. Reed, L. A. Curtiss, F. Weinhold, *Chem. Rev.* **1988**, *88*, 899; b) F. Weinhold, C. Landis, *Valency and Bonding – A Natural Bond Orbital Donor-Acceptor Perspective*, Cambridge University Press, Cambridge, **2005**.

[40] *MORPHY98*, a program written by P. L. A. Popelier with a contribution from R. G. A. Bone, UMIST, Manchester, England, **1998**.

[41] F. W. Biegler-König, R. F. W. Bader, T. Ting-Hua, *J. Comput. Chem.* **1982**, *3*, 317.

[42] F. W. Biegler-König, J. Schönbom, *AIM2000 Version 2.0*, University of Applied Sciences, Bielefeld, Germany, **2002**.

[43] *The Program System TURBOMOLE, Version 5-5*: R. Ahlrichs, M. Bär, M. Häser, H. Horn, C. Kölmel, *Chem. Phys. Lett.* **1989**, *162*, 165.

Received: September 5, 2006
Published Online: November 17, 2006

 © 2007 Wiley-VCH Verlag GmbH & Co. KGaA, Weinheim 

DOI: 10.1002/ejic.200600615

# Aminoalkylbis(phosphonates): Their Complexation Properties in Solution and in the Solid State

Vojtěch Kubíček,*[a] Jan Kotek,[a] Petr Hermann,[a] and Ivan Lukeš[a]

**Keywords:** Phosphonates / Complexation / Stability constants / Potentiometry

Five geminal bis(phosphonates) containing an amino group in the α, γ or δ position of the carbon chain have been synthesised and their acid–base and complexation properties with $Cu^{2+}$, $Zn^{2+}$, $Ca^{2+}$, $Mg^{2+}$ and $Na^{+}$ ions studied by potentiometry. Determination of the stability constants of the complexes with divalent metal ions is complicated by the formation of precipitates. The results of these studies show a negligible effect of the hydroxo group in the α position on the acid–base and complexation properties of the ligands. The presence of an amino group in the α position, however, decreases the basicity, which results in a lower complexation ability of the bis(phosphonates). The crystal structures of the three ligands with different degrees of protonation have also been determined. The structure of the triammonium salt of aminomethylbis(phosphonic acid) shows that the proton is bound to the nitrogen atom in monoprotonated species. The structure of the $Cu^{2+}$ complex of pamidronate $[\{Cu_2(H_2pam)_2\}\cdot H_2O]_n$ shows the presence of dimeric units with a relatively short distance (2.99 Å) between the metal centres. These units form a coordination polymeric chain.
(© Wiley-VCH Verlag GmbH & Co. KGaA, 69451 Weinheim, Germany, 2007)

## Introduction

Pyrophosphate is an important regulator of calcium metabolism in living organisms. Replacement of the bridging oxygen atom of pyrophosphate with methylene or a substituted methylene group results in the formation of geminal bis(phosphonic acids), hereafter referred to simply as bis(phosphonates). This group of compounds has been intensively studied over the last fifty years. As the central carbon atom can be substituted with many different organic groups, a huge number of bis(phosphonates) have been synthesised. Their low toxicity, high biological stability (they are not metabolized) and high affinity for calcium and calcified tissues have made them suitable for many biomedical applications.[1] After adsorption on the bone surface, bis(phosphonates) can affect the functioning of bone cells such as osteoclasts and osteocysts, which are responsible for bone formation and desorption. Because of this, bis(phosphonates) can be used in the treatment of osteoporosis, Paget disease and other diseases of calcified tissues. The large variability of bis(phosphonates) provides a wide scope of therapeutic effects, and some of the bis(phosphonates) used therapeutically nowadays are shown in Table 1. Bis(phosphonates) form complexes with divalent and trivalent transition metal ions, and these complexes have been applied in bone radiotherapy and for palliation of pain associated with metastatic bone cancer.[1]

Recently, attention has been paid to tissue-specific imaging and therapy. Attachment of a biologically active molecule to a molecule of contrast agent results in the binding of such species to specific tissue and increases their local concentration. This provides a better contrast and leads to the use of lower doses of the contrast agents and therapeutic agents. In these applications, bis(phosphonates) can play the role of a targeting group as their conjugate with the medically active molecule can be swiftly and strongly adsorbed on the surface of bones and other calcified tissues.[2,3] Recently, we have contributed to this field by studying the bis(phosphonate)-modified macrocyclic ligand $H_4$dota (1,4,7,10-tetraazacyclododecane-1,4,7,10-tetraacetic acid), which is useful for targeted visualisation of calcified tissues by magnetic resonance imaging (MRI) or other radiodiagnostic/therapeutic treatment.[4]

Most of the clinically used bis(phosphonates) contain an amino group in the carbon chain. These aminoalkylbis(phosphonates) strongly complex transition metal ions. Despite this fact, only a few studies have concentrated on their acid–base and complexation properties,[5–13] and generally only protonation constants have been determined. In the case of some ligands, their complexing behaviour with $Cu^{2+}$ ions has also been studied.[5,6,11,13] Unfortunately, the reported results are not always consistent. Some of the dissociation/protonation constants are beyond the lower or higher limits of the applied methods and, therefore, they were not determined. Furthermore, most of the studies were performed in presence of $Na^{+}/K^{+}$ ions.[5,6,9–13] As these ions are complexed by the bis(phosphonates),[14,15] all reported values of dissociation/protonation and complex stability

[a] Department of Inorganic Chemistry, Charles University, Hlavova 8, 12840 Prague 2, The Czech Republic
E-mail: vvvojta@volny.cz
Supporting information for this article is available on the WWW under http://www.eurjic.org or from the author.

 © 2007 Wiley-VCH Verlag GmbH & Co. KGaA, Weinheim 

Table 1. Bis(phosphonates) $[R^1R^2C(PO_3H_2)_2]$ used in medical practice.

| Commercial name | $-R^1$ | $-R^2$ | Commercial name | $-R^1$ | $-R^2$ |
|---|---|---|---|---|---|
| Aledronate | —OH | $—(CH_2)_3—NH_2$ | Pamidronate | —OH | $—(CH_2)_2—NH_2$ |
| Clodronate | —Cl | —Cl | Risedronate | —OH | |
| Etidronate | —OH | $—CH_3$ | Tiludronate | —H | |
| Ibandronate | —OH |  | Zoledronate | —OH | |

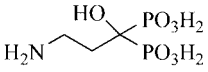

$H_4$pam
Pamidronate

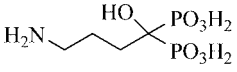

$H_4$ale
Aledronate

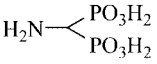

$H_4$meth

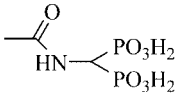

$H_4$aca

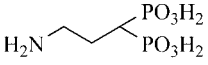

$H_4$prop

Figure 1. Structures of the ligands discussed.

constants are disturbed by the formation of such complexes.

In light of this we decided to use the non-complexing tetramethylammonium cation in the supporting electrolyte to avoid alkali metal complex formation. In this work, we report on the results of a solution study of four bis(phosphonates) containing an amino group in the side chain. Furthermore, as the bis(phosphonate) moiety is often connected by a peptidic bond in the bifunctional ligands, we chose a new amide derivative $H_4$aca as a model compound for comparison (Figure 1). The protonation constants and stability constants with $Cu^{2+}$, $Zn^{2+}$, $Ca^{2+}$, $Mg^{2+}$ and $Na^+$ ions are presented. The crystal structures of three ligands and one $Cu^{2+}$ complex have also been determined by single-crystal X-ray diffraction analysis.

## Results and Discussion

### Acid–Base Properties

Phosphonic acids undergo their first deprotonation in the strongly acidic ($pK_1 \leq 2$) and the second one in the weakly acidic region ($pK_2$ = 5–6).[16] A different situation occurs in the case of bis(phosphonates), where a strong electrostatic interaction between the two geminal phosphonic acid groups results in a large enhancement of the basicity of the moiety. Furthermore, the presence of an amino group brings another protonation site into the molecule, which affects the other protonation constants. The highest dissociation constants were determined by NMR titration following the procedure described recently in the literature.[17]

The ligands $H_4$pam, $H_4$ale, $H_4$meth and $H_4$prop exhibit similar acid–base behaviour, with five protonation constants spread over the whole pH range (Table 2). The first two $pK_a$'s lie in the strongly acidic region and correspond to the first deprotonation of each phosphonic acid group. The next constant is found close to the neutral region and represents release of the third proton from the bis(phosphonic acid) group, and the last two constants lie in the strongly alkaline region. The lower one is usually ascribed to the last deprotonation of the bis(phosphonic acid) moiety, and the last deprotonation occurs from the amino group.[18] The last proton is bound to the nitrogen atom in almost all poly(aminophosphonates).[19] This assignment can be supported by the crystal structure of the tris(ammonium) salt of $H_4$meth (see below), whose structure contains a fully deprotonated bis(phosphonic acid) group, whereas the amino group remains protonated. The $pK_a$ values of $H_4$meth are somewhat distinct from those of the other ligands, with the most significant difference being observed for the $pK_a(HL^{3-})$ and $pK_a(H_2L^{2-})$ values, which are between one and two units lower than those found for the other ligands. Such behaviour can be explained by steric and/or electronic effects. The protonated amino group on the same carbon atoms can efficiently interact intramolecularly (electrostatically and/or through hydrogen bonds[20]) with only one negatively charged phosphonate group. The

 © 2007 Wiley-VCH Verlag GmbH & Co. KGaA, Weinheim 

Table 2. Values of protonation/dissociation constants of the ligands.

| Species | $H_4$pam | | $H_4$ale | | $H_4$meth | | $H_4$aca | | $H_4$prop | |
|---|---|---|---|---|---|---|---|---|---|---|
| | log$\beta$ | p$K_a$ | log$\beta$ | p$K_a$ | log$\beta$ | p$K_a$ | log$\beta$ | p$K_a$ | log$\beta$ | p$K_a$ |
| $HL^{3-}$ | 13.06(3)[a] | 13.06 | 12.68(2)[a] | 12.68 | 11.43(2) | 11.43 | 10.73(4) | 10.73 | 12.76(2)[a] | 12.76 |
| $H_2L^{2-}$ | 23.36(5) | 10.30 | 23.75(1) | 11.07 | 19.72(3) | 8.29 | 18.22(6) | 7.49 | 23.42(2) | 10.66 |
| $H_3L^{-}$ | 29.21(7) | 5.85 | 30.11(1) | 6.36 | 25.07(3) | 5.35 | 23.98(7) | 5.76 | 29.57(3) | 6.15 |
| $H_4L$ | 31.01(9) | 1.80 | 32.30(2) | 2.19 | 26.25(6) | 1.18 | 25.34(8) | 1.36 | 31.68(4) | 2.11 |
| $H_5L^{+}$ | – | <1.2 | – | <1.2 | – | <1.2 | – | – | – | <1.2 |

[a] Determined by NMR titration. No control of the ionic strength.

other ligands with a more flexible carbon chain can be present in conformations where such convenient interaction(s) with both phosphonate groups are maximized. The strongest interaction should then be expected for $H_4$pam, which contains the shortest ethylene chain, and, indeed, it exhibits the most basic last deprotonation. Alternatively, the presence of electron withdrawing (protonated) amino and phosphonic acid moieties on the same carbon atom (α to each other) can decrease the values of all dissociation constants. A comparison of ligands $H_4$pam and $H_4$prop shows a small effect of the α-hydroxo group on the acid–base properties of ligands.

The ligand $H_4$aca contains an amide nitrogen atom instead of an amino group, which means that only four deprotonation steps can occur. The first one lies in the strongly acidic region, with two more in the neutral and the last one in the rather alkaline region. When compared with other bis(phosphonates) [e.g. methanediphosphonic acid: p$K$($HL^{3-}$) = 10.6, p$K$($H_2L^{2-}$) = 7.05, p$K$($H_3L^{-}$) = 2.77, p$K$($H_4L$) = 1.6],[21] $H_4$aca shows higher overall basicity due to the higher value of p$K$($H_3L^{-}$).

We carried out all measurements in the presence of non-complexing tetramethylammonium cations to avoid alkali metal ion complex formation, therefore our results differ from those reported in the literature (determined in the presence of $Na^+$ or $K^+$ ions).[5,6,9–13] The differences are particularly pronounced in the value of the last dissociation constant. In the presence of $Na^+/K^+$ ions, the values reported in the literature are lower by one or even two orders of magnitude due to alkali metal ion assisted deprotonation (see Table S2 in the Supporting Information). Although the stabilities of the $K^+$ complexes of bis(phosphonates) are much lower than those with $Na^+$, this interaction cannot be negligible[14,15] and the values of the dissociation/protonation constants should be changed.

## Complexation Properties

In order to simplify the following text we will use a three-digit code to describe the composition of the complexes. The first digit represents the number (stoichiometric coefficient) of protons, the second one is the number of ligand molecules and the third is the number of metal ions. A negative value of the first digit represents a hydroxo complex or untypical release of a proton(s) from, under common conditions, a fully deprotonated ligand molecule, for example alkoxide anion formation. As an example, a complex with an $[H_2L_2M]$ stoichiometry is referred to as [221] and the value of its overall stability constant as log$\beta_{221}$. The charges of the complexes are omitted, and throughout the following text pH means –log$[H^+]$.

### *Divalent Metal Ions*

Speciation of the complexes with biogenic metal ions ($Cu^{2+}$, $Zn^{2+}$, $Ca^{2+}$ and $Mg^{2+}$) in aqueous solution was studied by potentiometry (Figure 2). Following the procedure described in the Experimental Section, three sets of data with ligand-to-metal ratios 1:1, 2:1 and 1:2 were recorded for each ion. All these measurements were complicated by precipitate formation. In general, the precipitation started with increasing abundance of the uncharged [211] complex at a pH between 2.5 and 6.0. The precipitate was usually fully dissolved under basic conditions (pH 9–11, depending on the ligand and metal combination and ratio; see Table S1). Additionally, in some cases data could not be recorded due to extended precipitate formation over a wide pH range, especially for systems containing $H_4$meth or for mixtures with an excess of metal ion. Obviously, the stability constants of the species abundant mostly in the pH range where the precipitates were present were not accessible, which means that a chemical model for many systems does not involve non-protonated species and direct comparison of the complexation properties of different ligands is somewhat difficult. The results are compiled in Table 3, and all distribution diagrams are provided as Supporting Information (Figures S2–S7).

The chemical models for speciation of $H_4$pam, $H_4$ale, $H_4$meth and $H_4$prop complexes are similar. Complexation starts below pH 2 with formation of the [311] complex. At higher pH, less protonated species are present. The high negative charge of the fully deprotonated bis(phosphonate) group of the ligands disfavours formation of the [021] complexes and only the [121] and [221] species can be found in mixtures with an excess of the ligands. From a comparison of the constants corresponding to coordination of the first and second ligand molecules in their monoprotonated form (i.e. formation of the [111] and [221] complexes; Table 4), it is clear that the second consecutive stability constants are only slightly lower than the first ones. This fact indicates negligible steric crowding due to coordination of the first protonated ligand molecule.

In equimolar solutions and at metal excess, 1:2 L:M complexes are formed under neutral and alkaline conditions. As one ligand molecule binds two metal ions, all the protons

 © 2007 Wiley-VCH Verlag GmbH & Co. KGaA, Weinheim 

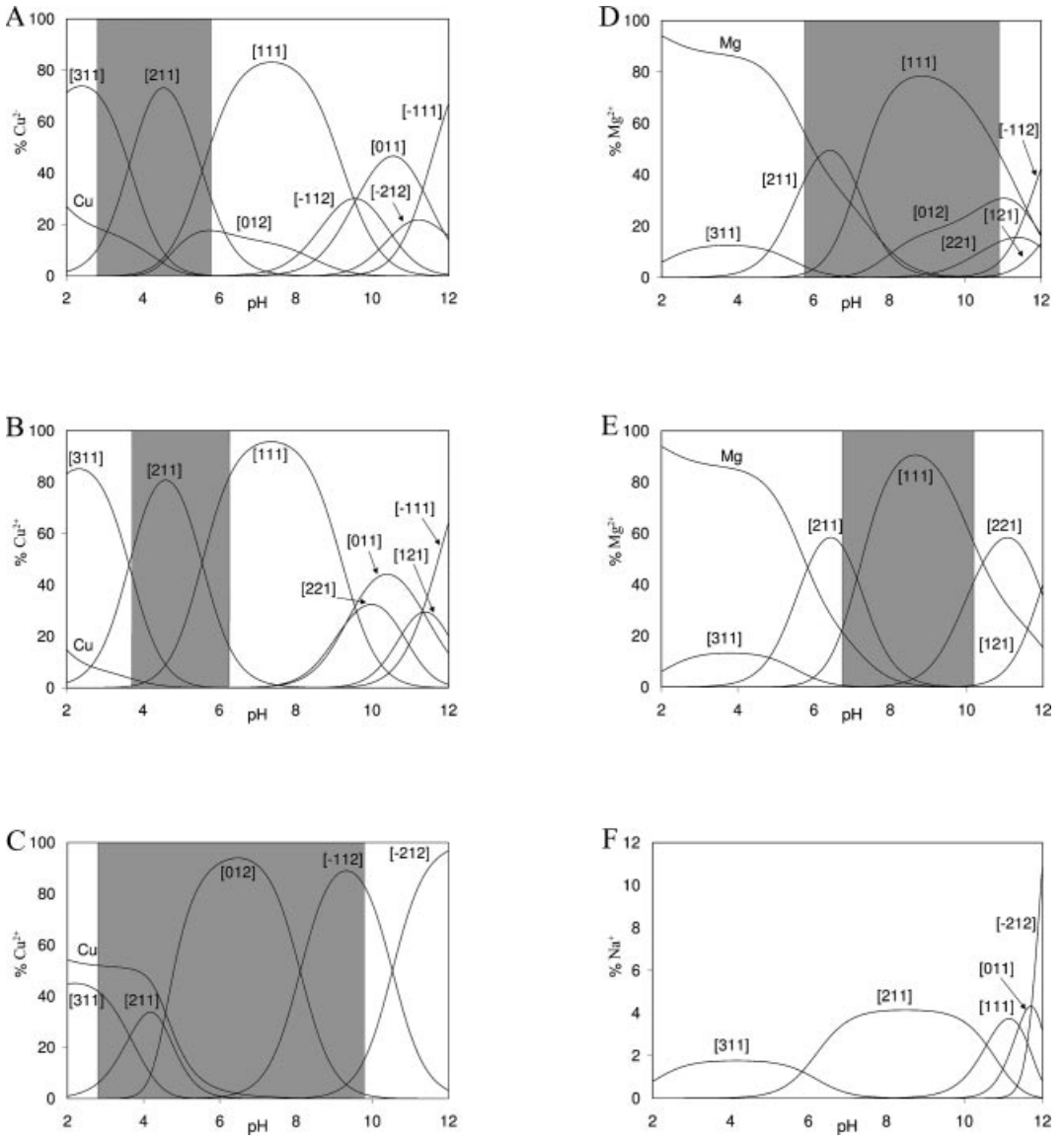


Figure 2. Species distribution plot for aqueous solutions of $Cu^{2+}$ and $H_4$ale with metal/ligand ratios of 1:1 (A), 1:2 (B) and 2:1 (C); $Mg^{2+}$ and $H_4$ale 1:1 (D) and 1:2 (E); $Na^+$ and $H_4$ale 10:1 (F). The grey areas were not studied during the experiment due to formation of a precipitate.

are released and these complexes do not exist in a protonated form. All systems containing $Cu^{2+}$ and $Zn^{2+}$ exhibit a high abundance of the [–111], [–112] and [–212] species in the alkaline region. In these complexes, deprotonation of the coordinated water molecule and/or deprotonation of the hydroxy group of ligands $H_4$pam and $H_4$ale has to occur, although these two possibilities could not be distinguished by potentiometry due to a proton ambiguity. As expected, the stability of the complexes follows the order $Cu^{2+} > Zn^{2+} > Mg^{2+} > Ca^{2+}$. The stabilities of the complexes with $H_4$pam, $H_4$ale and $H_4$prop are similar, whereas the presence of an amino group in the α position decreases the basicity of $H_4$meth and leads to a lower stability of its complexes.

As $H_4$aca contains an amide group instead of an amino group it prefers to form less protonated complexes and the complexation process starts at higher pH. The same effect was observed for 2:1 L:M complexes, where the [021] complex was found in all systems containing $H_4$aca. The stability constants of $H_4$aca complexes are between the values found for $H_4$meth and those found for the other ligands. In conclusion, the stabilities of the complexes follow the general order $H_4$pam ≈ $H_4$ale ≈ $H_4$prop > $H_4$aca > $H_4$meth.

The solid-state structures of bis(phosphonate) complexes typically show oligomeric or polymeric coordination chains with the bis(phosphonic acid) group acting as a bridging moiety.[22] Therefore, the presence of these complicated structures in solution is expected as well.[18] Unfortunately, the complexity of the studied systems did not allow us to take these multinuclear/polymeric complexes into account during the refinement of the potentiometric data.

### *Sodium*

As expected, the complexes with $Na^+$ ion exhibit the lowest stability constants of all the metal ions studied (Table 3),

 © 2007 Wiley-VCH Verlag GmbH & Co. KGaA, Weinheim 

Table 3. Stability constants of metal–ligand complexes.

| Cation | *h* | *l* | *m* | $\log\beta_{hlm}$ $H_4$pam | $H_4$ale | $H_4$meth | $H_4$aca | $H_4$prop |
|---|---|---|---|---|---|---|---|---|
| $Cu^{2+}$ | 3 | 1 | 1 | 32.66(8) | 33.82(3) | [a] | – | 32.90(3) |
| | 2 | 1 | 1 | 29.53(6) | 30.20(3) | [a] | 23.95(1) | 29.30(3) |
| | 1 | 1 | 1 | – | 24.65(4) | [a] | 19.40(3) | – |
| | 0 | 1 | 1 | – | 15.09(6) | [a] | 13.71(6) | – |
| | –1 | 1 | 1 | 5.30(9) | 3.78(5) | [a] | 2.98(6) | 3.14(6) |
| | 2 | 2 | 1 | 42.4(1) | 41.69(8) | [a] | – | 41.44(8) |
| | 1 | 2 | 1 | – | 30.90(7) | [a] | 29.02(8) | 30.60(8) |
| | 0 | 2 | 1 | – | – | [a] | 18.6(1) | – |
| | 0 | 1 | 2 | – | 23.4(1) | [a] | – | 24.63(4) |
| | –1 | 1 | 2 | 18.6(2) | 15.31(8) | [a] | – | 14.76(8) |
| | –2 | 1 | 2 | – | 4.76(8) | [a] | 2.60(7) | 4.13(6) |
| $Zn^{2+}$ | 3 | 1 | 1 | 31.48(4) | 32.52(2) | – | 26.74(9) | 31.75(2) |
| | 2 | 1 | 1 | 28.24(3) | 28.85(3) | 23.54(7) | 23.72(6) | – |
| | 1 | 1 | 1 | – | 22.68(7) | – | – | 24.36(6) |
| | 0 | 1 | 1 | 11.57(6) | 12.5(1) | – | 9.8(1) | 14.78(7) |
| | –1 | 1 | 1 | 1.12(8) | 1.23(8) | –1.34(1) | –0.79(8) | 3.91(7) |
| | 2 | 2 | 1 | 39.10(8) | 40.43(8) | 32.17(3) | – | 44.9(1) |
| | 1 | 2 | 1 | – | 29.30(9) | 22.46(7) | – | 33.9(1) |
| | 0 | 2 | 1 | – | – | – | 13.44(8) | 22.7(1) |
| | –1 | 1 | 2 | 9.0(2) | – | 5.83(4) | – | – |
| | –2 | 1 | 2 | – | –0.77(8) | – | –2.64(6) | – |
| $Ca^{2+}$ | 2 | 1 | 1 | [a] | 26.70(8) | [a] | [a] | 25.82(2) |
| | 1 | 1 | 1 | [a] | 17.25(8) | [a] | [a] | 15.72(8) |
| | 1 | 2 | 1 | [a] | 20.8(1) | [a] | [a] | 20.00(6) |
| | 0 | 1 | 2 | [a] | 9.1(1) | [a] | [a] | – |
| $Mg^{2+}$ | 3 | 1 | 1 | 30.6(2) | 31.56(6) | – | – | 30.78(9) |
| | 2 | 1 | 1 | 26.68(3) | 26.89(2) | – | – | 26.29(2) |
| | 1 | 1 | 1 | 20.08(7) | 19.78(5) | 18.2(4) | 19.79(3) | 18.80(4) |
| | 0 | 1 | 1 | – | – | 7.7(4) | 9.32(5) | – |
| | 2 | 2 | 1 | 37.3(2) | 36.19(9) | 32.6(4) | – | – |
| | 1 | 2 | 1 | 25.8(1) | 24.24(8) | 21.6(4) | – | – |
| | 0 | 2 | 1 | – | – | – | 12.54(9) | – |
| | 0 | 1 | 2 | 15.2(2) | 13.9(1) | – | – | 14.86(2) |
| | –1 | 1 | 2 | – | 2.3(1) | – | – | – |
| $Na^{+}$ | 3 | 1 | 1 | 29.5(1) | 30.73(6) | 25.8(1) | – | 30.31(8) |
| | 2 | 1 | 1 | 24.23(6) | 24.98(3) | 20.6(1) | 19.54(8) | 24.46(7) |
| | 1 | 1 | 1 | 14.82(3) | 14.43(3) | 12.83(5) | 12.36(7) | 14.53(4) |
| | 0 | 1 | 1 | 3.25(2) | 3.04(2) | 1.74(4) | 2.04(5) | – |
| | –1 | 1 | 2 | – | – | –9.51(6) | –8.52(4) | –7.20(2) |
| | –2 | 1 | 2 | –19.22(2) | –19.26(2) | – | – | – |

[a] These systems were not studied due to extensive precipitate formation.

Table 4. Formation constants of the [111] and [221] complexes.

| | $Cu^{2+}$:$H_4$ale | $Zn^{2+}$:$H_4$ale | $Zn^{2+}$:$H_4$prop | $Mg^{2+}$:$H_4$pam | $Mg^{2+}$:$H_4$ale | $Mg^{2+}$:$H_4$meth |
|---|---|---|---|---|---|---|
| $M + HL \rightleftharpoons MHL$ | 24.7 | 22.7 | 24.4 | 20.1 | 19.8 | 18.2 |
| $MHL + HL \rightleftharpoons M(HL)_2$ | 17.0 | 17.8 | 20.5 | 17.2 | 16.4 | 14.4 |

therefore a 1:10 L:M ratio was used to obtain a reasonable abundance of the complexes in solution. No precipitation was observed in these systems. For $H_4$pam, $H_4$ale, $H_4$meth and $H_4$prop, interaction starts below pH 2 with formation of the [311] complex. $H_4$aca exhibits similar differences to those described above (complexation starts at higher pH (3–4) with formation of the [211] complex). Despite a tenfold excess of $Na^+$ ions, less than 60% of the ligand is present in the form of complexes below pH 10, where only 1:1 L:M complexes are present. Under strongly alkaline conditions, the 1:2 L:M hydroxo species are present in significant abundance. Formation of the [–112] and [–212] species can be explained by deprotonation of the water molecules coordinated to the $Na^+$ ion and/or deprotonation of α-hydroxo group. Although formation of the $Na^+$ hydroxo complexes is unusual, their inclusion in the calculations significantly improves the fit of the experimental data (Figure S1). The presence of a hydroxide anion in the solid-state structure of trisodium phosphate is well known.[23,24] The stability order of the complexes is the same as that found for the divalent metal ions ($H_4$pam ≈ $H_4$ale ≈ $H_4$prop > $H_4$aca > $H_4$meth).

 © 2007 Wiley-VCH Verlag GmbH & Co. KGaA, Weinheim 

### Simulation of Speciation under Physiological Conditions

At physiological pH, all studied aminoalkylbis(phosphonates) are present mostly in their doubly protonated form $(H_2L)^{2-}$. As the third dissociation constant of the amide derivative $H_4aca$ is 7.49, both $(Haca)^{2-}$ and $(H_2aca)^-$ are present in almost equimolar concentrations at a pH of around 7. As strongly acidic conditions are necessary for protonation of bis(phosphonates) to form $H_4L$ species, these compounds remain in the ionised form in living organisms, thus disfavouring their absorption in the gastrointestinal tract upon oral administration.[1]

To demonstrate the speciation of aminoalkylbis(phosphonates) in body liquids, we chose the commercially applied ligand Aledronate ($H_4ale$). With the concentrations of metal ions commonly found in human blood plasma ($Cu^{2+}$: 0.15 μM; $Zn^{2+}$: 0.2 μM; $Ca^{2+}$: 3 mM; $Mg^{2+}$: 1 mM; $Na^+$: 0.138 M)[25] and at physiological pH (7.4), we obtained the abundances shown in Figure 3. It is evident that the majority of the ligand (approx. 90%) is bound in the form of $Ca^{2+}$, $Mg^{2+}$ and $Na^+$ complexes. The complexes are uncharged or singly negatively charged. As the form (free acid/complex, charge, polarity etc.) could dramatically change the pharmacological behaviour of the studied compound, formation of the above-mentioned complexes should be carefully taken into account during all medical and biological studies dealing with bis(phosphonates). Whereas alkali and alkaline earth metal complexes are preferentially formed due to high concentration of these metal ions at higher Aledronate concentrations, at lower Aledronate concentrations ($<10^{-5}$ M) the high stabilities of the transition metal complexes become important and increasing abundances of $Cu^{2+}$ and $Zn^{2+}$ complexes are obtained. The high stability of these complexes could decrease the bioavailability of the bis(phosphonate). In real living systems, we should expect a slightly lower abundance of these complexes due to the presence of many natural ligands (acetate, citrate, amino acids, phosphates etc.) that compete with bis(phosphonate) ligands. The effect of bioligands on the abundance of complexes with alkali and alkaline earth metal ions is probably negligible due to the low stability of the complexes with these bioligands.

### Crystal Structures

The crystal structures of $H_4meth$, $H_4aca$ and $H_4prop$ with various degrees of protonation and the $Cu^{2+}$ complex of $H_4pam$ were determined.

The phosphonate groups in the structure of $H_4aca{\cdot}thf$ are fully protonated (Figure 4). A lower hydrophilicity of the amide-containing ligand results in the formation of a solvate with one molecule of thf and two layers in the crystal. One layer consists of the ligand molecules, which are connected to each other by hydrogen bonds, and the second one is formed by thf molecules (Figure 5, Table S3). The

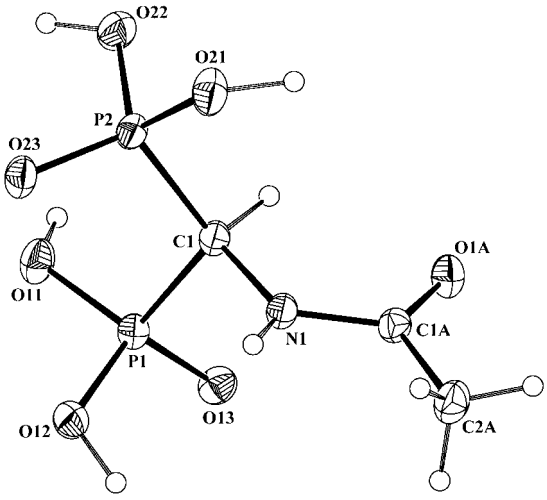


Figure 4. The molecular structure of $H_4aca$ in the crystal structure of $H_4aca{\cdot}thf$.

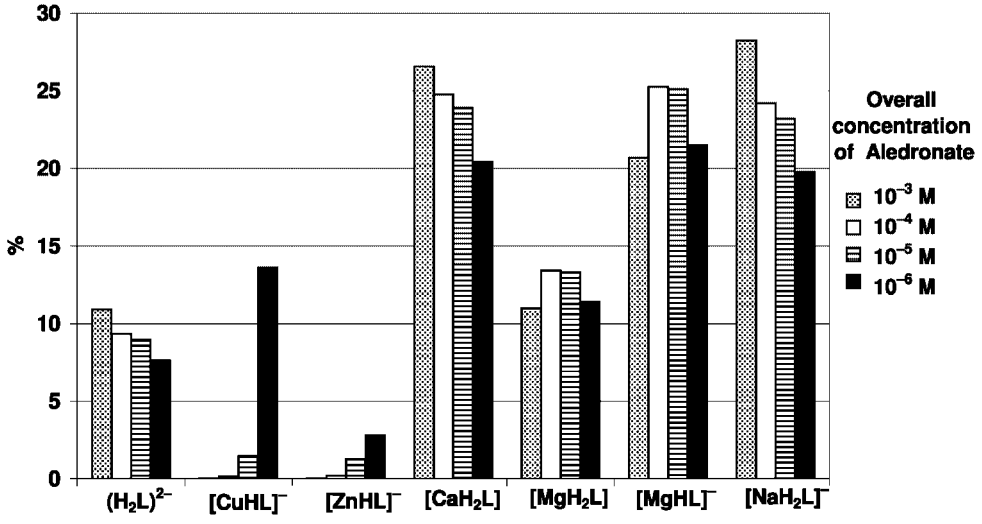


Figure 3. Simulation of the distribution of Aledronate ($H_4ale$)-containing species in human blood plasma.

 © 2007 Wiley-VCH Verlag GmbH & Co. KGaA, Weinheim 

position of the thf molecules is stabilized by hydrogen bonds between the ether oxygen atom and the phosphonate hydroxo groups of the ligand. The geometry around the phosphorus atoms is roughly tetrahedral, with slightly longer P–O distances to the protonated oxygen atoms than to the phosphoryl oxygen atom (Table 5).

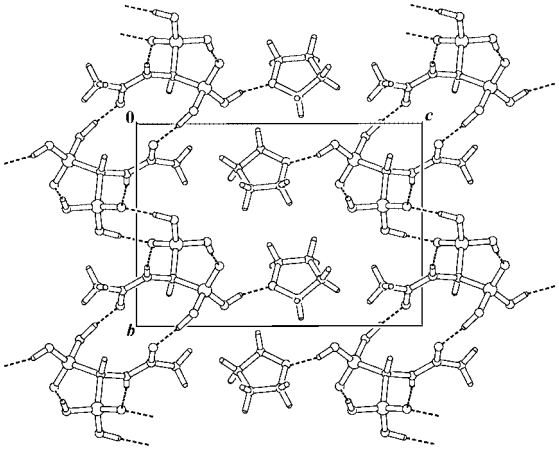


Figure 5. Crystal packing in the structure of $H_4$aca·thf.

Table 5. Geometry around the phosphorus atoms in the crystal structures of the free ligands.

| | $H_4$aca·thf | $(NH_4)(H_3prop)·H_2O$ | $(NH_4)_3(Hmeth)·H_2O$ |
|---|---|---|---|
| P1–O11 | 1.528(1) | 1.572(1) | 1.519(1) |
| P1–O12 | 1.551(1) | 1.510(1) | 1.529(1) |
| P1–O13 | 1.495(1) | 1.514(1) | 1.522(1) |
| P1–C1 | 1.825(2) | 1.812(2) | 1.842(1) |
| P2–O21 | 1.537(2) | 1.580(1) | 1.520(1) |
| P2–O22 | 1.542(2) | 1.500(1) | 1.524(1) |
| P2–O23 | 1.484(1) | 1.514(1) | 1.517(1) |
| P2–C1 | 1.826(2) | 1.827(2) | 1.839(1) |
| C1–P1–O11 | 108.6(1) | 106.6(1) | 107.0(1) |
| C1–P1–O12 | 106.3(1) | 109.4(1) | 103.5(1) |
| C1–P1–O13 | 107.5(1) | 107.0(1) | 109.0(1) |
| O11–P1–O12 | 113.2(1) | 108.0(1) | 112.2(1) |
| O11–P1–O13 | 115.9(1) | 109.6(1) | 112.0(1) |
| O12–P1–O13 | 104.9(1) | 115.9(1) | 112.5(1) |
| C1–P2–O21 | 105.8(1) | 104.4(1) | 105.8(1) |
| C1–P2–O22 | 104.6(1) | 108.1(1) | 107.4(1) |
| C1–P2–O23 | 112.7(1) | 111.0(1) | 103.8(1) |
| O21–P2–O22 | 108.7(1) | 109.6(1) | 113.3(1) |
| O21–P2–O23 | 111.7(1) | 109.4(1) | 113.1(1) |
| O22–P2–O23 | 112.8(1) | 113.9(1) | 112.6(1) |

A lower degree of protonation was found in $(NH_4)(H_3prop)·H_2O$ (Figure 6). Each phosphonic acid group and the amino group binds one proton. The P–O bonds are noticeably longer to the protonated oxygen atoms, and the geometry around the phosphorus atoms is tetrahedral (Table 5). The crystal structure is stabilized by an extensive three-dimensional framework of hydrogen bonds between the phosphonate oxygen atoms, the ligand amino group, the ammonia cations and co-crystallised water molecule (Table S4).

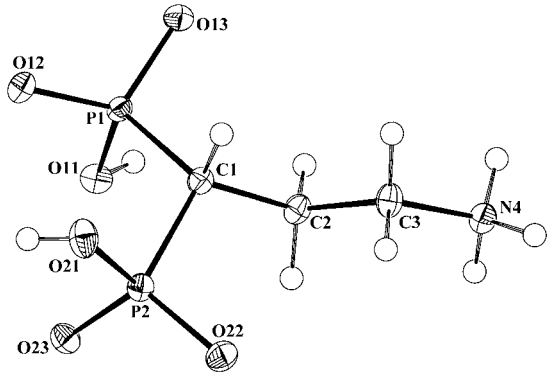


Figure 6. The molecular structure of $H_3prop^-$ in the crystal structure of $(NH_4)(H_3prop)·H_2O$.

The bis(phosphonic acid) group in the single crystals of $(NH_4)_3(Hmeth)·H_2O$ is fully deprotonated (Figure 7). The negative charge of the bis(phosphonic) unit is compensated by three ammonium cations and the protonated amino group of the ligand molecule. All phosphonate oxygen atoms are equivalent due to charge delocalisation (Table 5). An extended hydrogen-bond framework is also found in this structure. The ammonia cations are bound to phosphonate oxygen atoms by strong hydrogen bonds (O–N distances in the range 2.68–3.01 Å, Table S5). In addition, the co-crystallised water molecule forms hydrogen bonds with the phosphonate oxygen atoms (Ow–O distances of 2.77 and 2.90 Å, Table S5). This is the first reported structure to directly confirm the expected protonation scheme of aminoalkylbis(phosphonates). As the last proton is localised on the amino group, this supports the assumption that the final dissociation constant corresponds to a release of the proton from this group.

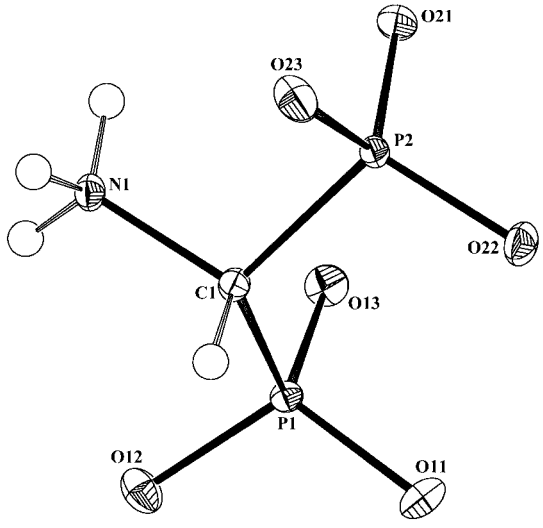


Figure 7. Molecular structure of $(Hmeth)^{3-}$ in the crystal structure of $(NH_4)_3(Hmeth)·H_2O$.

 © 2007 Wiley-VCH Verlag GmbH & Co. KGaA, Weinheim 

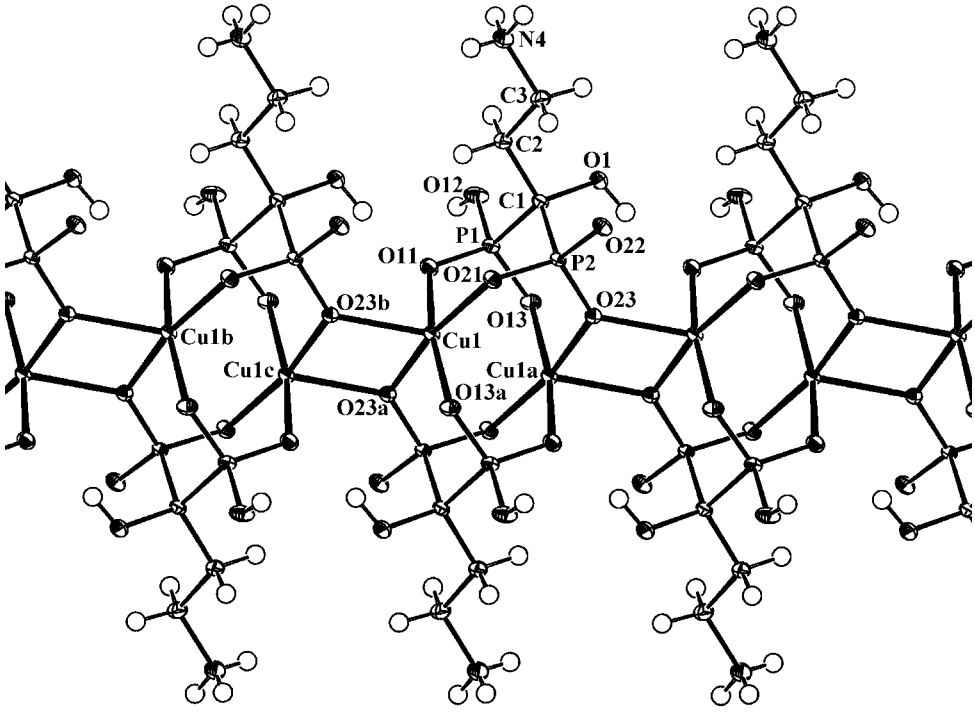


Figure 8. Chain design of $[Cu_2(H_2pam)_2]_n$ from the crystal structure of the $[\{Cu_2(H_2pam)_2\}\cdot H_2O]_n$. Symmetry operations: a: $-x + 2, -y + 1, -z + 1$; b: $x - 1, y, z$; c: $-x + 1, -y + 1, -z + 1$.

The crystal structure of $[\{Cu_2(H_2pam)_2\}\cdot H_2O]_n$ shows an infinite linear polymeric chain. The coordination sphere of the $Cu^{2+}$ ion is square-pyramidal (Figure 8, Table 6). The basal plane of the pyramid is formed by one oxygen atom of each phosphonic acid group of two different ligand molecules (O11, O21, O13a and O23a), and one of the oxygen atoms of the basal plane of the neighbouring unit is coordinated to the $Cu^{2+}$ ion in the apical position (O23b) to form a four-membered metallacycle with a Cu1–Cu1c separation of 3.21 Å. Each tetragonal pyramid is linked by a bridging ligand to a neighbouring molecule lying below the basal plane, with a Cu1–Cu1a separation of 2.99 Å. The geometrical parameter $\tau$ has a value of 0.005, which corresponds to an almost ideal square pyramid (theoretical value of $\tau = 0$, compared to an ideal trigonal bipyramid with $\tau = 1$).[26] One uncoordinated phosphonate oxygen atom is protonated as well as an amino group, and the coordination polymeric chains are connected by hydrogen bonds (Table S6).

Table 6. Bond lengths and angles found in the structure of $[\{Cu_2(H_2pam)_2\}\cdot H_2O]_n$.[a]

| | | | |
|---|---|---|---|
| P1–O11 | 1.530(1) | Cu1–O13a | 1.953(1) |
| P1–O12 | 1.539(2) | Cu1–O11 | 1.966(1) |
| P1–O13 | 1.522(2) | Cu1–O21 | 1.986(1) |
| P1–C1 | 1.838(2) | Cu1–O23a | 2.011(1) |
| P2–O21 | 1.532(1) | Cu1–O23b | 2.191(1) |
| P2–O22 | 1.520(1) | | |
| P2–O23 | 1.534(1) | | |
| P2–C1 | 1.852(2) | | |
| C1–P1–O11 | 107.1(1) | O13a–Cu1–O11 | 167.0(1) |
| C1–P1–O12 | 104.1(1) | O13a–Cu1–O21 | 90.1(1) |
| C1–P1–O13 | 108.4(1) | O13a–Cu1–O23a | 89.0(1) |
| O11–P1–O12 | 111.2(1) | O13a–Cu1–O23b | 100.7(1) |
| O11–P1–O13 | 113.6(1) | O11–Cu1–O21 | 90.5(1) |
| O12–P1–O13 | 111.9(1) | O11–Cu1–O23a | 87.7(1) |
| C1–P2–O21 | 106.2(1) | O11–Cu1–O23b | 91.1(1) |
| C1–P2–O22 | 109.0(1) | O21–Cu1–O23a | 167.4(1) |
| C1–P2–O23 | 104.6(1) | O21–Cu1–O23b | 112.2(1) |
| O21–P2–O22 | 113.4(1) | O23a–Cu1–O23b | 80.4(1) |
| O21–P2–O23 | 112.8(1) | | |
| O22–P2–O23 | 110.4(1) | | |

[a] Symmetry operations: a: $-x + 2, -y + 1, -z + 1$; b: $x - 1, y, z$; c: $-x + 1, -y + 1, -z + 1$.

The Cu1–Cu1a distance of 2.99 Å in the $Cu_2(pam)_2$ moiety is too long for metal–metal bond formation. A similar design was previously found for $Cu^{2+}$ complexes of 1-hydroxyethyl-1,1-bis(phosphonic acid),[27] with protonated diaminoalkanes as counter cations. These compounds show a moderately strong antiferromagnetic interaction.[27,28]

## Conclusions

We have reported the acid–base and complexation behaviour of five bis(phosphonate) ligands containing an amino group in the side chain. The protonation constants and stability constants of their complexes with $Cu^{2+}$, $Zn^{2+}$, $Ca^{2+}$, $Mg^{2+}$ and $Na^{+}$ ions have been determined by means of potentiometric titrations. The bis(phosphonic acid) group exhibits four dissociation constants — two in the strongly acidic region, the third in the neutral region and the last one in the alkaline region. The amino groups undergo deprotonation under strongly alkaline conditions. Determi-

 © 2007 Wiley-VCH Verlag GmbH & Co. KGaA, Weinheim 

nation of the stability constants was complicated by the precipitation of insoluble complexes. The stability constants of the complexes follow the order $H_4$pam ≈ $H_4$ale ≈ $H_4$prop > $H_4$aca > $H_4$meth. Complicated chemical models containing complexes with 1:1, 2:1 and 1:2 L:M ratios and various degrees of protonation were found for all systems with divalent metals. In $Na^+$-containing systems, 1:1 complexes cover the whole pH scale except strongly alkaline conditions, where 2:1 complexes are present. A comparison of the properties of the studied ligands has shown a negligible effect of the α-hydroxy group on the acid–base and coordination properties of the bis(phosphonates), whereas the presence of the amino group in the α position significantly decreases the overall basicity of the ligand and the stability of its complexes. Simulation of Aledronate ($H_4$ale) speciation in human blood plasma shows a high abundance of $Ca^{2+}$, $Mg^{2+}$ and $Na^+$ complexes. At lower overall concentrations of bis(phosphonate), increasing abundances of $Cu^{2+}$ and $Zn^{2+}$ complexes are expected. The crystal structures of the ligands show a different degree of protonation. The structure of the triammonium salt of aminomethylbis(phosphonic acid), which contains a monoprotonated ligand molecule, nicely documents the protonation scheme of the studied compounds — the last proton is released from the amino group. The crystal structure of the $Cu^{2+}$ complex of $H_4$pam shows a polymeric coordination chain. The square-pyramidal coordination sphere of $Cu^{2+}$ contains five oxygen atoms from five different phosphonic acid groups. In the polymeric chain, two tetragonal pyramids are oriented towards each other and their basal planes are linked together with a Cu–Cu distance of 2.99 Å.

## Experimental Section

**Materials and Methods:** Commercially available chemicals were of synthetic purity and were used as received. Acetonitrile was dried by distillation from $P_2O_5$. Elemental analyses were performed at the Institute of Macromolecular Chemistry (Academy of Science of the Czech Republic, Prague). $^1$H (400 MHz) and $^{31}$P (161.9 MHz) NMR spectra were recorded with a Varian UNITY *PLUS*-400 spectrometer in 5-mm sample tubes. NMR experiments were performed at 298 K. For the measurements in $D_2O$, *tert*-butyl alcohol was used as an internal standard with the methyl signal referenced to $\delta$ = 1.20 ppm ($^1$H). For the measurements in $CDCl_3$, tetramethylsilane was used as an internal standard with the methyl signal referenced to $\delta$ = 0.00 ppm ($^1$H). The $^{31}$P chemical shifts were measured with respect to 1% $H_3PO_4$ in $D_2O$ as an external standard (substitution method). Mass spectra were recorded with a Bruker Esquire 3000 spectrometer equipped with an electrospray ion source and an ion trap detector. All measurements were carried out in the positive-ion mode.

**Synthesis:** Ligands $H_4$pam,[29] $H_4$ale,[29] $H_4$meth[30] and $H_4$prop[31] were prepared by modification of reported procedures. The ligands were chemically pure (NMR, MS) and composition of the samples was checked by elemental analysis; see the Supporting Information for full experimental and analytical details, and discussion of the synthesis.

**Tetraethyl Acetamidomethylbis(phosphonate):** A solution of tetraethyl aminomethylbis(phosphonate)[30] (4.0 g, 13.2 mmol) in dry acetonitrile (50 mL) was added dropwise to a solution of acetyl chloride (3.0 g, 38.2 mmol) and $Na_2CO_3$ (5.2 g, 49 mmol) in dry acetonitrile (50 mL) at –40 °C. After the addition was finished, the mixture was warmed slowly to room temperature and stirred overnight. After treatment with charcoal and filtration, the unreacted acetyl chloride was removed by repeated vacuum evaporation with toluene. The product was obtained as a colourless oil in a yield of 4.4 g (97%). $C_7H_{17}NO_8P_2$: calcd. C 29.28, H 5.27, N 4.88; found C 29.42, H 5.41, N 4.25. $^1$H NMR ($CDCl_3$): $\delta$ = 1.34 (m, 12 H, $CH_2CH_3$), 2.08 (s, 3 H, $CH_3CO$), 4.19 (m, 8 H, $OCH_2$), 5.06 (td, $^2J_{P,H}$ = 21.4, $^3J_{H,H}$ = 10.4 Hz, 1 H, PC*H*P), 6.75 (br. s, 1 H, N*H*) ppm. $^{31}$P NMR ($CDCl_3$): $\delta$ = 17.0 ppm (d, $^2J_{H,P}$ = 21.4 Hz). ESI/MS: calculated 368.3; found 368.3 [M + $Na^+$].

**Acetamidomethylbis(phosphonic acid) ($H_4$aca):** Tetraethyl acetamidomethylbis(phosphonate) (3.0 g, 8.7 mmol) was dissolved in 30% HBr/AcOH (50 mL) in a 100-mL flask and stirred for 24 h at room temperature. After removal of the volatiles on a rotary evaporator, the resulting oil was dissolved in EtOH (30 mL). Precipitation of the crude product from solution occurred on standing. After 3 h, the precipitate was filtered off and extracted with boiling EtOH (100 mL). After filtration with charcoal, volatiles were removed in vacuo. The crude product was recrystallised from water by addition of thf. The product was filtered, washed with thf and dried at room temperature over $P_2O_5$. Yield: 1.7 g (63%) as adduct **6**·thf. $C_7H_{17}NO_8P_2$: calcd. C 27.55, H 5.61, N 4.59; found C 27.62, H 5.60, N 4.35. $^1$H NMR ($D_2O$/NaOD): $\delta$ = 1.63 (m, 4 H, $CH_2CH_2CH_2$ thf), $\delta$ = 1.94 (s, 3 H, $CH_3CO$), $\delta$ = 3.49 (m, 4 H, $CH_2CH_2O$ thf), 4.46 (t, $^2J_{P,H}$ = 21.3 Hz, 1 H, PC*H*P) ppm. $^{31}$P NMR ($D_2O$/NaOD): $\delta$ = 17.0 ppm (d, $^2J_{H,P}$ = 21.3 Hz). ESI/MS: calculated 256.0; found 255.8 [M + $Na^+$].

**Crystal-Structure Determination:** Single crystals of $H_4$aca·thf were selected from the recrystallised matter before the filtration. Single crystals of $(NH_4)(H_3prop)\cdot H_2O$ were prepared by the following method: $H_4$prop was dissolved in concentrated ammonia, the solution was evaporated, and the oily residue was dissolved in water and crystallised by slow vapour diffusion of *i*PrOH into the solution. Single crystals of $(NH_4)_3$(Hmeth)·$H_2O$ were prepared by slow vapour diffusion of EtOH into a solution of $H_4$meth in 5% ammonia. Single crystals of $[\{Cu_2(H_2pam)_2\}\cdot H_2O]_n$ were prepared by hydrothermal synthesis. Thus, $H_4$pam (352.5 mg, 1.50 mmol) and $CuCO_3$ (185.1 mg, 1.50 mmol) were suspended in water (30 mL) and the mixture was heated at 70 °C in a closed flask. After three weeks, shiny greenish-blue needles of $[\{Cu_2(H_2pam)_2\}\cdot H_2O]_n$ had formed. They were decanted off and dried in air. Yield: 446.3 mg (95%). $C_6H_{20}Cu_2N_2O_{15}P_4$: calcd. C 20.79, H 3.30, N 4.58; found C 21.05, H 3.48, N 4.39.

The selected crystals were mounted on glass fibres in a random orientation in silicone grease or epoxide glue. Diffraction data were collected using graphite-monochromated Mo-$K_\alpha$ radiation with an Enraf–Nonius KappaCCD diffractometer at 150(1) K [Cryostream Cooler (Oxford Cryosystem)] or 294(1) K and analysed using the HKL DENZO program package.[32] The structures were solved by direct methods, and refined by full-matrix least-squares techniques (SIR92,[33] SHELXL97[34]). The scattering factors used for neutral atoms were included in the SHELXL97 program. In the case of $[\{Cu_2(H_2pam)_2\}\cdot H_2O]_n$ a Gaussian absorption correction was applied.[35] Further details are given in Table 7.

All non-hydrogen atoms were refined anisotropically. In the structure of $H_4$aca·thf, the molecule of tetrahydrofuran solvate was found to be very disordered. This disorder was refined by splitting the carbon chain into two positions with occupancies of 61:39. The hydrogen atoms of the ligand molecule were localised in the electronic density difference map, however, they were fixed in theoreti-

 © 2007 Wiley-VCH Verlag GmbH & Co. KGaA, Weinheim 

Table 7. Experimental data of reported crystal structures.

| | $H_4$aca·thf | $(NH_4)(H_3$prop)·$H_2O$ | $(NH_4)_3$(Hmeth)·$H_2O$ | $\{[Cu_2(H_2pam)_2]\cdot H_2O\}_n$ |
|---|---|---|---|---|
| Formula | $C_7H_{17}NO_8P_2$ | $C_3H_{16}N_2O_7P_2$ | $CH_{18}N_4O_7P_2$ | $C_3H_{11}CuNO_8P_2$ |
| Molecular wt. | 305.16 | 254.12 | 260.13 | 314.61 |
| Colour | colourless | colourless | colourless | greenish blue |
| Shape | rod | plate | prism | rod |
| Dimensions [mm] | $0.10\times0.25\times0.50$ | $0.03\times0.20\times0.28$ | $0.33\times0.40\times0.50$ | $0.13\times0.15\times0.40$ |
| Crystal system | triclinic | monoclinic | orthorhombic | monoclinic |
| Space group | $P\bar{1}$ (no. 2) | $C2/c$ (no. 15) | $Pna2_1$ (no. 62) | $P2_1/c$ (no. 14) |
| $a$ [Å] | 5.2717(2) | 13.0593(3) | 17.9266(1) | 5.4824(1) |
| $b$ [Å] | 9.5220(3) | 7.2487(2) | 9.6087(2) | 14.3335(4) |
| $c$ [Å] | 13.1921(5) | 21.3368(5) | 6.2007(4) | 11.6411(3) |
| $\alpha$ [°] | 89.261(2) | 90 | 90 | 90 |
| $\beta$ [°] | 85.688(2) | 100.0962(15) | 90 | 103.1868(15) |
| $\gamma$ [°] | 76.917(3) | 90 | 90 | 90 |
| $V$ [Å$^3$] | 643.19(4) | 1988.53(9) | 1068.08(7) | 890.66(4) |
| Z | 2 | 8 | 4 | 4 |
| $D_c$ [g cm$^{-3}$] | 1.576 | 1.698 | 1.618 | 2.346 |
| $T$ [K] | 294(1) | 150(1) | 150(1) | 150(1) |
| $\theta$ range [°] | 3.10–27.50 | 1.94–27.48 | 2.40–27.49 | 3.36–27.48 |
| Index ranges | $-6 \le h \le 6$ | $-16 \le h \le 16$ | $-23 \le h \le 23$ | $-7 \le h \le 6$ |
| | $-11 \le k \le 12$ | $-9 \le k \le 9$ | $-12 \le k \le 12$ | $-18 \le k \le 18$ |
| | $-17 \le l \le 17$ | $-27 \le l \le 27$ | $-8 \le l \le 8$ | $-15 \le l \le 15$ |
| $\mu$ [mm$^{-1}$] | 0.370 | 0.455 | 0.430 | 2.839 |
| $F$(000) | 320 | 1072 | 552 | 636 |
| Independent data | 2920 | 2280 | 2325 | 2026 |
| Observed data [$I_o > 2\sigma(I_o)$] | 2530 | 1950 | 2285 | 1940 |
| Parameters | 191 | 128 | 200 | 137 |
| Gof on $F^2$ | 1.051 | 1.067 | 1.080 | 1.110 |
| $R$, $R'$ (all data) | 0.0389, 0.0462 | 0.0309, 0.0398 | 0.0183, 0.0190 | 0.0221, 0.0232 |
| w$R$, w$R'$ (all data) | 0.0993, 0.1056 | 0.0763, 0.0806 | 0.0470, 0.0477 | 0.0587, 0.0592 |

cal (H–C) or original (H–O,N) positions with thermal parameters $U_{eq}$(H) = 1.2 $U_{eq}$(C) or 1.3 $U_{eq}$(N,O) as the free refinement led to unrealistic bond lengths and angles. Hydrogen atoms belonging to solvate thf molecule were fixed in theoretical positions using a riding model. In the structure of $(NH_4)_3$(Hmeth)·$H_2O$, all hydrogen atoms were refined isotropically. In the structures of $(NH_4)(H_3$prop)·$H_2O$ and $[\{Cu_2(H_2pam)_2\}\cdot H_2O]_n$, the hydrogen atoms were localised in the electronic density difference map, but they were fixed in theoretical (H–C) or original (H–O,N) positions using a riding model with $U_{eq}$(H) = 1.2 $U_{eq}$(C) or 1.3 $U_{eq}$(N,O) as the free refinement led to unrealistic bond lengths and angles. The independent unit of $(NH_4)(H_3$prop)·$H_2O$ consists of a ligand molecule, two ammonium cations occupying special positions (with half-occupancy) and one water molecule. In the other structures, no special positions are occupied. The non-centrosymmetric structure of $(NH_4)_3$(Hmeth)·$H_2O$ was refined with a contribution of racemic twinning with a ratio between both antipodes 62:38.

CCDC-612685 ($H_4$aca·thf), -612687 [$(NH_4)(H_3$prop)·$H_2O$], -612686 [$(NH_4)_3$Hmeth·$H_2O$] and -612688 $[\{Cu_2(H_2pam)_2\}\cdot H_2O]_n$ contain the supplementary crystallographic data for this paper. These data can be obtained free of charge from The Cambridge Crystallographic Data Centre via www.ccdc.cam.ac.uk/data_request/cif.

### Determination of Dissociation and Stability Constants

**Chemicals and Stock Solutions for Potentiometric Titrations:** Water was purified with a Milli-Q (Millipore) purification system. The stock solution of hydrochloric acid (ca. 0.03 M) was prepared from a 35% aqueous solution (puriss., Fluka). Commercial $NMe_4Cl$ (99%, Fluka) was recrystallised from boiling *i*PrOH and the solid salt was dried with $P_2O_5$ in vacuo to constant weight (this dried salt is extremely hygroscopic).[36] Carbonate-free $NMe_4OH$ solution (ca. 0.2 M) was prepared from this $NMe_4Cl$ by ion exchange on Dowex 1 ($OH^-$ form, under argon, with carbonate-free water). The hydroxide solution was standardised against potassium hydrogen phthalate and the HCl solution against the approx. 0.2 M $NMe_4OH$ solution. Stock solutions of the individual metal cations were prepared by dissolving hydrates of $M(NO_3)_2$ or dried NaCl. The divalent metal ion contents in the stock solutions were determined by titration with standard $Na_2H_2$edta solution. The analytical concentration of ligand stock solution was determined together with refinement of protonation constants with the OPIUM[37] software package (see below).

**Potentiometric Titrations:** Titrations were carried out in a vessel thermostatted at 25.0 ± 0.1 °C, at an ionic strength $I$ = 0.1 M ($NMe_4Cl$) and in the presence of extra HCl in the pH range 1.7–11.9 (protonation constants and complex with $Na^+$) using a PHM 240 pH-meter, a 2-mL ABU 900 automatic piston burette and a GK 2401B combined electrode (all from Radiometer, Denmark). For systems with divalent metal ions, a precipitate was usually present at pH's between about 4 and 9, so data for this region were not collected. The initial volume was 5 mL and the concentration of the ligand was about 0.004 M. L:M molar ratios of 1:10 ($Na^+$ system), 1:1, 2:1 and 1:2 (other systems) were used. Five parallel titrations were carried out for each ratio, with each titration consisting of 40–50 points. An inert atmosphere was ensured by constant passage of argon saturated with the vapour of the solvent used in the measurements.

The constants (with their standard deviations) were calculated with the program OPIUM.[37] This program minimizes the criterion of the generalized least-squares method using the calibration function

$$E = E_0 + S\log[H^+] + j_1[H^+] + j_2 K_w/[H^+]$$

where the additive term $E_0$ contains the standard potentials of the electrodes used and the contributions of inert ions to the liquid-junction potential, $S$ corresponds to the Nernstian slope, the value

 © 2007 Wiley-VCH Verlag GmbH & Co. KGaA, Weinheim 

of which should be close to the theoretical value of 59.159 mV, and $j_1[H^+]$ and $j_2 K_w/[H^+] = j_2[OH^-]$ terms are contributions of the $H^+$ and $OH^-$ ions to the liquid-junction potential. The $j_1$ and $j_2$ parameters for the calibration titrations before and after each titration show only minor changes. It is clear that $j_1$ (values between –50 and 50) and $j_2$ (values between 100 and 200) cause deviation from a linear dependence between $E$ and pH only in strongly acidic and basic solutions. The calibration parameters were determined by titration of standard HCl with standard $NMe_4OH$ before each ligand or ligand-metal titration to give a pair calibration/titration, which was used for calculation of the constants. The protonation constants $\beta_n$ are defined by $\beta_n = [H_nL]/([H]^n[L])$ [they can be transferred to the dissociation constants by the relationships $pK_a(HL^{3-}) = \log\beta_1$ and $pK_a(H_nL^{n-4}) = \log\beta_n - \log\beta_{n-1}$]. The stability constants are defined by $\beta_{hlm} = [H_hL_lM_m]/([H]^h[L]^l[M]^m)$. The water ion product $pK_w$ used was 13.81. The stability constants of $M^{2+}$–$OH^-$ systems were included in the calculations and were taken from the literature.[21,38] Speciation of the studied systems was solved with the OPIUM[37] software package. The concentration of ligand supposed from the exactly weighed sample was in very good agreement with the concentration determined together with refinement of the protonation constants using OPIUM.

**NMR Titrations:** The $^{31}P\{^1H\}$ NMR titration experiments for determination of the highest protonation constant (pH in range 11.5–13.6, about 15 points) were carried out under conditions close to the potentiometric titrations (no control of ionic strength, $NMe_4Cl$, 25.0 °C, ligand concentration about 0.004 M). A coaxial capillary tube with $D_2O$ and $H_3PO_4$ was used for the lock and referencing. Protonation constants were calculated with OPIUM[37] from the dependence of $\delta_P$ of the phosphonate groups on $-\log[H^+]$.

**Supporting Information** (see also the footnote on the first page of this article): Discussion and experimental details dealing with the ligand synthesis. Figure S1 shows an example ($Na^+$:$H_4$prop system) of the fitting with and without hydroxo species. Table S1 shows the pH ranges skipped during titration due to the precipitate formation. Table S2 shows a comparison of the dissociation constant with those reported in the literature. The distribution diagrams of all systems studied are shown in Figures S2–S7. The hydrogen-bond parameters in the crystal structures are reported in Tables S3–S6.

## Acknowledgments

Support from the Grant Agency of the Czech Republic (no. 203/06/0467) and the Grant Agency of Academy of Science of the Czech Republic (no. KAN201110651; program "Nanotechnology for Society") is acknowledged. This work was carried out in the framework of COST D38 and the NoE projects supported by the European Union, EMIL (no. LSHC-2004-503569) and DiMI (no. LSHB-2005-512146). We thank Ms. M. Malíková for her help with the titration experiments.

[1] H. Fleisch, *Bisphosphonates in Bone Disease*, 4th ed., Academic Press London, **2000**.
[2] I. K. Adzamli, D. Johnson, M. Blau, *Invest. Radiol.* **1991**, *26*, 143–148.
[3] I. K. Adzamli, M. Blau, M. A. Pfeffer, M. A. Davis, *Magn. Reson. Med.* **1993**, *29*, 505–511.
[4] V. Kubíček, J. Rudovský, J. Kotek, P. Hermann, L. Vander Elst, R. N. Muller, Z. I. Kolar, H. T. Wolterbeek, J. A. Peters, I. Lukeš, *J. Am. Chem. Soc.* **2005**, *127*, 16477–16485.
[5] M. N. Rusina, T. M. Baleshova, B. V. Valeshov, A. J. Shitrina, I. A. Poljakova, *Zh. Obsch. Khim.* **1977**, *47*, 1721–1726.
[6] M. I. Kabashnik, T. J. Medved, N. M. Djatlova, J. M. Polikarpov, B. K. Sherbakov, F. I. Belskij, *Izv. Akad. Nauk Ser. Khim.* **1978**, 433–437.
[7] J. E. Bollinger, D. M. Roundhill, *Inorg. Chem.* **1993**, *32*, 2821–2826.
[8] J. E. Bollinger, D. M. Roundhill, *Inorg. Chem.* **1994**, *33*, 6421–6424.
[9] M. Dyba, H. Kozlowski, A. Tlalka, Y. Leroux, D. E. Manouni, *Pol. J. Chem.* **1998**, *72*, 1148–1153.
[10] Z. H. Kudzin, A. Kotynski, G. Andrijewski, *J. Organomet. Chem.* **1994**, *479*, 199–205.
[11] B. Boduszek, M. Dyba, M. Jezowska-Bojczuk, T. Kiss, H. Kozlowski, *J. Chem. Soc., Dalton Trans.* **1997**, 973–976.
[12] S. V. Mamveev, F. I. Beljskii, A. G. Mamveeva, A. Yu. Gukasova, Yu. M. Polikarpov, M. Kabachnik, *Izv. Akad. Nauk Ser. Khim.* **1998**, 1784–1787.
[13] M. Dyba, M. Jezowska-Bojczuk, E. Kiss, T. Kiss, H. Kozlowski, Y. Leroux, D. E. Manouni, *J. Chem. Soc., Dalton Trans.* **1996**, 1119–1123.
[14] H. Wada, Q. Fernando, *Anal. Chem.* **1972**, *44*, 1640–1643.
[15] R. L. Carroll, R. R. Irani, *Inorg. Chem.* **1967**, *6*, 1994–1998.
[16] *Aminophosphonic and Aminophosphinic Acids: Chemistry and Biological Activity* (Eds.: V. P. Kukhar, H. R. Hudson), John Wiley & Sons, **2000**.
[17] K. Popov, H. Rönkkömäki, L. H. J. Lajunen, *Pure Appl. Chem.* **2006**, *78*, 663–675.
[18] E. Matczak-Jon, B. Kurzak, P. Kafarski, A. Wozna, *J. Inorg. Biochem.* **2006**, *100*, 1155–1166.
[19] I. Lukeš, J. Kotek, P. Vojtíšek, P. Hermann, *Coord. Chem. Rev.* **2001**, *216–217*, 287–312.
[20] T. G. Appleton, J. R. Hall, A. D. Harris, M. A. Kimlin, I. J. Mc Mahon, *Aust. J. Chem.* **1984**, *37*, 1833.
[21] A. E. Martell, R. M. Smith, *Critical Stability Constants*, Plenum Press, New York, **1974–1989**, vol. 1–6; *NIST Standard Reference Database 46* (*Critically Selected Stability Constants of Metal Complexes*), Version 7.0, **2003**.
[22] E. Matczak-Jon, V. Videnova-Arabinska, *Coord. Chem. Rev.* **2005**, *249*, 2458–2488.
[23] E. Tillmanns, W. H. Baur, *Inorg. Chem.* **1970**, *9*, 1957–1958.
[24] N. N. Greenwood, A. Earnshaw, *Chemistry of the Elements*, Pergamon Press Plc, Oxford, **1984**.
[25] J. A. Cowan, *Inorganic Biochemistry*, VCH Publishers, Inc., New York, **1993**.
[26] A. W. Addison, T. N. Rao, J. Reedijk, J. van Rijn, G. C. Verschoor, *J. Chem. Soc., Dalton Trans.* **1984**, 1349–1356.
[27] H. Song, L. Zheng, Y. Liu, X. Xin, A. J. Jacobson, S. Decurtins, *J. Chem. Soc., Dalton Trans.* **2001**, 3274–3278.
[28] Z. C. Hu, H. Y. Wei, Z. D. Chen, *J. Mol. Struct.* **2004**, *668*, 235–242.
[29] G. R. Kieczykowski, D. F. Jobson, D. G. Melillo, D. F. Reinhold, V. J. Grenda, I. Shinkai, *J. Org. Chem.* **1995**, *60*, 8310–8312.
[30] D. Kantoci, J. K. Denike, W. J. Wechter, *Synth. Commun.* **1996**, *26*, 2037–2043.
[31] W. Winckler, T. Pieper, B. K. Keppler, *Phosphorus Sulfur Silicon Relat. Elem.* **1996**, *112*, 137–141.
[32] Z. Otwinowski, W. Minor, *HKL Denzo and Scalepack Program Package* by Nonius BV, Delft, **1997**; For a reference see: Z. Otwinowski, W. Minor, *Methods Enzymol.* **1997**, *276*, 307–326.
[33] A. Altomare, M. C. Burla, M. Camalli, G. Cascarano, C. Giacovazzo, A. Guagliardi, G. Polidori, *J. Appl. Crystallogr.* **1994**, *27*, 435.
[34] G. M. Sheldrick, *SHELXL97: Program for Crystal Structure Refinement from Diffraction Data*, University of Göttingen, Germany, **1997**.
[35] P. Coppens, *Crystallographic Computing*, Munksgaard, Copenhagen, **1970**, p. 255.
[36] P. Táborský, P. Lubal, J. Havel, J. Kotek, P. Hermann, I. Lukeš, *Collect. Czech. Chem. Commun.* **2005**, *70*, 1909–1942.

 © 2007 Wiley-VCH Verlag GmbH & Co. KGaA, Weinheim 

[37] M. Kývala, I. Lukeš, *International Conference on Chemometrics 95*, p. 63. Pardubice, Czech Republic, **1995**; the full version of OPIUM is available (free of charge) from http://www.natur.cuni.cz/~kyvala/opium.html.

[38] C. F. Baes Jr., R. E. Mesmer, *The Hydrolysis of Cations*, Wiley, New York, **1976**.

Received: June 29, 2006
Published Online: November 3, 2006

 © 2007 Wiley-VCH Verlag GmbH & Co. KGaA, Weinheim 

DOI: 10.1002/ejic.200600712

# Three Novel Functional $Cd^{II}$ Dicarboxylates with Nanometer Channels: Hydrothermal Synthesis, Crystal Structures, and Luminescence Properties

**Yu-Peng Tian,*[a–c] Yong-Min Zhu,[a] Hong-Ping Zhou,*[a] Peng Wang,[a] Jie-Ying Wu,[a] Xu-Tang Tao,[b] and Min-Hua Jiang[b]**

**Keywords:** Carboxylate / Supramolecular chemistry / Fluorescence / Coordination modes

Three novel functional transition-metal complexes with $H_2A$ ($H_2A$ = 9-ethylcarbazole-3,6-dicarboxylic acid), $Cd(HA)_2(H_2O)_2$ (**1**), $[Cd(A)(phen)]\cdot 1.5H_2O$ (**2**) (phen = 1,10-phenanthroline), and $Cd(HA)_2(bipy)$ (**3**) (bipy = 4,4′-bipyridine), have been successfully synthesized by a hydrothermal synthetic method and characterized by single-crystal X-ray diffraction, infrared spectroscopy, elemental analysis, thermogravimetric analysis, and photoluminescence. The results show that all of the complexes contain nanometer channels, while the coordination modes were changed by the addition of the mixed ligands. The 2D supramolecular open-framework **1** is constructed through hydrogen-bond and aromatic π–π interactions. 2D coordination polymer **2** is constructed by π–π interactions between adjacent metal-organic polymeric coordination chains. Interestingly, the 3D supramolecular architecture of **3** first formed 2D grid layers from 1D chains by intermolecular hydrogen bonds and then extended into a 3D structure through aromatic π–π interactions. Furthermore, strong emissions from these complexes were also changed by the coordination modes in the solid state. However, complexes **1**–**3** show high thermal stability.

(© Wiley-VCH Verlag GmbH & Co. KGaA, 69451 Weinheim, Germany, 2007)

## Introduction

In recent years, metal complexes have been investigated in luminescent materials for potential applications as light-emitting diodes (LEDs).[1] Metal carboxylate supramolecular open frameworks as a kind of metal complex have been the focus of recent research interest because of their interesting supramolecular compositions and versatile framework topologies, as well as their potential as functional materials in gas storage,[2] ion recognition,[3] catalysis,[4] sensor technology,[5] and nanotechnology.[6] The aromatic multicarboxylate ligands, such as 1,3,5-benzenetricarboxylic acid and 1,2,4,5-benzenetetracarboxylic acid, have been extensively introduced in the preparations of metal-organic supramolecular open frameworks.[7] However, the small π-conjugation system inhibited their potential application in luminescent materials. It is popular to extend the π-conjunction system of some widely used fluorophore precursors, such as rhodamine,[8] xylene,[9] and so forth, to get new analogs, although their synthesis and further modification may be difficult and laborious. On the other hand, emission properties of many luminescent materials can be tuned by incorporating the functional ligands into a polymeric structure, such as an all-organic polymer, or into a mixed inorganic/organic polymer.[10] Carbazole has been extensively exploited as a convenient basic building block for the application of the electroluminescent (EL) device because of its good hole transporting and luminescent properties.[11] Modification of the carbazole on the 3- and 6-positions represents a possible approach for designing carbazole-based luminescent materials.

On the other hand, $Cd^{II}$-containing coordination compounds have received considerable interest recently because of their ability to form bonds with different donors, their large radius, their various coordination modes, and the special properties of the $Cd^{II}$ ion. To date, four- to eight-coordinate $Cd^{II}$ complexes and their potential applications in catalysis,[12] luminescent materials,[13] and NLO materials[14] have been explored. Also, a hydrothermal synthetic method has been demonstrated as an effective, simple, and environmentally friendly technique in crystal engineering.[15] Considering all these aspects, we used a functional organic ligand that we had established previously,[16] 9-ethylcarbazole-3,6-dicarboxylic acid ($H_2A$), and cadmium nitrate as building blocks. 2D supramolecular open-framework $[Cd(HA)_2(H_2O)_2]_n$ (**1**) was obtained using hydrothermal synthesis. The skilful combination of carboxylates, the other coligands, and metal ions may generate many interesting coordination architectures as well as different emission properties. Pyridine, Schiff base, and polyamine derivatives were widely used as coligands. However, the selection of the

[a] Department of Chemistry, Anhui University, Hefei 230039, P. R. China
E-mail: yptian@ahu.edu.cn
[b] State Key Laboratory of Crystal Materials, Shandong University, Jinan 250100, P. R. China
[c] State Key Laboratory of Coordination Chemistry, Nanjing University, Nanjing 210093, P. R. China

 © 2007 Wiley-VCH Verlag GmbH & Co. KGaA, Weinheim 

coligand remains a challenge for us because two different kinds of ligands must coexist and compete in coordinating to the same metal ion. In this paper, we introduced a luminescent rigid chelated ligand (phen) and a flexible bridge ligand (bipy) into the reaction system, obtaining 2D coordination polymer $\{[Cd(A)(phen)]\cdot 1.5H_2O\}_n$ (**2**) and 3D supramolecular open framework $[Cd(HA)_2(bipy)]_n$ (**3**) respectively. The emission wavelengths are tuned by changing coordination architectures.

## Result and Discussion

### Synthesis

The hydrothermal synthetic method is a useful way of growing complex crystals because of its effectiveness, simplicity, and environmental friendliness. Also, the formation of these complexes is greatly influenced by the base. We have tried NaOH, $Na_2C_2O_4$, pyridine, and triethylamine, and only $Na_2C_2O_4$ was successfully used in the formation of these compounds, suggesting that it is a compatible base for deprotonation of $H_2A$. The formations of **1**–**3** are shown in Scheme 1.

$$H_2A + Cd(NO_3)_2\cdot 4H_2O + \begin{cases} \xrightarrow[165\ ^\circ C]{H_2O,C_2H_5OH} Cd(HA)_2(H_2O)_2 & (1) \\ \xrightarrow[phen\ \ 165\ ^\circ C]{H_2O,C_2H_5OH} Cd(A)(phen)\cdot 1.5H_2O & (2) \\ \xrightarrow[bipy\ \ 165\ ^\circ C]{H_2O,C_2H_5OH} Cd(HA)_2(bipy) & (3) \end{cases}$$

Scheme 1.

### Description of Crystal Structure

#### *$Cd(HA)_2(H_2O)_2$ (1)*

Complex **1** crystallized with a monoclinic space group *C*2/*c*. The crystallographic analysis of complex **1** featured a 2D framework containing nanometer channels with a repeating unit $[Cd(HA)_2(H_2O)_2]_n$. The symmetric unit contains one cadmium atom, two $H_2A$ groups, and two $H_2O$ molecules. Part a of Figure 1 illustrates the ORTEP structure of compound **1**. Each cadmium ion is hexacoordinated by four O atoms [Cd(1)–O(1) 2.247(2) Å; Cd(1)–O(2) 2.489(2) Å; Cd(1)–O(1A) 2.247(2) Å; Cd(1)–O(2A) 2.489(2) Å] from two different $H_2A$ ligands and two O atoms [Cd(1)–O(5) 2.187(3) Å; Cd(1)–O(5A) 2.187(3) Å] from two $H_2O$ molecules and forms a distorted octahedral geometry. The dihedral angle of the two carbazole planes of $H_2A$ is 83.57°. As for the $H_2A$ ligand, it shed one proton and chelated to the cadmium atom while the other carboxylate group connected to the coordinated $H_2O$ and carboxylate group of another $H_2A$ by intermolecular hydrogen bonds (Figure 1, b). The C–O bond [C2AC–O3AC 1.306 Å] is much longer than the C=O bond [C2AC–O4AC 1.219 Å] in the carboxy group, so C2AC–O4AC can be assigned as a double bond and C2AC–O3AC as a single bond, and H is linked to O3AC. The O–H···O intermolecular hydrogen bond formed by the $H_2A$ ligand and $H_2O$ has a O···O distance of 2.659 Å (O–H–O 172.53°), while the other O–H···O intermolecular hydrogen bond formed by two $H_2A$ ligands has a O···O distance of 2.686 Å (O–H–O 175.89°). Those units connected to each other and formed a 1D chain by intermolecular hydrogen bonds (O–H···O 2.712 Å, O–H–O 163.61°) (Figure 2). The 2D supramolecular open

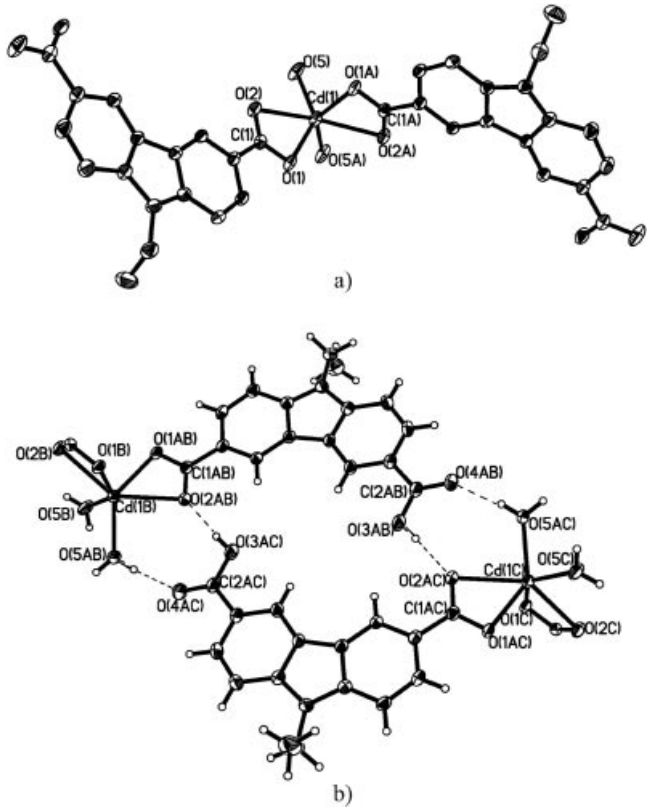


Figure 1. Perspective view of (a) the coordination environment of the cadmium atom in **1** and (b) the coordination mode of the $H_2A$ ligand; all hydrogen atoms in (a) are omitted for clarity.

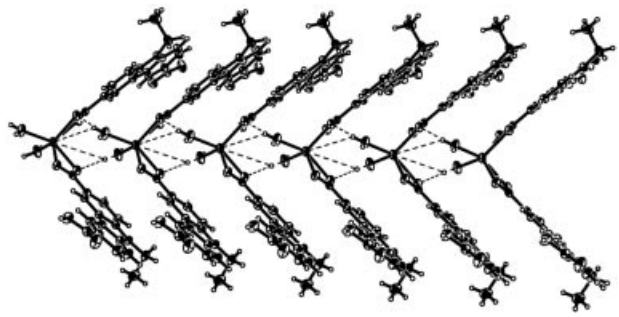

Figure 2. 1D structure of **1** along the *b* axis by intermolecular hydrogen bonds O–H···O.

 © 2007 Wiley-VCH Verlag GmbH & Co. KGaA, Weinheim 

framework contains 10.984 × 7.584 Å channels A formed by intermolecular hydrogen bonds and π–π interactions along the *b* axis with a distance of 3.41 Å (Figure 3).

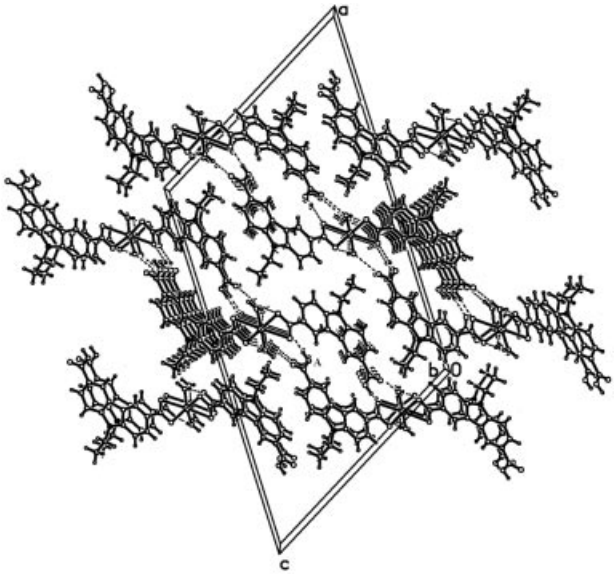


Figure 3. 2D structure containing nanometer channel A (10.984 × 7.584 Å) of **1** along the *a* axis by intermolecular hydrogen bonds O–H···O and π–π interactions.

### *[Cd(A)(phen)]·1.5H$_2$O (2)*

Complex **2** crystallized in the monoclinic space group *P*2/*c* with a formula $\{[Cd(A)(phen)]\cdot 1.5H_2O\}_n$. The structure featured a 2D polymeric pattern containing nanometer channels. The asymmetric unit contains one cadmium atom, one $H_2A$ group, and one phen molecule. Figure 4 illustrates the ORTEP structure of complex **2**. The cadmium atom is six-coordinate through coordination of one chelating carboxylate group [Cd(1)–O(1) 2.468(4) Å; Cd(1)–O(2) 2.315(3) Å], one chelating phen molecule [Cd(1)–N(2) 2.362(4) Å; Cd(1)–N(3) 2.372(4) Å], and two bridging carboxylate groups [Cd(1)–O(3A) 2.196(3) Å; Cd(1)–O(4B) 2.256(3) Å]. The coordination mode of $H_2A$ is different from complex **1**. It shed two protons and chelated to the metal atom [O(1B)–C(13B)–O(2B) 120.1(4)°] through one of the carboxylate groups, while the other carboxylate group bridged to two metal atoms [O(4B)–C(14B)–O(3B) 125.0(4)°]. The basic units first formed rings and then formed a zigzag 1D chain (Figure 5) with the 73.57° dihedral angle of the ring planes. The phen molecules chelated to the metals from the two sides of the chains one by one. Two adjacent phen molecules connected to each other by π–π stacking interactions with a plane–plane distance of 3.38 Å. The 2D open framework contains 10.537 × 9.232 Å nanometer channel B formed by π–π interactions along the *b* axis with a distance of 3.48 Å (Figure 6). Two kinds of distorted guest water molecules filled the channels. One kind filled the channel in the form of a distorted single $H_2O$ molecule (H–O–H 102.60°) by hydrogen bond (O–H···O 2.899 Å, O–H–O 128.47°) to the carboxylate group, while the other kind filled the channel in the form of distorted dimeric $H_2O$ molecules (H–O–H 107.22°) by hydrogen bond (O–H···O 2.695 Å, O–H–O 132.46°) to the carboxylate group.

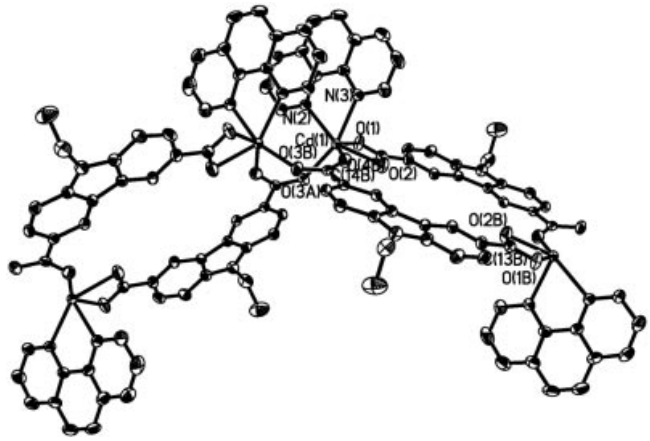


Figure 4. The ORTEP structure of **2** with atomic labeling scheme; all hydrogen atoms are omitted for clarity.

Figure 5. 1D zigzag chains of **2** formed by the basic units; all hydrogen atoms are omitted for clarity.

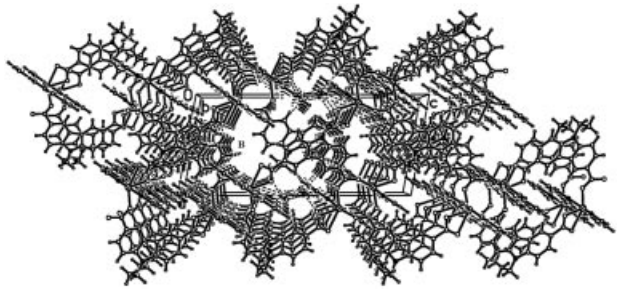

Figure 6. 2D structure containing nanometer channel B (10.537 × 9.232 Å) of **2** along the *b* axis by π–π interactions.

### *Cd(HA)$_2$(bipy) (3)*

Complex **3** (Figure 7) crystallized with a monoclinic space group *C*2/*c* with the formula $[Cd(HA)_2(bipy)]_n$. X-ray crystallographic analysis reveals that complex **3** is 3D open framework with nanometer channels. The symmetric unit contains one cadmium atom, two $H_2A$ groups, and two pyridine groups. The cadmium atom adopts a distorted octahedral geometry by coordinating to four oxygen atoms [Cd(1C)–O(1AC) 2.303(5) Å; Cd(1C)–O(2AC) 2.490(6) Å; Cd(1C)–O(1C) 2.303(5) Å; Cd(1C)–O(2C) 2.490(6) Å] of two chelating $H_2A$ ligands and two nitrogen atoms [Cd(1C)–N(2C) 2.218(8) Å; Cd(1C)–N(3C) 2.299(9) Å] of two different bipyridines. These basic units form a 1D chain. The coordination mode of $H_2A$ ligand is the same as that of complex **1**. It shed one proton and chelated to

 © 2007 Wiley-VCH Verlag GmbH & Co. KGaA, Weinheim 

the cadmium atom through one of the carboxylate groups while the other carboxylate group connected to the chelated carboxylate group by a hydrogen bond (O–H···O 2.583 Å, O–H–O 170.37°), combining the 1D chains into the 2D grid layer (Figure 8 and Figure 9). The C–O bond (C16A–O3A 1.324 Å) is much longer than the C=O bond (C16A–O4A 1.228 Å) in the carboxy group, so C16A–O4A can be assigned as a double bond and C16A–O3A as a single bond, and the hydrogen atom is linked to O3A. 2D grid layers were extended along the *a* axis and formed a 3D supramolecular framework with 9.437 × 7.620 Å nanometer channel C by π–π interactions with a distance of 3.47 Å (Figure 10).

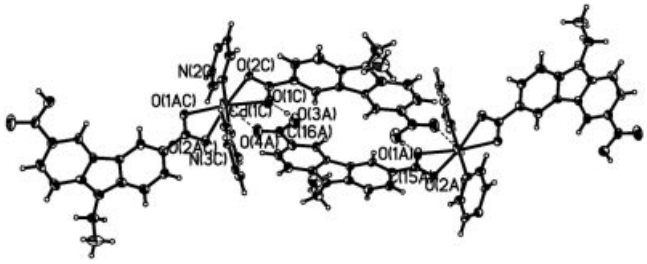


Figure 7. The ORTEP structure of **3** with atomic labeling scheme.

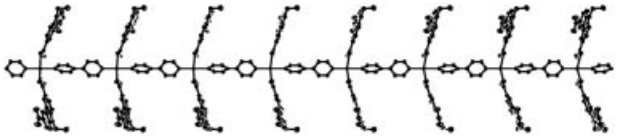

Figure 8. 1D chains of **3** formed by the basic units; all hydrogen atoms are omitted for clarity.

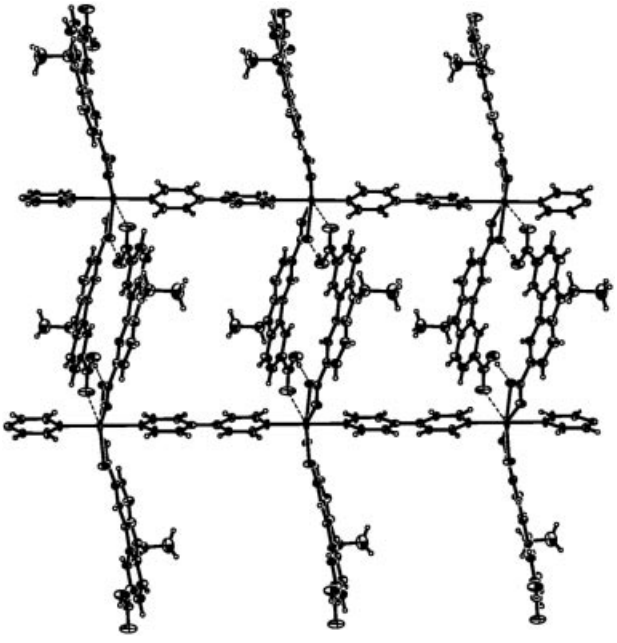

Figure 9. 2D grid layer based on 1D chains formed by intermolecular hydrogen bonds O–H···O.

Traditionally, flexible carboxylate ligands are able to produce more unique frameworks with aesthetic and useful properties than the rigid carboxylate ligands because of their flexibility and conformational freedom. However, in complexes **1**–**3**, the coordination modes were changed by the addition of the other ligand. With the exception of the different coordination mode in these complexes, many O–H···O hydrogen bonding interactions were observed in the crystal structure. Generally, the carboxylate groups are the main part of hydrogen-bonded networks. The hydrogen bonds of complex **1** are more numerous and more complicated than the others, because of the coordinated water. These strong O–H···O hydrogen bonds play an important role in the formation of the 2D or 3D supramolecular open frameworks containing nanometer channels. It should also be noted that, in comparison with **1** and **3**, the $H_2A$ ligand in **2** shed all the protons, which suggests that phen may potentially act as a base for deprotonation of $H_2A$. All of the nanometer channels had similar dimensions, which may be due to the formation of these channels by two $H_2A$ ligands. The small difference in size is a result of the different coordination modes and distorted stacking of aromatic rings.

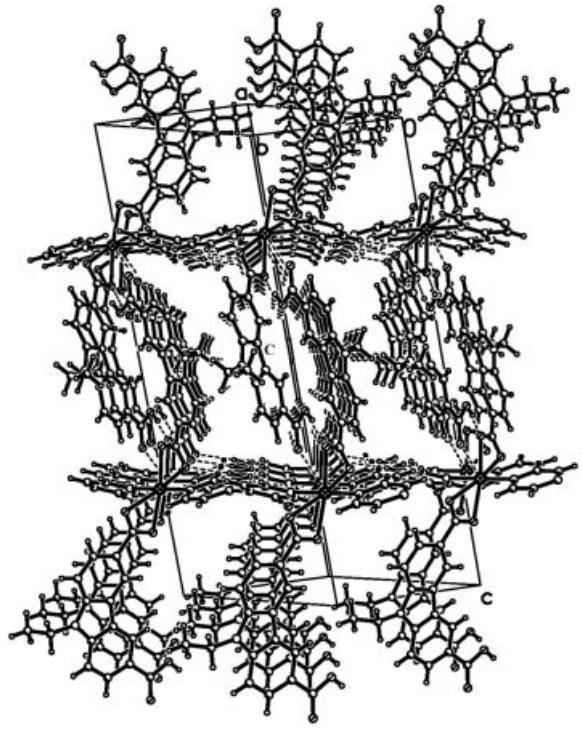

Figure 10. 3D structure containing nanometer channel C (9.437 × 7.620 Å) of **3**.

## Thermogravimetric Analysis

Thermogravimetric analyses (TGA) of complexes **1**–**3** were performed on single crystal samples in the range of 20–650 °C under nitrogen. Complexes **1**–**3** exhibit high thermal stability. For complex **1**, the first weight loss occurred in stages starting at 164 °C and completing at 227 °C, corresponding to the loss of two coordinated water molecules. The anhydrous complex suffered from serious mass loss upon heating to 277 °C, attributable to decomposition of

 © 2007 Wiley-VCH Verlag GmbH & Co. KGaA, Weinheim 

the organic composition. For complex **2**, the first major weight loss from 77 °C to 140 °C corresponded to the loss of guest water molecules. The main structure decomposed at 404 °C, exhibiting high thermal stability. Complex **3** also exhibits high thermal stability, as there is no weight loss below 361 °C.

## Fluorescent Properties

Fluorescent transition-metal complexes containing rigid multichromophoric ligands with a large π-conjugation system have been studied intensively because of their potential use. On the other hand, to extend the π-conjugation only by synthesis and modification of organic composition may be difficult and tedious. Synthesis of inorganic/organic coordination complexes by using functional ligands gained from simplified synthetic approaches, some coligands, and transition-metal centers can be a useful method to obtain new photoluminescent materials. The luminescent properties of the free ligand $H_2A$ and complexes **1**–**3** were investigated in solid state at room temperature (Figure 11). The nanosecond range of lifetime in the solid state at room temperature reveals that the emission is fluorescent in nature. The emission for free $H_2A$ ligand is at 422 nm ($\lambda_{exc}$ = 269 nm), which can be assigned to the $\pi^* \rightarrow \pi$ transition of the carbazole moiety.[17] Complex **1** exhibits a broad emission band with the maximal emission at 453 nm ($\lambda_{exc}$ = 268 nm), which is 31 nm red-shifted compared to the free ligand. These emissions may be attributed to ligand-to-ligand charge transfer (LLCT).[18] The shoulder at 390 and 369 nm may be assigned to the excimer emission of the ligand because of the interaction between the molecules.[19] The emission of complex **2** is at 492 nm ($\lambda_{exc}$ = 269 nm), which is red-shifted 70 nm compared to the free ligand; it can be assigned to the ligand-to-metal charge transfer (LMCT).[18] Generally, the intraligand and fluorescence emission is determined by the energy gap between π and π* molecular orbitals of the free ligand, which is simply related to the extent of π conjugation in the system.[20] Complex **3** exhibits strong emission at 396 nm ($\lambda_{exc}$ = 270 nm), which can be assigned to the intraligand fluorescent emission of coordinated $H_2A$ ligands. It is 26 nm blue-shifted compared to the free ligand and 57 nm blue-shifted compared to complex **1**, which may be due to the increase of the π–π stacking distance of the ligands [3.41 Å for **1**; 3.48 Å ($H_2A$), 3.38 Å (phen) for **2**; and 3.47 Å for **3**].

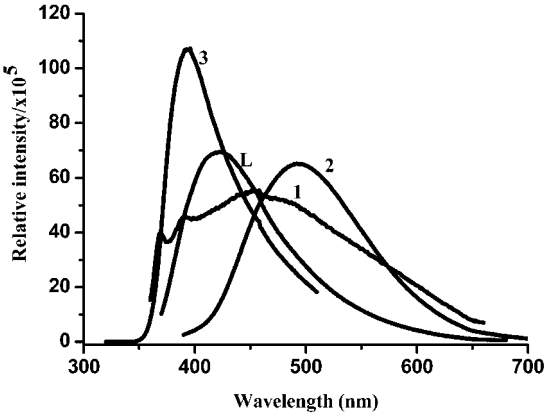


Figure 11. Photoluminescent spectra of $H_2A$ and complexes **1**–**3** in the solid state at room temperature.

## Conclusions

In this work, three supramolecular networks with strong luminescence as well as high thermal stability were obtained by hydrothermal synthesis. All of them contain nanometer channels formed by hydrogen bonds and π–π stacking. We have started to alter the luminescent properties and coordination modes by transforming the mixed ligands. This should lead to new, tunable, fluorescent materials. A novel 2D supramolecular network based on $H_2A$ ligand and $Cd(NO_3)_2{\cdot}4H_2O$ has been obtained by hydrothermal synthesis. When the phen molecule was added, the coordination mode was changed and a 2D coordination polymer was obtained. When phen was changed into bipy, a 3D supramolecular network was obtained. The maximum emission wavelengths of complexes **1**–**3** are 453, 492, and 396 nm, respectively. In addition to their strong emissions and reasonable thermal stability, they are almost insoluble in common polar and nonpolar solvents such as ethanol, chloroform, acetone, acetonitrile, benzene, and water. In conclusion, these compounds may be good candidates as advanced materials for light-emitting diode devices. The paper also shows that transforming the mixed ligands is an excellent way of changing the coordination modes and luminescent properties.

## Experimental Section

**General Remarks:** All chemicals and solvents were dried and purified by the usual methods. Elemental analysis data (C,H,N) were obtained using a Perkin–Elmer 240 analyzer. IR spectra were recorded with a Nicolet FTIR 170SX instrument (KBr discs) in the region of 4000–400 $cm^{-1}$. The luminescent spectra were measured on power samples at room temperature (room temp.) using a model Perkin–Elmer LS55 fluorescence spectrophotometer. TGA analyses were recorded with a Perkin–Elmer Pris-1 DMDA-V1 analyzer in nitrogen at a heating rate of 5 °C $min^{-1}$.

**9-Ethylcarbazole-3,6-dicarboxylic Acid:** The $H_2A$ ligand was synthesized using the established literature procedure.[16]

**Compound 1:** Complex **1** was synthesized using the established literature procedure.[16]

**Compound 2:** A mixture of $Cd(NO_3)_2{\cdot}4H_2O$ (0.117 g, 0.38 mmol), phen (0.0760 g, 0.38 mmol), $H_2A$ (0.0530 g, 0.19 mmol), $Na_2C_2O_4$ (0.0251 g (0.19 mmol), $H_2O$ (15 mL), and 15 drops of $C_2H_5OH$ was placed in a 25-mL Teflon-lined stainless steel vessel and then heated to 165 °C for 3 d and the reactant was cooled at a rate of 5 °C $min^{-1}$. The yellow crystals were obtained with a yield of 0.0780 g (70.2%) based on $H_2A$. $C_{28}H_{22}CdN_3O_{5.50}$ (600.89): calcd. C 55.97, H 3.69, N 6.99; found C 55.85, H 3.65, N 7.03. It is difficult to obtain reliable elemental analytical data because of the sensitivity of the analyzer. IR (KBr): $\tilde{\nu}$ = 3409 (m), 3066 (m), 2930

 © 2007 Wiley-VCH Verlag GmbH & Co. KGaA, Weinheim 

Table 1. Crystallographic data for compounds **1**–**3**.

| | **1** | **2** | **3** |
|---|---|---|---|
| Empirical formula | $C_{32}H_{28}CdN_2O_{10}$ | $C_{28}H_{22}CdN_3O_{5.50}$ | $C_{42}H_{32}CdN_4O_8$ |
| Formula mass | 712.96 | 600.89 | 833.12 |
| Crystal system | monoclinic | monoclinic | monoclinic |
| Space group | *C*2/*c* | *P*2/*c* | *C*2/*c* |
| Crystal size [mm] | 0.41 × 0.34 × 0.19 | 0.26 × 0.11 × 0.08 | 0.43 × 0.35 × 0.22 |
| *a* [Å] | 31.464(5) | 10.533(8) | 12.284(3) |
| *b* [Å] | 5.1789(7) | 10.138(8) | 11.609(3) |
| *c* [Å] | 20.453(3) | 23.817(18) | 26.995(4) |
| *β* [°] | 119.320(2) | 100.324(13) | 102.322(3) |
| *V* [Å$^3$] | 2905.8(7) | 2502(3) | 3761.0(14) |
| *Z* | 4 | 4 | 4 |
| $D_{calcd}$ [Mg m$^{-3}$] | 1.630 | 1.595 | 1.471 |
| $\mu$ [mm$^{-1}$] | 0.816 | 0.920 | 0.640 |
| *F* (000) | 1448 | 1212 | 1696 |
| *θ* range [°] | 1.48–25.10 | 2.01–5.01 | 2.44–25.01 |
| Collected reflections | 7161 | 11395 | 8513 |
| Unique reflections | 2573 | 4368 | 3037 |
| Parameters | 214 | 339 | 251 |
| Goodness-of-fit on $F^2$ | 0.997 | 1.002 | 1.022 |
| $R_1$, $wR_2$ [$I > 2\sigma(I)$] | 0.0343, 0.0898 | 0.0404, 0.0971 | 0.0931, 0.2217 |
| $R_1$, $wR_2$ [all data] | 0.0387, 0.0928 | 0.0720, 0.1077 | 0.1358, 0.2498 |
| Max., min. $\Delta\rho$ [e Å$^{-3}$] | 0.641, –0.593 | 1.070, –0.608 | 1.106, –1.071 |

(m), 1599 (vs), 1547 (s), 1460 (m), 1383 (vs), 1308 (s), 1265 (m), 1230 (m), 1142 (m), 849 (m), 779 (s), 720 (s), 665 (m) cm$^{-1}$.

**Compound 3:** The same synthesis procedure was used as for **2** except that phen was replaced by bipy. Yellow crystalline products were collected with a yield of 0.0950 g (60.3%) based on $H_2A$. $C_{42}H_{32}CdN_4O_8$ (833.12): calcd. C 60.55, H 3.87, N 6.72; found C 60.43, H 3.89, N 6.75. IR (KBr): $\tilde{\nu}$ = 3413 (m), 3056 (m), 2972 (m), 1699 (s), 1600 (vs), 1529 (s), 1486 (s), 1388 (vs), 1353 (s), 1305 (s), 1238 (s), 1150 (m), 814 (m), 775 (m), 648 (m), 510 (m) cm$^{-1}$.

Table 2. Selected bond lengths [Å] and angles [°] for **1**–**3**.

| | | | |
|---|---|---|---|
| **1** | | | |
| Cd(1)–O(1) | 2.247(2) | O(1A)–Cd(1)–O(2A) | 54.92(7) |
| Cd(1)–O(2) | 2.489(2) | O(5)–Cd(1)–O(1A) | 100.18(10) |
| Cd(1)–O(5) | 2.187(3) | O(5)–Cd(1)–O(2) | 84.76(8) |
| Cd(1)–O(1A) | 2.247(2) | O(1)–Cd(1)–O(2) | 54.92(7) |
| Cd(1)–O(2A) | 2.489(2) | O(5A)–Cd(1)–O(1) | 100.18(10) |
| Cd(1)–O(5A) | 2.187(3) | O(5A)–Cd(1)–O(2A) | 84.76(8) |
| **2** | | | |
| Cd(1)–O(1) | 2.468(4) | O(2)–Cd(1)–O(1) | 54.35(11) |
| Cd(1)–O(2) | 2.315(3) | N(3)–Cd(1)–O(1) | 93.06(12) |
| Cd(1)–O(3A) | 2.196(3) | N(2)–Cd(1)–N(3) | 70.56(14) |
| Cd(1)–O(4B) | 2.256(3) | O(3A)–Cd(1)–N(2) | 92.00(13) |
| Cd(1)–N(2) | 2.362(4) | O(3A)–Cd(1)–O(4B) | 98.29(13) |
| Cd(1)–N(3) | 2.372(4) | O(4B)–Cd(1)–O(2) | 88.30(12) |
| | | O(1B)–C(13B)–O(2B) | 120.1(4) |
| | | O(4B)–C(14B)–O(3B) | 125.0(4) |
| **3** | | | |
| Cd(1C)–O(1AC) | 2.303(5) | O(1AC)–Cd(1C)–O(2AC) | 54.46(19) |
| –O(2AC) | 2.490(6) | N(2C)–Cd(1C)–O(2C) | 97.41(14) |
| Cd(1C)–O(1C) | 2.303(5) | N(2C)–Cd(1C)–O(1AC) | 95.60(18) |
| Cd(1C)–O(2C) | 2.490(6) | O(1C)–Cd(1C)–O(2C) | 54.46(19) |
| Cd(1C)–N(2C) | 2.218(8) | N(3C)–Cd(1C)–O(2AC) | 82.59(14) |
| Cd(1C)–N(3C) | 2.299(9) | N(3C)–Cd(1C)–O(1C) | 84.40(18) |
| | | O(3A)–C(16A)–O(4A) | 121.7(8) |
| | | O(1A)–C(15A)–O(2A) | 121.0(7) |

**Single-Crystal Structure Determination:** Data collection was performed at 298 K for **2** and **3** and 293 K for **1** using a Siemens Smart CCD area detector diffractometer with Mo-$K_\alpha$ radiation with an $\omega$-scan mode ($\lambda$ = 0.71073 Å). The structure was solved with direct methods using the SHELXTL program and refined anisotropically with SHELXTL using full-matrix least-squares procedure. All non-hydrogen atoms were refined anisotropically. The hydrogen atoms were added theoretically and not refined. The crystallographic data for **1**–**3** are listed in Table 1, and selected bond lengths and angles for **1**–**3** are presented in Table 2.

CCDC-278329 (for $[Cd(HA)_2(H_2O)_2]$), -299277 (for $[Cd(A)(phen)]\cdot 1.5H_2O$), and -299279 (for $[Cd(HA)_2(bipy)]$) contain the supplementary crystallographic data for this paper. These data can be obtained free of charge from The Cambridge Crystallographic Data Centre via www.ccdc.cam.ac.uk/data_request/cif.

## Acknowledgments

This work was supported by grants from the National Natural Science Foundation of China(50532030, 50325311, 50335050), Doctoral Program Foundation of the Ministry of Education of China, Education Committee of Anhui Province(2006KJ032A, 2006KJ135B), Person with Ability Foundation of Anhui Province(2002Z021), the Team for Scientific Innovation Foundation of Anhui Province(2006KJ007TD), Key Laboratory of Opto-Electronic Information Acquisition and Manipulation (Anhui University), Ministry of Education, and Person with Ability Foundation of Anhui University.

[1] S.-N. Wang, *Coord. Chem. Rev.* **2001**, *215*, 79–98.
[2] a) J. L. C. Rowsell, O. M. Yaghi, *Angew. Chem. Int. Ed.* **2005**, *44*, 4670–4679; b) A. C. Sudik, A. R. Millward, N. W. Ockwig, A. P. Côté, J. Kim, O. M. Yaghi, *J. Am. Chem. Soc.* **2005**, *127*, 7110–7118.
[3] A. Lagunavicius, S. Grazulis, E. Balciunaite, D. Vainius, V. Siksnys, *Biochemistry* **1997**, *36*, 11093–11099.
[4] L.-G. Qiu, A.-J. Xie, L.-D. Zhang, *Adv. Mater.* **2005**, *17*, 689–692.

 © 2007 Wiley-VCH Verlag GmbH & Co. KGaA, Weinheim 

[5] a) U. Schlecht, Y. Nomura, T. Bachmann, I. Karube, *Bioconjugate Chem.* **2002**, *13*, 188–193; b) M. Boiocchi, M. Bonizzoni, L. Fabbrizzi, G. Piovani, A. Taglietti, *Angew. Chem.* **2004**, *116*, 1935–3940; *Angew. Chem. Int. Ed.* **2004**, *43*, 3847–3852.
[6] a) H. R. Moon, J. H. Kim, M. P. Suh, *Angew. Chem. Int. Ed.* **2005**, *44*, 1261–1265; b) M. P. Suh, H. R. Moon, E. Y. Lee, S. Y. Jang, *J. Am. Chem. Soc.* **2006**, *128*, 4710–4718.
[7] a) A. Vimont, J. M. Goupil, J. C. Lavalley, M. Daturi, S. Surblé, C. Serre, F. Millange, G. Férey, N. Audebrand, *J. Am. Chem. Soc.* **2006**, *128*, 3216–3227; b) X.-L. Wang, C. Qin, E.-B. Wang, *Cryst. Growth Des.* **2006**, *6*, 439–443.
[8] a) J. Liu, Z. Diwu, Y. Lu, B. Patch, P. P. Haughland, *Tetrahedron Lett.* **2003**, *44*, 4355–4359; b) J. W. Parker, O. Laksin, C. Yu, M. J. Lau, S. Klima, R. Fischer, I. Scott, B. W. Atwater, *Anal. Chem.* **1993**, *65*, 2329–2334.
[9] a) P. Schlichting, P. Duchscherer, G. Seisenberger, T. Basché, C. Bräuchle, K. Müllen, *Chem. Eur. J.* **1999**, *5*, 2388–2395; b) H. Langhals, H. Jaschke, U. Ring, P. von Unold, *Angew. Chem. Int. Ed.* **1999**, *38*, 201–203.
[10] a) E. Cariati, X. Bu, P. C. Ford, *Chem. Mater.* **2000**, *12*, 3385–3391; b) F. Wurthner, A. Sautter, *Chem. Commun.* **2000**, 445–446.
[11] N.-X. Hu, S. Xie, Z. Popovic, B. Ong, A. M. Hor, *J. Am. Chem. Soc.* **1999**, *121*, 5097–5098.
[12] M. Fujita, Y. J. Kwon, S. Washizu, K. Ogura, *J. Am. Chem. Soc.* **1994**, *116*, 1151–1152.
[13] a) J.-C. Dai, X.-T. Wu, Z.-Y. Fu, C.-P. Cui, S.-M. Hu, W.-X. Du, L.-M. Wu, H.-H. Zhang, R.-Q. Sun, *Inorg. Chem.* **2002**, *41*, 1391–1396; b) J. Zhang, Y.-R. Xie, Q. Ye, R.-G. Xiong, Z.-L. Xue, X.-Z. You, *Eur. J. Inorg. Chem.* **2003**, *14*, 2572–2577; c) X.-G. Meng, Y.-L. Song, H.-W. Hou, H.-Y. Han, B. Xiao, Y.-T. Fan, Y. Zhu, *Inorg. Chem.* **2004**, *43*, 3528–3536.
[14] a) O. R. Evans, W.-B. Lin, *Chem. Mater.* **2001**, *13*, 2705–2712; b) W.-B. Lin, Z.-Y. Wang, L. Ma, *J. Am. Chem. Soc.* **1999**, *121*, 11249–11250.
[15] X.-M. Zhang, *Coord. Chem. Rev.* **2005**, *249*, 1201–1219.
[16] H.-P. Zhou, Y.-M. Zhu, C.-M. Cui, P. Wang, H.-W. Li, J.-Y. Wu, Y. Xie, M.-H. Jiang, X.-T. Tao, Y.-P. Tian, *Inorg. Chem. Commun.* **2006**, *9*, 351–354.
[17] W.-F. Zhang, H. Guo, G.-H. Ma, Y.-B. Huang, Z.-L. Du, *Chem. J. Chin. University* **1998**, *19*, 591–594.
[18] A. Vogler, H. Kunkely, *Coord. Chem. Rev.* **2006**, *250*, 1622–1626.
[19] Z. R. Grabowski, K. Rotkiewicz, *Chem. Rev.* **2003**, *103*, 3899–4031.
[20] M. W. Perkovic, *Inorg. Chem.* **2000**, *39*, 4962–4968.

Received: August 1, 2006
Published Online: November 9, 2006

 © 2007 Wiley-VCH Verlag GmbH & Co. KGaA, Weinheim 

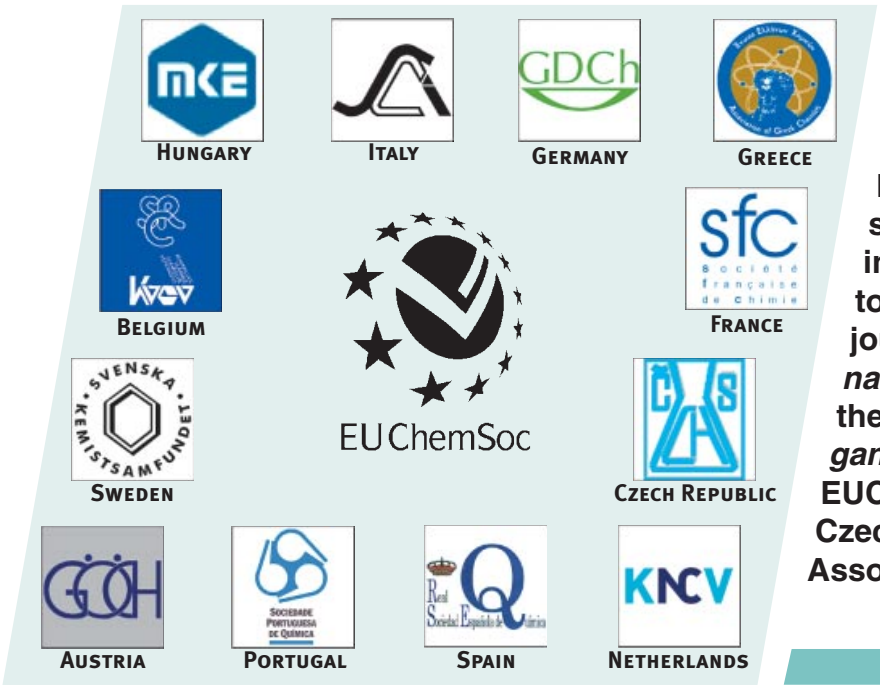


**The EUChemSoc Societies have taken the significant step into the future by merging their traditional journals, to form two leading chemistry journals, the *European Journal of Inorganic Chemistry* and the *European Journal of Organic Chemistry.* Three further EUChemSoc Societies (Austria, Czech Republic and Sweden) are Associates of the two journals.**

## COVER PICTURE

**The cover picture shows** the structure of a novel ruthenium complex with a μ-carbide ligand. This complex was obtained in an unexpected reaction from [(*p*-cymene)Ru(μ-Cl)$_3$RuCl($C_2H_4$)($PCy_3$)] and acetylene. The solid-state $^{13}C$ NMR spectrum of a μ-carbide complex obtained from fully $^{13}C$-labeled acetylene shows a strong peak at δ = 430.5 ppm. This confirms that acetylene was the source of the μ-carbide ligand and that the complex was formed by cleavage of the carbon triple bond. More details about this unusual reaction are described in the Short Communication by K. Severin et al. on p. 367ff.

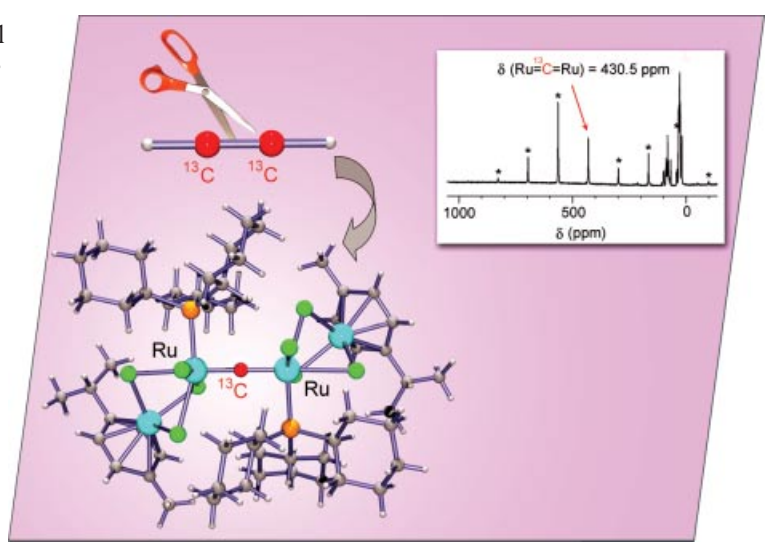


 © 2007 Wiley-VCH Verlag GmbH & Co. KGaA, Weinheim 

# CONTENTS

## SHORT COMMUNICATIONS


### Organometallic Chemistry

**E. Solari, S. Antonijevic, S. Gauthier, R. Scopelliti, K. Severin* ..... 367–371**

Formation of a Ruthenium μ-Carbide Complex with Acetylene as the Carbon Source

**Keywords:** Carbide ligands / Organometallic complexes / Ruthenium / Solid-state NMR spectroscopy / Vinylidene complexes

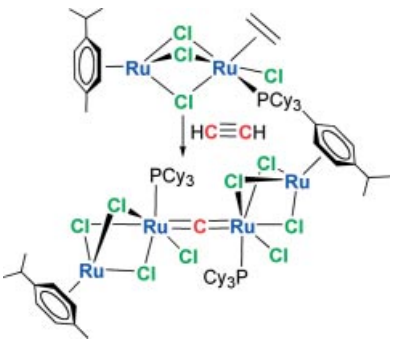


A tetranuclear μ-carbide complex was obtained by reaction of the dinuclear ruthenium complex [(*p*-cymene)Ru(μ-Cl)$_3$RuCl($C_2H_4$)($PCy_3$)] with acetylene as evidenced by single-crystal X-ray analysis as well as by solid-state NMR spectroscopy. Experiments with fully $^{13}$C-labelled acetylene demonstrate that acetylene was the carbon source for the carbide ligand.

### Light-Emitting Materials

**C. S. Chin,* M.-S. Eum, S. y. Kim, C. Kim, S. K. Kang ..... 372–375**

Blue-Light-Emitting Complexes: Cationic (2-Phenylpyridinato)iridium(III) Complexes with Strong-Field Ancillary Ligands

**Keywords:** Iridium / Luminescence / Blue-emitter / Strong field ligand

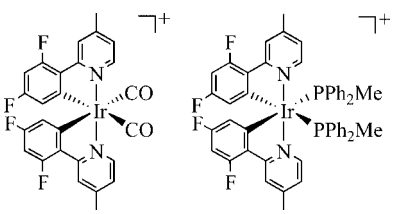


**2a$F_2$Me** **2b$F_2$Me**

Blue-light emission is obtained from cationic complexes **2a**$F_2$Me and **2b**$F_2$Me which contain strong-field ancillary ligands, CO and $PPh_2Me$, and a modified ppy ligand, $F_2$Meppy.


## FULL PAPERS


### Ti and Zr Coordination Polymers

**H. Fric, M. Puchberger, U. Schubert* ..... 376–383**

Two- and Three-Dimensional Coordination Polymers From the Reaction of Bis- and Tris(2-aminoethyl)amine with Titanium and Zirconium Alkoxides

**Keywords:** Titanium / Zirconium / Coordination polymers / N ligands

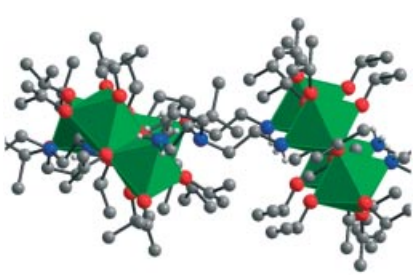

The chain-like coordination polymers [$M_2$-($OiPr)_8$($H_2NCH_2CH_2NHCH_2CH_2NH_2$)]$_\infty$, where only the $NH_2$ groups of the amine are coordinated to the $M_2(OiPr)_8$ units, are formed by reaction of the parent alkoxides [M($OiPr)_4$] (M = Ti, Zr) with an amine. These adducts dissociate into the starting compounds upon dissolution in $CD_2Cl_2$ but slowly re-form the solid-state structures over several weeks.


 © 2007 Wiley-VCH Verlag GmbH & Co. KGaA, Weinheim 

## Luminescent Platinum Complexes

**K. Zhang, J. Hu, K. C. Chan, K. Y. Wong, J. H. K. Yip* ..... 384–393**

Synthesis, Structures, and Electronic Spectroscopy of Luminescent Acetylene- and (Buta-1,3-diyne)platinum Complexes

**Keywords:** Spectroscopy / Luminescence / Platinum / Acetylene / Charge-transfer

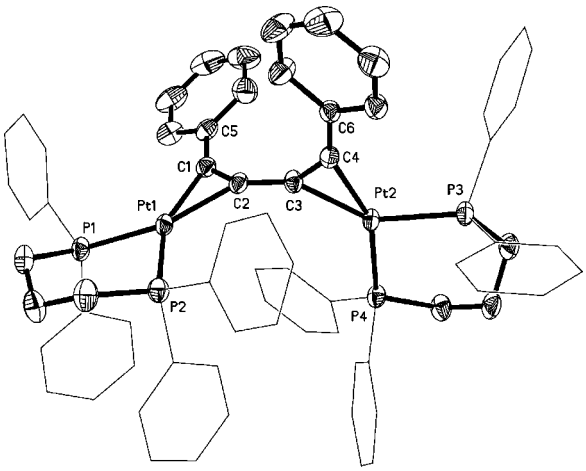


The absorption and emission spectroscopy of luminescent diphenylaceylene- and (buta-1,3-diyne)-$Pt^0$ complexes (L)Pt[(1,2-$\eta^2$)-R-(C≡C)$_n$-R] and [(L)Pt]$_2$[μ-(1,2-$\eta^2$):(3,4-$\eta^2$)-R-(C≡C)$_2$-R] [R = Ph or $CH_3$, L = dppp or $(PPh_3)_2$, $n$ = 1 or 2] were studied. The complexes display intense metal-to-ligand-charge-transfer (MLCT) absorptions and long-lived $^3$MLCT emissions.

## Medicinal Bioorganometallic Chemistry

**P. C. Kunz,* N. E. Brückmann, B. Spingler ..... 394–399**

Towards Polymer Diagnostic Agents – Copolymers of *N*-(2-Hydroxypropyl)-methacrylamide and Bis(2-pyridylmethyl)-4-vinylbenzylamine: Synthesis, Characterisation and $Re(CO)_3$-Labelling

**Keywords:** Rhenium / Carbonyl ligands / Polymer diagnostics / Copolymers / Cancer / Diagnosis / EPR effect

Copolymers of bis(2-pyridylmethyl)-4-vinylbenzylamine and *N*-(2-hydroxypropyl)-methacrylamide (HPMA) were prepared and characterised. Their capability of inert coordination towards $Re^I(CO)_3$ is demonstrated and a possible application in cancer diagnosis discussed.

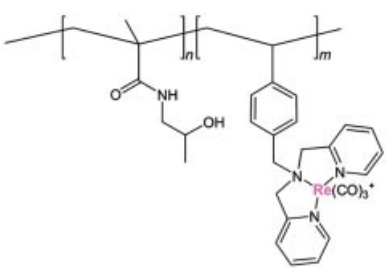


## Catalytic Hydration of Chloronitriles

**I. N. Stepanenko, B. Cebrián-Losantos, V. B. Arion,* A. A. Krokhin, A. A. Nazarov, B. K. Keppler* ..... 400–411**

The Complexes $[OsCl_2(azole)_2(dmso)_2]$ and $[OsCl_2(azole)(dmso)_3]$: Synthesis, Structure, Spectroscopic Properties and Catalytic Hydration of Chloronitriles

**Keywords:** Osmium / N ligands / Homogeneous catalysis / Hydration

Two families of mixed (azole)(chloro)(dimethyl sulfoxide)osmium(II) complexes, viz., *trans*,*cis*,*cis*-$[Os^{II}Cl_2(azole)_2(dmso)_2]$ and *cis*,*fac*-$[Os^{II}Cl_2(azole)(dmso)_3]$, where azole = indazole, pyrazole, benzimidazole and imidazole, have been prepared and fully characterised. The products catalyse the hydration of tri- and dichloroacetonitrile with high selectivity.

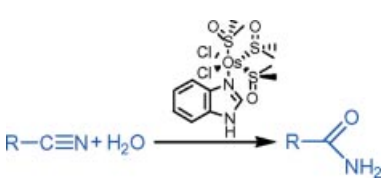


 © 2007 Wiley-VCH Verlag GmbH & Co. KGaA, Weinheim 

# CONTENTS

## Ruthenium-Promoted Reactions

**P. Banerjee, G. Mostafa, A. Castiñeiras, S. Goswami* ..... 412–421**

Two Novel Reactions of a Ruthenium-Coordinated Phenazine – Oxidative Aromatic Ring Hydroxylation and Dimerization via a New C–N Bond Formation

**Keywords:** Metal-mediated reaction / Phenazine / Ruthenium / Redox chemistry

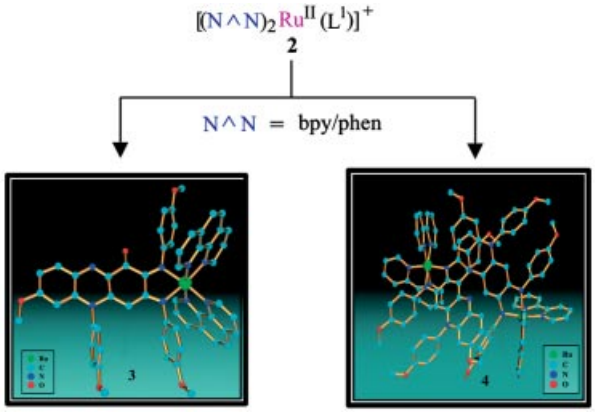


Ruthenium-mediated and unprecedented chemical transformations of a 2-amino-3-iminophenazine moiety via C–H activation are reported. The coordinated phenazine ligand undergoes oxidative hydroxylation and dimerization with the formation of a new C–N bond to produce the compounds **3** and **4**, respectively.

## Nickel-Based Microwires

**X. M. Ni, Q. B. Zhao, Y. F. Zhang, H. G. Zheng* ..... 422–428**

Reticular Nickel Microwires with Assembled Nanostructures: Synthesis, Magnetism and Catalysis for the Growth of Carbon Nanotubes

**Keywords:** Nickel / Nanostructures / Chemical reduction / Crystal growth

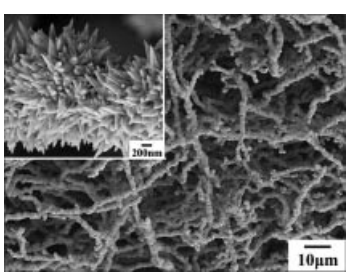


Reticular nickel microwires assembled from thorn-like nanocrystals are fabricated by a simple, complex-assisted chemical reduction route that does not require the use of surfactants or an external magnetic field. These nickel nanostructures exhibit high catalytic efficiency for the growth of carbon nanotubes in pyrolyzing acetone.

## A Versatile Ligand in Coordination Chemistry

**S. Foxon, J.-Y. Xu, S. Turba, M. Leibold, F. Hampel, F. W. Heinemann, O. Walter, C. Würtele, M. Holthausen, S. Schindler* ..... 429–443**

Syntheses, Characterization and Reactivity of Iron(II), Nickel(II), Copper(II) and Zinc(II) Complexes of the Ligand *N,N,N′,N′*-Tetrakis(2-pyridylmethyl)benzene-1,3-diamine (1,3-tpbd) and Its Phenol Derivative 2,6-Bis[bis(2-pyridylmethyl)amino]-*p*-cresol (2,6-tpcd)

**Keywords:** Iron / Copper / Zinc / Ligand effects

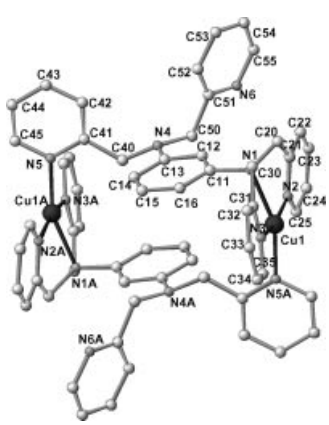


Redox active metal centers such as iron or copper ions demonstrate that *N,N,N′,N′*-Tetrakis(2-pyridyl methyl)benzene-1,3-diamine (1,3-tpbd) is a non-innocent ligand. Theoretical calculations support the formation of a dinuclear side-on copper peroxo complex during the reaction of the copper(I) complex with dioxygen. Most interestingly is a reaction if one equivalent of Cu(II) together with one equivalent of Zn(II) is reacted with one equivalent of 1,3-tbpd. Here $[Cu_2(1,3\text{-tpbd})_2(H_2O)_2](ClO_4)_4$ a so called "dimetallocyclophane" formed.

 © 2007 Wiley-VCH Verlag GmbH & Co. KGaA, Weinheim 

## Intercalated Vanadyl Phosphate

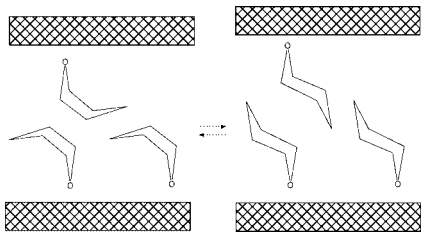

The thermal behavior of tetrahydropyran-(THP-)intercalated $VOPO_4$ was probed by a combination of experimental methods (XRD, DSC, FTIR, solid-state NMR) and quantum chemical calculations. Two temperature-induced transitions were detected and all polymorphs exhibit a high degree of molecular order and tight packing of THP in $VOPO_4$.

**K. Melánová, L. Beneš,* V. Zima, E. Černošková, J. Brus, M. Urbanová, M. Trchová, J. Dybal ..... 444–451**

Thermal Behavior of Tetrahydropyran-Intercalated $VOPO_4$: Structural and Dynamics Study

**Keywords:** Intercalations / NMR spectroscopy / IR spectroscopy / Thermal behavior / Quantum chemical calculations

## Epimerisation of CpRu(Josiphos)Cl

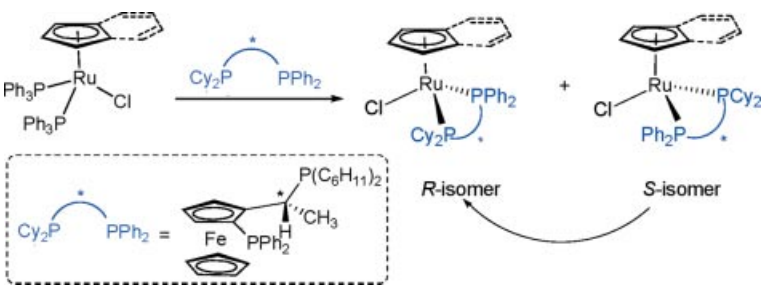


Phosphane substitution in [(Cp/Ind)Ru-$(PPh_3)_2$Cl] with the ferrocene-based chiral diphosphane ligand (*R*)-(*S*)-Josiphos led to the formation of (*R*) and (S) diastereomers, of which the thermodynamically stable (*R*) isomer was isolated pure.

**S. Y. Ng, G. Fang, W. K. Leong,* L. Y. Goh,* M. V. Garland ..... 452–462**

Reactivity and X-ray Structural Studies in Ligand Substitution of [Cp/(Ind)Ru-(dppf)Cl] – Epimerisation in [Cp/(Ind)Ru-(Josiphos)Cl] {Cp = $\eta^5$-$C_5H_5$, Ind = $\eta^5$-$C_7H_9$, dppf = 1,1′-Bis(diphenylphosphanyl)-ferrocene, Josiphos = (*R*)-(−)-1-[(*S*)-2-(Diphenylphosphanyl)ferrocenyl]ethyldicyclohexylphosphane}

**Keywords:** Indenyl / Ruthenium / dppf / Josiphos / Epimerisation / Phosphanes

## (Indenyl)ruthenium Thiolate Complexes

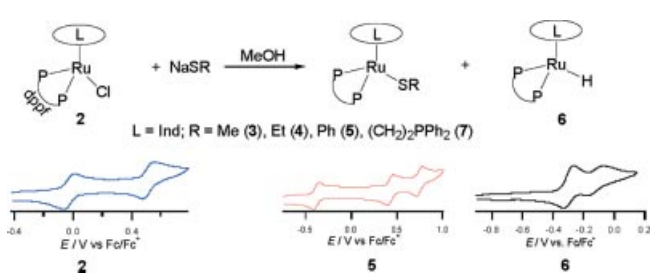


Chloro substitution of **2** with thiolates gave the thiolato derivatives, as well as the hydride **6** in R- and solvent-dependent yields. Cyclic voltammetry showed orders of ease of oxidation, as follows: L: Cp* < Ind < Cp and (diphos): dppm < dppe/dppf < $(PPh_3)_2$

**S. Y. Ng, W. K. Leong,* L. Y. Goh,* R. D. Webster ..... 463–471**

(Indenyl)ruthenium Complexes Containing 1,1′-Bis(diphenylphosphanyl)ferrocene (dppf) and Thiolato Ligands: Synthesis, X-ray Structure Analysis, Electrochemistry and Magnetic Studies

**Keywords:** (Indenyl)ruthenium / Thiolates / dppf / Cyclic voltammetry / ESR / Ruthenium

 © 2007 Wiley-VCH Verlag GmbH & Co. KGaA, Weinheim 

# CONTENTS

## Amido–Imine Chelates

**B. Neumann, C. Krinninger, I.-P. Lorenz* ..... 472–480**

Synthesis, Structures and Comparison of Neutral Complexes Formed by 2-(2′-Pyridyl)indole and $d^6$ Transition Metals

**Keywords:** Metallacycles / N ligands / Rhenium / Ruthenium / Rhodium / Iridium

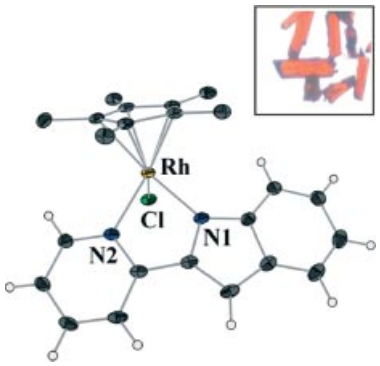


The 2-(2′-pyridyl)indolide anion (pyind) coordinates as an *N*,*N*′-bonded chelate ligand towards several suitable $d^6$ complex fragments of rhenium(I), ruthenium(II), rhodium(III) and iridium(III) to give new pyind complexes with potential catalytic activity.

## Metallacycles

**J. Blumhoff, R. Beckert,* D. Walther, S. Rau, M. Rudolph, H. Görls, W. Plass ..... 481–486**

Merocyanine-Like Chromophores as Ligands for Catalytic Active Metals of Group VIII

**Keywords:** N ligands / Chromophores / Palladium / Nickel / Electrochemistry

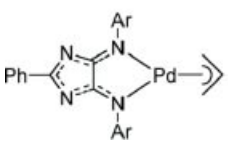


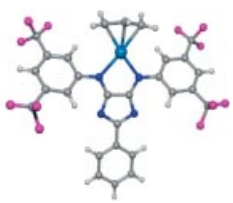

The synthesis, characterization and electrochemical properties of palladium complexes based on merocyanine-like ligands are described.

**If not otherwise indicated in the article, papers in issue 2 were published online on January 9, 2006**

 © 2007 Wiley-VCH Verlag GmbH & Co. KGaA, Weinheim 

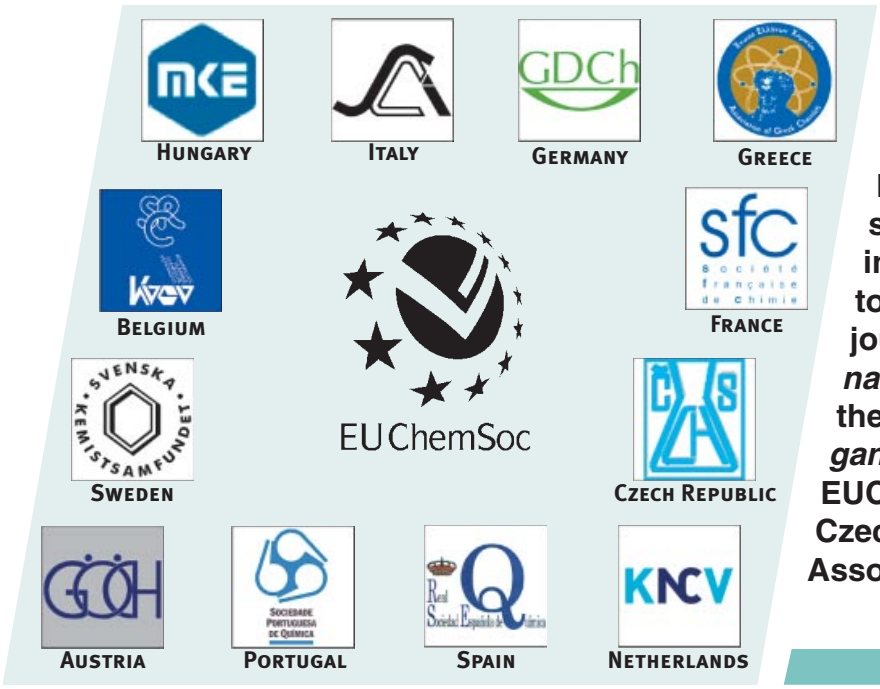


**The EUChemSoc Societies have taken the significant step into the future by merging their traditional journals, to form two leading chemistry journals, the *European Journal of Inorganic Chemistry* and the *European Journal of Organic Chemistry.* Three further EUChemSoc Societies (Austria, Czech Republic and Sweden) are Associates of the two journals.**

## COVER PICTURE

**The cover picture shows** the structure of a novel ruthenium complex with a μ-carbide ligand. This complex was obtained in an unexpected reaction from [(*p*-cymene)Ru(μ-Cl)$_3$RuCl($C_2H_4$)($PCy_3$)] and acetylene. The solid-state $^{13}C$ NMR spectrum of a μ-carbide complex obtained from fully $^{13}C$-labeled acetylene shows a strong peak at δ = 430.5 ppm. This confirms that acetylene was the source of the μ-carbide ligand and that the complex was formed by cleavage of the carbon triple bond. More details about this unusual reaction are described in the Short Communication by K. Severin et al. on p. 367ff.

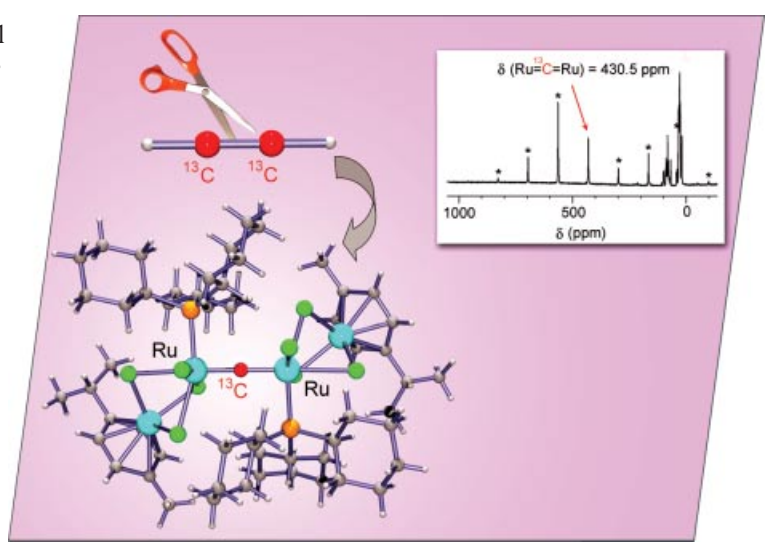


 © 2007 Wiley-VCH Verlag GmbH & Co. KGaA, Weinheim 

DOI: 10.1002/ejic.200600991

# Formation of a Ruthenium μ-Carbide Complex with Acetylene as the Carbon Source

**Euro Solari,[a] Sasa Antonijevic,[a] Sébastien Gauthier,[a] Rosario Scopelliti,[a] and Kay Severin*[a]**

**Keywords:** Carbide ligands / Organometallic complexes / Ruthenium / Solid-state NMR spectroscopy / Vinylidene complexes

Reactions of the dinuclear ruthenium complex [(*p*-cymene)-$Ru(\mu\text{-}Cl)_3RuCl(C_2H_4)(PCy_3)$] with phenylacetylene or *tert*-butylacetylene gave the vinylidene complexes [(*p*-cymene)-$Ru(\mu\text{-}Cl)_3RuCl(=C=CHR)(PCy_3)$] (R = *t*Bu, Ph), which were characterized crystallographically. With acetylene, however, a tetranuclear μ-carbide complex was obtained as evidenced by single-crystal X-ray analysis as well as by solid-state NMR spectroscopy. Experiments with fully $^{13}C$-labelled acetylene showed that acetylene was the carbon source for the carbide ligand.

(© Wiley-VCH Verlag GmbH & Co. KGaA, 69451 Weinheim, Germany, 2007)

A complex containing a single carbon atom as a bridging ligand between a metalloporphyrin and a second metal-fragment was described for the first time in 1979.[1] Since then, several structurally related compounds with porphyrinato or phthalocyaninato ligands have been reported.[2] Well-characterized μ-carbide complexes without these ligands are still rare.[3] An early example was published by Latesky and Selegue in 1987.[3e] They showed that the reaction between $[CpRu(C{\equiv}CMe)(CO)_2]$ and $[W(\equiv CEt)(OCMe_3)_3]$ proceeds with elimination of 2-pentyne to give the heteronuclear μ-carbide complex $[Cp(CO)_2Ru{-}C{\equiv}W(OCMe_3)_3]$ (**1**). More recently, it was observed that the terminal carbide complex $[RuCl_2(\equiv C)(PCy_3)_2]$[4] can act as a 'σ-donor ligand' for other metals to form bimetallic complexes such as **2** and **3**.[3b] In the following, we describe a tetranuclear complex containing an unusual {Ru=C=Ru} unit. This complex was obtained by a novel reaction from acetylene by cleavage of the carbon triple bond.

Over the last years, we investigated ruthenium complexes as catalysts for atom transfer radical reactions.[5] The halogeno-bridged complex [(*p*-cymene)$Ru(\mu\text{-}Cl)_3RuCl(C_2H_4)$-$(PCy_3)$] (**4**), which can easily be obtained from commercial $[(p\text{-cymene})RuCl_2]_2$, was found to display an exceptionally high activity for atom transfer radical addition reactions under mild conditions.[5c] In order to further explore the reactivity of this complex, we have investigated the reaction of **4** with alkynes. When phenylacetylene or *tert*-butylacetylene was added to a solution of complex **4** in $CH_2Cl_2$ or benzene, the rapid and quantitative formation of a new complex was observed as evidenced by in situ $^{31}P$ NMR spectroscopic experiments (Scheme 1). The products **5** and **6** were isolated in nearly quantitative yields by evaporation of the solvent and washing with hexane.

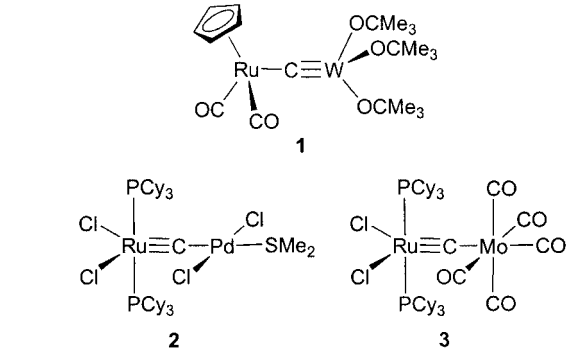


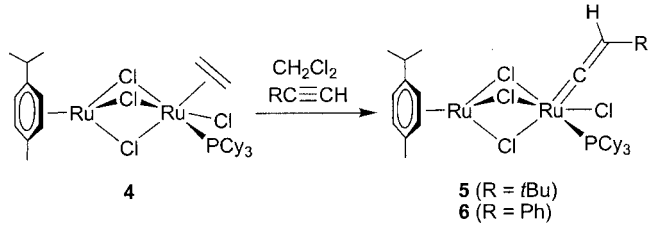


Scheme 1.

Both complexes were characterized by NMR spectroscopy ($^1H$, $^{13}C$, $^{31}P$; see Supporting Information), elemental analysis and single-crystal X-ray analysis (Figure 1 and Figure 2). The structures of **5** and **6** can be described as face-bridged dimers with a (*p*-cymene)Ru fragment con-

[a] Institut des Sciences et Ingénierie Chimiques, École Polytechnique Fédérale de Lausanne (EPFL)
1015 Lausanne, Switzerland
Fax: +41-21-6939305
E-mail: kay.severin@epfl.ch

Supporting information for this article is available on the WWW under http://www.eurjic.org or from the author.

 © 2007 Wiley-VCH Verlag GmbH & Co. KGaA, Weinheim 

nected by three chlorido bridges to a RuCl(=C=CHR)-($PCy_3$) fragment.[6] The Ru1–C1 distances [1.817(6) Å for **5**; 1.778(8) Å for **6**] are comparable to those of other coordinatively saturated Ru–vinylidene complexes such as [TpRuCl(=C=CHPh)($PPh_3$)] [1.801(4) Å][7] or [{RuCl($i$Pr$_2$-$PCH_2CH_2OMe)_2$(=C=CHPh)}(OTf)] [1.790(3) Å].[8] Apart from the vinylidene ligand, the bond lengths for **5** and **6** are similar to those for the starting material **4**. However, there is one notable exception: the Ru1–Cl1 bonds are significantly longer [2.6551(13) Å for **5**; 2.630(2) Å for **6**] than that of complex **4** [2.4878(6) Å]. This can be ascribed to the stronger *trans* influence of the vinylidene ligands relative to that of the ethylene ligand.

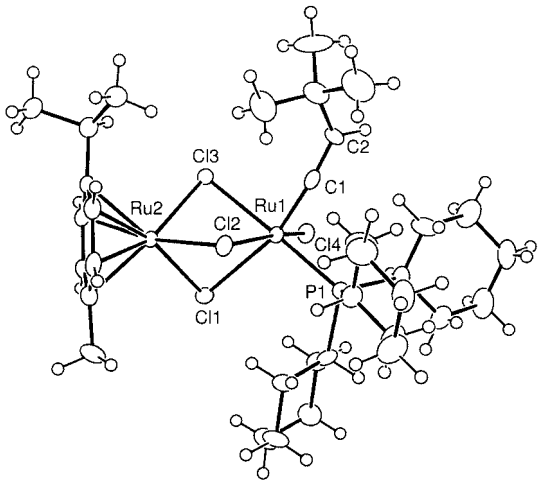


Figure 1. Graphical representation of the molecular structure of **5** in the crystal. The solvent molecules ($CH_2Cl_2$, 0.5 toluene) are not shown for clarity. Selected bond lengths [Å] and angles [°]: Ru1–Cl1 2.6551(13), Ru1–Cl2 2.4221(14), Ru1–Cl3 2.5246(13), Ru1–Cl4 2.3672(14), Ru1–P1 2.3129(14), Ru1–C1 1.817(6), C1–C2 1.299(8), Ru2–Cl1 2.4376(15), Ru2–Cl2 2.4607(12), Ru2–Cl3 2.4397(13); Cl1–Ru1–C1 163.93(17), Cl4–Ru1–Cl2 165.61(5), Cl4–Ru1–P1 91.33(5).

The formation of **5** and **6** can be rationalized by the displacement of the ethylene ligand by the respective acetylene followed by an alkyne-to-vinylidene transformation.[9] A related reaction with a face-bridged Ru dimer was reported by Fogg et al., who found that the addition of *tert*-butylacetylene to [(dcypb)ClRu(μ-Cl)$_3$Ru(dcypb)($N_2$)] {dcypb = 1,4-bis(dicyclohexylphosphanyl)butane} gave the vinylidene complex [(dcypb)ClRu(μ-Cl)$_3$Ru(=C=CH–$t$Bu)(dcypb)] by displacement of the dinitrogen ligand.[10]

When a solution of the olefin complex **4** in $CH_2Cl_2$ was treated with acetylene, the formation of a black product was observed, which was not characterized further. However, when a stoichiometric amount (1.2 equiv.) of acetylene was used in combination with thf as the solvent, a yellow-orange complex (**7**) precipitated.[11] Complex **7** displayed a very low solubility in all solvents. A detailed solution NMR analysis of **7** was therefore not possible, but crystals of sufficient quality for a single-crystal X-ray analysis were obtained from a dilute $CH_2Cl_2$ solution. Surprisingly, it was found that a tetranuclear μ-carbide complex had formed

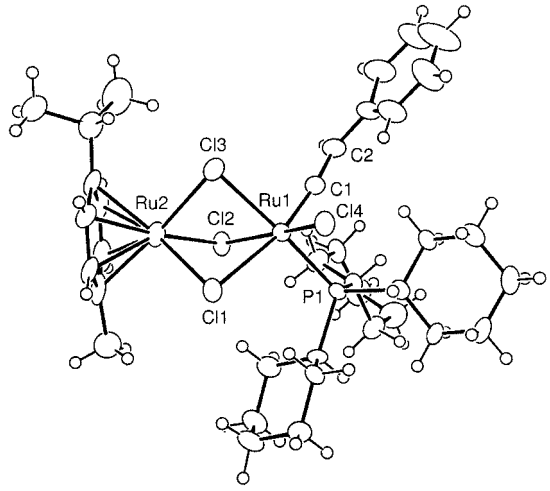


Figure 2. Graphical representation of the molecular structure of **6** in the crystal. The solvent molecules (2 toluene) are not shown for clarity. Selected bond lengths [Å] and angles [°]: Ru1–Cl1 2.630(2), Ru1–Cl2 2.403(2), Ru1–Cl3 2.541(2), Ru1–Cl4 2.362(2), Ru1–P1 2.325(2), Ru1–C1 1.778(8), C1–C2 1.329(11), Ru2–Cl1 2.427(2), Ru2–Cl2 2.428(2), Ru2–Cl3 2.437(2); Cl1–Ru1–C1 167.0(3), Cl4–Ru1–Cl2 164.32(8), Cl4–Ru1–P1 92.76(8).

(Scheme 2 and Figure 3). The elemental analysis of **7** was in agreement with this result, and the total yield with respect to the starting material was 56%.

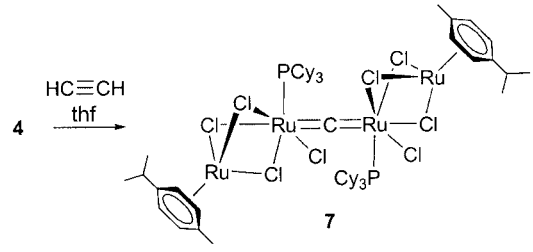


Scheme 2.

The molecular structure of complex **7** in the crystal consists of two symmetry-related[12] {(*p*-cymene)Ru(μ-Cl)$_3$-RuCl($PCy_3$)} fragments connected by a carbide ligand in a nearly linear fashion [Ru1–C1–Ru1_2 = 178.8(9)°] (Figure 3). The Ru1–C1 bond length [1.7877(9) Å] is longer than that of the carbide complex **2** [1.662(2) Å][3b] and similar to the Ru–C distances found for the vinylidene complexes **5** and **6**. This confirms the {Ru=C=Ru} structure of complex **7** as depicted in Scheme 2. The octahedral geometry around Ru1 is highly distorted. Noteworthy is the long Ru1–Cl1 distance of 2.685(3) Å, which demonstrates that the μ-carbide ligand also has a very strong *trans* influence.

A priori, the carbon atom sandwiched between the two ruthenium atoms could have resulted from an acetylene-induced splitting of the ethylene ligand of complex **4** or from acetylene itself. To clarify this issue, the reaction was repeated with fully $^{13}$C-labelled acetylene. The resulting product was investigated by solid-state MAS NMR spectroscopy. The $^{13}C\{^1H\}$ cross-polarized MAS NMR spectra of complex **7** show a strong signal at $\delta$ = 430.5 ppm (Figure 4), which can clearly be attributed to the bridging car-

 © 2007 Wiley-VCH Verlag GmbH & Co. KGaA, Weinheim 

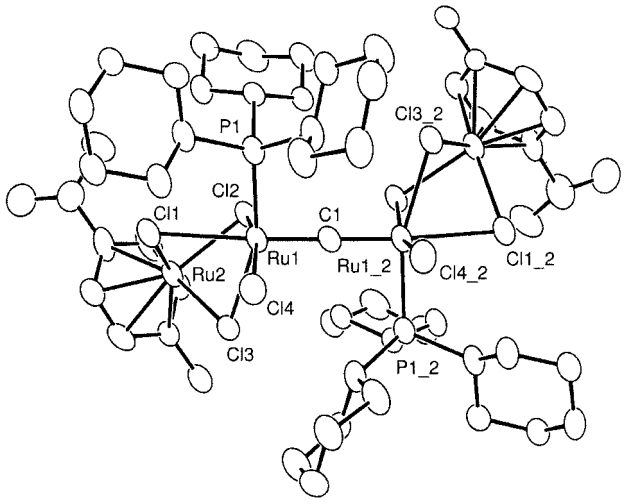


Figure 3. Graphical representation of the molecular structure of **7** in the crystal. The solvent molecules ($5\,CH_2Cl_2$) and the hydrogen atoms are not shown for clarity. Selected bond lengths [Å] and angles [°]: Ru1–C1 1.7877(9), Ru1–Cl1 2.685(3), Ru1–Cl2 2.439(3), Ru1–Cl3 2.548(3), Ru1–Cl4 2.365(3), Ru1–P1 2.350(4); Cl1–Ru1–C1 169.7(4), Cl4–Ru1–Cl2 162.99(11), Cl4–Ru1–P1 93.46(12), P1–Ru1–Cl3 161.75(11), Ru1–C1–Ru1_2 178.8(9).

bide ligand. The position of the signal is within the expected range as structurally related complexes such as **2** and **3** display resonances in the same region (**2**: $\delta$ = 381.2 ppm; **3**: $\delta$ = 446.3 ppm).[3b] These results demonstrate that the source of the μ-carbide ligand of complex **7** is indeed the acetylene.

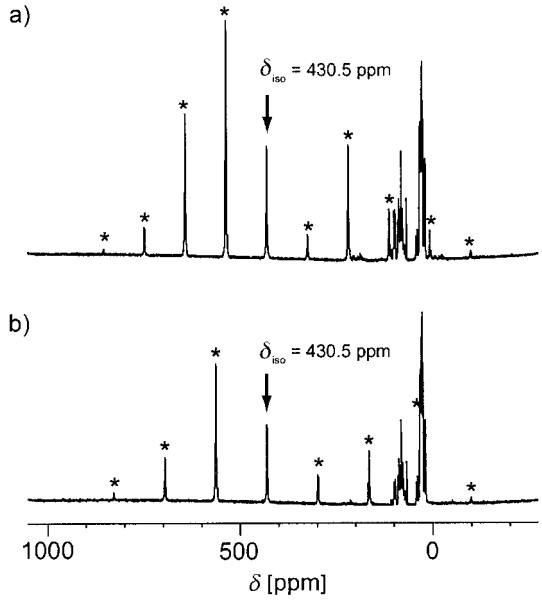


Figure 4. $^{13}C\{^1H\}$ cross-polarized (CP) MAS NMR spectra of solid complex **7** recorded at the spinning rates of (a) 8 kHz and (b) 10 kHz. The centreband, the isotropic chemical shift $\delta_{iso}$ = 430.5 ppm, of the C5 carbon resonance is indicated with an arrow, while the spinning sidebands are indicated by an *. The spectra are the result of averaging 12800 transients with a recycle interval of 3 s. The CP contact time was 5 ms.

In order to obtain information about possible side products of this unusual reaction, we investigated the mother liquor, from which complex **7** had precipitated, by solution NMR spectroscopy. The $^{31}P$ NMR spectrum shows several peaks with two dominant signals at $\delta$ = 61.82 and 66.00 ppm (see Supporting Information). The first signal appears as a doublet with a coupling constant of 17.9 Hz to a $^{13}C$ NMR signal at $\delta$ = 204.17 ppm. The second signal appears as a doublet of a doublet with a coupling constant of 20.2 Hz to a $^{13}C$ NMR signal at $\delta$ = 206.17 ppm and of 10.1 Hz to a $^{13}C$ signal at –10.46 ppm. The latter $^{13}C$ signal is assigned to a $CH_3$ group as evidenced by a $^{13}C$ NMR spectrum with coupling to $^1H$. The high-field position of the signal suggests a Ru-bound methyl group. On the basis of this data we propose that the two major phosphane complexes in solution contain a Ru($^{13}CX$)($PCy_3$) fragment (species at $\delta$ = 61.82 ppm) and a Ru($^{13}CX$)($^{13}CH_3$)($PCy_3$) fragment (species at $\delta$ = 66.00 ppm). The nature of the group/fragment 'X′ is currently not clear. From the chemical shift of the $^{13}C$ NMR signal at ca. 200 ppm, it can be excluded that X = Ru, and H-coupled spectra demonstrate that there are no protons directly bound to the $^{13}C$ carbon atom.

In summary, we have described the reaction of the dinuclear complex [(*p*-cymene)Ru(μ-Cl)$_3$RuCl($C_2H_4$)($PCy_3$)] (**4**) with alkynes. Whereas the vinylidene complexes **5** and **6** were obtained for phenylacetylene and *tert*-butylacetylene, the μ-carbide complex **7** was formed for reactions with acetylene. The latter represents a rare example of a structurally characterized Ru(μ-C)Ru complex. The available experimental data do not allow for the proposal of a mechanism for this unusual reaction. A plausible intermediate is the vinylidene complex [(*p*-cymene)Ru(μ-Cl)$_3$RuCl(C=$CH_2$)-($PCy_3$)], which undergoes subsequent transformations. It should be noted that Ru(=C=$CH_2$) complexes are not intrinsically unstable as evidenced by the isolation of, for example, the complex [RuHCl(=C=$CH_2$)(P*t*$Bu_2$Me)$_2$].[13] The fact that complex **4** can promote the splitting of a carbon triple bond of acetylene at room temperature is further evidence for its high reactivity,[5c] and other organometallic transformations of this complex are currently being investigated in our laboratory.

## Experimental Section

**General:** The synthesis of all complexes was performed under an atmosphere of dry argon by using standard Schlenk techniques. The complex [(*p*-cymene)Ru(μ-Cl)$_3$Ru($PCy_3$)($C_2H_4$)Cl] (**4**) was prepared as described before.[5c] The fully $^{13}C$-labelled acetylene (99%) was obtained from Cambridge Isotope Laboratories, Inc. The $^1H$- and $^{13}C$ NMR spectra in solution were recorded on Bruker Advance DPX 400, Advance 600 and Advance 800 instruments by using the residual protonated solvents as internal standards. Solid-state NMR spectra were recorded on a Bruker DRX 300 spectrometer equipped with a 7.0 widebore magnet and utilising a 4-mm CPMAS probehead. A nicely powdered sample was packed under a $N_2$ atmosphere into a 4-mm outer diameter $ZrO_2$ rotor. Chemical shifts of $^{13}C$ are reported in ppm relative to an external TMS standard.

 © 2007 Wiley-VCH Verlag GmbH & Co. KGaA, Weinheim 

**Synthesis of Complex 5:** [(*p*-cymene)Ru(μ-Cl)$_3$Ru(PCy$_3$)(C$_2$H$_4$)Cl] (**4**) (100 mg, 128 μmol) and *tert*-butylacetylene (19 μL, 154 μmol) in $CH_2Cl_2$ (5 mL) were stirred for 2 h under an inert atmosphere. After evaporation of the solvent under reduced pressure, the product was washed with hexane and dried under vacuum (isolated yield: 103 mg, 96%). Orange crystals were obtained from cold toluene. $^1$H NMR (400 MHz, $CDCl_3$): $\delta$ = 1.15 (s, 9 H, *t*Bu), 1.20–1.32 (m, 9 H, PCy$_3$), 1.32 [d, $^3J$ = 7 Hz, 3 H, CH(C$H_3$)$_2$], 1.34 [d, $^3J$ = 7 Hz, 3 H, CH(C$H_3$)$_2$], 1.54–2.13 (m, 24 H, PCy$_3$), 2.30 (s, 3 H, $CH_3$), 2.96 [sept, $^3J$ = 7 Hz, 1 H, C*H*(CH$_3$)$_2$], 3.83 (d, $^4J_{PH}$ = 3 Hz, 1 H, C*H*-*t*Bu), 5.37 (d, $^3J$ = 6 Hz, 2 H, CH, cymene), 5.50 (d, $^3J$ = 6 Hz, 1 H, CH, cymene), 5.58 (d, $^3J$ = 6 Hz, 1 H, CH, cymene) ppm. $^{13}$C NMR (101 MHz, $CDCl_3$): $\delta$ = 18.73 ($CH_3$, cymene), 22.07, 22.14 [CH(*C*H$_3$)$_2$, cymene], 26.32 ($CH_2$, PCy$_3$), 27.64 (d, $^3J_{PC}$ = 10 Hz, $CH_2$, PCy$_3$), 28.82 (d, $^2J_{PC}$ = 19 Hz, $CH_2$, PCy$_3$), 31.01 [*C*H(CH$_3$)$_2$, cymene], 33.13 (*t*Bu), 35.07 (d, $^1J_{PC}$ = 24 Hz, CH, PCy$_3$), 78.56, 78.78, 79.03, 79.78 (CH, cymene), 96.44, 101.19 (C, cymene), 122.23 (Ru=C=*C*), 352.55 (d, $^2J_{PC}$ = 19 Hz, Ru=C) ppm. $^{31}$P NMR (162 MHz, $CDCl_3$): $\delta$ = 54.48 (s) ppm. $C_{34}H_{57}Cl_4PRu_2$ (840.74): calcd. C 48.57, H 6.83; found C 48.84, H 6.73.

**Synthesis of Complex 6:** The synthesis was performed analogously to that of complex **5** by using phenylacetylene (18 μL, 154 μmol) (isolated yield: 105 mg, 95%). Orange crystals were obtained from cold toluene. $^1$H NMR (400 MHz, $CDCl_3$): $\delta$ = 1.12–1.35 (m, 9 H, PCy$_3$), 1.34 [d, $^3J$ = 7 Hz, 3 H, CH(C$H_3$)$_2$], 1.36 [d, $^3J$ = 7 Hz, 3 H, CH(C$H_3$)$_2$], 1.52–2.17 (m, 24 H, PCy$_3$), 2.29 (s, 3 H, $CH_3$), 2.96 [sept, $^3J$ = 7 Hz, 1 H, C*H*(CH$_3$)$_2$], 4.91 [d, $^4J_{PH}$ = 4 Hz, 1 H, C*H*(Ph)], 5.41 (d, $^3J$ = 6 Hz, 2 H, CH, cymene), 5.55 (d, $^3J$ = 6 Hz, 1 H, CH, cymene), 5.64 (d, $^3J$ = 6 Hz, 1 H, CH, cymene), 6.88–7.14 (m, 5 H, Ph) ppm. $^{13}$C NMR (101 MHz, $CDCl_3$): $\delta$ = 18.80 ($CH_3$, cymene), 22.06, 22.35 [CH(*C*H$_3$)$_2$, cymene], 26.28 ($CH_2$, PCy$_3$), 27.69 (d, $^3J_{PC}$ = 11 Hz, $CH_2$, PCy$_3$), 28.89 (d, $^2J_{PC}$ = 15 Hz, $CH_2$, PCy$_3$), 31.16 [*C*H(CH$_3$)$_2$, cymene], 35.07 (d, $^1J_{PC}$ = 24 Hz, CH, PCy$_3$), 78.28, 78.79, 79.52, 80.04 (CH, cymene), 97.03, 101.12 (C, cymene), 114.10 (Ru=C=*C*), 124.42, 125.85, 128.06, 131.07 (Ph), 356.11 (d, $^2J_{PC}$ = 19 Hz, Ru=C) ppm. $^{31}$P NMR (162 MHz, $CDCl_3$): $\delta$ = 54.21 (s) ppm. $C_{36}H_{53}Cl_4PRu_2$ (860.73): calcd. C 50.23, H 6.21; found C 50.14, H 6.24.

**Synthesis of Complex 7:** A fixed volume of acetylene (35 mL, 1.5 mmol) was connected to a 100-mL flask containing [(*p*-cymene)Ru(μ-Cl)$_3$Ru(PCy$_3$)(C$_2$H$_4$)Cl] (**4**) (1.00 g, 1.30 mmol) and thf (50 mL). The suspension was stirred for 24 h at room temperature during which the colour changed from orange-red to yellow-orange. The product was collected on a filter and dried in vacuo (yield: 560 mg, 56%). $C_{57}H_{94}Cl_8P_2Ru_4$ (1529.21): calcd. C 44.77, H 6.19; found C 44.65, H 6.11. Single crystals were obtained from $CH_2Cl_2$.

**X-ray Analyses:** Data collection was performed at 140(2) K with an Oxford Diffraction KM4 Sapphire CCD. Data reduction was carried out with CrysAlis RED, release 1.7.0.[14] Absorption correction was applied to both data sets. Structure solution and refinement were performed with the SHELXTL software package, release 5.1.[15] The structures were refined by using the full-matrix least-squares on $F^2$ with all non-H atoms anisotropically refined. H atoms were placed in calculated positions by using the 'riding model'. CCDC 624643–624645 contain the supplementary crystallographic data for this paper. These data can be obtained free of charge from The Cambridge Crystallographic Data Centre via www.ccdc.cam.ac.uk/data_request/cif.

**Crystal Data for Complex 5·$CH_2Cl_2$·0.5$C_6H_5CH_3$:** $C_{38.5}H_{63}Cl_6PRu_2$, $M$ = 971.70, triclinic, $a$ = 10.3246(7), $b$ = 13.0596(9), $c$ = 17.2481(10) Å, $\alpha$ = 77.248(5), $\beta$ = 85.836(5), $\gamma$ = 73.173(6)°, $V$ = 2171.1(2) Å$^3$, $T$ = 140(2) K, space group $P\bar{1}$, $Z$ = 2, $\mu$(Mo-$K_\alpha$) = 0.71073 Å, 13023 reflections collected, 6716 independent reflections, $R_{int}$ = 0.0307, $R_1$ [$I > 2\sigma(I)$] = 0.0457, $wR_2$ (all data) = 0.1281.

**Crystal Data for Complex 6·2$C_6H_5CH_3$:** $C_{50}H_{69}Cl_4PRu_2$, $M$ = 1044.96, monoclinic, $a$ = 9.6774(4), $b$ = 16.9682(9), $c$ = 30.2874(17) Å, $\beta$ = 97.243(4)°, $V$ = 4933.7(4) Å$^3$, $T$ = 140(2) K, space group $P2_1/c$, $Z$ = 4, $\mu$(Mo-$K_\alpha$) = 0.71073 Å, 28793 reflections collected, 7990 independent reflections, $R_{int}$ = 0.0587, $R_1$ [$I > 2\sigma(I)$] = 0.0648, $wR_2$ (all data) = 0.1549.

**Crystal Data for Complex 7·5$CH_2Cl_2$:** $C_{62}H_{104}Cl_{18}P_2Ru_4$, $M$ = 1953.77, monoclinic, $a$ = 17.8078(15), $b$ = 23.903(3), $c$ = 18.5150(17) Å, $\beta$ = 91.104(7)°, $V$ = 7879.7(13) Å$^3$, $T$ = 140(2) K, space group $C2/c$, $Z$ = 4, $\mu$(Mo-$K_\alpha$) = 0.71073 Å, 22389 reflections collected, 6566 independent reflections, $R_{int}$ = 0.1115, $R_1$ [$I > 2\sigma(I)$] = 0.0905, $wR_2$ (all data) = 0.2645.

**Supporting Information** (see footnote on the first page of this article): $^{13}$C- and $^{31}$P NMR spectra of the mother liquor of the reaction between complex **4** and fully $^{13}$C-labelled acetylene.

## Acknowledgments

The work was supported by the Swiss National Science Foundation and by the EPFL.

[1] I. Noda, S. Kato, M. Mizuta, N. Yasuoka, N. Kasai, *Angew. Chem. Int. Ed. Engl.* **1979**, *18*, 83.

[2] For selected examples see: a) L. Galich, A. Kienast, H. Hückstädt, H. Homborg, *Z. Anorg. Allg. Chem.* **1998**, *624*, 1235–1242; b) A. Kienast, L. Galich, K. S. Murray, B. Moubaraki, G. Lazerev, J. D. Cashion, H. Homborg, *J. Porph. Phthalocyan.* **1997**, *1*, 141–157; c) A. M. Paoletti, G. Pennesi, C. Ercolani, *Inorg. Chem.* **1995**, *34*, 4780–4784; d) W. Beck, W. Knauer, C. Robl, *Angew. Chem. Int. Ed. Engl.* **1990**, *29*, 318–320; e) C. Ercolani, M. Gardini, V. L. Goedken, G. Pennesi, G. Rossi, U. Russo, P. Zanonato, *Inorg. Chem.* **1989**, *28*, 3097–3099; f) D. Mansuy, J.-P. Lecomte, J.-C. Chottard, J.-F. Bartoli, *Inorg. Chem.* **1981**, *20*, 3119–3121.

[3] a) S. H. Hong, M. W. Day, R. H. Grubbs, *J. Am. Chem. Soc.* **2004**, *126*, 7414–7415; b) A. Hejl, T. M. Trnka, M. W. Day, R. H. Grubbs, *Chem. Commun.* **2002**, 2524–2525; c) R. L. Miller, P. T. Wolczanski, *J. Am. Chem. Soc.* **1993**, *115*, 10422–10423; d) M. Etienne, P. S. White, J. L. Templeton, *J. Am. Chem. Soc.* **1991**, *113*, 2324–2325; e) S. L. Latesky, J. P. Selegue, *J. Am. Chem. Soc.* **1987**, *109*, 4731–4733.

[4] a) S. R. Caskey, M. H. Stewart, J. E. Kivela, J. R. Sootsman, M. J. A. Johnson, J. W. Kampf, *J. Am. Chem. Soc.* **2005**, *127*, 16750–16751; b) R. G. Carlson, M. A. Gile, J. A. Heppert, M. H. Mason, D. R. Powell, D. V. Velde, J. M. Vilain, *J. Am. Chem. Soc.* **2002**, *124*, 1580–1581.

[5] a) L. Quebatte, K. Thommes, K. Severin, *J. Am. Chem. Soc.* **2006**, *128*, 7440–7441; b) M. Haas, E. Solari, Q. T. Nguyen, S. Gauthier, R. Scopelliti, K. Severin, *Adv. Synth. Catal.* **2006**, *348*, 439–442; c) L. Quebatte, E. Solari, R. Scopelliti, K. Severin, *Organometallics* **2005**, *24*, 1404–1406; d) L. Quebatte, M. Haas, E. Solari, R. Scopelliti, Q. T. Nguyen, K. Severin, *Angew. Chem. Int. Ed.* **2005**, *44*, 1084–1088; e) L. Quebatte, R. Scopelliti, K. Severin, *Eur. J. Inorg. Chem.* **2005**, 3353–3358; f) L. Quebatte, R. Scopelliti, K. Severin, *Angew. Chem. Int. Ed.* **2004**, *43*, 1520–1524.

[6] For Ru(μ-Cl)$_3$Ru complexes containing (arene)Ru and (PR$_3$)Ru fragments see: a) S. Gauthier, L. Quebatte, R. Scopelliti, K. Severin, *Chem. Eur. J.* **2004**, *10*, 2811–2821; b) M. P. de Araujo, E. M. A. Valle, J. Ellena, E. E. Castellano, E. N. dos Santos,

 © 2007 Wiley-VCH Verlag GmbH & Co. KGaA, Weinheim 

A. A. Batista, *Polyhedron* **2004**, *23*, 3163–3172; c) A. C. da Silva, H. Piotrowski, P. Mayer, K. Polborn, K. Severin, *Eur. J. Inorg. Chem.* **2001**, 685–691.
[7] C. Slugovc, K. Mereiter, E. Zobetz, R. Schmid, K. Kirchner, *Organometallics* **1996**, *15*, 5275–5277.
[8] M. Martin, O. Gevert, H. Werner, *J. Chem. Soc., Dalton Trans.* **1996**, 2275–2283.
[9] For a recent discussion of this transformation see: D. B. Grotjahn, X. Zeng, A. L. Cooksy, *J. Am. Chem. Soc.* **2006**, *128*, 2798–2799.
[10] D. Amoroso, G. P. A. Yap, D. E. Fogg, *Organometallics* **2002**, *21*, 3335–3343.
[11] Contrary to that which had been observed for reactions in $CH_2Cl_2$, a larger excess of acetylene (18 equiv.) also resulted in the formation of complex **7**. The yield was similar to that of reactions with equimolar amounts of acetylene, but the purity was slightly lower as evidenced by solid-state $^{31}P$ NMR spectroscopy.
[12] The symmetry operation is: $-x$, $y$, $-z+1/2$.
[13] M. Oliván, E. Clot, O. Eisenstein, K. G. Caulton, *Organometallics* **1998**, *17*, 897–901.
[14] Oxford Diffraction Ltd., Abingdon, Oxfordshire, UK, **2003**.
[15] G. M. Sheldrick, University of Göttingen, Germany, **1997**; Bruker AXS, Inc., Madison, Wisconsin, 53719, USA, **1997**.

Received: October 20, 2006
Published Online: December 12, 2006

 © 2007 Wiley-VCH Verlag GmbH & Co. KGaA, Weinheim 

DOI: 10.1002/ejic.200600920

# Blue-Light-Emitting Complexes: Cationic (2-Phenylpyridinato)iridium(III) Complexes with Strong-Field Ancillary Ligands

**Chong Shik Chin,*[a] Min-Sik Eum,[a] Song yi Kim,[a] Choongil Kim,[a] and Sung Kwon Kang[b]**

**Keywords:** Iridium / Luminescence / Blue-light emitter / Strong-field ligand

The emission $\lambda_{max}$ are strikingly shorter (451, 482 nm) for the cationic dicarbonyl complex $[Ir(ppy)_2(CO)_2]^+$ (**2a**) than those (473, 495 nm) of the anionic dicyano complex $[Ir(ppy)_2(CN)_2]^-$, where CO and $CN^-$ are both sp carbon coordinating ligands and known to be strong-field ligands showing a high *trans* effect. Sky-blue-light emission ($\lambda_{max}$ = 441–443 and 470–471 nm) could be obtained by modifying the ppy ligand to $F_2$Meppy (2,4-difluoro-2-phenyl-*m*-methylpyridinato anion) to prepare $[Ir(F_2Meppy)_2LL']^+$ [LL′ = $(CO)_2$ (**2a**$F_2$Me), $(PPh_2Me)_2$ (**2b**$F_2$Me)].
(© Wiley-VCH Verlag GmbH & Co. KGaA, 69451 Weinheim, Germany, 2007)

## Introduction

Research of blue-light-emitting materials is currently under thorough investigation because efficient blue-light emitters are in need in the display industry.[1] Iridium complexes of ppy (2-phenylpyridinato) have drawn much attention as they emit phosphorescence in the visible region with high quantum yields and the emission $\lambda_{max}$ can be tuned by modification of the ligands.[1–4] Theoretical calculations for $[Ir(ppy)_3]$,[2c] $[Ir(ppy)_2L_2]$,[4b] and [Pt(ppy)(acac)][5] suggest that the HOMO of these metal complexes include dπ-orbitals of the metal and orbitals of $L_2$[4b] or acac.[5] Spectroscopic data analysis for $Ir(C\text{^}N)_2LL'$ ($C\text{^}N$ = ppy and its derivatives)[4b] revealed that ancillary ligands (L, L′) alter the $^1$MLCT energy mainly by changing the HOMO energy level. The HOMO energy level may then be lowered by strong-field ancillary ligands, which causes a large d-orbital energy splitting. It is also likely that strong-field ancillary ligands L and L′ lengthen the bond lengths of Ir–C (ppy) *trans* to L and L′ to lower the energy levels of the dπ-orbitals of the metal as strong-field ligands are known to show a high *trans* effect.

Cationic complexes $[Ir(C\text{^}N)_2L_2]^+$ (L = neutral ligands such as CO) would be harder to oxidize than anionic complexes $[Ir(C\text{^}N)_2A_2]^-$ (A = anionic ligands such as $CN^-$) when L and A are the ligands having comparable ligand-field strength. One could expect, therefore, a larger energy gap between the HOMO and LUMO of the cationic complexes than that of the anionic complexes. A cationic complex such as $[Ir(C\text{^}N)_2(CO)_2]^+$ (not reported previously) would show a blueshifted emission $\lambda_{max}$ from that of the anionic complex $[Ir(C\text{^}N)_2(CN)_2]^-$ because both CO and $CN^-$ are well-known strong-field ligands that give large d-orbital energy splitting between dπ-orbitals ($e_g$) and dσ-orbitals ($t_{2g}$). One advantageous application of cationic complexes is their use for single-layer electroluminescent devices.[6]

We now wish to report new cationic complexes $[Ir(C\text{^}N)_2L_2]^+$ and $[Ir(C\text{^}N)_2LL']^+$ [$C\text{^}N$ = ppy, $F_2$ppy, $F_2$Meppy; L, L′ = strong-field ligands: CO, $PPh_2Me$, $P(OPh)_3$] and their photoluminescent characteristics in the blue color region.

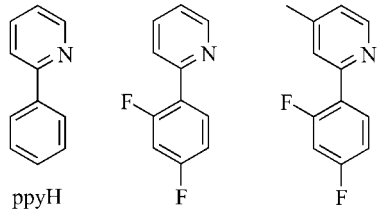


## Results and Discussion

Cationic complexes $[Ir(ppy)_2L_2]^+$ (**2**) and $[Ir(ppy)_2LL']^+$ (**3**, **4**) have been newly prepared (Scheme 1) and unambiguously characterized in detail by $^1$H-, $^{13}$C-, $^{31}$P NMR, IR spectral and elemental analysis data and also X-ray diffraction data analysis for single crystals of $[Ir(ppy)_2(PPh_3)(NCMe)]^+$ (**4a**). Assignment of the spectral signals is straightforward by comparison with those of related compounds previously reported (see Supporting Information).

[a] Chemistry Department, Sogang University,
Seoul 121-742, Korea
Fax: +82-2-701-0967
E-mail: cschin@sogang.ac.kr
[b] Chemistry Department, Chungnam National University
Daejeon 305-764, Korea
Supporting information for this article is available on the WWW under http://www.eurjic.org or from the author.


© 2007 Wiley-VCH Verlag GmbH & Co. KGaA, Weinheim

For example, the $Ir(ppy)_2$ moiety is unambiguously identified by detailed $^1H$- and $^{13}C$-NMR spectroscopic data while carbonyl (CO), cyano (CN), and MeCN complexes are characterized by IR absorptions due to ν(C≡O), ν(C≡N), and ν(N≡C).

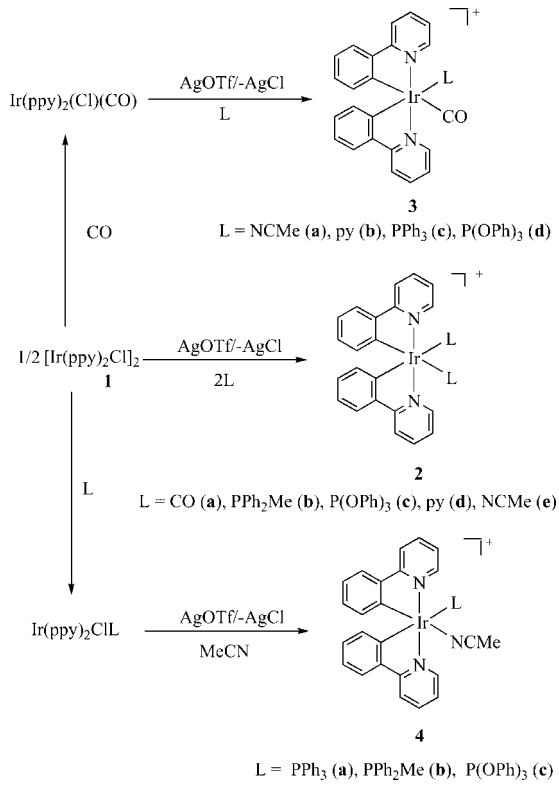


Scheme 1. Synthetic routes for $[Ir(ppy)_2L_2]^+$ (**2**), $[Ir(ppy)_2(CO)L]^+$ (**3**), and $[Ir(ppy)_2(NCMe)L]^+$ (**4**).

Attempts to prepare bis($PPh_3$) complex $[Ir(ppy)_2(PPh_3)_2]^+$ have been unsuccessful probably because $PPh_3$ is too large for the *cis*-$Ir(ppy)_2$ moiety to have two $PPh_3$ in the *cis* positions. Figure 1 shows that replacement of the MeCN ligand of **4a** with another $PPh_3$ would make the metal center too crowded to give the stable bis($PPh_3$) complex. A smaller phosphane ($PPh_2Me$) and a less congested phosphite [$P(OPh)_3$] fit into the *cis* positions of $[Ir(ppy)_2L_2]^+$ to give stable complexes, **2b** and **2c**.

Dicarbonyl complex $[Ir(ppy)_2(CO)_2]^+$ (**2a**) was the first complex synthesized in this study because the ligand-field strength of CO is as strong as that of $CN^-$ and photophysical data for the anionic complex $[Ir(ppy)_2(CN)_2]^-$ (**5**)[4a] are available to compare with those of **2a**.

Cationic complex **2a** shows emission $\lambda_{max}$ at 451 and 482 nm which are much shorter than those (473, 495 nm) of anionic complex **5** (see Table 1). Cationic complexes **2b** and **2c** with other strong-field ligands $PPh_2Me$ and $P(OPh)_3$ also emit blue color, whereas a longer emission $\lambda_{max}$ (480, 508 nm) is measured for complex **2d** containing the medium-strength-field ligand pyridine (Figure 2). Complex **2e** with the other N-based ligand MeCN shows the emission at $\lambda_{max}$ at 469 and 500 nm in MeCN where the dissociation of the labile MeCN ligand from **2** is suppressed, although no measurable emission is found in $CH_2Cl_2$ for **2e** as reported previously by Watts.[7]

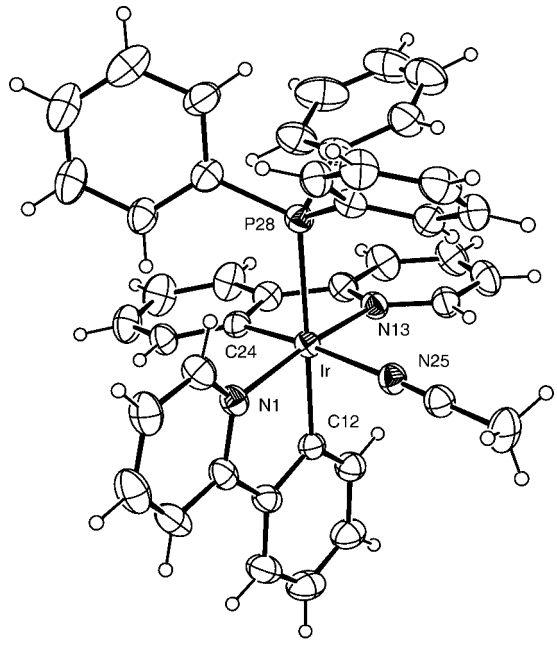


Figure 1. ORTEP drawing of $[Ir(ppy)_2(NCMe)(PPh_3)]^+$ (**4a**) with 50% thermal ellipsoids probability. Selected bond lengths [Å]: Ir–$N^1$ = 2.081(6); Ir–$N^{13}$ = 2.046(6); Ir–$N^{25}$ = 2.111(7); Ir–$C^{12}$ = 2.052(7); Ir–$C^{24}$ = 2.026(8), Ir–$P^{28}$ = 2.4342(19). Selected bond angles [°]: $N^1$–Ir–$N^{13}$ = 171.3(2); $C^{12}$–Ir–$P^{28}$ = 178.44(19); $C^{24}$–Ir–$N^{25}$ = 171.3(3).

Table 1. Photophysical data[a,b,c] for cationic complexes $[Ir(ppy)_2L_2]^+$ (**2**), $[Ir(ppy)_2(CO)(L)]^+$ (**3**), and $[Ir(ppy)_2(NCMe)(L)]^+$ (**4**).[a]

| | (**L**)(**L′**) | $\lambda_{max}$ [nm] | $\Phi_{PL}$ | $\tau$ [c] [μsec] |
|---|---|---|---|---|
| **2a** | (CO)(CO) | 451, 482 | 0.073 | 0.015 |
| **2b** | ($PPh_2Me$)($PPh_2Me$) | 460, 491 | 0.32 | 0.29 |
| **2c** | [$P(OPh)_3$][$P(OPh)_3$] | 458, 486 | 0.092 | 0.10 |
| **2d** | (py)(py) | 480, 508 | 0.73 | 0.15 |
| **2e** | (NCMe)(NCMe) | 469, 500 | 0.021 | 0.019 |
| **3a** | (CO)(NCMe) | 454, 485 | 0.054 | 0.10 |
| **3b** | (CO)(py) | 466, 487 | 0.41 | 0.80 |
| **3c** | (CO)($PPh_3$) | 455, 485 | 0.089 | 0.25 |
| **3d** | (CO)[$P(OPh)_3$] | 451, 482 | 0.19 | 1.1 |
| **4a** | ($PPh_3$)(NCMe) | 464, 495 | 0.034 | 0.027 |
| **4b** | ($PPh_2Me$)(NCMe) | 463, 493 | 0.040 | 0.029 |
| **4c** | [$P(OPh)_3$](NCMe) | 457, 488 | 0.13 | 0.34 |
| **5** | (CN)(CN) | 473, 495 | 0.79[b] | 2.6 |

[a] Compounds **2a**–**d** and **3b**–**d** in $CH_2Cl_2$ and **2e**, **3a**, **4a**–**4c**, and **5** in $CH_3CN$ at 298 K under an atmosphere of Ar. [b] Measured in this study and in agreement with the reported value,[4a] within experimental errors. [c] Calculated employing *fac*-$Ir(ppy)_3$ ($\Phi_{PL}$ = 0.40[8]) as the standard.

The quantum yields of complexes **2a**–**d** decrease significantly with a shift of the emission $\lambda_{max}$ to shorter wavelengths (see Table 1 and Figure 2). These results agree with the suggestion that the luminescence quantum yields decline with increasing emission energies.[4b] Among complexes prepared in this study, complex **2d** shows the longest emission $\lambda_{max}$ and the highest quantum yield. Both emis-

 © 2007 Wiley-VCH Verlag GmbH & Co. KGaA, Weinheim 

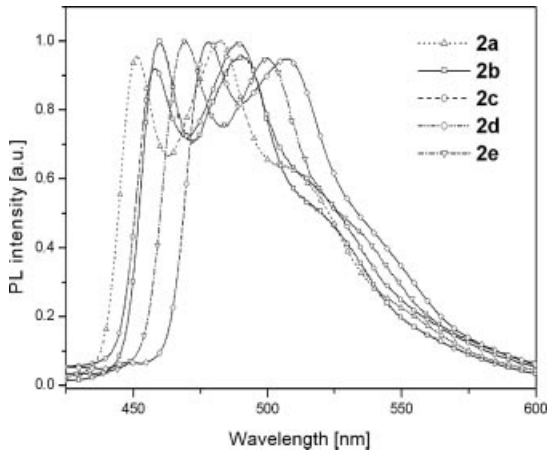


Figure 2. Normalized emission spectra of $[Ir(ppy)_2L_2](OTf)$ (**2**, $1 \times 10^{-4}$ M) in $CH_2Cl_2$ (**2a**–**d**), and MeCN (**2e**) at room temperature;·L = CO (**2a**), $PPh_2Me$ (**2b**), $P(OPh)_3$ (**2c**), py (**2d**), MeCN (**2e**).

sion $\lambda_{max}$ and quantum yield of cationic complex **2d** ($\lambda_{max}$ = 480, 508 nm; $_{PL}$ = 0.73 in $CH_2Cl_2$) are close to those of anionic complex **5** ($\lambda_{max}$ = 473, 495 nm; $\Phi_{PL}$ = 0.79 in MeCN) although pyridine is a much weaker-field ligand than $CN^-$. The lifetimes of cationic complexes prepared in this study are significantly shorter than that of anionic complex **5** and shorter lifetimes are measured for the complexes with relatively higher quantum yields (see Table 1).

The results observed for $[Ir(ppy)_2(L)_2]^+$ (**2**) agree with the anticipation that the emission $\lambda_{max}$ would be blueshifted by the strong-field (high *trans* effect) ancillary ligands L such as C- and P-based ligands, whereas a longer emission $\lambda_{max}$ would be seen for medium-field ligands L such as N-based ligands.

Complexes having two different strong-field ligands, $[Ir(ppy)_2(CO)(PPh_3)]^+$ (**3c**) and $[Ir(ppy)_2(CO)\{P(OPh)_3\}]^+$ (**3d**) also show shorter emission $\lambda_{max}$, whereas those with one MeCN or py (**3b** and **4a**–**c**) show $\lambda_{max}$ at relatively longer wavelengths (Table 1). It seems certain that among the N-based ligands, the sp N-based ligand MeCN gives shorter emission $\lambda_{max}$ than does the $sp^2$ N-based ligand pyridine as observed for **2d**, **2e**, **3a**, and **3b** (see Table 1). The effect of the field strength of the ancillary ligand on the emission energy is unambiguously confirmed again by replacing medium-field ligand pyridine with stronger-field ligand CO, which causes the emission $\lambda_{max}$ to be blueshifted from 480 and 508 nm for $[Ir(ppy)_2(py)_2]^+$ (**2d**) to 466 and 487 nm for $[Ir(ppy)_2(py)(CO)]^+$ (**3b**).

It is noticed that the quantum yield is relatively higher for $P(OPh)_3$ complex **3d** (0.19) than it is for both MeCN (**3a**) and $PPh_3$ (**3c**) complexes although the emission $\lambda_{max}$ is shorter for **3d** than it is for **3a** and **3c**, which may be understood by the fact that $P(OPh)_3$ is more basic than $PPh_3$ and MeCN and less dissociation of the ligand from the metal is expected for **3d** than for **3a** and **3c**.

Unlike bis-MeCN complex **2e**, mono-MeCN complexes **3a** and **4a**–**c** exhibit measurable emission in $CH_2Cl_2$ even in the absence of excess MeCN. Dissociation of the labile MeCN ligand, however, seems significant for most MeCN containing complexes and much lower quantum yields and redshifted emission $\lambda_{max}$ are observed in the absence of excess MeCN.

Cyclic voltammetric measurements for complexes prepared in this study show, in general, poorly resolved reversible waves for both oxidation and reduction. It is, however, confirmed that cationic complex **2a** clearly shows a more positive oxidation potential at 1.15 V than anionic complexes **5** (0.9 V)[4a] in $CH_2Cl_2$ (vs. $Fc^{2+}/Fc^+$) while **5** shows a more negative reduction potential (–1.70 V)[4a] than **2a** (–1.20 V) (see Supporting Information for voltammograms).

In order to see the effects of ppy ligand modification on the emission of $[Ir(ppy)_2L_2]^+$ (**2**), complexes of $F_2$ppy and $F_2$Meppy (**2a**$F_2$, **2a**$F_2$Me, **2b**$F_2$, **2b**$F_2$Me) have been prepared by the same method used for the preparation of **2** (Scheme 1). The blueshifts of the emission $\lambda_{max}$ caused by the modification of the ppy ligand are somewhat larger for the bisphosphane complexes (**2b**) than for the dicarbonyl complexes (**2a**) (see Table 2 and Figure 3). It should be

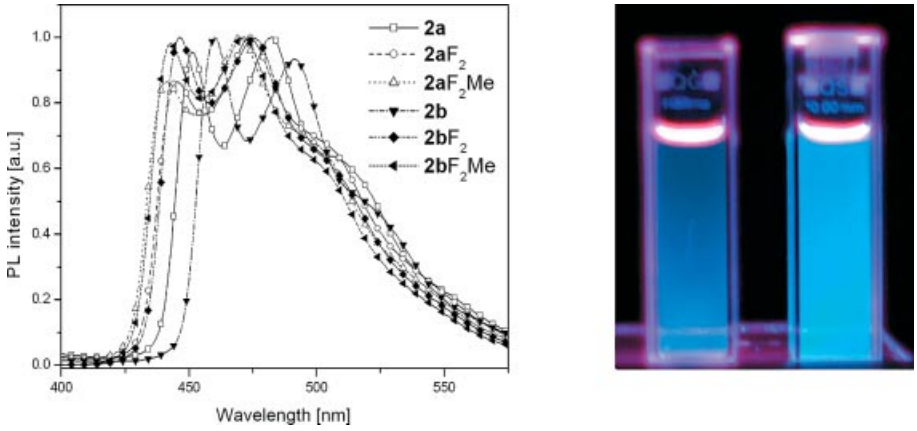


Figure 3. Normalized emission spectra of $[Ir(ppy)_2(CO)_2]^+$ (**2a**), $[Ir(F_2ppy)_2(CO)_2]^+$ (**2a**$F_2$), $[Ir(F_2Meppy)_2(CO)_2]^+$ (**2a**$F_2$Me), $[Ir(ppy)_2(PPh_2Me)_2]^+$ (**2b**), $[Ir(F_2ppy)_2(PPh_2Me)_2]^+$ (**2b**$F_2$) and $[Ir(F_2Meppy)_2(PPh_2Me)_2]^+$ (**2b**$F_2$Me) in $CH_2Cl_2$ at 25 °C. Complex **2a**$F_2$Me (left) displays somewhat of a more bluish emission than does **2b**$F_2$Me (right).

 © 2007 Wiley-VCH Verlag GmbH & Co. KGaA, Weinheim 

mentioned that blue-light emission is obtained by modification of the ppy ligand to produce **2a**$F_2$, **2a**$F_2$Me, **2b**$F_2$, and **2b**$F_2$Me while complexes **2a** and **2b** emit only greenish-blue light.

Increases in both the quantum yield and the lifetime of the emission are significant for phosphane complexes (**2b**, **2b**$F_2$, **2b**$F_2$Me), whereas no notable increase in the lifetime is observed for carbonyl complexes (**2a**, **2a**$F_2$, **2a**$F_2$Me) (see Table 2).

Table 2. Emission spectral data for $[Ir(C^{\wedge}N)_2L_2]^+$ (**2**) in $CH_2Cl_2$ at 25 °C.

| Complex | $C^{\wedge}N$ | L | $\lambda_{max}$ [nm] | $\Phi_{PL}$ | $\tau$ [μsec] |
|---|---|---|---|---|---|
| **2a**$F_2$ | $F_2$ppy | (CO) | 445, 474 | 0.079 | 0.17 |
| **2a**$F_2$Me | $F_2$Meppy | (CO) | 441, 470 | 0.097 | 0.15 |
| **2b**$F_2$ | $F_2$ppy | ($PPh_2$Me) | 446, 475 | 0.71 | 1.41 |
| **2b**$F_2$Me | $F_2$Meppy | ($PPh_2$Me) | 443, 471 | 0.80 | 1.16 |

In summary, the emission $\lambda_{max}$ of $[Ir(ppy)_2(L)_2]^+$ and $[Ir(ppy)_2(L)(L')]^+$ significantly shifts to shorter wavelengths with strong-ligand-field ancillary ligands (L and L′) such as CO and phosphorus-based ligands [$PPh_3$, $PPh_2$Me, $P(OPh)_3$] compared with the emission $\lambda_{max}$ of less-strong-field ligands such as nitrogen-based ligands (MeCN, py). For ancillary ligands of comparable ligand-field strengths such as CO and $CN^-$, the cationic complex $[Ir(ppy)_2(CO)_2]^+$ emits shorter wavelength than does the anionic one $[Ir(ppy)_2(CN)_2]^-$. Blue-light emission is obtained from cationic complexes **2a**$F_2$Me and **2b**$F_2$Me which contain strong-field ancillary ligands, CO and $PPh_2$Me, and a modified ppy ligand, $F_2$Meppy.

CCDC-619899 (for **4a**) contains the supplementary crystallographic data for this paper. These data can be obtained free of charge from The Cambridge Crystallographic Data Centre via www.ccdc.cam.ac.uk/data_request/cif.

**Supporting Information** (see footnote on the first page of this article): Experimental details and spectroscopic data for **2**–**4**. $^1$H- and $^{13}$C-NMR spectra of **2**–**4**. Photoluminescence decay diagrams and cyclic voltammograms of **2**.

## Acknowledgments

The authors wish to thank the Korea Research Foundation for their financial support of this study through the Basic Science Research Institute Program (Grant No. KRF-2005-015-C00222). Our appreciation also goes to Professor B. Lee, Phys. Dept., Sogang Univ. for the loan of the apparatus used to perform the phosphorescence lifetime measurements and Professor W. Shin, Chem. Dept., Sogang Univ. for the cyclic voltammetric measurements.

[1] a) N. Herron, N. S. Radu, E. M. Smith, Y. Wang, *US Patent* **2005/**0048312 A1; b) S. Lamansky, M. E. Thompson, V. Adamovich, P. I. Djurovich, C. Adachi, M. A. Baldo, S. R. Forrest, R. Kwong, *US Patent* **2002/**0182441 A1; c) T. Sajoto, P. I. Djurovich, A. Tamayo, M. Yousufuddin, R. Bau, M. E. Thompson, R. J. Holmes, S. R. Forrest, *Inorg. Chem.* **2005**, *44*, 7992–8003; d) P. Coppo, E. A. Plummer, L. De Cola, *Chem. Commun.* **2004**, 1774–1775; e) S. Chew, C. S. Lee, S.-T. Lee, P. Wang, J. He, W. Li, J. Pan, X. Zhang, H. Kwong, *Appl. Phys. Lett.* **2006**, *88*, 093510; f) C. Adachi, R. C. Kwong, P. Djurovich, V. Adamovich, M. A. Baldo, M. E. Thompson, S. R. Forrest, *Appl. Phys. Lett.* **2001**, *79*, 2082–2084.

[2] a) E. Holder, B. M. W. Langeveld, U. S. Schubert, *Adv. Mater.* **2005**, *17*, 1109–1121; b) M. A. Baldo, M. E. Thompson, S. R. Forrest, *Nature* **2000**, *403*, 750–753; c) A. B. Tamayo, B. D. Alleyne, P. I. Djurovich, S. Lamansky, I. Tsyba, N. N. Ho, R. Bau, M. E. Thompson, *J. Am. Chem. Soc.* **2003**, *125*, 7377–7387; d) A. Tsuboyama, H. Iwawaki, M. Furugori, T. Mukaide, J. Kamatani, S. Igawa, T. Moriyama, S. Miura, T. Takiguchi, S. Okada, M. Hoshino, K. Uneo, *J. Am. Chem. Soc.* **2003**, *125*, 12971–12979; e) J. Breu, P. Stössel, S. Schrader, A. Starukhin, W. J. Finkenzeller, H. Yersin, *Chem. Mater.* **2005**, *17*, 1745–1752; f) S. Okada, K. Okinaka, H. Iwawaki, M. Furugori, M. Hashimoto, T. Mukaide, J. Kamatani, S. Igawa, A. Tsuboyama, T. Takiguchi, K. Ueno, *Dalton Trans.* **2005**, 1583–1590; g) S. Lamansky, P. Djurovich, D. Murphy, F. Abdel-Razzaq, H.-E. Lee, C. Adachi, P. E. Burrows, S. R. Forrest, M. E. Thompson, *J. Am. Chem. Soc.* **2001**, *123*, 4304–4312.

[3] a) T. Tsuzuki, N. Shirasawa, T. Suzuki, S. Tokito, *Adv. Mater.* **2003**, *15*, 1455–1458; b) S. Jung, Y. Kang, H.-S. Kim, Y.-H. Kim, C.-L. Lee, J.-J. Kim, S.-K. Lee, S.-K. Kwon, *Eur. J. Inorg. Chem.* **2004**, 3415–3423; c) C.-H. Yang, K.-H. Fang, C.-H. Chen, I.-W. Sun, *Chem. Commun.* **2004**, 2232–2233; d) V. V. Grushin, N. Herron, D. D. LeCloux, W. J. Marshall, V. A. Petrov, Y. Wang, *Chem. Commun.* **2001**, 1494–1495; e) R. Ragni, E. A. Plummer, K. Brunner, J. W. Hofstraat, F. Babudri, G. M. Farinola, F. Naso, L. De Cola, *J. Mater. Chem.* **2006**, *16*, 1161–1170; f) I. R. Laskar, S.-F. Hsu, T.-M. Chen, *Polyhedron* **2006**, *25*, 1167–1176.

[4] a) M. K. Nazeeruddin, R. Humphrey-Baker, D. Berner, S. Rivier, L. Zuppiroli, M. Graetzel, *J. Am. Chem. Soc.* **2003**, *125*, 8790–8797; b) J. Li, P. I. Djurovich, B. D. Alleyne, M. Yousufuddin, N. N. Ho, J. C. Thomas, J. C. Peters, R. Bau, M. E. Thompson, *Inorg. Chem.* **2005**, *44*, 1713–1727; c) W. J. Finkenzeller, P. Stößel, H. Yersin, *Chem. Phys. Lett.* **2004**, *397*, 289–295; d) C.-L. Lee, R. R. Das, J.-J. Kim, *Chem. Mater.* **2004**, *16*, 4642–4646; e) C.-L. Lee, R. R. Das, J.-J. Kim, *Curr. Appl. Phys.* **2005**, *5*, 309–313.

[5] J. Brooks, Y. Babayan, S. Lamansky, P. I. Djurovivh, I. Tsyba, R. Bau, M. E. Thompson, *Inorg. Chem.* **2002**, *41*, 3055–3066.

[6] a) J. D. Slinker, A. A. Gorodetsky, M. S. Lowry, J. Wang, S. Parker, R. Rohl, S. Bernhard, G. G. Malliaras, *J. Am. Chem. Soc.* **2004**, *126*, 2763–2767; b) J. Slinker, D. Bernards, P. L. Houston, H. D. Abruña, S. Bernhard, G. G. Malliaras, *Chem. Commun.* **2003**, 2392–2399; c) S. Bernhard, J. A. Barron, P. L. Houston, H. D. Abruña, J. L. Ruglovksy, X. Gao, G. G. Malliaras, *J. Am. Chem. Soc.* **2002**, *124*, 13624–13628; d) J. D. Slinker, C. Y. Koh, G. G. Malliaras, M. S. Lowry, S. Bernhard, *Appl. Phys. Lett.* **2005**, *86*, 173506; e) M. S. Lowry, J. I. Goldsmith, J. D. Slinker, R. Rohl, R. A. Pascal Jr, G. G. Malliaras, S. Bernhard, *Chem. Mater.* **2005**, *17*, 5712–5719; f) H. J. Bolink, L. Cappelli, E. Coronado, A. Parham, P. Stössel, *Chem. Mater.* **2006**, *18*, 2778–2780.

[7] B. Schmid, F. O. Garces, R. J. Watts, *Inorg. Chem.* **1994**, *33*, 9–14 and references cited therein.

[8] K. A. King, P. J. Spellane, R. J. Watts, *J. Am. Chem. Soc.* **1985**, *107*, 1431.

Received: September 29, 2006
Published Online: December 12, 2006

 © 2007 Wiley-VCH Verlag GmbH & Co. KGaA, Weinheim 

DOI: 10.1002/ejic.200600743

# Two- and Three-Dimensional Coordination Polymers From the Reaction of Bis- and Tris(2-aminoethyl)amine with Titanium and Zirconium Alkoxides

**Helmut Fric,[a] Michael Puchberger,[a] and Ulrich Schubert*[a]**

*Dedicated to Professor Bernhard Kräutler on the occasion of his 60th birthday*

**Keywords:** Titanium / Zirconium / Coordination polymers / N ligands

The reaction of bis(2-aminoethyl)amine with M(O*i*Pr)$_4$ (M = Ti, Zr) affords the chain-like coordination polymers [M$_2$(O*i*Pr)$_8$(H$_2$NCH$_2$CH$_2$NHCH$_2$CH$_2$NH$_2$)]$_\infty$, where only the NH$_2$ groups of the amine are coordinated to the M$_2$(O*i*Pr)$_8$ units. 2D NMR spectroscopy shows that the adducts dissociate into the starting compounds when dissolved in CD$_2$Cl$_2$ but are slowly re-formed in solution over a period of two weeks. Puckered layers of condensed six-membered rings of [Ti$_2$(O*i*Pr)$_8$]$_3$[N(CH$_2$CH$_2$NH$_2$)$_3$]$_2$ are formed when [Ti(O*i*Pr)$_4$] is treated with tris(2-aminoethyl)amine. The voids in the center of the rings are filled by non-coordinated Ti$_2$(O*i*Pr)$_8$ guest molecules. In contrast, chains of [Zr$_2$(O*i*Pr)$_8$(H$_2$NCH$_2$CH$_2$NR′CH$_2$CH$_2$NH$_2$)]{R′=CH$_2$CH$_2$NH$_2$[Zr$_2$(O*i*Pr)$_8$(HO*i*Pr)]} are formed upon treatment of tris(2-aminoethyl)amine with [Zr(O*i*Pr)$_4$].

(© Wiley-VCH Verlag GmbH & Co. KGaA, 69451 Weinheim, Germany, 2007)

## Introduction

An understanding of the Lewis acidity of metal alkoxides is the key for understanding their chemistry, for example in sol–gel processes or as catalysts. One consequence of the acidic properties of the metal center in these alkoxides is their tendency to form oligomers [M(OR)$_x$]$_n$ with alkoxido bridges between two or three metal atoms, i.e. by interaction of the Lewis basic alkoxido groups with the Lewis acidic metal centers. The physical properties as well as the chemical reactivity of the metal alkoxides are influenced by the degree of aggregation. In alcoholic solution, for instance, addition of solvent molecules to the metal center competes with the formation of alkoxido bridges. The stability of the adducts increases for given alkoxido groups with increasing Lewis basicity of the alcohol, increasing Lewis acidity of the metal atom, and increasing coordination number of the metal. Thus, the adducts [M$_2$(O*i*Pr)$_8$(*i*PrOH)$_2$] (M = Ce,[1,2] Zr,[2] Hf[2,3]) can be isolated, whereas the analogous adducts [Ti$_2$(OR)$_8$(ROH)$_2$] are only stable when the Lewis acidity of the metal is raised by more electronegative substituents.[4–6] The metal atoms in the dimeric adducts [M$_2$(OR)$_8$(ROH)$_2$] are octahedrally coordinated owing to both the formation of alkoxido bridges and the coordination of alcohol molecules (Scheme 1, LH = ROH). The coordinated alcohol is stabilized by hydrogen bonding with the neighboring alkoxido ligand.

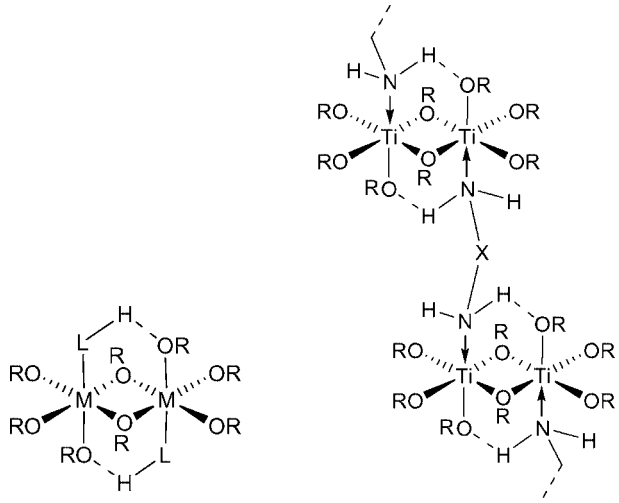

Scheme 1. General structure of the adducts [Ti$_2$(OR)$_8$(LH)$_2$] (LH = R′OH or R′NH$_2$; --- represents hydrogen bonds) and polymeric [Ti$_2$(OR)$_8$(NH$_2$XNH$_2$)].

The stability of the adducts can also be increased by stronger Lewis bases. We recently succeeded in crystallizing a number of amine adducts [M$_2$(OR)$_8$(NH$_2$R′)$_2$] (M = Ti, Zr) when M(OR)$_4$ was treated with the corresponding primary amines.[7,8] These amine adducts (Scheme 1, LH = R′NH$_2$) have similar structures to the alcohol adducts [M$_2$(OR)$_8$(ROH)$_2$], including the hydrogen bond between the amino group and the adjacent OR ligand. However, comparison of the adducts of different amines showed that

[a] Institute of Materials Chemistry, Vienna University of Technology,
Getreidemarkt 9, 1060 Wien, Austria

 © 2007 Wiley-VCH Verlag GmbH & Co. KGaA, Weinheim 

the Lewis basicity of the amine nitrogen is not the decisive parameter for the stability of the adducts. Instead, the strength of the NH···O hydrogen bond appears to be the main parameter. Any electronic or steric effect weakening the hydrogen bond thus weakens the stability of the adducts.

The general structure of $[Ti_2(OiPr)_8(NH_2R')_2]$ was extended to insoluble coordination polymers with the chain structures shown in Scheme 1 when $[Ti(OR)_4]$ was treated with diamines $H_2NXNH_2$ (X = hydrocarbon spacer).[7–9] An open question of previous work was whether the observed structures are retained in solution and whether coordination equilibria exist, because the obtained $^{15}N$ NMR spectra were rather inconclusive. The use of $NH(CH_2CH_2NH_2)_2$ and $N(CH_2CH_2NH_2)_3$ has now allowed us to answer this question. This is discussed in this paper, together with the interesting structural chemistry of the corresponding adducts.

## Results and Discussion

### Solid-State Structures

When bis(2-aminoethyl)amine was treated with an equimolar amount, or a slight excess, of $[Ti(OiPr)_4]$ in 2-propanol or $[Zr(OiPr)_4]$ in heptane, the compounds $[M_2(OiPr)_8(H_2NCH_2CH_2NHCH_2CH_2NH_2)]$ (**1**: M = Ti; **2**: M = Zr) were obtained in high yield. Although the starting amine contains three basic nitrogen atoms, only the two primary amino groups were found by X-ray structure analysis to coordinate to the metal alkoxide moieties. As a result, chain-like coordination polymers are formed (Figures 1 and 2), as previously found for $[Ti_2(OiPr)_8(H_2NXNH_2)]_\infty$ with hydrocarbon spacers (X) between the primary amino groups.

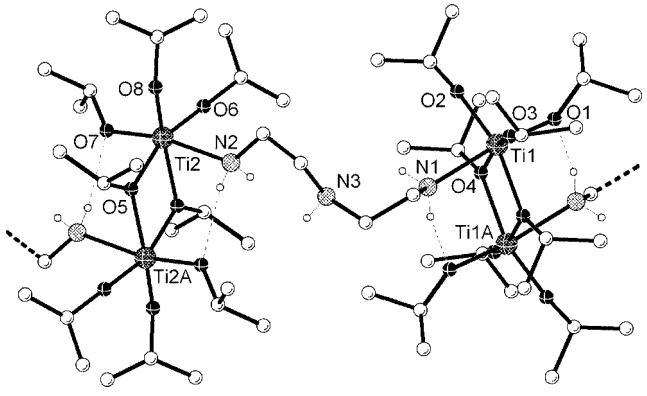


Figure 1. The chain structure of $[Ti_2(OiPr)_8(H_2NCH_2CH_2NHCH_2CH_2NH_2)]_\infty$ (**1**). The dotted lines represent NH···O hydrogen bonds. Selected bond lengths [pm] and angles [°]: Ti(1)–N(1) 229.2(2), Ti(1)–O(3) 180.7(2), Ti(1)–O(4) 205.0(2), Ti(1)–O(4A) 208.8(2), Ti(1)–O(1) 183.9(2), Ti(1)–O(2) 183.9(2), N(1)···O(1) 294.1(3), Ti(2)–N(2) 229.9(2), Ti(2)–O(7) 186.6(2), Ti(2)–O(5) 204.9(2), Ti(2)–O(4A) 209.8(2), Ti(2)–O(6) 181.4(2), Ti(2)–O(8) 182.6(2), N(2)···O(7) 293.7(3); N(1)–Ti(1)–O(1) 169.56(8), N(2)–Ti(2)–O(7) 168.65(9), N(1)–Ti(1)–Ti(1A) 77.97(6), N(2)–Ti(2)–Ti(2A) 76.75(7), O(1)–Ti(1)–Ti(1A) 91.75(6), O(7)–Ti(2)–Ti(2A) 92.42(7).

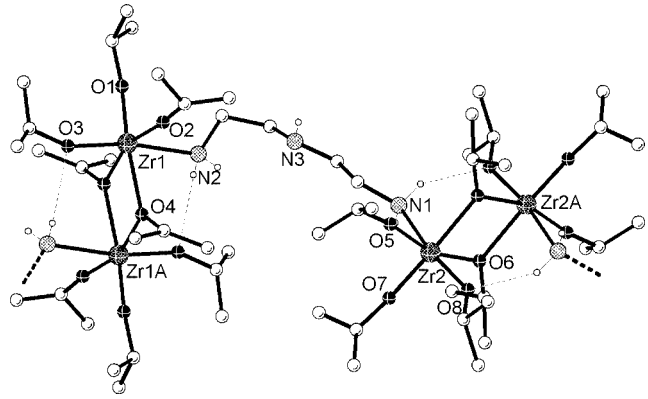


Figure 2. The chain structure of $[Zr_2(OiPr)_8(H_2NCH_2CH_2NHCH_2CH_2NH_2)]_\infty$ (**2**). The dotted lines represent NH···O hydrogen bonds. Selected bond lengths [pm] and angles [°]: Zr(1)–N(2) 241.7(3), Zr(1)–O(3) 196.9(3), Zr(1)–O(4) 219.0(2), Zr(1)–O(4A) 220.2(3), Zr(1)–O(1) 195.0(3), Zr(1)–O(2) 195.5(3), N(2)···O(3) 315.2(5), Zr(2)–N(1) 243.9(4), Zr(2)–O(8) 198.4(3), Zr(2)–O(6) 219.3(3), Zr(2)–O(6A) 219.2(3), Zr(2)–O(5) 195.1(3), Zr(2)–O(7) 195.0(3), N(1)···O(8) 308.8(5); N(2)–Zr(1)–O(3) 170.0(1), N(1)–Zr(2)–O(8) 168.4(1), N(2)–Zr(1)–Zr(1A) 76.77(9), N(1)–Zr(2)–Zr(2A) 76.24(9), O(3)–Zr(1)–Zr(1A) 93.41(9), O(8)–Zr(2)–Zr(2A) 92.70(9).

We have observed previously that secondary amines are less prone to coordinate to $M(OR)_4$ and have attributed this finding to the less pronounced ability of secondary amines to engage in the hydrogen bonding that stabilizes the M–N interaction.[8] Although the NH group in **1** and **2** does not interact with the metal alkoxides, it is probably responsible for the much better solubility of **1** and **2** compared to related coordination polymers with hydrocarbon spacers X. As will be discussed later, this fact allows us to investigate the solution structures by NMR spectroscopy.

Apart from different conformations of the bis(2-aminoethyl)amine units, the polymeric structures of **1** and **2** follow the same construction principle. The amine is a two-directional linker for the $M_2(OiPr)_8$ units, i.e. each $NH_2$ group of bis(2-aminoethyl)amine is coordinated to another $M_2(OiPr)_8$ unit. The chains are close-packed, with an interchain distance of about 870 pm in **1** and 910 pm in **2**

The metal alkoxide units are centrosymmetric dimers of the general composition $M_2(OR)_8(NH_2R)_2$ in which the octahedrally coordinated metal atoms are bridged by two OR groups. The amines are coordinated axially to the $M_2(\mu\text{-}OR)_2$ ring and hydrogen-bonded to neighboring alkoxido ligands (see Scheme 1 and Figures 1 and 2). The N···O separations [293.7(3) and 294.1(3) pm for **1**; 308.8(5) and 315.2(5) pm for **2**] are in the typical range of NH···O hydrogen bonds.[10] To enable hydrogen bonding, the M–M–N angles are reduced to 76–78° by bending of the amino ligand towards the center of the $M_2(\mu\text{-}OR)_2$ ring. The M–O distances *trans* to the amine ligand are in between the (long) M–O distances of the bridging OR groups and the (short) M–O distances of the equatorial terminal OR groups.

 © 2007 Wiley-VCH Verlag GmbH & Co. KGaA, Weinheim 

When $[Ti(OiPr)_4]$ was treated with 0.67 molar equivalents of tris(2-aminoethyl)amine, colorless crystals of $[\{Ti_2(OiPr)_8\}_3\{N(CH_2CH_2NH_2)_3\}_2 \cdot Ti_2(OiPr)_8]$ (**3**) were obtained after recrystallization from $CH_2Cl_2$. All $NH_2$ groups of tris(2-aminoethyl)amine coordinate to $Ti_2(OiPr)_8$ units. The crystal structure of **3** is thus a two-dimensional coordination polymer with $N(CH_2CH_2NH_2)_3$ as a three-directional linker and the $Ti_2(OR)_8$ units as two-directional connectors. The framework of **3** is formally related to that of black phosphorus, i.e. the framework of **3** is a puckered layer of condensed six-membered, centrosymmetric rings (Figures 3 and 4) with $CH_2CH_2NH_2[Ti_2(OiPr)_8]NH_2CH_2CH_2$ edges and pyramidal nitrogen atoms as the corners. The geometry of the $Ti_2(OiPr)_8(NH_2R)_2$ units of the framework structure corresponds to the general structure shown in Figure 1 (left), including the hydrogen bonds (N···O 297–302 pm). Furthermore, the Ti–N distances in **3** [230.5(4)–231.9(5) pm] are the same as in molecular or chain-like complexes with mono- or diamines.

The $[Ti_2(OiPr)_8]_3[N(CH_2CH_2NH_2)_3]_2$ network structure contains a large free volume due to the very large ring size (about 1.4 nm in diameter). In the crystals obtained in the reaction of $[Ti(OiPr)_4]$ with $N(CH_2CH_2NH_2)_3$, the voids in the center of the rings are filled with $Ti_2(OiPr)_8$ guest molecules, which do not undergo any bonding interaction with the host structure. The Ti–Ti vectors of the $Ti_2(OiPr)_8$

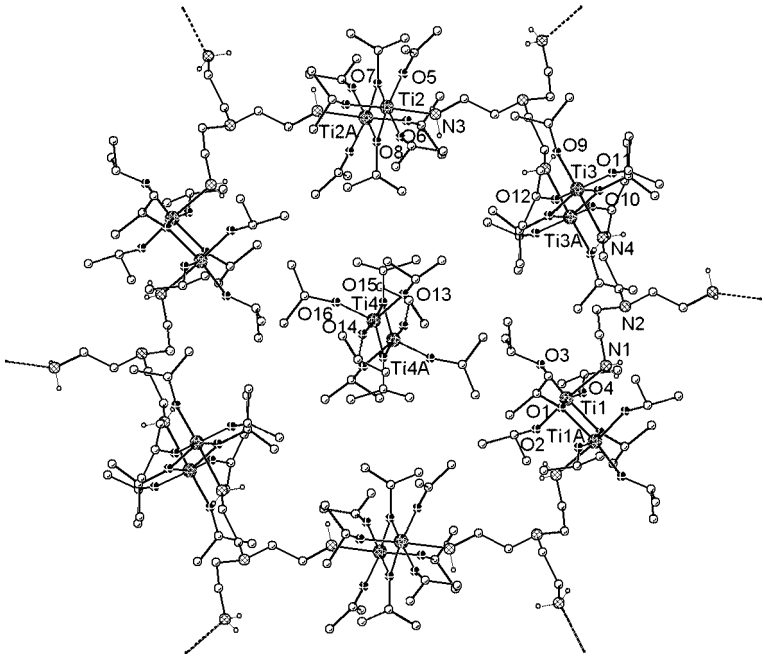


Figure 3. Perspective view (approximately perpendicular to the layer) of a six-membered ring from which the layer structure of **3** is composed. Most hydrogen atoms have been omitted for clarity. Selected bond lengths [pm]: Ti(1)–N(1) 233.5(5), Ti(2)–N(3) 231.4(4), Ti(3)–N(4) 231.7(4), N(1)···O(2) 302.0(6), N(3)···O(6) 296.7(6), N(4)···O(9) 298.2(6).

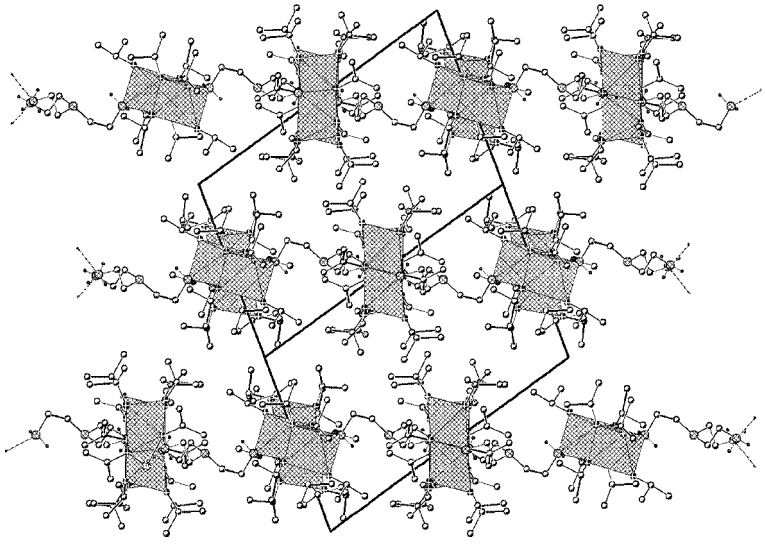

Figure 4. View of the layer structure of **3** parallel to the layers. The inter-layer distance is about 700 pm.

 © 2007 Wiley-VCH Verlag GmbH & Co. KGaA, Weinheim 

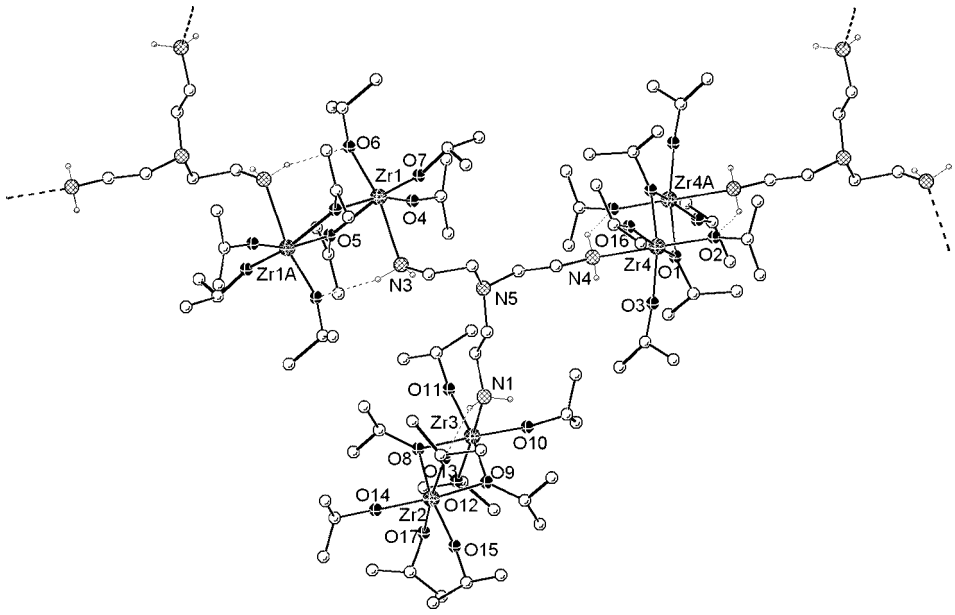


Figure 5. The chain structure of $[\{Zr_2(OiPr)_8\}\{Zr_2(OiPr)_8(HOiPr)\}\{(H_2NCH_2CH_2)_3N\}]_\infty$ (**4**). Selected bond lengths [pm]: Zr(1)–N(3) 244.8(6), Zr(3)–N(1) 243.0(7), Zr(4)–N(4) 243.3(6), Zr(2)–O(17) 232.1(6) (coordinated *i*PrOH), N(1)···O(13) 308(1), N(3)···O(6) 309.2(9), N(4)···O(2) 308(1), O(17)···O(12) 270.6(8).

guests are approximately perpendicular to the layer of the host structure. The structure of the entrapped titanium alkoxide dimers can be described as two trigonal bipyramids sharing a common axial–equatorial edge. Related structures of dimeric, nonsolvated titanium alkoxides with five-coordinate titanium atoms are known for bulky OR groups, such as $[Ti_2(OCH_2tBu)_8]$,[11] $[Ti_2(OiPr)_6(OAr)_2]$ (Ar = 2,4,6-$Me_3C_6H_2$[12] or 2,6-$iPr_2C_6H_3$[13]) and $[Ti_2(OiPr)_4\{OCH(CF_3)_2\}_4]$.[4] The crystal structure of **3** thus contains two structurally different $Ti_2(OiPr)_8$ moieties: the guest molecules with five-coordinate titanium atoms and the $Ti_2(OiPr)_8$ units with six-coordinate titanium atoms being part of the framework structure. Framework structures such as **3** have not yet been observed in the chemistry of transition metal alkoxides. It may be speculated that other guests could be incorporated in the same way into the host structure of $[Ti_2(OiPr)_8]_3[N(CH_2CH_2NH_2)_3]_2$.

The analogous reaction of $[Zr(OiPr)_4]$ with tris(2-aminoethyl)amine resulted in a compound with different composition and crystal structure. The structure of the obtained complex $[Zr_2(OiPr)_8][Zr_2(OiPr)_8(HOiPr)][(H_2NCH_2CH_2)_3N]$ (**4**) can be formally derived from the layer structure of **3** by decoordinating one $NH_2$ group per $N(CH_2CH_2NH_2)_3$ and replacing it with an 2-propanol molecule. This results in a chain structure of the type $Zr_2(OiPr)_8(H_2NCH_2CH_2NR'CH_2CH_2NH_2)$, where R′ is a $CH_2CH_2NH_2[Zr_2(OiPr)_8(HOiPr)]$ moiety (Figure 5). Formation of a layered structure is thus inhibited because one coordination site at one zirconium is blocked by an alcohol molecule. As mentioned in the Introduction, alcohol adducts of $[Zr(OiPr)_4]$ are stable while those of $[Ti(OiPr)_4]$ are not; this allows the alcohol to compete with the amine for coordination. It is interesting to note at this point that reaction of $M(OiPr)_4$ with benzylamine results in the same structure $[M_2(OiPr)_8(NH_2CH_2Ph)_2]$ for both Ti and Zr.[8] The bond lengths and angles of the zirconium atoms in **4** coordinated to $NH_2$ groups are basically the same as those in **2**, while those of the sixth zirconium atom, to which an 2-propanol molecule is coordinated, are very similar to those in $[Zr_2(OiPr)_8(iPrOH)_2]$, including the hydrogen bond between the coordinated alcohol and the adjacent O*i*Pr ligand.[2]

## NMR Investigations in Solution

The coordination polymers **1**–**4** described above can be recrystallized, which is a strong indication that the amine adducts are relatively stable and may persist in solution. Nevertheless, coordination equilibria may exist upon dissolution of the compounds. This is not simply an academic question but is also important for the use of metal alkoxides in sol–gel processes, where coordination polymers may offer the possibility to pre-organize metal alkoxides prior to hydrolytic polycondensation.

A section of the $^1H$ NMR spectrum of the dissolved crystals of **1** is reproduced at the top of Figure 6. The $^1H/^{13}C$ HSQC spectrum shows one correlation at $\delta$ = 4.51 ($^1H$) and 76.5 ppm ($^{13}C$) for a CH unit of the time-averaged isopropoxide ligands and two correlations at $\delta$ = 2.84 ($^1H$)/52.8 ppm ($^{13}C$) and 2.54 ($^1H$)/42.2 ppm ($^{13}C$) corresponding to the two $CH_2$ units of the amine ligand. The latter two signals are very similar to the signals of the free ligand at $\delta$ = 2.57/2.68 ppm ($^1H$) and 41.7/57.7 ppm ($^{13}C$), respectively. The $^1H/^{15}N$ HMBC spectrum of **1** (Figure 7, left) shows two correlations at $\delta$ = 9.1 (NH) and –3.2 ppm ($NH_2$), which are almost the same as the shifts for the uncoordi-

 © 2007 Wiley-VCH Verlag GmbH & Co. KGaA, Weinheim 

nated ligand ($\delta$ = 9.1 and –2.3 ppm). The two protons of the $NH_2$ groups appear as a broad signal at $\delta$ = 1.09 ppm. This indicates that most of the amine ligand is not coordinated to the metal center.

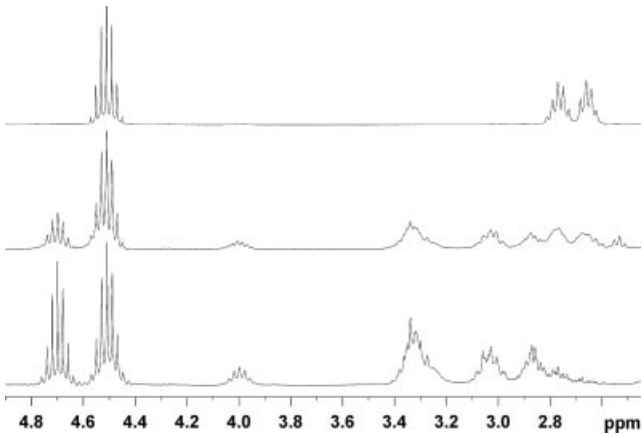


Figure 6. $^1$H NMR spectra of $[Ti_2(OiPr)_8(NH_2CH_2CH_2NHCH_2CH_2NH_2)]$ (**1**) in $CD_2Cl_2$. Top: immediately after dissolving the crystals; center: after one week; bottom: after two weeks.

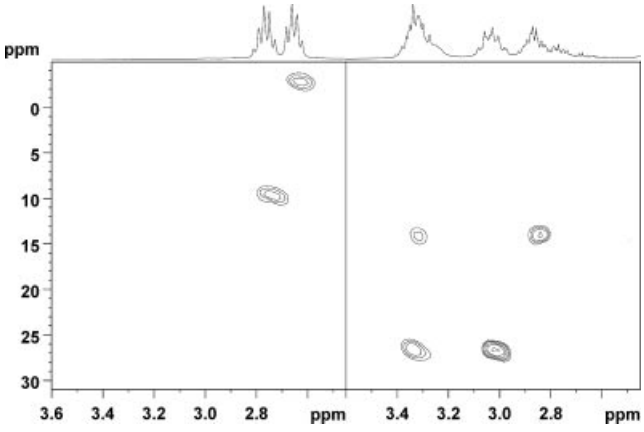


Figure 7. $^1$H/$^{15}$N HMBC spectrum of **1** in $CD_2Cl_2$. Left: immediately after dissolving the crystals; right: after two weeks.

This picture changed completely when NMR spectra of the same solution were recorded again after one week. The $CH_2$ region of the amine now showed five new broad and unresolved multiplets beside the previous two signals, which were broader (Figure 6, center) and with lower intensity. In a third spectrum measured after two weeks (Figure 6, bottom), nearly no starting signals were left, but instead four new broad multiplets were observed. The signals for the two nitrogen atoms had shifted to $\delta$ = 14.0 (typical shift range for coordinated $NH_2$) and 26.5 ppm (NH) (Figure 7, right). This indicated strongly that the amine is now coordinated. This conclusion was supported by the pair-wise splitting of the proton signals of the $CH_2$ groups in the $^1$H/$^{13}$C HSQC spectrum (Figure 8). Correlations were found at $\delta$ = 3.32/2.86 ($^1$H) and 48.7 ppm ($^{13}$C) as well as $\delta$ = 3.33/3.02 ($^1$H) and 39.6 ppm ($^{13}$C). The splitting of the proton resonance is due to the fact that the protons become non-equivalent upon coordination of the $NH_2$ groups to the metal centers.

The two protons of the $NH_2$ group are also split into two broad signals (proton trace in Figure 8) at $\delta$ = 5.69 and 2.39 ppm. This is evidence for the formation of stable N–H···O hydrogen bonds, as observed in the solid-state structure. Four different signals of isopropoxide groups were identified in the $^1$H/$^{13}$C HSQC spectrum at this point (Figure 8). Two signals overlap in the proton region at $\delta$ = 4.69 ppm ($^1$H) and show $^{13}$C correlations to the signals at $\delta$ = 78.3 and 76.7 ppm; the third is located at $\delta$ = 4.51 ($^1$H) and 76.1 ppm ($^{13}$C). The signals at $\delta$ = 3.97 ($^1$H) and 64.1 ppm ($^{13}$C) are due to non-coordinated *i*PrOH. The NMR spectra after two weeks, especially the number and intensity ratio of the O*i*Pr ligand signals, correspond with the local symmetry [two axial O*i*Pr (*trans* to $NH_2$), four equatorial and two bridging] of **1** in the solid-state structure. The presence of noncoordinated 2-propanol is either due to incomplete removal of adsorbed alcohol during drying of the crystals or minor hydrolysis during the long measuring period.

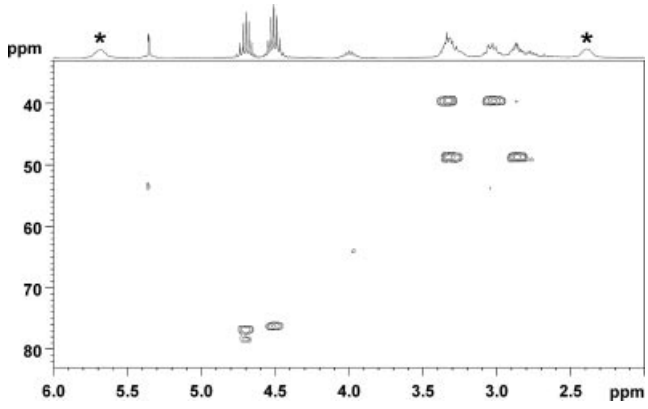


Figure 8. $^1$H/$^{13}$C HSQC spectrum of **1** in $CD_2Cl_2$ after two weeks. The two proton signals marked with an asterisk are from $NH_2$.

We interpret the spectroscopic findings by proposing that the polymeric adduct of **1** dissociates into $[Ti_2(OiPr)_8]$ and $NH(CH_2CH_2NH_2)_2$ upon dissolution in $CD_2Cl_2$. The NMR spectra measured immediately after dissolution of the crystals thus correspond to a mixture of the starting compounds. The adduct is formed again in a slow reaction in solution, and the NMR spectra after two weeks correspond to the amine adduct **1**. This notion was supported by the following experiment. When $[Ti(OiPr)_4]$ and bis(2-aminoethyl)amine were mixed in a 2:1 ratio (same Ti:amine ratio as in crystalline **1**) in $CD_2Cl_2$ the same changes in the spectra were observed over a period of two weeks as when crystals of **1** were dissolved. Only the signals of the starting materials were present after mixing, whereas an identical signal pattern was observed after two weeks as for the dissolved crystals.

The corresponding complex $[Zr_2(OiPr)_8(NH_2CH_2CH_2NHCH_2CH_2NH_2)]$ (**2**) shows almost the same solution behavior as **1**, with the exception that **2** is less soluble, which leads to rather faster crystallization in the NMR tube. The crystals recovered from the NMR tube had identical cell parameters as the original crystals.

 © 2007 Wiley-VCH Verlag GmbH & Co. KGaA, Weinheim 

As a result of the NMR investigations described above, it is now possible to prove adduct formation even if the compounds do not crystallize and thus no solid-state structures are available. Figure 9 shows the NMR spectra of a 1:1 mixture of $[Ti(OiPr)_4]$ and *N*-(trimethoxysilylpropyl)-ethylenediamine in $CD_2Cl_2$. To prove whether coordination occurs in solution, spectra were recorded over a period of two months. New signals were observed one week after mixing the starting compounds (Figure 9, center), and after two months (Figure 9, bottom) almost no signals of the starting compounds were left. $^{15}N$ NMR signals at $\delta$ = 14.3 (NH) and 2.7 ppm ($NH_2$) were found after mixing the compounds, compared to $\delta$ = 13.4 (NH) and –4.0 ppm ($NH_2$) for the ethylenediamine derivative before addition of $[Ti(OiPr)_4]$, which shifted to $\delta$ = 37.8 (NH) and 31.3 ppm ($NH_2$) after two months. The signals for the *i*OPr ligands after two months correspond roughly to the symmetry of a $[Ti_2(OiPr)_8(NH_2R)_2]$ complex. These NMR spectra thus strongly indicate that the ligand is almost completely coordinated and compound **5** is formed.

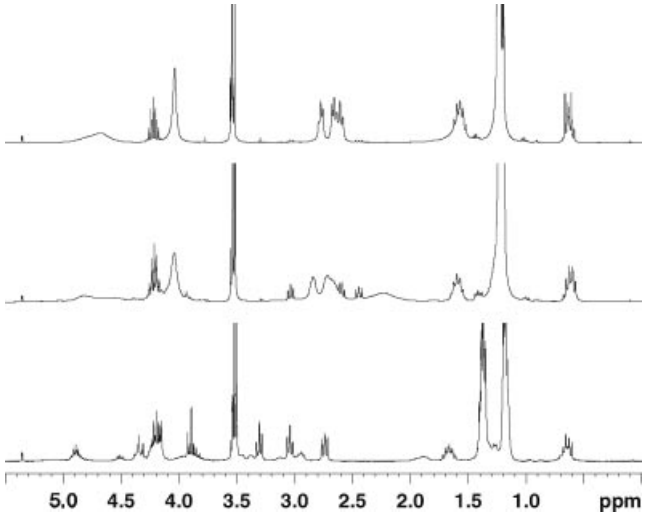


Figure 9. $^1H$ NMR spectrum of $[Ti(OiPr)_4]$ and $H_2NCH_2CH_2NHCH_2CH_2CH_2Si(OMe)_3$ in a 1:1 ratio in $CD_2Cl_2$. Top: after mixing; center: after one week; bottom: after two months.

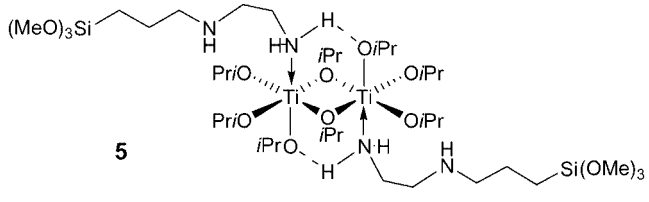


**5**

In the $^1H$ NMR spectrum of $[\{Ti_2(OiPr)_8\}_3\{N(CH_2CH_2NH_2)_3\}_2{\cdot}Ti_2(OiPr)_8]$ (**3**) (Figure 10, top) four broad multiplets were observed between $\delta$ = 3.40 and 2.80 ppm immediately after dissolving the crystals, and the $CH_2$ region in the $^1H/^{13}C$ HSQC spectrum (Figure 11) showed four different pairwise correlations to $^{13}C$ atoms, with two of them belonging to the same $CH_2CH_2$ unit ($\delta$ = 36.4–53.3 and 38.6–60.0 ppm). An EXSY spectrum of this compound showed exchange peaks between these $CH_2CH_2$ units along the diagonal. An explanation for this observation might be that not all three $CH_2CH_2$ units are coordinated in solution and therefore show time-averaged $^1H$ and $^{13}C$ signals. The $^{15}N$ signals were found at $\delta$ = 36.3 (N) and 14.8 ppm (coordinated $NH_2$).

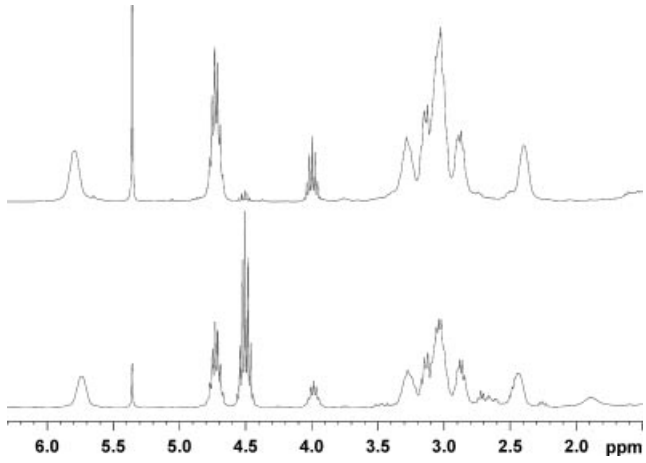


Figure 10. Top: $^1H$ NMR spectrum of $[\{Ti_2(OiPr)_8\}_3\{N(CH_2CH_2NH_2)_3\}_2{\cdot}Ti_2(OiPr)_8]$ (**3**) immediately after dissolving the crystals in $CD_2Cl_2$. Bottom: $[Ti(OiPr)_4]$ and tris(2-aminoethyl)-amine in $CD_2Cl_2$ mixed in a 2:1 ratio after two weeks.

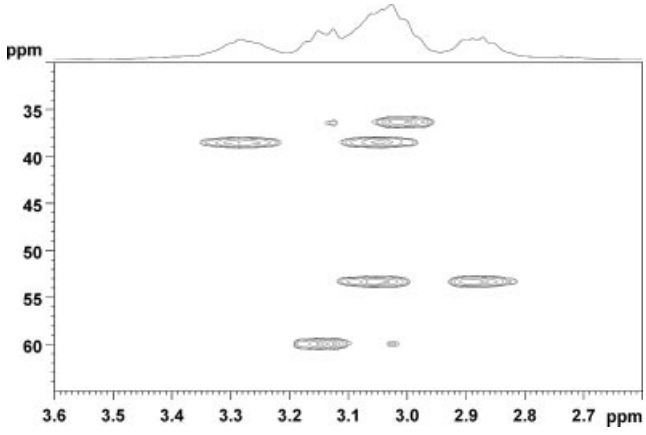


Figure 11. $^1H/^{13}C$ HSQC spectrum of the $CH_2$ region of **3** in $CD_2Cl_2$.

Mixing $[Ti(OiPr)_4]$ and tris(2-aminoethyl)amine in a 2:1 ratio in $CD_2Cl_2$ again showed a very similar peak pattern for the $CH_2$ region of the amine after two weeks (Figure 10, bottom). It is worth mentioning that the signals in the CH region of the isopropoxide ligand have different intensities, which might be due to either different concentrations of the product or to different amounts of free 2-propanol. The spectra of **3** suggests that this compound does not dissociate (completely) into the starting compounds, contrary to what had been observed for **1** and **2**. We cannot exclude that part of the $NH_2$ groups dissociate, but the observed spectra after dissolution of the crystals of **3** are distinctly different to a mixture of $[Ti(OiPr)_4]$ and tris(2-aminoethyl)-amine. The interpretation of the O*i*Pr signals in the spectra was complicated by the presence of the $Ti_2(OiPr)_8$ guests in the crystal lattice.

 © 2007 Wiley-VCH Verlag GmbH & Co. KGaA, Weinheim 

The corresponding zirconium derivative **4** is almost insoluble in $CD_2Cl_2$, therefore no detailed NMR investigations were carried out.

## Conclusions

We have shown that the previously observed formation of chain-like coordination polymers upon reaction of $[M(OR)_4]$ (M = Ti, Zr) with diamines can be extended to the formation of layered structures. Layers of $[Ti_2(OiPr)_8]_3$-$[N(CH_2CH_2NH_2)_3]_2$, consisting of condensed six-membered rings, are obtained from $[Ti(OiPr)_4]$ and tris(2-aminoethyl)amine. The voids of the rings are occupied by $Ti_2(OiPr)_8$ nonsolvated guest molecules.

The amine adducts of $[M(OR)_4]$ (M = Ti, Zr) are retained in solution. Although **1** and **2** dissociate into $[M(OiPr)_4]$ and bis(2-aminoethyl)amine when dissolved in $CD_2Cl_2$, the adducts slowly form again in solution. We are aware that this may be different in other solvents. There is strong spectroscopic evidence that the network structure of **3** is retained upon dissolution of the crystals, at least partially.

An important consequence for sol-gel processing is that amine adducts must be taken into account when $[M(OR)_4]$ is used in the presence of compounds with $NH_2$ groups. Adduct formation will probably influence the reactivity of the alkoxides and may also result in morphological changes of the gels. We will further investigate the possibility to preorganize gels by di- and triamine adducts.

## Experimental Section

All operations were carried out in a moisture- and oxygen-free atmosphere of argon. $[Ti(OiPr)_4]$ (97%, Aldrich), $[Zr(OiPr)_4]$ (70–75% in heptane, ABCR), bis(2-aminoethyl)amine (99%, Aldrich) and tris(2-aminoethyl)amine (96%, Aldrich ) were used as received. The solvents were dried and purified by standard techniques.

**Synthesis of $[Ti_2(OiPr)_8(H_2NCH_2CH_2NHCH_2CH_2NH_2)]$ (1):** Bis(2-aminoethyl)amine (315 mg, 3.05 mmol) was added, whilst stirring, to a solution of $[Ti(OiPr)_4]$ (882 mg, 3.10 mmol) in 1 mL of 2-propanol at room temperature. The clear reaction solution was then stored at 4 °C and colorless crystals were obtained after 12 h. The product was recrystallized twice from $CH_2Cl_2$ and dried in vacuo. Yield: 736 mg (83%).

**Dissolved Crystals or Mixture of Starting Compounds:** $^1$H NMR ($CD_2Cl_2$, 21 °C): $\delta$ = 4.51 (sept, $J$ = 6.1 Hz, OC*H*Me$_2$), 2.84–2.54 (m, C$H_2$C$H_2$NH$_2$), 1.26 [d, $J$ = 6.1 Hz, OCH(C$H_3$)$_2$], 1.08 (br., N$H_2$) ppm. $^{13}$C{$^1$H} NMR ($CD_2Cl_2$, 21 °C): $\delta$ = 76.5 (O*C*HMe$_2$), 52.8 [HN(*C*H$_2$)$_2$], 42.2 [H$_2$N(*C*H$_2$)$_2$], 26.5 [OCH(*C*H$_3$)$_2$] ppm. $^{15}$N{$^1$H} NMR ($CD_2Cl_2$, 21 °C): $\delta$ = –3.2 (H$_2$*N*), 9.1 (*N*H) ppm.

**After Two Weeks at Room Temperature:** $^1$H NMR ($CD_2Cl_2$, 21 °C): $\delta$ = 5.68 (br., N$H_2$/N*H*), 4.70, 4.51 (sept, $J$ = 6.1 Hz, OC*H*Me$_2$), 4.00 (sept, $J$ = 6.1 Hz, HOC*H*Me$_2$), 3.43–2.58 (m, C$H_2$C$H_2$NH$_2$), 2.39, 1.56 (br., N$H_2$/N*H*), 1.26 [d, $J$ = 6.1 Hz, OCH(C$H_3$)$_2$], 1.19 [d, $J$ = 6.1 Hz, HOCH(C$H_3$)$_2$] ppm. $^{13}$C{$^1$H} NMR ($CD_2Cl_2$, 21 °C): $\delta$ = 78.3, 76.7, 76.2 (O*C*HMe$_2$), 64.1 (HO*C*HMe$_2$), 48.7 (HN*C*H$_2$), 39.6 (H$_2$N*C*H$_2$), 26.1 [OCH(*C*H$_3$)$_2$/HOCH(*C*H$_3$)$_2$] ppm. $^{15}$N{$^1$H} NMR ($CD_2Cl_2$, 21 °C): $\delta$ = 14.0 (H$_2$*N*), 26.5 (*N*H) ppm.

**Synthesis of $[Zr_2(OiPr)_8(H_2NCH_2CH_2NHCH_2CH_2NH_2)]$ (2):** Bis(2-aminoethyl)amine (209 mg, 2.03 mmol) was slowly added, whilst stirring, to 1029 mg (2.20 mmol) of a 70–75% solution of $[Zr(OiPr)_4]$ in *n*-heptane that was diluted with 2 mL of *n*-heptane. The resulting white precipitate was dissolved in a mixture of 4 mL of 2-propanol and 2 mL of $CH_2Cl_2$ under reflux. The product was recrystallized twice from $CH_2Cl_2$ and dried in vacuo. Yield: 972 mg (94%).

**Dissolved Crystals:** $^1$H NMR ($CD_2Cl_2$, 21 °C): $\delta$ = 4.91, 4.39 (sept, $J$ = 6.1 Hz, OC*H*Me$_2$), 3.98 (sept, $J$ = 6.1 Hz, HOC*H*Me$_2$), 2.80 [br., HN(C$H_2$)$_2$], 2.69 [br., H$_2$N(C$H_2$)$_2$], 1.32, 1.30 [d, $J$ = 6.1 Hz, OCH(C$H_3$)$_2$], 1.20 [d, $J$ = 6.1 Hz, HOCH(C$H_3$)$_2$] ppm. $^{13}$C{$^1$H} NMR ($CD_2Cl_2$, 21 °C): $\delta$ = 69.8, 69.2 (O*C*HMe$_2$), 63.6 (HO*C*HMe$_2$), 42.1 [H$_2$N(C$H_2$)$_2$], 52.6 [HN(C$H_2$)$_2$], 32.1, 27.2 [OCH(C$H_3$)$_2$], 24.8 [HOCH(C$H_3$)$_2$] ppm.

**Synthesis of $[\{Ti_2(OiPr)_8\}_3\{(H_2NCH_2CH_2)_3N\}_2{\cdot}Ti_2(OiPr)_8]$ (3):** Tris(2-aminoethyl)amine (365 mg, 2.50 mmol) was added dropwise, whilst stirring, to a solution of 1051 mg (3.70 mmol) of $[Ti(OiPr)_4]$ in 2 mL of $CH_2Cl_2$ at room temperature under argon. The colorless solution was refluxed for 5 min and then concentrated to half its volume. The vessel was then stored at 4 °C to afford colorless crystals after 3 d. The product was recrystallized twice from $CH_2Cl_2$ and dried in vacuo. Yield: 732 mg (62%). The same product, but in lower yields, was obtained when 2-propanol was used as the solvent.

**Dissolved Crystals:** $^1$H NMR ($CD_2Cl_2$, 21 °C): $\delta$ = 5.81 (br., N$H_2$), 4.73, 4.51 (sept, $J$ = 6.1 Hz, OC*H*Me$_2$), 3.41–2.66 [m, N(C$H_2$C$H_2$NH$_2$)$_3$], 2.40 (br., N$H_2$), 1.26 [d, $J$ = 6.1 Hz, OCH(C$H_3$)$_2$], 0.96 (b, N$H_2$) ppm. $^{13}$C{$^1$H} NMR ($CD_2Cl_2$, 21 °C): $\delta$ = 79.0, 76.9, 76.3 (O*C*HMe$_2$), 60.2 (non-coordinated), 53.5 [N(*C*H$_2$CH$_2$NH$_2$)$_3$], 38.5 (non-coordinated), 36.5 [N(CH$_2$*C*H$_2$NH$_2$)$_3$], 26.0 [OCH(*C*H$_3$)$_2$] ppm. $^{15}$N{$^1$H} NMR ($CD_2Cl_2$, 21 °C): $\delta$ = 36.8 (*N*), 14.2, 13.5 (*N*H$_2$) ppm.

**Synthesis of $[Zr_2(OiPr)_8][Zr_2(OiPr)_8(HOiPr)][(H_2NCH_2CH_2)_3N]$ (4):** Tris(2-aminoethyl)amine (207 mg, 1.42 mmol) was slowly added, whilst stirring, to 737 mg (1.58 mmol) of a 70–75% solution of $[Zr(OiPr)_4]$ in *n*-heptane that was diluted with 3 mL of 2-propanol. The reaction solution was refluxed for 5 min and then concentrated to half its volume. The closed vessel was then stored at room temperature to yield colorless crystals after three weeks. The product was recrystallized twice from $CH_2Cl_2$ and dried in vacuo. Yield: 461 mg (89%).

**Dissolved Crystals:** $^1$H NMR ($CD_2Cl_2$, 21 °C): $\delta$ = 4.48, 4.35, 4.22 (sept, $J$ = 6.1 Hz, OC*H*Me$_2$), 3.13 (br., C$H_2$CH$_2$NH$_2$), 2.98 (br., CH$_2$C$H_2$NH$_2$), 1.44–0.98 [m, OCH(C$H_3$)$_2$/HOCH(C$H_3$)$_2$] ppm. $^{13}$C{$^1$H} NMR ($CD_2Cl_2$, 21 °C): $\delta$ = 71.4, 70.8, 70.3, 68.9 (O*C*HMe$_2$), 52.5 [N(*C*H$_2$CH$_2$NH$_2$)$_3$], 37.4 [N(CH$_2$*C*H$_2$NH$_2$)$_3$], 26.6, 26.3, 25.4 [OCH(*C*H$_3$)$_2$] ppm. $^{15}$N{$^1$H} NMR ($CD_2Cl_2$, 21 °C): $\delta$ = 30.85 (*N*), 9.09 (H$_2$*N*) ppm.

**X-ray Structure Analyses:** The crystals were mounted on a Siemens SMART diffractometer (area detector) and measured in a nitrogen stream. Mo-$K_\alpha$ radiation ($\lambda$ = 71.069 pm, graphite monochromator) was used for all measurements. The data collection at 173 K covered a hemisphere of the reciprocal space, by a combination of three or four sets of exposures. Each set had a different $\phi$ angle for the crystal, and each exposure took 15 or 20 s and covered 0.3° in $\omega$. The crystal-to-detector distance was 5 cm. Further details can be found in Table 1. The data were corrected for polarization and Lorentz effects, and an empirical absorption correction (SADABS) was employed. The cell dimensions were refined with all unique reflections. The structures were solved by direct methods

 © 2007 Wiley-VCH Verlag GmbH & Co. KGaA, Weinheim 

Table 1. Crystallographic parameters of **1**–**4**.

| | **1** | **2** | **3** | **4** |
|---|---|---|---|---|
| Empirical formula | $C_{28}H_{69}N_3O_8Ti_2$ | $C_{28}H_{69}N_3O_8Zr_2$ | $C_{108}H_{260}N_8O_{32}Ti_8$ | $C_{57}H_{138}N_4O_{17}Zr_4$ |
| Formula weight | 671.7 | 758.3 | 2566.4 | 1516.3 |
| Crystal system | triclinic | monoclinic | triclinic | triclinic |
| Space group | $P\bar{1}$ | $P2_1/c$ | $P\bar{1}$ | $P\bar{1}$ |
| $a$ [pm] | 9.6371(6) | 18.144(4) | 1234.4(5) | 12.269(3) |
| $b$ [pm] | 12.2646(7) | 18.238(4) | 1846.8(7) | 18.244(4) |
| $c$ [pm] | 17.055(1) | 12.366(3) | 1858.2(7) | 18.958(4) |
| $\alpha$ [°] | 99.820(1) | 90 | 63.522(7) | 90.875(4) |
| $\beta$ [°] | 95.970(1) | 92.98(3) | 83.637(8) | 92.723(5) |
| $\gamma$ [°] | 104.461(1) | 90 | 88.171(9) | 108.513(4) |
| Volume [$10^6$ pm$^3$] | 1900.5(2) | 4087(1) | 3767(2) | 4017(2) |
| $Z$ | 2 | 4 | 1 | 2 |
| Calcd. density [g cm$^{-3}$] | 1.174 | 1.233 | 1.131 | 1.254 |
| $\mu$ [mm$^{-1}$] | 0.463 | 0.550 | 0.464 | 0.560 |
| Crystal size [mm] | $0.26\times0.24\times0.22$ | $0.05\times0.03\times0.02$ | $0.29\times0.22\times0.19$ | $0.21\times0.18\times0.15$ |
| $2\theta$ range [°] | 2.42–25.00 | 2.78–25.00 | 2.02–25.00 | 2.11–25.00 |
| Reflections collected/unique | 15342/6657 | 14118/7184 | 20312/13064 | 20751/13995 |
| Data/parameters | 6657/374 | 7184/375 | 13064/703 | 13995/740 |
| GOF on $F^2$ | 1.054 | 1.039 | 1.01 | 0.888 |
| $R$ [$I > 2\sigma(I)$] | 0.050 | 0.050 | 0.088[a] | 0.078 |
| $wR_2$ | 0.135 | 0.138 | 0.140 | 0.155 |
| Largest diff. peak/hole [e Å$^{-3}$] | 1.233/–0.729 | 0.957/–0.562 | 0.929/–0.601 | 0.784/–0.922 |

[a] The high $R$ values of **3** are due to disorder of the guest $Ti_2(OiPr)_8$ molecule.

(SHELXS-97). Refinement was performed by the full-matrix least-squares method based on $F^2$ (SHELXL-97) with anisotropic thermal parameters for all non-hydrogen atoms. Hydrogen atoms were inserted in calculated positions and refined as riding on the corresponding atom. The C–O and C–C distances of the $Ti_2(OiPr)_8$ guest molecule in **3** were refined using geometric restraints (DFIX, DANG).

CCDC-616750 (for **1**), -616751 (for **2**), -269602 (for **3**) and -616752 (for **4**) contain the supplementary crystallographic data for this paper. These data can be obtained free of charge from The Cambridge Crystallographic Data Center via www.ccdc.cam.ac.uk/data_request/cif.

**NMR Investigations:** All NMR spectra were recorded with a Bruker Avance 300 spectrometer ($^1$H at 300.13, $^{13}$C at 75.47 MHz, $^{15}$N at 30.41 MHz) equipped with a 5 mm, inverse-broadband probe head with a $z$-gradient unit at room temperature. 2D NMR spectra (EXSY, mixing time was usually 1 s; HSQC; HMBC) were measured with Bruker standard pulse sequences. Gas-tight Young tubes were used for all measurements, and $CD_2Cl_2$ (99.8%, euriso-top) was used as the solvent. $^{15}$N shifts were referenced externally against an aqueous solution of $^{15}NH_4Cl$. To remove most of the residual amine and free alcohol previous to the measurement, the crystals were dissolved in $CD_2Cl_2$, the solvent was removed again in vacuo, and the residue was dried for more than 8 h at $4\times10^{-4}$ mbar. The dried precipitate was then used for NMR investigations.

## Acknowledgments

This work was supported by the Fonds zur Förderung der wissenschaftlichen Forschung (FWF), Austria. We thank Dr. Gerald Giester (University of Vienna) for his help with the X-ray diffraction measurement of **2**.

[1] P. Tolédano, F. Ribot, C. Sanchez, *Acta Crystallogr., Sect. C* **1990**, *46*, 1419.
[2] B. A. Vaartstra, J. C. Huffman, P. S. Gradeff, L. G. Hubert-Pfalzgraf, J. C. Daran, S. Parraud, K. Yunlu, K. G. Caulton, *Inorg. Chem.* **1990**, *29*, 3126.
[3] M. Veith, S. Mathur, C. Mathur, V. Huch, *J. Chem. Soc., Dalton Trans.* **1997**, 2101.
[4] J. Fisher, W. G. van der Sluys, J. C. Huffman, J. Sears, *Synth. React. Inorg. Met.-Org. Chem.* **1993**, *23*, 479.
[5] E. P. Turevskaya, N. Ya. Turova, *Bull. Acad. Sci. USSR Div. Chem. Sci. (Engl. Transl.)* **1977**, *26*, 1463; C. Campbell, S. G. Bott, R. Larsen, W. G. van der Sluys, *Inorg. Chem.* **1994**, *33*, 4950.
[6] G. W. Svetich, A. A. Voge, *Acta Crystallogr., Sect. B* **1972**, *28*, 1760.
[7] H. Fric, U. Schubert, *New J. Chem.* **2005**, *29*, 232.
[8] H. Fric, M. Puchberger, U. Schubert, *J. Sol-Gel Sci. Technol.* **2006**, *40*, 155.
[9] U. Schubert, U. Bauer, H. Fric, M. Puchberger, W. Rupp, V. Torma, *Mat. Res. Soc. Symp. Proc.* **2005**, *847*, 533.
[10] T. Steiner, *Angew. Chem. Int. Ed.* **2002**, *41*, 48.
[11] T. J. Boyle, T. M. Alam, E. R. Mechenbier, B. L. Scott, J. W. Ziller, *Inorg. Chem.* **1997**, *36*, 3293.
[12] S. C. James, N. C. Norman, A. G. Orpen, *Acta Crystallogr., Sect. C* **1998**, *54*, 1261.
[13] D. R. Click, B. L. Scott, J. G. Watkin, *J. Chem. Crystallogr.* **1999**, *29*, 921.

Received: August 8, 2006
Published Online: November 28, 2006

 © 2007 Wiley-VCH Verlag GmbH & Co. KGaA, Weinheim 

DOI: 10.1002/ejic.200600773

# Synthesis, Structures, and Electronic Spectroscopy of Luminescent Acetylene- and (Buta-1,3-diyne)platinum Complexes

**Ke Zhang,[a] Jian Hu,[a] Kwok Chu Chan,[b] Kwok Yin Wong,[b] and John H. K. Yip*[a]**

**Keywords:** Spectroscopy / Luminescence / Platinum / Acetylene / Charge-transfer

The electronic absorption and emission spectroscopy of a series of diphenylacetylene- and (buta-1,3-diyne)-$Pt^0$ complexes (L)Pt[(1,2-$\eta^2$)-R–(C≡C)$_n$–R] and [(dppp)Pt]$_2$[μ-(1,2-$\eta^2$):(3,4-$\eta^2$)-R–(C≡C)$_2$–R] {R = Ph or $CH_3$, L = dppp or $(PPh_3)_2$, $n$ = 1 or 2} was investigated. The structures of (dppp)Pt[(1,2-$\eta^2$)-Ph–C≡C–Ph], (dppp)Pt[(1,2-$\eta^2$)-PhC$_4$Ph] and [(dppp)Pt]$_2$[μ-(1,2-$\eta^2$):(3,4-$\eta^2$)-Ph–(C≡C)$_2$–Ph] were characterized by X-ray diffraction. The complexes all display intense absorptions that were attributed to Pt→P(dπ*) and Pt→acetylene($\pi_x$*) transitions. Except for the $CH_3C_4CH_3$ complexes, the complexes all exhibit two emissions at 380–550 nm and 500–800 nm. The higher energy emission could arise from the $^3$[P(dπ*)→Pt] transition, and the lower energy emission, which has a longer lifetime than the higher energy one, was attributed to the $^3$[acetylene($\pi_x$*)→Pt] transition. The energy of the MLCT absorption and emission was affected by the electronic properties of the acetylenes and the ancillary phosphanes.
(© Wiley-VCH Verlag GmbH & Co. KGaA, 69451 Weinheim, Germany, 2007)

## Introduction

Recent interest in linear organometallics that have a low-lying metal-to-ligand charge-transfer (MLCT) excited state arose from their potential as molecular devices.[1] For example, it had been demonstrated that the intense MLCT absorption of $Ru^{II}$ acetylides is associated with their large second-order nonlinear optical effect.[1c] In addition, MLCT excitation is accompanied with charge separation, which is pertinent for the operation of photonic wires.[2]

Currently, organometallic complexes containing π-conjugated ligands are receiving a lot of attention mainly because of their wire-like geometry and the ability of π-conjugated carbon chains to mediate electron transfer.[3] Most of the studies have focused on metal acetylides and metal polyyne σ complexes. One way to lower the MLCT energy is to increase π-conjugation of the polyyne ligand. For instance, the complex [Re(L)(CO)$_3$(C≡CC≡C)Re(L)(CO)$_3$] (L = 4,4′-di-*tert*-butyl-2,2′-bipyridine) displayed a low-energy MLCT transition [dπ(Re)→π*(C≡CC≡C–Re)] and $^3$MLCT emission.[4] However, a potential drawback of this approach is that the gap between the metal dπ- and the ligand π-orbitals is reduced, resulting in substantial mixing of the orbitals, and hence introduction of significant intraligand ππ* character to the MLCT excited state. In principle, the mixing could be subdued if the metal orbitals are much higher in energy than the ligand orbitals. This requires an electron-rich metal center. In search of organometallics showing low-energy MLCT transition, our attention was therefore drawn to acetyleneplatinum(0) π complexes, which possess an electron-rich metal center and low-lying π*-orbitals.

Although the π complexes have a fairly long history,[5] most studies to date focus on the structures and reactivity aspects of the compounds.[6] On the other hand, electronic spectroscopy and photophysics of the complexes remain sparsely studied.[7] The luminescent properties of a series of acetylene-$Pt^0$ complexes have been reported by Forniés and co-workers.[7a] They assigned the vibronic phosphorescence exhibited by [$(PPh_3)_2Pt_2$]$_2$(HC≡C–1,4-C$_6$H$_4$–C≡CH) to $^3$MLCT emission. The assignment was supported by extended Hückel calculations that showed that the HOMO contains a substantial metal character and the LUMO is mainly localized in the π*-orbital of the acetylene.

A better understanding of the electronic structures and photophysics of the complexes could be achieved by expanding the scope of spectroscopic study to cover molecules that contain different acetylenes and ancillary ligands. To this end, we have carried out a comparative study of a series of acetylene- and (buta-1,3-diyne)platinum(0) (LPt)[(1,2-$\eta^2$)-R–(C≡C)$_n$–R] {L = $(PPh_3)_2$ or dppp [1,3-bis(diphenylphosphanyl)propane]; R = Ph or $CH_3$; $n$ = 1 or 2} and binuclear [(dppp)Pt]$_2$[μ-(1,2-$\eta^2$):(3,4-$\eta^2$)-R–(C≡C)$_2$–R] complexes (Scheme 1). The complexes are different by the substituents attached to the C≡C bond, extent of conjugation, number of metal atoms or ancillary phosphane atoms.

[a] Department of Chemistry, National University of Singapore, 10 Kent Ridge Crescent, 119260 Singapore, Singapore
Fax: +65-7791691
E-mail: chmyiphk@nus.edu.sg
[b] Department of Applied Biology and Chemical Technology, Hong Kong Polytechnic University, Hunghom, Kowloon, Hong Kong SAR, People's Republic of China
Supporting information for this article is available on the WWW under http://www.eurjic.org or from the author.

 © 2007 Wiley-VCH Verlag GmbH & Co. KGaA, Weinheim 

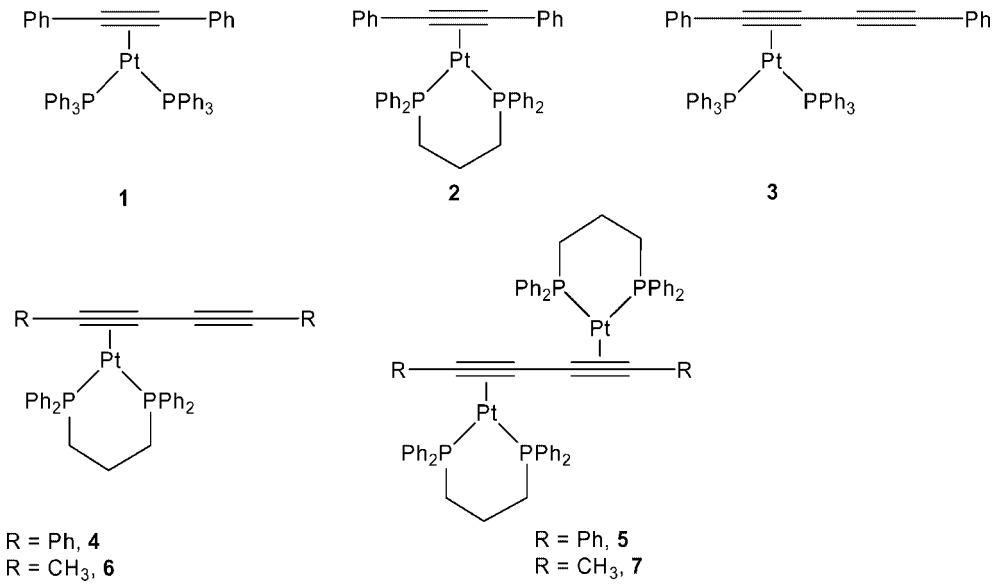


Scheme 1.

Except for complexes **1** and **3**, all of the complexes are new. While binuclear metal complexes of buta-1,3-diyne in μ-(1,2-$\eta^2$):(3,4-$\eta^2$) coordination mode are known, the complex **5** is the first $Pt_2$-butadiyne π complex ever characterized by X-ray crystallography.[8] The first diplatinum complex of $PhC_4Ph$, $[(PPh_3)_2Pt]_2$[μ-(1,2-$\eta^2$):(3,4-$\eta^2$)-$PhC_4Ph$], was synthesized by Stone but its crystal structure was not available.[9]

## Results and Discussion

### (A) Synthesis and Characterization

There are two literature methods for the preparation of acetylene-$Pt^0$ complexes. The first method[10] involves reduction of the $Pt(PPh_3)_2Cl_2$ ion by $N_2H_4$ in the presence of the acetylene ligand in alcohol. In this work, $(PPh_3)_2Pt$[(1,2-$\eta^2$)-$PhC_2Ph$] (**1**) and $(PPh_3)_2Pt$[(1,2-$\eta^2$)-$PhC_4Ph$] (**3**) were prepared by this method. However, synthesis of (dppp)-Pt[(1,2-$\eta^2$)-$PhC_2Ph$] (**2**) and (dppp)Pt[(1,2-$\eta^2$)-$PhC_4Ph$] (**4**) by the same methods was not successful. Instead the stronger reductant $NaBH_4$ is needed to reduce $Pt(dppp)Cl_2$ to $Pt^0$(dppp). This could be due to the fact that dppp is more electron-donating than $PPh_3$, making $Pt(dppp)Cl_2$ more difficult to reduce than $Pt(PPh_3)_2Cl_2$. Another literature method[9] involves substitution of ethylene in $(R_3P)_2$-$Pt(C_2H_4)$ by acetylenes. This method was used to prepare (dppp)Pt[(1,2-$\eta^2$)-$CH_3C_4CH_3$] (**6**) and the dinuclear $[(dppp)Pt]_2$[μ-(1,2-$\eta^2$):(3,4-$\eta^2$)-$PhC_4Ph$] (**5**) and $[(dppp)Pt]_2$-[μ-(1,2-$\eta^2$):(3,4-$\eta^2$)-$CH_3C_4CH_3$] (**7**).

The ESI-MS spectra of the complexes all show peaks attributable to the corresponding molecular ion $M^+$. The IR spectra of **1** and **2** display weak bands at 1741 and 1748 $cm^{-1}$, respectively, which are assigned to stretching of the coordinated C≡C bonds. Absorption bands of similar frequency and intensity have been observed for other reported acetylene-$Pt^0$ complexes.[5,6] The low stretching frequency is due to the metal-to-ligand π-back donation.[11] The IR spectra of **3**, **4** and **6** show two resonance signals at 1719–1749 and 2160–2196 $cm^{-1}$ arising from stretching of the coordinated and the uncoordinated C≡C bonds. The dinuclear complexes **5** and **7** show only a single peak at 1758 and 1705 $cm^{-1}$ for $\nu$(C≡C), respectively. This indicates that both C≡C bonds in the complexes are equivalent.

### (B) Structures

The complexes **2**, **4**, and **5** were characterized by single-crystal X-ray diffraction analysis, while crystal structures of **1**[12] and **3**[6b] have been previously reported by other research groups (Table 3). The selected bond lengths and angles are listed in Table 1.

#### (dppp)Pt[(1,2-$\eta^2$)-$PhC_2Ph$] (2)

There are two independent molecules **2a** and **2b** of very similar structure in a unit cell of crystal **2**·THF (Figure 1 for structure of **2a**).

Like the reported structure of **1**, complex **2** displays an approximate $C_{2v}$ symmetry. The acetylene bond length (C1–C1A) [1.301(7) Å] is significant longer than the average C≡C bond length (ca. 1.2 Å). This indicates a weakening of the bond due to σ-donation from the acetylene to the metal and π-back donation from the metal to the acetylene. The Pt center adopts a distorted square-planar coordination geometry with a small dihedral angle of 2.98° between the two C1–Pt1–C1A and P1–Pt1–P1A triangles. The Pt–C and the Pt–P bond lengths are normal. Similar to **1**, the linear C2–C1≡C1A–C2A backbone is distorted with the C2–C1–C1A angle being 144.5(2)°. It is slightly smaller

 © 2007 Wiley-VCH Verlag GmbH & Co. KGaA, Weinheim 

Table 1. Selected interatomic distances and angles in **2a**, **4**, and **5**.

| **2a** | | **4** | | **5** | |
|---|---|---|---|---|---|
| Distances [Å] | | | | | |
| Pt1–C1 | 2.041(3) | Pt1–C2 | 2.043(4) | Pt1–C1 | 2.034(3) |
| Pt1–P1 | 2.2705(9) | Pt1–C1 | 2.044(4) | Pt1–C2 | 2.051(3) |
| C1–C1A | 1.301(7) | Pt1–P1 | 2.2629(10) | Pt1–P1 | 2.2478(9) |
| C1–C2 | 1.464(5) | Pt1–P2 | 2.2686(10) | Pt1–P2 | 2.2581(9) |
| | | C1–C2 | 1.299(6) | Pt2–C4 | 2.017(3) |
| | | C1–C5 | 1.463(6) | Pt2–C3 | 2.063(3) |
| | | C2–C3 | 1.393(6) | Pt2–P3 | 2.2423(8) |
| | | C3–C4 | 1.201(6) | Pt2–P4 | 2.2755(9) |
| | | C4–C6 | 1.433(6) | C1–C2 | 1.303(5) |
| | | | | C1–C5 | 1.451(5) |
| | | | | C2–C3 | 1.411(4) |
| | | | | C3–C4 | 1.296(5) |
| | | | | C4–C6 | 1.454(5) |
| Angles [°] | | | | | |
| C1A–Pt1–C1 | 37.2(2) | C2–Pt1–C1 | 37.05(16) | C1–Pt1–C2 | 37.20(13) |
| C1–Pt1–P1A | 150.47(10) | C2–Pt1–P1 | 155.79(13) | C1–Pt1–P1 | 118.33(10) |
| C1–Pt1–P1 | 113.35(10) | C1–Pt1–P1 | 118.81(11) | C2–Pt1–P1 | 155.45(10) |
| P1–Pt1–P1A | 96.02(5) | C2–Pt1–P2 | 111.48(12) | C1–Pt1–P2 | 150.64(10) |
| C1A–C1–C2 | 144.5(2) | C1–Pt1–P2 | 148.40(11) | C2–Pt1–P2 | 113.44(10) |
| C2–C1–Pt1 | 144.0(3) | P1–Pt1–P2 | 92.44(4) | P1–Pt1–P2 | 91.00(3) |
| C1–C1A–Pt1 | 71.42(10) | C2–C1–C5 | 137.7(4) | C4–Pt2–C3 | 37.02(13) |
| | | C2–C1–Pt1 | 71.5(2) | C4–Pt2–P3 | 109.14(10) |
| | | C5–C1–Pt1 | 150.1(3) | C3–Pt2–P3 | 145.49(10) |
| | | C1–C2–C3 | 146.7(4) | C4–Pt2–P4 | 154.86(10) |
| | | C1–C2–Pt1 | 71.5(2) | C3–Pt2–P4 | 118.57(10) |
| | | C3–C2–Pt1 | 141.3(3) | P3–Pt2–P4 | 95.76(3) |
| | | C4–C3–C2 | 174.7(5) | C2–C1–C5 | 138.6(3) |
| | | C3–C4–C6 | 176.5(5) | C2–C1–Pt1 | 72.1(2) |
| | | | | C5–C1–Pt1 | 149.3(3) |
| | | | | C1–C2–C3 | 146.8(3) |
| | | | | C1–C2–Pt1 | 70.7(2) |
| | | | | C3–C2–Pt1 | 142.0(3) |
| | | | | C4–C3–C2 | 146.4(3) |
| | | | | C4–C3–Pt2 | 69.6(2) |
| | | | | C2–C3–Pt2 | 144.0(3) |
| | | | | C3–C4–C6 | 138.6(3) |
| | | | | C3–C4–Pt2 | 73.4(2) |
| | | | | C6–C4–Pt2 | 147.6(2) |

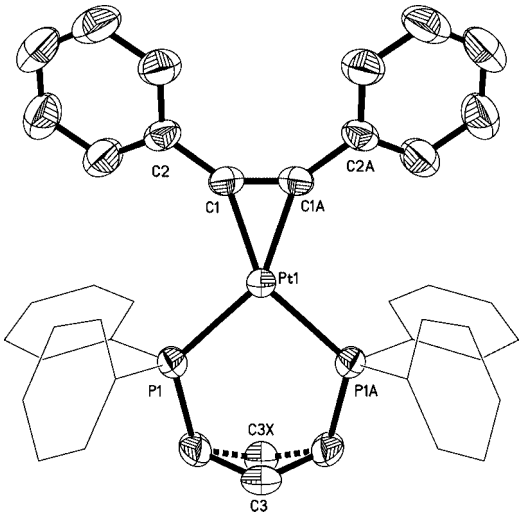


Figure 1. ORTEP diagram (thermal ellipsoid = 50%) of **2a**. H atoms and solvent molecules are omitted; C3 and C3X represent two positions of the disordered carbon atom, with 80% and 20% occupancy, respectively.

than the corresponding angles of 140 and 139° in **1**. The phenyl rings and the coordination triangle C1–Pt1–C1A are not coplanar, showing a dihedral angle of 26.89°.

### (dppp)Pt[(1,2-η$^2$)-PhC$_4$Ph] (4)

The molecular structure of complex **4** (Figure 2) is similar to that of {[(PPh$_3$)$_2$Pt](PhC$_4$Ph)} (**3**) reported by Deeming.[6b] The lengths of the coordinated C≡C bond (C1–C2) and the uncoordinated one (C3–C4) are 1.299(6) and 1.201(6) Å.

The coordination geometry at the Pt center in **4** is also nearly planar with the dihedral angle between triangles of C1–Pt1–C2 and P1–Pt1–P2 being 4.31°. The two Pt–C and Pt–P bond lengths are almost identical [Pt1–C1, 2.044(4) Å; Pt1–C2, 2.043(4) Å; Pt1–P1, 2.2629(10) Å; Pt1–P2, 2.2686(10) Å]. While the C5–C1–C2–C3 linkage is bent [∠C5–C1–C2 137.7(4)°; ∠C1–C2–C3 146.7(4)°] like that in **2a**, the uncoordinated triple bond remains linear [∠C2–C3–C4 = 174.7(5)°; ∠C3–C4–C6 176.5(5)°]. The dihedral angle between the coordination triangle of C1–Pt1–C2 and the adjacent phenyl ring of the acetylene is 18.36°.

 © 2007 Wiley-VCH Verlag GmbH & Co. KGaA, Weinheim 

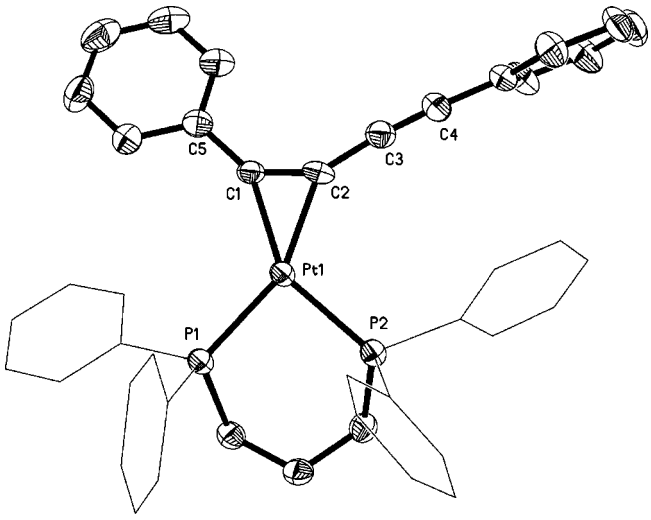


Figure 2. ORTEP diagram (thermal ellipsoid = 50%) of **4**. H atoms and solvent molecules are omitted.

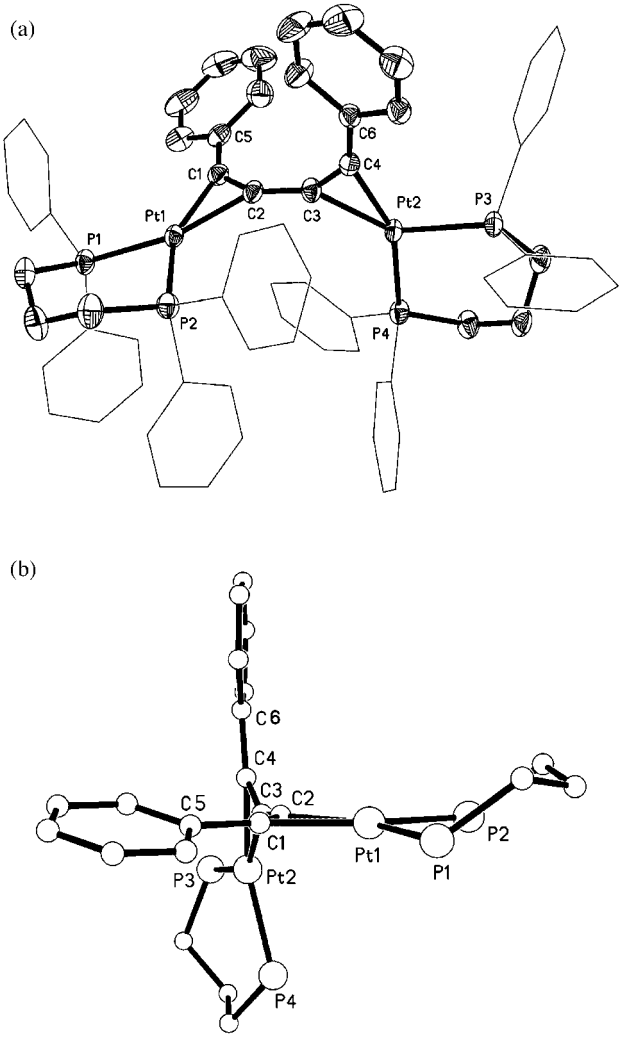


Figure 3. (a) ORTEP diagram (thermal ellipsoid = 50%) of **5**. H atoms and solvent molecules are omitted; (b) a side view showing the staggered conformation of **5**.

### [(dppp)Pt]$_2$[{μ-(1,2-η$^2$):(3,4-η$^2$)-PhC$_4$Ph}] (5)

The molecular structure of complex **5** is shown in Figure 3. The butadiyne is coordinated to the two Pt atoms in μ-(1.2-η$^2$):(3,4-η$^2$) mode. Both Pt atoms show nearly square-planar coordination geometry. The C1–C2–C3–C4 backbone of the butadiyne shows a *gauche* conformation with a torsion angle of 94.79°. Similar conformation has been observed in the μ-(1,2-η$^2$):(3,4-η$^2$)-butadiyne complexes (PyCl$_4$W)$_2$(Me$_3$SiC≡CC≡CPh),[8d] (Cp$_2$V)$_2$(Me$_3$Si–C≡CC≡C–SiMe$_3$),[8e] and [(R$_2$PCH$_2$CH$_2$PR$_2$)Ni]$_2$-(R′C≡CC≡CR′)[8f] (R = *i*Pr, R′ = H or R = *t*Bu, R′ = Ph) which display a torsion angle of 74–98°. The two Pt atoms are related by a $C_2$-rotation. The C1–Pt1–C2 and C3–Pt2–C4 metallacycles show a *gauche* conformation with a dihedral angle of 86.01°. The lengths of the two acetylene bonds are 1.303(5) Å (C1–C2) and 1.296(5) Å (C3–C4), similar to the acetylene bond lengths observed in **2a** and **4**.

Notably, the "inner" Pt–C bonds, Pt1–C2 [2.051(3) Å] and Pt2–C3 [2.063(3) Å] and the "inner" Pt–P bonds, Pt1–P2 [2.2581(9) Å] and Pt2–P4 [2.2755(9) Å], are slightly but consistently longer than the "outer" Pt1–C1 [2.034(3) Å], Pt2–C4 [2.017(3) Å], and Pt1–P1 [2.2478(9) Å] and Pt2–P3 [2.2423(8) Å], respectively. Such differences could be caused by the steric repulsions between two neighboring dppp ligands. Similar to compounds **1**–**4**, the carbon atoms at the two ends of the acetylene bond are bent away from the metal atom. The phenyl rings of the butadiyne are almost coplanar with the PtC$_2$ unit, showing dihedral angles of 15.14 and 16.95°.

### $^{31}$P-NMR Spectroscopy

The $^{31}$P NMR spectra of all the complexes are consistent with the X-ray crystal structures of the complexes. The spectra of **1** and **2** show only two singlets at $\delta$ = 27.07 and 4.11 with Pt satellites ($^1J_{Pt\text{-}P}$ = 3448 and 3155 Hz, respectively), and the spectrum of **3** shows two doublets of triplets at $\delta$ = 26.53 and 26.19 ppm ($^1J_{Pt\text{-}P}$ = 3521 and 3456 Hz, $^2J_{P\text{-}P}$ = 22.9 Hz). The spectra of **4** and **6** show similar [AB]$_2$ splitting patterns. On the other hand, the spectrum of **5** is poorly resolved, because of the similar chemical shifts of different P atoms in the complexes (4.18 and 3.94 ppm, $^2J_{P\text{-}P}$ = 26.7 Hz). In the spectrum of **7** the signals of the two phosphorus atoms are isochronous at $\delta$ = 8.54 ppm with very close $^1J_{Pt\text{-}P}$ (3227 and 3258 Hz). Although the X-ray crystal structures of **6** and **7** are not available, the similar NMR spectra suggest the molecular structures of **6** and **7** should resemble their PhC$_4$Ph counterparts, **4** and **5**, respectively.

### (C) Absorption Spectroscopy

The UV/Vis absorption spectra of complexes **1**, **2**, and the parent ligand diphenylacetyleme are shown in Figure 4. The ligand displays intense ($\varepsilon > 10^4$ M$^{-1}$cm$^{-1}$) vibronic absorptions at 250–310 nm. Similar vibronic bands are ob-

 © 2007 Wiley-VCH Verlag GmbH & Co. KGaA, Weinheim 

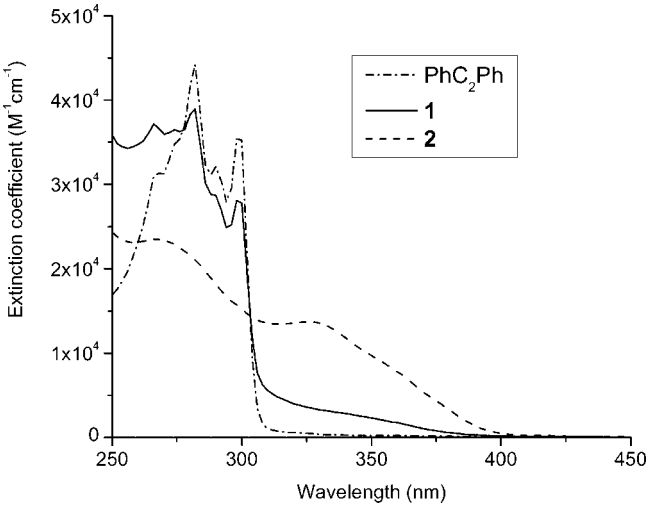


Figure 4. UV/Vis absorption spectra of complexes **1**, **2**, and ligand $PhC_2Ph$ in $CH_2Cl_2$ at room temperature.

served in the spectrum of **1**. In addition, the spectrum displays a broad and moderately intense absorption ($\varepsilon$ = 1–$3.5 \times 10^3$ M$^{-1}$cm$^{-1}$) ranging from 310–400 nm. No vibronic structure is observed in the spectrum of **2**. Instead the spectrum shows a broad and intense band peaked at 270 nm ($\varepsilon_{max} = 2.34 \times 10^4$ M$^{-1}$cm$^{-1}$) and a broad intense absorption at 300–420 nm. The latter absorption consists of more than one band, showing a peak at 327 nm ($\varepsilon_{max}$ = $1.38 \times 10^4$ M$^{-1}$cm$^{-1}$) and a shoulder at ca. 355 nm ($\varepsilon$ = $9.1 \times 10^3$ M$^{-1}$cm$^{-1}$).

The absorption spectrum of the ligand $PhC_4Ph$ shows a clear vibronic structured band at 270–340 nm with a progression of 2000 cm$^{-1}$ which should be associated with the vibration of the C≡C bond in the ππ* excited state (Figure 5). The three complexes exhibit very intense absorption around 250 nm with no distinct vibronic peak. While the parent ligand does not absorb beyond 350 nm, the complexes display broad intense absorption bands extending to 450 (**3** and **4**) or 500 nm (**5**). The low energy absorption

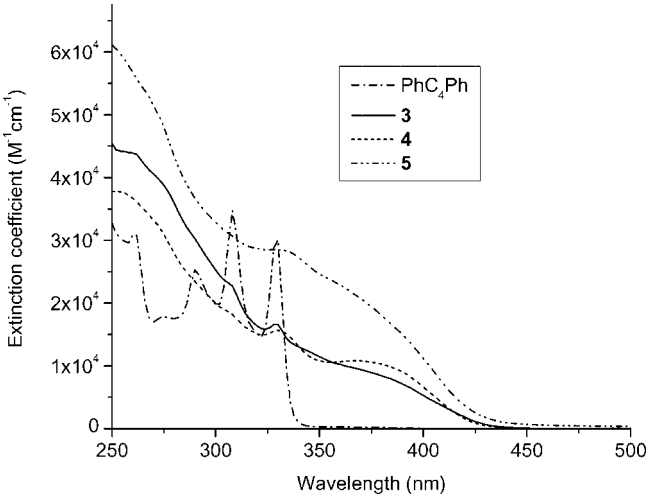


Figure 5. UV/Vis absorption spectra of complexes **3**, **4**, **5**, and ligand $PhC_4Ph$ in $CH_2Cl_2$ at room temperature.

bands of **3** and **4** maximize at 370 nm ($\varepsilon_{max}$ = $9 \times 10^3$ M$^{-1}$cm$^{-1}$) and 374 nm ($\varepsilon_{max}$ = $1.09 \times 10^4$ M$^{-1}$cm$^{-1}$), respectively. The low energy absorption ($\lambda_{max} \approx$ 360 nm, $\varepsilon_{max} = 2.31 \times 10^4$ M$^{-1}$cm$^{-1}$) of **5** is more intense than that of **3** and **4**.

The absorption spectra of **6**, **7**, and $CH_3C_4CH_3$ are shown in Figure 6. Unlike $PhC_2Ph$ and $PhC_4Ph$, the spectrum of $CH_3C_4CH_3$ shows little absorption at wavelengths longer than 250 nm ($\varepsilon < 200$ M$^{-1}$cm$^{-1}$). However, the spectra **6** and **7** show intense absorption bands around 250 nm and a less intense band at ca. 320 nm ($\varepsilon_{max}$ = $4.3 \times 10^3$ M$^{-1}$cm$^{-1}$) and 315 nm ($\varepsilon_{max}$ = $1.3 \times 10^4$ M$^{-1}$cm$^{-1}$), respectively.

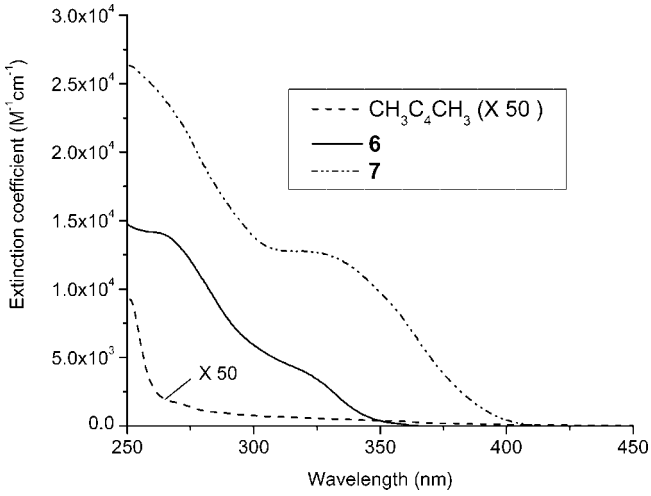


Figure 6. UV/Vis absorption spectra of complexes **6**, **7**, and $CH_3C_4CH_3$ in $CH_2Cl_2$ at room temperature.

### (D) Emission Spectroscopy

Table 2 summarizes the photophysical data of the complexes. The complexes are all not luminescent in degassed solution at room temperature. On the other hand, the solids of **1**–**5** are emissive at room temperature, showing two emission bands at 380–550 nm and 520–800 nm (Figure 7). The lifetimes ($\tau$) of the higher energy emissions are shorter than the detection limit of our nanosecond laser flash photolysis set-up (<0.1 μs), but the 520–800 nm emissions show long lifetimes ($\tau$ = 1.57–3.86 μs).

Table 2. Photophysical data of the acetylene-Pt complexes.

| | Emission (in EtOH, frozen at 77 K) $\lambda_{max}$ [nm] ($\tau$ [μs]) | Emission (solid state at 298 K) $\lambda_{max}$ [nm] ($\tau$ [μs]) |
|---|---|---|
| **1** | 447 (<0.1), 547 (58.32) | 446 (<0.1), 562 (3.86) |
| **2** | 429 (<0.1), 570 (39.97) | 443 (<0.1), 588 (2.19) |
| **3** | 404 (<0.1), 589 (21.76) | 457 (<0.1), 597 (2.72) |
| **4** | 475 (<0.1), 622 (10.07) | 459 (<0.1), 617 (1.57) |
| **5** | 468 (<0.1), 605 (5.65) | 458 (<0.1), 630 (too weak to be measured) |
| **6** | 490 (19.00) | No emission |
| **7** | 518 (29.20) | No emission |

 © 2007 Wiley-VCH Verlag GmbH & Co. KGaA, Weinheim 

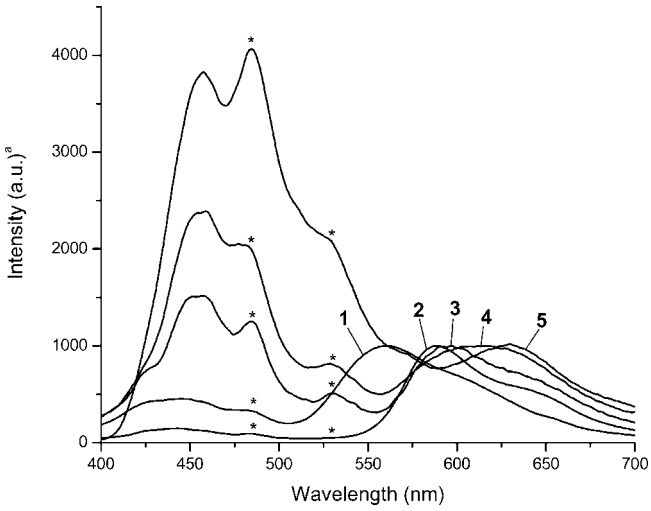


Figure 7. Solid-state emission spectra of complexes **1**–**5** at room temperature [a: intensities of the emission maximum in the low energy region (550–700 nm) are normalized; asterisks at ca. 485 and 529 nm denote instrumental artifacts]. The excitation wavelength is 320 nm.

The energy of the long-lived emissions of $PhC_4Ph$ complexes **3**, **4**, and **5** ($\lambda_{max}$ = 594–630 nm) is lower than $PhC_2Ph$ complexes **1** ($\lambda_{max}$ = 562 nm) and **2** ($\lambda_{max}$ = 588 nm). Apart from the acetylene, the emission energy is also affected by the ancillary phosphane atoms: the $PPh_3$-containing complexes **1** and **3** emit at slightly higher energy than their dppp counterparts **2** and **4**.

The emission spectra of 77 K frozen EtOH solutions of **1** and **2** are shown in Figure 8. Excitation at 320 nm leads to relatively weak emissions of short lifetimes ($\tau < 0.1$ μs) located at 350–500 nm. In addition, the spectra of **1** and **2** display more intense lower energy emissions of long lifetimes at 547 nm ($\tau$ = 58.32 μs) and 570 nm ($\tau$ = 39.97 μs), respectively.

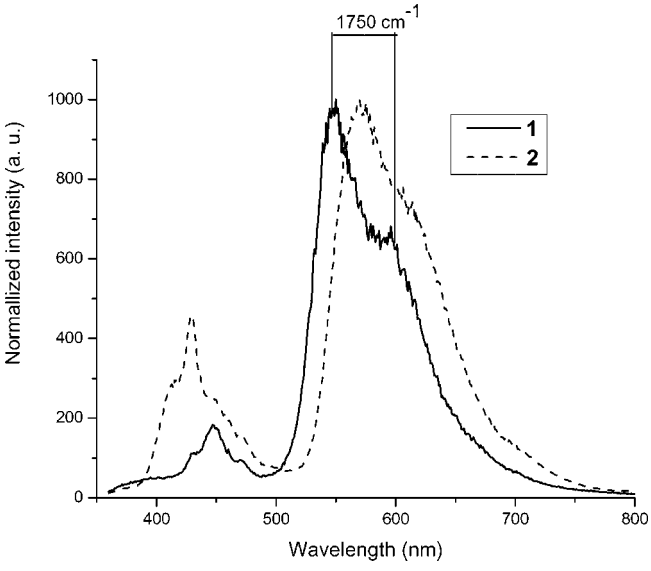


Figure 8. 77 K frozen ethanol solution emission spectra of complexes **1** and **2**. The excitation wavelength is 320 nm.

The lower energy emissions show vibronic shoulders. The spacing is estimated at 1750 $cm^{-1}$ in the spectrum of **1**.

The emission spectra of frozen solutions of **3**, **4**, and **5** at 77 K (supporting materials) also show two bands at 380–550 and 520–750 nm. Similar to the solid-state emission, the energy of the lower energy luminescence ($\lambda_{max}$ = 590–620 nm) is slightly lower than the corresponding emissions of **1** and **2**. The lifetime of the low energy emissions ($\tau$ = 5.65–21.76 μs) is much longer than that of the higher energy ones ($\tau < 0.1$ μs).

Unlike the $PhC_4Ph$ and $PhC_2Ph$ complexes, **6** and **7** are not emissive in the solid state at room temperature. At 77 K, the solids show weak emission at ca. 500 nm with $\tau$ of 5.10 μs (**6**) and 3.25 μs (**7**). The frozen solution spectra display similar emissions at 490 nm (**6**, $\tau$ = 19.00 μs) and 518 nm (**7**, $\tau$ = 29.20 μs) (Figure 9). The emissions of **6** and **7** are far less intense than those of **1**–**5**.

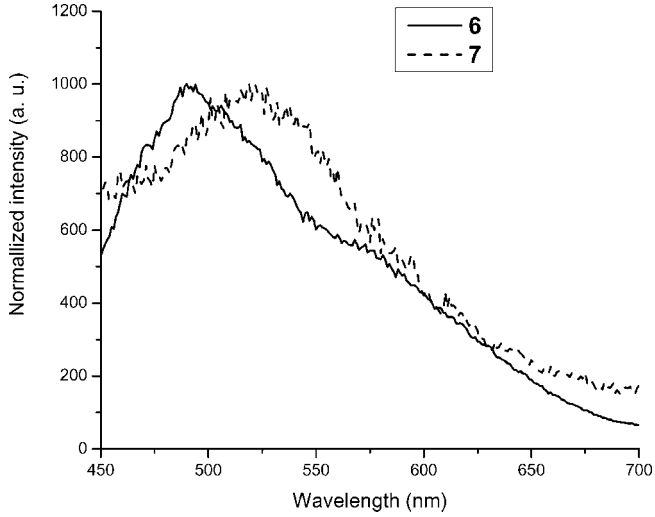


Figure 9. 77 K frozen ethanol solution emission spectra of complexes **6** and **7**. The excitation wavelength is 320 nm.

## Spectroscopic Assignments

In previous spectroscopic studies on acetylene-$Pt^0$ complexes, the low energy absorptions, which were absent in the spectra of the free acetylenes, were assigned to the Pt(5d)→acetylene(π*) charge transfer transition.[7a,7c] This assignment was further supported by semi-empirical calculations showing that the HOMO and LUMO are mainly composed of the $d_{z^2}$-orbital and acetylene π*-orbital.[7a] Likewise, the complexes **1**–**7** all exhibit intense absorption bands that are lower in energy than the ligand absorptions.

Scheme 2 shows a qualitative molecular orbital of acetylene-Pt complexes constructed from orbital interactions between a two-coordinate phosphane-$Pt^0$ and a bent acetylene.

Three metal orbitals $d_{z^2}$, $d_{xz}$, and $d_{x^2-y^2}$ are destabilized by interacting with either the $\pi_x$- or the $\pi_z$-orbital of the acetylenes. The $d_{z^2}$-orbital is expected to be the HOMO of the complexes as its energy is raised by the strong antibonding interactions with the $\pi_z$-orbital. Similarly, the $d_{x^2-y^2}$ or-

 © 2007 Wiley-VCH Verlag GmbH & Co. KGaA, Weinheim 

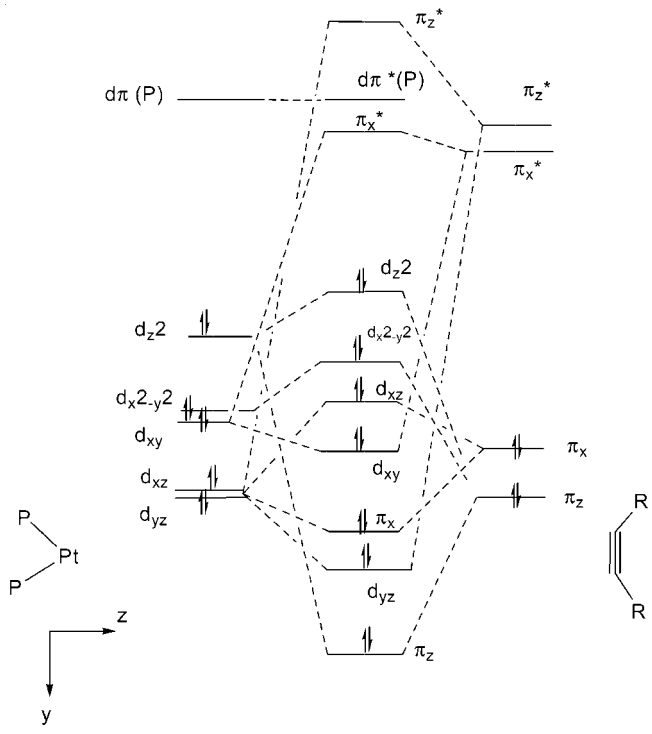


Scheme 2.

bital is involved in σ-interaction with the $\pi_z$-orbital but the interactions should be weak because of the poor overlap. The $d_{xz}$ is in the correct symmetry to overlap with the $\pi_x$-orbital. On the other hand, the $d_{yz}$-orbital should be strongly stabilized via π-back bonding with the $\pi_z$*-orbital. The $d_{yx}$-orbital is involved in δ-interactions with the $\pi_x$*-orbital and should be slightly lowered in energy.

The $\pi_z$*-orbital of the acetylene, strongly destabilized by the back bonding, should be higher energy than the $\pi_x$*-orbital which is slightly destabilized by the weak δ-interactions. In this molecular orbital picture, the lowest energy allowed Pt→acetylene transition is the $^1(d_{z^2}\rightarrow\pi_x^*)$ transition. The $^1(d_{xz}\rightarrow\pi_x^*)$ and $^1(d_{x^2-y^2}\rightarrow\pi_x^*)$ transitions should be close in energy to the $^1(d_{z^2}\rightarrow\pi_x^*)$. Because of the mixing between the metal and ligand orbitals, these transitions have some intraligand character. Especially the $^1(d_{xz}\rightarrow\pi_x^*)$ transition, which could mix with the $^1(\pi_x\rightarrow\pi_x^*)$ transition, should be more intense than the other two transitions. Apart from the Pt→acetylene transition, a Pt→P(dπ*) charge transfer from Pt to the dπ*-orbitals of the phosphane atoms is also possible. Gray showed that the complex $Pt^0(dppp)_2$ exhibited an intense $Pt(d_{x^2-y^2}, d_{z^2})\rightarrow(d\sigma^*, d\pi^*)$ charge transfer absorption ($\varepsilon_{max}$ = 24,000 $M^{-1}cm^{-1}$) at 360 nm.[13] As $PhC_2Ph$ and $PhC_4Ph$ are better π-acceptors and weaker σ-donors than dppp, it is likely that the Pt→P(dπ*) transitions in the present complexes locate at wavelengths shorter than 360 nm in view of the position and energy of the very intense bands peaked at ca. 320 nm in the spectra of **2**, **6**, and **7**. Both position and intensity of the absorption bands are consistent with the Pt→P(dπ*) transition.

The low energy absorption of the complexes at wavelengths longer than 320 nm should belong to the Pt→P(dπ*) and Pt→acetylene($\pi_x$*) transitions. The order of these MLCT transitions primarily depends on the energy gap between the d-orbitals and $\pi_x$*-orbitals. Results of semi-empirical calculations show that the HOMO and the LUMO of the acetylene are mainly composed of $\pi_x$ and $\pi_x$* of the acetylene, respectively. The HOMO–LUMO gap is 8.25, 8.38, and 10.48 eV for $PhC_4Ph$, $PhC_2Ph$, and $CH_3C_4CH_3$, respectively (supporting information), and is consistent with the order of the π→π* absorption energy of the acetylenes. Because of the π-conjugation, the order of the LUMO energy is $PhC_4Ph$ (–0.65) < $PhC_2Ph$ (–0.51 eV) < $CH_3C_4CH_3$ (0.73 eV). On the other hand, the HOMOs of $PhC_4Ph$ and $PhC_2Ph$ have almost the same energy (–8.89 eV) and are higher energy than the HOMO of $CH_3C_4CH_3$ (–9.75 eV). Although the acetylenes in the complexes are distorted from linearity, the energy order of the HOMOs and LUMOs should be the same as that of the free ligands. Accordingly, the Pt→acetylene($\pi_x$*) MLCT transition energy of the complexes should follow the order **3**, **4**, **5** < **1**, **2** < **6**, **7**. The same trend is observed in the absorption of the complexes. Given their low-lying $\pi_x$*-orbitals, the Pt→acetylene($\pi_x$*) transitions in **1**, **2**, **3**, **4**, and **5** should be lower in energy than the Pt→P(dπ*). In addition, it is reasonable to expect the MLCT transitions of **3** and **4** to be lower in energy than those of **1** and **2**. Indeed, the MLCT absorption of the $PhC_4Ph$ complexes extends to 500 nm while the $PhC_2Ph$ complexes do not absorb beyond 400 nm. On the other hand, the energy of the Pt→acetylene($\pi_x$*) transition could be close to or even higher than that of the Pt→P(dπ*) for the complexes **6** and **7** as the $\pi_x$*-orbitals of $CH_3C_4CH_3$ are high in energy.

The solid state and frozen solution emission spectra of **1**–**5** show emissions of short lifetimes at ca. 380–550 nm and of longer lifetimes at ca. 500–800 nm. The long lifetimes of the lower energy emission suggests that luminescence arises from a triplet excited state. It is further supported by the large Stoke shift between the absorption and the emission. The frozen solution spectrum of **1** shows a vibronic spacing of ca. 1750 $cm^{-1}$, that is close to the ground state stretching frequency of the coordinated acetylene. This suggests the excited state could be $^3$MLCT($\pi_x$*) arising from the Pt→acetylene($\pi_x$*) excitation. The order of the emission energy is **3**, **4**, **5** < **2** < **1** and is in agreement with the energy of the $\pi_x$*-orbitals of the complexes and hence the MLCT assignment. That the MLCT emission of **1** is slightly higher in energy than that of **2** could be due to the fact that the $PPh_3$ in **1** is a strong electron-acceptor and weaker electron-donor than the dppp in **2**.

The short-lived 350–550 nm emission displayed by **1**–**5** could arise from an intraligand (acetylene) ππ* excited state and/or a $^3$MLCT(dπ*). $PhC_2Ph$ and $PhC_4Ph$ fluoresce at 330 and 365 nm in solution, respectively (supporting information), while $CH_3C_4CH_3$ is not emissive. To a different extent, the metal–ligand interactions in the acetylene complexes stabilize the $\pi_x$- and $\pi_z$-orbitals and destabilize the $\pi_x$*- and $\pi_z$*-orbitals. Accordingly, the lowest energy intrali-

 © 2007 Wiley-VCH Verlag GmbH & Co. KGaA, Weinheim 

gand $\pi_x \rightarrow \pi_x^*$ transition, and hence the corresponding $\pi\pi^*$ emission should be blue shifted from that of the free acetylene. Possibly, the higher energy emissions of the complexes come from a $^3$MLCT(d$\pi^*$) that arises from the Pt→P(d$\pi^*$) transition. It should be noted that the complex $Pt^0(dppp)_2$ exhibits $^3$MLCT(d$\pi^*$) phosphorescence at 622 nm. As the Pt center in the acetylene complexes is less electron rich than the one in $Pt^0(dppp)_2$, it is reasonable for the $^3$MLCT(d$\pi^*$) emission to occur at a higher energy.

Unlike the other complexes, **6** and **7** are not luminescent at room temperature and show a single emission at low temperature. The emission energy is slightly higher than that of **1**–**5** by 1800–3800 cm$^{-1}$. Given the fact that the $\pi_x^*$-orbital of $CH_3C_4CH_3$ is about ca. 1.3 eV or 10000 cm$^{-1}$ higher than those of $PhC_4Ph$ and $PhC_2Ph$, it is unlikely the emissive state in **6** and **7** is $^3$MLCT($\pi_x^*$). The emissive excited state is therefore tentatively assigned to the $^3$MLCT($d\pi^*$).

## Concluding Remarks

In this work, MLCT emission of a series of phosphane-supported acetylene-$Pt^0$ complexes in both the solid state and frozen solution was observed. All of the complexes display intense charge transfer absorptions. Dual emissions are observed in the spectra of **1**–**5**. The higher energy emission could arise from intraligand $\pi\pi^*$ and/or $^3$MLCT(d$\pi^*$) excited states. It is demonstrated that the MLCT emission energy is subject to the electron-donating ability of the phosphane atom and the electronic structures of the acetylene. The lowest energy emissive excited state of **1**–**5** is assigned to $^3$MLCT($\pi_x^*$) as the $\pi_x^*$-orbitals of $PhC_4Ph$ and $PhC_2Ph$ are substantially stabilized via conjugation with the phenyl rings. On the other hand, we assign the phosphorescence of **6** and **7** to $^3$(d$\pi^*\rightarrow$Pt) transitions. It is believed that for the two complexes, the d$\pi^*$-orbitals of dppp are lower in energy than the $\pi_x^*$-orbitals.

## Experimental Section

**General Methods:** All reactions were carried out using standard Schlenk techniques. 1,4-diphenylbuta-1,3-diyne, $PPh_3$, dppp, $NaBH_4$, and $N_2H_4{\cdot}H_2O$ purchased from Aldrich, 2,4-hexa-1,3-diyne purchased from TCI, and $PtCl_2$ purchased from Oxkem were used without further purification. Diphenylacetylene and ethylene were obtained from Aldrich. All solvents used for syntheses and spectroscopic measurements were purified according to literature methods. $Pt(CH_3CN)_2Cl_2$ was prepared by refluxing $PtCl_2$ in a large excess of $CH_3CN$. *cis*-$Pt(PPh_3)_2Cl_2$ and $Pt(dppp)Cl_2$ were prepared by reacting 2 equiv. of $PPh_3$ and 1 equiv. of dppp, respectively, with $Pt(CH_3CN)_2Cl_2$ in $CH_2Cl_2$. (dppp)Pt[(1,2-$\eta^2$)-$CH_2$=$CH_2$] was prepared by reduction of $Pt(dppp)Cl_2$ in the presence of ethylene in ethanol. **1**[5a] and **3**[6b] were synthesized according to the reported methods. Their NMR spectra are identical to the reported ones.

### Synthesis

**(dppp)Pt[(1,2-$\eta^2$)-$PhC_2Ph$] (2):** $Pt(dppp)Cl_2$ (0.26 g, 0.39 mmol) was added to a 30-mL ethanolic solution of diphenylacetylene (0.085 g, 0.42 mmol). Slow addition of $NaBH_4$ (0.1 g, 2.6 mmol) to the mixture gave a pale yellow suspension. The reaction mixture was stirred overnight at room temperature. The yellow solid collected by filtration was washed with excess ethanol. Analytically pure product was obtained by recrystallization in THF/*n*-hexane. Yield: 0.25 g (80%). $C_{41}H_{36}P_2Pt$ (785.8): calcd. C 62.7, H 4.6; found C 62.5, H 4.5. $^1$H NMR (300 MHz, $CDCl_3$): $\delta$ = 7.66–6.96 (m, 30 H, Ph), 2.61–2.58 (m, 4 H, -$CH_2$-P-Pt-), 2.05–1.91 (m, 2 H, -C-$CH_2$-C-) ppm. $^{31}$P{$^1$H} NMR (121.5 MHz, $CDCl_3$): $\delta$ = 4.11 [$^1J$(PtP) = 3155 Hz] ppm. IR (KBr): $\nu$(C≡C) = 1748 (w) cm$^{-1}$. ESI-MS (*m*/*z*, assignment): 786 [M]$^+$. Single crystals of **2**·THF for X-ray diffraction analysis were obtained by slow diffusion of *n*-hexane into a concentrated THF solution of **2**.

**(dppp)Pt[(1,2-$\eta^2$)-$PhC_4Ph$] (4):** The procedures were similar to those for preparing **2**. Yield: 70%. $C_{43}H_{36}P_2Pt$ (809.8): calcd. C 63.8, H 4.5; found C 63.9, H 4.3. $^1$H NMR (300 MHz, $CDCl_3$): $\delta$ = 7.74–7.01 (m, 30 H, Ph), 2.64–2.55 (m, 4 H, -$CH_2$-P-Pt-), 2.09–1.94 (m, 2 H, -C-$CH_2$-C-) ppm. $^{31}$P{$^1$H} NMR (121.5 MHz, $CDCl_3$): $\delta$ = 4.87 [$^2J$(PP) = 15.3 Hz, $^1J$(PtP) = 3349 Hz], 3.20 [$^2J$(PP) = 15.3 Hz, $^1J$(PtP) = 3086 Hz] ppm. IR (KBr): $\nu$(C≡C) = 2160 (m, uncoordinated), 1719 (m, coordinated) cm$^{-1}$. ESI-MS (*m*/*z*, assignment): 810 [M]$^+$. Single crystals of **4** for X-ray diffraction analysis were obtained by slow diffusion of *n*-hexane into a concentrated $CH_2Cl_2$ solution of **4**.

**[(dppp)Pt]$_2$[μ-(1,2-$\eta^2$):(3,4-$\eta^2$)-$PhC_4Ph$] (5):** **4** (0.11 g, 0.14 mmol) and 1 mol equiv. of $Pt(dppp)(CH_2{=}CH_2)$ (0.086 g, 0.14 mmol) were added to diethyl ether (15 mL) and stirred at room temperature for 24 h. The pale yellow suspension was then filtered and washed with diethyl ether. The pale yellow crude product was recrystallized from THF/diethyl ether to give the pure product. Yield: 0.11 g (55%). $C_{70}H_{62}P_4Pt_2$ (1417.3): calcd. C 59.3, H 4.4; found C 59.2, H 4.4. $^1$H NMR (300 MHz, $C_6D_6$): $\delta$ = 6.81–7.91 (m, 50 H, Ph), 2.24 (m, 8 H, -$CH_2$-P-Pt-), 1.61–1.68 (m, 4 H, -C-$CH_2$-C-) ppm. $^{31}$P{$^1$H} NMR (121.5 MHz, $C_6D_6$): $\delta$ = 4.18 [$^2J$(PP) = 26.7 Hz, $^1J$(PtP) = 3258 Hz], 3.94 [$^2J$(PP) = 26.7 Hz, $^1J$(PtP) = 3267 Hz] ppm. IR (KBr): $\nu$(C≡C) = 1758 (m) cm$^{-1}$. ESI-MS (*m*/*z*, assignment): 1417 [M]$^+$. Single crystals of **5** for X-ray diffraction analysis were obtained by slow diffusion of diethyl ether into a concentrated THF solution of **5**.

**(dppp)Pt[(1,2-$\eta^2$)-$CH_3C_4CH_3$] (6):** $Pt(dppp)(CH_2{=}CH_2)$ (0.108 g, 0.17 mmol) was treated with twofold excess of 2,4-hexadiyne (0.027 g, 0.34 mmol) in diethyl ether at room temperature for 24 h. The pale yellow suspension was then filtered and washed with a small amount of diethyl ether. The product was purified by recrystallization in THF/diethyl ether. Yield: 0.08 g (70%). $C_{33}H_{32}P_2Pt$ (685.6): calcd. C 57.8, H 4.7; found C 57.5, H 4.5. $^1$H NMR (300 MHz, $C_6D_6$): $\delta$ = 7.98–7.92, 7.71–7.65 and 7.10–6.98 (m, 20 H, Ph), 2.76 [doublet of triplets, $^3J$(PtH) = 39.7 Hz, $^4J$(PH) = 7.6 Hz, 3 H, $CH_3$ on the coordinated C≡C], 2.15 (m, 4 H, -$CH_2$-P-Pt-), 1.90 [doublet of triplets, $^5J$(PtH) = 18.8 Hz, $^6J$(PH) = 3.5 Hz, 3 H, $CH_3$ on the uncoordinated C≡C], 1.62 (m, 2 H, -C-$CH_2$-C-) ppm. $^{31}$P{$^1$H} NMR (121.5 MHz, $C_6D_6$): $\delta$ = 8.47 [$^2J$(PP) = 31.1 Hz, $^1J$(PtP) = 3353 Hz], 7.29 [$^2J$(PP) = 31.1 Hz, $^1J$(PtP) = 3124 Hz] ppm. IR (KBr): $\nu$(C≡C) = 2196 w (uncoordinated), 1749 s (coordinated) cm$^{-1}$. ESI-MS (*m*/*z*, assignment): 686 [M]$^+$.

**[(dppp)Pt]$_2$[μ-(1,2-$\eta^2$):(3,4-$\eta^2$)-$CH_3C_4CH_3$] (7):** The preparative procedures for **7** were similar to those for preparing **5**. Yield: 40%. $C_{60}H_{58}P_4Pt_2$ (1293.2): calcd. C 55.7, H 4.5; found C 55.5, H 4.5. $^1$H NMR (300 MHz, $C_6D_6$): $\delta$ = 8.06–8.00, 7.86–7.80 and 7.10–6.93 (m, 40 H, Ph), 2.51 (m, 6 H, $CH_3$), 2.26 (br., 8 H, -$CH_2$-P-Pt-), 1.74 (br., 4 H, -C-$CH_2$-C-) ppm. $^{31}$P{$^1$H} NMR (121.5 MHz, $C_6D_6$): $\delta$ = 8.54 [$^1J$(PtP) = 3227 and 3258 Hz] ppm. IR (KBr): $\nu$(C≡C) = 1705 (w) cm$^{-1}$. ESI-MS (*m*/*z*, assignment): 1293 [M]$^+$.

 © 2007 Wiley-VCH Verlag GmbH & Co. KGaA, Weinheim 

Table 3. Crystal data and structure refinements for compounds **2**, **4**, and **5**.

| Compound | **2** | **4** | **5** |
|---|---|---|---|
| Empirical formula | $C_{45}H_{44}OP_2Pt$ | $C_{43}H_{36}P_2Pt$ | $C_{70}H_{62}P_4Pt_2$ |
| Formula weight | 857.83 | 809.75 | 1417.26 |
| Temperature [K] | 295(2) | 223(2) | 223(2) K |
| Wavelength [Å] | 0.71073 | 0.71073 | 0.71073 Å |
| Crystal system | orthorhombic | triclinic | monoclinic |
| Space group | *P*nma | $P\bar{1}$ | *P*2(1)/*n* |
| Unit cell dimensions (Å and deg) | $a$ = 30.0064(15)<br>$b$ = 23.4345(12)<br>$c$ = 10.7582(5)<br>$\alpha = \beta = \gamma = 90$ | $a$ = 10.7412(5)<br>$b$ = 12.6475(6)<br>$c$ = 13.7503(6)<br>$\alpha$ = 83.3900(10)<br>$\beta$ = 88.0370(10)<br>$\gamma$ = 66.3590(10) | $a$ = 10.8152(7)<br>$b$ = 20.0454(12)<br>$c$ = 26.8225(17)<br>$\alpha = \gamma = 90$<br>$\beta$ = 92.4740(10) |
| Volume [Å$^3$] | 7565.0(6) | 1699.68(14) | 5809.6(6) |
| $Z$ | 8 | 2 | 4 |
| Calculated density [mg/m$^3$] | 1.506 | 1.582 | 1.620 |
| Absorption coefficient [mm$^{-1}$] | 3.828 | 4.252 | 4.963 |
| $F$(000) | 3440 | 804 | 2792 |
| Crystal size [mm$^3$] | 0.38 × 0.26 × 0.20 | 0.40 × 0.10 × 0.08 | 0.50 × 0.20 × 0.20 |
| θ range for data collection [°] | 1.61 to 27.50 | 1.77 to 25.00 | 1.52 to 30.01 |
| Index ranges | $-38 \le h \le 36$, $-30 \le k \le 30$, $-12 \le l \le 13$ | $-12 \le h \le 12$, $-15 \le k \le 15$, $-16 \le l \le 16$ | $-14 \le h \le 15$, $-28 \le k \le 26$, $-20 \le l \le 37$ |
| Reflections collected | 51463 | 18338 | 46864 |
| Independent reflections | 8897 [$R$(int) = 0.0408] | 5990 [$R$(int) = 0.0271] | 16579 [$R$(int) = 0.0317] |
| Max. and min. transmission | 0.5148 and 0.3241 | 0.7272 and 0.2811 | 0.4368 and 0.1904 |
| Data/restraints/parameters | 8897/17/459 | 5990/0/556 | 16579/0/685 |
| Goodness-of-fit on $F^2$ | 1.021 | 1.080 | 1.025 |
| Final $R$ indices [$I > 2$sigma($I$)] | $R1$ = 0.0318, $wR2$ = 0.0664 | $R1$ = 0.0276, $wR2$ = 0.0695 | $R1$ = 0.0325, $wR2$ = 0.0752 |
| $R$ indices (all data) | $R1$ = 0.0461, $wR2$ = 0.0707 | $R1$ = 0.0287, $wR2$ = 0.0702 | $R1$ = 0.0440, $wR2$ = 0.0792 |
| Largest diff. peak and hole [e Å$^{-3}$] | 1.222 and –1.152 | 3.840 and –0.667 | 2.971 and –0.682 |

**Physical Measurements:** Elemental analyses of all the compounds prepared were carried out in the microanalysis laboratory in the Department of Chemistry, the National University of Singapore. $^1$H- and $^{31}$P{$^1$H}-NMR spectra were recorded at room temperature with a Bruker ACF 300 spectrometer. Electrospray ionization mass spectra (ESI-MS) were measured with a Finnigan MAT 731 LCQ spectrometer. IR spectra (KBr) were recorded using a Bio-Rad Win-IR spectrophotometer. UV/Vis absorption spectra were recorded with a Shimadzu UV-1601PC UV/Vis spectrophotometer. Emission spectra were recorded with a SPEX-Fluorolog2 model F111A1 fluorescence spectrofluorometer. The lifetimes were measured using the Quanta Ray DCR3 Nd:YAG laser with a pulsewidth of 8 ns and excitation wavelength of 355 nm. Sample solutions for 77 K frozen glass emission spectra measurement were prepared as follows: (i) a small amount of solid samples were added to ethanol solution; (ii) the solutions were then dissolved using the ultra-sonic bath; (iii) the solutions were filtered; (iv) the filtrates were introduced into a quartz tube; (v) the quartz tubes were immersed in liquid nitrogen in a quartz optical Dewar flask for measuring.

**Molecular Orbital Calculations:** The calculations were performed using the SPARTAN semiempirical program SGI/R10K, release 5.1.3, with geometry optimization. The model RHF/PM3 was used in the calculations.

**X-ray Crystallography:** The diffraction experiments were carried out with a Bruker AXS SMART CCD 3-circle diffractometer at $T$ = 223 K (except that: $T$ = 295 K for crystal **2**·THF), 2θ-ω scan with a sealed tube at 23 °C using graphite-monochromated Mo-$K_\alpha$ radiation ($\lambda$ = 0.71073 Å). The software used were: SMART[14] for collecting frames of data, indexing reflection, and determination of lattice parameters; SAINT[14] for integration of intensity of reflections and scaling; SADABS[15] for empirical absorption correction; and SHELXTL[16] for space group determination, structure solution, and least-squares refinements on $|F|^2$. The crystals were mounted at the end of glass fibers and used for the diffraction experiments. Anisotropic thermal parameters were refined for the rest of the non-hydrogen atoms. The hydrogen atoms were placed in their ideal positions. The X-ray crystal data and parameters used in structural refinements are summarized in Table 3.

CCDC-623835 (for **2**), -623836 (for **4**), and -623837 (for **5**) contain the supplementary crystallographic data. These data can be obtained free of charge from The Cambridge Crystallographic Data Centre via www.ccdc.cam.ac.uk/data_request/cif.

**Supporting Information** (see also the footnote on the first page of this article): Molecular orbitals of the acetylenes, emission spectra of diphenylacetylene and 1,4-diphenyl-buta-1,3-diyne, emission spectra of frozen glass solutions of **3**–**5** at 77 K, syntheses and characterizations of **1** and **3**.

## Acknowledgments

J. H. K. Y. thanks The National University of Singapore for financial support. K. Y. W. acknowledges the support from the Hong Kong Polytechnic University. We are grateful to Ms. Tan Geok Kheng (NUS) for her assistance with X-ray crystal structure determination.

[1] a) M. Y. Choi, M. C.-W. Chan, S. Zhang, K. K. Cheung, C.-M. Che, K. Y. Wong, *Organometallics* **1999**, *18*, 2074; b) G. B. Cunningham, Y. Li, S. Liu, K. S. Schanze, *J. Phys. Chem. B* **2003**, *107*, 12569; c) A. M. McDonagh, M. G. Humphrey, M. Samoc, B. Luther-Davies, S. Houbrechts, T. Wada, H. Sasabe, A. Persoons, *J. Am. Chem. Soc.* **1999**; *121*, 1405.

 © 2007 Wiley-VCH Verlag GmbH & Co. KGaA, Weinheim 

[2] a) V. W. W. Yam, K. M. C. Wong, *Top. Curr. Chem.* **2005**, *257*, 1; b) A. C. Benniston, A. Harriman, P. Li, C. A. Sams, *J. Phys. Chem. A* **2005**, *109*, 2302.
[3] a) I. R. Whittal, A. M. McDonagh, M. G. Humphrey, *Adv. Organomet. Chem.* **1998**, *42*, 291; b) J. Manna, K. J. John, M. D. Hopkins, *Adv. Organomet. Chem.* **1995**, *38*, 79; c) S. R. Marder, in *Inorganic Materials* (Eds.: D. W. Bruce, D. O'Hare), Wiley, Chichester, **1996**, p. 121; d) N. J. Long, C. K. Williams, *Angew. Chem. Int. Ed.* **2003**, *42*, 2586; e) C. R. Horn, J. A. Gladysz, *Eur. J. Inorg. Chem.* **2003**, 2211; f) J. H. K. Yip, J. Wu, K. Y. Wong, K. P. Ho, C. S. N. Pun, J. J. Vittal, *Organometallics* **2002**, *21*, 5292; g) H.-Y. Chao, W. Lu, Y. Li, M. C. W. Chan, C.-M. Che, K.-K. Cheung, N. Zhu, *J. Am. Chem. Soc.* **2002**; *124*, 14696; h) V. W.-W. Yam, *Acc. Chem. Res.* **2002**, *35*, 555; i) P. J. Low, *Dalton Trans.* **2005**, 2821; j) P. J. Low, M. I. Bruce, *Adv. Organomet. Chem.* **2001**, *48*, 71; k) W. Y. Wong, *J. Inorg. Organomet. Polym.* **2005**, *15*, 197.
[4] V. W. W. Yam, V. C. Y. Lau, K. K. Cheung, *Organometallics* **1996**, *15*, 1740.
[5] a) J. Chatt, G. A. Rowe, A. A. Williams, *Proc. Chem. Soc. London* **1957**, 208; b) J. Chatt, R. G. Guy, L. A. Duncanson, D. T. Thompson, *J. Chem. Soc.* **1963**, 5170.
[6] a) J. Klosin, K. A. Abboud, W. M. Jones, *Organometallics* **1995**, *14*, 2892; b) S. Yamazaki, A. J. Deeming, D. M. Speel, *Organometallics* **1998**, *17*, 775; c) S. Saito, K. Tando, C. Kabuto, Y. Yamamoto, *Organometallics* **2000**, *19*, 3704; d) C. Müller, R. J. Lachicotte, W. D. Jones, *Organometallics* **2002**, *21*, 1118; e) P. B. Tripathy, D. M. Roundhill, *J. Am. Chem. Soc.* **1970**, *92*, 3825; f) D. M. Barlex, R. D. W. Kemmitt, G. W. Littlecott, *J. Chem. Soc. C* **1969**, 613.
[7] a) I. Ara, J. R. Berenguer, E. Eguizábal, J. Forniés, J. Gómez, E. Lalinde, J. M. Sáez-Rocher, *Organometallics* **2000**, *19*, 4385; b) Z. Lu, K. A. Abboud, W. M. Jones, *J. Am. Chem. Soc.* **1992**, *114*, 10991; c) Y. Koie, S. Shinoda, Y. Saito, *J. Chem. Soc., Dalton Trans.* **1981**, 1802.
[8] a) R. M. Ward, A. S. Batsanov, J. A. K. Howard, T. B. Marder, *Inorg. Chim. Acta* **2006**, *359*, 3671; b) U. Rosenthal, S. Pulst, P. Arndt, A. Ohff, A. Tillack, W. Baumann, R. Kempe, V. V. Burlakov, *Organometallics* **1995**, *14*, 2961; c) C. M. Forsyth, S. P. Nolan, C. L. Stern, T. J. Marks, A. L. Rheingold, *Organometallics* **1993**, *12*, 3618; d) M. Kersting, K. Dehnicke, D. Fenske, *J. Organomet. Chem.* **1986**, *309*, 125; e) R. Choukroun, B. Donnadieu, I. Malfant, S. Haubrich, R. Frantz, C. Guerin, B. Henner, *Chem. Commun.* **1997**, 2315; f) W. Bonrath, K.-R. Pörschke, G. Wilke, K. Angermund, C. Kruger, *Angew. Chem. Int. Ed. Engl.* **1988**, *27*, 833.
[9] J. Bernardus, B. Heyns, F. G. A. Stone, *J. Organomet. Chem.* **1978**, *160*, 337.
[10] D. M. Blake, D. M. Roundhill, *Inorg. Synth.* **1978**, *18*, 120.
[11] a) J. H. Nelson, K. S. Wheelock, L. C. Cusachs, H. B. Jonassen, *J. Chem. Soc. C* **1969**, *18*, 1019.
[12] J. O. Glanville, J. M. Stewart, S. O. Grim, *J. Organomet. Chem.* **1967**, *7*, 9.
[13] P. D. Harvey, W. P. Schaefer, H. B. Gray, *Inorg. Chem.* **1988**, *27*, 1101.
[14] *SMART & SAINT Software Reference Manuals, Version 4.0*, Siemens Energy & Automation, Inc., Analytical Instrumentation, Madison, Wisconsin, USA, **1996**.
[15] G. M. Sheldrick, *SADABS*, software for empirical absorption correction, University of Gottingen, Gottingen, Germany, **1996**.
[16] *SHELXTL Reference Manual, Version 5.03*, Siemens Energy & Automation, Inc., Analytical Instrumentation, Madison, Wisconsin, USA, **1996**.

Received: August 19, 2006
Published Online: November 27, 2006

 © 2007 Wiley-VCH Verlag GmbH & Co. KGaA, Weinheim 

DOI: 10.1002/ejic.200600824

# Towards Polymer Diagnostic Agents − Copolymers of *N*-(2-Hydroxypropyl)-methacrylamide and Bis(2-pyridylmethyl)-4-vinylbenzylamine: Synthesis, Characterisation and $Re(CO)_3$-Labelling

**Peter C. Kunz,*[a] Nadine E. Brückmann,[a] and Bernhard Spingler[b]**

**Keywords:** Rhenium / Carbonyl ligands / Polymer diagnostics / Copolymers / Cancer / Diagnosis / EPR effect

Diagnosis of early stage angiogenic tumours is fundamental for cancer therapy. In this study we present the synthesis and characterisation of functionalised HPMA-copolymers with optimal molecular weights that meet the demands of the enhanced permeability and retention (EPR) effect. Rhenium tricarbonyl complexes of the tripodal ligands bis(2-pyridylmethyl)benzylamine (**1a**) and bis(2-pyridylmethyl)-4-vinylbenzylamine (**1b**) were prepared and characterised by $^1H$ NMR and IR spectroscopy, mass spectrometry and X-ray diffraction. Ligand **1b** was copolymerised with *N*-(2-hydroxypropyl)methacrylamide (HPMA), and the resulting copolymer was treated with $(nBu_4N)_2[Re(CO)_3Br_3]$ to yield a $Re(CO)_3$-labelled copolymer.

(© Wiley-VCH Verlag GmbH & Co. KGaA, 69451 Weinheim, Germany, 2007)

## Introduction

Polymer–drug conjugates are an interesting concept in medicinal chemistry. The conjugation of prodrugs to hydrophilic polymers provides an opportunity to solubilise poorly water-soluble drugs, improve tumour targeting and reduce drug toxicity.[1] Several polymer–drug conjugates have already entered phase-I/II clinical trials as anticancer agents.[2] The improved tumour targeting is due to the so called enhanced permeability and retention (EPR) effect, which concerns the passive accumulation of macromolecules in solid tumours because of the high vascular density in tumours, the increased permeability and defective architecture of tumour vessels, as well as suppressed lymphatic drainage from the tumour interestitium. The molecular weight ($M_w$) of macromolecular systems is more important than their nature (proteins, lipids or synthetic polymers) for the EPR effect. Macromolecules with molecular weights above 40 kDa are found to remain at high levels in circulating blood.[3] On the other hand, nephritic excretion is restricted to macromolecules with molecular weights below about 50 kDa.[4]

Although polymers are now widely used in therapeutic approaches, only a few examples of diagnostically used polymer conjugates exist.[5] We are interested in developing organometallic polymer-based tumour diagnostic agents. *N*-(2-Hydroxypropyl)methacrylamide (HPMA) was chosen as a copolymer base since its copolymers are water-soluble, biocompatible and non-immunogenic macromolecular carrier systems.[5a] Furthermore, the molecular weight of HPMA copolymers can be easily varied. Organometallic and coordination chemistry with relation to biological and medicinal chemistry is an increasingly important field. The use of technetium is of particular interest due to the short half-life of $^{99m}Tc$ ($T_{1/2}$ = 6 h, $E_\gamma$ = 140 keV), which makes this isotope one of the workhorses of diagnostic nuclear medicine.[6] The chemistry of this element is closest to its heavier congener rhenium, which itself has become interesting for therapeutic purposes as the isotope $^{188}Re$ ($T_{1/2}$ = 16.9 h, $E_\beta$ = 2.1 MeV). Since the development of new, simple routes for the synthesis of *fac*-$[^{99m}Tc(H_2O)_3(CO)_3]^+$ and *fac*-$[^{188}Re(H_2O)_3(CO)_3]^+$, several groups have begun to develop ligand systems for these $M(CO)_3$ fragments.[7] Therefore, a macromolecule that is able to bind $M(CO)_3$ (M = Tc, Re) would be interesting for diagnostic as well as therapeutic approaches.

Here, we report the synthesis and characterisation of HPMA-co-bis(2-pyridylmethyl)-4-vinylbenzylamine copolymers with different average molecular weights and the coordination of the $Re(CO)_3$ fragment to these copolymers.

## Results and Discussion

The ligand bis(2-pyridylmethyl)benzylamine (**1a**) was prepared from picolyl chloride and benzylamine by modifying a synthesis originally reported by Dick.[8] This ligand serves as a model for the coordination environment of the $Re(CO)_3$ moiety in the polymer. The co-monomer ligand

[a] Heinrich-Heine-Universität Düsseldorf,
Universitätsstr. 1, 40225 Düsseldorf, Germany
Fax: +49-211-811-2287
E-mail: Peter.Kunz@uni-duesseldorf.de
[b] Anorganisch-Chemisches Institut, Universität Zürich-Irchel,
Winterthurerstr. 190, 8057 Zürich, Switzerland
Fax: +41-44-635-6803
E-mail: spingler@aci.unizh.ch

 InterScience © 2007 Wiley-VCH Verlag GmbH & Co. KGaA, Weinheim 

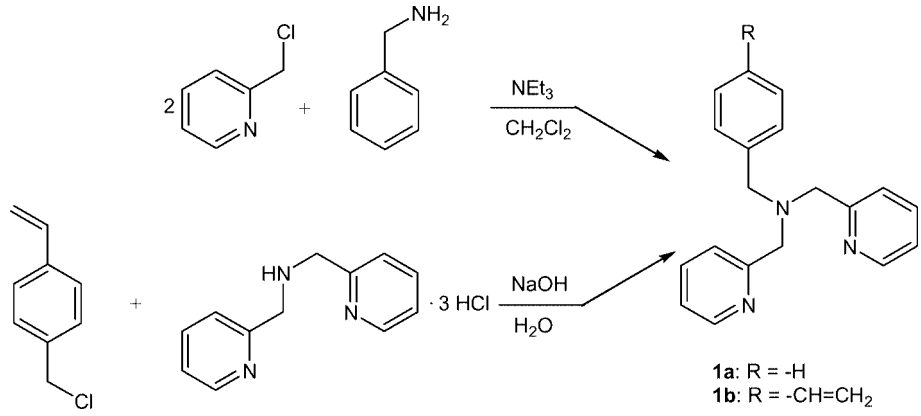


Scheme 1. Synthetic routes to the ligands **1a** and **1b**.

bis(2-pyridylmethyl)-4-vinylbenzylamine (**1b**) was prepared by the reaction of bis(2-pyridylmethyl)amine with 4-vinylbenzyl chloride (Scheme 1).

In the $^1$H NMR spectra in deuteriochloroform both ligands show singlets at $\delta$ = 3.7 and 3.8 ppm in a 2:4 ratio for the $CH_2$ groups attached to the amine. The aromatic protons of the phenyl ring and the protons of the pyridyl rings (H3, H4 and H5) appear in the region $\delta$ = 7.1–7.9 ppm, whereas $H6_{py}$ is at a lower field of $\delta$ = 8.6 ppm. In addition, **1b** exhibits signals for the three vinyl protons at $\delta$ = 5.23, 5.75 and 6.72 ppm, with the characteristic splitting pattern of two doublets ($^3J_{cis}$ = 11, $^3J_{trans}$ = 18 Hz) for the terminal protons and a doublet of doublets for the α-proton of the vinyl group. The FAB$^+$ mass spectra of **1a** and **1b** exhibit peaks for the molecular ion at the expected *m*/*z* value together with a characteristic fragmentation pattern.

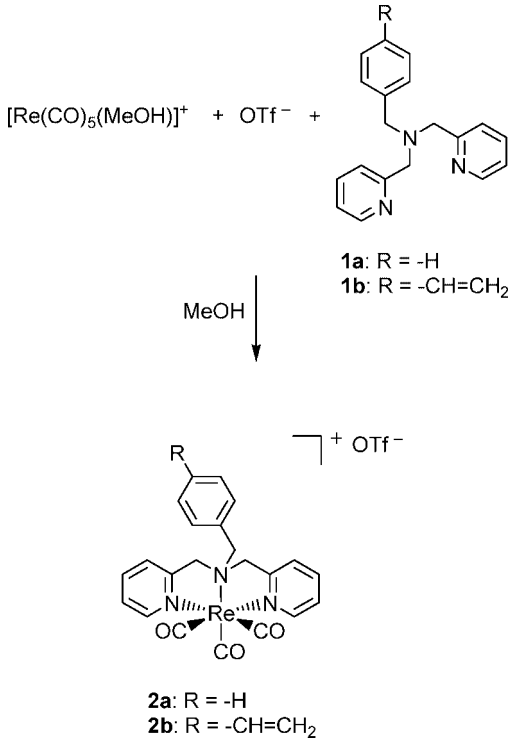


Scheme 2. Formation of complexes of **1a** and **1b** with [Re(CO)$_5$Br] in the presence of AgOTf.

Both **1a** and **1b** form complexes of the composition [LRe(CO)$_3$]OTf when Re(CO)$_5$Br, AgOTf and ligand are mixed in an equimolar stoichiometry in refluxing methanol (Scheme 2).

Upon coordination, the signals of the $CH_2$ groups directly bound to the amine nitrogen atom are shifted by about 1 ppm towards lower field. Additionally, the methylene protons of the 2-pyridylmethyl groups at $\delta$ = 4.8 ppm are no longer chemically equivalent due to the $C_s$-symmetry of complexes **2a** and **2b** and form an AB spin-system. The aromatic protons of the phenyl and pyridyl rings as well as the protons of the vinyl group in **2b** do not shift upon coordination. The IR spectra of **2a** and **2b** show the characteristic bands of the ligands and the two bands of a nearly $C_{3v}$-symmetrical Re(CO)$_3$ fragment, with the doubly degenerate *E* band slightly split (**2a**: 2028, 1922 cm$^{-1}$; **2b**: 2028, 1920 cm$^{-1}$). This splitting has also been observed in the Mo$^{I}$(CO)$_3$ complex of **1a**.[9] The FAB$^+$ mass spectra of **2a** and **2b** exhibit peaks for the molecular ion at the expected *m*/*z* values (both 100%) together with the characteristic $^{187/185}$Re isotope pattern.

## Solid-State Structures of 2a·$CH_2Cl_2$·$H_2O$ and 2b·$CH_2Cl_2$

For a better understanding of the Re(CO)$_3$ binding in the functionalised polymer we determined the structures of the molecular "model" complexes **2a** and **2b** by X-ray analysis. Both complexes can be crystallised by slow diffusion of *n*-hexane into a solution of the corresponding complex in dichloromethane. Complex **2a**·$CH_2Cl_2$·$H_2O$ crystallises in the triclinic space group $P\bar{1}$ (Figure 1). The co-crystallised water molecule is disordered. Interestingly, the achiral complex **2b**·$CH_2Cl_2$ crystallises in the chiral space group $P2_1$ (Figure 2). The rhenium centre in both structures is in a slightly distorted octahedral coordination environment, with the *N*,*N*,*N* ligands and the three carbonyl ligands coordinating facially. As expected, both structures are very similar at first glance. In the structure of **2a** the angles between the carbonyl ligands are close to 90° and

 © 2007 Wiley-VCH Verlag GmbH & Co. KGaA, Weinheim 

the maximum deviation of the Re1–$C_n$–$O_n$ ($n$ = 1–3) angles from 180° is less than 1.5°. Interestingly, the $Re(CO)_3$ fragment in **2b** shows significant distortion: the carbonyl groups are slightly bent towards each other and the C1–Re1–C3 angle is only 85.7°. In addition, the Re1–$C_n$–$O_n$ angles deviate significantly from 180°. The maximum deviation is found for the Re1–C3–O3 angle, which is 174.8°. Selected bond lengths and angles are summarised in Tables 1 and 2.

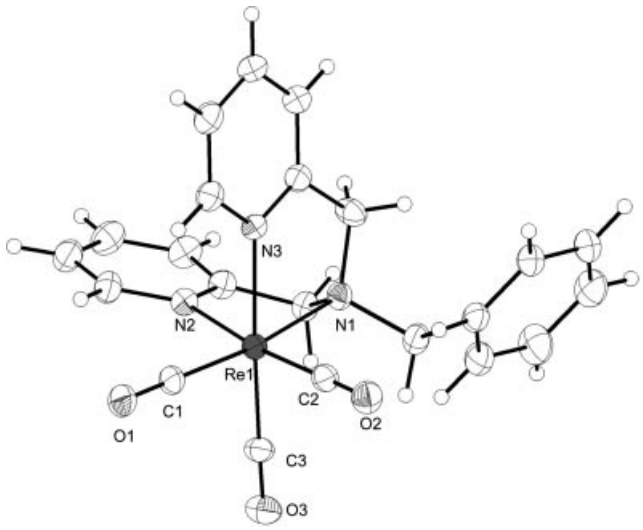


Figure 1. Structure of the cation [(**1a**)$Re(CO)_3$]$^+$ in **2a**·$CH_2Cl_2$·$H_2O$. Displacement ellipsoids are shown at the 30% probability level.

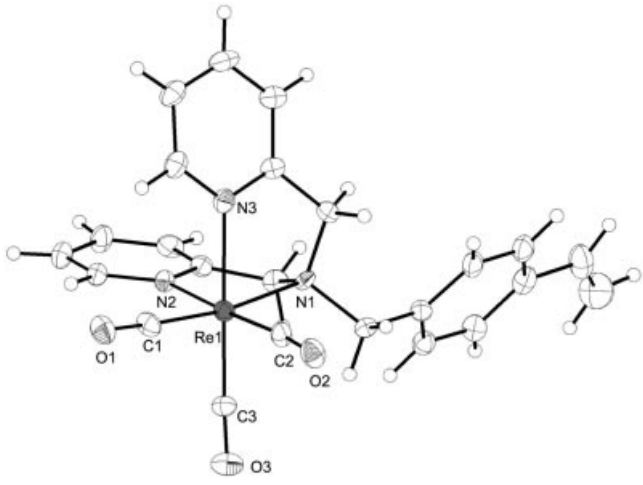


Figure 2. Structure of the cation [(**1b**)$Re(CO)_3$]$^+$ in **2b**·$CH_2Cl_2$. Displacement ellipsoids are shown at the 30% probability level.

Table 1. Selected bond lengths [Å] and angles [°] for **2a**·$CH_2Cl_2$·$H_2O$.

| | | | |
|---|---|---|---|
| Re1–N1 | 2.228(4) | Re1–C1 | 1.915(5) |
| Re1–N2 | 2.162(5) | Re1–C2 | 1.917(6) |
| Re1–N3 | 2.157(4) | Re1–C3 | 1.940(5) |
| C1–O1 | 1.151(6) | C2–O2 | 1.145(8) |
| C3–O3 | 1.133(7) | | |
| N1–Re1–N2 | 72.12(18) | N1–Re1–N3 | 78.43(16) |
| N2–Re1–N3 | 82.08(18) | C1–Re1–C2 | 88.7(2) |
| C1–Re1–C3 | 89.2(2) | C2–Re1–C3 | 89.7(3) |
| Re1–C1–O1 | 179.3(5) | Re1–C2–O2 | 179.3(5) |
| Re1–C3–O3 | 178.6(5) | | |

Table 2. Selected bond lengths [Å] and angles [°] for **2b**·$CH_2Cl_2$.

| | | | |
|---|---|---|---|
| Re1–N1 | 2.228(6) | Re1–C1 | 1.902(8) |
| Re1–N2 | 2.156(7) | Re1–C2 | 1.917(7) |
| Re1–N3 | 2.177(7) | Re1–C3 | 1.918(8) |
| C1–O1 | 1.148(11) | C2–O2 | 1.159(10) |
| C3–O3 | 1.158(11) | | |
| N1–Re1–N2 | 78.7(2) | N1–Re1–N3 | 78.0(2) |
| N2–Re1–N3 | 79.0(3) | C1–Re1–C2 | 89.6(4) |
| C1–Re1–C3 | 85.7(3) | C2–Re1–C3 | 87.1(4) |
| Re1–C1–O1 | 175.8(8) | Re1–C2–O2 | 177.1(8) |
| Re1–C3–O3 | 174.8(7) | | |

### $Re(CO)_3$-Labelled HPMA-Copolymer

In order to obtain HPMA-co-bis(2-pyridylmethyl)-4-vinylbenzylamine copolymer (**3**), freshly synthesised ligand **1b** and HPMA were dissolved in dry acetone and azobis(isobutyronitrile) (AIBN) added as initiator.[10] The reactions were carried out at 50 °C for 24 h. The resulting polymeric product was precipitated from a mixture of acetone and diethyl ether.

The $^1$H NMR spectrum of **3** (Figure 3) exhibits signals of the ligand as well as of HPMA. These signals are broadened due to the polymeric character of the examined molecules. Fortunately, there is almost no signal overlap and all signals can be assigned. The signals at $\delta$ = 3.8 and 3.9 ppm arise from the protons of the $CH_2$ groups attached to the amine, and the resonances deriving from the aromatic protons of the phenyl ring and the protons of the pyridyl rings appear in the region $\delta$ = 7.1–8.5 ppm. The other broad resonances can be assigned to HPMA and to the $CH_2$ group in the polymer backbone.

In the IR spectrum, the two $\nu_{C=C}$ bands of the aromatic pyridyl and phenyl rings occur at 1597 and 1572 cm$^{-1}$ and the carbonyl vibration deriving from the HPMA occurs at $\nu_{C=O}$ = 1730 cm$^{-1}$. Furthermore, the three aliphatic $CH_2$ and $CH_3$ vibrations are found in the region between 2980 and 2800 cm$^{-1}$. With monomer ratios of 10:1, 20:1 and 40:1 (HPMA:ligand) an average molecular weight of between 13.5 and 52 kDa can be obtained, as confirmed by size exclusion chromatography in DMF (Table 3).

The copolymer was labelled with $Re(CO)_3$ by refluxing $(n Bu_4N)_2[Re(CO)_3Br_3]$, AgOTf and copolymer in methanol. The IR spectrum clearly shows the vibrational bands of the copolymer as well as the two characteristic carbonyl bands from the pseudo $C_{3v}$-symmetrical $Re(CO)_3$ fragment.

In order to determine whether the $Re(CO)_3$ fragment is coordinated to the ligand system in the copolymer chain or whether it is non-specifically bound to the copolymer, the same reaction was carried out with poly-HPMA. In this case, the two bands of the carbonyl vibration can also be seen in the IR spectrum, thus indicating that $Re(CO)_3$ fragments are present in this sample as well. A Soxhlet extrac-

 © 2007 Wiley-VCH Verlag GmbH & Co. KGaA, Weinheim 

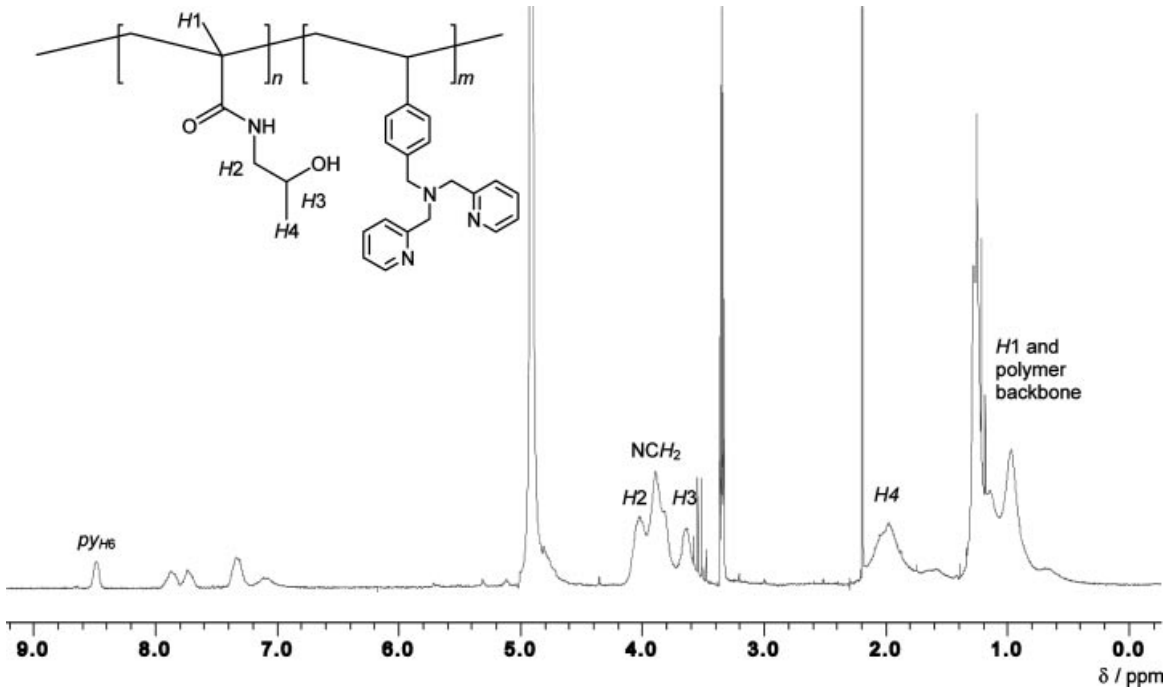


Figure 3. $^1$H NMR spectrum of HPMA-co-bis(2-pyridylmethyl)-4-vinylbenzylamine copolymer **3a**.

Table 3. Average molecular weights of the copolymers **3** obtained with different monomer and AIBN ratios.

| Copolymer | Monomer ratio | HPMA/**1b**/AIBN | $M_w$ [kDa] | Polydispersity |
|---|---|---|---|---|
| **3a** | 10:1 | 2 g/440 mg/30 mg | 13.5 | 1.4 |
| **3b** | 20:1 | 2 g/239 mg/15 mg | 20.0 | 1.2 |
| **3c** | 20:1 | 2 g/235 mg/20 mg | 18.0 | 1.6 |
| **3d** | 20:1 | 2 g/253 mg/20 mg | 22.5 | 1.5 |
| **3e** | 40:1 | 2 g/121 mg/15 mg | 52.0 | 1.8 |

tion of both labelled polymers was carried out using water as solvent. After extraction, only the IR spectrum of the copolymer sample shows the two carbonyl bands with high intensity (Figure 4); the IR spectrum of the extracted poly-HPMA sample shows the carbonyl bands with very low intensity (Figure 5). This proves that $Re(CO)_3$ is in fact coordinated to **3** and, in addition, that non-coordinated $Re(CO)_3$ can be washed out in order to obtain the pure product.

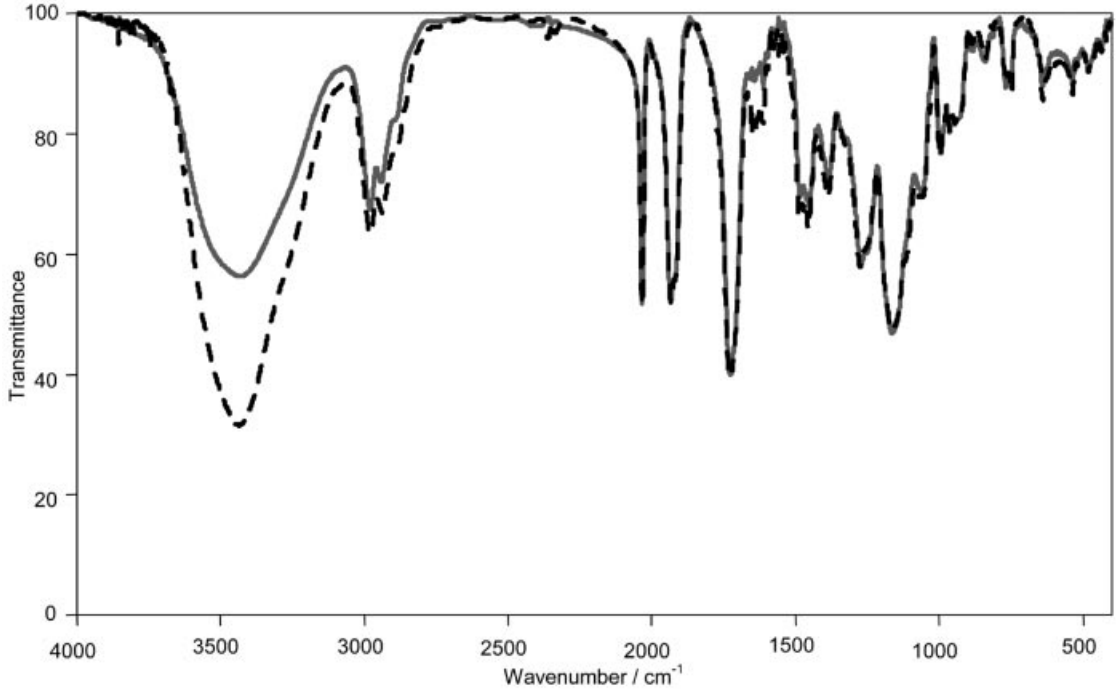


Figure 4. IR spectra of $Re(CO)_3$-labelled HPMA-co-bis(2-pyridylmethyl)-4-vinylbenzylamine copolymer **4a** before (dashed) and after Soxhlet extraction (solid).

 © 2007 Wiley-VCH Verlag GmbH & Co. KGaA, Weinheim 

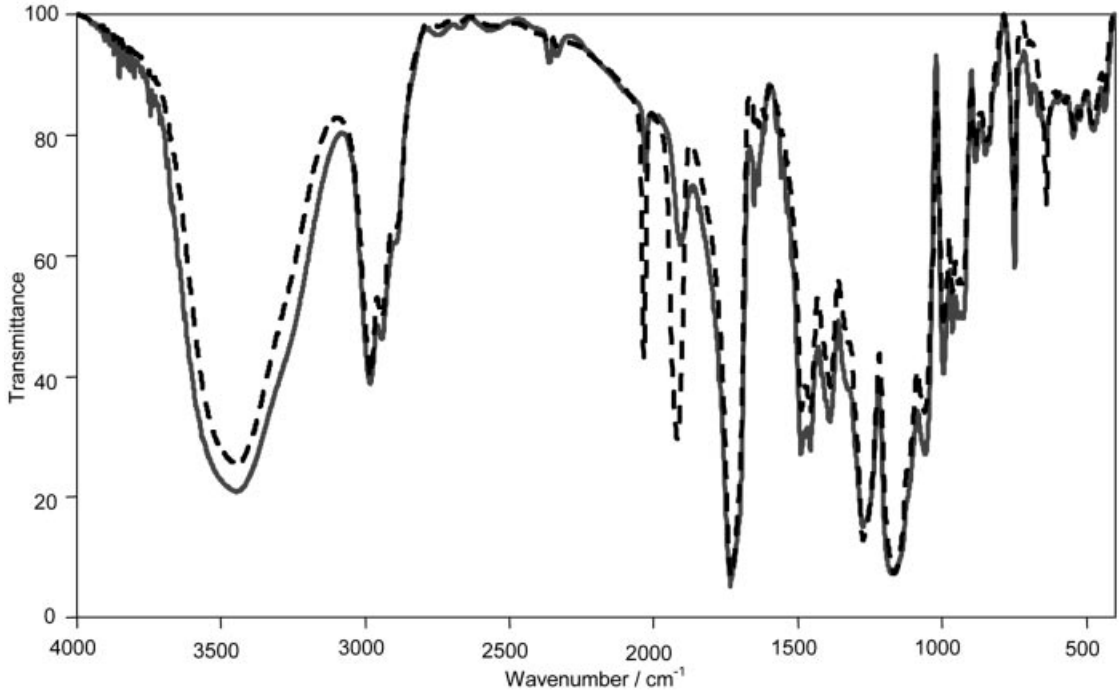


Figure 5. IR spectra of $Re(CO)_3$-labelled poly-HPMA before (dashed) and after Soxhlet extraction (solid).

## Conclusions

We have presented a novel, water-soluble co-polymer of HPMA, namely HPMA-co-bis(2-pyridylmethyl)-4-vinylbenzylamine. The average molecular weight can be controlled by variation of the co-monomers and radical starter. With copolymer **3e**, a polymer having a molecular weight (52 kDa) suitable for the EPR effect was obtained. The copolymers can be labelled with $[Re(CO)_3Br_3]^{2-}$ at the bis(2-pyridylmethyl)amine unit and it has been shown that the $Re(CO)_3$ labels are not easily lost in aqueous medium. This makes these copolymers interesting carriers for the diagnostically used $^{99m}Tc$.

The solid-state structures of the bis(2-pyridylmethyl)-amine-derived complexes **2a**·$CH_2Cl_2$·$H_2O$ and **2b**·$CH_2Cl_2$ have been determined by X-ray crystallography. The IR spectra of these complexes and the $Re(CO)_3$-labelled copolymer are identical, they therefore resemble the structure of the binding sites in the labelled copolymer.

## Experimental Section

2-Picolyl chloride hydrochloride, benzylamine and 4-vinylbenzyl chloride were used as purchased from Aldrich and Fluka. Bis(2-pyridylmethyl)amine tris(hydrochloride),[11] $Re(CO)_5Br$[12] and $(NBu_4)_2[Re(CO)_3Br_3]$[7a] were prepared according to literature procedures. The preparation of the complexes was carried out in Schlenk tubes under an atmosphere of dry nitrogen using anhydrous solvents purified according to standard procedures. Crystals suitable for X-ray structure analysis were prepared by slow diffusion of *n*-hexane into a solution of the complexes in dichloromethane. $^1H$ NMR spectra were recorded with a Bruker AM 200 and Bruker DRX 500 spectrometer. $^{13}C\{^1H\}$ NMR spectra were recorded with a Bruker DRX 500 spectrometer. The $^1H$ and $^{13}C\{^1H\}$ NMR spectra were calibrated against the residual proton signals and the carbon signals of the solvents as internal references ([$D_1$]chloroform: $\delta_H$ = 7.30 ppm and $\delta_C$ = 77.0 ppm). The FAB mass spectra were recorded with a Finnigan MAT 8200 mass spectrometer in an NBA matrix. IR spectra were recorded with a Bruker IFS 66 FT-IR spectrometer. Size-exclusion chromatography was performed with a Viskotec GPCmax VE 2001 GPC solvent/sample module with a Viskotec VE 3580 RI detector.

**Bis(2-pyridylmethyl)benzylamine (1a):** 2-Picolyl chloride hydrochloride (2.05 g, 12.5 mmol) and benzylamine (0.67 g, 6.3 mmol) were dissolved in 15 mL of water and heated to 60 °C. To this solution 5 mL of aqueous NaOH (5 M) were added dropwise over a period of 30 min and the resulting mixture stirred for an additional 60 min. The cooled solution was extracted three times with 20 mL of dichloromethane, the combined organic layers were dried with $Na_2SO_4$, filtered and the solvent removed in vacuo. The product was obtained as a viscous brown oil (1.51 g, 83%). $^1H$ NMR (500 MHz, $CDCl_3$): $\delta$ = 3.64 (s, 2 H, NC$H_2$Ph), 3.76 (s, 4 H, py$CH_2$), 7.1–7.9 (m, 11 H, aromatic *H*), 8.62 ppm (m, 2 H, py*H6*). $^{13}C\{^1H\}$ NMR (500 MHz, $CDCl_3$): $\delta$ = 58.9, 60.3, 122.5, 123.3, 127.5, 129.1, 129.4, 127.0, 139.1, 149.4, 160.0 ppm. IR (KBr): $\tilde{\nu}$ = 2923, 2819, 1590, 1570, 760, 699 $cm^{-1}$. $FAB^+$ MS (NBA matrix): *m*/*z* (%) 290 (100) $[(pyCH_2)_2NCH_2Ph + H]^+$, 197 (47) $[pyCH_2NCH_2Ph]^+$, 93 (49) $[pyCH_2]^+$, 91 (60) $[CH_2Ph]^+$.

**Bis(2-pyridylmethyl)-4-vinylbenzylamine (1b):** Under an inert gas atmosphere, 4-vinylbenzyl chloride (1.3 g, 8 mmol), bis(2-pyridylmethyl)amine trishydrochloride (2 g, 6.5 mmol) and triethylamine (4 mL, 40 mmol) were dissolved in 30 mL of dichloromethane and stirred for 8 h. The white precipitate of triethylamine hydrochloride was removed by filtration. The organic solution was extracted twice with 10 mL of water and dried with $Na_2SO_4$. The solvent was removed in vacuo to give the product as an orange viscous liquid (1.4 g, 68%). $^1H$ NMR (200 MHz, $CDCl_3$): $\delta$ = 3.71

 © 2007 Wiley-VCH Verlag GmbH & Co. KGaA, Weinheim 

(s, 2 H, NC$H_2$Ph), 3.84 (s, 4 H, pyC$H_2$), 5.23 (d, $^3J_{cis}$ = 11 Hz, 1 H, *cis*-C$H_2$CH), 5.75 (d, $^3J_{trans}$ = 18 Hz, 1 H, *trans*-C$H_2$CH), 6.72 (dd, 1 H, $CH_2CH$), 7.1–7.9 (m, 10 H, aromatic *H*), 8.56 ppm (m, 2 H, py*H*6). $^{13}C\{^1H\}$ NMR (500 MHz, $CDCl_3$): $\delta$ = 58.6, 60.4, 113.9, 123.2, 126.6, 129.4, 129.4, 136.9, 136.9, 137.0, 139.0, 149.4, 160.2 ppm. IR (KBr): $\tilde{\nu}$ = 2922, 2821, 1629, 1590, 1569, 825, 760 $cm^{-1}$. FAB$^+$ MS (NBA matrix): *m*/*z* (%) 316 (59) $[(pyCH_2)_2NCH_2PhCHCH_2 + H]^+$, 223 (45) $[pyCH_2NCH_2PhCHCH_2]^+$, 198 (26) $[(pyCH_2)_2N]^+$, 117 (100) $[CH_2C_6H_4CHCH_2]^+$, 93 (56) $[pyCH_2]^+$.

**General Procedure for the Preparation of Re(CO)$_3$ Complexes:** Under an inert gas atmosphere, AgOTf (129 mg, 500 μmol) and $Re(CO)_5Br$ (0.2 g, 0.5 mmol) in methanol were heated to reflux for 60 min. The AgBr precipitate was removed by filtration and 0.5 mmol of the ligand (**1a** or **1b**) dissolved in 5 mL methanol was added. The solution was refluxed for an additional hour. After cooling to ambient temperature the solvent was removed in vacuo and the residue dissolved in a minimum of dichloromethane. *n*-Hexane was added to the solution and colourless crystals deposited after a few days.

**[(1a)Re(CO)$_3$]OTf (2a):** Yield: 0.28 g (76%). $^1$H NMR (500 MHz, $CDCl_3$); $\delta$ = 4.69 (s, 2 H, PhC$H_2$), 4.82 (m, 4 H, $[AB]_2$, pyC$H_2$), 7.1–7.9 (m, 11 H, aromatic *H*), 8.6 ppm (m, 2 H, py*H*6). IR (KBr): $\tilde{\nu}$ = 2028, 1922, 1612 $cm^{-1}$. FAB$^+$ MS (NBA matrix): *m*/*z* (%) 560 (100) $[(\mathbf{1a})Re(CO)_3]^+$. $C_{23}H_{19}F_3N_3O_6ReS{\cdot}CH_2Cl_2{\cdot}C_6H_{14}$ (879.80): calcd. C 39.0, H 2.7, N 5.9; found C 38.6, H 2.7, N 5.8.

**[(1b)Re(CO)$_3$]OTf (2b):** Yield: 0.27 g (75%). $^1$H NMR (500 MHz, $CDCl_3$); $\delta$ = 4.67 (s, 2 H, PhC$H_2$), 4.82 (m, 4 H, $[AB]_2$, pyC$H_2$), 5.31 (d, $^3J_{cis}$ = 11 Hz, 1 H, *cis*-C$H_2$CH), 5.78 (d, $^3J_{trans}$ = 18 Hz, 1 H, *trans*-C$H_2$CH), 6.69 (dd, 1 H, $CH_2CH$), 7.1–7.9 (m, 10 H, aromatic *H*), 8.6 (m, 2 H, py*H*6). IR (KBr): $\tilde{\nu}$ = 2028, 1920, 1560 $cm^{-1}$. FAB$^+$ MS (NBA matrix): *m*/*z* (%) 585 (100) $[(\mathbf{1b})Re(CO)_3]^+$. $C_{25}H_{21}F_3N_3O_6ReS{\cdot}CH_2Cl_2{\cdot}C_6H_{14}$ (905.84): calcd. C 40.9, H 2.9, N 5.7; found C 40.1, H 2.6, N 5.6.

**General Procedure for the Preparation of HPMA-co-bis(2-pyridylmethyl)-4-vinylbenzylamine Copolymers (3):** HPMA and bis(2-pyridylmethyl)-4-vinylbenzylamine were dissolved in 15 mL of acetone in a Schlenk tube under an inert gas atmosphere. After addition of AIBN, the solution was heated to 50 °C and stirred for 24 h. The polymer was then precipitated by pouring the reaction mixture into a mixture of acetone and diethyl ether (1:1), the precipitate was filtered off and dried in vacuo to give **3a** (1.5 g, 67%). $^1$H NMR (200 MHz, [D$_4$]methanol): $\delta$ = 1.0 [C$H_2$ (polymer backbone), HPMA-H1], 2.0 (HPMA-H4), 3.6 (HPMA-H3), 3.8 (NC$H_2$Ph), 3.9 (pyC$H_2$), 4.0 (HPMA-H2), 7.1–7.9 (aromatic *H*), 8.6 ppm (py*H*6). IR (KBr): $\tilde{\nu}$ = 2980, 2800, 1597, 1572, 749 $cm^{-1}$.

**General Procedure for the Preparation of Re(CO)$_3$-Labelled HPMA-co-bis(2-pyridylmethyl)-4-vinylbenzylamine Copolymers (4):** Under an inert gas atmosphere, $(n\mathrm{Bu}_4\mathrm{N})_2[Re(CO)_3Br_3]$ (0.1 g, 0.13 mmol) and AgOTf (0.11 g, 0.39 mmol) were heated to reflux in methanol for 60 min. Precipitated AgBr was removed by filtration and 0.458 g of the copolymer **3a** dissolved in 10 mL methanol was added. The solution was refluxed for an additional hour and then cooled to room temperature. The polymer was then precipitated in a mixture of acetone and diethyl ether (1:1), filtered off and dried in vacuo (0.46 g, 93%). $^1$H NMR ([D$_4$]methanol): $\delta$ = 1.0 [C$H_2$ (polymer backbone), HPMA-H1], 2.0 (HPMA-H4), 3.6 (HPMA-H3), 3.9 (pyC$H_2$), 4.0 (HPMA-H2), 7.1–7.9 (aromatic *H*), 8.5 ppm (py*H*6). IR (KBr): $\tilde{\nu}$ = 2980, 2800, 2033 ($\nu_{CO}$), 1933 ($\nu_{CO}$), 1612, 1598, 749 $cm^{-1}$.

**X-ray Crystallographic Study:** Crystallographic data were collected with a Stoe IPDS diffractometer at 183(2) K using a graphite-monochromated Mo-$K_\alpha$ radiation ($\lambda$ = 0.71073 Å). Suitable crystals were covered with Paratone N oil, mounted on a glass fibre and immediately transferred to the diffractometer. 8000 Reflections distributed over the whole limiting sphere were selected by the program SELECT and used for unit cell parameter refinement with the program CELL.[13] Data were collected for Lorentz and polarisation effects as well as for absorption (numerical). Structures were solved by direct methods using SIR97[14] and were refined by full-matrix least-squares methods on $F^2$ with SHELXL-97.[15]

CCDC-617234 and -617235 contain the supplementary crystallographic data for this paper. These data can be obtained free of charge from The Cambridge Crystallographic Data Centre via www.ccdc.cam.ac.uk/data_request/cif.

## Acknowledgments

B. S. thanks the Swiss National Science Foundation and the University of Zürich for financial support.

[1] H. Ringsdorf, *J. Pharm. Sci. Polymer Symp.* **1975**, *51*, 135–153.
[2] a) R. Duncan, S. Gac-Brenton, R. Keane, R. Musila, Y. N. Sat, R. Satchi, F. Searle, *J. Controlled Release* **2001**, *74*, 135–146; b) R. Duncan, *Nat. Rev. Drug Discovery* **2003**, *2*, 347–360.
[3] H. Maeda, J. Wu, T. Sawa, Y. Matsumura, K. Hori, *J. Controlled Release* **2000**, *65*, 271–284.
[4] E. Oberdisse, E. Hackenthal, K. Kuschinsky, *Pharmakologie und Toxikologie*, 3rd ed., Springer, Berlin, **2002**.
[5] a) A. Mitra, A. Nan, H. Ghandehari, E. McNeill, J. Mulholland, B. R. Line, *Pharm. Res.* **2004**, *21*, 1153–1159; b) R. Satchi-Fainaro, M. Puder, J. W. Davis, H. T. Tran, D. A. Sampson, A. K. Greene, G. Corfas, J. Kolkman, *Nat. Med. (N.Y.)* **2004**, 255–261; c) Y. Huang, A. Nan, G. M. Rosen, C. S. Winalski, E. Schneider, P. Tsai, H. Ghandehari, *Macromol. Biosci.* **2003**, *3*, 647–652.
[6] K. Schwochau, *Technetium*, Wiley-VCH, Weinheim, **2000**.
[7] a) R. Alberto, K. Ortner, N. Wheatley, R. Schibli, A. P. Schubiger, *J. Am. Chem. Soc.* **2001**, *123*, 3135–3136; b) R. Schibli, R. Schwarzbach, R. Alberto, K. Ortner, H. Schmalle, C. Dumas, A. Egli, A. P. Schubiger, *Bioconjugate Chem.* **2002**, *13*, 750–756; c) S. R. Banerjee, M. K. Levadala, N. Lazarova, L. Wei, J. F. Valliant, K. A. Stephenson, J. W. Babich, K. P. Maresca, J. Zubieta, *Inorg. Chem.* **2002**, *41*, 64–6425; d) T. Storr, Y. Sugai, Y. Mikata, M. J. Adam, S. Yano, C. Orvig, *Inorg. Chem.* **2005**, *44*, 2698–2705; e) N. Lazavora, J. Babich, J. Valliant, P. Schaffer, S. James, J. Zubieta, *Inorg. Chem.* **2005**, *44*, 6763–6770.
[8] S. Dick, A. Weiss, *Z. Naturforsch., Teil B* **1997**, *52*, 188–192.
[9] D. R. van Staveren, E. Bothe, T. Weyhermüller, N. Metzler-Nolte, *Eur. J. Inorg. Chem.* **2002**, 1518–1529.
[10] Freshly prepared **1b** was used as **1b** homo-polymerises. Although **1b** has not been described in the literature, the homopolymer of **1b** is known as Dowex B by the Dow Chemical company.
[11] H. J. Hoorn, P. de Joode, W. L. Driessen, J. Reedijk, *Recl. Trav. Chim. Pays-Bas* **1996**, *115*, 191–197.
[12] D. Vitali, F. Calderazzo, *Gazz. Chim. Ital.* **1972**, *102*, 587–596; E. O. Brimm, M. A. Lynch Jr., W. J. Sesny, *J. Am. Chem. Soc.* **1954**, *76*, 3831–3835.
[13] "CELL" 2.87, 5/1998 ed., STOE & Cie, GmbH, Darmstadt, Germany, 1998.
[14] A. Altomare, M. C. Burla, M. Camalli, G. L. Cascarano, C. Giacovazzo, A. Guagliardi, A. G. G. Moliterni, G. Polidori, R. Spagna, *J. Appl. Crystallogr.* **1999**, *32*, 115–119.
[15] SHELXL-97, G. M. Sheldrick, University of Göttingen, Germany, **1997**.

Received: September 5, 2006
Published Online: November 29, 2006

 © 2007 Wiley-VCH Verlag GmbH & Co. KGaA, Weinheim 

DOI: 10.1002/ejic.200600859

# The Complexes $[OsCl_2(azole)_2(dmso)_2]$ and $[OsCl_2(azole)(dmso)_3]$: Synthesis, Structure, Spectroscopic Properties and Catalytic Hydration of Chloronitriles

**Iryna N. Stepanenko,[a] Berta Cebrián-Losantos,[a] Vladimir B. Arion,*[a] Artem A. Krokhin,[a] Alexey A. Nazarov,[a] and Bernhard K. Keppler*[a]**

**Keywords:** Osmium / N ligands / Homogeneous catalysis / Hydration

Two families of mixed-ligand osmium(II) complexes, namely *trans*,*cis*,*cis*-$[Os^{II}Cl_2(azole)_2(dmso)_2]$ [azole = indazole (**1**), pyrazole (**2**), benzimidazole (**3**) and imidazole (**4**)] and *cis*,*fac*-$[Os^{II}Cl_2(azole)(dmso)_3]$ [azole = indazole (**5**), pyrazole (**6**), benzimidazole (**7**) and imidazole (**8**)] have been prepared by taking advantage of the destabilising *trans* effect of the *S*-bonded dmso ligands. These complexes have been characterised by microanalysis, IR, UV/Vis, $^1H$ and $^{13}C$ NMR spectroscopy, electrospray mass spectrometry, cyclic voltammetry and X-ray crystallography. They have been found to catalyse the hydration of trichloroacetonitrile to trichloroacetamide and dichloroacetonitrile to dichloroacetamide with high selectivity. The catalyst efficiency depends strongly on the nature of the complex and the azole ligand present. The highest turnover (TON of 412 for trichloroacetamide and 578 for dichloroacetamide) and product yield (82.7 % for trichloroacetamide and 75.3 % for dichloroacetamide) have been achieved with complex **7**.
(© Wiley-VCH Verlag GmbH & Co. KGaA, 69451 Weinheim, Germany, 2007)

## Introduction

The coordination chemistry of dimethyl sulfoxide has been the subject of intensive studies in the past[1–3] and continues to attract the attention of researchers today.[4,5] Of the platinum group metals, the most extensively studied appear to be ruthenium-dmso complexes, some of which are endowed with potent antitumour properties[6,7] or have found application in catalytic processes.[8–10] In addition, $Ru^{II}$-dmso complexes have been successfully employed as precursors for the synthesis of a large variety of compounds, and, in particular, of $[Ru^{II}Cl_2(azole)_2(dmso)_2]$ geometric isomers,[11–16] with $[Ru^{II}Cl_2(4\text{-}NO_2Him)_2(dmso)_2]$ possessing radiosensitising properties. Quite recently, we discovered that *trans*,*trans*,*trans*-$[RuCl_2(Hind)_2(dmso)_2]$ (s in italics means coordination via sulfur) and *trans*,*cis*,*cis*-$[RuCl_2(Hind)_2(dmso)_2]$ species are able to mediate the insertion of the C≡N group of acetonitrile in the N1–H bond of the N2-coordinated indazole, these being the first examples of the metal-assisted iminoacylation of indazole.[17]

Comparison of the chemistry of ruthenium(II) dmso complexes with that of osmium(II) dmso species has permitted us to unravel expected similarities between these two types of complexes, but also remarkable, although less pronounced, differences. In particular, both ruthenium(II) and osmium(II) have been shown to form *cis*,*fac*-$[MCl_2(dmso)(dmso)_3]$ and *trans*-$[MCl_2(dmso)_4]$ isomers, the first of which contains three facially S-coordinated dmso ligands and one dmso molecule O-ligated to the metal ion, with the second containing four S-coordinated dmso ligands. However, the third (linkage) isomer *cis*-$[MCl_2(dmso)_4]$, with all dmso ligands coordinated via sulfur, has been isolated only for osmium(II).[18] In addition, it should be noted that despite the similarity between ruthenium(II) dmso and osmium(II) dmso complexes, the latter have, in general, rarely been used as precursors in inorganic synthesis. Examples reported in the literature have been confined to reactions of *trans*-$[OsCl_2(dmso)_4]$, *trans*-$[OsBr_2(dmso)_4]$ or *cis*,*fac*-$[OsCl_2(dmso)(dmso)_3]$ with chelating ligands containing Te, Sb or P as donor atoms.[19–21] This observed difference in the number of documented reactions can probably, in part, be explained by stronger Os–L bonds and higher ligand substitution activation energies in comparison with the case of ruthenium analogues.[22] In addition, it must be stressed that the position of the two metals in the periodic table is important, but not sufficient for the successful synthesis of the desired osmium complexes. This cannot be performed in a routine way simply by following the protocols for ruthenium species, and very often particular skills and experience are required. With this in mind, we set out to use the $Os^{II}$ dmso isomers available as starting compounds and to study their reactivity toward azole heterocycles, especially indazole (Hind), pyrazole (Hpz), benzimidazole (Hbzim) and imidazole (Him; see Scheme 1).

[a] Institute of Inorganic Chemistry, Faculty of Chemistry, University of Vienna,
Währingerstr. 42, 1090 Vienna, Austria
Fax: +43-1-4277-52680
E-mail: vladimir.arion@univie.ac.at
bernhard.keppler@univie.ac.at

Supporting information for this article is available on the WWW under http://www.eurjic.org or from the author.

 © 2007 Wiley-VCH Verlag GmbH & Co. KGaA, Weinheim 

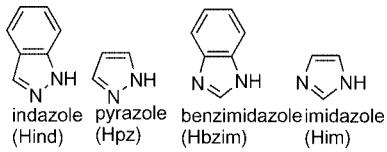


Scheme 1.

We anticipated (i) the isolation of "pure" isomers of composition [$OsCl_2$(azole)$_2$(dm*so*)$_2$], due to the distinct kinetic inertness of $Os^{II}$ complexes over $Ru^{II}$ species, without any competing isomerisation reactions interfering, (ii) the isolation of other species, the formation of which under similar reaction conditions does not occur in the case of ruthenium analogues, and (iii) the elucidation of previously unknown facets of the reactivity profile of the compounds prepared. In particular, in order to establish the scope of the recently discovered metal-assisted iminoacylation of indazole,[17] we checked the reactivity of the isolated *trans*,*cis*,*cis*-[$Os^{II}Cl_2$(Hind)$_2$(dm*so*)$_2$] isomer towards $CH_3CN$ and $CCl_3CN$. We show that no insertion of the C≡N group into the N1–H bond of the N2-coordinated indazole takes place. Instead, with trichloroacetonitrile we observed hydration of this solvent and set out to examine this reaction in more detail.

Herein we report the synthesis of two different families of compounds, namely *trans*,*cis*,*cis*-[$Os^{II}Cl_2$(azole)$_2$(dm*so*)$_2$] [azole = Hind (**1**), Hpz (**2**), Hbzim (**3**), Him (**4**)] and *cis*,*fac*-[$OsCl_2$(azole)(dm*so*)$_3$] [azole = Hind (**5**), Hpz (**6**), Hbzim (**7**) and Him (**8**)] and their structural and spectroscopic characterisation both in the solid state and in solution. In addition, the results of the study of the hydration reaction of chloronitriles catalysed by the prepared complexes are reported.

## Results and Discussion

### Synthesis

While treatment of *trans*-[$OsCl_2$(dm*so*)$_4$] with two equivalents of azole ligand in boiling absolute ethanol afforded the isomers *trans*,*cis*,*cis*-[$OsCl_2$(azole)$_2$(dm*so*)$_2$] (**1**–**4**) in 80–88% yield (Scheme 2), the reaction under similar conditions starting from *cis*-[$OsCl_2$(dmso)$_4$] resulted in the formation of complexes *cis*,*fac*-[$OsCl_2$(azole)(dm*so*)$_3$] (**5**–**8**) in 46–85% yield. We also discovered that heating complexes **1**–**4** in dimethyl sulfoxide at 125 °C led to their conversion into **5**–**8**, respectively, in 70–75% yield. It should be noted that the synthesis of ruthenium analogues of **5**–**8** is possible under mild conditions by selective replacement of the *O*-bonded dmso in *cis*,*fac*-[$RuCl_2$(dm*so*)(dm*so*)$_3$] by treatment with a stoichiometric amount of the corresponding azole ligand.[12,15a,16b] If, however, the azole ligand is added in excess and the reaction is carried out at elevated temperatures, isomers of the composition [$RuCl_2$(azole)$_2$(dm*so*)$_2$] are produced.[13,14,15a]

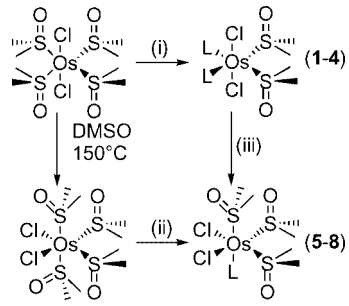


Scheme 2. Synthesis of complexes *trans*,*cis*,*cis*-[$OsCl_2L_2$(dm*so*)$_2$] [L = Hind (**1**), Hpz (**2**), Hbzim (**3**), Him (**4**)] and *cis*,*fac*-[$OsCl_2L$(dm*so*)$_3$] [L = Hind (**5**), Hpz (**6**), Hbzim (**7**) and Him (**8**)]. Reaction conditions: (i) 2 equiv. L, EtOH, 80–87 °C, 1–3 h; (ii) 2 equiv. L, EtOH, 80–87 °C, 40 min–2 h; (iii) dmso, 125 °C, 45 min–2 h. The complex *trans*-[$OsCl_2$(dm*so*)$_4$] at 150 °C undergoes isomerisation into *cis*-[$OsCl_2$(dmso)$_4$] in dmso.[21]

The formation of **1**–**4** from *trans*-[$OsCl_2$(dm*so*)$_4$] and **5**–**8** from *cis*-[$OsCl_2$(dmso)$_4$] can be explained by a remarkable destabilising *trans* effect of the *S*-bonded dmso molecules. The *trans* and *cis* isomers have two and one of these destabilising vectors, respectively, therefore substitution at these sites predetermined by structural differences between the isomers is favoured. Two pathways for the conversion of **1**–**4** into **5**–**8** can be proposed (Scheme 3): (a) the azole ligand is substituted by a molecule of dmso to give *trans*,*mer*-[$OsCl_2$(azole)(dm*so*)$_3$], which then isomerises to *cis*,*fac*-[$OsCl_2$(azole)(dm*so*)$_3$]; (b) another four isomers can theoretically exist along with *trans*,*cis*,*cis*-[$OsCl_2$(azole)$_2$(dm*so*)$_2$]. Taking into account that the *cis*,*cis*,*trans* and *cis*,*trans*,*cis* isomers have not been reported for ruthenium,[17] we postulate that the formation or emergence of the other two isomers (*trans*,*trans*,*trans* and *cis*,*cis*,*cis*) is more likely. Substitution of one of the two azole ligands by dmso, followed by isomerisation, results in *cis*,*fac*-[$OsCl_2$(azole)(dm*so*)$_3$]. The intermediate species could not be identified by the analyti-

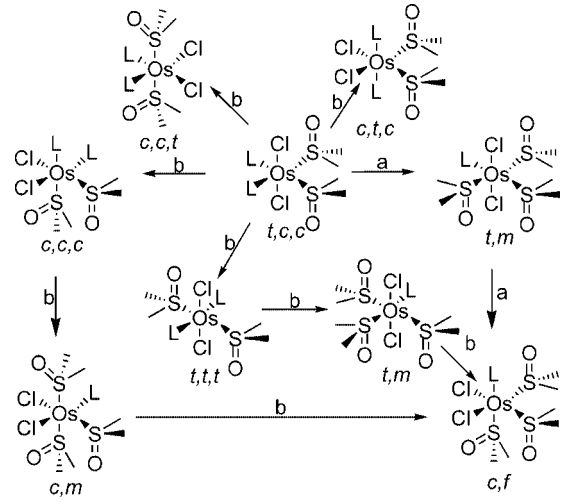


Scheme 3. Proposed transformation pathways (a and b) of **1**–**4** into **5**–**8**. Abbreviations used: *c* – *cis*, *t* – *trans*, *m* – *mer*, *f* – *fac*.

 © 2007 Wiley-VCH Verlag GmbH & Co. KGaA, Weinheim 

cal techniques available and the mechanism of this transformation remains uncertain. Nevertheless, the first pathway is shorter and simpler, which makes it more plausible.

### $^1$H and $^{13}$C NMR Spectra

In the $^1$H NMR spectra of **1/5** and **3/7** one set of signals of equal intensity for the Hind and Hbzim ligands [at $\delta$ = 12.74, 8.68, 7.65, 7.47, 7.40 and 7.16 ppm (**1**); $\delta$ = 14.43, 9.20, 7.73, 7.51, 7.43 and 7.19 ppm (**5**); $\delta$ = 12.87, 8.41, 7.87, 7.47, 7.13 and 6.91 ppm (**3**); $\delta$ = 13.18, 8.78, 8.21, 7.59, 7.29 and 7.24 ppm (**7**)] is observed. Likewise, one set of $^{13}$C resonances is seen for Hind in **1** and **5** and Hbzim in **3** and **7**. In addition, the singlet at $\delta$ = 3.37 (**1**) and 3.27 ppm (**3**), of sixfold intensity in comparison to the indazole or benzimidazole proton resonances present in the spectra, was assigned to the dmso methyl protons coordinated to osmium(II) via sulfur. Note that the downfield shift of dmso protons when coordinated through oxygen is much less with respect to the metal-free dmso.[18] In *cis*-[OsCl$_2$(dms*o*)(dm*s*o)$_3$], for example, this signal is observed at $\delta$ = 2.76 ppm. In the $^{13}$C NMR spectrum the dmso resonance is present at $\delta$ = 45.4 (**1**) and 45.6 ppm (**3**). Two resonances in the $^1$H NMR spectrum at $\delta$ = 3.64 and 3.35 ppm, with a 2:1 relative intensity in **5**, and three signals of equal intensity at $\delta$ = 3.59, 3.45 and 3.28 ppm in **7**, are indicative of the presence of three dmso ligands coordinated through sulfur. Three resonances for *S*-bonded dmso ligands at $\delta$ = 48.8, 48.1 and 45.8 (**5**) and 48.9, 47.1 and 45.7 ppm (**7**) are seen in the $^{13}$C NMR spectra of **5** and **7**. This is in agreement with the $C_2$ symmetry of **1** and **3** and the $C_1$ symmetry of **5** and **7** in solution. Significant downfield shifts of the resonances of the protons nearest to the Os$^{II}$ centre (NH and C3-H) in **1** and **5** with respect to the position of the same signals for the metal-free indazole ($\delta$ = 10.01 and 8.09 ppm) and in **3** and **7** with respect to the position of the NH, C2-H and C4-H/C7-H signals for the metal-free benzimidazole ($\delta$ = 12.44, 8.21 and 7.61 ppm) are also worthy of note.

The presence of singlet resonances at $\delta$ = 3.34 (**2**), 3.13 (**4**), 3.60, 3.59 and 3.29 (**6**), and 3.51, 3.45 and 3.25 ppm (**8**) in the $^1$H NMR spectra of **2**, **4**, **6** and **8** indicates coordination of the dmso ligands to osmium(II) through sulfur. In the $^{13}$C NMR spectra the resonances of the dmso carbon atoms are found at $\delta$ = 45.6 (**2**), 45.5 (**4**), 48.7, 47.9 and 45.8 (**6**) and 48.5, 47.2 and 46.0 ppm (**8**). Four signals for the pyrazole and imidazole protons and three carbon resonances in **2**, **4**, **6** and **8** (see Experimental Section) are indicative of the $C_2$ symmetry of molecules of **2** and **4** and the $C_1$ symmetry of **6** and **8** in solution. As for **1**, **3**, **5** and **7**, significant downfield shifts of the resonances of the protons nearest to the Os$^{II}$ centre (NH and C3-H in **2** and **6** and NH, C2-H and C4-H in **4** and **8**) with respect to the position of the same signals for the metal-free pyrazole [$\delta$ = 10.26 (NH) and 7.63 ppm (C3-H and C5-H)] and imidazole [$\delta$ = 12.03 (NH), 7.64 (C2-H) and 7.01 ppm (C4-H and C5-H)] are observed.

### Crystal Structures of 1–8

The asymmetric unit of **1** contains two crystallographically distinct [Os$^{II}$Cl$_2$(Hind)$_2$(dm*s*o)$_2$] molecules **1A** (Figure 1) and **1B** (Figure S1). Selected bond lengths and angles are listed in Table 1. Essentially octahedral coordination around the osmium atom is found in both molecules. The two chlorido ligands are mutually *trans*, while the two dmso and the two indazole ligands are correspondingly *cis* coordinated to each other. Thus, the configuration of the two independent complexes can be described as *trans*,*cis*,*cis*-[Os$^{II}$Cl$_2$(Hind)$_2$(dm*s*o)$_2$]. The Os–Cl bond lengths [2.4138(12) and 2.3984(11) Å in **1A** and 2.3989(12) and 2.4127(12) Å in **1B**] are similar to the Ru–Cl bond lengths in two independent molecules of *trans*,*cis*,*cis*-[Ru$^{II}$Cl$_2$(Hind)$_2$-(dm*s*o)$_2$] [2.4105(7), 2.4137(7), 2.4069(7) and 2.4147(7) Å], whereas the Os–S bond lengths [2.2250(11) and 2.2453(11) in **1A** and 2.2460(11) and 2.2245(11) Å in **1B**] are somewhat shorter than the Ru–S bond lengths [2.2439(13), 2.2588(8), 2.2477(7) and 2.2578(14) Å] and the Os–N interatomic distances [2.130(4), 2.137(4) (**1A**) and 2.122(4), 2.139(3) Å (**1B**)] are slightly longer than the Ru–N distances [2.1177(18), 2.1255(14), 2.1159(14) and 2.1244(19) Å]. The orientation of the *cis*-arranged indazole ligands in **1A** can be described by the torsion angles $\Theta_{Cl2–Os1–N1–N2}$ [17.5(3) °] and $\Theta_{Cl2–Os1–N3–N4}$ [–0.1(3)°] and is stabilised by the intramolecular hydrogen bonds N2–H2···Cl2 (N2–H2 0.880, H2···Cl2 2.572, N2···Cl2 3.115 Å; N2–H2–Cl2 120.69°) and

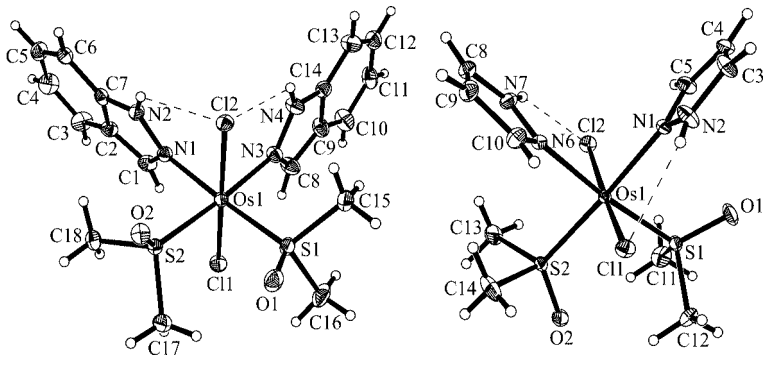


Figure 1. Molecular structures of the first independent molecule *trans*,*cis*,*cis*-[Os$^{II}$Cl$_2$(Hind)$_2$(dm*s*o)$_2$] (**1A**; left) and *trans*,*cis*,*cis*-[Os$^{II}$Cl$_2$(Hpz)$_2$(dm*s*o)$_2$] (**2**; right), showing the atom-numbering schemes. Thermal ellipsoids are drawn at the 50% probability level.

 © 2007 Wiley-VCH Verlag GmbH & Co. KGaA, Weinheim 

Table 1. Selected bond lengths [Å] and angles [°] in **1** and **2**.

| | **1A** | **1B** | **2** |
|---|---|---|---|
| Os1–N1/Os2–N5 | 2.130(4) | 2.122(4) | 2.1202(17) |
| Os1–N3/Os2–N7 | 2.137(4) | 2.139(3) | |
| Os1–N6 | | | 2.1365(17) |
| Os1–S1/Os2–S3 | 2.2250(11) | 2.2460(11) | 2.2498(6) |
| Os1–S2/Os2–S4 | 2.2453(11) | 2.2245(11) | 2.2386(6) |
| Os1–Cl1/Os2–Cl3 | 2.4138(12) | 2.4127(12) | 2.4293(8) |
| Os1–Cl2/Os2–Cl4 | 2.3984(11) | 2.3989(12) | 2.4053(8) |
| S1–O1/S3–O3 | 1.490(4) | 1.489(3) | 1.4819(17) |
| S2–O2/S4–O4 | 1.492(3) | 1.495(3) | 1.4855(16) |
| N1–Os1–N3/N5–Os2–N7 | 84.79(15) | 86.42(14) | |
| N1–Os1–N6 | | | 86.03(6) |
| S1–Os1–S2/S3–Os2–S4 | 91.47(4) | 91.01(4) | 94.51(2) |
| Cl1–Os1–Cl2/Cl3–Os2–Cl4 | 176.23(4) | 174.94(4) | 174.556(17) |

N4–H4A···Cl2 (N4–H4A 0.880, H4A···Cl2 2.530, N4···Cl2 3.086 Å; N4–H4A–Cl2 121.78°). The water molecules are involved in a number of hydrogen-bonding interactions with coordinated dmso and indazole molecules that stabilise the crystal lattice.

The X-ray diffraction study of **2** showed that the complex has a distorted octahedral geometry around the central metal ion (Figure 1). As in **1**, the two chlorido ligands are *trans* to each other, with Os1–Cl1 and Os1–Cl2 bond lengths of 2.4293(8) and 2.4053(8) Å, respectively. Two pyrazole ligands bind in a monodentate fashion with a *cis* arrangement [Os1–N1 2.1202(17) and Os1–N6 2.1365(17) Å] and the remaining positions of the coordination polyhedron are occupied by dmso ligands through the Os–S bond [Os1–S1 2.2498(6) and Os1–S2 2.2386(6) Å]. Intramolecular hydrogen bonding is evident between N2 and Cl1 [N2–H2 0.880, H2···Cl1 2.531, N2···Cl1 3.098 Å; N2–H2–Cl1 122.87°] and between N7 and Cl2 [N7–H7 0.880, H7···Cl2 2.518, N7···Cl2 3.086 Å; N7–H7–Cl2 123.00°]. These determine the orientation of the pyrazole rings, which can be described by the torsion angles $\Theta_{Cl1–Os1–N1–N2}$ [–12.59(15) °] and $\Theta_{Cl2–Os1–N6–N7}$ [3.67(14)°].

The results of X-ray diffraction studies of **3** and **4** are shown in Figure 2. Selected bond lengths and angles are listed in Table 2.

Table 2. Selected bond lengths [Å] and angles [°] in **3** and **4**.

| | **3** | **4** |
|---|---|---|
| Os1–N1 | 2.146(2) | 2.138(4) |
| Os1–N3 | 2.138(3) | 2.120(5) |
| Os1–S1 | 2.2273(7) | 2.2166(12) |
| Os1–S2 | 2.2282(8) | 2.2254(11) |
| Os1–Cl1 | 2.4170(8) | 2.402(2) |
| Os1–Cl2 | 2.4142(8) | 2.428(3) |
| S1–O1 | 1.480(2) | 1.495(4) |
| S2–O2 | 1.481(2) | 1.482(5) |
| N1–Os1–N3 | 83.44(9) | 84.25(17) |
| S1–Os1–S2 | 90.22(3) | 91.42(4) |
| Cl1–Os1–Cl2 | 175.69(3) | 175.24(10) |

The X-ray diffraction study of **5**–**8** revealed that the the $Os^{II}$ ion in all these complexes has a distorted octahedral geometry (see Figures 3 and 4). The coordination sites of osmium(II) are occupied by three sulfur atoms of three dmso molecules, one N atom of the corresponding azole heterocycle and two $Cl^-$ ligands, which are arranged *cis* to each other. Selected bond lengths and angles are given in Table 3. For the axial dmso and azole molecules the Cl2–Os1–S1 and Cl2–Os1–N1 bond angles are 89.53(4)° and 84.83(9)° (**5**), 89.52(3)° and 84.02(9)° (**6**), 91.55(3)° and 85.00(7)° (**7**) and 92.40(3)° and 85.68(6)° (**8**), respectively,

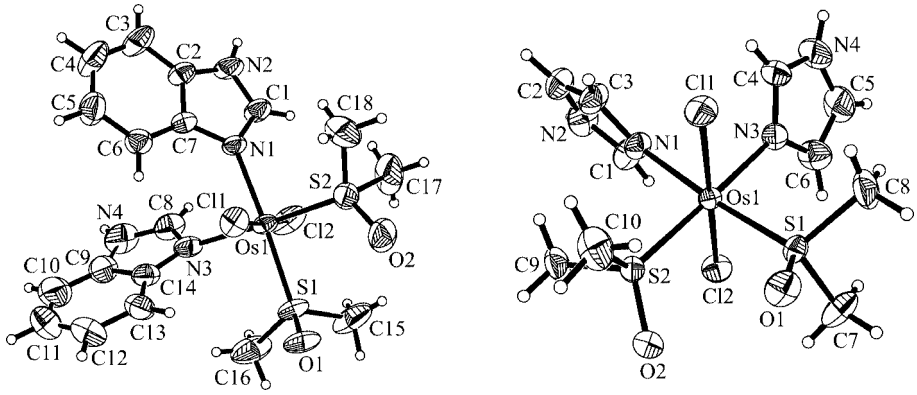


Figure 2. Molecular structures of *trans*,*cis*,*cis*-[$Os^{II}Cl_2$(Hbzim)$_2$(dmso)$_2$] (**3**; left) and *trans*,*cis*,*cis*-[$Os^{II}Cl_2$(Him)$_2$(dmso)$_2$] (**4**; right), showing the atom-numbering schemes. Thermal ellipsoids are drawn at the 50% probability level.

 © 2007 Wiley-VCH Verlag GmbH & Co. KGaA, Weinheim 

thus indicating notable steric constraints of the axial dmso group, which is pushed towards the chlorido ligands. The S2–Os1–S3 bond angle is 90.95(4)°, 91.40(4)°, 97.16(3)° and 93.55(3)° in **5**–**8**, respectively, while the Cl1–Os1–Cl2 angle of 86.41(3)°, 86.78(4)°, 86.92(3)° and 85.98(3)°, respectively, deviates more significantly from the ideal value of 90°. The $\Theta_{Cl2–Os1–N1–N2}$ torsion angle of –33.9°, which describes the orientation of the indazole ring in **5**, is probably determined by the bifurcated hydrogen bond between N2 and Cl2 [N2–H2 0.880, H2···Cl2 2.596, N2···Cl2 3.056 Å; N2–H2–Cl2 113.53°] and O2($x$ + 1/2, –$y$ + 2, $z$) [N2–H2 0.880, H2···O2 2.247, N2···Cl2 2.999 Å; N2–H2–O2 143.27°]. The significant difference (ca. 35 σ) in the bond lengths between Os1 and the two equatorial dmso ligands in **5** can probably be explained, in part, by the involvement of these dmso ligands in two different strong hydrogen-bonding interactions, the former with a lattice ethanol molecule [O4–H4 0.840, H4···O3($x$ + 1/2, –$y$ + 1, $z$) 1.921, O4···O3 2.753 Å; O4–H4–O3 170.49°] and the latter with N2 of the neighbouring indazole ligand (vide supra). The orientation of the pyrazole ring in **6** is determined by the intramolecular hydrogen bonding between N2 of the pyrazole and O3 of the

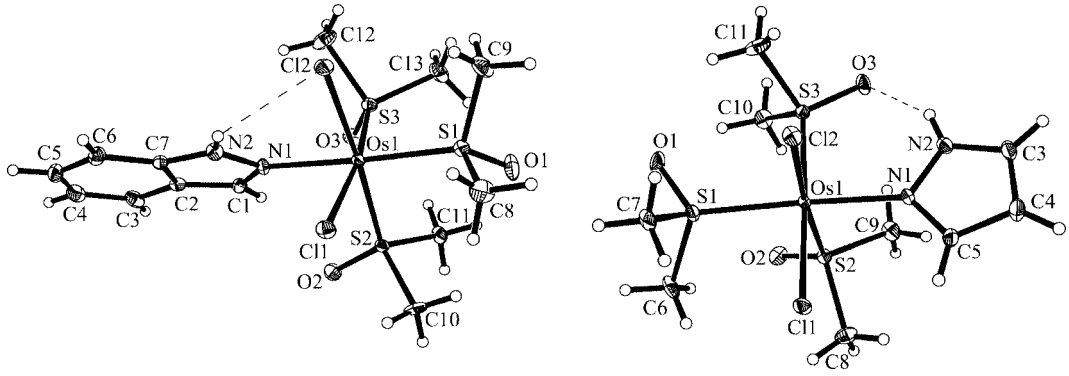


Figure 3. Molecular structures of *cis*,*fac*-[$Os^{II}Cl_2$(Hind)(dm*so*)$_3$] (**5**; left) and *cis*,*fac*-[$Os^{II}Cl_2$(Hpz)(dm*so*)$_3$] (**6**; right), showing the atom-numbering scheme. Thermal ellipsoids are drawn at the 50% probability level.

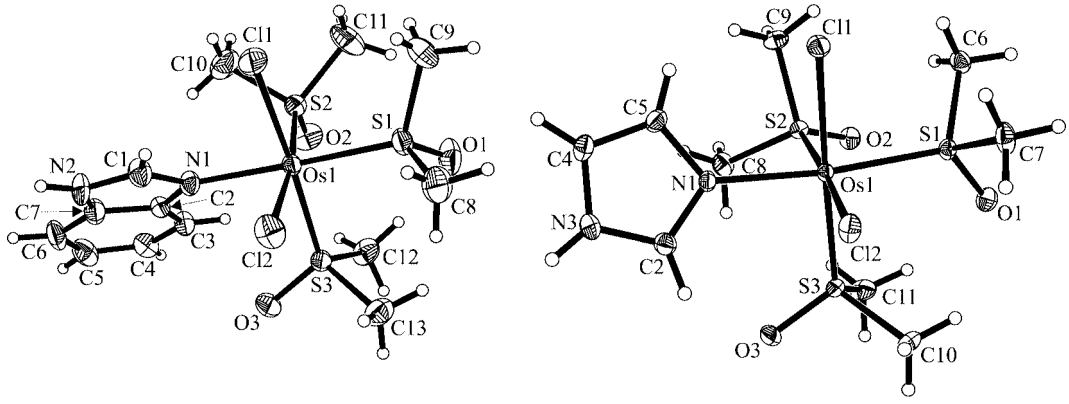


Figure 4. Molecular structures of *cis*,*fac*-[$Os^{II}Cl_2$(Hbzim)(dm*so*)$_3$] (**7**; left) and *cis*,*fac*-[$Os^{II}Cl_2$(Him)(dm*so*)$_3$] (**8**; right), showing the atom-numbering schemes. Thermal ellipsoids are drawn at the 50% probability level.

Table 3. Selected bond lengths [Å] and angles [°] in **5**–**8**.

| | **5** | **6** | **7** | **8** |
|---|---|---|---|---|
| Os1–N1 | 2.136(3) | 2.131(3) | 2.150(2) | 2.148(2) |
| Os1–S1 | 2.2821(10) | 2.2982(9) | 2.2878(8) | 2.2901(7) |
| Os1–S2 | 2.2899(8) | 2.2638(9) | 2.2746(7) | 2.2276(7) |
| Os1–S3 | 2.2480(9) | 2.2570(12) | 2.2804(7) | 2.2807(7) |
| Os1–Cl1 | 2.4302(10) | 2.4326(12) | 2.4202(7) | 2.4245(7) |
| Os1–Cl2 | 2.4232(8) | 2.4229(9) | 2.4364(8) | 2.4335(7) |
| S1–O1 | 1.475(4) | 1.486(3) | 1.477(2) | 1.4850(19) |
| S2–O2 | 1.481(3) | 1.485(3) | 1.472(2) | 1.4926(18) |
| S3–O3 | 1.492(3) | 1.501(2) | 1.482(2) | 1.4861(18) |
| S1–Os1–Cl1 | 92.07(4) | 85.97(3) | 89.86(3) | 87.22(2) |
| N1–Os1–Cl1 | 84.24(8) | 86.88(7) | 86.47(7) | 85.06(6) |
| S2–Os1–S3 | 90.95(4) | 91.40(4) | 97.16(3) | 93.55(3) |
| Cl1–Os1–Cl2 | 86.41(3) | 86.78(4) | 86.92(3) | 85.98(3) |

 © 2007 Wiley-VCH Verlag GmbH & Co. KGaA, Weinheim 

dmso ligand [N2–H2 0.880, H2···O3 1.850, N2···O3 2.635 Å; N2–H2–O3 147.58°], which results in a small $\Theta_{S3-Os1-N1-N2}$ torsion angle of 4.1(3)°. The imidazole ligand in **8** is hydrogen bonded to lattice ethanol [N3–H3 0.880, H3···O4(–*x* + 1, –*y*, –*z* + 2) 1.917, N3···O4 2.771 Å; N3–H3–O4 163.16°], which, in turn, acts as a hydrogen-bond donor to one of the dmso ligands [O4–H4 0.840, H4···O2 1.897, O4···O2 2.735 Å; O4–H4–O2 175.04°].

### Electrochemical Study

The electrochemical properties of osmium(II) complexes **1**, **2**, **5** and **6** and **3**, **4**, **7** and **8** were studied by cyclic voltammetry in acetonitrile (0.15 M [*n*$Bu_4$N][$BF_4$]) and dmf (0.15 M [*n*$Bu_4$N][$BF_4$]), respectively. Voltammetric data are given in Table 4, and the cyclic voltammogram of **2** is shown in Figure 5. One oxidative response is found for all complexes. Taking into account the similar responses in the analogous ruthenium complexes,[17] these electron-transfer processes are assigned to $Os^{II}$–$Os^{III}$ oxidation.

Table 4. Cyclic voltammetric data for **1**–**8**[a] and their estimated redox potential values.

| | $E_{1/2}^{ox}$ found[b,c] [V vs. NHE] | $E_{1/2}^{red}$ calcd. [V vs. NHE] |
|---|---|---|
| **1**[d] | 0.94 (60) | 0.79 |
| **2**[d] | 0.89 (60) | 0.67 |
| **3**[e] | 0.80 (70) | 0.61 |
| **4**[e] | 0.71 (60) | 0.51 |
| **5**[d] | 1.66 (65) | 1.10 |
| **6**[d] | 1.57 (60) | 1.04 |
| **7**[e] | 1.51 (70) | 1.01 |
| **8**[e] | 1.40 (60) | 0.96 |

[a] Supporting electrolyte: [*n*$Bu_4$N][$BF_4$]; scan rate: 0.2 V $s^{-1}$. [b] $E_{1/2} = 0.5(E_{pa} + E_{pc})$, where $E_{pa}$ and $E_{pc}$ are the anodic and cathodic peak potential, respectively. [c] $\Delta E_p = E_{pa} - E_{pc}$ [mV]. [d] In acetonitrile. [e] In dmf.

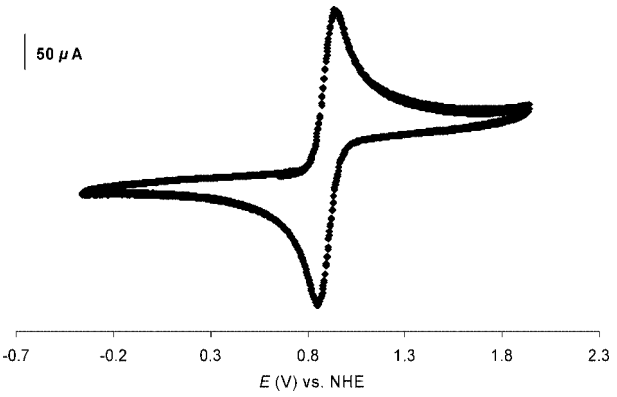


Figure 5. Cyclic voltammogram of *trans*,*cis*,*cis*-[$Os^{II}Cl_2$(Hpz)$_2$(dmso)$_2$] in acetonitrile solution (0.15 M [*n*$Bu_4$N][$BF_4$]) at a scan rate of 0.2 V $s^{-1}$.

The oxidation potentials for **1**–**4** (0.94–0.71 V) are markedly lower than those for **5**–**8** (1.66–1.40 V), which is in agreement with the stronger net electron-acceptor character of the S-coordinated dmso as compared with the azole ligands, which are more effective σ-donors. In addition, the redox potentials of the complexes are in the following order in the two series of compounds: $E_{1/2}^{ox}$(**1**, **5**) > $E_{1/2}^{ox}$(**2**, **6**) > $E_{1/2}^{ox}$(**3**, **7**) > $E_{1/2}^{ox}$(**4**, **8**), which agrees with the relative electron-donor character of the N-ligands [$E_L$(Hind) > $E_L$(Hpz) > $E_L$(Hbzim) > $E_L$(Him)] and their basicity [p$K_a$(Hind) < p$K_a$(Hpz) < p$K_a$(Hbzim) < p$K_a$(Him)[23]). The responses are reversible or quasi-reversible and are characterised by a peak-to-peak separation ($\Delta E_p$) of 60–70 mV and an anodic peak current ($i_{pa}$) that is almost equal to the cathodic peak current ($i_{pc}$) (or slightly different), as expected for reversible electron-transfer processes. The one-electron nature of the observed oxidation was verified by comparing its current height ($i_{pa}$) with that of a standard ferrocene/ferrocenium couple under identical experimental conditions.

The $E_{1/2}^{ox}$ values for complexes **1**–**4** and **5**–**8** are larger than those expected on the basis of the general Lever equation, by using the known values of $S_m$ and $I_m$ (1.01 and –0.40, respectively) for the $Os^{II}/Os^{III}$ redox couple and the $E_L$ values for the various ligands [$E_L$(Cl) = –0.24, $E_L$(dmso) = 0.57,[24] $E_L$(Hind) = 0.26, $E_L$(Hpz) = 0.20, $E_L$(Hbzim) = 0.17, $E_L$(Him) = 0.12[25]) due to the influence of the stereochemistry on the electronic distribution in the complexes.

### The Reactivity of Complexes 1–8 Towards Nitriles

Recently we have reported the first example of a ruthenium(II)-mediated coupling reaction of acetonitrile with 1*H*-indazole.[17] We found that the reaction of *trans*,*cis*,*cis*-[$Ru^{II}Cl_2$(Hind)$_2$(dmso)$_2$] with acetonitrile at room temperature proceeds with displacement of one indazole ligand from the coordination sphere of ruthenium and formation of an amidine ligand isolated as [$Ru^{II}Cl_2${HN=C(Me)-ind}(dmso)$_2$]·$H_2O$. As a logical consequence of this finding we studied the behaviour of the osmium analogue *trans*,*cis*,*cis*-[$Os^{II}Cl_2$(Hind)$_2$(dmso)$_2$] (**1**) and complexes **2**, **5** and **6** in acetonitrile. No amidine formation was observed in an acetonitrile solution of **1** at room temperature after five days. Even after heating the solutions of **1**, **2**, **5** and **6** at 80 °C for 1–2 h the complexes remained intact and could be recovered after evaporation of acetonitrile at reduced pressure, as verified by $^1$H NMR spectroscopy. It should, however, be noted that the solutions become coloured both at room temperature and on heating, although the minor species responsible for this colour change could not be identified. It is known[26] that the direct synthesis of amidines from a nitrile and an amine can be realised when the nitrile is activated by a strong electron-acceptor group such as $CCl_3$. With this in mind, we studied the reactivity of complexes **1** and **2** towards trichloroacetonitrile. Heating the solutions of **1** and **2** in $CCl_3CN$/methanol (1:1, v/v) at 65 °C for 1 h, $CCl_3CN$/hexane (1:6, v/v) at 80 °C for 2 h or prolonged refluxing (up to 16 h) of compounds **1** and **2** in neat $CCl_3CN$ at 85 °C did not result in the desired amidine. Removal of the volatiles after the reaction of **2** with neat $CCl_3CN$ left a solid residue, which was washed with diethyl

 © 2007 Wiley-VCH Verlag GmbH & Co. KGaA, Weinheim 

ether. This solid was shown by $^1$H NMR spectroscopy to contain the starting complex **2**. On slow evaporation of the diethyl ether washing solution a few colourless crystals separated, which proved to be suitable for an X-ray diffraction study. The determined cell parameters were in excellent agreement with those documented in the literature for trichloroacetamide.[27] Being intrigued by this disclosure, we decided to find out whether complexes **1**–**8** might play a catalytic role in the hydration of trichloroacetonitrile to give trichloroacetamide.

### Catalytic Hydration of Chloronitriles by 1–8

Trichloroacetamide and its derivatives exhibit fungicidal,[28] germicidal,[29] cardiovascular[30] and antitumour[31] activity. In addition, some of them are used as insect chemosterilants[32] or nitrification inhibitors.[33] They are also important agents and building blocks in preparative organic chemistry,[34] and, in particular, in peptide synthesis.[35] Although the synthetic approaches to trichloroacetamide are well-optimised,[36] they usually require the use of ammonia gas, which means that a route based on the catalytic hydration of trichloroacetonitrile would appear to be more appealing and environmentally friendly (Scheme 4).

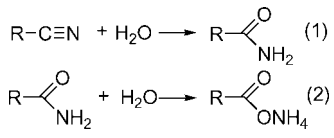

Scheme 4.

The selective hydration of nitriles to carboxamides is currently an important laboratory and industrial reaction.[37,38] The conversion of acrylonitrile into acrylamide, which is an important industrial reagent, for instance, is of considerable practical significance.[38,39] Such reactions are often base or acid catalysed. The main disadvantage of these catalysts is that the undesirable further hydrolysis of carboxamides into carboxylic acids (or their salts) occurs [Equation (2) in Scheme 4]. To avoid such a scenario transition metal complexes should be used in neutral conditions. Complexes **1**–**8** exhibit catalytic activity in the hydration of trichloroacetonitrile in solution. In our model reaction, we converted trichloroacetonitrile into trichloroacetamide and ammonium trichloroacetate. In the control experiments, the hydration of trichloroacetonitrile was carried out in the absence of osmium(II) complexes. A small amount of $CCl_3CONH_2$ (0.6%) was detected after the reaction of 1 mL of trichloroacetonitrile with 1.3 mL of water at 75 °C for 24 h. These conditions were found to be optimal for catalytic hydration of acetonitrile to acetamide by other osmium(II) compounds.[40] Depending on the azole ligands present in complexes **1**–**8**, the yields of the main product trichloroacetamide varied from 1.05 to 82.72%, with turnover numbers (TON) ranging from 6.22 to 412 (Table 5). The selectivity of formation of this product is remarkable (Table 5). The yields of ammonium trichloroacetate are commonly rather low and do not exceed 0.3%.

Complexes **5**–**8**, which contain three dmso ligands, are more efficient hydration catalysts than **1**–**4**, which contain two coordinated dmso ligands. Complexes **3** and **4** exhibit higher catalytic activity than **1** and **2**. Analogously, compounds **7** and **8** are significantly more efficient catalysts than **5** and **6**. It is worth noting that **7** shows the highest catalytic activity, with a turnover that is an order of magnitude higher than the second best catalyst and with good selectivity. Experiments with the hydrolysis of $CHCl_2CN$ mediated by complex **7** gave the following yields (%) and TON values for $CHCl_2CONH_2$ and $CHCl_2COONH_4$: 75.3, 578 and 1.7, 12.7, while those with $CH_2ClCN$ as substrate in the presence of the same complex afforded $CH_2ClCONH_2$ in a very low yield (2.2%) with low TON value (22) and the ammonium salt of monochloroacetate in 0.48% yield and very low turnover (TON = 5). The catalytic activity of the starting compound *trans*-[$OsCl_2$(dm*s*o)$_4$] has not been studied since its NMR spectrum showed full decomposition after heating the reaction mixture at 75 °C for 1 h.

Compounds **1**–**8** have no free coordination site to allow either water or trichloroacetonitrile binding to $Os^{II}$. As a possible mechanism for nitrile hydration we propose the substitution of one of the dmso molecules in light of the fact that traces of free dmso are found in the NMR spectra after performing the catalytic reaction. It should also be noted that *cis*,*fac*-[$RuCl_2$(Hind)(dm*s*o)$_3$] has been shown to

Table 5. Comparison of some catalysts for the hydrolysis of trichloroacetonitrile at 75 ± 1 °C.[a]

| Complex | Yield of $CCl_3CONH_2$ [mg (%)] | Turnover number | Yield of $CCl_3COONH_4$ [mg (%)] | Turnover number | Molar ratio $CCl_3CONH_2$/ $CCl_3COONH_4$ |
|---|---|---|---|---|---|
| **1** | 17 (1.1) | 6.2 ± 0.4 | 2.4 (0.13) | 0.8 ± 0.2 | 7.9 |
| **2** | 18.5 (1.2) | 6.4 ± 0.1 | 3.6 (0.20) | 1.1 ± 0.2 | 5.7 |
| **3** | 28 (1.7) | 10.5 ± 0.1 | 3.2 (0.18) | 1.1 ± 0.1 | 9.7 |
| **4** | 109 (6.7) | 36.4 ± 0.4 | 2.2 (0.12) | 0.6 ± 0.1 | 55.0 |
| **5** | 53 (3.3) | 19.4 ± 0.1 | 0.9 (0.05) | 0.3 ± 0.1 | 65.3 |
| **6** | 103.5 (6.4) | 35.0 ± 2.1 | 2.4 (0.13) | 0.7 ± 0.1 | 47.9 |
| **7** | 1090 (82.7) | 412 ± 30 | 5.4 (0.30) | 1.8 ± 0.1 | 224.2 |
| **8** | 147 (9.1) | 49 ± 3 | 1.2 (0.07) | 0.3 ± 0.1 | 136.0 |

[a] When the experiment was performed without catalyst under identical conditions (1 mL of $CCl_3CN$ and 1.3 mL of triply distilled water at 75 °C for 24 h), no more than 10 mg (0.6%) of $CCl_3CONH_2$ was obtained.

 © 2007 Wiley-VCH Verlag GmbH & Co. KGaA, Weinheim 

undergo replacement of indazole by acetonitrile at room temperature with formation of *cis*,*fac*-[$RuCl_2$(MeCN)-(dm*so*)$_3$].[17] This suggests another possible catalytic pathway for chloronitrile hydration, but does not explain the different efficiency of catalysts **5**–**8**. The catalytic nitrile hydration mechanism proposed by Chottard et al.[41] for cobalt(III) complexes with sulfenato-S ligands under mildly acidic conditions exploits the nucleophilic properties of coordinated sulfenates. This might be another option for osmium(II) sulfoxide-S complexes as well. Density functional calculations on the subject are currently underway in our laboratory.

## Conclusions

Two novel families of osmium(II) complexes, namely *trans*,*cis*,*cis*-[$OsCl_2$(azole)$_2$(dm*so*)$_2$] and *cis*,*fac*-[$OsCl_2$-(azole)(dm*so*)$_3$], have been prepared and characterised by exploring the destabilising *trans* effect of *S*-bonded dmso ligands to osmium in *trans*-[$Os^{II}Cl_2$(dm*so*)$_4$] and *cis*-[$Os^{II}$-$Cl_2$(dmso)$_4$]. In both series of complexes osmium(II) shows a preference for sulfur binding. In contrast to their ruthenium congeners, the complexes *trans*,*cis*,*cis*-[$OsCl_2$(Hind)$_2$-(dm*so*)$_2$] and *cis*,*fac*-[$OsCl_2$(Hind)(dm*so*)$_3$] do not undergo a coupling reaction with acetonitrile to give amidine chelate formation. Instead, complexes **1**–**8** have been found to catalyse the selective hydration of trichloroacetonitrile to trichloroacetamide, and dichloroacetonitrile to dichloroacetamide. The more acidic complexes of the type *cis*,*fac*-[$OsCl_2$(azole)(dm*so*)$_3$] commonly show higher activity than *trans*,*cis*,*cis*-[$OsCl_2$(azole)$_2$(dm*so*)$_2$]. In addition, the catalyst efficiency is also dependent on the azole ligand bonded to osmium(II). The highest yields (82.7 and 75.3%) and turnovers (TON values 412 and 578), with high selectivity for trichloroacetamide and dichloroacetamide, respectively, have been achieved with *cis*,*fac*-[$OsCl_2$(Hbzim)(dm*so*)$_3$]. These preliminary results are interesting and inspire us to investigate the hydration of acrylonitrile (where the selectivity is often not high), since the vinyl group resembles the $CHCl_2$ group in its electron-withdrawing ability.

## Experimental Section

**General:** The synthesis of all complexes was performed under an atmosphere of dry argon, using standard Schlenk techniques. *trans*-[$OsCl_2$(dm*so*)$_4$] and *cis*-[$OsCl_2$(dmso)$_4$] were prepared according to literature protocols.[18]

***trans*,*cis*,*cis*-[$OsCl_2$(Hind)$_2$(dm*so*)$_2$] (1):** A suspension of indazole (0.10 g, 0.85 mmol) and *trans*-[$OsCl_2$(dm*so*)$_4$] (0.20 g, 0.35 mmol) in dry ethanol (10 mL) was stirred at room temperature for 1 h and then heated at 80 °C for a further hour. The yellow-green solution was concentrated by evaporating part of the solvent off under reduced pressure until a yellow solid separated. The product was filtered off, washed with diethyl ether and dried in vacuo. Yield: 0.18 g (80%). $C_{18}H_{24}Cl_2N_4O_2OsS_2$ (653.64): calcd. C 33.08, H 3.70, N 8.57, S 9.81; found C 33.11, H 3.73, N 8.39, S 9.60. MS ($ESI^+$): *m*/*z* 677 $[M + Na]^+$; ($ESI^-$): *m*/*z* 653 $[M - H]^-$. IR (CsI): $\tilde{\nu}$ = 253 and 273 m ν(Os–N) and σ(Os–N–C); 315 m ν(Os–Cl); 382 m σ(C–S–O); 433 and 451 s ν(Os–S); 1018, 1072 s and 1091 vs ν(*S*–O); 1239 m, 1356 s, 1423, 1510 and 1627 m ν(C–C), ν(C–N) and σ(C–H); 3040, 3070 and 3125 w ν(C–H); 3239 and 3303 $cm^{-1}$ s ν(N–H). UV/Vis (MeOH): $\lambda_{max}$ (ε) = 210 nm (63676 $M^{-1}cm^{-1}$), 240 sh (18469), 277 (32733), 290 sh (29318), 302 sh (22529), 345 (5264). $^1H$ NMR (400.13 MHz, $CDCl_3$): δ = 12.74 (s, 2 H, NH), 8.68 (s, 2 H, CH=N), 7.65 (d, *J* = 8.0 Hz, 2 H, C4-H), 7.47 (d, *J* = 8.0 Hz, 2 H, C7-H), 7.40 (t, *J* = 7.3 Hz, 2 H, C6-H), 7.16 (t, *J* = 7.3 Hz, 2 H, C5-H), 3.37 (s, 12 H, $CH_3$) ppm. $^{13}C\{^1H\}$ NMR (100.63 MHz, $CDCl_3$): δ = 139.9 (C8), 135.5 (C3), 128.9 (C6), 122.6 (C9), 122.4 (C5), 121.3 (C4), 110.4 (C7), 45.4 ($CH_3$) ppm. Single crystals suitable for X-ray structure analysis were crystallised from an ethanol solution saturated with diethyl ether.

***trans*,*cis*,*cis*-[$OsCl_2$(Hpz)$_2$(dm*so*)$_2$] (2):** A suspension of pyrazole (0.05 g, 0.73 mmol) and *trans*-[$OsCl_2$(dm*so*)$_4$] (0.20 g, 0.35 mmol) in dry ethanol (10 mL) was stirred at room temperature for 2 h and then heated at 80 °C for a further 2 h. The yellow-green solution was concentrated under reduced pressure until a yellow solid separated. The product was filtered off, washed with diethyl ether and dried in vacuo. Yield: 0.16 g (85%). $C_{10}H_{20}Cl_2N_4O_2OsS_2$ (553.52): calcd. C 21.70, H 3.64, N 10.12, S 11.58; found C 21.67, H 3.43, N 9.82, S 11.49. MS ($ESI^+$): *m*/*z* 577 $[M + Na]^+$; ($ESI^-$): *m*/*z* 553 $[M - H]^-$. IR (CsI): $\tilde{\nu}$ = 217, 232 and 254 m ν(Os–N) and σ(Os–N–C); 319 m ν(Os–Cl); 394 m σ(C–S–O); 432 s and 451 m ν(Os–S); 1009 s, 1048, 1082 vs and 1127 s ν(*S*–O); 1353, 1411, 1471 and 1518 m ν(C–C), ν(C–N) and σ(C–H); 2926, 3018 w and 3126 m ν(C–H); 3286 and 3317 $cm^{-1}$ s ν(N–H). UV/Vis (MeOH): $\lambda_{max}$ (ε) = 232 nm (37020 $M^{-1}cm^{-1}$), 278 sh (8503), 344 (757). $^1H$ NMR (400.13 MHz, $CDCl_3$): δ = 13.05 (s, 2 H, NH), 7.83 (t, *J* = 2.0 Hz, 2 H, C3-H), 7.65 (t, *J* = 1.8 Hz, 2 H, C5-H), 6.40 (q, *J* = 2.3 Hz, 2 H, C4-H), 3.34 (s, 12 H, $CH_3$) ppm. $^{13}C\{^1H\}$ NMR (100.62 MHz, $CDCl_3$): δ = 139.1 (C3), 129.8 (C5), 106.4 (C4), 45.6 ($CH_3$) ppm. X-ray diffraction quality crystals of **2** were grown from ethanol solution.

***trans*,*cis*,*cis*-[$OsCl_2$(Hbzim)$_2$(dm*so*)$_2$] (3):** A suspension of benzimidazole (0.04 g, 0.35 mmol) and *trans*-[$OsCl_2$(dm*so*)$_4$] (0.10 g, 0.17 mmol) in dry ethanol (5 mL) was heated at 87 °C for 1.5 h. The solution was then cooled to room temperature. The yellow solid was collected by filtration, washed with ethanol (2 × 1 mL) and dried in vacuo. Yield: 0.10 g (88%). $C_{18}H_{24}Cl_2N_4O_2OsS_2$ (653.67): calcd. C 33.07, H 3.70, N 8.57, S 9.81; found C 33.05, H 3.73, N 8.52, S 9.55. MS ($ESI^+$): *m*/*z* 677 $[M + Na]^+$, 559 $[OsCl_2$-(Hbzim)(dm*so*)$_2$ + $Na]^+$; ($ESI^-$): *m*/*z* 535 $[OsCl_2$(Hbzim)(dm*so*)$_2$ – $H]^-$, 457 $[OsCl_2$(Hbzim)(dm*so*) – $H]^-$. IR (CsI): $\tilde{\nu}$ = 243 and 280 m ν(Os–N) and σ(Os–N–C); 307 m ν(Os–Cl); 397 m σ(C–S–O); 432 and 461 s ν(Os–S); 970, 1010 and 1063 b vs ν(*S*–O); 1247, 1271, 1306, 1421, 1464, 1505 and 1624 m ν(C–C), ν(C–N) and σ(C–H); 2921 and 3143 m ν(C–H); 3261 and 3410 $cm^{-1}$ s ν(N–H). UV/Vis (MeOH): $\lambda_{max}$ (ε) = 272 nm (24415 $M^{-1}cm^{-1}$), 278 (22390). $^1H$ NMR (400.13 MHz, [$D_6$]dmso): δ = 12.87 (s, 2 H, NH), 8.41 (s, 2 H, CH=N), 7.87 (d, *J* = 8.4 Hz, 2 H, C4-H), 7.47 (d, *J* = 8.00 Hz, 2 H, C7-H), 7.13 (t, *J* = 7.5 Hz, 2 H, C6-H), 6.91 (t, *J* = 7.5 Hz, 2 H, C5-H), 3.27 (s, 12 H, $CH_3$) ppm. $^{13}C\{^1H\}$ NMR (100.62 MHz, [$D_6$]dmso): δ = 147.4 (C2), 142.3 (C8 or C9), 133.2 (C8 or C9), 123.7 (C6), 122.2 (C5), 120.9 (C4), 113.1 (C7), 45.6 ($CH_3$) ppm. X-ray diffraction quality crystals of **3**·$CH_3CN$ were obtained from a solution of **3** in acetonitrile.

***trans*,*cis*,*cis*-[$OsCl_2$(Him)$_2$(dm*so*)$_2$] (4):** Imidazole (0.036 g, 0.53 mmol) was added to a solution of *trans*-[$OsCl_2$(dm*so*)$_4$] (0.15 g, 0.26 mmol) in dry ethanol (10 mL) and the reaction mixture heated at 87 °C for 3 h. After cooling the solution to room temperature, the brown solid was filtered off, washed with ethanol

 © 2007 Wiley-VCH Verlag GmbH & Co. KGaA, Weinheim 

(3 × 3 mL) and dried in vacuo. Yield: 0.13 g (88%). $C_{10}H_{20}Cl_2N_4O_2OsS_2$ (553.56): calcd. C 21.69, H 3.64, N 10.12, S 11.58; found C 21.90, H 3.55, N 9.82, S 11.39. MS (ESI$^+$): *m/z* 577 [M + Na]$^+$, 509 [$OsCl_2$(Him)(dm*so*)$_2$ + Na]$^+$; (ESI$^-$): *m/z* 553 [M – H]$^-$, 485 [$OsCl_2$(Him)(dm*so*)$_2$ – H]$^-$. IR (CsI): $\tilde{\nu}$ = 219, 258 and 274 m ν(Os–N) and σ(Os–N–C); 315 m ν(Os–Cl); 393 m σ(C–S–O); 433 and 455 s ν(Os–S); 1003, 1056 bs and 1140 s ν(*S*–O); 1292, 1309, 1326, 1432, 1498 and 1541 m ν(C–C), ν(C–N) and σ(C–H); 2924, 2963 and 3060 ν(C–H); 3137 b and 3455 cm$^{-1}$ sh ν(N–H). UV/Vis (MeOH): $\lambda_{max}$ (ε) = 223 nm (23993 M$^{-1}$ cm$^{-1}$), 349 (787). $^1$H NMR (400.13 MHz, [D$_6$]dmso): δ = 12.44 (s, 2 H, NH), 8.14 (s, 2 H, CH=N), 7.38 (s, 2 H, C4-H), 7.10 (s, 2 H, C5-H), 3.13 (s, 12 H, $CH_3$) ppm. $^{13}$C{$^1$H} NMR (100.62 MHz, [D$_6$]dmso): δ = 138.4 (C2), 128.3 (C4), 116.4 (C5), 45.5 ($CH_3$) ppm. X-ray diffraction quality crystals were obtained from a solution of **4** in ethanol.

***cis*,*fac*-[$OsCl_2$(Hind)(dm*so*)$_3$] (5). Method (a):** A suspension of indazole (0.045 g, 0.38 mmol) and *cis*-[$OsCl_2$(dmso)$_4$] (0.10 g, 0.18 mmol) in dry ethanol (10 mL) was heated at 80 °C for 40 min. The resulting colourless solution was cooled to room temperature and then concentrated by partial evaporation of the solvent under reduced pressure. The white product that separated was filtered off, washed with diethyl ether and dried in vacuo. Yield: 0.09 g (80%).

**Method (b):** A yellow-green solution of **1** (0.10 g, 0.15 mmol) in dimethyl sulfoxide (5 mL) was heated slowly to 125 °C and maintained at this temperature for 45 min. After evaporation of the solvent under reduced pressure at 100–110 °C, the white or light-grey residue was washed with a small amount of dry ethanol and diethyl ether and dried in vacuo. Yield: 0.07 g (75%). $C_{13}H_{24}Cl_2N_2O_3OsS_3$ (613.63): calcd. C 25.45, H 3.94, N 4.57, S 15.67; found C 25.56, H 3.96, N 4.56, S 15.68. MS (ESI$^+$): *m/z* 637 [M + Na]$^+$; (ESI$^-$): *m/z* 613 [M – H]$^-$. IR (CsI): $\tilde{\nu}$ = 226 and 256 m ν(Os–N) and σ(Os–N–C); 281 and 307 m ν(Os–Cl); 385 m σ (C–S–O); 441 and 471 s ν(Os–S); 953, 1024, 1048 s, 1091 and 1112 vs ν(*S*–O); 1217, 1315, 1365, 1416, 1516 and 1631 m ν(C–C), ν(C–N) and σ(C–H); 2928 and 3023 m ν(C–H); 3069, 3123 and 3144 cm$^{-1}$ w ν(N–H). UV/Vis (MeOH): $\lambda_{max}$ (ε) = 215 nm (20945 M$^{-1}$ cm$^{-1}$), 234 sh (6460), 268 sh (7947), 288 (9910), 305 sh (7531), 342 (428). $^1$H NMR (400.13 MHz, $CDCl_3$): δ = 14.43 (s, 1 H, NH), 9.20 (s, 1 H, CH=N), 7.73 (d, *J* = 8.0 Hz, 1 H, C4-H), 7.51 (d, *J* = 8.0 Hz, 1 H, C7-H), 7.43 (t, *J* = 7.5 Hz, 1 H, C6-H), 7.19 (t, *J* = 7.5 Hz, 1 H, C5-H), 3.64 (s, 12 H, $CH_3$), 3.35 (s, 6 H, $CH_3$) ppm. $^{13}$C{$^1$H} NMR (100.62 MHz, $CDCl_3$): δ = 140.4 (C8), 137.2 (C3), 129.2 (C6), 122.8 (C9), 122.6 (C5), 121.5 (C4), 110.9 (C7), 48.8 ($CH_3$), 48.1 ($CH_3$), 45.8 ($CH_3$) ppm. Crystals of **5**·$C_2H_5OH$ suitable for X-ray structure analysis were obtained from an ethanol solution of **5**.

***cis*,*fac*-[$OsCl_2$(Hpz)(dm*so*)$_3$] (6). Method (a):** A suspension of pyrazole (0.025 g, 0.37 mmol) and *cis*-[$OsCl_2$(dmso)$_4$] (0.10 g, 0.18 mmol) in dry ethanol (10 mL) was heated at 80 °C for 1 h. The resulting colourless solution was cooled to room temperature and then concentrated by partial evaporation of the solvent under reduced pressure. The white product that separated was filtered off, washed with diethyl ether and dried in vacuo. Yield: 0.08 g (85%).

**Method (b):** A yellow-green solution of **2** (0.10 g, 0.18 mmol) in dimethyl sulfoxide (5 mL) was heated slowly to 125 °C and maintained at this temperature for 45 min. After evaporation of the solvent under reduced pressure the remaining white solid was washed with a small amount of dry ethanol and diethyl ether and dried in vacuo. Yield: 0.07 g (70%). $C_9H_{22}Cl_2N_2O_3OsS_3$ (563.57): calcd. C 19.18, H 3.93, N 4.97, S 17.07; found C 19.32, H 3.88, N 4.93, S 17.09. MS (ESI$^+$): *m/z* 587 [M + Na]$^+$; (ESI$^-$): *m/z* 563 [M – H]$^-$. IR (CsI): $\tilde{\nu}$ = 234 and 254 m ν(Os–N) and σ(Os–N–C); 277 and 305 s ν(Os–Cl); 384 s σ (C–S–O); 429 and 470 s ν(Os–S); 935 s, 971 m, 1017 vs, 1062 m and 1098 vs ν(*S*–O); 1299 w, 1362 m, 1414 s and 1553 m ν(C–C), ν(C–N) and σ(C–H); 2807, 2922 and 3007 m ν(C–H); 3026, 3108 and 3126 cm$^{-1}$ m ν(N–H). UV/Vis (MeOH): $\lambda_{max}$ (ε) = 213 nm sh (15689 M$^{-1}$ cm$^{-1}$), 232 sh (11458), 296 (1165), 341 sh (194). $^1$H NMR (400.13 MHz, $CDCl_3$): δ = 14.44 (s, 1 H, NH), 8.60 (t, *J* = 1.8 Hz, 1 H, C3-H), 7.66 (t, *J* = 1.8 Hz, 1 H, C5-H), 6.40 (q, *J* = 2.3 Hz, 1 H, C4-H), 3.60 (s, 6 H, $CH_3$), 3.59 (s, 6 H, $CH_3$), 3.29 (s, 6 H, $CH_3$) ppm. $^{13}$C{$^1$H} NMR (100.62 MHz, $CDCl_3$): δ = 140.7 (C3), 130.7 (C5), 107.3 (C4), 48.7 ($CH_3$), 47.9 ($CH_3$), 45.8 ($CH_3$) ppm. Crystals of **6** suitable for X-ray structure analysis were grown from ethanol solution.

***cis*,*fac*-[$OsCl_2$(Hbzim)(dm*so*)$_3$] (7). Method (a):** Benzimidazole (0.038 g, 0.32 mmol) was added to a solution of *cis*-[$OsCl_2$-(dmso)$_4$] (0.086 g, 0.17 mmol) in dry ethanol (9 mL) and the reaction mixture heated at 87 °C for 1 h. After the solution had cooled to room temperature, the white solid was filtered off, washed with ethanol (3 × 5 mL) and dried in vacuo. Yield: 0.055 g (60%).

**Method (b):** A solution of **3** (0.07 g, 0.11 mmol) in dimethyl sulfoxide (2.5 mL) was heated slowly to 125 °C and maintained at this temperature for 1.5 h. The solvent was removed under reduced pressure and the white residue washed with a small amount of absolute ethanol and diethyl ether and dried in vacuo. Yield: 0.05 g (75%). $C_{13}H_{24}Cl_2N_2O_3OsS_3$ (613.67): calcd. C 25.44, H 3.94, N 4.56, S 15.67; found C 25.23, H 3.83, N 4.46, S 15.40. MS (ESI$^+$): *m/z* 637 [M + Na]$^+$; (ESI$^-$): *m/z* 613 [M – H]$^-$, 535 [$OsCl_2$(Hbzim)(dm*so*)$_2$ – H]$^-$, 457 [$OsCl_2$(Hbzim)(dm*so*) – H]$^-$. IR (CsI): $\tilde{\nu}$ = 217 sh and 267 m ν(Os–N) and σ(Os–N–C); 288 and 320 m ν(Os–Cl); 389 m σ (C–S–O); 433, 462 sh and 471 sh s ν(Os–S); 964, 975, 1012, 1073, 1033 sh and 1097 vs ν(*S*–O); 1243, 1273, 1302, 1322 sh, 1423, 1465, 1486, 1498, 1595 and 1618 m ν(C–C), ν(C–N) and σ(C–H); 2932 and 3036 sh m ν(C–H); 3153 and 3453 b cm$^{-1}$ w ν(N–H). UV/Vis (MeOH): $\lambda_{max}$ (ε) = 274 nm (23288 M$^{-1}$ cm$^{-1}$), 278 (23744). $^1$H NMR (400.13 MHz, [D$_6$]dmso): δ = 13.18 (s, 1 H, NH), 8.78 (s, 1 H, CH=N), 8.21 (d, *J* = 8.1 Hz, 1 H, C4-H), 7.59 (d, *J* = 7.1 Hz, 1 H, C7-H), 7.29 (t, *J* = 7.2 Hz, 1 H, C6-H), 7.24 (t, *J* = 7.0 Hz, 1 H, C5-H), 3.59 (s, 6 H, $CH_3$), 3.45 (s, 6 H, $CH_3$), 3.28 (s, 6 H, $CH_3$) ppm. $^{13}$C{$^1$H} NMR (100.62 MHz, [D$_7$]DMF): δ = 156.4 (C2), 141.4 (C8 or C9), 133.2 (C8 or C9), 123.7 (C6), 122.1 (C5), 122.1 (C4), 113.1 (C7), 48.9 ($CH_3$), 47.1 ($CH_3$), 45.7 ($CH_3$) ppm. X-ray diffraction quality crystals were obtained from a solution of **7** in ethanol.

***cis*,*fac*-[$OsCl_2$(Him)(dm*so*)$_3$] (8). Method (a):** Imidazole (0.036 g, 0.53 mmol) was added to a solution of *cis*-[$OsCl_2$(dmso)$_4$] (0.15 g, 0.26 mmol) in dry ethanol (20 mL) and the reaction mixture heated at 80 °C for 2 h. The solution volume was reduced to approximately 1 mL, the white solid was filtered off, washed with ethanol (2 × 2 mL) and dried in vacuo. Yield: 0.068 g (46%).

**Method (b):** A solution of **4** (0.08 g, 0.11 mmol) in dimethyl sulfoxide (2.5 mL) was heated slowly to 125 °C and maintained at this temperature for 2 h. The solvent was removed under reduced pressure and the white residue washed with a small amount of absolute ethanol and diethyl ether and dried in vacuo. Yield: 0.06 g (74%). $C_9H_{22}Cl_2N_2O_3OsS_3$ (563.61): calcd. C 19.17, H 3.93, N 4.97, S 17.06; found C 19.29, H 3.92, N 4.98, S 16.77. MS (ESI$^+$): *m/z* 587 [M + Na]$^+$; (ESI$^-$): *m/z* 563 [M – H]$^-$. IR (CsI): $\tilde{\nu}$ = 210 sh, 235 sh and 265 sh m ν(Os–N) and σ(Os–N–C); 280 and 299 m ν(Os–Cl); 393 m σ (C–S–O); 440 and 465 sh s ν(Os–S); 929, 974, 1015, 1062, 1073 sh and 1091 vs ν(*S*–O); 1261, 1300, 1316, 1413, 1451, 1490 and 1507 m ν(C–C), ν(C–N) and σ(C–H); 2929 and 3164 w ν(C–H); 3164 and 3292 cm$^{-1}$ m ν(N–H). UV/Vis (MeOH): $\lambda_{max}$ (ε) = 212 nm (1946 M$^{-1}$ cm$^{-1}$), 215 (1992), 293 (1694). $^1$H NMR (400.13 MHz, [D$_6$]dmso): δ = 12.62 (s, 1 H, NH), 8.35 (s, 1 H,

 © 2007 Wiley-VCH Verlag GmbH & Co. KGaA, Weinheim 

CH=N), 7.49 (s, 1 H, C4-H), 7.15 (s, 1 H, C5-H), 3.51 (s, 6 H, $CH_3$), 3.45 (s, 6 H, $CH_3$), 3.25 (s, 6 H, $CH_3$) ppm.$^{13}C\{^1H\}$ NMR (100.62 MHz, $D_2O$): $\delta$ = 140.2 (C2), 130.2 (C4), 117.0 (C5), 48.5 ($CH_3$), 47.2 ($CH_3$), 46.0 ($CH_3$) ppm. Crystals of **8**·$C_2H_5OH$ suitable for X-ray data collection were obtained from a solution of **8** in ethanol.

**Catalytic Hydration of Chloronitriles by a Metal Complex in Solution:** Typically, a solution/suspension of [$Os^{II}Cl_2$(azole)$_2$(dm*so*)$_2$] or [$Os^{II}Cl_2$(azole)(dm*so*)$_3$] (ca. 10 mg) in a mixture of chloronitrile (1 mL) and water (1.3 mL) was stirred at 75 °C for 24 h in a Schlenk flask equipped with a magnetic stirring bar. The metal complex:chloronitrile and chloronitrile:water molar ratios were 1:600 and 1:7, 1:650 and 1:6, 1:760 and 1:6 for trichloroacetonitrile, dichloroacetonitrile and chloroacetonitrile, respectively. Control experiments regarding hydration of the corresponding chloronitrile were carried out under similar conditions but in the absence of the osmium(II) complex. In all cases solvents were removed under reduced pressure and at moderate temperature (≤40 °C) to avoid sublimation of the carboxamide. The amount of product was determined by $^1H$ NMR experiments in [$D_6$]dmso by using 1,3,5-trimethoxybenzene as internal reference. The following lines were integrated: $CCl_3CONH_2$: $\delta$ = 8.35 (d, $J_{N,H}$ = 46.5 Hz) ppm; $CCl_3COONH_4$: $\delta$ = 7.12 (t, $J_{N,H}$ = 51.1 Hz) ppm; $CHCl_2CONH_2$: $\delta$ = 7.80 (d, $J_{N,H}$ = 82.1 Hz), 6.32 (s, H, $CHCl_2$) ppm; $CHCl_2COONH_4$: $\delta$ = 7.12 (t, $J_{N,H}$ = 50.1 Hz) ppm; $CH_2ClCONH_2$: $\delta$ = 7.50 (d, $J_{N,H}$ = 103.3 Hz), 4.02 (s, 2 H, $CH_2Cl$) ppm; $CH_2ClCOONH_4$: $\delta$ = 7.22 (t, $J_{N,H}$ = 51.1 Hz) ppm; $C_6H_3$-($OCH_3$)$_3$: $\delta$ = 6.08 (s, 3 H), 3.70 (s, 9 H) ppm.

**Physical Measurements:** Elemental analyses were carried out with a Carlo–Erba microanalyser at the Microanalytical Laboratory of the University of Vienna. Electrospray ionisation mass spectra were recorded with a Bruker esquire$_{3000}$ ion-trap mass spectrometer equipped with an orthogonal electrospray interface (Bruker Daltonics, Bremen, Germany) in both positive- and negative-ion modes. The Bruker Daltonics esquire 5.2 software bundle consisting of Bruker esquire Control 5.2 and Bruker Data Analysis 3.2 was used for acquiring spectra and data analysis, respectively. The sample solution in methanol was delivered at a flow rate of 3 μL min$^{-1}$ using a syringe pump 74900 from Cole–Parmer Instrument Company (Vernon Hills, IL, USA); $N_2$ was used as both drying and nebulising gas (flow rate: 5 L min$^{-1}$). Expected and experimental isotope distributions were compared. IR spectra were obtained from CsI pellets with a Perkin–Elmer FT-IR 2000 instrument (4000–200 cm$^{-1}$). UV/Vis spectra were recorded with a Perkin–Elmer Lambda 20 UV/Vis spectrophotometer from samples dissolved in methanol. $^1H$ NMR spectra were recorded with a Bruker DPX400 (Ultrashield™ Magnet) spectrometer at 298 K. The residual $^1H$ present in $CDCl_3$ ([$D_6$]dmso, [$D_7$]DMF, $D_2O$) was

Table 6. Crystal data and details of data collection for **1**–**8**.

| | **1** | **2** | **3** | **4** |
|---|---|---|---|---|
| Formula | $C_{18}H_{26}Cl_2N_4O_3OsS_2$ | $C_{10}H_{20}Cl_2N_4O_2OsS_2$ | $C_{20}H_{27}Cl_2N_5O_2OsS_2$ | $C_{10}H_{20}Cl_2N_4O_2OsS_2$ |
| *Fw* | 671.65 | 553.52 | 694.69 | 553.52 |
| Space group | $P2_1/n$ | $P2_1/n$ | $P2_1/n$ | $Cc$ |
| *a* [Å] | 23.386(5) | 8.796(2) | 10.1853(2) | 12.2467(2) |
| *b* [Å] | 11.732(2) | 16.397(3) | 20.7233(5) | 9.3749(2) |
| *c* [Å] | 17.422(3) | 12.266(2) | 12.3821(3) | 16.4373(3) |
| *β* [°] | 103.04(3) | 104.61(3) | 95.416(1) | 106.753(1) |
| *V* [Å$^3$] | 4656.7(15) | 1711.9(6) | 2601.86(10) | 1807.09(6) |
| *Z* | 8 | 4 | 4 | 4 |
| *λ* [Å] | 0.71073 | 0.71073 | 0.71073 | 0.71073 |
| $\rho_{calcd}$ [g cm$^{-3}$] | 1.916 | 2.148 | 1.773 | 2.035 |
| Crystal size [mm] | 0.22 × 0.22 × 0.17 | 0.20 × 0.14 × 0.11 | 0.17 × 0.11 × 0.09 | 0.19 × 0.16 × 0.14 |
| *T* [K] | 120 | 120 | 296 | 296 |
| *μ* [cm$^{-1}$] | 59.13 | 80.12 | 52.93 | 75.90 |
| $R_1$[a] | 0.0280 | 0.0174 | 0.0351 | 0.0261 |
| $wR_2$[b] | 0.1088 | 0.0425 | 0.0673 | 0.0602 |
| GOF[c] | 1.007 | 1.089 | 0.973 | 1.016 |
| | **5** | **6** | **7** | **8** |
| Formula | $C_{15}H_{30}Cl_2N_2O_4OsS_3$ | $C_9H_{22}Cl_2N_2O_3OsS_3$ | $C_{13}H_{24}Cl_2N_2O_3OsS_3$ | $C_{11}H_{28}Cl_2N_2O_4OsS_3$ |
| *Fw* | 659.69 | 563.57 | 613.62 | 609.63 |
| Space group | $Pca2_1$ | $P2_1$ | $P2_1/c$ | $P2_1/n$ |
| *a* [Å] | 14.242(3) | 8.403(2) | 10.1946(4) | 8.467(2) |
| *b* [Å] | 7.940(2) | 12.965(3) | 11.9361(5) | 21.599(4) |
| *c* [Å] | 19.685(4) | 8.858(2) | 15.9305(6) | 10.851(2) |
| *β* [°] | | 117.33(3) | 90.298(2) | 91.60(3) |
| *V* [Å$^3$] | 2226.0(9) | 857.3(3) | 1938.46(13) | 1983.6(7) |
| *Z* | 4 | 2 | 4 | 4 |
| *λ* [Å] | 0.71073 | 0.71073 | 0.71073 | 0.71073 |
| $\rho_{calcd}$ [g cm$^{-3}$] | 1.968 | 2.183 | 2.103 | 2.041 |
| Crystal size [mm] | 0.23 × 0.20 × 0.12 | 0.16 × 0.14 × 0.13 | 0.17 × 0.08 × 0.06 | 0.23 × 0.17 × 0.09 |
| *T* [K] | 120 | 120 | 296 | 120 |
| *μ* [cm$^{-1}$] | 62.74 | 81.20 | 71.92 | 70.31 |
| $R_1$[a] | 0.0201 | 0.0204 | 0.0272 | 0.0205 |
| $wR_2$[b] | 0.0464 | 0.0471 | 0.0538 | 0.0503 |
| GOF[c] | 1.048 | 1.045 | 1.019 | 1.072 |

[a] $R_1 = \Sigma||F_o| - |F_c||/\Sigma|F_o|$. [b] $wR_2 = \{\Sigma[w\,(F_o^2 - F_c^2)^2]/\Sigma[w(F_o^2)^2]\}^{1/2}$. [c] GOF = $\{\Sigma[w(F_o^2 - F_c^2)^2]/(n - p)\}^{1/2}$, where *n* is the number of reflections and *p* is the total number of parameters refined.

 © 2007 Wiley-VCH Verlag GmbH & Co. KGaA, Weinheim 

used as internal reference. The assignment was confirmed by 2D NMR ($^{13}C,^{1}H$; $^{1}H,^{1}H$ and $^{13}C,^{1}H$ via long-range couplings) and NOE (1D and 2D) spectroscopy. Cyclic voltammograms were measured in a three-electrode cell using a 0.2-mm-diameter platinum disc working electrode, a platinum auxiliary electrode and an $Ag|Ag^{+}$ reference electrode containing 0.1 M $AgNO_3$. Measurements were performed at room temperature using an EG&G PARC 273A potentiostat/galvanostat. Deaeration of solutions was accomplished by passing a stream of argon through the solution for 5 min prior to the measurement and then maintaining a blanket atmosphere of argon over the solution during the measurement. The potentials were measured in 0.15 M $[n\mathrm{Bu_4N}][\mathrm{BF_4}]/\mathrm{CH_3CN}$ (dmf) using $[\mathrm{Fe}(\eta^5\text{-}\mathrm{C_5H_5})_2]$ ($E_{1/2}^{ox}$ = +0.69 V vs. NHE)[42] as internal standard, and are quoted relative to NHE.

**Crystallographic Structure Determination:** X-ray diffraction measurements were performed with a Nonius Kappa CCD and X8AP-EXII CCD diffractometers. Single crystals were positioned at 35, 30, 40, 40, 35, 30, 40 and 35 mm from the detector, and 620, 344, 1001, 1089, 404, 344, 1885 and 538 frames were measured, each for 15, 30, 60, 60, 10, 10, 60 and 30 s over a 1, 2, 0.5, 0.5, 2, 2, 0.5 and 1.5° scan width for **1**–**8**, respectively. The data were processed using the Denzo-SMN or SAINT-Plus software package.[43,44] Crystal data, data collection parameters and structure-refinement details for **1**–**8** are given in Table 6. The structures were solved by direct methods and refined by full-matrix least-squares techniques. Non-hydrogen atoms were refined with anisotropic displacement parameters. H atoms were placed in geometrically calculated positions and refined as riding atoms in the subsequent least-squares model refinements. The isotropic thermal parameters were estimated to be 1.2-times the values of the equivalent isotropic thermal parameters of the atoms to which hydrogens are bonded. The following computer programs were used: structure solution: SHELXS-97;[45] refinement: SHELXL-97;[46] molecular diagrams: ORTEP;[47] computer CPU: Pentium® IV; scattering factors were taken from the literature.[48]

CCDC-606815 (for **1**), -606816 (for **2**), -606811 (for **3**), -606814 (for **4**), -606817 (for **5**), -606818 (for **6**), -606813 (for **7**) and -606812 (for **8**) contain the supplementary crystallographic data for this paper. These data can be obtained free of charge from The Cambridge Crystallographic Data Centre via www.ccdc.cam.ac.uk/data_request/cif.

**Supporting Information** (see also the footnote on the first page of this article): ORTEP view of the second independent molecule 1B (Figure S1); cyclic voltammograms of complexes **1** and **3**–**8** (Figures S2–S8).

## Acknowledgments

The authors are indebted to FWF and COST for financial support. We also thank Prof. G. Giester and Mr. A. Roller for X-ray data collection, and Dr. M. Galanski for NMR measurements. Dr. S. Shova and Mr. N. A. Sheddan are acknowledged for stimulating discussions.

[1] J. A. Davies, *Adv. Inorg. Chem. Radiochem.* **1981**, *24*, 115–187.
[2] H. B. Kagan, B. Ronan, *Rev. Heteroat. Chem.* **1992**, *7*, 92–116.
[3] M. Calligaris, O. Carugo, *Coord. Chem. Rev.* **1996**, *153*, 83–154.
[4] M. Calligaris, *Coord. Chem. Rev.* **2004**, *248*, 351–375.
[5] E. Alessio, *Chem. Rev.* **2004**, *104*, 4203–4242.
[6] G. Sava, E. Alessio, A. Bergamo, G. Mestroni, in *Topics in Biological Inorganic Chemistry*: *Metallo-Pharmaceuticals* (Eds.: M. J. Clarke, P. J. Sadler), Springer, Berlin, **1999**, vol. 1, p. 143–169.
[7] E. Alessio, G. Mestroni, A. Bergamo, G. Sava, in *Metal Ions in Biological Syst*ems: *Metal Complexes in Tumour Diagnosis and as Anticancer Agents* (Eds.: A. Sigel, H. Sigel, M. Dekker), New York, **2004**; vol. 42, p. 323–351.
[8] a) D. P. Riley, M. R. Thompson, J. Lyon III, *J. Coord. Chem.* **1988**, *19*, 49–59; b) R. S. Srivastava, *Appl. Organomet. Chem.* **2001**, *15*, 769–771; c) H. B. Henbest, J. Trocha-Grimshaw, *J. Chem. Soc., Perkin Trans. 1* **1974**, 607–608.
[9] a) M. Bressan, L. Forti, A. Morvillo, *J. Mol. Catal.* **1993**, *84*, 59–66; b) M. Bressan, L. Forti, F. Ghelfi, A. Morvillo, *J. Mol. Catal.* **1993**, *79*, 85–93; c) F. Porta, C. Crotti, S. Cenini, G. Palmisano, *J. Mol. Catal.* **1989**, *50*, 333–341.
[10] a) N. N. Dass, S. R. Sen, *J. Polym. Sci.* **1983**, *21*, 3381–3388; b) R. Castarlenas, I. Alaoui-Abdallaoui, D. Sémeril, B. Mernari, S. Guesmi, P. H. Dixneuf, *New J. Chem.* **2003**, *27*, 6–8; c) K. Kashiwagi, R. Sugise, T. Shimakawa, T. Matuura, M. Shirai, F. Kakiuchi, S. Murai, *Organometallics* **1997**, *16*, 2233–2235.
[11] a) P. K. L. Chan, K. A. Skov, B. R. James, N. P. Farrell, *Int. J. Radiat. Oncol. Biol. Phys.* **1986**, *12*, 1059–1062; b) P. K. L. Chan, K. A. Skov, B. R. James, *Int. J. Radiat. Biol.* **1987**, *52*, 49–55; c) P. K. L. Chan, P. K. H. Chan, D. C. Frost, B. R. James, K. A. Skov, *Can. J. Chem.* **1988**, *66*, 117–122; d) P. K. L. Chan, B. R. James, D. C. Frost, P. K. H. Chan, H.-L. Hu, K. A. Skov, *Can. J. Chem.* **1989**, *67*, 508–516.
[12] M. Henn, E. Alessio, G. Mestroni, M. Calligaris, W. M. Attia, *Inorg. Chim. Acta* **1991**, *187*, 39–50.
[13] M. Iwamoto, E. Alessio, L. G. Marzilli, *Inorg. Chem.* **1996**, *35*, 2384–2389.
[14] E. Alessio, E. Iengo, E. Zangrando, S. Geremia, P. A. Marzilli, M. Calligaris, *Eur. J. Inorg. Chem.* **2000**, 2207–2219.
[15] a) E. Alessio, M. Calligaris, M. Iwamoto, L. G. Marzilli, *Inorg. Chem.* **1996**, *35*, 2538–2545; b) L. G. Marzilli, M. Iwamoto, E. Alessio, L. Hansen, M. Calligaris, *J. Am. Chem. Soc.* **1994**, *116*, 815–816.
[16] a) M. M. T. Khan, P. S. Roy, K. Venkatasubramanian, N. H. Khan, *Inorg. Chim. Acta* **1990**, *176*, 49–55; b) M. M. T. Khan, N. M. Khan, R. I. Kureshy, K. Venkatasubramanian, *Polyhedron* **1992**, *11*, 431–441.
[17] E. Reisner, V. B. Arion, A. Rufińska, I. Chiorescu, W. F. Schmid, B. K. Keppler, *Dalton Trans.* **2005**, 2355–2364.
[18] E. Alessio, B. Serli, E. Zangrando, M. Calligaris, N. S. Panina, *Eur. J. Inorg. Chem.* **2003**, 3160–3166.
[19] A. J. Barton, W. Levason, G. Reid, V.-A. Tolhurst, *Polyhedron* **2000**, *19*, 235–240.
[20] T. Even, A. R. J. Genge, A. M. Hill, N. J. Holmes, W. Levason, M. Webster, *J. Chem. Soc., Dalton Trans.* **2000**, 655–662.
[21] A. M. McDonagh, M. G. Humphrey, D. C. R. Hockless, *Tetrahedron: Asymmetry* **1997**, *8*, 3579–3583.
[22] D. A. Freedman, D. J. Magneson, K. R. Mann, *Inorg. Chem.* **1995**, *34*, 2617–2624.
[23] E. Reisner, V. B. Arion, A. Eichinger, N. Kandler, G. Giester, A. J. L. Pombeiro, B. K. Keppler, *Inorg. Chem.* **2005**, *44*, 6704–6716.
[24] M. F. C. G. Guedes da Silva, A. J. L. Pombeiro, S. Geremia, E. Zangrando, M. Calligaris, A. V. Zinchenko, V. Yu. Kukushkin, *J. Chem. Soc., Dalton Trans.* **2000**, 1363–1371.
[25] A. B. P. Lever, *Inorg. Chem.* **1990**, *29*, 1271–1285.
[26] V. Yu. Kukushkin, A. J. L. Pombeiro, *Chem. Rev.* **2002**, *102*, 1771–1802.
[27] M. Hashimoto, K. Hamada, K. Mano, *Bull. Chem. Soc. Jpn.* **1987**, *60*, 1924–1926.
[28] E. A. Shomova, V. P. Rudavskii, I. G. Khaskin, *Mikrobiologiya* **1965**, *34*, 715–719.
[29] M. Nagasawa, M. Yoshido, R. Kubota, JP 32008650 19571007, **1957**.
[30] H. C. Englert, U. Gerlach, D. Mania, W. Linz, H. Gögelein, E. Klaus, P. Crause, EP 779288 A1 19970618, **1997**.

 © 2007 Wiley-VCH Verlag GmbH & Co. KGaA, Weinheim 

[31] D. Uemura, K. Yamada, A. Yamada, K. Suenaga, A. Takada, JP 11322593 A2 19991124, **1999**.
[32] P. C. Hamm, US Pat. 67-639657 19670519, **1971**.
[33] N. Komaki, Y. Hoshika, H. Taya, A. Fujinami, Y. Asano, N. Kameda, DE 2232176 19730111, **1973**.
[34] a) J. Quirante, C. Escolano, F. Diaba, J. Bonjoch, *J. Chem. Soc., Perkin Trans. 1* **1999**, 1157–1162; b) T. Nishikawa, N. Ohyabu, N. Yamamoto, M. Isobe, *Tetrahedron* **1999**, *55*, 4325–4340; c) N. Yamamoto, M. Isobe, *Chem. Lett.* **1994**, 2299–2302; d) A. J. Speziale, R. C. Freeman, *J. Am. Chem. Soc.* **1960**, *82*, 903–909.
[35] a) D. Albanese, D. Landini, M. Penso, *J. Org. Chem.* **1992**, *57*, 1603–1605; b) S. Takano, K. Ogasawara, M. Akyama, JP 61022053 A2 19860130, **1986**.
[36] a) E. B. Dol'berg, G. I. Kovalenko, B. G. Yasnitskii, *Metody Poluch. Khim. Reaktiv. Prep.* **1970**, 116–118; b) K. Maruyama, JP 44028889 19691126, **1969**; c) G. Popov, I. Knape, P. Mann, K. Peters, C. Pöschl, DE 10218603 A1 20031120, **2003**.
[37] N. V. Kaminskaia, N. M. Kostić, *J. Chem. Soc., Dalton Trans.* **1996**, 3677–3686.
[38] V. Yu. Kukushkin, A. J. L. Pombeiro, *Inorg. Chim. Acta* **2005**, *358*, 1–21.
[39] F. Matsuda, *Chemtech* **1977**, *7*, 306–308.
[40] E. Cariati, C. Dragonetti, L. Manassero, D. Roberto, F. Tessore, E. Lucenti, *J. Mol. Catal. A* **2003**, *204–205*, 279–285.
[41] L. Heinrich, A. Mary-Verla, Y. Li, J. Vaissermann, J.-C. Chottard, *Eur. J. Inorg. Chem.* **2001**, 2203–2206.
[42] W. C. Barrette Jr., H. W. Johnson Jr., D. T. Sawyer, *Anal. Chem.* **1984**, *56*, 1890–1898.
[43] Z. Otwinowski, W. Minor, in *Macromolecular Crystallography, Part A* (Eds.: C. W. Jr., Carter, R. M. Sweet), Academic Press, New York, **1997**, vol. 276, p. 307–326.
[44] SAINT-Plus (Version 7.06a) and APEX2, Bruker-Nonius AXS Inc. **2004**, Madison, Wisconsin, USA.
[45] G. M. Sheldrick, SHELXS-97, Program for Crystal Structure Solution, **1997**, University of Göttingen, Germany.
[46] G. M. Sheldrick, SHELXL-97, Program for Crystal Structure Refinement, **1997**, University of Göttingen, Germany.
[47] G. K. Johnson, Report ORNL-5138, Oak Ridge National Laboratory, Oak Ridge, TN, **1976**.
[48] *International Tables for X-ray Crystallography*, Kluwer Academic Press, Dordrecht, The Netherlands, **1992**; vol. C, Tables 4.2.6.8 and 6.1.1.4.9.

Received: September 14, 2006
Published Online: November 21, 2006

 © 2007 Wiley-VCH Verlag GmbH & Co. KGaA, Weinheim 

DOI: 10.1002/ejic.200600864

# Two Novel Reactions of a Ruthenium-Coordinated Phenazine – Oxidative Aromatic Ring Hydroxylation and Dimerization via a New C–N Bond Formation

**Priyabrata Banerjee,[a] Golam Mostafa,[b] Alfonso Castiñeiras,[c] and Sreebrata Goswami*[a]**

**Keywords:** Metal-mediated reaction / Phenazine / Ruthenium / Redox chemistry

The reaction of $[Ru(CH_3OH)_2(N\wedge N)_2]^{2+}$ [N∧N = 2,2′-bipyridine (bpy) and 1,10-*ortho*-phenanthroline(phen)] with the phenazine ligand, [$HL^1$ = 6-*p*-anisyl-2-(*p*-anisylamino)-3(4*H*)-*p*-anisylimine-9-methoxyphenazine] in the presence of a base ($NEt_3$) afforded two mononuclear ruthenium complexes, $[Ru(L^1)(N\wedge N)_2]X$ (**2**), and $[Ru(LO)(N\wedge N)_2]X_2$ (**3**), [LO = 7-methoxy-5-(4-methoxyphenyl)-2,3-bis(4-methoxyphenylimino)-3,5-dihydro-2*H*-phenazin-1-one] together with a diruthenium complex $[(N\wedge N)_2RuL^2Ru(N\wedge N)_2]X_3$ (**4**), [$L^2$ = 7,8′-dimethoxy-5,10′-bis(4-methoxyphenyl)-2,3′-bis(4-methoxyphenylamino)-3,2′-bis(4′-methoxyphenylimino)-3,5,2′,10′-tetrahydro-[1,5′]biphenazinyl-5′-ylium], (X = $ClO_4^-$ or $CF_3SO_3^-$). The complexes **3** and **4** were also obtained from the pure complex **2** under two different experimental conditions. Oxidative aromatic ring hydroxylation of the complex **2** produced **3** while the diruthenium complex, **4**, was formed by dimerization of **2** via a new C–N bond formation. The products were thoroughly characterized with the help of $^1H$ NMR and ESI-MS spectral measurements. Final authentication of the two complexes of the transformed phenazine ligands viz. **3** and **4** were made by single-crystal X-ray structure determination of the two representative complexes. These compounds are intensely colored and show transitions in the visible region, which are ascribed as metal-to-ligand charge transfer (MLCT). Notably, intensities of the two MLCT of the compound **4** are significantly higher than those of **2** and **3**. Redox properties of the complexes are reported. Electrochemical oxidation of compound **2**, even in the presence of trace moisture, produced compound **3**. Cyclic voltammetry of compound **3** shows a reductive response near –0.35 V. Its one-electron reduced product is blue and shows an intense EPR signal at $g$ = 2.001. The voltammogram of the diruthenium complex **4** consists of two responses near 0.70 and 0.85 V.
(© Wiley-VCH Verlag GmbH & Co. KGaA, 69451 Weinheim, Germany, 2007)

## Introduction

Transition-metal mediated functionalization of C–H bonds is one of the most vigorously pursued[1–4] areas of current synthetic research. In many instances these reactions lead to the synthesis of unusual molecules, which otherwise are difficult or even impossible to synthesize using conventional procedures. In recent years we have been working[5–6] on transition-metal promoted aromatic amine fusion reactions, via C–H functionalization, for the synthesis of new organic ligands whose coordination chemistry is rich with novel features. One such example[7] is the ferric chloride-mediated oxidative polymerization of *p*-anisidine, which produces *N*-substituted 2-amino-3-iminophenazines via a multiple C–N bond fusion reaction (Scheme 1).

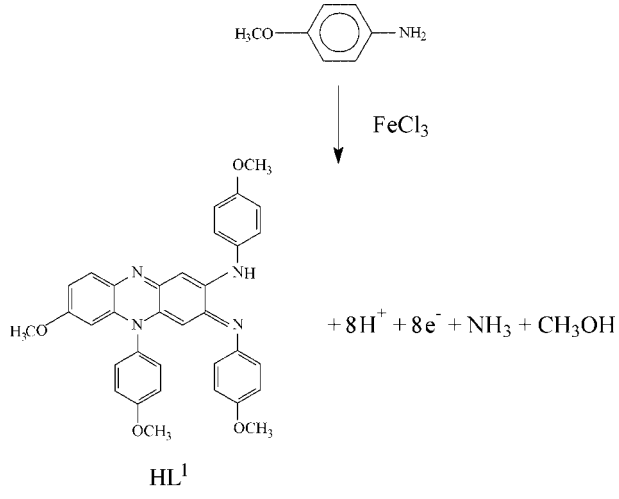


$HL^1$

Scheme 1.

Our interest[6] in the coordination chemistry of 1,2-diimine ligands and their redox partners prompted us to explore the ligand chemistry of [$HL^1$]. We have shown[7] that

[a] Department of Inorganic Chemistry, Indian Association for the Cultivation of Science,
Kolkata 700032, India
Fax: +91-33-2473-2805
E-mail: icsg@iacs.res.in
[b] Department of Physics, Jadavpur University,
Jadavpur, Kolkata 700032, India
[c] Departamento de Química Inorgánica, Universidade de Santiago de Compostela, Campus, Universitario Sur,
15782 Santiago de Compostela, Spain
Supporting information for this article is available on the WWW under http://www.eurjic.org or from the author.


© 2007 Wiley-VCH Verlag GmbH & Co. KGaA, Weinheim

the deprotonated phenazine ligand coordinates to the $[Ru(pap)_2]^{2+}$ moiety [pap = 2-(phenylazo)pyridine] spontaneously. The redox behavior of the resultant complex $[Ru(L^1)(pap)_2]^+$ (**1**) was of particular interest, since it seemed to follow[7] the EC-type pathway to produce a new ruthenium complex, following the oxidation of complex **1**. In practice, however, chemical oxidation of complex **1** resulted in a mixture of several products from which no pure compound could be isolated. The ESI-MS spectrum of the above crude mixture showed the presence of a moderately intense peak at $m/z$ = 1041 amu. For comparison we note here that the parent complex, **1**, showed a strong ESI-MS signal at $m/z$ = 1026 amu due to the $[Ru(L^1)(pap)_2]^+$ ion. The difference in mass between the two compounds indicates the addition of an oxygen atom to the parent complex **1**. Subsequently, we have found that the similar ruthenium complexes of $[L^1]^-$, $[Ru(L^1)(N\wedge N)_2]^+$ [N∧N = 2,2′-bipyridine (bpy) or 1,10-*ortho*-phenanthroline (phen)] also undergo similar chemical transformations upon oxidation. In these cases the transformed compounds are stable and suitable for following the above-mentioned metal-mediated redox reactions.

In this paper we report the results of the reaction of the 2-amino-3-iminophenazine, $HL^1$ and $[Ru(CH_3OH)_2(N\wedge N)_2]^{2+}$. The chemical reaction resulted in the formation of the three products **2**–**4**, of which the complexes **3** and **4** are formed due to an unprecedented type of chemical transformation of the coordinated ligand $[L^1]^-$ in the complex **2**. While oxidative hydroxylation of the ligand produced a ruthenium complex **3** of the oxidized phenazine ligand (LO), dimerization of it, on the other hand, produced a diruthenium complex **4** of a diphenazine bridge $[L^2]^-$. The latter reaction is associated with a new C–N bond fusion process. In the present context it is relevant to add that the coordination chemistry of the phenazine ligands, in general, has been developed in recent years; however, this work is confined[8] mostly to the complexes of pyridyl-containing phenazines. Some of these bind DNA and RNA and are an important class of molecular probes.[9] In contrast, the coordination chemistry of the related 2-amino-3-iminophenazine or its redox partners is not available in the literature. Thus, the reference reactions are noteworthy in the context of understanding the metal-mediated redox processes that are operative in amino-imino-phenazine[10] and related systems.

## Results and Discussion

The synthetic reaction involved refluxing a methanolic solution of $[Ru(N\wedge N)_2(CH_3OH)_2]^{2+}$, generated in situ,[11] with an equimolar quantity of $HL^1$ in the presence of a base ($NEt_3$) for 6 h. The initial red brown color of the solution mixture gradually turned bluish-violet and finally it became blue. The complexes were precipitated as their perchlorate or triflate salts. The crude mass, so formed, was a mixture of three major products: blue **2**, violet **3** and blue **4**, which were successfully separated on a preparative alumina TLC plate. The first blue complex **2** was unstable and with time slowly converted into the violet product **3** in air even at room temperature. The **2** → **3** conversion was much faster in boiling aqueous methanol.

Prolonged boiling of compound **2** in a dry and inert atmosphere, on the other hand, produced a stable blue compound **4** as the major product (vide infra). Schematic presentation of the reaction along with compound identification numbers are summarized in Scheme 2.

The sum total of the yields of the above three products exceeded 85%. There were a few minor fractions, which could not be purified and their identities remain uncertain.

The complexes gave satisfactory elemental analyses (see Exp. Sect.). These showed characteristic infrared stretches of the phenazine and coordinated ancillary ligands viz. bpy and phen. The most notable feature in the infrared spectra of **3a** and **3b** is the appearance of a sharp band at ca. 1680 $cm^{-1}$, which confirms the presence of a carbonyl function[12] (vide infra). These complexes are diamagnetic and displayed $^1H$ NMR resonances in the normal range. The spectral patterns in the aromatic region ($\delta$ = 5–9) are complex in nature (see Figure S1, supporting information) owing to the presence of a large number of unique protons. The methyl resonances were, however, diagnostic and useful for assessing their preliminary identities (Figure 1). For example, while the compounds **2** and **3** showed four –OMe signals each in the range $\delta$, 3.38–3.75, compound **4** displayed eight –OMe resonances in the range $\delta$ = 3.25–3.80. For comparison, the uncoordinated ligand, $[L^1]^-$, displayed four[7] such resonances at $\delta$ = 3.55–3.85. Thus, the $^1H$ NMR spectrum of complex **4** indicated the presence of two phenazine moieties. Electrospray mass spectra of the complexes were found to be informative for the identification of the complexes. The charge state distributions of these ranging from (+1) to (+3) are clearly observed, which exactly corroborated with the ionization of the respective complexes in the acetonitrile solution. For example an abundant peak, called a base peak, was observed for $[\mathbf{2a}\text{-}ClO_4^-]^+$ at $m/z$ = 971 amu. The complex **3a** showed a weak signal at $m/z$ = 1085 amu, and was accompanied by a strong signal at $m/z$ = 493 amu. These were ascribed to the $[\mathbf{3a} - ClO_4^-]^+$ and $[\mathbf{3a} - 2ClO_4^-]^{2+}$ ions, respectively. The compound **4a** exhibited peaks at 1020 and 647 amu, respectively. The peak at 647 amu was most intense and ascribed to the $[\mathbf{4a} - 3ClO_4^-]^{3+}$ ion. Similarly, the substituted complexes viz. **2b**, **3b** and **4b** displayed peaks at expected $m/z$ values (Exp. Sect.). From the ESI-MS spectral nature it is inferred that complex **4** is a dimetallic compound with a relatively high molecular weight. Notably, the experimental ESI-MS spectral features of the above compounds exactly corresponded to simulated patterns for the given formulations. Three representative ESI-MS spectra of **2**–**4**, are submitted as supplementary materials (Figure S2). Electrolytic natures of dilute acetonitrile (1 mM) solutions of the complexes were of different type: **2**, 1:1, **3**, 1:2 and **4**, 1:3.

Preliminary characterization of the above compounds was made from their physicochemical data. However, X-ray crystal analyses of the two complexes (**3** and **4**) of the

 © 2007 Wiley-VCH Verlag GmbH & Co. KGaA, Weinheim 

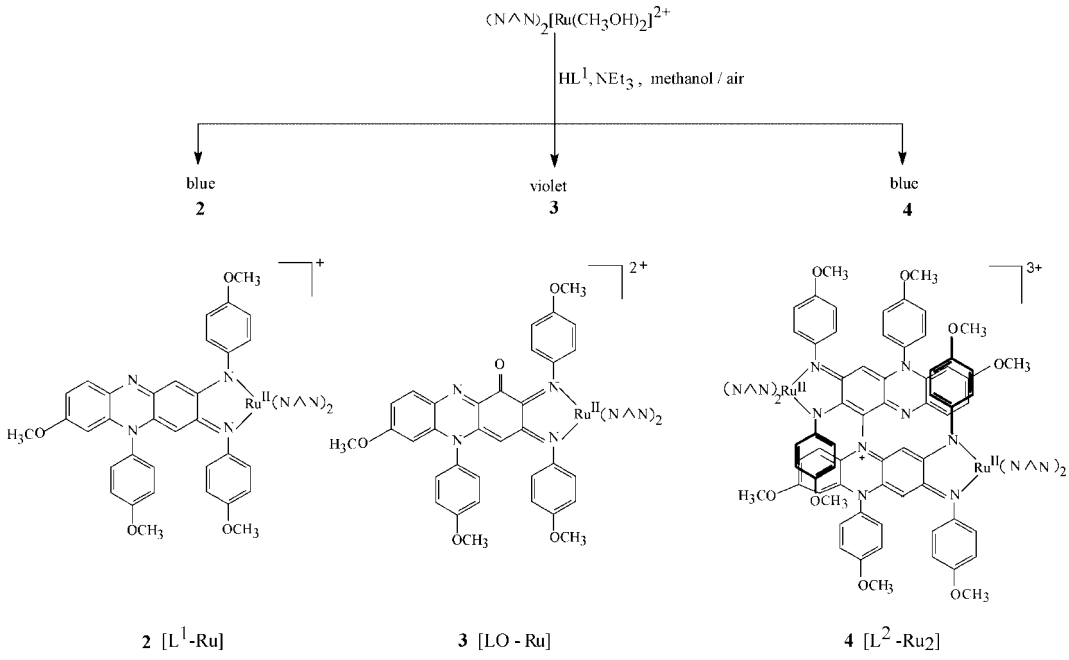


| compound | bpy | phen |
|---|---|---|
| **2** | **2a** | **2b** |
| **3** | **3a** | **3b** |
| **4** | **4a** | **4b** |

Scheme 2.

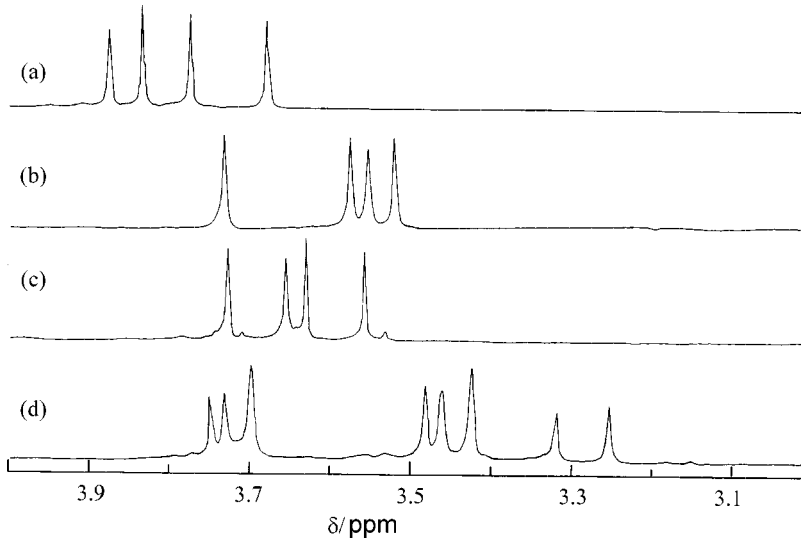


Figure 1. Segmented $^1$H NMR spectra of (a) HL$^1$, (b) **2a**, (c) **3a**, and (d) **4a** $CD_3CN$ at 298 K.

transformed ligands were indeed necessary for authentication of their formulations and structures.

The solutions of the complexes **2a** and **2b** were found to undergo chemical transformations to **3a** and **3b**, respectively, hence X-ray quality crystals of the parent complex, $[Ru(N\wedge N)_2(L^1)](X)$ (**2**) could not be grown. However, a complete characterization was obtained (vide supra) from the physicochemical data. The two representative complexes of the transformed ligands viz. **3b** and **4a** formed single crystals suitable for X-ray structure determination.

 © 2007 Wiley-VCH Verlag GmbH & Co. KGaA, Weinheim 

### $[Ru(phen)_2(LO)](CF_3SO_3)_2{\cdot}2H_2O$ (3b)

A view of the cationic part of the molecule $[Ru(phen)_2(LO)](CF_3SO_3)_2{\cdot}2H_2O$ is shown in Figure 2 and selected bond lengths and angles are collected in Table 1. In this complex, two bidentate 1,10-*ortho*-phenanthroline (phen) ligands and a neutral phenazine ligand [LO], formed via successive hydroxylation and oxidation of the coordinated ligand $[L^1]^-$, surround a ruthenium(II) center. The complex as a whole is dicationic and the crystallographic asymmetric unit also contains two triflate anions and two water molecules. Hydroxylation of the phenazine ligand occurred at the α-carbon (C13) to a *N*-aryl imine function [C(12)–N(11)]. The C(13)–O(130) bond length, 1.209(4) Å, indicates a localized double bond. The two C–N (imine) bond lengths, 1.300(4) Å [C(12)–N(11)] and 1.290(6) Å [C(25)–N(26)], respectively confirm[6a,13] their double bond character. The six Ru–N lengths are similar, and lie in the range 1.997–2.083 Å. The average of chelate bite angles of the phen ligand is 79.1(2)°, while the corresponding N(11)–Ru(1)–N(26) angle of the phenazine ligand has a value of 76.71(12)°.

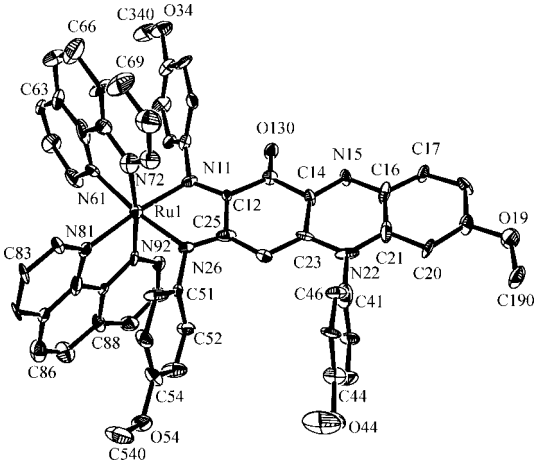


Figure 2. ORTEP and atom numbering scheme for **3b**. Hydrogen atoms are omitted for clarity.

### $[(bpy)_2RuL^2Ru(bpy)_2](ClO_4)_3$ (4a)

Figure 3 shows the ORTEP and atom numbering scheme for the cationic complex $[\mathbf{4a}]^{3+}$ and its bond parameters are collected in Table 1. Herein, two $[Ru^{II}(bpy)_2]$ moieties are bridged across a dimeric phenazine ligand $[L^2]^-$, formed via an unusual type of C–N fusion between the two $[Ru(bpy)_2L^1]^+$ units. In this reaction a new C–N bond is formed between the free pyrazine nitrogen N(9) of one unit and the α-carbon C(36) of the second unit. The bridging ligand, $[L^2]^-$, is a zwitterion with two anionic chelating sites and a cationic pyrazine nitrogen. The bridging ligand is thus mono-negative and coordinates to two ruthenium(II) centers in a bis chelating tetradentate fashion. The resulting diruthenium complex as a whole is tri-cationic and the asymmetric unit contains three perchlorate counterions. The C–N lengths viz. C(35)–N(5) 1.387(4) Å, C(40)–N(6) 1.314(4) Å, C(71)–N(11) 1.343(4) Å and C(72)–N(12) 1.348(4) Å are all longer than the corresponding distances in coordinated LO in the compound **3b** (Table 1). Notably, the C(35)–N(5) length is appreciably longer than C(40)–N(6) suggesting that the anionic charge in this part of the bridging ligand is localized on N(5). In contrast the two C–N lengths of the other part viz. C(71)–N(11) and C(72)–N(12) are nearly identical indicating effective charge delocalization over the N(11)–C(71)–C(72)–N(12) skeleton. The average of the above C–N lengths of $L^2$ lies in between a single and a double C–N bond length. The five-membered chelate rings of the bridging ligand have the expected bite angles, N(5)–Ru(1)–N(6) 76.12(9)° and N(11)–Ru(2)–N(12) 76.94(11)°.

The two reference chemical transformations, viz. **2** → **3** and **2** → **4**, occur due to induced C–H activation[6,14] at the ortho carbon of the coordinated phenazine. The plausible initial step for the formation of **3** is the oxidation reaction, **2** → $\mathbf{2}^+$. The oxidized product $\mathbf{2}^+$ is then converted to **3** in the presence of water and aerial oxygen. Water adds to the polarized phenazine ring and the hydroxo-intermediate, so formed, is oxidized to **3** in air. Exposure of an aqueous methanolic solution of **2** to air thus produces the com-

Table 1. Selected bond lengths [Å] and angles [°] for the complexes **3b** and **4a**.

| $[Ru(phen)_2(LO)](CF_3SO_3)_2{\cdot}2H_2O$ (**3b**) | | | | $[(bpy)_2RuL^2Ru(bpy)_2](ClO_4)_3$ (**4a**) | | | |
|---|---|---|---|---|---|---|---|
| Bond lengths | | | | Bond lengths | | | |
| Ru(1)–N(11) | 1.997(4) | N(11)–C(12) | 1.300(4) | Ru(1)–N(5) | 2.072(3) | C(35)-C(36) | 1.393(4) |
| Ru(1)–N(26) | 2.053(3) | C(12)–C(13) | 1.523(5) | Ru(1)–N(6) | 2.056(2) | C(39)–C(40) | 1.389(4) |
| Ru(1)–N(61) | 2.082(5) | C(12)–C(25) | 1.457(5) | Ru(2)–N(11) | 2.034(3) | C(35)–C(40) | 1.393(4) |
| Ru(1)–N(72) | 2.038(4) | N(26)–C(25) | 1.290(6) | Ru(2)–N(12) | 2.050(3) | C(70)–C(71) | 1.396(5) |
| Ru(1)–N(81) | 2.042(3) | C(25)–C(24) | 1.369(6) | N(6)–C(40) | 1.314(4) | C(71)–C(72) | 1.388(5) |
| Ru(1)–N(92) | 2.066(4) | C(13)–O(130) | 1.209(4) | N(9)–C(36) | 1.470(4) | C(72)–C(73) | 1.395(5) |
| | | | | N(11)–C(71) | 1.343(4) | C(35)–N(5) | 1.387(4) |
| | | | | N(12)–C(72) | 1.348(4) | | |
| Bond angles | | | | Bond angles | | | |
| N(11)–Ru(1)–N(26) | 76.71(12) | N(72)–Ru(1)–N(61) | 78.6(2) | N(1)–Ru(1)–N(2) | 78.27(10) | N(3)–Ru(1)–N(4) | 78.14(9) |
| N(92)–Ru(1)–N(81) | 79.64(15) | | | N(5)–Ru(1)–N(6) | 76.12(9) | N(11)–Ru(2)–N(12) | 76.94(11) |
| | | | | N(13)–Ru(2)–N(14) | 77.80(13) | N(15)–Ru(2)–N(16) | 79.52(13) |

 © 2007 Wiley-VCH Verlag GmbH & Co. KGaA, Weinheim 

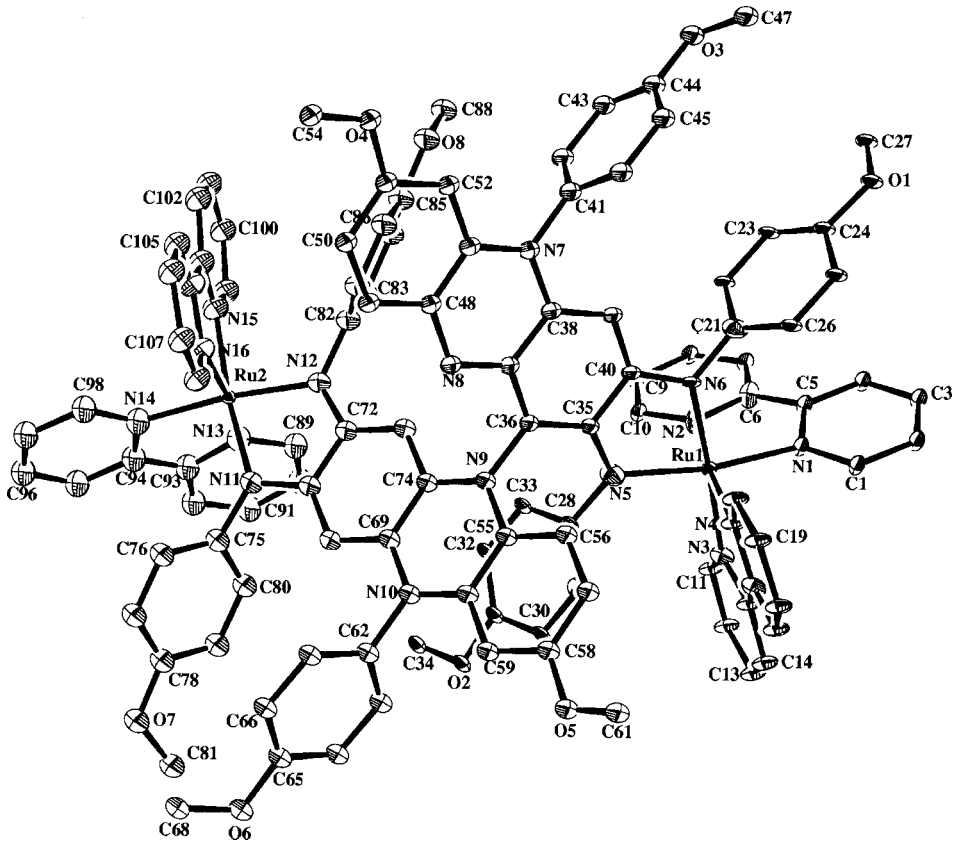


Figure 3. ORTEP and atom numbering scheme for **4a**. Hydrogen atoms are omitted for clarity.

pound **3** in almost quantitative yield. The plausible steps of this transformation[15] are shown in Scheme 3. Since the oxidation potential of complex **2** is low (vide infra), the aerial oxidation, $\mathbf{2} \rightarrow \mathbf{2}^{+}$ is reasonable and is believed to be the key step for the formation of **3** from **2**. Furthermore, the fact that electrochemical oxidation of the complex **2** (vide infra) produces the compound **3**, also supports our proposition. The conversion of **2** to **4** occurs only in dry and boiling methanol. Nucleophilic attack of the phenazine nitrogen of one molecule of **2** at the activated *ortho* C–H of another molecule followed by ($-H^{+} - 2e^{-}$) transfer produces the compound **4**.

Hence, we conclude that $\mathbf{2} \rightarrow \mathbf{3}$ conversion is facilitated by the initial oxidation of the ruthenium(II) center of **2**. However, if the initial oxidation of **2** is arrested, dimerization of the phenazine occurs preferably so as to initiate the formation of the dimetallic complex **4**. The results are summarized in Scheme 4.

The electronic spectroscopic data of all the complexes are collected in Table 2 and their representative spectra are displayed in Figure 4. The visible range spectra of these complexes consisted of strong absorptions. For example, the mononuclear complexes **2a** and **3a** each showed an allowed transition at 585 nm ($\varepsilon$ = 16385 $M^{-1}cm^{-1}$) and 565 nm ($\varepsilon$ = 23490 $M^{-1}cm^{-1}$), respectively. These are ascribed to charge transfer, $Ru^{II}(d\pi) \rightarrow \pi^{*}$(phenazine) (MLCT). The bimetallic compound **4a** displayed two intense transitions at 690 nm ($\varepsilon$ = 36450 $M^{-1}cm^{-1}$) and 645 nm ($\varepsilon$ = 32300 $M^{-1}cm^{-1}$), respectively. Notably, the two-phenazine moieties in the bridging ligand $[L^{2}]^{-}$ are not identical and hence the two major transitions in the visible region are believed to be due to the presence of two acceptor chromophores in the bridging ligand. Interestingly, the intensities of MLCT transitions in **4** are significantly higher than those of the mononuclear compounds **2** and **3**. This spectral behavior of the polynuclear complexes with repeating acceptor chromophores has been reported[6b] in the literature. The complexes also showed multiple UV-range transitions, which are assigned to inter- or intra-ligand transitions.

The redox behavior of the complexes **2**–**4** was studied in dichloromethane {maintaining $10^{-3}$ M concentration of the complex and $10^{-1}$ M concentration of the supporting electrolyte, $[n\mathrm{Bu_4N}](\mathrm{ClO_4})$} in the potential range 2.0 to –1.5 V by using platinum or glassy carbon working electrodes. The reported potentials (Table 2, Figure 5) are referenced to the saturated calomel electrode (SCE). The value for the ferrocene/ferrocenium couple under our experimental conditions was 0.39 V.

The mononuclear complex $[Ru(bpy)_2L^{1}]ClO_4$ (**2a**) showed an electrochemically reversible $Ru^{III}/Ru^{II}$ response at 0.15 V. Associated with it is an irreversible response, which appeared at a potential of 1.05 V. The redox behavior of the closely related system, $[Ru(phen)_2L^{1}]ClO_4$ **2b**, is similar to that of **2a**. Constant potential coulometry at 0.40 V of both **2a** and **2b** resulted in rapid transformations to **3a** and **3b**, respectively. The voltammetric behavior of the com-

 © 2007 Wiley-VCH Verlag GmbH & Co. KGaA, Weinheim 

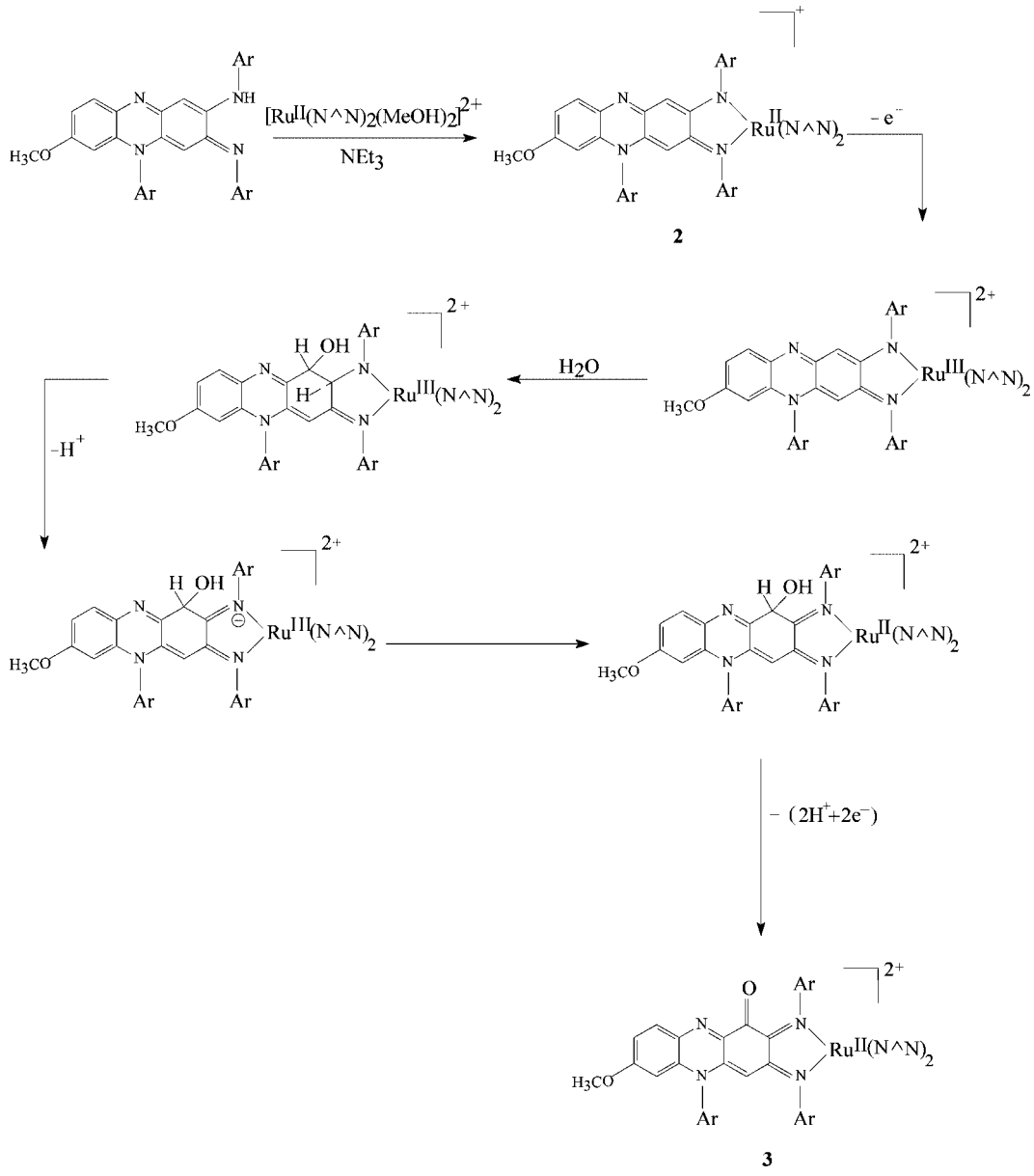


Scheme 3.

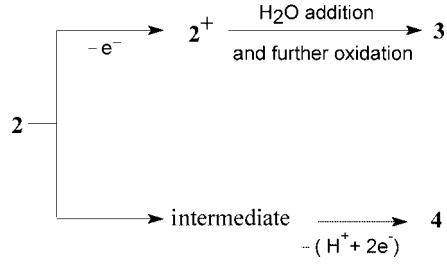


Scheme 4.

plexes, **3a** and **3b** was similar. These showed a reversible reductive response near –0.35 V. Exhaustive electrolysis of **3a** at –0.60 V produced a blue solution, which reverted to the parent bivalent complex, **3a** under our experimental conditions. However, we managed to record an EPR spectrum of the reduced complex, by performing the controlled potential bulk electrolysis of **3a** at 260 K and quickly freezing the electrolyzed solution at 77 K. The EPR spectrum showed (Figure S3) an intense signal at $g$ = 2.001 without any $g$-anisotropy, indicating large free radical[16] (ligand) contributions to the SOMO. We thus conclude that upon reduction of **3a**, an electron is added to the ketonic function of the phenazine ligand to result in a free radical-containing phenazine ligand $[LO^{\cdot}]^{-}$ that resembles[10] pyocyanine. The main feature of the cyclic voltammogram of the dimetallic complexes **4a** and **4b** consisted of two closely spaced responses at 0.70, 0.85 V and 0.75, 0.90 V, respectively. These are assigned to two successive electron transfers at the two

 © 2007 Wiley-VCH Verlag GmbH & Co. KGaA, Weinheim 

Table 2. Electronic spectra and cyclic voltammetric data.

| Compound | Abs. [$\lambda_{max}$ /nm ($\varepsilon$/M$^{-1}$ cm$^{-1}$)][a] | Cyclic voltammetry[c,d] Oxidation $E_{1/2}$ [V] ($\Delta E_p$ [mV]) | Reduction $E_{1/2}$ [V] ($\Delta E_p$ [mV]) |
|---|---|---|---|
| **2a** | 585 (16385), 420 (8770), 285 (41555) | 0.15 (70), 1.05[e] | –1.33 (90) |
| **3a** | 565 (23490), 400[b] (12085), 320[b] (18790), 290 (43830) | 0.85 (100) | –0.35 (100), –0.91[f] |
| **4a** | 690 (36450), 645 (32300), 340 (20480), 295 (36310) | 0.70 (80), 0.85 (90) | –0.88 (90) |
| **2b** | 585 (17390), 415 (8900), 285(44250) | 0.15 (75), 1.10[e] | –1.35 (100) |
| **3b** | 565(29610), 390[b] (12340), 320[b] (14640), 265 (45770), 225 (61135) | 0.90 (100) | –0.30 (80), –1.00[f] |
| **4b** | 690 (42155), 645 (36190), 325 (23060), 265 (116680), 225 (129170) | 0.75 (70), 0.90 (80) | –0.85 (80) |

[a] Solvent: acetonitrile. [b] Shoulder. [c] Solvent: dichloromethane, supporting electrolyte: [$n$Bu$_4$N](ClO$_4$) 10$^{-1}$ M; scan rate: 50 mV$^{-1}$ s$^{-1}$. [d] Sample concentration ca. 10$^{-3}$ M. [e] Irreversible, the value corresponds to $E_{pa}$. [f] Irreversible, the value corresponds to $E_{pc}$.

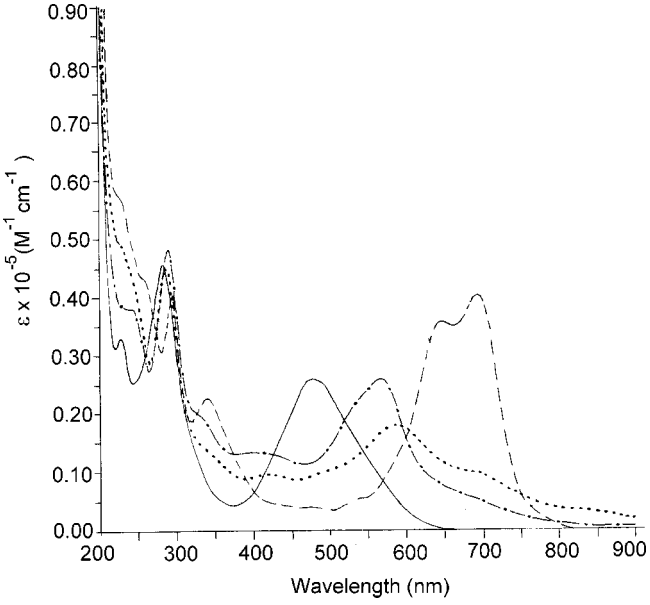


Figure 4. UV/Vis spectra of $(\mathbf{L^1})^-$, (−); (**2a**), (····); (**3a**), (-·-·-·); (**4a**), (-----) in acetonitrile.

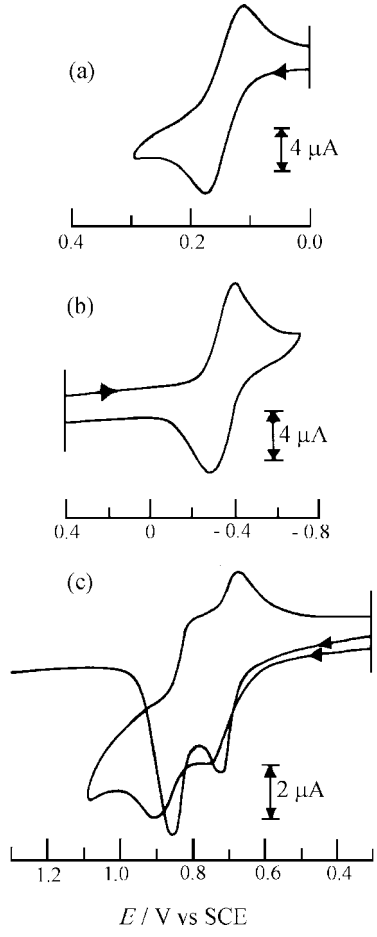


Figure 5. Cyclic voltammograms for the compounds (a) **2a**, (b) **3a**, and (c) **4a** in dichloromethane at a scan rate 50 mV s$^{-1}$.

ruthenium centers. The magnitude of $\Delta E$ signifies moderate electronic interactions between the ruthenium centers.

Our present work has demonstrated that the phenazine ligand [6-*p*-anisyl-2-(*p*-anisylamino)-3(4*H*)-*p*-anisylimine-9-methoxyphenazine], $HL^1$, upon coordination to ruthenium is susceptible to fascinating metal-mediated chemical transformations leading to isolation of the three new ruthenium complexes **2**–**4** of three different ligands (viz. $[L^1]^-$, LO and $[L^2]^-$) from the reaction of $[Ru(CH_3OH)_2(N\wedge N)_2]^{2+}$ and $HL^1$. The latter two ligands are formed in situ due to oxidative hydroxylation and dimerization reactions of the coordinated ligand, $[L^1]^-$. To authenticate these transformations, X-ray structure analyses of a mononuclear ruthenium complex of LO as well as a diruthenium complex of the bridging ligand $[L^2]^-$ were analyzed. Presently, we are pursuing our work to understand the effects of ancillary ligands and the metal ions on the chemical transformations of the reference phenazine ligands.

## Experimental Section

**Materials:** The precursor compounds *cis*-[Ru(bpy)$_2$Cl$_2$]·2H$_2$O and *cis*-[Ru(phen)$_2$Cl$_2$]·2H$_2$O were prepared according to the reported procedures.[17] The ligand $HL^1$ was synthesized as before.[7] Silica gel and aluminum oxide for TLC were obtained from Merck, India and Sisco Research Laboratories Pvt. Ltd., Bombay. RuCl$_3$·$n$H$_2$O was purchased from Arora Mathey Ltd., and 2,2′-bipyridine and 1,10-phenanthroline monohydrate were obtained from Qualigens and Merck, India, respectively. Tetrabutylammonium perchlorate (TBAP) was used as the supporting electrolyte, for spectroscopic

 © 2007 Wiley-VCH Verlag GmbH & Co. KGaA, Weinheim 

and electrochemical studies HPLC-grade solvents were used. Other chemicals and reagents were of reagent-grade and used as received.

**Physical Measurements**

Microanalytical data (C, H and N) were collected with a Perkin–Elmer 240C elemental analyzer. A Perkin–Elmer 783 spectrophotometer was used for the measurement of IR spectral data. $^1$H NMR spectroscopic data was recorded with a Bruker Avance 300 spectrometer using $SiMe_4$ as an internal standard. Electrochemical measurements were performed at 298 K under a dry nitrogen atmosphere on a PC-controlled PAR Model 273A electrochemistry system with a gas tight single-compartment cell. Voltammetric experiments were carried out in dichloromethane maintaining the sample concentration at ca. $10^{-3}$ M. The solution was degassed with the flow of dry nitrogen and the working electrode surface was polished before each measurement. A platinum disk working electrode, platinum wire auxiliary electrode and an aqueous saturated calomel reference electrode (SCE) were used in a three-electrode configuration. All redox potentials in this work are reported against the saturated calomel electrode. The value for the ferrocenium/ferrocene couple under our experimental conditions was 0.39 V. EPR spectral measurements were carried out with a Varian Model 109C E-line X-band spectrometer as described before,[18] fitted with a quartz Dewar for measurements at 77 K, and the spectroscopic data were calibrated against the spectrum of DPPH. Electrospray mass spectra were recorded with a micro mass Q-TOF mass spectrometer (Serial no. YA. 263). Electronic spectroscopic data were recorded with a Perkin–Elmer Lambda 950 UV/Vis spectrophotometer.

***CAUTION!*** *Although no problems were encountered in this work, transition metal perchlorate complexes with organic ligands are potentially explosive. Heating of dried samples must be avoided; handling of small quantities must proceed with great caution using proper protection.*

**Syntheses**

The complexes **2**–**4** were synthesized following a general procedure. Specific details for representative complexes are given below.

**Reactions of $[Ru(bpy)_2(MeOH)_2]^{2+}$with $HL^1$:** A mixture of *cis*-$[Ru(bpy)_2Cl_2]\cdot 2H_2O$ (0.065 g, 0.125 mmol) and $AgNO_3$ (0.042 g, 0.25 mmol) in dry methanol (25 mL) was heated at reflux for 2 h. The initial violet solution changed to orange red. The cooled solution was filtered through Whatman 42 filter paper to remove the precipitated AgCl. The ligand $HL^1$ (0.070 g, 0.125 mmol) along with two drops of $NEt_3$ was then added to the above filtrate. The resulting mixture was heated at reflux for 6 h. The solution finally became blue and its volume was reduced to ca. 10 mL. The concentrated solution was then poured into diethyl ether (50 mL) to precipitate a dark product. The crude product was then subjected to chromatography on a preparative alumina TLC plate for purification. It was first eluted with $CHCl_3$; a small band of unreacted phenazine ligand was first separated, which was followed by a blue (**2**) band. The unmoved dark band was collected and was again loaded on a fresh TLC plate and chloroform/acetonitrile (3:2) was then used as the eluent. This resulted in the separation of two distinct bands, viz. violet (**3**) and blue (**4**). The compounds **2**–**4** were collected by complete evaporation of the eluates. Recrystallization of these from different solvent mixtures yielded the products in their crystalline states. The yields and characterization data of the complexes are as follows.

**$[Ru(bpy)_2(L^1)](ClO_4)$ (2a):** This was crystallized from a dichloromethane/hexane (1:1) solvent mixture. Yield: 0.015 g (10%). $C_{54}H_{45}ClN_8O_8Ru$ (1069.50): calcd. C 60.58, H 4.20, N 10.47; found C 60.56, H 4.25, N 10.45. IR (KBr): $\tilde{\nu}$ = 1615 s, 1560 s, 1502 s, 1464 m, 1446 m, 1423 m, 1285 w, 1245 s, 1115 vs, 1100 vs, 838 m, 770 s, 625 s cm$^{-1}$. ESI-MS: *m*/*z* (%): 971 $[M - ClO_4^-]^+$, where *M* = molecular mass of the compound. $\Lambda_M$ in acetonitrile at 25 °C: 130 $\Omega^{-1}$ cm$^2$ M$^{-1}$.

**$[Ru(bpy)_2(LO)](ClO_4)_2$ (3a):** This was crystallized from an acetonitrile/toluene (1:4) solvent mixture. Yield: 0.069 g (45%). $C_{54}H_{44}Cl_2N_8O_{13}Ru$ (1184.10): calcd. C 54.72, H 3.71, N 9.46; found C 54.73, H 3.74, N 9.41. IR (KBr): $\tilde{\nu}$ = 1670 s, 1605 s, 1550 s, 1504 s, 1463 m, 1444 m, 1278 w, 1248 s, 1248 s, 1115 s, 1090 s, 836 m, 767 s, 620 s cm$^{-1}$. ESI-MS: *m*/*z* (%): 493 $[M - 2ClO_4^-]^{2+}$. $\Lambda_M$ in acetonitrile at 25 °C: 250 $\Omega^{-1}$ cm$^2$ M$^{-1}$.

**$[(bpy)_2RuL^2Ru(bpy)_2](ClO_4)_3$ (4a):** Evaporation of the third fraction from the TLC plate yielded the dimeric blue **4a**. Yield: 0.054 g (35%). This fraction was recrystallized from acetonitrile/toluene. $C_{108}H_{89}Cl_3N_{16}O_{20}Ru_2$ (2239.38): calcd. C 57.87, H 3.97, N 10.00; found C 57.95, H 4.00, N 10.01. IR (KBr): $\tilde{\nu}$ = 1605 s, 1565 w, 1504 s, 1481 m, 1464 w, 1445 m, 1382 vs, 1250 s, 1115 vs, 1030 s, 837 w, 768 s, 625 s cm$^{-1}$. ESI-MS: *m*/*z* (%): 647 $[M - 3ClO_4^-]^{3+}$. $\Lambda_M$ in acetonitrile at 25 °C: 370 $\Omega^{-1}$ cm$^2$ M$^{-1}$.

**Reactions of $[Ru(phen)_2(MeOH)_2]^{2+}$ with $HL^1$:** This reaction was performed as described above, except that *cis*-$Ru(phen)_2Cl_2$ was used in place of *cis*-$Ru(bpy)_2Cl_2$. The yields and characterization data of the complexes are collected below.

**$[Ru(phen)_2(L^1)](ClO_4)$ (2b):** This was recrystallized using a dichloromethane/THF/hexane solvent mixture (1:1:1). Yield: 0.013 g (8%). $C_{58}H_{45}ClN_8O_8Ru$ (1117.50): calcd. C 62.28, H 4.02, N 10.02; found C 62.25, H 4.10, N 9.98. IR (KBr): $\tilde{\nu}$ = 1610 s, 1548 m, 1504 s, 1427 s, 1384 s, 1245 s, 1175 m, 1100 m, 1027 w, 721 m, 620 s cm$^{-1}$. ESI-MS: *m*/*z* (%): 1018 $[M - ClO_4^-]^+$. $\Lambda_M$ in acetonitrile at 25 °C: 140 $\Omega^{-1}$ cm$^2$ M$^{-1}$.

**$[Ru(phen)_2(LO)](CF_3SO_3)_2\cdot 2H_2O$ (3b):** Crystalline compound of **3b** was obtained by slow evaporation of the solution of the compound in a dichloromethane/acetonitrile (1:2) solvent mixture. Yield: 0.075 g (47%). $C_{60}H_{48}F_6N_8O_{13}RuS_2$ (1368.21): calcd. C 52.62, H 3.50, N 8.18; found C 52.55, H 3.60, N 8.10. IR (KBr): $\tilde{\nu}$ = 1670 s, 1610 s, 1552 s, 1505 m, 1463 w, 1430 w, 1412 w, 1276 vs, 1250 s, 1163 m, 1116 s, 1030 s, 840 m, 721 w, 638 s cm$^{-1}$. ESI-MS: *m*/*z* (%): 517 $[M - 2CF_3SO_3^-]^{2+}$. $\Lambda_M$ in acetonitrile at 25 °C: 270 $\Omega^{-1}$ cm$^2$ M$^{-1}$.

**$[(phen)_2RuL^2Ru(phen)_2](ClO_4)_3$ (4b):** The thin rod-shaped crystalline compound was obtained from an acetonitrile/toluene (1:1) solvent mixture. Yield: 0.040 g (25%). $C_{116}H_{89}Cl_3N_{16}O_{20}Ru_2$ (2333.64): calcd. C 59.65, H 3.81, N 9.60; found C 59.63, H 3.87, N 9.55. IR (KBr): $\tilde{\nu}$ = 1605 s, 1564 w, 1502 s, 1481 s, 1427 w, 1408 m, 1383 vs, 1130 s, 1029 m, 842 m, 610 s cm$^{-1}$. ESI-MS: *m*/*z* (%): 678 $[M - 3ClO_4^-]^{3+}$. $\Lambda_M$ in acetonitrile at 25 °C: 400 $\Omega^{-1}$ cm$^2$ M$^{-1}$.

**Syntheses of Compounds 3 and 4 from 2. 2a→3a Conversion:** A solution of the compound $[Ru(bpy)_2(L^1)](ClO_4)$ (**2a**) [50 mg in 250-mL aqueous methanol (1:9)] was heated at reflux in air for 0.5 h. The blue solution became violet. The mixture was evaporated to dryness and the crude product was purified on an alumina TLC plate using a chloroform/acetonitrile (3:2) solvent mixture as the eluent. A violet band of the compound **3a** was collected. It was finally crystallized from an acetonitrile/toluene solvent mixture, yield 90%.

The compound **3b** was similarly obtained from **2b**, the yield was 86%.

**2a→4a Conversion:** A solution of the compound **2a** in dry methanol was heated at reflux under a dry nitrogen atmosphere for 6 h. The resultant blue solution was evaporated to dryness and was loaded on an $Al_2O_3$-TLC plate for purification. A minor violet

 © 2007 Wiley-VCH Verlag GmbH & Co. KGaA, Weinheim 

band (**3a**, yield 5%) and a major blue band (**4a**, yield 75%) were eluted using a chloroform/acetonitrile (3:2) solvent mixture.

The compound **4b** was similarly obtained from **2b**. The yield of **4b** was 80%.

**X-ray Crystallography:** Single crystals of $[Ru(phen)_2(LO)](CF_3SO_3)_2 \cdot 2H_2O$ (**3b**) were grown by slow evaporation of an acetonitrile/dichloromethane (2:1) solvent mixture and the single crystals of $[\{(bpy)_2Ru\}_2(L^2)^-](ClO_4)_3$ (**4a**) were grown by slow diffusion of an acetonitrile solution of **4a** into toluene. Crystallographic data are collected in Table 3 and further details are noted below.

Table 3. Crystallographic data and refinement results for **3b** and **4a**.

| Compound | **3b** | **4a** |
|---|---|---|
| Empirical formula | $C_{60}H_{48}F_6N_8O_{13}RuS_2$ | $C_{108}H_{89}Cl_3N_{16}O_{20}Ru_2$ |
| Molecular mass | 1368.25 | 2239.44 |
| $T$ [K] | 293(2) | 273(2) |
| Wavelengths [Å] | 0.71073 | 0.71073 |
| Crystal system | monoclinic | triclinic |
| Space group | $P21/c$ (no. 14) | $P$-1 (no. 2) |
| $a$ [Å] | 11.3828(13) | 11.6057(18) |
| $b$ [Å] | 22.640(2) | 15.236(2) |
| $c$ [Å] | 24.2105(19) | 33.086(5) |
| $\alpha$ [°] | 90 | 79.286(3) |
| $\beta$ [°] | 109.044(4) | 89.143(3) |
| $\gamma$ [°] | 90 | 75.031(3) |
| $V$ [Å$^3$] | 5897.7(10) | 5550.0(15) |
| $Z$ | 4 | 2 |
| $D_{calcd.}$ [mg m$^{-3}$] | 1.541 | 1.340 |
| Crystal dimensions [mm] | $0.23 \times 0.18 \times 0.16$ | $0.03 \times 0.16 \times 0.21$ |
| $\theta$ range for data collection [°] | 1.27–28.08 | 1.3–26.1 |
| Reflections collected | 28248 | 21643 |
| Unique reflections | 13468 | 15050 |
| Largest diff. between peak and hole [eÅ$^{-3}$] | –1.085, 2.731 | –0.64, 1.36 |
| Final $R$ indices $[I > 2\sigma(I)]$ | $R_1 = 0.0451$ $wR_2 = 0.1597$ | $R_1 = 0.0695$ $wR_2 = 0.1021$ |

**$[Ru(phen)_2(LO)](CF_3SO_3)_2 \cdot 2H_2O$ (3b):** X-ray quality crystals of **3b** were obtained by slow evaporation of an acetonitrile/dichloromethane (2:1) solvent mixture. A crystal of dimension ($0.23 \times 0.18 \times 0.16$ mm$^3$) was mounted, data were collected with a Bruker SMART CCD 1000 diffractometer equipped with a graphite crystal incident beam monochromator having Mo-$K_\alpha$ radiation ($\lambda$ = 0.71073 Å), and were processed with SAINT.[19] These were corrected for absorption using SADABS[20] (transmission factors: 1.000–0.742). A total of 24248 reflections were collected of which 13468 were unique ($R_{int}$ = 0.0436) and these were used in subsequent analysis. The structure was solved by direct methods using the program SHELXS-97[21] and refined by full-matrix least-squares techniques against $F^2$ using SHELXL-97.[22] Positional and anisotropic atomic displacement parameters were refined for all non-hydrogen atoms. Hydrogen atoms were included in geometrically idealized positions employing appropriate riding models with isotropic displacement parameters constrained. Crystallographic drawings were prepared using the programs PLATON[23] and SCHAKAL.[24]

**$[(bpy)_2RuL^2Ru(bpy)_2](ClO_4)_3$ (4a):** X-ray quality crystals of **4a** were obtained by slow diffusion of an acetonitrile solution of the compound into toluene. A crystal of dimension ($0.03 \times 0.16 \times 0.21$ mm$^3$) was mounted, and the data were collected with a Bruker Smart CCD diffractometer using graphite-monochromated Mo-$K_\alpha$ radiation ($\lambda$ = 0.71073 Å) at 273 K. These were corrected for Lorentz polarization effects and an empirical absorption correction was made with the help of the SAINT[19] program. A total of 21643 reflections were measured, of which 15050 reflections were unique ($R_{int}$ = 0.060). The data [$I > 2\sigma(I)$] were used for solution and refinement by full-matrix least-squares on $F^2$ using the SHELXL-97 package.[22] The non-hydrogen atoms having full occupancies were refined using anisotropic thermal parameters. Hydrogen atoms were included in the structure factor calculation at idealized positions, but not refined. The refinement was converged at $R$ = 0.0695 and $wR_2$ = 0.1021 with residual electron density 1.36 eÅ$^3$ and –0.64 eÅ$^3$. The maximum electron densities have no chemical significance as they were located at ca. 0.7 Å from a heavy atom. The calculations were performed using the Bruker Smart 5.63 software for data reduction, all other calculations and graphics were done using the PLATON[23] software package and ORTEP.[25]

Crystal data and refinement details are listed in Table 3. CCDC-290869 (for **3b**) and -290868 (for **4a**) contain the supplementary crystallographic data for this paper. These data can be obtained free of charge from The Cambridge Crystallographic Data Centre via www.ccdc.cam.ac.uk/data_request/cif.

**Supporting Information** (see also the footnote on the first page of this article): NMR spectra of a class of representative complexes (Figure S1). Observed ESI-MS spectra for representative complexes (a) $(\mathbf{2a})^+$, (b) $(\mathbf{3a})^{2+}$, (c) $(\mathbf{4a})^{3+}$ (Figure S2) and EPR spectrum of a frozen acetonitrile/toluene glass (1:1) of $(\mathbf{3a})^-$ at 77 K (Figure S3).

## Acknowledgments

Financial support received from the Department of Science and Technology, and the Council of Scientific and Industrial Research, New Delhi is gratefully acknowledged. P. B. is thankful to the Council of Scientific and Industrial Research, New Delhi, for his fellowship. We are also thankful to the School of Chemistry, University of Hyderabad, for X-ray data collection for one of the samples.

[1] For examples of recent reviews, see a) D. St. C. Black, in: *Comprehensive Coordination Chemistry* (Ed.: G. Wilkinson), Pergamon, Oxford, **1987**, vol. 6, p. 155; b) D. St. C. Black, in: *Comprehensive Coordination Chemistry* (Ed.: G. Wilkinson), Pergamon, Oxford, **1987**, vol. 1, p. 415; c) B. A. Arndtsen, R. G. Bergman, T. A. Mobley, T. H. Peterson, *Acc. Chem. Res.* **1995**, *28*, 154–162; d) E. C. Constable, *Metals and Ligand Reactivity. An Introduction to the Organic Chemistry of the Metal Complexes*, VCH, Weinheim, **1995**; e) A. J. L. Pombeiro, V. Yu. Kukushkin, in: *Comprehensive Coordination Chemistry* (Eds.: J. A. McCleverty, T. J. Meyer), Pergamon Press, Amsterdam, **2004**, vol. 1, chapter 29, p. 585–594.

[2] a) M. A. Lockwood, K. Wang, J. M. Mayer, *J. Am. Chem. Soc.* **1999**, *121*, 11894–11895; b) B. K. Bennett, S. Lovell, J. M. Mayer, *J. Am. Chem. Soc.* **2001**, *123*, 4336–4337; c) T. Suzuki, A. G. Dipasquale, J. M. Mayer, *J. Am. Chem. Soc.* **2003**, *125*, 10514–10515; d) I. J. Rhile, J. M. Mayer, *J. Am. Chem. Soc.* **2004**, *126*, 12718–12719.

[3] a) B. K. Santra, G. A. Thakur, P. Ghosh, A. Pramanik, G. K. Lahiri, *Inorg. Chem.* **1996**, *35*, 3050–3052; b) R. Acharyya, S.-M. Peng, G.-H. Lee, S. Bhattacharya, *Inorg. Chem.* **2003**, *42*, 7378–7380; c) S. Nag, P. Gupta, R. J. Butcher, S. Bhattacharya, *Inorg. Chem.* **2004**, *43*, 4814–4816; d) S. Patra, B. Sarkar, S. Ghumann, J. Fiedler, W. Kaim, G. K. Lahiri, *Inorg. Chem.* **2004**, *43*, 6108–6113; e) P. Gupta, S. Dutta, F. Basuli, S.-M. Peng, G.-H. Lee, S. Bhattacharya, *Inorg. Chem.* **2006**, *45*, 460–467.

[4] a) C. Pearson, A. L. Beauchamp, *Inorg. Chem.* **1998**, *37*, 1242–1248; b) T. Hashimoto, A. Endo, N. Nagao, G. P. Sato, K. Na-

 © 2007 Wiley-VCH Verlag GmbH & Co. KGaA, Weinheim 

trajan, K. Shimizu, *Inorg. Chem.* **1998**, *37*, 5211–5220; c) P. Paul, B. Tyagi, M. Balikakhiya, M. Bhadbhade, E. Suresh, G. Ramachandraiah, *Inorg. Chem.* **1998**, *37*, 5733–5742; d) A. Sundermann, O. Uzan, D. Milstein, J. M. L. Martin, *J. Am. Chem. Soc.* **2000**, *122*, 7095–7104; e) R. H. Crabtree, *Dalton Trans.* **2003**, 3985–3990; f) M. Lail, B. N. Arrowood, T. B. Gunnoe, *J. Am. Chem. Soc.* **2003**, *125*, 7506–7507; g) M. Lail, C. M. Bell, D. Conner, T. R. Cundari, T. B. Gunnoe, J. L. Petersen, *Organometallics* **2004**, *23*, 5007–5020.

[5] a) A. Saha, A. K. Ghosh, P. Majumdar, K. N. Mitra, S. Mondal, K. K. Rajak, L. R. Falvello, S. Goswami, *Organometallics* **1999**, *18*, 3772–3774; b) A. K. Ghosh, P. Majumdar, L. R. Falvello, G. Mostafa, S. Goswami, *Organometallics* **1999**, *18*, 5086–5090; c) C. Das, A. Saha, S.-M. Peng, G.-H. Lee, S. Goswami, *Inorg. Chem.* **2003**, *42*, 198–204.

[6] a) K. N. Mitra, P. Majumdar, S.-M. Peng, A. Castiñeiras, S. Goswami, *Chem. Commun.* **1997**, 1267–1268; b) K. N. Mitra, S.-M. Peng, S. Goswami, *Chem. Commun.* **1998**, 1685–1686; c) P. Majumdar, L. R. Falvello, M. Tomas, S. Goswami, *Chem. Eur. J.* **2001**, *7*, 5222–5228; d) C. Das, S. Goswami, *Comments Inorg. Chem.* **2003**, *24*, 137–163.

[7] A. K. Ghosh, K. N. Mitra, G. Mostafa, S. Goswami, *Eur. J. Inorg. Chem.* **2000**, 1961–1967.

[8] a) M. Yamada, Y. Tanaka, Y. Yoshimoto, S. Kuroda, I. Shimao, *Bull. Chem. Soc. Jpn.* **1992**, *65*, 1006–1011; b) S. Kawata, S. Kitagawa, H. Kumagai, C. Kudo, H. Kamesaki, T. Ishiyama, R. Suzuki, M. Kondo, M. Katada, *Inorg. Chem.* **1996**, *35*, 4449–4461; c) R. B. Nair, L. K. Yeung, C. J. Murphy, *Inorg. Chem.* **1999**, *38*, 2536–2538; d) N. Komatsuzaki, R. Katoh, Y. Himeda, H. Sugihara, H. Arakawa, K. Kasuga, *J. Chem. Soc., Dalton Trans.* **2000**, 3053–3054; e) M. Staffilani, P. Belser, L. D. Cola, F. Hartl, *Eur. J. Inorg. Chem.* **2002**, 335–339; f) T. Akasaka, H. Inoue, M. Kuwabara, T. Mutai, J. Otsuki, K. Araki, *Dalton Trans.* **2003**, 815–821; g) N. R. de Tacconi, R. O. Lezna, R. Konduri, F. Ongeri, K. Rajeshwar, F. M. Macdonnell, *Chem. Eur. J.* **2005**, *11*, 4327–4339.

[9] a) A. E. Friedman, J.-C. Chambron, J.-P. Sauvage, N. J. Turro, J. K. Barton, *J. Am. Chem. Soc.* **1990**, *112*, 4960–4962; b) E. Ruba, J. R. Hart, J. K. Barton, *Inorg. Chem.* **2004**, *43*, 4570–4578.

[10] J. B. Laursen, J. Nielsen, *Chem. Rev.* **2004**, *104*, 1663–1686 and references therein.

[11] B. P. Sullivan, D. J. Salmon, T. J. Meyer, *Inorg. Chem.* **1978**, *17*, 3334–3341.

[12] a) B. Halton, A. J. Kay, A. T. McNichols, P. J. Stang, Y. Apeloig, R. Boese, A. H. Maulitz, T. Hauman, *ARKIVOC* **2001**, *7*, 8–31; b) R. K. Agarwal, N. Goel, S. Prasad, *Turk. J. Chem.* **2004**, *28*, 405–413.

[13] a) J. Albert, A. González, J. Granell, R. Moragas, C. Puerta, P. Valerga, *Organometallics* **1997**, *16*, 3775–3778; b) N. M. Brunkan, P. S. White, M. R. Gagne, *J. Am. Chem. Soc.* **1998**, *120*, 11002–11003; c) M. Akazome, S. Suzuki, Y. Shimizu, K. Henni, K. Ogura, *J. Org. Chem.* **2000**, *65*, 6917–6921.

[14] a) W. D. Jones, F. J. Feher, *Acc. Chem. Res.* **1989**, *22*, 91–100; b) A. E. Shilov, G. B. Shul'pin, *Chem. Rev.* **1997**, *97*, 2879–2932; c) A. Shilov, A. A. Shteiman, *Acc. Chem. Res.* **1999**, *32*, 763–771; d) R. F. Moreira, P. M. Wehn, D. Sames, *Angew. Chem. Int. Ed.* **2000**, *39*, 1618–1621.

[15] S. E. Diamond, G. M. Tom, H. Taube, *J. Am. Chem. Soc.* **1975**, *97*, 2661–2664.

[16] A. K. Deb, S. Goswami, *J. Chem. Soc., Dalton Trans.* **1989**, 1635–1637.

[17] M. Kakoti, A. K. Deb, S. Goswami, *Inorg. Chem.* **1992**, *31*, 1302–1304.

[18] S. Goswami, R. Mukerjee, A. Chakravorty, *Inorg. Chem.* **1983**, *22*, 2825–2832.

[19] a) *SMART Software Users Guide, Version 5.0*, Bruker Analytical X-ray Systems, Madison, WI, **1999**; b) *SAINT Software Users Guide*, Bruker Analytical X-ray Systems, Madison, WI, USA, **1999**.

[20] G. M. Sheldrick, *SADABS*, program for empirical absorption correction of area detector data, University of Göttingen, Göttingen, Germany, **1997**.

[21] G. M. Sheldrick, *Acta Crystallogr., Sect. A* **1990**, *46*, 467–473.

[22] G. M. Sheldrick, *SHELXL-97*, program for the refinement of crystal structures, University of Göttingen, Göttingen, Germany, **1997**.

[23] A. L. Spek, *PLATON*, a multipurpose crystallographic tool, Utrecht University, Utrecht, The Netherlands, **2003**.

[24] E. Keller, *SCHAKAL-97*. A computer program for the graphic representation of molecular and crystallographic models, Kristallographisches Institut, Universität Freiburg, **1997**.

[25] C. K. Johnson, *ORTEP II*, Report *ORNL-5138*, Oak Ridge National Laboratory, Tennessee, USA, **1976**.

Received: September 15, 2006
Published Online: November 28, 2006

 © 2007 Wiley-VCH Verlag GmbH & Co. KGaA, Weinheim 

DOI: 10.1002/ejic.200600842

# Reticular Nickel Microwires with Assembled Nanostructures: Synthesis, Magnetism and Catalysis for the Growth of Carbon Nanotubes

Xiaomin Ni,[a] Qingbiao Zhao,[a] Yongfeng Zhang,[b] and Huagui Zheng*[a]

**Keywords:** Nickel / Nanostructures / Chemical reduction / Crystal growth

Reticular nickel microwires assembled from different-shaped building blocks are fabricated by a simple, one-pot method in the absence of any surfactants or external magnetic field. The synthetic process involves the chemical reduction of a nickel complex with hydrazine under controlled reaction conditions. Our strategy focuses on the modulation of the reaction rate to control the shape of the subunits and their spontaneous assembly behavior, which avoids the need for surfactants or an external force. The nickel wires can be reproducibly created with the assistance of various complexants, such as citrate, tartrate, lactate, ethylenediamine, triethanolamine and diethanolamine, which proves the generality of this method. These nickel wires show variable magnetic properties and catalysis for the growth of carbon nanotubes in pyrolyzing acetone due to the nature of their microstructures.
(© Wiley-VCH Verlag GmbH & Co. KGaA, 69451 Weinheim, Germany, 2007)

## Introduction

Assembled nanostructures have attracted considerable interest from materials scientists due to their potential applications in nanodevices.[1] In particular, magnetic assemblies have received more attention due to their unique properties and uses in electronic, magnetic, and biomedical applications, amongst others.[2] Generally, there are two routes for the assembly of magnetic nanoparticles into organized structures. The first of these harnesses the spontaneous noncovalent interactions between surfactants or polymer-modified building blocks, including van der Waals forces, π–π interactions, electrostatic forces, and hydrogen bonding.[3] For example, a three-dimensional spherical assembly of magnetite nanoparticles has been fabricated in the presence of ternary surfactant combinations[4] and the assembly of maghemite has been achieved in the presence of a block copolypeptide.[5] In the presence of polymers, monodisperse FePt nanoparticles self-assemble into films with controllable thicknesses and dimensions.[6] In these systems, the content of surfactants or polymers is relatively high, which usually damages their magnetic properties or makes their practical application difficult.[7] The other efficient method for the assembly of magnetic nanoparticles makes use of an external magnetic field. The application of a magnetic field to a suspension of magnetic particles typically produces one-dimensional (1D) chains of particles with their magnetic dipoles aligned head-to-tail and parallel to the magnetic field.[8] For instance, application of an external perpendicular magnetic field to a solution of $CoPt_3$ nanocrystals in toluene drives the formation of 1D microwires,[9] and $Fe_3O_4$ nanoparticles in the size range 8–12 nm self-assemble into elongated clusters on a GaAs substrate in the presence of a strong magnetic field, with the predominant orientation lengthwise along the field direction.[10] Colloidal nickel nanoparticles self-assemble into nanochains when subjected to a magnetic field with a strength of about 250 G.[11] However, these assemblies always require an external magnetic field to remain stable, and when the external magnetic field is removed they become unstable.[12] Currently, it is still challenging to explore simple and convenient approaches for the synthesis of assembled nanostructures.

Nanosized particles of nickel show diverse applications as catalysts, magnetic recording media, conducting materials, and in medical diagnosis.[13] In the past decades, many different-shaped nickel nanocrystals, including nanotubes, hollow spheres, nanobelts, nanorods, and nanoprisms, have been successfully created and their properties and applications found to depend on their morphology.[7,14] Some of these assembled nickel nanostructures, such as microwires assembled by acicular nanocrystals and chains consisting of nanospheres, were created with the aid of surfactants or an external magnetic field.[11,15] However, the assembly mechanism has not been investigated thoroughly and to date little work has been reported on the synthesis of assembled nickel architectures by methods other than those mentioned above.

[a] Department of Chemistry, University of Science and Technology of China,
Hefei, Anhui 230026, People's Republic of China
Fax: +86-551-360-1600
E-mail: hgzheng@ustc.edu.cn
[b] State Key Lab of Fire Science, University of Science and Technology of China,
Hefei, Anhui 230026, People's Republic of China
Supporting information for this article is available on the WWW under http://www.eurjic.org or from the author.

 © 2007 Wiley-VCH Verlag GmbH & Co. KGaA, Weinheim 

In this manuscript we report a facile kinetic-control method for the preparation of wire-like assembled nanostructures of nickel that does not require surfactants or an external magnetic field. This synthetic methodology focuses on the modulation of the reaction rate to control the shapes of the building blocks and their spontaneous assembly behavior and has the advantage of being simple to perform and easy to control. The thus-prepared nickel wires with different-shaped subunits show variable magnetic properties and catalytic activity for the formation of carbon nanotubes in pyrolyzing acetone, depending on their microstructures.

## Results and Discussion

Figure 1 shows a typical X-ray diffraction (XRD) pattern of sample1 (S1), in which all the diffraction peaks can be well indexed as ace-centered-cubic (fcc) nickel (JCPDS 01-1260). No peaks of nickel oxides or nickel hydroxides can be detected, thus indicating that pure fcc nickel is obtained by the current synthetic procedure.

The morphology of S1 is shown in Figure 2. The panoramic field emission scanning electron microscopy (FE-SEM) image in Figure 2 (a) indicates that the sample consists of reticular microwires with a diameter of about 2 μm and lengths of up to several hundred micrometers. The magnified images in parts b and c of Figure 2 demonstrate that the wires are prickly and are constructed from thorn-like particles with lengths of 200–400 nm. Figure 2 (d) is the TEM image of one wire and reveals the same characteristics as the SEM observations. Parts e, f and g of Figure 2 show a typical thorn-like subunit and the corresponding selected-area electron diffraction (SAED) and high-resolution TEM image. The pattern of spots reveals that the thorn is single-crystalline and the electron beam could be set along the

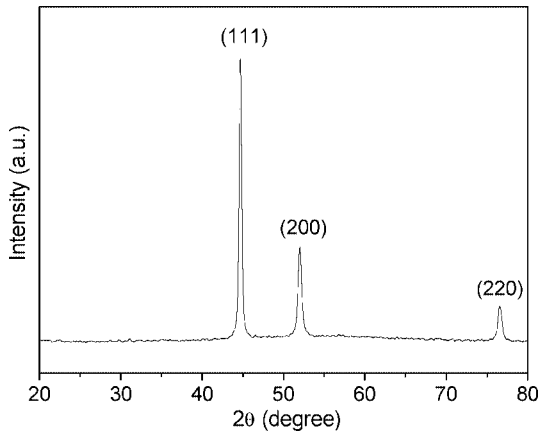


Figure 1. A typical XRD pattern of sample 1.

[$\bar{1}\bar{1}2$] zone axis. The spacing of the observed lattice planes is 0.20 nm, which is consistent with the separation of the (111) planes of fcc nickel. This demonstrates that the growth direction of the thorn is along the (111) plane. Analysis of several thorns gives a similar picture, thus suggesting that all the subunits have the same orientation.

In order to study the formation process of the wires, time-dependent TEM observations of the evolution of S1 were conducted; the results are shown in Figure 3. After 2 h, the product is present as small, granular nanocrystals with a diameter of 20–30 nm (Figure 3a). After heating the reaction mixture for 4 h thorns protrude from the particles and some prickly particles begin to aggregate due to their natural magnetic attraction, as shown in Figure 3b. After 8 h microwires consisting of thorn-like nanocrystals had formed (seen in Figure 3c). Figure 3d shows the HRTEM image recorded at the join of two neighboring subunits of the product heated for 8 h. It can be seen that the lattice

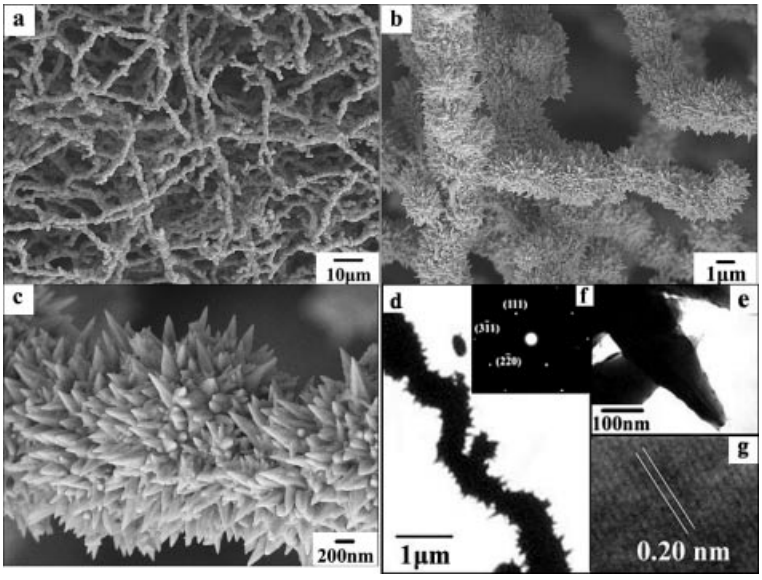


Figure 2. SEM and TEM images of sample 1: (a) a panoramic SEM image, (b) a low-magnification SEM image, (c) a high-magnification SEM image recorded on an individual wire, (d) a TEM image of a typical prickly wire, (e) a magnified TEM image of the thorn-like subunit, (f) the corresponding SAED image of the thorn, (g) the corresponding HRTEM image of the thorn.

 © 2007 Wiley-VCH Verlag GmbH & Co. KGaA, Weinheim 

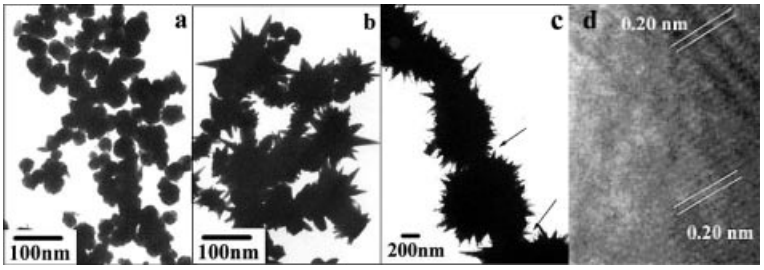


Figure 3. SEM images of the samples prepared at different reaction stages: (a) 2 h, (b) 4 h, (c) 8 h; (d) HRTEM image of the join of two neighboring thorn-like building blocks.

fringes prolongate across the two subunits without interruption by an apparent boundary, thus indicating that the building units have fused together. These results reveal that formation of the assembly wires occurs with a continuous aggregated growth rather than by direct aggregation of preformed, thorn-like particles.

Contrast experiments were carried out to investigate the factors that influence the formation of these nickel microwires. The redox reaction we employ here can be formulated as:

$$2\,[Ni(C_6H_5O_7)]^- + N_2H_4 + 4\,OH^- \rightarrow 2\,Ni + N_2 + 4\,H_2O + 2\,C_6H_5O_7^{3-}$$

Citrate was introduced here as the complexant to form the complex $[Ni(C_6H_5O_7)]^-$. Formation of this complex could sharply reduce the free $Ni^{2+}$ concentration in solution and thus result in a relatively slow reaction rate, which is favorable for the oriented growth of nickel crystals.[16] To examine the effect of citrate ions on the formation of the wires, SEM images of the samples obtained at different molar ratios of citrate to $Ni^{2+}$ ions ($\omega$) were compared. In the absence of citrate, the reaction was complete after 30 min and the product consisted of irregular spherical particles (Figure 4, a). When $\omega$ was set to 0.5, where the amount of citrate is not sufficient to form the complex, the reaction time was prolonged to 4 h and the product was found to be a mixture of dispersed spherical particles and microwires (Figure 4, b). When $\omega$ was increased to 1.0, about 7 h was needed to complete the reaction and the product was dominated by microwires. These results indicate that citrate ions play a significant role in the formation of the wires.

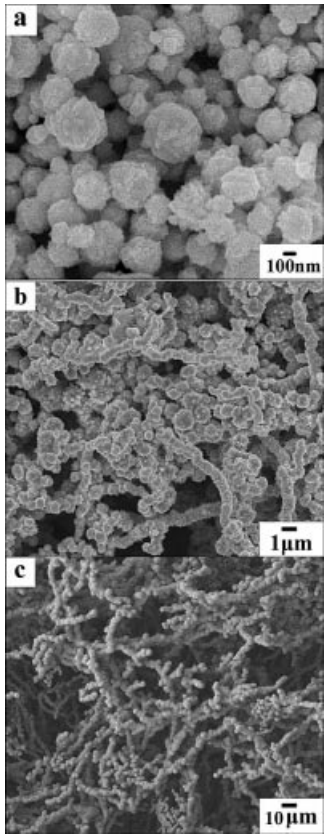


Figure 4. SEM images of the samples prepared at different molar ratios ($\omega$) of citrate to $Ni^{2+}$ ions: (a) $\omega$ = 0, (b) $\omega$ = 0.5, (c) $\omega$ = 1.0. The other reagent concentrations were kept the same.

The concentration of NaOH is another important parameter that affects the product morphology. It is known that a basic medium can increase the reducing power of hydrazine. Consequently, by adjusting the NaOH concentration, the reaction rate was correspondingly changed. Nickel wires were only obtained in a certain range of base concentrations when keeping the other conditions the same. Table 1 summarizes the reaction times and the product morphologies of the samples obtained at different base concentrations. The corresponding SEM images are shown in Figure 5. It can be seen that with an increase of base concentration the product gradually changes from wires into discrete particles and the reaction time is correspondingly shortened. A lower base concentration results in a relatively slow reaction rate, which facilitates the oriented growth of the nickel particles into thorns and their spontaneous assembly into wires. The fast reaction rate produced at high base concentrations only leads to bigger isolated particles.

The effect of temperature on the formation of the wires was also studied. It was found that the nickel wires could be fabricated in a wide temperature range of 70–140 °C. As the temperature decreases, the reaction time is obviously prolonged; for example, 2 h is sufficient to complete the reaction at 140 °C, while 36 h is needed for the reaction at 70 °C. No significant change of morphology and size was observed for the product obtained at different temperatures. In summary, an increase of reaction temperature accelerates the formation of the nickel wires but has little influence on their morphology and size.

Generally, nickel nanoparticles connect to each other due to magnetic interactions, although this magnetic dipole in-

 © 2007 Wiley-VCH Verlag GmbH & Co. KGaA, Weinheim 

Table 1. Reaction times and product morphologies of the samples prepared at different base concentration with the other conditions remaining the same.

| Sample | NaOH conc. [M] | Reaction time [h] | Product morphology |
|---|---|---|---|
| 1 | 0.05 | 10 | microwires consisting of nanoplates (diameter of the wire: 2 μm) |
| 2 | 0.10 | 8 | microwires consisting of nanoplates (diameter of the wire: 1 μm) |
| 3 | 0.15 | 5 | microwires consisting of nanoparticles (diameter of the wire: 0.5 μm) |
| 4 | 0.30 | 3 | pearl-necklace-like microwires (diameter of the wire: 0.3 μm) |
| 5 | 0.40 | 1 | discrete particles with a diameter of 100 nm |

teraction is rather weak and the aggregates can usually be dispersed by strong ultrasonication. Nevertheless, our wire-like assemblies show a high stability and even ultrasonication for 1 h could not destroy them. This indicates that the wire is not a loose aggregate of thorn-like nanocrystals but an integrated hierarchical structure. The assembly of magnetic particles is a complex process that is affected by several factors such as the velocity of crystal growth, dipolar interactions, spatial hindrance, and other kinetic factors. Based on the above studies of the evolution process and experimental parameters, the formation of our reticular hierarchical wires can be ascribed to the cooperative effect of the reaction rate and the inherent magnetic interactions. The reaction rate is controlled mainly by adjusting the reaction temperature and reagent concentration. During the first stage of the reaction spherical particles form as the nucleus. Then, anisotropic, thorn-like crystals develop from the active parts of the existing nuclei under the kinetic control of complexant and base and form prickly particles. Under the influence of the magnetic dipole interactions, the prickly particles tend to join with each other to acquire a low magnetic anisotropic energy. As the reaction proceeds, the contacting particles gradually fuse into each other and the separation between the joints disappears, which finally results in long wires. A schematic illustration of the possible formation process is presented in Scheme 1. During this process, there is a thermodynamic driving force for the aggregated growth because the surface energy is reduced substantially when the interface is eliminated.[17] As a result, reticular wires are observed.

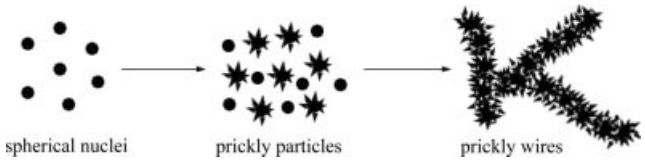


Scheme 1. Schematic illustration of the possible formation process of the prickly nickel microwires.

We have found that the diameter of the wire is not uniform and the narrower parts imply that the wires develop by the joining of discrete units. A relatively slow reaction rate is crucial for the formation of the thorn-like particles and their spontaneous aggregation into microwires. High base concentrations or low $\omega$ values lead to a high reaction rate, which means that the nucleus grows so fast into isolated spherical particles that oriented growth and simultaneous assembly essentially do not occur, while low base concentrations or high $\omega$ values allow a relatively slow reaction rate, which provides enough time for the oriented development of the nickel nuclei and their subsequent assembly. Such shape variations of nickel nanostructures with the basicity of the medium or complexant concentrations are the result of kinetic control of the crystal growth pro-

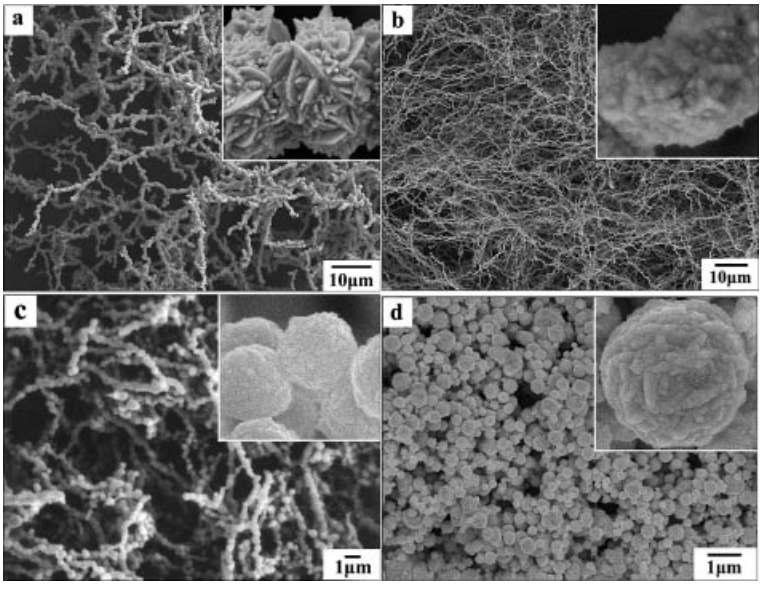


Figure 5. SEM images of the samples prepared at different NaOH concentrations: (a) 0.10 M, (b) 0.15 M, (c) 0.30 M, (d) 0.40 M. The other reagent concentrations were the same, namely $[NiCl_2]$ = 0.025 M, [citrate] = 0.10 M, $[N_2H_4]$ = 0.20 M.

 © 2007 Wiley-VCH Verlag GmbH & Co. KGaA, Weinheim 

cess. The wire formation observed within a specific range of base and complexant concentrations and temperatures therefore corresponds to an optimal combination of the reduction rate and crystal growth rate that allows organization of the building blocks.

In light of the formation mechanism proposed above, we conducted a series of experiments by replacing sodium citrate with other complexants such as sodium tartrate, sodium lactate, ethylenediamine, triethanolamine, and diethanolamine. In all cases we found similar results, namely that the base and complexant concentrations strongly influence the crystal morphology and assembly behavior. Wires with assembled nanostructures could only be reproducibly fabricated in a certain range of reagent concentrations. This result further proves the above aggregation growth mode, which is controlled by the complexant and inherent magnetic interactions. With the other conditions fixed, the base concentrations best suited to the formation of nickel wires in the presence of different complexants are summarized in Table 2 (their typical morphology images are given as Figure S1 in the Supporting Information).

Table 2. NaOH concentrations suitable for the formation of nickel microwires in the systems containing different complexants.[a]

| Complexant | Conc. of complexant | Conc. of NaOH |
|---|---|---|
| Citrate | 0.10 M | 0.03–0.3 M |
| Tartrate | 0.10 M | 0.03–0.4 M |
| Lactate | 0.10 M | 0.06–0.2 M |
| Ethyleneamine | 0.10 M | 0.50–2.0 M |
| Triethanolamine | 0.10 M | 0.40–1.2 M |
| Diethanolamine | 0.10 M | 0.40–1.0 M |

[a] The other reaction conditions were kept the same: $[NiCl_2]$ = 0.025 M, $[N_2H_4]$ = 0.2 M, hydrothermal treatment at 120 °C.

## Magnetic Properties

It is known that the magnetic properties of nanomaterials are strongly dependent on their size, morphology, crystallinity, synthetic methods, etc. Four samples (samples 1, 2, 3, and 5) with different morphologies were selected as the subjects for investigation; their M-H hysteresis loops are presented in Figure 6. These samples show a coercivity (Hc) of 268, 257, 202, and 173 Oe, respectively. The corresponding saturation magnetism (Ms) is about 29.21, 27.36, 22.96, and 15.81 emu $g^{-1}$. All four samples show a much higher coercivity than bulk nickel (Hc = 100 Oe).[18] As ultrafine ferromagnetic particles often exhibit enhanced coercivity relative to the corresponding bulk material, the small size of the samples may be responsible for the increased Hc values.[19] The lower Ms values with respect to that of bulk nickel (55 emu $g^{-1}$) can be ascribed to the surface spin disorder and inevitable slight surface oxidation of the nanoscale subunits, which significantly reduce the total magnetic moments.[20] Moreover, it was found that the Hc and Ms values decrease gradually from sample 1 (S1) to sample 5 (S5) and that the wires with the thorn-like subunits have the highest Hc and Ms values, possibly due to the relatively higher shape anisotropy of their subunits.[21] This demonstrates that the microstructure of the samples greatly influences their magnetic properties, and the building blocks with higher shape anisotropy can effectively improve the magnetic properties of the assembly.

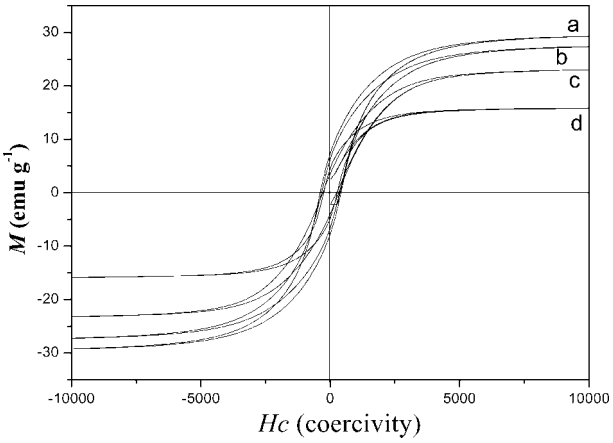


Figure 6. M–H hysteresis loops of four samples with different morphologies: (a) sample 1, (b) sample 2, (c) sample 4, (d) sample 5.

## Catalytic Activity for the Formation of Carbon Nanotubes

Nickel is a commonly used catalyst for the formation of carbon particles.[22] Here, we studied the catalysis of the as-prepared nickel wires for the growth of carbon nanotubes in pyrolyzing acetone. Figure 7 shows the SEM and the corresponding TEM images of the obtained carbon particles catalyzed by S1–S5. In contrast to the product obtained without any metal particles, which appears as aggregated carbon particles without regular shapes (Figure 7, f), the five nickel samples all show catalytic activity for the creation of carbon nanotubes, but with different performances. Samples 1 and 2 both give carbon nanotubes with a yield of above 95% according to SEM observations (Figure 7, a, b). In the product catalyzed by sample 3 (S3), however, the yield of carbon nanotubes is only about 70% and some irregular particles are observed (seen in Figure 7, c). As for the reaction catalyzed by sample 4 (pearl-necklace-like chain), the yield of the tubes decreased to 40% and the length of the nanotubes obviously shortened (Figure 7, d). When it came to the reaction catalyzed by sample 5 (dispersed particles), much more irregular carbon particles were formed and only a few nanotubes (about 10%) could be detected, as seen in Figure 7 (e). These contrasting results clearly demonstrate that the catalytic activity of these nickel samples depends strongly on their microstructure. Since the structure and surface area of the catalyst are important factors affecting their activity, the samples with a relatively high surface area have more surface accessible to the reagents, which is believed contributive to their improved activity for the nucleation of carbon nanotubes,[23] although further research is needed to explore the detailed mechanism.

 © 2007 Wiley-VCH Verlag GmbH & Co. KGaA, Weinheim 

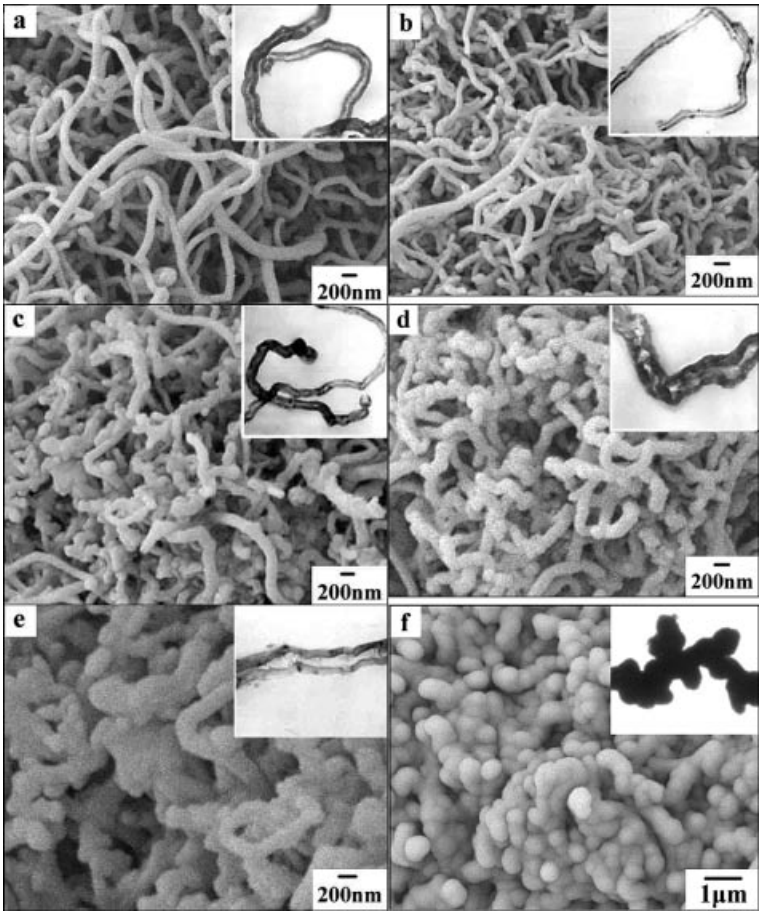


Figure 7. SEM images of the samples obtained in pyrolyzing acetone catalyzed by different nickel samples: (a) sample 1, (b) sample 2, (c) sample 3, (d) sample 4, (e) sample 5, (f) carbon particles fabricated without any nickel. The insets are the corresponding TEM images.

## Conclusion

In summary, we have reported a simple complex-assisted hydrazine reduction method for the synthesis of hierarchical nickel microwires by controlling the reaction rate. The morphological details of the building blocks and their assembly behavior can be tailored by adjusting the reagent concentration. These nickel wires can be reproducibly created with the aid of various complexants, which proves the generality of this approach. The thus-prepared nickel wires show microstructure-dependent magnetic properties and catalytic activity for the growth of carbon nanotubes in pyrolyzing acetone, and they show superior magnetic properties and catalytic performance to the discrete particles. Our synthetic methodology is a facile route for assembling nanosized building blocks into desired structures through kinetic control that avoids the use of any surfactants or an external magnetic field. Such a method is expected to be extendable to the synthesis of other magnetic nanostructures.

## Experimental Section

All chemicals were of analytical grade and were used without purification. A typical experiment for the preparation of nickel wires is as follows: trisodium citrate dihydrate ($Na_3C_6H_5O_7{\cdot}2H_2O$; 1.0 g) was dissolved in 30 mL of an aqueous solution of 0.025 M $NiCl_2$ whilst stirring. Then, 1.0 mL of hydrazine hydrate ($N_2H_4{\cdot}H_2O$ 80%) and a certain amount of dilute NaOH solution were added. The whole mixture was stirred for another 10 min to obtain a homogeneous solution and subsequently transferred into a 40-mL autoclave, which was sealed and maintained at 120 °C for 2–10 h. After the heating treatment was over, the black fluffy particles floating on the solution were collected, rinsed with distilled water and absolute ethanol, and finally dried under vacuum. The samples obtained at NaOH concentrations of 0.05, 0.10, 0.15, 0.30, and 0.40 M are denoted as samples 1 (S1), 2 (S2), 3 (S3), 4 (S4), and 5 (S5), respectively.

For the synthesis of carbon particles, 20 mg of the thus-prepared nickel sample was added to two 20-mL stainless autoclaves containing 12 mL of acetone. The autoclave was then sealed, heated at a rate of 5 °C $min^{-1}$ to 550 °C, and kept at this temperature for 10 h. After the heating treatment was over, the autoclave was cooled naturally to room temperature and the black precipitates were collected and immersed in dilute $HNO_3$ solution whilst stirring for 12 h. The product was then centrifuged, rinsed with distilled water and absolute ethanol, and finally vacuum dried at 50 °C for 2 h.

X-ray diffraction (XRD) patterns of the samples were recorded with a Philips X′pert diffractometer with Cu-$K_\alpha$ radiation ($\lambda$ = 1.5418 Å). The morphology and structure of the sample were studied by field emission scanning electron microscopy (FE-SEM, JEOL JSM-6300F) and transmission electron microscopy (TEM, Hitachi, H-800) with an accelerating voltage of 200 kV. High-reso-

 © 2007 Wiley-VCH Verlag GmbH & Co. KGaA, Weinheim 

lution TEM images were recorded with a JEOL-2010 TEM at an acceleration voltage of 200 kV. Magnetization–hysteresis (M-H) loops were recorded with a BHV-55 vibrating sample magnetometer (VSM) at room temperature.

**Supporting Information** (see also the footnote on the first page of this article): SEM images of the samples prepared with the assistance of different complexing agents (Figure S1).


[1] S. H. Sun, C. B. Murray, D. Weller, L. Folks, A. Moser, *Science* **2000**, *287*, 1989–1992.

[2] a) B. Z. Tang, Y. H. Geng, J. W. Y. Lam, B. S. Li, X. B. Jing, X. H. Wang, F. S. Wang, A. B. Pakhomov, X. X. Zhang, *Chem. Mater.* **1999**, *11*, 1581–1589; b) M. Kryszewski, J. K. Jeszka, *Synth. Met.* **1998**, *94*, 99–104; c) V. F. Puntes, P. Gorostiza, D. M. Aruguete, N. G. Bastus, A. P. Alivisatos, *Nat. Mater.* **2004**, *3*, 263–268; d) M. Bruchez, M. Moronne, P. Gin, S. Weiss, A. P. Alivisatos, *Science* **1998**, *281*, 2013–2016.

[3] a) R. P. Andres, J. D. Bielefeld, J. I. Henderson, D. B. Janes, V. R. Kolagunta, C. P. Kubiak, W. J. Mahoney, R. G. Osifchin, *Science* **1996**, *273*, 1690–1693; b) J. Jin, T. Iyoda, C. Cao, Y. Song, L. Jiang, T. J. Li, D. B. Zhu, *Angew. Chem. Int. Ed.* **2001**, *40*, 2135–2138; c) F. Caruso, R. A. Caruso, H. Mohwald, *Science* **1998**, *282*, 1111–1114; d) C. A. Mirkin, R. L. Letsinger, R. C. Mucic, J. J. Storhoff, *Nature* **1996**, *382*, 607–609.

[4] Y. L. Hou, S. Gao, T. Ohta, H. Kondoh, *Eur. J. Inorg. Chem.* **2004**, 1169–1173.

[5] L. E. Euliss, S. G. Grancharov, S. O'Brien, T. J. Deming, G. D. Stucky, C. B. Murray, G. A. Held, *Nano Lett.* **2003**, *3*, 1489–1493.

[6] S. H. Sun, S. Anders, H. F. Hamann, J. U. Thiele, J. E. E. Baglin, T. Thomson, E. E. Fullerton, C. B. Murray, B. D. Terris, *J. Am. Chem. Soc.* **2002**, *124*, 2284–2285.

[7] N. Cordente, R. M. Espaud, F. Secocq, M. J. Casanove, C. Amies, B. Chaudret, *Nano Lett.* **2001**, *1*, 565–568.

[8] M. Tanase, L. A. Bauer, A. Hultgren, D. M. Silevitch, L. Sun, D. H. Reich, P. C. Searson, G. J. Meyer, *Nano Lett.* **2001**, *1*, 155–158.

[9] E. V. Shevchenko, D. V. Talapin, A. L. Rogach, A. Komowski, M. Haase, H. Weller, *J. Am. Chem. Soc.* **2002**, *124*, 11480–11485.

[10] Y. Sahoo, M. Cheon, S. Wang, H. Luo, E. P. Furlani, P. N. Prasad, *J. Phys. Chem. B* **2004**, *108*, 3380–3383.

[11] S. Singamaneni, V. Bliznyuk, *Appl. Phys. Lett.* **2005**, *87*, 162511.

[12] W. X. Zhang, C. B. Wang, H. L. Lien, *Catal. Today* **1998**, *40*, 387–395.

[13] a) V. F. Puntes, K. M. Krishnan, A. P. Alivisatos, *Science* **2001**, *291*, 2115–2117; b) R. Hernandez, S. Polizu, S. Turenne, L. Yahia, *Bio-Med. Mater. Eng.* **2002**, *12*, 37–45; c) A. Smogunov, A. Dal Corso, E. Tosatti, *Surf. Sci.* **2002**, *507*, 609–614.

[14] a) J. S. Bradley, B. Tesche, W. Buser, M. Maase, M. T. Reetz, *J. Am. Chem. Soc.* **2000**, *122*, 4631–4636; b) J. Bao, C. Tie, Z. Xu, Q. Zhou, D. Shen, Q. Ma, *Adv. Mater.* **2001**, *13*, 1631–1633; c) J. Bao, Y. Liang, Z. Xu, L. Si, *Adv. Mater.* **2003**, *15*, 1832–1835; d) Z. Liu, S. Li, Y. Yang, S. Peng, Z. Hu, Y. Qian, *Adv. Mater.* **2003**, *15*, 1946–1948; e) X. M. Ni, Q. B. Zhao, H. G. Zheng, B. B. Li, J. M. Song, D. E. Zhang, X. J. Zhang, *Eur. J. Inorg. Chem.* **2005**, 4788–4793.

[15] a) H. Niu, Q. Chen, M. Ning, Y. Jia, X. Wang, *J. Phys. Chem. B* **2004**, *108*, 3996–3999; b) C. M. Liu, L. Guo, R. M. Wang, Y. Deng, H. B. Xu, S. H. Yang, *Chem. Commun.* **2004**, 2726–2727.

[16] S. M. Lee, Y. W. Jun, S. N. Cho, J. Cheon, *J. Am. Chem. Soc.* **2002**, *124*, 11244–11245.

[17] A. P. Alivisatos, *Science* **2000**, *289*, 736–737.

[18] L. Guo, C. M. Liu, R. M. Wang, H. B. Xu, Z. Y. Wu, S. H. Yang, *J. Am. Chem. Soc.* **2003**, *126*, 4530–4531.

[19] J. H. Hwang, V. P. Dravid, M. H. Teng, J. J. Host, B. R. Elliott, D. L. Johnson, T. O. Mason, *J. Mater. Res.* **1997**, *12*, 1076–1082.

[20] D. L. L. Pelecky, R. D. Rieke, *Chem. Mater.* **1996**, *8*, 1770–1783.

[21] S. H. Wu, D. H. Chen, *J. Colloid Interface Sci.* **2003**, *259*, 282–286.

[22] a) E. F. Kukovitsky, S. G. L'vov, N. A. Sainov, V. A. Shustov, *Appl. Surf. Sci.* **2003**, *215*, 201–208; b) H. Gao, J. Lin, H. Pan, G. Wu, Y. Feng, *Chem. Phys. Lett.* **2004**, *393*, 511–516; c) M. Han, W. Zhang, C. Gao, Y. Liang, Z. Xu, J. Zhu, J. He, *Carbon* **2006**, *44*, 211–215.

[23] C. Phan-Huu, R. Vieira, B. Louis, A. Carvalho, J. Amadou, T. Dintzer, M. J. Ledoux, *J. Catal.* **2006**, *240*, 194–202.


Received: September 9, 2006
Published Online: November 29, 2006

 © 2007 Wiley-VCH Verlag GmbH & Co. KGaA, Weinheim 

DOI: 10.1002/ejic.200600944

# Syntheses, Characterization and Reactivity of Iron(II), Nickel(II), Copper(II) and Zinc(II) Complexes of the Ligand *N*,*N*,*N*′,*N*′-Tetrakis(2-pyridylmethyl)-benzene-1,3-diamine (1,3-tpbd) and Its Phenol Derivative 2,6-Bis[bis(2-pyridylmethyl)amino]-*p*-cresol (2,6-tpcd)

**Simon Foxon,[a,b] Jing-Yuan Xu,[a,c] Sabrina Turba,[a] Michael Leibold,[d,e] Frank Hampel,[f] Frank W. Heinemann,[g] Olaf Walter,[d] Christian Würtele,[a] Max Holthausen,[h] and Siegfried Schindler*[a]**

**Keywords:** Iron / Copper / Zinc / Ligand effects

*N*,*N*,*N*′,*N*′-Tetrakis(2-pyridylmethyl)benzene-1,3-diamine (1,3-tpbd), a bis(tridentate) ligand, its protonated derivative, [1,3-tpbdH$_2$]$^{2+}$, and a series of new dinuclear complexes [Fe$_2$(1,3-tpbd)(CH$_3$CN)$_6$](ClO$_4$)$_4$·(CH$_3$CN)$_2$·(H$_2$O)$_{0.5}$ (**1**), [Fe$_2$(1,3-tpbd)(DMF)$_6$](ClO$_4$)$_4$ (**2**), [Ni$_2$(1,3-tpbd)(DMF)$_6$](ClO$_4$)$_4$ (**3**), [Zn$_2$(1,3-tpbd)(CH$_3$CN)$_2$(SO$_3$CF$_3$)$_2$(H$_2$O)](SO$_3$CF$_3$)$_2$ (**4**), [Zn$_2$(1,3-tpbd)Cl$_4$]·H$_2$O (**5**), [CuZn(1,3-tpbd)Cl$_4$] (**7**) and the tetranuclear copper(II) complex [Cu$_2$(1,3-tpbd)$_2$(H$_2$O)$_2$](ClO$_4$)$_4$·2H$_2$O (**8**) have been prepared and structurally characterized. Complex **8**, a so called "dimetallocyclophane", interestingly only formed in the presence of zinc ions and not when copper(II) ions were mixed stoichiometrically (1:1 mixtures) under aerobic conditions. Theoretical calculations provide evidence for the formation of a side-on dinuclear peroxido copper complex during the oxidation of the (1,3-tpbd)copper(I) complex. A possible reaction product, the dinuclear copper complex [Cu$_2$(2,6-tpcd)(H$_2$O)(Cl)](ClO$_4$)$_2$·2H$_2$O (**9**) of a phenolate derivative of 1,3-tpbd was synthesized and structurally characterized independently from oxidation reactions from copper(II) perchlorate and the ligand 2,6-bis[bis(2-pyridylmethyl)amino]-*p*-cresol.
(© Wiley-VCH Verlag GmbH & Co. KGaA, 69451 Weinheim, Germany, 2007)

## Introduction

Previously we have demonstrated that the ligand *N*,*N*,*N*′,*N*′-tetrakis(2-pyridylmethyl)benzene-1,3-diamine (1,3-tpbd) shown in Figure 1 can coordinate two copper ions in close proximity.[1–3] In this regard copper complexes of 1,3-tpbd or its phenol derivative 2,6-bis[bis(2-pyridylmethyl)-amino]-*p*-cresol (2,6-tpcd) (Figure 1) represent good structural models of the histidine-rich environments found in many dinuclear copper proteins (such as *hemocyanin and tyrosinase*).[1,4–7]

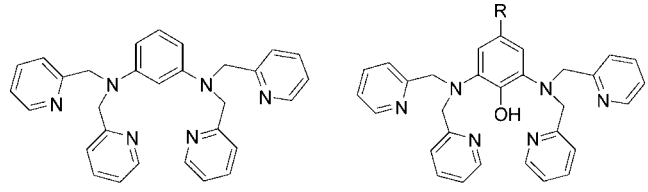


**1,3-tpbd** **2,6-tpcd**

Figure 1. The ligands *N*,*N*,*N*′,*N*′-tetrakis(2-pyridylmethyl)benzene-1,3-diamine (1,3-tpbd) and 2,6-bis[bis(2-pyridylmethyl)amino]-*p*-cresol (2,6-tpcd; R = CH$_3$).

Furthermore, the intramolecular magnetic coupling observed in a series of copper(II) complexes with 1,3-tpbd could be tuned from ferromagnetic to antiferromagnetic.[2,3] Similar ferromagnetic coupling has been observed for copper complexes with a related *m*-phenylenediamine-based ligand system.[8,9] Recently, a 1,3-tpbd platinum complex has been used in mechanistic studies.[10] However to date, only

[a] Institut für Anorganische und Analytische Chemie, Justus-Liebig-Universität Gießen,
Heinrich-Buff-Ring 58, 35392 Gießen, Germany
Fax: +49-641-9934149
E-mail: siegfried.schindler@chemie.uni-giessen.de
[b] Department of Chemistry, University of Sheffield, Sheffield, S3 7HF, United Kingdom
[c] College of Pharmacy, Tianjiin Medical University, 300070 Tianjiin, China
[d] Institut für Technische Chemie – Chemisch-Physikalische Verfahren (ITC-CPV), Forschungszentrum Karlsruhe, Postfach 3640, 76021 Karlsruhe, Germany
[e] Fachbereich Metallorganische Chemie, Universität Kassel, Heinrich-Plett-Strasse 40, 34132 Kassel, Germany
[f] Institut für Organische Chemie, Friedrich-Alexander-Universität Erlangen-Nürnberg, Henkestrasse 42, 91054 Erlangen, Germany
[g] Institut für Anorganische Chemie, Friedrich-Alexander-Universität Erlangen-Nürnberg, Egerlandstrasse 1, 91058 Erlangen, Germany
[h] Institut für Anorganische und Analytische Chemie, Johann-Wolfgang-Goethe-Universität Frankfurt/Main, Max-von-Laue-Strasse 7, 60438 Frankfurt, Germany
Supporting information for this article is available on the WWW under http://www.eurjic.org or from the author.

 © 2007 Wiley-VCH Verlag GmbH & Co. KGaA, Weinheim 

a small number of transition-metal complexes of related derivatives of the 1,3-tpbd ligand system have been investigated.[11–21]

To gain further understanding of the ligating ability of 1,3-tpbd, we herein describe the synthesis and characterization of a series of iron(II), zinc(II) and copper(II) complexes with 1,3-tpbd as well as a copper(II) complex of the phenol analogue of 1,3-tpbd. A similar complex with the phenol derivative ligand shown in Figure 1 (R = *tert*-butyl) and its interesting properties (e.g. interactions with DNA) was recently reported by Karlin and co-workers.[15,16]

## Results and Discussion

***N*,*N*,*N*′,*N*′-Tetrakis(2-pyridylmethyl)benzene-1,3-diamine (1,3-tpbd):** 1,3-tpbd was prepared in modest yields from commercially available *m*-phenylenediamine and picolyl chloride hydrochloride as previously reported.[1] Single crystals of 1,3-tpbd, suitable for structural characterization, were obtained by slow evaporation of a methanol solution of 1,3-tpbd in a glove box. Attempts to recrystallize the ligand outside of the glovebox often caused the formation of nearly colorless crystals in a slightly brown mother liquor. The solution turned to an intense red color during a couple of days affecting the crystals as well (most likely the ligand is partially oxidized) and as a consequence numerous attempts to solve the crystal structure failed due to poor refinement. A summary of crystal structure data and refinement parameters is presented in Table 2, selected bond lengths and angles in Table 1. The molecular structure of 1,3-tpbd is shown in Figure 2. The two pyridyl units bonded at each amine nitrogen atom are separated from each other by a large distance similar to the previously reported molecular structure of 1,4-tpbd.[18] 1,3-tpbd crystallizes with one additional methanol solvent molecule per unit, hydroxyl hydrogen atom of the methanol solvent molecule were located in a difference Fourier map and isotropically refined.

Protonation of 1,3-tpbd or coordination of 1,3-tpbd to metal ions has the consequence that the pyridyl units move much closer together. In Figure 3 the molecular structure of the cation of $[1,3\text{-tpbdH}_2](ClO_4)_2$ is shown (crystal structure data and refinement parameters, bond lengths and angles are presented in Table 2 and Table 1).

$[1,3\text{-tpbdH}_2](ClO_4)_2$ crystallizes with two molecules per crystallographically independent unit of the unit cell together with three molecules of acetonitrile. Two of the $ClO_4^-$ anions are disordered. The H atoms of the protonated N atoms were localized in a difference Fourier map and refined isotropically. The crystal structures of 1,3-tpbd and $[1,3\text{-tpbdH}_2]^{2+}$ display similar metrical parameters. The immediate geometry around the aliphatic amine nitrogen atoms is nearly planar with C1–N1 1.388(2) Å in 1,3-tpbd and C13–N1 1.396(4) Å in $[1,3\text{-tpbdH}_2](ClO_4)_2$ indicating delocalization of the nitrogen lone pair of electrons with the aromatic π systems. All the interbond angles around the aliphatic amine nitrogen atoms are close to 120°. However, as discussed above, the positions of the pyridine rings in 1,3-tpbd and its protonated derivative are quite different. In $[1,3\text{-tpbdH}_2]^{2+}$ adjacent pyridine nitrogen atoms on each ligand "arm" [N2 and N3, N5 and N6] are strongly hydrogen-bonded to one another. The average distance between the hydrogen-bonded pyridine nitrogen atoms is 2.741 Å. Additionally, we obtained the protonated triflate salt of 1,3-tpbd (see Supporting Information; for Supporting Information see also the footnote on the first page of this paper) of which the cation is identical to $[1,3\text{-tpbdH}_2](ClO_4)_2$. However, the two crystal structures differ from each other due to the crystal-packing arrangement of the anions, and furthermore the inclusion of additional solvent molecules. In principle these protonated ligand salts are comparable to the metal complexes (see below) and the protons in $[1,3\text{-tpbdH}_2]^{2+}$ can be regarded as small metal cations. The previously reported crystal structure of $[1,4\text{-tpbdH}_2]^{2+}$ displays similar bond lengths and angles to the $[1,3\text{-tpbdH}_2]^{2+}$ structure described above.[18]

**Iron Complexes:** Ligands capable of coordinating two iron ions in close proximity have been employed as structural models for dinuclear iron metalloproteins (e.g. the oxygen carrier protein hemerythrin).[22–24] Prior to the investigations of the oxygen-sensitive iron(II) model compounds, we tried to synthesize and structurally characterize an iron(III) complex of 1,3-tpbd. However, all our efforts to date in obtaining an 1,3-tpbd iron(III) complex were unsuccessful. Numerous attempts (employing different reaction conditions) to synthesize $[Fe_2(1,3\text{-tpbd})]^{6+}$ derivatives, such as $[Fe_2(1,3\text{-tpbd})(DMF)_6]^{6+}$ or $[Fe_2(1,3\text{-tpbd})(RCOO)_n]^{(6-n)+}$, by the reaction of 1,3-tpbd with $Fe(ClO_4)_3$ in different solvents (coordinating or non-coordinating), with and without addition of anions such as $AsO_4^{3-}$, $C_6H_5COO^-$, $CH_3COO^-$ or $Cl^-$, only afforded the protonated free ligand and unreacted iron salts. Over a period of weeks single crystals, suitable for X-ray structural analysis, of $[1,3\text{-tpbdH}_2](SO_3CF_3)_2$ (see supp. inf. and Experimental Section) and $[1,3\text{-tpbdH}_2](ClO_4)_2$ described above (Figure 3) were obtained. Furthermore, efforts in obtaining an 1,3-tpbd iron(III) complex by oxidizing the corresponding iron(II) precursor complex (described below) failed. These results clearly indicate that the 1,3-tpbd ligand has a low affinity for iron(III). In the presence of water, protonation of the ligand occurs, however in the absence of protons no complexation of the iron(III) ions was observed either. Other pyridyl containing ligands are known to stabilize iron(II) relative to iron(III), however in these cases it was still possible to synthesize, isolate and characterize the according iron(III) complexes.[25]

An iron(II) complex of 1,3-tpbd was prepared and single crystals of $[Fe_2(1,3\text{-tpbd})(CH_3CN)_6](ClO_4)_4{\cdot}2CH_3CN{\cdot}0.5H_2O$ (**1**) were grown. The molecular structure of the cation $[Fe_2(1,3\text{-tpbd})(CH_3CN)_6]^{4+}$ of **1** is shown in Figure 4 (crystal structure data and refinement parameters, bond lengths and angles are presented in Table 2 and Table 1). The unit cell of **1** consists of two sets of crystallographically independent dinuclear cations, $[Fe_2(1,3\text{-tpbd})(CH_3CN)_6]^{4+}$,

 © 2007 Wiley-VCH Verlag GmbH & Co. KGaA, Weinheim 

Table 1. Selected bond lengths [Å] and angles [°] for 1,3-tpbd ligand and compounds **1**–**9**.

| 1,3-tpbd | | | | | |
|---|---|---|---|---|---|
| N(1)–C(1) | 1.411(2) | N(5)–C(24) | 1.326(4) | C(1)–N(1)–C(7) | 120.7(2) |
| N(1)–C(7) | 1.451(2) | N(5)–C(20) | 1.336(2) | C(1)–N(1)–C(13) | 118.5(2) |
| N(1)–C(13) | 1.460(2) | N(6)–C(30) | 1.333(3) | C(7)–N(1)–C(13) | 115.1(2) |
| N(2)–C(8) | 1.345(2) | N(6)–C(26) | 1.339(2) | C(8)–N(2)–C(12) | 117.2(2) |
| N(2)–C(12) | 1.357(3) | C(7)–C(8) | 1.514(3) | C(18)–N(3)–C(14) | 117.2(2) |
| N(3)–C(18) | 1.342(3) | C(8)–C(9) | 1.382(3) | C(3)–N(4)–C(19) | 121.4(2) |
| N(3)–C(14) | 1.348(2) | C(9)–C(10) | 1.381(3) | C(3)–N(4)–C(25) | 120.4(2) |
| N(4)–C(3) | 1.388(2) | C(10)–C(11) | 1.370(3) | C(19)–N(4)–C(25) | 117.9(2) |
| N(4)–C(19) | 1.452(2) | C(11)–C(12) | 1.371(4) | C(24)–N(5)–C(20) | 117.1(2) |
| N(4)–C(25) | 1.454(2) | | | C(30)–N(6)–C(26) | 117.1(2) |
| $[H_2$1,3-tpbd$](ClO_4)_2$ | | | | | |
| N(2)–H(2A) | 0.84(4) | N(3)–C(8) | 1.336(4) | C(13)–N(1)–C(1) | 119.8(2) |
| N(5)–H(5A) | 0.94(4) | N(3)–C(12) | 1.343(4) | C(1)–N(1)–C(7) | 118.6(2) |
| N(1)–C(13) | 1.396(4) | C(7)–C(8) | 1.517(4) | C(13)–N(1)–C(7) | 119.7(2) |
| N(1)–C(1) | 1.449(4) | C(8)–C(9) | 1.386(5) | C(17)–N(4)–C(19) | 121.3(2) |
| N(1)–C(7) | 1.453(4) | C(9)–C(10) | 1.388(6) | C(17)–N(4)–C(25) | 119.6(2) |
| N(2)–C(6) | 1.340(4) | N(4)–C(17) | 1.397(4) | C(19)–N(4)–C(25) | 118.8(2) |
| N(2)–C(2) | 1.348(4) | N(4)–C(19) | 1.447(4) | C(6)–N(2)–H(2A) | 120(3) |
| C(1)–C(2) | 1.514(4) | N(4)–C(25) | 1.451(4) | C(2)–N(2)–H(2A) | 118(3) |
| C(2)–C(3) | 1.378(4) | N(5)–C(20) | 1.334(4) | C(24)–N(5)–H(5A) | 121(2) |
| C(3)–C(4) | 1.388(5) | N(5)–C(24) | 1.341(5) | C(20)–N(5)–H(5A) | 116(2) |
| C(4)–C(5) | 1.372(6) | N(6)–C(26) | 1.337(5) | | |
| C(5)–C(6) | 1.372(5) | N(6)–C(30) | 1.352(5) | | |
| $[Fe_2$(1,3-tpbd)$(CH_3CN)_6](ClO_4)_4 \cdot 2CH_3CN \cdot 0.5H_2O$ (**1**) | | | | | |
| Fe(1)–N(3) | 1.989(3) | N(3)–Fe(1)–N(9) | 171.8(2) | N(11)–Fe(2)–N(6) | 168.6(1) |
| Fe(1)–N(9) | 1.997(3) | N(3)–Fe(1)–N(7) | 95.0(2) | N(10)–Fe(2)–N(4) | 165.6(2) |
| Fe(1)–N(7) | 2.001(3) | N(9)–Fe(1)–N(7) | 90.7(2) | N(5)–Fe(2)–N(4) | 76.8(1) |
| Fe(1)–N(8) | 2.007(3) | N(3)–Fe(1)–N(8) | 84.5(2) | N(12)–Fe(2)–N(4) | 98.0(1) |
| Fe(1)–N(2) | 2.024(3) | N(9)–Fe(1)–N(8) | 89.6(2) | N(11)–Fe(2)–N(4) | 102.2(1) |
| Fe(1)–N(1) | 2.131(2) | N(7)–Fe(1)–N(8) | 90.4(2) | N(6)–Fe(2)–N(4) | 74.7(1) |
| Fe(2)–N(10) | 2.099(3) | N(3)–Fe(1)–N(2) | 94.3(2) | N(19)–Fe(3)–N(20) | 90.5(1) |
| Fe(2)–N(5) | 2.146(3) | N(9)–Fe(1)–N(2) | 91.3(2) | N(19)–Fe(3)–N(21) | 89.5(1) |
| Fe(2)–N(12) | 2.164(3) | N(7)–Fe(1)–N(2) | 92.6(2) | N(20)–Fe(3)–N(21) | 90.7(1) |
| Fe(2)–N(11) | 2.183(3) | N(8)–Fe(1)–N(2) | 176.8(2) | N(19)–Fe(3)–N(15) | 93.5(1) |
| Fe(2)–N(6) | 2.188(3) | N(3)–Fe(1)–N(1) | 83.0(1) | N(20)–Fe(3)–N(15) | 85.7(1) |
| Fe(2)–N(4) | 2.263(3) | N(9)–Fe(1)–N(1) | 92.3(1) | N(21)–Fe(3)–N(15) | 175.4(1) |
| Fe(3)–N(19) | 1.953(3) | N(7)–Fe(1)–N(1) | 171.4(1) | N(19)–Fe(3)–N(14) | 91.6(1) |
| Fe(3)–N(20) | 1.955(3) | N(8)–Fe(1)–N(1) | 97.7(1) | N(20)–Fe(3)–N(14) | 177.7(1) |
| Fe(3)–N(21) | 1.963(3) | N(2)–Fe(1)–N(1) | 79.2(1) | N(15)–Fe(3)–N(14) | 93.3(1) |
| Fe(3)–N(15) | 1.966(3) | N(10)–Fe(2)–N(5) | 95.6(2) | N(19)–Fe(3)–N(13) | 171.7(1) |
| Fe(3)–N(14) | 1.976(2) | N(10)–Fe(2)–N(12) | 90.3(2) | N(22)–Fe(4)–N(24) | 91.9(2) |
| Fe(3)–N(13) | 2.095(2) | N(5)–Fe(2)–N(12) | 173.6(2) | N(22)–Fe(4)–N(18) | 93.0(1) |
| Fe(4)–N(22) | 2.097(3) | N(10)–Fe(2)–N(11) | 90.4(2) | N(24)–Fe(4)–N(18) | 91.5(2) |
| Fe(4)–N(24) | 2.100(3) | N(5)–Fe(2)–N(11) | 93.6(1) | N(24)–Fe(4)–N(17) | 172.4(2) |
| Fe(4)–N(18) | 2.107(3) | N(12)–Fe(2)–N(11) | 83.9(2) | N(18)–Fe(4)–N(17) | 93.5(1) |
| Fe(4)–N(17) | 2.124(3) | N(10)–Fe(2)–N(6) | 94.3(2) | N(18)–Fe(4)–N(23) | 172.6(2) |
| Fe(4)–N(23) | 2.142(3) | N(5)–Fe(2)–N(6) | 96.3(1) | N(17)–Fe(4)–N(23) | 88.9(1) |
| Fe(4)–N(16) | 2.280(3) | N(12)–Fe(2)–N(6) | 85.6(1) | | |
| $[Fe_2$(1,3-tpbd)$(DMF)_6](ClO_4)_4$ (**2**) | | | | | |
| Fe(1)–O(1) | 2.075(2) | O(1)–Fe(1)–O(3) | 89.45(8) | O(1)–Fe(1)–N(3) | 177.19(8) |
| Fe(1)–O(2) | 2.112(2) | O(1)–Fe(1)–O(2) | 90.84(8) | O(3)–Fe(1)–N(3) | 89.44(8) |
| Fe(1)–O(3) | 2.110(2) | O(3)–Fe(1)–O(2) | 97.45(8) | O(2)–Fe(1)–N(3) | 86.74(8) |
| Fe(1)–N(1) | 2.312(2) | O(1)–Fe(1)–N(2) | 90.65(8) | N(2)–Fe(1)–N(3) | 92.03(8) |
| Fe(1)–N(2) | 2.152(2) | O(3)–Fe(1)–N(2) | 95.89(8) | O(1)–Fe(1)–N(1) | 105.90(7) |
| Fe(1)–N(3) | 2.174(2) | O(2)–Fe(1)–N(2) | 166.58(7) | O(3)–Fe(1)–N(1) | 163.39(7) |
| N(3)–Fe(1)–N(1) | 75.51(7) | O(2)–Fe(1)–N(1) | 88.79(7) | N(2)–Fe(1)–N(1) | 77.98(7) |
| $[Zn_2$(1,3-tpbd)$(CH_3CN)_2(SO_3CF_3)_2(H_2O)](SO_3CF_3)_2$ (**4**) | | | | | |
| Zn(1)–N(1) | 2.350(5) | N(1)–Zn(1)–N(2) | 78.3(2) | N(4)–Zn(2)–N(5) | 79.0(2) |
| Zn(1)–N(2) | 2.032(5) | N(1)–Zn(1)–N(3) | 78.9(2) | N(4)–Zn(2)–N(6) | 79.1(2) |
| Zn(1)–N(3) | 2.046(5) | N(2)–Zn(1)–N(3) | 156.1(2) | N(5)–Zn(2)–N(6) | 152.3(2) |
| Zn(1)–N(60) | 2.078(5) | N(1)–Zn(1)–O(12) | 93.1(2) | N(4)–Zn(2)–O(11) | 97.6(2) |
| Zn(1)–O(1) | 2.243(5) | N(2)–Zn(1)–O(12) | 89.0(2) | N(5)–Zn(2)–O(11) | 105.7(2) |
| Zn(1)–O(12) | 2.242(4) | N(3)–Zn(1)–O(12) | 99.4(2) | N(6)–Zn(2)–O(11) | 93.9(2) |

 © 2007 Wiley-VCH Verlag GmbH & Co. KGaA, Weinheim 

Table 1. (*Continued*)

| | | | | | |
|---|---|---|---|---|---|
| Zn(2)–N(4) | 2.346(4) | O(1)–Zn(1)–O(12) | 173.4(2) | O(11)–Zn(2)–O(21) | 167.3(2) |
| Zn(2)–N(5) | 2.024(4) | N(2)–Zn(1)–O(1) | 89.2(2) | N(4)–Zn(2)–O(21) | 88.3(2) |
| Zn(2)–N(6) | 2.021(5) | O(1)–Zn(1)–N(1) | 92.7(2) | N(5)–Zn(2)–O(21) | 86.5(2) |
| Zn(2)–N(70) | 2.104(5) | N(3)–Zn(1)–O(1) | 84.8(2) | N(70)–Zn(2)–O(11) | 90.1(2) |
| Zn(2)–O(11) | 2.122(4) | N(60)–Zn(1)–O(1) | 86.5(2) | N(5)–Zn(2)–N(70) | 100.2(2) |
| Zn(2)–O(21) | 2.578(4) | N(60)–Zn(1)–N(1) | 178.9(2) | N(70)–Zn(2)–O(21) | 84.0(2) |
| | | N(2)–Zn(1)–N(60) | 100.9(2) | N(6)–Zn(2)–O(21) | 76.1(2) |
| | | N(3)–Zn(1)–N(60) | 101.7(2) | N(70)–Zn(2)–N(4) | 172.3(2) |
| | | N(60)–Zn(1)–O(12) | 87.7(2) | N(6)–Zn(2)–N(70) | 99.3(2) |
| $[Zn_2(1,3\text{-tpbd})Cl_4]$ (**5**) | | | | | |
| Zn(1)–N(11) | 2.046(6) | N(11)–Zn(1)–N(21) | 120.1(3) | N(41)–Zn(2)–N(31) | 124.6(3) |
| Zn(1)–N(21) | 2.055(6) | N(11)–Zn(1)–Cl(1) | 116.6(2) | N(41)–Zn(2)–Cl(3) | 105.6(2) |
| Zn(1)–Cl(1) | 2.248(2) | N(21)–Zn(1)–Cl(1) | 113.0(2) | N(31)–Zn(2)–Cl(3) | 120.9(2) |
| Zn(1)–Cl(2) | 2.305(2) | N(11)–Zn(1)–Cl(2) | 98.3(2) | N(41)–Zn(2)–Cl(4) | 99.1(2) |
| Zn(1)–N(1) | 2.646(2) | N(1)–Zn(1)–N(11) | 71.7(2) | N(2)–Zn(2)–N(31) | 72.9(2) |
| Zn(2)–N(31) | 2.066(7) | N(21)–Zn(1)–Cl(2) | 100.8(2) | N(31)–Zn(2)–Cl(4) | 98.6(2) |
| Zn(2)–N(41) | 2.042(7) | Cl(1)–Zn(1)–Cl(2) | 103.5(1) | Cl(3)–Zn(2)–Cl(4) | 102.4(1) |
| Zn(2)–Cl(4) | 2.314(3) | Zn(1)–Cl(1)–O(1) | 89.9(2) | Zn(2)–Cl(3)–O(1) | 110.2(2) |
| Zn(2)–Cl(3) | 2.259(3) | C(16)–N(11)–Zn(1) | 122.0(6) | C(32)–N(31)–Zn(2) | 117.6(6) |
| Zn(2)–N(2) | 2.594(3) | N(1)–Zn(1)–Cl(1) | 94.8(2) | N(2)–Zn(2)–Cl(3) | 97.4(2) |
| $[CuZn(1,3\text{-tpbd})Cl_4]$ (**7**) | | | | | |
| Zn(1)–N(11) | 2.03(2) | N(11)–Zn(1)–N(21) | 145.4(4) | N(41)–Cu(1)–N(51) | 143.4(4) |
| Zn(1)–N(21) | 2.04(2) | N(11)–Zn(1)–Cl(2) | 95.1(3) | N(41)–Cu(1)–Cl(3) | 102.2(3) |
| Zn(1)–Cl(2) | 2.307(4) | N(21)–Zn(1)–Cl(2) | 96.4(3) | N(51)–Cu(1)–Cl(3) | 104.0(3) |
| Zn(1)–Cl(1) | 2.333(3) | N(11)–Zn(1)–Cl(1) | 99.2(3) | N(41)–Cu(1)–Cl(4) | 96.7(3) |
| Zn(1)–N(1) | 2.37(2) | N(21)–Zn(1)–Cl(1) | 109.6(3) | N(51)–Cu(1)–Cl(4) | 97.9(3) |
| Cu(1)–N(41) | 2.04(2) | Cl(2)–Zn(1)–Cl(1) | 103.3(2) | Cl(3)–Cu(1)–Cl(4) | 110.0(2) |
| Cu(1)–N(51) | 2.06(2) | N(11)–Zn(1)–N(1) | 76.9(4) | N(41)–Cu(1)–N(2) | 74.6(3) |
| Cu(1)–Cl(3) | 2.279(3) | N(21)–Zn(1)–N(1) | 77.2(4) | N(51)–Cu(1)–N(2) | 74.1(3) |
| Cu(1)–Cl(4) | 2.284(3) | Cl(2)–Zn(1)–N(1) | 150.8(3) | Cl(3)–Cu(1)–N(2) | 105.2(3) |
| Cu(1)–N(2) | 2.499(2) | Cl(1)–Zn(1)–N(1) | 105.6(3) | Cl(4)–Cu(1)–N(2) | 144.8(3) |
| $[Cu_2(1,3\text{-tpbd})_2(H_2O)_2](ClO_4)_4$ (**8**) | | | | | |
| Cu(1)–N(1) | 2.074(3) | N(3)–Cu(1)–N(2) | 164.8(2) | N(2)–Cu(1)–N(1) | 82.4(2) |
| Cu(1)–N(2) | 1.986(3) | N(3)–Cu(1)–N(5)[a] | 98.4(2) | N(3)–Cu(1)–O(1) | 89.4(2) |
| Cu(1)–N(3) | 1.976(3) | N(2)–Cu(1)–N(5)[a] | 96.8(2) | N(3)–Cu(1)–N(1) | 83.5(2) |
| Cu(1)–N(5) | 2.000(3) | N(5)[a]–Cu(1)–N(1) | 157.4(2) | N(2)–Cu(1)–O(1) | 87.0(2) |
| Cu(1)–O(1) | 2.286(3) | N(5)[a]–Cu(1)–O(1) | 104.1(2) | N(1)–Cu(1)–O(1) | 98.5(1) |
| $[Cu_2(2,6\text{-tpcd})(H_2O)(Cl)](ClO_4)_2\cdot 2H_2O$ (**9**) | | | | | |
| Cu(1)–O(2) | 1.993(2) | O(2)–Cu(1)–N(5) | 94.3(1) | N(3)–Cu(2)–N(2) | 159.1(1) |
| Cu(1)–N(5) | 2.003(2) | O(2)–Cu(1)–N(6) | 99.3(1) | N(3)–Cu(2)–N(1) | 82.9(1) |
| Cu(1)–N(6) | 2.013(2) | N(5)–Cu(1)–N(6) | 163.8(1) | N(2)–Cu(2)–N(1) | 81.9(1) |
| Cu(1)–N(4) | 2.064(2) | O(2)–Cu(1)–N(4) | 176.8(1) | N(3)–Cu(2)–O(1) | 96.0(1) |
| Cu(1)–O(1) | 2.153(2) | N(5)–Cu(1)–N(4) | 82.9(1) | N(2)–Cu(2)–O(1) | 96.5(1) |
| Cu(2)–N(3) | 1.996(2) | N(6)–Cu(1)–N(4) | 83.6(1) | N(1)–Cu(2)–O(1) | 84.0(1) |
| Cu(2)–N(2) | 2.007(2) | O(2)–Cu(1)–O(1) | 94.9(1) | N(3)–Cu(2)–Cl(1) | 97.8(1) |
| Cu(2)–N(1) | 2.076(2) | N(5)–Cu(1)–O(1) | 94.9(1) | N(2)–Cu(2)–Cl(1) | 96.6(1) |
| Cu(2)–O(1) | 2.106(2) | N(6)–Cu(1)–O(1) | 92.6(1) | N(1)–Cu(2)–Cl(1) | 176.7(1) |
| Cu(2)–Cl(1) | 2.280(1) | N(4)–Cu(1)–O(1) | 83.7(1) | O(1)–Cu(2)–Cl(1) | 99.1(1) |

[a] $-x+1$, $-y+1$, $-z+1$.

and uncoordinated perchlorate anions, four acetonitrile solvent molecules and one water molecule. There are only minor structural differences between the two dinuclear cations. In each cation, the intramolecular Fe···Fe separation is 7.488(1) and 7.697(2) Å, respectively. The 1,3-tpbd ligand coordinates each iron(II) center through two pyridine nitrogen atoms and one aliphatic amine nitrogen atom, displaying $N_{amine}$–Fe–$N_{pyridine}$ angles averaging ca. 81° to accommodate the five-membered chelate rings.

As has been observed previously for $Fe^{II}$TPA complexes, the Fe–$N_{amine}$ distances ranging from 2.095(2) to 2.280(3) Å are characteristically longer than the Fe–$N_{pyridine}$ bond lengths of 1.966(3) to 2.188(3) Å.[26–28] Three *fac*-coordinated acetonitrile molecules occupy the remaining coordination sites to complete the slightly distorted octahedral coordination geometry around each iron(II) center, with Fe–N–C angles ranging from 166.7(3) to 177.1(3)° and the Fe–N distances ranging from 1.953(3) to 2.183(3) Å. These

 © 2007 Wiley-VCH Verlag GmbH & Co. KGaA, Weinheim 

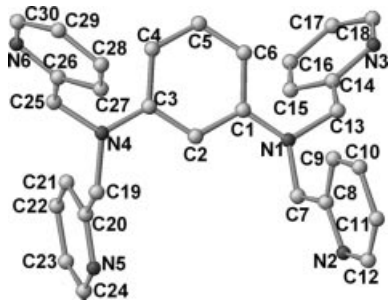


Figure 2. Molecular structure of 1,3-tpbd; hydrogen atoms are omitted for clarity.

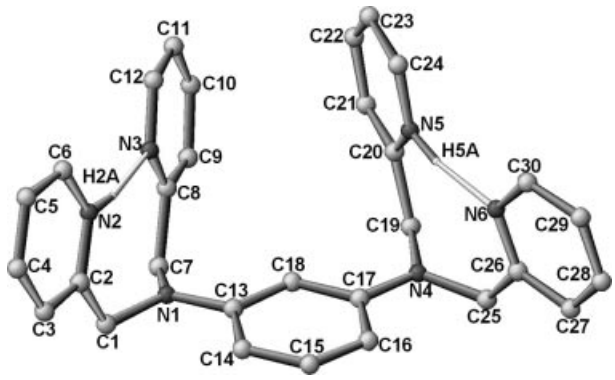


Figure 3. Molecular structure of the cation of $[1,3\text{-tpbdH}_2](ClO_4)_2$; only hydrogen atoms involved in hydrogen bonding are shown.

shorter Fe–N distances indicate that the nitrile groups of the acetonitrile solvent molecules are strongly coordinated to the iron(II) center. Intermolecular π···π interactions (ca. 3.675 Å) exist between C26–C27–C28–C29–C30–N6 and C56–C57–C58–C59–C60–N15 of adjacent pyridine rings from two independent dinuclear cations.

Furthermore, a second iron(II) complex, $[Fe_2(1,3\text{-tpbd})(DMF)_6](ClO_4)_4$ (**2**), was prepared. The molecular structure of the cation of complex **2** is shown in Figure 5 (crystal structure data and refinement parameters, bond lengths and angles are presented in Table 2 and Table 1). Compound **2** crystallizes with half a molecule per crystallographic independent unit of the unit cell, the other half is generated by the crystallographic twofold axis of the space group. Each iron(II) center lies in a distorted $N_3O_3$ octahedral coordination environment. The equatorial plane around Fe(1) comprises two pyridyl nitrogen atoms [N(2) and N(3)] from the *fac*-coordinated 1,3-tpbd ligand and two oxygen atoms [O(1) and O(2)] from coordinated DMF solvent molecules. Apical positions are occupied by the tertiary amine nitrogen N(1) of 1,3-tpbd and oxygen atom O(3) from a third DMF solvent molecule. The $Fe–N_{pyridine}$ bond lengths [2.152(2)–2.174(2) Å] are characteristically shorter than those of $Fe–N_{amine}$ [2.312(2) Å] and the *cis* $N_{pyridine}–Fe–N_{pyridine}$ angles [92.03°] are entirely consistent with

Table 2. Crystallographic data for 1,3-tpbd ligand and compounds **1**, **2** and **4**.

| Compound | 1,3-tpbd | $[1,3\text{-tpbdH}_2](ClO_4)_2$ | **1** | **2** | **4** |
|---|---|---|---|---|---|
| Empirical formula | $C_{31}H_{32}N_6O$ | $C_{66}H_{69}Cl_4N_{15}O_{16}$ | $C_{46}H_{53}Cl_4Fe_2N_{14}O_{16.5}$ | $C_{24}H_{35}Cl_2FeN_6O_{11}$ | $C_{40}H_{39}F_{12}N_9O_{13}S_4Zn_2$ |
| $M_r$ | 504.63 | 1470.16 | 1319.52 | 710.33 | 1340.78 |
| Temperature [K] | 193(2) | 200(2) | 100(2) | 200(2) | 293(2) |
| Radiation ($\lambda$ [Å]) | 0.71073 | 0.71073 | 0.71073 | 0.71073 | 0.71073 |
| Crystal size [mm] | $0.48\times0.32\times1.48$ | $0.8\times0.6\times0.6$ | $0.25\times0.21\times0.07$ | $0.8\times0.8\times0.4$ | $0.62\times0.50\times0.42$ |
| Crystal system | triclinic | monoclinic | monoclinic | monoclinic | orthorhombic |
| Space group | $P\bar{1}$ (no. 2) | $P2_1/c$ (no. 14) | $P2_1$ (no. 4) | $C2/c$ (no. 15) | $Pna2_1$ (no. 33) |
| $a$ [Å] | 8.0703(10) | 21.818(2) | 14.532(2) | 34.813(4) | 25.712(2) |
| $b$ [Å] | 13.2071(17) | 19.862(2) | 23.015(2) | 11.056(2) | 9.569(1) |
| $c$ [Å] | 14.379(2) | 16.294(2) | 17.284(2) | 19.807(2) | 21.901(2) |
| $\alpha$ [°] | 64.833(15) | 90 | 90 | 90 | 90 |
| $\beta$ [°] | 81.997(16) | 102.656(2) | 93.12(1) | 121.515(2) | 90 |
| $\gamma$ [°] | 88.423(15) | 90 | 90 | 90 | 90 |
| $V$ [Å$^3$] | 1372.7(3) | 6889.1(8) | 5772(1) | 6499(2) | 5388.5(9) |
| $Z$ | 2 | 4 | 4 | 8 | 4 |
| $\rho_{calcd.}$ [g cm$^{-3}$] | 1.221 | 1.417 | 1.518 | 1.452 | 1.653 |
| $\mu$ [mm$^{-1}$] | 0.077 | 0.251 | 0.767 | 0.692 | 1.154 |
| $F$(000) | 536 | 3064 | 2716 | 2952 | 2712 |
| Scan range $\theta$ [°] | 2.78 to 28.05 | 1.64 to 28.30 | 3.32 to 27.10 | 1.97 to 28.31 | 2.27 to 27.00 |
| Index ranges | $-9\le h\le9$ | $-29\le h\le28$ | $-18\le h\le18$ | $-46\le h\le46$ | $-32\le h\le32$ |
| | $-17\le k\le16$ | $-26\le k\le26$ | $-29\le k\le29$ | $-14\le k\le14$ | $-12\le k\le12$ |
| | $-18\le l\le18$ | $-21\le l\le21$ | $-22\le l\le22$ | $-26\le l\le26$ | $-27\le l\le27$ |
| Reflections collected | 12413 | 81510 | 140656 | 37816 | 12077 |
| Unique reflections | 6069 | 16875 | 25407 | 7966 | 11763 |
| $R_{int}$ | 0.0469 | 0.0513 | 0.0542 | 0.0431 | 0.0342 |
| Data/restraints/parameters | 6069/0/356 | 16875/42/933 | 25407/41/1536 | 7966/45/433 | 11763/3/730 |
| Goodness-of-fit on $F^2$ | 1.042 | 1.032 | 1.026 | 1.056 | 0.990 |
| $R_1$, $wR_2$ [$I>4\sigma(I)$] | 0.0511, 0.1290 | 0.0707, 0.1843 | 0.0412, 0.0818 | 0.0460, 0.1192 | 0.0577, 0.0944 |
| $R_1$, $wR_2$ (all data) | 0.0847, 0.1464 | 0.1153, 0.2218 | 0.0617, 0.0883 | 0.0709, 0.1308 | 0.1128, 0.1130 |
| Flack parameter[60] | – | – | 0.009(8) | – | –0.02(2) |
| Largest diff. peak/hole [e·Å$^{-3}$] | 0.262, –0.205 | 1.107, –0.771 | 0.689, –0.707 | 0.688, –0.846 | 0.373, –0.375 |

 © 2007 Wiley-VCH Verlag GmbH & Co. KGaA, Weinheim 

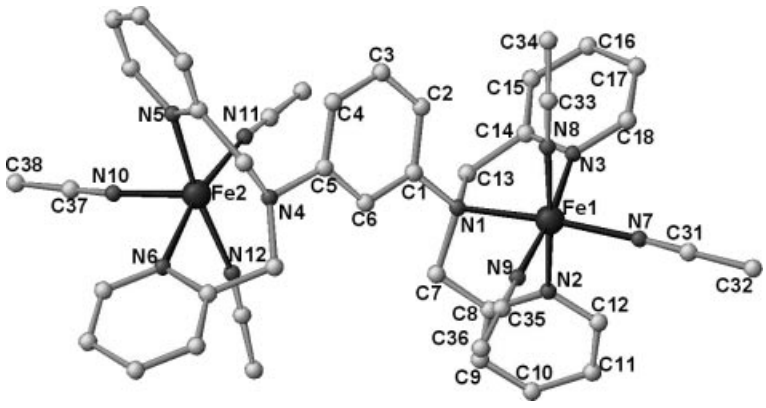


Figure 4. Molecular structure of the cation of $[Fe_2(1,3\text{-tpbd})(CH_3CN)_6](ClO_4)_4 \cdot 2CH_3CN \cdot 0.5H_2O$ (**1**); hydrogen atoms and solvent molecules are omitted for clarity.

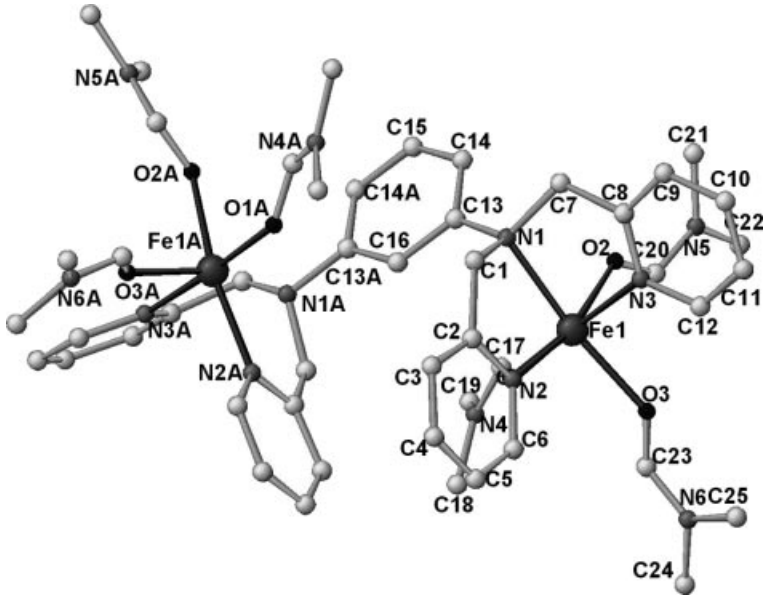


Figure 5. Molecular structure of the cation of $[Fe_2(1,3\text{-tpbd})(DMF)_6](ClO_4)_4$ (**2**); hydrogen atoms are omitted for clarity.

those found in **1**. The Fe–$O_{DMF}$ distances [2.075(2) to 2.112(2) Å] and the average *cis*-coordinated angles [O–Fe–O 92.58°] indicate that the DMF molecules are strongly coordinated to the iron(II) center. The Fe···Fe separation of 6.962 Å is shorter than in **1**, probably a consequence of the stronger π···π interaction (ca. 3.596 Å) between the two pyridine rings (C2–C3–C4–C5–C6–N2 and C2A–C3A–C4A–C5A–C6A–N2A) each from a different tridentate end of the 1,3-tpbd molecule.

Both iron(II) complexes were found to only react slowly with dioxygen, however much faster with hydrogen peroxide. Preliminary kinetic studies of both oxidation reactions indicated complex reaction mechanisms that could not be elucidated. Most likely this is a consequence that 1,3-tpbd is not an innocent ligand and is also involved in the oxidation reactions (see below). Furthermore, efforts to isolate reaction products from these oxidations, such as the according iron(III) complexes described above, were unsuccessful. In contrast with 1,4-tpbd as a ligand only polymeric iron(II) complexes were obtained.[19] With *N*,*N*-bis(2-pyridylmethyl)-aniline (phdpa), the half ligand system of 1,3-tpbd, a 2:1 ligand/metal ion ratio was observed, however, no crystal structures were reported.[20]

**Nickel Complexes:** Reacting $[Ni(DMF)_6](ClO_4)_2$ with 1,3-tpbd under anaerobic conditions in a glove box led to the nickel(II) analogue of **2**, $[Ni_2(1,3\text{-tpbd})(DMF)_6](ClO_4)_4$ (**3**). Crystals suitable for X-ray crystallography were grown and isolated. Compound **3** crystallizes with nearly identical cell parameters as **2** (Table 2), but the structure of **3** is much better described in the monoclinic space group *C*2 (**3**) than *C*2/*c* (**2**). Accordingly, the systematic absences for the glide plane in *C*2/*c* for **3** are not observed, whereas for **2** these systematic absence conditions are fulfilled absolutely so that the structure of **2** is described correctly in *C*2/*c*. However, a description of the structure of **3** in *C*2/*c* is possible but leads to a significant increase of the $R_1$ value from 10 to 16%. Therefore; even if it can be assumed from the cell parameters that **2** and **3** are isostructural, the crystal structure of **3** here is presented in the lower symmetric space group *C*2. A Figure of the molecular structure of the cation of **3** as

 © 2007 Wiley-VCH Verlag GmbH & Co. KGaA, Weinheim 

well as crystal structure data and refinement parameters, bond lengths and angles are presented in the Supporting Information.

The asymmetric unit of complex **3** comprises two crystallographically independent "half" cation units and four $ClO_4^-$ anions, of which three are disordered. The full contents of the unit cell is generated by applying symmetry operations to the asymmetric unit cell. As the structure of **3** is very similar to that of **2** and the calculations might be performed as well in the centrosymmetric space group *C*2/*c* the final absolute structure parameter is relatively high. The two crystallographically independent $[Ni_2(1,3\text{-tpbd})(DMF)_6]^{2+}$ cations of **3** differ only marginally with regard to their bond lengths and angles.

**Zinc Complexes:** In investigating redox-active metal complexes of iron and copper it is useful to study in comparison complexes with nonredox active centers such as zinc. Copper(II) ions can be substituted by zinc(II) ions and additionally show quite similar coordination behavior. Such zinc(II) complexes themselves can show interesting reaction properties, for example they can be used to hydrolyze diribonucleoside monophosphate diesters.[29] However, in contrast to our expectations the synthesis of a zinc(II) complex of 1,3-tpbd turned out to be more difficult than the synthesis of the according copper(II) complexes. Mixing zinc(II) perchlorate and 1,3-tpbd in alcoholic solution, immediately led to white gelatinous-like precipitates that could not be (re)crystallized. Only after a large number of experiments (applying different conditions), we obtained crystals of the zinc(II) complex $[Zn_2(1,3\text{-tpbd})(CH_3CN)_2(SO_3CF_3)_2(H_2O)](SO_3CF_3)_2$ (**4**) with triflate as a counter anion. The molecular structure of the cation of **4** in Figure 6 shows an unsymmetric di-zinc unit, both ions linked by the *m*-phenylenediamine group and a triflate ion giving an intramolecular Zn···Zn distance of 6.007(1) Å, which is much shorter than in those complexes that are only bridged by 1,3-tpbd. However, it is close to the Cu···Cu distance [5.873(1) Å] in the analogous complex $[Cu_2(1,3\text{-tpbd})(H_2O)_2(ClO_4)_3](ClO_4)$ with an additional perchlorate- in-

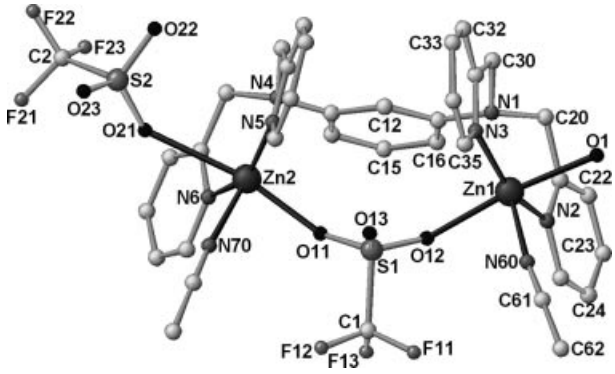


Figure 6. Molecular structure of the cation of $[Zn_2(1,3\text{-tpbd})(CH_3CN)_2(SO_3CF_3)_2(H_2O)](SO_3CF_3)_2$ (**4**). Hydrogen atoms are omitted for clarity.

Table 3. Crystallographic data for compounds **5**–**9**.

| Compound | **5** | **7** | **8** | **9** |
|---|---|---|---|---|
| Empirical formula | $C_{30}H_{30}Cl_4N_6OZn_2$ | $C_{30}H_{28}Cl_4CuN_6Zn$ | $C_{60}H_{64}Cl_4Cu_2N_{12}O_{20}$ | $C_{31}H_{35}Cl_3Cu_2N_6O_{12}$ |
| $M_r$ | 763.14 | 743.29 | 1542.11 | 917.08 |
| Temperature [K] | 173(2) | 173(2) | 293(2) | 200(2) |
| Radiation ($\lambda$ [Å]) | 0.71073 | 0.71073 | 0.71073 | 0.71073 |
| Crystal size [mm] | 0.20 × 0.10 × 0.10 | 0.30 × 0.20 × 0.20 | 0.65 × 0.50 × 0.32 | 0.25 × 0.35 × 0.2 |
| Crystal system | monoclinic | monoclinic | monoclinic | triclinic |
| Space group | $P2_1/n$ (no. 14) | $P2_1$ (no. 4) | $P2_1/n$ (no. 14) | $P\bar{1}$ (no. 2) |
| $a$ [Å] | 9.177(2) | 8.600(2) | 10.859(1) | 10.495(1) |
| $b$ [Å] | 27.304(6) | 13.002(3) | 22.660(2) | 12.184(2) |
| $c$ [Å] | 12.287(3) | 13.690(3) | 13.072(1) | 14.442(2) |
| $\alpha$ [°] | 90 | 90 | 90 | 93.880(1) |
| $\beta$ [°] | 91.79(2) | 103.24(3) | 94.54(1) | 95.284(1) |
| $\gamma$ [°] | 90 | 90 | 90 | 94.411(1) |
| $V$ [Å$^3$] | 3077.1(2) | 1490.1(5) | 3206.5(5) | 1828.3(3) |
| $Z$ | 4 | 2 | 2 | 2 |
| $\rho_{calcd.}$ [g cm$^{-3}$] | 1.647 | 1.657 | 1.597 | 1.666 |
| $\mu$ [mm$^{-1}$] | 1.943 | 1.910 | 0.916 | 1.453 |
| $F$(000) | 1552 | 754 | 1588 | 936 |
| Scan range $\theta$ [°] | 2.68 to 26.33 | 2.56 to 33.67 | 2.08 to 27.00 | 1.68 to 28.31 |
| Index ranges | $-11 \le h \le 11$ | $-10 \le h \le 0$ | $-1 \le h \le 13$ | $-13 \le h \le 13$ |
| | $-34 \le k \le 0$ | $-4 \le k \le 16$ | $-28 \le k \le 1$ | $-15 \le k \le 16$ |
| | $0 \le l \le 15$ | $-17 \le l \le 16$ | $-16 \le l \le 16$ | $-18 \le l \le 19$ |
| Reflections collected | 6543 | 3407 | 8527 | 16512 |
| Unique reflections | 6256 | 3196 | 7002 | 8570 |
| $R_{int}$ | 0.1193 | 0.0611 | 0.0214 | 0.0363 |
| Data/restraints/parameters | 6256/0/388 | 3196/1/379 | 7002/5/507 | 8570/0/518 |
| Goodness-of-fit on $F^2$ | 1.014 | 1.757 | 1.016 | 0.892 |
| $R_1$, $wR_2$ [$I > 4\sigma(I)$] | 0.0610, 0.1181 | 0.0569, 0.2133 | 0.0500, 0.0993 | 0.0388, 0.0848 |
| $R_1$, $wR_2$ (all data) | 0.1834, 0.1670 | 0.0704, 0.2198 | 0.0932, 0.1155 | 0.0693, 0.0923 |
| Flack parameter[60] | – | – | – | – |
| Largest diff. peak/hole [e Å$^{-3}$] | 0.829, –0.790 | 1.361, –1.294 | 0.459, –0.450 | 0.720, –0.651 |

 © 2007 Wiley-VCH Verlag GmbH & Co. KGaA, Weinheim 

stead of the triflate-bridge (crystal structure data and refinement parameters, selected bond lengths and angles are presented in Table 3 and Table 1).[1]

The coordination geometry around Zn1 is best described as distorted octahedral. The equatorial plane around the zinc(II) center is occupied by three N-donor atoms of the meridional capping ligand 1,3-tpbd (N1, N2 and N3). Apical positions are occupied by O12 of the bridging triflate anion and O1 of a water molecule. The nature of the ligands around Zn2 differs from Zn1 in that a terminal triflate, instead of a water molecule, occupies one of the apical coordination sites. The $N_{pyridine}$–Zn–$N_{pyridine}$ bond angles of 156.1(2)° and 152.3(2)° in **4** are smaller than $N_{pyridine}$–Cu–$N_{pyridine}$ in $[Cu_2(1,3\text{-tpbd})(H_2O)_2](ClO_4)_4\cdot 4H_2O$ [164.5(2)°] apparently owing to the bigger steric hindrance of the triflate ion. Accordingly, both distances of Zn–$N_{pyridine}$ in the range of 2.021(5)–2.046(5) Å and Zn–$N_{amine}$ at 2.350(5) and 2.346(4) Å are longer than those in $[Cu_2(1,3\text{-tpbd})(H_2O)_2](ClO_4)_4\cdot 4H_2O$ [av. Cu–$N_{pyridine}$ 1.969(5) Å; Cu–$N_{amine}$ 2.089(5) Å]. This also applies for the distance of the acetonitrile substituent [Zn–$N_{C\equiv N}$ av. 2.091(5) Å] instead of water [Cu–$O_w$ 1.985(5) Å] at the fourth equatorial site. A triflate anion bridges the two zinc(II) centers via O11 and O12 [Zn1–O12 2.242(4) Å and Zn2–O11 2.122(4) Å]. The structure is "capped" at the apical positions by a water molecule [Zn1–O1 2.243(5) Å] for Zn1 and by a terminal triflate anion [Zn2–O21 2.578(4) Å]. To the best of our knowledge there is only one further example of a crystal structure containing a bridging triflate anion linking two zinc(II) ions found in the Cambridge Crystallographic Database.[30] Efforts to obtain crystals of the (1,3-tpbd)copper(II) triflate analogue failed so far. Furthermore, using 1,4-tpbd as a ligand only a mononuclear zinc complex, $[ZnCl_2(1,4\text{-tpbd})]$, was obtained and its crystal structure has been reported.[19]

In contrast to the according copper(II) complexes, complex **4** is diamagnetic and can be studied in solution by $^1H$ NMR spectroscopy. Four types of pyridine proton resonances are found in the range 7.4–8.6 ppm (see Exp. Sect.). These four proton resonances represent four symmetry equivalent sets of the pyridine protons found in the complex. Two triplets and two doublets are formed by the splitting of each pyridine proton by its adjacent proton(s). The splitting scheme is depicted in Figure 7. $H_a$ is split into a doublet by $H_b$ ($J$ = 5 Hz), and $H_d$ is split into a doublet by $H_c$ ($J$ = 8 Hz). Proton $H_a$ is assigned to the downfield doublet, and $H_d$ as the upfield doublet. $H_b$ is split by both $H_a$ ($J$ = 6 Hz) and $H_c$ ($J$ = 7 Hz) to form a triplet, and $H_c$ is split by both $H_b$ ($J$ = 7 Hz) and $H_d$ ($J$ = 8 Hz) to form a triplet. $H_c$ is assigned to the downfield triplet, and $H_b$ is assigned to the upfield triplet. The assignments of $H_c$ and $H_b$ are based on greater stabilisation of electron withdrawal in the *para* position, compared to the *meta* position, and previous assignments of pyridine protons in related compounds.[31]

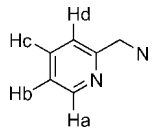


Figure 7. NMR assignment in complex **1**, **2** and **4**.

**Heterodinuclear Zinc(II) and Copper(II) Complexes:** After achieving the synthesis of a zinc(II) complex as well as the previously reported copper(I) and copper(II) complexes with the ligand 1,3-tpbd, it was obvious that we should try to prepare a heterodinuclear zinc(II) copper(II) complex as a model complex for the enzyme superoxide dismutase (CuZnSOD).[32–38] However, mixing stoichiometric amounts of 1,3-tpbd together with zinc(II) and copper(II) chloride did not lead to the isolation of pure $[CuZn(1,3\text{-tpbd})Cl_4]$, but instead to a mixture of the three dinuclear complexes: $[Zn_2(1,3\text{-tpbd})Cl_4]$ (**5**), $[Cu_2(1,3\text{-tpbd})Cl_4]$ (**6**) and $[CuZn(1,3\text{-tpbd})Cl_4]$ (**7**). Structural characterization of all three complexes was achieved by picking individual crystals (that were different in color) from the reaction mixture. The molecular structure of **5** is shown in Figure 8 and that of **7** in Figure 9 (crystal structure data and refinement parameters, bond lengths and angles are presented in Table 3 and Table 1).

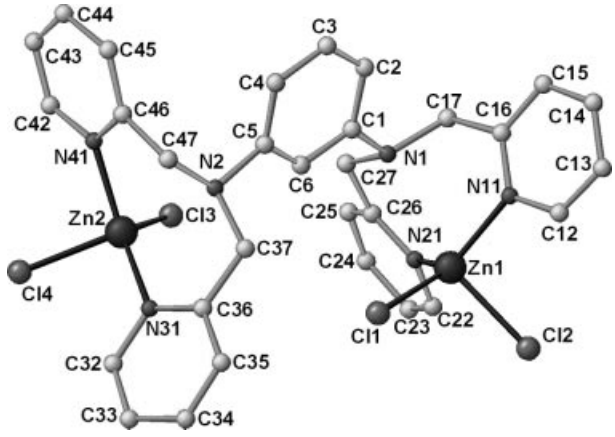


Figure 8. Molecular structure of $[Zn_2(1,3\text{-tpbd})Cl_4]$ (**5**); hydrogen atoms are omitted for clarity.

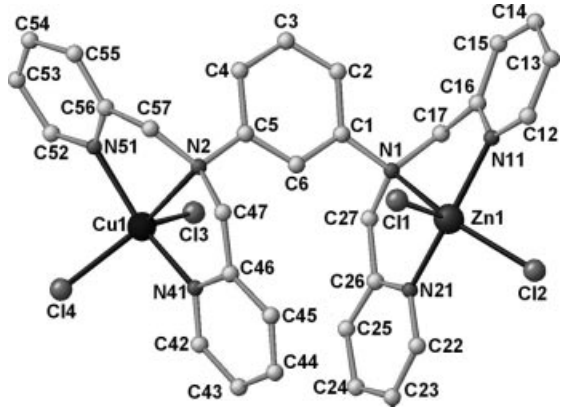


Figure 9. Molecular Structure of $[CuZn(1,3\text{-tpbd})Cl_4]$ (**7**); hydrogen atoms are omitted for clarity.

 © 2007 Wiley-VCH Verlag GmbH & Co. KGaA, Weinheim 

The crystal structure of $[Cu_2(1,3\text{-tpbd})Cl_4]$ (**6**) has been obtained previously in a different study and crystallographic details will be published elsewhere.[13] Due to the fact that here X-ray crystallography measurements do not allow the differentiation between zinc and copper ions, the presence of the different metal ions was further confirmed by photon-induced X-ray emission spectroscopy of the crystals of **5**, **6** and **7**.

The metal ions are linked through the 1,3-phenylenediamine group leading to an intramolecular Zn···Zn distance of 6.925 Å for **5** and Cu···Zn separation of 6.849 Å for **7**, both of them shorter than the Cu···Cu distance of 7.434 Å for **6**. In **5**, the zinc(II) ions are pentacoordinate by three nitrogen atoms of the 1,3-tpbd ligand and two chloride ions, with the following distances: Zn1–Cl1 2.248(2), Zn1–Cl2 2.305(2), average Zn1–$N_{pyridine}$ 2.050(6) and Zn1–$N_{amine}$ 2.646(2) Å. Considering such weak $N_{amine}$ ligation to zinc(II) ions, the coordination geometry around Zn1 and Zn2 can be described as distorted trigonal bipyramidal. The axial positions of the coordination sphere around Zn1 are occupied by N1 and Cl2 and the equatorial plane of the $ZnN_3Cl_2$ unit comprises N11, N22 and Cl1 with Zn1 lying out of the basal plane by 0.2956 Å. Compared to the mononuclear zinc(II) 1,4-tpbd complex with Zn–$N_{pyridine}$ average distance 2.14(1) Å and Zn–$N_{amine}$ 2.26(1) Å, where the Zn–$N_{pyridine}$ distance is significantly longer and the Zn–$N_{amine}$ distance is significantly shorter than in **5**.[19] In **7**, both coordination geometries around the copper(II) and zinc(II) centers are close to trigonal bipyramidal with N41 and N51 occupying the axial positions around Cu1 and N11 and N21 occupying the axial positions of Zn1. Similar to complex **5**, the three nitrogen atoms of one tridendate end of the 1,3-tpbd ligand and the metal center to which they are coordinated are almost coplanar, with Cu–$N_{pyridine}$ average distance 2.054(2) and Cu–$N_{amine}$ 2.499(2) Å, Zn–$N_{pyridine}$ average distance 2.034(2) and Zn–$N_{amine}$ 2.370(2) Å. The Cu–Cl distances are very close to each other [2.279(3) and 2.284(3) Å], likewise for the Zn–Cl bonds [2.307(4) and 2.333(3) Å]. The Zn–$N_{pyridine}$ and Cu–$N_{pyridine}$ distances are in accordance to those determined for related mononuclear analogues, in contrast the Zn–$N_{amine}$ and Cu–$N_{amine}$ distances in the mononuclear complexes of 2.142(2) Å and 2.207(6) Å are significantly shorter.[39,40] However, these complexes are complexes with a different ligand to metal cation ratio (one metal ion and two coordinated bispicolylamine ligands) at the amine nitrogen atom and the hydrogen atom is not substituted by an organic group.

**"Zinc-Ion-Assisted" Formation of a Dinuclear Copper Complex:** During our efforts to prepare model complexes for CuZnSOD described above, we observed a very surprising reaction behavior when stoichiometric mixtures of copper(II) and zinc(II) perchlorate salts were mixed with 1,3-tpbd. Instead of obtaining the heterodinuclear complex, we isolated a new dinuclear copper(II) complex, $[Cu_2(1,3\text{-tpbd})_2(H_2O)_2](ClO_4)_4$ (**8**), in which two copper(II) ions had reacted with two 1,3-tpbd ligand units. The molecular structure of the cation of complex **8** is shown in Figure 10 (crystal structure data and refinement parameters, bond lengths and angles are presented in Table 3 and Table 1).

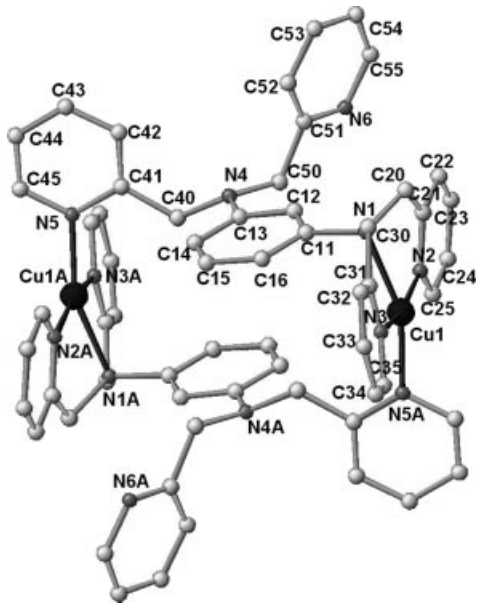


Figure 10. Molecular structure of the cation of $[Cu_2(1,3\text{-tpbd})_2(H_2O)_2](ClO_4)_4$ (**8**); water molecules and hydrogen atoms are omitted for clarity.

Complex **8** is a so called "dimetallocyclophane" and it is interesting to compare its structure with the dinuclear complex, $[Cu_2L'_2(H_2O)_2](ClO_4)_4{\cdot}2H_2O$, obtained previously from an impurity that was formed during the synthesis of 1,3-tpbd.[1] The "impurity" L′ is a derivative of the 1,3-tpbd ligand, missing one pyridyl "arm" (derived from incomplete formation of 1,3-tpbd during synthesis). A schematic presentation of the complex with the "impurity" as ligand in comparison with **8** is shown in Figure 11.

Complex **8** likewise crystallizes with an inversion center located in the middle of the "dimetallocyclophane" core. However, the metal coordination sphere is quite different to that of $[Cu_2L'_2(H_2O)_2](ClO_4)_4{\cdot}2H_2O$. The copper(II) ions in **8** exhibit a "4+1" square-based pyramidal geometry with three nitrogen atoms (N1, N2 and N3) from one tridentate end of 1,3-tpbd in the meridional form, and the pyridine (N5A) from the symmetry-related ligand completing the basal plane, while a water molecule (O1) occupies the apical site. In **8** the tertiary amine (N4A) from the symmetry-related ligand is not bound to the copper(II) center with a long distance of 4.472 Å, while the corresponding nitrogen (N2) as a secondary amine is coordinated to the copper(II) center with a bond length of 2.071(2) Å in the corresponding $[Cu_2L'_2(H_2O)_2](ClO_4)_4{\cdot}2H_2O$ complex.

The two pyridyl "arms" from the same tertiary amine are *trans* to one another [N2–Cu1–N3 164.8(2)°], [Cu1–N2 1.986(3), Cu1–N3 1.976(3) Å]. However, the corresponding two pyridyl nitrogen atoms in $[Cu_2L'_2(H_2O)_2](ClO_4)_4{\cdot}2H_2O$ are *cis*-coordinated to copper(II) with a N11–Cu1–N12 angle of 86.2(5)°. In complex **8**, all the Cu–$N_{pyridine}$ lengths are in general slightly shorter than the *trans* Cu–$N1_{amine}$ [2.074(3) Å]. The steric influence of the non-coordinated

 © 2007 Wiley-VCH Verlag GmbH & Co. KGaA, Weinheim 

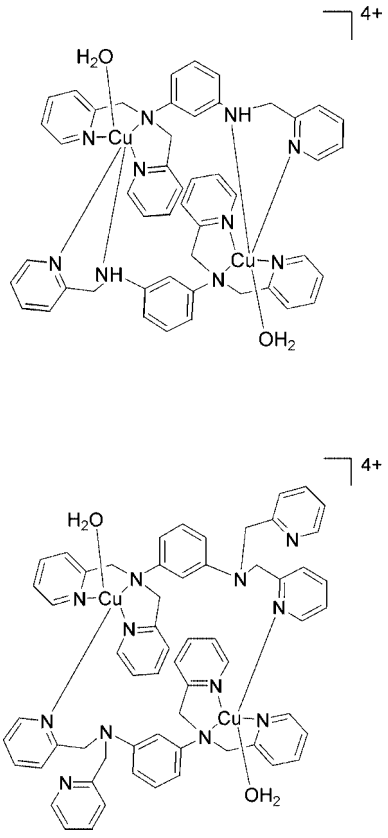

Figure 11. Schematic representation of the complex with the "impurity"L′ as ligand (top) in comparison to **8** (bottom).

pyridine ring results in the different coordination geometry and an intramolecular distance of Cu···Cu [8.820(1) Å] which is 1.3 Å longer than that of $[Cu_2L'_2(H_2O)_2](ClO_4)_4 \cdot 2H_2O$.

The finding that **8** forms despite the presence of zinc(II) ions is extremely surprising due to the results described above that zinc(II) can substitute copper(II) ions perfectly well in complexes of the ligand 1,3-tpbd. Furthermore, **8** can also be prepared if only a small amount (e.g. 5%) of zinc(II) ions are present. This result clearly suggests that zinc(II) ions should not be necessarily present and that it should be possible to synthesize **8** by mixing copper(II) perchlorate and 1,3-tpbd in a one to one stoichiometric ratio (Figure 12) because the reaction in a stoichiometric ratio of one (1,3-tpbd) to two $Cu(ClO_4)_2$ affords the dinuclear copper(II) complex $[Cu_2(1,3\text{-tpbd})(H_2O)_2(ClO_4)_3](ClO_4)$ that has been structurally characterized previously.[1]

However, in contrast a series of experiments showed that **8** cannot be prepared under aerobic conditions without the presence of zinc(II) ions. For example a mixture of 1,3-tpbd and one equivalent of copper(II) perchlorate in methanol/$H_2O$, acetonitrile or DMF exposed to air caused the effect that the green solutions rapidly started to turn to a deep-red color within a day.

Such a phenomenon has precedence with other related *m*-phenylendiamine derivatives where radical reactions were observed during oxidation reactions.[41–43] A possible mechanism (shown in Figure 13) can be postulated according to these previous findings (most likely an oxygen atom

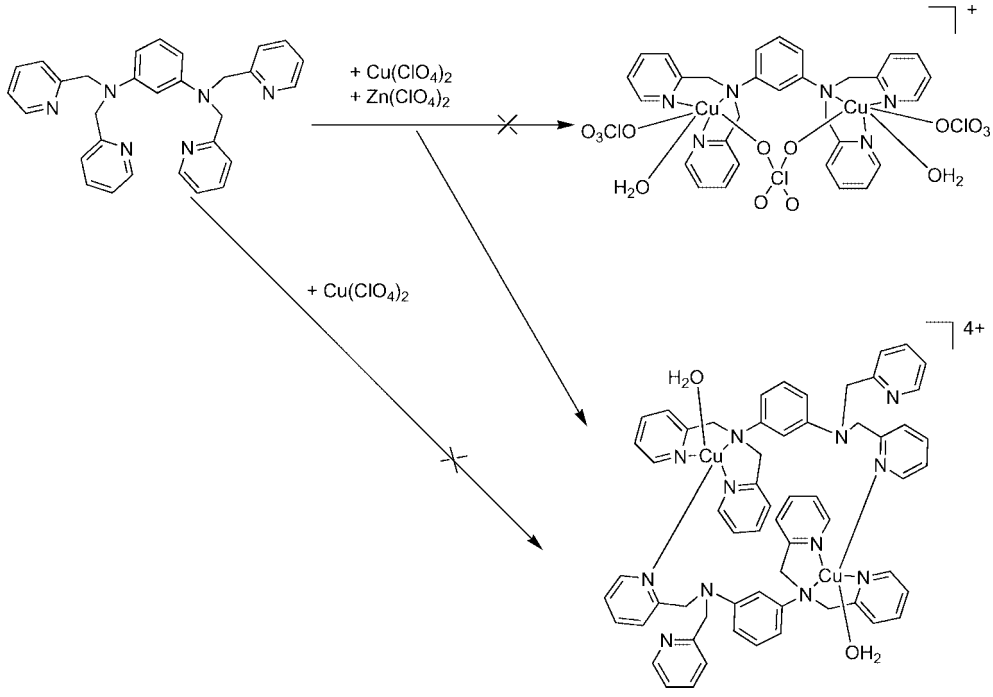

Figure 12. Scheme of reactions observed during the "zinc-assisted" formation of **8**.

 © 2007 Wiley-VCH Verlag GmbH & Co. KGaA, Weinheim 

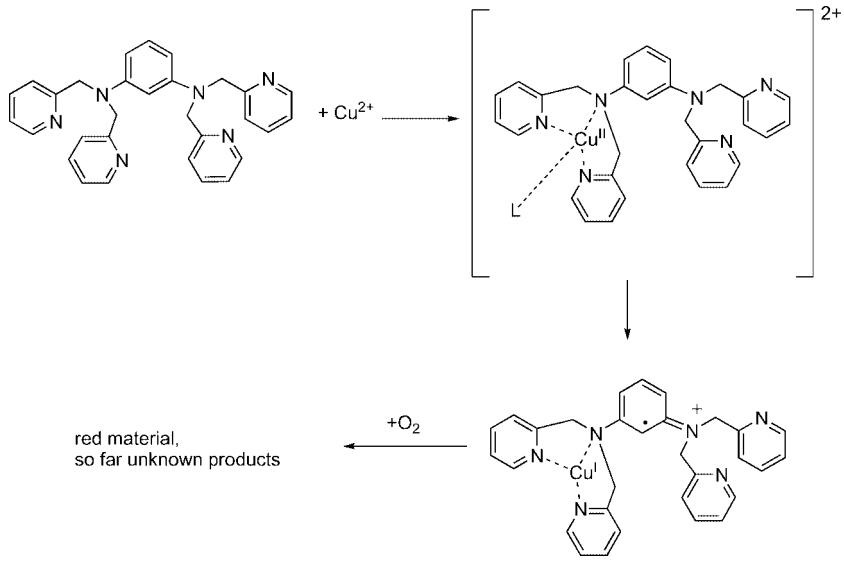


Figure 13. Possible reaction scheme for the formation of an oxidation product of 1,3-tpbd.

reacts with the benzene ring of the 1,3-tpbd ligand).[42] Unfortunately, all our efforts to identify this "red" material in order to ascertain whether 1,3-tpbd has been modified have been unsuccessful (only oily dark red reaction mixture products could be obtained so far).

However, this part of the postulated mechanism of ligand oxidation could readily explain the zinc(II) assisted crystallization of **8**. If enough copper(II) ions are present the formation of the radical intermediate shown in Figure 13 will be suppressed because both coordination sites are blocked with the copper(II) ions and dinuclear copper(II) complexes such as $[Cu_2(1,3\text{-tpbd})(H_2O)_2(ClO_4)_3]$-$ClO_4$ can be easily prepared.

If nonredox-active zinc(II) ions are present they will (as outlined above) coordinate to 1,3-tpbd as well. Most likely – and not for an obvious reason – they seem to prefer coordination only to one of the ligand sites as observed previously with the 1,4-tpbd derivative as ligand (see above), where even the crystal structure of this 1:1 complex was reported.[19] Then, the other coordination site will be filled with a copper(II) ion and in a consecutive reaction the zinc(II) ion will now be substituted by a copper(II) ion already coordinated to another 1,3-tpbd ligand molecule. Thus the zinc(II) ion will be liberated and can again interact with a different 1,3-tpbd ligand molecule [which would also explain why stoichiometric amounts of zinc(II) ions are not necessary]. Once complex **8** is formed, radical oxidations are again suppressed, and therefore allow the facile synthesis and isolation of complex **8**.

In our efforts to get a better understanding of the assumed ligand-oxidation processes we also reinvestigated the oxidation of the dinuclear 1,3-tpbd copper(I) complex with dioxygen described previously.[1] In the past this reaction has been studied in methanol, a solvent less suitable for stabilizing reactive intermediates such as copper "dioxygen adduct" complexes.[1] In our current experiments using more suitable solvents such as acetone we observed spectral changes that indicate the formation of a peroxido copper complex (even at ambient temperature), however, so far all efforts to isolate or to characterize this species in a pure form were unsuccessful.

As a complimentary means to obtain insights into the structure and energetics of possible dioxygen adduct complexes we performed quantum chemical calculations at the B3LYP/TZVP level of density functional theory. We optimized the structures of three isomers, i.e. the ($\eta^2$:$\eta^2$)-peroxido, the bis-μ-oxido, and the *trans*-($\eta^1$:$\eta^1$)-peroxido species. These calculations corroborate the interpretation of a side-on-bound ($\eta^2$:$\eta^2$)-peroxido species as the most stable complex formed. According to the quantum chemical results, the bis-μ-oxido species is 3.2 kcal/mol less stable, followed by the *trans*-peroxido species, which is 12.1 kcal/mol less stable than the side-on-bound peroxido isomer. Key parameters of the optimized structures are shown in Figure 14.

So far our efforts to isolate and characterize the final oxidation product(s) have been unsuccessful. A possible product that could arise from an intramolecular ligand hydroxylation similar to oxidation reactions observed previously for related systems[11] would lead to a phenol ligand shown in Figure 1 (R = H). Therefore we synthesized a derivative of this ligand (R = $CH_3$) from 2,6-diamino-*p*-cresol dihydrochloride[44] and 2-chloromethylpyridine hydrochloride. The copper(II) complex was obtained easily when copper(II) perchlorate was mixed with the ligand and crystals suitable for crystallographic characterization could be isolated. The crystal structure of $[Cu_2(2,6\text{-tpcd})(H_2O)(Cl)]$-$(ClO_4)_2 \cdot 2H_2O$ (**9**) is shown in Figure 15 (crystal structure data and refinement parameters, bond lengths and angles are presented in Table 3 and Table 1). The coordinated chloride ion is a consequence of the usage of the protonated ligand (isolation as the hydrochloride salt). The H atoms of water solvent molecules were derived from a difference Fou-

 © 2007 Wiley-VCH Verlag GmbH & Co. KGaA, Weinheim 

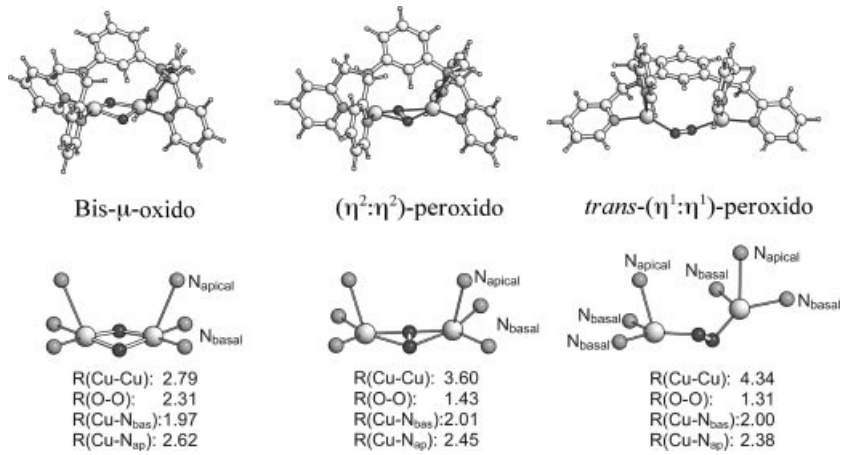


Figure 14. Calculated structures of the dioxygen copper adduct complex of 1,3-tpbd.

rier map and isotropically refined. **9** crystallizes with one coordinated and two additional water solvent molecules per unit.

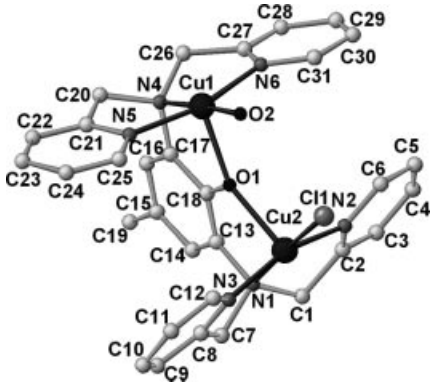


Figure 15. Molecular structure of the cation of $[Cu_2(2,6\text{-tpcd})(H_2O)(Cl)](ClO_4)_2$ (**9**).

In **9** both copper(II) ions are "4+1" coordinated forming a distorted square-pyramidal geometry. The basal plane consists of two pyridine nitrogen atoms (N2 and N3), the amine nitrogen N1 and the chloride anion Cl1 while the apical plane consists of the phenol oxygen atom O1. The distance between both copper(II) ions is 4.027 Å. Interestingly the distance Cu1–O1 with 2.153(1) Å is slightly longer than the corresponding distance Cu2–O1 [2.106(2) Å].

Parallel to our work, Karlin and co-workers investigated the reactivity of a dinuclear copper(I) complex with a nearly identical ligand (PD′OH) (Figure 1, R = *tert*-butyl). Besides selective DNA interactions of this complex[15] they furthermore reported in that regard a very interesting hydroxylation reaction of nitriles to aldehyde and cyanide during oxidation. A hydroperoxido complex has been postulated as reactive species in these reactions.[16]

## Conclusions

1,3-tpbd is a versatile ligand that can be used successfully to coordinate two metal ions in close proximity. While the nickel complex shows normal coordination behavior, redox active metal centers such as iron or copper ions demonstrate that 1,3-tpbd is a non-innocent ligand. Interestingly 1,3-tpbd does not coordinate iron(III) ions, instead protonation of the ligand is preferred. Oxidations of iron(II) complexes or copper(I) complexes of 1,3-tpbd led to reaction product mixtures that could not be characterized so far. Theoretical calculations support the formation of a dinuclear side-on peroxido copper complex during the reaction of the copper(I) complex with dioxygen. Intramolecular ligand hydroxylation might occur during the oxidation reaction, however, could not be proved experimentally. The possible reaction product, a phenolate-bridged derivative of the 1,3-tpbd complex could be synthesized in an independent way. Most interestingly is the reaction if only one equivalent of copper(II) salt is reacted with one equivalent of 1,3-tbpd. Under aerobic conditions a red product was formed after a short while, suggesting ligand oxidation. However, this reaction could be suppressed completely in the presence of zinc ions. Here $[Cu_2(1,3\text{-tpbd})_2(H_2O)_2](ClO_4)_4$ a so called "dimetallocyclophane" formed.

## Experimental Section

**General Remarks:** All chemicals were purchased from commercial sources and used as received.

***CAUTION!*** *The perchlorate salts used in this study are potentially explosive and should be handled with care.*

**Physical Measurements:** Elemental analyses were carried out with a Carlo Erba 1106 using a Mettler Toledo UMX-2. NMR spectra were recorded with a 400 MHz Bruker-Aspect 2000/3000. IR spectra were recorded with a Bruker Optics IFS25.

**Ligand Synthesis:** The ligand *N*,*N*,*N*′,*N*′-tetrakis(2-pyridylmethyl)-benzene-1,3-diamine (1,3-tpbd) was synthesized according to litera-

 © 2007 Wiley-VCH Verlag GmbH & Co. KGaA, Weinheim 

ture procedures.[1] Slow evaporation of a methanol solution of 1,3-tpbd in a glove box afforded single crystals suitable for X-ray diffraction studies.

**2,6-Bis[bis(2-pyridylmethyl)amino]-*p*-cresol (2,6-tpcd):** A solution of sodium hydroxide (4.18 g, 0.1050 mol) in water (30 mL) was added dropwise with stirring to a mixture of 2,6-diamino-*p*-cresole·2HCl[44] (2 g, 0.0095 mol) and 2-(chloromethyl)pyridine hydrochloride (7.82 g, 0.0475 mol) in 5 mL $H_2O$ under inert conditions. The crude product was recrystallized several times from acetone and 0.5 g (0.001 mol) 10.5% 2,6-tpcd were obtained. $^1$H NMR ($CDCl_3$/TMS, 400 MHz): $\delta$ = 8.48 (m, 4 H, pyr-$H_a$), 7.48 (m, 4 H, pyr-$H_c$), 7.45 (m, 8 H, pyr-$H_b$/$H_d$), 7.39 (s, 2 H, Ar-H), 4.75 (s, 8 H, –$CH_2$–), 2.15 (s, 3 H, -$CH_3$) ppm.

**$[H_4(1,3\text{-tpbd})_2](ClO_4)_4\cdot(CH_3CN)_3$:** A solution of iron(III) perchlorate hydrate (141.7 mg, 0.4 mmol) in water (3 mL) was added to a solution of 1,3-tpbd (95.2 mg, 0.2 mmol) in $CH_3OH$ (7 mL). The reaction mixture (a brown suspension) was stirred for 1 h at room temperature and filtered. The precipitate was dissolved in $CH_3CN$ (5 mL) and allowed to stand at room temperature for 2 d affording yellow block-shaped crystals suitable for X-ray diffraction analysis. $C_{66}H_{69}Cl_4N_{15}O_{16}$(1470.16): calcd. C 53.92, H 4.73, N 14.29; found C 53.78, H 4.94, N 14.51.

**$[H_4(1,3\text{-tpbd})_2](SO_3CF_3)_4$:** The complex was obtained in a similar way as for the perchlorate salt described above, however, for this compound no analytical data were collected. The crystal structure and data are reported in the Supporting Information.

**Synthesis of Complexes**

**$[Fe_2(1,3\text{-tpbd})(CH_3CN)_6](ClO_4)_4\cdot(CH_3CN)_2\cdot(H_2O)_{0.5}$ (1) and $[Fe_2(1,3\text{-tpbd})(DMF)_6](ClO_4)_4$ (2):** Complexes **1** and **2** were synthesized by the same procedure in a glove box differing only by the different solvents used. $Fe(ClO_4)_2\cdot H_2O$ (101.9 mg; 0.4 mmol) and 1,3-tpbd (95.2 mg, 0.2 mmol) were dissolved in 10 mL of $CH_3CN$ or DMF. The resulting clear, light-brown solution was stirred for 30 min at room temperature followed by vapor diffusion with diethyl ether (20 mL) at –11 °C. Nearly colorless square crystals of **1** and light yellow plate crystals of **2** suitable for X-ray diffraction analysis were grown after three weeks. Yield: 161 mg (0.12 mmol, 61%) for **1** and 159 mg (0.11 mmol, 56%) for **2**. $C_{46}H_{53}Cl_4Fe_2N_{14}O_{16.50}$ (1319.52) (**1**): calcd. C 41.87, H 4.05, N 14.86; found C 41.74, H 3.99, N 14.69. $C_{24}H_{35}Cl_2FeN_6O_{11}$ (710.33)(**2**): calcd. C 40.58, H 4.97, N 11.83; found C 40.65, H 4.84, N 11.87. $^1$H NMR ($CD_3CN$, 400 MHz): for **1**: $\delta$ = 9.78 (d, $J_{HH}$ = 1.9 Hz, 4 H, pyr-$H_a$), 8.97 (t, $^3J_{HH}$ = 7.7 Hz, 4 H, pyr-$H_c$), 8.55 (t, $^3J_{HH}$ = 5.5 Hz, 4 H, pyr-$H_b$), 8.49 (d, $J_{HH}$ = 7.4 Hz, 4 H, pyr-$H_d$), 8.07 (t, $^3J_{HH}$ = 14.6 Hz, 1 H, Ar-H), 7.32 (s, 1 H, Ar-H), 7.26 (dd, $J_{HH}$ = 6.99 Hz, 2 H, Ar-H), 6.00 (s, 8 H, –$CH_2$–) ppm; ($CD_3CN$, 400 MHz) for **2**: $\delta$ = 8.40 (d, 4 H, pyr-Ha), 8.00 (s, 1 H, DMF-H), 7.59 (t, 4 H, pyr-Hc), 7.05–7.16 (t/d, 8 H, pyr-Hb/–Hd), 6.70 (t, 1 H, Ar-H), 5.85–5.97 (s/d, 3 H, Ar-H), 4.61 (s, 8 H, –$CH_2$–), 2.71–2.87 (s, 36 H, DMF-$CH_3$) ppm.

**$[Ni_2(1,3\text{-tpbd})(DMF)_6](ClO_4)_4$ (3):** Similar to the above procedure for **1** and **2**, this complex was synthesized by adding a solution of $[Ni(DMF)_6](ClO_4)_2$[45] in DMF to a solution of 1,3-tpbd in DMF under the inert conditions of a glove box. Crystals suitable for X-ray diffraction analysis were obtained by slow diffusion of diethyl ether into the solution. $C_{48}H_{70}Cl_4N_{12}Ni_2O_{22}$ (1426.38): calcd. C 40.42, H 4.95, N 11.78; found C 39.77, H 4.48, N 11.60. UV/Vis (DMF): $\lambda_{max}$ = 612, 774, 937 nm. The crystal structure and data are reported in the Supporting Information.

**$[Zn_2(1,3\text{-tpbd})(CH_3CN)_2(SO_3CF_3)_2(H_2O)](SO_3CF_3)_2$ (4):** Zinc triflate (154 mg, 0.42 mmol) was added to a solution of 1,3-tpbd (100 mg, 0.21 mmol) in acetonitrile under an inert atmosphere. The solution was allowed to stir at room temperature for a further 2 h. The solvent was removed in vacuo and dichloromethane (5 mL) was added to the residual oil. Diethyl ether (20 mL) was added until the solution was slightly turbid. The vessel was placed in the freezer compartment of a fridge and within 3 d, large transparent blocks of 4 formed. IR (Nujol mull): $\tilde{\nu}$ 3631 (w), 3629 (w), 3627 (w), 3549 (w), 3434 (w), 3245 (m), 3120 (m), 2972 (s), 2948 (s), 2885 (s), 2845 (s), 2726 (m), 2676 (m), 2416 (w), 2394 (w), 2317 (m), 2288 (m), 2211 (w), 2038 (w), 1923 (w), 1610 (m), 1582 (m), 1456 (s), 1376 (s), 1287 (s), 1246 (s), 1167 (s), 1105 (m), 1031 (s), 957 (m), 901 (m), 850 (m), 817 (m), 774 (m), 726 (m), 696 (m), 634 (m), 574 (m), 544 (m), 517 (m), 472 (w) cm$^{-1}$. $^1$H NMR ($CD_3CN$, 300 MHz): $\delta$ = 8.60 (d, $^3J_{HH}$ = 4.9 Hz, 4 H, pyr-$H_a$), 8.10 (t, $^3J_{HH}$ = 7.5 Hz, 4 H, pyr-$H_c$), 7.63 (t, $J_{HH}$ = 6.0 Hz, 4 H, pyr-Hb), 7.44 (d, $^3J_{HH}$ = 7.9 Hz, 4 H, pyr-$H_d$), 6.90 (t, $^3J_{HH}$ = 8.3 Hz, 1 H, Ar-H), 6.33 (dd, $^3J_{HH}$ = 1.9 Hz, 1 H, 8.7 Hz, Ar-H), 5.96 (s, 1 H, Ar-H), 4.60 (s, 8 H, –$CH_2$–).

**$[Zn_2(1,3\text{-tpbd})Cl_4]\cdot H_2O$ (5), $[Cu_2(1,3\text{-tpbd})Cl_4]$ (6), $[CuZn(1,3\text{-tpbd})Cl_4]$ (7):** Slow evaporation of an aqueous methanolic solution of a stoichiometric mixture of $ZnCl_2$, $CuCl_2$ and 1,3-tpbd led to a mixture of yellow and two different green-colored crystals suitable for X-ray diffraction analysis.

**$[Cu_2(1,3\text{-tpbd})_2(H_2O)_2]\cdot(ClO_4)_4\cdot 2H_2O$ (8):** A methanolic suspension of 1,3-tpbd (95.2 mg, 0.2 mmol) was added to an aqueous methanol solution of $Cu(ClO_4)_2\cdot 6H_2O$ (64.1 mg, 0.2 mmol) and $Zn(ClO_4)_2\cdot 6H_2O$ (74.4 mg, 0.2 mmol). The mixture was stirred for 2 h, filtered and allowed to slowly evaporate at room temperature. Large green blocks formed within 48 h. A single-crystal X-ray diffraction analysis was performed and the structure of the green crystals was determined to be $[Cu_2(1,3\text{-tpbd})(OH_2)_2](ClO_4)_4$. That no zinc ions were present at all was further confirmed by photon-induced X-ray emission.

**$[Cu_2(2,6\text{-tpcd})(H_2O)(Cl)](ClO_4)_2\cdot 2H_2O$ (9):** A suspension of 2,6-tpcd (100 mg, 0.2 mmol) in 5 mL methanol was added to a solution of $Cu(ClO_4)_2\cdot 6\ H_2O$ (148.2 mg, 0.4 mmol) in 5 mL $H_2O$. The mixture was stirred for 30 min at room temperature and allowed to slowly evaporate at room temperature. Within two days small green needles of **9** suitable for X-ray diffraction analysis were formed.

**Computational Methods:** Density functional calculations have been performed employing the B3LYP functional[46–49] as implemented in the Turbomole program.[50–52] The TZVP basis set has been employed for all atoms.[53] Solvent effects have partially been included in these calculations employing the COSMO continuum solvent model (dielectric constant for acetone at room temperature: $\varepsilon$ = 36.64).[54]

**X-ray Crystallographic Studies:** X-ray crystallographic data for 1,3-tpbd were collected with a STOE IPDS-diffractometer at 193 K equipped with a low-temperature system (Karlsruher Glastechnisches Werk). Cell parameters were refined by using up to 5000 reflections. A sphere of data (210 frames) was collected with the $\varphi$ oscillation mode (0.9° frame width; Irradiation times/frame: 7 min.) No absorption corrections were applied. The structures were solved by direct methods in SHELXS97, and refined by using full-matrix least-squares in SHELXL97.[55] The hydrogen atoms were positioned geometrically and all non-hydrogen atoms were refined anisotropically, if not mentioned otherwise. All following data were corrected for Lorentz and polarization effects. Intensity data of **1** were collected with a Bruker-Nonius KappaCCD diffractometer, intensity data for **4** and **8** were collected with a Siemens P4 four circle diffractometer. Absorption effects were corrected either by semi-empirical methods based on multiple scans (**1**)[56] or on the

 © 2007 Wiley-VCH Verlag GmbH & Co. KGaA, Weinheim 

basis of Psi-scans.[57] The structures were solved by direct methods; full-matrix least-squares refinement was carried out on $F^2$ using SHELXTL NT 6.12.[58] All non-hydrogen atoms were refined anisotropically. Hydrogen atoms were geometrically positioned except for the hydrogen atoms of the water molecules or aqua ligands the positions of which were derived from a difference Fourier synthesis; their isotropic displacement parameters were tied to those of their corresponding carrier atoms by a factor of 1.2 or 1.5. One of the perchlorate anions of **1** is disordered; two preferred orientations were refined resulting in occupancy factors of 50.1(6) and 49.9(6) %. In **8** both of the two independent perchlorate anions are subjected to disorder. Two preferred orientations refined led to occupancy factors of 72(2) and 28(2)% around Cl1 and 61(2) and 39(2) % around Cl2, respectively.

Intensity data of protonated tpbd, **2**, **3** and **9** were collected with a Siemens SMART CCD 1000 diffractometer by the $\omega$-scan technique collecting a full sphere of data with irradiation times of 10 to 20 s per frame and $\Delta\omega$ ranges between 0.3° and 0.45°. The collected reflections were corrected for absorption effects.[56] All structures were solved by direct methods and refined by least-squares techniques using the SHELX97 programme package.[55] The hydrogen atoms were positioned geometrically and all non-hydrogen atoms were refined anisotropically, if not mentioned otherwise. Further data collection parameters are summarised in Tables 2, 3 and in the Supporting Information.

Intensity data of of **5** and **7** were collected with a Nonius MACH3 diffractometer. Cell parameters were obtained and refined from 25 reflections. Absorption corrections (psi-scans) were applied. The space groups were determined from systematic absences and subsequent least-squares refinement. The structures were solved by direct methods. The parameters were refined with all data by full-matrix-least-squares on $F^2$ using SHELXL-97.[55] Non-hydrogen atoms were refined with anisotropic thermal parameters. The hydrogen atoms were fixed in idealized positions using a riding model. Scattering factors were taken from the literature.[59] Figures of the molecular structures were obtained using Winray.[61]

CCDC-610594 (for 1,3-tpbd), -610424 (for $[1,3\text{-tpbdH}_2](ClO_4)_2$), -615270 (for **1**), -610425 (for **2**), -610426 (for $[1,3\text{-tpbdH}_2](CF_3SO_3)_2$), -610427 (for **3**), -615271 (for **4**), -611033 (for **5**), -611034 (for **7**), -615272 (for **8**) and -610428 (for **9**) contain the supplementary crystallographic data for this paper. These data can be obtained free of charge from The Cambridge Crystallographic Data Centre via www.ccdc.cam.ac.uk/data_request/cif.

**Supporting Information** (see also the footnote on the first page of this article): Crystallographic data and selected bond lenghts and angles of $[H_2]1,3\text{-tpbd}](SO_3CF_3)_2$ and **3**.

## Acknowledgments

The authors gratefully acknowledge financial support from the Deutsche Forschungsgemeinschaft (DFG). S. P. F. is thankful for a scholarship from the Deutscher Akademischer Austauschdienst (DAAD).

[1] S. Schindler, D. J. Szalda, C. Creutz, *Inorg. Chem.* **1992**, *31*, 2255–2264.
[2] S. P. Foxon, G. R. Torres, O. Walter, J. Z. Pedersen, H. Toftlund, M. Hueber, K. Falk, W. Haase, J. Cano, F. Lloret, M. Julve, S. Schindler, *Eur. J. Inorg. Chem.* **2004**, 335–343.
[3] S. P. Foxon, O. Walter, R. Koch, H. Rupp, P. Müller, S. Schindler, *Eur. J. Inorg. Chem.* **2004**, 344–348.
[4] E. A. Lewis, W. B. Tolman, *Chem. Rev.* **2004**, *104*, 1047–1076.
[5] L. M. Mirca, X. Ottenwaelder, T. D. P. Stack, *Chem. Rev.* **2004**, *104*, 1013–1045.
[6] S. Schindler, *Eur. J. Inorg. Chem.* **2000**, 2311–2326.
[7] L. Q. Hatcher, K. D. Karlin, *J. Biol. Inorg. Chem.* **2004**, *9*, 669–683.
[8] I. Fernández, R. Ruiz, J. Faus, M. Julve, F. Lloret, J. Cano, X. Ottenwaelder, Y. Journaux, M. C. Muñoz, *Angew. Chem. Int. Ed.* **2001**, *40*, 3039–3042.
[9] X. Ottenwaelder, J. Cano, Y. Journaux, E. Rivière, C. Brennan, M. Nierlich, R. Ruiz-Garcia, *Angew. Chem. Int. Ed.* **2004**, *43*, 850–852.
[10] A. Hoffmann, R. van Eldik, *Dalton Trans.* **2003**, 2979–2985.
[11] N. N. Murthy, M. Mahroof-Tahir, K. D. Karlin, *J. Am. Chem. Soc.* **1993**, *115*, 10404–10405.
[12] N. N. Murthy, K. D. Karlin, I. Bertini, C. Luchinat, *J. Am. Chem. Soc.* **1997**, *119*, 2156–2162.
[13] C. J. McKenzie, M. Julve, S. Schindler, unpublished results.
[14] T. N. Sorrell, M. L. Garrity, D. J. Ellis, *Inorg. Chim. Acta* **1989**, *166*, 71–75.
[15] L. Li, K. D. Karlin, S. E. Rokita, *J. Am. Chem. Soc.* **2005**, *127*, 520–521.
[16] L. Li, A. A. Narducci Sarjeant, M. A. Vance, L. N. Zakharov, A. N. Rheingold, E. I. Solomon, K. D. Karlin, *J. Am. Chem. Soc.* **2005**, *127*, 15360–15361.
[17] T. N. Sorrell, C. O'Connor, O. P. Anderson, J. H. Reibenspies, *J. Am. Chem. Soc.* **1985**, *107*, 4199–4206.
[18] T. Buchen, A. Hazell, L. Jessen, C. J. McKenzie, L. Preuss Nielsen, J. Z. Pedersen, D. Schollmeyer, *Dalton Trans.* **1997**, 2697–2704.
[19] A. Hazell, C. J. McKenzie, L. J. Preuss Nielsen, *J. Chem. Soc., Dalton Trans.* **1998**, 1751–1756.
[20] A. Hazell, C. J. McKenzie, L. Preuss Nielsen, *Polyhedron* **2000**, *19*, 1333–1338.
[21] A. Mederos, P. Gili, S. Domínguez, A. Benítez, M. Soledad Palacios, M. Hernández-Padilla, P. Martín-Zarza, M. L. Rodríguez, C. Ruíz-Pérez, F. J. Lahoz, L. A. Oro, F. Brito, J. M. Arrieta, M. Vlassi, G. Germain, *J. Chem. Soc., Dalton Trans.* **1990**, 1477–1491.
[22] E. Y. Tshuva, S. J. Lippard, *Chem. Rev.* **2004**, *104*, 987–1012.
[23] M. Costas, M. P. Mehn, M. P. Jensen, L. Que Jr., *Chem. Rev.* **2004**, *104*, 939–986.
[24] S. V. Kryatov, E. V. Rybak-Akimova, S. Schindler, *Chem. Rev.* **2005**, *105*, 2175–2226.
[25] I. Bernal, I. M. Jensen, K. B. Jensen, C. J. McKenzie, H. Toftlund, J. P. Tuchagues, *J. Chem. Soc., Dalton Trans.* **1995**, 3667–3675.
[26] C. R. Randall, L. Shu, Y.-M. Chiou, K. S. Hagen, M. Ito, N. Kitajima, R. J. Lachicotte, Y. Zang, L. Que Jr., *Inorg. Chem.* **1995**, *34*, 1036–1039.
[27] A. Diebold, K. S. Hagen, *Inorg. Chem.* **1998**, *37*, 215–223.
[28] D. Mandon, A. Nopper, T. Litrol, S. Goetz, *Inorg. Chem.* **2001**, *40*, 4803–4806.
[29] M. Yashiro, H. Kaneiwa, K. Onaka, M. Komiyama, *Dalton Trans.* **2004**, *4*, 605–610.
[30] M. L. Hlavinka, M. J. Mc Nevin, R. Shoemaker, J. R. Hagadorn, *Inorg. Chem.* **2006**, *45*, 1815–1822.
[31] J. B. Mandel, C. Maricondi, B. E. Douglas, *Inorg. Chem.* **1988**, *27*, 2990–2996.
[32] I. Fridovich, *Annu. Rev. Biochem.* **1995**, *64*, 97–112.
[33] D. P. Riley, *Chem. Rev.* **1999**, *99*, 2573–2587.
[34] D. Ghosh, N. Kundu, G. Maity, A. Caneschi, A. Endo, M. Chaudhury, *Inorg. Chem.* **2004**, *43*, 6015–6023.
[35] V. Pelmenschikov, P. E. M. Siegbahn, *Inorg. Chem.* **2005**, *44*, 3311–3320.
[36] H. Ohtsu, S. Itoh, S. Nagatomo, T. Kitagawa, S. Ogo, Y. Watanabe, S. Fukuzumi, *Chem. Commun.* **2000**, 1051–1052.
[37] H. Ohtsu, Y. Shimazaki, A. Odani, O. Yamauchi, W. Mori, S. Itoh, S. Fukuzumi, *J. Am. Chem. Soc.* **2000**, *122*, 5733–5741.
[38] S. Fukuzumi, H. Ohtsu, K. Ohkubo, S. Itoh, H. Imahori, *Coord. Chem. Rev.* **2002**, *226*, 71–80.

 © 2007 Wiley-VCH Verlag GmbH & Co. KGaA, Weinheim 

[39] Y. Gultneh, A. Raza Khan, D. Blaise, S. Chaudry, B. Ahvazi, B. B. Marvey, R. J. Butcher, *J. Inorg. Biochem.* **1999**, *75*, 7–18.
[40] M. Palaniandavar, R. J. Butcher, A. W. Addison, *Inorg. Chem.* **1996**, *35*, 467–471.
[41] A. Calder, A. R. Forrester, P. G. James, G. R. Luckhurst, *J. Am. Chem. Soc.* **1969**, *91*, 3724–3727.
[42] F. Effenberger, W.-D. Stohrer, K.-E. Mack, F. Reisinger, W. Seufert, H. E. A. Kramer, R. Föll, E. Vogelmann, *J. Am. Chem. Soc.* **1990**, *112*, 4849–4857.
[43] M. M. Wienk, R. A. J. Janssen, *J. Am. Chem. Soc.* **1996**, *118*, 10626–10628.
[44] E. Fromm, R. Ebert, *J. Prakt. Chem.* **1924**, *108*, 75–87.
[45] W. Fee, D. Elholum, A. McPherson, D. Rundle, *Aust. J. Chem.* **1973**, *26*, 1207–1225.
[46] A. D. Becke, *Phys. Rev. A* **1988**, *38*, 3098–3100.
[47] A. D. Becke, *J. Chem. Phys.* **1993**, *98*, 5648–5652.
[48] C. Lee, W. Yang, R. G. Parr, *Phys. Rev. B* **1988**, *37*, 785–789.
[49] P. J. Stephens, F. J. Devlin, C. F. Chabalowski, M. J. Frisch, *J. Phys. Chem.* **1994**, *98*, 11623–11627.
[50] R. Ahlrichs, M. Bär, H. P. Baron, R. Bauernschmitt, S. Becker, M. Ehrig, K. Eichkorn, S. Elliott, F. Furche, F. Haase, M. Häser, C. Hättig, H. Horn, C. Huber, U. Huniar, M. Kattanek, A. Köhn, C. Kölmel, M. Kollwitz, K. May, C. Ochsenfeld, H. Öhm, A. Schäfer, U. Schneider, O. Treutler, K. Tsereteli, B. Unterreiner, M. von Arnim, F. Weigend, P. Weis, H. Weiss, in *Turbomole – Program System for ab initio Electronic Structure Calculations*, version 5.6, University of Karlsruhe, **2002**.
[51] R. Ahlrichs, in: *Encyclopedia Computational Chemistry* (Ed.: P. v. R. Schleyer), Wiley, Chichester, **1998**, pp. 3123–3129.
[52] R. Ahlrichs, M. Bär, M. Häser, H. Horn, C. Kölmel, *Chem. Phys. Lett.* **1989**, *162*, 165–169.
[53] A. Schäfer, C. Huber, R. Ahlrichs, *J. Chem. Phys.* **1994**, *100*, 5829–5835.
[54] A. Klamt, G. Schüürmann, *J. Chem. Soc., Perkin Trans. 2* **1993**, 799–805.
[55] G. M. Sheldrick, *SHELX-97*, University of Göttingen, **1997**.
[56] *SADABS 2.06*, Bruker AXS, Inc., Madison, WI, USA, **2002**.
[57] A. T. C. North, D. C. Phillips, F. S. Matthews, *Acta Crystallogr., Sect. A* **1968**, *24*, 351–359.
[58] *SHELXTL NT 6.12*, Bruker AXS, Inc., Madison, WI, USA, **2002**.
[59] D. T. Cromer, J. T. Waber, in *International Tables for X-ray Crystallography* (Eds.: J. A. Ibers, W. C. Hamilton), Kynoch, Birmingham, **1974**.
[60] H. D. Flack, *Acta Crystallogr., Sect. A* **1983**, *39*, 876–881.
[61] Winray: R. Soltek, University of Heidelberg, **1997**; xpma: L. Zsolnai, University of Heidelberg, **1997**.

Received: October 5, 2006
Published Online: December 4, 2006

 © 2007 Wiley-VCH Verlag GmbH & Co. KGaA, Weinheim 

DOI: 10.1002/ejic.200600630

# Thermal Behavior of Tetrahydropyran-Intercalated $VOPO_4$: Structural and Dynamics Study

**Klára Melánová,[a] Ludvík Beneš,*[a] Vítězslav Zima,[a] Eva Černošková,[a] Jiří Brus,[b] Martina Urbanová,[b] Miroslava Trchová,[b] and Jiří Dybal[b]**

**Keywords:** Intercalations / NMR spectroscopy / IR spectroscopy / Thermal behavior / Quantum chemical calculations

The thermal behavior of tetrahydropyran-(THP-)intercalated $VOPO_4$ was probed by an extensive combination of experimental methods (XRD, DSC, FTIR, solid-state NMR) and quantum chemical calculations. Two temperature-induced transitions were detected and all polymorphs exhibit a high degree of molecular order and tight packing of THP in $VOPO_4$. The first reversible thermal transition at around 100 °C was attributed to boat/chair conformation changes of the THP molecules. Most probably, a low-temperature boat conformation of the guest molecules present in the interlayer space of $VOPO_4$ changes to a high-temperature chair conformation. This rearrangement of the THP molecules was confirmed by variable-temperature $^{13}C$ CP/MAS NMR spectroscopy. Quantum chemical calculations using a B3LYP functional and 6-31G(d) basis set also support this idea. The second change at around 140 °C is probably caused by a weakening of the donor–acceptor bond between the oxygen molecule of THP and the vanadium atom of the host and the formation of a disorder in packing of the THP molecules.

(© Wiley-VCH Verlag GmbH & Co. KGaA, 69451 Weinheim, Germany, 2007)

## Introduction

Vanadyl phosphate belongs to phosphates with a layered structure. The layers are formed of a tetragonal grid in which atoms of vanadium and phosphorus alternate. The atoms of vanadium and phosphorus are connected by oxygen atoms ($O_{host}$) of the phosphate groups.[1,2]

Thus, every vanadium atom is surrounded by four equatorial oxygen atoms. In addition, two oxygen atoms are bonded to the vanadium atoms forming a $VO_6$ octahedron. One of these two vanadium–oxygen bonds is shorter indicating the presence of a V=O bond, while the other is much longer and can be ascribed to the coordination of the oxygen atom from the V=O group of an adjacent $(VOPO_4)_\infty$ layer. The interlayer interactions are therefore accomplished by V=O···V bonds in anhydrous $VOPO_4$. In the vanadyl phosphate intercalates, the sixth position in the $VO_6$ octahedron is complemented by a donor atom of a guest molecule, which is then in a *trans* position to the oxygen atom of the V=O bond. Vanadyl phosphate forms a number of intercalation compounds with molecular guests having Lewis base character, among others also with ether oxygen as a donor atom.[3] Recently, tetrahydrofuran,[4,5] tetrahydropyran (THP),[5] 1,4-dioxane, 1,3,5-trioxane, and 18-crown-6[6] were intercalated into vanadyl phosphate. It is presumed that the guests are coordinated to the vanadium atoms of the host layer through the free electron pairs of the donor O atoms of the guests. These intercalates are generally very stable in air and the guest molecules are released at relatively high temperatures (for example the tetrahydrofuran intercalate decomposes at about 160 °C[5]). This indicates that the host–guest interaction is very strong.

Recently, we studied the thermal behavior of tetrahydropyran-intercalated $VOPO_4$. This intercalate was prepared by replacing 1-propanol in the $VOPO_4{\cdot}2C_3H_7OH$ intercalate with the THP. The lattice parameters of the tetragonal structure are $a$ = 6.201(2) Å and $c$ = 12.014(2) Å and the intercalate contains one THP molecule per formula unit. The probable arrangement of the THP molecules in the host interlayer space is derived from molecular simulations with the Cerius[2] 4.5 programme. The molecular simulations showed a bilayer arrangement of the THP molecules in the interlayer space, in which the guest layers are slightly overlapping.[5]

The thermal behavior of THP intercalated vanadyl phosphate was monitored by powder X-ray diffraction and TG-DTA. The basal spacing slightly increases up to 85 °C. At this temperature, a new phase with the basal spacing 12.8 Å appears. This effect is fully reversible during cooling. Another weak increase of the basal spacing up to 122 °C is followed by a significant increase of the basal spacing between 122–140 °C, which is accompanied by a broadening of the (00*l*) diffraction lines. At higher temperatures, the intensity of the (00*l*) diffraction lines decreases due to slow

[a] Joint Laboratory of Solid State Chemistry of Institute of Macromolecular Chemistry of Academy of Sciences and University of Pardubice,
Studentská 84, 53210 Pardubice, Czech Republic
[b] Institute of Macromolecular Chemistry, Academy of Sciences of the Czech Republic,
Heyrovský Sq. 2, 16206 Prague 6, Czech Republic

 © 2007 Wiley-VCH Verlag GmbH & Co. KGaA, Weinheim 

decomposition of the intercalate. The *a* parameter of the tetragonal lattice does not change up to 158 °C. The color of the intercalate does not change up to 122 °C at which point it changes to yellow-green. This indicates gradual reduction of vanadium(V).

As follows from the TG measurement, thermal decomposition of the intercalate starts at 140 °C, and THP is slowly released up to 600 °C. There are two endothermic effects on the DTA curve which occur at the temperatures (78 and 126 °C) when the step changes of the basal spacing are observed. No weight loss accompanies these effects. The exothermic effects at higher temperatures are probably due to the combustion of the released compounds.

The question is, what is the reason for the reversible effects that occur in the temperature range 60–130 °C and how these effects are connected to the presumed changes in the arrangement of the guest molecules in the interlayer space of the host. For this purpose, we utilized solid-state NMR spectroscopy together with other methods. Structural changes occurring in the investigated materials, in our case in the intercalated systems, can be easily inferred from the chemical shifts obtained by solid-state NMR spectroscopy. Besides, many NMR parameters are highly sensitive to the internal dynamics of molecular systems and for instance motional amplitudes of molecular segments can be directly extracted from the precise measurements of the site-specific motionally averaged one-bond dipolar couplings.

This paper reports the results of a DSC, IR, and NMR study of the thermal behavior of the THP intercalate. We focused also on the description of the basic structural motifs and motional states of the intercalated molecules of THP within the interlayer space of $VOPO_4$. For this task we used the analysis of the $^{13}C$ CP/MAS NMR spectra and the measurements of the $^{1}H$-$^{13}C$ and $^{1}H$-$^{31}P$ dipolar coupling constants. Furthermore, the conformational changes and the rearrangement of THP molecules that occur as the temperature is gradually elevated were probed by a variable-temperature measurement of the $^{13}C$ CP/MAS NMR spectra.

## Results and Discussion

The THP intercalate was prepared according to two methods: stirring at room temperature and refluxing. Both methods provide samples with the same composition $VOPO_4{\cdot}C_5H_{10}O$ but with slightly different basal spacings. The sample prepared at room temperature has a basal spacing of 12.02 Å and its lattice parameters are the same as those of the intercalate described in the previous paper.[5] The sample prepared by refluxing has a slightly higher basal spacing of 12.11 Å. Both samples were heated to 115 °C and then cooled to room temperature. After the thermal treatment, the basal spacing of the sample prepared at room temperature shifts from 12.02 to 12.11 Å (see Figure 1a). On the other hand, the diffractograms of the sample prepared by refluxing are practically the same before and after the thermal treatment and its thermal XRD behavior seems to be fully reversible (Figure 1b). Therefore, all other investigations were done with this sample.

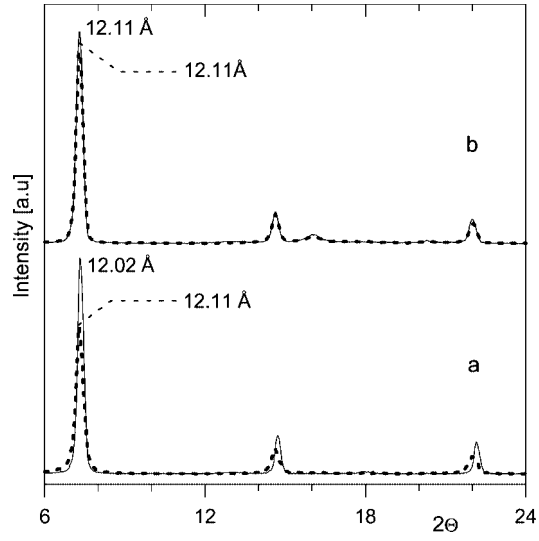


Figure 1. Comparison of the diffractograms measured before (solid line) and after (dashed line) thermal treatment for the THP intercalate prepared at room temperature (a) and by refluxing (b).

### DSC Measurements

Figure 2 shows the DSC curves for the intercalate. Three cycles of heating and cooling were carried out (curves 1–6). The first heating curve (dashed line 1) shows an endothermic peak at 98 °C with a shoulder at 102 °C. The second and third heating curves (3 and 5) are identical and differ

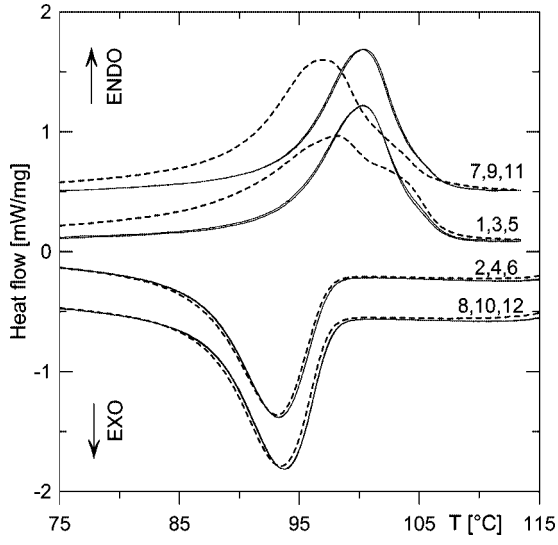


Figure 2. DSC curves of the intercalate prepared by refluxing. The curves are numbered as they were measured. The measurements 7–12 were repeated after 5 d with the same samples as measurements 1–6. The first cycles of heating (1 and 7) and cooling (2 and 8) are marked with dashed lines.

 © 2007 Wiley-VCH Verlag GmbH & Co. KGaA, Weinheim 

from the first heating curve. They have only one endothermic peak at 100.5 °C. All three cooling curves (2, 4, and 6) are nearly the same.

After 5 d, another three heating and cooling cycles were carried out with the same sample. The first heating curve in this series (dashed line 7) is similar to the first heating of the fresh sample. There is an endothermic peak at 97 °C but the shoulder at 102 °C is less marked. It indicates some slow relaxation at room temperature. The next two heating curves (9 and 11) and all cooling curves (8, 10, and 12) are practically the same and do not differ from those of the fresh sample.

### FTIR Spectroscopy

The phase transitions in $VOPO_4 \cdot C_5H_{10}O$ intercalate demonstrated by DSC analysis have been tested by FTIR spectroscopy. The FTIR spectra of the intercalate $VOPO_4 \cdot C_5H_{10}O$ during heating from 25 to 120 °C and of pure THP are shown in Figures 3 and 4.

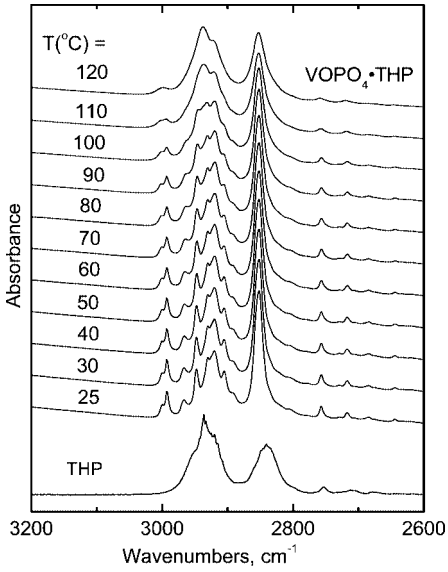


Figure 3. FTIR spectra of the intercalate $VOPO_4$ with THP in KBr pellets during heating from 25–120 °C and ATR FTIR spectrum of pure THP in the region from 3200 to 2600 $cm^{-1}$.

The infrared spectrum of the $VOPO_4 \cdot C_5H_{10}O$ intercalate at ambient temperature exhibits pronounced peaks which correspond to the THP vibrations. The intercalation of THP into vanadyl phosphate has been characterized by IR and Raman spectroscopy.[5] The band at 996 $cm^{-1}$ in the infrared spectrum of $VOPO_4 \cdot C_5H_{10}O$ has been assigned to the symmetric $\nu(PO_4)$ stretching vibration which is infrared-active due to the distortion of the phosphate tetrahedron in the intercalate. The shoulder at 1001 $cm^{-1}$ is most probably the V=O stretching band of the vanadyl group. Its position corresponds to the coordination of the oxygen atom of THP to the other axial position of the $VO_6$ octahedron. The band at 1149 $cm^{-1}$ in the infrared spectrum of the intercalate with THP is the asymmetric $\nu(PO_4)$ stretching vibration of the phosphate tetrahedron. The position of the main spectral bands of the host structure differs only slightly from those of anhydrous vanadyl phosphate or its hydrated form.[7] This confirms that the structure of the original $VOPO_4$ layers remains unchanged after the intercalation reaction.

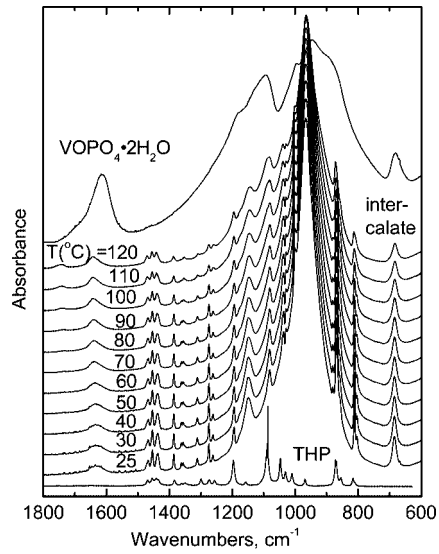


Figure 4. FTIR spectra of $VOPO_4 \cdot H_2O$ and of the intercalate $VOPO_4$ with THP in KBr pellets during heating from 25 to 120 °C and ATR FTIR spectrum of pure THP in the region from 1800 to 600 $cm^{-1}$.

The position, shape, and intensity of bands in the 3100–2700 $cm^{-1}$ region (see Figure 3) of the spectrum of the intercalate differs from those in the spectrum of pure THP.[8,9] Some changes of the $CH_2$ stretching vibrations have been observed when going from the liquid state to the intercalated form of THP. During the fixation of the intercalated molecules in the interlayer space, the asymmetric $CH_2$ stretching vibrations at 2936 and 2840 $cm^{-1}$ split into several bands and a new doublet shifted to 3002 and 2993 $cm^{-1}$ appears in the infrared spectrum of the intercalated THP (see Figure 3). Going from the liquid to the intercalated state of THP a change of the scissoring (several bands from 1380 to 1470 $cm^{-1}$), wagging (at about 1350 $cm^{-1}$), twisting (at about 1250 $cm^{-1}$), and rocking (at about 1150 $cm^{-1}$) vibrations of the $CH_2$ group have been observed in the infrared spectrum of the intercalate (see Figure 4).[8,9] The band of the asymmetric C–O–C ring vibrations at about 1090 $cm^{-1}$ is overlapped by $PO_4$ vibrations of vanadyl phosphate in the infrared spectrum. The position of the deformation ring vibration is shifted from 817 to 813 $cm^{-1}$ in the infrared spectrum. The peak of the deformation ring vibration at 872 $cm^{-1}$ of THP is shifted to 870 $cm^{-1}$ with a shoulder at 881 $cm^{-1}$.

The infrared spectra of the $VOPO_4$ intercalate with THP present some reversible changes during heating to 120 °C and cooling back to 25 °C. In the region 3100–2700 $cm^{-1}$, the asymmetric $CH_2$ stretching vibration, which is split into

 © 2007 Wiley-VCH Verlag GmbH & Co. KGaA, Weinheim 

several bands at ambient temperature, passes to two bands at 2936 and 2840 $cm^{-1}$ and the doublet at 3002 and 2993 $cm^{-1}$ passes to one band at 3001 $cm^{-1}$ during heating at about 110 °C. This transition occurs at 90 °C during cooling (see Figure 3). At the same temperatures we observe the reversible changes in the region from 1500 to 1100 $cm^{-1}$ of the scissoring, wagging, and twisting vibrations of $CH_2$ groups and in the region from 1000 to 800 $cm^{-1}$ of the ring deformation vibration (see Figure 4). The observed changes might be explained by the existence of two different conformations of the intercalated THP molecules. Basically, a six-membered ring of THP can adopt one of the two most common conformations: boat and chair. At ambient temperature, the attractive forces between the host layers compel the guest molecules to adopt the boat conformation, which is spatially less demanding. The corresponding low-temperature intercalate has therefore a lower basal spacing. On heating, the attractive forces between layers become less important and the THP molecule can adopt the energetically most favorable conformation, the chair conformation. The high-temperature chair conformation requires more space which results in a higher basal spacing of the intercalate at elevated temperature. This idea is strongly supported by the quantum mechanical calculations presented below.

## NMR Spectroscopy

### *Local Structure and Segmental Dynamics*

The standard $^{13}C$ CP/MAS NMR spectrum of the intercalate (Figure 5a) clearly reflects that the THP molecules intercalated between the layers of vanadyl phosphate are regularly arranged. This is indicated by relatively narrow and symmetric signals with a linewidth of about 0.59, 0.55, and 0.45 ppm for signals C1, C2, and C3, respectively. As these linewidths are almost comparable with the linewidths of $CH_2$ signals of highly crystalline substances measured under the same conditions (e.g. glycine: 0.42 ppm), this feature reflects a high degree of organization and packing of the THP molecules. The other possible explanation, a narrowing of the signals due to the fast rotation or fast ring interconversion of the THP molecules in the interlayer space, can be excluded. As reflected by the determined heteronuclear one-bond $^1H$-$^{13}C$ dipolar splitting $\nu_{CH}$ = 12.2–11.8 kHz (Figure 6), the THP molecules in the basic state at room temperature are fairly immobilized. This follows from the comparison with the expected rigid limit value of $\nu_{CH}$, found to be 12.3 kHz based on a model compound measurement (crystalline glycine).

Motional averaging of the dipolar splitting expressed by an order parameter[10]

$$S = \nu_{CH}/\nu_{CH,rig} = \nu_{CH}/12.3\ \text{kHz}$$

is a measure of the equilibrium distribution of orientations of the bond vector in a molecular reference frame. Assuming segmental motion to be axially symmetric and small in amplitude ($\langle \sin\theta \rangle \approx \langle \theta \rangle$), the order parameter can be converted to a root mean square (*r.m.s.*) angular fluctuation of the bond vector according to the following definition:[10,11]

$$S = 1 - {}^3/_2\langle\theta^2\rangle$$

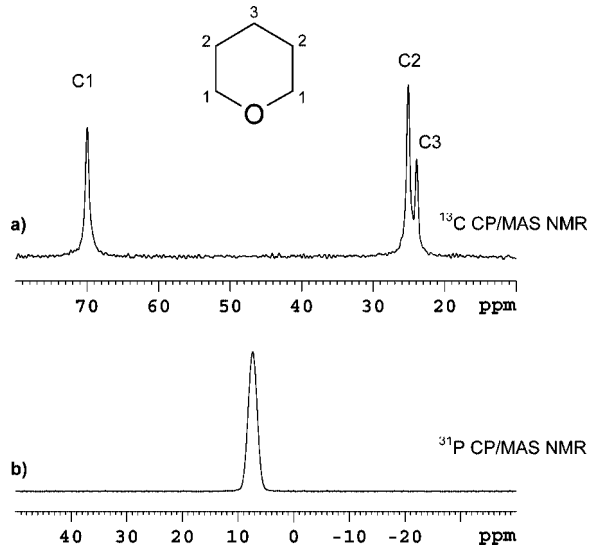


Figure 5. $^{13}C$ CP/MAS NMR spectrum (a) and $^{31}P$ CP/MAS NMR spectrum (b) of $VOPO_4$ with THP.

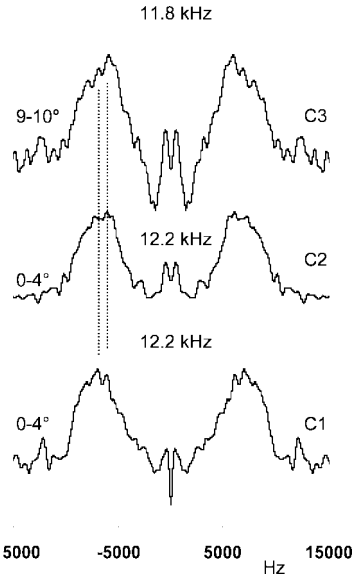


Figure 6. $^{13}C\{^1H\}$ NMR dipolar spectra of $CH_2$ units of the intercalated THP molecules measured at room temperature. The splitting in kHz ($\Delta\nu$) reflecting the motionally averaged dipolar coupling constant ($D_{CH}$) is shown between the maxima and calculated *r.m.s.* amplitudes at the left side of each spectrum.

In the case of the THP molecules intercalated in $VOPO_4$ the order parameter *S* ranges from 0.995 to 0.959. Applying the above-mentioned simplest but still physically realistic model, the determined motional amplitudes of the most rigid carbon atoms C1 and C2 of the THP molecule are about 0–4°. The motional amplitude of the most mobile segment C3 corresponds to a fluctuation angle of about 9–10°. This definitely confirms very low flexibility of THP

 © 2007 Wiley-VCH Verlag GmbH & Co. KGaA, Weinheim 

molecules at room temperature and therefore existence in one preferred conformation. The observed motional restrictions are probably induced by strong interaction with $VOPO_4$ layers.

The character of this intermolecular binding can be deduced from the $^{13}C$ NMR chemical shift. At room temperature the chemical shifts for the resonance peaks of THP trapped in as-synthesized vanadyl phosphate are significantly different from those of THP in the liquid state. It can be seen that the chemical shifts of the carbon atom connected to the oxygen atom in THP (C1), move to low field ($\delta$ = 69.9 ppm) in the $VOPO_4$ intercalate in comparison with $\delta$ = 68.4 ppm in the liquid state. Oppositely, the signals of C2 are significantly moved to high field ($\delta$ = 25.1 ppm), while the position of the signal of the C3 atom is almost unchanged ($\delta$ = 23.9 ppm). In the liquid state the carbon atoms C2 and C3 resonate at $\delta$ = 26.9 and 23.8 ppm. This phenomenon is caused by the nature of the interaction between the oxygen atom of THP and vanadyl phosphate. THP is a polar molecule in which the electronegativity of the oxygen atom is larger than that of the carbon atoms. As the oxygen atom of THP approaches the V atom, part of the electrons on the oxygen atom move to the vanadium atom, leaving the C1 atom with less negative charge. The deshielding effect causes the chemical shift to move to lower field, leading to a larger value of the chemical shift. Consequently, due to the inductive effects, electron density increases around the C2 atoms leading to a higher shielding of the nuclear spins and corresponding lower values of the chemical shifts. As the observed changes in the chemical shift are relatively large, +1.5 and –1.8 ppm for C1 and C2, respectively, the interaction between THP and the vanadyl phosphate framework must be strong.

A tight contact between the THP molecules and the $VOPO_4$ framework is further evidenced by a $^{31}P$ CP/MAS NMR experiment in which the nuclear polarization is transferred from hydrogen atoms of THP to spatially close phosphorus atoms (their distance must not exceed 6 Å). As this experiment can be easily performed (Figure 5b) and the obtained result is quite identical with the $^{31}P$ MAS NMR spectrum measured with a direct excitation of the $^{31}P$ magnetization (not shown here) the THP molecules must be regularly arranged over the whole sample and must be in close contact with all phosphorus atoms.

Average short distances between the hydrogen and phosphorus atoms were estimated from the measurement of $^{31}P$-$^{1}H$ dipolar profiles employing a recently developed and applied two-dimensional Lee–Goldburg cross-polarization experiment.[12,13] The obtained dipolar spectrum (Figure 7) probably corresponds to two superimposed dipolar doublets reflecting a superposition of two independent contributions. The most probable short-range $^{1}H$-$^{31}P$ pairs are reflected by the main splitting of the dipolar spectrum which is about 210 Hz. This corresponds to the average interatomic distance of 5.1 Å. The outer low-intensive doublet with the dipolar splitting of 460 Hz may reflect the shortest $^{1}H$-$^{31}P$ pairs, the interatomic distance of which is about 4.0 Å. The reliability of the applied analysis of the $^{1}H$-$^{31}P$ dipolar spectrum was confirmed by the measurement and subsequent simulation of the $^{1}H$-$^{31}P$ dipolar profiles for a four-spin system of $CaHPO_4$ for which the neutron-diffraction crystal structure is well known.[14]

### *Variable-Temperature $^{13}C$ CP/MAS NMR Spectroscopy*

Variable-temperature NMR experiments offer an interesting prospect to probe a temperature-induced rearrangement occurring in the investigated intercalated system. Gen-

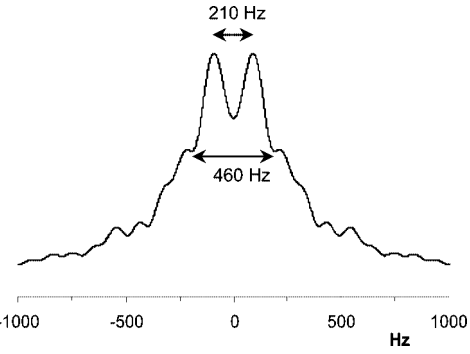


Figure 7. $^{31}P\{^{1}H\}$ dipolar spectrum of $VOPO_4$·THP intercalate measured at room temperature. The splitting in Hz ($\Delta\nu$) is shown between the maxima.

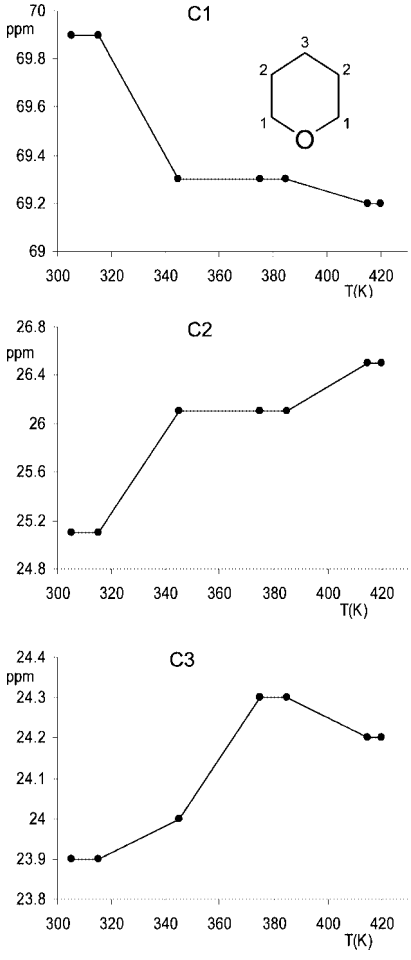


Figure 8. Temperature dependence of the $^{13}C$ NMR chemical shift of $VOPO_4$ with THP.

 © 2007 Wiley-VCH Verlag GmbH & Co. KGaA, Weinheim 

erally, an increase in temperature may help to overcome energy barriers and a reconstitution of the molecules – transition to another "polymorphic" form – can take place. Such changes can be simply monitored by two basic NMR parameters: chemical shift and linewidth of the $^{13}C$ NMR signals.

In our particular case the temperature dependence of the $^{13}C$ NMR chemical shifts (Figure 8) clearly revealed two conformation transitions. Both these transitions are not quite instant and rather occur in more or less broad temperature ranges. The first one occurs in the temperature range 70–85 °C and it is accompanied by a rearrangement of the THP molecules. This statement follows from three observed phenomena: (i) the $^{13}C$ NMR shifts of the C1 and C2 carbons signals substantially moved; (ii) the linewidth of all signals after the transition is significantly narrowed; and finally, (iii) in the temperature range of the phase transition it is almost impossible to record the $^{13}C$ NMR spectra.

The impossibility to detect the $^{13}C$ NMR spectra indicates that the molecules of THP are involved in the dynamic exchange process. The molecular motion, however, is neither very fast nor isotropic, because the $^{13}C$ MAS NMR spectrum measured with direct excitation provides only broad and unresolved signals. That is why this transformation could be attributed to the local conformation transition, for example boat/chair, which – at this temperature range – is reversible. At higher temperatures (95–130 °C) after the first transition, the molecules of THP are again stabilized and rearranged with a significantly higher degree of self-assembling. This is reflected by a high efficiency of the cross-polarization and very narrow signals with a linewidth of 0.48–0.38 ppm (Figure 9). The second transition occurring at about 130 °C is not so dramatic. We observe only slight changes in the $^{13}C$ NMR shift and slight broadening of the corresponding signals indicating increased disorder in packing of the THP molecules. The changes in the chemical shifts observed with increasing temperature further indicate a tendency of the molecules of THP to reach a relatively "free" state without the strong interaction with the $VOPO_4$ framework. Each transition is probably connected to a weakening of the intermolecular interactions between the THP molecules and vanadyl phosphate structure units.

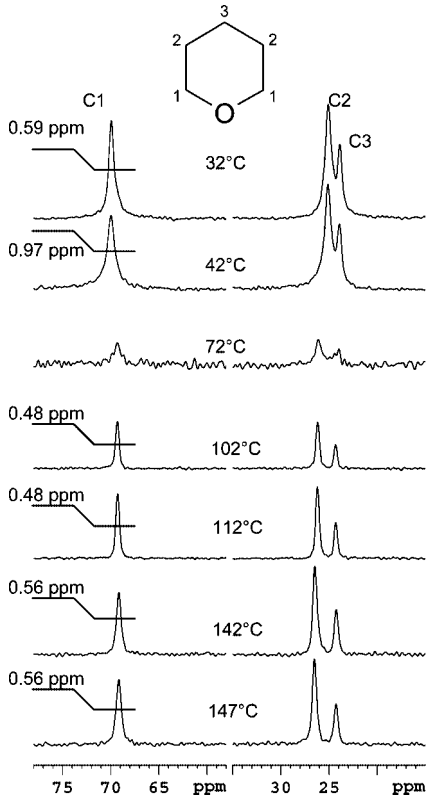


Figure 9. Variable-temperature $^{13}C$ CP/MAS NMR spectra of $VOPO_4$ with THP.

## Quantum Chemical Calculations

The character of the bonding between the guest molecules and the host layer in the THP intercalate was investigated by the methods of quantum chemical calculations. Figure 10 shows a DFT-optimized structure of the molecular segment representing local interactions of vanadyl phosphate with THP, using a B3LYP functional and 6-31G(d) basis set. In order to keep the overall planar structure of the segment during full geometry optimizations and to make the electronic structure in the segment close to the conditions appearing in the intercalates, an oxygen atom was inserted between two neighboring $PO_4$ groups and terminal oxygen atoms were substituted by OH groups.[15] The

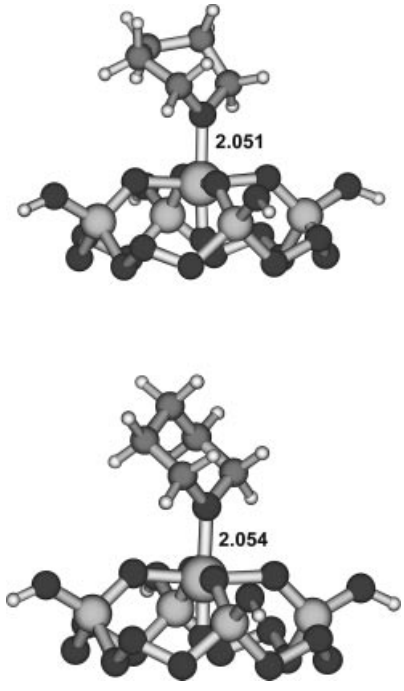


Figure 10. Optimized B3LYP/6-31G(d) structures of the molecular segment modeling the vanadyl phosphate–THP interaction with THP in boat and chair conformations.

 © 2007 Wiley-VCH Verlag GmbH & Co. KGaA, Weinheim 

total charge of the model compound was set to +3. It was found that all geometry optimizations with various starting orientations of THP with respect to the vanadyl group lead to the structures displayed in Figure 10, with the boat and chair conformations of THP. The structure with the chair conformation is energetically more favored by 4.9 kcal/mol.

## Conclusions

In summary, the following conclusions can be made:

(i) The donor-acceptor bond between the oxygen atom of THP and the vanadium atom of $VOPO_4$ has been confirmed by both IR and NMR spectroscopy. This bond loosens with increasing temperature.

(ii) The phase transition observed by the DSC and powder XRD methods is accompanied with changes in the infrared spectrum of the intercalate.

(iii) The existence of two phases (with the phase transition in the temperature region 80–120 °C) could be explained by the fact that the six-membered ring of THP forms two conformations: chair and boat. The chair conformation is energetically more favorable, as follows from the quantum chemical calculations, but is sterically more demanding. Thus, its existence can be presumed at higher temperature, when there is more space between the layers of the host as indicated by higher basal spacing observed for the high-temperature phase. The boat conformation, on the other hand, can be arranged in the interlayer space in such a way that the distance between layers is lower. Therefore, this boat conformation can be present in the low-temperature phase, where it is favored by steric conditions.

(iv) The second transition/change at around 140 °C is most probably caused by weakening of the donor–acceptor bond $O_{THP}$–V and formation of a disorder in packing of the THP molecules. These phenomena are followed by a slow decomposition of the intercalate.

## Experimental Section

**Sample Preparation:** The THP intercalate was prepared either by stirring a suspension of $VOPO_4{\cdot}2C_3H_7OH$ in THP at room temperature overnight or by refluxing a suspension of $VOPO_4{\cdot}2C_3H_7OH$ in THP for 1 h. The products were filtered off and dried under nitrogen at room temperature.

**XRD:** The powder data were obtained with a D8 Advance diffractometer (Bruker AXE, Germany) using Cu-$K_\alpha$ radiation with a secondary graphite monochromator. The diffraction angles were measured from 7 to 80° ($2\theta$). The temperature measurements from 25 to 200 °C were carried out on the heated corundum plate with a thermocouple. Each diffractogram was measured at constant temperature and each cycle of heating and measuring lasted about 60 min.

**DSC Measurements:** DSC experiments were performed with a Mettler DSC 12E instrument. The instrument was previously calibrated with indium, tin, and lead standards. A crystalline powder sample of about 1 mg was placed in an aluminum pan and measured with a heating and cooling rate of 5 K min$^{-1}$ in the range from 40 to 115 °C.

**Infrared Measurements:** The structural and optical properties of the samples were checked using Fourier transform infrared (FTIR) spectroscopy. Infrared measurements were performed with a Bruker IFS 55 EQUINOX FTIR spectrometer with a DLATGS detector. All spectra in the range 400–4000 cm$^{-1}$ with 2 cm$^{-1}$ spectral resolution were obtained from compressed KBr pellets in which the $VOPO_4{\cdot}$THP powders were evenly dispersed. Two hundred scans were used to record each FTIR spectrum. A variable-temperature-controlled cell (Specac Ltd.) in the range from 0 to +250 °C with solid holders was used for temperature-dependent measurements. The spectrum of the corresponding liquid THP was measured by the ATR technique on a ZnSe crystal. The spectra were corrected for the content of $H_2O$ and $CO_2$ in the optical path.

**Solid-State NMR Spectroscopy:** Standard one-dimensional (1D) experiments with cross-polarization (CP) and with direct excitation as well as two-dimensional (2D) recoupling experiments were performed with a Bruker Avance 500 NMR spectrometer (Karlsruhe, Germany, 2003) with a 4-mm $ZrO_2$ rotor. Magic-angle spinning (MAS) speed was 10–12 kHz, the nutation frequency of the $B_1(^{13}C)$ and $B_1(^{31}P)$ field was 62.5 kHz, and the repetition delay was 4 s. To detect site-specific $^1H$-$^{13}C$ and $^1H$-$^{31}P$ dipolar spectra, 2D PILGRIM (Phase Inverted LG Recoupling under MAS) experiments[12] were applied. Incremented off-resonance LG-CP with a 22.6 μs increment was used as a dipolar evolution period. The intensity of the $B_1(^1H)$ field for cross-polarization was $\omega_1/2\pi$ = 62.5 kHz and Hartman–Hahn matching conditions at the +1 spinning side-band were optimized experimentally. TPPM (two-pulse phase-modulated) decoupling was applied during the detection periods. The phase modulation angle was 15°, and the flip-pulse length was 4.7 μs. The applied nutation frequency of the $B_1(^1H)$ field was $\omega_1/2\pi$ = 89.3 kHz. The $^{13}C$ scale was calibrated with glycine as the external standard ($\delta$ = 176.03 ppm: low-field carbonyl signal). The $^{31}P$ scale was calibrated with $CaHPO_4$ ($\delta$ = –0.6 ppm). Taking into account frictional heating of the samples during fast rotation[16] precise temperature calibration was performed before variable-temperature experiments.

**Method of Calculation:** Quantum chemical calculations were carried out at the ab initio level of theory employing the Gaussian 98[17] program package. Local interactions and structures in the intercalates of vanadyl phosphate with THP were studied at a DFT level using a B3LYP functional with a 6-31G(d) basis set.

## Acknowledgments

This study was supported by the Academy of Sciences of the Czech Republic (AVOZ40500505) and Ministry of Education, Youth, and Sports of the Czech Republic (MSM0021627501). The help of the Grant Agency of the Academy of Sciences of the Czech Republic (grant IAA400500602) is also appreciated.

[1] H. R. Tietze, *Aust. J. Chem.* **1981**, *34*, 2035–2038.
[2] M. Tachez, F. Theobald, J. Bernard, A. W. Hewat, *Rev. Chim. Miner.* **1982**, *19*, 291–300.
[3] J. Kalousová, J. Votinský, L. Beneš, K. Melánová, V. Zima, *Collect. Czech. Chem. Commun.* **1998**, *63*, 1–19.
[4] K. Goubitz, P. Čapková, K. Melánová, W. Molleman, H. Schenk, *Acta Crystallogr., Sect. B* **2001**, *57*, 178–183.
[5] V. Zima, K. Melánová, L. Beneš, M. Trchová, P. Čapková, P. Matějka, *Chem. Eur. J.* **2002**, *8*, 1703–1709.
[6] L. Beneš, V. Zima, K. Melánová, M. Trchová, P. Čapková, B. Koudelka, P. Matějka, *Chem. Mater.* **2002**, *14*, 2788–2795.
[7] M. Trchová, P. Čapková, K. Melánová, L. Beneš, P. Matějka, E. Uhlířová, *J. Solid State Chem.* **1999**, *148*, 197–204.

 © 2007 Wiley-VCH Verlag GmbH & Co. KGaA, Weinheim 

[8] N. Bagget, S. A. Barker, A. B. Foster, R. H. Moore, D. H. Whiffen, *J. Am. Chem. Soc.* **1960**, *82*, 4565–4570.
[9] J. M. Eyster, *Spectrochim. Acta A* **1974**, *30*, 2041–2046.
[10] A. G. Palmer, J. Williams, A. McDermott, *J. Phys. Chem.* **1996**, *100*, 13293–13310.
[11] D. Huster, L. Xiao, M. Hong, *Biochemistry* **2001**, *40*, 7662–7674.
[12] M. Hong, X. Yao, K. Jakes, D. Huster, *J. Phys. Chem. B* **2002**, *106*, 7355–7364.
[13] B. J. van Rossum, C. P. de Groot, V. Ladizhansky, S. Vega, H. J. M. de Groot, *J. Am. Chem. Soc.* **2000**, *122*, 3465–3472.
[14] M. Catti, G. Ferraris, A. Filhol, *Acta Crystallogr., Sect. B* **1977**, *33*, 1223–1229.
[15] V. Zima, K. Melánová, L. Beneš, M. Trchová, J. Dybal, *Eur. J. Inorg. Chem.* **2004**, 570–574.
[16] J. Brus, *Solid State Nucl. Magn. Reson.* **2000**, *16*, 151–160.
[17] M. J. Frisch, G. W. Trucks, H. B. Schlegel, G. E. Scuseria, M. A. Robb, J. R. Cheeseman, J. A. Montgomery Jr, T. Vreven, K. N. Kudin, J. C. Burant, J. M. Millam, S. S. Iyengar, J. Tomasi, V. Barone, B. Mennucci, M. Cossi, G. Scalmani, N. Rega, G. A. Petersson, H. Nakatsuji, M. Hada, M. Ehara, K. Toyota, R. Fukuda, J. Hasegawa, M. Ishida, T. Nakajima, Y. Honda, O. Kitao, H. Nakai, M. Klene, X. Li, J. E. Knox, H. P. Hratchian, J. B. Cross, V. Bakken, C. Adamo, J. Jaramillo, R. Gomperts, R. E. Stratmann, O. Yazyev, A. J. Austin, R. Cammi, C. Pomelli, J. W. Ochterski, P. Y. Ayala, K. Morokuma, G. A. Voth, P. Salvador, J. J. Dannenberg, V. G. Zakrzewski, S. Dapprich, A. D. Daniels, M. C. Strain, O. Farkas, D. K. Malick, A. D. Rabuck, K. Raghavachari, J. B. Foresman, J. V. Ortiz, Q. Cui, A. G. Baboul, S. Clifford, J. Cioslowski, B. B. Stefanov, G. Liu, A. Liashenko, P. Piskorz, I. Komaromi, R. L. Martin, D. J. Fox, T. Keith, M. A. Al-Laham, C. Y. Peng, A. Nanayakkara, M. Challacombe, P. M. W. Gill, B. Johnson, W. Chen, M. W. Wong, C. Gonzalez, J. A. Pople, *Gaussian 03*, Revision C.02, Gaussian, Inc., Wallingford, CT, **2004**.

Received: July 4, 2006
Published Online: November 27, 2006

 © 2007 Wiley-VCH Verlag GmbH & Co. KGaA, Weinheim 

DOI: 10.1002/ejic.200600726

# Reactivity and X-ray Structural Studies in Ligand Substitution of [Cp/(Ind)Ru(dppf)Cl] – Epimerisation in [Cp/(Ind)Ru(Josiphos)Cl] {Cp = $\eta^5$-$C_5H_5$, Ind = $\eta^5$-$C_7H_9$, dppf = 1,1′-Bis(diphenylphosphanyl)ferrocene, Josiphos = (*R*)-(–)-1-[(*S*)-2-(Diphenylphosphanyl)ferrocenyl]ethyldicyclohexylphosphane}

**Sin Yee Ng,[a] Guihua Fang,[a] Weng Kee Leong,*[a] Lai Yoong Goh,*[a] and Marc V. Garland[b]**

**Keywords:** Indenyl / Ruthenium / dppf / Josiphos / Epimerisation / Phosphanes

Ligand substitution of [(Ind)Ru($PPh_3$)$_2$Cl] (**1**) led to the isolation of [(Ind)Ru($PPh_3$){$Ph_2P(CH_2)_2C_9H_7$}Cl] (**2**), [(Ind)Ru(dppf)Cl] (**3**) and [(Ind)Ru{$(Ph_2PCH_2)_3CMe$}]$PF_6$ ([**4**]$PF_6$), and diastereoisomers [(*R*)- and (*S*)-(Ind)Ru(Josiphos)Cl] [(*R*)-**5** and (*S*)-**5**], where (*R*)-(*S*)-Josiphos is the ferrocene-based chiral diphosphane ligand (*R*)-(–)-1-[(*S*)-2-(diphenylphosphanyl)ferrocenyl] ethyldicyclohexylphosphane. The Cp analogues of **5**, viz. (*R*)-**6** and (*S*)-**6**, were also obtained from [CpRu($PPh_3$)$_2$Cl] (**1a**). Josiphos-dependent epimerisation was observed, with conversion of the (*S*) isomer to the (*R*) isomer in both cases. Chloride abstraction of **3** with $NaPF_6$ in $CH_3CN$ and $NaN_3$ in EtOH gave [(Ind)Ru(dppf)($CH_3CN$)]$PF_6$ ([**7**]$PF_6$) and [(Ind)Ru(dppf)($N_3$)] (**8**), respectively. The azido ligand in **8** underwent [3+2] dipolar cycloaddition with dimethyl acetylenedicarboxylate to give a *N*-bound bis(methoxycarbonyl)-1,2,3-triazolato complex, **9**. X-ray crystal structures of the new complexes, except (*R*)-**5**, (*S*)-**5** and (*S*)-**6**, have been determined.
(© Wiley-VCH Verlag GmbH & Co. KGaA, 69451 Weinheim, Germany, 2007)

## Introduction

The chemistry of phosphane organometallic complexes has been well established in the last four decades,[1] interest being fuelled by their roles in medicinal and catalytic applications.[2] In particular, [CpRu($PPh_3$)$_2$Cl] (**1a**), first synthesised in 1969 by Gilbert and Wilkinson,[3] has attracted much attention. A rich chemistry has unfolded, based on the facile substitution of the $PPh_3$ ligand by two-electron donors, as well as the ready displacement of the chlorido ligand by both anionic and neutral ligands.[4] Its well-defined CpRu($PPh_3$)$_2$ moiety is an attractive auxiliary that can be used for the attachment of organic groups in studies of their steric and electronic effects on the chemical[4a] and catalytic[5] reactivity of the complex. More recently, the role of metallophosphane ligands, for example, of the symmetrical and unsymmetrical ferrocenyl type, in catalysis of organic reactions is increasingly being studied, as the ligands become more readily available.[6]

The marked effect of the capping ligand on reactivity of the complex came to light with the synthesis of [(Ind)Ru($PPh_3$)$_2$Cl] (**1**) (Ind = $\eta^5$-$C_9H_7$) some 16 years after that of its Cp analogue, **1a**.[7] The enhanced reactivity, commonly known as the "indenyl effect", was found to be largely brought about by ring slippage.[8] The combined effect of capping ligand and phosphane ligand variant would therefore be of interest. We note that research in recent years on (Ind)Ru chemistry has been focused on vinylidene and allenylidene complexes by the group of Gimeno,[8,9] and nitrogen-containing ligands, for example, amines, nitriles, *N*,*N*′-donor Schiff bases and azine ligands, by Kollipara and co-workers.[10] In this work, we have investigated the reactivity of **1** with the ferrocenyl diphosphane ligands 1,1′-bis(diphenylphosphanyl)ferrocene (dppf) and chiral ferrocenyl diphosphane ligand {(*R*)-(*S*)-Josiphos} and with the tripod ligand {$(Ph_2CH_2)_3CMe$}, and the reactivity of [(Ind)Ru(dppf)Cl] (**3**) towards N-containing ligands.

## Results and Discussion

### Phosphane Substitution

#### *Synthesis of [(Ind)Ru($PPh_3$){$Ph_2P(CH_2)_2C_9H_7$}Cl] (2), [(Ind)Ru(dppf)Cl] (3) and [(Ind)Ru(tripod)]$PF_6$ ([4]$PF_6$)*

As in [CpRu($PPh_3$)$_2$Cl] (**1a**), the substitution lability of $PPh_3$ in [(Ind)Ru($PPh_3$)$_2$Cl] (**1**) has provided an easy entry to various [(Ind)Ru] complexes. For instance, [(Ind)Ru(diphos)Cl] had been synthesised from a reaction of [(Ind)-

[a] Department of Chemistry, National University of Singapore, 3 Science Drive, Singapore 117543
Fax: +65-6779-1691
E-mail: chmgohly@nus.edu.sg
chmlwk@nus.edu.sg
[b] Institute of Chemical and Engineering Sciences, 1 Pesek Road, Jurong Island, Singapore 627833


© 2007 Wiley-VCH Verlag GmbH & Co. KGaA, Weinheim

$Ru(PPh_3)_2Cl$] by substitution with the desired diphos in refluxing toluene.[7] Adopting the reported procedure for the synthesis of (Ind)Ru(dppe)Cl [dppe = 1,2-bis(diphenylphosphanyl)ethane],[11] phosphane substitution of **1** at elevated temperature in toluene gave air- and moisture-stable red solids of the monophosphane-substituted complex [(Ind)-$Ru\{Ph_2P(CH_2)_2C_9H_7\}(PPh_3)Cl$] (**2**), containing the (1-indenylethyl)diphenylphosphane ligand **LH** (Scheme 1a), the diphosphane-substituted complex [(Ind)Ru(dppf)Cl] (**3**) with dppf (Scheme 1b), and a totally substituted complex [(Ind)-$Ru(Ph_2PCH_2)_3Me]PF_6$ ([**4**]$PF_6$) with the tripodal triphos ligand $(Ph_2PCH_2)_3CMe$ (Scheme 1c), in high yields.

It is anticipated that phosphane substitution of **1** will be facilitated by the release of steric stress in the coordination sphere by dissociation of one or both of the bulky $PPh_3$ ligands. This is very likely the driving force in the formation of **2**, as the ligand **LH** is less bulky than $PPh_3$. In the cases of **3** and [**4**]$PF_6$, the reactions are additionally assisted by the chelating effect of the incoming di- and triphosphane ligand, respectively.

The $^1H$ NMR spectrum of **2** shows four multiplets in the range $\delta$ = 1.79–3.52, assigned to the four inequivalent methylene protons of **LH**. The $CH_2$ protons of the five-membered ring of **LH** resonate at $\delta$ = 2.93, while the olefinic proton resonates at a higher field at $\delta$ = 6.5. On the other hand, the protons $H^{1-3}$ (see Experimental Section for numbering scheme) of the $\eta^5$-coordinated Ind ligand resonate at $\delta$ = 4.95–5.00 and $\delta$ = 5.78 ppm. The $^{31}P$ NMR spectrum shows two doublets at $\delta$ = 46.5 and $\delta$ = 50.0 with $^2J_{PP}$ = 42.9 Hz due to the coupling of the two inequivalent phosphorus atoms.

The $^1H$ NMR spectrum of **3** shows an ABCD pattern for the proton signals of the ferrocene rings at $\delta$ = 3.66, 3.83, 3.90 and 4.20, suggesting an eclipsed conformation for the chelating dppf ligand in **3**;[12] this was supported by the X-ray single-crystal diffraction analysis. The Cp proton signals of the $\eta^5$-indenyl ligand appear at $\delta$ = 4.66 ($H^1$) and 5.57 ($H^{2,3}$). The latter resonance is 1.67 ppm downfield shifted from that in the bis($PPh_3$) analogue, owing to relief from the shielding effect caused by the ring current of the Ph ring of $PPh_3$ on $H^2$ and $H^3$ in **1**.[13]

The $^1H$ NMR spectrum of [**4**]$PF_6$ shows a multiplet at $\delta \approx 1.5$ and a broad singlet at $\delta \approx 2.39$, assigned to the methyl and methylene groups of the tripod ligand, indicating the fluxionality of these groups in solution. However, a sharp singlet at $\delta$ = 39.9 in the $^{31}P$ NMR spectrum indicates an equivalent chemical environment for the three coordinated phosphorus atoms of tripod. The proton resonances of $H^1$ and $H^{2,3}$ of the indenyl ligand appear at $\delta$ = 5.51 and 5.57 ppm, while $H^{4-7}$ appear as two characteristic four-line multiplets at $\delta$ = 7.31–7.34 and $\delta$ = 7.43–7.47, respectively.

The molecular structures of **2**, **3** and [**4**]$^+$ have been determined by single-crystal X-ray crystallographic studies; their ORTEP diagrams are shown in Figures 1, 2 and 3, respectively, and selected bond parameters are compared with those of CpRu(dppf)Cl[14] in Table 1.

The molecular structures of **2** and **3** show Ru hexacoordinated to Ind, a Cl atom and two phosphorus atoms, that is, from $PPh_3$ and $C_9H_7(CH_2)_2PPh_2$ in **2** and from chelating dppf in **3**. The molecular structure of [**4**]$^+$ consists of a mononuclear cation [($\eta^5$-Ind)Ru(tripod)]$^+$ and $PF_6^-$ anion, to-

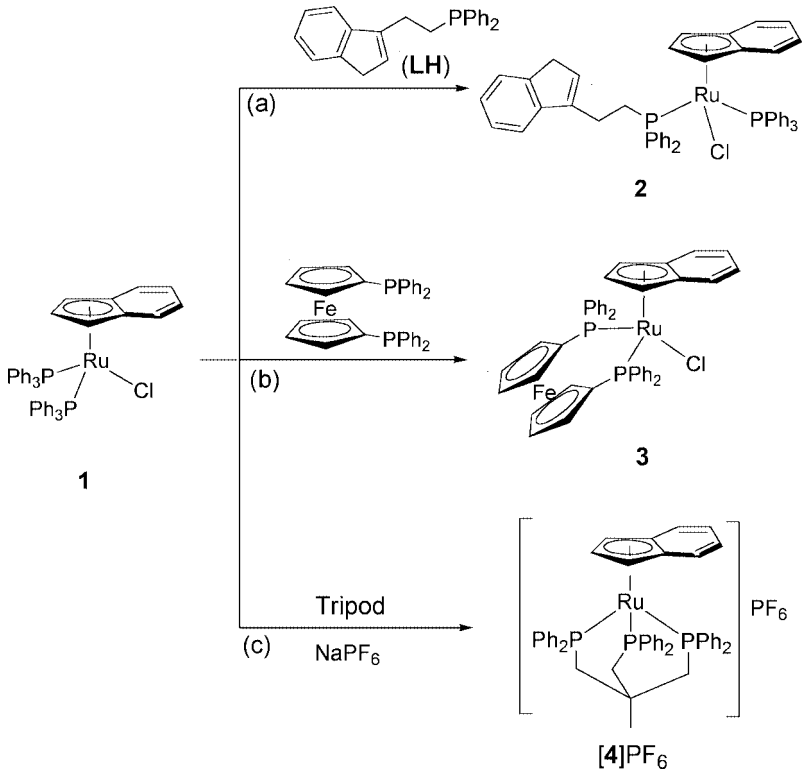


Scheme 1.

 © 2007 Wiley-VCH Verlag GmbH & Co. KGaA, Weinheim 

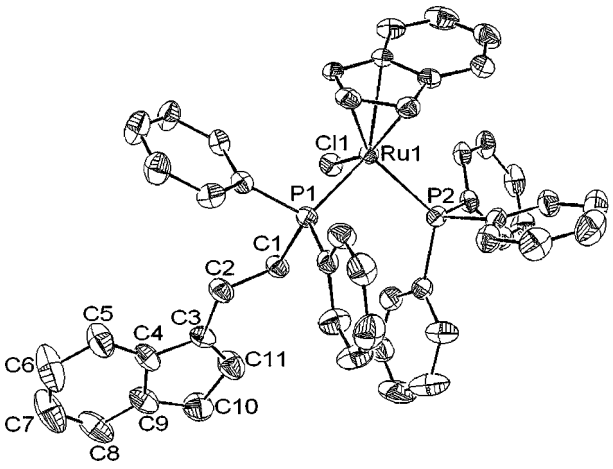


Figure 1. ORTEP diagram of **2**. Thermal ellipsoids are drawn to 50% probability level. Hydrogen atoms are omitted for clarity. Selected bond lengths: C1–C2 1.530(7) Å; C2–C3 1.506(6) Å; C3–C11 1.329(7) Å; C3–C4 1.454(7) Å; C4–C5 1.375(7) Å; C5–C6 1.388(8) Å; C6–C7 1.374(9) Å; C7–C8 1.368(9) Å; C8–C9 1.3859(8) Å; C9–C4 1.401(7) Å; C9–C10 1.513(8) Å; C10–C11 1.494(7) Å. Other bond parameters are given in Table 1.

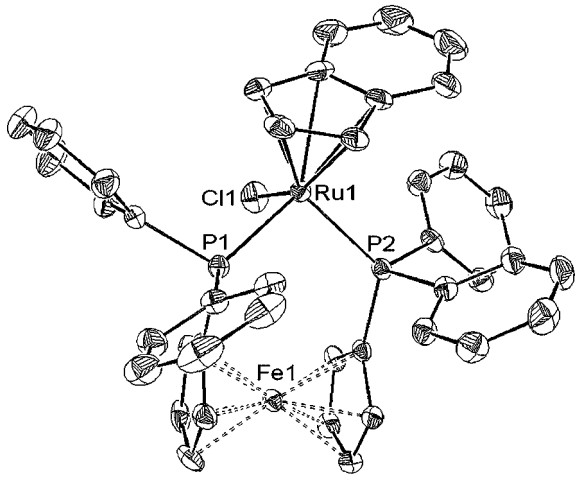


Figure 2. ORTEP diagram of **3**. Thermal ellipsoids are drawn to 50% probability level. Hydrogen atoms are omitted for clarity.

gether with two solvent molecules of dichloromethane, one of which is disordered.

A general, yet prominent structural feature of $\eta^5$-indenyl complexes is the distortion from $\eta^5$- to $\eta^3$-coordination, equivalent to an allyl-ene bonding description for the $C_5$ ring. Such a distortion is found in **2**, **3** and [**4**]$^+$, as evident from the values of their slip distortions ($\Delta$) and hinge angles (HA), which fall in the range of small or moderate distortion towards a $\eta^3$ binding mode.[15] The slightly larger distortion in **3** (longer $\Delta$) is probably a result of the stronger $\sigma$-donor capability of dppf.[8] The unusually large fold angle (FA) in [**4**]$^+$ likely arises from the steric congestion created by the phenyl rings of the tripod ligand, which causes the benzenoid ring of the indenyl ligand to twist upwards,

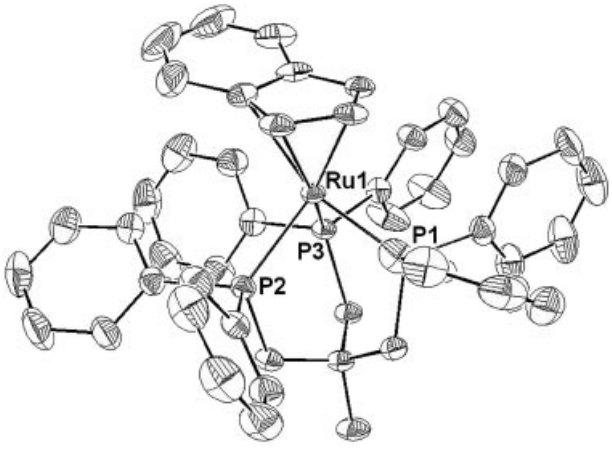


Figure 3. ORTEP diagram of [**4**]$^+$. Thermal ellipsoids are drawn to 50% probability level. Hydrogen atoms are omitted for clarity.

Table 1. Selected bond parameters of complexes **2**, **3**, [**4**]$^+$ and [CpRu(dppf)Cl].

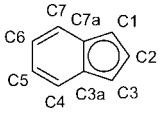


| Complexes | **2** | **3** | [**4**]$^+$ | [CpRu(dppf)Cl][14] |
|---|---|---|---|---|
| $\Delta$ [Å][a] | 0.182(5) | 0.193(4) | 0.182(5) | – |
| Hinge angle (HA) [°][a] | 7.43 | 7.69 | 7.71 | – |
| Fold angle (FA) [°][a] | 11.22 | 11.02 | 15.62 | – |
| | | | | |
| C*–Ru1[b] | 1.913(5) | 1.901(4) | 1.973(5) | – |
| Ru1–P1 | 2.2568(14) | 2.2556(9) | 2.3120(13) | 2.2858(14) |
| Ru1–P2 | 2.3160(14) | 2.2959(9) | 2.2479(14) | 2.2844(13) |
| Ru1–P3 | – | – | 2.3170(13) | – |
| Ru1–Cl1 | 2.4194(14) | 2.4434(9) | | 2.4443(13) |
| | | | | |
| P1–Ru1–P2 | 96.71(5) | 98.22(3) | 88.81(5) | 95.04(5) |
| P2–Ru1–P3 | – | – | 86.19(5) | – |
| P1–Ru1–P3 | – | – | 87.93(5) | – |
| P1–Ru1–Cl1 | 89.78(4) | 90.99(3) | – | 93.20(5) |
| P2–Ru1–Cl1 | 90.56(5) | 90.43(3) | – | 89.48(5) |

[a] Slip-fold parameters as defined in ref.[15]. [b] C* = centroid of the five-membered ring, C1, C2, C3, C3a and C7a.

 © 2007 Wiley-VCH Verlag GmbH & Co. KGaA, Weinheim 

thereby increasing the FA. This steric congestion is also reflected in the significantly longer C*–Ru1 bond length.

The "ene" character of the "dangling" ethylindene substituent of **LH** in **2** was indicated by the short C3–C11 bond length [1.329(7) Å], of C–C double bond character.[16] The C–C bond lengths of the benzenoid ring have an average of 1.382 Å, consistent with aromaticity of the ring.[16]

The metric data for the structures of **2**, **3** and [**4**]$^+$ are significantly different from those of CpRu(dppf)Cl.[14] While the Ru1–P bond lengths in the latter complex are almost identical, the two Ru1–P bond lengths in each of **2**, **3** and [**4**]$^+$ differ substantially, by 0.04–0.07 Å, probably because of the steric repulsion between the benzenoid ring of the indenyl ligand and the phenyl rings bonded to P2, which are situated directly below the benzenoid ring. The Cp rings of dppf in **3** are almost eclipsed (synperiplanar), with a torsional angle ($\tau$) of 4.3°, and the rings are tilted at an angle of 6.3°. The P1–Ru1–P2 angle of 98.22° is larger than those in **2** and [**4**]$^+$, undoubtedly because of the expanse of the dppf ligand. However, the value, like that of the Cp analogue (95.05°), falls in the range 91.6–102.2° reported for Ru(dppf) complexes.[17]

### *Synthesis of [(CpIInd)Ru(Josiphos)Cl]*

Phosphane substitution of **1** or **1a** by the ferrocene-based chiral diphosphane ligand (*R*)-(–)-1-[(*S*)-2-(diphenylphosphanyl)ferrocenyl]ethyldicyclohexylphosphane {(*R*)-(*S*)-Josiphos} can likewise be achieved at an elevated temperature (Scheme 2). Because of the inequivalence of the two phosphorus atoms in (*R*)-(*S*)-Josiphos and the pseudotetrahedral geometry of **1** and **1a**, a pair of diastereomers is formed, as displacement of $PPh_3$ by chiral Josiphos generates a chiral ruthenium centre.

It was found that an 8-h reflux generated a 1:1:3:2 equilibrium mixture of **1**, free Josiphos, (*R*)-**5** and (*S*)-**5** diastereomers. Prolonged reaction time did not lead to completion, but gave instead a decomposition product with a $^{31}P$ NMR resonance at $\delta$ = 24.9 ppm. Pure (*R*)-**5** can be isolated by liquid chromatography of the mixture, with 'loss' of the (*S*)-**5** isomer. Purification by fractional crystallisation was rendered impossible by the similar solubility of **1** and **5**.

A similar reaction of **1a** with (*R*)-(*S*)-Josiphos (1:1) for 1.5 h gave a 1.5:1 molar mixture of (*R*)- and (*S*)-[CpRu(Josiphos)Cl] (**6**) diastereomers. Further heating caused epimerisation of (*S*)-**6** to (*R*)-**6**, with complete conversion in 8 h, indicating that (*S*)-**6** is the kinetic product, while (*R*)-**6** is the thermodynamically more stable isomer (Scheme 3). The simultaneous appearance of two new sets of doublets in the $^{31}P$ NMR spectrum, corresponding to (*R*)-**6** and (*S*)-**6**, respectively, indicated that the chelation of Josiphos was a concerted process. This was unlike the stepwise process observed in the analogous displacement reactions of **1a** by other chiral diphosphanes.[18]

Pure (*R*)-**6** can be isolated by either liquid chromatography or by fractional crystallisation. Isolation of pure (*S*)-**6** was in vain, owing to epimerisation to (*R*)-**6**, despite attempts to slow down the process by the presence of a free ligand (see rate studies below); the process was found to be accelerated on a silica-gel column.

The configuration at the metal centre of **5** was determined by matching the coupling constants of the pair of doublets observed in the $^{31}P$ NMR spectrum to those of **6** [structurally determined (*R*)-**6** possesses $\delta$ = 37.5 and 67.2 ppm ($^2J_{PP}$ = 53.4 Hz) and (*S*)-**6**: $\delta$ = 49.3 and 68.1 ppm ($^2J_{PP}$ = 49.6 Hz)]. Based on these, the resonances for the diastereoisomers of **5** were assigned as follows: a pair of

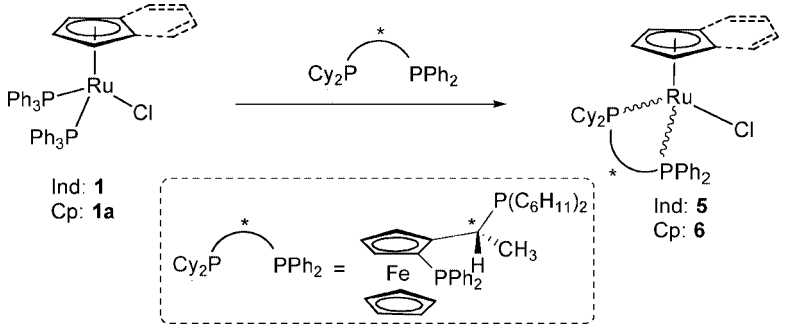


Scheme 2.

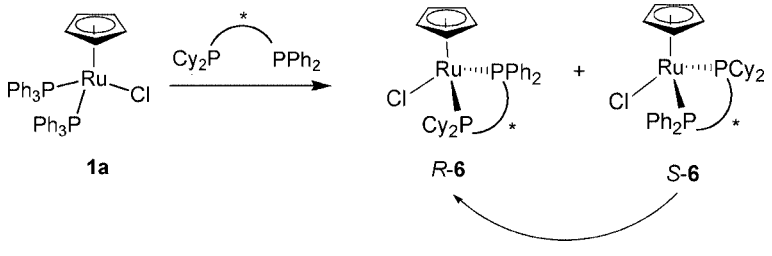


Scheme 3.

 © 2007 Wiley-VCH Verlag GmbH & Co. KGaA, Weinheim 

doublets at $\delta$ = 36.0 and 77.3 ppm ($^2J_{PP}$ = 53.4 Hz) for (*R*)-**5**, and $\delta$ = 60.5 and 68.4 ppm ($^2J_{PP}$ = 49.6 Hz) for (*S*)-**5**. In the $^1$H NMR spectra of (*R*)-**5** and (*R*)-**6**, the cyclohexyl protons resonate as broad signals in the range $\delta$ = 0.6–2.7; the Me resonance sits on top of one of the broad signals. The Cp protons of Josiphos in (*R*)-**5** and (*R*)-**6** resonate in the range $\delta$ = 3.68–4.30. Protons signals at $\delta$ = 5.34 ($H^1$) and 5.73 ($H^{2,3}$) are assignable to protons of $\eta^5$-Ind in (*R*)-**5**. In (*R*)-**6**, the protons of $\eta^5$-CpRu are observed at $\delta$ = 4.49 ppm.

The NMR spectroscopic data of (*S*) isomers of **5** and **6** were obtained from spectra of their diastereoisomeric mixtures by eliminating the resonances assigned to their (*R*) isomers and the starting materials. The $^{31}$P resonances of both (*S*)-**5** and (*S*)-**6** can be easily identified, as they are very well resolved. However, their $^1$H resonances overlapped extensively with those of the corresponding (*R*) isomer, with the exception of the singlets at $\delta$ = 3.56 in (*S*)-**5** and 3.89 in (*S*)-**6**, which belong to the protons of the Cp ring of Josiphos.

The X-ray crystal structure of (*R*)-**6** was obtained. A view of the molecule is shown in Figure 4, together with selected bond parameters. The cyclopentadienyl ring is slightly distorted, with a hinge angle of 2.22° and $\Delta$ of 0.037 Å. The bond lengths of Ru1–P, Ru1–Cl1 and average Ru1–C (of Cp ring) are comparable to those of (*S*)-{RuCl(Cp)[(*R*)-dppp]}.[19] The longer Ru1–P2 compared to Ru1–P1 is also observed in the crystal structure of *trans*-$RuCl_2${(*R*)-(*S*)-Josiphos}$(py)_2$.[20]

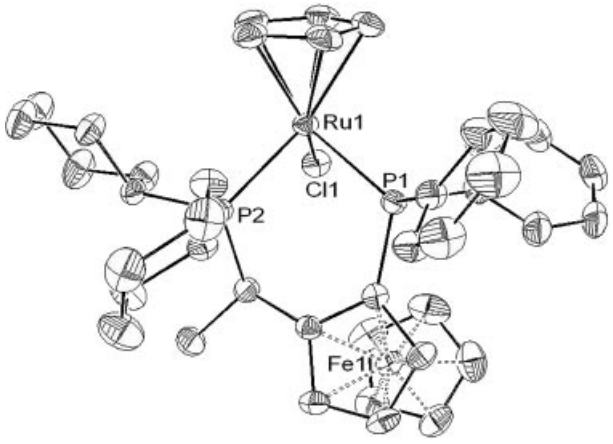


Figure 4. ORTEP diagram of (*R*)-**6**. Thermal ellipsoids are drawn to 50% probability level. Hydrogen atoms are omitted for clarity. Selected bond parameters: $\Delta$ = 0.037(4) Å; HA = 2.22°; C*–Ru1 1.858(4) Å; Ru1–P1 2.2804(11) Å; Ru1–P2 2.3115(11) Å; Ru1–Cl1 2.4525(11) Å; P1–Ru1–P2 90.22(4)°; P1–Ru1–Cl1 89.22(4)°; P2–Ru1–Cl1 90.41(4)°.

### Epimerisation of 6

As both complexes **5** and **6** undergo $S \rightarrow R$ epimerisation, it would be desirable to investigate their configurational stability and racemisation processes, as these processes often determine the potential of chiral-at-metal complexes in homogeneous catalysis. Complex **6** was chosen to be investigated rather than **5**, as the latter is thermally unstable.

$^1$H and $^{31}$P NMR spectral observations of the reaction of **1a** with Josiphos showed that the rate of epimerisation was markedly dependent on the concentration of free Josiphos in the reaction mixture. Thus, three experiments were carried out keeping Josiphos concentration [**J**] at 10 mM, and varying the molar ratio of **1a** to Josiphos. The results are given in Figure 5. In all three experiments, (*R*)-**6** and (*S*)-**6** were formed in about 1.2:1 ratio in the first 10 min of the reactions. Subsequently, the ratio of (*R*)-**6** to (*S*)-**6** increased rapidly in reactions **A** and **B**, as epimerisation proceeded at approximately similar rates, reaching a ratio of about 3 in 30 min, followed by a sharp increase to 118 at 90 min (reaction **A**), and 83.5 at 100 min (reaction **B**). It was observed that Josiphos was totally consumed at 30 min in reaction **A**, but was slowly consumed in reaction **B** to a negligible amount at about 50 min. In reaction **C**, using a 0.5 molar excess of Josiphos, epimerisation was observed to be extremely sluggish: the (*R*)-**6**/(*S*)-**6** ratio remained at about 1.5 up to 135 min, followed by a slow increase to about 10 in 500 min. This dramatic inhibition of epimerisation would suggest a dissociative type of mechanism, but the role of free Josiphos is currently still unclear to us. This case, involving a bidentate biphosphane, would not be expected to exactly parallel that for phosphane substitution in indenyl and $CpRu(PPh_3)_2$ complexes, for which a dissociative mechanism had been proposed by Gimeno on the basis of rate retardation by added $PPh_3$.[11] Nonetheless, the inhibitory effect of free Josiphos provides a useful way to control the rate of epimerisation.

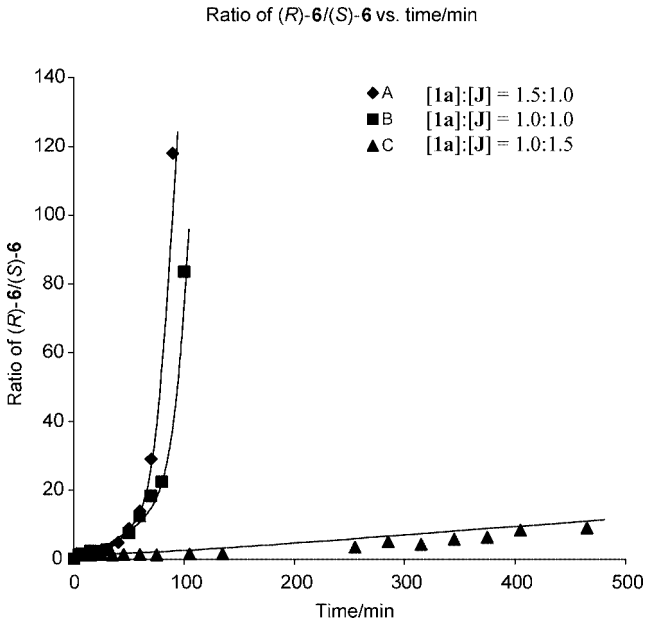


Figure 5. A plot of the ratio of (*R*)-**6**/(*S*)-**6** vs. time for the reaction of **1a** with Josiphos (**J**); [**J**] = 10 mM.

 © 2007 Wiley-VCH Verlag GmbH & Co. KGaA, Weinheim 

Complex (*R*)-**6** was observed to exhibit configurational stability in solution indefinitely, even at elevated temperature. As configurational stability is an asset for catalyst performance to give high enantioselectivity, (*R*)-**6** has good catalytic potential, especially for transfer hydrogenation of ketones, as was found for chiral-at-metal organoruthenium complexes.[21] Catalytic investigations of (*R*)-**6** are currently in progress in our laboratory.

### Chloro Lability of [(Ind)Ru(dppf)Cl] (3)

As in the case of **1** and **1a**, chloro substitution of **3** provides a convenient pathway to new derivatives. It was found that chloride abstraction with $NaPF_6$ occurred readily in $CH_3CN$ under reflux, giving the yellow acetonitrile solvento complex $[(Ind)Ru(dppf)(CH_3CN)]PF_6$ ([**7**]$PF_6$) (Scheme 4). This compound was fully characterised spectroscopically (see Experimental Section). The Cp protons of dppf display an ABCD pattern, similar to that in **3**.

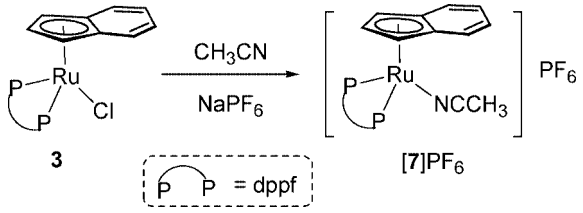


Scheme 4.

Treatment of **3** with $NaN_3$ in ethanol at reflux for 4 h afforded an 85% yield of **8** (Scheme 5), the spectral characteristics of which are given in Experimental Section. Here again, the Cp protons show an ABCD pattern.

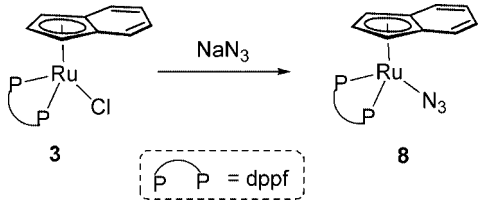


Scheme 5.

As at $Pt^{II}$[22] and $Pd^{II}$[23] centres, the azido ligand in **8** undergoes [3+2] dipolar cycloaddition reaction with dimethyl acetylenedicarboxylate, giving the N(2)-bound 4,5-bis(methoxycarbonyl)-1,2,3-triazolato complex **9** in 55% yield from an ambient temperature reaction (Scheme 6). Several cycloaddition reactions have been reported in half-sandwich ruthenium systems, like $[(Ind)Ru(LL)(N_3)]$, $[Cp^*Ru(LL)(N_3)]$ (LL = dppm, dppe)[10f] and $[CpRu(dppe)(N_3)]$.[24] This is a useful synthetic route to some heterocycles, but it should be noted that the viability of the method may be dependent on the substituents on the acetylenic carbons, as we found that the reaction of **8** with $(CN)_2C{\equiv}C(CN)_2$ or $HC{\equiv}C(CO_2Me)$ led to dissociation of the indenyl ligand and did not yield any isolable product.

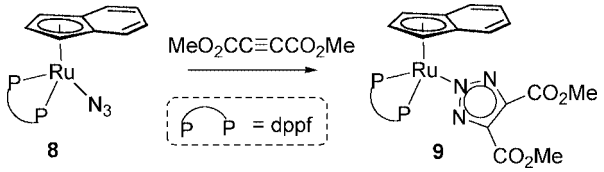


Scheme 6.

The ORTEP diagrams for the molecular structures of **8** and **9** are shown in Figures 6 and 7, respectively.

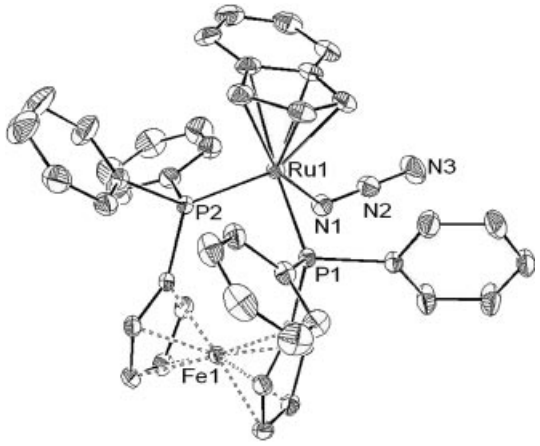


Figure 6. ORTEP diagram of **8**. Thermal ellipsoids are drawn to 50% probability level. Hydrogen atoms are omitted for clarity. Selected bond parameters: Δ = 0.163 Å; HA = 6.85°; FA = 8.70°; C*–Ru1 1.892 Å; Ru1–P1 2.2559(5) Å; Ru1–P 22.3251(6) Å; Ru–N1 2.1355(18) Å; N1–N2 1.192(3) Å; N2–N3 1.156(3) Å; P1–Ru1–P2 97.744(19)°; P1 Ru1–N1 84.42(5)°; P2–Ru1–N1 92.14(5)°; Ru1–N1–N2 117.96(15)°; N3–N2–N1 176.6(2)°.

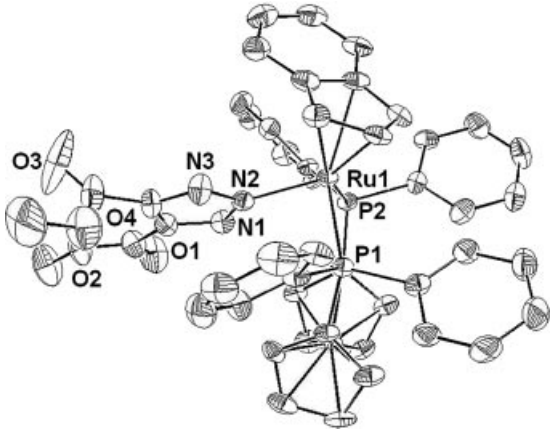


Figure 7. ORTEP diagram of **9**. Thermal ellipsoids are drawn to 50% probability level. Hydrogen atoms are omitted for clarity.

The slip-fold parameters of **8** fall in the normal range for $\eta^5$-coordination.[15] The Cp rings of the dppf ligand adopt a more stable synclinal staggered conformation, with tor-

 © 2007 Wiley-VCH Verlag GmbH & Co. KGaA, Weinheim 

Table 2. Selected bond lengths [Å] and angles [°] of **9** and [(Ind/Cp)Ru(dppe){$N_3C_2(CO_2Me)_2$}].

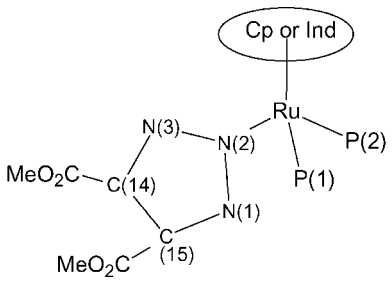


| Complexes | **9** | [(Ind)Ru(dppe){$N_3C_2(CO_2Me)_2$}][10f] | [CpRu(dppe){$N_3C_2(CO_2Me)_2$}][24] |
|---|---|---|---|
| Δ [Å] | 0.142 | 0.175 | – |
| Hinge angle (HA) [°] | 5.25 | – | – |
| Fold angle (FA) [°] | 9.63 | – | – |
| C*–Ru1 | 1.909(8) | 1.888(1) | – |
| Ru1–P1 | 2.3230(18) | 2.2396(6) | – |
| Ru1–P2 | 2.2646(18) | 2.2720(6) | – |
| Ru1–N2 | 2.070(6) | 2.0904(18) | 2.090(2) |
| N1–N2 | 1.306(8) | 1.336(3) | 1.331(3) |
| N2–N3 | 1.355(9) | 1.336(3) | 1.332(3) |
| N1–C15 | 1.352(10) | 1.348(3) | 1.351(3) |
| N3–C14 | 1.338(10) | 1.351(3) | 1.352(3) |
| C14–C15 | 1.385(11) | 1.395(3) | 1.400(4) |
| P1–Ru1–P2 | 98.08(6) | 84.92(2) | 85.13(3) |
| P1–Ru1–N2 | 91.35(17) | 86.38(5) | 86.48(6) |
| P2–Ru1–N2 | 87.54(16) | 89.73(5) | 89.89(6) |
| Ru1–N2–N1 | 126.4(5) | – | 121.4(2) |
| Ru1–N2–N3 | 121.1(4) | – | 125.2(2) |
| N1–N2–N3 | 112.2(6) | 112.95(17) | 113.4(2) |
| N2–N1–C15 | 106.8(6) | 105.83(18) | 105.6(2) |
| N2–N3–C14 | 105.3(6) | 108.29(19) | 105.5(2) |
| N1–C15–C14 | 107.2(6) | 107.67(19) | 107.7(2) |
| N3–C14–C15 | 108.5(7) | 108.29(19) | 107.8(2) |

sional angle 39.09°. The Ru1–N1 bond length of 2.1355(18) Å falls within the range of reported values for azido Ru complexes.[25] The coordinated terminal azido ligand is almost linear, the N3–N2–N1 angle being 176.6°.

In **9**, Ru is coordinated to two phosphorus atoms of the dppf ligand, heterocycle $N_3C_2(CO_2Me)_2$ through N(2) and an $\eta^5$-indenyl ligand. The coordination geometry of **9** is effectively similar to those of its Ind/Cp analogues containing dppe.[10f,24] The only noticeable difference lies in the irregularity of the pentagonal heterocyclic ring in **9**. This undoubtedly is caused by the steric demands of the bulky dppf ligand. It is seen in the structure of **9** that the heterocycle is hemmed in by the phenyl rings of dppf; moreover, N3, being nearer to the benzenoid ring of the indenyl ligand, suffers from additional steric encumbrance, hence the shortened N2–N3 bond length.

Selected metric data of **9**, including the slip-fold distortion parameters, are listed in Table 2, which also gives the metric data of its Ind/Cp dppe analogues for comparison. While these analogues possess very similar bond parameters, these differ appreciably from those of **9**, especially the bond angles. These significant differences are no doubt a consequence of the bulkiness of the dppf ligand.

## Conclusions

(Ind)Ru($PPh_3$)$_2$Cl has been prepared and mono-, di- and trisubstitution derivatives have been obtained with the monophosphane ligand **LH**, dppf and triphos, respectively. (*R*) and (*S*) diastereomers have been obtained with Josiphos, but only the thermodynamically stable (*R*) isomer could be isolated pure. A similar result was obtained with CpRu($PPh_3$)$_2$Cl. A rate study by $^1$H NMR spectroscopy showed Josiphos-dependent epimerisation of CpRu(Josiphos)Cl. Chloro substitution of (Ind)Ru(dppf)Cl with $CH_3CN$ and $N_3^-$ appears to indicate that this process is as facile as in the well-studied complex CpRu($PPh_3$)$_2$Cl. The [3+2] dipolar cycloaddition of the azido ligand provides an additional example for this uncommon occurrence at Ru.

## Experimental Section

**General:** All reactions were carried out using conventional Schlenk techniques under inert nitrogen or under argon in an M. Braun Labmaster 130 Inert Gas System. NMR spectra were measured on a Bruker 300 FT NMR spectrometer; for $^1$H and $^{31}$P spectra, chemical shifts were referenced to residual H-signals of the deuterated

 © 2007 Wiley-VCH Verlag GmbH & Co. KGaA, Weinheim 

solvents $C_6D_6$, $CD_3CN$. IR spectra in KBr pellets were measured in the range 4000–400 $cm^{-1}$ with a BioRad FTS-165 FTIR instrument. Mass spectra were run on a Finnigan Mat 95XL-T (FAB) or a Finnigan-MAT LCQ (ESI) spectrometer. Elemental analyses were performed by the microanalytical laboratory in-house. [(Ind)-$Ru(PPh_3)_2Cl$] (**1**)[7] and $C_9H_7(CH_2)_2PPh_2$[26] were prepared by the published methods. All other chemicals were obtained commercially and used without any further purification. All solvents were dried with sodium/benzophenone and distilled before use. Celite (Fluka AG), silica gel (Merck Kieselgel 60, 230–400 Mesh) were dried at 140 °C overnight before chromatographic use. Conventional numbering of indenyl protons is shown in Figure 8.

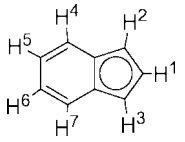


Figure 8. Numbering of indenyl protons.

**Synthesis of [(Ind)Ru(PPh$_3$){Ph$_2$P(CH$_2$)$_2$C$_9$H$_7$}Cl] (2):** $C_9H_7(CH_2)_2$-$PPh_2$ (35 mg, 0.11 mmol) was added to a red solution of **1** (70 mg, 0.09 mmol) in toluene (10 mL). The mixture was heated at 80 °C for 4 h. The resultant red solution was concentrated to about 1 mL and eluted through a silica gel column (2 × 2 cm) prepared in *n*-hexane with toluene/diethyl ether (10:1). From the red eluate, red microcrystals of [(Ind)Ru($PPh_3$){$Ph_2P(CH_2)_2C_9H_7$}Cl] (**2**) (57 mg, 75% yield) were obtained upon recrystallisation from THF/hexane. X-ray diffraction-quality crystals were obtained from a concentrated ether solution with hexane layering after 2 d at –30 °C.

**Data for 2:** $^1$H NMR (300 MHz, $C_6D_6$): $\delta$ = 1.73–1.90 (br. m, 1 H, C*H*$_2$), 2.18–2.30 (br. m, 1 H, C*H*$_2$), 2.93 (s, 2 H, C*H*$_2$ on IndH), 3.15 (s, 1 H, C*H*$_2$), 3.40–3.52 (m, 1 H, C*H*$_2$), 4.95–5.00 (m, 2 H, H$^{2,3}$), 5.78 (s, 1 H, H$^1$), 6.57–6.60 (d-like m, 1 H, IndH), 6.79–6.81, 6.84–6.94, 6.98–7.13, 7.19–7.22 (each m, total 29 H, H$^{4–7}$and Ph), 7.65–7.68 (d-like m, 1 H, Ph), 8.25 (t-like m, 2 H, Ph) ppm. $^{31}$P{$^1$H} NMR: $\delta$ = 46.5, 50.0 [each d, $^2J_{PP}$ = 42.9 Hz, $PPh_3$ and IndH$(CH_2)_2$-$PPh_2$] ppm. FAB$^+$-MS: *m*/*z* (%) = 842 [M]$^+$, 808 [M – Cl]$^+$, 691 [M – Ind]$^+$, 581 [M – $PPh_3$]$^+$, 545 [M – $PPh_3$ – Cl]$^+$, 479 [M – IndH$(CH_2)_2PPh_2$ – Cl]$^+$, 429 [M – Ind – $PPh_3$ – Cl]$^+$. $C_{50}H_{43}ClP_2Ru$ (842.35): calcd. C 71.3, H 5.2; found C 71.6, H 5.3.

**Synthesis of [(Ind)Ru(dppf)Cl] (3):** 1,1′-Bis(diphenylphosphanyl)ferrocene (dppf) (0.76 g, 1.37 mmol) was added to a red solution of **1** (1 g, 1.29 mmol) in toluene (15 mL) and the mixture refluxed for 2 h. Red air- and moisture-stable crystalline solids, [(Ind)Ru(dppf)-Cl] **3**, precipitated out from the solution and were filtered (0.62 g, 60% yield). The supernatant was concentrated to about 5 mL. Addition of hexane (about 2 mL) gave a second crop after 2 h at 0 °C (0.27 g, 26% yield). In solution, the red compound of **3** decomposed in air within a day to a brown species. X-ray diffraction-quality crystals were obtained from a saturated solution of **3** in $C_6D_6$ after a day at room temperature.

**Data for 3:** $^1$H NMR (300 MHz, $C_6D_6$): $\delta$ = 3.66, 3.83, 3.90 and 4.20 (each s, 2 H, $C_5H_4$), 4.66 (t, $^3J_{HH}$ = 2.5 Hz, 1 H, H$^1$), 5.57 (s, 2 H, H$^{2,3}$), 7.01–7.13 and 7.47–7.58 (m, 24 H, H$^{4–7}$ and Ph) ppm. $^{31}$P{$^1$H} NMR: $\delta$ = 51.9 (s, dppf) ppm. FAB$^+$-MS: *m*/*z* (5) = 806 [M]$^+$, 771 [M – Cl]$^+$, 655 [M – Cl – Ind]$^+$. $C_{43}H_{35}ClFeP_2Ru$ (806.05): calcd. C 64.1, H 4.4; found C 64.3, H 4.1.

**Synthesis of [(Ind)Ru(tripod)]PF$_6$ ([4]PF$_6$):** $NaPF_6$ (20 mg, 0.12 mmol) and tripod (40 mg, 0.06 mmol) were added to a red solution of **1** (50 mg, 0.06 mmol) in toluene/THF (5:1, 12 mL). The mixture was refluxed for 4 h, during which the colour of the mixture changed from red to yellow. The resultant yellow suspension was filtered through Celite. The filtrate was concentrated to about 5 mL. Addition of ether (2 mL) gave yellow microcrystals, [(Ind)-Ru(tripod)]$PF_6$ ([**4**]$PF_6$), after 1 d at –30 °C (51 mg, 83% yield). X-ray diffraction-quality crystals were obtained from a saturated solution of [**4**]$PF_6$ in $CH_2Cl_2$ with ether layering after 2 d at –30 °C.

**Data for [4]PF$_6$:** $^1$H NMR (300 MHz, $CD_3CN$): $\delta$ = 1.56–1.57 (m, 3 H, Me), 2.39 (br. s, 6 H, $CH_2$), 5.51 (d, $^3J_{HH}$ = 2.5 Hz, 2 H, H$^{2,3}$), 5.70 (t, $^3J_{HH}$ = 2.5 Hz, 1 H, H$^1$), 6.78–6.82 (br. s, 12 H, Ph), 7.04 (t, $^3J_{HH}$ = 7.4 Hz, 12 H, Ph), 7.22 (t, $^3J_{HH}$ = 7.4 Hz, 6 H, Ph), 7.31–7.34 and 7.43–7.47 (each m, 2 H, H$^{4–7}$) ppm. $^{31}$P{$^1$H} NMR: $\delta$ = 39.9 (s, tripod), –142.9 (septet, $PF_6$) ppm. IR (KBr): $\tilde{\nu}$ = 058 (w), 2923 (w), 2868 (w), 1482 (w), 1434 (m), 1092 (m), 839 [vs. ($PF_6$)], 744 (m), 697 (s), 557 [m ($PF_6$)], 517 (s) $cm^{-1}$. FAB$^+$-MS: *m*/*z* (%) = 841 [M]$^+$. FAB$^–$-MS: *m*/*z* (%) = 145 [$PF_6$]$^–$. $C_{50}H_{46}F_6P_4Ru$ (985.86): calcd. C 60.9, H 4.7; found C 60.5, H 5.2.

**Synthesis of [(Ind)Ru{(*R*)-(*S*)-Josiphos}Cl] (5):** (*R*)-(–)-1-[(*S*)-2-(Diphenylphosphanyl)ferrocenyl]ethyldicyclohexylphosphane {(*R*)-(*S*)-Josiphos} (23 mg, 0.04 mmol) was added to a red solution of **1** (30 mg, 0.04 mmol) in toluene (5 mL) and the mixture was refluxed. The reaction was monitored using $^{31}$P NMR spectroscopy. Refluxing was ceased when the ratio of starting materials and product remained constant (about 8 h). The solution was concentrated to about 2 mL and loaded onto a silica gel column (2 × 8 cm) prepared in *n*-hexane. Elution gave three fractions: (i) a yellow eluate in hexane/diethyl ether (1:1, about 4 mL), which recovered free (*R*)-(*S*)-Josiphos (2 mg, 9% recovery); (ii) an orange-red solution in hexane/diethyl ether (1:1, about 15 mL), which yielded [(*R*)-(Ind)-Ru{(*R*)-(*S*)-Josiphos}Cl] [(*R*)-**5**] (12 mg, 37% yield) as orange solids; and (iii) a red solution in THF (about 3 mL), which recovered unreacted **1** (2 mg, 7% recovery).

**Data for (*R*)-5:** $^1$H NMR (300 MHz, $C_6D_6$): $\delta$ = 0.87–1.10 (br. m, 6 H, Cy), 1.24–1.56 (br. m) with 1.47 (dd, sitting on top of br. m, $^3J_{HH}$ = 7.41, $^2J_{HP}$ = 9.9 Hz, total 11 H, Cy and Me), 1.63–1.68 (br. m, 1 H, Cy), 1.76–1.85 (br. m, 2 H, Cy), 1.94–1.98 (br. m, 2 H, Cy), 2.18–2.32, 2.37–2.50 and 2.60–2.68 (each br. m, 1 H, Cy), 3.68 (s, 5 H, Cp), 4.06 (t-linked m, 1 H, Cp), 4.19 and 4.23 (each br. s, 1 H, Cp), 5.22–5.29 [m, 1 H, C*H*MeP(Cy)$_2$], 5.34 (s, 1 H, H$^1$), 5.73 (s, 2 H, H$^{2,3}$), 6.89–6.94, 6.99–7.08, 7.11–7.16, 7.24–7.30, 7.44–7.49, 7.52–7.59 and 7.75–7.78 (each m, total 14 H, H$^{4–7}$ and Ph) ppm. $^{31}$P{$^1$H} NMR: $\delta$ = 36.0 (d, $^2J_{PP}$ = 53.4 Hz, Josiphos), 77.3 (d, $^2J_{PP}$ = 53.4 Hz, Josiphos) ppm. FAB$^+$-MS: *m*/*z* (%) = 846 [M]$^+$, 812 [M – Cl]$^+$. $C_{45}H_{51}ClFeP_2Ru$ (846.20): calcd. C 63.9, H 6.1; found C 63.9, H 6.3.

**Synthesis of [CpRu{(*R*)-(*S*)-Josiphos}Cl] (6):** (*R*)-(*S*)-Josiphos (18 mg, 0.03 mmol) was added to a yellow solution of **1a** (30 mg, 0.04 mmol) in toluene (5 mL) and the mixture was refluxed for 8 h. The solvent was removed in vacuo and the residue extracted using ether (3 × 2 mL).

**Purification Method (i):** The ether extract was concentrated to about 1 mL and loaded onto a silica gel column (2 × 4 cm) prepared in *n*-hexane. Elution gave two fractions: (i) a yellow eluate in hexane/diethyl ether (5:1, about 20 mL), which yielded [(*R*)-CpRu{(*R*)-(*S*)-Josiphos}Cl] [(*R*)-**6**] (28 mg, 85% yield) as orange microcrystals; and (ii) a yellow solution in hexane/diethyl ether (1:1, about 3 mL), which gave unreacted **1a** (6 mg, 20% recovery).

**Purification Method (ii):** The ether extract was concentrated to about 1 mL and hexane was added (about 2 mL). Orange solids of **1a** were recovered after 1 d at –30 °C, and removed by filtration (5 mg, 16% recovery). The mother liquor was concentrated to about 1 mL and hexane was added (about 4 mL). Orange yellow

 © 2007 Wiley-VCH Verlag GmbH & Co. KGaA, Weinheim 

solids of (*R*)-**6** were obtained after 1 d at –30 °C (15 mg, 46% yield). Subsequently, four additional crops of (*R*)-**6** were obtained, each about 3 mg (total 11 mg, 34% yield). X-ray diffraction-quality crystals were obtained from a concentrated ether solution with hexane layering after a day at –30 °C.

**Data for (*R*)-6:** $^1$H NMR (300 MHz, $C_6D_6$): $\delta$ = 0.61–0.77 (br. m, 2 H, Cy), 1.29–1.55 (br. m) with 1.52 (dd, sitting on top of br. m, $^3J_{HH}$ = 7.41, $^2J_{HP}$ = 9.06 Hz, total 13 H, Cy and Me), 1.65–1.92 (br. m, 6 H, Cy), 2.09–2.18 and 2.41–2.46 (each br. m, 2 H, Cy), 3.79 (s, 5 H, Cp), 4.11 (t, $^3J_{HH}$ = 2.49 Hz, 1 H, Cp), 4.27 and 4.30 (each br. s, 1 H, Cp), 4.49 (s, 5 H, $\eta^5$-*Cp*Ru), 5.23–5.34 [m, 1 H, C*H*MeP(Cy)$_2$], 6.85–6.90 and 7.20–7.23 (each m, 1 H, Ph), 6.93–6.97, 7.01–7.06 and 7.31–7.36 (each m, 2 H, Ph), 8.71 (br. s, 2 H, Ph) ppm. $^{31}$P{$^1$H} NMR: $\delta$ = 37.5 (d, $^2J_{PP}$ = 53.4 Hz, Josiphos), 67.2 (d, $^2J_{PP}$ = 53.4 Hz, Josiphos) ppm. FAB$^+$-MS: *m*/*z* (%) = 846 [M]$^+$, 812 [M – Cl]$^+$. $C_{41}H_{49}ClFeP_2Ru\cdot(CH_3CH_2)_2O$ (870.26): calcd. C 62.1, H 6.8; found C 62.2, H 6.8.

**Epimerisation Kinetics:** Complex **1a** [2.4 mg, 3.3 mmol (reaction **A**); 3.6 mg, 5 mmol (reaction **B**); 5.4 mg, 7.5 mmol (reaction **C**)] and (*R*)-(*S*)-Josiphos (3.0 mg, 5.0 mmol) were added to three different NMR tubes in three different ratios, that is, 1:1.5, 1:1 and 1.5:1. [D$_8$]toluene (0.5 mL) was added into each NMR tube. The initial $^1$H and $^{31}$P NMR spectrum of each reaction mixture was measured, and then at intervals during the reaction at 100 °C. The concentration of each component in the reaction mixtures was obtained from the integration of the Cp protons of the Josiphos [$\delta$ = 3.71 in (*R*)-**6** and $\delta$ = 3.89 in (*S*)-**6**], using as internal standard the residual 0.1% H-signal of 99.9% [D$_8$]toluene.

**Synthesis of [(Ind)Ru(dppf)(CH$_3$CN)]PF$_6$ ([7]PF$_6$):** $NaPF_6$ (16 mg, 0.09 mmol) was added to a red suspension of **3** (50 mg, 0.06 mmol) in $CH_3CN$ (10 mL) and the mixture was refluxed. The colour of the suspension changed slowly from red to yellow in 4 h. The suspension was filtered and the filtrate was evacuated to dryness. The residue was redissolved in THF (about 4 mL) and hexane (about 2 mL) was added. Yellow crystals of [(Ind)Ru(dppf)(CH$_3$CN)]PF$_6$ ([7]PF$_6$) (55 mg, 93% yield) were obtained after 1 d at –30 °C.

**Data for [7]PF$_6$:** $^1$H NMR (300 MHz, $CDCl_3$): $\delta$ = 2.15 (s, 3 H, C*H*$_3$CN), 4.22, 4.33 and 4.35 (each s, 2 H, $C_5H_4$), 4.44 (br. s, 3 H, $C_5H_4$ and H$^1$), 4.60 (d, $^3J_{HH}$ = 2.5 Hz, 2 H, H$^{2,3}$), 6.63–6.66 and 7.18–7.21 (each 4-line m, 2 H, H$^{4–7}$), 6.82–6.88, 7.28–7.33, 7.40–7.52 (m, 20 H, Ph) ppm. $^{31}$P{$^1$H} NMR: $\delta$ = 50.7 (s, dppf), –144.1 (septet, $PF_6$) ppm. IR (KBr): $\tilde{\nu}$ = 055 (w), 2974 (w), 2057 (w), 2276 [w (CN)], 1481 (m), 1435 (m), 1158 (m), 1092 (m), 840 [vs. ($PF_6$)], 749 (s), 699 (s), 557 [s ($PF_6$)], 514 (m) cm$^{-1}$. FAB$^+$-MS: *m*/*z* (%) = 812 [M]$^+$, 771 [M – $CH_3CN$]$^+$, 655 [M – $CH_3CN$ – $C_9H_7$]$^+$. FAB$^-$-MS: *m*/*z* (%) = 145 [$PF_6$]$^-$. $C_{45}H_{38}F_6FeNP_3Ru\cdot$½$CH_3CN$ (977.16): calcd. C 56.5, H 4.0, N 2.2; found C 56.0, H 3.9, N 2.1.

**Synthesis of [(Ind)Ru(dppf)N$_3$] (8):** $NaN_3$ (20 mg, 0.3 mmol) was added to a red suspension of **3** (50 mg, 0.06 mmol) in EtOH (10 mL) and the mixture was refluxed for 4 h. The solvent was removed in vacuo and the red residue extracted using $CH_2Cl_2$ (2 × 4 mL). The extract was concentrated to about 3 mL and hexane (about 10 mL) was added. After being kept overnight at –30 °C, red crystals of [(Ind)Ru(dppf)N$_3$] **8** (43 mg, 85% yield) were obtained. X-ray diffraction-quality crystals were obtained from a saturated solution in $CH_2Cl_2$ with hexane layering after 2 d at –30 °C.

**Data for 8:** $^1$H NMR (300 MHz, $C_6D_6$): $\delta$ = 3.79, 4.05, 4.21 and 4.29 (each s, 2 H, $C_5H_4$), 4.58 (s, 1 H, H$^1$), 4.79 (s, 2 H, H$^{2,3}$), 7.09–7.12, 7.14–7.23, 7.26–7.29, 7.39–7.44, 7.47–7.52 (each m, total 24

Table 3. Crystal and structure refinement data.

| | **2** | **3** | [**4**]PF$_6$ |
|---|---|---|---|
| Formula | $C_{54}H_{53}ClOP_2Ru$ | $C_{43}H_{35}ClFeP_2Ru$ | $C_{51.5}H_{49}Cl_3F_6P_4Ru$ |
| Formula mass | 916.42 | 806.02 | 1113.21 |
| Space group | $P2_1/c$ | $P2_1/c$ | $P\bar{1}$ |
| Crystal system | monoclinic | monoclinic | triclinic |
| Unit cell dimensions | | | |
| *a* [Å] | 12.433(5) | 11.5291(5) | 12.5364(5) |
| *b* [Å] | 15.543(6) | 29.8651(15) | 13.2396(5) |
| *c* [Å] | 23.785(9) | 11.3638(5) | 15.9901(6) |
| *α* [°] | 90 | 90 | 98.356(1) |
| *β* [°] | 101.836(10) | 118.9740(10) | 103.723(1) |
| *γ* [°] | 90 | 90 | 92.325(1) |
| Cell volume [Å$^3$] | 4499(3) | 3423.0(3) | 2543.08(17) |
| *Z* | 4 | 4 | 2 |
| $D_{calcd}$ [g cm$^{-3}$] | 1.353 | 1.564 | 1.454 |
| Absorption coefficient [mm$^{-1}$] | 0.518 | 1.069 | 0.648 |
| *F*(000) electrons | 1904 | 1640 | 1134 |
| Crystal size [mm$^3$] | 0.16 × 0.09 × 0.09 | 0.28 × 0.14 × 0.08 | 0.22 × 0.12 × 0.04 |
| *θ* range for data collection [°] | 2.13–25.00 | 2.02–27.50 | 2.20–26.37 |
| Index ranges | $-14 \le h \le 14$ | $-12 \le h \le 14$ | $-15 \le h \le 15$ |
| | $-18 \le k \le 17$ | $-28 \le k \le 38$ | $-16 \le k \le 16$ |
| | $-28 \le l \le 16$ | $-14 \le l \le 14$ | $0 \le l \le 19$ |
| Reflections collected | 26102 | 24177 | 36189 |
| Independent reflections | 7923 | 7849 | 10372 |
| Max. and min. transmission | 0.9549 and 0.9217 | 0.9194 and 0.7540 | 0.9745 and 0.8705 |
| Data/restraints/parameters | 7923/0/532 | 7849/0/433 | 10372/18/612 |
| Gof | 0.980 | 1.095 | 1.038 |
| Final *R* indices [$I > 2\sigma(I)$] | $R_1$ = 0.0542 | $R_1$ = 0.0491 | $R_1$ = 0.0648 |
| | $wR_2$ = 0.0965 | $wR_2$ = 0.0981 | $wR_2$ = 0.1862 |
| *R* indices (all data) | $R_1$ = 0.1004 | $R_1$ = 0.0649 | $R_1$ = 0.0845 |
| | $wR_2$ = 0.1097 | $wR_2$ = 0.1037 | $wR_2$ = 0.2032 |
| Largest diff. peak and hole [e Å$^{-3}$] | 0.565 and –0.400 | 0.738 and –0.500 | 2.127 and –0.421 |

 © 2007 Wiley-VCH Verlag GmbH & Co. KGaA, Weinheim 

Table 4. Crystal and structure refinement data.

| | (*R*)-**6** | **8** | **9** |
|---|---|---|---|
| Formula | $C_{43}H_{54}ClFeO_{0.50}P_2Ru$ | $C_{43}H_{35}FeN_3P_2Ru$ | $C_{51.50}H_{46}Cl_5FeN_3O_4P_2Ru$ |
| Formula mass | 833.17 | 897.53 | 1167.02 |
| Space group | $P2_12_12_1$ | $P2_1/n$ | $P2_1/c$ |
| Crystal system | orthorhombic | monoclinic | monoclinic |
| Unit cell dimensions | | | |
| *a* [Å] | 9.546(2) | 11.3220(3) | 17.8241(14) |
| *b* [Å] | 20.204(4) | 14.5824(3) | 11.6367(10) |
| *c* [Å] | 21.200(4) | 23.3452(5) | 25.689(2) |
| *α* [°] | 90 | 90 | 90 |
| *β* [°] | 90 | 96.5650(10) | 103.167(2) |
| *γ* [°] | 90 | 90 | 90 |
| Cell volume [Å$^3$] | 4088.9(15) | 3829.06(16) | 5188.2(7) |
| *Z* | 4 | 4 | 4 |
| $D_{calcd}$ [g cm$^{-3}$] | 1.353 | 1.557 | 1.494 |
| Absorption coefficient [mm$^{-1}$] | 0.897 | 1.034 | 0.937 |
| *F*(000) electrons | 1732 | 1824 | 2372 |
| Crystal size [mm$^3$] | 0.30 × 0.22 × 0.10 | 0.34 × 0.20 × 0.10 | 0.32 × 0.18 × 0.14 |
| *θ* range for data collection [°] | 2.02–30.51 | 2.10–26.37 | 2.11–26.37 |
| Index ranges | $-13 \le h \le 13$ | $-14 \le h \le 14$ | $-22 \le h \le 21$ |
| | $0 \le k \le 28$ | $0 \le k \le 18$ | $0 \le k \le 14$ |
| | $0 \le l \le 30$ | $0 \le l \le 29$ | $0 \le l \le 32$ |
| Reflections collected | 61668 | 35653 | 42001 |
| Independent reflections | 11860 | 7793 | 10631 |
| Max. and min. transmission | 0.9156 and 0.7746 | 0.9037 and 0.7201 | 0.8800 and 0.7537 |
| Data/restraints/parameters | 11860/2/434 | 7793/0/478 | 10631/28/625 |
| Gof | 1.199 | 1.056 | 1.137 |
| Final *R* indices [$I > 2\sigma(I)$] | $R_1$ = 0.0484 | $R_1$ = 0.0450 | $R_1$ = 0.0881 |
| | $wR_2$ = 0.1292 | $wR_2$ = 0.1091 | $wR_2$ = 0.2225 |
| *R* indices (all data) | $R_1$ = 0.0535 | $R_1$ = 0.0569 | $R_1$ = 0.1148 |
| | $wR_2$ = 0.1322 | $wR_2$ = 0.1159 | $wR_2$ = 0.2373 |
| Largest diff. peak and hole [e Å$^{-3}$] | 1.004 and –0.498 | 1.345 and –1.054 | 1.925 and –1.013 |

H, H$^{4-7}$ and Ph) ppm. $^{31}P\{^1H\}$ NMR: $\delta$ = 52.5 (s, dppf) ppm. IR (KBr): $\tilde{\nu}$ = 053 (w), 2025 [vs. ($N_3$)], 1433 (w), 1159 (w), 1091 (w), 1034 (w), 745 (m), 697 (m), 513 (m) cm$^{-1}$. FAB$^+$-MS: *m*/*z* (%) = 785 [M – $N_2$]$^+$, 771 [M – $N_3$]$^+$, 670 [M – Ind – $N_2$]$^+$, 655 [M – Ind – $N_3$]$^+$. $C_{43}H_{35}FeN_3P_2Ru$ (812.62): calcd. C 63.6, H 4.3, N 5.2; found C 63.5, H 4.8, N 5.2.

**Synthesis of [(Ind)Ru(dppf){$N_3C_2(CO_2Me)_2$}] (9):** Dimethyl acetylenedicarboxylate (38 μL, 0.31 mmol) was added into a red solution of **8** (50 mg, 0.06 mmol) in $CH_2Cl_2$ (10 mL) and the reaction mixture was stirred at room temperature for 24 h. The colour of the solution slowly changed from red to orange-red. The solution was concentrated to about 2 mL and hexane (8 mL) was added. Yellow crystals [(Ind)Ru(dppf){$N_3C_2(CO_2Me)_2$}] **9** (33 mg, 55% yield) were obtained after 18 h at –10 °C. X-ray diffraction-quality crystals were obtained from a saturated solution in $CH_2Cl_2$ with ether layering after 1 week at 4 °C.

**Data for 9:** $^1$H NMR (300 MHz, $C_6D_6$): $\delta$ = 3.52 (s, 6 H, Me), 3.76, 4.10, 4.31 and 4.34 (each s, 2 H, $C_5H_4$), 4.78 (s, 1 H, H$^1$), 5.35 (s, 2 H, H$^{2,3}$), 6.86–6.90 (m, 2 H, H$^{4-7}$), 6.96–6.97, 7.16–7.43, 7.72–7.78 (each m, total 22 H, H$^{4-7}$ and Ph) ppm. $^{31}P\{^1H\}$ NMR: $\delta$ = 56.8 (s, dppf) ppm. IR (KBr): $\tilde{\nu}$ = 057 (w), 2945 (w), 1736 [vs. (C=O)], 1434 [m (N=N)], 1292 [m (C–O)], 1165 (m), 1087 (s), 772 (m), 697 (m), 508 (m) cm$^{-1}$. FAB$^+$-MS: *m*/*z* 955 [M]$^+$, 771 [M – $N_3C_2(CO_2Me)_2$]$^+$. $C_{49}H_{41}FeN_3O_4P_2Ru$ (954.73): calcd. C 61.6, H 4.3, N 4.4; found C 61.7, H 3.8, N 4.4.

**Crystal Structure Determinations:** Crystals were mounted on quartz fibres. X-ray data were collected on a Bruker AXS APEX system, using Mo-$K_\alpha$ radiation, with the SMART suite of programs.[27] Data were processed and corrected for Lorentz and polarisation effects with SAINT,[28] and for absorption effects with SADABS.[29] Structural solution and refinement were carried out with the SHELXTL suite of programs.[30] Crystal and structure refinement data are summarised in Tables 3 and 4. The structures were solved by direct methods or Patterson maps to locate the heavy atoms, followed by difference maps for the light, non-hydrogen atoms. All non-hydrogen atoms were generally given anisotropic displacement parameters in the final model.

CCDC-616431 to -616436 contain the supplementary crystallographic data for this paper. These data can be obtained free of charge from The Cambridge Crystallographic Data Centre via www.ccdc.cam.ac.uk/data_request/cif.

## Acknowledgments

The authors acknowledge with thanks support from the Academic Research Fund (grant no. 143-000-209-112) to L. Y. G., Institute of Chemical and Engineering Sciences for a research scholarship to S. Y. N. and technical assistance from Dr. L. L. Koh and Ms. G. K. Tan for X-ray structure determinations of **2** and **3**.

[1] See for instance the following: a) C. A. Tolman, *Chem. Rev.* **1977**, *77*, 313; b) D. J. Darensbourg, A. H. Graves, *Inorg. Chem.* **1979**, *18*, 1257; c) J. D. Atwood, M. J. Wovkulich, D. C. Sonnenberger, *Acc. Chem. Res.* **1983**, *16*, 350; d) R. L. Harlow, R. J. McKinney, J. F. Whitney, *Organometallics* **1983**, *2*, 1839; e) A. G. Orpen, N. G. Connelly, *J. Chem. Soc., Chem. Commun.* **1985**, 1310.

[2] See for instance the following: a) L. Dahlenburg, *Coord. Chem. Rev.* **2005**, *249*, 2962; b) N. Mézailles, L. Ricard, F. Gagosz, *Org. Lett.* **2005**, *7*, 4133; c) A. D. Phillips, L. Gonsalvi, A. Romerosa, F. Vizza, M. Peruzzini, *Coord. Chem. Rev.* **2004**, *248*,

 © 2007 Wiley-VCH Verlag GmbH & Co. KGaA, Weinheim 

955; d) S. R. Klei, T. D. Tilley, R. G. Bergman, *Organometallics* **2002**, *21*, 4905; e) D. Ferraris, B. Young, T. Dudding, T. Lectka, *J. Am. Chem. Soc.* **1998**, *120*, 4548; f) J. P. Wolfe, S. Wagaw, S. L. Buchwald, *J. Am. Chem. Soc.* **1996**, *118*, 7215.
[3] J. D. Gilbert, G. Wilkinson, *J. Chem. Soc. A* **1969**, 1749.
[4] a) S. G. Davies, J. P. McNally, A. J. Smallridge, *Adv. Organomet. Chem.* **1990**, *30*, 1; b) T. Blackmore, M. I. Bruce, F. G. A. Stone, *J. Chem. Soc. A* **1971**, 2376; c) M. I. Bruce, N. J. Windsor, *Aust. J. Chem.* **1977**, *30*, 1601; d) G. S. Ashby, M. I. Bruce, I. B. Tomkins, R. C. Wallis, *Aust. J. Chem.* **1979**, *32*, 1003; e) M. I. Bruce, F. S. Wong, B. W. Skelton, A. H. White, *J. Chem. Soc., Dalton Trans.* **1981**, 1398; f) M. I. Bruce, M. G. Humphery, J. M. Patrick, A. H. White, *Aust. J. Chem.* **1983**, *36*, 2065.
[5] a) V. Cadierno, P. Crochet, S. E. García-Carrido, J. Gimeno, *Dalton Trans.* **2004**, 3635; b) Y. Wakatsuki, M. Tokunaga, *Angew. Chem. Int. Ed. Engl.* **1998**, *37*, 2867; c) D. B. Grotjahn, D. A. Lev, *J. Am. Chem. Soc.* **2004**, *126*, 12232; d) Y. Wakatsui, M. Tokunaga, T. Suzuki, *Org. Lett.* **2001**, *3*, 735; e) Y. Wakatsuki, A. Horiuchi, *J. Am. Chem. Soc.* **2001**, *123*, 11917.
[6] a) K.-S. Gan, T. S. A. Hor in *Ferrocenes: Homogeneous Catalysis, Organic Synthesis and Materials Science* (Eds.: A. Togni, T. Hayashi), Wiley-VCH, Weinheim, Germany, **1995**, p. 3; b) H.-U. Blaser, W. Brieden, B. Pugin, F. Spindler, M. Studer, A. Togni, *Top. Catal.* **2002**, *19*, 3.
[7] L. A. Oro, M. A. Ciriano, M. Campo, *J. Organomet. Chem.* **1985**, *289*, 117.
[8] V. Cadierno, J. Díez, M. P. Gamasa, J. Gimeno, E. Lastra, *Coord. Chem. Rev.* **1999**, *193–195*, 147 and references cited therein.
[9] See for example the following and references cited therein: a) J. Díez, M. P. Gamasa, J. Gimeno, E. Lastra, A. Villar, *Organometallics* **2005**, *24*, 1410; b) S. Conejero, J. Díez, M. P. Gamasa, J. Gimeno, *Organometallics* **2004**, *23*, 6299; c) M. Bassetti, P. Alvarez, J. Gimeno, E. Lastra, *Organometallics* **2004**, *23*, 5127; d) P. Alvarez, E. Lastra, J. Gimeno, M. Bassetti, L. R. Falvello, *J. Am. Chem. Soc.* **2003**, *125*, 2386; e) V. Cadierno, M. P. Gamasa, J. Gimeno, C. González-Bernardo, E. Pérez-Carreño, S. García-Granda, *Organometallics* **2001**, *20*, 5177.
[10] a) K. M. Rao, E. K. Rymmai, *Polyhedron* **2003**, *22*, 307; b) S. S. Keisham, Y. A. Mozharivskyj, P. J. Carroll, M. R. Kollipara, *J. Organomet. Chem.* **2004**, *689*, 1249; c) K. S. Singh, G. P. A. Yap, K. A. Kreisel, M. R. Kollipara, *J. Coord. Chem.* **2005**, *58*, 1607; d) P. Govindaswamy, C. Sinha, M. R. Kollipara, *J. Organomet. Chem.* **2005**, *690*, 3465; e) K. S. Singh, Y. A. Mozahrivskyj, C. Thöne, M. R. Kollipara, *J. Organomet. Chem.* **2005**, *690*, 3720; f) K. S. Singh, C. Thöne, M. R. Kollipara, *J. Organomet. Chem.* **2005**, *690*, 4222; g) K. S. Singh, C. Thöne, M. R. Kollipara, *J. Coord. Chem.* **2006**, *59*, 333.
[11] M. P. Gamasa, J. Gimeno, C. Gonzalez-Bernardo, B. M. Martin-Vaca, D. Monti, M. Bassetti, *Organometallics* **1996**, *15*, 302.
[12] J. J. Bishop, A. Davison, *Inorg. Chem.* **1971**, *10*, 826.
[13] a) D. Gareau, C. Sui-Seng, L. F. Groux, F. Brisse, D. Zargarian, *Organometallics* **2005**, *24*, 4003; b) D. Zargarian, *Coord. Chem. Rev.* **2002**, *233–234*, 157.
[14] X. L. Lu, Ph.D Thesis, National University of Singapore, Singapore, **2002**.
[15] For indenyl complexes containing undistorted $\eta^5$ rings: $\Delta$ = 0.03 Å, HA = 2.5°, FA = 4.4°; for those containing distorted $\eta^5$ rings: $\Delta$ = 0.11–0.42 Å, HA = 7–14°, FA = 6–13°; and for those wherein the five-membered ring is $\eta^3$-coordinated: $\Delta$ = 0.8 Å, FA = 28°. See: A. K. Kakkar, N. J. Taylor, T. B. Marder, J. K. Shen, N. Hallinan, F. Basolo, *Inorg. Chim. Acta* **1992**, *198–200*, 219.
[16] L. Pauling, *The Nature of the Chemical Bond*, Cornell University Press, Ithaca, NY, **1960**, chapter 7, p. 221.
[17] G. Bandoli, A. Dolmella, *Coord. Chem. Rev.* **2000**, *209*, 161.
[18] G. Consiglio, F. Morandini, F. Bangerter, *Inorg. Chem.* **1982**, *21*, 455.
[19] F. Morandini, G. Consiglio, B. Straub, G. Ciani, A. Sironi, *J. Chem. Soc., Dalton Trans.* **1983**, 2293.
[20] C. G. Leong, O. M. Akotsi, M. J. Ferguson, S. H. Bergens, *Chem. Commun.* **2003**, 750.
[21] J.-B. Sortais, V. Ritleng, A. Voelklin, A. Holuigue, H. Smail, L. Barloy, C. Sirlin, G. K. M. Verzijl, J. A. F. Boogers, A. H. M. de Vries, J. G. de Vries, M. Pfeffer, *Org. Lett.* **2005**, *7*, 1247.
[22] a) W. Beck, K. Schropp, *Chem. Ber.* **1975**, *108*, 3317; b) W. P. Fehlhammer, L. F. Dahl, *J. Am. Chem. Soc.* **1972**, *94*, 3370.
[23] T. Kemmerich, J. H. Nelson, N. E. Takach, H. Boeheme, B. Jablonski, W. Beck, *Inorg. Chem.* **1982**, *21*, 1226.
[24] C. W. Chang, G. H. Lee, *Organometallics* **2003**, *22*, 3107 and references cited therein.
[25] P. Govindaswamy, P. J. Carroll, Y. A. Mozharivskyj, M. R. Kollipara, *J. Organomet. Chem.* **2005**, *690*, 885.
[26] Y. Kataoka, Y. Iwato, T. Yamagata, K. Tani, *Organometallics* **1999**, *18*, 5423.
[27] *SMART* version 5.628, Bruker AXS Inc., Madison, WI, USA, **2001**.
[28] *SAINT*+ version 6.22a, Bruker AXS Inc., Madison, WI, USA, **2001**.
[29] G. M. Sheldrick, *SADABS*, University of Göttingen, Germany, **1996**.
[30] *SHELXTL* version 5.1, Bruker AXS Inc., Madison, WI, USA, **1997**.

Received: August 3, 2006
Published Online: November 28, 2006

 © 2007 Wiley-VCH Verlag GmbH & Co. KGaA, Weinheim 

DOI: 10.1002/ejic.200600879

# (Indenyl)ruthenium Complexes Containing 1,1′-Bis(diphenylphosphanyl)-ferrocene (dppf) and Thiolato Ligands: Synthesis, X-ray Structure Analysis, Electrochemistry and Magnetic Studies

**Sin Yee Ng,[a] Weng Kee Leong,*[a] Lai Yoong Goh,*[a] and Richard D. Webster[b]**

**Keywords:** (Indenyl)ruthenium / Thiolates / dppf / Cyclic voltammetry / ESR / Ruthenium

The reaction of [(Ind)Ru(dppf)Cl] (Ind = $\eta^5$-$C_9H_7$) (**2**) with RSNa {R = Me, Et, Ph, $Ph_2P(CH_2)_2$} proceeds in MeOH to give [(Ind)Ru(dppf)(SR)] {R = Me (**3**), Et (**4**), Ph (**5**), $Ph_2P(CH_2)_2$ (**7**)}, as well as [(Ind)Ru(dppf)H] (**6**), in all cases except for R = Ph. This R-dependence of the product mixture was rationalised on a $RS^-$/MeOH ↔ $MeO^-$/RSH equilibrium involving the interaction of thiolate ($RS^-$) with MeOH, and the relative nucleophilicities of $RS^-$ versus $MeO^-$; **6** arose from β-H elimination from an OMe derivative. Cyclic voltammetric measurements on **2**, **3**, **4** and **5**, as well as the Cp ($\eta^5$-$C_5H_5$) and Cp* ($\eta^5$-$C_5Me_5$) analogues of **2**, indicated that the formal oxidation potentials for [LRu(dppf)Cl] complexes {L = Ind (**2**), Cp (**2A**) and Cp* (**2B**)} occurred in the order Cp* < Ind < Cp, correlating with the more electron-donating groups lowering the oxidation potentials. EPR experiments performed on the one-electron oxidised forms of **3** and **5** indicated paramagnetic compounds with *g* values close to 2, while the two-electron oxidised forms of **3** and **5** were diamagnetic. All the complexes were characterised spectroscopically, and **5** and **6** also crystallographically.
(© Wiley-VCH Verlag GmbH & Co. KGaA, 69451 Weinheim, Germany, 2007)

## Introduction

The development of the chemistry of indenyl complexes of ruthenium(II) could be considered to date from the high-yield synthesis of [(Ind)Ru($PPh_3$)$_2$Cl] (Ind = $\eta^5$-$C_9H_7$) (**1**),[1] which superseded [(Ind)Ru(CO)$_2$]$_2$, a low-yield compound,[2] as the common source material for the synthesis of (indenyl)ruthenium complexes. A recently improved synthesis of [(Ind)Ru(COD)Cl][3] has provided yet another alternative starting material. The initial interest in the indenyl ligand stems from its resemblance to $\eta^5$-cyclopentadienyl Cp/Cp* ligands, the 'pillar' ligands of transition-metal organometallic chemistry; subsequent interest was heightened by the observation of the so-called indenyl effect, an enhancement of reactivity of the complex brought about by facile ring slippage from $\eta^5$ to $\eta^3$ involving aromatisation of the benzene ring.[4]

In the last decade Gimeno's group have carried out intensive studies, with emphasis on reactivity, including catalytic aspects, particularly of vinylidene and allenylidene derivatives of ruthenium half-sandwich complexes.[5] Prior to these, there had been limited reports from various groups on studies of indenyl complexes of Fe, followed by those of the Group 6, 7 and 9 metals.[6] Recently reports of a few (indenyl)Ru complexes carrying N-containing ligands have emerged,[7] but to date there is only one report of examples carrying S-donor ligands, viz. EtS and EtMeS.[8]

In recent work, we have performed a comparative study of the reactivity of [($\eta^6$-$C_6Me_6$)Ru(dppf)Cl] and [CpRu(dppf)Cl] (**2A**) with various nucleophiles, including S donor ligands.[9] It is therefore of interest to include the indenyl analogue of these in the comparison. This paper describes the reactions of [(Ind)Ru(dppf)Cl] (**2**) with simple alkyl/aryl monothiolates, $RS^-$ (R = Me, Et and Ph), to compare with reported analogous reactions of [(Ind)Ru($PPh_3$)$_2$-Cl] (**1**) with EtSNa,[8] and the comparative electrochemistry studies of [LRu(dppf)Cl] {L = Ind (**2**), Cp (**2A**) and Cp* (**2B**)} and [LRu(L′$_2$)Cl] (L = Ind, Cp and Cp*; L′$_2$ = dppm, dppe and dppf).

## Results and Discussion

[(Ind)Ru(dppf)Cl] (**2**) was synthesised from phosphane substitution of [(Ind)Ru($PPh_3$)$_2$Cl] (**1**), following a published procedure for the Cp analogue.[1]

### Chloro Substitution

#### *(a) Reaction of 2 with RSNa [R = Me (3), Et (4), Ph (5)] and Solvent Dependence*

The reaction of **2** with an excess of RSNa in alcoholic solvent (MeOH or EtOH) at room temperature gave

[a] Department of Chemistry, National University of Singapore, 3 Science Drive, Singapore 117543
Fax: +65-6779-1691
E-mail: chmgohly@nus.edu.sg
chmlwk@nus.edu.sg
[b] Division of Chemistry and Biological Chemistry, Nanyang Technological University, Singapore 637616

 © 2007 Wiley-VCH Verlag GmbH & Co. KGaA, Weinheim 

[(Ind)Ru(dppf)(SR)] in R-dependent yields. (NOTE: with 1 equiv. of RSNa, the reaction at r.t. did not reach completion even after 18 h.) In the cases of R = Me and Et, a hydride complex, [(Ind)Ru(dppf)H] (**6**), was also isolated in about 20% yield (Scheme 1).

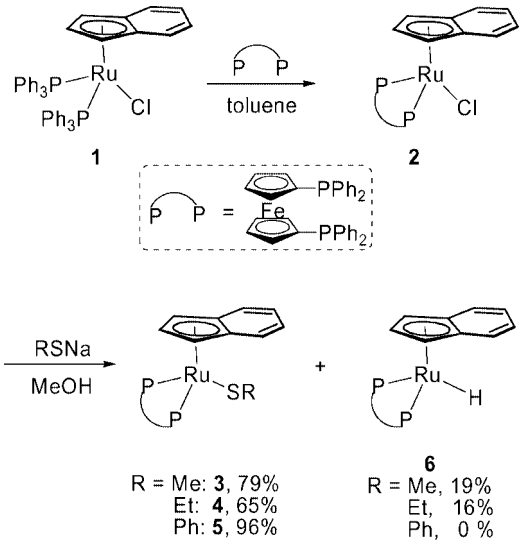


Scheme 1.

The latter complex was not anticipated, as hydride formation was not reported in the preparation of [(Ind)-$Ru(PPh_3)_2(SEt)$] from the reaction in refluxing THF of [(Ind)$Ru(PPh_3)_2Cl$] (**1**) with NaSEt,[8] or in similar syntheses of [$CpRu(PPh_3)_2(SR)$] (R = 1-$C_3H_7$, $CHMe_2$ and 4-$C_6H_4Me$).[10] Very recently, Gimeno and co-workers obtained mono- and diphosphane analogues of **6** from the reaction of [(Ind)Ru(P-P)Cl] {P-P = diphosphanes (dppm, dppe) or bis($PR_3$)} with an excess of MeONa in MeOH.[11] The formation of metal hydrides from alkoxide precursors by β-hydrogen elimination is a well-established phenomenon.[12,13] Invoking the role of alkoxide in this reaction involving the use of thiolates in MeOH will require the participation of an equilibrium represented by Equation (1).

$$RS^- + MeOH \overset{K}{\rightleftharpoons} MeO^- + RSH \quad (1)$$

In such a situation the competition of nucleophiles $RS^-$ and $MeO^-$ in displacement of X from [(Ind)Ru(dppf)X] (X = Cl or MeOH) comes into play. This will depend on their relative nucleophilicities ($RS^- > MeO^-$), as well as the preponderance of one species over the other, a direct consequence of the equilibrium constant *K*. This is in agreement with the order of $pK_a$'s in MeOH of the thiols as follows: MeSH (14.3)[14] ≤ EtSH (14.4)[15] > PhSH (10.9).[16] Thus, under similar concentrations of reactants, [$MeO^-$] in equilibrium (2) from $PhS^-$ will be about two orders of magnitude lower than that from $RS^-$ (S = Me or Et). This is in agreement with the observed absence of metal hydride formation for the R = Ph case. When both $RS^-$ (R = Me and Et) and $MeO^-$ are present, the higher nucleophilicity of the former anions qualitatively accounts for the preponderance of metal thiolate over metal hydride products.

This postulation is in agreement with our observation that the reaction of **2** with MeSNa *will not proceed in THF*, despite refluxing for 2 h, but went to completion within 15 min at 65 °C upon addition of 1/5 volume of MeOH. We similarly carried out, on an NMR scale, Hidai's reaction of **1**, using MeSNa, and found that in refluxing THF, [(Ind)-$Ru(PPh_3)_2(SMe)$] was the only product, while in refluxing MeOH, the hydride species [(Ind)$Ru(PPh_3)_2H$] was also formed [$^1$H NMR ($C_6D_6$): $\delta$ = –15.39 (t, $^2J_{HP}$ = 33.8 Hz) vs. lit. values in $CDCl_3$: $\delta$ = –15.40 (t, $^2J_{HP}$ = 31.6 Hz)[1]]. This indicates that nucleophilic substitution of $Cl^-$ with $MeS^-$ in THF is feasible in **1** but not in **2**, suggestive of the presence of a stronger Ru–Cl bond, which necessitates assistance from MeOH for cleavage. It is likely that **2**, like [$CpRu(PPh_3)_2Cl$] (**1A**), the Cp analogue of **1**, shows appreciable ionic behaviour in MeOH, as shown in Equation (2).

$$[CpRu(PPh_3)_2Cl] + MeOH \rightleftharpoons [CpRu(PPh_3)_2(MeOH)]^+ + Cl^- \quad (2)$$

Indeed, the MeOH complex had been isolated as the $BPh_4^-$ salt,[17] and nucleophilic displacement of chloride in **1A** by nitriles, tertiary phosphanes or phosphites has been shown to proceed by displacement of the weakly bound MeOH.[18] Such a dissociative tendency of the Ru–Cl bond will facilitate the dissociative pathways found to operate in substitution reactions of both Cp and indenyl complexes of Ru.[19] Incidentally, we have noted that the majority of reported reactions of (Ind)Ru complexes have been carried out in MeOH. In this present system, we have also observed, in a small-scale NMR tube reaction, that the solvent derivative of **2**, [(Ind)Ru(dppf)($CH_3CN$)]$PF_6$ (**2S**), reacted with MeSNa in THF at r.t. to give **3** as the sole product. In fact, Stone and co-workers had established that increasing donor ability of phosphane ligands strengthens the Ru–Cl bond sufficiently that displacement of chloride in [$CpRu(L)_2Cl$] (L = phosphane) cannot be effected.[20] Hence the observed stronger Ru–Cl bond in **2** versus its Cp analogue **2A** and versus its bis($PPh_3$) analogue **1** [here dppf vs. $(PPh_3)_2$] is in agreement with the recent finding that the indenyl ligand is more electron-donating than Cp towards Ru,[13] as is also confirmed by CV measurements in this study (see cyclic voltammetric and EPR measurements section).

Complex **5** crystallises with one $CH_2Cl_2$ and 0.5 MeOH in the orthorhombic *Fdd*2 space group, while **6** crystallises in the monoclinic $P2_1/n$ space group. Their molecular structures are very similar to those of their respective Cp analogues,[9b,21] and are illustrated in the ORTEP diagrams shown in Figures 1 and 2. The metal centres are coordinated to $\eta^5$-Ind, $\eta^2$-dppf and $\eta^1$-thiophenolate/hydrido ligands. Selected bond parameters are compared with those of the Cp analogues in Table 1.

The Ru–S distances in **5** and its Cp analogue are comparable and longer than in other examples of Ru–S(thiolate) bonds [2.30 Å (av.)].[23] The Cp rings of dppf in **5** are almost eclipsed (*syn* periplanar) to each other, with a torsional angle ($\tau$) of 2.1°. The phenyl ring on thiophenolate is almost parallel to the phenyl ring on P1, while the phenyl ring of

 © 2007 Wiley-VCH Verlag GmbH & Co. KGaA, Weinheim 

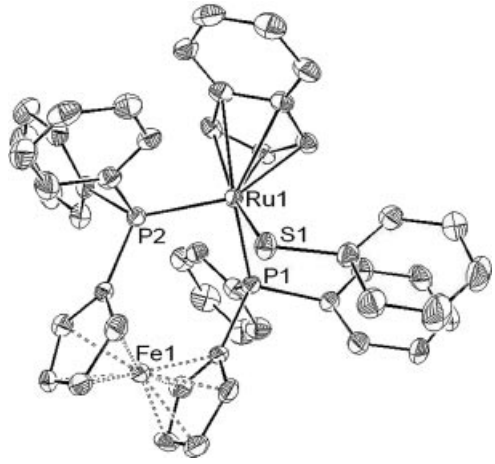


Figure 1. ORTEP diagram of **5**. Thermal ellipsoids are drawn to 50% probability level. Hydrogen atoms are omitted for clarity.

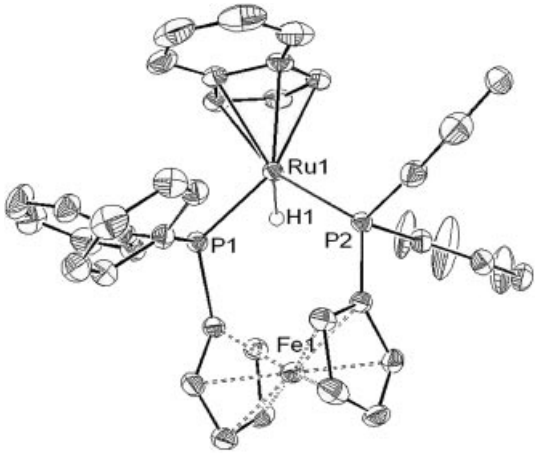


Figure 2. ORTEP diagram of **6**. Thermal ellipsoids are drawn to 50% probability level. Except for the metal hydride atom H1, all other hydrogen atoms are omitted for clarity.

thiophenolate in the Cp analogue points away from the phenyl rings on dppf. This is probably because of the steric bulk of the indenyl ligand, which restricts the orientation of the thiophenolate ligand in **5**.

The hydride ligand in **6** is located in the electron density map and refined with a Ru–H bond length of 1.499(6) Å and P–Ru–H angles of 80.19(2)° and 85.28(2)°. Compared to the eclipsed conformation in **5**, the Cp rings of the dppf in **6** adopt a more stable *syn* clinal (gauche) configuration. This is facilitated because the smaller terminal hydride relieves the steric stress around the Ru centre, enabling the dppf ligand to orientate to the lower-energy *syn* clinal configuration with a torsional angle ($\tau$) of 39.67°. The benzenoid ring of the indenyl ligand was predicted to arrange itself *trans* to the hydride, the higher *trans*-influence ligand,[4d] as shown in Figure 3.

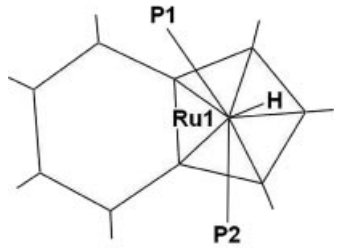


Figure 3. Top view of **6**.

### *(b) Reaction of 2 with the Mixed-Donor Ligand $^{-}S(CH_2)_2PPh_2$*

The reaction in MeOH of **2** with $Ph_2P(CH_2)_2S^-$, a 'hybrid' ligand with two coordinating sites, resulted in a mixture of [(Ind)Ru($\eta^2$-dppf){$\kappa^1$*S*-S$(CH_2)_2PPh_2$}] (**7**) and **6** in 54% and 15% yields respectively (Scheme 2), indicating an equilibrium between $Ph_2P(CH_2)_2S^-$ and $Ph_2P(CH_2)_2SH$ in MeOH. This reaction cannot be effected in THF at r.t. or at reflux, as previously observed. The amount of **6** isolated suggested that the p$K_a$ of $Ph_2P(CH_2)_2SH$ is similar to that of EtSH (see Scheme 1).

The $^1$H NMR and $^{31}$P NMR spectra of **7** indicate that the Ru centre is coordinated to $\eta^5$-Ind, $\eta^2$-dppf and $\kappa^1$*S*-2-(diphenylphosphanyl)ethylthiolate [$Ph_2P(CH_2)_2S^-$]; the coordinated phosphorus atoms of dppf resonate at $\delta$ = 56.1, while the low-field $^{31}$P signal ($\delta$ = –14.8 ppm) of the hybrid ligand pertains to a noncoordinating $PPh_2$ entity, in agreement with the higher nucleophilicity of thiolato sulfur, and hence its better coordinative capability to the Ru$^{II}$ centre when compared to phosphane P. The mixed-donor ligand

Table 1. Selected bond lengths [Å] and angles [°].

| Complex | **5**·$CH_2Cl_2$·0.5MeOH | [CpRu(dppf)(SPh)][9b] | **6** | [CpRu(dppf)H][21] |
|---|---|---|---|---|
| Δ [Å][22] | 0.192 | – | 0.1205 | – |
| Hinge angle (HA) [°][22] | 6.88 | – | 5.19 | – |
| Fold angle (FA) [°][22] | 9.87 | – | 7.56 | – |
| C*–Ru1[a] | 1.939 | – | 1.923 | – |
| Ru1–P1 | 2.2523(12) | 2.284(3) | 2.2446(9) | 2.263(4) |
| Ru1–P2 | 2.3085(12) | 2.302(3) | 2.2553(9) | 2.246(3) |
| Ru1–X | X = S1; 2.4193(12) | X = S1; 2.434(4) | X = H; 1.499(6) | X = H; 1.30 |
| P1–Ru1–P2 | 97.54(4) | 99.02(10) | 98.68(3) | 99.1(1) |
| P1–Ru1–X | X = S1; 86.21(4) | X = S1; 89.29(11) | X = H; 80.19(2) | – |
| P2–Ru1–X | X = S1; 86.08(4) | – | X = H; 85.28(2) | – |

[a] C* = centroid of the five-membered ring, C1, C2, C3, C3a and C7a.

 © 2007 Wiley-VCH Verlag GmbH & Co. KGaA, Weinheim 

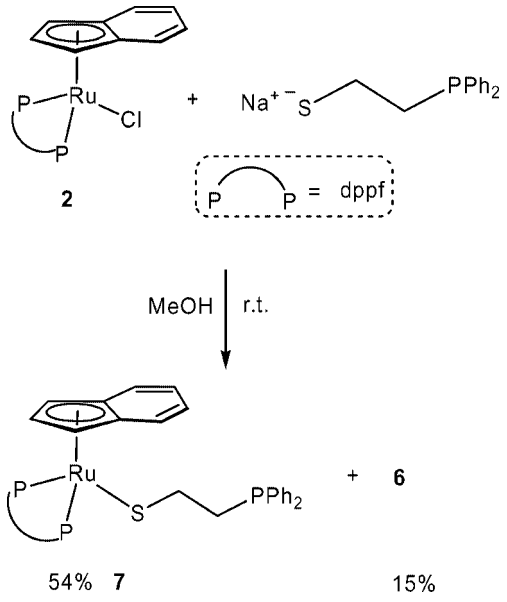


Scheme 2.

displaced neither the indenyl ligand nor dppf, indicating the stronger chelating effect of the dppf ligand versus $Ph_2P(CH_2)_2S^-$.

### Cyclic Voltammetric and EPR Measurements

Cyclic voltammograms obtained at a GC electrode in 0.5 mM solutions of **3**, **4**, **5**, **2**, **2A** and **2B** in $CH_2Cl_2$ at 233 K are shown in Figure 4. On the CV timescale, complexes **3**, **4** and **5** displayed chemically reversible oxidation processes at low temperatures, although at room temperature the third (most-positive) oxidation processes were only partially chemically reversible, suggesting chemical instability of the triply oxidised species. The expression "chemical reversibility", when used in connection with cyclic voltammetry experiments, relates to the ratio of the oxidative ($i_p^{ox}$) to reductive peak currents ($i_p^{red}$). The $i_p^{ox}/i_p^{red}$ ratio approaches unity for a fully chemically reversible process.

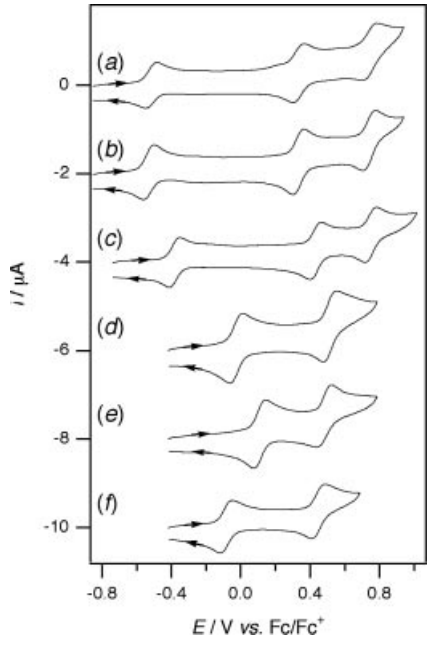


Figure 4. Cyclic voltammograms performed at a 1-mm diameter planar GC electrode in $CH_2Cl_2$ (0.25 M $Bu_4NPF_6$) at 233 K at a scan rate of 100 mV s$^{-1}$ for 0.5 mM (a) **3**, (b) **4** (c) **5**, (d) **2**, (e) **2A** and (f) **2B**. CVs in (b), (c), (d), (e) and (f) are offset by –2, –4, –6, –8 and –10 µA respectively.

Complexes **2**, **2A** and **2B** displayed two chemically reversible oxidation processes, except for **2A**, where the second more positive process was only partially chemically reversible at a scan rate of 100 mV s$^{-1}$ (suggesting instability of the more highly oxidised state). At scan rates >100 mV s$^{-1}$, the $i_p^{ox}/i_p^{red}$ ratio for the second process of **2A** became closer to one. Complexes **3**, **4** and **5** also displayed one chemically irreversible reduction process at about –2.5 V versus $Fc/Fc^+$ (data not shown), with a similar current magnitude to the first oxidation process (indicating that the same number of electrons were transferred).

Table 2 lists the reversible oxidation potentials ($E^r_{1/2}$) that were calculated from CV data under conditions where the $i_p^{ox}/i_p^{red}$ ratios were equal to unity and using the relationship (3)

$$E^r_{1/2} = (E_p^{ox} + E_p^{red})/2 \quad (3)$$

where $E_p^{ox}$ and $E_p^{red}$ are the anodic and cathodic peak potentials, respectively. In situations where no reverse peak was observed, only the peak potential is given. Voltammetric data from reports on several other related compounds are also given in Table 2. The $\Delta E$ values for several of the literature compounds are very large (>>100 mV), indicating complicated electrochemical behaviour, and suggesting that the reported $E^r_{1/2}$ values do not correspond closely to the formal potentials.

In most instances where the $E_p^{ox}$ and $E_p^{red}$ peak separation ($\Delta E$) could be measured, the values obtained were close to that expected for a one-electron transfer (Table 2). There were some variations detected in the peak current intensities for equivalent concentrations of different compounds (Figure 4), but this is likely to be due to differences in diffusion coefficients, as the peak currents appear to approximately inversely correlate with the size of the molecules. Coulometry measurements made during exhaustive controlled potential electrolysis (CPE) experiments at 233 K for the first oxidation process of **3** and **5**, at applied potentials 100 mV more positive than the $E^r_{1/2}$ values, confirmed the transfer of one electron per molecule, see Equation (4) in the Exp. Sect. The one-electron oxidised species were stable for at least 2–3 h at 233 K in $CH_2Cl_2$ and could be reversibly reduced back to their starting materials. The electrolysis experiments were performed at low temperatures to ensure increased stability of the oxidised compounds (compared to at ambient temperatures).

Free dppf is oxidised at about +200 mV more positive than ferrocene.[24] The product of this one-electron oxidation is not as stable as the $Fc/Fc^+$ system and moderate scan rates of around 3 V s$^{-1}$ are needed to obtain $i_p^{ox}/i_p^{red}$ ratios equal to unity.[24] When dppf is coordinated to other

 © 2007 Wiley-VCH Verlag GmbH & Co. KGaA, Weinheim 

Table 2. Cyclic voltammetric data obtained at a scan rate of 100 mV s$^{-1}$ at a 1-mm diameter glassy carbon electrode at 233 K in $CH_2Cl_2$ with 0.25 M $Bu_4NPF_6$ as the supporting electrolyte, together with some literature data.

| Compound | Oxidation process[a] | | | | Reduction process |
|---|---|---|---|---|---|
| | $E_p^{ox}$ [V][b] | $E_p^{red}$ [V][c] | $E^r_{1/2}$ [V][d] | $\Delta E$ [mV][e] | $E_p^{red}$ [V][c] |
| [($\eta^5$-Ind)Ru($PPh_3$)$_2$Cl] **1** | | | –0.01 | 66[13] | |
| [($\eta^5$-Ind)Ru(dppf)Cl] **2** | +0.010 | –0.062 | –0.03 | 72 | not detected |
| | +0.553 | +0.476 | +0.51 | 77 | |
| [($\eta^5$-Ind)Ru(dppf)(SMe)] **3** | –0.480 | –0.542 | –0.51 | 62 | |
| | +0.344 | +0.288 | +0.32 | 56 | |
| | +0.771 | +0.702 | +0.74 | 69 | |
| | | | | | –2.620 |
| [($\eta^5$-Ind)Ru(dppf)(SEt)] **4** | –0.498 | –0.560 | –0.53 | 62 | |
| | +0.364 | +0.300 | +0.33 | 64 | |
| | +0.776 | +0.708 | +0.74 | 68 | |
| | | | | | –2.610 |
| [($\eta^5$-Ind)Ru(dppf)(SPh)] **5** | –0.351 | –0.416 | –0.38 | 65 | |
| | +0.464 | +0.399 | +0.43 | 65 | |
| | +0.784 | +0.718 | +0.75 | 66 | |
| | | | | | –2.548 |
| [($\eta^5$-Ind)Ru(dppe)Cl] | | | –0.03 | 64[13] | |
| [($\eta^5$-Ind)Ru(dppm)Cl] | | | –0.07 | 62[13] | |
| [($\eta^5$-Cp)Ru(dppf)Cl] **2A** | +0.144 | 0.073 | +0.11 | 71 | not detected |
| | +0.521 | +0.436 | +0.48 | 85 | |
| [($\eta^5$-Cp)Ru(dppe)Cl] | | | +0.05 | 110[27] | |
| [($\eta^5$-Cp)Ru(dppm)Cl] | | | +0.03 | 340[27] | |
| [($\eta^5$-Cp)Ru($PPh_3$)$_2$Cl] **1A** | | | +0.10 | 360[27] | |
| [($\eta^5$-Cp*)Ru(dppf)Cl] **2B** | –0.050 | –0.115 | –0.08 | 65 | not detected |
| | +0.486 | +0.408 | +0.45 | 78 | |
| [($\eta^5$-Cp*)Ru(dppe)Cl] | | | –0.13 | 270[27] | |
| [($\eta^5$-Cp*)Ru($PPh_3$)$_2$Cl] | | | –0.03 | 240[27] | |
| [($\eta^5$-Ind)Ru(dppf)H] **6** | –0.262 | –0.328 | –0.30 | 66 | |
| | –0.072 | –0.174 | –0.12 | 102 | not detected |

[a] All potentials are relative to the $Fc/Fc^+$ redox couple. Data from literature reports[13,27] that were vs. SCE have been converted to vs. $Fc/Fc^+$ by adding 0.46 V (corrections for differences in temperature have not been made). [b] $E_p^{ox}$ = oxidative peak potential. [c] $E_p^{red}$ = reductive peak potential. [d] $E^r_{1/2} = (E_p^{ox} + E_p^{red})/2$. [e] $\Delta E = |E_p^{ox} - E_p^{red}|$.

metal ions through the phosphorus atoms, the oxidation potential increases to about +0.5 V versus $Fc/Fc^+$ and the stability of the oxidised dppf is substantially improved so that $i_p^{ox}/i_p^{red}$ ratios equal to unity are obtained at slow scan rates of 100 mV s$^{-1}$ (similar to $Fc/Fc^+$).[24,25] In the light of these previous observations,[24,25] we conclude that the oxidation process that occurs at +0.32–0.51 V versus $Fc/Fc^+$ in the CV's of **3**, **4**, **5**, **2**, **2A** and **2B** (i.e., the second process) is likely to be associated with the one-electron oxidation of [dppf] to $[dppf]^+$. Therefore, the first oxidation process observed in the CV's in Figure 4 is associated with the formal oxidation of $Ru^{2+}$ to $Ru^{3+}$ (although it is likely some electron delocalisation occurs). The conclusion that the first process is associated with localised oxidation of the Ru centre is consistent with a similar first oxidation potential for **3**, **4** and **5** (ca. –0.45 V vs. $Fc/Fc^+$) and for **2**, **2A** and **2B** (ca. 0 V vs. $Fc/Fc^+$) (Figure 4), as the potential is likely to be most sensitive to the substituents coordinated directly to the ruthenium. The third oxidation process for **3**, **4** and **5** is possibly again centred on the ruthenium ion, as an $Ru^{3+}$-to-$Ru^{4+}$ redox transformation is to be expected (although the exact location of the oxidation process is difficult to determine from CV experiments). Complexes **2**, **2A** and **2B** may also be further oxidised, but at a more positive potential than **3**, **4** and **5** (additional oxidation processes were not detected within the solvent/electrolyte potential window).

The $E^r_{1/2}$ values of the complexes (Table 2) indicate ease of oxidation of the complexes as follows: for [LRuCl(dppf)] complexes (L = Ind, Cp and Cp*), Cp* < Ind < Cp, in agreement with the decreasing electron-donor capability of the corresponding ligands. Similar trends have been observed for the dppe, dppm, $(PPh_3)_2$ and $(PMe_2Ph)_2$ analogues.[13,27] The data also show [(Ind)RuCl(dppf)SMe] (**3**) is more easily oxidised than its Ph analogue **5**, in agreement with decrease of electron density at the metal centre in **5**, caused by delocalisation into the Ph ring.

EPR experiments were performed at 10 K on frozen samples of $\mathbf{3}^+$ and $\mathbf{5}^+$ that were produced by electrochemically oxidising the starting materials by one electron at a constant potential at 233 K (Figure 5). The spectrum obtained for $\mathbf{5}^+$ showed additional hyperfine structure, suggesting that the unpaired electron was partially delocalised, possibly on the Ph group bonded to the S. Complex $\mathbf{3}^+$ did not display hyperfine structure, possibly because the unpaired electron was less able to be accommodated about the methyl group bonded to the sulfur. Interaction of the unpaired electron with the $^{31}P$ atoms ($I$ = ½, 100% abundance) is also possible, as has been observed in diastereomeric [($\eta^6$-arene)$Ru^{III}$(P-As)Cl] complexes in which the ruthenium atom is a chiral stereocentre.[26] EPR spectra of $\mathbf{3}^+$ or $\mathbf{5}^+$ were not detected at room temperature, indicting that the unpaired electron was mainly localised on the metal ion,

 © 2007 Wiley-VCH Verlag GmbH & Co. KGaA, Weinheim 

rather than on the organic ligands. The further one-electron oxidation of $\mathbf{3}^+$ and $\mathbf{5}^+$ at 233 K (two electrons overall) produced compounds that did not give an EPR signal at 10 K and above, either because they were diamagnetic or were paramagnetic with rapid relaxation times. Complex $\mathbf{4}^+$ was not examined by EPR spectroscopy because the cyclic voltammetry experiments indicated that its electrochemical behaviour was essentially identical to $\mathbf{3}^+$ (Figure 4).

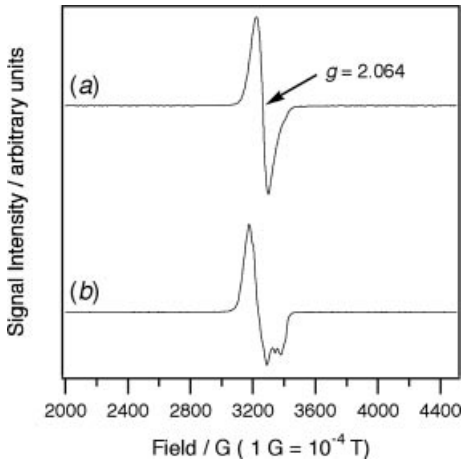


Figure 5. Continuous wave X-band EPR spectra obtained at 10 K with microwave frequency of 9.44 GHz and microwave power of 0.2 mW after the exhaustive electrochemical one-electron oxidation of (a) **3** to $\mathbf{3}^+$ and (b) **5** to $\mathbf{5}^+$ at –0.2 V vs. $Fc/Fc^+$ in $CH_2Cl_2$ (with 0.25 M $Bu_4NPF_6$) at 233 K.

Cyclic voltammograms of [(Ind)Ru(dppf)H] **6** obtained in $CH_2Cl_2$ solutions at 233 K at a GC electrode are displayed in Figure 6. The compound displayed two chemically reversible (or quasireversible) oxidation processes at about –0.3 and –0.1 V versus $Fc/Fc^+$. The second oxidation process had smaller peak currents than the first process, which may be caused by interactions between the oxidised compound and the electrode surface. On a Pt electrode, only one drawn out oxidation process was detected between –0.2 and 0.2 V, indicating that the oxidation processes were strongly influenced by the nature of the electrode surface. The cyclic voltammetry significantly changed from that shown in Figure 6 as the temperature was raised,

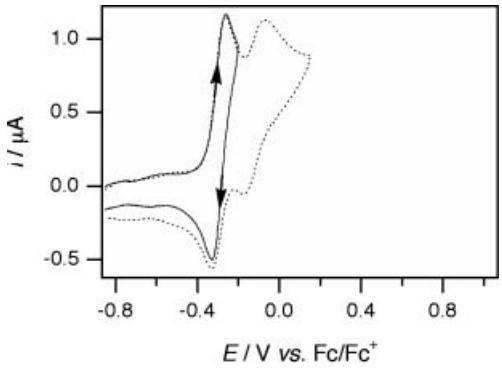


Figure 6. Cyclic voltammograms recorded at 100 $mV s^{-1}$ of a 1.2 mM $CH_2Cl_2$ solution of **6** with 0.5 M $Bu_4NPF_6$ at a 1-mm planar GC electrode at 233 K.

because of instability of oxidised **6** in $CH_2Cl_2$. At 293 K, only one chemically irreversible oxidation process was detected at about +0.6 V versus $Fc/Fc^+$.

[(Ind)Ru(dppf)H] (**6**) was approximately 0.3 V easier to oxidise than the corresponding Cl complex, [(Ind)Ru(dppf)-Cl] (**2**) (Table 2), which is a similar trend seen for other $\eta^5$ organometallic compounds containing the dppf ligand and Cl or H.[28]

## Conclusions

Chloro substitution of [(Ind)Ru(dppf)Cl] (**2**) with thiolates ($RS^-$) in MeOH was found to yield both thiolato derivatives and a hydrido complex, [(Ind)Ru(dppf)H] (**6**), the yield of which is both solvent- and R-dependent. From observations that the reaction could not proceed in the absence of MeOH, it was rationalised that **6** was formed by β-H elimination from ligated $MeO^-$, the latter being formed in equilibrium amounts by an interaction between $RS^-$ and MeOH. The product mixture therefore reflected the relative nucleophilicity of $RS^-$ and $MeO^-$. Voltammetry experiments indicated that the formal oxidation potentials for [LRu(dppf)Cl] compounds (L = Ind, Cp and Cp*) occurred in the order Cp* < Ind < Cp, with a 200 mV difference between the Cp* and Cp compounds. For [(Ind)Ru(L′)Cl] compounds {L′ = dppm, dppe, dppf, $(PPh_3)_2$}, the formal potentials decreased in the order dppm < dppe/dppf < $(PPh_3)_2$, although the total difference in oxidation potential spanning all the different diphosphanes [(Ind)Ru(L′)Cl] was a relatively small 60 mV. EPR experiments on $\mathbf{3}^+$ and $\mathbf{5}^+$ at 10 K indicated that the monocations were paramagnetic and the dications were EPR silent.

## Experimental Section

**General:** All reactions were carried out using conventional Schlenk techniques under inert nitrogen or argon in an M. Braun Labmaster 130 Inert Gas System.

NMR spectra were measured with a Bruker 300 FT NMR spectrometer; for $^1H$ and $^{31}P$ spectra, chemical shifts were referenced to residual solvent in the deuterio-solvents. IR spectra in KBr pellets were measured in the range 4000–400 $cm^{-1}$ by means of a BioRad FTS-165 FTIR instrument. Mass spectra were run on a Finnigan Mat 95XL-T (FAB) or a Finnigan-MAT LCQ (ESI) spectrometer. Elemental analyses were performed by the microanalytical laboratory in-house.

[(Ind)Ru($PPh_3$)$_2$Cl] (**1**)[1] and $Ph_2P(CH_2)_2SH$[29] were prepared by published methods. [(Ind)Ru(dppf)Cl] (**2**) was synthesised from phosphane substitution of **1**, while [(Ind)Ru(dppf)($CH_3CN$)]$PF_6$ (**2S**) was derived from **2** by reaction with $NaPF_6$ in refluxing $CH_3CN$.[30] All other chemicals were obtained commercially and used without any further purification. All solvents were dried with sodium/benzophenone and distilled before use. Celite (Fluka AG) and silica gel (Merck Kieselgel 60, 230–400 mesh) were dried at 140 °C overnight before chromatographic use.

**Electrochemical Studies:** Voltammetric experiments were conducted with a computer-controlled Eco Chemie µAutolab III potentiostat. Solutions of electrogenerated compounds for the EPR experiments

 © 2007 Wiley-VCH Verlag GmbH & Co. KGaA, Weinheim 

were prepared in a divided controlled potential electrolysis cell separated with a porosity no. 5 (1.0–1.7 μm) sintered glass frit. The working and auxiliary electrodes were identically sized Pt mesh plates symmetrically arranged with respect to each other. A silver wire reference electrode (isolated by a salt bridge containing 0.5 M $Bu_4NPF_6$ in $CH_3CN$) was positioned to within 2 mm of the surface of the working electrode. The electrolysis cell was jacketed in a glass sleeve and cooled to 233 K (for improved stability of the oxidised compounds) using a Lauda RL6 variable temperature methanol-circulating bath. The volumes of both the working and auxiliary electrode compartments were approximately 20 mL each. The number of electrons transferred during the bulk oxidation process was calculated from Equation (4)

$$N = Q/nF \quad (4)$$

where $N$ is the number of mols of the starting compound, $Q$ is the charge (coulombs), $n$ is the number of electrons and $F$ is the Faraday constant (96485 C mol$^{-1}$). The electrolysed solutions were transferred under vacuum into cylindrical 3-mm (id) EPR tubes that were immediately frozen in liquid $N_2$. EPR spectra were recorded with a Bruker ESP 300e spectrometer in a $TE_{102}$ cavity at 10 K using liquid He cooling.

**Synthesis of [(Ind)Ru(dppf)(SR)] {R = Me (3), Et (4), Ph (5)}:** RSNa {0.25 mmol: R = Me, 17 mg; R = Et [freshly prepared in situ from EtSH (19 μL) and MeONa obtained from 6 mg Na in 2 mL MeOH]; R = Ph, 33 mg} was added to a red suspension of [(Ind)-Ru(dppf)Cl] (**2**) (50 mg, 0.062 mmol) in MeOH (5 mL) and the mixture was stirred, whereupon the colour of the suspension changed immediately to green. After stirring at r.t. for 18 h, the solvent was removed in vacuo and the residue was extracted using toluene (2 × 5 mL). The extract was concentrated to about 2 mL and then loaded onto a silica gel column (2 × 5 cm) prepared in *n*-hexane. Elution gave two fractions: (i) a yellow eluate in toluene (about 8 mL), which yielded [(Ind)Ru(dppf)H] (**6**) (for the reaction in which R = Me, 9 mg, 19% yield; R = Et, 8 mg, 16% yield); (ii) a green eluate in toluene/THF (20:1, about 10 mL), which yielded [(Ind)Ru(dppf)(SR)] {R = Me (**3**), 40 mg, 79% yield; R = Et (**4**), 33.5 mg, 65% yield; R = Ph (**5**), 52 mg, 96% yield}; (iii) an orange-red eluate in THF (3 mL), which gave **2** in trace amounts.

Compound **3** was also formed from the reaction of [(Ind)-Ru(dppf)($CH_3CN$)]$PF_6$ (**2S**) with MeSNa as follows: MeSNa (2 mg, 0.029 mmol) was added to a yellow solution of **2S** (5 mg, 0.005 mmol) in THF (2 mL) and the mixture was stirred at r.t. The colour of the mixture slowly changed from yellow to green in 4 h. The $^1$H and $^{31}$P NMR spectra of an aliquot of the product mixture showed the sole presence of **3**.

**Data for 3:** $^1$H NMR ($C_6D_6$): $\delta$ = 1.96 (s, 3 H, SMe), 3.36, 3.89, 3.92 and 4.06 (each s, 2 H, $C_5H_4$), 5.29 (s, 1 H, Ind), 5.60 (s, 2 H, Ind), 7.04–7.58 (m, 24 H, Ind and Ph) ppm. $^{31}$P{$^1$H} NMR ($C_6D_6$): $\delta$ = 56.0 (s, dppf) ppm. FAB$^+$-MS: *m*/*z* (%) = 818 [M]$^+$, 771 [M – SMe]$^+$, 655 [M – SMe – Ind]$^+$. $C_{44}H_{38}FeP_2RuS$ (817.70): calcd. C 64.6, H 4.7, S 3.9; found C 64.7, H 4.8, S 3.9.

(*Note:* The proton resonances of the five-membered ring of Ind in this complex, as in others in this work, appear as singlets, although couplings are anticipated, most probably because these are too small to be resolved using the 300-MHz instrument.)

**Data for 4:** $^1$H NMR ($C_6D_6$): $\delta$ = 1.62 (t, $^3J_{HH}$ = 7.4 Hz, 3 H, $SCH_2CH_3$), 2.16 (q, $^3J_{HH}$ = 7.4 Hz, 2 H, $SCH_2CH_3$), 3.63, 3.89, 3.94 and 4.06 (each s, 2 H, $C_5H_4$), 5.27 (s, 1 H, Ind), 5.70 (s, 2 H, Ind), 7.04–7.57 (m, 24 H, Ind and Ph) ppm. $^{31}$P{$^1$H} NMR ($C_6D_6$): $\delta$ = 56.1 (s, dppf) ppm. FAB$^+$-MS: *m*/*z* (%) = 832 [M]$^+$, 771 [M – SEt]$^+$, 655 [M – SEt – Ind]$^+$. $C_{45}H_{40}FeP_2RuS$ (831.73): calcd. C 65.0, H 4.9, S 3.9; found C 65.5, H 5.1, S 3.4.

**Data for 5:** $^1$H NMR ($C_6D_6$): $\delta$ = 3.62, 3.79, 3.88 and 4.06 (each s, 2 H, $C_5H_4$), 5.25 (s, 1 H, Ind), 5.64 (s, 2 H, Ind), 6.38–6.40, 6.94–6.97 (each 4-line m, 2 H, Ind), 7.04–7.58 (m, 20 H, Ph) ppm. $^{31}$P{$^1$H} NMR ($C_6D_6$): $\delta$ = 54.9 (s, dppf) ppm. FAB$^+$-MS: *m*/*z* (%) = 880 [M]$^+$, 771 [M – SPh]$^+$, 655 [M – SPh–Ind]$^+$. $C_{49}H_{40}FeP_2RuS$ (879.77): calcd. C 66.9, H 4.6, S 3.6; found C 67.3, H 4.8, S 4.1.

**Small-Scale Reactions of 1 with MeSNa in MeOH and THF – Effect of Solvent:** MeSNa (2 mg, 0.029 mmol) was added to a red solution or suspension of **1** (5 mg, 0.006 mmol) in the selected solvent (1 mL), and the mixture was refluxed. After the reaction, the product mixture was evacuated to dryness and the respective residues extracted with toluene, for examination by $^1$H and $^{31}$P NMR spectroscopy.

(i) In MeOH: A reflux for 1 h produced a suspension of dark green solids in a faint yellow supernatant. The spectra indicated the product was a mixture of [(Ind)Ru($PPh_3$)$_2$(SMe)] (**3P**) and the hydride species [(Ind)Ru($PPh_3$)$_2$H] [$^1$H NMR ($C_6D_6$): $\delta$ = –15.39 ppm (t, $^2J_{HP}$ = 33.8 Hz), cf. lit. values in $CDCl_3$: $\delta$ = –15.40 ppm (t, $^2J_{HP}$ = 31.6 Hz)[1]] in the ratio of 1:1.

(ii) In THF: The solution changed slowly to dark green during reflux (2 h). The spectra indicated that [(Ind)Ru($PPh_3$)$_2$(SMe)] (**3P**) was the sole product.

**Data for 3P:** $^1$H NMR ($C_6D_6$): $\delta$ = 2.23 (s, 3 H, SMe), 4.30 (s, 2 H, Ind), 5.22 (s, 1 H, Ind), 6.88–7.47 (m, 34 H, Ind and Ph) ppm. $^{31}$P{$^1$H} NMR ($C_6D_6$): $\delta$ = 50.2 (s, $PPh_3$) ppm.

**Reaction of 2 with MeONa (in THF/MeOH):** Complex **2** (10 mg, 0.012 mmol) as a red solid was added to a suspension of dry MeONa [freshly prepared from Na (6 mg, 0.26 mmol) in MeOH (4 mL)] in THF (5 mL), and the slurry stirred at r.t. The $^1$H and $^{31}$P NMR spectra in $C_6D_6$ of aliquots of the reaction mixture at 2 h, and after reflux for an additional 4 h, revealed that the reaction did not proceed. MeOH (1 mL) was then added into the mixture and stirring continued at r.t. A slow colour change from orange-red to yellow occurred within 1 h. The $^1$H and $^{31}$P NMR spectra of an aliquot in $C_6D_6$ showed the formation of **6** as the sole product.

**Data for 6:** $^1$H NMR ($C_6D_6$): $\delta$ = –15.4 (t, $^2J_{HP}$ = 33 Hz, 1 H), 3.77 (s, 4 H, $C_5H_4$), 4.13 and 4.27 (each s, 2 H, $C_5H_4$), 4.34 (s, 2 H, Ind), 5.75 (s, 1 H, Ind), 6.28–6.31, 6.80–6.83 (each 4-line m, 2 H, Ind), 7.12–7.19, 7.28–7.33 and 8.03–8.08 (each m, total 20 H, Ph) ppm. $^{31}$P{$^1$H} NMR ($C_6D_6$): $\delta$ = 62.9 (s, dppf) ppm. ESI$^+$-MS: *m*/*z* (%) = 772 [M + H]$^+$. $C_{43}H_{36}FeP_2Ru$ (771.61): calcd. C 66.9, H 4.7; found C 66.9, H 4.5.

**Synthesis of [(Ind)Ru(dppf){S($CH_2$)$_2$$PPh_2$}] (7):** $Ph_2P(CH_2)_2SH$ (54 μL, 0.25 mmol) was added into excess NaH in THF (5 mL) and the suspension was stirred at r.t. overnight. The suspension was filtered through Celite into a red suspension of **2** (50 mg, 0.06 mmol) in MeOH (10 mL). The reaction mixture was stirred at r.t. for 18 h. A slow colour change from red suspension to dark green solution was observed. The solvent was removed in vacuo, and the residue extracted with toluene (2 × 5 mL). The toluene extract was concentrated to about 1 mL and loaded onto a silica gel column (2 × 10 cm) prepared in *n*-hexane. Elution gave two fractions: (i) a yellow eluate in toluene (about 4 mL), which gave **6** (7 mg, 15% yield); and (ii) a dark green eluate in toluene/diethyl ether (1:1, about 10 mL), which yielded [(Ind)Ru(dppf){S($CH_2$)$_2$-$PPh_2$}] (**7**) (34 mg, 54% yield).

**Data for 7:** $^1$H NMR ($C_6D_6$): $\delta$ = 2.31–2.39 and 2.75–2.80 (each m, 2 H, $CH_2$), 3.64, 3.88, 3.92 and 4.06 (each s, 2 H, $C_5H_4$), 5.18

 © 2007 Wiley-VCH Verlag GmbH & Co. KGaA, Weinheim 

Table 3. Crystal and structure refinement data.

| | 5·$CH_2Cl_2$·0.5MeOH | **6** |
|---|---|---|
| Formula | $C_{50.50}H_{44}Cl_2FeO_{0.50}P_2RuS$ | $C_{43}H_{36}FeP_2Ru$ |
| Formula mass | 980.68 | 771.58 |
| Space group (crystal system) | *Fdd*2 | $P2_1/n$ |
| Crystal system | orthorhombic | monoclinic |
| Unit cell dimensions | | |
| *a* [Å] | 27.452(3) | 11.8603(7) |
| *b* [Å] | 56.029(7) | 15.3521(10) |
| *c* [Å] | 11.6643(14) | 18.9672(12) |
| *α* [°] | 90 | 90 |
| *β* [°] | 90 | 98.300(2) |
| *γ* [°] | 90 | 90 |
| Cell volume [Å$^3$] | 17941(4) | 3417.4(4) |
| *Z* | 16 | 4 |
| $D_{calcd.}$ [g cm$^{-3}$] | 1.452 | 1.500 |
| Absorption coefficient [mm$^{-1}$] | 0.933 | 0.991 |
| *F*(000) electrons | 8016 | 1576 |
| Crystal size [mm] | 0.36 × 0.12 × 0.10 | 0.26 × 0.14 × 0.06 |
| *θ* range for data collection [°] | 2.08–26.37 | 2.17–26.37 |
| Index ranges | $0 \le h \le 34$, $0 \le k \le 70$, $-14 \le l \le 14$ | $-14 \le h \le 14$, $0 \le k \le 19$, $0 \le l \le 23$ |
| Reflections collected | 60968 | 27911 |
| Independent reflections | 9164 | 6985 |
| Max. and min. transmission | 0.9125–0.7300 | 0.9429–0.7827 |
| Data/restraints/parameters | 9164/3/520 | 6985/0/428 |
| Gof | 1.203 | 1.053 |
| Final *R* indices [$I > 2\sigma(I)$] | $R_1$ = 0.0440, $wR_2$ = 0.1091 | $R_1$ = 0.0465, $wR_2$ = 0.0927 |
| *R* indices (all data) | $R_1$ = 0.0462, $wR_2$ = 0.1102 | $R_1$ = 0.0640, $wR_2$ = 0.0994 |
| Largest diff. peak and hole [e Å$^{-3}$] | 0.954 and –0.522 | 0.618 and –0.443 |

(s, 1 H, Ind), 5.67 (s, 2 H, Ind), 7.03–7.05 (m, 8 H, Ph), 7.42 (br. s, 5 H, Ph), 7.56–7.61 (m, 7 H, Ph) ppm. $^{31}P\{^1H\}$ NMR ($C_6D_6$): $\delta$ = –14.8 [s, $S(CH_2)_2PPh_2$], 56.1 (s, dppf) ppm. FAB$^+$-MS: *m*/*z* (%) = 1016 [M]$^+$, 771 [M – $S(CH_2)_2PPh_2$]$^+$. $C_{57}H_{49}FeP_3RuS$ (1015.90): calcd. C 67.4, H 4.9, S 3.2; found C 67.7, H 5.0, S 3.2.

**Crystal Structure Determinations:** Crystals were mounted on quartz fibres. X-ray data were collected on a Bruker AXS APEX system, using Mo-$K_\alpha$ radiation, with the SMART suite of programs.[31] Data were processed and corrected for Lorentz and polarisation effects with SAINT,[32] and for absorption effects with SADABS.[33] Structural solution and refinement were carried out with the SHELXTL suite of programs.[34] Crystal and structure refinement data are summarised in Table 3. The structures were solved by direct methods or Patterson maps to locate the heavy atoms, followed by difference maps for the light, non-hydrogen atoms. All non-hydrogen atoms were generally given anisotropic displacement parameters in the final model.

Two solvent molecules were found for **5**: a dichloromethane and a half-molecule of methanol. The latter was refined with a common isotropic thermal parameter each for the O and C atoms, and the C–O bond length was restrained at 1.45(2) Å.

CCDC-621607 (for **5**·$CH_2Cl_2$·0.5MeOH) and -621608 (for **6**) contain the supplementary crystallographic data for this paper. These data can be obtained free of charge from The Cambridge Crystallographic Data Centre via www.ccdc.cam.ac.uk/data_request/cif.

## Acknowledgments

Support from the National University of Singapore under Academic Research Fund grant No. R-143-000-209-112 to L. Y. G. and a research scholarship to S. Y. N. from the Institute of Chemical and Engineering Sciences (ICES) are gratefully acknowledged. R. D. W. thanks the Australian National University for financial support.

[1] L. A. Oro, M. A. Ciriano, M. Campo, C. Foces-Foces, F. H. Cano, *J. Organomet. Chem.* **1985**, *289*, 117.
[2] a) O. A. Gansow, A. R. Burke, W. D. Vernon, *J. Am. Chem. Soc.* **1976**, *98*, 5817; b) A. Eisenstadt, F. Frolow, A. Efraty, *J. Chem. Soc., Chem. Commun.* **1982**, 642.
[3] P. Alvarez, J. Gimeno, E. Lastra, S. García-Granda, J. F. Van der Maelen, M. Bassetti, *Organometallics* **2001**, *20*, 3762.
[4] a) J. M. O'Connor, C. P. Casey, *Chem. Rev.* **1987**, *87*, 307; b) M. E. Rerek, L. N. Ji, F. Basolo, *J. Chem. Soc., Chem. Commun.* **1983**, 1208; c) V. Cadierno, J. Díez, M. P. Gamasa, J. Gimeno, E. Latra, *Coord. Chem. Rev.* **1999**, *193–195*, 147; d) J. W. Faller, R. H. Crabtree, A. Habib, *Organometallics* **1985**, *4*, 929; e) R. T. Baker, T. H. Tulip, *Organometallics* **1986**, *5*, 839.
[5] See the following and references cited therein: a) J. Díez, M. P. Gamasa, J. Gimeno, E. Lastra, A. Villar, *Organometallics* **2005**, *24*, 1410; b) S. Conejero, J. Díez, M. P. Gamasa, J. Gimeno, *Organometallics* **2004**, *23*, 6299; c) M. Bassetti, P. Alvarez, J. Gimeno, E. Lastra, *Organometallics* **2004**, *23*, 5127; d) P. Alvarez, E. Lastra, J. Gimeno, M. Bassetti, L. R. Falvello, *J. Am. Chem. Soc.* **2003**, *125*, 2386; e) V. Cadierno, M. P. Gamasa, J. Gimeno, C. González-Bernardo, E. Pérez-Carreño, S. García-Granda, *Organometallics* **2001**, *20*, 5177; f) M. P. Gamasa, J. Gimeno, B. M. Martín-Vaca, J. Borge, S. García-Granda, E. Pérez-Carreño, *Organometallics* **1994**, *13*, 4045.
[6] See leading references in: a) ref.[5f]; b) ref.[13]; c) A. Ceccon, S. Santi, L. Orian, A. Bisello, *Coord. Chem. Rev.* **2004**, *248*, 683.
[7] a) K. M. Rao, E. K. Rymmai, *Polyhedron* **2003**, *22*, 307; b) S. S. Keisham, Y. A. Mozharivskyj, P. J. Carroll, M. R. Kollipara, *J. Organomet. Chem.* **2004**, *689*, 1249; c) K. S. Singh, G. P. A. Yap, K. A. Kreisel, M. R. Kollipara, *J. Coord. Chem.* **2005**, *58*, 1607; d) P. Govindaswamy, C. Sinha, M. R. Kollipara, *J. Organomet. Chem.* **2005**, *690*, 3465; e) K. S. Singh, Y. A. Mozharivskyj, C. Thöne, M. R. Kollipara, *J. Organomet. Chem.* **2005**, *690*, 3720; f) K. S. Singh, C. Thöne, M. R. Kollipara, *J. Or-*

 © 2007 Wiley-VCH Verlag GmbH & Co. KGaA, Weinheim 

*ganomet. Chem.* **2005**, *690*, 4222; g) K. S. Singh, C. Thöne, M. R. Kollipara, *J. Coord. Chem.* **2006**, *59*, 333.
[8] T. Sato, M. Nishio, Y. Ishii, H. Yamazaki, M. Hidai, *J. Organomet. Chem.* **1998**, *569*, 98.
[9] a) X. L. Lu, J. J. Vittal, E. R. T. Tiekink, G. K. Tan, S. L. Kuan, L. Y. Goh, T. S. A. Hor, *J. Organomet. Chem.* **2004**, *689*, 1978; b) X. L. Lu, J. J. Vittal, E. R. T. Tiekink, L. Y. Goh, T. S. A. Hor, *J. Organomet. Chem.* **2004**, *689*, 1444.
[10] A. Shaver, P. V. Plouffe, P. Bird, E. Livingstone, *Inorg. Chem.* **1990**, *29*, 1826.
[11] M. P. Gamasa, J. Gimeno, C. Gonzalez-Bernardo, B. M. Martín-Vaca, J. Borge, S. Garcia-Granda, *Inorg. Chim. Acta* **2003**, *347*, 181.
[12] a) J. Chatt, B. L. Shaw, *Chem. Ind. (London)* **1960**, 931; b) J. Chatt, B. L. Shaw, *J. Chem. Soc.* **1962**, 5075 and references cited therein.
[13] a) M. I. Bruce, M. G. Humphrey, A. G. Swincer, R. C. Wallis, *Aust. J. Chem.* **1984**, *37*, 1747; b) T. Wilczewski, M. Bocheńska, J. F. Biernat, *J. Organomet. Chem.* **1981**, *215*, 87.
[14] Estimated from observed trends of $\Delta(pK_{a(MeOH)} - pK_{a(water)}) \approx 4.0$ for RSH and the known $pK_a$ value (10.3) of MeSH, in water. [See: E. P. Serjeant, B. Dempsey (Eds.), *Inoization Constants of Organic Acids in Solution, IUPAC Chemical Data Series No. 23*, Pergamon Press, Oxford, UK, **1979**.]
[15] J. F. Bunnett, L. A. Retallick, *J. Am. Chem. Soc.* **1967**, *89*, 423.
[16] B. W. Clare, D. Cook, E. C. F. Ko, Y. C. Mac, A. J. Parker, *J. Am. Chem. Soc.* **1966**, *88*, 1911 and references cited therein.
[17] R. J. Haines, A. L. Du Preez, *J. Organomet. Chem.* **1975**, *84*, 357.
[18] G. S. Ashby, M. I. Bruce, I. B. Tomkins, R. C. Wallis, *Aust. J. Chem.* **1979**, *32*, 1003.
[19] M. P. Gamasa, J. Gimeno, C. Gonzalez-Bernardo, B. M. Martín-Vaca, D. Monti, M. Bassetti, *Organometallics* **1996**, *15*, 302.
[20] T. Blackmore, M. I. Bruce, F. G. A. Stone, *J. Chem. Soc. A* **1971**, 2376.
[21] M. I. Bruce, I. R. Butler, W. R. Cullen, G. A. Koutsantonis, M. R. Snow, E. R. T. Tiekink, *Aust. J. Chem.* **1988**, *41*, 963.
[22] A. K. Kakkar, N. J. Taylor, T. B. Marder, J. K. Shen, N. Hallinan, F. Basolo, *Inorg. Chim. Acta* **1992**, *198–200*, 219.
[23] a) A. Shaver, P. V. Plouffe, D. C. Liles, E. Singleton, *Inorg. Chem.* **1992**, *31*, 997; b) R. Y. C. Shin, M. A. Bennett, L. Y. Goh, W. Chen, D. C. R. Hockless, W. K. Leong, K. Mashima, A. C. Willis, *Inorg. Chem.* **2003**, *42*, 96.
[24] B. Corain, B. Longato, G. Favero, D. Ajo, G. Pilloni, U. Russo, F. R. Kreissl, *Inorg. Chim. Acta* **1989**, *157*, 259.
[25] A. C. Ohs, A. L. Rheingold, M. J. Shaw, C. Nataro, *Organometallics* **2004**, *23*, 4655.
[26] P. A. Gugger, A. C. Willis, S. B. Wild, G. A. Heath, R. D. Webster, J. H. Nelson, *J. Organomet. Chem.* **2002**, *643–644*, 136.
[27] P. M. Treichel, D. A. Khomar, P. J. Vincenti, *Synth. React. Inorg. Met.-Org. Chem.* **1984**, *14*, 383.
[28] R. T. Hembre, J. S. McQueen, V. W. Day, *J. Am. Chem. Soc.* **1996**, *118*, 798.
[29] J. Chatt, J. R. Dilworth, J. A. Schmutz, J. A. Zubieta, *J. Chem. Soc., Dalton Trans.* **1979**, 1595.
[30] S. Y. Ng, G. Fang, W. K. Leong, L. Y. Goh, M. V. Garland, *Eur. J. Inorg. Chem.* **2007**, 452–462.
[31] *SMART* version 5.628, Bruker AXS Inc., Madison, WI, USA, **2001**
[32] *SAINT+* version 6.22a, Bruker AXS Inc., Madison, WI, USA, **2001**
[33] G. M. Sheldrick, *SADABS*, University of Göttingen, Germany, **1996**
[34] *SHELXTL* version 5.1, Bruker AXS Inc., Madison, WI, USA, **1997**

Received: September 20, 2006
Published Online: November 27, 2006

 © 2007 Wiley-VCH Verlag GmbH & Co. KGaA, Weinheim 

DOI: 10.1002/ejic.200600730

# Synthesis, Structures and Comparison of Neutral Complexes Formed by 2-(2′-Pyridyl)indole and $d^6$ Transition Metals

**Bernd Neumann,[a] Christoph Krinninger,[a] and Ingo-Peter Lorenz*[a]**

**Keywords:** Metallacycles / N ligands / Rhenium / Ruthenium / Rhodium / Iridium

2-(2′-Pyridyl)indole acts as an N,N-bidentate ligand when deprotonated and forms (1-amido-4-imine)metallacycles with $Re^{I}$, $Ru^{II}$, $Rh^{III}$ and $Ir^{III}$. The crystal structures of 2-(2′-pyridyl)indole and the complexes $[Re(C_{13}H_9N_2)(CO)_2(PPh_3)_2]$, $[Ru(C_{13}H_9N_2)(\eta^6\text{-}C_6Me_6)Cl]$, $[Rh(C_{13}H_9N_2)(\eta^5\text{-}C_5Me_5)Cl]$ and $[Ir(C_{13}H_9N_2)(\eta^5\text{-}C_5Me_5)Cl]$ are presented and their spectra discussed. This provides a foundation for the increased use of this ligand, which is a prototype of a monoanionic, bidentate N,N-chelating ligand. The introduction of negatively charged N,N-bidentate ligands can increase the possibility of synthesising complexes tailored to catalysis and other applications.
(© Wiley-VCH Verlag GmbH & Co. KGaA, 69451 Weinheim, Germany, 2007)

## Introduction

Chelating ligands play an important role both in classical coordination chemistry and in modern organometallic chemistry. Both symmetrical and asymmetrical chelates with the same type of donor atoms or asymmetrical ones with different donor atoms have been reported, and the formation of five-membered metallacycles has been found to be preferred due to the increased stability of the resulting complexes. A 1,4-relationship of the donor atoms allows complexation of a broad range of metal ions in tetrahedral, octahedral and square-planar geometries. This can be achieved by minor changes in the ligand's geometry. Asymmetric chelation with two identical donor atoms occurs in two different types. First, the backbone bridge of the chelating ligand can induce asymmetry, as is observed with the axially chiral BINAP and related ligands.[1] Second, the two donor atoms can be electronically different, with one being assigned a negative charge or coordinating with $sp^2$ or $sp^3$ free electron pairs. Among the N,N-bidentate ligands, two types of symmetrical ligands have found widespread use, namely neutral diamine ligands such as ethylenediamine (en) and neutral diimine ligands like bipyridine (bpy) or 1,10-phenanthroline (phen). However, nonsymmetric anionic bidentate ligands have so far been much less investigated even though ligands of this type should be useful for several reasons. Firstly, they can be used to adjust the overall charge of the complex, which allows high formal oxidation states of the central atom to remain stable within such complexes. Secondly, they may facilitate proton channelling in or out of the complex centre, with the overall complex remaining mostly intact. Most catalytic cycles known in homogeneous catalysis involve the formation and modification of metal hydrides and protons. Both substrate movement towards and away from the complex as isomerisation occurs within a catalytic cycle will be affected by a proton acceptor. Thirdly, a bidentate ligand allows the former process to take place without cleavage of the ligand from the complex as an anionic ligand is more likely to tolerate an intermediate protonated stage than a neutral ligand. We selected 2-(2′-pyridyl)indole (Hpyind) as the first ligand to be examined within a series of noble metal complexes. After deprotonation, Hpyind is capable of acting as a 1,4-chelate, with one of the nitrogen donor atoms being an imine and the other being an amido function (Scheme 1). Further N,N- and N,P-chelating ligands will be presented and discussed in future publications.

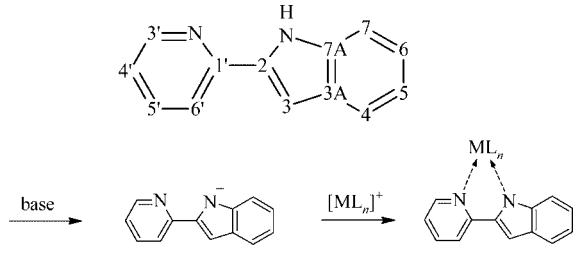


Scheme 1. General numbering (except crystal structures) and reaction scheme.

Hpyind is a well-known molecule that has been investigated in several recent publications. Indeed, complexes with pyind-like structures included in a larger molecule were described[2,3] even before the first detailed study on the behav-

[a] Ludwig Maximilian University Munich, Department of Chemistry and Biochemistry,
Butenandtstr. 5–13, 81377 Munich, Germany
Fax: +49-89-2180-77867
E-mail: ipl@cup.uni-muenchen.de
Supporting information for this article is available on the WWW under http://www.eurjic.org or from the author.

 © 2007 Wiley-VCH Verlag GmbH & Co. KGaA, Weinheim 

iour of Hpyind itself as a ligand was presented by Thummel et al.[4] Since the first isolated and structurally characterised pyind complex[5] with $Rh^I$ was described, some other related complexes have been reported.[6–9] Recent work has concerned not only pyind complexes as catalysts in hydroarylation[10] and the Heck reaction,[11] but also its use in optical devices.[12–16] It has also been used in an organometallic mimic for the protein kinase staurosporin.[17–21] The authors of the latter complex pointed out the "solely structural role" of an inert ruthenium complex in the biological activity of this pyind derivative, and they achieved enhanced activity and selectivity of the biologically active centre by modifying the distant ruthenium's ligand sphere. The promising idea of using such inert complexes within organic molecules is new[21] and supports the application of specially tailored chelate ligands such as Hpyind. In detail, such an anionic pyind-type ligand can form stable complexes with highly charged central atoms better than similar neutral ligands. It also leaves more space for varying the coligands at the metal centre than most neutral and anionic polydentate ligands and can easily be modified at several positions. We have therefore investigated the reactivity of rhenium(I), ruthenium(II), rhodium(III) and iridium(III) precursor complexes towards Hpyind in the presence of an appropriate base.

## Results and Discussion

In the synthesis of the complexes reported here, we first use a strong amide base or potassium hydride for the deprotonation of Hpyind in a nonprotic solvent to which we then add the precursor complex. The synthetic strategy shown in Scheme 2 for the rhodium complex **1** works well, although the stoichiometry of the amide has to be strictly controlled as some side-reactions may occur when excess base is present. We further established that even weak bases such as triethylamine are capable of quantitatively abstracting the proton of Hpyind when it is acidified by pre-coordination of the precursor complex to the pyridine ring (Scheme 3). The resulting triethylammonium halide is easily precipitated from toluene or separated from the product by extraction into a small amount of ethanol. Only one product was obtained in the reactions of $Ru^{II}$, $Rh^{III}$ and $Ir^{III}$, whereas the $Re^I$ complex **5** required purification by flash chromatography in a dry and oxygen-free environment. We were unable to obtain an analytically pure sample of complex **4** from the reaction of $[Re(CO)_5Br]$ with Hpyind and $NaN(SiMe_3)_2$ or $NEt_3$. The result of this reaction is summarised in Scheme 4. Complex **4**, which contains an $Re(CO)_4$ moiety, is likely to be less stable than **5**, which is stabilised by the bulky axial $PPh_3$ groups. The IR spectrum of **4** supports a pseudo-$C_{2v}$ symmetry and shows four ν(C=O) absorptions at 2015, 1936, 1912 and 1891 $cm^{-1}$. Upon evaporation of toluene, or in a more polar solvent like acetone, only two frequencies are observed [2011 and 1892 $cm^{-1}$ (br.)], thus suggesting a *fac*-$Re(CO)_3$ species. The DEI mass spectrum shows only an $[Re(CO)_3(pyind)]^+$ fragment as the highest peak.

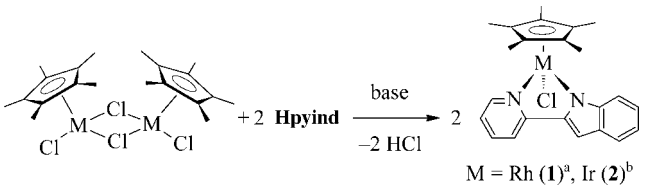


Scheme 2. Formation of rhodium and iridium complexes **1** and **2**; [a] toluene, $NaN(SiMe_3)_2$, 60 °C; [b] $CH_2Cl_2$, $NEt_3$, 25 °C.

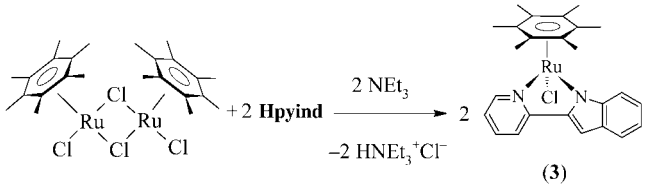


Scheme 3. Synthesis of ruthenium complex **3**.

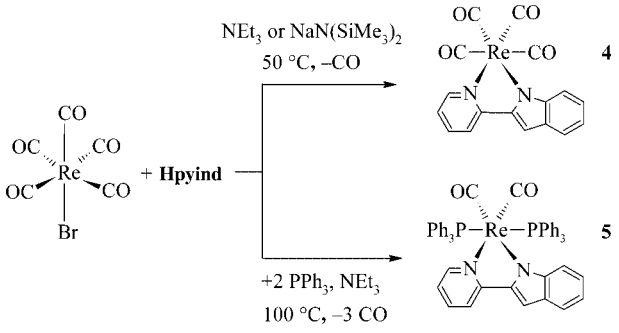


Scheme 4. Formation of complexes **4** and **5**.

The isolated complexes **1**–**3** are stable under argon at room temperature. However, some decomposition can be observed in moist air after several days. Solutions of these complexes in dichloromethane are stable for days, whereas the addition of methanol or moisture leads to the appearance of several new signals in the NMR spectra and decomposition. Complex **5** is somewhat more sensitive, and its decomposition is indicated by the formation of an intense green colour after a few seconds when the complex is exposed to moist air. All of the complexes show a high thermal stability, which makes them suitable for direct mass spectrometry.

The $^1H$ NMR spectrum of Hpyind has been described in the literature[4] but we have found some minor errors in the previous assignment concerning $H^{3'}$, $H^{4'}$, $H^4$ and $H^{6'}$. We therefore conducted H,H-COSY and HMQC measurements for both Hpyind and complex **1** in order to better understand the effect of complexation. These 2D NMR spectra of Hpyind and **1** are given as Supporting Information. Upon complexation, the NH signal of Hpyind disappears completely, the signals of $H^5$ and $H^6$ are shifted upfield by about 0.2 ppm, while those of $H^{5'}$, $H^{6'}$ and $H^7$ remain largely unaffected in complexes **1**–**3**. The signal of $H^3$ is affected only in the iridium complex **2**, where it is

 © 2007 Wiley-VCH Verlag GmbH & Co. KGaA, Weinheim 

shifted upfield by 0.1 ppm. Complex **5** shows a different picture due to the lower metal oxidation state, because the phosphane ligands are more electron-donating and the protons of pyind are affected by the phenyl groups of $PPh_3$ (ring current). The signals of the pyridine ring protons are shifted upfield by about 1.1 ppm on average, thereby indicating a highly electron-enriched aromatic system. All complexes give nearly identical peaks for the C–H carbon atoms in the $^{13}C$ NMR spectra, with $C^7$, which shows a 5 ppm downfield shift, being the only significantly shifted signal. The four quaternary carbon signals are shifted downfield, by about 7 ppm for $C^{1'}$, about 10 ppm for $C^2$ and $C^{7A}$ and about 3 ppm for $C^{3A}$, in all complexes. This effect is well known for metallacycle carbon atoms but somewhat surprising for the other ones. To conclude, the main effect of complexation is observed at the benzene ring of the indole moiety, and no major change is expected in the pyridylpyrrole moiety.

The mass spectra show no unexpected behaviour and are easily interpreted as a result of the metal and halide isotope distribution. The main fragmentation pattern is given by splitting off the ligands one after another.

The IR spectra of the complexes show a common strong band at around 1610 $cm^{-1}$ for ν(C=N) and lack the indole ν(NH) band of Hpyind at 3450 $cm^{-1}$. The two carbonyl bands of complex **5** indicate the sole presence of the *cis* conformation in solution, as was also observed in the crystal structure of **5**. They appear at very low energy ($\tilde{\nu}$ = 1905, 1823 $cm^{-1}$), in the range of terminal carbonyl ligands. Similar low frequencies have been reported for anionic complex radicals of rhenium(I).[22]

The electronic spectra of Hpyind have been discussed previously.[23–25] On complexation, the absorption maximum at 325 nm in Hpyind[4] shows a bathochromic shift of 40–65 nm. Table 1 shows this effect to be affected by the metal's charge and that it is stronger for complexes containing fifth-row metals than those with fourth-row metals.

Table 1. UV absorption data for pyind complexes in $CH_2Cl_2$.

| | $\lambda_{max}$ [nm] ($\varepsilon$ [$M^{-1}$ $cm^{-1}$]) | $\lambda_{max}$ [nm] ($\varepsilon$ [$M^{-1}$ $cm^{-1}$]) | $\lambda_{max}$ [nm] ($\varepsilon$ [$M^{-1}$ $cm^{-1}$]) |
|---|---|---|---|
| **1** | 363 (15890) | 314 (9000) | 260 (16680) |
| **2** | 377 (14620) | 326 (10800) | 260 (15240) |
| **3** | 374 (11670) | 331 (9860) | 248 (14760) |
| **5** | 367 (11335) | 323 (11430) | |

As several structure-related questions about Hpyind have been discussed in the literature, we were surprised to find that the crystal structure was unknown. In these studies, bridging methylene chains have been attached to restrain the nitrogen atoms in a *cis* conformation,[4] and tautomeric forms upon *N*-methylation have been studied.[26] After recrystallisation from chloroform/hexane we obtained colourless single crystals of Hpyind. An ORTEP plot of the molecular structure is displayed in Figure 1, which shows that Hpyind exists in a *cis* conformation in the solid state. The indole and pyridyl moieties are somewhat twisted by about 14°, as shown by the dihedral angle N(1)–C(1)–C(9)–N(2) given in Table 2. Within the crystal, two Hpyind molecules form a dimeric unit where the planes of the two Hpyind molecules form an angle of 110.8°. They are connected by two hydrogen bonds, where H(1) is refined freely between N(1) of one molecule and N(2) of the other molecule with an almost ideal N(1)–H(1)–N(2) angle of 170(2)° and an N(1)–N(2) distance of 2.988(3) Å, which indicates a strong interaction. The luminescent beryllium complex of pyind reported by Liu et al.[16] shows a similar structure. In order to compare the changes in the pyind moiety on complexation, some interatomic distances have been summarised in Table 3. In all our complexes the pyind ligand becomes planar, with the previously mentioned dihedral angle reduced to almost zero. This is accompanied by a significant shortening of the C(1)–C(9) bond. Together with these two carbon atoms, the two nitrogen donor atoms and

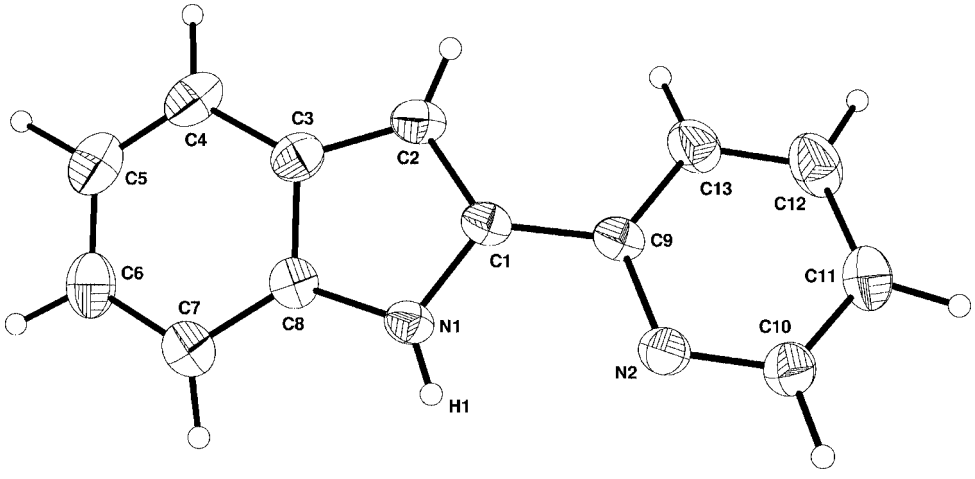


Figure 1. ORTEP plot (25% probability) of Hpyind. The numbering displayed is used in the discussion of all crystal structures for the pyind moiety.

 © 2007 Wiley-VCH Verlag GmbH & Co. KGaA, Weinheim 

Table 2. Selected angles [°] and dihedral angles [°].

| | Hpyind | 1 | 2 | 3 | 5 |
|---|---|---|---|---|---|
| Cl(1)–M(1)–N(1) | | 88.55(6) | 86.69(10) | 87.72(9) | |
| Cl(1)–M(1)–N(2) | | 87.45(5) | 85.62(10) | 88.70(9) | |
| N(1)–M(1)–N(2) | | 76.79(8) | 76.12(14) | 76.08(12) | 74.73(9) |
| M(1)–N(1)–C(1) | | 116.6(3) | 116.07(16) | 114.3(3) | 116.20(19) |
| M(1)–N(2)–C(9) | | 117.1(3) | 115.47(16) | 115.3(3) | 116.49(19) |
| N(1)–C(1)–C(9) | 121.28(17) | 115.9(2) | 115.4(4) | 114.9(3) | 117.6(2) |
| N(2)–C(9)–C(1) | 117.18(17) | 115.0(2) | 114.1(4) | 113.8(3) | 114.9(2) |
| N(1)–C(1)–C(9)–N(2) | –13.8(3) | –3.7(3) | 3.3(5) | –4.1(5) | –2.0(4) |

the metal atom form a coplanar five-membered metallacycle. The pyind ligand has quite a small bite angle of 74–77°, which makes it a nonideal ligand for large atoms. As it fits well into the octahedral coordination geometry of $d^6$ complexes, this deficiency seems to be compensated for by its charge transfer to the metal centre.

Table 3. Selected interatomic distances [Å].

| | Hpyind | 1 | 2 | 3 | 5 |
|---|---|---|---|---|---|
| M(1)–N(1) | | 2.073(2) | 2.050(3) | 2.082(3) | 2.153(2) |
| M(1)–N(2) | | 2.1343(19) | 2.103(3) | 2.108(3) | 2.202(2) |
| M(1)–Cl(1) | | 2.3987(8) | 2.3860(12) | 2.4142(10) | |
| N(1)–C(1) | 1.372(3) | 1.375(3) | 1.378(5) | 1.382(4) | 1.382(4) |
| C(1)–C(9) | 1.458(3) | 1.440(4) | 1.421(6) | 1.446(6) | 1.427(4) |
| C(9)–N(2) | 1.342(3) | 1.355(3) | 1.342(5) | 1.366(5) | 1.368(4) |

The $Rh^{III}$ complex **1** (Figure 2) and the $Ir^{III}$ complex **2** (Figure 3) are very similar, as would be expected, but some differences should be emphasised. The C(9)–N(2) distance increases in all complexes relative to the noncoordinated Hpyind ligand, but it remains unchanged in complex **2**. This is in agreement with the shorter metal–ligand contacts and the shorter C(1)–C(9) distance observed. As the $Rh^{III}$ centre in complex **1** should be smaller than $Ru^{II}$ in complex **3** (Figure 4), the latter would be expected to show larger metal–ligand distances. This is true for the slightly larger N(1)–Ru(1) distance, although the N(2)–Ru(1) distance is shortened by 0.05 Å. On the contrary, the shorter distances in complex **2** along with the shorter distances in the metallacycle mean that the ruthenium metallacycle of **3** has larger intraligand distances than found in **1**.

When complex **5** (Figure 5) is considered, the different co-ligand situation in this complex compared to the other complexes has to be taken in account. The two axial phosphane ligands show virtually identical Re–P distances of

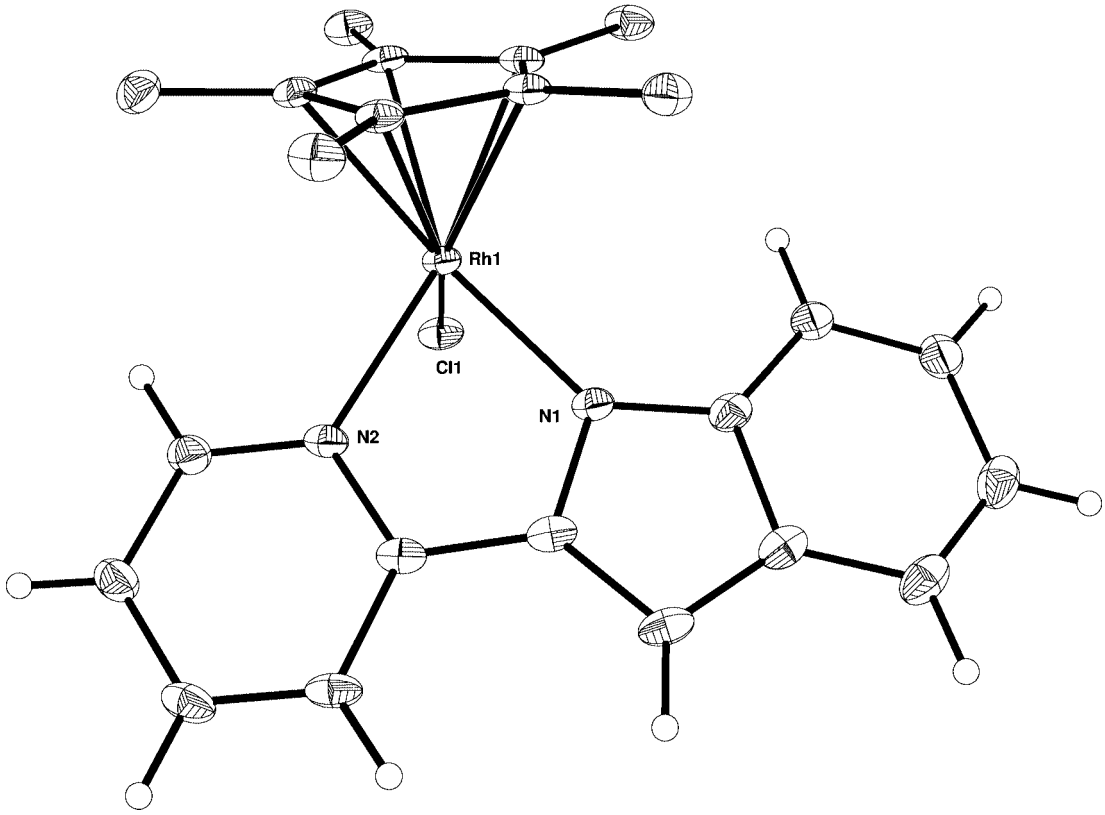


Figure 2. Molecular structure of rhodium complex **1** (25% probability). The methyl protons of $C_5Me_5$ are omitted for clarity.

 © 2007 Wiley-VCH Verlag GmbH & Co. KGaA, Weinheim 

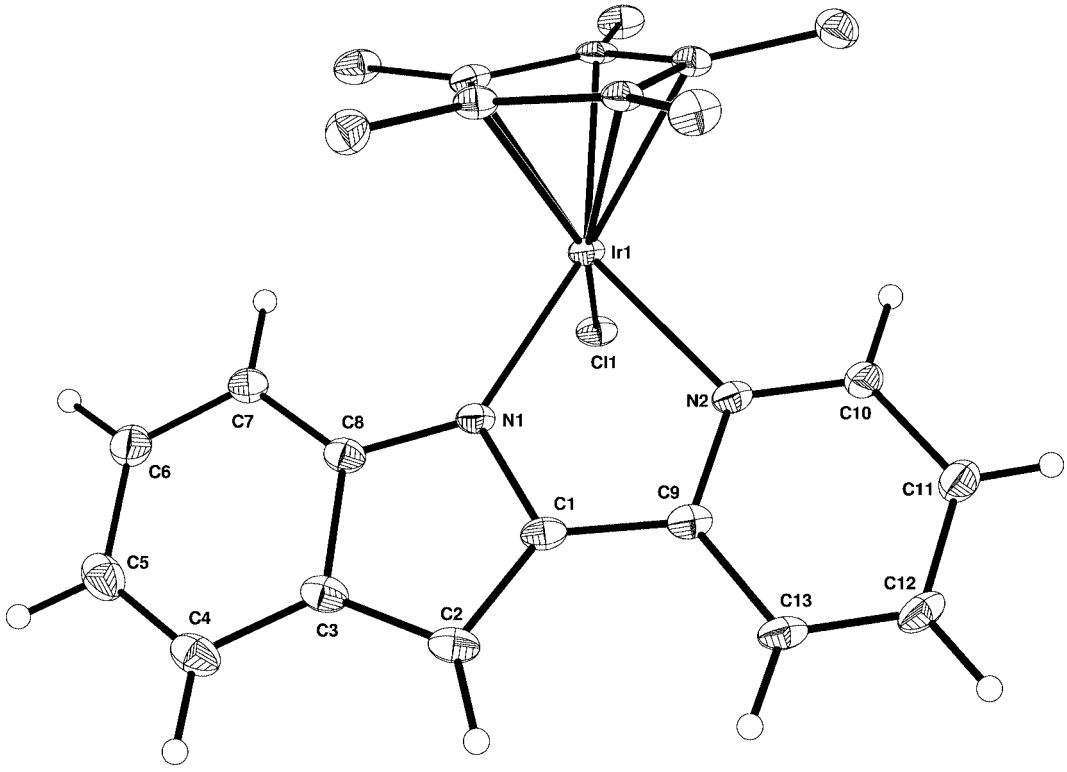


Figure 3. Molecular structure of complex **2** (25% probability). The methyl protons of $C_5Me_5$ are omitted.

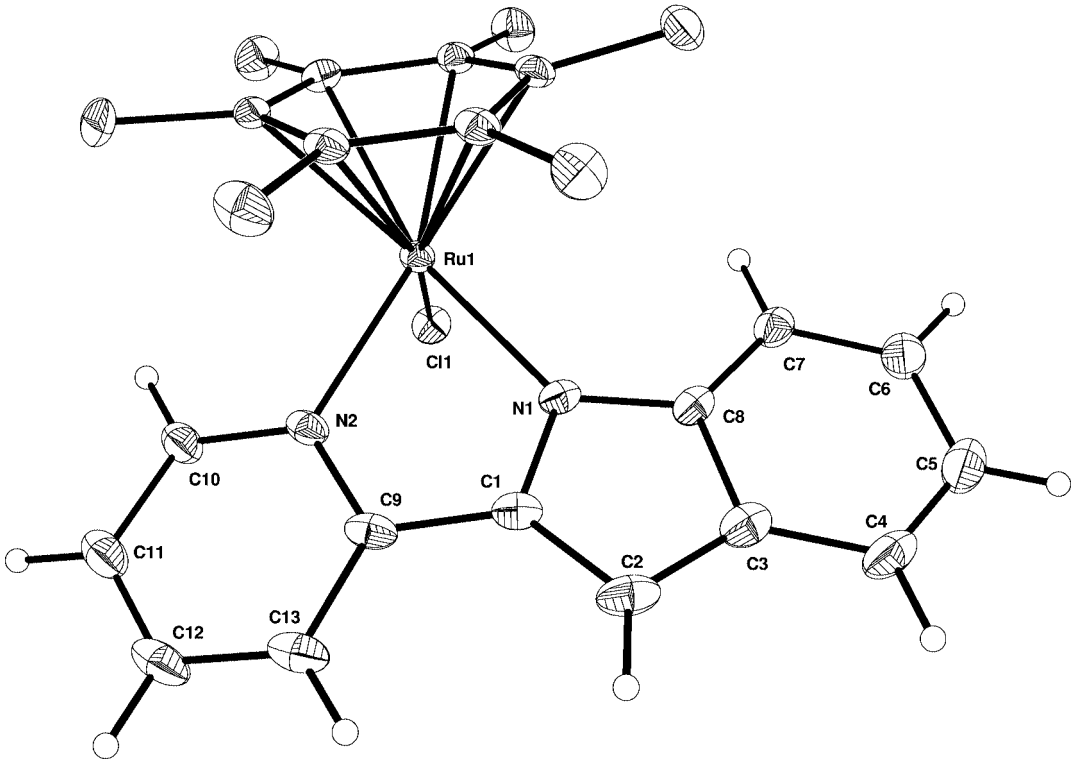


Figure 4. ORTEP plot of complex **3** (25% probability). The 18 disordered protons of the hexamethylbenzene moiety are omitted and a solvent molecule of $CH_2Cl_2$ is not included in the diagram.

2.4273(9) and 2.4324(9) Å, respectively, and all of the P–C distances of the phenyl groups lie between 1.832(3) and 1.837(3) Å. Two linear carbonyl ligands, which can act as both σ-donors and π-acceptors, are found in the *trans* positions with respect to the nitrogen donors. The very low C=O valence vibration energy observed suggests these car-

 © 2007 Wiley-VCH Verlag GmbH & Co. KGaA, Weinheim 

bonyl groups absorb a considerable amount of electron density. The low-valent rhenium(I) centre is larger than the optimum size for a chelating pyind ligand. Both of the Re–N distances are 0.10 Å longer than in the iridium complex **2**. However, the ligand shows both a shortened C(1)–C(9) bond, as was observed in compound **2**, as well as longer C=N bonds, as in **3**.

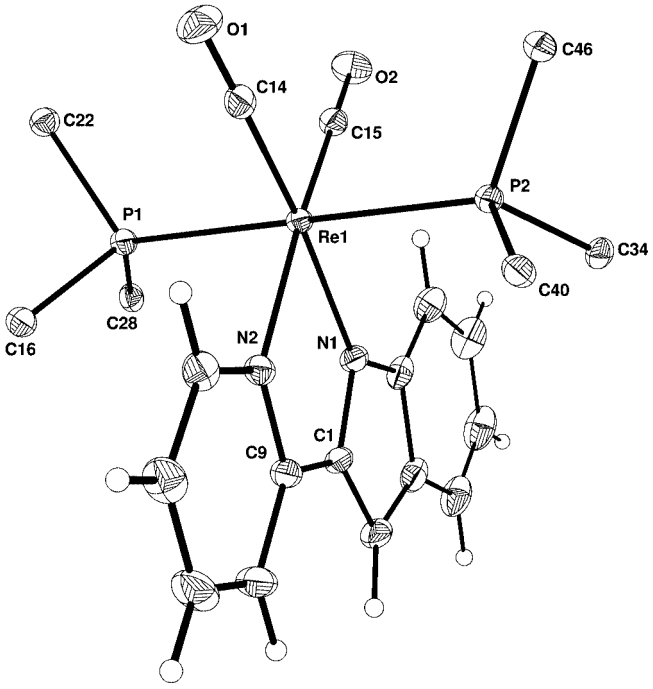


Figure 5. ORTEP plot of the rhenium compound **5** (25% probability). Only the terminal carbon atoms of both axial triphenylphosphane ligands are displayed. One disordered molecule of toluene is omitted.

## Conclusion

We have synthesised a series of novel transition metal complexes with the bidentate amido–imine ligand 2-(2′-pyridyl)indole. This is the first study to compare the properties that arise when different central atoms are used to form amido–imine complexes. Work on related anionic bidentate ligands, such as further modified amido–imine ligands and amido–phosphane ligands, is currently in progress. In addition, complexes containing different oxidation states for the central atoms, especially d$^8$ systems such as Rh$^{I}$, Ir$^{I}$ and Pd$^{II}$, will also be investigated. Investigations into the catalytic activity and optimisation of these complexes to improve certain catalytic processes are also underway.

## Experimental Section

**General:** All reactions were carried out under argon using standard Schlenk and vacuum-line techniques. Solvents were purified by standard procedures; dichloromethane was distilled from calcium hydride. The complexes $[RhCl_2Cp^*]_2$,[27] $[IrCl_2Cp^*]_2$,[27] $[Ru(CO)_2ClCp^*]$,[28] $[Ru(C_6Me_6)Cl_2]_2$[29] and $[Re(CO)_5Br]$[30] and Hpyind[4] were prepared and purified according to literature procedures. NMR spectra were measured with a Jeol Eclipse 270, Jeol Eclipse 400 or Jeol EX 400 spectrometer; the chemical shifts are given relative to external standards (TMS and 85% $H_3PO_4$). Mass spectra were recorded with a Jeol MStation JMS 700. IR spectra were recorded from KBr pellets or solutions in an NaCl cell using a Perkin–Elmer Spectrum One FT-IR spectrometer. UV/Vis spectra were measured in glass cuvettes with a Perkin–Elmer Lambda 16 spectrometer. The melting points, obtained with a Büchi 510 apparatus, are uncorrected. Elemental analysis was performed by the Microanalytical Laboratory of the Department of Chemistry and Biochemistry, LMU, using a Hereaus Elementar Vario El apparatus.

**2-(2′-Pyridyl)indol (Hpyind):** This compound was prepared according to the procedure reported by Thummel[4] and recrystallised from chloroform/hexanes. The following NMR assignments differ slightly from the literature. The 2D NMR spectra are given as Supporting Information. $^1$H NMR (400 MHz, $CD_2Cl_2$, 25 °C): $\delta$ = 9.79 (s, 1 H, NH), 8.57 (ddd, $^3J_{H,H}$ = 5.2, $^4J_{H,H}$ = 1.6, $^5J_{H,H}$ = 1.0 Hz, 1 H, H$^{3'}$), 7.82 (dt, $^3J_{H,H}$ = 8.0, $^{4,5}J_{H,H}$ = 1.0 Hz, H$^{6'}$), 7.73 (td, $^3J_{H,H}$ = 8.0, $^4J_{H,H}$ = 1.6 Hz, H$^{5'}$), 7.62 (dd, $^3J_{H,H}$ = 8.0, $^4J_{H,H}$ = 1.0 Hz, H$^4$), 7.38 (dd, $^3J_{H,H}$ = 8.0, $^4J_{H,H}$ = 1.0 Hz, H$^7$), 7.18 (td, $^3J_{H,H}$ = 8.0, $^4J_{H,H}$ = 1.0 Hz, 1 H, H$^6$), 7.18 (ddd, $^3J_{H,H}$ = 8.0, $^3J_{H,H}$ = 5.2, $^4J_{H,H}$ = 1.0 Hz, H$^{4'}$), 7.08 (td, $^3J_{H,H}$ = 8.0, $^4J_{H,H}$ = 1.0 Hz, 1 H, H$^5$), 7.02 (dd, $^4J_{H,H}$ = 2.0, $^5J_{H,H}$ = 1.0 Hz, 1 H, H$^3$) ppm. $^{13}$C NMR (100.62 MHz, $CD_2Cl_2$, 25 °C): $\delta$ = 150.3 (C$^{1'}$), 149.2 (C$^{3'}$), 136.9 (C$^2$), 136.7 (C$^{5'}$), 136.6 (C$^{7A}$), 129.2 (C$^{3A}$), 123.1 (C$^6$), 122.1 (C$^{4'}$), 121.1 (C$^4$), 120.1 (C$^5$), 119.9 (C$^{6'}$), 111.4 (C$^7$), 100.3 (C$^3$) ppm.

**Chlorido(η$^5$-pentamethylcyclopentadienido)[2-(2′-pyridyl)indolido-*N*,*N*′]rhodium(III) (1):** A 1 M solution of $NaN(SiMe_3)_2$ (280 μL, 0.28 mmol) was added to a solution of Hpyind (54 mg, 0.28 mmol) in toluene (10 mL). The mixture was stirred for 15 min and a solution of $[Rh_2Cl_4Cp^*_2]$ (85 mg, 0.14 mmol) in toluene (20 mL) was added dropwise. The red solution became darker and was stirred at 60 °C; after 10 min, an orange precipitate had formed. After 60 min, precipitation was complete and complex **1** was filtered, washed with cold toluene and dried in vacuo (115 mg, 0.25 mmol, 89%). $^1$H NMR (400 MHz, $CD_2Cl_2$, 25 °C): $\delta$ = 8.54 (br. d, $^3J_{H,H}$ = 5.7 Hz, 1 H, H$^{3'}$), 7.76 (ddd, $^3J_{H,H}$ = 8.1, $^4J_{H,H}$ = 1.7, $^4J_{H,H}$ = 0.8 Hz, 1 H, H$^{6'}$), 7.71 (ddd, $^3J_{H,H}$ = 8.1, $^3J_{H,H}$ = 7.0, $^4J_{H,H}$ = 1.5 Hz, 1 H, H$^{5'}$), 7.57 (dt, $^3J_{H,H}$ = 7.9, $^4J_{H,H}$ = 1.1 Hz, 1 H, H$^4$), 7.39 (dq, $^3J_{H,H}$ = 8.2, $^{4,5}J_{H,H}$ = 1.0 Hz, 1 H, H$^7$), 7.14 (ddd, $^3J_{H,H}$ = 7.0, $^3J_{H,H}$ = 5.7, $^4J_{H,H}$ = 1.7 Hz, 1 H, H$^{4'}$), 7.04 (ddd, $^3J_{H,H}$ = 8.2, $^3J_{H,H}$ = 6.8, $^4J_{H,H}$ = 1.1 Hz, 1 H, H$^6$), 7.00 (d, $^4J_{H,Rh}$ = 1.1 Hz, 1 H, H$^3$), 6.88 (ddd, $^3J_{H,H}$ = 7.9, $^3J_{H,H}$ = 6.8, $^4J_{H,H}$ = 1.0 Hz, 1 H, H$^5$), 1.62 (s, 15 H, Cp*) ppm. $^{13}$C NMR (100.52 MHz, $CD_2Cl_2$, 25 °C): $\delta$ = 157.4 (C$^{1'}$), 150.3 (C$^{3'}$), 145.8 (C$^2$), 144.9 (C$^{7A}$), 137.8 (C$^{5'}$), 132.5 (C$^{3A}$), 121.8 (C$^4$), 121.6 (C$^{4'}$), 120.9 (C$^6$), 119.8 (C$^{6'}$), 117.7 (C$^5$), 115.3 (C$^7$), 101.2 (C$^3$), 94.6 (d, $^1J_{C,Rh}$ = 7.7 Hz, Cp*), 9.4 (s, Cp*) ppm. DEI-MS (70 eV): *m*/*z* (%) = 466 (10) [M$^+$], 431 (100) [M$^+$ – Cl], 237 (17) [RhCp* – H], 235 (15) [RhCp* – 3 H], 194 (13) [pyind]. IR (KBr) $\tilde{\nu}$ = 3047 (w), 2984 (w), 2914 (w), 1607 (s), 1536 (s), 1449 (s), 1350 (m), 1310 (m), 1271 (w), 1199 (w), 1156 (m), 1119 (w), 1019 (m), 763 (s), 753 (m) cm$^{-1}$; ($CH_2Cl_2$) $\tilde{\nu}$ = 3049 (m), 2978 (w), 2918 (w), 1608 (s), 1537 (s), 1453 (s), 1361 (m), 1350 (m), 1312 (m), 1262 (m), 1200 (w), 1154 (m), 1141 (w), 1118 (w), 1077 (w), 1023 (m), 963 (w) cm$^{-1}$. UV/Vis ($CH_2Cl_2$, 25 °C): $\lambda$ ($\varepsilon$) = 363 (15890), 314 (9000), 260 (16680 M$^{-1}$ cm$^{-1}$) nm. $C_{23}H_{24}ClN_2Rh$ (466.81): calcd. C 59.18, H 5.18, N 6.00; found C 58.57, H 5.24, N 5.88. M.p. 305 °C (dec.). Single crystals suitable for X-ray structure determination were obtained by diffusion of pentane into a solution of **1** in $CH_2Cl_2$.

 © 2007 Wiley-VCH Verlag GmbH & Co. KGaA, Weinheim 

**Chlorido(η$^5$-pentamethylcyclopentadienido)[2-(2′-pyridyl)indolido-*N*,*N*′]iridium(III) (2):** Hpyind (59 mg, 0.3 mmol) and [$Ir_2Cl_4Cp^*_2$] (120 mg, 0.15 mmol) were dissolved in $CH_2Cl_2$ (5 mL) and $NEt_3$ (42 μL, 0.4 mmol) was added. After stirring at room temp. for 48 h, the solvent was evaporated. The yellow residue was stirred with EtOH (3 × 5 mL) to remove $HNEt_3Cl$ and the slightly yellow solution was discarded after centrifugation. Drying in vacuo yielded **2** (135 mg, 0.24 mmol, 81%). $^1$H NMR (400 MHz, $CD_2Cl_2$, 25 °C): $\delta$ = 8.55 (d, $^3J_{H,H}$ = 5.8 Hz, 1 H, H$^{3'}$), 7.81 (d, $^3J_{H,H}$ = 8.2 Hz, 1 H, H$^{6'}$), 7.70 (t, $^3J_{H,H}$ = 8.1 Hz, 1 H, H$^{5'}$), 7.54 (d, $^3J_{H,H}$ = 8.0 Hz, 1 H, H$^4$), 7.37 (d, $^3J_{H,H}$ = 8.4 Hz, 1 H, H$^7$), 7.09 (dd, $^3J_{H,H}$ = 6.5, $^3J_{H,H}$ = 5.8 Hz, 1 H, H$^{4'}$), 7.01 (dd, $^3J_{H,H}$ = 8.4, $^3J_{H,H}$ = 6.8 Hz, 1 H, H$^6$), 6.91 (s, 1 H, H$^3$), 6.90 (dd, $^3J_{H,H}$ = 7.8, $^3J_{H,H}$ = 6.8 Hz, 1 H, H$^5$), 1.66 (s, 15 H, Cp*) ppm. $^{13}$C NMR (100.52 MHz, $CD_2Cl_2$, 25 °C): $\delta$ = 158.1 (C$^{1'}$), 150.4 (C$^{3'}$), 145.3 (C$^2$), 144.9 (C$^{7A}$), 138.1 (C$^{5'}$), 131.5 (C$^{3A}$), 122.1 (*C*$^4$ and C$^{4'}$), 121.7 (C$^6$), 119.6 (C$^{6'}$), 118.1 (C$^5$), 115.2 (C$^7$), 101.8 (C$^3$), 86.8 (Cp*), 9.6 (Cp*) ppm. DEI-MS: *m*/*z* (%) = 556 (65) [M$^+$], 521 (100) [M$^+$ – Cl], 363 (20) [IrCp*Cl], 323 (17) [Ir(C$_7$H$_{11}$)Cl]. IR (KBr) $\tilde{\nu}$ = 3052 (w), 2986 (w), 1609 (s), 1541 (s), 1491 (w), 1447 (s), 1371 (w), 1349 (m), 1311 (m), 1266 (w), 1203 (w), 1155 (m), 1122 (m), 1082 (w), 1022 (m), 965 (w), 769 (s), 753 (s), 517 (w), 443 (w), 376 (w) cm$^{-1}$; ($CH_2Cl_2$) $\tilde{\nu}$ = 3047 (w), 2978 (w), 2921 (w), 1612 (s), 1453 (s), 1450 (s), 1381 (w), 1360 (w), 1359 (m), 1314 (m), 1202 (w), 1155 (w), 1120 (w), 1080 (w), 1030 (m) cm$^{-1}$. UV/Vis ($CH_2Cl_2$, 25 °C): $\lambda$ ($\varepsilon$) = 377 (14620), 326 (10800), 260 (15240), 226 (24740 M$^{-1}$ cm$^{-1}$) nm. $C_{23}H_{24}ClIrN_2$ (556.12): calcd. C 49.67, H 4.35, N 5.04; found C 49.43, H 4.15, N 4.90. M.p. 305–307 °C (dec.). Single crystals suitable for X-ray structure analysis were obtained by diffusion of pentane into a solution of **2** in $CH_2Cl_2$.

**Chlorido(hexamethylbenzene)[2-(2′-pyridyl)indolido-*N*,*N*′]-ruthenium(II) (3):** Hpyind (78 mg, 0.4 mmol) and [$Ru_2Cl_4(C_6Me_6)_2$] (134 mg, 0.2 mmol) were dissolved in $CH_2Cl_2$ (10 mL) and $NEt_3$ (30 μL, 0.4 mmol) was added. After stirring at room temp. for 24 h, the NMR spectrum indicated quantitative reaction. The solution was concentrated in vacuo and the residue was stirred with a small amount of EtOH (2 × 3 mL) to remove $HNEt_3Cl$. The EtOH solution was discarded after centrifugation from the insoluble residue, which was dried to give **3** as a yellow to orange powder (153 mg, 0.31 mmol, 78%). $^1$H NMR (270 MHz, $CD_2Cl_2$, 25 °C): $\delta$ = 8.49 (ddd, $^3J_{H,H}$ = 5.8, $^4J_{H,H}$ = 1.4, $^5J_{H,H}$ = 1.0 Hz, 1 H, H$^{3'}$), 7.65 (ddd, $^3J_{H,H}$ = 8.2, $^4J_{H,H}$ = 2.4, $^5J_{H,H}$ = 1.0 Hz, 1 H, H$^{6'}$), 7.62 (ddd, $^3J_{H,H}$ = 8.2, $^3J_{H,H}$ = 6.5, $^4J_{H,H}$ = 1.4 Hz, 1 H, H$^{5'}$), 7.53 (dt, $^3J_{H,H}$ = 8.1, $^4J_{H,H}$ = 1.0 Hz, 1 H, H$^4$), 7.30 (dq, $^3J_{H,H}$ = 8.4, $^{4,5}J_{H,H}$ = 1.0 Hz, 1 H, H$^7$), 7.06 (td, $^3J_{H,H}$ = 6.5, $^3J_{H,H}$ = 5.8, $^4J_{H,H}$ = 2.4 Hz, 1 H, H$^{4'}$), 7.00 (ddd, $^3J_{H,H}$ = 8.4, $^3J_{H,H}$ = 6.8, $^4J_{H,H}$ = 1.4 Hz, 1 H, H$^6$), 6.94 (d, $^4J_{H,H}$ = 0.8 Hz 1 H, H$^3$), 6.87 (ddd, $^3J_{H,H}$ = 7.8, $^3J_{H,H}$ = 6.8, $^4J_{H,H}$ = 1.1 Hz, 1 H, H$^5$), 1.98 (s, 18 H, C$_6$Me$_6$) ppm. $^{13}$C NMR (67.9 MHz, $CD_2Cl_2$, 25 °C): $\delta$ = 157.5 (C$^{1'}$), 151.9 (C$^{3'}$), 146.6 (C$^2$), 144.3 (C$^{7A}$), 137.0 (C$^{5'}$), 132.3 (C$^{3A}$), 121.6 (C$^4$), 120.7 (C$^{4'}$), 120.1 (C$^6$), 118.9 (C$^{6'}$), 117.6 (C$^5$), 116.0 (C$^7$), 101.2 (C$^3$), 93.1 (C$_6$Me$_6$), 15.8 (C$_6$Me$_6$) ppm. FAB-MS: *m*/*z* (%) = 493 (25) [MH$^+$], 492 (28) [M$^+$], 457 (100) [M$^+$ – Cl]. IR (KBr) $\tilde{\nu}$ = 3039 (w), 1605 (s), 1532 (s), 1446 (s), 1383 (w), 1360 (w), 1347 (m), 1309 (s), 1261 (m), 1226 (w), 1150 (w), 1115 (w), 1071 (m), 1036 (m), 1020 (m), 782 (m), 769 (m), 748 (m), 517 (w), 456 (w), 373 (w) cm$^{-1}$; ($CH_2Cl_2$) $\tilde{\nu}$ = 3052 (m), 2977 (w), 2923 (w), 1608 (s), 1534 (s), 1447 (s), 1386 (w), 1361 (w), 1348 (m), 1312 (m), 1199 (w), 1153 (w), 1118 (w), 1075 (w), 1021 (m), 960 (w), 895 (w) cm$^{-1}$. UV/Vis ($CH_2Cl_2$, 25 °C): $\lambda$ ($\varepsilon$) = 374 (11670), 331 (9860), 248 (14760), 229 (20135 M$^{-1}$ cm$^{-1}$) nm. $C_{25}H_{27}ClN_2Ru$ (492.02): calcd. C 61.03, H 5.53, N 5.69; found C 58.30, H 5.58, N 5.34. M.p. >320 °C. Single crystals suitable for X-ray structure analysis were obtained by diffusion of pentane into a solution of **3** in $CH_2Cl_2$. They contain one molecule of $CH_2Cl_2$ per formula unit.

**Tetracarbonyl[2-(2′-pyridyl)indolido-*N*,*N*′]rhenium(I) (4):** Hpyind (97 mg, 0.5 mmol) was dissolved in toluene (10 mL) and a solution of [$Re(CO)_5Cl$] (181 mg, 0.5 mmol) in toluene (10 mL) was added. A 0.1 M solution of $NaN(SiMe_3)_2$ in toluene (5.0 mL) or $NEt_3$ (75 μL, 0.5 mmol) was then added and the mixture stirred at 50 °C. Concentration of the solution after 16 h yielded a blue-green solid that dissolved readily in acetone or $CH_2Cl_2$. All our attempts to crystallise the substance by diffusion of a non-polar solvent into a solution of **4** or by cooling were not successful. NMR signals in the aromatic region are broad and could not be unambiguously interpreted. DEI-MS (70 eV): *m*/*z* (%) = 464 (89) [M$^+$ – CO], 436 (50) [M$^+$ – 2 CO], 408 (53) [M$^+$ – 3 CO], 380 (100) [Re(pyind)], 353 (25) [Re(pyind) – HCN]. IR (toluene) $\tilde{\nu}$ = 2015 (vs), 1936 (m), 1912 (vs), 1891 (vs) cm$^{-1}$; (acetone) $\tilde{\nu}$ = 2011 (vs), 1892 (vs) cm$^{-1}$; (toluene, from $NEt_3$ run) $\tilde{\nu}$ = 2010 (vs), 1891 (vs) cm$^{-1}$. Further details of the characterisation are not available.

**Dicarbonyl[2-(2′-pyridyl)indolido-*N*,*N*′]bis(triphenylphosphane)-rhenium(I) (5):** Hpyind (39 mg, 0.2 mmol), [$Re(CO)_5Br$] (81 mg, 0.2 mmol), $PPh_3$ (106 mg, 0.4 mmol) and $NEt_3$ (31 μL, 0.22 mmol) were dissolved in toluene (5 mL) and stirred in a sealed Schlenk tube at 100 °C for 48 h. The hot yellow-brown solution was separated from the colourless precipitate ($HNEt_3Cl$). The IR spectrum shows several carbonyl bands, thereby indicating that a mixture of species is present. The solution was cooled to –32 °C overnight and a yellow precipitate formed. This was separated (80 mg, 42%) from the solution and purified using a short chromatography column [$SiO_2$ 60, 70–230 mesh, 250 mL (!) $CH_2Cl_2$]. An air- and moisture-free environment must be maintained during the entire workup process as the crude product easily decomposes to form an intensely green oil, whereas the final pure product is considerably more stable. Drying yielded **5** as a yellow solid (70.2 mg, 73 μmol, 37%). $^1$H NMR (400 MHz, $CD_2Cl_2$, 25 °C): $\delta$ = 7.64–7.66 (m, 1 H, H$^4$), 7.46 (br. d, $^3J_{H,H}$ = 5.2 Hz, H$^{3'}$), 7.15 (dd, $^3J_{H,H}$ = 7.2, $^4J_{H,H}$ = 1.2 Hz, 1 H, H$^7$), 7.12 (ddd, $^3J_{H,H}$ = 8.0, $^3J_{H,H}$ = 7.2, $^4J_{H,H}$ = 1.2 Hz, H$^6$), 7.08–7.11 (m, 18 H, $PPh_3$), 6.99–7.01 (m, 12 H, $PPh_3$), 6.97–6.98 (m, 1 H, H$^5$), 6.85 (d, $^4J_{H,H}$ = 1.0 Hz, H$^3$), 6.63 (dd, $^3J_{H,H}$ = 6.0, $^3J_{H,H}$ = 5.2 Hz, 1 H, H$^{4'}$), 6.63 (d, $^3J_{H,H}$ = 7.4 Hz, 1 H, H$^{6'}$), 6.00 (ddd, $^3J_{H,H}$ = 7.4, $^3J_{H,H}$ = 6.0, $^4J_{H,H}$ = 1.6 Hz, 1 H, H$^{5'}$) ppm. $^{13}$C NMR (100.63 MHz, $CD_2Cl_2$, 25 °C): $\delta$ = 156.9 (C$^{1'}$), 151.6 (C$^{3'}$), 147.8 (C$^2$), 145.9 (C$^{7A}$), 135.3 (C$^{5'}$), 133.5 (t, $J_{C,P}$ = 5.3 Hz, $PPh_3$), 132.2 (C$^{3A}$), 129.1 ($PPh_3$), 127.7 (t, $J_{C,P}$ = 4.3 Hz, $PPh_3$), 120.49 (C$^4$), 120.47 (C$^{4'}$), 120.0 (C$^6$), 118.6 (C$^{6'}$), 117.8 (C$^5$), 117.1 (C$^7$), 101.4 (C$^3$) ppm. $^{31}$P NMR (162.00 MHz, $CD_2Cl_2$, 25 °C): $\delta$ = 21.05 ppm. DEI-MS (70 eV): *m*/*z* (%) = 960 (7) [M$^+$], 698 (5) [M$^+$ – $PPh_3$], 642 (9) [Re($PPh_3$)(pyind)], 262 (100) [$PPh_3$], 183 (45) [$PPh_2$]. IR (KBr) $\tilde{\nu}$ = 1905 (vs), 1823 (vs), 1609 (m), 1533 (m), 1481 (m), 1455 (w), 1444 (m), 1432 (s), 1367 (w), 1349 (w), 1318 (w), 1263 (w), 1153 (w), 1091 (m), 741 (s), 694 (s), 613 (w), 518 (s), 413 (w) cm$^{-1}$. UV/Vis ($CH_2Cl_2$, 25 °C) $\lambda$ ($\varepsilon$) = 367 (11335), 323 (11430 M$^{-1}$ cm$^{-1}$) nm. $C_{51}H_{39}N_2O_2P_2Re$ (960.02): calcd. C 63.81, H 4.09, N 2.92; found C 59.19, H 3.86, N 2.56. M.p. 211–214 °C (dec.). Single crystals suitable for X-ray structure determination were obtained from the initial toluene solution after separating the $HNEt_3Cl$ and cooling from 100 °C to room temp. within 10 h. The yellow, block-shaped crystals contain one molecule of toluene per formula unit.

**X-ray Crystallography:** X-ray crystallographic data (Table 4) were collected with a Nonius Kappa CCD and with an Oxford Diffraction Xcalibur S, both using graphite-monochromated Mo-$K_\alpha$ radiation ($\lambda$ = 0.71073 Å). Structures were solved by direct methods with

 © 2007 Wiley-VCH Verlag GmbH & Co. KGaA, Weinheim 

Table 4. Crystallographic data of Hpyind as well as complexes **1**–**3** and **5**.

| | Hpyind | **1** | **2** | **3** | **5** |
|---|---|---|---|---|---|
| Empirical formula | $C_{13}H_{10}N_2$ | $C_{23}H_{24}ClN_2Rh$ | $C_{23}H_{24}ClIrN_2$ | $C_{26}H_{29}Cl_3N_2Ru$ | $C_{58}H_{47}N_2O_2P_2Re$ |
| Formula mass [amu] | 194.232 | 466.808 | 556.120 | 576.95 | 1052.161 |
| Temperature [K] | 200(2) | 200(2) | 200(2) | 200(2) | 200(2) |
| Wavelength [Å] | 0.71073 | 0.71073 | 0.71073 | 0.71073 | 0.71073 |
| Crystal system | tetragonal | monoclinic | monoclinic | orthorhombic | monoclinic |
| Space group | $P4_12_12$ | $P2_1/n$ | $P2_1/n$ | *Pbca* | $P2_1/c$ |
| *a* [Å] | 8.4513(12) | 8.2365(16) | 8.2178(16) | 8.5237(17) | 12.278(3) |
| *b* [Å] | 8.4513(12) | 14.495(3) | 14.302(3) | 19.500(4) | 20.144(4) |
| *c* [Å] | 29.236(6) | 16.534(3) | 16.432(3) | 29.512(6) | 19.284(4) |
| $\alpha$ [°] | 90 | 90 | 90 | 90 | 90 |
| $\beta$ [°] | 90 | 95.75(3) | 96.35(3) | 90 | 95.97(3) |
| $\gamma$ [°] | 90 | 90 | 90 | 90 | 90 |
| *V* [Å$^3$] | 2088.2(6) | 1964.0(7) | 1919.4(7) | 4905.1(17) | 4743.7(17) |
| *Z* | 8 | 4 | 4 | 8 | 4 |
| $D_{calcd.}$ [g cm$^{-1}$] | 1.2356(4) | 1.5787(6) | 1.9245(7) | 1.5626(5) | 1.4733(5) |
| $\mu$ (Mo-$K_\alpha$) [mm$^{-1}$] | 0.075 | 1.016 | 7.106 | 0.984 | 2.675 |
| *F*(000) | 816 | 952 | 1080 | 2352 | 2120 |
| Crystal size [mm] | 0.24 × 0.16 × 0.09 | 0.45 × 0.25 × 0.18 | 0.40 × 0.1 × 0.05 | 0.18 × 0.09 × 0.04 | 0.14 × 0.09 × 0.02 |
| $\theta$ range [°] | 3.19–25.03 | 3.21–26.02 | 4.01–30.07 | 3.25–25.11 | 3.21–26.02 |
| Index ranges | $-10 \le h \le 10$ | $-10 \le h \le 9$ | $-11 \le h \le 11$ | $-10 \le h \le 10$ | $-15 \le h \le 15$ |
| | $-7 \le k \le 7$ | $-17 \le k \le 17$ | $-20 \le k \le 20$ | $-23 \le k \le 23$ | $-24 \le k \le 24$ |
| | $-28 \le l \le 34$ | $-20 \le l \le 20$ | $-23 \le l \le 23$ | $-34 \le l \le 35$ | $-23 \le l \le 23$ |
| Reflections collected | 3522 | 24467 | 25780 | 8110 | 18157 |
| Independent reflections | 1833 | 3848 | 5620 | 4328 | 9318 |
| *R*(int) | 0.0169 | 0.0466 | 0.0407 | 0.0302 | 0.0224 |
| Completeness to $\theta$ | 99.2% | 99.6% | 99.7% | 98.9% | 99.6% |
| Refinement method | Full-matrix least squares on $F^2$ | Full-matrix least squares on $F^2$ | Full-matrix least squares on $F^2$ | Full-matrix least squares on $F^2$ | Full-matrix least squares on $F^2$ |
| Data/restraints/parameters | 1833/0/166 | 3848/0/249 | 5620/0/244 | 4328/0/289 | 9318/0/614 |
| Goodness-of-fit on $F^2$ | 1.069 | 1.044 | 1.099 | 1.041 | 1.062 |
| Final *R* indices | $R_1$ = 0.0411 | $R_1$ = 0.0254 | $R_1$ = 0.0340 | $R_1$ = 0.0368 | $R_1$ = 0.0259 |
| [$I > 2\sigma(I)$] | $wR_2$ = 0.1101 | $wR_2$ = 0.0620 | $wR_2$ = 0.0768 | $wR_2$ = 0.0858 | $wR_2$ = 0.0549 |
| *R* indices | $R_1$ = 0.0550 | $R_1$ = 0.0322 | $R_1$ = 0.0471 | $R_1$ = 0.0621 | $R_1$ = 0.0352 |
| (all data) | $wR_2$ = 0.1184 | $wR_2$ = 0.0652 | $wR_2$ = 0.0828 | $wR_2$ = 0.0954 | $wR_2$ = 0.0582 |
| Absolute structure parameter | – | – | – | – | – |
| Largest difference peak/hole [e Å$^{-3}$] | 0.089/–0.136 | 0.933/–0.643 | 3.496/–0.930 | 0.830/–0.643 | 1.184/–0.812 |

the SHELXS[31] program and refined by full-matrix least-squares with SHELXL-97.[31] CCDC-616194 (Hpyind), -616193 (**1**), -616192 (**2**), -616195 (**3**) and -616196 (**5**) contain the supplementary crystallographic data for this paper. These data can be obtained free of charge from the Cambridge Crystallographic Data Centre via www.ccdc.cam.ac.uk/data_request/cif.

**Supporting Information** (see footnote on the first page of this article): H,H-COSY and HMQC spectra for Hpyind and rhodium(III) complex **1**; dimeric unit of Hpyind within the crystal structure as additional ORTEP plot.


[1] M. Berthod, G. Mignani, G. Woodward, M. Lemaire, *Chem. Rev.* **2005**, *105*, 1801–1836.
[2] D. S. C. Black, D. C. Craig, N. Kumar, L. C. H. Wong, *J. Chem. Soc., Chem. Commun.* **1985**, 1172–1173.
[3] B. Chiswell, *Inorg. Chim. Acta* **1972**, *6*, 629–634.
[4] R. P. Thummel, V. Hedge, *J. Org. Chem.* **1989**, *54*, 1720–1725.
[5] C. Crotti, S. Cenini, B. Rindone, S. Tollari, F. Demartin, *J. Chem. Soc., Chem. Commun.* **1986**, 784–786.
[6] S. Tollari, S. Cenini, A. Penoni, G. Granata, G. Palmisano, F. Demartin, *J. Organomet. Chem.* **2000**, *608*, 34–41.
[7] F. Wu, C. M. Chamchoumis, R. P. Thummel, *Inorg. Chem.* **2000**, *39*, 584–590.
[8] S. Jena, N. Rath, K. C. Dash, *Ind. J. Chem. A* **1999**, *38*, 350–354.
[9] J. C. Lee, B. Mueller, P. Pregosin, G. P. A. Yap, A. L. Rheingold, R. H. Crabtree, *Inorg. Chem.* **1995**, *34*, 6295–6301.
[10] D. Karshtedt, A. T. Bell, T. D. Tilley, *Organometallics* **2004**, *23*, 4169–4171.
[11] G. Cravotto, F. Demartin, G. Palmisano, A. Penoni, T. Radice, S. Tollari, *J. Organomet. Chem.* **2005**, *690*, 2017–2026.
[12] M. Scheibitz, J. B. Heilmann, R. F. Winter, M. Bolte, J. W. Bats, M. Wagner, *Dalton Trans.* **2005**, 159–170.
[13] J. E. Lee, G. C. Choi, B. O. Rim, S. M. Kim, N. G. Park, Y. K. Ha, Y. S. Kim, *Mater. Sci. Eng. C* **2004**, *24*, 269–273.
[14] W. L. Jia, Q. D. Liu, R. Wang, S. Wang, *Organometallics* **2003**, *22*, 4070–4078.
[15] Q. D. Liu, L. Thorne, I. Kozin, D. Song, C. Seward, M. D'Iorio, Y. Tao, S. Wang, *J. Chem. Soc., Dalton Trans.* **2002**, 3234–3240.
[16] S. F. Liu, Q. Wu, H. L. Schmider, H. Aziz, N. X. Hu, Z. Popovic, S. Wang, *J. Am. Chem. Soc.* **2000**, *122*, 3671–3678.
[17] H. Bregman, D. S. Williams, E. Meggers, *Synthesis* **2005**, *9*, 1521–1527.
[18] D. S. Williams, G. E. Atilla, H. Bregman, A. Arzoumanian, P. S. Klein, E. Meggers, *Angew. Chem. Int. Ed.* **2005**, *44*, 1984–1987.
[19] H. Bregman, D. S. Williams, G. E. Atilla, P. J. Carroll, E. Meggers, *J. Am. Chem. Soc.* **2004**, *126*, 13594–13595.
[20] H. Bregman, P. J. Carroll, E. Meggers, *J. Am. Chem. Soc.* **2006**, *128*, 877–884.
[21] U. Schatzschneider, N. Metzler-Nolte, *Angew. Chem. Int. Ed.* **2006**, *45*, 1504–1507.
[22] S. Frantz, J. Fiedler, I. Hartenbach, T. Schleid, W. Kaim, *J. Organomet. Chem.* **2004**, *689*, 3031–3039.


 © 2007 Wiley-VCH Verlag GmbH & Co. KGaA, Weinheim 

[23] Y. Nosenko, R. P. Thummel, A. Mordzinski, *Phys. Chem. Chem. Phys.* **2004**, *6*, 363–367.
[24] Y. Nosenko, Y. Stepanenko, R. P. Thummel, A. Mordzinski, *Chem. Phys. Lett.* **1999**, *315*, 87–94.
[25] J. Herbich, C. Y. Hung, R. P. Thummel, J. Waluk, *J. Am. Chem. Soc.* **1996**, *118*, 3508–3518.
[26] F. Wu, J. Hardesty, R. P. Thummel, *J. Org. Chem.* **1998**, *63*, 4055–4061.
[27] C. White, A. Yates, P. M. Maitlis, *Inorg. Synth.* **1992**, *29*, 228.
[28] H. Nagashima, K. Mukai, Y. Shiota, K. Yamaguchi, K. Ara, T. Fukahori, H. Suzuki, M. Akita, Y. Moro-oka, K. Itho, *Organometallics* **1990**, *9*, 799–807.
[29] M. A. Bennett, T.-N. Huang, T. W. Matheson, A. K. Smith, *Inorg. Synth.* **1982**, *21*, 74.
[30] G. Brauer, *Handbuch der Präparativen Anorganischen Chemie*, vol. 3, 3rd ed., Ferdinand Enke Verlag, Stuttgart, **1981**, p. 1951–1952.
[31] G. M. Sheldrick, *SHELX-97*, University of Göttingen, Germany, **1997**.

Received: August 4, 2006
Published Online: November 21, 2006

 © 2007 Wiley-VCH Verlag GmbH & Co. KGaA, Weinheim 

DOI: 10.1002/ejic.200600787

# Merocyanine-Like Chromophores as Ligands for Catalytic Active Metals of Group VIII

**Jörg Blumhoff,[a] Rainer Beckert,*[a] Dirk Walther,[b] Sven Rau,[b] Manfred Rudolph,[b] Helmar Görls,[b] and Winfried Plass[b]**

**Keywords:** N ligands / Chromophores / Palladium / Nickel / Electrochemistry

Nickel and palladium complexes that contain merocyanine-like 4*H*-imidazoles as ligands have been synthesized in good yields. The complexes were characterized by elemental analyses, mass spectrometry, $^1$H NMR, $^{13}$C NMR spectroscopy and in the solid state by single crystal diffraction analyses. The new palladium complexes of type **4** can be regarded as new functional dyes as well as deeply coloured and redox active metallacycles that display catalytic activity. In contrast to parent compounds **2**, the palladacycles of type **4** show two well-separated reductions that are fully reversible. The values of semiquinone formation constants of derivatives **4** (between $10^{11}$ and $10^{12}$) are only somewhat lower than those reported for similar boracycles.

(© Wiley-VCH Verlag GmbH & Co. KGaA, 69451 Weinheim, Germany, 2007)

## Introduction

Nitrogen-containing ligands based on oxalic amidines **1** have recently attracted increasing interest.[1–3] These bifunctional amidines can act as diamide or diamidinate ligands after deprotonation and the ligands can be easily modified in their electronic and steric effects by variation of the substituents on the nitrogen atoms. Moreover, they can adopt several possible coordination modes in their metal complexes. During the last decade we focussed our interests on the development of new cyclic versions of oxalic amidines. Thus, amidines without hydrogen in the α-position, such as benzamidines, can easily be cyclized with bis(imidoyl chlorides) derived from oxalic acid in order to yield 4*H*-imidazoles **2** (Figure 1).[4] A new class of chromophores/fluorophores was developed employing these diazafulvene imines.[5,6] In addition, the 4*H*-imidazoles **2** are reversible two-electron redox systems which have been optimized to powerful electron-accepting derivatives in the form of boratetraazapentalenes.[7] Their radical anions are characterized by an unusual thermodynamic stability as can be seen from semiquinone formation constants $K_{SEM}$ in the magnitude of $10^{15}$.

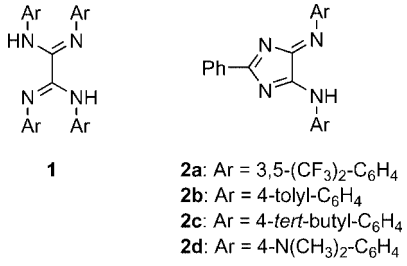


Figure 1. Oxalic amidines **1** and their cyclic versions 4*H*-imidazoles **2**.

The 4*H*-imidazoles **2** can therefore be regarded as multifunctional molecules in which the properties can easily be tuned by variation of the aryl substituents. Compared with derivatives of type **1**, they possess the same substructure which may serve as a donor site for metal complexation.

Because of the fact that open-chained oxalic amidines **1** have been successfully applied as ligands for cross-coupling methods,[8] their cyclic versions "cycloamidines" 4*H*-imidazoles **2**, should also be promising candidates. Zinc complexes of 4*H*-imidazoles have previously been reported.[9] Attempts to deprotonate derivatives **2** by lithium hydride[10] yielded unusual lithium complexes that surprisingly contain one molecule of water in their first complexation sphere.

Apart from porphyrins, phthalocyanines and related systems metal complexes in which the ligand is identical with an efficient chromophore are quite rare. Our aim was therefore to combine the redox active chromophore of 4*H*-imidazoles **2** with the catalytic activity of selected d-metals.

[a] Institut für Organische und Makromolekulare Chemie der Friedrich-Schiller-Universität,
Humboldtstr. 10, 07743 Jena, Germany
Fax: +49-3641-948212
E-mail: c6bera@uni-jena.de
[b] Institut für Anorganische und Analytische Chemie der Friedrich-Schiller-Universität,
Lessingstr. 8, 07743 Jena, Germany

 © 2007 Wiley-VCH Verlag GmbH & Co. KGaA, Weinheim 

## Results and Discussion

### Synthesis and Characterization

First we attempted to synthesize $Ni^{II}$ complexes starting from nickel$^{II}$-$(acac)_2$. This diketonato complex even reacts at room temperature with **2a**, the red solution changing to a deep purple. In order to complete the reaction, the mixture has to be heated under reflux for approx. 4 h (monitoring by TLC). It is remarkable that the complex formation takes place without addition of bases; most likely the acetylacetonato moiety functioned as a base for the deprotonation of the NH function. The X-ray structural analysis obtained from a single crystal of complex **3a** revealed a molecular structure as illustrated in Figure 2.

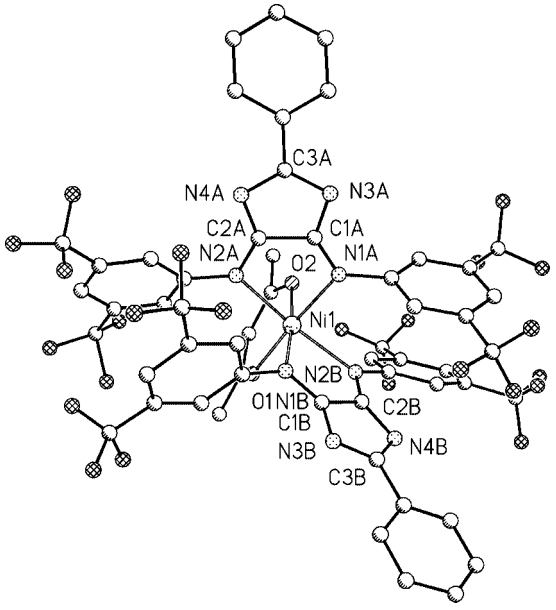


Figure 2. Molecular structure of complex **3a** (H atoms have been omitted for clarity). Selected bond lengths [Å]: Ni1–N1A 2.100(4), Ni1–N2A 2.197(4), Ni1–N1B 2.072(4), Ni1–N2B 2.201(4), Ni1–O1 2.009(3), Ni1–O2 2.042(3).

In the new chelate complex **3a** (Scheme 1) two 4*H*-imidazoles coordinate the nickel$^{II}$ centre, whereby the two remaining coordination sites are occupied by an acetylacetonato ligand. While one 4*H*-imidazole is coordinated in the deprotonated form, the other is bound as a neutral ligand. This fact could be verified by determining the Ni–N distances of the coordinating nitrogen atoms. This molecule is in agreement with the stoichiometry of the reaction. The octahedral nickel centre in **3a** exhibits paramagnetism and therefore, no NMR-data could be obtained. Characterization of complex **3a** via mass spectroscopy confirmed the results of the X-ray analysis. A high-resolution mass spectrum verified the chemical composition of compound **3a** ($C_{55}H_{30}F_{24}N_8NiO_2$). In addition, the complex **3a** shows a characteristic fragmentation due to the split-up of the ligands.

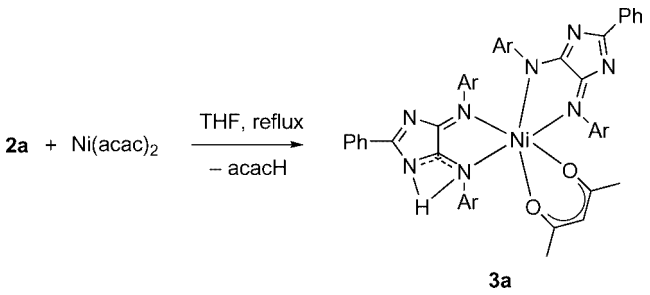


Scheme 1. Synthesis of complex **3a**.

Because of the fact that palladium plays a vital role as a catalytically active metal in cross-coupling methods, further investigations were directed towards the synthesis of analogous Pd complexes. As a starting metal complex, the easily accessible allyl palladium(II) chloride dimer was applied. Because of its tendency to dissociate in solution into two coordinative unsaturated fragments, it enables easy complexation of other ligands at the palladium(II) centre. Furthermore, the allyl palladium-fragment preferably forms complexes with an almost square-planar geometry showing diamagnetism that allows a detailed structural elucidation by NMR spectroscopy.

Even at room temperature the complex formation is visible by a colour change from red to purple. After heating under reflux conditions, for 2–4 h, chromatographic purification allowed the isolation of new complexes of type **4**. Elemental analysis, NMR spectroscopic data and MS data confirmed the composition of a 1:1 complex in **4a**. According to Scheme 2, the dimeric palladium species reacted with one molecule of the ligands **2a**–**d** to yield palladacycles **4a**–**d**. A high symmetry of the molecule was indicated by the $^1$H NMR spectrum of **4a**, which showed only five signals for the aromatic H-atoms in addition to the characteristic coupling pattern of the allyl substructure. Moreover, the $^{13}$C-NMR spectra confirm the symmetry of the molecule by a single set of signals. The signal for C-atom C4 is, compared to the ligand ($\delta$ = 190 ppm), shifted to a lower field in complex **4a** ($\delta$ = 199 ppm). This down-field shift is comparable to that in the corresponding boratetraazapentalenes,[7] thus indicating the change from the merocyanine to the cyanine chromophore.

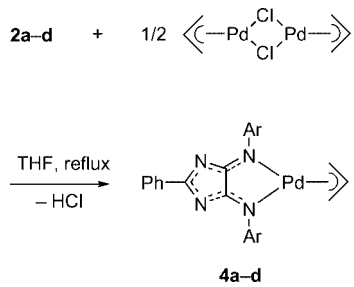


Scheme 2. Synthesis of complexes **4a**–**d**.

 © 2007 Wiley-VCH Verlag GmbH & Co. KGaA, Weinheim 

A single-crystal X-ray structure analysis of **4a** allowed an unambiguous assignment of these compounds, as shown in Figure 3. According to our presumptions, one 4*H*-imidazole is coordinated at the palladium(II) centre. Being a second ligand, the allyl-anion is $\eta^3$-bonded and causes square-planar coordination geometry in view to the palladium(II) centre and shows $C_2$ symmetry. In analogy to the synthesis of the bis(3,5-trifluoromethyl) derivative **4a**, complexes of 4*H*-imidazoles could be prepared that possess electron-donating substituents. The various aryl substituents have no significant influence on the complexation ability of the corresponding 4*H*-imidazole. Interestingly, all new synthesized Pd complexes of type **4** show high stabilities as solids as well as in solution. They can be handled under normal atmospheric conditions and tolerate slightly acidic and basic conditions. In comparison with the 4*H*-imidazoles the UV/Vis maxima of the palladium complexes are shifted to higher wavelengths (**2a**: $\lambda_{max}$ = 460, 515 nm; **4a**: $\lambda_{max}$ = 549, 590 nm) as shown in Figure 4. Furthermore, complex **4a** shows a weak fluorescence at 623 nm (THF).

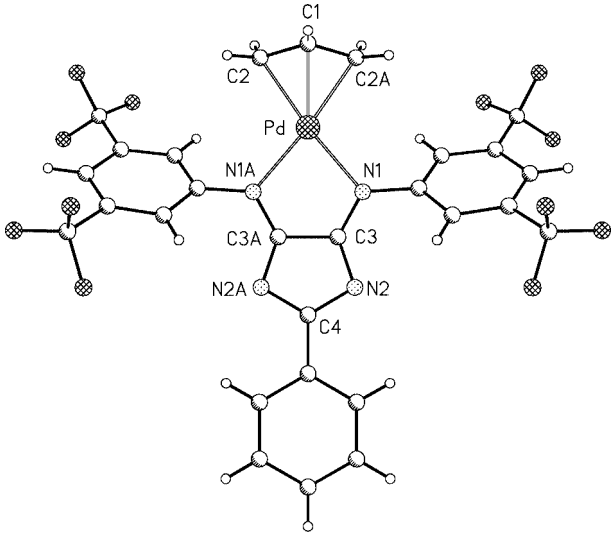


Figure 3. Molecular structure of complex **4a**. Selected bond lengths [Å]: Pd–N1 2.128(4), Pd–N1A 2.128(4), Pd–C2 2.120(5), Pd–C2A 2.120(5), Pd–C1 2.109(9).

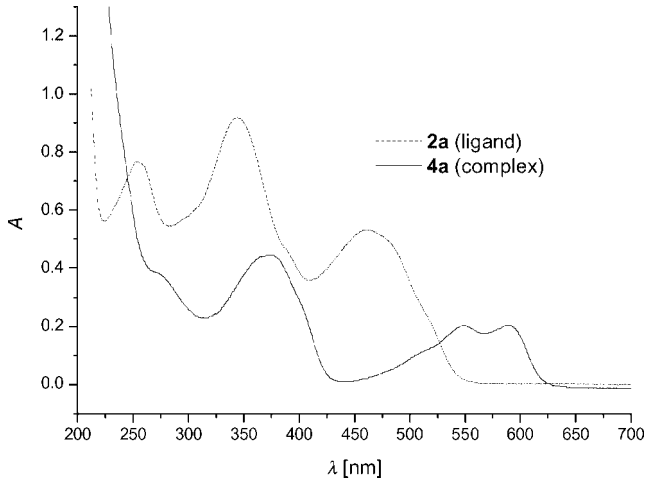


Figure 4. UV/Vis spectra of **2a** (···) and **4a** (—) in THF.

## Electrochemical Measurements of Complexes 4

The electrochemical reduction of the palladacycles **4** occurs in two one-electron steps. A typical series of cyclic square-wave voltammograms measured with square-wave frequencies from 25 to 800 Hz is shown in Figure 5. The half-wave potentials extracted from these measurements are summarized in Table 1.

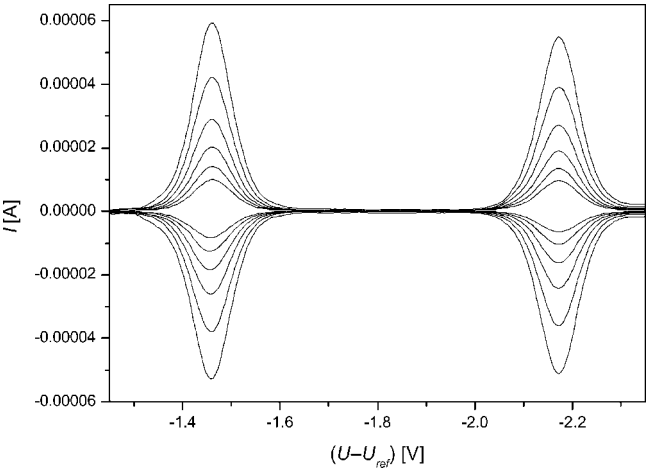


Figure 5. Cyclic square-wave voltammograms of the reduction of 1.5 mM of **4b** in DMF/tetrabutylammonium hexafluorophosphate at a mercury drop electrode using square-wave frequencies of 800, 400, 200, 100, 50 and 25 Hz. $U_{ref}$ is the potential of the ferrocenium/ferrocene couple in the same electrolyte.

Table 1. Half-wave potentials and semiquinone formation constants of complexes **4a**–**c**.

| Complex | $U_1^{1/2}$ | $U_2^{1/2}$ | $K_{sem}$ |
|---|---|---|---|
| **4b** | –1.460 V | –2.175 V | $1.26 \cdot 10^{12}$ |
| **4a** | –1.015 V | –1.670 V | $1.26 \cdot 10^{11}$ |
| **4c** | –1.455 V | –2.175 V | $1.58 \cdot 10^{12}$ |

If only the first reduction process is measured (by reversing the potential scan before the second reduction takes place), the experimental curves agree very well with those simulated for a fast (fully reversible) charge-transfer process followed by a slow first-order decomposition reaction. This means, as far as the charge transfer steps are concerned, a deviation from Nernstian behaviour cannot be detected up to square-wave frequencies of approx. 1000 Hz. However, the one-fold reduced species is chemically not fully stable in the solvent system. A second, (much faster) follow-up reaction is induced upon scanning over a potential range including the second reduction step. Interestingly, this follow-up reaction has a much larger effect on the re-oxidation wave associated with the second charge transfer reaction. The ratio between cathodic and anodic peak current remains close to 1 for the first charge transfer step even when using relatively low square-wave frequencies such as shown in Figure 6 ($f$ = 25 Hz). In the case of **4b** an almost perfect agreement between experimental and simulated curves was obtained on the basis of the reaction shown in Scheme 3.

 © 2007 Wiley-VCH Verlag GmbH & Co. KGaA, Weinheim 

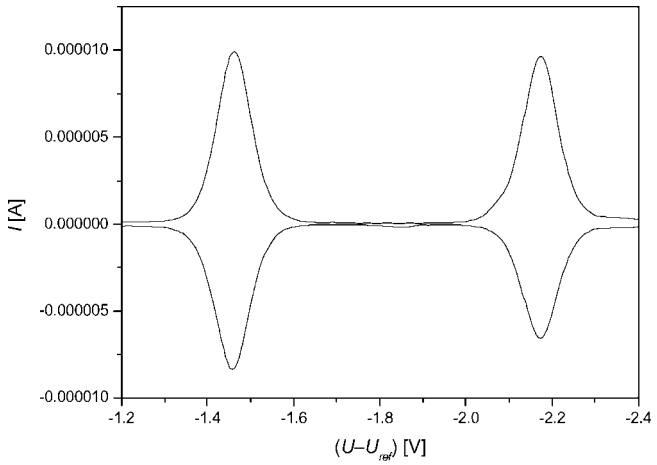


Figure 6. Cyclic square-wave voltammogram of the reduction of 1.5 mM of **4b** in DMF/tetrabutylammonium hexafluorophosphate at a mercury drop electrode using a square-wave frequency of 25 Hz. $U_{ref}$ is the potential of the ferrocenium/ferrocene couple in the same electrolyte.

$$O + e \rightleftarrows R_1 \quad \left(U_1^{1/2} = -1.46V, k_s^\circ \geq 1cm/s\right)$$

$$R_1 \longrightarrow P_1 \quad \left(k \approx 0.03s^{-1}\right)$$

$$R_1 + e \rightleftarrows R_2 \quad \left(U_2^{1/2} = -2.175V, k_s^\circ \geq 0.15cm/s\right)$$

$$R_2 \longrightarrow P_2 \quad \left(k \approx 0.65s^{-1}\right)$$

$$P_2 \longrightarrow R_1 \quad \left(k \approx 0.8s^{-1}\right)$$

Scheme 3. Reaction scheme for an almost perfect agreement between experimental and simulated curves.

We assume that the twofold reduced species reacts to give an intermediate from which the onefold reduced species is formed in a subsequent reaction; the data determined for **4c** are virtually identical. In the case of **4a**, the first reduction process is accompanied by a pre-wave. Since the latter could not be reproduced by digital simulation, only the half-wave potentials are reported in Table 1.

The lack of success of the Sonogashira and Suzuki reactions with these cross-conjugated heterocycles can now be explained due to the fact that the 4*H*-imidazoles act as very efficient chelating ligands for palladium. This means that required catalytic amounts of palladium were immobilized immediately by complexation and consequently no catalytic activity was observed. However, the palladacycles themselves are able to catalyze other types of cross-coupling reactions as shown by the Heck reaction.

In an initial experiment we used the substrates 4-bromoacetophenone and acrylic acid *n*-butylester in dimethylacetamide as the solvent at 120 °C, yielding the 4-substituted cinnamic acidester **5** (Scheme 4) to evaluate the catalytic activity of palladium complex **4a**. This complex belongs to the very rare group of Pd-catalysts with *N*,*N*-chelate ligands that are active in this C–C-coupling method. After 2 h of heating under reflux, 60% of the substrate was converted into cinnamic derivative **5**. Prolonged reaction times led to a nearly quantitative conversion.

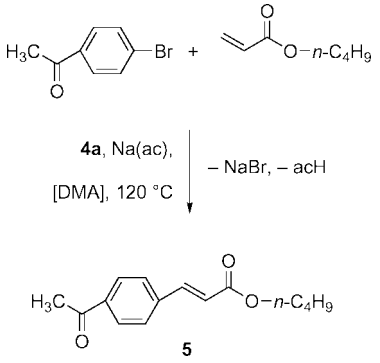


Scheme 4. The Heck coupling as a model reaction for the determination of the catalytic activity of **4a**.

On the basis of these experimental findings the subject of further research will be the synthesis of homo- and heterobimetallic complexes of 4*H*-imidazoles and studies directed to the electronic communication between both metal centres. Applications of molecular architectures similar to those described above could prove to be light-driven reactions and catalyses.

## Experimental Section

**General Comments:** All reactions were monitored by TLC, carried out on 0.25-mm Merck TLC aluminium sheets (aluminium oxide 150 $F_{254}$ neutral) using UV light. $^1$H and $^{13}$C NMR spectra were recorded with a Bruker DRX 400 (400 MHz) or a Bruker AC 250 (250 MHz) spectrometer. UV/Vis spectra were recorded with a Perkin–Elmer Lambda 19 spectrophotometer. MS spectra were taken from measurements on a Finnigan MAT SAQ 710 mass spectrometer. Elemental analyses were carried out in-house with an automatic analyzer LECO CHNS 932.

**Synthesis of the Nickel(II) Complex 3a:** In a 100-mL one-necked round flask, equipped with a magnetic stirrer, **2a** (1 mmol) was dissolved in THF (50 mL). Then, bis(acetylacetonato)nickel(II) (1 mmol) dissolved in THF (10 mL) was added dropwise at room temperature. A darkening of the reaction mixture indicated a fast complexation reaction. The reaction mixture was heated to completion under reflux for 3–5 h. HRMS of **3a**: $C_{55}H_{31}F_{24}N_8NiO_2$: $M$ = 1349.15401113 g mol$^{-1}$ (calculated), $M$ = 1349.15494000 g mol$^{-1}$ (found).

**Synthesis of the Palladium(II) Complexes 4a–d:** In a 100-mL one-necked round flask, equipped with a magnetic stirrer, 1 mmol of the corresponding 4*H*-imidazole **2a** was dissolved in THF (50 mL). Then, allylpalladium(II) chloride dimer (0.5 mmol) dissolved in THF (10 mL) was added dropwise at room temperature. The reaction mixture was heated to completion under reflux for 3–5 h and the progress of the reaction was monitored by TLC. For complex **4a**, the solvent was removed in vacuo and the residue was suspended in acetone. The resulting precipitate was filtered off and dried in vacuo. The complexes **4b–d** were purified by column chromatography (alumina, activity V, toluene).

**Complex 4a:** Yield: 587 mg (79%). $^1$H NMR ($CD_2Cl_2$, 250 MHz): $\delta$ = 8.34 (m, 2 H, aryl-H), 8.16 (s, 4 H, aryl-H), 7.59 (m, 3 H, aryl-

 © 2007 Wiley-VCH Verlag GmbH & Co. KGaA, Weinheim 

H), 7.45 (m, 2 H, aryl-H), 5.50 (m, 1 H, allyl C-H), 3.55 (d, $J$ = 7.5 Hz, 2 H, allyl $CH_2$), 3.03 (d, $J$ = 12.5 Hz, 2 H, allyl $CH_2$) ppm. $^{13}C$ NMR ($CD_2Cl_2$, 100 MHz): $\delta$ = 199.0, 178.8, 149.1, 134.9, 132.3, 131.5 [q, $^2J$(C,F) = 33.2 Hz], 130.9, 128.6, 125.8, 123.3 [q, $^1J$(C,F) = 272.7 Hz], 119.2, 116.1, 62.3 ppm. FAB-MS (NBA): $m/z$ (%) = 743 $[M]^+$, 702 $[M - allyl]^+$, 597 $[M - allyl - Pd + H]^+$. UV/Vis (THF): $\lambda_{max}$ (lg$\varepsilon$) = 549 (4.0), 590 nm (4.0). $C_{28}H_{16}F_{12}N_4Pd$ (742.86): calcd. C 45.27, H 2.17, N 7.54; found C 45.25, H 2.16, N 7.45.

**Complex 4b:** Yield: 274 mg (55%). $^1H$ NMR ($CD_2Cl_2$, 250 MHz): $\delta$ = 8.33 (m, 2 H, aryl-H), 7.51 (m, 7 H, aryl-H), 7.21 (m, 4 H, aryl-H), 5.63 (m, 1 H, allyl-CH), 3.62 (d, $J$ = 6.9 Hz, 2 H, allyl-$CH_2$), 3.16 (d, $J$ = 12.4 Hz, 2 H, allyl-$CH_2$), 2.40 (s, 6 H, $CH_3$) ppm. Micro-ESI-MS (methanol): $m/z$ (%) = 499 $[M + H]^+$. UV/Vis (THF): $\lambda_{max}$ (lg$\varepsilon$) = 560 (4.0), 600 nm (4.0). $C_{26}H_{24}N_4Pd$ (498.92): calcd. C 62.59, H 4.85, N 11.23; found C 62.55, H 4.80, N 11.31.

**Complex 4c:** Yield: 291 mg (50%). $^1H$ NMR ($CD_2Cl_2$, 250 MHz): $\delta$ = 8.35 (m, 2 H, aryl-H), 7.57 (m, 5 H, aryl-H), 7.43 (m, 6 H, aryl-H), 5.60 (m, 1 H, allyl-CH), 3.64 (d, $J$ = 6.9 Hz, 2 H, allyl-$CH_2$), 3.15 (d, $J$ = 12.4 Hz, 2 H, allyl-$CH_2$), 1.38 (s, 18 H, $CH_3$) ppm. Micro-ESI-MS (methanol): $m/z$ (%) = 582 $[M + H]^+$. UV/Vis (THF): $\lambda_{max}$ (lg$\varepsilon$) = 563 (4.1), 604 nm (4.1). $C_{32}H_{36}N_4Pd$ (583.08): calcd. C 65.92, H 6.22, N 9.61; found C 65.90, H 6.18, N 9.55.

**Complex 4d:** Yield: 362 mg (65%). $^1H$ NMR ($CD_2Cl_2$, 250 MHz): $\delta$ = 8.22 (m, 2 H, aryl-H), 7.61 (m, 4 H, aryl-H), 7.39 (m, 3 H, aryl-H), 6.64 (m, 4 H, aryl-H), 5.53 (m, 1 H, allyl-CH), 3.56 (d, $J$ = 6.9 Hz, 2 H, allyl-$CH_2$), 3.09 (d, $J$ = 12.4 Hz, 2 H, allyl-$CH_2$), 2.91 [s, 12 H, $N(CH_3)_2$] ppm. Micro-ESI-MS (methanol): $m/z$ (%) = 556 $[M]^+$. UV/Vis (THF): $\lambda_{max}$ = 630, 673 nm. $C_{28}H_{30}N_6Pd$ (557.01): calcd. C 60.38, H 5.43, N 15.09; found C 60.40, H 5.48, N 15.05.

**Heck Reaction Catalyzed by Complex 4a:** In a typical experiment, 4-bromoacetophenone (6.25 mmol) and anhydrous sodium acetate (7 mmol) were placed in a 25-mL two-necked flask equipped with a stirring bar, reflux condenser and septum. The flask was degassed under vacuum and purged with argon to ensure an inert reaction atmosphere. Then, *N*,*N*-dimethylacetamide (10 mL) as the solvent and *n*-butyl acrylate (0.5 g) were added through the septum. The reaction mixture was thoroughly stirred and heated to the appropriate reaction temperature at which it was held for 5 min followed by treatment with the catalyst solution containing complex **4a** (1.25 μmol in 0.5 mL of THF). After the appropriate time intervals samples (0.5 mL) of the reaction mixture were hydrolyzed with 2 M HCl (0.5 mL) and extracted with $CH_2Cl_2$ (0.5 mL). The organic phase was dried with $K_2CO_3$ and stored at –21 °C until GC analysis for determination of the yield.

**Crystal Structure Determination**: The intensity data for the compounds were collected with a Nonius KappaCCD diffractometer, using graphite-monochromated Mo-$K_\alpha$ radiation. Data were corrected for Lorentz and polarization effects, but not for absorption.[11,12] The structures were solved by direct methods (SHELXS[13]) and refined by full-matrix least-squares techniques against $F_o^2$ (SHELXL-97[14]). The hydrogen atoms of the structures were included at calculated positions with fixed thermal parameters. All non-hydrogen atoms were refined anisotropically.[14] XP (Siemens Analytical X-ray Instruments, Inc.) was used for structure representations.

**Crystal Data for 3a:**[15] $2C_{55}H_{31}F_{24}N_8NiO_2 \cdot C_{50}H_{82}Ni_8O_{30} \cdot 3CH_2Cl_2 \cdot H_2O$, $M$r = 4649.27 g mol$^{-1}$, red-brown prism, size 0.05 × 0.05 × 0.04 mm, monoclinic, space group $P2_1/c$, $a$ = 15.8755(2), $b$ = 20.4987(3), $c$ = 32.8158(4) Å, $\beta$ = 101.482(1)°, $V$ = 10465.4(2) Å$^3$, $T$ = –90 °C, $Z$ = 2, $\rho_{calcd.}$ = 1.475 g cm$^{-3}$, $\mu$ (Mo-$K_\alpha$) = 10.77 cm$^{-1}$, $F$(000) = 4714, 60125 reflections in $h$(–18/20), $k$(–26/26), $l$(–42/36), measured in the range 1.18° ≤ $\Theta$ ≤ 27.47°, completeness $\Theta_{max}$ = 99.3%, 23821 independent reflections, $R_{int}$ = 0.030, 18727 reflections with $F_o > 4\sigma(F_o)$, 1272 parameters, 0 restraints, $R_{1obs}$ = 0.087, $wR_{2obs}$ = 0.271, $R_{1all}$ = 0.111, $wR_{2all}$ = 0.289, GOOF = 2.184, largest difference peak and hole: 3.707/–1.610 e Å$^{-3}$.

**Crystal Data for 4a:**[15] $C_{28}H_{16}F_{12}N_4OPd \cdot H_2O$, $M$r = 759.86 g mol$^{-1}$, red-brown prism, size 0.04 × 0.04 × 0.03 mm, monoclinic, space group $C2/m$, $a$ = 18.7198(8), $b$ = 18.9056(8), $c$ = 9.8808(2) Å, $\beta$ = 120.749(2)°, $V$ = 3005.29(19) Å$^3$, $T$ = –90 °C, $Z$ = 4, $\rho_{calcd.}$ = 1.679 g cm$^{-3}$, $\mu$ (Mo-$K_\alpha$) = 7.22 cm$^{-1}$, $F$(000) = 1500, 10750 reflections in $h$(–24/24), $k$(–22/24), $l$(–12/12), measured in the range 1.66° ≤ $\Theta$ ≤ 27.50°, completeness $\Theta_{max}$ = 99.4%, 3540 independent reflections, $R_{int}$ = 0.039, 2996 reflections with $F_o > 4\sigma(F_o)$, 226 parameters, 0 restraints, $R_{1obs}$ = 0.064, $wR_{2obs}$ = 0.186, $R_{1all}$ = 0.077, $wR_{2all}$ = 0.203, GOOF = 1.055, largest difference peak and hole: 2.860/–0.943 e Å$^{-3}$.

**Cyclovoltammetric Instrumentation and Procedures:** Cyclic square-wave voltammetry was conducted with the 3-electrode technique using a home-built computer-controlled instrument based on the PCI 6110 data acquisition board (National Instruments). The experiments were performed in DMF containing 0.25-M tetrabutylammonium hexafluorophosphate (Merck, Darmstadt) under a blanket of solvent-saturated argon. The DMF was purified by stirring with NaH, distilled under reduced pressure and stored over molsieves 4A under argon.

The Ohmic resistance that had to be compensated was determined by measuring the impedance of the system at potentials where the Faradayic current was negligibly small. Background correction was accomplished by subtracting the current curves of the blank electrolyte (containing the same concentration of supporting electrolyte) from the experimental curves.

Working electrode: hanging mercury drop ($m_{Hg-drop}$ = 3.95–4.00 mg) produced by the CGME instrument (Bioanalytical Systems Inc., West Lafayette, USA). A platinum wire served as the counter electrode. Internal reference electrode: Ag/AgCl electrode in acetonitrile containing 0.25 M tetrabutylammonium chloride. However, for convenience all potentials reported in this paper refer to the ferrocenium/ferrocene couple. The latter was measured at the end of each experiment using a 1.5-mm Pt disk electrode. The evaluation of the experiments was accomplished by subjecting the experimental voltammograms to a nonlinear regression procedure using the freely available DigiElch software (htpp://www.DigiElch.de).

## Acknowledgments

This work was supported by Deutsche Forschungsgemeinschaft (SFB 436).

[1] a) M. Döhring, R. Beckert, H. Görls, *Z. Anorg. Allg. Chem.* **1994**, *620*, 551–560; b) P. Fehling, M. Döring, F. Knoch, R. Beckert, H. Görls, *Chem. Ber.* **1995**, *128*, 405–412; c) M. Döring, P. Fehling, H. Görls, W. Imhof, R. Beckert, D. Lindauer, *J. Prakt. Chem./Chem.-Ztg.* **1999**, *341*, 748–756.

[2] a) M. Ruben, S. Rau, A. Skirl, K. Krause, H. Görls, D. Walther, J. G. Vos, *Inorg. Chim. Acta* **2000**, *303*, 206–214; b) T. Döhler, H. Görls, D. Walther, *Chem. Commun.* **2000**, 945–946; c) M. Ruben, D. Walther, R. Knake, H. Görls, R. Beckert, *Eur.*

 © 2007 Wiley-VCH Verlag GmbH & Co. KGaA, Weinheim 

*J. Inorg. Chem.* **2000**, 1055–1060; d) D. Walther, M. Stollenz, L. Böttcher, H. Görls, *Z. Anorg. Allg. Chem.* **2001**, *627*, 1560–1570; e) D. Walther, M. Stollenz, H. Görls, *Organometallics* **2001**, *20*, 4221–4229; f) M. Stollenz, M. Rudolph, H. Görls, D. Walther, *J. Organomet. Chem.* **2003**, *687*, 153–160.
[3] M. Deng, Y. Yao, Y. Zhang, Q. Shen, *Chem. Commun.* **2004**, 2742–2743.
[4] J. Atzrodt, J. Brandenburg, C. Käpplinger, R. Beckert, W. Günther, H. Görls, J. Fabian, *J. Prakt. Chem./Chem.-Ztg.* **1997**, *339*, 729–734.
[5] J. Fabian, H. Görls, R. Beckert, J. Atzrodt, *J. Prakt. Chem./Chem.-Ztg.* **1997**, *339*, 735–741.
[6] J. Atzrodt, R. Beckert, W. Günther, H. Görls, *Eur. J. Org. Chem.* **2000**, 1661–1668.
[7] T. Gebauer, R. Beckert, D. Weiß, K. Knop, C. Käpplinger, H. Görls, *Chem. Commun.* **2004**, 1860–1861.
[8] S. Rau, K. Lamm, H. Görls, J. Schöffel, D. Walther, *J. Organomet. Chem.* **2004**, *689*, 3582–3592.
[9] J. Atzrodt, R. Beckert, H. Görls, *Heterocycles* **1991**, *51*, 763–783.
[10] J. Atzrodt, R. Beckert, K. Nordhoff, M. Bräuer, E. Anders, H. Görls, *Eur. J. Org. Chem.* **1998**, 2557–2563.
[11] *COLLECT*, Data Collection Software, Nonius B. V., Netherlands, **1998**.
[12] Z. Otwinowski, W. Minor, "Processing of X-ray Diffraction Data Collected in Oscillation Mode", in *Methods in Enzymology, vol. 276, Macromolecular Crystallography, Part A* (Eds.: C. W. Carter, R. M. Sweet), Academic Press, San Diego, **1997**, pp. 307–326.
[13] G. M. Sheldrick, *Acta Crystallogr., Sect. A* **1990**, *46*, 467–473.
[14] G. M. Sheldrick, *SHELXL-97*, University of Göttingen, Germany, **1993**.
[15] CCDC-614437 (for **3a**) -614438 (for **4a**) contain the supplementary crystallographic data for this paper. These data can be obtained free of charge from The Cambridge Crystallographic Data Centre via www.ccdc.cam.ac.uk/data_request/cif.

Received: August 25, 2006
Published Online: November 27, 2006

 © 2007 Wiley-VCH Verlag GmbH & Co. KGaA, Weinheim

**The EUChemSoc Societies have taken the significant step into the future by merging their traditional journals, to form two leading chemistry journals, the *European Journal of Inorganic Chemistry* and the *European Journal of Organic Chemistry.* Three further EUChemSoc Societies (Austria, Czech Republic and Sweden) are Associates of the two journals.**

## COVER PICTURE

**The cover picture shows** four substrates ($Cl^-$, $Br^-$, $I^-$, and dimethyl sulfide) that all pass through nearly identical transition states when oxidized by (hydroperoxido)(oxido)vanadium(V) 2,2′-[(2-hydroxyethyl)imino]diacetate [VO(OOH)Hheida]. The differences in the physical properties of the substrate are represented by the changes in the color scheme for each panel. Despite the different "colors", certain features of the transition states are always maintained, such as: nearly linear substrate peroxo oxygen bond angles, nucleophilic attack of the substrate on the unprotonated peroxo oxygen atom, and nearly complete hydroperoxo oxygen bond. This work lays the foundation for the development of more effective and potentially stereoselective catalysts based on the biomimetic catalyst V(OOH)Hheida. Details of this computational study can be found in the article by V. L. Pecoraro, and L. De Gioia on p. 515ff.

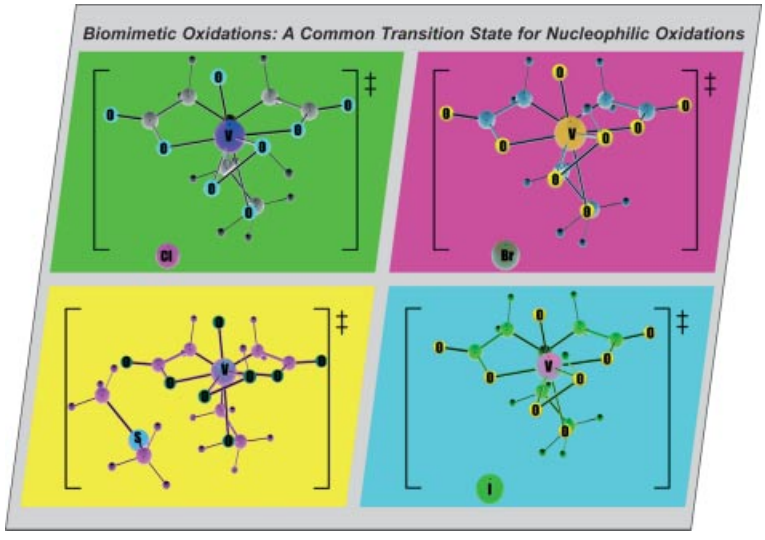


 © 2007 Wiley-VCH Verlag GmbH & Co. KGaA, Weinheim

**The EUChemSoc Societies have taken the significant step into the future by merging their traditional journals, to form two leading chemistry journals, the *European Journal of Inorganic Chemistry* and the *European Journal of Organic Chemistry.* Three further EUChemSoc Societies (Austria, Czech Republic and Sweden) are Associates of the two journals.**

## COVER PICTURE

**The cover picture shows** four substrates ($Cl^-$, $Br^-$, $I^-$, and dimethyl sulfide) that all pass through nearly identical transition states when oxidized by (hydroperoxido)(oxido)vanadium(V) 2,2′-[(2-hydroxyethyl)imino]diacetate [VO(OOH)Hheida]. The differences in the physical properties of the substrate are represented by the changes in the color scheme for each panel. Despite the different "colors", certain features of the transition states are always maintained, such as: nearly linear substrate peroxo oxygen bond angles, nucleophilic attack of the substrate on the unprotonated peroxo oxygen atom, and nearly complete hydroperoxo oxygen bond. This work lays the foundation for the development of more effective and potentially stereoselective catalysts based on the biomimetic catalyst V(OOH)Hheida. Details of this computational study can be found in the article by V. L. Pecoraro, and L. De Gioia on p. 515ff.

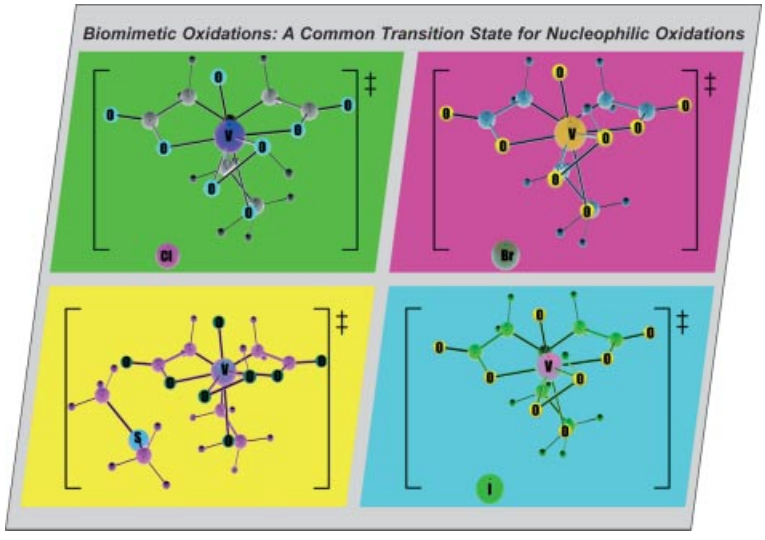


 © 2007 Wiley-VCH Verlag GmbH & Co. KGaA, Weinheim 

# CONTENTS

## SHORT COMMUNICATIONS


### Metal Complex–Fullerene Hybrids

**H. D. Lee, S. K. Oh, C. S. Choi, K.-Y. Kay* ..... 503–508**

A Novel Amphiphilic $Re^{I}$ Complex with Bis(fullerene)-Substituted Bipyridine Ligands: Synthesis, Electrochemistry, and Langmuir Film

**Keywords:** Rhenium / Fullerenes / Bipyridines / Cyclic voltammetry / Langmuir films


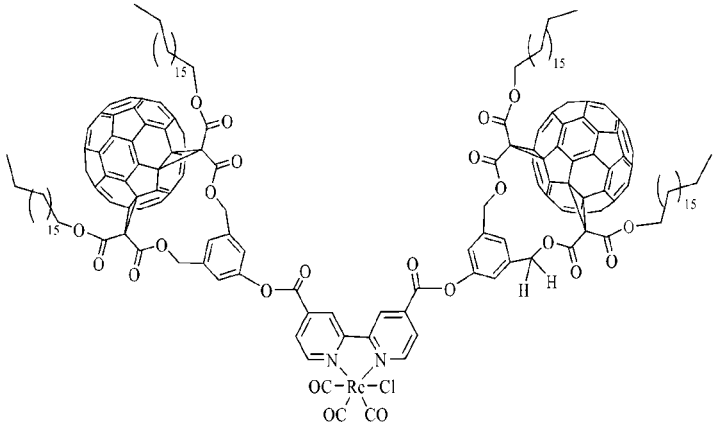
15
O
O
O

## ZnO Nanoparticles

**H. Thakuria, B. M. Borah, G. Das* ..... 524–529**

ZnO Nanoparticles From a Metal-Organic Framework Containing $Zn^{II}$ Metallacycles

**Keywords:** Metallacycles / Tripodal ligands / Hydrogen bonds / Metal-organic frameworks / Nanoparticles

Nitrilotriacetic acid ($H_3NTA$) reacts in the solid phase with zinc hydroxide (1:1) to form a 3D ladder-like metal-organic framework that forms wurtzite ZnO nanoparticles when heated above 600 °C. The same reaction with an excess of zinc hydroxide gives a mixed coordination network that gives ZnO microwires upon decomposition at around 500 °C.

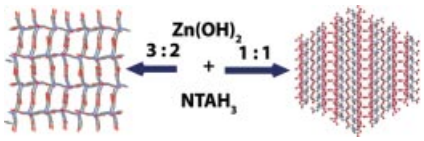


## Copper Redox Reactions

**A. Burg,* E. Maimon, H. Cohen, D. Meyerstein* ..... 530–536**

Ligand Effects on the Chemical Activity of Copper(I) Complexes: Outer- and Inner-Sphere Oxidation of $Cu^{I}L$

**Keywords:** Copper / Electron self exchange rate constant / Outer-sphere mechanism / Inner-sphere mechanism

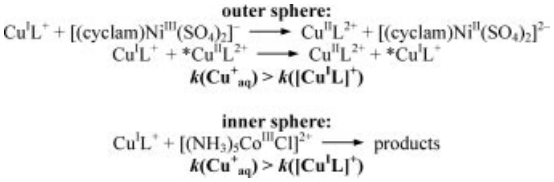


Ligand effects on the kinetics of reduction by $Cu^{I}$ by the outer- and inner-sphere mechanisms were studied. The results indicate that acetonitrile and alkenes should not be used as solvents for $[Cu^{I}L]^{+}$ redox-catalyzed processes. The results suggest that $[Cu^{I}$(2,5,8,11-tetraaza-2,5,8,11-tetramethyldodecane)$]^{+}$ is expected to be a good catalyst for such processes.

## Dinuclear Olefin Polymerization Catalysts

**S. K. Kim, H. K. Kim, M. H. Lee, S. W. Yoon, Y. Han, S. Park, J. Lee, Y. Do* ..... 537–545**

Dinuclear Metallocenes with a Modulated Biphenylene Bridge for Olefin Polymerization

**Keywords:** Homogeneous catalysis / Metallocenes / Olefins / Polymerization / Titanium / Zirconium

Well-defined novel dinuclear zirconocenes show comparable catalytic activity in ethylene polymerization and produce PE with increased molecular weight. In case of syndiotactic polystyrene preparation with the dinuclear half titanocenes, the decrease in the molecular weight and the activity was recognized as polymerization behavior.

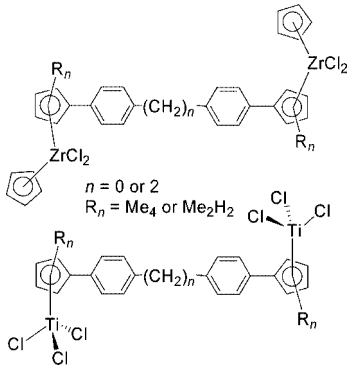


## Trinuclear Phthalocyanines

**S. G. Makarov, O. N. Suvorova, C. Litwinski, E. A. Ermilov, B. Röder, O. Tsaryova, T. Dülcks, D. Wöhrle* ..... 546–552**

Linear and Rectangular Trinuclear Phthalocyanines

**Keywords:** Phthalocyanines / NIR absorption / UV/Vis spectroscopy

Linear and rectangular trinuclear metal-free and zinc(II) phthalocyanines showing absorptions up to 940 nm with extinction coefficients of up to around 700000 $M^{-1}$ $cm^{-1}$ have been synthesized. Their electronic-absorption and fluorescence spectra have been recorded and compared to those of the corresponding mono- and dinuclear phthalocyanines.

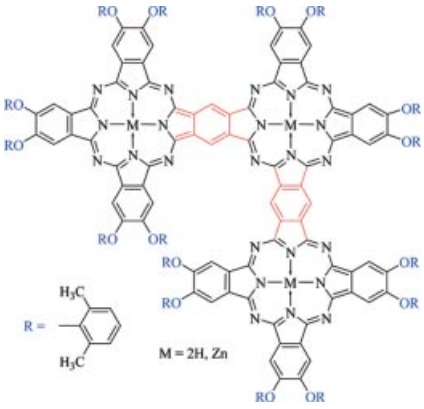


 © 2007 Wiley-VCH Verlag GmbH & Co. KGaA, Weinheim 

# CONTENTS


## Phosphametallocenes

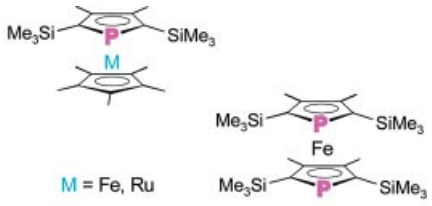


**R. Loschen, C. Loschen, W. Frank, C. Ganter* ..... 553–561**

Synthesis, Structure and Reactivity of Trimethylsilyl-Substituted Phosphametallocenes

**Keywords:** Metallocenes / P ligands / Silicon / Phosphaferrocenes / Conformation analysis

Phosphametallocenes with sterically demanding $Me_3Si$ groups have been prepared from the respective phospholyl anion and were characterized by X-ray diffraction. For complex **8** the barrier for internal ring–ring rotation was determined by low-temperature NMR spectroscopy and the result was confirmed by DFT calculations.

## Inversely Polarized Phosphaalkenes

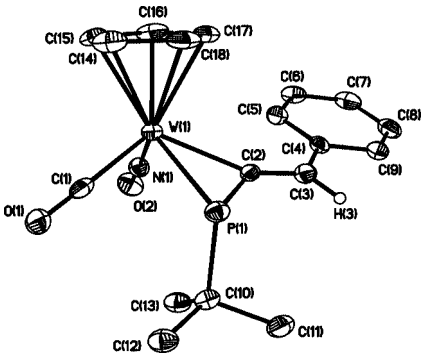


**L. Weber,* G. Noveski, T. Braun, H.-G. Stammler, B. Neumann .... 562–567**

Synthesis of the $\eta^2$-1-Phosphaallene Complexes $[(\eta^5\text{-}C_5H_5)(CO)(NO)W\{\eta^2\text{-}R^1P{=}C{=}C(R^2)H\}]$ ($R^1$ = *t*Bu, Cy; $R^2$ = Ph, H) from $[(\eta^5\text{-}C_5H_5)(CO)(NO)W{=}C{=}C(R^2)H]$ ($R^2$ = Ph, H) and Inversely Polarized Phosphaalkenes $R^1P{=}C(NMe_2)_2$ ($R^1$ = *t*Bu, Cy), and Their Structure

**Keywords:** Vinylidene complexes / Phosphaallene complexes / Phosphaalkenes / Tungsten

The reaction of vinylidene complexes $[(\eta^5\text{-}C_5H_5)(CO)(NO)W{=}C{=}C(H)R^1]$ ($R^1$ = Ph,H) with the phosphaalkenes $R^2P{=}C(NMe_2)_2$ ($R^2$ = *t*Bu, *c*-$C_6H_{11}$) affords the novel $\eta^2$-1-phosphaallene complexes $[\eta^2\text{-}\{R^1P{=}C{=}C(H)R^2\}W(CO)(NO)(\eta^5\text{-}C_5H_5)]$.

## Templated Octamolybdates

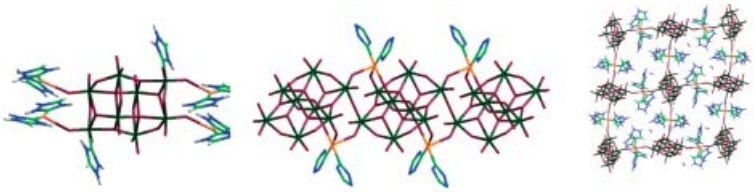

**K. Pavani, S. E. Lofland, K. V. Ramanujachary, A. Ramanan* ..... 568–578**

The Hydrothermal Synthesis of Transition Metal Complex Templated Octamolybdates

**Keywords:** Solvothermal synthesis / Molybdenum / Supramolecular chemistry / Organic–inorganic hybrid composites

The present work demonstrates the role of a transition metal complex and temperature in influencing the hydrothermal crystallization of octamolybdate cluster based solids with varying dimensionality. The crystal structures are rationalized in terms of supramolecular interactions between soluble molecular precursors.

## A Niobium Sol–Gel Precursor

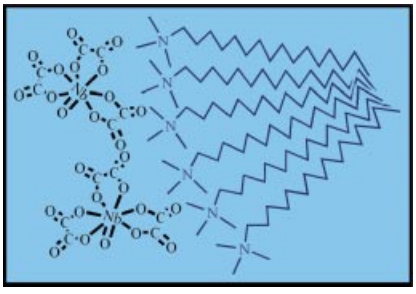

**M. A. Bizeto, V. R. L. Constantino* ..... 579–584**

Niobium Oxide Mesophases Obtained by Self-Assembly of an Aqueous Soluble Niobium Complex Precursor and Organic Templates

**Keywords:** Niobium / Mesophases / Organic–inorganic hybrid composites / Template synthesis / Sol–gel synthesis

The ammonium trioxalato(oxido)niobate is evaluated as a water-soluble inorganic precursor for the sol–gel-like synthesis of organized niobium oxide mesophases using organic templates as structure-directing agents. The benefits of using this precursor are the low cost, easy handling, and the opportunity to recycle the starting material directly from the niobium oxide.


 © 2007 Wiley-VCH Verlag GmbH & Co. KGaA, Weinheim 

Metal isobutylsilsesquioxanes containing $Ti^{IV}$ and $V^{V}$ prepared by direct corner-capping of a trisilanolisobutylsilsesquioxane precursor. The hybrid inorganic−organic nature of these compounds and the possibility of dispersing catalytically active metal centres in a highly efficient way within organic matrices have been investigated by dispersing these compounds in a polypropylene matrix by melt blending.

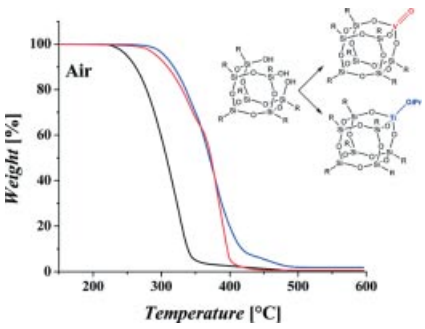


## Metal-Containing Isobutylsilsesquioxanes

**F. Carniato, E. Boccaleri,***
**L. Marchese, A. Fina, D. Tabuani,**
**G. Camino** ..... **585−591**

Synthesis and Characterisation of Metal Isobutylsilsesquioxanes and Their Role as Inorganic−Organic Nanoadditives for Enhancing Polymer Thermal Stability

**Keywords:** Silsesquioxanes / Titanium / Vanadium / Polymers / Nanocomposites

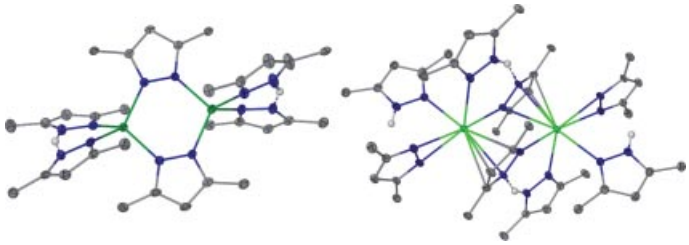

Stabilization through hydrogen bonding between neutral pyrazole and anionic pyrazolato ligands is the main structure-determining force in a group of novel alkaline earth and rare earth metal diisopropylpyrazolates.

## Pyrazolate Complexes

**J. Hitzbleck, G. B. Deacon,**
**K. Ruhlandt-Senge*** ..... **592−601**

Structural Trends in Alkaline Earth and Rare Earth Metal 3,5-Diisopropylpyrazolates

**Keywords:** Alkaline earth metals / Lanthanoids / N ligands / Coordination modes

The versatility in the bonding modes of the trifluoroacetate ligand is reflected in the X-ray structures of the complexes $[Y_3Cu(\eta^3\text{-}OH)(mdeaH)_5(TFA)_3](TFA)_2(H_2O)$ (**1**) and $[Ba_3(mdeaH_2)_4(TFA)_6]_{1\infty}$ (**2**), where it acts not only in a terminal ($\eta^1$ and $\eta^2$) or bridging-chelating ($\mu,\eta^2$ and $\mu_3\text{-}\eta^2\text{:}\eta^2\text{:}\eta^1$) manner but also as a counterion. The unique $\mu_3\text{-}\eta^2(O,O')\text{:}\eta^2(O,F)\text{:}\eta^1(O)$ bonding mode in **2** shows the metal···F interaction, observed for the first time for a TFA ligand.

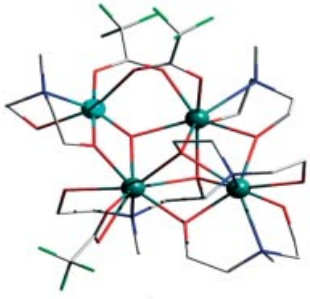

**1**

## Coordination Modes

**S. Mishra,* J. Zhang,**
**L. G. Hubert-Pfalzgraf, D. Luneau,**
**E. Jeanneau** ..... **602−608**

The Interplay between Yttrium and Barium or Copper Trifluoroacetates and *N*-Methyldiethanolamine: Synthesis of a Heterometallic $Y_3Cu$ Trifluoroacetate Complex and a Homometallic Ba-TFA 1D Polymer

**Keywords:** Heterometallic complexes / Yttrium / Copper / Barium / N,O ligands

Hierarchical self-assembly is an appropriate tool in order to obtain oligonuclear coordination compounds. In the presented example, lithium cations act as a "glue", which connects simple mononuclear complexes to supramolecular aggregates.

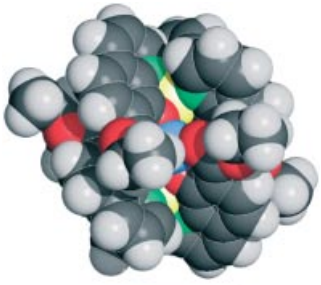

$[Li_3(ligand)_6Ni_2]^+$

## Metallosupramolecular Chemistry

**M. Albrecht,* M. Fiege, M. Baumert,**
**M. de Groot, R. Fröhlich, L. Russo,**
**K. Rissanen** ..... **609−616**

Hierarchical, Lithium-Templated Assembly of Helicate-Type Complexes: How Versatile Is This Reaction?

**Keywords:** Dinuclear complexes / Helicates / Hierarchical assembly / Chelate ligands / N,O ligands

 © 2007 Wiley-VCH Verlag GmbH & Co. KGaA, Weinheim 

# CONTENTS

## Ferrocene Peptides

**K. Heinze,* U. Wild, M. Beckmann ..... 617–623**

Solid-Phase Synthesis of Chiral Modular Ferrocene-Based Peptides

**Keywords:** Conformation analysis / Hydrogen bonds / Metallocenes / Molecular modelling / Solid-phase synthesis

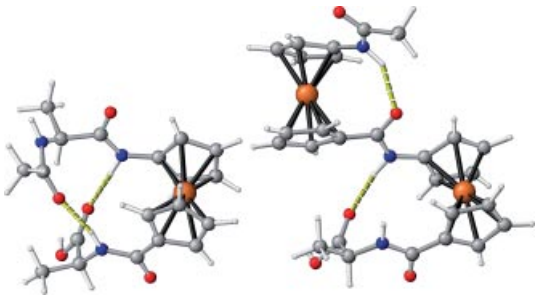

The development of solid-phase peptide synthesis for ferrocene amino acids, conformational analyses of the peptides, on-bead oxidation procedures and on-bead binding assays paves the way for devising selective redox-controlled receptor and transporter systems, which, by synthetic design, are amenable to parallel solid-phase peptide synthesis and on-bead oxidation and screening assays.

**If not otherwise indicated in the article, papers in issue 3 were published online on January 11, 2007**

 © 2007 Wiley-VCH Verlag GmbH & Co. KGaA, Weinheim 

DOI: 10.1002/ejic.200600875

# A Novel Amphiphilic $Re^{I}$ Complex with Bis(fullerene)-Substituted Bipyridine Ligands: Synthesis, Electrochemistry, and Langmuir Film

**Hwi Deuk Lee,[a] Sang Keun Oh,[a] Chan Soo Choi,[b] and Kwang-Yol Kay*[a]**

**Keywords:** Rhenium / Fullerenes / Bipyridines / Cyclic voltammetry / Langmuir films

An amphiphilic fullerene ($C_{60}$) derivative with a (bipyridine)-tricarbonylrhenium(I) chloride polar head group has been prepared. Electrochemical studies indicate that some ground state electronic interactions between the fullerene subunit and the metal complexed moiety are present in $Re^{I}$ complex **1**. The Langmuir film of this compound has been characterized by its surface pressure versus molecular area isotherm and Brewster angle microscopy (BAM) observations.
(© Wiley-VCH Verlag GmbH & Co. KGaA, 69451 Weinheim, Germany, 2007)

## Introduction

The fullerene ($C_{60}$) is an attractive functional group for a large number of multicomponent molecular architectures with photoinduced electron transfer processes[1] because of its electro- and photophysical properties. Fullerene is especially attractive because it can efficiently induce a rapid charge separation accompanied by a slow charge recombination.[2] Various donors such as porphyrin,[1f,3] TTFs,[4] ferrocene,[5] pyrene,[6] carbazol,[7] oligothiophenes,[8] *N*,*N*′-dialkylaniline,[9] carotenoid,[10] and phthalocyanine[11] have mainly been attached to fullerene ($C_{60}$) to investigate energy- and electron-transfer interactions. Recently, further efforts have been made to produce long-lived and high-energy intramolecular charge separated states, which can be exploited for practical applications such as solar energy conversion.[12] Among these, hybrid systems combining the fullerene with coordination compounds of metal ions such as $Ru^{II}$,[13] $Re^{I}$,[13e] and $Cu^{I}$[1g,14] are interesting because the long-lived metal-to-ligand charge transfer (MLCT) excited state of such complexes has a marked reducing character and is capable of initiating photoinduced electron transfer to the fullerene subunit. In fact, the photoelectrochemical (PEC) devices prepared from fullerene-substituted tris(2,2′-bipyridine)ruthenium(II) derivatives have shown the possibility for a controlled fabrication of the molecular level devices with high energy conversion efficiencies.[15]

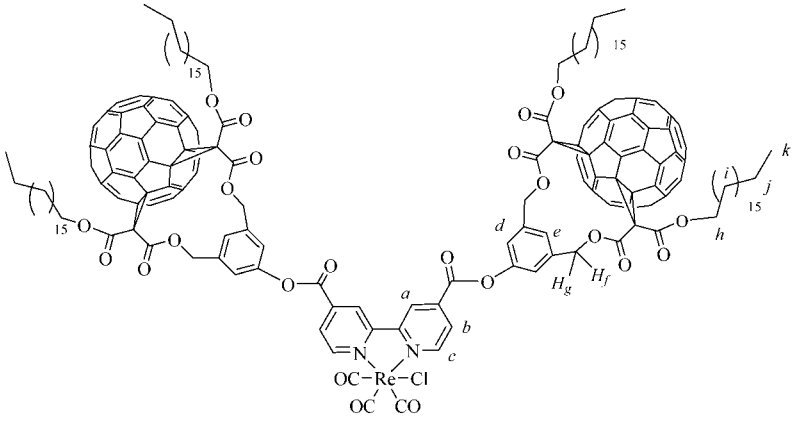


**1**

However, only one multicomponent system of such an array with a $Re^{I}$ complex[13e] has been reported to date. In this hybrid system, one fullerene and $Re^{I}$ complex are connected by a long, flexible alkyl linker and have mutual inter-

[a] Department of Molecular Science and Technology, Ajou University,
Suwon 443-749, South Korea
Fax: +82-31-219-1615
E-mail: kykay@ajou.ac.kr
[b] Department of Applied Chemistry, Daejeon University,
Daejeon 300-716, South Korea

 © 2007 Wiley-VCH Verlag GmbH & Co. KGaA, Weinheim 

actions through spatial arrangement of the two components. Also, no $Re^{I}$ complex with more than one fullerene substituent has been reported until now, to the best of our knowledge. On the other hand, studies on Langmuir and Langmuir–Blodgett films from amphiphilic fullerene derivatives have already been reported by Diederich, Nierengarten and others.[16] However, only a limited number of the Langmuir films from fullerene–metal conjugates, such as monofullerene–ruthenium(II) coordination compound has been reported so far.[13g] In line with these aspects, we report herein the first synthesis of $Re^{I}$ coordination compound **1** that possesses a bis(fullerene)-substituted bipyridine ligand, which has short and relatively rigid linkages between fullerene and the $Re^{I}$ complex. Furthermore, we also report its electrochemical properties and Langmuir films.

## Results and Discussion

The synthetic route leading to the bis(fullerene)-substituted 2,2′-bipyridine ligand used for the preparation of rhenium(I) complex **1** is depicted in Scheme 1. Commercially available 5-hydroxyisophthalic acid (**2**) was esterified to give diester **3** (93% yield), and subsequent reduction of **3** with LAH produced 3,5-bis(hydroxymethyl)phenol (**4**) in a yield of 85%. Octadecanol (**5**) reacted with meldrum's acid (**6**) to afford malonic acid monooctadecyl ester (**7**) in 89% yield. Esterification of **4** with monoester **7** of malonic acid in the presence of *N*,*N*′-dicyclohexylcarbodiimide (DCC) yielded bis(malonate) **8** (73% yield). The functionalization of $C_{60}$ was based on the highly regioselective Diederich reaction,[17] which led to macrocyclic bis adducts of $C_{60}$ through macrocyclization of the carbon sphere with the bis(malonate) derivatives in a double Bingel addition.[18] Treatment of $C_{60}$ with **8**, iodine, and 1,8-diazabicyclo[5.4.0]undec-7-ene (DBU) in toluene at room temperature afforded mono adduct **9**[11b] in 28% yield. The reaction of mono adduct **9** with 2,2′-bipyridine-4,4′-dicarbonyl dichloride (**10**)[19] which was prepared by oxidation of 4,4′-dimethyl-2,2′-bipyridine with $K_2Cr_2O_7$ and subsequent conversion of the diacid to diacyl dichloride **10**, went smoothly in the presence of triethylamine to produce bis adduct **11**[20] in 83% yield. Finally, fullerene-functionalized ligand **11** reacted with pentacarbonylrhenium(I) chloride in toluene to afford complex **1**[20] in 92% yield.

To compare the electrochemical and photochemical properties of ligand **11** and its $Re^{I}$ complex **1**, model compounds **12**[20] and **13**[20] that lack fullerene moieties were synthesized in an analogous method (Scheme 2).

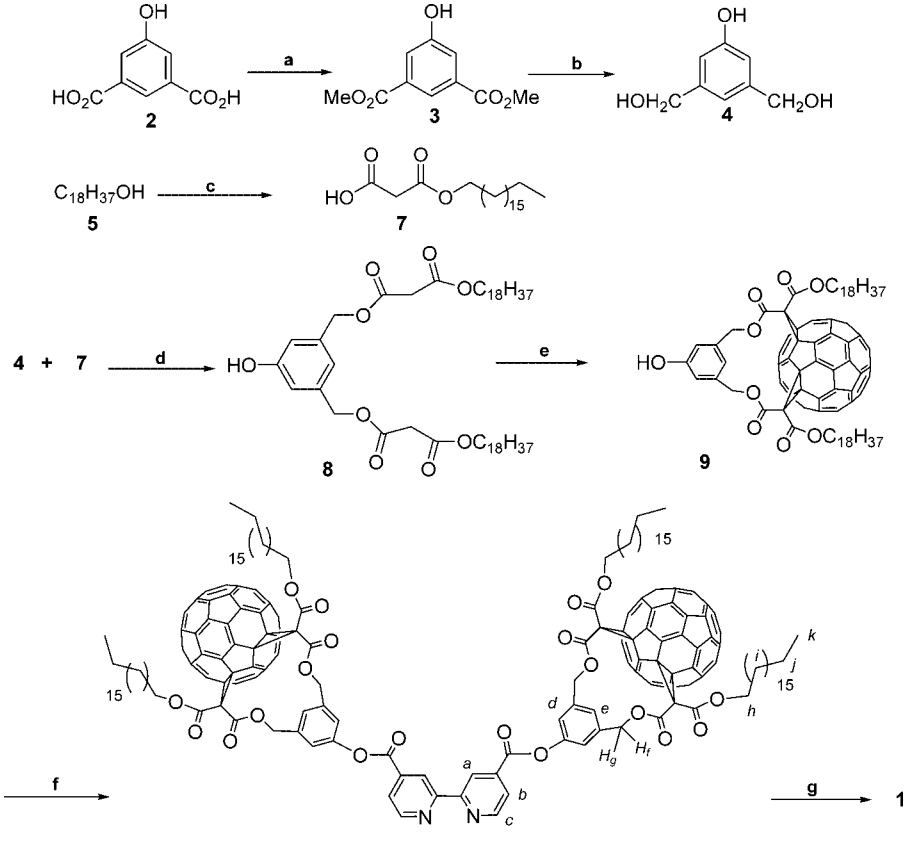


Scheme 1. Synthesis of ligand **11** and complex **1**: a) MeOH, $H_2SO_4$, reflux, 24 h, 93%; b) $LiAlH_4$, THF, reflux, 48 h, 85%; c) Meldrum's acid (**6**), 110–120 °C, 2 h, 89%; d) DCC, DMAP, HOBT, THF, room temp., 12 h, 73%; e) $C_{60}$, $I_2$, DBU, room temp., 24 h, 28%; f) **10**, $Et_3N$, $CHCl_3$, room temp., 12 h, 83%; g) $Re(CO)_5Cl$, toluene, 80 °C, 12 h, 92%;.

 © 2007 Wiley-VCH Verlag GmbH & Co. KGaA, Weinheim 

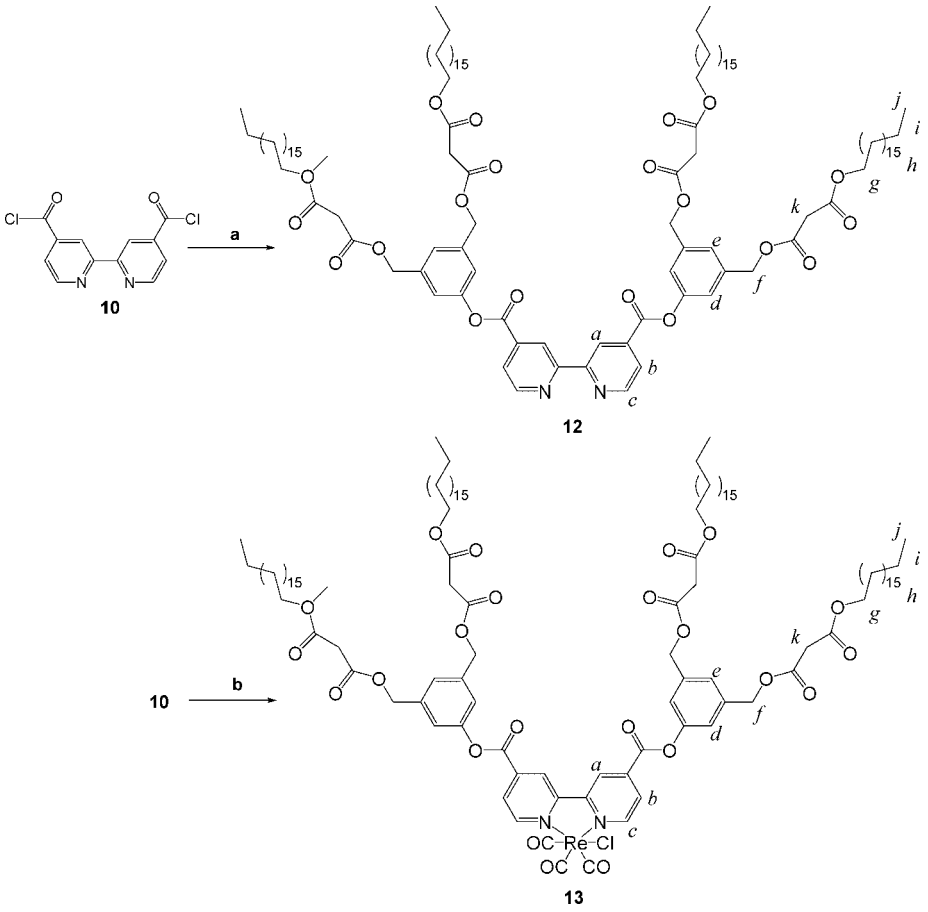


Scheme 2. Synthesis of model compounds **12** and **13**: a) **8**, $Et_3N$, $CHCl_3$, room temp., 12 h, 29%; b) $Re(CO)_5Cl$, EtOH, reflux, 12 h, 86%.

The structure and purity of the new compounds were confirmed by $^1H$ NMR and IR spectroscopy, MALDI-TOF mass spectrometry, and elemental analysis.[20] The $^1H$ NMR spectra of **11** and **1** show the characteristic features of the 1,3-phenylenebis(methylene)-tethered fullerene *cis*-2 bis adduct substituent.[11b,13g] In **11** and **1**, a set of AB quartets are clearly observed for the benzylic $CH_2$ groups ($H_f$ and $H_g$) and an $AX_2$ system is revealed for the aromatic protons ($H_d$ and $H_e$) of the 1,3,5-trisubstituted bridging phenyl ring. The spectra are also characterized by three sets of aromatic signals in a typical pattern for a 4,4′-disubstituted 2,2′-bipyridine ($H_a$, $H_b$, and $H_c$). Thus, the $^1H$-NMR spectrum of complex **1** is consistent with the proposed structure. Detailed assignments of the peaks in **11** and **1** are given and compared with model compounds **12** and **13**.[20]

The structure of **1** was also confirmed by mass spectrometry. The MALDI-TOF MS of **1** is characterized by a singly charged peak at $m/z$ = 3574.81, which can be assigned to **1** after loss of one chlorine atom.

The electrochemical properties of rhenium(I) complex **1** and ligand **11** were investigated and compared with those of model compounds **12** and **13** by cyclic voltammetry (CV) together with differential pulse voltammetry (DPV) in tetrahydrofuran (THF) with tetrabutylammonium tetrafluoroborate ($TBABF_4$) as a supporting electrolyte (Table 1). In the negative potential region, complex **1** shows nine reduction processes. As shown by comparison with corresponding ligand **11**, which lacks rhenium moiety, complex **1** showed five waves (–0.21, –0.69, –1.29, –1.62, and –2.11 V), which correspond to $C_{60}$-centered reductions. These reduction waves are regularly spaced around 500 mV. The first three fullerene-centered reduction waves of triad compound **1** are shifted about 30 mV more cathodically with respect to those (–0.19, –0.66, and –1.25 V) of the corresponding fullerene model compound, ligand **11**. This indicates that the LUMO energy levels of the ground state of the fullerene moiety are elevated by $Re^I$ complexation. However, Armaroli et al.[13e] reported that the first two fullerene-centered reductions of a $C_{60}$–$Re^I$ dyad showed opposite shifts. They suggested that this observation could be a consequence of a small electronic interaction due to spatial proximity for the two chromophores (more facile fullerene reduction) in $C_{60}$–$Re^I$. The triad of the present work seems to have adopted an extended conformation through rigid linkers between fullerene and the $Re^I$ complex, which prevents spatial interactions among the chromophores. So, our electrochemical results suggest that the electron donation from $Re^I$ to fullerene chromophores mainly occurs through the bonds. We have to mention that Armaroli et al.[13e] used a fullerene model compound without a bipyridine ligand, which does not provide a background for the representation of only a difference in $Re^I$. Thus, it is difficult to directly

 © 2007 Wiley-VCH Verlag GmbH & Co. KGaA, Weinheim 

compare their results with the results of the present work. Therefore, the present work only provides more convincing results to explain the electron donating effects of $Re^{I}$. The additional waves at –1.00 and –1.48 V that originated from the bipyridine–malonate domain also shifted negatively compared with those of ligand **11** (–0.98, –1.43 V). This indicates that the complexation of rhenium to the bipyridine ligand can influence this negative shift. However, the corresponding waves of model compound **13** (–0.97, –1.47 V) showed a relatively large positive shift by the complexation of rhenium of corresponding ligand **12** (–1.22, –1.57 V). The redox processes of ligand **11** were found to have also shifted positively from those of ligand **12**. These results indicate that the electron-withdrawing $C_{60}$ group strongly affects the characteristics of ligand **11**. In model compounds **12** and **13** there are oxidation processes at the redox potentials of 0.81 V ($\Delta E_p$ = 100 mV) and 0.77 V ($\Delta E_p$ = 110 mV), respectively (not shown in Table 1). This may be caused by a redox reaction of the aromatic ester group. Interestingly, the negative potential shift of compound **13** shows that the oxidation of this group is easier, probably because of an electron donating function of rhenium. On the other hand, the additional waves $E_2$ and $E_8$ in Table 1 seem to originate from the metal center because only the compounds with rhenium metal show these waves.

Table 1. Electrochemical properties of **1**, **11**, **12**, and **13**.[a]

| Compound | Reduction $E_1$ | $E_2$ | $E_3$ | $E_4$ | $E_5$ | $E_6$ | $E_7$ | $E_8$ | $E_9$ |
|---|---|---|---|---|---|---|---|---|---|
| **1** | – | – | – | – | – | – | – | – | – |
| | 0.21 | 0.51 | 0.69 | 1.00 | 1.29 | 1.48 | 1.62 | 1.80 | 2.11 |
| | (175) | (i) | (102) | (138) | (106) | (118) | (61) | (98) | (146) |
| **11** | – | | – | – | – | – | – | | – |
| | 0.19 | | 0.66 | 0.98 | 1.25 | 1.43 | 1.75 | | 2.27 |
| | (93) | | (96) | (96) | (111) | (98) | (125) | | (114) |
| **12** | | | | – | | – | | | |
| | | | | 1.22 | | 1.57 | | | |
| | | | | (200) | | (100) | | | |
| **13** | | – | | – | | – | | – | |
| | | 0.49 | | 0.97 | | 1.47 | | 1.90 | |
| | | (100) | | (110) | | (100) | | (120) | |

[a] Cyclic voltammetric measurements: glassy carbon disk working electrode (3 mm in diameter), Pt wire counter electrode, and silver wire pseudoreference electrode ($Ag/Ag^+$) were used. The electrolyte contained degassed THF, 0.1 M $Bu_4NBF_4$ and $3 \times 10^{-4}$ M synthesized compounds. The scan rate was 100 mV/s. Values for $E_{1/2}$ (in V) as $(E_{pa} + E_{pc})/2$ and $\Delta E_p$ (in mV) are given in parentheses. DPV technique was also used to confirm redox potentials, and the results were in good agreement with CV technique within the first decimal point. (i) denotes irreversible. The experiments were performed at ambient temperature and pressure.

The UV/Vis spectrum of **1** in a $CHCl_3$ solution shows the characteristic absorption features of the fullerene units as well as the diagnostic MLCT band of the 2,2′-bipyridine rhenium(I) complex at 380 nm. Interestingly, preliminary luminescence measurements of **1** in $CHCl_3$ solution ($\lambda_{exc}$ = 292 and 380 nm) show strong quenching of the emission by introducing the fullerene moieties in **1**, which indicates the occurrence of intramolecular photoinduced processes. Detailed photophysical studies are currently under investigation and will be reported in due time.

Langmuir films of compound **1** have been characterized by their surface pressure versus molecular area (π/A) isotherms and Brewster angle microscopy (BAM) observation.[21] Figure 1 shows a surface pressure/area isotherm (π-A isotherm) of compound **1** on a water surface. Under continuous compression, the surface pressure started to increase steeply around 200 $Å^2$/molecule and the Langmuir film collapsed around $\pi_c \approx 50$ mN/m. The results suggest that compound **1** forms very stable monolayers on the water surface because of the balance between the hydrophobicity of the fullerene surrounded by two long alkyl chains and the hydrophilicity of the bipyridine $Re^{I}$ complex. Good reversible behavior in the successive compression/expansion cycles (data not shown) is also consistent with the amphiphilic structure of compound **1**, where aggregation of fullerenes is largely prevented by the long alkyl chains. These results are in a good agreement with the previous findings on a related amphiphilic fullerene derivative with ruthenium(II).[13g] The occupied surface area obtained by extrapolation of the steeply rising portion of the π-A isotherm to zero pressure is 166 $Å^2$/molecule, which is very close to the molecular area estimated by molecular modeling of compound **1**. A Brewster angle microscope was used to monitor the structural change of the Langmuir films during compression. The insets of Figure 1 show the BAM images of the Langmuir films at 200, 300, and 500 $Å^2$/molecule. The images clearly show that the domain size (brighter regions in the images) becomes larger as the surface pressure is increased, and a homogeneous monolayer is formed below 200 $Å^2$/molecule.

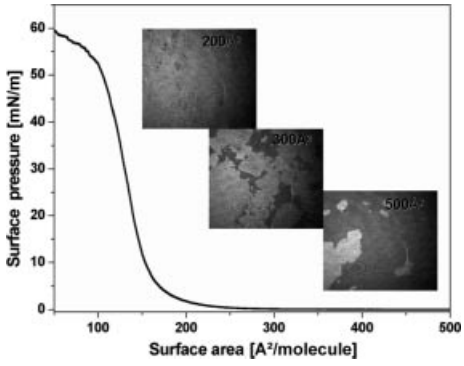


Figure 1. π-A isotherm recorded during compression of the monolayer of compound **1**. The insets are the BAM images of the Langmuir films at 200, 300, and 500 $Å^2$/molecule.

## Conclusions

We have synthesized a new $Re^{I}$ complex with bis(fullerene)-substituted bipyridine ligands, which is a suitable amphiphilic derivative for the preparation of stable Langmuir films. Electrochemical properties of this compound have also shown that some ground state electronic interactions between the fullerene subunit and the metal complexed moiety are present in this complex. We are currently investi-

 © 2007 Wiley-VCH Verlag GmbH & Co. KGaA, Weinheim 

gating the physical properties of Langmuir–Blodgett films of this molecule and attempting to apply their behavior in PEC cells for solar energy conversion.

## Acknowledgments

This work was supported by the Ministry of Education of Korea (Brain Korea 21 program).

[1] a) D. Gust, T. A. Moore, A. L. Moore, *Acc. Chem. Res.* **2001**, *34*, 40–48; b) H. Imahori, Y. Sakata, *Eur. J. Org. Chem.* **1999**, 2445–2457; c) D. M. Guldi, *Chem. Commun.* **2000**, 321–327; d) N. Martin, L. Sanchez, B. Illescas, I. Perez, *Chem. Rev.* **1998**, *98*, 2527–2547; e) H. Imahori, D. M. Guldi, K. Tamaki, Y. Yoshida, C. P. Luo, Y. Sakata, S. Fukuzumi, *J. Am. Chem. Soc.* **2001**, *123*, 6617–6628; f) D. Kuciauskas, P. A. Liddell, S. Lin, T. E. Johnson, S. J. Weghorn, J. S. Lindsey, A. L. Moore, T. A. Moore, D. Gust, *J. Am. Chem. Soc.* **1999**, *121*, 8604–8614; g) N. Armaroli, C. Boudon, D. Felder, J. P. Gisselbrecht, M. Gross, G. Marconi, J. F. Nicoud, J. F. Nierengarten, V. Vicinelli, *Angew. Chem. Int. Ed.* **1999**, *38*, 3730–3733.

[2] a) I. Hiroshi, S. Yoshiteru, *Eur. J. Org. Chem.* **1999**, 2445–2457; b) F. D'Souza, R. Chitta, S. Gadde, M. E. Zandler, A. S. D. Sandanayaka, Y. Araki, O. Ito, *Chem. Commun.* **2005**, 1279–1281; c) M.-S. Choi, T. Aida, H. Luo, Y. Araki, O. Ito, *Angew. Chem. Int. Ed.* **2003**, *42*, 4060–4063.

[3] a) M. Wedel, F.-P. Montforts, *Tetrahedron Lett.* **1999**, *40*, 7071–7074; b) Y. Koji, I. Hiroshi, N. Yoshinobu, Y. Iwao, S. Yoshiteru, *Chem. Lett.* **1999**, 895–896; c) F. Manoru, O. Ito, I. Hiroshi, Y. Koji, Y. Hiroko, S. Yoshiteru, *Chem. Lett.* **1999**, 721–722; d) P. Cheng, S. R. Wilson, D. I. Schuster, *Chem. Commun.* **1999**, 89–90; e) T. Koichi, I. Hiroshi, N. Yoshinobu, Y. Iwao, S. Yoshiteru, *Chem. Commun.* **1999**, 625–626; f) N. V. Tkachenka, L. Rantala, A. Y. Tauber, J. Helaja, P. H. Hynninen, H. Lemmetyinen, *J. Am. Chem. Soc.* **1999**, *121*, 9378–9387; g) G. D. L. Torre, F. Giacalone, J. L. Segura, N. Martin, D. M. Guldi, *Chem. Eur. J.* **2005**, *11*, 1267–1280; h) A. S. D. Sandanayaka, K.-I. Ikeshita, N. Araki, Y. Furusho, T. Takata, O. Ito, *J. Mater. Chem.* **2005**, *15*, 2276–2287.

[4] a) N. Martin, L. Sanchez, C. Seoane, R. Andreu, I. Garin, J. Orduna, *Tetrahedron Lett.* **1996**, *37*, 5979–5982; b) K. B. Simonsen, V. V. Konovalov, T. A. Konovalova, T. Kawai, M. P. Cava, L. D. Kispert, R. M. Metzger, J. Becher, *J. Chem. Soc., Perkin Trans. 2* **1999**, 657–665; c) S. Chopin, Z. Gan, J. Cousseau, Y. Araki, O. Ito, *J. Mater. Chem.* **2005**, *15*, 2288–2296; d) L. Sanchez, M. Sierra, N. Martin, D. M. Guldi, M. W. Wienk, R. A. J. Janssen, *Org. Lett.* **2005**, *7*, 1691–1694.

[5] a) D. M. Guldi, M. Maggini, G. Scorrano, M. Prato, *J. Am. Chem. Soc.* **1997**, *119*, 974–980; b) F. Hauke, A. Hirsch, S.-G. Liu, L. Echegoyen, A. Schwartz, C. Luo, D. M. Guldi, *ChemPhysChem* **2002**, *3*, 195–205; c) K.-Y. Kay, L. H. Kim, I. C. Oh, *Tetrahedron Lett.* **2000**, *41*, 1397–1400; d) B. Dardel, R. Deschenaux, M. Even, E. Serrano, *Macromolecules* **1999**, *32*, 5193–5198.

[6] M. Fujitsuka, H. Luo, Y. Murato, N. Kato, O. Ito, K. Komatsu, *Chem. Lett.* **2002**, 968–969.

[7] S. Wang, Y. Li, Z. Shi, C. Du, H. Fang, S. Xiao, Y. Zhou, D. Zhu, *Synth. Commun.* **2002**, *32*, 2507–2512.

[8] a) N. Negishi, K. Yamada, K. Takimiya, Y. Aso, T. Otsubo, Y. Harima, *Chem. Lett.* **2003**, *32*, 404–405; b) J. Ikemoto, K. Takimiya, Y. Aso, T. Otsubo, M. Fujitsuka, O. Ito, *Org. Lett.* **2002**, *4*, 309–311; c) T. Yamazaki, Y. Murata, K. Komatsu, K. Furukawa, M. Morita, N. Maruyama, T. Yamao, S. Fugita, *Org. Lett.* **2004**, *6*, 4865–4868.

[9] a) P. V. Kamat, S. Barazzouk, S. Hotchandani, K. G. Thomas, *Chem. Eur. J.* **2000**, *6*, 3914–3921; b) R. M. Williams, J. M. Zwier, J. W. Verhoeven, *J. Am. Chem. Soc.* **1995**, *117*, 4093–4099; c) D. Liu, J. Li, H. Pan, Y. Li, Z.-X. Guo, D. Zhu, *Synth. Met.* **2003**, *135–136*, 851–852.

[10] D. Kuciauskas, P. A. Liddel, S. Lin, S. G. Stone, A. L. Moore, T. A. Moore, D. Gust, *J. Phys. Chem. B* **2000**, *104*, 4307–4321.

[11] a) Y. Chen, M. E. El-Khouly, M. Sasaki, Y. Araki, O. Ito, *Org. Lett.* **2005**, *7*, 1613–1616; b) K. N. Kim, C. S. Choi, K.-Y. Kay, *Tetrahedron Lett.* **2005**, *46*, 6791–6795; c) D. M. Guldi, A. Gouloumis, P. Vazquez, T. Torres, V. Georgakilas, M. Prato, *J. Am. Chem. Soc.* **2005**, *127*, 5811–5813.

[12] a) L. C. Sun, L. Hummarstrom, B. Akermark, S. Styrings, *Chem. Soc. Rev.* **2001**, *30*, 36–49; b) C. J. Brabec, N. S. Sariciftci, J. C. Hummelen, *Adv. Funct. Mater.* **2001**, *11*, 15–26; c) J. F. Eckert, J. F. Nicoud, J. F. Nierengarten, S. G. Liu, L. Echegoyen, F. Barigelletti, N. Armaroli, L. Ouali, V. Kranikov, G. Hadziioannou, *J. Am. Chem. Soc.* **2000**, *122*, 7467–7479.

[13] a) D. Armspach, E. C. Constable, F. Diederich, C. E. Housecrott, J.-F. Nierengarten, *Chem. Eur. J.* **1998**, *4*, 723–739; b) M. Maggini, D. M. Guldi, S. Mondini, G. Scorrano, F. Paolucci, P. Ceroni, S. Roffia, *Chem. Eur. J.* **1998**, *4*, 1992–2000; c) A. Polese, S. Mondini, A. Bianco, C. Toniolo, G. Scorrano, D. M. Guldi, M. Maggini, *J. Am. Chem. Soc.* **1999**, *121*, 3446–3452; d) C. Du, Y. Li, S. Wang, Z. Shi, S. Xiao, D. Zhu, *Synth. Met.* **2001**, *124*, 287–289; e) N. Armaroli, G. Accorsi, D. Felder, J.-F. Nierengarten, *Chem. Eur. J.* **2002**, *8*, 2314–2323; f) F. Cardinali, J.-F. Nierengarten, *Tetrahedron Lett.* **2003**, *44*, 2673–2676; g) F. Cardinali, J.-L. Gallani, S. Schergna, M. Maggini, J.-F. Nierengarten, *Tetrahedron Lett.* **2005**, *46*, 2969–2972.

[14] a) N. Armaroli, F. Diederich, C. O. Dietrich-Bucheker, L. Flamigni, G. Marconi, J.-F. Nierengarten, J.-P. Sauvage, *Chem. Eur. J.* **1998**, *4*, 406–416; b) Y. Rio, G. Enderlin, C. Bourgogne, J.-F. Nierengarten, J.-P. Gisselbrecht, M. Gross, G. Accorsi, N. Armaroli, *Inorg. Chem.* **2003**, *42*, 8783–8793; c) F. Cardinali, H. Mamlouk, Y. Rio, N. Armaroli, J.-F. Nierengarten, *Chem. Commun.* **2004**, 1582–1583; d) D. I. Schuster, K. Li, D. M. Guldi, J. Ramey, *Org. Lett.* **2004**, *6*, 1919–1922; e) K. Li, D. I. Schuster, D. M. Guldi, M. A. Herranz, L. Echegoyen, *J. Am. Chem. Soc.* **2004**, *126*, 3388–3389; f) K. Li, P. J. Bracher, D. M. Guldi, M. A. Herranz, L. Echegoyen, D. I. Schuster, *J. Am. Chem. Soc.* **2004**, *126*, 9156–9157.

[15] C. Luo, D. M. Guldi, M. Maggini, E. Menna, S. Mondini, N. A. Kotov, M. Prato, *Angew. Chem. Int. Ed.* **2000**, *39*, 3905–3909.

[16] a) F. Cardullo, F. Diederich, L. Echegoyen, T. Habicher, N. Jayaraman, R. M. Leblanc, J. F. Stoddart, S. Wang, *Langmuir* **1998**, *14*, 1955–1959; b) J. F. Nierengarten, *New J. Chem.* **2004**, *28*, 1177–1191 and references cited therein; c) J.-F. Nierengarten, J. Eckert, Y. Rio, M. del Pilar Carreon, J. Gallani, D. Guillon, *J. Am. Chem. Soc.* **2001**, *123*, 9743–9748; d) D. Felder, M. del Pilar Carreon, J. Gallani, D. Guillon, J.-F. Nierengarten, T. Chuard, R. Deschenaux, *Helv. Chim. Acta* **2001**, *84*, 1119–1132.

[17] J.-F. Nierengarten, V. Gramlich, F. Cardullo, F. Diederich, *Angew. Chem. Int. Ed. Engl.* **1996**, *35*, 2101–2103.

[18] C. Bingel, *Chem. Ber.* **1993**, *126*, 1957–1959.

[19] V. Penicaud, F. Odobel, B. Bujoli, *Tetrahedron Lett.* **1998**, *39*, 3689–3692.

[20] Selected physical data for **1**, **11**, **12**, and **13**. Compound **1**: M.p. 162 °C. $^1$H NMR (200 MHz, $CDCl_3$, 25 °C): $\delta$ = 9.38 (d, 1 H, *c*ArH), 9,02 (s, 1 H, *a*ArH), 8.30 (d, $J$ = 5.1 Hz, 1 H, *b*ArH), 7.68 (s, 1 H, *e*ArH), 7.27 (s, 2 H, *d*ArH), 5.85 (d, $J$ = 12.8 Hz, 2 H, *f*$CH_2$), 5.25 (d, $J$ = 12.8 Hz, 2 H, *g*$CH_2$), 4.35 (t, $J$ = 5.2 Hz, 4 H, *h*$OCH_2$), 1.70 (m, 4 H, *j*$CH_2$), 1.25 (s, 60 H, *i*$CH_2$), 0.85 (t, $J$ = 6.4 Hz, 6 H, *k*$CH_3$) ppm. FTIR (KBr): $\tilde{\nu}$ = 2021, 1924, 1905, 1750 $cm^{-1}$. MALDI-TOF MS: $m/z$ = 3574.81 [M – Cl]$^+$, 721 [$C_{60}$ + H]$^+$. $C_{235}H_{168}ClN_2O_{23}Re$ (3609.58): calcd. C 78.20, H 4.69; found C 78.32, H 4.64. Compound **11**: M.p. 120 °C. $^1$HNMR (200 MHz, $CDCl_3$, 25 °C): $\delta$ = 9.25 (s, 1 H, *c*ArH), 9.00 (d, $J$ = 5.1 Hz, 1 H, *a*ArH), 8.10 (d, $J$ = 5.1x Hz, 1 H, *b*ArH), 7.55 (s, 1 H, *e*ArH), 7.27 (s, 2 H, *d*ArH), 5.85 (d, $J$ = 13.6 Hz, 2 H, *f*$CH_2$), 5.25 (d, $J$ = 13.6 Hz, 2 H, *g*$CH_2$),

 © 2007 Wiley-VCH Verlag GmbH & Co. KGaA, Weinheim 

4.40 (t, $J$ = 6.2 Hz, 4 H, $h$OCH$_2$), 1.75 (m, 4 H, $j$CH$_2$), 1.25 (s, 60 H, $i$CH$_2$), 0.85 (t, $J$ = 6.4 Hz, 6 H, $k$CH$_3$) ppm. FTIR (KBr): $\tilde{\nu}$ = 1750 cm$^{-1}$. MALDI-TOF MS: $m/z$ = 3304.21 [M$^+$]. $C_{232}H_{168}N_2O_{20}$ (3303.89): calcd. C 84.34, H 5.13; found C 84.41, H 4.98. Compound **12**: M.p. 84 °C. $^1$H NMR (200 MHz, $CDCl_3$, 25 °C): $\delta$ = 9.25 (s, 1 H, $c$ArH), 8.96 (d, $J$ = 5.1 Hz, 1 H, $a$ArH), 8.05 (d, $J$ = 5.1 Hz, 1 H, $b$ArH), 7.31 (s, 1 H, $e$ArH), 7.27 (s, 2 H, $d$ArH), 5.25 (s, 4 H, $f$CH$_2$), 4.15 (t, $J$ = 6.5 Hz, 4 H, $g$CH$_2$), 3.45 (d, $J$ = 4.7 Hz, 2 H, $k$CH$_2$), 1.60 (m, 4 H, $i$CH$_2$), 1.25 (s, 60 H, $h$CH$_2$), 0.85 (t, $J$ = 6.4 Hz, 6 H, $j$CH$_3$) ppm. FTIR (KBr): $\tilde{\nu}$ = 1738 cm$^{-1}$. $C_{112}H_{176}N_2O_{20}$ (1870.63): calcd. C 71.91, H 9.48; found C 71.88, H 9.43. Compound **13**: M.p.95 °C. $^1$H NMR (200 MHz, $CDCl_3$, 25 °C): $\delta$ = 9.32 (d, $J$ = 5.1 Hz, 1 H, $c$ArH), 9.00 (s, 1 H, $a$ArH), 8.27 (d, $J$ = 5.1 Hz, 1 H, $b$ArH), 7.36 (s, 1 H, $e$ArH), 7.27 (s, 2 H, $d$ArH), 5.23 (s, 4 H, $f$CH$_2$), 4.12 (t, $J$ = 6.5 Hz, 4 H, $g$CH$_2$), 3.45 (d, $J$ = 4.7 Hz, 2 H, $k$CH$_2$), 1.60 (m, 4 H, $i$CH$_2$), 1.25 (s, 60 H, $h$CH$_2$), 0.85 (t, $J$ = 6.4 Hz, 6 H, $i$CH$_3$) ppm. FTIR (KBr): $\tilde{\nu}$ = 2030, 1910, 1900, 1750 cm$^{-1}$. $C_{115}H_{176}ClN_2O_{23}Re$ (2176.32): calcd. C 63.47, H 8.15; found C 63.50, H 8.18.

[21] An LB trough (KSV 5000, KSV instruments, Finland) was used to form Langmuir monolayers of compound **1** at the water/air interface. A chloroform solution of compound **1** at a concentration of 0.05 mM was spread onto the water surface of the LB trough, and then compressed to a surface pressure of about 60 mN/m. A Brewster angle microscope (BAM, Nanofilm Technology, Germany) equipped with a CCD camera was used to examine the morphology of the Langmuir films.

Received: September 19, 2006
Published Online: December 19, 2006

 © 2007 Wiley-VCH Verlag GmbH & Co. KGaA, Weinheim 

DOI: 10.1002/ejic.200600926

# A Surprising Reaction of Trimethylphosphane with the Unsaturated Diruthenium Complex $[(\eta^6\text{-}C_6Me_6)_2Ru_2(\mu_2\text{-}H)_3]^+$: Synthesis and Molecular Structure of the Cations $[(\eta^6\text{-}C_6Me_6)Ru_2(PMe_3)_3(\mu_2\text{-}H)_3]^+$ and $[(\eta^6\text{-}C_6Me_6)_2Ru_2(PMe_3)_2(\mu_2\text{-}H)(H)_2]^+$

**Mathieu J.-L. Tschan,[a] Frédéric Chérioux,[b] Bruno Therrien,[a] and Georg Süss-Fink*[a]**

**Keywords:** Ruthenium complexes / Arene complexes / Phosphane ligands / Hydrido ligands

Whereas aromatic or aliphatic phosphanes undergo cleavage of the P–C bond in the reaction with $[(\eta^6\text{-}C_6Me_6)_2Ru_2(\mu_2\text{-}H)_3]^+$ to give phosphido-bridged diruthenium cations of the type $[(\eta^6\text{-}C_6Me_6)_2Ru_2(\mu_2\text{-}PR_2)(\mu_2\text{-}H)_2]^+$, trimethylphosphane surprisingly yields the substitution product $[(\eta^6\text{-}C_6Me_6)Ru_2(PMe_3)_3(\mu_2\text{-}H)_3]^+$ (**1**), as well as the racemic intermediate $[(\eta^6\text{-}C_6Me_6)_2Ru_2(PMe_3)_2(\mu_2\text{-}H)(H)_2]^+$ (**2**), in the form of the tetrafluoroborate salts. In complex **2**, the hydrido ligands are fluxional in solution, as shown by variable-temperature $^1H$ NMR spectroscopy. Cation **1** reacts with *p*-bromothiophenol to give the complex $[(\eta^6\text{-}C_6Me_6)_2Ru_2(PMe_3)_3\{\mu_2\text{-}(p\text{-}Br\text{-}C_6H_4)\text{-}S\}(\mu_2\text{-}H)_2]^+$ (**3**), isolated as the tetrafluoroborate salt.

(© Wiley-VCH Verlag GmbH & Co. KGaA, 69451 Weinheim, Germany, 2007)

## Introduction

Tertiary phosphanes are without any doubt among the most important ligand systems used in organometallic chemistry or in molecular catalysis.[1] The cleavage of the carbon–phosphorus bond has been observed in numerous cases, essentially by reacting metal carbonyl complexes with aromatic phosphanes.[2] Recently, we found that trisubstituted (aliphatic or aromatic) phosphanes, $PR_3$, undergo facile P–C bond cleavage with the unsaturated complex $[(\eta^6\text{-}C_6Me_6)_2Ru_2(\mu_2\text{-}H)_3]^+$ to give the phosphido-bridged complexes $[(\eta^6\text{-}C_6Me_6)_2Ru_2(\mu_2\text{-}PR_2)(\mu_2\text{-}H)_2]^+$.[3] In the reaction of triphenylphosphane with $[(\eta^6\text{-}C_6Me_6)_2Ru_2(\mu_2\text{-}H)_3]^+$ to give $[(\eta^6\text{-}C_6Me_6)_2Ru_2(\mu_2\text{-}PPh_2)(\mu_2\text{-}H)_2]^+$, we were able to isolate an intermediary complex containing a bridging phenyl ligand, $[(\eta^6\text{-}C_6Me_6)_2Ru_2(\mu_2\text{-}PPh_2)(\mu_2\text{-}Ph)(\mu_2\text{-}H)]^+$, and to perform a single-crystal X-ray structure analysis of the tetrafluoroborate salt. In the reaction of trialkylphosphanes with $[(\eta^6\text{-}C_6Me_6)_2Ru_2(\mu_2\text{-}H)_3]^+$ to give $[(\eta^6\text{-}C_6Me_6)_2Ru_2(\mu_2\text{-}PR_2)(\mu_2\text{-}H)_2]^+$ (R = *n*Oct, *n*Bu), we were able to show that the reaction produces the corresponding olefins (*n*-octene or *n*-butene) and not the expected alkanes. This suggests that the P–C bond cleavage in trialkylphosphanes at the diruthenium centre occurs by β-H elimination from the alkyl group. In order to confirm this hypothesis, we decided to study the reaction of $[(\eta^6\text{-}C_6Me_6)_2Ru_2(\mu_2\text{-}H)_3]^+$ with trimethylphosphane, in which β-H elimination is impossible.

## Results and Discussion

The reaction of $[(\eta^6\text{-}C_6Me_6)_2Ru_2(\mu_2\text{-}H)_3]^+$ with $PMe_3$ indeed does not yield the expected complex $[(\eta^6\text{-}C_6Me_6)_2Ru_2(\mu_2\text{-}PMe_2)(\mu_2\text{-}H)_2]^+$, but surprisingly leads to the formation of the cation $[(\eta^6\text{-}C_6Me_6)Ru_2(PMe_3)_3(\mu_2\text{-}H)_3]^+$ (**1**), in which one of the two hexamethylbenzene ligands has been replaced by three trimethylphosphane ligands. Cation **1** is obtained in 28% yield and it can be isolated as the tetrafluoroborate salt (Scheme 1). The substitution of an $\eta^6$-arene ligand at a ruthenium atom by three phosphane ligands has been observed so far for benzene,[4] toluene[5] and *p*-cymene[6] ligands, but never for the strongly bound $\eta^6\text{-}C_6Me_6$ ligand.

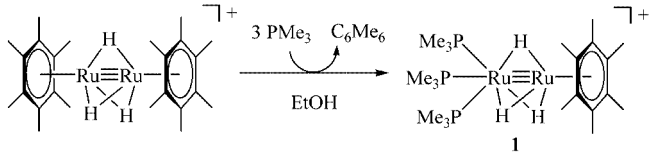


Scheme 1. Synthesis of **1**.

The single-crystal X-ray structure analysis of [**1**][$BF_4$], crystallised by slow diffusion of diethyl ether in a concentrated acetone solution of [**1**][$BF_4$], reveals for cation **1** the presence of three bridging hydrido ligands coordinated to

[a] Institut de Chimie, University of Neuchâtel,
Case postale 158, 2009, Switzerland
Fax: +41-32-718-2511
E-mail: georg.suess-fink@unine.ch
[b] Laboratoire FEMTO-ST/LPMO, CNRS UMR 6174,
32 Avenue de l'Observatoire, 25044 Besançon cedex, France

 © 2007 Wiley-VCH Verlag GmbH & Co. KGaA, Weinheim 

the two ruthenium atoms, one ruthenium atom being coordinated to an $\eta^6$-$C_6Me_6$ ligand and the other one to three $PMe_3$ ligands. The molecular structure of cation **1** is shown in Figure 1.

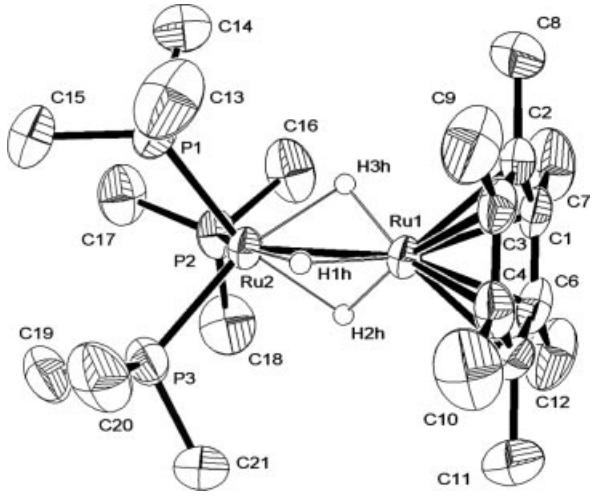


Figure 1. Molecular structure of cation **1** (ORTEP drawing of **1** at the 50% probability level with hydrogen atoms and tetrafluoroborate anion omitted for clarity).

The Ru–Ru distance [2.4934(6) Å] is within the range of a ruthenium–ruthenium triple bond.[7] The replacement of a hexamethylbenzene ligand by three $PMe_3$ ligands does not significantly affect the geometrical parameters of the $Ru_2(\mu_2\text{-}H)_3$ backbone as compared to $[(\eta^6\text{-}C_6Me_6)_2Ru_2(\mu_2\text{-}H)_3]^+$.[7b] The three independent Ru–P lengths (ca. 2.258 Å) are comparable to those found in $[Ru_2(PMe_3)_6(\mu_2\text{-}H)_3]^+$.[8] In the $^1$H NMR spectrum the nine methyl protons give rise to a broad signal, each carbon atom of the three equivalent $PMe_3$ ligands can be differentiated in the $^{13}$C NMR spectrum (i.e. $\delta$ = 24.59, 24.69 and 24.79 ppm). This is probably due to the steric hindrance of the methyl groups (see Figure 2) and suggests a restricted rotation of the three $PMe_3$ ligands, which gives rise to three independent signals in the $^{13}$C NMR spectrum.

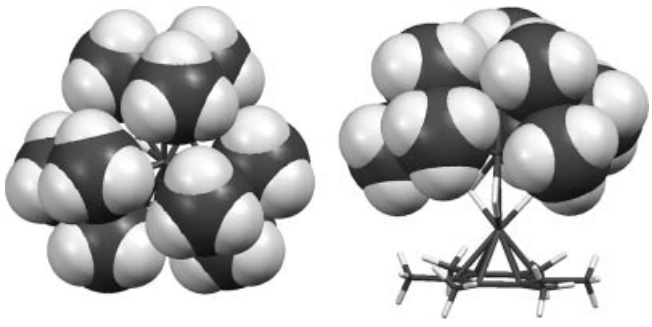

Figure 2. Mixed van der Waals and capped sticks representation of **1** with hydrogen atoms.

The molar ratio of $[(\eta^6\text{-}C_6Me_6)_2Ru_2(\mu_2\text{-}H)_3]^+$ and $PMe_3$ in the synthesis of **1** is critical: Although the stoichiometry of the reaction requires 3 equiv. of $PMe_3$ (see Scheme 1), the reaction must be carried out with an excess of $[(\eta^6\text{-}C_6Me_6)_2Ru_2(\mu_2\text{-}H)_3][BF_4]$.

The best yield (28%) is obtained with 2.5 equiv. of $PMe_3$, 3 equiv. or more leads to decomposition. In order to shine light on this strange observation, we carried out the reaction of $[(\eta^6\text{-}C_6Me_6)_2Ru_2(\mu_2\text{-}H)_3]^+$ with 2 equiv. of $PMe_3$ in ethanol at room temperature. In this case, the reaction quantitatively gives the cation $[(\eta^6\text{-}C_6Me_6)_2Ru_2(PMe_3)_2(\mu_2\text{-}H)(H)_2]^+$ (**2**), in which both hexamethylbenzene are still present (Scheme 2). Cation **2** can be considered as an intermediate in the formation of cation **1** (see below), and its conversion with $PMe_3$ into **1** is accompanied by the formation of mononuclear complexes, mainly $[(\eta^6\text{-}C_6Me_6)\text{-}Ru(PMe_3)_2H]^+$.[9] This explains why any local excess of trimethylphosphane has to be avoided for the synthesis of **1**.

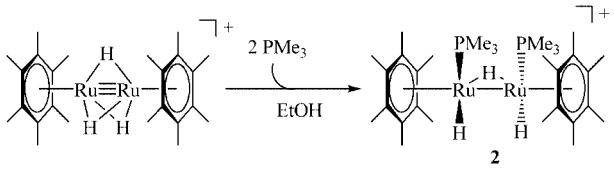


Scheme 2. Synthesis of **2**.

The single-crystal X-ray structure analysis of [**2**][$BF_4$], crystallised by slow diffusion of diethyl ether in a concentrated acetone solution of [**2**][$BF_4$], reveals for cation **2** only one hydrido bridge, each ruthenium atom being coordinated also to a terminal hydride, an $\eta^6$-$C_6Me_6$ ligand and a $PMe_3$ ligand. The molecular structure of cation **2** is shown in Figure 3.

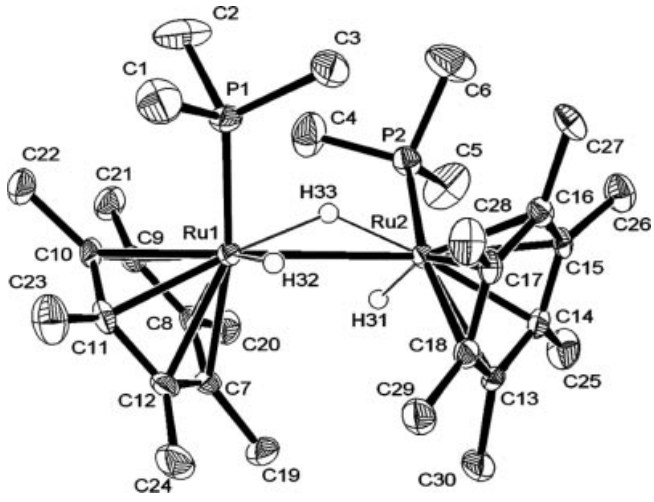


Figure 3. Molecular structure of cation **2** (ORTEP drawing of **2** at the 50% probability level with hydrogen atoms and tetrafluoroborate anions omitted for clarity).

The two $C_6Me_6$ arene ligands are not parallel to each other, and the angle between the $C_6Me_6$ planes is 56.6(2)°. Accordingly, to reduce the steric hindrance, the phosphorus atoms adopt a staggered conformation, the P1–Ru1–Ru2–P2 torsion angle being 67.79° (Figure 3). Interestingly, in **2**, the Ru–Ru distance [3.2230(8) Å] is very long. As the electron count of 34 e suggests a formal metal–metal single bond, this would be the longest Ru–Ru bond observed in a dinuclear complex. In the absence of DFT calculations,

 © 2007 Wiley-VCH Verlag GmbH & Co. KGaA, Weinheim 

however, the question of metal–metal bonding interaction remains a debatable point.

At room temperature, no hydride resonances can be observed in the $^1$H NMR spectrum of [**2**][$BF_4$], which suggests a fluxional behaviour of the hydrido ligands. This is confirmed by variable-temperature NMR experiments down to –40 °C (Figure 4). At 0 °C, two badly-defined signals centred at $\delta$ = –13.00 and –25.25 ppm appear, which sharpen at –40 °C, to give a doublet of doublets at $\delta$ = –13.10 ppm [dd, $^2J_{(H,H)}$ = 7.6 Hz, $^2J_{(H,P)}$ = 51.8 Hz, 2 H], which corresponds to the two terminal hydrides, and a triplet of triplets at –25.24 ppm [tt, $^2J_{(H,H)}$ = 7.6 Hz, $^2J_{(H,P)}$ = 23.4 Hz, 1 H], which is assigned to the bridging hydride in the $^1$H NMR spectra.

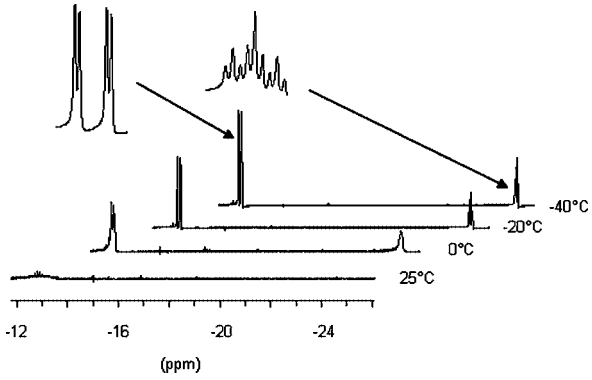


Figure 4. Variable $^1$H NMR temperature for [**2**][$BF_4$] in [$D_6$]acetone.

The two ruthenium atoms in **2** are stereogenic, the crystal structure analysis of [**2**][$BF_4$] reveals a racemic mixture of the (*R*,*R*) and the (*S*,*S*) enantiomers, the *meso* (*R*,*S*) isomer being absent. This observation shows that the addition of the trimethylphosphane ligands to [($\eta^6$-$C_6Me_6$)$_2$Ru$_2$($\mu_2$-H)$_3$]$^+$ occurs diastereospecifically.

This can be explained by step-wise attack of the two $PMe_3$ molecules: In the first step, one $PMe_3$ molecule coordinates to one ruthenium atom, which forces the two hexamethylbenzene ligands to adopt a tilted geometry in the *trans* configuration with respect to each other, and pushes one of the three hydrido ligands from a bridging into a terminal position at the second ruthenium atom, in an *anti* configuration with respect to the $PMe_3$ ligand. In the second step, the next $PMe_3$ molecule enters the complex coordinating to the second ruthenium atom, *trans* with respect to the $\eta^6$-$C_6Me_6$ ligand, which pushes a second hydrido ligand from a bridging into a terminal position. As the coordination of the first trimethylphosphane ligand does not favour the (*R*) or (*S*) enantiomers, the racemic mixture is obtained (Scheme 3). Alternatively, an intermediate containing a bridging trimethylphosphane ligand may be considered.[10]

At 80 °C in the presence of $PMe_3$ (0.1 equiv.), cation **2** converts into cation **1** with liberation of one equivalent of hexamethylbenzene (10% yield), which suggests **2** to be an intermediate in the reaction between [($\eta^6$-$C_6Me_6$)$_2$Ru$_2$($\mu_2$-H)$_3$]$^+$ and $PMe_3$ to give **1** (Scheme 4). However, no evidence

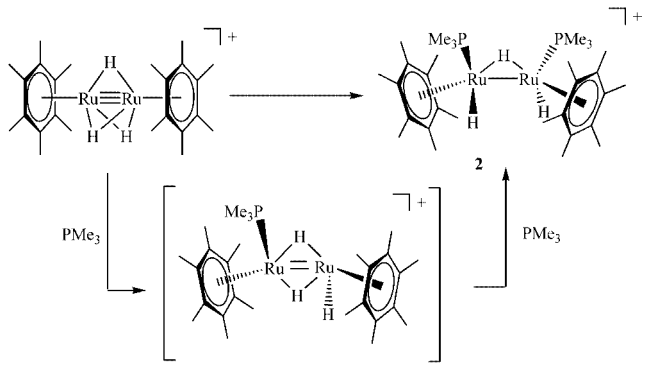


Scheme 3. Mechanistic proposal for the diastereospecific addition of two $PMe_3$ ligands to [($\eta^6$-$C_6Me_6$)$_2$Ru$_2$($\mu_2$-H)$_3$]$^+$.

for the direct transfer of one $PMe_3$ ligand from one ruthenium atom to the other one in **2** to give **1**, could be obtained.

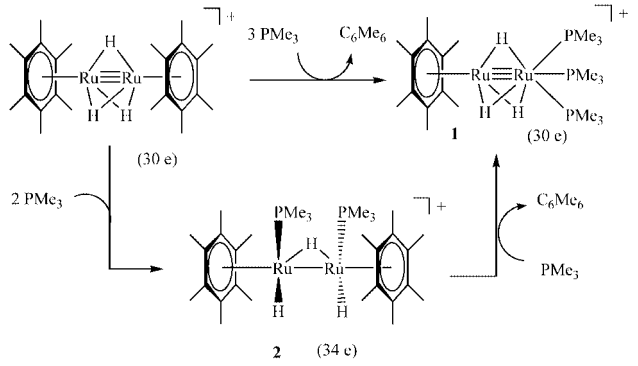


Scheme 4. Mechanistic hypothesis for the synthesis of **1**.

In order to study the reactivity of unsaturated complex **1** (30 e), we reacted **1** with *p*-bromothiophenol given that the parent cation [($\eta^6$-$C_6Me_6$)$_2$Ru$_2$($\mu_2$-H)$_3$]$^+$ (30 e) reacts with *p*-bromothiophenol to give [($\eta^6$-$C_6Me_6$)$_2$Ru$_2${$\mu_2$-(*p*-Br-$C_6H_4$)-S}($\mu_2$-H)$_2$]$^+$ and [($\eta^6$-$C_6Me_6$)$_2$Ru$_2${$\mu_2$-(*p*-Br-$C_6H_4$)-S}$_2$($\mu_2$-H)]$^+$.[11] Indeed, complex **1** reacts in refluxing ethanol with *p*-bromothiophenol to give, with elimination of molecular hydrogen, the thiolato-bridged derivative [($\eta^6$-$C_6Me_6$)Ru$_2$($PMe_3$)$_3${$\mu_2$-(*p*-Br-$C_6H_4$)-S}($\mu_2$-H)$_2$]$^+$ (**3**), isolated as the tetrafluoroborate salt (Scheme 5) in 45% yield. Unlike the reaction of [($\eta^6$-$C_6Me_6$)$_2$Ru$_2$($\mu_2$-H)$_3$]$^+$ with *p*-bromothiophenol, analogous complex **1** gives only the monosubstituted product even with a large excess (10 equiv.) of *p*-bromothiophenol, probably for steric reasons.

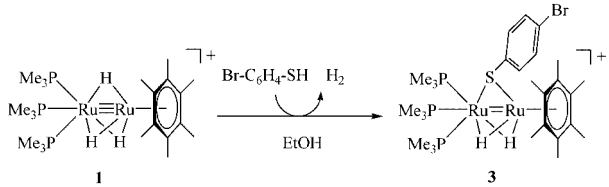


Scheme 5. Synthesis of **3**.

 © 2007 Wiley-VCH Verlag GmbH & Co. KGaA, Weinheim 

The two hydrido ligands in **3** are not equivalent due to the tetrahedral geometry of the sulfur atom, which gives rise to two signals in the hydride region ($\delta$ = –14.29 and –15.48 ppm) in the $^1$H NMR spectrum.

## Conclusions

In conclusion, we studied the reactivity of the unsaturated cation $[(\eta^6\text{-}C_6Me_6)_2Ru_2(\mu_2\text{-}H)_3]^+$ toward trimethylphosphane, which shows that even the strongly bound $\eta^6$-$C_6Me_6$ ligand can be replaced by three trimethylphosphane ligands in $[(\eta^6\text{-}C_6Me_6)_2Ru_2(\mu_2\text{-}H)_3]^+$ to give $[(\eta^6\text{-}C_6Me_6)\text{-}Ru_2(PMe_3)_3(\mu_2\text{-}H)_3]^+$ (**1**). A possible intermediate $[(\eta^6\text{-}C_6Me_6)_2Ru_2(PMe_3)_2(\mu_2\text{-}H)(H)_2]^+$ (**2**), obtained as a racemic mixture of both (*R*,*R*) and (*S*,*S*) enantiomers, has been isolated by reacting $[(\eta^6\text{-}C_6Me_6)_2Ru_2(\mu_2\text{-}H)_3]^+$ and trimethylphosphane at room temperature.

## Experimental Section

**General Remarks:** All manipulations were carried out in an inert atmosphere of nitrogen by using standard Schlenk techniques. All solvents were degassed with nitrogen prior to use. Silica gel (type G) used for preparative thin-layer chromatography was purchased from Macherey–Nagel GmbH. Trimethylphosphane solution (1 M) in thf was purchased from Aldrich. The dinuclear trihydrido complex $[(\eta^6\text{-}C_6Me_6)_2Ru_2(\mu_2\text{-}H)_3][BF_4]$ was synthesised by a previously described method.[12] Deuterated NMR solvents were purchased from Cambridge Isotope Laboratories, Inc. NMR spectra were recorded with a Bruker 400 MHz spectrometer and ESI mass spectra were recorded at the University of Fribourg by Prof. Titus Jenny. Microanalyses were carried out by the Laboratory of Pharmaceutical Chemistry, University of Geneva.

**Synthesis of $[(\eta^6\text{-}C_6Me_6)Ru_2(PMe_3)_3(\mu_2\text{-}H)_3][BF_4]$ ([1][BF$_4$]):** In a pressure Schlenk tube, $[(\eta^6\text{-}C_6Me_6)_2Ru_2(\mu_2\text{-}H)_3][BF_4]$ (100 mg, 0.16 mmol) was dissolved in ethanol (20 mL, puriss.) and a solution of trimethylphosphane (1 M) in thf (0.4 mmol, 0.4 mL) was then added. The resulting solution, which turned red after a few minutes, was stirred at 80 °C for 18 h. The reaction mixture was then cooled to room temperature, and the solvent was evaporated under reduce pressure. The resulting orange-red solid was purified by preparative thin-layer chromatography on silica (acetone/dichloromethane, 1:10). The pure product was extracted with acetone from the main orange band and evaporation of the solvent gave [**1**][BF$_4$]. Yield: 30 mg, 0.044 mmol (28%). $^1$H NMR (400 MHz, [D$_6$]acetone, 25 °C): $\delta$ = –13.24 (q, $^2J_{(H,P)}$ = 4.5 Hz, hydride), 1.51 [br., 27 H, P(C$H_3$)$_3$], 2.46 [s, 18 H, $C_6$(C$H_3$)$_6$] ppm. $^{13}$C{$^{31}$P, $^1$H} NMR (100 MHz, [D$_6$]acetone, 25 °C): $\delta$ = 18.05 [$C_6$(*C*H$_3$)$_6$], 24.59 [P(*C*H$_3$)$_3$], 24.79 [P(*C*H$_3$)$_3$], 24.89 [P(*C*H$_3$)$_3$], 93.53 [$C_6$(CH$_3$)$_6$] ppm. $^{31}$P{$^1$H} NMR (160 MHz, [D$_6$]acetone, 25 °C): $\delta$ = 18.69 (s) ppm. MS (ESI): *m*/*z* = 597 [M + H]$^+$. $C_{21}H_{48}BF_4P_3Ru_2$ (682.47): calcd. C 36.95, H 7.08; found C 36.88, H 7.02.

**Synthesis of $[(\eta^6\text{-}C_6Me_6)_2Ru_2(PMe_3)_2(\mu_2\text{-}H)(H)_2][BF_4]$ ([2][BF$_4$]):** In a pressure Schlenk tube, $[(\eta^6\text{-}C_6Me_6)_2Ru_2(\mu_2\text{-}H)_3][BF_4]$ (100 mg, 0.16 mmol) was dissolved in ethanol (20 mL, puriss) and a solution of trimethylphosphane (1 M) in thf (0.33 mmol, 0.33 mL) was added. The resulting solution, which turns red after a few minutes, was stirred at room temperature for 18 h. The solvent was evaporated to dryness under reduced pressure. The red solid was washed with diethyl ether (3 × 60 mL), dissolved in acetone, and filtered through celite under an inert atmosphere by using a Mülheim apparatus. The solvent was then evaporated to dryness to give quantitatively [**2**][BF$_4$] (115 mg, 0.15 mmol). $^1$H NMR (400 MHz, [D$_6$]-acetone, –40 °C): $\delta$ = –25.24 (tt, $^2J_{(H,H)}$ = 7.6 Hz, $^2J_{(H,P)}$ = 23.4 Hz, 1 H, hydride), –13.10 (dd, $^2J_{(H,H)}$ = 7.6 Hz, $^2J_{(H,P)}$ = 51.8 Hz, 2 H, hydride), 1.40 [d, $^2J_{(H,P)}$ = 9.16 Hz, 18 H, P(C$H_3$)$_3$], 2.28 [s, 36 H, $C_6$(C$H_3$)$_6$] ppm. $^{13}$C{$^{31}$P, $^1$H} NMR (100 MHz, [D$_6$]acetone, 25 °C): $\delta$ = 18.14 [$C_6$(*C*H$_3$)$_6$], 23.45 [d, $^1J_{(P\text{-}C)}$ = 32 Hz, P(*C*H$_3$)$_3$], 99.26 [$C_6$(CH$_3$)$_6$] ppm. $^{31}$P{$^1$H} NMR (160 MHz, [D$_6$]-acetone, 25 °C): $\delta$ = 8.61 (s) ppm. MS (ESI): *m*/*z* = 681 [M]$^+$ (and decomposition signals). $C_{30}H_{57}BF_4P_2Ru_2$ (768.66): calcd. C 46.87, H 7.47; found C 46.94, H 7.39.

**Conversion of 2 into 1:** In a pressure Schlenk tube, $[(\eta^6\text{-}C_6Me_6)_2\text{-}Ru_2(\mu_2\text{-}H)_3][BF_4]$ (100 mg, 0.16 mmol) was dissolved in ethanol (20 mL, puriss.) and a solution of trimethylphosphane (1 M) in thf (0.34 mmol, 0.34 mL) was added. The resulting red solution was stirred at room temperature for 18 h. The solution containing [**2**][BF$_4$] was heated at 80 °C for 8 h, and the solvent was then evaporated to dryness under reduce pressure. The resulting orange-red solid was purified by preparative thin-layer chromatography on silica (acetone/dichloromethane, 1:10). The product was extracted with acetone from the main orange band and evaporation of the solvent gave [**1**][BF$_4$]. Yield: 11 mg, 0.016 mmol (10%).

**Synthesis of $[(\eta^6\text{-}C_6Me_6)Ru_2(PMe_3)_3\{\mu_2\text{-}(p\text{-}Br\text{-}C_6H_4)\text{-}S\}(\mu_2\text{-}H)_2]\text{-}[BF_4]$ ([3][BF$_4$]):** $[(\eta^6\text{-}C_6Me_6)Ru_2(PMe_3)_3(\mu_2\text{-}H)_3][BF_4]$ (30 mg, 0.044 mmol) and *para*-bromothiophenol (26.6 mg, 0.14 mmol) were dissolved in ethanol (25 mL, puriss.), and the red solution was heated at reflux for 18 h. After cooling to room temperature, the solvent was evaporated to dryness, and the red solid was washed with diethyl ether (3 × 40 mL). The red solid was purified by preparative thin-layer chromatography on silica (acetone/dichloromethane, 1:10). The product was extracted with acetone from the main orange fraction and evaporation of the solvent gave the pure product. Yield: 18 mg, 0.02 mmol (45%). $^1$H NMR (400 MHz, [D$_6$] acetone, 25 °C): $\delta$ = –15.48 (m, 1 H, hydride), –14.29 (m, 1 H, hydride), 1.14 [d, $^2J_{(H,P)}$ = 9.0 Hz, 9 H, P(C$H_3$)$_3$], 1.47 [d, $^2J_{(H,P)}$ = 9.4 Hz, 9 H, P(C$H_3$)$_3$], 1.69 [d, $^2J_{(H,P)}$ = 8.7 Hz, 9 H, P(C$H_3$)$_3$], 2.22 [s, 18 H, $C_6$(C$H_3$)$_6$], 7.48 (br., 4 H, *H*-Ar) ppm. $^{13}$C{$^{31}$P, $^1$H} NMR (100 MHz, [D$_6$] acetone, 25 °C): $\delta$ = 17.75 [$C_6$(*C*H$_3$)$_6$], 21.64 [P(*C*H$_3$)$_3$], 21.92 [P(*C*H$_3$)$_3$], 22.01 [P(*C*H$_3$)$_3$], 22.31 [P(*C*H$_3$)$_3$], 24.03 [P(*C*H$_3$)$_3$], 24.32 [P(*C*H$_3$)$_3$], 94.97 [$C_6$(CH$_3$)$_6$], 121.53 (*C*-Br), 132.67 (*C*-Ar), 133.11 (*C*-Ar), 146.25 (*C*-S) ppm. $^{31}$P{$^1$H} NMR (160 MHz, [D$_6$]acetone, 25 °C): $\delta$ = 10.89 (dd, $^2J_{(H,P)}$ = 28 Hz, $^2J_{(H,P)}$ = 32 Hz), 12.68 (dd, $^2J_{(H,P)}$ = 32 Hz, $^2J_{(H,P)}$ = 43 Hz), 16.40 (dd, $^2J_{(H,P)}$ = 30 Hz, $^2J_{(H,P)}$ = 44 Hz) ppm. MS (ESI) *m*/*z* = 783 [M + H]$^+$. $C_{27}H_{51}BBrF_4P_3Ru_2S$ (869.53): calcd. C 37.29, H 5.91; found C 37.34, H 5.94.

**X-ray Crystallography:** Crystals of [**1**][BF$_4$] and [**2**][BF$_4$] were mounted on a Stoe Image Plate Diffraction System equipped with a φ circle goniometer by using Mo-$K_\alpha$ graphite monochromated radiation ($\lambda$ = 0.71073 Å) with φ range 0–200°, increment of 1.0 and 1.5°, respectively, 2$\theta$ range from 2.0–26°, $D_{max}/D_{min}$ = 12.45/0.81 Å. The two structures were solved by direct methods by using the program SHELXS-97.[13] Refinement and all further calculations were carried out by using SHELXL-97.[14] The H-atoms were included in calculated positions and treated as riding atoms with the use of the SHELXL default parameters. The non-H atoms were refined anisotropically by using weighted full-matrix least-square on $F^2$. Crystallographic details are summarised in Table 1. Figure 1 and Figure 3 (ORTEP[15] drawing) show the labelling scheme for [**1**][BF$_4$] and [**2**][BF$_4$]. Figure 3 is drawn with MERCURY.[16]

 © 2007 Wiley-VCH Verlag GmbH & Co. KGaA, Weinheim 

Table 1. Crystallographic and selected experimental data for [**1**][$BF_4$] and [**2**][$BF_4$].

| | [**1**][$BF_4$] | [**2**][$BF_4$] |
|---|---|---|
| Chemical formula | $C_{21}H_{48}BF_4P_3Ru_2$ | $C_{30}H_{57}BF_4P_2Ru_2$ |
| Formula weight | 682.45 | 768.64 |
| Crystal system | Monoclinic | Monoclinic |
| Space group | $P2_1/n$ | $P2_1/n$ |
| Crystal colour and shape | Red block | Orange block |
| Crystal size | $0.25 \times 0.20 \times 0.20$ | $0.30 \times 0.22 \times 0.12$ |
| $a$ [Å] | 9.379(2) | 14.612(3) |
| $b$ [Å] | 12.812(3) | 15.260(3) |
| $c$ [Å] | 26.127(5) | 15.000(3) |
| $\beta$ [°] | 95.40(3) | 94.03(3) |
| $V$ [Å$^3$] | 3125.6(12) | 3336.4(12) |
| $Z$ | 4 | 4 |
| $T$ [K] | 293(2) | 173(2) |
| $D_c$ [g cm$^{-3}$] | 1.450 | 1.528 |
| $\mu$ [mm$^{-1}$] | 1.151 | 1.042 |
| Scan range [°] | $4.46 < 2\theta < 51.90$ | $3.82 < 2\theta < 52.12$ |
| Unique reflections | 6084 | 6462 |
| Reflections used [$I > 2\sigma(I)$] | 3454 | 3857 |
| $R_{int}$ | 0.0622 | 0.0760 |
| Final $R$ indices [$I > 2\sigma(I)$][a] | 0.0297, $wR_2$ 0.0525 | 0.0344, $wR_2$ 0.0620 |
| $R$ indices (all data) | 0.0730, $wR_2$ 0.0578 | 0.0740, $wR_2$ 0.0670 |
| Goodness-of-fit | 0.755 | 0.798 |
| Max, Min $\Delta\rho$/e [Å$^{-3}$] | 0.596, –0.492 | 0.870, –0.731 |

[a] Structures were refined on $F_o^2$: $wR_2 = [\Sigma[w(F_o^2 - F_c^2)^2]/\Sigma w(F_o^2)^2]^{1/2}$, where $w^{-1} = [\Sigma(F_o^2) + (aP)^2 + bP]$ and $P = [\max(F_0^2, 0) + 2F_c^2]/3$.

CCDC-615022 (**1**)[$BF_4$] and CCDC-615023 (**2**)[$BF_4$] contain the supplementary crystallographic data for this paper. These data can be obtained free of charge from The Cambridge Crystallographic Data Centre via www.ccdc.cam.ac.uk/data_request/cif.

## Acknowledgments

Financial support of the Fond National Suisse de la Recherche Scientifique is gratefully acknowledged. The authors are also indebted to the Johnson Mathey Technology Centre for a loan of ruthenium trichloride hydrate and to Professor H. Stoeckli-Evans for free access to X-ray facilities.

[1] a) P. W. N. M. van Leeuwen, P. C. J. Kamer, J. N. H. Reek, P. Dierkes, *Chem. Rev.* **2000**, *100*, 2741–2769; b) C. A. Tolman, J. W. Faller in *Homogeneous Catalysis with Metal Phosphine Complexes* (Ed.: L. H. Pignolet), Plenum Press **1983**, p. 13; c) D. Evans, J. A. Osborn, G. Wilkinson, *J. Chem. Soc. A* **1968**, 3133–3142; d) J. F. Young, J. A. Osborn, F. H. Jardine, G. Wilkinson, *J. Chem. Soc., Chem. Commun.* **1965**, 131–132; e) L. G. Cannell, L. H. Slaugh, R. D. Mullineaux, *Chem. Abstr.* **1965**, *62*, 16054.

[2] a) P. E. Garrou, *Chem. Rev.* **1985**, *85*, 171–185; b) G. Lavigne in *The Chemistry of Metal Cluster Complexes* (Eds.: D. F. Shriver, R. D. Adams, H. D. Kaesz), VCH Publishers, New York, **1990**; c) K.-C. Kong, C.-H. Cheng, *J. Am. Chem. Soc.* **1991**, *113*, 6313–6315; d) D. K. Morita, J. K. Stille, J. R. Norton, *J. Am. Chem. Soc.* **1995**, *117*, 8576–8581; e) F. E. Goodson, T. I. Wallow, B. M. Novak, *J. Am. Chem. Soc.* **1997**, *119*, 12441–12453.

[3] M. J.-L. Tschan, F. Chérioux, L. Karmazin-Brelot, G. Süss-Fink, *Organometallics* **2005**, *24*, 1974–1981.

[4] S. Takemoto, H. Kawamura, Y. Yamada, T. Okada, A. Ono, E. Yoshikawa, Y. Mizobe, M. Hidai, *Organometallics* **2002**, *21*, 3897–3904.

[5] M. Okazaki, N. Yamahira, J. J. G. Minglana, H. Tobita, *Organometallics* **2004**, *23*, 4531–4533.

[6] K. D. Redwine, J. H. Nelson, *Organometallics* **2000**, *19*, 3054–3061.

[7] a) B. Chaudret, J. Devillers, R. Poilblanc, *Organometallics* **1985**, *4*, 1727–1732; b) M. Jahncke, A. Neels, H. Stoeckli-Evans, G. Süss-Fink, *J. Organomet. Chem.* **1998**, *561*, 227–235; c) T. Takao, M.-A. Amako, H. Suzuki, *Organometallics* **2003**, *22*, 3855–3876.

[8] R. A. Jones, G. Wilkinson, I. J. Colquohoun, W. McFarlane, A. M. R. Galas, M. B. Hursthouse, *J. Chem. Soc., Dalton Trans.* **1980**, 2480–2487.

[9] R. Werner, H. Werner, *Chem. Ber.* **1982**, *115*, 3781–3795.

[10] a) H. Werner, *Angew. Chem. Int. Ed.* **2004**, *43*, 938–954; *Angew. Chem.* **2004**, *116*, 956–972 and references cited therein; b) T. Pechmann, C. D. Brandt, H. Werner, *Chem. Eur. J.* **2004**, *10*, 728–736.

[11] M. J.-L. Tschan, F. Chérioux, B. Therrien, G. Süss-Fink, *Eur. J. Inorg. Chem.* **2004**, *12*, 2405–2411.

[12] a) M. A. Bennett, P. J. Ennett, *Inorg. Chim. Acta* **1992**, *198–200*, 583–592; b) M. Jahncke, G. Meister, G. Rheinwald, H. Stoeckli-Evans, G. Süss-Fink, *Organometallics* **1997**, *16*, 1137–1143.

[13] G. M. Sheldrick, *Acta Crystallogr., Sect. A* **1990**, *46*, 467.

[14] G. M. Sheldrick, *SHELXL-97*, University of Göttingen, Göttingen, Germany, **1999**.

[15] L. J. Farrugia, *J. Appl. Crystallogr.* **1997**, *30*, 565.

[16] I. J. Bruno, J. C. Cole, P. R. Edgington, M. Kessler, C. F. Macrae, P. McCabe, J. Pearson, R. Taylor, *Acta Crystallogr., Sect. B* **2002**, *58*, 389–397.

Received: October 2, 2006
Published Online: December 21, 2006

 © 2007 Wiley-VCH Verlag GmbH & Co. KGaA, Weinheim 

DOI: 10.1002/ejic.200600739

# Mechanistic Analysis of Nucleophilic Substrates Oxidation by Functional Models of Vanadium-Dependent Haloperoxidases: A Density Functional Theory Study

**Curtis J. Schneider,[a] Giuseppe Zampella,[b] Claudio Greco,[b] Vincent L. Pecoraro,*[a,c] and Luca De Gioia*[b]**

**Keywords:** Peroxido ligands / Tripodal ligands / Oxidation / Vanadium / Density functional calculations

Density functional theory has been used to investigate the structural, electronic, and reactivity properties of an established functional model for vanadium-dependent haloperoxidases, K[VO($O_2$)Hheida] (Hheida$^{2-}$ = 2,2′-[(2-hydroxyethyl)imino]diacetate). Possible solution species were determined on the basis of potential exogenous donors present under the conditions necessary for reactivity. The energetically favored solution-state species is a 1:1 complex of Hheida and vanadium with a coordinated hydroxyethyl donor *trans* to the vanadium–oxido bond which is in agreement with the reported solid-state structure for K[VO($O_2$)Hheida]. Transition states of the oxidation reaction were located for four substrates: chloride, bromide, iodide, and dimethyl sulfide. The role of protonation and its effects on reactivity were examined for each substrate. Protonation of the peroxido moiety leads to a significant drop in the activation barrier for oxidation. In contrast no transition states could be located for an oxido-transfer process involving the oxido ligand. Barriers of activation calculated for halide oxidation were similar, providing support to the hypothesis that the p$K_a$ of the halide in acetonitrile is responsible for the decrease in reactivity between $I^-$, $Br^-$, and $Cl^-$. The results presented herein provide a mechanistic correlation between a functional model and the enzyme, making K[VO($O_2$)Hheida] a "complete" functional model for vanadium-dependent haloperoxidase.

(© Wiley-VCH Verlag GmbH & Co. KGaA, 69451 Weinheim, Germany, 2007)

## Introduction

Vanadium complexes have been used in a number of oxidative transformations[1] relevant to organic synthesis, including but not limited to alcohol oxidation, halide oxidation, and sulfoxidation. Of these reactions, the oxidation of achiral sulfides to chiral sulfoxides[1–4] has sparked the most attention in recent years because of the potential applications of chiral sulfoxides.[5] Peroxido-vanadium complexes are capable of the single oxidation of organic sulfides to sulfoxides with little double oxidation product (sulfone).[1,6,7] A number of catalysts have been presented in the literature[3,8–11] to be competent with respect to sulfide oxidation and in some cases to be stereoselective. To date the best peroxido vanadium-based catalyst is K[VO($O_2$)Hheida], showing the highest rates of sulfide oxidation of any reported catalyst for bromide and organic sulfide oxidation. The mechanism of both halide and sulfide oxidation with this complex have been extensively studied. Thus, the K[VO($O_2$)Hheida] serves as an effective functional mimic for the vanadium-dependent haloperoxidase class of enzyme and is an excellent catalyst in its own right.

Vanadium-dependent haloperoxidases (VHPO) are metalloenzymes containing a mononuclear vanadium(V) cofactor[12] that catalyze the oxidation of halides in the presence of hydrogen peroxide. The oxidized species (HOX, $X_3^-$, or $X_2$) subsequently adds to organic molecules, yielding halogenated marine products.[13] The first example of this vanadoenzyme class was a bromoperoxidase isolated from the marine algae *Ascophyllum nodosum*.[14] The enzyme nomenclature is based upon the most electronegative halide that the enzyme is capable of oxidizing. VHPO's can also catalyze the stereospecific two-electron oxidation of organic sulfides to chiral sulfoxides.[15] The importance of a protonation of the active site for reactivity is suggested by the catalytically relevant p$K_a$ of 5.9[16] for a vanadium bromoperoxidase. A number of X-ray crystal structures are now available for VHPO,[17–20] including peroxide-bound and unbound forms of a vanadium chloroperoxidase from the fungus *Curvularia inaequalis*.[19] The vanadate co-factor is covalently coordinated to an enzyme-bound histidine. The coordination geometry is trigonal bipyramidal, with an oxygen atom in the axial position *trans* to N atom of histidine, three other oxygen atoms complete the coordination sphere. The peroxide-bound form is best described as having a distorted tetragonal geometry when treating the per-

[a] Department of Chemistry, University of Michigan, Ann Arbor, Michigan, 48109-1055, USA
[b] Department of Biotechnology and Biosciences, University of Milano-Bicocca, Piazza della Scienza 2, 20126 Milano, Italy
[c] Biophysics Research Division, University of Michigan, Ann Arbor, Michigan, 48109-1055, USA

 © 2007 Wiley-VCH Verlag GmbH & Co. KGaA, Weinheim 

oxido ligand as a single donor ligand. The coordination sphere is completed by an imidazole nitrogen donor, one oxido, and one hydroxido oxygen atoms.

Recently, computational methods have been employed to examine the resting and catalytically active states for simple models of the enzyme[21–26] active site. The limitations of X-ray crystallography left some ambiguity as to the protonation state of the vanadate co-factor in the resting and peroxido-bound forms. Density functional theory was used to explore the energetic consequences of protonation of a quantum chemical (QC) model for the vanadate co-factor with fixed nearby donor residues.[25] The results of this study indicate the resting state to contain a *cis*-dioxido vanadium(V) species with one axial hydroxido group, an equatorial hydroxido, with an imidazole completing the first coordination sphere. Recent QM/MM calculations have indicated another isoenergetic potential resting state configuration that is stabilized by long range electrostatic interactions, and which contains three oxido moiety plus an axial water.[22,23] $^{51}V$ solid state NMR spectroscopy was used in conjunction with DFT methods to examine the resting state configuration of vanadium chloroperoxidase; these studies confirm the resting state structure proposed in the aforementioned DFT and QM/MM studies.[21]

A number of mechanisms have been proposed for these enzyme based on small molecule mimics, including $KVO(O_2)$Hheida, which generally invoke oxido-transfer catalysis. It has been shown that protonation of the peroxido moiety is essential for reactivity. Thus, in the catalytically active form there exists on the vanadium a terminal oxido and a protonated and unprotonated peroxido oxygen atoms. The question that then arises is which of these oxygen atoms is transferred to the substrate.[27] Colpas et al. proposed that the transferred oxygen originated from the hydroperoxido moiety; however, these authors could not identify whether the protonated or unprotonated oxygen was involved. Computational methods have been employed to differentiate these two possibilities in QC models of VHPO.[26] These studies indicate that oxido-transfer proceeded through the unprotonated peroxido atom through an $S_N2$-like process and that protonation of the peroxide ligand significantly lowered the barrier of activation for both halide and sulfide oxidation. These computational studies are in full agreement with reported catalytic abilities of the enzyme system.[16]

As previously mentioned, considerable effort has been expended to clarify the enzymatic mechanism, relatively little attention has been focused on the understanding the mechanism of the original catalysts described by Colpas and co-workers. These complexes are not only important for further our understanding of VHPO's, but in their own right as useful catalysts in organic synthesis. These vanadium tripodal amine complexes are the most effective sulfoxidation catalysts reported in the literature.[6,27] Mechanistic studies have shown the maximal rate of substrate oxidation occurs when one equivalent of proton with respect to vanadium is present. A red shift in the peroxido-vanadium charge-transfer band indicates the direct protonation of the vanadium complex. $V^{51}$ NMR showed a single resonance with a chemical shift and a linewidth consistent with a single mono-peroxido oxidovanadium(V) species under the reaction conditions; however, this does not rule out rapidly interconverting isoenergetic species. These observations were incorporated into a mechanistic proposal that was developed on the basis of the previously proposed halide oxidation mechanism, involving a hydroperoxido vanadium species undergoing an oxido transfer reaction with organic sulfides[6] (Figure 1). Despite these extensive mechanistic studies solution speciation under the reported reaction conditions, the site of catalyst protonation, the role of the protonated peroxido moiety in oxidative catalysis and the geometry of the transition state, still require further scrutiny.

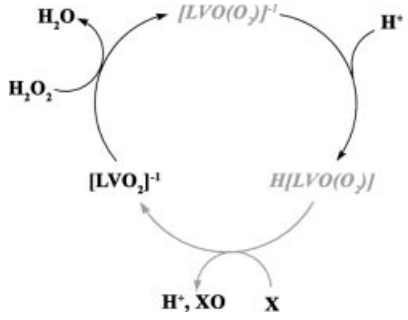


Figure 1. Diagram of the proposed mechanism for oxidation of a nucleophilic substrate by tripodal amino complexes of vanadium(V). X = $Br^-$, $I^-$, or $R_2S$. Steps highlighted in grey are the focus of this study.

Density functional theory has been used to address questions regarding reactivity and spectroscopic properties of transition-metal systems related to biology[28] and catalysis.[29] Balcells et al. reported computational studies of a truncated QC models for vanadium(V)-containing Schiff base complexes[30] and its ability to oxidize organic disulfides in the presence of hydrogen peroxide. This study was later expanded to determine the factors controlling the stereoselectivity of disulfide oxidation using QM/MM methods[31] on sterically hindered Schiff bases often employed in vanadium catalysis literature.[7,9–11,32] Balcells et. al demonstrated the characteristics of an $S_N2$-like transition state, where oxido-transfer occurs from the unprotonated oxygen of the peroxido moiety to organic sulfides. Although the coordination environment of the Schiff base complex is significantly different from the enzyme system, it does bear some similarities (side-bound peroxido, similar transition state) and lends support to a peroxido atom transfer to the substrate. Schiff base vanadium(V) complexes have been shown to be functional mimics for VHPO based on their ability to oxidize bromide and organic sulfide,[9,11,32] but kinetic analysis and, therefore, detailed mechanistic studies are not possible due to bromination of the ligand system.[33]

$K(VO(O_2)$Hheida) has been studied extensively with respect to both bromide[27] and sulfide[6] oxidation, despite these synthetic results mechanistic questions relevant to future catalyst design based on these systems (i.e. protonation state of the catalytically active species and transition-state

 © 2007 Wiley-VCH Verlag GmbH & Co. KGaA, Weinheim 

geometries). We present herein a detailed computational investigation of this catalyst. Treating the entire complex quantum mechanically, we provide a better understanding of the mechanism for substrate oxidation allowing more efficient catalyst design and providing a mechanistic correlation between these functional mimics and VHPO's.

## Results

### Quantum Chemical System

The X-ray coordinates for K[VO($O_2$)Hheida][34] were used as a starting point to set up a quantum chemical model of this system. Waters of crystallization were removed, as was the potassium ion. Under the reaction conditions used by Colpas et al., there are two equivalents of 18-crown-6 which chelate the potassium ion in acetonitrile, limiting the potential interactions of the cation with the vanadium complex during the catalytic cycle. The resulting energy-minimized geometry of [VO($O_2$)Hheida]$^{-1}$ (**1**), depicted in Figure 2 is nearly identical to the bond lengths reported in the crystal structure (Table 1).

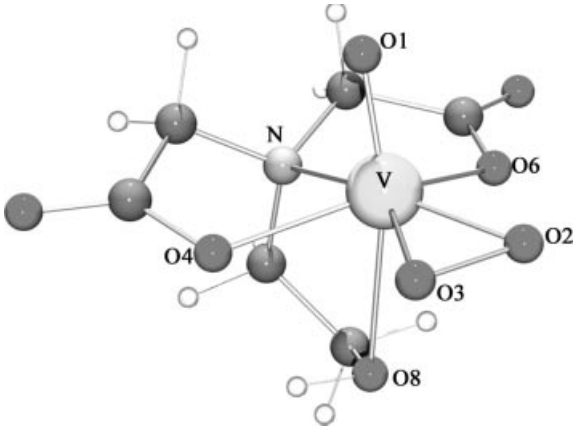


Figure 2. Ball-and-stick representation of geometry optimized **1**.

Table 1. Bond lengths [Å] of [VO($O_2$)Hheida]$^{-1}$.

| | X-ray structure | Optimized **1** |
|---|---|---|
| V–O1 | 1.60 | 1.62 |
| V–O2 | 1.87 | 1.85 |
| V–O3 | 1.86 | 1.85 |
| V–O4 | 2.05 | 2.10 |
| V–O6 | 2.04 | 2.05 |
| V–O8 | 2.24 | 2.45 |
| V–N1 | 2.19 | 2.28 |
| O3–O2 | 1.43 | 1.44 |

### Protonation and Solution Speciation

Before exploring the oxidative chemistry of **1**, a better understanding of the solution-state speciation for this pre-catalytic species is necessary. The crystal structure of K[VO($O_2$)Hheida] shows a disordered hydroxyethyl arm due to two ring conformation of a five-membered chelate ring. The interconversion between these two states is rapid compared to the rate of oxidation, therefore, the left- and right-hand sides of **1** are treated as equivalent for optimizations involving an Hheida$^{-2}$ ligand. The weakest coordinating and therefore most labile donor atom is the oxygen associated with the hydroxyethyl arm of Hheida$^{2-}$. Geometry-optimized structures were obtained initially both with a coordinated hydroxy oxygen atom and a completely dissociated hydroxy group. The former being the more stable of the two by 1.3 kcal/mol. Given the two potential pre-catalytic isomers, a coordinated hydroxy and the uncoordinated hydroxy group and the presence of sigma donor ligands under the reaction conditions (water, acetonitrile, and substrate), a vacant coordination site is not likely. As there is no experimental evidence supporting coordination of substrate molecules in VHPO or in the small molecule models, substrate coordination was ruled out as possibility. A comparison of the energetic differences between the van der Waals complex of the exogenous donors, water and acetonitrile, with the coordinated exogenous donor in place of the hydroxy group was made. These comparisons were made using the most stable protonated species to reduce the electronic repulsion created by the approach of a sigma donor to an anionic vanadium species. The results of this comparison are presented later.

Five potential sites of protonation were identified on the basis of the areas of highest electron density for **1**: oxido (**0c**), peroxido left (**0b**), peroxido right (**0a**), carboxylate oxygen (**0d**), and the carbonyl oxygen (**0e**) (Figure 3). Only one of the carboxylate donors was protonated due to the previously mentioned conformational isomerism. Protonation of the peroxido can occur in four possible locations as illustrated in part b of Figure 3. The most stable optimized structures involved protonation of the peroxido ligand **0a** or **0b**. The four possible orientations of the proton around

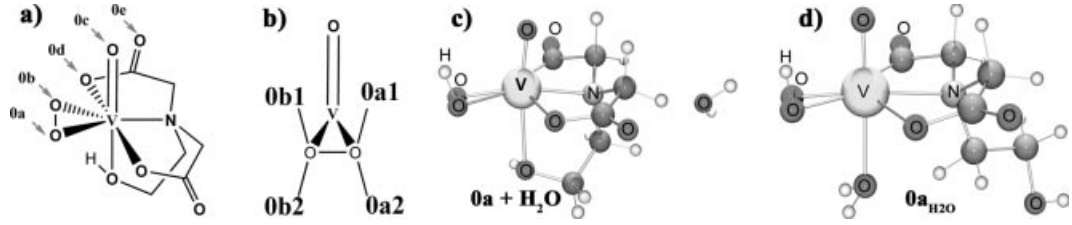


Figure 3. (a) Proton acceptors in **1**. (b) Nomenclature for the orientation of proton with respect to V=O bond (c) Representative ball-and-stick diagram of a non-coordinated exogenous donor, in this the exogenous donor is water. (d) Representative cartoon for coordination of an exogenous donor to vanadium. White atoms are hydrogens and unlabeled atoms are carbon.

 © 2007 Wiley-VCH Verlag GmbH & Co. KGaA, Weinheim 

the peroxido ligand were isoenergetic when ring conformations were taken into account. There is significant contraction of the vanadium hydroxy bond (V–O8) upon protonation of the complex in **0a**, **0b**, or **0c**, a decrease of 0.1 Å for **0a** and **0b**, and 0.2 Å for **0c.**

The most stable optimized geometry, **0a**, was used to determine whether exogenous ligands can bind *trans* to the oxido moiety. Three exogenous donors were tested in place of hydroxy coordination to the vanadium center: water, acetonitrile, and bromide. In all cases, a van der Waals complex of the exogenous donor and **0a** is more stable than coordination of the respective donor in place of the hydroxy. In the case of water coordination to **0a**, (Figure 3, parts c, d), hydroxy coordination to vanadium over water was favored by 4.0 kcal/mol. A coordinatively unsaturated species, dissociation of the hydroxy group with no *trans* donor, was less favored by 4.6 kcal/mol.

### Halide Transition States

Transition states corresponding to the nucleophilic attack of halide ions ($Cl^-$, $Br^-$, $I^-$) on the peroxido ligand of the vanadium atom were located for both **1** and **0a**. Due to the anionic character of both the halide and **1**, starting materials were calculated on the basis of two infinitely separated species, as any attempt to minimize a van der Waals complex resulted in the two ions rapidly diverging. The transition-state geometry found for **1** with all three halides (**1_cl**, **1_br**, **1_i**) are nearly identical, therefore, a representative case will be presented for the oxidation of bromide. The transition state for bromide oxidation is characterized by a linear halide peroxido bond angle (173°), where the dihedral angle between the peroxido ligand and the vanadium–oxido is 100° (Figure 4). The rest of the vanadium coordination sphere is significantly perturbed in comparison to **1**, there is a dramatic lengthening of all bonds in the first coordination sphere, in the case of **1_br** the carboxylate donors have bond lengths of 2.27 Å whereas the carboxylate-vanadium distances in **1** are 2.04 Å. Additionally the tertiary nitrogen bond lengthened by 0.3 Å in relation to **1** (Table 2). The computed barrier of activation, $\Delta G^{\ddagger}$, for bromide oxidation is 38.1 kcal/mol.

Table 2. Bond lengths [Å] of the transition states for bromide oxidation.

| | 1 | 1_br | 0a_br |
|---|---|---|---|
| V–O1 | 1.62 | 1.64 | 1.62 |
| V–O2 | 1.85 | 1.71 | 2.05 |
| V–O3 | 1.86 | 1.90 | 1.90 |
| V–O4 | 2.10 | 2.27 | 2.02 |
| V–O6 | 2.05 | 2.27 | 1.99 |
| V–O8 | 2.45 | 2.48 | 2.30 |
| V–N1 | 2.28 | 2.50 | 2.29 |
| O3–O2 | 1.44 | 1.87 | 1.69 |
| O3–Br | – | 2.27 | 2.38 |

Protonation of **1** at the most stable site (**0a**) yields an earlier transition state (**0a_br**), in which the Br–O bond is only partially formed with a nearly complete O–OH bond in the peroxido moiety, with a significantly lower barrier of activation (21.1 kcal/mol). The bromide–peroxido oxygen bond lengths is longer by 0.11 Å than **1_br**, with a comparably shorter peroxide bond length. The Br–O3–O2 bond angle is 163.4° while the dihedral angle between the peroxido ligand and the vanadium–oxido is 123.8°. Transitions states were only located in the protonated case where a hydrogen bond formed between the halide and the hydroxy ligand. No transition states related to halide oxidation could be located for attack of the substrate on the protonated peroxido ligand. This is true for all anionic halide transition states (**0a_cl**, **0a_br**, **and 0a_i**), where the corresponding barriers to activation are 23.0 kcal/mol for $Cl^-$ and 19.0 kcal/mol for $I^-$.

To explore the reactivity of **0a_x** further, a coordinatively unsaturated geometry was used as the starting point, in which a halide can weakly coordinate to vanadium(V) center. Bromide was used as the substrate and positioned to weakly coordinate to the vanadium center. **0a_br2** is characterized by a distortion of the dihedral angle V–O1–O2–O3 (149°) allowing a weak interaction of the bromide with vanadium 3.03 Å. A reasonable reactant structure could be located with bromide coordinating to the vanadium, and the computed barrier of activation is 8.6 kcal/mol. The barrier is significantly lower in energy because the coordination of bromine to an coordinatively unsaturated vanadium complex (**0a_br2**) is 10 kcal/mol higher energy than the corresponding hydrogen-bonded starting materials (**0a_br**).

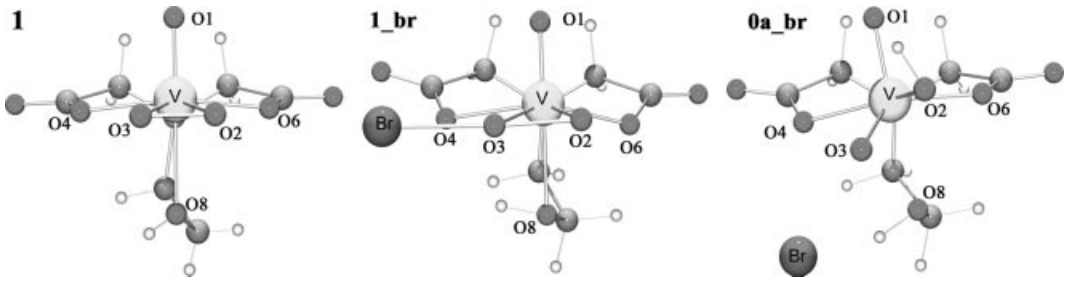


Figure 4. Ball-and-stick cartoons showing pre-catalytic anionic complex (left), dianionic transition state for bromide oxidation (middle) and the corresponding monoanionic transition state.

 © 2007 Wiley-VCH Verlag GmbH & Co. KGaA, Weinheim 

Table 3. Comparison of relevant bond lengths and $\Delta E_{scf}$ [kcal/mol] for transition states associated with halide oxidation.

| | **1** | **1a_cl** | **1a_br** | **1a_i** | **0a** | **0a_cl** | **0a_br** | **0a_i** | **0a_br2** |
|---|---|---|---|---|---|---|---|---|---|
| O3–X | – | 2.17 Å | 2.27 Å | 2.39 Å | – | 2.29 Å | 2.38 Å | 2.55 Å | 2.48 Å |
| O3–O2 | 1.44 Å | 1.85 Å | 1.87 Å | 1.90 Å | 1.46 Å | 1.77 Å | 1.69 Å | 1.69 Å | 1.70 Å |
| V–O1–O2–O3 | 98.5° | 100.3° | 100.0° | 100.0° | 103.7° | 124.5° | 123.7° | 121.8° | 149.0° |
| $\Delta E_{scf}^{\ddagger}$ [kcal/mol] | – | 39.2 | 38.1 | 36.0 | – | 23.0 | 21.1 | 19.0 | 20.05 |

The geometries and respective energy differences between starting materials and transition states for all located halide transition states are presented in Table 3. No transition states could be located corresponding to attack of the halide on the oxido ligand of **1**, **0a**, or **0c**.

### Sulfide Transition States

The effects of protonation on the barrier of activation were also explored for the oxidation of dimethyl sulfide. Transition states calculated for dimethyl sulfide oxidation are less distorted from the energy minimized structures of **1** or the appropriate protonated species **0(a**,**b)** than the corresponding halide transition state. Figure 5 shows two representative transition states located for sulfide oxidation by anionic and neutral vanadium species.

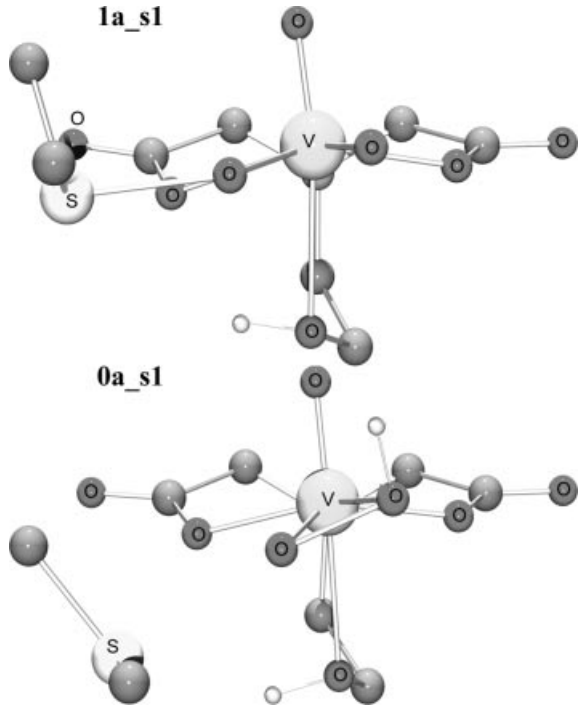


Figure 5. Ball-and-stick representation of an anionic (top) and neutral (bottom) transition state located for dimethyl sulfide oxidation.

The transition-state geometry **1_s** is characterized by a nearly linear S–O2–O3 bonding angle, identical to that identified for the case of halide oxidation. Due to the asymmetry associated with upper and lower halves of **1**, multiple transition states with slightly different energies could be located, the only difference being related to relative orientation of the methyl groups of dimethyl sulfide. Approach of dimethyl sulfide to the left or right hand side of **1** yielded nearly isoenergetic transition states, with a barrier of activation of 18.3 kcal/mol. Starting materials were minimized from each located transition state generating a van der Waals complex of dimethyl sulfide and **1**.

Transition states were located for the protonated complexes **0a_s** and **0b_s**. As was the case for **1**, multiple rotational isomers could be located and are related to orientation of the methyl groups on the substrate. The neutral transition states located for dimethyl sulfide oxidation are less distorted than **0a_X**, with dihedral angles approx. V–O1–O2–O3 111.8° and a S–O3–O2 of 166.6° where the sulfide attacks the unprotonated peroxido oxygen. To calculate the barrier of activation, van der Waals complexes of dimethyl sulfide and the appropriately protonated vanadium species were optimized. The lowest energy starting material complex located contained a hydrogen bond forms between dimethyl sulfide and the hydroxy group of the complex the barrier of activation for the oxidation reaction is 9.4 kcal/mol. The barrier of activation drops significantly (by 9 kcal/mol), when the peroxido moiety is protonated, leading to four isoenergetic transition coordinates differing in the approach of sulfide to the neutral vanadium complex and orientation of the sulfide. No transition states could be located related to attack of the sulfide on the unprotonated oxido group (**0c**) or attack of the sulfide on the protonated peroxido oxygen.

## Discussion

Although many model complexes[27,32,33,35,36] have been presented in the literature, the pre-catalytic species K[VO($O_2$)Hheida][34] isolated by Colpas and co-workers is the most thoroughly investigated system. Detailed mechanistic studies have shown the importance of protonation of the complex with respect to halide[27] and sulfide oxidation.[6] These studies established K[VO($O_2$)Hheida] as a functional mimic of the vanadium-dependent haloperoxidases and as an excellent catalyst for organic transformations. We have undertaken a thorough computational investigation of the mechanism for halide and sulfide oxidation, specifically with respect to the effects of protonation of the complex on the activation barrier for these processes in order to develop future asymmetric oxidation catalysts based on the $H_3$heida architecture.

Starting coordinates are taken from the crystallographically characterized pre-catalyst, we optimized chemically reasonable solution state species. The crystal structure of K[VO($O_2$)Hheida] shows a hydroxy group *trans* to the ox-

 © 2007 Wiley-VCH Verlag GmbH & Co. KGaA, Weinheim 

ido, with tertiary nitrogen *trans* to the peroxido moiety, a typical binding mode for oxidovanadium(V) peroxido complexes with tripodal amino ligands. The experimental conditions have been taken into account when setting up the QM investigation, both regarding solvent polarizing power, and to explore the possibility of binding by exogenous donor ligand to vanadium. Potassium is chelated by 18-C-6 allowing K[VO($O_2$)Hheida] to be solubilized in acetonitrile. On the basis of this condition, the quantum chemical model, **1**, excluded potassium in all geometry optimizations. The weakest donor group in **1** is the hydroxy group *trans* to the oxido. As there is no ligand field stabilization energy for a vanadium(V) complex, a coordinatively unsaturated species is potentially feasible. Geometry optimization was performed on an anionic complex in which the hydroxy group was completely dissociated from the complex, the resulting optimized structure is 1.3 kcal/mol higher in energy when enthalpic and entropic corrections are taken into account. Under the reaction conditions a number of exogenous donors are present in at least equimolar quantities with respect to the vanadium complex, making a coordinately unsaturated species less likely.

Before examining the energetic preference for exogenous donors, we explored the energetics of monoprotonated **1**. The potential proton acceptors in the complex are all of the oxygen atoms associated with the ligand, this generates five potential sites of protonation. Protonation of the peroxido ligand is the most energetically favored, there is a slight difference between protonation of O3 and O2 this effect is negligible when chelate ring conformations of the hydroxyethyl arm of **1** are taken into account. Protonation of the peroxido (**0a** and **0b**) is favored by 3 kcal/mol over protonation of the oxido ligand (**0c**), while protonation of either carboxylate oxygen generates a species 6 kcal/mol higher in energy.

Using the energetically favored protonation states of the complex, two optimizations were performed for exogenous donors, one in which a van der Waals complex of the donor was made with a coordinated hydroxy species **0a**, and one with the exogenous donors coordinated in place of the hydroxy. For all the exogenous donors tested (water, acetonitrile, and bromide), the van der Waals complex was more stable by 2, 7, and 15 kcal/mol, respectively. Thus a coordinated hydroxy species is likely to be the dominate solution species present. Previously $^{51}$V NMR has been used to explore the number of vanadium species present under the reaction conditions, suggesting only one species is present or there is an exchange process faster than the $^{51}$V NMR timescale. All factors considered, the loss of entropy is higher in the cases of exogenous donor molecules. Since the enthalpic contribution is roughly similar when considering exogenous and endogenous ligands (on binding to V) a larger gain in the entropy is expected when a water, bromide, or other exogenous ligand dissociates, compared to an endogenous ligand.

Using the most stable unprotonated (**1**) and protonated species (**0a**) as a starting point, transition-state searches were performed for chloride, bromide and iodide. Transition state located for **1** showed a significant lengthening of all ligand bonds to the vanadium, due to the increased electron density of the complex in the transition state. All bond lengths are still within a weak bonding distance. The transition state corresponded to the $S_N2$-like attack on the peroxido ligand of the vanadium complex as determined by examining the single negative vibrational eigenvalue. No transition state could be located for bromide attack on the vanadium–oxido bond. The energy of **1** and the appropriate halide at infinite separation were used as starting materials, as any attempt to generate a van der Waals complex resulted in a rapid divergence of the two anions. The resulting energies of activation were 39, 38, and 36 kcal/mol for chloride, bromide, and iodide, respectively.

Upon protonation of the complex, a pre-reaction adduct is formed, in which a hydrogen bond between the halide ion and the complex is present and, most importantly, the barriers of activation decreased dramatically. The resulting monoanionic transition states are $S_N2$-like with the nearly linear V–O3–O2H bond angle and have strongly distorted V–O1–O3–O2 dihedral angle. The hydrogen bond is maintained in all anionic halide transition states, and no transition states could be located for complexes in which this hydrogen bond was not present. Due to the large electron density surrounding the carboxylate donors of **0a**, it is necessary to stabilize the negative charge of the halide in this early transition state. Under the experimental reaction conditions this stabilization could be accomplished by the presence of hydrogen-bond donors (water or hydrogen peroxide) or cations (tetraethylammonium or potassium).

Zampella et al. located transition states for the oxidation of bromide using quantum chemical models of the active site of a VHPO.[26] Their results showed that nucleophilic attack of the halide on the unprotonated oxygen of a hydroperoxido species had the lowest barrier of activation. Transition states were located for the peroxido vanadium adduct; protonation of the peroxido moiety yielded a significantly more stable transition geometry resulting in a lower barrier of activation. The hydroperoxido transition state occurred significantly earlier with respect to halide–oxygen formation than the peroxido transition state. The transition states located for bromide oxidation by **1** and **0a** show the same trend with respect to the halide–oxygen bond formation. The resulting transition state **0a_br** shows a longer halide–oxygen bond than **1_br**, indicating an earlier transition state. Additionally, there is dramatic decrease in the barrier of activation from **1_br** to **0a_br** (Table 3); this observed decrease in the barrier of activation is likely an oversimplification of experimental barrier because of the interaction between two anionic species (vanadium complex and the halide) in the case of **1_br**. Indeed, under reaction conditions it may be possible to carry out this reaction by offsetting the negative charge with strongly associated cations or hydrogen-bond donors. These results now correlate the mechanism of halide oxidation for the best reported functional model for VHPO, K[VO($O_2$)Hheida], with the proposed mechanism for halide oxidation by the enzyme. The importance of offsetting the negative charge on the anionic

 © 2007 Wiley-VCH Verlag GmbH & Co. KGaA, Weinheim 

halide is observed in the case of **0a_br** transition state, where a hydrogen bond forms between the bromide and the hydroxy group of the ligand resulting in a distorted dihedral angle for the peroxido moiety with respect to the vanadium–oxido bond. This is further supported by the location of a nearly isoenergetic reaction pathway, in which the bromide weakly coordinates to coordinatively unsaturated vanadium species **0a_br2**.

Given that VClPO is capable of oxidizing chloride, bromide and iodide, and K[VO($O_2$)Hheida] has been shown to be competent with respect to only bromide and iodide oxidation, we chose to explore the differences in barrier of activation for the oxidation of the aforementioned halides. Reactivity studies demonstrate the protonated K[VO($O_2$)-Hheida] is capable of oxidizing bromide and iodide, but not chloride. Two possible factors could contribute to this inability to oxidize chloride: 1. The reduction potential of the chloride is sufficiently high to prevent oxidation, 2. The active protonated form of the complex can not be generated in presence of chloride. The latter hypothesis was presented by Colpas et al. to explain this reactivity.[27] Slebodnick et al. demonstrated the ability of a tripodal amino complex to oxidize chloride when a mixture of acetonitrile (94%) and water (6%) was used as the solvent system.[37] Because chloride oxidation is not observed in either pure solvent it appears that in a mixture of the two solvents the basicity of the peroxido vanadium species increases with respect to chloride, allowing the catalytically active protonated species to be formed. On the basis of the transition-state energies presented herein, there is not a large difference in the energies of activation for each of the halides, therefore, differences in the reactivity can not be explained solely on the differences in reduction potentials of the oxidized halides. As protonation of the complex generates an early transition state, in which formation of the halide–oxygen bond is very weak, there is less contribution of halide orbital character in the transition state leading to smaller differences in the barrier of activation for halide oxidation (Table 3). These energies of activation presented here provide further support for this hypothesis.

To complete the functional correlation between the quantum-chemical models of the enzyme system and functional models for the enzyme, we examined the effects of protonation of the complex on organic sulfide oxidation. In the case of halide oxidation, the effects of protonation on the reaction barriers are masked to some degree by a highly charged dianionic transition state in the case of **1_x**, although this does represent the experimental conditions quite well, considering the chelation of potassium ions by 18-crown-6 preventing strong ion pair formation.

The organic sulfide oxidation system does not suffer from this highly charged transition state, resulting in a better understanding on the effects of protonation of the peroxido with respect to the barrier of activation for oxidation. Dimethyl sulfide was used as the organic sulfide to explore a number of transition-state geometries for both anionic and neutral catalytic species. The anionic transition states located were similar to those located for halide oxidation, a nearly linear S–O–O bond angle (175°) with V–O–O–O dihedral angle of 101°. The S–O bond length at the transition state was 2.08 Å indicating a high degree of sulfide–oxygen bonding character. These geometric parameters were conserved across the four anionic transition states located, two transitions for nucleophilic attack of DMS on the left- and right-hand side of the complex with two rotational isomers of DMS per side. Protonation of the peroxido moiety of **1** yielded lower energy transitions states (**0a_s**, **0b_s**), again exhibiting a lower degree of sulfur–oxygen bond formation leading to an earlier transition state identical to the trend observed for halide oxidation. The decrease in the barrier of activation of 8 kcal/mol is consistent with the dramatic increase in the rate of sulfide oxidation by K[VO($O_2$)Hheida] upon protonation. As the transition states located for the anionic catalytic species (**1_s1**, **1_s2**, etc.) are monoanionic, there is an overestimation of the barrier of activation for this pathway, though this overestimation is less dominant that it was in the case of the dianionic halide transition states. The anionic catalytic species may still present a viable reaction path in the presence of strong hydrogen bonding or ionic effects that could stabilize the transition state. This being said, the energy differences between the **1_s** and **0a_s** or **0b_s** are significant enough to consider the latter to be the dominant catalytic pathway.

The results presented above provide a direct correlation between the proposed transition-state geometries for VHPO's with the best known functional mimic for the same enzymes, making K[VO($O_2$)Hheida] a complete functional model for vanadium-dependent bromoperoxidases. As was the case for the enzyme studies, protonation of the peroxido moiety leads an early transition state and a dramatic decrease in the barrier of activation for substrate oxidation (substrate = halide or sulfide). Typical features of the transition states from enzyme model system are maintained (i.e. nearly linear O–O–S angle, similar bonding distances). Additionally, we provide support to the reactivity hypothesis presented by Colpas et al. describing the halide oxidation ability of K[VO($O_2$)Hheida]. The early transition states generated by protonation of the complex lead to small differences in the barrier of activation for halide oxidation; in contrast to the large difference in reduction potential for chloride, bromide, and iodide.

A comparison of van der Waals reactants adducts obtained with the hydrido-peroxido species of enzyme and synthetic models show that in both cases the substrate has a suitable spatial orientation to react with the hydroperoxido moiety. In particular, in the enzyme models, the atom of the substrate which undergoes oxidation (S, Br, I, Cl) is weakly coordinated to the vacant coordination position of vanadium and the interaction with vanadium place the substrate in the proper spatial orientation to act as attacking group in the $S_N2$ reaction.[26] In the synthetic model, the role of vanadium in positioning the substrate is played by the hydroxido ligand coordinated to the metal. In fact, the structure of the pre-reaction adducts obtained with the hydroperoxido form of the synthetic complex show that the atom of the substrate that will undergo oxidation is involved in a

 © 2007 Wiley-VCH Verlag GmbH & Co. KGaA, Weinheim 

hydrogen bond with the hydroxido group. Formation of this hydrogen bond positions the substrate in the proper location to act as a nucleophile in the $S_N2$ reaction. Therefore, in both cases (enzyme and synthetic models) the vanadium complex plays a role in properly positioning the substrate in the transiently formed pre-reaction adduct.

The calculated barriers to activation for K[VO($O_2$)-Hheida], in the case of both bromide and sulfide oxidation, are slightly higher than that calculated for the enzyme system (Table 4). The differences in the barriers of activations between the enzyme and synthetic model systems can be explained by the polarization of the peroxido bond and the torsional angle of the peroxido ligand in the transition state. The hydroperoxido moiety is more activated in the enzyme model, in particular, the O–O bond is longer (1.467 enzyme model vs. 1.458 Å synthetic model) and the peroxido bond is more polarized ($Dq$ = 0.12 enzyme model vs. 0.02 synthetic model). Additionally, in the transition states computed for the synthetic model, the hydroperoxido group is slightly tilted (see Figure 5 above) due to simultaneous formation of the hydrogen bond with the hydroxido group and $S_N2$-type oxido transfer reaction. The tilting of the hydroperoxido group in the transition state is possibly another factor responsible for increasing the energy of the transition state thereby increasing the barrier to activation.

Table 4. Comparison of computed $\Delta G^{\ddagger}$ for thioether (DMS) and bromide (Br) oxidation using the enzyme and synthetic models (energies in kcal/mol). All energy values are obtained as difference between TS energies and Van der Waals reactant adducts.

| | Enzyme model | Synthetic model |
|---|---|---|
| DMS | 2.9 | 9.4 |
| $Br^-$ | 3.7 | 21.1 |

These results demonstrate the importance of protons in catalytic process. Many vanadium catalysts have been presented in the literature for a variety of oxidations: alcohol oxidations,[38] olefin epoxidation,[1,39–41] sulfide oxidation,[6,7,9,11,41] and phosphane oxidation.[1,8] Many of these processes use in-situ-derived catalytic systems from vanadium starting materials, vanadyl sulfate and vanadyl acetylacetonate being the most common, with a variety of ligands. The reported rates and turnover numbers for sulfide oxidation are significantly lower than those presented for K[VO($O_2$)Hheida], despite the similarities in coordination environments and terminal oxidant (hydrogen peroxide). The difference between other systems and the Hheida system is often the protonation of the peroxido ligand; which as shown herein decrease the barrier of activation and has experimentally been shown to increase the rate of reaction. To design better oxidation catalysts using vanadium, care should be taken to limit potential competitive protonation states. Additionally, steric bulk and H-bond acceptors should be added in such a way as to encourage selective protonation of one side of peroxido ligand thereby limiting the potential orientations a pro-chiral can adopt in the linear $S_N2$ type transition state. The computational results contained herein make it possible to design ligand sets capable of stereoselective oxidations using non-redox active $d^0$ metal–peroxido coordination complexes rationally.

## Conclusions

Our group has shown K[VO($O_2$)Hheida] to be an effective functional model and biomimetic catalyst for thioether and halide oxidation. Density functional theory was used to explore the chemically feasible pre-catalytic species, protonation states, and transition-state geometries. We have shown that coordination of the hydroxyethyl arm of Hheida is energetically favored over coordination of an exogenous donor such as acetonitrile or water. All chemically reasonable protonation states were examined on the basis of the precatalytic species. These results showed that protonation of the peroxido moiety is favored over protonation of Hheida or the oxido ligand. Transition states were located for thioether and halide oxidations (halide = $I^-$, $Br^-$, and $Cl^-$), all transition states were $S_N2$-like, with a nearly linear substrate–peroxido oxygen bond angles. Protonation of the peroxido moiety dramatically reduces the barrier to activation for both thioether and halides; however barriers are insensitive to the identity of the halide. This further supports the hypothesis that the inability of K[VO(OOH)-Hheida] to oxidize chloride is the result of the increasing basicity of the substrate, which leads to deprotonation of the catalytically active hydroperoxido species. These results provide the necessary information regarding the transition-state geometry and the importance of protons in the catalytic cycle to develop the class of catalysts based upon K[VO(OOH)Hheida] for asymmetric oxidations.

## Experimental Section

DFT geometry optimization of molecular structures were performed using the BP86 functional[42] and an all-electron triple-ζ basis set with polarization functions on all atoms (TZVP).[43] Calculations were carried out using the Turbomole suite of programs[44] in conjunction with the resolution of identity technique.[45,46]

Optimizations of the transition-state structures were performed using a procedure based on a pseudo Newton–Raphson method. Initial starting structures of a guessed transition state were optimized by constraining the distances related to the reaction coordinate, specifically the peroxido O–O and the substrate X–O or S–O (where X = $I^-$, $Br^-$, $Cl^-$ S = sulfur of dimethyl sulfide) interatomic distances. The initial Hessian matrix was calculated at the classical level, whereas the BP86-RI/TZVP was used to compute the Hessian matrix of the minimum energy structures. Full vibrational analysis of the stationary points were carried out to ensure the presence of one eigenmode featuring an imaginary frequency corresponding to the reaction coordinate. This point was then used as a starting point for the transition-state searches, which were conducted using an eigenvector-following strategy.

Transition states are labeled on the basis of the number negative charges present on vanadium complex (–1 or **0**), site of protonation (Figure 6, a), and the substrate. In the case of dimethyl sulfide transition states a number has been assigned to the rotational confor-

 © 2007 Wiley-VCH Verlag GmbH & Co. KGaA, Weinheim 

mation of the methyl groups, **P** indicating a methyl group parallel to the vanadium peroxido group or **A** indicating an antiparallel methyl group (Figure 6, b). A transition state corresponding to protonation of the left-side peroxido oxygen atom with dimethyl sulfide in a parallel methyl group orientation would be **0a_sP**, while the anionic transition state for bromide oxidation would be **1_br**.

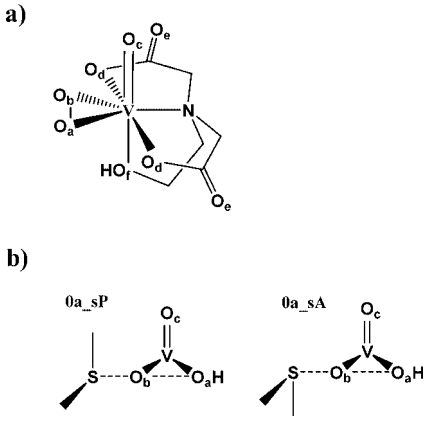


Figure 6. Illustration of the nomenclature adopted for this manuscript.

Full vibrational analysis has been carried out to characterize each stationary point. The effects of solvation were evaluated with the solvent continuous model approach COSMO[47,48] as implemented in the Turbomole suite. The polarizable continuum medium is expected to mimic the effects of a pure solvent environment to this purpose the dielectric constant for acetonitrile ($\varepsilon$ = 36.64) was used as previous studies[6,27] have employed it as the solvent to explore the reactivity of monoperoxido oxidovanadium complexes. Corrections have been computed to estimate $\Delta G$ from $\Delta E$, by calculating roto-vibrational partition function of the different molecular species.

## Acknowledgments

CJS would like thank the National Institutes of Health (NIH) (GM008597, CBI Training Program) and the Sokol International Summer Research Fellowship for funding.

[1] C. Bolm, *Coord. Chem. Rev.* **2003**, *237*, 245–256.
[2] S. A. Blum, R. G. Bergman, J. A. Ellman, *J. Org. Chem.* **2003**, *68*, 153–155.
[3] G. Santoni, G. Licini, D. Rehder, *Chem. Eur. J.* **2003**, *9*, 4700–4708.
[4] F. Van de Velde, I. W. C. E. Arends, R. A. Sheldon, *J. Inorg. Biochem.* **2000**, *80*, 81–89.
[5] I. Fernandez, N. Khiar, *Chem. Rev.* **2003**, *103*, 3651–3705.
[6] T. S. Smith, V. L. Pecoraro, *Inorg. Chem.* **2002**, *41*, 6754–6760.
[7] A. Barbarini, R. Maggi, M. Muratori, G. Sartori, R. Sartorio, *Tetrahedron: Asymmetry* **2004**, *15*, 2467–2473.
[8] G. Du, J. H. Espenson, *Inorg. Chem.* **2005**, *44*, 2465–2471.
[9] Y.-C. Jeong, S. Choi, Y. D. Hwang, K.-H. Ahn, *Tetrahedron Lett.* **2004**, *45*, 9249–9252.
[10] P. Plitt, H. Pritzkow, R. Kraemer, *Dalton Trans.* **2004**, 2314–2320.
[11] J. Sun, C. Zhu, Z. Dai, M. Yang, Y. Pan, H. Hu, *J. Org. Chem.* **2004**, *69*, 8500–8503.
[12] H. Vilter, *Met. Ions Biol. Syst.* **1995**, *31*, 325–362.
[13] A. Butler, J. N. Carter-Franklin, *Nat. Prod. Rep.* **2004**, *21*, 180–188.
[14] H. Vilter, *Phytochemistry* **1984**, *23*, 1387–1390.
[15] M. Andersson, A. Willetts, S. Allenmark, *J. Org. Chem.* **1997**, *62*, 8455–8458.
[16] R. R. Everett, J. R. Kanofsky, A. Butler, *J. Biol. Chem.* **1990**, *265*, 4908–4914.
[17] C. Rush, A. Willetts, G. Davies, Z. Dauter, H. Watson, J. Littlechild, *FEBS Lett.* **1995**, *359*, 244–246.
[18] M. Weyand, H. J. Hecht, H. Vilter, D. Schomburg, *Acta Crystallogr., Sect. D.* **1996**, *D52*, 864–865.
[19] A. Messerschmidt, L. Prade, R. Wever, *Biol. Chem.* **1997**, *378*, 309–315.
[20] A. Mueller-Fahrnow, W. Hinrichs, W. Saenger, H. Vilter, *FEBS Lett.* **1988**, *239*, 292–294.
[21] N. Pooransingh-Margolis, R. Renirie, Z. Hasan, R. Wever, A. J. Vega, T. Polenova, *J. Am. Chem. Soc.* **2006**, *128*, 5190–5208.
[22] T. Borowski, W. Szczepanik, M. Chruszcz, E. Broclawik, *Int. J. Quantum Chem.* **2004**, *99*, 864–875.
[23] J. Y. Kravitz, V. L. Pecoraro, H. A. Carlson, *J. Chem. Theory Comput.* **2005**, *1*, 1265–1274.
[24] S. Raugei, P. Carloni, *J. Phys. Chem.* **2005**, ACS ASAP.
[25] G. Zampella, J. Y. Kravitz, C. E. Webster, P. Fantucci, M. B. Hall, H. A. Carlson, V. L. Pecoraro, L. De Gioia, *Inorg. Chem.* **2004**, *43*, 4127–4136.
[26] G. Zampella, P. Fantucci, V. L. Pecoraro, L. De Gioia, *J. Am. Chem. Soc.* **2005**, *127*, 953–960.
[27] G. J. Colpas, B. J. Hamstra, J. W. Kampf, V. L. Pecoraro, *J. Am. Chem. Soc.* **1996**, *118*, 3469–3478.
[28] P. E. M. Siegbahn, M. R. A. Blomberg, *Chem. Rev.* **2000**, *100*, 421–437.
[29] S. Niu, M. B. Hall, *Chem. Rev.* **2000**, *100*, 353–405.
[30] D. Balcells, F. Maseras, A. Lledos, *J. Org. Chem.* **2003**, *68*, 4265–4274.
[31] D. Balcells, F. Maseras, G. Ujaque, *J. Am. Chem. Soc.* **2005**, *127*, 3624–3634.
[32] A. Butler, M. J. Clague, G. E. Meister, *Chem. Rev.* **1994**, *94*, 625–638.
[33] M. J. Clague, N. L. Keder, A. Butler, *Inorg. Chem.* **1993**, *32*, 4754–4761.
[34] G. J. Colpas, B. J. Hamstra, J. W. Kampf, V. L. Pecoraro, *J. Am. Chem. Soc.* **1994**, *116*, 3627–3628.
[35] V. Conte, F. Di Furia, S. Moro, S. Rabbolini, *J. Mol. Catal. A* **1996**, *113*, 175–184.
[36] V. Conte, O. Bortolini, M. Carraro, S. Moro, *J. Inorg. Biochem.* **2000**, *80*, 41–49.
[37] C. Slebodnick, V. L. Pecoraro, *Inorg. Chim. Acta* **1998**, *283*, 37–43.
[38] C. Li, P. Zheng, J. Li, H. Zhang, Y. Cui, Q. Shao, X. Ji, J. Zhang, P. Zhao, Y. Xu, *Angew. Chem. Int. Ed.* **2003**, *42*, 5063–5066.
[39] R. F. De la Pradilla, A. Castellanos, J. Fernandez, M. Lorenzo, P. Manzano, P. Mendez, J. Priego, A. Viso, *J. Org. Chem.* **2006**, *71*, 1569–1575.
[40] J. Hartung, S. Drees, M. Greb, P. Schmidt, I. Svoboda, H. Fuess, A. Murso, D. Stalke, *Eur. J. Org. Chem.* **2003**, 2388–2408.
[41] A. G. J. Ligtenbarg, R. Hage, B. L. Feringa, *Coord. Chem. Rev.* **2003**, *237*, 89–101.
[42] A. D. Becke, *Phys. Rev. A* **1988**, *38*, 3098–3100.
[43] A. Schaefer, C. Huber, R. Ahlrichs, *J. Chem. Phys.* **1994**, *100*, 5829–5835.
[44] R. Ahlrichs, M. Baer, M. Haeser, H. Horn, C. Koelmel, *Chem. Phys. Lett.* **1989**, *162*, 165–169.
[45] K. Eichkorn, F. Weigend, O. Treutler, R. Ahlrichs, *Theor. Chem. Acc.* **1997**, *97*, 119–124.
[46] K. Eichkorn, O. Treutler, H. Oehm, M. Haeser, R. Ahlrichs, *Chem. Phys. Lett.* **1995**, *240*, 283–290.
[47] A. Klamt, *J. Phys. Chem.* **1996**, *100*, 3349–3353.
[48] A. Klamt, *J. Phys. Chem.* **1995**, *99*, 2224–2235.

Received: August 7, 2006
Published Online: December 15, 2006

 © 2007 Wiley-VCH Verlag GmbH & Co. KGaA, Weinheim 

DOI: 10.1002/ejic.200600623

# ZnO Nanoparticles From a Metal-Organic Framework Containing $Zn^{II}$ Metallacycles

**Harjyoti Thakuria,[a] Ballav Moni Borah,[a] and Gopal Das*[a]**

**Keywords:** Metallacycles / Tripodal ligands / Hydrogen bonds / Metal-organic frameworks / Nanoparticles

Nitrilotriacetic acid ($H_3NTA$) reacts in the solid phase with zinc hydroxide (1:1) to form a 3D ladder-like metal-organic framework that forms wurtzite ZnO nanoparticles when heated above 600 °C. Complex **1** contains a 1D zig-zag water chain. A mixed coordination network **2** is formed with excess $Zn^{II}$ hydroxide, which, on decomposition at about 500 °C, forms microwires of ZnO.

(© Wiley-VCH Verlag GmbH & Co. KGaA, 69451 Weinheim, Germany, 2007)

## Introduction

In the past decade, the design and synthesis of functional molecule analogues by the self-assembly of metal-connecting points and organic linkers under controlled reaction conditions has attracted a great deal of attention among the inorganic, materials, and supramolecular chemistry communities.[1] As a result of these concerted efforts, the studies on the syntheses of metal-organic frameworks (MOFs) have undergone tremendous development by virtue of their attractive topologies and potential application in areas such as magnetism, non-linear optics, electrical conductivity, host–guest chemistry, gas storage, nonlinear optics, ion-exchange, and catalysis.[2,3]

The development of metal complexes that assemble into predictable supramolecular structures in the crystal is of great interest because of their potential in designing new materials with desirable optical and magnetic properties.[4] Nitrilotriacetate ($H_3NTA$) is a multidentate $C_3$-symmetric tripodal ligand that has been attracting much attention.[5] The self-complementary character of this ligand controls its assembly into aggregates by intermolecular hydrogen bonds and its threefold symmetry is maintained upon complexation.

The physical properties such as electric conductivity and magnetic, optical, and mechanical characteristics of nanosized metal oxide particles are known to be substantially different from those of bulk materials. The preparation methods of metal oxide nanoparticles have been extensively studied to precisely control the morphology at the nanometer scale. ZnO is one of the most important oxide materials for such wide ranging industrial applications as transparent conductors, UV-protection films, and chemical sensors.[6] Synthetic routes that have been employed to prepare ZnO nanoparticles include a liquid-phase method, vapor deposition, and a precursor process.[7]

Here we report the solid-phase synthesis of $Zn^{II}$-containing metallacycles using simple yet versatile acid-base chemistry with the $C_3$-symmetric tripodal ligand nitrilotriacetic acid ($H_3NTA$) in a 1:1 ratio. The resulting complex **1** forms a ladder-like 3D polymeric metal-organic framework (MOF). The macrocyclic pores host a zig-zag 1D infinite chain of lattice water. Complex **1** forms wurtzite ZnO nanoparticles when heated above 600 °C. A mixed coordination network **2** is formed with excess $Zn^{II}$ hydroxide, which, on decomposition at around 500 °C, forms microwires of ZnO.

## Results and Discussion

### Synthesis and Characterization

Complex **1** was synthesized by a simple acid-base reaction in the solid phase. A mixture of nitrilotriacetic acid (1 mmol, 0.191 g) and anhydrous freshly prepared zinc hydroxide (1 mmol, 0.099 g) was ground thoroughly with a pestle in an open mortar at room temperature under air. The mixture was ground for 5 min until the mixture turned into a slurry. X-ray quality single crystals of Zn complex **1** were grown from water within a day at room temperature in quantitative yield. Complex **2** was synthesized following the same procedure as **1**, only the metal to ligand ratio was different (3:2).

### $[(HNTA)(H_2O)_3Zn^{II}]\cdot H_2O$ (1)

The molecular structure of complex **1** consists of a $Zn^{II}$ ion, partially deprotonated NTA, and water molecules (Fig-

[a] Department of Chemistry, Indian Institute of Technology Guwahati,
Guwahati, Assam 781039, India
Fax: +91-361-258-2349
E-mail: gdas@iitg.ernet.in

Supporting information for this article is available on the WWW under http://www.eurjic.org or from the author.

 © 2007 Wiley-VCH Verlag GmbH & Co. KGaA, Weinheim 

ure 1). The X-ray structure determination shows that compound **1** contains hexacoordinate $Zn^{II}$ with a distorted octahedral geometry. The angular distortion around Zn from the octahedral geometry is significant. The N(1)–Zn–O angles deviate considerably from 90° and range between 78.22(7)° and 100.02(8)° while the N(1)–Zn–O(7) angle is only 162.19(11)°. The metal ion is bonded to two carboxylates from the ligand, each of which donates a single O atom. The third coordination site is occupied by the tertiary amine bridgehead N-atom of the ligand, while the remaining coordination sites of the octahedral geometry are occupied with water molecules. The resulting coordination polymer looks like an array of zinc-containing metallomacrocycles (see Supporting Information). The Zn–O(carboxylate) and Zn–N bond lengths are 2.068(3), 2.074(2), and 2.222(2) Å, respectively, in good agreement with other $Zn^{II}$ carboxylate complexes.[8] The Zn–O(water) bond lengths are 2.0671(17), 2.107(3), and 2.105(3) Å, and are also similar to other Zn–$OH_2$ bond lengths reported in the literature.[9] The bond lengths and bond angles are found to be within normal statistical errors.[8]

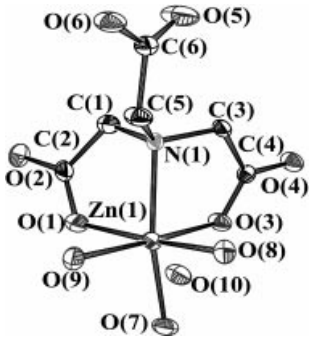


Figure 1. An ORTEP view of complex **1**.

Figure 2 shows an illustration of the 3D assembly of an infinite ladder framework. The rails of the ladder are made of almost linear, seven-atom units consisting of intermolecularly hydrogen bonded O(4)–C(4)–O(3)–Zn(1)–O(1)–C(2)–O(2) groups of NTA. The rungs of the ladder are made of an O atom of the axial water molecule. The distance between the rails of the ladder is 7.652 Å (distance between two adjacent Zn atoms forming the rail) and the two adjacent ladders are separated by 11.218 Å (distance between two Zn atoms of neighboring rails). However, the separation between the rungs of the ladder is 5.093 Å (forming the rail distance between two axial water oxygen atoms). Adjacent rails of the ladders are interconnected by intermolecular hydrogen bonds (Figure 2).

A crystal water molecule (O10) forms strong hydrogen bonds with neighboring metal-coordinated water molecules as well as with the coordinated O atom of the carboxylic acid group. Each of the crystal water molecules is hydrogen bonded to the four neighboring molecules in an almost tetrahedral arrangement (see Supporting Information). The hydrogen bonding between the crystal water molecules is comparatively weak in nature and forms a 1D zig-zag infinite water chain along the *b* axis (Figure 3), which is one

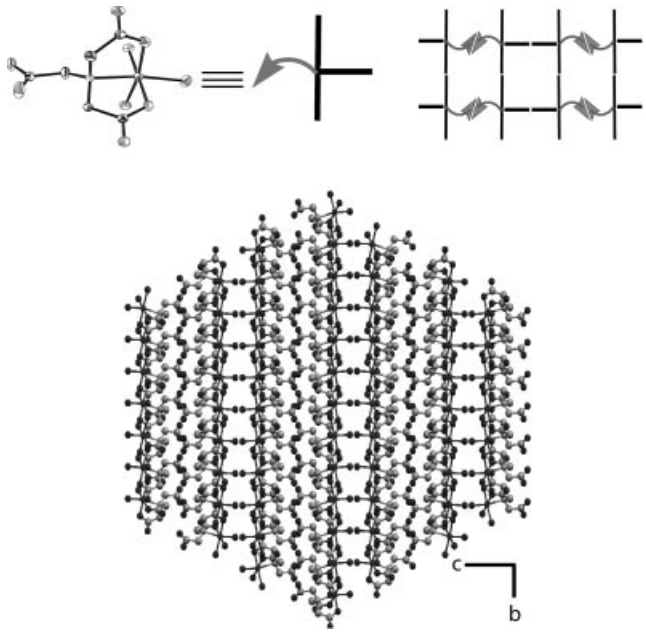


Figure 2. An infinite ladder framework along the *a* axis of **1**.

of the probable proton wire structures found in biological systems.[10] A zig-zag motif of a water chain has also been reported for nonbiological system.[11]

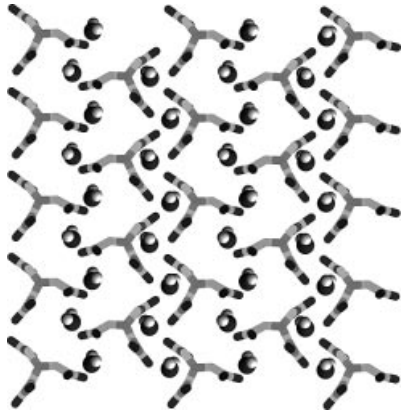

Figure 3. Perspective view of the zig-zag water chain in the crystal lattice of complex **1**.

The uncoordinated carboxylic acid group of NTA forms strong intramolecular hydrogen bonds with the neighboring O atom of the coordinated carboxylate group [O4···H4 1.793(5), O4–O6 2.604(7) Å and O6–H4–O4 170.23°]. O4 is acting as a H-bond acceptor and O6 as a H-bond donor and they act together like a clip (see Supporting Information), which eventually helps to form the 3D hydrogen-bonded MOF. Here, both water–MOF and water–water interactions are important for the stability of the overall polymeric structure.

The interaction between the MOF and the water chain is moderate, as thermogravimetric analysis of complex **1** under $N_2$ shows a 22.67% weight loss at around 100 °C, which corresponds to the loss of four water molecules (calculated 22.08%). Among the three carboxylic acid groups present

 © 2007 Wiley-VCH Verlag GmbH & Co. KGaA, Weinheim 

in the ligand, two are coordinated to the metal ion as carboxylate. TG analysis shows the sequential removal of one $CO_2$ molecule from the uncoordinated carboxylic acid group and two $CO_2$ molecules from the two coordinated carboxylate groups in the ranges 260–330 °C (loss of 17.24%; calcd. 17.32%) and 330–420 °C (loss of 41.66%; calcd. 41.79%) respectively, which is in good agreement with the X-ray crystal structure. Complete decomposition is achieved at about 600 °C. The DSC plot shows an endothermic peak at 100 °C due to the loss of water molecules. It also shows two exothermic peaks at 310 and 370 °C due to the decomposition of the carboxylic acid groups.

The FT-IR spectrum of complex **1** shows a broad band centered at 3300 $cm^{-1}$ due to the presence of water molecules; this vanishes when the compound is heated under vacuum (0.1 mm) at 150 °C for 6 h. Two types of carboxylic acid groups are present in complex **1**: uncoordinated, unionized and coordinated, ionized. The FT-IR spectrum clearly shows the presence of uncoordinated, unionized COOH at 1740 $cm^{-1}$ and coordinated, ionized $COO^-$ at 1590 $cm^{-1}$; these values agree well with those in the literature (see Supporting Information).[12] The $^1H$ NMR spectrum shows a broad singlet in $D_2O$ at $\delta$ = 3.49 ppm ($NCH_2COOH$), which proves the dynamic complexation and decomplexation behavior of the third carboxylic acid group at room temperature in solution.

The powder X-ray diffraction patterns of **1** show significant changes in the peak positions as well as intensities before and after water removal (Figure 4), which match well with the simulated pattern.

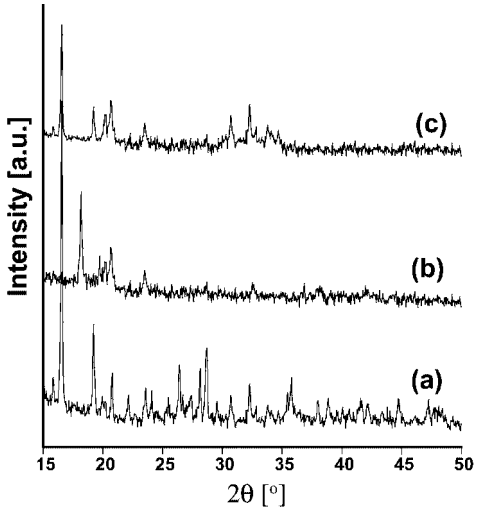


Figure 4. The powder XRD pattern of complex **1** before water removal (a), after water removal (b), and after re-hydration (c).

Thermal decomposition of complex **1** at 700 °C for 6 h in a muffle furnace forms wafers of ZnO with lengths ranging from 0.2 to 1.2 mm. The average size of these wafers remains unchanged with longer reaction time, up to 14 h. SEM images taken of several batches of samples showed that the entire wafer is formed from a uniform and densely packed array of ZnO nanoparticles (Figure 5). The nanoparticles' crystallinity was analyzed by powder X-ray diffraction techniques. The diffraction peaks (Figure 6) can be indexed as the wurtzite structure of ZnO (JCPDS 36-1451), thereby indicating that the zinc NTA complex has been thermally decomposed into ZnO.[13] The X-ray diffraction pattern shows an enhanced (101) peak resulting from the linear orientation of the nanoparticles. A typical synthesis yields particles with diameters ranging between 10 and 60 nm.

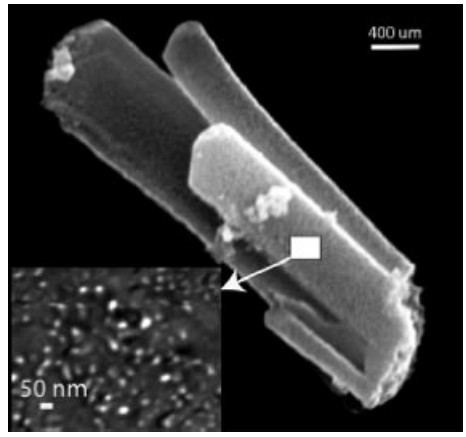


Figure 5. SEM micrographs of microwafers made of ZnO nanoparticles.

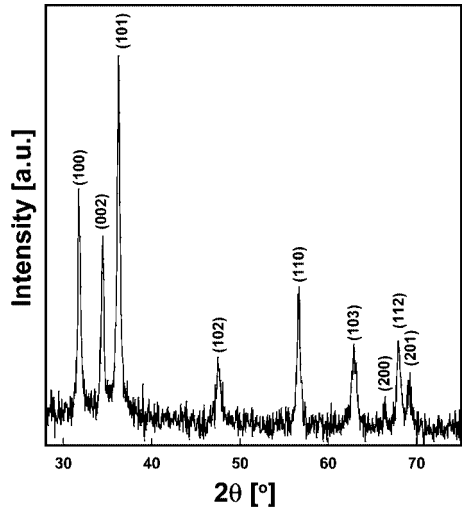


Figure 6. Powder XRD pattern of ZnO (wurtzite) nanoparticles.

### $[(H_2O)_6Zn][(NTA)_2Zn_2]\cdot 2H_2O$ (2)

The dimeric Zn nitrilotriacetato complex **2** is formed in the presence of an excess of zinc hydroxide. The asymmetric unit contains the hexaaquazinc(II) cation, the dimeric Zn-NTA complex anion, and crystal water. There are three symmetry-independent Zn sites in the structure. The first two of them (Zn1 and Zn2) are distorted octahedral with five carboxyl oxygens and one amine nitrogen making up the coordination environment. The other zinc cation, Zn3, is coordinated to six water molecules. Zn1 and Zn2 are bridged together by the carboxylic O3, O4, O11, and O12

 © 2007 Wiley-VCH Verlag GmbH & Co. KGaA, Weinheim 

atoms to form an infinite metal-organic framework. Among these four oxygen atoms, O3 and O11 form very rare μ-oxo carboxylato type bridges where each carboxylate ligand is bonded to three metal centers. Atom O3 forms a stronger bond with Zn2 [Zn(1)–O(3) 2.365(2), Zn(2)–O(3) 1.947(2) Å] while O11 forms a stronger bond with Zn1 [Zn(1)–O(11) 1.948(2) and Zn(2)–O(11) 2.351(2) Å]. Atom O3 occupies the axial position of Zn1 but the equatorial position of Zn2, whereas O11 occupies the axial position of Zn2 and the equatorial position of Zn1. The remaining four carboxylic oxygen atoms (O2, O6, O8, and O10) are not coordinated to the metal cation but form strong hydrogen bonds with the water molecules coordinated to the Zn3 cation. The carboxylic acid of one arm of each NTA unit is coordinated to the three zinc centers simultaneously along the crystallographic *ab* plane, which results in the formation of a complicated 3D polymeric rectangular network (Figures 7 and 8). The other two arms of each NTA unit form extensive hydrogen bonds with water molecules along the crystallographic *bc* plane. The overall 3D network is built up with the help of water of hydration (O19 and O20). The crystal water molecule O19 acts as a double hydrogen-bond donor as well as acceptor, while O20 acts as a single hydrogen-bond donor and acceptor. Both of these water molecules are strongly hydrogen bonded to the carboxylate as well as another coordinated water molecule. Unlike the mononuclear Zn-NTA complex **1**, there is no direct hydrogen bond between two crystal water molecules, which, in turn, prevents the formation of any water network in the solid-state structure. Two of the alternate rectangular void spaces in the 2D rectangular network are filled with these water molecules. Alternating Zn-aqua and Zn-NTA moieties form this 2D network.

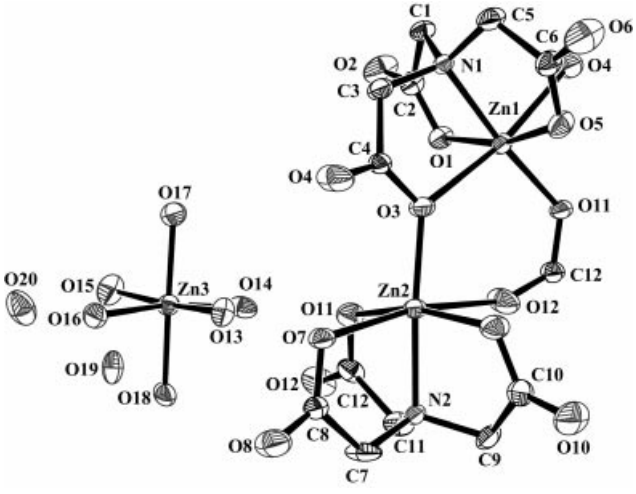


Figure 7. An ORTEP view of the Zn-NTA complex **2**.

Thermogravimetric analysis of complex **2** under $N_2$ shows a 21.08% weight loss between 30 and 100 °C corresponding to the loss of eight water molecules (calcd. 20.09%). All six coordinated carboxylic acid groups are removed between 100 and 240 °C with a weight loss of 47.08% (calcd. 46.11%), which is in good agreement with the X-ray crystal structure. Complete decomposition is achieved at about 480 °C and shows the formation of ZnO as the decomposed product. The DSC plot shows an endothermic peak at 75 °C due to the loss of water molecules. It also shows two exothermic peaks at 200 and 340 °C due to the decarboxylation and complete decomposition, respectively.

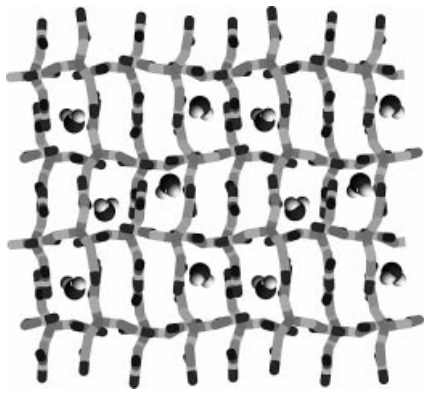

Figure 8. An infinite rectangular network along the *ab* plane of **2**.

The FT-IR spectrum of complex **2** shows a broad band centered at 3500 $cm^{-1}$ due to the presence of water molecules, which also vanishes when heated, as for complex **1**. Unlike complex **1**, however, it contains only coordinated, ionized types of carboxylic acid groups, which absorb at 1620 $cm^{-1}$.[12]

Complex **2** decomposes above 500 °C to form microwires of ZnO with lengths ranging from 200 nm to 8 μm. The average size and shape of these fibers does not change with temperature and reaction time. The powder X-ray diffraction pattern of these microwires also confirms the presence of the wurtzite structure of ZnO (Figure 9).

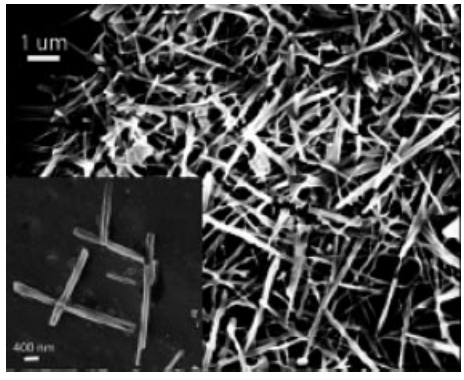


Figure 9. SEM micrographs of ZnO microwires.

## Conclusions

We have been able to synthesize two different metal-organic frameworks in the solid state by changing the metal to ligand ratio. An infinite array of metallacycles forms an interesting ladder and rectangular net like structures. The mononuclear complex **1** contains a 1D zig-zag infinite water

 © 2007 Wiley-VCH Verlag GmbH & Co. KGaA, Weinheim 

chain. The stability of the water chain is derived from strong H-bonding interactions with the carboxylate group and the metal-bound water molecules. The binuclear complex **2** contains a very rare μ-oxo carboxylato bridge, where one carboxylate ligand binds to three metal centers simultaneously. Several other combinations of metal and ligand to synthesize MOFs of interest in solvent-free methods are currently under investigation in our laboratory. We have also demonstrated a precursor synthesis of ZnO nanoparticles and microwires with a wurtzite structure. The crystal lattice deposition temperatures for ZnO are very high because of the formation of extensive coordination networks of these supramolecular complexes. The technique demonstrated here can be extended to the synthesis of a wide range of nanomaterials having similar structures. These studies are currently underway in our laboratory.

## Experimental Section

**Materials and Methods:** Reagents were purchased from commercial sources and, unless otherwise stated, were used as received. Nitrilotriacetic acid was purchased from Sigma–Aldrich Co. and used without further purification. The IR spectra were recorded with a Perkin–Elmer Spectrum One FT-IR Spectrometer as KBr disks in the range 4000–400 $cm^{-1}$. The thermogravimetric analyses (TGA) of the compounds were performed with an SDTA 851e TGA thermal analyzer (Mettler Toledo) with a heating rate of 2 °C $min^{-1}$ under $N_2$ with 5–10 mg of sample per run. Scanning electron micrograph (SEM) images were obtained with a LEO-1430 VP electron microscope on samples glued onto an aluminum stub and gold sputtered. Powder XRD data were recorded with a Seifert powder X-ray diffractometer (XRD, 3003TT) with Cu-$K_\alpha$ source ($\lambda$ = 1.54 Å) on a glass surface for an air-dried sample.

**X-ray Crystallography:** Colorless single crystals of **1** and **2** were grown by slow evaporation of an aqueous solution of the complexes at room temperature. The X-ray diffraction data were collected at room temp. with a Bruker three-circle diffractometer (Bruker Nonius SMART APEX-II) equipped with CCD area detectors, and using graphite-monochromated Mo-$K_\alpha$ radiation ($\lambda$ = 0.71073 Å) from a 60-W microfocus Siemens Microsource with glass polycapillary optics. The SMART[14] software was used for data acquisition and the SAINT[14] software for data extraction. The structures were solved by direct methods and refined by full-matrix least-squares against $F^2$. Absorption corrections were done using SADABS. Structures were solved and refined using SHELX 97.[15] All non-hydrogen atoms were refined anisotropically. The hydrogen atoms were located from the difference Fourier maps and refined.

**Compound 1:** $C_6H_{15}NO_{10}Zn$, $M$ = 326.58, orthorhombic, $a$ = 12.2958(10), $b$ = 6.6129(10), $c$ = 27.846(2) Å, $V$ = 2262.4(4) $Å^3$, space group $Pbca$, $Z$ = 8, $T$ = 298(2) K, $\mu$ (Mo-$K_\alpha$) = 2.288 $mm^{-1}$, $F(000)$ = 1170, GOF = 1.103; final $R$ indices: $R_1$ = 0.0213 [$I > 2\sigma(I)$], $wR_2$ = 0.0610; $R$ indices (all data): $R_1$ = 0.0224, $wR_2$ = 0.0604.

**Compound 2:** $C_{12}H_{28}N_2O_{20}Zn_3$, $M$ = 716.53, orthorhombic, $a$ = 12.7369(10), $b$ = 11.3290(10), $c$ = 16.4424(14) Å, $V$ = 2372.6(3) $Å^3$, space group $Pna2_1$, $Z$ = 4, $T$ = 298(2) K, $\mu$ (Mo-$K_\alpha$) = 3.120 $mm^{-1}$, $F(000)$ = 1272, GOF = 0.931; final $R$ indices: $R_1$ = 0.0282 [$I > 2\sigma(I)$], $wR_2$ = 0.0980; $R$ indices (all data): $R_1$ = 0.0291, $wR_2$ = 0.0997.

CCDC-280983 (for **1**) and -612885 (for **2**) contain the supplementary crystallographic data for this paper. These data can be obtained free of charge from The Cambridge Crystallographic Data Center via www.ccdc.cam.ac.uk/data_request/cif.

**Supporting Information** (see footnote on the first page of this article): The TGA-DSC curves, FT-IR spectra, powder XRD patterns, and selected figures.

## Acknowledgments

Financial support from the Council of Scientific and Industrial Research (CSIR) of India to GD and HT [grant no. 01(1948)/04/EMR-II] is gratefully acknowledged. We thank the Central Instrument Facility, Center for Nanotechnology and Department of Chemistry IIT Guwahati for SEM, powder XRD, and single-crystal XRD measurements.

[1] a) G. R. Desiraju, *Crystal Engineering: The Design of Organic Solids*, Elsevier, Amsterdam, **1989**; b) M. J. Zaworotko, *Chem. Soc. Rev.* **1994**, *23*, 283–288; c) B. Moulton, M. J. Zaworotko, *Chem. Rev.* **2001**, *101*, 1629–1658; d) S. Kitagawa, R. Kitaura, S. I. Noro, *Angew. Chem. Int. Ed.* **2004**, *43*, 2334–2375; e) S. Lee, A. B. Mallik, Z. E. Xu, B. Lobkovsky, L. Tran, *Acc. Chem. Res.* **2005**, *38*, 251–261.

[2] a) N. L. Rosi, J. Eckert, M. Eddaoudi, D. T. Vodak, J. Kim, M. O'Keeffe, O. M. Yaghi, *Science* **2003**, *300*, 1127–1130; b) L. Pan, M. B. Sander, X. Huang, J. Li, M. Smith, E. Bittner, B. Bockrath, J. K. Johnson, *J. Am. Chem. Soc.* **2004**, *126*, 1308–1309; c) D. N. Dybtsev, H. Chun, S. H. Yoon, D. Kim, K. Kim, *J. Am. Chem. Soc.* **2004**, *126*, 32–33; d) G. Férey, M. Latroche, C. Serre, F. Millange, T. Loiseau, A. Percheron-Guégan, *Chem. Commun.* **2003**, 2976–2977.

[3] a) O. R. Evans, W. Lin, *Acc. Chem. Res.* **2002**, *35*, 511–522; b) K. S. Suslick, P. Bhyrappa, J. H. Chou, M. E. Kosal, S. Nakagaki, D. W. Smithenry, S. R. Wilson, *Acc. Chem. Res.* **2005**, *38*, 283–291; c) D. Bradshaw, T. J. Prior, E. J. Cussen, J. B. Claridge, M. J. Rosseinsky, *J. Am. Chem. Soc.* **2004**, *126*, 6106–6114; d) J. S. Seo, D. Whang, H. Lee, S. I. Jun, J. Oh, Y. J. Jeon, K. Kim, *Nature* **2000**, *404*, 982–986; e) O. Ohmori, M. Fujita, *Chem. Commun.* **2004**, 1586–1587; f) O. R. Evans, H. L. Ngo, W. Lin, *J. Am. Chem. Soc.* **2001**, *123*, 10395–10396.

[4] a) J. M. Lehn, *Angew. Chem. Int. Ed. Engl.* **1990**, *29*, 1304–1319; b) *Supramolecular Architecture* (Eds.: R. Robson, B. F. Abrahams, S. R. Batten, R. W. Gabe, B. F. Hoskins, T. Bein), American Chemical Society, Washington, D.C., **1992**, p. 256; c) *Transition Metals in Supramolecular Chemistry* (Eds.: L. Fabbrizzi, A. Poggi), Kluwer Academic, Dordrecht, **1994**.

[5] a) L. Pan, N. Ching, X. Huang, *Chem. Eur. J.* **2001**, *7*, 4431–4437; b) Y. Chen, B. Q. Ma, Q. D. Liu, J. R. Li, S. Gao, *Inorg. Chem. Commun.* **2000**, *3*, 319–321.

[6] a) D. R. Clarke, *J. Am. Ceram. Soc.* **1999**, *82*, 485–502; b) T. K. Gupta, *J. Am. Ceram. Soc.* **1990**, *73*, 1817–1840.

[7] a) S. M. Haile, D. W. Johnson, G. H. Wiseman Jr., H. K. Bowen, *J. Am. Ceram. Soc.* **1989**, *72*, 2004–2008; b) Y. Suyama, Y. Tomokiyo, T. Manabe, E. Takana, *J. Am. Ceram. Soc.* **1988**, *71*, 391–395.

[8] a) B. Sun, Z. Wang, S. Gao, *Inorg. Chem. Commun.* **2001**, *4*, 79–81; b) J. Kim, B. Chen, T. M. Reineke, H. Li, M. Eddaoudi, D. B. Molar, M. O'Keeffe, O. M. Yaghi, *J. Am. Chem. Soc.* **2001**, *123*, 8239–8247; c) C. N. R. Rao, S. Natarajan, R. Vaidhyanathan, *Angew. Chem. Int. Ed.* **2004**, *43*, 1466–1496.

[9] a) N. Diaz, D. Suarez, K. M. Merz Jr., *Chem. Phys. Lett.* **2000**, *326*, 288–292; b) C. W. Bock, A. K. Katz, J. P. Glusker, *J. Am. Chem. Soc.* **1995**, *117*, 3754–3765.

[10] J. F. Nagle, H. J. Morowitz, *Proc. Natl. Acad. Sci. USA* **1978**, *75*, 298–302.

[11] a) L. E. Cheruzel, M. S. Pometun, M. R. Cecil, M. S. Mashuta, R. J. Wittebort, R. M. Buchanan, *Angew. Chem. Int. Ed.* **2003**,

 © 2007 Wiley-VCH Verlag GmbH & Co. KGaA, Weinheim 

*42*, 5452–5455; b) P. A. Kuz′min, M. D. Surazhskaya, M. A. Golubnichaya, I. B. Baranovskii, *Zh. Neorg. Khim.* **2003**, *48*, 276–280; c) E. W. Hughes, H. L. Yakel, H. Freeman, *Acta Crystallogr.* **1961**, *14*, 345–352.
[12] K. Nakamoto, *Infrared and Ramman Spectra of Inorganic and Coordination Compounds*, 5th ed., John Wiley & Sons Inc., New York, **1997**.
[13] M. Yin, Y. Gu, I. L. Kuskovsky, T. Andelman, Y. Zhu, G. F. Neumark, S. O'Brien, *J. Am. Chem. Soc.* **2004**, *126*, 6206–6207.
[14] *SMART and SAINT*, Siemens Analytical X-ray Instruments Inc., Madison, Wisconsin, USA, **1995**.
[15] G. M. Sheldrick, *SHELXL-97*: *Program for Crystal Structures Refinement*; University of Göttingen: Göttingen, Germany, **1997**.

Received: July 3, 2006
Published Online: December 7, 2006

 © 2007 Wiley-VCH Verlag GmbH & Co. KGaA, Weinheim 

DOI: 10.1002/ejic.200600702

# Ligand Effects on the Chemical Activity of Copper(I) Complexes: Outer- and Inner-Sphere Oxidation of $Cu^{I}L$

**Ariela Burg,*[a] Eric Maimon,[b,c] Haim Cohen,[b,d] and Dan Meyerstein*[b,d]**

**Keywords:** Copper / Electron self exchange rate constant / Outer-sphere mechanism / Inner-sphere mechanism

The effect of the ligands acetonitrile (AN), fumaric acid ($H_2$fum) and 2,5,8,11-tetramethyl-2,5,8,11-tetraazadodecane ($L^1$) on the kinetics of oxidation of $Cu^{I}$ complexes by $[(cyclam)Ni^{III}(SO_4)_2]^-$ and $[(NH_3)_5Co^{III}Cl]^{2+}$ in aqueous solutions via an outer- and inner-sphere mechanism, respectively, has been studied. The effects of the ligands on the electron self-exchange rate constants have also been evaluated. All ligands studied stabilize $Cu^{I}$ in aqueous solution but affect the redox potential of the $Cu^{II/I}L$ couple differently. The ligands decrease the rate of the redox reactions and the electron self-exchange rate constants. The results indicate that acetonitrile and alkenes should not be used as solvents for $[Cu^{I}L]^{+}$-catalyzed processes that involve redox steps. On the other hand, the results also suggest that $[Cu^{I}L^{1}]^{+}$ should be a good catalyst for such processes.

(© Wiley-VCH Verlag GmbH & Co. KGaA, 69451 Weinheim, Germany, 2006)

## Introduction

Copper complexes are used as catalysts for a variety of important redox processes[1–18] such as the Ullmann reaction and are present in various enzymes. As $Cu^{+}_{aq}$ is not stable due to its disproportionation to $Cu^{2+}_{aq}$ and $Cu^{0}$,[19] and as the solubility product of $Cu_2O$ in neutral and alkaline solutions is very low,[20] ligands are required in order to stabilize it. The electron transfer in these processes involves an unusually large change in the coordination geometry: $Cu^{II}$ complexes generally exist as Jahn–Teller distorted octahedra (though other configurations are known), while $Cu^{I}$ complexes are usually four-coordinate tetrahedral or linear species. These large changes in the complex geometry during redox processes are expected to slow them down, therefore the choice of ligands has a major effect on the rates of catalytic processes involving copper complexes.

In general, redox processes proceed by one of two mechanisms: outer sphere or inner sphere. It therefore seemed of interest to study the effect of different types of ligands on the kinetics of oxidation of $[Cu^{I}L^{i}]^{+}$ complexes by an outer sphere and an inner sphere oxidizing agent. For this purpose, the following reactions were studied:

$$[(cyclam)Ni^{III}(SO_4)_2]^- + [Cu^{I}L]^{+} \xrightarrow{k_1} [(cyclam)Ni^{II}(SO_4)_2]^{2-} + [Cu^{II}L]^{2+} \quad (1)$$

$$[(NH_3)_5Co^{III}Cl]^{2+} + [Cu^{I}L]^{+} \xrightarrow{k_2} \text{Products} \quad (2)$$

as $[(cyclam)Ni^{III}(SO_4)_2]^-$ and $[(NH_3)_5Co^{III}Cl]^{2+}$ are known to be an outer-sphere and an inner-sphere oxidant, respectively.[21–23]

In the present study the effect of several ligands that are used, or have been recommended for use, in catalytic processes on the electron self-exchange rate of the $Cu^{II/I}L$ couple has been studied. The ligands chosen affect the redox potential of the $Cu^{II/I}_{aq}$ couple differently — two of them shift it anodically and the other cathodically. They bind to $Cu^{I}$ and $Cu^{II}$ ions in different modes. The first ligand, acetonitrile (AN), which is used as a solvent in many industrial synthetic processes catalyzed by copper(I),[24–26] is a σ donor and a π acceptor in its complexes with $Cu^{I}$ and is not a ligand of $Cu^{II}$ in aqueous solutions at acetonitrile concentrations below 1 M. The second ligand is fumaric acid (fum). Many polymerization processes and other synthetic processes catalyzed by $Cu^{I}$ complexes involve alkenes as substrates,[27,28] and it has been suggested that in order to decrease pollution these reactions should be carried out using the neat alkenes without any solvent.[28] However, alkenes form relatively stable π complexes with $Cu^{I}$,[9,29–31] therefore it is of interest to study the effect of an alkene on the kinetics of the reaction. Fumaric acid was chosen as a model for this study as it is known to bind to copper ions via its π system[29–33]). 2,5,8,11-Tetramethyl-2,5,8,11-tetra-

[a] Department of Chemical Engineering, Sami Shamoon College of Engineering, Beer-Sheva, Israel
[b] Chemistry Department, Ben-Gurion University of the Negev, Beer-Sheva, Israel
[c] Nuclear Research Centre Negev, Beer-Sheva, Israel
[d] Biological Chemistry Department, The College of Judea and Samaria, Ariel, Israel

 © 2007 Wiley-VCH Verlag GmbH & Co. KGaA, Weinheim 

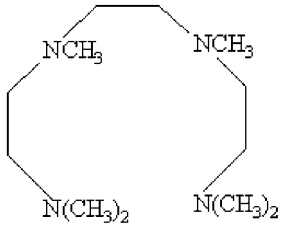


Figure 1. $L^1$ = 2,5,8,11-tetramethyl-2,5,8,11-tetraazadodecane.

azadodecane ($L^1$; Figure 1) shifts the redox potential of the $Cu^{II/I}{}_{aq}$ couple cathodically.[9,29,30,34–37] However, it shifts equilibrium (3) to the left:

$$2Cu^{+}{}_{aq} \leftrightarrows Cu^{2+}{}_{aq} + Cu^{0}\ K_3{}^{[19]} = 1 \times 10^6\ \text{M}^{-1} \quad (3)$$

this stems from

$$2Cu^{I}L_n \leftrightarrows Cu^{II}L_m + Cu^{0} + (2n - m)L\ K_4 \quad (4)$$

where $K_4 = ([Cu^{II}L_m][L]^{2n-m})/[Cu^{I}L_n]^2 = (K^{II}[Cu^{2+}{}_{aq}][L]^m\text{-}[L]^{2n-m})/(K^{I}[Cu^{+}{}_{aq}][L]^n)^2 = K^{II}[Cu^{2+}{}_{aq}]/(K^{I})^2[2Cu^{+}{}_{aq}]^2 = 10^6K^{II}/(K^{I})^2$, and $K^{II}$ and $K^{I}$ are $[Cu^{II}L_m]/([Cu^{2+}{}_{aq}][L]^m)$ and $[Cu^{I}L_n]/([Cu^{+}{}_{aq}][L]^n)$, respectively.

Equilibrium (4) will be shifted to the left if $(K^{I})^2 > K^{II}$, whereas the redox potential of the $Cu^{II}L_m/Cu^{I}L_n$ couple is shifted cathodically if $K^{II} > K^{I}$. Thus, the addition of ligands for which both of these criteria are fulfilled to a mixture of $Cu^{2+}{}_{aq}$ and $Cu^0$ should improve the catalytic properties of this mixture as they stabilize $Cu^{I}$ and increase its reducing power. With regards to this property, $L^1$ is special.

Each of the ligands chosen for this study affects the redox potential of the copper complex differently (Table 1) as each has a different effect on the geometric structure and the electronic configuration of the copper complex. Thus, $[Cu^{I}AN]^+$, $[Cu^{I}(AN)_2]^+$, and $[Cu^{I}(fum)]$ complexes are probably linear, whereas the $(Cu^{I}L^1)^+$ complex is tetrahedral, therefore it was expected that each of them would affect the rate constant of the redox reactions differently. Awareness of the effect of the ligands on the rate constants of outer- and inner-sphere reactions is essential for the design of good copper catalysts.

Table 1. The rate constants for reactions (1) and (2).

| $[Cu^{I}L]^+$ | $E^0$ [V][a] | $k_1$ [$M^{-1}s^{-1}$] | $k_{-11}$ [$M^{-1}s^{-1}$] | $k_2$ [$M^{-1}s^{-1}$] |
|---|---|---|---|---|
| $Cu^{+}{}_{aq}$ | 0.15 | $3.0\times10^4$ | $2.7\times10^{-4}$ | $5.4\times10^4$ |
| $[Cu^{I}fum]^+$ | 0.38[29] | $\leq3.0\times10^1$ | $\leq3.0\times10^{-7}$ | $1.0\times10^2$ |
| $[Cu^{I}AN]^+$ | 0.35[38–41] | $\approx8.5\times10^2$ | $\approx9.7\times10^{-5}$ | $2.2\times10^2$ |
| $[Cu^{I}(AN)_2]^+$ | 0.41[38–41] | $\approx5.0\times10^1$ | $\approx2.2\times10^{-6}$ | 9.3 |
| $[Cu^{I}L^1]^+$ | 0.08[35] | $2.3\times10^4$ | $1.4\times10^{-5}$ | $2.4\times10^4$ |

[a] $E^0$ is the redox potential for the $[Cu^{II/I}L]^{2+/+}$ couple with respect to NHE.

## Results

$[(cyclam)Ni^{III}(SO_4)_2]^-$ and $[(NH_3)_5Co^{III}Cl]^{2+}$ in excess were used as reagents, each one separately, with $Cu^{I}L$ (L = AN, fum, $L^1$). We decided to study systems with an excess of these complexes due to the possibility of some dioxygen leakage, which means that the $[Cu^{I}L]^+$ concentration is less accurate (the reactions with $L^1$ and fum were also studied with $[Cu^{I}L]^+$ in excess — the rate constants are the same). The observed rate constants depend linearly on the $[(cyclam)Ni^{III}(SO_4)_2]^-$ and $[(NH_3)_5Co^{III}Cl]^{2+}$ concentrations (see, for example, Figure 2). The slope of these lines equals the rate constant of the reaction under the experimental conditions. The rate constants thus obtained for all the complexes studied are summarized in Table 1.

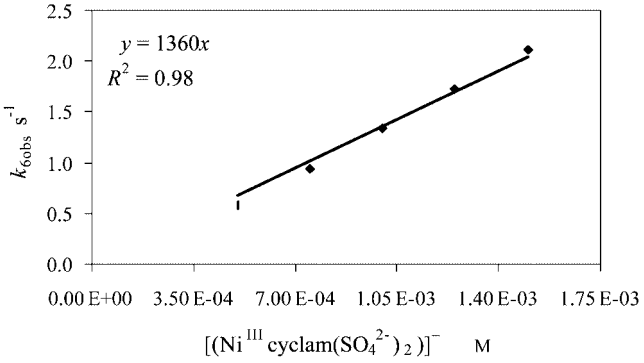


Figure 2. Dependence of $k_6$obs on $[(cyclam)Ni^{III}(SO_4)_2]^-$. The experiments were performed in solutions containing $2.0\times10^{-4}$ M $[Cu^{I}]_T$, $2.5\times10^{-3}$ M fum, $\mu$ = 0.30 M, He-saturated at pH 3.0. As $[(cyclam)Ni^{III}(SO_4)_2]^-$ is stable in the absence of $[Cu^{I}L]^+$, the slope was calculated assuming that the line passes through the origin.

### Derivation of $k(Cu^{+}{}_{aq})$, the Rate Constant of Reactions (5) and (9)

$$[(cyclam)Ni^{III}(SO_4)_2]^- + Cu^{+}{}_{aq} \xrightarrow{k(Cu^{+}{}_{aq})} [(cyclam)Ni^{II}(SO_4)_2]^{2-} + Cu^{2+}{}_{aq} \quad (5)$$

The effect of fum concentration on the rate of reaction (6) was measured by changing its concentration $[(0.25\text{–}1.13)\times10^{-2}$ M].

$$[(cyclam)Ni^{III}(SO_4)_2]^- + [Cu^{I}L]^+ \xrightarrow{k_6} [(cyclam)Ni^{II}(SO_4)_2]^{2-} + [Cu^{II}L]^{2+} \quad (6)$$

$[Cu^{I}]_T = [Cu^{I}L] = [[Cu^{I}(H_2fum)]^+ + [Cu^{I}(Hfum)] + Cu^{+}{}_{aq}]$ (It should be noted that at pH 3.0 the equilibrium reaction $HO_2CCH{=}CHCO_2H \rightleftarrows HO_2CCH{=}CHCO_2^- + H^+$; $pK_{a1}$ = 2.9[29] dictates that about 50% of the two species exist in the solution. The $pK_a$ of fumarate bound to $Cu^{I}$ is similar.[29])

$$[(cyclam)Ni^{III}(SO_4)_2]^- + [Cu^{I}(H_2fum)]^+/Cu^{I}(Hfum) \xrightarrow{k_7} [(cyclam)Ni^{II}(SO_4)_2]^{2-} + [Cu^{II}(H_2fum)]^{2+}/[Cu^{II}(Hfum)]^+ \quad (7)$$

The rate law for reaction (6) is $-d[Ni^{III}]/dt = k_6[Cu^{I}]_T[Ni^{III}]$. As $[Cu^{I}]_T << [Ni^{III}]$, this rate law can be rewritten as $-d[Ni^{III}]/dt = k_{6obs}[Cu^{I}]_T$, where $k_{6obs} = k_6[Ni^{III}]$.

The rate constants $k_{6obs}$ at each fum concentration depend linearly on the $[(cyclam)Ni^{III}(SO_4)_2]^-$ concentration (Figure 2). The dependence of $k_6$ on fum concentration is plotted in Figure 3.

 © 2007 Wiley-VCH Verlag GmbH & Co. KGaA, Weinheim 

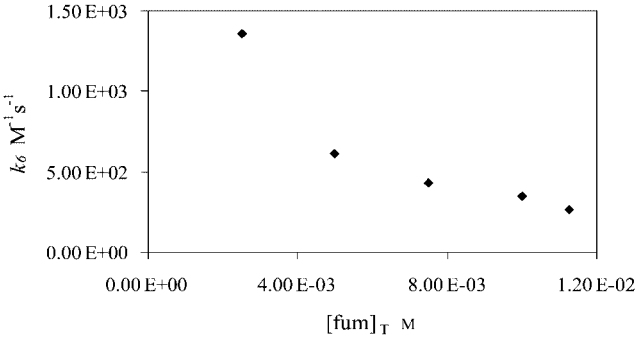


Figure 3. $k_6$ as a function of fumaric acid concentration. The experiments were carried out at $[Cu^I]_T = 2.0 \times 10^{-4}$ M, $\mu = 0.30$ M, pH 3.0; the solutions were He-saturated.

It was decided to assume, as a first approximation, that the contribution of $[Cu^I(fumH_2)]^+$ and $[Cu^I(fumH)]$ species to the rate is negligible, i.e. $k_7 = 0$ and reaction (5) is the only reaction which contributes to $k_6$. Therefore, the rate law can be written $-d[Ni^{III}]/dt = k_5[Cu^+_{aq}][Ni^{III}]$.

From the equilibrium constant of reaction (8):

$$Cu^+_{aq} + fumH_2/fumH^- \leftrightarrows [Cu^I(fumH_2)]^+/[Cu^I(fumH)]; \quad K_8 \text{ (at pH 3.0)}^{[29]} = 8.70 \times 10^3 \text{ M}^{-1} \quad (8)$$

$[Cu^+_{aq}]$ can be expressed as

$K_8 = [Cu^IL]/([Cu^+_{aq}][L])$

$[Cu^+_{aq}] = [(Cu^IL)]/(K_8[L]) = ([Cu^I]_T - [Cu^+_{aq}])/K_8[L]$

$[Cu^+_{aq}] = [Cu^I]_T/(K_8[L] + 1)$

Therefore, under these assumptions, $-d[Ni^{III}]/dt = k_5[Cu^I]_T/(K_8[L] + 1)[Ni^{III}]$.

Plotting $k_6$ (at different fum concentrations) as a function of $1/(K_8[L] + 1)$ (Figure 4) yields a straight line with a slope which equals $k_5$. Thus, the rate constant of reaction (5), $k_5$, is found to be $(3.0 \pm 0.3) \times 10^4$ M$^{-1}$ s$^{-1}$.

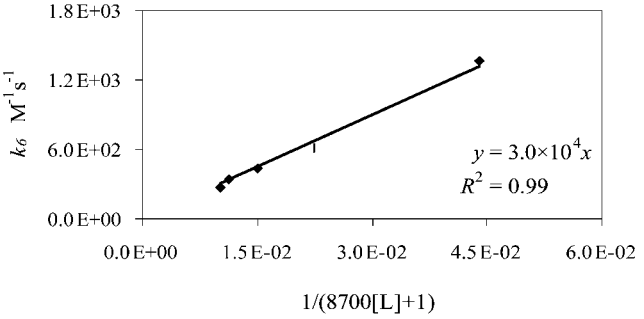


Figure 4. $k_6$ as a function of 1/(8700[fum] + 1). The experiments were carried out at $[Cu^I]_T = 2.0 \times 10^{-4}$ M, $\mu = 0.30$ M, pH 3.0; the solutions were He-saturated.

From the fact that no intercept is obtained in Figure 4 one can calculate that $k_7 \leq 30$ M$^{-1}$ s$^{-1}$ (this is the upper limit of the rate constant assuming that the error of the experiments is ±10%).

The rates of reactions (9) and (10) were studied using an analogous approach.

$$[(NH_3)_5Co^{III}Cl]^{2+} + Cu^+_{aq} \xrightarrow{k_9} \text{products} \quad (9)$$

$$[(NH_3)_5Co^{III}Cl]^{2+} + [Cu^I(fumH_2)]^+/[Cu^I(fumH)] \xrightarrow{k_{10}} \text{products} \quad (10)$$

The results yield $k_9 = (5.4 \pm 0.5) \times 10^4$ M$^{-1}$ s$^{-1}$. This rate constant is in good agreement with an earlier study.[23] The intercept in Figure 5 gives a value for $k_{10}$ of $\leq 100$ M$^{-1}$ s$^{-1}$.

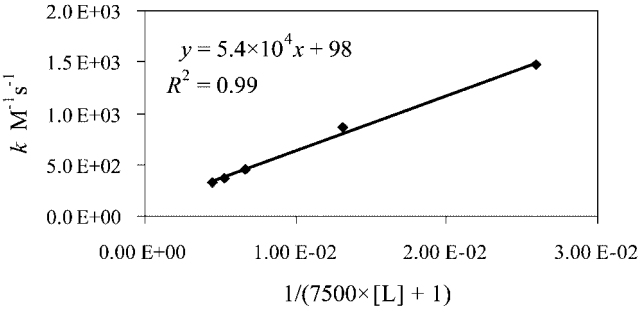


Figure 5. $k$ as a function of 1/(7500[L] + 1), for the reduction of $[(NH_3)_5Co^{III}Cl]^{2+}$ by $Cu^I$ in the presence of fumarate. The experiments were carried out at $[Cu^I]_T = 4.0 \times 10^{-4}$ M, $\mu = 0.20$ M, pH 2.0; the solutions were saturated with He. $k$ = the rate constant observed at each fumaric acid concentration.

### Oxidation of $[Cu^I(AN)_n]^+$

The apparent rate constants of reaction (11) were measured at different acetonitrile concentrations. The results are summed up in Table 2.

$$[(cyclam)Ni^{III}(SO_4)_2]^- + [Cu^I(AN)_n]^+ \xrightarrow{k_{11}} [(cyclam)Ni^{II}(SO_4)_2]^{2-} + [Cu^{II}(AN)_n]^{2+} \quad (11)$$

The results show that $k_{11}$ decreases with an increase in acetonitrile concentration (Figure 6). Under the experimental conditions used here four $Cu^I$ complexes are present in the solution,[38–41] namely $Cu^+_{aq}$, $[Cu^I(AN)]^+$, $[Cu^I(AN)_2]^+$, and $[Cu^I(AN)_3]^+$. Therefore, it is reasonable to assume that the dependence of $k_{11}$ on acetonitrile concentration stems from the relative concentrations of these complexes in the solutions and the rate constants of reactions (5), (12), (13), and (14).

$$[(cyclam)Ni^{III}(SO_4)_2]^- + [Cu^I(AN)]^+ \xrightarrow{k_{12}} [(cyclam)Ni^{II}(SO_4)_2]^{2-} + [Cu^{II}(AN)]^{2+} \quad (12)$$

$$[(cyclam)Ni^{III}(SO_4)_2]^- + [Cu^I(AN)_2]^+ \xrightarrow{k_{13}} [(cyclam)Ni^{II}(SO_4)_2]^{2-} + [Cu^{II}(AN)_2]^{2+} \quad (13)$$

$$[(cyclam)Ni^{III}(SO_4)_2]^- + [Cu^I(AN)_3]^+ \xrightarrow{k_{14}} [(cyclam)Ni^{II}(SO_4)_2]^{2-} + [Cu^{II}(AN)_3]^{2+} \quad (14)$$

The stability constants of the different $[Cu^I(AN)_n]^+$ complexes are known, although their accuracy is not very high, as can be seen from the different values given by different authors.[38–42] The results in Table 2 suggest that (1) the observed rate constants approach a limiting value at high acetonitrile concentration, i.e. the observed reaction is not due

 © 2007 Wiley-VCH Verlag GmbH & Co. KGaA, Weinheim 

Table 2. The observed rate constants for reaction (11).

| AN [M] | $[Cu^{+}_{aq}]$ [M] | $[[CuAN]^{+}]$ [M] | $[[Cu(AN)_2]]^{+}$ [M] | $[[Cu(AN)_3]^{+}]$ [M] | $k_{11}$ [$M^{-1}s^{-1}$] | $k_{11}$ calculated [$M^{-1}s^{-1}$] |
|---|---|---|---|---|---|---|
| 0.096 | $4.9\times10^{-7}$ | $8.8\times10^{-5}$ | $1.01\times10^{-4}$ | $1.05\times10^{-5}$ | 630 | 470 |
| 0.14 | $2.5\times10^{-7}$ | $6.7\times10^{-5}$ | $1.15\times10^{-4}$ | $1.8\times10^{-5}$ | 420 | 370 |
| 0.17 | $1.9\times10^{-7}$ | $5.9\times10^{-5}$ | $1.19\times10^{-4}$ | $2.2\times10^{-5}$ | 390 | 330 |
| 0.19 | $1.5\times10^{-7}$ | $5.3\times10^{-5}$ | $1.20\times10^{-4}$ | $2.5\times10^{-5}$ | 220 | 290 |
| 0.24 | $9.6\times10^{-8}$ | $4.3\times10^{-5}$ | $1.24\times10^{-4}$ | $3.2\times10^{-5}$ | 125 | 240 |
| 0.29 | $6.7\times10^{-8}$ | $3.6\times10^{-5}$ | $1.25\times10^{-4}$ | $3.9\times10^{-5}$ | 120 | 200 |
| 0.38 | $3.7\times10^{-8}$ | $2.7\times10^{-5}$ | $1.22\times10^{-4}$ | $5.1\times10^{-5}$ | 95 | 160 |
| 0.67 | $1.1\times10^{-8}$ | $1.4\times10^{-5}$ | $1.08\times10^{-4}$ | $7.9\times10^{-5}$ | 88 | 90 |

The $[Cu^{I}(AN)_n]^{+}$ concentrations were calculated from the stability constant of the following reactions:

$Cu^{+}_{aq} + AN \leftrightarrows [Cu^{I}AN]^{+}$ $K$[42] = $1.9\times10^{3}$ $M^{-1}$

$Cu^{+}_{aq} + 2AN \leftrightarrows [Cu^{I}(AN)_2]^{+}$ $\beta_2$[42] = $2.2\times10^{4}$ $M^{-2}$

$Cu^{+}_{aq} + 3AN \leftrightarrows [Cu^{I}(AN)_3]^{+}$ $\beta_3$[42] = $2.4\times10^{5}$ $M^{-3}$

by the following equations:

$[Cu^{I}]_T = 2.0\times10^{-4}\ M = [Cu^{+}_{aq}](1 + K_1[AN] + \beta_2[AN]^2 + \beta_3[AN]^3)$

$[[Cu^{I}AN]^{+}] = [Cu^{+}_{aq}]\times\beta_1\times[AN]$

$[[Cu^{I}(AN)_2]^{+}] = [Cu^{+}_{aq}]\times\beta_2\times[AN]^2$

$[[Cu^{I}(AN)_3]^{+}] = [Cu^{+}_{aq}]\times\beta_3\times[AN]^3$

This set of equilibria constants was chosen as they were measured at similar ionic strengths to those used in this study. The use of the stability constants reported by Jordan et al.[41] does not affect the derived rate constants considerably.

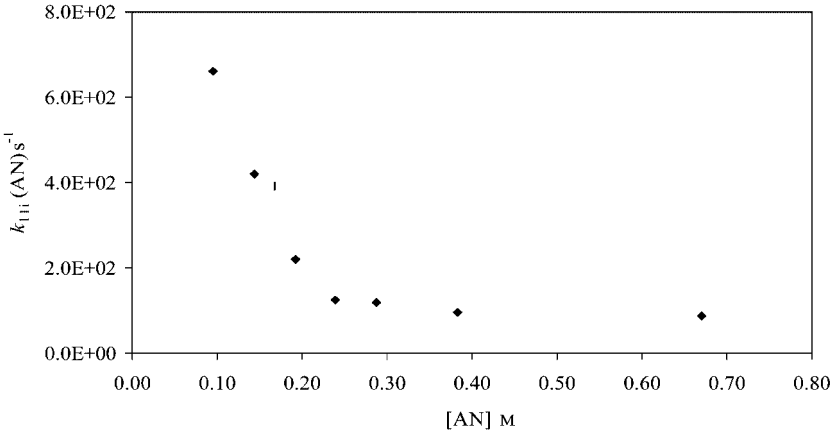


Figure 6. $k_{11}$ as a function of acetonitrile concentration. The experiments were carried out at $[Cu^{I}]_T = 2.0\times10^{-4}$ M, $\mu$ = 0.30 M, pH 3.0; the solutions were He-saturated.

only to reaction (5) and (2) the observed rates at high acetonitrile concentration seem to be independent of $[Cu^{I}(AN)_3]^{2+}$, i.e. one can assume that $k_{14}$ is negligible. Following these assumptions, and with $k_5$ determined above, $k_{12}$ and $k_{13}$ were calculated by repetitive approximations. The deviations of the calculated rate constants from the experimental ones are probably due mainly to the uncertainties in $K([Cu^{I}(AN)]^{+})$, $K([Cu^{I}(AN)_2]^{+})$ and $K([Cu^{I}(AN)_3]^{+})$.

The rate constants of reactions (15), (16), and (17) were evaluated analogously.

$$[(NH_3)_5Co^{III}Cl]^{2+} + [Cu^{I}(AN)]^{+} \xrightarrow{k_{15}} \text{products} \quad (15)$$

$$[(NH_3)_5Co^{III}Cl]^{2+} + [Cu^{I}(AN)_2]^{+} \xrightarrow{k_{16}} \text{products} \quad (16)$$

$$[(NH_3)_5Co^{III}Cl]^{2+} + [Cu^{I}(AN)_3]^{+} \xrightarrow{k_{17}} \text{products} \quad (17)$$

The rate constants are summed up in Table 3.

Table 3. Basicity of the ligands and stability constants of their copper complexes in aqueous solutions.

| | log $K$ | |
|---|---|---|
| | $L^{1}$[35,37] | fum[29] |
| $LH^{+} + H^{+} \rightleftarrows LH_2^{+}$ | 8.50 | 3.1 |
| $LH_2^{+} + H^{+} \rightleftarrows LH_3^{+}$ | 5.40 | |
| $LH_3^{+} + H^{+} \rightleftarrows LH_4^{+}$ | 1.70 | |
| $L + Cu^{+} \rightleftarrows CuL^{+}$ | 11.0 | 3.94 (pH 3.0), 3.88 (pH 2.0) |

### Evaluation of the Self-Exchange Rate Constants, $k'_{11}$, of Reaction (18) for the Complexes Studied

According to the Marcus theory,[43–46] for reactions proceeding by the outer-sphere mechanism, $k'_{12}$, the rate constant of the cross reaction, reaction (1), depends on three parameters: the equilibrium constant of the cross reaction ($K_{12}$) and the electron self-exchange rate constants $k'_{11}$ [reaction (18)] and $k'_{22}$ (the electron self-exchange rate con-

 © 2007 Wiley-VCH Verlag GmbH & Co. KGaA, Weinheim 

stant for the $[(cyclam)Ni^{III/II}(SO_4)_2]^{-/2-}$ couple). The equilibria constants $K_{12}$ are known from the redox potentials of the different complexes. Some of them were calculated from the known stability constants of the different complexes using the Nernst equation,[29,35,37,41] and $k'_{22}$ was measured by the following procedure: the rate of the reaction of ascorbate ($HA^-$) with $[(cyclam)Ni^{III}(SO_4)_2]^-$ at pH 4.9 was measured [reaction (19)].

$$[Cu^{I}L]^+ + [*Cu^{II}L]^{2+} \rightarrow [Cu^{II}L]^{2+} + [*Cu^{I}L]^+ \quad (18)$$

$$HA^- + [(cyclam)Ni^{III}(SO_4)_2]^- \rightarrow HA^{\cdot} + [(cyclam)Ni^{II}(SO_4)_2]^{2-};\ k_{19} = 2.7\times10^4\ M^{-1}s^{-1} \quad (19)$$

The electron self-exchange rate constant for the ascorbate couple is known.[47] From these values, a value of $k'_{22} = 1.1\times10^3\ M^{-1}s^{-1}$ for $[(cyclam)Ni^{III}(SO_4)_2]^-$ at $\mu = 0.30$ M is obtained. Using these data and the measured rate constants for reaction (1) (neglecting the electrostatic work term, which is small for reactions of relatively large ions with small charges in solutions with a relatively high ionic strength) the self-exchange rate constants, $k'_{11}$, of the $Cu^{II}L/Cu^{I}L$ couples, reaction (18), were calculated by applying the Marcus cross relation. These results are summed up in Table 1.

The results obtained for the self exchange of $Cu^{2+/+}_{aq}$ [reaction (20)] are in very good agreement with those of Davies et al.,[48] who obtained $k'_{11} = 2.0\times10^{-4}\ M^{-1}s^{-1}$.

$$Cu_{aq}^{+} + *Cu_{aq}^{2+} \overset{k'_{11}}{\rightarrow} Cu_{aq}^{+} + *Cu_{aq}^{2+} \quad (20)$$

This observation suggests that the value used for $k'_{22}$ and the experimental approach used are adequate, although the value reported by Sisley and Jordan,[49] $k'_{11} = 5\times10^{-7}\ M^{-1}s^{-1}$, is considerably lower. Recently,[40] the electron self-exchange of $[Cu^{II/I}(AN)_n]^+$ ($n$ = 3 or 4) was reported to be around $5\times10^{-9}\ M^{-1}s^{-1}$ in solutions containing 50–97.5% AN. The authors state that "the various $Cu^{II}$ solvates have similar self-exchange constants", although this is clearly not the case for $[Cu^{I}(AN)]^+$ and $[Cu^{I}(AN)_2]^+$ measured in the present study, which shows that $k'_{11}$ decreases with an increase in $n$. The value reported for $n$ = 3–4 is orders of magnitude smaller than that for $n$ = 2, and this observation is in agreement with the assumption that $k_{14}$ is very small and can be neglected.

It is of interest to note that all the ligands studied by us lower the self-exchange rate constant relative to that of $Cu^{2+/+}_{aq}$. This observation is not general,[50] and the self-exchange rate constants of copper enzymes are about ten orders of magnitude higher.[51–53]

## Discussion

The three ligands chosen for this study slow down the rates of reduction of both $[(cyclam)Ni^{III}(SO_4)_2]^-$, an outer-sphere oxidant, and $[(NH_3)_5Co^{III}Cl]^{2+}$, an inner-sphere oxidant, although this is clearly not a general observation as $L^1$ accelerates the rate of reduction of $NO_2^-$ by $Cu^{I}$.[18] The effect of $L^1$, which shifts the redox potential of the $Cu^{2+/+}_{aq}$ couple cathodically,[34–36] on the rate constants is considerably smaller than would be expected.

It is of interest to note that AN and $H_2$fum not only shift the redox potential of the $Cu^{2+/+}_{aq}$ couple anodically but also considerably decrease the rate of the electron self-exchange reaction [reaction (18)]. The combination of the effect of these ligands on the redox potential and on the electron self-exchange rate constants suggests that their complexes are poor catalysts for $Cu^{I}$-catalyzed processes that involve a redox process. Thus, it is concluded that acetonitrile and alkenes should not be used as solvents for such processes. On the other hand, the electron self-exchange rate of the $[Cu^{II/I}L^1]^{2+/+}$ couple is only slightly lower than that of the $Cu^{2+/+}_{aq}$ couple and $L^1$ shifts the redox potential of the $Cu^{II/I}$ couple cathodically. The contribution of these effects explains the observation that $[Cu^{I}L^1]^+$ is a very good catalyst[54] for $Cu^{I}$-catalyzed processes.

## Experimental Section

**Materials:** $CuSO_4$, $Cu^0$, acetonitrile (AN), fumaric acid ($H_2$fum), $L^1$, sodium perchlorate, and perchloric acid were ordered from Aldrich. $[(cyclam)Ni^{III}(SO_4)_2]H$[55] and $[(NH_3)_5Co^{III}Cl](ClO_4)_2$[23] were synthesized according to literature procedures. All solutions were prepared from A.R. grade chemicals and from deionized water further purified by passing through a Milli Q Millipore setup (final resistivity > 10 MΩ cm$^{-1}$).

Solutions of the $[Cu^{I}L]^+$ complexes were prepared by a comproportionation process [reaction (4)]. The solutions' color changed after several hours from blue (indicating $[Cu^{II}L]^{2+}$ complexes) to colorless (indicating $[Cu^{I}L]^+$ complexes). Solid copper metal was added to deaerated solutions containing $CuSO_4$ and an excess of L.

Reaction (1) was studied at $\mu = 0.30$ M, maintained by the addition of $Na_2SO_4$ in order to stabilize $[(cyclam)Ni^{III}(SO_4)_2]^-$. The stability constant of $[(cyclam)Ni^{III}(SO_4)_2]^-$ is $K = [[(cyclam)Ni^{III}(SO_4)_2]^-]/[[(cyclam)Ni^{III}(H_2O)_2]^{3+}[SO_4^{2-}]^2] = 5\times10^6\ M^{-2}$,[56,57] therefore a high concentration of $SO_4^{2-}$ is essential. Solutions of $[(cyclam)Ni^{III}(SO_4)_2]^-$ were prepared by literature procedures.[56,58] Reaction (2) was studied at $\mu = 0.20$ M. The reactions were carried out at the appropriate pH, i.e. that at which the ligands bind to the copper ion. The experiments with AN and $H_n$fum ($n$ = 0–2) as ligands were carried out at pH 3.0. The experiments with $L^1$ were carried out at pH 6, where $L^1$ also acts as a buffer. Table 3 sums up the p$K$'s of the ligands and the binding constants of $[Cu^{I}L]^+$. All $[Cu^{I}L]^+$, $[(cyclam)Ni^{III}(SO_4)_2]^-$, and $[(NH_3)_5Co^{III}Cl]^{2+}$ complexes were handled under strictly anaerobic conditions, using the syringe technique. All experiments were carried out at room temperature (22 °C). Blank experiments demonstrated, as expected, that the different $[Cu^{II}L]^{2+}$ complexes do not react with $[(cyclam)Ni^{III}(SO_4)_2]^-$ or $[(NH_3)_5Co^{III}Cl]^{2+}$.

**Kinetic Measurements:** Stopped-flow experiments were carried out using an SX.18 Applied PhotoPhysics stopped flow machine that enables kinetic measurements of reactions with half lifetimes above 2 ms. A 05-109 Spectra Kinetics Monochromator, which enables measurements in the range 200–700 nm, was used. The optical path was 10 mm.

The absorbance was followed as a function of time at the appropriate absorption bands of the complexes. The disappearance of [(cy-

 © 2007 Wiley-VCH Verlag GmbH & Co. KGaA, Weinheim 

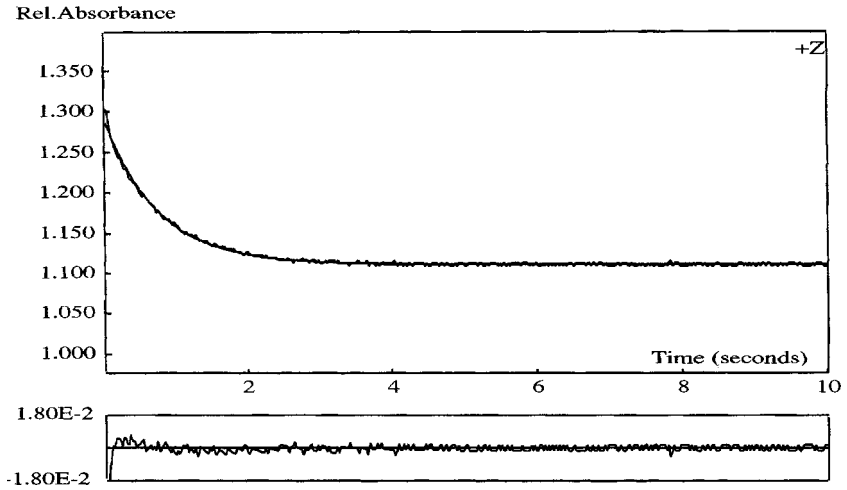


Figure 7. Dependence of $[(cyclam)Ni^{III}(SO_4)_2]^-$ concentration on time. The experiments were carried out at $[Cu^{I}]_T = 2.0 \times 10^{-4}$ M, $2.5 \times 10^{-3}$ M fum, $\mu = 0.30$ M, pH 3.0; the solutions were He-saturated.

clam)$Ni^{III}(SO_4)_2]^-$ and $[(NH_3)_5Co^{III}Cl]^{2+}$ was followed at 435 and 530 nm, respectively (Figure 7). The formation of $[Cu^{II}L]^{2+}$ was followed at $\lambda > 600$ nm. Each kinetic run was repeated at least five times using at least two independently prepared stock solutions. The error limit of the measured rates is $\leq 10\%$.

The Δ(absorbance) observed was always in agreement with expectations based on $[Cu^{I}L]^+$ and $\varepsilon[Ni^{III}L(SO_4)_2]^-$ and $\varepsilon[(NH_3)_5Co^{III}Cl]^{2+}$.

## Acknowledgments

This study was supported, in part, by a grant from the Budgeting and Planning Committee of The Council of Higher Education. D. M. wishes to express his thanks to Irene Evens for her ongoing interest and support.

[1] A. Burg, H. Cohen, D. Meyerstein, *J. Biol. Inorg. Chem.* **2000**, *5*, 213–217.
[2] E. T. Adman and M. E. Murphy, *Handbook of Metalloproteins*, Wiley, New York, **2001**.
[3] C. G. Bates, P. Saejueng, M. Q. Doherty, D. Venkataraman, *Org. Lett.* **2004**, *6*, 5005–5008.
[4] R. J. F. Branco, P. A. Fernandes, M. J. Ramos, *Theor. Chem. Acc.* **2006**, *115*, 27–31.
[5] U. H. F. Bunz, K. P. Gwaltney, K. K. Arrowood, *Polymer* **2006**, *47*, 598.
[6] Y. Tokita, A. Okamoto, K. Nishiwaki, M. Kobayashi, E. Nakamura, *Bull. Chem. Soc. Jpn.* **2004**, *77*, 1395–1399.
[7] D. Bellus, *Pure Appl. Chem.* **1985**, *57*, 1827–1838.
[8] J. Lindley, *Tetrahedron* **1984**, *40*, 1433–1456.
[9] N. Navon, A. Burg, H. Cohen, R. V. Eldik, D. Meyerstein, *Eur. J. Inorg. Chem.* **2002**, 423–429.
[10] A. A. Moroz, M. S. Shvartsberg, *Russ. Chem. Rev.* **1974**, *43*, 679–689.
[11] M. Saphier, A. Burg, S. Sheps, H. Cohen, D. Meyerstein, *J. Chem. Soc., Dalton Trans.* **1999**, 1845–1849.
[12] D. A. Zuberbuhler, *Micron* **2004**, *35*, 137–139.
[13] N. V. Kramareva, E. D. Finashina, A. V. Kucherov, L. M. Kustov, *Kinet. Catal.* **2003**, *44*, 793–800.
[14] E. Fadda, N. Chakrabarti, R. Pomes, *J. Phys. Chem. B* **2005**, *109*, 22629–22640.
[15] S. Fukuzumi, *Pure Appl. Chem.* **2003**, *75*, 577–587.
[16] H. J. Cristau, A. Ouali, J. F. Spindler, M. Taillefer, *Chem. Eur. J.* **2005**, *11*, 2483–2492.
[17] V. Pelmenschikov, P. E. M. Siegbahn, *Inorg. Chem.* **2005**, *44*, 3311–3320.
[18] A. Burg, E. Lozinsky, H. Cohen, D. Meyerstein, *Eur. J. Inorg. Chem.* **2004**, *18*, 3675–3680.
[19] F. A. Cotton, G. Wilkinson, *Advanced Inorganic Chemistry*, John Wiley & Sons, New York, **1972**, p. 905.
[20] J. A. Dean, *Lange's Handbook of Chemistry*, 14th ed., McGraw-Hill, New York, **1992**, section 8.8.
[21] P. S. Myunghyun, *Adv. Inorg. Chem.* **1997**, *44*, 93–146.
[22] A. G. Lappin, A. McAuley, *Adv. Inorg. Chem.* **1988**, *32*, 241–295.
[23] O. J. Parker, J. H. Espenson, *J. Am. Chem. Soc.* **1969**, *91*, 1968.
[24] P. Aslanidis, P. J. Cox, S. Davanidis, P. Karagiannidis, *Inorg. Chim. Acta* **2004**, *357*, 1063–1076.
[25] T. Yukitoshi, Y. Yoshikazu, K. Kosuke, D. Hiroshi, Y. Kentaro, I. Tsuneo, *J. Org. Chem.* **2005**, *70*, 9009–9012.
[26] V. Ali, R. Kaur, N. Kamal, S. Singh, S. C. Jain, H. P. S. Kang, M. Zulfequar, M. Husain, *J. Phys. Chem. Solids* **2006**, *67*, 659–664.
[27] D. Batt-Coutrot, D. M. Haddleton, A. P. Jarvis, R. L. Kelly, *Eur. Polym. J.* **2003**, *39*, 2243–2252.
[28] T. Wei, N. A. Kumar, M. Krzysztof, *Macromol. Chem. Phys.* **2005**, *206*, 1171–1177.
[29] N. Navon, A. Masarwa, H. Cohen, D. Meyerstein, *Inorg. Chim. Acta* **1997**, *261*, 29–35.
[30] N. Navon, G. Golub, H. Cohen, P. Paoletti, B. Valtancoli, D. Meyerstein, *Inorg. Chem.* **1999**, *38*, 3484–3488.
[31] D. Meyerstein, *Inorg. Chem.* **1975**, *14*, 1716–1717.
[32] R. M. Keefer, L. J. Andrews, R. E. Kepner, *J. Am. Chem. Soc.* **1949**, *71*, 3906–3909.
[33] J. K. Hurst, R. H. Lane, *J. Am. Chem. Soc.* **1973**, *95*, 1703–1709.
[34] G. Golub, H. Cohen, D. Meyerstein, *J. Chem. Soc., Chem. Commun.* **1992**, 397–398.
[35] G. Golub, H. Cohen, P. Paoletti, A. Bencini, L. Messori, I. Bertini, D. Meyerstein, *J. Am. Chem. Soc.* **1995**, *117*, 8353–8361.
[36] G. Golub, I. Zilbermann, H. Cohen, D. Meyerstein, *Supramol. Chem.* **1996**, *6*, 275–279.
[37] G. Golub, H. Cohen, A. Bencini, B. Valtancoli, D. Meyerstein, *Inorg. Chim. Acta* **1997**, *255*, 111–115.
[38] P. Hemmerich, C. Sigwart, *Experientia* **1963**, *19*, 488–489.
[39] A. Zuberbuhler, *Helv. Chim. Acta* **1970**, *53*, 473–485.
[40] J. Irangu, M. J. Ferguson, R. B. Jordan, *Inorg. Chem.* **2005**, *44*, 1619–1625.
[41] P. Kamau, R. B. Jordan, *Inorg. Chem.* **2001**, *40*, 3879–3883.
[42] A. Gunter, A. Zuberbuhler, *Chimia* **1970**, *24*, 340–342.

 © 2007 Wiley-VCH Verlag GmbH & Co. KGaA, Weinheim 

[43] R. A. Marcus, *J. Chem. Phys.* **1956**, *24*, 741–746.
[44] R. A. Marcus, *J. Chem. Phys.* **1957**, *26*, 867–871.
[45] R. A. Marcus, *J. Chem. Phys.* **1966**, *45*, 2630–2638.
[46] R. A. Marcus, *Angew. Chem. Int. Ed. Engl.* **1993**, *32*, 1111–1121.
[47] A. McAuley, T. Oswald, R. I. Haines, *Can. J. Chem.* **1983**, *61*, 1120–1125.
[48] K. M. Davies, *Inorg. Chem.* **1983**, *22*, 615–619.
[49] M. J. Sisley, R. B. Jordan, *Inorg. Chem.* **1992**, *31*, 2880–2884.
[50] D. B. Rorabacher, *Chem. Rev.* **2004**, *104*, 651–697.
[51] P. Kyritsis, W. McFarlane, A. G. Sykes, *Inorg. Chem.* **1995**, *34*, 5371–5374.
[52] C. M. Groeneveld, S. Dahlin, B. Reinhammar, G. W. Canters, *J. Mol. Biol.* **1988**, *200*, 189–199.
[53] C. M. Groeneveld, S. Dahlin, B. Reinhammar, G. W. Canters, *J. Am. Chem. Soc.* **1987**, *109*, 3247–3250.
[54] I. Rusonik, H. Cohen, D. Meyerstein, *Dalton Trans.* **2003**, 2024–2028.
[55] E. K. Barefield, F. Wagner, A. W. Herlinger, A. R. Dahl, *Inorg. Synth.* **1976**, *16*, 220–225.
[56] E. Zeigerson, L. J. Kirschenbaum, D. Meyerstein, *J. Electroanal. Chem.* **1981**, *127*, 113–126.
[57] E. Zeigerson, I. Bar, J. Bernstein, L. J. Kirschenbaum, D. Meyerstein, *Inorg. Chem.* **1982**, *21*, 73–80.
[58] I. Zilbermann, H. Cohen, D. Meyerstein, *Chem. Rev.* **2005**, *105*, 2609–2625.

Received: July 28, 2006
Published Online: November 6, 2006

 © 2007 Wiley-VCH Verlag GmbH & Co. KGaA, Weinheim 

DOI: 10.1002/ejic.200600833

# Dinuclear Metallocenes with a Modulated Biphenylene Bridge for Olefin Polymerization

**Seong Kyun Kim,[a] Hwa Kyu Kim,[a] Min Hyung Lee,[a][‡] Seung Woong Yoon,[a] Yonggyu Han,[a] Sungjin Park,[a] Junseong Lee,[a] and Youngkyu Do*[a]**

**Keywords:** Homogeneous catalysis / Metallocenes / Olefins / Polymerization / Titanium / Zirconium

Dinuclear group 4 metallocene catalysts linked by a biphenylene or 1,2-diphenylethylene bridge, namely [4,4′-$(C_5Me_4)_2$-$(C_6H_4)_2$][$CpZrCl_2$]$_2$ (**2a**), [*p*-$(C_5Me_4)C_6H_4CH_2$]$_2$[$CpZrCl_2$]$_2$ (**2b**), [*p*-(3,4-$Me_2C_5H_2$)$C_6H_4CH_2$]$_2$[$CpZrCl_2$]$_2$ (**2c**), [$(C_5Me_4)_2$-$(C_6H_4)_2$][$TiCl_3$]$_2$ (**3a**), [*p*-$(C_5Me_4)C_6H_4CH_2$]$_2$[$TiCl_3$]$_2$ (**3b**), and [*p*-(3,4-$Me_2C_5H_2$)$C_6H_4CH_2$]$_2$[$TiCl_3$]$_2$ (**3c**), have been prepared and the crystal structures of **2b** and **3b** determined by X-ray diffraction methods. The crystal structures reveal that these complexes consist of two equivalent metal units inverted with respect to the center of the bridge. All the complexes were tested for the polymerization of ethylene and styrene in the presence of methylaluminoxane (MAO), and direct comparisons of their catalytic properties with those of the corresponding mononuclear analogues [$(PhC_5Me_4)$-$CpZrCl_2$] (**4a**), [(*p*-$TolC_5Me_4$)$CpZrCl_2$] (**4b**), [(1-*p*-Tol-3,4-$Me_2C_5H_2$)$CpZrCl_2$] (**4c**), [$(PhC_5Me_4)TiCl_3$] (**5a**), [(*p*-$TolC_5Me_4$)$TiCl_3$] (**5b**), and [(1-*p*-Tol-3,4-$Me_2C_5H_2$)$TiCl_3$] (**5c**) were performed. The dinuclear zirconocenes show a high activity in ethylene polymerization comparable with those of the corresponding mononuclear catalysts and give an increased molecular weight of polyethylene. The dinuclear half-sandwich titanocenes exhibit similar or slightly lower activity and molecular weight in styrene polymerization compared with their mononuclear analogues.
(© Wiley-VCH Verlag GmbH & Co. KGaA, 69451 Weinheim, Germany, 2007)

## Introduction

Single-site catalytic systems for olefin polymerization based on group 4 metal complexes have become well established during the last two decades and have provided various opportunities to tailor the polymer properties, especially molecular weight, molecular weight distribution, and stereochemistry, as well as high catalytic activity.[1–6] The fruits of these endeavors are the various kinds of catalyst systems that are now being used in practical applications. Syndiotactic polystyrene (sPS) from half-sandwich metallocene catalysts and linear low-density polyethylene (LLDPE) from constrained-geometry catalysts are typical products available commercially from single-site catalyst systems. Most of these catalyst systems, however, involve mononuclear complexes, as dinuclear systems that consist of two active centers linked within the same molecule have become a focus of attention only since the first report by Mülhaupt et al.[7] on a phenylene-bridged dinuclear zirconocene system for propylene polymerization. Initial efforts made by several groups have shown that these catalyst systems are effective in olefin polymerization[8–11] but they have still remained much less defined in terms of structural aspects, class of catalysts, and kinds of polymerization they can perform in comparison with the well-known mononuclear systems.

Recently, it has been found that dinuclear systems are able to show interesting catalytic behaviors that are different from those of mononuclear systems. Systematic polymerization studies by Noh et al. using polysiloxane- and polymethylene-bridged dinuclear complexes have demonstrated that the catalytic activity[12,13] and co-monomer incorporation ratio[14–16] are strongly correlated with both the nature and the length of the bridging group employed. Marks et al. have revealed that dinuclear constrained-geometry catalysts connected by ethylene and/or methylene bridges exhibit unique polymerization behaviors such as high α-olefin incorporation,[17,18] high activity in styrene polymerization,[19] and branched or significantly increased molecular weights in ethylene polymerization[18,20–22] mainly due to the cooperative interactions between two active centers. Alt et al. have also reported asymmetric dinuclear zirconocenes that are capable of producing polyethylene with a bimodal molecular weight distribution.[23,24]

Although it has been suggested from the foregoing studies that the catalytic properties of dinuclear complexes can be strongly affected by the nature of the bridging group and possible cooperative metal–metal interactions, very few studies on the variation of the bridging group have been

[a] Department of Chemistry, School of Molecular Science BK-21, Center for Molecular Design and Synthesis, Korea Advanced Institute of Science and Technology,
Daejeon, 305-701, Republic of Korea
Fax: +82-42-869-2810
E-mail: ykdo@kaist.ac.kr
[‡] Current address: Department of Chemistry, Texas A&M University,
College Station, TX 77843, USA

 © 2007 Wiley-VCH Verlag GmbH & Co. KGaA, Weinheim 

performed. Flexible alkylene groups still constitute the majority of bridges,[7–26] therefore it is of great value to examine the electronic and/or steric effects of the bridging group that play an important role in governing the catalytic properties of dinuclear complexes and thereby rationalize the cooperative reactivity of dinuclear catalysts. In this regard, our group recently reported the well-defined dinuclear group 4 metal complexes [4,4′-$(C_5Me_4)_2(C_6H_4)_2$][$CpZrCl_2$]$_2$ (**2a**) and [4,4′-$(C_5Me_4)_2(C_6H_4)_2$][$TiCl_3$]$_2$ (**3a**), which are linked by a rigid biphenylene bridge, and the direct comparison of their catalytic properties with those of the corresponding mononuclear analogues in ethylene and styrene polymerization.[27] We observed an increase of both molecular weight of polymer and catalytic activity, irrespective of the co-catalyst employed, especially in ethylene polymerization.

In the present report, which includes a further investigation of the polymerization behavior of the biphenylene-bridged system, we aim to endow the existing biphenylene group with flexibility that could provide additional metal–metal interactions and at the same time to keep each metal center highly active by minimizing the steric hindrance between the two active centers. To this end, we have developed novel dinuclear group 4 catalysts containing bis(cyclopentadienido) ligands bound to a rigid but flexible 1,2-diphenylethylene bridge. A complete set of comparative polymerization studies in olefin polymerization with the corresponding mononuclear catalysts is also reported.

## Results and Discussion

### Complexes Synthesis and Characterization

Two new ligands (**1b** and **1c**) were synthesized by a procedure analogous to that for ligand **1a** reported in our previous communication.[27] These ligands are poorly soluble in common organic solvents but are more soluble than **1a**, thus reflecting their flexible nature. The zirconium complexes **2b** and **2c** were prepared in a straightforward manner by the direct transmetalation of dilithium salts of the ligands with two equivalents of [$CpZrCl_3$] in thf. Complexes **2b** and **2c** have much better solubility then **1a** in hydrocarbon solvents, which could be an important advantage when the immobilization of the catalysts is considered for industrial applications. Reaction of the dilithium salt of the ligands with two equivalents of $ClTi(OiPr)_3$ in thf, followed by in situ chlorination with an excess of $Me_3SiCl$ or $Me_2SiCl_2$ in $CH_2Cl_2$, also afforded the final titanium trichloride complexes **3b** and **3c** (Scheme 1). Complex **3c** is less soluble in $CHCl_3$ and $CH_2Cl_2$ than **3a** and **3b**, which suggests that the sterically less congested nature of **3c** allows the retention of planarity between the phenyl and cyclopentadienido rings in the ligand backbone. Two singlets for the methyl proton resonance in the $^1H$ NMR spectra of **2a**, **2b** and **3a**, **3b**, and one singlet methyl resonance for **2c** and **3c** indicate that the two metal units in these dinuclear complexes are in an identical chemical environment in solution.

### X-ray Crystallographic Structures of 2b and 3b

The molecular structures of **2b** and **3b** are depicted in Figure 1 and selected interatomic distances and angles are listed in Table 1. The zirconium complex **2b** crystallizes in the space group *C*2/*c* with only one half of the molecule in the asymmetric unit. Interestingly, the diphenylethylene bridge adopts a *gauche* conformation in which the molecule has a $C_2$-symmetric axis perpendicular to the C(16)–C(16′) bond. Thus, two [Cp′$CpZrCl_2$] (Cp′ = $C_5Me_4Ph$) fragments are perfectly inverted along the rotation axis, which indicates that complex **2b** consists of two equivalent units in the solid state. The detailed structural analysis indicates that the bonding geometry around the zirconium center, such as the Cl(1)–Zr–Cl(2) and Cg(1)–Zr–Cg(2) bond angles and Zr–Cl and Zr–Cg bond lengths shown in Table 1, are in a similar range to those of mononuclear, unbridged zirconocene complexes.[28–30] The dihedral angle of 41.28(18)° between the $C_5Me_4$ ring [Cp(1)] and the adjacent phenylene ring [Ph(1)] is closer to that of the phenyl-substituted mo-

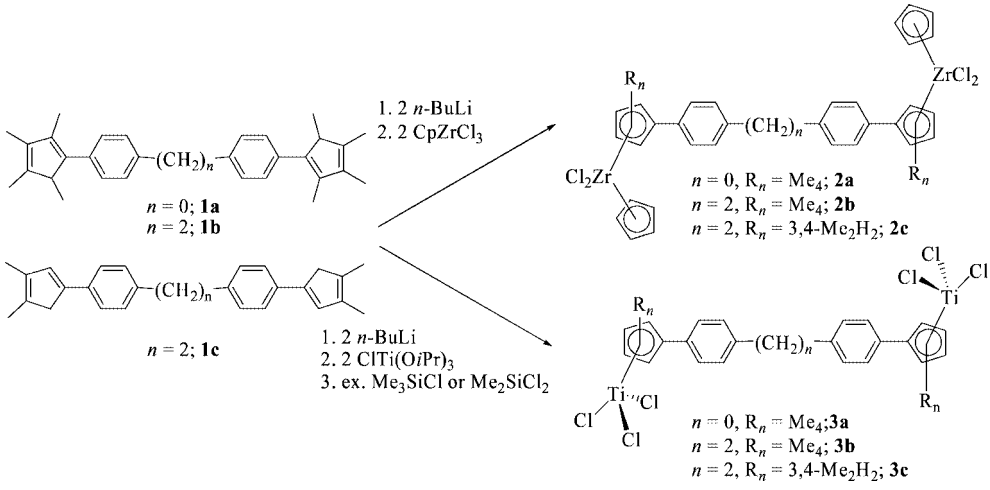


Scheme 1.

 © 2007 Wiley-VCH Verlag GmbH & Co. KGaA, Weinheim 

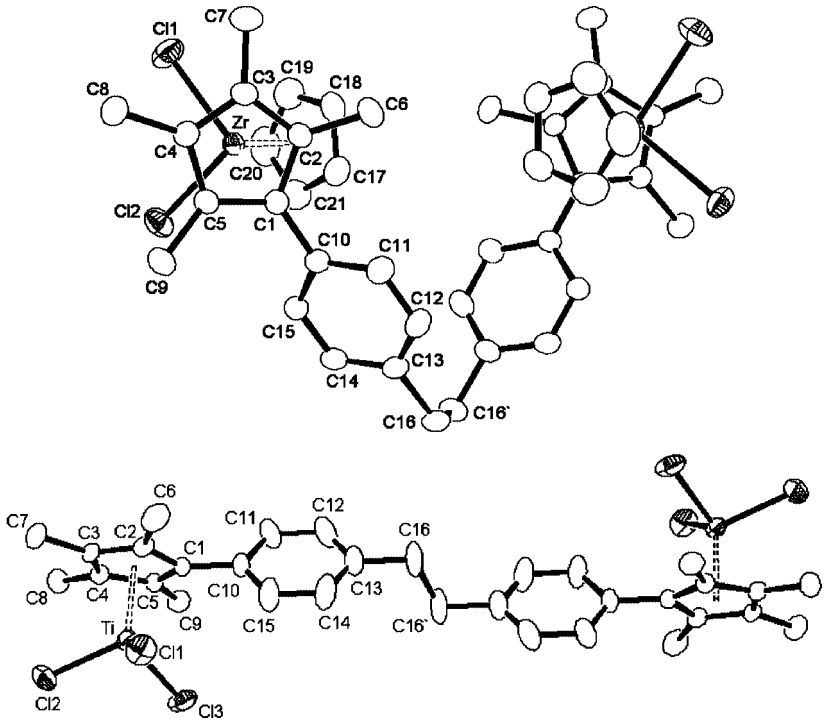


Figure 1. Molecular structures of **2b** (top) and **3b** (bottom).

nonuclear zirconocene **4a** (47.2°)[31] than that observed in the biphenylene-bridged **2a** [63.6(2)°],[27] which suggests that flexible nature of the bridging group makes the steric environment of each metallocene unit of **2b** similar to that of the mononuclear **4a**.

Table 1. Selected bond lengths [Å] and angles [°] for **2b** and **3b**.

| Compound | **2a** (M = Zr)[a] | **2b** (M = Zr) | **3b** (M = Ti) |
|---|---|---|---|
| Cl(1)–M–Cl(2) | 96.5(0) | 97.07(3) | 103.57(11) |
| Cg(1)–M–Cg(2)[b] | 129.8 | 130.98 | – |
| Cp′(1)–Ph(1)[c] | 63.6(2) | 41.28(18) | 62.6(3) |
| M–Cl(1) | 2.429(1) | 2.4337(11) | 2.242(4) |
| M–Cl(2) | 2.440(1) | 2.467(10) | 2.245(4) |
| M–Cl(3) | – | – | 2.240(4) |
| M–Cg(1) | 2.224(1) | 2.2231(15) | 2.026(4) |
| M–Cg(2) | 2.199(2) | 2.213(2) | – |

[a] Data taken from ref.[27] [b] Cg(1) and Cg(2) are the centroids of the $C_5Me_4$ (C1–C5) and Cp (C21–C25) rings, respectively. [c] Cp′(1) is the plane of $C_5Me_4$ (C1–C5) and Ph(1) the plane of $C_6H_4$ (C10–C15).

The titanium complex **3b** crystallizes in the space group *C*2/*c* and contains half of each of two independent molecules in the asymmetric unit. Similarly to **2a** and **3a**, two $Cp'TiCl_3$ ($Cp' = C_5Me_4Ph$) fragments are also perfectly inverted with respect to the C(16)–C(16′) bond axis, thus indicating that complex **3b** consists of two equivalent units in the solid state. According to the solid-state structure, **3b** adopts an *anti* conformation of the diphenylethylene bridge. The bond angles and distances around titanium are also similar to those for mononuclear complexes but, interestingly, the dihedral angle between the $C_5Me_4$ ring [Cp(1)] and the adjacent phenylene ring [Ph(1)] is much larger [62.6(3)°] than those of the corresponding dinuclear zirconocene **2b** [41.28(18)°] and $[(C_6H_4C_5Me_4)TiCl_2]_2(\mu\text{-}O)$ (50.4°).[32]

### Ethylene Polymerization

Ethylene polymerizations with the dinuclear zirconocene complexes **2a**–**c** were carried out in toluene solution under 1 bar of ethylene. To compare their catalytic properties with those of the corresponding mononuclear catalysts, polymerizations with **4a**–**c** were also performed under identical conditions (Table 2). All the catalysts show high activities that are in a range similar to that of the corresponding mononuclear complexes **4a**–**c** at all reaction temperatures. The polyethylenes produced by the dinuclear zirconocenes also show a narrow molecular weight distribution ($M_w/M_n$) similar to that of polyethylenes obtained with the mononuclear complexes, which suggests that the two zirconium centers in the dinuclear complexes behave as independent single active sites, as expected from the crystal structures and NMR spectra. In particular, biphenylene-bridged **2a** shows higher activity than mononuclear **4a** at high temperature, while diphenylethylene-bridged **2b** and **2c** show lower activity than mononuclear **4b** and **4c** at the low- and high-temperature limits. Thus, an enhanced thermal stability of the active species is seen only for biphenylene-bridged **2a** among the three dinuclear systems. Moreover, the activity of **2a** is higher than that of **2b** at all temperatures, while the corresponding mononuclear analogues **4a** and **4b** exhibit a similar activity. In addition, in the case of the flexible diphenylethylene-bridged systems, a higher activity was observed for di-

 © 2007 Wiley-VCH Verlag GmbH & Co. KGaA, Weinheim 

Table 2. Ethylene polymerization results with catalysts **2a**–**c** and **4a**–**c**.[a]

| Entry | Cat. [μmol] | $T_p$ [°C] | Yield [g] | $A$ ($\times 10^{-3}$)[b] | $M_w$ ($\times 10^{-3}$) | $M_w/M_n$ | $T_m$ [°C] |
|---|---|---|---|---|---|---|---|
| 1 | **2a** (1.0) | 30 | 0.628 | 9.42 | 732 | 1.97 | 131.9 |
| 2 | **2a** (1.0) | 50 | 0.631 | 9.47 | 392 | 2.23 | 135.1 |
| 3 | **2a** (1.0) | 70 | 1.035 | 15.53 | 135 | 1.96 | 134.0 |
| 4 | **2a** (1.0) | 90 | 0.548 | 8.22 | 54 | 2.02 | 133.3 |
| 5 | **4a** (1.0) | 30 | 0.615 | 9.23 | 534 | 2.10 | 135.7 |
| 6 | **4a** (2.0) | 50 | 0.782 | 11.73 | 317 | 2.28 | 134.9 |
| 7 | **4a** (2.0) | 70 | 0.633 | 9.50 | 121 | 2.14 | 134.5 |
| 8 | **4a** (2.0) | 90 | 0.426 | 6.39 | 67 | 2.54 | 132.9 |
| 9 | **2b** (1.0) | 30 | 0.383 | 5.75 | 821 | 1.93 | 131.2 |
| 10 | **2b** (1.0) | 50 | 0.556 | 8.34 | 525 | 2.31 | 133.7 |
| 11 | **2b** (1.0) | 70 | 0.935 | 14.03 | 230 | 2.2 | 134.1 |
| 12 | **2b** (1.0) | 90 | 0.238 | 3.57 | 88 | 2.72 | 133.8 |
| 13 | **4b** (2.0) | 30 | 0.545 | 8.18 | 413 | 2.02 | 136.8 |
| 14 | **4b** (2.0) | 50 | 0.582 | 8.73 | 298 | 2.87 | 135.8 |
| 15 | **4b** (2.0) | 70 | 0.850 | 12.75 | 222 | 3.85 | 133.8 |
| 16 | **4b** (2.0) | 90 | 0.451 | 6.77 | 73 | 3.22 | 134.2 |
| 17 | **2c** (1.0) | 30 | 0.496 | 7.44 | 654 | 2.21 | 135.7 |
| 18 | **2c** (1.0) | 50 | 0.798 | 11.97 | 334 | 2.57 | 135.4 |
| 19 | **2c** (1.0) | 70 | 0.897 | 13.46 | 114 | 2.90 | 133.2 |
| 20 | **2c** (1.0) | 90 | 0.546 | 8.19 | 47 | 2.99 | 131.6 |
| 21 | **4c** (2.0) | 30 | 0.690 | 10.35 | 552 | 2.39 | 136.0 |
| 22 | **4c** (2.0) | 50 | 0.714 | 10.71 | 267 | 2.92 | 135.8 |
| 23 | **4c** (2.0) | 70 | 1.026 | 15.39 | 147 | 3.65 | 134.3 |
| 24 | **4c** (2.0) | 90 | 0.560 | 8.40 | 59 | 3.97 | 131.8 |
| 25 | $Cp_2ZrCl_2$ (2.0) | 50 | 0.571 | 8.57 | 235 | 2.92 | 134.7 |

[a] Conditions: *P*(ethylene): 1 bar; solvent: 50 mL of toluene; $t_p$: 2.0 min; MAO: s-MAO; [Al]/[Zr]: 1000. [b] Activity: kg of PE per mol of Zr per hour per bar.

methyl-substituted **2c** than for tetramethyl-substituted **2b**, which implies that the steric effect of the ligand strongly influences the activity. These results may indicate that the lower steric hindrance and the possible electronic stabilization caused by the rigid and conjugative nature of the biphenylene bridge in **2a** lead to the higher activity.

Thus, it can be suggested that the biphenylene group acts as a much more effective bridge in terms of catalytic activity. Noh et al. have pointed out that the more electron releasing and the longer the bridge, the higher the activity of the dinuclear zirconium complexes compared with that of the mononuclear catalyst in ethylene polymerization.[13] In our case, the rigidity, coupled with the appropriate length of the bridging unit, provides favorable electronic stabilization and steric effects and thus likely plays an important role in governing catalytic activity when compared with the flexible diphenylethylene-bridged systems.

The characteristic most noteworthy of mention is the molecular weight of the polyethylene: the polyethylenes produced by **2a**–**c** have a higher molecular weight than those of **4a**–**c**, especially at temperatures below 50 °C, while at high temperature (>70 °C), the values are similar to those of the mononuclear analogues. Between two diphenylethylene-bridged systems, the more electron-releasing **2b** gives higher molecular weights than **2c** at all temperatures, as expected. However, in contrast to the trend in activity, the molecular weight given by **2b** is greater than the biphenylene-bridged **2a** under identical conditions. Note that the ratio of molecular weights between **2b** and **4b** is about 2.0 while that between **2a** and **4a** is about 1.5 (Figure 2). This result can be mainly explained by steric reasons, as for the activity. Due to the flexible nature of the bridge, the two metal centers in **2b** can exert mutual steric hindrance by being located in proximal positions despite the partial relief of such an interaction due to the presence of an additional phenylene linkage. This increased steric hindrance towards the growing polymer chains presumably leads to a reduced rate of chain-transfer reactions.[33] This assumption also appears to be valid for the higher molecular weight produced by **2b** and **2c** in comparison to mononuclear **4b** and **4c**, respectively.

### Styrene Polymerization

From the polymerization results in Table 3, it can be seen that dinuclear half-sandwich titanocenes behave as highly active, single-site catalysts for styrene polymerization, and the syndiotactic index (SI) and melting temperature ($T_m$) of the polystyrenes suggest that the syndiospecific stereocontrol is also well maintained. For a given Cp ligand, a biphenylene bridge appears to form a more efficient dinuclear catalytic system than a diphenylethylene bridge, as judged from the polymerization behavior of **3a** and **3b** at all temperatures (note the higher activity of biphenylene-bridged **3a** than diphenylethylene-bridged **3b** and the retention of the high activity of **3a** even at 90 °C). For a given bridging ligand, the sterically less congested dimethyl-substituted Cp ligand fragment affords a catalytically more active system than the tetramethyl-substituted Cp ligand fragment, as exemplified by **3b** and **3c**. A similar effect of the Cp ligand on the catalytic system has been observed with **5c** and **5b** and other reported mononuclear catalyst systems.[34–36]

 © 2007 Wiley-VCH Verlag GmbH & Co. KGaA, Weinheim 

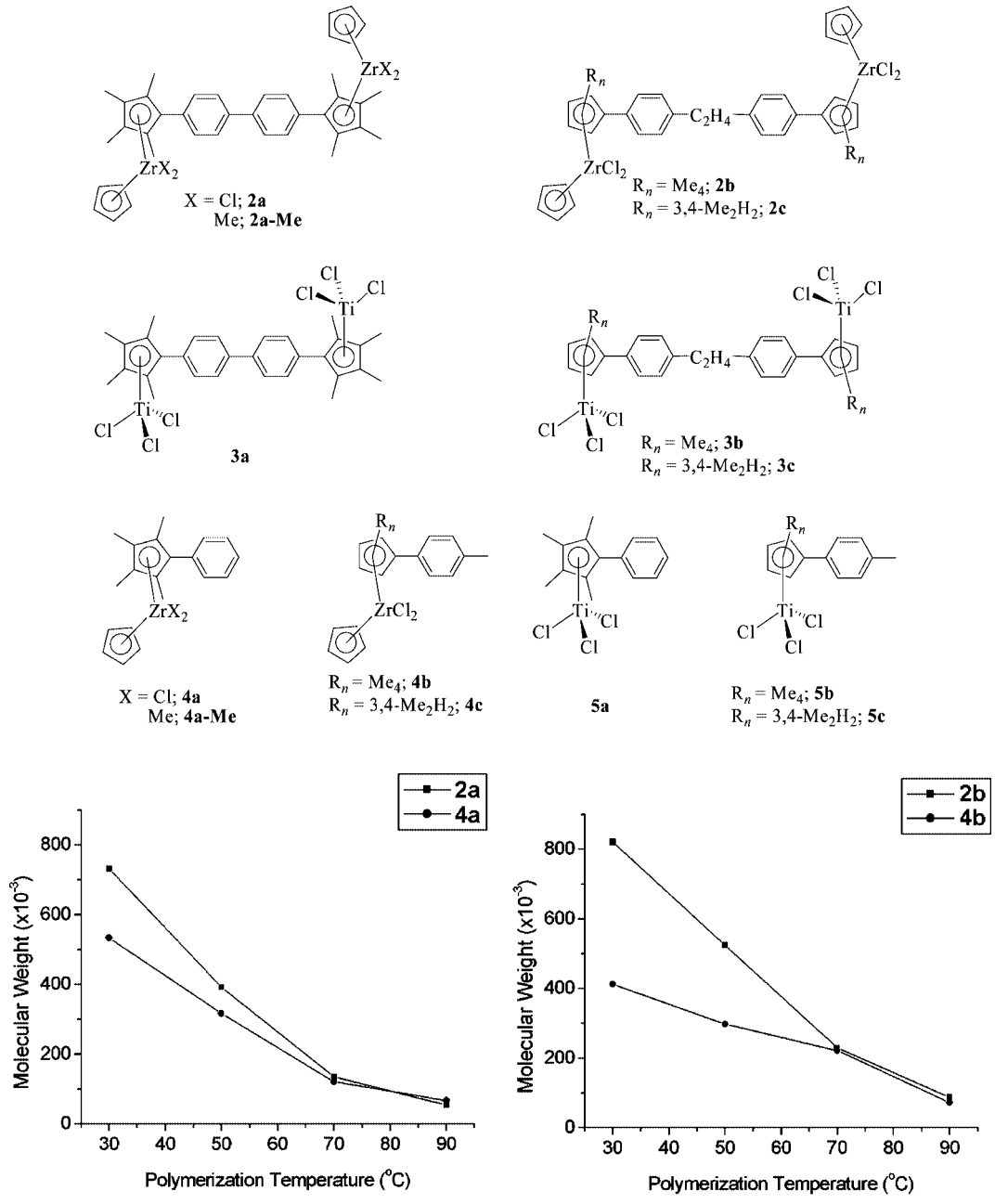


Figure 2. Molecular weight difference between the polymers obtained with **2a** and **4a** (left) and **2b** and **4b** (right).

The activities of the dinuclear complexes are slightly lower than those of the corresponding mononuclear systems. The extent of the activity decrease is more significant in **3b** and **3c**, which have a flexible diphenylethylene bridge, than in **3a**, which has a rigid biphenylene bridge, thereby indicating the effect of the steric influence on the catalytic activity in styrene polymerization.[37] Rausch et al. have also reported that ethylene-bridged dinuclear indenyltitanium trichloride shows much lower activity than the corresponding mononuclear compound in spite of similar syndioselectivity of these two complexes.[38] This result may imply that the bridge flexibility in **3b** and **3c** makes the two polymer chains growing at the two active centers exert a steric influence on each other which slows down the rate of chain propagation.[39]

The polystyrenes produced by dinuclear **3a**–**c** have a lower molecular weight than those of the corresponding mononuclear **5a**–**c** at all reaction temperatures. This can be explained in terms of the steric effect of the ligand, which means that β-H elimination becomes preferred to propagation as the steric hindrance between the polymer chain and ligand in half-sandwich metallocenes increases.[39] However, in contrast to the activity trend, the molecular weights of the polymers formed by the dinuclear systems are in the order **3a** > **3b** > **3c**, which is similar to the order of the mononuclear systems (**5a** ≈ **5b** > **5c**). The low molecular

 © 2007 Wiley-VCH Verlag GmbH & Co. KGaA, Weinheim 

Table 3. Styrene polymerization results with catalysts **3a**–**3c** and **5a**–**5c**.[a]

| Entry | Cat. [μmol] | $T_p$ [°C] | Yield [g] | Activity[b] | $M_w$ ($\times 10^{-3}$) | $M_w/M_n$ | $T_m$ [°C] | SI [%][c] |
|---|---|---|---|---|---|---|---|---|
| 1 | **3a** (5.0) | 50 | 1.334 | 400.2 | 297 | 1.99 | 267 | 93 |
| 2 | **3a** (5.0) | 70 | 1.694 | 508.2 | 214 | 1.81 | 267 | 96 |
| 3 | **3a** (5.0) | 90 | 1.636 | 490.8 | 98.7 | 1.91 | 272 | 95 |
| 4 | **5a** (10.0) | 50 | 1.153 | 345.9 | 460 | 1.82 | 268 | 93 |
| 5 | **5a** (10.0) | 70 | 1.996 | 598.8 | 246 | 1.95 | 268 | 99 |
| 6 | **5a** (10.0) | 90 | 1.872 | 561.6 | 151 | 1.88 | 268 | 95 |
| 7 | **3b** (5.0) | 50 | 1.055 | 316.5 | 267 | 1.77 | 268 | 98 |
| 8 | **3b** (5.0) | 70 | 1.694 | 508.2 | 182 | 1.77 | 269 | 93 |
| 9 | **3b** (5.0) | 90 | 1.400 | 420.0 | 93.8 | 1.92 | 271 | 95 |
| 10 | **5b** (10.0) | 50 | 1.192 | 357.6 | 420 | 1.86 | 269 | 92 |
| 11 | **5b** (10.0) | 70 | 2.671 | 801.3 | 269 | 2.03 | 272 | 96 |
| 12 | **5b** (10.0) | 90 | 2.565 | 769.5 | 139 | 1.92 | 272 | 97 |
| 13 | **3c** (5.0) | 50 | 1.640 | 492.0 | 279 | 1.94 | 268 | 95 |
| 14 | **3c** (5.0) | 70 | 2.804 | 851.2 | 119 | 2.05 | 270 | 97 |
| 15 | **3c** (5.0) | 90 | 2.119 | 635.7 | 57.9 | 1.92 | 268 | 96 |
| 16 | **5c** (10.0) | 50 | 2.672 | 801.6 | 347 | 2.01 | 271 | 96 |
| 17 | **5c** (10.0) | 70 | 3.256 | 976.8 | 147 | 2.02 | 270 | 98 |
| 18 | **5c** (10.0) | 90 | 3.083 | 924.9 | 58.5 | 1.91 | 266 | 96 |
| 19 | $Cp^*TiCl_3$ | 50 | 0.963 | 288.9 | 310 | 1.90 | 266 | 96 |

[a] Conditions: solvent: 50 mL of toluene; [Al]/[Ti]: 1000; styrene: 5.0 mL; $t_p$: 20 min; MAO: s-MAO. [b] Activity: kg of PS per mol of Ti per hour. [c] Syndiotacticity determined from the amount of polymer insoluble in 2-butanone.

weight obtained with both the most active complexes (**3c** and **5c**) appears to be mainly ascribed to the lower electron-donating effect of the dimethyl-substituted ligand. The molecular weight trend **3a** > **3b** can be considered to be a manifestation of the reduced steric effects in **3a** compared to **3b**.

## Conclusions

The biphenylene- and diphenylethylene-bridged dinuclear zirconocenes [4,4′-$(C_5Me_4)_2(C_6H_4)_2$][$CpZrCl_2]_2$ (**2a**), [*p*-$(C_5Me_4)C_6H_4CH_2]_2$[$CpZrCl_2]_2$ (**2b**), and [*p*-(3,4-$Me_2C_5H_2)C_6H_4CH_2]_2$[$CpZrCl_2]_2$ (**2c**) consistently provide high molecular weight polymers and have a high catalyst activity in ethylene polymerization, although there are some differences, including both structural and polymerization properties, between rigid and flexible bridged dinuclear complexes in terms of activity and molecular weight trends. In contrast, the corresponding dinuclear half-sandwich titanocenes [$(C_5Me_4)_2(C_6H_4)_2$][$TiCl_3]_2$ (**3a**), [*p*-$(C_5Me_4)$-$C_6H_4CH_2]_2$[$TiCl_3]_2$ (**3b**), and [*p*-(3,4-$Me_2C_5H_2)C_6H_4CH_2]_2$-[$TiCl_3]_2$ (**3c**) do not show any enhanced polymerization properties in styrene polymerization compared to their mononuclear analogues. Indeed, they show a significant decrease in the molecular weight of the polymer produced and a slight decrease of catalytic activity. These results appear to be due to the cooperative participation of the electronic effect of the two cationic metal centers through the biphenylene or diphenylethylene bridge and/or the steric effects between them.

## Experimental Section

**General:** Tetrahydrofuran, toluene, *n*-hexane, and *n*-pentane were distilled from Na-K alloy, $Et_2O$ from Na-benzophenone ketyl, and $CH_2Cl_2$ from $CaH_2$. All solvents were stored over activated molecular sieves (5 Å). All other chemicals were used without any further purification. 3,4-Dimethylcyclopent-2-enone,[40] 4,4′-$(C_6H_4)_2$-$(C_5Me_4H)_2$ (**1a**),[27] ($p$-$BrC_6H_4CH_2)_2$,[41] [4,4′-$(C_5Me_4)_2(C_6H_4)_2$]-[$CpZrCl_2]_2$ (**2a**),[27] [4,4′-$(C_5Me_4)_2(C_6H_4)_2$][$TiCl_3]_2$ (**3a**),[27] [$(PhC_5Me_4)CpZrCl_2$] (**4a**),[31] [(*p*-tolyl$C_5Me_4)CpZrCl_2$] (**4b**),[31] 1-tolyl-3,4-$Me_2C_5H_3$,[7] [(1-tolyl-3,4-$Me_2C_5H_2)CpZrCl_2$] (**4c**),[7] [$(PhC_5Me_4)TiCl_3$] (**5a**),[42] and [(*p*-tolyl$C_5Me_4)TiCl_3$] (**5b**)[43] were prepared according to literature procedures. Methylaluminoxane (MAO) was used as a solid (s-MAO). This was obtained by complete evaporation of the solvent and residual $AlMe_3$ from a toluene solution of PMAO (Witco, EUROCEN 30T) and a toluene solution of PMAO (Witco, EUROCEN 10T). Polymerization-grade ethylene monomer from Honam Petrochemical Corporation was used after purification by passing through Labclear™ and Oxiclear™ filters. Styrene monomer purchased from Aldrich was used after purification by passing through an alumina column. $^1H$ and $^{13}C$ NMR spectra were recorded with a Bruker Spectropin 400 spectrometer at ambient temperature. All chemical shifts are reported in $\delta$ units with reference to the residual peaks of $CDCl_3$ for proton ($\delta$ = 7.24 ppm) and carbon ($\delta$ = 77.0 ppm). Elemental analyses were carried out with an EA 1110-FISONS (CE Instruments) at KAIST.

**Synthesis of [*p*-$(C_5Me_4H)C_6H_4CH_2]_2$ (1b):** A solution of (*p*-$BrC_6H_4CH_2)_2$ (3.40 g, 10 mmol) in 50 mL of diethyl ether was treated with 2.2 equiv. of *n*BuLi (8.8 mL) at 0 °C and the reaction mixture was stirred at this temperature for 1 h. The slow formation of a white precipitate was observed and the reaction mixture was then warmed to room temperature and stirred for a further 2 h. The colorless solution was then decanted off and 30 mL of thf was added to the resulting dilithium salt. Subsequently, two equivalents of 2,3,4,5-tetramethylcyclopent-2-enone (2.76 g) in 20 mL of thf was added slowly through a cannula at –78 °C. The reaction mixture was slowly warmed to room temperature and stirred overnight. The resulting light orange solution was treated with 30 mL of a saturated aqueous solution of $NH_4Cl$. The organic portion was separated and the aqueous layer was further extracted with diethyl ether (50 mL). The combined organic portions were dried with anhydrous $MgSO_4$, filtered, and the solvents evaporated to dryness to afford a colorless oily product. The crude product was redissolved in $CH_2Cl_2$ (30 mL) and a catalytic amount of solid *p*-TsOH (0.1 g)

 © 2007 Wiley-VCH Verlag GmbH & Co. KGaA, Weinheim 

was added to the solution at room temperature. A yellow solid was immediately formed, and the stirring was continued for a further hour. The volume of the resulting reaction mixture was reduced to 10%, and 30 mL of *n*-hexane was poured into the flask in order to precipitate the product and dissolve the unreacted materials. The large amount of yellow solid obtained was filtered through a glass frit and washed successively with ethanol (30 mL), diethyl ether (30 mL), and *n*-pentane (30 mL). Drying in vacuo afforded 2.83 g of **1b** in 67% yield. $^1$H NMR (400.13 MHz, $CDCl_3$): $\delta$ = 7.18 (m, 8 H), 3.17 (q, 2 H), 2.93 (m, 4 H), 2.02 (s, 6 H), 1.91 (s, 6 H), 1.85 (s, 6 H), 0.95 (d, 6 H) ppm. $^{13}C\{^1H\}$ NMR (100.62 MHz, $CDCl_3$): $\delta$ = 142.7, 140.4, 139.0, 136.7, 135.0, 134.8, 128.4, 128.1, 50.1, 37.6, 14.9, 12.7, 11.9, 11.1 ppm. EIMS: *m*/*z* 422 (85) [$M^+$], 408 (9) [$M^+ - CH_2$], 225 (15) [$M^+ - C_6H_4C_5Me_4H$], 211 (100) [$M^+/2$]. $C_{32}H_{38}$ (422.64): calcd. C 90.94, H 9.06; found C 90.33, H 9.44.

**Synthesis of [*p*-(3,4-$Me_2C_5H_3$)$C_6H_4CH_2$]$_2$ (1c):** An identical procedure to that for the synthesis of **1b** was employed with 3,4-dimethylcyclopent-2-enone (2.18 g) instead of 2,3,4,5-tetramethylcyclopent-2-enone. This afforded 2.31 g of an ivory solid (**1c**) in 63% yield. $^1$H NMR (400.13 MHz, $CDCl_3$): $\delta$ = 7.35 (d, 4 H), 7.09 (d, 4 H), 6.60 (s, 2 H), 3.24 (s, 4 H), 2.86 (s, 4 H), 1.96 (s, 6 H), 1.87 (s, 6 H) ppm. $^{13}C\{^1H\}$ NMR (100.62 MHz, $CDCl_3$): $\delta$ = 142.4, 139.7, 135.5, 135.4, 134.2, 131.0, 128.6, 124.5, 45.3, 37.6, 13.4, 12.6 ppm. EIMS: *m*/*z* 366 (76) [$M^+$], 183 (100) [$M^+/2$], 167 (61) [$M^+/2 - CH_3$]. $C_{28}H_{30}$ (366.54): calcd. C 91.75, H 8.25; found C 91.23, H 8.52.

**Synthesis of [{[*p*-($C_5Me_4$)$C_6H_4CH_2$][$CpZrCl_2$]}$_2$] (2b):** A slurry of **1b** (0.422 g, 1.00 mmol) in 20 mL of thf was treated with two equivalents of *n*BuLi (0.8 mL) at –78 °C. The reaction mixture was warmed to room temperature and stirred for 4 h. Two equivalents of [$CpZrCl_3$] (2.0 mmol, 0.525 g) dissolved in 10 mL of thf was added to the resulting yellow suspension through a cannula at –78 °C. The reaction mixture was then warmed to room temperature and stirred for 24 h. The golden-yellow solution formed was then evaporated to dryness and extracted with 30 mL of toluene. The mixture was filtered through a Celite pad, and the light-yellow filtrate was evaporated to dryness. The crude product was washed twice with 10 mL of a mixture of *n*-hexane and diethyl ether (2:1, v/v). Drying in vacuo afforded spectroscopically pure **2b** as a light-yellow solid (0.639 g, 73%). Recrystallization of a concentrated $CH_2Cl_2$ solution of **2b** layered with *n*-hexane at room temperature afforded light golden colored, single crystals suitable for an X-ray diffraction study. $^1$H NMR (400.13 MHz, $CDCl_3$): $\delta$ = 7.19 (d, 4 H), 7.05 (d, 4 H), 6.13 (s, 10 H), 2.99 (s, 4 H), 2.21 (s, 12 H), 2.04 (s, 12 H) ppm. $^{13}C\{^1H\}$ NMR (100.62 MHz, $CDCl_3$): $\delta$ = 140.5, 131.6, 129.7, 128.5, 126.5, 126.1, 124.2, 116.7, 37.3, 14.0, 12.3 ppm. $C_{42}H_{46}Cl_4Zr_2$ (875.07): calcd. C 57.65, H 5.30; found C 56.64, H 5.72.

**Synthesis of [{[*p*-(3,4-$Me_2C_5H_2$)$C_6H_4CH_2$][$CpZrCl_2$]}$_2$] (2c):** An identical procedure to that used for the synthesis of **2b** was employed with the ligand **1c** (0.366 g, 1.00 mmol) to afford **2c** as a light-yellow solid (0.573 g, 70%). $^1$H NMR (400.13 MHz, $CDCl_3$): $\delta$ = 7.36 (d, 4 H), 7.12 (d, 4 H), 6.49 (s, 4 H), 6.11 (s, 10 H), 2.86 (s, 4 H), 2.15 (s, 12 H) ppm. $^{13}C\{^1H\}$ NMR (100.62 MHz, $CDCl_3$): $\delta$ = 140.8, 131.4, 129.4, 128.7, 125.1, 122.6, 116.5, 114.0, 37.3, 13.8 ppm. $C_{38}H_{38}Cl_4Zr_2$ (818.97): calcd. C 55.73, H 4.68; found C 55.74, H 4.87.

**Synthesis of [*p*-($C_5Me_4$)$C_6H_4CH_2$]$_2$[$TiCl_3$]$_2$ (3b):** A slurry of **1b** (0.422 g, 1.00 mmol) in 20 mL of thf was treated with two equivalents of *n*BuLi (0.8 mL) at –78 °C. The reaction mixture was warmed to room temperature and stirred for 4 h to give a yellow suspension. Two equivalents of [$ClTi(OiPr)_3$] (2.0 mmol, 0.521 g) dissolved in 10 mL of thf was added to the reaction mixture through a cannula at –78 °C. The resulting reaction mixture was then warmed to room temperature and stirred for 24 h. The golden-yellow solution formed was evaporated to dryness and extracted with 30 mL of $CH_2Cl_2$. The mixture was subsequently treated with an excess amount of $Me_3SiCl$ (3 to 4 equiv.) at 0 °C. After warming to room temperature, the reaction mixture was further stirred overnight. During the course of the reaction, the slow formation of a red precipitate was observed. The resulting red mixture was evaporated, and the shiny red product was washed twice with 20 mL of a mixture of *n*-hexane and $CH_2Cl_2$ (4:1, v/v). Drying in vacuo afforded 0.445 g of scarlet microcrystals of **3b** in 61% yield. Recrystallization of a concentrated $CH_2Cl_2$ solution of **3b** layered with *n*-hexane at room temperature afforded red single crystals suitable for an X-ray diffraction study. $^1$H NMR (400.13 MHz, $CDCl_3$): $\delta$ = 7.24 (m, 8 H), 2.99 (s, 4 H), 2.46 (s, 12 H), 2.41 (s, 12 H) ppm. $^{13}C\{^1H\}$ NMR (100.62 MHz, $CDCl_3$): $\delta$ = 142.9, 142.0, 138.7, 136.1, 130.8, 130.3, 128.4, 37.3, 15.5, 14.6 ppm. $C_{32}H_{36}Cl_6Ti_2$ (729.08): calcd. C 52.72, H 4.98; found C 52.65, H 5.44.

**Synthesis of [{[*p*-(3,4-$Me_2C_5H_2$)$C_6H_4CH_2$][$TiCl_3$]}$_2$] (3c):** A similar procedure to that used for the synthesis of **3b** was employed with the ligand **1c** (0.366 g, 1.00 mmol), but with an excess of $Me_2SiCl_2$ instead of $Me_3SiCl$, to afford **3c** as a dark-red solid (0.451 g, 67%). $^1$H NMR (400.13 MHz, $CDC_{l3}$): $\delta$ = 7.57 (d, 4 H), 7.17 (s, 4 H), 7.10 (d, 4 H), 2.93 (s, 4 H), 2.47 (s, 12 H) ppm. $^{13}C\{^1H\}$ NMR (100.62 MHz, $CDCl_3$): $\delta$ = 143.3, 140.6, 139.3, 130.8, 129.2, 126.1, 119.1, 37.4, 16.0 ppm. $C_{28}H_{28}Cl_6Ti_2$ (672.97): calcd. C 49.97, H 4.19; found C 49.60, H 5.02.

**Synthesis of [(1-*p*-tolyl-3,4-$Me_2C_5H_2$)$TiCl_3$] (5c):** A similar procedure to that used for the synthesis of **3b** was employed with 1-tolyl-3,4-$Me_2C_5H_3$ (0.366 g, 1.00 mmol), but with an excess of $Me_2SiCl_2$ instead of $Me_3SiCl$, to afford **6c** as dark red microcrystals (0.432 g, 64% yield). $^1$H NMR (400.13 MHz, $CDCl_3$): $\delta$ = 7.61 (d, 2 H), 7.22 (d, 2 H), 7.18 (s, 2 H), 2.47 (s, 6 H), 2.37 (s, 3 H) ppm. $^{13}C\{^1H\}$ NMR (100.62 MHz, $CDCl_3$): $\delta$ = 140.8, 140.4, 139.2, 130.2, 129.6, 126.0, 119.0, 21.4, 15.9 ppm. $C_{14}H_{15}Cl_3Ti$ (337.49): calcd. C 49.82, H 4.48; found C 49.42, H 4.61.

**Ethylene Polymerization:** Freshly distilled toluene (48 mL) was placed in a degassed 250-mL glass reactor charged with a pre-weighed amount of s-MAO (Al/Zr = 1000) and the temperature was adjusted using an external bath. The flask was then filled with ethylene monomer at 1 bar with vigorous stirring after degassing with the monomer several times. Polymerization was started by addition of a toluene solution of catalyst (2.0 mL, 2.0 μmol of Zr). After 2 min, all the reactions were quenched by addition of an acidified ethanol solution (10% HCl in EtOH) and the resulting polyethylene was precipitated by the addition of 200 mL of ethanol. After stirring for 1 to 2 h, the polyethylenes were filtered off, washed with ethanol several times, and dried under vacuum to a constant weight at 80 °C.

**Styrene Polymerization:** Freshly distilled toluene (48 mL) and styrene (5.0 mL) were successively added to a degassed, 250-mL glass reactor charged with a pre-weighed amount of s-MAO (Al/Ti = 1000) with vigorous stirring. The temperature was adjusted using an external bath. Polymerization was started by addition of a toluene solution of catalyst (2.0 mL, 10.0 μmol of Ti). After 20 min, all the reactions were quenched by addition of an acidified ethanol solution (10% HCl in EtOH) and the resulting polystyrene was further precipitated by addition of 200 mL of ethanol. After stirring for 1 to 2 h, polystyrenes were filtered off, washed with ethanol several times, and dried under vacuum to a constant weight at

 © 2007 Wiley-VCH Verlag GmbH & Co. KGaA, Weinheim 

80 °C. The crude polymer was extracted with refluxing 2-butanone for 12 h, and the insoluble fraction was filtered and dried under vacuum overnight at 80 °C in order to determine the syndiotactic polystyrene portion.

**Polymer Analysis:** The molecular weight ($M_w$) and molecular weight distribution ($M_w/M_n$) of polypropylenes were determined by GPC (Polymer Laboratories PL-GPC 220) in 1,2,4-trichlorobenzene using standard polystyrenes as a reference. The melting temperatures ($T_m$) of polypropylenes were measured by DSC (TA Instrument, 2910 MDSC).

**X-ray Structure Determination:** X-ray diffraction measurements were performed with a Bruker AXS diffractometer with a CCD area detector, using graphite-monochromated Mo-$K_\alpha$ radiation ($\lambda$ = 0.71073 Å) at 293 K. A hemisphere of data was collected using ω scans. The frame data sets were processed using the SAINT and XPREP processing package. An empirical absorption correction was applied to each data set with the program SADABS. All the intensity data were corrected for Lorentz and polarization effects. The structure was solved by direct methods and refined by full-matrix least-squares methods using the SHELXTL program package with anisotropic thermal parameters for all non-hydrogen atoms. Hydrogen atoms were placed at their geometrically calculated positions and refined as riding on the corresponding carbon atoms with isotropic thermal parameters. For **2b**, final refinement based on the reflections with $I > 2\sigma(I)$ converged at $R1$ = 0.0348, $wR2$ = 0.0851, GOF = 0.963, and for **3b**, $R1$ = 0.0506, $wR2$ = 0.1156 and GOF = 0.845 (Table 4).[44]

Table 4. X-ray crystallographic data.

| Compound | **2b** | **3b** |
|---|---|---|
| Formula | $C_{42}H_{46}Cl_4Zr_2$ | $C_{32}H_{36}Cl_6Ti_2$ |
| Formula weight | 875.07 | 729.08 |
| Crystal system; space group | monoclinic; *C*2/*c* | monoclinic; *C*2/*c* |
| *a* [Å] | 21.509(5) | 36.11(6) |
| *b* [Å] | 16.944(4) | 6.625(11) |
| *c* [Å] | 12.933(3) | 15.33(2) |
| $\alpha, \beta, \gamma$ [°] | 90, 124.370(4), 90 | 90, 94.59(9), 90 |
| *V* [Å$^3$] | 3890.5(16) | 3656(10) |
| *Z* | 4 | 8 |
| $D_{calcd.}$ [g cm$^{-3}$] | 1.494 | 1.325 |
| *F*(000) | 1784 | 1496 |
| *T* [K] | 293 | 293 |
| $\mu$ (Mo-$K_\alpha$) [mm$^{-1}$] | 0.839 | 0.895 |
| $\theta$ range [°] | 1.66–28.37 | 1.13–27.97 |
| No. of unique/observed $[I > 2\sigma(I)]$ reflections | 4499/12111 | 4059/10577 |
| No. of parameters refined | 221 | 193 |
| $R1$, $wR2$[a] | 0.0348, 0.0851 | 0.0506, 0.1156 |
| GOF | 1.045 | 0.845 |
| Min./max. electron density [e Å$^{-3}$] | –0.692/0.302 | –0.360/0.313 |

[a] $R1 = \sum||F_o| - |F_c||/\sum|F_o|$; $wR2 = [\sum[w(F_o^2 - F_c^2)^2]/\sum[w(F_o^2)^2]]^{1/2}$.

## Acknowledgments

Financial support from Center for Molecular Design and Synthesis (CMDS), Korea Advanced Institute of Science and Technology and the BK-21 project is gratefully acknowledged. We also thank Honam Petrochemical Corporation for high quality ethylene monomer and financial support. S. K. K thanks Dr. J.-W. Hwang for help in obtaining the X-ray crystal structures.

[1] Special issue on "Frontiers in Metal-Catalyzed Polymerization" (Ed.: J. A. Gladysz), *Chem. Rev.* **2000**, *100*, 1167–1604.
[2] S. Park, Y. Han, S. K. Kim, J. Lee, H. K. Kim, Y. Do, *J. Organomet. Chem.* **2004**, *689*, 4263–4276.
[3] V. C. Gibson, S. K. Spitzmesser, *Chem. Rev.* **2003**, *103*, 283–316.
[4] W. Kaminsky, *Adv. Catal.* **2001**, *46*, 89–159.
[5] T. J. Marks, J. C. Stevens (Eds.), *Top. Catal.* **1999**, *7*, 1–208.
[6] G. J. P. Britovsek, V. C. Gibson, D. F. Wass, *Angew. Chem. Int. Ed.* **1999**, *38*, 428–447.
[7] S. Jüngling, R. Mülhaupt, H. Plenio, *J. Organomet. Chem.* **1993**, *460*, 191–195.
[8] K. Soga, T. H. Ban, T. Uozumi, *J. Mol. Catal. A* **1998**, *128*, 273–278.
[9] W. Spaleck, F. Kuber, B. Bachmann, C. Firtze, A. Winter, *J. Mol. Catal. A* **1998**, *128*, 279–287.
[10] T. Ushioda, M. L. H. Green, J. Haggitt, X. Yan, *J. Organomet. Chem.* **1996**, *518*, 155–166.
[11] M. L. H. Green, N. H. Popham, *J. Chem. Soc., Dalton Trans.* **1999**, 1049–1059.
[12] S. K. Noh, J. Kim, J. Jung, C. S. Ra, D. H. Lee, H. B. Lee, S. W. Lee, W. S. Huh, *J. Organomet. Chem.* **1999**, *580*, 90–97.
[13] S. K. Noh, S. Kim, J. Kim, D. H. Lee, K. B. Yoon, H. B. Lee, S. W. Lee, W. S. Huh, *J. Polym. Sci. Part A: Polym. Chem.* **1997**, *35*, 3717–3728.
[14] S. K. Noh, M. Lee, D. H. Kum, W. S. Lyoo, D. H. Lee, *J. Polym. Sci. Part A: Polym. Chem.* **2004**, *42*, 1712–1723.
[15] S. K. Noh, Y. Yang, W. S. Lyoo, *J. Appl. Polym. Sci.* **2003**, *90*, 2469–2474.
[16] S. K. Noh, J. Lee, D. H. Lee, *J. Organomet. Chem.* **2003**, *667*, 53–60.
[17] H. Li, L. Li, T. J. Marks, L. Liable-Sands, A. L. Rheingold, *J. Am. Chem. Soc.* **2003**, *125*, 10788–10789.
[18] L. Li, M. V. Metz, H. Li, M.-C. Chen, T. J. Marks, L. Liable-Sands, A. L. Rheingold, *J. Am. Chem. Soc.* **2002**, *124*, 12725–12741.
[19] N. Guo, L. Li, T. J. Marks, *J. Am. Chem. Soc.* **2004**, *126*, 6542–6543.
[20] H. Li, L. Li, T. J. Marks, *Angew. Chem. Int. Ed.* **2004**, *43*, 4937–4940.
[21] J. Wang, H. Li, N. Guo, L. Li, C. L. Stern, T. J. Marks, *Organometallics* **2004**, *23*, 5112–5114.
[22] H. Li, C. L. Stern, T. J. Marks, *Macromolecules* **2005**, *38*, 9015–9027.
[23] H. G. Alt, R. Ernst, *Inorg. Chim. Acta* **2003**, *350*, 1–11.
[24] H. G. Alt, R. Ernst, *J. Mol. Catal. A* **2003**, *195*, 11–27.
[25] J. C. Sierra, D. Hüerländer, M. Hill, G. Kehr, G. Erker, R. Fröhlich, *Chem. Eur. J.* **2003**, *9*, 3618–3622.
[26] J. Kuwabara, D. Takeuchi, K. Osakada, *Organometallics* **2005**, *24*, 2705–2712.
[27] M. H. Lee, S. K. Kim, Y. Do, *Organometallics* **2005**, *24*, 3618–3620.
[28] J. L. M. Petoff, M. D. Bruce, R. M. Waymouth, A. Masood, T. K. Lal, R. W. Quan, S. J. Behrend, *Organometallics* **1997**, *16*, 5909–5916.
[29] K. Kimura, K. Takaishi, T. Matsukawa, T. Yoshimura, H. Yamazaki, *Chem. Lett.* **1998**, 571–572.
[30] M. H. Lee, Y. Do, *J. Organomet. Chem.* **2005**, *690*, 1240–1248.
[31] X. Deng, B. Wang, S. Xu, X. Zhou, L. Yang, Y. Li, Y. Hu, Y. Li, F. Zou, *J. Mol. Catal. A* **2002**, *184*, 57–64.
[32] M. Björgvinsson, S. Halldorsson, I. Arnason, J. Magull, D. Fenske, *J. Organomet. Chem.* **1997**, *544*, 207–215.
[33] As usual, a higher degree of steric bulk gives a higher molecular weight of polyethylene: H. G. Alt, A. Köppl, *Chem. Rev.* **2000**, *100*, 1205–1222.
[34] W. Kaminsky, V. Scholz, R. Werner, *Macromol. Symp.* **2000**, *159*, 9–18.
[35] K. Nomura, T. Komatsu, Y. Imanishi, *Macromolecules* **2000**, *33*, 8122–8124.
[36] D. J. Byun, A. F. Fudo, A. Tanaka, M. Fujiki, K. Nomura, *Macromolecules* **2004**, *37*, 5520–5530.

 © 2007 Wiley-VCH Verlag GmbH & Co. KGaA, Weinheim 

[37] K. Yokota, T. Inoue, S. Naganuma, H. Shozaki, N. Tomotsu, M. Kuramoto, N. Ishihara, *Syndiospecific Polymerization of Styrene*, in *Metal-Organic Catalysts for Synthesis and Polymerization* (Ed.: W. Kaminsky), Springer, Berlin, **1999**, p. 435–446.
[38] J. C. Flores, T. E. Ready, J. C. W. Chien, M. D. Rausch, *J. Organomet. Chem.* **1998**, *562*, 11–15.
[39] J. Schellenberg, N. Tomotsu, *Prog. Polym. Sci.* **2002**, *27*, 1925–1982 and references therein.
[40] J. M. Conia, M. L. Leriverend, *Bull. Soc. Chim. Fr.* **1970**, 2981–2991.
[41] Y. Suh, J.-S. Lee, S.-H. Kim, R. D. Rieke, *J. Organomet. Chem.* **2003**, *684*, 20–36.
[42] M. Bjoergvinsson, S. Halldorsson, I. Arnason, J. Magull, D. Fenske, *J. Organomet. Chem.* **1997**, *544*, 207–215.
[43] Y. Kim, Y. Han, J.-W. Hwang, M. W. Kim, Y. Do, *Organometallics* **2002**, *21*, 1127–1135.
[44] CCDC-617759 (for **2b**) and -617760 (for **3b**) contain the supplementary crystallographic data for this paper. These data can be obtained free of charge from The Cambridge Crystallographic Data Center via www.ccdc.cam.ac.uk/data_request/cif.

Received: September 7, 2006
Published Online: December 12, 2006

 © 2007 Wiley-VCH Verlag GmbH & Co. KGaA, Weinheim 

DOI: 10.1002/ejic.200600843

# Linear and Rectangular Trinuclear Phthalocyanines

Sergey G. Makarov,[a,b] Olga N. Suvorova,[b] Christian Litwinski,[c] Eugeny A. Ermilov,[c] Beate Röder,[c] Olga Tsaryova,[a] Thomas Dülcks,[a] and Dieter Wöhrle*[a]

**Keywords:** Phthalocyanines / NIR absorption / UV/Vis spectroscopy / Semiempirical calculations / Fused-ring systems

Isomeric linear and rectangular trinuclear metal-free and zinc(II) phthalocyanine complexes connected by common annulated benzene rings have been synthesized by the mixed cyclotetramerization of a 1,2,4,5-tetracyanobenzene derivative and 4,5-bis(2,6-dimethylphenoxy)phthalonitrile. Their electronic-absorption and fluorescence spectra have been studied in comparison with the corresponding mono- and dinuclear phthalocyanines. For the zinc complexes, the molecular orbitals and electronic spectra have been calculated semi-empirically. The trinuclear phthalocyanines exhibit absorptions up to 940 nm with extinction coefficients up to about 700000 $M^{-1}cm^{-1}$, which shows the extension of the π-electron system.

(© Wiley-VCH Verlag GmbH & Co. KGaA, 69451 Weinheim, Germany, 2007)

## Introduction

Conjugated porphyrin oligomers are the subject of significant interest due to their potential uses as molecular wires, materials for optical limiting, and other advanced technologies.[1] Accordingly, many compounds have been synthesized and studied in recent years. However, much less is known[2] about such systems based on phthalocyanines (Pcs) − the most common porphyrin analogues. Pcs have many applications, such as in dyes and pigments,[3a] catalysts and photocatalysts,[3b–3d] photoconductors in laser printers,[3e] and photosensitizers in photodynamic therapy.[3f] They are also of significant interest as potential molecular conductors and semiconductors,[4a] electrochromic[4b,4c] and non-linear optical[4d,4e] materials, components of organic photovoltaic cells,[4f] and light-emitting diodes.[4g] The high overall stability and exceptional electronic properties of Pcs are responsible for most of their actual and potential applications. The synthesis of conjugated oligomers as a way of modifying the electronic structure of phthalocyanines by increasing the dimensions of the conjugated π-electron system is of substantial interest for the design of new functional materials.

Changes in the electronic structure of Pcs are well indicated by their electronic absorption spectra. Most Pcs in solution have a sharp intense absorption band (Q band) in the red spectral region ($\lambda_{max} \approx 680$ nm). The extension of the Pc π-conjugated system causes a bathochromic shift and, depending on the resulting symmetry, splitting of the Q band. To understand these spectral changes MO calculations, which are normally in good agreement with experimental data, are often performed.

One possible way to extend the Pc π-system is annulation of further benzene rings at the periphery of the molecule, which leads to naphthalocyanines (Ncs), anthracocyanines (Acs),[5a] and different unsymmetrical analogues such as phthalonaphthalocyanines.[5b,5c] Unsymmetrical annulation gives more flexibility when it comes to tuning the electronic properties. However, this approach also leads to decreased stability.[5a,5b] The other possibility is the construction of conjugated Pc oligomers. Some dimers of Pcs and their close analogues have been described[2] but only a very few conjugated trimers are known: a diacetylene-bridged "Pc triangle", a benzo-annulated SubPc trimer, and only one conjugated benzo-annulated Pc trimer (described by us).[2a,2b,2g–2i,2l] It has been shown that the strongest known interaction between Pc units is probably achieved if they are connected through a common annulated benzene ring.[2b] It is interesting to point out that further annulation of a Pc ring to a dimer of this type will lead to isomeric linear and rectangular trimers with different symmetries and electronic properties. In our previous work,[2b] a substituted metal-free dimer and a linear metal-free trimer were prepared and their photophysical properties were described. To the best of our knowledge, a rectangular trimer of this type has not yet been reported and neither have metal-containing linear and rectangular trimers. In this work, we describe the preparation and basic photophysical properties of linear and rectangular metal-free and zinc Pc trimers in comparison

[a] FB2, Biologie/Chemie
Universität Bremen
P. O. Box 330440, 28334 Bremen, Germany
Fax: +49-421-218-4935
E-mail: woehrle@chemie.uni-bremen.de
[b] G.A. Razuvaev Institute of Organometallic Chemistry
Russian Academy of Sciences
Nizhniy Novgorod, Russia
[c] Institut für Physik, Photobiophysik
Humboldt-Universität zu Berlin
Newtonstr. 15, 12489 Berlin, Germany


© 2007 Wiley-VCH Verlag GmbH & Co. KGaA, Weinheim

with their mono- and dinuclear analogues. For the zinc complexes, molecular orbitals and electronic spectra have been calculated semi-empirically.

## Results and Discussion

The metal-free linear trinuclear phthalocyanine $H_6$**5** was described in our previous work.[2b] It was isolated in 0.2% yield from the Pc mixture obtained by co-cyclotetramerization of the tetracyanobenzene derivative **1** and the substituted phthalonitrile **2**. Bulky 2,6-dimethylphenoxy groups in the phthalonitrile derivative **2** were selected to avoid or reduce aggregation of the corresponding Pcs. Compared to Pcs prepared from a mono-substituted phthalonitrile, a Pc synthesized from **2** exists as single isomer, which allows easier isolation and better characterization. The corresponding rectangular metal-free trimer was not isolated but was detected from a peak at around 900 nm in the UV/Vis/NIR spectrum of the reaction mixture.[2b] In the present work more careful gradient elution from a silica gel column with a toluene/hexane mixture, followed by column chromatography of all mixed fractions, allowed us to isolate both $H_6$**5** and $H_6$**6** in yields of 0.9 and 1.7%, respectively. Their zinc complexes were prepared by the usual metalation with zinc acetate in toluene/dmf (Scheme 1).

All compounds prepared in this work are stable in air and to light in solution as well as in the solid state. They are soluble in aromatic solvents, thf and halogenated hydrocarbons. Linear trinuclear Pcs, especially $Zn_3$**5**, have significantly lower solubility and higher aggregation tendency than the other Pcs described previously and here.[2b] This becomes significant in toluene (concentration dependence of the extinction coefficient, broad bands at around 850 and 1000 nm) at concentrations higher than $10^{-6}$ M. This tendency is not so pronounced in chloroform for $H_6$**5** or in thf for both $H_6$**5** and $Zn_3$**5**. Generally, zinc complexes $Zn_2$**4**–$Zn_3$**6** tend to aggregate more strongly than the corresponding free ligands.

The electrospray ionization (ESI) method was used for mass-spectrometric characterization of the prepared compounds. This method is widely employed for high-molecular-weight ($M > 1000$) compounds such as biomacromolecules,[6a] supramolecular systems,[6b] fullerenes[6c,6e] etc. It is known that ESI is sensitive only to ions already present in the solution or compounds that easily ionize through acid/base (Brønsted or Lewis) or redox chemistry.[6c,6d] To enhance the sensitivity to compounds that are more difficult to ionize, different reagents that convert the substrate into an ionic form (oxidants,[6c] salts,[6b,6d,6e] even in combination with chemical derivatization of analyte[6b,6d]) are used. In the present work, we found that the use of pyridine as a basic co-solvent for $H_6$**6**, or a small amount of sodium cyanide ($\approx 10^{-4}$ M) for $Zn_3$**5** and $Zn_3$**6**, facilitates their ionization to produce [$M^{2-}$ – 2H] and [$M^{2-}$ + 2CN], respectively. Pyridine is expected to deprotonate pyrrole fragments and cyanide coordinate to Zn. An interesting example of using

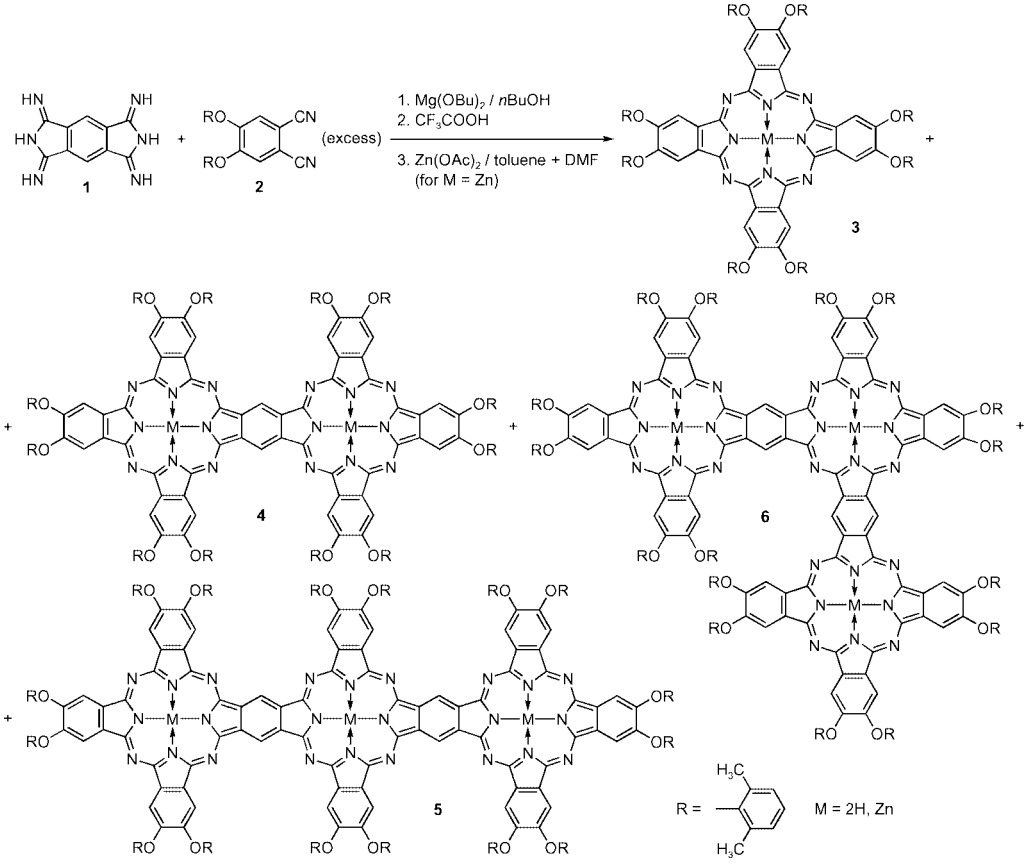


Scheme 1. Synthesis of **3**–**6** (M = 2 H, Zn).

 © 2007 Wiley-VCH Verlag GmbH & Co. KGaA, Weinheim 

NaCN in ESI MS is the analysis of higher fullerenes.[6e] In this case the nucleophilic addition of cyanide to fullerene is responsible for ionization. In summary, the molecular ions of the annulated dinuclear and trinuclear Pcs were clearly identified by the ESI MS method, although it was not possible to distinguish by mass spectrometric means between the isomeric trinuclear linear **5** and rectangular **6**.

The difference between linear and rectangular trinuclear Pcs can be clearly seen in their $^1$H NMR spectra, where Pc ring currents help to resolve the spectra of di- and trinuclear Pcs by deshielding the protons of the neighboring Pc fragments.[2b] The $^1$H NMR spectrum of $H_6$**5** has been described previously.[2b] The spectrum of $H_6$**6** (Figure 1) is more complicated due to its lower symmetry. The signals of the methyl protons are only partially resolved,[7a] in contrast to the clearly resolved group of four singlets in the case of the linear $H_6$**5**. In the aromatic region of the spectrum, two signals of (two types of) protons of the bridging benzene rings appear at $\delta$ = 11.46 and 11.25 ppm, and two groups of signals of the other Pc aromatic protons (eight types, resolved only partially) at $\delta$ = 8.99–9.08 and 8.17–8.37 ppm. In the case of $H_6$**5** there are only five types of Pc ring protons that give separate singlets. The aromatic protons of the substituents show a broad signal at $\delta$ = 7.32–7.54 ppm. In the rectangular trimer, one pair of substituents get very close to each other and, in one of the possible conformations, their tails can be located over the neighboring benzene rings of the remote Pc fragments. The doublet at $\delta$ = 6.96 ppm and the triplet at $\delta$ = 6.63 ppm in the spectrum of $H_6$**6**, which disappear upon increasing temperature, can be assigned to the aromatic protons of these substituents. Zinc complexes $Zn_3$**5** and $Zn_3$**6** show similar spectra to the corresponding free ligands except for the two signals of the pyrrole protons near $\delta$ = 0 ppm (1:2 ratio), which belong to central and peripheral Pc rings, respectively.

The UV/Vis/NIR absorption spectra of **3**–**6** (M = Zn) are shown in Figure 2. The values for the most intense bands are given in Table 1. The spectrum of $H_6$**6** is very similar to that of $Zn_3$**6** [for **3**–**5** (M = 2 H) see ref.[2b]]. The spectral changes on going from Zn**3** to $Zn_2$**4** and further to $Zn_3$**5** are similar to the changes reported[2b] for their metal-free analogues, namely a strong red shift of the Q band [166 nm (2900 cm$^{-1}$) from Zn**3** to $Zn_2$**4** and 102 nm (1300 cm$^{-1}$) from $Zn_2$**4** to $Zn_3$**5**], and an increase of its ex-

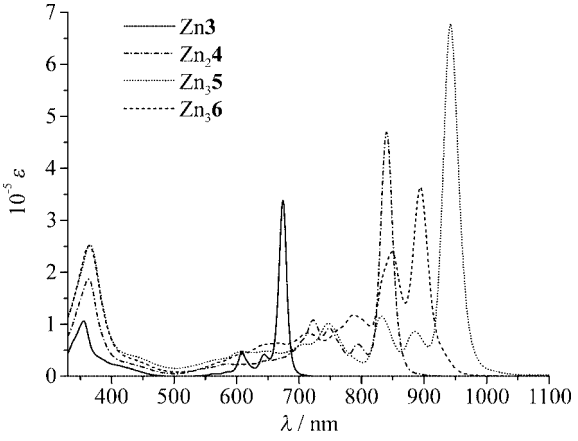


Figure 2. Electronic absorption spectra of **3**–**6** (M = Zn) in thf.

Table 1. Main electronic absorption bands of **3**–**6** (M = Zn).

| | Q band | | B band | |
|---|---|---|---|---|
| | $\lambda$ [nm] (cm$^{-1}$) | $\varepsilon$ [M$^{-1}$ cm$^{-1}$] | $\lambda$ [nm] (cm$^{-1}$) | $\varepsilon$ [M$^{-1}$ cm$^{-1}$] |
| Zn**3** | 674 (14800) | 338000 | 355 (28200) | 106000 |
| $Zn_2$**4** | 840 (11900) | 470000 | 363 (27500) | 187000 |
| $Zn_3$**5** | 942 (10600) | 680000 | 365 (27800) | 253000 |
| $Zn_3$**6** | 894 (11200) | 364000 | 364 (27500) | 251000 |
| | 849 (11800) | 239000 | | |

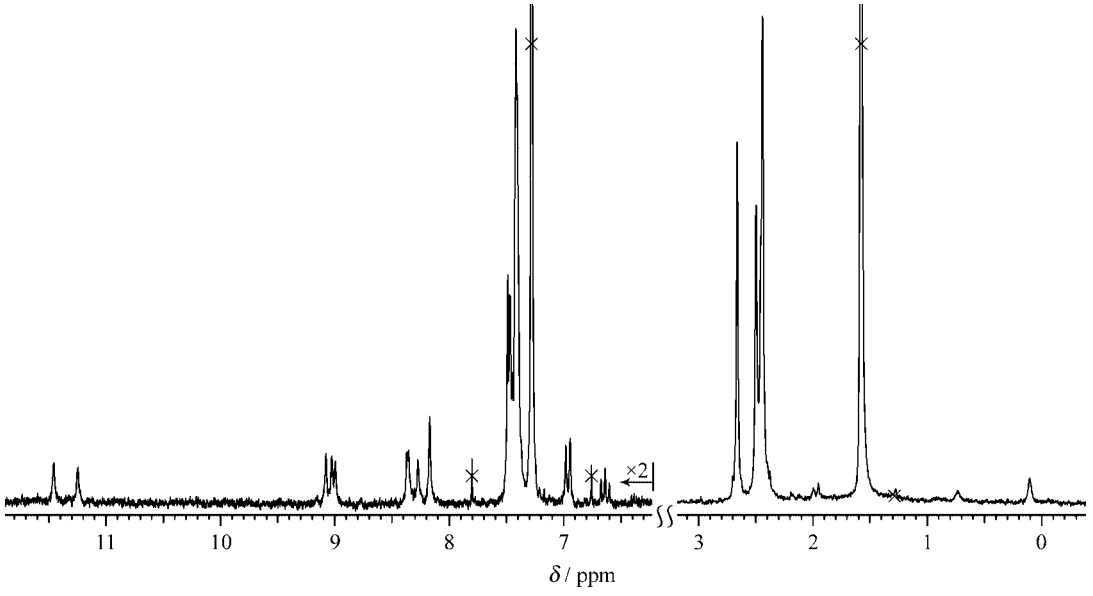


Figure 1. $^1$H NMR spectrum of $H_6$**6** in $CDCl_3$.

 © 2007 Wiley-VCH Verlag GmbH & Co. KGaA, Weinheim 

tinction coefficient. The spectrum of $Zn_3$**6** is more complex. The Q band appears between those of $Zn_2$**4** and $Zn_3$**5**, thus indicating that the rectangular annulation of the third Pc ring has less effect on the frontier orbitals than the linear one. In contrast to $D_{2h}$-symmetric $Zn_2$**4** and $Zn_3$**5**, the Q band of $C_{2v}$-symmetric[8] $Zn_3$**6** is split into two sub-bands of similar intensity; its maximal extinction coefficient is lower than that of $Zn_3$**5**. The Soret band position is not significantly influenced by π-system extension, which indicates only a weak perturbation of the higher excited singlet state. The intensity of the Soret band increases with molecular size − the intensity ratios for Zn**3**/$Zn_2$**4**/$Zn_3$**5**/$Zn_3$**6** are 1:1.76:2.38:2.36, i.e. not proportional to the number of Pc rings but more likely to the number of benzene rings (ratios 1:1.75:2.50:2.50).

For better understanding of the observed spectral changes semi-empirical MO calculations (ZINDO/s method) were carried out for the unsubstituted analogues Zn**3a**–$Zn_3$**6a** of Zn**3**–$Zn_3$**6**, respectively. The initial geometries were constructed from the crystal structure of the unsubstituted ZnPc (Zn**3a**)[9] by making the molecules perfectly planar and adopting $D_{4h}$ (Zn**3a**), $D_{2h}$ ($Zn_2$**4a** and $Zn_3$**5a**), or $C_{2v}$ symmetry ($Zn_3$**6a**), as described for dinuclear Pc.[2f] The distance between the closest hydrogen atoms located at the first and the third Pc ring of $Zn_3$**6a** is only 2.8 Å, which means that bulky substituents at these positions in **6** have to escape each other (see discussion of NMR spectra), perhaps also distorting the Pc rings. This more sterically hindered and less symmetrical structure could be the reason for the much higher solubility of **6** compared to **5**. The calculated spectra are shown in Figure 3 and the partial orbital diagrams in Figure 4. The results obtained for Zn**3a** and $Zn_2$**4a** are similar to data reported previously.[2c,2e,2f] The shapes of the theoretical spectra are in good agreement with the experimental ones, although the transition energies are underestimated by around 10% for the Q bands of $Zn_2$**4**–$Zn_3$**6**. The splitting of the Q band for $Zn_3$**6** is predicted. Also, the higher-energy transitions at around 700 nm calculated for $Zn_2$**4**–$Zn_3$**6** can be seen in their spectra as broad bands of low intensity. The observed strong Q band changes can be explained by considering a simplified orbital model (Figure 4). The Pc Q band is essentially a HOMO–LUMO transition. A series of two HOMOs and four LUMOs of **4a** can be described as a linear combination of frontier orbitals of two mononuclear Pc molecules.[2f] The splitting of the corresponding energy levels reduces the HOMO–LUMO gap, and this effect increases with addition of the third Pc ring. Whereas the HOMO splitting pattern is similar for $Zn_3$**5a** and $Zn_3$**6a**, the LUMO splitting is different: it is stronger for $Zn_3$**5a**, and in the case of $Zn_3$**6a** two lowest unoccupied levels have very similar energy values, which is responsible for the Q band splitting. This is very similar to the observed difference between opposite and adjacent annulation of benzene rings at the Pc:[5b,5c] the splitting of the LUMO (and, as a consequence, of the Q band) in the latter case is much weaker. This can be explained by the orthogonality of the Pc LUMOs ($E_{gx}$ and $E_{gy}$). In the case of rectangular (adjacent) annulation they interact with the orbitals of annulated fragments (Pc or benzene rings) almost independently, which results in a rather small splitting. This is in contrast to linear (opposite) annulation along the $x$ axis, where the $E_{gx}$ LUMO interacts

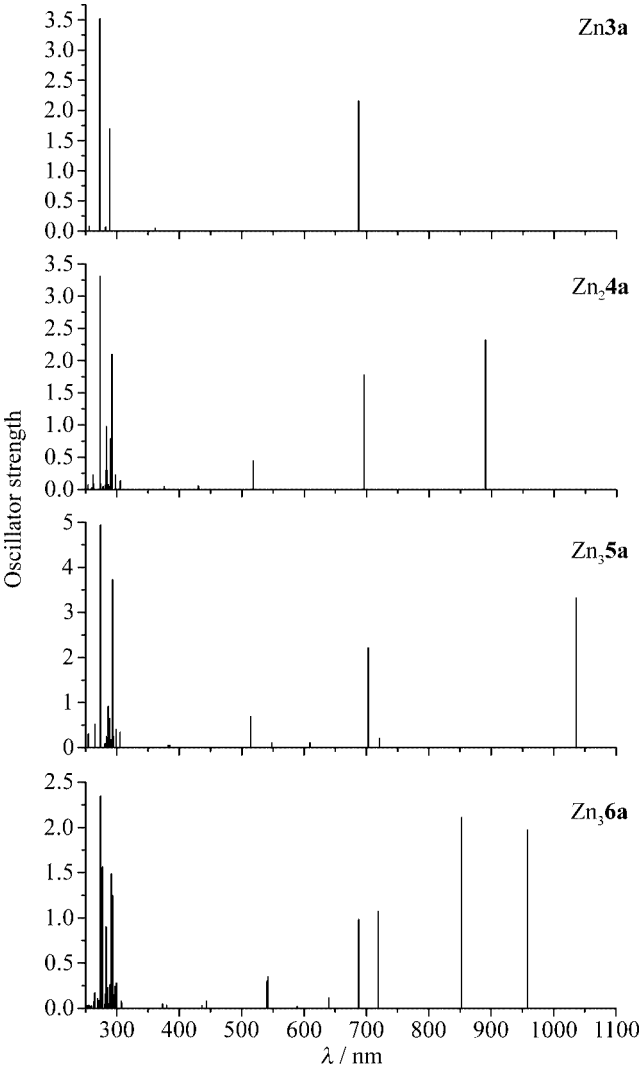


Figure 3. Calculated electronic spectra (ZINDO/s method) for unsubstituted analogues **3a**–**6a** (M = Zn) of **3**–**6** (M = Zn).

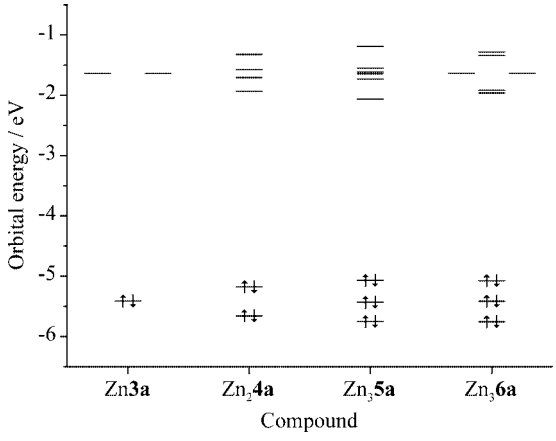


Figure 4. Partial orbital diagrams of **3a**–**6a** (M = Zn).

 © 2007 Wiley-VCH Verlag GmbH & Co. KGaA, Weinheim 

strongly with both fragments, resulting in strong red shift of the *x*-polarized Q sub-band. Since the Pc HOMO ($A_{1u}$) is symmetric relative to all four $C_2$ axes within the plane, its interaction with the orbitals of additional Pc or benzene rings, which results in splitting or destabilization[5b] of the corresponding energy levels, is similar for both types of annulation. Each trimer has one occupied and two unoccupied orbitals with energies very similar to the HOMO and LUMOs of Zn**3a**. These "unperturbed" orbitals are located on peripheral Pc rings.

The fluorescence spectra of compounds **3**–**6** (M = Zn) in thf are shown in Figure 5. The maximum of the fluorescence spectrum of the mononuclear Pc Zn**3** ($\lambda_{max}$ = 687 nm) shifts to 846 nm for the dinuclear Pc $Zn_2$**4**, 902 nm for the rectangular trimer $Zn_3$**6**, and to 948 nm for the linear trimer $Zn_3$**5** (Table 2). The fluorescence quantum yield ($\Phi_{fl}$) of the mononuclear Pc Zn**3** is 0.28, that of the dinuclear Pc $Zn_2$**4** is 0.08, and those for the linear ($Zn_3$**5**) and rectangular ($Zn_3$**6**) trinuclear Pcs less than 0.03 (Table 2). The fluorescence lifetime ($\tau_{fl}$) of Zn**3** is 3.05 ns, whereas it is 0.68 ns for $Zn_2$**4**, 0.35 ns for $Zn_3$**5**, and 0.56 ns for $Zn_3$**6**. The values of the fluorescence quantum yield of the dinuclear and trinuclear ZnPcs are reduced compared with that of the mononuclear Pc. This reduction is in agreement with a decrease of the fluorescence lifetime. The decrease of the HOMO–LUMO gap and a more extended vibrational level structure of larger molecules, which increase the probability of nonradiative decay, are the reasons for this effect.[2b,2f,2j,10] Compared to the values for $H_2$**3** reported in our previous publication,[2b] the fluorescence lifetime and fluorescence quantum yield of Zn**3** are strongly reduced due to the heavy-atom effect, which is usual for Pcs with a closed-shell central metal.[10] Due to the strongly increased probability of nonradiative deactivation of the first excited singlet state of **4** and **5**, the difference between the fluorescence lifetime and quantum yield for metal-free and Zn di- and trinuclear Pcs becomes negligible.[11]

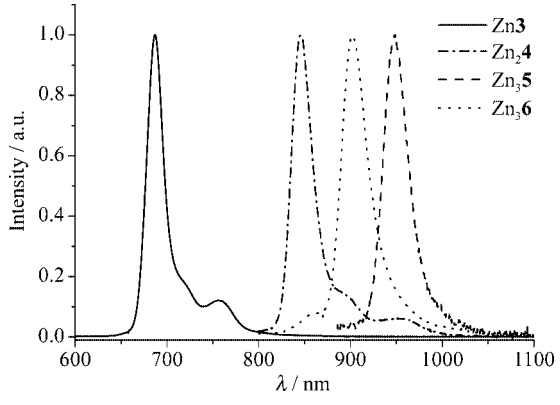


Figure 5. Fluorescence spectra (uncorrected) of **3**–**6** (M = Zn) in thf.

Table 2. Photophysical properties of **3**–**6** (M = Zn) in thf.

| | Fluorescence max. $\lambda$ [nm] ($cm^{-1}$) | $\Phi_{fl}$ | $\tau_{fl}$ [ns] |
|---|---|---|---|
| Zn**3** | 687 (14550) | 0.28 | 3.05 |
| $Zn_2$**4** | 846 (11800) | 0.08 | 0.68 |
| $Zn_3$**5** | 948 (10550) | <0.03 | 0.35 |
| $Zn_3$**6** | 902 (11100) | <0.03 | 0.56 |

## Conclusions

Isomeric linear and rectangular trinuclear phthalocyanines connected through common annulated benzene rings have been obtained by the mixed condensation of a tetracyanobenzene derivative and 4,5-bis(2,6-dimethylphenoxy)-phthalonitrile together with mono- and dinuclear Pcs. The different annulated Pcs could be separated by column chromatography. Metal-free rectangular and zinc linear and rectangular trinuclear Pcs of this type have been prepared for the first time. The annulated zinc complexes show intense ($\varepsilon = 2\times10^5$–$7\times10^5$ $M^{-1}cm^{-1}$) NIR absorption bands at $\lambda \approx 950$ nm for the linear and $\lambda \approx 850$ and 900 nm for the rectangular trimer, whereas the dinuclear Pc absorbs at $\lambda \approx 850$ nm. This clearly reflects the extension of the π-electron system. An exceptionally long wavelength shift and decreasing HOMO–LUMO gap is also observed for triply linked fused porphyrins due to conjugation over the whole planar π-system.[1b,1e,1f] Compared to the linear trimer, the less symmetrical rectangular one shows a more complex spectrum with a splitting of the lowest energy absorption band. The observed spectral changes are in good agreement with semi-empirical MO calculations (ZINDO/s method). The difference between the orbitals and spectra of linear and rectangular trinuclear Pcs is analogous to that in opposite and adjacent dibenzo-annulated Pc analogues.[5b,5c] The fluorescence quantum yields and lifetimes decrease with increasing molecular size. The rectangular trimer $Zn_3$**6** has a longer fluorescence lifetime than the linear $Zn_3$**5**. Work is now in progress to study the electronic properties of these trinuclear Pcs in more detail.

## Experimental Section

**Measurements:** Electronic absorption spectra were recorded with a Perkin–Elmer Lambda 2 spectrophotometer, IR spectra with a Perkin–Elmer Spectrum 1000 FT-IR spectrometer, NMR spectra with a Bruker Avance DPX 200 (200 MHz), and ESI mass spectra with a Bruker Esquire LC mass spectrometer. The experimental setups for steady-state and time-resolved fluorescence measurements have been described previously.[2b] The excitation source for the time-resolved measurements was a pulsed frequency doubled linear polarized Nd:$VO_4$ laser (Cougar, Time Bandwidth Products) with a wavelength of 532 nm, a pulse width of 12 ps, and a repetition rate of 60 MHz. The steady-state fluorescence spectra of **3**–**6** were recorded at an excitation wavelength of 360 nm.

Molecular Orbital Calculations were performed using the ZINDO/s method within the HyperChem R 5.02[12] software program. The σ–σ and π–π overlap weighing factors were 1.267 and 0.585, respectively. The electronic spectra were calculated using the configuration interaction method including all singly excited configurations with excitation energies up to 8 eV, as described previously.[2c] The initial geometries were constructed from the X-ray crystal structure

 © 2007 Wiley-VCH Verlag GmbH & Co. KGaA, Weinheim 

of the unsubstituted PcZn[9] by making the molecules perfectly planar and adopting $D_{4h}$ (Zn**3a**), $D_{2h}$ ($Zn_2$**4a** and $Zn_3$**5a**), or $C_{2v}$ symmetry ($Zn_3$**6a**), as described previously for $Zn_2$**4a**.[2f]

**Materials:** Zinc acetate dihydrate (Fluka) purchased in the highest available grade was used without further purification. The solvents (Fluka, analytical reagent grade) were dried, distilled, and stored under nitrogen. Merck silica gel 60 (40–63 μm) was used for chromatographic separations. The compounds Zn**3** and $Zn_2$**4** were prepared as described previously.[2l]

The phthalocyanines **3**–**6** (M = 2 H) were prepared by the mixed condensation procedure described by us previously.[2b] After demetalation of the obtained mixture of MgPcs with trifluoroacetic acid, the resulting mixture of metal-free Pcs was chromatographed on silica gel eluting with toluene/hexane and *very slowly* reducing the hexane content from 15 to 5 vol.-%. The eluate content was analyzed by UV/Vis/NIR spectroscopy, the fractions containing peaks at about 900 and 950 nm were collected, and the ones with almost identical spectra were mixed and re-chromatographed to obtain two fractions whose spectra did not change during elution from the column. The solvents were then evaporated under reduced pressure. Compound $H_6$**5** (less soluble) was recrystallized from toluene and $H_6$**6** re-precipitated from toluene with hexane; both were then dried under vacuum ($10^{-2}$ mbar) at 60 °C.

**$H_6$5:** Dark-green powder; yield: 8.5 mg (0.9%). $^1$H NMR: identical to previous data.[2b] UV/Vis (thf): $\lambda_{max}$ ($\varepsilon$) = 944 (400000), 890 (89000), 836 (100000), 754 (85000), 660 (sh, 45000), 608 (41000), 418 (sh, 72000), 356 nm (215000 $M^{-1}cm^{-1}$).[13] MS (ESI, $CH_2Cl_2$/dmf, 1:10, negative mode): *m*/*z* 1652.5 [$M^{2-}$ – H].

**$H_6$6:** Dark-green powder; yield: 16 mg (1.7%). $^1$H NMR (200 MHz, $CDCl_3$, 25 °C, TMS):[7a] $\delta$ = 11.46 (s, 2 H), 11.25 (s, 2 H), 9.08 (s, 2 H), 9.02 (s, 2 H), 8.99 (s, 2 H), 8.37 (s, 2 H), 8.35 (s, 2 H), 8.27 (s, 2 H), 8.17 (br., 4 H), 7.32–7.54 (br. m, 42 H), 6.96 (d, $J_{H,H}$ = 7.6 Hz, 4 H), 6.63 (t, $J_{H,H}$ = 7.6 Hz, 2 H), 2.36–2.72 (m, 96 H), 0.73 (br. s, 2 H), 0.10 (br. s, 4 H) ppm. UV/Vis (thf): $\lambda_{max}$ ($\varepsilon$) = 907 (288000), 860 (209000), 810 (118000) 773 (sh, 102000), 729 (107000), 668 (sh, 66000), 420 (sh, 84000), 357 nm (232000 $M^{-1}cm^{-1}$). MS (ESI, pyridine/dmf, 1:10, negative mode): *m*/*z* 1652 [$M^{2-}$ – 2 H].

**Compound $Zn_3$5:** $H_6$**5** (5.1 mg, 1.5 μmol) was suspended in toluene (2 mL) by sonication. A solution of zinc acetate dihydrate (30 mg, 0.14 mmol) in dmf (1 mL) was then added and the resulting mixture was refluxed for 15 h. The cooled mixture was diluted with methanol (10 mL) and the precipitate was collected by centrifugation, washed with methanol, vacuum-dried, dissolved in toluene containing 8 vol.-% of diethyl ether, and chromatographed on silica gel eluting with toluene/diethyl ether (approx. 10 vol.-% of diethyl ether). The solvents were then evaporated under reduced pressure and the compound was recrystallized from toluene and vacuum-dried ($10^{-2}$ mbar, 60 °C) to obtain a black powder. Yield: 2.3 mg (42%). $^1$H NMR (200 MHz, $C_6D_6$, 65 °C, TMS):[7b] $\delta$ = 11.71 (s, 4 H), 9.82 (s, 4 H), 8.68 (br., 8 H), 7.25–7.49 (br. m, 48 H), 2.73 (s, 24 H), 2.64 (s, 24 H), 2.40 (s, 24 H), 2.28 (s, 24 H) ppm. UV/Vis (thf): $\lambda_{max}$ ($\varepsilon$) = 942 (680000), 885 (86000), 832 (115000), 746 (102000), 709 (sh, 62000), 648 (48000), 607 (48000), 365 nm (253000 $M^{-1}cm^{-1}$). MS (ESI, dmf + NaCN, negative mode): *m*/*z* 1772 [$M^{2-}$ + 2CN].

**Compound $Zn_3$6:** Similarly, a mixture of $H_6$**6** (10.9 mg, 3.3 μmol) in toluene (2 mL) was treated with zinc acetate dihydrate (44 mg, 0.20 mmol) in dmf (1 mL). The crude product was chromatographed on silica gel eluting with toluene/diethyl ether (approx. 9 vol.-% of diethyl ether), re-precipitated from toluene with hexane, and vacuum-dried ($10^{-2}$ mbar, 60 °C) to obtain $Zn_3$**6** as a dark-green powder. Yield: 5.1 mg (44%). $^1$H NMR (200 MHz, $C_6D_6$, 60 °C, TMS):[7a] $\delta$ = 11.91 (s, 2 H), 11.81 (s, 2 H), 9.77 (s, 2 H), 9.74 (s, 2 H), 9.55 (s, 2 H), 8.71 (br., 10 H), 7.24–7.52 (m, 48 H), 2.25–2.80 (m, 96 H) ppm. UV/Vis (thf): $\lambda_{max}$ ($\varepsilon$) = 894 (364000), 849 (239000), 787 (118000), 715 (83000), 664 (sh, 64000), 364 nm (251000 $M^{-1}cm^{-1}$). MS (ESI, dmf + NaCN, negative mode): *m*/*z* 1772 [$M^{2-}$ + 2CN].

## Acknowledgments

We thank the Deutsche Forschungsgemeinschaft for financial support (WO 237/32-3, RO 1042/9-4).

[1] a) P. D. Harvey, in *The Porphyrin Handbook*, vol. 18 (Eds.: K. M. Kadish, K. M. Smith, R. Guilard), Academic Press, San Diego, California, **2003**, pp. 63–250; b) H. L. Anderson, *J. Am. Chem. Soc.* **2002**, *124*, 14642–14654; c) H. L. Anderson, *Chem. Commun.* **1999**, 2323–2330; d) M. G. Vicente, L. Jaquinod, K. M. Smith, *Chem. Commun.* **1999**, 1771–1782; e) A. Tsuda, H. Furuta, A. Osuka, *J. Am. Chem. Soc.* **2001**, *123*, 10304–10321; f) A. Tsuda, A. Osuka, *Adv. Mater.* **2002**, *14*, 75–79; g) A. K. Burrell, D. L. Officer, P. G. Plieger, D. C. W. Reid, *Chem. Rev.* **2001**, *101*, 2751–2796.

[2] a) N. Kobayashi, *Coord. Chem. Rev.* **2002**, *227*, 129–152; b) S. Makarov, Ch. Litwinski, E. A. Ermilov, O. Suvorova, B. Röder, D. Wöhrle, *Chem. Eur. J.* **2006**, *12*, 1468–1474; c) N. Kobayashi, H. Ogata, *Eur. J. Inorg. Chem.* **2004**, 906–914; d) M. Calvete, M. Hanack, *Eur. J. Inorg. Chem.* **2003**, 2080–2083; e) N. Kobayashi, T. Fukuda, D. Lelievre, *Inorg. Chem.* **2000**, *39*, 3632–3637; f) N. Kobayashi, H. Lam, W. A. Nevin, P. Janda, C. C. Leznoff, T. Koyama, A. Monden, H. Shirai, *J. Am. Chem. Soc.* **1994**, *116*, 879–890; g) M. J. Cook, M. J. Heeney, *Chem. Eur. J.* **2000**, *6*, 3958–3964; h) E. M. Garcia-Frutos, F. Fernandez-Lazaro, E. M. Maya, P. Vazquez, T. Torres, *J. Org. Chem.* **2000**, *65*, 6841–6846; i) C. G. Claessens, T. Torres, *Angew. Chem.* **2002**, *114*, 2673–2677; *Angew. Chem. Int. Ed.* **2002**, *41*, 2561–2565; j) N. Kobayashi, Y. Higashi, T. Osa, *Chem. Lett.* **1994**, 1813–1816; k) G. de la Torre, V. M. Martinez-Diaz, T. Torres, *J. Porphyrins Phthalocyanines* **1999**, *3*, 560–568; l) S. G. Makarov, A. V. Piskunov, O. N. Suvorova, G. Schnurpfeil, G. A. Domrachev, D. Wöhrle, *Chem. Eur. J.*, in press.

[3] a) P. Erk, H. Hengelsberg, in *The Porphyrin Handbook*, vol. 19 (Eds.: K. M. Kadish, K. M. Smith, R. Guilard), Academic Press, San Diego, California, **2003**, pp. 105–149; b) D. Wöhrle, O. Suvorova, R. Gerdes, O. Bartels, Ł. Łapok, N. Baziakina, S. Makarov, A. Słodek, *J. Porphyrins Phthalocyanines* **2004**, *8*, 1020–1041; c) J. H. Zagal, *Coord. Chem. Rev.* **1992**, *119*, 89–136; d) R. Gerdes, O. Bartels, G. Schneider, D. Wöhrle, G. Schulz-Ekloff, *Polym. Adv. Technol.* **2001**, *12*, 152–160; e) K.-Y. Law, *Chem. Rev.* **1993**, *93*, 449–486; f) E. Ben-Hur, W. Shun Chan, in *The Porphyrin Handbook*, vol. 19 (Eds.: K. M. Kadish, K. M. Smith, R. Guilard), Academic Press, San Diego, California, **2003**, pp. 1–36.

[4] a) T. Inabe, H. Tajima, *Chem. Rev.* **2004**, *104*, 5503–5533; b) R. J. Mortimer, *Chem. Soc. Rev.* **1997**, *26*, 147–156; c) M. M. Nicholson, in *Phthalocyanines – Properties and Applications*, vol. 3 (Eds.: C. C. Leznoff, A. B. P. Lever), VCH Publishers, New York, **1993**, pp. 71–117; d) G. de la Torre, P. Vazquez, F. Agullo-Lopez, T. Torres, *Chem. Rev.* **2004**, *104*, 3723–3750; e) S. Flom, in *The Porphyrin Handbook*, vol. 19 (Eds.: K. M. Kadish, K. M. Smith, R. Guilard), Academic Press, San Diego, California, **2003**, pp. 179–190; f) D. Wöhrle, L. Kreienhoop, D. Schlettwein, in *Phthalocyanines – Properties and Applications*, vol. 4 (Eds.: C. C. Leznoff, A. B. P. Lever), VCH Publishers,

 © 2007 Wiley-VCH Verlag GmbH & Co. KGaA, Weinheim 

New York, **1996**, pp. 219–284; g) W. H. Flora, H. K. Hall, N. R. Armstrong, *J. Phys. Chem. B* **2003**, *107*, 1142–1150.
[5] a) N. Kobayashi, S. Nakajima, H. Ogata, T. Fukuda, *Chem. Eur. J.* **2004**, *10*, 6294–6312; b) N. Kobayashi, H. Miwa, V. N. Nemykin, *J. Am. Chem. Soc.* **2002**, *124*, 8007–8020; c) N. Kobayashi, J. Mack, K. Ishii, M. J. Stillman, *Inorg. Chem.* **2002**, *41*, 5350–5363.
[6] a) J. B. Fenn, M. Mann, C. K. Meng, S. F. Wong, C. M. Whitehouse, *Science* **1989**, *246*, 64–71; b) K. C. Russell, E. Leize, A. V. Dorsselaer, J.-M. Lehn, *Angew. Chem. Int. Ed. Engl.* **1995**, *34*, 209–213; c) S. R. Wilson, Y. Wu, *J. Am. Soc. Mass Spectrom.* **1993**, *4*, 596–603; d) G. I. Van Berkel, F. Zhou, *Anal. Chem.* **1994**, *66*, 3408–3415; e) G. Khairallah, J. B. Peel, *Int. J. Mass Spectrom.* **2000**, *194*, 115–120.
[7] a) The low-intensity, temperature-dependent satellites around the signals of the methyl protons in the spectra of $H_6$**6** and $Zn_3$**6** could be due to aggregation and/or hindered rotation of the substituents; b) The peaks in the spectrum of $Zn_3$**5** appear on a background of broad bands of aggregates; the integration is only approximate.
[8] $C_{2v}$ is the symmetry of the idealized flat structure. The real symmetry is probably lower ($C_2$) due to the steric hindrance of the substituents.
[9] J. F. Kirner, W. Dow, W. R. Scheidt, *Inorg. Chem.* **1976**, *15*, 1685–1690.
[10] K. Ishii, N. Kobayashi, in *The Porphyrin Handbook*, vol. 16 (Eds.: K. M. Kadish, K. M. Smith, R. Guilard), Academic Press, San Diego, California, **2003**, pp. 1–42.
[11] There is an error in our previous paper (ref.[2b]): The fluorescence quantum yield of $H_2$**3** is 0.66 and that of $H_4$**4** is 0.08.
[12] *HyperChem. R.5.02 Pro*, Hypercube Inc., Gainesville, FL, USA, **1997**.
[13] The $\varepsilon$ values were underestimated in our previous work,[2b] probably due to incomplete disaggregation: the sample dissolution requires sonication, then the solution must stand for several hours until the slowly increasing optical density stabilizes; the reported values (ref.[2b]) were obtained immediately after dissolution.

Received: September 11, 2006
Published Online: December 11, 2006

 © 2007 Wiley-VCH Verlag GmbH & Co. KGaA, Weinheim 

DOI: 10.1002/ejic.200600914

# Synthesis, Structure and Reactivity of Trimethylsilyl-Substituted Phosphametallocenes

**Rebekka Loschen,[a] Christoph Loschen,[a][‡] and Walter Frank,[a][‡‡] and Christian Ganter*[a]**

*Dedicated to Prof. Dr. Gerhard E. Herberich on the occasion of his 70th birthday*

**Keywords:** Metallocenes / P ligands / Silicon / Phosphaferrocenes / Conformation analysis

New sterically crowded phosphaferrocene and -ruthenocene derivatives were synthesized via the 2,5-bis(trimethylsilyl)-phospholide anion **5**. Their reactivity with regard to the exchange of the $Me_3Si$ groups for other functional groups was examined. X-ray structures were determined for the mono- (**6**) and the 1,1′-diphosphaferrocene (**8**). The activation barrier for ring–ring rotation in **8** was determined by NMR spectroscopy and supported by DFT calculations. Attempts to prepare 2,5-difunctional phosphaferrocenes through electrophilic substitutions were unsuccessful, but yielded en route a new bidentate P,P ligand (**3**) and its $Mo(CO)_4$ complex, which were both characterized by X-ray diffraction.
(© Wiley-VCH Verlag GmbH & Co. KGaA, 69451 Weinheim, Germany, 2007)

## Introduction

Phosphametallocenes are interesting compounds that show remarkable equivalence with their carbocyclic analogues regarding some of the physical and chemical properties but also show markedly different behaviour with regard to other properties. The Fe containing phosphaferrocenes are by far the most intensively studied phosphametallocenes, which were discovered in 1977 and still continue to be of interest.[1] In particular, the use of phosphaferrocene building blocks for the construction of multidentate, chiral chelate ligands has brought about a renewed interest within the last decade.[2] The chemical reactivity of phosphaferrocenes in view of synthetically useful transformations is restricted to electrophilic aromatic substitutions, which provide access to derivatives with one additional functional group attached to the phosphole ring, thereby rendering the phosphaferrocene a planar-chiral moiety. In this paper we report our attempts to prepare phosphaferrocene and phospharuthenocene derivatives with two functional groups at the 2,5-position of the phosphole ring. Related compounds were prepared earlier by converting suitable phosphole precursors into the respective phosphametallocenes[3] and this strategy was successfully employed in this work. The sought-after 2,5-difunctionalized phosphaferrocenes are synthetically interesting compounds and may be used for the assembly of extended structures like macrocycles containing several individual phosphaferrocene units. Such compounds would significantly expand the class of known macrocyclic ligands, which mainly consist of oxygen, sulfur or nitrogen containing derivatives.[4] In contrast, much less is known about phosphorus containing macrocycles although the first example was prepared as early as 1975.[5,6] While the O, N and S containing compounds feature strong σ-donor properties, the P derivatives are of special interest because they may exhibit a more or less pronounced π-acceptor character, depending on the nature of the phosphorus subunit. For example, a macrocycle comprising four phosphinine rings with strong acceptor properties[7] has been reported by Mathey et al.[8] This ligand formed stable complexes with low-valent transition-metal fragments of $Rh^I$, $Ir^I$, $Au^I$ and $Au^0$.[8a,9] Phosphaferrocenes also feature $sp^2$-hybridized P atoms with a significant π-acceptor capacity[1] and have been used recently as building blocks for the construction of bi- and oligodentate chiral chelate ligands. In view of their potential use for the assembly of macrocycles we decided to elaborate on the synthesis of 2,5-disubstituted phosphaferrocenes.

## Results and Discussion

A potential retrosynthetic fragmentation of a phosphaferrocene containing macrocycle is presented in Scheme 1. Disconnection leads to 2,5-disubstituted phosphaferrocene derivatives with suitable functional groups. Thus, a 2,5-diformyl or diacyl derivative, or compounds derived thereof, appear to be attractive synthetic targets.

[a] Institut für Anorganische Chemie, Heinrich-Heine-Universität Düsseldorf,
Universitätsstrasse 1, 40225 Düsseldorf, Germany
E-Mail: christian.ganter@uni-duesseldorf.de
[‡] DFT calculations.
[‡‡] X-ray structure determinations.

 © 2007 Wiley-VCH Verlag GmbH & Co. KGaA, Weinheim 

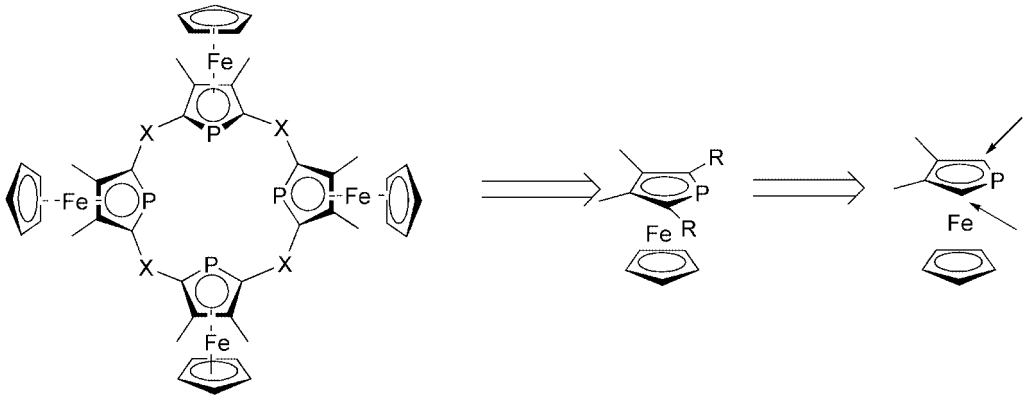


Scheme 1.

**Modification of an Existent Phosphaferrocene**

In contrast to ferrocene, which can be deprotonated and treated with a great variety of electrophiles, this protocol is not applicable to phosphaferrocenes,[10] thus preventing an easy and general access to functionalized derivatives. As mentioned above, electrophilic substitution is the only reported method for the introduction of a substituent into the phosphole ring of a given phosphaferrocene unit. For example, the electrophilic formylation,[11] acylation[12] and carboxylation[13] of 3,4-dimethylphosphaferrocene under Friedel–Crafts or Vilsmeyer conditions have been reported to occur selectively on the phosphole ring giving the monofunctionalized products with the additional substituent at the 2-position in good yield, thereby rendering the phosphaferrocene a planar-chiral moiety. The deactivating nature of the formyl, acyl and carboxylic ester functional groups prevents the formation of disubstituted derivatives. We thought that transformation of these functional groups into less deactivating or even activating ones might overcome this situation and allow the introduction of a second functional group via electrophilic substitution. Therefore, we prepared the ether derivatives **2** and **3** in good yield after initial reduction of the aldehyde **1** to the corresponding alcohol (Scheme 2).

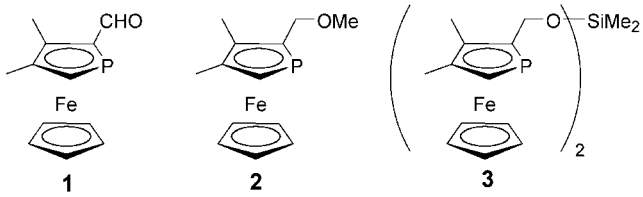


Scheme 2.

The spectroscopic characterization revealed that compound **3** was obtained as a *rac*/*meso* mixture in the ratio of 2:1 because of the racemic nature of the starting aldehyde **1**. The *rac* isomer of **3** could be characterized by an X-ray diffraction analysis. It crystallizes in the triclinic space group $P\bar{1}$ with both enantiomers in the asymmetric unit ($Z$ = 4). The geometrical data for the two independent molecules are identical within experimental precision and values are reported for one molecule only. Bond lengths and angles fall in the range typically observed for phosphaferrocene derivatives. The suitability of the dinuclear phosphaferrocene **3** to act as a bidentate-P,P ligand was demonstrated by the formation of the complex **3**·Mo(CO)$_4$. Again, the X-ray structure of the complex containing the *rac*-ligand could be determined and the two structures are depicted in Figure 1 and Figure 2, relevant geometrical data are compiled in Table 1 and Table 2. The Mo complex lacks any molecular symmetry in the solid state (point group $C_1$), but features effective $C_2$ symmetry in solution leading to a singlet resonance for the two phosphorus atoms in the $^{31}$P NMR spectrum. A Similar behaviour has been observed before for other Mo(CO)$_4$ complexes with $C_2$-symmetric bisphosphaferrocenes.[14,15] The deviations of the central MoL$_6$ core from regular octahedral symmetry in terms of bond angles are rather small since the P,P ligand is highly flexible because of the extended backbone. The Mo–P and Mo–CO distances are in agreement with values observed for related complexes with phosphaferrocene or other π-acidic P-ligands.[16] The changes of intra-ligand geometrical parameters upon coordination are small but typical and mainly

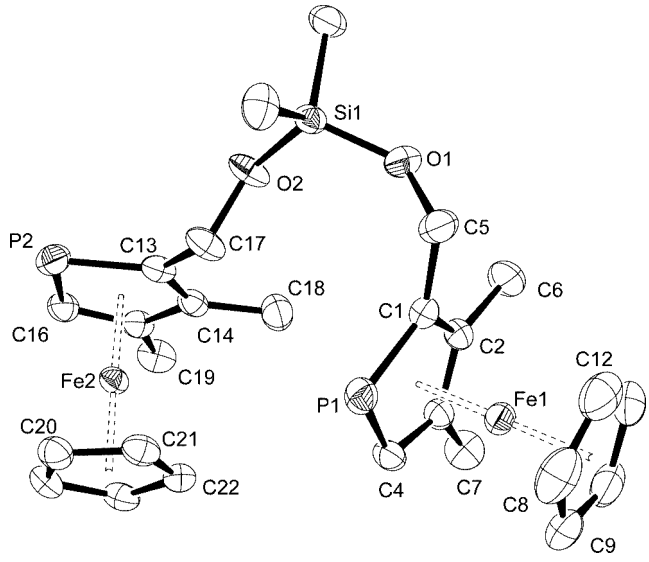


Figure 1. Molecular structure of complex **3**.

 © 2007 Wiley-VCH Verlag GmbH & Co. KGaA, Weinheim 

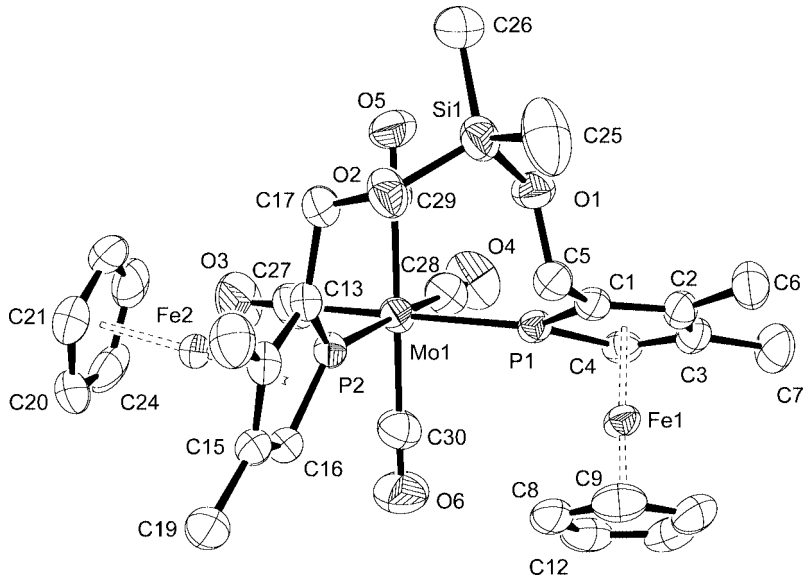


Figure 2. Molecular structure of complex (*rac*-**3**)·[$Mo(CO)_4$].

involve the increase of the C–P–C angle in the phosphole ring from 88.3 to 90.2°.

Table 1. Selected bond lengths [Å] and angles [°] for complexes **3** and **3**·$Mo(CO)_4$.

| | **3** | **3**·$Mo(CO)_4$ |
|---|---|---|
| P1–C4 | 1.753(4) | 1.737(5) |
| P1–C1 | 1.775(4) | 1.756(5) |
| P2–C16 | 1.766(4) | 1.756(5) |
| P2–C13 | 1.778(4) | 1.758(5) |
| C1–C2 | 1.410(5) | 1.420(6) |
| C3–C4 | 1.402(5) | 1.416(7) |
| C2–C3 | 1.414(4) | 1.419(7) |
| C13–C14 | 1.412(5) | 1.435(6) |
| C15–C16 | 1.406(5) | 1.396(7) |
| C14–C15 | 1.420(5) | 1.423(7) |
| Si1–O1 | 1.622(2) | 1.629(4) |
| Si1–O2 | 1.631(2) | 1.632(4) |
| C4–P1–C1 | 88.35(17) | 90.2(2) |
| C16–P2–C13 | 88.17(17) | 90.2(2) |
| C2–C1–C5 | 123.2(3) | 124.4(4) |
| C14–C13–C17 | 123.6(3) | 122.7(5) |
| O1–Si1–O2 | 112.89(14) | 109.13(19) |

Table 2. Unique bond lengths [Å] and angles [°] for complex **3**·$Mo(CO)_4$.

| | | | |
|---|---|---|---|
| Mo1–P1 | 2.4938(14) | Mo1–P2 | 2.5187(14) |
| Mo1–C27 | 1.989(7) | Mo1–C28 | 1.959(7) |
| Mo1–C30 | 2.010(7) | Mo1–C29 | 2.019(7) |
| O3–C27 | 1.174(7) | O4–C28 | 1.167(7) |
| O5–C29 | 1.152(6) | O6–C30 | 1.151(7) |
| C30–Mo1–C29 | 178.9(3) | C27–Mo1–P1 | 174.6(2) |
| C28–Mo1–P2 | 177.9(2) | P1–Mo1–P2 | 92.93(4) |

Unfortunately, all attempts to introduce a second functional group into the derivatives **2** and **3** by electrophilic formylation or acylation have met with failure. Furthermore, the dinuclear derivative 1,1′-bis[(3,4-dimethylphosphaferrocene-2-yl)methyl]ferrocene[15] could also neither be formylated nor acylated.

### *2,5-Disubstituted Phosphaferrocenes from Preformed Phospholes*

Because of the unsuccessful attempts described in the preceding paragraph a different synthetic approach was envisaged. An alternative access to 2,5-disubstituted phosphaferrocenes is the synthesis of a suitable 2,5-disubstituted phospholide anion in a first step and subsequent coordination to a CpFe source. For this purpose we chose the well-known zirconocene-mediated coupling of alkynes: with 1-trimethylsilylpropyne as a coupling partner, the zirconacyclopentadiene with the $Me_3Si$ groups in α-positions is formed regioselectively in high yield and can be converted into the corresponding bromophosphole (**4**) by treatment with $PBr_3$ (Scheme 3).[17,18]

Reduction of bromophosphole (**4**) by elemental lithium proceeds straightforwardly to the corresponding phospholide anion **5**, the conversion can easily be monitored by $^{31}P$ NMR spectroscopy [$\delta$ = 141 (**5**), 78 ppm (**4**)]. Subsequent coordination of anion **5** to suitable Cp-metal fragments gave access to new TMS-substituted phosphametallocenes (Scheme 4): 2,5-bis(trimethylsilyl)-3,4-dimethylphosphaferrocene (**6**), the analogous ruthenocene (**7**) and 2,2′,5,5′-tetrakis(trimethylsilyl)-3,3′,4,4′-tetramethyl-1,1′-diphosphaferrocene (**8**), which has been synthesized before but was only characterized by $^1H$ NMR spectroscopy.[19]

### *2,5-Bis(trimethylsilyl)-3,4-dimethylphosphaferrocene (6)*

In order to prepare 2,5-bis(silyl)monophosphaferrocene derivatives the phospholide anion **5** was treated with different iron precursors. While the reaction with [(mesitylene)$FeCp^+$]$PF_6$ was unsuccessful, treatment with $[Cp^*FeCl]_n$ (Scheme 3) – prepared in situ from Cp*Li and $FeCl_2$ in THF according to the literature[2g] – proceeded straightforwardly to produce the Cp*-phosphaferrocene **6** in 55% yield as red crystals after crystallization from MeOH, which was completely characterized by NMR spectroscopy, mass spectroscopy, elemental analysis and X-ray diffraction. An

 © 2007 Wiley-VCH Verlag GmbH & Co. KGaA, Weinheim 

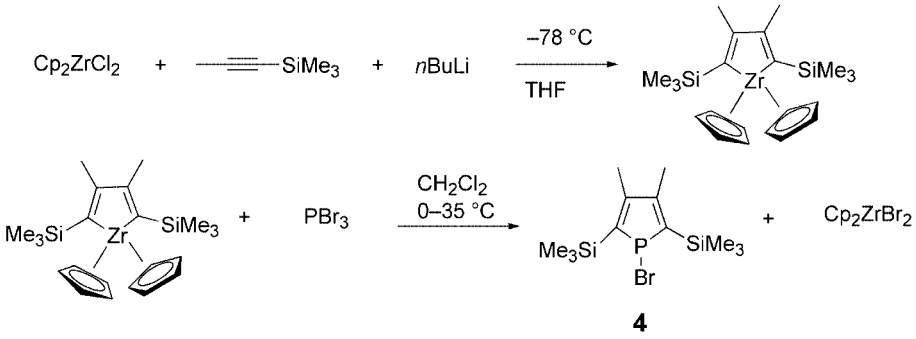


Scheme 3.

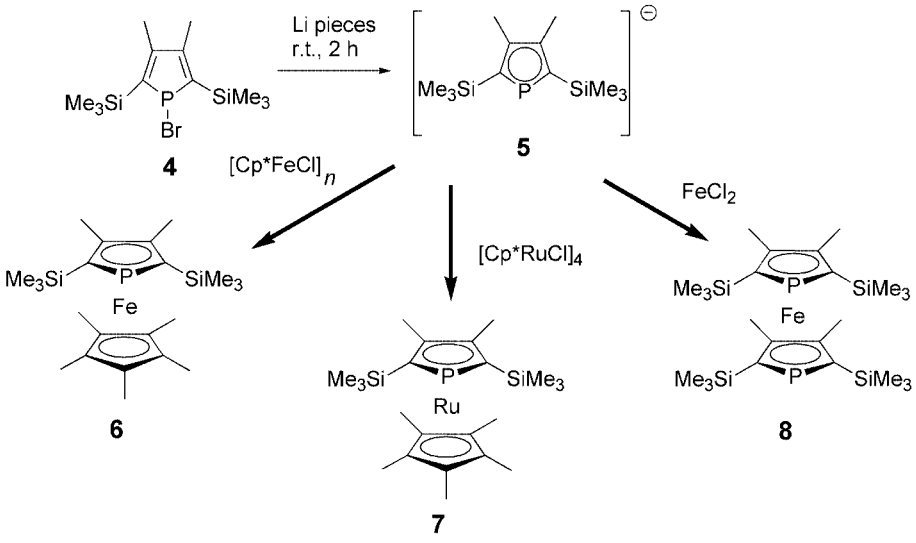


Scheme 4.

ORTEP plot of the molecular structure of **6** is depicted in Figure 3, relevant geometrical data can be found in Table 3. Complex **6** features a typical sandwich-type structure with an almost planar phospholyl ring parallel to the Cp* ring. The distances between the Fe atom and the phospholyl centroid Ct1 (1.668 Å) and the Cp* centroid Ct2 (1.690 Å), respectively, are very similar. As is usually observed in phosphametallocene complexes, the C1–P1–C4 angle (91.4°) is close to 90°, the mean P–C distances are 1.790 Å and the C–C bonds in the phospholyl ring are very similar. The steric bulk of the $SiMe_3$ groups becomes apparent from the angles Fe–Ct1–Si (95.7°, 96.8°), which exceed the ideal value of 90°, while the deviation for the β-Me groups is significantly smaller (90.9°, 91.1°). In conclusion, the structural parameters of the parent compound differ only very slightly from those observed for the related phosphaferrocene and ruthenocene ([Cp*M{(2,5-$t$Bu$_2$)$C_4H_2P$}], M = Fe,[20] Ru[21]) with $t$Bu groups in place of the $Me_3Si$ groups. A closely related molecule with alkynyldimethylsilyl substituents was obtained by Mathey et al. via [CpFe($\eta^6$-$C_9H_{12}$)][$PF_6$].[18]

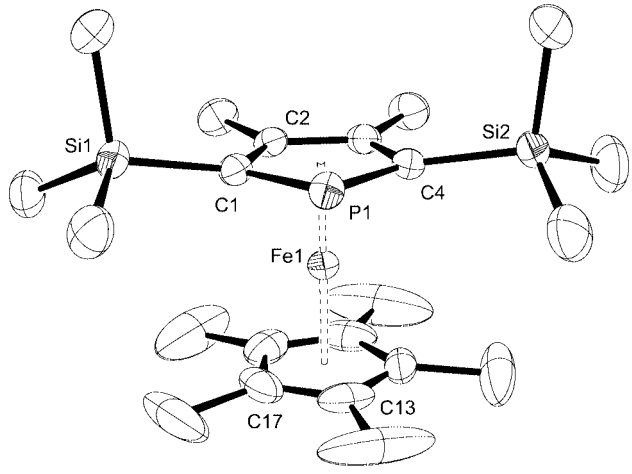


Figure 3. Molecular structure of complex **6**.

The bis(trimethylsilyl) complex **6** may serve as a source for other 2,5-difunctionalized phosphaferrocenes suitable for macrocyclization reactions by exchange of the $Me_3Si$

 © 2007 Wiley-VCH Verlag GmbH & Co. KGaA, Weinheim 

Table 3. Selected bond lengths [Å] and angles [°] for complexes **6** and **8**.

| | **6** | **8** |
|---|---|---|
| P1–C1 | 1.792(3) | 1.750(4) |
| P1–C4 | 1.788(3) | 1.751(3) |
| C1–C2 | 1.430(4) | 1.401(5) |
| C2–C3 | 1.437(4) | 1.390(5) |
| C3–C4 | 1.439(4) | 1.421(5) |
| Fe1–Ct($C_4$P) | 1.668(2) | 1.672(2) |
| Fe1–Ct($C_5$) | 1.690(2) | |
| C4–P1–C1 | 91.42(13) | 92.5(2) |
| Fe1–Ct($C_4$P)–Si1 | 96.8(2) | 95.0(2) |
| Fe1–Ct($C_4$P)–Si2 | 95.7(2) | 97.6(2) |

groups for other functional groups, although the small polarity of the C–Si bond limits the reaction bandwidth.[22] For example, the conversion of an *i*$Pr_3$Si group attached to a phosphametallocene into a trifluoroacetyl group has recently been reported[23] and the bis(trifluoroacetyl) derivative derived from **6** would be of high synthetic value. However, upon treatment of complex **6** with trifluoroacetic anhydride and $BF_3$·$OEt_2$ only one TMS group is substituted, the other one is protodesilylated by the acid formed during the reaction.

An even simpler approach to 2,5-difunctionalized phosphaferrocenes with substituents suitable for further transformation might involve the preparation of 2,5-diacyl- or dicarboxylic ester derivatives. Although the syntheses of the appropriate phospholide anions with two acyl or ester groups have been elaborated by Mathey et al.,[24] we were unsuccessful in transforming these functional phospholide anions into the respective Fe or Ru sandwich complexes.

### *2,5-Bis(trimethylsilyl)-3,4-dimethylphospharuthenocene (7)*

Phospharuthenocenes are much less investigated than phosphaferrocenes. The first example, [Cp*Ru{(2,5-*t*$Bu_2$)-$C_4$P}], was prepared by Carmichael et al. in 1994[21] and some mixed Ru/Fe tripledecker[25] complexes were reported later. Meanwhile, a couple of additional derivatives with bulky groups in 2,5-positions like naphthyl,[26] triisoproplylsilyl,[23] cyclohexyl or menthyl[27] could be prepared as well. To prevent $\eta^1$-P-coordination in the complexation reaction, the phosphole has to bear either bulky substituents at the α-position or, as was found out later, an electron-withdrawing group.[28] Once the phosphole is coordinated to ruthenium, the α-substituents can be transformed into other sterically less demanding functional groups. Treatment of anion **5** with $[Cp^*RuCl]_4$ afforded the new 2,5-bis(trimethylsilyl)ruthenocene (**7**) (Scheme 4) as a brown solid after chromatographic workup. Interestingly, the $^{31}$P resonance of complex **7** ($\delta$ = 0.95 ppm) is drastically shifted to lower field as compared to the 2,5-*t*$Bu_2$ analogue ($\delta$ = –63.0 ppm).[21]

In analogy to **6** the reactivity of **7** towards electrophilic desilylation was tested in a trifluoroacylation reaction. However, the only product isolated from this reaction was the protodesilylated complex, as was evident from the appearance of a doublet in the $^1$H NMR spectrum due to the α protons.

### *2,2′,5,5′-Tetrakis(trimethylsilyl)-3,3′,4,4′-tetramethyl-1,1′-diphosphaferrocene (8)*

This compound has been synthesized before, but was only poorly characterized.[19] We found that treatment of anion **5** with anhydrous $FeCl_2$ in THF at low temperature provides ready access to complex **8**, which was completely characterized by NMR and mass spectroscopy, elemental analysis and X-ray diffraction. An ORTEP view of the molecular structure is given in Figure 4 and selected geometrical data are given in Table 3. The compound crystallizes in the orthorhombic space group *Pnna* with the Fe atom sitting on a crystallographic twofold axis ($Z$ = 4). Bond lengths and angles are within the range of values usually observed for 1,1′-diphosphaferrocenes in general and compare well in particular with the closely related molecules [{2,5-($SiMe_2CCMe$)$_2$-3,4-$Me_2$-$C_4P$}$_2$Fe] (**A**)[18] and [{2,5-$Cy_2$-$C_4H_2P$}$_2$Fe] (**B**).[27] Again, as observed for compound **6**, the deviation of the Fe–Ct–Si angles from 90° (95.0 and 97.6°) is more pronounced than that for the β-Me groups (91.1 and 91.5°), reflecting the increased steric bulk of the silyl groups. The most interesting feature of the structure is the conformation of the two phospholyl rings with a P–Ct–Ct′–P′ torsion angle of $\alpha$ = 85.4°, which means that the P atom of one ring is roughly eclipsing the α-C atom of the other (P/$C_\alpha$-conformation). Several conformations are conceivable for 1,1′-diphosphaferrocenes:[29] the limiting high-symmetry conformations $C_{2v}$ and $C_{2h}$, with the P atoms in a *syn* ($\alpha$ = 0°) or *anti* ($\alpha$ = 180°) arrangement, respectively, and two $C_2$-symmetric conformations in which the P atoms are superposed either with the α carbon (P/$C_\alpha$, $\alpha$ = 90–100°) or with the β carbon of the other ring (P/$C_\beta$, $\alpha$ = 140–145°). Indeed, examples for all of these conformations have been observed in the solid state and the question of which conformation is preferred has been addressed on various levels of theory. Both extended Hückel[30] and Fenske–Hall[31] calculations indicated that the $C_{2h}$-symmetric conformation has the highest relative energy for the unsubstituted derivative, lying some 10 kcal/mol above a $C_2$-symmetric arrangement with $\alpha > 100°$. However, for substituted derivatives the substitution pattern may also influence the relative stability of conformers by the avoidance of sterically unfavourable interactions of the substituents. For example, for the 3,3′,4,4′-tetramethyl derivative the P/$C_\beta$ conformation is found in the solid state in accordance with theory,[11] minimizing the steric interference of the Me groups. For 2,2′,5,5′-tetraphenyl-1,1′-diphosphaferrocene, however, an exceptional P,P-*syn* conformation is found ($\alpha$ = 0°), which is stabilized presumably by additional π–π interactions between the two pairs of parallel phenyl rings.[29] This contradicts nicely with the structure of the 2,2′,5,5′-tetracyclohexyl derivative, for which a P,P-*anti* arrangement has been identified.[27] However, this conformation seems to be the exception rather than the rule, because many other 1,1′-diphosphaferrocenes with sterically demanding groups in the 2,5 positions show the P/$C_\alpha$ conformation as observed for complex **8**. Examples include the alkynylsilyl derivative **A**,[18] the 2,5-*t*$Bu_2$-diphosphametallocenes with Sn and Pb,[32] the Sb analogue of **8**[17b] and the parent 1,1′,3,3′-

 © 2007 Wiley-VCH Verlag GmbH & Co. KGaA, Weinheim 

tetrakis(trimethylsilyl)ferrocene.[33] DFT calculations on a B3LYP level were performed for complex **8** and exhibited a P/$C_\alpha$ minimum energy conformation with a torsion angle of $\alpha \approx 86°$. The highest relative energy (11.6 kcal/mol) was identified for the $C_{2v}$ symmetric conformation ($\alpha = 0°$).

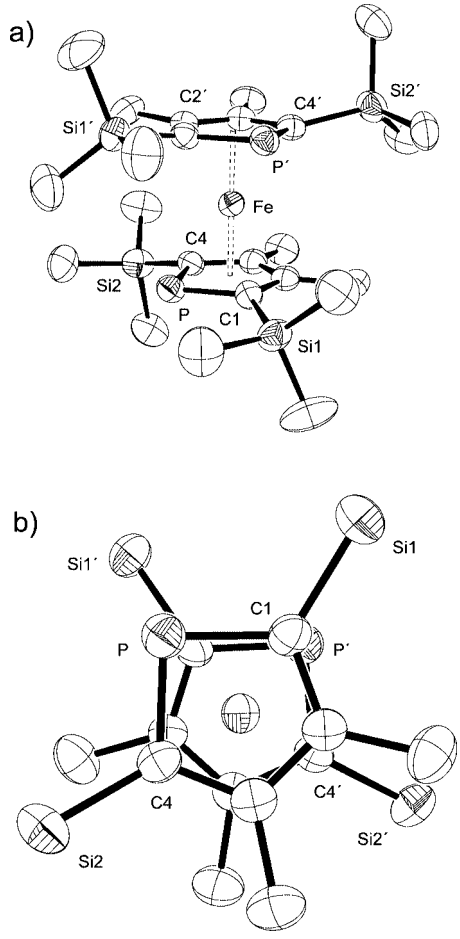


Figure 4. Two views of the molecular structure of complex **8**.

*Solution Dynamics of **8***

The proton NMR spectrum of **8** at room temperature shows two singlets corresponding to the methyl and to the TMS groups in a ratio 6:18. Obviously, ring rotation at ambient temperature is fast on the NMR time-scale. On cooling a sample in [$D_8$]toluene coalescence was observed (500 MHz) at ca. –5 °C for the $SiMe_3$ signals ($\Delta\nu = 125$ Hz) and at –20 °C for the β-Me signals ($\Delta\nu = 34$ Hz). At –50 °C the signals were clearly separated. The value of $12.6 \pm 0.3$ kcal/mol for the rotational barrier calculated from these data is in agreement with the value determined by Al-Taweel[19] and lies well within the range of 10–14 kcal/mol observed for other ferrocenes and diphosphaferrocenes with bulky substituents (Table 4) and fits nicely with the value obtained from the DFT calculations of 11.6 kcal/mol. No substantial differences between ferrocenes and diphosphaferrocenes are recognizable.

Table 4. Activation barriers ($\Delta G^{\ddagger}$) for ring rotation in 1,1′-diphosphaferrocenes and ferrocenes with bulky substituents.

| Substituents | $\Delta G^{\ddagger}$ [kcal mol$^{-1}$] | Reference |
|---|---|---|
| **1,1′-Diphosphaferrocenes** | | |
| 2,2′,5,5′-$(TMS)_4$-3,3′,4,4′-$Me_4$ | 12.6 | this work[a] |
| | 12.5 | [19][a] |
| | 11.6 | this work[b] |
| None | 8.8 | [30][d] |
| 2,2′,5,5′-$Ph_4$ | < 6.5 | [29][c] |
| 2,2′,5,5′-[(–)-menthyl]$_4$ | 12.9 | [44][a] |
| **Ferrocenes** | | |
| 1,1′3,3′-$(TMS)_4$ | 11.0 | [33][a] |
| 1,1′,2,2′,4,4′-$(TMS)_6$ | 11.0 | [45][a] |
| 1,1′,2,2′,3,3′,4,4′-(*i*Pr)$_8$ | 13.7 | [46][a] |
| 1,1′,2,2′-$(TMS)_4$-4,4′-(*t*Bu)$_2$ | 9.8 | [47][a] |

[a] Low-temperature NMR spectroscopy. [b] DFT calculation. [c] Calculated value. [d] EHT calculation.

Treatment of **8** with DMSO/KOtBu[34] in order to examine the reactivity of the complex towards desilylation resulted in decomposition of the starting material and no product could be isolated.

## Experimental Section

**DFT Calculations:** In order to determine the rotational barrier B3LYP[35] single point energies with Ahlrichs TZVP basis set[36] on top of BP86[37] geometries, optimized with a SVP basis set[38] have been carried out, as implemented in the program package Turbomole.[39] For the BP86 calculations the resolution of the identity (RI) approach has been used to fit the density within the Coulomb potential with an auxiliary basis set.[40] The phosphaferrocene backbone has been kept frozen at different torsional orientations of the two rings whereas the remainder of the molecule has been relaxed to its equilibrium geometry. The minimum structure has been characterized by calculating the Hessian matrix.

Reactions were carried out under an atmosphere of dry nitrogen by means of conventional Schlenk techniques. Solvents were dried and purified by standard methods. Alumina was heated at 220 °C for 12 h, cooled to room temp. under high vacuum, deactivated with 5% water and stored under nitrogen. NMR spectra were recorded with a Bruker Avance DRX 500 ($^1$H NMR, 500 MHz; $^{31}$P{$^1$H} NMR, 202 MHz; $^{13}$C{$^1$H} NMR, 126 MHz) and a Bruker Avance DRX 200 spectrometer ($^1$H NMR, 200 MHz; $^{31}$P{$^1$H} NMR, 81 MHz). $^1$H NMR spectra are referenced to the residual solvent signal and $^{31}$P NMR spectra to external $H_3PO_4$ (85%). Mass spectra were recorded with a Varian MAT 311A spectrometer (EI, 70 eV electron energy). 2,5-Bis(trimethylsilyl)-3,4-dimethyl-1,1-bis(cyclopentadienyl)zirconacyclopentadiene,[17] **4**,[18] [Cp*FeCl]$_n$,[2g] 2-Hydroxymethyl-3,4-dimethyl-1-phosphaferrocene[11] and [Cp*RuCl]$_4$[41] were prepared according to the literature.

**Synthesis of 2:** A suspension of NaH (60 wt.-% in mineral oil, 0.21 g, 5.25 mmol) in THF was added dropwise to a mixture of 2-hydroxymethyl-3,4-dimethyl-1-phosphaferrocene (1.01 g, 3.86 mmol) and methyliodide (2.4 mL, 38.6 mmol) in THF at –55 °C. The mixture was slowly warmed to room temp. while stirring overnight and was subsequently heated to reflux for 30 min. After cooling to room temp. water (10 mL) was added and the product was extracted with dichloromethane. The organic phase was dried with $Na_2SO_4$, filtered and the solvent was removed under high vacuum. Column chromatography on alumina (hexane/ether, 5:1) gave pure

 © 2007 Wiley-VCH Verlag GmbH & Co. KGaA, Weinheim 

**2** as an orange oil (1.003 g, 95%). $^1$H NMR (200 MHz, $CDCl_3$): $\delta$ = 2.215, 2.222 (s, 6 H, 3,4-$CH_3$), 3.35 (s, 3 H, O-$CH_3$), 3.78 (d, $^2J_{CP}$ = 35.89 Hz, 1 H, α-H), 4.12 (s, 5 H, Cp), 3.86–4.24 (m, 2 H, $CH_2$) ppm. $^{13}$C NMR (126 MHz, $CDCl_3$): $\delta$ = 13.48 and 16.86 (s, 3,4-$CH_3$), 57.78 (s, $OCH_3$), 71.02 (d, $^2J_{CP}$ = 21.80 Hz, $CH_2$), 71.85 (s, Cp), 76.92 (d, $^1J_{CP}$ = 58.13 Hz, α-CH), 92.69 (d, $^1J_{CP}$ = 55.71 Hz, α-C), 94.20 (d, $^2J_{CP}$ = 4.84 Hz, β-C), 96.75 (d, $^2J_{CP}$ = 7.26 Hz, β-C) ppm. $^{31}$P{$^1$H} NMR (81 MHz, $CDCl_3$): $\delta$ = –73.24 (s) ppm. $C_{13}H_{17}FePO$ (276.10), EI-MS: *m*/*z* = 276 ($M^+$), 246 ($M^+$ – 2 $CH_3$), 231 ($M^+$ – $CH_2OMe$). Calcd. C 56.55, H 6.21; found C 56.57, H 6.30.

**Synthesis of 3:** Triethylamine (328 μL, 2.36 mmol) was added to a solution of 2-hydroxymethyl-3,4-dimethyl-1-phosphaferrocene (620 mg, 2.36 mmol) in THF (20 mL) at room temp. Dichlorodimethylsilane (143 μL, 1.18 mmol) was added slowly via syringe and the mixture was refluxed for 3 h. After cooling to room temp. water was added and the product extracted with diethyl ether and dried with $Na_2SO_4$. Filtration and removal of the solvent under high vacuum gave the *rac*/*meso* mixture of **3** in a 2:1 ratio as an analytically pure orange oil (411 mg, 0,71 mmol, 60%). Cooling an ether solution gave the pure *rac* isomer as orange crystals suitable for X-ray diffraction. $^1$H NMR (200 MHz, $CDCl_3$); *rac*/*meso* mixture: $\delta$ = 0.115 (s, 3 H, $SiCH_3$), 0.122 (s, 3 H, $SiCH_3$), 2.173, 2.183, 2.193, 2.205 (4s, 12 H, $CCH_3$), 3.75 (d(br), $^1J_{HP}$ = 35.89 Hz, 2 H, α-H), 4.114, 4.121 (2s, 10 H, Cp), 4.155–4.365 (m, 4 H, $CH_2$-O) ppm; *rac* isomer: $\delta$ = 0.121 (s, 6 H, $SiCH_3$), 2.173 (s, 6 H, $CCH_3$), 2.184 (s, 6 H, $CCH_3$), 3.75 (d, 2 H, α-H, $^2J_{HP}$ = 35.89 Hz), 4.120 (s, 10 H, Cp), 4.26 (m, 4 H, $CH_2$-O) ppm. $^{13}$C NMR (125 MHz, $CDCl_3$); *rac*/*meso* mixture: $\delta$ = –2.53 (br. s, $SiCH_3$), –0.597 (br. s, $SiCH_3$), 13.54 (s, $CH_3$), 16.92 (s, $CH_3$), 61.18 (d, $^2J_{CP}$ = 24.2 Hz, $CH_2$), 71.81 (s, Cp), 71.83 (s, Cp), 76.70 (d, $^1J_{CP}$ = 58.1 Hz, α-CH), 76.58 (d, $^1J_{CP}$ = 58.1 Hz, α-CH) ppm. $^{31}$P{$^1$H} NMR ($CDCl_3$, 81 MHz): $\delta$ = –74.18 (*rac*); –74.34 (*meso*) ppm. EI-MS (80 eV, 150 °C), *m*/*z* = 580 ($M^+$), 515 ($M^+$ – Cp), 262 (PFc – $CH_2O^+$), 245 ($PFcCH_2^+$), 179 ($PFcCH_2^+$-Cp), 124 (179 – Fe). $C_{26}H_{34}Fe_2O_2P_2Si$ (580.28): calcd. C 53.82, H 5.91; found C 53.00, H 5.83. The too small value for C is probably due to the formation of some SiC, which is rather frequently encountered.

**Synthesis of [(*rac*-3)·Mo(CO)$_4$]:** A solution of [(nbd)Mo(CO)$_4$] (65 mg, 0.217 mmol) in THF was added to a solution of *rac*-**3** (126 mg, 0.217 mmol) in THF, the mixture was stirred at room temp. for 30 min and subsequently refluxed for two hours. The solvent was removed under high vacuum and the residue was recrystallized from ether. $^1$H NMR (200 MHz, $CDCl_3$): $\delta$ = 0.06 (s, 6 H, $SiCH_3$), 2.20, 2.21 (s, 6 H, $CH_3$), 3.84 (d, 2 H, $^2J_{HP}$ = 32.12 Hz, α-H), 4.21 (s, 10 H, Cp), 4.19 (m, 4 H, $CH_2$) ppm. $^{31}$P{$^1$H} NMR (81 MHz, $CDCl_3$): –22,74 (s) ppm. IR ($CDCl_3$): 2029 (mst), 1935 (st), shoulders at 1920 and 1900 cm$^{-1}$. $C_{30}H_{34}Fe_2MoO_6P_2Si$ (788.20): calcd. C 45.71, H 4.35; found C 45.49, H 4.50.

**Synthesis of 6:** Freshly cut lithium pieces (excess) were added to a solution of bromophosphole (**4**) (400 mg, 1.19 mmol) in THF at room temp. After complete conversion of the phosphole to the phospholide anion (monitored by $^{31}$P NMR, **5**: 141 ppm, ca. 3 h) the solution was transferred by cannula to a freshly prepared solution of $[Cp^*FeCl]_n$ at 0 °C and the mixture was stirred overnight at room temp. and refluxed for 1 h. Water was added and the product was extracted with diethyl ether. The organic phase was dried with $Na_2SO_4$, filtered and the solvent was removed under high vacuum. The crude product was purified by column chromatography over alumina (hexane). Recrystallization from methanol yielded bright red crystals (ca. 290 mg, 55%) contaminated with trace amounts of decamethylferrocene. $^1$H NMR (200 MHz, $CDCl_3$): $\delta$ = 0.20 (d, $^4J_{HP}$ = 0.75 Hz, 18 H, $SiMe_3$), 1.81 (s, 15 H, Cp*), 2.03 (s, 6 H, $CH_3$) ppm. $^{31}$P{$^1$H} NMR (81 MHz, $CDCl_3$): $\delta$ = –8.18 ppm (s). $C_{22}H_{39}FePSi_2$ (446): calcd. C 59.17, H 8.80; found C 58.99, H 8.88. EI-MS: *m*/*z* = 446 ($M^+$), 374 ($M^+$ – TMS + H), 326 (374 – $SiMe_2$).

**Synthesis of 7:** A solution of phospholide (**5**) was prepared as described above from bromophosphole (**4**) (111 mg, 0.33 mmol). $[Cp^*RuCl]_4$ (90 mg, 0.083 mmol) was suspended in THF and added to the phospholide solution at –78 °C. The reaction mixture turned from red to brown and was warmed to room temp. while stirring overnight. The solvent was removed under high vacuum and the crude product was purified by column chromatography over alumina (hexane/ether = 5:1). Compound **7** (120 mg, 36%) was obtained as a brown powder after the removal of the solvent in vacuo. $^1$H NMR (200 MHz, $CDCl_3$): $\delta$ = 0.20 (d, $^4J_{HP}$ = 0.75 Hz, 18 H, $SiMe_3$), 1.87, (s, 15 H, Cp*), 1.93 (s, 6 H, 3,4-$CH_3$) ppm. $^{13}$C NMR (126 MHz, $CDCl_3$): $\delta$ = 1.6 (d, $^3J_{CP}$ = 5.5 Hz, $SiMe_3$), 11.6 (s, Cp*-$CH_3$), 13.8 (d, $^3J_{CP}$ = 1.8 Hz, 3,4-$CH_3$), 87.4 (s, Cp*-C), 88.6 (d, $^1J_{CP}$ = 79.7 Hz, α-C), 100.1 (d, $^2J_{CP}$ = 4.6 Hz, β-C) ppm. $^{31}$P{$^1$H} NMR (81 MHz, $CDCl_3$): $\delta$ = 0.95 (s) ppm. EI-MS ($C_{22}H_{39}PRuSi_2$, 491.77): *m*/*z* = 492 ($M^+$), 477 ($M^+$ – $CH_3$), 419 ($M^+$ – $SiMe_3$). Calcd. C 53.73, H 7.99; found C 54.01, H 8.15.

**Synthesis of 8:** A solution of phospholide (**5**) was prepared as described above from bromophosphole (**4**) (0.51 g, 1.52 mmol). Anhydrous $FeCl_2$ (0.096 g, 0,76 mmol) was added to the phospholide solution at –78 °C. The solution was stirred overnight and warmed to room temp. The solvent was removed under high vacuum and the crude product purified by chromatography over alumina (hexane). Recrystallization from methanol yielded **8** (0.150 g, 35%) as red crystals suitable for X-ray diffraction. $^1$H NMR (200 MHz, $CDCl_3$): $\delta$ = 0.27 (s, 36 H, $SiMe_3$), 2.08 (s, 12 H, 3,4-$CH_3$) ppm. $^{31}$P{$^1$H} NMR (81 MHz, $CDCl_3$): $\delta$ = –26.13 (s) ppm. $^{13}$C NMR (126 MHz, 298 K, $CDCl_3$): $\delta$ = 1.80, 1.82, 1.84, 1.86 (s, $SiMe_3$), 16.5 (br. s, 3,4-$CH_3$), 103.8 (d, $^2J_{CP}$ = 4.6 Hz, β-C) ppm. EI-MS ($C_{24}H_{48}FeP_2Si_4$, 566.78): *m*/*z* = 566 ($M^+$), 494 ($M^+$ – H – $SiMe_3$) 405 ($M^+$ – H – $SiMe_3$ – $CH_3$). Calcd. C 50.86, H 8.54; found C 51.02, H 8.50.

**X-ray Crystallographic Study:** Crystals of compounds **3**, **3**·Mo(CO)$_4$, **6** and **8** suitable for X-ray studies were investigated with a Stoe IPDS using graphite-monochromated Mo-$K_\alpha$ radiation ($\lambda$ = 0.71073 Å) at 291 K. In the cases of **3**·Mo(CO)$_4$ and **6** a space group type of $P2_1/n$ and in the case of **8** the space group *Pnna* were uniquely determined. In the case of **3** the symmetry of the diffraction pattern was compatible with space group types $P1$ and $P\bar{1}$. The latter proved to be the correct one after structure refinement. Lorentz polarization corrections were applied to all the intensity data. In the case of **3**·Mo(CO)$_4$ and **8** absorption corrections using symmetry equivalent reflections and a face-indexed Gaussian integration procedure, respectively, were applied. The structures were solved by direct methods[42] and the positions of all but the H atoms of the pentamethylcyclopentadienyl group of **6** were found via $\Delta F$ syntheses. Refinements[43] by full-matrix least-squares calculations on $F^2$ converged to the indicators given in Table 5. Anisotropic displacement parameters were refined for all atoms heavier than hydrogen. Idealized bond lengths and angles were used for the $CH_3$, $CH_2$ and CH groups; the riding model was applied for their H atoms. In addition, the H atoms of the $CH_3$ groups were allowed to rotate around the neighbouring C–C bonds. The isotropic displacement parameters of the H atoms were kept equal to 120% of the equivalent isotropic displacement parameters of the parent "aromatic" or secondary carbon atom and equal to 150% of the parent primary carbon atom, respectively. A summary of

 © 2007 Wiley-VCH Verlag GmbH & Co. KGaA, Weinheim 

Table 5. Crystallographic data for compounds **3**, **3·Mo(CO)$_4$**, **6** and **8**.

| Compound | **3** | **3·Mo(CO)$_4$** | **6** | **8** |
|---|---|---|---|---|
| Formula | $C_{26}H_{34}Fe_2O_2P_2Si$ | $C_{30}H_{34}Fe_2MoO_6P_2Si$ | $C_{22}H_{39}FePSi_2$ | $C_{24}H_{48}FeP_2Si_4$ |
| $M_r$ [g mol$^{-1}$] | 580.26 | 788.24 | 446.53 | 566.77 |
| Crystal system | triclinic | monoclinic | monoclinic | orthorhombic |
| Space group | $P\bar{1}$ | $P2_1/n$ | $P2_1/n$ | $Pnna$ |
| $a$ [Å] | 11.1473(8) | 10.9670(16) | 9.7586(6) | 19.0769(19) |
| $b$ [Å] | 13.9223(10) | 17.7718(14) | 13.2369(9) | 16.6026(11) |
| $c$ [Å] | 17.4988(12) | 17.7603(19) | 19.9071(13) | 10.2037(6) |
| $\alpha$ [°] | 92.111(8) | 90 | 90 | 90 |
| $\beta$ [°] | 100.862(8) | 94.514(18) | 93.781(8) | 90 |
| $\gamma$ [°] | 90.298(9) | 90 | 90 | 90 |
| $V$ [Å]$^3$ | 2665.1(3) | 3450.8(7) | 2565.9(3) | 3231.8(4) |
| $Z$ | 4 | 4 | 4 | 4 |
| $D_c$ [g cm$^{-3}$] | 1.446 | 1.517 | 1.156 | 1.165 |
| $F$(000) | 1208 | 1600 | 960 | 1216 |
| $\mu$(Mo-$K_\alpha$) [mm$^{-1}$] | 1.275 | 1.353 | 0.748 | 0.725 |
| $2\theta_{max}$ [°] | 50.00 | 50.00 | 50.00 | 50.00 |
| Total reflections | 35124 | 26649 | 32998 | 2844 |
| Independent reflections | 8846 | 5984 | 4516 | 2844 |
| Observed reflections [$I > 2\sigma(I)$] | 5768 | 3189 | 3285 | 906 |
| Parameters refined | 607 | 385 | 248 | 149 |
| $R_1/wR_2$ [$I > 2\sigma(I)$] | 0.0337, 0.0764 | 0.0367, 0.0731 | 0.0453, 0.1129 | 0.0336, 0.0456 |
| $R_1/wR_2$ (all data) | 0.0512, 0.0780 | 0.0709, 0.0759 | 0.0584, 0.1156 | 0.0824, 0.0484 |

further crystallographic data, data collection parameters and refinement parameters is collected in Table 5.

CCDC-622213 (for **3**), -622214 [for **3·Mo(CO)$_4$**], -622216 (for **6**) and -622215 (for **8**) contain the supplementary crystallographic data for this paper. These data can be obtained free of charge from The Cambridge Crystallographic Data Centre via www.ccdc.cam.ac.uk/data_request/cif.

## Acknowledgments

Financial support of this work by the Deutsche Forschungsgemeinschaft (DFG) (GA 597/1) is gratefully acknowledged. We gratefully acknowledge computer time granted by the HRZ Philipps-Universität Marburg and the CSC Frankfurt. We thank M. Schilling and E. Hammes for assistance with the X-ray structure determinations.

[1] For comprehensive reviews see for example: a) F. Mathey, *Coord. Chem. Rev.* **1994**, *137*, 1; b) F. Mathey, *Top. Curr. Chem.* **2002**, *220*, 27; c) P. Le Floch, *Coord. Chem. Rev.* **2006**, *250*, 627.

[2] a) C. Ganter, L. Brassat, C. Glinsböckel, B. Ganter, *Organometallics* **1997**, *16*, 2862; b) C. Ganter, *Chem. Soc. Rev.* **2003**, *32*, 130; c) C. Ganter, *J. Chem. Soc., Dalton Trans.* **2001**, 3541; d) J. Bitta, S. Fassbender, G. Reiss, W. Frank, C. Ganter, *Organometallics* **2005**, *24*, 5176; e) R. Shintani, G. C. Fu, *J. Am. Chem. Soc.* **2003**, *125*, 10778; f) R. Shintani, G. C. Fu, *Angew. Chem.* **2003**, *115*, 4216; g) R. Shintani, G. C. Fu, *Org. Lett.* **2002**, *4*, 3699.

[3] a) S. Holand, M. Jeanjean, F. Mathey, *Angew. Chem.* **1997**, *109*, 117; b) P. Toullec, F. Mathey, *Synlett* **2001**, 1977; c) M. Melaimi, L. Ricard, F. Mathey, P. Le Floch, *Org. Lett.* **2002**, *4*, 1245.

[4] a) J.-M. Lehn, *Angew. Chem.* **1988**, *100*, 91; b) C. J. Pedersen, *Angew. Chem.* **1988**, *100*, 1053; c) D. J. Cram, *Angew. Chem.* **1988**, *100*, 1041; d) R. Cooper (Ed.), *Crown Compounds: Toward Future Application*, Wiley Interscience: New York, **1992**; e) J. S. Bradshaw, R. M. Izatt, *Acc. Chem. Res.* **1997**, *30*, 338; f) J.-M. Lehn, *Acc. Chem. Res.* **1978**, *11*, 49; g) N. S. Pooma, A. V. Baja, *Chem. Rev.* **1979**, *79*, 389.

[5] L. Horner, P. Walach, H. Kunz, *Phosphorus* **1975**, *6*, 63.

[6] a) For a review see: A.-M. Caminade, J. P. Majoral, *Chem. Rev.* **1994**, *94*, 1183; b) S. Ekici, M. Nieger, R. Glaum, E. Niecke, *Angew. Chem.* **2003**, *115*, 451; c) P. G. Edwards, R. Haigh, D. Li, V. Newman, *J. Am. Chem. Soc.* **2006**, *128*, 3818.

[7] F. Mathey, P. Le Floch, *Chem. Ber.* **1996**, *129*, 263.

[8] a) N. Avarvari, N. Mézailles, L. Ricard, F. Mathey, *Science* **1998**, *280*, 1587; b) N. Avarvari, N. Maigrot, L. Ricard, F. Mathey, P. Le Floch, *Chem. Eur. J.* **1999**, *5*, 2109.

[9] N. Mézailles, N. Avarvari, N. Maigrot, L. Ricard, F. Mathey, P. Le Floch, L. Cataldo, T. Berclaz, M. Geoffrey, *Angew. Chem.* **1999**, *111*, 3390.

[10] a) B. Dechamps, J. Fischer, F. Mathey, A. Mitschler, *Inorg. Chem.* **1981**, *20*, 3252; b) B. Dechamps, J. Fischer, F. Mathey, A. Mitschler, L. Ricard, *Organometallics* **1982**, *1*, 312.

[11] G. de Lauzon, B. Deschamps, J. Fischer, F. Mathey, A. Mitschler, *J. Am. Chem. Soc.* **1980**, *102*, 994.

[12] F. Mathey, A. Mitschler, R. Weiss, *J. Am. Chem. Soc.* **1977**, *99*, 3537.

[13] G. de Lauzon, B. Deschamps, F. Mathey, *Nouv. J. Chim.* **1980**, *4*, 683.

[14] S. O. Agustsson, C. Hu, U. Englert, T. Marx, L. Wesemann, C. Ganter, *Organometallics* **2002**, *21*, 2993.

[15] C. Ganter, C. Kaulen, U. Englert, *Organometallics* **1999**, *18*, 5444.

[16] a) ref.[14]; b) ref.[15]; c) C. Ganter, L. Brassat, B. Ganter, *Chem. Ber./Recueil* **1997**, *130*, 1771; d) T. G. Hill, C. Haltiwanger, T. R. Prout, A. D. Norman, *Inorg. Chem.* **1989**, *28*, 3461; e) E. H. Wong, F. C. Bradley, E. J. Gabe, *J. Organomet. Chem.* **1983**, *244*, 235; f) M. S. Balakrishna, T. K. Prakasha, S. S. Krishnamurthy, U. Siriwardane, N. S. Hosmane, *J. Organomet. Chem.* **1990**, *390*, 203.

[17] a) M. Westerhausen, M. H. Digeser, C. Gückel, H. Nöth, J. Knizek, W. Ponikwar, *Organometallics* **1999**, *18*, 2491; b) A. J. Ashe III, J. W. Kampf, S. M. Al-Taweel, *Organometallics* **1992**, *11*, 1491; c) A. J. Ashe III, J. W. Kampf, S. M. Al-Taweel, *J. Am. Chem. Soc.* **1992**, *114*, 372.

[18] X. Sava, N. Mézailles, N. Maigrot, F. Nief, L. Ricard, F. Mathey, P. Le Floch, *Organometallics* **1999**, *18*, 4205.

[19] S. M. Al-Taweel, *Phosphorus, Sulphur Silicon Relat. Elem.* **1997**, *130*, 203.

[20] C. Burney, D. Carmichael, K. Forissier, J. C. Green, F. Mathey, L. Ricard, *Chem. Eur. J.* **2005**, *11*, 5381.

 © 2007 Wiley-VCH Verlag GmbH & Co. KGaA, Weinheim 

[21] D. Carmichael, L. Ricard, F. Mathey, *J. Chem. Soc., Chem. Commun.* **1994**, 1167.
[22] a) For cross-coupling reactions with aryl-X see: E. Hagiwara, K. Gouda, Y. Hatanaka, T. Hiyama, *Tetrahedron Lett.* **1997**, *38*, 439; b) for silyl-halogen exchange see: B. Bennetau, J. Dunogues, *Synlett* **1993**, 171; c) T. H. Chan, I. Fleming, *Synthesis* **1979**, 761.
[23] D. Carmichael, F. Mathey, L. Ricard, N. Seeboth, *Chem. Commun.* **2002**, 2976.
[24] For the preparation by treatment of the 3,4-dimethylphospholide anion with electrophiles see ref.[3a,3b]; For preparations by $CO_2$ insertion into the C–Si bonds of phospholide **5** see ref.[3c].
[25] a) G. E. Herberich, B. Ganter, *Organometallics* **1997**, *16*, 522; b) G. E. Herberich, B. Ganter, U. Englert, *Struct. Chem.* **1998**, *9*, 359.
[26] D. Carmichael, L. Ricard, N. Seeboth, J. M. Brown, T. D. W. Claridge, B. Odell, *Dalton Trans.* **2005**, 2173.
[27] M. Ogasawara, T. Nagano, K. Yoshida, T. Hayashi, *Organometallics* **2002**, *21*, 3062.
[28] D. Carmichael, J. Klankermeyer, L. Ricard, N. Seeboth, *Chem. Commun.* **2004**, 1144.
[29] P. B. Hichcock, G. A. Lawless, I. Marziano, *J. Organomet. Chem.* **1997**, *527*, 305.
[30] G. Guimon, D. Gonbeau, G. Pfister-Guillouzo, G. de Lauzon, F. Mathey, *Chem. Phys. Lett.* **1984**, *104*, 560.
[31] N. M. Kostic, R. F. Fenske, *Organometallics* **1983**, *3*, 1008.
[32] K. Forissier, L. Ricard, D. Carmichael, F. Mathey, *Chem. Commun.* **1999**, 1273.
[33] J. Okuda, E. Herdtweck, *J. Organomet. Chem.* **1989**, *373*, 99.
[34] C. Ganter, T. Wagner, *Chem. Ber.* **1995**, *128*, 1157.
[35] a) A. D. Becke, *J. Chem. Phys.* **1993**, *98*, 1372; b) C. Lee, W. Yang, R. G. Parr, *Phys. Rev. B* **1988**, *37*, 785; c) P. J. Stephens, F. J. Devlin, C. F. Chabalowski, M. J. Frisch, *J. Phys. Chem.* **1994**, *98*, 11623.
[36] A. Schäfer, C. Huber, R. Ahlrichs, *J. Chem. Phys.* **1994**, *100*, 5829.
[37] a) A. D. Becke, *Phys. Rev. A* **1988**, *38*, 3098; b) J. P. Perdew, *Phys. Rev. B* **1986**, *33*, 8822; c) J. P. Perdew, *Phys. Rev. B* **1986**, *34*, 7406.
[38] A. Schäfer, H. Horn, R. Ahlrichs, *J. Chem. Phys.* **1992**, *97*, 2571.
[39] a) R. Ahlrichs, M. Bär, M. Häser, H. Horn, C. Kölmel, *Chem. Phys. Lett.* **1989**, *162*, 165; b) O. Treutler, R. Ahlrichs, *J. Chem. Phys.* **1995**, *102*, 346.
[40] a) K. Eichkorn, O. Treutler, H. Öhm, M. Häser, R. Ahlrichs, *Chem. Phys. Lett.* **1995**, *240*, 283; b) K. Eichkorn, O. Treutler, H. Öhm, M. Häser, R. Ahlrichs, *Chem. Phys. Lett.* **1995**, *242*, 652; c) K. Eichkorn, F. Weigend, O. Treutler, R. Ahlrichs, *Theor. Chem. Acc.* **1997**, *97*, 119.
[41] P. J. Fagan, M. D. Ward, J. C. Calabrese, *J. Am. Chem. Soc.* **1989**, *111*, 1698.
[42] G. M. Sheldrick, *SHELXS86. Program for the Solution of Crystal Structures*, University of Göttingen, Germany, **1985**.
[43] G. M. Sheldrick, *SHELXL97. Program for the Refinement of Crystal Structures*, University of Göttingen, Germany, **1997**.
[44] M. Ogasawara, K. Yoshida, T. Hayashi, *Organometallics* **2003**, *22*, 1783.
[45] J. Okuda, E. Herdtweck, *Chem. Ber.* **1988**, *121*, 1899.
[46] H. Sitzmann, *J. Organomet. Chem.* **1988**, *354*, 203.
[47] J. Okuda, *Chem. Ber.* **1989**, *122*, 1075.

Received: September 28, 2006
Published Online: December 19, 2006

 © 2007 Wiley-VCH Verlag GmbH & Co. KGaA, Weinheim 

DOI: 10.1002/ejic.200600922

# Synthesis of the η²-1-Phosphaallene Complexes [(η⁵-$C_5H_5$)(CO)(NO)W{η²-$R^1P$=C=C($R^2$)H}] ($R^1$ = *t*Bu, Cy; $R^2$ = Ph, H) from [(η⁵-$C_5H_5$)(CO)(NO)-W=C=C($R^2$)H] ($R^2$ = Ph, H) and Inversely Polarized Phosphaalkenes $R^1P$=C($NMe_2$)$_2$ ($R^1$ = *t*Bu, Cy), and Their Structure

**Lothar Weber,*[a] Gabriel Noveski,[a] Thomas Braun,[a] Hans-Georg Stammler,[a] and Beate Neumann[a]**

**Keywords:** Vinylidene complexes / Phosphaallene complexes / Phosphaalkenes / Tungsten

The reaction of the vinylidene complex [(η⁵-$C_5H_5$)(CO)(NO)-W=C=C(H)Ph] (**9**) with the phosphaalkenes RP=C($NMe_2$)$_2$ (**1a**: R = *t*Bu; **1c**: R = *c*-$C_6H_{11}$) affords the novel η²-1-phosphaallene complexes [η²-{RP=C=C(H)Ph}W(CO)(NO)(η⁵-$C_5H_5$)] (**14**: R = *t*Bu; **15**: R = *c*-$C_6H_{11}$) in addition to the carbene complex [(η⁵-$C_5H_5$)(CO)(NO)W=C($NMe_2$)C(Ph)=C(H)-$NMe_2$] (**16**). Similarly, treatment of [(η⁵-$C_5H_5$)(CO)(NO)-W=C=$CH_2$] (**12**) with the phosphaalkenes gives rise to the formation of [η²-{RP=C=$CH_2$}W(CO)(NO)(η⁵-$C_5H_5$)] (**17**: R = *t*Bu; **18**: R = *c*-$C_6H_{11}$). The novel compounds **14**, **15**, **17**, and **18** were characterized by elemental analysis and by spectroscopy (IR, $^1$H, $^{13}$C NMR, MS). Moreover, the molecular structures of **14** and **16** were determined by X-ray diffraction analyses.
(© Wiley-VCH Verlag GmbH & Co. KGaA, 69451 Weinheim, Germany, 2007)

## Introduction

Inversely polarized phosphaalkenes (**I**) with an electron-distribution $P^{\delta-}C^{\delta+}$ about the P=C double bond may be described by two canonical formulae (**I** and **I′**).[1] This situation mirrors the bonding in phosphorus ylides **II** (Scheme 1).[2]

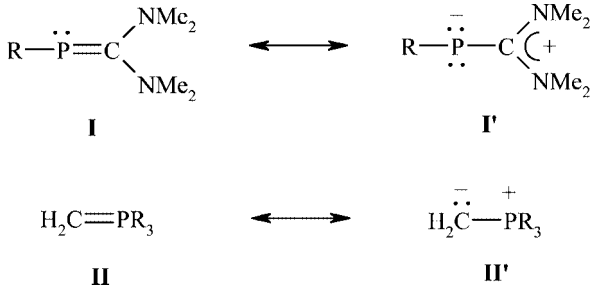


Scheme 1. Mesomeric structures of inversely polarized phosphaalkenes (**I**) and phosphorus ylides (**II**).

The chemical behavior of both classes of compounds (e.g. protonation, alkylation, complexation) can be rationalized by considering the zwitterionic structures **I′** and **II′**. Phosphorus ylides are nucleophilic transfer reagents of alkylidene groups to electrophilic functionalities (e.g. Wittig reaction). The combination of phosphorus ylides and aryl(alkoxy)carbene complexes affords enol ethers.[3] Recently, we discovered that the inversely polarized phosphaalkenes RP=C($NMe_2$)$_2$ [R = *t*Bu (**1a**), $Me_3Si$ (**1b**)] react with aryl(alkoxy)carbene complexes to yield novel phosphaalkene complexes by a formal transfer of the phosphinidene unit to the carbene ligand (Scheme 2).[4]

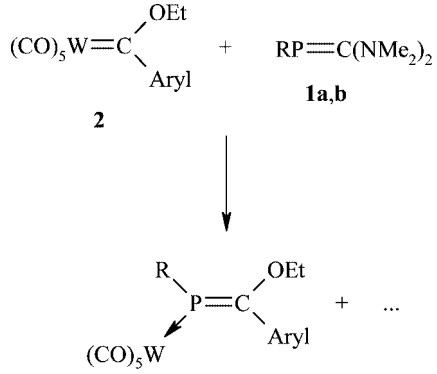


**3** (R = *t*Bu; Aryl = 2-$MeOC_6H_4$)
**4** ($Me_3Si$; 2-$MeOC_6H_4$)
**5** ($Me_3Si$; 2-$MeC_6H_4$)

Scheme 2. Reaction of Fischer carbene complexes with inversely polarized phosphaalkenes.

We have since described the smooth transfer of phosphinidine units from phosphaalkenes **1a** (R = *t*Bu) and **1c** (R = Cy) to the electrophilic ligand in the phosphavinylidene complexes **6** and **7** to produce the first η³-1,2-diphosphaallyl complexes (Scheme 3).[5] Similar transformations have been effected with inversely polarized arsaalkenes.[6]

[a] Fakultät für Chemie der Universität Bielefeld,
Universitätsstrasse 25, 33615 Bielefeld, Germany
Fax: +49-521-106-6146
E-mail: lothar.weber@uni-bielefeld.de


© 2007 Wiley-VCH Verlag GmbH & Co. KGaA, Weinheim

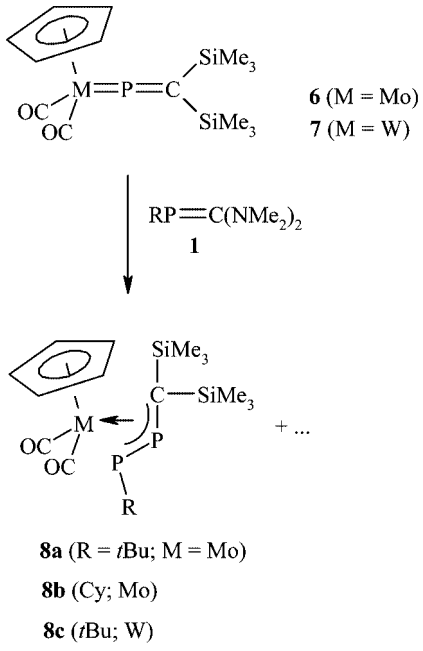


Scheme 3. Formation of 1,2-diphosphaallyl complexes **8a**–**c**.

The obvious next step was to extend our studies on the nucleophilic transfer of phosphinidenes from inversely polarized phosphaalkenes to the electrophilic ligand of vinylidene complexes. This extension seemed particularly promising in light of the previous synthesis of $\eta^2$-1-arsaallene complexes **11a**–**c** from vinylidene complexes **9** and **10** and arsaalkenes (Scheme 4).[7]

Moreover, Ipaktschi et al. have succeeded in the transformation of vinylidene complex **12** into $\eta^2$-allene complexes **13a**–**c** by treating them with diazomethane and ethyl diazoacetate (Scheme 5).[8] In this contribution we present our results on the smooth phosphinidene transfer from phosphaalkenes **1a** and **1c** to the vinylidene ligands of complexes **9** and **12**.

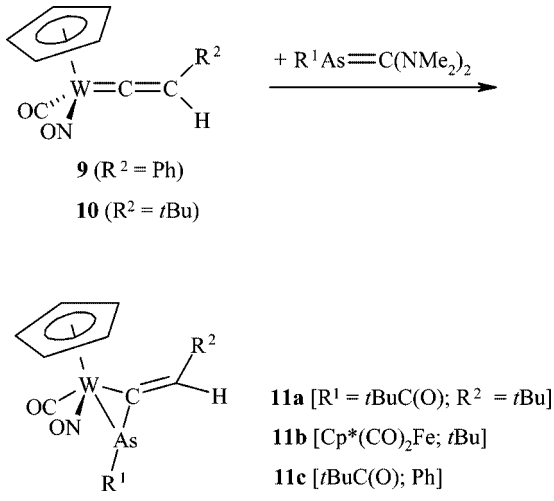


Scheme 4. Synthesis of $\eta^2$-1-arsaallene complexes **11a**–**c**.

## Results and Discussion

Treatment of [Cp(CO)(NO)W=C=C(H)Ph] (**9**)[9] with half a molar equivalent of phosphaalkenes $RP=C(NMe_2)_2$ (**1a**: R = *t*Bu;[4a] **1c**: R = Cy[5]) in tetrahydrofuran (**1a**) or diethyl ether (**1c**) in the range 0 to 20 °C afforded the crystalline $\eta^2$-1-phosphaallene complexes **14** (20% yield) and **15** (19% yield), respectively. Purification of the products was effected by column chromatography on Florisil with hexane as an eluent (Scheme 6).

Red, crystalline carbene complex **16** was formed as a by-product in these reactions. During this process it appears that the nucleophilic carbene $C(NMe_2)_2$ is released and attacks a second equivalent of **9**. In keeping with this, if the precursors are employed in a 1:1 molar ratio half of the phosphaalkene remains unaffected. Carbene complex **16** can be eluted from the column with diethyl ether. However, only impure samples were obtained by this method. In a more efficient protocol, the phosphaallene complex **15** was extracted from the solid, red reaction residue with a diethyl ether/pentane mixture and the remaining orange residue

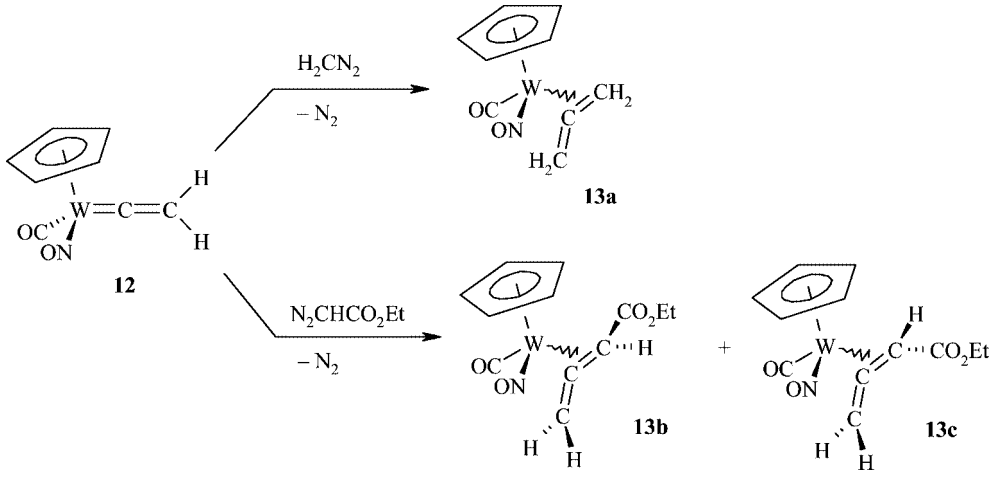


Scheme 5. Synthesis of $\eta^2$-allene complexes **13a**–**c** from **12** and diazoalkanes.

 © 2007 Wiley-VCH Verlag GmbH & Co. KGaA, Weinheim 

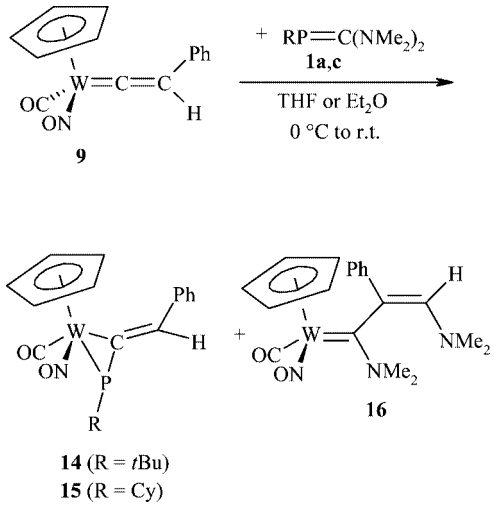


Scheme 6. Formation of the 1-phosphaallene complexes **14** and **15** and carbene complex **16**.

was dissolved in a dichloromethane/pentane mixture (3:1). Storage of the filtered solution at 4 °C afforded red crystalline **16**. The air- and moisture-sensitive complexes **14** and **15** are well soluble in saturated hydrocarbon, ethereal, and aromatic solvents. Complex **16** has been generated previously by the treatment of **9** with $[Cp^*(CO)_2FeAs{=}C(NMe_2)_2]$ in 69% yield,[7] and characterized by means of spectroscopy and elemental analyses. Similarly, yellow crystalline **17** resulted from the reaction of phosphaalkene **1a** and vinylidene complex **12**[10] in a molar ratio of 1:2 in thf at 20 °C (Scheme 7). The synthesis of **18** from **12** and **1c** was accomplished in diethyl ether at –30 °C.

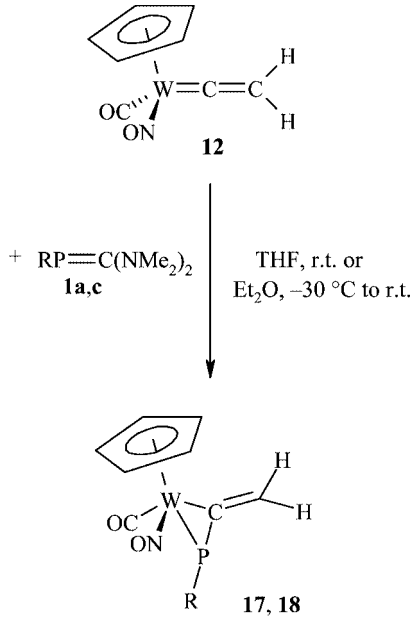


Scheme 7. Preparation of the 1-phosphaallene complexes **17** and **18**.

Doublets at $\delta$ = 8.66 ($^3J_{P,H}$ = 8.2 Hz) and 8.77 ppm ($^3J_{P,H}$ = 8.8 Hz) in the $^1$H NMR spectra of **14** and **15**, respectively, can be assigned to the proton of the exocyclic methylene group. In precursor **9** this proton gives rise to singlets at significantly higher field ($\delta$ = 6.54 and 6.59 ppm; ratio 4:5).[9] In the unsupported phosphaallene Mes*P=C=C(Ph)H a doublet at $\delta$ = 6.67 ($^3J_{P,H}$ = 27 Hz) accounts for this proton.[11] The singlets at $\delta$ = 5.81 and 5.84 ppm (ratio 5:4) for the $C_5H_5$ protons in **9** are markedly deshielded [$\delta$ = 4.76 (**14**), 4.79 ppm (**15**)], which is taken as an indication of the improved donor character of the $\eta^2$-phosphaallene over the vinylidene ligand in **9**. The resonances at $\delta$ = 344.64, 209.2 (210.6), and 130.95 (131.3) ppm in the $^{13}C\{^1H\}$ NMR spectrum of **9** are assigned to $C_\alpha$, the carbonyl ligands, and $C_\beta$ in the two isomers, respectively. The $C_\alpha$ atom in the $\eta^2$-phosphaallene complexes **14** and **15** is strongly shielded [**14**: $\delta$ = 166.5 ppm (d, $^1J_{P,C}$ = 97.7 Hz); **15**: $\delta$ = 167.6 ppm (d, $^1J_{P,C}$ = 94.9 Hz)], whereas the $C_\beta$ atom is slightly deshielded in **14** [$\delta$ = 142.2 ppm (d, $^2J_{P,C}$ = 6.9 Hz)] and **15** [$\delta$ = 142.2 ppm (d, $^2J_{P,C}$ = 7.4 Hz)]. The $C_\alpha$ and $C_\beta$ resonances in free phosphaallene Mes*P=C=C(Ph)H are observed as doublets at $\delta$ = 239.3 (d, $^1J_{P,C}$ = 25 Hz) and $\delta$ = 112.9 (d, $^2J_{P,C}$ = 10 Hz) ppm.[11] The carbonyl ligands in complexes **14** and **15** give rise to doublets at $\delta$ = 218.7 ($^2J_{P,C}$ = 16.1 Hz) and 218.8 ppm ($^2J_{P,C}$ = 17.3 Hz). The shift to high field of about 8 ppm in comparison to **9** [$\delta$(CO) = 209.2 (210.6) ppm] is easily explained by the more pronounced donor capacity of the organophosphorus ligand. Pronounced bathochromic shifts of the CO and NO stretching frequencies of **14** and **15** relative to those of **9** additionally support the NMR findings. In the $^{31}P\{^1H\}$ NMR spectra of **14** and **15** singlet resonances appear at $\delta$ = –130.0 and –158.0 ppm, in the characteristic region for three-membered, phosphorus-containing rings.[12] A similar situation is encountered for the phosphaalkene complexes **17** and **18**. In the $^{31}$P NMR spectra the phosphorus atoms of the three-membered rings give rise to singlets at $\delta$ = –124.0 and –153.6 ppm, respectively. Two doublets at $\delta$ = 6.48 ($^3J_{P,H}$ = 19.5 Hz) and 7.18 ppm ($^3J_{P,H}$ = 6.9 Hz) in the $^1$H NMR spectrum of **17** and at $\delta$ = 6.46 ($^3J_{P,H}$ = 20.7 Hz) and 7.41 ppm ($^3J_{P,H}$ = 6.9 Hz) account for the magnetically different protons of the terminal methylene unit of **18**. Singlets in the $^{13}$C NMR spectrum of the complexes at $\delta$ = 126.0 and 125.9 ppm account for the $^{13}$C nuclei of these groups. The carbon atom $C_\alpha$ is observed as a doublet at $\delta$ = 169.3 ($^1J_{P,C}$ = 94.8 Hz) in **17** and at $\delta$ = 172.5 ppm ($^1J_{P,C}$ = 93.6 Hz) in **18**.

### X-ray Structural Investigations

Single crystals of **14** suitable for X-ray diffraction analysis were grown from hexane at 4 °C. The analysis (Figure 1) shows a molecule with a distorted piano-stool geometry [P(1)–W(1)–C(1) 72.3(1)°, C(1)–W(1)–N(1) 91.3(2)°, N(1)–W(1)–C(2) 91.8(1)°], with nearly linear carbonyl and nitrosyl ligands [W(1)–C(1)–O(1) 178.8(4)°, W(1)–N(1)–O(2) 174.4(3)].

The most interesting part of the molecule is the 1-phosphaallene ligand, which is unsymmetrically linked to the metal atom in an $\eta^2$-fashion by the W(1)–P(1) [2.568(1) Å] and W(1)–C(2) [2.175(4) Å] bonds. The latter bond is

 © 2007 Wiley-VCH Verlag GmbH & Co. KGaA, Weinheim 

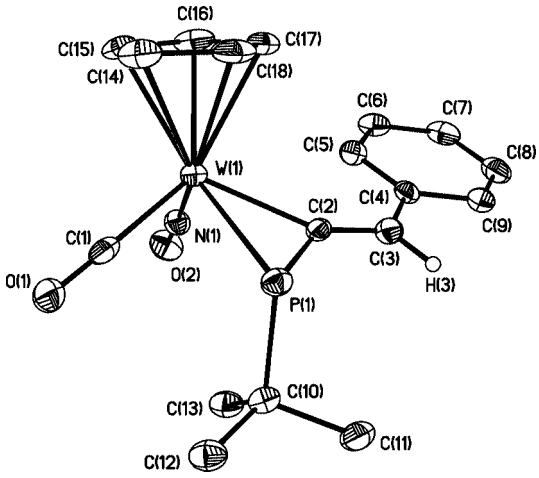


Figure 1. Molecular structure of **14** in the crystal. Selected bond lengths [Å] and angles [°]: W(1)–C(1) 2.007(4), W(1)–N(1) 1.801(3), W(1)–C(2) 2.175(4), W(1)–P(1) 2.568(1), W(1)–C(14–18) 2.335(4) – 2.382(4), P(1)–C(2) 1.742(4), P(1)–C(10) 1.904(4), C(2)–C(3) 1.353(6), C(3)–C(4) 1.468(5); W(1)–C(1)–O(1) 178.8(4), W(1)–N(1)–O(2) 174.4(3), W(1)–C(2)–P(1) 81.1(2), W(1)–C(2)–C(3) 142.2(3), C(2)–W(1)–P(1) 42.1(1), C(2)–W(1)–N(1) 91.8(1), N(1)–W(1)–C(1) 91.3(2), C(1)–W(1)–P(1) 72.3(1), W(1)–P(1)–C(10) 115.1(1), W(1)–P(1)–C(2) 56.8(1), P(1)–C(2)–C(3) 136.7(3), C(10)–P(1)–C(2) 105.3(2).

significantly shorter than the W(1)–C distances of the [$C_5H_5W$] part of the molecule [2.335(4)–2.382(4) Å]. The W(1)–C(2) bond length is comparable to that in complex **19** [2.178(7) Å],[13] but much smaller than in the ($\eta^3$-2-phospha-1-arsaallyl)tungsten complex **20** [2.439(2) Å].[6]

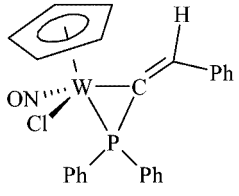


**19**

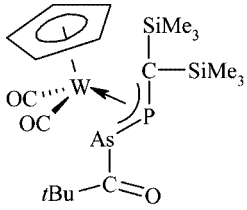


**20**

Thus, the situation of a π complex involving the W atom and the P=C double bond is not reflected satisfactorily by the structural data of **14**. Moreover, inspection of the W=C bond lengths in a series of carbene–tungsten complexes [1.859(4)–2.23(2) Å][14] reveals some degree of WC multiple bonding in our new complex. A similar observation was made in the molecular structure of **11b**.[7] The W(1)–P(1) separation [2.568(1) Å] markedly exceeds the WP bond length in **19** [2.434(2) Å] and may be compared with the endocyclic WP bond lengths in complexes **21** [2.5352(7) and 2.5695(7) Å][5] or **22** [2.573(4) and 2.582(4) Å].[15]

The endocyclic P(1)–C(2) bond length [1.742(4) Å] may be regarded as being a π-coordinated multiple bond. Generally, unsupported P=C bonds in acyclic phosphaalkenes range from 1.65–1.72 Å,[16] and a value of 1.63 Å has been reported for the P=C distance in the 1-phosphaallene Mes*P=C=$CPh_2$.[17] The carbon-carbon double bond C(2)–C(3) [1.353(6) Å] is lengthened with respect to that in Mes*P=C=$CPh_2$ (1.31 Å),[17] and the P(1)–C(2)–C(3) angle

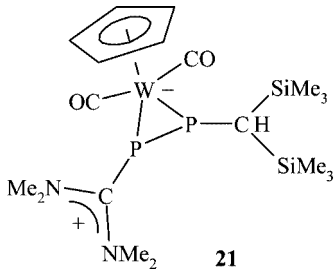


**21**

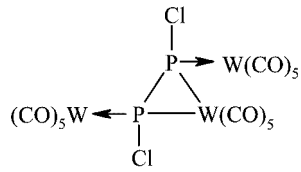


**22**

of 136.7(3)° is strongly compressed when compared with that in the free 1-phosphaallene (167°). Carbon atoms C(3) and C(4) are located in the plane defined by the atoms W(1), P(1), and C(2), and atom P(1) is roughly placed in a *trans* disposition to the nitrosyl ligand whereas C(2) and the carbonyl group are *trans* oriented.

Wine-red, single crystals of carbene complex **16** were grown by slow diffusion of pentane into a $CH_2Cl_2$ solution during a period of seven days. The analysis (Figure 2) reveals a molecule with a distorted, three-legged piano-stool geometry [N(1)–W(1)–C(6) 91.6(1)°, N(1)–W(1)–C(7) 101.1(1)°, C(6)–W(1)–C(7) 80.7(1)°] with nearly linear carbonyl and nitrosyl ligands [W(1)–C(6)–O(2) 176.5(2)°, W(1)–N(1)–O(1) 173.7(2)°]

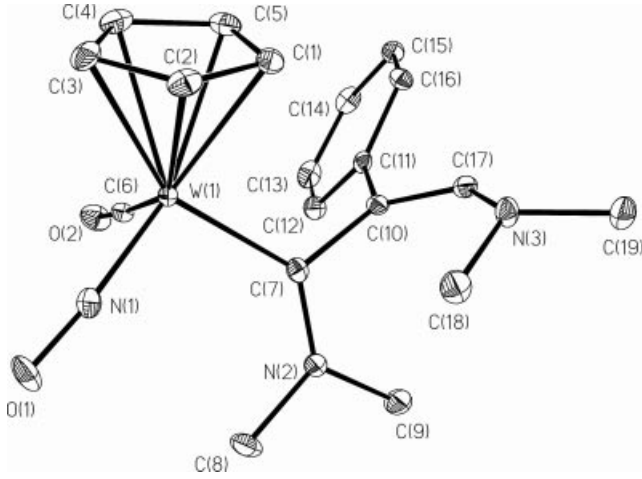


Figure 2. Molecular structure of **16** in the crystal. Selected bond lengths [Å] and angles [°]: W(1)–N(1) 1.802(2), W(1)–C(6) 1.979(2), W(1)–C(7) 2.126(2), W(1)–C(1–5) 2.373(2) – 2.407(2), N(2)–C(7) 1.339(3), N(2)–C(8) 1.478(3), N(2)–C(9) 1.481(3), C(7)–C(10) 1.516(3), C(10)–C(11) 1.491(3), C(10)–C(17) 1.369(3), N(3)–C(17) 1.383(3), N(3)–C(18) 1.437(3), N(3)–C(19) 1.467(3); N(1)–W(1)–C(6) 91.6(1), N(1)–W(1)–C(7) 101.1(1), C(6)–W(1)–C(7) 86.7(1), W(1)–C(7)–N(2) 130.4(2), W(1)–C(7)–C(10) 115.6(1), N(2)–C(7)–C(10) 114.0(2), C(7)–C(10)–C(17) 124.3(1), C(7)–C(10)–C(11) 117.8(2), C(11)–C(10)–C(17) 117.8(2), C(10)–C(17)–N(3) 132.3(2), C(17)–N(3)–C(18) 123.0(2), C(17)–N(3)–C(19) 116.5(2), C(18)–N(3)–C(19) 113.6(2).

The third leg is a dimethylamino vinylcarbene ligand which is attached to the metal by the W(1)–C(7) double bond [2.126(2) Å]. The plane defined by the atoms C(7), C(8), C(9), C(10), and N(2) is nearly coplanar with the vector W(1)–N(1) (torsion angle 7.5°). The contact N(2)–C(7) of 1.339(3) Å represents multiple bonding. An accepted average value for a $C_{sp^2}$–$N_{sp^2}$ single bond amounts to

 © 2007 Wiley-VCH Verlag GmbH & Co. KGaA, Weinheim 

1.41 Å.[18] Within the β-aminoalkenyl substituents the C(7)–C(17) bond [1.516(3) Å] has a bond order of unity. The C(10)–C(17) double bond of 1.369(3) Å is lengthened by conjugation with the lone pair at the slightly pyramidalized N(3) atom (sum of angles: 353.1°). As a consequence, the N(3)–C(17) distance [1.383(3) Å] is a shortened single bond. The plane defined by the atoms N(3), C(17), C(10), C(11), and C(7) is oriented nearly orthogonally to the plane of the carbene moiety.

## Conclusions

The previously observed transition-metal-induced cleavage of inversely polarized phosphaalkenes to give $\eta^3$-1,2-diphosphaallyl complexes[5] has been extended to the smooth generation of $\eta^2$-1-phosphaallene complexes **14**, **15**, **17**, and **18**. This reaction underlines the ability of phosphaalkenes to act as convenient sources for phosphanediyl (phosphinidene) units under mild conditions.

## Experimental Section

**General:** All experiments were performed under dry, oxygen-free dinitrogen using standard Schlenk techniques. Solvents were carefully dried with the appropriate drying agent and freshly distilled under $N_2$ before use. The following compounds were prepared according to literature procedures: [Cp(CO)(NO)W=C=C(H)Ph] (**9**),[9] [Cp(CO)(NO)W=C=$CH_2$] (**12**),[10] *t*BuP=C($NMe_2$)$_2$ (**1a**),[4a] CyP=C($NMe_2$)$_2$ (**1c**).[5] IR spectra were recorded with a Bruker FT-IR VECTOR 22 spectrometer. $^1$H, $^{13}$C, and $^{31}$P NMR spectra were recorded at room temperature with a Bruker AM Avance DRX 500 instrument ($^1$H: 500.13, $^{13}$C: 125.75, $^{31}$P: 202.46 MHz). References: $SiMe_4$ ($^1$H, $^{13}$C) and 85% $H_3PO_4$ ($^{31}$P). MS: Bruker Esquire Ion Trap mass spectrometer. Florisil was purchased from Merck.

**[Cp(CO)(NO)W{$\eta^2$-*t*BuP=C=CHPh}] (14):** A solution of phosphaalkene **1a** (0.16 g, 0.83 mmol) in thf was added dropwise at 0 °C to a well stirred solution of complex **9** (0.61 g, 1.5 mmol) in thf (15 mL). Stirring was continued at 0 °C for 1 h. The solution was then warmed up to ambient temp. and stirred for another 2.5 h at room temp. The solvents were removed in vacuo to afford a red solid residue. The latter was suspended in hexane (150 mL) and filtered through a pad of Florisil (*l* = 1.5 cm, *d* = 2 cm). A yellow zone was eluted with hexane (4 × 30 mL). Concentration of the elute to about 15 mL and storage at 4 °C for 14 h led to the separation of product **14** as big yellow crystals. (Yield: 0.15 g, 20%). IR (KBr): $\tilde{\nu}$ = 1972 s (CO), 1630 s (NO) cm$^{-1}$. $^1$H NMR ($C_6D_6$): $\delta$ = 1.29 (d, $^3J_{P,H}$ = 13.2 Hz, 9 H, *t*Bu), 4.76 (s, 5 H, Cp), 7.12 (t, $^3J_{H,H}$ = 7.5 Hz, 1 H, *p*-H-Ph), 7.26 (t, $^3J_{H,H}$ = 7.5 Hz, 2 H, *m*-H-Ph), 7.70 (d, $J_{H,H}$ = 6.9 Hz, 2 H, *o*-H-Ph), 8.66 [d, $^3J_{P,H}$ = 8.2 Hz, 1 H, =C(*H*)Ph] ppm. $^{13}$C{$^1$H} NMR ($C_6D_6$): $\delta$ = 30.4 [d, $^2J_{P,C}$ = 16.1 Hz, C(*C*H$_3$)$_3$], 35.5 [d, $^1J_{P,C}$ = 47.1 Hz, *C*(CH$_3$)$_3$], 96.7 (s, $C_5H_5$), 127.3 (s, Ph), 128.1 (s, Ph), 128.5 (s, Ph), 139.9 (d, $^3J$ = 5.7 Hz, *i*-C-Ph), 142.2 (d, $^2J_{P,C}$ = 6.9 Hz, P–C=*C*), 166.5 (d, $^2J_{P,C}$ = 97.7 Hz, P=*C*), 218.7 (d, $^2J_{P,C}$ = 16.1 Hz, CO) ppm. $^{31}$P{$^1$H} NMR $\delta$ = –130.0 ppm. EI-MS: *m*/*z* 498 [M + H$^+$]. $C_{18}H_{20}NO_2PW$ (497.17): calcd. C 43.49, H 4.05, N 2.82; found C 43.51, H 4.14, N 2.86.

Compound **16** with low purity may be extracted from the column with neat diethyl ether. The preparation of analytically pure **16** in an acceptable yield requires a slightly modified protocol. Thus, a solution of **1a** (0.33 g, 1.75 mmol) in thf (15 mL) was added dropwise to chilled solution of complex **9** (1.45 g, 3.54 mmol) in thf (15 mL). After stirring the reaction mixture for 2.5 h at room temp., solvents and other volatile components were removed in vacuo. The red solid residue was triturated with 32 mL of a diethyl ether/pentane mixture, and then the liquid phase was decanted. The solid was washed with pentane (6 × 10 mL) and dried at $10^{-6}$ bar. The orange solid was dissolved in a dichloromethane/pentane mixture (3:1), filtered, and the filtrate was stored at +4 °C. Carbene complex **16** separated as red crystals (0.65 g, 36% yield). The spectroscopic data were identical with a sample obtained previously by another method.

**[Cp(CO)(NO)W{$\eta^2$-CyP=C=CHPh}] (15):** A solution of phosphaalkene **1c** (0.24 g, 1.12 mmol) in diethyl ether (30 mL) was slowly added to a chilled solution (0 °C) of complex **9** (0.83 g, 2.03 mmol) in diethyl ether (30 mL). Stirring at 0 °C was continued for 2.5 h before the mixture was warmed to room temp. It was then evaporated to dryness and the orange-red solid residue was suspended in hexane (125 mL). It was filtered through a pad of Florisil (*l* = 1.5 cm, *d* = 2 cm). A yellow zone was eluted with hexane (4 × 30 mL). The elute was concentrated to about 15 mL and stored for 12 h at 4 °C to afford 0.20 g (19%) of orange-yellow crystalline **15**. IR (KBr): $\tilde{\nu}$ = 1990 s (CO), 1625 s (NO) cm$^{-1}$. $^1$H NMR ($C_6D_6$): $\delta$ = 0.88–2.29 (br., 11 H, $C_6H_{11}$), 4.79 (s, 5 H, Cp), 7.11 (t, $^3J_{H,H}$ = 7.2 Hz, 1 H, *p*-H-Ph), 7.24 (t, $^3J_{H,H}$ = 7.5 Hz, 2 H, *m*-H-Ph), 7.71 (d, $^3J_{H,H}$ = 7.5 Hz, 2 H, *o*-H-Ph), 8.77 [d, $^3J_{P,H}$ = 8.8 Hz, =C(*H*)Ph] ppm. $^{13}$C{$^1$H} NMR ($C_6D_6$): $\delta$ = 96.7 (s, $C_5H_5$), 127.3 (s, Ph), 128.1 (s, Ph), 128.5 (s, Ph), 140.1 (d, $^3J_{P,C}$ = 6.2 Hz, *i*-C-Ph), 142.2 (d, $^3J_{P,C}$ = 7.4 Hz, P=C=*C*), 167.6 (d, $^1J_{P,C}$ = 94.9 Hz, P=C), 218.8 (d, $^2J_{P,C}$ = 17.3 Hz, CO) ppm. $^{31}$P{$^1$H} NMR $\delta$ = –158.0 (s) ppm. EI-MS: *m*/*z* 524.2 [M + H$^+$], 496.2 [M – CO + H$^+$]. $C_{20}H_{22}NO_2PW$ (523.21): calcd. C 45.91, H 4.24, N 2.68; found C 46.04, H 4.27, N 2.67.

**[Cp(CO)(NO)W{$\eta^2$-*t*BuP=C=$CH_2$}] (17):** A solution of phosphaalkene **1a** (0.11 g, 0.58 mmol) in thf (5 mL) was added dropwise at ambient temp. to a solution of complex **12** (0.37 g, 1.11 mmol) in thf (10 mL). Stirring was continued for 2.5 h before the reaction mixture was evaporated to dryness. The yellow solid residue was chromatographed on a small column charged with Florisil (*l* = 4 cm, *d* = 2 cm). A yellow zone was eluted with hexane/diethyl ether (30:2). The elute was concentrated to 15 mL and stored at 4 °C for 18 h to give **17** as yellow crystals (0.14 g, 30% yield). IR (KBr): $\tilde{\nu}$ = 1979 s (CO), 1618 s (NO) cm$^{-1}$. $^1$H NMR ($CDCl_3$): $\delta$ = 1.11 (d, $^3J_{P,H}$ = 13.2 Hz, 9 H, *t*Bu), 5.63 (s, 5 H, Cp), 6.48 (d, $^3J_{P,H}$ = 19.5 Hz, 1 H, =$CH_2$), 7.18 (d, $^3J_{P,H}$ = 6.9 Hz, 1 H, =$CH_2$) ppm. $^{13}$C{$^1$H} NMR ($CDCl_3$): $\delta$ = 30.2 [d, $^2J_{P,C}$ = 16.2 Hz, C(*C*H$_3$)$_3$], 34.4 [d, $^1J_{P,C}$ = 42.8 Hz, *C*(CH$_3$)$_3$], 96.8 (s, Cp), 126.0 (s, P=C=*C*), 169.3 (d, $^1J_{P,C}$ = 94.8 Hz, P=*C*=C), 217.3 (d, $^2J_{P,C}$ = 12.7 Hz, CO) ppm. $^{31}$P{$^1$H} NMR ($CDCl_3$): $\delta$ = –124.0 ppm. EI-MS: *m*/*z* 422.1 [M + H$^+$]. $C_{12}H_{16}NO_2PW$ (421.08): calcd. C 34.23, H 3.83, N 3.33; found C 33.51, H 3.87, N 3.30.

**[Cp(CO)(NO)W{$\eta^2$-CyP=C=$CH_2$}] (18):** A solution of phosphaalkene **1c** (0.22 g, 1.04 mmol) in diethyl ether (25 mL) was added dropwise to a chilled solution (–30 °C) of complex **12** (0.62 g, 1.86 mmol) in diethyl ether (30 mL). Stirring was continued at –30 °C for 1 h, and then at room temp. for another 2.5 h. The mixture was evaporated to dryness. The red solid residue was suspended in pentane (150 mL) and filtered through a pad of Florisil (*l* = 1.5 cm, *d* = 2 cm). A yellow zone was eluted with a diethyl ether/pentane mixture (1:3). The elute was concentrated to 20 mL and stored at 4 °C for 14 h, whereby product **18** separated as yellow crystals (0.10 g, 12%). IR (KBr): $\tilde{\nu}$ = 1973 s (CO), 1618 s (NO)

 © 2007 Wiley-VCH Verlag GmbH & Co. KGaA, Weinheim 

$cm^{-1}$. $^1H$ NMR ($C_6D_6$): $\delta$ = 1.10–2.29 (m, 11 H, $C_6H_{11}$), 4.76 (s, 5 H, Cp), 6.46 (d, $^3J_{P,H}$ = 20.7 Hz, 1 H, =$CH_2$), 7.41 (d, $^3J_{P,H}$ = 6.9 Hz, 1 H, =$CH_2$) ppm. $^{13}C\{^1H\}$ NMR ($C_6D_6$): $\delta$ = 26.4 (s, Cy), 27.2 (d, $J_{P,C}$ = 6.9 Hz, Cy), 27.4 (d, $J_{P,C}$ = 13.9 Hz, Cy), 32.3 (d, $J_{P,C}$ = 6.9 Hz, Cy), 33.6 (d, $J_{P,C}$ = 20.8, Cy), 40.3 (d, $J_{P,C}$ = 40.5 Hz, Cy), 95.5 (s, $C_5H_5$), 125.9 (s, P=C=*C*), 175.5 (d, $^1J_{P,C}$ = 93.6 Hz, P=C), 219.5 (d, $^2J_{P,C}$ = 15.0 Hz, CO) ppm. $^{31}P\{^1H\}$ NMR $\delta$ = –153.6 (s) ppm. EI-MS: *m/z* 448.1 [$M^+$]. $C_{14}H_{18}NO_2PW$ (447.11): calcd. C 37.61, H 4.06, N 3.13; found C 37.33, H 4.09, N 3.15.

**X-ray Crystallography:**[19] Crystallographic data were collected with a Nonius KappaCCD diffractometer with Mo-$K_\alpha$ radiation (graphite monochromator, $\lambda$ = 0.71073 Å) at 100 K. The crystallographic programs used for structure solution and refinement were SHELXS-97 and SHELXL-97. The structures were solved by direct methods and refined by full-matrix least-squares on $F^2$ of all unique reflections with anisotropic thermal parameters for all non-hydrogen atoms. Hydrogen atoms were included at calculated positions with $U$(H) = 1.2 $U_{eq}$ for $CH_2$ groups and $U$(H) = 1.5 $U_{eq}$ for $CH_3$ groups. The largest difference peaks for **14** are located near W(1) (0.82 and 0.89 Å). Other crystal data for both compounds are listed in Table 1.

Table 1. Crystal data and collection parameters.

| | **14** | **16** |
|---|---|---|
| Empirical formula | $C_{18}H_{20}NOPW$ | $C_{19}H_{23}N_3O_2W$ |
| $M_r$ [g mol$^{-1}$] | 497.17 | 509.25 |
| Crystal dimensions [mm] | 0.30 × 0.29 × 0.26 | 0.18 × 0.17 × 0.10 |
| Crystal system | monoclinic | monoclinic |
| Space group | $P2_1/c$ | $P2_1/n$ |
| *a* [Å] | 9.9120(3) | 9.1310(4) |
| *b* [Å] | 23.2500(3) | 20.026(2) |
| *c* [Å] | 7.6980(7) | 9.9290(9) |
| $\beta$ [°] | 97.6080(11) | 91.245(6) |
| *V* [Å$^3$] | 1758.42(17) | 1815.2(3) |
| *Z* | 4 | 4 |
| $\rho_{calcd.}$ [g m$^{-3}$] | 1.878 | 1.863 |
| $\mu$ [mm$^{-1}$] | 6.668 | 6.381 |
| *F*(000) | 960 | 992 |
| $\Theta$ [°] | 3.00–25.00 | 2.00–30.00 |
| Reflections collected | 34975 | 73776 |
| Reflections unique | 3064 | 5277 |
| *R*(int) | 0.043 | 0.0582 |
| Refined parameters | 211 | 230 |
| GOF | 1.085 | 1.021 |
| $R_F$ [$I > 2\sigma(I)$] | 0.0244 | 0.0203 |
| $wR_{F^2}$ [all data] | 0.0664 | 0.0332 |
| $\Delta\rho_{max/min}$ [e Å$^{-3}$] | 2.476/–1.206 | 0.659/–0.740 |

CCDC-622264 (for **14**) and -622265 (for **16**) contain the supplementary crystallographic data for this paper. These data can be obtained free of charge from The Cambridge Crystallographic Data Centre via www.ccdc.cam.ac.uk/data_request/cif.


[1] Review: L. Weber, *Eur. J. Inorg. Chem.* **2000**, 2425–2441.
[2] *Ylides and Imines of Phosphorus* (Ed.: A. W. Johnson), Wiley, New York, **1993**.
[3] C. P. Casey, T. J. Burkhardt, *J. Am. Chem. Soc.* **1972**, *94*, 6543–6544.
[4] a) L. Weber, M. Meyer, H.-G. Stammler, B. Neumann, *Chem. Eur. J.* **2001**, *7*, 5401–5408; b) L. Weber, M. Meyer, H.-G. Stammler, B. Neumann, *Organometallics* **2003**, *22*, 5063–5068.
[5] L. Weber, G. Noveski, U. Lassahn, H.-G. Stammler, B. Neumann, *Eur. J. Inorg. Chem.* **2005**, 1940–1946.
[6] L. Weber, P. Bayer, S. Uthmann, T. Braun, H.-G. Stammler, B. Neumann, *Eur. J. Inorg. Chem.* **2006**, 137–143.
[7] L. Weber, P. Bayer, G. Noveski, H. G. Stammler, B. Neumann, *Eur. J. Inorg. Chem.* **2006**, 2299–2305.
[8] J. Ipaktschi, P. Rooshenas, A. Dülmer, *Eur. J. Inorg. Chem.* **2006**, 1456–1459.
[9] J. Ipaktschi, G. J. Demuth-Eberle, F. Mirzaei, B. G. Müller, J. Beck, M. Serafin, *Organometallics* **1995**, *14*, 3335–3341.
[10] J. Ipaktschi, P. Rooshenas, T. Klotzbach, A. Dülmer, E. Hüseynova, *Organometallics* **2005**, *24*, 1351–1354.
[11] R. Appel, V. Winkhaus, F. Knoch, *Chem. Ber.* **1986**, *119*, 2466–2472.
[12] M. Baudler, J. Hahn, H. Dietsch, G. Fürstenberg, *Z. Naturforsch., Teil B* **1976**, *31*, 1305–1310.
[13] J. Ipaktschi, T. Klotzbach, A. Dülmer, *Organometallics* **2000**, *19*, 5281–5286.
[14] U. Schubert, in *Transition Metal Carbene Complexes*, VCH, Weinheim, **1973**, p. 103.
[15] V. Vogel, G. Stößer, M. Scheer, *Angew. Chem.* **2001**, *113*, 1476–1478; *Angew. Chem. Int. Ed.* **2001**, *40*, 1443–1445.
[16] Review: L. Weber, *Angew. Chem.* **1996**, *108*, 292–310; *Angew. Chem. Int. Ed. Engl.* **1996**, *35*, 271–288.
[17] R. Appel, P. Fölling, B. Josten, M. Siray, U. Winkhaus, F. Knoch, *Angew. Chem.* **1984**, *96*, 620–621; *Angew. Chem. Int. Ed. Engl.* **1984**, *23*, 619–620.
[18] A. N. Chernega, A. V. Ruban, V. D. Romanenko, L. N. Markovskii, A. A. Korkin, M. Y. Antipin, Y. T. Struchkov, *Heteroat. Chem.* **1991**, *2*, 229–241.
[19] G. M. Sheldrick, *SHELX-97, program for crystal structure refinement*, University of Göttingen, Germany, **1997**.


Received: September 29, 2006
Published Online: December 12, 2006

 © 2007 Wiley-VCH Verlag GmbH & Co. KGaA, Weinheim 

DOI: 10.1002/ejic.200600829

# The Hydrothermal Synthesis of Transition Metal Complex Templated Octamolybdates

**Katikaneani Pavani,[a] Samuel E. Lofland,[b] Kandalam V. Ramanujachary,[c] and Arunachalam Ramanan*[a]**

**Keywords:** Solvothermal synthesis / Molybdenum / Supramolecular chemistry / Organic–inorganic hybrid composites

The hydrothermal reaction of an aqueous ammonium heptamolybdate solution with cobalt or copper metal salts in the presence of imidazole (imi) or pyrazole (pz) in the temperature range 120–180 °C and at autogenous pressure yields four fully oxidized metal-complex-templated octamolybdates, namely $[\{Cu^{I}(imi)_2\}_4(imi)_2Mo_8O_{26}]\cdot 4H_2O$ (**1**), $(Himi)_2[\{Cu^{II}(imi)_2\}_2Mo_8O_{27}]$ (**2**), $[\{Co^{II}(pz)_4\}_2(pz)_2Mo_8O_{26}]$ (**3**), and $[\{Cu^{II}(pz)_4\}_2Mo_8O_{26}]\cdot 2H_2O$ (**4**). The single-phase nature of the solids was established by single-crystal and powder X-ray diffraction, thermal analysis, and spectroscopic techniques. Compounds **1**, **3**, and **4** are neutral composite solids – **1** is a discrete molecular unit while **3** and **4** are 2D sheets. Compound **2** consists of anionic chains with imidazolium counter cations. The influence of the metal complex and temperature of the hydrothermal reaction on the formation of the different hybrid solids built of octamolybdate clusters is discussed. We also provide plausible mechanisms for the self-assembly of the crystals in terms of supramolecular organization between metal complexes and soluble molybdenum precursors in the initial stages of the reaction. The magnetic properties of **2**, **3**, and **4** confirm the presence of Cu and Co in the divalent state with no appreciable long-range order down to 5 K, whereas **1** is diamagnetic.

(© Wiley-VCH Verlag GmbH & Co. KGaA, 69451 Weinheim, Germany, 2007)

## Introduction

Polyoxomolybdate (POM) cluster anions are ideal nanobuilding blocks to assemble giant molecular crystals exhibiting compositional variation and structural diversity.[1,2] A contemporary interest in this area is to employ organic components or metal complexes to dictate the formation of novel organic–inorganic hybrid composites as these show promising applications in the areas of catalysis, magnetism, photochemistry, sensors, and energy storage.[3–6] A large number of POM-based solids have been self-assembled from aqueous solution in the presence of organic molecules as structure directors.[7–9] In particular, the role of organic diamines in the formation of discrete POM clusters to three-dimensional networks of molybdenum oxide based materials has been investigated extensively.[10–12] It is well established that solids crystallized from aqueous molybdate solution under either ambient or hydrothermal conditions in the presence of organic diamines are predominantly based on organic–inorganic hybrid salts. These may be salts between organic ammonium cations and discrete POM anions or composite solids with extended POM anions incorporated with organic cations.[13,14] If an additional transition metal ion is present, the metal complex formed in situ can either occur as the counter cation or derivatise the POM anion, or they can also be part of the extended network linking POM cluster anions.[15–17] In selected cases, the organic ammonium ions can take part in unusual hydrogen bonding and/or π-π interactions, which, in turn, can direct the crystal packing.[18] In an attempt to rationalize the reactivity pattern in the formation of these solids under hydrothermal conditions, we have been systematically analyzing the chemistry involved in controlling the reaction and hence the structure of molybdates, even though hydrothermal reactions are commonly termed as "black box" in nature. Apart from pH, molybdenum's ability to coordinate with aromatic diamines to form either pillared or composite solids is also important.[19] Another issue is the nature of the complex formed between the organic amine and the transition metal ion and its stability under hydrothermal conditions. Frequently, some of these organic amines can reduce transition metals under hydrothermal conditions and hence can lead to a different metal complex in situ. In addition, the temperature of crystallization is important. Apart from these, nonbonding interactions taking place between molybdate cluster anions and organic groups along with water molecules will influence the crystal structure packing. In our earlier work,[20] we have shown how a weak

[a] Department of Chemistry, Indian Institute of Technology, New Delhi 110016, India
Fax: +91-11-2658-2277
E-mail: aramanan@chemistry.iitd.ac.in
[b] Department of Physics and Astronomy, Rowan University, Glassboro, New Jersey 08028, USA
[c] Department of Chemistry and Biochemistry, Rowan University, Glassboro, New Jersey 08028, USA

Supporting information for this article is available on the WWW under http://www.eurjic.org or from the author.


InterScience®
© 2007 Wiley-VCH Verlag GmbH & Co. KGaA, Weinheim

ligand such as 2-aminopyridine ($pK_a \approx 6.9$) affects the hydrolysis and condensation reactions taking place in aqueous molybdate solution containing first-row transition metal ions.

Acidification of aqueous molybdate solution in the presence of organic cations yields a variety of POM cluster anions with varying numbers of molybdenum atoms. Among them, the octamolybdate anion **A** (Figure 1, left) with the composition $[Mo_8O_{26}]$ is predominant.[21–23] This cluster anion exhibits different isomeric structures; the cluster can occur either as discrete entities (zero-dimensional) or act as building blocks for 1D chains, 2D sheets, or 3D frameworks.[24–26] Another octamolybdate cluster, **B**, which has a different composition $[Mo_8O_{28}]$ (Figure 1, right), is observed in a few solids although in only one example does it exist as a discrete cluster.[27] While $Mo_8O_{26}$ is rarely protonated,[28,29] the cluster anion $Mo_8O_{28}$ is possibly protonated in aqueous solution and hence has a strong tendency to become derivatized or condensed under suitable conditions.[30–32] In this paper, we explore the reaction conditions necessary to form the octamolybdate cluster anion as a versatile inorganic building block for the construction of new hybrid molybdates in the presence of imidazole and its isomer pyrazole as templates. We also discuss the formation of **1**–**4** in terms of ideas recently proposed by Ramanan and Whittingham[33] for the formation of metal organic polymers and later extended to explain the formation of copper coordination polymers based on molybdates crystallized under hydrothermal conditions.[34]

## Results and Discussion

The hydrothermal reaction of copper and cobalt salts in the presence of imidazole (imi) or pyrazole (pz) at different temperatures leads to different products. Powder and single crystal XRD, TGA, and FTIR analysis were employed to establish the crystal structure, phase purity, and composition. Scheme 1 summarizes the optimal reaction conditions employed to obtain monophasic solids.

### Crystal Structure of 1

The crystal structure of $[\{Cu^{I}(imi)_2\}_4(imi)_2Mo_8O_{26}]\cdot 4H_2O$ (**1**) shows the presence of a discrete octamolybdate cluster (type **B**) derivatized by two imidazole moieties and

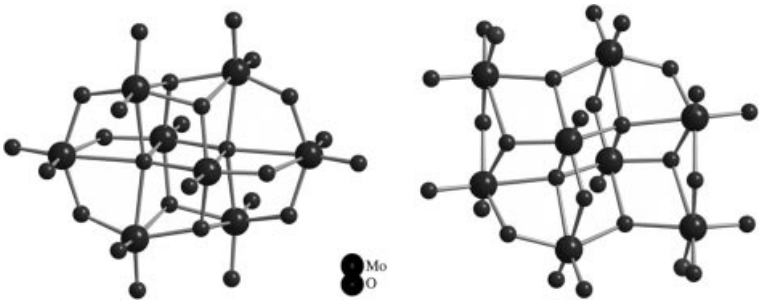


Figure 1. A view of (a) the β-octamolybdate anion $[Mo_8O_{26}]$ (type **A**) and (b) the octamolybdate anion $[Mo_8O_{28}]$ (type **B**).

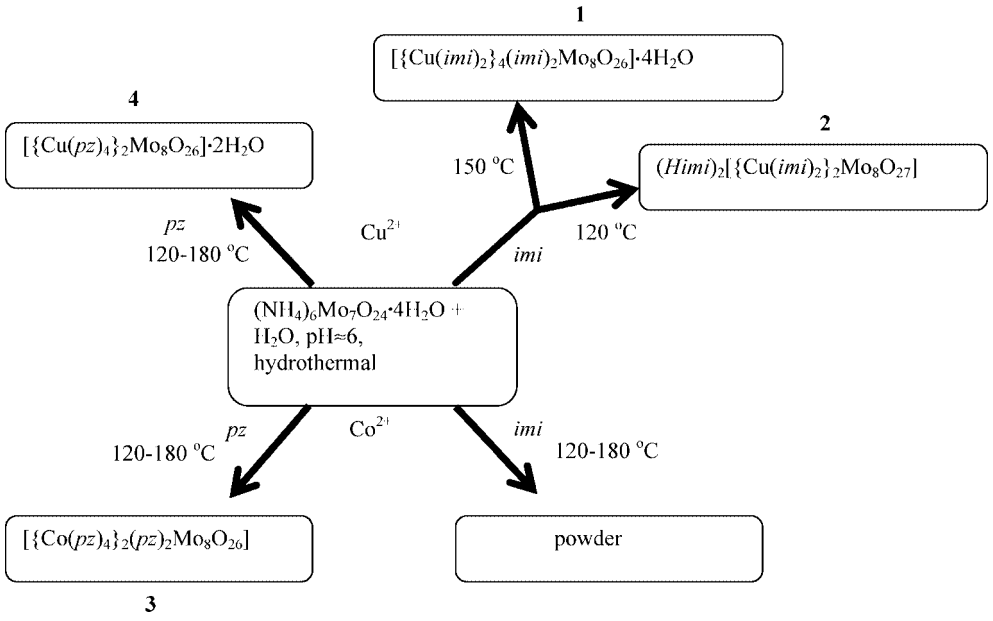


Scheme 1. Experimental details.

 © 2007 Wiley-VCH Verlag GmbH & Co. KGaA, Weinheim 

four tricoordinate copper imidazole complexes (Figure 2). An inversion center occurs in the center of the cluster anion. Each molybdenum atom in the $\{Mo_8O_{26}N_2\}^{4-}$ cluster anion has a distorted octahedral environment with six oxygen atoms. The thirteen asymmetric oxygen atoms in this cluster anion fall into four groups: seven are terminal, three are doubly bridging, two are triply bridging, and one is a quadruply bridging ligand. The copper(I) imidazole complex has two imidazole ligands and the third coordination is to the terminal oxygen of the cluster anion. In all the examples reported in the literature, derivatization of the cluster anion with an organic moiety (e.g. acetate or formate groups) appears to take place only on the molybdenum containing three terminal oxygens.[35,36] An interesting feature of this structure is that copper occurs in the +1 oxidation state and is tricoordinate. The supramolecular assemblies based on the derivatized octamolybdate unit $[\{Cu^{I}(imi)_2\}_4(imi)_2Mo_8O_{26}]$ are further connected to each other through strong H-bonding interactions of the type N–H···O (see Figure S1 in the Supporting Information). Apart from these, C–H···π interactions with an angle of 123.17° also dominate the crystal packing (Figure 3). Such copper(I) tricoordination is seen in the literature for β- and γ-octamolybdate cluster anions.[37–39] Complex **1** appears to be similar to one reported in the literature even though we have prepared it under different reaction conditions.[40]

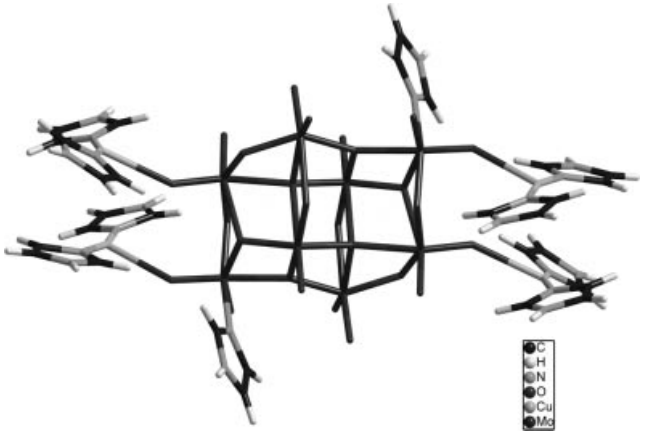


Figure 2. Crystal structure of the discrete octamolybdate **B** in **1** derivatized by two imidazole groups and four tricoordinate copper imidazole complexes.

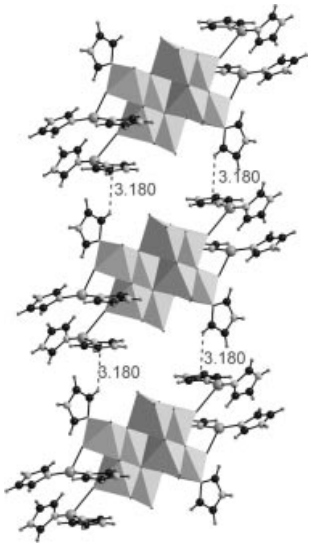


Figure 3. C–H···π interactions (Å, dotted lines) dominating the packing of the unit cell in **1**.

## Crystal Structure of 2

The crystal structure of $(Himi)_2[\{Cu^{II}(imi)_2\}_2Mo_8O_{27}]$ (**2**) consists of imidazolium cations and infinite $\{Mo_8O_{27}\}_\infty$ chains connected to square-pyramidal copper complexes (Figure 4). The $\{Mo_8O_{27}\}_\infty$ chain propagates along the *a*-axis and is surrounded by six others (see Figure S2 in the Supporting Information). The inter-chain regions are filled with imidazolium cations that participate extensively in strong hydrogen bonding with the cluster oxygens. An interesting feature observed in the crystal structure is the strong π···π interaction between the imidazole groups coordinated to the copper atoms of two adjacent chains (Figure 5). The Mo–O distances are significantly different due to their multiple bonding character and range from 1.687(3) to 2.504

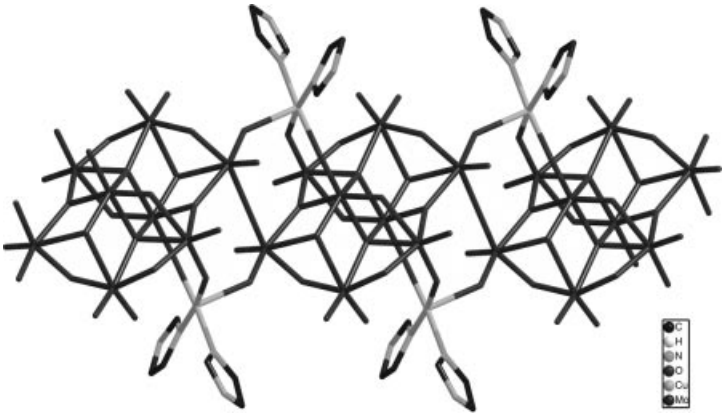


Figure 4. Anionic molybdenum oxide chains $\{Mo_8O_{27}\}^{6-}$ built from the octamolybdate clusters of type **B** sharing corners and also coordinated to square-pyramidal copper complexes in **2**.

 © 2007 Wiley-VCH Verlag GmbH & Co. KGaA, Weinheim 

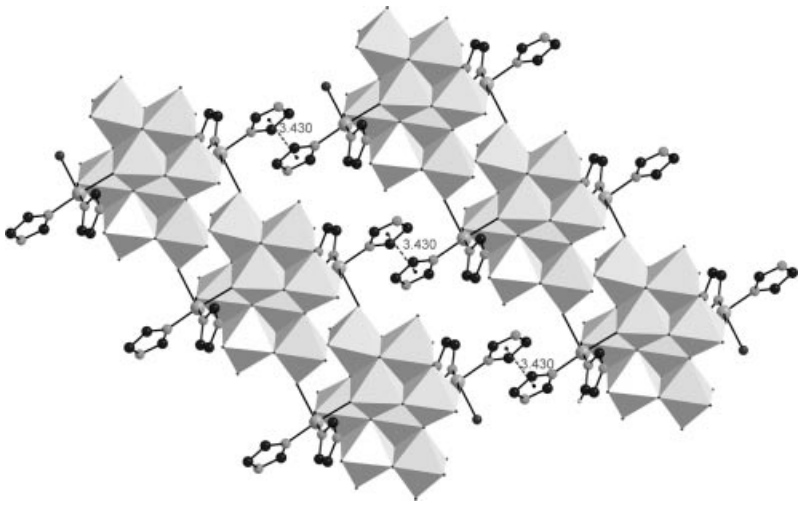


Figure 5. Strong π···π interactions (Å, dotted lines) between copper-coordinated imidazole groups of two adjacent chains in **2**.

(3) Å; the Cu–O distances range from 2.134 to 2.315 Å. A sixth Cu–O distance is 2.705 Å. The octamolybdate chains found in **2** are similar to those of $(NH_4)_6Mo_8O_{27}\cdot 4H_2O$[41] and $(C_4H_{12}N_2)_3Mo_8O_{27}$,[42] which are built from type **B** clusters, but with different counter cations such as ammonium or protonated amines. A similar metal coordination to the molybdate chain has been found previously in the case of rare-earth metals like samarium[43] and europium.[44] However, this is the first example of a transition metal organic complex coordinating with the chain. The structure is also special as the same organic group occurs as the counter cation as well as a coordinating unit during self-assembly.

### Crystal Structure of 3

The single-crystal analysis of $[\{Co^{II}(pz)_4\}_2(pz)_2Mo_8O_{26}]$ (**3**) shows the presence of octamolybdate (type **B**) derivatized by two pyrazole moieties and covalently bonded to the four cobalt pyrazole square-planar complexes (see Figure S3 in the Supporting Information). Each cobalt complex in this structure is covalently linked to two octamolybdate cores by a singly bridging oxo ligand. The $Co^{II}$ sites exhibit octahedral geometry $\{CoN_4O_2\}$ in such a way that each cobalt ion is coordinated to four nitrogen donors of pyrazole in the basal plane and two bridging oxo groups of the octamolybdate clusters at the apical position, thereby forming the 2D network shown in Figure 6. Linkage of cobalt complexes through molybdate clusters has rarely been reported in the literature, and this is the first example where a cobalt complex is covalently linking the derivatized octamolybdate. There are two other examples where cobalt complexes are linked to the β-octamolybdate cluster anion $[Mo_8O_{26}]$ (type **A** in Figure 1a).[24] This structure is a unique example where the derivatized $[Mo_8O_{28}]^{[8]-}$ is covalently linked to metal complexes to extend it into a 2D network.

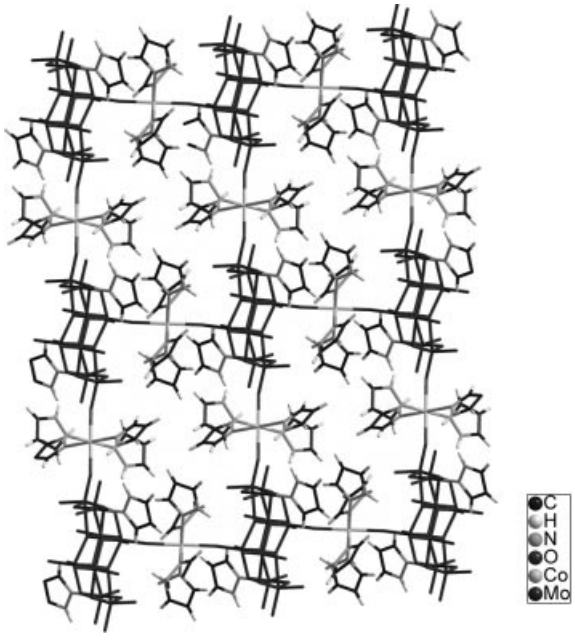


Figure 6. Pyrazole-derivatized octamolybdate cluster **B** linked through square-planar cobalt pyrazole complexes forming 2D sheets in **3**.

### Crystal Structure of 4

Solid $[\{Cu^{II}(pz)_4\}_2Mo_8O_{26}]\cdot 2H_2O$ (**4**) contains β-octamolybdate clusters (type **A**) that are covalently linked to four square-planar $\{Cu(pz)_4\}^{2+}$ complexes to form 2D sheets with isolated water molecules (Figure 7). The $\{Mo_8O_{26}\}^{4-}$ cluster unit is identical to the well-documented β form, with eight edge-sharing $MoO_6$ octahedra where all molybdenum atoms are in the +6 oxidation state. Each copper complex in this structure is covalently linked to two octamolybdate cores by a singly bridging oxo ligand (see Figure S4 in the Supporting Information). The $Cu^{II}$ sites exhibit an octahedral geometry $\{CuN_4O_2\}$ such that each copper center is

 © 2007 Wiley-VCH Verlag GmbH & Co. KGaA, Weinheim 

coordinated to four nitrogen donors of pyrazole in the basal plane and two bridging oxo groups of the octamolybdate clusters at the apical positions, thus extending it into a 2D network. A number of structures where octamolybdate clusters are covalently bonded to $\{M(ligand)\}^{n+}$ complexes have been described previously,[24–26] although the framework in **4** is unique. There are a few other solids based on β-octamolybdate clusters covalently linked through copper. In $[\{Cu(2,2'\text{-bipy})_2\}_2Mo_8O_{26}]$,[45] the β-octamolybdate cluster is linked to two square-pyramidal copper bipyridyl complexes and occurs as a supramolecular entity. In $[\{Cu_2(C_8H_6N_2)_2(C_7H_6N_2)\}_2Mo_8O_{26}]$,[46] the copper complex with two bidentate ligands links β-octamolybdate clusters into 1D chains. On the other hand, in $[\{Cu(o\text{-phen})_2\}_2Mo_8O_{26}]$ and $[\{Cu(en)_2\}_2Mo_8O_{26}]$, octamolybdate clusters are reported to adopt the α and γ forms, respectively.[47]

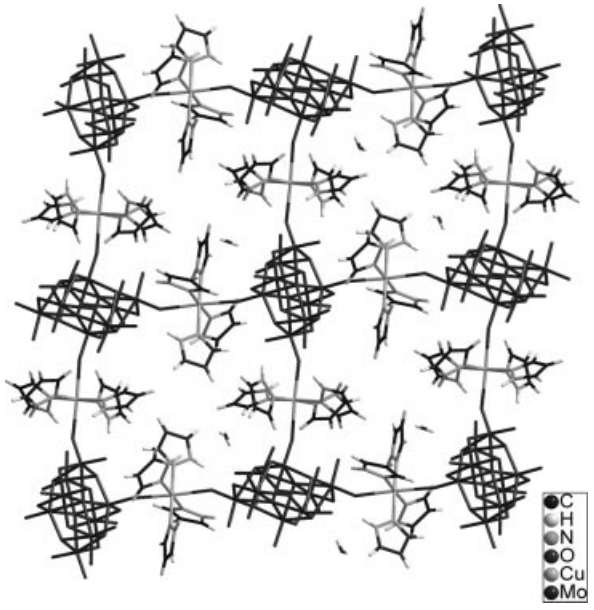


Figure 7. The 2D network observed in **4** involving the linkage of the octamolybdate anion $[Mo_8O_{26}]$ (type **A**) to square-planar copper pyrazole complexes.

### Chemistry of Formation of Hybrid Solids Based on Octamolybdate Anions

The cobalt or copper salts and the amines used as templates in this work were employed under identical reaction conditions (in terms of molybdate precursor, concentration, volume of the solution, molar ratios of the reacting species) to examine the nature of the molybdates formed. The selected amines act as good complexing agents and are stable under hydrothermal conditions. In addition, they have similar $pK_b$ values and therefore do not affect the pH of the reaction medium considerably. We also varied the tempera-

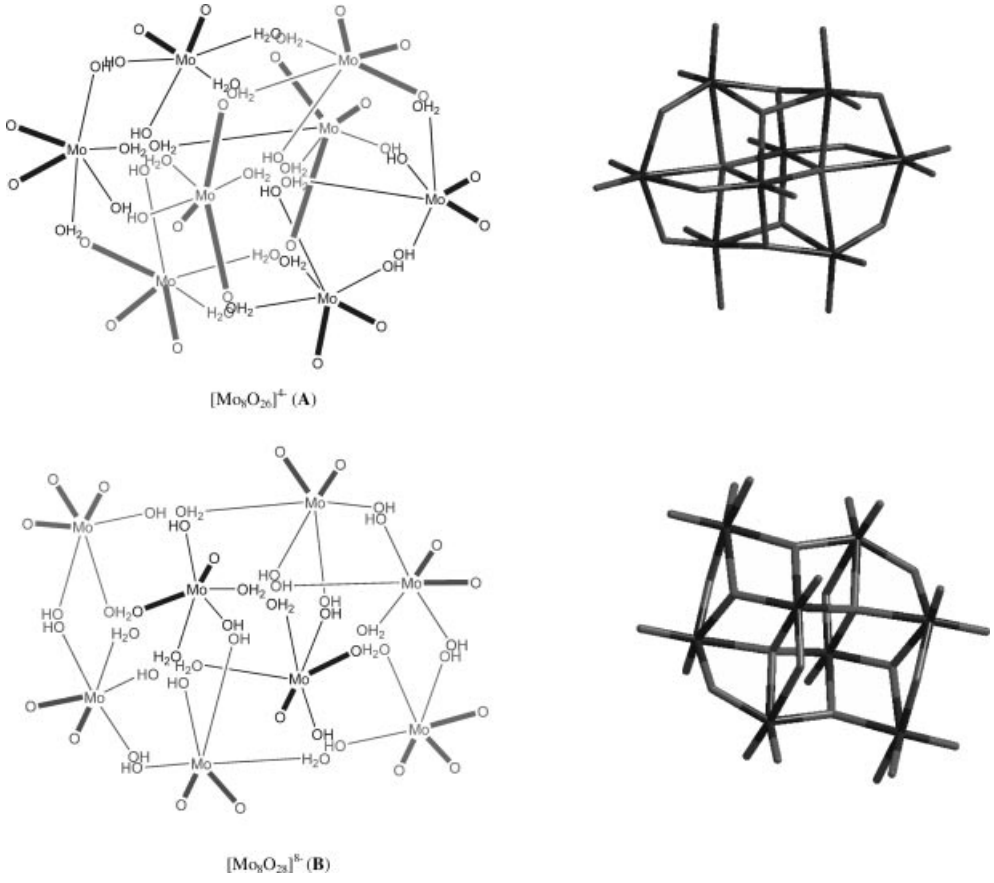


Scheme 2. A hypothetical scheme for the self-assembly of octamolybdate cluster anions **A** and **B** from the condensation of neutral molybdenum precursors.

 © 2007 Wiley-VCH Verlag GmbH & Co. KGaA, Weinheim 

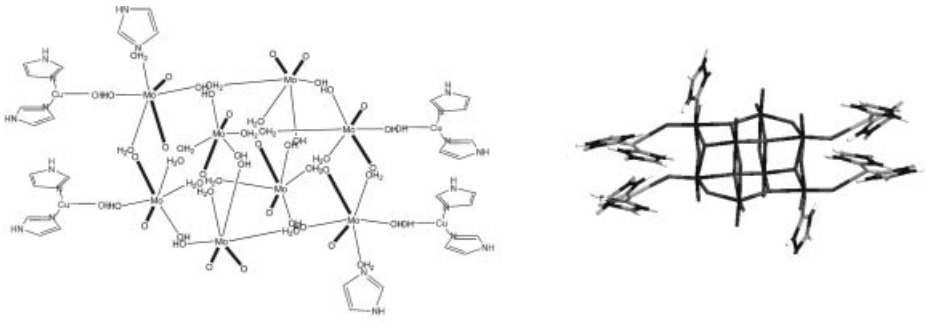

Molecular assembly leading to discrete neutral clusters based on **B** in $[\{Cu(imi)_2\}_4(imi)_2Mo_8O_{26}]\cdot 4H_2O$, **1**

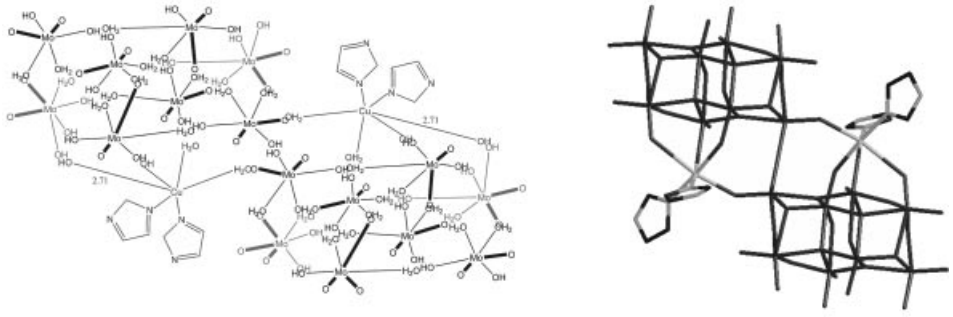

Molecular assembly leading to anionic 1D chains in $[\{Cu(imi)_2\}_2Mo_8O_{27}]^{2-}$, **2.** The counter cations (*Himi*) are not shown.

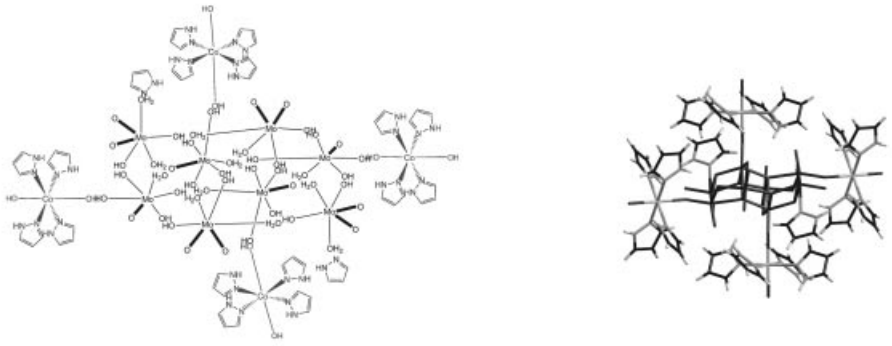

Molecular assembly leading to neutral 2D sheets based on **B** in $[\{Co(pz)_4\}_2(pz)_2Mo_8O_{26}]$. **3**

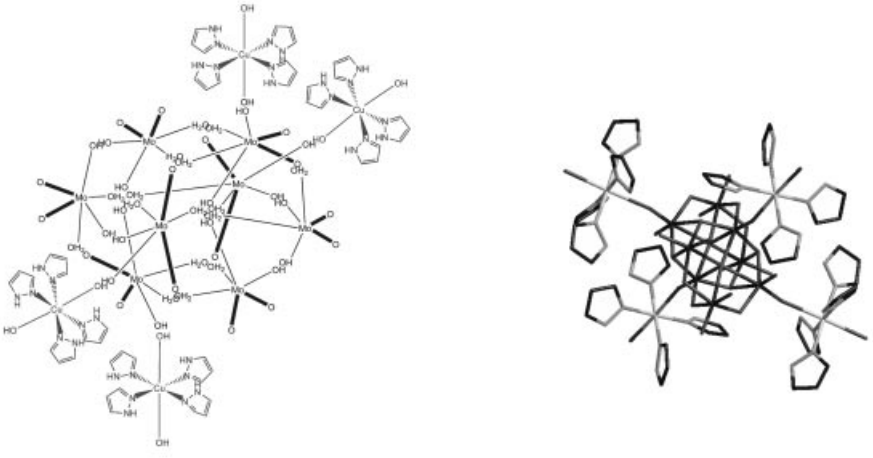

Molecular assembly leading to neutral 2D sheets based on **A** in $[\{Cu(pz)_4\}_2Mo_8O_{26}].2H_2O$, **4**

Scheme 3. A hypothetical scheme for the self-assembly of compounds **1**–**4** from the molecular precursors.

 © 2007 Wiley-VCH Verlag GmbH & Co. KGaA, Weinheim 

ture (and indirectly the autogenous pressure) to understand its effect on the nature of the products formed. When the heptamolybdate cluster anion is dissolved in aqueous solution in the presence of an organic diamine (pz or imi) and a cobalt or copper salt, a number of cluster anions, including $[Mo_8O_{26}]^{4-}$ (**A**) or $[H_xMo_8O_{28}]^{-(8-x)}$ (**B**), self-assemble due to hydrolysis and condensation of neutral and/or anionic molybdenum precursors, the assembly of which depends on the pH, ionic strength, and polarity of the medium. An examination of the literature shows that **A** is the dominant cluster found in several solids crystallized from acidified aqueous molybdate solution. However, in the majority of these solids **A** occurs as a discrete unit, whereas **B** occurs as a discrete protonated cluster in only one example[27] as it invariably gets derivatized by the organic group or condensed to form a 1D chain through three kinds of linkages, i.e. sharing edges, corners and pair –M–O–M– bridges,[20] or links through metal complexes to form 2D sheets (see Figure S5 in the Supporting Information). This is probably due to the large negative charge present on the anion **B**. Crystallization of **1**–**3** as well our previous report suggests that cluster **B** can also act as a building block to form multidimensional structures under favorable conditions. One can interpret the formation of **1**–**3** based on the complexing strength of the ligand and their lability with hydroxy groups in aqueous solution. In our earlier work, we also observed that in the presence of a better leaving group, such as 2-aminopyridine, cobalt yielded a heptamolybdate while copper yielded Lindgrenite-type copper molybdate as both cobalt and copper complex weakly with 2-aminopyridine.[20] In the presence of imi, copper forms a bis complex by *cis* addition. This prefers to derivatize cluster **B** and form the supramolecular assembly in **1** (Figure 2). In contrast, the reaction in the presence of pz leads to the formation of the square-planar complex $\{Cu(pz)_4\}^{2+}$, which crystallizes with the counter anion **A** to yield the solid **4**. On the other hand, the reaction of imi with cobalt yields only a powder that could not be structurally characterized. Reaction of cobalt with pz forms the complex $\{Co(pz)_4\}^{2+}$, which coordinates with **B** and crystallizes as **3**. We also note that the heteroatom of the organic moiety plays two roles: it provides a coordination linkage and acts as a charge compensator if necessary. The temperature does not affect the product if the metal complexes formed are stable in the presence of the organic amine (**3** and **4**). Imidazole is a better reducing agent than pyrazole, and hence $[Cu(H_2O)_4(imi)_2]^{2+}$ is readily reduced at higher temperature to form $[Cu(H_2O)(imi)_2]^{+}$, which derivatises **B** to form **1**.

Ramanan and Whittingham[33] have recently postulated a hypothetical mechanism for the formation of metal organic polymers from soluble molecular species. Pavani et al. have extended this approach to rationalize the formation of cop-

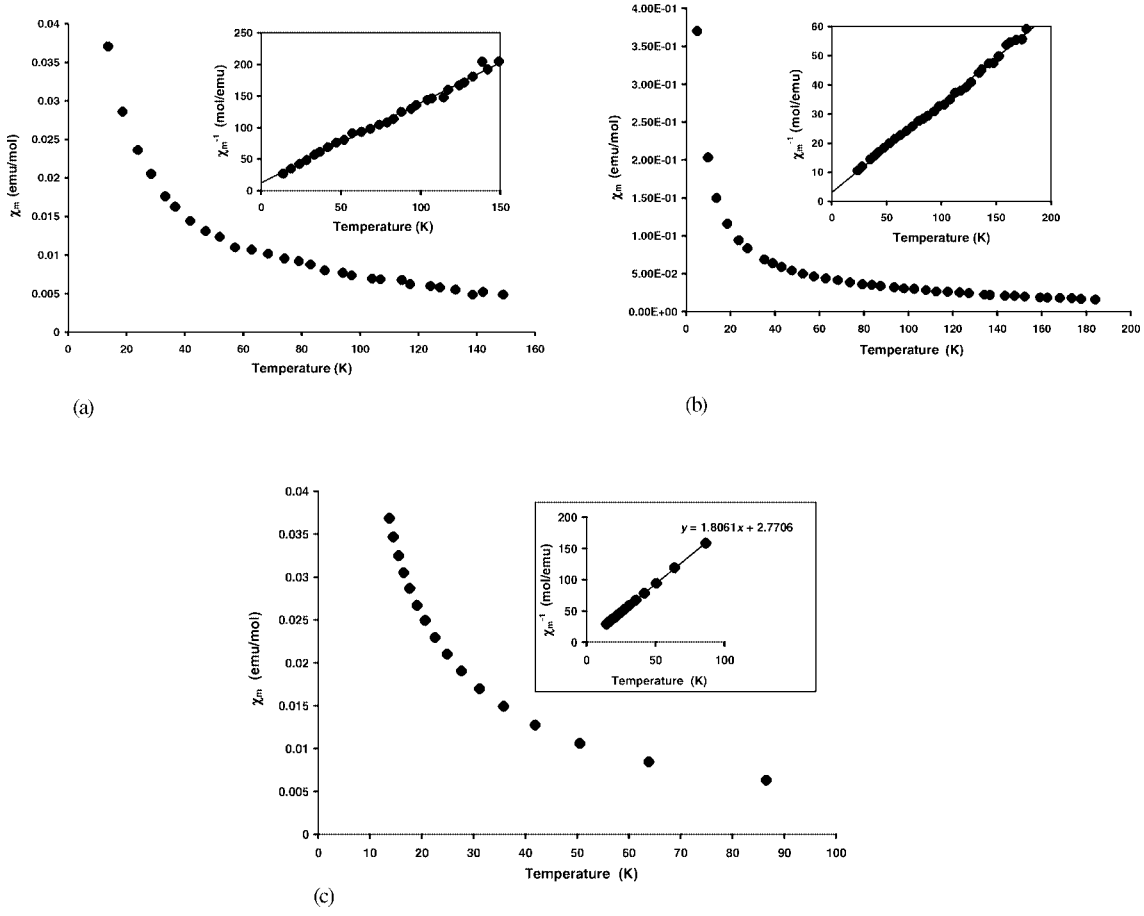


Figure 8. $\chi_m$ and $\chi_m^{-1}$ (insets) vs. *T* plots for (a) **2**, (b) **3**, and (c) **4**.

 © 2007 Wiley-VCH Verlag GmbH & Co. KGaA, Weinheim 

per coordination polymers based on molybdates under hydrothermal conditions.[34] Here, we have employed a similar strategy to understand the self-assembly of octamolybdate complexes that incorporate a copper/cobalt amine complex and/or the amine. Scheme 2 shows the proposed formation of the two cluster anions **A** and **B** from the condensation (dehydration) of monomeric molybdenum precursors. While **A** is built from two precursors, one neutral and another anionic, **B** forms from three types of molybdenum precursors. The formation of hybrid salts based on **A** can be visualized in terms of supramolecular aggregation of ion pairs formed between a molybdenum anionic precursor and organic cation along with a neutral molybdenum precursor. The presence of a large negative charge on **B** makes it unstable and the supramolecular aggregation is redefined to yield extended molybdate chains through edge-shared, pairs of vertex-shared, or vertex-shared clusters with K, $NH_4$, 2-ampy, picolinium, hexylammonium, etc. cations (as shown in Scheme S1 in the Supporting Information). However, when the solutions contain metal amine complexes and uncomplexed amines different supramolecular assemblies occur. In Scheme 3 we have proposed a plausible model to account for the formation of **1**–**4**.

### Magnetic Properties

The presence of $Cu^{II}(d^9)$ in **2**, **4** and $Cu^{II}(d^7)$ in **3** prompted us to carry out a magnetic study of these materials. The vast structural diversity of polyoxomolybdates and their ability to incorporate a large number of 3d metal cations opens synthetic routes to new magnetic molecules in which a diamagnetic molybdate framework acts as an efficient mediator of magnetic superexchange. The thermal variations of $\chi_m$ and $\chi_m^{-1}$ in the temperature range 5–160 K for **2**, **3**, and **4** are shown in Figure 8. The molar magnetic susceptibility was corrected for the diamagnetic corrections of the core electrons of the ions and functional groups. The linear portions of the plots were fitted to the Curie–Weiss relation given below, where $\theta$ is the Weiss constant and $C$ is the Curie constant. The Weiss constants are –10, –10, and –1.5 K for **2**, **3**, and **4** respectively.

$$\chi_m = C/(T - \theta)$$

The negative values of the Weiss constant indicate that the precursor exchange interactions are dominantly antiferromagnetic, although no long-range ordering was observed down to 5 K in these samples. As already mentioned, the structures consist of copper complexes that are well separated by the diamagnetic octamolybdate cluster units $\{Mo_8O_{28}\}^{8-}$ and $\{Mo_8O_{26}\}^{4-}$. The exchange correlations can be attributed to the superexchange couplings between the copper(II) or cobalt(II) ions. The effective magnetic moments calculated for **2**, **3**, and **4** are 2.51, 5.10, and 2.22, respectively, per formula unit and are consistent with divalent copper and cobalt ions.

## Conclusions

In conclusion, our results suggest that hybrid molybdates can be crystallized in the presence of cobalt or copper pyrazole (or imidazole) complexes as templates. A pH value of about 6 is crucial for the formation of octamolybdate anion as well as for the stability of the metal complex. At this stage, predicting the exact nature of the metal complex and the type of octamolybdate anion (**A** or **B**) formed in a particular solid is difficult to rationalize. Reduction of the copper complex under hydrothermal conditions is apparent. However, it is almost impossible to determine beforehand whether a metal complex or organic moiety will act as a counter cation or derivatize the anion during crystallization. In this context, our proposal of hypothetical mechanisms for the occurrence of various hybrid crystals not only underlines the role of molecular recognition but also simplifies the crystal structure in terms of molecular bricks. The present work demonstrates how condensation of $[Mo_8O_{28}]$ cluster anions into 1D chains or 2D sheets is facilitated by hydrothermal conditions. We strongly believe that recognition of such molecular building blocks will allow us to rationalize the synthetic protocols to be employed for the design of such solids.

## Experimental Section

**Materials and Methods:** All the starting materials were reagent grade and were used as purchased. The IR spectra were recorded with a Nicolet 5DX spectrophotometer with pressed KBr pellets. TG analyses were carried out with a Perkin–Elmer TGA7 and DTA7 system on well ground samples under flowing nitrogen with a heating rate of 10 °C min$^{-1}$. Room-temperature X-ray powder diffraction data were collected with a Bruker D8 Advance diffractometer using Ni-filtered Cu-$K_\alpha$ radiation. Data were collected with a step size of 0.02° and a count time of 2 s per step over the range $2° < 2\theta < 60°$. The susceptibility measurements as a function of temperature were performed with a SQUID magnetometer. Diamagnetic corrections were estimated from Pascal's constants.

**Synthesis:** A mixture of $(NH_4)_6Mo_7O_{24}{\cdot}4H_2O$ (0.7724 g, 0.625 mmol), $CuCl_2{\cdot}2H_2O$ (0.8524 g, 5 mmol), imidazole (imi; 0.5106 g, 7.5 mmol) and water (18 mL) was sealed in a Teflon-lined stainless-steel reactor and heated at various temperatures between 120 and 180 °C for three days. After the reaction, the system was slowly cooled down to room temperature. To rationalize the effect of the organic component as well as the metal ion, reactions with similar molar compositions were also carried out with pyrazole (pz) instead of imidazole and cobalt chloride instead of copper chloride. The reaction mixtures containing copper chloride and imidazole yielded two phases **1** (68% yield based on Mo) and **2** (71% yield based on Mo) at 150 and 120 °C, respectively, but the reaction between copper and pyrazole yielded **4** (84% yield based on Mo) at all temperatures between 120 and 180 °C. While the reaction mixture containing pyrazole and cobalt salt yielded **3** (87% yield based on Mo), the reaction between imidazole and cobalt resulted in a powder that could not be structurally characterized due to lack of suitable single crystals.

**Crystallographic Studies:** Single-crystal diffraction studies were carried out with a Bruker AXS SMART Apex CCD diffractometer

 © 2007 Wiley-VCH Verlag GmbH & Co. KGaA, Weinheim 

fitted with a Mo-$K_\alpha$ (0.71073 Å) radiation source at 28 °C for **1**–**4**. The software SADABS was used for absorption correction and SHELXTL for space group and structure determination and refinements.[48,49] The molybdenum atoms were located first and then remaining atoms were deduced from subsequent difference Fourier syntheses. The hydrogen atoms were located using geometrical constraints. All the atoms except H were refined anisotropically. The least-squares refinement cycles on $F^2$ were performed until the model converged. Experimental conditions and crystal data are provided in Tables 1 and 2, respectively.

Table 1. Experimental details.

| Reactants/molar ratio | Phase | Color | Temperature (°C) | pH Initial[a] | Final[b] |
|---|---|---|---|---|---|
| $(NH_4)_6Mo_7O_{24}{\cdot}4H_2O$ + $CuCl_2{\cdot}2H_2O$ + imidazole + $H_2O$/18:12:1600 | $[\{Cu(imi)_2\}_4(imi)_2Mo_8O_{26}]{\cdot}4H_2O$ (**1**) | brown | 150 | ≈6 | ≈6 |
| $(NH_4)_6Mo_7O_{24}{\cdot}4H_2O$ + $CuCl_2{\cdot}2H_2O$ + imidazole + $H_2O$/1:8:12:1600 | $(Himi)_2[\{Cu(imi)_2\}_2Mo_8O_{27}]$ (**2**) | green | 120 | ≈6 | ≈6 |
| $(NH_4)_6Mo_7O_{24}{\cdot}4H_2O$ + $CoCl_2{\cdot}6H_2O$ + imidazole + $H_2O$/1:8:12:1600 | Crystalline powder with no known phases. No suitable single crystals. | violet | 120–180 | ≈6 | ≈6 |
| $(NH_4)_6Mo_7O_{24}{\cdot}4H_2O$ + $CoCl_2{\cdot}6H_2O$ + pyrazole + $H_2O$/1:8:12:1600 | $[\{Co(pz)_4\}_2(pz)_2Mo_8O_{26}]$ (**3**) | red | 120–180 | ≈6 | ≈6 |
| $(NH_4)_6Mo_7O_{24}{\cdot}4H_2O$ + $CuCl_2{\cdot}6H_2O$ + pyrazole + $H_2O$/1:8:12:1600 | $[\{Cu(pz)_4\}_2Mo_8O_{26}]{\cdot}2H_2O$ (**4**) | blue | 120–180 | ≈6 | ≈6 |

[a] pH of the initial reaction mixture before hydrothermal treatment. [b] pH of the filtrate after the crystals or solids have been separated.

Table 2. Crystallographic details.

| | **1** | **2** | **3** | **4** |
|---|---|---|---|---|
| Crystal system | triclinic | triclinic | monoclinic | monoclinic |
| Space group | $P\bar{1}$ | $P\bar{1}$ | $P2_1/n$ | $P2_1/n$ |
| $T$ [K] | 300(2) | 300(2) | 300(2) | 300(2) |
| $a$ [Å] | 9.6867(19) | 9.429(3) | 10.6172(16) | 11.5849(8) |
| $b$ [Å] | 12.835(2) | 9.875(4) | 14.017(2) | 18.4697(13) |
| $c$ [Å] | 12.981(3) | 12.591(4) | 19.030(3) | 12.2645(9) |
| $\alpha$ [°] | 67.868(3) | 71.427(7) | 90 | 90 |
| $\beta$ [°] | 84.964(3) | 81.358(7) | 91.695(2) | 94.18(0) |
| $\gamma$ [°] | 84.943(3) | 72.474(7) | 90 | 90 |
| $V$ [Å$^3$] | 1486.6(5) | 1057.7(6) | 2831.0(7) | 2617.25(30) |
| $Z$ | 1 | 1 | 2 | 2 |
| Collected reflections | 9087 | 6541 | 16800 | 15695 |
| Unique reflections | 5982 | 4285 | 6295 | 5994 |
| Observed reflections | 4629 | 2911 | 5204 | 4941 |
| $R_1$ [$I > 2\sigma(I)$] | 0.0395 | 0.0578 | 0.0350 | 0.0381 |
| w$R_2$ (all) | 0.0754 | 0.0984 | 0.0738 | 0.0837 |

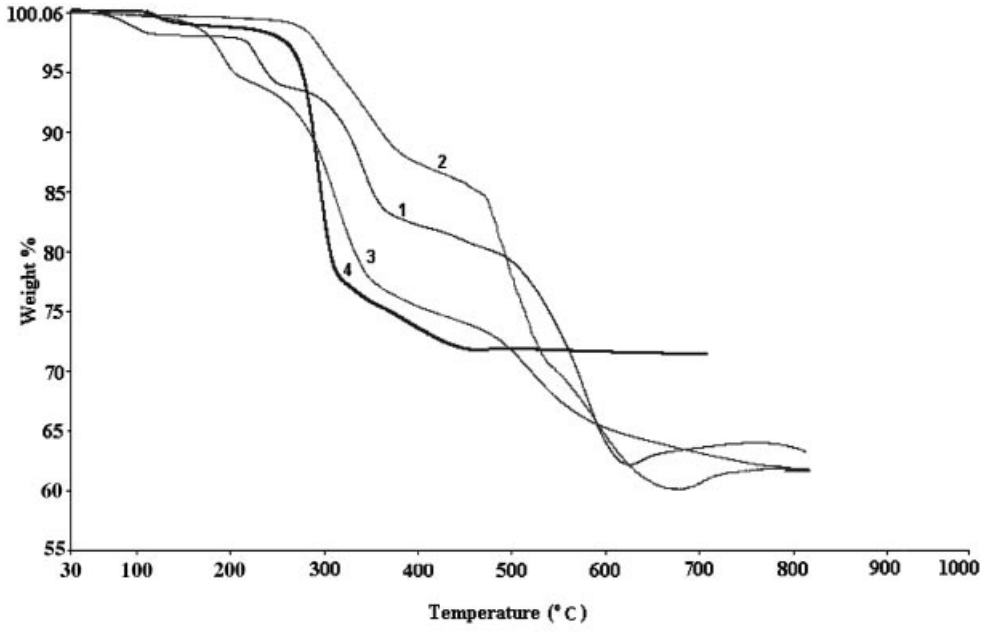


Figure 9. Thermogravimetric analysis for compounds **1**–**4**.

 © 2007 Wiley-VCH Verlag GmbH & Co. KGaA, Weinheim 

CCDC-284102 (for **1**), -284101 (for **2**), -284103 (for **3**) and -269635 (for **4**) contain the supplementary crystallographic data for this paper. These data can be obtained free of charge from The Cambridge Crystallographic Data Center via www.ccdc.cam.ac.uk/data_request/cif.

**Vibrational Spectroscopy:** In the IR spectrum of **1**, the peaks at 933, 890, 845, and 651 $cm^{-1}$ are attributed to the $\nu(Mo\text{-}O_t)$ and $\nu(Mo\text{-}O_b)$ vibrational modes of the $[Mo_8O_{28}]^{8-}$ anion. Features at 3132, 2946, 1630, 1540, 1504, 1435, 1326, 1257, and 1181 $cm^{-1}$ are characteristic absorptions of copper-coordinated imidazoles. The broad band at around 3371 $cm^{-1}$ can be ascribed to the absorption of lattice water molecules. The IR spectra of **2** and **3** are similar to **1** expect that the peak at 3371 $cm^{-1}$ is absent in the former, thus showing that there are no water molecules. The IR spectrum of **4** shows characteristic peaks at 945, 910, 849, 710, 666, and 551 $cm^{-1}$ due to β-octamolybdate; the bands at 3132, 2946, 1630, 1540, 1504, 1435, 1326, 1257, and 1181 $cm^{-1}$ are characteristic of copper-coordinated pyrazoles.

**Thermal Stability of 1–4:** The thermal dehydrations of **1**–**4** are quite different (Figure 9). All samples show a weight loss in multiple steps. For **1**, the loss of water molecules and free organic molecules and the decomposition of metal complexes occur in multiple steps. This observation clearly reflects the strength of hydrogen-bonding and other weak interactions noticed in the single crystal structure of the solids and was further confirmed by powder XRD and FTIR studies. The first two steps correspond to the loss of four water molecules and one organic group. The third and fourth steps correspond to degradation of the assembly. In **2**, the first step corresponds to the loss of two imidazole groups (≈ 200 °C) and the second step corresponds to the collapse of the structure with the loss of remaining organic groups. Complex **3** loses its organic groups in three steps. In the case of **4**, the loss of organic and water molecules was observed in the range 100–450 °C. In all cases the phase purity of the samples was further established by simulating powder X-ray diffraction patterns on the basis of the single-crystal structure data.

**Supporting Information** (see also the footnote on the first page of this article): Figures S1–S5 show additional figures for **1**–**4**, Figures S6–S9 show simulated and experimental powder X-ray diffraction patterns for **1**–**4**, and bond lengths and bond angles for **1**–**4** are given in Tables S10–S13.

## Acknowledgments

K. P. thanks the Council of Scientific and Industrial Research, Government of India (CSIR) for a research fellowship and A. R. acknowledges the Department of Science and Technology, Government of India (DST), for financial support. We thank Dr. N. G. Ramesh for helpful discussion. A. R. also thanks the DST for funding a powder X-ray diffractometer under IRHPA and a Smart Apex CCD single-crystal X-ray diffractometer under FIST to the Department of Chemistry at IIT, Delhi. A. R. thanks Professor M. S. Whittingham for his support and encouragement during his sabbatical leave. S. E. L. acknowledges support from National Science Foundation and Materials Research Science and Engineering Centres (NSF MRSEC) DMR 0520471 and DMR 0603644.

[1] A. Müller, P. Kogerler, *Coord. Chem. Rev.* **1999**, *182*, 3–17.
[2] A. Müller, S. Roy, *Coord. Chem. Rev.* **2003**, *245*, 153–166.
[3] R. K. Grasselli, *Catal. Today* **1999**, *49*, 141–153.
[4] P. Kogerler, A. Müller, *J. Appl. Phys.* **2003**, *93*, 7101–7102.
[5] S. S. Kim, S. Ogura, H. Ikuta, Y. Uchimoto, M. Wakihara, *Solid State Ionics* **2002**, *146*, 249–256.
[6] Y. Song, P. Zhang, X. M. Ren, X. F. Shen, Y. Z. Li, X. Z. You, *J. Am. Chem. Soc.* **2005**, *127*, 3708–3709.
[7] J. B. Strong, G. P. A. Yap, R. Ostrander, L. M. L. Sands, A. L. Rheingold, R. Thouvenot, P. Gouzerh, E. A. Maatta, *J. Am. Chem. Soc.* **2000**, *122*, 639–649.
[8] T. Duraisamy, A. Ramanan, J. J. Vittal, *J. Mater. Chem.* **1999**, *9*, 763–767.
[9] B. Modec, J. V. Brencic, J. Zubieta, P. J. Hagrman, *Inorg. Chem. Commun.* **2001**, *4*, 537–540.
[10] P. Gili, P. A. L. Luis, A. Mederos, J. M. Arrieta, G. Germain, A. Castineiras, R. Carballo, *Inorg. Chim. Acta* **1996**, *295*, 106–114.
[11] Z. Kong, L. Weng, D. Tan, H. He, B. Zhang, J. Kong, B. Yue, *Inorg. Chem.* **2004**, *43*, 5676–5680.
[12] S. Upreti, A. Ramanan, *Inorg. Chim. Acta* **2005**, *358*, 1241–1246.
[13] B. Modec, J. V. Brencic, J. Zubieta, *Inorg. Chem. Commun.* **2003**, *6*, 506–512.
[14] N. Guillou, G. Ferey, *J. Solid State Chem.* **1997**, *132*, 224–227.
[15] C. D. Wu, C. Z. Lu, S. M. Chen, H. H. Zhang, J. S. Huang, *Polyhedron* **2003**, *22*, 3091–3095.
[16] C. Z. Lu, C. D. Wu, H. H. Zhang, J. S. Huang, *Chem. Mater.* **2002**, *14*, 2649–2655.
[17] D. Hagrman, C. Sangregorio, C. J. O'Connor, J. Zubieta, *J. Chem. Soc., Dalton Trans.* **1998**, 3707–3710.
[18] S. Upreti, A. Ramanan, *Cryst. Growth Des.* **2005**, *5*, 1837–1843; S. Upreti, A. Ramanan, *Cryst. Growth Des.* **2006**, *6*, 2066–2071.
[19] P. J. Hagrman, D. Hagrman, J. Zubieta, *Angew. Chem. Int. Ed.* **1999**, *38*, 2638–2684.
[20] K. Pavani, A. Ramanan, *Eur. J. Inorg. Chem.* **2005**, 3080 –3087.
[21] S. Randy Jr., R. S. Rarig, J. Zubieta, *J. Solid State Chem.* **2002**, *167*, 370–375.
[22] D. G. Allis, R. S. Rarig, E. Burkholder, J. Zubieta, *J. Mol. Struct.* **2004**, *688*, 11–31.
[23] S. M. Chen, C. Z. Lu, Y. Q. Yu, Q. Z. Zhang, X. He, *Inorg. Chem. Commun.* **2004**, *7*, 1041–1044.
[24] W. Yang, C. Lu, H. Zhuang, *J. Chem. Soc., Dalton Trans.* **2002**, 2879–2884.
[25] C. Z. Lu, C. D. Wu, H. H. Zhuang, J. S. Huang, *Chem. Mater.* **2002**, *14*, 2649–2655.
[26] R. S. Rarig, J. Zubieta, *Polyhedron* **2003**, *22*, 177–188.
[27] M. Isobe, F. Marumo, T. Yamase, T. Ikawa, *Acta Crystallogr., Sect. B* **1978**, *34*, 2728–2731.
[28] W. Wang, L. Xu, Y. Wei, F. Lia, G. Gao, E. Wang, *J. Solid State Chem.* **2005**, *178*, 608–612.
[29] D. Attanasio, M. Bonamico, V. Fares, L. Suber, *J. Chem. Soc., Dalton Trans.* **1992**, 2523–2528.
[30] B. M. Gatehouse, P. Leverette, *J. Chem. Soc. A* **1971**, 2107–2112.
[31] R. Benchrifa, M. Leblanc, R. de Pape, *Eur. J. Solid State Inorg. Chem.* **1989**, *26*, 593–601.
[32] J. Kang, Q. Z. Zhang, C. D. Wu, W. B. Yang, X. P. Zhan, Y. Q. Yu, C. Z. Lu, *Chin. J. Struct. Chem.* **2003**, *22*, 190–194.
[33] A. Ramanan, M. S. Whittingham, *Cryst. Growth Des.* **2006**, *6*, 2419–2421.
[34] K. Pavani, A. Ramanan, M. S. Whittingham, *J. Mol. Struct.* **2006**, *796*, 179–186.
[35] X. You, J. Chen, Z. Xu, J. Huang, *Acta Crystallogr., Sect. C* **1989**, *45*, 413–415.
[36] R. D. Adams, W. G. Klemperer, R. S. Lui, *J. Chem. Soc., Chem. Commun.* **1979**, 256–257.
[37] C. D. Wu, C. Z. Lu, H. H. Zuang, J. S. Huang, *Inorg. Chem.* **2002**, *41*, 5636–5637.
[38] J. Luo, M. Hong, R. Wang, Q. Shi, R. Cao, J. Weng, R. Sun, H. Zhang, *Inorg. Chem. Commun.* **2003**, *6*, 702–705.
[39] X. B. Cui, K. Lu, Y. Fan, J. O. Xu, L. Yeb, Y. H. Sun, Y. Li, H. H. Yu, Z. H. Yi, *J. Mol. Struct.* **2005**, *743*, 151–155.
[40] C. D. Wu, C. Z. Lu, W. B. Yang, S. F. Lu, H. H. Zhaung, J. Huang, *J. Cluster. Sci.* **2002**, *13*, 55–62.

 © 2007 Wiley-VCH Verlag GmbH & Co. KGaA, Weinheim 

[41] I. Boeschen, B. Buss, B. Krebs, *Acta Crystallogr., Sect. B* **1974**, *30*, 48–56.
[42] W. T. A. Harrison, L. L. Dussack, A. J. Jacobson, *Acta Crystallogr., Sect. C* **1996**, *52*, 1075–1077.
[43] T. Yamase, T. Ozeki, I. Kawashima, *Acta Crystallogr. Sect. C* **1995**, *51*, 545–547.
[44] T. Yamase, H. Naruke, *J. Chem. Soc., Dalton Trans.* **1991**, 285–292.
[45] D. Hagrman, P. J. Hagrman, J. Zubieta, *Comments Inorg. Chem.* **1999**, *21*, 225–261.
[46] C. D. Wu, C. Z. Lu, H. Zhuang, J. Huang, *Inorg. Chem.* **2002**, *41*, 5636–5637.
[47] J. R. D. DeBord, R. C. Haushalter, L. M. Meyer, D. J. Rose, P. J. Zapf, J. Zubieta, *Inorg. Chim. Acta* **1997**, *256*, 165–168.
[48] G. M. Sheldrick, *Acta Crystallogr., Sect. A* **1990**, *46*, 467–473.
[49] G. M. Sheldrick, SHELXTL-NT2000, version 6.12, reference manual, University of Göttingen, Germany.

Received: September 6, 2006
Published Online: December 7, 2006

 © 2007 Wiley-VCH Verlag GmbH & Co. KGaA, Weinheim 

DOI: 10.1002/ejic.200600529

# Niobium Oxide Mesophases Obtained by Self-Assembly of an Aqueous Soluble Niobium Complex Precursor and Organic Templates

**Marcos A. Bizeto[a] and Vera R. L. Constantino*[a]**

**Keywords:** Niobium / Mesophases / Organic–inorganic hybrid composites / Template synthesis / Sol–gel synthesis

In this paper the use of triammonium trioxalato(oxido)-niobate $\{(NH_4)_3[NbO(C_2O_4)_3]\}$ as an inorganic precursor to assemble organized hybrid niobium oxide mesophases using *n*-octylamine (OCT) and cetyltrimethylammonium (CTA) bromide as structure-directing agents is described for the first time. The niobium complex is water-soluble and its hydrolysis at controlled pH and in the presence of organic templates leads to the formation of hybrid mesophases. A lamellar mesophase is produced by a neutral route based on the interaction of hydrolyzed units with the octylamine micelles. On the other hand, a hexagonal (*p*6*m*) mesophase is obtained when hydrolyzed species interact with CTA micelles through a charge-matching route (ionic route). This is the first time that such an ionic route has been described for the production of organized niobium oxide hybrids.

(© Wiley-VCH Verlag GmbH & Co. KGaA, 69451 Weinheim, Germany, 2007)

## Introduction

Organic–inorganic hybrid materials obtained by soft chemistry routes are the basis for the production of hierarchical inorganic structures that are of great interest in scientific and industrial areas. The molding of an inorganic structure around templates constituted of micellar aggregates produces organized mesophases that are precursors of periodic porous materials. Upon template removal, the mesophase can be transformed into an inorganic structure full of voids with regular shapes and sizes that are useful for applications in some industrial and technological fields, such as catalysis, separations, sensing, and others.[1] The approach to tailor-made porous structures started with Mobil corporation researchers, who created a family of mesoporous silicas called M41S.[2] These materials are obtained by controlling the hydrolysis of an inorganic precursor, generally silicon alkoxides such as tetraethylorthosilicate, around surfactant micelles. Since the discovery of mesoporous silicas, much effort has been devoted to the development of new mesoporous systems based on non-silicate materials. A great deal of work has concentrated on the synthesis of transition metal mesoporous oxides due to the possibility of these metal centers participating in chemical reactions. However, these materials are difficult to synthesize due to their tendency to crystallize and undergo chemical reactions that lead to mesostructure collapse.[3] The critical step of the process is the mesostructure formation as it is necessary to provide experimental conditions where the interaction between the inorganic species and organic template is established at the interface and is strong enough to promote the self-assembly of the moieties. There are different ways for these interactions to occur. The simplest one happens when the inorganic and organic moieties have opposite charges under the synthesis condition,[4] known as the "ionic route". The interaction can also take place by H-bonding or dipolar forces − the "neutral route".[5] A third possibility is exclusive for some transition metals where interaction can occur by coordination of a structure-directing agent to the metal center, leading to the so-called "ligand-assisted crystal templating".[6] One of the first successful examples of a stable mesoporous structure based on a transition metal oxide was mesoporous niobium oxide.[6] Ordered porous niobium oxide phases have been obtained by synthetic procedures where inorganic precursors, such as niobium alkoxides or chlorides, are used together with neutral structure-directing agents based on alkylamines or non-ionic surfactant micelles.[6,7] Mesoporous niobium oxides present interesting properties that can be used in many technological applications. The confinement of species into their pores, such as fullerides,[8] metallocenes,[9] or biomolecules,[10] produces materials with interesting electronic, magnetic, catalytic, and sensing properties. Taking these properties into account, the development of simple synthetic routes employing cheap and easy to handle reactants is an important issue to be resolved. The inorganic precursors normally used for this purpose are expensive, not easy to synthesize, and require controlled humidity conditions to be manipulated.

The niobium compound $(NH_4)_3[NbO(C_2O_4)_3]\cdot 3H_2O$ (Figure 1) has some interesting chemical properties that are useful not only for the assembly of mesoporous solid pre-

[a] Instituto de Química, Universidade de São Paulo,
C. P. 26077, CEP 05513-970, São Paulo – SP, Brazil
Fax: +55-11-3815-5579
E-mail: vrlconst@iq.usp.br

 © 2007 Wiley-VCH Verlag GmbH & Co. KGaA, Weinheim 

cursors (mesophases) but also in sol–gel-like soft-chemical routes. First of all triammonium trioxalato(oxido)niobate is water-soluble and stable in acid solution. Secondly, the niobium oxalate moiety has a negative charge and labile water molecules in the niobium coordination sphere when the aqueous equilibrium with the two oxalato ligands is considered.[11] These properties make this compound suitable for self-assembly with organic species by coordination and electrostatic interactions. The third and most important point is that triammonium trioxalato(oxido)niobate can be synthesized directly from niobium oxide by simple chemical procedures,[12,13] which means that the starting material can be easily recycled. Considering the possible interaction modes of trioxalato(oxido)niobate with organic moieties, in this paper we describe the use of a cationic surfactant and a long carbon chain amine as structure-directing agents for the generation of niobium oxide mesophases that might be further converted into mesoporous phases by template removal. A previous attempt at using a water-soluble niobium precursor derived from niobium pentoxide was not successful in a similar process.[6b]

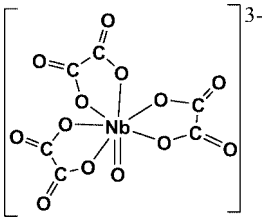


Figure 1. Chemical structure of $[NbO(C_2O_4)_3]^{3-}$.

## Results and Discussion

Triammonium trioxalato(oxido)niobate is soluble in water and is in equilibrium[11] with dioxalate species in solution, according to the chemical equation below.

$$[NbO(C_2O_4)_3]^{3-} + 2\ H_2O \rightleftharpoons [NbO(C_2O_4)_2(H_2O)_2]^{-} + C_2O_4^{2-}$$

Both species in equilibrium have a heptacoordinate niobium atom.[14] The initial pH of an aqueous solution of the compound is very acid due to partial hydrolysis of the compound. Upon increasing the pH to near 4 with a hydroxide solution, the niobium oxalate hydrolysis reaction is favored and leads to the formation of a hydrated amorphous niobium oxide bulk phase.[11] Figure 2 shows the typical sodium hydroxide titration curve of an aqueous triammonium trioxalato(oxido)niobate solution. According to this curve, trioxalato(oxido)niobate hydrolysis occurs in the pH range 4.2–5.8. Thus, it is possible to modulate the interaction of the oxide phase with structure-directing agents by controlling the hydrolysis process by adjusting the amount of base added.

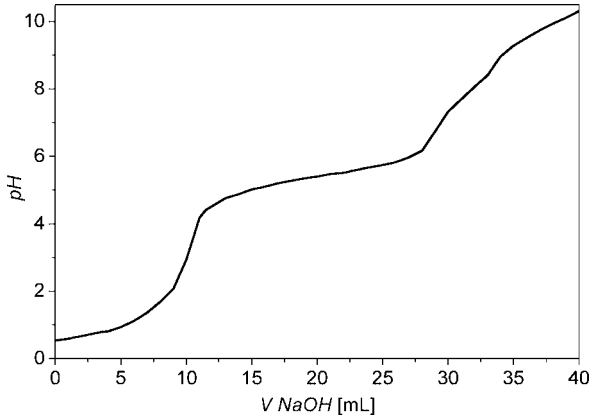


Figure 2. Titration curve of an aqueous solution of triammonium trioxalato(oxido)niobate (0.2 M) with a 3 M NaOH solution.

The crystal structure of triammonium trioxalato(oxido)-niobate belongs to the triclinic crystal system with the niobium atom heptacoordinate in a pentagonal-bipyramidal arrangement.[13] The high crystallinity of the solid can be seen in the powder XRD pattern shown in Figure 3. The solid isolated at a pH of around 5.5 is amorphous (Figure 3), while the solid isolated at higher pH (excess of base) is crystalline with a diffraction pattern very different from the pristine material (Figure 3). It is possible to produce an organized mesophase characterized by an amorphous inorganic framework with a regular repetition of voids filled with template micelles by performing the hydrolysis in the presence of a structure-directing agent. This synthetic approach was tested using cetyltrimethylammonium (CTA) bromide and *n*-octylamine (OCT) as structure-directing agents.

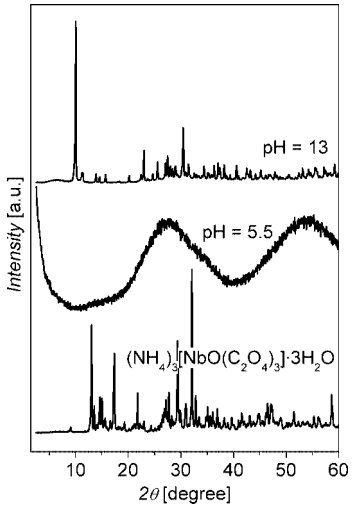


Figure 3. XRD patterns of triammonium trioxalato(oxido)niobate and its hydrolysis products isolated at different pH values.

CTA is a common template used in the synthesis of mesoporous silica, such as MCM-41, by a charge-matching ionic route. However, for niobium oxide hybrid mesostructures, only neutral routes with non-ionic surfactants have been performed until now. As can be seen in Figure 4, hy-

 © 2007 Wiley-VCH Verlag GmbH & Co. KGaA, Weinheim 

drolysis of the trioxalato(oxido)niobate in the presence of the CTA template produces a hexagonally packed mesostructure. The XRD pattern of this phase shows reflection peaks at low angles related to the long-range order of the assembled hybrid material (Figure 4). Two types of hexagonal phases are known for silica-based systems: 2D hexagonal *p6m* (MCM-41) and 3D $P6_3/mmc$ (SBA).[15] The diffraction peak distances in Figure 4 are in a ratio close to 1:3, which can be attributed to a *p6m* hexagonal phase. The diffraction pattern also indicates that the assembled hybrid structure is not highly ordered. Hexagonal phases with regular parallel channels filled with the template provide intense diffraction patterns with many peak orders.[16] In the case of the synthesized CTA/niobium oxide phase, however, only two diffraction peaks are observed in the low-angle region, which suggests a non-fully parallel channel architecture. According to the diffraction data, the most organized mesophases are generated when an Nb/CTA molar ratio of 1:1 is used. The $d_{100}$ distance related to the first-order peak of the hexagonal mesophases has a mean value of 42.5 Å, while the mean $d_{110}$ value is 23.3 Å.

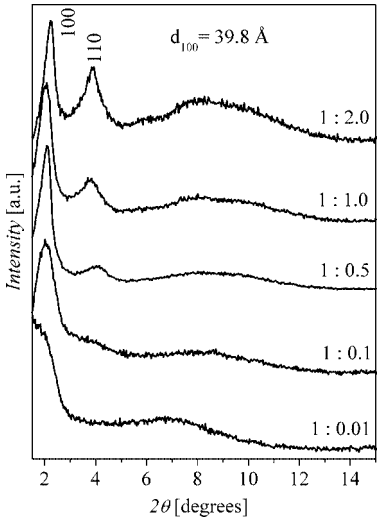


Figure 4. XRD patterns of the as-synthesized niobium oxide mesophase with CTA template at different Nb/CTA molar ratios.

The partial disorder of the porous architecture was confirmed by TEM (Figure 5). In the micrograph shown in Figure 5a, it is possible to observe that pores (elongation aligned parallel to the observer's view) are irregularly distributed along the material, like a wormhole pattern. In Figure 5b, the pores' elongation is parallel to the grid plane and some domains with well-ordered porous organization can be observed.

In the neutral-route synthesis the CTA template was replaced by *n*-octylamine (OCT), which resulted in a mesophase with a lamellar arrangement for Nb/OCT molar ratios above 1:0.5 (Figure 6). As can be seen from the XRD patterns in Figure 6, the distances of the diffraction peaks have a ratio of 1:2:3, which corresponds to a lamellar mesophase ($d_{001} \approx 24.5$, $d_{002} \approx 12.1$, and $d_{003} \approx 8.2$ Å). The TEM micrographs (Figure 7) also reveal a well-organized lamellar mesophase.

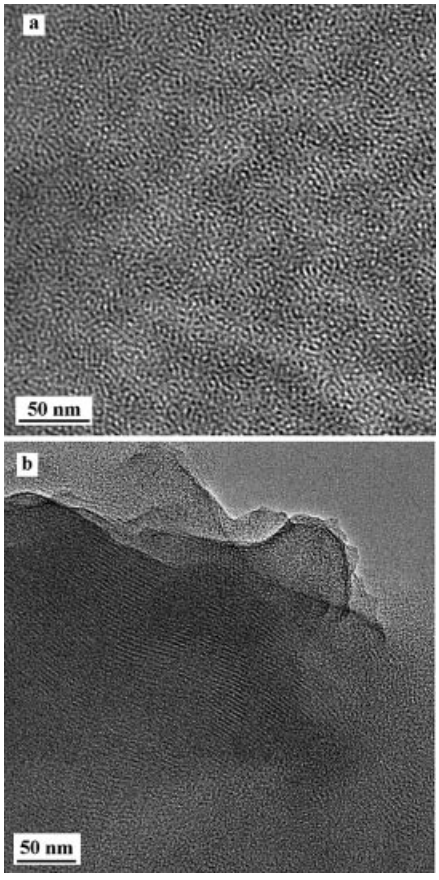


Figure 5. TEM images of the as-synthesized niobium oxide mesostructure (Nb/CTA molar ratio of 1:1): (a) porous elongation parallel to the view; (b) porous elongation perpendicular to the view.

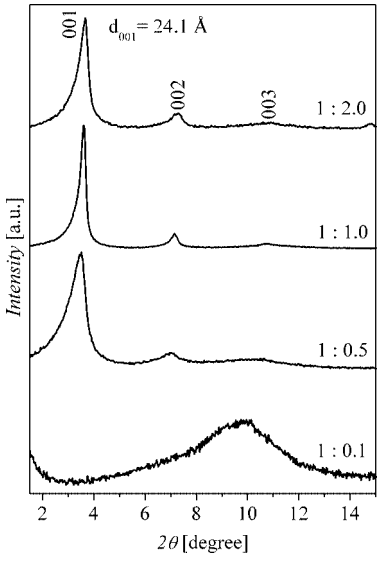


Figure 6. XRD patterns of the as-synthesized niobium oxide mesophase with *n*-octylamine as template at different Nb/OCT molar ratios.

To generate a mesoporous niobium oxide it is necessary to remove the template from the material to produce empty voids with regular shape and size along the mesostructure.

 © 2007 Wiley-VCH Verlag GmbH & Co. KGaA, Weinheim 

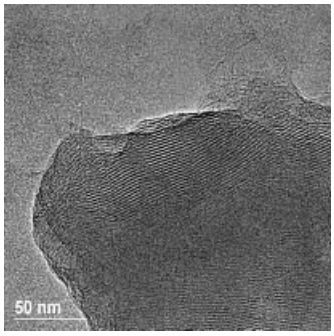


Figure 7. TEM image of the as-synthesized niobium oxide mesostructure (Nb/OCT molar ratio of 1:1).

This procedure is not possible in lamellar mesophases since the mesoporous phase is not stable after template removal due to the absence of species that keep the inorganic slabs apart. The collapse of lamellar mesostructures has already been observed in niobium oxide[6b] and silica MCM-50[17] phases.

The first attempt at CTA removal was made by solvent extraction, but due to the strong interaction between inorganic and organic moieties in the charge-matching mechanism of mesophase formation this solvent-template extraction was not an efficient process. Therefore, calcination of the hexagonal mesophase was performed based on thermogravimetric data obtained in air. According to thermogravimetric analysis (not shown), the complete removal of CTA occurs above 600 °C. The thermal stability of the generated mesoporous phase is closely related to the Tammann temperature of the respective oxide structure, which for $Nb_2O_5$ is 892 K (ca. 620 °C).[18] In the vicinity of the Tammann temperature the mobility of the atoms in the oxide structure increases significantly, thereby favoring the mesostructure collapse. Thus, the temperature requirement for complete template elimination is close to the Tammann temperature of niobium oxide, which makes calcination an unsuitable process for template removal in this case. In fact, when the mesophase calcination was performed at 600 °C we observed mesostructure collapse and production of an orthorhombic crystalline niobium oxide phase. The amorphous niobium oxide phase turns into a crystalline T-phase[12b] at around 500–600 °C, and this process could be the reason for the mesostructure collapse since the bridging Nb–O–Nb bond angles might change with crystallization. Other methods described in the literature[6b] for template removal by calcination also promoted the mesostructure collapse. In the charge-matching mechanism of mesophase formation, removal of the template leaves behind an unbalanced charge in the inorganic framework that contributes to the structure instability.[5] Considering this feature, the CTA removal was performed by combining a process of solvent extraction and ion exchange by using a mixture of ethanol and HCl, but also without success. Template extraction from the hexagonal mesophase was only possible when the ethanol/HCl solution was replaced by an ethanol solution of a large organic cationic species such as tetrabutylammonium (TBA) hydroxide. The organic cation provides the structural charge neutralization but, due to its large size, the porous voids are still occluded, thereby producing a material with low porosity, as confirmed by the desorption/adsorption isotherm experiments (not shown). Further calcination of the TBA-exchanged phase also promoted the mesostructure collapse.

In light of these results, an investigation of the causes of the low thermal stability of the hexagonal mesostructure was performed using vibrational Raman spectroscopy to determine the condensation degree of the inorganic framework. Intense bands between 900 and 1000 $cm^{-1}$ are attributed to terminal Nb=O stretching modes, with the respective bending modes in the region 200–400 $cm^{-1}$.[11,19] The range between 500 and 700 $cm^{-1}$ is dominated by Nb–O–Nb stretching modes of corner- or edge-shared octahedral $NbO_6$ units.[11,19] The presence of bands in this region indicates the condensation degree of the octahedral units that constitute the mesophase inorganic framework. Figure 8 shows the Raman spectra recorded for the mesophases. For comparison purposes, we have included the spectrum of $HNb_2O_5$, which is a thermodynamically stable niobium oxide crystalline phase.[12] Figure 8a presents the spectral region dominated by Nb–O vibrations. Thus, comparing the Raman spectra of the mesophases with that of $HNb_2O_5$ (Figure 8a) it is possible to determine a low condensation degree of the inorganic framework in mesophases due to the absence of strong bands in the region 500–700 $cm^{-1}$.

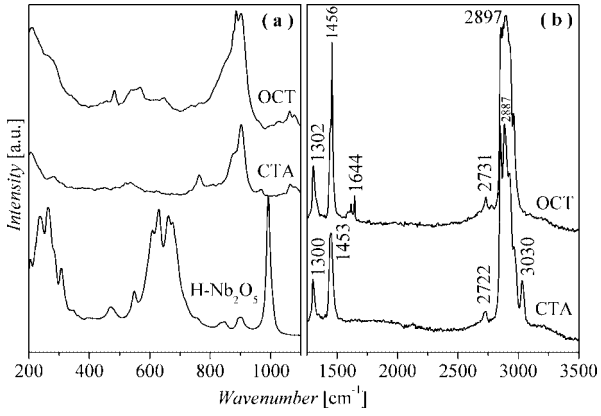


Figure 8. Raman spectra of niobium oxide mesophases (Nb/template molar ratio of 1:1) compared to $HNb_2O_5$: (a) region dominated by Nb–O vibrations; (b) vibrational region of organic templates.

The spectral region dominated by vibrational bands related to the organic moieties (1200–3500 $cm^{-1}$) is shown in Figure 8b, where it is possible to observe intense vibrational bands around 2900 $cm^{-1}$ attributed to the ν(C–H) vibrational modes of the template's carbon chains. Figure 8b also shows vibrational bands in the region 1200–1500 $cm^{-1}$ attributed to the oxalate $\nu_a$(C=O), $\nu_s$(C–O) and δ(O–C=O) modes,[20] thus indicating that the hydrolysis process of the

 © 2007 Wiley-VCH Verlag GmbH & Co. KGaA, Weinheim 

inorganic precursor is not complete. This could be one of the factors that affect the mesostructure stability. So, modifications of experimental procedures are necessary to achieve a better condensation of skeletal inorganic units and also to ensure complete trioxalato(oxido)niobate hydrolysis.

Some information about the local structure of poorly crystalline solids can be obtained by X-ray absorption techniques. Figure 9 shows the X-ray absorption near-niobium *K*-edge (XANES) spectra of the *n*-octylamine niobium oxide mesophase, the starting triammonium trioxalato(oxido)niobate, and the crystalline $HNb_2O_5$ phase. The absorption edge outline is mainly related to the element oxidation state but some local structural information can be obtained by simple comparison with XANES spectra of compounds whose structures are already known. The intensity of the pre-edge peak at the low-energy side of the spectra is related to the coordination site distortions around Nb.[21] This pre-edge peak is low in intensity for an octahedral geometry.[22] Some authors assume that it is related to the presence of Nb=O bonds and its absence is related to the presence of tetrahedral $NbO_4$ units.[23] Extended niobium oxides are mainly constituted of joined distorted $NbO_5$ and $NbO_6$ octahedral units. As determined by Raman spectroscopy, the synthesized niobium mesophases have bands in the region attributed to Nb=O bonds. The beyond-edge peaks shown in Figure 9 indicate that niobium in the $Nb_2O_5$ mesophase has neighboring atoms in an arrangement similar to niobium in $HNb_2O_5$, which is expected by the hydrolysis of trioxalato(oxido)niobate and condensation of the generated hexacoordinate niobium octahedral centers. As previously mentioned, the starting triammonium trioxalato(oxido)niobate has heptacoordinate niobium centers in a pentagonal-bipyramidal arrangement.[13]

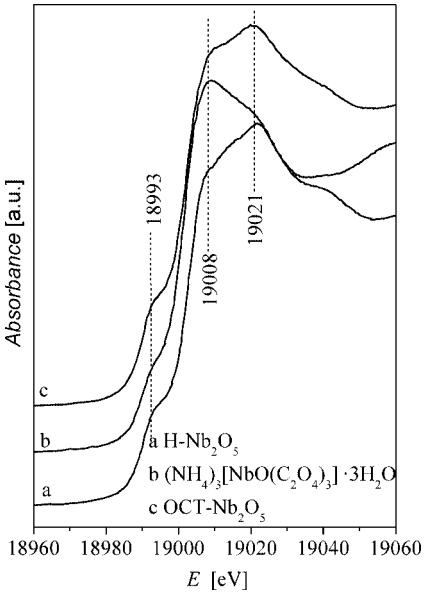


Figure 9. Niobium *K*-edge XANES spectra of (a) $HNb_2O_5$, (b) triammonium trioxalato(oxido)niobate, and (c) the OCT/$Nb_2O_5$ mesophase (Nb/OCT molar ratio of 1:1).

Other ways to achieve a better consolidation of the inorganic framework are under investigation. One of the synthetic changes tried comprises the use of a nonionic surfactant based on copolymers such as Brij56 (Aldrich). According to the literature,[5] nonionic routes produce mesostructures with thicker walls with a better thermal stability and easy template removal. When using Brij56 as structure-directing agent and triammonium trioxalato(oxido)niobate as inorganic precursor (Nb/Brij56 molar ratio of 1:0.5), the interaction at the interface of the inorganic and organic domains is very weak and no organized mesophase is produced, as shown in Figure 10 and also confirmed by X-ray diffractometry (not shown). The as-synthesized mesophase is even less stable than the mesophases described above since it crystallizes under the electron beam while registering the micrograph (TEM micrograph with higher magnification not shown). Maybe an organized mesophase with Brij56 as template can be obtained under experimental conditions (solvent/template/Nb molar ratios, pH, and temperature) distinct to those reported here.

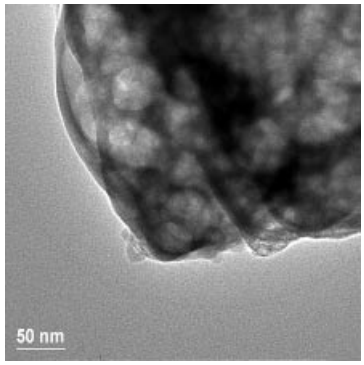


Figure 10. TEM image of the as-synthesized niobium oxide mesostructure using Brij56 as template (Nb/Brij56 molar ratio of 1:0.5).

Other synthetic modifications are still under investigation, such as the use of hydrothermal conditions, slow addition of the hydroxide to pH = 5.5, with constant monitoring of the pH, the use of other sources of base, such $NH_4OH$ and tetraethylammonium hydroxide, and templates, pre-hydrolysis of the trioxalato(oxido)niobate before mixing with the template, and thermal treatment of the mesophase under an inert gas before template removal. All the products generated by these synthetic modifications are now being characterized.

## Conclusions

In conclusion, this paper shows that it is possible to use triammonium trioxalato(oxido)niobate as an inorganic precursor to synthesize niobium oxide mesostructures by means of a neutral or an ionic route. The advantage of using this niobium compound instead of metal alkoxides or chloride precursors is related to its low cost, stability in water, easy manipulation, and possibility of recycling. Triammonium trioxalato(oxido)niobate can interact with neutral and cationic templates to produce organized mesophases under

 © 2007 Wiley-VCH Verlag GmbH & Co. KGaA, Weinheim 

controlled pH conditions. To obtain mesoporous niobium oxides from the synthesized mesophases, further studies are necessary to define experimental conditions that promote a better condensation and consolidation of the skeletal inorganic units, since attempts at template removal by calcination or solvent extraction lead to the collapse of the mesostructure.

## Experimental Section

In a typical synthesis, 12.0 g of triammonium trioxalato(oxido)-niobate, $(NH_4)_3[NbO(C_2O_4)_3]\cdot 3H_2O$ (CBMM; Companhia Brasileira de Metalurgia e Mineração) was dissolved in 200 mL of deionized water. The template [CTAB (Aldrich) or OCT (Merck)] was dissolved in 100 mL of a 3 M aqueous NaOH solution. The Nb/template molar ratios were varied from 1:0.1 to 1:2 to determine the influence of this parameter on mesophase formation. The solution of niobium complex was poured into the template solution (NaOH/Nb molar ratio of 4:1) and constantly stirred at room temperature for 48 h and at 80 °C for another 24 h to promote the decomposition of any remaining oxalate anion. After this period, the solid was filtered off, washed with water, and dried at 120 °C for 5 h. The obtained solids were characterized by X-ray diffractometry (XRD), transmission electron microscopy (TEM), Raman spectroscopy, and XANES. The standard $HNb_2O_5$ was obtained by treating a sample of $Nb_2O_5$ at 1200 °C for 2 h and its structure was confirmed by X-ray diffractometry.

X-ray diffraction patterns of the powdered samples were recorded with a Rigaku diffractometer model Miniflex using Cu-$K_\alpha$ radiation (1.541 Å, 30 kV and 15 mA), a step of 0.03°, and Ni filter. TEM images were recorded with a 300 kV JEM-3010 ARP microscope (1.7 Å point resolution) at the LME/LNLS (Laboratory of Electron Microscopy of the Brazilian Synchrotron Light National Laboratory, Campinas, Brazil). Samples were prepared by dispersing solids in ethanol in an ultrasonic bath followed by deposition on a carbon-coated Cu microgrid. Raman spectra were recorded with a Renishaw Raman Microscope model 3000, fitted with an Olympus metallurgical microscope (BH2-UMA) and a CCD camera (Wright, 600 × 400 pixels), with laser excitation line at 632.8 nm of an He-Ne laser (Spectra Physics, model 127). The XANES measurements at room temperature were performed at the XAFS beam line of Brazilian Synchrotron Light Laboratory (ring energy of 1.37 GeV and a beam current of about 175 mA). The monochromator was an Si(220) crystal and the recorded energy steps were 0.5 eV for the 18980–19060 eV XANES region in fluorescence mode. All energy values in the Nb *K*-edge spectra were calibrated against niobium metal.

## Acknowledgments

The authors acknowledge the Brazilian agencies FAPESP (Fundação de Amparo à Pesquisa do Estado de São Paulo) and CNPq (Conselho Nacional de Desenvolvimento Científico e Tecnológico) for financial support and fellowships. We are thankful to LNLS for recording the HRTEM images and XANES spectra (projects TEM-2173 and D04B-XAFS1 4337/05). We are also grateful to the Companhia Brasileira de Metalurgia e Mineração (CBMM) for the triammonium trioxalato(oxido)niobate sample and the Laboratório de Espectroscopia Molecular (IQ-USP) for recording the Raman spectra.

[1] a) M. A. Davis, *Nature* **2002**, *417*, 813–821; b) F. Fajula, A. Galarneau, F. D. Renzo, *Microporous Mesoporous Mater.* **2005**, *82*, 227–239; c) C. Sanchez, B. Julián, P. Belleville, M. Popall, *J. Mater. Chem.* **2005**, *15*, 3559–3592.
[2] C. T. Kresge, M. E. Leonowicz, W. J. Roth, J. C. Vartulli, J. S. Beck, *Nature* **1992**, *359*, 710–712.
[3] G. J. de A. A. Soler-Illia, C. Sanchez, B. Lebeau, J. Patarin, *Chem. Rev.* **2002**, *102*, 4093–4138.
[4] Q. Huo, D. I. Margolese, U. Ciesla, P. Feng, T. E. Gier, P. Sieger, R. Leon, P. M. Petroff, F. Schüth, G. D. Stucky, *Nature* **1994**, *368*, 317–321.
[5] P. T. Tanev, M. Chibwe, T. J. Pinnavaia, *Nature* **1994**, *368*, 321–323.
[6] a) D. M. Antonelli, J. Y. Ying, *Angew. Chem. Int. Ed. Engl.* **1996**, *35*, 426–430; b) D. M. Antonelli, A. Nakahira, J. Y. Ying, *Inorg. Chem.* **1996**, *35*, 3126–3136; c) S. Tao, J. Y. Ying, *Nature* **1997**, *389*, 704–706.
[7] B. Lee, D. Lu, J. N. Kondo, K. Domen, *J. Am. Chem. Soc.* **2002**, *124*, 11256–11257.
[8] a) B. Ye, M. Trudeau, D. Antonelli, *Adv. Mater.* **2001**, *13*, 29–33; b) B. Ye, M. Trudeau, D. Antonelli, *Chem. Mater.* **2001**, *13*, 2730–2741; c) B. Ye, M. Trudeau, D. Antonelli, *Chem. Mater.* **2002**, *14*, 2774–2781.
[9] a) S. Murray, M. Trudeau, D. Antonelli, *Adv. Mater.* **2000**, *12*, 1339–1341; b) S. Murray, M. Trudeau, D. Antonelli, *Inorg. Chem.* **2000**, *39*, 5901–5908; c) M. Vettraino, B. Ye, M. Trudeau, D. Antonelli, *J. Mater. Chem.* **2001**, *11*, 1755–1759; d) X. He, M. Trudeau, D. Antonelli, *J. Mater. Chem.* **2003**, *13*, 75–79.
[10] a) L. Washmon-Kriel, V. L. Jimenez, K. J. Balkus Jr, *J. Mol. Catal. B: Enzym.* **2000**, *10*, 453–469; b) X. Xu, B. Tian, J. Kong, S. Zhang, B. Liu, D. Zhao, *Adv. Mater.* **2003**, *15*, 1932–1936; c) X. Xu, B. Tian, S. Zhang, J. Kong, D. Zhao, B. Liu, *Anal. Chim. Acta* **2004**, *519*, 31–38.
[11] J. M. Jehng, I. E. Wachs, *ACS Symp. Ser.* **1990**, *437*, 232–242.
[12] a) F. Fairbrother, J. B. Taylor, *J. Chem. Soc.* **1956**, 4946–4954; b) F. Fairbrother, *The Chemistry of Niobium and Tantalum*, Elsevier, Amsterdam, **1967**.
[13] G. Mathern, R. Weiss, *Acta Crystallogr., Sect. B* **1971**, *27*, 1610–1618.
[14] B. K. Prodic, R. Liminga, S. Scavnicar, *Acta Crystallogr., Sect. B* **1973**, *29*, 864–869.
[15] Q. Huo, D. I. Margolese, G. D. Stucky, *Chem. Mater.* **1996**, *8*, 1147–1160.
[16] C. Y. Chen, S. Q. Xiao, M. E. Davis, *Microporous Mater.* **1995**, *4*, 1–20.
[17] J. C. Vartuli, K. D. Schmitt, C. T. Kresge, W. J. Roth, M. E. Leonowicz, S. B. McCullen, S. D. Hellring, J. S. Beck, J. L. Schlenker, D. H. Olson, E. H. Sheppardt, *Chem. Mater.* **1994**, *6*, 2317–2326.
[18] M. A. Carreon, V. V. Guliants, *Eur. J. Inorg. Chem.* **2005**, 27–43.
[19] J. M. Jehng, I. E. Wachs, *Chem. Mater.* **1991**, *3*, 100–107.
[20] R. L. Frost, *Anal. Chim. Acta* **2004**, *517*, 207–214.
[21] T. Tanaka, T. Yoshida, H. Yoshida, H. Aritani, T. Funabiki, S. Yoshida, J. M. Jehng, I. E. Wachs, *Catal. Today* **1996**, *28*, 71–78.
[22] M. S. P. Francisco, R. Landers, Y. Gushikem, *J. Solid State Chem.* **2004**, *177*, 2432–2439.
[23] T. Ushikubo, Y. Koike, K. Wada, L. Xie, D. Wang, X. Guo, *Catal. Today* **1996**, *28*, 59–69.

Received: June 6, 2006
Published Online: December 4, 2006

 © 2007 Wiley-VCH Verlag GmbH & Co. KGaA, Weinheim 

DOI: 10.1002/ejic.200600683

# Synthesis and Characterisation of Metal Isobutylsilsesquioxanes and Their Role as Inorganic–Organic Nanoadditives for Enhancing Polymer Thermal Stability

**Fabio Carniato,[a] Enrico Boccaleri,*[a] Leonardo Marchese,[a] Alberto Fina,[b] Daniela Tabuani,[b] and Giovanni Camino[b]**

*Dedicated to the memory of Roberto Piazza*[†]

**Keywords:** Silsesquioxanes / Titanium / Vanadium / Polymers / Nanocomposites

Metal isobutylsilsesquioxanes (M-POSS) with $Ti^{IV}$ and $V^{V}$ metal centres have been prepared by direct corner-capping of trisilanolisobutyl-POSS (**1**). The synthetic procedure has been followed in solution by FTIR spectroscopy and samples have been characterised by $^{29}Si\{^{1}H\}$ NMR, FTIR, FT-Raman and UV/Vis spectroscopy in order to study the structure and the chemical properties of the transition metal centres incorporated in the synthesised compounds. The corner-capping reaction basically lead to tetrahedrally coordinated metal centres inserted in the siliceous cage. The hybrid inorganic–organic nature of these compounds and the possibility of dispersing catalytically active metal centres in a highly efficient way within organic matrices have been investigated by dispersing the title compounds at 3 wt.-% in a polypropylene matrix by melt blending, which leads to nanocomposite materials. A study of the thermal degradation of polypropylene, trisilanolisobutyl-POSS and metal-isobutyl-POSS composites shows a significantly enhanced thermal stability under oxidative conditions only when metal-containing silsequioxanes are dispersed, along with an extended formation of condensed polyaromatic compounds (charring products). This evidence is consistent with a possible catalytic effect favouring oxidative dehydrogenation of the polymeric organic chains occurring in the condensed phase under combustion conditions, and highlights a possible promising use of M-POSS as fire-retardant additives for polymers.
(© Wiley-VCH Verlag GmbH & Co. KGaA, 69451 Weinheim, Germany, 2007)

## Introduction

Polyhedral oligomeric silsesquioxanes (POSS) are a class of condensed, three-dimensional oligomeric organosilica compounds with cage frameworks having different degrees of symmetry. These materials are present in most of the up-to-date research topics in the field of advanced materials development as they combine a nanodimensional, well-defined geometry (given by their molecular nature) with the structural and chemical properties of both inorganic siliceous materials and organic molecules. The stoichiometry of these compounds shows each silicon atom bonded to one-and-a-half oxygens (sesqui-) and to a hydrocarbon (-ane), which leads to ($RSiO_{1.5}$) units.[1–3] Besides fully condensed polyhedral silsesquioxanes, which are essentially centred on cubic $R_8Si_8O_{12}$ molecules, open-corner POSS compounds with incompletely condensed silanol groups [with general formula $R_7Si_7O_9(OH)_3$], which can generally be obtained by direct synthesis from specific chlorosilanes[1–5] or by cleavage of completely condensed POSS,[6–7] are far more interesting due to the possibility of further functionalisation both with specific organosilanes and with heteroelements. In particular, these compounds (Figure 1) are suitable for reaction with a variety of transition metal complexes (in the form of alkoxides or chlorides) to form completely condensed metal-silsesquioxanes (M-POSS).[8–12] These metal-containing cage structures have proved to be promising both as homogeneous catalysts and as precursors for highly efficient metal-based heterogeneous catalysts.[13–16]

Since a wide variety of organic groups can be bound to the silicon, the inorganic cage can also show a tunable chemical affinity towards several organic solvents and also for polymeric matrices. Thus, these inorganic–organic hybrid molecular materials may be made chemically compatible towards polymers and become suitable for preparing nanocomposites. The use of cubic silsesquioxanes in the

[a] Dipartimento di Scienze e Tecnologie Avanzate, Interdisciplinary Center Nano-Sistemi, Università del Piemonte Orientale, INSTM Local Research Unit,
Via V. Bellini 25G, 15100 Alessandria, Italy
E-mail: enrico.boccaleri@mfn.unipmn.it
[b] Centro di Cultura per l'Ingegneria delle Materie Plastiche – Politecnico di Torino, INSTM Local Research Unit,
V.le T. Michel 5, 15100 Alessandria, Italy
[†] This young chemist died recently at the age of 34. Most of us have known him as a student or as a study companion and feel glad to honour his memory in this work.

 © 2007 Wiley-VCH Verlag GmbH & Co. KGaA, Weinheim 

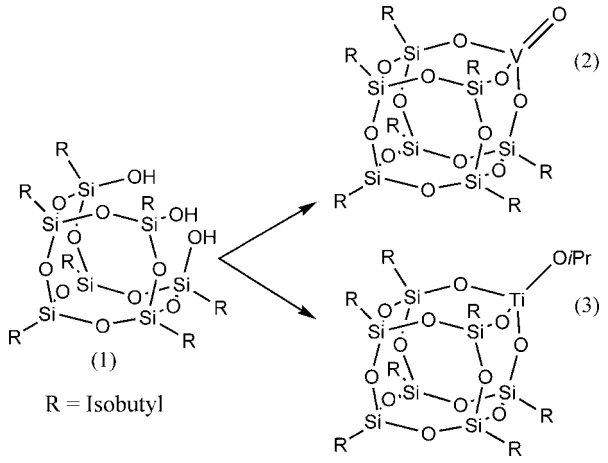


Figure 1. Trisilanolisobutyl-POSS (**1**), V-isobutyl-POSS (V-POSS; **2**) and Ti-isobutyl-POSS (Ti-POSS; 3); dimeric forms (see Figure 3 for instance) can also be present.

preparation of polymer nanocomposites has resulted in physicochemical properties that are significantly different to those of the parent polymer.[17–20] For this reason, the ability to disperse homogeneous metal-containing silsesquioxanes in polymeric matrices can lead to the distribution of well-exposed, coordinatively defined metallic centres within the organic matrix which, by acting as condensed-phase catalytic centres, can further modify the chemical behaviour of polymers, in particular at high temperatures (i.e. combustion conditions). In particular, M-POSS can deliver important flame retarding properties as they are able to activate, for instance, oxidative dehydrogenation reactions, thus reducing polymer ablation by the formation of carbonaceous and ceramic layers (given by the silica cage) on the polymer surface. Fina et al., for example, have recently shown that Al- and Zn-isobutyl-POSS are catalytic promoters of the formation of charring products during thermal oxidation of polypropylene.[21,22] Hence, interesting results can be expected when catalytically active transition metals are inserted in the siliceous cage and dispersed.

Some papers in the literature show the use of metal oxide species as additives for polymeric matrices different from polypropylene.[23] In particular, composites containing $TiO_2$ particles dispersed in poly(methyl methacrylate) or polystyrene have been investigated.[24–26] When reported, the presence of this inorganic filler showed interesting effects on the thermal stability of composites (for instance in the study of oxidative thermal degradation with TGA), giving a temperature shift on oxidative thermal degradation of about 50 °C for PMMA with 5–20 wt.-% of $TiO_2$. However, the net amount of transition metal inserted and the type of dispersion and interfacial interactions occurring with the polymer are extremely different and hard to relate to the selected M-POSS. Furthermore, as reported previously,[17–20] the introduction of silsesquioxane nanostructures can also modify other properties of the polymeric materials (i.e. mechanical behaviour).

This work focuses on the synthesis of V and Ti isobutyl-silsesquioxanes by corner-capping reactions.[27–29] The synthetic conditions for the insertion of $[(n\text{PrO})_3\text{VO}]$ and $[\text{Ti}(\text{O}i\text{Pr})_4]$ within the cage of isobutyl-POSS have been optimised (solvent, temperature and reaction time) and followed by FTIR spectroscopy. The products have been thoroughly characterised by $^{29}\text{Si}\{^1\text{H}\}$ NMR, FTIR, FT-Raman and UV/Vis spectroscopy. The materials obtained, together with the unmodified parent silsesquioxane, have been blended with polypropylene (to the best of our knowledge, the preparation of these composites is reported here for the first time) and the composites have been characterised by thermogravimetric analysis (TGA) under nitrogen and air in order to investigate the role of the dispersed metal during thermal and thermo-oxidative degradation.

## Results and Discussion

The occurrence of the corner-capping reaction of the open cage silsesquioxane was observed in the $^{29}\text{Si}\{^1\text{H}\}$ NMR spectra. The products were diluted with the appropriate deuterated solvents at about 5 wt.-% concentration. For example, sample **1** (Figure 2, A) gave a $^{29}\text{Si}\{^1\text{H}\}$ NMR spectrum (in $C_6D_6$ at 25 °C) that contains three distinct multiplet signals at $\delta$ = –58, –66.5 and –68 ppm in a 3:1:3 ratio. After functionalisation with a metal centre [part B of Figure 2, shows the $^{29}\text{Si}\{^1\text{H}\}$ NMR spectrum of V-isobutyl-POSS], the changes in the NMR spectrum are clear. Thus, the signal at $\delta$ = –58 ppm due to Si–OH is substituted by a

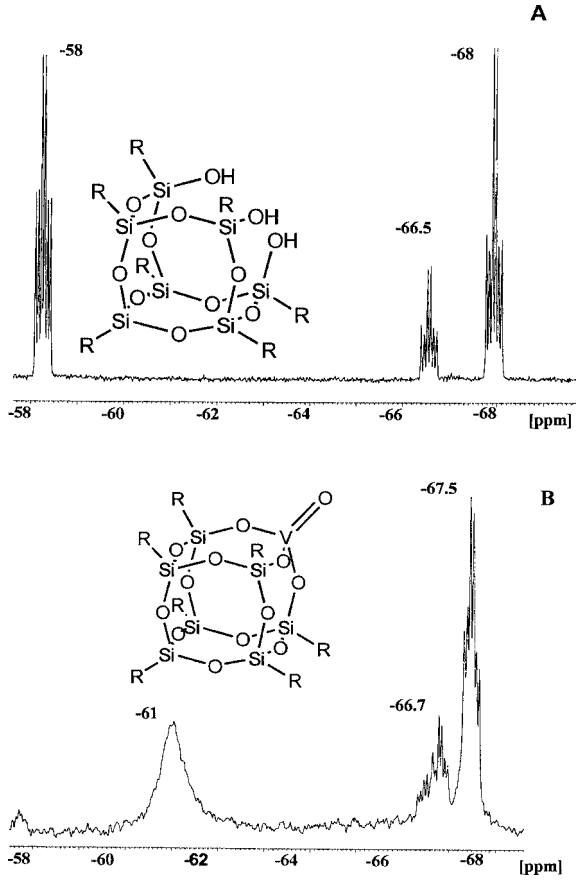


Figure 2. $^{29}\text{Si}\{^1\text{H}\}$NMR spectra of **1** (A) and **2** (B).

 © 2007 Wiley-VCH Verlag GmbH & Co. KGaA, Weinheim 

broader signal at $\delta$ = –61 ppm in the V-containing silsesquioxane and, as expected, the fine structure of the multiplet signal disappears due to the presence of dipolar interactions with the $^{51}V$ nucleus. This result strongly supports the introduction of a tricoordinate vanadyl group into the cage corner of the trisilanolisobutyl-POSS, and that this is the main product. Moreover, these signals are typical of a monomeric structure of V-isobutyl-POSS, although possible changes of solution concentration and temperature can favour a dimer structure in equilibrium with the monomeric one.[28]

The Si–OH signal is also absent in the $^{29}Si\{^1H\}$ NMR spectrum of the titanium derivative **3**, thus suggesting that the corner-capping reaction is also successful for this compound. However, the spectrum shows a complex multiplet centred at around $\delta$ = –66.5 ppm, which was attributed to the presence of an equilibrium between dimeric and monomeric Ti-isobutyl-POSS molecules (Figure 3). This assignment was suggested by the fact that similar results have been reported for Ti-cyclohexyl-POSS.[27]

In order to evaluate the reaction evolution, and to optimise the synthesis time of V-isobutyl-POSS, the process was followed by IR spectroscopy (Figure 4A) in the liquid phase by collecting small amounts of the reaction medium. The IR spectra collected at increasing reaction time show a rapid disappearance of the broad absorption in the 3400–3100 $cm^{-1}$ range that is attributable to the O–H stretching of H-bonded silanols of the POSS cage. The maximum of this absorption could not be detected due to overlap with the C–H stretching modes of the aromatic ring of the solvent. However, it is very clear that this absorption disappears almost completely within five minutes.

The reaction times are longer for the synthesis of Ti-isobutyl-POSS, and 90 minutes are necessary to the complete corner-capping reaction of partially condensed isobutyl-POSS (Figure 4B).

The IR spectra of M-POSS in KBr pellets (Figure 5) show a clear similarity to that of the parent open-cage POSS in the fingerprint region (1500 and 1000 $cm^{-1}$), where the stretching and bending modes of the isobutyl chains and of the cage framework [$\nu_{as}$(Si–O–Si) around 1100 $cm^{-1}$] absorb. However, only the parent trisilanolisobutyl-POSS

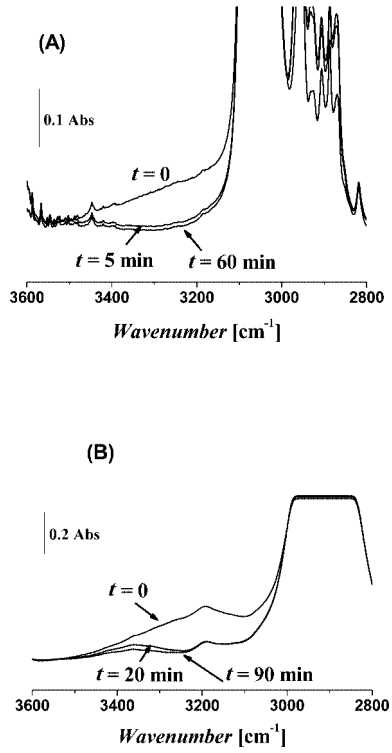


Figure 4. (A) IR spectra of the reaction mixture (in $C_6H_6$ solution) for the preparation of V-isobutyl-POSS; (B) IR spectra of the reaction mixture (in *n*-hexane solution) for the preparation of Ti-isobutyl-POSS.

(**1**) shows a clear band at 890 $cm^{-1}$ (Figure 5, curve 1) due to the bending mode of the Si–O–H groups, which is replaced by bands at 910 and 920 $cm^{-1}$ in the case of V- and Ti-POSS respectively (Figure 5, curves 2 and 3). These absorptions, which appear with the disappearance of the Si–OH bending mode[27] of **1**, can be assigned to $\nu_{as}$(Si–O–V)[30] and $\nu_{as}$(Si–O–Ti),[31] respectively.

Raman spectroscopy (Figure 6) confirmed that the vanadyl group is present in V-POSS. In fact, a sharp new peak at 1020 $cm^{-1}$, due to the V=O stretching vibration, is found in the Raman spectrum of V-POSS. The remaining part of the spectrum is almost unchanged with respect to the parent trisilanolisobutyl-POSS **1**. The NMR, FTIR and Ra-

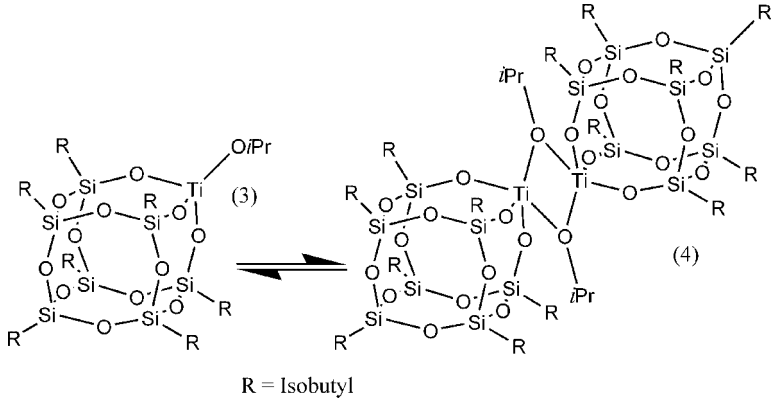


Figure 3. Schematic representation of monomeric **3** and dimeric Ti-isobutyl-POSS (**4**).

 © 2007 Wiley-VCH Verlag GmbH & Co. KGaA, Weinheim 

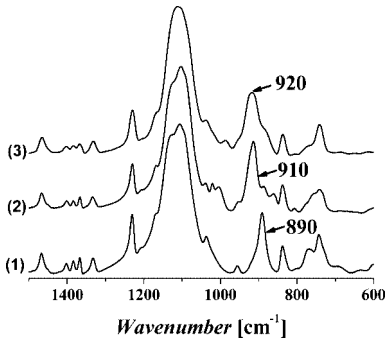


Figure 5. IR spectra (KBr pellet) of **1**–**3**.

man spectra therefore provide clear evidence that silanol groups are complexed with Ti or V metal centres leading to the closure of the isobutyl-POSS polyhedral cage.

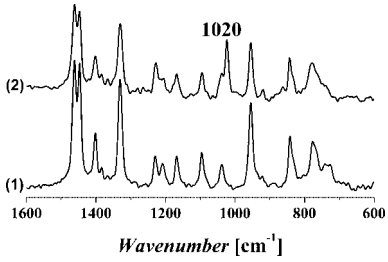


Figure 6. Raman spectra of **1** and **2**.

Diffuse-reflectance UV/Vis spectroscopy was used to monitor the oxidation states of the metals in **2** and **3**. Two bands at 250 and 300 nm are found in the spectrum of V-isobutyl-POSS (Figure 7, dotted line). These bands are assigned to low-energy charge-transfer (CT) transitions associated with framework vanadium species in a tetrahedral coordination environment.[32] In particular, the absorption at 250 nm is correlated to an electron-transfer transition between the bridging oxygens and the metal centre, while the band at 300 nm is an n → π* transition due to the terminal V=O bond.

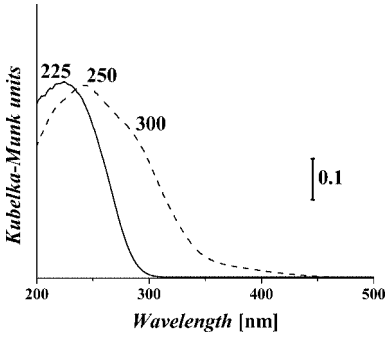


Figure 7. Diffuse reflectance UV/Vis spectra of **2** (dotted line) and **3** (solid line) mixed with anhydrous $BaSO_4$.

The vanadium centre within this material is sensitive to the presence of water, undergoing expansion of its coordination number in the presence of humidity. This was proved by recording the UV/Vis spectrum of V-isobutyl-POSS mixed with hydrated KBr. The band at 400 nm confirms a change of coordination of the metal centre, which passes from tetrahedral to fivefold coordination. It should be noted, however, that under these conditions the formation of oxide aggregation by-products is not observed. On the basis of these observations, the M-POSS complexes were stored under nitrogen in order to prevent any interaction with water.

The diffuse-reflectance UV/Vis spectrum of Ti-isobutyl-POSS (Figure 7, solid line) is characterised by a broad band at 225 nm, which is typical of tetrahedrally coordinated $Ti^{IV}$, as reported in the literature for similar samples[33] and mesoporous titanosilicates.[34]

## Polypropylene/M-POSS Nanocomposites: Thermogravimetric Analysis

Thermogravimetry is a well-established technique for the assessment of the ability of nanoadditives to favour the activation of degradation pathways suitable to protect the polymeric matrix and delay its weight loss upon heating.[35–37] In particular, the comparative analysis of the thermal behaviour of pure polymer and nanocomposite under inert or oxidative conditions is straightforward. On the other hand, these materials may activate catalytic reactions in the condensed phase due to the presence of peculiar surface and interfacial properties, such as surface acidity or redox catalytic sites, when in contact with oxygen at a given temperature. In particular, besides oxidative phenomena (which lead to the formation of small volatile molecules or CO, $CO_2$ and water), oxidative dehydrogenation reactions (ODH), which can be responsible for the formation of carbonaceous products, may occur. Moreover, the inorganic fillers can provide a physical protection to the polymeric matrix by limiting the oxygen diffusion, and thus the oxidation processes, by the formation of thermally stable siliceous or carbosiliceous surface layers (physical effect).

Due to the high affinity of isobutyl-POSS for polypropylene,[38] the prepared M-isobutyl-POSS complexes were dispersed in a polypropylene matrix by melt blending to give inorganic–organic nanocomposite materials. During the preparation of composite materials in a microextruder, the extrusion process was performed in the absence of humidity at 190 °C in order to avoid possible interactions between the metal centres and the water molecules. On the basis of the results of the NMR spectra collected on solutions (discussed above) in which the concentration of M-isobutyl-POSS is higher than in the composites, assuming a similar efficient dispersion of the nanofiller within the polymeric organic matrix, it can reasonably be expected that a large amount of M-POSS within PP exists as the monomeric species. The polymer was also blended with open cage trisilanolisobutyl-POSS (i.e. without metals in the siliceous cages), following the same procedure, for comparison. This proved to be helpful to discriminate the physical and chemical role of the dispersed nanofillers (e.g. the role of metal centres in promoting ODH reactions).

TGA measurements run under nitrogen showed that the maximum decomposition rate of pure polypropylene (Fig-

 © 2007 Wiley-VCH Verlag GmbH & Co. KGaA, Weinheim 

ure 8, curve A) occurs at about 454 °C (see the weight loss derivative curves, DTG, in the bottom panel). The addition of trisilanolisobutyl-POSS (Figure 8, B) and Ti-isobutyl-POSS (Figure 8, D) does not significantly change the thermal behaviour of the polypropylene, whereas in the presence of V-isobutyl-POSS (Figure 8, C) the degradation occurs at slightly higher temperature (464 °C).

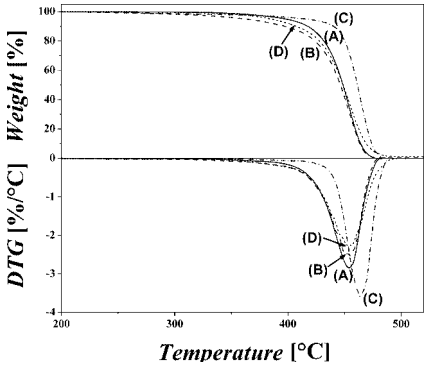


Figure 8. TGA measurements (10 °C min$^{-1}$) under nitrogen (the derivative curves, DTG, are shown in the bottom panel) for PP (A), PP-trisilanolisobutyl-POSS (3 wt.-%; B), PP-V-isobutyl-POSS (3 wt.-%; C) and PP-Ti-isobutyl-POSS (3 wt.-%; D).

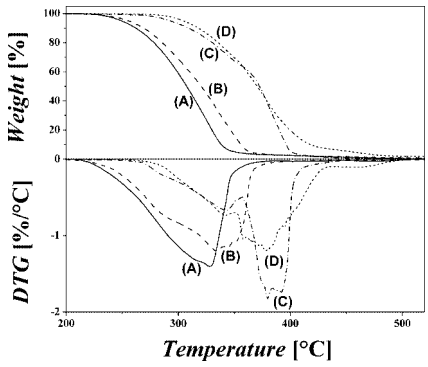


Figure 9. TGA measurements (10 °C min$^{-1}$) under air (the derivative curves, DTG, are shown in the bottom panel) for PP (A), PP-trisilanolisobutyl-POSS (3 wt.-%; B), PP-V-isobutyl-POSS (3 wt.-%; C) and PP-Ti-isobutyl-POSS (3 wt.-%; D).

Table 1. Comparison of the degradation processes of PP, PP-trisilanolisobutyl-POSS and PP-M-isobutyl-POSS composites from TGA data under oxidative conditions.

| | $T_{onset}$ [°C] | $T_{max}$ [°C] | Residue at 400 °C |
|---|---|---|---|
| Polypropylene (PP) | 247 | 327 | 2.5% |
| PP-trisilanolisobutyl-POSS | 255 | 335 | 2.5% |
| PP-V-isobutyl-POSS | 290 | 390 | 6% |
| PP-Ti-isobutyl-POSS | 303 | 375 | 20% |

On the other hand, large modifications of the thermal degradation behaviour were observed with both Ti- and V-isobutyl-POSS when heating the composites in air (Figure 9). In an oxidative atmosphere, the thermal oxidation of pure polypropylene occurs with maximum rate (measured from the DTG curve) at 327 °C (Figure 9, A) and the presence of trisilanolisobutyl-POSS (Figure 9, B) has only a limited effect, shifting the maximum weight loss rate to 335 °C. The effect of the presence of V-isobutyl-POSS (Figure 9, C) and Ti-isobutyl-POSS (Figure 9, D) is well evident from curves C and D in Figure 9, where a significant shift of the whole thermal oxidation process towards higher temperature can be observed. In detail, the degradation onset temperature (calculated when the decomposition reaches 5% of weight loss) for composites with M-isobutyl-POSS, reported in Table 1, are shifted to 290 and 303 °C, respectively, an increase of 43 and 56 °C with respect to pure polypropylene (onset temperature: 247 °C). The temperatures of maximum decomposition rate (by DTG profiles), which were found to be 327 °C for the pristine PP matrix, 390 °C for the PP-Ti-isobutyl-POSS composite and 375 °C for the PP-V-isobutyl-POSS composite, further confirmed this evidence. This effect can be attributed to the presence of Ti and V catalytic centres, which are active in ODH reactions and promote the formation of thermally stable char products. This is demonstrated by the presence of a meaningful amount of degradation products, which are oxidised only at temperatures higher than 400 °C. Indeed, while the residues of polypropylene and the PP-trisilanolisobutyl-POSS composite oxidised above 400 °C are very low, a far greater amount (about 20 wt.-%) can be detected with M-isobutyl-POSS (in particular Ti-isobutyl-POSS; Table 1).

Further evidence for the role of M-POSS on the oxidative thermal degradation of the polymeric matrix can be found by monitoring the weight loss under isothermal conditions in air (Figure 10). When setting the temperature to the beginning of the degradation of the pure matrix (i.e. 250 °C), neat PP and trisilanolisobutyl-POSS showed a very similar behaviour, with a rapid degradation that led to a residue of around 10 wt.-% in only 50 min (Figure 10, curves A and B). On the contrary, polypropylene composites containing both V- and Ti-isobutyl-POSS showed a massive formation of thermally stable products. After 250 min, in fact, residues of 28 and 42 wt.-% were found for V-isobutyl-POSS (Figure 10, C) and Ti-isobutyl-POSS (Figure 10, D), respectively. These results can be explained by the presence of catalytically active metal centres dispersed within the polymeric matrix, which result in the formation of thermally stable charring products, and suggest that the phenomenon is sensitive to the chemical nature of the metal centres.

The μ-ATR-IR spectroscopic data of composites containing Ti- and V-isobutyl-POSS were recorded on the residues at 250 °C. As shown in Figure 11, the presence of a band at 1600 cm$^{-1}$ suggests that the metal-containing nanofillers activate the early formation of unsaturated moieties as degradation products of the polypropylene matrix in the presence of oxygen. The bands observed at 1770 and 1710 cm$^{-1}$ can be attributed to the formation of oxidised species (i.e. γ-lactones and ketones).[39] The formation of extended conjugated unsaturated regions, which is favoured by the catalytic role of the metal centres, could be responsible for the stabilization of the thermal behaviour of the polymer, in agreement with the thermogravimetric analysis.

 © 2007 Wiley-VCH Verlag GmbH & Co. KGaA, Weinheim 

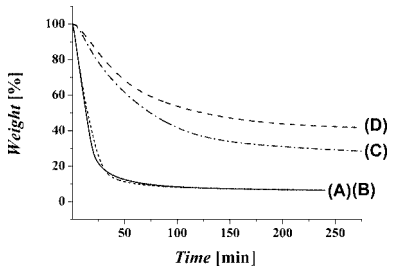


Figure 10. TGA measurements under isothermal conditions (250 °C) in air for PP (3 wt.-%; A), PP-trisilanolisobutyl-POSS (3 wt.-%; dotted line, B), PP-V-isobutyl-POSS (3 wt.-%; C) and PP-Ti-isobutyl-POSS (3 wt.-%; D).

Further studies on the mechanism acting within the M-POSS polypropylene composites carried out with several spectroscopic techniques highlight and confirm the solid-state catalytic activity of the nanofillers within the polymeric matrix.[40]

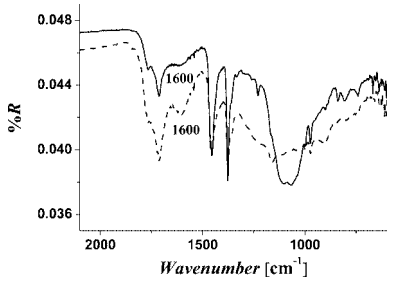


Figure 11. μ-ATR-IR spectra of the residues obtained at 250 °C under air flow for PP-Ti-isobutyl-POSS (solid line) and PP-V-isobutyl-POSS (dashed line).

When polypropylene is blended with Ti-POSS, the stabilisation effect on the polymer is more effective. These results are far more remarkable when the extremely low amount of metal dispersed in the material is considered (less than 0.2 wt.-%).

## Conclusions

This article focuses on the synthesis of V- and Ti-functionalised cubic silsesquioxanes, which are reported for the first time with an isobutyl substituent on the cage corners. A detailed characterisation during the synthetic procedure has highlighted that the reaction times are very short with respect to the results published on POSS with different organic substituents. Besides solution $^{29}Si\{^1H\}$ NMR, FTIR spectroscopy is a sensitive probe for the monitoring of the corner-capping reaction and the characterisation of the products, while Raman spectroscopy can often provide complementary information about the nature of the transition metal centres inserted into the cage. The coordination state of the metallic centres has been investigated by diffuse reflectance UV/Vis spectroscopy.

Due to their chemical affinity, these compounds have been used as additives (3 wt.-%) in polypropylene by melt blending to give nanocomposite materials. The thermal degradation of these materials under an inert or oxidative atmosphere was followed by thermogravimetric analysis. Whilst metal-free additives (i.e. trisilanolisobutyl-POSS) have limited effects on the degradation pathway of the polymeric matrix, Ti-POSS and V-POSS shift the oxidative degradation significantly to higher temperature (around 70–80 °C). Moreover, under isothermal conditions, while neat polypropylene and metal-free PP-POSS composites degrade rapidly at 250 °C in air (leaving less than 10% of residue after 50 min), in the presence of V- and Ti-POSS the degradation is significantly slower and leads to large amounts of residues: 28% and 42% respectively after 250 min. This suggests that metal-bearing nanofillers can operate chemically on the polymeric matrix degradation pathway, thereby inducing significant modifications to the high temperature oxidative processes. In particular, oxidative dehydrogenation reactions, which lead to thermally stable charring products, are seemingly favoured in this case.

A more detailed multi-technique investigation, which is currently in progress, is needed to highlight the chemical reactivity induced by the presence of M-POSS and the related evolution of the species that are formed within the polymeric matrix.

## Experimental Section

**Materials:** Trisilanolisobutyl-POSS (**1**) from Hybrid Plastics Company was used as precursor for the preparation of M-isobutyl-POSS by a corner-capping reactions. The preparation was performed under inert conditions (nitrogen). All solvents, freshly opened, were used without further purification.

**V-Isobutyl-POSS (2):** An equimolar solution of $[(n\mathrm{PrO})_3\mathrm{VO}]$ (98%, Sigma Aldrich) and trisilanolisobutyl-POSS was prepared by adding a 2-mL solution of $[(n\mathrm{PrO})_3\mathrm{VO}]$ (288 μL, $1.27\times10^{-3}$ mol) in benzene to a solution of **1** (1.00 g, $1.27\times10^{-3}$ mol) in 20 mL of benzene under vigorous stirring. As found by IR spectroscopy, trisilanolisobutyl-POSS was almost completely transformed within a few minutes; however, the mixture was stirred for 1.5 h to complete the reaction. Filtration through a fine sintered glass funnel, and solvent removal in vacuo, led to the isolation of 900 mg of V-isobutyl-POSS as a white amorphous foam.

**Ti-Isobutyl-POSS (3):** $[\mathrm{Ti}(O\mathit{i}\mathrm{Pr})_4]$ (375 μL, $1.27\times10^{-3}$ mol; 97%, Sigma Aldrich) was added with vigorous stirring to a solution of **1** (1.00 g, $1.27\times10^{-3}$ mol) in 160 mL of *n*-hexane. The reaction solution was carefully purged with nitrogen to prevent the rapid hydrolysis of $[\mathrm{Ti}(O\mathit{i}\mathrm{Pr})_4]$. After addition, the temperature was raised to 60 °C and the mixture stirred for 90 min. In this case, FTIR spectroscopy showed that the transformation of trisilanolisobutyl-POSS was almost complete within 1.5 h. Subsequently, the solvent was evaporated until a white powder (900 mg) was obtained.

Both complexes were stored under nitrogen in order to prevent any interaction with water.

Melt blending of M-isobutyl-POSS in a polypropylene matrix (3 wt%) was performed using a Basell Moplen HP501L Polypropylene Homopolymer (density: 0.9 $g\,cm^{-3}$). The melt flow rate (MFR) (230 °C/2.16 kg) was 6.0 g/10 min. The mixing was performed using a Haake twin screw microextruder at 190 °C for 10 min. The extruder was driven at 100 rpm.

**Characterisation:** $^{29}Si\{^1H\}$ NMR spectra of the samples dissolved in $C_6D_6$ (concentration: 0.1 M) at room temperature were recorded

 © 2007 Wiley-VCH Verlag GmbH & Co. KGaA, Weinheim 

with a Jeol Eclipse Plus spectrometer equipped with an 8-T magnet.

Infrared (IR) spectra of solid samples in KBr pellets were recorded in the range 4000–400 $cm^{-1}$ at 4-$cm^{-1}$ resolution with a Bruker Equinox 55 spectrometer.

ATR spectra of the samples were recorded in the range 4000–500 $cm^{-1}$ at 4-$cm^{-1}$ resolution with a Perkin–Elmer Spectrum GX FTIR SystemMultiscope FTIR Microscope.

Raman spectra were recorded in the range 4000–50 $cm^{-1}$ at 4-$cm^{-1}$ resolution (500 scans) with a RFS 100 Bruker FT-Raman spectrometer equipped with a 1064-nm wavelength excitation laser. The laser power was set at 100 mW.

UV/Vis spectra were recorded in the range 190–750 nm with a Perkin–Elmer Lambda 900 spectrometer equipped with a diffuse reflectance sphere attachment (DR-UV/Vis). The samples were dispersed in anhydrous $BaSO_4$ (10 wt.-%).

Thermogravimetric analyses (TGA) of composite materials (M-isobutyl-POSS dispersed in polypropylene) were performed in air or nitrogen (60 mL $min^{-1}$) with a Q500 TA Instruments thermobalance, heating from 50 to 600 °C at 10 °C $min^{-1}$ or under isothermal conditions, with 10-mg samples.

## Acknowledgments

The authors thanks Dr. Nadia Tzankova Dintcheva of the University of Palermo for blending M-POSS in PP. The authors are grateful to the European Commission for financial support by means of the Specific Targeted Research or Innovation Project (STRP) project "Nanofire" (proposal no. 505637-1) in the context of the 6th Framework Programme. Financial support by the Ministero per l'Università e la Ricerca Scientifica (MIUR) through a PRIN 2002 project is gratefully acknowledged.

[1] R. H. Baney, M. Itoh, A. Sakakibara, T. Suzuki, *Chem. Rev.* **1995**, *95*, 1409.
[2] P. G. Harrison, *J. Organomet. Chem.* **1997**, *542*, 141.
[3] P. P. Pescarmona, T. Maschmeyer, *Aust. J. Chem.* **2001**, *54*, 583.
[4] F. J. Feher, T. A. Budzichowski, R. L. Blanski, K. J. Weller, J. W. Ziller, *Organometallics* **1991**, *10*, 2526.
[5] P. A. Agaskar, *Colloids Surf.* **1992**, *63*, 131.
[6] F. J. Feher, R. Terroba, J. W. Ziller, *Chem. Commun.* **1999**, 2309.
[7] F. J. Feher, D. Soulivong, G. T. Lewis, *J. Am. Chem. Soc.* **1997**, *119*, 11323.
[8] R. W. J. M. Hanssen, R. A. van Santen, H. C. L. Abbenhuis, *Eur. J. Inorg. Chem.* **2004**, 675.
[9] F. J. Feher, J. F. Walzer, *Inorg. Chem.* **1991**, *30*, 1689.
[10] K. Wada, M. Nakashita, A. Yamamoto, T. Mitsudo, *Chem. Commun.* **1998**, 133.
[11] T. Maschmeyer, M. C. Klunduk, C. M. Martin, D. S. Shephard, J. M. Thomas, B. F. G. Johnson, *Chem. Commun.* **1997**, 1847.
[12] P. Smet, B. Devreese, F. Verpoort, T. Pauwels, I. Svoboda, S. Foro, J. Van Beeumen, L. Verdonck, *Inorg. Chem.* **1998**, *37*, 6583.
[13] H. C. L. Abbenhuis, *Chem. Eur. J.* **2000**, *6*, 25.
[14] S. Krijnen, H. C. L. Abbenhuis, R. W. J. M. Hanssen, J. H. C. van Hooff, R. A. van Santen, *Angew. Chem. Int. Ed.* **1998**, *37*, 356.
[15] N. Maxim, A. Overweg, P. J. Kooyman, J. H. M. C. van Wolput, R. W. J. M. Hanssen, R. A. van Santen, H. C. L. Abbenhuis, *J. Phys. Chem. B* **2002**, *106*, 2203.
[16] M. D. Skowronska-Ptasinska, M. L. W. Vorstenbosch, R. A. van Santen, H. C. L. Abbenhuis, *Angew. Chem. Int. Ed.* **2002**, *41*, 637.
[17] P. T. Mather, H. G. Jeon, A. Romo-Uribe, T. S. Haddad, J. D. Lichtenhan, *Macromolecules* **1999**, *32*, 1194.
[18] S. H. Phillips, T. S. Haddad, S. J. Tomczak, *Curr. Opin. Solid State Mater. Sci.* **2004**, *8*, 21.
[19] J. Pyun, K. Matyjaszewski, *Macromolecules* **2000**, *33*, 217.
[20] J. D. Lichtenhan, J. J. Schwab, W. A. Reinerth, *Chem. Innovation* **2001**, *31*, 3.
[21] A. Fina, H. C. L. Abbenhuis, D. Tabuani, A. Frache, G. Camino, *Polym. Degrad. Stab.* **2006**, *91*, 1064.
[22] A. Fina, H. C. L. Abbenhuis, D. Tabuani, G. Camino, *Polym. Degrad. Stab.* **2006**, *91*, 2275.
[23] U. Schubert, *Chem. Mater.* **2001**, *13*, 3487.
[24] A. Laachachi, E. Leroy, M. Cochez, M. Ferriol, J. M. Lopez Cuesta, *Polym. Degrad. Stab.* **2005**, *89*, 344.
[25] A. Laachachi, M. Cochez, M. Ferriol, J. M. Lopez Cuesta, E. Leroy, *Mater. Lett.* **2005**, *59*, 36.
[26] Y. Yang, P. Wang, *Polymer* **2006**, *47*, 2683.
[27] T. Maschmeyer, M. C. Klunduk, C. M. Martin, D. S. Shephard, J. M. Thomas, B. F. G. Johnson, *Chem. Commun.* **1997**, 1847.
[28] F. J. Feher, J. F. Walzer, *Inorg. Chem.* **1991**, *30*, 1689.
[29] B. A. Morrow, A. J. McFarlan, *J. Phys. Chem.* **1996**, *92*, 1395.
[30] P. R. H. P. Rao, A. V. Ramaswamy, P. Ratnasamy, *J. Catal.* **1992**, *137*, 225.
[31] C. Perego, G. Bellussi, C. Corno, M. Taramasso, F. Buonuomo, A. Esposito, *Stud. Surf. Sci. Catal.* **1986**, *28*, 129.
[32] A. Albuquerque, H. O. Pastore, L. Marchese, *Stud. Surf. Sci. Catal.* **2005**, *155*, 45.
[33] Gianotti, A. Frache, S. Coluccia, J. M. Thomas, T. Maschmeyer, L. Marchese, *J. Mol. Catal. A* **2003**, *204*, 483.
[34] E. Gianotti, V. Dellarocca, L. Marchese, G. Martra, S. Coluccia, T. Maschmeyer, *Phys. Chem. Chem. Phys.* **2002**, *4*, 6109.
[35] M. Zanetti, G. Camino, P. Reichert, R. Mülhaupt, *Macromol. Rapid Commun.* **2001**, *22*, 176.
[36] M. Zanetti, G. Camino, R. Thomann, R. Mülhaupt, *Polymer* **2001**, *42*, 4501.
[37] A. Riva, M. Zanetti, M. Braglia, G. Camino, L. Falqui, *Polym. Degrad. Stab.* **2002**, *77*, 299.
[38] A. Fina, D. Tabuani, A. Frache, G. Camino, *Polymer* **2005**, *46*, 7855.
[39] G. A. George, M. Celina, A. M. Vassallo, P. A. Cole-Clarke, *Polym. Degrad. Stab.* **1995**, *48*, 199.
[40] F. Carniato, E. Boccaleri, L. Marchese, A. Fina, D. Tabuani, G. Camino, manuscript in preparation.

Received: July 21, 2006
Published Online: December 15, 2006

 © 2007 Wiley-VCH Verlag GmbH & Co. KGaA, Weinheim 

DOI: 10.1002/ejic.200600767

# Structural Trends in Alkaline Earth and Rare Earth Metal 3,5-Diisopropylpyrazolates

**Julia Hitzbleck,[a,b] Glen B. Deacon,[b] and Karin Ruhlandt-Senge*[a,b]**

**Keywords:** Alkaline earth metals / Lanthanoids / N ligands / Coordination modes

A series of 3,5-diisopropylpyrazolates of magnesium, calcium, and strontium in addition to a divalent europium analog continues our investigation on the differences and similarities between the alkaline earth and divalent rare earth metal elements. The alkane elimination reaction between dibutylmagnesium and excess 3,5-diisopropylpyrazole (*i*Pr$_2$pzH) in toluene afforded the dinuclear magnesium pyrazolate [{Mg(*i*Pr$_2$pz)$_2$(*i*Pr$_2$pzH)}$_2$] (**1**). [{Ca(*i*Pr$_2$pz)$_2$(*i*Pr$_2$pzH)$_2$}$_2$] (**2**) and [{Eu(*i*Pr$_2$pz)$_2$(*i*Pr$_2$pzH)$_2$}$_2$] (**3**) were obtained as the product of redox-transmetallation/ligand-exchange reactions between an excess of the corresponding metal, 2 equiv. of *i*Pr$_2$pzH, and Hg(C$_6$F$_5$)$_2$ in toluene. This reaction with Sr metal led to the isolation of a unique byproduct, [Hg$_3$(*i*Pr$_2$pz)$_4$(C$_6$F$_5$)$_2$] (**4**). High-temperature direct metallation of barium with *i*Pr$_2$pzH afforded [{Ba(*i*Pr$_2$pz)$_2$(py)$_3$}$_2$] (**5**) upon treatment of the hydrocarbon-insoluble homoleptic [{Ba(*i*Pr$_2$pz)$_2$}$_n$] with pyridine (py). X-ray crystal structure analyses revealed dinuclear structures for compounds **1**–**3** and **5** with μ-η$^n$:η$^m$ bridging pyrazolato ligands, including the new μ-η$^1$:η$^5$ linkage, and further stabilization of **1**–**3** by intramolecular hydrogen bonding between the terminal pyrazole donor and terminal **1** or bridging pyrazolato ligands in **2** and **3**. The trinuclear **4** displays the first example of a complex with an *open*, triangular Hg$_3$ unit. It has μ-η$^1$:η$^1$ bridging pyrazolato ligands and terminal pentafluorophenyl groups.

(© Wiley-VCH Verlag GmbH & Co. KGaA, 69451 Weinheim, Germany, 2007)

## Introduction

The coordination chemistry of the pyrazolate ligand system has been a point of interest for quite some time, and the recognized array of binding modes keeps increasing as this work continues.[1] Many of the pyrazolato complexes reported in the literature to date involve transition metals,[1b,1d,2] followed by a much smaller number of lanthanoid pyrazolates.[3] Nevertheless, triggered by the potential use of this ligand system for chemical vapor deposition (CVD) precursor materials,[3i,4] the pyrazolate series was extended to the more electropositive alkaline earth metals in recent years.[4c,5] Despite the numerous coordination modes reported (e.g. *C*- or *N*-η$^1$, η$^2$, η$^5$, μ-η$^n$:η$^m$)[3,5,6] and the close structural similarities with the analogous lanthanoid pyrazolates, suitable group 2 CVD precursor materials have not been obtained as of yet, because of the thermal instability of the compounds.[5] Hence the custom design of such materials still requires a more in-depth understanding of the coordination chemistry of alkaline earth metals and the resulting structure–reactivity relationship of their compounds.

[a] Syracuse University, Department of Chemistry, CST 1-014, Syracuse, NY, 13244-4100, USA
Fax: +1-315-443-4070
E-mail: kruhland@syr.edu
[b] School of Chemistry, Monash University, Victoria 3800, Australia
Fax: +61-3-9905 4597
E-mail: glen.deacon@sci.monash.edu.au

Considerable effort in our laboratories has shed light on the chemistry of alkaline earth and rare earth metal pyrazolates, and we recently reported on several metal-based syntheses of alkaline earth 3,5-diphenyl- and 3,5-dimethylpyrazolates Ph$_2$pz and Me$_2$pz.[5c] Structural analysis revealed the expected similar coordination modes to the previously reported rare earth metal pyrazolates[3e,3k,3m,6f] and identical structures for metals with similar ionic radii (e.g. Ca$^{2+}$/Yb$^{2+}$; Sr$^{2+}$/Sm$^{2+}$/Eu$^{2+}$).[7] Alternatively, where the Yb$^{2+}$ complexes have not been crystallized,[3j] a prediction can be made from the structure of the Ca complex and vice versa.[5c,5d,5f] Furthermore, we could show that, in the absence of suitable donor solvents, or if ideal steric saturation cannot be achieved by co-solvent coordination, formation of oligonuclear species is observed.[5d,5f] While the sterically demanding alkaline earth metal diphenylpyrazolates [M(Ph$_2$pz)$_2$(thf)$_4$] (M = Ca, Sr, Ba) form exclusively mononuclear complexes in the presence of thf,[5c] the corresponding di-*tert*-butylpyrazolates [{M(*t*Bu$_2$pz)$_2$(thf)$_n$}$_2$] crystallize as dinuclear species with an array of μ-η$^2$:η$^n$-bridging pyrazolato modes.[5f] An even greater variety of coordination modes is observed in the products of high-temperature metallation, affording linear, homoleptic alkaline earth metal 3,5-di-*tert*-butylpyrazolates [{M(*t*Bu$_2$pz)$_2$}$_n$] (M = Ca, Sr, Ba; *n* = 3, 4, 6 respectively).[5d] Where the corresponding pyrazoles are coligands,[3l,3m] hydrogen bonding also plays a major role in determining the structures of alkaline earth metal derivatives.[5b,5c,8] The coordination of a neutral li-

 © 2007 Wiley-VCH Verlag GmbH & Co. KGaA, Weinheim 

gand is also an important design element of potential CVD precursor molecules.[3i,8] Deposition experiments have shown that the addition of the free ligand to the vapor frequently results in increased complex stability,[8] and we recently reported on enhanced vapor transport of complexes containing free pyrazole as a donor.[5f] Nevertheless, the effect of ligand bulk on the synthesis of alkaline earth metal pyrazolates as well as on their structures is incompletely understood. We now report a study of the synthesis and structures of alkaline earth and a rare earth metal 3,5-diisopropylpyrazolates. *i*Pr$_2$pz has steric bulk intermediate between the Ph$_2$pz and Me$_2$pz ligands, further assisting an understanding of this important class of complexes. Particular features are the influence of the thermal stability of the ligand in high-temperature syntheses, and the effect of hydrogen bonding as well as π-Ar–M pyrazolate coordination on the geometry of the resulting structures.

## Results and Discussion

The commercial availability of a variety of magnesium alkyls offers a straightforward and clean synthetic route to magnesium amides.[5b,9] Hence the magnesium pyrazolate [{Mg(*i*Pr$_2$pz)$_2$(*i*Pr$_2$pzH)}$_2$] (**1**) (Figure 1) was prepared by alkane elimination from dibutylmagnesium in toluene in the presence of four equivalents of 3,5-diisopropylpyrazole (Scheme 1). Despite excess pyrazole (sixfold also examined), dimerization and coordination of only one pyrazole group per metal center is observed. This contrasts with the report on monomeric [Mg(*t*Bu$_2$pz)$_2$(*t*Bu$_2$pzH)$_2$], in which two equivalents of free pyrazole coordinate to the metal center.[5b]

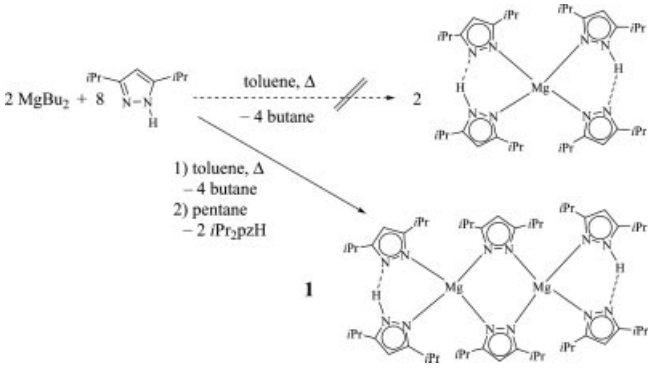


Scheme 1.

For the heavier congeners, metal dialkyls or "heavy Grignard" reagents are less accessible because of their inherent higher reactivity. Even though dibenzyl complexes of the heavier group 2 metals have been reported,[10] their synthesis is quite involved, making these reagents less competitive starting materials for our target compounds. To expand the synthetic schemes on hand for the alkaline earth metals, we recently reported on metal-based routes to heavy group 2 pyrazolates, circumventing problems encountered in salt metathesis.[5a] One of these, redox-transmetallation/ligand-exchange, has now been employed to prepare [{Ca(*i*Pr$_2$pz)$_2$-(*i*Pr$_2$pzH)$_2$}$_2$] (**2**) and [{Eu(*i*Pr$_2$pz)$_2$(*i*Pr$_2$pzH)$_2$}$_2$] (**3**) (Figure 2 and Figure 3). However, the redox-transmetallation/ligand-exchange reaction of excess metal, *i*Pr$_2$pzH and Hg(C$_6$F$_5$)$_2$ (mol ratio 2:1) in toluene (M = Ca, Eu) did not go to completion to yield [{M(*i*Pr$_2$pz)$_2$}$_n$]. Instead, only 50% conversion of the organomercurial and the pyrazole was observed under these conditions, leading to the isolation of complexes **2** and **3** in good yields with respect to the pyrazole used (Scheme 2). Redox-transmetallation/ligand-exchange syntheses are normally carried out in polar solvents (S), giving [Ln(L)$_n$S$_m$] complexes,[3e,3g,3j,3l,5c,11] but use of a nonpolar solvent such as toluene enabled the preparation of homoleptic compounds, as demonstrated with [La(Odpp)$_3$] (Odpp = 2,6-diphenylphenolate).[12]

The phenomenon of an incomplete reaction due to the preferred formation of a "free-ligand" stabilized species is a recurring feature of group 2 pyrazolates syntheses.[5b,5c] In a similar fashion, the transamination reaction between alkaline earth metal bis[bis(trimethylsilylamido)] complexes [M{N(SiMe$_3$)$_2$}$_2$(thf)$_2$] (M = Ca, Sr, Ba) and Me$_2$pzH in thf yielded monomeric Me$_2$pz analogs [M(Me$_2$pz)$_2$(Me$_2$pzH)$_4$], instead of the expected Lewis base donor adducts [M(Me$_2$pz)$_2$(thf)$_n$].[5c] The formation of pyrazole adducts is a likely consequence of the stabilizing effect of hydrogen bonding (vide infra) between the anionic ligand and the free pyrazole, in addition to the strong donor properties of the latter, as also observed for compounds **1**–**3**. The energy gain through such a hydrogen bonding stabilization prevents the complete ligand-exchange reaction since all pyrazole is consumed when 50% of the mercurial is converted.

Surprisingly, the same reaction with either strontium or ytterbium metal repeatedly did not afford analogs of **2** and **3** (Scheme 3), even though this route has been successful with Ca and Sr in combination with thf or dme and 3,5-diphenylpyrazole,[5c] or with Yb, 3,5-diphenylpyrazole and HgPh$_2$.[3j,13] The redox-transmetallation/ligand-exchange reaction at room temperature led repeatedly to the recovery

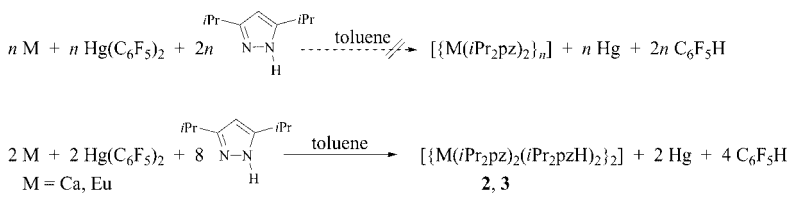


Scheme 2.

 © 2007 Wiley-VCH Verlag GmbH & Co. KGaA, Weinheim 

of unreacted metal, $i$Pr$_2$pzH, and Hg(C$_6$F$_5$)$_2$. The use of more forcing conditions in refluxing toluene initiated the ligand rearrangement between the already formed strontium pyrazolate and remaining mercurial to form a unique heteroleptic trinuclear organomercurial [Hg$_3$($i$Pr$_2$pz)$_4$(C$_6$F$_5$)$_2$] (**4**) (Figure 5).

$$Sr + Hg(C_6F_5)_2 + 2\ i\mathrm{Pr}_2\mathrm{pzH} \longrightarrow Sr(i\mathrm{Pr}_2\mathrm{pz})_2 + Hg + 2\ C_6F_5H$$

$$2\ Sr(i\mathrm{Pr}_2\mathrm{pz})_2 + 3\ Hg(C_6F_5)_2 \longrightarrow [Hg_3(i\mathrm{Pr}_2\mathrm{pz})_4(C_6F_5)_2] + 2\ Sr(C_6F_5)_2$$

Scheme 3.

In the presence of unreacted bis(pentafluorophenyl)mercury, a rearrangement reaction can occur, leading to preferential crystallization of the novel complex **4**. Bis(pentafluorophenyl)mercury is normally resistant to protolysis[14] and in particular does not react with 3,5-diphenylpyrazole.[15] The Sr(C$_6$F$_5$)$_2$ from the rearrangement may undergo protolysis to Sr($i$Pr$_2$pz)$_2$ or decompose to SrF$_2$ by C–F activation.

A third synthetic route involving direct metallation at elevated temperatures (Scheme 4) was attempted for the synthesis of homoleptic 3,5-diisopropylpyrazolato complexes [{M($i$Pr$_2$pz)$_2$}$_n$] (M = Ca, Sr, Ba). Contrasting the straightforward syntheses of the corresponding 3,5-di-*tert*-butylpyrazolates [{M($t$Bu$_2$pz)$_2$}$_n$] (M = Ca, Sr, Ba),[5d] 3,5-diisopropylpyrazole failed to react with calcium and strontium under elevated-temperature conditions, suggesting a slightly less acidic character for $i$Pr$_2$pzH than for $t$Bu$_2$pzH. The addition of a drop of elemental mercury to the reaction mixture for surface amalgamation of the metal has been proven to be useful in combination with the slightly less reactive rare earth metals (e.g.[3h,3k–m]). In contrast, for the group 2 metals, direct metallation reactions under such conditions proceeded without the addition of mercury in other pyrazole systems (Ph$_2$pzH, $t$Bu$_2$pzH).[5c,d,f] Nevertheless, with $i$Pr$_2$pzH even mercury addition did not result in the desired reaction, and only ligand decomposition was observed in the reaction of Ca and Sr upon increasing temperature. Only for the most reactive alkaline earth metal barium metallation occurred, as indicated by the slowly solidifying reaction mixture. In contrast to the 3,5-di-*tert*-butylpyrazolates, the homoleptic species could not be sublimed in the Carius tube. Several extractions with hot toluene were also unsuccessful, thus indicating an oligo- or polynuclear structure comparable to [{Ba($t$Bu$_2$pz)$_2$}$_6$].[5d] Extraction of the crude material with pyridine afforded the toluene-soluble dinuclear [{Ba($i$Pr$_2$pz)$_2$(py)$_3$}$_2$] (**5**).

All compounds were analyzed by spectroscopic methods (IR; NMR except for **3**); **1**, **2**, and **5** show the expected signals corresponding to the pyrazole/pyrazolato ligands (**1**, **2**), or the pyridine donor and pyrazolato ligand in **5** in the $^1$H and $^{13}$C NMR spectra of the respective compounds. Variable temperature NMR studies indicated the fluxional behavior of complexes **1** and **2** in solution, forfeiting the differentiation between bridging and terminal pyrazolato or pyrazole [CH(pzH) and CH(pz)] ligands even at low temperature (–60 °C). This is in contrast to the homoleptic 3,5-di-*tert*-butylpyrazolate [{M($t$Bu$_2$pz)$_2$}$_n$] (M = Ca, Sr, Ba) analogs where a clear separation of the pyrazolate CH signals has been observed upon cooling, and they correspond to the different types of terminal and bridging pyrazolato ligands in the multinuclear species.[5d] Compound **4** reveals the characteristic signals of the pentafluorophenyl group, with $^3J_{(Hg,F)}$ appropriate for a mono(pentafluorophenyl)-mercury compound.[16]

The solid-state structures of the 3,5-diisopropylpyrazolate compounds **1**–**5** were determined by single-crystal X-ray crystallography; perspective views of **1**–**5** are shown in Figures 1–5. Compounds **1**–**3** are all dinuclear; **1** contains one pyrazole per metal center, while the larger metals satisfy their coordination sphere with two pyrazole donors in **2** and **3**, or three pyridine donors in **5**. Crystal data are given in Table 5, and selected bond lengths and angles are summarized in Tables 1–4.

The metal centers in the dinuclear compounds [{M($i$Pr$_2$pz)$_2$($i$Pr$_2$pzH)$_n$}$_2$] ($n$ = 1, M = Mg **1**; $n$ = 2, M = Ca **2**, Eu **3**, Figure 1) are further stabilized by intramolecular hydrogen bonding involving the acidic proton of the pyrazole donor and the lone pair on the pyridine-like nitrogen of the η$^1$-bonded pyrazolates. In contrast to the heavier analogs **2** and **3**, but in accordance with the dinuclear magnesium *tert*-butylpyrazolates [{Mg($t$Bu$_2$pz)$_2$}$_2$] and [{Mg($t$Bu$_2$pz)$_2$(thf)}$_2$],[4c] the bridging ligands in **1** bind fairly symmetrically in a μ-η$^1$:η$^1$-fashion and are slightly twisted out of plane (Mg1, Mg2, pz3, pz4) to reduce steric interactions of the pendant isopropyl groups with the terminal ligands. This results in a distorted tetrahedral coordination environment for magnesium [maximum deviation from the ideal tetrahedral angle 9.7(1)°]. Surprisingly, the terminal Mg–N bonds for the σ-η$^1$-pyrazolates [Mg–N

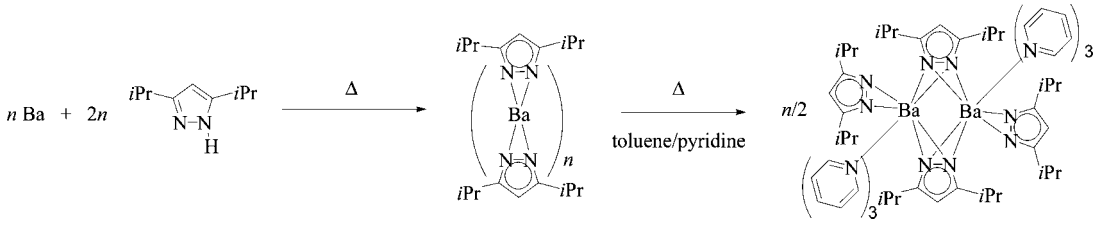


Scheme 4.

 © 2007 Wiley-VCH Verlag GmbH & Co. KGaA, Weinheim 

2.077(2)–2.088(2) Å] are slightly elongated as compared with the bridging ligands [Mg–N 2.053(2)–2.061(2) Å]. In addition, there is no marked difference in Mg–N bond length (within experimental error) between the terminal anionic ligand pz2 and the neutral donor pzH1 [Δ(Mg–N) 0.003(4) Å]. Pz2 and pzH1 display short hydrogen-bonding contacts between H12 and N22 [1.56(5) Å; N12–H12–N22 155.66°]. Even though the corresponding pz5 and donor pzH6 on Mg2 show slightly larger differences [Δ(Mg–N) 0.011(4) Å], the hydrogen-bonding contacts are very similar [H62···N52 1.58(4) Å, N62–H62–N52 154.76°].

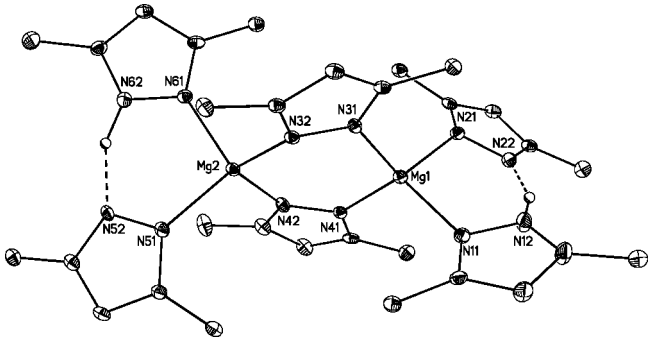


Figure 1. X-ray crystal structure of [{Mg(*i*Pr$_2$pz)$_2$(*i*Pr$_2$pzH)}$_2$] (**1**); the isopropyl groups and hydrogen atoms have been removed for clarity, except for those involved in hydrogen bonding.

A dinuclear structural motif identical to **1** has been reported for the zinc dimethylpyrazolate complex [{Zn(Me$_2$pz)$_2$(Me$_2$pzH)$_2$}$_2$], with a pseudotetrahedral geometry around the zinc atoms [N–Zn–N 99.6(2)° –113.8(2)°].[2a] Analogous to the magnesium complex **1**, the metal centers are bridged by two μ-η$^1$:η$^1$-Me$_2$pz ligands, but with significantly shorter bridging bond lengths [Zn–N 1.991(3) Å] than the terminal ligand [Zn–N 2.025(3) Å]. The zinc atoms are capped by a Me$_2$pz/Me$_2$pzH pair, which is linked together by hydrogen bonding [N1–H1···N2 141°; H1···N2 1.77 Å], where the position of the hydrogen atom is disordered over two possible sites (Table 1).

The effect of metal size on the pyrazolato binding mode is nicely demonstrated in the heavier analogs **2** and **3**. Here, the larger size of calcium and europium (Ca$^{2+}$ = 1.14 Å, Eu$^{2+}$ = 1.31 Å, Mg$^{2+}$ = 0.860 Å; CN = 6)[7] requires the coordination of two equivalents of pyrazole to afford the dinuclear structures [{Ca(*i*Pr$_2$pz)$_2$(*i*Pr$_2$pzH)$_2$}$_2$] (**2**, Figure 2) and [{Eu(*i*Pr$_2$pz)$_2$(*i*Pr$_2$pzH)$_2$}$_2$] (**3**, Figure 3). The larger metals also display a more pronounced side-on coordination of the pyrazolate ring, as well as a π-bonding interaction of the europium metal centers with the aromatic core of the ligand, leading to an increased torsion angle between the N–N ligand moiety and the metal–metal axis (N1–N2–M1–M2 18° **1**, 55° **2**, 80° **3**). The same trend has been reported previously for the structures of [{M(*t*Bu$_2$pz)$_2$(thf)}$_2$] (M = Ca/Yb; Sr/Eu)[3e,5f] and [{M(*t*Bu$_2$pz)}$_n$] (M = Ca, *n* = 3; M = Sr/Eu, *n* = 4), where a more extended π-coordination of the bridging pyrazolato ligand is observed upon increasing metal size (Ca/Yb to Sr/Eu (μ-η$^2$:η$^2$ Ca/Yb, μ-η$^5$:η$^2$ Sr/Eu) in the former complexes, or an overall increase in metal–ligand contact sites in the latter compounds [Ση$^n$ = 8 (Ca2), 9 (Ca1,3); Ση$^n$ = 12 (Sr1), 9 (Sr2)].[3e,3k,5d,5f]

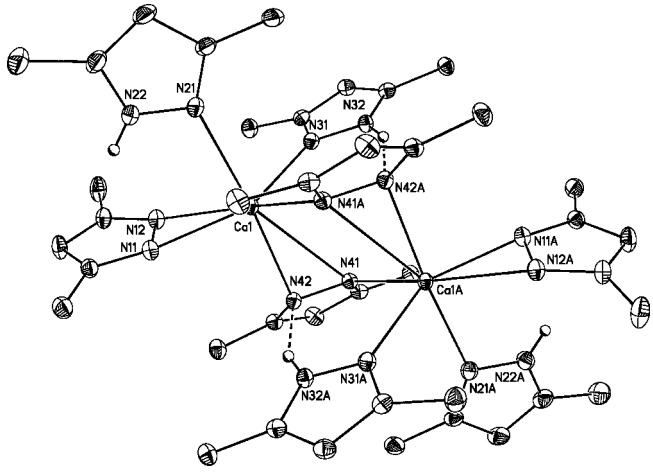


Figure 2. X-ray crystal structure of [{Ca(*i*Pr$_2$pz)$_2$(*i*Pr$_2$pzH)$_2$}$_2$] (**2**); the isopropyl groups and hydrogen atoms have been removed for clarity, except for those involved in hydrogen bonding.

The additional donor in **2** and **3**, in comparison to **1**, also leads to binding modes of μ-η$^2$:η$^1$-pyrazolato ligands in **2** and new μ-η$^5$:η$^1$-pyrazolato ligands in **3** further stabilized by hydrogen bonding between the pyrazole donor and the bridging ligand [N32–H···N42# 2.138(3) Å, 147.88° **2**, 2.012(5) Å, 151.20° **3**] but *not* between the terminal *i*Pr$_2$pz and *i*Pr$_2$pzH ligands. To better indicate this novel type of bridging coordination of the pyrazolato ligand, the coordination mode could also be expressed as μ$_3$-η$^1$(H):η$^2$(Ca):η$^1$(Ca) in **2** and μ$_3$-η$^1$(H):η$^5$(Eu):η$^1$(Eu) in **3**. This arrangement prevents the second pyrazolate nitrogen from bridging the metal centers [M1–N42# closest contact 3.292(1) Å **2**, 3.471(4) Å **3**, cf. M–N$_{br}$ 2.405(2)–3.003(2) Å **2**, 2.684(4)–2.794(4) Å **3**] and results in rather unsymmetrical M–N bond lengths induced by the twisting of the bridging pyrazolato ligand. The hydrogen bonding of pzH3 to the bridging pyrazolato ligand pz4 leads to closer M–N(pzH3) contacts relative to those of the second pyrazole

Table 1. Selected bond lengths [Å] and angles [°] for compound **1**.

| | | | | | |
|---|---|---|---|---|---|
| Mg1–N11 | 2.080(2) | N11–Mg1–N21 | 99.79(9) | N32–Mg2–N42 | 107.87(9) |
| Mg1–N21 | 2.083(2) | N11–Mg1–N31 | 105.97(9) | N32–Mg2–N51 | 119.07(9) |
| Mg1–N31 | 2.053(2) | N11–Mg1–N41 | 118.21(9) | N32–Mg2–N61 | 106.04(8) |
| Mg1–N41 | 2.056(2) | N21–Mg1–N31 | 117.11(9) | N42–Mg2–N51 | 108.98(9) |
| Mg2–N32 | 2.056(2) | N21–Mg1–N41 | 107.91(9) | N42–Mg2–N61 | 114.41(9) |
| Mg2–N42 | 2.061(2) | N31–Mg1–N41 | 108.19(9) | N51–Mg2–N61 | 100.59(9) |
| Mg2–N51 | 2.077(2) | | | | |
| Mg2–N61 | 2.088(2) | | | | |

 © 2007 Wiley-VCH Verlag GmbH & Co. KGaA, Weinheim 

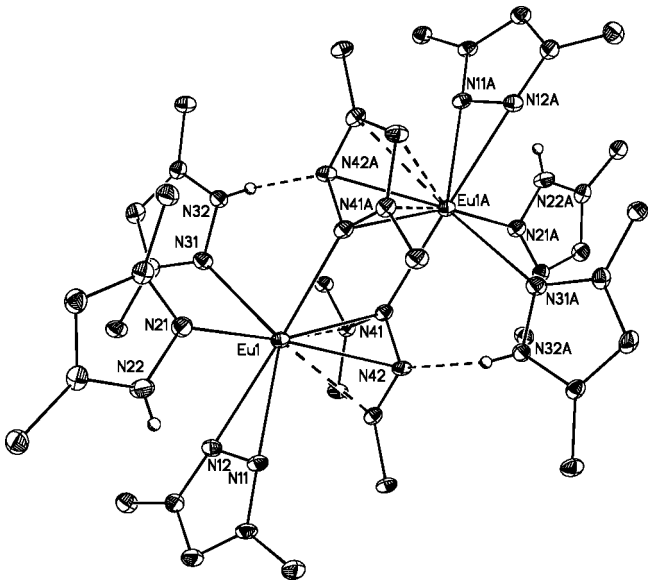


Figure 3. X-ray crystal structure of [{Eu($i$Pr$_2$pz)$_2$($i$Pr$_2$pzH)$_2$}$_2$] (**3**); the isopropyl groups and hydrogen atoms have been removed for clarity, except for those involved in hydrogen bonding.

donor pzH2, which also binds to the metal by means of its pyridine-like nitrogen [2.567(2) Å **2**, 2.693(4) Å **3**; cf. pzH3 2.455(2) Å **2**, 2.659(4) Å **3**] in an almost perpendicular orientation to the σ-bonded pyrazolate pz1 [dihedral angle 88.9(1)° **2**, 82.9(1)° **3**], thereby preventing further hydrogen-bonding contacts. Hence the novel type of bridging coordination of the pyrazolato ligand, μ-$\eta^2$:$\eta^1$ in **2** and μ-$\eta^5$:$\eta^1$ in **3**, is enforced by hydrogen bonding as one pz(N) is unable to further bridge the metal centers. A related structural feature of hydrogen-bonded, enforced $\eta^1$-pyrazolato coordination has been observed previously in [Nd($\eta^2$-Me$_2$pz)$_2$($\eta^1$-Me$_2$pz)(Me$_2$pzH)$_2$(py)].[31] The Eu–C43,45 distances in **3** are comparable with π-Eu–C bonds in [{Eu($t$Bu$_2$pz)$_2$}$_4$],[3k] which is consistent with the proposal of $\eta^5$-bonding, whereas the longer Ca–C distances for the smaller divalent metal are nonbonding (Table 2).

The coordination environment of the metal (formal coordination numbers 7 for **2**, and 8 for **3**) can be described in a simplified manner as a distorted trigonal bipyramid by considering the bonding through the center of the N–N bond for the σ-bonded pyrazolato ligand pz1 to be justified by the small bite angle [pz1 33.89(6)° **2**, 31.5(1)° **3**] and through the centroid (cen) of the N–N bond (**2**) or pyrazolate core (**3**) of the bridging ligand pz4. The pz4 ($\eta^2$ **2**, $\eta^5$ **3**) and N21 occupy the axial positions (169.4° **2**, 174.1° **3**), whereas the angle between N31–M–N41A (92.9° **2**, 87.6° **3**) in the equatorial plane is smaller than the others [cen(N11,12)–M–N31, cen(N11,12)–M–N41A 128.7°, 135.6° **2**, 113.7°, 151.1° **3**] because of hydrogen bonding.

The heteroleptic complex [{Ba($i$Pr$_2$pz)$_2$(py)$_3$}$_2$] (**5**, Figure 4) is a centrosymmetric dinuclear compound having nine-coordinate barium centers bridged by two chelating μ-$\eta^2$:$\eta^2$-pyrazolato ligands. Due to steric interactions with the third donor, the terminal $\eta^2$-pyrazolato ligands coordinate rather unsymmetrically to the metal [Ba–N 2.739(4) Å, 2.838(4) Å]. In contrast, the chelating, bridging ligand binds more symmetrically [Ba–N 2.806(4) Å, 2.884(4) Å; Ba–N# 2.991(4) Å, 3.060(4) Å], and the pyrazolate core is slightly inclined by 9.7(5)° towards Ba1 from an ideal perpendicular μ-$\eta^2$:$\eta^2$-bridging mode. This ligand inclination only provides very weak π-interactions between Ba1 and

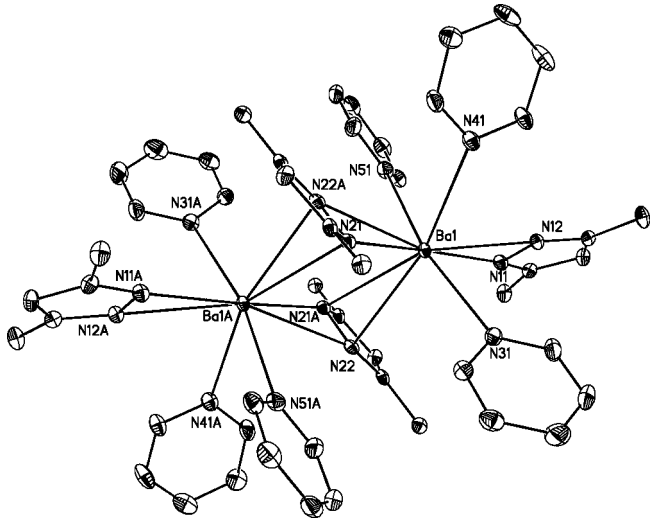


Figure 4. X-ray crystal structure of [{Ba($i$Pr$_2$pz)$_2$(py)$_3$}$_2$] (**5**); the isopropyl groups and hydrogen atoms have been removed for clarity.

Table 2. Selected bond lengths [Å] and angles [°] for compounds **2**, **3**.

| | | | | | |
|---|---|---|---|---|---|
| Ca1–N11 | 2.391(1) | Ca1–N41 | 3.003(1) | N11–Ca1–N12 | 33.89(6) |
| Eu1–N11 | 2.550(4) | Eu1–N41 | 2.794(4) | N11–Eu1–N12 | 31.46(12) |
| Ca1–N12 | 2.388(1) | Ca1–N42 | 2.467(1) | N11–Ca1–N21 | 82.43(6) |
| Eu1–N12 | 2.590(4) | Eu1–N42 | 2.760(4) | N11–Eu1–N21 | 75.95(12) |
| Ca1–N21 | 2.567(1) | Ca1–C43* | 3.367(2) | N12–Ca1–N21 | 80.87(6) |
| Eu1–N21 | 2.693(4) | Eu1–C43 | 3.019(4) | N12–Eu1–N21 | 77.84(12) |
| Ca1–N31 | 2.455(1) | Ca1–C44* | 4.209(2) | N21–Ca1–N31 | 87.36(6) |
| Eu1–N31 | 2.659(4) | Eu1–C44 | 3.178(5) | N21–Eu1–N31 | 82.72(11) |
| | | Ca1–C45* | 3.992(2) | N31–Ca1–N41 | 75.88(6) |
| | | Eu1–C45 | 3.051(4) | N31–Eu1–N41 | 94.92(11) |
| | | Ca1–N41# | 2.405(1) | N31–Ca1–N41A | 92.93(6) |
| | | Eu1–N41# | 2.684(4) | N31–Eu1–N41A | 87.65(11) |
| | | | | N41–Ca1–N42 | 27.39(5) |
| | | | | N41–Eu1–N42 | 29.13(10) |

#1 indicates symmetry generated atoms: 2–$x$, 1–$y$, 1–$z$: **2**; 1–$x$, 1–$y$, 1–$z$: **3**. * nonbonding distance.

 © 2007 Wiley-VCH Verlag GmbH & Co. KGaA, Weinheim 

C23, 25 [3.464(4) Å, 3.499(4) Å], contrasting the strong π-coordination observed in the absence of additional donors in the related complex [{Ba(*t*Bu$_2$pz)$_2$}$_6$] [Ba–C 3.10(1)–3.39(1) Å].[5d] The overall coordination sphere around the metal in **5** can be described as distorted octahedral with three pyridine donors and the N–N centroid (Ncen) of the bridging pyrazolato ligand in the equatorial plane [angles between neighboring ligands N31, N41, N51, Ncen(21,22), N31 94.1°, 82.0°, 90.9°, 97.1° respectively], whereas the axial positions are occupied by the terminal and the symmetry-generated bridging pyrazolato ligands [Ncen(21A,22A)–Ba–Ncen(11,12) 164.2°]. The Ba–N distances of the neutral pyridine donors range from 2.856(4) Å to 2.959(4) Å and thus lie between the bond lengths for the bridging pyrazolato ligand [2.806(4) Å–3.060(4) Å], though they are significantly longer than those for the terminal pyrazolato ligand [2.739(4) Å, 2.838(4) Å], as anticipated for a neutral donor (Table 3).

Table 3. Selected bond lengths [Å] and angles [°] for compound **5**.

| | | | |
|---|---|---|---|
| Ba1–N11 | 2.739(4) | N11–Ba1–N12 | 28.8(1) |
| Ba1–N12 | 2.838(4) | N21–Ba1–N22 | 79.9(1) |
| Ba1–N21 | 2.806(4) | N21#–Ba1–N22# | 74.3(1) |
| Ba1–N22 | 2.884(4) | N31–Ba1–N41 | 94.1(1) |
| Ba1–C23 | 3.464(4) | N41–Ba1–N51 | 82.0(1) |
| Ba1–C24 | 3.937(4) | N31–Ba1–N51 | 168.7(1) |
| Ba1–C25 | 3.499(4) | Ba1–N21–Ba1# | 96.6(1) |
| Ba1–N21# | 3.060(4) | Ba1–N22–Ba1# | 96.5(1) |
| Ba1–N22# | 2.991(4) | | |
| Ba1–N31 | 2.914(4) | | |
| Ba1–N41 | 2.959(4) | | |
| Ba1–N51 | 2.856(4) | | |

#1 indicates symmetry generated atoms: 2–*x*, 2–*y*, 1–*z*.

The difference in steric demand of *i*Pr$_2$pz compared with that of the *t*Bu$_2$pz ligand is apparent in the monomeric structure of the magnesium complex [Mg(*t*Bu$_2$pz)$_2$-(*t*Bu$_2$pzH)$_2$] [H···N 2.745(2) Å, N–H···N 153(3)°],[5b] which, despite the common metal, shows more similarity to the heavier monomeric dimethylpyrazolato analogs [M(Me$_2$pz)$_2$-(Me$_2$pzH)$_4$] (M = Ca, Sr) with hydrogen bonding between the terminal η$^1$-pyrazolato ligands and pyrazole donors [H···N 2.01(2) Å, N–H···N 156(2)° for Ca].[5c] The preferential formation of the present dinuclear, hydrogen-bonded complexes can be explained by the additional stabilization provided by the bridging of the metal centers, as the average bond length in **1** is shorter than in the monomeric [Mg(*t*Bu$_2$pz)$_2$(*t*Bu$_2$pzH)$_2$] whereas the overall metal coordination number is the same.[5b] The dinuclear formulation enables the formation of stronger/shorter hydrogen bonds. As the formation of **1** was also observed with an excess of *i*Pr$_2$pzH, targeting the formation of a monomeric [Mg(*i*Pr$_2$pz)$_2$(*i*Pr$_2$pzH)$_2$], the role of secondary interactions in coordination compounds must play a crucial role, a fact also observed in lanthanoid pyrazolate Nd(η$^2$-Me$_2$pz)$_2$-(η$^1$-Me$_2$pz)(Me$_2$pzH)$_2$(py)].[3l] For the larger analogs the dimerization leads to an increase in coordination number (**2** CN = 7, **3** CN = 8; cf. CN = 6 in [M(Me$_2$pz)$_2$(Me$_2$pzH)$_4$] M = Ca, Sr),[5c] while the average bond lengths are comparable despite the difference in coordination number.

In the structure of [Hg$_3$(*i*Pr$_2$pz)$_4$(C$_6$F$_5$)$_2$] (**4**, Figure 5), an open triangle of mercury atoms (Hg···Hg···Hg 55.66–67.22°) displays Hg1,2 as well as Hg2,3 [Hg···Hg 3.6395(6) Å, 3.7026(6) Å] each linked by two μ-η$^1$:η$^1$-3,5-diisopropylpyrazolato ligands, one nearly in the Hg$_3$ plane [Hg1,3, pz5 7.2(5)°; Hg2,3, pz3 26.9(5)°] and the other above or below the plane [Hg1,2, pz4 65.9(2)°; Hg2,3, pz2 77.0(3)°]. Both Hg1 and Hg3 have terminal C$_6$F$_5$ groups, and they form the open edge of the Hg$_3$ triangle [Hg···Hg 4.0644(7) Å]. It could be considered that the structure arises from the coordination of a [Hg(*i*Pr$_2$pz)$_4$]$^{2-}$ moiety to two [Hg-(C$_6$F$_5$)]$^+$ ions.

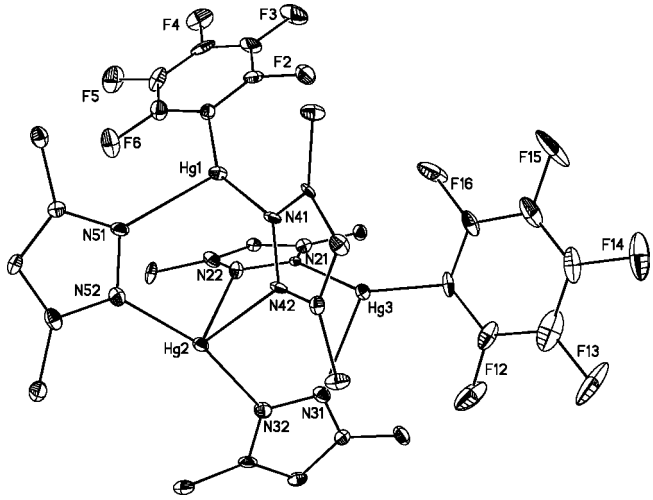


Figure 5. The crystal structure of [Hg$_3$(*i*Pr$_2$pz)$_4$(C$_6$F$_5$)$_2$] (**4**); the isopropyl groups and hydrogen atoms have been omitted for clarity.

Each terminal mercury atom, Hg1,3, is strongly bonded to a carbon and a nitrogen donor atom [Hg–C(N) ≈ 2.10 Å] and a further, more distant, nitrogen atom [Hg–N ≈ 2.43 Å]. Even the larger Hg–N bonds are well within the sum of the van der Waals radii of mercury (1.73 Å,[17] which is a conservative value, see also 1.9–2.0 Å,[17,18] or 2.1–2.2 Å[19]) and nitrogen (1.60 Å[20]). The geometry deviates considerably from the expected T-shape[21] (where the strongly bound ligands are linear) towards trigonal (angles ≈ 154°, 116°, 90°). Although coordination of the more distant nitrogen causes considerable bending of C1,11–Hg1,3–N41,21, any effect on the Hg–C distances [2.09(1) Å, 2.08(1) Å] is marginal, as they are near the Hg–C bond lengths observed in the homoleptic organomercurial Hg(C$_6$F$_5$)$_2$ [Hg–C 2.047(6)–2.052(6) Å][22] in the trinuclear [{Hg(C$_6$F$_4$)}$_3$]·(C$_6$H$_6$) [Hg–C 2.058(8) Å][23] or in the T-shaped three-coordinate [Hg(C$_6$F$_4$OH-*p*)$_2$(OH$_2$)] [Hg–C 2.047(7), 2.058(7) Å].[21b] Both the short and longer Hg–N distances are close to the values (ca. 2.15 Å, ca. 2.5 Å from X-ray powder diffraction data) for pseudo-polymeric mercuric pyrazolate.[24] By contrast with Hg1,3, Hg2 is four-coordinate with two short Hg–N bonds in a *transoid* arrangement [N32–Hg2–N52 163.5(4)°] and with two more distant nitrogen donors each nearly perpendicular to the N32–Hg2–N52 vector, resulting in overall sawhorse geometry. This is as expected for two strong and two weak donors

 © 2007 Wiley-VCH Verlag GmbH & Co. KGaA, Weinheim 

bound to mercury,[21a,22,23] though distorted square planar geometry has also been observed.[21b,25] Both short and long Hg–N bond lengths compare favorably to those observed at Hg1,3 (Table 4).

Table 4. Selected bond lengths [Å] and angles [°] for compound **4**.

| | | | |
|---|---|---|---|
| Hg1–C1 | 2.086(10) | N41–Hg1–N51 | 91.1(3) |
| Hg3–C11 | 2.079(10) | N41–Hg1–C1 | 152.6(4) |
| Hg1–N41 | 2.101(8) | N51–Hg1–C1 | 115.7(4) |
| Hg1–N51 | 2.422(9) | N22–Hg2–N32 | 92.2(3) |
| Hg2–N22 | 2.489(8) | N22–Hg2–N42 | 85.0(3) |
| Hg2–N32 | 2.066(9) | N22–Hg2–N52 | 96.3(3) |
| Hg2–N42 | 2.472(8) | N32–Hg2–N42 | 96.1(3) |
| Hg2–N52 | 2.051(9) | N32–Hg2–N52 | 163.5(4) |
| Hg3–N21 | 2.113(8) | N42–Hg2–N52 | 98.8(3) |
| Hg3–N31 | 2.442(9) | N21–Hg3–N31 | 87.7(3) |
| | | N21–Hg3–C11 | 155.0(4) |
| | | N31–Hg3–C11 | 116.7(4) |

The structural motif of trinuclear mercury complexes has been reported for a number of compounds,[26] although many structures contain mixed-valent or fractional valence species,[27] as seen in a series of $[\{Hg[P(Ph_2)CH_2P(Ph_2)]\}_3][A]_n$ with a range of different counterions (A = $CH_3SO_3$, $CF_3SO_3$, $PF_6$, $SiF_6$, $CF_3CO_2$),[27a] leaving the (*ortho*-phenylene)mercury derivatives $[\{Hg(C_6F_4)\}_3]$ and $[\{Hg(C_6H_4)\}_3]$ as the most closely related species.[23,26] However, these display closed $Hg_3$ unit, whereas **4** is open. Another difference of such compounds from **4** is the planar metal/ligand arrangement, favoring π-stacking with a variety of arenes (benzene, toluene, naphthalene, etc.).[23,26k] In the heteroleptic complex **4**, the trinuclear metal center is shielded by two pyrazolato ligands above and below the plane. In addition, the steric bulk provided by the isopropyl substituents prevents any potential stabilizing arene–Hg interactions.

## Conclusions

The increasing metal size in the 3,5-diisopropylpyrazolates **1**–**3** and **5** leads to a stepwise increase in coordination number [Mg 4, Ca 7, Eu 8, Ba 9], in addition to changes in the bridging ligand orientation from the exobidentate pyrazolato ligands in the magnesium complex **1**, via the already tilted, hydrogen-bonded μ-$\eta^1$:$\eta^2$-bridging pyrazolato ligands in the heavier metal analog **2** and μ-$\eta^1$:$\eta^5$ in **3**, to the almost perpendicular μ-$\eta^2$:$\eta^2$-bridging ligand and three pyridine donors in the barium complex **5**. These compounds display further examples of the amazing variety of binding modes of the pyrazolato ligand system and illustrate the unique role of secondary interactions in the stabilization of labile or highly reactive compounds. Intramolecular hydrogen bonding in pyrazolato complexes has previously only been reported between terminal ligands,[2a,4c,5b] enforcing an $\eta^1$-coordination over the otherwise preferred terminal $\eta^2$-chelation. The interaction with the μ-$\eta^1$:$\eta^n$ bridging ligands is a new structural feature and implies that minor steric effects or the potential of additional stabilization via hydrogen bonding of the ligand/donor can significantly influence the overall complex geometry. It is interesting to note that compounds **1**–**3** form preferentially over analogs of the oligonuclear $[M(t\mathrm{Bu}_2\mathrm{pz})_2]_n$ (M = Ca, Sr, Ba; $n$ = 3–6),[5d] as rationalized by the decreased steric demand of the $i\mathrm{Pr}_2$pz ligand and hence insufficient shielding of the metal centers. A polynuclear formulation for $[Ba(i\mathrm{Pr}_2\mathrm{pz})_2]_x$ provides an explanation for its hydrocarbon insolubility and the need for additional donors as in **5** to induce solubility and enable crystallization.

## Experimental Section

**General Remarks:** All preparations were carried out under an atmosphere of purified nitrogen. Pentane and toluene were predried with sodium, distilled under nitrogen from sodium/benzophenone, and stored in Schlenk flasks fitted with Teflon taps, or freshly distilled from sodium/potassium alloy and degassed in three freeze-pump-thaw cycles; pyridine was distilled from $CaH_2$ under nitrogen and stored in Schlenk flasks fitted with Teflon taps. 3,5-Diisopropylpyrazole, dibutylmagnesium (1.0 M solution in heptane), calcium, strontium, ytterbium, and europium metals were obtained commercially (+99.9% distilled ingots; europium ingots stored under oil); $Hg(C_6F_5)_2$ was prepared by a literature method.[28] IR data (4000–650 $cm^{-1}$) were obtained for Nujol or mineral oil mulls sandwiched between NaCl plates with a Perkin–Elmer 1600 or Perkin–Elmer Paragon FTIR spectrometer. $^1$H and $^{13}$C NMR spectra were recorded with Bruker Avance spectrometers (300 MHz; 25 °C) in [$D_6$]benzene and the chemical shifts referenced to the residual solvent signals. Melting points of air-sensitive compounds were obtained in capillaries sealed under nitrogen and are uncorrected.

**Synthesis of Compounds 1–5**

**$[\{Mg(i\mathrm{Pr}_2\mathrm{pz})_2(i\mathrm{Pr}_2\mathrm{pzH})\}_2]$ (1):** 3,5-Diisopropylpyrazole (0.63 g, 4.0 mmol) was dissolved in toluene (30 mL), dibutylmagnesium (1.0 M in heptane; 1.0 mL, 1.0 mmol) was added with a syringe, and the reaction mixture was heated at reflux for 2 h. Filtration, removal of the solvent, and recrystallization from hot pentane yielded very thin, colorless plates of **1** at room temperature (0.40 g, 84%). M.p. 76–79 °C. $^1$H NMR (300 MHz, $C_6D_6$, 25 °C): $\delta$ = 1.22 [s, 72 H, CH(C$H_3$)$_2$], 3.02–2.87 [m, 12 H, C$H$(CH$_3$)$_2$], 5.86 [s, 2 H, C4-H(pzH)], 5.88 [s, 2 H, C4-H($pz_{ter}$)], 5.99 [s, 2 H, C4-H($pz_{br}$)], 11.02 [br. s, 2 H, (pz)NH] ppm. $^{13}$C NMR (300 MHz, $C_6D_6$, 25 °C): $\delta$ = 23.3 [pzH, CH(*C*H$_3$)$_2$], 24.7 [pz, CH(*C*H$_3$)$_2$], 27.6 [pzH, *C*H(CH$_3$)$_2$], 28.7 [pz, *C*H(CH$_3$)$_2$], 97.3 [*C*H(pzH)], 97.6 [*C*H($pz_{ter}$)], 98.6 [*C*H($pz_{br}$)], 159.0 [*ipso*-*C*(pzH)], 165.0 [*ipso*-*C*(pz)] ppm. IR (Nujol): $\tilde{\nu}$ = 3307 (w), 3166 (m), 3087 (m), 1867 (m), 1728 (w), 1674 (w), 1575 (m), 1522 (s), 1504 (s), 1467 (s), 1422 (m), 1360 (m), 1302 (s), 1263 (s), 1176 (m), 1102 (s), 959 (w), 922 (m), 866 (s), 786 (s), 725 (m), 700 (m), 665 (m) $cm^{-1}$.

Attempted preparation of $[Mg(i\mathrm{Pr}_2\mathrm{pz})_2(i\mathrm{Pr}_2\mathrm{pzH})_4]$ by reaction of 3,5-diisopropylpyrazole (0.95 g, 6.0 mmol) and dibutylmagnesium (1.0 M in heptane; 1.0 mL, 1.0 mmol) in toluene (30 mL) led to the cocrystallization of thin plates of **1** and thin needles of $i\mathrm{Pr}_2$pzH.

**$[\{Ca(i\mathrm{Pr}_2\mathrm{pz})_2(i\mathrm{Pr}_2\mathrm{pzH})_2\}_2]$ (2):** Calcium metal in pieces (0.20 g, 5.0 mmol), bis(pentafluorophenyl)mercury (0.54 g, 1.0 mmol), and 3,5-diisopropylpyrazole (0.31 g, 2.0 mmol) were stirred in toluene (40 mL) for two days. Filtration, reduction of the solvent volume (20 mL), and cooling to –20 °C yielded colorless rods of **2** (0.29 g, 89% on pyrazole). M.p. 116–120 °C. $^1$H NMR (300 MHz, $C_6D_6$, 25 °C): $\delta$ = 1.21 [bd, 96 H, CH(C$H_3$)$_2$], 3.03 [br. s, 16 H, C*H*(CH$_3$)$_2$], 5.92 [s, 8 H, C4-H(pz)], 11.86 (b, 4 H, N-H) ppm. $^{13}$C

 © 2007 Wiley-VCH Verlag GmbH & Co. KGaA, Weinheim 

NMR (300 MHz, $C_6D_6$, 25 °C): $\delta$ = 24.0 [$CH(CH_3)_2$], 28.2 [$CH(CH_3)_2$], 97.8 [*C*H(pz)], 157.8 [*ipso*-C(pz)] ppm. IR (Nujol): $\tilde{\nu}$ = 3338 (m), 3167 (m), 3100 (w), 1638 (m), 1612 (w), 1561 (m), 1510 (s), 1460 (s), 1416 (m), 1303 (m), 1293 (m), 1276 (m), 1251 (m), 1176 (m), 1134 (s), 1070 (s), 1050 (m), 1011 (m), 991 (m), 966 (s), 892 (w), 878 (w), 805 (m), 782 (m), 726 (m), 692 (w), 669 (w) $cm^{-1}$.

**[{Eu(*i*Pr$_2$pz)$_2$(*i*Pr$_2$pzH)$_2$}$_2$] (3):** Europium metal in pieces (0.76 g, 5.0 mmol), bis(pentafluorophenyl)mercury (0.54 g, 1.0 mmol), and 3,5-diisopropylpyrazole (0.31 g, 2.0 mmol) were stirred in toluene (40 mL) for two days. Filtration, reduction of the solvent volume (20 mL), and cooling to –20 °C yielded dark yellow rods of **3** (0.37 g, 96% on pyrazole). M.p. 88 °C. IR (Nujol): $\tilde{\nu}$ = 3329 (m), 3088 (m), 1930 (w), 1860 (w), 1819 (w), 1763 (w), 1713 (w), 1638 (m), 1556 (m), 1506 (s), 1464 (s), 1373 (s), 1275 (m), 1178 (m), 1135 (m), 1069 (s), 1019 (m), 967 (s), 805 (m), 721 (m) $cm^{-1}$.

**[Hg$_3$(*i*Pr$_2$pz)$_4$(C$_6$F$_5$)$_2$] (4):** Strontium metal in pieces (0.44 g, 5.0 mmol), bis(pentafluorophenyl)mercury (0.27 g, 0.5 mmol), 3,5-diisopropylpyrazole (0.32 g, 2.0 mmol) were heated at reflux in toluene (30 mL) for 48 h. Filtration and reduction of the solvent volume (20 mL) led to the isolation of very small, colorless plates after several days at room temperature. Yield 0.09 g (18% on mercury). M.p. 76–82 °C (melted), >110 °C (clear). IR (Nujol): $\tilde{\nu}$ = 3180 (m), 3097 (m), 1634 (m), 1573 (m), 1506 (s), 1362 (s), 1300 (m), 1263 (m), 1177 (m), 1128 (m), 1097 (s), 1076 (s), 1044 (s), 1010 (s), 963 (s), 874 (w), 792 (s), 718 (s) $cm^{-1}$. $^1$H NMR (300 MHz, [D$_6$]benzene, 25 °C): $\delta$ = 5.89 [s, 4 H, C4-H(pz)], 2.83 [m, 8 H, $CH(CH_3)_2$], 1.18 [d, 48 H, $CH(CH_3)_2$] ppm. $^{13}$C NMR: $\delta$ = 129.8 [*ipso*-*C*(pz)*i*Pr], 98.1 [*C*H(pz)], 28.6 [$CH(CH_3)_2$], 24.0 [$C(CH_3)_2$] ppm; $C_6F_5$ undetected. $^{19}$F NMR: $\delta$ = –115.8 (td, $^3J_{(F\text{-}F)}$ = 20 Hz, $^3J_{(Hg\text{-}F)}$ = 502 Hz, 4 F, F2,6), –155.3 (t, $^3J_{(F\text{-}F)}$ = 20 Hz, 2 F, F4), –161.9 (t, $^3J_{(F\text{-}F)}$ = 20 Hz, 4 F, F3,5) ppm.

**[{Ba(*i*Pr$_2$pz)$_2$(py)$_3$}$_2$] (5):** Barium metal in pieces (0.65 g, 5 mmol) and 3,5-diisopropylpyrazole (0.31 g, 2 mmol) were heated to 170 °C for 5 d in a sealed and evacuated (approx. $1 \times 10^{-3}$ Torr) Carius tube until the contents of the tube solidified. Extraction of the crude product [{Ba(*i*Pr$_2$pz)$_2$}$_n$] with a mixture of toluene (30 mL) and pyridine (15 mL) led to the isolation of colorless plates upon cooling to –20 °C. Yield 0.26 g (56%). M.p. 63–65 °C, 115 °C (solidifies again), >235 °C (decomposition). IR (Nujol): $\tilde{\nu}$ = 3178 (m), 3101 (m), 1858 (w), 1574 (s), 1502 (s), 1405 (s), 1360 (s), 1304 (s), 1261 (s), 1218 (w), 1177 (s), 1129 (sh), 1105 (s), 1047 (w), 994 (s), 882 (m), 846 (m), 725 (s), 747 (w), 699 (s), 682 (sh), 673 (w) $cm^{-1}$. $^1$H NMR (300 MHz, [D$_6$]benzene, 25 °C): $\delta$ = 8.48 [td, $^3J_{(H,H)}$ = 3.0 Hz, 6 H, *o*-H(py)], 6.98 [tt, $^3J_{(H,H)}$ = 8.0 Hz, 3 H, *p*-H(py)], 6.66 [tt, $^3J_{(H,H)}$ = 4.0 Hz, 6 H, *m*-H(py)], 5.97 (s, 4 H, H4-pz), 3.02 [sept, 8 H, $CH(CH_3)_2$], 1.26 [d, 48 H, $CH(CH_3)_2$] (partially desolvated) ppm. $^{13}$C NMR: $\delta$ = 157.2 [*ipso*-*C*(pz)-*i*Pr], 150.6 [*o*-*C*(py)], 135.7 [*p*-*C*(py)], 123.9 [*m*-*C*(py)], 98.1 [*C*H(pz)], 28.3 [$CH(CH_3)_2$], 24.0 [$CH(CH_3)_2$] ppm.

**Attempted Preparation of [{Yb(*i*Pr$_2$pz)$_2$(*i*Pr$_2$pzH)$_2$}$_2$]:** Ytterbium metal in pieces (0.88 g, 5.0 mmol), bis(pentafluorophenyl)mercury (0.54 g, 1.0 mmol), and 3,5-diisopropylpyrazole (0.31 g, 2.0 mmol) were stirred in toluene (40 mL) for two days. Filtration, reduction of the solvent volume (20 mL), and cooling to –20 °C led to the subsequent recovery of 3,5-diisopropylpyrazole and bis(pentafluorophenyl)mercury toluene solvate.

**Attempted Preparation of [{Sr(*i*Pr$_2$pz)$_2$(*i*Pr$_2$pzH)$_2$}$_2$]:** Strontium metal in pieces (0.44 g, 5.0 mmol), bis(pentafluorophenyl)mercury (0.54 g, 1.0 mmol), and 3,5-diisopropylpyrazole (0.31 g, 2.0 mmol) were stirred in toluene (40 mL) for two days. Filtration, reduction of the solvent volume (20 mL), and cooling to –20 °C led to recovery of 3,5-diisopropylpyrazole and bis(pentafluorophenyl)mercury. Changing the ligand/mercurial stoichiometry to a ratio of 4:1 and heating the reaction mixture at reflux led to the isolation of **4**.

**X-ray Crystallography:** For compounds **1**–**5** a hemisphere of low temperature data was collected (monochromatic Mo-$K_\alpha$ radiation, $\lambda$ = 0.71073 Å) by using a Bruker AXS SMART system, complete with 3-circle goniometer and APEX-CCD detector, for **1** and **4** and an Enraf–Nonius CCD area-detector instrument for **2**, **3**, **5** (Table 5). A total of $N$ unique reflections ($N_o$ [$I > 2\sigma(I)$] "observed") were used in least-squares refinement [anisotropic $U$ for non-hydrogen atoms, ($x$, $y$, $z$, $U_{iso}$)$_H$ constrained] after structure solution by Direct Methods as included in the XSEED or SHELXTL-Plus program package.[29] Absorption corrections were performed with the programs SADABS (**1**, **4**) and maXus (**2**, **3**,

Table 5. Experimental crystallographic data for compounds **1**–**5**.

| | **1** | **2** | **3** | **4** | **5** |
|---|---|---|---|---|---|
| Empirical formula | $C_{54}H_{92}Mg_2N_{12}$ | $C_{72}H_{124}Ca_2N_{16}$ | $C_{72}H_{124}Eu_2N_{16}$ | $C_{48}H_{60}F_{10}Hg_3N_8$ | $C_{66}H_{90}Ba_2N_{14}$ |
| Formula weight | 958.02 | 1294.03 | 1517.79 | 1540.81 | 1354.20 |
| Crystal system | triclinic | monoclinic | triclinic | triclinic | triclinic |
| Space group | $P\bar{1}$ (No. 2) | $P2_1/a$ (No. 14) | $P\bar{1}$ (No. 2) | $P\bar{1}$ (No. 2) | $P\bar{1}$ (No. 2) |
| $a$ [Å] | 10.860(1) | 13.9033(2) | 11.8046(3) | 10.398(1) | 11.9467(1) |
| $b$ [Å] | 14.508(2) | 20.8058(4) | 11.8805(4) | 12.550(1) | 13.2047(2) |
| $c$ [Å] | 20.711(3) | 14.5525(3) | 15.3057(5) | 22.846(2) | 13.9593(2) |
| $\alpha$ [°] | 73.904(3) | 90 | 90.978(2) | 79.775(2) | 114.553(1) |
| $\beta$ [°] | 87.431(3) | 107.131(1) | 101.478(2) | 88.313(2) | 92.137(1) |
| $\gamma$ [°] | 70.313(3) | 90 | 111.050(2) | 71.375(2) | 116.411(1) |
| $V$ [Å$^3$] | 2947.7(7) | 4022.83(13) | 1954.0(1) | 2779.1(4) | 1725.96(5) |
| $Z$ | 2 | 2 | 1 | 2 | 1 |
| $T$ [K] | 87(2) | 123(2) | 123(2) | 123(2) | 91(2) |
| Density $\delta_{calcd.}$ [g cm$^{-3}$] | 1.079 | 1.068 | 1.290 | 1.841 | 1.303 |
| Absorption coefficient [mm$^{-1}$] | 0.084 | 0.189 | 1.639 | 8.338 | 1.181 |
| Reflections collected | 24216 | 38992 | 28465 | 22783 | 26109 |
| Reflections unique | 10365 ($R_{int}$ = 0.0605) | 7075 ($R_{int}$ = 0.0597) | 6823 ($R_{int}$ = 0.0738) | 9780 ($R_{int}$ = 0.0543) | 6055 ($R_{int}$ = 0.0923) |
| Final R-indices [$I > 2\sigma(I)$][a] | $R$ = 0.0609 | $R$ = 0.0483 | $R$ = 0.0420 | $R$ = 0.0742 | $R$ = 0.0593 |
| | $R_w$ = 0.1268 | $R_w$ = 0.1079 | $R_w$ = 0.0955 | $R_w$ = 0.1241 | $R_w$ = 0.1499 |

[a] $R = \Sigma||F_o| - |F_c||/\Sigma|F_o|$; $Rw = [\Sigma w(F_o^2 - F_c^2)^2/\Sigma w(F_o^2)^2]^{1/2}$.

 © 2007 Wiley-VCH Verlag GmbH & Co. KGaA, Weinheim 

**5**).[30] All carbon-bound hydrogen atoms were placed geometrically and refined, including free rotation about C–C bonds for methyl groups with $U_{iso}$ constrained at 1.2 for non-methyl groups, and 1.5 for methyl groups times $U_{eq}$ of the carrier C atom. The pyrazole N–H hydrogen atoms were located in the respective difference Fourier maps and refined isotropically.

CCDC-283035 to -283037 (for **1**–**3**), -608636 (for **4**), -299836 (for **5**) contain the supplementary crystallographic data for this paper. These data can be obtained free of charge from The Cambridge Crystallographic Data Centre via www.ccdc.cam.ac.uk/data_request/cif.

## Acknowledgments

We gratefully acknowledge support from the Monash University Small Grant Scheme, the Australian Research Council, and the National Science Foundation [Grants CHE-0108098 (including a supplement) and CHE-0505863], enabling the collaboration between Monash University and Syracuse University. Purchase of the X-ray diffraction equipment at Syracuse was made possible with grants from the National Science Foundation (Grants CHE-9527858 and CHE-0234912), Syracuse University, and the W. M. Keck Foundation.

[1] a) S. Trofimenko, *Chem. Rev.* **1972**, *72*, 497–509; b) S. Trofimenko, *Prog. Inorg. Chem.* **1986**, *34*, 115–210; c) A. P. Sadimenko, S. S. Basson, *Coord. Chem. Rev.* **1996**, *147*, 247–297; d) G. LaMonica, G. A. Ardizzoia, *Prog. Inorg. Chem.* **1997**, *46*, 151–238; e) J. E. Cosgriff, G. B. Deacon, *Angew. Chem.* **1998**, *110*, 298–299; *Angew. Chem. Int. Ed.* **1998**, *37*, 286–287; f) F. Nief, *Eur. J. Inorg. Chem.* **2001**, 891–904; g) A. P. Sadimenko, *Adv. Heterocycl. Chem.* **2001**, *81*, 167–252.

[2] a) M. K. Ehlert, S. J. Rettig, A. Storr, R. C. Thompson, J. Trotter, *Can. J. Chem.* **1990**, *68*, 1494–1498; b) D. Röttger, G. Erker, M. Grehl, R. Fröhlich, *Organometallics* **1994**, *13*, 3897–3902; c) D. Carmona, J. Ferrer, F. J. Lahoz, L. A. Oro, M. P. Lamata, *Organometallics* **1996**, *15*, 5175–5178; d) I. A. Guzei, A. G. Baboul, G. P. A. Yap, A. L. Rheingold, H. B. Schlegel, C. H. Winter, *J. Am. Chem. Soc.* **1997**, *119*, 3387–3388; e) I. A. Guzei, G. P. A. Yap, C. H. Winter, *Inorg. Chem.* **1997**, *36*, 1738; f) C. Yelamos, M. J. Heeg, C. H. Winter, *Inorg. Chem.* **1999**, *38*, 1871–1878; g) C. Yelamos, M. J. Heeg, C. H. Winter, *Organometallics* **1999**, *18*, 1168–1176; h) J. R. Perera, M. J. Heeg, H. B. Schlegel, C. H. Winter, *J. Am. Chem. Soc.* **1999**, *121*, 4536–4537; i) N. C. Mösch-Zanetti, R. Krätzner, C. Lehmann, T. R. Schneider, I. Usón, *Eur. J. Inorg. Chem.* **2000**, 13–16; j) K. R. Gust, M. J. Heeg, C. H. Winter, *Polyhedron* **2001**, *20*, 805–813; k) K. R. Gust, J. E. Knox, M. J. Heeg, H. B. Schlegel, C. H. Winter, *Angew. Chem.* **2002**, *114*, 1661–1664; *Angew. Chem. Int. Ed.* **2002**, *41*, 1591–1594; l) T. Beringhelli, G. D′Alfonso, M. Panigati, P. Mercandelli, A. Sironi, *Chem. Eur. J.* **2002**, *8*, 5340–5350; m) K. Most, N. C. Mösch-Zanetti, D. Vidovic, J. Magull, *Organometallics* **2003**, *22*, 5485–5490; n) G. Zhu, J. M. Tanski, G. Parkin, *Polyhedron* **2003**, *22*, 199–203; o) C. L. I. V. Dezelah, O. M. El-Kadri, M. J. Heeg, C. H. Winter, *J. Mater. Chem.* **2004**, *14*, 3167–3176; p) Y. Kawamura, Y. Tsukahara, S. Nasu, S. Marimoto, A. Fuyuhiro, S. Kaizaki, *Inorg. Chim. Acta* **2004**, *357*, 2437–2440; q) E. Sebe, I. A. Guzei, M. J. Heeg, L. M. Liable-Sands, A. L. Rheingold, C. H. Winter, *Eur. J. Inorg. Chem.* **2005**, 3955–3961; r) G. B. Deacon, E. E. Delbridge, D. J. Evans, R. Harika, P. C. Junk, B. W. Skelton, A. H. White, *Chem. Eur. J.* **2004**, *10*, 1193–1204; s) K. Most, J. Hoßbach, D. Vidovic, J. Magull, N. C. Mösch-Zanetti, *Adv. Synth. Catal.* **2005**, *347*, 463–472; t) N. C. Mösch-Zanetti, A. Sachse, R. Pfoh, D. Vidovic, J. Magull, *Dalton Trans.* **2005**, 2124–2129; u) J. Vela, S. Vaddadi, S. Kingsley, C. J. Flaschenriem, R. J. Lachicotte, T. R. Cundar, P. L. Holland, *Angew. Chem.* **2006**, *118*, 1637–1641; *Angew. Chem. Int. Ed.* **2006**, *45*, 1607–1611.

[3] a) H. Schumann, P. R. Lee, J. Loebel, *Angew. Chem.* **1989**, *101*, 1073–1074; *Angew. Chem. Int. Ed. Engl.* **1989**, *28*, 1033–1035; b) G. B. Deacon, B. M. Gatehouse, S. Nickel, S. N. Platts, *Aust. J. Chem.* **1991**, *44*, 613–621; c) J. E. Cosgriff, G. B. Deacon, B. M. Gatehouse, H. Hemling, H. Schumann, *Angew. Chem.* **1993**, *105*, 906–907; *Angew. Chem. Int. Ed. Engl.* **1993**, *32*, 874–875; d) J. E. Cosgriff, G. B. Deacon, B. M. Gatehouse, *Aust. J. Chem.* **1993**, *46*, 1881–1896; e) G. B. Deacon, E. E. Delbridge, B. W. Skelton, A. H. White, *Angew. Chem.* **1998**, *110*, 2372–2373; *Angew. Chem. Int. Ed.* **1998**, *37*, 2251–2252; f) G. B. Deacon, E. E. Delbridge, C. M. Forsyth, P. C. Junk, B. W. Skelton, A. H. White, *Aust. J. Chem.* **1999**, *52*, 733–739; g) G. B. Deacon, E. E. Delbridge, C. M. Forsyth, *Angew. Chem.* **1999**, *111*, 1880–1882; *Angew. Chem. Int. Ed.* **1999**, *38*, 1766–1767; h) G. B. Deacon, A. Gitlits, B. W. Skelton, A. H. White, *Chem. Commun.* **1999**, 1213–1214; i) D. Pfeiffer, B. J. Ximba, L. M. Liable-Sands, A. L. Rheingold, M. J. Heeg, D. M. Coleman, H. B. Schlegel, T. F. Kuech, C. H. Winter, *Inorg. Chem.* **1999**, *38*, 4539–4548; j) G. B. Deacon, E. E. Delbridge, B. W. Skelton, A. H. White, *Eur. J. Inorg. Chem.* **1999**, 751–761; k) G. B. Deacon, A. Gitlits, P. W. Roesky, M. R. Bürgstein, K. C. Lim, B. W. Skelton, A. H. White, *Chem. Eur. J.* **2001**, *7*, 127–138; l) G. B. Deacon, C. M. Forsyth, A. Gitlits, R. Harika, P. C. Junk, B. W. Skelton, A. H. White, *Angew. Chem.* **2002**, *114*, 3383–3385; *Angew. Chem. Int. Ed.* **2002**, *41*, 3249–3251; m) G. B. Deacon, C. M. Forsyth, A. Gitlits, B. W. Skelton, A. H. White, *Dalton Trans.* **2004**, 1239–1247; n) S. Beaini, G. B. Deacon, M. Hilder, P. C. Junk, D. R. Turner, *Eur. J. Inorg. Chem.* **2006**, *17*, 3434–3441.

[4] a) J. G. Cederberg, T. D. Culp, B. Bieg, D. Pfeiffer, C. H. Winter, K. L. Bray, T. F. Kuech, *J. Cryst. Growth* **1998**, *195*, 105–111; b) T. D. Culp, J. G. Cederberg, B. Bieg, T. F. Kuech, K. L. Bray, D. Pfeiffer, C. H. Winter, *J. Appl. Phys.* **1998**, *83*, 4918–4927; c) D. Pfeiffer, M. J. Heeg, C. H. Winter, *Angew. Chem.* **1998**, *110*, 2674–2676; *Angew. Chem. Int. Ed.* **1998**, *37*, 2517–2519; d) J. G. Cederberg, T. D. Culp, B. Bieg, D. Pfeiffer, C. H. Winter, K. L. Bray, T. F. Kuech, *J. Appl. Phys.* **1999**, *85*, 1825–1831; e) Y. Chi, H.-L. Yu, W.-L. Ching, C.-S. Liu, Y.-L. Chen, T.-Y. Chou, S.-M. Peng, G.-H. Lee, *J. Mater. Chem.* **2002**, *12*, 1363–1369; f) Y.-H. Song, Y.-L. Chen, Y. Chi, C.-S. Liu, W.-L. Ching, J.-J. Kai, R.-S. Chen, Y.-S. Huang, A. J. Carty, *Chem. Vap. Deposition* **2003**, *9*, 162–169; g) Y. Chi, E. Lay, T.-Y. Chou, Y.-H. Song, A. J. Carty, *Chem. Vap. Deposition* **2005**, *11*, 206–212.

[5] a) D. Pfeiffer, M. J. Heeg, C. H. Winter, *Inorg. Chem.* **2000**, *39*, 2377–2384; b) N. C. Mösch-Zanetti, M. Ferbinteanu, J. Magull, *Eur. J. Inorg. Chem.* **2002**, 950–956; c) J. Hitzbleck, A. Y. O'Brien, G. B. Deacon, K. Ruhlandt-Senge, *Chem. Eur. J.* **2004**, *10*, 3315–3323; d) J. Hitzbleck, G. B. Deacon, K. Ruhlandt-Senge, *Angew. Chem.* **2004**, *116*, 5330–5332; *Angew. Chem. Int. Ed.* **2004**, *43*, 5218–5220; e) H. M. El-Kaderi, M. J. Heeg, C. H. Winter, *Polyhedron* **2005**, *24*, 645–653; f) J. Hitzbleck, G. B. Deacon, A. Y. O'Brien, K. Ruhlandt-Senge, *Inorg. Chem.* **2006**, *45*, 10329.

[6] a) L. R. Falvello, J. Fornies, A. Martin, R. Navarro, V. Sicilia, P. Villarroya, *Chem. Commun.* **1998**, 2429–2430; b) C. Yelamos, M. J. Heeg, C. H. Winter, *Inorg. Chem.* **1998**, *37*, 3892–3894; c) J. R. Perera, M. J. Heeg, H. B. Schlegel, C. H. Winter, *J. Am. Chem. Soc.* **1999**, *121*, 4536–4537; d) G. B. Deacon, E. E. Delbridge, C. M. Forsyth, B. W. Skelton, A. H. White, *J. Chem. Soc., Dalton Trans.* **2000**, 745–751; e) A. Steiner, G. T. Lawson, B. Walfort, D. Leusser, D. Stalke, *J. Chem. Soc., Dalton Trans.* **2001**, 219–221; f) G. B. Deacon, E. E. Delbridge, D. J. Evans, R. Harika, P. C. Junk, B. W. Skelton, A. H. White, *Chem. Eur. J.* **2004**, *10*, 1193–1204.

 © 2007 Wiley-VCH Verlag GmbH & Co. KGaA, Weinheim 

[7] R. D. Shannon, *Acta Crystallogr., Sect. A* **1976**, *32*, 751–767.
[8] a) L. G. Hubert-Pfalzgraf, *Appl. Organomet. Chem.* **1992**, *6*, 627–643; b) S. B. Turnipseed, R. M. Barkley, R. E. Sievers, *Inorg. Chem.* **1991**, *30*, 1164–1170.
[9] a) M. Gillett-Kunnath, W. Teng, W. Vargas, K. Ruhlandt-Senge, *Inorg. Chem.* **2005**, *44*, 4862–4870, and references cited herein; b) V. U. Wannagat, H. Autzen, H. Kuckertz, H.-J. Wismar, *Z. Anorg. Allg. Chem.* **1972**, *394*, 254–262; c) L. M. Engelhardt, B. S. Jolly, P. C. Junk, C. L. Raston, B. W. Skelton, A. H. White, *Aust. J. Chem.* **1986**, *39*, 1337–1345; d) R. A. Bartlett, M. M. Olmstead, P. P. Power, *Inorg. Chem.* **1994**, *33*, 4800–4803; e) W. Vargas, U. Englich, K. Ruhlandt-Senge, *Inorg. Chem.* **2002**, *41*, 5602–5608.
[10] a) Harder, F. Feil, *Organometallics* **2002**, *21*, 2268–2274; b) Harder, S. Mueller, E. Huebner, *Organometallics* **2004**, *23*, 178–183.
[11] G. B. Deacon, C. M. Forsyth, S. Nickel, *J. Organomet. Chem.* **2002**, *647*, 50–60.
[12] G. B. Deacon, T. Feng, C. M. Forsyth, A. Gitlits, D. C. R. Hockless, Q. Shen, B. W. Skelton, A. H. White, *J. Chem. Soc., Dalton Trans.* **2000**, 961–966.
[13] G. B. Deacon, E. E. Delbridge, B. W. Skelton, A. H. White, *Eur. J. Inorg. Chem.* **1998**, 543–545.
[14] R. D. Chambers, G. E. Coates, J. G. Livingstone, W. K. R. Musgrave, *J. Chem. Soc.* **1962**, 4367–5371.
[15] J. E. Cosgriff, G. B. Deacon, B. M. Gatehouse, *Aust. J. Chem.* **1993**, *46*, 1881–1896.
[16] a) H. B. Albrecht, G. B. Deacon, M. J. Tailby, *J. Organomet. Chem.* **1974**, *70*, 313–321; b) W. Kitching, M. Glenn, *Science of Synthesis* **2004**, *3*, 133–303.
[17] A. J. Canty, G. B. Deacon, *Inorg. Chim. Acta* **1980**, *45*, L225–L227.
[18] K. R. Flower, V. J. Howard, S. Naguthney, R. G. Prichard, J. E. Warren, A. T. McGown, *Inorg. Chem.* **2002**, *41*, 1907–1912.
[19] S. S. Batsanov, *J. Chem. Soc., Dalton Trans.* **1998**, *10*, 1541–1546.
[20] S. C. Nyburg, C. H. Faerman, *Acta Crystallogr., Sect. B* **1985**, 274276.
[21] a) G. B. Deacon, C. M. Forsyth, D. M. M. Freckmann, G. Meyer, D. Stellfeldt, *Z. Anorg. Allg. Chem.* **2000**, *626*, 540–546; b) G. B. Deacon, P. W. Felder, P. C. Junk, K. Mueller-Buschbaum, T. J. Ness, C. C. Quitmann, *Inorg. Chim. Acta* **2005**, *358*, 4389–4393.
[22] D. L. Wilkinson, J. Riede, G. Mueller, *Z. Naturforsch., Teil B* **1991**, *46*, 285–288.
[23] M. Tsunoda, F. P. Gabbai, *J. Am. Chem. Soc.* **2000**, *122*, 8335–8336.
[24] N. Masciocchi, G. A. Ardizzoia, A. Maspero, G. LaMonica, A. Sironi, *Inorg. Chem.* **1999**, *38*, 3657–3664.
[25] G. B. Deacon, P. C. Junk, P. Turner, *J. Chem. Crystallogr.* **2004**, *34*, 405–408.
[26] a) P. Sartori, A. Golloch, *Chem. Ber.* **1968**, *101*, 2004–2009; b) A. Streitwieser, P. J. Scannon, H. M. Niemeyer, *J. Am. Chem. Soc.* **1972**, *94*, 7926–7937; c) D. S. Brown, A. G. Massey, D. A. Wickens, *Acta Crystallogr., Sect. B* **1978**, *34*, 1695–1697; d) M. C. Ball, D. S. Brown, A. G. Massey, D. A. Wickens, *J. Organomet. Chem.* **1981**, *206*, 265–277; e) J. Catalan, J. L. M. Abboud, J. Elguero, *Adv. Heterocycl. Chem.* **1987**, *41*, 187–274; f) M. F. Hawthorne, *Pure Appl. Chem.* **1994**, *66*, 245–254; g) J. Vaugeois, M. Simard, J. D. Wuest, *Coord. Chem. Rev.* **1995**, *95*, 55–73; h) M. F. Hawthorne, Z. Zhang, *Acc. Chem. Res.* **1997**, *30*, 267–276; i) A. L. Chistyakov, I. V. Stankevich, N. P. Gambaryan, Yu. T. Struchkov, A. I. Yanovsky, I. A. Tikhoanova, V. B. Shur, *J. Organomet. Chem.* **1997**, *536*, 413–424; j) J. D. Wuest, *Acc. Chem. Res.* **1999**, *32*, 81–89; k) M. R. Haneline, M. Tsunoda, F. P. Gabbai, *J. Am. Chem. Soc.* **2002**, *124*, 3737–3742; l) M. R. Haneline, F. P. Gabbai, *Z. Naturforsch., Teil B* **2004**, *59*, 1483–1487.
[27] a) A. Knoepfler-Muhlecker, B. Scheffter, H. Kopacka, K. Wurst, P. Peringer, *J. Chem. Soc., Dalton Trans.* **1999**, 2525–2528; b) M. L. Cole, G. B. Deacon, P. C. Junk, K. Konstas, P. W. Roesky, *Eur. J. Inorg. Chem.* **2005**, 1090–1098.
[28] G. B. Deacon, J. E. Cosgriff, E. T. Lawrenz, C. M. Forsyth, D. L. Wilkinson in *Synthetic Methods of Organometallic and Inorganic Chemistry (Herrmann/Brauer), Vol. 6,* 3rd ed. (Ed.: W. A. Herrmann), G. Thieme, Stuttgart, **1997**, p. 48.
[29] a) L. J. Barbour, *J. Supramol. Chem.* **2003**, *1*, 189–191; b) G. M. Sheldrick, Siemens, Madison, WI (USA), **1999**.
[30] a) G. M. Sheldrick, University of Göttingen, Göttingen, Germany, **1996**; b) C. F. G. S. Mackay, C. Edwards, M. Tremayne, N. Stewart, K. Shankland, University of Glasgow (Scotland); Nonius BV, Delft (The Netherlands); MacScience Co. Ltd., Yokohama (Japan), **1998**.

Received: August 17, 2006
Published Online: December 27, 2006

 © 2007 Wiley-VCH Verlag GmbH & Co. KGaA, Weinheim 

DOI: 10.1002/ejic.200600825

# The Interplay between Yttrium and Barium or Copper Trifluoroacetates and *N*-Methyldiethanolamine: Synthesis of a Heterometallic $Y_3Cu$ Trifluoroacetate Complex and a Homometallic Ba-TFA 1D Polymer

**Shashank Mishra,*[a] Jianyong Zhang,[a] Liliane G. Hubert-Pfalzgraf,[a][†] Dominique Luneau,[b] and Erwann Jeanneau[b]**

**Keywords:** Heterometallic complexes / Yttrium / Copper / Barium / N,O ligands

The reactions between $[Y(TFA)_3(H_2O)_3]$ and either $[Cu(TFA)_2(MeOH)]$ or $[Ba(TFA)_2]_\infty$ in the presence of excess *N*-methyldiethanolamine ($mdeaH_2$) have been investigated in relation with their use as precursors for high Tc superconductors. They afford the heterometallic $Y_3Cu$ complex $[CuY_3(\mu_3\text{-}OH)(\mu\text{-}\eta^3\text{:}\eta^1\text{-}mdeaH)_3(\mu_3\text{-}\eta^3\text{:}\eta^1\text{:}\eta^1\text{-}mdeaH)_2(\eta^2\text{-}TFA)(\mu,\eta^2\text{-}TFA)_2](TFA)_2(H_2O)$ (**1**) and the homometallic Ba-TFA 1D polymer $[Ba_3(\eta^3\text{-}mdeaH_2)_2(\mu\text{-}\eta^3\text{:}\eta^1\text{-}mdeaH_2)_2(\eta^1\text{-}TFA)_2(\eta^2\text{-}TFA)_2(\mu_3\text{-}\eta^2\text{:}\eta^2\text{:}\eta^1\text{-}TFA)_2]_{1\infty}$ (**2**), respectively, in high yield. These compounds were characterised by X-ray diffraction and FT-IR, ESR (for **1**) and NMR (for **2**) spectroscopy. Single-crystal X-ray diffraction studies show the versatile bonding modes of the trifluoroacetate and *N*-methyldiethanolamine ligands, with the former acting not only as a terminal ($\eta^1$ and $\eta^2$) or bridging-chelating ($\mu,\eta^2$ and $\mu_3\text{-}\eta^2\text{:}\eta^2\text{:}\eta^1$) ligand but also as a counterion, whereas the latter, either protonated or partially deprotonated, binds the metal centres in a chelating ($\eta^3$) or bridging-chelating ($\mu,\eta^3\text{:}\eta^1$ and $\mu_3\text{-}\eta^3\text{:}\eta^1\text{:}\eta^1$) manner. The triangular $Y_3$ unit [3.480(6)–3.550(6) Å] in the cation of **1** consists of one nine-coordinate and two eight-coordinate Y atoms, the former of which are quite scarce in alkoxide chemistry. The unique feature of the 1D polymeric structure of **2** is the secondary F···cation bond, which has not been observed so far for TFA ligands. In addition, it is the only example where the Ba atom is linked to monodentate, bidentate and bridging trifluoroacetate ligands simultaneously.
(© Wiley-VCH Verlag GmbH & Co. KGaA, 69451 Weinheim, Germany, 2007)

## Introduction

Fluorinated carboxylates, especially fluoroacetates, are the most common precursors for the elaboration of high Tc superconductor coatings.[1] For barium, their preferential decomposition into $BaF_2$ represents a means to avoid the formation of highly stable barium carbonate, which is detrimental to the superconducting properties. Mixed-metal species are a means to provide homogeneity at a molecular level in order to modify the reactivity pattern and solubility.[2] Various amino alcohols, such as 2,6-bis[(dimethylamino)methyl]-4-methylphenol (bdmmpH) and 1,3-bis(dimethylamino)propan-2-ol (bdmapH), have been shown to stabilize lanthanide–copper and alkaline-earth metal–copper heterometallic complexes with trifluoroacetate (TFA) ancillary ligands.[3] Compounds of different nuclearity, such as $[LaCu(TFA)_3(bdmmp)(bdmmpH)(OH)]_2$,[4] $LaCu_2(TFA)_4(bdmap)_3$,[5] $[LnCu(bdmapH)_2(hfacac)_2(TFA)L]$ [Ln = Y, Pr; hfacac = hexafluoroacetylactonate; L = 2-methyl-2,4,6-tris(trifluoromethyl)-1,3-dioxane-4,6-diolato],[6] $[LnCu_2(hfacac)(hfacacH)(bdmap)_3(OAc)(TFA)]$ (Ln = Pr, Nd),[6,7] $[Cu_3(bdmap)_3(TFA)_2]_2[Y_2(bdmap)_2(TFA)_6]$,[8] $[MCu(TFA)_2(bdmap)_2(H_2O)]_x$ (M = Ca, $x$ = 1; M = Sr, $x$ = 2),[9] $[Sr_2Cu_4(TFA)_4(bdmap)_6(OH)_2]$,[9] $[SrCu_2(TFA)_3(bdmap)_3]$[10] and $[BaCu_4(bdmap)_4(2\text{-}PyO)_4(TFA)_2]$,[11] have been isolated. To the best of our knowledge, no amino alcohol has been shown to bridge yttrium and barium (or a lanthanide and an alkaline-earth metal) so far. Further studies are desirable to have a better understanding of the reactivity of these TFA species and to access heterometallic complexes with the right stoichiometry for the formation of $YBa_2Cu_3O_{7-x}$ films.

We have been interested in the design and synthesis of new homo- and heterometallic TFA derivatives related to high Tc superconductors.[12–14] The 1D coordination polymer $[Ba_3Cu_2(\mu,\eta^2\text{-}TFA)_6(\mu,\eta^2\text{-}dmea)_4(MeOH)_2\cdot 2MeOH]_{1\infty}$ was recently reported by our lab from the reaction between copper powder and $[Ba(TFA)_2]_\infty$ in methanol under air and in the presence of *N*-dimethylethanolamine (dmeaH).[12] The use of *N*-methyldiethanolamine ($mdeaH_2$) instead of dmeaH led to co-crystallisation of $[Ba(\eta^1\text{-}TFA)_2(mdeaH_2)_2]$ and $[Cu(mdeaH)_2]$.[12] In continuation, we now wish to report the reactions between Y and Cu or Ba trifluoroacetates in the presence of *N*-methyldiethanolamine. These reactions afford the heterometallic, tetranuclear complex $[CuY_3(\mu_3\text{-}OH)(\mu\text{-}\eta^3\text{:}\eta^1\text{-}mdeaH)_3(\mu_3\text{-}\eta^3\text{:}\eta^1\text{:}\eta^1\text{-}mdeaH)_2$-

[a] Université de Lyon1, IRC,
2 av. A. Einstein, 69626 Villeurbanne Cédex, France
Fax: +33-4-72445399
E-mail: mishrashashank74@rediffmail.com
[b] Université de Lyon1, Centre de Diffractométrie,
69629 Villeurbanne Cédex, France
[†] Deceased.

($\eta^2$-TFA)($\mu$,$\eta^2$-TFA)$_2$](TFA)$_2$($H_2O$) (**1**) and the homometallic Ba TFA 1D polymer [$Ba_3$($\eta^3$-mdea$H_2$)$_2$($\mu$-$\eta^2$:$\eta^1$:$\eta^1$-mdea$H_2$)$_2$($\eta^1$-TFA)$_2$($\eta^2$-TFA)$_2$($\mu_3$-$\eta^2$:$\eta^2$:$\eta^1$-TFA)$_2$]$_{1\infty}$ (**2**), respectively, which were characterised by X-ray diffraction and FT-IR, X-band ESR (for **1**) and NMR (for **2**) spectroscopy.

## Results and Discussion

### Reactions between TFA Derivatives

The reaction between [Y(TFA)$_3$($H_2O$)$_3$] and [Cu(TFA)$_2$-(MeOH)] in the presence of mdea$H_2$ afforded the heterometallic $CuY_3$ complex **1**. The reaction in the right stoichiometry improved the yield of the product [Equation (1)].

$$[Cu(TFA)_2(MeOH)] + 3\,[Y(TFA)_3(H_2O)_3] + 5\ mdeaH_2 \xrightarrow{thf} \underset{\mathbf{1}}{[CuY_3(\mu_3\text{-}OH)(mdeaH)_5(\eta^2\text{-}TFA)(\mu,\eta^2\text{-}TFA)_2](TFA)_2(H_2O)} + 6\ TFAH + 7\ H_2O \quad (1)$$

In contrast, no heterometallic Y-Ba species was obtained by treating [Y(TFA)$_3$($H_2O$)$_3$] with [Ba(TFA)$_2$]$_\infty$, even in the presence of excess mdea$H_2$. Instead, the 1D barium coordination polymer **2** was isolated and no yttrium derivative could be crystallised out. Complex **2**, which can also be obtained by treating [Ba(TFA)$_2$]$_\infty$ with 4/3 mol of mdea$H_2$ in thf, is different from the previously reported Ba TFA derivatives with mdea$H_2$ as ligand, namely the neutral complex [Ba(TFA)$_2$(mdea$H_2$)$_2$] (**3**)[12] or the ionic complex [Ba(mdea$H_2$)$_3$](TFA)$_2$ (**4**; Scheme 1).[13]

Heterometallic Y(Ln)-Ba derivatives are quite scarce when compared to heterometallic Y(Ln)-Cu[4–8,15] or Ba-Cu[16] derivatives and are limited to compounds where the connection between the metals is ensured by classical[17] or fluorinated[18] alkoxides or siloxides.[19] Lanthanide–alkaline-earth metal heterometallic derivatives stabilized by hydroxyquinoline or aminocarboxylic acids are also known.[20]

### Spectroscopic Characterisation

The FT-IR spectra of **1** and **2** show the presence of alcohol functionalities [$\nu$(OH) absorptions at 3413 and 3330 for **1** and 3313 cm$^{-1}$ for **2**] as well as trifluoroacetate groups in the metal coordination sphere. The $\nu_{as}(CO_2)$ absorption at high frequency (1698 cm$^{-1}$) suggests the presence of ionic TFA ligands, whereas that at 1660 cm$^{-1}$ indicates a chelating-bridging TFA in **1**. The overlap of the $\nu_{as}(CO_2)$ absorptions due to the presence of different TFA ligands (monodentate, bidentate and bridging) in **2** results in a strong broad absorption centred at 1680 cm$^{-1}$. Strong C–F and C–O absorption bands in the 1120–1210 cm$^{-1}$ range also characterise the spectra of **1** and **2**. Three characteristic absorptions for TFA derivatives are found in the 850–720 cm$^{-1}$ region.[12–14] The low-frequency absorptions at 632–404 cm$^{-1}$ are due to the $\nu$(M–O) and $\nu$(M–N) vibrations.[12–14] The $^1$H NMR spectrum of **2** indicates the presence of protonated *N*-methyldiethanolamine ligands in at least two different environments. It exhibits a broad peak at $\delta$ = 5.30 ppm, two triplets ($J$ = 6.0 Hz) at $\delta$ = 3.85 and 3.75 ppm, two broad peaks at $\delta$ = 2.82 and 2.53 ppm and a singlet at $\delta$ = 1.86 ppm due to OH, $OCH_2$, $NCH_2$ and NMe groups, respectively. The X-band ESR spectrum of polycrystalline **1** at room temperature exhibits a well-resolved hyperfine structure ($A_\parallel$ = 47 G) due to interaction of the unpaired electron with the nuclear spin ($I$ = 3/2) of both $^{63}$Cu and $^{65}$Cu (Figure 1). It reveals that the Cu$^{II}$ centre is indeed axial ($2.0 < g_\perp < g_\parallel$) with a $d_{x^2-y^2}$ ground state. The

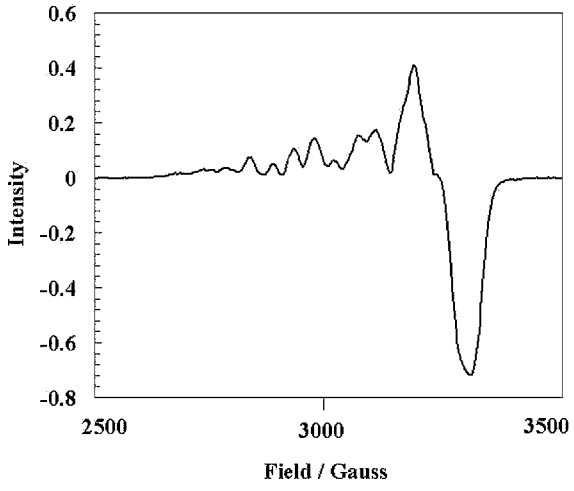


Figure 1. Room-temperature ESR spectrum of **1**.

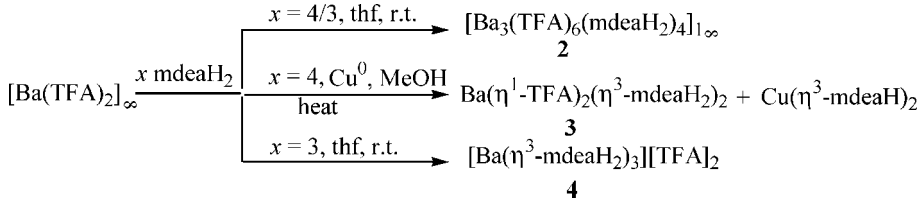


Scheme 1. Reactions of [Ba(TFA)$_2$]$_\infty$ with mdea$H_2$ with different stoichiometries and conditions.

 © 2007 Wiley-VCH Verlag GmbH & Co. KGaA, Weinheim 

values of the spin Hamiltonian parameters, $g_{\perp}$ = 2.047 and $g_{\parallel}$ = 2.281, are typical for a tetragonally distorted octahedral $Cu^{II}$ ion.[21]

### Molecular Structures of $[CuY_3(\mu_3\text{-}OH)(\mu\text{-}\eta^3\text{:}\eta^1\text{-}mdeaH)_3(\mu_3\text{-}\eta^3\text{:}\eta^1\text{:}\eta^1\text{-}mdeaH)_2(\eta^2\text{-}TFA)(\mu,\eta^2\text{-}TFA)_2](TFA)_2(H_2O)$ (1) and $[Ba_3(\eta^3\text{-}mdeaH_2)_2(\mu\text{-}\eta^3\text{:}\eta^1\text{-}mdeaH_2)_2(\eta^1\text{-}TFA)_2(\eta^2\text{-}TFA)_2(\mu_3\text{-}\eta^2\text{:}\eta^2\text{:}\eta^1\text{-}TFA)_2]_{1\infty}$ (2)

A single-crystal X-ray diffraction study of $[CuY_3(\mu_3\text{-}OH)(\mu\text{-}\eta^3\text{:}\eta^1\text{-}mdeaH)_3(\mu_3\text{-}\eta^3\text{:}\eta^1\text{:}\eta^1\text{-}mdeaH)_2(\eta^2\text{-}TFA)(\mu,\eta^2\text{-}TFA)_2](TFA)_2(H_2O)$ (**1**) revealed that it is an ionic complex (Figure 2, Table 1). All five amino alcohols are only partially deprotonated to afford mdeaH ligands. These are of two types, which act either in a doubly or triply bridging-chelating manner. The cationic species can be described as a regular triangular $Y_3$ unit [3.4805(6)–3.5503(6) Å] capped by oxygen atoms O10 and O6 of the mdeaH ligands. The Y atoms are eight-coordinate for Y1 and Y3 and nine-coordinate for Y2. Nine-coordinate yttrium atoms are rare in alkoxide chemistry, although they have been observed with poly(amino alkoxides).[22] The connection between yttrium atoms Y1, Y2 and the copper atom is achieved through oxygen atom O1M3, which is actually a hydroxide ligand, with a tetrahedral configuration, as well as by the oxygen atoms of two $\mu,\eta^2$-trifluoroacetates and one deprotonated oxygen of an *N*-methylethanolaminate ligand. The third trifluoroacetate ligand is linked in a chelating manner to Y2. The six-coordinate copper atom has an $O_5N$ environment where the Cu–O1 [2.549(4) Å] and Cu–O13 [2.453(4) Å] bond lengths are longer than the other Cu–O bond lengths (1.948 Å av.) as a combined result of the coordination with an alcohol functionality and a Jahn–Teller distortion.[23] The Cu–N1 bond length [2.028(4) Å] is in good agreement with those found in other copper complexes with N-heterocyclic ligands.[23] The Y–O bond lengths vary from 2.245(3)

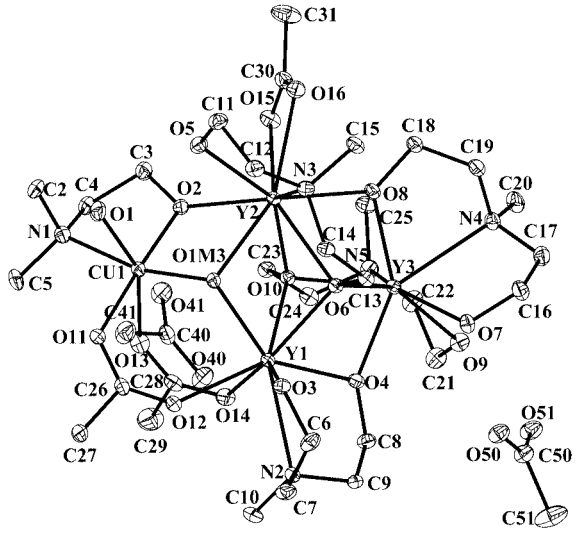


Figure 2. Molecular structure of **1** with atom labelling and ellipsoids at 30% probability. Hydrogen atoms have been omitted for clarity.

Table 1. Selected bond lengths [Å] and bond angles [°] for **1**.

| | | | |
|---|---|---|---|
| Cu1–O2 | 1.906(3) | Cu1–O1M3 | 1.956(3) |
| Cu1–O11 | 1.983(3) | Cu1–N1 | 2.028(4) |
| Cu1–O13 | 2.453(4) | Cu1–O1 | 2.549(4) |
| Y3–O8 | 2.245(3) | Y3–O4 | 2.272(3) |
| Y3–O6 | 2.346(3) | Y3–O7 | 2.348(3) |
| Y3–O10 | 2.385(3) | Y3–O9 | 2.404(3) |
| Y3–N5 | 2.576(4) | Y3–N4 | 2.643(4) |
| Y3···Y1 | 3.4805(6) | Y3···Y2 | 3.5503(6) |
| Y2–O2 | 2.313(3) | Y2–O8 | 2.332(3) |
| Y2–O10 | 2.337(3) | Y2–O1M3 | 2.414(3) |
| Y2–O5 | 2.458(3) | Y2–O6 | 2.487(3) |
| Y2–O16 | 2.488(3) | Y2–O15 | 2.520(4) |
| Y2–N3 | 2.616(4) | Y1–O1M3 | 2.308(3) |
| Y1–O4 | 2.255(3) | Y1–O14 | 2.322(3) |
| Y1–O6 | 2.363(3) | Y1–O3 | 2.402(3) |
| Y1–O12 | 2.417(3) | Y1–O10 | 2.416(3) |
| Y1–N2 | 2.626(4) | | |
| O2–Cu1–O1M3 | 84.2 (1) | O2–Cu1–O11 | 177.3(1) |
| O1M3–Cu1–O11 | 93.7(1) | O2–Cu1–N1 | 87.1(1) |
| O1M3–Cu1–N1 | 164.3(2) | O11–Cu1–N1 | 95.3(2) |
| O2–Cu1–O13 | 97.7(1) | O1M3–Cu1–O13 | 105.6(1) |
| O11–Cu1–O13 | 81.2(1) | N1–Cu1–O13 | 88.5 (2) |
| O2–Cu1–O1 | 100.1(1) | O1M3–Cu1–O1 | 88.8(1) |
| O11–Cu1–O1 | 81.6(1) | N1–Cu1–O1 | 79.9(2) |
| O13–Cu1–O1 | 158.2(1) | O8–Y3–O4 | 140.6(1) |
| O8–Y3–O6 | 71.2(1) | O4–Y3–O6 | 73.4(1) |
| O8–Y3–O7 | 109.4(1) | O4–Y3–O7 | 82.0(1) |
| O6–Y3–O7 | 82.3(1) | O8–Y3–O10 | 74.7(1) |
| O4–Y3–O10 | 74.2(1) | O6–Y3–O10 | 62.8(1) |
| O7–Y3–O10 | 142.0(1) | O8–Y3–O9 | 139.0(1) |
| O4–Y3–O9 | 79.7(1) | O6–Y3–O9 | 147.8(1) |
| O7–Y3–O9 | 76.7(1) | O10–Y3–O9 | 125.9(1) |
| O8–Y3–N5 | 92.1(1) | O4–Y3–N5 | 100.2(1) |
| O6–Y3–N5 | 133.7(1) | O7–Y3–N5 | 143.3(1) |
| O10–Y3–N5 | 71.3(1) | O9–Y3–N5 | 67.8(1) |
| O8–Y3–N4 | 69.7(1) | O4–Y3–N4 | 144.8(1) |
| O6–Y3–N4 | 117.6(1) | O7–Y3–N4 | 67.7(1) |
| O10–Y3–N4 | 141.0(1) | O9–Y3–N4 | 76.4(1) |
| N5–Y3–N4 | 94.2(1) | Y1···Y3···Y2 | 61.65(1) |
| O2–Y2–O8 | 135.6(1) | O2–Y2–O10 | 77.0(1) |
| O8–Y2–O10 | 74.0(1) | O2–Y2–O1M3 | 66.4(1) |
| O8–Y2–O1M3 | 133.4(1) | O10–Y2–O1M3 | 74.4(1) |
| O2–Y2–O5 | 71.1(1) | O8–Y2–O5 | 141.3(1) |
| O10–Y2–O5 | 144.3(1) | O1M3–Y2–O5 | 78.4(1) |
| O2–Y2–O6 | 124.2(1) | O8–Y2–O6 | 67.3(1) |
| O10–Y2–O6 | 61.4(1) | O1M3–Y2–O6 | 67.7(1) |
| O5–Y2–O6 | 126.9(1) | O2–Y2–O16 | 107.3(1) |
| O8–Y2–O16 | 76.7(1) | O10–Y2–O16 | 140.0(1) |
| O1M3–Y2–O16 | 144.7(1) | O5–Y2–O16 | 67.2(1) |
| O6–Y2–O16 | 128.5(1) | O2–Y2–O15 | 73.4(1) |
| O8–Y2–O15 | 75.8(1) | O10–Y2–O15 | 94.1(1) |
| O1M3–Y2–O15 | 139.7(1) | O5–Y2–O15 | 92.0(1) |
| O6–Y2–O15 | 139.9(1) | O16–Y2–O15 | 52.3(1) |
| O2–Y2–N3 | 132.5(1) | O8–Y2–N3 | 91.8(1) |
| O10–Y2–N3 | 130.0(1) | O1M3–Y2–N3 | 83.2(1) |
| O5–Y2–N3 | 67.5(1) | O6–Y2–N3 | 68.9(1) |
| O16–Y2–N3 | 77.0(1) | O15–Y2–N3 | 129.2(1) |
| Cu1···Y2···Y3 | 113.52(2) | O4–Y1–O1M3 | 140.9(1) |
| O4–Y1–O14 | 85.2(1) | O1M3–Y1–O14 | 111.6(1) |
| O4–Y1–O6 | 73.3(1) | O1M3–Y1–O6 | 71.5(1) |
| O14–Y1–O6 | 139.8(1) | O4–Y1–O3 | 104.9(1) |
| O1M3–Y1–O3 | 84.2(1) | O14–Y1–O3 | 141.2(1) |
| O6–Y1–O3 | 78.3(1) | O4–Y1–O12 | 143.8(1) |
| O1M3–Y1–O12 | 75.3(1) | O14–Y1–O12 | 75.7(1) |
| O6–Y1–O12 | 138.7(1) | O3–Y1–O12 | 74.6(1) |
| O4–Y1–O10 | 73.9(1) | O1M3–Y1–O10 | 74.9(1) |
| O14–Y1–O10 | 79.6(1) | O6–Y1–O10 | 62.1(1) |
| O3–Y1–O10 | 139.2(1) | O12–Y1–O10 | 130.3(1) |
| O4–Y1–N2 | 70.5(1) | O1M3–Y1–N2 | 144.6(1) |
| O14–Y1–N2 | 80.8(1) | O6–Y1–N2 | 120.9(1) |
| O3–Y1–N2 | 68.2(1) | O12–Y1–N2 | 76.2(1) |
| O10–Y1–N2 | 140.5(1) | Y3···Y1···Cu1 | 112.21(2) |
| Y3···Y1···Y2 | 60.13(1) | Cu1···Y1···Y2 | 57.02(1) |
| Cu1–O2–Y2 | 107.2(1) | Y1–O4–Y3 | 100.5(1) |
| Y3–O6–Y1 | 95.3(1) | Y3–O6–Y2 | 94.5(1) |
| Y1–O6–Y2 | 95.9(1) | Y3–O8–Y2 | 101.7(1) |
| Y2–O10–Y3 | 97.5(1) | Y2–O10–Y1 | 98.6(1) |
| Y3–O10–Y1 | 92.9(1) | Cu1–O1M3–Y1 | 111.4(1) |
| Cu1–O1M3–Y2 | 101.8(1) | Y1–O1M3–Y2 | 99.4(1) |

 © 2007 Wiley-VCH Verlag GmbH & Co. KGaA, Weinheim 

to 2.520(3) Å, the order of variation being Y–O(μ,η²-mdeaH) < Y–O($\mu_3$-OH) ≈ Y–O($\mu_3$,η³-mdeaH) ≈ Y–O(η¹-mdeaH) ≈ Y–O(μ,η²-TFA) < Y–O(η²-TFA). The transannular Y–N bond lengths are longer (av. 2.615 Å) but are comparable to those reported for $[Y_2Cu_6(bdmap)_8(TFA)_{10}]$.[8] The distance between one TFA counteranion (O41) and the oxygen of the $\mu_3$-hydroxo group O1M3···O41 is 2.802(6) Å, which suggests hydrogen bonding. The $\mu_3$-OH must originate from the coordinated water of $[Y(TFA)_3(H_2O)_3]$ since **1** was obtained by treating $[Y(TFA)_3(H_2O)_3]$ with $[Cu(TFA)_2(MeOH)]$ and $mdeaH_2$ in anhydrous thf. This further confirms that the yttrium starting material is easily hydrolysed to form trinuclear $Y_3$ units.[14]

The structure of **2** is that of a homometallic Ba 1D coordination polymer of formula $[Ba_3(\eta^3\text{-}mdeaH_2)_2(\mu\text{-}\eta^3{:}\eta^1\text{-}mdeaH_2)_2(\eta^1\text{-}TFA)_2(\eta^2\text{-}TFA)_2(\mu_3\text{-}\eta^2{:}\eta^2{:}\eta^1\text{-}TFA)_2]_{1\infty}$. It contains two types of barium atoms, namely Ba1 and Ba2, which are present in a 2:1 ratio and form a zig-zag chain (Figures 3, 4 and 5). Selected bond lengths and angles are collected in Table 2. Polymer **2** can be seen formally as the association between $[Ba_2(\eta^3\text{-}mdeaH_2)_2(\mu\text{-}\eta^3{:}\eta^1\text{-}mdeaH_2)_2(\mu,\eta^2{:}\eta^1\text{-}TFA)_2]^{2+}$ and $[Ba(\eta^2\text{-}TFA)_2(\eta^1\text{-}TFA)_2]^{2-}$ units through one oxygen and one fluorine atom [Ba2···F = 3.010(3) Å] of μ,η²:η¹-TFA ligands, which overall act as unique triply bridging TFA ligands bonded in two different chelating manners [η²(O,O) and η²(O,F); Figures 3 and 4). The triply bridging $\mu_3$-η¹:η²:η¹ coordination mode is known for TFA (Scheme 2) for a Ba[24] and few other complexes,[25] but no secondary F···cation bond has been reported so far. Such metal–fluorine interactions appear to be a common feature for compounds of large elements such as alkaline-earth metals or lanthanides with fluorinated alkoxides or β-diketonates,[26] but are reported here for the first time with TFA.

Two types of amino alcohols coordinating to Ba1 are not deprotonated: one $mdeaH_2$ acts in a tridentate mode and

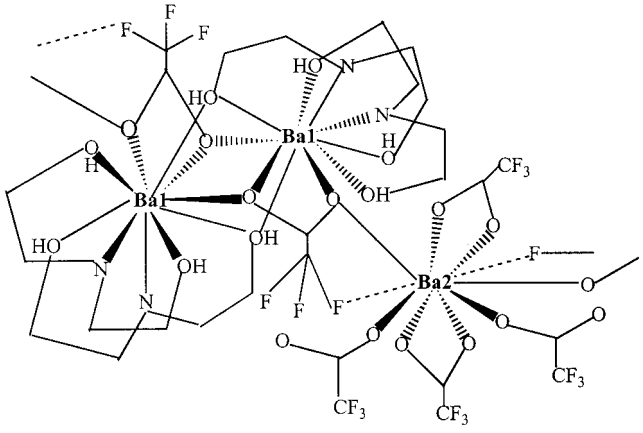


Figure 3. ChemDraw structure of $[Ba_3(\eta^3\text{-}mdeaH_2)_2(\mu\text{-}\eta^3{:}\eta^1\text{-}mdeaH_2)_2(\eta^1\text{-}TFA)_2(\eta^2\text{-}TFA)_2(\mu_3\text{-}\eta^2{:}\eta^2{:}\eta^1\text{-}TFA)_2]_{1\infty}$ (**2**).

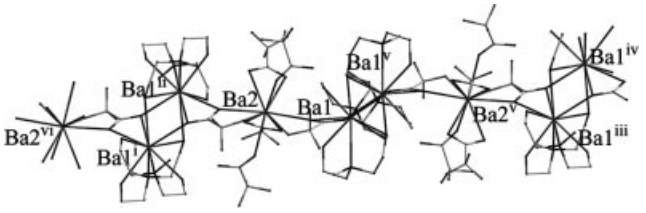


Figure 5. View of the 1D polymer chains of **2**. Symmetry elements: (i) $^1/_2 + x$, $^1/_2 - y$, $^1/_2 + z$; (ii) $2 - x$, $y$, $^1/_2 - z$; (iii) $-^1/_2 + x$, $^1/_2 - y$, $-^1/_2 + z$; (iv) $1 - x$, $y$, $-^1/_2 - z$; (v) $^3/_2 - x$, $^1/_2 - y$, $-z$; (vi) $^5/_2 - x$, $^1/_2 - y$, $1 - z$.

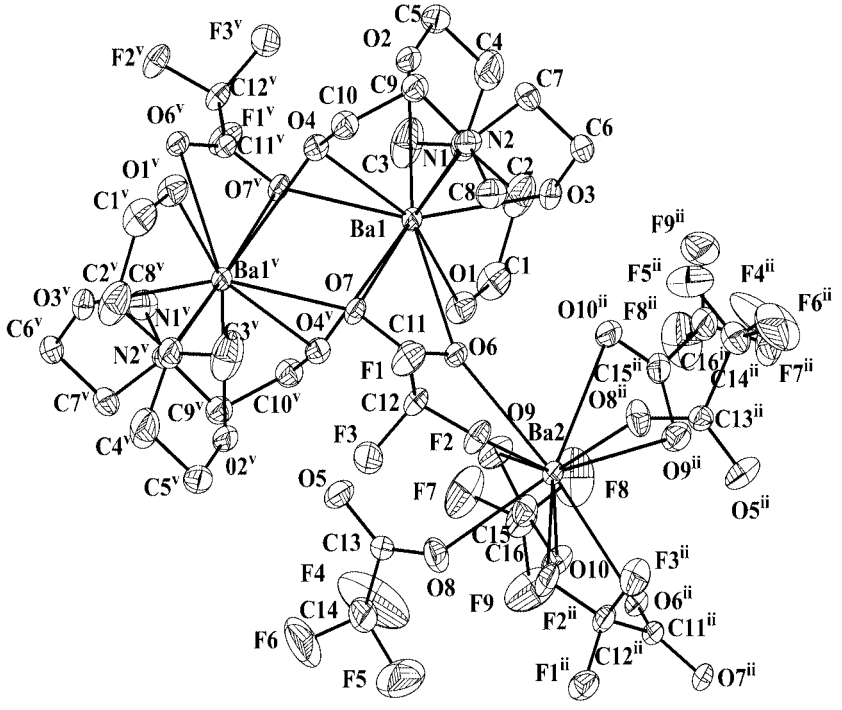


Figure 4. Molecular structure of **2** with atom labelling and ellipsoids at 30% probability. Hydrogen atoms have been omitted for clarity.

 © 2007 Wiley-VCH Verlag GmbH & Co. KGaA, Weinheim 

Table 2. Selected bond lengths [Å] and bond angles [°] for **2**.[a]

| | | | |
|---|---|---|---|
| Ba1–O1 | 2.721(4) | Ba2–O8 | 2.668(4) |
| Ba1–O2 | 2.769(4) | Ba2–O8$^{i}$ | 2.668(4) |
| Ba1–O3 | 2.733(4) | Ba2–O9 | 2.833(4) |
| Ba1–O4 | 2.906(4) | Ba2–O9$^{i}$ | 2.833(4) |
| Ba1–O4$^{ii}$ | 2.929(4) | Ba2–O10 | 2.863(5) |
| Ba1–O6 | 2.952(3) | Ba2–O10$^{i}$ | 2.863(5) |
| Ba1–O7 | 3.064(4) | Ba1–N1 | 3.001(6) |
| Ba1–O7$^{ii}$ | 2.778(3) | Ba1–N2 | 3.034(5) |
| Ba2–O6 | 2.795(3) | Ba2–F2 | 3.010(3) |
| Ba2–O6$^{i}$ | 2.795(3) | Ba2–F2$^{i}$ | 3.010(3) |
| O1–Ba1–O3 | 79.952(1) | O4$^{ii}$–Ba1–O7 | 58.137(9) |
| O1–Ba1–O2 | 117.042(1) | O4$^{ii}$–Ba1–N1 | 133.874(1) |
| O1–Ba1–O7$^{ii}$ | 101.527(1) | O4$^{ii}$–Ba1–N2 | 78.129(1) |
| O1–Ba1–O4 | 160.582(1) | O6–Ba1–O7 | 43.667(9) |
| O1–Ba1–O4$^{ii}$ | 72.268(1) | O6–Ba1–N1 | 133.874(1) |
| O1–Ba1–O6 | 82.185(1) | O6–Ba1–N2 | 78.129(1) |
| O1–Ba1–O7 | 114.982(1) | N1–Ba1–N2 | 113.029(1) |
| O1–Ba1–N1 | 59.043(1) | N1–Ba1–O7 | 173.267(1) |
| O1–Ba1–N2 | 137.554(1) | N2–Ba1–O7 | 73.358(1) |
| O3–Ba1–O2 | 83.301(1) | O8$^{i}$–Ba2–O8 | 134.73(1) |
| O3–Ba1–O7$^{ii}$ | 156.180(9) | O8$^{i}$–Ba2–O6$^{i}$ | 79.106(1) |
| O3–Ba1–O4 | 119.412(1) | O8$^{i}$–Ba2–O6 | 93.776(1) |
| O3–Ba1–O4$^{ii}$ | 138.345(1) | O8$^{i}$–Ba2–O9$^{i}$ | 75.120(1) |
| O3–Ba1–O6 | 77.365(1) | O8$^{i}$–Ba2–O9 | 146.984(1) |
| O3–Ba1–O7 | 110.523(9) | O8$^{i}$–Ba2–O10 | 139.910(1) |
| O3–Ba1–N1 | 72.422(1) | O8$^{i}$–Ba2–O10$^{i}$ | 75.770(1) |
| O3–Ba1–N2 | 59.271(1) | O8–Ba2–O6$^{i}$ | 93.776(1) |
| O2–Ba1–O7$^{ii}$ | 74.823(1) | O8–Ba2–O6 | 79.106(1) |
| O2–Ba1–O4 | 69.989(9) | O8–Ba2–O9$^{i}$ | 146.984(1) |
| O2–Ba1–O4$^{ii}$ | 137.004(9) | O8–Ba2–O9 | 75.120(1) |
| O2–Ba1–O6 | 149.897(9) | O8–Ba2–O10 | 75.770(1) |
| O2–Ba1–O7 | 127.738(9) | O8–Ba2–O10$^{i}$ | 139.910(1) |
| O2–Ba1–N1 | 58.021(1) | O6$^{i}$–Ba2–O6 | 161.585(9) |
| O2–Ba1–N2 | 72.172(1) | O6$^{i}$–Ba2–O9$^{i}$ | 76.608(1) |
| O7$^{ii}$–Ba1–O4 | 61.621(9) | O6$^{i}$–Ba2–O9 | 118.261(1) |
| O7$^{ii}$–Ba1–O4$^{ii}$ | 62.230(9) | O6$^{i}$–Ba2–O10 | 72.525(1) |
| O7$^{ii}$–Ba1–O6 | 126.455(9) | O6$^{i}$–Ba2–O10$^{i}$ | 121.076(1) |
| O7$^{ii}$–Ba1–O7 | 90.603(9) | O6–Ba2–O9$^{i}$ | 118.261(1) |
| O7$^{ii}$–Ba1–N1 | 87.818(1) | O6–Ba2–O9 | 76.608(1) |
| O7$^{ii}$–Ba1–N2 | 120.435(1) | O6–Ba2–O10 | 121.076(1) |
| O4–Ba1–O4$^{ii}$ | 90.341(9) | O6–Ba2–O10$^{i}$ | 72.525(1) |
| O4–Ba1–O6 | 99.841(9) | O9$^{i}$–Ba2–O9 | 81.806(1) |
| O4–Ba1–O7 | 59.204(9) | O9$^{i}$–Ba2–O10 | 71.214(1) |
| O4–Ba1–N1 | 125.190(1) | O9$^{i}$–Ba2–O10$^{i}$ | 45.754(1) |
| O4–Ba1–N2 | 61.00(1) | O9–Ba2–O10 | 45.754(1) |
| O4$^{ii}$–Ba1–O6 | 68.744(9) | O9–Ba2–O10$^{i}$ | 71.214(1) |
| | | O10–Ba2–O10$^{i}$ | 95.152(1) |

[a] Symmetry codes: (i) $2 - x, y, {}^{1}/_{2} - z$; (ii) ${}^{3}/_{2} - x, {}^{1}/_{2} - y, - z$.

the other one acts as a bridging ligand with one OH as well as a tridentate ligand. The coordination number of 10 around each Ba1 is achieved by two $\eta^3$-mdeaH$_2$ ligands, one $\eta^2$-TFA [actually the triply bridging one bonded in an $\eta^2$(O,O) manner], one $\eta^1$-mdeaH$_2$ (bridging) and an $\eta^1$-TFA (actually the triply bridging one bonded in a μ-O manner). Two $\eta^1$-TFA, two $\eta^2$-TFA and two triply bridging TFA ligands bonded in an $\eta^2$(O,F) manner provide a coordination number of 10 around Ba2 as well. The Ba1···Ba1# distance is 4.115(9) Å, whereas the Ba1···Ba2 ones are longer [5.292(1) Å]. The Ba–O(μ-mdeaH$_2$) bond lengths [2.906(4)–2.929(4) Å] are longer than the terminal Ba–OH [2.721(4)–2.769(4) Å] one (Table 2). The Ba1–O(TFA) bond lengths vary from 2.779(4) to 3.064(4) Å. The transannular Ba–N coordination bond lengths [3.001(6)–3.034(5) Å] are comparable with those reported in [Ba($\eta^1$-TFA)$_2$-(mdeaH$_2$)$_2$].[12] The Ba2 atom bears two monodentate and two bidentate trifluoroacetate ligands. The Ba2–O($\eta^1$-TFA) bond length [2.668(4) Å] is shorter than those for bidentate TFA [2.833(4)–2.863(5) Å] and bridging TFA [2.795(3)]. Compound **2** is the only example thus far where Ba is linked to both mono- and bidentate as well as bridging trifluoroacetate ligands.

The structure of **2** shows the versatility of the reactions between [Ba(TFA)$_2$]$_\infty$ and *N*-methyldiethanolamine (mdeaH$_2$) since it is the third Ba-TFA-mdeaH$_2$ derivative (Scheme 1). The two other derivatives have recently been reported by us.[12,13] The eight-coordinate Ba centre in [Ba($\eta^1$-TFA)$_2$(mdeaH$_2$)$_2$] (**3**) bears two monodentate dangling trifluoroacetate and two *N*-methyldiethanolamine ligands,[12] whereas ionic [Ba(mdeaH$_2$)$_3$][TFA]$_2$ (**4**) has a nine-coordinate $Ba^{2+}$ cation surrounded by three tridentate *N*-methyldiethanolamines, with two trifluoroacetate ligands acting as counterions.[13] No Ba···F short interactions are found in the solid. Strict control of the stoichiometry is required for access to a specific Ba-TFA adduct with the neutral mdeaH$_2$ ligand. The absence of deprotonation of amino alcohols in Ba-TFA adducts, probably due to the large radius of $Ba^{2+}$ cation, precludes the formation of Y-Ba heterometallic complexes. In contrast, the reaction between Y and Cu TFA derivatives proceeds with partial deprotonation of amino alcohols and removal of some TFA as TFAH to form heterometallic compounds.

## Experimental Section

All reactions were carried out under argon by using standard Schlenk-tube and vacuum-line techniques. Solvents were purified by standard methods. Trifluoroacetic acid (TFAH) was stored over molecular sieves. [Ba(TFA)$_2$], [Cu(TFA)$_2$(MeOH)][12,13] and [Y(TFA)$_3$(H$_2$O)$_3$][14] were prepared as reported previously. Analytical data were obtained from the Service Central d′Analyses du CNRS. FT-IR spectra were recorded as Nujol mulls with a Perkin–Elmer Paragon 500 spectrometer. NMR spectra were recorded with a Bruker AC-300 spectrometer. The ESR spectrum (X-band, 9.4 GHz) was obtained at room temp. for the powder with a Bruker spectrometer (microwave power of 10 mW, modulation frequency of 100 kHz). Diphenylpicrylhydrazyl (DPPH) was used as an internal reference ($g$ = 2.0036).

**Synthesis of [CuY$_3$(μ$_3$-OH)(mdeaH)$_5$($\eta^2$-TFA)(μ,$\eta^2$-TFA)$_2$](TFA)$_2$(H$_2$O) (1):** MeN(C$_2$H$_4$OH)$_2$ (0.5 mL, excess) was added dropwise to a greenish blue solution of [Cu(TFA)$_2$(MeOH)] (0.276 g, 0.85 mmol) and [Y(TFA)$_3$(H$_2$O)$_3$] (0.408 g, 0.85 mmol) in thf (20 mL). The colour of the solution changed to blue in a few minutes. After stirring overnight, blue crystals were obtained by layering the medium with Et$_2$O (0.29 g, 67% based on Y). The reaction in the right stoichiometry {[Cu(TFA)$_2$(MeOH)] (0.095 g, 0.26 mmol), [Y(TFA)$_3$(H$_2$O)$_3$] (0.381 g, 0.73 mmol), MeN(C$_2$H$_4$OH)$_2$ (0.5 mL, excess)} improved the yield of the product (0.31 g, 78%). $C_{35}H_{62}CuF_{15}N_5O_{22}Y_3$ (1520.1): calcd. C 27.65, H 4.11, N 4.61; found C 27.35, H 4.09, N 4.57. IR (nujol): $\tilde{\nu}$ = 3413 cm$^{-1}$ w, 3330 m [ν(OH)]; 1698 s, 1660 m [$\nu_{as}$(CO$_2$)], 1462 s [$\nu_s$(CO$_2$)], 1213 s, 1195 s, 1139 s [ν(C–F)], 844 w, 800 m, 723 m, 632 w, 615 w, 597 w, 588 w, 557 w, 541 w, 521 w, 459 m.

 © 2007 Wiley-VCH Verlag GmbH & Co. KGaA, Weinheim 

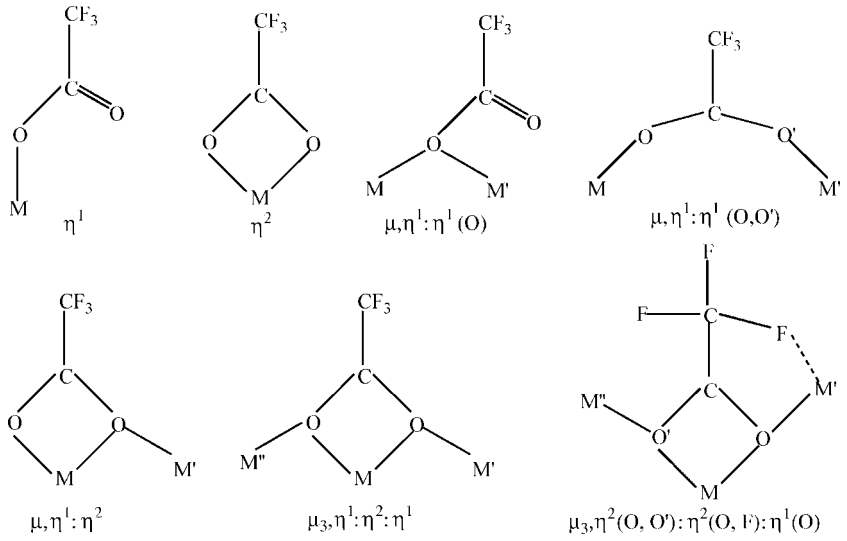


Scheme 2. Various bonding modes observed in TFA complexes.

**$[Ba_3(\eta^3\text{-mdeaH}_2)_2(\mu\text{-}\eta^3\text{:}\eta^1\text{-mdeaH}_2)_2(\eta^1\text{-TFA})_2(\eta^2\text{-TFA})_2(\mu_3\text{-}\eta^2\text{:}\eta^2\text{:}\eta^1\text{-TFA})_2]_{1\infty}$ (2):** $MeN(CH_2CH_2OH)_2$ (0.5 mL, excess) was added to a solution of $[Y(TFA)_3(H_2O)_3]$ (0.88 g, 1.83 mmol) and $[Ba(TFA)_2]$ (0.67 g, 1.84 mmol) in thf (20 mL) and the medium was stirred overnight. Colourless needles (0.81 g, 84% based on Ba) were obtained at room temp. by concentration (3 mL). Anal: found (calcd.) for $C_{32}H_{52}Ba_3F_{18}N_4O_{20}$ (1566.76): calcd. C 24.50, H 3.31, N 3.57; found C 24.39, H 3.27, N 3.56. IR (nujol): $\tilde{\nu}$ = 3313 $cm^{-1}$ br [ν(OH)], 1670 s [$\nu_{as}(CO_2)$], 1461 s [$\nu_s(CO_2)$], 1194 s, 1130 s [ν(C–F)], 836 s, 787 s, 763 m, 714 s, 598 m, 512 m, 404 m. $^1H$ NMR (300 MHz, $CDCl_3$, 25 °C): $\delta$ = 5.30 (br., 8 H, OH), 3.85, 3.75 (t, $J$ = 6.0 Hz, 16 H, $OCH_2$), 2.82, 2.53 (br., 16 H, $NCH_2$), 1.86 ppm (s, 12 H, NMe). Compounds **1** and **2** are soluble in thf but insoluble in toluene, *n*-hexane and diethyl ether. Unlike **2**, which is moderately soluble in chloroform and dichloromethane, **1** is completely insoluble in these solvents.

**Crystallography:** Suitable crystals of **1** were obtained by layering its thf solution with $Et_2O$ whereas a concentrated thf solution of **2** gave crystals at room temp. suitable for X-ray crystallography. X-ray single-crystal diffraction data were collected with a Nonius Kappa CCD diffractometer ($\lambda$ = 0.71073 Å) using the COLLECT software (Nonius BV, 1997–2000) and processed with the DENZO reduction software.[27] The structure of **1** was solved and refined on $F^2$ using SHELXTL[28] whereas **2** was solved with the SIR97 program[29] and refined with CRYSTALS.[30] All non-hydrogen atoms were refined with anisotropic thermal parameters. The hydrogen atoms were included in the final refinement in calculated positions with isotropic thermal parameters. Crystal data for $C_{35}H_{62}CuF_{15}N_5O_{22}Y_3$ (**1**): $M_w$ = 1520.17, $T$ = 163(2) K, triclinic, $P\bar{1}$, $a$ = 12.646(2), $b$ = 15.100(3), $c$ = 15.793(3) Å, $\alpha$ = 104.134(1)°, $\beta$ = 90.185(1)°, $\gamma$ = 96.564(1)°, $V$ = 2903.68(9) $Å^3$, $Z$ = 2, $\mu$(Mo-$K_\alpha$) = 3.451 $mm^{-1}$, reflections collected 24438, independent reflections 13214 [$R$(int) = 0.043], data/restraints/parameters 13214/0/766, $R$ [$F^2 > 2\sigma(F^2)$] = 0.055, $wR$ ($F^2$) = 0.150, $R$ (all data) = 0.078, $wR$ (all data) = 0.168, GOF = 1.17, residual electron density: –0.996 and 1.424 e $Å^{-3}$.

$C_{32}H_{52}Ba_3F_{18}N_4O_{20}$ (**2**): $M_w$ = 1566.76, $T$ = 150(2) K, monoclinic, $C2/c$, $a$ = 17.008(5), $b$ = 18.376(5), $c$ = 17.659(5) Å, $\beta$ = 92.436(5), $V$ = 5514(3) $Å^3$, $Z$ = 4, $\mu$(Mo-$K_\alpha$) = 2.25 $mm^{-1}$, reflections collected 8528, independent reflections 8324 [$R$(int) = 0.069], data/restraints/parameters 5887/6/348, $R$ [$F^2 > 2\sigma(F^2)$] = 0.056, $wR(F^2)$ = 0.060, $R$ (all) = 0.087, $wR$ (all data) = 0.076, GOF 1.08, residual electron density: –1.01 and 1.57 e $Å^{-3}$.

CCDC-244549 (for **1**) and -296883 (for **2**) contain the supplementary crystallographic data for this paper. These data can be obtained free of charge from The Cambridge Crystallographic Data Centre via www.ccdc.cam.ac.uk/data_request/cif.

## Acknowledgments

The authors are grateful to the Region Rhone Alpes for financial support (Project Superflex) and a postdoctoral fellowship to S. M.

[1] a) T. Araki, I. Hirabayaski, J. Shibata, Y. Ikuhara, *Supercond. Sci. Technol.* **2002**, *15*, 913–916; b) T. Araki, I. Hirabayashi, *Supercond. Sci. Technol.* **2003**, *16*, R71–R94; c) T. Araki, I. Hirabayashi, T. Niwa, *Supercond. Sci. Technol.* **2004**, *17*, 135–139.
[2] L. G. Hubert-Pfalzgraf, *Inorg. Chem. Commun.* **2003**, *6*, 102–120.
[3] S. Wang, *Polyhedron* **1998**, *17*, 831–843.
[4] L. Chen, S. R. Breeze, R. J. Rousseau, S. Wang, L. K. Thompson, *Inorg. Chem.* **1995**, *34*, 454–465.
[5] a) S. Wang, K. D. L. Smith, Z. Pang, M. J. Wagner, *J. Chem. Soc., Chem. Commun.* **1992**, 1594–1596; b) S. Wang, Z. Pang, K. D. L. Smith, M. J. Wagner, *J. Chem. Soc., Dalton Trans.* **1994**, 955–964.
[6] S. Wang, Z. Pang, K. D. L. Smith, *Inorg. Chem.* **1993**, *32*, 4992–4993.
[7] S. Wang, Z. Pang, K. D. L. Smith, Y.-S. Hua, C. Deslippe, M. J. Wagner, *Inorg. Chem.* **1995**, *34*, 908–917.
[8] S. Wang, Z. Pang, K. D. L. Smith, M. J. Wagner, *J. Chem. Soc., Dalton Trans.* **1994**, 955–964.
[9] S. R. Breeze, S. Wang, *Inorg. Chem.* **1994**, *33*, 5113–5121.
[10] S. R. Breeze, S. Wang, L. K. Thompson, *Inorg. Chim. Acta* **1996**, *250*, 163–171.
[11] S. Wang, S. J. Trepanier, M. J. Wagner, *Inorg. Chem.* **1993**, *32*, 833–840.
[12] J. Zhang, L. G. Hubert-Pfalzgraf, D. Luneau, *Inorg. Chem. Commun.* **2004**, *7*, 979–984.
[13] J. Zhang, L. G. Hubert-Pfalzgraf, D. Luneau, *Polyhedron* **2005**, *24*, 1185–1195.
[14] J. Zhang, S. Morlens, L. G. Hubert-Pfalzgraf, D. Luneau, *Eur. J. Inorg. Chem.* **2005**, 3928–3935.

 © 2007 Wiley-VCH Verlag GmbH & Co. KGaA, Weinheim 

[15] a) C. Benelli, A. Caneschi, D. Gatteschi, O. Guillou, L. Pardi, *Inorg. Chem.* **1990**, *29*, 1750–1755; b) S. Wang, *Inorg. Chem.* **1991**, *30*, 2252–2253; c) S. Wang, Z. Pang, M. J. Wagner, *Inorg. Chem.* **1992**, *31*, 5381–5388; d) W. Bidell, J. Doring, H. W. Bosch, H. U. Hund, E. Plappert, H. Berke, *Inorg. Chem.* **1993**, *32*, 502–507; e) Y. Cui, J.-T. Chen, J.-S. Huang, *Inorg. Chim. Acta* **1999**, *293*, 129–139; f) H. Guillon, L. G. Hubert-Pfalzgraf, J. Vaissermann, *Eur. J. Inorg. Chem.* **2000**, 1243–1252; g) A. C. Rizzi, R. Calvo, R. Baggio, M. T. Garland, O. Pena, M. Perec, *Inorg. Chem.* **2002**, *41*, 5609–5614; h) G. Novitchi, S. Shova, A. Caneschi, J.-P. Costes, M. Gdaniec, N. Stanica, *Dalton Trans.* **2004**, 1194–1200.

[16] a) N. N. Sauer, E. Garcia, K. V. Salazar, R. R. Ryan, J. A. Martin, *J. Am. Chem. Soc.* **1990**, *112*, 1524–1528; b) W. Bidell, V. Shklover, H. Berke, *Inorg. Chem.* **1992**, *31*, 5561–5571; c) W. Bidell, H. W. Bosch, D. Veghini, H. U. Hund, J. Doring, H. Berke, *Helv. Chim. Acta* **1993**, *76*, 596–606; d) F. Labrize, L. G. Hubert-Pfalzgraf, J. Vaissermann, C. B. Knobler, *Polyhedron* **1996**, *15*, 577–589; e) S. R. Breeze, S. Wang, J. E. Greedan, N. P. Raju, *J. Chem. Soc., Dalton Trans.* **1998**, 2327–2333.

[17] a) P. Miele, J. D. Foulon, N. Hovnanian, L. Cot, *J. Chem. Soc., Chem. Commun.* **1993**, 29–31; b) B. Borup, W. E. Streib, K. G. Caulton, *Chem. Ber.* **1996**, *129*, 1003–1005; c) P. Miele, G. Foulon, N. Hovnanian, *Inorg. Chim. Acta* **1997**, *255*, 289–294; d) W. J. Evans, D. G. Giarikos, M. A. Greci, J. W. Ziller, *Eur. J. Inorg. Chem.* **2002**, 453–456.

[18] a) F. Labrize, L. G. Hubert-Pfalzgraf, J.-C. Daran, S. Halut, *J. Chem. Soc., Chem. Commun.* **1993**, 1556–1558; b) F. Labrize, L. G. Hubert-Pfalzgraf, J.-C. Daran, S. Halut, P. Tobaly, *Polyhedron* **1996**, *15*, 2707–2718; c) H. Guillon, L. G. Hubert-Pfalzgraf, J. Vaissermann, *Eur. J. Inorg. Chem.* **2000**, 1243–1252.

[19] J. D. Foulon, P. Miele, N. Hovnanian, *Z. Kristallogr.* **1994**, *209*, 282–284.

[20] a) C. K. Schauer, O. P. Anderson, *J. Chem. Soc., Dalton Trans.* **1989**, 185–191; b) Y. Inomata, D. Okamura, K. Morita, Y. Yukawa, F. S. Howell, *J. Mol. Struct.* **2003**, *659*, 23–34; c) G. B. Deacon, P. C. Junk, S. G. Leary, *Z. Anorg. Allg. Chem.* **2004**, *630*, 1541–1543.

[21] a) D. S. Rawat, P. J. Benites, C. D. Incarvito, A. L. Rheingold, J. M. Zaleski, *Inorg. Chem.* **2001**, *40*, 1846–1857; b) J. Fawcett, S. H. Laurie, C. Simpson, M. C. R. Symons, F. A. Taiwo, I. Hawkins, *Inorg. Chim. Acta* **2001**, *312*, 245–248; c) G. A. van Albada, A. Mohamadou, I. Mutikainen, U. Turpeinen, J. Reedijk, *Eur. J. Inorg. Chem.* **2004**, 3733–3742; d) J. Moncol, P. Segla, D. Miklos, M. Mazur, M. Melnik, T. Glowiak, M. Valko, M. Koman, *Polyhedron* **2006**, *25*, 1561–1566.

[22] M. K. Thompson, A. J. Lough, A. J. P. White, D. J. Williams, I. A. Kahwa, *Inorg. Chem.* **2003**, *42*, 4828–4841.

[23] a) M. Kavana, D. R. Powell, J. N. Burstyn, *Inorg. Chim. Acta* **2000**, *297*, 351–361; b) B. Murphy, G. Roberts, S. Tyagi, B. J. Hathaway, *J. Mol. Struct.* **2004**, *698*, 25–36; c) Y. Akhriff, J. Server-Carrio, J. Garcia-Lozano, J. V. Folgado, A. Sancho, E. Escriva, P. Vitoria, L. Soto, *Cryst. Growth Des.* **2006**, *6*, 1124–1133.

[24] W. A. Wojtczak, P. Atanassova, M. J. Hampden-Smith, E. Duesler, *Inorg. Chem.* **1996**, *35*, 6995–7000.

[25] a) F. Li, Y. Jin, C. Song, Y. Lin, F. Pei, F. Wang, N. Hu, *Appl. Organomet. Chem.* **1996**, *10*, 761–771; b) L. Brammer, M. D. Burgard, M. D. Eddleston, C. S. Rodger, N. P. Rath, H. Adams, *Cryst. Eng. Commun.* **2002**, *4*, 239–248; c) E. V. Dikarev, K. W. Andreini, M. A. Petrukhina, *Inorg. Chem.* **2004**, *43*, 3219–3224.

[26] a) J. A. Samuels, J. W. Zwanziger, E. B. Lobkovsky, K. G. Caulton, *Inorg. Chem.* **1992**, *31*, 4046–4047; b) D. C. Bradley, M. Hasan, M. B. Hursthouse, M. Motevalli, O. F. Z. Khan, R. G. Pritchard, J. O. Williams, *J. Chem. Soc., Chem. Commun.* **1992**, 575–576; c) D. C. Bradley, H. Chudzynska, M. E. Hammond, M. B. Hursthouse, M. Motevalli, W. U. Ruowen, *Polyhedron* **1992**, *11*, 375–379; d) H. Vincent, F. Labrize, L. G. Hubert-Pfalzgraf, *Polyhedron* **1994**, *13*, 3323–3327.

[27] a) B. V. Nonius, Collect Software, **1997**–**2000**; b) Z. Otwinowski, W. Minor, *Processing of X-ray Diffraction Data Collected in Oscillation Mode*, in *Methods in Enzymology*, 276: Macromolecular Crystallography, part A (Eds.: C. W. Carter Jr., R. M. Sweet), Academic Press, **1997**, p. 307–326.

[28] G. M. Sheldrick, *Program for the refinement of crystal structures*, University of Göttingen, Germany (Bruker AXS, Madison, Wisconsin, USA), **1997**.

[29] A. Altomare, M. C. Burla, G. Camalli, G. Cascarano, C. Giacovazzo, M. A. Guagliardi, G. Polidori, R. Rizzi, *J. Appl. Crystallogr.* **1999**, *32*, 115–119.

[30] P. W. Betteridge, J. R. Carruthers, R. I. Cooper, K. Prout, D. J. Watkin, *J. Appl. Crystallogr.* **2003**, *36*, 1487.

Received: September 6, 2006
Published Online: December 4, 2006

 © 2007 Wiley-VCH Verlag GmbH & Co. KGaA, Weinheim 

DOI: 10.1002/ejic.200600852

# Hierarchical, Lithium-Templated Assembly of Helicate-Type Complexes: How Versatile Is This Reaction?

**Markus Albrecht,*[a] Marcel Fiege,[a] Miriam Baumert,[a] Marita de Groot,[a] Roland Fröhlich,[b] Luca Russo,[c] and Kari Rissanen[c]**

**Keywords:** Dinuclear complexes / Helicates / Hierarchical assembly / Chelate ligands / N,O ligands

Catechol ligands that bear carbonyl functions such as esters or aldehydes in the 3-position (**1a**–**c**-$H_2$) form triple-stranded, helicate-type complexes $[Li_3(\mathbf{1a}–\mathbf{c})_6Ti_2]^-$ with titanium(IV) and the corresponding double-stranded compounds $[Li_2(\mathbf{1a}–\mathbf{c})_4B_2]$ with boron(III) in hierarchical, lithium-templated processes. The related 8-hydroxyquinoline ligands **2a**,**b**-H can be used for the formation of similar complexes $[Li_3(\mathbf{2a},\mathbf{b})_6M_2]^+$ with cobalt(II), nickel(II), or zinc(II). A prerequisite for the formation of the lithium-bridged dimers is a negative charge of the mononuclear complexes, which are able to electrostatically attract the lithium cations and thus compensate the repulsion between the cations.
(© Wiley-VCH Verlag GmbH & Co. KGaA, 69451 Weinheim, Germany, 2007)

## Introduction

Hierarchical processes are frequently observed in the formation of natural and non-natural aggregates.[1–7] The build-up of viruses or proteins, for example, depends on the specific interplay of binding interactions of different strength.[8]

Recently, we described the hierarchical assembly of dinuclear, helicate-type coordination compounds[9–15] that possess three lithium cations bridging mononuclear building blocks. Here, in a first "recognition event", mononuclear catechol complexes are formed that bear carbonyl units in the 3-position of the ligands. These provide a second binding site (Figure 1) that is ideal for the coordination of lithium cations that form three bridging units between two mononuclear moieties in a second "recognition event".[16–26]

Coordination compounds of this type have been found for derivatives of 3-carbonyl-substituted catechols (carbonyl = aldehyde, ketone, ester) with titanium(IV) and gallium(III) ions. The resulting dinuclear, helicate-type dimers $[Li_3\{(ligand)_6M_2\}]^{n-}$ (M = Ti, $n$ = 1; M = Ga, $n$ = 3), are in equilibrium with the monomeric complex units. This equilibrium has been thoroughly investigated by NMR spectroscopic and ESI FT-ICR MS methods.[16]

In addition, a related equilibrium was found for monomeric and dimeric catecholate complexes with molybdenum(VI) centers. Here, only two catechols bind to each of the metal centers as the remaining coordination site is blocked by two *cis* arranged oxo units. In case of the dimer, the dioxomolybdenum units take part in the bridging of the three lithium cations.[27]

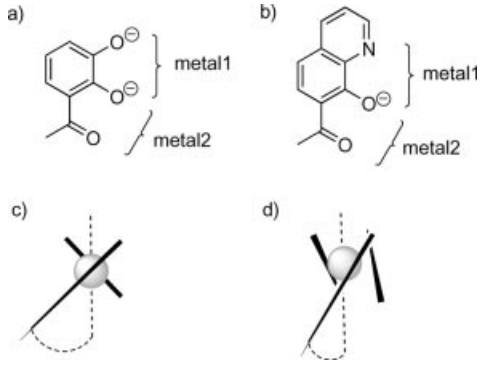


Figure 1. Representation of the two metal binding sites in carbonyl-substituted catecholate (a) and related 8-quinolinate ligands (b) and schematic representations of the relative orientation of chelating ligands in tetrahedral bis-ligand (c) or octahedral tris-ligand complexes (d).

At first sight the hierarchical assembly of helicates seems to be limited to very special examples. However, in this manuscript we report some new compounds to show that the formation of such helicate-type complexes is more general and is not limited to triple-stranded systems or catechol ligands. We also show that the dimerization depends strongly on the electrostatic attraction between negatively charged metal complexes and lithium cations.

[a] Institut für Organische Chemie der RWTH-Aachen, Landoltweg 1, 52074 Aachen, Germany
Fax: +49-241-80-92385
E-mail: markus.albrecht@oc.rwth-aachen.de
[b] Organisch-Chemisches Institut, Universität Münster, Corrensstr. 40, 48149 Münster, Germany
[c] Nanoscience Center, Department of Chemistry, University of Jyväskylä, Survontie 9, 40014 Jyväskylä, Finland

 © 2007 Wiley-VCH Verlag GmbH & Co. KGaA, Weinheim 

## Results and Discussion

### General Considerations

In our recent studies on the hierarchical, lithium-templated assembly of dinuclear, helicate-type complexes, 3-carbonyl-substituted catechol derivatives were used as ligands (see Figure 1, a).[16,27] Compounds of this type provide two binding sites for metal ions: a first metal can be bound to the catecholate unit, while a second metal ion might coordinate to the chelating unit formed by the internal catecholate oxygen atom and the carbonyl oxygen. A tilt angle of 90° between the two chelating units seems to be appropriate in order to allow the formation of the dimeric, lithium-bridged compounds.

A similar geometry to that of the catechol derivatives can be found for 7-carbonyl-substituted 8-hydroxyquinolines (Figure 1, b). Although this ligand has different electronic features compared to the catecholates, it should be able to coordinate two different metal ions and form hierarchically assembled heteronuclear coordination compounds.

Another problem that will be addressed in this study is the formation of double-stranded vs. triple-stranded lithium-bridged dinuclear complexes. Double-stranded coordination compounds are formed if metal cations are introduced that prefer a tetrahedral coordination geometry, while the corresponding triple-stranded systems are formed with octahedral metal centers. Due to the different tilt angles of the projection of the ligand planes on the main axis of the complex unit (see Figure 1c,d), one kind of ligand can form both double- and triple-stranded compounds if the spacer with the lithium cations possesses some flexibility.

In earlier studies we have shown that, due to the donor strength of the carbonyl unit, ester-substituted ligands are the most appropriate to obtain a monomer–dimer equilibrium of lithium-bridged complexes, with the dimer being the dominant species.[16] Therefore we now mainly discuss complexes with the ester-substituted ligands **1a**,**b**-$H_2$ and **2a**,**b**-H. In addition, we have used 2,3-dihydroxybenzaldehyde (**1c**-$H_2$) for comparison studies (Figure 2).

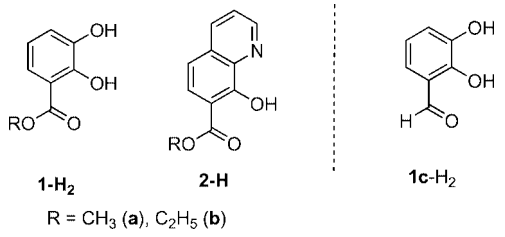


Figure 2. Ester-substituted catechol (**1a**,**b**-$H_2$) and 8-hydroxyquinoline ligands (**2a**,**b**-H) and 2,3-dihydroxybenzaldehyde (**1c**-$H_2$).

### Triple- and Double-Stranded, Helicate-Type Complexes Based on Catecholate Ligands

Recently we described a series of X-ray structures of dinuclear titanium(IV) complexes of carbonyl-substituted catecholate ligands with aldehyde, ketone, or ester sidechains.[16,28,29]

A representation of the dimers Li[$Li_3${(**1a**–**c**)$_3$Ti}$_2$] is shown in Figure 3. The side view of the complex shows the two pseudo-octahedral titanium(IV) centers and the bridging tetrahedral lithium cations binding to the carbonyl and to the internal catecholate oxygens.

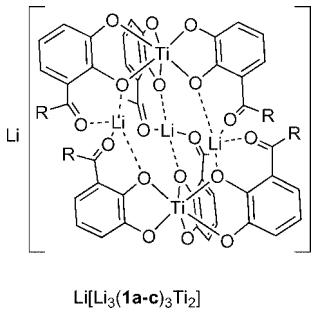


Figure 3. Schematic representation of the dimers Li[$Li_3${(**1a**–**c**)$_3$-Ti}$_2$].

In order to obtain a double-stranded system, we substituted the titanium(IV) ions by boron(III). This ion can only bind two catecholates to form a pseudo-tetrahedral coordination compound. Two of the carbonyl-substituted mononuclear units [(ligand)$_2$B]$^-$ should be able to form a double lithium-bridged dinuclear complex. We performed the reaction of the catechol ligands **1a**–**c** with boric acid in the presence of lithium carbonate.[30] The complexes are still contaminated with free ligand in most cases, and pure material can only be obtained in minor amounts by crystallization (Scheme 1).

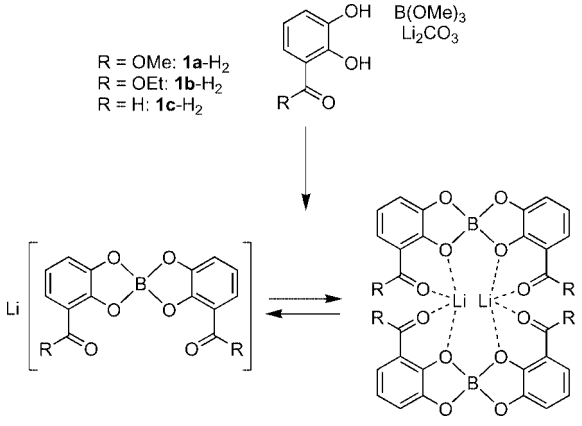


Scheme 1.

Well resolved NMR spectra of "Li[(**1a**–**c**)$_2$B]" can be obtained in deuterated chloroform. For example, only one set of signals can be observed for the complex of the aldehyde derivative **1c** in this solvent at $\delta$ = 9.08 (s, 1 H), 7.01 (dd, $J$ = 7.7, 1.1 Hz, 1 H), 6.82 (t, $J$ = 7.7 Hz, 1 H) and 6.67 ppm (dd, $J$ = 7.7, 1.1 Hz, 1 H). The high-field shift of the signal of the aldehyde proton to $\delta$ = 9.08 ppm seems to be indicative of a dimeric structure for this complex.[16] In this case the aldehyde proton of one complex unit is located in the anisotropic region of the aromatic moieties of the second.

 © 2007 Wiley-VCH Verlag GmbH & Co. KGaA, Weinheim 

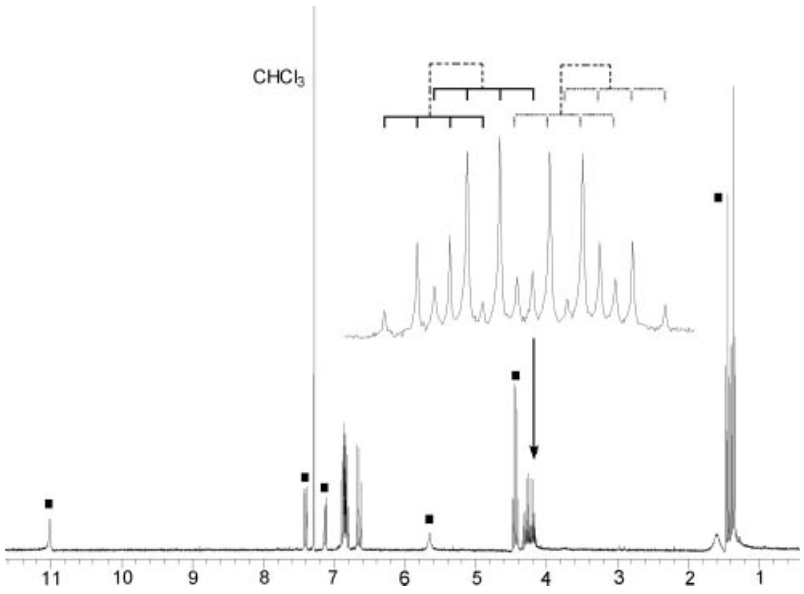


Figure 4. $^1$H NMR spectrum of "Li[(**1b**)$_2$B]" in deuterated chloroform showing the signals of the complex and the free ligand **1b**-H$_2$ (■). The inset shows the doublet of quartets of the diastereotopic methylene protons in the complex.

Figure 4 shows the $^1$H NMR spectrum of "Li[(**1b**)$_2$B]" in deuterated chloroform as a representative example. Signals of the free ligand can be observed together with the resonances of the complex. The aromatic protons are observed in the region $\delta$ = 6.6–6.9 ppm as multiplets. The most informative resonances can be observed for the ethyl group. The methyl signal is detected as a triplet ($J$ = 7.2 Hz) at $\delta$ = 1.37 ppm, while the methylene protons are diastereotopic and appear as two doublets of quartets at $\delta$ = 4.19 and 4.28 ppm ($J_{gem}$ = 10.8 Hz). The high-field shifts of the protons of the ethyl ester indicate that a dimeric complex should be present, although no final decision can be made based on the NMR spectra.

The dimeric species [Li$_2${(**1a**–**c**)$_2$B}$_2$] possess no charge and therefore cannot be detected directly by mass spectrometry. However, we were able to detect characteristic fragments by ESI MS. Peaks of the complexes with ligand **1a** are observed in the negative detection mode at *m*/*z* 343 [(**1a**)$_2$B]$^-$ and 693 [Li{(**1a**)$_2$B}$_2$]$^-$; [K{(**1a**)$_2$B}$_2$]$^-$ is found at *m*/*z* 725 as an impurity. The positive ESI mass spectrum shows a peak for [Li$_3${(**1b**)$_2$B}$_2$]$^+$ at *m*/*z* 763. Fortunately, we were able to obtain X-ray quality crystals of dimeric [Li$_2${(**1a**)$_2$B}$_2$] from chloroform.

The dimer crystallizes in the space group *Cc*, with a noncrystallographic twofold axis perpendicular to the plane formed by the four centers (Li and B). This results in two nonequivalent catecholate ligands, which is in contrast to the high-symmetry spectrum that is observed by NMR spectroscopy. Two of the ligands in the crystal are orientated more or less parallel to the B–B axis, while the others are severely tilted with respect to this axis (Figure 5). This unsymmetrical orientation of the ligands is probably due to the tendency to reduce strain at the bridging lithium cations. The boron and lithium cations adopt a distorted tetrahedral coordination geometry, with B–B, Li–Li, and Li–B separations of 4.456, 4.255, and 3.158–3.187 Å, respectively.

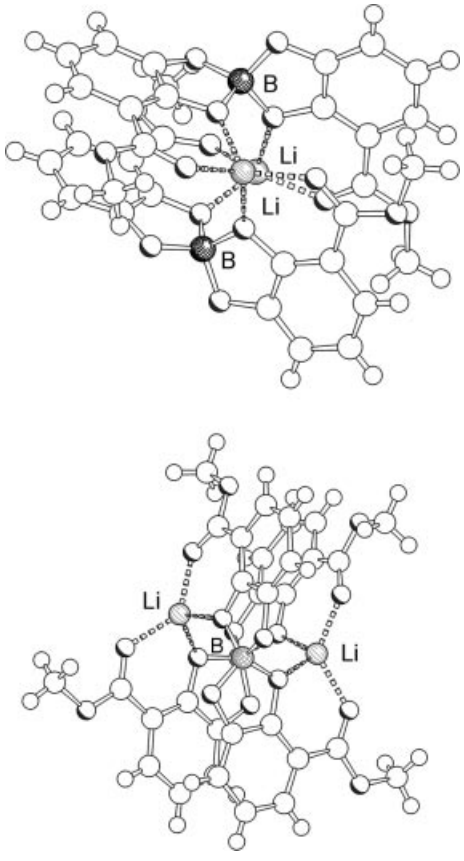


Figure 5. Views of the solid-state structure of dimeric [Li$_2${(**1a**)$_2$B}$_2$] down the Li–Li (top) and down the B–B axis (bottom).

The catecholate complexes with boron show a green or blue fluorescence in chloroform solution. Thus, upon excitation at $\lambda$ = 265 or 363 nm the aldehyde Li[(**1c**)$_2$B] shows an emission maximum at $\lambda$ = 476 nm. The corresponding

 © 2007 Wiley-VCH Verlag GmbH & Co. KGaA, Weinheim 

methyl ester shows emission at $\lambda$ = 393 nm when excited either at $\lambda$ = 248 or 326 nm.

### Triple-Stranded Complexes Based on 8-Hydroxyquinolinate Ligands

8-Hydroxyquinoline and catechol are sterically similar chelating units for metal ions[31] as a five-membered heterocycle is formed upon coordination of the metal. However, their electronic features are severely different. In the deprotonated form, catecholate possesses a charge of 2– while 8-hydroxyquinolinate is a mono anion (see Figure 1). In order to test the versatility of the lithium-templated dimerization of complex units, we decided to substitute the catecholate moiety by 8-hydroxyquinolinate.

The methyl and ethyl esters **2a**-H and **2b**-H were prepared by simple sulfuric acid catalyzed esterification of 8-hydroxyquinoline-7-carboxylic acid in the corresponding alcohol as solvent.[32]

In initial experiments, coordination studies of ligands **2a/b**-H were performed with aluminium(III) and gallium(III) salts. Elemental analysis of the resulting complexes showed a 3:1 ligand-to-metal ratio. NMR spectroscopy revealed complicated spectra with broad signals, probably due to a *syn*/*anti* isomerization. However, the positive-ion ESI mass spectra showed the formation of the complexes [(**2a**,**b**)$_3$Ga/Al]. Cationic species can be observed at *m*/*z* 656 [(**2a**)$_3$AlNa]$^+$, 676 [(**2b**)$_3$AlH]$^+$, 676 [(**2a**)$_3$GaH]$^+$, and 718 [(**2b**)$_3$GaH]$^+$.[33]

Addition of lithium perchlorate to solutions of [(**2a**,**b**)$_3$Ga/Al] in [D$_4$]MeOH does not alter the NMR spectra, and the ESI mass spectra do not show the formation of "{Li$_3$[(**2a**,**b**)$_3$Ga/Al]$_2$}$^{3+}$" dimers. The neutral complex units are obviously not good binders for the lithium cations due to a lack of the electrostatic attraction that it is present in the corresponding compounds of titanium(IV) or gallium(III) with catecholate ligands.

In order to introduce negative charge at the complexes, we switched to cobalt(II), nickel(II), and zinc(II) ions as metal centers (Scheme 2).

The reaction of cobalt(II), nickel(II), or zinc(II) acetate with ligands **2a**,**b**-H in methanol in the presence of lithium carbonate leads, after work-up, to coordination compounds

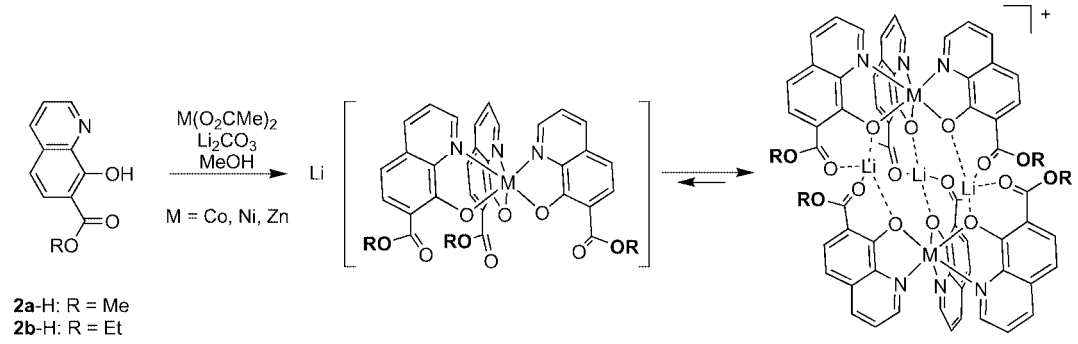


Scheme 2.

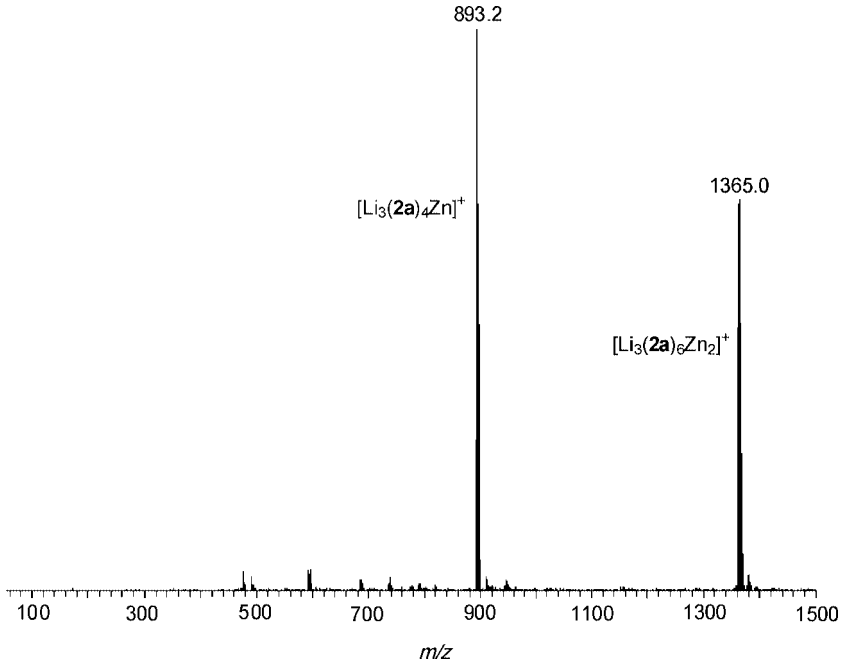


Figure 6. ESI mass spectrum of [Li$_3$(**2**)$_6$Zn$_2$][OAc] in methanol/chloroform.

 © 2007 Wiley-VCH Verlag GmbH & Co. KGaA, Weinheim 

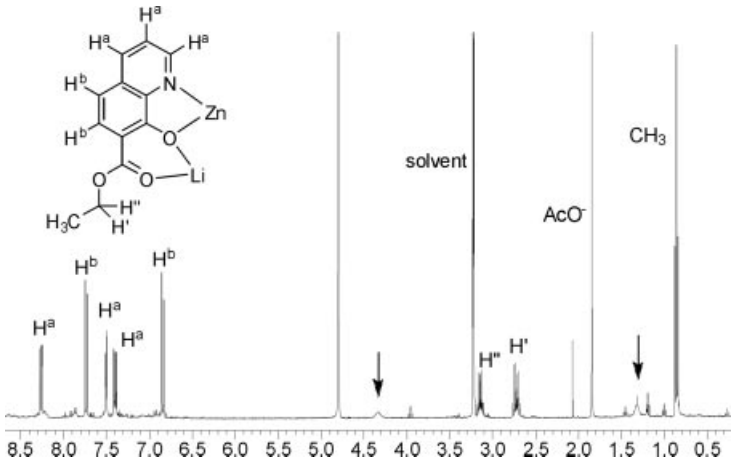


Figure 7. $^1$H NMR spectrum of $[Li_3(\mathbf{3b})_6Zn_2][O_2CCH_3]$ in $[D_4]$MeOH. The signals of the dimeric complex are assigned. The broad signalsarked with arrows are probably due to monomeric complexes.

that show peaks for the dimeric species $[Li_3(\mathbf{2})_6M_2]^+$ (M = Co, Ni, Zn) at *m/z* 1365 $[Li_3(\mathbf{2a})_6Zn_2]^+$, 1449 $[Li_3(\mathbf{2b})_6Zn_2]^+$, 1349 $[Li_3(\mathbf{2a})_6Ni_2]^+$, 1433 $[Li_3(\mathbf{2b})_6Ni_2]^+$, and 1351 $[Li_3(\mathbf{2a})_6Co_2]^+$ in the positive-ion ESI mass spectra. All signals possess the expected isotopic patterns. The spectrum of the zinc(II) complex with ligand **2a** is shown in Figure 6.

A monomeric complex with three ligands is observed only for $[Li_2(\mathbf{2b})_3Ni]^+$ (*m/z* 720). The dominating fragmentation is the formation of different mononuclear species. Mononuclear transition metal complexes with four ligands and three lithium cations can be detected in the gas phase at *m/z* 893 $[Li_3(\mathbf{2a})_4Zn]^+$, 949 $[Li_3(\mathbf{2b})_4Zn]^+$, 887 $[Li_3(\mathbf{2a})_4Ni]^+$, 943 $[Li_3(\mathbf{2b})_4Ni]^+$, and 889 $[Li_3(\mathbf{2a})_4Co]^+$. This shows an unsymmetrical decomposition of the dimer under these ionization conditions with loss of the neutral mononuclear $[(\mathbf{2a},\mathbf{b})_2Zn/Ni/Co]$.[16]

The diamagnetic zinc(II) complexes can be studied by NMR spectroscopy. The spectrum of "Li$[(\mathbf{2b})_3Zn]$" in $[D_4]$-MeOH is shown in Figure 7 as a representative example.

The dinuclear zinc(II) complex $[Li_3(\mathbf{3b})_6Zn_2][O_2CCH_3]$ is observed as the dominant species. The signals of the three pyridine protons $H^a$ appear at $\delta$ = 8.26 (dd, $J$ = 8.2, 1.7 Hz), 7.50 (dd, $J$ = 4.2, 1.7 Hz), and 7.39 ppm (dd, $J$ = 8.2, 4.2 Hz) while the doublets ($J$ = 9.5 Hz) of the phenolic unit $H^b$ are detected at $\delta$ = 7.73 and 6.82 ppm. The terminal $CH_3$ group of the ethyl ester is found as a triplet ($J$ = 7.1 Hz) at $\delta$ = 0.86 ppm. The methylene group results in two doublets of quartets at $\delta$ = 2.72 and 3.14 ppm, with a geminal coupling constant 11.0 Hz. The high-field shift and the diastereotopicity of those two signals show that the dimeric complex is present, as (1) in the dimeric complex the ethyl groups of one complex unit are located close to the aromatic system of the second. This leads to an anisotropic shift to low field. This effect is also observed for the resonance of the methyl group. (2) In the dimeric complex the stereochemistry at the complex units is fixed so no fast racemization between the Λ and Δ isomers takes place. In the monomers this isomerization as well as a *syn–anti* isomerization should proceed much more rapidly. According to this, broad signals at $\delta$ = 4.33 and 1.31 ppm (marked by an arrow in Figure 7) can be tentatively assigned to the ethyl groups of a highly dynamic mononuclear complex.

We were able to obtain X-ray quality crystals of $[Li_3(\mathbf{2b})_6Ni_2][HSO_4]\cdot Et_2O$ from ethanol/diethyl ether. The structure of the $[Li_3(\mathbf{2b})_6Ni_2]^+$ cation is depicted in Figure 8.[34] This compound is built up from two pseudo-octahedral nickel(II) complexes $[(\mathbf{2b})_3Ni]^-$ with the quinolinate ligands **2b** orientated in a *syn* fashion. This enables the binding of three lithium cations to the phenolate carbonyl

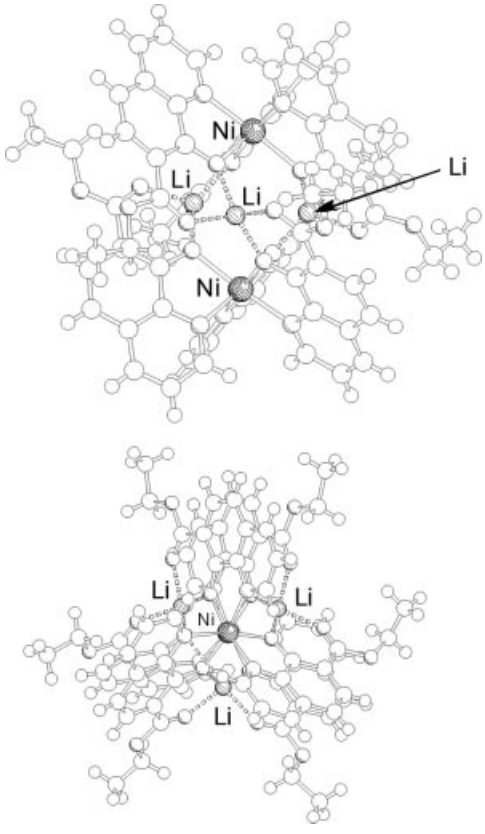


Figure 8. Views of the solid-state structure of the cation $[Li_3\{(\mathbf{2b})_3Ni\}_2]$ down the Li–Li (top) and down the Ni–Ni axis (bottom).

 © 2007 Wiley-VCH Verlag GmbH & Co. KGaA, Weinheim 

chelate of each of the two units and formation of the triply bridged dimer, with nickel–nickel separations of 5.276 Å. The three lithium cations form a triangle with distances of 3.607, 3.804, and 3.825 Å, respectively. The alkali metal ions are located 3.374–3.462 Å away from the transition metals.

The structure of the hydroxyquinoline complex $[Li_3(\mathbf{2b})_6Ni_2]^+$ is very similar to those observed for titanium(IV) catechol derivatives like $[Li_3\{(\mathbf{1b})_3Ti\}_2]^-$.

## Conclusions

We have studied the versatility of the lithium-templated hierarchical assembly of dinuclear, helicate-type complexes. As described earlier, titanium(IV) catecholate complexes that bear carbonyl substituents in the 3-position of the ligand are able to form triple-stranded dimers in the presence of lithium cations.[16] Substitution of the titanium(IV) centers by boron results in the formation of the analogous double-stranded complexes, which, although they are labile and are often obtained in a mixture with free ligand, can be readily characterized.

Furthermore, this approach to oligonuclear complexes is not restricted to catecholate ligands as 8-hydroxyquinolines with a carbonyl in the 7-position can form related compounds with late transition metals. With aluminum(III) or gallium(III) ions neutral 8-hydroxyquinolinate complexes are obtained, which do not show a tendency to lithium-mediated dimerization. This indicates that the electrostatic attraction between anionic complex units and lithium cations is an essential driving force in the dimerization process.

We have a broad set of different kinds of ligands and different metal centers available for future studies. We will investigate whether we can use "combinatorial" approaches to obtain specific heterodinuclear complexes and we will functionalize the periphery of the complexes in order to tune their properties.

## Experimental Section

NMR spectra were recorded with a Varian Mercury 300 or Inova 400 spectrometer. FT-IR spectra were recorded with a Bruker IFS spectrometer. Mass spectra were recorded with a Thermo Deca XP mass spectrometer. Elemental analyses were obtained with a Heraeus CHN-O-Rapid analyser. Fluorescence measurements were performed on a Perkin–Elmer LS-50B spectrofluorimeter.

**$Li[Li_3(\mathbf{1a–c})_6Ti_2]$:** The titanium(IV) complexes were prepared as described earlier.[16]

**General Procedure for the Preparation of Boron Complexes:** Catechol **1a**–**c**-$H_2$ (2 equiv.), boric acid (1 equiv.), and lithium carbonate (1 equiv.) were dissolved in methanol (10 mL) and the solution stirred overnight. The solvent was then removed and the residue was recrystallized from chloroform and dried in vacuo. Attempts to purify the compounds over Sephadex LH20 did not result in pure material.

**$Li_2[B_2(\mathbf{1a})_4]$:** Yield: 40 mg (42%). $^1$H NMR ($CDCl_3$, 400 MHz): $\delta$ = 6.77 (m, 8 H), 6.57 (t, $J$ = 8.0 Hz, 4 H), 3.71 ppm (s, 12 H). IR (KBr): $\tilde{\nu}$ = 3460, 2361, 2340, 1678, 1469, 1322, 1262, 1227, 1143, 1107, 1031, 744 cm$^{-1}$. Negative ESI MS (dmf, MeOH): $m/z$ 693 $[LiB_2(\mathbf{1a})_4]^-$, 343 $[B(\mathbf{1a})_2]^-$. Fluorescence data: ($CHCl_3$): $\lambda_{ex}$ (nm) = 248, 326; $\lambda_{em}$ (nm) = 395. $C_{32}H_{24}B_2Li_2O_{16}\cdot 4H_2O$ (772.10): calcd. C 49.77, H 4.18; found C 49.98, H 4.69. A single crystal of the product was selected and mounted on a cryo-loop for single-crystal X-ray data collection on a Bruker–Nonius KAPPACCD diffractometer equipped with a graphite-monochromated Mo-$K_\alpha$ radiation source ($\lambda$ = 0.71073 Å), an APEXII area detector, and an Oxford Cryostream cryogenic device (data collected at 173 K). Structure solution was performed with SHELXS-97,[35] with subsequent refinement on $F^2$ by full-matrix least-squares (SHELXL-97[35]). Hydrogen atoms were calculated at their idealized positions and refined with a riding model (isotropic displacement parameters 1.2- or 1.5-times C anisotropic displacement parameters). Multiscan absorption correction was applied to the data (SADABS[12]). Crystal system: monoclinic; space group: $Cc$; $a$ = 9.2853(19), $b$ = 23.783(5), $c$ = 14.844(3) Å, $\beta$ = 106.70(3)°; cell volume: 3139.7(11) Å$^3$; $Z$ = 4; calculated density: 1.481 g cm$^{-3}$; absorption coefficient: 0.117 mm$^{-1}$; $F$(000) = 1440; crystal color: colorless; size: 0.40 × 0.20 × 0.10 mm$^3$; reflections for cell refinement: 1005 ($\theta$ range 2.5 to 27.5°); data collection method: &phis; and $\omega$ scans; $\theta$ range for data collection: 3.4 to 27.4°; index ranges: $-11 \le h \le 11$, $0 \le k \le 30$, $0 \le l \le 19$; completeness to $\theta$ = 27.4°: 97.2%; reflections collected: 3470; independent reflections: 3470 ($R_{int}$ = 0.0654, before merging); reflections with $F^2 > 2\sigma$: 2416; absorption correction: semi-empirical from equivalents; Min. and max. transmission: 0.9546 and 0.9884; structure solution: direct methods; full-matrix least-squares on $F^2$; weighting parameters: $a$ = 0.0449, $b$ = 0.1095; data/restraints/parameters: 3470/2/470; final $R$ indices [$F^2 > 2\sigma$] $R_1$ = 0.0632, $wR_2$ = 0.1064; $R$ indices (all data) $R_1$ = 0.1141, $wR_2$ = 0.1293; goodness-of-fit on $F^2$: 1.190; absolute structure parameter: 1.0(14); extinction coefficient: 0.0020(4); largest and mean shift/su: 0.001 and 0.000; largest diff. peak and hole: 0.23 and –0.28 e Å$^{-3}$.

**$Li_2[B_2(\mathbf{1b})_4]$:** Yield: 39 mg (38%). $^1$H NMR ($CDCl_3$, 300 MHz): $\delta$ = 6.85 (m, 8 H), 6.64 (t, $J$ = 7.2 Hz, 4 H), 4.19 (qd, $J$ = 7.2, 10.8 Hz, 4 H), 4.28 (qd, $J$ = 7.2, 10.8 Hz, 4 H), 1.36 ppm (t, $J$ = 7.2 Hz, 12 H). IR (KBr): $\tilde{\nu}$ = 3474, 2983, 2361, 2369, 1675, 1468, 1372, 1263, 1222, 1102, 1033, 885, 742 cm$^{-1}$. Positive ESI MS ($CHCl_3$, MeOH): $m/z$ 763 $[Li_3B_2(\mathbf{1b})_4]^+$, 385 $[Li_2B(\mathbf{1b})_2]^+$. Fluorescence data: ($CHCl_3$): $\lambda_{ex}$ (nm) = 255, 328; $\lambda_{em}$ (nm) = 395. $C_{36}H_{32}B_2Li_2O_{16}\cdot 7H_2O$ (882.25): calcd. C 49.01, H 5.25; found C 48.86, H 5.46.

**$Li_2[B_2(\mathbf{1c})_4]$:** Yield: 57 mg (54%). $^1$H NMR ($CDCl_3$, 400 MHz): $\delta$ = 9.08 (s, 1 H), 7.00 (dd, $J$ = 7.6, 1.1 Hz, 1 H), 6.83 (t, $J$ = 7.6 Hz, 1 H), 6.67 ppm (dd, $J$ = 7.6, 1.1 Hz, 1 H). IR (KBr): $\tilde{\nu}$ = 3854, 3744, 3420, 2361, 2340, 1661, 1621, 1585, 1467, 1403, 1266, 1214, 1086, 880, 737, 680 cm$^{-1}$. Negative ESI MS (dmf, MeOH): $m/z$ 573 $[LiB_2(\mathbf{1c})_4]^-$, 283 $[B(\mathbf{1c})_2]^-$. Fluorescence data: ($CHCl_3$): $\lambda_{ex}$ (nm) = 265, 363; $\lambda_{em}$ (nm) = 471. $C_{28}H_{16}B_2Li_2O_{12}$ (579.93): calcd. C 57.99, H 2.78; found C 58.21, H 3.26.

**General Procedure for the Preparation of Aluminum(III) and Gallium(III) Complexes of the 8-Hydroxyquinoline Ligands 2a,b-H:** 8-Hydroxyquinoline derivative **2a**-H or **2b**-H (3 equiv.) and gallium nitrate or aluminum trichloride (1 equiv.) were dissolved in methanol or ethanol and stirred overnight. The solvent was then removed under reduced pressure to obtain solid materials in close to quantitative yields.

**$[(\mathbf{2a})_3Al]$:** Yield: 59.1 mg (92%). $^1$H NMR (400 MHz, $CD_3OD$): $\delta$ = 3.96 (s, 3 H), 7.34 (d, $J$ = 8.8 Hz, 1 H), 7.60 (dd, $J$ = 4.2, 8.3 Hz, 1 H), 7.86 (d, $J$ = 8.8 Hz, 1 H), 8.26 (dd, $J$ = 1.1, 8.3 Hz, 1 H), 8.80 ppm (dd, $J$ = 1.1, 4.2 Hz, 1 H). Positive ESI MS: $m/z$ 656

 © 2007 Wiley-VCH Verlag GmbH & Co. KGaA, Weinheim 

$[Na(\mathbf{2a})_3Al]^+$. IR (KBr): $\tilde{\nu}$ = 3431, 3056, 2990, 2948, 2843, 1702, 1629, 1605, 1572, 1501, 1459, 1397, 1317, 1291, 1247, 1195, 1123, 1055, 1009, 984, 916, 882, 789, 757, 667, 621, 575, 474, 458 $cm^{-1}$. $C_{33}H_{24}AlN_3O_9 \cdot 1.5\,H_2O \cdot 1.5\,CH_3OH$ (708.64): calcd. C 58.48, H 4.69, N 5.93; found C 58.56, H 4.73, N 5.93.

**$[(\mathbf{2b})_3Al]$:** Yield: 52.2 mg (98%). $^1H$ NMR (400 MHz, $CD_3OD$): Due to the presence of different isomers only an uninformative spectrum with broad signals is obtained. Positive ESI MS: *m/z* 676 $[H(\mathbf{2b})_3Al]^+$. IR (KBr): $\tilde{\nu}$ = 3791, 3447, 3066, 2980, 2931, 2901, 1707, 1603, 1572, 1501, 1458, 1399, 1311, 1292, 1244, 1197, 1112, 1055, 1024, 948, 884, 833, 755, 666, 622, 573, 529, 492 $cm^{-1}$. $C_{36}H_{30}AlN_3O_9 \cdot H_2O$ (693.65): calcd. C 62.34, H 4.65, N 6.06; found C 62.35, H 4.98, N 5.97.

**$[(\mathbf{2a})_3Ga]$:** Yield: 56.7 mg (97%). $^1H$ NMR (400 MHz, $CD_3OD$): $\delta$ = 3.59 (s, 3 H), 7.23 (d, $J$ = 8.8 Hz, 1 H), 7.45 (d, $J$ = 8.8 Hz, 1 H), 7.61 (d, $J$ = 8.2 Hz, 1 H), 7.63 (d, $J$ = 8.2 Hz, 1 H), 7.95 ppm (d, $J$ = 8.8 Hz, 1 H). Positive ESI MS: *m/z* 676 $[H(\mathbf{2a})_3Ga]H^+$. IR (KBr): $\tilde{\nu}$ = 3898, 3854, 3744, 3694, 3674, 3620, 3589, 3565, 3437, 2948, 2360, 2339, 1842, 1700, 1652, 1564, 1504, 1456, 1391, 1317, 1293, 1243, 1197, 1117, 1058, 1005, 884, 834, 748, 666, 610, 561, 509 $cm^{-1}$. $C_{33}H_{24}GaN_3O_9 \cdot 2\,H_2O$ (712.32): calcd. C 55.64, H 3.96, N 5.90; found C 55.69, H 3.99, N 6.01.

**$[(\mathbf{2b})_3Ga]$:** Yield: 49.1 mg (89%). $^1H$ NMR (400 MHz, $CD_3OD$): Due to the presence of different isomers only an uninformative spectrum with broad signals was obtained. Positive ESI MS: *m/z* 718 $[H(\mathbf{2b})_3Ga]^+$. IR (KBr): $\tilde{\nu}$ = 3511, 3408, 3063, 2979, 2934, 2901, 1711, 1603, 1569, 1500, 1452, 1395, 1311, 1291, 1243, 1196, 1119, 1054, 1022, 948, 833, 788, 747, 665, 607, 563, 521 $cm^{-1}$. No correct elemental analysis was obtained.

**General Procedure for the Preparation of Cobalt(II), Nickel(II), and Zinc(II) Complexes of the 8-Hydroxyquinoline Ligands 2a,b-H:** 8-Hydroxyquinoline derivative **2a**-H or **2b**-H (3 equiv.), lithium carbonate, and cobalt(II), nickel(II) or zinc(II) acetate (1 equiv.) were dissolved in methanol or ethanol and stirred overnight. The solvent was removed under reduced pressure to obtain solid materials in close to quantitative yields.

**$[Li_3(\mathbf{2a})_6Co_2][O_2CCH_3]$:** Yield: 24 mg (97%) as crude product. IR (KBr): $\tilde{\nu}$ = 3448, 2952, 1680, 1600, 1562, 1500, 1449, 1404, 1384, 1307, 1245, 1198, 1117, 1008, 833, 797, 752, 671, 616, 536, 462 $cm^{-1}$. Positive ESI MS: *m/z* 1351 $[Li_3(\mathbf{2a})_6Co_2]^+$. No correct elemental analysis was obtained, probably due to the exchange of acetate by other anions.

**$[Li_3(\mathbf{2a})_6Ni_2][O_2CCH_3]$:** Yield: 56.9 mg (98%). Positive ESI MS: *m/z* 1349 $[Li_3(\mathbf{2a})_6Ni_2]^+$. IR (KBr): $\tilde{\nu}$ = 3411, 3049, 2999, 2949, 1680, 1601, 1556, 1500, 1447, 1403, 1308, 1246, 1193, 1152, 1116, 1051, 1006, 883, 829, 788, 746, 669, 611, 536, 472 $cm^{-1}$. $C_{66}H_{48}Li_3N_6Ni_2O_{18} \cdot OCOCH_3 \cdot 2\,CH_3OH$ (1474.5): calcd. C 57.02, H 4.03, N 5.70; found C 57.36, H 4.26, N 5.93.

**$[Li_3(\mathbf{2b})_6Ni_2][HSO_4]$:** The complex was prepared using **2b**-H·$H_2SO_4$ as ligand. Yield: 55.8 mg (95%). Positive ESI MS: *m/z* 1432.9 $[Li_3(\mathbf{2b})_6Ni_2]^+$. IR (KBr): $\tilde{\nu}$ = 3425, 3056, 2979, 2932, 1677, 1599, 1557, 1500, 1450, 1406, 1361, 1305, 1244, 1191, 1157, 1115, 1026, 950, 828, 785, 744, 667, 616, 538, 493, 458 $cm^{-1}$. $C_{72}H_{60}Li_3N_6Ni_2O_{18} \cdot HSO_4 \cdot C_2H_5OH$ (1578.66): calcd. C 56.30, H 4.28, N 5.32; found C 56.54, H 4.47, N 5.21.

**X-ray Crystal Structure Analysis for $[Li_3(\mathbf{2b})_6Ni_2][HSO_4]$:** Formula: $[C_{72}H_{60}Li_3N_6Ni_2O_{18}][HSO_4] \cdot C_4H_{10}O$; $M$ = 1606.69; yellow crystal, 0.20 × 0.15 × 0.06 $mm^3$; $a$ = 12.763(1), $b$ = 16.435(1), $c$ = 18.420(1) Å, $\alpha$ = 83.93(1)°, $\beta$ = 78.12(1)°, $\gamma$ = 87.00(1)°; $V$ = 3758.0(4) $Å^3$; $\rho_{calc}$ = 1.420 $g\,cm^{-3}$; $\mu$ = 0.610 $mm^{-1}$; empirical absorption correction (0.888 ≤ $\theta$ ≤ 0.964); $Z$ = 2, triclinic, space group $P\bar{1}$ (no. 2); $\lambda$ = 0.71073 Å; $T$ = 198 K; $\omega$ and $\varphi$ scans, 24802 reflections collected ($\pm h$, $\pm k$, $\pm l$), [(sin$\theta$)/$\lambda$] = 0.54 $Å^{-1}$; 9777 independent ($R_{int}$ = 0.078) and 6454 observed reflections [$I \geq 2\sigma(I)$]; 1008 refined parameters, $R$ = 0.078, $wR_2$ = 0.231, max. residual electron density 2.51 (–0.82) e $Å^{-3}$ in the region of the disordered anion, which was refined with geometrical and thermal constraints; hydrogen atoms were calculated and refined as riding. The data set was collected with a Nonius KappaCCD diffractometer equipped with a rotating anode generator. Programs used: data collection: COLLECT (Nonius B.V., 1998); data reduction: Denzo-SMN;[36] absorption correction: SORTAV;[37,38] structure solution: SHELXS-97;[39] structure refinement: SHELXL-97 (G. M. Sheldrick, University of Göttingen, 1997); graphics: SCHAKAL (E. Keller, University of Freiburg, 1997).

**$[Li_3(\mathbf{2a})_6Zn_2][O_2CCH_3]$:** Yield: 56.1 mg (96%). $^1H$ NMR (400 MHz, $CD_3OD$): $\delta$ = 1.79 (s, 3 H), 2.64 (s, 3 H), 6.86 (d, $J$ = 9.0 Hz, 1 H), 7.40 (dd, $J$ = 3.9, 8.2 Hz, 1 H), 7.50 (dd, $J$ = 1.2, 3.9 Hz, 1 H), 7.69 (d, $J$ = 9.0 Hz, 1 H), 8.26 ppm (dd, $J$ = 1.2, 8.2 Hz, 1 H). positive ESI MS: *m/z* 1365.4 $[Li_3(\mathbf{3a})_6Zn_2]^+$. IR (KBr): $\tilde{\nu}$ = 3986, 3946, 3661, 3428, 3053, 2949, 1682, 1601, 1557, 1500, 1449, 1405, 1308, 1248, 1194, 1153, 1116, 1056, 1008, 908, 827, 788, 743, 701, 670, 616, 543, 479 $cm^{-1}$. $C_{66}H_{48}Li_3N_6O_{18}Zn_2 \cdot OCOCH_3 \cdot 3\,H_2O \cdot 3\,CH_3OH$ (1573.9): calcd. C 54.18, H 4.42, N 5.34; found C 54.10, H 4.33, N 5.48.

**$[Li_3(\mathbf{2b})_6Zn_2][O_2CCH_3]$:** Yield: 56.5 mg (98%). $^1H$ NMR (400 MHz, $CD_3OD$): $\delta$ = 0.86 (t, $J$ = 7.1 Hz, 3 H), 1.84 (s, 3 H), 2.72 (dd, $J$ = 3.5, 7.1 Hz, 1 H), 3.14 (dd, $J$ = 3.5, 7.1 Hz, 1 H), 6.84 (d, $J$ = 8.8 Hz, 1 H), 7.40 (dd, $J$ = 4.7, 8.2 Hz, 1 H), 7.50 (dd, $J$ = 1.4, 4.7 Hz, 1 H), 7.73 (d, $J$ = 8.8 Hz, 1 H), 8.26 ppm (d, $J$ = 1.4, 8.2 Hz, 1 H). Positive ESI MS: *m/z* 1449 $[Li_3(\mathbf{3b})_6Zn_2]^+$. IR (KBr): $\tilde{\nu}$ = 3415, 3057, 2979, 2932, 2902, 1678, 1601, 1556, 1500, 1450, 1408, 1362, 1304, 1245, 1190, 1156, 1116, 1027, 950, 828, 786, 742, 672, 616, 539, 494, 468 $cm^{-1}$. $C_{72}H_{60}Li_3N_6O_{18}Zn_2 \cdot OCOCH_3 \cdot 2\,H_2O \cdot CH_3OH$ (1576.0): calcd. C 57.16, H 4.54, N 5.33; found C 57.14, H 4.78, N 5.42.

CCDC-620597 and -620598 contain the supplementary crystallographic data for this paper. These data can be obtained free of charge from The Cambridge Crystallographic Data Centre via www.ccdc.cam.ac.uk/data_request/cif.

## Acknowledgments

Financial support by the Deutsche Forschungsgemeinschaft (DFG) is gratefully acknowledged. We thank Prof. Elmar Weinhold for the opportunity to measure the fluorescence spectra.

[1] V. Percec, W.-D. Cho, G. Ungar, D. J. P. Yeardley, *Angew. Chem.* **2000**, *112*, 1662; *Angew. Chem. Int. Ed.* **2000**, *39*, 1597.
[2] J. A. A. W. Elemans, A. E. Rowan, R. J. M. Nolte, *J. Mater. Chem.* **2003**, *13*, 2661.
[3] F. Würthner, S. Yao, U. Beginn, *Angew. Chem.* **2003**, *115*, 3368; *Angew. Chem. Int. Ed.* **2003**, *42*, 3247.
[4] J. A. A. W. Elemans, A. E. Rowan, R. J. M. Nolte, *J. Am. Chem. Soc.* **2002**, *124*, 1532.
[5] V. Berl, M. J. Krische, I. Huc, J.-M. Lehn, M. Schmutz, *Chem. Eur. J.* **2000**, *6*, 1938.
[6] T. Kawasaki, M. Tokuhiro, N. Kimizuka, T. Kunitake, *J. Am. Chem. Soc.* **2001**, *123*, 6792.
[7] O. Ikkala, G. ten Brinke, *Chem. Commun.* **2004**, 2131.
[8] A. Klug, *Angew. Chem.* **1983**, *95*, 579; *Angew. Chem. Int. Ed. Engl.* **1983**, *22*, 565.

 © 2007 Wiley-VCH Verlag GmbH & Co. KGaA, Weinheim 

[9] J.-M. Lehn, A. Rigault, J. Siegel, J. Harrowfield, B. Chevrier, D. Moras, *Proc. Natl. Acad. Sci. USA* **1987**, *84*, 2565.
[10] E. C. Constable, *Tetrahedron* **1992**, *48*, 10013.
[11] C. Piguet, G. Bernardinelli, G. Hopfgartner, *Chem. Rev.* **1997**, *97*, 2005.
[12] M. Albrecht, *Chem. Rev.* **2001**, *101*, 3457.
[13] M. J. Hannon, L. J. Childs, *Supramol. Chem.* **2004**, *16*, 7.
[14] M. Albrecht, I. Janser, R. Fröhlich, *Chem. Commun.* **2005**, 157.
[15] R. W. Saalfrank, B. Demleitner, in *Transition Metals in Supramolecular Chemistry* (Ed.: J.-P. Sauvage), John Wiley & Sons, New York, **1999**; vol. 5, p. 1.
[16] M. Albrecht, S. Mirtschin, M. de Groot, I. Janser, J. Runsink, G. Raabe, M. Kogej, C. A. Schalley, R. Fröhlich, *J. Am. Chem. Soc.* **2005**, *127*, 10371.
[17] X. Sun, W. J. Darren, D. Caulder, R. E. Powers, K. N. Raymond, E. H. Wong, *Angew. Chem.* **1999**, *111*, 1386; *Angew. Chem. Int. Ed.* **1999**, *38*, 1303.
[18] X. Sun, D. W. Johnson, D. Caulder, K. N. Raymond, E. H. Wong, *J. Am. Chem. Soc.* **2001**, *123*, 2752.
[19] X. Sun, D. W. Johnson, K. N. Raymond, E. H. Wong, *Inorg. Chem.* **2001**, *40*, 4504.
[20] S. G. Telfer, R. Kuroda, *Chem. Eur. J.* **2005**, *11*, 57.
[21] M. Albrecht, K. Witt, H. Röttele, R. Fröhlich, *Chem. Commun.* **2001**, 1330.
[22] A. K. Das, A. Rueda, L. R. Falvello, S.-M. Peng, S. Batthacharya, *Inorg. Chem.* **1999**, *38*, 4365.
[23] J. Heinicke, N. Peulecke, K. Karaghiosoff, P. Mayer, *Inorg. Chem.* **2005**, *44*, 2137.
[24] T. Konno, K. Tokuda, T. Suzuki, K. I. Okamoto, *Bull. Chem. Soc. Jpn.* **1998**, *71*, 1049.
[25] T. Konno, K. Tokuda, K. Okamoto, *Chem. Commun.* **1998**, 1697.
[26] M. H. W. Lam, S. T. C. Cheung, K.-M. Fung, W.-T. Wong, *Inorg. Chem.* **1997**, *36*, 4618.
[27] M. Albrecht, M. Baumert, J. Klankermayer, M. Kogej, C. A. Schalley, R. Fröhlich, *Dalton Trans.* **2006**, 4395.
[28] B. A. Borgias, S. R. Cooper, Y. B. Koh, K. N. Raymond, *Inorg. Chem.* **1984**, *23*, 1009.
[29] A. V. Davis, T. K. Firman, B. P. Hay, K. N. Raymond, *J. Am. Chem. Soc.* **2006**, *128*, 9484.
[30] E. Graf, M. W. Hosseini, A. De Cian, J. Fischer, *Bull. Soc. Chim. Fr.* **1996**, *133*, 743.
[31] M. Albrecht, O. Blau, *Synthesis* **1997**, 213.
[32] Z. Eckstein, B. Kanik, E. Leszczynska, E. Lipczynska-Kochany, J. Pajak, M. Zawadzka, *Pol. J. Chem.* **1979**, *53*, 2373.
[33] H. Schmidbaur, J. Lettenbauer, D. L. Wilkinson, G. Müller, O. Kumberger, *Z. Naturforsch., Teil B* **1991**, *46*, 901.
[34] For helicates with 8-hydroxyquinoline ligands see: M. Albrecht, O. Blau, R. Fröhlich, *Proc. Natl. Acad. Sci. USA* **2002**, *99*, 4867.
[35] G. M. Sheldrick, SHELXTL (**2001**), Madison, USA.
[36] Z. Otwinowski, W. Minor, *Methods Enzymol.* **1997**, *276*, 307.
[37] R. H. Blessing, *Acta Crystallogr., Sect. A* **1995**, *51*, 33.
[38] R. H. Blessing, *J. Appl. Crystallogr.* **1997**, *30*, 421.
[39] G. M. Sheldrick, *Acta Crystallogr., Sect. A* **1990**, *46*, 467.

Received: September 13, 2006
Published Online: December 5, 2006

 © 2007 Wiley-VCH Verlag GmbH & Co. KGaA, Weinheim 

DOI: 10.1002/ejic.200600857

# Solid-Phase Synthesis of Chiral Modular Ferrocene-Based Peptides

Katja Heinze,*[a] Ute Wild,[a] and Manuela Beckmann[a]

**Keywords:** Conformation analysis / Hydrogen bonds / Metallocenes / Molecular modelling / Solid-phase synthesis

Ferrocene-containing tripeptides with one to two ferrocene building blocks were prepared by solid-phase peptide synthesis (SPPS) using Fmoc-protected 1′-aminoferrocene-1-carboxylic acid (Fca). The conformations of the tripeptides were analysed by spectroscopic and theoretical methods. The immobilised ferrocene compounds can be reversibly oxidised on-bead to positively charged peptides and were analysed for anion-binding affinities by a solid-phase binding assay.
(© Wiley-VCH Verlag GmbH & Co. KGaA, 69451 Weinheim, Germany, 2007)

## Introduction

In contrast to organic-based receptors[1] with carboxylate binding sites, which are either charged (e.g. guanidinium or pyridinium ions[2]) or uncharged (e.g. pyrroles, amides or diketopiperazines[3]), suitably substituted ferrocene derivatives create the possibility to switch between the neutral ferrocene (low-affinity state) and charged ferricinium (high-affinity state) simply by applying an external voltage or by chemically induced redox reactions (redox control of molecular recognition[4]). Application of the reverse concept for cation binding to a ferrocene derivative has been recently demonstrated.[5]

With this idea in mind we set out to prepare chemically diverse chiral ferrocene-based two-armed receptors preferably in a combinatorial fashion using state-of-the-art solid-phase peptide synthesis methods (SPPS). For this application we have recently prepared a SPPS-compatible ferrocene building block, namely the fluorenylmethoxycarbonyl-protected 1,1′-ferrocene amino acid Fmoc-Fca-OH (Scheme 1).[6]

Peptides incorporating the artificial amino acid Fca have been previously synthesised by Metzler-Nolte, Kraatz, Rapić and by us using solution-phase methods.[7,8] Fca derivatives have been employed as transition-state analogues for formation of catalytic antibodies.[9] Simple neutral ferrocene-containing amides were shown to bind anions with moderate affinity while the charged ferricinium counterparts bind anions much more strongly because of additional electrostatic interactions between host and guest.[10,11] Fca derivatives bind chloride anions in an induced fit binding process.[11]

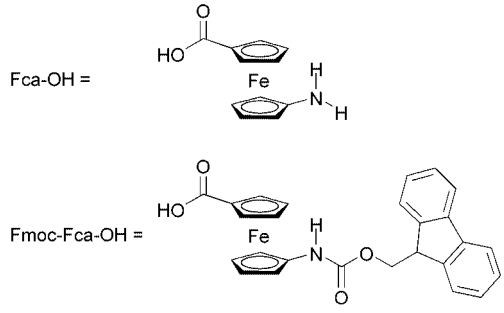


Scheme 1.

## Results and Discussion

### Solid-Phase Synthesis of Ferrocene-Containing Peptides

Here we report a general and modular synthetic approach to peptides containing ferrocene in the backbone compatible with standard SPPS based on the Fmoc-protection strategy.[12] As solid support/linker TentaGel-Wang resins turned out to be superior to polystyrene/divinyl benzene-Wang resins both for SPPS and on-bead reactions. After Fmoc removal from the TentaGel support using piperidine, Fmoc-Fca-OH is preactivated with DIC/HOBt and coupled to the free amine (Scheme 2, DIC = 1,3-diisopropylcarbodiimide, HOBt = 1-hydroxybenzotriazole). Because of the orange colour of the immobilised ferrocene, a Kaiser test for free amines proved impossible. Capping of unreacted amino groups was done using $Ac_2O$/pyridine (see Experimental Section).

Fmoc deprotection of the immobilised ferrocene occurs under standard conditions, as does DIC/HOBt-promoted coupling with an *N*-acetylated L-α-amino acid. Cleavage of the resulting tripeptide from the support with trifluoroacetic acid (TFA) gives tripeptides **1**–**3**. Attaching Ac-Fca-OH[6] instead of an α-amino acid yields the diferrocene peptide **4**. After chromatographic workup the orange peptides

[a] Anorganisch-Chemisches Institut der Universität Heidelberg, Im Neuenheimer Feld 270, 69120 Heidelberg, Germany
Fax: +49-6221-545707
E-mail: katja.heinze@urz.uni-heidelberg.de
Supporting information for this article is available on the WWW under http://www.eurjic.org or from the author.

 © 2007 Wiley-VCH Verlag GmbH & Co. KGaA, Weinheim 

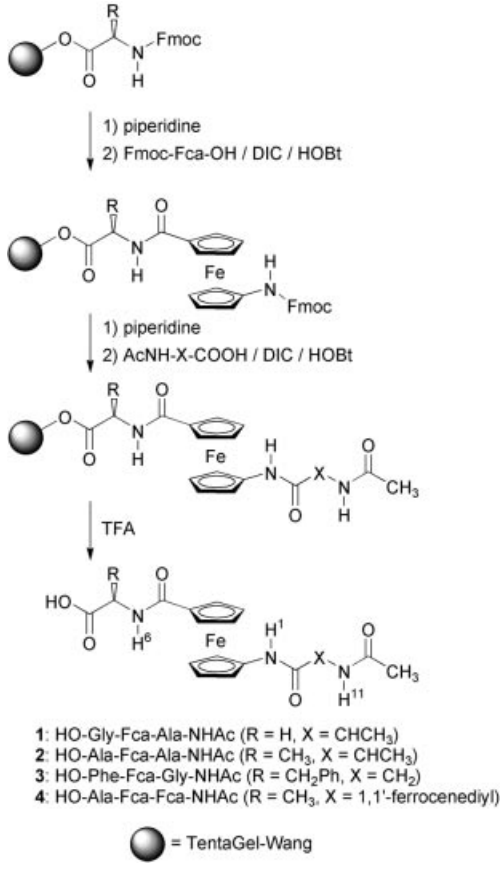


Scheme 2.

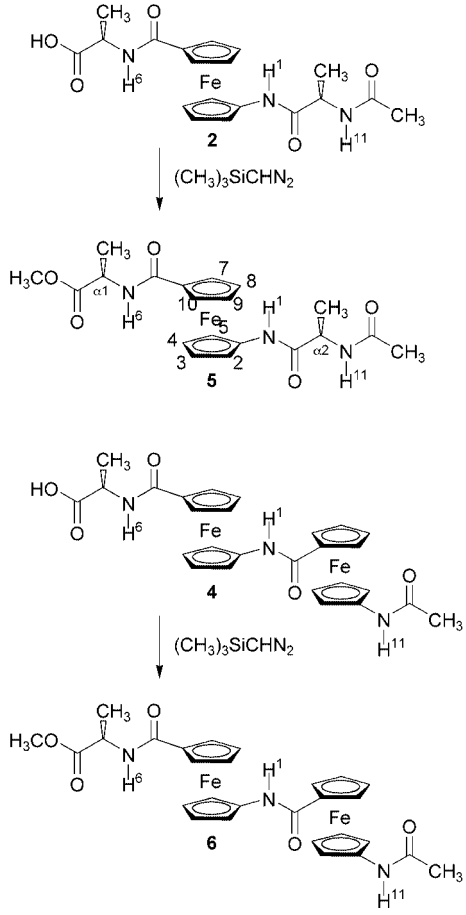


Scheme 3.

**1**–**4** were characterised by spectroscopic and mass spectrometric techniques. The data fully prove the composition and sequence of the peptides.

### Conformational Analysis of Ferrocene-Containing Peptides

Negative ion ESI mass spectra of **1**–**4** display, in addition to the $[M - H]^-$ peaks, signals corresponding to $[2M - H]^-$ consistent with the formation of carboxylic acid dimers in solution.[13] The dimer motif is also the most stable arrangement in the solid state as the signal for the $C{=}O_{acid}$ stretching vibration is found at 1725 $cm^{-1}$.[6]

To allow a detailed conformational analysis, the acid groups of **2** and **4** were methylated with (trimethylsilyl)diazomethane, giving esters **5** and **6** (Scheme 3). This increases the solubility of the tripeptides and eliminates the interference of the OH group. The IR spectra of **5** and **6** in $CH_2Cl_2$ indicate free and hydrogen-bonded NH groups (**5**: $\tilde{\nu}_{NH}$ = 3439, 3353, 3323 $cm^{-1}$; **6**: $\tilde{\nu}_{NH}$ = 3432, 3373, 3291 $cm^{-1}$) as well as hydrogen-bonded $CO_{ester}$ groups for **5** but not for **6** (**5**: $\tilde{\nu}_{CO}$ = 1727 $cm^{-1}$; **6**: $\tilde{\nu}_{CO}$ = 1741 $cm^{-1}$).

For ester **5** the chemical shifts of the amide protons $H^1$ and $H^6$ in $CD_2Cl_2$ ($\delta$ = 9.19, 7.95; for atom numbering see Scheme 3 and Figure 3) show that these two protons engage in (intramolecular) hydrogen bonds while $H^{11}$ ($\delta$ = 7.08 ppm) does not. This is also supported by the finding that $H^6$ exchanges more slowly against deuterium than $H^{11}$, with half-lives of $\tau_{1/2}(H^6)$ = 6.8 min and $\tau_{1/2}(H^{11})$ = 5.6 min in $CD_2Cl_2/D_2O$. In addition the chemical shift of proton $H^{11}$ is significantly different in the hydrogen-bond-forming solvent [D$_6$]DMSO as compared to the shift in $CD_2Cl_2$ [$\Delta\delta(H^{11}$, [D$_6$]DMSO, $CD_2Cl_2$) = 1.05] while $H^1$ and $H^6$ form hydrogen bonds in both solvents [$\Delta\delta(H^1$, [D$_6$]DMSO, $CD_2Cl_2$) = 0.08; $\Delta\delta(H^6$, [D$_6$]DMSO, $CD_2Cl_2$) = 0.08].[7]

However, $H^{11}$ forms an intermolecular hydrogen bond in concentrated $CD_2Cl_2$ solution [$\delta(H^{11})$ = 7.08 in concentrated solution; $\delta(H^{11})$ = 6.39 in diluted solution], at lower temperature, as the proton resonance is strongly temperature-dependent [$\Delta\delta(H^{11})$ = –24 ppb $K^{-1}$ in concentrated $CD_2Cl_2$ solution and $\Delta\delta(H^{11})$ = –27 ppb $K^{-1}$ in diluted $CD_2Cl_2$ solution; Figure 1], as well as in the solid state ($\tilde{\nu}_{NH}$ = 3316 $cm^{-1}$).

NOE contacts *between* the two ferrocene substituents of **5** are observed in $CD_2Cl_2$ but not in [D$_6$]DMSO, namely cross-peaks between $H^6$–$H^1$ and $H^6$–$H^{\alpha 2}$ (Figure 2). Thus the NMR and IR data of **5** suggest a conformation with two intramolecular hydrogen bonds $H^1\cdots O^4$ and $H^6\cdots O^1$ between the two substituents – a pattern similar to that found in the crystalline state of the tetrapeptide Boc-Ala-Fca-Ala-Ala-OMe.[7] The hydrogen bond between $H^1$ and $O^4$ is also found in short dipeptides of the type Ac-Fca-AA-OMe (AA = L-Val, L-Ile).[8] DFT calculations (B3LYP, LANL2DZ) additionally indicate this (*P*)-helical conformation with two

 © 2007 Wiley-VCH Verlag GmbH & Co. KGaA, Weinheim 

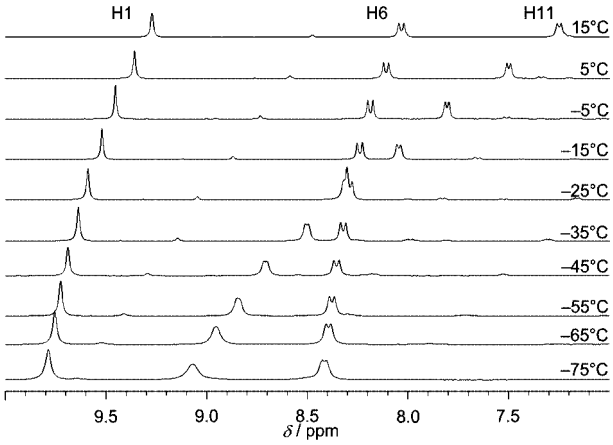


Figure 1. VT $^1$H NMR spectra of **5** in concentrated $CD_2Cl_2$ solution.

intramolecular hydrogen bonds to be the global minimum of seven hydrogen-bonded conformations of **2** (Figure 3). Other folded conformations for **1**–**3** with one to three intramolecular hydrogen bonds are calculated higher in energy by 6–39 kJ mol$^{-1}$ (see Supporting Information).

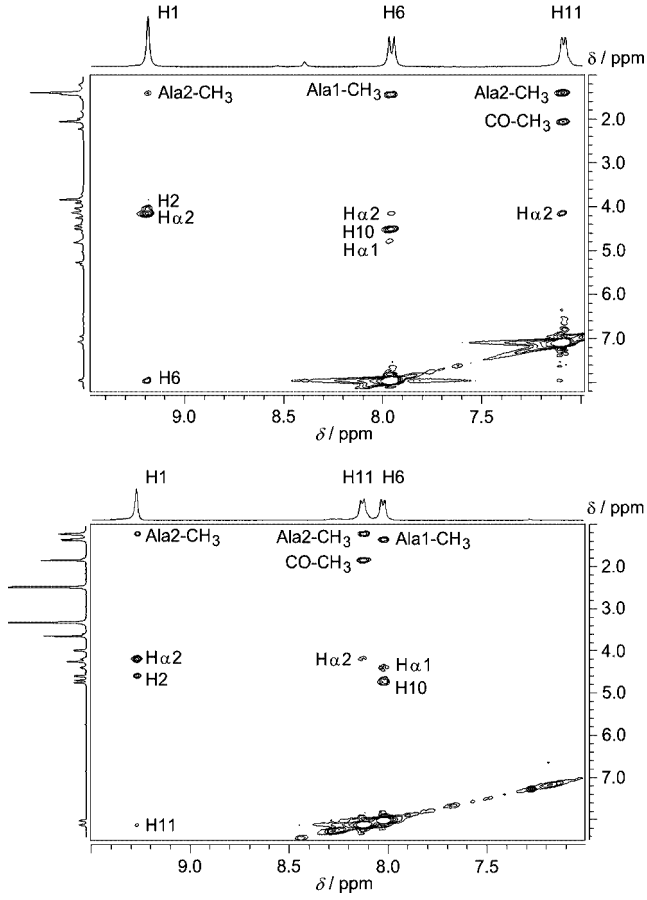


Figure 2. NOESY spectra of **5** in $CD_2Cl_2$ (top) and in [$D_6$]DMSO (bottom).

The observed vicinal coupling constants $^3J(H^6\text{-}H^{\alpha1})$ = 7.7 Hz and $^3J(H^{11}\text{-}H^{\alpha2})$ = 6.0 Hz in $CD_2Cl_2$ and the derived torsion angles[14] C–N–C$^{\alpha1}$–C = –86° and C–N–C$^{\alpha2}$–C = –76° fit well to the DFT calculated angles C–N–C$^{\alpha1}$–C = –90° and C–N–C$^{\alpha2}$–C = –73° of the preferred conformer. In THF similar vicinal coupling constants are observed [$^3J(H^6\text{-}H^{\alpha1})$ = 7.5 Hz and $^3J(H^{11}\text{-}H^{\alpha2})$ = 5.4 Hz] while in [$D_6$]DMSO the folded structure is completely disrupted [$^3J(H^6\text{-}H^{\alpha1})$ = 6.9 Hz and $^3J(H^{11}\text{-}H^{\alpha2})$ = 6.7 Hz]. These findings support the assumption that even the TentaGel immobilised peptides in THF retain this preferred conformation.

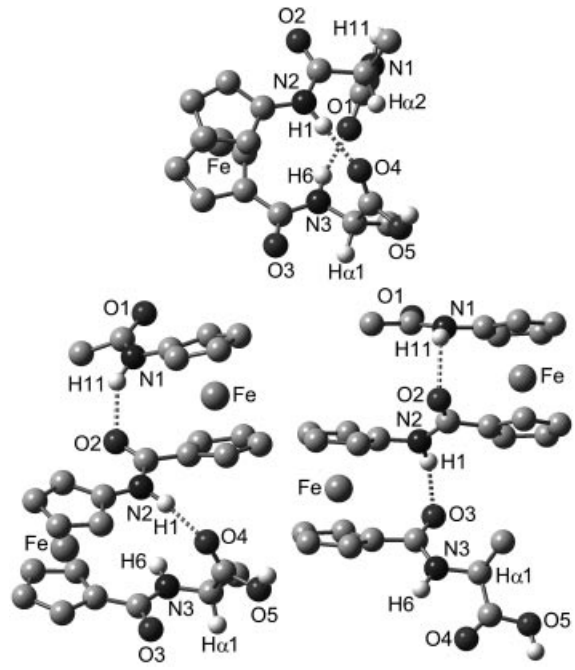


Figure 3. DFT calculated minimum conformations of **2** (top) and **4** (bottom) (Cp and methyl H atoms omitted).

For diferrocene **4** several different conformations were calculated with similar energy (Figure 3, Supporting Information). This is also supported by NMR and IR spectroscopy of ester **6**. The amide proton H$^1$ engages prevalently in hydrogen bonds ($\delta$ = 8.54; $\Delta\delta$ = –10.5 ppb K$^{-1}$; $\tau_{1/2}$ = 26 min) as compared to H$^{11}$ ($\delta$ = 7.61; $\Delta\delta$ = –13.7 ppb K$^{-1}$; $\tau_{1/2}$ = 5.8 min). However, even H$^6$ participates in hydrogen bonding ($\delta$ = 7.10; $\Delta\delta$ = –14.5 ppb K$^{-1}$). The finding that all amide protons form hydrogen bonds can only be accomplished by an ensemble of conformations in solution (two of the low-energy conformations of **4** are shown in Figure 3).

### Electrochemistry of Ferrocene-Containing Peptides

Monoferrocenes **1**–**3** are reversibly oxidised to the corresponding ferricinium cations around 500 mV versus SCE in $CH_3CN$ almost independently of the α-amino acids employed, while diferrocene **6** displays two oxidation waves at 470 and 590 mV versus SCE (Figure 4). The difference in the redox potentials of **6** ($\Delta E_{1/2}$ = 590 – 470 = 120 mV) is significantly smaller than that observed for Fc-NHCO-Fc-NHAc with differently substituted ferrocene moieties ($\Delta E_{1/2}$ = 305 mV[6]). The similarly substituted ferrocene

 © 2007 Wiley-VCH Verlag GmbH & Co. KGaA, Weinheim 

units in **6** (in contrast to Fc-NHCO-Fc-NHAc) allow estimation of the comproportionation constant for the monocation $\mathbf{6}^+$ as $K_C = 107$, which characterises $\mathbf{6}^+$ as a class II mixed-valent species with moderate delocalisation of the electron hole.

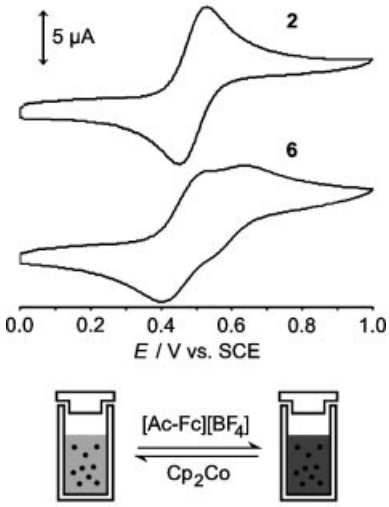


Figure 4. Cyclic voltammograms of tripeptides **2** and **6** (top) and chemical on-bead oxidation/reduction of ferrocene-containing tripeptide **2** (bottom).

To test binding affinities of neutral and charged peptides directly on-resin, it is necessary to chemically oxidise the peptides on the solid support. On-bead oxidation is performed by adding soluble [Ac-Fc][$BF_4$] ($E_{1/2}$ = 730 mV vs. SCE in $CH_2Cl_2$[15]) in $CH_2Cl_2$ solution to the immobilised tripeptide. Progress of the oxidation reaction is monitored UV/Vis-spectrophotometrically as the 633 nm absorption band of $[Ac\text{-}Fc]^+$ disappears while the 449 nm band of Ac-Fc increases (Figure 5, top). The reaction is finished within minutes. EPR spectroscopy[16] confirms the formation of the immobilised ferricinium cation as the typical axial pattern with $g_{\|} = 4.30$ and $g_{\perp} = 1.99$ is observed.[17]

Chemical reversibility is checked on-bead by re-reduction to the neutral peptides employing $CoCp_2$ as reductant and UV/Vis-spectrophotometric monitoring (disappearance of the 512 nm band of $CoCp_2$ and development of the 400 nm absorption band of $[CoCp_2]^+$). Reduction requires hours to be completed, probably because of the hydrophobic character of $CoCp_2$ and the hydrophilic nature of the Tentagel resin employed (Figure 5, bottom).

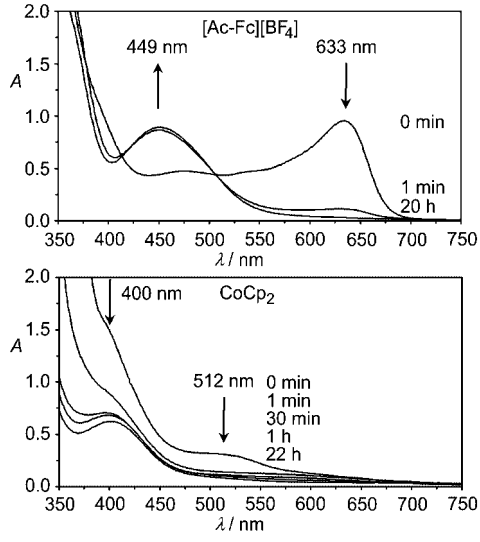


Figure 5. UV/Vis spectra during oxidation of immobilised **2** with [AcFc][$BF_4$] and during reduction of immobilised $\mathbf{2}^+$ with $CoCp_2$.

## Preliminary Solution and On-Bead Binding Studies

The conformation analysis suggests that binding of a guest to Fca peptides should occur by an induced fit process rather than being governed by the static lock and key concept.[11] ESI mass spectra of **5** and an equimolar mixture of five *N*-acetylated α-amino acids (Ac-Gly, Ac-Ala, Ac-Val, Ac-Ile, Ac-Phe; **5**: Ac-NH-CHR-COOH, 10:1) in $CH_3CN$ provide a first hint that Fca peptides bind these guests as carboxylates (*m*/*z* = 559.3, 573.3, 601.2, 615.3 and 649.4 for [**5** + Ac-Gly – H]$^+$, [**5** + Ac-Ala – H]$^+$, [**5** + Ac-Val – H]$^+$, [**5** + Ac-Ile – H]$^+$ and [**5** + Ac-Phe – H]$^+$, respectively; Figure 6; the peak at *m*/*z* = 556.3 corresponds to [**5** + TFA – H]$^+$ with TFA present in the mass spectrometer).

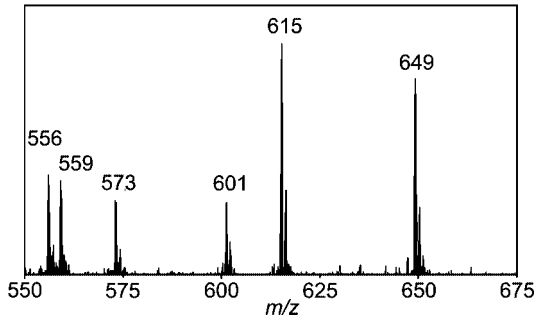


Figure 6. Partial ESI (neg.) mass spectrum of **5** and a mixture of five *N*-acetylated α-amino acids.

On-bead analysis[18] of immobilised peptide **2** using the chromophoric substrates pyrene-$(CH_2)_3$-COOH/$P_1t$Bu [$\lambda_{max}$ = 344 nm (60000 $M^{-1}cm^{-1}$) in THF] and coumarin-3-COOH/$P_1t$Bu[19] [$\lambda_{max}$ = 315 nm (12000 $M^{-1}cm^{-1}$) in THF] allowed determination of binding affinities by absorption spectroscopy. Equilibrium is reached after about 10 h in both cases according to spectroscopic measurements (Figure 7). Binding constants $K_a$ were calculated with the assumption of a 1:1 receptor substrate complex by Equation (1).

$$K_a = [RS]/\{([R]_0 - [RS])([S]_0 - [RS])\} \quad (1)$$

where [RS] is the concentration of receptor/substrate complex at equilibrium, $[R]_0$ is the initial receptor concentration and $[S]_0$ is the initial substrate concentration.

 © 2007 Wiley-VCH Verlag GmbH & Co. KGaA, Weinheim 

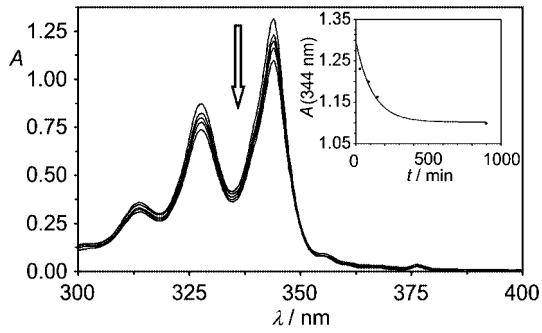


Figure 7. UV/Vis absorption spectra during reaction of immobilised **2** with pyrene-$(CH_2)_3$-COOH/$P_1t$Bu in THF (the inset shows the corresponding $t$ vs. $A$ plot).

Tripeptide **2** binds the coumarin derivative significantly stronger than the pyrene derivative [$K_a$(coumarin) = 670 $M^{-1}$, $K_a$(pyrene) = 200 $M^{-1}$]. This is probably due to the presence of additional hydrogen acceptors (oxygen atoms) in the coumarin dye as compared to the pyrene dye, which complements the three NH groups of peptide **2** (three-point binding vs. two-point-binding). A detailed analysis of the binding modes of different (chiral) substrates to ferrocene peptides as well as to charged ferricinium peptides is currently in progress. For the latter investigation, redox-stable chromophoric substrates have to be used as the coumarin and pyrene dyes employed in this study undergo chemical degradation when reacted with immobilised $\mathbf{2}^+$.

## Conclusions

The development of SPPS for ferrocene amino acids, conformational analyses of the peptides, on-bead oxidation procedures and on-bead binding assays paves the way for devising selective redox-controlled receptor and transporter systems, which, by synthetic design, are amenable to parallel solid-phase peptide synthesis and on-bead oxidation and screening assays.

## Experimental Section

Unless noted otherwise, all manipulations were carried out under argon by means of standard Schlenk techniques. All solvents were dried by standard methods and distilled under argon prior to use. All other reagents were used as received from commercial sources.

NMR: Bruker Avance DPX 200 at 200.15 MHz and Varian Unity Plus 400 at 399.89 MHz ($^1$H); chemical shifts ($\delta$) in ppm with respect to residual solvent peaks as internal standard: $CD_2Cl_2$ ($^1$H: $\delta$ = 5.32; $^{13}$C: $\delta$ = 53.5 ppm), [$D_8$]THF ($^1$H: $\delta$ = 1.73, 3.58; $^{13}$C: $\delta$ = 25.5, 67.7), [$D_6$]DMSO ($^1$H: $\delta$ = 2.49 ppm). IR spectra were recorded with a BioRad Excalibur FTS 3000 spectrometer using $CaF_2$ cells in $CH_2Cl_2$ and as CsI disks. Cyclic voltammetry was performed using a glassy carbon electrode, a platinum electrode and a SCE electrode, $10^{-3}$ M in 0.1 M $n$Bu$_4$NPF$_6$/$CH_2Cl_2$; potentials are given relative to that of SCE. ESI mass spectra were recorded with a Finnigan TSQ 700 spectrometer. EPR spectra were recorded with a Bruker ELEXSYS E500 spectrometer (X-band). UV/Vis spectra were recorded with a Perkin–Elmer Lambda 19, 0.2-cm cells (Hellma, suprasil). Melting points were determined with a Gallenkamp capillary melting point apparatus MFB 595 010 and are uncorrected.

**Computational Method:** Density functional calculations were carried out with the Gaussian03/DFT[20] series of programs. The B3LYP formulation of density functional theory was used employing the LanL2DZ basis set.[20] This functional/basis set combination has been successfully applied previously to investigate the conformational preference of substituted ferrocenes.[6,8,11,21,22] All points were characterised as minima ($N_{imag}$ = 0) by frequency analysis.

**Solid-Phase Peptide Synthesis of 1–4**

TentaGel-Wang-AA$^1$-Fmoc [1 g; AA$^1$ = Gly (**1**), Ala (**2**, **4**), Phe (**3**); 0.17–0.24 mmol g$^{-1}$] was deprotected with 20% piperidine in $CH_2Cl_2$/DMF (9:1). The loading was determined spectrophotometrically at 290 nm. The resin was washed with DMF (2×), $CH_2Cl_2$ (1×), DMF (1×) and $CH_2Cl_2$ (2×). Fmoc-Fca-OH (1.5 equiv.) was activated by using DIC (1.8 equiv.) and HOBt (1.8 equiv.) in $CH_2Cl_2$/DMF (1:1) for 10 min and added to the resin. The resin was shaken for 12 h, washed with DMF (2×), $CH_2Cl_2$ (1×), DMF (1×) and $CH_2Cl_2$ (2×) treated with acetic anhydride/pyridine (10:1) for 30 min and washed with DMF (2×), $CH_2Cl_2$ (1×), DMF (1×) and $CH_2Cl_2$ (2×). Fmoc was removed with 20% piperidine in $CH_2Cl_2$/DMF (9:1). Ac-AA$^2$-OH [1.5 equiv.; AA$^2$ = Ala (**1**, **2**), Phe (**3**), Fca (**4**)] activated with HOBt (1.8 equiv.) and DIC (1.8 equiv.) in $CH_2Cl_2$/DMF (1:1) for 10 min was added and the resin shaken for 12 h. After washing with DMF (2×), $CH_2Cl_2$ (1×), DMF (1×) and $CH_2Cl_2$ (2×) the tripeptide was cleaved from the resin with 50% TFA in dichloromethane (1 h) and purified on silica gel (EtOAc/MeOH or EtOAc/THF) to give an orange powder.

**Complex 1:** 51 mg, 61%; m.p. 128 °C; $R_f$ ($SiO_2$, EtOAc/MeOH, 7:3) = 0.55. $^1$H NMR ([$D_8$]THF): $\delta$ = 9.17 (s, 1 H, H$^1$), 7.99 (dvd, 1 H, H$^6$), 7.78 (m, 1 H, H$^{11}$), 5.15 (pt, 1 H, H$^5$), 4.75 (pt, 1 H, H$^7$), 4.45 (pt, 1 H, H$^{10}$), 4.35 (pt, 1 H, H$^9$), 4.33 (dvd, $^2J_{HH}$ = 17.5, $^3J_{HH}$ = 6.8 Hz, 1 H, H$^{\alpha 1}$), 4.20 (pt, 1 H, H$^8$), 4.14 (pt, 1 H, H$^2$), 4.09 (q, $^3J_{HH}$ = 6.9 Hz, 1 H, H$^{\alpha 2}$), 4.01 (pt, 1 H, H$^3$), 3.87 (pt, 1 H, H$^4$), 3.71 (dvd, $^2J_{HH}$ = 17.5, $^3J_{HH}$ = 5.0 Hz, 1 H, H$^{\alpha 1}$), 1.96 (s, 3 H, $COCH_3$), 1.27 (d, $^3J_{HH}$ = 6.9 Hz, 3 H, Ala2-$CH_3$) ppm. $^{13}$C{$^1$H} NMR ([$D_8$]THF): $\delta$ = 175.7 (s, COOH), 174.6 (s, CO), 171.9 (s, CO), 170.3 (s, CO), 97.7 (s, $C_{Cp}$-N), 77.6 (s, $C_{Cp}$-CO), 72.9 (s, C$^9$), 71.5 (s, C$^{10}$), 71.0 (s, C$^8$), 70.5 (s, C$^7$), 66.1 (s, C$^3$), 65.7 (s, C$^4$), 64.6 (s, C$^2$), 63.4 (s, C$^5$), 51.2 (s, C$^{\alpha 2}$), 41.5 (s, C$^{\alpha 1}$), 22.7 (s, $COCH_3$), 17.7 (s, Ala2-$CH_3$) ppm. Complex **1** exists as a mixture of two NMR-discernible conformers; resolved signals for the minor conformer: $^1$H NMR ([$D_8$]THF): $\delta$ = 8.94 (s, 1 H, H$^1$), 5.11 (pt, 1 H, H$^5$), 4.73 (pt, 1 H, H$^7$), 4.40 (dvd, $^2J_{HH}$ = 17.5, $^3J_{HH}$ = 6.8 Hz, 1 H, H$^{\alpha 1}$), 4.10 (q, $^3J_{HH}$ = 6.9 Hz, 1 H, H$^{\alpha 2}$), 3.78 (dvd, $^2J_{HH}$ = 17.5, $^3J_{HH}$ = 5.0 Hz, 1 H, H$^{\alpha 1}$), 1.95 (s, 3 H, $COCH_3$), 1.29 (d, $^3J_{HH}$ = 6.9 Hz, 3 H, Ala2-$CH_3$) ppm. IR (CsI): $\tilde{\nu}$ = 3504 (OH), 3373, 3309, 3258 (NH), 1727 (C=$O_{acid}$), 1666, 1629 (amide I), 1574, 1546 (amide II), 1262 (C–O) cm$^{-1}$. IR ($CH_2Cl_2$): $\tilde{\nu}$ = 3687, 3601, 3440, 3365, 3321, 1771, 1732, 1663, 1655, 1605, 1572, 1531, 1522 cm$^{-1}$. UV (THF): $\lambda_{max}$ = 445 nm (190 $M^{-1}$ cm$^{-1}$). CV ($CH_3CN$, $n$Bu$_4$NPF$_6$): $E_{1/2}$ = 505 mV ($\Delta E$ = 80 mV) versus SCE. Neg.-ESI-MS ($CH_3CN$): $m/z$ (%) = 414.2 (100) [M – H]$^-$, 829.3 (8) [2M – H]$^-$.

**Complex 2:** 71 mg, 83%; m.p. 113 °C; $R_f$ ($SiO_2$, EtOAc/MeOH, 7:3) = 0.32. $^1$H NMR ([$D_8$]THF): $\delta$ = 9.39 (s, 1 H, H$^1$), 7.98 (br. s, 1 H, H$^6$), 7.99 (m, 1 H, H$^{11}$), 5.16 (pt, 1 H, H$^5$), 4.77 (pt, 1 H, H$^7$), 4.71 (q, $^3J_{HH}$ = 7.5 Hz, 1 H, H$^{\alpha 1}$), 4.60 (pt, 1 H, H$^{10}$), 4.36 (pt, 1 H, H$^9$), 4.23 (q, $^3J_{HH}$ = 7.0 Hz, 1 H, H$^{\alpha 2}$), 4.20 (pt, 1 H, H$^8$), 4.14

 © 2007 Wiley-VCH Verlag GmbH & Co. KGaA, Weinheim 

(pt, 1 H, $H^2$), 4.00 (pt, 1 H, $H^3$), 3.86 (pt, 1 H, $H^4$), 1.97 (s, 3 H, $COCH_3$), 1.42 (d, $^3J_{HH}$ = 7.5 Hz, 3 H, Ala1-$CH_3$), 1.28 (d, $^3J_{HH}$ = 7.0 Hz, 3 H, Ala2-$CH_3$) ppm. $^{13}C\{^1H\}$ NMR ([D$_8$]THF): $\delta$ = 172.3 (s, COOH), 171.7 (s, CO), 170.7 (s, CO), 170.6 (s, CO), 97.7 (s, $C_{Cp}$-N), 77.4 (s, $C_{Cp}$-CO), 72.7 (s, $C^9$), 71.8 (s, $C^{10}$), 70.9 (s, $C^8$), 70.6 (s, $C^7$), 66.0 (s, $C^3$), 65.7 (s, $C^4$), 64.7 (s, $C^2$), 63.5 (s, $C^5$), 51.3 (s, $C^{\alpha 2}$), 48.2 (s, $C^{\alpha 1}$), 22.7 (s, $COCH_3$), 17.6 (s, Ala2-$CH_3$), 17.5 (s, Ala1-$CH_3$) ppm. IR (CsI): $\tilde{\nu}$ = 3518 (OH), 3310 (NH), 1725 (C=O$_{acid}$), 1656, 1637 (amide I), 1570, 1544 (amide II), 1262 (C–O) cm$^{-1}$. IR ($CH_2Cl_2$): $\tilde{\nu}$ = 3687, 3600, 3434, 3408, 3318, 1773, 1724, 1684, 1668, 1653, 1605, 1570, 1539, 1523 cm$^{-1}$. UV (THF): $\lambda_{max}$ = 444 nm (290 M$^{-1}$ cm$^{-1}$). CV ($CH_3CN$, $n$Bu$_4$NPF$_6$): $E_{1/2}$ = 490 mV ($\Delta E$ = 73 mV) versus SCE. Neg.-ESI-MS (MeOH): *m*/*z* (%) = 428.2 (100) [M – H]$^-$, 857.3 (6) [2M – H]$^-$.

**Complex 3:** 36 mg, 37%; m.p. 125 °C; $R_f$ ($SiO_2$, EtOAc/MeOH, 7:3) = 0.59. $^1H$ NMR ([D$_8$]THF): $\delta$ = 8.99 (s, 1 H, $H^1$), 7.72 (dvd, 1 H, $H^6$), 7.96 (m, 1 H, $H^{11}$), 7.35 (m, 2 H, Phe-$CH_{ortho}$), 7.23 (m, 2 H, Phe-$CH_{meta}$), 7.14 (m, 1 H, Phe-$CH_{para}$), 4.93 (pt, 1 H, $H^5$), 4.88 (m, 1 H, $H^{\alpha 1}$), 4.66 (pt, 1 H, $H^7$), 4.59 (pt, 1 H, $H^{10}$), 4.32 (pt, 1 H, $H^9$), 4.26 (pt, 1 H, $H^2$), 4.18 (pt, 1 H, $H^8$), 4.04 (m, 1 H, $H^{\alpha 2}$), 3.97 (pt, 1 H, $H^3$), 3.86 (pt, 1 H, $H^4$), 3.91 (m, 1 H, $H^{\alpha 2}$), 3.23 (m, 1 H, Phe-$CH_2$), 3.11 (m, 1 H, Phe-$CH_2$), 2.01 (s, 3 H, $COCH_3$) ppm. $^{13}C\{^1H\}$ NMR ([D$_8$]THF): $\delta$ = 176.8 (s, COOH), 171.8 (s, CO), 170.5 (s, CO), 168.6 (s, CO), 139.4 (s, Phe-CH), 130.2 (s, Phe-CH), 129.2 (s, Phe-CH), 127.3 (s, Phe-CH), 97.5 (s, $C_{Cp}$-N), 77.7 (s, $C_{Cp}$-CO), 72.5 (s, $C^9$), 71.4 (s, $C^{10}$), 71.1 (s, $C^8$), 70.5 (s, $C^7$), 66.2 (s, $C^3$), 65.9 (s, $C^4$), 64.7 (s, $C^2$), 63.3 (s, $C^5$), 55.1 (s, $C^{\alpha 1}$), 45.0 (s, $C^{\alpha 2}$), 37.8 (s, Phe-$CH_2$), 22.8 (s, $COCH_3$) ppm. Complex **3** exists as a mixture of two NMR-discernible conformers; resolved signals for the minor conformer: $^1H$ NMR ([D$_8$]THF): $\delta$ = 8.83 (s, 1 H, $H^1$), 3.75 (m, 1 H, $H^{\alpha 2}$), 3.64 (m, 1 H, $H^{\alpha 2}$), 2.88 (m, 1 H, Phe-$CH_2$), 2.77 (m, 1 H, Phe-$CH_2$), 1.94 (s, 3 H, $COCH_3$) ppm. IR (CsI): $\tilde{\nu}$ = 3511 (OH), 3323 (NH), 1725 (C=O$_{acid}$), 1657, 1637 (amide I), 1560, 1544 (amide II), 1263 (C–O), 703 (Ph$_{def}$) cm$^{-1}$. IR ($CH_2Cl_2$): $\tilde{\nu}$ = 3687, 3601, 3447, 3322, 1723, 1696, 1668, 1656, 1605, 1571, 1522 cm$^{-1}$. UV (THF): $\lambda_{max}$ = 444 nm (170 M$^{-1}$ cm$^{-1}$). CV ($CH_3CN$, $n$Bu$_4$NPF$_6$): $E_{1/2}$ = 515 mV ($\Delta E$ = 79 mV) versus SCE. Neg.-ESI-MS ($CH_3CN$): *m*/*z* (%) = 490.3 (100) [M – H]$^-$, 981.3 (7) [2M – H]$^-$.

**Complex 4:** 65 mg, 56%; $R_f$ ($SiO_2$, EtOAc/MeOH, 7:3) = 0.48. $^1H$ NMR ([D$_6$]DMSO): $\delta$ = 10.24 (s, 1 H, $H^1$), 9.74 (s, 1 H, $H^{11}$), 7.41 (d, $^3J_{HH}$ = 6.5 Hz, 1 H, $H^6$), 4.96 (br. s, 1 H), 4.89 (br. s, 2 H), 4.68 (br. s, 2 H), 4.60 (br. s, 2 H), 4.52 (br. s, 1 H), 4.29, 4.22, 4.20 (m, 5 H), 3.99 (br. s, 2 H), 3.93 (br. s, 2 H), 1.86 (s, 3 H, $COCH_3$), 1.32 (d, $^3J_{HH}$ = 6.8 Hz, 3 H, Ala-$CH_3$) ppm. Poor solubility prevented recording of $^{13}C$ NMR spectra. IR (CsI): $\tilde{\nu}$ = 3509 (OH), 3341 (NH), 1733 (C=O$_{acid}$), 1642 (amide I), 1546 (amide II), 1262 (C–O) cm$^{-1}$. UV (THF): $\lambda_{max}$ = 447 nm (360 M$^{-1}$ cm$^{-1}$). Neg.-ESI-MS ($CH_3CN$): *m*/*z* (%) = 584.2 (100) [M – H]$^-$, 1169.1 (8) [2M – H]$^-$.

**Synthesis of 5 by Methylation of 2**

(Trimethylsilyl)diazomethane (0.1 mL; 2 M in $Et_2O$, 0.2 mmol) was added to **2** (50 mg, 0.117 mmol) in MeOH (10 mL) and the mixture was stirred at 25 °C for 2 h. The solvent was removed in vacuo and the residue was purified on silica gel (THF/PE, 7:3) to give **5** as an orange powder.

**Complex 5:** 47 mg 90%; $R_f$ ($SiO_2$, EtOAc/MeOH, 7:3) = 0.66. $^1H$ NMR ($CD_2Cl_2$): $\delta$ = 9.19 (s, 1 H, $H^1$), 7.95 (d, $^3J_{HH}$ = 7.7 Hz, 1 H, $H^6$), 7.08 (d, $^3J_{HH}$ = 6.0 Hz, 1 H, $H^{11}$), 5.27 (pt, 1 H, $H^5$), 4.82 (br. s, 1 H, $H^7$), 4.77 (q, $^3J_{HH}$ = 6.3 Hz, 1 H, $H^{\alpha 1}$), 4.51 (br. s, 1 H, $H^{10}$), 4.43 (br. s, 1 H, $H^9$), 4.26 (br. s, 1 H, $H^8$), 4.16 (q, $^3J_{HH}$ = 6.9 Hz, 1 H, $H^{\alpha 2}$), 4.14 (br. s, 1 H, $H^3$), 4.04 (br. s, 1 H, $H^2$), 3.92 (br. s, 1 H, $H^4$), 3.84 (s, 3 H, $OCH_3$), 2.07 (s, 3 H, $COCH_3$), 1.44 (br. s, 3 H, Ala1-$CH_3$), 1.42 (br. s, 3 H, Ala2-$CH_3$) ppm. $^{13}C\{^1H\}$ NMR ($CD_2Cl_2$): $\delta$ = 177.4 (s, COOMe), 171.6 (s, CO), 170.9 (s, CO), 170.1 (s, CO), 95.6 (s, $C_{Cp}$-N), 75.7 (s, $C_{Cp}$-CO), 72.5 (s, $C^9$), 71.0 (s, $C^{10}$), 70.5 (s, $C^8$), 69.7 (s, $C^7$), 65.8 (s, $C^3$), 65.3 (s, $C^4$), 64.2 (s, $C^2$), 62.8 (s, $C^5$), 52.8 (s, $OCH_3$), 50.8 (s, $C^{\alpha 2}$), 48.2 (s, $C^{\alpha 1}$), 22.6 (s, $COCH_3$), 17.2 (s, Ala2-$CH_3$), 16.7 (s, Ala1-$CH_3$) ppm. $^1H$ NMR ([D$_8$]THF): $\delta$ = 8.94 (s, 1 H, $H^1$), 7.97 (d, $^3J_{HH}$ = 7.5 Hz, 1 H, $H^6$), 7.77 (d, $^3J_{HH}$ = 5.4 Hz, 1 H, $H^{11}$), 5.15 (pt, 1 H, $H^5$), 4.74 (pt, 1 H, $H^7$), 4.72 (q, $^3J_{HH}$ = 7.6 Hz, 1 H, $H^{\alpha 1}$), 4.56 (pt, 1 H, $H^{10}$), 4.36 (pt, 1 H, $H^9$), 4.18 (pt, 1 H, $H^8$), 4.12 (q, $^3J_{HH}$ = 6.8 Hz, 1 H, $H^{\alpha 2}$), 4.07 (pt, 1 H, $H^2$), 4.02 (pt, 1 H, $H^3$), 3.86 (pt, 1 H, $H^4$), 3.79 (s, 3 H, $OCH_3$), 1.96 (s, 3 H, $COCH_3$), 1.41 (d, $^3J_{HH}$ = 7.6 Hz, 3 H, Ala1-$CH_3$), 1.30 (d, $^3J_{HH}$ = 6.8 Hz, 3 H, Ala2-$CH_3$) ppm. $^1H$ NMR ([D$_6$]DMSO): $\delta$ = 9.27 (s, 1 H, $H^1$), 8.13 (d, $^3J_{HH}$ = 6.7 Hz, 1 H, $H^{11}$), 8.03 (d, $^3J_{HH}$ = 6.9 Hz, 1 H, $H^6$), 4.76 (br. s, 1 H, $H^{10}$), 4.70 (br. s, 1 H, $H^7$), 4.61 (br. s, 1 H, $H^5$), 4.59 (br. s, 1 H, $H^2$), 4.40 (q, $^3J_{HH}$ = 7.0 Hz, 1 H, $H^{\alpha 1}$), 4.26 (br. s, 2 H, $H^{9,10}$), 4.19 (q, $^3J_{HH}$ = 6.8 Hz, 1 H, $H^{\alpha 2}$), 4.00, 3.98 (br. s, 1 H, $H^{3,4}$), 3.65 (s, 3 H, $OCH_3$), 1.85 (s, 3 H, $COCH_3$), 1.37 (d, $^3J_{HH}$ = 7.0 Hz, 3 H, Ala1-$CH_3$), 1.23 (d, $^3J_{HH}$ = 6.8 Hz, 3 H, Ala2-$CH_3$) ppm. $^{13}C\{^1H\}$ NMR ($CD_2Cl_2$): $\delta$ = 173.8 (s, COOMe), 171.4 (s, CO), 169.4 (s, CO), 169.2 (s, CO), 96.3 (s, $C_{Cp}$-N), 76.0 (s, $C_{Cp}$-CO), 71.9, 71.8 (s, $C^{8,9}$), 69.4 (s, $C^7$), 69.1 (s, $C^{10}$), 66.0, 65.9 (s, $C^{3,4}$), 62.3, 62.1 (s, $C^{2,5}$), 52.0 (s, $OCH_3$), 49.1 (s, $C^{\alpha 2}$), 47.9 (s, $C^{\alpha 1}$), 22.6 (s, $COCH_3$), 18.1 (s, Ala2-$CH_3$), 17.0 (s, Ala1-$CH_3$) ppm. IR (CsI): 3316 (NH), 1743 (C=O$_{ester}$), 1657, 1638 (amide I), 1570, 1543 (amide II), 1263 (C–O) cm$^{-1}$; N-deuterated analogue: $\tilde{\nu}$ = 2455 (ND) cm$^{-1}$. IR ($CH_2Cl_2$): $\tilde{\nu}$ = 3439, 3353, 3323 (NH), 1727 (C=O$_{ester}$), 1690, 1668, 1651 (amide I), 1571, 1527 (amide II) cm$^{-1}$. UV (THF): $\lambda_{max}$ = 443 nm (310 M$^{-1}$ cm$^{-1}$). Pos.-ESI-MS ($CH_3CN$): *m*/*z* (%) = 444.3 (39) [M + H]$^+$, 466.3 (100) [M + Na]$^+$, 482.2 (10) [M + K]$^+$, 887.1 (3) [2M + H]$^+$, 909.8 (39) [2M + Na]$^+$, 925.0 (4) [2M + K]$^+$.

**Synthesis of 6 by Methylation of 4**

(Trimethylsilyl)diazomethane (0.1 mL; 2 M in $Et_2O$, 0.2 mmol) was added to crude **4** (50 mg, 0.085 mmol) in MeOH (10 mL) and the mixture was stirred at 25 °C for 2 h. The solvent was removed in vacuo and the residue was purified on silica gel (EtOAc/MeOH, 7:3) or alternatively by TLC (EtOAc/MeOH, 7:3) to give **6** as an orange powder.

**Complex 6:** 40 mg, 79%; $R_f$ ($SiO_2$, EtOAc/MeOH, 7:3) = 0.72. $^1H$ NMR ($CD_2Cl_2$): $\delta$ = 8.54 (s, 1 H, $H^1$), 7.61 (s, 1 H, $H^{11}$), 7.10 (d, $^3J_{HH}$ = 7.1 Hz, 1 H, $H^6$), 4.79 (br. s, 1 H), 4.67 (br. s, 1 H), 4.49 (br. s, 1 H), 4.47 (br. s, 1 H) [$H^{2,2',5,5'}$], 4.75 (br. s, 1 H), 4.69 (br. s, 2 H), 4.61 (br. s, 1 H) [$H^{7,7',10,10'}$], 4.62 (m, 1 H, $H^{\alpha 1}$), 4.42 (br. s, 2 H), 4.41 (br. s, 2 H) [$H^{8,8',9,9'}$], 4.15 (br. s, 2 H), 4.13 (br. s, 2 H) [$H^{3,3',4,4'}$], 3.76 (s, 3 H, $OCH_3$), 2.00 (s, 3 H, $COCH_3$), 1.51 (d, $^3J_{HH}$ = 7.2 Hz, 3 H, Ala-$CH_3$) ppm. $^{13}C\{^1H\}$ NMR ($CD_2Cl_2$): $\delta$ = 71.6, 71.5, 71.3, 71.2 (s, $C^{8,9,8',9'}$), 70.0, 69.9, 69.8, 69.6 (s, $C^{7,10,7',10'}$), 66.4, 66.3, 66.2, 66.1 (s, $C^{3,4,3',4'}$), 65.2, 64.5, 64.4, 64.3 (s, $C^{2,5,2',5'}$), 52.5 (s, $OCH_3$), 48.6 (s, $C^{\alpha}$), 23.8 (s, $COCH_3$), 17.7 (s, Ala-$CH_3$) ppm. Poor solubility prevented observation of all quaternary C signals. IR (CsI): $\tilde{\nu}$ = 3299 (NH), 1742 (C=O$_{ester}$), 1654, 1638 (amide I), 1560, 1542 (amide II), 1262 (C–O) cm$^{-1}$. IR ($CH_2Cl_2$): $\tilde{\nu}$ = 3432, 3373, 3291 (NH), 1741 (C=O$_{ester}$), 1676, 1655, 1606 (amide I), 1557, 1538, 1517 (amide II) cm$^{-1}$. CV ($CH_3CN$, $n$Bu$_4$NPF$_6$): $E_{1/2}$ = 470 mV, 590 mV versus SCE. Pos.-ESI-MS ($CH_3CN$): *m*/*z* (%) = 600.3 (100) [M + H]$^+$, 622.2 (30) [M + Na]$^+$, 638.3 (6) [M + K]$^+$, 1199.3 (2) [2M + H]$^+$, 1221.4 (2) [2M + Na]$^+$.

**Supporting Information** (see also the footnote on the first page of this article): Selected NMR spectra of **3**, temperature-dependent NMR shifts of NH protons of **1**–**3**, **5** and **6**, $^1H$ NMR spectra during reaction of **5** with $D_2O$ in $CD_2Cl_2$, time dependence of

 © 2007 Wiley-VCH Verlag GmbH & Co. KGaA, Weinheim 

H/D exchange of **5** in $CD_2Cl_2/D_2O$, X-band EPR spectrum of immobilised $\mathbf{2}^+$, DFT-calculated minimum structures and relative energies of **1**–**3** and **4**.

## Acknowledgments

We thank the German Science Foundation (Heisenberg fellowship to K. H.) and the Dr. Otto Röhm Gedächtnisstiftung for financial support.

[1] a) T. Schrader, A. D. Hamilton (Eds.), *Functional Synthetic Receptors*, Wiley-VCH, Weinheim, **2005**; b) P. A. Gale, *Coord. Chem. Rev.* **2003**, *240*, 1; c) M. W. Peczuh, A. D. Hamilton, *Chem. Rev.* **2000**, *100*, 2479–2494; d) W. C. Still, *Acc. Chem. Res.* **1996**, *29*, 155–163.

[2] a) M. H. Filby, T. D. Humphries, D. R. Turner, R. Kataky, J. Kruusma, J. W. Steed, *Chem. Commun.* **2006**, 156–158; b) J. Shepherd, T. Gale, K. B. Jensen, J. D. Kilburn, *Chem. Eur. J.* **2006**, *12*, 713–720; c) C. Schmuck, P. Wich, *Angew. Chem.* **2006**, *118*, 4383–4387; *Angew. Chem. Int. Ed.* **2006**, *45*, 4277–4281; d) C. Schmuck, P. Frey, M. Heil, *ChemBioChem* **2005**, *6*, 628–631; e) C. Schmuck, U. Machon, *Chem. Eur. J.* **2005**, *11*, 1109–1118; f) C. Schmuck, *Chem. Commun.* **1999**, 843–844.

[3] a) J. L. Sessler, D. An, W.-S. Cho, V. Lynch, M. Marquez, *Chem. Eur. J.* **2005**, *11*, 2001–2011; b) J. L. Sessler, L. R. Eller, W.-S. Cho, S. Nicolaou, A. Aguilar, J. T. Lee, V. M. Lynch, D. J. Magda, *Angew. Chem.* **2005**, *117*, 6143–6146; *Angew. Chem. Int. Ed.* **2005**, *44*, 5989–5992; c) P. A. Gale, *Chem. Commun.* **2005**, 3761–3772; d) S. Otto, S. Kubik, *J. Am. Chem. Soc.* **2003**, *125*, 7804–7805; e) H. Wennemers, M. C. Nold, M. M. Conza, K. J. Kulicke, M. Neuburger, *Chem. Eur. J.* **2003**, *9*, 442–448; f) H. Wennemers, M. Conza, M. Nold, P. Krattiger, *Chem. Eur. J.* **2001**, *7*, 3342–3347.

[4] A. E. Kaifer, *Acc. Chem. Res.* **1999**, *32*, 62–71.

[5] A. Caballero, V. Lloveras, A. Tárraga, A. Espinosa, M. D. Velasco, J. Vidal-Gancedo, C. Roviran, K. Wurst, P. Molina, J. Veciana, *Angew. Chem.* **2005**, *117*, 2013–2017; *Angew. Chem. Int. Ed.* **2005**, *44*, 1977–1981.

[6] K. Heinze, M. Schlenker, *Eur. J. Inorg. Chem.* **2004**, 2974–2988.

[7] a) L. Barišić, M. Dropucic, V. Rapić, H. Pritzkow, S. I. Kirin, N. Metzler-Nolte, *Chem. Commun.* **2004**, 2004–2005; b) L. Barišić, M. Čakić, K. A. Mahmoud, Y. Liu, H.-B. Kraatz, H. Pritzkow, S. I. Kirin, N. Metzler-Nolte, V. Rapić, *Chem. Eur. J.* **2006**, *12*, 4965–4980.

[8] K. Heinze, M. Beckmann, *Eur. J. Inorg. Chem.* **2005**, 3450–3457.

[9] a) C. E. Cannizzaro, J. A. Ashley, K. D. Janda, K. N. Houk, *J. Am. Chem. Soc.* **2003**, *125*, 2489–2506; b) J. T. Yli-Kauhaluoma, J. A. Ashley, C.-H. Lo, L. Tucker, M. M. Wolfe, K. D. Janda, *J. Am. Chem. Soc.* **1995**, *117*, 7041–7047; c) A. Heine, E. A. Stura, J. T. Yli-Kauhaluoma, C. Gao, Q. Deng, B. R. Beno, K. N. Houk, K. D. Janda, I. A. Wilson, *Science* **1998**, *279*, 1934–1940.

[10] a) M.-C. Daniel, J. Ruiz, S. Nlate, J.-C. Blais, D. Astruc, *J. Am. Chem. Soc.* **2003**, *125*, 2617–2628; b) P. D. Beer, P. A. Gale, *Angew. Chem.* **2001**, *113*, 502–532; *Angew. Chem. Int. Ed.* **2001**, *40*, 486–516; c) K. Kavallieratos, S. Hwang, R. H. Crabtree, *Inorg. Chem.* **1999**, *38*, 5184–5186; d) P. D. Beer, *Acc. Chem. Res.* **1998**, *31*, 71–80.

[11] K. Heinze, M. Schlenker, *Eur. J. Inorg. Chem.* **2005**, 66–71.

[12] W. C. Chan, P. D. White (Eds.), *Fmoc Solid Phase Peptide Synthesis*, Oxford University Press, Oxford, **2000**.

[13] N. Kubota, T. Fukuo, R. Akawa, *J. Am. Soc. Mass. Spectrom.* **1999**, *10*, 557–560.

[14] V. F. Bystrov, *Prog. Nucl. Magn. Reson. Spectrosc.* **1976**, *10*, 41–81.

[15] N. G. Connelly, W. E. Geiger, *Chem. Rev.* **1996**, *96*, 877–910.

[16] K. Heinze, A. Reinhart, *Inorg. Chem.* **2006**, *45*, 2695–2703.

[17] D. M. Duggan, D. N. Hendrickson, *Inorg. Chem.* **1975**, *14*, 955–970.

[18] M. Conza, H. Wennemers, *Chem. Commun.* **2003**, 866–867.

[19] $P_1t$Bu = *tert*-butylimino-tris(dimethylamino)phosphorane as base.

[20] M. J. Frisch, G. W. Trucks, H. B. Schlegel, G. E. Scuseria, M. A. Robb, J. R. Cheeseman, J. A. Montgomery Jr, T. Vreven, K. N. Kudin, J. C. Burant, J. M. Millam, S. S. Iyengar, J. Tomasi, V. Barone, B. Mennucci, M. Cossi, G. Scalmani, N. Rega, G. A. Petersson, H. Nakatsuji, M. Hada, M. Ehara, K. Toyota, R. Fukuda, J. Hasegawa, M. Ishida, T. Nakajima, Y. Honda, O. Kitao, H. Nakai, M. Klene, X. Li, J. E. Knox, H. P. Hratchian, J. B. Cross, C. Adamo, J. Jaramillo, R. Gomperts, R. E. Stratmann, O. Yazyev, A. J. Austin, R. Cammi, C. Pomelli, J. W. Ochterski, P. Y. Ayala, K. Morokuma, G. A. Voth, P. Salvador, J. J. Dannenberg, V. G. Zakrzewski, S. Dapprich, A. D. Daniels, M. C. Strain, O. Farkas, D. K. Malick, A. D. Rabuck, K. Raghavachari, J. B. Foresman, J. V. Ortiz, Q. Cui, A. G. Baboul, S. Clifford, J. Cioslowski, B. B. Stefanov, G. Liu, A. Liashenko, P. Piskorz, I. Komaromi, R. L. Martin, D. J. Fox, T. Keith, M. A. Al-Laham, C. Y. Peng, A. Nanayakkara, M. Challacombe, P. M. W. Gill, B. Johnson, W. Chen, M. W. Wong, C. Gonzalez, J. A. Pople, *Gaussian 03, Revision B.03*, Gaussian, Inc., Pittsburgh, PA, **2003**.

[21] S. I. Kirin, U. Schatzschneider, X. de Hatten, T. Weyhermüller, N. Metzler-Nolte, *J. Organomet. Chem.* **2006**, *691*, 3451–3457.

[22] K. Heinze, M. Beckmann, *J. Organomet. Chem.* **2006**, *691*, 5588–5596.

Received: September 14, 2006
Published Online: December 19, 2006

 © 2007 Wiley-VCH Verlag GmbH & Co. KGaA, Weinheim

**The EUChemSoc Societies have taken the significant step into the future by merging their traditional journals, to form two leading chemistry journals, the *European Journal of Inorganic Chemistry* and the *European Journal of Organic Chemistry.* Three further EUChemSoc Societies (Austria, Czech Republic and Sweden) are Associates of the two journals.**

## COVER PICTURE

**The cover picture shows** the result of the electrochemical oxidation of a square-planar nickel(II) complex. The oxidation state of the metal remains largely unchanged, and the phenoxy ligand is oxidized to the depicted radical cation. Details are discussed in the Short Communication by J. Reedijk et al. on p. 637ff.

 © 2007 Wiley-VCH Verlag GmbH & Co. KGaA, Weinheim

**The EUChemSoc Societies have taken the significant step into the future by merging their traditional journals, to form two leading chemistry journals, the *European Journal of Inorganic Chemistry* and the *European Journal of Organic Chemistry.* Three further EUChemSoc Societies (Austria, Czech Republic and Sweden) are Associates of the two journals.**

## COVER PICTURE

**The cover picture shows** the result of the electrochemical oxidation of a square-planar nickel(II) complex. The oxidation state of the metal remains largely unchanged, and the phenoxy ligand is oxidized to the depicted radical cation. Details are discussed in the Short Communication by J. Reedijk et al. on p. 637ff.

 © 2007 Wiley-VCH Verlag GmbH & Co. KGaA, Weinheim 

# CONTENTS

## SHORT COMMUNICATIONS


### Monoradical Complexes

**L. Benisvy, R. Kannappan, Y.-F. Song, S. Milikisyants, M. Huber, I. Mutikainen, U. Turpeinen, P. Gamez, L. Bernasconi, E. J. Baerends, F. Hartl, J. Reedijk*** ..... **637–642**

A Square-Planar Nickel(II) Monoradical Complex with a Bis(salicylidene)diamine Ligand

**Keywords:** Phenoxyl radicals / Nickel(II) complexes / Redox chemistry / Spectroelectrochemistry / EPR spectroscopy / Density functional calculations


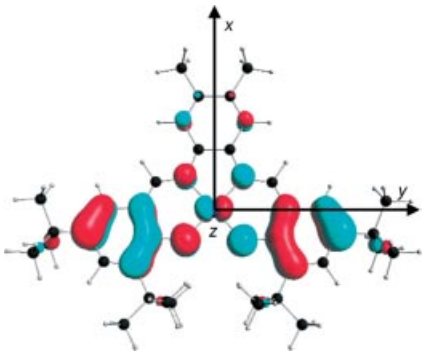


The square complex [Ni($^{Me}$L)] (**1**$^{Me}$) [$^{Me}$L = the dianionic phenolato form of *N*,*N*′-bis(3,5-di-*tert*-butylsalicylidene)-4,5-dimethyl-1,2-phenylenediamine ($^{Me}$LH$_2$)] has been synthesised and characterised. Electrochemical one-electron oxidation of **1**$^{Me}$ produces thermally stable (**1**$^{Me}$)$^+$ [10–295 K]. UV/Vis and EPR spectroscopy, supported by DFT calculations, indicate that (**1**$^{Me}$)$^+$ is best described as a Ni$^{II}$ monoradical complex and does NOT exist in a Ni$^{III}$ ground state, in contrast to its demethylated counterpart [Ni($^{H}$L)]$^+$ (**1**$^{H}$)$^+$ below 170 K.


### Polymorphism

**A. Karmakar, R. J. Sarma, J. B. Baruah*** ..... **643–647**

Polymorphism in an Aqua-Bridged, Dinuclear 2-Nitrobenzoate Complex of Cobalt(II)

**Keywords:** Dinuclear cobalt complexes / Aqua-bridged complexes / Polymorphism / Conformers


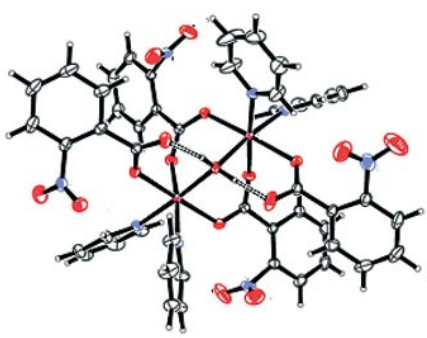

Three polymorphs of a dinuclear, aqua-bridged cobalt complex [$Co_2$(μ-$OH_2$)-($C_5H_5N$)$_4$(μ-$O_2CC_6H_4$-2-$NO_2$)$_2$($O_2CC_6H_4$-2-$NO_2$)$_2$] are structurally characterised. Selective crystallisation of the polymorphs is achieved by controlling the reaction conditions and the crystallisation processes. Reaction of cobalt(II) acetate tetrahydrate with 2-nitrobenzoic acid followed by treatment with excess pyridine leads to the mononuclear complex [$Co(H_2O)_2(C_5H_5N)_2$-($O_2CC_6H_4$-2-$NO_2$)$_2$].


### Antimony Anions

**D. Fenske,* A. Rothenberger, S. Wieber** ..... **648–651**

Synthesis and Characterization of the First Silver Complexes with Antimony Anions

**Keywords:** Silver / Antimony / Clusters


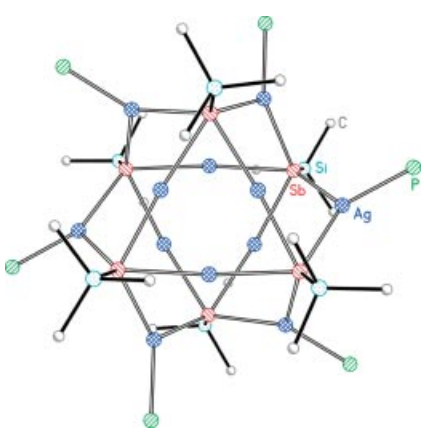


The synthesis and characterization of the silver antimony complexes [$Ag_{12}${Sb-($SiMe_3$)}$_6$($Pi Pr_3$)$_6$] (**1**), [$Ag_4(Sb_4Ph_4)_2$-($Pi Pr_3$)$_4$] (**2**) and [$Ag_4(Sb_6Ph_6)_2$($Pn Bu_3$)$_4$] (**3**) is reported.

 © 2007 Wiley-VCH Verlag GmbH & Co. KGaA, Weinheim 

$K^+$ salts of the square-planar noble metal iodate $[M(IO_3)_4]^{n-}$ (M = $Pd^{II}$, $Au^{III}$; $n$ = 2, 1) anions have been prepared under mild hydrothermal conditions, and the structures elucidated to demonstrate that while both are highly polar anions, polar and centrosymmetric extended architectures can form using these building units.

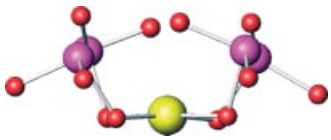

### Noble Metal Iodates

**J. Ling,**
**T. E. Albrecht-Schmitt* ..... 652–655**

Square-Planar Noble Metal Iodate $[M(IO_3)_4]^{n-}$ (M = $Pd^{II}$, $Au^{III}$; $n$ = 2, 1) Anions and Their Ability to Form Polar and Centrosymmetric Architectures

**Keywords:** Gold / Palladium / Iodate / Oxo ligands

# FULL PAPERS

Peroxidovanadium(V) or superoxidovanadium(IV)? Crystallography, spectroscopy and oxidation reactivity are used to answer this question.

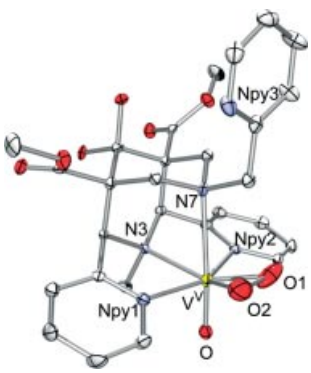


### Vanadium Bispidine Complexes

**P. Comba,* S. Kuwata, G. Linti, M. Tarnai, H. Wadepohl ..... 657–664**

Synthesis and Oxidation of Vanadyl Complexes Containing Bispidine Ligands

**Keywords:** Peroxido complexes / Superoxido complexes / Rigid ligand / Bispidine

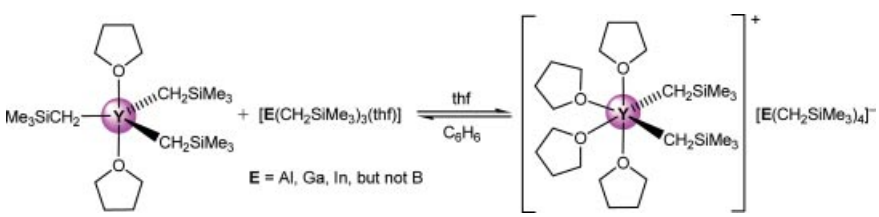


The alkyl abstraction reaction of $[YR_3(thf)_2]$ (R = $CH_2SiMe_3$) with group-13 trialkyl complexes $[(ER_3)_n]$ (E = B, Ga, In: $n$ = 1; E = Al: $n$ = 2) leading to cationic yttrium species $[YR_2(thf)_4]^+[ER_4]^-$ (E = Al, Ga, In) shows a strong dependence on the solvent basicity.

### Cationic Alkylyttrium

**M. U. Kramer, D. Robert, Y. Nakajima, U. Englert, T. P. Spaniol, J. Okuda* ..... 665–674**

Alkyl Abstraction from a Trialkylyttrium Complex $[YR_3(thf)_2]$ (R = $CH_2SiMe_3$) Using a Group-13 Element Lewis Acid $ER_3$ (E = B, Al, Ga, In) – Structural Characterisation of the Ion Pair $[YR_2(thf)_4]^+[GaR_4]^-$ and of $ER_3$ (E = B, Al, Ga)

**Keywords:** Yttrium / Lewis acids / Alkyl abstraction / Group-13 elements / Cationic complexes

 © 2007 Wiley-VCH Verlag GmbH & Co. KGaA, Weinheim 

# CONTENTS

## $CO_2$ Fixation

**H.-J. Himmel* ..... 675–683**

$CO_2$ Fixation by Alkylzinc Amides: A Quantum Chemical Study Motivated by Recent Experimental Results

**Keywords:** $CO_2$ fixation / Zinc / Reaction mechanisms / Quantum chemical calculations

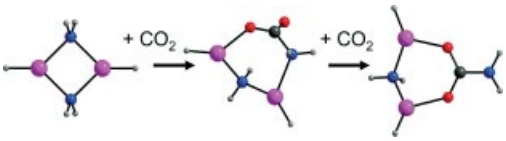


The mechanism of $CO_2$ fixation by monomeric as well as dimeric alkylzinc amides was studied by quantum chemical calculations. The results of this work help us in the understanding of $CO_2$ fixation by synthesized alkylzinc amides and also shed light on enzymatic reactivity.

## Metal-Organic Polymers

**M. C. Bernini, E. V. Brusau, G. E. Narda,* G. E. Echeverria, C. G. Pozzi, G. Punte, C. W. Lehmann ..... 684–693**

The Effect of Hydrothermal and Non-Hydrothermal Synthesis on the Formation of Holmium(III) Succinate Hydrate Frameworks

**Keywords:** Lanthanides / Hydrothermal synthesis / Hybrid frameworks / Coordination polymers

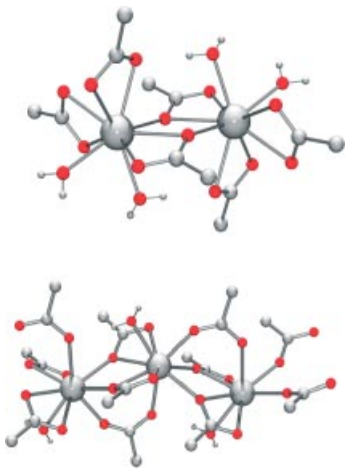

Holmium(III) succinates $[Ho_2(C_4H_4O_4)_3(H_2O)_4]\cdot 6H_2O$ (**1**) and $[Ho_2(C_4H_4O_4)_3(H_2O)_2]\cdot H_2O$ (**2**) have been synthesized under ambient and hydrothermal conditions, respectively. Single-crystal XRD shows that **1** is a 2D hybrid polymer and **2** presents a 3D architecture showing that hydrothermal conditions favor increasing dimensionality. They were characterized by FTIR and Raman spectroscopy, thermal analysis and magnetic measurements.

## Supramolecular Chemistry

**Z. Grote, R. Scopelliti, K. Severin* ..... 694–700**

Controlled Formation of Mixed-Metal Macrocycles Using Dynamic Exchange Processes and Steric Constraints

**Keywords:** Dynamic combinatorial chemistry / Metallamacrocycle / Organometallic complex / Rhodium / Ruthenium

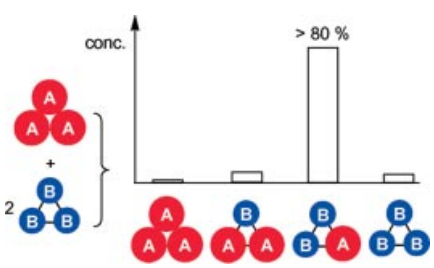


Size matters: Steric interactions in combination with dynamic exchange processes can be used to generate mixed-metal macrocycles in high yield. This is demonstrated by the controlled formation of organometallic macrocycles containing different (π-ligand)M fragments (M = Rh, Ru).

## Phosphinic Acid Derivatives

**G. Tircsó,* A. Bényei, R. Király, I. Lázár, R. Pál, E. Brücher ..... 701–713**

Complexation Properties of the Di-, Tri-, and Tetraacetate Derivatives of Bis(aminomethyl) Acid

**Keywords:** Phosphinic acid derivatives / Divalent metal ions / Synthesis / Protonation constants / Stability constants

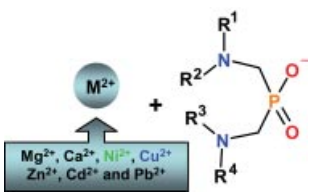


Acetate derivatives of bis(aminomethyl)-phosphinic acid are synthesized and the stability of the complexes formed with these diamino-di-, -tri-, and -tetracarboxylates involving some endogenous ($Mg^{2+}$, $Ca^{2+}$, $Cu^{2+}$, $Zn^{2+}$) and toxic ($Ni^{2+}$, $Pb^{2+}$, and $Cd^{2+}$) doubly charged metal ions, are reported. The structure of the ligand $L^3$ (tricarboxylate) and the $Cu^{2+}$ complex of $L^1$ are studied in the solid state.

 © 2007 Wiley-VCH Verlag GmbH & Co. KGaA, Weinheim 

## Anion-Dependent Structural Diversity

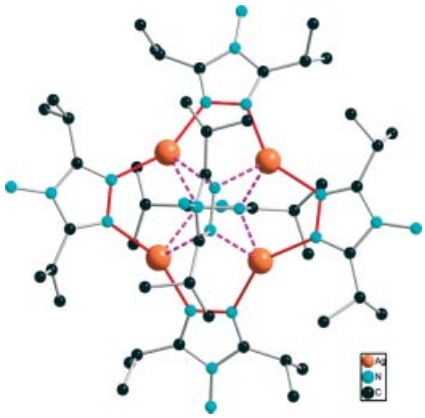

Reactions of silver(I) salts with 4-amino-3,5-diisopropyl-1,2,4-triazole (L) yield, based on the anion used, dinuclear, triangular or cyclic tetranuclear complexes. Shown here is the tetranuclear cation $[Ag_4L_6]^{4+}$, anions (not shown) are $BF_4^-$.

**G. Yang,* Y.-L. Wang, J.-P. Li, Y. Zhu, S.-M. Wang, H.-W. Hou, Y.-T. Fan, S. W. Ng ..... 714–719**

Anion-Dependent Structural Diversity in Silver(I) Complexes of 4-Amino-3,5-diisopropyl-1,2,4-triazole

**Keywords:** Silver / Triazole / Anions

## Thioether Aminophosphonite Complexes

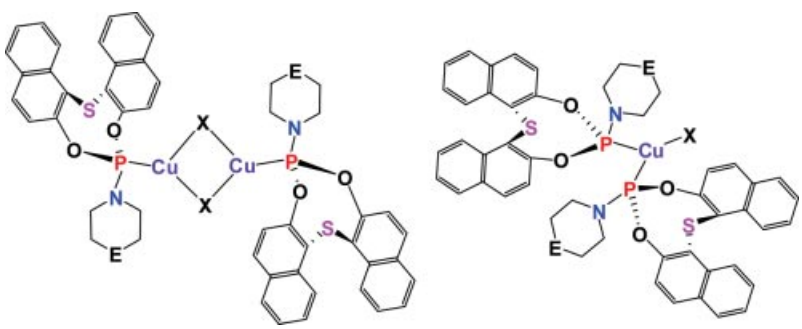

The reactivity of thioether aminophosphonites (L) with group 11 metal derivatives is described. A series of three-coordinate monomeric and dimeric complexes with or without the sulfur coordination are reported. Halogen exchange is observed between [LAuCl] and CuI to form [LAuI] and CuCl.

**B. Punji, J. T. Mague, M. S. Balakrishna* ..... 720–731**

Group 11 Metal Complexes of the Mesocyclic Thioether Aminophosphonites $[-OC_{10}H_6(\mu\text{-}S)C_{10}H_6O-]PNC_4H_8E$ (E = O, NMe)

**Keywords:** Thioether-aminophosphonites / P,S ligands / Copper / Gold

## Half-Sandwich Ruthenium(II) Complexes

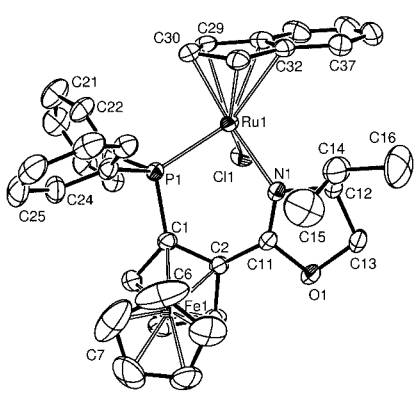


Chiral-at-metal indenyl- and areneruthenium(II) complexes containing the chiral ligand (4*S*)-2-[($S_P$)-2-(diphenylphosphanyl)ferrocenyl]-4-(methylethyl)oxazoline (FcPN) have been synthesised diastereoselectively. The reported complexes include those containing alkynyl, allenylidene, and Fischer-type carbene ligands. The absolute configuration of the ruthenium atoms in representative complexes has been determined by X-ray analyses.

**A. García-Fernández, J. Gimeno, E. Lastra,* C. A. Madrigal, C. Graiff, A. Tiripicchio ..... 732–741**

Half-Sandwich $\eta^5$-Indenyl- and $\eta^6$-Areneruthenium(II) Complexes Bearing the Chiral Ligand (4*S*)-2-[($S_p$)-2-(Diphenylphosphanyl)-ferrocenyl]-4-(methylethyl)oxazoline (FcPN)

**Keywords:** N,P ligands / Phosphanes / Indenyl complexes / Arene complexes / Ruthenium

 © 2007 Wiley-VCH Verlag GmbH & Co. KGaA, Weinheim 

# CONTENTS

## Cadmium Coordination Polymers

**Z. Guo, R. Cao,* X. Li, D. Yuan, W. Bi, X. Zhu, Y. Li ..... 742–748**

A Series of Cadmium(II) Coordination Polymers Synthesized at different pH Values

**Keywords:** Cadmium / Polymers / Self-assembly / Photoluminescence

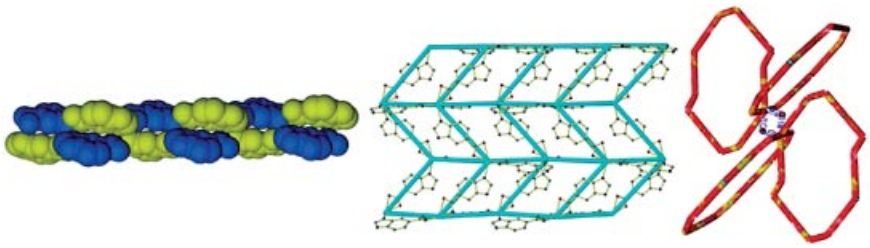

A new family of cadmium(II) coordination polymers has been hydrothermally prepared by the assembly of $Cd^{II}$ with 1H-benzimidazole-5-carboxylic acid. A change in the pH values resulted in a series of compounds with different compositions and dimensionalities.

## Ruthenium/Manganese Complexes

**A. D. Bond, B. S. Creaven, D. F. Donlon, T. L. Gernon, J. McGinley,* H. Toftlund ..... 749–756**

Metal Complexation of Calix[4]azacrown Derivatives – Evidence for Communication Between Upper and Lower Functionalised Rims

**Keywords:** Calix[4]arene / Macrocyclic ligands / Heterometallic compounds / Copper(II) / Manganese(II) / Ruthenium(II) / EPR spectroscopy

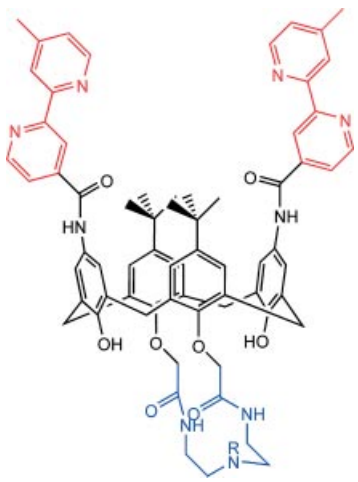


The first example of a binuclear ruthenium(II)/manganese(II) complex, involving the calix[4]arene framework as the bridging ligand (showing two different metal binding centres), is reported.

**If not otherwise indicated in the article, papers in issue 4 were published online on January 22, 2007**

 © 2007 Wiley-VCH Verlag GmbH & Co. KGaA, Weinheim 

DOI: 10.1002/ejic.200601015

# A Square-Planar Nickel(II) Monoradical Complex with a Bis(salicylidene)-diamine Ligand

**Laurent Benisvy,[a] Ramu Kannappan,[a] Yu-Fei Song,[a] Sergey Milikisyants,[b] Martina Huber,[b] Ilpo Mutikainen,[c] Urho Turpeinen,[c] Patrick Gamez,[a] Leonardo Bernasconi,[d] Evert Jan Baerends,[d] František Hartl,[e] and Jan Reedijk*[a]**

**Keywords:** Phenoxyl radicals / Nickel(II) complexes / Redox chemistry / Spectroelectrochemistry / EPR spectroscopy / Density functional calculations

The new square-planar $Ni^{II}$–$N_2O_2$ complex [Ni($^{Me}$L)] (**1**$^{Me}$), where $^{Me}$L stands for the dianionic phenolato form of *N*,*N*′-bis(3,5-di-*tert*-butyl-salicylidene)-4,5-dimethyl-1,2-phenylenediamine ($^{Me}LH_2$), has been synthesised and fully characterised. X-ray crystallography was also used for the characterisation. The electrochemical one-electron oxidation of **1**$^{Me}$ produces the thermally stable (within the temperature range 10–295 K) cationic species (**1**$^{Me}$)$^+$. The UV/Vis and X-band EPR experimental data, supported by DFT calculations, indicate that (**1**$^{Me}$)$^+$ is best described as a $Ni^{II}$ monoradical complex and, thus, does NOT exist in a $Ni^{III}$ ground state, in contrast to its demethylated counterpart [Ni($^{H}$L)]$^+$ (**1**$^{H}$)$^+$ below 170 K.

(© Wiley-VCH Verlag GmbH & Co. KGaA, 69451 Weinheim, Germany, 2007)

There has been much current interest in the nature and properties of d-transition-metal complexes in which one or more of the ligands are present in a radical state.[1] This interest has been stimulated by the observation and study of so-called "radical enzymes" in nature,[2] as illustrated by galactose oxidase (GO) that uses, in its active form, a phenoxyl radical directly bound to a $Cu^{II}$ centre to perform two-electron oxidation reactions.[3] Further, metal complexes bearing radical-type ligands may exhibit novel physical properties. In some cases, valence tautomerism [$M^{n+1}$–$^-$OPh] ↔ [$M^{n+}$–$^{\cdot}$OPh] occurs, which is of relevance for the construction of molecular switches.[4] For these reasons, a thorough understanding of the factors governing the locus of the oxidation (metal versus ligand) is of importance.

Consequently, various suitably protected phenol-containing ligands were designed and successfully applied to stabilise a phenoxyl radical state when coordinated to a transition metal.[1a] With nickel, various $Ni^{III}$ species have been characterised.[5] Recently, De Castro et al. investigated bis(salicylidene)diamine-type ligands at $Ni^{II}$ centres. Oxidation of the complexes in various polar solvents ($S_Y$) yielded the corresponding octahedral $Ni^{III}$ species [$Ni^{III}$(L)$(S_Y)_2$]$^+$.[5i–5n] At the same time, two research groups have independently reported that one-electron oxidation of the square-planar complexes [$Ni^{II}$($^{R}$L)] {$^{R}$L = a dianionic Schiff-base ligand with a cyclohexylene-1,2-diamine backbone ($^{Cy}$L*)[6] and a phenylene-1,2-diamine ($^{H}$L) backbone[7]} (see structure below) produces, in dichloromethane, a $Ni^{III}$ complex [$Ni^{III}$($^{R}$L)]$^+$ at sufficiently low temperature and a $Ni^{II}$ radical complex [$M^{II}$($^{R}$L$^{\cdot}$)]$^+$ ($^{R}$L$^{\cdot}$ = phenoxyl radical anion of $^{R}$L) above 190 K. These interesting results have been interpreted in terms of temperature-dependent tautomerism.[6,7]

Herein we report the synthesis and characterisation of the analogous dimethylated complex [Ni($^{Me}$L)] (**1**$^{Me}$) ($^{Me}$L contains the 4,5-dimethylphenylene-1,2-diamine backbone) and its one-electron oxidised product [Ni($^{Me}$L)]$^+$. Surprisingly, experimental EPR spectroscopic and UV/Vis spectroelectrochemical data reveal that the oxidised species does NOT exist in a $Ni^{III}$ ground state in the studied low-temperature range, in contrast to its counterparts [Ni($^{H}$L)]$^+$ and [Ni($^{Cy}$L)]$^+$.[6,7] Instead, it can be best formulated as a $Ni^{II}$ monoradical complex [$Ni^{II}$($^{Me}$L$^{\cdot}$)]$^+$. DFT calculations support this assignment, pointing to the negligible effect of the methyl groups when the electronic structures of [Ni($^{H}$L)]$^+$ and [Ni($^{Me}$L)]$^+$ are compared.

[a] Leiden Institute of Chemistry, Gorlaeus Laboratories, Leiden University,
P. O. Box 9502, 2300 RA Leiden, The Netherlands
Fax: +31-715274671
E-mail: reedijk@chem.leidenuniv.nl
[b] Department of Molecular Physics, Huygens Laboratory, Leiden University,
P. O. Box 9504, 2300 RA Leiden, The Netherlands
[c] Department of Chemistry, Laboratory of Inorganic Chemistry, University of Helsinki,
P. O. Box55, A. I. Virtasenaukio 1, 00014 Helsinki, Finland
[d] Theoretische Chemie, Vrije Universiteit Amsterdam,
De Boelelaan 1083, 1081 HV Amsterdam, The Netherlands
[e] Van't Hoff Institute for Molecular Sciences, Homogeneous and Supramolecular Catalysis, Universiteit van Amsterdam,
Nieuwe Achtergracht 166, 1018 WV Amsterdam, The Netherlands

Supporting information for this article is available on the WWW under http://www.eurjic.org or from the author.

 © 2007 Wiley-VCH Verlag GmbH & Co. KGaA, Weinheim 

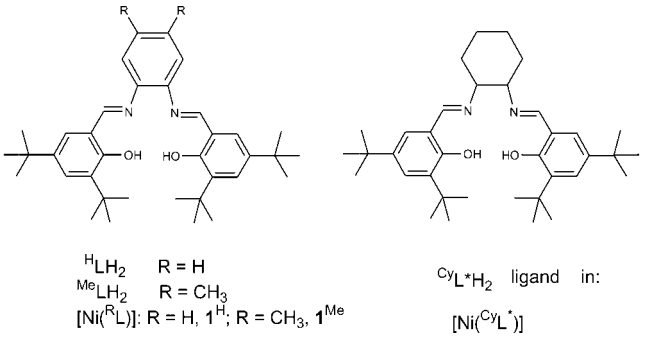


The tetradentate ligand *N*,*N*′-bis(3,5-di-*tert*-butyl-salicylidene)-4,5-dimethylphenylene-1,2-diimine ($^{Me}LH_2$) was synthesised by the condensation of 4,5-dimethylphenylene-1,2-diamine with 3,5-di-*tert*-butyl-salicylaldehyde, as previously reported.[8] The reaction of $^{Me}LH_2$ with $Ni(ClO_4)_2{\cdot}6H_2O$ (1:1) in methanol leads to the formation of red, needlelike crystals of [Ni($^{Me}$L)] ($\mathbf{1}^{Me}$) in 77% yield. The molecular structure of $\mathbf{1}^{Me}$ (Figure 1), determined by X-ray crystallography at 173 K, reveals a $Ni^{II}$ centre with a square-planar $N_2O_2$ coordination sphere defined by the two imine nitrogen atoms [N(30), N(40)] and the two phenolate oxygen atoms [O(10), O(20)] of $^{Me}$L. As expected, the structure and molecular dimensions of $\mathbf{1}^{Me}$ are almost identical to those of $\mathbf{1}^{H}$ (see Table S1).[7] Thus, the Ni–O and Ni–N bond lengths [1.853(3)–1.861(2) Å] are short. The mean deviation from the least-squares plane defined by Ni(1), O(10), O(20), N(30) and N(40) is 0.11 Å, with a dihedral angle of 9.6° between the O(10)–Ni(1)–N(30) and O(20)–Ni(1)–N(40) planes.

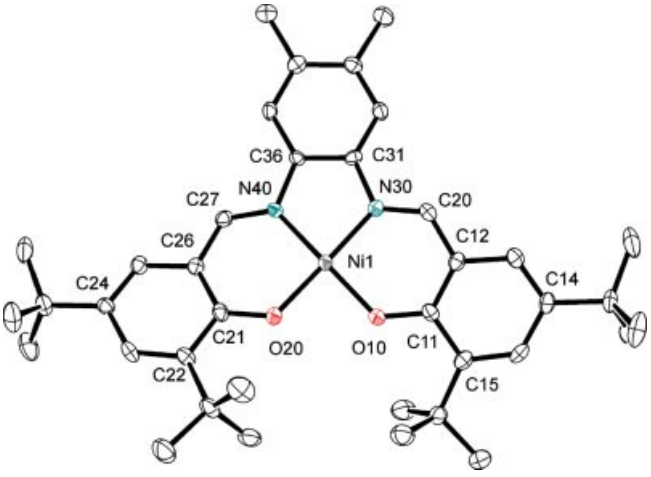


Figure 1. ORTEP representation of [Ni($L^{Me}$)] ($\mathbf{1}^{Me}$) shown with 50% thermal ellipsoids, as determined at 173 K. The hydrogen atoms are omitted for clarity. Selected bond lengths [Å] and angles [°] for **1**: Ni(1)–O(10), 1.856(2); Ni(1)–O(20), 1.861(2); Ni(1)–N(30), 1.856(3); Ni(1)–N(40), 1.853(3); C(11)–O(10), 1.327(4); C(21)–O(20), 1.327(4); C(27)–N(40), 1.321(4); C(36)–N(40), 1.428(4); C(31)–N(30), 1.421(4); C(17)–N(30), 1.318(4) Å. O(10)–Ni(1)–N(40), 173.03(11); O(10)–Ni(1)–N(30), 94.07(11); N(40)–Ni(1)–N(30), 85.63(12); O(10)–Ni(1)–O(20), 86.86(9); N(40)–Ni(1)–O(20), 94.25(11); N(30)–Ni(1)–O(20), 173.37(11)°.

Complex $\mathbf{1}^{Me}$ exhibits no EPR signal, neither in the solid state nor in $CH_2Cl_2$ solution, at room temperature or at 77 K. This result indicates that $\mathbf{1}^{Me}$ is diamagnetic ($S = 0$), as expected for a low-spin $d^8$ square-planar $Ni^{II}$ complex. In $CDCl_3$ solution, $\mathbf{1}^{Me}$ exhibits a well-defined $^1$H NMR spectrum with resonances between 0 and 10 ppm, which also confirms its diamagnetic nature. Similar to that of complex $\mathbf{1}^{H}$,[7] the UV/Vis spectrum of $\mathbf{1}^{Me}$ in $CH_2Cl_2$ (Figure 2) displays an absorption band at $\lambda_{max}$ = 385 nm ($\varepsilon_{max}$ = 29800 $M^{-1}cm^{-1}$) due to a $\pi\rightarrow\pi^*$ intraligand transition. Another intense absorption band at 499 nm ($\varepsilon_{max}$ = 8900 $M^{-1}cm^{-1}$) and a shoulder at 475 nm ($\varepsilon$ = 6700 $M^{-1}cm^{-1}$) are assigned to a phenolate→$Ni^{II}$ charge transfer. A weak shoulder at about 600 nm ($\varepsilon < 200\ M^{-1}cm^{-1}$) may correspond to a largely metal-centred (MC) transition. These spectroscopic observations suggest that the square-planar $Ni^{II}$–$N_2O_2$ coordination sphere is retained in $CH_2Cl_2$ solution.

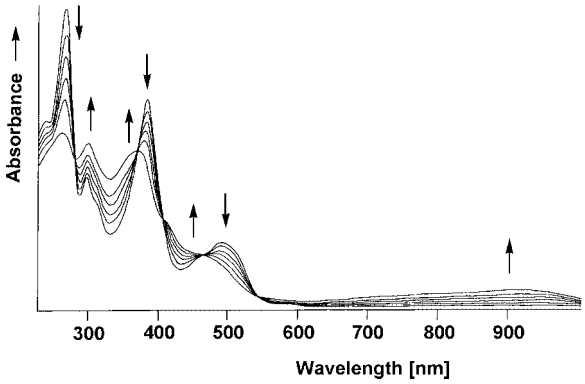


Figure 2. UV/Vis spectroelectrochemistry for the first oxidation of $\mathbf{1}^{Me}$ in $CH_2Cl_2$ containing $[NBu^n_4][ClO_4]$ (0.3 M) at 293 K.

The cyclic voltammogram (CV) of complex $\mathbf{1}^{Me}$ in dichloromethane ($v$ = 100 mV/s, $T$ = 293 K) exhibits two reversible ($I_{p,c}/I_{p,a}$ = 1) one-electron anodic processes at $E_{1/2}$ = +0.49 V ($\Delta E_p$ = 80 mV) and 0.78 V ($\Delta E_p$ = 110 mV) vs. $Fc/Fc^+$ ($\Delta E_p$ = 80 mV) used as an internal standard (see Figure S1). These oxidation processes are associated with the formation of $(\mathbf{1}^{Me})^+$ and $(\mathbf{1}^{Me})^{2+}$, respectively. The larger peak-to-peak separation for the second anodic step producing $(\mathbf{1}^{Me})^{2+}$ indicates a slower electron transfer, most likely associated with a change in the molecular structure of the dicationic product. This difference between the anodic steps became more apparent on the longer time scale of the spectroelectrochemical experiments (see below). Interestingly, the $E_{1/2}$ values determined for $\mathbf{1}^{Me}$ are lower than those observed for $\mathbf{1}^{H}$ by 90 and 20 mV for the first and second couple, respectively,[7] and reveal a stabilisation effect of the methyl groups at the phenyl-diene backbone on the oxidised species.

Corresponding UV/Vis spectroelectrochemical experiments with $\mathbf{1}^{Me}$ in the anodic region were performed in dichloromethane at 293 K (Figure 2) and 233 K, with almost identical results. The one-electron-oxidised species

 © 2007 Wiley-VCH Verlag GmbH & Co. KGaA, Weinheim 

$(\mathbf{1}^{Me})^+$ remains fully stable at both temperatures, as revealed by the completely reversible thin-layer cyclic voltammetric response (with a small $\Delta E_p$ value of about 20 mV, which is comparable to that of the $Fc/Fc^+$ couple) recorded in the course of the anodic and reverse cathodic scans. In the UV/Vis spectral region, the conversion of $\mathbf{1}^{Me}$ to $(\mathbf{1}^{Me})^+$ at room temperature is accompanied by the disappearance of the absorption bands of the parent complex (see Experimental Section) and the growth of new intense bands of the cationic product at $\lambda_{max}$ ($\varepsilon_{max}$, $M^{-1}\,cm^{-1}$) = 300 (23 200), 374 (22 400), 411 (sh., better resolved at 233 K) and 468 nm(7300); in addition, a broad absorption band of lower intensity appears at a low energy, with poorly resolved maxima at $\lambda_{max}$ ($\varepsilon_{max}$, $M^{-1}\,cm^{-1}$) = 810 (2100) and 920 nm (2500). The reversibilty of the first anodic step is reflected by the presence of isosbestic points at 280, 375, 405, 466 and 543 nm (Figure 2) and the full recovery of the initial UV/Vis spectrum of $\mathbf{1}^{Me}$ after "back reduction" of $(\mathbf{1}^{Me})^+$. It is important to note that absorption bands at ca. 400 nm ($\varepsilon_{max}$ ca. 10 000 $M^{-1}\,cm^{-1}$) are typically found for phenoxyl radical complexes and have been attributed to a $\pi\rightarrow\pi^*$ electronic transition of the phenoxyl ligand.[1a,9] The broad low-energy bands may have their origin in an electron transfer to the phenoxyl singly occupied molecular orbital (SOMO) from lower-lying occupied levels.[10] Thus, one-electron-oxidised $(\mathbf{1}^{Me})^+$ shows the spectroscopic signature of a phenoxyl radical complex, which suggests that the oxidation of $\mathbf{1}^{Me}$ to $(\mathbf{1}^{Me})^+$ is predominantly ligand-centred.

The second anodic step, i.e. the oxidation of $(\mathbf{1}^{Me})^+$ to $(\mathbf{1}^{Me})^{2+}$, is characterised by a large separation between the anodic and reverse cathodic peaks of the couple observed in the thin-layer cyclic voltammogram exceeding 500 mV at 233 K. This result points to a significant difference between the ultimate molecular structures of $(\mathbf{1}^{Me})^+$ and $(\mathbf{1}^{Me})^{2+}$. The electronic absorption spectrum of $(\mathbf{1}^{Me})^{2+}$ (not shown) exhibits a very intense band at 300 nm with a shoulder at 325 nm, two less intense bands of similar intensities at 420 and 455 nm and a weak band at 558 nm. The absorption maximum at 820 nm disappeared and the broad, low-energy absorption band shifted more to the NIR region relative to $(\mathbf{1}^{Me})^+$ (Figure 2). These absorption features indicate the presence of the coordinated phenoxyl radical chromophore also in the dicationic product $(\mathbf{1}^{Me})^{2+}$. The subsequent oxidation of $(\mathbf{1}^{Me})^+$ is presumably localised more at the nickel(II) centre, causing changes in the coordination sphere, which may explain the electrochemically irreversible nature of the second anodic step. However, detailed investigation of this process is beyond the scope of this work. Back reduction of $(\mathbf{1}^{Me})^{2+}$ resulted in the smooth recovery of $(\mathbf{1}^{Me})^+$, thereby excluding any decomposition or irreversible structural change induced by the second anodic reaction.

The X-band EPR spectra of $(\mathbf{1}^{Me})^+$ − generated electrochemically (Figure 3) by bulk electrolysis in $CH_2Cl_2$ (see Experimental Section) − were recorded in the temperature range 10–240 K. Above the freezing point of $CH_2Cl_2$ (170–190 K), the EPR spectrum exhibits a single unresolved isotropic signal centred at $g_{iso}$ = 2.04 with a peak-to-peak line width of ca. 100 G. This spectrum resembles those obtained for $[Ni(^{H}L)]^{+}$[7] and $[Ni(^{Cy}L)]^{+}$[6] at T > 190 K. The $g_{av}$ values for the latter spectra (2.03–2.04) are much lower than those expected for a $Ni^{III}$ species ($g_{av}$ values ranging from 2.13 to 2.17),[5] but higher than $g$ factors reported for free[11] or Zn-coordinated[7,10] phenoxyl radicals (2.004–2.005), which are typically close to the free electron value ($g_e$ = 2.0023).[10b] At temperatures below the freezing point of $CH_2Cl_2$ (10–170 K), the EPR spectrum of $(\mathbf{1}^{Me})^+$ displays a rhombic signal with $g_{11}$ = 2.00, $g_{22}$ = 2.02, $g_{33}$ (broad) = 2.10 and a $g_{av}$ value of 2.04 (obtained from numerical calculation of the average over the whole spectrum). The values $g_{11}$ = 2.00 and $g_{22}$ = 2.02 were obtained directly from the spectrum, and $g_{33}$ was calculated from $g_z = 3g_{av} - g_x - g_y$. Thus, the $g_{av}$ value in frozen $CH_2Cl_2$ is identical to that obtained above 190 K in fluid solution. This observation is in sharp contrast with the EPR spectra recorded for $[Ni(^{H}L)]^+$ and $[Ni(^{Cy}L)]^+$ at $T < 170$ K, which exhibit an axial signal with $g_\perp > g_\parallel$ and $g_{av}$ of 2.17 and 2.18, respectively.[6,7] The latter spectra are typically observed as a result of a $(d_{z^2})^1$ ground state, which, to the best of our knowledge, can only be achieved for six-coordinate tetragonally elongated nickel(III) compounds,[5] as predicted by the theory.[12]

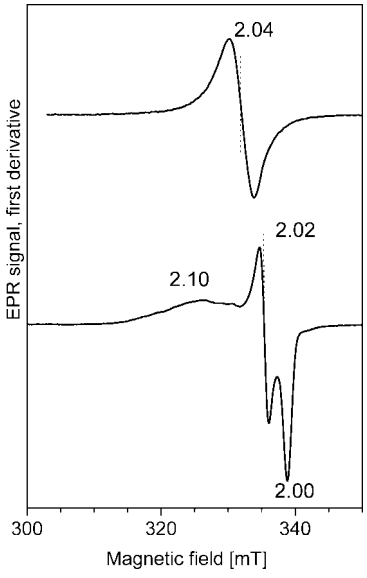


Figure 3. X-band EPR spectrum of electrochemically generated$(\mathbf{1}^{Me})^+$ recorded in frozen $CH_2Cl_2$ at 30 K (bottom) and at 255 K (top). The numbers indicate the $g$ values (see text).

Thus, the experimental data obtained for $(\mathbf{1}^{Me})^+$ indicate that the electronic structure of the complex remains unchanged in the 10–240 K temperature range. In frozen $CH_2Cl_2$, the anisotropy becomes resolved. The anisotropy of $(\mathbf{1}^{Me})^+$ and the low $g_{av}$ value are consistent with a $Ni^{II}$ radical complex; the metal centre has a partial $Ni^{III}$ character (vide infra) with a $(dp)^1$ configuration (dp = $d_{xy}$, $d_{xz}$ or $d_{yz}$) in a square-planar coordination environment. Such interpretation agrees well with the rhombic or axial EPR

 © 2007 Wiley-VCH Verlag GmbH & Co. KGaA, Weinheim 

spectra obtained for $Ni^{II}$–$(N_2O_2)^{\cdot}$ complexes bearing oxamato ($g_{\|} = 2.040 > g_{\perp} = 2.005$;[13] $g_{av} = 2.028$), salicylamidato ($g = 2.09, 2.03, 1.95$; $g_{av} = 2.023$)[7] or semiquinonato ($g_x = 2.0098, 2.0384, 2.1097$; $g_{av} = 2.019$)[14] radical ligands.

DFT calculations were performed with all core states explicitly included, and exchange-correlation effects were treated at the BP86[15a,15b] level of theory. Geometry optimisation, frontier orbitals and EPR parameters were calculated for both parent ($\mathbf{1}^{Me}$) and oxidised compound $(\mathbf{1}^{Me})^+$, and similar treatments were applied for $\mathbf{1}^{H}$ and $(\mathbf{1}^{H})^+$ for comparison. The calculated structural parameters for geometry optimised $\mathbf{1}^{Me}$ and $\mathbf{1}^{H}$ have been found to agree appreciably with the corresponding data obtained by X-ray crystallography: bond lengths are reproduced within ±0.02 Å and bond angles within ±0.2° (Table S1). The calculated *g*-tensor parameters for $(\mathbf{1}^{Me})^+$ are $g_{xx} = 2.1341$, $g_{yy} = 2.0027$, $g_{zz} = 1.9822$. The *z* axis is perpendicular to the plane of the molecule and the *x* axis is the $C_2$ axis of the system along the plane of the molecule, as indicated in Figure 4. The result is in good agreement (within 0.03) with the experimental data. In particular, the anisotropy in the *g* values has been well reproduced, with the two *g* values close to $g_e$ separated by ca. 0.02 ($g_{yy} - g_{zz}$) and $g_{xx} > g_{yy}$, $g_{zz}$. We thus tentatively assign the principal *g*-tensor orientations as $g_{11}(2.00) = g_{zz}$, $g_{22}(2.02) = g_{yy}$ and $g_{33}(2.10) = g_{xx}$. This finding supports the validity of the theoretical model and rules out unambiguously a $(d_{z^2})^1$ low-spin $Ni^{III}$ ground state, as had been proposed for $(\mathbf{1}^{H})^+$[7] and $(\mathbf{1}^{Cy})^+$.[6] The calculated singly occupied molecular orbital (SOMO) and the corresponding unpaired spin density distribution of $(\mathbf{1}^{Me})^+$ were also analysed. The SOMO is mainly delocalised on both phenoxy rings, with appreciable contributions of the nickel $d_{xz}$ (6.49%) and $d_{yz}$ (6.33%) orbitals (Figure 4). Consequently, ca. 75% of the unpaired spin is located on the ligand and 25% on the nickel centre. For each phenoxy ring, the typical phenoxy radical pattern with an alternating spin density distribution was obtained; a significant amount of positive spin population at the O (0.115), $C_{ortho}$ (0.08 and 0.06) and $C_{para}$ (0.11) atoms (Figure S2 and Table S2) accounts for ca. 72% of the total spin density. Hence, the calculations agree well with the experimental findings, and $(\mathbf{1}^{Me})^+$ is best described as a nickel(II) complex with a phenoxyl-type radical ligand. In addition, the DFT calculation on $(\mathbf{1}^{H})^+$ shows that the calculated bond parameters of the complex, the nature of the SOMO and the anisotropy in the *g* tensor (calculated *g* values are $g_{zz} = 1.97771$, $g_{yy} = 2.0027$, $g_{xx} = 2.1329$) are essentially identical to the corresponding parameters obtained for $(\mathbf{1}^{Me})^+$. This result is consistent with the calculated absence of spin density on the methyl groups in $(\mathbf{1}^{Me})^+$ and rules out any significant electronic effect of the methyl groups that can explain the EPR discrepancies between $(\mathbf{1}^{Me})^+$ and $(\mathbf{1}^{H})^+$ in frozen $CH_2Cl_2$. Moreover, in the case of $(\mathbf{1}^{H})^+$, the EPR data in MeOH remain essentially unchanged relative to those obtained in $CH_2Cl_2$, which suggest a six-coordinate species.[7] Such a coordination environment may have been achieved by either axial coordination of remnant water molecules or intermolecular interactions that may have been prevented by the presence of the methyl groups in the case of $(\mathbf{1}^{Me})^+$.

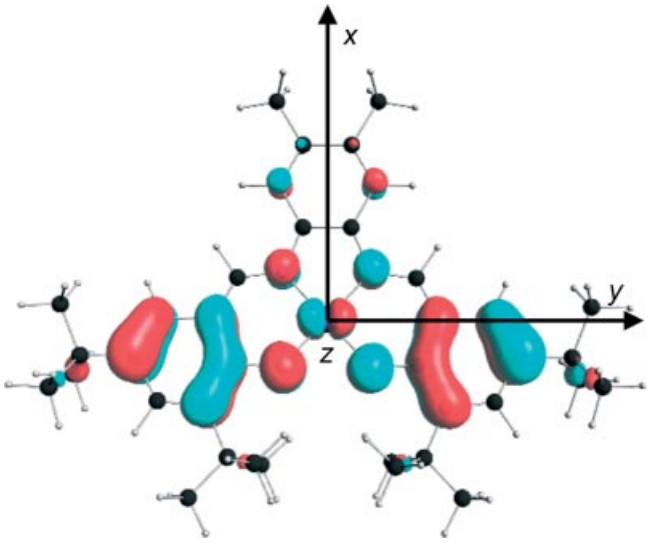


Figure 4. Calculated SOMO for geometry-optimised $(\mathbf{1}^{Me})^+$.

## Conclusions

In this communication, we have demonstrated that the one-electron oxidation of the diamagnetic $S = 0$, $d^8$, low-spin $Ni^{II}$ square-planar compound $[Ni^{II}(^{Me}L)]$ occurs largely on the Schiff-base ligand, yielding $[Ni^{II}(^{Me}L^{\cdot})]^+$. The latter cation is the first example of a thermally stable (within the temperature range 10–295 K) $Ni^{II}$ phenoxyl radical complex. The EPR discrepancies observed (below 170 K) for the reported related complexes $[Ni^{III}(^{H}L)]^+$ and $[Ni^{III}(^{Cy}L)]^+$ cannot be explained by electronic effects. Rather, they may be the result of axial coordination by water (present as impurities) and/or intermolecular interactions, which allow the stabilisation of a six-coordinate $Ni^{III}$ complex. Apparently, this coordination is not stable at higher temperatures and leads to a *g* value in liquid solution that is close to the $g_{av}$ value observed in the present study. Several new bis(salicylidene)diaminenickel(II) complexes with various substituents on the phenylene backbone are being synthesised in order to shed more light on the factors that govern the "spectroscopic" oxidation states of their one-electron oxidation product.

## Experimental Section

**Synthesis of [Ni($^{Me}$L)] ($\mathbf{1}^{Me}$) and Characterisation by NMR Spectroscopy, MS and Elemental Analysis:** $H_2L$ (0.568 g, 0.001 mol) in $CHCl_3$ (25 mL) was added to a solution of nickel(II) perchlorate hexahydrate (0.365 g, 0.001 mol) in methanol (10 mL), and the resulting red solution was stirred for 2 h at room temperature. Slow evaporation of the solvent yielded red, needle-shaped crystals within one day, which were isolated, washed with diethyl ether and dried in air. The crystals appeared to be suitable for X-ray structural determination. Yield: 0.46 g (77%). $C_{38}H_{50}N_2NiO_2$ (625.51): calcd. C 72.97, H 8.06, N 4.48; found C 73.04, H 7.71, N 4.40.

 © 2007 Wiley-VCH Verlag GmbH & Co. KGaA, Weinheim 

ES(+)-MS: $m/z$ = 624.36 [$M^+$]. IR (neat solid): $\nu$(C=N): 1616 $cm^{-1}$. UV/Vis ($CH_2Cl_2$): $\lambda_{max}$ ($\varepsilon_{max}$, $M^{-1}cm^{-1}$) = 268 (42 400), 299 (18 300), 312 (sh.), 385 (29 800), 475 (sh.), 499 (8 900) nm. $^1H$ NMR (300 MHz, $CDCl_3$): $\delta$ = 8.14 (s, 2 H, H–C=N), 7.44 (s, 2 H, $H_{PhN_2}$), 7.39 (d, $^4J$ = 2.7 Hz, 2 H, $H_{PhO}$), 7.09 (d, $^4J$ = 2.7 Hz, 2 H, $H_{PhO}$), 2.30 (s, 6 H, $CH_3$), 1.46 [s, 18 H, $C(CH_3)_3$], 1.30 [s, 18 H, $C(CH_3)_3$] ppm. All measurements were performed on locally available standard instruments.

**Electrochemistry:** Each experiment was performed under dinitrogen using dry, distilled and degassed $CH_2Cl_2$. The cyclic voltammogram of the studied compound $\mathbf{1}^{Me}$ ($10^{-3}$ M) in $CH_2Cl_2$ containing [$NBu^n_4$][$ClO_4$] ($4\times10^{-1}$ M) as the background electrolyte was recorded at room temperature with a glassy carbon working electrode, a Pt plate auxiliary electrode and a Ag/AgCl reference electrode. The electrode potentials are referenced against the $Fc/Fc^+$ couple that was used as the internal standard. The oxidised species $(\mathbf{1}^{Me})^+$ was generated by controlled potential electrolysis (CPE) performed on $\mathbf{1}^{Me}$ ($10^{-3}$ M) at 263 K in a $CH_2Cl_2$ solution containing [$NBu^n_4$][$ClO_4$] ($4\times10^{-1}$ M) as the background electrolyte. The electrolytic cell consisted of a Pt gauze basket working electrode, a Pt gauze auxiliary electrode and a Ag/AgCl reference electrode. Both CV and CPE measurements were performed by using an Autolab PGSTAT20 potentiostat.

**UV/Vis Spectroelectrochemistry:** UV/Vis spectroelectrochemical experiments at low temperatures were performed with a cryostatted optically transparent thin-layer electrochemical (OTTLE) cell equipped with $CaF_2$ windows and a Pt minigrid working electrode (32 wires per cm).[16a] The electrolysis at room temperature was conducted with another home-made demountable OTTLE cell.[16b] The concentrations of the solutions were typically $3\times10^{-1}$ M in the supporting electrolyte ([$NBu^n_4$][$ClO_4$]) and $10^{-3}$ M in the analyte. The working electrode potential of the spectroelectrochemical cells was controlled with a PA4 potentiostat (EKOM, Polná, Czech Republic). A thin-layer cyclic voltammogram was recorded during the course of each spectroelectrochemical experiment. The electronic absorption spectra were obtained with a HP 8453 diode array spectrophotometer.

**EPR Spectroscopy:** X-band (9.48 GHz) cw-EPR spectra were recorded by using a ELEXSYS E680 (Bruker, BioSpin, Rheinstetten) spectrometer with a TE102 resonator. Sample solutions of electrochemically generated $(\mathbf{1}^{Me})^+$ (vide ultra) were rapidly transferred under exclusion of dioxygen into an X-band quartz tube (4-mm inner diameter), which was immediately frozen and stored in liquid nitrogen. The measurements were performed at temperatures from 10 to 240 K using an Oxford ESR 900H cryostat. The microwave power supplied to the resonator was varied in the range 0.2–2 mW; a 100-kHz magnetic field modulation with a peak-to-peak amplitude of 0.5 mT was used.

**DFT Calculations:** The calculations were performed with the Amsterdam Density Functional (ADF 2005) program system.[15c,15d] A Slater-type orbital basis set of triple zeta quality for the valence orbitals was used, augmented with a polarization function, cf. the standard TZP basis.[15e] Calculations were performed on isolated molecules, without inclusion of solvent molecules.[15f]

**X-ray Crystallographic Study of $\mathbf{1}^{Me}$:** Crystal data: $C_{38}H_{50}N_2NiO_2$, red, needle, $F_w$ = 625.51, triclinic, space group $P\bar{1}$, $a$ = 9.2500(10) Å, $b$ = 14.865(2) Å, $c$ = 14.951(2) Å, $\alpha$ = 119.220(10)°, $\beta$ = 101.650(10)°, $\gamma$ = 92.310(10)°, $V$ = 1733.9(4) $Å^3$, $d$ = 1.198 $g\,cm^{-3}$, $Z$ = 2, $T$ = 173(2) K, $F(000)$ = 627, $\mu$(Mo-$K_\alpha$) = 0.593 $mm^{-1}$. A transparent, red, needlelike single crystal of $0.25\times0.05\times0.05$ mm was mounted on a Lindemann glass capillary and transferred into the cold nitrogen stream of a Nonius KappaCCD diffractometer on a rotating anode (Mo-$K_\alpha$ radiation, graphite monochromator, $\lambda$ = 0.71073 Å). 27617 independent reflections (7944 unique; $R_{int}$ = 0.117) were collected. The intensity data were corrected for Lorentz and polarisation effects and for absorption. The structure was solved by direct methods. The programs COLLECT[17a] SHELXS-97[17b] and SHELXL-97[17c] were used for data reduction, structure solution and structure refinement, respectively. The final agreement factors are $R_1$ = 0.0657 for 4241 data with $F > 4\sigma(F)$ and $R_1$ = 0.1554, $wR_2$ = 0.1433 for 7944 data. All non-hydrogen atoms were refined anisotropically. Hydrogen atoms were placed at idealised positions and allowed to ride on the connecting atom. CCDC-622859 contains the supplementary crystallographic data for this paper. These data can be obtained free of charge from The Cambridge Crystallographic Data Centre via www.ccdc.cam.ac.uk/data_request/cif.

**Supporting Information** (see footnote on the first page of this article): Cyclic voltammogram of $\mathbf{1}^{Me}$, in $CH_2Cl_2$, containing [$NBu^n_4$][$ClO_4$] (0.4 M), plot of the distribution of the non-zero spin populations, calculated bond lengths [Å] and angles [°] for the optimised structure of $\mathbf{1}^{Me}$ and $\mathbf{1}^{H}$, list of individual atomic electron spin density calculated for $(\mathbf{1}^{Me})^+$.

## Acknowledgments

This work has been supported financially by the Graduate Research School Combination "Catalysis", a joint activity of the graduate research schools NIOK, HRSMC and PTN. Financial support from COST Action D21/003/01 and the Netherlands Technology Research Foundation (STW) applied science division of the Netherlands Organisation for Scientific Research (NWO) are thankfully acknowledged (grant number 5751).

[1] Recent reviews: a) P. Chaudhuri, K. Wieghardt, *Prog. Inorg. Chem.* **2001**, *50*, 151–216; b) C. G. Pierpont, *Coord. Chem. Rev.* **2001**, *216–217*, 99–125; c) C. G. Pierpont, *Coord. Chem. Rev.* **2001**, *219–221*, 415–433; d) W. Kaim, *Dalton Trans.* **2003**, 761–768.

[2] Recent reviews: a) J. Stubbe, W. A. van der Donk, *Chem. Rev.* **1998**, *98*, 705–762; b) J. Stubbe, D. G. Nocera, C. S. Yee, M. C. Y. Chang, *Chem. Rev.* **2003**, *103*, 2167–2201.

[3] J. W. Whittaker, *Chem. Rev.* **2003**, *103*, 2347–2363.

[4] a) P. Gütlich, A. Dei, *Angew. Chem. Int. Ed. Engl.* **1997**, *36*, 2734–2736; b) P. Gütlich, Y. Garcia, T. Woike, *Coord. Chem. Rev.* **2001**, *219–221*, 839–879; c) D. A. Shultz, in *Magnetoscience – From Molecules to Materials* (Eds.: S. Miller, M. Drillon), Wiley-VCH, New York, **2001**.

[5] a) R. S. Drago, E. I. Baucom, *Inorg. Chem.* **1972**, *11*, 2064–2069; b) N. Takvoryan, K. Farmery, V. Katovic, F. V. Lovecchio, E. S. Gore, L. A. Anderson, F. V. Lovecchio, E. S. Gore, D. H. Busch, *J. Am. Chem. Soc.* **1974**, *96*, 731–742; c) D. H. Busch, *J. Am. Chem. Soc.* **1974**, *96*, 3109–3118; d) A. Bencini, L. Fabbrizzi, A. Poggi, *Inorg. Chem.* **1981**, *20*, 2544–2549; e) S. A. Jacobs, D. W. Margerum, *Inorg. Chem.* **1984**, *23*, 1195–1201; f) H. J. Krüger, R. H. Holm, *Inorg. Chem.* **1987**, *26*, 3645–3647; g) P. A. Connick, K. A. Macor, *Inorg. Chem.* **1991**, *30*, 4654–4663; h) T. J. Collins, T. R. Nichols, E. S. Uffelman, *J. Am. Chem. Soc.* **1991**, *113*, 4708–4709; i) F. Azevedo, M. A. Carrondo, B. Castro, M. Convery, D. Domingues, C. Freire, M. T. Duarte, K. Nielsen, I. C. Santos, *Inorg. Chim. Acta* **1994**, *219*, 43–54; j) D. Pinho, P. Gomes, C. Freire, B. De Castro, *Eur. J. Inorg. Chem.* **2001**, 1483–1493; k) B. De Castro, C. Freire, *Inorg. Chem.* **1990**, *29*, 5113–5119; l) C. Freire, B. De Castro, *J. Chem. Soc., Dalton Trans.* **1998**, 1491–1498; m) I. C. Santos, M. Vilas-Boas, M. F. M. Piedade, C. Freire, M. T. Duarte, B. De Castro, *Polyhedron* **2000**, *19*, 655–664; n) M. A. Carrondo,

 © 2007 Wiley-VCH Verlag GmbH & Co. KGaA, Weinheim 

B. De Castro, A. M. Coelho, D. Domingues, C. Freire, J. Morais, *Inorg. Chim. Acta* **1993**, *205*, 157–166; o) K. Nag, A. Chakravorty, *Coord. Chem. Rev.* **1980**, *33*, 87–147; p) Z. Xiao, B. O. Patrick, D. Dolphin, *Inorg. Chem.* **2003**, *42*, 8125–8127; q) P. J. Alonso, L. R. Falvello, J. Fornies, A. Martin, B. Menjon, G. Rodriguez, *Chem. Commun.* **1997**, 503–504; r) H.-J. Krüger, G. Peng, R. H. Holm, *Inorg. Chem.* **1991**, *30*, 734–742.

[6] Y. Shimazaki, F. Tani, K. Fukui, Y. Naruta, O. Yamauchi, *J. Am. Chem. Soc.* **2003**, *125*, 10512–10513.

[7] O. Rotthaus, O. Jarjayes, F. Thomas, C. Philouze, C. Perez Del Valle, E. Saint-Aman, J.-L. Pierre, *Chem. Eur. J.* **2006**, *12*, 2293–2302.

[8] R. Kannappan, S. Tanase, D. M. Tooke, A. L. Spek, I. Mutikainen, U. Turpeinen, J. Reedijk, *Polyhedron* **2004**, *23*, 2285–2291.

[9] E. R. Altwicker, *Chem. Rev.* **1967**, *67*, 475–531.

[10] a) L. Benisvy, E. Bill, A. J. Blake, D. Collison, E. S. Davies, C. D. Garner, G. McArdle, E. J. L. McInnes, J. McMaster, S. Ross, C. Wilson, *Dalton Trans.* **2006**, 258–267; b) It should be noted that an apparent typical "$Ni^{III}$" $g_{av}$ value of 2.13 has been obtained for an octahedral $Ni^{II}$ phenoxyl radical complex; the reported spectrum was in sharp contrast to that of a $Ni^{III}$ species and covered the 100–400 mT region and was assigned to an $S = 3/2$ ground state originating from strong intramolecular ferromagnetic coupling between the $Ni^{II}$ $S = 1$ and the radical $S = 1/2$ centres. See J. Müller, A. Kikuchi, E. Bill, T. Weyhermüller, P. Hildebrandt, L. Ould-Moussa, K. Wieghardt, *Inorg. Chim. Acta* **2000**, *297*, 265–277.

[11] a) T. Maki, Y. Araki, Y. Ishida, O. Onomura, Y. Matsumura, *J. Am. Chem. Soc.* **2001**, *123*, 3371–3372; b) F. Thomas, O. Jarjayes, H. Jamet, S. Hamman, E. Saint-Aman, C. Duboc, J.-L. Pierre, *Angew. Chem. Int. Ed.* **2004**, *43*, 594–597; c) L. Benisvy, R. Bittl, E. Bothe, C. D. Garner, J. McMaster, S. Ross, C. Teutloff, F. Neese, *Angew. Chem. Int. Ed.* **2005**, *44*, 5314–5317.

[12] A. H. Maki, N. Edelstein, A. Davidson, R. H. Holm, *J. Am. Chem. Soc.* **1964**, *86*, 4580–4587.

[13] X. Ottenwaelder, R. Ruiz-García, G. Blondin, R. Carasco, J. Cano, D. Lexa, Y. Journaux, A. Aukauloo, *Chem. Commun.* **2004**, 504–505.

[14] K. S. Min, T. Weyhermüller, E. Bothe, K. Wieghardt, *Inorg. Chem.* **2004**, *43*, 2922–2931.

[15] a) A. D. Becke, *Phys. Rev. A* **1988**, *38*, 3098–3100; b) J. P. Perdew, *Phys. Rev. B* **1986**, *33*, 8822–8824; c) E. J. Baerends, D. E. Ellis, P. Ros, *Chem. Phys.* **1973**, *2*, 41–51; d) C. Fonseca Guerra, J. G. Snijders, G. te Velde, E. J. Baerends, *Theor. Chem. Acc.* **1998**, *99*, 391–403; e) Scientific Computing and Modeling (SCM), Theoretical Chemistry, Vrije Universiteit Amsterdam, URL: http://www.scm.com; f) For details on the procedure for computing EPR parameters and ADF implementations, the reader is referred to the online documentation of ADF.[15e]

[16] a) F. Hartl, R. P. Groenestein, T. Mahabiersing, *Collect. Czech. Chem. Commun.* **2001**, *66*, 52–66; b) M. Krejčík, M. Daněk, F. Hartl, *J. Electroanal. Chem.* **1991**, *317*, 179–187.

[17] a) B. V. Nonius, *COLLECT*, Software Suite, Delft University, Delft, **2004**; b) G. M. Sheldrick, *SHELXS-97, Program for Crystal Structure Determination*, University of Göttingen, Germany, **1997**; c) G. M. Sheldrick, *SHELXL-97, Program for Crystal Structure Refinement*, University of Göttingen, Germany, **1997**.

Received: October 27, 2006
Published Online: January 8, 2007

 © 2007 Wiley-VCH Verlag GmbH & Co. KGaA, Weinheim 

DOI: 10.1002/ejic.200600915

# Polymorphism in an Aqua-Bridged, Dinuclear 2-Nitrobenzoate Complex of Cobalt(II)

**Anirban Karmakar,[a] Rupam J. Sarma,[a] and Jubaraj B. Baruah*[a]**

**Keywords:** Dinuclear cobalt complexes / Aqua-bridged complexes / Polymorphism / Conformers

Three polymorphs of a dinuclear, aqua-bridged cobalt complex with the composition $[Co_2(\mu\text{-}OH_2)(C_5H_5N)_4(\mu\text{-}O_2CC_6H_4\text{-}2\text{-}NO_2)_2(O_2CC_6H_4\text{-}2\text{-}NO_2)_2]$ are identified and the crystal structures are determined by X-ray crystallography. Selective crystallisation of the polymorphs can be achieved by controlling the reaction conditions as well as the crystallisation processes. The reaction of cobalt(II) acetate tetrahydrate with 2-nitrobenzoic acid followed by treatment with excess pyridine leads to a mononuclear complex with the composition $[Co(H_2O)_2(C_5H_5N)_2(O_2CC_6H_4\text{-}2\text{-}NO_2)_2]$.
(© Wiley-VCH Verlag GmbH & Co. KGaA, 69451 Weinheim, Germany, 2007)

## Introduction

Polymorphism of a molecule (or compound) may be related to the ability of it having different crystalline phases. The crystallisation process leading to a polymorph is generally sensitive to variation in the conditions of temperature, pressure and/or the manner in which the crystals are obtained.[1] Polymorphism in organic crystals,[2] including crystals of pharmaceutically active compounds,[3] is an active area of research, which is driven by the rationale that such a study would provide insight/understanding into the kinetic and thermodynamic factors that govern nucleation and crystal growth. Subsequently, this may enable us to gain control of the crystallisation process, and in particular, the production/exclusion of the specific polymorph. Studies have shown that interconversion between polymorphs is possible through the mechanochemical processing of solid compounds[4] or through the mixing of several components in the solid phase.[5] Consequently, aspects related to the synthesis, structure and polymorphism in metal coordination complexes is emerging as an active field of research.[6] In this communication, we report three polymorphs of an aqua–bridged, dinuclear cobalt(II) complex **1** and describe their synthetic and structural aspects. From a structural perspective, such aqua-bridged dinuclear cobalt(II) complexes may be regarded as synthetic mimics of the active sites of certain metalloenzymes[7] such as leucine aminopeptidase as they contain a dinuclear cobalt core that has an aqua as well as a carboxylate group as bridged ligands, along with monodentate nitrogen-containing ligands at two ends. This makes their study quite relevant. While the complex itself [having the same coordination environment about the two cobalt(II) ions] may be synthesised by grinding the solid reactants followed by solution processing or by solution processing alone, the polymorphs may be identified from differences in the relative orientation of the 2-nitrobenzoate groups that are coordinated to the cobalt(II) ions in the complex. A similar phenomenon is known for organic compounds,[8] but is less known for coordination complexes of cobalt(II) carboxylate compounds.[9a]

## Results and Discussion

We have found that the reaction of cobalt(II) chloride hexahydrate with 2-nitrobenzoic acid, sodium hydroxide and pyridine in methanol gives complex **1** [Equation (1)], which crystallises as pink rods in the triclinic space group $P\bar{1}$ (polymorph **I**).

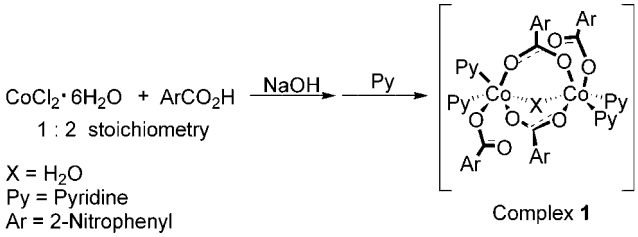


(1)

In this complex, each cobalt(II) ion is coordinated to a monodentate benzoate molecule and two pyridine molecules; the six-coordinate octahedral geometry is completed by two bridging 2-nitrobenzoate groups and a bridging aqua ligand. The monodentate 2-nitrobenzoate molecule is intramolecularly hydrogen bonded to the bridging aqua group {O(17)–H···O(14) [2.578(2) Å, 167(3)°] and O(17)–

[a] Department of Chemistry, Indian Institute of Technology Guwahati,
Guwahati 781039, Assam, India
E-mail: juba@iitg.ernet.in
Supporting information for this article is available on the WWW under http://www.eurjic.org or from the author.

 © 2007 Wiley-VCH Verlag GmbH & Co. KGaA, Weinheim 

H···O(2) [2.508(3) Å, 177(4)°]}. The corresponding Co(1)–O(17) and Co(2)–O(17) bond lengths are found to be 2.1255(15) and 2.1278(15) Å, respectively, while the Co(1)–O(17)–Co(2) bond angle is 114.55(7)°. Moreover, weak intramolecular C(6)–H···O(3) [3.255(4) Å, 158°], C(6)–H···O(1) [3.103(3) Å, 124°], C(10)–H···O(10) [3.104(4) Å, 125°], C(10)–H···O(12) [3.281(5) Å, 150°] and C(17)–H···O(5) [2.722(3) Å, 101°] interactions are also observed in this polymorph. These interactions stabilise the *out-out* orientation of the nitro groups of 2-nitrobenzoate ligand relative to the Co(1)–O(17)–Co(2) fragment in the complex. These molecules have a self-assembled structure in the lattice through weak C(14)–H···O(12) [3.429(4) Å, 158°] and C(2)–H···O(7) [3.279(5) Å, 139°] interactions, and the corresponding packing diagram is shown in Figure 2a. We have also found two other polymorphs of this compound, and the synthesis of these polymorphs is highly dependent on the reaction conditions, as illustrated in Scheme 1. The crystal structures of all the three polymorphs were determined and are shown in Figure 1.

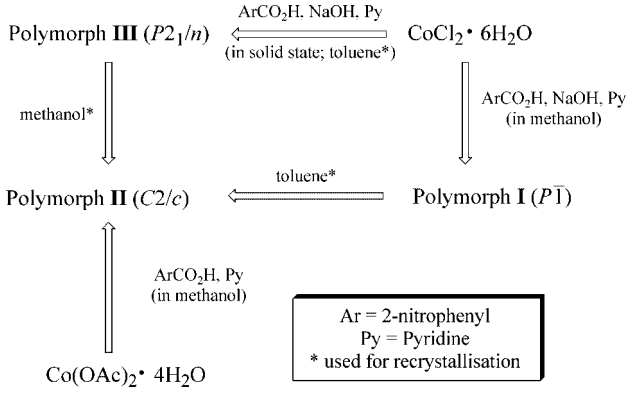


Scheme 1.

Complex **1** was also prepared by reaction of cobalt(II) acetate tetrahydrate with 2-nitrobenzoic acid and pyridine in methanol. However, this complex crystallises, from methanol, as pink plates in the monoclinic *C*2/*c* space group (polymorph **II**). In polymorph **II**, each cobalt(II) ion is coordinated to a monodentate 2-nitrobenzoate molecule and two pyridine molecules; two bridged 2-nitrobenzoate groups and the aqua bridge complete the six-coordinate octahedral geometry. The crystal structure of **II** shows that the complex is stabilised [such that the Co(1)···Co(1′) distance is 3.616(3) Å] by intramolecular hydrogen bonding between the monodentate 2-nitrobenzoate and bridging aqua groups {O(9)–H···O(2) [2.582(16) Å, 157°]}. The corresponding Co(1)···O(9) distance is 2.142(9) Å, while the Co(1)–O(9)–Co(1′) bond angle is 115.11(8)°. The packing structure of **II** is shown in Figure 2b, wherein the molecules are held in the lattice through weak intermolecular C3–H···O2 [3.229(3) Å, 156°] and C4–H···O4 [3.292 Å, 127°] interactions. In polymorph **II**, the nitro groups of each carboxylate ligand projects inwards and they therefore may be described as having *in-in* orientations.

Reaction of cobalt(II) chloride hexahydrate, 2-nitrobenzoic acid and sodium hydroxide in the solid state followed by addition of pyridine (in a 1:2:2 stoichiometry) also gave the dinuclear cobalt(II) complex **1**. This complex is soluble in toluene and could subsequently be crystallised as pink plates in the $P2_1/n$ space group (polymorph **III**). The packing diagram of this polymorph is given in Figure 2c.

It is noteworthy that in polymorph **I**, each of the nitro groups adopts an *out-out* orientation in the dinuclear cobalt(II) complex. On the other hand, polymorph **III** can be identified by two of the 2-nitrobenzoate groups adopting an *out-out* orientation and two adopting an *out-in* orientation relative to the Co–O–Co fragment. The corresponding powder XRD patterns of the polymorphs were recorded and compared with the calculated patterns, which substantiated our observation of distinct crystalline phases. Surprisingly, recrystallisation of polymorph **I** from methanol gave pink "square" plates, and structural analysis led to the identification of polymorph **II** (monoclinic *C*2/*c*). Similarly, recrystallisation experiments of polymorph **III** from toluene also gave pink "square" plates in the *C*2/*c* space group. Subsequently, we performed powder XRD analysis of the samples (see Supporting Information), which confirmed the

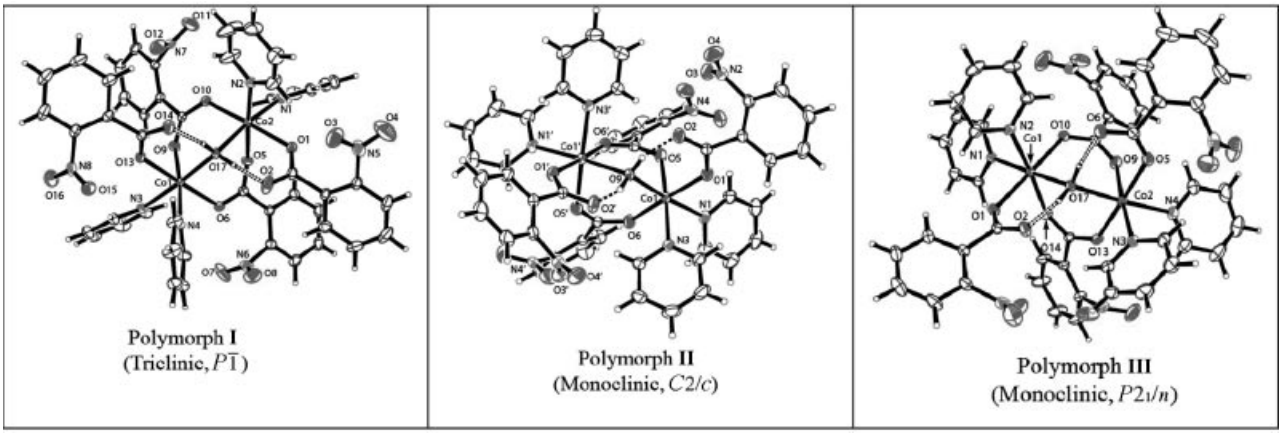


Figure 1. Crystal structures of three dinuclear polymorphs of **1** (30% thermal ellipsoid).

 © 2007 Wiley-VCH Verlag GmbH & Co. KGaA, Weinheim 

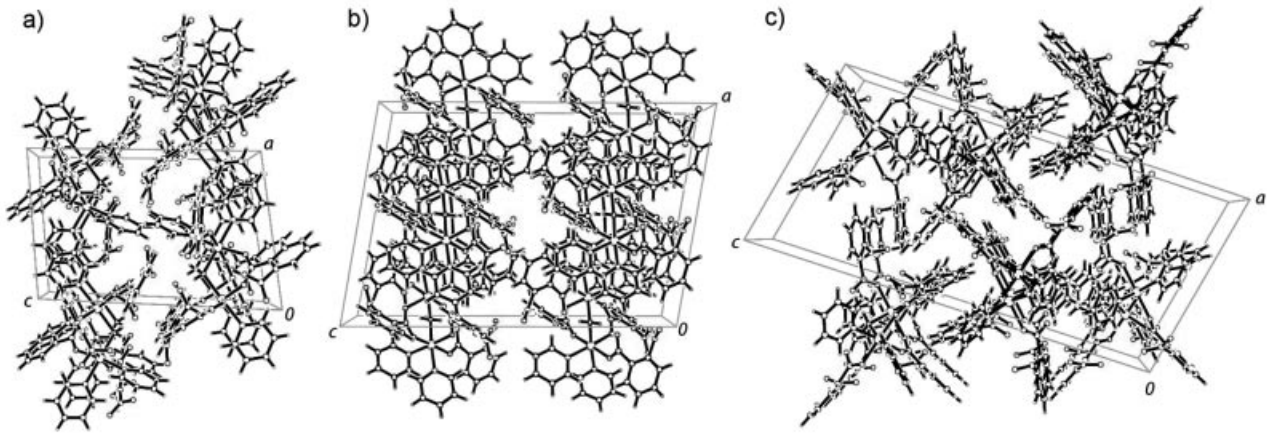


Figure 2. Packing structures of complex **1**: a) polymorph **I**, (b) polymorph **II** and (c) polymorph **III**.

conversion of both polymorphs **I** and **III** into **II**, as illustrated in Scheme 1.

A close inspection of the bond lengths (Table 1) in the three polymorphs of complex **1** shows that the coordination environment around each cobalt(II) ions is similar; the cobalt(II) ions are coordinated to a monodentate benzoate group and two N-donor pyridine ligands. The two cobalt(II) ions are bridged by two 2-nitrobenzoate ligands and an aqua group that is intramolecularly hydrogen bonded to the carboxyl group of the monodentate 2-nitrobenzoate.

Table 1. Selected bond lengths [Å] and angles [°] in **I**–**III**.[a]

| | Polymorph **I** ($P\bar{1}$) | Polymorph **II** ($C2/c$) | Polymorph **III** ($P2_1/n$) |
|---|---|---|---|
| Co(1)–O(X) | 2.120(1) | 2.091(1) | 2.127(2) |
| Co(1)–O(Y) | 2.114(1) | 2.108(1) | 2.086(2) |
| Co(1)–O(Y′) | 2.078(1) | 2.075(1) | 2.105(1) |
| Co(2)–O(X) | 2.148(1) | 2.091(1)[b] | 2.122(2) |
| Co(2)–O(Y) | 2.096(1) | 2.108(1)[b] | 2.063(2) |
| Co(2)–O(Y′) | 2.102(1) | 2.075(1)[b] | 2.076(2) |
| Co(1)–N′(#1) | 2.147(2) | 2.138(1) | 2.164(2) |
| Co(1)–N′′(#2) | 2.158(2) | 2.147(1) | 2.156(2) |
| Co(2)–N′(#1) | 2.151(2) | 2.138(1)[b] | 2.140(2) |
| Co(2)–N′(#2) | 2.146(2) | 2.147(1)[b] | 2.162(2) |
| Co(1)–O(aqua) | 2.126(2) | 2.142(8) | 2.136(2) |
| Co(2)–O(aqua) | 2.128(2) | 2.142(8)[b] | 2.157(2) |
| Co(1)···Co(2) | 3.578 | 3.616 | 3.651 |
| Co(1)–O–Co(2) | 114.55(7) | 115.12(7)[b] | 116.49(7) |

[a] X = (2-nitrobenzoate); Y, Y′ = μ-(2-nitrobenzoate). [b] $-x$, $y$, $-z+1/2$.

Each of the polymorphs (**I**–**III**) described above obtained from complex **1** shows broad signals centred at 3407 $cm^{-1}$ (O–H stretching) in their solid-state FTIR spectra. This apparently corresponds to the presence of intramolecular hydrogen-bonding interactions involving the 2-nitrobenzoate group and the bridging aqua ligand. Solid-state FTIR spectra of polymorphs **II** and **III** exhibit similar absorptions in the carbonyl C=O (1531 and 1635 $cm^{-1}$, respectively) and nitro N–O stretching regions (1364 and 1395 $cm^{-1}$, respectively). While the corresponding C=O absorptions of polymorph **I** are similar to those of **II** and **III**, the N–O stretching bands appear as a broad absorption at 1390 $cm^{-1}$ with a shoulder at about 1356 $cm^{-1}$.

In order to study the influence of the solvent on the crystallisation process, we performed the reaction of the cobalt(II) salts with 2-nitrobenzoic acid and sodium hydroxide in the presence of excess pyridine rather than by using the stoichiometric amount. In each case, two concomitant complexes were obtained both by solid-state synthesis and by solution processing. One of the complexes, which was obtained as orange prisms, turned out to be the mononuclear cobalt(II) complex **IV**, as depicted in Figure 3. The other complex was found to be the dinuclear complex **1** that crystallises as pink rods in the $P\bar{1}$ space group.

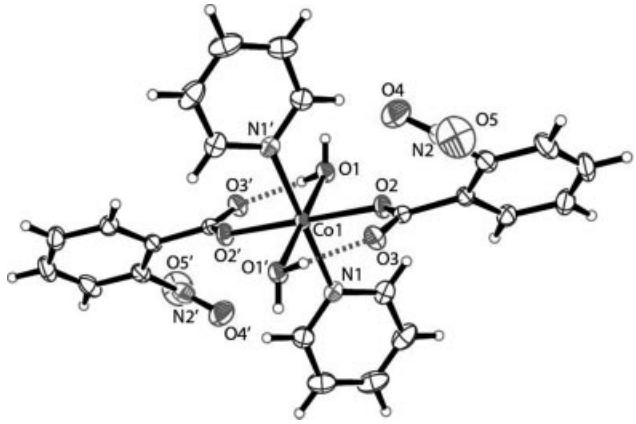


Figure 3. Structure of the mononuclear complex **IV**.

The mononuclear complex **IV** is formed preferentially during the reaction of cobalt(II) sulfate heptahydrate with 2-nitrobenzoic acid in the presence of sodium hydroxide and excess pyridine in methanol. Similarly, reactions of cobalt(II) chloride with 2-nitrobenzoic acid and sodium hydroxide in excess pyridine led to mononuclear complex **IV**, which suggests that the role of anion in the synthesis through the solution route is not prominent. However, the formation of polymorph **I** from the reaction of cobalt chloride with 2-nitrobenzoic acid in the presence of sodium hydroxide and pyridine and the formation of polymorph **II** directly from the reaction of cobalt(II) acetate with 2-nitrobenzoic acid and pyridine clearly indicates that the reaction conditions and the crystallisation procedures can influence

 © 2007 Wiley-VCH Verlag GmbH & Co. KGaA, Weinheim 

the formation and isolation of crystal(s) of the complexes with different orientations of the nitro groups. The polymorphs **I**–**III** isolated in this study are three conformers of several possible conformers that can be envisaged by imagining the dimeric core as a rigid unit and by fixing the 2-nitrophenyl groups in different orientations at two ends of the rigid unit – similar to those for cubane-type organic molecules with different orientations of nitro groups.[8b]

In conclusion, we have shown that depending on the method of synthesis and crystallisation, three distinct polymorphs (**I**–**III**) of an aqua–bridged, dinuclear 2-nitrobenzoate cobalt(II) complex **1** may be obtained. In this case, the formation of polymorphs originates from the orientations of the nitro group in the 2-nitrobenzoate units in the complex. The formation of the polymorphs is controlled by three factors: (a) the synthetic route (solid- or solution phase), (b) the solvent of crystallisation and (c) the stoichiometry of the auxiliary ligand pyridine.

## Experimental Section

X-ray crystallographic data were collected at 296 K with a Mo-$K_\alpha$ radiation source ($\lambda$ = 0.71073 Å) by using a Bruker Nonius SMART CCD diffractometer equipped with a graphite monochromator. The SMART software was used for data collection, for indexing the reflections and for determining the unit cell parameters; the collected data were integrated by using the SAINT software. The structures were solved by direct methods and refined by full-matrix least-squares calculations ($F^2$) by using the SHELXTL-97 software. All non-H atoms were refined in the anisotropic approximation against $F^2$ for all reflections. All H atoms, except those attached to O atoms, were placed at their calculated positions and refined in the isotropic approximation; those attached to heteroatoms were located in the difference Fourier maps and refined with isotropic displacement coefficients. Crystal data for the cobalt complexes is given in Table 2. CCDC-619774, CCDC-619773, CCDC-608665 and CCDC-620812 (for compounds **I**–**IV**) contain the supplementary crystallographic data for this paper. These data can be obtained free of charge from The Cambridge Crystallographic Data Centre via www.ccdc.cam.ac.uk/data_request/cif.

**Synthesis of Polymorphs I:** 2-Nitrobenzoic acid (0.34 g, 2 mmol) was dissolved in methanol (10 mL) and sodium hydroxide (0.081 g, 2 mmol) was added to it. The mixture was stirred vigorously for 5 min, and cobalt(II) chloride hexahydrate (0.238 g, 1 mmol) was then added. The reaction mixture became pink, and subsequently pyridine (0.158 g, 2 mmol) was added. The solution was filtered, and the pink filtrate was kept at room temperature. Pink, rodlike crystals were obtained after 3 d, which were then collected and dried in air. Yield 44% (based on Co).

**Synthesis of Polymorph II:** 2-Nitrobenzoic acid (0.34 g, 2 mmol) was added to a solution of cobalt acetate tetrahydrate (0.249 g, 1 mmol) in methanol (20 mL), and the mixture was stirred overnight. To this solution, pyridine (0.158 g, 2 mmol) was added, and the mixture stirred for 10 min. On standing for 2 d, square–shaped, pink crystals were obtained from the reaction mixture. Yield 41% (based on Co).

**Synthesis of Polymorph III:** 2-Nitrobenzoic acid (0.34 g, 2 mmol), sodium hydroxide (0.081 g, 2 mmol) and $CoCl_2{\cdot}6H_2O$ (0.238 g, 1 mmol) was finely ground with a mortar and pestle and heated at 100 °C for 15 min – the pink colour turns to blue. The reaction mixture was cooled to room temperature and transferred into a

Table 2. Crystal parameters and refinement data for polymorphs **I**–**III** and complex **IV**.

| | **I** | **II** | **III** | **IV** |
|---|---|---|---|---|
| Formula | $C_{48}H_{38}Co_2N_8O_{17}$ | $C_{48}H_{38}Co_2N_8O_{17}$ | $C_{48}H_{38}Co_2N_8O_{17}$ | $C_{24}H_{22}CoN_4O_{10}$ |
| $M_w$ | 1116.72 | 1116.72 | 1116.72 | 585.39 |
| Crystal system | triclinic | monoclinic | monoclinic | triclinic |
| Space group | $P\bar{1}$ | $C2/c$ | $P2_1/n$ | $P\bar{1}$ |
| Temperature [K] | 296 | 296 | 296 | 296 |
| Wavelength [Å] | 0.71073 | 0.71073 | 0.71073 | 0.71073 |
| $a$ [Å] | 11.8668(2) | 16.0312(3) | 13.6133(4) | 7.2206(5) |
| $b$ [Å] | 13.8387(2) | 13.5441(3) | 13.3201(4) | 8.5518(6) |
| $c$ [Å] | 17.8115(3) | 23.7144(5) | 28.6728(9) | 11.0026(7) |
| $\alpha$ [°] | 68.727(10) | 90 | 90 | 97.169(1) |
| $\beta$ [°] | 75.229(10) | 99.850(10) | 101.746(2) | 98.233(1) |
| $\gamma$ [°] | 66.628(10) | 90 | 90 | 108.126(1) |
| $V$ [Å$^3$] | 2480.91(7) | 5073.16(18) | 5090.4(3) | 628.59(7) |
| $Z$ | 2 | 4 | 4 | 1 |
| Density [Mg m$^{-3}$] | 1.495 | 1.462 | 1.457 | 1.546 |
| Abs. coeff. [mm$^{-1}$] | 0.750 | 0.734 | 0.731 | 0.748 |
| Abs. correction | none | none | none | none |
| $F$(000) | 1144 | 2288 | 2288 | 301 |
| Total no. of reflections | 29432 | 23519 | 60000 | 4750 |
| max. 2$\theta$ [°] | 28.28 | 28.27 | 28.21 | 25.9 |
| Ranges ($h$, $k$, $l$) | $-15 \le h \le 15$ | $-21 \le h \le 21$ | $-17 \le h \le 17$ | $-8 \le h \le 8$ |
| | $-18 \le k \le 18$ | $-17 \le k \le 12$ | $-17 \le k \le 17$ | $-10 \le k \le 10$ |
| | $-23 \le l \le 21$ | $-31 \le l \le 29$ | $-38 \le l \le 35$ | $-12 \le l \le 13$ |
| Completeness to 2$\theta$ [%] | 95.0 | 95.5 | 99.1 | 89.9 |
| Refinement method | full-matrix least-squares on $F^2$ | full-matrix least-squares on $F^2$ | full-matrix least-squares on $F^2$ | full-matrix least-squares on $F^2$ |
| Data/restraints/parameters | 11705/0/684 | 5991/0/339 | 12446/0/684 | 2221/0/187 |
| Goof ($F^2$) | 1.019 | 0.942 | 1.006 | 1.006 |
| $R$ indices [$I > 2\sigma(I)$] | 0.0384 | 0.0323 | 0.0417 | 0.0254 |
| $R$ indices (all data) | 0.0921 | 0.0632 | 0.0787 | 0.0616 |

 © 2007 Wiley-VCH Verlag GmbH & Co. KGaA, Weinheim 

round-bottomed flask, and toluene (20 mL) was added to it. The heterogeneous mixture was stirred at room temperature for 5 min followed by the addition of pyridine (0.158 g, 2 mmol). The blue supernatant liquid turned pink. The residue was filtered off, and the pink filtrate was left undisturbed. Pink crystals were collected after 3 d and dried in air. Yield: 34% (based on Co). IR (KBr): $\tilde{\nu}$ = 3412 (b), 3076 (ms), 1636 (s), 1603 (ms), 1531 (s), 1447 (ms), 1395 (s), 1218 (ms), 1154 (ms), 1040 (ms), 821 (s), 735 (s), 700 (s) $cm^{-1}$. Magnetic moment: 6.56 BM at 25 °C. UV/Vis: $\lambda_{max}$ ($\varepsilon$, $M^{-1} cm^{-1}$) = 521 nm (39.23).

**Synthesis of IV:** 2-Nitrobenzoic acid (0.34 g, 2 mmol) was dissolved in methanol (20 mL), and to this solution, sodium hydroxide (0.08 g, 2 mmol) was added. After 10 min of stirring, cobalt(II) sulfate heptahydrate (0.281 g, 1 mmol) was added to the solution, and the heterogeneous mixture was stirred for 30 min. To this heterogeneous mass, pyridine (0.15 g, 2 mmol) was added, and the mixture stirred for 10 min. The residue was filtered and discarded. Orange crystals were collected after 4 d from the filtrate. The crystals were collected and dried in air. Yield: 51% (based on Co). $\mu_{eff}$ = 3.952 BM at 25 °C. IR (KBr): $\tilde{\nu}$ = 3414 (wb), 3064 (w), 1604 (m), 1582 (s), 1555 (s), 1526 (s), 1484 (m), 1448 (s), 1400 (s), 1356 (s), 1303 (w), 1069 (w), 1041 (w), 911 (wb), 818 (s), 759 (w), 738 (s), 695 (s) $cm^{-1}$. UV/Vis (methanol): $\lambda_{max}$ ($\varepsilon$, $M^{-1} cm^{-1}$)= 515 nm (6.7).

**Supporting Information** (see footnote on the first page of this article): The X-ray powder diffraction pattern of polymorphs **I**–**III** and the solid-state FTIR spectra of the polymorphs **I**–**III** are given.

## Acknowledgments

The authors acknowledge DST for financial support, while R. J. S. acknowledges CSIR (India) for a Research Fellowship.

[1] a) I. Weissbuch, M. Lahav, L. Leiserowitz, *Cryst. Growth Des.* **2003**, *3*, 125–150; b) J. A. R. P. Sarma, G. R. Desiraju in *Crystal Engineering: The Design and Application of Functional Solids* (Eds.: K. R. Seddon, M. J. Zaworotko), Kluwer, Dordrecht, **1999**, vol. 539, pp. 325–356; c) J. Bernstein in *Polymorphism in Molecular Crystals*, Oxford University Press, **2002**; d) N. Blagden, R. J. Davey, *Cryst. Growth Des.* **2003**, *3*, 873–885.

[2] a) A. Dey, G. R. Desiraju, *CrystEngComm* **2006**, 478–482; b) J. Bernstein, R. J. Davey, J.-O. Henck, *Angew. Chem. Int. Ed.* **1999**, *38*, 3440–3461; c) G. S. McGrady, M. Odlyha, P. D. Prince, J. W. Steed, *CrystEngComm* **2002**, 271–276; d) R. J. Sarma, J. B. Baruah, *Chem. Eur. J.* **2006**, *12*, 4994–5000; e) R. J. Davey, N. Blagden, G. D. Potts, R. Docherty, *J. Am. Chem. Soc.* **1997**, *119*, 1767–1772.

[3] a) O. Almarsson, M. J. Zaworotko, *Chem. Commun.* **2004**, 1889–1894; b) T. Beyer, G. M. Day, S. L. Price, *J. Am. Chem. Soc.* **2001**, *123*, 5086–5094.

[4] a) C. M. Reddy, S. Basavoju, G. R. Desiraju, *Chem. Commun.* **2005**, 2439–2441; b) J. A. McMahon, M. J. Zaworotko, J. F. Remenar, *Chem. Commun.* **2004**, 278–279; c) A. V. Trask, N. Shan, W. D. S. Motherwell, W. Jones, S. Feng, R. B. H. Tan, K. J. Carpenter, *Chem. Commun.* **2005**, 880–882.

[5] a) F. Calderazzo, L. Labella, F. Marchetti, *J. Chem. Soc., Dalton Trans.* **1998**, 1485–1490; b) D. Braga, G. Cojazzi, A. Abati, L. Maini, M. Polito, L. Scaccianoce, F. Grepioni, *J. Chem. Soc., Dalton Trans.* **2000**, 3969–3975.

[6] a) B. Moulton, M. J. Zaworotko, *Chem. Rev.* **2001**, *101*, 1629–1658; b) K. M. Fromm, J. L. S. Doimeadios, A. Y. Robin, *Chem. Commun.* **2005**, 4548–4550; c) D. Braga, F. Grepioni, *Chem. Commun.* **2005**, 3635–3645; d) K. M. Fromm, E. D. Gueneau, A. Y. Robin, W. Maudez, J. Sague, B. Remi, *Z. Anorg. Allg. Chem.* **2005**, *631*, 1725–1740; e) J. A. Bis, P. Visheshwar, R. A. Middleton, M. J. Zaworotoko, *Cryst. Growth Des.* **2006**, *6*, 1048–1053; f) D. Barga, F. Grepioni, S. Ellena, R. Gobetto, *Organometallics* **2006**, *25*, 4627–4633.

[7] a) R. C. Holz, *Coord. Chem. Rev.* **2002**, *232*, 5–26; b) D. Lee, P.-L. Hung, B. Spingler, S. J. Lippard, *Inorg. Chem.* **2002**, *41*, 521–531; c) D. E. Wilcox, *Chem. Rev.* **1996**, *96*, 2435–2458.

[8] a) L. Yu, G. A. Stephenson, C. A. Mitchell, C. A. Bunnell, S. V. Snorek, J. J. Bowyer, T. B. Borchardt, J. G. Stowell, S. R. Byrn, *J. Am. Chem. Soc.* **2000**, *122*, 585–591; b) P. E. Eaton, K. Pramod, T. Emrick, R. Gilardi, *J. Am. Chem. Soc.* **1999**, *121*, 4111–4123.

[9] a) A. Karmakar, R. J. Sarma, J. B.Baruah, *Polyhedron*, in press; b) A. Karmakar, K. Deka, R. J. Sarma, J. B. Baruah, *Inorg. Chem. Commun.* **2006**, *9*, 836–838.

Received: September 28, 2006
Published Online: January 4, 2007

 © 2007 Wiley-VCH Verlag GmbH & Co. KGaA, Weinheim 

DOI: 10.1002/ejic.200601083

# Synthesis and Characterization of the First Silver Complexes with Antimony Anions

**Dieter Fenske,*[a] Alexander Rothenberger,[a,b] and Stephan Wieber[b]**

*Dedicated to Joachim Strähle on the occasion of his 70th birthday*

**Keywords:** Silver / Antimony / Clusters

The synthesis and characterization of the silver antimony complexes $[Ag_{12}\{Sb(SiMe_3)\}_6(PiPr_3)_6]$ (**1**), $[Ag_4(Sb_4Ph_4)_2(PiPr_3)_4]$ (**2**) and $[Ag_4(Sb_6Ph_6)_2(PnBu_3)_4]$ (3) is reported.

(© Wiley-VCH Verlag GmbH & Co. KGaA, 69451 Weinheim, Germany, 2007)

## Introduction

In 1989 Cowley et al. had synthesized the first copper complex containing an antimony anion by the metathesis reaction of a $Cu^I$ salt with lithium dimesitylantimonide.[1] More recent developments in the area of complexes containing antimony anions represent the discovery of a new class of compounds with unstoichiometric mixtures of Cu and Sb atoms and a range of novel group 13 metal complexes.[2,3] The synthesis of complexes e.g., $[Cu_{40}Sb_{12}(PMe_3)_{20}]$ and $[Cu_{45}Sb_{16}(PEt_2Me)_{16}]$, was achieved by reactions of silylated stibanes with phosphane complexes of $Cu^I$ salts. For the heavier coinage metals, only very few complexes with stibanes as ligands are known and a common feature of them is the interaction of the coinage metal (Ag or Au) with the lone pair of a neutral trisubstituted stibane.[4]

In contrast to antimony, several examples for arsenic anions bridging silver or gold centres are known.[5] The silver arsinidene cluster $[Ag_{14}(AsPh)_6Cl_2(PEt_3)_8]$ or the isostructural complexes $[Ag_4(As_4Ph_4)_2(PEt_3)_4]$ and $[Au_4(As_4Ph_4)_2(PnPr_3)_4]$ can be obtained by the reaction of coinage metal salts with $PhAs(SiMe_3)_2$ in the presence of tertiary phosphanes.[6] This prompted us to attempt the synthesis of silver and gold complexes containing antimony anions. In the following first results of mixed-metal Ag/Sb complexes are described.

[a] Institut für Anorganische Chemie, Universität Karlsruhe, Geb. 30.45,
Engesserstr. 15a, 76131 Karlsruhe
E-mail: dieter.fenske@chemie.uni-karlsruhe.de
[b] Institut für Nanotechnologie, Forschungszentrum Karlsruhe GmbH,
P. O. Box 3640, 76021 Karlsruhe, Germany

## Results and Discussion

The reactions of silver nitrate with stibanes produced the silver antimony compounds $[Ag_{12}\{Sb(SiMe_3)\}_6(PiPr_3)_6]$ (**1**), $[Ag_4(Sb_4Ph_4)_2(PiPr_3)_4]$ (**2**) and $[Ag_4(Sb_6Ph_6)_2(PnBu_3)_4]$ (**3**) (Scheme 1).

$$AgNO_3 + Sb(SiMe_3)_3 \xrightarrow{PiPr_3} [Ag_{12}(SbSiMe_3)_6(PiPr_3)_6]\ (\mathbf{1})$$

$$AgNO_3 + PhSb(SiMe_3)_2 \xrightarrow{PiPr_3} [Ag_4(Sb_4Ph_4)_2(PiPr_3)_4]\ (\mathbf{2})$$

$$AgNO_3 + PhSb(SiMe_3)_2 \xrightarrow{PnBu_3} [Ag_4(Sb_6Ph_6)_2(PnBu_3)_4]\ (\mathbf{3})$$

Scheme 1. Synthesis of the Ag/Sb complexes **1**, **2** and **3**.

The complex **1** crystallizes from diethyl ether as orange blocks in the trigonal space group $P\bar{3}$ with three molecules in the unit cell. It can be described by a distorted triangular antiprism of antimony atoms in which every edge is capped by a silver atom (Ag1) (Figure 1). The other six silver atoms (Ag2) are coordinated by phosphane ligands.

On each Sb atom a trimethylsilyl group is retained. The Sb–Si bond length of 2.527(1) Å is in the range of commonly observed Sb–Si bond lengths.[2] The Sb–Ag distances in **1** are also similar to reported average Ag–Sb distances of 2.72 Å in 75 compounds with most of them of the general type $[R_3Sb–AgX]$ (R = organic group, X = anion).[7,8] The stability of the cluster compounds increased when $PhSb(SiMe_3)_2$ was used as antimony source. By the reaction of $AgNO_3$ with $PhSb(SiMe_3)_2$ and four equivalents of $PiPr_3$ in diethyl ether the cluster compound $[Ag_4(Sb_4Ph_4)_2(PiPr_3)_4]$ (**2**) is obtained as red crystals together with colourless blocks of the silver phosphane complex $[Ag(NO_3)(PiPr_3)_2]$ (Table 1) and $[PhSb]_6$.[9] **2** crystallizes in the triclinic space group $P\bar{1}$ with one molecule in the unit cell and

 © 2007 Wiley-VCH Verlag GmbH & Co. KGaA, Weinheim 

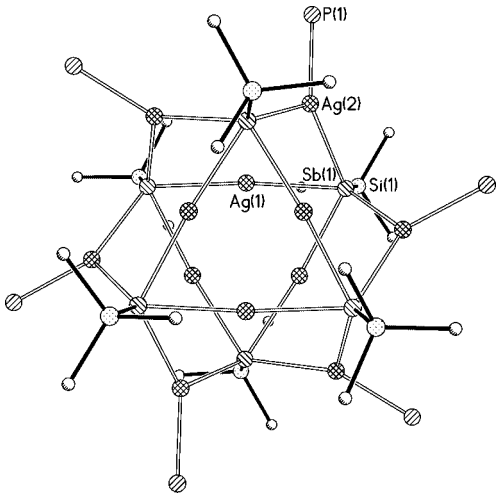


Figure 1. Molecular structure of **1** in the crystal (without C atoms of phosphane ligands and disordered components). Selected bond lengths [Å] and angles [°]: Sb(1)–Ag(1) 2.7183(6), Sb(1)–Ag(2) 2.754(1), Si(1)–Sb(1) 2.527(1), Ag(1)···Ag(2) 2.902(1), Ag(2)–P(1) 2.446(2), Si(1)–Sb(1)–Ag(1) 104.53(4), Si(1)–Sb(1)–Ag(2) 119.56(4), Ag(1)–Sb(1)–Ag(2) 64.04(3), Sb–Ag(1)–Sb 171.86(2), P(1)–Ag(2)–Sb(1) 133.90(5).

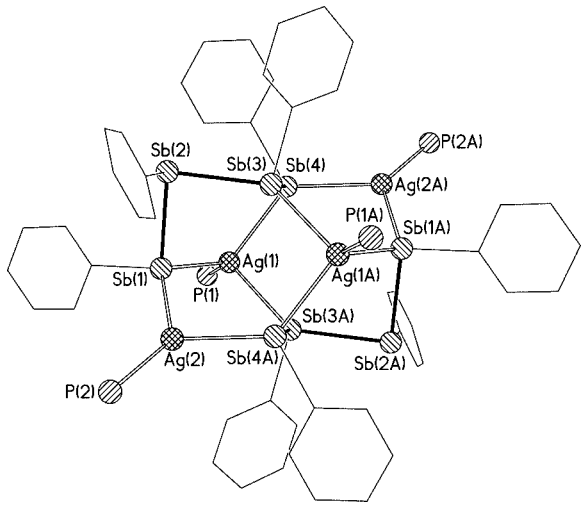


Figure 2. Molecular structure of **2** in the crystal (without C atoms of phosphane ligands). Final label letter A denotes the symmetry operation $-x, -y, -z+1$. Selected bond lengths [Å] and angles [°]: Sb(1)–Ag(2) 2.7220(10), Sb(1)–Ag(1) 2.7452(12), Sb(1)–Sb(2) 2.7987(11), Sb(2)–Sb(3) 2.8301(11), Sb(3)–Sb(4) 2.8031(12), Sb(3)–Ag(1A) 2.8567(12), Sb(4)–Ag(2A) 2.7144(11), Sb(4)–Ag(1) 2.7463(10), Ag(1)–P(1) 2.454(2), Ag(2)–P(2) 2.430(2), Ag(2)–Sb(1)–Ag(1) 118.18(3), Ag(2)–Sb(1)–Sb(2) 112.04(3), Ag(1)–Sb(4)–Sb(3) 92.09(3), Ag(1)–Sb(1)–Sb(2) 98.29(3), Sb(1)–Sb(2)–Sb(3) 89.24(3), Sb(4)–Sb(3)–Sb(2) 95.32(3), P(1)–Ag(1)–Sb(1) 119.41(6), P(1)–Ag(1)–Sb(4) 116.69(6), Sb(1)–Ag(1)–Sb(4) 109.63(4), P(1)–Ag(1)–Sb(3A) 118.84(7), Sb(1)–Ag(1)–Sb(3A) 92.43(3), Sb(4)–Ag(1)–Sb(3A) 95.03(3), P(2)–Ag(2)–Sb(4A) 128.74(7), P(2)–Ag(2)–Sb(1) 133.03(7), Sb(4A)–Ag(2)–Sb(1) 98.15(3).

two lattice-bound ether molecules (Figure 2). The molecular structure of **2** is isostructural to the structure of $[Ag_4(As_4Ph_4)_2(PEt_3)_4]$ in the solid state.[6]

The structure of **2** can be described as a centrosymmetric dimer of a $[(PhSb)_4]^{2-}$ anion and two Ag-phosphane units. Each $[(PhSb)_4]^{2-}$ anion chelates Ag(1,1A) by terminal Sb atoms. Ag(2) is coordinated by Sb atoms of different anions. The longest Ag–Sb bond in **2**, which is observed between Sb(3) and Ag(1A), corresponds to distances commonly observed between neutral stibanes and $Ag^I$ centres.[4a,4b] These interactions are slightly longer than bonds between silver and terminal antimony atoms. The coordination sphere of the four silver atoms is completed by additional P*i*Pr$_3$ ligands. The formation of the $[(PhSb)_4]^{2-}$ anion in **2** is intriguing, and it is currently assumed that **2** represents an intermediate of the $Ag^I$-induced oxidation of $PhSb(SiMe_3)_2$ to *cyclo*-$[PhSb]_6$. The Sb–Sb distances are in the range of reported Sb–Sb bond lengths of about 2.8 Å.[9]

Table 1. Details of the X-ray data collection and refinements.

| Compound | **1** | **2** | **3** | $[Ag(NO_3)(PiPr_3)_2]$ |
|---|---|---|---|---|
| Formula | $C_{72}H_{180}Ag_{12}P_6Sb_6Si_6$ | $C_{92}H_{144}Ag_4O_2P_4Sb_8$ | $C_{120}H_{168}Ag_4P_4Sb_{12}$ | $C_{18}H_{42}AgNO_3P_2$ |
| Formula weight | 3425.46 | 2811.43 | 3626.90 | 490.34 |
| $T$ [K] | 100(2) | 110(2) | 150(2) | 150(2) |
| Crystal system | trigonal | triclinic | triclinic | triclinic |
| Space group | *R*-3 | $P\bar{1}$ | $P\bar{1}$ | $P\bar{1}$ |
| $a$ [Å] | 18.589(3) | 13.176(4) | 15.980(2) | 8.3773(5) |
| $b$ [Å] | 18.589(3) | 14.823(3) | 16.758(3) | 10.0485(7) |
| $c$ [Å] | 31.487(6) | 15.128(4) | 24.559(4) | 14.485(1) |
| $\alpha$ [°] | 90 | 65.508(19) | 90.793(12) | 95.259(6) |
| $\beta$ [°] | 90 | 77.09(2) | 90.689(12) | 95.940(6) |
| $\gamma$ [°] | 120 | 86.72(2) | 90.960(12) | 98.329(6) |
| $V$ [Å$^3$] | 9423(3) | 2618.7(12) | 6574.7(17) | 1192.93(14) |
| $Z$ | 3 | 1 | 2 | 1 |
| $\mu$ [mm$^{-1}$] | 3.251 | 2.858 | 3.091 | 0.994 |
| $F$(000) | 4968 | 1368 | 3496 | 516 |
| Reflections collected | 22270 | 15930 | 43872 | 9274 |
| Unique data | 4122 | 9536 | 26763 | 5197 |
| $R_{int}$ | 0.0499 | 0.0631 | 0.0454 | 0.0518 |
| Parameters | 159 | 509 | 673 | 238 |
| $wR_2$ (all data) | 0.0950 | 0.0992 | 0.1499 | 0.1160 |
| $R_1$ [$I > 2\sigma(I)$] | 0.0364 | 0.0450 | 0.0570 | 0.0333 |

 © 2007 Wiley-VCH Verlag GmbH & Co. KGaA, Weinheim 

The use of the phosphane P*n*Bu$_3$ instead of P*i*Pr$_3$ leads to the cluster compound [Ag$_4$(Sb$_6$Ph$_6$)$_2$(P*n*Bu$_3$)$_4$] (**3**). Compound **3** crystallizes in the triclinic space group $P\bar{1}$ with two molecules in the unit cell (Figure 3).

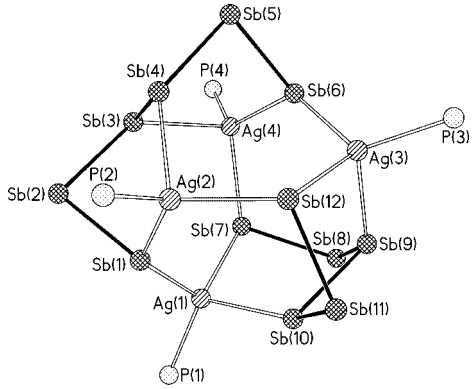


Figure 3. Molecular structure of **3** in the crystal (without organic substituents). Selected bond lengths [Å] and angles [°]: Sb(1)–Ag(2) 2.7462(11), Sb(1)–Ag(1) 2.7635(10), Sb(3)–Ag(4) 2.9944(10), Sb(4)–Ag(2) 2.9331(12), Sb(6)–Ag(4) 2.7433(10), Sb(6)–Ag(3) 2.7853(11), Sb(7)–Ag(1) 2.7248(11), Sb(7)–Ag(4) 2.7620(12), Sb(1)–Sb(2) 2.8012(10), Sb(2)–Sb(3) 2.8234(10), Sb(3)–Sb(4) 2.8446(10), Sb(4)–Sb(5) 2.8197(10), Sb(5)–Sb(6) 2.7868(10), Sb(7)–Sb(8) 2.7946(9), Sb(8)–Sb(9) 2.8161(10), Sb(9)–Sb(10) 2.8359(11), Sb(9)–Ag(3) 2.9445(11), Sb(10)–Sb(11) 2.8354(10), Sb(10)–Ag(1) 2.9237(11), Sb(11)–Sb(12) 2.8035(11), Sb(12)–Ag(2) 2.7631(10), Sb(12)–Ag(3) 2.7666(11), Ag–P 2.459(3)–2.481(3), Sb–Sb–Sb 88.06(3)–92.95(3).

The molecular structure of **3** consists like **2** of two *oligo*-[(PhSb)$_6$]$^{2-}$ anions and four Ag atoms. Compound **3**, however, represents, in comparison to **2**, an intermediate where the [PhSb]$_6$ chain is preformed at metal centres and "ready to cyclize" to *cyclo*-[PhSb]$_6$, which is formed in all the investigated reactions between Ag$^{I}$ salts and PhSb(SiMe$_3$)$_2$. The almost tetrahedral arrangement of the four Ag atoms in **3** is favoured by the sterically demanding anions over the centrosymmetric arrangement in the solid-state structure of **2** or other possibilities. Each of the [(PhSb)$_6$]$^{2-}$ anions in **3** chelates two Ag atoms forming five-membered rings as observed in **2** and all Ag atoms are coordinated by Sb atoms of both dianions. Bond lengths between silver atoms and inner antimony atoms in **3** are ca. 0.2 Å longer than distances Ag–Sb(terminal).

## Conclusions

In this contribution the first examples of silver complexes containing antimony anions are reported. A common feature of the compounds is their thermal instability and rather difficult syntheses. Currently, attempts are made to optimise the reactions towards a selective formation of a particular complex in high yield in order to allow subsequent investigations of physical properties.

## Experimental Section

**General Remarks:** All operations were carried out under purified nitrogen. Hexane and diethyl ether were dried with LiAlH$_4$ and freshly distilled. AgNO$_3$ and P*n*Bu$_3$ were purchased from Sigma–Aldrich. P*n*Bu$_3$ was distilled prior use. P*i*Pr$_3$, PhSb(SiMe$_3$)$_2$ and Sb(SiMe$_3$)$_3$ were prepared according to published procedures.[10]

**1:** AgNO$_3$ (0.18 g, 1.06 mmol) was dissolved in Et$_2$O (15 mL) and P*i*Pr$_3$ (0.79 mL, 4.2 mmol) by briefly heating to reflux. The clear, colourless solution was cooled to –78 °C and Sb(SiMe$_3$)$_3$ (1.467 mL, 0.66 mmol, 0.45 mol/L in hexane) was added. The brown reaction mixture was stored at –78 °C for four days. Sensitive red crystals of **1** could be isolated for crystallographic measurements.

**2:** AgNO$_3$ (0.18 g, 1.06 mmol) was dissolved in Et$_2$O (15 mL) and P*i*Pr$_3$ (0.79 mL, 4.2 mmol) by briefly heating to reflux. The clear, colorless solution was cooled to –78 °C and PhSb(SiMe$_3$)$_2$ (0.27 mL) was added. The brown reaction mixture was stored at –78 °C for one day. Then it was warmed up to –40 °C. After one week red crystals of **2** besides colourless crystals of the silver phosphane complex could be isolated for crystallographic measurements.

**3:** AgNO$_3$ (0.18 g, 1.06 mmol) was dissolved in Et$_2$O (15 mL) and P*i*Pr$_3$ (0.79 mL, 4.2 mmol) by briefly heating to reflux. The clear, colorless solution was cooled to –78 °C and PhSb(SiMe$_3$)$_2$ (0.27 mL) was added. The brown reaction mixture was stored at –78 °C for one day. Then it was warmed up to –8 °C. After three weeks red crystals of **3** could be isolated for crystallographic measurements.

Due to thermal instability of **1**–**3** (slow decomposition even at –80 °C) characterization was restricted to X-ray crystallography.

**X-ray Crystallographic Study:** Data were collected with a STOE IPDS II diffractometer by using graphite-monochromated Mo-$K_\alpha$ radiation ($\lambda$ = 0.71073 Å). The structures were solved by direct methods and refined by full-matrix least-squares on $F^2$ (all data) using the SHELXTL programme package (Table 1).[11] Hydrogen atoms were placed in calculated positions, non-hydrogen atoms were assigned anisotropic thermal parameters. Disordered components were refined with isotropic thermal parameters.

CCDC-627012 to -627014 and CCDC-627632 contain the supplementary crystallographic data for this paper. These data can be obtained free of charge from The Cambridge Crystallographic Data Centre via www.ccdc.cam.ac.uk/data_request/cif.

## Acknowledgments

We gratefully acknowledge the DFG Center for Functional Nanostructures, the Forschungszentrum Karlsruhe and the Fonds der Chemischen Industrie for financial support.

[1] A. H. Cowley, R. A. Jones, C. M. Nunn, D. L. Westmoreland, *Angew. Chem.* **1989**, *101*, 1089–1090; *Angew. Chem. Int. Ed. Engl.* **1989**, *28*, 1018–1019.
[2] R. Ahlrichs, D. Fenske, M. McPartlin, A. Rothenberger, C. Schrodt, S. Wieber, *Angew. Chem.* **2005**, *117*, 4002–4005; *Angew. Chem. Int. Ed. Engl.* **2005**, *44*, 3932–3936.
[3] S. Schulz, F. Thomas, M. Nieger, *Chem. Commun.* **2006**, 1860–1861.
[4] a) A. M. Hill, W. Levason, M. Webster, *Inorg. Chem.* **1996**, *35*, 3428–3430; b) A. Cingolani, E. Effendy, J. V. Hanna, M. Pellei, C. Pettinari, C. Santini, B. W. Skelton, A. H. White, *Inorg. Chem.* **2003**, *42*, 4938–4948; c) Au–Sb: J. Vicente, A. Arcas, P. G. Jones, J. Lautner, *J. Chem. Soc., Dalton Trans.* **1990**, 451–456.
[5] a) P. Sevillano, O. Fuhr, M. Kattannek, P. Nava, O. Hampe, S. Lebedkin, R. Ahlrichs, D. Fenske, M. Kappes, *Angew. Chem.*

 © 2007 Wiley-VCH Verlag GmbH & Co. KGaA, Weinheim 

**2006**, *118*, 3785–3791; *Angew. Chem. Int. Ed. Engl.* **2006**, *45*, 3702–3708; b) D. Fenske, W. Holstein, *Angew. Chem.* **1994**, *106*, 1311–1312; *Angew. Chem. Int. Ed. Engl.* **1994**, *33*, 1290–1292; c) J. Besinger, D. Fenske, *Z. Anorg. Allg. Chem.* **2001**, *627*, 1487–1494.
[6] D. Fenske, F. Simon, *Z. Anorg. Allg. Chem.* **1996**, *622*, 45–52.
[7] F. H. Allen, *Acta Crystallogr., Sect. B* **2002**, *58*, 380–388.
[8] I. J. Bruno, J. C. Cole, P. R. Edgington, M. Kessler, C. F. Macrae, P. McCabe, J. Pearson, R. Taylor, *Acta Crystallogr., Sect. B* **2002**, *58*, 389–397.
[9] H. J. Breunig, K. H. Ebert, S. Gülec, J. Probst, *Chem. Ber.* **1995**, *128*, 599–603.
[10] a) W. C. Davies, *J. Chem. Soc.* **1933**, 1043–1044; b) M. Ates, H. J. Breunig, S. Gülec, *Phosphorus Sulfur Silicon Relat. Elem.* **1989**, *44*, 129–133; c) G. Becker, H. Freudenblum, O. Mundt, M. Reti, M. Sachs, in: *Synthetic Methods of Organometallic and Inorganic Chemistry* (Eds.: Herrmann, Brauer), vol. 3 (Ed.: H. H. Karsch), Thieme, Stuttgart, **1996**, p. 193–198.
[11] G. M. Sheldrick, SHELXTL-97, University of Göttingen, **1997**.

Received: November 19, 2006
Published Online: January 4, 2007

 © 2007 Wiley-VCH Verlag GmbH & Co. KGaA, Weinheim 

DOI: 10.1002/ejic.200601146

# Square-Planar Noble Metal Iodate $[M(IO_3)_4]^{n-}$ ($M = Pd^{II}$, $Au^{III}$; $n = 2, 1$) Anions and Their Ability to Form Polar and Centrosymmetric Architectures

**Jie Ling[a] and Thomas E. Albrecht-Schmitt*[a]**

**Keywords:** Gold / Palladium / Iodate / Oxo ligands

$K^+$ salts of the square-planar noble metal iodate $[M(IO_3)_4]^{n-}$ ($M = Pd^{II}$, $Au^{III}$; $n = 2, 1$) anions have been prepared under mild hydrothermal conditions, and the structures elucidated to demonstrate that while both are highly polar anions, polar and centrosymmetric extended architectures can form using these building units.
(© Wiley-VCH Verlag GmbH & Co. KGaA, 69451 Weinheim, Germany, 2007)

## Introduction

Iodate compounds have been the subject of intense interest because of their propensity for adopting noncentrosymmetric structures that are often polar,[1–8] a feature that is aptly illustrated by $A[MoO_3(IO_3)]$ (A = Rb, Cs),[9] $A[(VO)_2(IO_3)_3O_2]$ (A = $NH_4$, Rb, Cs),[10] and $NaYI_4O_{12}$.[11] This structural attribute can be exploited in the development of new nonlinear optical, pyroelectric, piezoelectric, and ferroelectric materials, with the first property being the most heavily investigated. Structure–property relationships in early d-block and f-block iodates are becoming well-developed.[1–11] However, noble metal iodates are virtually unknown.[12]

Renewed interest in noble metal oxoanion compounds has led to the discovery of a plethora of remarkable solids including $AuSO_4$, which contains a $Au^{II}$–$Au^{II}$ dimer,[13] and polar $Au_2(SeO_3)_2(SeO_4)$, which is constructed from square-planar $Au^{III}$ and both selenite and selenate anions.[14] Despite repeated attempts over the past eight years, gold iodates have remained elusive for several reasons. First, common anions employed in gold reactions such as chloride and nitrate can interfere with the formation of these compounds. Second, iodate and periodate do not react appreciably with elemental gold, even under acidic compounds. Finally, as with many iodates, gold iodates are quite insoluble under normal conditions precluding simple crystallization techniques.

## Results and Discussion

The solution to the synthesis of a gold iodate proved to be the use of a strongly oxidizing mixed-anion system. In this case the reaction of elemental gold with concentrated selenic acid and $KIO_4$ under mild hydrothermal conditions results in the formation of $K[Au(IO_3)_4]$. As is shown in Figure 1, single crystals of $K[Au(IO_3)_4]$ grow directly off of the surface of the gold metal and ultimately passivate the surface. We speculate that selenic acid dissolves small quantities of the gold metal to yield a halo of $Au^{III}$ that rapidly reacts with iodate to yield $K[Au(IO_3)_4]$ crystals. The in situ generation of iodate by the reduction of periodate by water is a critical feature of this reaction, because it allows for the slow introduction of the key reactant that controls solubility.[9,10,15]

Figure 1. A photograph showing yellow crystals of $K[Au(IO_3)_4]$ that have grown directly on the surface of elemental gold under hydrothermal conditions. Crystals typically have maximum dimensions of several millimeters.

The structure of $K[Au(IO_3)_4]$ is quite unusual in that it crystallizes in the lowest symmetry space group $P1$. The origin of the asymmetry becomes obvious by viewing the $[Au(IO_3)_4]^{1-}$ anion shown in Figure 2, and the packing of these anions in Figure 3. The $[Au(IO_3)_4]^{1-}$ anions contain square-planar $Au^{III}$ bound by four monodentate iodate

[a] Department of Chemistry and Biochemistry, Auburn University, 179 Chemistry Building,
Auburn, AL 36849, USA
Fax: +1-334-844-6959
E-mail: albreth@auburn.edu

 InterScience © 2007 Wiley-VCH Verlag GmbH & Co. KGaA, Weinheim 

anions. As can be viewed in Figure 2, all of the iodate anions in the $[Au(IO_3)_4]^{1-}$ anions are aligned on one side of the $AuO_4$ square plane. Hence, these anions are highly polar, and pack in the lattice with identical orientation yielding a polar structure consistent with the space group. The Au–O bond lengths range from 1.981(9) Å to 1.987(9) Å, and are normal.[16] We have surveyed 28 high-resolution iodate crystal structures to arrive at a value of 1.792(5) Å for terminal I–O bonds. The terminal I–O bonds in the $[Au(IO_3)_4]^{1-}$ anions are normal in this respect. In contrast, I–O bond lengths for bridging or $\mu_2$-O bonds from 32 different structures, show an average distance 1.831(5) Å. The bridging I–O bond lengths strain the normal limits and average 1.882(9) Å. The bridging I–O bond lengths are of a length expected for protonated moieties, suggesting polarization in the Au–O–I bonds. There are several other $Au^{III}$ compounds with monodentate oxoanions that share features in common with the bonding found in $K[Au(IO_3)_4]$; these compounds include $K[Au(NO_3)_4]$,[17] $(H_5O_2)[Au(NO_3)_4]\cdot H_2O$,[18] and $(ClO_2)[Au(ClO_4)_4]$.[19] In all three examples significant lengthening of the bridging E–O (E = N, Cl) bonds is observed.

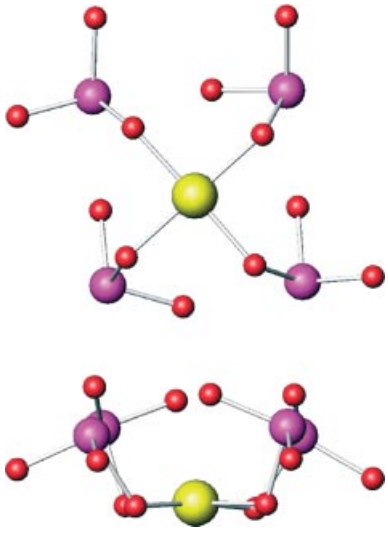

Figure 2. Two views of the $[Au(IO_3)_4]^{1-}$ anion in the structure of $K[Au(IO_3)_4]$. Gold is shown in yellow, iodine in magenta, and oxygen in red.

Short contacts on the order of 2.5 to 2.8 Å between the oxygen atom from one iodate anion and the iodine atom of a neighboring iodate play a critical role in the structures of iodate compounds and minerals.[20] The importance of iodate···iodate interactions in the structure of $K[Au(IO_3)_4]$ can not be underestimated. We have previously shown that these interactions can lead to alignment of the lone pair of electrons on the iodate anions in $Na_2[UO_2(IO_3)_4(H_2O)]$.[21] This also occurs in the structure of $K[Au(IO_3)_4]$ where there are numerous intermolecular iodate···iodate interactions. These interactions stitch what appears to be a molecular structure into a complex polar network.

The IR vibrational spectrum of $K[Au(IO_3)_4]$ shows four weak bands at 519, 514, 503 and 499 $cm^{-1}$ that are attributed to vibrations within the $[AuO_4]$ unit.[22,23] Iodate stretching vibrations ($\nu_1$ and $\nu_3$) are found at 822, 803, 778, 765, 741, and 664 $cm^{-1}$.[24–26] The Raman spectrum shows a broad peak centered at 508 $cm^{-1}$ that coincides well with the IR features. In addition, there is a broad envelope for the various iodate modes with discernible vibrational modes at 860, 821, 773, and 741 $cm^{-1}$.

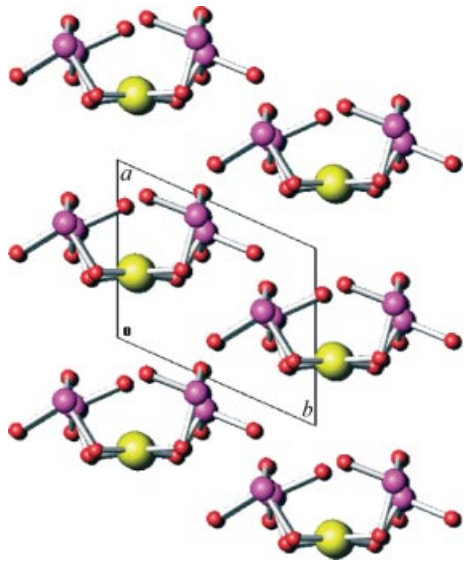


Figure 3. A view down the *c* axis of the structure of $KAu(IO_3)_4$ showing the polar stacking of the $[Au(IO_3)_4]^{1-}$ anions. $K^+$ cations have been omitted for clarity. Gold is shown in yellow, iodine in magenta, and oxygen in red.

The thermal behavior of $K[Au(IO_3)_4]$ was addressed using differential scanning calorimetry (DSC), and shows that it is stable to 375 °C. Two sharp endotherms are then observed at 387 and 518 °C, which are ascribed to the decomposition of $K[Au(IO_3)_4]$ to elemental gold and thermal disproportionation of iodate, respectively. The first endotherm is immediately followed by an exothermic event, again consistent with the formation of elemental gold, which can be visually observed in the sample containers at the end of the thermal analysis.

In contrast to the difficulties in synthesizing $K[Au(IO_3)_4]$, the synthesis of its $Pd^{II}$ analog, $K_{2.5}[Pd(IO_3)_4]\cdot H_{0.5}IO_3$, proved to be quite straightforward as it can be prepared from the reaction of $Pd(NO_3)_2\cdot 2H_2O$ with $KIO_4$ under mild hydrothermal conditions. Again the in situ reduction of $IO_4^-$ to $IO_3^-$ is utilized. The complexation of $Pd^{II}$ by four iodate anions yields $[Pd(IO_3)_4]^{2-}$ anions. Unlike the $[Au(IO_3)_4]^{1-}$ anion, in which the bridging I–O bonds are slightly polarized with an average bond length of 1.882(9) Å, all I–O bond lengths in the $[Pd(IO_3)_4]^{2-}$ anions are within the range of 1.790(4) to 1.865(5) Å, and no excessive lengthening of the bridging I–O bonds are observed. The $[Pd(IO_3)_4]^{2-}$ anions are similar to $[Au(IO_3)_4]^{1-}$ in that all of the four iodate anions in the $[Pd(IO_3)_4]^{2-}$ anions are aligned on one side of the $PdO_4$ square plane, as is shown in Figure 4. However, individual anions are related through inversion centers, and it crystallizes in the centrosymmetric space group *C*2/*m* (Figure 5).

 © 2007 Wiley-VCH Verlag GmbH & Co. KGaA, Weinheim 

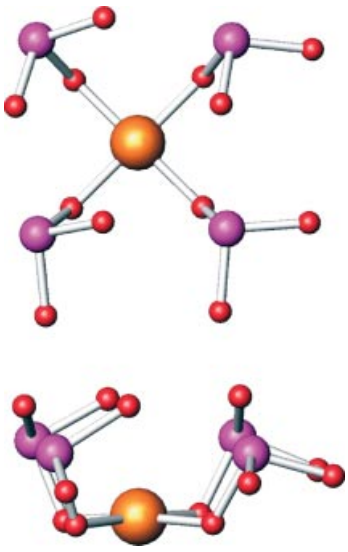

Figure 4. Two depictions of the $[Pd(IO_3)_4]^{2-}$ anion in the structure of $K_{2.5}Pd(IO_3)_4{\cdot}H_{0.5}IO_3$. Palladium is shown in orange, iodine in magenta, and oxygen in red.

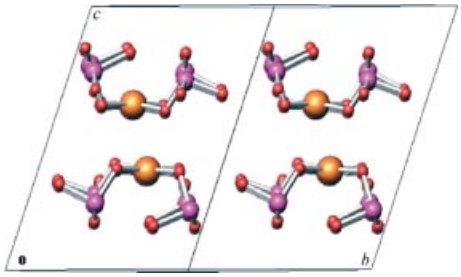


Figure 5. An illustration of the centrosymmetric packing of the $[Pd(IO_3)_4]^{2-}$ anions in $K_{2.5}Pd(IO_3)_4{\cdot}H_{0.5}IO_3$. $K^+$ cations and iodate/iodic acid units have been omitted for clarity. Palladium is shown in orange, iodine in magenta, and oxygen in red.

The critical feature of the vibrational spectrum of $K_{2.5}[Pd(IO_3)_4]{\cdot}H_{0.5}IO_3$ is the presence of a I–OH stretch at 1180 $cm^{-1}$, confirming the protonation of the co-crystallized iodate moiety.[27] In addition, a low frequency band at 495 $cm^{-1}$ is observed that might be attributable to a stretch mode of Pd–O. A set of weak bands centered at 560 $cm^{-1}$ can potentially be assigned to distortions of the $[PdO_4]$ square plane.[28,29] Iodate stretching vibrations ($\nu_1$ and $\nu_3$) are found at 797, 782, 728, 696, 673 and 659 $cm^{-1}$.

## Conclusions

In conclusion, we have demonstrated that two new noble metal iodates can be prepared under mild hydrothermal conditions by using in situ reduction of periodate to iodate. These compounds are the first members a new family of noble metal iodate compounds containing square-planar metal ions. The importance of these compounds lies in their ability to form polar structures that will allow for the development of new nonlinear optical, pyroelectric, piezoelectric, and ferroelectric materials.

## Experimental Section

**$K[Au(IO_3)_4]$:** Prepared by loading gold (70 mg, 0.355 mmol), $KIO_4$ (300 mg, 1.304 mmol), 0.2 mL concentrated $H_2SeO_4$ solution, and 0.05 mL of distilled and filtered water (Millipore) in 23 mL PTFE-lined autoclave. The autoclave was heated at 200 °C for 4 d, and slowly cooled to 9 °C/h to 22 °C. The product consisted of yellow crystals of $K[Au(IO_3)_4]$ that had grown on the surface of unreacted gold metal, and a bright yellow solution, that was converted into a yellow precipitate of $Au_2(SeO_3)_3$ when water was added. Yield for $K[Au(IO_3)_4]$: 50 mg (15% based on Au). EDX analysis provided a K/Au/I ratio of 1:1:4.

**$K_{2.5}[Pd(IO_3)_4]{\cdot}H_{0.5}IO_3$:** Prepared by loading $Pd(NO_3)_2{\cdot}2H_2O$ (105.8 mg, 0.397 mmol), $KIO_4$ (284.2 mg, 1.236 mmol), and 0.5 mL distilled and filtered water (Millipore) in 23 mL PTFE-lined autoclave. The autoclave was heated at 200 °C for 3 d, and slowly cooled to 9 °C/h to 22 °C. The product consisted of dark orange plates of $K_{2.5}[Pd(IO_3)_4]{\cdot}H_{0.5}IO_3$ and unreacted $Pd(NO_3)_2{\cdot}2H_2O$. Yield for $K_{2.5}[Pd(IO_3)_4]{\cdot}H_{0.5}IO_3$: 54 mg (12% based on Pd). EDX analysis provided a K/Pd/I ratio of 2.3:1:5.1.

**X-ray Structural Analyses**

**$K[Au(IO_3)_4]$ (1):** Yellow block, crystal dimensions $0.084 \times 0.048 \times 0.046$ mm, triclinic, $P\bar{1}$, $Z = 1$, $a = 5.6484(5)$, $b = 7.1935(7)$, $c = 8.1377(8)$ Å, $\alpha = 105.264(2)°$, $\beta = 93.585(2)°$, $\gamma = 111.840(2)°$, $V = 291.30(5)$ $Å^3$ ($T = 193$ K), $\mu = 236.39$ $cm^{-1}$, $R_1 = 0.0289$, $wR_2 = 0.0762$.

**$K_{2.5}[Pd(IO_3)_4]{\cdot}H_{0.5}IO_3$ (2):** Dark orange plate, crystal dimensions $0.055 \times 0.020 \times 0.012$ mm, monoclinic, $C2/m$, $Z = 4$, $a = 11.3270(13)$, $b = 11.8246(14)$, $c = 12.9665(15)$ Å, $\beta = 114.417(2)°$ $V = 1581.4(3)$ $Å^3$ ($T = 193$ K), $\mu = 116.67$ $cm^{-1}$, $R_1 = 0.0277$, $wR_2 = 0.0635$. Bruker APEX CCD diffractometer: $\theta_{max} = 56.58°$ (for **1**) and 56.62° (for **2**), Mo-$K_\alpha$, $\lambda = 0.71073$ Å, 0.3° $\omega$ scans, 2796 (for **1**) and 7413 (for **2**) reflections measured, 2440 (**1**) and 2007 (**2**) independent reflections all of which were included in the refinement. The data were corrected for Lorentz polarization effects and for absorption (numerical and SADABS), solutions were solved by direct methods, anisotropic refinement on all heavy atoms of $F^2$ by full-matrix least-squares, 164 (**1**) and 125 (**2**) parameters. Further details of the crystal structure investigation may be obtained from the Fachinformationzentrum Karlsruhe, 76344 Eggenstein-Leopoldshafen, Germany [Fax: (+49)-7247-808-666; E-mail: crysdata@fiz-karlsruhe.de] on quoting depository numbers CSD-417267 and -417268. G. M. Sheldrick, SHELXTL PC, Version 5.0, Siemens Analytical X-ray Instruments, Inc., Madison, WI, 1994.

## Acknowledgments

This research was sponsored by the U.S. Department of Energy, Heavy Elements Program, Grant No. DE-FG02-01ER15187.

[1] C. Svenson, S. C. Abrahams, J. L. Bernstein, *J. Solid State Chem.* **1981**, *36*, 195–204.
[2] K. Nassau, J. W. Shiever, B. E. Prescott, *J. Solid State Chem.* **1973**, *7*, 186–204.
[3] K. Nassau, J. W. Shiever, B. E. Prescott, A. S. Cooper, *J. Solid State Chem.* **1974**, *11*, 314–318.
[4] R. Liminga, S. C. Abrahams, J. L. Bernstein, *J. Chem. Phys.* **1975**, *62*, 755–763.
[5] K. Nassau, J. W. Shiever, B. E. Prescott, *J. Solid State Chem.* **1975**, *14*, 122–132.
[6] S. C. Abrahams, J. L. Bernstein, K. Nassau, *J. Solid State Chem.* **1976**, *16*, 173–184.

 © 2007 Wiley-VCH Verlag GmbH & Co. KGaA, Weinheim 

[7] R. Liminga, S. C. Abrahams, J. L. Bernstein, *J. Chem. Phys.* **1977**, *67*, 1015–1023.
[8] P. K. S. Gupta, H. L. Ammon, S. C. Abrahams, *Acta Crystallogr., Sect. C* **1989**, *45*, 175–178.
[9] R. E. Sykora, K. M. Ok, P. S. Halasyamani, T. E. Albrecht-Schmitt, *J. Am. Chem. Soc.* **2002**, *124*, 1951–1957.
[10] R. E. Sykora, K. M. Ok, P. S. Halasyamani, D. M. Wells, T. E. Albrecht-Schmitt, *Chem. Mater.* **2002**, *14*, 2741–2749.
[11] K. M. Ok, P. S. Halasyamani, *Inorg. Chem.* **2005**, *44*, 9353–9359.
[12] F. Schellhaas, R. Frydrych, *Chem. Ber.* **1975**, *108*, 364–366.
[13] M. S. Wickleder, *Z. Anorg. Allg. Chem.* **2001**, *627*, 2112–2114.
[14] M. S. Wickleder, O. Buechner, C. Wickleder, S. El Sheik, G. Brunklaus, H. Eckert, *Inorg. Chem.* **2004**, *43*, 5860–5964.
[15] a) A. L. Hector, S. J. Henderson, W. Levason, M. Webster, *Z. Anorg. Allg. Chem.* **2002**, *628*, 198–202; b) P. Douglas, A. L. Hector, W. Levason, M. E. Light, M. L. Matthews, M. Webster, *Z. Anorg. Allg. Chem.* **2004**, *630*, 479–483.
[16] J. Geb, M. Jansen, *J. Solid State Chem.* **1996**, *122*, 364–370.
[17] a) C. C. Addison, G. S. Brownlee, N. Logan, *J. Chem. Soc., Dalton Trans.* **1972**, *14*, 1440–1445; b) C. D. Garner, S. C. Wallwork, *J. Chem. Soc.* **1970**, *18*, 3092–3095.
[18] O. Buechner, M. S. Wickleder, *Z. Anorg. Allg. Chem.* **2004**, *630*, 1079–1083.
[19] F. Cunin, C. Deudon, F. Favier, B. Mula, J. L. Pascal, *Inorg. Chem.* **2002**, *41*, 4173–4178.
[20] a) P. C. Burns, F. C. Hawthorne, *Can. Mineral.* **1993**, *31*, 313–319; b) M. A. Cooper, F. C. Hawthorne, A. C. Roberts, J. D. Grice, J. A. R. Stirling, E. A. Moffatt, *Am. Mineral.* **1998**, *83*, 390–399.
[21] T. H. Bray, J. V. Beitz, A. C. Bean, Y. Yu, T. E. Albrecht-Schmitt, *Inorg. Chem.* **2006**, *45*, 8251–8257.
[22] E. Schwarzmann, E. Z. Fellwock, *Naturforsch., Teil B* **1971**, *26*, 1369–1370.
[23] M. Jansen, A. V. Mudring, in *Gold, Process in Chemistry, Biochemistry and Technology* (Ed.: H. Schmidbaur), John Wiley & Sons, Chichester, **1999**, p. 753.
[24] G. Pracht, N. Lange, H. D. Lutz, *Thermochim. Acta* **1997**, *293*, 13–24.
[25] H. D. Lutz, E. Suchanek, *Spectrochim. Acta* **2000**, *A56*, 2707–2713.
[26] V. Schellenschlarger, G. Pracht, H. D. Lutz, *J. Raman Spectrosc.* **2001**, *32*, 373–382.
[27] W. Levason, *Coord. Chem. Rev.* **1997**, *161*, 33–78.
[28] K. Panagiotidis, R. Glaum, J. Schmedt auf der Guenne, W. Hoffbauer, H. Goerzel, *Z. Anorg. Allg. Chem.* **2005**, *631*, 2371–2376.
[29] K. Nakamoto, *Infrared and Raman Spectra of Inorganic and Coordination Compounds–Part A: Theory and Applications in Inorganic Chemistry*, 5th ed., John Wiley & Sons, **1997**.

Received: November 15, 2006
Published Online: January 8, 2007

 © 2007 Wiley-VCH Verlag GmbH & Co. KGaA, Weinheim 

DOI: 10.1002/ejic.200600927

# Synthesis and Oxidation of Vanadyl Complexes Containing Bispidine Ligands

**Peter Comba,*[a] Shigemasa Kuwata,[a] Gerald Linti,[a] Máté Tarnai,[a] and Hubert Wadepohl[a]**

**Keywords:** Peroxido complexes / Superoxido complexes / Rigid ligand / Bispidine

The reaction of 3-methyl-9-oxo-7-picolyl-2,4-di(2-pyridyl)-3,7-diazabicyclo[3.3.1]nonane-1,5-dicarboxylate ($L^2$) with vanadyl sulfate in methanol yields the purple complex $[V^{IV}{=}O(L^{2'})](ClO_4)_2$, where $L^2$ is hydrated to the corresponding 9-diol $L^{2'}$. The crystal structure of $[V^{IV}{=}O(L^{2'})](ClO_4)_2$ has a saturated coordination sphere with a long bond to the tertiary amine N7 *trans* to the oxido group (2.36 Å). Oxidation of $[V^{IV}{=}O(L^{2'})](ClO_4)_2$ with an excess of aqueous hydrogen peroxide yields the orange complex $[V^{V}{=}O(O_2)(L^{2'})]ClO_4$. This can be further oxidized with $Ce^{4+}$ in MeCN at –40 °C to the unstable vanadium(V)-oxidosuperoxido complex $[V^{V}{=}O(O_2)(L^{2'})]^{2+}$, as shown by EPR spectroscopy. The X-ray crystal structure of $[V^{V}{=}O(O_2)(L^{2'})]ClO_4$ shows that the N7-pendant pyridine donor is dissociated and the V–N7 bond is elongated (2.56 Å). The O–O distance of the side-on bound peroxide in $[V^{V}{=}O(O_2)(L^{2'})]ClO_4$ is unexpectedly short (1.28 Å) and is therefore in the range which is typical for a superoxido group. However, the IR spectrum of $[V^{V}{=}O(O_2)(L^{2'})]ClO_4$ shows $^{18}O$ isotope shifts, which support the assignment as a peroxido complex, and this is also supported by EPR and UV/Vis spectroscopic analysis. The short O–O bond is attributed to a static disorder rather than to libration of the "non-rigid" peroxido group.

(© Wiley-VCH Verlag GmbH & Co. KGaA, 69451 Weinheim, Germany, 2007)

## Introduction

Oxidation states up to +5 are accessible for vanadium, and in the high valent vanadium(IV) ($d^1$, vanadyl) and vanadium(V) ($d^0$, vanadate) forms the hard metal centers form stable oxido complexes. There is a considerable interest and activity in developing vanadium complexes as models for a variety of metalloenzymes, specifically for the mononuclear haloperoxidases, which catalyze the peroxide-dependent halogenation of organic substrates.[1,2] Vanadium(V) oxido-peroxido complexes have also been found to be catalytically active in the oxidation of organic substrates (e.g., epoxidation of alkenes and hydroxylation of alkanes and aromatic compounds).[3,4] In addition, mononuclear vanadyl(IV) and peroxidovanadium(V) complexes are known to have insulin-mimetic properties.[5,6]

Three pentadentate bispidine-based ligands with tertiary amine, pyridine, and phenolate donors have been used for the isolation and characterization of oxido- and peroxidovanadium(IV) and -vanadium(V) complexes (see Scheme 1). Upon complexation, the 9-keto group of the ligands is hydrated to the corresponding 9-diol, and in methanolic solution the hemiacetal structure (9-hydroxy-9-methoxy) can be formed; the hydrated diol ligands are denoted as $L^{1'}$, $L^{2'}$, and $L^{3'}$, respectively. Bispidine ligands are relatively soft and therefore prefer relatively large metal ions,[7] which means that they are not optimal for vanadium(IV/V) chemistry and quite rigorous methods have to be used for their preparation. Several methods have been reported for the preparation of vanadyl complexes;[8] of special interest are those for the synthesis of complexes with similar amine/pyridine-based ligands.[9]

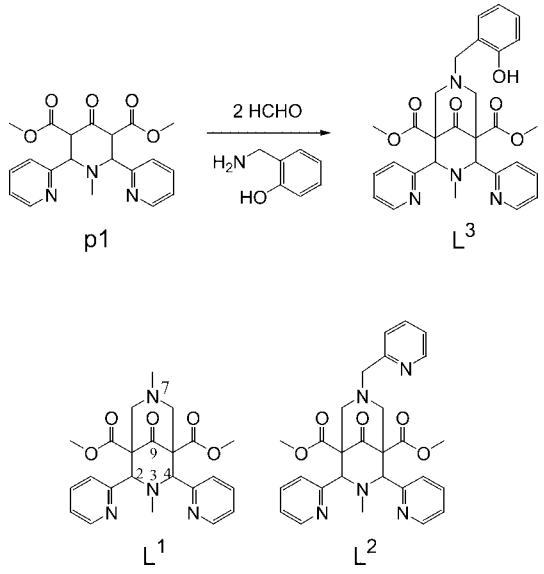


Scheme 1.

[a] Universität Heidelberg, Anorganisch-Chemisches Institut,
Im Neuenheimer Feld 270,
69120 Heidelberg, Germany
Fax: +49-6221-546617
E-mail: peter.comba@aci.uni-heidelberg.de

 © 2007 Wiley-VCH Verlag GmbH & Co. KGaA, Weinheim 

We report here the synthesis and properties of vanadium complexes of the three ligands shown in Scheme 1. Specifically, we have been interested in the structural and spectroscopic properties of the oxidovanadium(V) peroxide complex and the possibility of oxidizing it to the corresponding superoxide complex. Possible applications in the area of oxidation catalysis are briefly discussed on the basis of preliminary test reactions.

## Results and Discussion

### Synthesis and Structure of the Vanadyl Complexes

The vanadyl complexes with the pentadentate ligands $L^2$ and $L^3$ were prepared from vanadyl sulfate. These complexes are easily obtained from hot methanolic or acetonitrile ($L^3$) solutions (with addition of one equivalent of triethylamine to deprotonate the phenolic group donor). The complexes were purified by ion-exchange chromatography. Attempts to use vanadium(III) salts (chloride, acetylacetonate) did not produce any of the desired products. Interestingly, the method found to be successful for the pentadentate ligands did not succeed for the tetradentate ligand $L^1$. Treatment of $L^1$ with an ethanolic solution of [VO(OEt)$_3$] produced a deep-green solution after refluxing overnight, from which a dark green solid precipitated after several days in the refrigerator (4 °C). Characterization of the product confirmed the formation of the vanadyl complex of $L^1$ ([V=O($L^{1'}$)(OH$_2$)]$^{2+}$).

A plot of the molecular structure of [$V^{IV}$=O($L^{2'}$)](ClO$_4$)$_2$·H$_2$O, as determined by X-ray crystal structure analysis, is shown in Figure 1; the structural data are presented in Table 1. Only one of the two independent complex ions is discussed because they do not differ much in their structural parameters. The vanadyl ion coordinates to $L^{2'}$ in a distorted octahedral geometry. The vanadium center lies almost in the plane defined by Npy1, Npy2, and N3. The distance between vanadium and this plane is 0.074 Å, although the two pyridyl rings are twisted by 14.0° and 13.5° with respect to this plane. The length of the V=O bond (1.59 Å) is consistent with values found for other vanadyl complexes.[10] The V–N7 bond length (2.36 Å) is rather long for a $V^{IV}$–$N_{amine}$ bond, whereas that of V–N3 (2.10 Å) is as expected.[11] The average $V^{IV}$–N bond length (2.15 Å) is ideal for the $L^2$ bispidine ligand cavity, which means that almost no strain is induced in the ligand by the vanadyl center.[7] Long bonds to N7 are quite common in bispidine coordination chemistry,[12–14] probably due to the bispidine-ligand-enforced angular distortion of the N7–V–O axis and, to a lesser extent, to π-bonding involving the two in-plane pyridine donors.[15] Long bonds in vanadyl complexes *trans* to the yl oxygen donor are also common, therefore the bispidine ligands $L^2$ and $L^3$, which enforce the yl oxygen group *trans* to N7, have a high complementarity with respect to the vanadyl fragment and form stable vanadyl complexes.

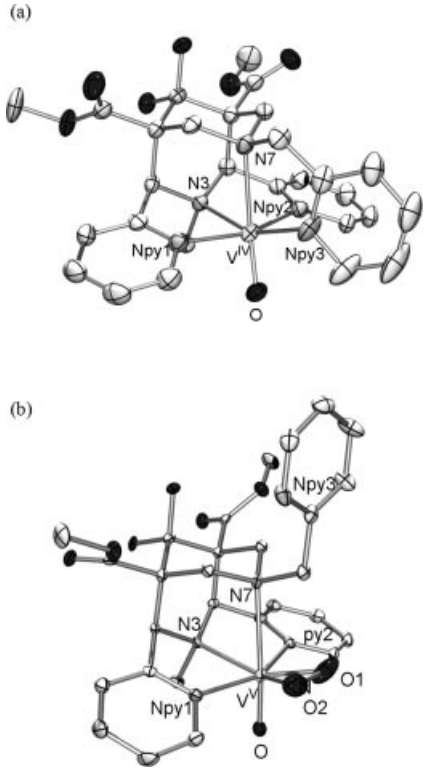


Figure 1. Molecular structures of [V=O($L^{2'}$)]$^{2+}$ (a) and [V=O(O$_2$)($L^{2'}$)]$^+$ (b). Displacement ellipsoids are scaled to 50% probability.

Table 1. Selected bond lengths and angles for [V=O($L^2$)](ClO$_4$)$_2$·H$_2$O (a) and [V=O(O$_2$)($L^2$)]ClO$_4$·H$_2$O (b).

| | a | b |
|---|---|---|
| Distances [Å] | | |
| V–N3 | 2.098(3) | 2.192(2) |
| V–N7 | 2.364(3) | 2.557(3) |
| V–Npy1 | 2.109(4) | 2.112(3) |
| V–Npy2 | 2.097(4) | 2.113(3) |
| V–Npy3 | 2.078(4) | – |
| V=O | 1.589(3) | 1.602(2) |
| $(V–N)_{av}$ | 2.149 | 2.244 |
| V–O1 | – | 1.810(3) |
| V–O2 | – | 1.838(3) |
| O1–O2 | – | 1.281(5) |
| N3···N7 | 2.836(5) | 2.909(3) |
| Npy1···Npy2 | 4.131(5) | 4.087(3) |
| Angles [°] | | |
| N3–V–N7 | 78.69(12) | 75.07(9) |
| N3–V–Npy1 | 79.61(13) | 75.95(10) |
| N3–V–Npy2 | 78.89(13) | 74.62(10) |
| N3–V–Npy3 | 154.55(14) | – |
| N3–V=O | 108.32(15) | 98.34(11) |
| N7–V=O | 172.70(15) | 172.55(9) |
| Npy1–V–Npy2 | 158.28(13) | 150.51(11) |
| Torsion angles [°] | | |
| C1–C2–CA–Npy1 | 84.31(40) | 89.77(34) |
| C5–C4–CA2–Npy2 | –86.99(39) | –94.65(34) |

 © 2007 Wiley-VCH Verlag GmbH & Co. KGaA, Weinheim 

### Spectroscopy of the Vanadyl Complexes

The IR spectra for all complexes, as expected, have no Bohlmann band (ca. 2600 $cm^{-1}$), which typically appears for the metal-free bispidine ligand (interaction between the lone pairs of the tertiary amine nitrogen donors); this is usually missing when a metal is coordinated.[16] The vibrational band at 986 $cm^{-1}$ in the spectrum of $[V^{IV}{=}O(L^{2'})](ClO_4)_2$ is assigned to the V=O stretching mode, and this is consistent with known five- and six-coordinate vanadyl complexes, where $\nu_{V=O}$ appears around 980 $cm^{-1}$ and 950 $cm^{-1}$, respectively.[17,18] As expected from the structural data (see above) $[V^{IV}{=}O(L^{2'})](ClO_4)_2$, due to the long V–N7 distance, has a V=O stretching mode similar to that expected for a five-coordinate vanadyl complex.

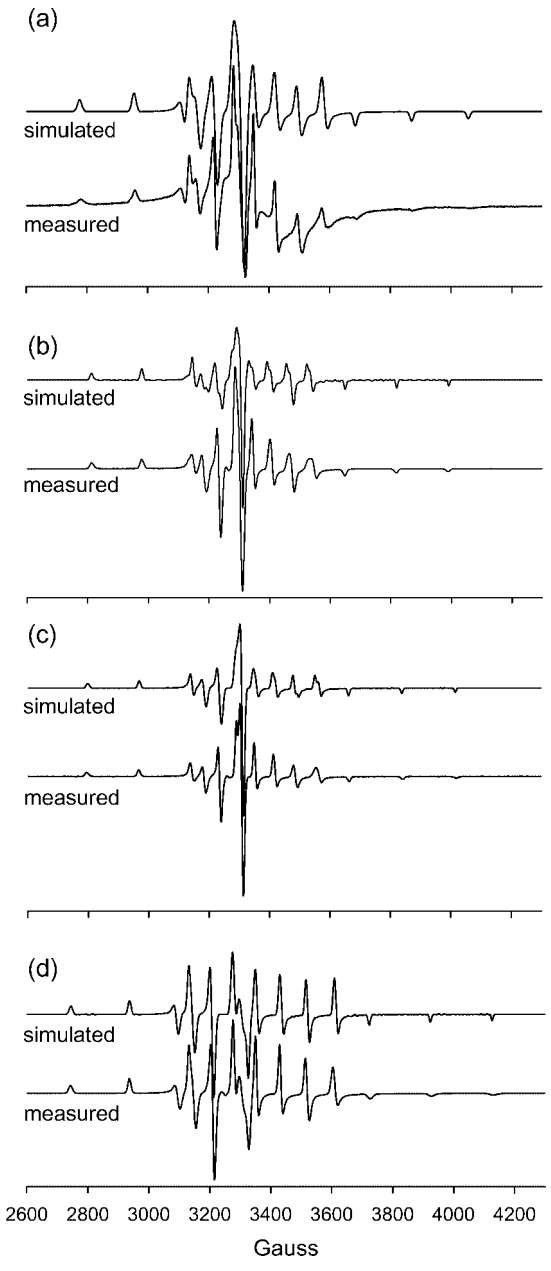


Figure 2. Experimental and simulated EPR spectra of $[V{=}O(L^{1'})]^{2+}$ (a), $[V{=}O(L^{2'})]^{2+}$ (b), $[V{=}O(L^{3'})]^{+}$ (c), and $[V{=}O(OH_2)_5]^{2+}$ (d) (dmf/$H_2O$, 2:1, 125 K, X-band).

The three d–d transitions expected for a distorted octahedral $d^1$ system are observed in the UV/Vis spectrum of $[V^{IV}{=}O(L^{2'})](ClO_4)_2$. The highest energy transition, which appears as a shoulder of the high intensity charge-transfer band at 363 nm, is assigned to the $d_{xy} \rightarrow d_{z^2}$ transition. Two weaker transitions at 514 and 695 nm are assigned to $d_{xy} \rightarrow d_{x^2-y^2}$ and $d_{xy} \rightarrow d_{xz,yz}$, respectively. A moderate ligand field in the expected range ($D_q$ = 1950 $cm^{-1}$) emerges [$D_q(VOSO_4{\cdot}H_2O)$ = 1600 $cm^{-1}$] from this.[19,20] For $[V^{IV}{=}O(L^{3'})]^{+}$, only one dd transition is observed at 571 nm. The others are probably not resolved due to the strong charge-transfer transition at 386 nm, and this supports the coordination of the phenolate donor group.

The EPR spectra of the three bispidine vanadyl compounds and of the vanadyl aqua ion are shown in Figure 2. The spin-Hamiltonian parameters, obtained by spectral simulation,[21] are given in Table 2. The spectra are typical for $d^1$ vanadyl systems with a $d_{xy}$ ground state and a compressed tetragonal geometry.[22–24] The trend of the *g*- and *A*-tensor parameters (in particular of the *z* components) with decreasing values along the series $L^2 > L^3 > L^1 > (H_2O)_5$ depends on the type of chromophore ($N_aO_b$, $a + b = 5$), and is consistent with the expected level of delocalization of the unpaired electron to the donor groups, with the softer N donors leading to more covalent interactions than the harder O donors.

### Oxidation of the Vanadium(IV) Bispidine Complexes

The oxidation of a methanolic solution of $[V^{IV}{=}O(L^{2'})]^{2+}$ with a large excess of 30% aqueous $H_2O_2$ was studied by time-dependent UV/Vis/NIR spectroscopy. The series of spectra (see Figure 3) show a gradual decrease of the d–d transitions of the vanadyl complex (695 nm) and the appearance of a more intense single band at 429 nm (the color of the solution changes from light purple to orange). These changes indicate that metal-centered oxidation occurs. The reaction shows two isosbestic points at 390 and 547 nm and a pseudo-first-order behavior. The rate

Table 2. EPR parameters of the vanadyl complexes.[a]

| | $A_{xx}$ [$10^{-4}$ $cm^{-1}$] | $A_{yy}$ [$10^{-4}$ $cm^{-1}$] | $A_{zz}$ [$10^{-4}$ $cm^{-1}$] | $g_{xx}$ | $g_{yy}$ | $g_{zz}$ |
|---|---|---|---|---|---|---|
| $[V{=}O(L^2)]^{2+}$ | –51 | –50 | –153 | 1.988 | 1.977 | 1.950 |
| $[V{=}O(L^3)]^{+}$ | –54 | –55 | –158 | 1.979 | 1.972 | 1.947 |
| $[V{=}O(L^1)(OH_2)]^{2+}$ | –60 | –60 | –166 | 1.977 | 1.977 | 1.943 |
| $[V{=}O(OH_2)_5]^{2+}$ | –68 | –68 | –178 | 1.977 | 1.972 | 1.932 |

[a] Obtained by simulation of the experimental spectra.[21]

 © 2007 Wiley-VCH Verlag GmbH & Co. KGaA, Weinheim 

of disappearance of the d–d band at 700 nm and increase of the charge-transfer band at 430 nm leads to a reaction rate, $k_{obs}$, of $1.02 \times 10^{-3}$ s$^{-1}$. The product formed was purified by ion-exchange chromatography and characterized as a oxidovanadium(V) peroxide complex. The transition at 430 nm is assigned to a peroxide-to-vanadium charge-transfer transition. This is in the range typical for oxidovanadium(V) peroxide complexes.[8,30]

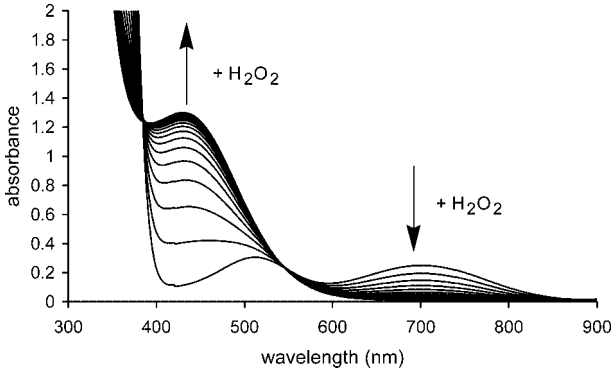


Figure 3. Time-dependent UV/Vis NIR spectra of the oxidation of $[VO(L^{2'})]^{2+}$ (11 mM MeOH) at 25 °C by $H_2O_2$ (170 equiv. of 30% aqueous solution) recorded at 5 min time intervals.

The CT band at 430 nm formed during oxidation is shifted to 456 nm in a much slower process (approx. one day). This is assigned to a rearrangement of an initially formed oxidohydroperoxido intermediate, which produces the oxidovanadium(V) peroxide complex (see Scheme 2).[4] This intramolecular rearrangement is expected to be a slow process because it involves ligand substitution at the vanadium(V) center. No intermediates were detected by EPR spectroscopy, which indicates that the first, relatively fast process is probably the oxidation of the $V^{IV}$=O complex and that no vanadyl peroxide intermediates can be trapped.

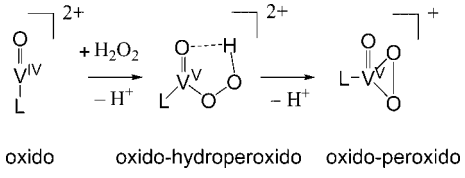


Scheme 2.

The oxidation products were analyzed with various oxidant concentrations, in a number of different solvents, and after quenching the reactions after various time intervals. Maximum yields of the vanadium(V) product were obtained with rather large amounts of $H_2O_2$ as oxidant (170 equiv.) and when the reaction was quenched after 2 h. When these reaction mixtures were left for two days, ESI mass spectrometry indicated that the orange product had completely decomposed (yellow solution). Aprotic solvents seem to lead to more side products than protic solvents, and the highest yields were obtained in MeOH and MeCN. This is not unexpected since vanadyl/$H_2O_2$ systems are known to produce OH radicals[25] and the yields of the vanadium(V) product seem to correlate with the ability of the solvent to quench these radicals.

Three transitions are found in the low energy part of the IR spectrum, at 890, 932, and 962 cm$^{-1}$. Based on published data, the absorption at 962 cm$^{-1}$ can be attributed to the V=O stretching vibration. The other two are tentatively assigned to O–O modes. To confirm this assignment, an $^{18}$O-labeling study was performed with $H_2{}^{18}O_2$ as oxidant (see Figure 4). In the IR spectrum of the $[V^{V}=O(^{18}O_2)(L^{2'})]^{+}$ complex, the transitions originally seen at 932 and 890 cm$^{-1}$ are shifted to 887 and 850 cm$^{-1}$, respectively. These experimental isotope shifts are close to those expected theoretically. Similar isotope shifts are also observed in the nitrate salt of the complex.

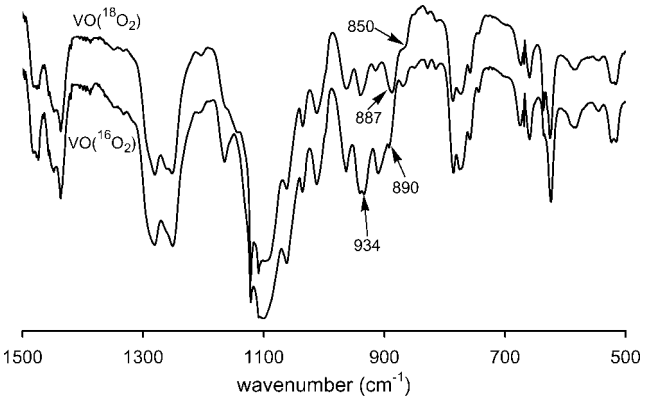


Figure 4. FT-IR spectra (KBr pellet) of $[V=O(O_2)(L^{2'})]^{+}$; top: synthesis with $H_2{}^{18}O_2$; bottom: synthesis with $H_2{}^{16}O_2$.

Single crystals of $[V^{V}=O(O_2)(L^{2'})]ClO_4 \cdot H_2O$ suitable for an X-ray structure determination were obtained by slow evaporation of the solvent (water/acetonitrile, 1:10). The resulting orange crystals are stable in air for several days. The structure of the cation $[V^{V}=O(O_2)(L^{2'})]^{+}$ is shown in Figure 1; selected geometric parameters are given in Table 1. The V–Npy1 and V–Npy2 distances are similar to the values determined for the corresponding vanadyl complex (see Table 1). The V–N3 distance is somewhat longer than in the vanadium(IV) complex and this may be due to the peroxido group, which leads to five in-plane donor atoms attached to the vanadium(V) center. This also leads to a smaller Npy1–V–Npy2 angle in the oxidovanadium(V) peroxide complex. The structure shows that the side-on coordination of the peroxido group requires the dissociation of the third pyridine group Npy3. As a result, there is a marked elongation of the V–N7 bond (2.56 vs. 2.36 Å) and, as a consequence, the distance between the two tertiary amino nitrogen donors increases from 2.84 to 2.91 Å. This value is very similar to that in the metal-free ligand $L^1$ (N3···N7 = 2.901 Å) and indicates that the oxidation of the vanadium center and the coordination of the peroxido group are assisted by the rigid bispidine ligand structure. The V=O distance, as expected, is rather insensitive to the oxidation state and coordination environment of vanadium.[10]

The description of the complex as an oxidovanadium(V) peroxide species is not unambiguous − it might alternatively be assigned as an oxidovanadium(IV) superoxide complex. There is a linear correlation between the O–O

 © 2007 Wiley-VCH Verlag GmbH & Co. KGaA, Weinheim 

stretching frequency and the bond length in this type of complexes:[26] peroxido complexes generally have O–O distances of 1.4–1.5 Å and O–O stretching frequencies of 1050–1200 $cm^{-1}$.[26] Therefore, judging from the apparent bond length in the crystal [1.281(5) Å] the assignment should rather be $[V^{IV}{=}O(O_2)(L^{2'})]^+$ (superoxide), while the IR spectra (see above) indicate that $[V^{V}{=}O(O_2)(L^{2'})]^+$ (peroxide) is the correct formulation. Close inspection of the crystal structure reveals much larger atomic displacement parameter (ADPs) for O1 and O2 than for the other oxygen, nitrogen, and carbon atoms. In addition, there is a systematic deviation of the shapes of the "thermal" envelopes for O1 and O2 from spherical (Figure 5). Normally, such effects can be attributed to thermally induced libration of "non-rigid groups".[27] Such libration leads to a systematic shortening of the apparent bond lengths between the affected atoms. This effect has indeed been observed in some $\eta^2$-$O_2$ metal complexes.[26] In the present case, the Hirshfeld Δ parameters indicate a highly correlated displacement of the $O_2$ moiety relative to the rest of the molecule. However, the diffraction data were collected at low temperature (100 K), which should greatly diminish the amplitude of librational motion. Indeed, attempts to model the effects by libration around the obvious axis joining V and the mid-point between O1 and O2 were unsuccessful. Dynamic effects (i.e. thermal motion) cannot be ruled out completely, but the ADPs also reflect static displacements of the atoms in many individual unit cells from their macroscopic space-averaged positions. We therefore tentatively assign the high ADPs of O1 and O2 to static disorder effects and do not see any particular significance in the apparently short oxygen–oxygen bond. In addition to the infrared spectroscopic data discussed above, there are no low intensity dd transitions in the 600–1000 nm range in the UV/Vis spectrum. Furthermore, the charge-transfer transition at 456 nm is in the area expected for vanadium(V) peroxide compounds.

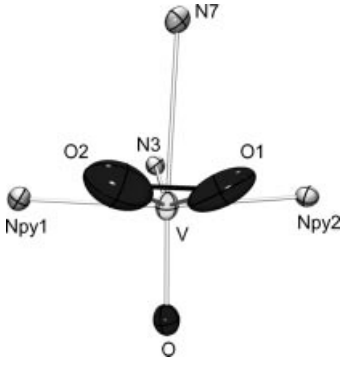


Figure 5. Displacement ellipsoids (50%) for the $N_4OVO_2$ core of the complex cation $[V{=}O(O_2)(L^{2'})]^+$.

It should be possible to oxidize oxidovanadium(V) peroxide complexes to the corresponding superoxido compounds.[28,29] Various oxidants were investigated ($Co^{3+}$, $KO_2$, $Ce^{4+}$), but only the preliminary experiments with $Ce^{4+}$ were partially successful. Thus, addition of one equivalent of $Ce^{4+}$ at –40 °C to an orange solution of $[V{=}O(O_2)$-$(L^{2'})]^+$ leads to a pale-yellow solution. Both $Ce^{3+}$ and oxidovanadium(V) superoxide complexes are expected to be yellowish. Addition of $H_2O_2$ to this solution brings the orange color back. The EPR spectrum of the yellow solution shows a signal for $Ce^{3+}$. No other signals were observed after five minutes at 230 K. When the sample is left for a longer time at 230 K (10 min, see Figure 6) additional signals appeared, which were assigned to a $VO^{2+}$ complex. These increase in intensity with longer reaction times whereas the intensity of the $Ce^{3+}$ signal does not change. We tentatively interpret these observations as being due to the oxidation of $[V^{V}{=}O(O_2)(L^{2'})]^+$ (peroxide) to $[V^{V}{=}O(O_2)(L^{2'})]^{2+}$ (superoxide) and assume that the EPR signal of the superoxide is hidden under the $Ce^{3+}$ signal. The vanadyl spectrum is a result of the decomposition of the metastable vanadium(V) superoxide complex to a vanadyl complex and dioxygen.

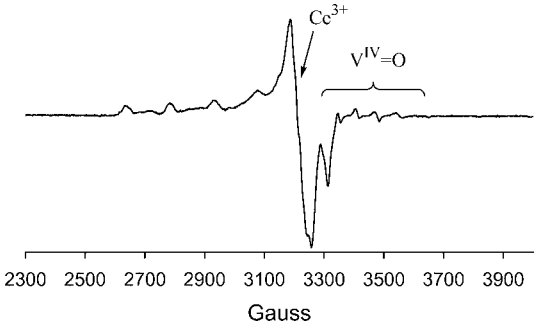


Figure 6. EPR spectrum of $[V^{V}{=}O(O_2)(L^{3'})]$ + 1 equiv. of $Ce^{4+}$ (reaction for 10 min at 230 K; spectrum recorded at 100 K) in MeCN/dmf (1:2).

## Reactivity

The vanadium(V) complexes were used for a number of catalytic oxidation test reactions (see Experimental Section). These include the bromination of phenol red (haloperoxidase test reaction)[30] and the oxidation of cyclohexene (epoxidation, hydroxylation).[4] There was no activity in the haloperoxidase test reaction and for cyclohexene oxidation the vanadium(V) complexes were also inactive. However, vanadyl complexes are also known to be able to oxidize olefins in the presence of $H_2O_2$.[31,32] Indeed, $[V^{IV}{=}O(L^{2'})]^{2+}$ has been shown to be able to oxidize cyclohexane but with a very low activity [0.7 mM catalyst, 7 mM $H_2O_2$, TON (cyclohexen-1-ol) = 0.1, TON (cyclohexen-1-one) = 0.3]. The vanadyl cations are believed to form hydroxyl radicals with $H_2O_2$,[25] and the allylic products probably emerge from these. The larger fraction of ketone product probably results from subsequent oxidation of the alcohol. The allylic products are likely to be, at least partially, the result of an autoxidation process involving dioxygen from air.[33] A possible reason for the low activity of the $[V^{IV}{=}O(L^{2'})]^{2+}/H_2O_2$ and $[V^{V}{=}O(O_2)(L^{2'})]^{+}/H_2O_2$ oxidation catalysis system is the saturated coordination sphere. A vacant coordination site has been proposed as

 © 2007 Wiley-VCH Verlag GmbH & Co. KGaA, Weinheim 

an active intermediate for the epoxidation process.[22] This might then explain the observed selectivity for allylic products.

## Experimental Section

**General:** The ligands $L^1$,[34] $L^2$,[35] and $L^3$ [35] were synthesized according to known procedures.

$H_2{}^{18}O_2$ (90% $^{18}O$ enriched, 2% solution in $H_2{}^{16}O$) was obtained from ICON services, USA. Commercially available chemicals were used without further purification.

UV/Vis spectra were recorded with a V-570 Jasco instrument. $^1H$ and $^{13}C$ NMR spectra at 200.13 and 50.54 MHz, respectively, were recorded with a Bruker AS 200 spectrometer in $CDCl_3$, [$D_6$]-DMSO, or $D_2O$ using TMS as an internal standard. Elemental analyses were obtained by the microanalytical laboratory of the chemical institutes of the University of Heidelberg. Mass spectra were measured with a Finnigan 8400 mass spectrometer. EPR spectra were recorded with a Bruker Elexsys E500 spectrometer at 110 K. Spectral parameters were determined by simulation using the program XSophe.[21] GC analyses were performed on a Varian 3900 gas chromatograph instrument equipped with a flame ionization detector, using a capillary column of Phenomenes Zebron ZB-1701 (length: 30 m; internal diameter: 0.25 mm). Temperature program: after 1 min, heating at a rate of 15 °C min$^{-1}$ from 40 to 130 °C; after 11 min at this temperature, heating at a rate of 49 °C min$^{-1}$ to 250 °C.

**Crystal Structure Determination:** Intensity data were collected with a STOE IPDS I or a Bruker AXS Smart1000 CCD diffractometer, and corrected for absorption and other effects.[36] Crystal data are compiled in Table 3. The structures were solved by direct methods and refined by full-matrix least-squares based on $F^2$. All non-hydrogen atoms were given anisotropic displacement parameters. Hydrogen atoms (except those of the solvent water molecule) were input in calculated positions. The calculations were performed using the programs SHELXS-86,[37,38] SHELXL-97.[39] Analysis of thermal motion was carried out with the program THMA11.[40]

CCDC-615579 ($[V^{IV}{=}O(L^{2'})](ClO_4)_2{\cdot}H_2O$) and -615580 ($[V^{V}{=}O(O_2)(L^{2'})]ClO_4{\cdot}H_2O$) contain the supplementary crystallographic data for this paper. These data can be obtained free of charge from The Cambridge Crystallographic Data Center via www.ccdc.cam.ac.uk/data_request/cif.

**$[V^{IV}{=}O(L^{1'})](ClO_4)_2$:** $V_2O_5$ (608 mg, 3.34 mmol) was added to MeOH (150 mL) and the resulting yellow suspension was refluxed overnight. Unreacted solid $V_2O_5$ was removed from the green suspension obtained by filtration, and a solution of $L^1$ (2.485 g, 5.67 mmol) in EtOH (100 mL) was added to the hot solution containing the $VO(OEt)_3$ product (0.5157 g, 5.67 mmol, 84.8%). The yellowish/greenish mixture was refluxed for 20 h, then $NaClO_4$ (1.593 g, 11.34 mmol) was added, and the solution was left at 4 °C overnight. The precipitate which formed was removed by filtration, washed with small portions of cold EtOH, and dried in vacuo. Yield: 260 mg (0.37 mmol, 7%). ESI-MS (MeOH): *m/z* 521.3 $[V^{IV}{=}O(L^1)(OH)]^+$, 539.3 $[V^{IV}{=}O(L^{1\prime})(OH)]^+$, 553.3 $[V^{IV}{=}O(L^1)(OH)(MeOH)]^+$. $C_{23}H_{26}Cl_2N_4O_{14}V$ (704.34): calcd. C 39.22, H 3.72, N 7.96; found C 39.30, H 4.07, N 8.30. IR (KBr): $\tilde{\nu}$ = 3436 br. s, 3078 w (CH), 2974 ($CH_2$), 1734 (C=O), 1604 m, 1474 m, 1444 m, 1270 m, 1090 ($ClO_4$), 964 m, 780 m, 624 m. UV (MeOH): $\lambda$ ($\varepsilon$) = 370 nm (910 M$^{-1}$ cm$^{-1}$), 470 (350, sh), 590 (190), 680 (190).

**$[V^{IV}{=}O(L^{2'})](ClO_4)_2{\cdot}H_2O$:** $L^2$ (1.00 g, 1.94 mmol) was dissolved in MeOH (30 mL) and a solution of $VOSO_4{\cdot}H_2O$ (0.49 g, 1.94 mmol)

Table 3. Crystal data for $[V^{IV}{=}O(L^{2'})](ClO_4)_2{\cdot}H_2O$ and $[V^{V}{=}O(O_2)(L^{2'})]ClO_4{\cdot}H_2O$.

| | $[V^{IV}{=}O(L^{2'})](ClO_4)_2{\cdot}H_2O$ | $[V^{V}{=}O(O_2)(L^{2'})]ClO_4{\cdot}H_2O$ |
|---|---|---|
| Empirical formula | $C_{28}H_{31}Cl_2N_5O_{19}V$ | $C_{28}H_{33}ClN_5O_{14}V$ |
| Formula weight | 863.42 | 749.98 |
| Temperature [K] | 293(2) | 100(2) |
| $\lambda$ [Å] | 0.71073 | 0.71073 |
| Crystal system | triclinic | triclinic |
| Space group | $P\bar{1}$ | $P\bar{1}$ |
| $a$ [Å] | 14.478(3) | 8.8221(5) |
| $b$ [Å] | 14.707(3) | 11.9404(7) |
| $c$ [Å] | 18.380(4) | 16.1571(10) |
| $\alpha$ [°] | 79.57(3) | 71.039(1) |
| $\beta$ [°] | 74.30(3) | 86.580(1) |
| $\gamma$ [°] | 70.01(3) | 75.568(1) |
| Volume [Å$^3$]; $Z$ | 3523.6(12); 4 | 1571.79(16); 2 |
| Density (calculated) [Mg m$^{-3}$] | 1.628 | 1.585 |
| Absorption coefficient [mm$^{-1}$] | 0.524 | 0.480 |
| Absorption correction | numerical | semi-empirical from equivalents |
| Min./max. transmission | 0.722/0.798 | 0.942/0.988 |
| $F$(000) | 1772 | 776 |
| Crystal size [mm$^3$] | 0.619 × 0.596 × 0.471 | 0.125 × 0.125 × 0.025 |
| $\theta$ range for data collection | 1.7 to 24.04° | 1.84 to 27.10° |
| Index ranges | $-16 \le h \le 16$<br>$-16 \le k \le 16$<br>$-20 \le l \le 20$ | $-11 \le h \le 11$<br>$-14 \le k \le 15$<br>$0 \le l \le 20$ |
| Reflections collected | 22605 | 20669 |
| Independent reflections | 10390 [$R_{int}$ = 0.0283] | 6932 [$R_{int}$ = 0.0504] |
| Goodness-of-fit on $F^2$ | 1.074 | 1.078 |
| Parameters | 991 | 447 |
| Final $R$ indices [$I > 2\sigma(I)$] | $R_1$ = 0.0616, $wR_2$ = 0.1770 | $R_1$ = 0.0534, $wR_2$ = 0.1372 |
| $R$ indices (all data) | $R_1$ = 0.0759, $wR_2$ = 0.1881 | $R_1$ = 0.0815, $wR_2$ = 0.1486 |
| Largest diff. peak and hole [e Å$^{-3}$] | 1.085/–1.328 | 1.178/–1.212 |

 © 2007 Wiley-VCH Verlag GmbH & Co. KGaA, Weinheim 

in MeOH (5 mL) was added. After refluxing for 1 h, the purple solution was evaporated to dryness and the product was separated on a CM Sephadex C-25 ion-exchange column with 0.1 M $NaClO_4$ as eluent. After partial solvent removal from the eluted purple band the product precipitated and was filtered and dried in vacuo. Yield: 0.81 g (0.99 mmol, 51%). ESI-MS (MeOH): *m/z* 291.5 $[V^{IV}{=}O\text{-}(L^2)]^{2+}$, 300.4 $[V^{IV}{=}O\ (L^{2'})]^{2+}$. $C_{28}H_{35}Cl_2N_5O_{17}V$ (835.42): calcd. C 40.25, H 4.22, N 8.38; found C 40.65, H 4.11, N 8.43. IR (KBr): $\tilde{\nu}$ = 3484 br. s, 3092 w, 2956 w, 1728 vs (C=O), 1608 s, 1479 m, 1437 w, 1286 s, 1281 w, 1253 w, 1205 w, 1098 vs, 1086 w, 986 w, 774 m, 658 w, 624 s, 538 w. CV (MeCN): $E$ = –1.10 V (quasi rev.), –0.24 V (irrev.), 1.60 V (irrev.). UV (MeOH): $\lambda$ ($\varepsilon$) = 254 nm (591 $M^{-1}cm^{-1}$), 363 (sh, 290), 514 (30), 695 (29)

**$[V^{IV}{=}O(L^{2'})](BF_4)_2{\cdot}H_2O$:** The reaction was performed in a similar fashion to that of $[V^{IV}{=}O(L^{2'})](ClO_4)_2{\cdot}H_2O$ but with 0.1 M $NaBF_4$ as eluent. Yield: 34%. ESI-MS: *m/z* 291.5 $[V^{IV}{=}O(L^2)]^{2+}$, 300.4 $[V^{IV}{=}O(L^{2'})]^{2+}$, 599.4 $[V^{IV}{=}O(L^2)(OH)]^{+}$. $C_{28}H_{35}B_2F_8N_5O_9V$ (810.13): calcd. C 41.50, H 4.35, N 8.65; found C 41.37, H 4.44, N 8.57. UV (MeOH): $\lambda$ ($\varepsilon$) = 363 nm (290 $M^{-1}cm^{-1}$), 514 (30), 695 (29). IR (KBr): $\tilde{\nu}$ = 3432 br. s, 3112 w, 2962 w, 1732 s, 1608 m, 1482 m, 1438 s, 1284 s, 1258 s, 1060 vs, 776 m, 658 m.

**$[V^{IV}{=}O(L^{3'})]Cl{\cdot}Et_3NHCl{\cdot}1.5H_2O$:** A solution of $VOSO_4$ (239 mg, 0.942 mmol) in MeCN (40 mL) was added to a MeCN solution (50 mL) of $L^3$ (500 mg, 0.942 mmol), followed by triethylamine (131.1 µL, 0.942 mmol). The reaction mixture was refluxed for 1 h, whereupon the color of the solution turned deep green. After the solution had cooled down, water (200 mL) was added and the mixture was transferred to a CM Sephadex C-25 ion-exchange column. The blue band eluted with 0.1 M NaCl was collected. Yield: 513 mg (0.63 mmol, 67%). ESI-MS (MeOH): *m/z* 596.4 $[VO(L^3H_{-1})]^{+}$, 614.4 $[VO(L^{3'}H_{-1})]^{+}$, 628.4 $[VO(L^3H_{-1})(MeOH)]^{+}$. $C_{35}H_{50}Cl_2N_5O_{9.5}V$ (814.65): calcd. C 51.60, H 6.18, Cl 8.71, N 8.60; found C 51.47, H 5.97, Cl 8.83, N 8.79. UV (MeOH): $\lambda$ ($\varepsilon$) = 386 nm (305 $M^{-1}cm^{-1}$), 571 (65), 766 (15, sh). IR (KBr): $\tilde{\nu}$ = 3422 br. s, 3070 w, 2980 w, 2950 w, 2676 m, 2624 m, 2498 w, 1734 vs (C=O), 1606 s, 1482 s, 1458 s, 1274 vs, 1100 vs, 974 s, 770 m, 622 m.

**$[V^{V}{=}O(O_2)(L^{2'})]ClO_4{\cdot}H_2O$:** 30% hydrogen peroxide (300 µL, 10 equiv.) was added to $[V^{IV}{=}O(L^{2'})](ClO_4)_2{\cdot}H_2O$ (0.25 g, 0.30 mmol) in MeOH (30 mL). After stirring at room temp. for 2 h, the formed orange product was purified on a CM Sephadex C-25 ion-exchange column. The orange band was collected by eluting with 0.1 M $NaClO_4$. After partial solvent removal, the precipitated orange solid was collected, washed with water, and dried in vacuo. Yield: 0.43 g (0.14 mmol, 47%). ESI-MS: *m/z* 632.3 $[VO(O_2)\text{-}(L^{2'})]^{+}$. $C_{28}H_{33}ClN_5O_{14}V$ (749.96): calcd. C 44.84, H 4.44, N 9.34; found C 44.59, H 4.55, N 9.20. $^1$H NMR ([D$_6$]DMSO): $\delta$ = 7.23–9.92 (m, 12 H, Ar-H), 5.59 (s, 2 H, N-C*H*), 3.81 (s. 2 H, N-C$H_2$), 3.69 (s, 6 H, O-C$H_3$), 3.57 (s, 3 H, N-C$H_3$), 2.65 (d, 2 H, C$H_2$), 1.95 ppm (d, 2 H, C$H_2$). UV (MeOH): $\lambda$ ($\varepsilon$) = 456 nm (137 $M^{-1}cm^{-1}$). IR (KBr): $\tilde{\nu}$ = 3378 s, 2952 w, 1734 vs, 1608 s, 1475 m, 1450 w, 1436 w, 1286 s, 1250 s, 1164 w, 1098 s, 1061 w, 1035 w, 1012 w, 963 w, 932 w, 890 w, 785 w, 771 w, 675 w, 623 m, 523 m.

**$[V^{V}{=}O(O_2)(L^{2'})NO_3{\cdot}H_2O]$:** The reaction was performed in a similar fashion to that of $[V^{V}{=}O(O_2)(L^{2'})]ClO_4{\cdot}H_2O$ but with 0.1 M $NaNO_3$ as eluent. ESI-MS(+): *m/z* 614.3 $[VO_3(L^2)]^{+}$, 632.4 $[VO_3(L^{2'})]^{+}$, 646.4 $[VO_3(L^2)(MeOH)]^{+}$; ESI-MS(–): *m/z* 738.2 $[VO_3(L^2)(NO_3)_2]^{-}$, 756.2 $[VO_3(L^{2'})(NO_3)_2]^{-}$, 770.2 $[VO_3(L^2)(NO_3)_2\text{-}(MeOH)]^{-}$. $C_{28}H_{33}N_6O_{13}V$ (712.51): calcd. C 47.20, H 4.67, N 11.80; found C 47.02, H 4.56, N 12.62. UV (MeOH): $\lambda$ ($\varepsilon$) = 450 nm (350 $M^{-1}cm^{-1}$, sh). IR (KBr): $\tilde{\nu}$ = 3430 br. s, 3070 w, 2956 m, 1730 vs, 1606 s, 1480 m, 1436 m, 1384 s, 1278 m, 1250 m, 1204 w, 1158 m, 1106 m, 1060 s, 1032 m, 1006 w, 961 s, 937 m, 923 w, 830 w, 788 m, 674 m, 657 m, 585 m, 527 w.

**$[V^{V}{=}O(^{18}O_2)(L^{2'})]ClO_4{\cdot}H_2O$:** The reaction was performed in a similar fashion to that of $[V^{V}{=}O(O_2)(L^{2'})]ClO_4{\cdot}H_2O$ but with 2% $H_2{}^{18}O_2$ as oxidant. IR (KBr): $\tilde{\nu}$ = 3422 br. s, 3120 w, 2958 w, 2852 w, 1734 vs, 1608 m, 1482 m, 1436 m, 1282 s, 1252 s, 1098 vs, 1036 sh, 1012 m, 964 m, 936 w, 914 w, 886 m, 786 m, 772 m, 624 s.

**$[V^{V}{=}O(O_2)(L^{3'}H_{-1})]Cl{\cdot}Et_3NHCl{\cdot}3.5H_2O$:** A 30% (w/w) $H_2O_2$ solution (3.09 mL, 116 equiv.) was added to a solution of $[V^{IV}{=}O(L^{3'}H_{-1})]Cl{\cdot}Et_3NHCl{\cdot}1.5H_2O$ (211 mg, 0.259 mmol) in MeOH (40 mL). The reaction mixture was stirred for one week at room temp., whereupon the color turned orange. After dilution with water the mixture was transferred to a CM Sephadex C-25 ion-exchange column, and the main orange band was collected with 0.1 M NaCl as eluent. Yield: 64 mg (0.049 mmol, 19%). ESI-MS: *m/z* 629.3 $[V^{V}{=}O(O_2)(L^3H_{-1})]^{+}$, 647.4 $[V^{V}{=}O(O_2)(L^{3'}H_{-1})]^{+}$, 661.3 $[V^{V}{=}O(O_2)(L^3H_{-1})(MeOH)]^{+}$. $C_{53}H_{103}Cl_5N_8O_{13.5}V$ (1296.7): calcd. C 49.09, H 8.00, Cl 13.67, N 8.64; found C 49.09, H 7.35, Cl 13.67, N 8.66. IR (KBr): $\tilde{\nu}$ = 3430 br. s, 2977 w, 2942 w, 2678 m, 2623 w, 2604 w, 2495 m, 1734 m, 1607 m, 1473 m, 1442 m, 1279 br m, 1261 br m, 1106 w, 1036 w, 959 w. UV (MeOH): $\lambda$ ($\varepsilon$) = 431 nm (240 $M^{-1}cm^{-1}$).

**$[V^{V}{=}O(^{18}O_2)(L^{2'})]NO_3{\cdot}H_2O$:** The reaction was performed in a similar fashion to that of $[V^{V}{=}O(O_2)(L^{2'})]NO_3{\cdot}H_2O$ but with 2% $H_2{}^{18}O_2$ as oxidant. IR (KBr): $\tilde{\nu}$ = 3420 br. s, 3080 br. m, 2952 m, 2852 w, 1732 s, 1608 m, 1480 w, 1436 m, 1384 vs, 1278 s, 1250 s, 1162 m, 1106 m, 1060 s, 1034 m, 1012 w, 962 m, 938 m, 886 s, 786 m sh, 776 sh, 758 m, 674 m, 658 m, 584 m, 517 m

**Catalysis Test Reactions**

**Haloperoxidase Test:** Bromination of the organic dye Phenol Red was carried out under conditions reported in the literature.[30]

**Cyclohexene Oxidation:** An $H_2O_2$ solution (0.3 mL; prepared by mixing 60 µL of 35% $H_2O_2$ and 10 mL of dry acetonitrile) was injected over 30 min with a syringe pump to a mixture of 2.1 µmol of vanadium complex and 2.1 mmol of cyclohexene in 2.7 mL of dry acetonitrile. After a given reaction time 1 mL of 6.8 mM naphthalene in acetonitrile was added as internal standard. The mixture was passed through a silica column, washed with ethyl acetate, and the eluate was directly analyzed by GC.[41]

## Acknowledgments

Financial support by the German Science Foundation (DFG) is gratefully acknowledged.

[1] A. Butler, J. V. Walker, *Chem. Rev.* **1993**, *93*, 1937.
[2] D. Rehder, *Angew. Chem.* **1991**, *103*, 152; *Angew. Chem. Int. Ed. Engl.* **1991**, *30*, 148.
[3] A. Butler, M. J. Clague, G. E. Meister, *Chem. Rev.* **1994**, *94*, 625.
[4] H. Mimoun, L. Saussine, E. Daire, M. Postel, J. Fischer, R. Weiss, *J. Am. Chem. Soc.* **1983**, *105*, 3101.
[5] A. Shaver, J. B. Ng, A. Hall, B. S. Lum, B. I. Posner, *Inorg. Chem.* **1993**, *32*, 3109.
[6] P. Caravan, L. Gelmini, N. Glover, F. G. Herring, H. J. H. McNeill, S. J. Rettig, I. A. Setyawati, Y. E. Sun, S. Tracey, V. G. Yuen, C. Orvig, *J. Am. Chem. Soc.* **1995**, *117*, 127.
[7] C. Bleiholder, H. Börzel, P. Comba, R. Ferrari, A. Heydt, M. Kerscher, S. Kuwata, G. Laurenczy, G. A. Lawrance, A. Lienke, B. Martin, M. Merz, B. Nuber, H. Pritzkow, *Inorg. Chem.* **2005**, *44*, 8145.

 © 2007 Wiley-VCH Verlag GmbH & Co. KGaA, Weinheim 

[8] G. J. Colpas, B. J. Hamstra, J. W. Kampf, V. L. Pecoraro, *J. Am. Chem. Soc.* **1996**, *118*, 3469.
[9] H. Kelm, H.-J. Krüger, *Inorg. Chem.* **1996**, *35*, 3533.
[10] J. Selbin, *Coord. Chem. Rev.* **1966**, *1*, 293.
[11] H. Kelm, H.-J. Krüger, *Angew. Chem.* **2001**, *113*, 2406; *Angew. Chem. Int. Ed.* **2001**, *40*, 2344.
[12] P. Comba, M. Kerscher, M. Merz, V. Müller, H. Pritzkow, R. Remenyi, W. Schiek, Y. Xiong, *Chem. Eur. J.* **2002**, *8*, 5750.
[13] M. R. Bukowski, P. Comba, C. Limberg, M. Merz, L. Que Jr, T. Wistuba, *Angew. Chem.* **2004**, *116*, 1303; *Angew. Chem. Int. Ed.* **2004**, *43*, 1283.
[14] M. R. Bukowski, P. Comba, A. Lienke, C. Limberg, C. Lopez de Laorden, R. Mas-Balleste, M. Merz, L. Que Jr, *Angew. Chem.* **2006**, *118*, 3524; *Angew. Chem. Int. Ed.* **2006**, *45*, 3446.
[15] M. Atanasov, P. Comba, manuscript in preparation.
[16] F. Bohlmann, *Chem. Ber.* **1958**, *91*, 2157.
[17] X. Li, M. S. Lah, V. L. Pecoraro, *Inorg. Chem.* **1988**, *27*, 4657.
[18] J. A. Bonadies, C. J. Carrano, *J. Am. Chem. Soc.* **1986**, *108*, 4088.
[19] L. E. Orgel, *J. Chem. Phys.* **1955**, *23*, 1819.
[20] T. S. Piper, R. L. Carlin, *J. Chem. Phys.* **1960**, *33*, 1208.
[21] D. Wang, G. R. Hanson, *J. Magn. Reson. Ser. A* **1995**, *117*, 1.
[22] C. J. Ballhausen, H. B. Gray, *Inorg. Chem.* **1962**, *1*, 111.
[23] P. Comba, L. M. Engelhardt, J. M. Harrowfield, G. A. Lawrance, L. L. Martin, A. M. Sargeson, A. H. White, *J. Chem. Soc., Chem. Commun.* **1985**, 174.
[24] P. Comba, A. M. Sargeson, *Aust. J. Chem.* **1986**, *39*, 1029.
[25] R. Ma, A. Bakac, J. H. Espenson, *Inorg. Chem.* **1992**, *31*, 1925.
[26] C. J. Cramer, W. B. Tolman, K. H. Theopold, A. L. Rheingold, *Proc. Natl. Acad. Sci. USA* **2003**, *100*, 3635.
[27] J. D. Dunitz, E. F. Maverick, K. N. Trueblood, *Angew. Chem.* **1988**, *100*, 910; *Angew. Chem. Int. Ed. Engl.* **1988**, *27*, 880.
[28] R. C. Thompson, *Inorg. Chem.* **1982**, *21*, 859.
[29] R. C. Thompson, *Inorg. Chem.* **1983**, *22*, 584.
[30] G. J. Colpas, B. J. Hamstra, J. W. Kampf, V. L. Pecoraro, *J. Am. Chem. Soc.* **1994**, *116*, 3627.
[31] U. Schuchardt, M. C. Guerreiro, G. B. Shul′pin, *Russ. Chem. Bull.* **1998**, *47*, 247.
[32] D. M. Boghaei, S. Mohebi, *J. Mol. Catal. A: Chem.* **2002**, *179*, 41.
[33] H. Weiner, A. Trovarelli, R. G. Finke, *J. Mol. Catal. A: Chem.* **2003**, *191*, 217.
[34] U. Holzgrabe, E. Ericyas, *Arch. Pharm.* **1992**, *325*, 657.
[35] H. Börzel, P. Comba, K. S. Hagen, M. Merz, Y. D. Lampeka, A. Lienke, G. Linti, H. Pritzkow, L. V. Tsymbal, *Inorg. Chim. Acta* **2002**, *337*, 407.
[36] G. M. Sheldrick, University of Göttingen, Germany, **2004**.
[37] G. M. Sheldrick, University of Göttingen, Germany, **1986**.
[38] G. M. Sheldrick, *Acta Crystallogr., Sect. A* **1990**, *46*, 467.
[39] G. M. Sheldrick, University of Göttingen, Germany, **1997**.
[40] K. N. Trueblood, UCLA, CA, USA, **1987**.
[41] M. Merz, Dissertation, University of Heidelberg.

Received: October 1, 2006
Published Online: December 27, 2006

 © 2007 Wiley-VCH Verlag GmbH & Co. KGaA, Weinheim 

DOI: 10.1002/ejic.200601025

# Alkyl Abstraction from a Trialkylyttrium Complex $[YR_3(thf)_2]$ ($R = CH_2SiMe_3$) Using a Group-13 Element Lewis Acid $ER_3$ (E = B, Al, Ga, In) – Structural Characterisation of the Ion Pair $[YR_2(thf)_4]^+[GaR_4]^-$ and of $ER_3$ (E = B, Al, Ga)

**Mathias U. Kramer,[a] Dominique Robert,[a] Yumiko Nakajima,[a] Ulli Englert,[a] Thomas P. Spaniol,[a] and Jun Okuda*[a]**

**Keywords:** Yttrium / Lewis acids / Alkyl abstraction / Group-13 elements / Cationic complexes

The alkyl abstraction reaction of $[YR_3(thf)_2]$ ($R = CH_2SiMe_3$) with group-13 trialkyl complexes $[(ER_3)_n]$ (E = B, Ga, In: $n$ = 1; E = Al: $n$ = 2) forming cationic yttrium species $[YR_2(thf)_4]^+[ER_4]^-$ (E = Al, Ga, In) shows a strong dependence on the Lewis acidic metal centre E and on the solvent basicity. Whilst the boron compound does not react with $[YR_3(thf)_2]$, the heavier homologues form the ion pairs $[YR_2(thf)_4]^+[ER_4]^-$ (E = Al, Ga, In) which dissociate to give the neutral compounds in apolar solvents such as benzene. Single-crystal structure analysis of the gallate $[YR_2(thf)_4]^+[GaR_4]^-$ shows the presence of an ion pair with *cis*-arranged alkyl ligands in the octahedral yttrium cation and a tetrahedral gallate anion. Group-13 trialkyl compounds $[(ER_3)_n]$ (E = B, Al, Ga), all liquids at room temperature, and $[Li(12\text{-crown-}4)_2]^+[AlR_4]^-$ were characterised by single-crystal X-ray diffraction and NMR spectroscopy.
(© Wiley-VCH Verlag GmbH & Co. KGaA, 69451 Weinheim, Germany, 2007)

## Introduction

There has recently been an increasing interest in cationic alkyl complexes of rare-earth metals, due to their enhanced electrophilicity and application in homogeneous catalysis, most prominently in α-olefin polymerisation catalysis.[1] One way to generate and isolate the cationic species is to irreversibly react neutral trialkyl complexes $[LnR_3(L)_n]$ with a weak Brønsted acid such as $[NEt_3H][BPh_4]$ or a strong Lewis acid such as $[Ph_3C][B(C_6F_5)_4]$. Another way is an alkyl abstraction with neutral Lewis acids, in particular group-13 organometallic compounds such as $[B(C_6X_5)_3]$ (X = H, F). The resulting ion pairs are either charge-separated or consist of contact ion pairs, such as $[ScMe_2(Me_3\text{-}TACN)(\mu\text{-}Me)B(C_6F_5)_3]$, (TACN = 1,4,7-triazacyclononane) prepared from $[ScMe_3(Me_3\text{-}TACN)]$ and $[B(C_6F_5)_3]$ in thf.[2] In the context of studying homogeneous ethylene polymerisation catalysis by $[Y(CH_2SiMe_3)_3(thf)_2]$/$[PhNMe_2H][B(C_6F_5)_4]$/$[AlR_3]$ we isolated a charge-separated ion pair $[Y(CH_2SiMe_3)_2(thf)_4]^+[Al(CH_2SiMe_3)_4]^-$ (**1a**) from the reaction of $[Y(CH_2SiMe_3)_3(thf)_2]$ and $[Al(CH_2SiMe_3)_3(thf)]$ that underwent further protonolysis to afford the dication $[Y(CH_2SiMe_3)(thf)_5]^+[B(C_6F_5)_4]^-{}_2$.[3,4] We report here a solvent dependent reversible equilibrium between ionic **1a** and its neutral precursors $[Y(CH_2SiMe_3)_3(thf)_2]$ and $[Al(CH_2SiMe_3)_3(thf)]$ and an extension of this alkyl abstraction reaction to the use of homologous group-13 trialkyl compounds $[\{E(CH_2SiMe_3)_3\}_n]$ (E = B, **3**, $n$ = 1; E = Al, **4**, $n$ = 2; E = Ga, **5**, $n$ = 1; E = In, **6**, $n$ = 1). In addition, we present the crystal structures of the group-13 trialkyl complexes **3**–**5**.[5]

[a] Institute of Inorganic Chemistry, RWTH Aachen University
Landoltweg 1, 52074 Aachen, Germany
Fax: +49-241-8092644
E-mail: jun.okuda@ac.rwth-aachen.de

## Results and Discussion

### Cationic Yttrium Complexes

Encouraged by the facile formation of **1a** by reaction of the trialkyl compound $[Y(CH_2SiMe_3)_3(thf)_2]$ with a stoichiometric amount of the trialkylaluminium **4** in thf,[3,4] attempts were made to synthesise yttrium cationic complexes bearing the analogous borate, gallate and indate anions, $[B(CH_2SiMe_3)_4]^-$, $[Ga(CH_2SiMe_3)_4]^-$, and $[In(CH_2SiMe_3)_4]^-$ respectively. It was found, however, that whilst the reaction proceeds at ambient temperature for the gallium and indium species **5** and **6** in thf, no reaction was observed with the borane **3** in $[D_8]$thf or $[D_5]$bromobenzene at elevated temperatures up to 60 °C. The lack of reactivity of **3** is not only due to insufficient Lewis acidity of the boron atom in **3**, as $[B(CH_2SiMe_3)_4]^-$ is a known species with a variety of cations,[6] but it appears that the neutral boron compound is not sufficiently electrophilic to abstract an alkyl group from the yttrium centre. A possible explanation is the formation of a very stable adduct with thf, as is the case in the alkyl abstraction from $[Y(CH_2SiMe_3)_3(thf)_2]$

 © 2007 Wiley-VCH Verlag GmbH & Co. KGaA, Weinheim 

using $[B(C_6F_5)_3]$, where heating of the reaction mixture was necessary for the abstraction to proceed.[4] The low reactivity of **3** towards Lewis bases compared to the remaining group-13 species is also illustrated in its negligible water sensitivity, whereas **4**–**6** all react with water.[5] The formation of alkyl gallates and indates $[Y(CH_2SiMe_3)_2(thf)_4]^+$-$[E(CH_2SiMe_3)_4]^-$ (E = Ga, **1b**; In, **1c**) as charge-separated ion pairs in thf solutions (vide infra) represents the first cationic rare-earth metal alkyl complexes with these anions (Table 1). Previously only neutral complexes with bridging alkyl groups bound to gallium were reported.[7]

Table 1. Selected bond lengths [Å] and bond angles [°] for **1b**[a] and **7c**.

| $[Y(CH_2SiMe_3)_2(thf)_4]^+$ $[Ga(CH_2SiMe_3)_4]^-$ (**1b**) | | $[Li(12\text{-crown-}4)_2]^+$ $[Al(CH_2SiMe_3)_4]^-$ (**7c**) | |
|---|---|---|---|
| Y2–C41 | 2.400(3) | | |
| Y2–C45 | 2.368(3) | | |
| Y2–O5 | 2.479(2) | | |
| Y2–O6 | 2.3349(19) | | |
| Y2–O7 | 2.3243(19) | | |
| Y2–O8 | 2.424(2) | | |
| C41–Y2–C45 | 102.94(11) | | |
| Ga1–C25 | 2.038(3) | Al–C17 | 2.0300(13) |
| Ga1–C29 | 2.040(3) | Al–C18 | 2.0247(14) |
| Ga1–C33 | 2.057(3) | Al–C19 | 2.0278(14) |
| Ga1–C37 | 2.031(3) | Al–C20 | 2.0311(14) |
| C33–Ga1–C37 | 108.06(11) | C17–Al–C18 | 114.80(6) |
| C37–Ga1–C25 | 107.98(13) | C17–Al–C19 | 106.43(6) |
| C37–Ga1–C29 | 109.59(11) | C17–Al–C20 | 107.58(6) |

[a] For **1b** only one of the two crystallographically independent ion pairs chosen.

Based on the results from X-ray crystallographic and NMR spectroscopic analysis in $[D_8]$thf, complex **1a** was described previously as a charge-separated ion pair.[3,4] When measured in less donating solvents, such as $[D_6]$benzene, $[D_8]$toluene and $[D_5]$bromobenzene, the previously isolated complex **1a** dissociates to form $[Y(CH_2SiMe_3)_3(thf)_2]$ and $[Al(CH_2SiMe_3)_3(thf)]$ (Scheme 1). The NMR spectra are exact superpositions of the spectra of the corresponding neutral species.[8] A notable feature for the $AlCH_2$ signal in the $^1H$ NMR spectra ($[D_8]$thf) is that the signal in $[Al(CH_2SiMe_3)_3(thf)]$ is a singlet, whilst the corresponding resonance in the anion $[Al(CH_2SiMe_3)_4]^-$ is a distorted sextet due to coupling to quadrupolar aluminium ($I$ = 5/2) that collapses to a singlet in the $^1H\{^{27}Al\}$ decoupled spectrum (Figure 1). Correspondingly, the $^{27}Al$ NMR shows a nonet at $\delta$ = 150.9 ppm with $^2J_{Al,H}$ = 9.0 Hz. The same NMR spectroscopic features are found for the lithium salts containing the anion $[Al(CH_2SiMe_3)_4]^-$ (vide infra), confirming the ion separation in thf solution.

Addition of one equivalent of 12-crown-4 to a $[D_6]$benzene solution of **1a** results in complete ionisation of the neutral species to form the previously reported ion pair $[Y(CH_2SiMe_3)_2(12\text{-crown-}4)(thf)]^+[Al(CH_2SiMe_3)_4]^-$ (**2a**).[4] Similarly, upon addition of $[D_8]$thf to the $[D_6]$benzene solution of the neutral compounds, dissociation occurs, depending on the solvent mixture and temperature. An investigation of **1a** in a range of $[D_6]$benzene/$[D_8]$thf mixtures (composition range 40–60 mol-% of $[D_8]$thf) and at different temperatures was therefore conducted. However, even inside this reduced range, an exact quantification of equilibrium constants $K = c([Y(CH_2SiMe_3)_2(thf)_4][Al(CH_2SiMe_3)_4])/c([Y(CH_2SiMe_3)_3(thf)_2])\cdot c([Al(CH_2SiMe_3)_3(thf)])$ for the equilibrium depicted in Scheme 1 remained difficult due to peak overlapping in the $^1H$ NMR spectra. An increase in the amount of $[D_8]$thf leads to an increase in the dissociation constant $K$. Using a 60:40 mixture $[D_8]$thf/$[D_6]$benzene, variable-temperature NMR measurements were conducted at 25 °C, 35 °C, and 45 °C. Using the van't Hoff equation $d(\ln K)/dT = \Delta_r H°/RT^2$, the standard enthalpy change for the ionisation $\Delta_r H°$ is estimated as about –70 kJ mol$^{-1}$ at 308 K. The exchange equilibrium is slow on the NMR timescale, as coupling patterns of the neutral and cationic yttrium species are observed.

Similarly to the aluminate **1a**, both gallate **1b** and indate **1c** form charge-separated complexes in thf solutions. The signals in their NMR spectra belonging to the $[Y(CH_2SiMe_3)_2(thf)_4]^+$ cation are identical to those reported for the aluminate **1a** and similar to those of compounds containing other anions (Table 2), indicating that the anions are only weakly coordinating in the $[D_8]$thf solutions.[9] Probably due to the quadrupolar nature of Ga ($I$ = 3/2) and In ($I$ = 9/2), the $^1H$ NMR signals assigned to the $ECH_2$ (E = Ga, In) protons are very broad (Figure 2). The corresponding signal for the indate **1c** in the $^{13}C$ NMR spectrum is not detected, as was previously noted for the $^{13}C$ signals of $BCH_2$ in similar complexes containing the $[B(C_6X_5)_3(CH_2SiMe_3)]^-$ (X = H, F) anions.[4]

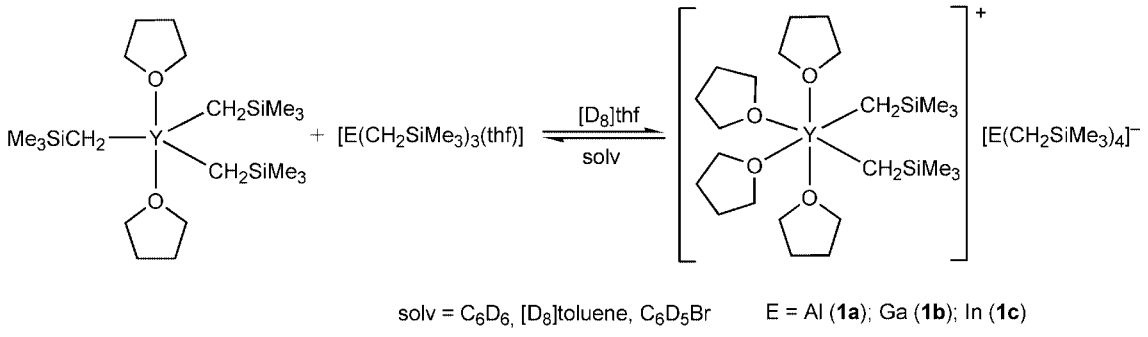


Scheme 1.

 © 2007 Wiley-VCH Verlag GmbH & Co. KGaA, Weinheim 

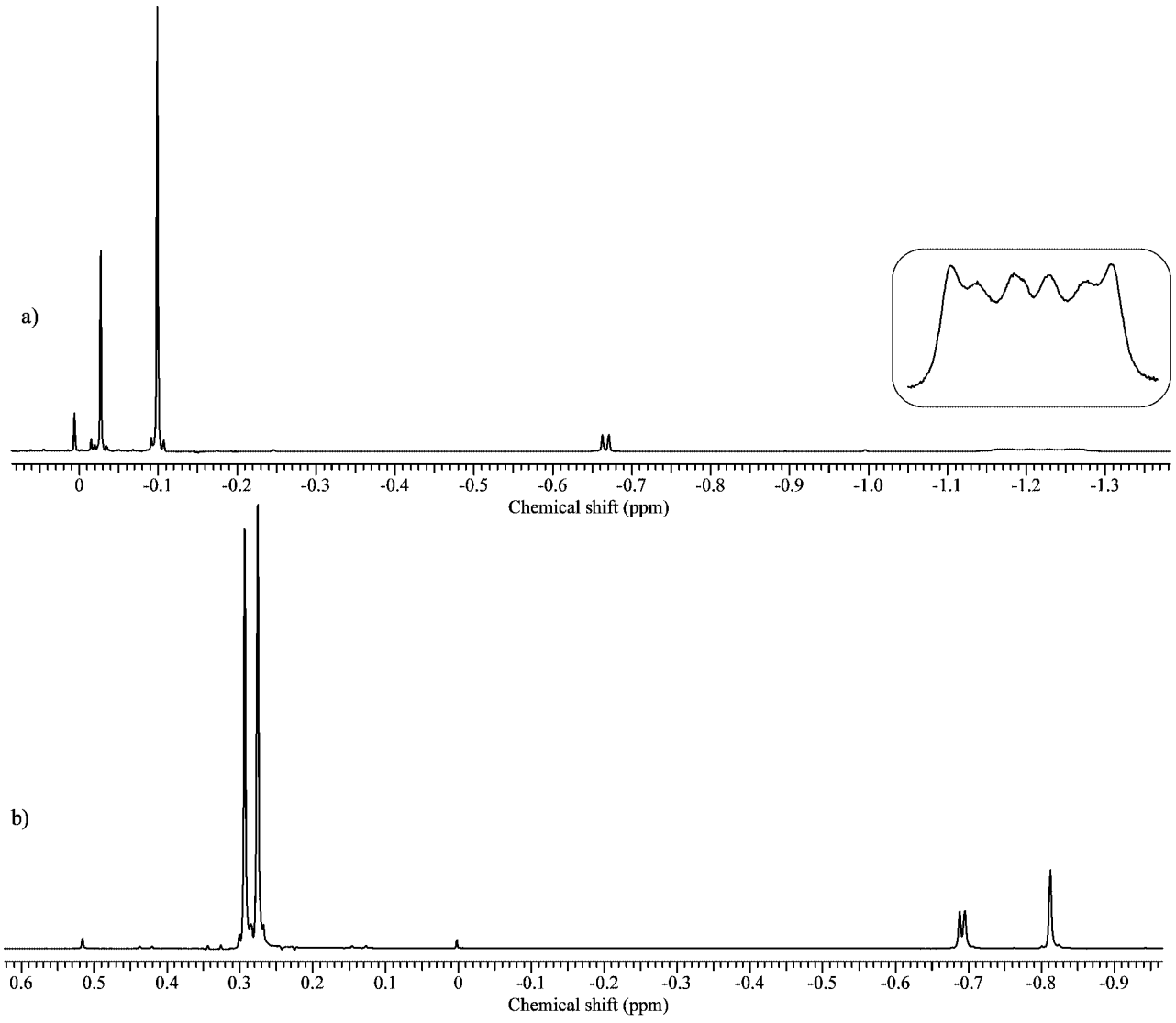


Figure 1. $^1$H NMR spectra at 25 °C of $[Y(CH_2SiMe_3)_2(thf)_4]^+[Al(CH_2SiMe_3)_4]^-$ (**1a**) in a) $[D_8]$thf and b) in $C_6D_6$.

Table 2. $^1$H NMR spectroscopic data (25 °C, $[D_8]$thf) for $[Y(CH_2SiMe_3)_2(thf)_4]^+[A]^-$.

| Anion [A] | $\delta_H$ of $YCH_2$ (ppm) | $^2J_{Y,H}$ (Hz) | Ref. |
|---|---|---|---|
| $[Ga(CH_2SiMe_3)_4]$ | –0.68 | 3.0 | this work |
| $[In(CH_2SiMe_3)_4]$ | –0.68 | 3.3 | this work |
| $[Al(CH_2SiMe_3)_4]$ | –0.68 | 3.2 | this work |
| $[B(C_6F_5)_4]$ | –0.69 | 3.2 | [4] |
| $[BPh_4]$ | –0.77 | 3.3 | [4] |
| $[B(C_6F_5)_3(CH_2SiMe_3)]$ | –0.70 | 2.9 | [4] |
| $[BPh_3(CH_2SiMe_3)]$ | –0.80 | 3.2 | [4] |

When NMR spectra of **1b** and **1c** are measured in $[D_6]$benzene, $[D_8]$toluene, and $[D_5]$bromobenzene, it is found that on the NMR timescale all $CH_2$ protons and all $SiMe_3$ protons are equivalent in these solvents. The peaks in the $^1$H NMR spectra appear broad, and lack any coupling pattern to yttrium. It is therefore postulated that the molecules are fluxional and exchange alkyl groups intermolecularly (due to the lack of coupling) fast on the NMR timescale. Spectra of **1b** in $[D_8]$thf and $[D_6]$benzene are shown in Figure 2. This situation is similar to that found in compounds of the type $MR_2{\cdot}ZnR_2$ (M = Sr or Ba; R = $CH_2SiMe_3$).[10] NMR spectroscopic analysis of these compounds showed that all alkyl groups are chemically and magnetically equivalent on the NMR timescale and an equilibrium between neutral alkyl complexes, "ate" complexes, contact ion pairs and solvent separated ions was proposed in the literature.[10–12]

A further example for solvent dependence of the structures and for intra-/intermolecular exchange was reported for $[La(\eta^5\text{-}C_5Me_5)\{CH(SiMe_3)_2\}BPh_4]$, where the tetraphenylborate anion is coordinating to the lanthanum centre in aromatic solvents. In constrast to the case of **1b** and **1c**, irreversible charge separation is achieved by solvation to give $[La(\eta^5\text{-}C_5Me_5)\{CH(SiMe_3)_2\}(thf)_3][BPh_4]$ in thf.[13]

 © 2007 Wiley-VCH Verlag GmbH & Co. KGaA, Weinheim 

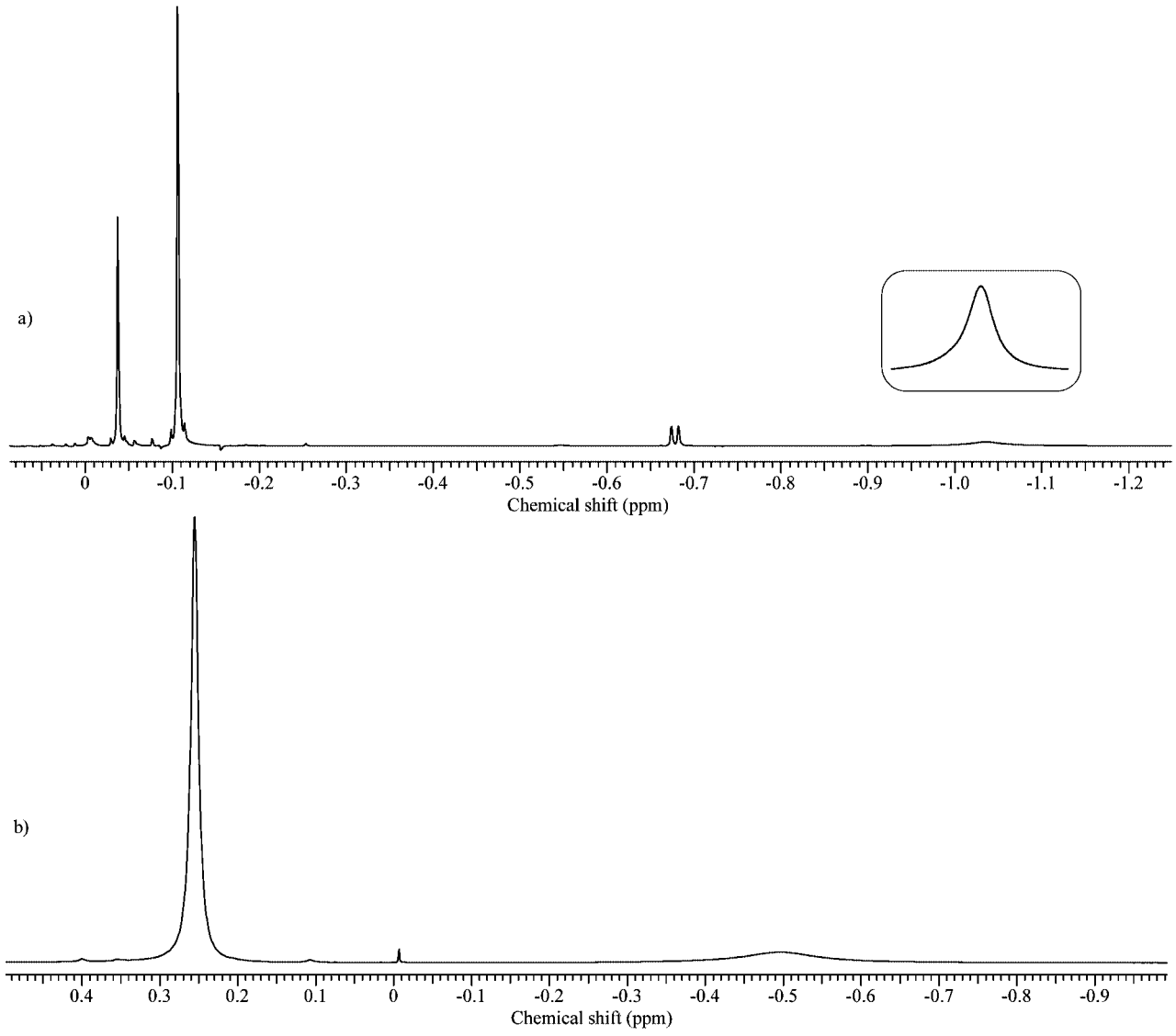


Figure 2. $^1$H NMR spectra at 25 °C of $[Y(CH_2SiMe_3)_2(thf)_4][Ga(CH_2SiMe_3)_4]$ (**1b**) in a) $[D_8]$thf and b) in $C_6D_6$.

Upon addition of one equivalent of 12-crown-4 to $[D_6]$-benzene solutions of **1b** and **1c** the molecules separate into the charge-separated ion pairs $[Y(CH_2SiMe_3)_2(12\text{-crown-4})(thf)]^+[E(CH_2SiMe_3)_4]^-$ (E = Ga, **2b**; In, **2c**), as was observed for **1a**. The peaks arising from the cationic yttrium species are similar in all three cases, implying only weakly coordinating anions.

Single crystals of the gallate **1b** suitable for X-ray analysis were grown by slowly cooling a thf/pentane solution to –30 °C. The unit cell contains two sets of independent ion pairs, each expressing slightly distorted tetrahedral geometry around the gallium atom and distorted octahedral geometry around the yttrium centre (Figure 3). Whilst the cationic fragments express a similar octahedral geometry with *cis*-arranged alkyl groups to that observed in $[Y(CH_2SiMe_3)_2(thf)_4]^+[Al(CH_2SiMe_3)_4]^-$ (**1a**),[3] the anionic fragments are slightly more distorted from perfect tetrahedral geometry than their aluminate counterparts, with C–Ga–C angles ranging from 107.98(13)° to 111.02(11)°, compared to C–Al–C bond angles only ranging from 108.9(2)° to 109.8(3)° (vide infra).

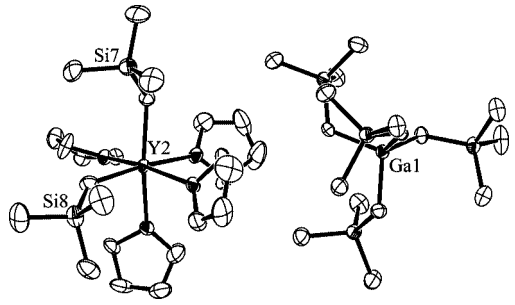


Figure 3. ORTEP representation of one ion pair of $[Y(CH_2SiMe_3)_2(thf)_4]^+[Ga(CH_2SiMe_3)_4]^-$ (**1b**). Displacement ellipsoids drawn at the 50% probability level, hydrogen atoms omitted for clarity.

 © 2007 Wiley-VCH Verlag GmbH & Co. KGaA, Weinheim 

The Y–C bond lengths range from 2.375(3) Å to 2.400(3) Å and thus lie within the range of distances reported in the literature for cationic and neutral (trimethylsilymethyl)yttrium complexes as are the Y–O distances [2.324(2) Å to 2.478(2) Å].[4] The Ga–C distances found in the two anions range from 2.031(3) Å to 2.058(3) Å (mean 2.042 Å) and are very similar to those found for the sterically less demanding benzyl ligand in $[Mg_3Br_{2.4}Cl_{1.6}(OEt_2)_6][Ga(CH_2Ph)_4]_2$·0.5 toluene (2.039 Å mean),[14] the terminal trimethylsilylmethyl ligand in $[Li(dioxane)_{1.5}][Ga(CH_2SiMe_3)_4]$ (2.025 Å mean),[15] and the bulky fluorenyl ligand in $[Li(DME)_3][Ga(C_{13}H_9)_4]$ (2.062 Å mean).[16] Compared to the parent molecule **5** the bonds have increased in length by about 5%.

### Structure of Tris(trimethylsilylmethyl) Group-13 Metal Complexes

To compare the Lewis acidity of the group-13 complexes we have carried out structural comparison of the (trimethylsilylmethyl)boron, -aluminium and -gallium compounds **3**–**5**. As expected, only the aluminium compound turned out to be dinuclear (Table 3).

Table 3. Selected bond lengths [Å] and bond angles [°] for **3**, **4** and **5**.

| | $[B(CH_2SiMe_3)_3]$ | $[\{Al(CH_2SiMe_3)_3\}_2]$ | $[Ga(CH_2SiMe_3)_3]$ |
|---|---|---|---|
| M–M | – | 2.8328(13) | – |
| M–C1 | 1.567(3) | 2.031(2) | 1.954(4) |
| M–C2 | 1.563(3) | 1.958(2) | 1.971(3) |
| M–C3 | 1.573(3) | 1.958(2) | 1.952(4) |
| M–C1′ | – | 2.336(2) | – |
| C1–Si1 | 1.871(2) | 1.909(2) | 1.852(4) |
| C2–Si2 | 1.8820(19) | 1.854(2) | 1.855(4) |
| C3–Si3 | 1.874(2) | 1.858(2) | 1.852(4) |
| C1–M–C2 | 119.01(17) | 116.46(10) | 118.61(16) |
| C2–M–C3 | 121.12(17) | 115.35(9) | 121.82(16) |
| C3–M–C1 | 119.82(18) | 111.53(9) | 119.56(15) |
| M–C1–M′ | – | 80.55(7) | – |
| M–C1–Si1 | 117.13(13) | 109.10(10) | 116.60(19) |
| M–C2–Si2 | 114.27(14) | 130.21(12) | 114.82(19) |
| M–C3–Si3 | 119.73(15) | 124.75(11) | 118.24(19) |
| M–C1′–Si1′ | – | 167.57(12) | – |

#### *Tris(trimethylsilylmethyl)boron*

As expected, the crystal structure of tris(trimethylsilylmethyl)boron (**3**), Figure 4, revealed discrete molecules, structurally similar to $BEt_3$ with respect to the arrangement of the ligands around the central atom.[17] The three B–C–Si angles [117.04° on average, ranging from 114.27(14)° to 119.73(15)°] deviate from the ideal tetrahedral angle 109.47° at the carbon, which was already observed in other tris(alkyl) boron compounds (cf. $BEt_3$: B–C–C average: 118.9°,[17] or B*t*Bu$_3$: B–C–C 120.6(2)°[18]). In these compounds, hyperconjugation was invoked to justify these abnormally large values. In **3** however, it is more likely that the important steric bulk of the trimethylsilyl groups dictates their orientation, rather than hyperconjugation. Indeed, the B–C–Si angles of the two groups pointing towards each other [B–C1–Si1 117.13(13)° and B–C3–Si3 119.73(15)°] are found to be larger than the corresponding angle in the third alkyl group [B–C2–Si2 114.27(14)°].

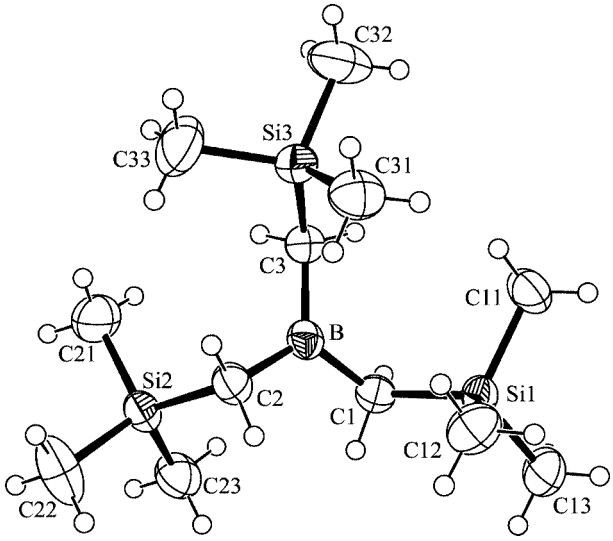


Figure 4. ORTEP representation of the molecular structure of $[B(CH_2SiMe_3)_3]$ (**3**). Displacement ellipsoids of non-H atoms drawn at the 50% probability level.

The B–C bond lengths [1.568 Å mean, ranging from 1.563(3) Å to 1.573(3) Å] do not present any particular deviation from the values typically observed in homoleptic boron compounds. The same was observed for the C–B–C angles, the planar geometry around the boron centre being almost perfect ($\Sigma_{C-B-C}$ = 359.95°).

#### *Tris(trimethylsilylmethyl)aluminium*

As many other homoleptic (e.g. $[(AlMe_3)_2]$,[19] $[(AlPh_3)_2]$,[20] $[\{Al(cyclo\text{-}Pr)_3\}_2]$,[21] $[\{Al(C_6H_4\text{-}2\text{-}Me)_3\}_2]$[22]) and mixed-alkyl (e.g. $[\{AlMe_2(\mu\text{-}Ph)\}_2]$,[23] $[\{Al\textit{i}Bu_2(\mu\text{-}C{=}C\textit{t}Bu)\}_2]$[24]) aluminium species, $[\{Al(CH_2SiMe_3)_3\}_2]$ (**4**), Figure 5, was found to adopt a dimeric structure. The molecule shows crystallographic inversion symmetry and exhibits in addition two non-equivalent C–Al bonds for each bridging carbon in the solid state. Only few organoaluminium compounds have so far been reported to exhibit such unsymmetrical bridges (e.g. $[\{AlPh_2(\mu\text{-}C{\equiv}CPh)\}_2]$,[25] or $[\{AlMe_2(\mu\text{-}C{\equiv}CMe)\}_2]$[26]). Until now, to the best of our knowledge, no homoleptic dimeric trialkylaluminium compound featuring non-equivalent bridges has been reported. Thus **4** appears to be the first example for this coordination mode in the solid state. These findings are in agreement with a previous report that **4** is only partially dimerised in benzene solution based on cryoscopic measurements.[27]

Due to steric bulk of the $CH_2SiMe_3$ groups, the Al–Al distance observed in $[\{Al(CH_2SiMe_3)_3\}_2]$ of 2.8328(13) Å is amongst the longest reported. As a consequence, the Al–C1–Al′ bridge angle of 80.55(7)° is also slightly larger than usually observed (Table 4). Only heteroleptic aluminium de-

 © 2007 Wiley-VCH Verlag GmbH & Co. KGaA, Weinheim 

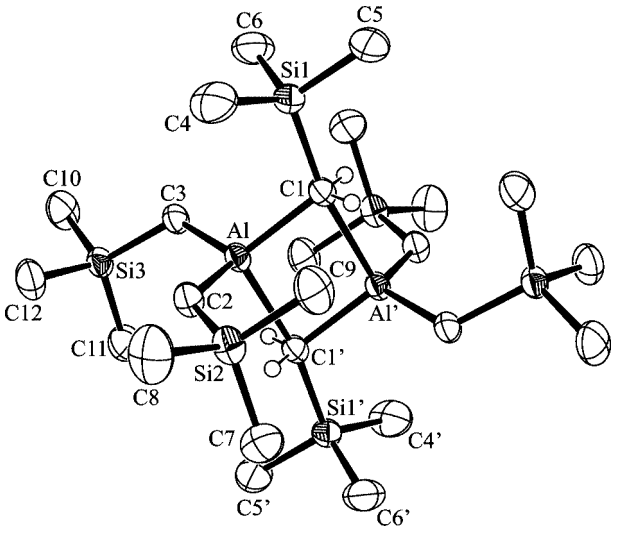


Figure 5. ORTEP representation of the molecular structure of $[\{Al(CH_2SiMe_3)_3\}_2]$ (**4**). Displacement ellipsoids of non-H atoms drawn at the 50% probability level; only hydrogen atoms bonded to bridging carbons shown.

rivatives bearing rigid bridging groups like $[\{AlPh_2(\mu\text{-}C{\equiv}CPh)\}_2]$ (Al–$C_b$–Al 91.73°)[25] or $[\{AlMe_2(\mu\text{-}C{\equiv}CMe)\}_2]$ [Al–$C_b$–Al 92.0(1)°],[26] or bulky bridging groups, like $[\{Al(C_6H_4\text{-}2\text{-}Me)_3\}_2]$ [Al–$C_b$–Al 81.9(1)°],[22] display larger bridge angles.

Table 4. Al–Al bond lengths [Å] and Al–$C_b$–Al angles [°] for dimeric organoaluminium compounds.

| Compound | Al–Al [Å] | Al–$C_b$–Al [°] | Ref. |
|---|---|---|---|
| $[\{Al(CH_2SiMe_3)_3\}_2]$ | 2.8328(13) | 80.55(7) | this work |
| $[(AlMe_3)_2]$ | 2.700(10) | 78.0(3) | [19] |
| $[\{AlMe_2(\mu\text{-}Ph)\}_2]$ | 2.690(4) | 77.8(2) | [23] |
| $[(AlPh_3)_2]$ | 2.702(2) | 76.5(2) | [20] |
| $[\{Al(C_6H_4\text{-}2\text{-}Me)_3\}_2]$ | 2.817(2) | 81.9(1) | [22] |
| $[\{Al(cyclo\text{-}Pr)_3\}_2]$[a] | 2.618(3)/2.607(3) | 78.2(3)/77.9(2) | [21] |

[a] First value determined at 22 °C, second at –67 °C.

In **4** the $SiMe_3$ fragment of the bridging ligands is oriented away from the second aluminium centre [Al–$C_b$–Si1 109.10(10)° and Al′–$C_b$–Si1 167.57(12)°]. The two protons and the trimethylsilyl group bonded to the bridging carbons are in a staggered conformation with the silicon being located 0.2539(8) Å outside of the plane defined by Al, $C_b$, Al′ and $C_b$′. The sum of the C–Al–C angles around the aluminium ($\Sigma_{C-Al-C}$ = 343.34°) represents a non-negligible deviation from planarity, with the aluminium situated 0.4748 Å above the C1–C2–C3 plane. The bonds to the terminal alkyl groups [Al–C2 and Al–C3 1.958(2) Å] were found to be in the typical range for this type of compound. The Al–C bond of the bridging ligand [Al–C1 2.031(2) Å] shows considerable elongation; the second bridging contact [Al–C1′ 2.336(2) Å] is the longest ever reported in such a dimer. $[(AlPh_3)_2]$ is the only other known compound with bridging contacts of that magnitude [Al–$C_b$ 2.180(5) and Al–$C_b$′ 2.184(5) Å].[20]

### *Tris(trimethylsilylmethyl)gallium*

$[Ga(CH_2SiMe_3)_3]$ (**5**), Figure 6, crystallises with four equivalent monomeric molecules per unit cell. Unlike in $[GaEt_3]$,[28] in which the three ethyl groups adopt a propeller-like configuration (in only three of the four independent molecules of the unit cell however), the $CH_2SiMe_3$ groups in **5** adopt a structure resembling that of **3**. Two alkyl groups occupy the same side of the molecule, and display enlarged Ga–C–Si angles [116.60(19)° and 118.24(19)°] whilst the third one lies on the opposite side and is more bent towards the gallium centre [Ga–C2–Si2 114.82(19)°]. With an average value of 116.55°, the Ga–C–Si angles express the same deviation from the expected value as does the boron homologue (117.04° mean). In **5** hyperconjugation again has smaller influence on the molecular geometry than the steric requirements of the ligands. The Ga–C bond lengths [1.959 Å mean, ranging from 1.952(4) Å to 1.971(3) Å] fall within the range of already reported values, as well as the C–Si bonds. The three groups define a perfectly planar skeleton around the gallium ($\Sigma_{C-Ga-C}$ = 359.99°).

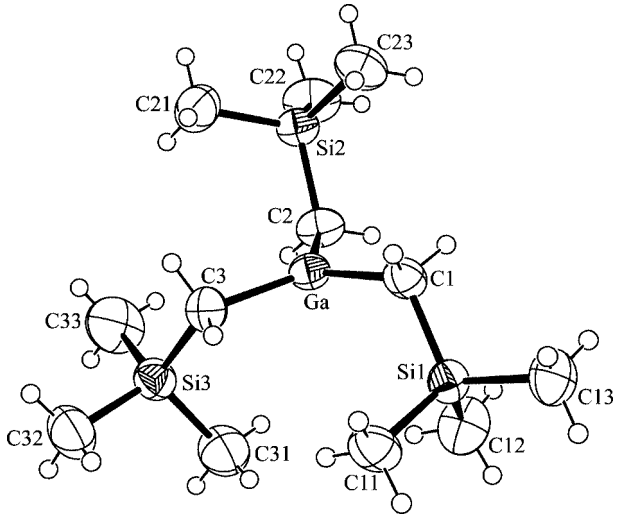


Figure 6. ORTEP representation of the molecular structure of $[Ga(CH_2SiMe_3)_3]$ (**5**). Displacement ellipsoids drawn at the 50% probability level.

That $[Ga(CH_2SiMe_3)_3]$ is monomeric is of no great surprise, since other structurally characterised trialkylgallium compounds which do not contain ligand-based electron pairs tend to be monomeric. $[GaEt_3]$ exhibits short intermolecular contacts in the solid-state structure, and $[GaMe_3]$ shows a tetrameric arrangement of the molecules in the lattice, the interactions in both compounds being however very weak.[28] Dimeric gallium compounds require electron-donating bridging ligands, such as $[\{GaMe_2(\mu\text{-}C{\equiv}CMe)\}_2]$,[29] $[\{Ga(CH{=}CH_2)_3\}_2]$,[30] $[\{GaMe_2(\mu\text{-}C{\equiv}CPh)\}_2]$,[31] $[\{Ga(CH_2Ph)_2Br\}_2]$ or $[\{Ga(CH_2Ph)_2(NHtBu)\}_2]$.[32] The solid-state structure of a TMEDA adduct of $[Ga(CH_2SiMe_3)_3]$, $[\{Ga(CH_2SiMe_3)_3\}_2]\cdot Me_2NCH_2CH_2NMe_2$[33] shows slightly elongated Ga–C bonds (by 1.6% on average) compared to the parent mole-

 © 2007 Wiley-VCH Verlag GmbH & Co. KGaA, Weinheim 

cule $[Ga(CH_2SiMe_3)_3]$, but no significant influence of the TMEDA coordination could be seen in the length of the C–Si bonds.

### Lithium Tetrakis(trimethylsilylmethyl)aluminates

To compare with the structure of the ion pair $[Y(CH_2SiMe_3)_2(thf)_4]^+[Al(CH_2SiMe_3)_4]^-$ (**1a**), solvent separated lithium derivatives of the $[Al(CH_2SiMe_3)_4]^-$ anion were prepared.[3] Upon addition of two equivalents of TMEDA or 12-crown-4 to $[Li]^+[Al(CH_2SiMe_3)_4]^-$ (**7a**),[34] obtained by reaction of $[\{Al(CH_2SiMe_3)_3\}_2]$ with $LiCH_2SiMe_3$, the corresponding adducts $[Li(TMEDA)_2]^+[Al(CH_2SiMe_3)_4]^-$ (**7b**) and $[Li(12\text{-crown-}4)_2]^+[Al(CH_2SiMe_3)_4]^-$ (**7c**) were isolated. Crystals of **7c** were obtained from cooling a saturated thf solution. The geometry around the aluminium centre is further shifted towards a regular tetrahedral arrangement compared to that in the neutral parent $[\{Al(CH_2SiMe_3)_3\}_2]$ (Figure 7). Thus, the three C–Al–C angles of the alkyl groups composing the "base" of the tetrahedron display very close values [106.43(6)°, 107.32(6)° and 107.58(6)°] whilst the fourth alkyl group (involving C18) forms together with the three other ligands angles of 110.02(6)°, 110.35(6)° and 114.80(6)°. All four Al–C bonds are almost equal (2.028 Å on average).

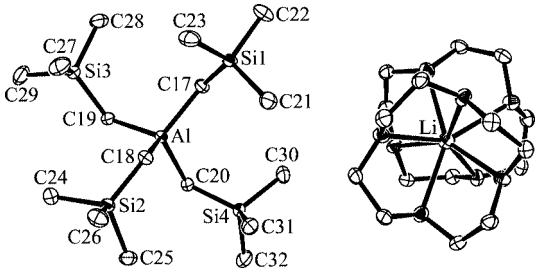


Figure 7. ORTEP representation of the molecular structure of $[Li(12\text{-crown-}4)_2]^+[Al(CH_2SiMe_3)_4]^-$ (**7c**). Displacement ellipsoids drawn at the 50% probability level, hydrogen atoms omitted for clarity.

The anionic part of $[Y(CH_2SiMe_3)_2(thf)_4]^+[Al(CH_2SiMe_3)_4]^-$ (**1a**)[3] displays a geometry much closer to a regular tetrahedral arrangement. The three alkyl groups defining the base of the structure show C–Al–C angles of 109.7(2)°, 109.7(2)° and 109.8(3)°. Angles of 109.19° in average ($\sigma$ = 0.2°) are measured between the fourth group and each of the three others. The aluminate anion in complex **1a** seems to be less influenced by the presence of the counter cation, and therefore adopts a perfectly tetrahedral geometry. Similar Al–C bond lengths and Al–C–Si angles were measured in **1a** (2.033 Å mean, cf. 2.029 Å in **7c**; 122.20° mean, cf. 124.17° in **7c**).

## Conclusions

The Lewis acid induced alkyl transfer reaction of the prototypical rare earth metal alkyl complex $[Y(CH_2SiMe_3)_3(thf)_2]$ with group-13 metal compounds $[\{E(CH_2SiMe_3)_3\}_n]$ proceeds to give an ion pair $[Y(CH_2SiMe_3)_2(thf)_4]^+[E(CH_2SiMe_3)_4]^-$ for E = Al, Ga and In in thf solution. In the presence of aromatic hydrocarbons, however, recombination to form the neutral precursors $[Y(CH_2SiMe_3)_3(thf)_2]$ and $[E(CH_2SiMe_3)_3(thf)]$ occurs. The small boron compound $[B(CH_2SiMe_3)_3]$ failed to react with $[Y(CH_2SiMe_3)_3(thf)_2]$ for kinetic reasons as well as for reduced Lewis acidity. The present results may be relevant to the reversible chain transfer reaction between rare earth metal alkyl catalyst and cocatalyst such as aluminium and zinc alkyl during olefin polymerisation.[1,3,4,35]

## Experimental Section

**General:** All operations were performed under an inert atmosphere of argon using standard Schlenk-line or glovebox techniques. Thf and pentane were distilled from sodium benzophenone ketyl and sodium benzophenone ketyl triglyme, respectively. Deuterated thf and benzene were dried with sodium, distilled and degassed prior to use; deuterated dichloromethane was dried with $CaH_2$, then distilled and degassed. Anhydrous $AlBr_3$, $GaCl_3$, $InCl_3$, $YCl_3$, and $BF_3{\cdot}OEt_2$ (STREM) were used as received. $LiCH_2SiMe_3$[36] and $[Y(CH_2SiMe_3)_3(thf)_2]$[37] were prepared according to literature procedure. All other chemicals were commercially available and used after appropriate purification. NMR spectra were recorded at room temperature on a Bruker DRX 400 spectrometer ($^1H$ 400.1 MHz, $^{13}C$ 100.6 MHz) or on a Varian Unity 500 spectrometer ($^1H$ 499.6 MHz, $^{13}C$ 125.6 MHz, $^{11}B$ 160.3 MHz, $^7Li$ 194.2 MHz, $^{27}Al$ 130.2 MHz) unless otherwise stated. All chemical shifts are given in ppm. Chemical shifts for $^1H$ and $^{13}C$ NMR spectra were referenced internally using the residual solvent resonances and reported relative to $SiMe_4$. $^{11}B$ NMR spectra were referenced externally to a saturated solution of $NaBH_4$ in $D_2O$. $^7Li$ NMR spectra were referenced externally to a 1 mol $L^{-1}$ solution of LiCl in $D_2O$. $^{27}Al$ NMR spectra were referenced externally to a 1.5 mol $L^{-1}$ solution of $Al(NO_3)_3$ in $D_2O$.

**$[Y(CH_2SiMe_3)_2(thf)_4][Al(CH_2SiMe_3)_4]$ (1a):** The compound was prepared according to the literature procedure.[3,4] $^1H$ NMR (200 MHz; [D$_8$]thf): $\delta$ = –1.22 (sextet, $AlCH_2$, $^2J_{Al,H}$ = 9.0 Hz, 8 H), –0.68 (d, $^2J_{Y,H}$ = 3.2 Hz, 4 H, $YCH_2$), –0.11 [s, 36 H, $AlCH_2Si(CH_3)_3$], 0.03 [s, 18 H, $YCH_2Si(CH_3)_3$], 1.77 (16 H, β-$CH_2$, thf), 3.62 (16 H, α-$CH_2$, thf) ppm. $^{27}Al$ NMR (130 MHz; [D$_8$]thf): $\delta$ = 150.9 (nonet, $^2J_{Al,H}$ = 9.0 Hz) ppm. $^1H$ NMR (400 MHz; $C_6D_6$): $\delta$ = –0.81 (s, 6 H, $AlCH_2$), –0.69 (d, $^2J_{Y,H}$ = 2.8 Hz, 6 H, $YCH_2$), 0.28 [s, 27 H, $AlCH_2Si(CH_3)_3$], 0.29 [s, 27 H, $YCH_2Si(CH_3)_3$], 1.27 (16 H, β-$CH_2$, thf), 3.72 (16 H, α-$CH_2$, thf) ppm. $^{13}C\{^1H\}$ NMR (100 MHz; $C_6D_6$): $\delta$ = –0.67 ($AlCH_2$), 3.30 [$AlCH_2Si(CH_3)_3$], 4.58 [$YCH_2Si(CH_3)_3$], 25.14 (β-$CH_2$, thf), 33.70 (d, $^1J_{Y,C}$ = 35.5 Hz, $YCH_2$), 69.99 (α-$CH_2$, thf) ppm.

**$[Y(CH_2SiMe_3)_2(thf)_4][Ga(CH_2SiMe_3)_4]$ (1b):** To a solution of $[Y(CH_2SiMe_3)_3(thf)_2]$ (974 mg, 1.969 mmol) in thf (5 mL), $[Ga(CH_2SiMe_3)_3]$ (653 mg, 1.969 mmol) in thf (5 mL) was added dropwise whilst stirring. Upon complete addition, the reaction mixture was stirred for further 10 min and all volatiles were subsequently removed under reduced pressure to yield a colourless solid, which was washed with pentane and dried under vacuum to yield **1b** as a colourless solid (1650 mg, 86%). Single crystals suitable for X-ray diffraction analysis could be obtained by slow cooling of a saturated thf/pentane solution of **1b**. $^1H$ NMR (400 MHz; [D$_8$]thf): $\delta$ = –1.04 (br. s, 8 H, $GaCH_2$), –0.68 (d, $^2J_{Y,H}$ = 3.0 Hz, 4 H, $YCH_2$), –0.11 [s, 36 H, $GaCH_2Si(CH_3)_3$], –0.04 [s, 18 H, $YCH_2$-

 © 2007 Wiley-VCH Verlag GmbH & Co. KGaA, Weinheim 

$Si(CH_3)_3$], 1.77 (16 H, β-$CH_2$, thf), 3.62 (16 H, α-$CH_2$, thf) ppm. $^{13}C$ NMR (100 MHz; [$D_8$]thf): $\delta$ = 2.67 ($GaCH_2$), 4.02 [$GaCH_2Si(CH_3)_3$], 4.07 [$YCH_2Si(CH_3)_3$], 26.31 (β-$CH_2$, thf), 37.47 (d, $^1J_{Y,C}$ = 41.6 Hz, $YCH_2$), 68.21 (α-$CH_2$, thf) ppm. $^1H$ NMR (400 MHz; $C_6D_6$): $\delta$ = –0.49 (br. s, 12 H, $GaCH_2$ and $YCH_2$), 0.26 [br. s, 54 H, $YCH_2Si(CH_3)_3$ and $GaCH_2Si(CH_3)_3$], 1.31 (16 H, β-$CH_2$, thf), 3.70 (16 H, α-$CH_2$, thf) ppm. $^{13}C\{^1H\}$ NMR (100 MHz; $C_6D_6$): $\delta$ = 3.64 [br., $GaCH_2Si(CH_3)_3$ and $YCH_2Si(CH_3)_3$], 25.24 (β-$CH_2$, thf), 33.82 (v br, $GaCH_2$ and $YCH_2$), 69.56 (α-$CH_2$, thf) ppm. $C_{40}H_{98}GaO_4Si_6Y$ (970.36): calcd. C 49.51, H 10.17; found C 48.61, H 10.43%.

**[Y(CH$_2$SiMe$_3$)$_2$(thf)$_4$][In(CH$_2$SiMe$_3$)$_4$] (1c):** To a solution of [$Y(CH_2SiMe_3)_3(thf)_2$] (487 mg, 0.984 mmol) in thf (5 mL), [$In(CH_2SiMe_3)_3$] (371 mg, 0.984 mmol) in thf (5 mL) was added dropwise whilst stirring. Upon complete addition, the reaction mixture was stirred for a further 10 min and volatiles were subsequently removed under reduced pressure to yield an oily solid, which was washed with pentane and dried under vacuum to yield **1c** as a colourless solid (823 mg, 82.4%). $^1H$ NMR (400 MHz; [$D_8$]-thf): $\delta$ = –1.07 (br. s, 8 H, $InCH_2$), –0.68 (d, $^2J_{Y,H}$ = 3.3 Hz, 4 H, $YCH_2$), –0.10 [s, 36 H, $InCH_2Si(CH_3)_3$], –0.04 [s, 18 H, $YCH_2Si(CH_3)_3$], 1.77 (16 H, β-$CH_2$, thf), 3.62 (16 H, α-$CH_2$, thf) ppm. $^{13}C$ NMR (100 MHz; [$D_8$]thf): $\delta$ = 4.02 [$InCH_2Si(CH_3)_3$], 4.06 [$YCH_2Si(CH_3)_3$], 26.31 (β-$CH_2$, thf), 37.47 (d, $^1J_{Y,C}$ = 42.5 Hz, $YCH_2$), 68.20 (β-$CH_2$, thf), the signal for the $InCH_2$ carbons was not detected ppm. $^1H$ NMR (400 MHz; $C_6D_6$): $\delta$ = –0.48 (br. s, 12 H, In$CH_2$ and Y$CH_2$), 0.28 [br. s, 54 H, $InCH_2Si(CH_3)_3$ and $YCH_2Si(CH_3)_3$], 1.34 (16 H, β-$CH_2$, thf) 3.65 (16 H, α-$CH_2$, thf) ppm. $^{13}C\{^1H\}$ NMR (100 MHz; $C_6D_6$): $\delta$ = 3.79 [br., $InCH_2Si(CH_3)_3$ and $YCH_2Si(CH_3)_3$], 25.38 (β-$CH_2$, thf), 69.12 (β-$CH_2$, thf) ppm. the signals for the $InCH_2$/$YCH_2$ carbons were not detected. $C_{40}H_{98}InO_4Si_6Y$ (1015.45): calcd. C 47.31, H 9.72; found C 46.28, H 9.94%.

**NMR-Tube Synthesis of [Y(CH$_2$SiMe$_3$)$_2$(12-crown-4)(thf)][Al(CH$_2$SiMe$_3$)$_4$] (2a):** To a solution of [$Y(CH_2SiMe_3)_2(thf)_4$][$Al(CH_2SiMe_3)_4$] (20 mg, 21.6 μmol) in $C_6D_6$, neat 12-crown-4 (3.5 μL, 21.6 μmol) was added and the reaction mixture was shaken. $^1H$ NMR (400 MHz; $C_6D_6$): $\delta$ = –0.68 (d, $^2J_{Y,H}$ = 3.0 Hz, 4 H, $YCH_2$), –0.62 (br. s, 8 H, $AlCH_2$), 0.23 [s, 18 H, $YCH_2Si(CH_3)_3$], 0.50 [s, 36 H, $AlCH_2Si(CH_3)_3$], 1.42 (16 H, β-$CH_2$, thf), 3.36 (br. s, 16 H, $CH_2$, 12-crown-4), 3.58 (16 H, α-$CH_2$, thf) ppm. $^{13}C\{^1H\}$ NMR (100 MHz; $C_6D_6$): $\delta$ = 3.30 ($AlCH_2$), 4.30 [$YCH_2Si(CH_3)_3$], 4.83 [$AlCH_2Si(CH_3)_3$], 25.68 (β-$CH_2$, thf), 36.73 (d, $^1J_{Y,C}$ = 40.7 Hz, $YCH_2$), 68.00 (br., $CH_2$, 12-crown-4), 68.37 (α-$CH_2$, thf) ppm.

**[Y(CH$_2$SiMe$_3$)$_2$(12-crown-4)(thf)][Ga(CH$_2$SiMe$_3$)$_4$] (2b):** To a solution of [$Y(CH_2SiMe_3)_3(thf)_2$] (200 mg, 0.38 mmol) in thf (2 mL) were successively added [$Ga(CH_2SiMe_3)_3$] (131 mg, 0.38 mmol) in thf (1 mL) and neat 12-crown-4 (70 mg, 0.38 mmol). The resulting clear solution was stirred for five minutes, after which the volatiles were removed under vacuum. Washing with pentane (2 × 10 mL) and drying afforded **2b** as a white powder (315 mg, 89%). $^1H$ NMR (400 MHz; $C_6D_6$): $\delta$ = –0.68 (d, $^2J_{Y,H}$ = 3.1 Hz, 4 H, $YCH_2$), –0.43 (s, 8 H, $GaCH_2$), 0.22 [s, 18 H, $YCH_2Si(CH_3)_3$], 0.49 [s, 36 H, $GaCH_2Si(CH_3)_3$], 1.44 (4 H, β-$CH_2$, thf), 3.17 and 3.43 (2 × 8 H, m, $CH_2$, 12-crown-4), 3.59 (4 H, α-$CH_2$, thf) ppm. $^{13}C\{^1H\}$ NMR (100 MHz; $C_6D_6$): $\delta$ = 2.5–3.8 (br. m, $GaCH_2$), 4.32 [$YCH_2Si(CH_3)_3$], 4.65 [$GaCH_2Si(CH_3)_3$], 25.64 (β-$CH_2$, thf), 36.85 (d, $^1J_{Y,C}$ = 41.6 Hz, $YCH_2$), 67.58 (12-crown-4), 68.61 (α-$CH_2$, thf) ppm. $C_{36}H_{90}GaO_5Si_6Y$ (930.25): calcd. C 46.48, H 9.75; found C 45.83, H 9.43%.

**[Y(CH$_2$SiMe$_3$)$_2$(12-crown-4)(thf)][In(CH$_2$SiMe$_3$)$_4$] (2c):** Following the procedure described for **2b**, [$Y(CH_2SiMe_3)_3(thf)_2$] (200 mg, 0.38 mmol) in thf (2 mL) was treated with [$In(CH_2SiMe_3)_3$] (131 mg, 0.38 mmol) in thf (1 mL) and neat 12-crown-4 (70 mg, 0.38 mmol). Identical work-up afforded **2c** as a white powder (333 mg, 90%). $^1H$ NMR (400 MHz; $C_6D_6$): $\delta$ = –0.68 (d, $^2J_{Y,H}$ = 3.2 Hz, 4 H, $YCH_2$), –0.47 (br. s, 8 H, $InCH_2$), 0.22 [s, 18 H, $YCH_2Si(CH_3)_3$], 0.48 [s, 36 H, $InCH_2Si(CH_3)_3$], 1.44 (4 H, β-$CH_2$, thf), 3.17 and 3.41 (m, 2 × 8 H, $CH_2$, 12-crown-4), 3.59 (4 H, α-$CH_2$, thf) ppm. $^{13}C\{^1H\}$ NMR (100 MHz; $C_6D_6$): $\delta$ = 4.30 [$YCH_2Si(CH_3)_3$], 4.60 [$InCH_2Si(CH_3)_3$], 25.66 (β-$CH_2$, thf), 36.79 (d, $^1J_{Y,C}$ = 41.6 Hz, $YCH_2$), 67.57 (12-crown-4), 68.53 (α-$CH_2$, thf) ppm. the signal for the $InCH_2$ carbons was not detected. $C_{36}H_{90}InO_5Si_6Y$ (975.35): calcd. C 44.33, H 9.30; found C 43.78, H 9.15%.

**[B(CH$_2$SiMe$_3$)$_3$] (3):** This compound was synthesised according to the procedure described in the literature[5a] and isolated as a colourless liquid (9745 mg, 74.5%), m.p. –32 °C. $^1H$ NMR (500 MHz; $C_6D_6$): $\delta$ = 0.12 [s, 27 H, $Si(CH_3)_3$], 0.93 (s, 6 H, $BCH_2$) ppm. $^{13}C\{^1H\}$ NMR (125 MHz, $C_6D_6$): $\delta$ = 0.02 [$Si(CH_3)_3$], 23.80 ($BCH_2$) ppm. $^{11}B$ NMR (160 MHz, $C_6D_6$): $\delta$ = 78.8 ppm.

**[{Al(CH$_2$SiMe$_3$)$_3$}$_2$] (4):** The product was synthesised according to the procedure described in literature[5b] and isolated as a colourless liquid (6490 mg, 75.0%), m.p. –18 °C. $^1H$ NMR (500 MHz; $C_6D_6$): $\delta$ = –0.54 (s, 6 H, $AlCH_2$), 0.00 [s, 27 H, $Si(CH_3)_3$] ppm. $^{13}C\{^1H\}$ NMR (125 MHz; $C_6D_6$): $\delta$ = 0.27 [$Si(CH_3)_3$], 2.65 ($AlCH_2$) ppm. $^{27}Al$ NMR (130 MHz; $C_6D_6$): $\delta$ = 290.3 ppm.

**[Ga(CH$_2$SiMe$_3$)$_3$] (5):** The product was synthesised according to the published procedure[5c] and isolated as a colourless liquid (2575 mg, 65.2%), m.p. –42 °C. $^1H$ NMR (400 MHz. $CD_2Cl_2$): $\delta$ = 0.06 [s, 27 H, $Si(CH_3)_3$], 0.08 (s, 6 H, $GaCH_2$) ppm. $^{13}C\{^1H\}$ NMR (100 MHz. $CD_2Cl_2$): $\delta$ = 2.4 [$Si(CH_3)_3$], 12.5 ($GaCH_2$) ppm.

**[In(CH$_2$SiMe$_3$)$_3$] (6):** The product was synthesised according to the published procedure[5d] and isolated as a colourless liquid (4701 mg, 55.2%), m.p. –45 °C. $^1H$ NMR (400 MHz. $CD_2Cl_2$): $\delta$ = –0.06 (s, 6 H, $InCH_2$), 0.03 [s, 27 H, $Si(CH_3)_3$] ppm. $^{13}C\{^1H\}$ NMR (100 MHz. $CD_2Cl_2$): $\delta$ = 2.47 [$Si(CH_3)_3$], 10.79 ($InCH_2$) ppm.

**[Li][Al(CH$_2$SiMe$_3$)$_4$] (7a):** The procedure described in the literature[34] for the synthesis of **4** was slightly modified: In the glovebox, $Al(CH_2SiMe_3)_3$ (289 mg, 1 mmol) was dissolved in pentane (3 mL); $Li(CH_2SiMe_3)$ (94 mg, 1 mmol) in pentane (3 mL) was added dropwise at room temperature. A colourless precipitate formed immediately and the suspension was stirred for 1 h. Filtration, washing with pentane (2 × 5 mL) and drying in vacuo afforded **4** (328 mg, 86%) as a colourless powder. $^1H$ NMR (500 MHz; [$D_8$]thf): $\delta$ = –1.22 (br. m, 8 H, $AlCH_2$), –0.11 [s, 36 H, $Si(CH_3)_3$] ppm. $^{13}C\{^1H\}$ NMR (100 MHz; [$D_8$]thf): $\delta$ = 1.51 (sextet, $^1J_{Al,C}$ = 60 Hz, $CH_2$), 3.78 [s, $Si(CH_3)_3$] ppm. $^{27}Al$ NMR (130 MHz; [$D_8$]thf): $\delta$ = 150.1 (nonet, $^2J_{Al,H}$ = 9.0 Hz) ppm. $^7Li$ NMR (194 MHz, [$D_8$]thf): $\delta$ = –0.54 ppm.

**[Li(tmeda)$_2$][Al(CH$_2$SiMe$_3$)$_4$] (7b):** In the glovebox, neat tmeda (191 mg, 1.65 mmol) was added at once to a solution of **4** (315 mg, 0.82 mmol) in thf (3 mL), and the resulting clear solution stirred overnight. After all volatiles were removed in vacuo, the residue was washed three times with 5 mL of pentane, and dried in vacuo. The product was isolated as a colourless powder (255 mg, 51%). $^1H$ NMR (500 MHz, [$D_8$]thf): $\delta$ = –1.22 (br. m, 8 H, $AlCH_2$), –0.10 [s, 36 H, $Si(CH_3)_3$], 2.15 [s, 24 H, $(CH_3)_2N$], 2.31 (s, 8 H, $NCH_2CH_2N$) ppm. $^{13}C\{^1H\}$ NMR (125 MHz, [$D_8$]thf): $\delta$ = 2.00 (sextet, $^1J_{Al,C}$ = 60 Hz, $AlCH_2$), 4.23 [s, $Si(CH_3)_3$], 46.2 [$(CH_3)_2N$], 58.9 ($NCH_2CH_2N$) ppm. $^{27}Al$ NMR (130 MHz, [$D_8$]thf): $\delta$ = 150.2 (nonet, $^2J_{Al,H}$ = 9.0 Hz) ppm. $^7Li$ NMR (194 MHz, [$D_8$]thf): $\delta$ = –0.53 ppm. $C_{28}H_{76}AlLiN_4Si_4$ (615.20): calcd. C 54.67, H 12.45, N 9.11; found C 55.00, H 12.94, N 9.78%.

 © 2007 Wiley-VCH Verlag GmbH & Co. KGaA, Weinheim 

Table 5. Crystallographic and data collection parameters for compounds **1b**, **3**, **4**, **5**, and **7c**.

| Compound | **1b** | **3** | **4** | **5** | **7c** |
|---|---|---|---|---|---|
| Empirical formula | $C_{40}H_{98}GaO_4Si_6Y$ | $C_{12}H_{33}BSi_3$ | $C_{24}H_{66}Al_2Si_6$ | $C_{12}H_{33}GaSi_3$ | $C_{32}H_{76}AlLiO_8Si_4$ |
| $M_r$ | 970.35 | 272.46 | 577.27 | 331.37 | 735.21 |
| Crystal system | monoclinic | monoclinic | triclinic | monoclinic | monoclinic |
| Space group | $P2_1/n$ | $P2_1/c$ | $P$-1 | $P2_1/c$ | $P2_1/c$ |
| $a$ [Å] | 21.548(3) | 6.5339(11) | 10.009(2) | 6.5482(5) | 10.4405(10) |
| $b$ [Å] | 15.689(3) | 16.378(3) | 10.4113(16) | 16.9374(17) | 21.327(2) |
| $c$ [Å] | 34.434(5) | 18.764(3) | 11.3479(18) | 18.838(3) | 20.566(2) |
| $\alpha$ [°] | | | 108.780(13) | | |
| $\beta$ [°] | 102.661(5) | 105.097(13) | 103.538(16) | 101.271(10) | 104.481(2) |
| $\gamma$ [°] | | | 111.771(15) | | |
| $V$ [Å$^3$] | 11358(3) | 1938.7(6) | 952.0(3) | 2049.0(4) | 4433.8(7) |
| Z | 8 | 4 | 1 | 4 | 4 |
| $D_{calc}$ [g cm$^{-3}$] | 1.135 | 0.933 | 1.007 | 1.074 | 1.101 |
| $T$ [K] | 133(2) | 223(2) | 248(2) | 223(2) | 115(2) |
| $\mu$(Mo-$K_\alpha$) [mm$^{-1}$] | 1.649 | 0.226 | 0.277 | 1.501 | 0.194 |
| $F$(000) | 4192 | 608 | 320 | 712 | 1616 |
| $\theta$ Range [°] | 1.80–27.05 | 2.25–28.22 | 3.11–28.09 | 2.20–28.01 | 2.17–29.67 |
| Number of reflections collected | 138759 | 13002 | 9202 | 11146 | 62561 |
| Number of reflections observed [$I>2\sigma(I)$] | 12522 | 3097 | 3830 | 3640 | 8661 |
| Number of independent reflections ($R_{int}$) | 24727 (0.1409) | 4721 (0.0840) | 4601 (0.0318) | 4697 (0.0541) | 12168 (0.0880) |
| Data/restraints/parameters | 24727/18/973 | 4721/0/154 | 4601/0/162 | 4697/0/154 | 12168/0/415 |
| Goodness-of-fit on $F^2$ | 0.831 | 1.008 | 1.011 | 1.071 | 0.938 |
| $R_1$, $wR_2$ [$I>2\sigma(I)$] | 0.0404, 0.0709 | 0.0520, 0.1110 | 0.0471, 0.1119 | 0.0484, 0.1179 | 0.0412, 0.0930 |
| $R_1$, $wR_2$ (all data) | 0.1105, 0.0802 | 0.0930, 0.1209 | 0.0615, 0.1182 | 0.0684, 0.1351 | 0.0591, 0.0974 |
| Largest difference in peak and hole [e Å$^{-3}$] | 0.628 and –0.573 | 0.372 and –0.172 | 0.434 and –0.308 | 0.616 and –1.191 | 0.564 and –0.453 |

**[Li(12-crown-4)$_2$][Al(CH$_2$SiMe$_3$)$_4$] (7c):** Following the same protocol as for **7b**, this compound was obtained by addition of two equivalents of neat 12-crown-4 (290 mg, 1.65 mmol) to a solution of **4** (315 mg, 0.82 mmol) in thf (3 mL). After work-up, the product was isolated as a colourless powder (320 mg, 53%). A saturated thf solution was cooled down to –40 °C to afford crystals suitable for X-ray diffraction. $^1$H NMR (500 MHz, [D$_8$]thf): $\delta$ = –1.22 (br. m, 8 H, AlCH$_2$), –0.10 [s, 36 H, Si(CH$_3$)$_3$], 3.68 (s, 32 H, 12-crown-4) ppm. $^{13}$C{$^1$H} NMR (125 MHz, [D$_8$]thf): $\delta$ = 2.00 (sextet, $^1J_{Al,C}$ = 60 Hz, AlCH$_2$), 4.23 [s, Si(CH$_3$)$_3$], 70.2 (12-crown-4) ppm. $^{27}$Al NMR (130 MHz, [D$_8$]thf): $\delta$ = 150.2 (nonet, $^2J_{Al,H}$ = 9.0 Hz) ppm. $^7$Li NMR (194 MHz, [D$_8$]thf): $\delta$ = –0.21 ppm. $C_{32}H_{76}AlLiO_8Si_4$ (735.22): calcd. C 52.28, H 10.42; found C 52.54, H 10.44%.

**X-ray Diffraction:** Data collections were performed with graphite-monochromated Mo-$K_\alpha$ radiation ($\lambda$ = 0.71073 Å). Single crystals of **3**, **4**, and **5** were directly grown on a NONIUS CAD4 diffractometer. Capillaries containing ca. 2 μL of **3**, **4**, and **5** were exposed in appropriate geometry ($\chi$ = 90°) to a cold stream of $N_2$; the samples completely solidified. The temperature of the gas stream was gradually increased to the melting point, retaining only a small fraction of solid in the tip of the capillary. Slow cooling resulted in a crystalline sample. The procedure was repeated until single crystals of satisfactory quality were obtained; their diffraction pattern was directly registered on the CAD4 diffractometer. The structures of **3** and **5** are closely related and probably isomorphous. Intensity data for **1b** and **7c** were collected on a Bruker CCD D8 goniometer equipped with a SMART APEX CCD detector. Data were processed using SAINT and SADABS to yield the reflection data file.[38] Subsequent calculations were carried out using the SHELXS and SHELXL programs.[39] Analytical scattering factors for neutral atoms were used throughout the analysis.[40] The hydrogen atoms attached to the bridging carbon atom in **4** were freely refined; all other H atoms were included at calculated positions. Crystal data, parameters of data collection and convergence results for the diffraction experiments are compiled in Table 5.

CCDC-621523 (for **1b**), -620839 (for **3**), -620838 (for **4**), -620840 (for **5**), -620841 (for **7c**) contain the supplementary crystallographic data for this paper. These data can be obtained free of charge from The Cambridge Crystallographic Data Centre via www.ccdc.cam.ac.uk/data_request/cif.

## Acknowledgments

We thank the Deutsche Forschungsgemeinschaft (DFG), the Fonds der Chemischen Industrie (Kekulé fellowship to M. U. K.) and the Alexander von Humboldt Foundation (postdoctoral fellowship to Y. N.) for financial support.

[1] For recent reports, see: a) S. Bambirra, A. Meetsma, B. Hessen, *Organometallics* **2006**, *25*, 3454–3462; b) S. Bambirra, A. Meetsma, B. Hessen, A. P. Bruins, *Organometallics* **2006**, *25*, 3486–3495. For reviews, see: c) P. M. Zeimentz, S. Arndt, B. R. Elvidge, J. Okuda, *Chem. Rev.* **2006**, *106*, 2404–2433; d) S. Arndt, J. Okuda, *Adv. Synth. Catal.* **2005**, *347*, 339–354.
[2] S. Hajela, W. P. Schaefer, J. E. Bercaw, *J. Organomet. Chem.* **1997**, *532*, 45–53.
[3] S. Arndt, T. P. Spaniol, J. Okuda, *Angew. Chem. Int. Ed.* **2003**, *42*, 5075–5079.
[4] B. R. Elvidge, S. Arndt, P. M. Zeimentz, T. P. Spaniol, J. Okuda, *Inorg. Chem.* **2005**, *44*, 6777–6788.

 © 2007 Wiley-VCH Verlag GmbH & Co. KGaA, Weinheim 

[5] For the preparation of [{E($CH_2SiMe_3$)$_3$}$_n$], see: a) E = B: D. Seyferth, *J. Am. Chem. Soc.* **1959**, *81*, 1844–1847; b) E = Al: C. Tessier-Youngs, O. T. Beachley Jr, *Inorg. Synth.* **1986**, *24*, 92–93; c) E = Ga: O. T. Beachley Jr, R. G. Simmons, *Inorg. Chem.* **1980**, *19*, 1021–1025; d) E = In: J. P. Kopasz, R. B. Hallock, O. T. Beachley Jr, *Inorg. Synth.* **1986**, *24*, 89–91.
[6] a) G. A. Artamkina, A. B. Tuzikov, I. P. Beletskaya, O. A. Reutov, *Izv. Akad. Nauk SSSR, Ser. Khim.* **1980**, *10*, 2429; b) D. V. Yandulov, J. C. Huffman, K. G. Caulton, *Organometallics* **2002**, *21*, 4030–4049.
[7] a) H. M. Dietrich, G. Raudaschl-Sieber, R. Anwander, *Angew. Chem.* **2005**, *117*, 5437–5440; b) W. J. Evans, R. Anwander, R. J. Doedens, J. W. Ziller, *Angew. Chem. Int. Ed. Engl.* **1994**, *33*, 1641–1644; c) M. A. Busch, R. Harlow, P. L. Watson, *Inorg. Chim. Acta* **1987**, *140*, 15–20.
[8] The chemical shifts for [Al($CH_2SiMe_3$)$_3$(thf)] were determined as $^1$H NMR (200 MHz, $C_6D_6$): $\delta$ = –0.82 ppm (6 H, s, $AlCH_2$), 0.27 [27 H, s, $AlCH_2Si(CH_3)_3$], 1.25 (4 H, m, β-$CH_2$, thf), 3.49 (4 H, m, α-$CH_2$, thf).
[9] For a discussion of coordination of anions, see: a) A. Macchioni, *Chem. Rev.* **2005**, *105*, 2039–2073; b) S. H. Strauss, *Chem. Rev.* **1993**, *93*, 927–942.
[10] M. Westerhausen, C. Gückel, T. Habereder, M. Vogt, M. Warchhold, H. Nöth, *Organometallics* **2001**, *20*, 893–899.
[11] F. Kaufmann, A. Geraudelle, B. Kaempf, F. Schué, A. Deluzarche, A. Maillard, *J. Organomet. Chem.* **1970**, *24*, 13–31.
[12] Y. Kawakami, Y. Yasuda, T. Tsuruta, *Bull. Chem. Soc. Jpn.* **1971**, *44*, 1164–1165.
[13] C. J. Schaverien, *Organometallics* **1992**, *11*, 3476–3478.
[14] M. R. Kopp, B. Neumüller, *Z. Naturforsch., Teil B* **1998**, *53*, 545–551.
[15] W. Uhl, K.-W. Klinkhammer, M. Layh, W. Massa, *Chem. Ber.* **1991**, *124*, 279–284.
[16] K. Niediek, B. Neumüller, *Z. Anorg. Allg. Chem.* **1994**, *620*, 2088–2098.
[17] R. Boese, D. Bläser, N. Niederprüm, M. Nüsse, W. A. Brett, P. von Ragué Schleyer, M. Bühl, N. van Eikema Hommes, *Angew. Chem. Int. Ed. Engl.* **1992**, *31*, 314–316.
[18] A. R. Cowley, A. J. Downs, S. Marchant, V. A. Macrae, R. A. Taylor, S. Parsons, *Organometallics* **2005**, *24*, 5702–5709.
[19] G. S. McGrady, J. F. C. Turner, R. M. Ibberson, M. Prager, *Organometallics* **2000**, *19*, 4398–4401.
[20] J. F. Malone, W. S. McDonald, *J. Chem. Soc., Dalton Trans.* **1972**, 2646–2648.
[21] a) J. W. Moore, D. A. Sanders, P. A. Scherr, M. D. Glick, J. P. Oliver, *J. Am. Chem. Soc.* **1971**, *93*, 1035–1037; b) W. H. Ilsley, M. D. Glick, J. P. Oliver, J. W. Moore, *Inorg. Chem.* **1980**, *19*, 3572–3577.
[22] M. Barber, D. Liptak, J. P. Oliver, *Organometallics* **1982**, *1*, 1307–1311.
[23] J. F. Malone, W. S. McDonald, *J. Chem. Soc., Dalton Trans.* **1972**, 2649–2652.
[24] M. J. Albright, W. M. Butler, T. J. Anderson, M. D. Glick, J. P. Oliver, *J. Am. Chem. Soc.* **1976**, *98*, 3995–3996.
[25] G. D. Stucky, A. M. McPherson, W. E. Rhine, J. J. Eisch, J. L. Considine, *J. Am. Chem. Soc.* **1974**, *96*, 1941–1942.
[26] The structure of [{Al($Me$)$_2$(μ-C≡C$Me$)}$_2$] was determined in the gas phase: A. Almenningen, L. Fernholt, A. Haaland, *J. Organomet. Chem.* **1978**, *155*, 245–257.
[27] J. Z. Nyathi, J. M. Ressner, J. D. Smith, *J. Organomet. Chem.* **1974**, *70*, 35–38.
[28] N. W. Mitzel, C. Lustig, R. J. F. Berger, N. Runeberg, *Angew. Chem. Int. Ed.* **2002**, *41*, 2519–2522.
[29] T. Fjeldberg, A. Haaland, R. Seip, J. Weidlein, *Acta Chem. Scand., Ser. A* **1981**, *35*, 437–441.
[30] T. Fjeldberg, A. Haaland, R. Seip, J. Weidlein, *Acta Chem. Scand., Ser. A* **1981**, *35*, 637–638.
[31] B. Tecle, W. H. Ilsley, J. P. Oliver, *Inorg. Chem.* **1981**, *20*, 2335–2337.
[32] T. Kräuter, B. Werner, B. Neumüller, *Z. Naturforsch., Teil B* **1996**, *51*, 637–645.
[33] R. B. Hallock, W. E. Hunter, J. L. Atwood, O. T. Beachley Jr, *Organometallics* **1985**, *4*, 547–549.
[34] R. L. Kieft, T. L. Brown, *J. Organomet. Chem.* **1974**, *77*, 289–298.
[35] a) J. F. Pelletier, A. Mortreux, X. Olonde, K. Bujadoux, *Angew. Chem. Int. Ed. Engl.* **1996**, *35*, 1854–1856; b) G. J. P. Britovsek, S. A. Cohen, V. C. Gibson, M. van Meurs, *J. Am. Chem. Soc.* **2004**, *126*, 10701–10712 and references cited therein.
[36] a) C. Tessier-Youngs, O. T. Beachley Jr, *Inorg. Synth.* **1986**, *24*, 95–97; b) B. Teclé, A. F. M. Maqsudur Rahman, J. P. Oliver, *J. Organomet. Chem.* **1986**, *317*, 267–275.
[37] a) M. F. Lappert, R. Pearce, *J. Chem. Soc., Chem. Commun.* **1973**, 126; b) W. J. Evans, J. C. Brady, J. W. Ziller, *J. Am. Chem. Soc.* **2001**, *123*, 7711–7712.
[38] *ASTRO, SAINT and SADABS. Data Collection and Processing Software for the SMART System*, Siemens Analytical X-ray Instruments Inc. Madison, WI, USA, **1996**.
[39] a) G. M. Sheldrick, *SHELXS-86, Program for Crystal Structure Solution*, University of Göttingen, Germany, **1986**; b) G. M. Sheldrick, *SHELXL-97, Program for Crystal Structure Refinement*, University of Göttingen, Germany, **1997**.
[40] *International Tables for X-ray Crystallography*, Kluwer Academic Publishers, Dordrecht, **1992**, vol. C.

Received: October 31, 2006
Published Online: January 4, 2007

 © 2007 Wiley-VCH Verlag GmbH & Co. KGaA, Weinheim 

DOI: 10.1002/ejic.200600840

# $CO_2$ Fixation by Alkylzinc Amides: A Quantum Chemical Study Motivated by Recent Experimental Results

**Hans-Jörg Himmel*[a]**

**Keywords:** $CO_2$ fixation / Zinc / Reaction mechanisms / Quantum chemical calculations

Herein the insertion of $CO_2$ into the Zn–N bond of alkylzinc amides of the general formula $RZnNR'_2$ (R = H, $CH_3$, $CF_3$, R′ = $CH_3$, *i*Pr, H, F, $C_6H_5$) is discussed on the basis of quantum chemical calculations. Several possible reaction pathways were considered, starting from monomeric as well as dimeric alkylzinc amides. Special consideration is given to the influence of the electronic properties of the amido group on the reaction energy. The mechanisms were studied in detail starting with the model compounds $HZnNH_2$ and $H_3CZnN(CH_3)_2$ as well as the dimer $[HZnNH_2]_2$. The reaction of monomeric compounds with $CO_2$ first leads to an intermediate featuring a Zn–N–C–O four-membered ring. This first step requires an activation energy $\Delta G$ of ca. 60 kJ·mol$^{-1}$ and turns out to be the rate-determining step. In the second step, which requires a much smaller activation energy, the carbamate product is formed. Reactions of dimeric alkylzinc amides are subject to a significantly higher activation barrier (with a $\Delta G$ value of 103 kJ·mol$^{-1}$), with a four-membered ring as the transition-state structure. The activation energy is slightly higher than the energy required for decomposition of the dimer into two monomers, and therefore it is plausible that the alkylzinc amides react as monomers with $CO_2$. The calculations for the dimer reaction again gave evidence for the formation of an intermediate exhibiting in this case a six-membered ring. The barrier to formation of the carbamate from this intermediate is very small. The results of this work contribute to the knowledge of $CO_2$ fixation by alkylzinc amides and might shed some light on enzymatic reactivity.
(© Wiley-VCH Verlag GmbH & Co. KGaA, 69451 Weinheim, Germany, 2007)

## Introduction

The reduction of $CO_2$ emission, a gas that besides others is responsible for global warming, is continuing to be an extremely important issue, especially since no real alternatives to fossil fuels[1] have yet been discovered. Therefore, there is a great demand for methods to either reduce $CO_2$ production or for suitable materials that help to reduce the release of the produced $CO_2$ into the air (and ideally turn $CO_2$ into something useful at the same time). There are now numerous examples of transition-metal complexes that can bind $CO_2$.[2] In the case of mononuclear complexes three coordination modes can be realized (see Scheme 1). The first authenticated example for the $\eta^1$-OCO binding mode was discovered only very recently,[3] although it seems to play an important role in enzymes. In this example a linear $CO_2$ unit is bound to a trivalent uranium atom in the center of a sterically crowded complex. The unusual coordination mode most likely results from the restricted space that the ligand shell offers to the incoming $CO_2$.

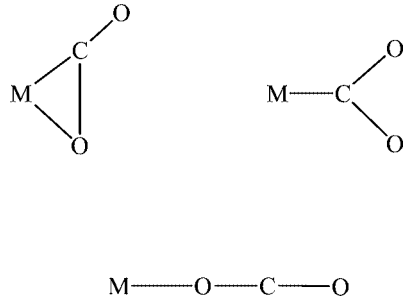

Scheme 1.

Several main-group element compounds are also known to react with $CO_2$. Very recently it was claimed that the reaction of $Mg[N(SiMe_3)_2]_2$ with $AlR_3$ (R = Me or Et) and $CO_2$ in THF affords aluminium–magnesium complexes with linearly bridging $CO_2$ units, viz. $[\{R_2Al(\mu\text{-}NSiMe_3)(\mu\text{-}OSiMe_3)Mg(thf)_2(\mu\text{-}O_2C)\}_3]$.[4] However, this result was questioned by a later analysis,[5] according to which the compound exhibits bridging $NCO^-$ ligands instead of the isoelectronic neutral $CO_2$ ligands. Zn compounds, especially pyrazolylborate zinc hydroxides,[6] dinuclear complexes that should mimic the reactive center of enzymes,[7] and zinc amides (see below), were also the focus of recent research, particularly because of their biological relevance.

[a] Anorganisch-Chemisches Institut, Ruprecht-Karls-Universität Heidelberg
Im Neuenheimer Feld 270, 69120 Heidelberg, Germany
Fax: +49-6221-54-5707
E-mail: hans-jorg.himmel@aci.uni-heidelberg.de

 © 2007 Wiley-VCH Verlag GmbH & Co. KGaA, Weinheim 

Several amides of main group elements (such as Li or Mg) have been shown to react with $CO_2$ to give carbamate molecules. Generally four bonding modes can be realized (see Scheme 2).[8] The enzyme rubisco (ribulose-1,5-biphosphate-carboxylase/oxygenase) features a $Mg^{2+}$ ion in the center to which a monodentate carbamato ligand is bound (thus realizing bonding mode **A**).[9,10] Bonding mode **C** is realized, for example, in the enzymes urease and phosphotriesterase in which a carbamato ligand (formed from a lysine) bridges two nickel (urease) or zinc (phosphotriesterase) ions.[10,11] The first example for bonding mode **B** was found only very recently in the unsymmetrical dinuclear compound $[Mg_2(O_2CNCy_2)_4(HMPA)]$, where Cy = cyclohexyl and HMPA = hexamethylphoshoramide.[12] There are several synthetic routes to carbamates, one of which is a direct reaction of amides with $CO_2$.[2] It was shown that chiral carbamates can be synthesized from the reaction between chiral lithium amides and $CO_2$.[13] The mechanism for these reactions was recently analyzed on the basis of quantum chemical (B3LYP) calculations.[14]

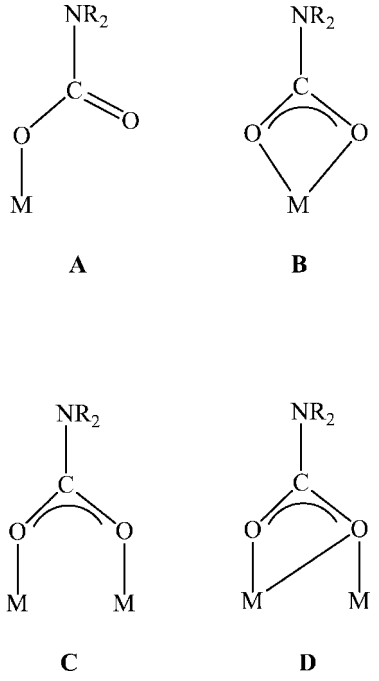


Scheme 2.

The reactions between alkylzinc amides of the formula $RZnNEt_2$ (R = Me, Et) and $CO_2$ were reported to first give the tetramer $[R_2Zn_4O_2C(NEt_2)_6]$,[15] which reacts with an excess of $ZnMe_2$ to give the compound $[Zn_4Me_4(O_2CNEt_2)_4]$ featuring an approximately tetrahedral arrangement of the four Zn atoms.[16] Very recently it was shown that $CO_2$ inserts into the metal–nitrogen bond of $H_3CZnNR_2$ (R = *i*Pr, *i*Bu or piperidinyl) to give tetrameric cage compounds of the formula $[H_3CZnO_2CNR_2]_4$,[17] which seem to contradict previously obtained results. Interestingly, addition of pyridine achieves a breakage of the tetramer into two dimeric units. In light of all these findings a theoretical analysis of the reaction pathways is highly desirable.

## Results and Discussion

The discussion is divided into two sections. In the first one it is assumed that the alkylzinc amide reacts as a monomer with $CO_2$, although of course the majority of alkylzinc amides are generally expected to be dimeric or even trimeric. However, monomeric alkylzinc amides containing sterically demanding alkyl groups are known, e.g. $(Me_3Si)_3CZnN(H)Si(iPr_3)$.[18] It is assumed that the reaction first leads to a monomeric zinc carbamate, which oligomerizes afterwards. In the second section $CO_2$ fixation by dimeric alkylzinc amides is discussed.

### 1. Reactions Starting from Monomeric Alkylzinc Amides

Although monomeric alkylzinc amides can only be isolated in the case of sterically demanding alkyl groups, they could in other cases exist in solution (in small quantities) in equilibrium with the dimeric form.[19] The general consensus in the case of mononuclear transition-metal complexes is that electrophilic attack at the amide nitrogen by the carbon atom of $CO_2$ initiates reaction. However, the role of the metal has not yet been accessed in sufficient depth. In the case of *fac*-$(CO)_3$(dppe)MnOR derivatives featuring an alkoxide or aryloxide (OR) group in place of an amide a four-membered transition state has been postulated.[20] In this transition state, the C atom of the $CO_2$ group interacts with the O atom of the OR group, and one of the O atoms of $CO_2$ interacts with the metal center. This suggestion might imply that the metal–oxygen interaction is already established at an early stage of the reaction. One of the objectives of the following discussion is therefore to analyze the role of the metal–oxygen bond during the reactions of alkylzinc amides with $CO_2$. However, other questions concerning the mechanism arise. In the case of insertion of $CO_2$ into the metal–nitrogen bond of the transition-metal complex $(Ph)(PCy_3)_2PtNH_2$[21] it was claimed, on the basis of spectroscopic (IR, NMR) evidence, that in benzene a nitrogen-bonded carbamate is first formed. This species was reported to rearrange readily when dissolved in dichloromethane to the more stable oxygen-bonded carbamate. Thus the calculations in this paper also have to answer the question whether or not the nitrogen-bonded carbamate represents an intermediate in the course of the reaction with alkylzinc amides.

The analysis starts with the simplest possible model compound, cf. $HZnNH_2$. Two different initial orientations of the $CO_2$ molecule were considered. In the first one the O–C–O axis is oriented perpendicular to the H–Zn–N plane ("vertical" approach). The $CO_2$ axis at the start of the reaction has roughly the same relative orientation as in the product. The symmetry is constrained to $C_{2v}$ throughout the approach of the $CO_2$ toward the alkylzinc amide. Figure 1 displays the energy as calculated using BP/TZVPP relative to that of the two separated reactants ($HZnNH_2$ and $CO_2$) versus the Zn–N–C angle. The $CO_2$ molecule already occurs at large values of the reaction coordinate, slightly attracted by the lone pair at the N atom. For a Zn–N–C

 © 2007 Wiley-VCH Verlag GmbH & Co. KGaA, Weinheim 

angle of 112.2°, a minimum is reached at a relative energy of not more than –8 kJ·mol$^{-1}$ (according to BP/TZVPP). The N···C separation at this point amounts to 295.7 pm. The C–O distances (117.2 pm) are almost identical to those in free $CO_2$ (117.1 pm according to our BP/TZVPP calculations, exp. value: 116.32 pm). The Zn–N distance measures 183.7 pm and is also only very slightly elongated relative to the distance in free $HZnNH_2$ (183.1 pm). If the molecule is restricted to $C_{2v}$ symmetry the energy again increases for smaller values of the reaction coordinate, and no binding interaction between the O atoms and the Zn atom is established. The interaction energy between the amido group and the $CO_2$ under these conditions is thus only –8 kJ·mol$^{-1}$, a value too weak to bring about reaction. This is a first result underlining the importance of an early formation of a metal–oxygen interaction for any further reaction to occur.

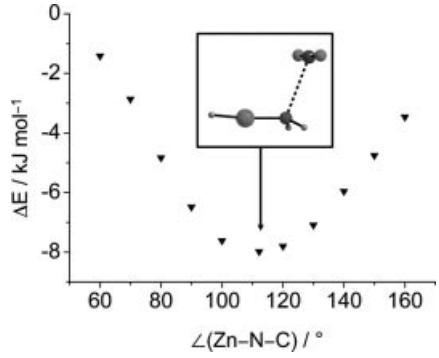


Figure 1. Energy versus the Zn–N–C angle and relative to the separated reactants for the "vertical" approach of the $CO_2$ molecule toward monomeric $HZnNH_2$ as calculated with BP/TZVPP. The inlet shows the structure of the minimum.

The second possibility is that at an early stage of the reaction the three atoms of the $CO_2$ molecule are located roughly in the same plane as the H, Zn, and N atoms of the alkylzinc amide ("parallel" approach). Of course, in this case the symmetry has to change somewhere along the reaction coordinate and therefore all calculations were carried out in $C_1$ symmetry.[22] Figure 2 shows the relative energy calculated versus the N–C distance. Again a shallow minimum ($\Delta E$ of ca. 8 kJ·mol$^{-1}$ without ZPE corrections) occurs at large N–C distances (centered at 280 pm). However, after the system has passed a first transition state (with $\Delta E$ being +7 without and +18 kJ·mol$^{-1}$ with ZPE corrections, and $\Delta G$ being +59 kJ·mol$^{-1}$) it reaches a local minimum that is bound with respect to the reactants by –19 kJ·mol$^{-1}$ without and –8 kJ·mol$^{-1}$ with ZPE corrections. At +33 kJ·mol$^{-1}$ the $\Delta G$ value is still positive at this point. This local minimum features a four-membered [ZnNCO] ring and is characterized by the following bond lengths (in pm, for BP/TZVPP): 155.1 (N–C), 102.4 (N–H), 120.8/129.6 (C–O), 151.7 (Zn–H), 196.1 (Zn–O), and 252.7 (Zn–N). The C–O bond as part of the four-membered ring is significantly elongated (129.6 pm) to a value that falls in between the typical regions for CO single (ca. 142 pm) and double bonds. At 132.0° the O–C–O bond angle is already quite small. A significant Zn–O interaction is already established and, together with a larger C–N interaction, is responsible for the decrease in energy. The Zn–N distance at this point is substantially elongated with respect to that in free $HZnNH_2$ (183.1 pm). However, the formation of new bonds can more than compensate the decrease of the Zn–N bond strength. For N–C distances shorter than 155.1 pm, the relative energy first slightly rises until, at ca. 145 pm, a second transition state is reached. The energy at this transition state is not more than 6 kJ·mol$^{-1}$ higher than that of the preceding local minimum. Relative to the reactants the energy at this point amounts to –13 without and –1 kJ·mol$^{-1}$ with ZPE corrections, and $\Delta G$ is +40 kJ·mol$^{-1}$. Finally, at an N–C distance of 135.5 pm, the carbamate product is reached, which adopts the structure type **B** (see Scheme 2). The energy of the carbamate is by –79 or –67 kJ·mol$^{-1}$ (without or with ZPE corrections, respectively) lower than that of the two separated reactants. $\Delta G$ for the complete reaction is –26 kJ·mol$^{-1}$. The Zn–H, Zn–O, C–O, and N–H distances were calculated to be 151.8, 204.6, 128.9, and 101.0 pm, respectively. The Zn···N separation now amounts to 236.2 pm and the O–C–O angle measures 119.9°. This compares to an O–C–O angle of 119.63(16)° in the compound $[Mg_2(O_2CNCy_2)_4(HMPA)]$ (see Introduction), the only known example of mode **B** in Mg chemistry.[12]

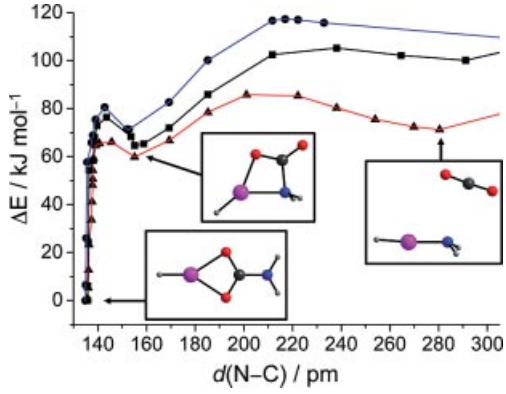


Figure 2. Energy relative to the carbamate product versus the N–C distance as calculated for the reaction of $CO_2$ with $HZnNH_2$ (BP/TZVPP calculation, red line), $H_3CZnN(CH_3)_2$ (BP/TZVPP calculation, black line) and $H_3CZnN(CH_3)_2$ (B3LYP/TZVPP calculation, blue line).

There is no evidence for the formation of a nitrogen-bonded carbamate as an intermediate in the course of the reaction. Nevertheless, we have calculated the geometry and energy of such a species. Its energy turned out to be 12 kJ·mol$^{-1}$ according to BP/SVP and 7 kJ·mol$^{-1}$ according to BP/TZVPP higher than that of the intermediate four-membered ring that is formed during the reaction. This value is higher than the barrier to carbamate formation (second TS, see Table 1) and it is not likely that interaction with the solvent (toluene) leads to a significant stabilization. Therefore any engagement of the nitrogen-bonded carbamate in the reaction can be ruled out. Figure 3 summarizes the reaction pathway.[23]

 © 2007 Wiley-VCH Verlag GmbH & Co. KGaA, Weinheim 

Table 1. Energy, $\Delta E$, zero-point energy corrected energy, $\Delta E_{ZPE}$, and $\Delta G$ (at 298 K, 1 bar), all in kJ·mol$^{-1}$, relative to the reactants for the reaction between $HZnNH_2$ or $H_3CZnN(CH_3)_2$ and $CO_2$ as calculated with BP/TZVPP and B3LYP/TZVPP.

| | $HZnNH_2$ | $H_3CZnN(CH_3)_2$ | |
|---|---|---|---|
| | BP/TZVPP $\Delta E$, $\Delta E_{ZPE}$, $\Delta G$ | BP/TZVPP $\Delta E$, $\Delta E_{ZPE}$, $\Delta G$ | B3LYP/TZVPP $\Delta E$, $\Delta E_{ZPE}$, $\Delta G$ |
| First TS[a] | +7, +18, +59 | +1, +12, +56 | +8, +19, +63 |
| Intermediate | –19, –8, +33 | –40, –29, +15 | –38, –27, +17 |
| Second TS[a] | –13, –1, +40 | –28, –16, +29 | –29, –17, +28 |
| Product | –79, –67, –26 | –105, –93, –50 | –109, –97, –54 |

[a] TS: transition state.

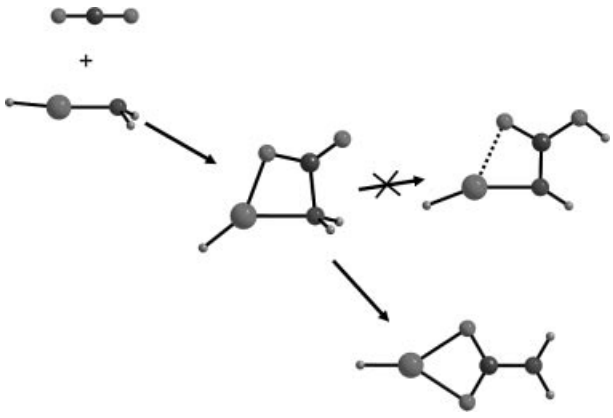

Figure 3. Pathway calculated for the reaction between $HZnNH_2$ with $CO_2$ leading to the carbamate $HZnO_2CNH_2$.

The calculations were repeated with the more realistic model compound methylzinc dimethylamide, $H_3CZnN(CH_3)_2$. For this molecule the effect of changing the method from the pure DFT method BP to the hybrid method B3LYP, which generally gives more accurate energies, was also analyzed. The energy curves resulting from these calculations are included in Figure 2. It can be seen that the reaction mechanism is qualitatively and in some important details also quantitatively similar to that obtained for $HZnNH_2$. Again, a $\Delta G$ barrier of ca. 60 kJ·mol$^{-1}$ leads from the separated reactants to the intermediate, which is, however, this time more strongly bound ($\Delta E$ = –40 kJ·mol$^{-1}$, instead of –19 kJ·mol$^{-1}$ in the case of $HZnNH_2$). A small barrier separates this intermediate from the carbamate product, which is now bound by $\Delta E$ = –105 kJ·mol$^{-1}$ (instead of –79 kJ·mol$^{-1}$ in the case of $HZnNH_2$). The values calculated for the relative energies with and without zero-point energy corrections, and for the standard Gibbs energy are summarized in Table 1. BP and B3LYP give similar relative energies.

Table 2 summarizes the energy changes calculated for reactions of several different monomeric model alkylzinc amides with $CO_2$ to give monomeric carbamates. All carbamates prefer structure type **B** (see Scheme 2). Facile oligomerization reactions of the monomeric carbamates should therefore be responsible for the fact that this mode is so seldom realized (see Introduction). On the other hand, the hypothesis that the electron density donated by the two oxygen atoms is so great that the highly strained four-membered ring of **B** generally cannot form[24] can be ruled out. It can be seen that the reaction energy is very sensitive to variations of the amide group (see Figure 4). Thus the reaction energy increases in the order $NF_2 < N(Ph)_2 < N(H)Ph < NH_2 < N(iPr)_2$, a trend that can easily be explained by the increasing basicity. On the other hand, the reaction energy is not significantly different for $HZnNH_2$, $CH_3ZnNH_2$, and $CF_3ZnNH_2$ indicating that the energies are less sensitive to alterations on the alkyl side. Table 3 compares the Zn–N distances in the initial alkylzinc amides and the Zn–O distances in the carbamate products with the reaction energy. In general large Zn–N distances of the alk-

Table 2. Reaction energies (in kJ·mol$^{-1}$) as calculated with BP/SVP and BP/TZVPP for reactions starting with monomeric $HZnNH_2$.

| Reaction | BP/SVP | BP/TZVPP |
|---|---|---|
| $HZnNH_2 + CO_2 \rightarrow HZnO_2CNH_2$ | –115 | –79 |
| $H_3CZnNH_2 + CO_2 \rightarrow H_3CZnO_2CNH_2$ | –114 | –78 |
| $H_3CZnN(CH_3)_2 + CO_2 \rightarrow H_3CZnO_2CN(CH_3)_2$ | –132 | –105 |
| $F_3CZnNH_2 + CO_2 \rightarrow F_3CZnO_2CNH_2$ | –112 | –76 |
| $H_3CZnNF_2 + CO_2 \rightarrow H_3CZnO_2CNF_2$ | –43 | –8 |
| $HZnN(iPr)_2 + CO_2 \rightarrow HZnO_2CN(iPr)_2$ | –124 | –97 |
| $H_3CZnN(iPr)_2 + CO_2 \rightarrow H_3CZnO_2CN(iPr)_2$ | –123 | –96 |
| $HZnN(H)Ph + CO_2 \rightarrow HZnO_2CN(H)Ph$ | –88 | –61 |
| $HZnN(Ph)_2 + CO_2 \rightarrow HZnO_2CN(Ph)_2$ | –71 | –31 |
| $2\,[HZnO_2CNH_2] \rightarrow [HZnO_2CNH_2]_2$ | –116 | –76 |
| $2\,[HZnO_2CNH_2]_2 \rightarrow [HZnO_2CNH_2]_4$ | –162 | –103 |
| $4\,HZnO_2CNH_2 \rightarrow [HZnO_2CNH_2]_4$ | –393 | –255 |
| $H_3CZnO_2CN(iPr)_2 \rightarrow [H_3CZnO_2CN(iPr)_2]_4$ | –325 | [a] |

[a] Because of computational restrictions the calculation for this special reaction has been performed exclusively with BP/SVP.

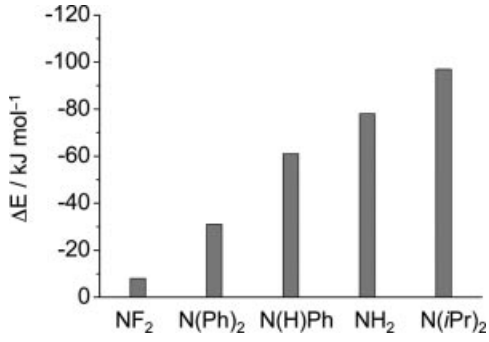


Figure 4. Energy changes for the reactions between $CO_2$ and Zn amides of the general formula HZnNRR′ (R, R′ = H, F, Ph, *i*Pr).

Table 3. Zn–N distance (in pm) in the reactant and Zn–N distance (also in pm) in the product as well as reaction energies (in kJ·mol$^{-1}$) as calculated with BP/TZVPP for some zinc amides.

| Reactant | *d*(Zn–N), reactant | *d*(Zn–O), product | $\Delta E$ |
|---|---|---|---|
| $HZnNF_2$ | 195.4 | 210.5 | –8 |
| HZnN(H)F | 188.0 | 205.6/208.1 | –56 |
| $HZnNPh_2$ | 186.6 | 204.4 | –31 |
| HZnN(H)Ph | 183.8 | 203.1/207.3 | –61 |
| $HZnNH_2$ | 183.1 | 204.6 | –78 |
| $HZnN(iPr)_2$ | 183.3 | 203.4 | –97 |

 © 2007 Wiley-VCH Verlag GmbH & Co. KGaA, Weinheim 

ylzinc amide reactant lead to large Zn–O distances in the carbamate product and consequently smaller values of the absolute reaction energies.

### *Oligomerization of Monomeric Carbamates*

The final step in our model reaction pathway is oligomerization of the monomeric carbamates. Tetramers seem to represent the preferred end products. Figure 5 visualizes the oligomerization process for the simplest model reactant $HZnNH_2$ leading first to dimers and finally to tetramers. Dimerization of two carbamate monomers is associated with an energy change of –116 (BP/SVP) or –76 kJ·mol$^{-1}$ (BP/TZVPP). The zero-point corrected energy change and the $\Delta G$ value for this process are –71 and –19 kJ·mol$^{-1}$, respectively (BP/TZVPP). The dimer is unsymmetrical ($C_1$ symmetry) and features C–O, Zn–H, Zn–O, and C–N bond lengths of 127.8–128.7, 153.0, 197.5–199.3, and 136.2 pm, respectively. The O–Zn–O and O–C–O bond angles measure 99.8° and 124.3/125.0°. Further dimerization of these dimers to give tetramers is even more exothermic [reaction energies of –162 (BP/SVP) or –103 kJ·mol$^{-1}$ (BP/TZVPP) and $\Delta G$ = –36 kJ·mol$^{-1}$ (BP/TZVPP)]. To test the accuracy of our calculations we have also calculated the structure of

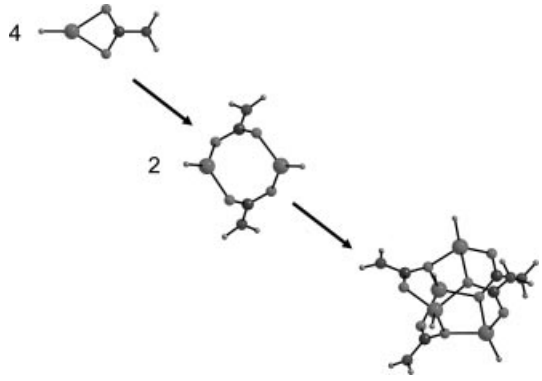


Figure 5. Pathway leading to the $[HZnO_2CNH_2]_4$ tetramer starting with a $HZnNH_2$ monomer.

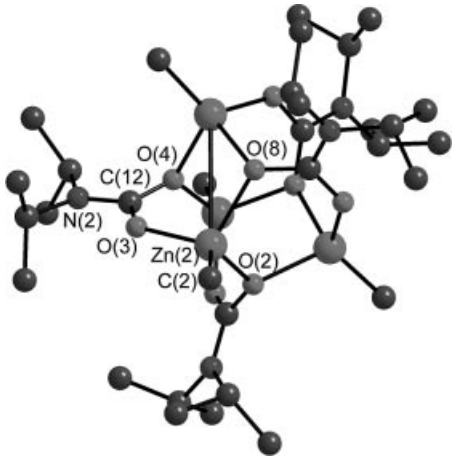


Figure 6. Experimentally determined structure of the $[MeZnO_2CN(iPr)_2]_4$ tetramer (see ref.[14]). H atoms are omitted for the sake of clarity.

$[H_3CZnO_2CN(iPr)_2]_4$ (only with BP/SVP because of computational restrictions) and compared it to the experimentally observed one. Figure 6 shows the structure of $[CH_3ZnO_2CN(iPr)_2]_4$ from the literature[17] and Table 4 compares the experimentally obtained dimensions with the corresponding calculated ones for $[MeZnO_2CN(iPr)_2]_4$ and $[HZnO_2CNH_2]_4$. The labeling of the atoms as shown in Figure 6 and Table 4 is taken from ref.[17] It can be seen that the general level of agreement between the calculated and experimentally observed dimensions is already good with BP/SVP.

Table 4. Comparison between experimental dimensions (bond lengths in pm, bond angles in °) for $[MeZnO_2CN(iPr)_2]_4$ (from ref.[14]) and calculated ones for $[MeZnO_2CN(iPr)_2]_4$ and $[HZnO_2CNH_2]_4$.

| Parameter[a] | $[MeZnO_2CN(iPr)_2]_4$ exp.[b] | $[MeZnO_2CN(iPr)_2]_4$ calcd. | $[HZnO_2CNH_2]_4$ calcd. |
|---|---|---|---|
| Zn(2)–C(2) | 195.0(3) | 197.7 | – |
| Zn(2)–O(2) | 208.8(2) | 210.5 | 215.7 |
| Zn(2)–O(3) | 199.2(2) | 201.5 | 202.0 |
| Zn(2)–O(8) | 205.5(2) | 210.3 | 208.7 |
| O(3)–C(12) | 125.9(3) | 127.4 | 126.8 |
| C(12)–O(4) | 130.8(3) | 131.3 | 130.4 |
| C(12)–N(2) | 133.9(3) | 136.7 | 135.5 |
| O(3)–Zn(2)–O(8) | 101.98(7) | 100.0 | 99.2 |
| O(2)–Zn(2)–O(3) | 100.54(7) | 98.4 | 96.9 |
| O(2)–Zn(2)–O(8) | 93.45(6) | 92.9 | 91.8 |
| O(3)–C(12)–O(4) | 121.0(2) | 122.3 | 124.7 |

[a] See Figure 6 for atom numbering. [b] Ref.[14]

### 2. Reactions Starting from Dimeric Alkylzinc Amides

There are numerous examples of authenticated dimeric alkylzinc amides. However, their structural analysis using X-ray diffraction is limited. Just to name two of them, the crystal structures of dimeric methylzinc and ethylzinc triisopropylsilylamide have recently been reported.[25] Dimerization of the model compound $HZnNH_2$ to give cyclic $[HZnNH_2]_2$ is associated with an energy change of –189 kJ·mol$^{-1}$ according to BP/SVP and –133 kJ·mol$^{-1}$ according to BP/TZVPP calculations. In addition to DFT calculations using the BP functional ab initio (MP2) calculations were performed in this special case to test the accuracy of our calculated methods. MP2/TZVPP calculations gave a dimerization energy of –157 kJ·mol$^{-1}$. Thus the energies calculated with DFT methods are relatively close to those calculated with MP2. The standard Gibbs energy change for dimerization, $\Delta G°$, was calculated to be –75 kJ·mol$^{-1}$ according to BP/TZVPP and –99 kJ·mol$^{-1}$ according to MP2/TZVPP. The Zn–H, Zn–N, and N–H distances in the dimer amount to 154.6, 204.6, and 102.3 pm, respectively, and the N–Zn–N and Zn–N–Zn bond angles were calculated to be 86.9° and 93.1°, respectively. In the case of $[MeZnN(iPr)_2]_2$, an example for which crystal structures are available,[28] the Zn–N distances, and N–Zn–N and Zn–N–Zn bond angles were experimentally determined to be 201.5–204.0 pm, 89.8–90.0°, and 90.1–90.2°, respec-

 © 2007 Wiley-VCH Verlag GmbH & Co. KGaA, Weinheim 

tively. Thus the experimental values are in good agreement with the ones calculated for the model dimer $[HZnNH_2]_2$.

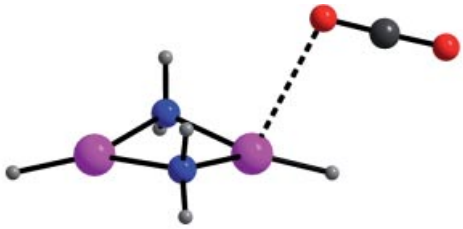

Structure of the complex $[(HZnNH_2)_2(CO_2)]$

$CO_2$ first forms only a weakly bound complex with $[HZnNH_2]_2$. The binding energy amounts to no more than –11 kJ·mol$^{-1}$ according to BP/SVP and –5 kJ·mol$^{-1}$ according to BP/TZVPP. In this complex, the Zn atom interacts with one of the O atoms of $CO_2$, the distance being ca. 298 pm. The N and C atoms are separated by ca. 460 pm. As anticipated, the dimer does not allow any attractive N···C interaction to be established (all valence orbitals on the N atoms are engaged in bonding with the H and Zn atoms of the $[HZnNH_2]_2$ unit). A vibrational analysis (at the BP/SVP level) confirmed that this complex defines a minimum on the potential energy surface.

Part a of Figure 7 displays the relative energy versus the separation between the carbon atom of the $CO_2$ molecule and one of the N atoms. It can be seen that the energy first increases (extremely sharply between 240 and 232 pm) until a transition state is reached at 232.8 pm. The sharp increase coincides with a large increase in the Zn–N bond length into which $CO_2$ first inserts (from 208.9 pm at an N···C distance of 238.1 pm to 285.5 pm for an N···C distance of 232.8 pm). The transition state energy is 51 kJ·mol$^{-1}$ higher than the sum of the energies of the separated reactants. $\Delta G$ at this point amounts to +103 kJ·mol$^{-1}$ (see Table 5) The barrier is caused by the weakening of the strong Zn–N bonds, which cannot be compensated by the newly formed C–N and O–Zn interactions. The transition state is further characterized by Zn···O and N···C distances of 228.9 and 232.9 pm, respectively. The C–O distances measure 120.1 and 117.6 pm. Thus one of the C–O distances is already significantly elongated with respect to the distance in free $CO_2$ (117.1 pm). We therefore conclude that the reaction of the dimeric alkylzinc amide is subjected to a significantly higher barrier than that starting from the monomer. It is also higher than that calculated for the reaction between dimeric lithium amides and $CO_2$ (a Gibbs free energy barrier of +41 kJ·mol$^{-1}$ was obtained in this work).[14] In the case of the lithium amides, the Li–N distance seems to be insignificantly elongated at the transition state.

For smaller distances the energy decreases again, but not steadily, until the carbamate is formed. A local minimum is reached at 148.6 pm exhibiting a relative energy of –19 kJ·mol$^{-1}$ ($\Delta G$ = +33 kJ·mol$^{-1}$) and featuring a six-membered [ZnNZnNCO] ring. A vibrational analysis confirms that it is a real minimum (no imaginary frequencies occurred). The Zn–N–C angle at this point amounts to 105.9°. If we introduce the atom numbers N1, N2, Zn1, Zn2, O1, and O2, with Zn1 being bound to O1 and N1, and Zn2 being bound to N1 and N2, the bond lengths (in pm) are as follows: 203.7 (Zn1–N1), 197.2 (Zn2–N1), 218.2 (Zn2–N2), 148.6 (N2–C), 129.0 (C–O1), 122.3 (C–O2), 198.2 (O1–Zn1). The Zn1···N2 separation amounts to 351.7 pm. The changes in the C–N distance between the structure of this local minimum (148.6 pm) and the carbamate product (136.9 pm) are relatively small. In fact toward the end of the reaction the C–N distance remains almost unchanged although the energy still decreases. Therefore for this stage of the reaction, the C–N distance is not the optimal choice for the reaction coordinate and the Zn–N–C bond angle was taken instead. The corresponding energy curve is displayed in Figure 7b. It can be seen that the barrier separating the intermediate from the heterodimer $[H_2Zn(NH_2)(O_2CNH_2)]$ amounts to no more than 1.3 kJ·mol$^{-1}$. The overall reaction to give the heterodimer product is associated with an energy change of –102 kJ·mol$^{-1}$ according to BP/SVP and –75 kJ·mol$^{-1}$ according to BP/TZVPP. $\Delta G$ for the overall reaction is –24 kJ·mol$^{-1}$ (BP/TZVPP). The nonplanar product is char-

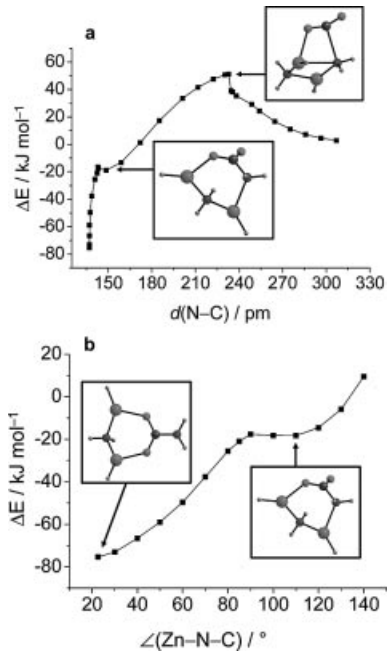


Figure 7. (a) Energy versus the N–C separation and relative to the separated reactants for the reaction of the $[HZnNH_2]_2$ dimer with $CO_2$. (b) Energy versus the Zn–N–C angle and relative to the separated reactants for the reaction of the $[HZnNH_2]_2$ dimer with $CO_2$.

Table 5. Energy, $\Delta E$, zero-point energy corrected energy, $\Delta E_{ZPE}$, and $\Delta G$ (at 298 K, 1 bar), all in kJ·mol$^{-1}$, relative to the reactants for the reaction between $[HZnNH_2]_2$ and $CO_2$ as calculated with BP/TZVPP.

| | $\Delta E$ | $\Delta E_{ZPE}$ | $\Delta G$ |
|---|---|---|---|
| First TS[a] | +51 | +65 | +103 |
| Intermediate | –19 | –5 | +34 |
| Second TS[a] | –18 | –4 | +35 |
| Product | –75 | –63 | –24 |

[a] TS: transition state.

 © 2007 Wiley-VCH Verlag GmbH & Co. KGaA, Weinheim 

acterized by the following distances (in pm) and angles: 128.1 (C–O), 200.2 (Zn–O), 200.0 (Zn–N), 136.9 (C–N), 127.2° (O–C–O), and 106.5° (Zn–N–Zn). In summary, the rate-determining step again turns out to be the formation of the intermediate, which is opposed by a barrier $\Delta G$ of +103 kJ·mol$^{-1}$.

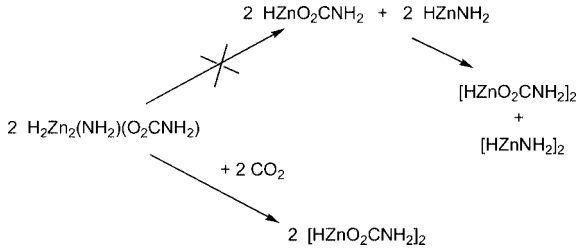


### *Further Reaction with $CO_2$ and Oligomerization*

Two possible routes lead from the heterodimer $H_2Zn_2(O_2CNH_2)(NH_2)$ to the homodimer $[HZnO_2CNH_2]_2$. The first one includes dissociation of $H_2Zn_2(O_2CNH_2)(NH_2)$ to give monomeric $HZnO_2CNH_2$ and $HZnNH_2$, which afterwards dimerize to $[HZnO_2CNH_2]_2$ and $[ZnNH_2]_2$, respectively. The energy needed to form the monomers is, however, 176 (BP/SVP) or 129 kJ·mol$^{-1}$ (BP/TZVPP). The subsequent dimerization is, of course, exothermic, but the overall formation of $[HZnO_2CNH_2]_2$ and $[ZnNH_2]_2$ is still endothermic (see Table 6). The second possibility is that $[HZnO_2CNH_2]_2$ is formed by the reaction between $H_2Zn_2(O_2CNH_2)(NH_2)$ and a second $CO_2$ molecule. This reaction is calculated to be exothermic [reaction energy of –55 (BP/SVP) or –26 kJ·mol$^{-1}$ (BP/TZVPP)], and therefore this most likely represents the preferred path. It is worth mentioning that our calculations show that the fixation of the first $CO_2$ molecule (reaction energy of –75 kJ·mol$^{-1}$ according to BP/TZVPP) is significantly more exothermic than the fixation of the second one (reaction energy of only –26 kJ·mol$^{-1}$). While $\Delta G$ for the fixation of the first $CO_2$ is negative (–24 kJ·mol$^{-1}$), it is positive (+34 kJ·mol$^{-1}$) for the fixation of the second one. It has been shown that in enzymes the presence of a carbamato ligand is important for $CO_2$ fixation. Carbamate formation preorganizes the active center e.g. of the $Mg^{2+}$ complex in the center of the enzyme rubisco. The carbamato ligand adopts in this special case an end-on monodentate rather than a bidentate coordination mode, which is different from our model compounds. Figure 8 shows the reaction pathway leading first to $[H_2Zn_2(NH_2)(O_2CNH_2)]$ and then to $[HZnO_2CNH_2]_2$. This molecule dimerizes finally to the tetramer as shown in Figure 5. This dimerization is accompanied by an energy change of –103 kJ·mol$^{-1}$. $\Delta G$ for this process is –36 kJ·mol$^{-1}$.

Table 6. Reaction energies (in kJ·mol$^{-1}$) as calculated with BP/SVP and BP/TZVPP for reactions involving the $[HZnNH_2]_2$ dimer.

| Reaction | BP/SVP | BP/TZVPP |
|---|---|---|
| 2 $HZnNH_2 \rightarrow [HZn(\mu\text{-}NH_2)]_2$ | –189 | –133 |
| $[HZn(\mu\text{-}NH_2)]_2 + CO_2 \rightarrow$ $H_2Zn_2(O_2CNH_2)(NH_2)$ | –102 | –75 |
| $H_2Zn_2(O_2CNH_2)(NH_2) + CO_2 \rightarrow$ $[HZn(O_2CNH_2)]_2$ | –55 | –26 |
| $H_2Zn_2(O_2CNH_2)(NH_2) \rightarrow$ $HZn(O_2CNH_2) + HZnNH_2$ | +176 | +129 |
| $[HZn(O_2CNH_2)]_2 \rightarrow 2\ HZn(O_2CNH_2)$ | +116 | +76 |
| 2 $H_2Zn_2(O_2CNH_2)(NH_2) \rightarrow$ $[HZn(O_2CNH_2)]_2 + [HZnNH_2]_2$ | +48 | +49 |

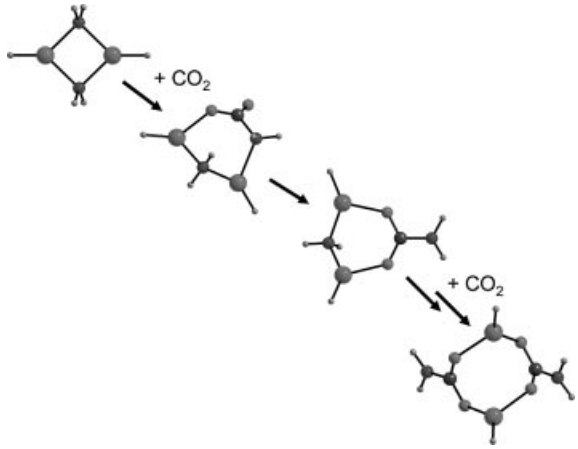


Figure 8. Pathway from $[HZnNH_2]_2$ and $CO_2$ leading to the $[HZnO_2CNH_2]_2$ homodimer that later dimerizes as shown in Figure 5.

## Conclusions

Quantum chemical calculations were used to obtain detailed insight into $CO_2$ fixation by monomeric as well as dimeric alkylzinc amides. The reaction of monomeric alkylzinc amides first leads to an intermediate featuring a four-membered [ZnNCO] ring. The activation energy $\Delta G$ of this first, rate-determining step is around +60 kJ·mol$^{-1}$. From this local minimum on the potential energy surface the system has to pass a much smaller barrier to proceed to the monomeric carbamate product. Dimerization and tetramerization of the monomeric carbamates follow (both exhibiting negative $\Delta G$ values). Any engagement of an N-bonded carbamato species during the reaction can be ruled out. $CO_2$ fixation by several different alkylzinc amide molecules bearing the overall formula RZnNR′R′′ was then compared. The reaction energies were found to be highly sensitive to changes in the electronic properties of the amido group, while modifications on the alkyl (R) side bear almost no influence.

The calculations indicate that the reaction of dimeric alkylzinc amides with $CO_2$ is opposed by a larger barrier ($\Delta G$ value more than +100 kJ·mol$^{-1}$). In this case the transition state features a four-membered [ZnNCO] ring. A six-membered ring then follows as a local minimum on the potential energy curve. The barrier separating this intermediate from the product is again very small. Surprisingly, the calculations indicate that the barrier for $CO_2$ fixation by dimeric alkylzinc amides is higher than the negative dimerization energy of the monomeric alkylzinc amide. It is also higher than the barrier for $CO_2$ fixation by monomeric alkylzinc

 © 2007 Wiley-VCH Verlag GmbH & Co. KGaA, Weinheim 

amide (ca. 60 kJ·mol$^{-1}$). Therefore, although dimeric alkylzinc amides are preferred over monomers, reaction with $CO_2$ could very well predominantly occur from the monomeric state.

## Computational Details

Calculations were carried out with the aid of the TURBOMOLE program package.[26] Pure DFT calculations relied on the BP method (BP is the short notation for Becke–Perdew and is a nonlocal DFT method employing the Becke exchange and Perdew correlation functionals). In addition the hybrid-method B3LYP (DFT using Becke exchange functional and Lee–Yang–Parr correlation functional, as well as Hartree–Fock exchange)[27] was used in the mechanistic studies since this method generally leads to more accurate energies.

It has been shown in the case of quantum chemical studies on $CO_2$ fixation by lithium amides[14] that the choice of basis set is important and that large basis sets (ideally including polarization functions) are necessary. Therefore for all our calculations we have used not only an SVP (split-valence, polarized), but also a TZVPP (triple-zeta valence, doubly-polarized) basis set.[28] It turned out that the reaction energies as calculated with the SVP basis set are in some cases different from those calculated with the TZVPP basis set.

It should be mentioned that for the mechanistic studies it is assumed, as in almost all mechanistic studies of this kind, that the reaction can be divided into several steps, e.g. the dimeric alkylzinc amide reacts in the first step with one equivalent of $CO_2$ and afterwards in a second step with another equivalent of $CO_2$. Of course it is plausible that the reaction with a second $CO_2$ already occurs before completion of the reaction with the first one, and this should indeed happen if it leads to lower energies. However, it is almost impossible to consider all reaction pathways. The "step-by-step" hypothesis thus leads to an upper limit for the true reaction barrier.

In the mechanistic studies a vibrational analysis was carried out at each point to make sure that the approach of the two reactants occurs along a low-energy path. The relative energies, zero-point corrected energies, and the Gibbs energies of all the important points along the reaction path are included in the discussion (see also Tables 1 and 5). Solvent effects were not considered. The solvent used in most of the synthetic work is toluene. The interaction between toluene and the two reactants is expected to be small. In addition, the accurate description of interactions of this kind, which involve the π system of toluene, is extremely difficult and requires highly sophisticated and practically unusable methods to model the complete reaction mechanism.

## Acknowledgments

Financial support from the Deutsche Forschungsgemeinschaft (DFG) and the Fonds der Chemischen Industrie is gratefully acknowledged.

[1] See, for example: P. B. Reich, S. E. Hobbie, T. Lee, D. S. Ellsworth, J. B. West, D. Tilman, J. M. H. Knops, S. Naeem, J. Trost, *Nature* **2006**, *440*, 922; and references therein.
[2] See, for example: a) K. K. Pandey, *Coord. Chem. Rev.* **1995**, *140*, 37–114; b) W. Leitner, *Coord. Chem. Rev.* **1996**, *153*, 257.
[3] I. Castro-Rodriguez, H. Nakai, L. N. Zakharov, A. L. Rheingold, K. Meyer, *Science* **2004**, *305*, 1757.
[4] C.-C. Chang, M.-C. Liao, T.-H. Chang, S.-M. Peng, G.-H. Lee, *Angew. Chem.* **2005**, *117*, 7584; *Angew. Chem. Int. Ed.* **2005**, *44*, 7418.
[5] H. Phull, D. Alberti, I. Korabkov, S. Gambarotta, P. H. M. Budzelaar, *Angew. Chem.* **2006**, *118*, 5457.
[6] See, for example: a) M. Ruf, H. Vahrenkamp, *Inorg. Chem.* **1996**, *35*, 6571; b) M. Ruf, F. A. Schell, R. Walz, H. Vahrenkamp, *Chem. Ber./Recueil* **1997**, *130*, 101; c) H. Vahrenkamp, *Acc. Chem. Res.* **1999**, *32*, 589; d) A. Peter, H. Vahrenkamp, *Z. Anorg. Allg. Chem.* **2005**, *631*, 2347, and references therein.
[7] See, for example: B. Bauer-Siebenlist, F. Meyer, E. Farkas, D. Vidovic, S. Dechert, *Chem. Eur. J.* **2005**, *11*, 4349.
[8] C.-C. Chang, M. S. Ameerunisha, *Coord. Chem. Rev.* **1999**, *189*, 199.
[9] a) T. C. Taylor, I. Andersson, *Nat. Struct. Biol.* **1996**, *3*, 95; b) J. Newman, S. Gutteridge, *Structure* **1994**, *2*, 495; c) W. W. Cleland, T. J. Andrews, S. Gutteridge, F. C. Hartman, G. H. Lorimer, *Chem. Rev.* **1998**, *98*, 549, and references therein.
[10] D. Walther, M. Ruben, S. Rau, *Coord. Chem. Rev.* **1999**, *182*, 67; and references therein.
[11] a) E. Jabry, M. B. Car, P. Hausinger, P. A. Karplus, *Science* **1995**, *268*, 998; b) L. S. Park, R. P. Hausinger, *Science* **1995**, *267*, 1156.
[12] Y. Tang, L. N. Zakharov, A. L. Rheingold, R. A. Kemp, *Organometallics* **2004**, *23*, 4788.
[13] U. Köhn, E. Anders, *Tetrahedron Lett.* **2002**, *43*, 9585.
[14] S. O. N. Lill, U. Köhn, E. Anders, *Eur. J. Org. Chem.* **2004**, 2868.
[15] M. B. Hursthouse, M. A. Malik, M. Motevalli, P. O'Brien, *J. Chem. Soc., Chem. Commun.* **1991**, 1690.
[16] I. Abrahams, M. A. Malik, M. Motevalli, P. O'Brien, *J. Chem. Soc., Dalton Trans.* **1995**, 1043.
[17] Y. Tang, W. S. Kassel, L. N. Zakharov, A. L. Rheingold, R. A. Kemp, *Inorg. Chem.* **2005**, *44*, 359.
[18] M. Westerhausen, M. Wieneke, W. Schwarz, *J. Organomet. Chem.* **1999**, *572*, 249.
[19] Variable-temperature NMR spectroscopic studies have shown that the dimeric structure of the amide $\{[(PhCH_2)_2N]_2Zn\}_2$ fails to remain wholly intact in arene solution and a dynamic monomer–dimer equilibrium exists. See: D. R. Armstrong, G. C. Forbes, R. E. Mulvey, W. Clegg, D. M. Tooke, *J. Chem. Soc., Dalton Trans.* **2002**, 1656.
[20] D. J. Darensbourg, W.-Z. Lee, A. L. Phelps, E. Guidry, *Organometallics* **2003**, *22*, 5585.
[21] S. Park, A. L. Rheingold, D. M. Roundhill, *Organometallics* **1991**, *10*, 615.
[22] The start and end geometries exhibit both $C_{2v}$ symmetry, but the mirror plane changes.
[23] Calculations were also carried out for $CO_2$ fixation by the analogue magnesium model compound $HMgNH_2$ to obtain information on the effect that variation of the metal atom brings about. This reaction was shown to follow the same pattern as that of the Zn compound. The "vertical" approach again leads to a small minimum, which this time adopts a Mg–N–C angle of 109.8° and an energy relative to the sum of the energies of the separated reactants of –25 (BP/SVP) or –6 kJ·mol$^{-1}$ (BP/TZVPP). The interatomic distances (Mg–N 191.6, C–O 117.3, C···N 302.3 pm) and the O–C–O angle (176.1°) again indicate that the geometries of the two reactants are only slightly influenced by this adduct formation. The intermediate featuring a four-membered Mg–N–C–O ring formed in the course of the "parallel" approach now exhibits a relative energy of –127 (BP/SVP) or –79 kJ·mol$^{-1}$ (BP/TZVPP). It is reached at a Zn–N–C angle of 84.5°. The Mg–N, N–C, and C–O distances are 215.2, 157.4, and 128.8/120.9 pm, respectively, and the O–C–O bond angle measures 132.9°. With –198 (BP/SVP) or –153 kJ·mol$^{-1}$ (BP/TZVPP) the overall reaction energy for carbamate formation is almost twice as large as that for the Zn compound.
[24] K.-C. Yang, C.-C. Chang, C.-S. Yeh, G.-H. Lee, S.-M. Peng, *Organometallics* **2001**, *20*, 126.

 © 2007 Wiley-VCH Verlag GmbH & Co. KGaA, Weinheim 

[25] M. Westerhausen, T. Bollwein, A. Pfitzner, T. Nilges, H.-J. Deiseroth, *Inorg. Chim. Acta* **2001**, *312*, 239.
[26] a) R. Ahlrichs, M. Bär, M. Häser, H. Horn, C. Kölmel, *Chem. Phys. Lett.* **1989**, *162*, 165; b) K. Eichkorn, O. Treutler, H. Öhm, M. Häser, R. Ahlrichs, *Chem. Phys. Lett.* **1995**, *240*, 283; c) K. Eichkorn, O. Treutler, H. Öhm, M. Häser, R. Ahlrichs, *Chem. Phys. Lett.* **1995**, *242*, 652; d) K. Eichkorn, F. Weigend, O. Treutler, R. Ahlrichs, *Theor. Chem. Acc.* **1997**, *97*, 119; e) F. Weigend, M. Häser, *Theor. Chem. Acc.* **1997**, *97*, 331; f) F. Weigend, M. Häser, H. Patzelt, R. Ahlrichs, *Chem. Phys. Lett.* **1998**, *294*, 143.
[27] a) A. D. Becke, *J. Chem. Phys.* **1993**, *98*, 5648; b) P. J. Stephens, F. J. Devlin, C. F. Chabalowski, M. J. Frisch, *J. Phys. Chem.* **1994**, *98*, 11623.
[28] A. Schäfer, H. Horn, R. Ahlrichs, *J. Chem. Phys.* **1992**, *97*, 2571.

Received: September 8, 2006
Published Online: January 4, 2007

 © 2007 Wiley-VCH Verlag GmbH & Co. KGaA, Weinheim 

DOI: 10.1002/ejic.200600860

# The Effect of Hydrothermal and Non-Hydrothermal Synthesis on the Formation of Holmium(III) Succinate Hydrate Frameworks

**Maria C. Bernini,[a] Elena V. Brusau,[a] Griselda E. Narda,*[a] Gustavo E. Echeverria,[b,c] C. Gustavo Pozzi,[b] Graciela Punte,[b] and Christian W. Lehmann[d]**

**Keywords:** Lanthanides / Hydrothermal synthesis / Hybrid frameworks / Coordination polymers

Two novel hydrated holmium(III) succinates with formula $[Ho_2(C_4H_4O_4)_3(H_2O)_4]\cdot 6H_2O$ (**1**) and $[Ho_2(C_4H_4O_4)_3(H_2O)_2]\cdot H_2O$ (**2**) have been synthesized from aqueous solution under ambient and hydrothermal conditions, respectively. Single-crystal X-ray diffraction shows that $Ho^{III}$ is nine-coordinate in both compounds even though their structures are markedly different, the main distinctive features being the $[H_2O]/[C_4H_4O_4^{2-}]$ ratio in the coordination sphere, the conformation and coordination ability of the succinate ions, and the resulting framework dimensionality. Compound **1** is a 2D hybrid polymer and its crystal structure is unprecedented for rare-earth succinates. It consists of centrosymmetric dimers of edge-sharing $HoO_7(H_2O)_2$ polyhedra linked by succinate ions in the [100] and [101] directions. Hydrogen-bonded hydration water molecules connect layers to give three-dimensional stability. Compound **2** is built up from infinite chains of $HoO_8(H_2O)$ polyhedra linked by succinates that result in a 3D architecture. This structure shows that hydrothermal conditions favor an increase in the overall dimensionality of these hybrids, in agreement with theoretical considerations. The compounds were characterized by FTIR and Raman spectroscopy, thermal analysis, and variable-temperature magnetic susceptibility measurements and the results are discussed in connection with the structural findings. The effect of the dimensionality on the thermal stability of both structures after removal of the hydration water molecules is also analyzed.

(© Wiley-VCH Verlag GmbH & Co. KGaA, 69451 Weinheim, Germany, 2007)

## Introduction

The last few years have witnessed a great effort dedicated to the investigation, design, and prediction of open hybrid organic/inorganic frameworks with metal cations and multifunctional anions as structural agents.[1–8] Such molecular-based porous materials have potential utility in catalysis, optics, gas separation/storage, and host–guest chemistry.[9–14]

The observed wide use of dicarboxylates to build open framework systems is due to the versatility of these anions' interactions. Their different coordination modes with metals, many of which can coexist, and their ability to act as hydrogen-bond acceptors and donors make them capable of generating supramolecular assemblies and account for their multifunctionality. The synthesis of specific rare-earth dicarboxylates allows us to expand the range of applications of this kind of compounds by constructing smart materials with attractive optical or magnetic properties, depending on the nature of the metal ion.[15–17]

One important limitation for the practical application of hybrid materials is their thermal stability, although this can be considerably improved by the formation of extended metal–oxygen–metal arrays.[13] In the case of lanthanide dicarboxylates, the combination of lanthanide ions with a high coordination number and relatively flexible ligands, like aliphatic dicarboxylates, is expected to prevent collapse of the structure upon removal of guest molecules as well as interpenetration of networks, which obstructs the pores.

A large variety of coordination polymers have been synthesized by crystallization under mild conditions, and hydrothermal techniques allow the variety of structural types to be considerably extended. Although the synthesis conditions are known to play an important role in the framework dimensionality and hydration grade, the way in which all the variables influence the framework development is not yet clear. According to the literature, hydrothermal conditions are more suitable for preparing 3D solids with extended M–O–M networks, which favors better thermal stability since they enhance metal–ligand interactions rather

[a] Area de Química General e Inorgánica "Dr. G. F. Puelles", Facultad de Química, Bioquímica y Farmacia, Universidad Nacional de San Luis,
5700 San Luis, Argentina
E-mail: gnarda@unsl.edu.ar
[b] LANADI e IFLP, Departamento de Física, Facultad de Ciencias Exactas,
1900 La Plata, Argentina
[c] Facultad de Ingeniería, Universidad Nacional de La Plata, CC67,
1900 La Plata, Argentina
[d] Max-Planck-Institut für Kohlenforschung,
45470 Mülheim an der Ruhr, Germany

Supporting information for this article is available on the WWW under http://www.eurjic.org or from the author.

 © 2007 Wiley-VCH Verlag GmbH & Co. KGaA, Weinheim 

than metal–water coordination.[18,19] According to Férey et al.,[20] although helping the formation of M–O–M networks, hydrothermal conditions preclude the assistance of computer simulations in the rational design of this kind of compounds as hydrothermal conditions modify the nature of the species in solution.

Lanthanide succinates have been examined by various authors and several compounds have been reported in the literature, especially $[Ln_2(C_4H_4O_4)_3(H_2O)_2]$ (Ln = Ce,[21] Eu,[22] Gd[23] and Er;[24] type 1), $[Ln_2(C_4H_4O_4)_3(H_2O)_2]\cdot H_2O$ (Ln = Y, La,[14] Pr,[25] Sm,[21,25] Gd[23] and Tb;[22] type 2), and $[Lu_2(C_4H_4O_4)_3(H_2O)_4]\cdot 4H_2O$[26] (type 3). All of these have been obtained by hydrothermal synthesis or under high-temperature conditions and are 3D hybrid frameworks with channels that can host hydrogen-bonded hydration water molecules. Structural analyses have indicated that type-1 compounds, which crystallize in the triclinic system (space group $P\bar{1}$) and do not host hydration waters, present a framework with important structural similarities with type-2 compounds, which crystallize in the monoclinic $C2/c$ space group. Both structural types include infinite 1D inorganic networks (running along a crystallographic axis) that are built up from edge-sharing $LnO_8(H_2O)$ polyhedra interconnected by succinate dianions, with channels parallel to the chains. On the other hand, the lutetium succinate structure (type 3) consists of isolated, irregular $LuO_6(H_2O)_2$ polyhedra linked by organic moieties to form a three-dimensional framework.

To better understand the factors that influence the way of binding and the formation and stability of polymeric structures with different dimensionalities in hybrid systems we decided to explore the self-assembly of $Ho^{III}$ and succinate ligands under ambient and hydrothermal conditions. Two novel dicarboxylate complexes, formulated as $[Ho_2(C_4H_4O_4)_3(H_2O)_4]\cdot 6H_2O$ (**1**) and $[Ho_2(C_4H_4O_4)_3(H_2O)_2]\cdot H_2O$ (**2**), were obtained and their thermal stability was studied. Their characterization by single-crystal X-ray diffraction, thermal and magnetic measurements, and FTIR and Raman spectroscopy are presented here. It is worth noting that the crystal structure of compound **1**, which was obtained under mild conditions, has not been observed previously and therefore it is the first lanthanide succinate with a 2D open structure.

## Results and Discussion

### Crystal Structures

Compound **1** crystallizes in the triclinic space group $P\bar{1}$ with $Z = 2$, although its structure is different from type 1 described above. Compound **2** crystallizes in the monoclinic space group $C2/c$ and is isostructural with all the $Ln^{III}$ succinates that crystallize in the type-2 structure mentioned above (see Experimental Section).

There are two crystallographically independent anions in compound **1**. One (A) is located on an inversion center such that the anion has a perfect *trans* conformation (torsion angle: 180°) with a distance between the α and ω carbon atoms of 3.902(7) Å and the other anion (B) adopts a *gauche* conformation, with a torsion angle of –60.4(5)° and a distance between the α and ω carbon atoms of 2.999(7) Å. Both oxygens of both carboxylates of anion A are bound in a chelating mode, while although both O atoms of both carboxylates in anion B bind in a chelating mode, one oxygen atom of one of the carboxylates also acts in a bridging mode (see Scheme 1).

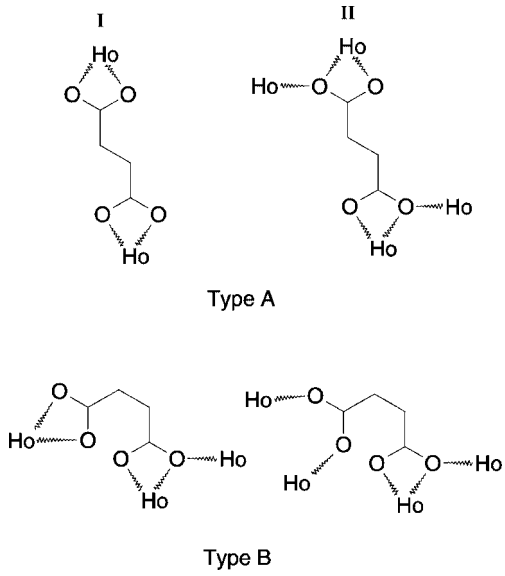


Scheme 1.

The $Ho^{III}$ cations are coordinated by nine oxygen atoms, seven of them belonging to four succinate anions and the others to the two crystallographically inequivalent water molecules (Figure 1 and Table 1). The $HoO_7(H_2O)_2$ coordination polyhedra can be described as a monocapped square antiprism. Edge-sharing polyhedra, related by an inversion

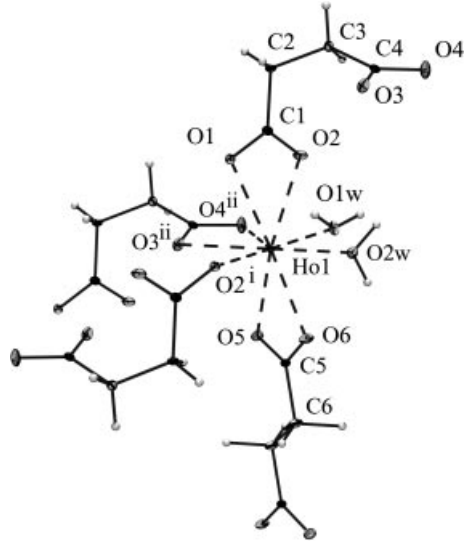


Figure 1. ORTEP-III view of the coordination polyhedron of $Ho^{III}$ in **1** showing the atom-labeling scheme. Displacement ellipsoids are drawn at 50% probability. See footnote to Table 2 for symmetry codes.

 © 2007 Wiley-VCH Verlag GmbH & Co. KGaA, Weinheim 

Table 1. Selected intramolecular bond lengths [Å] and bond, torsion, and dihedral angles [°] for **1** and **2**. See footnote to Table 2 for symmetry codes.

| | | | | | |
|---|---|---|---|---|---|
| Compound **1** | | | | | |
| Ho1–O1W | 2.361(3) | C1–O2 | 1.280(5) | Ho1–O2–Ho1$^{i}$ | 112.4(1) |
| Ho1–O2W | 2.317(3) | C1–C2 | 1.492(6) | O1–C1–C2–C3 | –25.1(6) |
| Ho1–O1 | 2.419(3) | C2–C3 | 1.519(6) | O2–C1–C2–C3 | 155.5(4) |
| Ho1–O2 | 2.532(3) | C3–C4 | 1.500(6) | C1–C2–C3–C4 | –60.4(5) |
| Ho1–O2$^{i}$ | 2.348(3) | C4–O3 | 1.272(5) | C2–C3–C4–O3 | –24.4(6) |
| Ho1–O3$^{ii}$ | 2.399(3) | C4–O4 | 1.261(5) | C2–C3–C4–O4 | 157.7(4) |
| Ho1–O4$^{ii}$ | 2.459(3) | C5–O5 | 1.261(6) | O5–C5–C6–C6$^{iii}$ | –177.1(5) |
| Ho1–O5 | 2.397(3) | C5–O6 | 1.269(6) | O6–C5–C6–C6$^{iii}$ | 3.1(8) |
| Ho1–O6 | 2.472(3) | C5–C6 | 1.504(6) | C5–C6–C6$^{iv}$–C5$^{iv}$ | –180.0(4) |
| C1–O1 | 1.256(6) | C6–C6$^{iii}$ | 1.510(9) | | |
| Compound **2** | | | | | |
| Ho1–O1W | 2.434(5) | C1–C2 | 1.499(9) | C4–O4–Ho1$^{x}$ | 135.1(5) |
| Ho1–O1 | 2.497(5) | C2–C3 | 1.53(1) | O3–C4–O4 | 124.8(6) |
| Ho1–O1$^{vi}$ | 2.391(5) | C3–C4 | 1.516(8) | C4–O3–Ho1$^{v}$ | 145.0(4) |
| Ho1–O2 | 2.445(5) | C4–O3 | 1.247(8) | O1–C1–C2–C3 | –68.5(7) |
| Ho1–O3$^{v}$ | 2.274(5) | C4–O4 | 1.265(9) | O2–C1–C2–C3 | 113.8(7) |
| Ho1–O4$^{vii}$ | 2.391(5) | C5–O5 | 1.281(8) | C1–C2–C3–C4 | –73.1(8) |
| Ho1–O5 | 2.428(5) | C5–O6 | 1.495(10) | C2–C3–C4–O3 | 2.6(9) |
| Ho1–O5$^{vi}$ | 2.388(4) | C5–C6 | 1.495(11) | C2–C3–C4–O4 | –178.0(6) |
| Ho1–O6 | 2.438(5) | C6–C6$^{viii}$ | 1.511(11) | O5–C5–C6–C6$^{viii}$ | –176.2(8) |
| C1–O1 | 1.280(8) | Ho1$^{ix}$–O1–Ho1 | 110.1(2) | O6–C5–C6–C6$^{viii}$ | 1.8(12) |
| C1–O2 | 1.250(8) | Ho1$^{ix}$–O5–Ho1 | 112.6(2) | C5–C6–C6$^{viii}$–C5$^{viii}$ | –180.0(6) |
| Plane P1: atoms: | | Plane P2: atoms: | | Plane P3: atoms: | |
| Ho, O1, Ho$^{ii}$, O1$^{ii}$ | | Ho, O1$^{ii}$, O2$^{ii}$ | | Ho, O1w, O3$^{iii}$, Ho$^{ii}$ | |
| <P1,P2> = 17.5(2)° | | <P2,P3> = 89.3(1)° | | | |

center, form centrosymmetric dimers (see Figure 2) where the Ho$^{III}$ cations are connected by two chelating bridging carboxylates, with the chelating plane (CP) departing 17.5(2)° from the bridging plane (BP; see Table 1 for plane labeling). These dimers are further strengthened by a hydrogen bond (HB) interaction involving the coordinated water W1 and the carboxylate oxygen O3 (see Table 2). The Ho···Ho distance within the dimer is 4.0579(2) Å. The distances between Ho$^{III}$ and the coordinated succinate oxygen atoms range between 2.348(3) and 2.532(3) Å; these extreme values correspond to the bridging oxygen atoms O1 and O1$^{ii}$ [O1–Ho–O1$^{ii}$ angle: 112.4(1)°; ii: 1 – *x*, 1 – *y*, –*z*]. The overall structure can therefore be described as consisting of 2D organic–inorganic polymeric layers, as shown in Figure 3.

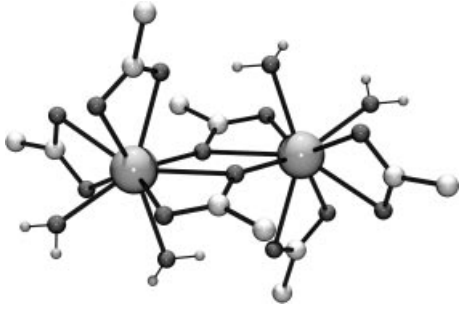

Figure 2. Perspective diagram showing the Ho$^{III}$ and succinate ion connections in the dimer together with the bridging and chelating planes. For reasons of clarity only the relevant succinate fragments are shown. The Ho$^{III}$ ions (bulky spheres) are medium color, while the carbon and oxygen atoms are light and dark gray, respectively.

Table 2. Hydrogen-bond interactions in **1** and **2**.[a]

| | D–H [Å] | H···A [Å] | D···A [Å] | D–H···A [°] |
|---|---|---|---|---|
| Compound **1** | | | | |
| O1W–H11W···O6$^{ii}$ | 0.777 | 2.141 | 2.790(5) | 141.1 |
| O1W–H12W···O3$^{viii}$ | 0.821 | 1.831 | 2.650(4) | 175.1 |
| O2W–H21W···O3W | 0.924 | 1.829 | 2.719(5) | 160.8 |
| O2W–H22W···O5W | 0.857 | 1.814 | 2.663(4) | 170.1 |
| O3W–H31W···O4W | 0.850 | 2.212 | 2.852(5) | 132.0 |
| O3W–H32W···O5W$^{xi}$ | 0.849 | 2.125 | 2.809(5) | 137.4 |
| O4W–H41W···O4$^{xii}$ | 0.850 | 2.098 | 2.925(5) | 164.4 |
| O5W–H51W···O5$^{xiii}$ | 0.850 | 1.939 | 2.740(5) | 156.5 |
| O5W–H52W···O4W$^{xiv}$ | 0.850 | 2.185 | 2.694(6) | 118.3 |
| C6–H61···O4W$^{xiii}$ | 0.932 | 2.582 | 3.471(6) | 159.6 |
| C6–H62···O1W$^{xiii}$ | 1.149 | 2.519 | 3.449(5) | 137.8 |
| Compound **2** | | | | |
| O1W–H11W···O4$^{xv}$ | 0.850 | 2.099 | 2.862(8) | 149.1 |
| O1W–H12W···O2$^{v}$ | 0.850 | 1.882 | 2.709(7) | 164.2 |
| O2W–H21W···O1W | 0.998 | 2.129 | 2.939(8) | 137.1 |
| C2–H22···O6$^{ix}$ | 0.970 | 2.586 | 3.15(1) | 117.6 |
| C3–H31···O2W$^{xiv}$ | 0.970 | 2.575 | 3.51(2) | 161.2 |
| C6–H62···O2$^{ix}$ | 0.975 | 2.494 | 3.13(1) | 122.7 |

[a] Symmetry codes: (i) –*x* + 1, – *y* + 1, –*z* + 2; (ii) *x* – 1, *y*, *z*; (iii) –*x*, –*y* + 1, –*z* + 1; (iv) 2 – *x*, 1 – *y*, 1 – *z*; (v) –*x* + 1/2, –*y* + 3/2, –*z* + 1; (vi) –*x* + 1/2, *y* + 1/2, –*z* + 1/2; (vii) *x*, –*y* + 1, *z* – 1/2; (viii) –*x*, 1 – *y*, –*z*; (ix) –*x* + 1/2, *y* – 1/2, –*z* + 1/2; (x) *x*, –*y* + 1, *z* + 1/2; (xi) 1 – *x*, –*y*, 1 – *z*; (xii) –*x*, –*y*, 1 – *z*; (xiii) 1 – *x*, 1 – *y*, 1 – *z*; (xiv) 1 + *x*, *y*, *z*; (xv) 1/2 – *x*, 1/2 – *y*, 1 – *z*.

Within a layer the dimers are connected by succinates A along [100] and succinates B along [101]. The connection along [100] is further stabilized by a HB between W1 and the succinate oxygen O5 (see Table 2). The hydration water molecules (W3, W4, and W5) are located between the 2D

 © 2007 Wiley-VCH Verlag GmbH & Co. KGaA, Weinheim 

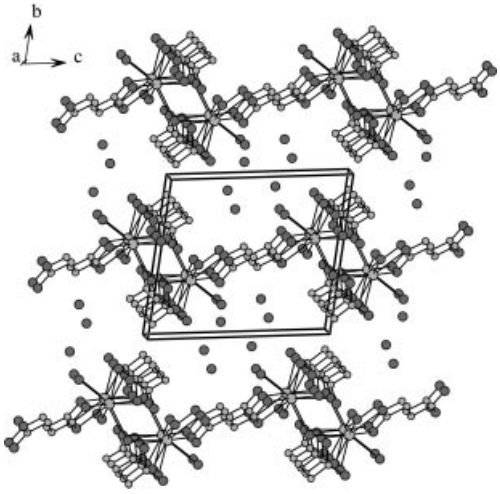


Figure 3. Projection of the framework along the *a* direction of **1**.

organic–inorganic polymeric layers. Hydration waters are connected by HBs to form six-membered clusters, which are located around the inversion centers at (0,0,1/2) and equivalent positions. The coordinated water W2 links clusters through two HBs, thus generating hydrogen-bonded chains of hydration water clusters running in the [100] direction. Hydration waters are further hydrogen bonded to succinate anions, providing in this way the connection between the layers and the stabilization of the three-dimensional arrangement. In spite of the differences in coordination number and coordination modes, we have observed a similar 2D structure in diaquasuccinatocadmium(II).[27,28]

There are also two crystallographically independent anions in compound **2**. One (A) is also located on an inversion center (perfect *trans* conformation) with a distance between the α and ω carbon atoms of 3.838(12) Å and the other (B) adopts a *gauche* conformation with a torsion angle of –73.1(8)° and a distance between the α and ω carbon atoms of 3.21(1) Å. Different to **1**, both carboxylates belonging to anion A in compound **2** coordinate the cations through a chelating and a bridging mode, while one carboxylate of anion B coordinates the cation through a chelating and a bridging mode and the two O atoms of the other carboxylate are only involved in a bridging interaction (see Scheme 1). The $Ho^{III}$ cations in this compound are also coordinated to nine oxygen atoms, in this case adopting a tricapped trigonal prismatic geometry. In this structure just one oxygen of the coordination polyhedra belongs to a water molecule, with the other eight belong to six different carboxylate groups (see Figure 4 and Table 1). Neighboring $Ho^{III}$ cations are connected by two chelating bridging carboxylates and by an additional bidentate carboxylate, which is oriented with the O–C–O plane almost perpendicular to the corresponding BP [the angle is 87.0(9)°; see Figure 5]. This connectivity, different from that observed in **1**, is extended by the twofold screw axis parallel to the *b* axis to build infinite chains where all $Ho^{III}$ ions are at the same distance [4.007(1) Å]. In spite of this, bridging Ho–O–Ho geometries within adjacent polyhedra are different within three esd's. The bridging Ho–O distances are 2.391(5) and 2.388(4) Å [2.497(5) and 2.428(5) Å] and the Ho–O–Ho angle is 112.6(2)° [110.1(2)°; see Table 1]. The chains are connected by anions of type A running perpendicular to the (101) planes and by anions of type B situated along the [101] direction. Adjacent chains along *a* are 8.920(5) and 11.002(5) Å apart and those along *b* 6.016(7) and 7.894(6) Å apart. This arrangement helps the development of an open-framework with two set of channels of different cross-section size [28.8(5) and 20.8(5) $Å^2$], both of which run parallel to the $HoO_2$ chains with the hydration waters located in the largest channel, as can be seen in Figure 6. The hydration waters are linked to the framework by hydrogen bonds (see Table 2). They interact as donors with coordination waters and as H-acceptors from type-B succinate anions.

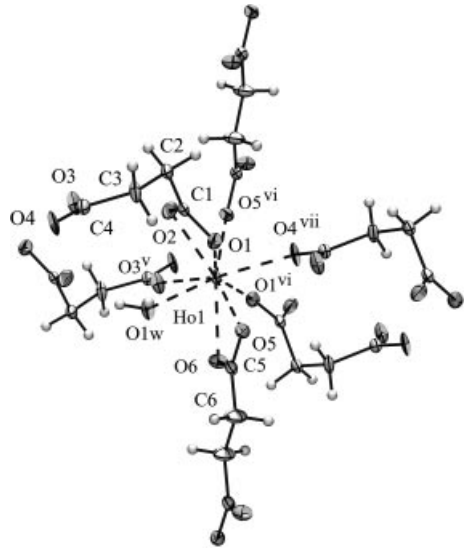


Figure 4. ORTEP-III view of the coordination polyhedron of $Ho^{III}$ in **2** showing the atom-labeling scheme. Displacement ellipsoids are drawn at 50% probability. See footnote to Table 2 for symmetry codes.

Figure 5. Perspective diagram showing the $Ho^{III}$ and succinate ion connections along the chain together with the bridging and chelating planes. Similar to Figure 2, the relevant succinate fragments and gray shades are used.

Taking into account the synthesis conditions that give rise to each structure, it can be inferred that the presence of a higher number of coordination waters, the smaller Ho–OW distances, and the less rich coordination modes of the dicarboxylate anions in **1** are favored by the milder conditions of the solution. This synthesis path leads to the devel-

 © 2007 Wiley-VCH Verlag GmbH & Co. KGaA, Weinheim 

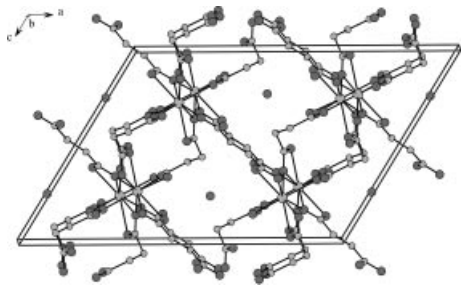

Figure 6. Projection of the framework along the *b* direction of **2**.

opment of 2D organic–inorganic polymeric layers whose hydrophilic surfaces are linked by the hydration waters. On the other hand, the hydrothermal conditions used for the synthesis of **2** help to prevent the presence of a high number of coordination waters and enhance carboxylate coordination, thereby facilitating the formation of infinite Ho–O–Ho networks (see Figure 5) and a 3D framework structure. A comparison of the densities reported in Table 3 shows that they increase with the temperature employed during the synthesis. This correlates with the increasing dimensionality and is in accordance with the results reported in the literature for other metal dicarboxylates.[18,19,29]

### Vibrational Spectra

Figure 7 shows the FTIR and Raman spectra of both compounds. IR and Raman frequencies values for compound **2** are reported in parentheses below. The interpretation of the IR and Raman spectra is performed by considering the internal vibrations of water molecules, carboxylates, and methylene groups and their comparison with those observed in succinic acid and other related compounds. According to structural data, both structures are centrosymmetric ($P\bar{1}$ and $C2/c$) and no coincidences between IR and Raman frequencies (or at least only a few) can be expected, in agreement with the mutual exclusion rule.

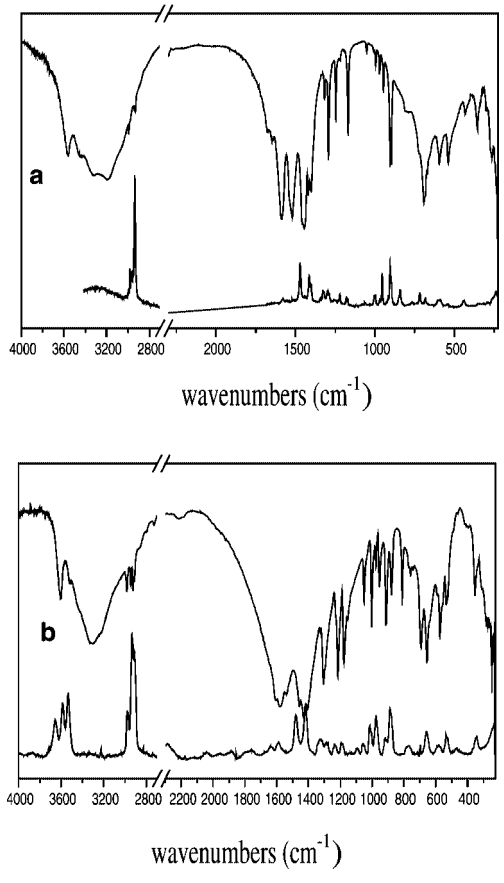


Figure 7. FTIR (top) and Raman (bottom) spectra of a) **1** and b) **2**.

### *Water Modes*

The assignment of these modes, particularly the librational ones, was performed by comparing the spectra of partially and completely dehydrated samples, which were obtained by using a variable-temperature IR cell (the thermal diagrams were taken into account; see Figure 8).

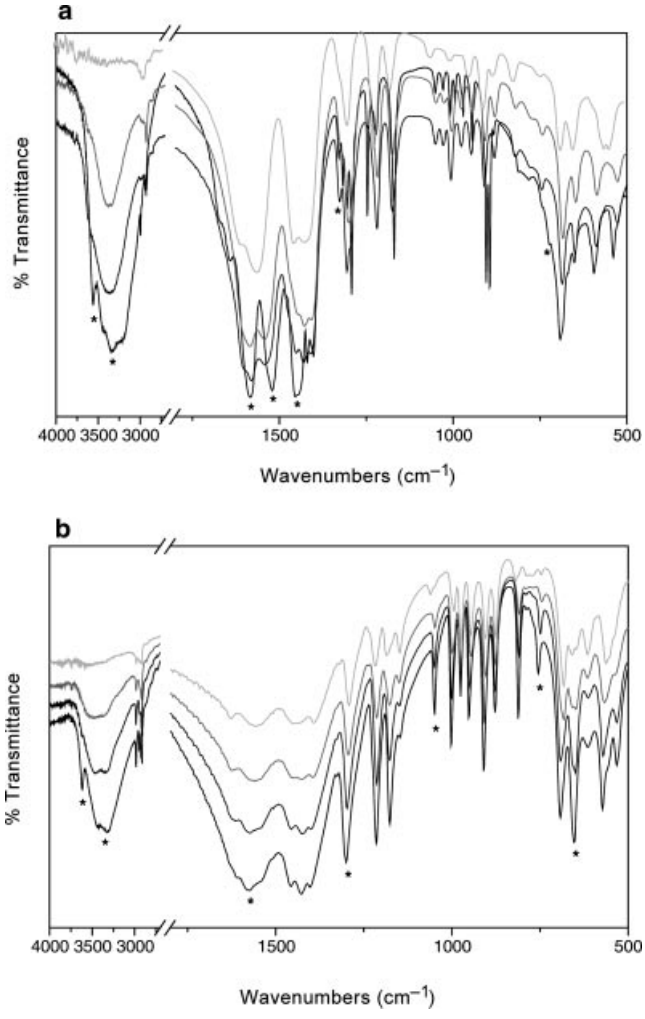


Figure 8. FTIR spectra recorded as a function of temperature during the dehydration of a) **1** and b) **2**. The most notable changes are indicated with asterisks.

The ν(OH) absorption can be identified in the FTIR spectrum of compound **1** as one broad, markedly asymmetric band that involves several components. This fact is consistent with the structural data, where four different kinds

 © 2007 Wiley-VCH Verlag GmbH & Co. KGaA, Weinheim 

of water molecules are seen to be present. The components centered at 3560 and 3460 $cm^{-1}$ (3560, 3520, and 3445 $cm^{-1}$ for **2**) are mainly associated with hydration water since they disappear after partial dehydration; on the contrary, those centered at 3330 and 3175 $cm^{-1}$ (3315 and 3210 $cm^{-1}$ for **2**), which are absent upon complete dehydration, can be attributed to the remaining coordinated water.

The two low-intensity bands located at 1675 and 1645 $cm^{-1}$ are associated with the bending mode; the former is related to those water molecules that are eliminated first during thermal treatment since it is absent in the spectra of partially dehydrated samples.

### *OCO Group Modes*

Both carboxylate stretching modes are present in the FTIR spectra as broad, asymmetric bands with various components included. The splitting of these modes can be explained in terms of the different types of interactions between the carboxylate groups and the $Ho^{III}$ cations found in the crystals of both compounds (see Scheme 1). Two bands at 1585 and 1520 $cm^{-1}$ (1610, 1580, and 1540 $cm^{-1}$) are assigned to $\nu_{as}$(OCO), with the bands at 1330, 1315, and 1305 $cm^{-1}$ (1300 $cm^{-1}$) being associated with the corresponding symmetric mode. Splitting of the OCO stretching modes is not observed in the IR spectra of metal succinates where a unique binding mode for carboxylate groups has been reported.[28,30] No evidence for a carbonyl absorption is present, in agreement with the observed C–O distances (see Table 1).

### Thermal Analysis

TGA curves and thermodiffractograms up to complete dehydration for compounds **1** and **2** are shown in Figures 9 and 10, respectively. The temperature values were selected with reference to TG and *d*TG data; experimental $\Delta m$ percentages and temperature values for compound **2** are presented in parentheses. The differences between the $\Delta m$ percentages found for both compounds and the calculated ones do not exceed 1%. Dehydration proceeds in two stages at 68 °C (55 °C) and 115 °C (176 °C), as expected from the structural data. The first weight loss of 12.5% (1.93%) is related to loss of hydration water whereas the second mass decay of 8% (4.97%) corresponds to the elimination of coordinated water molecules. Differential water removal has also been observed in other type-2 lanthanide succinates, such as the La and Gd ones, whereas in those of Y, Pr, Sm, and Tb hydration and coordinated water molecules are lost in a single step.

A comparison of the dehydration events in **1** and **2** highlights noticeable differences. The continuous loss of weight between 40 and 87 °C for compound **1** accounts for the different interactions of the clustered hydration water molecules, and a rather narrow range of temperatures separates it from the next dehydration step. On the contrary, compound **2** exhibits an extended plateau of stability in the range 60–150 °C after hydration water elimination. These differences in the thermal behaviors of **1** and **2** can be explained as a consequence of the hydrogen bonds inside the framework and the interactions with the water molecules in the channels. These results show that the hydration water in **2** is looser than in other type-2 compounds such as that of

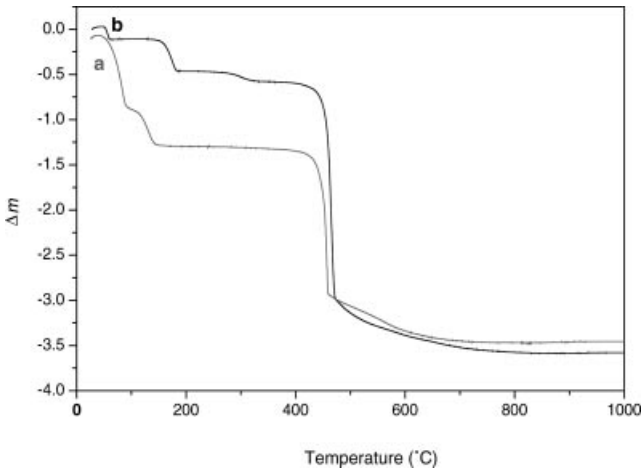


Figure 9. TG curves of **1** and **2**.

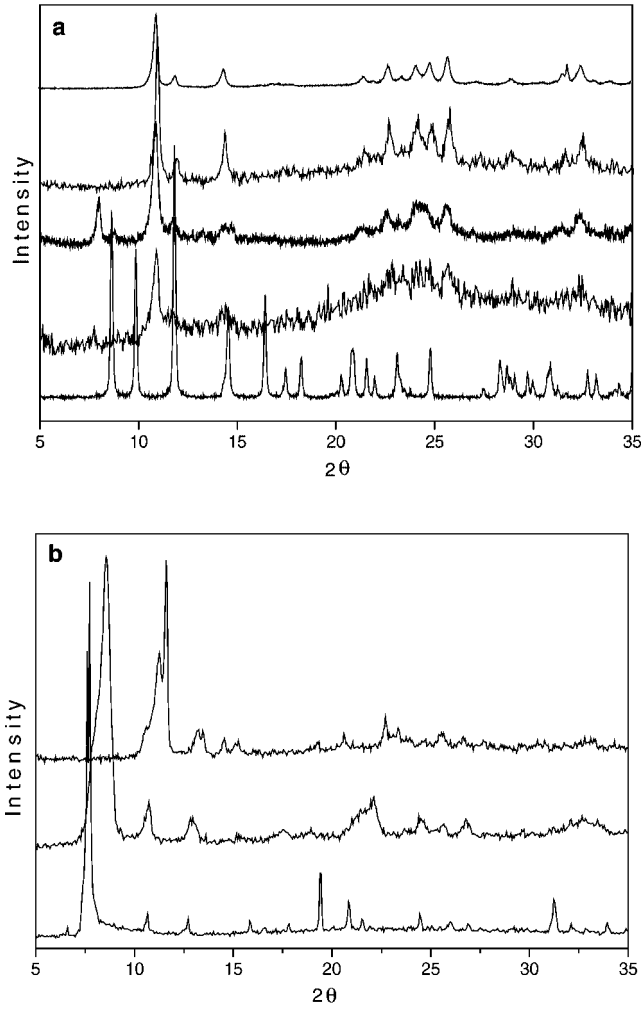


Figure 10. XRD patterns as a function of temperature of a) **1** and b) **2** thermolyzed to dehydration.

 © 2007 Wiley-VCH Verlag GmbH & Co. KGaA, Weinheim 

$Sm^{III}$, where the DTA curve only shows one peak at 214 °C due to loss of both hydration and coordinated waters, or $Gd^{III}$, where lattice and coordinated water molecules are lost in the 200–240 °C and 270–325 °C ranges, respectively.

Dehydration of compounds **1** and **2** was also followed by variable-temperature FTIR spectroscopy (Figure 8). The broad band assigned to the ν(OH) stretching gradually decreases in intensity until its complete disappearance at higher temperature. The OCO stretching bands are strongly affected by dehydration of compound **1** due to the progressive degradation of the H-bond network. Thermally induced changes in these modes are less significant for compound **2**, where a shift to lower frequencies is observed in the main component of the $\nu_{as}$(OCO) and in the corresponding $\nu_s$(OCO) band. The spectra recorded at the highest temperature for both compounds do not display the librational modes of water molecules below 1100 $cm^{-1}$.

The removal of hydration water molecules in **1** leads to an amorphous phase that recrystallizes on further heating and remains stable, with increasing crystallinity, up to succinate ion decomposition, as has been observed for other 2D metallic dicarboxylates (see Figure 10a).[27,30] An extremely weak endothermic DSC signal at 165 °C is related to this transition (see Supporting Information). The X-ray powder diffraction pattern of the new crystalline phase, corresponding to the anhydrous compound, was indexed in the monoclinic space group *P*2/*m* (no. 10), using the TREOR program,[31] with the following cell parameters: $a$ = 19.378(5), $b$ = 8.157(4), $c$ = 4.236(1) Å, and $\beta$ = 92.22(1)°. Taking into account the structural features of compound **1** (described above), it is reasonable to expect that removal of hydration water implies loss of crystallinity.

Compound **2** essentially retains its crystalline structure when the first water molecule is lost, with the decrease in the XRPD intensity being the most outstanding difference between patterns corresponding to different temperature treatments (see Figure 10b).

The thermal evolution of both compounds presents a final event at 442 °C for **1** (460 °C for **2**) which is associated with succinate ion decomposition to give cubic holmium oxide as the final product; this is stable up to 1000 °C (PDF card 43-1018). A change in the slope of the TG trace around 500 °C suggests the formation of an intermediate product. A carbonated phase, which further decomposes to the oxide, appears upon heating to 500 °C and its identification was performed by FTIR spectroscopy, which exhibits characteristic bands at 1390 and 860 $cm^{-1}$.[32]

## Magnetic Measurements

The magnetic behavior of **1** and **2** is shown in Figure 11, where the real component of the AC magnetic susceptibility ($\chi'$) and the product $\chi'T$ are plotted against temperature. In both cases, at temperatures below 100 K, the $\chi'T$ curve departs from a Curie–Weiss law. The Curie constant, $C$, and Curie temperature, $\theta$, were determined from a linear fit of the inverse of $\chi'^{-1}$ in the range of temperatures where the Curie–Weiss law stands. This fit yields the values $C$ = 14.27(7) and 13.49(3) $cm^3\,K\,mol^{-1}$ and $\theta$ = –2.5(5) and –3.6(6) K for **1** and **2**, respectively. The negative value of the Curie temperature and the temperature dependence of $\chi'T$ indicate that an antiferromagnetic ordering is reached at lower temperatures. The effective magnetic moments ($\mu_{eff}$) calculated from the Curie constants are 10.68(1) $\mu_B$ for **1** and 10.37(1) $\mu_B$ for **2**, both of which are very close to the effective magnetic moment of the free $Ho^{III}$ cation (10.6 $\mu_B$). The observed lower $\mu_{eff}$ value in **2** might be a consequence of the higher delocalization of the $Ho^{III}$ electrons in this compound due to the higher number of oxy-

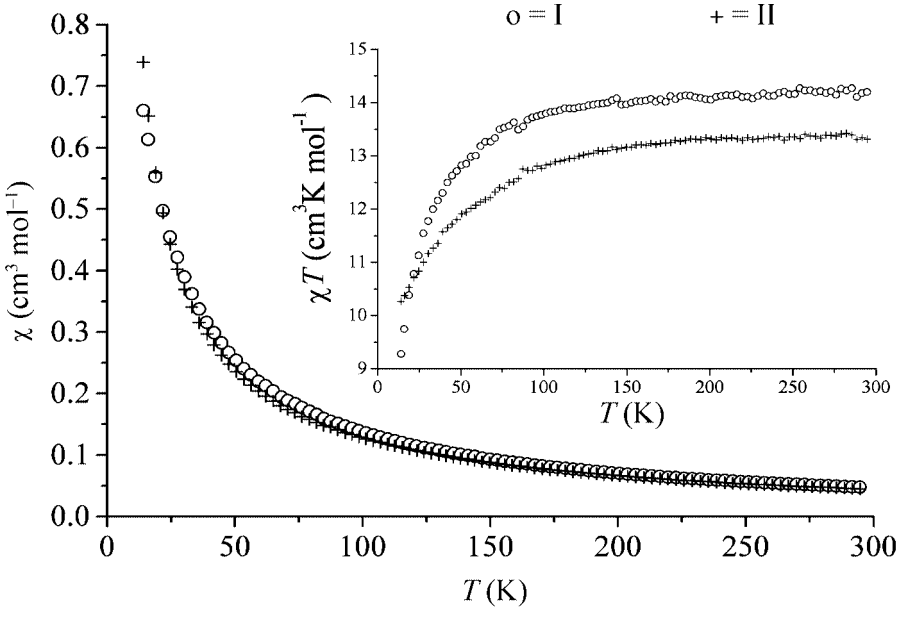


Figure 11. Thermal dependence of $\chi'$ for **1** and **2**. The inset shows the $\chi'T$ curves, which display the Curie–Weiss antiferromagnetic behavior of both compounds.

 © 2007 Wiley-VCH Verlag GmbH & Co. KGaA, Weinheim 

gens belonging to succinate anions in the coordination sphere.

At low temperatures, where the $\chi' T$ curves deviate from the Curie–Weiss law, the calculated $\mu_{eff}$ values at 14 K are 8.62(4) $\mu_B$ for **1** and 9.06(1) $\mu_B$ for **2**. A deviation of the magnetic behavior from a Curie–Weiss law and a decrease of the $\chi' T$ product with temperature have been observed in other $Ho^{III}$ carboxylates[33] and have been mainly ascribed to crystal field effects, which induce a depopulation of the rare-earth cation Stark components at low temperatures.

## Conclusions

Two $Ho^{III}$ succinate coordination polymers, namely $[Ho_2(C_4H_4O_4)_3(H_2O)_4]\cdot 6H_2O$ (**1**) and $[Ho_2(C_4H_4O_4)_3(H_2O)_2]\cdot H_2O$ (**2**), have been prepared and characterized employing mild and hydrothermal conditions, respectively. $Ho^{III}$ is nine-coordinate in both compounds. The structure of **1** consists of 2D organic–inorganic polymeric layers where coordination polyhedra form dimers that are connected by hydrogen-bonded hydration waters. In **2**, neighboring $Ho^{III}$ ions build infinite Ho–O–Ho chains linked by *trans* and *gauche* succinates. Chain formation supports the development of a hybrid open framework with two set of channels of different size, the largest of which contains the hydration waters. Thus, the multidentate character of the succinate ions in this compound, together with the substitution of a water ligand by an oxygen of the OCO groups, favors the formation of infinite M–O–M networks and plays an important role in the inorganic condensation. This also allows us to explain the observed difference in the magnetic results as being due to the presence of a dissimilar number of oxygens belonging to the succinate anions in the coordination sphere.

A crystalline anhydrous phase is obtained upon heating **1** after water removal, while the partially dehydrated compound obtained upon heating **2** shows a plateau of thermal stability, which indicates the potential capability of the dehydrated form of **2** to act as a stable open-framework material with empty channels.

All the above results show the effect of the synthesis conditions on the dimensionality and thermal stability of the metal-organic polymers and reinforce the necessity of the hydrothermal method for the formation of inorganic networks and open channels. However, other parameters, at present under study, need to be looked at to understand the relationship between synthesis temperature and the structure and properties of the products.

## Experimental Section

**Synthesis:** Reagents of analytical grade were used in the synthesis of compounds **1** and **2** according to the following procedures.

**$[Ho_2(C_4H_4O_4)_3(H_2O)_4]\cdot 6H_2O$ (1):** $HoCl_3\cdot 6H_2O$ (2 mmol) was dissolved in distilled water (100 mL) and then added to an aqueous solution containing succinic acid (3 mmol, 100 mL) whilst stirring; the resulting pH was raised to 4.5 by NaOH addition. The solution was then left to evaporate slowly at room temperature. A large number of pale-orange, needle-shaped single crystals (70% yield) suitable for a crystallographic study were obtained after several days. These were filtered, washed with distilled water, and dried at room temperature. $C_6H_{16}HoO_{11}$ (429.12): calcd. C 16.39, H 3.81; found C 16.78, H 3.73.

**$[Ho_2(C_4H_4O_4)_3(H_2O)_2]\cdot H_2O$ (2):** A solution prepared as described above (50 mL) was allowed to react under autogenous pressure for 3 d at 180 °C. Pale-orange, prismatic single crystals (58% yield) suitable for a crystallographic study were obtained. These were filtered, washed with distilled water, and dried at room temperature. $C_6H_{10}HoO_{7.5}$ (367.07): calcd. C 19.71, H 2.58; found C 19.63, H 2.45.

**X-ray Powder Diffraction (XRPD):** X-ray powder diagrams were obtained with a Rigaku D-MAX-IIIC diffractometer using Cu-$K_\alpha$ radiation (Ni filter) and NaCl and quartz as external calibration standards.

**Single-Crystal Structure Determination:** Single-crystal X-ray data for compound **1** were collected using a KappaCCD area detector diffractometer equipped with a Bruker AXS FR591 rotating anode. Data collection and determination of the unit cell parameters were performed with the Nonius collect software package, while integration of the data frames and scaling of the intensities were performed using the DENZO suite of programs.[34] Room temperature data did not provide a flat difference-Fourier synthesis map, proba-

Table 3. Crystal data, structure determination, and refinement summary for $[Ho_2(C_4H_4O_4)_3(H_2O)_4]\cdot 6H_2O$ (**1**) and $[Ho_2(C_4H_4O_4)_3(H_2O)_2]\cdot H_2O$ (**2**).

| | **1** | **2** |
|---|---|---|
| Crystal system | triclinic | monoclinic |
| Empirical formula | $C_6H_{16}HoO_{11}$ | $C_6H_{10}HoO_{7.5}$ |
| Formula mass | 429.12 | 367.07 |
| Space group | $P\bar{1}$ | $C2/c$ |
| $a$ [Å] | 6.49590(10) | 19.899(2) |
| $b$ [Å] | 9.6737(2) | 7.681(2) |
| $c$ [Å] | 10.4356(2) | 13.813(2) |
| $\alpha$ [°] | 79.5780(10) | 90 |
| $\beta$ [°] | 89.7050(10) | 121.534(10) |
| $\gamma$ [°] | 70.8820(10) | 90 |
| $V$ [Å$^3$] | 608.34(2) | 1799.5(6) |
| $\rho_{calcd.}$ [g cm$^{-3}$] | 2.343 | 2.710 |
| $Z$ | 2 | 8 |
| $F(000)$ | 414 | 1376 |
| $\mu$ (Mo-$K_\alpha$/Cu-$K_\alpha$) [mm$^{-1}$] | 6.554 | 16.683 |
| Crystal size [mm] | 0.14 × 0.08 × 0.04 | 0.40 × 0.03 × 0.02 |
| $T_{min}/T_{max}$ | 0.259/0.596 | 0.133/0.613 |
| Temperature [K] | 100(1) | 293(2) |
| $\lambda$ (Mo-$K_\alpha$/Cu-$K_\alpha$) [Å] | 0.71073 | 1.54184 |
| Monochromator | graphite | graphite |
| $\theta$ range for data collection [°] | 3.29 to 31.02 | 5.22 to 67.91 |
| Completeness to $\theta$ = 31.02/67.91° | 99.8% | 94.2% |
| Limiting indices | $-9 \le h \le 9$ | $-23 \le h \le 20$ |
| | $-14 \le k \le 14$ | $-1 \le k \le 9$ |
| | $-15 \le l \le 15$ | $0 \le l \le 16$ |
| Reflections collected/unique with $I > 2\sigma(I)$ | 14505/3872 | 1886/1538 |
| Refined parameters | 164 | 136 |
| Goodness-of-fit on $F^2$ | 1.236 | 0.956 |
| $R$ | 0.0278 | 0.0603 |
| $R_w$ | 0.1210 | 0.1739 |
| $(\Delta/\rho)_{max}/(\Delta/\rho)_{min}$ [e Å$^{-3}$] | 2.313/–3.685 | 2.146/–2.339 |

 © 2007 Wiley-VCH Verlag GmbH & Co. KGaA, Weinheim 

bly due to thermal smearing induced by motion of the hydration waters. The crystal was therefore cooled down to 100 K in a stream of cold nitrogen gas using a Cryostream cooler from Oxford Cryosystems. Data collected at that temperature were used for structure refinement. Data for compound **2** were collected on an automatic four-circle CAD-4 diffractometer at ambient temperature (293 K). CAD-4 software was used for data collection and cell refinement.[35] The program XCAD4[36] was employed for data reduction. Both structures were solved by direct methods using SHELXS-86[37] and refined by full-matrix least-squares based on $F^2$ using SHELXL-93.[38] The succinate hydrogen atoms in both structures were located from a difference-Fourier synthesis, while the program CALC-OH[39] was employed to calculate the position of the hydrogen atoms of water. Further refinements were performed with the hydrogen atoms riding on bound atoms. The structural analyses were performed with PLATON[40] and PARST.[41] The molecular graphics were produced with ORTEP[42] and POV-Ray.[43] Crystal data and details of data collection and structure refinement are given in Table 3. Selected interatomic distances and bond, torsion, and dihedral angles are listed in Table 1. Table 2 lists the H-bonds' geometry.

CCDC-618378 and -618379 contain the supplementary crystallographic data for this paper. These data can be obtained free of charge from The Cambridge Crystallographic Data Center via www.ccdc.cam.ac.uk/data_request/cif.

**Infrared and Raman Spectroscopy:** FTIR spectra were recorded with a Nicolet Protégé 460 spectrometer in the 4000–225 $cm^{-1}$ range with 32 scans, using the KBr pellet technique; spectral resolution was 4 $cm^{-1}$. Raman spectra were recorded with a Raman Jobin–Yvon T64000 equipped with a CCD and an Ar laser operating at 514.5 nm.

**Thermal Analysis:** TG curves and DSC measurements were recorded with a Shimadzu TGA-50H thermal analyzer apparatus and a Shimadzu DSC-60 apparatus under flowing oxygen at 50 mL $min^{-1}$ at a heating rate of 10 °C $min^{-1}$. Appropriate combinations of X-ray powder diffraction and FTIR spectroscopy were used for further characterization of the pyrolysis products.

**Magnetic Measurements:** Magnetic measurements were carried out in the range 14–330 K with a LakeShore 7130 AC Susceptometer with an alternating field of 1 Oe and 825 Hz.

**Supporting Information** (see footnote on the first page of this article): DSC diagram of compound **1** to support the thermal analysis.

## Acknowledgments

The authors thank the Consejo Nacional de Investigaciones Científicas y Técnicas (CONICET: PID 4929 and PID 6007), the Agencia Nacional de Promoción Científica y Tecnológica (PICT 03041), the Comisión de Investigaciones Científicas de la Provincia de Buenos Aires (CICPBA), Universidad Nacional de La Plata (UNLP), Universidad Nacional de San Luis (UNSL), Republica Argentina and Consejo Superior de Investigaciones Científicas (CSIC), Spain, for financial support. Dr. A. P. Ayala is acknowledged for his assistance in measuring the Raman spectra. The authors are grateful to the Comisión Nacional de Energía Atómica (CNEA) for providing the TXRD equipment. G. P., G. E. E., and G. E. N. are members of the CONICET. C. G. P. and M. C. B. acknowledge a CONICET fellowship.

[1] B. F. Abrahams, V. Hoskins, D. M. Michail, R. Robson, *Nature* **1994**, *369*, 727.
[2] M. L. MacGillavray, S. Subramanian, M. J. Zaworotko, *J. Chem. Soc., Chem. Commun.* **1994**, 1325.
[3] A. K. Cheetham, G. Férey, T. Loiseau, *Angew. Chem. Int. Ed.* **1999**, *38*, 3268.
[4] C. N. R. Rao, S. Natarajan, R. Vaidhyanathan, *Angew. Chem. Int. Ed.* **2004**, *43*, 1466.
[5] R. Vaidhyanathan, S. Natarajan, C. N. R. Rao, *Dalton Trans.* **2003**, 1459.
[6] G. Férey, *Chem. Mater.* **2001**, *13*, 3084.
[7] G. Shimizu, *J. Solid State Chem.* **2005**, *178*, 2519.
[8] P. M. Forster, A. K. Cheetham, *Top. Catal.* **2003**, *24*, 79.
[9] O. M. Yaghi, G. Li, H. Li, *Nature* **1995**, *378*, 703.
[10] N. L. Rosi, M. Eddaudi, J. Kim, M. O'Keefe, O. M. Yaghi, *CrystEngComm* **2002**, *4*, 401.
[11] R. Eberhardt, M. Allmendinger, M. Zintl, C. Troll, G. Luinstra, B. Rieger, *Macromol. Chem. Phys.* **2004**, *205*, 42.
[12] M. Eddaoudi, H. Li, T. Reineke, M. Fehr, D. Kelley, T. Groy, O. M. Yaghi, *Top. Catal.* **1999**, *9*, 105.
[13] P. M. Forster, A. K. Cheetham, *Angew. Chem. Int. Ed.* **2002**, *41*, 457.
[14] J. Perles, M. Iglesias, C. Ruiz-Valero, N. Snejko, *J. Mater. Chem.* **2004**, *14*, 2683.
[15] J. Legendziewicz, B. Keller, I. Turowska-Tyrk, W. Wojciechowski, *New J. Chem.* **1999**, *23*, 1097.
[16] Y. Kim, M. Suh, D.-Y. Jung, *Inorg. Chem.* **2004**, *43*, 245.
[17] R. Hill, D.-L. Long, P. Hubberstey, M. Schröder, N. Champness, *J. Solid State Chem.* **2005**, *178*, 2414.
[18] C. Livage, C. Egger, G. Férey, *Chem. Mater.* **2001**, *13*, 410.
[19] P. M. Forster, A. Burbank, C. Livage, G. Férey, A. K. Cheetham, *Chem. Commun.* **2004**, 368.
[20] G. Férey, C. Mellot-Draznieks, C. Serre, F. Millange, *Acc. Chem. Res.* **2005**, *38*, 217.
[21] A. Seguatni, M. Fakhfakh, M. Vauley, N. Jouini, *J. Solid State Chem.* **2004**, *177*, 3402.
[22] G.-H. Cui, J.-R. Li, R.-H. Zhang, X.-H. Bu, *J. Mol. Struct.* **2005**, *740*, 187.
[23] Y.-F. Zhou, F.-L. Jiang, D.-Q. Yuan, B.-L. Wu, M.-C. Hong, *J. Mol. Struct.* **2005**, *743*, 21.
[24] G.-Y. Dong, G.-H. Cui, J. Lin, *Acta Crystallogr., Sect. E* **2006**, *62*, 738.
[25] F. Serpaggi, G. Férey, *Microporous Mesoporous Mater.* **1999**, *32*, 311.
[26] M. Fleck, *Z. Kristallogr.* **2002**, *NCS 217*, 569.
[27] E. V. Brusau, J. C. Pedregosa, G. Echeverría, G. Punte, G. E. Narda, *J. Solid State Chem.* **2000**, *153*, 1.
[28] E. V. Brusau, J. C. Pedregosa, G. Echeverría, G. Pozzi, G. Punte, G. E. Narda, *J. Coord. Chem.* **2001**, *54*, 469.
[29] L. A. Borkowski, C. L. Cahill, *Inorg. Chem. Commun.* **2004**, *7*, 725.
[30] Y. J. Kim, D.-Y. Jung, *Inorg. Chem.* **2000**, *39*, 1470.
[31] P. E. Werner, L. Eriksson, M. Westdahl, *J. Appl. Crystallogr.* **1985**, *18*, 367.
[32] K. Nakamoto, *Infrared and Raman Spectra of Inorganic and Coordination Compounds*, 5th ed., John Wiley & Sons, Inc., USA, **1997**, 182.
[33] R. Baggio, M. T. Garland, O. Peña, M. Perec, *Inorg. Chim. Acta* **2005**, *358*, 2332.
[34] Z. Otwinowski, W. Minor, "Processing of X-ray Diffraction Data Collected, in Oscillation Mode", *Methods in Enzymology*, vol. 276: Macromolecular Crystallography, part A, p. 326 (Eds.: C. W. Carter Jr., R. M. Sweet), Academic Press, New York, **1997**, 307.
[35] CAD4 Express Software, Enraf–Nonius, Delft, The Netherlands, **1994**.
[36] K. Harms, S. Wocadlo, *XCAD-4*, *Program for Processing CAD-4 Diffractometer Data*, University of Marburg, Germany, **1995**.

 © 2007 Wiley-VCH Verlag GmbH & Co. KGaA, Weinheim 

[37] G. M. Sheldrick, *SHELXS86, Program for Crystal Structure Solution*, Institut für Anorganische Chemie der Universität, Tammannstrasse 4, Göttingen, Germany, **1986**.
[38] G. M. Sheldrick, *SHELXL93, Program for the Refinement of Crystal Structures*, University of Göttingen, Göttingen, Germany, **1993**.
[39] M. Nardelli, *J. Appl. Crystallogr.* **1999**, *32*, 563.
[40] A. L. Spek, *Acta Crystallogr., Sect. A* **1990**, *46*, C34.
[41] PARST: M. Nardelli, *J. Appl. Crystallogr.* **1995**, *28*, 659.
[42] M. N. Burnett, C. K. Johnson, *ORTEP-III Report ORNL-6895*, Oak Ridge National Laboratory, Oak Ridge, Tennessee, U. S. A., **1996**.
[43] C. J. Cason, *Persistence of Vision Ray Tracer* (POV-Ray™), Version 3.1e.watcom.win32 (optimized for Pentium® II processor), **1999**.

Received: September 14, 2006
Published Online: January 4, 2007

 © 2007 Wiley-VCH Verlag GmbH & Co. KGaA, Weinheim 

DOI: 10.1002/ejic.200600863

# Controlled Formation of Mixed-Metal Macrocycles Using Dynamic Exchange Processes and Steric Constraints

Zacharias Grote,[a] Rosario Scopelliti,[a][‡] and Kay Severin*[a]

**Keywords:** Dynamic combinatorial chemistry / Metallamacrocycle / Organometallic complex / Rhodium / Ruthenium

The exchange reaction of the trinuclear macrocycles $[(C_6H_3iPr_3)Ru(C_5H_3NO_2)]_3$ (**AAA**) and $[(cymene)Ru(C_5H_3NO_2)]_3$ (**BBB**) has been studied. It was found that the equilibration proceeds in two steps and that the final mixture is completely dominated by the mixed-metal macrocycles $[\{(C_6H_3iPr_3)Ru\}_2\{(cymene)Ru\}(C_5H_3NO_2)_3]$ (**AAB**) and $[\{(C_6H_3iPr_3)Ru\}\{(cymene)Ru\}_2(C_5H_3NO_2)_3]$ (**ABB**). The results are rationalized by assuming unfavorable steric interactions between adjacent $(C_6H_3iPr_3)Ru$ fragments. It is shown that interactions of this kind can be used to bias scrambling processes in such a way that mixed-metal macrocycles are obtained in over 80% yield. The structures of $[\{(C_6Me_6)Ru\}\{(C_6H_6)Ru\}_2(C_5H_3NO_2)_3]$ and $[(Cp^*Rh)\{(C_6H_6)Ru\}_2(C_5H_3NO_2)_3]$ have been determined by single-crystal X-ray analysis.

(© Wiley-VCH Verlag GmbH & Co. KGaA, 69451 Weinheim, Germany, 2007)

## Introduction

Transition metal-based self-assembly processes have been used extensively to build macrocyclic compounds with diverse structures and functionalities.[1] In the majority of these cases, metal complexes M with available coordination sites were combined with bridging ligands L to give symmetrical macrocycles of the type $M_nL_n$. These reactions are typically performed in a single step under thermodynamic control. Macrocycles containing two different metal fragments M and M′, however, are generally constructed in a two-step procedure.[2,3] For mixed-metal squares and rectangles, this is illustrated in Scheme 1. In a first step, a ditopic ligand is coordinated to a metal M. The resulting complex $ML_2$ is then reacted with a metal M′ to give the tetranuclear complex $M_2M'_2L_4$. Usually, the preformed metal complex $ML_2$ is kinetically inert under the reaction conditions employed in the second step (Scheme 1, a).[2] This avoids scrambling reactions, which would lead to mixtures of assemblies with variable M-M′ content and position. Alternatively, the formation of mixed-metal assemblies can be favored by the utilization of ligands having two distinct donor sites, each of which with a pronounced selectivity for the respective metal fragment M or M′, respectively (Scheme 1, b).[3] Additional specificity can be achieved by template effects. For the latter case, one-step syntheses of heterometallic macrocycles under thermodynamic control have been reported.[4]

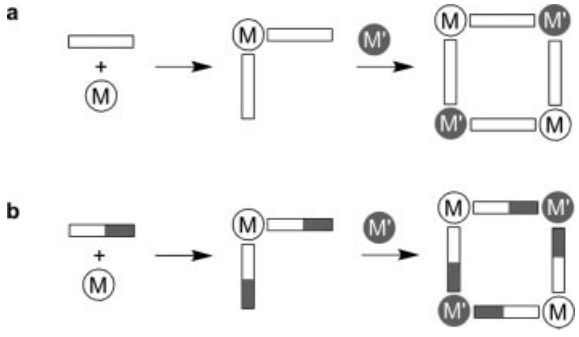


Scheme 1. Stepwise synthesis of tetranuclear macrocycles containing two different metal fragments M and M′.

Over the last few years, we have reported in a number of publications the synthesis and host–guest chemistry of trinuclear metallamacrocycles comprised of (arene)$Ru^{II}$ or (cyclopentadienyl)$M^{III}$ (M = Rh, Ir) complexes and bridging 2,3-dihydroxypyridine ligands.[5] These complexes represent organometallic analogues of 12-crown-3 and show an outstanding affinity for lithium ions, even in aqueous solutions.[6] During the course of our studies we observed that in polar solvents, these metallacrown complexes undergo exchange reactions. This was used to create dynamic combinatorial libraries[7] of macrocycles and to investigate the adaptive behavior of such mixtures.[8] In the following we show that steric interactions can be used to guide the scrambling process in such a fashion that a defined mixed-metal macrocycle can be obtained in synthetically interesting yields.

[a] Institut des Sciences et Ingénierie Chimiques, École Polytechnique Fédérale de Lausanne,
1015 Lausanne, Switzerland
Fax: +41-21-693-9305
E-mail: kay.severin@epfl.ch
[‡] X-ray structural analysis.


© 2007 Wiley-VCH Verlag GmbH & Co. KGaA, Weinheim

## Results and Discussion

In a first experiment, we investigated the scrambling reaction of the two trimeric (arene)Ru complexes $[(C_6H_3iPr_3)Ru(C_5H_3NO_2)]_3$ (**AAA**) and $[(cymene)Ru(C_5H_3NO_2)]_3$ (**BBB**) (Scheme 2). The complexes were mixed in a 1:1 ratio in $CD_3OD$, with an initial concentration of 5.0 mM each. To accelerate the exchange process, the solution was gently heated to 40 °C. The reaction was followed by $^1H$ NMR spectroscopy and the time course is shown in Figure 1.

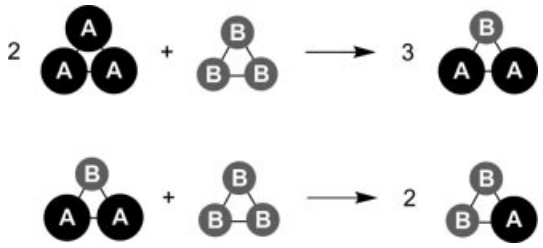


Scheme 2. The equilibration of $[(C_6H_3iPr_3)Ru(C_5H_3NO_2)]_3$ (**AAA**) and $[(cymene)Ru(C_5H_3NO_2)]_3$ (**BBB**) proceeds in two steps. First, the sterically encumbered **AAA** is converted into **AAB**. This is followed by a second, much slower transformation, in which **ABB** is formed.

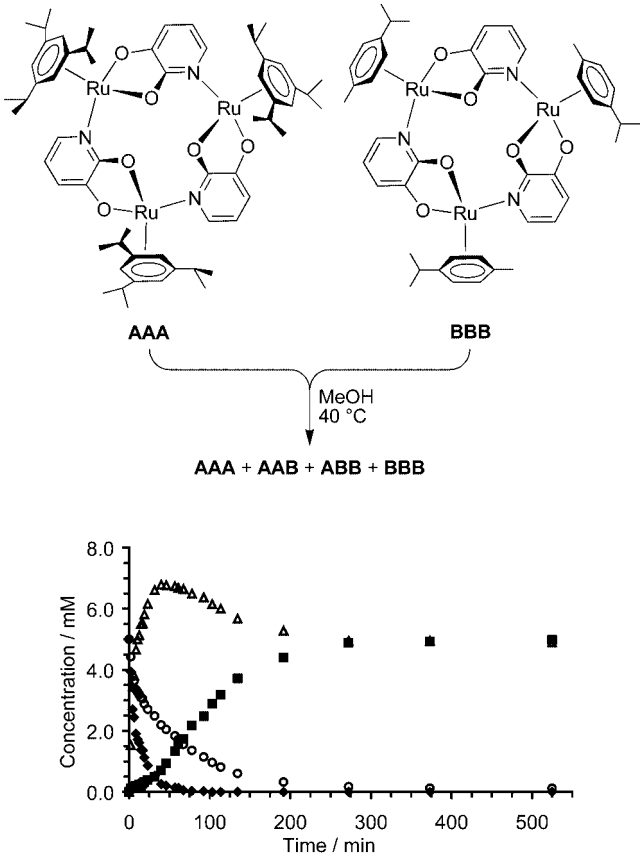


Figure 1. Time course of the reaction between $[(C_6H_3iPr_3)Ru(C_5H_3NO_2)]_3$ (**AAA**; ♦) and $[(cymene)Ru(C_5H_3NO_2)]_3$ (**BBB**, ○) to give the mixed-metal macrocycles **AAB** (Δ) and **ABB** (■) as determined by $^1H$ NMR spectroscopy. The reaction was performed in $CD_3OD$ at 40 °C with initial concentrations of [**AAA**] = [**BBB**] = 5.0 mM.

The beginning of the reaction was marked by a fast decrease of **AAA** and a rapid increase of **AAB**. The formation of **ABB** was almost negligible in the first 15 min. During this period, the decrease of **AAA** was almost twice as fast as the decrease of **BBB**. After 40 min, a turning point was reached. The concentration of **AAB** was at its maximum and represented 68% of the total trimer concentration. Subsequently, a decrease of **AAB** and a concomitant increase of **ABB** were observed. Accordingly, the concentration-time profile of **ABB** shows a sigmoidal form. After six hours, the mixture was at equilibrium and only the two mixed complexes **AAB** and **ABB** were present in significant amounts.

For equally stable macrocycles, a statistical mixture of **AAA/AAB/ABB/BBB** = 1:3:3:1 would be expected. At first glance, the complete dominance of **AAB** and **ABB** after equilibration might suggest a preferential stabilization of the mixed complexes with respect to the homotrimers **AAA** and **BBB** (situation a, Figure 2). But there is another explanation for such a distribution: the B-rich species **ABB** and **BBB** are stabilized and the homotrimer **AAA** is significantly destabilized (situation b, Figure 2). For $\Delta\Delta G1 = \Delta\Delta G2 = 1/2\ \Delta\Delta G3$, the two situations result in the same equilibrium distribution with equal amounts of heterotrimers being the dominant species in solution. It is interesting to note that for the situation described in Figure 2 (b), the concentration of the stable homotrimer **BBB** is as low as that of the disfavored **AAA**. A more detailed discussion of this phenomenon can be found in a recent theoretical study.[9]

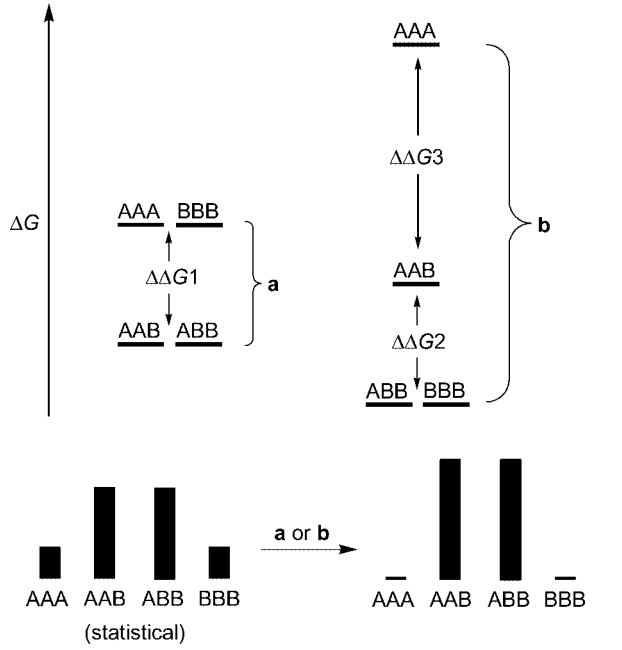


Figure 2. For equally stable trimers **AAA**, **AAB**, **ABB**, and **BBB**, a statistical 1:3:3:1 distribution is expected. The energetic situations shown in **a** and **b** both result in selective formation of the mixed trimers **AAB** and **ABB**.

 © 2007 Wiley-VCH Verlag GmbH & Co. KGaA, Weinheim 

An energy distribution similar to what is described in Figure 2 (b) is more likely to account for the dynamic mixture described above. Complex $[(C_6H_3iPr_3)Ru(C_5H_3NO_2)]_3$ (**AAA**) has three sterically demanding triisopropylbenzene ligands. The π-ligands approach each other and destabilize the aggregate. For the mixed trimer **AAB**, only one unfavorable A···A interaction is found, whereas the aggregates **ABB** and **BBB** display no intramolecular A···A contacts at all. The kinetic data support this picture. The sterically encumbered trimer **AAA** rapidly reacts with the smaller cymene complex **BBB** to give **AAB**. This first reaction is followed by a second, much slower reaction, in which **AAB** is converted into **ABB** (Scheme 2). It should be noted that the sequential formation of first **AAB** and then **ABB** excludes a simple bimolecular reaction mechanism in which two trimers **AAA** and **BBB** exchange fragments.

An interesting consequence from an asymmetric free energy distribution is the possibility to bias the equilibration process in favor of a certain species. For a dynamic mixture of equally stable trimers **AAA**, **AAB**, **ABB**, and **BBB**, the relative concentration of the mixed trimer **ABB** after equilibration can be increased from 37.5% to a maximum theoretical value of 44.3% by using two equivalents of **BBB** and only one equivalent of **AAA**. For a system such as the one described in Figure 2 (b), the maximum relative concentration of a mixed trimer after equilibration can be much higher.

To demonstrate this point, we have investigated the scrambling reaction of $[(C_6H_3iPr_3)Ru(C_5H_3NO_2)]_3$ (**AAA**) and $[(C_6H_6)Ru(C_5H_3NO_2)]_3$ (**CCC**) (Figure 3). The small benzene complex **CCC** was chosen to further accentuate the difference between the π-ligands. This time, the complexes were mixed in a 1:2 ratio with initial concentrations of [**AAA**] = 2.0 mM and [**CCC**] = 4.1 mM. The time course of the reaction is shown in Figure 3. The beginning of the equilibration process was again marked by the fast formation of the mixed complex **AAC** comprised of two large $(C_6H_3iPr_3)Ru$ moieties and the simultaneous rapid decrease of **AAA**. After 26 min, more than 95% of the initial amount of complex **AAA** was converted and the concentration of **AAC** reached its maximum. Then, its concentration decreased in favor of **ACC**. The equilibrium was reached after 10 h, after which the heterotrimer **ACC** completely dominated the mixture (83 ± 2%). Only minor amounts of **AAC** (7 ± 2%) and **CCC** (10 ± 2%) were found in the solution.

The results described above suggest that equilibration processes with 2:1 stoichiometries of complexes having significantly different π-ligands can be used for the controlled formation of mixed-metal macrocycles in preparative amounts. The following results show that this is indeed the case. Solutions containing two equivalents of the small benzene complex $[(C_6H_6)Ru(C_5H_3NO_2)]_3$ (**CCC**) and one equivalent of the trimers $[(C_6Me_6)Ru(C_5H_3NO_2)]_3$ (**DDD**) or $[Cp^*Rh(C_5H_3NO_2)]_3$ (**EEE**), both of which have sterically demanding π-ligands, were tempered in $CD_3OD$ at 45 °C overnight. Similar to what was found in experiments with **AAA**, the mixed-metal complexes **DCC** and **ECC** were

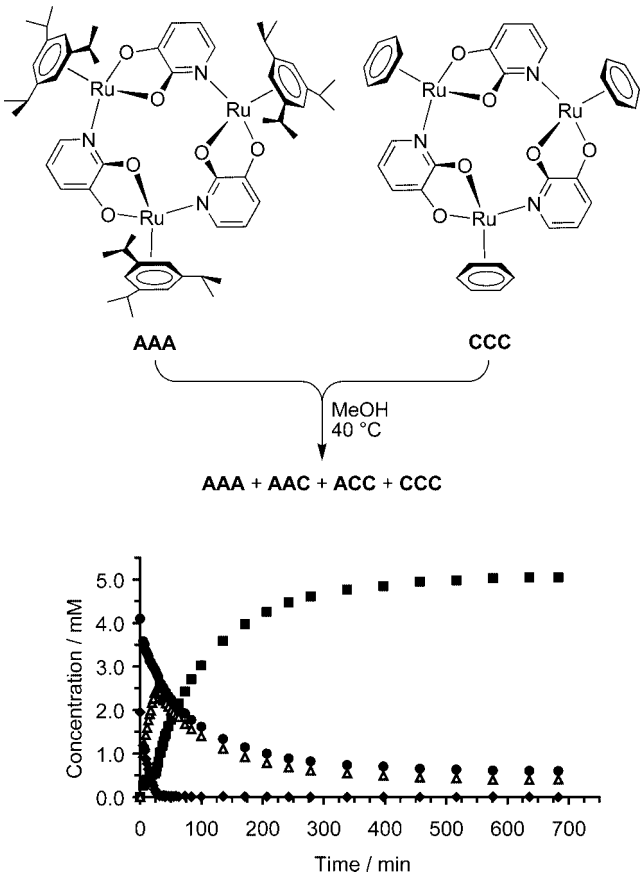


Figure 3. Time course of the reaction between $[(C_6H_3iPr_3)Ru(C_5H_3NO_2)]_3$ (**AAA**; ♦) and $[(C_6H_6)Ru(C_5H_3NO_2)]_3$ (**CCC**, ●) to give the mixed-metal macrocycles **AAC** (Δ) and **ACC** (■) as determined by $^1H$ NMR spectroscopy. The reaction was performed in $CD_3OD$ at 40 °C with initial concentrations of [**AAA**] = 4.1 mM and [**CCC**] = 2.0 mM.

formed almost exclusively (>80%) as evidenced by $^1H$ NMR spectroscopy.

The complexes **ACC**, **DCC**, and **ECC** can not only be obtained by scrambling of preformed homotrimers but also directly from appropriate amounts of the respective building blocks. Thus, when two equivalents of the dimer $[(C_6H_6)RuCl_2]_2$,[10] one equivalent of $[(C_6H_3iPr_3)RuCl_2]_2$, $[(C_6Me_6)RuCl_2]_2$, or $[Cp^*RhCl_2]_2$ and six equivalents of the 2,3-dihydroxypyridine ligand were reacted in methanol in the presence of $Cs_2CO_3$, the products **ACC**, **DCC**, and **ECC** could be isolated with yields of ca. 60% and in good purity. It was also possible to obtain mixed-metal trimers with two large metal fragments and one small fragment. This was corroborated by the synthesis of complex **AAC** using two equivalents of $[(C_6H_3iPr_3)RuCl_2]_2$ and one equivalent of $[(C_6H_6)RuCl_2]_2$. It should be noted that exchange processes were found to be significantly slower in less polar solvents such as benzene and chloroform as compared to methanol. This allowed the characterization of the mixed-metal trimers in pure form.

The $^1H$ NMR spectroscopic data of all three products were in agreement with the anticipated structure: three sets of signals were observed for aromatic protons of the bridging pyridonate ligands and two singlets were found for the

 © 2007 Wiley-VCH Verlag GmbH & Co. KGaA, Weinheim 

chemically distinct benzene π-ligands. The complexes **DCC** and **ECC** were also characterized by a single-crystal X-ray analysis (Figure 4, Figure 5, and Figure 6).

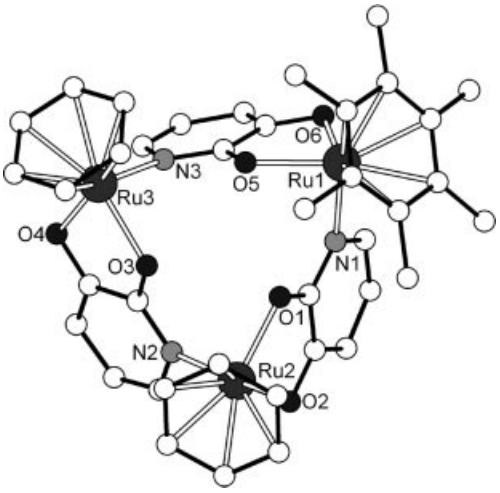


Figure 4. Ball-and-stick representation of the molecular structure of **DCC** in the crystal. The hydrogen atoms and the solvent molecules ($2CHCl_3$) are omitted for clarity. Selected bond lengths [Å]: Ru1–N1 2.130(6), Ru1–O5 2.086(4), Ru1–O6 2.065(5), Ru2–O1 2.060(5), Ru2–O2 2.069(5), Ru2–N2 2.118(6), Ru3–O3 2.069(5), Ru3–O4 2.073(5), Ru3–N3 2.139(6).

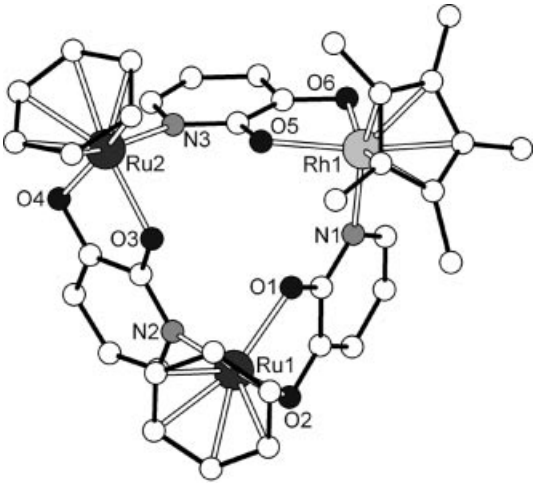


Figure 5. Ball-and-stick representation of the molecular structure of **ECC** in the crystal. The hydrogen atoms and the solvent molecules ($H_2O$, MeOH, $C_6H_5CH_3$) are omitted for clarity. Selected bond lengths [Å]: Rh1–O5 2.080(7), Rh1–O6 2.088(8), Rh1–N1 2.122(9), Ru1–O2 2.067(6), Ru1–O1 2.078(7), Ru1–N2 2.106(8), Ru2–O3 2.072(6), Ru2–O4 2.076(7), Ru2–N3 2.104(9).

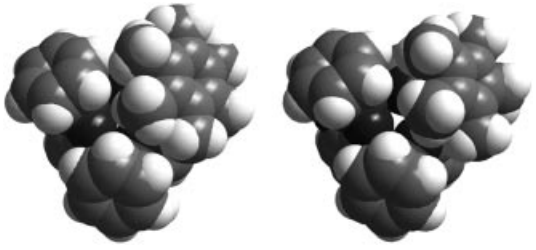

Figure 6. Space filling representation of the molecular structure of **DCC** (left) and **ECC** (right) in the crystal. The solvent molecules have been omitted for clarity.

The bond lengths and angles found for the macrocyclic core of **DCC** and **ECC** are comparable to what has been observed for the corresponding homotrimeric complexes.[5] Additional structural anisotropy due to the presence of different half-sandwich complexes was not observed. Indirect evidence for the reduced steric strain of the mixed-metal macrocycles **DCC** and **ECC** is the fact that their average metal–metal distances (**DCC**: 5.26 Å; **ECC**: 5.26 Å) are shorter than what has been observed for the homotrimers **DDD** (5.46 Å) and **EEE** (5.35 Å).[5g] The importance of the size of the π-ligand for the stability of the trimeric aggregates is also evident from the space filling representations of **DCC** and **ECC** (Figure 6).

## Conclusions

The synthesis of metallamacrocycles containing two different metal fragments M and M′ is mostly performed in two or more steps under kinetic control. We have shown that steric interactions can be used to bias dynamic exchange processes in such a way that mixed-metal macrocycles are obtained in over 80% yield under thermodynamic control. The results are conceptually related to work on *mixed-ligand* metallamacrocycles and cages. Navarro and Romero et al. have shown that scrambling of symmetrical (en)$Pd^{II}$-based macrocycles with bridging 4,7-phenanthroline and 2-pyrimidinolate ligands can lead to the dominant formation of a single product given that appropriate stoichiometries are employed;[11] and Fujita et al. and James et al. have used steric interactions between ligands to achieve the quantitative formation of macrocycles and coordination cages containing two different heterocyclic ligands.[12,13] It should be noted that rather small differences in free energy of the various aggregates can be sufficient to bias dynamic mixtures of metallamacrocycles (or cages) towards the formation of a defined product. For the system described in Figure 2 (b), for example, a difference of $\Delta\Delta G2 = 1/2\ \Delta\Delta G3 = 3.0\ kcal\,mol^{-1}$ results in an increase of the relative concentration of mixed product **ABB** from 44.3% (statistical) to 91.6% (for $[\mathbf{AAA}]_{initial} = 1/2\ [\mathbf{BBB}]_{initial}$).[14] In view of the fact that asymmetric metallamacrocycles may display interesting functional differences (host–guest chemistry etc.) when compared to their symmetrical $M_nL_n$ counterparts, the strategy discussed above should be regarded as an attractive alternative to step-wise synthetic procedures.

## Experimental Section

**General:** All reactions were performed under dry dinitrogen. The complexes $[(C_6H_3iPr_3)Ru(C_5H_3NO_2)]_3$ (**AAA**),[8c] [(cymene)-$Ru(C_5H_3NO_2)]_3$ (**BBB**),[5h] $[(C_6H_6)Ru(C_5H_3NO_2)]_3$ (**CCC**),[5g] $[(C_6Me_6)Ru(C_5H_3NO_2)]_3$ (**DDD**),[5g] $[Cp^*Rh(C_5H_3NO_2)]_3$ (**EEE**),[5g] $[(C_6H_3iPr_3)RuCl_2]_2$,[15] $[(C_6Me_6)RuCl_2]_2$,[16] $[Cp^*RhCl_2]_2$[17] and $[(C_6H_6)RuCl_2]_2$[18] were prepared according to literature procedures. 2,3-Dihydroxypyridine (95%) was purchased from Fluka and $Cs_2CO_3$ (99.9%) was purchased from Aldrich. The $^1H$ and $^{13}C$ NMR spectra were recorded with a Bruker Advance DPX

 © 2007 Wiley-VCH Verlag GmbH & Co. KGaA, Weinheim 

400 spectrometer with the residual protonated solvent as internal standard. All spectra were recorded at room temperature.

**Synthesis of Complex [{($C_6H_3iPr_3$)Ru}{($C_6H_6$)Ru}$_2$($C_5H_3NO_2$)$_3$] (ACC):** A suspension of [($C_6H_3iPr_3$)$RuCl_2$]$_2$ (75 mg, 0.10 mmol), [($C_6H_6$)$RuCl_2$]$_2$ (110 mg, 0.22 mmol), 2,3-dihydroxypyridine (69 mg, 0.60 mmol), and $Cs_2CO_3$ (489 mg, 1.50 mmol) in degassed MeOH (25 mL) was stirred overnight at 45 °C. After evaporation of the solvent under reduced pressure, the product was extracted with $CH_2Cl_2$ (30 mL). A small amount of precipitate was observed after addition of hexane (60 mL), which was removed by filtration. The clear solution was concentrated to 15 mL and the resulting precipitate was filtered off and dried in vacuo. The mixed trimer was obtained as an orange powder in 60% yield (126 mg, 0.12 mmol) and 96% purity. $^1$H NMR (400 MHz, $CDCl_3$): $\delta$ = 1.40 [d, $^3J$ = 7 Hz, 9 H, CH(C$H_3$)$_2$], 1.44 [d, $^3J$ = 7 Hz, 9 H, CH(C$H_3$)$_2$], 2.81 [sept, br, $^3J$ = 7 Hz, 3 H, C$H$(C$H_3$)$_2$], 4.97 (s, 3 H, $C_6H_3iPr_3$), 5.44 (s, 6 H, $C_6H_6$), 5.45 (s, 6 H, $C_6H_6$), 5.62–5.69 (m, 3 H, pyridone), 6.08 (dd, $^3J$ = 7 Hz, $^4J$ = 2 Hz, 1 H, pyridone), 6.12 (dd, $^3J$ = 7 Hz, $^4J$ = 2 Hz, 1 H, pyridone), 6.16 (dd, $^3J$ = 7 Hz, $^4J$ = 1 Hz, 1 H, pyridone), 6.60 (dd, $^3J$ = 6 Hz, $^4J$ = 1 Hz, 1 H, pyridone), 6.63 (dd, $^3J$ = 6 Hz, $^4J$ = 2 Hz, 1 H, pyridone), 6.67 (dd, $^3J$ = 6 Hz, $^4J$ = 1 Hz, 1 H, pyridone) ppm. $^{13}$C NMR (101 MHz, $CDCl_3$): $\delta$ = 22.60, 23.28 ($CH_3$), 31.51 (CH), 71.09 ($C_6H_3iPr_3$), 81.60, 81.66 ($C_6H_6$), 107.10 ($C_6H_3iPr_3$), 109.99, 110.24, 110.30, 114.82, 115.09, 115.33, 132.11, 132.81, 133.11, 156.05, 156.28, 157.43, 171.06, 171.07, 171.62 (pyridone) ppm. $C_{42}H_{45}N_3O_6Ru_3\cdot 2CH_3OH$ (1055.12): calcd. C 50.09, H 5.06, N 3.98; found C 49.84, H 4.89, N 4.08.

**Synthesis of Complex [{($C_6Me_6$)Ru}{($C_6H_6$)Ru}$_2$($C_5H_3NO_2$)$_3$] (DCC):** A suspension of [($C_6Me_6$)$RuCl_2$]$_2$ (67 mg, 0.10 mmol), [($C_6H_6$)$RuCl_2$]$_2$ (110 mg, 0.22 mmol), 2,3-dihydroxypyridine (69 mg, 0.60 mmol), and $Cs_2CO_3$ (489 mg, 1.50 mmol) in degassed MeOH (25 mL) was stirred overnight at 45 °C. After evaporation of the solvent under reduced pressure, the product was extracted with $CH_2Cl_2$ (30 mL). A small amount of precipitate was observed after addition of hexane (60 mL), which was removed by filtration. The clear solution was concentrated to 15 mL and the resulting precipitate was filtered off and dried in vacuo. The mixed trimer was obtained as an orange powder in 50% yield (113 mg, 0.10 mmol) and 92% purity. The complex was crystallized from $CHCl_3$/pentane. $^1$H NMR (400 MHz, $CDCl_3$): $\delta$ = 2.16 (s, 18 H, $C_6Me_6$), 5.46 (s, 6 H, $C_6H_6$), 5.48 (s, 6 H, $C_6H_6$), 5.60 (dd, $^3J$ = 7 Hz, $^3J$ = 6 Hz, 1 H, pyridone), 5.67 (t, $^3J$ = 7 Hz, 1 H, pyridone), 5.71 (dd, $^3J$ = 7 Hz, $^3J$ = 6 Hz, 1 H, pyridone), 6.03 (dd, $^3J$ = 7 Hz, $^4J$ = 1 Hz, 1 H, pyridone), 6.16 (dd, $^3J$ = 7 Hz, $^4J$ = 1 Hz, 1 H, pyridone), 6.17 (dd, $^3J$ = 7 Hz, $^4J$ = 2 Hz, 1 H, pyridone), 6.47 (dd, $^3J$ = 6 Hz, $^4J$ = 2 Hz, 1 H, pyridone), 6.60 (dd, $^3J$ = 6 Hz, $^4J$ = 2 Hz, 1 H, pyridone), 6.60 (dd, $^3J$ = 6 Hz, $^4J$ = 2 Hz, 1 H, pyridone) ppm. $^{13}$C NMR (101 MHz, $CDCl_3$): $\delta$ = 15.71 ($CH_3$), 81.47, 81.62 ($C_6H_6$), 89.11 ($C_6Me_6$), 109.51, 110.14, 110.53, 113.38, 114.73, 115.05, 131.36, 132.23, 132.21, 156.10, 156.13, 158.39, 170.28, 171.19, 171.76 (pyridone) ppm. $C_{39}H_{39}N_3O_6Ru_3\cdot 2CH_2Cl_2$ (1118.82): calcd. C 44.01, H 3.87, N 3.76; found C 44.27, H 4.53, N 3.95.

**Synthesis of Complex [{Cp*Rh}{($C_6H_6$)Ru}$_2$($C_5H_3NO_2$)$_3$] (ECC):** A suspension of [Cp*$RhCl_2$]$_2$ (62 mg, 0.10 mmol), [($C_6H_6$)$RuCl_2$]$_2$ (150 mg, 0.30 mmol), 2,3-dihydroxypyridine (69 mg, 0.60 mmol), and $Cs_2CO_3$ (489 mg, 1.50 mmol) in degassed MeOH (25 mL) was stirred overnight at 45 °C. After evaporation of the solvent under reduced pressure, the product was extracted with $CH_2Cl_2$ (30 mL). A small amount of precipitate was observed after addition of hexane (60 mL), which was removed by filtration. The clear solution was concentrated to 15 mL and the resulting precipitate was filtered off and dried in vacuo. The mixed trimer was obtained as brown-red powder in 59% yield (114 mg, 0.12 mmol) and 83% purity. The complex was crystallized from toluene/pentane. $^1$H NMR (400 MHz, $CDCl_3$): $\delta$ = 1.77 (s, 18 H, Cp*), 5.45 (s, 6 H, $C_6H_6$), 5.46 (s, 6 H, $C_6H_6$), 5.65 (t, $^3J$ = 7 Hz, 1 H, pyridone), 5.69 (t, $^3J$ = 7 Hz, 1 H, pyridone), 5.79 (t, $^3J$ = 7 Hz, 1 H, pyridone), 6.10 (dd, $^3J$ = 7 Hz, $^4J$ = 1 Hz, 1 H, pyridone), 6.19 (dd, $^3J$ = 7 Hz, $^4J$ = 1 Hz, 1 H, pyridone), 6.23 (dd, $^3J$ = 7 Hz, $^4J$ = 1 Hz, 1 H, pyridone), 6.62 (dd, $^3J$ = 6 Hz, $^4J$ = 1 Hz, 1 H, pyridone), 6.64 (dd, $^3J$ = 6 Hz, $^4J$ = 1 Hz, 1 H, pyridone), 6.73 (dd, $^3J$ = 6 Hz, $^4J$ = 1 Hz, 1 H, pyridone) ppm. $^{13}$C NMR (101 MHz, $CDCl_3$): $\delta$ = 14.26 ($CH_3$), 81.57, 81.77 ($C_6H_6$), 90.32 (d, $^1J$(C,Rh) = 8 Hz, C, Cp*), 109.72, 110.24, 110.96, 113.99, 115.12, 115.21, 131.76, 131.84, 132.38, 156.25, 156.63, 157.93, 169.95, 171.22, 171.88 (pyridone) ppm. $C_{37}H_{36}N_3O_6RhRu_2\cdot CH_3OH\cdot H_2O$ (973.80): calcd. C 46.87, H 4.35, N 4.32; found C 46.57, H 4.59, N 4.29.

**Synthesis of Complex [{($C_6H_3iPr_3$)Ru}$_2$(benzene)Ru}($C_5H_3NO_2$)$_3$] (AAC):** A suspension of [($C_6H_3iPr_3$)$RuCl_2$]$_2$ (151 mg, 0.20 mmol), [($C_6H_6$)$RuCl_2$]$_2$ (50 mg, 0.1 mmol), 2,3-dihydroxypyridine (69 mg, 0.60 mmol), and $Cs_2CO_3$ (489 mg, 1.50 mmol) in degassed MeOH (25 mL) was stirred overnight at 45 °C. After evaporation of the solvent under reduced pressure, the product was extracted with $CH_2Cl_2$ (30 mL). After addition of hexane (60 mL), the solution was concentrated to 15 mL and the resulting precipitate filtered off and dried in vacuo. The mixed trimer was obtained as a brown powder in 45% yield (100 mg, 0.09 mmol) and 90% purity. $^1$H NMR (400 MHz, $CDCl_3$): $\delta$ = 1.16 [d, $^3J$ = 7 Hz, 9 H, CH(C$H_3$)$_2$], 1.33 [d, $^3J$ = 7 Hz, 9 H, CH(C$H_3$)$_2$], 1.38 [d, $^3J$ = 7 Hz, 9 H, CH(C$H_3$)$_2$], 1.52 [d, $^3J$ = 7 Hz, 9 H, CH(C$H_3$)$_2$], 2.81 [sept, $^3J$ = 7 Hz, 3 H, C$H$(C$H_3$)$_2$], 3.22 [sept, $^3J$ = 7 Hz, 3 H, C$H$(C$H_3$)$_2$], 4.86 (s, 3 H, $C_6H_3iPr_3$), 4.90 (s, 3 H, $C_6H_3iPr_3$), 5.39 (s, 6 H, $C_6H_6$), 5.56 (t, $^3J$ = 7 Hz, 1 H, pyridone), 5.61 (t, $^3J$ = 7 Hz, 1 H, pyridone), 5.65 (t, $^3J$ = 7 Hz, 1 H, pyridone), 6.01 (dd, $^3J$ = 7 Hz, $^4J$ = 1 Hz, 1 H, pyridone), 6.03 (dd, $^3J$ = 7 Hz, $^4J$ = 2 Hz, 1 H, pyridone), 6.12 (dd, $^3J$ = 7 Hz, $^4J$ = 2 Hz, 1 H, pyridone), 6.57 (dd, $^3J$ = 6 Hz, $^4J$ = 2 Hz, 1 H, pyridone), 6.63 (dd, $^3J$ = 6 Hz, $^4J$ = 2 Hz, 1 H, pyridone), 6.64 (dd, $^3J$ = 6 Hz, $^4J$ = 1 Hz, 1 H, pyridone) ppm. $^{13}$C NMR (1010 MHz, $CDCl_3$): $\delta$ = 21.48, 22.42, 22.73, 24.19 ($CH_3$), 30.85, 31.64 (CH), 69.27, 69.87 ($C_6H_3$), 81.41 ($C_6H_6$), 107.96, 108.25 ($C_6H_3$), 109.55, 109.63, 110.14, 113.75, 114.12, 114.84, 132.03, 132.92, 133.09, 156.02, 156.64, 157.65, 171.02, 171.47, 171.29 (pyridone) ppm. $C_{51}H_{63}N_3O_6Ru_3\cdot 2CH_2Cl_2$ (1287.13): calcd. C 49.46, H 5.25, N 3.26; found C 49.07, H 5.41, N 3.61.

**X-ray Crystallography:** Details for the crystals and their structure refinement are listed in Table 1 whereas some relevant geometrical parameters are included in the picture captions. Data collection was performed at 140(2) K by means of a Mar345 imaging plate detector. Data reduction was carried out with CrysAlis RED, release 1.7.0.[19] Absorption correction has been applied to both data sets. Structure solution and refinement were performed with the SHELXTL software package, release 5.1.[20] The structures were refined using the full-matrix least-squares on $F^2$ with all non-H atoms anisotropically defined except the toluene molecule of complex **ECC**, which has been retained as isotropic with a fixed geometry. H atoms were placed in calculated positions using the riding model.

CCDC-617057 and -617058 contain the supplementary crystallographic data for this paper. These data can be obtained free of charge from The Cambridge Crystallographic Data Centre via www.ccdc.cam.ac.uk/data_request/cif.

 © 2007 Wiley-VCH Verlag GmbH & Co. KGaA, Weinheim 

Table 1. Crystallographic data for the complexes **DCC** and **ECC**.

| | **DCC**·2CHCl$_3$ | **ECC**·MeOH·C$_7$H$_8$·H$_2$O |
|---|---|---|
| Empirical formula | $C_{41}H_{41}Cl_6N_3O_6Ru_3$ | $C_{45}H_{50}N_3O_8RhRu_2$ |
| Molecular weight [g mol$^{-1}$] | 1187.68 | 1065.93 |
| Crystal size [mm$^3$] | 0.20 × 0.12 × 0.09 | 0.17 × 0.17 × 0.13 |
| Crystal system | triclinic | monoclinic |
| Space group | $P\bar{1}$ | $P2_1/n$ |
| $a$ [Å] | 9.2537(14) | 13.273(5) |
| $b$ [Å] | 12.040(3) | 18.718(5) |
| $c$ [Å] | 20.007(5) | 18.668(4) |
| $\alpha$ [°] | 85.44(2) | 90 |
| $\beta$ [°] | 80.731(16) | 110.09(3) |
| $\gamma$ [°] | 88.110(16) | 90 |
| Volume [Å$^3$] | 2192.5(8) | 4356(2) |
| $Z$ | 2 | 4 |
| Density [g cm$^{-3}$] | 1.799 | 1.625 |
| Temperature [K] | 140(2) | 140(2) |
| Absorption coeff. [mm$^{-1}$] | 1.436 | 1.115 |
| $\Theta$ range [°] | 3.09 to 25.03 | 2.73 to 25.03 |
| Index ranges | $-10 \le 10$, $-14 \le 14$, $-23 \le 23$ | $-15 \le 15$, $-22 \le 22$, $-21 \le 22$ |
| Reflections collected | 14091 | 26761 |
| Independent reflections | 7271 ($R_{int}$ = 0.0439) | 7694 ($R_{int}$ = 0.0626) |
| Absorption correction | semi-empirical | semi-empirical |
| Max. and min. transmission | 0.9528 and 0.7704 | 0.8564 and 0.7350 |
| Data / restraints / parameters | 7271 / 0 / 533 | 7694 / 3 / 492 |
| Goodness-of-fit on $F^2$ | 1.08 | 0.998 |
| Final $R$ indices [$I > 2\sigma(I)$] | $R_1$ = 0.0638, $wR_2$ = 0.1757 | $R_1$ = 0.0688, $wR_2$ = 0.1885 |
| $R$ indices (all data) | $R_1$ = 0.0769, $wR_2$ = 0.1941 | $R_1$ = 0.1118, $wR_2$ = 0.2197 |
| Large diff. peak/hole [e·Å$^{-3}$] | 1.152 and –1.076 | 0.946 and –0.957 |

## Acknowledgments

We gratefully acknowledge support by the Swiss National Science Foundation, by the COST action D31 and by the Ecole Polytechnique Fédérale de Lausanne (EPFL).

[1] For reviews see: a) S. J. Lee, J. T. Hupp, *Coord. Chem. Rev.* **2006**, *250*, 1710–1723; b) C. H. M. Amijs, G. P. M. van Klink, G. van Koten, *Dalton Trans.* **2006**, 308–327; c) N. C. Gianneschi, M. S. Masar III, C. A. Mirkin, *Acc. Chem. Res.* **2005**, *38*, 825–837; d) P. Thanasekaran, R.-T. Liao, Y.-H. Liu, T. Rajendran, S. Rajagopal, K.-L. Lu, *Coord. Chem. Rev.* **2005**, *249*, 1085–1110; e) F. Würthner, C.-C. You, C. R. Saha-Möller, *Chem. Soc. Rev.* **2004**, *33*, 133–146; f) B. J. Holliday, C. A. Mirkin, *Angew. Chem. Int. Ed.* **2001**, *40*, 2022–2043; g) G. F. Swiegers, T. J. Malefetse, *Chem. Rev.* **2000**, *100*, 3483–3538; h) S. Leininger, B. Olenyuk, P. J. Stang, *Chem. Rev.* **2000**, *100*, 853–908.

[2] For selected examples see: a) G. N. Newkome, P. Wang, C. N. Moorefield, T. J. Cho, P. P. Mohapatra, S. Li, S.-H. Hwang, O. Lukoyanova, L. Echegoyen, J. A. Palagallo, V. Iancu, S.-W. Hla, *Science* **2006**, *312*, 1782–1785; b) D. Guo, C.-Y. Duan, F. Lu, Y. Hasegawa, Q.-J. Meng, S. Yanagida, *Chem. Commun.* **2004**, 1486–1487; c) G. R. Newkome, T. J. Cho, C. N. Moorefield, P. P. Mohapatra, L. A. Godínez, *Chem. Eur. J.* **2004**, *10*, 1493–1500; d) J. Forniés, J. Gómez, E. Lalinde, M. T. Moreno, *Chem. Eur. J.* **2004**, *10*, 888–898; e) H. Oshio, H. Onodera, T. Ito, *Chem. Eur. J.* **2003**, *9*, 3946–3950; f) R. D. Sommer, A. L. Rheingold, A. J. Goshe, B. Bosnich, *J. Am. Chem. Soc.* **2001**, *123*, 3940–3952; g) M. M. Ali, F. M. MacDonnell, *J. Am. Chem. Soc.* **2000**, *122*, 11527–11528; h) C. Müller, J. A. Whiteford, P. J. Stang, *J. Am. Chem. Soc.* **1998**, *120*, 9827–9837; i) K. K. Klausmeyer, T. B. Rauchfuss, S. R. Wilson, *Angew. Chem. Int. Ed. Engl.* **1998**, *37*, 1694–1696; j) J. A. Whiteford, C. V. Lu, P. J. Stang, *J. Am. Chem. Soc.* **1997**, *119*, 2524–2533; k) R. V. Slone, D. I. Yoon, R. M. Calhoun, J. T. Hupp, *J. Am. Chem. Soc.* **1995**, *117*, 11813–11814.

[3] For selected examples see: a) M. C. Álvarez-Vergara, M. A. Casado, M. L. Martín, F. J. Lahoz, L. A. Oro, J. J. Pérez-Torrente, *Organometallics* **2005**, *24*, 5929–5936; b) J. K. Bera, J. Bacsa, B. W. Smucker, K. R. Dunbar, *Eur. J. Inorg. Chem.* **2004**, 368–375; c) N. C. Gianneschi, C. A. Mirkin, L. N. Zakharov, A. L. Reingold, *Inorg. Chem.* **2002**, *41*, 5326–5328; d) J. K. Bera, B. W. Smucker, R. A. Walton, K. R. Dunbar, *Chem. Commun.* **2001**, 2562–2563; e) P. J. Stang, N. E. Persky, *Chem. Commun.* **1997**, 77–78.

[4] a) E. Doxiadi, R. Vilar, A. J. P. White, D. J. Williams, *Polyhedron* **2003**, *22*, 2991–2998; b) S.-T. Cheng, E. Doxiadi, R. Vilar, A. J. P. White, D. J. Williams, *J. Chem. Soc., Dalton Trans.* **2001**, 2239–2244.

[5] a) K. Severin, *Chem. Commun.* **2006**, 3859–3867; b) M.-L. Lehaire, A. Schulz, R. Scopelliti, K. Severin, *Inorg. Chem.* **2003**, *42*, 3576–3581; c) K. Severin, *Coord. Chem. Rev.* **2003**, *245*, 3–10; d) M.-L. Lehaire, R. Scopelliti, K. Severin, *Chem. Commun.* **2002**, 2766–2767; e) M.-L. Lehaire, R. Scopelliti, K. Severin, *Inorg. Chem.* **2002**, *41*, 5466–5474; f) M.-L. Lehaire, R. Scopelliti, H. Piotrowski, K. Severin, *Angew. Chem. Int. Ed.* **2002**, *41*, 1419–1422; g) H. Piotrowski, G. Hilt, A. Schulz, P. Mayer, K. Polborn, K. Severin, *Chem. Eur. J.* **2001**, *7*, 3197–3208; h) H. Piotrowski, K. Polborn, G. Hilt, K. Severin, *J. Am. Chem. Soc.* **2001**, *123*, 2699–2700.

[6] a) Z. Grote, R. Scopelliti, K. Severin, *J. Am. Chem. Soc.* **2004**, *126*, 16959–16972; b) Z. Grote, M.-L. Lehaire, R. Scopelliti, K. Severin, *J. Am. Chem. Soc.* **2003**, *125*, 13638–13639; c) H. Piotrowski, K. Severin, *Proc. Natl. Acad. Sci. USA* **2002**, *99*, 4997–5000.

[7] For reviews on dynamic combinatorial chemistry see: a) P. T. Corbett, J. Leclaire, L. Vial, K. R. West, J.-L. Wietor, J. K. M. Sanders, S. Otto, *Chem. Rev.* **2006**, *106*, 3652–3711; b) S. Otto, *J. Mater. Chem.* **2005**, *15*, 3357–3361; c) O. Ramström, T. Bunyapaiboonsri, S. Lohmann, J.-M. Lehn, *Biochim. Biophys. Acta*

 © 2007 Wiley-VCH Verlag GmbH & Co. KGaA, Weinheim 

**2002**, *1572*, 178–186; d) S. J. Rowan, S. J. Cantrill, G. R. L. Cousins, J. K. M. Sanders, J. F. Stoddart, *Angew. Chem. Int. Ed.* **2002**, *41*, 898–952; e) S. Otto, R. L. E. Furlan, J. K. M. Sanders, *Curr. Opin. Chem. Biol.* **2002**, *6*, 321–327; f) J.-M. Lehn, *Chem. Eur. J.* **1999**, *5*, 2455–2463.
[8] a) I. Saur, R. Scopelliti, K. Severin, *Chem. Eur. J.* **2006**, *12*, 1058–1066; b) I. Saur, K. Severin, *Chem. Commun.* **2005**, 1471–1473; c) Z. Grote, R. Scopelliti, K. Severin, *Angew. Chem. Int. Ed.* **2003**, *42*, 3821–3825.
[9] K. Severin, *Chem. Eur. J.* **2004**, *10*, 2565–2580.
[10] The utilization of slightly more than two equivalents of $[(C_6H_6)RuCl_2]_2$ was found to be advantageous, possibly due to some impurities in the starting material.
[11] M. A. Galindo, S. Galli, J. A. R. Navarro, M. A. Romero, *Dalton Trans.* **2004**, 2780–2785.
[12] a) M. Yoshizawa, M. Nagao, K. Kumazawa, M. Fujita, *J. Organomet. Chem.* **2005**, *690*, 5383–5388; b) M. Yoshizawa, J. Nakagawa, K. Kumazawa, M. Nagao, M. Kawano, T. Ozeki, M. Fujita, *Angew. Chem. Int. Ed.* **2005**, *44*, 1810–1813.
[13] J. Zhang, P. W. Miller, M. Nieuwenhuyzen, S. L. James, *Chem. Eur. J.* **2006**, *12*, 2448–2453.
[14] The equilibrium concentrations were calculated with the program *Gepasi*, version 3.30. See: a) P. Mendes, *Comput. Appl. Biosci.* **1993**, *9*, 563–571; b) P. Mendes, *Trends Biochem. Sci.* **1997**, *22*, 361–363.
[15] J. W. Hull, W. L. Gladfelter, *Organometallics* **1984**, *3*, 605–613.
[16] M. A. Bennett, T. N. Huang, T. W. Matheson, A. K. Smith, *Inorg. Synth.* **1982**, *21*, 74–78.
[17] C. White, A. Yates, P. M. Maitlis, *Inorg. Synth.* **1992**, *29*, 228–234.
[18] R. A. Zelonka, M. C. Baird, *Can. J. Chem.* **1972**, *50*, 3063–3072.
[19] Oxford Diffraction Ltd., Abingdon, Oxfordshire, UK, **2003**.
[20] G. M. Sheldrick, *SHELXTL*, University of Göttingen, **1997**; Bruker AXS, Inc., Madison, Wisconsin, **1997**.

Received: September 14, 2006
Published Online: December 19, 2006

 © 2007 Wiley-VCH Verlag GmbH & Co. KGaA, Weinheim 

DOI: 10.1002/ejic.200600891

# Complexation Properties of the Di-, Tri-, and Tetraacetate Derivatives of Bis(aminomethyl)phosphinic Acid

Gyula Tircsó,*[a][‡] Attila Bényei,[b] Róbert Király,[a] István Lázár,[a] Róbert Pál,[a] and Ernő Brücher*[a]

**Keywords:** Phosphinic acid derivatives / Divalent metal ions / Synthesis / Protonation constants / Stability constants

Four ligands, which can be considered as di- [both symmetric ($L^1$) and asymmetric ($L^2$)], tri- ($L^3$), and tetraacetate ($L^4$) derivatives of bis(aminomethyl)phosphinic acid ($L^0$) have been synthesized and their complexation equilibria involving $Mg^{2+}$, $Ca^{2+}$, $Ni^{2+}$, $Cu^{2+}$, $Zn^{2+}$, $Cd^{2+}$, and $Pb^{2+}$ have been studied by pH potentiometry. The first two protonation constants of the ligands are lower than those of the analogous diaminopolycarboxylates due to the electron-withdrawing effect of the phosphinate group. The asymmetric ligands $L^2$ and $L^3$ and their complexes are protonated first at the primary ($NH_2$) and secondary (NH) amine groups, respectively. The ligands $L^0$, $L^1$, $L^2$, and $L^3$ form the species ML, MLH, $ML_2$, and $ML_2H$ whereas heptadentate $L^4$ forms very stable ML complexes, protonated (MLH and $MLH_2$) species and, unlike the other ligands, it also forms dinuclear $M_2L$ complexes. The stability constants of the complexes of $L^0$, $L^1$, $L^2$, and $L^3$ are generally lower, while those of the $L^4$ are similar or higher, than those of the analogous diaminocarboxylate derivatives. The phosphinate group is not directly coordinated to the metal ions but may contribute to the stability by increasing the electrostatic interaction, which is significant for the complexes of $L^4$. The $^1H$ NMR spectra of complexes $ZnL^2$, $ZnL^3$, and $ZnL^4$ show an AB multiplet pattern for the protons of the iminodiacetate moiety of the ligands, which indicates the long half-life of the $Zn^{2+}$–N bond and the rigid structure of this segment of the complexes. The solid-state structure of the ligand $[H_5L^3]Cl$ and complex $K[CuL^1]\cdot H_2O$ have been determined by X-ray diffraction techniques. The arrangement of the ligand $L^1$ is square planar around $Cu^{2+}$ with two nitrogen and carboxylate oxygen donor atoms, although the axial proximity of a carboxylate and a phosphinate oxygen atom in two neighboring molecules results in a distorted octahedral coordination.

(© Wiley-VCH Verlag GmbH & Co. KGaA, 69451 Weinheim, Germany, 2007)

## Introduction

Due to their biological importance there has been a growing interest in recent years in the coordination chemistry of ligands containing phosphinate functional groups.[1] The charge of the phosphinate group, $PO_2^-$, is minus one, similar to that of the carboxylate, and thus the complexation properties of aminoalkylphosphinate ligands are similar to those of aminocarboxylates in many respects. However, as phosphinate groups are less basic than carboxylates, the stability constants of the complexes formed with aminoalkylphosphinates are lower than those of aminocarboxylates.[2–8]

[a] University of Debrecen, Department of Inorganic and Analytical Chemistry,
P. O. Box 21, Egyetem tér 1, Debrecen 4010, Hungary
Fax: +36-52-489-667
E-mail: gyulat@gmail.com
ebrucher@delfin.klte.hu
[b] University of Debrecen, Department of Chemistry, Laboratory for X-ray Diffraction,
P. O. Box 7, Egyetem tér 1, Debrecen 4010, Hungary
[‡] Present address of the corresponding author: Department of Chemistry, University of Texas at Dallas,
P. O. Box 830660, Richardson, Texas 75080, USA
Fax: +1-972-883-2925

Supporting information for this article is available on the WWW under http://www.eurjic.org or from the author.

The successful use of some tri- and tetraacetate derivatives of cyclen in medical diagnosis and therapy has drawn attention to the tetramethylenephosphinates of cyclen, and a number of cyclen derivatives have been synthesized with different phosphinate functional groups. The $Gd^{3+}$ complexes of these ligands have been proposed as contrast enhancing agents in magnetic resonance imaging.[9–15] Since the methylenephosphinate groups [$CH_2P(R)O_2^-$, where R is H, alkyl, or aryl] in these cyclen derivatives are attached to the ring nitrogens, the phosphinate groups are in terminal position, similar to open-chain ligands. However, in contrast to the carboxylate and phosphonate groups, phosphinate groups may also occupy an "in-chain" position and some multidentate aminocarboxylate ligands that contain $PO_2^-$ groups as linkers have attracted considerable interest in recent years.[16–26] Phosphinic acid peptides are specific inhibitors of peptide hydrolytic enzymes (e.g. Zn metalloproteinases and aspartic acid proteinases) because the non-hydrolyzable $>PO_2^-$ moiety resembles the transition state of the hydrolyzable peptides.[18,19]

The complexation properties of bis(aminomethyl)phosphinic acid and some of its derivatives have already been investigated. Complex formation between the ligands bis(aminomethyl)-, bis(*N*-methylsarcozinato)-, bis(*N*-methyl-

 © 2007 Wiley-VCH Verlag GmbH & Co. KGaA, Weinheim InterScience 

prolinato)-, and bis(*N*-methyliminodiacetato)phosphinate and some divalent metal ($Co^{2+}$, $Cu^{2+}$, $Zn^{2+}$, $Cd^{2+}$, $Pb^{2+}$) and lanthanide(III) ($Ln^{3+}$) ions has been studied in solution by pH potentiometry and $^1H$ NMR and EPR spectroscopy.[20–24] Although the coordination of the phosphinate group to $M^{2+}$ ions has been detected in some cases, it is more important in the formation of complexes with $Ln^{3+}$ ions.[21,22] The $PO_2^-$ group has also been incorporated into macrocyclic rings. Eight- and fourteen-membered functionalized bis(aminomethyl)phosphinate macrocycles have recently been synthesized by Aime et al. and Song et al., respectively.[25,26] The stability constant of the $Gd^{3+}$ complex formed with the eight-membered diphosphinate ligand was found to be relatively high ($\log K_{GdL} = 17.6$).[25] The fourteen-membered ligand does not form highly stable complexes.[26]

The ligand $HL^0$ (Scheme 1) was first synthesized by Maier and somewhat later by Natchev.[27,28] More recently, Kubiček et al. have published a new procedure for the synthesis of $HL^0$ and they also studied its $Co^{II}$, $Ni^{II}$, $Cu^{II}$, and $Zn^{II}$ complexes in solution and in the solid state.[24] The ligand $H_3L^1$ was also prepared by Maier but its complexation was studied only with $Ni^{II}$.[29] The same author prepared the ligand $H_5L^4$ from the reaction of iminodiacetic acid ($H_2$imda) and paraformaldehyde in the presence of hypophosphorus acid.[30] Similar conditions were used previously in our laboratory by Varga to obtain some bis(aminomethyl)phosphinic acid derivatives from various imino(di)acids.[20] The experimental conditions were found to have a great influence on these reactions. Thus, high concentrations of the reactants at reflux temperature led to the formation of a number of by-products and purification of the final products was difficult.[20]

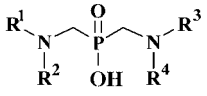

| $R^1$ | $R^2$ | $R^3$ | $R^4$ | Ligand |
|---|---|---|---|---|
| H | H | H | H | $HL^0$ |
| H | $CH_2COOH$ | H | $CH_2COOH$ | $H_3L^1$ |
| H | H | $CH_2COOH$ | $CH_2COOH$ | $H_3L^2$ |
| H | $CH_2COOH$ | $CH_2COOH$ | $CH_2COOH$ | $H_4L^3$ |
| $CH_2COOH$ | $CH_2COOH$ | $CH_2COOH$ | $CH_2COOH$ | $H_5L^4$ |

Scheme 1. Structure of the ligands synthesized and investigated in this work.

One of our goals was to find a procedure which would allow the large-scale preparation of bis(aminomethyl)phosphinic acid derivatives from readily available, inexpensive starting materials without expensive instrumental purification methods. Similarly, the bis(aminomethyl)phosphinic acid itself can be considered as a building block for the synthesis of macrocycles containing linker phosphinate group(s) when the macrocycle itself has a negative charge. By dividing the Mannich-type synthesis into two consecutive steps we have successfully synthesized the ligands $H_3L^1$, $H_3L^2$, and $H_3L^3$ (Scheme 1). These compounds can be regarded as fragments of the edta analog $H_5L^4$, which was reported earlier.[21,22] In the present study, the stability constants of the complexes formed between some endogenous ($Mg^{2+}$, $Ca^{2+}$, $Cu^{2+}$, and $Zn^{2+}$) and toxic ($Ni^{2+}$, $Cd^{2+}$, and $Pb^{2+}$) divalent metal ions and bis(aminomethyl)phosphinic acid derivatives are examined by pH potentiometry. The structures of the ligand $[H_5L^3]Cl$ and the complex $K[CuL^1]\cdot H_2O$ have been determined in the solid state by X-ray diffraction methods and the $Zn^{2+}$ complexes studied by $^1H$ and $^{31}P$ NMR spectroscopy in solution.

## Results and Discussion

### Synthesis of the Ligands

Synthesis of the symmetric bis(aminomethyl)phosphinic acid derivatives was achieved in a multi-step reaction starting from *N*,*N*-dibenzylamine according to Scheme 2. The monohydrochloride of the intermediate **1** was obtained in high yields by a Mannich reaction in 6 M HCl. The debenzylation of this key intermediate by catalytic hydrogenolysis can be carried out in different ways depending on the solvent selected. Using acetic acid/water as a solvent in the presence of EtOH with slight heating to achieve complete dissolution of the starting material the bis(aminomethyl)-phosphinic acid hydrochloride **2** could be prepared in very high yields. Another advantage of this synthesis is that it does not use expensive materials or instrumentation and can be scaled up easily. The debenzylation of **1** in MeOH in the presence of formic acid was found to be controlled by solubility and the hydrochloride salt of the selectively protected bis(benzylaminomethyl)phosphinic acid **3** crystallized out quantitatively from the reaction mixture during the reduction process. An analytical sample of **3** was obtained by recrystallization of crude **3** from hot water. Compound **3** proved to be a valuable intermediate for the synthesis of new carboxy- or phosphonomethyl derivatives of bis(aminomethyl)phosphinic acid. Alkylation of **3** with bromoacetic acid in the presence of NaOH afforded the trisodium salt of **4**. The monohydrochloride salt of the free acid was prepared by crystallizing **4** from fairly acidic solutions ($pH < 2$). Debenzylation of **4** in a water/acetic acid mixture afforded compound **5** ($H_3L^1$).

The synthesis of the asymmetric bis(aminomethyl)phosphinic acid derivatives **7**–**10** is presented in Scheme 3. They are all new compounds that have not been published previously. The intermediate **6** was obtained from the reaction of iminodicarboxylic acid with paraformaldehyde in a Mannich-type reaction in ethanol in the presence of excess hypophosphorus acid, which also acts as an acid catalyst. In this particular case (when $H_2$imda was used as starting material), the reaction was found to be solubility controlled and at the end of the reaction the product crystallized out from the reaction mixture. The remaining P–H bond in the molecule can be reacted further in a second Mannich-type reaction in 6 M HCl to replace the H with another aminomethyl

 © 2007 Wiley-VCH Verlag GmbH & Co. KGaA, Weinheim 

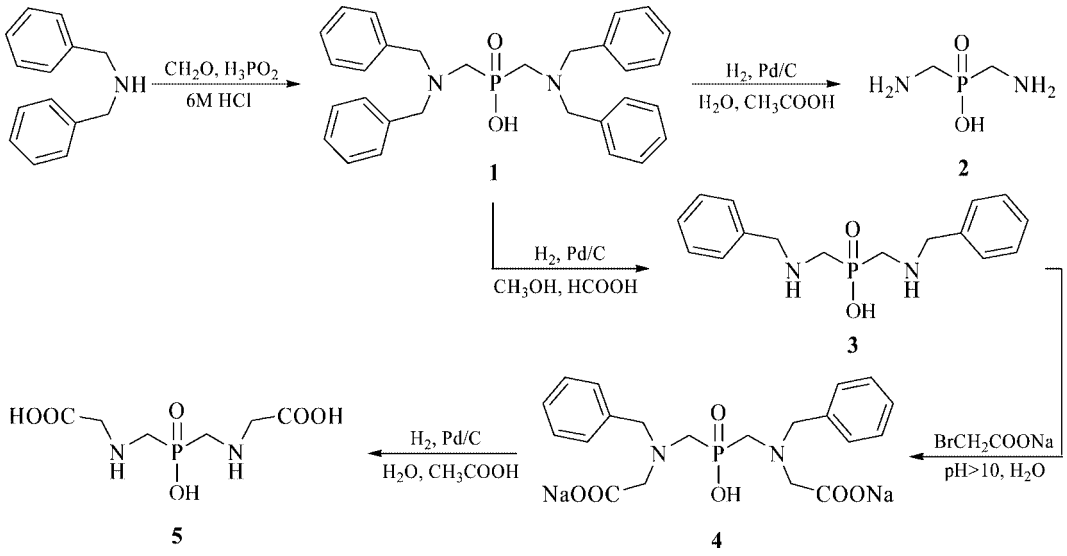


Scheme 2. Synthesis of the symmetric bis(aminomethyl)phosphinic acid derivatives studied in this work.

segment. This process allowed us to synthesize hitherto unknown asymmetric bis(aminomethyl)phosphinic acid derivatives (Scheme 3). The best yields for this reaction were obtained when short reaction times (about 1.5 h) were used as the number of by-products in the reaction mixture increased with an increase of the reaction time while the amount of desired products (**7** and **9**) decreased. When longer reaction times (up to 6 h) were used the reaction mixtures yielded compounds **4** and $H_5L^4$, respectively, after the workup and separation procedure. The formation of these compounds is evidence that the phosphorus–carbon bond [$CH_2P(O)(OH)H$] is not stable under Mannich conditions and *trans*-aminomethylation occurs. The debenzylation of **7** and **9** to **8** ($H_4L^3$) and **10** ($H_3L^2$), respectively, was achieved by catalytic hydrogenation under similar conditions to those described for compound **2**.

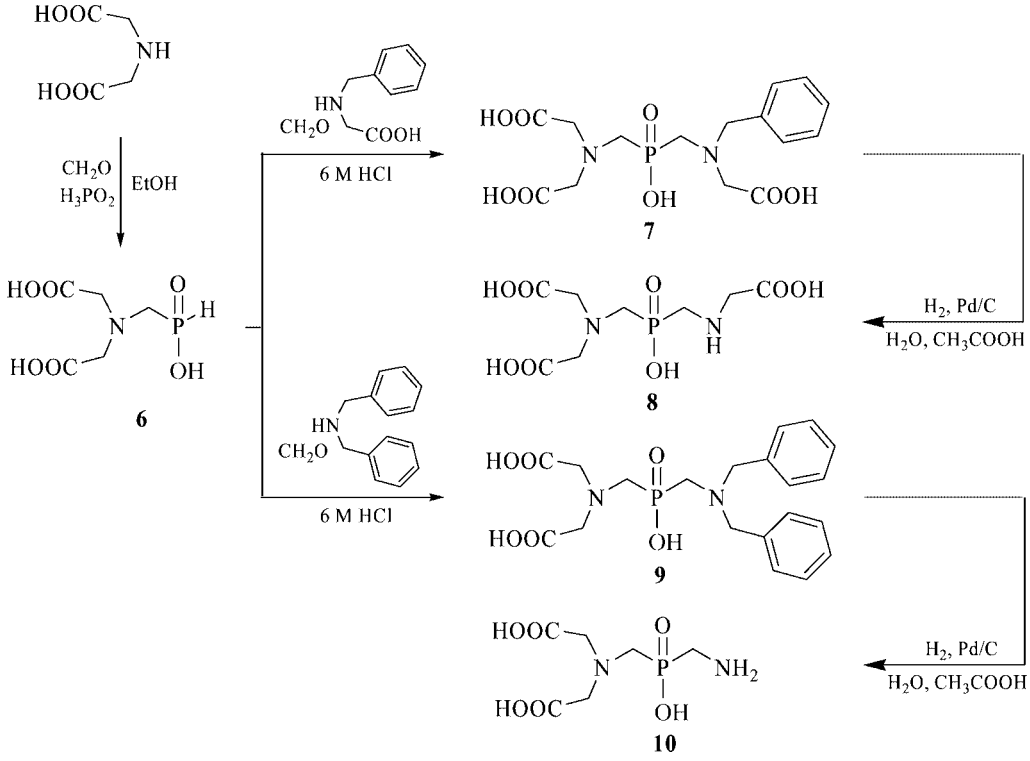


Scheme 3. Synthesis of the asymmetric bis(aminomethyl)phosphinic acid derivatives studied in this work.

 © 2007 Wiley-VCH Verlag GmbH & Co. KGaA, Weinheim 

### X-ray Crystal Structure of $[H_5L^3]Cl$ and $K[CuL^1]\cdot H_2O$

The structures of $[H_5L^3]Cl$ and $K[CuL^1]\cdot H_2O$ were established by single-crystal X-ray diffraction studies (see Figures 1 and 2, Tables 1 and 2, and the Supporting Information). The most important feature of the structure of the protonated ligand of $[H_5L^3]Cl$ is the extensive H-bonding network (Table S1) and the related disordered position of the chloride ions (see below). The compound crystallizes in the noncentrosymmetric space group $Pn2_1a$ (no. 33). It is important to note that the position of the carboxylate hydrogen atoms as well as the protons at the nitrogen atoms could be found in the difference electron density maps of both structures. However, these hydrogen atoms were placed in geometric positions in the final refinement cycle. The C–O bond length data (Table 3) of $[H_5L^3]Cl$ show C3–O4, C6–O6, and C8–O8 bond lengths of 1.298(10), 1.316(9), and 1.310(10) Å, respectively, which also indicate the sites of protonation. Besides the electronic and steric factors of the phosphinate moiety, the higher values of the P–C bond lengths compared to C–C bonds as well as the slightly different bond angles are another tool for the fine tuning of the ligand that could be important in applications. For example, the water exchange rate and thereby the relaxivity of $Gd^{III}$ complexes formed with poly(amino)carboxylates depends on the steric crowding in the complex.[31] In our case, the significant difference between the P1–C1 and P1–C4 distances [1.803(7) and 1.821(8) Å, respectively] also shows the electronic and steric effects of the mono- and bis(diacatate) arms on the N1 and N2 nitrogen atoms, respectively as these bond lengths are the same in the analogous symmetric bis(aminomethyl)phosphinate hydrochloride structure.[24]

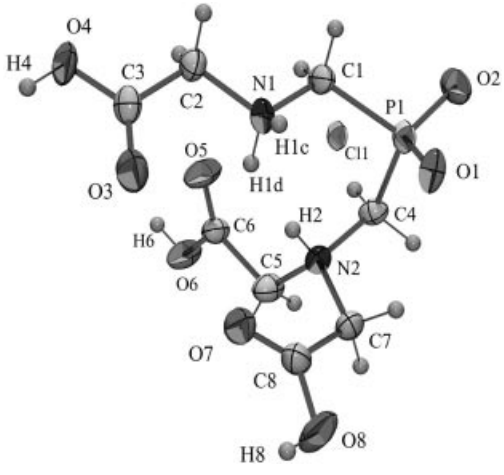


Figure 1. ORTEP view of the asymmetric unit in the structure of $[H_5L^3]Cl$ with thermal ellipsoids at the 50% probability level, with atom-numbering scheme.

The packing of $[H_5L^3]Cl$ is shown in Figure S1 and the data of the H-bonding network are listed in Table S1 (see Supporting Information). The high max/min atomic displacement parameter ratio of the chloride ions in the structure of $[H_5L^3]Cl$ can be explained by the fact that the chloride ion is not fixed in the lattice but loosely occupies a polar channel. Strong N–H···Cl hydrogen bonds fix the anion in the analogous layered structure of bis(aminomethyl)phosphinate hydrochloride, although the long range Cl–Cl distances are similar in the two structures (approx. 3.96 Å). In our case, however, the three strong hydrogen bonds with the participation of carboxylate donors and P1–O1 or P1–O2 as acceptors as well as the steric restraints prevent the formation of N–H···Cl hydrogen bonds (Table S1).

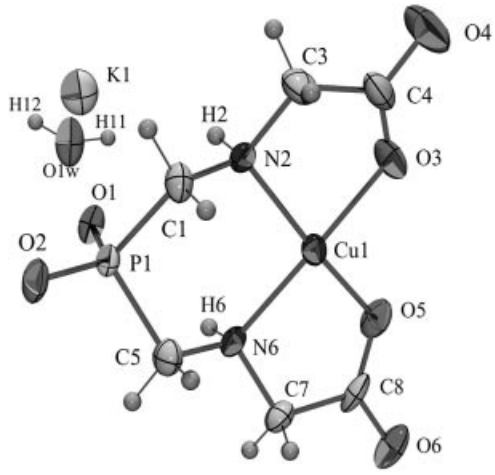


Figure 2. ORTEP view of the asymmetric unit in the structure of $K[CuL^1]\cdot H_2O$ with thermal ellipsoids at the 50% probability level, with atom-numbering scheme.

Table 1. Selected bond lengths [Å] and angles [°] for $[H_5L^3]Cl$.[a]

| | | | |
|---|---|---|---|
| P1–O1 | 1.503(6) | P1–C1 | 1.821(8) |
| P1–O2 | 1.493(5) | P1–C4 | 1.803(7) |
| C3–O3 | 1.204(10) | C8–O7 | 1.188(10) |
| C3–O4 | 1.298(10) | C8–O8 | 1.310(10) |
| C6–O5 | 1.188(9) | C1–N1 | 1.477(9) |
| C6–O6 | 1.316(9) | C4–N2 | 1.469(8) |
| O1–P1–O2 | 115.7(4) | C2–C3–O3 | 123.7(7) |
| C1–P1–C4 | 103.7(4) | C5–C6–O5 | 125.7(7) |
| C5–N2–C4 | 112.8(6) | C7–C8–O7 | 125.5(7) |
| C4–N2–C7 | 111.8(6) | C1–N1–C2 | 111.8(6) |

[a] See Figure 1 for numbering scheme.

Table 2. Selected bond lengths [Å] and angles [°] for $[K(CuL^1)]\cdot H_2O$.[a]

| | | | |
|---|---|---|---|
| Cu1–N2 | 2.008(6) | O1–P1 | 1.504(6) |
| Cu1–N6 | 2.013(6) | O2–P1 | 1.491(5) |
| Cu1–O3 | 1.940(6) | C1–P1 | 1.811(8) |
| Cu1–O5 | 1.961(5) | C5–P1 | 1.799(8) |
| Cu1–O2$^{i}$ | 2.249(5) | O1–K1 | 2.648(6) |
| Cu1–O5$^{ii}$ | 2.945(5) | O1w–K1 | 2.714(7) |
| O1w–K1$^{iii}$ | 2.731(8) | O6–K1$^{i}$ | 3.012(7) |
| O4–K1 | 2.726(8) | O6–K1 | 2.780(7) |
| O3–Cu1–O5 | 90.1(3) | O2–P1–O1 | 119.8(3) |
| O5–Cu1–N2 | 166.0(2) | O2–P1–C5 | 108.8(3) |
| N2–Cu1–N6 | 99.4(2) | O1–K1–O1w | 107.9(2) |
| N2–Cu1–O2$^{i}$ | 89.7(2) | C5–P1–C1 | 104.6(4) |
| O5–Cu1–N6 | 83.5(2) | C1–N2–C3 | 111.2(6) |

[a] See Figure 2 for numbering scheme. Symmetry transformations used to generate equivalent atoms: i: 1/3 + *y*, 2/3 – *x* + *y*, 2/3 – *z*; ii: –*x*, –*y*, –*z*; iii: 4/3 – *x* + *y*, 2/3 – *x*, *z* – 1/3.

 © 2007 Wiley-VCH Verlag GmbH & Co. KGaA, Weinheim 

$K[CuL^1]\cdot H_2O$ crystallizes in the trigonal centrosymmetric space group $R\bar{3}$ (no. 148). The configuration of the nitrogen atoms N2 and N6 is mixed, and the complex exists as a racemate with equal amounts of (*R*,*S*) and (*S*,*R*) enantiomers present in the lattice. Selected bond lengths and angles are summarized in Table 2. The coordination of the $Cu^{2+}$ in $K[CuL^1]\cdot H_2O$ is best described as elongated distorted octahedral. N2, N6, O3, and O5 form the basal square-planar coordination and the copper is positioned out of this plane by 0.211 Å. The carboxylate oxygen atom $O5^{i}$ and phosphinate oxygen atom $O2^{ii}$ of symmetry-related molecules (i: $-x, -y, -z$; ii: $y + 1/3, -x + y + 2/3, -z + 2/3$) are coordinated in the axial positions with Cu–O distances of 2.945 and 2.249 Å, respectively. In this way, two O5 atoms serve as bridging ligands that hold together two copper complexes with a Cu–Cu distance of 3.827 Å and give rise to a supramolecular polymer structure. This bridging role of O5 also supports an octahedral rather than a square-pyramidal coordination. The coordination of O2 of the next complex in the lattice can be attributed to the electron-withdrawing properties of the phosphinate group as well as the increase in the length of the side arm due to the P–C bonds.

The hydrogen-bond data are summarized in the Supporting Information (Table S2). In this web, the H2 and H6 participate in bifurcating hydrogen bonds while O1 is a bifurcating acceptor. However, the N2–H2···O1 hydrogen bond has an unfavorable angle of 107°.

Tetradentate ligands analogous to 1,3-propanediamine-*N*,*N*′-diacetate can form square-pyramidal copper(II) complexes.[32] However, a search in the Cambridge Structural Database (version 5.27, November 2005; update May 2006) revealed that octahedral coordination may also occur in similar compounds.[33] This is especially important in the case of a $Cu^{II}$ complex containing a small, sterically undemanding ligand such as in (3-hydroxy-1,5-diazacycloheptane-*N*,*N*′-diacetato)copper(II), where the coordination is N2O4.[34] Here, the hydroxyl oxygen and a water molecule complete the octahedral coordination with Cu–O distances of 2.456 and 2.564 Å, respectively. The deposited data do not contain hydrogen atoms, which may indicate some ambiguity, but similar octahedral coordination has also been observed in another case where an axial water molecule and another axial carboxylate oxygen complete the coordination sphere of the copper ion with Cu–O distances of 2.275 and 2.780 Å, respectively.[35]

The coordination of potassium is also octahedral, with carboxylate, phosphinate, and water oxygen atoms ($O6^{i}$, $O6^{iii}$, O4, O1, O1w, and $O1w^{iv}$; i: $-x, -y, -z$; iii: $x - y + 1/3, -x + 2/3, -z + 2/3$; iv: $-y + 2/3, x - y + 1/3, z + 1/3$) with K···O distances in the range o2.65–3.01 Å. O6 and O1w serve as bridges between the potassium ions and the K···K distance is 4.046 Å. Altogether, the complicated supramolecular structure of $K[CuL^1]\cdot H_2O$ is stabilized by interpenetrating ionic and coordination interactions as well as a strong hydrogen bond network. In the polymer there are hexagonal channels with a diameter of approximately 8.5 Å (Figure S2, Supporting Information), which are filled with disordered water molecules.

**Protonation Constants and Protonation Sites of the Ligands**

The protonation equilibria of the ligands, $L^0$, $L^1$, $L^2$, $L^3$, and $L^4$ were studied by pH-potentiometry and $^1H$ (in some cases $^{31}P$) NMR spectroscopy (Figures S3–S7 in the Supporting Information). The titrations were performed in the pH range of about 1.8–11.5 in the presence of 1.0 M $Me_4NCl$. The protonation constants, defined as $K_i^H = [H_iL]/[H_{i-1}L][H^+]$, were also determined in 1.0 M $KNO_3$ since the complexation with $Cd^{2+}$ and $Pb^{2+}$ was studied in $KNO_3$ solution in order to avoid the formation of chloro complexes. For the calculation of the protonation constants of the ligands, the number of data points was between 160 and 250. The $\log K_i^H$ values obtained are presented in Table 3, where the standard deviations are shown in parentheses. The protonation constants of the ligands $L^0$ and $L^4$, which have been determined previously (Table 3),[22–24] are comparable with the ones obtained in this work when the different experimental conditions are taken into account.

As was expected, we found by $^1H$ (and $^{31}P$) NMR studies that the most basic donor atoms in all derivatives of $L^0$ are the two nitrogens, which are protonated first (Figures S4 and S5).[21,22,24] The protonation of these nitrogens is followed by protonation of the carboxylates, while the strongly acidic phosphinate group is protonated only in strongly acidic solution.[22,24] The protonation constants of $L^0$ are lower than those of 1,3-diaminopropane ($\log K_1^H = 10.52$ and $\log K_2^H = 8.74$), in which the two nitrogen donors are also separated from each other by three atoms. The behavior of the derivatives of $L^0$ is similar. The first two protonation constants of $L^4$ (Table 3) are significantly lower than those of 1,3-diaminopropane-*N*,*N*′,*N*′′,*N*′′′-tetraacetic acid (10.41 and 8.02).[36] Similarly, the $\log K_1^H$ and $\log K_2^H$ values of $L^1$ are lower than the first two protonation constants of ethylenediamine-*N*,*N*′-diacetic acid ($L^6$; 9.69 and 6.72).[36] The lower basicity of the nitrogen atoms of the phosphinate ligands is probably due to the electron-withdrawing effect of the phosphinate group.

Table 3. Protonation constants of the ligands $L^0$, $L^1$, $L^2$, $L^3$, and $L^4$ (25 °C).

| L | $\log K_1^H$ | $\log K_2^H$ | $\log K_3^H$ | $\log K_4^H$ |
|---|---|---|---|---|
| $L^0$ [a,f] | 8.73 (0.01) | 7.35 (0.01) | – | – |
| $L^0$ [b] | 8.74 (0.01) | 7.38 (0.01) | 0.91 (0.08) | – |
| $L^0$ [c] | 8.51 | 7.07 | 0.77 | – |
| $L^1$ [a] | 9.00 | 6.53 | 2.53 | 1.66 |
| $L^1$ [b] | 8.93 (0.02) | 6.80 (0.03) | 2.65 (0.05) | 1.77 (0.05) |
| $L^2$ [a] | 9.97 (0.01) | 5.62 (0.02) | 2.42 (0.02) | – |
| $L^2$ [b] | 9.94 (0.01) | 5.68 (0.01) | 2.23 (0.01) | – |
| $L^3$ [a] | 10.17 (0.01) | 5.52 (0.01) | 2.49 (0.02) | 2.03 (0.04) |
| $L^3$ [b] | 9.79 (0.01) | 5.67 (0.02) | 2.68 (0.03) | 1.43 (0.04) |
| $L^4$ [a] | 10.01 | 6.50 | 2.68 | 2.17 |
| $L^4$ [b] | 9.44 (0.01) | 6.56 (0.01) | 2.54 (0.01) | 1.98 (0.01) |
| $L^4$ [d] | 8.87 (0.01) | 6.41 (0.01) | 2.49 (0.01) | 1.69 (0.05) |
| $L^4$ [e] | 9.27 | 6.56 | 2.84 | 2.32 |

[a] 1.0 M $Me_4NCl$. [b] 1.0 M $KNO_3$. [c] 0.1 M $KNO_3$.[24] [d] 1.0 M NaCl. [e] 0.16 M NaCl.[22] [f] Redetermined in the present study ($I$ = 1.0 M $Me_4NCl$).

 © 2007 Wiley-VCH Verlag GmbH & Co. KGaA, Weinheim 

A comparison of the data in Table 3 reveals that the difference between the protonation constants $\log K_1^H$ and $\log K_2^H$ is lower for the symmetric ligands $L^0$, $L^1$, and $L^4$ than for asymmetric $L^2$ and $L^3$, which show a larger difference in the basicity of the nitrogen atoms. Parallel with this finding, the question arises regarding the protonation order of the nitrogens in the asymmetric ligands $L^2$ and $L^3$. The protonation scheme of $L^2$ and $L^3$ was determined by $^1$H NMR titrations in the pH range of about 1–12. The $^1$H NMR titration curves of ligands $L^2$ and $L^3$ are shown in Figures 3 and 4, respectively. In Figure 3, the chemical shift of the -C$H_2$NH$_2$ methylene protons (the center of the doublet) increases with a decrease of pH from about 12 to 8.5, while the signals of both the phosphinate and acetate methylene protons [-C$H_2$N(C$H_2$COO$^-$)$_2$] are practically not shifted. This finding indicates that the first proton is attached to the $NH_2$ group of $L^2$. In the pH range of about 4 to 7 the signals of both the phosphinate and acetate methylene protons [-C$H_2$N(C$H_2$COO$^-$)$_2$] are strongly shifted to higher frequencies due to the protonation of the imda nitrogen. A further decrease of pH below about 3 results in a shift of the signal of the acetate methylene protons to higher frequencies, which indicates the protonation of the carboxylate groups.

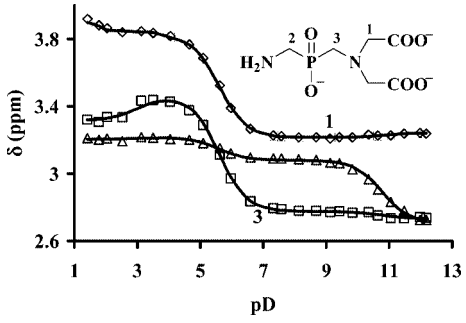


Figure 3. $^1$H NMR titration curves of ligand $L^2$ ($C_L$ = 0.05 M, 25 °C) showing the change in the chemical shifts of the protons indicated in the figure.

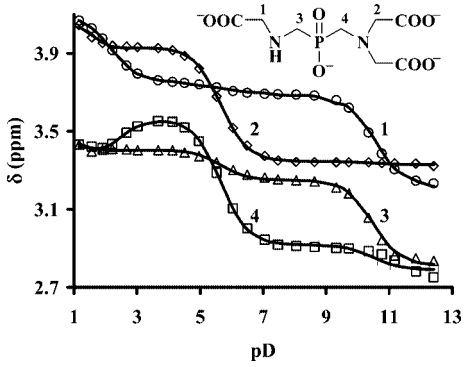


Figure 4. $^1$H NMR titration curves of ligand $L^3$ ($C_L$ = 0.05 M, 25 °C) showing the change in the chemical shifts of the protons indicated in the figure.

In Figure 4, a decrease of the pH from about 12 to 8 leads to a significant change in the chemical shifts of the glycinate and phosphinate methylene protons (-C$H_2$NHC$H_2$COOH), which indicates the protonation of the glycinate nitrogen of $L^3$. In the pH range 4–7 a strong change can be observed in the chemical shifts of the imda and phosphinate methylene protons, which shows that the second proton is attached to the nitrogen of the imda group. At a pH of around 3.5 the signal of the glycinate methylene protons starts to move to higher frequencies due to the protonation of the glycinate carboxylate.

The protonation constants $\log K_1^H$ determined in $KNO_3$ solution are generally lower than those obtained in $Me_4NCl$ solution, and the $\log K_1^H$ value of $L^4$ determined in NaCl solution is even lower. These results indicate that at higher pH values the ligands form very poorly stable complexes with $K^+$ and somewhat more stable complexes with $Na^+$ ions.

### Stability Constants of the Complexes

To characterize the complexation properties of $L^0$, $L^1$, $L^2$, $L^3$, and $L^4$ the formation equilibria between these ligands and the metal ions $Mg^{2+}$, $Ca^{2+}$, $Ni^{2+}$, $Cu^{2+}$, $Zn^{2+}$, $Cd^{2+}$, and $Pb^{2+}$ were studied by pH potentiometry. The titrations were performed at three or four different metal-to-ligand concentration ratios. The number of data points for the calculations were usually between 250 and 500. Some typical titration curves are presented in Figure 5, which shows the formation of complexes with $L^1$. The equilibrium models used for the calculation of the stability constants were selected on the basis of the properties of the metal ions and the ligands by taking into consideration the quality and number of the donor atoms. The results of the EPR study of the $Cu^{2+}$ complexes with $L^0$, $L^1$, and $L^4$ were also used to assume the species formed in these systems.[23] For characterizing the solution equilibria, the formation of the following complexes was considered: $MLH_2$, MLH, ML, M(OH)L, $ML_2H$, $ML_2$, and $M_2L$. The stability constants that describe the equilibria were defined as follows (the charges of the species have been omitted for simplicity):

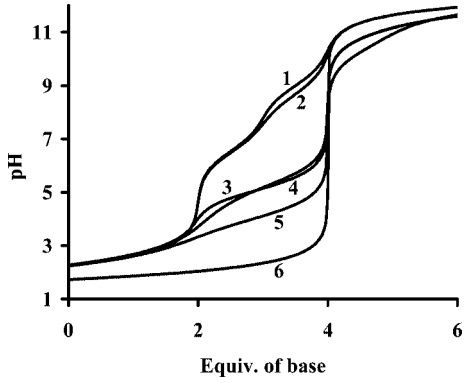


Figure 5. Titration curves of a $5 \times 10^{-3}$ M solution of $L^1$ in the absence of metal ions (1) and in the presence of one equivalent of $Ca^{2+}$ (2), $Pb^{2+}$ (3), $Cd^{2+}$ (4), $Zn^{2+}$ (5), and $Cu^{2+}$ (6).

 © 2007 Wiley-VCH Verlag GmbH & Co. KGaA, Weinheim 

$$K_{ML} = \frac{[ML]}{[M][L]} \quad ; \quad K_{ML}{}^{H} = \frac{[MLH]}{[ML][H]}$$

$$K_{MLH}{}^{H} = \frac{[MLH_2]}{[MLH][H]} \quad ; \quad K_{M(OH)L} = \frac{[M(OH)L][H]}{[ML]}$$

$$K_{ML_2} = \frac{[ML_2]}{[ML][L]} \quad ; \quad K_{ML_2}{}^{H} = \frac{[ML_2H]}{[ML_2][H]}$$

$$K_{M_2L} = \frac{[M_2L]}{[ML][M]}$$

The equilibrium constants $\beta_{pqr} = [M_pH_qL_r]/[M]^p[H]^q[L]^r$ were calculated with the program PSEQUAD.[37] Tables 4, 5, 6, and 7 present the stepwise stability constants related to the formation of ML, $ML_2$ and $M_2L$ complexes as calculated from the $\beta_{pqr}$ values. We also calculated the protonation constants of the complexes, $K_{ML}{}^{H}$, $K_{MHL}{}^{H}$, and $K_{ML_2}{}^{H}$ because these values give some information about the site of protonation (nitrogen or carboxylate oxygen). By fitting the titration data to the assumed equilibrium model we obtained the equilibrium constants $\beta_{pqr}$ and also the standard deviation values (given in parentheses in Tables 4–7).

Table 4. Stability constants of the complexes formed between $L^0$ and $Ni^{2+}$, $Cu^{2+}$, $Zn^{2+}$ (25 °C, 1.0 M $Me_4NCl$), $Cd^{2+}$, and $Pb^{2+}$ (25 °C, 1.0 M $KNO_3$).

| | $\log K_{ML}$ | $\log K_{ML}{}^{H}$ | $\log K_{ML_2}$ | $\log K_{ML_2}{}^{H}$ |
|---|---|---|---|---|
| $Ni^{2+}$ | 5.63 (0.01) | 6.12 (0.06) | 3.99 (0.03) | 7.46 (0.05) |
| $Ni^{2+}$[a] | 5.58 | 5.4 | 3.83 | – |
| $Cu^{2+}$[b] | 8.30 | 5.01 | 6.35 | 6.59 |
| $Cu^{2+}$[a] | 7.64 | 5.07 | 5.41 | 6.74 |
| $Zn^{2+}$ | 4.28 (0.02) | 6.59 (0.04) | 2.97 (0.02) | 7.95 (0.05) |
| $Zn^{2+}$[a] | 4.12 | 6.5 | 3.41 | – |
| $Cd^{2+}$ | 4.25 (0.04) | 7.52 (0.02) | 3.73 (0.02) | 7.79 (0.03) |
| $Pb^{2+}$ | 4.20 (0.04) | 7.46 (0.03) | 3.01 (0.04) | 8.02 (0.08) |

[a] $I$ = 0.1 M $KNO_3$.[24] [b] $I$ = 1.0 M $Me_4NCl$.[23]

### *Complexes of L⁰*

The formation of complexes between the $L^0$ and $Mg^{2+}$ or $Ca^{2+}$ could not be detected by pH potentiometry up to a pH of around 10. This is probably due to the fact that the nitrogens of the two $NH_2$ groups do not coordinate to $Mg^{2+}$ or $Ca^{2+}$ and the binding of the phosphinate oxygen is very weak. The titration curves obtained in the presence of $Ni^{2+}$, $Cu^{2+}$, $Zn^{2+}$, $Cd^{2+}$, and $Pb^{2+}$ can be interpreted by assuming the formation of complexes ML and $ML_2$ and the protonated species MLH and $ML_2H$. The possible formation of hydroxo complexes was taken into consideration when calculating the stability constants by using the equilibrium constants known for the species $M(OH)^+$.[38] The stability constants of the complexes of $Ni^{2+}$, $Cu^{2+}$, and $Zn^{2+}$ determined by Kubiček et al. and in our laboratory are similar (Table 4). The $\log K_{ML}$ and $\log K_{ML_2}$ values are lower than those of the complexes formed with 1,3-diaminopropane ($L^5$). The stability constants ($\log K$) of the species ML, $ML_2$, and $ML_3$ formed, for example, between $Ni^{2+}$ and $Cd^{2+}$ and $L^5$ are 6.47, 4.43, and 1.2 and 4.50, 2.70, and 0.8, respectively.[36] The lower stabilities of the complexes of $L^0$ indicate that the phosphinate group does not play a role in the complexation. It is more probable that $L^0$ is coordinated to the two N donor atoms to form a six-membered chelate ring.[24] However, the ligand $L^5$ forms $ML_3$ species and the absence of the formation of 1:3 complexes with $L^0$ shows that some weak interaction may exist between the metal ion and the phosphinate group and the steric requirement of the $L^0$ is larger than that of $L^5$, which hinders the coordination of a third $L^0$ ligand.

The $K_{ML}{}^{H}$ and $K_{ML_2}{}^{H}$ protonation constants of the complexes are relatively large (Table 4), which suggests that the protonation occurs at one of the two $NH_2$ groups while the ligand $L^0$ is coordinated only through its other $NH_2$ group. The negatively charged phosphinate group may contribute to the stability of the protonated complex.

### *Complexes of L¹ and L²*

The ligands $L^1$ and $L^2$ possess two amine nitrogens, two carboxylate oxygens, and one phosphinate oxygen as donor atoms. The structure of $L^1$ and the asymmetric $L^2$ resemble the structure of ethylenediamine-*N*,*N*′-diacetate ($L^6$) and ethylenediamine-*N*,*N*-diacetate ($L^7$), with the difference that the latter do not contain a phosphinate moiety. For comparison, therefore, the diacetate derivatives of 1,3-diaminopropane would be more suitable, but unfortunately these ligands have not been studied to date. The titration data obtained for $L^1$ in the presence of $Mg^{2+}$, $Ca^{2+}$, $Ni^{2+}$, and $Cu^{2+}$ can be interpreted by assuming the formation of the species ML only, while $Zn^{2+}$, $Cd^{2+}$, and $Pb^{2+}$ form hydroxo complexes M(OH)L and very weak $ML_2$ complexes as well at a pH above 9. The stability constants are shown in Table 5. Ligand $L^1$ has been prepared earlier and the stability constant of its $Ni^{2+}$ complex, $\log K_{NiL}$ = 12.24, agrees well with the value found by us (Table 5).[17] The stability constants of the ML complexes formed with $L^1$ are somewhat lower than those formed with $L^6$ (the $\log K_{ML}$ values for the complexes of $L^6$ formed with $Mg^{2+}$, $Ni^{2+}$, $Zn^{2+}$, and $Cd^{2+}$ are 3.95, 13.65, 11.22, and 8.99, respectively).[36] The lower $\log K_{ML}$ values of the complexes can be interpreted as being due to the lower protonation constants of the ligand $L^1$ (the protonation constants for $L^6$ are 9.69, 6.72, 2.37, and 1.66).[36] Considering these findings, it is surprising that the stability constant $\log K_{ML}$ of the $Cu^{2+}$ complex of $L^1$ is higher than that of $CuL^6$ ($\log K_{CuL}$ = 16.2).[36] This unexpected result can not be interpreted by assuming participation of the phosphinate group in the complexation. It is more likely that the formation of two five-membered ($>NCH_2COO^-$) and a six-membered ($>NCH_2PO_2-CH_2N<$) chelate ring around the $Cu^{2+}$ ion leads to a more stable square-planar arrangement than the coordination of $L^6$, which involves the formation of three five-membered chelate rings. Similar results are known for the formation

 © 2007 Wiley-VCH Verlag GmbH & Co. KGaA, Weinheim 

Table 5. Stability constants of the complexes formed between the ligands $L^1$ and $L^2$ and $Mg^{2+}$, $Ca^{2+}$, $Cu^{2+}$, $Zn^{2+}$ (25 °C, 1.0 M $Me_4NCl$), $Cd^{2+}$, and $Pb^{2+}$ (25 °C, 0.1 M $KNO_3$).

| | $L^1$ | | $L^2$ | | | |
|---|---|---|---|---|---|---|
| $M^{2+}$ | $\log K_{ML}$ | $\log K_{M(OH)L}$ | $\log K_{ML}$ | $\log K_{ML}{}^{H}$ | $\log K_{M(OH)L}$ | $\log K_{ML_2}$ |
| $Mg^{2+}$ | 2.50 (0.05) | – | 3.98 (0.06) | 8.44 (0.05) | – | 3.00 (0.07) |
| $Ca^{2+}$ | 2.61 (0.02) | – | 4.62 (0.04) | 8.00 (0.03) | – | 2.69 (0.08) |
| $Ni^{2+}$ | 12.22 (0.03) | – | 12.89 (0.05) | 4.44 (0.09) | – | 2.80 (0.08) |
| $Cu^{2+}$ | 17.40[a] | – | 13.76 (0.07) | 5.21 (0.01) | –9.63 (0.07) | – |
| $Zn^{2+}$[b] | 9.82 (0.01) | –10.27 (0.02) | 10.37 (0.04) | 5.80 (0.01) | –10.80 (0.04) | – |
| $Cd^{2+}$[b,c] | 7.82 (0.01) | –11.40 (0.05) | 9.00 (0.04) | 6.50 (0.03) | –10.51 (0.05) | 3.61 (0.06) |
| $Pb^{2+}$[b,c] | 8.19 (0.03) | –10.87 (0.07) | 9.59 (0.03) | 7.32 (0.02) | –11.27 (0.03) | 2.87 (0.05) |

[a] Ref.[23] [b] The stability constants of $ML_2$ complexes formed with $L^1$ are as follows: $\log K_{ZnL_2}$ = 1.94 (0.06), $\log K_{CdL_2}$ = 2.47 (0.05), $\log K_{PbL_2}$ = 2.95 (0.04). [c] The studies with $Cd^{2+}$ and $Pb^{2+}$ were performed in 1.0 M $KNO_3$.

of $Cu^{2+}$ complexes with *N*,*N*′-bis(2-aminoethyl)dimethylenediamine ($\log K_{CuL}$ = 23.9) and triethylenetetramine ($\log K_{CuL}$ = 20.1).[36]

The structure and donor atoms of ligand $L^1$ and those of bis(*N*-methylsarcosinato)phosphinic acid, which was synthesized previously in our laboratory, are similar, although the stability constants of the complexes formed with $L^1$ are higher.[20,21] This difference is probably a result of the steric hindrance caused by the two methyl groups attached to the nitrogen donor atoms of the bis(*N*-methylsarcosinato)phosphinate ligand.

The titration data obtained for $L^2$ in the presence of the metal ions were interpreted by assuming the formation of the species ML, MLH, $ML_2$, and M(OH)L. The stability constants of ML complexes are generally higher than those of the complexes of $L^1$. The only exception is complex $CuL^2$, which exhibits much lower stability than $CuL^1$. This difference in the behavior of $Cu^{2+}$ complexes is understandable if we take into account the propensity $Cu^{2+}$ to form square-planar complexes. The other metal ions studied prefer octahedral (or some other) geometry. Due to its linear structure, $L^1$ forms a high stability square-planar complex with $Cu^{2+}$. The ligand $L^2$ can not occupy four coordination sites in one plane if the phosphinate is not involved in complexation. For metal ions other than $Cu^{2+}$, the coordination of the two nitrogen and two carboxylate oxygen donor atoms of $L^2$ is possible at four apices of an octahedron, which results in relatively high $\log K_{ML}$ values. The fourth coordination site of $CuL^2$ in the equatorial position is probably occupied by a water molecule as, in contrast to $CuL^1$, $CuL^2$ starts to hydrolyze at about pH 8.

All the metal ions except $Cu^{2+}$ and $Zn^{2+}$ form $ML_2$ complexes with $L^2$. The $\log K_{ML_2}$ values are much lower than those for ligand $L^7$ (the $\log K_{ML_2}$ values for the $ML_2$ complexes of $Ni^{2+}$ and $Cd^{2+}$ are 5.91 and 6.01, respectively).[36] The low $\log K_{ML_2}$ values indicate that the first ligand probably coordinates in the equatorial plane and hinders the coordination of the second ligand. As a result, the second ligand is coordinated through only two donor atoms for steric reasons.

### *Complexes of $L^3$ and $L^4$*

Ligands $L^3$ and $L^4$ are structurally similar. While the symmetric $L^4$ possesses two nitrogen, four carboxylate, and one phosphinate oxygen donor atoms, the asymmetric $L^3$ contains only three carboxylate groups. Because of its heptadentate nature, $L^4$ does not form $ML_2$ complexes, and the $ML_2$ species formed with hexadentate $L^3$ have very low stability ($Cu^{2+}$ does not even form such a complex). The $L^3$ ligands in the $ML_2$ complexes are probably coordinated through their imda groups and the coordination of two imda groups is more favorable than formation of the ML complex.

The titration data obtained for the ligand $L^3$ in the presence of metal ions can be interpreted by the formation of the complexes MLH, ML, M(OH)L, $ML_2$, and $ML_2H$. The calculated stability constants are presented in Table 6. The $\log K_{ML}$ values are significantly lower than those of the hexadentate edta (ethylenediamine-*N*,*N*,*N*′,*N*′-tetraacetate). The only exception is $CuL^3$, whose stability constant is similar to that of $Cu(edta)^{2-}$ ($\log K_{CuL}$ = 18.80).[36]

The $\log K_{ML}$ values of the complexes $CuL^3$ and $CuL^1$ are practically identical, which suggests that $L^3$ is coordinated to $Cu^{2+}$ through two nitrogen and two carboxylate oxygen donor atoms and that the third carboxylate (and phosphinate) group does not participate in the complexation. The protonation constant of the complex $CuL^3$ is very low, which indicates protonation of the free carboxylate. The protonation constants of the other complexes of $L^3$ are higher (particularly those of $MgL^3$ and $CaL^3$) as in these species the nitrogen atom of the glycinate is most likely protonated.

In an earlier study of complexes of the ligand $L^4$ with some divalent metal ions the formation of ML and MLH species was assumed.[21] The results of a recent, more detailed pH potentiometric titration study were interpreted by the formation of ML, MLH, $MLH_2$, and $M_2L$ species. The number of data points used for the calculations, which were obtained at three or four metal-to-ligand ratios, are given in parenthesis for the respective metals as follows: $Mg^{2+}$ (338), $Ca^{2+}$ (355), $Ni^{2+}$ (347), $Cu^{2+}$ (665), $Zn^{2+}$ (513), $Cd^{2+}$ (476), and $Pb^{2+}$ (493). The calculated stability constants as well as the data reported for the analogous propylenediamine-*N*,*N*,*N*′,*N*′-tetraacetate ($L^8$) are shown in Table 7. We have also determined the protonation constants of $L^8$ and found that at 25 °C in 1.0 M KCl the $\log K_i^H$ values are 10.50 (0.03), 8.17 (0.04), 2.78 (0.05), and 1.96 (0.05). These $\log K_i^H$ values are significantly higher than those of $L^4$

 © 2007 Wiley-VCH Verlag GmbH & Co. KGaA, Weinheim 

Table 6. Stability constants of the complexes formed between $L^3$ and $Mg^{2+}$, $Ca^{2+}$, $Cu^{2+}$, $Zn^{2+}$ (25 °C, 1.0 M $Me_4NCl$), $Cd^{2+}$, and $Pb^{2+}$ (25 °C, 0.1 M $KNO_3$).

| | $\log K_{ML}$ | $\log K_{ML}^{H}$ | $\log K_{M(OH)L}$ | $\log K_{ML_2}$ | $\log K_{ML_2}^{H}$ |
|---|---|---|---|---|---|
| $Mg^{2+}$ | 4.83 (0.04) | 7.40 (0.05) | – | 3.63 (0.04) | 8.97 (0.07) |
| $Ca^{2+}$ | 5.35 (0.04) | 7.66 (0.03) | – | 3.80 (0.05) | 9.02 (0.08) |
| $Cu^{2+}$ | 18.32 (0.25) | 1.75 (0.09) | – | – | – |
| $Zn^{2+}$ | 12.66 (0.01) | 3.47 (0.01) | –12.16 (0.04) | 1.90 (0.16) | – |
| $Cd^{2+}$ | 10.04 (0.03) | 5.11 (0.03) | –11.47 (0.04) | 2.44 (0.09) | – |
| $Pb^{2+}$ | 10.34 (0.03) | 5.60 (0.02) | –10.92 (0.04) | 2.77 (0.06) | – |

Table 7. Stability constants of the complexes of the ligands $L^4$ and $L^{8}$[a] formed with $Mg^{2+}$, $Ca^{2+}$, $Ni^{2+}$, $Cu^{2+}$, $Zn^{2+}$, $Cd^{2+}$, and $Pb^{2+}$. The data for $L^4$ were obtained at 25 °C, in 1.0 M $Me_4NCl$[b] and for $L^8$ at 20 °C, in 0.1 M $Me_4NCl$.

| | $L^4$ | | | | $L^{8}$[a] | |
|---|---|---|---|---|---|---|
| | $\log K_{ML}$ | $\log K_{ML}^{H}$ | $\log K_{MLH}^{H}$ | $\log K_{M_2L}$ | $\log K_{ML}$ | $\log K_{ML}^{H}$ |
| $Mg^{2+}$ | 7.65 (0.03) | 6.42 (0.04) | 4.28 (0.02) | 3.23 (0.03) | 6.21 | 7.30 |
| $Ca^{2+}$ | 7.66 (0.03) | 6.41 (0.02) | 4.28 (0.02) | 3.23 (0.03) | 7.28 | 6.34 |
| $Ni^{2+}$ | 17.77 (0.05) | 2.64 (0.07) | – | 3.30 (0.09) | 18.15 | 2.20 |
| $Cu^{2+}$ [b] | 19.30 | 2.80 | – | 3.70 | 18.92 | 2.20 |
| $Zn^{2+}$ | 15.94 (0.01) | 2.14 (0.01) | 1.96 (0.02) | 1.61 (0.05) | 15.26 | 2.50 |
| $Cd^{2+}$ [c] | 13.07 (0.01) | 3.16 (0.01) | 2.53 (0.02) | 3.00 (0.02) | 13.90 | 3.06 |
| $Pb^{2+}$ [c] | 11.29 (0.04) | 5.66 (0.05) | 2.26 (0.09) | 6.31 (0.04) | 13.78 | 3.86 |

[a] Propylenediamine-*N*,*N*,*N*′,*N*′-tetraacetate.[36] [b] Ref.[23] [c] The studies with $Cd^{2+}$ and $Pb^{2+}$ were performed in 1.0 M $KNO_3$.

(Table 3). In spite of the lower protonation constants, the stability constants of the complexes of $L^4$ are very similar or higher than those of $L^8$. The phosphinate oxygen is not coordinated directly to the metal ion and the high stability constants probably result from the higher negative charge of the ligand and the two coordinated imda groups, which pull the phosphinate closer to the metal ion. However, the complexes of smaller and larger metal ions ($Ni^{2+}$, $Cu^{2+}$, and $Zn^{2+}$ vs. $Cd^{2+}$and $Pb^{2+}$) behave differently, which is particularly evident when the stability constants are compared with those of the edta complexes. The $\log K_{ML}$ values for the edta complexes of $Zn^{2+}$ and $Pb^{2+}$ are 16.50 and 18.04, respectively, while ligand $L^4$ shows an unexpectedly high selectivity for $Zn^{2+}$ over $Pb^{2+}$ ($\log K_{ML}$ values of 15.94 and 11.29, respectively; Table 7). These results can be interpreted according to Hancock, who found that larger metal ions prefer five-membered chelate rings while smaller metal ions form high stability complexes with both five- and six-membered chelate rings.[39] In the dinuclear complexes formed with $L^4$ both metal ions are attached to an iminodiacetate group of the ligand, as was found for the $Cu^{2+}$ complexes by EPR spectroscopy.[23] The formation of dinuclear complexes was also unambiguously detected by pH potentiometry. Typical titration curves obtained in the presence of one and two equivalents of $Pb^{2+}$ are shown in Figure 6. Because of the strong competition between protons and $Pb^{2+}$ in the presence of one extra equivalent of $Pb^{2+}$, the buffer region observed at a 1:1 metal-to-ligand ratio disappears completely, which indicates the formation of dinuclear species in solution. The $K_{ML}^{H}$ protonation constants imply the protonation of the acetate group in the complexes of $Ni^{2+}$, $Cu^{2+}$, $Zn^{2+}$, and $Cd^{2+}$ while the protonation is more probable at a nitrogen in the complexes of $Mg^{2+}$, $Ca^{2+}$, and $Pb^{2+}$.

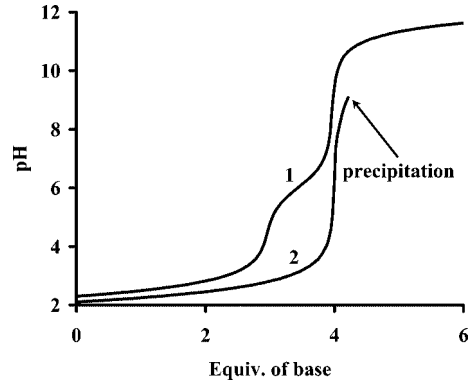


Figure 6. Titration curves of $5 \times 10^{-3}$ M solutions of $L^4$ in the presence of one (1) and two equivalents (2) of $Pb^{2+}$ ions ($I$ = 1.0 M $KNO_3$, $T$ = 25 °C).

## $^1$H NMR Spectra of the $Zn^{2+}$ Complexes

The formation of complexes between $Zn^{2+}$ and the ligands $L^1$, $L^2$, $L^3$, and $L^4$ results in a significant change in the $^1$H NMR spectra. The doublet signals of the phosphinate ($-[CH_2]_2PO_2^-$) methylene protons are shifted slightly to low field but their multiplicity does not change. The shift of the signals of the methylene protons is due to the inductive effect of the $Zn^{2+}$ ion. Upon formation of $ZnL^1$ the signal of the glycinate methylene protons is shifted to $\delta$ = 3.48 ppm but is not split. With a decrease of temperature from 50 °C to close to 0 °C the signals broaden significantly, however an AB multiplet pattern could not be observed even at this temperatures (Figure S8). Similarly, the signal of the glycinate methylene protons for $ZnL^3$ is not split by the formation of the complex and it appears at about $\delta$ = 3.30 ppm (pH 7.05) as a broad signal (Figure 8). The shift of the signals for the acetate methylene protons

 © 2007 Wiley-VCH Verlag GmbH & Co. KGaA, Weinheim 

of the iminodiacetate groups are usually larger and often appear in the form of AB multiplets (Figures 7 and 8). The formation of an AB multiplet indicates the inequivalence of the acetate methylene protons of the imda group, which is the result of the relatively long lifetime of the $Zn^{2+}$–N bond on the NMR timescale.[40] The chemical shifts of the non-equivalent A and B protons of $ZnL^2$ at pH 7.02 (Figure 7) are $\delta$ = 3.62 and 3.23 ppm, respectively. The exceptionally large H–C–H geminal coupling constant between these protons ($^2J_{H,H}$ = 17.3 Hz) suggests a dihedral angle of about 180° for the coordinated acetate arms (positions of the $CH_2$ H atoms towards the $p_z$ orbital of the carbon atom of $COO^-$).[41] The signals of the phosphinate methylene protons give a "pseudo-triplet" consisting of two overlapping doublets centered at $\delta$ = 2.99 and 2.96 ppm ($^2J_{P,H}$ = 8.6 and $^2J_{P,H}$ = 11.5 Hz). Since these signals are doublets due to coupling with phosphorus, the value of the geminal coupling constants for the $CH_2$ protons ($^2J_{H,H}$) can not be determined from the spectra (the values appear to be less than 0.8 Hz), which indicates a very weak interaction between the phosphinate oxygen and $Zn^{2+}$ in these complexes (presumably of an electrostatic nature). Figure 8 shows the $^1H$ NMR spectrum of $ZnL^3$ recorded at pH 7.05. The AB multiplet pattern of the iminodiacetate methylene protons appears at $\delta$ = 3.57 and 3.19 ppm (the geminal coupling constant is $^2J_{H,H}$ = 17.3 Hz), and the broad singlet at $\delta$ = 3.30 ppm is due to the glycinate methylene protons, while the doublets of the phosphinate methylene protons are centered at $\delta$ = 2.95 and 2.93 ppm ($^2J_{P,H}$ = 12.6 and $^2J_{P,H}$ = 13.3 Hz). For $ZnL^4$ the imda methylene protons appear as an AB multiplet ($^2J_{H,H}$ = 17.5 Hz), which shows the rigid structure of the complex (Figure S9). These carboxymethyl groups may occupy equivalent positions on the coordination polyhedron around $Zn^{2+}$. In summary, we can state that in complexes $ZnL^2$, $ZnL^3$, and $ZnL^4$ the $Zn^{2+}$–N bond of the coordinated imda fragment has a long lifetime while the $Zn^{2+}$–N bonds formed by the coordination of the $-NHCH_2COO^-$ group in $ZnL^1$ and $ZnL^3$ and the $-CH_2NH_2$ group in $ZnL^2$ appear to be more labile. These findings demonstrate that the lifetime of the $Zn^{2+}$–N bond is long on the NMR timescale as the coordination of the two carboxylate groups keeps the N atom in the vicinity of the $Zn^{2+}$ ion.

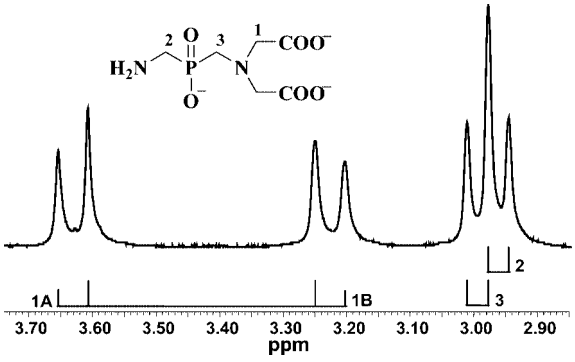


Figure 7. $^1H$ NMR spectrum of a 0.05 M $ZnL^2$ solution at 25 °C (pH 7.02).

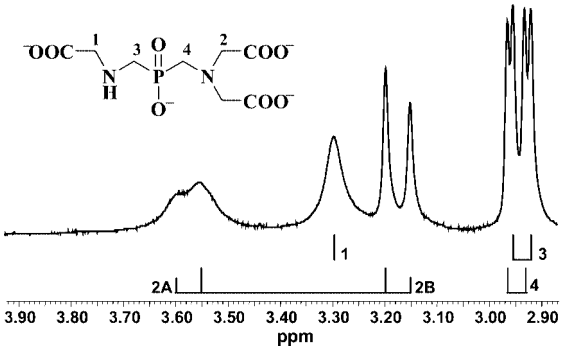


Figure 8. $^1H$ NMR spectrum of a 0.05 M $ZnL^3$ solution at 25 °C (pH 7.05).

## Conclusions

A new synthetic method has been developed that starts from inexpensive materials and gives reasonable yields of bis(aminomethyl)phosphinic acid as well as its derivatives containing the phosphinate group in a linker position. In addition, two consecutive Mannich reactions afford asymmetric bis(aminomethyl)phosphinic acids. These procedures can easily be scaled up and do not require inert atmosphere techniques. This synthetic method will likely be applicable to the synthesis of macrocyclic ligands that incorporate a bis(aminomethyl)phosphinic acid moiety in the macrocycle.

The basicities of the nitrogen atoms of the symmetric and asymmetric diacetate ($L^1$ and $L^2$) and tri- ($L^3$) and tetraacetate ($L^4$) derivatives of bis(aminomethyl)phosphinic acid ($L^0$) are lower than those of the analogous diaminopolycarboxylates mainly due to the electron-withdrawing effect of the phosphinate group. For a given ligand, the basicity of the nitrogen atoms decreases in the order primary > secondary > tertiary.

The stability constant of complexes formed between $L^0$, $L^1$, $L^2$, $L^3$, and $L^4$ and the metal ions $Mg^{2+}$, $Ca^{2+}$, $Ni^{2+}$, $Cu^{2+}$, $Zn^{2+}$, $Cd^{2+}$, and $Pb^{2+}$ increase with an increasing number of carboxylate groups of the ligands. The complexes formed with ligands $L^0$, $L^1$, $L^2$, and $L^3$ generally have lower stability constants than those of the analogous diaminopolycarboxylates, which indicates the unimportant role of the phosphinate group in the complexation. On the other hand, the presence of the phosphinate group has a significant effect on the complexation properties of $L^4$. In spite of the lower basicities of the two nitrogen atoms of $L^4$, it forms complexes of similar or higher stability with the smaller metal ions than the analogous 1,3-diaminopropane-*N*,*N*,*N*′,*N*′′-tetraacetate ($L^8$). $L^4$ also shows an unusually high selectivity for $Zn^{2+}$ over $Pb^{2+}$, unlike edta or $L^8$. Its stability constants are higher probably because of the higher charge of the ligand, and there is a strong electrostatic interaction between the phosphinate and the metal ion due to the coordination of both imda groups. Furthermore, $L^4$ shows a strong propensity for the formation of dinuclear $M_2L$ complexes, which indicates that in the presence of the

 © 2007 Wiley-VCH Verlag GmbH & Co. KGaA, Weinheim 

phosphinate group the two imda groups behave more independently than in the case of edta or L[8].

Of the two diacetate derivatives the asymmetric $L^2$ forms complexes of higher stability with the metal ions that prefer octahedral coordination. However, the metal ions that prefer square-planar coordination, like $Cu^{2+}$, form more stable complexes with the symmetric ligand $L^1$. The equatorial coordination of $L^1$ to $Cu^{2+}$ has been confirmed by X-ray crystallography in the solid state for $K[CuL^1]\cdot H_2O$, which has a polymer structure with hexagonal channels.

The ligands $L^2$ and $L^3$ form ML and $ML_2$ complexes but the stability constants of the $ML_2$ species are relatively low, probably due to the larger steric requirement of the phosphinate-containing ligands.

In the $^1H$ NMR spectra of the complexes of $Zn^{2+}$ formed with $L^1$, $L^2$, $L^3$, and $L^4$ the acetate methylene protons of the coordinated imda groups appear as an AB multiplet, thus indicating the long lifetime of the $Zn^{2+}$–N bond on the NMR timescale, while the signal of the glycinate methylene protons is a singlet.

## Experimental Section

**Synthesis of the Ligands:** All reagents and solvents used in this paper were commercially available and used without further purification, unless noted otherwise. The synthesis of ligands $L^0$, $L^1$, $L^2$, and $L^3$ is outlined in Schemes 1 and 2. Ligand $L^4$ was prepared following a previously published procedure.[20] A detailed description of the synthetic procedures for compounds **1**–**10** is included in the Supporting Information (SI). The purity of the ligands was controlled by multinuclear ($^1H$, $^{13}C$, and $^{31}P$) NMR spectroscopy; the spectra obtained together with the results of pH potentiometric studies indicated the suitable purity of the ligands (higher than 99%).

**X-ray Diffraction Studies:** Large crystals of approx. 1 cm × 5 mm × 3 mm were obtained from saturated solution after the purification of $L^3$. Equivalent amounts (0.3 mmol) of $H_3L^1$ and $CuCl_2$ stock solutions were mixed and the pH of the mixture was increased to about pH 7.5 by addition of KOH solution. The solution was evaporated to dryness and a weighed amount (0.1 mmol) of the dried complex was redissolved in doubly distilled water (0.5 mL) and placed into a narrow tube. Anhydrous ethanol was carefully layered on the aqueous phase and the tube was placed in a refrigerator at around 4 °C. Navy blue crystals suitable for X-ray crystallography grew in three weeks.

X-ray quality crystals of $[H_5L^3]Cl$ and $K[CuL^1]\cdot H_2O$ were mounted on a glass fiber using epoxy resin. Data were collected at 293(1) K with an Enraf Nonius MACH3 diffractometer using monochromated Mo-$K_\alpha$ radiation ($\lambda$ = 0.71073 Å) in the $\omega$–$2\theta$ mode. The absorption correction was made using psi scans. The structure was solved by direct methods with the SIR-92 software and refined on $F^2$ by full-matrix least-squares methods with the program SHELX-97.[42,43] All non-hydrogen atoms were refined anisotropically. Hydrogen atoms were included using a riding model. Some of the water hydrogen atoms were found in the difference electron density map while others were placed in calculated positions for strong hydrogen bonds. For the final refinement the O–H bond lengths were restrained at 0.85 Å but otherwise the coordinates of O–H hydrogen atoms were refined. Publication material was prepared with the WINGX-97 suite.[44] Some other details of data collection and structure determination are shown in Table 8.

Table 8. X-ray crystallographic data and structure refinement for $[H_5L^3]Cl$ and $[K(CuL^1)]\cdot H_2O$.

| | $[H_5L^3]Cl$ | $K[CuL^1]\cdot H_2O$ |
|---|---|---|
| Chemical formula | $C_8H_{16}ClN_2O_8P$ | $C_6H_{12}CuKN_2O_7P$ |
| Molecular weight | 334.65 | 357.79 |
| Crystal color and habit | colorless block | blue block |
| Crystal size [mm] | 0.45 × 0.4 × 0.36 | 0.55 × 0.35 × 0.27 |
| Crystal system | orthorhombic | trigonal |
| Space group | $Pn2_1a$ (no. 33) | $R\bar{3}$ (no. 148) |
| $a$ [Å] | 7.877(3) | 28.477(2) |
| $b$ [Å] | 13.564(3) | 28.477(2) |
| $c$ [Å] | 13.837(5) | 8.681(2) |
| $\alpha$ [°] | 90.00 | 90.00 |
| $\beta$ [°] | 90.00 | 90.00 |
| $\gamma$ [°] | 90.00 | 120.00 |
| $V$ [Å$^3$] | 1478.4(8) | 6096.6(15) |
| $Z$ | 4 | 18 |
| Temperature [K] | 293 | 293 |
| $D_{calcd.}$ [g cm$^{-3}$] | 1.504 | 1.754 |
| $\mu$ [mm$^{-1}$] | 0.403 | 2.062 |
| $F(000)$ | 696 | 3257 |
| $2\theta_{max}$ [°] | 50.4 | 52 |
| Index ranges | $-4 \le h \le 9$ | $-35 \le h \le 30$ |
| | $-2 \le k \le 15$ | $-15 \le k \le 35$ |
| | $0 \le l \le 15$ | $-10 \le l \le 5$ |
| Reflections collected | 1391 | 4275 |
| Unique reflections with $I > 2\sigma(I)$ | 1244 | 1731 |
| Completeness of data | 97.5 | 95.4 |
| Decay [%] | 2 | 0 |
| Parameters | 181 | 169 |
| Refinement method | Full-matrix least-squares on $F^2$ | |
| $R$[a] | 0.053 | 0.057 |
| $Rw$ (all data)[b] | 0.154 | 0.193 |
| GOF on $F^2$ | 1.292 | 1.082 |
| Largest diff. peak/hole [e Å$^{-3}$] | 0.583/–0.587 | 0.994/–0.924 |

[a] $R = \Sigma|F_o - F_c|/\Sigma F_o$. [b] $R_w = \{\Sigma[w(F_o^2 - F_c^2)^2]/\Sigma[w(F_o^2)^2]\}^{1/2}$, where $w = 1/[\sigma^2\{F_o^2 = +(aP)^2 + bP\}]$, $P = (F_o^2 + F_c^2)/3$; $a$ and $b$ are given in the Supporting Information.

CCDC-616444 (for $[H_5L^3]Cl$) and -616445 (for $K[CuL^1]\cdot H_2O$) contain the supplementary crystallographic data for this paper. These data can be obtained free of charge from The Cambridge Crystallographic Data Centre via www.ccdc.cam.ac.uk/data_request/cif.

**Materials and Preparation of Solutions:** Stock solutions of $MgCl_2$, $CaCl_2$, $NiCl_2$, $CuCl_2$, $ZnCl_2$, $Cd(NO_3)_2$, $Pb(NO_3)_2$, $Me_4NOH$, and KOH were prepared with the highest analytical grade reagents. The concentrations of the metal-ion solutions were determined by complexometric titration with standardized $Na_2H_2edta$ solution using eriochrome black T, murexide or xylenol orange indicator. Aqueous solutions of the ligands were prepared by weight and the concentrations were determined by pH potentiometric titrations.

**Equilibrium Studies:** The protonation constants of the ligands and stability constants of complexes were determined by pH potentiometric titration in vessels thermostatted at 25 °C. The ionic strength of the solutions was kept constant at 1.0 M $Me_4NCl$ or, in the case of $Cd^{2+}$ and $Pb^{2+}$, at 1.0 M $KNO_3$. Titration experiments were performed at two to four different metal-to-ligand ratios (1:1, 1:2, 1:3, and 2:1) by varying the ligand concentration in the range 0.0025–0.006 M. The titrations were performed with a Radiometer pHM 85 pH-meter equipped with pHG 211 glass and REF 201 Ag/AgCl electrodes and a Radiometer ABU 80 autoburette. The

 © 2007 Wiley-VCH Verlag GmbH & Co. KGaA, Weinheim 

samples (in general 15 mL) were stirred and argon was bubbled through the solutions. KH-phthalate (pH = 4.005) and borax (pH = 9.180) buffers were used to calibrate the pH meter. The $H^+$ ion concentration was obtained from the measured pH data by the method suggested by Irving et al. A 0.01 M HCl solution was titrated in 1.0 M $Me_4NCl$ (or 1.0 M $KNO_3$) with the $Me_4NOH$ (or KOH) solution used for the titrations.[45] The difference between the calculated and measured pH values was used to obtain the $H^+$ ion concentrations from the pH values measured in the titration experiments.[45] The ionic product of water ($pK_w$) was also calculated from the data obtained in the titration of the 0.01 M HCl solution. The $pK_w$ values obtained in 1.0 M $Me_4NCl$ and 1.0 M $KNO_3$ are 13.99 and 13.88, respectively. The protonation constants of the ligands and stability constants of the complexes were calculated from the titration data with the computer program PSEQUAD.[37]

**NMR Measurements:** The solutions of complexes were prepared by mixing equivalent amounts of the ligands and $ZnCl_2$ solutions. After evaporation of the $H_2O$ the solid material was dissolved in $D_2O$. The pD of the solutions was monitored by the addition of KOD or DCl (Cambridge Isotope Laboratories, Inc.) solutions and the readings were corrected for the deuterium isotope effect using the relationship pH = 0.4 + pD. Both one- and two-dimensional NMR spectra were recorded on a Bruker Avance DRX-360 spectrometer operating at 360.0 and at 90.5 MHz for $^1H$ and $^{13}C$, respectively. A Bruker DRX-500 spectrometer equipped with a Eurotherm variable temperature unit (±0.1 K), which was calibrated by the methanol method,[46] was used for variable-temperature measurements. Two-dimensional $^1H$-$^1H$ correlation spectra (COSY-45, DQF-COSY, NOESY, EXSY) were recorded using standard pulse sequences in direct mode with a 5-mm QNP probehead. $^{13}C$ NMR spectra were recorded in *J*-modulated or inverse gated decoupling mode. Data processing was performed with the Bruker WinNMR software package.

**Supporting Information** (see footnote on the first page of this article): Description of the synthetic procedures for compounds **1**–**10**; H-bond network in $[H_5L^3]Cl$ (Figure S1); data of the H-bond network in $[H_5L]Cl$ (Table S1); the H-bond network and long-range packing in $K[CuL^1]\cdot H_2O$ (Figure S2); the H-bond network in $K[CuL^1]\cdot H_2O$ (Table S2); $^1H$ and $^{31}P$ NMR titration curves for the ligands $L^0$, $L^1$, and $L^4$ (Figures S3–S7); temperature dependence of the $^1H$ NMR spectra of $ZnL^1$ (Figure S8); $^1H$-$^1H$ COSY spectrum of $ZnL^4$ (Figure S9).

## Acknowledgments

This work was supported by the Hungarian Science Foundation (OTKA T-038364 and OTKA T-043365) and performed within the framework of the EU COST Action D18. I. L. is grateful to the Hungarian Academy of Sciences for an István Széchenyi Fellowhip and A. B. is grateful for an Öveges József Fellowship from the Hungarian Research and Technology Foundation. The helpful discussions with Dr. Zoltán Kovács (University of Texas Southwestern Medical Center) are gratefully acknowledged.

[1] V. P. Kukhar, H. R. Hudson, *Aminophosphonic and Aminophosphinic Acids: Chemistry and Biological Activity* (Eds.: V. P. Kukhar, H. R. Hudson), John Wiley & Sons, New York, **2000**, p. 660.
[2] T. Kiss, E. Farkas, M. Jezowska-Bojczuk, H. Kozlowski, E. Kowalik, *J. Chem. Soc., Dalton Trans.* **1990**, 377–379.
[3] T. Kiss, M. Jezowska-Bojczuk, H. Kozlowski, P. Kafarski, K. Antczak, *J. Chem. Soc., Dalton Trans.* **1991**, 2275–2279.
[4] I. Lukes, K. Bazakas, P. Hermann, P. Vojtisek, *J. Chem. Soc., Dalton Trans.* **1992**, 939–944.
[5] P. Hermann, I. Lukes, *J. Chem. Soc., Dalton Trans.* **1995**, 2605–2610.
[6] a) J. Rohovec, I. Lukes, P. Vojtisek, I. Cisarova, P. Hermann, *J. Chem. Soc., Dalton Trans.* **1996**, 2685–2691; b) P. Hermann, I. Lukes, P. Vojtisek, I. Cisarova, *J. Chem. Soc., Dalton Trans.* **1995**, 2611–2618.
[7] G. B. Bates, E. Cole, D. Parker, R. Kataky, *J. Chem. Soc., Dalton Trans.* **1996**, 2693–2698.
[8] M. Lukas, M. Kyvala, P. Hermann, I. Lukes, D. Sanna, G. Micera, *J. Chem. Soc., Dalton Trans.* **2001**, 2850–2857.
[9] C. J. Broan, K. J. Jankowski, R. Kataky, D. Parker, A. M. Randall, A. Harrison, *J. Chem. Soc., Chem. Commun.* **1990**, 1739–1741.
[10] I. Lázár, A. D. Sherry, R. Ramasamy, E. Brücher, R. Király, *Inorg. Chem.* **1991**, *30*, 5016–5019.
[11] D. Parker, K. Pulukkody, T. J. Norman, A. Harrison, L. Royle, C. Walker, *J. Chem. Soc., Chem. Commun.* **1992**, 1441–1443.
[12] K. P. Pulukkody, T. J. Norman, D. Parker, L. Royle, C. J. Broan, *J. Chem. Soc., Perkin Trans. 2* **1993**, 605–620.
[13] K. Bazakas, I. Lukes, *J. Chem. Soc., Dalton Trans.* **1995**, 1133–1137.
[14] J. Rohovec, P. Vojtisek, P. Hermann, J. Ludvik, I. Lukes, *J. Chem. Soc., Dalton Trans.* **2000**, 141–148.
[15] J. Rohovec, M. Kyvala, P. Vojtisek, P. Hermann, I. Lukes, *Eur. J. Inorg. Chem.* **2000**, 195–203.
[16] M. A. Dhansay, P. W. Linder, R. G. Torrington, T. A. Modro, *J. Phys. Org. Chem.* **1990**, *3*, 248–254.
[17] M. A. Dhansay, P. W. Linder, *J. Coord. Chem.* **1993**, *28*, 133–145.
[18] A. Peyman, K. H. Budt, J. Spanig, B. Stowasser, D. Ruppert, *Tetrahedron Lett.* **1992**, *33*, 4549–4552.
[19] M. Collinsova, J. Jiracek, *Curr. Med. Chem.* **2000**, *7*, 629–647.
[20] T. R. Varga, *Synth. Commun.* **1997**, *27*, 2899–2903.
[21] T. R. Varga, R. Király, E. Brücher, V. Hietapelto, *ACH – Models in Chemistry* **1999**, *136*, 431–439.
[22] L. Xu, S. J. Rettig, C. Orvig, *Inorg. Chem.* **2001**, *40*, 3734–3738.
[23] N. V. Nagy, T. Szabó-Plánka, G. Tircsó, R. Király, Z. Árkosi, A. Rockenbauer, E. Brücher, *J. Inorg. Biochem.* **2004**, *98*, 1655–1666.
[24] V. Kubicek, P. Vojtisek, J. Rudovsky, P. Hermann, I. Lukes, *Dalton Trans.* **2003**, 3927–3938.
[25] S. Aime, C. Cavallotti, E. Gianolio, G. B. Giovenzana, G. Palmisano, M. Sisti, *Tetrahedron Lett.* **2002**, *43*, 8387–8389.
[26] B. Song, T. Storr, S. Liu, C. Orvig, *Inorg. Chem.* **2002**, *41*, 685–692.
[27] L. Maier, *J. Organomet. Chem.* **1979**, *178*, 157–169.
[28] A. I. Natchev, *Liebigs Ann. Chem.* **1988**, 861–867.
[29] L. Maier, M. J. Smith, *Phosphorus Sulfur Silicon Relat. Elem.* **1980**, *8*, 67–72.
[30] L. Maier, *Helv. Chim. Acta* **1967**, *50*, 1742–1746.
[31] Z. Jászberényi, A. Sour, É. Tóth, A. E. Merbach, *Dalton Trans.* **2005**, 2713–2719.
[32] Z. D. Matovic, G. Pelosi, S. Ianelli, G. Ponticelli, D. D. Radanovic, D. J. Radanovic, *Inorg. Chim. Acta* **1998**, *268*, 221–230 (ref. code: POWHOY in CSD).
[33] F. H. Allen, *Acta Crystallogr., Sect. B* **2002**, *58*, 380–388.
[34] S. H. Liu, E. Q. Fu, L. R. Chen, C. T. Wu, *Jiegou Huaxue (Chinese J. Struct. Chem.)* **1999**, *18*, 38–40 (ref. code: HOGSOL in CSD).
[35] N. D. Villanueva, M. Z. Chiang, J. R. Bocarsly, *Inorg. Chem.* **1998**, *37*, 685–692 (ref. code: PUQGIR in CSD).
[36] A. E. Martell, R. M. Smith, *Critical Stability Constants*, vol. 1–6, Plenum Press, New York, **1974**..
[37] L. Zékány, I. Nagypál, *Computational Methods for Determination of Formation Constants* (Ed.: D. J. Legett), Plenum Press, New York, **1985**, p. 291.

 © 2007 Wiley-VCH Verlag GmbH & Co. KGaA, Weinheim 

[38] C. F. Baes Jr, R. E. Mesmer, *The Hydrolysis of Cations*, John Wiley & Sons Inc., New York, **1976**, p. 512.
[39] R. D. Hancock, P. W. Wade, M. P. Ngwenya, A. S. de Sousa, K. V. Damu, *Inorg. Chem.* **1990**, *29*, 1968–1974.
[40] R. J. Day, C. N. Reilley, *Anal. Chem.* **1964**, *36*, 1073–1076.
[41] W. A. Thomas, *Prog. Nucl. Magn. Reson. Spectrosc.* **1997**, *30*, 183–207.
[42] A. Altomare, G. Cascarano, C. Giacovazzo, A. Guagliardi, *J. Appl. Crystallogr.* **1993**, *26*, 343–350.
[43] G. M. Sheldrick, *SHELX-97, A Program for Crystal Structure Refinement*; University of Göttingen, Germany, **1997**.
[44] L. J. Farrugia, *WINGX-97 system*, University of Glasgow, U. K., **1996**.
[45] H. M. Irving, M. G. Miles, L. D. Pettit, *Anal. Chim. Acta* **1967**, *38*, 475–488.
[46] A. L. Van Geet, *Anal. Chem.* **1970**, *42*, 679–680.

Received: September 24, 2006
Published Online: January 4, 2007

 © 2007 Wiley-VCH Verlag GmbH & Co. KGaA, Weinheim 

DOI: 10.1002/ejic.200600898

# Anion-Dependent Structural Diversity in Silver(I) Complexes of 4-Amino-3,5-diisopropyl-1,2,4-triazole

Guang Yang,*[a] Ying-Li Wang,[a] Jin-Peng Li,[a] Yu Zhu,[a] Shao-Min Wang,[a] Hong-Wei Hou,[a] Yao-Ting Fan,[a] and Seik Weng Ng[b]

**Keywords:** Silver / Triazole / Anions

Reactions of silver salts with 4-amino-3,5-diisopropyl-1,2,4-triazole (L) afford dinuclear complex $[Ag_2L_2(NO_3)_2(CH_3CN)]$, triangular complex $[Ag_3L_3](CF_3SO_3)_3$, and cyclic tetranuclear complexes $[Ag_4L_6](BF_4)_4$ and $[Ag_4L_6](ClO_4)_4$. On the basis of the X-ray analyses, anions are found to play an important role in determining the structures. Through coordination/noncoordination, anions can impart their influence on the coordination geometry of Ag atoms and the angles of N–Ag–N, which seems to be the main factor controlling the nuclearity of the reaction products in this system. $^1$H NMR and MS measurements suggest that these complexes probably retain their structural integrities in $CH_3CN$ solution.
(© Wiley-VCH Verlag GmbH & Co. KGaA, 69451 Weinheim, Germany, 2007)

## Introduction

With the coordination complexes of metals, the anions serve more than merely balancing the charges of a cationic species;[1–8] anions impart their influence on the structure of a given supramolecular system through coordinative bonding to metal ions or through weak interaction with organic ligands. Leob et al. reported that a molecular square, rectangle and an infinite helical chain have been obtained by the reaction of 4-(2-pyridyl)pyrimidine with various silver salts and the degree of aggregation is dependent on the anion used.[2] Dunbar et al. found that reaction of 3,6-di(2-pyridyl)-1,2,4,5-tetrazine with first-row transition metals could yield a molecular square and a pentagon with one anion accommodated in the cavities of the polygons. In this case, anions function as templates through anion-π interactions.[3] It seems promising that one can, to some extent, control or tune the structures of some supramolecules by simply changing anions. Obviously, before the use of anions can become a powerful tool for synthetic chemists in the construction of supramolecules, more work is needed towards understanding the mechanism of anion action.

Recent years have seen a rapidly increasing interest in the structures and properties of metal complexes of 1,2,4-triazole and its derivatives.[9] 1,2,4-Triazole is believed to unite the coordination geometries of both pyrazoles and imidazoles, and exhibit versatile coordination modes upon ligation to metals. 4-Amino-3,5-diisopropyl-1,2,4-triazole (4-$NH_2$-3,5-*i*$Pr_2$-tz) has been known for some time,[10] however, so far only few of its metal complexes have appeared in the literature to the best of our knowledge.[11] On the other hand, the less-crowded analogues with methyl or ethyl groups in place of the isopropyl groups are common ligands that furnish a large number of adducts with metal salts.[9] We report herewith the syntheses and crystal structures of four $Ag^I$-4-$NH_2$-3,5-*i*$Pr_2$-tz complexes; the structural outcomes of these adducts appear to be dependent on the nature of anions used.

[a] Department of Chemistry, Zhengzhou University, Zhengzhou, China 450001
E-mail: yang@zzu.edu.cn
[b] Department of Chemistry, University of Malaya, 50603, Kuala Lumpur, Malaysia

## Results and Discussion

### Structure of $[Ag_2(\mu_2\text{-}4\text{-}NH_2\text{-}3,5\text{-}i Pr_2\text{-}tz)_2(NO_3)_2(CH_3CN)]$ (1)

The product of stoichiometric quantities of $AgNO_3$ and 4-$NH_2$-3,5-*i*$Pr_2$-tz is the dinuclear complex **1**; the two Ag atoms are four-coordinate in different environments (Figure 1). The Ag(1) atom is coordinated by two triazole N atoms, two O atoms from the chelating nitrate, while the Ag(2) atom is coordinated by two triazole N atoms, one N atom of acetonitrile, and one O atom from the monodentate nitrate; each triazole bridges two Ag atoms (Scheme 1, a). The distance between Ag(1) and Ag(2) is 3.2867(5) Å, less than the sum of the van der Waals radii for the Ag atoms (3.44 Å). Complex **1** features a $(Ag–N–N–)_2$ ring having a boat conformation with the two Ag atoms forming the ring tips. Such a six-membered ring is also observed in other (triazole)silver complexes, e.g. $[Ag_2(\mu_2\text{-}tzH)_2(NO_3)_2]$[15] and $[Ag_2(\mu_2\text{-}4\text{-}NH_2\text{-}3,5\text{-}Me_2\text{-}tz)_2(CF_3COO)_2]$[16] (tzH = 1,2,4-triazole; 4-$NH_2$-3,5-$Me_2$-tz = 4-amino-3,5-dimethyl-1,2,4-triazole). A number of dinuclear pyrazolato complexes also have this feature.[17,18]

 © 2007 Wiley-VCH Verlag GmbH & Co. KGaA, Weinheim 

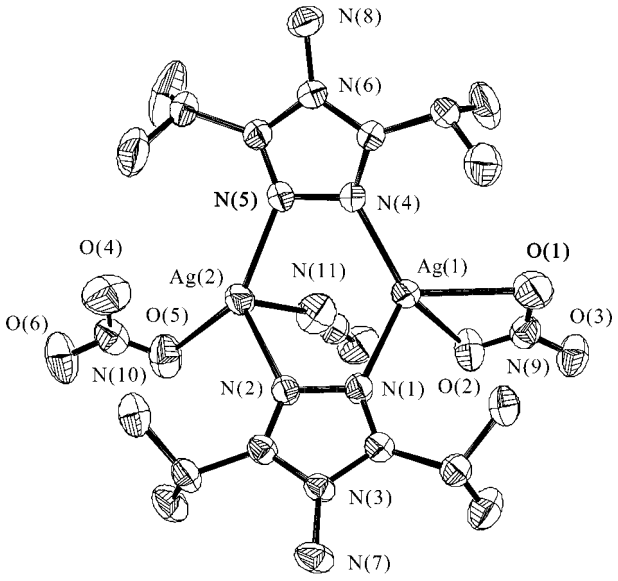


Figure 1. ORTEP diagram (at 35% probability) of the X-ray structure of $[Ag_2(\mu_2\text{-}4\text{-}NH_2\text{-}3,5\text{-}i\text{Pr}_2\text{-}tz)_2(NO_3)_2(CH_3CN)]$ (**1**). Selected distances [Å] and angles [°]: Ag(1)···Ag(2) 3.2867(5), Ag(1)–N(1) 2.282(3), Ag(1)–N(4) 2.213(3), Ag(1)–O(1) 2.567(4), Ag(1)–O(2) 2.471(3), Ag(2)–N(2) 2.325(3), Ag(2)–N(5) 2.275(3), Ag(2)–N(11) 2.526(5), Ag(2)–O(5) 2.507(4), N(1)–Ag(1)–N4 110.56(11), N(2)–Ag(2)–N(5) 109.88(11), N(2)–N(1)–Ag(1) 113.4(2), N(1)–N(2)–Ag(2) 115.0(2), N(5)–N(4)–Ag(1) 116.6(2), N(4)–N(5)–Ag(2) 113.0(2).

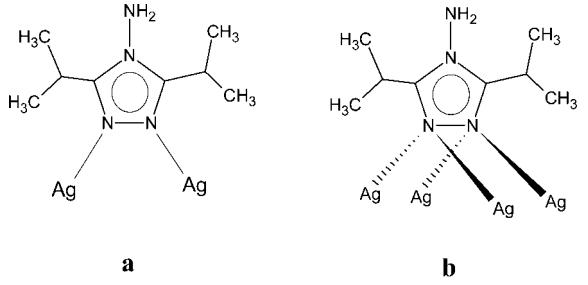


Scheme 1.

From the structure of **1**, we can see that nitrates participate in the distorted four-coordinate environment around the Ag atoms, the N–Ag–N angles of ca. 110° are critical for the formation of the six-membered ring. For a given system like this one containing silver(I) and an *exo*-bidentate ligand, other cyclic products or 1D complexes might be formed,[19] depending on the angles of N–Ag–N. It is thus possible to obtain other products by using weaker coordinating or noncoordinating anions, which would have an influence on the coordination geometry of Ag atoms and the angles of N–Ag–N.

### Structure of $[Ag_3(\mu_2\text{-}4\text{-}NH_2\text{-}3,5\text{-}i\text{Pr}_2\text{-}tz)_3](CF_3SO_3)_3$ (2)

Trifluoromethylsulfonates are weaker coordinating anions than nitrates owing to the electron-withdrawing $CF_3^-$ entity. In the $AgCF_3SO_3$ adduct, **2**, the $(Ag–N–N–)_n$ ring is a nine-membered, triangular-shaped ring. The Ag atoms are two-coordinate in a linear geometry, and the triazoles act as *exo*-bidentate bridging ligands (see parts a in Figure 2 and Scheme 1). The $(Ag–N–N–)_3$ ring is roughly planar, the mean deviation from the plane defined by three Ag atoms and six triazole N atoms being 0.0853 Å.

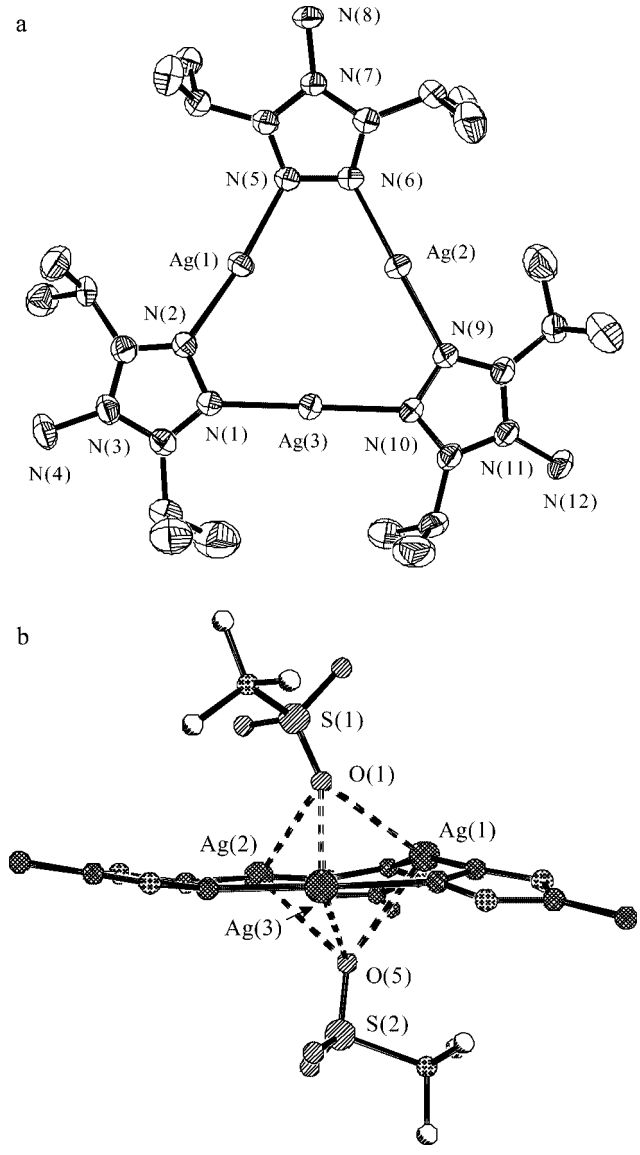


Figure 2. (a) ORTEP diagram (at 35% probability) of the X-ray structure of the cationic triangular $[Ag_3(\mu_2\text{-}4\text{-}NH_2\text{-}3,5\text{-}i\text{Pr}_2\text{-}tz)_3]^{3+}$ in **2**. (b) An edge-on-view with the two closest anions of $CF_3SO_3^-$. Selected distances [Å] and angles [°]: Ag(1)···Ag(2) 3.4316(9), Ag(1)···Ag(3) 3.4579(8), Ag(2)···Ag(3) 3.5573(8), Ag(1)–N(2) 2.132(3), Ag(1)–N(5) 2.129(3), Ag(2)–N(6) 2.159(3), Ag(2)–N(9) 2.168(3), Ag(3)–N(1) 2.165(3), Ag(3)–N(10) 2.168(3), N(5)–Ag(1)–N(2) 165.36(14), N(6)–Ag(2)–N(9) 176.02(14), N(1)–Ag(3)–N(10) 178.72(14), N(1)–N(2)–Ag(1) 121.5(2), N(6)–N(5)–Ag(1) 119.4(2), N(5)–N(6)–Ag(2) 117.8(2), N(10)–N(9)–Ag(2) 119.6(2), N(2)–N(1)–Ag(3) 116.3(2), N(9)–N(10)–Ag(3) 120.4(2).

Two of the three $CF_3SO_3^-$ anions are located on each side of the $(Ag–N–N–)_3$ ring with one O atom pointing to the centre of the triangle defined by three Ag atoms; contacts are O(1)···Ag(1) 2.668 Å, O(1)···Ag(2) 2.711 Å, O(1)···Ag(3) 2.742 Å, $O(5^i)$···Ag(1) 2.696 Å, $O(5^i)$···Ag(2)

 © 2007 Wiley-VCH Verlag GmbH & Co. KGaA, Weinheim 

2.736 Å, O(5$^{i}$)···Ag(3) 2.684 Å (symmetry code: *i*: –*x*, –*y* + 1, –*z* + 1) (Figure 2, b). Interestingly, while the above-mentioned two weakly coordinated $CF_3SO_3^-$ anions are in full occupancy in the X-ray structure, the third one, which has no contacts with Ag atoms, is disordered and has been refined as two parts with an occupancy factor of 0.5 each. Since the structure motif of the 1D chain may compete with the triangle when the angular units of ca. 60° (the triazole ligand) are combined with the ditopic linear units (the two-coordinate $Ag^I$ atoms),[19] the triangular arrangement observed in **2** is possibly the result of the pre-organization of the Ag atoms and triazoles through weak Ag···O interactions.

A number of neutral triangular silver-pyazolates have been known for a long time,[20] however, a triangular silver-triazole compound has not been reported; on the other hand several $Pd^{II}$, $Cu^{II}$-triazole compounds do adopt this triangular motif.[21]

### Structures of $[Ag_4(\mu_2\text{-}4\text{-}NH_2\text{-}3,5\text{-}i Pr_2\text{-}tz)_6](ClO_4)_4\cdot H_2O$ (3) and $[Ag_4(\mu_2\text{-}4\text{-}NH_2\text{-}3,5\text{-}i Pr_2\text{-}tz)_6](BF_4)_4$ (4)

Since two different anions ($NO_3^-$ and $CF_3SO_3^-$) give two different structures of silver complexes of 4-$NH_2$-3,5-*i*$Pr_2$-tz, the possibility exists that other structural arrangements may be discovered in this system when other anions with different shapes and different coordinating abilities are used. Perchlorate and tetrafluoroborate anions have been proven to be weaker or noncoordinate ligands for silver(I), therefore $AgClO_4$ and $AgBF_4$ were used in the reaction with 4-$NH_2$-3,5-*i*$Pr_2$-tz. X-ray analyses demonstrate that the resulting two new compounds **3** and **4** are structurally similar, however, different from **1** and **2**. They are tetranuclear compounds with the formula $Ag_4L_6X_4$, featuring a (Ag–N–N–)$_4$ ring (L = 4-$NH_2$-3,5-*i*$Pr_2$-tz; X = $ClO_4^-$, $BF_4^-$). Figure 3 shows the structure of compound **3**. In both complexes the four Ag atoms are approximately coplanar defining a rhombus with Ag–Ag distances in the range of 3.374(1)–3.444(1) Å in **3** and 3.303(1)–3.477(1) Å in **4**, Ag–Ag–Ag angles of 88.02(2)–88.77(2)° in **3** and 86.93(2)–93.00(2)° in **4**. The $Ag_4$ rhombus in **3** is actually a little butterfly-distorted while that in **4** is almost planar, as indicated by the mean deviations of Ag atoms from the best-fit $Ag_4$ planes being 0.2823 Å (for **3**) and 0.0460 Å (for **4**). For both, the four bridging triazole ligands alternate above and below the $Ag_4$-plane forming a (Ag–N–N–)$_4$ ring of roughly $S_4$ symmetry (Scheme 1, a). The best-fit planes of the opposite triazoles form dihedral angles of 46.0, 54.0° and 30.5, 53.9° for **3** and **4**, respectively. A similar (Ag–N–N–)$_4$ ring is observed in the pyrazole complex $[Ag(\mu_2\text{-}3,5\text{-}t Bu_2pz)]_4$,[22] however, the rings in **3** and **4** are flatter than that in $[Ag(\mu_2\text{-}3,5\text{-}t Bu_2pz)]_4$. Additionally, two triazole ligands are placed nearly orthogonally on each side of the $Ag_4$ plane with the Ag···N contacts falling in the range of 2.513(5)–2.845(5) Å (for **3**) and 2.428(5)–2.859(5) Å (for **4**). These values are much longer than the Ag–N distances of the (Ag–N–N–)$_4$ rings, thus these two triazoles are only weakly bound to Ag atoms in an uncommon $\eta^2,\eta^2,\mu_4$ fashion (Scheme 1, b).

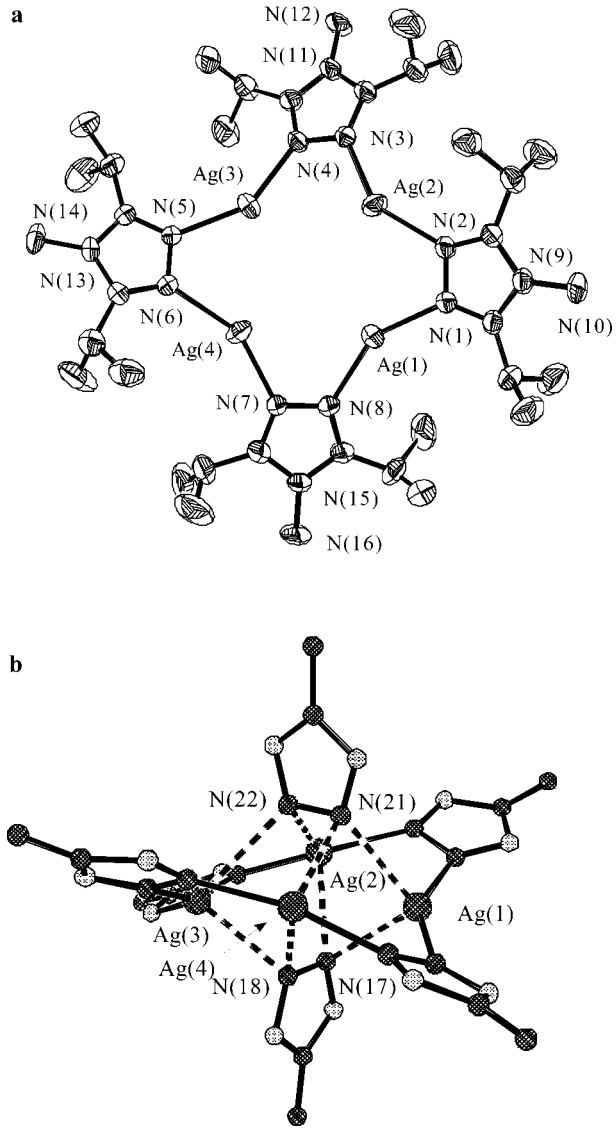


Figure 3. (a) ORTEP diagram (at 35% probability) of the X-ray structure of the cationic tetranuclear ring $[Ag_4(\mu_2\text{-}4\text{-}NH_2\text{-}3,5\text{-}i Pr_2\text{-}tz)_4]^{4+}$ in **3**. (b) A side view of $[Ag_4(\mu_2\text{-}4\text{-}NH_2\text{-}3,5\text{-}i Pr_2\text{-}tz)_6]^{4+}$ in **3** showing two weakly bound triazoles (the isopropyl groups are omitted for clarity). Selected distances [Å] and angles [°]: Ag(1)···Ag(2) 3.3754(9), Ag(3)···Ag(4) 3.3743(9), Ag(2)···Ag(3) 3.4436(9), Ag(1)···Ag(4) 3.4399(9), Ag(1)–N(1) 2.220(5), Ag(1)–N(8) 2.240(5), Ag(2)–N(3) 2.206(5), Ag(2)–N(2) 2.238(5), Ag(3)–N(5) 2.190(5), Ag(3)–N(4) 2.204(5), Ag(4)–N(7) 2.186(5), Ag(4)–N(6) 2.198(5), Ag(1)···N(17) 2.570(5), Ag(1)···N(21) 2.626(5), Ag(2)···N(22) 2.513(5), Ag(2)···N(17) 2.678(5), Ag(3)···N(18) 2.555(5), Ag(3)···N(22) 2.845(5), Ag(4)···N(21) 2.621(5), Ag(4)···N(18) 2.768(5), N(1)–Ag(1)–N(8) 148.80(18), N(3)–Ag(2)–N(2) 147.04(18), N(5)–Ag(3)–N(4) 148.91(18), N(7)–Ag(4)–N(6) 149.99(18).

Considering all the close contacts, the coordinate geometry of Ag atoms is better described as highly distorted tetrahedral. The N–Ag–N angles in (Ag–N–N–)$_4$ rings fall in the range of 146.4(2)–157.6(2)°. These values are less than those in (Ag–N–N–)$_3$ (ca. 180°), but larger than those in (Ag–N–N–)$_2$ (ca. 110°), which might account for the formation of the (Ag–N–N–)$_4$ ring in **3** and **4**. Very recently, Ag-triazole complexes with the same formula of $Ag_4L_6X_4$ have

 © 2007 Wiley-VCH Verlag GmbH & Co. KGaA, Weinheim 

been reported by Cheng et al.[23] Interestingly, their complexes could be considered as two dinuclear units (similar to that in **1**), which are further connected via two additional $N^1$,$N^2$-bridged triazoles and therefore are structurally different from those we report in this paper.

Hydrogen bonds are found in the crystal structures of the four complexes. In complexes **1**, **2** and **4**, some of the amino groups of the triazole ligands serve as donors and the O atoms and/or F atoms of anions as acceptors for the hydrogen bonds. In **3**, only one amino group [N(24)] is found to form a hydrogen bond with the lattice water molecule [O(17)]; the water molecule is further H-bonded with two O atoms [O(2), O(13)] from two perchlorates. Therefore, this water molecule acts as both acceptor and donor in the hydrogen bonds presenting in **3**. The distances of N(24)···O(17), O(17)···O(2) and O(17)···O(13) are 2.846(13), 2.977(15) and 2.763(19) Å, respectively. The hydrogen bonds observed here, although relatively weaker, might contribute to the stabilisation and packing of the molecules in the crystals.

### Solution Study

Free 4-$NH_2$-3,5-*i*$Pr_2$-tz exhibits resonances of *i*Pr protons at $\delta$ = 3.15 [m, H-C(Me)$_2$] and 1.27 (d, Me) ppm in $CD_3CN$; complexes **1**–**4** show only one set of slightly downfield-shifted resonances for the corresponding *i*Pr protons at 3.28, 1.32 (**1**); 3.25, 1.32 (**2**); 3.22, 1.29 (**3**); 3.21, 1.29 ppm (**4**), respectively. The resonances are interpreted in terms of the triazoles binding to $Ag^I$ atoms in a symmetric fashion in $CD_3CN$ solution.

The ESI-MS spectrum of **1** in $CH_3CN$/MeOH exhibits peaks at *m*/*z* = 275, 316 and 443, with the appropriate isotopic distributions, that correspond to [Ag(4-$NH_2$-3,5-*i*$Pr_2$-tz)]$^+$, [Ag(4-$NH_2$-3,5-*i*$Pr_2$-tz)($CH_3CN$)]$^+$ and [Ag(4-$NH_2$-3,5-*i*$Pr_2$-tz)$_2$]$^+$, respectively. No disilver species could be observed in this case. On the other hand, complex **2** exhibits peaks at *m*/*z* = 275, 316, 443, 699 and 1123 in its ESI MS spectrum in $CH_3CN$, which are assigned to [Ag(4-$NH_2$-3,5-*i*$Pr_2$-tz)]$^+$, [Ag(4-$NH_2$-3,5-*i*$Pr_2$-tz)($CH_3CN$)]$^+$, [Ag(4-$NH_2$-3,5-*i*$Pr_2$-tz)$_2$]$^+$, [$Ag_2$(4-$NH_2$-3,5-*i*$Pr_2$-tz)$_2$($CF_3SO_3$)]$^+$ and [$Ag_3$(4-$NH_2$-3,5-*i*$Pr_2$-tz)$_3$($CF_3SO_3$)$_2$]$^+$, respectively (Figure 4). The presence of trisilver species in the ESI MS spectrum of **2**, together with the fact that there was only one set of proton resonances in its $^1$H NMR spectrum, implies that the complex of **2** retains the integrity of its triangular nature in $CH_3CN$ solution. Besides the peaks at *m*/*z* = 275, 316 and 443, the tetranuclear complex **3** also exhibits weak peaks at *m*/*z* = 649, 1023, and 1397 in $CH_3CN$, which could be assigned to [$Ag_2$(4-$NH_2$-3,5-*i*$Pr_2$-tz)$_2$($ClO_4$)]$^+$, [$Ag_3$(4-$NH_2$-3,5-*i*$Pr_2$-tz)$_3$($ClO_4$)$_2$]$^+$ and [$Ag_4$(4-$NH_2$-3,5-*i*$Pr_2$-tz)$_4$($ClO_4$)$_3$]$^+$. The presence of $Ag_4L_4$ species instead of the crystallographically characterized $Ag_4L_6$ in the ESI MS spectrum of **3** indicates that two of the six triazoles are easily dissociated from the $Ag_4$ cluster under the conditions of MS measurement. This is in agreement with the crystal structure of **3**. However, since only one set of proton resonances is observed in the $^1$H NMR spectrum of **3**, we therefore propose that the complex **3** is a fluxional molecule. All the triazoles (the weakly bound and tightly bound ones) exchange their positions very quickly in $CH_3CN$ solution at room temperature.

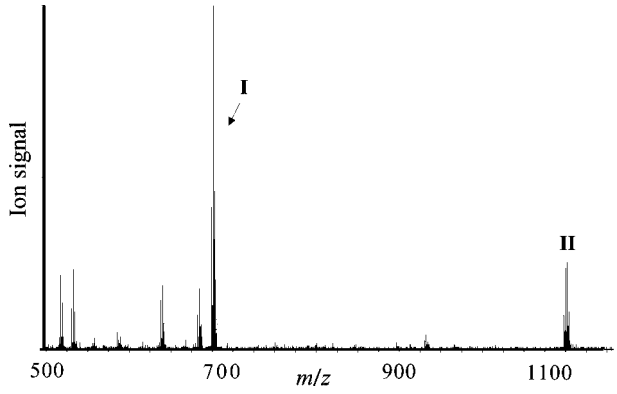


Figure 4. Electrospray mass spectrum of complex **2** in MeCN/MeOH. The ion signals displayed correspond to [$Ag_2$(4-$NH_2$-3,5-*i*$Pr_2$-tz)$_2$($CF_3SO_3$)]$^+$ (**I**) at *m*/*z* = 699, and [$Ag_3$(4-$NH_2$-3,5-*i*$Pr_2$-tz)$_3$($CF_3SO_3$)$_2$]$^+$ (**II**) at *m*/*z* = 1123.

## Conclusion

In this paper, we describe an interesting case of anion-dependent structural diversity. We found the reaction of $Ag^I$ salts with 4-amino-3,5-diisopropyl-1,2,4-triazole produce complexes of different nuclearity, dependent on the anions employed. The role of the anions consists of determining the coordination geometry of the Ag-centres, namely the N–Ag–N angles in the (Ag–N–N–)$_n$ rings. Furthermore, we also found that 4-amino-3,5-diisopropyl-1,2,4-triazole acts as an *exo*-bidentate N-ligand in a somewhat similar way as pyrazolates, although the former is a neutral species.

## Experimental Section

4-Amino-3,5-diisopropyl-1,2,4-triazole was prepared according to literature methods.[10] Other reagents were commercially available and used as received.

The CHN microanalyses were carried out with an ELEMENTAR vario EL elemental analyser. IR spectra (KBr pellets) were recorded with a Niclolet Impact 420 FT-IR spectrometer. $^1$H NMR spectra were recorded with a Bruker DPX-400 spectrometer (400 MHz). Positive ESI mass spectra were recorded with a Waters Q-Tof micro mass spectrometer.

### Syntheses

**[$Ag_2$($\mu_2$-4-$NH_2$-3,5-*i*$Pr_2$-tz)$_2$($NO_3$)$_2$($CH_3CN$)] (1):** A solution of $AgNO_3$ (0.1 mmol, 17 mg) in MeCN (2 mL) was mixed with a 2-mL ethanol solution of 4-$NH_2$-3,5-*i*$Pr_2$-tz (0.1 mmol, 17 mg). The resulting mixture was allowed to evaporate for one week to yield colourless crystals of **1** (30 mg), suitable for X-ray work. Yield: 42%. IR (KBr): $\tilde{\nu}$ = 3222 (m) ($NH_2$), 2974 (m) (*i*Pr), 1645 (w), 1518 (w), 1383 (s) ($NO_3^-$), 1110 (w), 1041 (w) cm$^{-1}$. $^1$H NMR ($CD_3CN$): $\delta$ = 1.32 (d, 12 H, Me), 3.28 [m, 2 H, H-C(Me)$_2$] ppm.

 © 2007 Wiley-VCH Verlag GmbH & Co. KGaA, Weinheim 

Table 1. Crystallographic data for **1**, **2**, **3** and **4**.

| | **1** | **2** | **3** | **4** |
|---|---|---|---|---|
| Formula | $C_{18}H_{35}Ag_2N_{11}O_6$ | $C_{27}H_{48}Ag_3F_9N_{12}O_9S_3$ | $C_{48}H_{98}Ag_4Cl_4N_{24}O_{17}$ | $C_{48}H_{96}Ag_4B_4F_{16}N_{24}$ |
| Molecular weight | 717.31 | 1275.56 | 1856.78 | 1788.21 |
| Crystal system | monoclinic | triclinic | monoclinic | monoclinic |
| Space group | $P2_1/c$ | $P\bar{1}$ | $P2_1/c$ | $P2_1/n$ |
| $a$ [Å] | 10.0878(9) | 11.519(3) | 24.305(5) | 11.996(2) |
| $b$ [Å] | 11.0001(10) | 14.550(3) | 24.296(5) | 22.899(5) |
| $c$ [Å] | 25.927(2) | 14.810(3) | 13.153(3) | 27.986(6) |
| $\alpha$ [°] | | 99.651(12) | | |
| $\beta$ [°] | 93.016(2) | 94.281(15) | 91.41(3) | 93.36(3) |
| $\gamma$ [°] | | 90.706(16) | | |
| $V$ [Å$^3$] | 2873.0(5) | 2439.4(9) | 7765(3) | 7675(3) |
| $Z$ | 4 | 2 | 4 | 4 |
| $T$ [K] | 298 | 298 | 298 | 298 |
| $\rho_{calcd.}$ [mg/m$^3$] | 1.658 | 1.737 | 1.588 | 1.548 |
| $\mu$ [mm$^{-1}$] | 1.414 | 1.411 | 1.205 | 1.093 |
| Reflections collected | 16960 | 23941 | 19892 | 20638 |
| Reflections | 6266 | 11031 | 11601 | 12343 |
| Unique | ($R_{int}$ = 0.0224) | ($R_{int}$ = 0.0170) | ($R_{int}$ = 0.0421) | ($R_{int}$ = 0.0414) |
| Final $R$ indices | $R1$ = 0.0363 | $R1$ = 0.0427 | $R1$ = 0.0507 | $R1$ = 0.0430 |
| [$I > 2\sigma(I)$] | $wR2$ = 0.0850 | $wR2$ = 0.1230 | $wR2$ = 0.1195 | $wR2$ = 0.0859 |
| $S$ | 1.024 | 1.087 | 1.022 | 0.852 |
| $\Delta\rho_{max}$ [e Å$^{-3}$] | 1.010 | 0.944 | 0.708 | 0.571 |

$C_{18}H_{35}Ag_2N_{11}O_6$ (717.31): calcd. C 30.21, H 4.90, N 21.54; found C 29.53, H 4.86, N 21.58.

**$[Ag_3(\mu_2\text{-}4\text{-}NH_2\text{-}3,5\text{-}i Pr_2\text{-}tz)_3](CF_3SO_3)_3$ (2):** A 2-mL aqueous solution of $AgCF_3SO_3$ (0.1 mmol, 26 mg) was mixed with a 2-mL ethanol solution of 4-$NH_2$-3,5-$i$Pr$_2$-tz (0.1 mmol, 17 mg). The resulting mixture was allowed to evaporate for several days to yield colourless crystals of **2** (76 mg). Yield: 60%. IR (KBr): $\tilde{\nu}$ = 3233 (m), 3122 (m) ($NH_2$), 2976 (s), 2935 (w) ($i$Pr), 1625 (w), 1517 (m), 1460 (m), 1251 (s) ($CF_3$), 1172 (s), 1109 (w), 1045 (s), 653 (s), 579 (w), 522 (m) cm$^{-1}$. $^1$H NMR ($CD_3CN$): $\delta$ = 1.32 (d, 12 H, Me), 3.25 [m, 2 H, H-C(Me)$_2$] ppm. $C_{27}H_{48}Ag_3F_9N_{12}O_9S_3$ (1275.56): calcd. C 25.47, H 3.77, N 13.21; found C 25.44, H 3.73, N 13.23.

**$[Ag_4(\mu_2\text{-}4\text{-}NH_2\text{-}3,5\text{-}i Pr_2\text{-}tz)_6](ClO_4)_4\cdot H_2O$ (3):** This compound was prepared as **2** using $AgClO_4$ instead of $AgCF_3SO_3$. Yield: 55% (based on ligand). IR (KBr): $\tilde{\nu}$ = 3232 (m), 3121 (m) ($NH_2$), 2975 (m), 2935 (w) ($i$Pr), 1662 (w), 1517 (m), 1461 (w), 1385 (w), 1145 (s), 1089 (s) ($ClO_4^-$), 631 (m), 549 (w) cm$^{-1}$. $^1$H NMR ($CD_3CN$): $\delta$ = 1.29 (d, 12 H, Me), 3.22 [m, 2 H, H-C(Me)$_2$] ppm. $C_{48}H_{98}Ag_4Cl_4N_{24}O_{17}$ (1856.78): calcd. C 31.14, H 5.30, N 18.16; found C 31.11, H 5.38, N 18.11.

**$[Ag_4(\mu_2\text{-}4\text{-}NH_2\text{-}3,5\text{-}i Pr_2\text{-}tz)_6](BF_4)_4$ (4):** This compound was prepared as **2** using $AgBF_4$ instead of $AgCF_3SO_3$. Yield: 53% (based on ligand). IR (KBr): $\tilde{\nu}$ = 3235 (m), 3122 (m) ($NH_2$), 2976 (s), 2935 (w), 1660 (w), 1518 (m), 1462 (m), 1385 (w), 1077 (s) ($BF_4^-$), 527 (w) cm$^{-1}$. $^1$H NMR ($CD_3CN$): $\delta$ = 1.29 (d, 12 H, Me), 3.21 [m, 2 H, H-C(Me)$_2$] ppm. $C_{48}H_{96}Ag_4B_4F_{16}N_{24}$ (1788.21): calcd. C 32.29, H 5.38, N 18.83; found C 32.04, H 5.62, N 18.75.

**X-ray Crystallography:** Diffraction intensities were collected with a Bruker SMART Apex CCD diffractometer (for **1**), Rikagu RAXIS-RAPID imaging plate diffractometer (for **2**) and a Rikagu RAXIS IV imaging plate diffractometer (for **3** and **4**), with graphite-monochromated Mo-$K_\alpha$ radiation. The data collected by CCD diffractometer were processed by *SAINT*;[12] while those collected by Rikagu diffractometers were corrected by "multi-scan" absorption corrections.[13] The structures were solved by direct methods and refined by least-squares on $F^2$ using the SHELXL program.[14] All non-hydrogen atoms were refined with anisotropic displacement parameters; hydrogen atoms were treated as riding. For complexes **2** and **4**, some of the anions and isopropyl groups have been split into two parts with an occupancy factor of 0.5. The lower completeness and lower redundancy of the data for **3** and **4** are probably caused by (a) the poorer quality of crystals of **3** and **4**; (b) the aged detector of the diffractometer used for collection of the intensities. The crystal data for the complexes reported here are summarised in Table 1.

CCDC-620543 to -620546 (for **1**–**4**) contain the supplementary crystallographic data for this paper. These data can be obtained free of charge from The Cambridge Crystallographic Data Centre via www.ccdc.cam.ac.uk/data_request/cif.

## Acknowledgments

This work was supported by the Scientific Research Foundation for Returned Overseas Chinese Scholars, State Education Ministry, China.

[1] B. L. Schottel, H. T. Chifotides, M. Shatruk, A. Chouai, L. M. Perez, J. Bacsa, K. R. Dunbar, *J. Am. Chem. Soc.* **2006**, *128*, 5895–5912; B. L. Schottel, J. Bacsa, K. R. Dunbar, *Chem. Commun.* **2005**, 46–47.
[2] D. A. Beauchamp, S. J. Loeb, *Chem. Commun.* **2002**, 2484–2485.
[3] C. S. Campos-Fernandez, B. L. Schottel, H. T. Chifotides, J. K. Bera, J. Bacsa, J. M. Koomen, D. H. Russell, K. R. Dunbar, *J. Am. Chem. Soc.* **2005**, *127*, 12909–12923.
[4] M. A. Withersby, A. J. Blake, N. R. Champness, P. Hubberstey, W. S. Li, M. Schröder, *Angew. Chem. Int. Ed. Engl.* **1997**, *36*, 2327–2327.
[5] O.-S. Jung, Y. J. Kim, Y.-A. Lee, K.-M. Park, S. S. Lee, *Inorg. Chem.* **2003**, *42*, 844–850.
[6] D. A. Beauchamp, S. J. Loeb, *Supramol. Chem.* **2005**, *17*, 617–622.
[7] L. Yi, X. Yang, T. Lu, P. Cheng, *Cryst. Growth Des.* **2005**, *5*, 1215–1219.
[8] G. Yang, S.-L. Zheng, X.-M. Chen, H. K. Lee, Z.-Y. Zhou, T. C. W. Mak, *Inorg. Chim. Acta* **2000**, *303*, 86–93.

 © 2007 Wiley-VCH Verlag GmbH & Co. KGaA, Weinheim 

[9] J. G. Haasnoot, *Coord. Chem. Rev.* **2000**, *200–202*, 131–185; J.-P. Zhang, S.-L. Zheng, X.-C. Huang, X.-M. Chen, *Angew. Chem. Int. Ed.* **2004**, *43*, 206–209; J.-P. Zhang, Y.-Y. Lin, X.-C. Huang, X.-M. Chen, *J. Am. Chem. Soc.* **2005**, *127*, 5495–5506; G. Yang, R. G. Raptis, *Chem. Commun.* **2004**, 2058–2059; K. Müller-Buschbaum, Y. Mokaddem, *Chem. Commun.* **2006**, 2060–2062; W. Ouellette, J. R. Galán-Mascarós, K. Dunbar, J. Zubieta, *Inorg. Chem.* **2006**, *45*, 1909–1911; L. Yi, B. Ding, B. Zhao, P. Cheng, D.-Z. Liao, S.-P. Yan, Z.-H. Jiang, *Inorg. Chem.* **2004**, *43*, 33–43; Y.-B. Dong, H.-Y. Wang, J.-P. Ma, R.-Q. Huang, M. D. Smith, *Cryst. Growth Des.* **2005**, *5*, 789–800.
[10] R. M. Herbst, J. A. Garrison, *J. Org. Chem.* **1953**, *18*, 872–877.
[11] W. Zheng, M. J. Heeg, C. H. Winter, *Angew. Chem. Int. Ed.* **2003**, *42*, 2761–2764.
[12] *SAINT*, Bruker AXS Inc., Madison, WI, **2000**.
[13] T. Higashi, *ABSCOR*, Rigaku Corporation, Tokyo, Japan, **1995**.
[14] *SHELXTL* version 6.10, Bruker AXS Inc., Madison, WI, **2000**.
[15] H. Schmidbaur, A. Mair, G. Müller, J. Lachmann, S. Gamper, *Z. Naturforsch., Teil B* **1991**, *46*, 912–918.
[16] J.-C. Liu, G.-C. Guo, H.-W. Ma, C. Yang, G.-W. Zhou, F.-K. Zheng, S.-H. Lin, M.-S. Wang, J.-S. Huang, *Chinese J. Struct. Chem.* **2002**, *21*, 371–373.
[17] G. La Monica, G. A. Ardizzoia, *Prog. Inorg. Chem.* **1997**, *46*, 151–238.
[18] A. P. Sadimenko, *Adv. Heterocycl. Chem.* **2001**, *80*, 157–240.
[19] S. Leininger, B. Olenyuk, P. J. Stang, *Chem. Rev.* **2000**, *100*, 853–908.
[20] N. Masciocchi, M. Moret, P. Cairati, A. Sironi, G. A. Ardizzoia, G. La Monica, *J. Am. Chem. Soc.* **1994**, *116*, 7668–7676; H. H. Murray, R. G. Raptis, J. P. Fackler Jr, *Inorg. Chem.* **1988**, *27*, 26–33; A. A. Mohamed, L. M. Pérez, J. P. Fackler Jr, *Inorg. Chim. Acta* **2005**, *358*, 1657–1662; H. V. R. Dias, S. A. Polach, Z. Wang, *J. Fluorine Chem.* **2000**, *103*, 163–169; F. Meyer, A. Jacobi, L. Zsolnai, *Chem. Ber./Recueil* **1997**, *130*, 1441–1447; K. Singh, J. R. Long, P. Stavropoulos, *J. Am. Chem. Soc.* **1997**, *119*, 2942–2943.
[21] S. R. Grap, L. G. Kuz'mina, O. Yu. Burtseva, M. A. Porai-Koshits, A. P. Kurbakova, I. A. Efimenko, *Russ. J. Inorg. Chem.* **1991**, *36*, 810–815; S. Ferrer, J. G. Haasnoot, J. Reedijk, E. Müller, M. B. Cingi, M. Lanfranchi, A. M. M. Lanfredi, J. Ribas, *Inorg. Chem.* **2000**, *39*, 1859–1867; J.-C. Liu, G.-C. Guo, J.-S. Huang, X.-Z. You, *Inorg. Chem.* **2003**, *42*, 235–243; W. Ouellette, M. H. Yu, C. J. O'Connor, D. Hagrman, J. Zubieta, *Angew. Chem. Int. Ed.* **2006**, *45*, 3497–3500; B. Ding, L. Yi, P. Cheng, D.-Z. Liao, S.-P. Yan, *Inorg. Chem.* **2006**, *45*, 5799–5803; Q.-G. Zhai, C.-Z. Lu, S.-M. Chen, X.-J. Xu, W.-B. Yang, *Cryst. Growth Des.* **2006**, *6*, 1393–1398; A. B. Lysenko, E. V. Govor, H. Krautscheid, K. V. Domasevitch, *Dalton Trans.* **2006**, 3772–3776.
[22] G. Yang, R. G. Raptis, *Inorg. Chim. Acta*, DOI: 10.1016/j.ica.2006.10.032.
[23] Y. Wang, L. Yi, X. Yang, B. Ding, P. Cheng, D.-Z. Liao, S.-P. Yan, *Inorg. Chem.* **2006**, *45*, 5822–5829.

Received: September 25, 2006
Published Online: January 5, 2007

 © 2007 Wiley-VCH Verlag GmbH & Co. KGaA, Weinheim 

DOI: 10.1002/ejic.200600913

# Group 11 Metal Complexes of the Mesocyclic Thioether Aminophosphonites [-$OC_{10}H_6$(μ-S)$C_{10}H_6O$-]$PNC_4H_8E$ (E = O, NMe)

**Benudhar Punji,[a] Joel T. Mague,[b] and Maravanji S. Balakrishna*[a]**

**Keywords:** Thioether-aminophosphonites / P,S ligands / Copper / Gold

Group 11 metal complexes of the mesocyclic thioether aminophosphonites [-$OC_{10}H_6$(μ-S)$C_{10}H_6O$-]$PNC_4H_8E$ {**2a**: E = O; **2b**: E = NMe; IUPAC names: 4-(dinaphtho[2,1-*d*:1′,2′-*g*][1,3,6,2]dioxathiaphosphocin-4-yl)morpholine (**2a**), 1-(dinaphtho[2,1-*d*:1′,2′-*g*][1,3,6,2]dioxathiaphosphocin-4-yl)-4-methylpiperazine (**2b**)} are reported. Thioether aminophosphonites **2a** and **2b** react with CuX (X = Cl, Br, and I) in a 1:1 molar ratio to give the tricoordinate, dimeric complexes [{[{-$OC_{10}H_6$(μ-S)$C_{10}H_6O$-}$PNC_4H_8E$-κ*P*]Cu(μ-X)}$_2$] (**4a**: E = O, X = Cl; **4b**: E = NMe, X = Cl; **5a**: E = O, X = Br; **5b**: E = NMe, X = Br; **6a**: E = O, X = I; **6b**: E = NMe, X = I), whereas with 2:1 molar ratios monomeric complexes of the type [{[-$OC_{10}H_6$(μ-S)$C_{10}H_6O$-]$PNC_4H_8O$-κ*P*}$_2$CuX] (**7a**: E = O, X = Cl; **7b**: E = NMe, X = Cl; **8a**: E = O, X = Br; **8b**: E = NMe, X = Br; **9a**: E = O, X = I; **9b**: E = NMe, X = I) are obtained in excellent yield. The P,S-chelated cationic complexes [{[-$OC_{10}H_6$(μ-S)$C_{10}H_6O$-]$PNC_4H_8E$-κ*P*,κ*S*}$_2$Cu]$BF_4$ (**10a**: E = O; **10b**: E = NMe) are obtained when **2a** and **2b** are treated with half an equivalent of [$(MeCN)_4$Cu]$BF_4$. Similarly, the silver complexes [{[{-$OC_{10}H_6$(μ-S)$C_{10}H_6O$-}$PNC_4H_8E$-κ*P*,κ*S*]-Ag$CF_3SO_3$}$_2$] (**11a**: E = O: **11b**: E = NMe) and [{[-$OC_{10}H_6$(μ-S)$C_{10}H_6O$-]$PNC_4H_8E$-κ*P*,κ*S*}Ag($PPh_3$)]$CF_3SO_3$ (**12a**: E = O; **12b**: E = NMe) are synthesized by the treatment of thioether aminophosphonites **2a** and **2b** with AgOTf and [Ag($PPh_3$)][OTf], respectively. Reactions of **2a** and **2b** with [AuCl($SMe_2$)] produce the simple monomeric gold(I) complexes [{[-$OC_{10}H_6$(μ-S)$C_{10}H_6O$-]$PNC_4H_8E$-κ*P*}AuCl] (**13a**: E = O; **13b**: E = NMe). The iodo derivatives [{[-$OC_{10}H_6$(μ-S)-$C_{10}H_6O$-]$PNC_4H_8E$-κ*P*}AuI] (**14a**: E = O; **14b**: E = NMe) are obtained by the halide-exchange reaction of **13a** and **13b** with CuI at room temperature. The structures of complexes **5a**, **7a**, **8a**, **13a**, **13b**, and **14a** are confirmed by single-crystal X-ray diffraction studies. In all of these complexes, the sulfur atom in the mesocyclic ring shows coordinative interaction towards the phosphorus atom, and in **5a**, **7a**, **8a**, and **14a** towards the metal center as well.
(© Wiley-VCH Verlag GmbH & Co. KGaA, 69451 Weinheim, Germany, 2007)

## Introduction

In recent years, complexes of mixed-donor ligands have been found to be more advantageous than those of ligands having only one type of donor atom because of their catalytic potential in various organic transformations.[1] In principle, those ligands containing donor atoms with different binding abilities are ideally suited to provide temporary coordinative saturation to the metal center via chelation until it is required to furnish an active site at the metal center prior to oxidative addition, an important step in homogeneous catalysis. Among various mixed-donor ligands of the type P,O,[2] P,N,[3] and P,S,[4] ligands combining phosphorus and sulfur centers are especially interesting. Both phosphorus and sulfur are excellent donor atoms for a wide range of metals while the low ionization energy of sulfur and the existence of several lone pairs of electrons (three in the case of a thiolate anion) offer the possibility of a rich sulfur-based chemistry of the complexes. Although, the coordination chemistry of P,S ligands with various transition metal derivatives has been well studied and some complexes have proved to be active catalysts,[5] P,S ligand chemistry with the group 11 metals is limited. Of the few complexes of mixed P,S donor ligands with group 11 metal derivatives that are known, some show excellent catalytic activity and offer interesting structural features (only P or both P and S coordination), and some bimetallic complexes show metallophilic interactions that can make them ideal candidates for luminescence studies.[6]

We recently reported the synthesis of the mesocyclic mixed P,S ligands **2a** and **2b**, which exhibit an interesting coordination behavior towards palladium and platinum derivatives that results in cationic, anionic (**3a**, **3b**), and neutral complexes (Scheme 1).[7] In all compounds, the sulfur atom present as part of an eight-membered thioether aminophosphonite ring system shows a coordinative interaction with phosphorus, which creates a pseudo trigonal bipyramidal (TBP) geometry at the phosphorus center. All the palladium complexes synthesized are promising catalysts for Suzuki cross-coupling reactions, with the anionic complexes **3a** and **3b** being particularly active (TONs of up to 92000). Since group 11 metal complexes of P,S ligands are

[a] Department of Chemistry, Indian Institute of Technology Bombay,
Powai, Mumbai 400076, India
Fax: +91-22-2576-7152, -2572-3480
E-mail: krishna@chem.iitb.ac.in
[b] Tulane University,
New Orleans, Lousiana 70118, USA

 © 2007 Wiley-VCH Verlag GmbH & Co. KGaA, Weinheim 

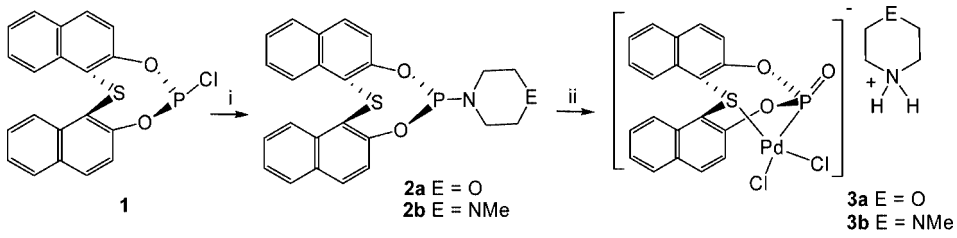


Scheme 1.

few in number, we sought to examine the reactivity of these thioether aminophosphonites with the group 11 metals. As part of our interest in organometallic chemistry[8] and catalytic investigations,[7,9] we report here on the reactivity of the mesocyclic thioether aminophosphonites **2a** and **2b** with group 11 metal centers as well as halide-exchange reactions of gold(I) complexes. X-ray structures of copper(I) (**5a**, **7a**, **8a**) and gold(I) (**13a**, **13b**, **14a**) complexes are also described.

## Results and Discussion

### Synthesis of Copper(I) Complexes

Treatment of thioether aminophosphonites **2a** and **2b** with one equivalent of CuX (X = Cl, Br, and I) in dichloromethane/acetonitrile mixtures leads to the formation of the halide-bridged dinuclear $Cu^{I}$ complexes [{[{-$OC_{10}H_6$(μ-S)-$C_{10}H_6O$-}$PNC_4H_8$E-κ*P*]Cu(μ-X)}$_2$] (**4a**: E = O, X = Cl; **4b**: E = NMe, X = Cl; **5a**: E = O, X = Br; **5b**: E = NMe, X = Br; **6a**: E = O, X = I; **6b**: E = NMe, X = I) in good yields, as shown in Scheme 2. Both the chloro derivatives (**4a** and **4b**) and iodo derivative **6b** precipitated from the reaction mixture as white insoluble solids, whereas the remaining complexes (**5a**, **5b**, and **6a**) crystallize from the mother liquor either at –25 °C or at room temperature. Most of the complexes (except for **4a** and **6b**) are soluble only in DMSO, which allows us to carry out spectroscopic studies. The $^{31}P$ NMR spectra of complexes **4b**, **5a**, **5b**, and **6a** show single resonances at $\delta$ = 114.4, 113.3, 110.5, and 110.4 ppm, respectively. In the $^{1}H$ NMR spectra of these complexes, two broad singlets are observed in the region $\delta$ = 2.49–3.71 ppm for the $CH_2$ protons of the morpholine and piperazine moieties. The mass spectrum of complex **5a** shows two peaks at *m*/*z* 576.0 and 496.0 for the ions corresponding to [$M^+$ – (**2a** + CuBr)] and [$M^+$ – (**2a** + $CuBr_2$)], respectively. Spectroscopic studies on complexes **4a** and **6b** could not be carried out because of their poor solubility in most organic solvents; however, their chemical compositions were established by elemental analysis. The molecular structure of complex **5a** was confirmed by a single-crystal X-ray diffraction study.

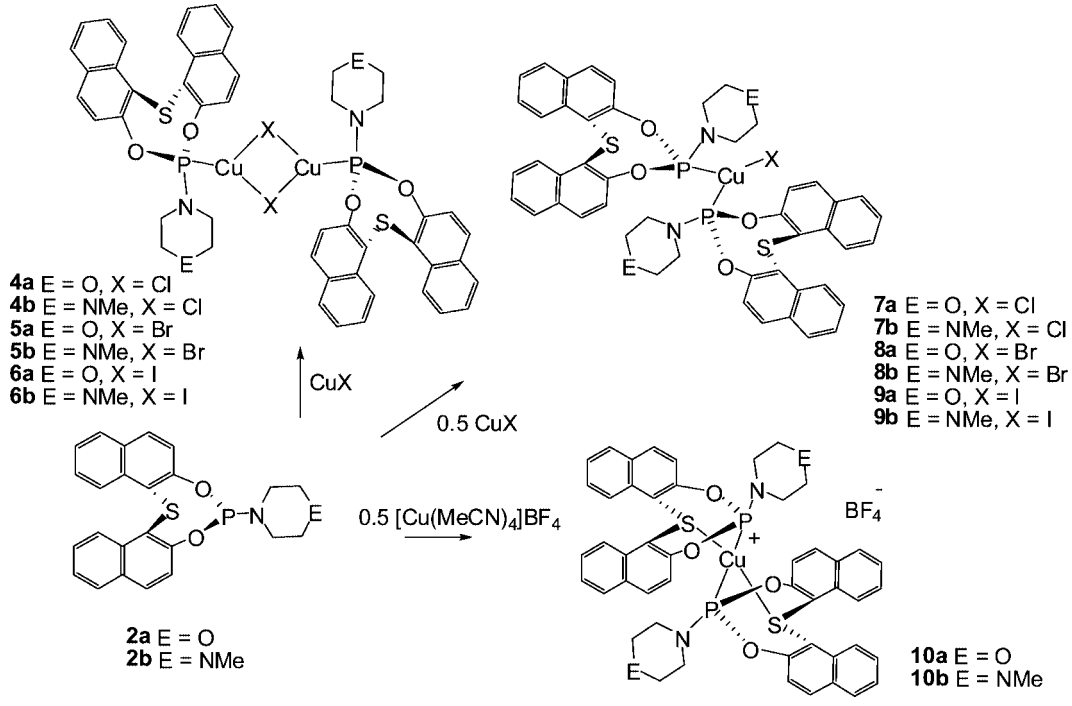


Scheme 2.

 © 2007 Wiley-VCH Verlag GmbH & Co. KGaA, Weinheim 

The reactions of **2a** with CuX (X = Cl, Br, and I) in a 2:1 ratio in dichloromethane afford the tricoordinate mononuclear complexes [{[-$OC_{10}H_6$(μ-S)$C_{10}H_6$O-]$PNC_4H_8$O-κ*P*}$_2$CuX] (**7a**: X = Cl; **8a**: X = Br; **9a**: X = I; Scheme 2). The $^{31}$P NMR spectra of complexes **7a**, **8a**, and **9a** show single resonances at $\delta$ = 115.8, 112.3, and 111.8 ppm, respectively. In the $^1$H NMR spectra of these complexes, two broad singlets are observed in the region $\delta$ = 3.29–3.66 ppm for the $CH_2$ protons of the morpholine moiety, although two distinct triplets ($\delta$ = 3.41 and 3.79 ppm) are observed for ligand **2a**. Similarly, the reactions of **2b** with half an equivalent of CuX (X = Cl, Br, and I) produce the mononuclear complexes [{[-$OC_{10}H_6$(μ-S)$C_{10}H_6$O-]$PNC_4H_8NCH_3$-κ*P*}$_2$CuX] (**7b**: X = Cl; **8b**: X = Br; **9b**: X = I) in good yields The chloro and bromo derivatives precipitate during the course of reaction while the iodo derivative crystallizes from the mother liquor. The $^{31}$P NMR spectra of complexes **7b**, **8b**, and **9b** show single resonances at $\delta$ = 112.2, 113.4, and 116.9 ppm, respectively. Further support for the structural composition of these complexes comes from their $^1$H NMR spectra and elemental analyses, while single-crystal X-ray structure determinations established the structures of complexes **7a** and **8a**.

Surprisingly, ligands **2a** and **2b** in the above complexes (**4a**–**9b**) are monodentate with only phosphorus coordination and do not form chelate rings with the P and S centers despite these centers being in close proximity [P···S nonbonding distances in **2a** and **2b** are 3.089(1) and 3.040(1) Å, respectively].[7] However, the P,S-chelated cationic complexes [{[-$OC_{10}H_6$(μ-S)$C_{10}H_6$O-]$PNC_4H_8$O-κ*P*,κ*S*}$_2$Cu]$BF_4$ (**10a**) and [{[-$OC_{10}H_6$(μ-S)$C_{10}H_6$O-]$PNC_4H_8NCH_3$-κ*P*,κ*S*}$_2$Cu]$BF_4$ (**10b**) are formed when ligands **2a** and **2b** are treated with half an equivalent of [Cu(MeCN)$_4$]$BF_4$, as shown in Scheme 2. Both these complexes are moderately stable in the solid state but decompose slowly in solution. The $^{31}$P NMR spectra of complexes **10a** and **10b** show single resonances at $\delta$ = 112.2 and 113.7 ppm, respectively. The mass spectrum of complex **10a** shows peaks at *m*/*z* 929.1 and 496.0 for the ions [$M^+$ – $BF_4$] and [$M^+$ – (**2a** + $BF_4$)], respectively. Similarly, for complex **10b** peaks are observed at *m*/*z* 955.2 and 509.1 for the ions [$M^+$ – $BF_4$] and [$M^+$ – (**2b** + $BF_4$)], respectively.

### Synthesis of Silver(I) Complexes

Treatment of thioether aminophosphonites **2a** and **2b** with one equivalent of AgOTf gives complexes with the composition [(**2a**)Ag(OTf)] (**11a**) and [(**2b**)Ag(OTf)] (**11b**), respectively. These complexes are highly light sensitive in solution, whereas they are moderately stable in the solid state. In the room-temperature $^{31}$P NMR spectrum of com-

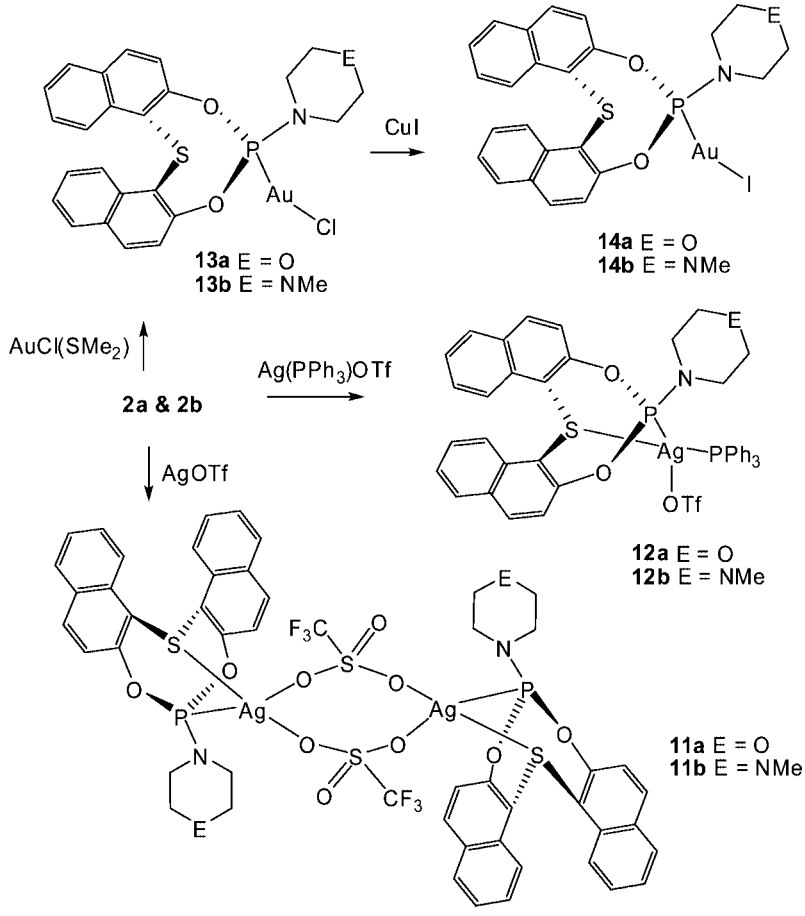


Scheme 3.

 © 2007 Wiley-VCH Verlag GmbH & Co. KGaA, Weinheim 

plex **11b**, two broad resonances separated by about 594 Hz are observed centered at $\delta$ = 123.3 ppm, while one broad singlet is observed at $\delta$ = 118.8 ppm for complex **11a**. Previous $^{31}$P NMR studies of phosphane and phosphite complexes of $Ag^I$ salts involving both coordinating and noncoordinating anions[6d,10] have shown the existence of ligand dissociation and/or exchange processes at or below room temperature that lead to broad resonances due to the loss of the expected $^1J_{Ag,P}$ couplings. Typically, the low-temperature limiting spectra consist of two doublets for each group of chemically equivalent phosphorus nuclei due to coupling with both $^{109}$Ag and $^{107}$Ag. Unfortunately, due to the poor solubility and stability of **11a** and **11b**, low-temperature NMR studies could not be carried out, so that while with **11a** there is probably only one phosphorus environment, in the case of **11b** it is not clear whether there are two different phosphorus environments or simply one where the dynamic process occurring is sufficiently slow that an average $^1J_{Ag,P}$ coupling is observed. Structural studies of the silver complexes of another P,S ligand [Fc(PPh$_2$)(SPh)] show a preference for a four-coordinate tetrahedral geometry.[6d] Although only tentatively because of the limited data available, we suggest that complexes **11a** and **11b** contain a chelating P,S ligand and are either monomeric with a bidentate trifluoromethanesulfonate or dinuclear with bridging trifluoromethanesulfonate ligands. Similarly, the P,S chelated complexes [{[-OC$_{10}$H$_6$(μ-S)C$_{10}$H$_6$O-]PNC$_4$H$_8$E-κ*P*,κ*S*}Ag(PPh$_3$)]CF$_3$SO$_3$ (**12a**: E = O; **12b**: E = NMe) can be synthesized by treatment of **2a** and **2b** with [Ag(PPh$_3$)][OTf] in a 1:1 molar ratio. The $^{31}$P NMR spectrum of complex **12a** shows two sets of broad doublets centered at $\delta$ = 123.9 and 9.7 ppm with $^1J_{Ag,P}$ coupling constants of about 512 and 394 Hz for coordinated **2a** and PPh$_3$, respectively. However, the $^{31}$P NMR spectrum of complex **12b** shows broad singlets at $\delta$ = 130.3 and 8.2 ppm for coordinated **2b** and PPh$_3$, respectively. In the mass spectra of complexes **12a** and **12b**, peaks are observed at *m*/*z* 803.1 and 816.9, respectively, for the ion [M$^+$ – CF$_3$SO$_3$]. By analogy with the complex [Ag(PPh$_3$){Fc(PPh$_2$)(SPh)}(OTf)],[6d] which contains a chelating P,S ligand and coordinated triflate, we propose that **12a** and **12b** are monomeric, four-coordinate species with chelating P,S ligands and monodentate trifluoromethanesulfonate. Further support for the composition of these complexes comes from their $^1$H NMR spectra and elemental analysis data (Scheme 3).

### Synthesis of Gold(I) Complexes

The reactions of thioether aminophosphonites **2a** and **2b** with [AuCl(SMe$_2$)] in dichloromethane afford the mononuclear P-coordinated complexes [{[-OC$_{10}$H$_6$(μ-S)C$_{10}$H$_6$O-]PNC$_4$H$_8$E-κ*P*}AuCl] (**13a**: E = O; **13b**: E = NMe). Both complexes are white, crystalline solids and are light sensitive while in solution. Attempt to synthesize three-coordinate gold complexes akin to [(PPh$_3$)$_2$AuCl][11] were unsuccessful and resulted in the formation of complexes **13a** and **13b**. This may be due to the bulkiness of the ligand, with the closeness of the sulfur atom to the gold center (vide infra) preventing another ligand from approaching the gold center. The $^{31}$P NMR spectra of complexes **13a** and **13b** show single resonances at $\delta$ = 113.1 and 115.3 ppm, respectively. When these complexes are treated with CuI in dichloromethane at room temperature, they undergo halide exchange to form the iodo derivatives [{[-OC$_{10}$H$_6$(μ-S)C$_{10}$H$_6$O-]PNC$_4$H$_8$E-κ*P*}AuI] (**14a**: E = O; **14b**: E = NMe). The $^{31}$P NMR spectra of complexes **14a** and **14b** show singlets at $\delta$ = 118.1 and 118.9 ppm, which are considerably deshielded compared to their chloro analogs. The molecular compositions of these complexes (**13a**,**b** and **14a**,**b**) were further confirmed by their $^1$H NMR spectra, elemental analysis data, and X-ray diffraction studies for complexes **13a**, **13b**, and **14a**. Other groups have also reported similar halogen-exchange reactions of gold complexes with KI at elevated temperature,[12] although halogen exchange of gold(I) complexes with CuI is not known in the literature.

### Crystals Structures of Complexes 5a, 7a, 8a, 13a, 13b, and 14a

Perspective views of the molecular structures of compounds **5a**, **7a**, **8a**, **13a**, **13b**, and **14a** with the atom-numbering schemes are shown in Figures 1, 2, 3, 4, 5, and 6, respectively. Selected bond lengths and bond angles for complexes **5a**, **7a**, and **8a** appear in Table 1, whereas those of complexes **13a**, **13b**, and **14a** are listed in Table 2. Crystal data and the details of the structure determinations are given in the Experimental Section.

In the molecular structure of complex **5a**, each of the copper centers is coordinated to one phosphorus center and two bromine atoms and exists as a centrosymmetric dimer. The morpholine rings adopt a chair conformation and the sulfur atoms connecting the naphthalene groups face towards the Cu$_2$Br$_2$ ring with a Cu···S separation of 3.0901(14) Å. As this is less than the sum of the van der Waals radii for copper and sulfur (3.20 Å),[13] there may be a weak Cu···S interaction. The backbones of two aminophosphonite ligands are in the staggered conformation, while the PCu(μ-Br)$_2$CuP unit is almost planar. Several trigonal planar dinuclear copper complexes of this type containing monophosphanes have been well characterized,[14] however those of aminophosphonites or phosphites are rare. The Cu–P bond length [2.171(1) Å] in complex **5a** is comparable with that in the tetrahedral copper complex of the monophosphite 4-nitro,2,6,7-trioxa-1-phosphabicyclo-[2.2.2]octane [Cu–P 2.1683(6) Å].[15] The Cu···Cu and Br···Br distances are 3.108 and 3.758 Å, respectively, indicating a possible weak Cu···Cu interaction. The core angles Cu–Br–Cu$_a$ [79.17(2)°] and Br–Cu–Br$_a$ [100.83(2)°] are significantly distorted from those of the above-mentioned monophosphite complex [Cu–Br–Cu$_a$ 75.183(12); Br–Cu–Br$_a$ 104.817(12)°].[15]

Interestingly, the sulfur atom also appears to show a weak coordinative interaction with phosphorus, as indi-

 © 2007 Wiley-VCH Verlag GmbH & Co. KGaA, Weinheim 

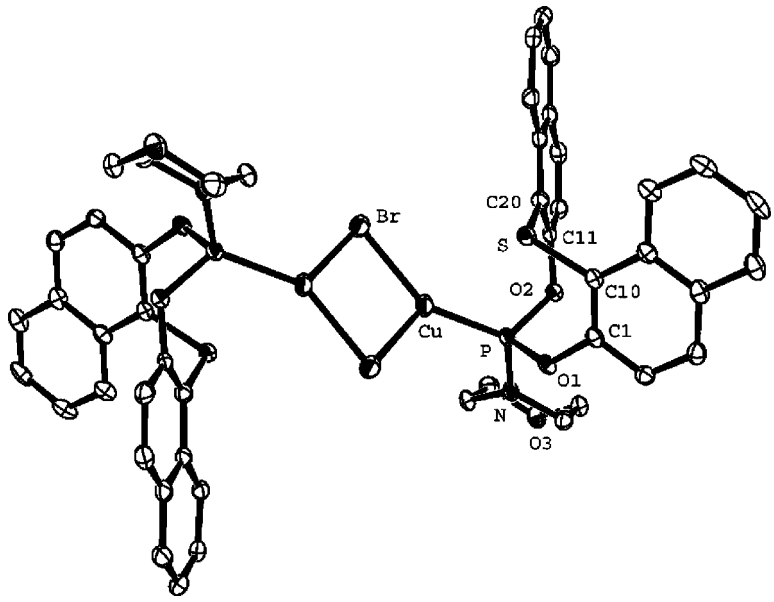


Figure 1. Molecular structure of **5a**. All hydrogen atoms have been omitted for clarity. Displacement ellipsoids are drawn at the 50% probability level.

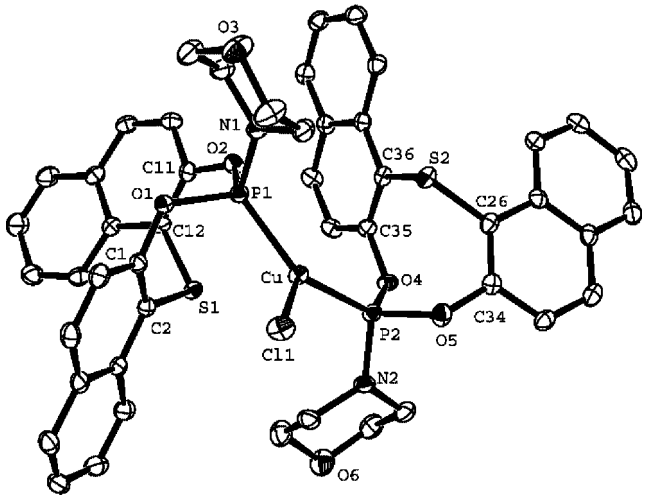


Figure 2. Molecular structure of **7a·$CH_2Cl_2$**. Solvent molecules and all hydrogen atoms have been omitted for clarity. Displacement ellipsoids are drawn at the 50% probability level.

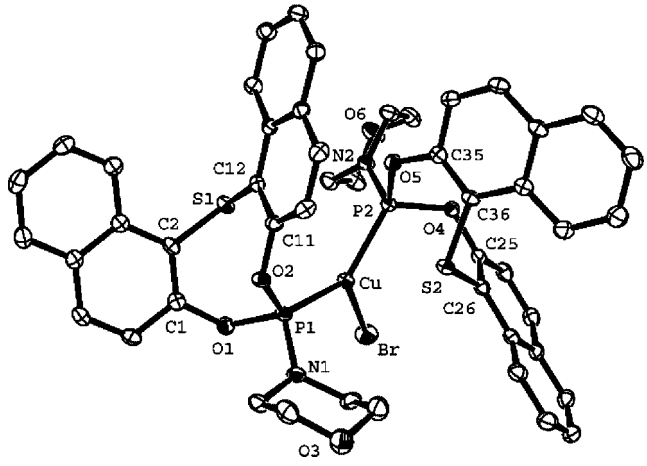


Figure 3. Molecular structure of **8a**. Solvent molecules and all hydrogen atoms have been omitted for clarity. Displacement ellipsoids are drawn at the 50% probability level.

cated by the P···S distance [3.098(2) Å]. This P···S distance is comparable to that observed in our previous report[7] and that of others[16] (see Table 3). While considerably greater than the sum of the covalent radii for sulfur and phosphorus (2.12 Å),[17] this distance is less than the sum of van der Waals radii (3.65 Å)[13] for these two elements. This interaction leads to the structural displacement of phosphorus from pyramidal to a pseudo TBP. The degree to which the TBP is approached can be seen from the axial S–P–R angle and can be quantified by the procedure of Holmes and coworkers.[18] In this procedure, the degree of displacement from pyramidal toward TBP can be calculated by noting how far the P···S distance departs from the sum of the van der Waals radii (3.65 Å) toward the sum of the covalent radii (2.12 Å). For complex **5a** the %TBP displacement is calculated to be 36.1% (Table 3).

The molecular structures of the chloride (**7a**) and bromide (**8a**) complexes are isomorphous; they crystallize in the monoclinic space group $P2_1/n$. In both structures the copper centers are coordinated through two aminophosphonite ligands and a halide ion and exist as monomers. The geometries around the copper center are almost planar. The Cu–P bond lengths in complex **7a** [Cu–P1 2.2062, Cu–P2 2.1897(7) Å] and complex **8a** [Cu–P1 2.1884(6), Cu–P2 2.2063(5) Å] are almost identical. As seen in complex **5a**, the sulfur atoms in complexes **7a** and **8a** show coordinative interaction towards the phosphorus centers [**7a**: S1–P1 3.088(1), S2–P2 3.199(1) Å; **8a**: S1–P1 3.1918(8), S2–P2 3.0874(8) Å], which forces the phosphorus centers to as-

 © 2007 Wiley-VCH Verlag GmbH & Co. KGaA, Weinheim 

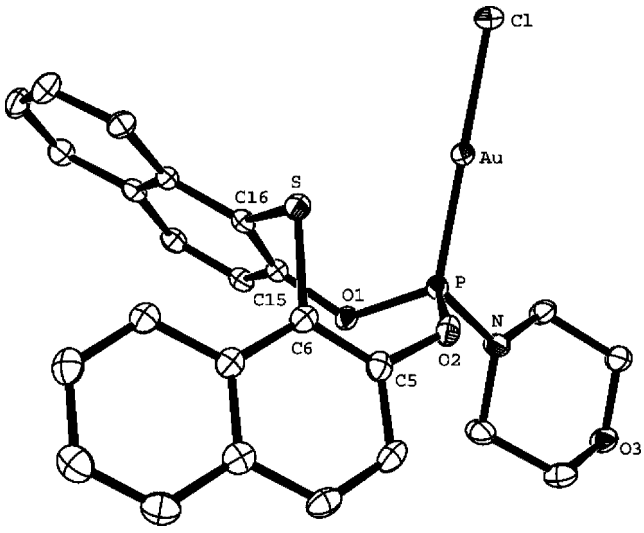


Figure 4. Molecular structure of **13a**. All hydrogen atoms have been omitted for clarity. Displacement ellipsoids are drawn at the 50% probability level.

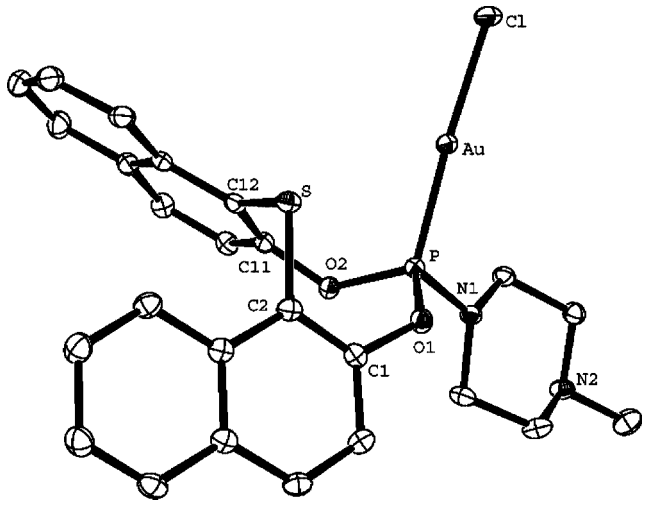


Figure 5. Molecular structure of **13b**. All hydrogen atoms have been omitted for clarity. Displacement ellipsoids are drawn at the 50% probability level.

sume pseudo TBP geometries (Table 3). Although the sulfur atoms in both complexes are pointing towards the copper center, no sulfur to copper bonding interaction is observed as the Cu···S separations are 0.17–0.42 Å greater than the sum of the van der Waals radii. The P1–Cu–P2 bond angle in bromo derivative **8a** [130.20(2)°] is slightly greater than that of the chloro complex **7a** [128.61(3)°]. Structural data are available for a number of three-coordinate complexes of

Table 1. Selected bond lengths [Å] and bond angles [°] for complexes **5a**, **7a**, and **8a**. Symmetry operation: _a: 0.5 – *x*, 0.5 + *y*, 0.5 – *z*.

| **5a** | | **7a** | | **8a** | |
|---|---|---|---|---|---|
| Br–Cu | 2.3828(9) | Cu–Cl1 | 2.2307(8) | Br–Cu | 2.3374(4) |
| Br–Cu_a | 2.4931(9) | Cu–P1 | 2.2062(8) | Cu–P1 | 2.1884(6) |
| Cu–P | 2.171(1) | Cu–P2 | 2.1897(7) | Cu–P2 | 2.2063(5) |
| S–C10 | 1.793(5) | S1–C2 | 1.774(2) | S1–C2 | 1.772(2) |
| S–C20 | 1.792(4) | S1–C12 | 1.768(2) | S1–C12 | 1.773(2) |
| P–O1 | 1.632(3) | P1–O2 | 1.636(2) | P1–O2 | 1.637(1) |
| P–O2 | 1.663(3) | P1–O1 | 1.650(2) | P1–O1 | 1.645(2) |
| P–N | 1.639(4) | P1–N1 | 1.631(2) | P1–N1 | 1.636(2) |
| Cu–Br–Cu_a | 79.17(2) | Cl1–Cu–P1 | 116.73(3) | Br–Cu–P1 | 114.13(2) |
| Br–Cu–P | 142.15(4) | Cl1–Cu–P2 | 114.66(3) | Br–Cu–P2 | 115.66(2) |
| Br–Cu–Br_a | 100.83(2) | P1–Cu–P2 | 128.61(3) | P1–Cu–P2 | 130.20(2) |
| Br_a–Cu–P | 116.96(4) | C2–S1–C12 | 102.2(1) | C2–S1–C12 | 102.68(9) |
| C10–S–C20 | 102.8(2) | C26–S2–C36 | 102.7(1) | C26–S2–C36 | 102.46(9) |
| Cu–P–O1 | 110.9(1) | Cu–P1–O1 | 114.07(7) | Cu–P1–O1 | 115.52(6) |
| Cu–P–O2 | 120.2(1) | Cu–P1–O2 | 124.53(7) | Cu–P1–O2 | 120.95(5) |
| | | Cu–P1–N1 | 113.80(8) | Cu–P1–N1 | 115.99(7) |

Table 2. Selected bond lengths [Å] and bond angles [°] for complexes **13a**, **13b**, and **14a**.

| **13a** | | **13b** | | **14a** | |
|---|---|---|---|---|---|
| Au–Cl | 2.2725(7) | Au–Cl | 2.2786(5) | Au–I | 2.5603(3) |
| Au–P | 2.2002(7) | Au–P | 2.2038(5) | Au–P | 2.2291(8) |
| S–C6 | 1.776(2) | S–C2 | 1.775(2) | S–C10 | 1.780(3) |
| S–C16 | 1.783(2) | S–C12 | 1.781(2) | S–C11 | 1.773(3) |
| P–O1 | 1.611(2) | P–O1 | 1.612(1) | P–O1 | 1.634(3) |
| P–O2 | 1.618(2) | P–O2 | 1.618(1) | P–O2 | 1.618(2) |
| P–N | 1.628(2) | P–N1 | 1.630(2) | P–N | 1.621(3) |
| Cl–Au–P | 178.73(2) | Cl–Au–P | 176.67(2) | I–Au–P | 170.41(2) |
| C6–S–C16 | 101.3(1) | C2–S–C12 | 100.54(8) | C10–S–C11 | 102.8(2) |
| Au–P–O1 | 117.17(7) | Au–P–O1 | 116.93(5) | Au–P–O1 | 111.36(9) |
| Au–P–O2 | 117.07(8) | Au–P–O2 | 117.57(5) | Au–P–O2 | 119.69(9) |
| Au–P–N | 114.44(8) | Au–P–N1 | 112.70(6) | Au–P–N | 117.8(1) |
| O1–P–O2 | 100.78(8) | O1–P–O2 | 101.12(7) | O1–P–O2 | 99.9(1) |

 © 2007 Wiley-VCH Verlag GmbH & Co. KGaA, Weinheim 

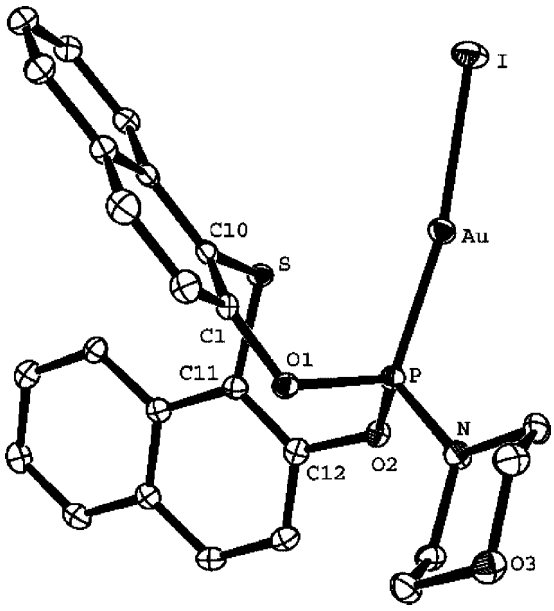


Figure 6. Molecular structure of **14a**. All hydrogen atoms have been omitted for clarity. Displacement ellipsoids are drawn at the 50% probability level.

the type $[CuX(PR_3)_2]$ containing tertiary phosphanes[14] but analogous complexes containing aminophosphonites or phosphites are not present in the literature.

Table 3. Comparison of P–S bond parameters and ring conformations obtained from the X-ray studies for cyclic phosphites (in increasing order of %TBP).

| Compound | *d*(P–S) /Å | % TBP[a] | S–P–$R_{ax}$ /° [b] | Ref. |
|---|---|---|---|---|
| 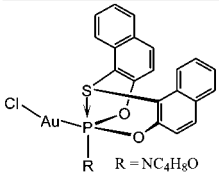 | 3.1820(8) | 30.6 | 166.94 | this work |
| 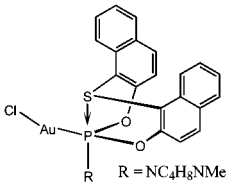 | 3.1673(7) | 31.5 | 168.78 | this work |
| 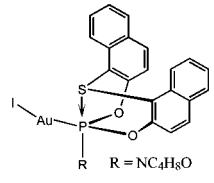 | 3.1566(13) | 32.2 | 168.22 | this work |
| 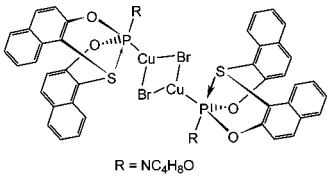 | 3.0978(17) | 36.1 | 168.34 | this work |

Table 3. *(continued)*

| Compound | *d*(P–S) /Å | % TBP[a] | S–P–$R_{ax}$ /° [b] | Ref. |
|---|---|---|---|---|
| 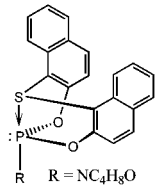 | 3.089(1) | 36.7 | 164.47 | [7] |
| 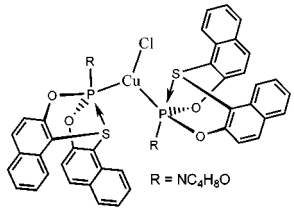 | 3.0879(10)<br>3.1992(10) | 36.7<br>29.5 | 168.24<br>162.11 | this work |
| 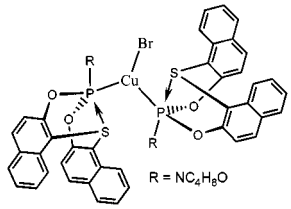 | 3.0874(8)<br>3.1918(8) | 36.8<br>29.9 | 168.79<br>162.75 | this work |
| 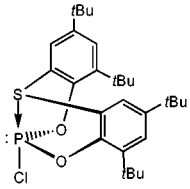 | 3.043(2) | 39.7 | 172.22(8) | [16a] |
| 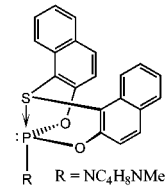 | 3.040(1) | 39.8 | 166.68 | [7] |
| 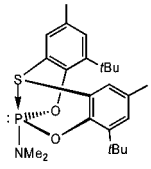 | 2.952(9) | 47.1 | 173.3(9) | [16a] |
| 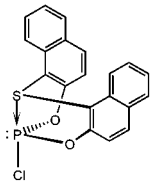 | 2.887(1) | 49.9 | 165.55 | [7] |
| 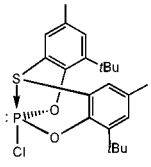 | 2.816(2) | 54.5 | 169.24(7) | [16b] |

[a] Percent geometrical displacement from a pyramid towards a TBP. [b] With reference to a TBP with sulfur in an axial site.

 © 2007 Wiley-VCH Verlag GmbH & Co. KGaA, Weinheim 

For complexes **13a** and **13b** the unit cell contains two molecules arranged in an anti-parallel manner with no intermolecular gold–gold interaction [a common feature among linear mononuclear gold(I) complexes][12b] present (Au···Au 5.017 and 5.511 Å, respectively). The Au–Cl [2.2725(7) and 2.2786(5) Å] and Au–P bond lengths [2.2002(7) and 2.2038(5) Å] in complexes **13a** and **13b** are comparable with those observed for [(PhO)$_3$PAuCl] [Au–Cl 2.273(5), Au–P 2.192(5) Å][19a] as well as for [{2,4,6-*t*Bu$_3$C$_6$H$_2$P=C(Cl)PPh$_2$}AuCl] [Au–Cl 2.283(1), Au–P 2.229(1) Å].[19b] The S···Au separations observed in **13a** and **13b** are 3.4876(6) and 3.4508(5) Å, respectively, which are comparable to the sum of the van der Waals radii for gold and sulfur (3.46 Å).[13] There is thus only a minimal Au···S interaction at best. As with the previous complexes, the sulfur atoms in **13a** and **13b** show a coordinative interaction towards phosphorus, with S···P separations of 3.1820(8) (for **13a**) and 3.1673(7) Å (for **13b**), which are markedly shorter than the sum of the van der Waals radii for sulfur and phosphorus (3.65 Å).[13] The geometries around gold are not quite linear, with Cl–Au–P bond angles of 178.73(2)° and 176.67(2)°, respectively, for **13a** and **13b**. Again, these are comparable with that found in [(PhO)$_3$PAuCl] [Cl–Au–P 178.5(2)°].[19a]

The molecular structure of complex **14a** is shown in Figure 6. The unit cell contains two molecules that are somewhat more closely packed (Au···Au 4.285 Å) than is observed for the chloro derivative **13a**. The Au–P bond [2.2291(8) Å] is somewhat longer than that found in the chloro derivative **13a**, possibly reflecting the increased size and polarizability of iodine compared with chlorine. The sulfur shows weak interactions with the gold and phosphorus centers since the S···Au and S···P distances [3.2976(9) and 3.1566(13) Å, respectively] are less than the sum of the van der Waals radii (S···Au 3.46 and S···P 3.65 Å).[13] There is a C–H···I contact of 3.075 Å with a C17–H17–I angle of 139.82°. As this distance lies between the outer limits proposed by Steiner[20] and by Brammer et al.[21] for C–H···I hydrogen bonds, and as the C–H···I angle is rather small, this is a weak interaction at best. The coordination about the gold center is less linear, with an I–Au–P bond angle of 170.41(2)°.

## Conclusions

Group 11 metal complexes of thioether aminophosphonite ligands have been synthesized. The aminophosphonites **2a** and **2b**, which contain a hemilabile thioether functionality, show versatile coordination properties. By choosing appropriate metal reagents and reaction conditions both mono- and chelating bidentate modes of coordination can be achieved. With copper halides both the mononuclear and dinuclear trigonal planar complexes are obtained. In these complexes only phosphorus takes part in coordination, leaving the sulfur center uncoordinated. The uncoordinated sulfur atom is pointing towards the metal center in all complexes, and in some cases there is an interaction with the metal. Structurally characterized dinuclear trigonal-planar copper complexes of phosphites or aminophosphonites of the type **5a** are rare. Silver and cationic copper complexes (**10a** and **10b**) have also been synthesized where sulfur is also involved in coordination. Gold complexes of both the thioether aminophosphonite ligands undergo halide exchange with copper(I) iodide to form the iodide derivatives in quantitative yield at room temperature. Generally, the halogen-exchange reactions of platinum metal derivatives are carried out at high temperature using an excess of NaI or KI. In all the complexes, the sulfur atom present in the eight-membered mesocycle shows a tendency to coordinate to phosphorus. As a consequence, the tricoordinate geometry of phosphorus is displaced towards TBP.

## Experimental Section

**Reagents and Technique:** All experimental manipulations were carried out under an atmosphere of dry nitrogen or argon using Schlenk techniques. Solvents were dried and distilled prior to use by conventional methods. The thioether aminophosphonites (**2a** and **2b**) were prepared as reported previously.[7] The metal precursors CuX (X = Cl and Br),[22] [Cu(MeCN)$_4$]BF$_4$,[23] [AuCl(SMe$_2$)][24] and [Ag(OTf)PPh$_3$][25] were prepared according to the published procedures. The $^1$H and $^{31}$P{$^1$H} NMR spectra ($\delta$ in ppm) were obtained with a Varian VXR 300 or VRX 400 spectrometer operating at frequencies of 300 or 400 ($^1$H) and 121 or 162 MHz ($^{31}$P), respectively. The spectra were recorded for $CDCl_3$ (or [D$_6$]DMSO or [D$_6$]acetone) solutions with $CDCl_3$ (or [D$_6$]-DMSO or [D$_6$]acetone) as an internal lock; TMS and 85% $H_3PO_4$ were used as internal and external standards for $^1$H and $^{31}$P{$^1$H} NMR, respectively. Positive shifts lie downfield of the standard in all cases. IR spectra were recorded with a Nicolet Impact 400 FTIR instrument as KBr disks. Microanalyses were carried out with a Carlo–Erba Model 1106 elemental analyzer. Q-Tof Micromass experiments were carried out with a Waters Q-Tof micro (YA-105). Melting points of all compounds were determined with a Veego melting point apparatus and are uncorrected.

**Synthesis of [{[{-OC$_{10}$H$_6$(μ-S)C$_{10}$H$_6$O-}PNC$_4$H$_8$O-κ*P*]Cu(μ-Cl)}$_2$] (4a):** A solution of **2a** (0.087 g, 0.202 mmol) in dichloromethane (10 mL) was added dropwise to a solution of CuCl (0.02 g, 0.202 mmol) in acetonitrile (4 mL) and the reaction mixture was stirred for 1 h. The white precipitate formed was filtered and dried under vacuum. Yield: 85% (0.091 g); m.p. 208 °C (dec.). C$_{48}$H$_{40}$Cl$_2$Cu$_2$N$_2$O$_6$P$_2$S$_2$ (1064.9): calcd. C 54.14, H 3.79, N 2.63, S 6.02; found C 54.08, H 3.75, N 2.61, S 5.97.

**Synthesis of [{[{-OC$_{10}$H$_6$(μ-S)C$_{10}$H$_6$O-}PNC$_4$H$_8$NCH$_3$-κ*P*]Cu(μ-Cl)}$_2$] (4b):** This compound was synthesized by a procedure similar to that for **4a** from **2b** (0.090 g, 0.202 mmol) and CuCl (0.02 g, 0.202 mmol). Yield: 83% (0.091 g); m.p. 186 °C (dec.). C$_{50}$H$_{46}$Cl$_2$Cu$_2$N$_4$O$_4$P$_2$S$_2$ (1091.0): calcd. C 55.04, H 4.25, N 5.14, S 5.88; found C 54.98, H 4.22, N 5.11, S 5.81. $^1$H NMR (400 MHz, [D$_6$]DMSO): $\delta$ = 8.62 (d, $^3J_{H,H}$ = 8.8 Hz, 4 H, ArH), 7.92 (d, $^3J_{H,H}$ = 8.4 Hz, 8 H, ArH), 7.22–7.65 (m, 12 H, ArH), 3.33 (br. s, 8 H, CH$_2$), 2.49 (br. s, 8 H, CH$_2$), 2.06 (s, 6 H, CH$_3$) ppm. $^{31}$P{$^1$H} NMR (162 MHz, [D$_6$]DMSO): $\delta$ = 114.4 (s) ppm.

**Synthesis of [{[{-OC$_{10}$H$_6$(μ-S)C$_{10}$H$_6$O-}PNC$_4$H$_8$O-κ*P*]Cu(μ-Br)}$_2$] (5a):** This compound was synthesized by a procedure similar to that for **4a** from **2a** (0.06 g, 0.139 mmol) and CuBr (0.02 g,

 © 2007 Wiley-VCH Verlag GmbH & Co. KGaA, Weinheim 

0.139 mmol). Yield: 85% (0.068 g); m.p. 228 °C (dec.). $C_{48}H_{40}Br_2Cu_2N_2O_6P_2S_2$ (1153.8): calcd. C 49.97, H 3.49, N 2.43, S 5.56; found C 49.92, H 3.45, N 2.41, S 5.51. $^1$H NMR (400 MHz, [D$_6$]DMSO): $\delta$ = 8.67 (d, $^3J_{H,H}$ = 8.4 Hz, 4 H, ArH), 7.97 (t, $^3J_{H,H}$ = 9.2 Hz, 8 H, ArH), 7.67 (d, $^3J_{H,H}$ = 6.8 Hz, 4 H, ArH), 7.51 (d, $^3J_{H,H}$ = 6.8 Hz, 4 H, ArH), 7.37 (d, $^3J_{H,H}$ = 8.4 Hz, 4 H, ArH), 3.71 (br. s, 8 H, $CH_2$), 3.37 (br. s, 8 H, $CH_2$) ppm. $^{31}$P{$^1$H} NMR (162 MHz, [D$_6$]DMSO): $\delta$ = 113.3 (s) ppm. MS (EI): *m*/*z* 576.0 [M$^+$ – (L + CuBr)], 496.0 [M$^+$ – (L + CuBr$_2$)].

**Synthesis of [{[{-OC$_{10}$H$_6$(μ-S)C$_{10}$H$_6$O-}PNC$_4$H$_8$NCH$_3$-κ*P*]Cu(μ-Br)}$_2$] (5b):** This compound was synthesized by a procedure similar to that for **4a** from **2b** (0.062 g, 0.139 mmol) and CuBr (0.02 g, 0.139 mmol). Yield: 83% (0.068 g); m.p. 196 °C (dec.). $C_{50}H_{46}Br_2Cu_2N_4O_4P_2S_2$ (1179.9): calcd. C 50.89, H 3.93, N 4.75, S 5.44; found C 50.82, H 3.89, N 4.71, S 5.42. $^1$H NMR (400 MHz, [D$_6$]DMSO): $\delta$ = 8.75 (d, $^3J_{H,H}$ = 8.8 Hz, 4 H, ArH), 7.05 (d, $^3J_{H,H}$ = 8.4 Hz, 4 H, ArH), 7.36–7.99 (m, 16 H, ArH), 3.37 (br. s, 8 H, $CH_2$), 2.50 (br. s, 8 H, $CH_2$), 2.29 (s, 6 H, $CH_3$) ppm. $^{31}$P{$^1$H} NMR (162 MHz, [D$_6$]DMSO): $\delta$ = 110.5 (s) ppm.

**Synthesis of [{[{-OC$_{10}$H$_6$(μ-S)C$_{10}$H$_6$O-}PNC$_4$H$_8$O-κ*P*]Cu(μ-I)}$_2$] (6a):** This compound was synthesized by a procedure similar to that for **4a** from **2a** (0.068 g, 0.157 mmol) and CuI (0.03 g, 0.157 mmol) and was stirred for 2 h. Yield: 89% (0.087 g); m.p. 232 °C (dec.). $C_{48}H_{40}Cu_2I_2N_2O_6P_2S_2$ (1247.8): calcd. C 46.20, H 3.23, N 2.24, S 5.14; found C 46.15, H 3.21, N 2.22, S 5.11. $^1$H NMR (400 MHz, [D$_6$]DMSO): $\delta$ = 8.67 (d, $^3J_{H,H}$ = 8.4 Hz, 4 H, ArH), 7.96 (t, $^3J_{H,H}$ = 7.2 Hz, 8 H, ArH), 7.39–7.67 (m, 12 H, ArH), 3.71 (br. s, 8 H, $CH_2$), 3.35 (br. s, 8 H, $CH_2$) ppm. $^{31}$P{$^1$H} NMR (162 MHz, [D$_6$]DMSO): $\delta$ = 110.4 (s) ppm.

**Synthesis of [{[{-OC$_{10}$H$_6$(μ-S)C$_{10}$H$_6$O-}PNC$_4$H$_8$NCH$_3$-κ*P*]Cu(μ-I)}$_2$] (6b):** This compound was synthesized by a procedure similar to that for **4a** from **2b** (0.07 g, 0.157 mmol) and CuI (0.03 g, 0.157 mmol). Yield: 88% (0.088 g); m.p. 192 °C (dec.). $C_{50}H_{46}Cu_2I_2N_4O_4P_2S_2$ (1273.9): calcd. C 47.14, H 3.64, N 4.39, S 5.03; found C 47.03, H 3.57, N 4.32, S 4.98.

**Synthesis of [{[-OC$_{10}$H$_6$(μ-S)C$_{10}$H$_6$O-]PNC$_4$H$_8$O-κ*P*}$_2$CuCl] (7a):** CuCl (0.01 g, 0.101 mmol) was added to a solution of **2a** (0.09 g, 0.207 mmol) in dichloromethane (12 mL) and the reaction mixture was stirred for 3 h. The colorless solution obtained was concentrated (5 mL) under vacuum and 1 mL of acetonitrile was added. Slow evaporation of the solution at room temperature gave colorless crystals of **7a**. Yield: 88% (0.093 g); m.p. 218 °C (dec.). $C_{48}H_{40}ClCuN_2O_6P_2S_2{\cdot}CH_2Cl_2$ (1050.9): calcd. C 56.00, H 4.03, N 2.67, S 6.10; found C 55.96, H 4.01, N 2.59, S 5.96. $^1$H NMR (400 MHz, [D$_6$]DMSO): $\delta$ = 8.60 (d, $^3J_{H,H}$ = 8.4 Hz, 4 H, ArH), 7.89 (d, $^3J_{H,H}$ = 8.8 Hz, 8 H, ArH), 7.62 (t, $^3J_{H,H}$ = 7.2 Hz, 4 H, ArH), 7.45 (t, $^3J_{H,H}$ = 7.2 Hz, 4 H, ArH), 7.23 (d, $^3J_{H,H}$ = 8.8 Hz, 4 H, ArH), 3.64 (br. s, 8 H, $CH_2$), 3.30 (br. s, 8 H, $CH_2$) ppm. $^{31}$P{$^1$H} NMR (121.4 MHz, [D$_6$]DMSO): $\delta$ = 115.8 (s) ppm.

**Synthesis of [{(-OC$_{10}$H$_6$(μ-S)C$_{10}$H$_6$O-)PNC$_4$H$_8$NCH$_3$-κ*P*}$_2$CuCl] (7b):** This compound was synthesized by a procedure similar to that for **7a** from **2b** (0.092 g, 0.207 mmol) and CuCl (0.01 g, 0.101 mmol). Yield: 87% (0.087 g); m.p. 188 °C (dec.). $C_{50}H_{46}ClCuN_4O_4P_2S_2$ (992.00): calcd. C 60.54, H 4.67, N 5.65, S 6.46; found C 60.49, H 4.63, N 5.61, S 6.40. $^1$H NMR (400 MHz, [D$_6$]DMSO): $\delta$ = 8.65 (d, $^3J_{H,H}$ = 7.6 Hz, 4 H, ArH), 7.95 (d, $^3J_{H,H}$ = 8.4 Hz, 8 H, ArH), 7.67 (t, $^3J_{H,H}$ = 8.4 Hz, 4 H, ArH), 7.50 (t, $^3J_{H,H}$ = 8.4 Hz, 4 H, ArH), 7.31 (d, $^3J_{H,H}$ = 7.6 Hz, 4 H, ArH), 3.33 (br. s, 8 H, $CH_2$), 2.50 (br. s, 8 H, $CH_2$), 2.08 (s, 6 H, $CH_3$) ppm. $^{31}$P{$^1$H} NMR (162 MHz, [D$_6$]DMSO): $\delta$ = 112.2 (s) ppm.

**Synthesis of [{[-OC$_{10}$H$_6$(μ-S)C$_{10}$H$_6$O-]PNC$_4$H$_8$O-κ*P*}$_2$CuBr] (8a):** This compound was synthesized by a procedure similar to that for **7a** from CuBr (0.015 g, 0.105 mmol) and **2a** (0.093 g, 0.214 mmol). Yield: 90% (0.104 g); m.p. 242 °C (dec.). $C_{48}H_{40}BrCuN_2O_6P_2S_2{\cdot}CH_2Cl_2$ (1095.30): calcd. C 53.73, H 3.87, N 2.56, S 5.86; found C 53.65, H 3.82, N 2.51, S 5.82. $^1$H NMR (400 MHz, [D$_6$]DMSO): $\delta$ = 8.71 (d, $^3J_{H,H}$ = 8.8 Hz, 4 H, ArH), 7.26–8.01 (m, 20 H, ArH), 3.65 (br. s, 8 H, $CH_2$), 3.31 (br. s, 8 H, $CH_2$) ppm. $^{31}$P{$^1$H} NMR (162 MHz, [D$_6$]DMSO): $\delta$ = 112.3 (s) ppm.

**Synthesis of [{[-OC$_{10}$H$_6$(μ-S)C$_{10}$H$_6$O-]PNC$_4$H$_8$NCH$_3$-κ*P*}$_2$CuBr] (8b):** This compound was synthesized by a procedure similar to that for **7a** from CuBr (0.015 g, 0.105 mmol) and **2b** (0.096 g, 0.214 mmol) and was stirred for 4 h. Yield: 85% (0.092 g); m.p. 196 °C (dec.). $C_{50}H_{46}BrCuN_4O_4P_2S_2$ (1036.5): calcd. C 57.94, H 4.47, N 5.41, S 6.19; found C 57.89, H 4.41, N 5.36, S 6.10. $^1$H NMR (400 MHz, [D$_6$]DMSO): $\delta$ = 8.63 (d, $^3J_{H,H}$ = 8.4 Hz, 4 H, ArH), 7.92 (d, $^3J_{H,H}$ = 8.8 Hz, 8 H, ArH), 7.33–7.66 (m, 12 H, ArH), 3.34 (br. s, 8 H, $CH_2$), 2.52 (br. s, 8 H, $CH_2$), 2.09 (s, 6 H, $CH_3$) ppm. $^{31}$P{$^1$H} NMR (121.4 MHz, [D$_6$]DMSO): $\delta$ = 113.4 (s) ppm.

**Synthesis of [{[-OC$_{10}$H$_6$(μ-S)C$_{10}$H$_6$O-]PNC$_4$H$_8$O-κ*P*}$_2$CuI] (9a):** This compound was synthesized by a procedure similar to that for **7a** from CuI (0.02 g, 0.105 mmol) and **2a** (0.093 g, 0.215 mmol) and was stirred for 6 h. Yield: 81% (0.09 g); m.p. 220 °C (dec.). $C_{48}H_{40}CuIN_2O_6P_2S_2$ (1057.4): calcd. C 54.52, H 3.81, N 2.65, S 6.07; found C 54.49, H 3.78, N 2.62, S 5.98. $^1$H NMR (400 MHz, [D$_6$]DMSO): $\delta$ = 8.71 (d, $^3J_{H,H}$ = 8.8 Hz, 4 H, ArH), 8.02 (d, $^3J_{H,H}$ = 8.4 Hz, 4 H, ArH), 7.96 (d, $^3J_{H,H}$ = 8.0 Hz, 4 H, ArH), 7.31–7.91 (m, 12 H, ArH), 3.66 (br. s, 8 H, $CH_2$), 3.29 (br. s, 8 H, $CH_2$) ppm. $^{31}$P{$^1$H} NMR (121.4 MHz, [D$_6$]DMSO): $\delta$ = 111.8 (s) ppm.

**Synthesis of [{[-OC$_{10}$H$_6$(μ-S)C$_{10}$H$_6$O-]PNC$_4$H$_8$NCH$_3$-κ*P*}$_2$CuI] (9b):** This compound was synthesized by a procedure similar to that for **7a** from CuI (0.02 g, 0.105 mmol) and **2b** (0.096 g, 0.215 mmol). Yield: 83% (0.095 g); m.p. 232 °C (dec.). $C_{50}H_{46}CuIN_4O_4P_2S_2$ (1083.5): calcd. C 55.43, H 4.28, N 5.17, S 5.92; found C 55.38, H 4.27, N 5.15, S 5.88. $^1$H NMR (400 MHz, [D$_6$]DMSO): $\delta$ = 8.71 (d, $^3J_{H,H}$ = 8.4 Hz, 4 H, ArH), 7.76 (d, $^3J_{H,H}$ = 8.0 Hz, 4 H, ArH), 7.64 (d, $^3J_{H,H}$ = 9.2 Hz, 4 H, ArH), 7.61 (t, $^3J_{H,H}$ = 8.0 Hz, 4 H, ArH), 7.44 (t, $^3J_{H,H}$ = 7.2 Hz, 4 H, ArH), 6.94 (d, $^3J_{H,H}$ = 8.4 Hz, 4 H, ArH), 3.47 (br. s, 8 H, $CH_2$), 2.49 (br. s, 8 H, $CH_2$), 2.13 (s, 6 H, $CH_3$) ppm. $^{31}$P{$^1$H} NMR (162 MHz, [D$_6$]DMSO): $\delta$ = 116.9 (s) ppm.

**Synthesis of [{[-OC$_{10}$H$_6$(μ-S)C$_{10}$H$_6$O-]PNC$_4$H$_8$O-κ*P*,κ*S*}$_2$Cu]BF$_4$ (10a):** [Cu(MeCN)$_4$]BF$_4$ (0.025 g, 0.079 mmol) was added to a solution of **2a** (0.07 g, 0.162 mmol) in dichloromethane (15 mL) and the reaction mixture was stirred for 2 h. The resultant solution was concentrated to 5 mL under vacuum and layered with petroleum ether (1 mL) to give **10a** as a white crystalline product at –25 °C. Yield: 89% (0.072 g); m.p. 170–172 °C (dec.). $C_{48}H_{40}BCuF_4N_2O_6P_2S_2$ (1017.3): calcd. C 56.67, H 3.96, N 2.75, S 6.30; found C 56.59, H 3.92, N 2.73, S 6.26. $^1$H NMR (400 MHz, $CDCl_3$): $\delta$ = 8.52 (d, $^3J_{H,H}$ = 7.6 Hz, 4 H, ArH), 7.77 (d, $^3J_{H,H}$ = 8.4 Hz, 8 H, ArH), 7.26–7.54 (m, 8 H, ArH), 7.12 (d, $^3J_{H,H}$ = 8.0 Hz, 4 H, ArH), 3.74 (br. s, 8 H, $CH_2$), 3.37 (br. s, 8 H, $CH_2$) ppm. $^{31}$P{$^1$H} NMR (121.4 MHz, $CDCl_3$): $\delta$ = 112.2 (s) ppm. MS (EI): *m*/*z* 929.1 [M$^+$ – BF$_4$], 496.0 [M$^+$ – (L + BF$_4$)].

**Synthesis of [{[-OC$_{10}$H$_6$(μ-S)C$_{10}$H$_6$O-]PNC$_4$H$_8$NCH$_3$-κ*P*,κ*S*}$_2$-Cu]BF$_4$ (10b):** This compound was synthesized by a procedure similar to that for **10a** from **2b** (0.072 g, 0.162 mmol) and [Cu(MeCN)$_4$]-BF$_4$ (0.025 g, 0.079 mmol). Yield: 90% (0.075 g); m.p. 158–160 °C (dec.). $C_{50}H_{46}BCuF_4N_4O_4P_2S_2$ (1043.35): calcd. C 57.56, H 4.44, N 5.37, S 6.15; found C 57.48, H 4.41, N 5.32, S 6.09. $^1$H NMR (400 MHz, $CDCl_3$): $\delta$ = 8.55 (d, $^3J_{H,H}$ = 8.4 Hz, 4 H, ArH), 7.59

 © 2007 Wiley-VCH Verlag GmbH & Co. KGaA, Weinheim 

(d, $^3J_{H,H}$ = 8.0 Hz, 8 H, ArH), 6.88–7.56 (m, 12 H, ArH), 3.35 (br. s, 8 H, $CH_2$), 2.52 (br. s, 8 H, $CH_2$), 2.01 (s, 6 H, $CH_3$) ppm. $^{31}P\{^1H\}$ NMR (162 MHz, $CDCl_3$): $\delta$ = 113.7 (s) ppm. MS (EI): *m*/*z* 955.2 [$M^+ - BF_4$], 509.1 [$M^+ - (L + BF_4)$].

**Synthesis of [{[{-OC$_{10}$H$_6$(μ-S)C$_{10}$H$_6$O-}PNC$_4$H$_8$O-κ*P*,κ*S*]Ag(CF$_3$SO$_3$)}$_2$] (11a):** AgOTf (0.04 g, 0.156 mmol) was added to a solution of **2a** (0.067 g, 0.156 mmol) in dichloromethane (12 mL) and the reaction mixture was stirred for 3 h. The resultant solution was concentrated to 3 mL under vacuum and petroleum ether (5 mL) was added to precipitate **11a** as a white crystalline product, which was then filtered off and dried under high vacuum. Yield: 91% (0.097 g); m.p. 138 °C (dec.). $C_{25}H_{20}AgF_3NO_6PS_2$ (690.39): calcd. C 43.49, H 2.92, N 2.03, S 9.29; found C 43.41, H 2.89, N 1.99, S 9.21. $^1H$ NMR (400 MHz, $CDCl_3$): $\delta$ = 8.79 (d, $^3J_{H,H}$ = 8.4 Hz, 2 H, ArH), 7.15–8.32 (m, 10 H, ArH), 3.91 (br. s, 4 H, $CH_2$), 3.28 (br. s, 4 H, $CH_2$) ppm. $^{31}P\{^1H\}$ NMR (121.4 MHz, $CDCl_3$): $\delta$ = 118.8 (br. s) ppm.

**Synthesis of [{[{-OC$_{10}$H$_6$(μ-S)C$_{10}$H$_6$O-}PNC$_4$H$_8$NCH$_3$-κ*P*,κ*S*]Ag(CF$_3$SO$_3$)}$_2$] (11b):** This compound was synthesized by a procedure similar to that for **11a** from **2b** (0.069 g, 0.156 mmol) and AgOTf (0.04 g, 0.156 mmol). Yield: 89% (0.097 g); m.p. 192 °C (dec.). $C_{26}H_{23}AgF_3N_2O_5PS_2$ (703.44): calcd. C 44.39, H 3.29, N 3.98, S 9.12; found C 44.31, H 3.22, N 3.91, S 9.03. $^1H$ NMR (400 MHz, $CDCl_3$): $\delta$ = 8.52 (d, $^3J_{H,H}$ = 8.8 Hz, 4 H, ArH), 8.28 (d, $^3J_{H,H}$ = 8.4 Hz, 8 H, ArH), 6.86–7.58 (m, 12 H, ArH), 3.19 (br. s, 8 H, $CH_2$), 2.67 (br. s, 8 H, $CH_2$), 2.33 (s, 6 H, $CH_3$) ppm. $^{31}P\{^1H\}$ NMR (162 MHz, $CDCl_3$): $\delta$ = 123.3 (2 br. s, $^1J_{Ag,P} \approx$ 594 Hz, 2 P) ppm.

**Synthesis of [{[-OC$_{10}$H$_6$(μ-S)C$_{10}$H$_6$O-]PNC$_4$H$_8$O-κ*P*,κ*S*}Ag(PPh$_3$)]CF$_3$SO$_3$ (12a):** [Ag(PPh$_3$)][OTf] (0.05 g, 0.096 mmol) was added to a solution of **2a** (0.042 g, 0.096 mmol) in dichloromethane (12 mL), and the reaction mixture was stirred for 2 h. The solution was concentrated under vacuum and diethyl ether (5 mL) was added to precipitate a white crystalline product. This was filtered off and dried under vacuum. Yield: 82% (0.075 g); m.p. 140–142 °C (dec.). $C_{43}H_{35}AgF_3NO_6P_2S_2$ (952.69): calcd. C 54.21, H 3.70, N 1.47, S 6.73; found C 54.16, H 3.64, N 1.44, S 6.69. $^1H$ NMR (400 MHz, $CDCl_3$): $\delta$ = 8.76 (d, $^3J_{H,H}$ = 8.4 Hz, 2 H, ArH), 7.09–8.34 (m, 10 H, ArH, 15 H, $PPh_3$), 3.89 (br. s, 4 H, $CH_2$), 3.24 (br. s, 4 H, $CH_2$) ppm. $^{31}P\{^1H\}$ NMR (121.4 MHz, $CDCl_3$): $\delta$ = 123.9 (2 br. d, $J_{Ag,P} \approx$ 512 Hz, 1 P), 9.7 (2 br. d, $J_{Ag,P} \approx$ 394 Hz, 1 P, $PPh_3$) ppm. MS (EI): *m*/*z* 803.1 [$M^+$ – OTf].

**Synthesis of [{[-OC$_{10}$H$_6$(μ-S)C$_{10}$H$_6$O-]PNC$_4$H$_8$NCH$_3$-κ*P*,κ*S*}Ag(PPh$_3$)]CF$_3$SO$_3$ (12b):** This complex was synthesized by a procedure similar to that for **12a** from **2b** (0.0043 g, 0.096 mmol) and [Ag(PPh$_3$)][OTf] (0.05 g, 0.096 mmol). Yield: 78% (0.073 g); m.p. 144 °C (dec.). $C_{44}H_{38}AgF_3N_2O_5P_2S_2$ (965.73): calcd. C 54.72, H 3.97, N 2.90, S 6.64; found C 54.68, H 3.92, N 2.88, S 6.59. $^1H$ NMR (400 MHz, $CDCl_3$): $\delta$ = 8.64 (d, $^3J_{H,H}$ = 8.4 Hz, 2 H, ArH), 7.04–7.75 (m, 10 H, ArH, 15 H, $PPh_3$), 3.45 (br. s, 4 H, $CH_2$), 2.61 (br. s, 4 H, $CH_2$), 2.36 (s, 3 H, $CH_3$) ppm. $^{31}P\{^1H\}$ NMR (162 MHz, $CDCl_3$): $\delta$ = 130.3 (br. s, 1 P), 8.2 (br. s, 1 P, $PPh_3$) ppm. MS (EI): *m*/*z* 816.9 [$M^+$ – OTf].

**Synthesis of [{[-OC$_{10}$H$_6$(μ-S)C$_{10}$H$_6$O-]PNC$_4$H$_8$O-κ*P*}AuCl] (13a):** A solution of **2a** (0.051 g, 0.119 mmol) in $CH_2Cl_2$ (8 mL) was added dropwise to a dichloromethane (5 mL) solution of [AuCl(SMe$_2$)] (0.035 g, 0.119 mmol) and the reaction mixture was stirred for 3 h at room temperature. The solution was concentrated to 3 mL and layered with petroleum ether to give colorless crystals of **13a** on cooling to –25 °C. Yield: 90% (0.071 g); m.p. 178–180 °C (dec.). $C_{24}H_{20}AuClNO_3PS$ (665.88): calcd. C 43.29, H 3.03, N 2.10, S 4.82; found C 43.19, H 2.99, N 2.08, S 4.79. $^1H$ NMR (400 MHz, $CDCl_3$): $\delta$ = 8.77 (d, $^3J_{H,H}$ = 8.4 Hz, 2 H, ArH), 7.63–7.87 (m, 6 H, ArH), 7.51 (t, $^3J_{H,H}$ = 7.2 Hz, 2 H, ArH), 7.24 (d, $^3J_{H,H}$ = 8.0 Hz, 2 H, ArH), 3.84 (t, $^3J_{H,H}$ = 4.8 Hz, 4 H, $CH_2$), 3.65 (t, $^3J_{H,H}$ = 5.2 Hz, 4 H, $CH_2$) ppm. $^{31}P\{^1H\}$ NMR (121.4 MHz, $CDCl_3$): $\delta$ = 113.1 (s) ppm.

**Synthesis of [{[-OC$_{10}$H$_6$(μ-S)C$_{10}$H$_6$O-]PNC$_4$H$_8$NCH$_3$-κ*P*}AuCl] (13b):** This was synthesized by a procedure similar to that for **13a** from **2b** (0.053 g, 0.119 mmol) and [AuCl(SMe$_2$)] (0.035 g, 0.119 mmol). Yield: 89% (0.072 g); m.p. 158 °C (dec.). $C_{25}H_{23}AuClN_2O_2PS$ (678.92): calcd. C 44.23, H 3.41, N 4.13, S 4.72; found C 44.18, H 3.37, N 4.09, S 4.69. $^1H$ NMR (400 MHz, [D$_6$]acetone): $\delta$ = 8.84 (d, $^3J_{H,H}$ = 8.0 Hz, 2 H, ArH), 8.08 (d, $^3J_{H,H}$ = 8.8 Hz, 2 H, ArH), 7.99 (d, $^3J_{H,H}$ = 8.0 Hz, 2 H, ArH), 7.52–7.76 (m, 4 H, ArH), 7.49 (d, $^3J_{H,H}$ = 7.6 Hz, 2 H, ArH), 3.72 (br. s, 4 H, $CH_2$), 2.91 (br. s, 4 H, $CH_2$), 2.37 (s, 3 H, $CH_3$) ppm. $^{31}P\{^1H\}$ NMR (121.4 MHz, [D$_6$]acetone): $\delta$ = 115.3 (s) ppm.

**Synthesis of [{[-OC$_{10}$H$_6$(μ-S)C$_{10}$H$_6$O-]PNC$_4$H$_8$O-κ*P*}AuI] (14a):** A solution of CuI (0.014 g, 0.075 mmol) in acetonitrile (5 mL) was added dropwise to a solution of **13a** (0.05 g, 0.075 mmol) in dichloromethane (8 mL) and the reaction mixture was stirred for 3 h. The solution obtained was concentrated to 5 mL to give a crystalline product on cooling to –25 °C. Yield: 74% (0.042 g); m.p. 208–210 °C (dec.). $C_{24}H_{20}AuINO_3PS$ (757.33): calcd. C 38.06, H 2.66, N 1.85, S 4.23; found C 37.98, H 2.63, N 1.81, S 4.19. $^1H$ NMR (400 MHz, $CDCl_3$): $\delta$ = 8.78 (d, $^3J_{H,H}$ = 8.0 Hz, 2 H, ArH), 7.43–7.81 (m, 8 H, ArH), 7.28 (d, $^3J_{H,H}$ = 8.4 Hz, 2 H, ArH), 3.85 (br. s, 4 H, $CH_2$), 3.68 (br. s, 4 H, $CH_2$) ppm. $^{31}P\{^1H\}$ NMR (162 MHz, $CDCl_3$): $\delta$ = 118.1 (s) ppm.

**Synthesis of [{[-OC$_{10}$H$_6$(μ-S)C$_{10}$H$_6$O-]PNC$_4$H$_8$NCH$_3$-κ*P*}AuI] (14b):** This complex was synthesized by a procedure similar to that for **14a** from CuI (0.014 g, 0.075 mmol) and **13b** (0.051 g, 0.075 mmol). Yield: 69% (0.04 g); m.p. 192–194 °C (dec.). $C_{25}H_{23}AuIN_2O_2PS$ (770.37): calcd. C 38.98, H 3.01, N 3.64, S 4.16; found C 38.92, H 2.97, N 3.59, S 4.12. $^1H$ NMR (400 MHz, $CDCl_3$): $\delta$ = 8.76 (d, $^3J_{H,H}$ = 8.4 Hz, 2 H, ArH), 7.80–7.85 (m, 4 H, ArH), 7.64 (t, $^3J_{H,H}$ = 7.6 Hz, 2 H, ArH), 7.48 (t, $^3J_{H,H}$ = 7.6 Hz, 2 H, ArH), 7.22 (d, $^3J_{H,H}$ = 8.8 Hz, 2 H, ArH), 3.67 (br. s, 4 H, $CH_2$), 2.55 (br. s, 4 H, $CH_2$), 2.39 (s, 3 H, $CH_3$) ppm. $^{31}P\{^1H\}$ NMR (162 MHz, $CDCl_3$): $\delta$ = 118.9 (s) ppm.

**X-ray Crystallography:** Crystals of **5a**, **7a**, **8a**, **13a**, **13b**, and **14a** were mounted in a Cryoloop™ with a drop of Paratone oil and placed in the cold nitrogen stream of the Kryoflex™ attachment of a Bruker APEX CCD diffractometer. A full sphere of data was collected using 606 scans in $\omega$ (0.3° per scan) at $\phi$ = 0, 120, and 240° (for **5a**, **7a**, and **14a**) or 400 scans in $\omega$ (0.5° per scan) at $\phi$ = 0, 90, and 180° plus 800 scans in $\phi$ (0.45° per scan) at $\omega$ = 0 and 210° (for **8a**, **13a**, and **13b**) using the SMART software package.[26] The raw data were reduced to $F^2$ values using the SAINT+ software[27] and global refinements of unit cell parameters using 4630–9050 reflections chosen from the full data sets were performed. Multiple measurements of equivalent reflections provided the basis for empirical absorption corrections as well as corrections for any crystal deterioration during the data collection (SADABS[28]). The structures were solved by direct methods (for **5a**, **7a**, **8a**, **13a**, and **13b**) or the position of the metal atoms was obtained from a sharpened Patterson function (for **14a**) and refined by full-matrix least-squares procedures using the SHELXTL program package.[29] Hydrogen atoms were placed in calculated positions and included as riding contributions with isotropic displacement parameters tied to those of the attached non-hydrogen atoms. Pertinent crystallographic data and other experimental details are summarized in Tables 4 and 5.

 © 2007 Wiley-VCH Verlag GmbH & Co. KGaA, Weinheim 

Table 4. Crystallographic data for complexes **5a**, **7a**, and **8a**.

| | **5a** | **7a** | **8a** |
|---|---|---|---|
| Formula | $C_{48}H_{40}Br_2Cu_2N_2O_6P_2S_2$ | $C_{48}H_{40}ClCuN_2O_6P_2S_2{\cdot}CH_2Cl_2$ | $C_{48}H_{40}BrCuN_2O_6P_2S_2{\cdot}CH_2Cl_2$ |
| Molecular weight | 1153.80 | 1050.83 | 1095.26 |
| Crystal system | triclinic | monoclinic | monoclinic |
| Crystal size [mm] | $0.11\times0.11\times0.14$ | $0.17\times0.17\times0.32$ | $0.14\times0.15\times0.28$ |
| Space group | $P\bar{1}$ (no. 2) | $P2_1/n$ (no. 14) | $P2_1/n$ (no. 14) |
| $a$ [Å] | 9.574(2) | 13.638(1) | 13.582(1) |
| $b$ [Å] | 11.357(2) | 21.690(2) | 21.839(2) |
| $c$ [Å] | 11.462(2) | 16.002(2) | 16.042(1) |
| $\alpha$ [°] | 98.769(2) | 90 | 90 |
| $\beta$ [°] | 108.777(2) | 103.633(2) | 103.437(1) |
| $\gamma$ [°] | 101.580(2) | 90 | 90 |
| $V$ [Å$^3$] | 1123.8(4) | 4600.1(8) | 4628.1(7) |
| $Z$ | 1 | 4 | 4 |
| $\rho_{calcd}$ [g cm$^{-3}$] | 1.705 | 1.517 | 1.572 |
| $\mu$(Mo-$K_\alpha$) [mm$^{-1}$] | 2.941 | 0.863 | 1.663 |
| $F$(000) | 1160 | 2160 | 2232 |
| Temp. [K] | 100 | 100 | 100 |
| $\theta_{min,max}$ [°] | 2.4, 28.4 | 2.2, 28.2 | 2.4, 28.3 |
| GOF ($F^2$) | 0.99 | 1.03 | 1.04 |
| $R_1$[a] | 0.0504 | 0.0444 | 0.0352 |
| $wR_2$[b] | 0.1371 | 0.1220 | 0.0931 |

[a] $R_1 = \Sigma|F_o| - |F_c|/\Sigma|F_o|$. [b] $wR_2 = \{\Sigma w[(F_o^2 - F_c^2)^2]/\Sigma[w(F_o^2)^2]\}^{1/2}$.

Table 5. Crystallographic data for complexes **13a**, **13b**, and **14a**.

| | **13a** | **13b** | **14a** |
|---|---|---|---|
| Formula | $C_{24}H_{20}AuClNO_3PS$ | $C_{25}H_{23}AuClN_2O_2PS$ | $C_{24}H_{20}AuINO_3PS$ |
| Molecular weight | 665.86 | 678.90 | 757.32 |
| Crystal system | triclinic | triclinic | triclinic |
| Crystal size [mm] | $0.09\times0.14\times0.21$ | $0.14\times0.17\times0.21$ | $0.12\times0.15\times0.22$ |
| Space group | $P\bar{1}$ (no. 2) | $P\bar{1}$ (no. 2) | $P\bar{1}$ (no. 2) |
| $a$ [Å] | 9.9857(9) | 9.945(1) | 9.5688(8) |
| $b$ [Å] | 10.817(1) | 10.500(1) | 11.2775(9) |
| $c$ [Å] | 11.704(1) | 13.220(1) | 11.648(1) |
| $\alpha$ [°] | 76.089(1) | 103.775(1) | 99.422(1) |
| $\beta$ [°] | 67.262(1) | 95.073(1) | 99.004(1) |
| $\gamma$ [°] | 71.899(1) | 104.354(1) | 106.991(1) |
| $V$ [Å$^3$] | 1097.8(2) | 1282.9(2) | 1157.7(2) |
| $Z$ | 2 | 2 | 2 |
| $\rho_{calcd}$ [g cm$^{-3}$] | 2.014 | 1.757 | 2.172 |
| $\mu$(Mo-$K_\alpha$) [mm$^{-1}$] | 7.019 | 6.006 | 7.874 |
| $F$(000) | 644 | 660 | 716 |
| Temp. [K] | 100 | 100 | 100 |
| $\theta_{min,max}$ [°] | 2.6, 28.3 | 2.9, 28.3 | 2.3, 28.2 |
| GOF ($F^2$) | 1.05 | 1.05 | 1.05 |
| $R_1$[a] | 0.0164 | 0.0141 | 0.0236 |
| $wR_2$[b] | 0.0399 | 0.0356 | 0.0568 |

[a] $R_1 = \Sigma|F_o| - |F_c|/\Sigma|F_o|$. [b]$wR_2 = \{\Sigma w[(F_o^2 - F_c^2)^2]/\Sigma[w(F_o^2)^2]\}^{1/2}$.

CCDC-622054 (for **5a**), -622055 (for **7a**), -622056 (for **8a**), -622057 (for **13a**), -622058 (for **13b**), and -622059 (for **14a**) contain the supplementary crystallographic data for this paper. These data can be obtained free of charge from The Cambridge Crystallographic Data Centre via www.ccdc.cam.ac.uk/data_request/cif.

## Acknowledgments

We are grateful to the Department of Science and Technology (DST), New Delhi, for funding through grant SR/S1/IC-05/2003. B. P. thanks the Council of Scientific and Industrial Research (CSIR), India, for a Senior Research Fellowship (SRF). We also thank SAIF, Mumbai, Department of Chemistry Instrumentation Facilities, Bombay, for spectral and analytical data and the Louisiana Board of Regents through grant LEQSF(2002-03)-ENH-TR-67 for funds to purchase the CCD diffractometer and the Chemistry Department of Tulane University for support of the X-ray laboratory.

[1] a) P. Braunstein, F. Naud, *Angew. Chem. Int. Ed.* **2001**, *40*, 680–699; b) A. M. Masdeu-Bultó, M. Diéguez, E. Martin, M. Gómez, *Coord. Chem. Rev.* **2003**, *242*, 159–201; c) H. Chen, Y. Liu, S. Peng, S. Liu, *Dalton Trans.* **2003**, 1419–1424; d) D. S. McGuinness, P. Wasserscheid, D. H. Morgan, J. T. Dixon, *Organometallics* **2005**, *24*, 552–556; e) M. C. Aragoni, M. Arca, A. Bencini, A. J. Blake, C. Caltagirone, A. Decortes, F. Demartin, F. A. Devillanova, E. Faggi, L. S. Dolci, A. Garau, F. Isaia, V. Lippolis, L. Prodi, C. Wilson, B. Valtancoli, N. Zaccheroni, *Dalton Trans.* **2005**, 2994–3004.

 © 2007 Wiley-VCH Verlag GmbH & Co. KGaA, Weinheim 

[2] For recent example of P,O ligands, see: a) N. Oberbeckmann-Winter, X. Morise, P. Braunstein, R. Welter, *Inorg. Chem.* **2005**, *44*, 1391–1403; b) C. Muller, L. J. Ackerman, J. N. H. Reek, P. C. J. Kamer, P. W. N. M. van Leeuwen, *J. Am. Chem. Soc.* **2004**, *126*, 14960–14963; c) F. Goettmann, D. Grosso, F. Mercier, F. Mathey, C. Sanchez, *Chem. Commun.* **2004**, 1240–1241; d) W. Dai, Y. Li, Y. Zhang, K. W. Lai, J. Wu, *Tetrahedron Lett.* **2004**, *45*, 1999–2001; e) P. Braunstein, B. T. Heaton, C. Jacob, L. Manzi, X. Morise, *Dalton Trans.* **2003**, 1396–1401.

[3] For recent example of P,N ligands, see: a) R. J. Kloetzing, P. Knochel, *Tetrahedron: Asymmetry* **2006**, *17*, 116–123; b) F. Speiser, P. Braunstein, L. Saussine, *Dalton Trans.* **2004**, 1539–1545; c) W. Tang, W. Wang, X. Zhang, *Angew. Chem. Int. Ed.* **2003**, *42*, 943–946; d) G. Chelucci, G. Orru, G. A. Pinna, *Tetrahedron* **2003**, *59*, 9471–9515; e) P. Braunstein, J. Zhang, R. Welter, *Dalton Trans.* **2003**, 507–509; f) T. Bunlaksananusorn, K. Polborn, P. Knochel, *Angew. Chem. Int. Ed.* **2003**, *42*, 3941–3943.

[4] For recent example of P,S ligands, see: a) O. Piechaczyk, M. Doux, L. Ricard, P. Le Floch, *Organometallics* **2005**, *24*, 1204–1213; b) H. Liang, S. Ito, M. Yoshifuji, *Org. Lett.* **2004**, *6*, 425–427; c) A. Dervisi, R. L. Jenkins, K. M. A. Malik, M. B. Hursthouse, S. Coles, *Dalton Trans.* **2003**, 1133–1142; d) M. Doux, N. Mézailles, M. Melaimi, L. Ricard, P. Le Floch, *Chem. Commun.* **2002**, 1566–1567; e) J. R. Dilworth, N. Wheatley, *Coord. Chem. Rev.* **2000**, *199*, 89–158; f) X. Verdaguer, A. Moyano, M. A. Pericas, A. Riera, M. A. Maestro, J. Mahia, *J. Am. Chem. Soc.* **2000**, *122*, 10242–10243; g) D. Morales-Morales, R. Redón, Y. Zheng, J. R. Dilworth, *Inorg. Chim. Acta* **2002**, *328*, 39–44; h) J. R. Dilworth, D. Morales-Morales, Y. Zheng, *J. Chem. Soc., Dalton Trans.* **2000**, 3007–3015.

[5] a) J. R. Dilworth, C. A. M. von Beckh Widmanstetter, S. I. Pascu, *Dalton Trans.* **2005**, 2151–2161; b) X. Verdaguer, M. A. Pericas, A. Riera, M. A. Maestro, J. Mahia, *Organometallics* **2003**, *22*, 1868–1877; c) D. Enders, R. Peters, J. Runsink, J. W. Bats, *Org. Lett.* **1999**, *1*, 1863–1866; d) A. Albinati, P. S. Pregosin, K. Wick, *Organometallics* **1996**, *15*, 2419–2421; e) P. Barbaro, A. Currao, J. Herrmann, R. Nesper, P. S. Pregosin, R. Salzmann, *Organometallics* **1996**, *15*, 1879–1888; f) E. Guimet, M. Diéguez, A. Ruiz, C. Claver, *Tetrahedron: Asymmetry* **2005**, *16*, 959–963; g) E. Guimet, M. Diéguez, A. Ruiz, C. Claver, *Dalton Trans.* **2005**, 2557–2562; h) M. Dieguez, O. Pamies, C. Claver, *Tetrahedron: Asymmetry* **2005**, *16*, 3877–3880; i) D. A. Evans, K. R. Campos, J. S. Tedrow, F. E. Michael, M. R. Gagne, *J. Org. Chem.* **1999**, *64*, 2994–2995; j) D. A. Evans, F. E. Michael, J. S. Tedrow, K. R. Campos, *J. Am. Chem. Soc.* **2003**, *125*, 3534–3543; k) O. Pamies, M. Diéguez, G. Net, A. Ruiz, C. Claver, *Organometallics* **2000**, *19*, 1488–1496; l) K. Selvakumar, M. Valentini, P. S. Pregosin, A. Albinati, *Organometallics* **1999**, *18*, 4591–4597.

[6] a) M. Doux, L. Ricard, P. Le Floch, N. Mézailles, *Dalton Trans.* **2004**, 2593–2600; b) M. Diéguez, O. Pamies, G. Net, A. Ruiz, C. Claver, *J. Mol. Catal. A* **2002**, *185*, 11–16; c) S. Cabrera, R. G. Arrayas, J. C. Carretero, *J. Am. Chem. Soc.* **2005**, *127*, 16394–16395; d) J. E. Aguado, S. Canales, M. C. Gimeno, P. G. Jones, A. Laguna, M. D. Villacampa, *Dalton Trans.* **2005**, 3005–3015; e) N. Mezailles, L. Ricard, F. Gagosz, *Org. Lett.* **2005**, *7*, 4133–4136.

[7] B. Punji, J. T. Mague, M. S. Balakrishna, *Inorg. Chem.* **2006**, *45*, 9454–9464.

[8] a) M. S. Balakrishna, R. Panda, J. T. Mague, *Inorg. Chem.* **2001**, *40*, 5620–5625; b) M. S. Balakrishna, R. Panda, J. T. Mague, *J. Chem. Soc., Dalton Trans.* **2002**, 4617–4621; c) S. Priya, M. S. Balakrishna, J. T. Mague, S. M. Mobin, *Inorg. Chem.* **2003**, *42*, 1272–1281; d) P. Chandrasekaran, J. T. Mague, M. S. Balakrishna, *Organometallics* **2005**, *24*, 3780–3783; e) P. Chandrasekaran, J. T. Mague, M. S. Balakrishna, *Inorg. Chem.* **2005**, *44*, 7925–7932; f) P. Chandrasekaran, J. T. Mague, M. S. Balakrishna, *Inorg. Chem.* **2006**, *45*, 5893–5897; g) P. Chandrasekaran, J. T. Mague, M. S. Balakrishna, *Inorg. Chem.* **2006**, *45*, 6678–6683; h) B. Punji, M. S. Balakrishna, *Indian J. Chem.* **2006**, *45A*, 1390–1394.

[9] a) S. Priya, M. S. Balakrishna, S. M. Mobin, R. McDonald, *J. Organomet. Chem.* **2003**, *688*, 227–235; b) S. Mohanty, B. Punji, M. S. Balakrishna, *Polyhedron* **2006**, *25*, 815–820; c) B. Punji, J. T. Mague, M. S. Balakrishna, *Dalton Trans.* **2006**, 1322–1330; d) B. Punji, C. Ganesamoorthy, M. S. Balakrishna, *J. Mol. Catal. A* **2006**, *259*, 78–83; e) B. Punji, J. T. Mague, M. S. Balakrishna, *J. Organomet. Chem.* **2006**, *691*, 4265–4272.

[10] E. L. Muetterties, C. W. Alegranti, *J. Am. Chem. Soc.* **1972**, *94*, 6386–6391.

[11] G. A. Bowmaker, J. C. Dyason, P. C. Healy, L. M. Engelhardt, C. Pakawatchai, A. H. White, *J. Chem. Soc., Dalton Trans.* **1987**, 1089–1097.

[12] a) T. L. Stott, M. O. Wolf, B. O. Patrick, *Inorg. Chem.* **2005**, *44*, 620–627; b) H. Xiao, Y. Weng, W. Wong, T. C. W. Mak, C. Che, *J. Chem. Soc., Dalton Trans.* **1997**, 221–226; c) H. Schmidbaur, A. Wohlleben, F. Wagner, O. Orama, G. Huttner, *Chem. Ber.* **1977**, *110*, 1748–1754.

[13] A. Bondi, *J. Phys. Chem.* **1964**, *68*, 441–451.

[14] G. A. Bowmaker, S. E. Boyd, J. V. Hanna, R. D. Hart, P. C. Healy, B. W. Skelton, A. H. White, *J. Chem. Soc., Dalton Trans.* **2002**, 2722–2730.

[15] J. R. Cole, M. E. Dellinger, T. J. Johnson, B. A. Reinecke, R. D. Pike, W. T. Pennington, M. Krawiec, A. L. Rheingold, *J. Chem. Crystallogr.* **2003**, *33*, 341–347.

[16] a) D. J. Sherlock, A. Chandrasekaran, R. O. Day, R. R. Holmes, *Inorg. Chem.* **1997**, *36*, 5082–5089; b) D. J. Sherlock, A. Chandrasekaran, R. O. Day, R. R. Holmes, *J. Am. Chem. Soc.* **1997**, *119*, 1317–1322.

[17] L. Sutton, *Tables of Interatomic Distances and Configuration*, in *Molecules and Ions*, Special Publication Nos. 11 and 18, The Chemical Society, London, **1958** and **1965**.

[18] R. O. Day, T. K. Prakasha, R. R. Holmes, H. Eckert, *Organometallics* **1994**, *13*, 1285–1293.

[19] a) P. B. Hitchcock, P. L. Pye, *J. Chem. Soc., Dalton Trans.* **1977**, 1457–1460; b) M. Freytag, S. Ito, M. Yoshifuji, *Chem. Asian J.* **2006**, *1*, 693–700.

[20] T. Steiner, *Acta Crystallogr., Sect. B* **1998**, *54*, 456–463.

[21] L. Brammer, E. A. Bruton, P. Sherwood, *Cryst. Growth Des.* **2001**, *1*, 277–290.

[22] B. S. Furniss, A. J. Hannaford, P. W. G. Smith, A. R. Tatchell, *Vogel's Textbook of Practical Organic Chemistry*, Fifth Edition, ELBS, England, **1989**, p. 428–429.

[23] R. A. Heintz, J. A. Smith, P. S. Szalay, A. Weisgerber, K. R. Dunbar, K. Beck, D. Coucouvanis, *Inorg. Synth.* **2002**, *33*, 75–83.

[24] M. C. Brandys, M. C. Jennings, R. J. Puddephatt, *J. Chem. Soc., Dalton Trans.* **2000**, 4601–4606.

[25] M. Bardaji, O. Crespo, A. Laguna, A. K. Fischer, *Inorg. Chim. Acta* **2000**, *304*, 7–16.

[26] Bruker-AXS, *SMART*, Version 5.625, Madison, WI, **2000**.

[27] Bruker-AXS, *SAINT+*, Version 6.35A, Madison, WI, **2002**.

[28] G. M. Sheldrick, *SADABS*, Version 2.05, University of Göttingen, Germany **2002**.

[29] a) Bruker-AXS, *SHELXTL*, Version 6.10, Madison, WI, **2000**; b) G. M. Sheldrick, *SHELXS97* and *SHELXL97*, University of Göttingen, Germany **1997**.

Received: September 26, 2006
Published Online: December 19, 2006

 © 2007 Wiley-VCH Verlag GmbH & Co. KGaA, Weinheim 

DOI: 10.1002/ejic.200600934

# Half-Sandwich $\eta^5$-Indenyl- and $\eta^6$-Areneruthenium(II) Complexes Bearing the Chiral Ligand (4*S*)-2-[($S_p$)-2-(Diphenylphosphanyl)ferrocenyl]-4-(methylethyl)-oxazoline (FcPN)

**Almudena García-Fernández,[a] José Gimeno,[a] Elena Lastra,*[a] Cesar A. Madrigal,[a] Claudia Graiff,[b] and Antonio Tiripicchio[b]**

**Keywords:** N,P ligands / Phosphanes / Indenyl complexes / Arene complexes / Ruthenium

Chiral indenylruthenium(II) [Ru($\eta^5$-$C_9H_7$){$\kappa^2$(*P*,*N*)-FcPN}(PPh$_3$)][PF$_6$] (**1**), [Ru($\eta^5$-$C_9H_7$)Cl{$\kappa^2$(*P*,*N*)-FcPN}] (**2**) and areneruthenium(II) [RuX($\eta^6$-arene){$\kappa^2$(*P*,*N*)-FcPN}][PF$_6$] [$\eta^6$-arene = *p*-cymene, X = Cl (**6a**), H (**7**), N$_3$ (**8**); $\eta^6$-arene = 1,2,3,4-tetramethylbenzene, X = Cl (**6b**)] complexes containing the chiral ligand (4*S*)-2-[($S_P$)-2-(diphenylphosphanyl)ferrocenyl]-4-(methylethyl)oxazoline (FcPN) have been synthesised diastereoselectively. Reaction of **2** with terminal alkynes allows the synthesis of alkynyl [Ru($\eta^5$-$C_9H_7$)(C≡CR){$\kappa^2$(*P*,*N*)-FcPN}] [R = Ph (**3a**), *p*-$CH_3C_6H_4$ (**3b**)], allenylidene [Ru($\eta^5$-$C_9H_7$)-{$\kappa^2$(*P*,*N*)-FcPN}(=C=C=CPh$_2$)][PF$_6$] (**4**) and Fischer-type carbene [Ru($\eta^5$-$C_9H_7$){$\kappa^2$(*P*,*N*)-FcPN}{=C(OMe)CH=CHPh}][PF$_6$] (**5**) complexes. The structures of complexes **2**, **3a** and **6a** have been determined by X-ray diffraction methods.
(© Wiley-VCH Verlag GmbH & Co. KGaA, 69451 Weinheim, Germany, 2007)

## Introduction

Metal-mediated asymmetric catalysis has emerged as a very valuable synthetic tool to obtain enantiomerically pure substances.[1] Chiral ferrocene-based ligands incorporating both planar and central chirality are especially attractive due to their potential use in asymmetric induction.[2] Phosphanylferrocenyloxazoline derivatives[3,4] (Scheme 1) belong to this class of ligands and show a remarkable versatility since the substituents in the oxazoline group allow the modulation of the stereogenic centre located close to the N donor atom. Hybrid hemilabile phosphorus–nitrogen ligands are also gaining increasing relevance in coordination and organometallic chemistry since they can reversibly create and/or occupy a vacant coordination site at the metal.[5] In particular, ruthenium complexes containing chiral phosphanylferrocenyloxazoline ligands have proven to be good catalysts in hydrogenation,[6] hydrosilylation,[7] and transfer hydrogenation[8,9] of ketones, imines and ketoximes. However, most of the active species are formed in situ and therefore their coordination chemistry has been scarcely studied.

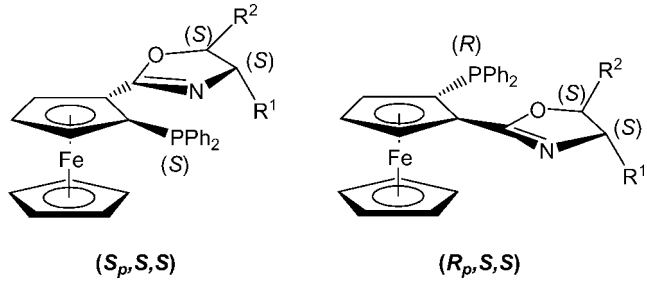


($S_p$,*S*,*S*) ($R_p$,*S*,*S*)

Scheme 1.

The only isolated ruthenium(II) derivatives with FcPN ligands are either five-coordinate, such as [RuCl$_2${$\kappa^2$(*P*,*N*)-FcPN}(PPh$_3$)],[9] or octahedral complexes, such as [RuX$_2${$\kappa^2$(*P*,*N*)-FcPN}(PR$_3$)$_2$], [RuCl$_2${$\kappa^2$(*P*,*N*)-FcPN}-(dppm)], [RuCl$_2$(CO){$\kappa^2$(*P*,*N*)-FcPN}(L)] and [RuCl(CO)-{$\kappa^2$(*P*,*N*)-FcPN}(dppm)][PF$_6$] [dppm = bis(diphenylphosphanyl)methane].[10,11] It is interesting to note that no half-sandwich species have been described to date.

Following our interest in the chemistry of half-sandwich ruthenium(II) fragments and their use as promoters of catalytic[12] and stoichiometric C–C coupling reactions,[13] we report herein the diastereoselective synthesis of the first half-sandwich $\eta^5$-indenyl- and $\eta^6$-areneruthenium(II) complexes containing the chiral ligand FcPN (Scheme 2).

[a] Departamento de Química Orgánica e Inorgánica, Instituto de Química Organometálica "Enrique Moles" (Unidad Asociada al CSIC), Universidad de Oviedo,
Oviedo, Principado de Asturias, Spain
Fax: +34-985-103-446
E-mail: elb@uniovi.es
[b] Dipartimento di Chimica Generale ed Inorganica, Chimica Analitica, Chimica Fisica, Università di Parma,
Parco Area delle Scienze 17/A, 43100, Parma, Italy
E-mail: tiri@unipr.it

 © 2007 Wiley-VCH Verlag GmbH & Co. KGaA, Weinheim 

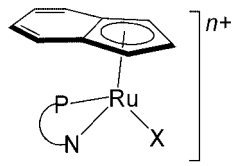


X = Cl, C≡CR, $n$ = 0;
X = $PPh_3$, =C=C=$CPh_2$,
=C(OMe)CH=CHPh, $n$ = 1

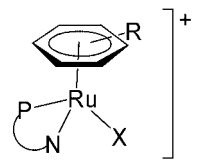


$\eta^6$-arene = *p*-cymene,
X = Cl, H, $N_3$; arene =
1,2,3,4-tetramethylbenzene;
X = Cl

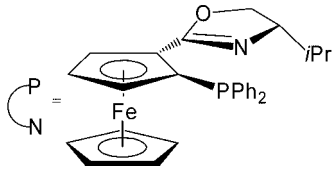


Scheme 2.

## Results and Discussion

### Synthesis of Indenyl Complexes

#### *Synthesis of [Ru($\eta^5$-$C_9H_7$){$\kappa^2$(P,N)-FcPN}($PPh_3$)][$PF_6$] (1)*

The lability of the triphenylphosphane ligands in the complex [Ru($\eta^5$-$C_9H_7$)Cl($PPh_3$)$_2$] allows their ready exchange and the synthesis of a large series of mixed and chelating diphosphane complexes such as [Ru($\eta^5$-$C_9H_7$)-Cl($PPh_3$)L] and [Ru($\eta^5$-$C_9H_7$)Cl(L–L)].[14] Following this methodology, the reaction of [Ru($\eta^5$-$C_9H_7$)Cl($PPh_3$)$_2$] with FcPN in refluxing toluene does not lead, however, to the expected phosphane exchange. Rather, the cationic complex [Ru($\eta^5$-$C_9H_7$){$\kappa^2$(*P*,*N*)-FcPN}($PPh_3$)][Cl] is formed. Subsequent treatment with $NaPF_6$ in methanol leads to the hexafluorophosphate salt [Ru($\eta^5$-$C_9H_7$){$\kappa^2$(*P*,*N*)-FcPN}($PPh_3$)]-[$PF_6$] (**1**) in 81% yield, which was isolated as a red, air-stable solid (Scheme 3).

[Ru($\eta^5$-$C_9H_7$)Cl($PPh_3$)$_2$] —(i) FcPN, toluene, Δ; (ii) $NaPF_6$, MeOH→ [Ru($\eta^5$-$C_9H_7$){$\kappa^2$(*P*,*N*)-FcPN}($PPh_3$)][$PF_6$]

**1**

Scheme 3.

Complex **1** is soluble in dichloromethane and thf and insoluble in diethyl ether and hexane. It was characterised by analytical and spectroscopic methods (see Experimental Section for details). The most remarkable spectroscopic features are: i) the IR spectrum (KBr) shows a strong absorption at 841 $cm^{-1}$ due to the $PF_6^-$ group, and ii) the $^{31}P\{^1H\}$ NMR spectrum displays two doublet resonances at $\delta$ = 34.7 and 58.8 ppm ($^2J_{P,P}$ = 36.5 Hz), as expected for an AB system arising from the presence of the inequivalent phosphorus nuclei.

#### *Synthesis of [Ru($\eta^5$-$C_9H_7$)Cl{$\kappa^2$(P,N)-FcPN}] (2)*

The neutral, chelating FcPN complex [Ru($\eta^5$-$C_9H_7$)-Cl{$\kappa^2$(*P*,*N*)-FcPN}] (**2**) was readily obtained by displacement of the labile COD ligand in [Ru($\eta^5$-$C_9H_7$)Cl-(COD)][12e] (COD = 1,5-cyclooctadiene) by treatment with one equivalent of FcPN in refluxing thf (Scheme 4). Complex **2** was isolated (95% yield) as an air-stable, red solid that is soluble in dichloromethane, thf and diethyl ether and insoluble in hexane. It was fully characterised by analytical and spectroscopic methods and X-ray crystallography, which confirmed the chelating coordination mode of FcPN. Slow diffusion of hexane into a solution of **2** in dichloromethane resulted in crystals suitable for X-ray diffraction studies. An ORTEP view of the molecule is shown in Figure 1; selected bond lengths are listed in the caption.

[Ru($\eta^5$-$C_9H_7$)Cl(COD)] —FcPN, THF, Δ→ [Ru($\eta^5$-$C_9H_7$)Cl{$\kappa^2$(*P*,*N*)-FcPN}]

**2**

Scheme 4.

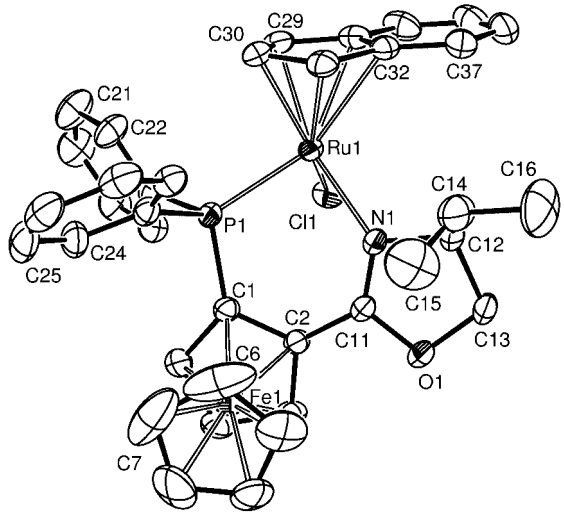


Figure 1. Molecular structure and atom-labelling scheme for complex **2**. Non-hydrogen atoms are represented by their 30% probability ellipsoids. Hydrogen atoms have been omitted for clarity. Selected bond lengths [Å]: Ru(1)–C* 1.884(4), Ru(1)–N(1) 2.137(2), Ru(1)–P(1) 2.228(1), Ru(1)–Cl(1) 2.434(1), N(1)–C(11) 1.284(3), P(1)–C(1) 1.813(3), C(1)–C(2) 1.444(4), C(2)–C(11) 1.444(4). Selected bond angles [°]: C*–Ru(1)–P(1) 126.27(6), C*–Ru(1)–N(1) 132.78(8), C*–Ru(1)–Cl(1) 120.73(6), N(1)–Ru(1)–P(1) 90.65(6), N(1)–Ru(1)–Cl(1) 83.56(6), P(1)–Ru(1)–Cl(1) 88.60(3), C(1)–P(1)–Ru(1) 112.94(9), N(1)–C(11)–C(2) 128.8(2), C(1)–C(2)–C(11) 125.8(2), C(2)–C(1)–P(1) 123.6(2). C* means the centroid of atoms C(29), C(30), C(31), C(32) and C(33).

The complex adopts a three-legged piano-stool structure with P and N atoms from the bidentate chelating FcPN ligand and the Cl atom as the legs. The Ru–N, Ru–P and

 © 2007 Wiley-VCH Verlag GmbH & Co. KGaA, Weinheim 

Ru–Cl bond lengths are 2.137(2), 2.227(1) and 2.434(1) Å respectively. The ruthenium atom interacts in an $\eta^5$ fashion with the five-membered C29–C33 ring of the indenyl ligand, although in an asymmetric way as the Ru–C bond lengths range from 2.134(3) to 2.382(3) Å. The chelating six-membered ring shows an envelope conformation. The crystal structure of **2** indicates that only one diastereoisomer ($S_{Ru}$,*S*,$S_P$) is present in the crystal.

Although the crystallisation of complex **2** gives rise to the isolation of only one diastereoisomer, the $^1H$, $^{31}P\{^1H\}$ and $^{13}C\{^1H\}$ NMR spectra in $CD_2Cl_2$ (see Experimental Section) indicate the presence of two isomers. In particular, the $^{31}P\{^1H\}$ NMR spectrum shows two signals at $\delta$ = 63.8 and 60.7 ppm whose ratio is dependent on the solvent, thereby suggesting a potential epimerisation of the $S_{Ru}$,*S*,$S_P$ into the $R_{Ru}$,*S*,$S_P$ diastereoisomer, a behaviour that is typical for configurationally unstable chiral-at-metal complexes.[15] Chloride dissociation as well as the opening of the Ru–P–N chelate ring could promote this isomerisation. However, complex **2** behaves as a neutral species since its conductivity values in dichloromethane (4.2 $\Omega^{-1}cm^2mol^{-1}$) and acetone (1.5 $\Omega^{-1}cm^2mol^{-1}$) are rather low. Provided that no ring opening is observed for ruthenium complexes with the FcPN ligand,[10,11] we assume that two rotamers[16] arising from different favoured conformations of the indenyl ring[14] are formed in solution.

### *Synthesis of the Alkynyl Derivatives [Ru(η⁵-C₉H₇)-(C≡CR){κ²(P,N)-FcPN}] [R = Ph (3a), p-CH₃C₆H₄ (3b)]*

Reaction of complex **2** with HC≡CR and KOH in methanol affords the alkynyl complexes [Ru($\eta^5$-$C_9H_7$)-(C≡CR){$\kappa^2$(*P*,*N*)-FcPN}] [R = Ph (**3a**), *p*-$CH_3C_6H_4$ (**3b**)], which were isolated as air-stable brown solids [Yields: 79% (**3a**) and 69% (**3b**); Scheme 5].

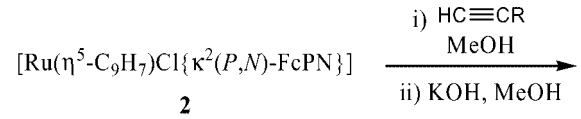


[Ru($\eta^5$-$C_9H_7$)(C≡CR){$\kappa^2$(*P*,*N*)-FcPN}]

R = Ph (**3a**), *p*-$CH_3C_6H_4$ (**3b**)

Scheme 5.

Complexes **3a**,**b** are soluble in dichloromethane, thf and diethyl ether and insoluble in hexane. Both complexes were characterised analytically and spectroscopically (see the Experimental Section for details). In contrast to its chloride precursor **2**, all spectroscopic data are consistent with the presence of only one diastereoisomer. The following observations are of particular interest: i) the singlet resonances observed at $\delta$ = 69.3 (**3a**) and 68.4 ppm (**3b**) in the $^{31}P\{^1H\}$ NMR spectra remain unchanged within the range –90 to 20 °C, thus obviating the possibility of a dynamic process in solution; ii) the $^{13}C\{^1H\}$ NMR spectrum shows the expected resonances of the alkynyl groups (doublet signals for $C_\alpha$ [$\delta$ = 82.8 ppm ($J_{C,P}$ = 44.0 Hz) for **3a**; $\delta$ = 82.1 ppm ($J_{C,P}$ = 44.7 Hz) for **3b**] and singlets for $C_\beta$ [$\delta$ = 110.7 (**3a**) and 109.9 ppm (**3b**)]). In addition, the IR spectra (KBr) show the characteristic ν(C≡C) absorption at 2073 (**3a**) and 2074 $cm^{-1}$ (**3b**).

The absolute configuration of the ruthenium atom in these complexes was determined from an X-ray diffraction study of complex **3a**. Single crystals suitable for X-ray diffraction analysis were obtained by slow diffusion of hexane into a solution of complex **3a** in dichloromethane. An ORTEP-type view of the complex is shown in Figure 2; selected bonding data are listed in the caption.

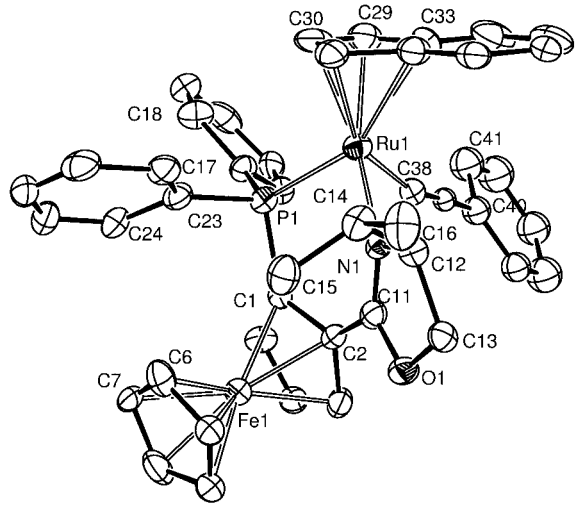


Figure 2. Molecular structure and atom-labelling scheme for complex **3a**. Non-hydrogen atoms are represented by their 10% probability ellipsoids. Hydrogen atoms have been omitted for clarity. Selected bond lengths [Å]: Ru(1)–C* 1.894(4), Ru(1)–N(1) 2.098(11), Ru(1)–P(1) 2.207(4), Ru(1)–C(38) 2.042(14), C(38)–C(39) 1.11(2) [1.27(3)], N(1)–C(11) 1.438(16), P(1)–C(1) 1.867(14), C(1)–C(2) 1.446(17), C(2)–C(11) 1.462(18). Selected bond angles [°]: C*–Ru(1)–P(1) 127.77(7), C*–Ru(1)–N(1) 132.33(5), C*–Ru(1)–C(38) 119.27(7), N(1)–Ru(1)–P(1) 89.6(3), N(1)–Ru(1)–C(38) 88.0(4), P(1)–Ru(1)–C(38) 84.6(4), C(1)–P(1)–Ru(1) 111.5(4), N(1)–C(11)–C(2) 124.8(14), C(1)–C(2)–C(11) 127.4(13), C(2)–C(1)–P(1) 120.5(11). C* means the centroid of atoms C(29), C(30), C(31), C(32) and C(33).

The complex is very similar to complex **2**. The Ru–N and Ru–P bond lengths are 2.098(11) and 2.207(4) Å, respectively, very similar to those found in **2**. The alkynyl ligand is disordered and is distributed over two positions with an equal occupancy factor. The two images have C38 as common atom [the Ru–C(38) bond length is 2.042(14) Å]. The Ru–C bond lengths involving the asymmetric $\eta^5$ interaction of the Ru atom with the five-membered ring of the indenyl ligand span from 2.10(2) to 2.34(2) Å. The stereochemistry around the ruthenium atom is $S_{Ru}$,*S*,$S_P$ and therefore no change occurs with respect to the precursor complex **2**.

 © 2007 Wiley-VCH Verlag GmbH & Co. KGaA, Weinheim 

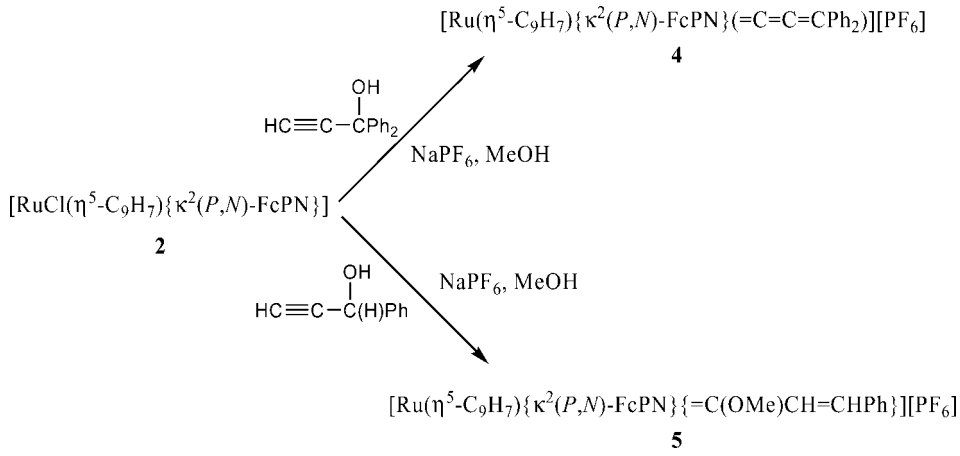


Scheme 6.

### *Synthesis of Allenylidene [Ru(η⁵-C₉H₇)[κ²(P,N)-FcPN](=C=C=CPh₂)][PF₆] (4) and Methoxycarbene [Ru(η⁵-C₉H₇){κ²(P,N)-FcPN}{=C(OMe)CH=CHPh}][PF₆] (5) Complexes*

The activation of terminal alkynes with ruthenium(II) complexes is the most direct route to cumulenylidene and related carbene complexes.[17] Following this methodology we explored the reactivity of [Ru($\eta^5$-$C_9H_7$)Cl{$\kappa^2$(*P*,*N*)-FcPN}] (**2**) towards propargylic alcohols. As expected, the reaction of equimolecular amounts of complex **2** and 1,1-diphenyl-2-propyn-1-ol in methanol in the presence of $NaPF_6$ yields the allenylidene derivative [Ru($\eta^5$-$C_9H_7$){$\kappa^2$(*P*,*N*)-FcPN}(=C=C=$CPh_2$)][$PF_6$] (**4**), which was isolated as a purple-red solid in 65% yield after work-up (Scheme 6). However, the reaction with 1-phenyl-2-propyn-1-ol gives the alkenyl carbene [Ru($\eta^5$-$C_9H_7$){$\kappa^2$(*P*,*N*)-FcPN}{=C(OMe)CH=CHPh}][$PF_6$] (**5**), which was isolated as a yellow solid in 73% yield after work-up (Scheme 6).

Complexes **4** and **5** are soluble in dichloromethane and thf and insoluble in diethyl ether and hexane. The elemental analysis and IR and NMR spectroscopic data are in accordance with the proposed formulations (see Experimental Section for details). The most representative spectroscopic data are as follows. The IR spectrum of complex **4** shows the ν(C=C=C) absorption at 1926 $cm^{-1}$ and the absorption corresponding to the $PF_6^-$ group at 841 $cm^{-1}$. Its $^{31}P\{^1H\}$ spectrum displays a singlet resonance at $\delta$ = 50.7 ppm and its $^{13}C\{^1H\}$ NMR spectrum shows a low-field signal for $C_\alpha$ [doublet at $\delta$ = 286.9 ppm ($J_{C,P}$ = 21.0 Hz)] and two broad singlet resonances at $\delta$ = 215.9 and 154.5 ppm for $C_\beta$ and $C_\gamma$, respectively. The IR spectrum of complex **5** shows the ν(Ru=C) absorption at 1955 $cm^{-1}$ and the ν(P–F) absorption at 841 $cm^{-1}$. The expected singlet in the $^{31}P\{^1H\}$ NMR spectra appears at $\delta$ = 57.4 ppm, and the $^1H$ NMR spectrum shows a singlet at $\delta$ = 3.75 ppm due to the methoxy group and two doublets at $\delta$ = 5.09 and 5.97 ppm ($J_{H,H}$ = 16.0 Hz) for the hydrogen atoms of the alkenyl group. The coupling constant for these doublets indicates a *trans* disposition. The $^{13}C\{^1H\}$NMR spectrum shows a low-field doublet at $\delta$ = 305.9 ppm ($J_{C,P}$ = 16.4 Hz) due to the $C_\alpha$ resonance.

The formation of **5** probably proceeds through the nucleophilic addition of one methanol molecule to the intermediate cationic allenylidene complex [Ru($\eta^5$-$C_9H_7$){$\kappa^2$(*P*,*N*)-FcPN}(=C=C=CHPh)]$^+$.[17]

## Synthesis of $\eta^6$-Arene Complexes

### *Synthesis of [RuX(η⁶-arene){κ²(P,N)-FcPN}][PF₆] [arene = p-cymene, X = Cl (6a), H (7), N₃ (8); arene = 1,2,3,4-tetramethylbenzene, X = Cl (6b)]*

The reaction of two equivalents of FcPN with [RuCl(μ-Cl)($\eta^6$-arene)]$_2$ ($\eta^6$-arene = *p*-cymene, 1,2,3,4-tetramethylbenzene) in refluxing ethanol leads to the complexes [RuCl($\eta^6$-arene){$\kappa^2$(*P*,*N*)-FcPN}][Cl]. Subsequent chloride exchange with $NaPF_6$ gives the hexafluorophosphate salts [RuCl($\eta^6$-arene){$\kappa^2$(*P*,*N*)-FcPN}][$PF_6$] [$\eta^6$-arene = *p*-cymene (**6a**), 1,2,3,4-tetramethylbenzene (**6b**)], which were isolated as air-stable orange solids in yields of 89% (**6a**) and 86% (**6b**; Scheme 7).

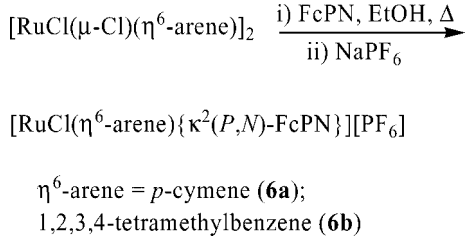


Scheme 7.

Complex **6a** has been shown to be a good precursor of analogous derivatives by metathesis of the chloride ligand. Thus, the reaction with an excess of Li[$BHEt_3$] leads to the hydride derivative [RuH($\eta^6$-*p*-cymene){$\kappa^2$(*P*,*N*)-FcPN}][$PF_6$] (**7**), which was isolated as an air-stable green solid in 75% yield. Likewise, the treatment of **6a** with sodium azide in refluxing methanol gives [Ru($N_3$)($\eta^6$-*p*-cymene){$\kappa^2$(*P*,*N*)-

 © 2007 Wiley-VCH Verlag GmbH & Co. KGaA, Weinheim 

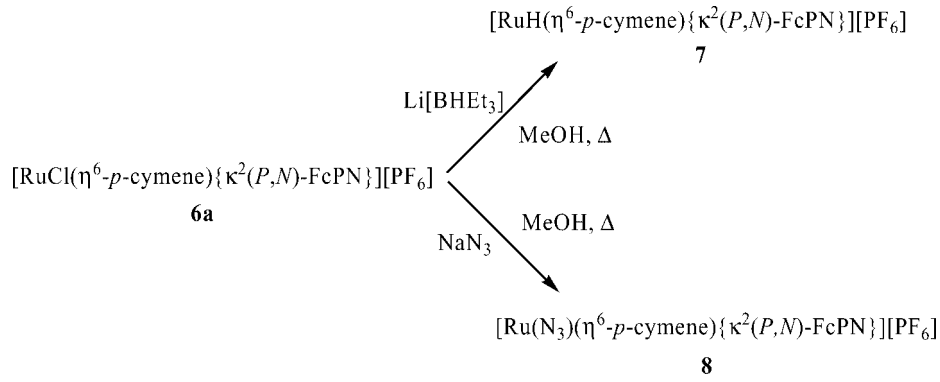


Scheme 8.

FcPN}][$PF_6$] (**8**), which was isolated as a brown solid in 71% yield (Scheme 8).

The analytical and spectroscopic data support these formulations (see Experimental Section for details). The syntheses are diastereoselective, as determined from the NMR spectra ($^1H$, $^{31}P\{^1H\}$ and $^{13}C\{^1H\}$). In particular, the $^{31}P\{^1H\}$ NMR spectra display only a singlet resonance at $\delta$ = 24.9 (**6a**) 26.5 (**6b**) 50.7 (**7**) and 23.1 ppm (**8**) at room temperature. The spectra of the complexes remain unchanged in the range –90 to 20 °C, thus indicating that, as for the analogous indenyl complex **1**, no dynamic processes take place in this temperature range. The most characteristic spectroscopic features are the ν(Ru–H) absorption at 1967 $cm^{-1}$ in the IR spectrum (KBr) and a high-field doublet for the hydride resonance at $\delta$ = –8.66 ($^2J_{H,P}$ = 43.7 Hz) in the $^1H$ NMR spectrum of complex **7**, and the ν(N=N=N) absorption at 2035 $cm^{-1}$in the IR spectrum (KBr) of complex **8**.

NOESY experiments performed on complex **6a** show cross-peaks between the $OCH_2$ and CHN protons of the oxazoline and the isopropyl group of the *p*-cymene ligand, thus indicating thier spatial proximity and suggesting that the stereochemistry around the metal is $R_{Ru}$ (see Scheme 9).

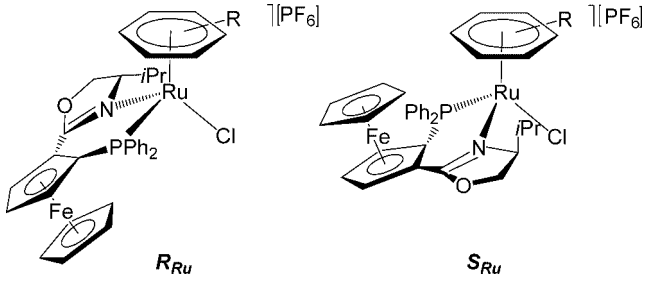


Scheme 9.

This stereochemistry was confirmed by an X-ray crystal diffraction study. Single crystals suitable for X-ray diffraction analysis were obtained by slow diffusion of hexane into a solution of complex **6a** in dichloromethane. Two crystallographically independent cations (A and B) and two $PF_6^-$ anions are present in the crystals of **6a**. The two independent complexes are very similar but differ in the coordination of the *p*-cymene: in the former the isopropyl substituent is almost eclipsed with respect to the Cl atom whereas in the latter the methyl substituent is almost eclipsed with the Cl atom. Practically, the *p*-cymene ligand is rotated by 180° in the two complexes. An ORTEP view of one of the two independent cationic complexes (B) is shown in Figure 3; selected bonding data for both complexes are listed in the caption.

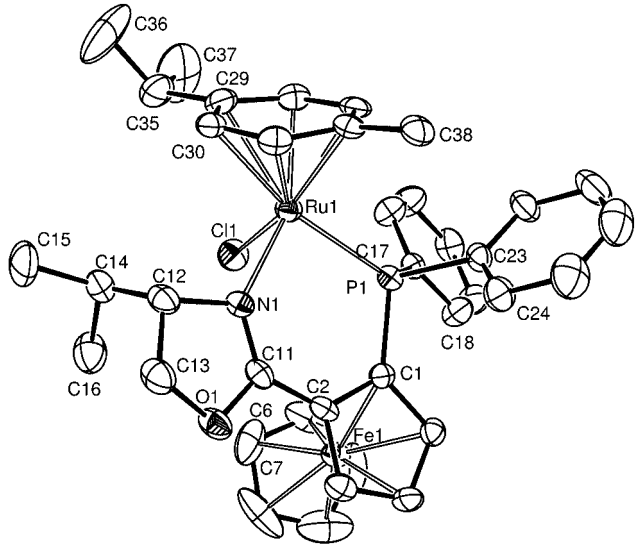


Figure 3. Molecular structure and atom-labelling scheme for complex **6a**. Non-hydrogen atoms are represented by their 30% probability ellipsoids. Hydrogen atoms have been omitted for clarity. Selected bond lengths [Å]: Ru(1)–C* 1.749(4) [1.744(5)], Ru(1)–N(1) 2.150(4) [2.122(3)], Ru(1)–P(1) 2.349(1) [2.347(1)], Ru(1)–Cl(1) 2.374(1) [2.390(1)], N(1)–C(11) 1.270(5) [1.283(5)], P(1)–C(1) 1.806(4) [1.824(5)], C(1)–C(2) 1.433(6) [1.427(6)], C(2)–C(11) 1.445(6) [1.443(6)]. Selected bond angles [°]: C*–Ru(1)–P(1) 127.66(6) [129.30(5)], C*–Ru(1)–N(1) 129.99(4) [126.22(4)], C*–Ru(1)–Cl(1) 122.58(8) [125.27(5)], N(1)–Ru(1)–P(1) 89.41(10) [91.54(11)], N(1)–Ru(1)–Cl(1) 84.23(10) [84.99(10)], P(1)–Ru(1)–Cl(1) 89.35(5) [85.68(4)], C(1)–P(1)–Ru(1) 114.27(15) [113.32(15)], N(1)–C(11)–C(2) 131.5(5) [129.0(5)], C(1)–C(2)–C(11) 127.3(4) [129.8(4)], C(2)–C(1)–P(1) 122.6(4) [122.9(4)]. C* means the centroid of atoms C(29), C(30), C(31), C(32), C(33), C(34). Data in square brackets refer to complex B.

As shown in Figure 3, the absolute configuration at the ruthenium atom ($R_{Ru}$) is the opposite to that found for the indenyl complexes **2** and **3a**. The Ru–N bond lengths [2.150(4) and 2.122(3) Å for cation B] do not differ significantly from those observed in **2** and **3a**, while the Ru–P

 © 2007 Wiley-VCH Verlag GmbH & Co. KGaA, Weinheim 

ones are longer [2.349(1) and 2.347(1) Å]. The Ru–Cl bond lengths [2.374(1) and 2.390(1) Å] are slightly shorter than that found in **2** [2.434(1) Å]. The Ru–C bond lengths of the *p*-cymene ligand span from 2.180(5) to 2.321(4) Å.

The stereochemistry $R_{Ru}$ found for complex **6a** can also be tentatively assigned to be the same for the chloride (**6b**), hydride (**7**) and azide (**8**) complexes.

## Conclusions

In summary, we have described the diastereoselective synthesis of new chiral-at-metal $\eta^5$ and $\eta^6$ half-sandwich ruthenium(II) complexes containing the chiral ligand (4*S*)-2-[($S_p$)-2-(diphenylphosphanyl)ferrocenyl]-4-(methylethyl)-oxazoline (FcPN). The absolute configuration of the ruthenium atoms has been determined by X-ray analyses of complexes **2**, **3a** and **6a**.

## Experimental Section

**General Procedures:** All manipulations were performed under an atmosphere of dry nitrogen using standard vacuum-line and Schlenk techniques. All reagents were obtained from commercial suppliers and used without further purification. Solvents were dried by standard methods and distilled under nitrogen before use. The compounds [Ru($\eta^5$-$C_9H_7$)Cl(COD)],[12e] [Ru($\eta^5$-$C_9H_7$)Cl($PPh_3$)],[18] [RuCl(μ-Cl)($\eta^6$-$C_{10}H_{14}$)]$_2$ [19] and (4*S*)-2-[($S_p$)-2-(diphenylphosphanyl)ferrocenyl]-4-(methylethyl)oxazoline (FcPN).[4] were prepared by previously reported methods. IR spectra were recorded with a Perkin–Elmer FT-IR Paragon 1000 spectrometer. The conductivities were measured at room temperature, for approximately $5 \times 10^{-4}$ M water solutions, with a Jenway PCM3 conductimeter. The C, H and N analyses were carried out with a Perkin–Elmer 240-B microanalyzer. NMR spectra were recorded with a Bruker AC300 or 300DPX instrument at 300 ($^1$H), 121.5 ($^{31}$P) or 75.4 MHz ($^{13}$C) using $SiMe_4$ or 85% $H_3PO_4$ as standards. DEPT experiments were carried out for all compounds. The following atom labels are used for the indenyl $^1$H and $^{13}$C{$^1$H} spectroscopic data. The label Ind-6 is used for the benzo ring.

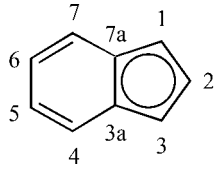


**Synthesis of [Ru($\eta^5$-$C_9H_7$){$\kappa^2$(*P*,*N*)-FcPN}($PPh_3$)][$PF_6$] (1):** FcPN (859 mg, 1.8 mmol) was added to a solution of [Ru ($\eta^5$-$C_9H_7$)-Cl($PPh_3$)$_2$] (1320 mg, 1.7 mmol) in toluene (80 mL) and the reaction mixture was refluxed for 2.5 h. The solvents were removed under vacuum and the resulting solid was dissolved in methanol (65 mL). $NaPF_6$ (857 mg, 5.1 mmol) was added and the solution was stirred for 1 h at room temperature. The solvents were then removed under vacuum and the solid residue extracted with $CH_2Cl_2$. The solution was filtered through kieselguhr, concentrated under vacuum to a volume of about 5 mL, and diethyl ether (80 mL) was added. The solid was washed with diethyl ether ($2 \times 80$ mL) and dried under vacuum to afford complex **1** as an orange-red solid. Yield: 1.521 g (81%). Conductivity [$(CH_3)_2CO$, 20 °C]: 123 $\Omega^{-1}$ cm$^2$ mol$^{-1}$. FTIR (KBr): $\tilde{\nu}$ = 841 cm$^{-1}$ ($PF_6^-$). $^1$H NMR (300 MHz, $CD_2Cl_2$, 20 °C): $\delta$ = 7.77–7.05 (m, 28 H, Ph, Ind-6), 5.91 (m, 1 H, H-1 or H-3), 5.65 (d, $^3J_{H,H}$ = 8.3 Hz, 1 H, Ind-6), 5.32 (m, 1 H, H-1 or H-3), 4.94 (m, 1 H, $C_5H_3$), 4.68 (t, $^3J_{H,H}$ = 5.0 Hz, 1 H, $C_5H_3$), 4.66 (m, 1 H, $C_5H_3$), 4.34 (dd, $^2J_{H,H}$ = 1.9, $^3J_{H,H}$ = 8.7 Hz, 1 H, $OCH_2$), 3.64 (s, 5 H, $C_5H_5$), 3.60 (d, $^3J_{H,H}$ = 8.7 Hz, 1 H, $OCH_2$), 3.18 (m, 1 H, H-2), 3.03 (t, $^3J_{H,H}$ = 8.7 Hz, 1 H, CHN), 2.89 [sept d, $^3J_{H,H}$ = 2.6, $^3J_{H,H}$ = 7.0 Hz, 1 H, C*H*($CH_3$)$_2$], 1.28 (d, $^3J_{H,H}$ = 7.0 Hz, 3 H, $CH_3$), 1.26 (d, $^3J_{H,H}$ = 7.0 Hz, 3 H, $CH_3$) ppm. $^{13}$C NMR (75.4 MHz, $CD_2Cl_2$, 20 °C): $\delta$ = 170.8 (s, *C*$OCH_2$), 143.6–128.0 (Ph, Ind-6), 124.6 (s, Ind-6), 124.4 (s, Ind), 116.8 (d, $^2J_{C,P}$ = 3.8 Hz, C-3a or C-7a), 112.3 (m, C-3a or C-7a), 93.7 (s, C-2), 79.0 (d, $J_{C,P}$ = 39.4 Hz, $CPPh_2$), 75.7 (s, $C_5H_3$), 75.3 (s, $C_5H_3$), 74.5 (d, $^2J_{C,P}$ = 19.1 Hz, *C*$CPPh_2$), 73.2 (d, $^3J_{C,P}$ = 6.4 Hz, CHN), 72.9 (d, $^2J_{C,P}$ = 7.0 Hz, $C_5H_3$), 72.3 (s, $C_5H_5$), 68.4 (d, $^2J_{C,P}$ = 12.7 Hz, C-1 or C-3), 67.7 (s, $OCH_2$), 63.6 (s, C-1 or C-3), 29.2 [s, *C*H($CH_3$)$_2$], 19.5 (s, $CH_3$), 15.2 (s, $CH_3$) ppm. $^{31}$P{$^1$H} NMR (121.5 MHz, $CD_2Cl_2$, 20 °C): $\delta$ = 58.8 (d, $^2J_{P,P}$ = 36.5 Hz), 34.7 (d, $^2J_{P,P}$ = 36.5 Hz) ppm. $C_{55}H_{50}F_6FeNOP_3Ru$ (1104.82): calcd. C 59.79, H 4.56, N 1.27; found C 59.42, H 4.48, N 1.27.

**Synthesis of [Ru($\eta^5$-$C_9H_7$)Cl{$\kappa^2$(*P*,*N*)-FcPN}] (2):** FcPN (1203 mg, 2.5 mmol) was added to a solution of [RuCl($\eta^5$-$C_9H_7$)(COD)] (900 mg, 2.5 mmol) in thf (90 mL) and the reaction mixture was refluxed for 7 h. The solvents were removed under vacuum to a volume of about 5 mL, and hexane (50 mL) was added. The solid was washed with hexane ($2 \times 50$ mL) and dried under vacuum to afford complex **2** as a red solid. Yield: 1.741 g (95%). $C_{37}H_{35}ClFeNOPRu$ (733.02): calcd. C 60.63, H 4.81, N 1.91; found C 60.47, H 4.72, N 1.83.

**Rotamer 2a:** $^1$H NMR (300 MHz, $CDCl_3$, 20 °C): $\delta$ = 8.67–7.01 (m, 14 H, Ph, Ind-6), 5.07 (m, 1 H, H-1 or H-3), 4.87 (m, 1 H, H-1 or H-3), 4.49–4.38 (m, 3 H, CHN, $C_5H_3$), 4.32 (dd, $^2J_{H,H}$ = 4.1, $^3J_{H,H}$ = 8.7 Hz, 1 H, $OCH_2$), 4.10 (br. s, 1 H, $C_5H_3$), 4.04 (s, 5 H, $C_5H_5$), 3.74 (m, 1 H, $OCH_2$), 3.05 (m, 1 H, H-2), 2.37 [m, 1 H, C*H*($CH_3$)$_2$], 0.76 (d, $^3J_{H,H}$ = 6.4 Hz, 3 H, $CH_3$), 0.69 (d, $^3J_{H,H}$ = 6.9 Hz, 3 H, $CH_3$) ppm. $^{13}$C NMR (75.4 MHz, $CD_2Cl_2$, 20 °C): $\delta$ = 166.4 (s, *C*$OCH_2$), 145.6–124.6 (Ph, Ind-6), 121.1 (s, Ind-6), 117.4 (d, $^2J_{C,P}$ = 6.0 Hz, C-3a or C-7a), 111.6 4 (m, C-3a or C-7a), 85.7 (s, C-6), 77.7 (br. s, $C_5H_3$), 75.8 (d, $J_{C,P}$ = 37.0 Hz, $CPPh_2$), 75.0 (d, $^2J_{C,P}$ = 18.1 Hz, *C*$CPPh_2$), 73.8 (d, $^2J_{C,P}$ = 3.8 Hz, $C_5H_3$), 71.8 (s, $C_5H_5$), 71.6 (m, CHN), 71.0 (s, $C_5H_3$), 68.0 (s, $OCH_2$), 63.6 (s, C-1 or C-3), 50.8 (s, C-1 or C-3), 28.0 [s, *C*H($CH_3$)$_2$], 19.4 (s, $CH_3$), 15.8 (s, $CH_3$) ppm. $^{31}$P{$^1$H} NMR (121.5 MHz, $CD_2Cl_2$, 20 °C): $\delta$ = 60.7 (s) ppm.

**Rotamer 2b:** $^1$H NMR (300 MHz, $CDCl_3$, 20 °C): $\delta$ = 8.67–7.01 (m, 14 H, Ph, Ind-6), 4.82 (m, 1 H, H-1 or H-3), 4.72 (m, 1 H, H-1 or H-3), 4.56 (m, 2 H, CHN, $C_5H_3$), 4.53 (t, $^3J_{H,H}$ = 2.7 Hz, 1 H, $C_5H_3$), 4.24 (m, 1 H, $OCH_2$), 4.14 (br. s, 1 H, $C_5H_3$), 3.61 (m, 1 H, $OCH_2$), 3.56 (m, 1 H, H-2), 3.52 (s, 5 H, $C_5H_5$), 2.73 [m, 1 H, C*H*($CH_3$)$_2$], 1.13 (d, $^3J_{H,H}$ = 6.9 Hz, 3 H, $CH_3$), 1.03 (d, $^3J_{H,H}$ = 6.9 Hz, 3 H, $CH_3$) ppm. $^{13}$C NMR (75.4 MHz, $CD_2Cl_2$, 20 °C): $\delta$ = 168.0 (s, *C*$OCH_2$), 140.1–124.6 (Ph, Ind-6), 122.5 (s, Ind-6), 114.3 (d, $^2J_{C,P}$ = 5.3 Hz, C-3a or C-7a), 111.6 (d, $^2J_{C,P}$ = 7.6 Hz, C-3a or C-7a), 82.3 (s, C-2), 80.7 (d, $J_{C,P}$ = 37.8 Hz, $CPPh_2$), 75.3 (br. s, $C_5H_3$), 74.4 (d, $^2J_{C,P}$ = 18.9 Hz, *C*$CPPh_2$), 73.3 (br. s, $C_5H_3$), 73.2 (m, CHN), 71.3 (s, $C_5H_5$), 71.1 (s, $C_5H_3$), 67.7 (s, $OCH_2$), 57.8 (s, C-1 or C-3), 55.2 (s, C-1 or C-3), 29.4 [s, *C*H($CH_3$)$_2$], 19.1 (s, $CH_3$), 14.3 (s, $CH_3$) ppm. $^{31}$P{$^1$H} NMR (121.5 MHz, $CD_2Cl_2$, 20 °C): $\delta$ = 63.8 (s) ppm.

**Synthesis of [Ru($\eta^5$-$C_9H_7$)(C≡CR){$\kappa^2$(*P*,*N*)-FcPN}] [R = Ph (3a), *p*-$CH_3C_6H_4$ (3b)]:** HC≡CR (0.55 mmol) was added to a solution of complex **2** (367 mg, 0.5 mmol) in MeOH (35 mL), and the reaction mixture was stirred at room temperature for 10 min. A solution of

 © 2007 Wiley-VCH Verlag GmbH & Co. KGaA, Weinheim 

KOH in MeOH (5 mL, 0.11 M) was then added and the resulting solution stirred at room temperature for 5 h (**3a**) or 1.5 h (**3b**). The solvents were removed under vacuum and the resulting solid extracted with $CH_2Cl_2$. The solution was filtered through kieselguhr, concentrated under vacuum to a volume of about 2 mL, and hexane (20 mL) was added. The solid was washed with hexane (20 mL) and dried under vacuum to afford complexes **3a**,**b** as brown solids.

**3a:** Yield: 0.315 g (79%). FTIR (KBr): $\tilde{\nu}$ = 2073 $cm^{-1}$ (C≡C). $^1H$ NMR (300 MHz, $CDCl_3$, 20 °C): $\delta$ = 8.08–6.99 (m, 16 H, Ph, Ind-6), 6.88 (d, $^3J_{H,H}$ = 7.4 Hz, 1 H, Ind-6), 6.75 (d, $^3J_{H,H}$ = 7.4 Hz, 2 H, Ind-6), 5.34 (br. s, 1 H, H-1 or H-3), 4.73 (m, 2 H, $C_5H_3$ and H-1 or H-3), 4.62 (br. s, 1 H, $C_5H_3$), 4.56 (m, 1 H, $C_5H_3$), 4.22 (dd, $^2J_{H,H}$ = 4.2, $^3J_{H,H}$ = 8.9 Hz, 1 H, $OCH_2$), 4.06 (t, $^3J_{H,H}$ = 8.9 Hz, 1 H, CHN), 3.49 (s, 5 H, $C_5H_5$), 3.28 (br. s, 1 H, H-2), 3.22 (m, 1 H, $OCH_2$), 2.78 [m, 1 H, C*H*$(CH_3)_2$], 1.08 (d, $^3J_{H,H}$ = 7.0 Hz, 3 H, $CH_3$), 0.93 (d, $^3J_{H,H}$ = 6.8 Hz, 3 H, $CH_3$) ppm. $^{13}C$ NMR (75.4 MHz, $CD_2Cl_2$, 20 °C): $\delta$ = 165.9 (s, *C*$OCH_2$), 141.3–125.1 (Ph), 124.9 (s, Ind), 123.2 (s, Ind), 123.0 (s, Ind), 120.7 (s, Ind), 113.9 (d, $^2J_{C,P}$ = 6.1 Hz, C-3a or C-7a), 112.0 (d, $^2J_{C,P}$ = 4.6 Hz, C-3a or C-7a), 110.7 (br. s, $C_\beta$) 87.4 (s, C-2), 82.8 (d, $^2J_{C,P}$ = 44.0 Hz, $C_\alpha$), 74.9 (br. s, $C_5H_3$), 74.7 (m, *C*$CPPh_2$), 73.4 (br. s, $C_5H_3$), 73.2 (m, $CPPh_2$), 71.0 (s, $C_5H_5$), 70.5 (m, CHN, $C_5H_3$), 66.6 (s, $OCH_2$), 63.6 (s, C-1 or C-3), 58.4 (s, C-1 or C-3), 28.8 [s, *C*$H(CH_3)_2$], 18.9 (s, $CH_3$), 14.5 (s, $CH_3$) ppm. $^{31}P\{^1H\}$ NMR (121.5 MHz, $CD_2Cl_2$, 20 °C): $\delta$ = 69.3 (s) ppm. $C_{45}H_{40}FeNOPRu{\cdot}CH_2Cl_2$ (883.63): calcd. C 62.53, H 4.79, N 1.59; found C 62.39, H 4.63, N 1.50.

**3b:** Yield: 0.280 g (69%). FTIR (KBr): $\tilde{\nu}$ = 2074 $cm^{-1}$ (C≡C). $^1H$ NMR (300 MHz, $CD_2Cl_2$, 20 °C): $\delta$ = 8.07–7.01 (m, 14 H, Ph), 6.82 (m, 2 H, Ind-6), 6.64 (d, $^3J_{H,H}$ = 8.1 Hz, 2 H, Ind-6), 5.32 (br. s, 1 H, H-1 or H-3), 4.72 (m, 2 H, $C_5H_3$ and H-1 or H-3), 4.61 (br. s, 1 H, $C_5H_3$), 4.54 (m, 1 H, $C_5H_3$), 4.22 (dd, $^2J_{H,H}$ = 4.4, $^3J_{H,H}$ = 9.0 Hz, 1 H, $OCH_2$), 4.05 (t, $^3J_{H,H}$ = 9.0 Hz, 1 H, CHN), 3.48 (s, 5 H, $C_5H_5$), 3.27 (br. s, 1 H, H-2), 3.22 (dd, $^2J_{H,H}$ = 4.4, $^3J_{H,H}$ = 9.0 Hz, 1 H, $OCH_2$), 2.79 [sept d, $^3J_{H,H}$ = 2.8, $^3J_{H,H}$ = 7.0 Hz, 1 H, C*H*$(CH_3)_2$], 2.21 (s, 3 H, $C_6H_4CH_3$) 1.07 (d, $^3J_{H,H}$ = 7.0 Hz, 3 H, $CH_3$), 0.92 (d, $^3J_{H,H}$ = 7.0 Hz, 3 H, $CH_3$) ppm. $^{13}C$ NMR (75.4 MHz, $CD_2Cl_2$, 20 °C): $\delta$ = 166.1 (s, *C*$OCH_2$), 141.6–127.1 (Ph), 126.3 (s, Ind), 125.1 (s, Ind), 123.2 (s, Ind), 121.0 (s, Ind), 113.3 (d, $^2J_{C,P}$ = 6.5 Hz, C-3a or C-7a), 111.9 (d, $^2J_{C,P}$ = 4.4 Hz, C-3a or C-7a), 109.9 (br. s, $C_\beta$) 87.7 (s, C-2), 82.1 (d, $^2J_{C,P}$ = 44.7 Hz, $C_\alpha$), 74.9 (br. s, $C_5H_3$), 74.5 (d, $^2J_{C,P}$ = 18.5 Hz, *C*$CPPh_2$), 73.6 (br. s, $C_5H_3$), 73.3 (m, $CPPh_2$), 71.2 (s, $C_5H_5$), 70.8 (m, CHN, $C_5H_3$), 67.3 (s, $OCH_2$), 66.6 (s, C-1 or C-3), 57.4 (s, C-1 or C-3), 29.1 [s, *C*$H(CH_3)_2$], 21.3 (s, $C_6H_4CH_3$), 19.2 (s, $CH_3$), 14.7 (s, $CH_3$) ppm. $^{31}P\{^1H\}$ NMR (121.5 MHz, $CD_2Cl_2$, 20 °C): $\delta$ = 68.4 (s) ppm. $C_{46}H_{42}FeNOPRu$ (812.72): calcd. C 67.98, H 5.21, N 1.72; found C 67.53, H 5.12, N 1.66.

**Synthesis of [Ru(η⁵-$C_9H_7$){κ²(*P*,*N*)-FcPN}(=C=C=$CPh_2$)][$PF_6$] (4):** A solution of complex **2** (220 mg, 0.3 mmol) and $NaPF_6$ (55 mg, 0.33 mmol) in methanol (25 mL) was stirred at room temperature for 10 min and 1,1-diphenyl-2-propyn-1-ol (69 mg, 0.33 mmol) was then added. The reaction mixture was stirred at room temperature for 1.5 h. The solvents were removed under vacuum and the resulting solid extracted with $CH_2Cl_2$. The solution was filtered through kieselguhr, concentrated under vacuum to a volume of about 2 mL, and diethyl ether (50 mL) was added. The solid was washed with diethyl ether (2 × 50 mL) and dried under vacuum to afford complex **4** as a purple solid. Yield: 0.201 g (65%). Conductivity [$(CH_3)_2CO$, 20 °C]: 103 $\Omega^{-1}cm^2mol^{-1}$. FTIR (KBr): $\tilde{\nu}$ = 1926 (C=C=C), 841 ($PF_6^-$) $cm^{-1}$. $^1H$ NMR (300 MHz, $CDCl_3$, 20 °C): $\delta$ = 8.07–7.15 (m, 22 H, Ph, Ind-6), 5.76 (m, 2 H, Ind-6), 5.21 (br. s, 1 H, Ind), 5.16 (br. s, 1 H, Ind), 5.10 (m, 1 H, $C_5H_3$), 5.00 (br. s, 1 H, Ind), 4.65 (dd, $^2J_{H,H}$ = 3.6, $^3J_{H,H}$ = 9.1 Hz, 1 H, $OCH_2$), 4.38 (s, 5 H, $C_5H_5$), 4.33 (t, $^3J_{H,H}$ = 9.1 Hz, 1 H, CHN), 4.10 (br. s, 1 H, $C_5H_3$), 3.70 (s, 5 H, $C_5H_5$), 3.49 (m, 1 H, $OCH_2$), 2.57 [m, 1 H, C*H*$(CH_3)_2$], 1.18 (d, $^3J_{H,H}$ = 6.8 Hz, 3 H, $CH_3$), 1.00 (d, $^3J_{H,H}$ = 6.6 Hz, 3 H, $CH_3$) ppm. $^{13}C$ NMR (75.4 MHz, $CD_2Cl_2$, 20 °C): $\delta$ = 286.9 (d, $^2J_{C,P}$ = 21.0 Hz, $C_\alpha$), 215.9 (s, $C_\beta$), 171.3 (s, *C*$OCH_2$), 154.5 (s, $C_\gamma$), 145.6–128.4 (Ph, Ind-6), 126.3 (s, Ind-6), 124.4 (s, Ind-6), 118.4 (br. s, C-3a or C-7a), 117.8 (br. s, C-3a or C-7a), 99.0 (s, C-2), 80.6 (d, $J_{C,P}$ = 50.7 Hz, $CPPh_2$), 77.1 (m, *C*$CPPh_2$, C-1, C-3), 76.0 (s, $C_5H_3$), 74.0 (m, CHN, $C_5H_3$), 72.8 (s, $C_5H_5$), 68.8 (s, $OCH_2$), 30.7 [s, *C*$H(CH_3)_2$], 18.9 (s, $CH_3$), 14.8 (s, $CH_3$) ppm. $^{31}P\{^1H\}$ NMR (121.5 MHz, $CD_2Cl_2$, 20 °C): $\delta$ = 50.7 (s) ppm. $C_{52}H_{45}F_6FeNOP_2Ru$ (1032.77): calcd. C 60.47, H 4.39, N 1.36; found C 61.02, H 4.61, N 1.32.

**Synthesis of [Ru(η⁵-$C_9H_7$){κ²(*P*,*N*)-FcPN}{=C(OMe)CH=CHPh}][$PF_6$] (5):** A solution of complex **2** (357 mg, 0.5 mmol) and $NaPF_6$ (92 mg, 0.55 mmol) in methanol (40 mL) was stirred at room temperature for 10 min. 1-Phenyl-2-propyn-1-ol (67 μL, 0.55 mmol) was then added and the reaction mixture stirred at room temperature for 3 h. The solvents were removed under vacuum and the resulting solid extracted with $CH_2Cl_2$. The solution was filtered through kieselguhr, concentrated under vacuum to a volume of about 2 mL, and diethyl ether (50 mL) was added. The solid was washed with diethyl ether (2 × 50 mL) and dried under vacuum to afford complex **5** as a yellow solid. Yield: 0.361 g (73%). Conductivity [$(CH_3)_2CO$, 20 °C]: 107 $\Omega^{-1}cm^2mol^{-1}$. FTIR (KBr): $\tilde{\nu}$ = 1955 (Ru=C), 841 ($PF_6^-$) $cm^{-1}$. $^1H$ NMR (300 MHz, $CDCl_3$, 20 °C): $\delta$ = 7.87–7.03 (m, 19 H, Ph, Ind-6), 5.97 (d, $^3J_{H,H}$ = 16.0 Hz, 1 H, =CH), 5.39 (br. s, 1 H, Ind), 5.09 (d, $^3J_{H,H}$ = 16.0 Hz, 1 H, =CH), 4.88 (br. s, 2 H, Ind, $C_5H_3$), 4.81 (br. s, 2 H, Ind, $C_5H_3$), 4.73 (br. s, 2 H, Ind, $C_5H_3$), 4.28 (m, 2 H, $C_5H_3$, $OCH_2$), 4.09 (br. s, 1 H, $C_5H_3$), 3.82 (m, 1 H, $OCH_2$), 3.75 (s, 1 H, $OCH_3$), 3.73 (m, 1 H, CHN), 3.52 (s, 5 H, $C_5H_5$), 2.82 [m, 1 H, C*H*$(CH_3)_2$], 1.22 (d, $^3J_{H,H}$ = 6.7 Hz, 3 H, $CH_3$), 0.94 (d, $^3J_{H,H}$ = 6.7 Hz, 3 H, $CH_3$) ppm. $^{13}C$ NMR (75.4 MHz, $CD_2Cl_2$, 20 °C): $\delta$ = 305.9 (d, $^2J_{C,P}$ = 16.4 Hz, $C_\alpha$), 170.3 (s, *C*$OCH_2$), 140.8 (s, =CH), 139.3–126.9 (Ph, Ind-6, =CH), 123.6 (s, Ind-6), 123.4 (s, Ind-6), 115.4 (br. s, C-3a or C-7a), 112.9 (d, $^2J_{C,P}$ = 4.6 Hz, C-3a or C-7a), 96.7 (s, C-2), 80.4 (d, $J_{C,P}$ = 44.6 Hz, $CPPh_2$), 76.4 (s, $C_5H_3$), 75.7 (s, $C_5H_3$), 73.5 (d, $^2J_{C,P}$ = 19.5 Hz, *C*$CPPh_2$), 72.5 (m, CHN, $C_5H_3$), 72.2 (s, $C_5H_5$), 70.0 (s, C-1 or C-3), 68.0 (s, $OCH_2$), 63.6 (s, $OCH_3$), 63.5 (s, C-1 or C-3), 29.3 [s, *C*$H(CH_3)_2$], 19.4 (s, $CH_3$), 15.0 (s, $CH_3$) ppm. $^{31}P\{^1H\}$ NMR (121.5 MHz, $CD_2Cl_2$, 20 °C): $\delta$ = 57.4 (s) ppm. $C_{47}H_{45}F_6FeNO_2P_2Ru{\cdot}CH_2Cl_2$ (1073.65): calcd. C 53.70, H 4.41, N 1.30; found C 54.18, H 4.53, N 1.33.

**Synthesis of [RuCl(η⁶-arene){κ²(*P*,*N*)-FcPN}][$PF_6$] [arene = *p*-cymene (6a), 1,2,3,4-tetramethylbenzene (6b)]:** FcPN (770 mg, 1.6 mmol) was added to a solution of [RuCl(μ-Cl)(η⁶-arene)]$_2$ (490 mg, 0.8 mmol) in ethanol (100 mL), and the reaction mixture was refluxed for 2 h. After cooling, $NaPF_6$ (269 mg, 1.6 mmol) was added and the solution was stirred for 1 h at room temperature. The solvents were removed under vacuum and the solid residue extracted with $CH_2Cl_2$. The solution was filtered through kieselguhr, concentrated under vacuum to a volume of about 5 mL, and diethyl ether (50 mL) was added. The solid residue was washed with diethyl ether (2 × 50 mL) and dried under vacuum to afford complexes **6a**,**b** as orange solids.

**6a:** Yield: 1.277 g (89%). Conductivity [$(CH_3)_2CO$, 20 °C]: 101 $\Omega^{-1}cm^2mol^{-1}$. FTIR (KBr): $\tilde{\nu}$ = 841 ($PF_6^-$) $cm^{-1}$. $^1H$ NMR (300 MHz, $CDCl_3$, 20 °C): $\delta$ = 8.23 (m, 2 H, Ph), 7.62 (m, 3 H, Ph), 7.41 (m, 3 H, Ph), 6.92 (m, 2 H, Ph), 5.82 (d, $^3J_{H,H}$ = 6.3 Hz,

 © 2007 Wiley-VCH Verlag GmbH & Co. KGaA, Weinheim 

1 H, CH), 5.59 (d, $^3J_{H,H}$ = 6.3 Hz, 1 H, CH), 5.55 (d, $^3J_{H,H}$ = 6.0 Hz, 1 H, CH), 5.16 (br. s, 1 H, $C_5H_3$), 4.80 (t, $^3J_{H,H}$ = 2.6 Hz, 1 H, $C_5H_3$), 4.77 (m, 1 H, $OCH_2$), 4.55 (m, 4 H, $C_5H_3$, $OCH_2$, CHN, CH), 4.05 (s, 5 H, $C_5H_5$), 2.93 [m, 1 H, C*H*$(CH_3)_2$], 2.08 [m, 1 H, C*H*$(CH_3)_2$], 1.94 (s, 3 H, $CH_3$), 1.14 (d, $^3J_{H,H}$ = 7.1 Hz, 3 H, $CH_3$), 1.03 (d, $^3J_{H,H}$ = 6.8 Hz, 3 H, $CH_3$), 0.96 (d, $^3J_{H,H}$ = 6.3 Hz, 3 H, $CH_3$), 0.85 (d, $^3J_{H,H}$ = 6.8 Hz, 3 H, $CH_3$) ppm. $^{13}$C NMR (75.4 MHz, $CD_2Cl_2$, 20 °C): $\delta$ = 171.0 (br. s, *C*$OCH_2$), 141.1–128.7 (Ph), 110.4 (s, *C*CH), 102.3 (s, *C*CH), 98.6 (d, $^2J_{C,P}$ = 7.6 Hz, CH), 92.5 (m, CH), 89.4 (br. s, CH), 85.1 (m, CH), 80.3 (br. s, $C_5H_3$), 76.0 (d, CHN, $^3J_{C,P}$ = 5.1 Hz), 75.2 (br. s, $C_5H_3$), 74.2 (d, $J_{C,P}$ = 7.6 Hz, $C_5H_3$), 73.4 (d, $J_{C,P}$ = 17.2 Hz, *C*$CPPh_2$), 72.8 (s, $C_5H_5$), 70.7 (d, $^2J_{C,P}$ = 47.7 Hz, $CPPh_2$), 68.6 (s, $OCH_2$), 30.8 [s, *C*H$(CH_3)_2$], 29.2 [s, *C*H$(CH_3)_2$], 23.8 (s, *C*$CH_3$), 21.6 (s, $CH_3$), 20.1 (s, $CH_3$), 18.1 (s, $CH_3$), 16.2 (s, $CH_3$) ppm. $^{31}$P{$^1$H} NMR (121.5 MHz, $CD_2Cl_2$, 20 °C): $\delta$ = 24.9 (s) ppm. $C_{38}H_{42}ClF_6FeNOP_2Ru$ (897.05): calcd. C 50.88, H 4.72, N 1.56; found C 51.12, H 4.86, N 1.40.

**6b:** Yield: 1.234 g (86%. Conductivity [$(CH_3)_2CO$, 20 °C]: 115 $\Omega^{-1}$ cm$^2$ mol$^{-1}$. FTIR (KBr): $\tilde{\nu}$ = 846 ($PF_6^-$) cm$^{-1}$. $^1$H NMR (300 MHz, $CDCl_3$, 20 °C): $\delta$ = 8.26 (m, 2 H, Ph), 7.70–7.61 (m, 3 H, Ph), 7.43 (m, 3 H, Ph), 7.04 (m, 2 H, Ph), 5.13 (br. s, 1 H, $C_5H_3$), 4.96 (m, 1 H, CH), 4.79 (br. s, 1 H, $C_5H_3$), 4.59 (m, 2 H, $C_5H_3$, CH), 4.40 (m, 1 H, $OCH_2$), 4.17 (m, 1 H, $OCH_2$), 4.01 (s, 5 H, $C_5H_5$), 3.03 (s, 1 H, CHN), 2.47 [m, 1 H, C*H*$(CH_3)_2$], 2.22 (s, 3 H, $CH_3$), 2.09 (br. s, 3 H, $CH_3$), 2.07 (br. s, 3 H, $CH_3$), 1.70 (br. s, 3 H, $CH_3$), 1.07 (d, $^3J_{H,H}$ = 6.3 Hz, 3 H, $CH_3$), 0.97 (d, $^3J_{H,H}$ = 6.3 Hz, 3 H, $CH_3$) ppm. $^{13}$C NMR (75.4 MHz, $CD_2Cl_2$, 20 °C): $\delta$ = 171.3 (s, *C*$OCH_2$), 142.9–128.5 (Ph), 113.5 (d, $^2J_{C,P}$ = 8.3 Hz, *C*Me), 112.5 (d, $^2J_{C,P}$ = 7.4 Hz, *C*Me), 96.9 (d, $^2J_{C,P}$ = 8.3 Hz, 2 *C*Me), 90.8 (s, CH), 83.6 (s, CH), 77.8 (d, $J_{C,P}$ = 51.8 Hz, $CPPh_2$), 76.4 (br. s, $C_5H_3$), 76.0 (d, $^2J_{C,P}$ = 5.6 Hz, CHN), 74.3 (br. s, $C_5H_3$), 74.2 (d, $^2J_{C,P}$ = 8.3 Hz, $C_5H_3$), 73.3 (d, $^2J_{C,P}$ = 17.6 Hz, *C*$CPPh_2$), 72.6 (s, $C_5H_5$), 69.2 (br. s, $OCH_2$), 28.6 [s, *C*H$(CH_3)_2$], 19.5(s, $CH_3$), 19.0 (s, $CH_3$), 18.4 (s, $CH_3$), 16.6 (s, $CH_3$), 16.3 (s, $CH_3$), 14.6 (s, $CH_3$) ppm. $^{31}$P{$^1$H} NMR (121.5 MHz, $CD_2Cl_2$, 20 °C): $\delta$ = 26.5 (s) ppm. $C_{38}H_{42}ClF_6FeNOP_2Ru$ (897.05): calcd. C 50.88, H 4.72. N 1.56; found C 50.18, H 4.40, N 1.34.

**Synthesis of [RuH($\eta^6$-*p*-cymene){$\kappa^2$(*P*,*N*)-FcPN}][$PF_6$] (7):** $Li[BHEt_3]$ (1.3 mL of a 1 M solution in thf, 1.3 mmol) was added to a solution of **6a** (897 mg, 1.0 mmol) in thf (100 mL) and the reaction mixture was stirred at room temp. for 14 h. The solvents were removed under vacuum and the solid residue extracted with $CH_2Cl_2$. The solution was filtered through kieselguhr, concentrated under vacuum to a volume of about 5 mL, and diethyl ether (50 mL) was added. The solid was washed with diethyl ether (2 × 50 mL) and dried under vacuum to afford complex **7** as a green solid. Yield: 0.647 g (75%). Conductivity [$(CH_3)_2CO$, 20 °C]: 96 $\Omega^{-1}$ cm$^2$ mol$^{-1}$. FTIR (KBr): $\tilde{\nu}$ = 1967 (RuH), 842 ($PF_6^-$) cm$^{-1}$. $^1$H NMR (300 MHz, $CD_2Cl_2$, 20 °C): $\delta$ = 8.12 (m, 2 H, Ph), 7.64 (m, 3 H, Ph), 7.40 (m, 3 H, Ph), 7.06 (m, 2 H, Ph), 5.12 (m, 1 H, CH), 5.02 (br. s, 1 H, $C_5H_3$), 4.98 (m, 2 H, CH), 4.90 (m, 1 H, CH), 4.74 (t, $^3J_{H,H}$ = 2.4 Hz, 1 H, $C_5H_3$), 4.52 (br. s, 1 H, $C_5H_3$), 4.42 (dd, $^2J_{H,H}$ = 4.0, $^3J_{H,H}$ = 9.1 Hz, 1 H, $OCH_2$), 4.31 (t, $^3J_{H,H}$ = 9.1 Hz, 1 H, CHN), 3.73 (m, 6 H, $C_5H_5$, $OCH_2$), 2.55 [sept d, $^3J_{H,H}$ = 3.2, $^3J_{H,H}$ = 7.2 Hz, 1 H, C*H*$(CH_3)_2$], 2.30 [m, 1 H, C*H*-$(CH_3)_2$], 1.86 (br. s, 3 H, $CH_3$), 1.26 (d, $^3J_{H,H}$ = 6.8 Hz, 3 H, $CH_3$), 1.16 (d, $^3J_{H,H}$ = 6.8 Hz, 3 H, $CH_3$), 1.02 (d, $^3J_{H,H}$ = 7.2 Hz, 3 H, $CH_3$), 0.84 (d, $^3J_{H,H}$ = 7.2 Hz, 3 H, $CH_3$), –8.66 (d, $^2J_{H,P}$ = 43.7 Hz, 1 H, RuH) ppm. $^{13}$C NMR (75.4 MHz, $CD_2Cl_2$, 20 °C): $\delta$ = 168.6 (br. s, *C*$OCH_2$), 141.9–128.7 (Ph), 119.7 (s, *C*CH), 106.3 (m, *C*CH), 93.4 (s, 2 C, CH), 92.3 (s, 2 C, CH), 78.3 (br. s, $C_5H_3$), 75.6 (d, $^3J_{C,P}$ = 4.5 Hz, CHN), 75.0 (br. s, $C_5H_3$), 74.2 (d, $J_{C,P}$ = 46.7 Hz, $CPPh_2$), 73.7 (m, *C*$CPPh_2$, $C_5H_3$), 71.8 (s, $C_5H_5$), 67.5 (s, $OCH_2$), 32.2 [s, *C*H$(CH_3)_2$], 24.5 [s, *C*H$(CH_3)_2$], 24.4 (s, $CH_3$), 23.6 (s, $CH_3$), 19.1 (s, $CH_3$), 18.8 (s, $CH_3$), 13.8 (s, $CH_3$) ppm. $^{31}$P{$^1$H} NMR (121.5 MHz, $CD_2Cl_2$, 20 °C): $\delta$ = 50.7 (s) ppm. $C_{40}H_{47}F_6FeNOP_2Ru{\cdot}2CH_2Cl_2$ (1032.5): calcd. C 46.53, H 4.59, N 1.36; found C 46.05, H 4.29, N 1.61.

**Synthesis of [Ru($N_3$)($\eta^6$-*p*-cymene){$\kappa^2$(*P*,*N*)-FcPN}][$PF_6$] (8):** A solution of **6a** (449 mg, 0.5 mmol) and $NaN_3$ (49 mg, 0.75 mmol) in methanol (50 mL) was refluxed for 4 h. After cooling, the solvents were removed under vacuum and the solid residue extracted with $CH_2Cl_2$. The solution was filtered through kieselguhr, concentrated under vacuum to a volume of about 5 mL, and diethyl ether (70 mL) was added. The solid was washed with diethyl ether (2 × 70 mL) and dried under vacuum to afford complex **8** as a brown solid. Yield: 0.321 g (71%). Conductivity [$(CH_3)_2CO$, 20 °C]: 84 $\Omega^{-1}$ cm$^2$ mol$^{-1}$. FTIR (KBr): $\tilde{\nu}$ = 2035 ($N_3$), 841 ($PF_6^-$) cm$^{-1}$. $^1$H NMR (300 MHz, $CD_2Cl_2$, 20 °C): $\delta$ = 8.10 (m, 2 H, Ph), 7.70 (m, 3 H, Ph), 7.45 (m, 3 H, Ph), 7.03 (m, 2 H, Ph), 5.89 (d, $^3J_{H,H}$ = 6.0 Hz, 1 H, 1 H, CH), 5.81 (d, $^3J_{H,H}$ = 6.0 Hz, 1 H, 1 H, CH), 5.39 (br. s, 1 H, CH), 5.17 (br. s, 1 H, $C_5H_3$), 4.84 (br. s, 1 H, $C_5H_3$), 4.64 (m, 1 H, $OCH_2$), 4.57 (br. s, 1 H, $C_5H_3$), 4.45 (t, $^3J_{H,H}$ = 9.0 Hz, 1 H, CHN), 4.33 (m, 1 H, $OCH_2$), 4.12 (br. s, 1 H, CH), 3.98 (s, 5 H, $C_5H_5$), 2.70 [m, 1 H, C*H*$(CH_3)_2$], 2.38 [m, 1 H, C*H*$(CH_3)_2$], 2.32 (s, 3 H, $CH_3$), 1.17 (d, $^3J_{H,H}$ = 6.3 Hz, 3 H, $CH_3$), 1.11 (d, $^3J_{H,H}$ = 6.3 Hz, 3 H, $CH_3$), 1.02 (d, $^3J_{H,H}$ = 6.3 Hz, 3 H, $CH_3$), 0.67 (d, $^3J_{H,H}$ = 6.3 Hz, 3 H, $CH_3$) ppm. $^{13}$C NMR (75.4 MHz, $CD_2Cl_2$, 20 °C): $\delta$ = 171.3 (br. s, *C*$OCH_2$), 139.7–129.2 (Ph), 119.4 (s, *C*CH), 99.9 (m, CH), 99.2 (s, *C*CH), 94.3 (m, CH), 88.4 (br. s, CH), 85.4 (s, CH), 79.7 (s, $C_5H_3$), 76.4 (d, $^3J_{C,P}$ = 5.4 Hz, CHN), 75.2 (s, $C_5H_3$), 74.4 (d, $^2J_{C,P}$ = 7.2 Hz, $C_5H_3$), 72.5 (m, $C_5H_5$, *C*$CPPh_2$), 69.4 (d, $J_{C,P}$ = 33.2 Hz, $CPPh_2$), 68.4 (s, $OCH_2$), 31.0 [s, *C*H$(CH_3)_2$], 29.9 [s, *C*H$(CH_3)_2$], 24.4 (s, $CH_3$), 21.1 (s, $CH_3$), 19.9 (s, $CH_3$), 17.4 (s, $CH_3$), 14.0 (s, $CH_3$) ppm. $^{31}$P{$^1$H} NMR (121.5 MHz, $CD_2Cl_2$, 20 °C): $\delta$ = 23.1 (s) ppm. $C_{38}H_{42}F_6FeN_4OP_2Ru$ (903.62): calcd. C 50.51, H 4.68, N 6.20; found C 49.9, H 4.75, N 6.24.

**X-ray Crystal Structure Determination of Complexes 2·$CH_2Cl_2$, 3a and 6a:** Data for **2**·$CH_2Cl_2$ and **6a** were collected at 293 K with a Bruker AXS SMART 1000 single-crystal diffractometer (Mo-$K_\alpha$ graphite-monochromated radiation, $\lambda$ = 0.71073 Å) equipped with an area detector,[20] while data for compound **3a** were collected at 293 K with a Philips PW1100 single-crystal diffractometer (Mo-$K_\alpha$ graphite-monochromated radiation, $\lambda$ = 0.71073 Å). Crystals of **3a** were of poor quality, so the collection of the reflections was limited to $\theta$ = 22°. Details of the X-ray data collections are reported in Table 1. The structures were solved by Patterson and direct methods with SHELXS-97 and refined against $F^2$ with SHELXL-97,[21] with anisotropic thermal parameters for all non-hydrogen atoms. The dichloromethane molecule in **2**·$CH_2Cl_2$ was found to be disordered over two positions with occupancy factors of 0.60 and 0.40 and refined isotropically. The C≡CPh moiety in **3a** was found to be disordered over two positions with occupancy factors of 0.5 and refined with geometrical restraints (idealised planar ring). Four fluorine atoms of the two independent $PF_6^-$ anions in **6a** were found to be disordered and distributed over two positions (occupancy factors of 0.7 and 0.3). The absolute configuration of the three structures was confirmed by refining the Flack parameter, which showed the enantiopure character of the crystal.

CCDC-608692 (for **2**), -608693 (for **3a**) and -608694 (for **6a**) contain the supplementary crystallographic data for this paper. These data can be obtained free of charge from The Cambridge Crystallographic Data Centre via www.ccdc.cam.ac.uk/data_request/cif.

 © 2007 Wiley-VCH Verlag GmbH & Co. KGaA, Weinheim 

Table 1. Crystallographic data for **2**, **3a** and **6a**.[a]

| | **2**·$CH_2Cl_2$ | **3a** | **6a** |
|---|---|---|---|
| Formula | $C_{37}H_{35}ClFeNOPRu{\cdot}CH_2Cl_2$ | $C_{45}H_{40}FeNOPRu$ | $C_{38}H_{42}ClFeNOPRu{\cdot}PF_6$ |
| Formula weight | 817.93 | 798.67 | 897.04 |
| Crystal system | orthorhombic | tetragonal | orthorhombic |
| Space group | $P2_12_12_1$ | $P4_32_12$ | $P2_12_12_1$ |
| $a$ [Å] | 11.399(3) | 13.802(2) | 10.778(3) |
| $b$ [Å] | 16.106(5) | 13.802(2) | 19.283(5) |
| $c$ [Å] | 19.434(5) | 42.161(7) | 36.654(9) |
| $V$ [Å$^3$] | 3568(2) | 8031(2) | 7618(3) |
| $Z$, $D_{calcd}$ [g cm$^{-3}$] | 4, 1.523 | 8, 1.321 | 4, 1.564 |
| $F$(000) | 1664 | 3280 | 3648 |
| $\mu$ [cm$^{-1}$] | 11.31 | 8.10 | 9.93 |
| Reflections collected | 54445 | 5424 | 72709 |
| Reflections unique | 10623 [$R_{int}$ = 0.0365] | 4862 [$R_{int}$ = 0.0487] | 13434 [$R_{int}$ = 0.0852] |
| Observed reflections [$I > 2\sigma(I)$] | 9535 | 2559 | 8666 |
| Parameters | 414 | 419 | 1001 |
| Final $R$ indices [$I > 2\sigma(I)$] | $R_1$ = 0.0329<br>$wR_2$ = 0.0909 | $R_1$ = 0.0658<br>$wR_2$ = 0.1516 | $R_1$ = 0.0366<br>$wR_2$ = 0.0480 |
| Final $R$ indices [all data] | $R_1$ = 0.0392<br>$wR_2$ = 0.0965 | $R_1$ = 0.1292<br>$wR_2$ = 0.1936 | $R_1$ = 0.0705<br>$wR_2$ = 0.0529 |
| Flack parameter | –0.02 | –0.03 | –0.008 |

[a] $R_1 = \Sigma||F_o| - |F_c||/\Sigma(F_o)$; $wR_2 = [\Sigma\{w(F_o^2 - F_c^2)^2\}/\Sigma\{w(F_o^2)^2\}]^{1/2}$.

## Acknowledgments

This work was supported by the Spanish Ministerio de Ciencia y Tecnología (M.C.T) (BQU2003-00255) and Fondo Europeo de Desarrollo Regional (FEDER) (1FD97-0565).

[1] a) R. Noyori, *Angew. Chem. Int. Ed.* **2002**, *41*, 2008–2022; b) *Catalytic Asymmetric Synthesis*, 2nd ed. (Ed.: I. Ojima), Wiley VCH, **2000**; c) *Comprehensive Asymmetric Catalysis*, vols. I–III (Eds.: E. N. Jacobsen, A. Pfaltz, H. Yamamoto), Springer-Verlag, **1999**.

[2] a) S. Cabrera, O. G. Mancheno, R. G. Arrayas, I. Alonso, P. Mauleon, J. C. Carretero, *Pure Appl. Chem.* **2006**, *78*, 257–265; b) G. C. Fu, *Acc. Chem. Res.* **2004**, *37*, 542–547; c) P. Barbaro, C. Bianchini, G. Giambastiani, S. L. Parisel, *Coord. Chem. Rev.* **2004**, *248*, 2131–2150; d) L. X. Dai, T. Tu, S. L. You, W. P. Deng, X. L. Hou, *Acc. Chem. Res.* **2003**, *36*, 659–667; e) T. J. Colacot, *Chem. Rev.* **2003**, *103*, 3101–3118.

[3] a) O. B. Sutclife, M. R. Bryce, *Tetrahedron: Asymmetry* **2003**, *14*, 2297–2325; b) W. Deng, X. Hou, L. Dai, Y. Yu, W. Xia, *Chem. Commun.* **2000**, 285–286; c) E. L. Stangeland, T. Sammakia, *Tetrahedron* **1997**, *53*, 16503–16510; d) T. Sammakia, E. L. Stangeland, *J. Org. Chem.* **1997**, *62*, 6104–6105; e) C. J. Richards, A. W. Mulvaney, *Tetrahedron: Asymmetry* **1996**, *7*, 1419–1430; f) C. J. Richards, T. Damalidis, D. E. Hibbs, M. B. Hursthouse, *Synlett* **1995**, 74; g) T. Sammakia, H. A. Latham, *J. Org. Chem.* **1995**, *60*, 6002–6003.

[4] a) Y. Nishibayashi, K. Segawa, Y. Arikawa, K. Ohe, M. Hidai, S. Uemura, *J. Organomet. Chem.* **1997**, *545–546*, 381–398; b) Y. Nishibayashi, S. Uemura, *Synlett* **1995**, 79–81.

[5] a) P. Braunstein, *Chem. Rev.* **2006**, *106*, 134–159; b) V. V. Grushin, *Chem. Rev.* **2004**, *104*, 1629–1662; c) A. Caballero, F. A. Jalón, B. R. Manzano, G. Espino, M. Perez-Manrique, A. Mucientes, F. J. Poblete, M. Maestro, *Organometallics* **2004**, *23*, 5694–5706; d) M. S. Rahman, M. Oliana, K. K. Hii, *Tetrahedron: Asymmetry* **2004**, *15*, 1835–1840; e) M. Kuriyama, K. Nagai, K. Yamada, Y. Miwa, T. Taga, K. Tomioka, *J. Am. Chem. Soc.* **2002**, *124*, 8932–8939; f) P. Braunstein, F. Naud, *Angew. Chem. Int. Ed.* **2001**, *40*, 680–699; g) P. Braunstein, F. Naud, S. J. Rettig, *New J. Chem.* **2001**, *25*, 32–39; h) C. Standfest-Hauser, C. Slugovc, K. Mereiter, R. Schmid, K. Kirchner, L. Xiao, W. Weissensteiner, *J. Chem. Soc., Dalton Trans.* **2001**, 2989–2995; i) P. Espinet, K. Soulantica, *Coord. Chem. Rev.* **1999**, *193–195*, 499–556.

[6] F. Naud, C. Malan, F. Spindler, C. Rüggeberg, A. T. Schmidt, H. U. Blaser, *Adv. Synth. Catal.* **2006**, *348*, 47–50.

[7] a) I. Takei, Y. Nishibayashi, Y. Ishii, Y. Mizobe, S. Uemura, M. Hidai, *Chem. Commun.* **2001**, 2360–2361; b) I. Takei, Y. Nishibayashi, Y. Arikawa, S. Uemura, M. Hidai, *Organometallics* **1999**, *18*, 2271–2274.

[8] a) G. Onodera, Y. Nishibayashi, S. Uemura, *Angew. Chem. Int. Ed.* **2006**, *45*, 3819–3822; b) Y. Nishibayashi, A. Yamauchi, G. Onodera, S. Uemura, *J. Org. Chem.* **2003**, *68*, 5875–5880; c) P. Braunstein, F. Naud, S. J. Rettig, *New J. Chem.* **2001**, *25*, 32–39; d) G. Helmchen, A. Pfaltz, *Acc. Chem. Res.* **2000**, *33*, 336–345; e) T. Sammakia, E. L. Stangeland, *J. Org. Chem.* **1997**, *62*, 6104–6105.

[9] a) Y. Nishibayashi, I. Takei, S. Uemura, M. Hidai, *Organometallics* **1999**, *18*, 2291–2293; b) Y. Arikawa, M. Ueoka, K. Matoba, Y. Nishibayashi, M. Hidai, S. Uemura, *J. Organomet. Chem.* **1999**, *572*, 163–168; c) Y. Nishibayashi, I. Takei, S. Uemura, M. Hidai, *Organometallics* **1998**, *17*, 3420–3422.

[10] J. Gimeno, E. Lastra, C. Madrigal, C. Graiff, A. Tiripicchio, *J. Organomet. Chem.* **2002**, *663*, 204–212.

[11] J. Gimeno, E. Lastra, C. Madrigal, C. Graiff, A. Tiripicchio, *J. Organomet. Chem.* **2001**, *637–639*, 463–468.

[12] a) J. Díez, M. P. Gamasa, E. Lastra, A. García-Fernández, M. P. Tarazona, *Eur. J. Inorg. Chem.* **2006**, 2855–2864; b) P. Crochet, J. Díez, M. A. Fernández Zúmel, J. Gimeno, *Adv. Synth. Catal.* **2006**, *348*, 93–100; c) V. Cadierno, P. Crochet, S. E. García-Garrido, J. Gimeno, *Dalton Trans.* **2004**, 3635–3641; d) P. Álvarez, J. Gimeno, E. Lastra, *Organometallics* **2002**, *21*, 5678–5680; e) P. Álvarez, J. Gimeno, E. Lastra, S. García-Granda, J. F. Van der Maelen, M. Bassetti, *Organometallics* **2001**, *20*, 3762–3771.

[13] a) J. Díez, M. P. Gamasa, J. Gimeno, E. Lastra, A. Villar, *Organometallics* **2005**, *24*, 1410–1418; b) P. Álvarez, E. Lastra, J. Gimeno, M. Bassetti, L. R. Falvello, *J. Am. Chem. Soc.* **2003**, *125*, 2386–2387.

[14] V. Cadierno, J. Díez, M. P. Gamasa, J. Gimeno, E. Lastra, *Coord. Chem. Rev.* **1999**, *193–195*, 147–205 and references cited therein.

[15] a) C. Ganter, *Chem. Soc. Rev.* **2003**, *32*, 130–138; b) H. Brunner, *Eur. J. Inorg. Chem.* **2001**, 905–912.

 © 2007 Wiley-VCH Verlag GmbH & Co. KGaA, Weinheim 

[16] We have also observed the presence of two rotamers in $C_6D_6$ solution for $[OsH(\eta^5\text{-}C_9H_7)(PPh_3)_2]$ (J. Gimeno, M. Gonzalez-Cueva, E. Lastra, E. Perez-Carreño, S. García-Granda, *Inorg. Chim. Acta* **2003**, *347*, 99–106) and $CD_2Cl_2$ solution for complexes $[RuI(\eta^5\text{-}C_9H_7)(CO)(PR_3)]$ (R = P*i*Pr$_3$, PCy$_3$) (C. Gonzalez-Bernardo, PhD Thesis, Universidad de Oviedo, **1999**).

[17] a) V. Cadierno, M. P. Gamasa, J. Gimeno, *Coord. Chem. Rev.* **2004**, *248*, 1627–1657; b) M. I. Bruce, *Coord. Chem. Rev.* **2004**, *248*, 1603–1625; c) M. I. Bruce, *Chem. Rev.* **1998**, *98*, 2797–2858.

[18] a) L. A. Oro, M. A. Ciriano, M. Campo, C. Foces-Foces, F. H. Cano, *J. Organomet. Chem.* **1985**, *289*, 117–131; b) M. P. Gamasa, J. Gimeno, C. Gonzalez-Bernardo, B. M. Martín-Vaca, D. Monti, M. Bassetti, *Organometallics* **1996**, *15*, 302–308.

[19] a) M. A. Bennett, A. K. Smith, *J. Chem. Soc., Dalton Trans.* **1974**, 233–241; b) J. W. Hull Jr, W. L. Gladfelter, *Organometallics* **1984**, *3*, 605–613.

[20] *SMART Software Users Guide*, *Version 5.1*, Bruker Analytical X-ray Systems, Madison, WI, **1999**; *SAINT Software Users Guide, Version 6.0*, Bruker Analytical X-ray Systems, Madison, WI, **1999**; G. M. Sheldrick, *SADABS*, Bruker Analytical X-ray Systems, Madison, WI, **1999**.

[21] G. M. Sheldrick, *SHELX-97, Programs for Crystal Structure Analysis (release 97-2)*, Göttingen, Germany, **1997**.

Received: October 3, 2006
Published Online: January 3, 2007

 © 2007 Wiley-VCH Verlag GmbH & Co. KGaA, Weinheim 

DOI: 10.1002/ejic.200600844

# A Series of Cadmium(II) Coordination Polymers Synthesized at different pH Values

Zhengang Guo,[a] Rong Cao,*[a] Xiaoju Li,[a] Daqiang Yuan,[a] Wenhua Bi,[a] Xiandong Zhu,[a] and Yafeng Li[a]

**Keywords:** Cadmium / Polymers / Self-assembly / Photoluminescence

A new family of cadmium(II) coordination polymers, $\{[Cd(Hbic)_2\cdot(H_2O)_2]\cdot 2H_2O\}_n$ (**1**), $[Cd(Hbic)_2]_n$ (**2**), $[Cd(Hbic)_2\cdot(H_2O)]_n$ (**3**), $H_2bic$ = 1H-benzimidazole-5-carboxylic acid, has been hydrothermally prepared by the assembly of $Cd^{II}$ with $H_2bic$. A change in the pH values resulted in a series of compounds with different compositions and dimensionalities. Formed at the lowest pH, compound **1** has a two-dimensional supramolecular structure, which contains 1D chains extended by hydrogen bonds. At a slightly higher pH, compound **2** is synthesized with a higher number of deprotonated carboxylate groups per cadmium atom. A further increase in the pH leads to 3D dinuclear compound **3** with yellow-green emitting fluorescence.

(© Wiley-VCH Verlag GmbH & Co. KGaA, 69451 Weinheim, Germany, 2007)

## Introduction

The rational design and synthesis of metal–organic frameworks (MOFs) has undergone tremendous development owing to their structural and functional motifs,[1] which include magnetism,[2] catalysis,[3] luminescence,[4] and gas sorption.[5] The utilization of organic aromatic moieties containing carboxylic and nitrogen donor groups, for example imidazolecarboxylate or pyridylcarboxylate groups, can result in many intriguing polymers.[6] To obtain designed and predictable frameworks with potential properties, the observation of coordination polymers constructed from organic ligands and metal ions through a self-assembly route has been explored intensively, but it is still a challenge to date. The aromatic organic ligands with carboxy groups and nitrogen donors, on one hand, have been extensively employed in the construction of inorganic/organic hybrid materials for thermal stability and, on the other hand, can result in structures with high dimensions because of the multifunctional coordination sites.[7] The structure chemistry of functional groups such as carboxylates and nitrogen-donor groups are sensitive to pH values and the protonation states of these ligands. The formation of novel coordination compounds markedly depends on the metal ions.[8]

In order to have a better understanding of the effects of the pH value on the aromatic nitrogen-donor ligands, the reaction system of $H_2bic$ ($H_2bic$ = 1H-benzimidazole-5-carboxylic acid) and $Cd(NO_3)_2\cdot 4H_2O$ was studied. As a hybrid ligand, $Hbic^-$ possesses two kinds of resonance structures (Scheme 1). The conformation of polymorphism is worthy to explore.[9] Furthermore, there are four potentially coordinating sites: two oxygen atoms of the carboxylate group and two nitrogen atoms of the imidazole ring. Two protons, one from the carboxylate and the other from the nitrogen donor, should play an important role in the process of assembly. Consequently, $H_2bic$ is a good candidate for the investigation of the relation between the pH value and the coordination geometry. The diverse geometries of different metal ions may play critical roles in the assembly of metal–organic frameworks with various structures. The choice of metal ions in the systems is very important.[10] In the present work, we have selected cadmium(II) as metal nodes because of the luminescent characteristics. Other factors of the system such as the temperature, the amount of distilled water, and the type of stainless steel reactor are kept critically constant. Herein, we report the syntheses and characterizations of a new family of cadmium(II) coordination polymers: compounds $\{[Cd(Hbic)_2\cdot(H_2O)_2]\cdot 2H_2O\}_n$ (**1**), $[Cd(Hbic)_2]_n$ (**2**), and $[Cd(Hbic)_2\cdot(H_2O)]_n$ (**3**), built from the aromatic nitrogen-donor ligands $H_2bic$ and $Cd(NO_3)_2\cdot 4H_2O$. The three compounds have been characterized by IR

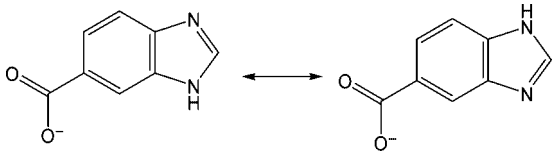

Scheme 1. Resonance structures of $Hbic^-$ ligand.

[a] State Key Laboratory of Structural Chemistry, Fujian Institute of Research on the Structure of Matter, Chinese Academy of Sciences,
Fujian, Fuzhou, 350002, China
Fax: +86-591-3714946
E-mail: rcao@ms.fjirsm.ac.cn

Supporting information for this article is available on the WWW under http://www.eurjic.org or from the author.



© 2007 Wiley-VCH Verlag GmbH & Co. KGaA, Weinheim

spectra, elemental analysis, thermogravimetric analysis, and fluorescent spectroscopy, as well as single-crystal X-ray diffraction analysis.[11–12] Discussion of the subtleties is addressed below.

## Results and Discussions

### Syntheses

Our aim is to investigate the effects of the pH value on the coordination behavior of aromatic nitrogen-donor ligands and the structures of the compounds thus formed. $H_2$bic and $Cd(NO_3)_2{\cdot}4H_2O$ were selected as starting materials in our study. We first carried out the reaction at a pH value of 5.0, compound **1** with a 2D supramolecular assembly was obtained, in which the carboxylic proton was deprotonated and $Hbic^-$ adopted a single coordination mode (Figure S1, a). We raised the pH value to 6.5 and compound **2** with a $4^4$ rhombus network structure was obtained, in which $Hbic^-$ adopted two different coordination modes (Figure S1, b and c). If the pH value was raised to 7.2, compound **3** with a 3D architecture was isolated, in which $Hbic^-$ also adopted two different coordination modes (Figure S1, d and e). The results illustrate that the pH value plays a crucial role on the coordination mode of $Hbic^-$ and the structures of the products. To confirm this, the reaction was carried out at a pH value between 5.0 and 6.5, a mixture of compounds **1** and **2** was obtained. If the reaction was carried out at a pH value between 6.5 and 7.2, a mixture of **2** and **3** was obtained. However, our efforts to obtain a compound constructed from $bic^{2-}$, in which both nitrogen atoms of $H_2$bic were deprotonated, at high pH values was unsuccessful. Among the three compounds, only compound **1** has coordinated water molecules which formed at the lowest pH value. The higher the pH value, the more difficult it is for water molecules to coordinate to the metal ions.

### Structural Descriptions

#### *{[Cd(Hbic)$_2$·(H$_2$O)$_2$]·2H$_2$O}$_n$ (1)*

Structure determination shows that compound **1** crystallizes in the monoclinic space group $C_2/c$ and has a 1D chain architecture with guest water molecules. The coordination environment of the metal ion and the coordination mode of $Hbic^-$ are shown in Figure 1 and Figure S1, respectively. The $Cd^{II}$ ion is coordinated by two nitrogen atoms, two water molecules and two *syn* carboxylate oxygen atoms in a distorted octahedral environment. The bond lengths of Cd–N1, Cd–OW1, and Cd–O2B are 2.280(3), 2.325(4), and 2.338(3) Å, respectively, which are the typical distances of Cd–N and Cd–O bonds. Linked by two $Hbic^-$ ligands, these metal nodes are extended into 1D chains along the [010] direction (Figure 2, a). In addition, each guest water is hydrogen bonded to one coordinated water molecule [OW2–OW1A distance: 2.702 Å; symmetry code: A: $x + 1/2, -y + 1/2, z - 1/2$] and two monodentate carboxylate oxygen atoms: one from the same polymeric chain with the coordinated water molecule [OW2–O2 distance 2.751 Å; symmetry code: B: $-x + 1/2, y + 1/2, -z - 1/2$] and the other from a neighboring polymeric chain [OW2–O1 distance: 2.795 Å] (Figure 2, b). The hydrogen bonds lead the 1D

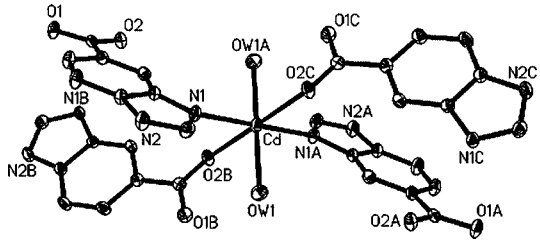


Figure 1. The coordination environment around $Cd^{II}$ in compound **1** with the thermal ellipsoids drawn at the 30% probability level. The guest water molecules are omitted for clarity. Symmetry codes: A: $-x, -y, -z$; B: $-x, y, -z-1/2$.

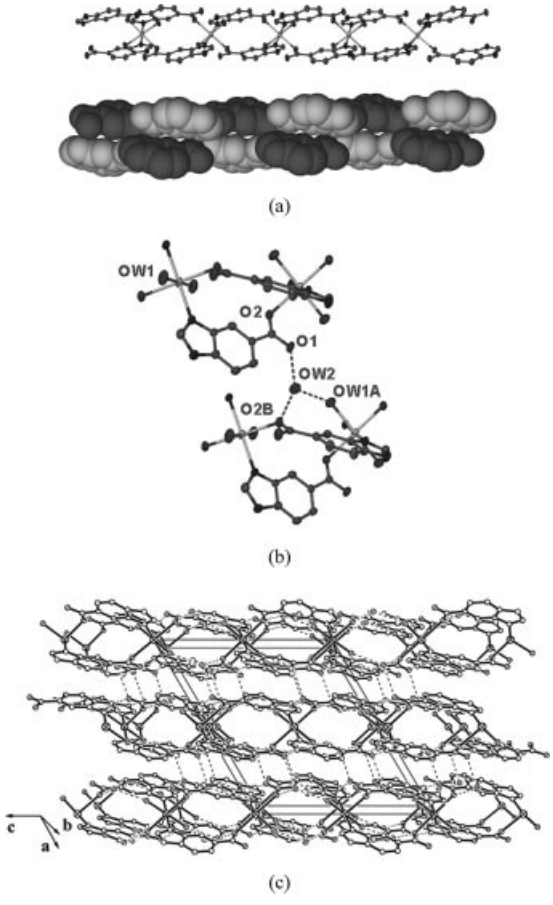


Figure 2. The 1D polymeric chain architecture in compound **1** (a). View of the supramolecular assembly along the [010] direction in compound **1** (b), the guest water molecules are omitted for clarity. Details of H-bond (dotted lines) for compounds **1** (c), hydrogen atoms are omitted for clarity, and thermal ellipsoids are drawn at the 50% probability level. Symmetry codes: A: $x+1/2, -y+1/2, z-1/2$; B: $-x+1/2, y+1/2, -z-1/2$.

 © 2007 Wiley-VCH Verlag GmbH & Co. KGaA, Weinheim 

chains to a supramolecular architecture (Figure 2, c).[13] Ping Liu and coworkers have synthesized a Co compound that is isostructural to compound **1**.[14]

### *[Cd(Hbic)$_2$]$_n$ (2)*

Single-crystal X-ray diffraction analysis reveals that compound **2** crystallizes in the orthorhombic space group *Pbcn* and is composed of a 2D coordination network. The asymmetric unit of compound **2** is shown in Figure 3, which contains one $Cd^{II}$ and two $Hbic^-$ ligands showing two different coordination modes (Figure S1). Similar to compound **1**, the central $Cd^{II}$ ions in **2** are six-coordinate in a distorted octahedral coordination geometry. The equatorial plane is defined by one nitrogen atom, a chelating carboxylate group, and one oxygen atom from another chelating carboxylate group. One nitrogen atom and one oxygen atom from the chelating carboxylate group occupy the axial positions of the octahedron with an O2–Cd–N1B bond angle of 146.96(10)°. The bond lengths of Cd–O1, Cd–O2, and Cd–N3 are 2.330(3), 2.335(3), and 2.278(3) Å, respectively, which are all within the normal ranges. The ligands link adjacent $Cd^{II}$ nodes into the formation of a $4^4$ rhombus network, which is different from other square-grid frameworks (Figure 4, a).[15] Furthermore, the distance between benzene rings is 3.585 Å, which indicates that there are weak face-to-face π–π stacking interactions between the neighboring layers (Figure 4, b and c).[16] We have reported a weak antiferromagnetic coordination polymer synthesized from $Ni(NO_3)_2{\cdot}6H_2O$ and $H_2bic$,[17] which is an allomer of **2**.

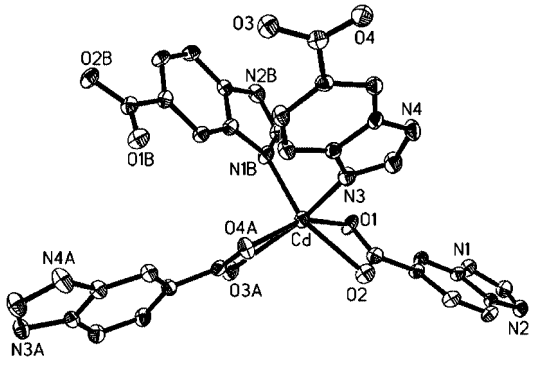


Figure 3. Perspective view of the asymmetric unit of compound **2** (30% probability ellipsoids). Symmetry codes: A: $x$, $-y$, $z-1/2$; B: $-x+3/2$, $y-1/2$, $z$.

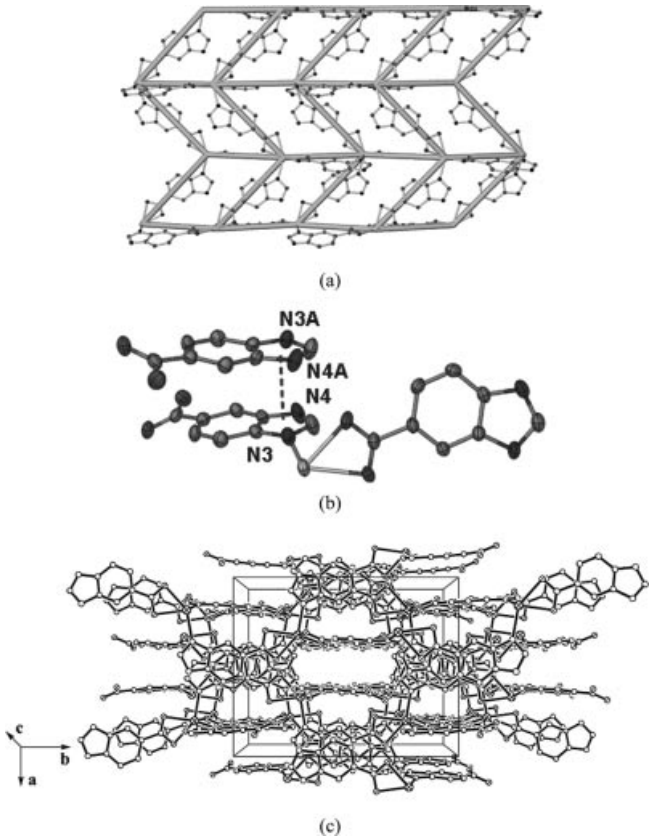


Figure 4. The $4^4$ rhombus network (a) along the [100] direction. Details of π–π stacking interactions (dotted lines) for compound **2** (b), hydrogen atoms are omitted for clarity, and the thermal ellipsoids are drawn at the 50% probability level. Symmetry code: A: $2-x$, $y$, $1/2-z$. Packing of the 2D framework of compound **2** (c) along the [001] direction.

### *[Cd(Hbic)$_2$·(H$_2$O)]$_n$ (3)*

The framework of compound **3** crystallizes in the monoclinic space group *P21/c* and has a 3D architecture with guest water molecules. The structure is built up of dinuclear units in which the cadmium atoms are joined by two oxygen atoms from the chelating/bridging carboxylate groups (Figure 5). Each cadmium atom is six-coordinate through two nitrogen atoms of $Hbic^-$ at apical positions and four oxygen atoms in the equatorial basal plane: one from monodentate carboxylate group and three from two chelating/bridging carboxylate groups (Cd–N, Cd–O). The coordination geometries for $Hbic^-$ are shown in Figure S1 and act as bridging and chelating/bridging ligands, respectively. With a head-to-head aggregation, four $Hbic^-$ ligands link $Cd^{II}$ centers into a $[Cd(Hbic^-)]_4$ ring, in which four metal ions and four ligands are approximately coplanar. On the basis of $Cd^{II}$ distances, the ring is $7.922 \times 10.259$ Å$^2$. In addition, every couple of neighboring $Cd^{II}$ ions is involved in another kind of building unit which consists of two metal joints and two oxygen atoms from chelating/bridging carboxylate groups. Two types of rings form the butterfly framework (Figure 6, a). Interestingly, each $[Cd(Hbic^-)]_4$ is surrounded by four other perpendicular $[Cd(Hbic^-)]_4$ rings through sharing $Cd^{II}$ joints, which may be due to the proper geometry of the metal ion. The 3D network can be classified as a $4^{28}$ topological-type based on eight connected nodes. As hydrogen bonding donors, the water molecules are involved in interactions with the nitrogen atoms and chelating carboxylate oxygen atoms to stabilize the framework furthermore [OW–N1, 2.825 Å; OW–O2A, 3.009 Å; symmetry code: A: $-x+1$, $-y+2$, $-z-1$].[13] Finally, the weak face-to-face π–π stacking interactions between adjacent $Hbic^-$ ligands (distance, 3.600 Å) stabilize the whole framework further (Figure 6, b and c).[16]

 © 2007 Wiley-VCH Verlag GmbH & Co. KGaA, Weinheim 

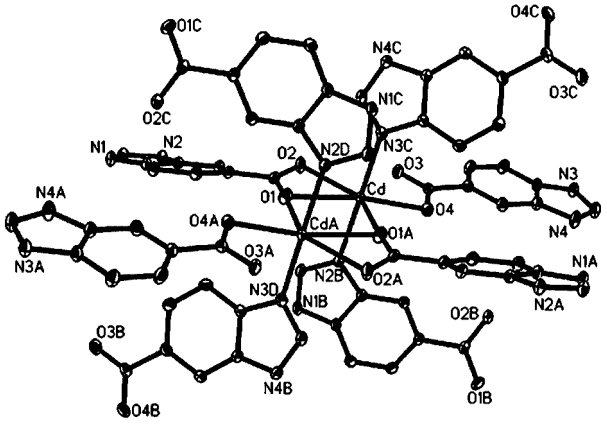


Figure 5. The coordination environment around $Cd^{II}$ in compound **3** with the thermal ellipsoids drawn at the 30% probability level. The guest water molecules are omitted for clarity. Symmetry codes: A: $-x+2$, $y+1/2$, $-z+1/2$; B: $x$, $-y+3/2$, $z+1/2$.

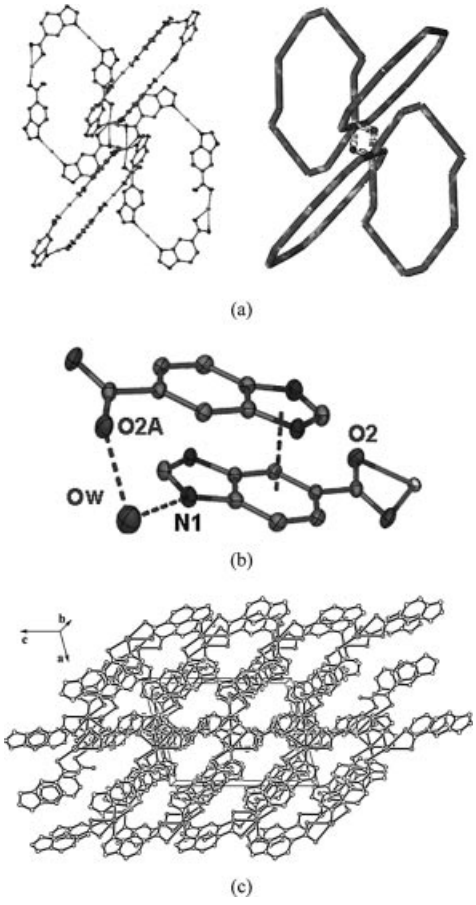


Figure 6. View of the butterfly framework generated from four $[Cd(Hbic^{-})]_4$ rings (a). Details of H-bond and π–π stacking interactions (dotted lines) for compound **3** (b), hydrogen atoms are omitted for clarity, and the thermal ellipsoids are drawn at the 50% probability level. Symmetry code: A: $-x+1$, $-y+2$, $-z-1$. Packing of the 3D framework of compound **3** along the [010] direction (c), the guest water molecules are omitted for clarity.

### Characterization of Vibrational Spectra

In the IR spectrum of compound **1**, a strong and broad peak at 3467 $cm^{-1}$ indicates the presence of water molecules. The antisymmetric and symmetric stretching vibrations of carboxylate group at 1530 $cm^{-1}$ and 1384 $cm^{-1}$, respectively, show that all $Hbic^{-}$ ligands adopt a monodentate coordination mode that is consist with the crystal structure. The IR spectrum of compound **2** shows typical chelating carboxylate antisymmetric and symmetric stretching bands at 1530 $cm^{-1}$ and 1417 $cm^{-1}$, respectively. The IR spectrum of compound **3** shows a broad peak at 3451 $cm^{-1}$ that also testifies to the existence of guest water molecules. The antisymmetric and symmetric stretching vibrations at 1532 $cm^{-1}$ and 1418 $cm^{-1}$, and at 1383 $cm^{-1}$, respectively, show that the carboxylate groups employ the chelating and monodentate coordination geometry.[18]

### Thermogravimetric Analysis

To access the thermal stability of the three compounds, thermogravimetric analyses were carried out with a NETZSCH STA 449C unit, at a heating rate of 10 °C/min under an air atmosphere. As shown in Figure S2, the TGA curve of compound **1** exhibits two significant weight losses. The first weight loss occurs between 81 °C and 185 °C, which can be attributed to the loss of guest water molecules. The observed weight loss of 6.79% is in good agreement with the calculated value (7.11%). From 304 °C to 631 °C, the weight loss of 65.74% suggests the decomposition of compound **1**. The residue weight (24.55%) is ascribed to CdO (calculated 25.34%). The TGA curve of compound **2** indicates only one weight loss stage. The weight loss of 70.2% covers a temperature range from 251 °C to 545 °C, which is possibly due to the collapse of compound **2**. The TGA curve of compound **3** indicates two obvious weight loss stages: 4.04% between 94 °C and 148 °C, and 66.02% between 296 °C and 647 °C. The former is in accordance with the loss of the guest water molecules (calculated 3.98%). The latter suggests the chemical decomposition of compound **3**. The residue weight (27.8%) is attributed to CdO (calculated 28.3%).

### Fluorescent Properties

At room temperature, the luminescent spectra of compounds **1**–**3** and the $H_2bic$ ligand in solid state are shown in Figure 7. The fluorescence spectrum of compound **1** is shown in Figure 7 and exhibits one emission maxima at 443 nm. The emission spectrum of compound **2**, shown in Figure 7 and redshifted relative to **1**, appears at 572 nm. Also shown in Figure 7, the emission spectrum of compound **3** is redshifted compared with those of compounds **1** and **2** to 576 nm. As previously reported, the emission of compound **1** may be attributed to σ-donation from the coordination environment of the $Cd^{II}$ centers, and may be assigned to a ligand-to-metal charge-transfer (LMCT).[19] To ascertain the adscription of the emission spectra, the photoluminescence of pure $H_2bic$ is measured with one emission maxima at 550 nm under the same conditions (Figure 7, ligand). We speculate that the maximum emis-

 © 2007 Wiley-VCH Verlag GmbH & Co. KGaA, Weinheim 

sions bands of compounds **2** and **3** may be caused by the intraligand π–π* transition. Owing to the yellow-green emissions of compounds **2** and **3**, the remarkable feature demonstrates that they may be potential candidates for yellow-green emitting fluorescent materials.[20]

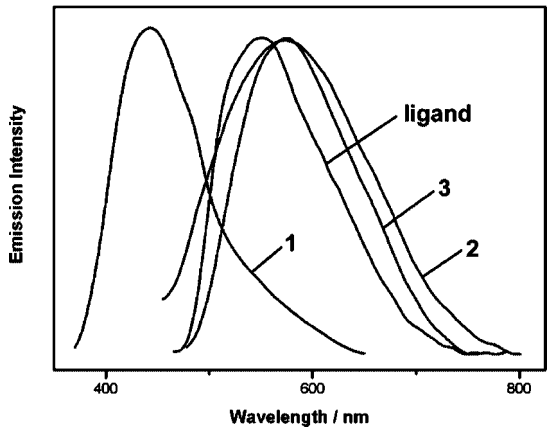


Figure 7. Solid-state emission spectra for compounds **1**–**3** and the $H_2$bic ligand at room temperature.

## Conclusions

A new family of compounds, $\{[Cd(Hbic)_2{\cdot}(H_2O)_2]{\cdot}2H_2O\}_n$ (**1**), $[Cd(Hbic)_2]_n$ (**2**), $[Cd(Hbic)_2{\cdot}(H_2O)]_n$ (**3**), has been synthesized hydrothermally and characterized during our investigation of the $Cd(NO_3)_2{\cdot}4H_2O$/$H_2$bic/NaOH reaction system. The pH values played an important role in the formation of these compounds. At 165 °C, the reaction at a pH value of 5.0 led to the formation of compound **1** with a 2D supramolecular assembly consisting of one-dimensional chains and hydrogen bonded water molecules. When the pH value was raised to 6.5, the reaction gave rise to the formation of compound **2** with a $4^4$ rhombus network structure. Further increase in the pH to a value of 7.2 led to the formation of compound **3** with a 3D architecture based on dinuclear cadmium units. With yellow-green emissions, compounds **2** and **3** may be good candidates for fluorescent materials.

## Experimental Section

**Materials and General Methods:** $H_2$bic = 1H-benzimidazole-5-carboxylic acid was purchased from Acros and used without further purification; all other reagents are commercially available and used as purchased. IR spectra as KBr pellets were recorded with a Magna 750 FTIR spectrophotometer. Elemental analysis of C, H, and N were determined by using a Perkin–Elmer 240C elemental analyzer. Fluorescence spectroscopy was performed with an Edinburgh Analytical instrument FLS920.

**Synthesis:** A mixture of $Cd(NO_3)_2{\cdot}4H_2O$ (0.25 mmol, 77.1 mg), $H_2$bic (0.25 mmol, 40.5 mg), NaOH (0–0.37 mmol, 0–14.8 mg), and distilled water (12 mL) was sealed in a 18 mL stainless steel vessel with a Teflon liner and heated at 165 °C for 72 h. After cooling at a rate of 3 °C/h to 25 °C, the crystals were obtained and washed with water and ethanol. Optimized syntheses of compounds **1**, **2**, and **3** are given below.

**Synthesis of $\{[Cd(Hbic)_2{\cdot}(H_2O)_2]{\cdot}2H_2O\}_n$ (1):** A mixture of $Cd(NO_3)_2{\cdot}4H_2O$ (0.25 mmol, 77.1 mg), $H_2$bic (0.25 mmol, 40.5 mg), and $H_2O$ (12 mL) was placed in a Teflon-lined stainless steel vessel then heated at 165 °C for 72 h. After cooling the reac-

Table 1. Crystal data and structure determination summary for **1**, **2**, and **3**.

| | **1** | **2** | **3** |
|---|---|---|---|
| Formula | $C_{16}H_{18}CdN_4O_8$ | $C_{16}H_{10}CdN_4O_4$ | $C_{16}H_{12}CdN_4O_5$ |
| *Fw* | 506.74 | 434.68 | 452.70 |
| Crystal size [mm] | 0.15 × 0.10 × 0.05 | 0.15 × 0.10 × 0.05 | 0.50 × 0.33 × 0.25 |
| Crystal system | monoclinic | orthorhombic | monoclinic |
| Space group | *C2/c* | *Pbcn* | *P21/c* |
| *a* [Å] | 16.338(4) | 12.542(4) | 10.834(3) |
| *b* [Å] | 9.157(1) | 15.743(5) | 10.743(3) |
| *c* [Å] | 14.328(3) | 15.190(5) | 14.456(4) |
| *β* [°] | 120.079(5) | | 104.343(3) |
| *V* [Å$^3$] | 1854.9(6) | 2999(2) | 1630.1(7) |
| *Z* | 8 | 8 | 4 |
| $D_{calcd.}$ [g cm$^{-3}$] | 1.815 | 1.925 | 1.845 |
| $\mu$ [mm$^{-1}$] | 1.232 | 1.488 | 1.377 |
| *F*(000) | 1016 | 1712 | 896 |
| *T* [K] | 173(2) | 173(2) | 173(2) |
| $\lambda$(Mo-$K_a$) [Å] | 0.71073 | 0.71073 | 0.71073 |
| Reflections collected | 6907 | 21949 | 12063 |
| Unique reflections | 2119 | 3440 | 3725 |
| $R_{int}$ | 0.0468 | 0.0470 | 0.0136 |
| Parameters | 133 | 228 | 235 |
| S on $F^2$ | 1.118 | 1.213 | 1.100 |
| $R_1$ [$I > 2\sigma(I)$][a] | 0.0511 | 0.0481 | 0.0219 |
| $wR_2$ [$I > 2\sigma(I)$][b] | 0.0816 | 0.0786 | 0.0544 |
| $R_1$ (all data) | 0.0758 | 0.0628 | 0.0234 |
| $wR_2$ (all data)[b] | 0.0913 | 0.0831 | 0.0554 |
| $\Delta\rho_{min}$ and $\Delta\rho_{max}$ [e Å$^3$] | 0.479 and –0.487 | 0.610 and –0.385 | 0.999 and –0.437 |

[a] $R = \Sigma||F_o| - |F_c||/\Sigma|F_o|$. [b] $wR = [\Sigma w(F_o^2 - F_c^2)^2/\Sigma w(F_o^2)^2]^{1/2}$.

 © 2007 Wiley-VCH Verlag GmbH & Co. KGaA, Weinheim 

tion system to 25 °C over 48 h, yellow prism crystals of **1** were obtained and washed with water and ethanol. The final pH value of the reaction medium was 5.0. Yield: 15.8 mg, 25% (based on Cd). IR (KBr): 3467 (bs), 1625 (s), 1530 (m), 1458 (s), 1384 (m), 1283 (w), 848 (w), 782 (w), 730 (w), 697 (w) $cm^{-1}$. $C_8H_9Cd_{0.5}N_2O_4$ (253.37): calcd. C 37.92, H 3.58, N 11.05; found C 37.87, H 3.61, N 11.00.

**Synthesis of $[Cd(Hbic)_2]_n$ (2):** A mixture of $Cd(NO_3)_2{\cdot}4H_2O$ (0.25 mmol, 77.1 mg), $H_2bic$ (0.25 mmol, 40.5 mg), $H_2O$ (12 mL), and NaOH (0.27 mmol, 10.8 mg) was placed in a Teflon-lined stainless steel vessel then heated at 165 °C for 72 h. After cooling the reaction system to 25 °C over 48 h, light yellow block crystals of **2** were obtained and washed with water and acetone. The final pH value of the reaction medium was 6.5. Yield: 44.5 mg, 41% (based on Cd). IR (KBr): 3451 (bs), 1626 (s), 1530 (s), 1417 (m), 1382 (s), 967 (w), 777 (m), 671 (w), 539 (w) $cm^{-1}$. $C_{16}H_{10}CdN_4O_4$ (434.67): calcd. C 44.21, H 2.31, N 12.89; found C 44.16, H 2.48, N 12.81.

**Synthesis of $[Cd(Hbic)_2{\cdot}(H_2O)]_n$ (3):** A mixture of $Cd(NO_3)_2{\cdot}4H_2O$ (0.25 mmol, 77.1 mg), $H_2bic$ (0.25 mmol, 40.5 mg), $H_2O$ (12 mL), and NaOH (0.37 mmol, 14.8 mg) was placed in a Teflon-lined stainless steel vessel then heated at 165 °C for 72 h. After cooling at a rate of 3 °C/h to room temperature, yellow prism crystals of **3** were obtained. The final pH value of the reaction medium was 7.2. The resulting product was recovered by filtration, washed with ethanol, and dried in air. Yield: 39.6 mg, 35% (based on Cd). IR (KBr): 3451 (bs), 1626 (s), 1532 (s), 1418 (m), 1383 (s), 936 (w), 776 (s), 623 (s), 539 (w) $cm^{-1}$. $C_{16}H_{12}CdN_4O_5$ (452.68): calcd. C 42.45, H 2.67, N 12.38; found C 42.39, H 2.72, N 12.29.

**X-ray Crystallographic Studies:** Measurements of compounds **1**, **2**, and **3** were collected with a Rigaku CCD. The absorption corrections were performed with the procedure contained within the CrystalClear software package.[11] The structures were solved by direct methods with the SHELXL-97 program package.[12] All data were refined by full-matrix least-squares minimizations of $\sum(F_o - F_c)^2$ with anisotropic thermal parameters for all non-hydrogen atoms. The hydrogen atoms were generated geometrically (C–H 0.95 Å). The crystallographic data and structure determination summaries for compounds **1**, **2**, and **3** are listed in Table 1. Selected bond lengths and angles for the three compounds are listed in Table 2. CCDC-609811, CCDC-609812, and CCDC-609813 for compounds **1**, **2**, and **3**, respectively, contain the supplementary crystallographic data for this paper. These data can be obtained free of charge from The Cambridge Crystallographic Data Centre via www.ccdc.cam.ac.uk/data_request/cif.

**Supporting Information** (see footnote on the first page of this article): The coordination modes of $Hbic^-$ and TGA curves for compounds **1**–**3**.

Table 2. Selected bond lengths [Å] and angles [°] for **1**–**3**.[a]

| | | | |
|---|---|---|---|
| Compound **1** | | | |
| Cd–N1 | 2.280(3) | Cd–OW1 | 2.325(4) |
| Cd–O2B | 2.338(3) | | |
| N1A–Cd–N1 | 180.0(2) | N1A–Cd–O2B | 95.1(1) |
| N1–Cd–O2B | 84.9(1) | OW1–Cd–O2B | 86.4(1) |
| N1–Cd–OW1A | 97.6(1) | O2B–Cd–O2C | 180.0(2) |
| N1–Cd–OW1 | 82.4(1) | OW1–Cd–O2C | 93.6(1) |
| OW1A–Cd–OW1 | 180.0(2) | | |
| Compound **2** | | | |
| Cd–O4A | 2.239(3) | Cd–O1 | 2.330(3) |
| Cd–N1B | 2.269(4) | Cd–O2 | 2.335(3) |
| Cd–N3 | 2.278(3) | Cd–O3A | 2.561(3) |
| O4A–Cd–N1B | 102.5(1) | N3–Cd–O2 | 89.6(1) |
| O4A–Cd–N3 | 94.8(1) | O1–Cd–O2 | 55.8(1) |
| N1B–Cd–N3 | 94.7(1) | O4A–Cd–O3A | 54.2(1) |
| O4A–Cd–O1 | 154.5(1) | N1B–Cd–O3A | 91.0(1) |
| N1B–Cd–O1 | 91.7(1) | N3–Cd–O3A | 148.9(1) |
| N3–Cd–O1 | 105.3(1) | O1–Cd–O3A | 105.1(1) |
| O4A–Cd–O2 | 109.9(1) | O2–Cd–O3A | 102.0(1) |
| N1B–Cd–O2 | 147.0(1) | | |
| Compound **3** | | | |
| Cd–O4 | 2.279(1) | Cd–O2 | 2.349(2) |
| Cd–N3A | 2.299(2) | Cd–O1C | 2.387(1) |
| Cd–N2B | 2.298(2) | Cd–O1 | 2.576(2) |
| O4–Cd–N3A | 88.9(1) | N2BCd–O1C | 86.1(1) |
| O4–Cd–N2B | 92.6(1) | O2–Cd–O1C | 135.3(1) |
| N3A–Cd–N2B | 176.9(1) | O4–Cd–O1 | 167.4(1) |
| O4–Cd–O2 | 139.5(1) | N3A–Cd–O1 | 94.8(1) |
| N3A–Cd–O2 | 88.7(1) | N2B–Cd–O1 | 83.2(1) |
| N2B–Cd–O2 | 92.0(1) | O2–Cd–O1 | 52.7(1) |
| O4–Cd–O1C | 85.2(1) | O1C–Cd–O1 | 82.8(1) |
| N3A–Cd–O1C | 91.3(1) | | |

[a] Symmetry codes: **1**: A: $-x, -y, -z$; B: $-x, y, -z-1/2$; C: $x, -y, z+1/2$. **2**: A: $x, -y, z-1/2$; B: $-x+3/2, y-1/2, z$. **3**: A: $-x+2, y+1/2, -z+1/2$; B: $x, -y+3/2, z+1/2$; C: $-x+1, -y+2, -z$.

## Acknowledgments

We are grateful for the financial support of the National Nature Science Foundation of China, Chinese Academy of Sciences (No. 90206040, 20325106, 20521101), the Nature Science Foundation of Fujian Province (2005HZ01-1, E0520003), Key Project from MOST (2006CB932903) and "One Hundred Talent Project" from CAS.

[1] a) B. F. Abrahams, B. F. Hoskins, J. Liu, R. Robson, *J. Am. Chem. Soc.* **1991**, *113*, 3045–3051; b) O. M. Yaghi, G. Li, H. Li, *Nature* **1995**, *378*, 703–706; c) S. Wang, D. B. Mitzi, C. A. Field, A. M. Guloy, *J. Am. Chem. Soc.* **1995**, *117*, 5297–5302; d) S. S. Y. Chui, S. M. F. Lo, J. P. H. Charmant, A. G. Orpen, I. D. Williams, *Science* **1999**, *283*, 1148–1150.

[2] a) S. M. Humphrey, P. T. Wood, *J. Am. Chem. Soc.* **2004**, *126*, 13236–13237; b) A. Galet, A. B. Gaspar, G. Agusti, M. C. Muñoz, G. Levchenko, J. A. Real, *Eur. J. Inorg. Chem.* **2006**, 3571–3573; c) M. Riou-Cavellec, C. Lesaint, M. Nogués, J. Grenéche, G. Férey, *Inorg. Chem.* **2003**, *42*, 5669–5674; d) M. E. Chapman, P. Ayyappan, B. M. Foxman, G. T. Yee, W. B. Lin, *Cryst. Growth Des.* **2001**, *1*, 159–163; e) A. K. Ghosh, D. Ghoshal, E. Zangrando, J. Ribas, N. Ray Chaudhuri, *Inorg. Chem.* **2005**, *44*, 1786–1793.

[3] B. Gomez-Lor, E. Gutiérrez-Puebla, M. Lglesias, M. A. Monge, C. Ruiz-Valero, N. Snejko, *Inorg. Chem.* **2002**, *41*, 2429–2432.

[4] a) J. Pang, E. J. P. Marcotte, C. Seward, R. S. Brown, S. N. Wang, *Angew. Chem. Int. Ed.* **2001**, *40*, 4042–4045; b) H. J. Tracy, J. L. Mullin, W. T. Klooster, J. A. Martin, J. Haug, S. Wallace, I. Rudloe, K. Watts, *Inorg. Chem.* **2005**, *44*, 2003–2011.

[5] M. Dincă, J. Long, *J. Am. Chem. Soc.* **2005**, *127*, 9376–9377.

[6] a) Y. L. Liu, V. Kravtsov, R. D. Walsh, P. Poddar, H. Srikanth, M. Eddaoudi, *Chem. Commun.* **2004**, 2806–2807; b) R. Custelcean, M. Gorbunova, *J. Am. Chem. Soc.* **2005**, *127*, 16362–16363; c) Y. L. Liu, V. Ch. Kravtsov, D. A. Beauchamp, J. F.

 © 2007 Wiley-VCH Verlag GmbH & Co. KGaA, Weinheim 

Eubank, M. Eddaoudi, *J. Am. Chem. Soc.* **2005**, *127*, 7266–7267.
[7] Y. Q. Sun, J. Zhang, Y. M. Chen, G. Y. Yang, *Angew. Chem. Int. Ed.* **2005**, *44*, 5814–5817.
[8] a) C. Y. Su, X. P. Yang, B. S. Kang, T. C. W. Mak, *Angew. Chem. Int. Ed.* **2001**, *40*, 1725–1728; b) R. H. Wang, M. C. Hong, J. H. Luo, R. Cao, J. B. Weng, *Chem. Commun.* **2003**, 1018–1019; c) B. Sreenivasulu, J. J. Vittal, *Cryst. Growth Des.* **2003**, *3*, 635–637.
[9] a) J. Bernstein, A. T. Hagler, *J. Am. Chem. Soc.* **1978**, *100*, 673–681; b) T. Hennigar, D. MacQuarrie, P. Losier, R. Rogers, M. Zaworotko, *Angew. Chem. Int. Ed. Engl.* **1997**, *36*, 972–973.
[10] D. F. Sun, R. Cao, Y. C. Liang, Q. Shi, W. P. M. C. Hong, *J. Chem. Soc., Dalton Trans.* **2001**, 2335–2340.
[11] *Molecular Structure Corporation and Rigaku*, **2000**, CrystalClear, v 1.36. MSC, Texas, USA, and *Rigaku Corporation*, 3–9–12 Akishima, Tokyo, Japan.
[12] G. M. Sheldrick, *SHELXS 97*, *Program for Crystal Structure Solution*, University of Göttingen, Göttingen, **1997**.
[13] a) C. V. Sharma, M. J. Zaworotko, *Chem. Commun.* **1996**, 2655–2656; b) S. Nagahama, K. Inoue, K. Sada, M. Miyata, A. Matsumoto, *CrystGrowthDes* **2003**, *3*, 247–256.
[14] Z. Liu, Y. Chen, P. Liu, J. Wang, M. H. Wang, *J. Solid State Chem.* **2005**, *178*, 2306–2312.
[15] a) M. L. Tong, H. J. Chen, X. M. Chen, *Inorg. Chem.* **2000**, *39*, 2235–2238; b) M. Fujita, Y. J. Kwon, S. Washizu, K. Ogura, *J. Am. Chem. Soc.* **1994**, *116*, 1151–1152; c) D. Hagrman, R. P. Hammond, R. Haushalter, J. Zubieta, *Chem. Mater.* **1998**, *10*, 2091–2100.
[16] a) Y. B. Go, X. Q. Wang, E. V. Anokhina, A. J. Jacobson, *Inorg. Chem.* **2004**, *43*, 5360–5367; b) A. C. B. Lucassen, M. Vartanian, L. Gregory, M. E. Boom, *CrystGrowthDes.* **2005**, *5*, 1671–1673.
[17] Z. G. Guo, D. Q. Yuan, W. H. Bi, X. J. Li, Y. Q. Wang, R. Cao, *J. Mol. Struct.* **2006**, *782*, 106–109.
[18] a) F. A. Almeida Paz, J. Klinowski, *Inorg. Chem.* **2004**, *43*, 3948–3954; b) Y. B. Go, X. Q. Wang, E. V. Anokhina, A. J. Jacobson, *Inorg. Chem.* **2005**, *44*, 8265–8271.
[19] a) C. S. Liu, X. S. Shi, J. R. Li, J. J. Wang, X. H. Bu, *Cryst. GrowthDes.* **2006**, *6*, 656–663; b) J. H. Luo, M. C. Hong, R. H. Wang, R. Cao, L. Han, Z. Z. Lin, *Eur. J. Inorg. Chem.* **2003**, 2705–2710; c) R. Q. Zou, X. H. Bu, R. H. Zhang, *Inorg. Chem.* **2004**, *43*, 5382–5386.
[20] S. Kyushin, Y. Ishikita, H. Matsumoto, H. Horiuchi, H. Hiratsuka, *Chem. Lett.* **2006**, *35*, 64–65.

Received: September 11, 2006
Published Online: December 21, 2006

 © 2007 Wiley-VCH Verlag GmbH & Co. KGaA, Weinheim 

DOI: 10.1002/ejic.200601000

# Metal Complexation of Calix[4]azacrown Derivatives – Evidence for Communication Between Upper and Lower Functionalised Rims

**Andrew D. Bond,[a] Bernadette S. Creaven,[b] Denis F. Donlon,[b,c] Tammy L. Gernon,[b,c] John McGinley,*[c] and Hans Toftlund[a]**

*Dedicated to the memory of Des Cunningham*[†]

**Keywords:** Calix[4]arene / Macrocyclic ligands / Heterometallic compounds / Copper(II) / Manganese(II) / Ruthenium(II) / EPR spectroscopy

The coordination chemistry of calix[4]azacrowns obtained from the reaction of a diester calix[4]arene with diethylenetriamine provided unusual copper(II) and manganese(II) complexes in which calix[4]azacrown acts as a bidentate N,O-donor ligand, in some cases, but as a unidentate N-donor ligand, in other cases. The first example of a binuclear ruthenium(II)/manganese(II) complex, involving the calix[4]arene framework as the bridging ligand, is also reported. The calix[4]arene framework consists of a bipyridyl unit connected at the upper rim of the calix[4]arene, through an amide linkage, and an azacrown unit at the lower rim, also connected through amide groups.
(© Wiley-VCH Verlag GmbH & Co. KGaA, 69451 Weinheim, Germany, 2007)

## Introduction

Calix[4]arenes are versatile host molecules for supramolecular chemistry, which have been incorporated into numerous elaborate structures.[1] Double calix[4]arenes,[2] for example, have been constructed covalently through upper rim/upper rim linkage,[3] lower rim/lower rim linkage[4] or upper rim/lower rim linkage,[5] and also noncovalently through hydrogen bonding.[6] Incorporation of a crown ether into a rigid calix[4]arene creates a new type of supramolecular host, with interesting prospects for binding metal ions.[7] The family of calix[4]azacrowns combine calix[4]arenes with azaethylene chains attached to the phenolic oxygen atoms by acetamido groups, which serve both as covalent linking functions and as potential chelating

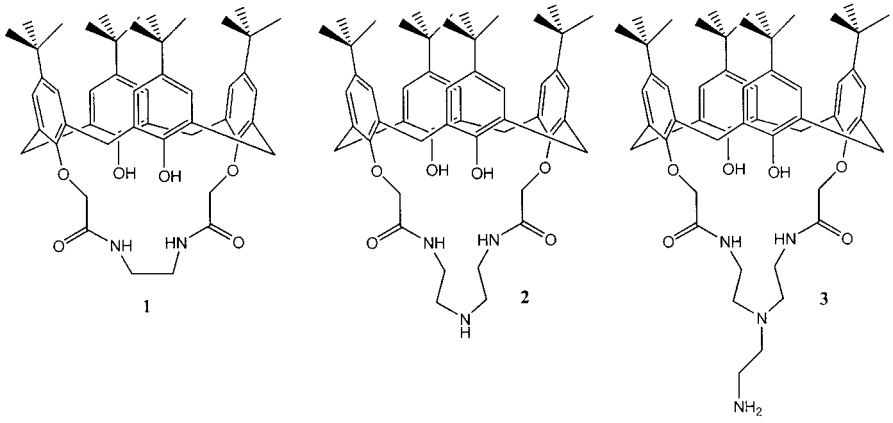


Figure 1. Calix[4]azacrowns.

[a] Department of Physics and Chemistry, University of Southern Denmark,
5230 Odense M, Denmark
[b] Department of Applied Science, Institute of Technology, Tallaght, Dublin 24, Ireland
[c] Department of Chemistry, National University of Ireland Maynooth,
Maynooth, Co. Kildare, Ireland
[†] Our teacher, mentor and friend who passed away on September 18, 2006.

 © 2007 Wiley-VCH Verlag GmbH & Co. KGaA, Weinheim 

groups. The first calix[4]azacrowns of type **1** (Figure 1) were prepared by reaction of either a calix[4]arene dimethyl ester or calix[4]arene diacyl chloride derivative with the appropriate diamine and were shown by FAB-mass spectrometry to complex divalent ($Be^{2+}$, $Mg^{2+}$, $Ca^{2+}$, $Sr^{2+}$, $Ba^{2+}$) and trivalent ($Sc^{3+}$, $Y^{3+}$, $In^{3+}$, $Gd^{3+}$, $Bi^{3+}$) metal cations.[8]

We have previously reported upper- and lower-rim functionalised calix[4]arenes, capable of binding transition-metal and alkali-metal salts, as well as ligands capable of attachment to calix[4]arenes.[9] One such calix[4]arene contained picolyl groups.[9c] In extending this theme, we targeted the design of calix[4]azacrowns and, in particular, the calix[4]arenes **2** and **3** which are capped by a diamide bridge at the 1,3-position on the lower rim.

Transition-metal ions which are covalently linked to each other through a ligand system are of interest and importance for a variety of purposes.[10–17] They can be used for studies into light-induced energy and electron transfer, as well as model systems for the development of supramolecular compounds which are capable of performing useful light induced processes such as photochemical devices. Indeed, the conversion of light energy into chemical energy is of current interest with particular focus on the development of efficient solar energy conversion schemes. To observe such transfer processes between the metal centres, they must be linked by a bridging ligand. These ligands have varied from chelating units linked by either flexible or rigid chains or by rod-like spacers.[14,18–21] More recently, the cage compound 1,12-dicarba-*closo*-dodecaborane, known as *p*-carborane, has been used as the linker molecule.[22] These linker or spacer molecules determine the spatial arrangement of the whole molecule while their chemical properties are important in influencing the spectroscopic and redox properties of the two metal centres as well as determining the rate of the electron/electron transfer process. We have focused our efforts on the construction of polynuclear complexes in which a photoactive and redox-active metal are linked by bridges based on a calix[4]arene derivative.[9a] Extensive functionalisation has been carried out at both the upper and lower rims of the calix[4]arene. A calix[4]arene, with appropriate functionalisation at both the wide and narrow rims, is capable of maintaining a well-defined distance between two metal centres positioned at each rim. By the simple modification of the synthesis of the functionalised calix[4]arene, this distance can be easily altered. To the best of our knowledge, there has been no report of a calix[4]arene derivative as a spacer molecule in energy/electron transfer reactions.

## Results and Discussion

### Lower-Rim Complexes

The method used for preparation of lower-rim functionalised calix[4]azacrown (**2**) is shown in Scheme 1. Base-promoted reaction of *p*-*tert*-butylcalix[4]arene with ethyl bromoacetate in acetonitrile produced the diester 5,11,17,23-tetra-*tert*-butyl-25,27-bis(ethoxycarbonylmethyloxy)calix[4]-arene (diester calix[4]arene),[9a,23] which was then stirred for 72 h with either diethylenetriamine or tris(2-aminoethyl)-amine in a methanol/toluene solvent mixture to give the cyclic amides **2** and **3** as white solids in good yield, similar to that described by Bitter et al.[24] The IR spectra of **2** and **3** exhibit a strong C=O signal at 1678 and 1681 $cm^{-1}$ respectively (compared to 1746 $cm^{-1}$ in the starting diester calix[4]arene), indicative of the amide functional group, together with a sharp N–H signal at 3372 and 3399 $cm^{-1}$, which is not present in the spectrum of the starting diester derivative. The $^1H$ NMR spectrum suggests that the calix-[4]arene molecules in **2** and **3** adopt a distorted cone conformation:[25] a pair of AB-type doublets is observed for the diastereotopic methylene protons at $\delta$ = 4.16 and 3.36 ppm in **2** and at $\delta$ = 4.17 and 3.39 ppm in **3**, respectively, compared to $\delta$ = 4.43 and 3.30 ppm for the corresponding signals in the starting diester calix[4]arene.

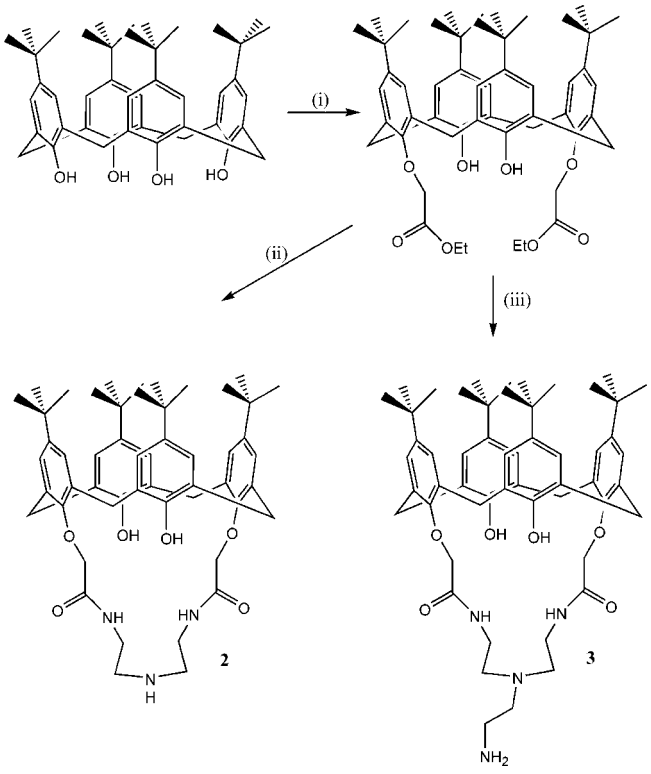


Scheme 1. Reagents and conditions: (i) $K_2CO_3$, ethyl bromoacetate, MeCN, reflux, 18 h; (ii) diethylenetriamine, MeOH, toluene, 48 h; (iii) tris(2-aminoethyl)amine, MeOH, toluene, 48 h.

$^1H$ NMR studies have previously indicated that macrocycles of this type show interesting binding properties;[7c,7d,26] for example, while the tetra(*p*-*tert*-butyl)calix-[4]azacrown **1** does not extract transition-metal ions, the corresponding 1,3-dimethoxy-*p*-*tert*-butylcalix[4]azacrown extracts $Cu^{2+}$ ions selectively with respect to $Co^{2+}$ and $Ni^{2+}$ ions.[7c,7d] Complexation behaviour of **2** towards alkaline-earth and transition-metal ions has been recently described[26] and the X-ray crystal structure of the complex with $Mg^{2+}$ revealed that the metal ion was not bound to any of the nitrogen atoms, but lay outside of the crown loop, forming a coordination polymer through metal–oxy-

 © 2007 Wiley-VCH Verlag GmbH & Co. KGaA, Weinheim 

gen bonds to carbonyl O atoms from different calix[4]arene entities. Oueslati et al.[7d] found that metal extraction did not occur on attempted complexation of **2** with copper, nickel and cobalt picrates. Instead, crystals were formed in which a water molecule lies within the crown loop of **2** and picric acid accepts a hydrogen bond from this water molecule. In an effort to understand the binding, or lack thereof, of $Cu^{2+}$ to calix[4]azacrowns, we undertook complexation reactions of **2** and **3** with various copper(II) salts, as well as investigating the complexation behaviour of $MnCl_2$.

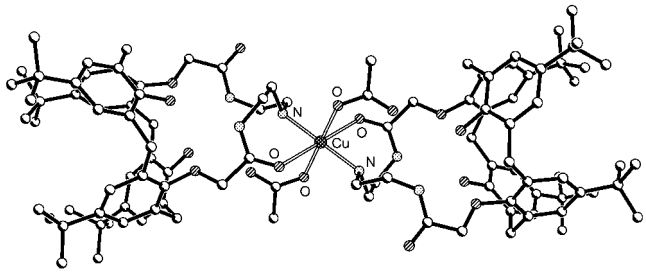


Figure 2. Molecular structure of **4** (H atoms omitted).

### Copper(II) Complexes

Complexation reactions of **2** and **3** were carried out in MeOH at reflux temperature, using copper(II) acetate hydrate, copper(II) chloride dihydrate and copper(II) perchlorate hexahydrate, respectively, in each case in a 1:1 ratio. Intense blue solutions were obtained in all cases and most of the solvent had to be removed under reduced pressure before precipitation occurred. For the reaction involving **2** with copper(II) acetate, a blue/green complex **4** was obtained, which was shown by X-ray diffraction to be $Cu(\mathbf{2})_2(CH_3CO_2)_2(MeOH)_2$ (Figure 2). The $Cu^{2+}$ ion is not complexed within the calix[4]azacrown, but instead is bound to two such units through interactions with the lone pairs on the NH of the crown ring and the C=O groups of the amide units. Thus, **2** acts as a bidentate N,O-donor ligand. The complex is centrosymmetric, and $Cu^{2+}$ adopts a typical [4+2] distorted octahedral geometry. The Cu–N and Cu–O(acetate) bond lengths are 2.052(4) and 1.957(3) Å, respectively, while the axial Cu–O=C distances are 2.715(3) Å. The monomeric nature of the copper acetate unit, in contrast to the bridging structures, usually associated with simple copper(II) acetate salts,[27] may be attributed to the steric bulk of the calix[4]azacrown ligand, which prevents further association. The coordinated amine group of **2** retains its proton, forming an N–H···O hydrogen bond to the unbound O atom of the acetate group. An O–H···O hydrogen bond is also formed from the phenolic OH group of **2** to the acetate group. In the solid state, MeOH molecules form O–H···O hydrogen bonds to the Cu-bound and unbound C=O groups of the amide bridge. The infrared spectrum of **4** shows two bands in the carbonyl region, as was expected from the X-ray crystal structure, at 1690 $cm^{-1}$, representative of an amide carbonyl bond, and also at 1578 $cm^{-1}$, representing the acetate carbonyl group. The reaction of **3** with copper(II) acetate also results in a green solid **5** which showed similar bands in the infrared spectrum, particularly in the carbonyl region at 1676 and 1555 $cm^{-1}$ suggesting that the acetate was binding to the copper in an analogous manner. A broad band at 3360 $cm^{-1}$ was also evident implying that the copper was bonding to **3** through the pendant amine. Elemental analysis on this compound also suggested a 1:2 metal/ligand complex as observed in **4**.

The complexation reactions of **2** and **3** with copper(II) perchlorate hexahydrate gave the green complexes **6** and **7**. Comparison of the IR spectrum of **6** and **7** with that of **4** reveals slight differences in the spectra. The differences suggest that the mode of complexation of the calixazacrown derivative is not determined solely by the metal ion (although this clearly will have some bearing), but is also influenced by the anion and its coordinating ability. The more strongly complexing acetate anion remains bound to $Cu^{2+}$ in **4**, while the weakly complexing perchlorate anions may be less likely to do so in **6** and **7**. Elemental analyses of both **6** and **7** suggest the presence of one perchlorate anions per $Cu^{2+}$ ion as well as the presence of only one calix[4]-azacrown unit, requiring that the ligands of **2** and **3** be neutral, possibly using the lone pairs on the nitrogen atoms in the ring to bind $Cu^{2+}$ internally in the calixazacrown loop. Furthermore, the metal complexes crystallise along with a molecule of methanol in both cases. To date, we have not been able to obtain suitable crystals of **6** or **7** to establish this conclusively.

For the complexation reaction of **2** with copper(II) chloride, a mixture of green **8** and blue **9** solids was obtained when the reaction was allowed to proceed for 120 min. On decreasing the reaction time to 20 min, the major product was **8**. The green material **8** has an IR spectrum similar to that of **4** (with the exception of the carbonyl stretching frequency due to the acetate group). This suggests that **8** comprises of copper(II) chloride bound between two calixazacrown ligands in a similar manner to the copper(II) acetate complex **4**. Since **8** is the major product obtained from the reaction after only a the short time period, complexation of copper(II) chloride by **2** appears to be the initial outcome. When the reaction proceeds for a longer time, the blue solid **9** is formed. Single crystals of **9** were obtained from the mother liquor after 90 min reaction, and single-crystal X-ray analysis[28] confirmed that cleavage of the amide bonds had occurred, resulting in the simple copper-diethylenetriamine complex shown in Figure 3. This complex can also be obtained by direct reaction of diethylenetriamine with copper(II) chloride dihydrate in a 1:1 ratio.[29] Cleavage of amide bonds by copper(II) chloride has been described previously.[30] On repeating the reaction, we were also able to obtain the calix[4]arene di-acid derivative[31] that is formed in the cleavage reaction. We have only observed the formation of **9** when the reaction mixture is heated for long periods of time. This suggests that the green complex **8** is relatively stable, and that it requires a considerable amount of energy before the cleavage reaction pro-

 © 2007 Wiley-VCH Verlag GmbH & Co. KGaA, Weinheim 

ceeds. One probable mechanism for this process involves $Cu^{2+}$ moving from being externally coordinated (in the manner of **4**) to being internally coordinated, with this movement allowing the amide bonds to cleave.

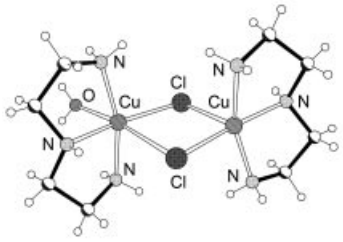


Figure 3. Molecular structure of the cleavage product **9**.

The complexation reaction of **3** with copper(II) chloride results only in a single green complex **10**. The infrared spectrum of this compound was very similar to that obtained for **8** which suggested that the copper was bonded to the free amine of the calix[4]azacrown. Microanalysis suggested the presence of only one chloride anion which would mean that the calix[4]azacrown was acting as a unidentate ligand through loss of a proton from the pendant amine group. The remaining coordination sites about the copper atom were occupied by water molecules. There was no evidence in this case of any cleavage reactions occurring or of two calix[4]azacrown units bonding to the copper atom.

### Manganese(II) Complexes

As in the case of the copper complexations described above, the complexation reactions of **2** and **3** with manganese(II) chloride tetrahydrate were carried out in MeOH at reflux temperature, respectively, in each case in a 1:1 ratio. Brown solutions were obtained in both cases and most of the solvent had to be removed under reduced pressure before precipitation occurred. Compound **11** crystallises with a molecule of methanol present as solvent of crystallisation. Elemental analyses for **11** and **12** suggest the presence of only one chloride anion which would mean that the calix[4]azacrown **3**, in each case, was acting as a unidentate ligand through loss of a proton from the pendant amine group. The remaining coordination sites about the metal atom were occupied by water molecules.

The EPR spectra of the $Mn^{II}$ complexes without any functionalisation on the upper rim (**11**–**12**) were obtained as glasses in dimethylformamide (DMF) at 120 K. Both spectra were almost identical, showing jagged six-line spectra; the six-line spectrum in each case arising from the fact that $Mn^{II}$ has $I = 5/2$. These spectra indicate that the coordination of $Mn^{II}$ is very similar in each case. We believe that the manganese atom is bonded to the amine nitrogen of the azacrown ring, either NH or $NH_2$ depending on the calix[4]arene derivative **2** or **3**, similar to the bonding of the copper metal in the X-ray crystal structure of **4**. The remaining coordination sites around the manganese metal are occupied by water molecules. Elemental analyses and the infrared spectra of these complexes support this hypothesis.

### Ruthenium(II)/Manganese(II) Complexes

We have previously investigated the complexation of copper(I) to a pyridyl derivative of a calix[4]arene and were able to oxidise the metal centre while retaining complexation.[9c] Retention of this bonding is important, because if energy or electron transfer occurs from one rim to the other, then a change in the oxidation state of the metal at the lower rim must happen. Thus, it is essential that the metal–ligand bonding is retained at the lower rim. To achieve a scaffold capable of holding two different metals at different coordination sites, we have functionalised both the upper and lower rim of a calix[4]arene (Scheme 2); the synthesis of **13** has been reported previously.[9a]

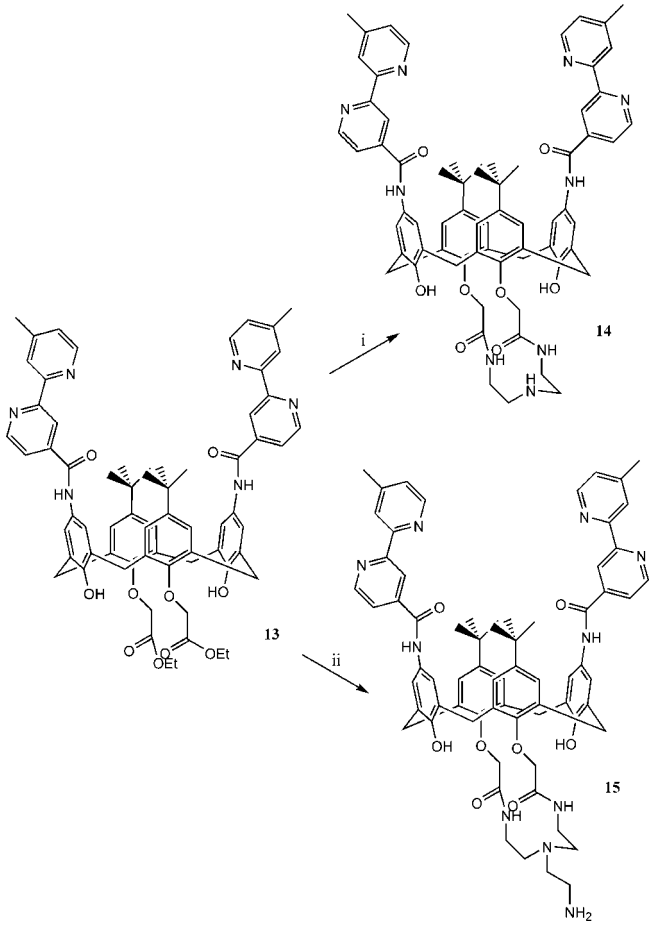


Scheme 2. Reagents and conditions: (i) diethylenetriamine, MeOH, toluene, 48 h; (ii) tris(2-aminoethyl)amine, MeOH, toluene, 48 h.

The bis(bipy) diester calix[4]arene **13** was treated with 0.5 equiv. of either diethylenetriamine or tris(2-aminoethyl)-amine in methanol/toluene[24] to give the calix[4]azacrown derivatives **14** and **15**. The $Ru^{II}$ complexes **16** and **17** were prepared by reacting **14** or **15** with 1.1 equiv. of Ru(bipy)-$Cl_4$[32] in refluxing absolute ethanol and, on cooling, a

 © 2007 Wiley-VCH Verlag GmbH & Co. KGaA, Weinheim 

brown solid precipitated in each case and recrystallised from chloroform. These solids were kept in the dark during the filtering and drying stages and were stored at room temperature in the dark. All efforts to obtain $^1$H NMR spectra of both **16** and **17** failed in all solvents, due to lack of solubility in the deuterated solvents. Elemental analyses for both products showed the presence of three molecules of chloroform. The $Ru^{II}/Mn^{II}$ complexes **18** and **19** were prepared by the reaction of the appropriate $Ru^{II}$ complexes **16** or **17** with manganese(II) chloride tetrahydrate in refluxing methanol. Elemental analyses for **18** and **19** suggest the presence of only one chloride anion which would mean that the calix[4]azacrowns **16** and **17**, in each case, were acting as a unidentate ligand through loss of a proton from the pendant amine group. The remaining coordination sites about the metal atom were occupied by water molecules. Furthermore, in both cases, two molecules of chloroform were also present as solvent of crystallisation, the chloroform being present from the washing of the solid to remove any unreacted calix[4]azacrown scaffold. Interestingly, the two metal centres are not directly connected through the same aromatic ring of the calix[4]arene. This is simply due to the synthetic path chosen. The first step in the functionalisation process is the etherification reaction at the lower rim, which has a dual role; firstly, it protects two of the phenol groups on the narrow rim while conferring cone conformation on the molecule, and secondly, it directs the functionalisation of the wide rim opposite the remaining free hydroxy groups of the narrow rim. It is this second function which does not allow a direct connection between both metal centres.

The EPR spectra of the complexes **18** and **19** were obtained as glasses in DMF at 120 K. Both spectra were almost identical. Some very small peaks for $Ru^{III}$ were observed, which was not unexpected as it was impossible to keep the sample under light-free conditions at all times during the preparation of the sample for the experiment. The very similar, jagged six-line spectra for **18** and **19** indicate that the coordination of $Mn^{II}$ is very similar in both complexes. We believe that, in both cases, the Mn atom is bonded to one nitrogen atom from the azacrown unit and that the remaining five coordination sites of the manganese are occupied by water molecules. These results are similar to those observed by Berg et al., where they had synthesised $[Ru(bipy)_3]^{2+}$ complexes covalently attached to bis(picolylamine) or tris(picolylamine) functional groups to which $Mn^{II}$ could be attached.[33]

The $Ru^{II}/Mn^{II}$ complexes **18** and **19** were partially oxidised to obtain the mixed valence $Ru^{III}/Mn^{II}$ complexes. The reactions were preformed using ammonium cerium(IV) nitrate as the oxidant in a 3:1 mixture of DMF and methanol, similar to that described by Ghirotti et al.[22] Dimethylformamide was one of the two solvents in which these compounds would dissolve, the other was methyl sulfoxide. The oxidation was monitored using EPR spectroscopy. On cooling the partially oxidised sample, no decrease in the signal intensity of the six-line region of the spectra, associated with the $Mn^{II}$ signals, was observed. There was, however, a substantial increase in the signals for a $Ru^{III}$ species, which indicated that the oxidation had occurred only at the $Ru^{II}$ sites. The samples were then warmed to 273 K and recooled to 120 K. This was to allow any energy or electron transfer to occur. On recording the spectra again, the spectra looked identical to the initial partially oxidised spectra. However, closer examination revealed that the intensity of both the $Mn^{II}$ and $Ru^{III}$ species had decreased by ca. 30%, indicating that either energy or electron transfer was occurring from the $Mn^{II}$ centre to the $Ru^{III}$ centre, with consequent oxidation of the $Mn^{II}$ to $Mn^{III}$, an EPR-silent species. Importantly, this suggests that the two metals are in communication with each other, despite the fact that there is no direct pathway between them, since they are not attached to the same benzene ring. More unprecedented was that the result could be observed using the relative slow EPR spectroscopy technique, instead of having to use transient spectroscopy with nanoseceond laser flash photolysis. This would indicate that the charge recombination reaction in this case is very slow, implying that the charge-separation between the metal species is close to an optimum distance.

## Conclusions

We have shown that binding of copper(II) and manganese(II) to calixazacrowns can be achieved, and that the particular mode of coordination appears to be influenced by the coordination ability of the associated anion. We have also synthesised mixed metal complexes with ruthenium(II) at the upper rim of our calix[4]arene scaffold and manganese(II) at the lower rim. Furthermore, initial EPR studies of these complexes indicate that the metals are able to communicate with each other, although they are not bound to the same aromatic ring of the calix[4]arene structure. We are currently examining the amide cleavage reaction in more detail and also looking at the coordination chemistry of other transition metals with **2** and **3**, as well as carrying out transient spectroscopy on the mixed metal species in an effort to understand the communication processes being undertaken.

## Experimental Section

$^1$H and $^{13}$C NMR ($\delta$ in ppm; $J$ in Hz) spectra were recorded with either a JEOL JNM-LA300 FT-NMR spectrometer or a Bruker Avance 300 MHz spectrometer using saturated $CDCl_3$ solutions with $Me_4Si$ reference, unless indicated otherwise, with resolutions of 0.18 Hz and 0.01 ppm, respectively. Infrared spectra ($cm^{-1}$) were recorded as KBr discs or liquid films between KBr plates with a Nicolet Impact 410 FT-IR. All UV/Vis spectra were recorded on a Shimadzu UV-160A spectrometer. Melting point analysis was carried out using a Stewart Scientific SMP 1 melting point apparatus and are uncorrected. The EPR spectra were recorded either at room temperature or in frozen glass at 120 K using a Bruker EMX spectrometer operating at the X-band. Microanalysis was carried out at the Microanalytical Laboratory of either University College, Dublin or the National University of Ireland Cork. Standard Schlenk techniques were used throughout. Starting materials were

 © 2007 Wiley-VCH Verlag GmbH & Co. KGaA, Weinheim 

commercially obtained and used without further purification. The synthesis of compounds 4-*tert*-butylcalix[4]arene,[34] 5,11,17,23-tetra-*tert*-butyl-25,27-diethoxycarbonylmethyloxycalix[4]arene,[9a,23] calix[4]azacrown **2**,[35] and 5,17-di-*tert*-butyl-11,23-bis[(4′-methyl-2,2′-bipyridin-4-yl)carbonylamino]-25,27-bis(ethoxycarbonylmethoxy)calix[4]arene (**13**)[9a] and $Ru^{II}(bipy)Cl_4$[32] have been described in the literature previously.

**Synthesis of Calix[4]azacrown 3:** A solution of diester calix[4]arene (2.0 g, 2.5 mmol) and tris(2-aminoethyl)amine (2.26 mL, 15.1 mmol) in a mixture of methanol (25 mL) and toluene (25 mL) was stirred at room temperature for 3 d. After this time, the solution was concentrated under reduced pressure. The solid residue was suspended in methanol and filtered to give a white solid.

**Calix[4]azacrown 3:** Yield 1.23 g (56.4%). $C_{54}H_{74}N_4O_6$ (875.19): calcd. C 74.10, H 8.52, N 6.40; found C 74.25, H 8.40, N 6.43; m.p. 262–264 °C. IR (KBr): $\tilde{\nu}_{max}$ = 3390 (NH), 1680 (amide C=O) $cm^{-1}$. $^1H$ NMR (300 MHz, $CDCl_3$): $\delta$ = 8.29 (br. t, 2 H, CON*H*$CH_2$), 7.12 (s, 4 H, Ar-*H*), 6.70 (s, 4 H, Ar-H), 6.33 (s, 2 H, OH), 4.48 (s, 4 H, $OCH_2CO$), 4.18 (d, $^1J$ = 13.0 Hz, 4 H, Ar-$CH_aH_b$-Ar), 3.52 (m, 6 H, $CH_2$), 3.39 (d, $^1J$ = 13.0 Hz, 4 H, Ar-C$H_aH_b$-Ar), 2.95 (m, 6 H, $CH_2$), 1.33 (s, 18 H, *t*Bu), 0.88 (s, 18 H, *t*Bu) ppm.

**General Synthesis of Copper(II) Complexes 4–10:** To a solution of the calix[4]azacrown (0.5 mmol) in chloroform (5 mL) was added the appropriate copper(II) salt (0.5 mmol) in methanol (5 mL) and the resulting blue solution was heated to reflux for 2 h. On cooling, the solution was allowed to stand and, after several days, either a powder or crystals appeared, which was collected by filtration and dried.

**4:** Blue solid, yield 0.39 g (84%). $C_{112}H_{160}CuN_6O_{20}$ (1974.04): calcd. C 68.14, H 8.17, N 4.26; found C 67.78, H 8.00, N 4.43; m.p. 179–180 °C. IR (KBr): $\tilde{\nu}_{max}$ = 3360 (NH), 1690 (amide C=O) $cm^{-1}$, 1578 ($COO_{asym}$) $cm^{-1}$, 1448 ($COO_{sym}$) $cm^{-1}$.

**5:** Green/blue solid, yield 0.42 g (88%). $C_{112}H_{154}CuN_6O_{16}$ (1932.01): calcd. C 69.62, H 8.03, N 5.80, found C 69.78, H 8.00, N 5.43; m.p. 179–180 °C. IR (KBR): $\tilde{\nu}_{max}$ = 3360 (NH), 1690 (amide C=O) $cm^{-1}$, 1578 ($COO_{asym}$) $cm^{-1}$, 1448 ($COO_{sym}$) $cm^{-1}$.

**6:** Green solid, yield 0.42 g (86%). $C_{53}H_{72}ClCuN_3O_{11}$ (1026.15): calcd. C 62.03, H, 7.07, N 4.09; found C 61.93, H 6.98, N 4.32; m.p. 200 °C (dec.). IR (KBr): $\tilde{\nu}_{max}$ = 3359 (NH), 1677 (amide C=O), 1109 ($ClO_4$) $cm^{-1}$, 625 ($ClO_4$) $cm^{-1}$.

**7:** Green solid, yield 0.41 g (78%). $C_{55}H_{77}ClCuN_4O_{11}$ (1069.22): calcd. C 61.78, H 7.22, N 5.24, found C 62.19, H 6.83, N 5.32; m.p. 212 °C (dec.). IR (KBr): $\tilde{\nu}_{max}$ = 3355 (NH) $cm^{-1}$, 1668 (amide C=O) $cm^{-1}$, 1110 ($ClO_4$) $cm^{-1}$, 625 ($ClO_4$) $cm^{-1}$.

**8:** Green solid, yield 0.38 g (85%). $C_{104}H_{138}Cl_2CuN_6O_{12}$ (1798.69): calcd. C 69.45, H 7.73, N 4.67; found C 69.68, H 7.36, N 5.01; m.p. 150 °C (dec.). IR (KBr): $\tilde{\nu}_{max}$ = 3340 (NH), 1678 (amide C=O) $cm^{-1}$.

**9:** Blue solid, yield 0.18 g (88%). $C_8H_{26}Cl_2Cu_2N_6O$ (420.33): calcd. C 22.86, H 6.23, N 19.99; found C 22.87, H 5.84, N 19.90; m.p. 160 °C (dec.). IR (KBr): $\tilde{\nu}_{max}$ = 3240 (NH) $cm^{-1}$.

**10:** Green solid, yield 0.24 g (80%). $C_{54}H_{84}ClCuN_4O_{11}$ (1064.26): calcd. C 60.94, H 7.96, N 5.26; found C 60.42, H 7.47, N 5.64; m.p. 160 °C (dec.). IR (KBr): $\tilde{\nu}_{max}$ = 3340 (NH, OH), 1681 (C=O amide) $cm^{-1}$.

**General Synthesis of Manganese(II) Complexes 11–12:** To a solution of the calix[4]azacrown (0.5 mmol) in chloroform (5 mL) was added manganese(II) chloride (0.5 mmol) in methanol (10 mL) and the resulting brown solution was stirred for 2 h. The solution was allowed to stand and, after several days, a brown powder precipitated, which was collected by filtration and dried.

**11:** Brown solid, yield 0.39 g (75%). $C_{53}H_{82}ClMnN_3O_{12}$ (1043.62): calcd. C 61.00, H 7.92, N 4.03; found C 61.19, H 8.15, N 4.48; m.p. 220 °C (dec.). IR (KBr): $\tilde{\nu}_{max}$ = 3343 (NH) $cm^{-1}$, 1680 (amide C=O) $cm^{-1}$.

**12:** Brown solid, yield 0.40 (76%). $C_{54}H_{83}ClMnN_4O_{11}$ (1054.65): calcd. C 61.50, H 7.93, N 5.31; found C 61.99, H 7.55, N 5.74; m.p. 220 °C (dec.). IR (KBr): $\tilde{\nu}_{max}$ = 3357 (NH) $cm^{-1}$, 1667 (amide C=O) $cm^{-1}$.

**Synthesis of Extended Calix[4]azacrown 14:** A solution of the bis(bipy) calix[4]arene **13** (0.4 mmol) and diethylenetriamine (1.6 mmol) in a mixture of methanol (20 mL) and toluene (20 mL) was stirred at room temperature for 5 d. After this time, the solution was concentrated under reduced pressure. The solid residue was dissolved in methanol, recrystallised and filtered to give a white solid.

**Calix[4]azacrown 14:** Yield 0.26 g (67%). $C_{68}H_{71}N_9O_8$ (1142.35): calcd. C 71.50, H 6.26, N 11.04; found C 71.39, H 6.04, N 11.09; m.p. 250 °C (dec.). IR: (KBr): $\tilde{\nu}_{max}$ = 3400 (NH, OH), 1671 (amide C=O) $cm^{-1}$. $^1H$ NMR (300 MHz, $CDCl_3$): $\delta$ = 8.89 (d, $^1J$ = 7.2 Hz, 2 H, 6-H), 8.78 (s, 2 H, 3-H), 8.59 (d, $^1J$ = 7.2 Hz, 2 H, 6′-H), 8.35 (s, 2 H, 3′-H), 8.20 (s, 2 H, OH), 8.05 (br. t, 2 H, CON*H*$CH_2$), 7.94 (d, $^1J$ = 7.2 Hz, 2 H, 5-H), 7.52 (s, 4 H, Ar-H), 7.23 (d, $^1J$ = 7.2 Hz, 2 H, 5′-H), 6.79 (s, 4 H, Ar-H), 6.28 (s, 1 H, NH), 4.47 (s, 4 H, $OCH_2CO$), 4.21 (d, $^1J$ = 14.0 Hz, 4 H, Ar-$CH_aH_b$-Ar), 3.55 (m, 4 H, $CH_2$), 3.47 (d, $^1J$ = 14.0 Hz, 4 H, Ar-C$H_aH_b$-Ar), 2.94 (m, 4 H, $CH_2$), 2.49 (s, 6 H, $CH_3$), 0.96 (s, 18 H, *t*Bu) ppm.

**Synthesis of Extended Calix[4]azacrown 15:** A solution of **13** (0.5 mmol) and diethylenetriamine (2.0 mmol) in a mixture of methanol (15 mL) and toluene (15 mL) was stirred at room temperature for 5 d. After this time, the solution was concentrated under reduced pressure. The solid residue was dissolved in methanol, recrystallised and filtered to give a white solid.

**Calix[4]azacrown 15:** Yield 0.21 g (44%); m.p. 200 °C (dec.). $C_{70}H_{76}N_{10}O_8$ (1185.42): calcd. C 70.92, H 6.46, N 11.82; found C 71.39, H 6.04, N 11.59. IR (KBr): $\tilde{\nu}_{max}$ = 3360 (NH, OH), 1666 (amide C=O) $cm^{-1}$. $^1H$ NMR (300 MHz, $CDCl_3$): $\delta$ = 8.85 (d, $^1J$ = 7.2 Hz, 2 H, 6-H), 8.80 (s, 2 H, 3-H), 8.55 (d, $^1J$ = 7.2 Hz, 2 H, 6′-H), 8.31 (s, 2 H, 3′-H), 8.13 (br. t, 2 H, CON*H*$CH_2$), 7.92 (d, $^1J$ = 7.2 Hz, 2 H, 5-H), 7.53 (s, 4 H, Ar-H), 7.30 (s, 2 H, OH), 7.18 (d, $^1J$ = 7.2 Hz, 2 H, 5′-H), 6.84 (s, 4 H, Ar-H), 4.52 (s, 4 H, O$CH_2$CO), 4.18 (d, $^1J$ = 14.0 Hz, 4 H, Ar-$CH_aH_b$-Ar), 3.53 (m, 6 H, $CH_2$), 3.46 (d, $^1J$ = 14.0 Hz, 4 H, Ar-C$H_aH_b$-Ar), 2.76 (m, 6 H, $CH_2$), 2.50 (s, 6 H, $CH_3$), 0.97 (s, 18 H, *t*Bu) ppm.

**General Synthesis of Ruthenium(II) Complexes 16 and 17:** To a solution of the calix[4]azacrown **14** or **15** (0.185 mmol) in absolute ethanol (20 mL) was added $Ru^{II}(bipy)Cl_4$ (0.37 mmol) in absolute ethanol (20 mL) and the resulting brown solution was heated to reflux for 3 h. On cooling, a brown precipitate resulted in each case. The precipitate was collected by filtration, dried and stored in the dark.

**16:** Red/brown solid, yield 0.32 g (83%). $C_{91}H_{90}Cl_{13}N_{13}O_8Ru_2$ (2156.8): calcd. C 50.68, H 4.21, N 8.44; found C 50.78, H 4.00, N 8.73; m.p. > 300 °C. IR (KBr): $\tilde{\nu}_{max}$ = 3385 (NH, OH), 1663 (amide C=O) $cm^{-1}$.

**17:** Red/brown solid, yield 0.30 g (76%). $C_{93}H_{95}Cl_{13}N_{14}O_8Ru_2$ (2180.8): calcd. C 50.78, H 4.32, N 8.91; found C 50.48, H 4.01, N 8.43; m.p. > 300 °C. IR (KBr): $\tilde{\nu}_{max}$ = 3385 (NH, OH), 1661 (amide C=O) $cm^{-1}$.

 © 2007 Wiley-VCH Verlag GmbH & Co. KGaA, Weinheim 

**General Synthesis of Ruthenium(II)/Manganese(II) Complexes 18 and 19:** To a solution of the ruthenium(II) calix[4]azacrown **16** or **17** (0.11 mmol) in methanol (10 mL) was added manganese(II) chloride tetrahydrate (0.11 mmol) in methanol (10 mL) and the resulting brown solution was stirred at room temperature for 2 h. During the course of the reaction, a dark brown solid precipitated in each case. The precipitate was collected by filtration, washed with $CHCl_3$, dried and stored in the dark.

**18:** Brown solid, yield (62%). $C_{90}H_{98}Cl_{11}MnN_{13}O_{13}Ru_2$: calcd. C 48.76, H 4.46, N 8.21; found C 48.21, H 4.39, N 8.72; m.p. > 300 °C: IR (KBr): $\tilde{\nu}_{max}$ = 3374 (NH, OH), 1662 (amide C=O) $cm^{-1}$.

**19:** Brown solid, yield 0.14 g (57%). $C_{92}H_{103}Cl_{11}MnN_{14}O_{13}Ru_2$ (2216.9): calcd. C 48.89, H 4.59, N 8.68; found C 49.19, H 4.63, N 9.17; m.p. > 300 °C. IR (KBr): $\tilde{\nu}_{max}$ = 3378 (NH, OH), 1660 (amide C=O) $cm^{-1}$.

**X-ray Crystallography:** Crystal data for **4**: $C_{112}H_{160}CuN_6O_{20}$, $M$ = 1974.00, monoclinic, $a$ = 12.2259(8) Å, $b$ = 24.0471(17) Å, $c$ = 19.5251(13) Å, $\beta$ = 101.262(3)°, $U$ = 5629.8(7) Å$^3$, $T$ = 180(2) K, space group $P2_1/n$, $Z$ = 2, $\mu$(Mo-$K_\alpha$) = 0.261 $mm^{-1}$. 66796 reflections measured, 9751 unique ($R_{int}$ = 0.0913) which were used in all calculations. The final $R_1$ = 0.0824, $wR_2$ (all data) = 0.2874, goodness-of-fit on $F^2$ = 1.09. Data were collected at 180(2) K with a Bruker Nonius X8 APEX II diffractometer,[36] and a multi-scan correction was applied.[37] The structures were refined against $F^2$ using all data.[38] Hydrogen atoms were placed at calculated positions and refined using a riding model.

CCDC-616020 contains the supplementary crystallographic data for this paper. These data can be obtained free of charge from The Cambridge Crystallographic Data Centre via www.ccdc.cam.ac.uk/data_request/cif.

## Acknowledgments

The authors are grateful to the Technological Sector Research Programme, Strand I (2002–2005), under the European Social Fund Operational Programme for Industrial Development, the PhD continuation of IT Tallaght and the Enterprise Ireland, International Collaboration Fund for financial assistance. A. D. B. is grateful to the Danish Natural Sciences Research Council and the Carlsberg Foundation for provision of the X-ray equipment.

[1] a) Z. Asfari, V. Böhmer, J. Harrowfield, J. Vicens, *Calixarene* **2001**, Kluwer Academic, Dordrecht, **2001**; b) L. Mandolini, R. Ungaro, *Calixarene in Action*, Imperial College, London, **2000**; c) C. D. Gutsche, *Calixarenes Revisited: Monographs in Supramolecular Chemistry*, Royal Society of Chemistry, London, **1998**; d) J. Vicens, V. Böhmer, *Calixarenes, A Versatile Class of Macrocyclic Compounds*, Kluwer Academic, Dordrecht, **1991**; e) C. D. Gutsche, *Calixarenes: Monographs in Supramolecular Chemistry*, Royal Society of Chemistry, London, **1989**.

[2] a) I. Higler, P. Timmerman, W. Verboom, D. N. Reinhoudt, *Eur. J. Org. Chem.* **1998**, 2689–2702; b) A. Ikeda, S. Shinkai, *Chem. Rev.* **1997**, *97*, 1713–1734.

[3] See, for example, a) J.-M. Liu, Y.-S. Zheng, Q.-Y. Zheng, J. Xie, M.-X. Wang, Z.-T. Huang, *Tetrahedron* **2002**, *58*, 3729–3736; b) A. Arduini, A. Pochini, A. Secchi, *Eur. J. Org. Chem.* **2000**, 2325–2334; c) M. Pitarch, V. McKee, M. Nieuwenhuyzen, M. A. McKervey, *J. Org. Chem.* **1998**, *63*, 946–951; d) P. Lhoták, S. Shinkai, *Tetrahedron Lett.* **1996**, *37*, 645–648; e) D. M. Rudkevich, W. Verboom, D. N. Reinhoudt, *J. Org. Chem.* **1995**, *60*, 6585–6587.

[4] See, for example, a) T. Ceyhan, A. Altindal, A. R. Özkaya, M. K. Erbil, B. Salih, Ö. Bekaroğlu, *Chem. Commun.* **2006**, 320–322; b) N. Cheriaa, R. Abidi, J. Vicens, *Tetrahedron Lett.* **2005**, *46*, 1533–1536; c) H. Al-Saraierh, D. O. Miller, P. E. Georghiou, *J. Org. Chem.* **2005**, *70*, 8273–8280; d) M. Kumar, V. Sharma, J. N. Babu, *Tetrahedron* **2003**, *59*, 3267–3273; e) S. E. Matthews, V. Felix, M. G. B. Drew, P. D. Beer, *Org. Biomol. Chem.* **2003**, *1*, 1232–1239; f) S. E. Matthews, V. Felix, M. G. B. Drew, P. D. Beer, *New J. Chem.* **2001**, *25*, 1355–1358; g) F. Santoyo-González, A. Torres-Pinedo, A. Sanchéz-Ortega, *J. Org. Chem.* **2000**, *65*, 4409–4414.

[5] See, for example, a) V. Štasný, I. Stibor, H. Dvořáková, P. Lhoták, *Tetrahedron* **2004**, *60*, 3383–3391; b) F. Szemes, M. G. B. Drew, P. D. Beer, *Chem. Commun.* **2002**, 1228–1229; c) O. Mogck, P. Parzuchowski, M. Nissinen, V. Böhmer, G. Rokicki, K. Rissanen, *Tetrahedron* **1998**, *54*, 10053–10068.

[6] See, for example, a) A. M. Rincon, P. Prados, J. de Mendoza, *J. Am. Chem. Soc.* **2001**, *123*, 3493–3498; b) M. O. Vysotsky, I. Thondorf, V. Bohmer, *Angew. Chem. Int. Ed. Angew. Chem. Int. Ed. Engl.* **2000**, *39*, 1264–1267; c) J. Rebek Jr, *Chem. Commun.* **2000**, 637–643.

[7] See, for example, a) S. Banthia, A. Samanta, *Org. Biomol. Chem.* **2005**, *3*, 1428–1434; b) K. No, H. J. Lee, K. M. Park, S. S. Lee, K. H. Noh, S. K. Kim, J. Y. Lee, J. S. Kim, *J. Heterocycl. Chem.* **2004**, *41*, 211–219; c) R. Abidi, I. Oueslati, H. Amri, P. Thuéry, M. Nierlich, Z. Asfari, J. Vicens, *Tetrahedron Lett.* **2001**, *42*, 1685–1689; d) I. Oueslati, R. Abidi, P. Thuéry, M. Nierlich, Z. Asfari, J. Harrowfield, J. Vicens, *Tetrahedron Lett.* **2000**, *41*, 8263–8267; e) J. S. Kim, O. J. Shon, J. W. Ko, M. H. Cho, I. Y. Yu, J. Vicens, *J. Org. Chem.* **2000**, *65*, 2386–2392.

[8] R. Ostaszewski, T. W. Stephens, W. Verboom, D. N. Reinhoudt, *Recl. Trav. Chim. Pays-Bas* **1991**, *110*, 294–298.

[9] a) B. S. Creaven, T. L. Gernon, J. McGinley, A.-M. Moore, H. Toftlund, *Tetrahedron* **2006**, *62*, 9066–9071; b) B. S. Creaven, M. F. Mahon, J. McGinley, A.-M. Moore, *Inorg. Chem. Commun.* **2006**, *9*, 231–234; c) B. S. Creaven, T. L. Gernon, T. McCormac, J. McGinley, A.-M. Moore, H. Toftlund, *Inorg. Chim. Acta* **2005**, *358*, 2661–2670; d) D. Tobin, B. S. Creaven, C. McKenna, M. Deasy, B. A. Murray, *Eur. J. Inorg. Chem.* **2005**, 1282–1292; e) B. S. Creaven, M. Deasy, J. F. Gallagher, J. McGinley, B. A. Murray, *Tetrahedron* **2001**, *57*, 8883–8887; f) M. Pitarch, A. Walker, J. F. Malone, J. J. McGarvey, M. A. McKervey, B. Creaven, D. Tobin, *Gazz. Chim. Ital.* **1997**, *127*, 717–721.

[10] V. Balzani, G. Bergamini, F. Marchioni, P. Ceroni, *Coord. Chem. Rev.* **2006**, *250*, 1254–1266.

[11] M. Elvington, K. J. Brewer, *Inorg. Chem.* **2006**, *45*, 5242–5244.

[12] J. H. Alstrum-Acevedo, M. K. Brennaman, T. J. Meyer, *Inorg. Chem.* **2005**, *44*, 6802–6827.

[13] S. Welter, N. Salluce, P. Belser, M. Groeneveld, L. De Cola, *Coord. Chem. Rev.* **2005**, *249*, 1360–1371.

[14] R. T. F. Jukes, V. Adamo, F. Hartl, P. Belser, L. De Cola, *Coord. Chem. Rev.* **2005**, *249*, 1327–1335.

[15] L. Sun, B. Åkermark, S. Ott, *Coord. Chem. Rev.* **2005**, *249*, 1653–1663.

[16] F. Weldon, L. Hammarström, E. Mukhtar, R. Hage, E. Gunneweg, J. G. Haasnoot, J. Reedijk, W. R. Browne, A. L. Guckian, J. G. Vos, *Inorg. Chem.* **2004**, *43*, 4471–4481.

[17] B. Geiβer, R. Alsfasser, *Dalton Trans.* **2003**, 612–618.

[18] M. Furue, K. Maruyama, Y. Kanematsu, T. Kushida, M. Kamachi, *Coord. Chem. Rev.* **1994**, *132*, 201–208.

[19] B. Schlicke, L. De Cola, P. Belser, V. Balzani, *Coord. Chem. Rev.* **2000**, *208*, 267–275.

[20] A. Beyeler, P. Belser, *Coord. Chem. Rev.* **2002**, *230*, 28–38.

[21] P. Belser, A. von Zelewsky, M. Frank, C. Seel, F. Vögtle, L. De Cola, F. Barigelletti, V. Balzani, *J. Am. Chem. Soc.* **1993**, *115*, 4076–4086.

[22] M. Ghirotti, P. F. H. Schwab, M. T. Indelli, C. Chiorboli, F. Scandola, *Inorg. Chem.* **2006**, *45*, 4331–4333.

[23] E. M. Collins, M. A. McKervey, S. J. Harris, *J. Chem. Soc., Perkin Trans. 1* **1989**, 372–374.

 © 2007 Wiley-VCH Verlag GmbH & Co. KGaA, Weinheim 

[24] B. Balázs, G. Tóth, G. Horváth, A. Grün, V. Csokai, L. Töke, I. Bitter, *Eur. J. Org. Chem.* **2001**, 61–71.
[25] F. Benevelli, J. Klinowski, I. Bitter, A. Grün, B. Balázs, G. Tóth, *J. Chem. Soc., Perkin Trans. 2* **2002**, 1187–1192.
[26] I. Oueslati, R. Abidi, P. Thuéry, J. Vicens, *J. Inclusion Phenom. Macrocyclic Chem. J. Inclusion Phenom.* **2003**, *47*, 173–178.
[27] See, for example, a) M.-L. Tong, W. Li, X.-M. Chen, S.-L. Zheng, S. W. Ng, *Acta Crystallogr., Sect. C* **2002**, *58*, m232–m234; b) H.-L. Hu, M.-C. Suen, C.-W. Yeh, J.-D. Chen, *Polyhedron* **2005**, *24*, 1497–1502; c) R. Horikoshi, K. Okazawa, T. Mochida, *J. Organomet. Chem.* **2005**, *690*, 1793–1799; d) L. P. Battaglia, A. B. Corradi, L. Menabue, *J. Chem. Soc., Dalton Trans.* **1986**, 1653–1657.
[28] T. L. Gernon, B. S. Creaven, J. McGinley, A. D. Bond, *Acta Crystallogr., Sect. E* **2006**, *62*, m1958–m1960.
[29] R. D. Willett, *Acta Crystallogr., Sect. E* **2001**, *57*, 605–606.
[30] N. Niklas, F. W. Heinemann, F. Hampel, T. Clark, R. Alsfasser, *Inorg. Chem.* **2004**, *43*, 4663–4673.
[31] a) C.-C. Zeng, J. Y. Becker, *Tetrahedron* **2004**, *60*, 1643–1650; b) A. B. Salem, J. B. Regnouf-de-Vains, *Tetrahedron Lett.* **2001**, *42*, 7033–7036; c) F. Arnaud-Neu, G. Barrett, S. Cremin, M. Deasy, G. Ferguson, S. J. Harris, A. J. Lough, L. Guerra, M. A. McKervey, M. J. Schwingweill, P. Schwinte, *J. Chem. Soc., Perkin Trans. 2* **1992**, 1119–1125; d) M. Dudic, P. Lhoták, I. Stibor, H. Dvoráková, K. Lang, *Tetrahedron* **2002**, *58*, 5475–5482.
[32] R. A. Krause, *Inorg. Chim. Acta* **1977**, *22*, 209–213.
[33] K. E. Berg, A. Tran, M. K. Raymond, M. Abrahamsson, J. Wolny, S. Redon, M. Andersson, L. Sun, S. Styring, L. Hammarström, H. Toftlund, B. Åkermark, *Eur. J. Inorg. Chem.* **2001**, 1019–1029.
[34] C. D. Gutsche, D. E. Johnston Jr, D. R. Stewart, *J. Org. Chem.* **1999**, *64*, 3747–3750.
[35] I. Bitter, A. Grün, G. Tóth, B. Balázs, L. Tőke, *Tetrahedron* **1997**, *53*, 9799–9812.
[36] Bruker Nonius, APEX2, version 1.0-22, Bruker Nonius BV, Delft, The Netherlands, **2004**.
[37] G. M. Sheldrick, SADABS, version 2.10, Bruker AXS Inc., Madison, Wisconsin, USA, **2003**.
[38] G. M. Sheldrick, SHELXTL, version 6.10, Bruker AXS Inc., Madison, Wisconsin, USA, **2000**.

Received: October 24, 2006
Published Online: January 5, 2007

 © 2007 Wiley-VCH Verlag GmbH & Co. KGaA, Weinheim

**The EUChemSoc Societies have taken the significant step into the future by merging their traditional journals, to form two leading chemistry journals, the *European Journal of Inorganic Chemistry* and the *European Journal of Organic Chemistry.* Three further EUChemSoc Societies (Austria, Czech Republic and Sweden) are Associates of the two journals.**

## COVER PICTURE

**The cover picture shows** how mechanistic insight into the activation of NO by biological and model metal complexes can be gained through volume profile analysis. The presented volume profile describes the binding of NO to the high-spin, five-coordinate $Fe^{III}$ centre in cytochrome P450 in the presence of camphor to form a low-spin (diamagnetic), six-coordinate $Fe^{II}-NO^{+}$ product. Details are presented in the Microreview by R. van Eldik et al. on p. 773ff.

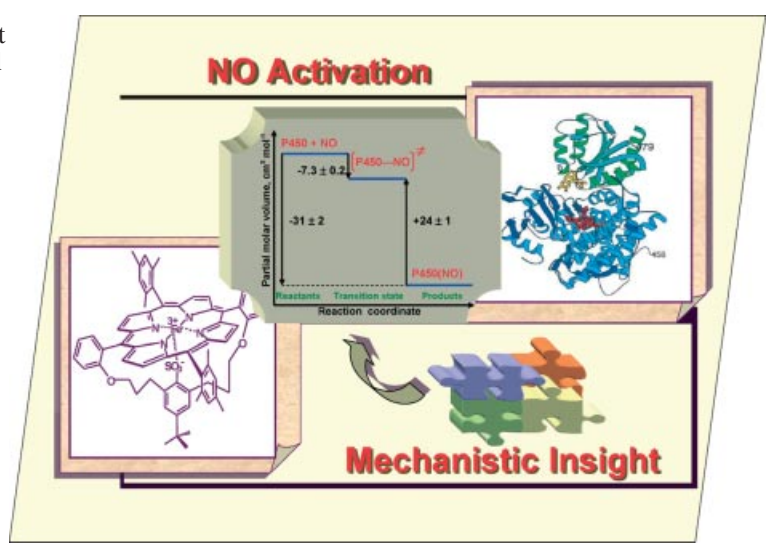


 © 2007 Wiley-VCH Verlag GmbH & Co. KGaA, Weinheim

**The EUChemSoc Societies have taken the significant step into the future by merging their traditional journals, to form two leading chemistry journals, the *European Journal of Inorganic Chemistry* and the *European Journal of Organic Chemistry.* Three further EUChemSoc Societies (Austria, Czech Republic and Sweden) are Associates of the two journals.**

## COVER PICTURE

**The cover picture shows** how mechanistic insight into the activation of NO by biological and model metal complexes can be gained through volume profile analysis. The presented volume profile describes the binding of NO to the high-spin, five-coordinate $Fe^{III}$ centre in cytochrome P450 in the presence of camphor to form a low-spin (diamagnetic), six-coordinate $Fe^{II}-NO^{+}$ product. Details are presented in the Microreview by R. van Eldik et al. on p. 773ff.

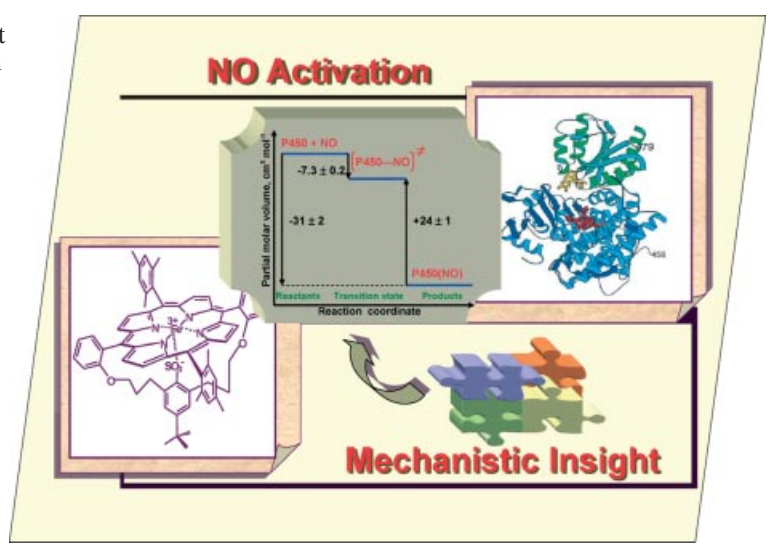


 © 2007 Wiley-VCH Verlag GmbH & Co. KGaA, Weinheim 

# CONTENTS

## MICROREVIEW


### NO Activation

**A. Franke, F. Roncaroli, R. van Eldik* ..... 773–798**

Mechanistic Studies on the Activation of NO by Iron and Cobalt Complexes

**Keywords:** Activation of NO / Reductive nitrosylation / Kinetics / Cytochrome P450 / Vitamin $B_{12}$ / Porphyrins / Chelates


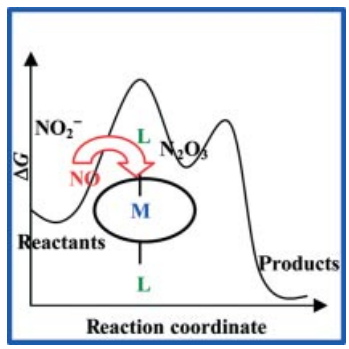



The reactions of NO with selected Fe and Co chelates and porphyrins, as well as with cytochrome P450, vitamin $B_{12}$ and model complexes are reviewed. Throughout, the focus is on mechanistic details of the binding and release of NO from metal complexes and on the nature of the stable metal–NO complexes produced in solution.


## FULL PAPERS


### Reorientation of Guests

**G. Q. Wu, L. Y. Wang*, L. Yang, J. J. Yang ..... 799–808**

Factors Affecting the Interlayer Arrangement of Transition Metal–Ethylenediaminetetraacetate Complexes Intercalated in Mg/Al Layered Double Hydroxides

**Keywords:** Layered compounds / Intercalation / Metal–edta complexes / Reorientation / Organic–inorganic hybrid composites


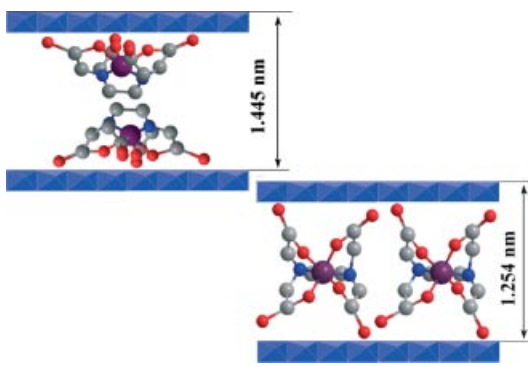



Guests on the Move: Transition metal–edta complex $\{[M(edta)]^{2-}\}$ intercalates of layered double hydroxide (LDH) were obtained by a hydrothermal synthesis method. The observed basal spacings of the LDH complexes, 1.445 nm in $Mg_2Al$–M(edta) LDH and 1.254 nm in $Mg_3Al$–M(edta) LDH, were ascribed to bilayer and monolayer arrangements of the incorporated $[M(edta)]^{2-}$, respectively. Heat treatment of the $Mg_2Al$–M(edta) LDH resulted in similar monolayer arrangements to that found in the $Mg_3Al$–M(edta) LDH. Rehydration of the calcined solids allows for the recovery of their original bilayer structures upon cooling to room temperature in air.



### 1D Metal Complexes

**K. Uemura, K. Yamasaki, K. Fukui, K. Matsumoto* ..... 809–815**

Synthesis, Crystal Structures, and Oxidation States of MM′X-Type Platinum–Rhodium Dinuclear Complexes Having Amidate Bridging Ligands

**Keywords:** Platinum / Rhodium / 1D Chains / Dinuclear complexes


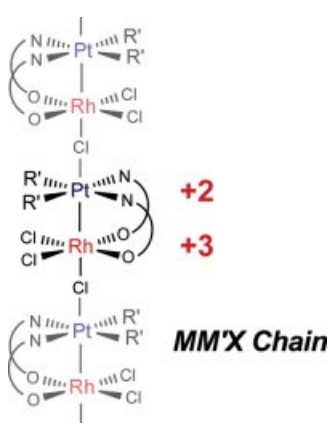



Two kinds of metal ions are bridged by amidate ligands to form Pt–Rh dinuclear complexes, which exist as pseudo 1D chains (MM′X chain), $[-Pt-Rh-Cl-]_n$, in the crystals. The dinuclear complexes have close metal–metal bond lengths with Pt(+2)–Rh(+3) formal oxidation states.

## Metal Azide → Nitrido Complex?

**D. Schröder,* H. Schwarz, N. Aliaga-Alcalde, F. Neese ..... 816–821**

Fragmentation of the (Cyclam-acetato)iron Azide Cation in the Gas Phase

**Keywords:** N ligands / Iron / Azides / Mass spectrometry

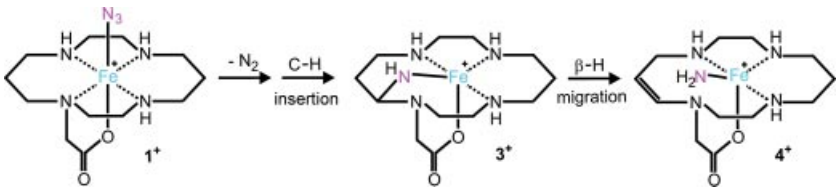


Collision-induced decomposition of the azido complex $\mathbf{1}^+$ in the gas phase to afford an iron(V) nitrido species appears to be followed by subsequent hydrogen rearrangements to afford isomers $\mathbf{3}^+$and $\mathbf{4}^+$.

## Chemical Nucleases

**J. Borrás,* G. Alzuet, M. González-Alvarez, J. L. García-Giménez, B. Macías, M. Liu-González ..... 822–834**

Efficient DNA Cleavage Induced by Copper(II) Complexes of Hydrolysis Derivatives of 2,4,6-Tri(2-pyridyl)-1,3,5-triazine in the Presence of Reducing Agents

**Keywords:** Copper triazine complexes / Oxidative DNA damage / ROS scavengers / Oxidation

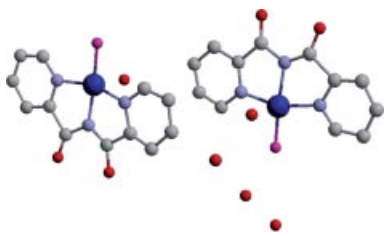

The complexes $[Cu(ptN_2)(OAc)]\cdot 3H_2O$ (**1**), $[Cu(ptO_2)(OAc)(H_2O)]\cdot H_2O$ (**2**), $[Cu(ptN_2)(for)]\cdot 3H_2O$ (**3**), $[Cu(ptO_2)(for)(H_2O)]$ (**4**), $[Cu(ptO_2)(benz)]\cdot H_2O$ (**5**), and $[Cu(ptO_2)F(H_2O)]_2\cdot 3H_2O$ (**6**) are obtained from the reaction of 2,4,6-tri(pyridyl)-1,3,5-triazine (ptz) and copper(II) salts in dmf/water (1:1) as a result of the hydrolysis of ptz. Efficient oxidative DNA cleavage by these compounds is observed in the presence of ascorbate and dioxygen.

## Coordination Polymers

**P. Banerjee, S. Kar, A. Bhaumik, G.-H. Lee, S.-M. Peng, S. Goswami* ..... 835–845**

Isolation and Characterization of $Zn^{II}$ and $Hg^{II}$ Coordination Polymers with a Designed Azo-Aromatic Ligand: Identification of Micrometer- and Nanometer-Sized Particles

**Keywords:** Coordination polymers / Azo-aromatic ligands / $d^{10}$ metal ions / X-ray structures / Nanostructures / Fluorescence

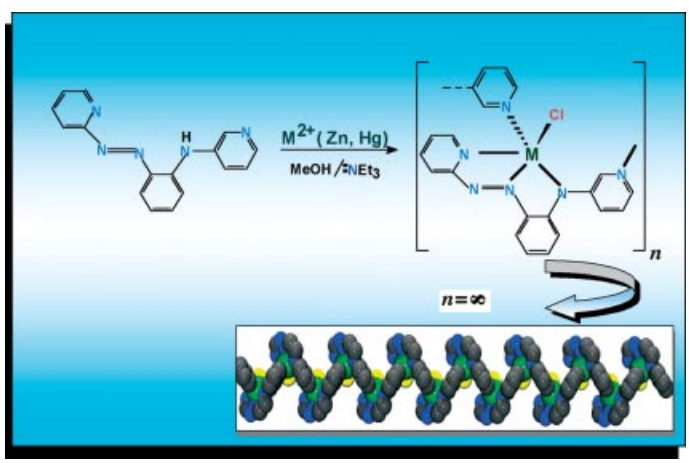


Isolation and characterization of one-dimensional, *zigzag*-chain, metal–organic framework of zinc ($Zn^{II}$) and mercury ($Hg^{II}$) with the bridging azo-aromatic ligand 2-[3-(pyridylamino)phenylazo]pyridine is described.

## Ferromagnetic Copper Complex

**S.-L. Ma, X.-X. Sun, S. Gao, C.-M. Qi,* H.-B. Huang, W.-X. Zhu ..... 846–851**

A New Chloro-Bridged $Cu^{II}$ Schiff Base Complex with Ferromagnetic Exchange Interaction

**Keywords:** Copper / Schiff bases / Dinuclear complex / Crystal structure / Magnetic properties

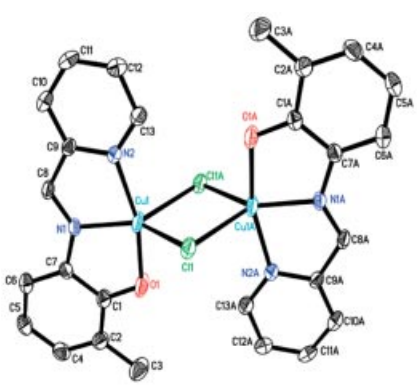

One μ-Cl-bridged dimer $[CuLCl]_2$ with distorted trigonal-bipyramidal geometry and ferromagnetic coupling is reported. A comparison for the magnetic coupling of $[CuLCl]_2$ with other $Cu(\mu\text{-}Cl)_2Cu$ compounds with square-pyramidal and trigonal-bipyramidal geometry is discussed.

 © 2007 Wiley-VCH Verlag GmbH & Co. KGaA, Weinheim 

# CONTENTS


## Bio-Inspired Oxidation Catalysts

**E. A. Duban, K. P. Bryliakov, E. P. Talsi* ..... 852–857**

The Active Intermediates of Non-Heme-Iron-Based Systems for Catalytic Alkene Epoxidation with $H_2O_2/CH_3COOH$

**Keywords:** Oxidoiron(IV) complexes / Acylperoxido complexes / EPR spectroscopy / Paramagnetic NMR spectroscopy / Intermediates / Oxidation

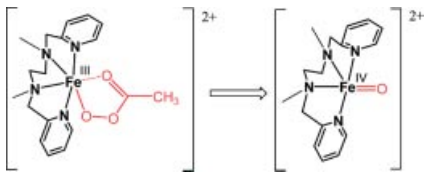

Using $^{1,2}H$ NMR and EPR spectroscopy, it was shown that the active species of the catalytic systems $[(BPMEN)Fe^{II}](ClO_4)_2/H_2O_2/CH_3COOH$ and $[(TPA)Fe^{II}](ClO_4)_2/H_2O_2/CH_3COOH$ are the respective mononuclear iron(IV)-oxido complexes $[(BPMEN)Fe^{IV}{=}O]^{2+}$ and $[(TPA)Fe^{IV}{=}O]^{2+}$.

## Tin(II) Phosphate Frameworks

**X.-j. Yuan, Y.-Z. Li, Y. Xu, X.-z. You,* R. J. Linhardt* ..... 858–864**

Synthesis of Tin(II) Phosphate Open Frameworks Using Isomers of 1,2-Diaminocyclohexane as Template

**Keywords:** Tin(II) phosphate / Open framework / Templated hydrothermal synthesis / Leaching

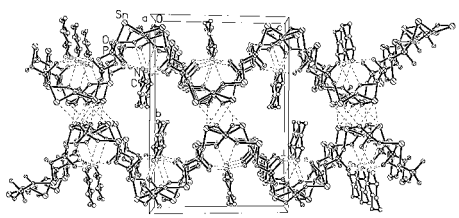

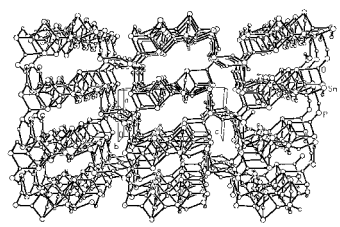

A novel layered framework of tin(II) phosphate, $[Sn_4(PO_4)_3(OH)]^{2-}\cdot$ [*trans*-1,2-$C_6H_{10}(NH_3)_2]^{2+}$ and a neutral inorganic phosphate framework, $(Sn_3O)_2(Sn_2O)_2(PO_4)_4$, are reported.

## Cationic $Au^I$ Alkanethiolates

**A. Battisti, O. Bellina, P. Diversi,* S. Losi, F. Marchetti, P. Zanello ..... 865–875**

Preparation, Structure and Reactivity of Polynuclear Gold(I) Phosphanyl Alkanethiolates

**Keywords:** Gold(I) complexes / Tertiary phosphane complexes / Thiolates / Aurophilicity / Redox behaviour

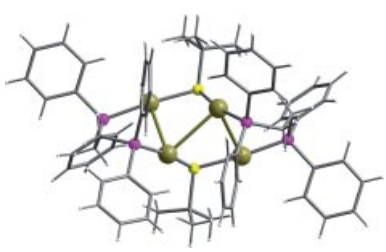

The cationic gold(I) phosphanyl alkanethiolates of formula $[Au_2(SR)_2(phosphane)_2][BF_4]$ (R = $CMe_3$, $CH_2CMe_3$, $CH_2CHMe_2$) have been prepared and characterized. Their structures in the solid state are dimeric with the arrangement of the tetragold core depending on the phosphane. Their reactivity with nucleophiles has also been studied.

## Sm-Based Polymerization Catalysts

**M. Wiecko, P. W. Roesky,* V. V. Burlakov, A. Spannenberg* ..... 876–881**

Bis(phosphinimino)methanides as Ligands in Divalent Samarium Chemistry: Synthesis, Structures and Catalysis

**Keywords:** Catalysis / Caprolactone / N,P ligands / Polymerization / Samarium

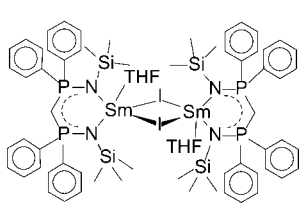

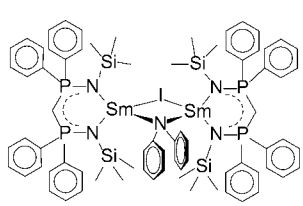

Three bis(phosphinimino)methanide complexes of divalent samarium, namely $[\{(Me_3SiNPPh_2)_2CH\}Sm(\mu\text{-}I)(thf)]_2$, $[\{(Me_3SiNPPh_2)_2CH\}_2Sm]$, and $[(\{(Me_3SiNPPh_2)_2CH\}Sm)_2(\mu\text{-}I)(\mu\text{-}NPh_2)]$, are synthesized and the former is investigated as a catalyst for the polymerization of ε-caprolactone.


 © 2007 Wiley-VCH Verlag GmbH & Co. KGaA, Weinheim 

## Stereochemical Activity of $e^-$ Lone Pairs

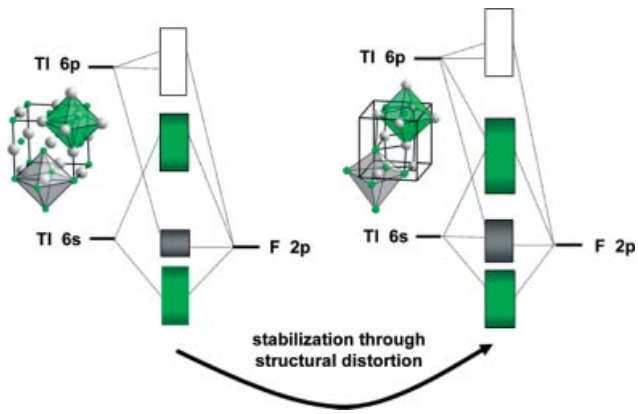


The stereochemical activity of lone pairs of heavier main-group elements is determined by the antibonding interaction with their surroundings. These unfavourable interactions can be minimised by structural distortions, which lead to a net stabilisation of the compound.

**A.-V. Mudring*** ..... **882–890**

Thallium Halides – New Aspects of the Stereochemical Activity of Electron Lone Pairs of Heavier Main-Group Elements

**Keywords:** Halides / Thallium / Electron lone pairs

## Selenium Chemistry

Reaction of $[PhP(Se)(\mu\text{-}Se)]_2$ (Woollins' reagent) with alkynes gives new vinylic $C_2P(Se)Se_2$ rings and an unexpected intramolecular cycloaddition product.

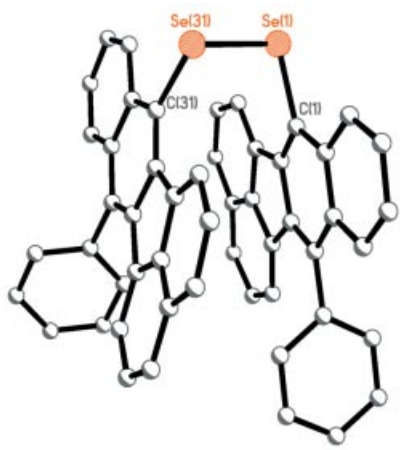


**G. Hua, Y. Li, A. M. Z. Slawin, J. D. Woollins*** ..... **891–897**

Synthesis of Novel Vinylic P–Se Heterocycles from Selenation of Alkynes by $[PhP(Se)(\mu\text{-}Se)]_2$

**Keywords:** Selenium / Heterocycles / Alkynes / Woollins' reagent / Cycloaddition

**If not otherwise indicated in the article, papers in issue 5 were published online on January 30, 2007**

 © 2007 Wiley-VCH Verlag GmbH & Co. KGaA, Weinheim 

DOI: 10.1002/ejic.200600921

# Mechanistic Studies on the Activation of NO by Iron and Cobalt Complexes

Alicja Franke,[a] Federico Roncaroli,[a,b] and Rudi van Eldik*[a]

**Keywords:** Activation of NO / Reductive nitrosylation / Kinetics / Cytochrome P450 / Vitamin $B_{12}$ / Porphyrins / Chelates

In this review, the reactions of nitric oxide with selected Fe and Co complexes of biological and environmental importance are reviewed. Fundamental chemical kinetics and mechanisms of reactions that lead to the formation and decay of nitrosyl complexes are illustrated and discussed on the basis of studies on $Fe^{II}$ chelates, $Fe^{II/III}$ pentacyano complexes, $Fe^{III}$ porphyrins, cytochrome P450 and model complexes, $Co^{II/III}$ porphyrins and vitamin $B_{12}$. Throughout the review, the focus is on mechanistic details of the binding of NO to and the release of NO from metal complexes and on the nature of the stable metal–NO complexes produced in solution. As will be seen for most of the presented reactions, the interaction of NO with the metal complex involves activation of the small NO molecule so that charge transfer occurs as a result of the formation of the metal–NO bond.

(© Wiley-VCH Verlag GmbH & Co. KGaA, 69451 Weinheim, Germany, 2007)

[a] Institute for Inorganic Chemistry, University of Erlangen-Nürnberg,
Egerlandstr. 1, 91058 Erlangen, Germany
E-mail: vaneldik@chemie.uni-erlangen.de
[b] Department of Inorganic, Analytical and Physical Chemistry, INQUIMAE, Faculty of Exact and Natural Sciences, University of Buenos Aires,
C1428EHA Buenos Aires, Argentina

## 1. Introduction

In recent years, we developed an interest in the interaction of NO with complexes of Fe, Co and Ru, and in their mechanistic understanding. Since this was a new research area for us, we were confronted with many fundamental questions that forced us to make a critical evaluation of the

*Alicja Franke was born in Biecz, a small town in south-eastern Poland, in 1972. After completing her M.Sc. in 1996 from the Jagiellonian University, Krakow, she was awarded TEMPUS (1997) and DAAD (1998) Fellowships to perform research work at the University of Erlangen-Nürnberg, Germany, in the group of Prof. Rudi van Eldik. In 2001 she received her PhD in the kinetics and mechanism of nitric oxide donation and binding in model systems of biological relevance, under the supervision of Prof. Grazyna Stochel (Jagiellonian University). In 2002 she joined the research group of Prof. Rudi van Eldik as a post-doctoral fellow. She continues to work in Erlangen on the kinetics and mechanism of small-molecule activation by iron-heme centres, as well as on the activation of organic peracids by cytochrome P450 and model complexes in the "peroxide-shunt" catalytic cycle.*

*Federico Roncaroli was born in Buenos Aires, Argentina, in 1976. He graduated as a chemist in 2000 at the University of Buenos Aires. In 2001 he was awarded a doctoral fellowship from the Scientific Research Council of Argentina (CONICET) to perform research work at the University of Buenos Aires and at the University of Erlangen-Nürnberg, Germany. At the first institution, he studied the reactivity and spectroscopic properties of metal–nitrosyl complexes under the direction of Professor José Olabe, which allowed him to earn a PhD degree in 2004. At the second institution, under the supervision of Professor Rudi van Eldik, his work focused on the reactions of nitric oxide with biologically relevant complexes like vitamin $B_{12}$ and metal porphyrins, for which he was awarded a Dr. rer. nat. in 2005. His current interests are bioinorganic chemistry, homogeneous catalysis and activation of small molecules.*

*Rudi van Eldik was born in 1945 in Amsterdam and grew up in Johannesburg (South Africa). He received his chemistry education and Ph.D. at Potchefstroom University (SA), followed by post-doctoral work with Gordon M. Harris (SUNY at Buffalo, NY) and Hartwig Kelm (University of Frankfurt, Germany). After completing his habilitation in physical chemistry at the University of Frankfurt in 1982, he was appointed as Professor of Inorganic Chemistry at the private University of Witten/Herdecke in 1987. In 1994 he accepted his present position as Professor of Inorganic and Analytical Chemistry at the University of Erlangen-Nürnberg. His research interests cover the elucidation of inorganic, organometallic and bioinorganic reaction mechanisms, with special emphasis on the application of high-pressure thermodynamic and kinetic techniques. He is presently editor of Advances in Inorganic Chemistry and author of ca. 680 research papers and reviews in international journals (www.chemie.uni-erlangen.de/vaneldik). He has developed a promotional activity for chemistry and related experimental sciences in the form of chemistry edutainment over the past ten years (www.magic-chemistry-lecture.com).*

 © 2007 Wiley-VCH Verlag GmbH & Co. KGaA, Weinheim 

existing literature data at that time. One aspect that was particularly disturbing was the fact that for many metal–NO complexes the exact oxidation state of both components was not stated and the Enemark and Feltham notation[1] was adopted in which the product is written as $\{M–NO\}^{(n+1)}$, where $n$ represents the number of d electrons of the metal ion [one is added ($n$ + 1) for the unpaired electron on the NO radical]. From a basic coordination chemistry viewpoint, this situation was not very satisfying since the oxidation state of the metal centre is very crucial for the understanding of its chemical behaviour and for analysing the extent to which the coordinated NO is 'activated' during the binding process. Another aspect that caused us to run into severe problems was the fact that in aqueous solutions of NO there are always unavoidable traces of nitrite that can totally inhibit or overrule the reaction with NO. Thus, we wondered whether it is really NO that reacts under the selected conditions, and if it is NO, what is the nature of the M–NO complex that is formed in terms of the formal-oxidation-state assignment. Along these lines, the first review of our work was entitled: 'To be or not to be NO in coordination chemistry? A mechanistic approach'.[2]

In this microreview, we focus on our most recent mechanistic studies dealing with the interaction of NO with complexes of $Fe^{II}$, $Fe^{III}$, $Co^{II}$ and $Co^{III}$, which also include the enzymes cytochrome P450 and vitamin $B_{12}$, as well as suitable model systems. The interaction will describe the reversible binding kinetics of NO, the characterization of the produced metal–nitrosyl complex, and provide information on subsequent reactions that lead to stable product species. The employed kinetic techniques (stopped-flow and laser flash photolysis at ambient and high pressure) allowed the extraction of the appropriate rate constants and activation parameters for the forward ("on") and back ("off") reactions for the reversible binding of NO and enabled us to discuss mechanisms underlying NO-substitution processes. In general, substitution reactions involving the displacement of a ligand coordinated to a metal centre by a free ligand in solution can be visualized as presented schematically in Figure 1.

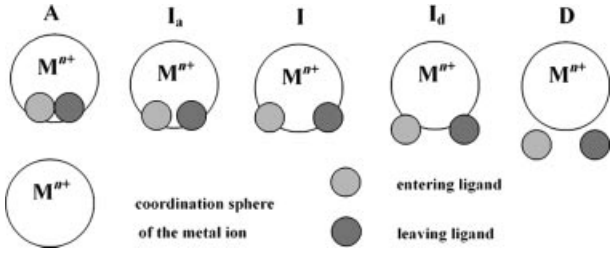


Figure 1. Schematic representation of the transition states of different substitution mechanisms.

If the activation parameters for the "on" and "off" reactions support an intermediate of higher and lower coordination number than in the reactant state, the mechanisms are of the limiting type denoted as associative (A) and dissociative (D), respectively. When the association and dissociation of the entering and leaving ligand, respectively, occur to an equal extent, then the mechanism can be described as an interchange (I) process. However, a "pure" interchange mechanism occurs very rarely and more often associative interchange ($I_a$) and dissociative interchange ($I_d$) mechanisms are observed in which the entering and leaving ligands are either firmly ($I_a$) or weakly ($I_d$) embedded in the coordination sphere of the metal ion.

## 2. Structure and Properties of Metal Nitrosyls

Binding of NO to a metal centre must result in the stabilisation of NO, a radical species in the ground state. Such stabilisation can be achieved by a shift of electron density to the metal centre or to the nitrosyl ligand and can formally be described as the formation of the nitrosyl cation ($NO^+$) or the nitroxyl anion ($NO^–$), respectively, as depicted by the mesomeric structures in reactions (1a) and (1b).

$$(L)M^{n+} + NO \rightleftharpoons (L)M^{n+}–NO \leftrightarrow (L)M^{(n-1)+}–NO^+;$$
linear M–N–O group (1a)

$$(L)M^{n+} + NO \rightleftharpoons (L)M^{n+}–NO \leftrightarrow (L)M^{(n+1)+}–NO^–;$$
bent M–N–O group (1b)

In reaction (1a), the $NO^+$ group is isoelectronic with CO, whereas in reaction (1b) the $NO^–$ group is isoelectronic with $O_2$. These two formal descriptions of the M–N–O bond are extreme and ideal, since metal–nitrosyl complexes usually show M–NO angles between 180° and 120°, and their electronic structures cannot be described as $M–NO^+$ or $M–NO^–$. Moreover, some complexes can be described as $(L)M^{n+}–NO^{\cdot}$, where the odd electron is *mainly* located on the metal. Nevertheless, in terms of the coordination chemistry at hand, it is in many cases useful to think in terms of formal oxidation states in order to understand the mechanistic behaviour of the complexes. A detailed account of the formal description of these limiting situations along with the description introduced by Enemark and Feltham have been published in an earlier account from our group.[2] The characterization of the produced metal–nitrosyl complexes has, in general, been done on the basis of EXAFS, XAS Fe-edge, resonance Raman, EPR and Mössbauer spectroscopic and magnetic circular dichroism data. Spin-crossover and spin-coupling phenomena account for the overall observed spin behaviour of the investigated complexes.

## 3. Interaction of NO with $Fe^{II}$ Chelate Complexes

Before we discuss the results of the interaction of NO with $Fe^{II}$ chelate complexes, we would like to refer to the interaction of NO with aquated $Fe^{II}$ in acidic medium, a classical text book example that forms part of the well-known brown-ring test for nitrate. A detailed kinetic and spectroscopic study[3] revealed that the overall reaction can be formulated as shown in reaction (2), where the product is formally an $Fe^{III}–NO^–$ species in which the high-spin $Fe^{III}$ ($S$ = 5/2) is antiferromagnetically coupled to the two un-

 © 2007 Wiley-VCH Verlag GmbH & Co. KGaA, Weinheim 

paired electrons on $NO^-$ ($S = 1$) to result in the overall $S = 3/2$ spin state of the product.

$$[Fe^{II}(H_2O)_6]^{2+} + NO \underset{k_{off}}{\overset{k_{on}}{\rightleftharpoons}} [Fe^{III}(H_2O)_5(NO^-)]^{2+} + H_2O \quad (2)$$

The 'on' reaction is controlled by water exchange on $[Fe(H_2O)_6]^{2+}$ and follows an $I_d$ mechanism as can be clearly seen from the volume profile for this reaction reported in Figure 2.

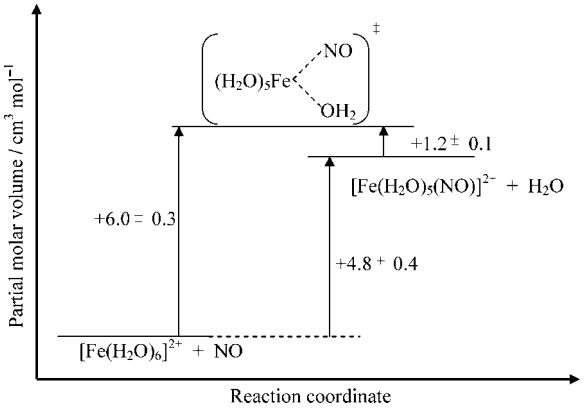


Figure 2. Volume profile for the binding of NO to aquated $Fe^{II}$ as given in reaction (2).[3]

The introduction of a chelate such as a polyaminocarboxylate labilizes the $Fe^{II}$ complex and significantly increases the water-exchange rate constant. The nitrosation of such complexes can be formulated as shown in reaction (3). Spectroscopic data suggested that the reaction product is formally $Fe^{III}$–$NO^-$.

$$[Fe^{II}L(H_2O)]^{2+} + NO \underset{k_{off}}{\overset{k_{on}}{\rightleftharpoons}} [Fe^{II}L(NO)]^{2+} + H_2O \quad (3)$$

A systematic study of the series of $Fe^{II}(L)$ complexes with different polyaminocarboxylate ligands indicated that their ability to reversibly bind NO is strongly affected by the selected chelating ligand. This influence is apparent from the large variation in the overall binding constant $K_{NO}$ ($= k_{on}/k_{off}$), which spans a wide range from ca. $1 \times 10^3$ to $2 \times 10^7$ $M^{-1}$ for the studied complexes (see Figure 3).[4] In addition, an interesting correlation was found between the stability of the $Fe^{III}(L)(NO^-)$ complexes and the oxygen sensitivity of the parent $Fe^{II}(L)$ complexes, in other words, their tendency to form $Fe^{III}(L)(O_2^-)$ species. From the comparison presented in Figure 3, it can, in general, be concluded that the higher the $K_{NO}$ value for a given metal–nitrosyl complex, the larger the oxygen sensitivity of the parent $Fe^{II}(L)$ complex. Clearly, an increasing inductive effect of the chelate ligand causes an increase in stability of the $Fe^{III}$–$NO^-$ bond and also an enhancement of the shift of electron density from iron to oxygen atom in the corresponding $Fe^{III}(L)(O_2^-)$ complex.

A quantitative basis for the observed trends in the stability of the $Fe^{III}(L)(NO^-)$ complexes was provided by kinetic and mechanistic studies on the binding and release of NO from selected $Fe^{II}(L)$ complexes. The complexes exhib-

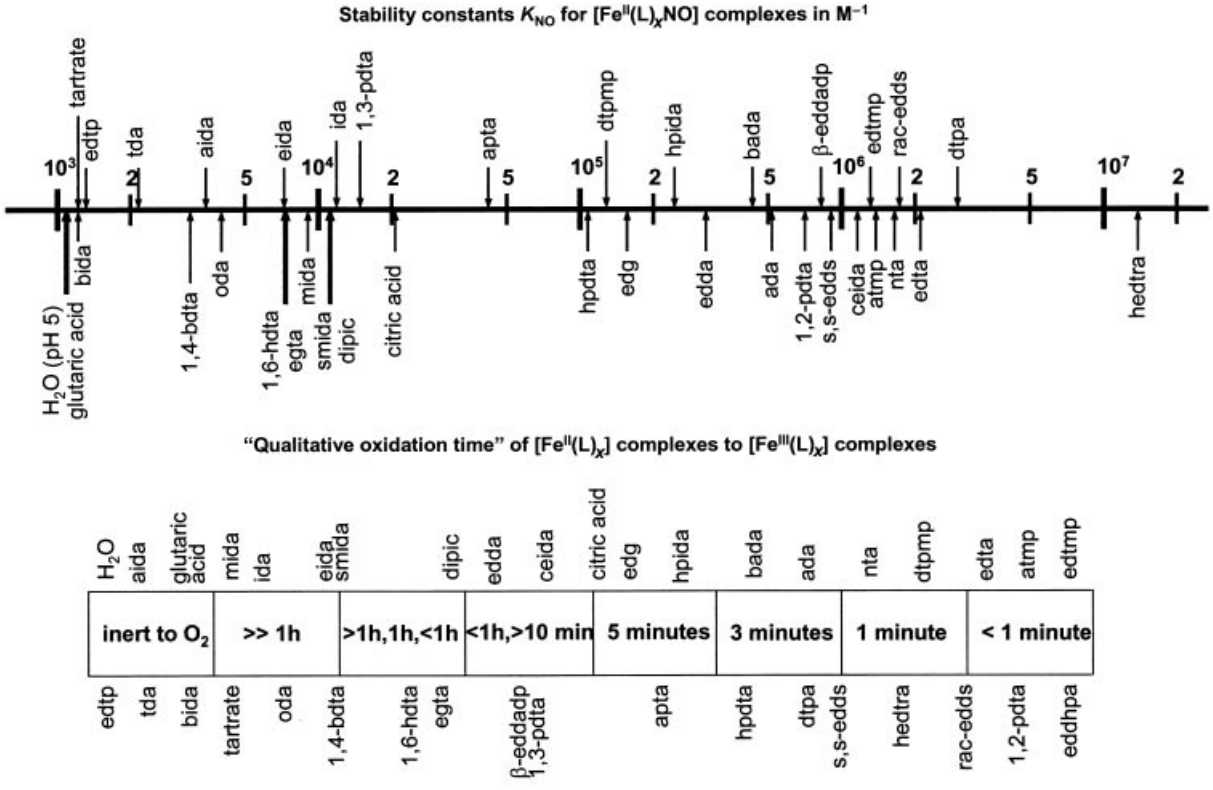


Figure 3. Correlation between $K_{NO}$ [defined by reaction (3)] and qualitative oxidation time of selected $Fe^{II}(L)$ complexes.[4]

 © 2007 Wiley-VCH Verlag GmbH & Co. KGaA, Weinheim 

ited quite different behaviour in their reactions with NO. The observed differences are particularly large in the case of the $Fe^{II}$(mida) and $Fe^{II}$(edta) complexes: the mida complex shows almost no oxygen sensitivity, exhibits a low binding affinity for NO and releases NO almost completely on passing an inert gas through the solution. In contrast, the edta complex is extremely oxygen sensitive, shows a very high binding affinity for NO and releases NO only slowly when treated with an inert gas.

More detailed insight into the mechanisms of the thermal reactions in which NO binds and dissociates from the iron centre in the studied $Fe^{II}$(L) systems comes from activation parameters for the "on" and "off" reactions, obtained from systematic studies of $k_{on}$ and $k_{off}$ as a function of temperature and pressure.[5] The positive volumes of activation found in most cases clearly indicate that the complex-formation reactions can be best described by a dissociative interchange ($I_d$) mechanism. The exception is the reaction of $Fe^{II}$(nta)$(H_2O)_2$ with NO, which exhibits a definite (Figure 4) negative volume of activation, suggesting that the reaction occurs through an associative interchange ($I_a$) mechanism. The difference in the mechanism of nitrosylation observed for the $Fe^{II}$(nta)$(H_2O)_2$ complex relative to the other studied complexes becomes clear from a comparison of the volume profiles for the edta and nta systems shown in Figure 4. Such a variation in the mechanism presumably reflects the fact that $Fe^{II}$(nta)$(H_2O)_2$ is a six-coordinate complex, whereas it is known that $Fe^{II}$(edta)$H_2O$ is seven-coordinate. This would mean that some complexes react according to an $I_d$ mechanism as a result of their seven-coordinate, 20-valence-electron character, whereas the six-coordinate nta complex reacts according to an $I_a$ mechanism because of its 18-valence-electron character. These results suggest that water-exchange reactions on the studied $Fe^{II}$(L) complexes presumably control the kinetics and mechanism of the NO binding.

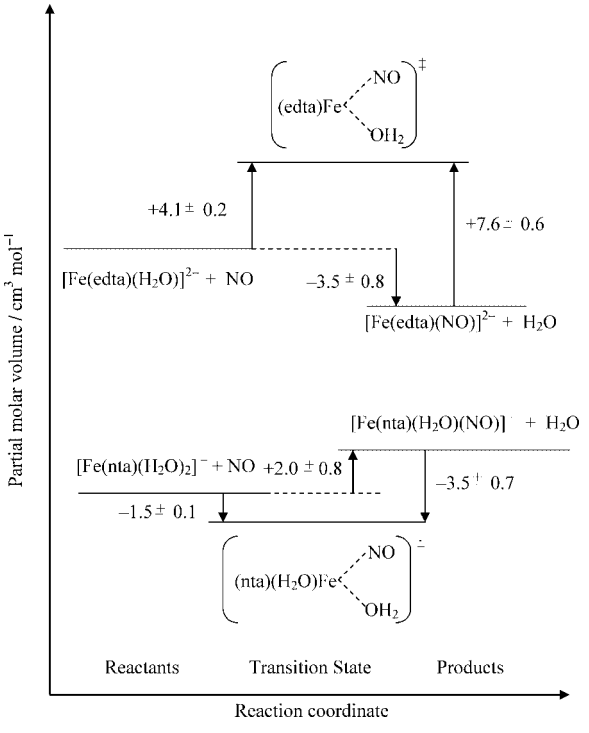


Figure 4. Volume profiles for the reversible binding of NO to $[Fe^{II}(edta)H_2O]^{2-}$ (top) and $[Fe^{II}(nta)(H_2O)_2]^{-}$ (bottom).[5]

## 4. Interaction of NO with Pentacyanoferrate(II)

Complex-formation and -dissociation reactions of the $[Fe^{II}(CN)_5(H_2O)]^{3-}$ complex have been extensively studied over the past decades for a good variety of ligands.[6,7] For this reason, this complex seemed to be an attractive choice for studying the reaction with NO and for comparing its binding, reactivity and coordination properties with other ligands; a comparison which, to the best of our knowledge, was missing or not addressed thoroughly enough in the literature. In this way, the investigated reaction is shown in reaction (4).

$$[Fe^{II}(CN)_5(H_2O)]^{3-} + NO \rightleftharpoons [Fe^{II}(CN)_5(NO^{\cdot})]^{3-} + H_2O;\ k_f,\ k_d \quad (4)$$

The product of reaction (4), the $[Fe^{II}(CN)_5(NO^{\cdot})]^{3-}$ complex, which can also be generated upon reduction of nitroprusside with several reducing agents or with different techniques (i.e. electrochemical, pulse radiolysis),[8,9] was characterized by different spectroscopic methods (UV/Vis, IR, EPR).[8,9] This compound was postulated to be responsible for the hypotensive effect of nitroprusside, i.e. $[Fe^{II}(CN)_5(NO^{+})]^{2-}$ is reduced in biological fluids to the $[Fe^{II}(CN)_5(NO^{\cdot})]^{3-}$ complex, which eventually releases NO.[10] This complex shows a *trans*-labilization effect which can be formulated as shown in reaction (5).

$$[Fe^{II}(CN)_5(NO^{\cdot})]^{3-} \rightleftharpoons [Fe^{I}(CN)_4(NO^{+})]^{2-} + CN^{-};\ k_5,\ k_{-5},\ K_5 \quad (5)$$

The parameters of reaction (5) were determined at 25 °C: $k_5 = 2.7 \times 10^2\ s^{-1}$, $k_{-5} = 4 \times 10^6\ M^{-1}\,s^{-1}$, $K_5 = 6.8 \times 10^{-5}$ M.[9] They indicate that the equilibrium is driven to the formation of the $[Fe^{II}(CN)_5(NO^{\cdot})]^{3-}$ species at high pH (>8) and in the presence of $CN^-$.

UV/Vis and EPR spectroscopic data at pH > 8 showed that the $[Fe^{II}(CN)_5(NO^{\cdot})]^{3-}$ complex is the product of reaction (4).[11] Between pH 4 and 8, the $[Fe(CN)_5(NO)]^{3-}$ complex could not be detected, which is in agreement with reaction (5).[12] However, a systematic study of the reaction between $[Fe^{II}(CN)_5(H_2O)]^{3-}$ and NO as a function of the pH allowed us to conclude that the reaction is controlled by the substitution of the coordinated water molecule by NO, i.e. the decay of the $[Fe(CN)_5(H_2O)]^{3-}$ complex was independent of the pH (4–10).[11]

From a systematic study as a function of the NO concentration, the complex-formation rate constant $k_f = 250 \pm 10\ M^{-1}\,s^{-1}$ (25.4 °C, $I$ = 0.1 M, pH = 7.0) was obtained. As shown in Table 1, this value is very close to the complex-formation rate constant for several neutral ligands. Experiments at different temperatures and pressures afforded the activation parameters $\Delta H^{\#} = 70 \pm 1\ kJ\,mol^{-1}$, $\Delta S^{\#} = +34 \pm 4\ J\,K^{-1}\,mol^{-1}$ and $\Delta V^{\#} = +17.4 \pm 0.3\ cm^3\,mol^{-1}$. In Table 1, the activation parameters are also compared with

 © 2007 Wiley-VCH Verlag GmbH & Co. KGaA, Weinheim 

the corresponding values for other ligands. Several mechanisms have been proposed to explain these complex-formation reactions (Scheme 1).

Table 1. Complex-formation rate constants and activation parameters for different $[Fe^{II}(CN)_5L]^{n-}$ complexes.[a]

| Ligand | $k_f$ [$M^{-1}s^{-1}$] | $\Delta H_f^{\#}$ [$kJ\,mol^{-1}$] | $\Delta S_f^{\#}$ [$J\,K^{-1}mol^{-1}$] | $\Delta V_f^{\#}$ [$cm^3\,mol^{-1}$] | Ref. |
|---|---|---|---|---|---|
| *N*-Mepz$^{+}$[b,c] | 550[b] | 70.3 | +42 | | [7] |
| | 2350[c] | | | | [6] |
| CO[c] | 310 | 63 | +15 | | [7] |
| NO[c] | 250 | 70 | +34 | +17.4 | [11] |
| dmso[b] | 240 | 64.4 | +16.7 | | [7] |
| pz[d] | 380 | 64.4 | +20.9 | | [7] |
| his[c] | 315 | 64.4 | +21 | +17.0 | [7,14] |
| py[d] | 365 | 67.4 | +29.3 | | [7] |
| $NH_3$[c] | 365 | 62 | +10 | | [7] |
| | 452 | 78 | +67 | +14.4 | |
| Im[c] | 242 | 63.5 | +12.5 | +15.5 | [7,14] |
| $CN^-$[b] | 30 | 76.9 | +42 | +13.5 | [16] |

[a] For the reaction: $[Fe(CN)_5H_2O]^{3-} + L \rightarrow [Fe(CN)_5L]^{n-} + H_2O$, $T$ = 25.0 °C, with the exception of L = NO where $T$ = 25.4 °C. [b] $I$ = 1 M. [c] $I$ = 0.1 M. [d] $I$ = 0.5 M.

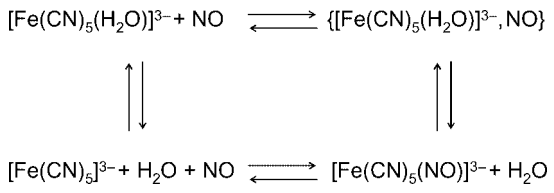


Scheme 1.

In the limiting dissociative mechanism (D), the reaction is controlled by the release of the water molecule, generating a pentacoordinate intermediate (left side of Scheme 1), followed by fast coordination of NO (bottom of Scheme 1).[13] The dissociative interchange mechanism ($I_d$) implies the rapid formation of a precursor complex between $[Fe(CN)_5(H_2O)]^{3-}$ and NO (top of Scheme 1), followed by the rate-determining ligand interchange between the first and the second coordination spheres of the precursor complex (right side of Scheme 1).[13] Finally, in a variation of the last mechanism ($D_{pc}$), the slow dissociation of the water molecule occurs within a precursor complex.[6] All of these mechanisms agree with the second-order behaviour of the rate law and with the dependence of $k_f$ on the charge of the coordinating ligand. The consistent rate constants found for the complex-formation reactions with different ligands of the same charge, and the significantly large and positive values for the activation entropies and volumes, suggest the operation of a D mechanism.[13] An additional argument presented in favour of the D mechanism is based on the principle of microscopic reversibility, since strong evidence, i.e. large activation volumes, supports the operation of a D mechanism in the complex-dissociation reaction ($k_d$). Moreover, the activation volumes in Table 1 range from +14 to +18 $cm^3\,mol^{-1}$.[14] These values are consistent with the theoretical activation volume calculated for the dissociation of a water molecule in an octahedral metal centre (+13.1 $cm^3\,mol^{-1}$).[15]

From the complex-formation rate constants, we conclude that NO behaves like a normal Lewis base. Since the complex-formation rate constant is controlled by the dissociation of water, it is not possible to obtain specific information on the coordination properties of NO, and no specific influence of the unpaired electron on NO is observed when it is compared with the coordination ability of diamagnetic ligands.

The $[Fe(CN)_5(NO)]^{3-}$ complex is the product of reaction (4), and we were able to generate it through the reaction between $[Fe(CN)_5(H_2O)]^{3-}$ and NO at pH > 8. The addition of $CN^-$ allowed us to prevent the formation of the $[Fe(CN)_4NO]^{2-}$ complex and its subsequent reactions.[12] In this way, it was possible to study the complex-dissociation reaction ($k_d$). The overall reaction of the former complex in the presence of $CN^-$ is shown in reaction (6).

$$[Fe(CN)_5(NO)]^{3-} + CN^- \rightleftharpoons [Fe(CN)_6]^{4-} + NO \quad (6)$$

During reaction (6), the characteristic bands of the reactant at 347 and 440 nm decayed according to a first order process. Only a shoulder at 320 nm, assignable to $[Fe(CN)_6]^{4-}$, remained. NO was detected by mass spectrometry and electrochemical techniques.[11] With excess cyanide, the observed rate constant is independent of the concentration of this ligand, and reaction (6) is controlled by the dissociation of NO, i.e. $k_d$. At pH 10 (25.0 °C, $I$ = 0.1 M), the observed rate constant was $(1.58 \pm 0.06) \times 10^{-5}\ s^{-1}$. The activation parameters were $\Delta H^{\#} = 106.4 \pm 0.8\ kJ\,mol^{-1}$, $\Delta S^{\#} = +20 \pm 2\ J\,K^{-1}mol^{-1}$ and $\Delta V^{\#} = +7.1 \pm 0.2\ cm^3\,mol^{-1}$. Table 2 summarizes the data for the complex-dissociation rate constants for similar complexes with different ligands that show different σ–π interactions with the metal centre. The activation enthalpies and entropies are consistent with those reported for the release of other ligands in the pentacyanoferrate(II) fragment. Although the activation volume for NO is significantly smaller than for other ligands, it is still indicative of a D mechanism. In Table 2, we can appreciate that $k_d$ for NO is significantly lower than for most ligands, comparable to that for the π-acceptor ligand DMSO, but faster than those for the strong π-acceptor ligands such as CO, $CN^-$ or $NO^+$ (the release of $NO^+$ is, in principle, undetectable in $M^{II}NO^+$ complexes).

In view of the presented value of $k_d$, we conclude that NO is not released from the $[Fe(CN)_5(NO)]^{3-}$ complex after biological reduction of nitroprusside. In vitro experiments showed that conditions favouring the release of $CN^-$ after reduction of nitroprusside are required to allow the release of NO.[12] Figure 5 shows the volume profile for reaction (4) constructed with the activation volumes determined for $k_f$ and $k_d$. Evidently, the partial molar volume of the transition state is much larger than that of the reactant and the product states, which is consistent with the proposal of a D mechanism. This mechanism is in agreement with that expected for a pentacyano fragment, where the σ-donor and π-acceptor properties of the ligands cause significant *trans*- and *cis* labilization of water or NO.[7]

Several volume profiles for the reversible binding of NO to different iron complexes have been recently reported,

 © 2007 Wiley-VCH Verlag GmbH & Co. KGaA, Weinheim 

Table 2. Dissociation rate constants and activation parameters for different $[Fe^{II}(CN)_5L]^{n-}$ complexes.[a]

| Ligand | $k_d$ [$s^{-1}$] | $\Delta H_d^{\#}$ [kJ mol$^{-1}$] | $\Delta S_d^{\#}$ [J K$^{-1}$ mol$^{-1}$] | $\Delta V_d^{\#}$ [cm$^3$ mol$^{-1}$] | Ref. |
|---|---|---|---|---|---|
| CO[b,c] | $<10^{-8}$ | | | | [7] |
| $CN^-$[c,d] | ca.$4\times10^{-7}$ | | | | [17] |
| NO[c] | $1.58\times10^{-5}$ | $106.4\pm0.8$ | $+20\pm2$ | $+7.1\pm0.2$ | [11] |
| dmso[c] | $7.5\times10^{-5}$ | 110.0 | +46.0 | | [7] |
| *N*-Mepz$^+$[e] | $2.8\times10^{-4}$ | 115 | +75 | +0.9 | [7,18] |
| pz[e] | $4.2\times10^{-4}$ | 110.5 | +58.6 | +13.0 | [7,18] |
| his[c] | $5.3\times10^{-4}$ | 105.4 | +46.0 | | [7] |
| 2-Mepz[e] | $7.7\times10^{-4}$ | 114 | +44 | +19.4 | [19] |
| 4-CNpy[e] | $1\times10^{-3}$ | 105 | +50 | +20.6 | [19] |
| py[e] | $1.1\times10^{-3}$ | 103.8 | +46.0 | | [7] |
| 3,5-$Me_2$py[e] | $1.2\times10^{-3}$ | 108 | +60 | +20.5 | [7,20] |
| 3-CNpy[e] | $2.2\times10^{-3}$ | 93 | +16 | +20.6 | [20] |
| $NO_2^-$[c] | $1\times10^{-2}$ | 97 | +42 | +20.1 | [21] |
| $NH_3$[c] | $1.75\times10^{-2}$ | 102 | +68 | +16.4 | [7] |

[a] $T$ = 25.0 °C. [b] Estimated number, measured using pz as a scavenger. [c] $I$ = 0.1 M. [d] Extrapolated from data reported at higher temperatures. [e] $I$ = 0.5 M.

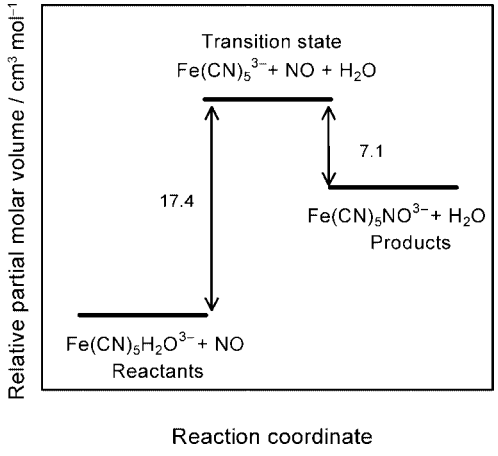


Figure 5. Volume profile for the overall reaction (4).

some of them support the operation of a D mechanism. Examples are the reaction of NO with metmyoglobin and some iron(III) porphyrin complexes. It is important to note that the volume profile shown in Figure 5 is the first reported for a reversible reaction with NO where no formal charge transfer occurs during the reaction, as is the case for the previously reported data.

## 5. Interaction of NO with Pentacyanoferrate(III)

The reaction between the $[Fe(CN)_5(H_2O)]^{2-}$ complex and NO produces quantitatively $[Fe(CN)_5NO]^{2-}$ (nitroprusside).[24] Thus, the overall reaction can be described by reaction (7) ($k_f$ and $k_d$ are redefined for this reaction).

$$[Fe^{III}(CN)_5(H_2O)]^{2-} + NO \rightleftharpoons [Fe^{II}(CN)_5(NO^+)]^{2-} + H_2O;\ k_f,\ k_d \quad (7)$$

Several attempts were made to determine $k_d$ by using trapping agents for the released NO, but they were unsuccessful, probably due to the slowness of the release reaction. When the $[Fe(CN)_5(H_2O)]^{2-}$ complex reacted with excess NO, the characteristic bands of the reactant at 394 and 340 nm decayed and a new band at 264 nm, assignable to nitroprusside, grew following a first-order behaviour. By working at different NO concentrations, $k_f$ was found to be $0.252\pm0.004$ M$^{-1}$ s$^{-1}$ (25.5 °C, $I$ = 0.1 M). From the pressure and temperature dependence of reaction (7), the activation parameters were obtained: $\Delta H^{\#} = 52\pm1$ kJ mol$^{-1}$, $\Delta S^{\#} = -82\pm4$ J K$^{-1}$ mol$^{-1}$ and $\Delta V^{\#} = -13.9\pm0.5$ cm$^3$ mol$^{-1}$.[24]

Although the coordination chemistry of the pentacyanoferrate(III) system has not been disclosed as deeply as for the $Fe^{II}$ analogue, there are studies with several other ligands that allow a comparison with our results for NO. In general, substitution reactions of this complex are slow reactions with second-order rate constants that range from $10^{-4}$ to $10^{-7}$ M$^{-1}$ s$^{-1}$.[21–23] The activation entropies and volumes for the substitution reaction with some nucleosides were studied. The values were in the range 5–120 J K$^{-1}$ mol$^{-1}$ and 3–6 cm$^3$ mol$^{-1}$, respectively.[23] These data were interpreted in terms of a dissociative interchange mechanism ($I_d$) and proposed to be generally valid for water-substitution reactions of $[Fe(CN)_5(H_2O)]^{2-}$. These slow reactions can be catalyzed by $Fe^{II}$ or other reducing species.[21,22]

In contrast, $k_f$ is several orders of magnitude faster than the typical values for substitution reactions of this complex. Moreover, the activation entropy and volume are negative.[24] On the basis of these discrepancies, we propose that reaction (7) is controlled by an electron-transfer reaction that produces the $[Fe^{II}(CN)_5(H_2O)]^{3-}$ complex, which in turn reacts with the ligands present in the medium generating nitroprusside (see Scheme 2).

The $[Fe^{II}(CN)_5(H_2O)]^{3-}$ complex was not detected as an intermediate; in fact no intermediates were observed during the reaction. This complex is labile; the rate of water exchange was estimated to be ca. 300 s$^{-1}$,[6] and this is consistent with the fact that the reported values of $k_{NO_2^-}$ (Scheme 2) are at least one order of magnitude faster than $k_{NO}$.[6,7] The rate constant $k_{H^+}$ is also reported to be very fast under the selected conditions.[25] According to this information, the reduction by NO must be rate determining in the overall reaction (7), and $k_f = k_{NO}$. Although NO reduction of the $[Fe(CN)_5(H_2O)]^{2-}$ complex through an outer-sphere reaction is very unfavourable,[24] the possibility of an inner-sphere path can explain why the reaction is still observable.[11] Kinetic studies on the reduction of the $[Fe(CN)_5(NO_2)]^{3-}$ and $[Fe(CN)_6]^{3-}$ complexes with ascorbic acid afforded very similar activation parameters to those obtained in our study, namely $\Delta S^{\#} = -119$ J K$^{-1}$ mol$^{-1}$ and $\Delta V^{\#} = -10$ cm$^3$ mol$^{-1}$ for the reaction of $[Fe(CN)_5(NO_2)]^{3-}$ to generate nitroprusside.[26]

Another possibility is that NO, which is in excess, reacts with the $[Fe(CN)_5(H_2O)]^{3-}$ complex (Scheme 2) to generate the $[Fe(CN)_5NO]^{3-}$ complex [reaction (4)]. The latter complex would be oxidized by the starting compound to nitroprusside, and the reaction would be autocatalytic.[11,24,27] Nevertheless, this intermediate was not detected. Moreover, experiments done in the presence of pyrazine (vide infra) showed that neutral ligands cannot compete effectively with

 © 2007 Wiley-VCH Verlag GmbH & Co. KGaA, Weinheim 

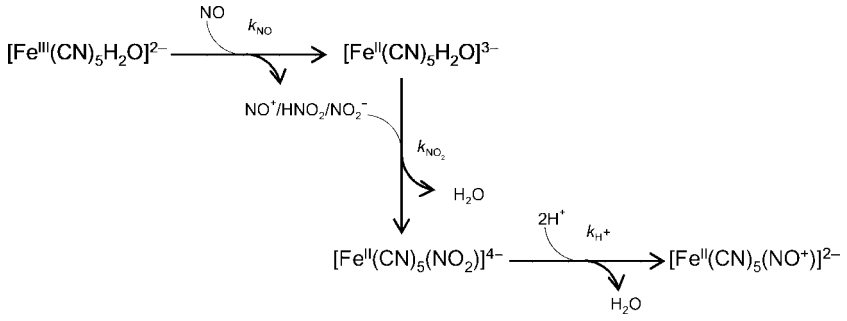


Scheme 2.

$NO^+/HNO_2/NO_2^-$ present in the second coordination sphere, since concentrations as high as 50 mM were insufficient to convert all of the reactant into the pyrazine complex.[24] On the other hand, the yield of nitroprusside for the reaction between $[Fe(CN)_5H_2O]^{3-}$ and NO at pH 3–5 was quite low: 35–45%,[11] while the reaction with the $Fe^{III}$ complex under similar conditions generated nitroprusside quantitatively.[24] Finally, we would expect a quadratic NO concentration dependence for such an autocatalytic mechanism, according to Scheme 2 and Equation (8) (vide infra).

Reaction (7) was studied in the presence of other ligands (pyrazine and $SCN^-$) that could scavenge the $[Fe(CN)_5(H_2O)]^{3-}$ complex and give evidence of its presence during the reaction.[24] When $SCN^-$ was used, a first order decay of the bands characteristic of the $[Fe(CN)_5(H_2O)]^{2-}$ complex was accompanied by formation of the $[Fe^{III}(CN)_5SCN]^{3-}$ complex, which was evidenced by its typical absorption band at 598 nm. Working at constant NO concentration, the observed rate constant depended linearly on the $SCN^-$ concentration, with a slope of $2.3 \times 10^{-3}$ M$^{-1}$ s$^{-1}$. The intercept was $2.17 \times 10^{-4}$ s$^{-1}$, which is very similar to the value obtained in the absence of $SCN^-$, as expected. By using pyrazine instead of $SCN^-$, a very similar picture was obtained, and a first-order reaction with a linear dependence on the pyrazine concentration was also observed. It is important to note that such reactions in the absence of NO are orders of magnitude slower.[22] To explain these findings, we propose the mechanism depicted in Scheme 3, where pyrazine or $SCN^-$ compete with $NO^+$, $HNO_2$ or $NO_2^-$ to react with the $[Fe(CN)_5(H_2O)]^{3-}$ complex. The $Fe^{II}$ complexes thus produced are oxidized by the reactant to form the corresponding $Fe^{III}$ compounds.

Assuming that the $Fe^{II}$ complexes are in steady state, Equation (8) was derived.[24]

$$k_{obs} = k_{NO}[NO]\left(1 + \frac{k_L[SCN^-/pz]}{k_{NO_2^-}[HNO_2]}\right) \quad (8)$$

The rate law predicts a linear dependence of $k_{obs}$ on the pyrazine and $SCN^-$ concentrations, as was observed, which provides evidence for the role of the $[Fe(CN)_5(H_2O)]^{3-}$ complex as an intermediate and strong support for the proposed mechanism.

To obtain additional information in favour of this proposal, the reaction of NO with other $[Fe^{III}(CN)_5L]$ complexes was studied. When L = pyridine, the corresponding $Fe^{II}$ complex was observed as an intermediate. Moreover, the $[Fe(CN)_5(NO_2)]^{3-}$ complex generates nitroprusside quantitatively when it reacts with NO at pH 5.[24]

The present reaction and the proposed mechanism were discussed in a recent review, and an alternative mechanism was proposed.[27] It involves the formation of a seven-coordinate intermediate between NO and the starting compound $[Fe^{II}(CN)_5(H_2O)(NO^+)]^{2-}$. This intermediate would lead to the formation of nitroprusside through the release of water or would lead to the formation of $[Fe(CN)_5(H_2O)]^{3-}$ through the release of $NO^+$. As we mentioned before, the $Fe^{II}$–$NO^+$ bond is very stable, and we find it rather unlikely that the $[Fe(CN)_5(H_2O)]^{3-}$ complex would be generated as an intermediate in this way. Alternatively, the formation of a related precursor between NO and the starting complex could be proposed, in which NO interacts with the

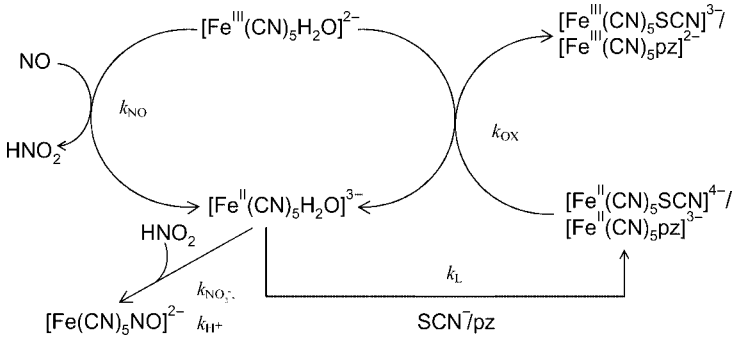


Scheme 3.

 © 2007 Wiley-VCH Verlag GmbH & Co. KGaA, Weinheim 

$CN^-$ ligands without changing the first coordination sphere of the Fe centre.[11] In this way, the reaction would proceed through an inner-sphere electron-transfer reaction, generating also the $[Fe(CN)_5(H_2O)]^{3-}$ complex. This mechanism would provide an explanation why neutral ligands like pyrazine cannot effectively compete with $HNO_2$. This mechanism does not change our conclusions and the main argument in favour of a prior reduction of the $Fe^{III}$ complex, in the absence of a change in the first coordination sphere, followed by coordination of $HNO_2/NO_2^-$ and final conversion into nitroprusside.

## 6. Reactions of NO with Iron(III) Porphyrin Complexes

In terms of biological activity, the most significant property of NO is its interactions with iron centres of hemoproteins. It has been suggested that many heme-based enzymes have their activity modulated by NO in vivo. Under bioregulatory conditions, two important target enzymes of NO action in biological systems such as mammalian guanylate cyclase[28] and fungal nitric oxide reductase[29] utilize the iron-heme-cofactors. NO–iron-porphyrin interactions have been shown to be responsible for the inhibition of certain hemoproteins that under physiological conditions bind/or activate dioxygen, including hemoglobin, myoglobin and the cytochrome P450 super family.[30] Moreover, NO binding to the iron-heme centre of a ferriheme salivary protein (nitrophorins) is considered to play an important role in vasodilating effects of blood sucking insects.[31] Since in vivo interactions of NO with iron centres of hemoproteins affect physiological and pathophysiological actions, numerous mechanistic and structural studies on NO binding to iron hemes and their biomimetic models have been undertaken.[32] However, because of the close interplay of many factors that govern the dynamics of NO binding to iron heme centres and of NO release from heme nitrosyls (e.g. oxidation state and spin state of the iron centre, type of the heme ring, number and identity of the axial ligands, interactions of the amino acid residues around the active site in the protein pocket, protein superstructure, accessibility of the iron heme centre to the NO ligand, polarity of the reaction media, etc.), the elucidation of the details of the molecular pathways followed during NO coordination to and dissociation from iron hemes is very difficult and far from complete.

Our own contribution to the understanding of the role of these factors involves in-depth mechanistic and kinetic investigations of the reversible NO binding to selected ferriheme proteins and model iron(III) porphyrins that can supplement other results from structural, kinetic and thermodynamic studies available to date on this topic. In contrast to the NO reactions with iron(II) centres, which are inconvenient to measure because of slow NO dissociation kinetics, the kinetic behaviour of the reactions with iron(III) centres enables the determination of both association and dissociation processes of NO under physiological conditions. In this context, we present an overview of some developments in the mechanistic chemistry involving reactions of selected iron(III) porphyrin complexes [hemoproteins and synthetic iron(III) porphyrin models] with NO, which gives an opportunity to gain insight into the mechanisms of formation and decay of nitrosyl hemoproteins in vivo.

In acidic aqueous solution, NO reversibly binds to six-coordinate, water-soluble iron(III) porphyrin complexes such as $(TPPS^{4-})Fe(H_2O)_2$, $(TMPS^{4-})Fe(H_2O)_2$ and $(TMPyP^{4+})Fe(H_2O)_2$, where TPPS = tetraphenylporphyrinato-4-sulfonate, TMPS = tetramesitylporphyrinato-4-sulfonate and TMPyP = tetra(4-*N*-methylpyridyl)porphyrin.[33,34] Coordination of NO to these hemoproteins induces a low-spin electronic configuration of the metal centre in the resulting nitrosyl derivative.[35] According to the Enemark and Feltham formalism,[1] the nitrosyl products of NO binding to iron(III) porphyrins are typically diamagnetic complexes (type $\{Fe–NO\}^6$) with a linear $Fe^{II}–NO^+$ unit, as has been demonstrated by $^{15}N$ NMR and IR spectroscopy.[36,37] In general, the kinetic behaviour of NO binding to the above-mentioned iron(III) porphyrins is described by the relatively high values for the association and dissociation rate constants (Table 3). The "on" rates for NO binding to these complexes are, however, about three orders of magnitude lower than those found for the iron(II) analogues.[33] In addition, the $(TMPyP^{4+})Fe(H_2O)_2$ complex with a 4+ charge on the porphyrin ring reacts with nitric oxide 25–100 slower than the other two systems, $\{(TPPS^{4-})Fe(H_2O)_2$ and $(TMPS^{4-})Fe(H_2O)_2\}$, in which the porphyrin carries a 4– charge. A close examination of the activation parameters, especially the activation volumes, determined for these reactions appears to be very helpful in understanding the kinetic trends observed in NO binding reactions for the studied iron(III) porphyrins.

The reactions of NO binding to $(TPPS^{4-})Fe(H_2O)_2$ and $(TMPS^{4-})Fe(H_2O)_2$ are described by large and positive values for the activation entropy and activation volume for both the "on" and "off" processes (Table 3), which are signatures for ligand substitution dominated by dissociation of a water molecule as depicted in Scheme 4 ("D" mechanism).[33]

Thus, in acidic medium the dynamics of the reversible binding of NO to the iron(III) centres of $(TPPS^{4-})Fe(H_2O)_2$ and $(TMPS^{4-})Fe(H_2O)_2$ seems to be mainly controlled by the lability of the metal centre. An analogous dissociatively activated mechanism was also proposed for NO release from the nitrosyl complexes of these iron(III) porphyrins. A dissociative mechanism requires that the exchange of the water molecule proceeds in a comparable way. Indeed, variable temperature/pressure NMR studies on the water-exchange kinetics of these iron(III) porphyrin diaqua species[38] very nicely confirmed that activation parameters found for the nitrosylation reaction of these two complexes are largely defined by a dissociative mechanism and the limiting step is the dissociation of the coordinated water molecule. On the basis of this mechanism, it can be explained why NO association reactions with iron(II) porphyrins are

 © 2007 Wiley-VCH Verlag GmbH & Co. KGaA, Weinheim 

Table 3. Rate constants and activation parameters for reversible binding of NO to water-soluble iron(III) porphyrins.

| Complex | $k_{on}$ [$M^{-1}s^{-1}$][a]<br>$k_{off}$ [$s^{-1}$][a] | $\Delta H^{\#}$ [$kJ\,mol^{-1}$] | $\Delta S^{\#}$ [$J\,K^{-1}\,mol^{-1}$] | $\Delta V^{\#}$ [$cm^3\,mol^{-1}$] | Proposed mechanism | Ref. |
|---|---|---|---|---|---|---|
| $(TPPS^{4-})Fe(H_2O)_2$ | $4.5\times10^5$ | $69\pm3$ | $95\pm10$ | $9\pm1$ | D | [33] |
| Int[a] = 20% | $500\pm400$ | $76\pm6$ | $60\pm11$ | $18\pm2$ | D | |
| $(TMPS^{4-})Fe(H_2O)_2$ | $2.8\times10^6$ | $57\pm3$ | $69\pm11$ | $13\pm1$ | D | [33] |
| Int[a] = 26% | $900\pm200$ | $84\pm3$ | $94\pm10$ | $17\pm3$ | D | |
| $(TMPS^{4-})Fe(OH)$ | $1.3\times10^4$[b] | $28\pm1$ | $-71\pm2$ | $-16\pm0.4$ | A | [43] |
| | $7.0\pm0.1$[b] | $90\pm1$ | $76\pm3$ | $7.4\pm1$ | | |
| $(TMPyP^{4+})Fe(H_2O)_2$ | $2.9\times10^4$ | $67\pm4$ | $67\pm13$ | $3.9\pm1$ | $I_d$ | [34] |
| Int[a] = 7% | $59\pm4$ | $113\pm5$ | $169\pm18$ | $17\pm0.2$ | D | |
| $(P^{8+})Fe(H_2O)_2$ | $1.5\times10^4$ | $77\pm3$ | $94\pm12$ | $1.5\pm0.3$ | $I_d$ or I | [41] |
| Int[a] = 10% | $26\pm0.5$ | $83\pm4$ | $61\pm14$ | $9.3\pm0.5$ | $I_d$ | |
| $(P^{8+})Fe(OH)(H_2O)$ | $1.6\times10^3$ | $41\pm1$ | $-45\pm2$ | $-13.8\pm0.4$ | A | [41] |
| | $6.2\pm0.1$ | $72\pm2$ | $12\pm5$ | $2.6\pm0.2$ | | |
| $(P^{8-})Fe(H_2O)_2$ | $8.2\times10^5$ | $51\pm0.5$ | $40\pm2$ | $6.1\pm0.1$ | $I_d$ or D | [40] |
| Int[a] = 24% | $220\pm2$ | $107\pm3$ | $160\pm10$ | $16.8\pm0.4$ | D | |
| $(P^{8-})Fe(OH)$ | $5.1\times10^4$ | $35\pm0.4$ | $-39\pm1$ | $-6.1\pm0.2$ | A | [40] |
| | $11\pm0.3$ | $107\pm2$ | $136\pm7$ | $17\pm3$ | | |
| metMb | $4.8\times10^4$ | $71\pm2$ | $82\pm7$ | $21\pm1$ | D | [45] |
| | $29\pm1.5$ | $78\pm2$ | $46\pm7$ | $16\pm1$ | D | |

[a] Contribution of the intermediate-spin state ($S$ = 3/2) in the corresponding spin-admixed iron(III) diaqua porphyrin complex. [b] Determined at 22 °C.

$$Fe^{III}(Por)(H_2O)_2 \underset{k_{-1}}{\overset{k_1}{\rightleftharpoons}} Fe^{III}(Por)(H_2O) + H_2O$$

$$Fe^{III}(Por)(H_2O) + NO \underset{k_{-2}}{\overset{k_2}{\rightleftharpoons}} Fe^{III}(Por)(H_2O)(NO)$$

Scheme 4.

several orders of magnitude faster than those with the iron(III) analogues. Since high-spin iron(II) porphyrins may be five-coordinate, NO binding to the metal centre can proceed without first displacing another ligand [for example a water molecule in the iron(III) porphyrin diaqua species]. Another important conclusion that can be drawn from these studies is that the free radical nature of NO appears to have only a minor (if any) influence on the NO substitution dynamics at the metal centres of iron(III) porphyrins, thus NO behaves as a typical Lewis base donor.

Another mechanistic scenario was observed for the NO interaction with the positively charged $(TMPyP^{4+})Fe(H_2O)_2$.[34] The much slower bond cleavage observed for this system [both NO association and dissociation rate constants are significantly lower than those for the iron(III) porphyrins carrying a 4– charge] must be closely related to the electrophilicity of the iron centre in the TMPyP complex. From the activation parameters found for this system (Table 3), it is clear that in this case the substitution of a coordinated water molecule by NO follows a dissociative interchange ($I_d$) mechanism. The changeover from a limiting dissociative substitution mechanism observed for the corresponding iron(III) TPPS and -TMPS complexes to an $I_d$ mechanism found in this case can be ascribed to the lower lability of the coordinated water molecule in the $(TMPyP^{4+})Fe(H_2O)_2$ complex. This finding appears to be in line with the trend observed for the rate constants and activation parameters measured for water-exchange reactions of these three complexes,[38] where the water-exchange reaction at the iron(III) centre of the positively charged porphyrin is much slower than for the other studied systems with a 4– charge on the porphyrin rings. It seems that in acidic medium, water-exchange processes control the rate and mechanism of the nitrosylation reactions of all three diaqua iron(III) porphyrins in which the labilization of the $Fe–OH_2$ bond is determined by the electron-donating/withdrawing properties of the substituted porphyrin, which in turn depend on the anionic/cationic nature of the substituents, respectively.

In order to better understand the influence of the porphyrin microenvironment in iron(III) porphyrin systems on the rate and mechanism of NO binding and release, as well as to establish the relationship between the structure of the prosthetic group and its reactivity toward NO in various hemoproteins in vivo, two new iron(III) porphyrin models, a highly negatively charged {$(P^{8-})Fe^{III}$ = [5⁴,10⁴,15⁴,20⁴-tetra-*tert*-butyl-5²,5⁶,15²,15⁶-tetrakis(2,2-biscarboxylatoethyl)-5,10,15,20-tetraphenylporphyrin]iron(III)} and a highly positively charged {$(P^{8+})Fe^{III}$ = [5,10,15,20-tetrakis(4′-*tert*-butyl-2′,6′-bis(4-*tert*-butylpyridine)phenyl)porphyrinato]iron(III)} water-soluble porphyrin, have been synthesized[39,40] (see Figure 6). A detailed kinetic and mechanistic description of the reversible binding of NO to these complexes in aqueous solution at low and high pH has been presented recently.[40,41]

In general, iron(III) porphyrins may occur as five- and six-coordinate complexes in which the iron atom can exist in three different spin states, the low-spin state ($S$ = 1/2, typically six-coordinate with short axial and equatorial bonds), high-spin state ($S$ = 5/2, often five-coordinate with elongated equatorial bonds and displacement of the iron atom out of the porphyrin plane) and intermediate-spin state ($S$ = 3/2 with short equatorial and elongated axial bonds). In addition, depending on the nature of the axial ligands and porphyrin-ring substituents, the spin state of

 © 2007 Wiley-VCH Verlag GmbH & Co. KGaA, Weinheim 

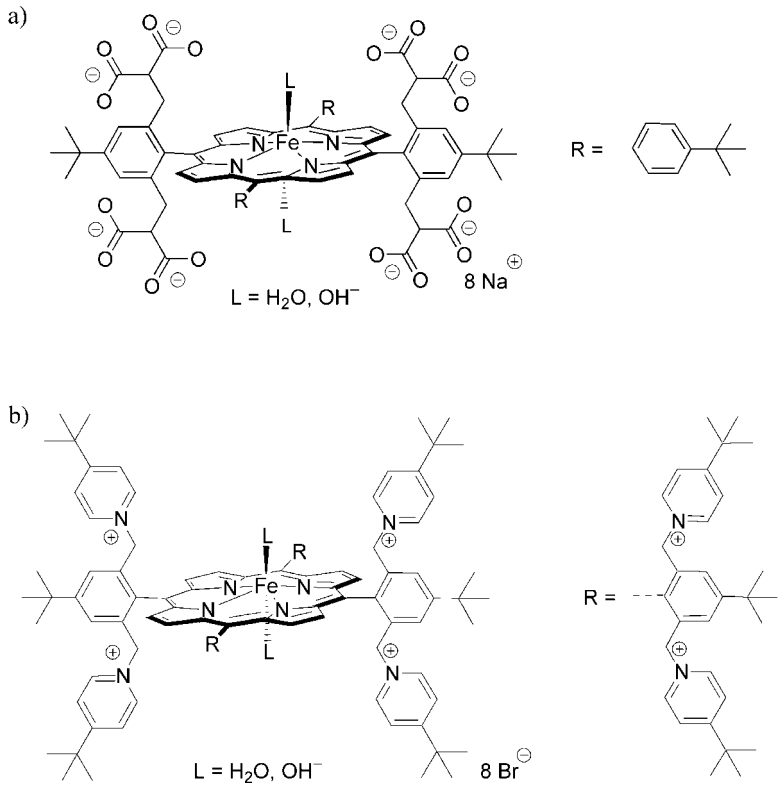


Figure 6. Structures of (a) a highly negatively charged $(P^{8-})Fe^{III}(L)_2$[40] and (b) a highly positively charged $(P^{8+})Fe^{III}(L)_2$[39] iron(III) porphyrin model.

the iron(III) in many iron(III) porphyrins can be described as admixed intermediate, in which varying ratios of $S = 5/2$ and $S = 3/2$ admixing were noted.[42] In this context, it was revealed that introduction of four flexible malonate substituents on the highly negatively charged porphyrin $(P^{8-})Fe^{III}(H_2O)_2$ (in buffered, aqueous solution at pH = 7) leads to significant electronic effects on the iron(III) centre, which are reflected by the relatively high contribution of the $S = 3/2$ spin state in the spin-admixed intermediate.[40] Moreover, these electronic effects together with the possible through-space interactions of negatively charged substituents with coordinated water resulted in an increase in the $pK_a$ value of the coordinated $H_2O$ to the highest value reported to date. With regard to the kinetic behaviour of $(P^{8-})Fe^{III}(H_2O)_2$ in its reaction with NO, a relatively high contribution of the $S = 3/2$ spin state in the spin-admixed state of this complex in comparison with those of other iron(III) porphyrins correlates very well with high NO coordination rates (see Table 3) and the high lability of coordinated water measured for this system.[40] A comparison of the rate and activation parameters for the binding and release of NO for $(P^{8-})Fe^{III}(H_2O)_2$ in aqueous solution at pH = 7 (Table 3) with those reported for other diaqua-ligated iron(III) porphyrin species leads to the conclusion that the reactivity of this complex toward NO is described by the same dissociative (D or $I_d$) mechanism, in which the NO association reaction is controlled by substitution of a water molecule. Similarly, the release of NO from the corresponding nitrosyl complex also follows a dissociative mechanism.

Markedly smaller (in absolute values) NO association and dissociation rate constants as well as activation parameters (especially activation volumes) were obtained for a highly positively charged water-soluble porphyrin, viz. $(P^{8+})Fe^{III}(H_2O)_2$ (Table 3) in which the $Fe^{III}$ centre is weakly spin-admixed with only a 10-% contribution of the intermediate $S = 3/2$ spin state.[41] NO coordination to the iron(III) centre of this highly positively charged porphyrin appears to follow an $I_d$ or even I mechanism (without a predominant a- or d-character). In a similar way, the substantially smaller value of the activation volume determined for NO release from the nitrosyl complex of $(P^{8+})Fe^{III}(H_2O)_2$ than the corresponding values reported for other porphyrin nitrosyls clearly implies a less dissociative mode for NO dissociation from the highly positively charged iron(III) porphyrin.

In summary, the results from the kinetic and mechanistic studies presented above for reversible NO binding to the water-soluble iron(III) diaqua-ligated porphyrins (Table 3) clearly demonstrate that the identity and charge of the substituents in the porphyrin periphery strongly affect the dynamics of both the binding and release of NO. These effects can be summarized as follows: (i) Electron-donating *meso* substituents on the porphyrin rings increase and electron-withdrawing groups decrease electron density on the iron(III) centres, which is reflected by an increase or a decrease in the contribution of the $S = 3/2$ spin state in the spin-admixed system, respectively. (ii) Electron density on the iron(III) centre influences the lability of the coordinated

 © 2007 Wiley-VCH Verlag GmbH & Co. KGaA, Weinheim 

water molecule. Thus, a porphyrin-induced increase in electron density on the iron(III) centre facilitates breakage of the Fe–$H_2O$ bond, whereas for porphyrins with electron-withdrawing *meso* substituents, this bond is more stabilized. (iii) As a result of (i) and (ii), the rate of NO binding to iron(III) diaqua-ligated porphyrins increases with increasing electron donation from the porphyrin *meso* substituents, which is also reflected by the change in the mechanism of NO coordination to the iron(III) centre from predominantly dissociative for the porphyrins with electron-donating *meso* substituents to interchange ($I_d$ or I) for the systems carrying electron-withdrawing *meso* substituents on the porphyrin rings. (iv) Electron-donating groups on the porphyrin rings destabilize, whereas electron-withdrawing substituents stabilize, the $Fe^{II}$–$NO^+$ bond in the nitrosyl complexes of (P)Fe($H_2O$)$_2$, which is illustrated by the variation in $k_{off}$ for the complexes studied. In general, NO dissociation from nitrosyl porphyrins is interpreted in terms of a dissociative mechanism. However, a decrease in the electron-donation from the porphyrin substituents was shown to result in a less dissociative mode for NO release from the corresponding nitrosyl complex.

The reactivity pattern presented above for the iron(III) diaqua-ligated porphyrins points to a crucial role of the lability of the coordinated water molecule in the dynamics of the reversible binding of NO to model iron(III) porphyrins. However, our recent systematic studies on the reactivity of various water-soluble (P)$Fe^{III}$ species towards NO revealed that interactions of NO with heme centres need not always be controlled by the lability/accessibility of the metal centre, but can be determined by electronic and structural factors such as reorganization of the spin density of the iron centre and the accompanying structural changes.[40,41,43]

It has been demonstrated that the rate and mechanism of nitrosylation of water-soluble iron(III) porphyrin complexes can be nicely tuned by the pH of the solution, which determines the nature and number of the axial ligands on the (P)$Fe^{III}$ species and thereby controls the coordination number, spin state and reactivity of the iron(III) centre toward NO.[43] In this context, kinetic and mechanistic investigations on the reactions of NO with monohydroxo-ligated forms of (P)$Fe^{III}$ [formed by deprotonation of coordinated water in (P)Fe($H_2O$)$_2$ at pH > p$K_a$] were performed for the first time.[40,41,43] In general, according to the known *trans*-labilizing effect of the hydroxo ligand, it can be expected that the presence of a more labile water molecule in the position *trans* to $OH^-$ [or even its absence as revealed for example in the ($TMPS^{4-}$)$Fe^{III}$ and ($P^{8-}$)$Fe^{III}$ species, which exist as five-coordinate monohydroxo complexes at high pH] should result in a significant increase in the NO binding rate constants relative to those measured for the corresponding iron(III) diaqua-ligated species. Surprisingly, NO rate constants and activation parameters determined for the monohydroxo forms of (P)$Fe^{III}$ appear to be significantly smaller than those found for the (P)Fe($H_2O$)$_2$ species, indicating that NO coordination to these complexes is no longer controlled by the lability or accessibility of the iron(III) centre. Obviously, this must involve a changeover

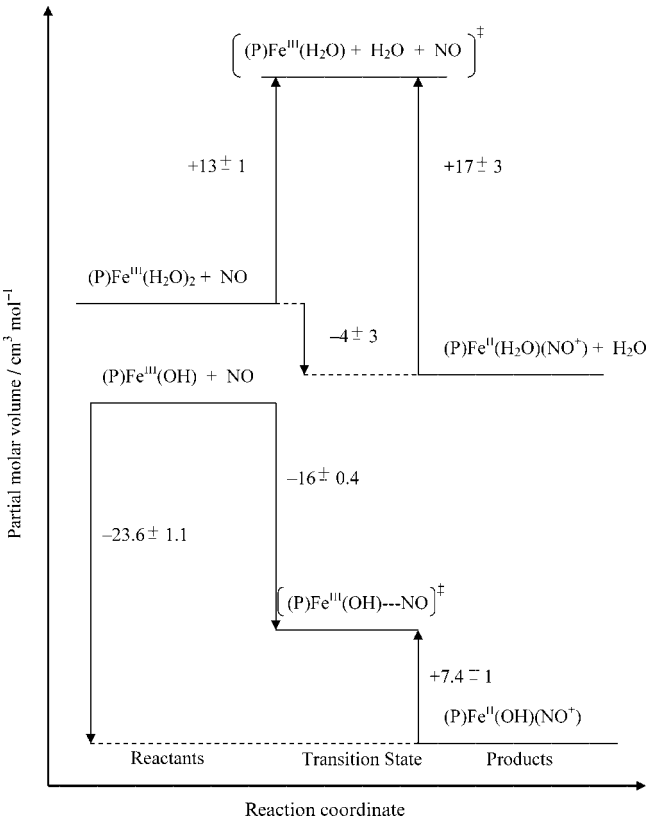


Figure 7. Volume profiles for reversible NO binding to ($TMPS^{4-}$)-$Fe^{III}(H_2O)_2$[33c] (top) and ($TMPS^{4-}$)$Fe^{III}$(OH) (bottom).[43]

in the mechanism of NO binding from dissociative in iron(III) diaqua-ligated species to associatively activated in the (P)$Fe^{III}$(OH) forms. This mechanistic difference can be nicely illustrated by a comparison of the volume profiles constructed for the reactions of reversible binding of NO to ($TMPS^{4-}$)$Fe^{III}(H_2O)_2$ and ($TMPS^{4-}$)$Fe^{III}$(OH), as depicted in Figure 7.

The associatively activated mechanism proposed for NO coordination to ($TMPS^{4-}$)$Fe^{III}$(OH) involves the diffusion-controlled formation of an encounter complex, {(P)-$Fe^{III}$(OH)‖NO}, and subsequent rate-determining $Fe^{II}$–$NO^+$ bond formation. A similar mechanism was proposed previously for NO binding to the high-spin iron(II) porphyrins[32b,33c] and to substrate-bound cytochrome P450.[44] The significantly slower (and therefore rate-limiting) $Fe^{II}$–$NO^+$ bond formation during NO coordination to monohydroxo iron(III) porphyrins than those observed for the nitrosylation reactions of (P)Fe($H_2O$)$_2$ species (in this case $Fe^{II}$–$NO^+$ bond formation is fast and a less energetically demanding process) can be ascribed to the difference in the spin reorganization of the iron(III) centre upon NO binding at low and high pH. Accordingly, the overall spin-state change accompanying the formation of low-spin ($TMPS^{4-}$)-$Fe^{II}(NO^+)$ from purely high-spin ($TMPS^{4-}$)$Fe^{III}$(OH) ($S$ = 5/2 → $S$ = 0) is larger than that occurring upon binding of NO to the spin-admixed, diaqua-ligated complex ($S$ = 5/2, 3/2 → $S$ = 0). This marked difference in the spin reorganiza-

 © 2007 Wiley-VCH Verlag GmbH & Co. KGaA, Weinheim 

tion and the accompanying structural changes [in the purely high-spin $(TMPS^{4-})Fe^{III}(OH)$, the iron atom is displaced out of the porphyrin plane] can be responsible for the observed ca. 100-fold decrease in the NO rate constants at high pH and for the changeover in the mechanism of NO coordination to the complexes studied.

In addition to the effects associated with the lability/accessibility of the metal centre, the spin reorganization of the iron atom and the structural changes that were discussed above in detail, a number of other factors resulting from the presence of the protein coat, such as hydrogen-bonding interactions of the amino acid residues around the active site, polarity of the protein pocket, accessibility of the heme prosthetic group to the solvent, etc., should be considered in the interpretation of reactivity patterns observed for the reversible binding of NO to iron(III) centres of hemoproteins. Indeed, the results from mechanistic studies on the interactions of NO with native ferriheme proteins and comparison to those obtained for "free" iron(III) model porphyrins revealed the important role of the heme pocket in NO interactions with hemoproteins.[45,46] This can be illustrated by mechanistic studies on the reversible binding to metmyoglobin (metMb).[45] Like the iron(III) models $[(TPPS^{4-})Fe^{III}(H_2O)_2$ and $(TMPS^{4-})Fe^{III}(H_2O)_2]$, the iron(III) centre of metmyoglobin is six-coordinate and a water molecule occupies the site at which NO will coordinate. Activation parameters found for NO interaction with metMb (Table 3) clearly evidence the similar mechanistic behaviour of metmyoglobin and model iron(III) porphyrins at low pH, i.e. NO coordination to the iron(III) centre follows a dissociative mechanism controlled by the lability of the water molecule. However, close inspection of the activation volumes determined for these systems indicate that the value of $\Delta V^{\#}_{on}$ observed for the binding of NO to metMb is significantly larger than the corresponding values observed for "free" iron(III) porphyrins (see Figure 8) and therefore cannot reflect only the volume changes associated with dissociation of the water molecule from an octahedral complex (≈13 $cm^3 mol^{-1}$[47]) as was thought for the model complexes. This finding suggests that the protein may undergo some structural rearrangement upon release of coordinated water prior to the binding of NO, which can lead to a further increase in the size of the protein pocket in the transition state. This conclusion was confirmed by the results from XAFS structural studies on nitrosylated metMb.[48] The importance of the protein pocket in the interaction of NO with metmyoglobin can also be demonstrated by a comparison of the NO dissociation rate constants observed for the nitrosyl complexes of metMb and iron(III) porphyrin models $(TPPS^{4-})Fe^{III}(H_2O)_2$ and $(TMPS^{4-})Fe^{III}(H_2O)_2$ (Table 3). The much lower values of $k_{off}$ reported for the metMb/NO system than the corresponding values observed for porphyrin models can be interpreted in terms of the stabilization of the $Fe^{II}$–$NO^+$ moiety by hydrogen-bonding interactions with the residues of the amino acids in the protein pocket. Obviously, the NO molecule cannot be as effectively "caged" after coordination to the iron(III) centres of "free" porphyrin models.

The essential contribution of the protein architecture in the dynamics of reversible NO binding to heme proteins has also been revealed by flash photolysis studies of the analogous nitrosyl complex of ferrous myoglobin (Mb).[49] The existence of multiple geminate-type intermediates in the recombination pathway of Mb(NO) has been ascribed to the presence of the protein pocket from which NO released after the laser flash cannot escape significantly from the protein as recombination occurs much faster than dissociation of the {Mb, NO} geminate pair.

Another important example of protein influence on the kinetics of NO binding to heme centres in hemoproteins can be illustrated by the reaction of NO with ferric and ferrous cytochrome *c* (Cyt *c*) in which the protein limits access of NO molecules to the iron centre.[33a,50] Since the axial ligands in Cyt *c* are occupied by histidine and methionine residues in both oxidation states of the iron centre, coordination of NO must involve displacement of a relatively tightly bound axial ligand (methionine or histidine). As a result, NO binding rate constants observed for Cyt $c^{II}$

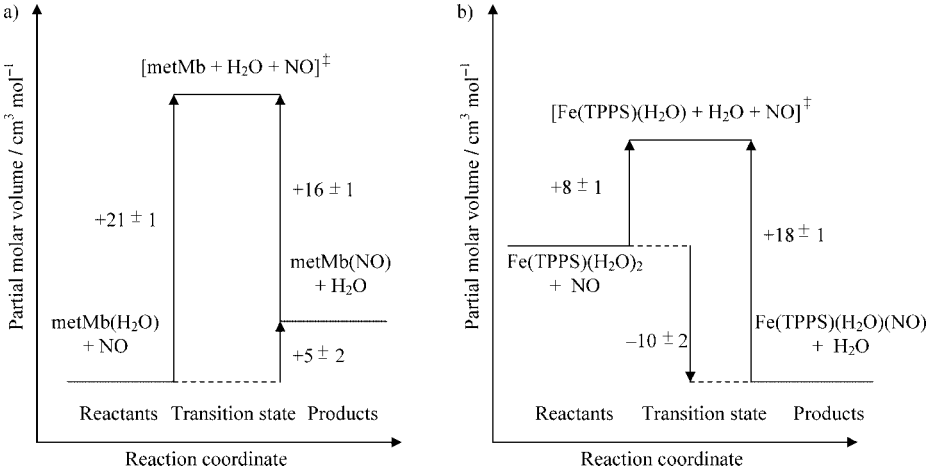


Figure 8. Comparison of the volume profiles constructed for the reversible binding of NO to (a) metmyoglobin[45] and (b) water-soluble $Fe^{III}(TPPS)(H_2O)_2$.[33]

 © 2007 Wiley-VCH Verlag GmbH & Co. KGaA, Weinheim 

and Cyt $c^{III}$ are unusually small relative to rate constants obtained for ferric and ferrous hemoproteins in which access to the metal centre for the entering NO ligand is not limited by the protein (or the coordination site is occupied by a very labile ligand such as a water molecule in metMb).

## 7. Reactions of NO with $P450_{cam}$ and Model Complexes

Since the nature of the anionic proximal ligand coordinated to the iron(III) centre plays a crucial role in controlling the properties and reactivity of hemoproteins in numerous catalytic processes,[51] the super-family of cytochromes P450 with its quite unusual thiolate ligation attracts particular attention with regard to the spin-state equilibria of the resting state, the redox potential of the iron(III) porphyrin and the electronic nature of the high-valent iron(IV) oxo species. In order to elucidate the mechanism of action of cytochrome P450 in vivo and to understand the essence of its biological function, it is very important to gain detailed mechanistic insight into binding of small molecules such as $O_2$, NO and CO to the catalytic site of this enzyme. Unlike carbon monoxide and dioxygen, NO can bind to both oxidation states of cytochrome P450; the nitrosyl complexes of the ferrous forms with their electronic structure and geometry resemble the physiologically important dioxygen complexes of P450 enzymes. Furthermore, several pieces of evidence revealed that cytochromes P450 might be primary targets for NO action in vivo.[52] Since the reactions of ferrous cytochromes P450 with small molecules have already been extensively investigated, we have focused our attention on the kinetics and mechanistic interpretation of the reversible binding of NO to ferric cytochrome $P450_{cam}$ (isolated from bacterium *Pseudomonas putida*) in the absence and presence of the substrate (1*R*-camphor).[44] The substrate-free ferric $P450_{cam}$ is a low-spin ($S$ = 1/2), six-coordinate complex with a water cluster bound at the distal site *trans* to the cysteine axial ligand in the proximal position. Upon binding of camphor to the active site, water molecules are expelled from the coordination sphere, which leads to the formation of a high-spin ($S$ = 5/2), five-coordinate iron-heme centre. Coordination of NO to the substrate-free or camphor-bound form of $P450_{cam}$ results in the formation of the relatively stable, six-coordinate nitrosyl complex. Earlier EPR[53] and resonance Raman[54] studies on the NO adduct of $P450_{cam}$ showed that the nitrosyl complex of $P450_{cam}$ is a low-spin complex (EPR silent) in which the Fe–NO group adopts a linear structure in the absence of substrate, but becomes slightly bent upon binding of camphor. However, subsequent crystallographic characterization of the Fe–N–O linkage in the $\{FeNO\}^6$ species (models and enzymes)[55] revealed that such systems can also display an axial NO bending feature coupled with tilting of the Fe–NO group. The tilting/bending mode of the axial NO ligand in nitrosyl complexes of iron(III) porphyrins was found to be intrinsic to species of the type $(Por)Fe^{III}(NO)X$, where X is a strong σ-donor ligand.[55a]

Binding of NO to the substrate-free $P450_{cam}$ was shown to exhibit biphasic kinetics, which can be interpreted in terms of an equilibrium between conformational substates in cytochrome P450 (which is the effect of different hydrogen-bonding networks between differently packed water molecules in the heme pocket).[44] The NO binding rate constants and activation parameters determined for both reaction steps (Table 4) are consistent with the operation of a limiting dissociative ligand-substitution mechanism, in which the lability of coordinated water dominates the reactivity of the iron(III) centre with NO.

It should be noted that a similar mechanism was proposed for NO binding to metMb and synthetic water-soluble $(P)Fe^{III}(H_2O)_2$ complexes. In agreement with the principle of microscopic reversibility, the activation parameters found for the release of NO from the nitrosyl complex of substrate-free $P450_{cam}$ also indicate a rate-limiting dissociative mechanism. The overall reaction volume determined for this system is close to zero and is very similar to that found for NO binding to metmyoglobin. The apparent larger value for $\Delta V^{\#}_{on}$ (which represents volume changes associated with a pathway in which a water molecule is dissociated) reported for the reaction between NO and substrate-free $P450_{cam}$ relative to that found for the metMb/NO system can be accounted for in terms of much higher structural rearrangement in the protein pocket of $P450_{cam}$ during dissociation of the water molecule that is additionally bound to the ordered water cluster. Formation of the five-coordinate transition-state $Fe^{III}$ complex is associated with a change in spin state from low-spin to high-spin, which is accompanied by a volume increase of between 12 and 15 $cm^3 mol^{-1}$ on the basis of literature data for such spin-state changes.

A different mechanistic scenario was observed for the reversible binding of NO to the camphor-bound form of cytochrome $P450_{cam}$.[44] As already mentioned, the substrate-bound $P450_{cam}$ is a five-coordinate, high-spin complex with no water molecule occupying the sixth coordination position of the iron(III) centre. The NO association rate constants determined for this complex appear to be significantly higher than those reported for the substrate-free $P450_{cam}$ (Table 4). Moreover, the presence of camphor markedly affects not only the NO binding rate constants but also NO release from the corresponding nitrosyl complex. The substantial negative values for the activation entropy and activation volume found for the "on" reaction (Table 4) clearly indicate that the mechanistic pathways for NO coordination to the iron(III) centres of the substrate-free and camphor-bound form of $P450_{cam}$ are completely different. Since the $Fe^{III}$-heme centre in substrate-bound $P450_{cam}$ is five-coordinate, formation of an Fe–NO bond does not require initial displacement of a water molecule, and therefore the ligation cannot be limited by the rate of $H_2O$ dissociation as was observed for the reaction with substrate-free $P450_{cam}$. These features are consistent with the associatively activated mechanism in which an encounter complex, $\{(P)Fe^{III}\|NO\}$, is formed prior to NO bond formation, as was also proposed for the reaction of NO with

 © 2007 Wiley-VCH Verlag GmbH & Co. KGaA, Weinheim 

Table 4. Comparison of the rate and equilibrium constants, and thermodynamic and kinetic parameters for NO binding to the iron(III) centre in $P450_{cam}$ (in the absence and presence of camphor)[17] and model complexes.

| | $P450_{cam}$ resting state[44] | $P450_{cam}$ + camphor ($E{\cdot}S\text{-}P450_{cam}$)[44] | SR complex in methanol[62] | Complex **3** in toluene[67] | Complex **4** in methanol[67] |
|---|---|---|---|---|---|
| $k_{on}$ [$M^{-1}s^{-1}$][a] | $(3.20 \pm 0.02) \times 10^5$ | $(3.2 \pm 0.5) \times 10^6$ | $(2.7 \pm 0.2) \times 10^6$ | $(1.80 \pm 0.05) \times 10^6$ | $(0.6 \pm 0.05) \times 10^5$ |
| $\Delta H^{\#}_{on}$ [kJ mol$^{-1}$] | $92 \pm 1$ | $14. 1 \pm 0.1$ | $75 \pm 3$ | $4 \pm 2$ | $14 \pm 1$ |
| $\Delta S^{\#}_{on}$ [J mol$^{-1}$ K$^{-1}$] | $+169 \pm 4$ | $-73.1 \pm 0.4$ | $+130 \pm 11$ | $-111 \pm 6$ | $-107 \pm 3$ |
| $\Delta G^{\#}_{on}$ [kJ mol$^{-1}$][a] | $42 \pm 1$ | $35.9 \pm 0.1$ | $36 \pm 3$ | $37 \pm 2$ | $46 \pm 1$ |
| $\Delta V^{\#}_{on}$ [cm$^3$ mol$^{-1}$] | $+28 \pm 2$ | $-7.3 \pm 0.2$ | $+6.4 \pm 1$ | $-25 \pm 1$ | $-21 \pm 4$ |
| $k_{off}$ [$s^{-1}$][a] | $0.35 \pm 0.02$ | $1.93 \pm 0.02$ | $1.8 \pm 2.1$ | $12470 \pm 120$ | $2249 \pm 167$ |
| $\Delta H^{\#}_{off}$ [kJ mol$^{-1}$] | $122 \pm 4$ | $83.8 \pm 0.7$ | | $58 \pm 1$ | $44 \pm 5$ |
| $\Delta S^{\#}_{off}$ [J mol$^{-1}$ K$^{-1}$] | $+155 \pm 15$ | $+41 \pm 2$ | | $+29 \pm 5$ | $-34 \pm 22$ |
| $\Delta G^{\#}_{off}$ [kJ mol$^{-1}$][a] | $76 \pm 4$ | $71.6 \pm 0.7$ | | $50 \pm 1$ | $54 \pm 5$ |
| $\Delta V^{\#}_{off}$ [cm$^3$ mol$^{-1}$] | $+31 \pm 1$ | $+24 \pm 1$ | | $+7 \pm 3$ | $+7 \pm 3$ |
| $K_{NO}$ [$M^{-1}$][a] | $(9.0 \pm 0.2) \times 10^5$ | $(1.2 \pm 0.4) \times 10^6$ | | $122 \pm 10$ | $26.9 \pm 2.9$ |
| $\Delta H°$ [kJ mol$^{-1}$] | $-30 \pm 5$ | $-69.7 \pm 0.8$ | | $-71 \pm 3$ | $-59 \pm 4$ |
| $\Delta S°$ [J mol$^{-1}$ K$^{-1}$] | $+14 \pm 19$ | $-114 \pm 2$ | | $-197 \pm 10$ | $-169 \pm 13$ |
| $\Delta G°$ [kJ mol$^{-1}$][a] | $-34 \pm 4$ | $-35.7 \pm 0.7$ | | $-12 \pm 3$ | $-9 \pm 4$ |
| $\Delta V°$ [cm$^3$ mol$^{-1}$] | $+3 \pm 3$ | $-31.3 \pm 1.2$ | | $-39 \pm 2$ | $-28 \pm 1$ |

[a] At 25 °C.

ferroheme proteins[56] and their model complexes[32b,33c] or with the water-soluble monohydroxo iron(III) porphyrin models.[40,41,43] The value of the second-order rate constant for the binding of NO to camphor-bound $P450_{cam}$ is relatively small relative to the rate constants known for the diffusion-controlled reactions in water. This observation, along with the negative activation entropy and activation volume values, supports an activation-controlled reaction mechanism in which Fe–NO bond formation is the rate-determining step. In such a case, Fe–NO bond formation and the concomitant change in spin-state from high- ($S$ = 5/2) to low spin ($S$ = 0) should result in negative contributions to the activation entropy and activation volume. Notably, the large and positive values for the activation parameters found for the release of NO from the nitrosyl complex of camphor-bound $P450_{cam}$ are consistent with a reaction mechanism in which the iron–nitrosyl bond is broken. This process should formally involve charge transfer from iron(II) to the nitrosyl ligand (i.e. formal oxidation of $Fe^{II}$ to $Fe^{III}$) with concomitant solvational changes as a result of charge distribution. The difference in the mechanistic mode observed during NO coordination to the iron(III) centre of $P450_{cam}$ in the absence and presence of substrate can be illustrated nicely by comparison of volume profiles constructed on the basis of kinetic data determined for both reactions (see Figure 9a and Figure 10a). The importance of NO bond-formation/bond-breakage processes coupled to changes in the spin state of the iron(III) centre in camphor-bound $P450_{cam}$ is reflected by a drastic volume decrease on going from the reactant to the product states, whereas the overall reaction volume measured for the nitrosylation reaction of substrate-free $P450_{cam}$ is close to zero, indicating no overall spin-state change occurs during NO binding to the low-spin, six-coordinate $P450_{cam}$. Moreover, the transition states for these reactions differ significantly in terms of the contribution arising from Fe–NO bond formation. In the case of NO binding to $P450_{cam}$ in the presence of camphor, the transition state can be described as "early", i.e. close in nature to the reactant state, which indicates that only partial bond formation accounts for this position. Subsequently, bond formation is completed and accompanied by a change in spin state.

Comparison of the NO association and dissociation rate constants obtained for the reversible binding of NO to $P450_{cam}$ with those found for other iron(III) thiolate- and imidazole-ligated proteins, led to the conclusion that it is very problematic to quantify the real *trans* effect of proximal imidazole and thiolate coordination in such systems. Taking into account that iron(III) heme proteins with even the same thiolate ligation can display quite a wide range of NO binding and release rate constants, it is clear that apart from factors arising from the coordination mode and spin state of the iron(III) centre [i.e. the lability of the leaving group (or its absence) and the identity of the axial and porphyrin ligands], other effects associated with different protein architecture of the heme active sites and their accessibility to ligands should be considered in the dynamics of reactions of NO with metal centres of biological relevance. It seems very likely that nature uses the simultaneous interplay of all these factors to achieve a desired goal, viz. regulation (facilitation or slowing down) of the rates of NO binding or release processes, depending on the physiological requirements. For example, the binding of NO to ferric $P450_{cam}$ was found to be significantly faster in the presence of camphor than in its absence. As mentioned above, this feature can be ascribed to the vacant position in the coordination sphere of the camphor-bound cytochrome. However, considering the fact that the reactions of NO with five-coordinate ferrous hemoporphyrins are about three orders of magnitude larger than those for the six-coordinate ferric analogues, the effect of the vacant distal position of iron(III) in camphor-bound $P450_{cam}$ does not seem to be so large (the NO binding rate constant is only 10 times larger in the presence of camphor than in its absence). It is likely that in this case the effect of facilitation of NO binding as a result of the free coordination site is partially compensated by other opposite effects such as the greater rigidity of the active site (binding of camphor to $P450_{cam}$ causes the pro-

 © 2007 Wiley-VCH Verlag GmbH & Co. KGaA, Weinheim 

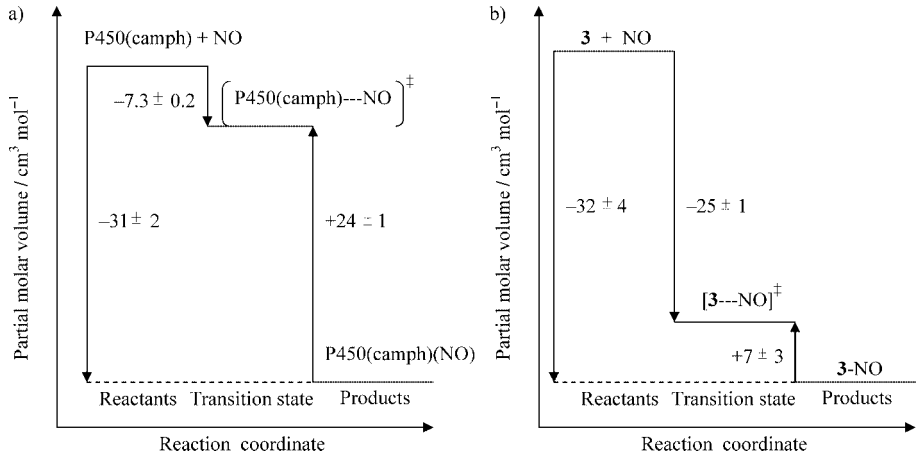


Figure 9. Comparison of volume profiles for NO binding to (a) camphor-bound $P450_{cam}$[44] and (b) complex **3** in toluene.[67]

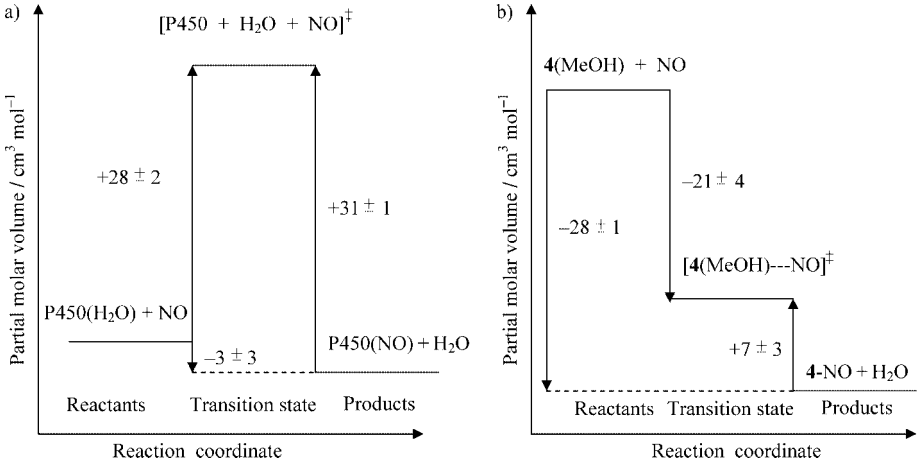


Figure 10. Volume profiles for reversible NO binding to (a) the substrate-free form of $P450_{cam}$[44] and (b) complex **4** in methanol.[67]

tein and the heme pocket to be more rigid and less compressible[57]) and/or the much larger reorganization of spin multiplicity upon NO binding to substrate-bound $P450_{cam}$ (from $S = 5/2$ to $S = 0$) than that observed for the substrate-free analogue (from $S = 1/2$ to $S = 0$).

In order to elucidate the extent to which NO binding to P450 enzymes is controlled by the metal–ligand system and the extent to which the protein heme environment can influence the dynamics of NO binding and release processes, our interest focused on mechanistic studies of NO binding to synthetic models relevant to P450 cytochrome enzymes that do not possess a protein coat. Although a number of sophisticated thiolate-ligated iron(III) porphyrins have been synthesized, most of them tend to be unstable under the employed experimental conditions, mainly because of the axial sulfur atom, which was found to be very sensitive to oxidation.[58] In this context, Higuchi and coworkers[59] prepared a stable, low-spin $Fe^{III}$-porphyrin alkanethiolate complex (SR complex, see complex **1** in Figure 11), in which the thiolate ligand is sterically protected by bulky pivaloyl groups. It was shown that the SR complex displays a reactivity that is similar to that of cytochrome P450 enzymes, and its bulky, protected axial thiolate ligand remains stable during the catalytic cycle.[60] Moreover, the first synthetic SR–NO complex was prepared and was characterized with the application of spectroscopic and electrochemical methods.[61] The study revealed that NO binds reversibly to the $Fe^{III}$ centre of SR (when an equivalent amount of NO was introduced into the reaction medium), and the resulting nitrosyl complex is diamagnetic (EPR silent) with $\nu$(N–O) and $\nu$(Fe–N) modes that are similar to those of natural heme-thiolate-containing enzymes.

These results motivated us to investigate the mechanistic aspects of the reversible binding of NO to the SR complex in coordinating (methanol) and non-coordinating (toluene) solvents.[62] During the course of the systematic kinetic studies involving concentration-, temperature- and pressure dependences, we revealed that the interaction of the SR complex with NO cannot be described as a simple reversible binding of NO to the iron(III) centre as was reported earlier for the $P450_{cam}$/NO system.[44] Even for a low excess of NO, a rather complex reactivity pattern with several reaction steps was clearly observed. Under the conditions of low NO concentrations, NO reversibly coordinates to the SR complex in methanol with a binding rate constant that is similar to that found for the related reaction with $P450_{cam}$

 © 2007 Wiley-VCH Verlag GmbH & Co. KGaA, Weinheim 

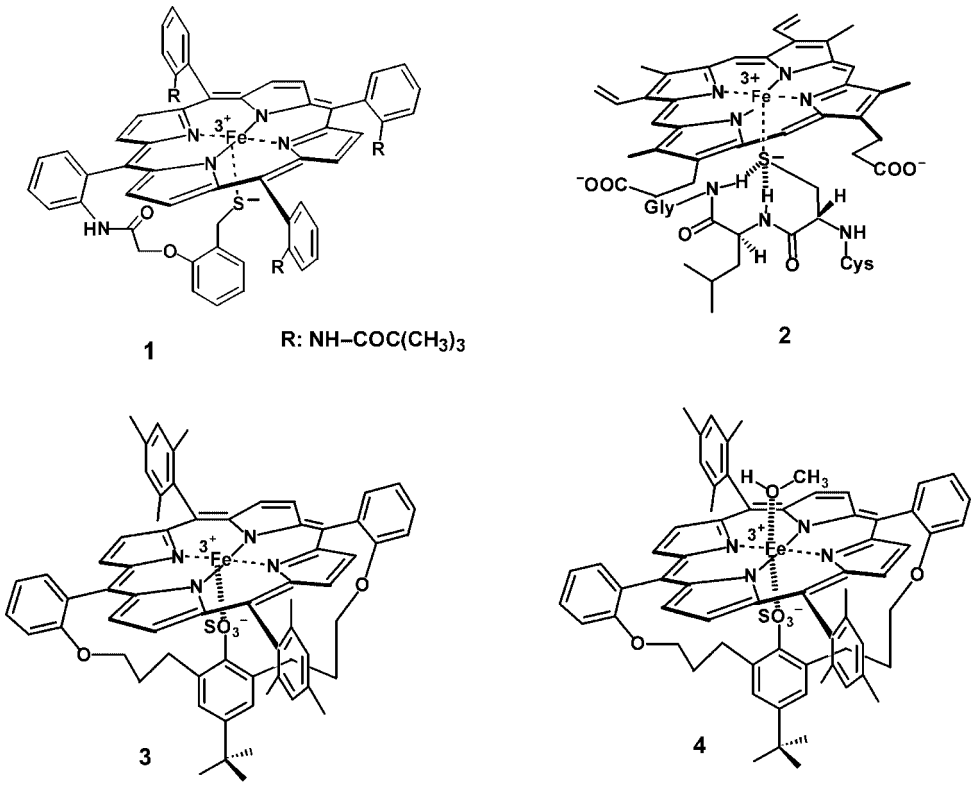


Figure 11. P450 enzyme models [**1** (SR complex),[59] **3**[65] and **4**[65]] and coordination sphere of $P450_{cam}$ (**2**).

(Table 4). The NO dissociation rate constant, although determined with a relatively large extrapolation error (because of subsequent reactions it was impossible to measure this value directly with the use of NO scavengers), is also of the same order of magnitude as that reported for the $P450_{cam}$/NO system.

The activation parameters determined for the formation of the SR–NO complex in methanol (Table 4) indicate a limiting dissociative mechanism that is dominated by dissociation of a coordinated methanol molecule. The value for the NO binding rate constant determined for this reaction in a non-coordinating solvent such as toluene is almost three orders of magnitude higher and clearly supports that the NO binding dynamics is, in this case, governed by the coordination mode of the iron(III) centre.

Under conditions of excess NO, the rapid formation of the SR–NO complex is followed by subsequent slower processes. The second observed reaction step can be accounted for in terms of direct attack of a second NO molecule at the sulfur atom of the thiolate ligand in the initially formed SR–NO complex. This leads to the formation of the five-coordinate $SR(Fe^{II})$ nitrosyl complex, which was characterized by EPR and IR spectroscopy. Although the thiolate ligand in SR is sterically protected by bulky groups, formation of the S-nitrosylated derivative under conditions of a large excess of NO does not seem unusual. It should be noted that a similar scenario was observed for the reactions between NO and the stable glutathionylcobalamin[63] and insect nitrophorins.[64] The following two slower reactions appeared to be strongly accelerated by a large excess of NO or by the presence of higher nitrogen oxides ($NO_x$) in the reaction medium. They can be accounted for in terms of the dynamic equilibria between higher nitrogen oxides and the reactive SR species, which results in the formation of a nitrosyl–nitrite complex of $SR(Fe^{II})$ as the final product.

In summary, although $P450_{cam}$ and the SR model display similar NO association and dissociation rate constants, their reactivity towards NO differs, leading to several $NO_x$-induced reaction steps in the latter case. The use of NO even in a large excess did not result in the nitrosylation of the proximal thiolate group of cytochrome $P450_{cam}$. This observation reflects very well the importance of the protein structure in the neighbourhood of the iron centre not only in controlling the coordination mode and spin state of the metal centre, but also in stabilizing thiolate coordination to the iron(III) heme centre. On the other hand, the multiple reaction steps observed for the SR/NO system can be regarded as a good model for the reactions occurring in vivo, where the dynamic equilibria involving iron(III) hemoproteins and redox-related $NO_x$ species present under aerobic physiological conditions can lead to the rather complex reactivity pattern in which $NO_x$ can act (i) as a ligand that coordinates to the metal centre, (ii) as a S-nitrosylation agent or (iii) as a nucleophile (catalyst), leading to the reductive nitrosylation of the iron(III) heme centres.

More suitable and inert towards oxidation and S-nitrosylation appears to be an enzyme mimic in which the thiolate group is replaced by a $RSO_3^-$ group (complex **3**, Figure 11).[65] DFT calculations[65d] revealed that introduction of the $RSO_3^-$ ligand significantly reduces the negative

 © 2007 Wiley-VCH Verlag GmbH & Co. KGaA, Weinheim 

charge localized on the oxygen atom that coordinates to the iron(III) centre. Therefore, such a system can better mimic the coordination sphere of several native P450 enzymes, in which electron donation from the sulfur atom is also reduced because of the presence of hydrogen bonding between the thiolate ligand and residues of the amino acids in the protein pocket (compare complex **2** and **3** in Figure 11). Moreover, preliminary UV/Vis[65f] and kinetic[66] experiments showed that upon treatment of complex **3** with peracid (peroxide shunt pathway), the oxoiron(IV) porphyrin π-cation radical is produced, which is regarded in the literature as a reactive intermediate responsible for the oxygen atom transfer to hydrocarbons in P450-catalyzed reactions.

To investigate the influence of the identity of the proximal and distal ligands on the dynamics of NO binding to the new synthetic model carrying the $RSO_3^-$ group in the axial position, we performed thermodynamic and kinetic studies on NO coordination to complexes **3** (in non-coordinating toluene) and **4** (in coordinating methanol).[67] In toluene, the five-coordinate, high-spin complex **3** reminiscent of the camphor-bound $P450_{cam}$ is formed, whereas in methanol the six-coordinate complex **4** (see Figure 11) is produced, which resembles the resting state of $P450_{cam}$. As can be seen from Table 4, model complex **3**, although having no protein pocket and possessing a $SO_3^-$ group as proximal ligand, displays a NO binding rate constant in a non-coordinating solvent that is similar to that measured for the NO association reaction of camphor-bound $P450_{cam}$. However, the rate constants for the NO release from the nitrosyl complexes of **3** and camphor-bound $P450_{cam}$ differ by almost four orders of magnitude; **3** has a significantly lower value for the NO binding constant at room temperature. However, the binding constant increases significantly as the temperature decreases. Activation parameters found for NO binding to complex **3** and to native camphor-bound $P450_{cam}$ support the same mechanism for both reactions; the mechanism is dominated by $Fe^{III}$–NO bond formation accompanied by a change in the iron(III) spin state (from $S = 5/2$ to $S = 0$). However, despite the similarity in the reaction volume and entropy, the volume profiles for NO binding to these complexes (Figure 9) differ substantially in terms of the position of the transition state, which can reflect different contributions arising from bond formation and change in spin state. In contrast to the volume profile constructed for the reaction between NO and camphor-bound $P450_{cam}$, reversible binding of NO to **3** is described by a "late" transition state for the association reaction and an "early" transition state for the dissociation reaction. This feature is in agreement with relatively slow "on" and fast "off" reactions and results in the much lower binding constant for NO coordination to **3** than to the native $P450_{cam}$.

When the reaction between NO and the model complex **3** was carried out in a coordinating solvent (methanol), a different mechanistic scenario was observed, indicating the importance of the spin state and the coordination mode of the iron(III) centre in the NO binding process.[67] In methanol, complex **4** is a six-coordinate, high-spin species. The presence of methanol coordinated to iron(III) slows down the binding of NO to **4** by about a factor of 10 relative to the binding of NO to **3**, which lacks the sixth ligand (Table 4). A similar substitution behaviour was noted for the reversible binding of NO to the substrate-free and camphor-bound forms of $P450_{cam}$.[44] However, the activation parameters determined for NO coordination to **4** (Table 4) indicate a different mechanism than that proposed for the reversible binding of NO to substrate-free $P450_{cam}$. Whereas NO binding to the resting form of $P450_{cam}$ is controlled by dissociation of a coordinated water molecule, the displacement of a methanol molecule in **4** follows an associative interchange process in which the volume collapse reflects $Fe^{III}$–NO bond formation with a concomitant change from a high-spin to low-spin state. As already mentioned, NO coordination to substrate-free $P450_{cam}$ does not involve a high-spin to low-spin rearrangement of the iron(III) centre.[44] These opposite effects are clearly seen by comparison of the volume profiles constructed for these two reactions (Figure 10).

The NO binding constants determined for the enzyme models **3** and **4** are about four orders of magnitude smaller than those found for the native $P450_{cam}$/NO system, which can be explained in terms of the very effective NO dissociation from the nitrosyl complexes of **3** and **4**. Because of the exothermic nature of NO coordination to **3** and **4**, the NO binding constants for these complexes increase significantly with decreasing temperature. This is a general observation noted also for other model enzymes (for instance, the binding of dioxygen to hemocyanine and tyrosinase) where intermediate oxidant or substrate-bound species can be stabilized only at very low temperatures. This feature clearly evidences the important role of the enzyme pocket of $P450_{cam}$ in stabilizing the $NO^+$ state and in forming more stable nitrosyl complexes at ambient temperature relative to those observed for many protein free model complexes. Thus, although the ligand-substitution behaviour of synthetic iron(III) porphyrin complexes can to some extent be regulated by tuning the electronic nature of the porphyrin ring, by the identity and number of axial ligands and by selection of experimental conditions (coordinating/non-coordinating solvent, pH, temperature, etc.), comparison of the kinetic and thermodynamic data for the native iron(III)-thiolate hemoproteins with those obtained for protein-free enzyme models clearly highlights the unique features of the protein architecture in controlling the dynamics of NO binding to P450 cytochromes according to their physiological activity.

## 8. Reductive Nitrosylation Reactions of $Fe^{III}$ Porphyrin Complexes

As mentioned in earlier sections, the binding of NO to the iron(III) centres of hemoproteins and model systems results in the formation of nitrosyl products with a linear coordination mode of the Fe–NO bond and significant charge transfer from NO to the metal centre. This leads formally to the one-electron reduction of the $Fe^{III}$ centre

 © 2007 Wiley-VCH Verlag GmbH & Co. KGaA, Weinheim 

and to the formation of a $(P)Fe^{II}(NO^+)$ complex with a coordinated nitrosyl ($NO^+$) ligand, which is isoelectronic to carbon monoxide. Clearly, $NO^+$ as an electrophilic ligand (much more electrophilic than free NO) may be susceptible to nucleophilic attack in aqueous and nonaqueous solution, which can result in the apparent instability of the nitrosyl complexes of iron(III) porphyrins relative to their analogous $(P)Fe^{II}(NO)$ species. Indeed, it has long been known that ferriheme proteins (methemoglobin and ferricytochrome *c*) undergo autoreduction when exposed to NO in aqueous solution.[68] Although many groups have systematically investigated NO reduction processes of various ferriheme proteins,[50,69] the mechanisms of these reactions are still far from completely understood. Hoshino et al.[70] reported detailed kinetic studies on the NO reductions of some ferriheme proteins in buffered solutions at various pH and proposed a plausible reaction sequence for the reductive nitrosylation of iron(III) centres. This involves attack of a nucleophile (Nu), viz. a water molecule or hydroxide ion as a general base, on the ferrous nitrosonium complex to produce a ferrous porphyrin species [which reacts very rapidly with excess NO to give (P)Fe(NO)] and the nitrosylated nucleophile as shown in Scheme 5.

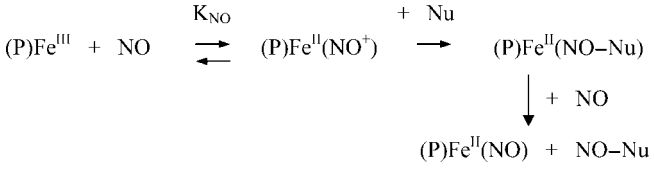


Scheme 5.

This finding has motivated many researchers to study, in detail, the role of general base buffer and hydroxide ion catalysis on the reductive nitrosylation of many ferriheme proteins and iron(III) porphyrin models.[71,72] During the course of these studies, a very important discovery was made that the nitrite ion (present in the reaction medium as a reaction product or as an ubiquitous impurity in aqueous NO solutions) can also be regarded as a catalyst for this reaction.[72] In order to account for the catalytic effect of nitrite, two mechanistic proposals were made.[72] The first involves an inner-sphere pathway proceeding by nucleophilic attack of the nitrite ion on the electrophilic, coordinated $NO^+$ to produce the iron(II) complex of the $N_2O_3$ species ($Fe–N_2O_3$) as a key intermediate. Dissociation of this complex followed by subsequent fast reactions [i.e. hydrolysis of $N_2O_3$ to nitrous acid and very rapid nitrosylation of the iron(II) porphyrin complex] lead to the reaction products and regeneration of catalytic nitrite. Another possible mechanism is described by an outer-sphere electron-transfer process between the nitrite ion and the ferrous nitrosonium complex to give a nitrosyl iron(II) porphyrin and nitrogen dioxide. $NO_2$ would then react very rapidly with the excess NO to form $N_2O_3$, which further undergoes hydrolysis to nitrite. Notably, a common aspect of these two mechanisms is the formation of $N_2O_3$ as a reactive intermediate. In aqueous solution, it can very easily undergo hydrolysis to nitrous acid; however, in the hydrophobic protein pocket, $N_2O_3$ formed during reductive nitrosylation of ferriheme proteins can offer other possibilities, for example, as an important nitrosating agent for protein amines or thiols.

All these interesting results have inspired us to investigate the reactions of reductive nitrosylation of iron(III) porphyrin models in more detail. Our contribution in this area involves temperature and pressure studies on the reductive nitrosylation reactions following the binding of NO to $(TMPyP^{4+})Fe^{III}(H_2O)_2$ (at pH = 4)[34] and to the highly negatively $[(P^{8-})Fe^{III}]$ and highly positively $[(P^{8+})Fe^{III}]$ charged ferric porphyrins (at high and low pH).[73] Estimation of the activation parameters for the nitrite-catalyzed reductive nitrosylation of these iron(III) models enabled us to discuss the validity of the above-mentioned inner- and outer-sphere mechanisms proposed for the catalytic effect of the $NO_2^-$ ion, as well as allowed us to establish the role of the overall charge on the porphyrin ring and iron centre on the rate and mechanism of reductive nitrosylation reactions.

Nitrite concentration dependence studies of the reaction between the nitrosyl complex of $(TMPyP^{4+})Fe^{III}(H_2O)_2$ and $NO_2^-$ at pH = 4 revealed that positively charged $(TMPyP^{4+})Fe^{II}(H_2O)(NO^+)$ undergoes reductive nitrosylation (in the presence of added nitrite) significantly faster than that already reported for the negatively charged $(TPPS^{4-})Fe^{II}(H_2O)(NO^+)$ complex[72] (Table 5). Activation parameters determined for this reaction are significantly positive (Table 5), which can indicate the significant role of electrostriction effects as a result of charge neutralization during binding of $NO_2^-$ to coordinated $NO^+$. The substantial contribution of these effects on the rate of reductive nitrosylation processes can be better understood in terms of the more recent results from mechanistic studies on the nitrite-catalyzed reductive nitrosylation of $(P^{8-})Fe^{III}$ and $(P^{8+})Fe^{III}$ complexes.[73] It was shown that exposure of aqueous solutions of $(P^{8-})Fe^{III}(H_2O)_2$ at pH = 7 and of $(P^{8+})Fe^{III}(H_2O)_2$ at pH = 2 leads to rapid nitrosylation reactions to produce $(P^{8-})Fe^{II}(H_2O)(NO^+)$ and $(P^{8+})Fe^{II}(H_2O)(NO^+)$, respectively. The NO binding reaction is, in both cases, followed by the slower subsequent reductive nitrosylation reaction, which leads to the formation of five-coordinate nitrosyl adducts as the final products, $(P^{8-})Fe^{II}(NO)$ and $(P^{8+})Fe^{II}(NO)$, respectively. The NO concentration dependence of the observed rate constant for reductive nitrosylation of these complexes enabled the calculation of the first-order rate constants for the reduction reactions ($k_{red}$). It was revealed that the value of $k_{red}$ is almost two orders of magnitude larger for the reduction of the positively charged $(P^{8+})Fe^{II}(NO^+)$ species than for that of the negatively charged $(P^{8-})Fe^{II}(NO^+)$ porphyrin. This observation is in line with the results obtained earlier for the reductive nitrosylation of $(TPPS^{4-})Fe^{III}$ and $(TMPyP^{4+})Fe^{III}$[34,72] and can be explained in terms of the electrophilicity of the iron(III) centres in both complexes. The accelerated reductive nitrosylation observed for $(P^{8+})Fe^{II}(NO^+)$ can be ascribed to the higher electrophilicity of

 © 2007 Wiley-VCH Verlag GmbH & Co. KGaA, Weinheim 

Table 5. Rate constants and activation parameters for the nitrite-catalyzed reductive nitrosylation reactions of $(P)Fe^{II}(H_2O)(NO^+)$ complexes.

| Starting complex | pH | $k_{nit}$ (25 °C) [$M^{-1}s^{-1}$] | $\Delta H^{\#}$ [kJ mol$^{-1}$] | $\Delta S^{\#}$ [J mol$^{-1}$ K$^{-1}$] | $\Delta V^{\#}$ [cm$^3$ mol$^{-1}$] | Ref. |
|---|---|---|---|---|---|---|
| $(P^{8+})Fe(H_2O)_2$ | 2 | 155 ± 8 | 90 ± 3 | 99 ± 10 | 7.2 ± 0.5 | [73] |
| $(P^{8+})Fe(H_2O)_2$ | 4 | 242 ± 3 | 73 ± 2 | 92 ± 7 | 12.3 ± 0.7 | [73] |
| $(P^{8+})Fe(OH)(H_2O)$ | 8 | 22 ± 1 | 68 ± 1 | 5 ± 2 | 2.2 ± 0.2 | [73] |
| $(TMPyP^{4+})Fe(H_2O)_2$ | 4 | 159 ± 12 | 88 ± 2 | 92 ± 6 | 8.8 ± 0.1 | [34] |
| $(TMPyP^{4+})Fe(H_2O)_2$ | 5 | 83 ± 3 | – | – | – | [72] |
| $(TPPS^{4-})Fe(H_2O)_2$ | 5 | 3.1 | – | – | – | [72] |
| $(P^{8-})Fe(H_2O)_2$ | 7 | 2.1 ± 0.2 | 60 ± 2 | –36 ± 7 | –8.6 ± 0.4 | [73] |

the metal centre and of coordinated $NO^+$, which is the result of the presence of the positively charged electron-withdrawing *meso* substituents in the heme environment. Conversely, electron-donating groups in $(P^{8-})Fe^{II}(NO^+)$ seem to stabilize the nitrosyl complex by the increased electron density at the iron(II) centre and therefore slow down the reductive nitrosylation reaction. Similarly, the presence of the $OH^-$ group in the position *trans* to $NO^+$ in $(P^{8+})$-$Fe^{II}(OH)(NO^+)$ (at pH = 8) has been shown to reduce $k_{red}$ significantly for this complex, mainly because of the induced electron density (coming from the *trans* $OH^-$ ligand) on the nitrosyl ligand and the decrease in electrophilic character.[73]

Since the reductive nitrosylation reactions observed for the above systems can be catalyzed by nitrite ions present in the solution as a final reaction product, a detailed study of the nitrite-catalyzed reduction of $(P^{8-})Fe^{II}(NO^+)$ and $(P^{8+})Fe^{II}(NO^+)$ was performed.[73] The values of the reduction rate constant with nitrite ion as catalyst ($k_{nit}$) obtained for these complexes and related systems are summarized in Table 5.

During the course of these studies, it was revealed that the rates of reductive nitrosylation are sensitive to the nature of the reactant, viz. HONO or $NO_2^-$ [see for example the rate constants determined for the $(P^{8+})Fe(H_2O)_2$ complex at pH = 2 and 4, where nitrous acid exists mainly as HONO and $NO_2^-$, respectively], and to the protonated/deprotonated form of the coordinated water molecule [see rate constants determined for $(P^{8+})Fe(H_2O)_2$ and $(P^{8+})$-$Fe(OH)(H_2O)$ at pH = 4 and 8, respectively]. All these observations indicate that nitrite-catalyzed reductive nitrosylation of the complexes studied proceeds according to an inner-sphere mechanism described by direct nucleophilic attack of the $HONO/NO_2^-$ species on coordinated $NO^+$ to form the $Fe^{II}$–$N_2O_3$ complex, which subsequently dissociates $N_2O_3$ and rapidly binds NO (present in excess in solution) to form the final product $(P)Fe^{II}(NO)$. Such a mechanism is also strongly supported by the activation parameters determined for $k_{nit}$ (Table 5). Activation entropies and activation volumes for the nitrite-catalyzed reductive nitrosylation of cationic complexes are substantially positive, whereas those for the negatively charged porphyrin complexes are significantly negative. This correlates very well with the electrophilicity of coordinated $NO^+$, which in turn controls the contribution of changes in electrostriction that accompanies bond formation between the electrophilic nitrosonium ligand and the $HONO/NO_2^-$ species. For example, the electrophilicity of the $NO^+$ ligand in $(P^{8-})$-$Fe^{II}(H_2O)(NO^+)$ is not expected to be high because of the overall negative charge on the porphyrin ring, such that charge neutralization and decrease in the electrostriction during bond formation is relatively small in comparison to the intrinsic contributions arising from bond formation. This means that positive contributions to the activation entropy and activation volume arising from the decrease in electrostriction (accompanied by the release of solvent molecules) can only partially compensate the negative intrinsic contributions associated with bond formation, which finally leads to the substantially negative values of the activation parameters and relatively small value of $k_{nit}$. In contrast, bond formation between $HONO/NO_2^-$ and the highly electrophilic $NO^+$ in $(P^{8+})Fe^{II}(H_2O)(NO^+)$ (because of the additional positive charge on the heme environment) will result in more effective charge neutralization. Thus, in this case, the positive contributions arising from the significant decrease in electrostriction are expected to play a major role. This is reflected by the substantially positive values for the activation parameters and high $k_{nit}$ values found for this system. In summary, the observed trend in the $k_{nit}$ values for a series of $(P^n)Fe^{III}$ complexes [$(P^{8+})Fe^{III}$ > $(TMPyP^{4+})$-$Fe^{III}$ > $(TPPS^{4-})Fe^{III}$ > $(P^{8-})Fe^{III}$] along with the activation parameters determined for these systems strongly support the operation of an inner-sphere electron-transfer mechanism for the reductive nitrosylation reactions of iron(III) porphyrins, as opposed to an outer-sphere electron-transfer mechanism, which was proposed in recent reports.[71c,72]

## 9. Reductive Nitrosylation of Water-Soluble Cobalt Porphyrins

Vitamin $B_{12a}$, aquacobalamin [$Cbl(H_2O)$], was proposed to react with NO under biological conditions and to regulate its physiological functions in this way.[74] Experimental and theoretical work from our laboratory proved that $Cbl(H_2O)$ does not react with NO at pH 7.[75,76] Nevertheless, it was reported later that $Cbl(H_2O)$ reacts with NO at low pH, under conditions in which the dimethylbenzimidazole group is protonated and subsequently dechelates.[77] The final product of this reaction was not a $Co^{III}$–(NO) complex but $Co^{II}$–(NO), or better described as $Co^{III}$–$(NO^-)$. This complex is also obtained when reduced $Cbl(H_2O)$ reacts with NO;[78] in this way, the reaction is a reductive nitrosylation process. Co porphyrins react in a

 © 2007 Wiley-VCH Verlag GmbH & Co. KGaA, Weinheim 

manner similar to that for Cbl($H_2O$) at low pH, generating $Co^{III}$–($NO^-$) complexes as final products.[33c,79] In this way, the reaction under study can be described by reaction (9).

$$Co^{III}(P) + 2\,NO \rightarrow\!\!\rightarrow Co^{III}(P)(NO^-) + NO_2^- \quad (9)$$

From titrations of the $[Co^{III}(TPPS)(H_2O)_2]^{3-}$ complex solution with NO, the stoichiometry of the consumption of NO was determined to be close to 2. Quantification of the $NO_2^-$ concentration at the end of the reaction allowed us to conclude that approximately 1 mol of $NO_2^-$ is produced per mol of complex, which gives strong support to the overall stoichiometry described by reaction (9).[80]

Three different Co-porphyrin complexes were studied [TPPS, TMPyP and TCPP = *meso*-tetra(4-carboxyphenyl)-porphyrin]; all of them react with NO and show, qualitatively, a very similar picture.[80] The reactivity difference correlates with the electron density on the metal centre. The reaction with NO proceeds through an apparently single first-order reaction; however, the isosbestic points are not clean, the observed rate constants are not reproducible and, in some cases, the kinetic traces had to be fitted to a two-exponential function. These findings suggest a more complex behaviour. For this reason the influence of $NO_2^-$/$HNO_2$ on the kinetics was studied in detail, since these species are typical and unavoidable impurities in aqueous NO solutions.[72c,75] The reactions of the three complexes under study were strongly pH dependent. At pH > 3, two reaction steps were clearly observed, whereas at pH < 3, a single reaction step was observed.

At pH < 3, in contrast to the behaviour at higher pH, formation of the final product is observed from the beginning of the reaction. The kinetic data show that the reaction is controlled by the reversible substitution of coordinated water to produce the $[Co^{III}(P)(NO)(H_2O)]$ complex, i.e. the product of the primary interaction between NO and the starting compound.[80] A weak EPR signal obtained at pH 1 with a $[Co(TPPS)(H_2O)_2]^{3-}$ sample saturated with NO gives some evidence for the presence of this intermediate.[80,81c] These complexes were obtained by electrochemical methods in organic solvents and characterized in situ,[81] since they are very unstable towards NO dissociation, to generate $[Co(P)(solvent)_2]$ complexes.[81b] We propose that the $[Co^{III}(P)(NO)(H_2O)]$ complex reacts with a second NO molecule to generate the dinitrosyl species $[Co^{III}(P)(NO)_2]$ (see left side of Scheme 6). This compound produces the final product through an inner-sphere electron-transfer reaction. These $[Co(P)(L)_2]$ compounds were observed for all the ligands studied, viz. $SCN^-$, $I^-$, pyridine.[82] Moreover, we observed the formation of $[Co(P)(NO_2^-)_2]$ complexes.[80] In all of these cases, the coordination of the second ligand molecule is faster than that of the first because of the increase in electron density on the metal centre, which is in agreement with the fact that coordination of the first NO molecule is the rate-determining step and with the observation of a single reaction step.

At pH > 3, two reactions were clearly observed when mixtures of NO and $NO_2^-$ were used. It was concluded that the first reaction is controlled by the competition between these two species to substitute one of the coordinated water molecules in the complex.[80] In this way, the expression of the observed rate constant for this reaction ($k_{1(obs)}$) can be written as in Equation (10) [see Figure 12].

$$k_{1(obs)} = k_{NO}[NO] + k_{NO_2^-}[NO_2^-] \quad (10)$$

The values of $k_{NO}$ obtained at pH 1 are in agreement with those obtained at higher pH in the presence of $NO_2^-$. This is also true for the values of $k_{NO_2^-}$ obtained in the absence and presence of NO (see Figure 12). The proposed rate law in Equation (10) is supported by the kinetic data and activation parameters obtained for the first reaction step at pH 5 and 1 and is in agreement with the data reported in the literature for the reaction of the same Co(P)

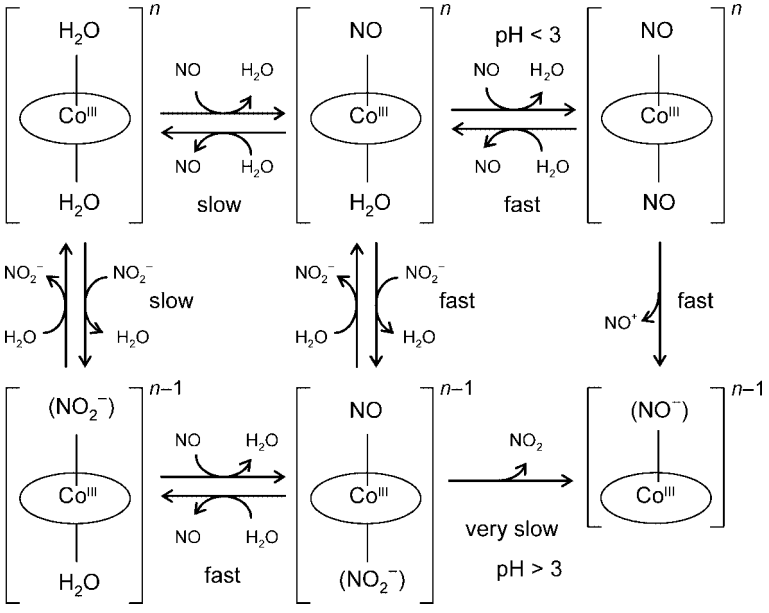


Scheme 6.

 © 2007 Wiley-VCH Verlag GmbH & Co. KGaA, Weinheim 

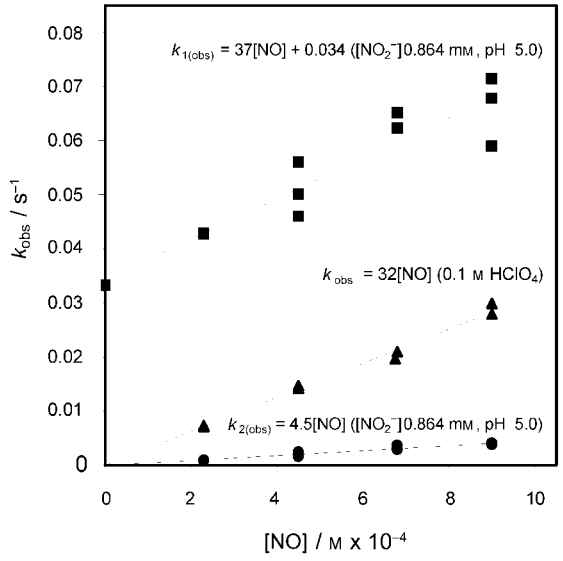


Figure 12. NO concentration dependence for the reaction with $[Co(TPPS)(H_2O)_2]^{3-}$ studied under different conditions: pH = 5.0 (0.01 M acetate buffer) or pH = 1.0 ($HClO_4$), $I$ = 0.1 M ($NaClO_4$), $T$ = 25.0 °C, $[Co(TPPS)(H_2O)_2^{3-}]$ = 1–5 × $10^{-6}$ M. Different values of $k_{obs}$ represent the spread in the measurements at a particular NO concentration (each data point is the average of 4 to 10 kinetic runs).

complexes with other ligands (see Table 6 and Table 7).[82] The first reaction step for the three complexes correlates with the electron density on the metal centre as was previously observed. The spectrum of the intermediate generated during the reaction was very similar to that of the $[Co(P)(NO_2^-)(H_2O)]$ complex; no final product, i.e. $[Co^{III}(P)(NO^-)]$, was produced and no EPR signals could be detected either. According to Equation (10), the $[Co(P)(NO_2^-)(H_2O)]$ and $[Co(P)(NO)(H_2O)]$ complexes should be the products of the first reaction, where $NO_2^-$ and NO compete. Nevertheless, only the first compound was detected. We propose that the second intermediate is unstable under these conditions, even more than at pH 1, and the presence of $NO_2^-$ leads to the decomposition of this intermediate thus releasing NO and generating $[Co(P)(NO_2^-)(H_2O)]$ (see central part of Scheme 6). This decomposition of the intermediate by $NO_2^-$ is prevented at low pH through protonation, where formation of the final product is observed from the beginning of the reaction.

The second reaction was observed at pH > 3. The observed rate constants for this reaction ($k_{2(obs)}$) are very similar to those observed for the reaction between the $[Co(P)(NO_2^-)(H_2O)]$ complexes and NO under similar conditions. On the other hand, they do not depend significantly on the $NO_2^-$ concentration, they depend linearly on the NO concentration (see Figure 12) and the activation parameters support a dissociative mechanism. The nature of this reaction is discussed elsewhere, and several possible mechanisms are considered, among them the oxo-transfer reaction.[80] We propose that the $[Co(P)(NO_2^-)(H_2O)]$ complex is, in the presence of NO, in equilibrium with small amounts of the $[Co(P)(NO_2^-)(NO)]$ intermediate (see lower part of Scheme 6). This last intermediate slowly decomposes through an inner-sphere electron-transfer reaction to generate the final product $[Co^{III}(P)(NO^-)]$ and $NO_2$. Thus, this reaction would be the rate-determining step for the second reaction. This proposal is consistent with the NO- and $NO_2^-$ concentration dependences, as well as with the activation parameters.

In the reductive nitrosylation of $Fe^{III}$ porphyrins, where general base catalysis was observed, it was proposed that the $[Fe^{III}(P)NO]$ complex is attacked by nucleophiles such as $NO_2^-$, different bases and even solvents to generate the $Fe^{II}(P)$ complex.[71,72] The latter complex reacts under diffusion-controlled conditions with NO to produce the final product. We do not have any evidence in favour of such catalysis in our system. If this was the case, we would expect different $NO_2^-$ concentration- and pH dependences. We believe that the reason why reductive nitrosylation of Co porphyrins is so different from that of the Fe analogues is the instability of the $[Co^{III}(P)(NO)(H_2O)]$ intermediate.[80,81] Although the electronic structure of this compound may have some contribution from the $[Co^{II}(P)(NO^+)(H_2O)]$

Table 6. Kinetic data for reactions of NO and $NO_2^-$ with the $[Co(TPPS)(H_2O)_2]^{3-}$ complex.[a]

| Reaction | $k_1$ [$M^{-1}s^{-1}$] [Intercept, $s^{-1}$] | $k_2$ [$M^{-1}s^{-1}$] [Intercept, $s^{-1}$] | $\Delta H^{\neq}_1$ kJ mol$^{-1}$ | $\Delta H^{\neq}_2$ kJ mol$^{-1}$ | $\Delta S^{\neq}_1$ J K$^{-1}$ mol$^{-1}$ | $\Delta S^{\neq}_2$ J K$^{-1}$ mol$^{-1}$ | $\Delta V^{\neq}_1$ cm$^3$ mol$^{-1}$ | $\Delta V^{\neq}_2$ cm$^3$ mol$^{-1}$ |
|---|---|---|---|---|---|---|---|---|
| NO (pH 1.0) | 32 ± 1 | | 101 ± 2 | | +121 ± 6 | | +13 ± 1 | |
| $NO_2^-$ (pH 5.0) | 38.5 ± 0.8 | | 90.2 ± 0.6 | | +88 ± 2 | | +11 ± 1 | |
| $HNO_2$ (pH 1.0) | 14.2 ± 0.4 [(7 ± 1) × $10^{-3}$] | | 93 ± 2 | | +91 ± 5 | | +15 ± 1 | |
| NO ([$NO_2^-$] 1 mM, pH 5.0) | 37 ± 5 [(3.4 ± 0.4) × $10^{-2}$] | 4.5 ± 0.5 | 94 ± 3 | 98 ± 3 | +100 ± 10 | +97 ± 9 | +13 ± 1 | +14 ± 1 |
| $NO_2^-$ ([NO] 0.9 mM, pH 5.0) | 41 ± 4 [(3.0 ± 0.4) × $10^{-2}$] | [(4.2–3.2) × $10^{-3}$] | | | | | | |
| $HNO_2$ ([NO] 0.9 mM, pH 1.0) | 13 ± 1 [(3.4 ± 0.5) × $10^{-2}$] | | | | | | | |
| $SCN^-$ | 179[b] | | 77[c] | | +60[c] | | +15.4[d] | |
| Py | 520[b] | | 74[c] | | +60[c] | | | |
| $I^-$ | 118[c] | | 87[c] | | +87[c] | | | |

[a] $I$ = 0.1 M, unless otherwise stated; subscripts 1 and 2 refer to the first and second observed reaction steps. [b] From ref.[82a] [c] From ref.[82b] $I$ = 1.0 M. [d] from ref.[82h] $I$ = 1.0 M.

 © 2007 Wiley-VCH Verlag GmbH & Co. KGaA, Weinheim 

Table 7. Kinetic data for the different $Co^{III}$ porphyrin complexes studied.[a]

| Reaction | $[Co(TPPS)(H_2O)_2]^{3-}$ | | $[Co(TCPP)(H_2O)_2]^{3-}$ | | $[Co(TMPyP)(H_2O)_2]^{5+}$ | |
|---|---|---|---|---|---|---|
| | $k_1$ [$M^{-1}s^{-1}$] [Intercept, $s^{-1}$] | $k_2$ [$M^{-1}s^{-1}$] [Intercept, $s^{-1}$] | $k_1$ [$M^{-1}s^{-1}$] [Intercept, $s^{-1}$] | $k_2$ [$M^{-1}s^{-1}$] [Intercept, $s^{-1}$] | $k_1$ [$M^{-1}s^{-1}$] [Intercept, $s^{-1}$] | $k_2$ [$M^{-1}s^{-1}$] [Intercept, $s^{-1}$] |
| NO (pH 1.0) | $32 \pm 1$ | | | | $(1.5 \pm 0.1) \times 10^{-1}$ | |
| $NO_2^-$ | $38.5 \pm 0.8$[b] | | $54.1 \pm 0.2$[c] | | $8.4 \pm 0.2$[d] | |
| $HNO_2$ (pH 1.0) | $14.2 \pm 0.4$ $[(7 \pm 1) \times 10^{-3}]$ | | | | | |
| NO ([$NO_2^-$] 1 mM) | $37 \pm 5$[b] $[(3.4 \pm 0.3) \times 10^{-2}]$ | $4.5 \pm 0.5$[b] | $130 \pm 10$[c] $[(5.3 \pm 0.1) \times 10^{-2}]$ | $7.2 \pm 0.5$[c] | $1.6 \pm 0.2$[d] $[(8.4 \pm 0.1) \times 10^{-3}]$ | $2.2 \pm 0.3$[d] |
| $NO_2^-$ ([NO] 0.9 mM) | $41 \pm 4$[b] $[(3.0 \pm 0.4) \times 10^{-2}]$ | $[(3.2–4.2) \times 10^{-3}]$ | $47 \pm 6$[c] $[(1.2 \pm 0.1) \times 10^{-1}]$ | $[(5.3–6.7) \times 10^{-3}]$ | $8.8 \pm 0.8$[d] | $[(1.6–2.4) \times 10^{-3}]$ |
| $SCN^-$ | 179[e] | | 450[g] | | 2.1[h] | |
| Py | 520[e] | | 1400[g] | | 0.7[h] | |
| $I^-$ | 118[f] | | | | 1.6[i] | |
| p$K_a$ | 7.0[f] | | 7.5[g] | | 6.0[h] | |

[a] $T$ = 25.0 °C, $I$ = 0.1 M, unless otherwise stated; subscripts 1 and 2 refer to the first and second observed reaction steps. [b] pH 5.0. [c] pH 6.0. [d] pH 4.7. [e] From ref.[82a] [f] From ref.[82b] $I$ = 1.0 M. [g] From ref.[82g] $I$ = 0.5 M. [h] From ref.[82d] $I$ = 0.5 M. [i] From ref.[82f] $I$ = 1.0 M.

structure, its instability prevents any further reaction with nucleophiles. In fact, such reactions are quite slow and they are about $10^{-3}$ $s^{-1}$ for the reactions with solvent (water), acetate, etc.[71,72]

## 10. Reductive Nitrosylation of Aquacobalamin at Low pH

As mentioned in the previous section, aquacobalamin, [Cbl($H_2O$)], does not react with NO at pH 7,[75,76] nevertheless, it was reported that it can undergo reductive nitrosylation at low pH to generate a $Co^{III}$–$NO^-$ complex or Cbl($NO^-$)[77] in a manner similar to that of Co porphyrins.[79] As a natural extension of the kinetic and mechanistic studies on Co porphyrins,[80] the reductive nitrosylation of Cbl($H_2O$) at low pH was revisited.[83] Many similarities between Cbl($H_2O$) and the previously studied Co porphyrins, as well as some important differences, were found.

In the preliminary experiments, kinetic traces obtained during the reaction with NO were irreproducible, which shows, in many cases, a more complex behaviour than a simple first-order process. The influence of $HNO_2$ impurities was studied by using mixtures of NO and $HNO_2$. As previously found for Co porphyrins, two reaction steps were observed. The first reaction shows very small absorption changes and proceeds on the stop-flow timescale. The UV/Vis spectrum of the intermediate generated during the first reaction is very similar to that of the Cbl($NO_2^-$) complex generated for the same $HNO_2$ concentration. The observed rate constants obtained for this reaction ($k_{1(obs)}$) are independent of the NO concentration. On the other hand, they show a linear dependence on the $HNO_2$ concentration with a slope of $110 \pm 2$ $M^{-1}s^{-1}$ and an intercept of $(4.0 \pm 0.2) \times 10^{-2}$ $s^{-1}$. Very similar parameters were obtained if no NO (only $HNO_2$) is present in the medium, i.e. $106 \pm 5$ $M^{-1}s^{-1}$ and $3.3 \pm 0.6$ $s^{-1}$, respectively. In other words, NO does not react with Cbl($H_2O$) even at pH 1.[83]

The second reaction step shows the spectral changes reported in the literature for the reductive nitrosylation of Cbl($H_2O$) at low pH, and the Cbl($NO^-$) complex is produced as final product.[77] It was previously reported that this reaction was independent of the NO concentration.[77] We found, however, that the observed rate constant for this reaction ($k_{2(obs)}$) depends on the NO and $HNO_2$ concentrations, but the dependence on the concentration of each species is quite surprising and unexpected.[83] For example, when the $HNO_2$ concentration was kept constant, the $k_{2(obs)}$ values decreased with increasing NO concentration. As the yield of the reaction decreased as the NO concentration decreased, quantitative information was not obtained. On the other hand, when the NO concentration was kept constant, the $k_{2(obs)}$ values increased with increasing $HNO_2$ concentration, and a non-linear, quadratic dependence was observed (see Figure 13). The yield of the final product decreased also when the $HNO_2$ concentration increased, which is in agreement with the previous finding. The second reaction step is strongly pH dependent. As was previously reported, the reaction rate decreases with increasing pH, and the reaction is no longer observed at pH > 4.[77] The pH dependence correlates with the spectral changes observed for the Cbl($NO_2^-$) complex as a function of pH. From the UV/Vis data, the p$K_a$ of the protonated Cbl($NO_2^-$) complex is estimated to be close to 1.[83] In contrast, the p$K_a$ of protonated Cbl($H_2O$) is –2.5.[84] We propose that the dimethylbenzimidazole group is protonated at low pH and dissociates from the metal centre to leave a vacant site for the coordination of NO. The dissociation of this group after protonation is a fast reaction [ca. 0.3 $s^{-1}$ at pH 1 for the Cbl($NO_2^-$) complex].[83] In this way, the reactive species towards NO is not Cbl($H_2O$) but the Cbl($NO_2^-$) complex (see Scheme 7), since the concentration of the protonated form of Cbl($H_2O$) is extremely low at pH 1.

The effect of the $HNO_2$ concentration on $k_{2(obs)}$ and on the yield of the reaction revealed the possibility of a reaction between $HNO_2$ and the Cbl($NO^-$) complex, i.e. a *back reaction*. Interestingly, the observed rate constants for this last reaction ($k_{obs}$) do not differ significantly from $k_{2(obs)}$ obtained for identical $HNO_2$ and NO concentrations (see

 © 2007 Wiley-VCH Verlag GmbH & Co. KGaA, Weinheim 

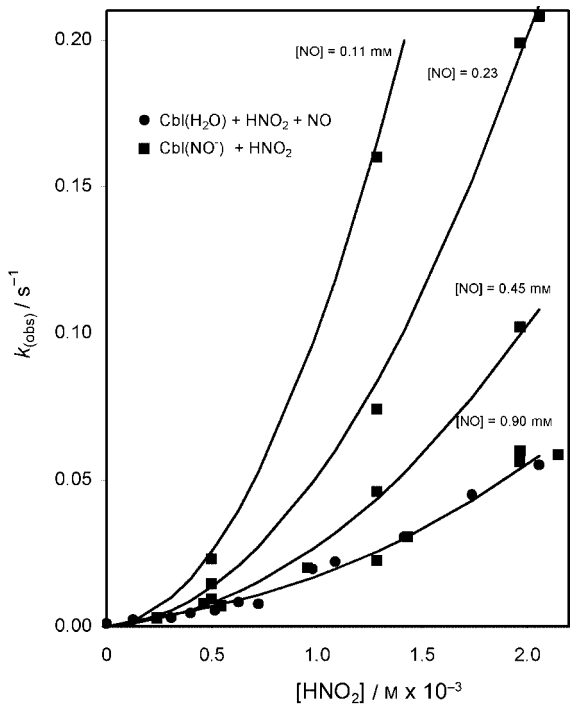


Figure 13. $[HNO_2]$ dependence of the observed rate constant for the second reaction step ($k_{2(obs)}$) and of the reaction between $Cbl(NO^-)$ and $HNO_2$ ($k_{obs}$). The solid line corresponds to the simulated data according to Equation (12), by using $K_{HNO_2}$ = 2800 $M^{-1}$ (fixed variable), $k_{NO} = 7 \pm 2$ $M^{-1} s^{-1}$ and $K = 0.6 \pm 0.2$. Experimental conditions: pH = 1.0, $I$ = 0.1 M ($HClO_4$), $T$ = 25.0 °C. $[Cbl(H_2O)]$ = 0.01–0.05 mM.

Figure 13).[83] Moreover, $k_{obs}$ values show a quadratic dependence on the $HNO_2$ concentration and decrease when the NO concentration increases. The product of the *back reaction* must be $Cbl(NO_2^-)$ in equilibrium with $Cbl(H_2O)$, since $HNO_2$ is in excess and no consecutive reactions are observed. In this way, the reductive nitrosylation is a reversible reaction and can be expressed by reaction (11).

$$Cbl(NO_2^-) + 2\,NO + H_2O \rightleftharpoons Cbl(NO^-) + 2\,HNO_2;\ K \qquad (11)$$

According to the kinetic data and the earlier work on Co porphyrins, the proposed mechanism for the reaction of $Cbl(H_2O)$ with NO at low pH is summarized in Scheme 7.

According to this mechanism and the assumptions described elsewhere,[83] Equation (12) can be derived, where $K_{HNO_2}$ is the equilibrium constant for the formation of the $Cbl(NO_2^-)$ complex, $K$ is the equilibrium constant for the reductive nitrosylation expressed in reaction (11) and $k_{NO}$ expresses the rate constant for the release of $NO_2^-$ from the $Cbl(NO_2^-)(NO)$ intermediate (see Scheme 7), which is the rate-determining step in the second reaction step.

$$k_{2(obs)} = \frac{K_{HNO_2}[HNO_2]}{1 + K_{HNO_2}[HNO_2]}\, k_{NO}[NO] + \frac{k_{NO}[HNO_2]^2}{K\,[NO]} \qquad (12)$$

Equation (12) can account for the dependence of $k_{2(obs)}$ for the reductive nitrosylation and of $k_{obs}$ for the *back reaction* on the NO and $HNO_2$ concentrations. Moreover, by fitting the experimental data with this equation, the values of $7 \pm 2$ $M^{-1} s^{-1}$ and $0.6 \pm 0.2$ were obtained for $k_{NO}$ and $K$, respectively. This latter parameter was confirmed by direct equilibrium measurements.[83] These measurements were also consistent with the stoichiometry expressed in reaction (11). In summary, the reductive nitrosylation is dominated by its *back reaction*, and this is the reason for its strange NO- and $HNO_2$ concentration dependences.

DFT calculations were performed on the present system.[83] Earlier studies concluded that $Cbl(H_2O)$ cannot interact with NO in aqueous solution.[76] The more recent work focused on the effect of the coordination of NO, $NO_2^-$, $H_2O$ and $OH^-$ on the lengthening of the Co–dimethylbenzimidazole bond.[83] On deprotonation of the coordinated water molecule in the $Cbl(H_2O)$ complex, significant lengthening of the Co–dimethylbenzimidazole bond occurs. A similar effect is observed upon coordination of $NO_2^-$. On the other hand, the Co–dimethylbenzimidazole bond length in the Cbl(NO) complex is similar to that in $Cbl(H_2O)$. In this way, lengthening of the Co–dimethylbenzimidazole bond in the $Cbl(NO_2^-)$ complex allows its protonation and dechelation at low pH. This is evidently not possible for the $Cbl(H_2O)$ and Cbl(NO) complexes.

In conclusion, we confirmed that $Cbl(H_2O)$ cannot react with NO even at low pH. We propose that the active species towards NO is $Cbl(NO_2^-)$ and not $Cbl(H_2O)$. A mechanism based on (and consistent with) previous work on Co porphyrins is proposed. This mechanism accounts for the NO- and $HNO_2$ concentration dependences of the observed rate constant for the reductive nitrosylation ($k_{2(obs)}$) as well as for the pH dependence. As we mentioned in the previous section, $Co^{III}$–(NO) complexes are very unstable compounds.[81] This is the main reason why the reductive nitrosylation in Co porphyrins is so different from that in the Fe analogues.[71,72] This instability of the $Co^{III}$–(NO) complexes determines why $Cbl(H_2O)$ does not react with NO as well.[76,83]

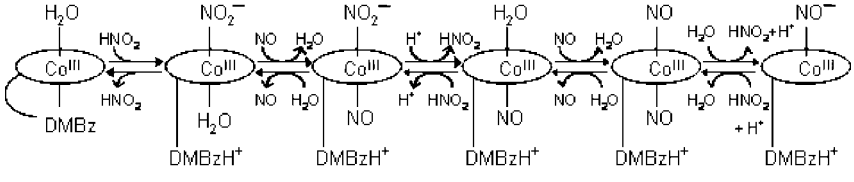


Scheme 7.

 © 2007 Wiley-VCH Verlag GmbH & Co. KGaA, Weinheim 

## 11. Conclusions and Future Outlook

The work summarized in this microreview has greatly assisted the mechanistic clarification of the interaction of NO with Fe and Co complexes and of the observed subsequent reactions. It forms an excellent basis for the clarification of observations in the literature that are of significant biological and environmental importance. In this process the application of volume-profile analysis has been extremely useful, especially in cases where the activation of NO is accompanied by changes in the spin state of the metal centre. Presently, we are extending this work to water-soluble model complexes of P450 that closely resemble the coordination environment of P450. Although NO is a radical, the presented work clearly shows that it behaves like any other nucleophile, with the exception that once it is bound to the metal centre there is a redistribution of charge density, which results in a formal redox reaction. Furthermore, the fundamental work involving the binding of NO to P450 and model complexes forms a basis for the understanding of the more complex reaction sequences observed during the activation of peroxides by such systems, a topic that is now being studied in more detail in our group.

## Acknowledgments

We gratefully acknowledge financial support from the National Research Council of Argentina (CONICET) and the Deutsche Forschungsgemeinschaft within SFB 583 on "Redox-Active Metal Complexes". We appreciate the productive collaboration with Norbert Jux (Institute for Organic Chemistry, University of Erlangen-Nürnberg).

[1] J. H. Enemark, R. D. Feltham, *Coord. Chem. Rev.* **1974**, *13*, 339.
[2] M. Wolak, R. van Eldik, *Coord. Chem. Rev.* **2002**, *230*, 263.
[3] A. Wanat, T. Schneppensieper, G. Stochel, R. van Eldik, B. Eckhard, K. Wieghardt, *Inorg. Chem.* **2002**, *41*, 4.
[4] T. Schneppensieper, S. Finkler, A. Czap, R. van Eldik, M. Heus, P. Nieuwenhuizen, C. Wreesman, W. Abma, *Eur. J. Inorg. Chem.* **2001**, 491.
[5] T. Schneppensieper, A. Wanat, G. Stochel, R. van Eldik, *Inorg. Chem.* **2002**, *41*, 2565.
[6] a) D. H. Macartney, *Rev. Inorg. Chem.* **1988**, *9*, 101; b) L. M. Baraldo, P. Forlano, A. R. Parise, L. D. Slep, J. A. Olabe, *Coord. Chem. Rev.* **2001**, *219–221*, 881; c) A. G. Sharpe, *The Chemistry of Cyano Complexes of the Transition Metals*, Academic Press, London, **1976**.
[7] a) H. E. Toma, J. M. Malin, *Inorg. Chem.* **1974**, *13*, 1772; b) H. E. Toma, *Inorg. Chim. Acta* **1975**, *15*, 205; c) H. E. Toma, A. A. Batista, H. B. Gray, *J. Am. Chem. Soc.* **1982**, *104*, 7509; d) I. Maciejowska, R. van Eldik, G. Stochel, Z. Stasicka, *Inorg. Chem.* **1997**, *36*, 5409; e) H. E. Toma, N. M. Moroi, N. Y. M. Iha, *An. Acad. Brasil. Cienc.* **1982**, *54*, 315; f) H. E. Toma, J. M. Malin, E. Giesbrecht, *Inorg. Chem.* **1973**, *12*, 2084; g) E. H. Toma, J. M. Malin, *Inorg. Chem.* **1973**, *12*, 1039; h) H. E. Toma, J. M. Malin, *Inorg. Chem.* **1973**, *12*, 2080; i) H. E. Toma, J. M. Martins, E. Giesbrecht, *J. Chem. Soc., Dalton Trans.* **1981**, 1610.
[8] a) R. Nast, J. Schmidt, *Angew. Chem. Int. Ed. Engl.* **1969**, *8*, 383; b) J. D. W. van Voorst, P. Hemmerich, *J. Chem. Phys.* **1966**, *45*, 3914; c) J. R. Bertolino, C. O. Della Védova, O. Sala, *Polyhedron* **1989**, *8*, 361; d) J. Masek, E. Maslova, *Collection Czechoslov. Chem. Commun.* **1974**, *39*, 2141.
[9] R. P. Cheney, M. G. Simic, M. Z. Hoffman, I. A. Taub, K. D. Asmus, *Inorg. Chem.* **1977**, *16*, 2187.
[10] a) M. J. Clarke, J. B. Gaul, *Struct. Bonding (Berlin)* **1993**, *81*, 147; b) A. R. Butler, C. Glidewell, *Chem. Soc. Rev.* **1987**, *16*, 361.
[11] F. Roncaroli, J. A. Olabe, R. van Eldik, *Inorg. Chem.* **2003**, *42*, 4179.
[12] a) F. Roncaroli, R. van Eldik, J. A. Olabe, *Inorg. Chem.* **2005**, *44*, 2781; b) The $[Fe(CN)_5NO]^{3-}$ complex reacts with NO to generate nitroprusside. The $[Fe(CN)_4NO]^{2-}$ complex is responsible for this behaviour, which can be prevented by the addition of $CN^-$. These reactions are discussed in ref.[12a]
[13] C. H. Langford, H. B. Gray, *Ligand Substitution Processes*, W. A. Benjamin, Inc., **1965**.
[14] G. Stochel, J. Chatlas, P. Martínez, R. van Eldik, *Inorg. Chem.* **1992**, *31*, 5480.
[15] T. W. Swaddle, *Inorg. Chem.* **1983**, *22*, 2663.
[16] M. I. Finston, H. G. Drickamer, *J. Phys. Chem.* **1981**, *85*, 50.
[17] J. Legros, *J. Chim. Phys. Phys.-Chim. Biol.* **1964**, *61*, 909.
[18] S. Alsheri, J. Burgess, *Inorg. Chim. Acta* **1991**, *181*, 153.
[19] T. R. Sullivan, D. R. Stranks, J. Burgess, R. I. Haines, *J. Chem. Soc., Dalton Trans.* **1977**, 1460.
[20] M. J. Blandamer, J. Burgess, K. W. Morcom, R. Sherry, *Transition Met. Chem.* **1983**, *8*, 354.
[21] G. Stochel, R. van Eldik, E. Hejmo, Z. Stasicka, *Inorg. Chem.* **1988**, *27*, 2767.
[22] a) A. D. James, R. S. Murray, *J. Chem. Soc., Dalton Trans.* **1977**, 326; b) A. D. James, R. S. Murray, W. C. E. Higginson, *J. Chem. Soc., Dalton Trans.* **1974**, 1273.
[23] G. Stochel, R. van Eldik, *Inorg. Chim. Acta* **1991**, *190*, 55.
[24] F. Roncaroli, J. A. Olabe, R. van Eldik, *Inorg. Chem.* **2002**, *41*, 5417.
[25] I. Maciejowska, Z. Stasicka, G. Stochel, R. van Eldik, *J. Chem. Soc., Dalton Trans.* **1999**, 3643.
[26] A. Wanat, R. van Eldik, G. Stochel, *J. Chem. Soc., Dalton Trans.* **1998**, 2497.
[27] P. C. Ford, L. E. Laverman, *Coord. Chem. Rev.* **2005**, *249*, 391.
[28] J. R. Stone, M. A. Marletta, *Biochemistry* **1994**, *33*, 5636.
[29] K. Nakahara, K. Tanimoto, K. Hatano, K. Usuda, H. Shoun, *J. Biol. Chem.* **1993**, *268*, 8350.
[30] a) R. Cassoly, Q. H. Gibson, *J. Mol. Biol.* **1975**, *91*, 301; b) E. G. Moore, Q. H. Gibson, *J. Biol. Chem.* **1976**, *251*, 2788; c) P. Ascenzi, M. Colleta, R. Santucci, F. Polizio, A. Desideri, *J. Inorg. Biochem.* **1994**, *53*, 273; d) M. Hoshino, K. Ozawa, H. Seki, P. C. Ford, *J. Am. Chem. Soc.* **1993**, *115*, 9568.
[31] J. F. Andersen, X. D. Ding, C. Balfour, T. K. Shokhireva, D. E. Champagne, F. A. Walker, W. R. Montfort, *Biochemistry* **2000**, *39*, 10118.
[32] a) W. R. Scheidt, M. K. Ellison, *J. Am. Chem. Soc.* **2001**, *123*, 6314; b) P. C. Ford, I. M. Lorkovic, *Chem. Rev.* **2002**, *102*, 993 and references cited therein; c) P. C. Ford, L. E. Laverman, I. M. Lorkovic, *Adv. Inorg. Chem.* **2003**, *54*, 2003 and references cited therein.
[33] a) M. Hoshino, K. Ozawa, H. Seki, P. C. Ford, *J. Am. Chem. Soc.* **1993**, *115*, 9568; b) L. E. Laverman, M. Hoshino, P. C. Ford, *J. Am. Chem. Soc.* **1997**, *119*, 12663; c) L. E. Laverman, P. C. Ford, *J. Am. Chem. Soc.* **2001**, *123*, 11614.
[34] A. Theodoridis, R. van Eldik, *J. Mol. Catal. A* **2004**, *224*, 197.
[35] M. Hoshino, L. Laverman, P. C. Ford, *Coord. Chem. Rev.* **1999**, *187*, 75 and references cited therein.
[36] a) P. A. Duffin, L. F. Larkworthy, J. Mason, A. N. Stephens, R. M. Thompson, *Inorg. Chem.* **1987**, *26*, 2034; b) Y. Chen, F. Lin, R. E. Shepherd, *Inorg. Chem.* **1999**, *38*, 973; c) D. S. Bohle, Ch. Hung, B. D. Smith, *Inorg. Chem.* **1998**, *37*, 5798.

 © 2007 Wiley-VCH Verlag GmbH & Co. KGaA, Weinheim 

[37] W. R. Scheidt, M. K. Ellison, *Acc. Chem. Res.* **1999**, *32*, 350 and references cited therein.
[38] T. Schneppensieper, A. Zahl, R. van Eldik, *Angew. Chem. Int. Ed.* **2001**, *40*, 1678.
[39] D. M. Guldi, G. M. A. Rahman, N. Jux, D. Balbinot, U. Hartnagel, N. Tagmatarchis, M. Prato, *J. Am. Chem. Soc.* **2005**, *127*, 9830.
[40] J.-E. Jee, S. Eigler, F. Hampel, N. Jux, M. Wolak, A. Zahl, G. Stochel, R. van Eldik, *Inorg. Chem.* **2005**, *44*, 7717.
[41] J.-E. Jee, M. Wolak, D. Balbinot, N. Jux, A. Zahl, R. Van Eldik, *Inorg. Chem.* **2006**, *45*, 1326.
[42] a) W. R. Scheidt, Ch. A. Reed, *Chem. Rev.* **1981**, *81*, 543; b) W. R. Scheidt, S. R. Osvath, Y. J. Lee, Ch. A. Reed, B. Shaevitz, G. P. Gupta, *Inorg. Chem.* **1989**, *28*, 1591; c) D. R. Evans, Ch. A. Reed, *J. Am. Chem. Soc.* **2000**, *122*, 4660 and references cited therein.
[43] M. Wolak, R. van Eldik, *J. Am. Chem. Soc.* **2005**, *127*, 13312.
[44] A. Franke, G. Stochel, C. Jung, R. van Eldik, *J. Am. Chem. Soc.* **2004**, *126*, 4181.
[45] L. E. Laverman, A. Wanat, J. Oszajca, G. Stochel, P. C. Ford, R. van Eldik, *J. Am. Chem. Soc.* **2001**, *123*, 285.
[46] A. Wanat, M. Wolak, Ł. Orzeł, M. Brindell, R. van Eldik, G. Stochel, *Coord. Chem. Rev.* **2002**, *229*, 37 and references cited therein.
[47] a) A. Drljaca, C. D. Hubbard, R. van Eldik, T. Asano, M. V. Basilevsky, W. J. le Noble, *Chem. Rev.* **1998**, *98*, 2167; b) L. Helm, A. E. Merbach, *J. Coord. Chem.* **1999**, *187*, 151.
[48] A. M. Rich, R. S. Armstrong, P. J. Ellis, P. A. Lay, *J. Am. Chem. Soc.* **1998**, *120*, 10827.
[49] a) M. L. Calrson, R. Regen, E. Elber, H. Li, G. N. Phillips, J. L. Olson, Q. H. Gibson, *Biochemistry* **1994**, *33*, 10597; b) T. G. Traylor, D. Magde, J. Marsters, K. Jongeward, G. Wu, K. Walda, *J. Am. Chem. Soc.* **1993**, *115*, 4808.
[50] T. Yoshimura, S. Suzuki, *Inorg. Chim. Acta* **1988**, *152*, 241.
[51] a) J. H. Dawson, *Science* **1988**, *240*, 433; b) T. L. Poulus, *J. Biol. Inorg. Chem.* **1996**, *1*, 356; c) D. B. Goodin, *J. Biol. Inorg. Chem.* **1996**, *1*, 360; d) S. Franzen, M. P. Roach, Y.-P. Chen, R. B. Dyer, W. H. Woodruff, J. H. Dawson, *J. Am. Chem. Soc.* **1998**, *120*, 4658.
[52] a) C. J. Hanke, J. G. Drewett, C. R. Myers, W. B. Campbell, *Endocrinology* **1998**, *139*, 4053; b) K. del Punta, E. H. Charreau, O. Pignataro, *Endocrinology* **1996**, *137*, 5337.
[53] a) R. E. Ebel, D. H. O'Keeffe, J. A. Peterson, *FEBS Lett.* **1975**, *55*, 198; b) D. H. O'Keeffe, R. E. Ebel, J. A. Peterson, *J. Biol. Chem.* **1978**, *253*, 3509.
[54] S. Hu, J. R. Kincaid, *J. Am. Chem. Soc.* **1991**, *113*, 2843.
[55] a) G. B. Richter-Addo, R. A. Wheeler, C. A. Hixson, L. Chen, M. A. Khan, M. K. Ellison, C. E. Schulz, W. R. Scheidt, *J. Am. Chem. Soc.* **2001**, *123*, 6314; b) S. A. Roberts, A. Weichsel, Y. Qiu, J. A. Shelnutt, F. A. Walker, W. R. Montfort, *Biochemistry* **2001**, *40*, 11327; c) M. K. Ellison, C. E. Schulz, W. R. Scheidt, *J. Am. Chem. Soc.* **2002**, *124*, 13833.
[56] D. J. Taube, H. D. Projahn, R. van Eldik, D. Magde, T. G. Traylor, *J. Am. Chem. Soc.* **1990**, *112*, 6880.
[57] C. Jung, N. Bec, R. Lange, *Eur. J. Biochem.* **2002**, *269*, 2989.
[58] a) S. C. Tang, S. Koch, G. C. Papaefthymiou, S. Foner, R. B. Frankel, J. A. Ibers, R. H. Holm, *J. Am. Chem. Soc.* **1976**, *98*, 2414; b) C. Caron, A. Mitschler, G. Riviere, L. Ricard, M. Schapacher, R. Weiss, *J. Am. Chem. Soc.* **1979**, *101*, 7401; c) H. Ogoshi, H. Sugimoto, Z. Yoshida, *Tetrahedron Lett.* **1975**, *16*, 2289.
[59] T. Higuchi, S. Uzu, M. Hirobe, *J. Am. Chem. Soc.* **1990**, *112*, 7051.
[60] a) T. Higuchi, K. Shimada, N. Maruyama, M. Hirobe, *J. Am. Chem. Soc.* **1993**, *115*, 7551; b) Y. Urano, T. Higuchi, M. Hirobe, T. Nagano, *J. Am. Chem. Soc.* **1997**, *119*, 12008; c) T. Higuchi, M. Hirobe, *J. Mol. Catal. A* **1996**, *113*, 403.
[61] N. Suzuki, T. Higuchi, Y. Urano, K. Kikuchi, T. Uchida, M. Mukai, T. Kitagawa, T. Nagano, *J. Am. Chem. Soc.* **2000**, *122*, 12059.
[62] A. Franke, G. Stochel, N. Suzuki, T. Higuchi, K. Okuzono, R. van Eldik, *J. Am. Chem. Soc.* **2005**, *127*, 5360.
[63] D. Zheng, R. L. Birke, *J. Am. Chem. Soc.* **2002**, *124*, 9066.
[64] F. A. Walker, *J. Inorg. Biochem.* **2005**, *99*, 216.
[65] a) W.-D. Woggon, T. Leifels, L. Sbaragli, *Cytochromes P450: Biochemistry Biophysics and Drug Metabolism*, International Conference on Cytochromes P450, 13th, Prague, Czech Republic, June 29-July 3; b) D. N. Meyer, W.-D. Woggon, *Chimia* **2005**, *59*, 85; c) W.-D. Woggon, *Acc. Chem. Res.* **2005**, *38*, 127; d) S. Kozuch, T. Leifels, D. Meyer, L. Sbaragli, S. Shaik, W.-D. Woggon, *Synlett* **2005**, *4*, 675; e) L. Sbaragli, W.-D. Woggon, *Synthesis* **2005**, *9*, 1538; f) D. Meyer, T. Leifels, L. Sbaragli, W.-D. Woggon, *Biochem. Biophys. Res. Commun.* **2005**, *338*, 372.
[66] N. Hessenauer-Ilicheva, A. Franke, D. Meyer, W.-D. Woggon, R. van Eldik, manuscript in preparation.
[67] A. Franke, N. Hessenauer-Ilicheva, D. Meyer, G. Stochel, W.-D. Woggon, R. van Eldik, *J. Am. Chem. Soc.* **2006**, *128*, 13611.
[68] a) J. C. W. Chien, *J. Am. Chem. Soc.* **1969**, *91*, 2166; b) A. Ehrenberg, T. W. Szczepkowski, *Acta Chem. Scand.* **1960**, *14*, 1.
[69] a) A. J. Gow, B. P. Luchsinger, J. R. Pawloski, D. J. Singel, J. S. Stamler, *Proc. Natl. Acad. Sci. USA* **1999**, *96*, 9027; b) V. S. Sharma, R. A. Isaacson, M. E. John, M. R. Waterman, M. Chevion, *Biochemistry* **1983**, *22*, 3897; c) A. W. Addison, J. J. Stephanos, *Biochemistry* **1986**, *25*, 4104.
[70] M. Hoshino, M. Maeda, R. Konishi, H. Seki, P. C. Ford, *J. Am. Chem. Soc.* **1996**, *118*, 5702.
[71] a) D. Tran, B. W. Skelton, A. H. White, L. E. Laverman, P. C. Ford, *Inorg. Chem.* **1998**, *37*, 2505; b) K. M. Miranda, R. W. Nims, D. D. Thomas, M. G. Espay, D. Citrin, M. D. Bartberger, N. Paolocci, J. M. Fukuto, M. Feelisch, D. A. Wink, *J. Inorg. Biochem.* **2003**, *93*, 52; c) P. C. Ford, B. O. Fernandez, M. D. Lim, *Chem. Rev.* **2005**, *105*, 2439 and references cited therein; d) M. D. Lim, I. M. Lorkovic, P. C. Ford, *J. Inorg. Biochem.* **2005**, *99*, 151 and references cited therein.
[72] a) B. O. Fernandez, P. C. Ford, *J. Am. Chem. Soc.* **2003**, *125*, 10510; b) B. O. Fernandez, I. M. Lorkovic, P. C. Ford, *Inorg. Chem.* **2003**, *42*, 2; c) B. O. Fernandez, I. M. Lorkovic, P. C. Ford, *Inorg. Chem.* **2004**, *43*, 5393.
[73] J.-E. Jee, R. van Eldik, *Inorg. Chem.* **2006**, *45*, 6523.
[74] a) L. G. Rochelle, S. J. Morana, H. Kruszyna, M. A. Russell, D. E. Wilcox, R. P. Smith, *J. Pharmacol. Exp. Ther.* **1995**, *275*, 48; b) M. Brouwer, W. Chamulitrat, G. Ferruzi, D. L. Sauls, J. B. Weinberg, *Blood* **1996**, *88*, 1857; c) S. S. Greenberg, J. M. Xie, D. R. Kapusta, M. J. S. Miller, *J. Pharmacol. Exp. Ther.* **1995**, *273*, 257; d) D. Zheng, R. Birke, *J. Am. Chem. Soc.* **2001**, *123*, 4637; e) H. Kruszyna, J. S. Magyar, L. G. Rochelle, M. A. Russell, R. P. Smith, *J. Pharmacol. Exp. Ther.* **1998**, *285*, 665.
[75] M. Wolak, G. Stochel, M. Hamza, R. van Eldik, *Inorg. Chem.* **2000**, *39*, 2018.
[76] C. Selcuki, R. van Eldik, T. Clark, *Inorg. Chem.* **2004**, *43*, 2828.
[77] V. S. Sharma, R. B. Pilz, G. R. Boss, D. Madge, *Biochemistry* **2003**, *42*, 8900.
[78] M. Wolak, A. Zahl, T. Schneppensieper, G. Stochel, R. van Eldik, *J. Am. Chem. Soc.* **2001**, *123*, 9780.
[79] L. E. Laverman, *PhD Dissertation*, University of California Santa Barbara, USA, **1999**.
[80] F. Roncaroli, R. van Eldik, *J. Am. Chem. Soc.* **2006**, *128*, 8042.
[81] a) E. Fujita, J. Fajer, *J. Am. Chem. Soc.* **1983**, *105*, 6743; b) S. Kelly, D. Lancon, K. M. Kadish, *Inorg. Chem.* **1984**, *23*, 1451; c) E. Fujita, C. K. Chang, J. Fajer, *J. Am. Chem. Soc.* **1985**, *107*, 7665; d) K. M. Kadish, X. H. Mu, X. Q. Lin, *Inorg. Chem.* **1988**, *27*, 1489; e) X. H. Mu, K. M. Kadish, *Inorg. Chem.* **1990**, *29*, 1031; f) S. Cheng, Y. O. Su, *Inorg. Chem.* **1994**, *33*, 5847.
[82] a) J. Abwao-Konya, A. Cappelli, L. Jacobs, M. Krishnamurthy, M. Smith, *Transition Met. Chem.* **1984**, *9*, 270; b) K. R. Ashley, J. G. Leipoldt, *Inorg. Chem.* **1981**, *20*, 2326; c) K. R. Ashley, S. Au-Young, *Inorg. Chem.* **1976**, *15*, 1937; d) R. F. Pasternack, M. A. Cobb, N. Sutin, *Inorg. Chem.* **1975**, *14*, 866; e) R. F. Pasternack, M. A. Cobb, *J. Inorg. Nucl. Chem.* **1973**, *35*, 4327;


 © 2007 Wiley-VCH Verlag GmbH & Co. KGaA, Weinheim 

f) R. K. Ashley, M. Berggren, M. Cheng, *J. Am. Chem. Soc.* **1975**, *97*, 1422; g) R. F. Pasternack, G. R. Parr, *Inorg. Chem.* **1976**, *15*, 3087; h) J. G. Leipoldt, R. van Eldik, H. Kelm, *Inorg. Chem.* **1983**, *22*, 4146.
[83] F. Roncaroli, T. E. Shubina, T. Clark, R. van Eldik, *Inorg. Chem.* **2006**, *45*, 7869.
[84] a) M. S. A. Hamza, X. Zou, K. L. Brown, R. van Eldik, *Eur. J. Inorg. Chem.* **2003**, 268; b) M. S. A. Hamza, R. van Eldik, *Dalton Trans.* **2004**, 1.

Received: September 29, 2006
Published Online: February 2, 2007

 © 2007 Wiley-VCH Verlag GmbH & Co. KGaA, Weinheim 

DOI: 10.1002/ejic.200600946

# Factors Affecting the Interlayer Arrangement of Transition Metal–Ethylenediaminetetraacetate Complexes Intercalated in Mg/Al Layered Double Hydroxides

**Guoqing Wu,[a] Lianying Wang,*[a] Lan Yang,[a] and Junjiao Yang[a]**

**Keywords:** Layered compounds / Intercalation / Metal–edta complexes / Reorientation / Organic–inorganic hybrid composites

Transition metal (M)–ethylenediaminetetraacetate (edta) complexes {$[M(edta)]^{2-}$} have been intercalated in layered double hydroxides (LDHs) by a hydrothermal method using $MgAl–NO_3$ LDH as the precursor. The factors affecting the orientation of the incorporated $[M(edta)]^{2-}$ in the resulting well-ordered materials were investigated. Whilst varying the metal cation in the intercalated complex has no major influence on the orientation of the $[M(edta)]^{2-}$ (M = Co, Ni, Cu, Zn) anion in the interlayer galleries, there is a marked dependence on layer charge density. The observed basal spacings of 1.402–1.461 nm for $Mg_2Al$–M(edta) LDH and 1.254 nm for $Mg_3Al$–Zn(edta) LDH can be ascribed to bilayer and monolayer arrangements, respectively, of the $[M(edta)]^{2-}$ anion. When the Mg/Al ratio is varied in the range 2.2–2.7 the two guest arrangements coexist. The evolution of the interlayer arrangement of $[M(edta)]^{2-}$ in LDHs with increasing temperature was studied by variable-temperature in-situ XRD measurements, variable-temperature in-situ FT-IR, and combined thermogravimetric analysis and mass spectrometry (TGA-MS). In the case of $Mg_2Al$–M(edta) LDH, a metastable phase with a similar monolayer structure to that found in $Mg_3Al$–M(edta) LDH was detected by XRD in the range 140–300 °C. Cooling of the calcined solid to room temperature in air leads to the recovery of the original bilayer structure. The reversible nature of the structural transformation indicates that a reorientation of the guest $[M(edta)]^{2-}$ complex in the interlayer galleries occurs on heating, rather than a grafting process. Heat treatment of $Mg_3Al$–M(edta) LDH results only in a gradual contraction of the basal spacing associated with the loss of interlayer water without any reorientation of the guest $[M(edta)]^{2-}$ complex.

(© Wiley-VCH Verlag GmbH & Co. KGaA, 69451 Weinheim, Germany, 2007)

## Introduction

By virtue of their anion-exchange properties, layered double hydroxides (LDHs) have potential applications as catalysts or precursors to new catalytic materials, such as ion exchangers, adsorbents, or hosts for nanoscale reactions as well as in medicine.[1] LDHs can be represented by the general formula $[M^{II}_{1-x}M^{III}_{x}(OH)_2]^{x+}(A^{n-})_{x/n}\cdot yH_2O$. Their structure is based on the stacking of positively charged layers arising from the substitution of trivalent cations for part of the divalent cations in brucite-like layers, and exchangeable anions ($A^{n-}$) in hydrated interlayer galleries.

In recent years, great attention has been paid to the intercalation of metal complex anions in LDHs in an effort to develop new functional materials such as heterogeneous catalysts, photocatalytic materials, magnetic nanocomposites, and luminescent materials.[2–5] In particular, intercalation of metal–edta complexes into LDHs has been extensively studied due to the strong chelating ability of the edta ligand with almost any metal cation.[6–14] O'Hare et al.[6] have recently prepared LDHs containing such complexes, either directly by intercalation of the transition metal–edta complex or indirectly by forming the metal complex in situ in the interlayer galleries of Li–Al LDH pre-intercalated with edta. Tsyganok et al.[7] have studied the catalytic activity in dry reforming of methane of a material derived from LDH-intercalated $[Ni(edta)]^{2-}$ complexes. Lukashin et al.[3] have reported the magnetic properties of anisotropic metal nanoparticles prepared from an LDH containing an edta complex of $Fe^{III}$ or $Ni^{II}$. The synthesis and characterization of an $Mg_2Al$ LDH intercalated by luminescent $[Eu(edta)]^-$ complexes was recently reported.[8]

In general, the arrangement of interlayer guest anions can dramatically influence the physicochemical properties of LDH materials.[15–18] For example, in the case of poly(diacetylenecarboxylates) incorporated in LDHs, the possibility of having different arrangements of interlayer guests is responsible for the observed reversible thermal color changes.[18] In developing such functional materials it is important to be able to control the orientation of functional guest anions in the interlayer galleries in order to fully uti-

[a] State Key Laboratory of Chemical Resource Engineering, Beijing University of Chemical Technology,
Box 98, 15 Beisanhuan Dong Lu, Beijing 100029, China
Fax: +86-1064425385
E-mail: wangliany@mail.buct.edu.cn

 © 2007 Wiley-VCH Verlag GmbH & Co. KGaA, Weinheim InterScience 

lize their anisotropic properties. An understanding of the factors controlling the interlayer arrangement is important if tailored applications in areas such as those mentioned above are to be found for LDHs containing $[M(edta)]^{2-}$ complexes, but no such study has been reported to date.

In addition, thermal treatment is a key step in the synthesis of LDH-derived catalysts. Despite numerous investigations of the structural evolution of LDHs with temperature the process of thermal decomposition of LDHs, in particular the origin of thermally metastable intermediate phases, is still a matter of debate. The possible role of grafting simple or complex anions to the slabs in the formation of the thermally metastable phase has been extensively discussed. Whilst a grafting phenomenon at low temperature has been reported for LDHs with both oxygen-containing and non-oxygen-containing anions,[19–24] other authors have suggested that the thermally metastable phase originates from a reorientation of the anions in the interlayer domains rather than from such a grafting process.[25–30]

In this work, we report the intercalation of transition metal complexes $[ZnY]^{2-}$, $[NiY]^{2-}$, $[CoY]^{2-}$, and $[CuY]^{2-}$ (where Y denotes $edta^{4-}$) into MgAl LDHs with different Mg/Al ratios, by a hydrothermal synthesis method. Our aim is to clarify the factors affecting the orientation of the complexes, particularly in the temperature interval 30–400 °C, in order to understand the evolution of the interlayer phase with temperature. Structural changes arising from thermal treatment are monitored by variable-temperature in-situ XRD, variable-temperature in-situ FT-IR, and combined thermogravimetric analysis and mass spectrometry (TGA-MS). Such information should enable a better understanding of the LDH–M(edta) structure and provide a framework for the synthesis of new functional materials.

## Results and Discussion

Three methods for the intercalation of the $[MY]^{2-}$ complex in LDH materials, namely ion exchange, coprecipitation, and reconstruction, have been described in the literature. In order to obtain a pure LDH phase containing the $[MY]^{2-}$ complex, a large (tenfold) excess of the $[MY]^{2-}$ complex has typically been employed.[3,7] If the amount of $[MY]^{2-}$ complex is low it has been reported that the materials suffer from poor crystallinity and the coexistence of more than one phase, which makes it impossible to study their structures in detail.[8,31] In an attempt to overcome this problem we chose to employ a hydrothermal synthesis using only a twofold excess of the $[MY]^{2-}$ complex.

### Effect of Varying the Metal Cation in the Complex Anion on Interlayer Orientation

Chemical analysis (see Table 1) confirms both that the nitrate anions in the LDH-2.0-$NO_3$ precursor have been completely exchanged by anionic edta complexes and that there is no contamination by co-intercalated carbonate ions. The composition of the LDH-2.0-$NO_3$ precursor (where 2.0 refers to the $Mg^{2+}/Al^{3+}$ molar ratio in the synthesis mixture) and intercalated materials are given in Table 1. The Mg/Al molar ratio in LDH-2.0-[MY] (M = Zn, Ni, Co, Cu) is essentially the same as that in the LDH-2.0-$NO_3$ precursor (2.04), which excludes the possibility of partial dissolution of the magnesium in the layers during the hydrothermal synthesis.

The XRD patterns of the LDH-2.0-$NO_3$ precursor and its exchanged products (LDH-2.0-[MY]) are shown in Figure 1. The patterns are typical of lamellar materials, with a basal reflection and associated harmonics at low angles $2\theta$ and weaker nonbasal reflections at higher angles. Intercalation of $[MY]^{2-}$ leads to an increase in basal spacing for all the exchanged LDHs and the values of the basal spacing in LDH-2.0-[MY] (M = Zn, Cu, Co) are rather similar, whilst that for LDH-2.0-[NiY] is slightly lower (see Table 1). This is indicative of a similar orientation of the $[MY]^{2-}$ anions within the interlayer galleries. No change is observed in the value of the unit cell parameter *a*, calculated from the posi-

Table 1. Chemical composition, cell parameter *a*, and basal spacing *d*(003) for the LDH materials.

| Sample | Mg/Al | Chemical composition (found/calcd.) [wt-%] and proposed formula | *a* [nm] | *d*(003) [nm] |
|---|---|---|---|---|
| LDH-2.0-[$NO_3$] | 2.04 | Mg 18.58/18.51, Al 10.27/10.11, N 5.14/5.24, H 3.25/3.34<br>$[Mg_{0.68}Al_{0.33}(OH)_2](NO_3)_{0.33}\cdot 0.47H_2O$ | 0.303(0) | 0.867 |
| LDH-2.0-[ZnY] | 2.03 | Mg 12.45/12.50, Al 6.89/6.84, Zn 8.27/8.38, C 15.21/15.38, N 3.61/3.70, H 4.23/4.15<br>$[Mg_{0.67}Al_{0.33}(OH)_2][Zn(C_{10}H_{12}N_2O_8)]_{0.16}\cdot 0.71H_2O$ | 0.302(8) | 1.445 |
| LDH-2.0-[NiY] | 2.00 | Mg 12.52/12.57, Al 7.03/6.97, Ni 7.63/7.57, C 15.39/15.48, N 3.68/3.61, H 4.15/4.13<br>$[Mg_{0.67}Al_{0.33}(OH)_2][Ni(C_{10}H_{12}N_2O_8)]_{0.16}\cdot 0.65H_2O$ | 0.302(7) | 1.402 |
| LDH-2.0-[CuY] | 2.01 | Mg 12.38/12.25, Al 6.94/6.89, Cu 8.05/8.10, C 15.23/15.30, N 3.64/3.57, H 4.25/4.16<br>$[Mg_{0.66}Al_{0.33}(OH)_2][Cu(C_{10}H_{12}N_2O_8)]_{0.16}\cdot 0.70H_2O$ | 0.302(8) | 1.461 |
| LDH-2.0-[CoY] | 1.99 | Mg 12.41/12.29, Al 6.97/6.90, Co 7.50/7.53, C 15.18/15.30, N 3.67/3.58, H 4.31/4.21<br>$[Mg_{0.66}Al_{0.33}\ (OH)_2][Co(C_{10}H_{12}N_2O_8)]_{0.16}\cdot 0.73H_2O$ | 0.303(1) | 1.440 |
| LDH-2.2-[ZnY] | 2.19 | Mg 13.60/13.65, Al 6.96/6.90, Zn 8.02/8.09, C 14.91/14.84, N 3.52/3.46, H 4.05/3.99<br>$[Mg_{0.69}Al_{0.31}(OH)_2][Zn(C_{10}H_{12}N_2O_8)]_{0.15}\cdot 0.52H_2O$ | 0.303(2) | 1.401 |
| LDH-2.5-[ZnY] | 2.46 | Mg 14.70/14.66, Al 6.72/6.64, Zn 7.69/7.77, C 14.34/14.26, N 3.55/3.45, H 4.10/3.94<br>$[Mg_{0.72}Al_{0.29}(OH)_2][Zn(C_{10}H_{12}N_2O_8)]_{0.14}(NO_3)_{0.02}\cdot 0.48H_2O$ | 0.303(3) | 1.350 |
| LDH-2.7-[ZnY] | 2.72 | Mg 15.51/15.41, Al 6.43/6.41, Zn 6.94/6.90, C 12.58/12.66, N 3.40/3.32, H 4.01/4.06<br>$[Mg_{0.73}Al_{0.27}\ (OH)_2][Zn(C_{10}H_{12}N_2O_8)]_{0.12}(NO_3)_{0.03}\cdot 0.59H_2O$ | 0.303(5) | 1.299 |
| LDH-3.0-[ZnY] | 2.97 | Mg 16.50/16.48, Al 6.26/6.18, Zn 5.91/5.82, C 11.09/10.98, N 3.28/3.20, H 4.25/4.16<br>$[Mg_{0.75}Al_{0.25}(OH)_2][Zn(C_{10}H_{12}N_2O_8)]_{0.10}(NO_3)_{0.05}\cdot 0.67H_2O$ | 0.304(2) | 1.254 |

 © 2007 Wiley-VCH Verlag GmbH & Co. KGaA, Weinheim 

tion of the $d(110)$ reflection near $2\theta = 60°$, suggesting that the average cation–cation distance in the layers of LDH-2.0-[MY] remains unaffected (Table 1). This is consistent with the result from chemical analysis. An inversion of the relative intensities between the (006) and (009) reflections in the XRD pattern of LDH-2.0-[MY] is observed relative to those in the LDH-2.0-$NO_3$ precursor. This phenomenon has been ascribed to the presence of atoms with large scattering power in the interlayer region.[2,25] This will be discussed in detail below. The observation that the Mg/Al ratio in the layers is not affected by the incorporation of the edta complexes and that the orientation of the anions within the interlayer galleries is essentially independent of the identity of the metal M may be attributed to the similar coordination mode and high stability constants of the metal–edta complexes.[32,33]

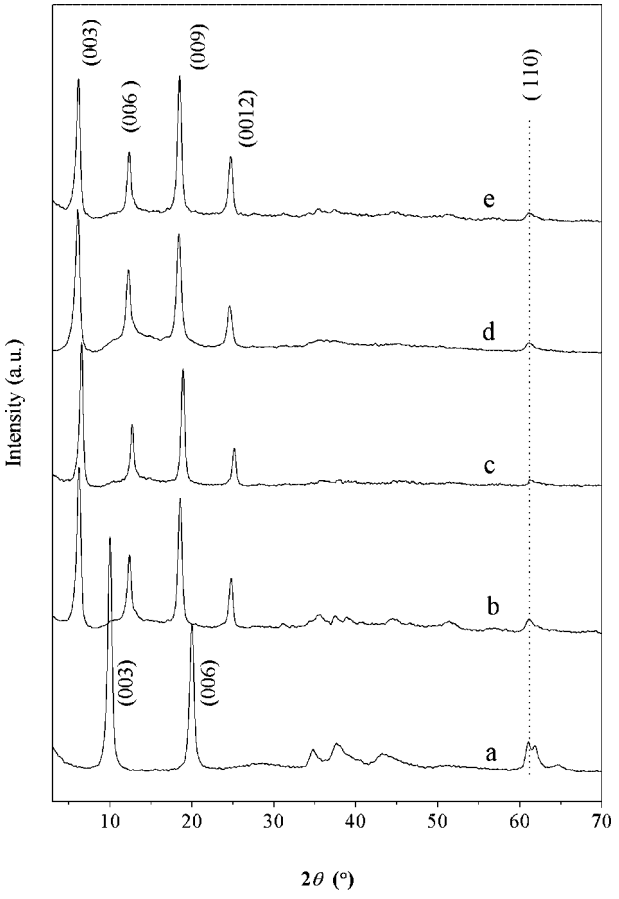


Figure 1. Powder XRD patterns of (a) LDH-2.0-$NO_3$, (b) LDH-2.0-[ZnY], (c) LDH-2.0-[NiY], (d) LDH-2.0-[CuY], and (e) LDH-2.0-[CoY].

The LDH materials were also characterized by FT-IR and selected spectra are shown in Figure 2. For the LDH nitrate precursor (Figure 2a), the intense and broad absorption band centered at 3445 $cm^{-1}$ corresponds to the stretching vibrations of the hydroxyl groups of both the layer hydroxide moieties and interlayer water molecules. The broadening of this band is due to hydrogen-bond formation.[34] The band close to 1640 $cm^{-1}$ corresponds to the deformation mode ($\delta H_2O$) of water molecules. The absorption peaks at 1384 and 839 $cm^{-1}$ are usually assigned to the $\nu_3$ and $\nu_2$ vibration modes, respectively, of $NO_3^-$ with $D_{3h}$ symmetry,[35] whilst bands around 447 and 675 $cm^{-1}$ are from Al–O and Mg–O lattice vibrations, respectively.[36]

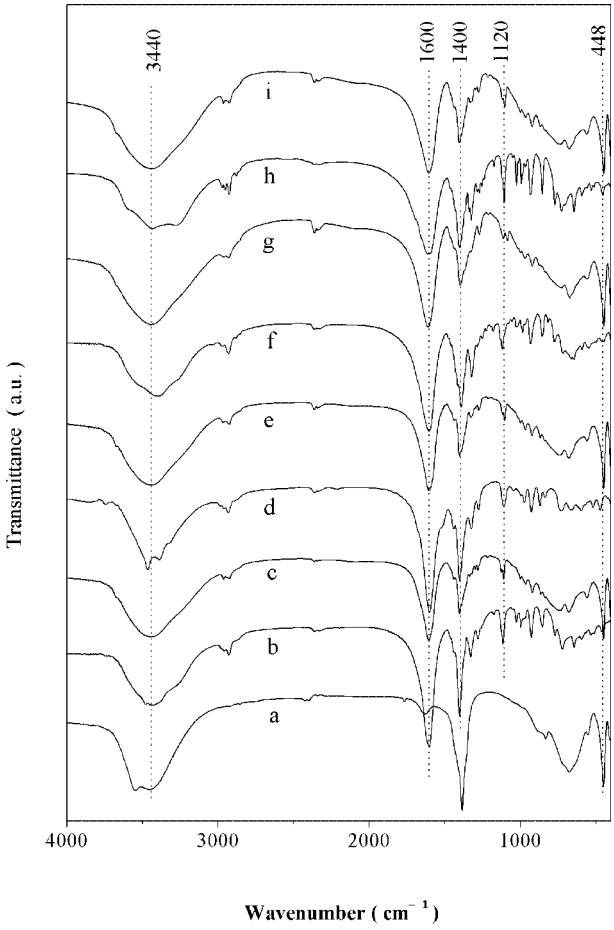


Figure 2. FT-IR spectra of (a) LDH–$NO_3$-2.0, (b) $Na_2$[ZnY], (c) LDH-2.0-[ZnY], (d) $Na_2$[NiY] (e) LDH-2.0-[NiY], (f) $Na_2$[CuY], (g) LDH-2.0-[CuY], (h) $Na_2$[CoY], and (i) LDH-2.0-[CoY].

After exchange of $Mg_2Al$–$NO_3$ LDH with $Na_2$[MY]·$3H_2O$ the $\nu_3$ vibration of $NO_3^-$ disappears, and the asymmetric $\nu_{as}$(COO) and symmetric $\nu_s$(COO) stretching modes of the carboxylate groups, at 1600 and 1400 $cm^{-1}$, respectively, appear (Figure 2c). The wavenumber difference $\Delta\nu = \nu_{as} - \nu_s$ gives information about the coordination environment of the carboxylate group.[37,38] The value of $\Delta\nu$ in both $Na_2$[MY]·$3H_2O$ and LDH-2.0-[MY] is greater than 200 $cm^{-1}$, indicating the presence of deprotonated carboxylate groups coordinated to the metal ion in a monodentate fashion.[37,38] Furthermore, the similar values of $\Delta\nu$ for LDH-2.0-[MY] and $Na_2$[MY]·$3H_2O$ suggest that the coordination mode of the carboxylate groups is unchanged after intercalation. The slight difference in the value of $\Delta\nu$ may be a reflection of the different intermolecular hydrogen-bonding environments experienced by the anion in the sodium salt and in the interlayer galleries of the LDH.[38–40] This result clearly confirms the presence of $[MY]^{2-}$ anions between the layers.

 © 2007 Wiley-VCH Verlag GmbH & Co. KGaA, Weinheim 

### Effect of Varying the Layer Charge Density on the Orientation of the Guest Anions

The layer charge density is often an important factor in determining the orientation of the guest anions in the interlayer galleries.[16,41] For further insight into the structure of the LDH-intercalated $[MY]^{2-}$ complexes samples of LDH-*X*-[ZnY] (with Mg/Al ratio in the synthesis mixture $X = 2.0$, 2.2, 2.5, 2.7, 3.0) were chosen. Elemental compositions of the resulting LDH-*X*-[ZnY] materials are given in Table 1. The Mg/Al molar ratios in LDH-*X*-[ZnY] are essentially the same as those in the corresponding LDH-*X*-$NO_3$ precursors (not shown in Table 1) which excludes the possibility of partial dissolution of the magnesium in the layers during the hydrothermal synthesis. Elemental analysis confirms that small amounts of $NO_3^-$ anion are co-intercalated with $[ZnY]^{2-}$ at high Mg/Al molar ratios, suggesting that intercalation of the bulky $[ZnY]^{2-}$ anion becomes less favorable as the layer-charge density decreases.[41,42]

The XRD results of LDH-*X*-[ZnY] (see Figure 3) show that there is not only a progressive decrease in the basal spacing for samples from 1.445 nm in LDH-2.0-[ZnY] (Figure 3a) to 1.254 nm in LDH-3.0-[ZnY] (Figure 3e) but also a significant variation in the relative intensities of the (00*l*) ($l$ = 3, 6, 9, 12) reflections with the Mg/Al mol ratio, suggesting different orientations of $[MY]^{2-}$ within the interlayer galleries. In general, when atoms with large scattering power are located at different positions along the *c* axis, the usual pattern of decreasing intensities of successive (00*l*) reflections with increasing *l* is not observed because of the fluctuations in the one-dimensional electron-density distribution along the *c* axis.[2,4,25,43–45] When the intensity of the (006) reflection is greater than that of (003), as is the case for LDH-3.0-[ZnY], it has been proposed that the heavy metal atom is located at the midpoint of the interlayer galleries.[2,4,25,44] In LDH-2.0-[ZnY], the intensity of the (009) reflection is greater than that of (006), suggesting that the alternate heavy metal centers are located above and below the midpoint of the interlayer galleries.[4,43,45]

When the Mg/Al molar ratio is increased to 2.2 no significant changes are observed (Figure 3b), suggesting there is only a single phase corresponding to a basal spacing of 1.445 nm. However, on further increasing the Mg/Al molar ratio, LDH-2.5-[ZnY] shows a complicated pattern of broad XRD reflections suggesting that two or more phases (Figure 3c), with different basal spacings, are present; the intensity of the third harmonic reflection (009) also decreases much more than that of the other (00*l*) reflections. These results indicate that some variation in the arrangement of the guest anions is associated with the decrease in layer-charge density. In the case of LDH-2.7-[ZnY] (see Figure 3d), the asymmetric (00*l*) reflections and the splitting of the (006) reflection are also consistent with the presence of at least two LDH phases. When the Mg/Al molar ratio is increased to 3.0, with the exception of a weak shoulder on the (006) reflection peak centered at $2\theta \approx 12°$, the reflections are characteristic of a single phase with a basal spacing of 1.254 nm. The elemental analysis results also

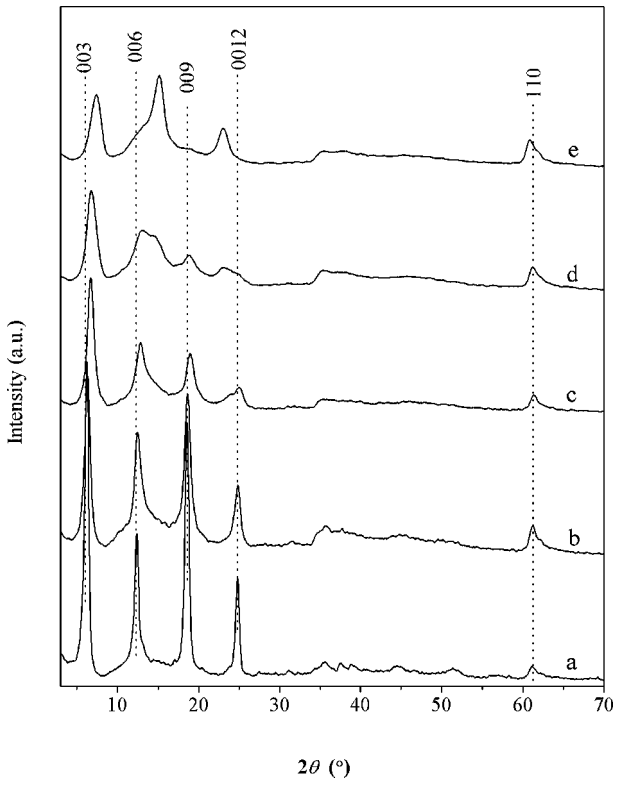


Figure 3. Powder XRD patterns of (a) LDH-2.0-[ZnY], (b) LDH-2.2-[ZnY], (c) LDH-2.5-[ZnY], (d) LDH-2.7-[ZnY], and (e) LDH-3.0-[ZnY].

show that LDH-3.0-[ZnY] in contrast to LDH-2.0-[ZnY] contains a significant amount of $NO_3^-$. This can perhaps also contribute to the asymmetric shape of the peaks in the XRD pattern of the former sample. The XRD data suggest that the phase LDH-2.0-[ZnY] involves the heavy metal centers located alternately above and below the midpoint of the interlayer galleries and the phase LDH-3.0-[ZnY] has the heavy metal centers located at the midpoint of the interlayer galleries. For intermediate Mg/Al molar ratios (2.2–2.7) the two LDH phases are both present; there is no evidence for a new phase with a third guest arrangement in LDH–[ZnY].

### Structural Model for LDH–MY

The observed basal spacings are 1.445 nm in LDH-2.0-[ZnY] and 1.254 nm in LDH-3.0-[ZnY], respectively. If the thickness of the LDH layer is taken as 0.48 nm,[46] the gallery heights are 0.97 nm and 0.77 nm, respectively. A gallery height of 0.97 nm is in close agreement with the maximal dimensions (0.90–1.00 nm) of the complex anion in salts such as $K_2[CuY]\cdot 3H_2O$, $Ca[NiY]\cdot 4H_2O$, and $Ca[Co(H_2O)Y]\cdot 4H_2O$ as determined by single-crystal XRD.[32,23] On this basis O'Hare et al.[6] proposed that the interlayer of $LiAl_2$–[MY] LDH consists of a monolayer of metal–edta complexes with the maximal dimension of each anion perpendicular to the hydroxide layers. This model, with the heavy

 © 2007 Wiley-VCH Verlag GmbH & Co. KGaA, Weinheim 

metal atom located at the midpoint of the interlayer galleries, is not consistent with the observed inversion of the relative intensities between the (006) and (009) reflections in the LDH-2.0-[MY]. However, this indicates that the heavy metal atom is located at sites alternately above and below the midpoint of the interlayer galleries in LDH-2.0-[MY], as discussed above.

A gallery height of 0.97 nm in LDH-2.0-[ZnY] is, however, almost twice as long as the minimal dimensions (0.5 nm) of the complex anion in the above salts.[32,33] Therefore it is reasonable to assume that the interlayer galleries consist of a condensed bilayer of guest species with the minimal dimension of each anion perpendicular to the brucite-like layers in the LDH-2.0-[ZnY], as shown schematically in Figure 4a. In this model the four carboxylate groups of individual anions all interact with the same hydroxide layer, maximizing the interaction with the layers through both electrostatic attractions with the positive charge and hydrogen bonding with the layer hydroxyl groups. The inversion of the relative intensities between the (006) and (009) reflections in the XRD pattern of LDH-2.0-[ZnY] is consistent with this model of a bilayer arrangement of $[ZnY]^{2-}$ guests. In the bilayer orientation, the corresponding cross-sectional area occupied by each anion in the *ab* plane is in the range 0.81–1.00 $nm^2$ (see Figure 4a). The area per unit charge of the host lattice with an Mg/Al ratio of 2.0, calculated from the crystallographic data, is 0.25 $nm^2$.[16,47] Since the guests are orientated in a bilayer (as shown in Figure 4a), the area available per two divalent anions is approximately 1.0 $nm^2$ ($4 \times 0.25$ $nm^2$). It follows that in a bilayer of $[ZnY]^{2-}$ anions, the host layer charge can be balanced, although relatively close packing of guest anions in the *c* axis direction is required.

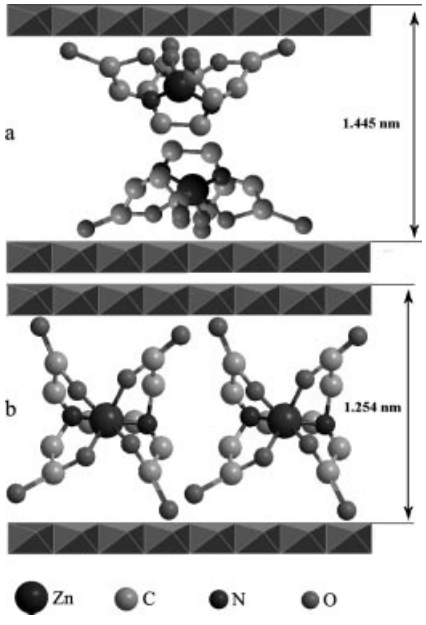


Figure 4. Schematic illustration of the structures of (a) LDH-2.0-[ZnY] and (b) LDH-3.0-[ZnY].

Taking into account the gallery height (0.77 nm) and the observed inversion of intensity between the first two (00*l*) peaks in LDH-3.0-[ZnY], we propose that in LDH-3.0-[ZnY] the metal–edta complexes form a monolayer of guest species with two carboxylate groups of individual anions attracted electrostatically to the upper hydroxide layer and the other two attracted to the lower one, as shown schematically in Figure 4b. This model also allows a favorable interaction between the four carboxylate groups of the guest and the host layers through both electrostatic attraction with the positively charged layers and hydrogen bonding with the layer hydroxyl groups. The height (0.77 nm) in LDH-3.0-[ZnY] probably arises from a monolayer assembly, with the maximal dimension of each anion tilted with respect to the hydroxide layers. Calculations show that the $[ZnY]^{2-}$ anion is capable of balancing the host layer charge of LDH-3.0-[ZnY] when arranged in a monolayer, since the cross-sectional area occupied by each anion in the *ab* plane is in the range 0.45–0.50 $nm^2$, whereas the area available per divalent anion is approximately 0.66 $nm^2$ ($2 \times 0.33$ $nm^2$).[16,47]

The above two guest arrangements maximize the interaction between the four carboxylate groups of the guest and the host layers and this is consistent with the absence of a new phase corresponding to a third guest arrangement at intermediate Mg/Al molar ratios. Other arrangements, such as two carboxylate groups of individual anions being fixed to upper and lower hydroxide layers and the other carboxylate groups extending into the interlayer galleries without any interaction with hydroxide layers, as proposed by O& apos;Hare et al., are less likely on energetic grounds.

The monolayer and bilayer orientation observed for the guest anions in the gallery have been reported in the literature.[4,43] Benzoate anions form bilayer-like structures[41] or monofilms of interdigitated species as found for methyl orange.[17] In all cases, the preferred orientation of the guest species is such as to permit the maximum interaction of the carboxylate groups with the layers through hydrogen bonding with the layer hydroxyl groups and, at the same time, the hydrophobic aromatic groups are located at the center of the galleries as far apart as possible from the hydrophilic layer hydroxyl groups.

### Reorientation of $[MY]^{2-}$ in the Interlayer Space under Thermal Treatment

The in situ variable-temperature powder X-ray diffraction patterns of LDH-2.0-[ZnY] and LDH-3.0-[ZnY] in the temperature range 30–900 °C in an ambient atmosphere are shown in Figures 5 and 6, respectively. The relationship between the *d*(003) basal spacings of LDH–[ZnY] and the temperature is shown in Figure 7. It can be observed that the basal reflections in both LDH-2.0-[ZnY] and LDH-3.0-[ZnY] move to a higher angle with increasing temperature indicating a contraction in the interlayer spacing. However, the magnitudes and evolution of the contraction observed on heating the two samples are very different (see Figure 7). A significant contraction in basal spacing (0.244 nm) is ob-

 © 2007 Wiley-VCH Verlag GmbH & Co. KGaA, Weinheim 

served for LDH-2.0-[ZnY] over a very small temperature range, between 110 and 140 °C, with the basal spacing remaining nearly constant before and after the transition. In contrast, LDH-3.0-[ZnY] shows only a gradual small contraction (0.082 nm) on heating from room temperature up to 150 °C, which can be associated with loss of water. TGA-MS (see below) indicates that similar amounts of water are released over the temperature range 30–150 °C for both LDH-2.0-[ZnY] and LDH-3.0-[ZnY], suggesting that the much larger contraction observed for the former cannot be ascribed to the loss of interlayer water alone. Above 140 °C the basal spacing of LDH-2.0-[ZnY] (1.201 nm) is similar to that of LDH-3.0-[ZnY] at room temperature (1.254 nm). This suggests that a reorientation of the $[MY]^{2-}$ anions in the interlayer galleries, probably induced by the loss of the interlayer water, is the real origin of the significant contraction in LDH-2.0-[ZnY].

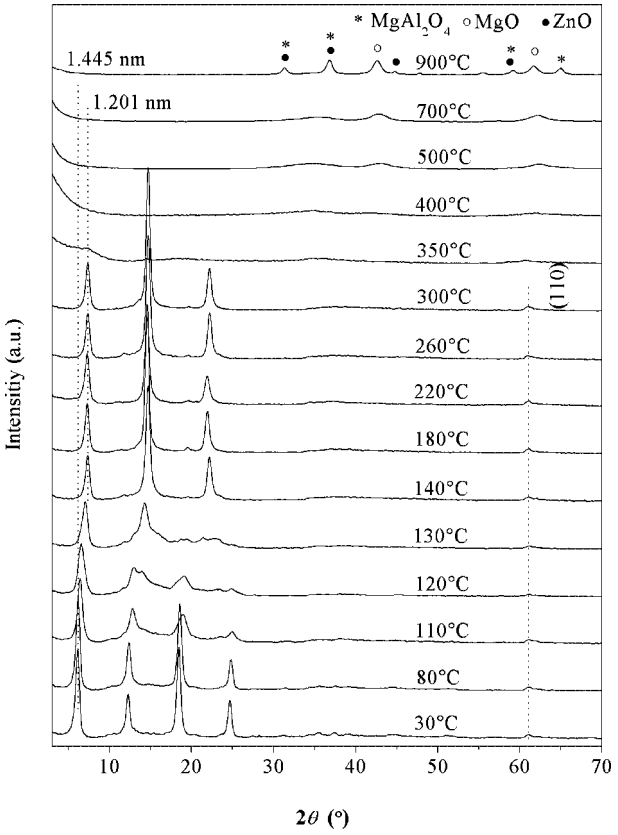


Figure 5. In-itu powder XRD patterns of LDH-2.0-[ZnY] over the temperature range 30–900 °C.

The occurrence of such a guest reorientation is confirmed by the significant variation in the relative intensities of the (00*l*) reflections in the XRD patterns of LDH-2.0-[ZnY] with increasing temperature. The inversion in intensity between the (006) peak and (009) peak in LDH-2.0-[ZnY] disappears on heating from 30 °C to 130 °C. Especially in the range 120–130 °C, the (00*l*) reflections broaden significantly and become asymmetric, which possibly corresponds to an unstable intermediate resulting from disorder in the arrangement of guests induced by loss of interlayer water from the hydrogen-bonded framework in the interlayer galleries. However, the intensity of the (006) reflections becomes significantly stronger between 140 and 300 °C and in addition a series of symmetric and strong (00*l*) reflections, with the pattern resembling that of LDH-3.0-[ZnY], emerge. Therefore it can be concluded that removal of interlayer water occurs upon heating, resulting in stronger electrostatic and hydrogen-bonding interactions between $[ZnY]^{2-}$ and LDH layer hydroxyl groups. This will

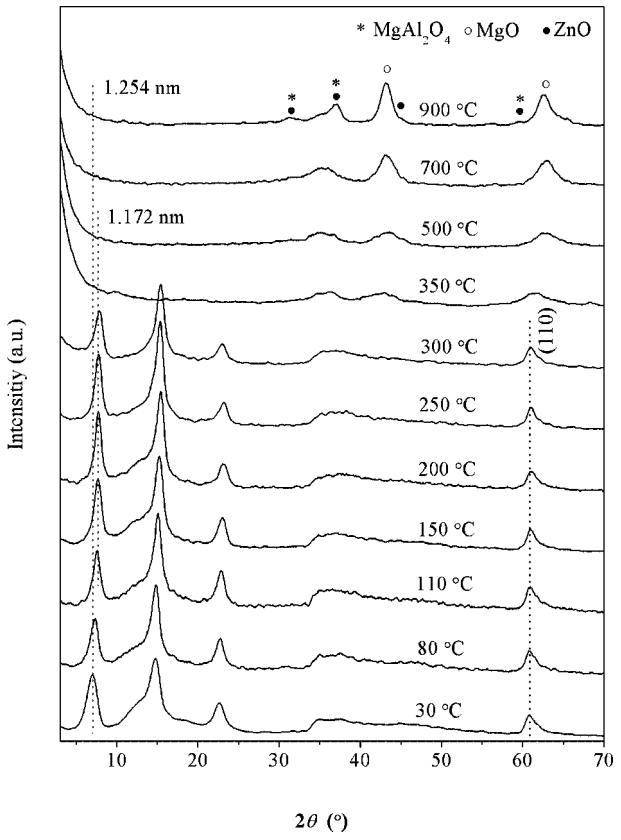


Figure 6. In-situ powder XRD patterns of LDH-3.0-[ZnY] over the temperature range 30–900 °C.

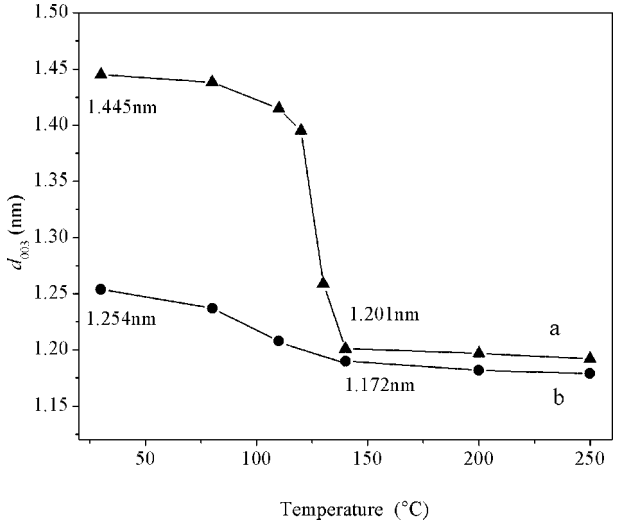


Figure 7. Relationship between *d*(003) basal spacing and temperature for (a) LDH-2.0-[ZnY] and (b) LDH-3.0-[ZnY].

 © 2007 Wiley-VCH Verlag GmbH & Co. KGaA, Weinheim 

cause the bilayer $[ZnY]^{2-}$ to adopt a thermodynamically more stable monolayer orientation. Pillar reorientation at 140 °C, therefore, appears to be responsible for the observed gallery contraction of 0.244 nm for the LDH-2.0-[ZnY]. In the case of LDH-3.0-[ZnY], the relative intensities of the (00*l*) reflections are almost unchanged with increasing temperature, confirming that the orientation of $[ZnY]^{2-}$ in the interlayer galleries of LDH-3.0-[ZnY] does not vary with temperature. In addition, a weak shoulder on the (006) reflection peak centered at $2\theta \approx 12°$ in the pattern for LDH-3.0-[ZnY] gradually disappears with increasing temperature, indicating that the small amount of bilayer phase initially present is completely converted into the monolayer form.

The monolayer structure in LDH–[ZnY] is retained on heating up to 300 °C. On further heating above 300 °C, however, the absence of (00*l*) diffraction peaks corresponding to an LDH phase indicates that the layer structure is completely destroyed. This is consistent with TGA-MS data (see below), which suggest that dehydroxylation of the brucite-like layers along with anion decomposition occurs above 300 °C. At 400 °C, reflections characteristic of a cubic MgO-like phase begin to appear and at 900 °C reflections from an $MgAl_2O_4$ spinel phase and MgO are present, as is generally observed for calcined MgAl LDHs.[48] In addition, peaks that can be assigned to ZnO (JCPDS Card 01-1136), resulting from the decomposition of $[ZnY]^{2-}$, can be observed.

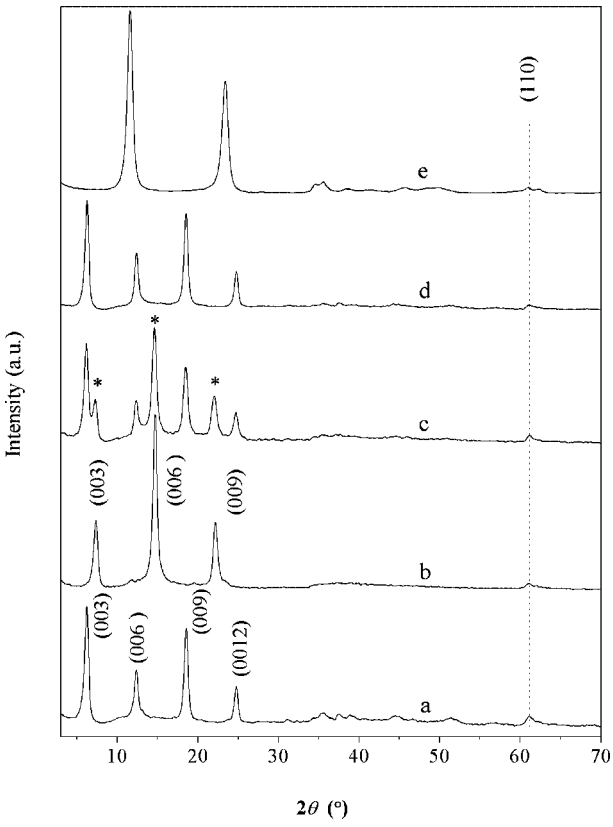


Figure 8. Powder XRD patterns of LDH-2.0-[ZnY] at (a) room temperature, (b) 140 °C, (c) room temperature (after cooling the sample from 140 °C in moist air for 20 min), (d) room temperature (after cooling the sample from 140 °C in moist air for 1 h), and (e) LDH–$CO_3$–[ZnY].

### A Reversible Structural Transformation

Although we have suggested above that the origin of the observed metastable phase is a reorientation of the $[MY]^{2-}$ anion in the interlayers, the possibility remains that it could be because of grafting of the anion to the hydroxyl layers as has been claimed by some authors for other anions in describing the formation of similar metastable phases associated with a significant interlayer contraction.[19–24] In order to provide further insight into the origin of the metastable phase, a sample of LDH-2.0-[ZnY] was heated to 140 °C and, after recording the powder XRD pattern at this temperature, subsequently cooled to room temperature over either 20 min or 1 h (in moist air), and the powder XRD patterns measured again (see Figure 8). The results show that the original phase and the metastable phase coexist when the sample is cooled in moist air for 20 min (Figure 8c), indicating that the structural transformation is reversible upon hydration. When the hydration reaction time is extended to 1 h the structural transformation is completely reversed as shown by the disappearance of peaks associated with the metastable phase (Figure 8d).

The recovery of the original phase on cooling demonstrates that heat treatment (up to 140 °C) does not result in covalent grafting of the anions to the hydroxyl layers. The absence of grafting is further confirmed by the observation that the $[MY]^{2-}$ anions in the metastable phase are readily exchanged with carbonate anions (Figure 8e). This would not be expected to be the case if the ions were actually grafted to the layers. The reversible structural transformation observed on heating and cooling is shown schematically in Figure 9.

To further study the evolution of the interlayer arrangement in this reversible transition the thermal behavior of LDH-2.0-[ZnY] was investigated by TGA, coupled with mass spectrometry. The TGA curves, as well as the analysis of the evolved decomposition products by mass spectrometry, are presented in Figure 10. Generally, four steps are observed in the thermal evolution of LDHs: desorption of physically adsorbed water, removal of the interlayer structural water, dehydroxylation of the brucite-like sheets, and the decomposition of the interlayer anions, although the first two steps may overlap in the low-temperature range. The thermal decomposition of LDH-2.0-[ZnY] is indeed characterized by three mass-loss steps. The first one from room temperature to 300 °C corresponds to the removal of surface adsorbed water and interlayer water molecules with their respective DTG peaks centered at 88 and 134 °C. The coupled mass spectrometry confirms this result since the ion current peak ($m/z$ = 18 $[H_2O^+]$) is assigned to the evolution of water. The temperature range of the loss of interlayer water is similar to that associated with the large contraction associated with guest reorientation (see Figure 5). This suggests that loss of water molecules may play an im-

 © 2007 Wiley-VCH Verlag GmbH & Co. KGaA, Weinheim 

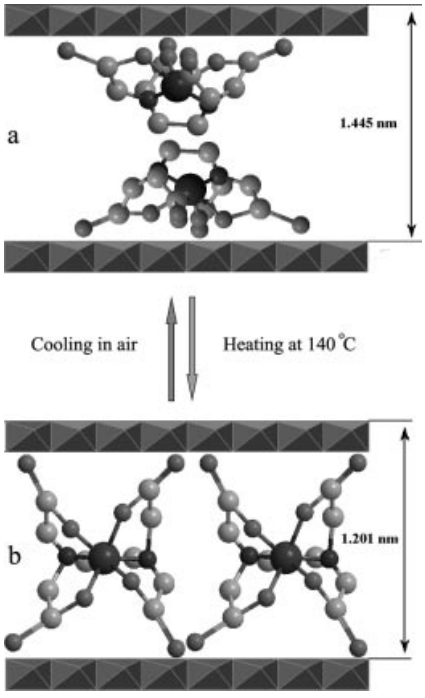


Figure 9. Schematic illustration of the reversible structural transformation of LDH-2.0-[ZnY] at (a) room temperature and (b) 140 °C.

portant role in initiating the reorientation. The sharp mass loss observed in the range 300–600 °C is due to the dehydroxylation of the brucite-like layers as well as combustion of the organic materials, with a corresponding sharp peak centered at 396 °C in the DTG curve (Figure 10a). This is confirmed by the mass spectrometry results (Figure 10b), which show strong $CO_2^+$, $NO^+$, and $H_2O^+$ ion currents over the entire decomposition range. The final gradual mass loss in the range 600–950 °C is a result of the oxidation of residual organic material as shown by the evolution of $CO_2$ alone in the MS trace. The thermal decomposition data is in good agreement with the in-situ HT-XRD data discussed above.

The in-situ FT-IR spectra of LDH-2.0-[ZnY] heated in the temperature range 30–550 °C are shown in Figure 11, and are also indicative of a reorientation taking place upon heating rather than a grafting process. On heating, the first change in the FT-IR spectra occurs between 30 and 150 °C. The band at 3444 $cm^{-1}$ moves to a higher frequency (3506 $cm^{-1}$) and its intensity decreases. This may be attributed to an increase in the force constant of the OH bond as a result of the loss of hydrogen bonding with interlayer

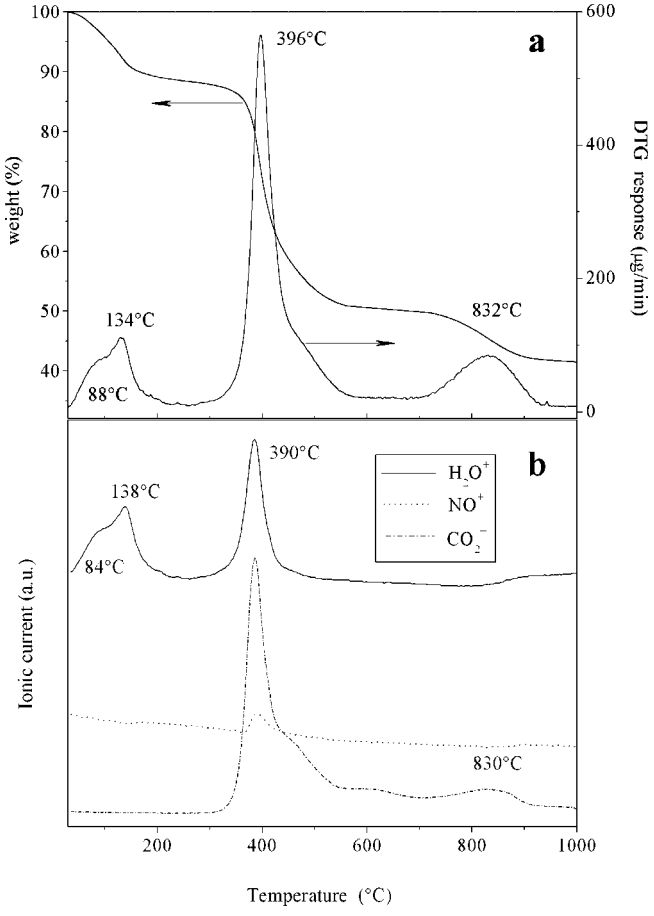


Figure 10. TGA curve (a) and coupled mass spectrometry trace (b) for LDH-2.0-[ZnY].

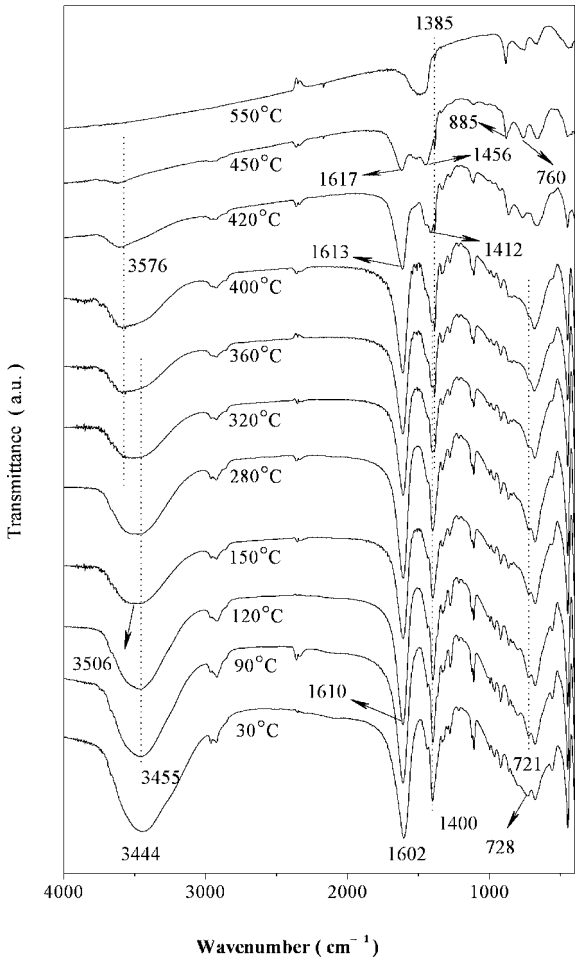


Figure 11. In-situ variable-temperature FT-IR spectra of LDH-2.0-[ZnY].

 © 2007 Wiley-VCH Verlag GmbH & Co. KGaA, Weinheim 

water. The asymmetric and symmetric stretching vibrations of the carboxylate group show slight shifts to higher frequency and lower frequency, respectively. As discussed above, the wavenumber difference $\Delta\nu = \nu_{as} - \nu_s$ gives information about the coordination environment of the carboxylate group. The value of $\Delta\nu$ shows only a marginal increase, from 202 $cm^{-1}$ at 30 °C to 210 $cm^{-1}$ at 150 °C, which suggests that the coordination environment of the carboxylate group remains nearly unaffected; this is consistent with the proposed reorientation of the $[ZnY]^{2-}$ anions on heating. If the carboxylate groups actually became covalently grafted to the hydroxyl layers a much more dramatic change in the value of $\Delta\nu$ would be expected.[23]

On heating from 320 to 550 °C there is a gradual decrease in the intensity of hydroxyl and carboxylate vibration bands, consistent with the dehydroxylation and decomposition processes observed by TGA-MS in this temperature range. The emergence of bands at 885 and 760 $cm^{-1}$ above 450 °C can be assigned to M–O vibrations in mixed oxide phases.

## Conclusions

Highly ordered MgAl LDHs intercalated by $[MY]^{2-}$ guest anions have successfully been prepared by a hydrothermal synthesis method. Charge matching between the $[MY]^{2-}$ anions and the LDH layers controls the gallery orientation of the $[MY]^{2-}$ anions. In the case of LDH-2.0-[MY], the interlayer separation for the fully hydrated material indicates that the guest species are arranged in a bilayer with the minimal dimension perpendicular to the host layers. In contrast, in LDH-3.0-[MY] the guest species are arranged in a monolayer with the maximal dimension tilted with respect to the host layers. Heating LDH-2.0-[MY] at 140 °C results in a reorientation of the $[MY]^{2-}$ complex in the interlayer giving a similar monolayer structure to that found in LDH-3.0-[MY]. The metastable monolayer phase is quite stable and the layered structure can still be identified by powder XRD after heat treatment at 300 °C. Rehydration of the calcined solids upon cooling to room temperature in air leads to the recovery of materials with the original values of the gallery heights. The reversible nature of the transformation is inconsistent with a grafting process and strongly supports a mechanism involving reorientation of the anion in the interlayer galleries. Calcination at 400 °C gives rise to a collapse of the layered structure and amorphous phases are formed. Further heat treatment of LDH-2.0-MY leads to a mixture of MgO, MO, and $MgAl_2O_4$ spinel phases above 750 °C.

## Experimental Section

### Synthesis

**Preparation of $Na_2[MY]\cdot xH_2O$:** The $Na_2[MY]\cdot xH_2O$ (M = Zn, Ni, Co, Cu; Y = $edta^{4-}$) complexes were prepared by mixing the appropriate molar equivalents of aqueous solutions of the corresponding metal nitrate, $Na_2C_{10}H_{14}N_2O_8\cdot 2H_2O$ ($Na_2H_2Y$), and $Na_2CO_3$, which is similar to the method described by Sawyer and Paulsen.[49] The resulting solution was adjusted to pH = 7.0 with dilute $HNO_3$ solution and warmed to boiling point. After concentration of the solution to one-third of the initial volume, absolute ethanol was added until a slight turbidity appeared. Finally, the solution was cooled in a refrigerator. The resulting crystalline material was filtered and recrystallized from a water/ethanol mixture. The recrystallized complexes were isolated by filtration and dried under air.

**Preparation of LDH–Nitrate Precursor:** MgAl–$NO_3$ LDH with different Mg/Al molar ratios (designated LDH-*X*-$NO_3$, where *X* = value of Mg/Al molar ratios in the mixed solution) were prepared by a coprecipitation method at controlled pH as described in the literature.[50] These preparations were carried out under constant nitrogen flow using freshly decarbonated, deionized water. Mixed solutions of $Mg(NO_3)_2$ and $Al(NO_3)_3$ with the required Mg/Al molar ratio, having total cation concentrations equal to 1 M, have been used at constant pH = 9.5. After precipitation, the suspension was aged at 100 °C for 8 h while stirring. The resulting white precipitate was collected by centrifugation, washed several times with carbonate-free deionized water, and dried in air at 50 °C for 24 h.

**Preparation of $[MY]^{2-}$-Intercalated MgAl LDH:** LDH-2.0-[MY] was obtained by anion exchange of the LDH-2.0-$NO_3$ precursors under hydrothermal conditions. As an example, the intercalation of the $[NiY]^{2-}$ anion into the LDH-2.0-$NO_3$ precursor is described. In the first step, a mixture of the LDH precursor (0.550 g, 0.002 mol) and $Na_2[NiY]\cdot 3H_2O$ (1.788 g, 0.004 mol) in a twofold molar excess over the anion exchange capacity was crushed in an agate mortar for 5 min and placed in an autoclave (22 $cm^3$) with distilled and decarbonated water (20 $cm^3$). The autoclave was then heated at 120 °C for 24 h developing an autogenous pressure. The powdered products were collected by centrifugation, washed three times with carbonate-free deionized water, and finally dried in air at 50 °C for 24 h. Other LDH-*X*-[ZnY] materials were obtained by the same procedure using the corresponding LDH-*X*-$NO_3$ precursors and $Na_2[ZnY]\cdot xH_2O$.

### Characterization

Elemental analyses for metals were performed by inductively coupled plasma (ICP) emission spectroscopy with a Shimadzu ICPS-7500 instrument using solutions prepared by dissolving the samples in dilute $HNO_3$. C, H, and N analyses were carried out using an Elementarvario elemental analysis instrument. The in-situ powder X-ray diffraction (in-situ XRD) data were recorded with a Shimadzu XRD-6000 powder diffractometer over the temperature range 30–900 °C in air, using Cu-$K_\alpha$ radiation ($\lambda$ = 0.154 nm) at 40 kV and 30 mA. The samples, as unoriented powders, were step-scanned in steps of 5°/min in the $2\theta$ range from 3 to 70° using a count time of 4 s per step. The rate of temperature increase was 10 °C/min with a holding time of 5 min before each measurement. The in situ Fourier transform infrared (in-situ FT-IR) spectra were recorded with a Nicolet 605XB FT-IR spectrometer in the range 4000–400 $cm^{-1}$ with 4 $cm^{-1}$ resolution under flowing $N_2$ (65 $cm^3$/min) with a heating rate of 5 °C/min in the range 25–450 °C. The KBr pellet technique, with a typical pellet containing ca. 1 wt% sample in KBr, was employed. Thermogravimetric analysis coupled to mass spectrometry was performed using a Perkin–Elmer Diamond TG apparatus linked to a ThermoStar mass spectrometer by a quartz capillary transfer line heated at 190 °C. The heating rate was 10 °C/min with an $N_2$ flow rate of 200 $cm^3$/min. The TG apparatus was at atmospheric pressure, and the mass spectrometer at a working pressure of $6\times10^{-6}$ Torr. The mass of sample used was 10 mg in each case.

 © 2007 Wiley-VCH Verlag GmbH & Co. KGaA, Weinheim 

## Acknowledgments

We are grateful to the National Natural Science Foundation of China (Grant No. 20401002) and to the National Natural Science Foundation Major International Joint Research Program (Project No. 20620130108).

[1] *Layered Double Hydroxides: Present and Future* (Ed.: V. Rives), Nova Science Publishers Inc., New York, **2001**. pp. 251–431.
[2] P. Beaudot, M. E. De Roy, J. P. Besse, *Chem. Mater.* **2004**, *16*, 935–945.
[3] A. V. Lukashin, A. A. Vertegel, A. A. Eliseev, M. P. Nikiforov, P. Gornert, Y. D. Tretyakov, *J. Nanopart. Res.* **2003**, *5*, 455–464.
[4] S. Gago, M. Pillinger, R. A. Sá Ferreira, L. D. Carlos, T. M. Santos, I. S. Gonçalves, *Chem. Mater.* **2005**, *17*, 5803–5809.
[5] V. Rives, M. A. Ulibarri, *Coord. Chem. Rev.* **1999**, *181*, 61–115.
[6] K. A. Tarasov, D. O'Hare, V. P. Isupov, *Inorg. Chem.* **2003**, *42*, 1919–1927.
[7] A. I. Tsyganok, T. Tsunoda, S. Hamakawa, K. Suzuki, K. Takehira, T. Hayakawa, *J. Catal.* **2003**, *213*, 191–203.
[8] C. Li, G. Wang, D. G. Evans, X. Duan, *J. Solid State Chem.* **2004**, *177*, 4569–4575.
[9] A. I. Tsyganok, M. Inaba, T. Tsunoda, S. Hamakawa, K. Suzuki, T. Hayakawa, *Catal. Commun.* **2003**, *4*, 493–498.
[10] A. I. Tsyganok, K. Suzuki, S. Hamakawa, K. Takehira, T. Hayakawa, *Catal. Lett.* **2001**, *77*, 75–86.
[11] K. A. Tarasov, V. P. Isupov, B. B. Bokhonov, Y. A. Gaponov, B. P. Tolochko, M. R. Sharafutdinov, S. S. Shatskaya, *J. Mater. Synth. Process.* **2000**, *8*, 21–27.
[12] V. P. Isupov, R. P. Mitrofanova, L. E. Chupakhina, E. V. Starikova, K. A. Tarasov, M. M. Yulikov, *J. Struct. Chem.* **2005**, *46* (suppl.), S165–S170.
[13] E. V. Starikova, V. P. Isupov, K. A. Tarasov, L. E. Chupakhina, M. M. Yulikov, *J. Struct. Chem.* **2004**, *45* (suppl.), S115–S120.
[14] M. R. Perez, I. Pavlovic, C. Barriga, J. Cornejo, M. C. Hermosin, M. A. Ulibari, *Appl. Clay Sci.* **2006**, *32*, 245–251.
[15] L. Ukrainczyk, M. Chibwe, T. J. Pinnavaia, S. A. Boyd, *J. Phys. Chem.* **1994**, *98*, 2668–2676.
[16] N. Iyi, K. Kurashima, T. Fujita, *Chem. Mater.* **2002**, *14*, 583–589.
[17] U. Costantino, N. Coletti, M. Nocchetti, G. G. Aloisi, F. Elisei, *Langmuir* **1999**, *15*, 4454–4460.
[18] T. Itoh, T. Shichi, T. Yui, H. Takahashi, Y. Inui, K. Takagi, *J. Phys. Chem. B* **2005**, *109*, 3199–3206.
[19] C. Vaysse, L. Guerlou-Demourgues, C. Delmas, *Inorg. Chem.* **2002**, *41*, 6905–6913.
[20] F. Malherbe, J. P. Besse, *J. Solid State Chem.* **2000**, *155*, 332–341.
[21] M. Del Arco, D. Carriazo, S. Gutiérrez, C. Martín, V. Rives, *Inorg. Chem.* **2004**, *43*, 375–384.
[22] C. Vaysse, L. Guerlou-Demourgues, A. Demourgues, C. Delmas, *J. Solid State Chem.* **2002**, *167*, 59–72.
[23] V. Prévot, C. Forano, J. P. Besse, *Appl. Clay Sci.* **2001**, *18*, 3–15.
[24] L. Vieille, I. Rousselot, F. Leroux, J. P. Besse, C. Taviot-Guého, *Chem. Mater.* **2003**, *15*, 4361–4368.
[25] T. Hibino, A. Tsunashima, *Chem. Mater.* **1997**, *9*, 2082–2089.
[26] D. Carriazo, C. Domingo, C. Martín, V. Rives, *Inorg. Chem.* **2006**, *45*, 1243–1251.
[27] S. Gago, M. Pillinger, T. M. Santos, J. Rocha, I. S. Gonçalves, *Eur. J. Inorg. Chem.* **2004**, 1389–1395.
[28] J. J. Bravo-Suárez, E. A. Páez-Mozo, S. T. Oyama, *Chem. Mater.* **2004**, *16*, 1214–1225.
[29] S. K. Yun, T. J. Pinnavaia, *Inorg. Chem.* **1996**, *35*, 6853–6860.
[30] V. Prévot, C. Forano, J. P. Besse, *Inorg. Chem.* **1998**, *37*, 4293–4301.
[31] A. Tsyganok, A. Sayari, *J. Solid State Chem.* **2006**, *179*, 1830–1841.
[32] M. A. Porai-Koshits, T. N. Polynova, *Koord. Khim.* **1984**, *10*, 725–772.
[33] H. A. Weakliem, J. L. Hoard, *J. Am. Chem. Soc.* **1959**, *81*, 549–555.
[34] F. M. Labajos, V. Rives, M. A. Ulibarri, *J. Mater. Sci.* **1992**, *27*, 1546–1552.
[35] Z. P. Xu, H. C. Zeng, *J. Phys. Chem. B* **2001**, *105*, 1743–1749.
[36] V. Rives, in: *Layered Double Hydroxides: Present and Future* (Ed.: V. Rives), Nova Science Publishers Inc., New York, **2001**, pp. 139–192.
[37] K. Nakamoto, *Infrared and Raman Spectra of Inorganic and Coordination Compounds*, 4th ed., Wiley, New York, **1986**, pp. 231–248.
[38] G. B. Deacon, R. J. Phillips, *Coord. Chem. Rev.* **1980**, *33*, 227–250.
[39] N. Gutmann, B. Müller, H. J. Tiller, *J. Solid State Chem.* **1995**, *119*, 331–338.
[40] Y. Tomita, K. Ueno, *Bull. Chem. Soc. Jpn.* **1963**, *36*, 1069–1073.
[41] F. Kooli, I. C. Chisem, M. Vucelic, W. Jones, *Chem. Mater.* **1996**, *8*, 1969–1977.
[42] M. Kaneyoshi, W. Jones, *J. Mater. Chem.* **1999**, *9*, 805–811.
[43] S. Bonnet, C. Forano, A. De Roy, J. P. Besse, *Chem. Mater.* **1996**, *8*, 1962–1968.
[44] M. Del Arco, S. Gutiérrez, C. Martín, V. Rives, *Inorg. Chem.* **2003**, *42*, 4232–4240.
[45] G. Q. Wu, L. Y. Wang, D. G. Evans, X. Duan, *Eur. J. Inorg. Chem.* **2006**, 3185–3196.
[46] Q. Yuan, M. Wei, D. G. Evans, X. Duan, *J. Phys. Chem. B* **2004**, *108*, 12381–12387.
[47] R. Allmann, *Acta Crystallogr., Sect. B* **1968**, *24*, 972–977.
[48] B. Rebours, J. B. d'Espinose de la Caillerie, O. Clause, *J. Am. Chem. Soc.* **1994**, *116*, 1707–1717.
[49] D. T. Sawyer, P. J. Paulsen, *J. Am. Chem. Soc.* **1959**, *81*, 816–820.
[50] S. Miyata, *Clays Clay Miner.* **1975**, *23*, 369–375.

Received: October 6, 2006
Published Online: January 4, 2007

 © 2007 Wiley-VCH Verlag GmbH & Co. KGaA, Weinheim 

DOI: 10.1002/ejic.200600902

# Synthesis, Crystal Structures, and Oxidation States of MM′X-Type Platinum–Rhodium Dinuclear Complexes Having Amidate Bridging Ligands

**Kazuhiro Uemura,[a][‡] Kana Yamasaki,[a] Kôichi Fukui,[a][‡‡] and Kazuko Matsumoto*[a][‡‡‡]**

**Keywords:** Platinum / Rhodium / 1D Chains / Dinuclear complexes

Six novel Pt–Rh dinuclear complexes (**1**–**6**), $[PtRh(PVM)_2(NH_3)_2Cl_3]\cdot 4H_2O$ (**1**, PVM = *t*BuCONH$^-$), $[PtRh(PVM)_2(en)Cl_3]\cdot 3H_2O$ (**2**, en = ethylenediamine), $[PtRh(PVM)_2(NH_2CH_3)_2Cl_3]\cdot 3H_2O$ (**3**), $[PtRh(PVM)_2(NH_2tBu)_2Cl_3]\cdot 3H_2O$ (**4**), $[PtRh(TCM)_2(NH_3)_2Cl_3]$ (**5**, TCM = $Cl_3CCONH^-$), and $[PtRh(BZM)_2(NH_3)_2Cl_3]\cdot H_2O$ (**6**, BZM = PhCONH$^-$), have been synthesized from Pt mononuclear complexes having nitrogen-coordinated amidate ligands with noncoordinated amidate oxygen atoms. X-ray analysis revealed that compounds **1** and **2** form zigzag one-dimensional chains in the form $[–Pt–Rh–Cl–]_n$. The oxidation states of the metal ions have been determined by X-ray photoelectron spectroscopy (XPS) and $^{195}$Pt NMR spectroscopic analysis, and are Pt(+2, $d^8$)···Rh(+3, $d^6$). In comparison with the Pt–Rh distances found in the literature, it has become apparent that the Pt–Rh dinuclear complexes have a dative Pt($d^8$)→Rh($d^6$) bond, where the Pt $d_{z^2}$ orbital is stabilized by the overlap with the $d_{z^2}$ orbital of the Rh atom.
(© Wiley-VCH Verlag GmbH & Co. KGaA, 69451 Weinheim, Germany, 2007)

## Introduction

One-dimensional (1D) metal complexes have been one of the intriguing subjects for the last several decades owing to their unusual electrical properties that are based on a variety of possible metal oxidation states.[1] Most of the 1D chains are made up of Rh(+1/+2) and/or Pt(+2/+3) because partial oxidation or reduction of the $d_{z^2}$ orbital attributed to the $d^8 \leftrightarrow d^7$ redox change affords partially filled valence bands. Several 1D metal complexes comprising infinite –Pt–Pt– bonds[2] or –Rh–Rh– bonds[3] and halogen-bridged Pt (MX and MMX) chains[4,5] have been synthesized and investigated to present. MMX chains have mixed-valence states of the dinuclear units and adopt a variety of electronic structures represented by the four extreme valence-ordering states.[4] Control of the electronic structures by tailoring the ligands with subtle chemical modifications has been attempted with MMX chains.[4] However, control of the electronic structures by introduction of another metal (M′) to the MMX chains to make so-called MM′X chains has not been reported, to the best of our knowledge (Scheme 1). A series of MM′X chains is considered to be a new class of 1D metal complexes and is expected to have interesting electrical properties.

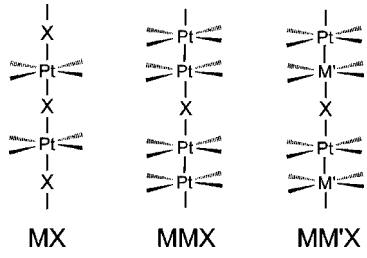


Scheme 1.

On the basis of the background above, we have tried to synthesize MM′X chains by starting with Pt mononuclear complexes with amidate ligands such as $[Pt(PVM)_2(NH_3)_2]\cdot 2H_2O$ (PVM = *t*BuCONH$^-$),[6] which can easily bind a second metal ion with the noncoordinated oxygen atoms in the amide moieties and afford various dinuclear and trinuclear Pt complexes (Scheme 2).[7] When M′ is one of the first transition metals (e.g. Co, Ni, Cu), trinuclear Pt–M′–Pt complexes are obtained because of their thermal stabilities and the ease of substitution of the ligands, even if the mixing ratio is 1:1 (Pt:M′).[6] Considering the undesired trimerization and the necessity of mixed valency for 1D chains, we selected Rh atoms as M′. Herein, we show the synthesis, crystallographic characterization, and determination of the formal metal oxidation states in Cl$^-$ ion bridged Pt–Rh dinuclear complexes.

[a] Department of Chemistry, Graduate School of Science and Engineering, Waseda University,
3-4-1, Ohkubo, Shinjuku, Tokyo 169-8555, Japan
Fax: +81-3-3413-5352
E-mail: kmatsu@yf6.so-net.ne.jp
[‡] Current address: Environmental Science and Engineering, Graduate School of Science and Engineering, Yamaguchi University,
Tokiwadai 2-16-1, Ube-shi, Yamaguchi, 755-8611, Japan
[‡‡] Current address: Graduate School of Life Science and Systems Engineering, Kyushu Institute of Technology,
Hibikino 2-4, Wakamatsu-ku, Kitakyushu 808-0196, Japan
[‡‡‡] Current address: 3-9-12-105, Daizawa,
Setagaya-ku, Tokyo 155-0032, Japan
Supporting information for this article is available on the WWW under http://www.eurjic.org or from the author.

 © 2007 Wiley-VCH Verlag GmbH & Co. KGaA, Weinheim 

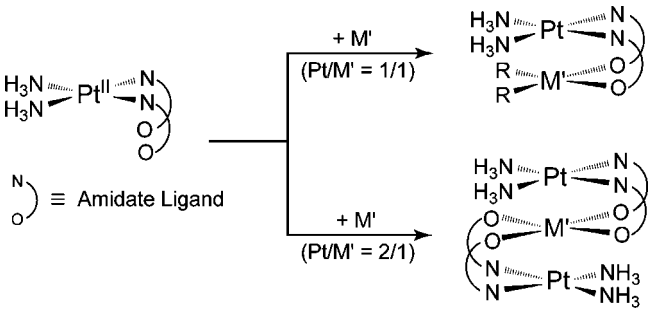


Scheme 2.

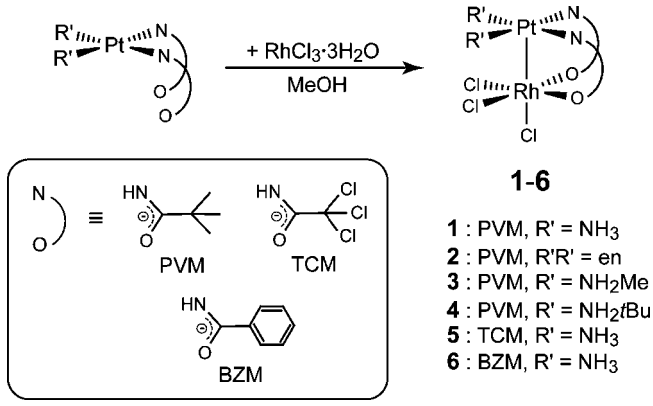


Scheme 3.

## Results and Discussion

### Synthesis and Characterization

Mixing of $[Pt(PVM)_2(NH_3)_2]\cdot 2H_2O$[6] with $RhCl_3\cdot 3H_2O$ in MeOH provided a dinuclear Pt–Rh complex, $[PtRh(PVM)_2(NH_3)_2Cl_3]\cdot 4H_2O$ (**1**) (Scheme 3). The reaction was stoichiometrically complete within 3 d at 40 °C, where the solution color changed from dark red to dark brown. The dark brown MeOH solution was concentrated, and then excess KCl in $H_2O$ was added to yield the pure product, which was confirmed by $^1H$ NMR spectroscopic analysis. The $^1H$ NMR spectra of **1** shows a single peak at $\delta$ = 1.19 ppm for the *t*Bu moieties,[8] which is apparently shifted from the peak at $\delta$ = 1.10 ppm for the *t*Bu moieties in $[Pt(PVM)_2(NH_3)_2]\cdot 2H_2O$.[6a] Figure 1a shows the ESI-MS (positive) spectra of **1** by dilution in MeOH. The peak at *m*/*z* = 1241, attributed to the dinuclear complex, was observed and the simulated isotope pattern based on the dinuclear complex apparently coincides with the observed one.

Other Pt–Rh dinuclear complexes with various amidates (TCM = $Cl_3CCONH^-$, BZM = $PhCONH^-$) and coligands, $[PtRh(PVM)_2(en)Cl_3]\cdot 3H_2O$ (**2**), $[PtRh(PVM)_2(NH_2CH_3)_2Cl_3]\cdot 3H_2O$ (**3**), $[PtRh(PVM)_2(NH_2tBu)_2Cl_3]\cdot 3H_2O$ (**4**), $[PtRh(TCM)_2(NH_3)_2Cl_3]$ (**5**), and $[PtRh(BZM)_2(NH_3)_2Cl_3]\cdot H_2O$ (**6**), were also obtained in a similar manner from the Pt mononuclear complexes having the noncoordinated oxygen atoms in the amide moieties; *cis*-$[Pt(PVM)_2(en)]\cdot 4H_2O$, *cis*-$[Pt(PVM)_2(NH_2CH_3)_2]\cdot H_2O$, *cis*-$[Pt(PVM)_2(NH_2tBu)_2]$, *cis*-$[Pt(TCM)_2(NH_3)_2]$, and *cis*-$[Pt(BZM)_2(NH_3)_2]$.[9] As shown in Figure 1, the ESI-MS peaks attributed to each dinuclear complex (**2**–**6**) were observed.

### Crystal Structure of $[PtRh(PVM)_2(NH_3)_2Cl_3]\cdot 4H_2O$ (1)

Figure 2 shows the crystal structure of **1**, and Table 1 summarizes the selected bond lengths and angles for **1**. The single-crystal consists of Pt and Rh dinuclear complexes in which the two metal ions are doubly bridged by two PVM

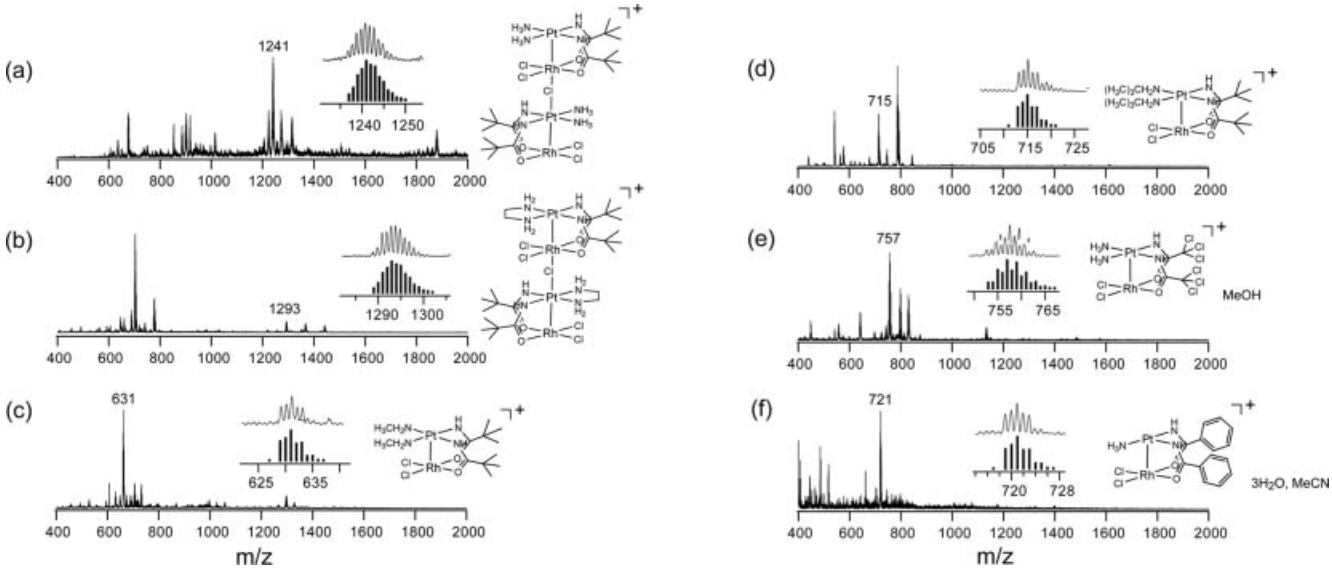


Figure 1. ESI-MS (positive) spectra for (a) **1**, (b) **2**, (c) **3**, (d) **4**, (e) **5**, and (f) **6**. Complexes **1**–**5** and **6** were measured by dilution in MeOH and MeOH/MeCN (v/v = 1:1), respectively.

 © 2007 Wiley-VCH Verlag GmbH & Co. KGaA, Weinheim 

ligands (Figure 2a). The asymmetric unit consists of Pt(1), Rh(1), Cl(1–3), one amine [N(1)], and one PVM [including O(1), O(2), N(2), and C(1)] ligand, with a crystallographic mirror along the *ab* plane [along the Pt(1)–Rh(1)–Cl(1) line]. The *cis* coordinated Cl(2)/Cl(3) and O(1)/O(2) atoms are in a disordered relationship with the 0.50/0.50 occupancy level, which means that two kinds of Rh(1) coordination planes, O(2)–O(1′)–Cl(2′)–Cl(3) and O(1)–O(2′)–Cl(3′)–Cl(2), are present in the crystal with a 50:50 ratio.

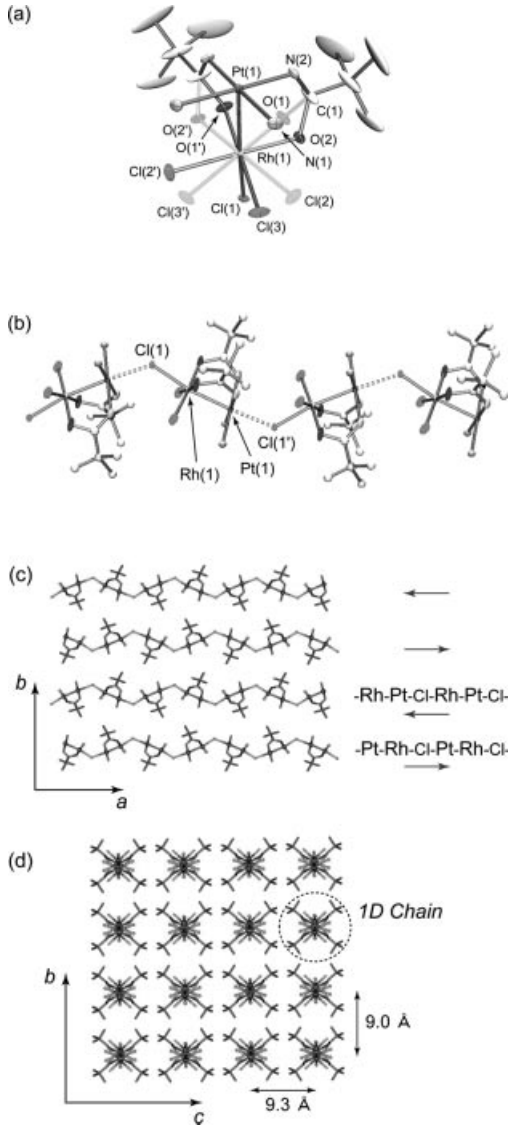


Figure 2. Crystal structure of $[PtRh(PVM)_2(NH_3)_2Cl_3]\cdot 4H_2O$ (**1**). (a) ORTEP drawing of **1** at the 30% probability level. Hydrogen atoms and water molecules are omitted for clarity. O(1) and O(2), and Cl(2) and Cl(3) atoms are in a disordered relationship. (b) Pseudo 1D chain where axially coordinated Cl(1) atoms bridge the dinuclear complexes. (c) Four pseudo 1D chains are aligned in parallel. Arrows indicate the chain directions. (d) Crystal packing diagram along the *a* axis. Water molecules are omitted for clarity.

Within the dimer, the Pt and Rh atoms are separated by 2.5704(7) Å (**1**). The Pt atom is *cis* coordinated with two amine ligands and two deprotonated nitrogen atoms of the PVM ligands. The Rh atom is coordinated by three $Cl^-$ ions, two *cis* in the equatorial plane and one axially coordinated to Rh with the distances Rh(1)–Cl(1) = 2.4127(18), Rh(1)–Cl(2) = 2.333(3), and Rh(1)–Cl(3) = 2.329(3) Å. The coordination planes of the two metals are slightly tilted by 11.9°.

Table 1. Selected distances [Å] and angles [°] for $[PtRh(PVM)_2(NH_3)_2Cl_3]\cdot 4H_2O$ (**1**).[a]

| | | | |
|---|---|---|---|
| Bond lengths | | | |
| Pt(1)–Rh(1) | 2.5704(7) | Pt(1)–Cl(1)[1] | 2.6328(17) |
| Pt(1)–N(1) | 2.078(5) | Pt(1)–N(2) | 1.995(5) |
| Rh(1)–Cl(1) | 2.4127(18) | Rh(1)–Cl(2) | 2.333(3) |
| Rh(1)–Cl(3) | 2.329(3) | Rh(1)–O(1) | 2.039(8) |
| Rh(1)–O(2) | 2.026(9) | C(1)–N(2) | 1.276(9) |
| C(1)–O(1) | 1.372(12) | C(1)–O(2) | 1.358(11) |
| Bond angles | | | |
| N(2)–Pt(1)–N(1) | 88.5(2) | N(2)[2]–Pt(1)–N(2) | 90.6(3) |
| N(2)–C(1)–O(1) | 115.8(7) | N(2)–C(1)–O(2) | 118.5(7) |
| Rh(1)–Pt(1)–Cl(1)[1] | 176.92(4) | Cl(1)–Rh(1)–Pt(1) | 171.08(5) |
| Rh(1)–Cl(1)–Pt(1)[3] | 127.42(7) | | |

[a] Symmetry operators: (1) $x-1/2, -y+1/2, z$; (2) $x, y, -z$; (3) $x+1/2, -y+1/2, z$.

As shown in Figure 2b, the axially coordinated $Cl^-$ ion on the Rh atom contacts the neighboring Pt atom with a distance of 2.6328(17) Å and bridges two Pt–Rh dimers. As to the packing of the Pt–Rh dimers, infinite strands of the head–head dimers are formed to give chains with the expression $[–Pt–Rh–Cl–]_n$. All chains run along the *a* axis, where adjacent chains run in the opposite direction as shown in Figure 2c. The one-dimensional chains are not linear but zigzag; the bridging $Cl^-$ ions form the zigzag chains with the angle Rh(1)–Cl(1)–Pt(1′) = 127.42(7)°. All the chains run along the *a* axis without significant interaction between them (Figure 2d); the distances between the chain centers are about 9.0 and 9.3 Å.

### Crystal Structure of $[PtRh(PVM)_2(en)Cl_3]\cdot 3H_2O$ (2)

Figure 3 shows the crystal structure of **2**, and Table 2 summarizes the selected bond lengths and angles for **2**. Compound **2** contains two individual dinuclear complexes in the unit cell. The asymmetric unit consists of Cl(1), Rh(1), Pt(1), Cl(3), Rh(2), Pt(2), two amines, and two PVM ligands, with a crystallographic mirror along the *ac* plane [along the Cl(1)–Rh(1)–Pt(1)–Cl(3)–Rh(2)–Pt(2) line] (Figure 3a). The carbon atoms C(1)/C(2) and C(8)/C(9) in the en ligands are disordered with the 0.58/0.42 occupancy level. Similar to **1**, the Pt and Rh ions in the dinuclear complexes are doubly bridged by two PVM ligands. The Pt atom is *cis* coordinated by four N-donor ligands; one en and two PVM ligands. The Rh atom is coordinated by three $Cl^-$ ions, of which the axially coordinated $Cl^-$ ion bridges two Pt–Rh dimers (Figure 3b). The distances between Pt and Rh are 2.5796(19) and 2.5771(17) Å. The coordination planes of the two metals are slightly tilted by 11.8 and 13.8°.

 © 2007 Wiley-VCH Verlag GmbH & Co. KGaA, Weinheim 

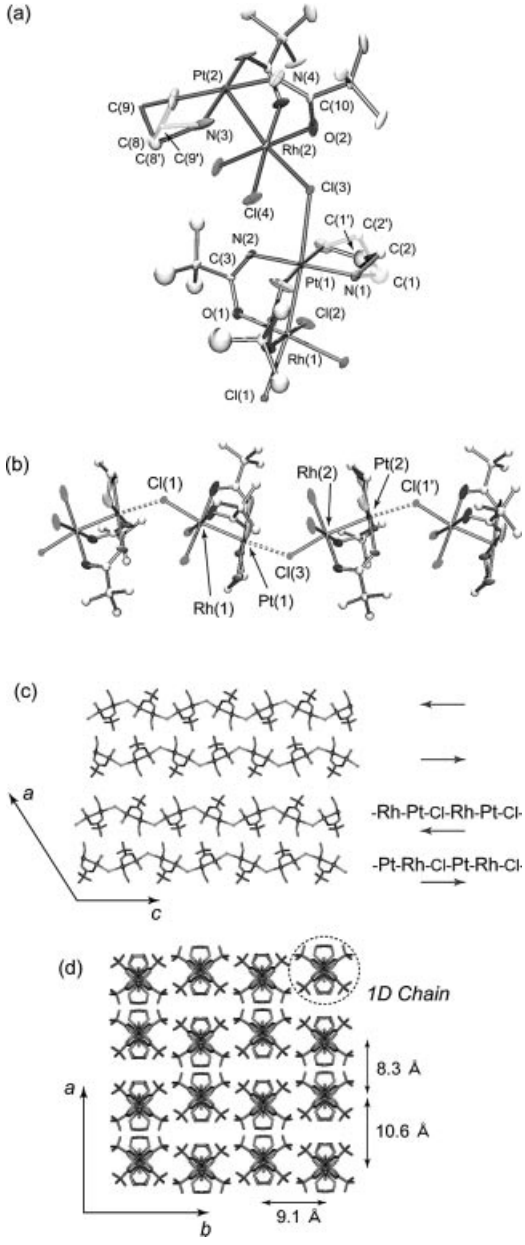


Figure 3. Crystal structure of $[PtRh(PVM)_2(en)Cl_3]\cdot 3H_2O$ (**2**). (a) ORTEP drawing of **2** at the 30% probability level. Hydrogen atoms and water molecules are omitted for clarity. C(1) and C(2), and C(8) and C(9) atoms are in a disordered relationship. (b) Pseudo 1D chain where axially coordinated Cl(1) and Cl (3) atoms bridge the dinuclear complexes. (c) Four pseudo 1D chains are aligned in parallel. Arrows indicate the chain directions. (d) Crystal packing diagram along the *c* axis. Water molecules are omitted for clarity.

As found in the packing structure of **2** (Figure 3c and Figure 3d), the pseudo 1D chain consists of the repetition of head–head dimers with the expression $[–Pt–Rh–Cl–]_n$, in a similar manner to **1**. The one-dimensional chains of **2** also zigzag, where the $Cl^–$ ions form bent bridges between the dimers with the angles of 128.08(18) and 129.26(19)°. The distances between Pt and axially contacted Cl atoms [Pt(1)···Cl(3) = 2.662(5), Pt(2)···Cl(1′) = 2.692(4) Å] in **2** are slightly longer than the corresponding one in **1**: Pt(1)···Cl(1′) = 2.6328(17) Å. As shown in Figure 3d, two

Table 2. Selected distances [Å] and angles [°] for $[PtRh(PVM)_2(en)Cl_3]\cdot 3H_2O$ (**2**).[a]

| Bond lengths | | | |
|---|---|---|---|
| Pt(1)–Rh(1) | 2.5796(19) | Pt(2)–Rh(2) | 2.5771(17) |
| Pt(1)–Cl(3) | 2.662(5) | Pt(2)–Cl(1)[1] | 2.692(4) |
| Pt(1)–N(1) | 2.058(13) | Pt(1)–N(2) | 1.977(13) |
| Pt(2)–N(3) | 2.055(14) | Pt(2)–N(4) | 1.988(13) |
| Rh(1)–Cl(1) | 2.410(4) | Rh(1)–Cl(2) | 2.328(4) |
| Rh(2)–Cl(3) | 2.420(5) | Rh(2)–Cl(4) | 2.308(4) |
| Rh(1)–O(1) | 2.033(10) | Rh(2)–O(2) | 2.022(10) |
| C(3)–N(2) | 1.266(19) | C(3)–O(1) | 1.252(15) |
| C(10)–N(4) | 1.264(18) | C(10)–O(2) | 1.265(16) |
| **Bond angles** | | | |
| N(2)–Pt(1)–N(1) | 90.5(8) | N(2)–Pt(1)–N(2)[2] | 93.1(13) |
| N(4)–Pt(2)–N(3) | 91.6(9) | N(4)[2]–Pt(2)–N(4) | 89.9(11) |
| O(1)–Rh(1)–Cl(2) | 86.7(3) | O(1)–Rh(1)–O(1)[2] | 92.7(6) |
| O(2)–Rh(2)–Cl(4) | 90.5(5) | O(2)[2]–Rh(2)–O(2) | 87.3(8) |
| N(2)–C(3)–O(1) | 121.6(14) | N(4)–C(10)–O(2) | 121.9(13) |
| Rh(1)–Pt(1)–Cl(3) | 174.81(10) | Rh(2)–Pt(2)–Cl(1)[1] | 175.50(10) |
| Cl(1)–Rh(1)–Pt(1) | 170.76(12) | Cl(3)–Rh(2)–Pt(2) | 171.25(13) |
| Rh(1)–Cl(1)–Pt(2)[3] | 128.08(18) | Rh(2)–Cl(3)–Pt(1) | 129.26(19) |

[a] Symmetry operators: (1) *x*, *y*, *z* + 1; (2) *x*, –*y* + 1, *z*; (3) *x*, *y*, *z*– 1.

parallel chains run in the opposite directions, $[–Pt–Rh–Cl–]_n$ and $[–Cl–Rh–Pt–]_n$, in close proximity of about 8.3 Å.

Both **1** and **2** give pseudo 1D infinite chains expressed as –MM′X–. A substantial number of halogen bridged chains have been thoroughly investigated to date, namely: (1) –MX– type chains,[5] (2) –MMX– type chains,[4] (3) the $Cl^–$-bridged platinum tan {= HH-$[Pt(2.5+)_4(NH_3)_8(\mu\text{-}C_4H_6NO)_4(Cl)]_n^{5n+}$, "platinum tan"[10] is the dark red amidate-bridged Pt tetranuclear complex containing the $Pt(2.5+)_4$ mixed valency} expressed as the $M_4X$-type chain.[11] In contrast, the present quasi 1D system is distinctly different from the previous systems on the ground that two kinds of metal ions are conjugated in the system (–MM′X– type chain).

## Determination of the Oxidation States

The X-ray analysis of **1** and **2** revealed that the three $Cl^–$ ions and two amidate ligands are coordinated in the dinuclear unit, which indicates that the total oxidation state of the Pt–Rh core is +5. Considering the general oxidation states of the Pt and Rh atoms, possible formal oxidation states of **1** and **2** are Pt(+3)–Rh(+2) and Pt(+2)–Rh(+3). In order to determine the oxidation state of the metal ions in the Pt–Rh dinuclear complexes, XPS and $^{195}Pt$ NMR measurements were carried out.

Figure 4 shows the Rh $3d_{5/2}$ and $3d_{3/2}$, and Pt $4f_{7/2}$ and $4f_{5/2}$ core level spectra for **1**–**6** at room temperature. In the $3d_{3/2}$ region of rhodium, Pt $4d_{5/2}$ signals also exist but are overlapped with the Rh signals. The Pt $4f_{7/2}$ binding energies were determined as 73.4 (**1**) and 73.3 (**2**), which are closer to that of the Pt(+2) complex $[Pt^{II}(en)_2(\alpha\text{-pyridonato})_2](NO_3)_2$ (72.6 eV) than that of the Pt(+3) complex $[Pt^{III}(NH_3)_4(\alpha\text{-pyrrolidonato})_2(NO_3)_2](NO_3)_2$ (75.0 eV).[12] On the other hand, the Rh $3d_{5/2}$ binding energies obtained

 © 2007 Wiley-VCH Verlag GmbH & Co. KGaA, Weinheim 

are 309.4 (**1**) and 309.2 (**2**), which are close to the value of Rh(+3) in $RhCl_3 \cdot 3H_2O$ (310.0 eV).[13] As shown in Table 3, compounds **3**–**6** have binding energies similar to those of **1** and **2**.

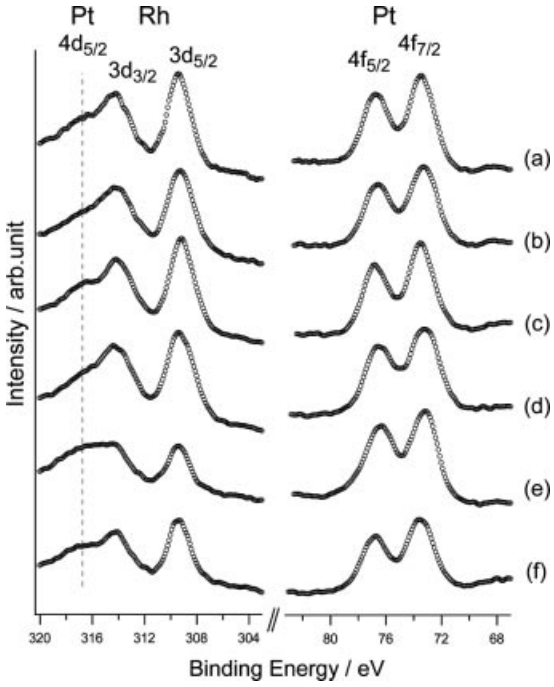


Figure 4. Rh $3d_{5/2}$ and $3d_{3/2}$ (left), Pt $4f_{7/2}$ and $4f_{5/2}$ (right) core levels of XPS for (a) **1**, (b) **2**, (c) **3**, (d) **4**, (e) **5**, and (f) **6**.

Table 3. Binding energy (eV) for 3d region of rhodium and 4f region of platinum in **1**–**6**.

| Complex | Rh $3d_{3/2}$ | Rh $3d_{5/2}$ | Pt $4f_{5/2}$ | Pt $4f_{7/2}$ |
|---|---|---|---|---|
| **1** | 314.2 | 309.4 | 76.7 | 73.4 |
| **2** | 314.1 | 309.2 | 76.5 | 73.3 |
| **3** | 314.2 | 309.1 | 76.8 | 73.5 |
| **4** | 314.4 | 309.4 | 76.6 | 73.2 |
| **5** | 314.2 | 309.4 | 76.3 | 73.1 |
| **6** | 314.1 | 309.3 | 76.7 | 73.6 |

Furthermore, the $^{195}Pt$ NMR chemical shifts obtained in MeOD by using an aqueous solution of $K_2[PtCl_6]$ as the external reference are –2452 (**1**), –2590 (**2**), –2365 (**3**), –2642 (**4**), and –2371 ppm (**5**), which are in the expected range for Pt(+2) complexes.[14,15] The broad line widths of the $^{195}Pt$ NMR signals are probably due to the interactions with $^{14}N$ nuclear spins. Compounds **4** and **5** did not show well-defined $^{195}Pt$ NMR signals in MeOD because of equilibrium mixing.[15] Interestingly, the $^{195}Pt$ chemical shifts for **1**–**5** are dispersed in a rather wide range (–2365 to –2642 ppm), which shows that there is a significant difference in the electronic states among them. Considering the results of XPS and $^{195}Pt$ NMR, we conclude that the formal oxidation state of the metal ions in **1**–**6** is Pt(+2, $d^8$)···Rh(+3, $d^6$).

### Comparison with Other Pt–Rh Dinuclear Complexes

Previously, we reported unique heterometal chains with mixed valence (so-called HMMs), $\{[PtRh(PVM)_2(NH_3)_2Cl_{2.5}]_2[Pt_2(PVM)_2(NH_3)_4]_2(PF_6)_6 \cdot 2MeOH \cdot 2H_2O\}_n$ (HMM-**1**), that comprised Pt–Rh and Pt–Pt dinuclear complexes possessing an unpaired electron over the octanuclear unit.[16] Compound **1** corresponds to a fragment of the octanuclear repetition unit in HMM-**1**. Because the HOMO is in the Pt–Rh dinuclear metal orbital part in HMM-**1**,[16] comparison between **1** and HMM-**1** is meaningful. As shown in Table 4, the Pt–Rh distances in **1** and **2** are slightly shorter than that of Pt(+3, $d^7$)···Rh(+2.5, $d^{6.5}$) in HMM-**1**.[16]

Table 4. Pt–Rh oxidation states and distances [Å].

| Compound | Oxidation states | Pt–Rh distance | Ref. |
|---|---|---|---|
| [a] | Pt(+2, $d^8$)···Rh(+1, $d^8$) | 3.043(1) | [17] |
| [b] | Pt(+2, $d^8$)···Rh(+1, $d^8$) | 3.079(2) | [18] |
| HMM-**1** | Pt(+3, $d^7$)···Rh(+2.5, $d^{6.5}$) | 2.5987(11) | [19] |
| **1** | Pt(+2, $d^8$)···Rh(+3, $d^6$) | 2.5704(7) | this work |
| **2** | Pt(+2, $d^8$)···Rh(+3, $d^6$) | 2.5796(19) | this work |

[a] = *trans*-Rh–(CO)Cl(μ-$Ph_2AsCH_2PPh_2)_2$-*cis*-$PtCl_2$. [b] = $[(NC)_2PtRh(CNtBu)_2(\mu\text{-dpm})_2](PF_6)$ [μ-dpm = bis(diphenylphosphanyl)methane].

In addition, the Pt–Rh distances in **1** and **2** are about 0.5 Å shorter than those reported in other Pt–Rh dinuclear complexes, *trans*-Rh–(CO)Cl(μ-$Ph_2AsCH_2PPh_2)_2$-*cis*-$PtCl_2$ (***a***)[17] and $[(NC)_2PtRh(CNtBu)_2(\mu\text{-dpm})_2](PF_6)$ (***b***, μ-dpm = bis(diphenylphosphanyl)methane),[18] where the formal oxidation states are Pt(+2, $d^8$)···Rh(+1, $d^8$). It has been shown that an occupied $d_{z^2}$ orbital in the $d^8$ transition metal ion with square-planar coordination geometry can act as a donor to other metal ions (M′) to form a dative Pt($d^8$)→M′ bond.[19] Considering the short Pt–Rh distances, compounds **1** and **2** are considered to have a dative Pt($d^8$)→Rh($d^6$) bond, where the Pt $d_{z^2}$ orbital is stabilized by the overlap with the $d_{z^2}$ orbital of Rh.

## Conclusions

The present study is focused on the synthesis and single-crystal X-ray analysis of novel Pt–Rh dinuclear complexes having a Pt–Rh bond doubly bridged by amidate ligands, and we have succeeded in obtaining six dinuclear complexes with various amidate and amine ligands. Compounds **1** and **2** are zigzag MM′X chains, and XPS and $^{195}Pt$ NMR spectroscopic measurements revealed that the dinuclear complexes have the formal oxidation state of Pt(+2, $d^8$)···Rh(+3, $d^6$). Apparently, there is no electronic interaction between the Pt–Rh dinuclear complex units bridged by $Cl^-$ ions in the zigzag chain. Because linear 1D chains constructed from Pt and a heterometal are expected to have unique physical properties, attempts to straighten the alignment of the Pt–Rh dinuclear complexes in the chain by modifying the axial ligand is currently in progress.

## Experimental Section

**Synthesis of $[PtRh(PVM)_2(NH_3)_2Cl_3] \cdot 4H_2O$ (1):** A MeOH solution (200 mL) of $[Pt(PVM)_2(NH_3)_2] \cdot 2H_2O$ (1 mmol, 0.47 g) was stirred

 © 2007 Wiley-VCH Verlag GmbH & Co. KGaA, Weinheim 

with $RhCl_3 \cdot 3H_2O$ (1 mmol, 0.26 g) for 3 d at 40 °C. The resulting brown solution was concentrated to yield a brown solid. The brown solid was stirred with an aqueous solution (10 mL) of KCl (4.0 mmol, 0.30 g) to give the brown product. Yield: 0.28 g (39%). The product was recrystallized by diffusing excess KCl into the aqueous solution to give suitable single crystals. IR (KBr pellet): C=O stretching, $\tilde{\nu}$ = 1639 (m), 1574 (s) $cm^{-1}$. $C_{10}H_{34}Cl_3N_4O_6PtRh$ (711): calcd. C 16.90, H 4.82, N 7.88; found C 17.12, H 4.51, N 7.09.

**Synthesis of $[PtRh(PVM)_2(en)Cl_3] \cdot 3H_2O$ (2):** A MeOH solution (300 mL) of $[Pt(PVM)_2(en)] \cdot 4H_2O$ (1.5 mmol, 0.79 g) was stirred with $RhCl_3 \cdot 3H_2O$ (1.5 mmol, 0.395 g) for 2 d at 40 °C. The resulting brown solution was concentrated to yield a brown solid. The brown solid was stirred with an aqueous solution (10 mL) of KCl (4.0 mmol, 0.30 g) to give the dark green product. Yield: 0.29 g (27%). The product was recrystallized by diffusing excess KCl into the aqueous solution to give suitable single crystals. IR (KBr pellet): C=O stretching, $\tilde{\nu}$ = 1635 (m), 1574 (s) $cm^{-1}$. $C_{12}H_{34}Cl_3N_4O_5PtRh$ (719): calcd. C 20.05, H 4.77, N 7.79; found C 20.30, H 4.43, N 7.64.

**Synthesis of $[PtRh(PVM)_2(NH_2CH_3)_2Cl_3] \cdot 3H_2O$ (3):** A MeOH solution (136 mL) of $[Pt(PVM)_2(NH_2CH_3)_2] \cdot H_2O$ (0.68 mmol, 0.32 g) was stirred with $RhCl_3 \cdot 3H_2O$ (0.68 mmol, 0.18 g) for 2 d at 40 °C. The resulting dark violet solution was concentrated to yield a dark violet solid. The dark violet solid was stirred with an aqueous solution (6.5 mL) of KCl (6.7 mmol, 0.50 g) to give the brown product. Yield: 0.15 g (31%). IR (KBr pellet): C=O stretching, $\tilde{\nu}$ = 1645 (m), 1570 (s) $cm^{-1}$. $C_{12}H_{36}Cl_3N_4O_5PtRh$ (721): calcd. C 20.00, H 5.03, N 7.77; found C 20.40, H 4.50, N, 7.17.

**Synthesis of $[PtRh(PVM)_2(NH_2tBu)_2Cl_3] \cdot 3H_2O$ (4):** A MeOH solution (90 mL) of $[Pt(PVM)_2(NH_2tBu)_2]$ (0.45 mmol, 0.24 g) was stirred with $RhCl_3 \cdot 3H_2O$ (0.45 mmol, 0.12 g) for 2 d at 40 °C. The resulting brown solution was concentrated to yield a brown solid. The brown solid was stirred with an aqueous solution (5 mL) of KCl (1.3 mmol, 0.10 g) to give the brown product. Yield: 0.23 g (63%). IR (KBr pellet): C=O stretching, $\tilde{\nu}$ = 1647 (m), 1571 (s) $cm^{-1}$. $C_{18}H_{48}Cl_3N_4O_5PtRh$ (805): calcd. C 26.86, H 6.01, N, 6.96; found C 25.90, H 5.16, N 6.01.

**Synthesis of $[PtRh(TCM)_2(NH_3)_2Cl_3]$ (5):** A MeOH solution (150 mL) of $[Pt(TCM)_2(NH_3)_2]$ (0.75 mmol, 0.41 g) was stirred with $RhCl_3 \cdot 3H_2O$ (0.75 mmol, 0.20 g) for 3 d at 40 °C. The resulting brown solution was concentrated to yield a brown solid. The brown solid was stirred with an aqueous solution (4 mL) of NaCl (10.3 mmol, 0.60 g) to give the dark green product. Yield: 0.25 g (43%). IR (KBr pellet): C=O stretching, $\tilde{\nu}$ = 1716 (m), 1628 (s) $cm^{-1}$. $C_4H_8Cl_9N_4O_2PtRh$ (761): calcd. C 6.31, H 1.06, N, 7.36; found C 6.31, H 1.50, N 7.33.

**Synthesis of $[PtRh(BZM)_2(NH_3)_2Cl_3] \cdot H_2O$ (6):** A MeOH solution (120 mL) of $[Pt(BZM)_2(NH_3)_2]$ (0.6 mmol, 0.28 g) was stirred with $RhCl_3 \cdot 3H_2O$ (0.6 mmol, 0.16 g) for 3 d at 40 °C. The resulting brown solution was concentrated to yield a brown solid. The brown solid was stirred with an aqueous solution (4 mL) of KCl (9.3 mmol, 0.70 g) to give the brown product. Yield: 0.18 g (42%). IR (KBr pellet): C=O stretching, $\tilde{\nu}$ = 1597 (m), 1558 (s) $cm^{-1}$. $C_{14}H_{20}Cl_3N_4O_3PtRh$ (697): calcd. C 24.14, H 2.89, N 8.04; found C 24.38, H 2.91, N 7.48.

**X-ray Structure Determination for 1 and 2:** Measurements were carried out with a Bruker SMART APEX CCD diffractometer equipped with a normal focus Mo-target X-ray tube ($\lambda$ = 0.71073 Å) operated at 2000 W power (50 kV, 40 mA) and a CCD two-dimensional detector. A total of 1315 frames were collected with a scan width of 0.3° in $\omega$ with an exposure time of 20 (**1**) and 40 (**2**) s/frame. The frames were integrated with the SAINT software package with a narrow frame algorithm.[20] Absorption correction was applied by using SADABS.[21] All the structures were solved by direct methods with the subsequent difference Fourier syntheses and the refinement with the SHELXTL (version 5.1) software package.[22] For all compounds, the non-hydrogen atoms were refined anisotropically and all hydrogen atoms were placed in the ideal positions. In **1**, O(1) and O(2), Cl(2) and Cl(3) atoms were refined with disorder relationship. In **2**, C(1) and C(2), C(8) and C(9) atoms were refined with disorder relationship. In **2**, C(1), C(2), C(5)–(9), O(4) and O(6) were isotropically refined under rigid conditions (Table 5). CCDC-618494 (for **1**) and -618495 (for **2**) contain the supplementary crystallographic data for this paper. These data can be obtained free of charge from The Cambridge Crystallographic Data Centre via www.ccdc.cam.ac.uk/data_request/cif.

Table 5. Crystal data and structure refinement for $[PtRh(PVM)_2(NH_3)_2Cl_3] \cdot 4H_2O$ (**1**) and $[PtRh(PVM)_2(en)Cl_3] \cdot 3H_2O$ (**2**).

| Compound | **1** | **2** |
|---|---|---|
| Formula | $C_{10}H_{20}Cl_3N_4O_6PtRh$ | $C_{12}H_{20}Cl_3N_4O_5PtRh$ |
| Formula mass | 696.65 | 704.67 |
| Crystal system | orthorhombic | monoclinic |
| Space group | *Ibam* (no. 72) | *C2/m* (no. 12) |
| *a* [Å] | 13.7371(17) | 22.050(10) |
| *b* [Å] | 18.002(2) | 18.260(8) |
| *c* [Å] | 18.541(2) | 13.865(6) |
| $\alpha$ [°] | 90 | 90 |
| $\beta$ [°] | 90 | 122.138(7) |
| $\gamma$ [°] | 90 | 90 |
| *V* [Å$^3$] | 4585.1(10) | 4727(4) |
| *Z* | 8 | 8 |
| $D_{calcd.}$ [g cm$^{-3}$] | 2.018 | 1.980 |
| $\mu$ [mm$^{-1}$] | 7.193 | 6.975 |
| $R_1$[a] [$I > 2.0\sigma(I)$] | 0.0266 | 0.0710 |
| $wR_2$[b] [all data] | 0.1034 | 0.2001 |
| *T* [°C] | –153 | –153 |

[a] $R_1 = \Sigma(|F_o| - |F_c|)/\Sigma(|F_o|)$. [b] $wR_2 = \{\Sigma[w(F_o^2 - F_c^2)^2]/\Sigma[w(F_o^2)^2]\}^{1/2}$.

**Physical Measurements:** The X-ray photoelectron spectroscopy measurements were carried out with a JEOL JPS-9010. Binding energies were measured relative to the C 1s peak (284.8 eV) of internal hydrocarbon.

**Supporting Information** (see footnote on the first page of this article): $^1$H NMR spectra for **1**–**4**, IR spectra for **1**–**6**, $^{195}$Pt NMR spectra for **1**–**5**.

## Acknowledgments

This work was supported by Iketani Science and Technology Foundation, Grants-in-Aid for Scientific Research [Young Scientist (B) No. 17750058], and the 21COE program "Practical Nano-Chemistry" from MEXT, Japan.

[1] a) J. S. Miller, *Extended Linear Chain Compounds, Vols. 1–3*, Plenum, New York, **1982**.; b) J. K. Bera, K. R. Dunbar, *Angew. Chem. Int. Ed.* **2002**, *41*, 4453–4457.

[2] a) K. Sakai, M. Takeshita, Y. Tanaka, T. Ue, M. Yanagisawa, M. Kosaka, T. Tsubomura, M. Ato, T. Nakano, *J. Am. Chem. Soc.* **1998**, *120*, 11353–11363; b) K. Sakai, E. Ishigami, Y. Konno, T. Kajiwara, T. Ito, *J. Am. Chem. Soc.* **2002**, *124*, 12088–12089; c) M. Yamashita, D. Kawakami, S. Matsunaga, Y. Nakayama, M. Sasaki, S. Takaishi, F. Iwahori, H. Miyasaka, K. Sugiura, Y. Wada, H. Miyamae, H. Matsuzaki, H.

 © 2007 Wiley-VCH Verlag GmbH & Co. KGaA, Weinheim 

Okamoto, H. Tanaka, K. Marumoto, S. Kuroda, *Angew. Chem. Int. Ed.* **2004**, *43*, 4763–4767.
[3] a) G. M. Finniss, E. Canadell, C. Campana, K. R. Dunbar, *Angew. Chem. Int. Ed. Engl.* **1996**, *35*, 2772–2774; b) M. E. Prater, L. E. Pence, R. Clerac, G. M. Finniss, C. Campana, P. Auban-Senzier, D. Jerome, E. Canadell, K. R. Dunbar, *J. Am. Chem. Soc.* **1999**, *121*, 8005–8016; c) F. A. Cotton, E. V. Dikarev, M. A. Petrukhina, *J. Organomet. Chem.* **2000**, *596*, 130–135; d) F. A. Cotton, E. V. Dikarev, M. A. Petrukhina, *J. Chem. Soc., Dalton Trans.* **2000**, 4241–4243; e) F. P. Pruchnik, P. Jakimowicz, Z. Ciunik, *Inorg. Chem. Commun.* **2001**, *4*, 726–729; f) M. Mitsumi, S. Umebayashi, Y. Ozawa, M. Tadokoro, H. Kawamura, K. Toriumi, *Chem. Lett.* **2004**, *33*, 970–971; g) M. Mitsumi, H. Goto, S. Umebayashi, Y. Ozawa, M. Kobayashi, T. Yokoyama, H. Tanaka, S.-i. Kuroda, K. Toriumi, *Angew. Chem. Int. Ed.* **2005**, *44*, 4164–4168.
[4] a) H. Kitagawa, N. Onodera, T. Sonoyama, M. Yamamoto, T. Fukawa, T. Mitani, M. Seto, Y. Maeda, *J. Am. Chem. Soc.* **1999**, *121*, 10068–10080; b) H. Kitagawa, T. Mitani, *Coord. Chem. Rev.* **1999**, *190–192*, 1169–1184; c) M. Mitsumi, T. Murase, H. Kishida, T. Yoshinari, Y. Ozawa, K. Toriumi, T. Sonoyama, H. Kitagawa, T. Mitani, *J. Am. Chem. Soc.* **2001**, *123*, 11179–11192.
[5] M. Yamashita, D. Kawakami, S. Matsunaga, Y. Nakayama, M. Sasaki, S. Takaishi, F. Iwahori, H. Miyasaka, K. Sugiura, Y. Wada, H. Miyamae, H. Matsuzaki, H. Okamoto, H. Tanaka, K. Marumoto, S. Kuroda, *Angew. Chem. Int. Ed.* **2004**, *43*, 4763.
[6] a) W. Chen, K. Matsumoto, *Inorg. Chim. Acta* **2003**, *342*, 88–96; b) W. Chen, F. Liu, T. Nishioka, K. Matsumoto, *Eur. J. Inorg. Chem.* **2003**, 4234–4243.
[7] a) A. Erxleben, I. Mutikainen, B. Lippert, *J. Chem. Soc., Dalton Trans.* **1994**, 3667–3675; b) E. Zangrando, F. Pichierri, L. Randaccio, B. Lippert, *Coord. Chem. Rev.* **1996**, *156*, 275–332.
[8] The $^{1}$H NMR spectrum is shown in the Supporting Information.
[9] K. Uemura, K. Yamasaki, K. Fukui, K. Matsumoto, unpublished work; Similarly to the previous procedure,[6a] five new mononuclear platinum complexes with noncoordinated oxygen atoms in the amide ligands were successfully obtained.
[10] K. Matsumoto, K. Fuwa, *J. Am. Chem. Soc.* **1982**, *104*, 897–898.
[11] K. Sakai, Y. Tanaka, Y. Tsuchiya, K. Hirata, T. Tsubomura, S. Iijima, A. Bhattacharjee, *J. Am. Chem. Soc.* **1998**, *120*, 8366–8379.
[12] K. Matsumoto, K. Sakai, K. Nishio, Y. Tokisue, R. Ito, T. Nishide, Y. Shichi, *J. Am. Chem. Soc.* **1992**, *114*, 8110–8118.
[13] C. Furlani, G. Mattogno, G. Polzonetti, G. Braca, G. Valentini, *Inorg. Chim. Acta* **1983**, *69*, 199–205.
[14] P. S. Pregosin, *Coord. Chem. Rev.* **1982**, *44*, 247–291.
[15] $^{195}$Pt NMR spectra are shown in the Supporting Information. Compounds **4** and **5** (asterisk) did not show well-defined $^{195}$Pt NMR signals in MeOD because of equilibrium mixing and the limited solubility. It seems that dissociation and coordination of the axial $Cl^{-}$ ion occurs in equilibrium, which induces two species, $[PtRh(Amid)_2(Am)_2Cl_2]^{+}$ and $[PtRh(Amid)_2(Am)_2Cl_3]$ (Amid = amidate, Am = amine). Low solubility of **6** precluded $^{195}$Pt NMR measurements.
[16] a) K. Uemura, K. Fukui, H. Nishikawa, S. Arai, K. Matsumoto, H. Oshio, *Angew. Chem. Int. Ed.* **2005**, *44*, 5459–5464; b) K. Uemura, K. Fukui, K. Yamasaki, K. Matsumoto, *Sci. Technol. Adv. Mater.* **2006**, 461–467.
[17] a) R. R. Guimerans, F. E. Wood, A. L. Balch, *Inorg. Chem.* **1984**, *23*, 1307–1308; b) A. L. Balch, R. R. Guimerans, J. Linehan, F. E. Wood, *Inorg. Chem.* **1985**, *24*, 2021–2026.
[18] A. L. Balch, V. J. Catalan, *Inorg. Chem.* **1992**, *31*, 3934–3942.
[19] a) F. A. Cotton, L. R. Falvello, R. Uson, J. Fornies, M. Tomas, J. M. Casas, I. Ara, *Inorg. Chem.* **1987**, *26*, 1366–1370; b) T. Yamaguchi, F. Yamazaki, T. Ito, *J. Am. Chem. Soc.* **1999**, *121*, 7405–7406; c) T. Yamaguchi, F. Yamazaki, T. Ito, *J. Am. Chem. Soc.* **2001**, *123*, 743–744.
[20] *SMART & SAINT Software Package v. 5.625*, Siemens Energy & Automation, Inc., Analytical Instrumentation, Madison, WI, **2001**.
[21] G. M. Sheldrick, *SADABS, Software for Empirical Absorption Corrections*, University of Göttingen, Germany, **1996**.
[22] *SHELXTL Reference Manual v. 5.1: Bruker AXS*, Analytical X-ray Systems, Madison, WI, **1997**.

Received: September 26, 2006
Published Online: January 5, 2007

 © 2007 Wiley-VCH Verlag GmbH & Co. KGaA, Weinheim 

DOI: 10.1002/ejic.200600805

# Fragmentation of the (Cyclam-acetato)iron Azide Cation in the Gas Phase

Detlef Schröder,*[a] Helmut Schwarz,[b] Núria Aliaga-Alcalde,[c] and Frank Neese[c]

**Keywords:** N ligands / Iron / Azides / Mass spectrometry

Mass spectrometry is used to investigate the fragmentation of the ligated azidoiron cation [(cyclam-acetato)Fe($N_3$)]$^+$, which is accessible in the gas phase by electrospray ionization of a solution of its hexafluorophosphate salt in methanol/water. Upon collisional activation, mass-selected [(cyclam-acetato)Fe($N_3$)]$^+$ undergoes competing loss of dinitrogen or $HN_3$ as the prevailing fragmentations. The former dissociation pathway is investigated in detail in order to determine whether or not the free, high-valent iron nitride [(cyclam-acetato)FeN]$^+$ is formed. The evidence obtained indeed supports the formation of the iron nitride species as an intermediate, although the long-lived ion sampled after mass selection may also have undergone further rearrangements.

(© Wiley-VCH Verlag GmbH & Co. KGaA, 69451 Weinheim, Germany, 2007)

## Introduction

High-valent iron species are of long-standing interest in coordination chemistry due to their occurrence as reaction intermediates in metalloenzyme reactions.[1] The field has gained significant momentum since the discovery of the first proven $Fe^{IV}$ intermediate in mononuclear nonheme iron enzymes[2] and the first crystal structure of an elusive $Fe^{IV}$-oxo species by Rohde et al.[3] More recently, it has proven possible to proceed beyond the oxidation state $Fe^{IV}$ and to obtain definitive spectroscopic evidence for genuine $Fe^{V}$[4,5] and even $Fe^{VI}$ species.[6,7] The high-valent iron sites in these compounds are stabilized in a distorted octahedral environment by an innocent framework provided by ligands designed on the basis of the cyclam motif together with an extremely basic axial nitrido ligand, which is generated in situ by photolysis of the corresponding iron azide precursors. For the time being these species can only be generated in an immobilized state in solids or frozen solutions, therefore their chemistry cannot yet be explored in detail. In this work we take a first step towards studying the reactivity of these elusive species by generating them in the gas phase. In addition to the interest from biological chemists, the chemistry of transition-metal nitride compounds is attracting ongoing attention due to their potential in organic synthesis, with the formation of C–N bonds being particularly important.[8–10] The evidence for metal nitride species is, however, often only circumstantial because of the intrinsically high reactivity of these species. Recently, the photolysis of solid [(cyclam-acetato)Fe($N_3$)][$PF_6$] ([**1**][$PF_6$]), was described to yield the [(cyclam-acetato)FeN]$^+$ cation **2**$^+$ according to Equation (1).[5]

[(cyclam-acetato)Fe($N_3$)][$PF_6$] → [(cyclam-acetato)FeN][$PF_6$] + $N_2$ (1)

Cation **2**$^+$ can be viewed as an example of a genuine and isolated nitridoiron cation and hence offers a possibility for the investigation of the gas-phase reactivity of these compounds. In this context, it has been demonstrated previously[11,12] that the bare imidoiron cation $FeNH^+$ provides an excellent model system for the examination of transition-metal-mediated imine transfer in the gas phase. The chemical behavior of $FeNH^+$ towards oxygen, water, hydrogen, various aliphatic hydrocarbons (including methane), benzene, and toluene reveals an intrinsically high reactivity of $FeNH^+$, even under thermal conditions. Thus, reactions are brought about which are otherwise difficult to realize, such as the direct amination of organic substrates (RH) according to Equation (2).

RH + ‹NH› → $RNH_2$ (2)

Compared to $FeNH^+$, much less is known about the gas-phase chemistry of the diatomic iron nitride FeN.[13] Given the availability of the precursor salt [**1**][$PF_6$], electrospray ionization (ESI) appeared to be a promising method to probe the occurrence of reaction (1) in the gas phase and to subsequently investigate the gas-phase reactivity of such a rare transition-metal nitrido complex.

## Results and Discussion

Under mild ionization conditions, ESI of [(cyclam-acetato)Fe($N_3$)][$PF_6$] dissolved in methanol/water provides an intense signal for the molecular cation [(cyclam-acetato)-Fe($N_3$)]$^+$ (**1**$^+$) at *m*/*z* 355 for the most abundant $^{56}$Fe isotope

[a] Institute of Organic Chemistry and Biochemistry, Flemingovo nám. 2, 16610 Prague 6, Czech Republic
[b] Institut für Chemie der Technischen Universität Berlin, Strasse des 17. Juni 135, 10623 Berlin, Germany
[c] Lehrstuhl für Theoretische Chemie, Universität Bonn, 53115 Bonn, Germany

 InterScience © 2007 Wiley-VCH Verlag GmbH & Co. KGaA, Weinheim 

with the expected isotope pattern.[14,15] Under increasingly harsher ionization conditions, $\mathbf{1}^+$ undergoes consecutive dissociations, and ESI under enforced conditions can hence be used to generate these fragment ions (see below).[16,17] CID of mass-selected [(cyclam-acetato)$Fe(N_3)]^+$ shows mass differences, $\Delta m$, of –28 and –43 as the major fragmentation pathway in the CID spectra over the whole range of collision energies studied (Figure 1). Phenomenological analysis of the energy behavior reveals an appearance energy of $1.0 \pm 0.2$ eV for the $\Delta m$ = –28 fragmentation and $1.9 \pm 0.4$ eV for the $\Delta m$ = –43 fragmentation. Accordingly, the fragmentation with $\Delta m$ = –28 is the lowest-energy dissociation pathway of $\mathbf{1}^+$.

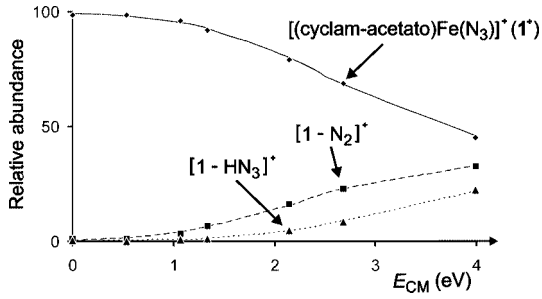


Figure 1. Collision-induced fragmentation of mass-selected [(cyclam-acetato)$Fe(N_3)]^+$ ($\mathbf{1}^+$) as a function of collision energy (center-of-mass frame). The lines connecting the experimental data points show the result of the fits using sigmoid functions (see Experimental Section).

Given the elemental composition of $\mathbf{1}^+$ ($C_{12}H_{25}N_7O_2Fe$), the mass difference of –43 can be associated with various combinations of neutral molecules lost. However, the presence of an azido group very much implies the expulsion of $HN_3$ according to reaction (3).

$$\underset{m/z\ 355}{[(\text{cyclam-acetato})Fe(N_3)]^-} \rightarrow \underset{m/z\ 312}{[(\text{cyclam-acetato} - H)Fe]^+} + HN_3 \quad (3)$$

$$\rightarrow \underset{m/z\ 327}{[(\text{cyclam-acetato})FeN]^+} + N_2 \quad (4)$$

The additional proton required for the formation of neutral $HN_3$ must come from the ligand backbone, most probably from one of the three NH groups. This view is supported by an analogous and moreover exclusive loss of $CH_3OH$ from the related species [(cyclam-acetato)-$Fe(OCH_3)]^+$, which is formed upon slow solvolysis of [**1**][$PF_6$] in methanol/water solution (half-life of about 5 days at ambient temperature). If the $\Delta m$ = –43 fragmentation were instead due to a facile degradation of the cyclam ligand itself (e.g. a loss of vinylamine), the same mass difference would also be expected for [(cyclam-acetato)-$Fe(OCH_3)]^+$; however, such a fragmentation is not observed even in traces. By the same line of reasoning, the $\Delta m$ = –28 fragmentation is attributed to the expulsion of a nitrogen molecule from the azido group, see reaction (4), which is in perfect analogy to the occurrence of reaction (1) in the condensed phase.[5] If this mass loss were instead due to a fragmentation of the cyclic ligand, it would also be expected to occur for the methoxido complex, for which it is not observed experimentally.

The key question which we will pursue in the following is the nature of the ionic fragment $[\mathbf{1} - N_2]^+$ formed in reaction (4) because it could either correspond to the elusive nitridoiron cation $\mathbf{2}^+$ or an isomeric product of a subsequent rearrangement (see below). While mass spectrometry alone cannot provide an unambiguous answer in this respect, analysis of the fragmentation pattern might provide insight into the isomeric structures conceivable from an experimental point of view.[18] Hence, the fragment ion $[\mathbf{1} - N_2]^+$ (*m*/*z* 327) formed in the ESI source under slightly enforced ESI conditions was mass-selected and subjected to CID.

Not unexpectedly, the fragmentation pattern of $[\mathbf{1} - N_2]^+$ is rather rich, and the most significant dissociation pathways are associated with mass differences of –16, –17, –30, –44, –61, –99, and –142. Most of these routes cannot be explained in a straightforward manner, although this is to be expected if $\mathbf{2}^+$ were indeed formed. Thus, $\Delta m$ = –16, for example, can correspond to either losses of neutral $CH_4$, $NH_2$, or O. Likewise, $\Delta m$ = –17 may account for expulsion of $NH_3$ or OH, and for $\Delta m$ = –30 neutral fragments like $C_2H_6$, $CH_2NH_2$, $CH_2O$, or even NO are conceivable. In the case of the larger mass differences, the options become increasingly more complex. Due to the manifold of fragments, the collision-energy dependence of the fragmentation behavior is also not analyzed in detail. Qualitatively, however, it can be noted that the fragments associated with $\Delta m$ = –17, –30, –44, and –99 already appear at lower collision energies (Figure 2, a), whereas those with $\Delta m$ = –16, –61, and –142 are more pronounced at elevated collision energies (Figure 2, b); the comparison indicates that the latter are either due to consecutive fragmentations or correspond to entropically favored, but energy-demanding, direct bond cleavages.[19]

In general, isotopic labeling would appear to be an ideal strategy for the identification of the various neutral losses. Selective isotope labeling of the ligand is, however, not easily applicable here because the precursor synthesis is not trivial and our major interest concerns the nature of the putative nitridoiron species rather than the degradation of the ligand backbone. Therefore, only three isotopic ions were considered. At first, the ion with *m*/*z* 325 was mass-selected as this can be attributed exclusively to the $^{54}Fe$ isotope of $[\mathbf{1} - N_2]^+$ and shows the same mass differences as listed above. Accordingly, none of the neutrals lost upon CID contain the iron atom of $[\mathbf{1} - N_2]^+$. Next, the precursor [**1**][$PF_6$] was dissolved in $D_2O$ and the solution was stored for 2 h at room temperature. In the resulting mass spectrum, the signal due to $\mathbf{1}^+$ is cleanly shifted three mass units higher, which is attributed to the exchange of all amino hydrogen atoms by deuterium, i.e. [*N*,*N*,*N*-$D_3$]-$\mathbf{1}^+$ (*m*/*z* 358). CID of mass-selected [*N*,*N*,*N*-$D_3$]-$\mathbf{1}^+$ yields the loss of $N_2$ ($\Delta m$ = –28) and $DN_3$ ($\Delta m$ = –44), as expected from the occurrence of reactions (3) and (4) for the unlabeled ion.

 © 2007 Wiley-VCH Verlag GmbH & Co. KGaA, Weinheim 

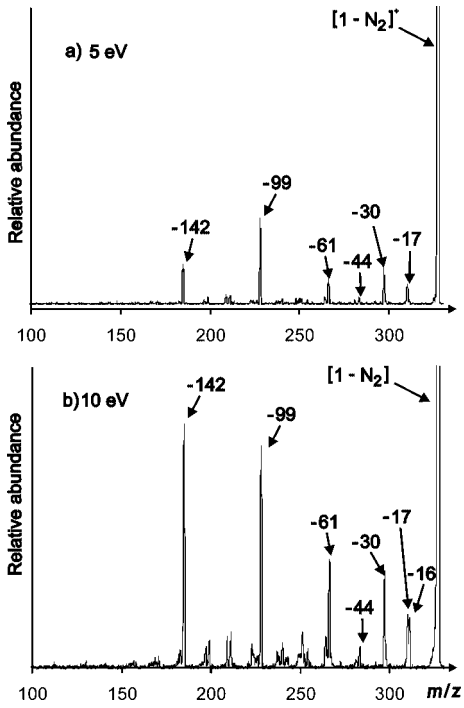


Figure 2. CID spectra of mass-selected $[\mathbf{1} - N_2]^+$ at a collision energy of a) 5 and b) 10 eV. In both spectra, the parent ion is 20-fold off-scale.

For the fragment ion $[\{N,N,N\text{-}D_3\}\text{-}\mathbf{1}^+ - N_2]^+$, mass differences of –17, –19, –30, –31, –32, –44, –63, –99, –100, –142, and –143 are observed (Table 1). Likewise, a sample of the precursor was investigated in which the azido ligand is $^{15}N_1$-labeled − terminally $^{15}N_1$-labeled azide was used in the preparative synthesis to afford a 1:1 mixture of [(cyclam-acetato)Fe($^{15}N^{14}N^{14}N$)]$^+$ and [(cyclam-acetato)-Fe($^{14}N^{14}N^{15}N$)]$^+$. CID of the mass selected ion $[^{15}N_1]$-$\mathbf{1}^+$ (*m*/*z* 356) shows a 1:1 ratio of $^{14}N_2$ and $^{14}N^{15}N$ losses ($\Delta m$ = –28 and – 29) as well as an expulsion of neutral $[^{15}N_1]$-$HN_3$ ($\Delta m$ = –44). Hence, the fragmentations of $\mathbf{1}^+$ exclusively involve the azido group, as already concluded above from the behavior of the methoxido complex [(cyclam-acetato)Fe($OCH_3$)]$^+$. Mass selection of $[\{^{15}N_1\}\text{-}\mathbf{1} - N_2]^+$ and subsequent CID lead to mass differences of –17, –18, –30, –44, –62, –100, and –143, thus indicating the participation of the labeled nitrogen atom in most of the neutral losses.

The following conclusions can be drawn from the mass shifts observed for the ions compared to the unlabeled species (Table 1): (i) The mass differences $\Delta m$ = –16 and –17 are most likely associated with loss of an amino radical and ammonia, respectively, with exclusive participation of the azido N-atom and incorporation of one H-atom from the hydrocarbon linkers while the other hydrogen(s) stem(s) from the amino groups; (ii) with the given elemental composition of $[\mathbf{1} - N_2]^+$, the mass difference $\Delta m$ = –30 can correspond to the formation of either $C_2H_6$, $[CH_4N]$, $CH_2O$, or NO. Based on the results for the deuterated compound, participation of the amino groups is obvious and hence implies loss of $[CH_4N]$ (e.g. an aminomethyl radical $CH_2NH_2$ or $CH_3NH$),[20] although a definitive assignment of the neutral fragment cannot be made; (iii) even though other options cannot be rigorously excluded, the labeling patterns as well as the known structure of $[\mathbf{1}][PF_6]$ imply that $\Delta m$ = –44 corresponds to decarboxylation, which is further supported by the fragment with $\Delta m$ = –61, whose genesis can be explained by combined losses of $CO_2$ and ammonia; (iv) $\Delta m$ = –99 and $\Delta m$ = –142 are assigned to fragmentations of the ligand backbone after initial decarboxylation, with only limited participation of the amino protons. It is noteworthy that the azido N-atom is incorporated in the neutral fragment lost; (v) investigation of the $^{54}$Fe isotope demonstrates that iron is not contained in any of the neutral fragments lost.

Some additional information can be derived by inspecting the CID spectra of some of the major fragment ions of $[\mathbf{1} - N_2]^+$ which are formed under more drastic ionization conditions. For example, the ion at *m*/*z* 310 formally corresponding to loss of ammonia from $[\mathbf{1} - N_2]^+$ shows a mass loss of –44 as the most abundant mass difference upon CID. Further, the relationship of $\Delta m$ = –99 and –142 as consecutive processes is supported by the observation of $\Delta m$ = –43 as a major fragmentation pathway in the CID spectrum of $[\mathbf{1} - N_2 - 99]^+$. Not all fragment ions of interest can be investigated by this approach, however, because of interfering isobaric ions formed in the course of ESI.

Combining the insights derived from the CID spectra together with the data of the isotopologs, a sequence for the successive fragmentation of $\mathbf{1}^+$ can be suggested (Scheme 1). While such a scenario is necessarily also based on several assumptions derived from chemical plausibility considerations, it can provide a consistent explanation for most of the fragmentations observed. Thus, in the first step, molecular nitrogen is lost from $\mathbf{1}^+$ to afford the elusive nitridoiron species $\mathbf{2}^+$. Next, this nitridoiron species is suggested to undergo an intramolecular insertion into one of the C–H bonds of the methylene groups in one of the $C_3$ bridges

Table 1. Mass differences[a] and relative abundances observed in the CID spectra of mass-selected $[\mathbf{1} - N_2]^+$ and some of its isotopologs at a collision energy of 10 eV.

| Precursor ion | *m*/*z* | Mass difference (abundance)[b] |
|---|---|---|
| $[\mathbf{1} - N_2]^+$ | 327 | –16 (20), –17 (25), –30 (40), –44 (8), –61 (45), –99 (90), –142 (100) |
| $[\{^{54}Fe\}\text{-}\mathbf{1} - N_2]^+$ | 325 | –16 (20), –17 (30), –30 (40), –44 (10), –61 (55), –99 (100), –142 (90) |
| $[\{D_3\}\text{-}\mathbf{1} - N_2]^+$ | 330 | –17 (45), –19 (25), –30 (10), –31 (25), –32 (35), –44 (12), –63 (30), –99 (100), –100 (35), –142 (70), –143 (30) |
| $[\{^{15}N\}\text{-}\mathbf{1} - N_2]^+$[c] | 328 | –17 (40), –18 (60), –30 (45), –44 (10), –61 (45), –100 (95), –143 (100) |

[a] Only selected peaks are listed; the complete CID spectrum of the unlabeled ion $[\mathbf{1} - N_2]^+$ (*m*/*z* 327) is shown in Figure 2b. [b] Given relative to the base peak of the CID spectrum (100). [c] The CID spectrum is corrected for interfering isotopes of $[\mathbf{1} - N_2]^+$ which is also formed from $[^{15}N\text{-}\mathbf{1}]^+$ upon loss of $^{14}N^{15}N$.

 © 2007 Wiley-VCH Verlag GmbH & Co. KGaA, Weinheim 

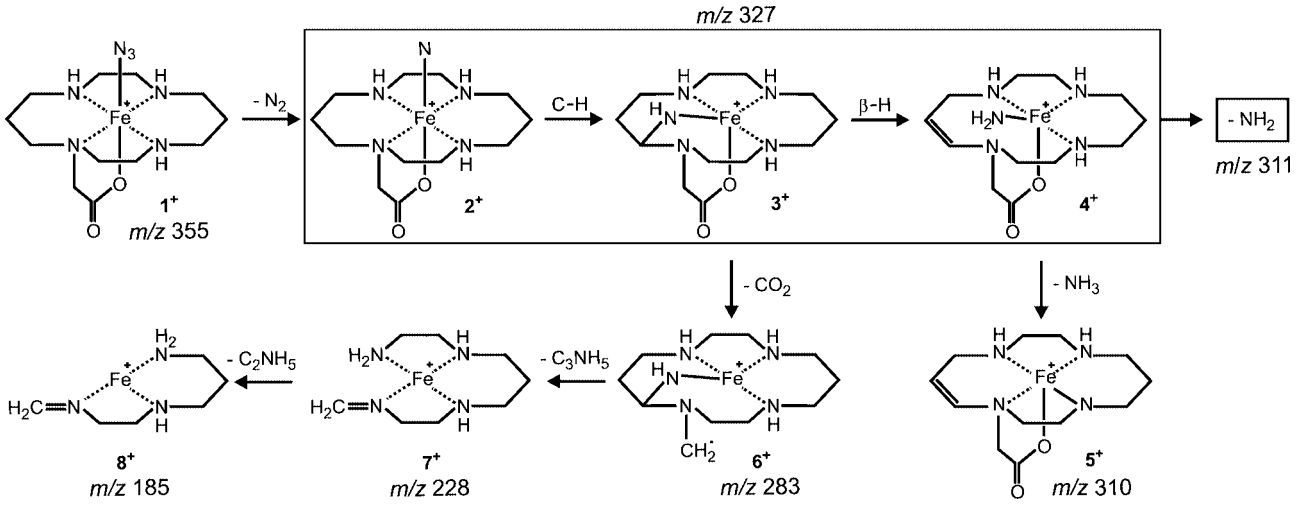


Scheme 1.

(here it is shown in the vicinity of the carboxymethyl substituent). The thus-formed insertion intermediate $\mathbf{3}^+$ can subsequently undergo β-hydrogen transfer to afford structure $\mathbf{4}^+$, from which either an $NH_2$ group can be lost directly at higher collision energies ($\Delta m$ = –16) or ammonia is released ($\mathbf{4}^+ \rightarrow \mathbf{5}^+$; $\Delta m$ = –17). As an alternative, decarboxylation of intermediate $\mathbf{3}^+$ is suggested to afford the aminoalkyl radical $\mathbf{6}^+$ ($\Delta m$ = –44), which then loses a $[C_3H_5N]$ unit in a rapid consecutive reaction to afford $\mathbf{7}^+$ ($\Delta m$ = –99); note that the latter process already has a related precedent in the mass spectra of $CH^+$ adducts of the cyclam ligand.[21] Eventual degradation of the neighboring $C_2$ bridge can then lead to $\mathbf{8}^+$ ($\Delta m$ = –142). Note, however, that we have deliberately not included the loss of $CH_2NH_2$ because the labeling patterns (particularly the lack of a mass shift upon $^{15}N$-labeling) preclude us from even proposing a speculative pathway.

The entire fragmentation sequence is thus fully in accordance with the formation of the genuine nitridoiron cation $\mathbf{2}^+$. Specifically, the suggested C–H bond insertions and the formations of $NH_2$ and $NH_3$ are indicative of the presence of a highly reactive intermediate which is capable of bond-activation processes such as the bare iron oxide cation $FeO^+$[22,23] or the iminoiron cation $FeNH^+$.[11,12] It is of crucial importance to note, however, that this chemical evidence very much supports the presence of structure $\mathbf{2}^+$ as an intermediate but does not prove that the long-lived $[\mathbf{1} - N_2]^+$ ion sampled in the MS/MS experiments described here still exhibits this particular structure. In fact, the experimental data reported so far are consistent with all isomeric structures $\mathbf{2}^+$–$\mathbf{4}^+$ suggested in Scheme 1 in that the reactions considered to be characteristic for the nitridoiron cation will also occur for the products of consecutive rearrangements.

In light of this, we finally attempted to probe the structure of $[\mathbf{1} - N_2]^+$ by investigating its ion/molecule reactions at thermal energy. To this end, mass-selected $[\mathbf{1} - N_2]^+$ was allowed to interact with butane, 1-butene, as well as deuterated methanol, where the order of the neutral reagents parallels the ease of bond-activation processes.[24,25] No reactions were observed at all with the two hydrocarbons, however, and with $CD_3OD$ only a very slow formation of the formal adduct $[\mathbf{1} - N_2 + CD_3OD]^+$ was observed. While again not providing unambiguous evidence, these preliminary reactivity studies suggest that long-lived $[\mathbf{1} - N_2]^+$ may indeed exist in an already rearranged structure such as $\mathbf{3}^+$ or $\mathbf{4}^+$. We would like to point out that this conclusion is all but trivial because it is quite often simply assumed that well-known reactions, such as the decomposition of an azide, lead to the species anticipated by analogies from other media. However, it needs to be tested in every instance that the particular structures are also maintained on a unimolecular level and are not altered by subsequent rearrangements. In the present case, for example, we do not have any reasonable doubt that the nitrido species $\mathbf{2}^+$ is formed as an intermediate – in fact it has been observed in frozen matrices[5] – but the experimental evidence obtained for the gaseous ion at least indicates that the long-lived ions bears a different connectivity.

## Conclusions

Electrospray mass spectrometry has been used to show that the decomposition of gaseous [(cyclam-acetato)Fe-$(N_3)$]$^+$ leads to the bare, high-valent $Fe^V$ nitride cation [(cyclam-acetato)FeN]$^+$, as already suggested for the condensed phase. Analysis of the fragmentation pattern implies, however, that this iron nitride species undergoes further rearrangements which mean that the long-lived ion might have a different structure. This question cannot be solved unambiguously with the mass spectrometric methods used here, and further studies of mass-selected [(cyclam-acetato)-FeN]$^+$ would hence be desirable in order to investigate

 © 2007 Wiley-VCH Verlag GmbH & Co. KGaA, Weinheim 

whether or not the cyclam-acetato ligand has indeed lost his "innocence", i.e. has undergone degradation processes due to the close vicinity of the free iron nitride unit. In this respect, the CID experiments reported here are not ideal for a distinction of isomeric structures,[18] and this question is perhaps best addressed by the appropriate spectroscopic experiments in the gas phase coupled with quantum chemical calculations; work along these lines is in progress in our laboratories.[26]

## Experimental Section

The experiments were performed using a VG BIO-Q mass spectrometer as described in detail elsewhere.[27] Briefly, the VG BIO-Q is a commercial instrument which consists of an electrospray ionization source combined with a tandem mass spectrometer of QHQ configuration (Q stands for quadrupole and H for hexapole). In the present experiments, millimolar solutions of [(cyclam-acetato)Fe($N_3$)][$PF_6$] in methanol/water (4:1) were introduced through a fused-silica capillary to the ESI source with a syringe pump (ca. 5 μL min$^{-1}$). Nitrogen was used as nebulizing and drying gas at a source temperature of about 80 °C. Maximal yields of the desired ions $\mathbf{1}^+$ and $\mathbf{2}^+$ (see below) were achieved by adjusting the cone voltage to about 30 and 60 V, respectively. For collision-induced dissociation (CID) at low collision energies, the ions of interest were mass-selected using Q1, interacted with xenon as a collision gas in the hexapole H under single-collision conditions (typically $2 \times 10^{-4}$ mbar) at variable collision energies ($E_{lab}$ = 0–20 eV), while scanning Q2 to monitor the ionic products. At $E_{lab}$ = 0 eV, no significant fragmentations of either mass-selected $\mathbf{1}^+$ or $\mathbf{2}^+$ were observed under these conditions. We note in passing that the sample examined contains some traces of potassium, which lowers the yield of Fe-containing cations in the ESI spectra somewhat but does not hinder the experiments.

As pointed out previously, the VG Bio-Q does not allow the direct extraction of quantitative threshold information from CID experiments due to several limitations of the commercial instrument.[27] For weakly bound ions,[28] for example, a non-negligible amount of ion decay is observed even at $E_{lab}$ = 0 eV, which is in part attributed to the presence of collision gas not only in the hexapole but also in the focusing regions between the mass analyzers. Note that this dissociation does not correspond to metastable ions because it does not occur in the absence of collision gas. To a first approximation, however, the energy dependence of the product distributions in the CID spectra can be modeled by a sigmoid function,[29] which allows the extraction of some semi-quantitative information about the energetics of the ions examined.[30] Nevertheless, the energy dependence of the CID fragments can be approximated by sigmoid functions of the type $I_i(E_{CM}) = \{BR_i/[1 + e^{(E_{1/2} - E_{CM})/b}]\}$ using a least-squares criterion; for the parent ion M, the relation is $I_M(E_{CM}) = \{1 - \Sigma(BR_i/[1 + e^{(E_{1/2,i} - E_{CM})/b}_i]\}$, where $BR_i$ is the branching ratio of a particular product ion ($\Sigma BR_i = 1$), $E_{1/2}$ is the energy at which the sigmoid function of ion intensities has reached half of its maximum, $E_{CM}$ is the collision energy in the center-of-mass frame [$E_{CM} = m_T/(m_T + m_I) \times E_{lab}$, where $m_T$ and $m_I$ stand for the masses of the collision gas and the ion, respectively], and $b$ describes the rise of the sigmoid curve. In consecutive dissociations, all secondary product ions were added to the intensity of the primary fragment. Further, non-negligible ion decay at $E_{lab}$ = 0 eV as well as some fraction of nonfragmenting parent ions at large collision energies were acknowledged by means of appropriate scaling and normalization procedures. This empirical, yet physically reasonable, approach is able to reproduce the measured ion yields quite well; note, however, that this simplified formalism does not explicitly include a treatment of competitive branching ratios at elevated energies. It is obvious, however, that the term $E_{1/2}$ used in the exponent corresponds neither to the intrinsic appearance energy of the fragmentation of interest nor to the thermochemical thresholds at 0 K. The phenomenological threshold energies given below were derived from linear extrapolations of the rise of the sigmoid curves at $E_{1/2}$ to the base line.

## Acknowledgments

Financial support by the Deutsche Forschungsgemeinschaft (SFB 546) and the Fonds der Chemischen Industrie is gratefully acknowledged. We gratefully acknowledge generous support by Prof. Karl Wieghardt and skilful technical assistance by Bernd Mienert.

[1] M. Costas, M. P. Mehn, M. P. Jenser, L. Que Jr, *Chem. Rev.* **2004**, *104*, 939.
[2] J. C. Price, E. W. Barr, B. Tirupati, J. M. Bollinger, C. Krebs, *Biochemistry* **2003**, *42*, 7497.
[3] J.-U. Rohde, J.-H. In, M. H. Lim, W. W. Brennessel, M. R. Bukowski, A. Stubna, E. Münck, W. Nam, L. Que Jr, *Science* **2003**, *299*, 1037.
[4] K. Meyer, E. Bill, B. Mienert, T. Weyhermüller, K. Wieghardt, *J. Am. Chem. Soc.* **1999**, *121*, 4859.
[5] N. Aliaga-Alcalde, S. DeBeer George, B. Mienert, E. Bill, K. Wieghardt, F. Neese, *Angew. Chem. Int. Ed.* **2005**, *44*, 2908.
[6] J. F. Berry, E. Bill, E. Bothe, S. DeBeer George, B. Miernert, F. Neese, K. Wieghardt, *Science* **2006**, *312*, 1937.
[7] P. J. Chirik, *Angew. Chem.* **2006**, *118*, 7110; *Angew. Chem. Int. Ed.* **2006**, *45*, 6956.
[8] J. A. Halfen, *Curr. Org. Chem.* **2005**, *9*, 657.
[9] H. Lebel, O. Leogane, K. Huard, S. Lectard, *Pure Appl. Chem.* **2006**, *78*, 363.
[10] S. Cenini, E. Gallo, A. Caselli, F. Ragaini, S. Fantauzzi, C. Piangiolino, *Coord. Chem. Rev.* **2006**, *250*, 1234.
[11] S. W. Buckner, J. R. Gord, B. S. Freiser, *J. Am. Chem. Soc.* **1988**, *110*, 6606.
[12] M. Brönstrup, I. Kretzschmar, D. Schröder, H. Schwarz, *Helv. Chim. Acta* **1998**, *81*, 2348.
[13] A. Fiedler, S. Iwata, *Chem. Phys. Lett.* **1997**, *271*, 143.
[14] Calculated with the Chemputer program developed by M. Winter, University of Sheffield; see: http://winter.group.shef.ac.uk/chemputer/.
[15] For a recent investigation of the gas-phase thermochemistry of cyclam complexes, see: A. T. Blades, P. Kebarle, *J. Phys. Chem. A* **2006**, *110*, 12055.
[16] N. Tsierkezos, D. Schröder, H. Schwarz, *J. Phys. Chem. A* **2003**, *107*, 9575.
[17] J. Roithová, J. Hrušak, D. Schröder, H. Schwarz, *Inorg. Chim. Acta* **2005**, *358*, 4287.
[18] D. Schröder, in *Encyclopedia of Mass Spectrometry*, vol. 1 (Ed.: P. B. Armentrout), Elsevier, Amsterdam, **2003**, 460.
[19] C. Trage, M. Diefenbach, D. Schröder, H. Schwarz, *Chem. Eur. J.* **2006**, *12*, 2454.
[20] J. Roithová, D. Schröder, H. Schwarz, *Eur. J. Org. Chem.* **2005**, 3304.
[21] H.-F. Wu, C.-H. Chen, M.-T. Wu, *J. Mass Spectrom.* **2004**, *39*, 396.
[22] T. C. Jackson, D. B. Jacobson, B. S. Freiser, *J. Am. Chem. Soc.* **1984**, *106*, 1252.
[23] Reviews: a) D. Schröder, H. Schwarz, *Angew. Chem. Int. Ed. Engl.* **1995**, *34*, 1973; b) D. Schröder, S. Shaik, H. Schwarz,

 © 2007 Wiley-VCH Verlag GmbH & Co. KGaA, Weinheim 

*Struct. Bond.* **2000**, *97*, 91; c) D. Schröder, H. Schwarz, *Top. Organomet. Chem.*, in press.
[24] H. H. Cornehl, C. Heinemann, D. Schröder, H. Schwarz, *Organometallics* **1995**, *14*, 992.
[25] S. Feyel, D. Schröder, H. Schwarz, *J. Phys. Chem. A* **2006**, *110*, 2647.
[26] D. Schröder, H. Schwarz, J. Roithová, P. Milko, *J. Phys. Chem. A* **2006**, *110*, 8346.
[27] D. Schröder, T. Weiske, H. Schwarz, *Int. J. Mass Spectrom.* **2002**, *219*, 729.
[28] D. Schröder, M. Semialjac, H. Schwarz, *Int. J. Mass Spectrom.* **2002**, *233*, 103.
[29] G. Bouchoux, D. Leblanc, J. Y. Salpin, *Int. J. Mass Spectrom.* **1996**, *153*, 37.
[30] D. Schröder, M. Engeser, M. Brönstrup, C. Daniel, J. Spandl, H. Hartl, *Int. J. Mass Spectrom.* **2003**, *228*, 743.

Received: August 31, 2006
Published Online: January 8, 2007

 © 2007 Wiley-VCH Verlag GmbH & Co. KGaA, Weinheim 

DOI: 10.1002/ejic.200600821

# Efficient DNA Cleavage Induced by Copper(II) Complexes of Hydrolysis Derivatives of 2,4,6-Tri(2-pyridyl)-1,3,5-triazine in the Presence of Reducing Agents

**Joaquín Borrás,*[a] Gloria Alzuet,[a] Marta González-Alvarez,[a] Jose L. García-Giménez,[a] Benigno Macías,[b] and Malva Liu-González[c]**

**Keywords:** Copper triazine complexes / Oxidative DNA damage / ROS scavengers / Oxidation

The reaction of 2,4,6-tri(pyridyl)-1,3,5-triazine (ptz) and copper(II) salts in dmf/water (1:1) results in the hydrolysis of ptz and formation of the anions bis(2-pyridylcarbonyl)amide ($ptO_2^-$) and bis(2-pyridylamine)amide ($ptN_2^-$), which are found in the complexes $[Cu(ptN_2)(OAc)]\cdot 3H_2O$ (**1**), $[Cu(ptO_2)(OAc)(H_2O)]\cdot H_2O$ (**2**), $[Cu(ptN_2)(for)]\cdot 3H_2O$ (**3**) (for = formate), $[Cu(ptO_2)(for)(H_2O)]$ (**4**), $[Cu(ptO_2)(benz)]\cdot H_2O$ (**5**) (benz = benzoate), and $[Cu(ptO_2)F(H_2O)]_2\cdot 3H_2O$ (**6**). This report includes the chemical and spectroscopic characterization of all these complexes along with the crystal structures of **4**–**6**. The coordination spheres of $Cu^{II}$ in **4** and **5** are best described as distorted tetragonal square pyramidal for the former and distorted square planar for the latter. The crystal structure of **6** shows the presence of two discrete monomeric $[Cu(ptO_2)F(H_2O)]$ entities in the crystallographic asymmetric unit in which both copper(II) ions have a distorted square-pyramidal coordination geometry. The binding of the complexes to DNA has been investigated with the aid of viscosity and thermal denaturation studies, both of which indicate that the interaction is probably due to the outer-sphere mechanism. The ability of the compounds to cleave DNA has also been tested. Efficient oxidative cleavage was observed in the presence of a mild reducing agent (ascorbate) and dioxygen. Mechanistic studies with reactive oxygen species (ROS) scavengers confirm that hydrogen peroxide, the hydroxyl radical, singlet oxygen-like species, and the superoxide anion are necessary diffusible intermediates in the scission process. A mechanism involving either the Fenton or the Haber–Weiss reaction plus the formation of copper oxene species is proposed for the DNA cleavage mediated by these compounds.

(© Wiley-VCH Verlag GmbH & Co. KGaA, 69451 Weinheim, Germany, 2007)

## Introduction

The interaction of reactive oxygen species (ROS) with DNA is of considerable interest because of the potential pathobiological significance of ROS-induced DNA damage. Such damage may be promutagenic and has been linked to the pathogenesis of human diseases such as cancer and aging.[1,2]

The transition metal ion catalyzed reduction of hydrogen peroxide has served as a useful model reaction for generating ROS. Reduction of $H_2O_2$ by copper ion produces highly reactive DNA-damaging species.[3] Copper ion induces significantly more DNA base damage in the presence of $H_2O_2$ than does ferrous ion, the other biologically relevant transition metal ion.[4,5] Moreover, copper is an important structural metal ion in chromatin,[6–8] which contains about one copper ion per kilobase.[6] For these reasons, there is an increased interest in the ability of copper ion to participate in DNA-damaging reactions in vivo.[8,9]

Kinetic,[9–11] inhibitor,[4,5,9] and sequence-context[12–15] studies have all suggested that DNA damage induced by copper ion in the presence of $H_2O_2$ occurs site-specifically at the sites of DNA-associated copper. However, the nature of the last DNA-oxidizing species produced by the interaction of the DNA-$Cu^I$ complex with $H_2O_2$ remains uncertain. Some investigators have suggested that the hydroxyl radical is the principal reactive intermediate,[9,16] while others have proposed less reactive intermediates such as an oxidocopper complex[11,14,15] or cupryl ion.[10] Regardless of the true nature of the reaction mechanism, exposure of DNA to copper has been reported to result in single- and double-strand breaks, modified bases, abasic sites, and DNA-protein crosslinks.[17,18]

2,4,6-Tri(2-pyridyl)-1,3,5-triazine (ptz; Scheme 1) is of current interest due to its utility as a spacer for designing multinuclear metal complexes. Compounds of this family of 2,4,6-triaryltriazines are usually stable against hydrolysis;

[a] Departament de Química Inorgànica, Facultat de Farmàcia, Universitat de València,
Vicent Andrés Estellés s/n, 46100 Burjassot, Spain
Fax: +34-963-544-960
E-mail: Joaquin.Borras@uv.es
[b] Departamento de Química Inorgánica, Facultad de Farmacia, Universidad de Salamanca
Campus Unamuno, 37007 Salamanca, Spain
[c] SCSIE, RX. Universitat de València,
50 Dr. Moliner, 46100 Burjassot, Spain

Supporting information for this article is available on the WWW under http://www.eurjic.org or from the author.

 © 2007 Wiley-VCH Verlag GmbH & Co. KGaA, Weinheim 

indeed, their hydrolysis requires the presence of a concentrated mineral acid and temperatures above 150 °C.[19] Lerner and Lippard[20,21] have found that ptz undergoes hydrolysis in the presence of $Cu^{II}$ in aqueous media. They have also reported the crystal structure of a copper(II) complex with a hydrolysis product of ptz. On the basis of the Cu–N bond lengths and angles of the carbonyl carbon atoms within the chelate ring, they suggested that the coordination of ptz induces an angular strain which allows a nucleophilic attack at the carbon atoms of the triazine ring by the solvent, which, in turn, results in the hydrolysis of ptz.[20,22] Kinetic and thermodynamic data have revealed that such a reaction probably occurs by nucleophilic attack at the triazine ring by $OH^-$ or $H_2O$.[23] However, a comparison of the structural and NMR spectroscopic data of rhodium and ruthenium complexes with ptz and a ptz derivative have led to the conclusion that a decrease in electron density at the carbon atoms of the triazine ring due to the electron-withdrawing effect (L→M) of the metal ion is a more predominant factor than angular strain in the metal-assisted hydrolysis of ptz.[24,25] Very recently, Li et al. have confirmed by a theoretical study that the hydrolysis of ptz is affected by the electron-withdrawing effect of the metal ions.[26]

The hydrolysis of ptz (Scheme 1) involves the formation of several intermediates containing either two imino nitrogens ($ptN_2^-$), one imino and one carbonyl ($ptNO^-$), and finally two carbonyl groups ($ptO_2^-$). The literature contains reports of metal complexes of the $ptO_2^-$ ligand, usually described as $bpca^-$, which is formed upon deprotonation of bis(2-pyridylcarbonyl)amine (Hbpca; Scheme 1). Mono-, di- (homo- and heteronuclear), and trinuclear complexes have been reported for various divalent and trivalent metal ions ($M^{II}$ = $Cu^{II}$, $Fe^{II}$, $Mn^{II}$, $Co^{II}$, $Ni^{II}$, and $Zn^{II}$; $M^{III}$ = $Fe^{III}$, $Rh^{III}$).[27–33] Among these, a ternary complex of copper(II) with one $bpca^-$ and another derivative formed during the hydrolysis process, namely 2-picolinamide, has been described.[28] The $ptO_2^-$ anion is obtained by means of a Cannizzaro-type reaction of pyridine-2-carboxaldehyde and NaNCO in the presence of copper metal ion.[34] Kawijara et al. have described the $ptN_2^-$ ligand,[35] which forms when ptz is mixed with copper(II) acetate at reflux in dry MeOH in the presence of $NaClO_4$. This ligand links the copper(II) ions to form a polymer chain.

In this paper we describe the crystal structures of copper(II) complexes with $ptO_2^-$ and other new copper complexes with $ptN_2^-$. The ptz and the ptz-derived ligands present a planar structure and can interact with the bases of DNA through stacking, which is one of the well-known conditions for interaction with DNA in order to give rise to ROS that then cleave the DNA. In this vein, Thorp et al.[36] have reported the DNA-cleavage activity of $Ru^{II}$-ptz complexes based on the formation of oxidoruthenium(IV). Our group has also published numerous papers about the nuclease activity of copper(II) complexes in the presence of reducing agents.[37–42] In this paper we assay the nuclease activity of the synthesized copper(II) complexes in the presence of reducing agents such as mercaptopropionic acid, ascorbic acid, and glutathione.

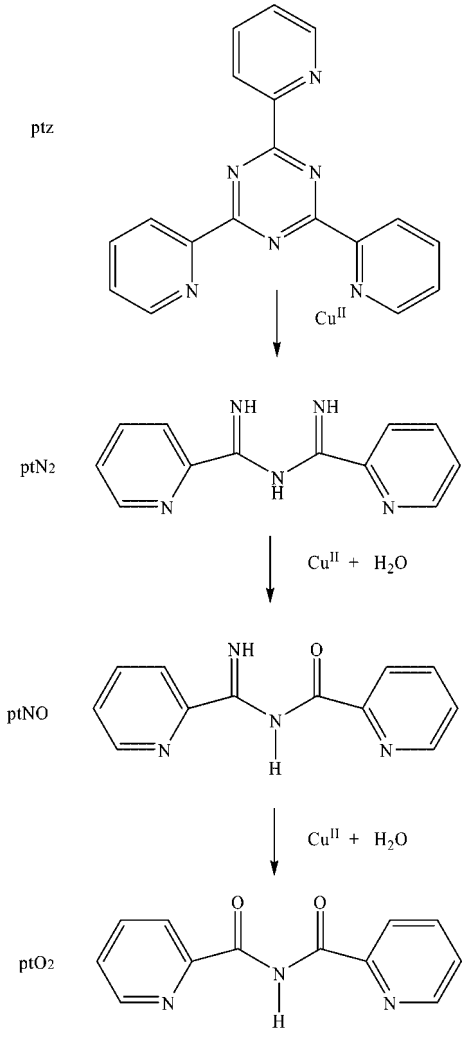


Scheme 1. Hydrolysis of 2,4,6-tri(2-pyridyl)-1,3,5-triazine.

## Results and Discussion

### Synthesis

The reaction of copper salts and ptz in dmf/$H_2O$ (4:1) resulted in the hydrolysis of ptz to $ptO_2^-$ or $ptN_2^-$ anions and afforded complexes of composition $[Cu(ptO_2)(X)(H_2O)]$, $[Cu(ptN_2)(X)]\cdot 3H_2O$ (X = acetate or formate), $[Cu(ptO_2)(benz)]\cdot H_2O$, and $[Cu(ptO_2)(F)(H_2O)]_2\cdot 3H_2O$.

### Crystal Structures

#### *[Cu(ptO$_2$)(for)(H$_2$O)] (4)*

Figure 1 shows an ORTEP view of the molecule with the atomic numbering scheme. Selected bond lengths and angles are listed in Table 1. The coordination sphere of copper(II) is best described as a distorted tetragonal square pyramid, as can be deduced from the $\tau$ value of 0.24.[43] The basal positions are occupied by the three nitrogen atoms of the $ptO_2^-$ ligand and one oxygen atom of the monodentate formate (for) anion. The apical site is occupied by the oxygen atom from the coordinated water molecule. The Cu–N

 © 2007 Wiley-VCH Verlag GmbH & Co. KGaA, Weinheim 

bond lengths, which range from 1.942(3) to 2.022(2) Å, are very similar to those found in other previously reported copper(II) complexes with $ptO_2^-$.[27] The Cu–$O_{for}$ and the Cu–$O_{water}$ bond lengths are 1.933(2) and 2.329(4) Å, respectively. The four basal atoms are quasi coplanar, and the copper ion is displaced 0.106 Å below the plane. The second oxygen of the formate group is located a long distance away from copper(II) [2.882(4) Å].

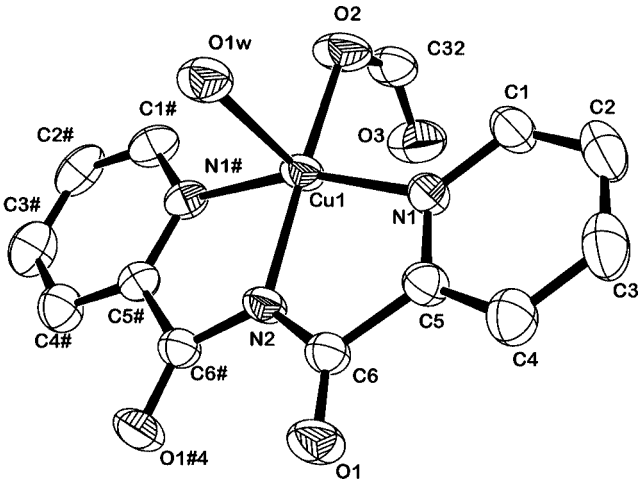


Figure 1. ORTEP drawing of [Cu($ptO_2$)(for)($H_2O$)] (**4**).

The crystal packing is stabilized by intermolecular hydrogen bonds. A moderate hydrogen bond is formed between O1W and O3 of the formate anion [O1W···O3 2.792(5) Å, O1W–H1A–O3 174.92(4.60)°]. In addition, O1W forms a moderately strong hydrogen bond with the carbonyl O1 [O1W···O1 2.944(3) Å, O1W–H1B–O1 137.56(6)°].[44]

### *[Cu($ptO_2$)(benz)]·$H_2O$ (5)*

An ORTEP view of the complex with the atom numbering scheme is shown in Figure 2. Selected bond lengths and angles are listed in Table 1. The geometry of the copper(II) ion can be described as distorted square planar. The coordination polyhedron is formed by a $ptO_2^-$, which functions as a tridentate ligand through the nitrogen atoms, and one carboxylate O atom from the benzoate (benz) ligand. The three Cu–N bond lengths, which are within the range 1.9268(13)–2.0007(16) Å, are similar to those of the complex described above and to those found for other copper(II) $ptO_2$ complexes.[27] The distortion of the square-planar geometry can be determined by the dihedral angle between the $CuN_2$ and CuNO planes. When the dihedral angle is 0° the geometry is planar while when the angle is 90° the stereochemistry is tetrahedral. In this complex, the dihedral angle value of 3.48(6)° indicates a very slightly distorted square planar configuration. A distorted square pyramid could be considered due to fact that the Cu–O4

Table 1. Selected bond lengths [Å] and angles [°] for [Cu($ptO_2$)(for)($H_2O$)] (**4**), [Cu($ptO_2$)(benz)]·$H_2O$ (**5**), and [Cu($ptO_2$)F($H_2O$)]$_2$·3$H_2O$ (**6**).[a]

| [Cu($ptO_2$)(for)($H_2O$)] (**4**) | | [Cu($ptO_2$)(benz)]·$H_2O$ (**5**) | | [Cu($ptO_2$)F($H_2O$)]$_2$·3$H_2O$ (**6**) | |
|---|---|---|---|---|---|
| Cu(1)–O(2) | 1.933(2) | Cu(1)–O(3) | 1.9268(13) | Cu(1)–N(2A) | 1.87(2) |
| Cu(1)–N(2) | 1.942(3) | Cu(1)–N(2) | 1.9279(14) | Cu(1)–F(1) | 1.933(12) |
| Cu(1)–N(1) | 2.022(2) | Cu(1)–N(1) | 1.9927(15) | Cu(1)–N(3A) | 1.95(3) |
| Cu(1)–N(1)#1 | 2.022(2) | Cu(1)–N(3) | 2.0007(16) | Cu(1)–N(1A) | 2.02(2) |
| Cu(1)–O(1W)#2 | 2.329(4) | Cu(1)–O(4) | 2.690(2) | Cu(1)–O(1) | 2.290(10) |
| | | | | Cu(2)–F(2) | 1.902(11) |
| | | | | Cu(2)–N(2B) | 1.94(2) |
| | | | | Cu(2)–N(3B) | 1.98(2) |
| | | | | Cu(2)–N(1B) | 2.03(2) |
| | | | | Cu(2)–O(2) | 2.283(11) |
| O(2)–Cu(1)–N(2) | 176.2(3) | O(3)–Cu(1)–N(2) | 178.09(6) | N(2A)–Cu(1)–F(1) | 173.1(6) |
| O(2)–Cu(1)–N(1) | 98.28(6) | O(3)–Cu(1)–N(1) | 99.37(7) | N(2A)–Cu(1)–N(3A) | 80.0(13) |
| N(2)–Cu(1)–N(1) | 81.46(6) | N(2)–Cu(1)–N(1) | 82.13(7) | F(1)–Cu(1)–N(3A) | 98.3(10) |
| O(2)–Cu(1)–N(1)#1 | 98.28(6) | O(3)–Cu(1)–N(3) | 96.25(6) | N(2A)–Cu(1)–N(1A) | 82.7(16) |
| N(2)–Cu(1)–N(1)#1 | 81.46(6) | N(2)–Cu(1)–N(3) | 82.19(6) | F(1)–Cu(1)–N(1A) | 97.8(11) |
| N(1)–Cu(1)–N(1)#1 | 161.35(12) | N(1)–Cu(1)–N(3) | 164.01(6) | N(3A)–Cu(1)–N(1A) | 160.6(13) |
| O(2)–Cu(1)–O(1W)#2 | 91.25(19) | | | N(2A)–Cu(1)–O(1) | 91.2(6) |
| N(2)–Cu(1)–O(1W)#2 | 92.51(17) | | | F(1)–Cu(1)–O(1) | 95.5(4) |
| N(1)–Cu(1)–O(1W)#2 | 94.08(9) | | | N(3A)–Cu(1)–O(1) | 94.5(7) |
| N(1)#1–Cu(1)–O(1W)#2 | 94.08(9) | | | N(1A)–Cu(1)–O(1) | 94.7(5) |
| | | | | F(2)–Cu(2)–N(2B) | 170.2(6) |
| | | | | F(2)–Cu(2)–N(3B) | 102.6(10) |
| | | | | N(2B)–Cu(2)–N(3B) | 77.5(14) |
| | | | | F(2)–Cu(2)–N(1B) | 94.1(12) |
| | | | | N(2B)–Cu(2)–N(1B) | 84.3(13) |
| | | | | N(3B)–Cu(2)–N(1B) | 160.5(14) |
| | | | | F(2)–Cu(2)–O(2) | 95.5(4) |
| | | | | N(2B)–Cu(2)–O(2) | 94.2(6) |
| | | | | N(3B)–Cu(2)–O(2) | 94.3(7) |
| | | | | N(1B)–Cu(2)–O(2) | 94.0(6) |

[a] Symmetry transformations used to generate equivalent atoms: #1 $x$, $y$, $-z + 2$; #2 $x + 1$, $y$, $z$.

 © 2007 Wiley-VCH Verlag GmbH & Co. KGaA, Weinheim 

distance is 2.690(2) Å. In this case, the carboxylate acts as a bidentate ligand, in contrast to that observed for $[Cu(ptO_2)(for)(H_2O)]$ (**4**) and for the previously reported complex $[Cu(ptO_2)(OAc)(H_2O)]\cdot H_2O$.[27] The four basal atoms deviate slightly from planarity, and the copper ion is displaced 0.037 Å below the plane.

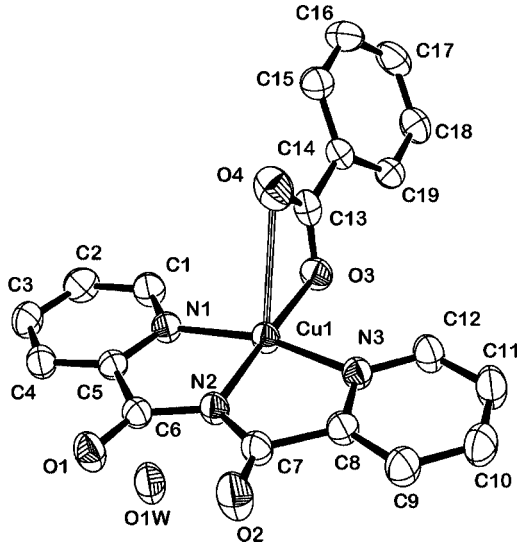


Figure 2. ORTEP drawing of $[Cu(ptO_2)(benz)]\cdot H_2O$ (**5**).

The molecule is stabilized by moderate and weak hydrogen bonds formed by O1W and two O carbonyl groups [O1W···O1 3.112(3) Å, O1W–H1A–O1 129.67(2.35)°; O1W···O2 2.858(2) Å, O1W–H1A–O2 150.18(2.45)°; O1W···O1 3.112(3) Å, O1W–H1B–O1 101.46(2.35)°].[44]

### *$[Cu(ptO_2)F(H_2O)]_2\cdot 3H_2O$ (6)*

Figure 3 displays the structure of complex $[Cu(ptO_2)F(H_2O)]_2\cdot 3H_2O$ with the labeling scheme. Selected interatomic distances and angles are listed in Table 1. The crystal structure shows the presence of two discrete monomeric $[Cu(ptO_2)F(H_2O)]$ entities and three lattice water molecules in the crystallographic asymmetric unit. Both copper(II) ions have a distorted square-pyramidal coordination geometry. The equatorial planes are defined by three nitrogen atoms of the $ptO_2^-$ ligand [Cu–N in the range 1.87(2)–2.02(2) Å for Cu(1) and 1.94(2)–2.03(3) Å for Cu(2)] and one fluoride anion [Cu(1)–F(1) 1.933(12), Cu(2)–F(2) 1.902(11) Å]. The apical position is occupied by the O atom of a water molecule [Cu(1)–O1 2.290(10), Cu(2)–O2 2.283(11) Å]. The equatorial plane displays a slight tetrahedral distortion as Cu(1) is displaced 0.1407 Å below the plane while Cu(2) lies 0.1559 Å above the plane. These two monomeric $[Cu(ptO_2)F(H_2O)]$ entities show different trigonality parameters ($\tau$). These different $\tau$ values − 0.24 for Cu(1) and 0.16 for Cu(2) − are due to crystal packing effects.

The $CuN_3F$ plane in each entity is coplanar to the $ptO_2^-$ ligand [angle between planes of 179.74° in Cu(1) and 178.63° in Cu(2)]. Moreover, both $[Cu(ptO_2)F(H_2O)]$ entities are also coplanar (the angle between the $Cu1N_3F$ and $Cu2N_3F$ planes is 178.70°).

The crystal structure is stabilized by many hydrogen-bonding interactions involving the fluoride anions (F1, F2), the oxygen atoms of the $ptO_2^-$ ligand (O2, O3), and the oxygen atoms of the water molecules (O1W, O2W, and O3W), some of which are of moderate strength.[44]

### Spectroscopic Properties

The IR spectra of $[Cu(ptN_2)(for)]\cdot 3H_2O$ (**3**; violet) and $[Cu(ptO_2)(for)(H_2O)]$ (**4**; blue) are significantly different (see Figure S1 in the Supporting Information). Thus, while the presence of a strong band at 1712 $cm^{-1}$, attributable to the ν(C=O) vibrations characteristic of the $ptO_2^-$ ligand,[27] is a significant feature in the IR spectrum of **4**, the IR spectrum of **3** does not show this band but rather shows a band

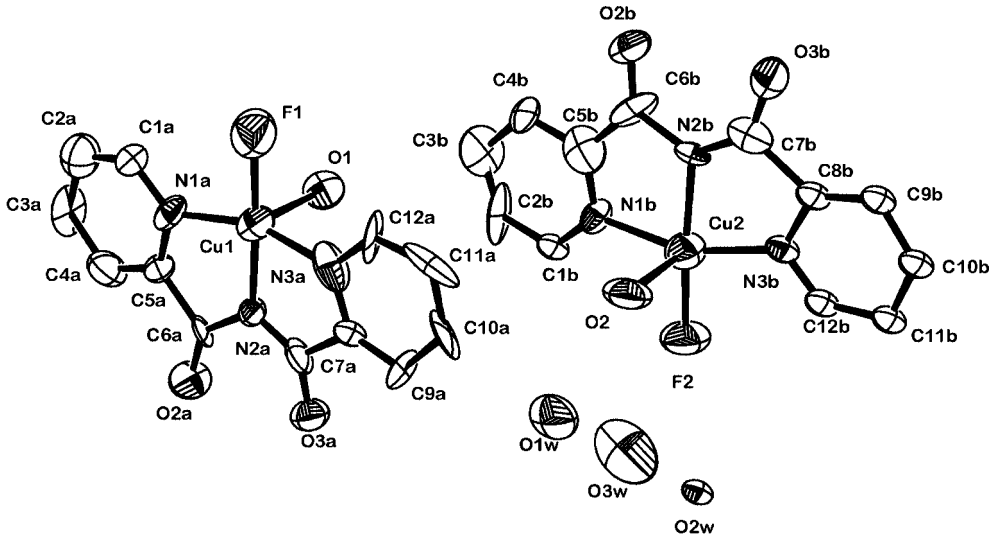


Figure 3. ORTEP drawing of $[Cu(ptO_2)F(H_2O)]_2\cdot 3H_2O$ (**6**).

 © 2007 Wiley-VCH Verlag GmbH & Co. KGaA, Weinheim 

at 1666 $cm^{-1}$ due to the $\delta$(N–H) vibrations. Another domain in which noteworthy differences exist between the IR spectra of both complexes is that between 3500 and 3000 $cm^{-1}$. For example, in the spectrum of **4**, a strong band with two peaks is observed at 3500 and 3440 $cm^{-1}$, attributable to ν(O–H) vibrations of the water molecules, while in the IR spectrum of **3** two bands appear at 3300 and 3100 $cm^{-1}$. These can most likely be assigned to ν(N–H) and ν(O–H) vibrations of the lattice water molecules, respectively. Both spectra exhibit bands at 1600 and 1350 $cm^{-1}$ that correspond to the $\nu_{as}(COO^-)$ and $\nu_s(COO^-)$ vibrations of the formate group.

The interpretation of the IR spectrum of **4** is corroborated by the corresponding IR spectra of $[Cu(ptO_2)(benz)]\cdot H_2O$ (**5**) and $[Cu(ptO_2)F(H_2O)]_2\cdot 3H_2O$ (**6**), which both show the strong band at 1712 $cm^{-1}$ and the two peaks at 3500 and 3440 $cm^{-1}$. In contrast, the IR spectrum of $[Cu(ptN_2)(OAc)]\cdot 3H_2O$ (**1**) shows no bands at 3500, 3440, or 1712 $cm^{-1}$, but rather at 3300, 3100, and 1660 $cm^{-1}$, similar to those of $[Cu(ptN_2)(for)]\cdot 3H_2O$ (**3**). In the IR spectrum of **5**, the bands attributable to the $\nu_{as}(COO^-)$ and $\nu_s(COO^-)$ vibrations of the benzoate group appear at 1600 and 1350 $cm^{-1}$, respectively.

Differences between complexes **3** and **4** are also found in their reflectance spectra. Thus, while the spectrum of **4** shows an unresolved broad d–d band at about 637 nm, that of **3** presents the d–d transition at about 565 nm. The same pattern is observed for the d–d bands of **2** (620 nm) and **1** (565 nm). Complexes **5** and **6** show the d–d band at 582 and 627 nm, respectively. The position of the d–d maximum thus follows the order **5** < **2** < **6** < **4**. The order of the d–d maximum position for the three latter complexes is in good agreement with the extent of geometrical distortion defined by the $\tau$ parameter: 0.16 (**2**), 0.16 and 0.24 (**6**), and 0.24 (**4**). In addition to the d–d band, a shoulder appears at about 420 nm in complexes **2**, **4**, and **5**; this can be assigned to an LMCT band. While the spectrum for the complex **1** does not exhibit this band, that of **6** shows a very strong band at 400 nm that can be attributed to an F–Cu LMCT band.

As the complexes are soluble in $H_2O$, we also recorded their UV/Vis spectra in aqueous solution. The spectra of aqueous solutions of complexes **5**, **2**, and **4** show the same maxima at 646 nm ($\varepsilon$ = 45, 91, and 90 $M^{-1}cm^{-1}$, respectively), thus suggesting that all three compounds contain the same chromophore in solution. The shift of the d–d band position with respect to that in the diffuse reflectance spectra is probably a consequence of the coordination of water molecules and the dissociation of the carboxylate anions. Moreover, a weak LMCT band at about 400 nm, similar to that observed in the solid-state spectra, is present, which indicates the interaction between the metal ion and the $ptO_2^-$ anion. Finally, the UV/Vis spectrum of an aqueous solution of complex **1**, while showing a band at 590 nm ($\varepsilon$ = 49 $M^{-1}cm^{-1}$), shows none around 400 nm (see Figure S2 in the Supporting Information), thus confirming the results in the solid state.

## EPR Spectroscopy

The X- and Q-band spectra of polycrystalline samples of the complexes were recorded at room temperature. Powder samples of **2**, **4**, **5**, and **6** were prepared from the single crystals. The EPR parameters obtained by simulation with WINSimphonia[45] are given in Table 2. The Q-band EPR spectrum of **5** is the axial-only spectrum, with $g_\parallel > g_\perp$. This indicates a mainly copper(II) $d_{x^2-y^2}$ orbital ground state. The other Q-band EPR spectra are rhombic, with $g_x < g_y < g_z$ and $R$ values ranging from 0.07 to 0.38, which suggests that the unpaired electron is in the $d_{x^2-y^2}$ orbital. The pattern of the EPR spectra is in good agreement with the square-planar geometry of **5** and the square-pyramidal geometry of **4** and **6**. Interestingly, the better resolution of the Q-band spectra allowed us to deduce the rhombic nature of the EPR spectrum of **2**, which had been hypothesized to be axial in a previous paper.[27]

It is also interesting to note that the EPR spectra of the complexes with the $ptO_2^-$ ligands (**2** and **4**) are different from those of the complexes with the $ptN_2^-$ ligand (**1** and **3**; see Figure S3 in the Supporting Information).

## Mass Spectral Analysis

The FAB spectra of complexes **2**, **4**, **5**, and **6** show a major peak at *m*/*z* 289 that corresponds to the $[Cu(ptO_2)]^+$ fragment due to the dissociation of the carboxylate or $F^-$ anions. There are, however, other significant peaks in the spectra. The FAB spectrum of **2**, for example, shows peaks at *m*/*z* 349 and 307 attributable to the $[Cu(ptO_2)(OAc) + H]^+$ and $[Cu(ptO_2) + H_2O]^+$ fragments. The FAB mass spectrum of **6**, which is similar to that of **2**, shows a peak at *m*/*z* 309 that can be attributed to the $[Cu(ptO_2)F + H]^+$ fragment. The FAB spectrum of complex **4** displays a peak at *m*/*z* 335 that corresponds to the $[Cu(ptO_2)(for)H]^+$ entity. The FAB spectrum of **5** shows a peak at *m*/*z* 411 that is

Table 2. X- and Q-band EPR data for the complexes.

| Compound | Q-band | | | | X-band | | | |
|---|---|---|---|---|---|---|---|---|
| | $g_x$ | $g_y$ | $g_z$ | $R$ | $g_\parallel$ | $g_\perp$ | $g_\parallel$ | $g_\perp$ |
| $[Cu(ptN_2)(OAc)]\cdot 3H_2O$ (**1**) | 2.045 | 2.062 | 2.217 | 0.11 | | | 2.060 | 2.208 |
| $[Cu(ptO_2)(OAc)(H_2O)]\cdot H_2O$ (**2**) | 2.046 | 2.049 | 2.230 | 0.07 | | | 2.211 | 2.060 |
| $[Cu(ptN_2)(for)]\cdot 3H_2O$ (**3**) | 2.043 | 2.064 | 2.216 | 0.14 | | | – | – |
| $[Cu(ptO_2)(for)(H_2O)]$ (**4**) | 2.044 | 2.064 | 2.238 | 0.17 | | | 2.063 | 2.19 |
| $[Cu(ptO_2)(benz)]\cdot H_2O$ (**5**) | – | – | – | – | 2.207 | 2.046 | 2.191 | 2.056 |
| $[Cu(ptO_2)F(H_2O)]\cdot H_2O$ (**6**) | 2.047 | 2.094 | 2.218 | 0.38 | | | – | – |

 © 2007 Wiley-VCH Verlag GmbH & Co. KGaA, Weinheim 

assigned to the $[Cu(ptO_2)(benz) + H]^+$ fragment. Interestingly, the mass spectrum of **1** presents a peak at *m*/*z* 305, which corresponds to the $[Cu(ptN_2) + H_2O]^+$ fragment. The presence of this peak agrees with the difference in mass between $ptO_2^-$ (226.06) and $ptN_2^-$ (224.09).

### Electrochemical Behavior

In the electroactivity domain of acetonitrile/$Bu_4NClO_4$, the cyclic voltammograms of complexes **2** and **5** have the same shape. A reduction peak is observed around –0.90 mV (vs. SCE) towards cathodic potentials; this can be attributed to the reduction of $Cu^{II}$ to $Cu^{I}$. The same $E_{cat}$ value for both complexes indicates that **2** and **5** give identical species in acetonitrile solution, probably the $[Cu(ptO_2)]^+$ entity, thus confirming the UV/Vis and FAB data. On the reverse scan, an anodic peak was found at about –0.2 mV. The voltammogram is clearly irreversible, probably because the $Cu^{I}$ species formed upon reduction of $Cu^{II}$ is unstable. The reduction peak at –0.90 mV relative to SCE corresponds to –0.68 mV relative to NHE. Such a value indicates a higher stabilization of the $Cu^{II}$ species with respect to those of $Cu^{I}$.

Attempts to determine the electrochemical behavior of the complexes in cacodylate buffer, the medium used in the biological studies, were unsuccessful because a solid precipitated in the electrolytic cell.

### DNA-Binding Interactions

The mode and propensity of binding of the complexes to calf-thymus DNA (CT-DNA) were studied with the aid of various techniques.

#### *Viscosity Measurements*

Viscosity measurements were carried out on CT-DNA by varying the concentration of the complexes. Hydrodynamic measurements that are sensitive to length changes are regarded as the least ambiguous and most critical tests of binding in solution. One classic intercalation model results in the lengthening of the DNA helix as the base-pairs are separated to accommodate the binding ligand, thus leading to the increase of DNA viscosity. In contrast, complexes that bind exclusively in DNA grooves by means of partial and/or nonclassical intercalation under the same conditions typically cause either a less pronounced change (positive or negative) of DNA solution viscosity or none at all.[46] The results obtained with our compounds reveal that the presence of complexes **3**, **5**, or **6** has no effect on the relative viscosity of CT-DNA. This indicates that the interaction of these complexes follows the general pattern of complexes that bind in DNA grooves by either a partial or nonclassical intercalation.

#### *Thermal Denaturation*

In order to obtain a better understanding of the interaction of the compounds, the binding of complexes **3**, **5**, and **6** to CT-DNA was studied by examining the thermal denaturation profile of DNA. The melting temperature ($T_m$) of CT-DNA upon addition of **3**, **5**, or **6** was found to be 75.7, 78.5, and 75.6 °C respectively. The complexes thus produce no increase in $T_m$ upon addition to DNA ($T_m$ = 76.6 °C in cacodylate buffer 0.1 M, NaCl 2 mM, pH 6.0). These results suggest that the complexes do not effect duplex stabilization through intercalation between the DNA base-pairs.

In summary, both viscosity and $T_m$ measurements indicate that the complexes do not intercalate between the DNA base-pairs. Most probably, the interaction of the complexes is mainly electrostatic through the phosphate backbone of the DNA since the compounds are present in solution as the positive $[Cu(ptO_2)]^+$ or $[Cu(ptN_2)]^+$ species.

### Nuclease Activity of Complexes and Mechanistic Investigations

#### *Oxidative DNA Cleavage Mediated by the Compounds*

The ability of complexes **1**–**6** to cleave DNA was investigated by means of gel electrophoresis with supercoiled pUC18 in 0.1 M cacodylate buffer (pH 6.0) and with ascorbate activation. Control experiments with $CuSO_4$ were also carried out under the same experimental conditions. The DNA cleavage activity of the complexes was assayed by the conversion of supercoiled DNA (SC, form I) to nicked circular (NC, form II) or linearized DNA (LC, form III). All the complexes were found to exhibit nuclease activity (Figure 4). At 6, 18, and 30 μM the compounds present the same cleavage pattern (lanes 2–4, parts a–f of Figure 4). The fact that the complexes exhibit similar nuclease activity is not surprising since they are dissociated in solution into $[Cu(ptO_2)]^+$ or $[Cu(ptN_2)]^+$. The $[Cu(ptO_2)]^+$ or $[Cu(ptN_2)]^+$ entities derived from the complexes must therefore be the active species that mediate DNA-strand scission since $CuSO_4$ at the highest concentration assayed is only able to produce a partial conversion of SC DNA into NC DNA (lane 6, Figure 4, g). Thus, the DNA cleavage activity of the compounds can be ascribed to the cooperative effect between $Cu^{II}$ and the $ptO_2^-$ or $ptN_2^-$ ligands.

Because certain copper(II) complexes are able to bring about hydrolytic cleavage of DNA, the possibility of a hydrolytic mechanism for the DNA damage mediated by these compounds must be taken into account. In order to clarify this point, the nuclease activity of complexes **1**–**6** was assayed without ascorbate activation. No DNA cleavage was observed, which indicates that a hydrolytic mechanism is not involved (lane 1, parts a–f of Figure 4).

The nuclease efficiency of a large number of $Cu^{II}$ complexes is known to depend on the reducing agent used for initiating the DNA cleavage. We thus tested the activity of **4** in the presence of various activators [ascorbate, hydrogen peroxide, 3-mercaptopropionic acid (MPA), and glutathione] at a 50-fold excess relative to the complex concentration. The results, shown in Figure 5 (A), indicate the following increasing order of efficiency: hydrogen peroxide < glutathione < MPA < ascorbate (cf. lanes 8, 10, 12, and 14 in Figure 5, A). By way of comparison, the same assays were

 © 2007 Wiley-VCH Verlag GmbH & Co. KGaA, Weinheim 

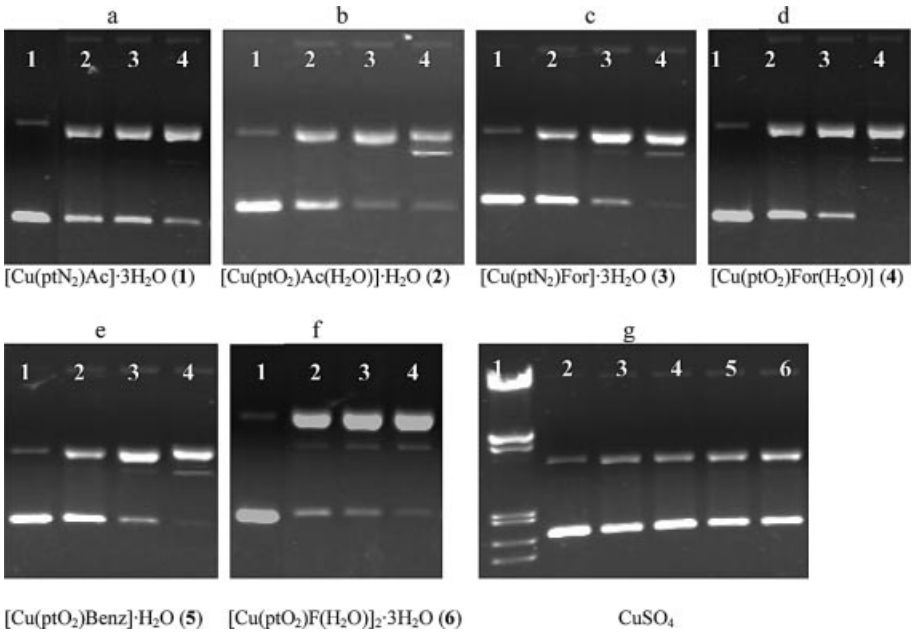


Figure 4. Agarose gel electrophoresis of pUC18 plasmid DNA treated with the complexes or $CuSO_4$ with [ascorbate]:[tested compound] = 100:1 or without ascorbate. Incubation time: 1 h (37 °C). (a) $[Cu(ptN_2)(OAc)]\cdot 3H_2O$ (**1**), (b) $[Cu(ptO_2)(OAc)(H_2O)]\cdot H_2O$ (**2**) (c) $[Cu(ptN_2)(for)]\cdot 3H_2O$ (**3**), (d) $[Cu(ptO_2)(for)(H_2O)]$ (**4**), (e) $[Cu(ptO_2)(benz)]\cdot H_2O$ (**5**), (f) $[Cu(ptO_2)F(H_2O)]_2\cdot 3H_2O$ (**6**), (g) $CuSO_4$; **a**–**f**: lane 1: 60 μM complex without ascorbate; lane 2: 6 μM complex with ascorbate 100×; lane 3: 18 μM complex with ascorbate 100×, 30 μM complex with ascorbate 100×; **g**: lane 1: λDNA/EcoRI + Hind III Marker; lane 2: supercoiled DNA; lane 3: supercoiled DNA with 3 mM ascorbate; lane 4: 6 μM $CuSO_4$ with ascorbate 100×; lane 5: 18 μM $CuSO_4$ with ascorbate 100×; lane 6: 30 μM $CuSO_4$ with ascorbate 100×.

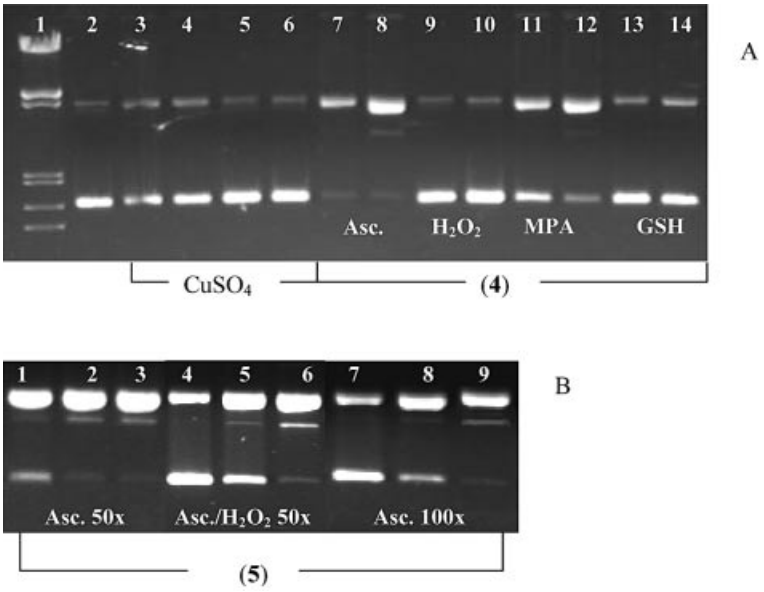


Figure 5. A) Agarose gel electrophoresis of pUC18 plasmid DNA treated with $[Cu(ptO_2)(for)(H_2O)]$ (**4**) in the presence of different reducing agents. Incubation time: 1 h (37 °C). Lane 1: λDNA/EcoRI + Hind III Marker; lane 2: supercoiled DNA; lane 3: $CuSO_4$ 30 μM + ascorbate 50×; lane 4: $CuSO_4$ 30 μM + $H_2O_2$ 50×; lane 5: $CuSO_4$ 30 μM + MPA 50×; lane 6: $CuSO_4$ 30 μM + glutathione 50×; lane 7: **4** 18 μM + ascorbate 50×; lane 8: **4** 30 μM + ascorbate 50×; lane 9: **4** 18 μM + $H_2O_2$ 50×; lane 10: **4** 30 μM + $H_2O_2$ 50×; lane 11: **4** 18 μM + MPA 50×; lane 12: **4** 30 μM + MPA 50×; lane 13: **4** 18 μM + glutathione 50×; lane 14: **4** 30 μM + glutathione 50×. B) Agarose gel electrophoresis of pUC18 plasmid DNA treated with $[Cu(ptO_2)(benz)]\cdot H_2O$ (**5**) in the presence of ascorbate and ascorbate/$H_2O_2$. Incubation time: 1 h (37 °C). Lane 1: **5** 6 μM + ascorbate 50×; lane 2: **5** 18 μM + ascorbate 50×; lane 3: **5** 30 μM + ascorbate 50×; lane 4: **5** 6 μM + ascorbate/$H_2O_2$ 50×; lane 5: **5** 18 μM + ascorbate/$H_2O_2$ 50×; lane 6: **5** 30 μM + ascorbate/$H_2O_2$ 50×; lane 7: **5** 6 μM + ascorbate 100×; lane 8: **5** 18 μM + ascorbate 100×; lane 9: **5** 30 μM + ascorbate 100×.

 © 2007 Wiley-VCH Verlag GmbH & Co. KGaA, Weinheim 

performed with $CuSO_4$. Lanes 3–6 (Figure 5, A) show that $CuSO_4$ at 30 μM is not an efficient chemical nuclease in the presence of these activating agents. Several authors have studied the influence of different reducing agents on the cleavage of DNA by copper(II) complexes.[47–50] Sigman et al.,[47] for example, examined the influence of the activating agent on the nuclease activity of a bis(*o*-phenanthroline)-copper(II) complex and deduced that ascorbic acid and 3-mercaptopropionic acid are the most efficient reducing agents. However, while these same authors found MPA to be superior to ascorbic acid because it produces less background cleavage, in our study ascorbic acid is clearly more efficient than MPA. Chiou et al.[48] have indicated that ascorbate is more effective in cleaving DNA than other reducing agents such as MPA and dithiothreitol even though the latter compounds possess higher reducing powers than ascorbate. The uniqueness of ascorbate as a reducer in the scission reaction may depend on its ability to generate hydrogen peroxide in the presence of oxygen and metal ions, whereas other reducing agents with a thiol group are known to produce superoxide, which rapidly undergoes dismutation in aqueous solution. Detmer et al.[49] have found that a combination of ascorbate and $H_2O_2$ is a more effective activating agent than ascorbate alone. In order to elucidate the influence of mixing ascorbate with $H_2O_2$, the cleavage process of **5** was studied with ascorbate/$H_2O_2$ (50×) or ascorbate (50× and 100×) as activators (Figure 5, B). No significant differences in DNA damage were found.

### *Mechanistic Studies*

The mechanism of pUC18 DNA cleavage by the compounds was studied using inhibiting reagents. The results for complexes **3** and **5** are shown in Figure 6. The involvement of ROS was investigated with standard hydroxyl radical scavengers (DMSO, *tert*-butyl alcohol, potassium iodide, and urea), singlet oxygen scavengers (azide and DABCO), superoxide radical scavengers (Tiron), and catalase. The groove binding preferences were tested in the presence of the minor groove binder distamycin and the major groove binder methyl green. The reduction of $Cu^{II}$ to $Cu^{I}$ during the cleavage process was evaluated with neocuproine, a ligand that chelates strongly to copper(I).

A strong inhibition of DNA cleavage mediated by **5** is observed upon addition of DMSO, *tert*-butyl alcohol, potassium iodide, or urea, thereby indicating that hydroxyl radical is involved in the cleavage process (lanes 4–7, Figure 6, A). The addition of sodium azide or DABCO (lanes 8 and 9, Figure 6, A) also decreases the cleavage efficiency, which indicates that either $^1O_2$ or a singlet-oxygen-like entity is one of the active oxygen intermediates responsible for the cleavage. The inhibitory activity of sodium azide can be ascribed to the affinity of the azide anion for transition metals.[51] Adding Tiron to the reaction mixture decreases the DNA damage slightly, which suggests that the superoxide anion is involved in the DNA scission (lane 10, Figure 6, A). Catalase also inhibits the nucleolytic process, which confirms that hydrogen peroxide is also necessary in the DNA strand scission (lane 14, Figure 6, A).

Treatment of pUC18 DNA with distamycin prior to the addition of **5** has no effect on the cleavage reaction mediated by the compound (lane 11, Figure 6, A). In contrast, prior treatment with methyl green attenuates the DNA strand scission (lane 12, Figure 6, A). It can thus be inferred from these results that **5** prefers major groove binding. Finally, neocuproine does not inhibit the DNA damage (lane 13, Figure 6, A). This is probably due to the strong redox stability of the $[Cu(ptO_2)]^+$ species, as was deduced from the electrochemical studies.

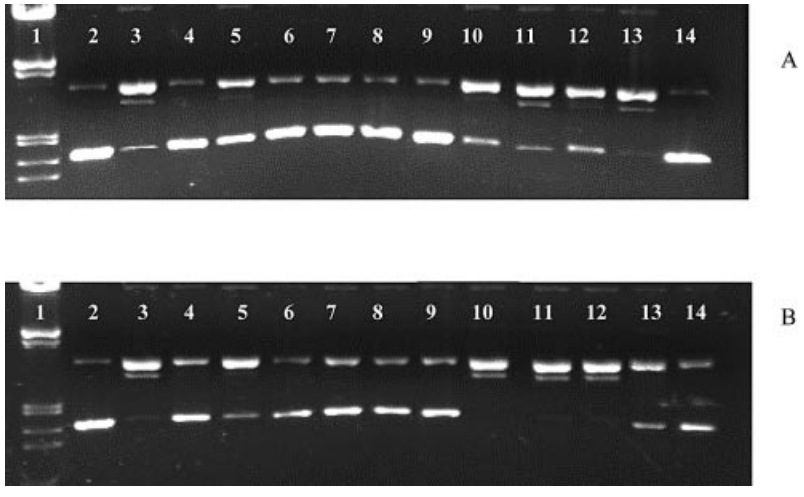


Figure 6. A) Agarose gel electrophoresis of pUC18 plasmid treated with 30 μM $[Cu(ptO_2)(benz)]\cdot H_2O$ (**5**) and 1.5 mM ascorbate/$H_2O_2$ in the presence of potential inhibitors. Incubation time: 1 h (37 °C). B) Agarose gel electrophoresis of pUC18 plasmid treated with 30 μM $[Cu(ptN_2)(for)]\cdot 3H_2O$ (**3**) and 1.5 mM ascorbate/$H_2O_2$ in the presence of potential inhibitors. Incubation time: 1 h (37 °C). Lane 1: λDNA/EcoRI + Hind III Marker; lane 2: supercoiled DNA; lane 3: complex without inhibitors; lane 4: complex + DMSO (1 M); lane 5: complex + *tert*-butyl alcohol (1 M); lane 6: complex + IK (0.4 M); lane 7: complex + urea (0.4 M); lane 8: complex + $NaN_3$(100 mM); lane 9: complex + DABCO (0.4 M); lane 10: complex + Tiron (10 mM); lane 11: complex + distamycin (8 μM); lane 12: complex + methyl green (2.5 μL of a 0.01 mg mL$^{-1}$ solution); lane 13: complex + neocuproine (75 μM); lane 14: complex + catalase (6.5 units).

 © 2007 Wiley-VCH Verlag GmbH & Co. KGaA, Weinheim 

The results for complex **3** (Figure 6, B) indicate that, as was the case for **5**, hydroxyl radical, $^1O_2$, and hydrogen peroxide are the active species responsible for the DNA damage (lanes 4–7, 8, 9, and 14, Figure 6, B). However, the cleavage scission process mediated by this compound is somewhat different from that of **5**. First of all, the superoxide anion does not seem to be involved in the DNA scission (lane 10, Figure 6, B). Also, since neocuproine attenuates the DNA cleavage in this case (lane 13, Figure 6, B), it seems likely that the reduction of $Cu^{II}$ to $Cu^{I}$ takes place, probably due to a lower stability of $[Cu(ptN_2)]^+$ with respect to that of $[Cu(ptO_2)]^+$. Moreover, in contrast to **5**, complex **3** does not show major or minor groove binding preferences (lanes 11 and 12, Figure 6, B).

The involvement of hydroxyl radicals was subjected to further studies. The hydroxyl release by **5** was studied by using 2-deoxy-D-ribose as a radical trap.[52] 2-Deoxy-D-ribose provides a chemically equivalent model for the oxidative target in DNA strand scission chemistry. The quantitation of 2-deoxy-D-ribose under sodium ascorbate/$H_2O_2$ activation conditions is displayed in Figure 7, where it can be seen that the calculated production of hydroxyl radicals increases to about 700 nM at 60 min.

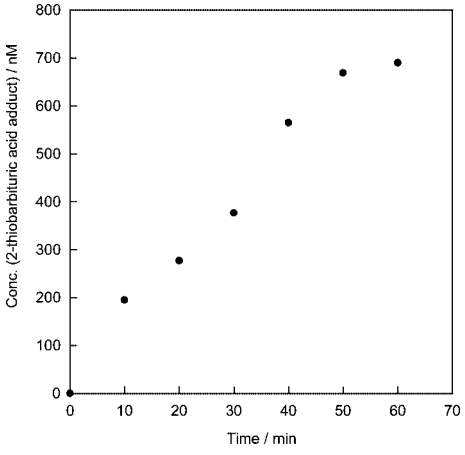


Figure 7. Production of hydroxyl radicals by $[Cu(ptO_2)(benz)]\cdot H_2O$ (**5**) as assayed by the 2-deoxy-D-ribose/2-thiobarbituric acid system.

In general, two mechanisms can be proposed for $Cu^{II}$ complexes that mediate oxidative DNA cleavage, one involving hydroxyl radicals and another involving metal-oxido species. Bocarsly et al.[49,50,53] have suggested that hydroxyl radicals are generated by a variety of chemical and physical processes. Transition-metal-mediated hydroxyl radical production is known to occur by a number of routes; two well-known pathways are the Fenton and the Haber–Weiss mechanism. In the Fenton mechanism, the metal acts as a catalyst for hydroxyl radical generation from hydrogen peroxide:

$$Cu^{II}L + ascH_2 \rightarrow Cu^{I}L + ascH^-$$

$$Cu^{I}L + H_2O_2 \rightarrow Cu^{II}L + OH^- + OH^{\cdot}$$

whereas the Haber–Weiss reaction involves the reaction between superoxide anion and hydrogen peroxide:

$$Cu^{I}L + O_2 \rightarrow Cu^{II}L + O_2^-$$

$$O_2^- + H_2O_2 \rightarrow O_2 + OH^- + OH^{\cdot}$$

On the other hand, Sigman has suggested that bis(*o*-phenanthroline)copper(II), the classic nuclease system, follows a different mechanistic pathway.[54] Thus, reduction of the copper to cuprous state leads to the generation of superoxide anion. The $O_2^-$ then dismutates to $H_2O_2$ and dioxygen and the hydrogen peroxide reacts with another equivalent of copper(I) to produce hydroxyl radical-like species, which may be bound to the metal. This species, which could be considered analogous to a metal-oxido species, is responsible for initiating DNA strand scission.[55]

Bocarsly et al. have compared their proposed mechanism with that of Cu-phenanthroline. They concluded that the differences between the two mechanisms are most likely related to the electronic differences between the ligands. Their mechanism is related to complexes with ligands that present σ character, while the mechanism proposed by Sigman is related to complexes with ligands that present π character (phen). Since the $ptO_2^-$ and the $ptN_2^-$ ligands in the title complexes present both σ and π character, both mechanisms can be proposed. This could explain why both hydroxyl radical scavengers and scavengers of singlet oxygen or singlet-oxygen-like species inhibit the DNA damage and strand breakage.

## Conclusions

Ternary copper(II) complexes with 2,4,6-tri(2-pyridyl)-1,3,5-triazine hydrolytic derivatives have been prepared and structurally characterized with the aid of X-ray crystallography. The binding of DNA has been studied with the aid of viscosity and $T_m$ measurements, which indicate that the complexes do not intercalate between the DNA base pairs. In contrast, an electrostatic interaction of the complexes with the phosphate backbone of the DNA can be deduced since the compounds are present in solution as the cationic $[Cu(ptO_2)]^+$ or $[Cu(ptN_2)]^+$ species. The complexes act as efficient chemical nucleases upon ascorbate activation. The participation of $H_2O_2$, hydroxyl radical, superoxide anion, and singlet-oxygen-like entities in the scission process mediated by the compounds suggests a mechanism pathway involving a Fenton or a Haber–Weiss reaction and copper(II)-oxene species.

## Experimental Section

**Materials and Physical Measurements:** Reagents and solvents were commercially available and used without further purification. pUC18 was purchased from Roche Diagnostics. Calf-thymus DNA (CT-DNA) was supplied by Sigma–Aldrich.

Elemental analyses (C,N,H) were performed with a Carlo–Erba AAS instrument. IR spectra (KBr disks) were recorded with a Mattson satellite FT-IR spectrometer in the range 4000–400 $cm^{-1}$. Diffuse reflectance spectra (nujol mulls) of the complexes were recorded with a Shimadzu UV-2101 PC spectrophotometer. UV/Vis

 © 2007 Wiley-VCH Verlag GmbH & Co. KGaA, Weinheim 

spectra of the complex solutions were recorded with an HP 8453 spectrophotometer. FAB mass spectra were obtained with a VG Autospec spectrometer with 3-nitrobenzyl alcohol as matrix. EPR spectra were recorded at the X- and Q-band frequencies at room temperature with a Bruker ELEXSYS spectrometer. Electrochemical measurements were performed with the aid of a Princeton Applied Research Model 273A potentiostat/galvanostat. Cyclic voltammograms were obtained for acetonitrile solutions of the complexes with [TBA][$ClO_4$] as the supporting electrolyte under argon. The electrochemical cell employed had a standard three-electrode configuration, with a platinum working electrode, a platinum wire counter electrode, and an Ag/AgCl reference electrode.

**[Cu(ptN$_2$)(OAc)]·3H$_2$O (1):** An aqueous solution of $Cu_2Ac_4{\cdot}2H_2O$ (10 mL; 200 mg, 1 mmol) was added with continuous stirring to 40 mL of a yellow dmf solution of ptz (312 mg, 1 mmol). A dark green solution was formed immediately; after 30 min it turned blue-green in color and overnight it became blue with a small amount of violet precipitate. The precipitate was isolated by filtration, washed, and dried until constant weight. Yield: 20%. $C_{14}H_{19}CuN_5O_5$: calcd. C 41.94, H 4.77, N 17.47; found C 41.15, H 4.59, N 17.76.

Slow evaporation of the filtrate yielded blue, needle-like crystals that correspond to [Cu(ptO$_2$)(OAc)(H$_2$O)]·H$_2$O (**2**), which has previously been reported as [Cu(bpca)(OAc)(H$_2$O)]·H$_2$O.[26]

**[Cu(ptN$_2$)(for)]·3H$_2$O (3) and [Cu(ptO$_2$)(for)(H$_2$O)] (4):** An aqueous solution of [Cu$_2$(for)$_4$]·4H$_2$O (10 mL; 225 mg, 1 mmol) was added to 40 mL of a yellow dmf solution of ptz (312 mg, 1 mmol). A dark green solution was formed immediately; after 30 min it turned blue-green in color and overnight it became blue with a small amount of violet precipitate. The precipitate was isolated by filtration, washed, and dried until constant weight. Yield: 16%. $C_{13}H_{16}CuN_5O_5$: calcd. C 42.43, H 3.92, N 18.20; found C 42.43, H 4.14, N 18.12.

Slow evaporation of the filtrate yielded blue, needle-like crystals that correspond to [Cu(ptO$_2$)(for)(H$_2$O)] (**4**). Yield: 47%. $C_{13}H_{11}CuN_3O_5$: calcd. C 44.26, H 3.14, N 11.47; found calcd. C 44.10, H 3.09, N 11.90.

**[Cu(ptO$_2$)(benz)]·H$_2$O (5):** This compound was obtained by a procedure similar to that described above, but with $Cu_2(benz)_4$ (611 mg, 1, mmol), which was obtained either by mixing copper(II) perchlorate with sodium benzoate or by electrochemical synthesis. Slow evaporation of the resulting blue solution gave rise to blue, needle-like crystals after four or five days. Yield: 65%. $C_{19}H_{15}CuN_3O_5$: calcd. C 53.21, H 3.52, N 9.75; found C 52.99, H 3.44, N 9.75.

**[Cu(ptO$_2$)F(H$_2$O)]·1.5H$_2$O (6):** The synthesis of this compound is similar to that described above, but with $CuF_2{\cdot}2H_2O$ (137 mg, 1 mmol). Blue crystals formed 4 or 5 days after its preparation. Yield: 22%. $C_{12}H_{13}CuFN_3O_{4.5}$: calcd. C 40.74, H 3.70, N 11.88; found C 41.50, H 3.38, N 12.03.

**X-ray Crystallography**

**[Cu(ptO$_2$)(for)(H$_2$O)] (4):** Greenish-blue crystal, size $0.2\times0.2\times0.2$ mm, orthorhombic, space group $A2_1am$ (determined from the systematic absences). Data collection was performed at 293 K with a Nonius Kappa-CCD single crystal diffractometer, with Mo-$K_\alpha$ radiation ($\lambda$ = 0.7173 Å). The crystal–detector distance was fixed at 45 mm, and a total of 148 images were collected by means of the oscillation method, with a scan angle per frame of 2° oscillation and a 10-s exposure time per image. Unit cell dimensions were determined from 895 reflections between $\theta$ = 2.91° and 27.49°. Unit cell parameters: $a$ = 6.575(5), $b$ = 13.462(5), $c$ = 15.516(5) Å, $V$ = 1373.4(12) Å$^3$, $Z$ = 4, $D_x$ = 1.701 mg m$^{-3}$, $\mu$ = 1.619 mm$^{-1}$. Multiple observations were averaged, $R_{merge}$ = 0.000, resulting in 1533 unique reflections of which 1390 were observed with $I > 2\sigma(I)$. Final mosaicity was 0.42. Data completeness was 99.4%. All non-hydrogen atoms were refined anisotropically. Hydrogen atoms were located in the difference Fourier map and located geometrically. The final cycle of full-matrix least-squares refinement based on 1533 reflections and 131 parameters converged to a final value of $R1$ [$F^2 > 2\sigma(F^2)$] = 0.0291, $wR2$ [$F^2 > 2\sigma(F^2)$] = 0.0732, $R1$ ($F^2$) = 0.0338, $wR2$ ($F^2$) = 0.0754. The final difference Fourier maps showed no peaks higher than 0.323 e Å$^{-3}$ at 1.56 Å from C32 and no troughs deeper than –0.513 e Å$^{-3}$ at 0.72 Å from Cu1.

**[Cu(ptO$_2$)(benz)]·H$_2$O (5):** Violet crystal, size $0.8\times0.16\times0.008$ mm, monoclinic, space group $P2_1/a$ (determined from the systematic absences). Data collection was performed at 293 K with a Nonius Kappa-CCD single crystal diffractometer, with Mo-$K_\alpha$ radiation ($\lambda$ = 0.7173 Å). The crystal–detector distance was fixed at 30.4 mm, and a total of 175 images were collected by means of the oscillation method, with a scan angle per frame of 1.7° oscillation and a 25-s exposure time per image. Unit cell dimensions were determined from 6088 reflections between $\theta$ = 0.998° and 33.142°. Unit cell parameters: $a$ = 10.359(5), $b$ = 10.295(5), $c$ = 16.555(5) Å, $\beta$ = 99.482(5)°, $V$ = 1741.4(13) Å$^3$, $Z$ = 4, $D_x$ = 1.636 mg m$^{-3}$, $\mu$ = 1.293 mm$^{-1}$. Multiple observations were averaged, $R_{merge}$ = 0.027, resulting in 6517 unique reflections of which 4279 were observed with $I > 2\sigma(I)$. Final mosaicity was 0.6. Data completeness was 98.5%. All non-hydrogen atoms were refined anisotropically. Hydrogen atoms were located in the difference Fourier map and located geometrically. The final cycle of full-matrix least-squares refinement based on 6517 reflections and 315 parameters converged to a final value of $R1$ [$F^2 > 2\sigma(F^2)$] = 0.0381, $wR2$ [$F^2 > 2\sigma(F^2)$] = 0.0887, $R1$ ($F^2$) = 0.0701, $wR2$ ($F^2$) = 0.0997. The final difference Fourier maps showed no peaks higher than 0.43 e Å$^{-3}$ at 0.71 Å from C5 and no troughs deeper than 0.56 e Å$^{-3}$ at 0.66 Å from Cu1.

**[Cu(ptO$_2$)F(H$_2$O)]$_2$·3H$_2$O (6):** Blue crystal, size $0.4\times0.25\times0.15$ mm, triclinic, space group $P\bar{1}$. Data collection was performed at 293 K with a Nonius Kappa2000 single crystal diffractometer, with Cu-$K_\alpha$ radiation ($\lambda$ = 1.54184 Å). The crystal–detector distance was fixed at 35 mm, and a total of 261 images were collected by means of the oscillation method, with a scan angle per frame of 2° oscillation and 2-s exposure time per image. Unit cell dimensions were determined from 1136 reflections between $\theta$ = 0.999° and 47.840°. Unit cell parameters: $a$ = 6.7680(4), $b$ = 10.2740(5), $c$ = 20.8690(10) Å, $\alpha$ = 98.635(2)°, $\beta$ = 90.641(2)°, $\gamma$ = 107.633(2)°, $V$ = 1364.78(12) Å$^3$, $Z$ = 2, $D_x$ = 1.722 mg m$^{-3}$, $\mu$ = 2.621 mm$^{-1}$. Multiple observations were averaged, $R_{merge}$ = 0.000, resulting in 1477 unique reflections of which 745 were observed with $I > 2\sigma(I)$. Final mosaicity was 0.65. Data completeness was 59.4%. All non-hydrogen atoms were refined anisotropically. Hydrogen atoms were located in the difference Fourier map and located geometrically. The final cycle of full-matrix least-squares refinement based on 1477 reflections and 407 parameters converged to a final value of $R1$ [$F^2 > 2\sigma(F)^2$] = 0.048, $wR2$ [$F^2 > 2\sigma(F^2)$] = 0.122, $R1$ ($F^2$) = 0.108, $wR2$ ($F^2$) = 0.162. The final difference Fourier maps showed no peaks higher than 0.36 e Å$^{-3}$ at 0.92 Å from H3B and no troughs deeper than –0.37 e Å$^{-3}$ at 0.31 Å from H2A.

Data collection for all complexes was performed with the program Collect.[56] Data reduction and cell refinement were performed with the programs HKL Denzo and Scalepack.[57] The crystal structure was solved by direct methods with the program SIR-97.[58] Aniso-

 © 2007 Wiley-VCH Verlag GmbH & Co. KGaA, Weinheim 

Table 3. Crystal and structure refinement data for [Cu(ptO$_2$)(for)(H$_2$O)] (**4**), [Cu(ptO$_2$)(benz)]·H$_2$O (**5**) and [Cu(ptO$_2$)F(H$_2$O)]$_2$·3H$_2$O (**6**).

| | [Cu(ptO$_2$)(for)(H$_2$O)] (**4**) | [Cu(ptO$_2$)(benz)]·H$_2$O (**5**) | [Cu(ptO$_2$)F(H$_2$O)]$_2$·3H$_2$O (**6**) |
|---|---|---|---|
| Empirical formula | $C_{13}H_{11}CuN_3O_5$ | $C_{19}H_{15}CuN_3O_5$ | $C_{24}H_{26}Cu_2F_2N_6O_9$ |
| Formula weight | 351.78 | 428.88 | 707.59 |
| Temperature [K] | 293(2) | 293(2) | 293(2) |
| Wavelength [Å] | 0.71069 | 0.71069 | 1.54184 |
| Crystal system, space group | cba, $A2_1am$ | monoclinic, $P2_1/a$ | triclinic, $P\bar{1}$ |
| $a$ [Å] | 6.575(5) | 10.359(5) | 6.7680(4) |
| $b$ [Å] | 13.462(5) | 10.295(5) | 10.2740(5) |
| $c$ [Å] | 15.516(5) | 16.555(5) | 20.8690(10) |
| $\alpha$ [°] | 90.000(5) | 90.000(5) | 98.635(2) |
| $\beta$ [°] | 90.000(5) | 99.482(5) | 90.641(2) |
| $\gamma$ [°] | 90.000(5) | 90.000(5) | 107.633(2) |
| Volume [Å$^3$] | 1373.4(12) | 1741.4(13) | 1364.78(12) |
| $Z$, calculated density [Mg m$^{-3}$] | 4, 1.701 | 4, 1.636 | 2, 1.722 |
| Absorption coefficient [mm$^{-1}$] | 1.619 | 1.293 | 2.621 |
| $F$(000) | 712 | 876 | 720 |
| Limiting indices | $8 \le h \le 8$ | $-15 \le h \le 15$ | $-6 \le h \le 6$ |
| | $-17 \le k \le 17$ | $-15 \le k \le 14$ | $-9 \le k \le 9$ |
| | $-19 \le l \le 20$ | $-25 \le l \le 25$ | $0 \le l \le 16$ |
| Reflections collected/unique | 1568/1533 [$R_{int}$ = 0.0000] | 10399/6517 [$R_{int}$ = 0.0272] | 2561/1477 [$R_{int}$ = 0.0000] |
| Data/restraints/parameters | 1533/2/131 | 6517/0/315 | 1477/3/407 |
| Final $R$ indices [$I > 2\sigma(I)$] | $R1$ = 0.0291, $wR2$ = 0.0732 | $R1$ = 0.0381, $wR2$ = 0.0887 | $R1$ = 0.0476, $wR2$ = 0.1218 |
| $R$ indices (all data) | $R1$ = 0.0338, $wR2$ = 0.0754 | $R1$ = 0.0701, $wR2$ = 0.0977 | $R1$ = 0.1079, $wR2$ = 0.1615 |

tropic least-squares refinement was carried out with SHELXL-97.[59] Geometrical calculations were made with PARST.[60] The crystallographic plots were made with ORTEP.[61] A summary of the crystallographic data of the complexes is given in Table 3.

CCDC-615303, -615304, and -615305 (for **4**–**6**, respectively) contain the supplementary crystallographic data for this paper. These data can be obtained free of charge from The Cambridge Crystallographic Data Centre via www.ccdc.cam.ac.uk/data_request/cif.

**Viscosity Measurements:** Viscosity experiments were carried out with a Cannon 25 L97 viscometer immersed in a Julabo thermostatted water bath maintained at 25.0 ± 0.1 °C. Solutions of the complexes (1–10 μM) in cacodylate buffer (pH 6.0) were added to a calf-thymus DNA (50 μM base pairs) solution in cacodylate buffer. The flow times were measured with a digital stopwatch. The flow measurements were performed in triplicate. Data are presented as $(\eta/\eta_0)^{1/3}$ vs. the ratio of the concentration of complex and DNA, where $\eta$ is the viscosity of DNA in the presence of the complex and $\eta_0$ is the viscosity of DNA alone. Viscosity values were calculated from the observed flow time of a DNA-containing solution corrected for the flow time of buffer alone ($t_0$), $\eta = t - t_0$.

**Thermal Denaturation Experiments:** DNA-melting experiments were carried out by monitoring the absorbance (260 nm) of CT-DNA (100 μM base-pairs) at different temperatures in the absence and presence of the complexes in a 4:1 DNA/complex ratio. Measurements were performed with an Agilent 8453 UV/Vis spectrophotometer equipped with a Peltier temperature-controlled sample cell and driver (Agilent 89090A). The solution containing the ternary complex and CT-DNA in 0.1 M cacodylate buffer (2 mM NaCl, pH 6.0) was stirred continuously and heated with a rate of temperature increase of 1 °C min$^{-1}$. The temperature interval studied ranged from 25 to 90 °C.

**pUC18 DNA Cleavage:** A typical reaction with the complexes was undertaken by mixing 7 μL of 0.1 M cacodylate buffer (pH 6.0), 1 μL of pUC18 (0.25 μg μL$^{-1}$), 6 μL of a solution of the tested complex at increasing concentrations between 20 and 100 μM, and 6 μL of ascorbate (100-fold molar excess relative to the concentration of the complex) in cacodylate buffer. The mixtures were allowed to stand for 1 h at 37 °C, then 3 μL of a quench buffer solution consisting of 0.25% bromophenol blue, 0.25% xylene cyanole, and 30% glycerol was added. The solution was then subjected to electrophoresis on a 0.8% agarose gel in 0.5× TBE buffer (0.045 M tris, 0.045 M boric acid, and 1 mM EDTA) containing 2 μL per 100 mL of a solution of ethidium bromide (10 mg mL$^{-1}$) at 80 V for about 2 h. The gel was photographed on a capturing gel printer plus TDI.

To test for the presence of reactive oxygen species (ROS) generated during strand scission, various scavengers were added to the reaction mixtures. The scavengers used were Tiron (10 mM), DMSO (1 M), *tert*-butyl alcohol (1 M), potassium iodide (0.4 M), urea (0.4 M), sodium azide (100 mM), DABCO (0.4 M), and catalase (6.5 units). An assay in the presence of the minor groove binder distamycin (8 μM) and the major groove binder methyl green (2.5 μL of a 0.01 mg mL$^{-1}$ solution) was also performed. Neocuproine, a ligand that chelates strongly to copper(I), was tested at 75 μM. Samples were treated as described above.

**Hydroxyl Radical Assay by 2-Deoxy-D-ribose Degradation:** Hydroxyl radical production by the complexes was assayed by degradation of 2-deoxy-D-ribose followed by quantitation of the 2-thiobarbituric acid adduct.[62] A 100 μM solution of metal complex was treated at room temperature with 4 mM 2-deoxy-D-ribose with activation by 50 mM sodium ascorbate and $H_2O_2$. Reactions were performed in a 4 mL volume of 0.1 M cacodylate buffer (pH 6.0). Reaction solutions were quenched with EDTA (2.4 mM final concentration) and stored in ice for 5 min. Each aliquot was then treated with 2-thiobarbituric acid (1.1 mM final concentration) at 95 °C for 15 min. The chromophore concentration was measured from its fluorescence intensity at 553 nm (excitation at 532 nm). The fluorescence intensity was used due to its sensitivity and also to the fact that ascorbate by-products absorb in the visible region and therefore interfere with visible quantitation of the thiobarbituric adduct. Fluorescence intensity was converted to concentration with a standard fluorescence curve constructed from known concentrations of the chromophore, synthesized from malondialdehyde and 2-thiobarbituric acid.[63] Blank reactions lacking a cleavage agent were included in each run and the blank intensity was subtracted from each experimental point.

 © 2007 Wiley-VCH Verlag GmbH & Co. KGaA, Weinheim 

**Supporting Information** (see also the footnote on the first page of this article): IR spectra of $[Cu(ptN_2)(for)]\cdot 3H_2O$ (**3**) and the $[Cu(ptO_2)(for)(H_2O)]$ (**4**; Figure S1); UV/Vis spectra of aqueous solutions of $[Cu(ptN_2)(OAc)]\cdot 3H_2O$ (**1**) and $[Cu(ptO_2)(OAc)(H_2O)]\cdot H_2O$ (**2**; Figure S2); EPR spectra of $[Cu(ptN_2)(for)]\cdot 3H_2O$ (**3**) and $[Cu(ptO_2)(for)(H_2O)]$ (**4**; Figure S3).

## Acknowledgments

J. B., G. A., and J. L. G.-G acknowledge financial support from the Spanish Centro de Investigación Científica y Tecnólogica (CICYT) (CTQ2004-03735). M. G.-A. wishes to thank the city government of Valencia (Spain) for a Carmen and Severo Ochoa postdoctoral fellowship. B. M. acknowledges financial support from the Junta de Castilla y León (SA056A05).

[1] S. S. Wallace, *Int. J. Radiat. Biol.* **1994**, *66*, 579–589.
[2] K. Z. Guyton, T. W. Kensler, *Br. Med. Bull.* **1993**, *49*, 523–544.
[3] O. I. Arouma, B. Haliwell, E. Gajewski, M. Dizdaroglu, *Biochem. J.* **1991**, *273*, 601–604.
[4] M. Dizdaroglu, G. Rao, D. A. Beary, R. A. LaBiche, K. J. Hardy, *Arch. Biochem. Biophys.* **1991**, *285*, 317–324.
[5] S. E. Bryant, D. A. Vizard, D. A. Beary, R. A. LaBiche, K. J. Hardy, *Nucleic Acid Res.* **1981**, *9*, 5811–5823.
[6] C. D. Lewis, U. K. Laemli, *Cell* **1982**, *29*, 171–181.
[7] A. M. George, S. A. Sabovijev, L. E. Hart, W. A. Cramp, G. Harris, S. Homsey, *Br. J. Cancer* **1987**, *55*, 141–144.
[8] R. Stoewe, W. A. Prutz, *Free Rad. Biol. Med.* **1987**, *3*, 97–105.
[9] M. Dizdaroglu, O. I. Arouma, B. Haliwell, *Biochemistry* **1990**, *29*, 8447–8451.
[10] M. Masarwa, H. Cohen, D. Meyerstein, D. L. Hickman, A. Bakac, J. H. Espenson, *J. Am. Chem. Soc.* **1988**, *110*, 4293–4297.
[11] J. Sagripanti, K. H. Kraemer, *J. Biol. Chem.* **1989**, *264*, 1729–1734.
[12] K. Yamamoto, S. Kawanishi, *J. Biol. Chem.* **1989**, *264*, 15435–15440.
[13] G. R. A. Johnson, N. B. Nazat, R. A. Saadalla-Nazhat, *J. Chem. Soc., Faraday Trans. 1* **1988**, *84*, 501–510.
[14] N. C. Thomas, B. L. Iolcy, A. L. Rheingold, *Inorg. Chem.* **1988**, *27*, 3426–3429.
[15] S. Chirayil, V. Hegde, Y. Jahng, R. P. Thummel, *Inorg. Chem.* **1991**, *30*, 2821–2823.
[16] N. Gupta, N. Grover, G. A. Neyhart, P. Singh, H. B. Thorp, *Inorg. Chem.* **1993**, *32*, 310–316.
[17] R. M. Berger, J. R. Holcombe, *Inorg. Chim. Acta* **1995**, *232*, 217–221.
[18] R. M. Berger, D. D. Ellis II, *Inorg. Chim. Acta* **1996**, *241*, 1–4.
[19] E. M. Smolin, L. Rapoport, *S-Triazines and Derivatives*, Interscience, New York, **1959**, p. 163.
[20] E. I. Lerner, S. J. Lippard, *J. Am. Chem. Soc.* **1976**, *98*, 5397–5398.
[21] E. I. Lerner, S. J. Lippard, *Inorg. Chem.* **1977**, *16*, 1546–1551.
[22] J. Faus, M. Julve, J. M. Amigo, T. Debaerdemaeker, *J. Chem. Soc., Dalton Trans.* **1989**, 1681–1687.
[23] P. A. Gillard, P. A. Williams, *Transition Met. Chem.* **1979**, *4*, 18–23.
[24] P. Paul, B. Tyagi, M. M. Bhadbhade, E. Suresh, *J. Chem. Soc., Dalton Trans.* **1997**, 2273–2277.
[25] P. Paul, B. Tyagi, A. K. Bilakhiya, M. M. Bhadbade, G. Ramachandaiah, *Inorg. Chem.* **1998**, *37*, 5733–5742.
[26] X.-P. Zhou, D. Li, S.-L. Zheng, X. Zhang, T. Wu, *Inorg. Chem.* **2006**, *45*, 7119–7125.
[27] J. V. Folgado, E. Coronado, D. Beltrán-Porter, R. Burriel, A. Fuertes, C. Miratvilles, *J. Chem. Soc., Dalton Trans.* **1988**, 3041–3045.
[28] A. Cantarero, J. M. Amigo, J. Faus, M. Julve, T. Debaerdemaeker, *J. Chem. Soc., Dalton Trans.* **1988**, 2033–2039.
[29] J. V. Folgado, E. Martinez-Tamayo, A. Beltrán-Porter, D. Beltrán-Porter, *Polyhedron* **1989**, *8*, 1077–1083.
[30] A. Kamiyama, T. Noguchi, T. Kajiwara, T. Ito, *Inorg. Chem.* **2002**, *41*, 507–512.
[31] T. Glaser, T. Lugger, R. Fröhlich, *Eur. J. Inorg. Chem.* **2004**, 394–400.
[32] B. Casellas, F. Constantino, A. Mandonnet, A. Caneschi, D. Gatteschi, *Inorg. Chim. Acta* **2005**, *358*, 177–185.
[33] S. A. Cotton, V. Franckevicius, M. F. Mahon, L. L. Ooi, P. R. Raithby, S. A. Teat, *Polyhedron* **2006**, *25*, 1057–1068.
[34] S. R. Dey, C. R. Choudhury, S. P. Dey, D. K. Dey, N. Mondal, S. O. G. Mahalli, K. M. A. Malik, S. Mitra, *J. Chem. Res. (S)* **2002**, 496–499.
[35] T. Kawijara, A. Kamiyama, T. Ito, *Chem. Commun.* **2002**, 1256–1257.
[36] N. Gupta, N. Grover, G. A. Neyhart, P. Singh, H. B. Thorp, *Inorg. Chem.* **1993**, *32*, 310–316.
[37] M. González-Álvarez, G. Alzuet, J. Borrás, B. Macías, M. Del Olmo, M. Liu-González, F. Sanz, *J. Inorg. Biochem.* **2002**, *89*, 29–35.
[38] B. Macías, I. García, M. J. Villa, M. González-Álvarez, J. Borrás, A. Castiñeiras, *J. Inorg. Biochem.* **2003**, *96*, 367–374.
[39] M. González-Álvarez, G. Alzuet, J. Borrás, B. Macías, A. Castiñeiras, *Inorg. Chem.* **2003**, *42*, 2992–2998.
[40] M. González-Álvarez, G. Alzuet, J. Borrás, M. Pitié, B. Meunier, *J. Biol. Inorg. Chem.* **2003**, *8*, 644–652.
[41] B. Macías, M. V. Villa, F. Sanz, J. Borrás, M. González-Álvarez, G. Alzuet, *J. Inorg. Biochem.* **2005**, *99*, 1441–1448.
[42] R. Cejudo, G. Alzuet, M. González-Álvarez, J. L. García-Giménez, J. Borrás, M. Liu-González, *J. Inorg. Biochem.* **2006**, *100*, 70–79.
[43] A. W. Addison, T. N. Rao, J. Reedijk, J. van Rijn, C. G. Verschoor, *J. Chem. Soc., Dalton Trans.* **1984**, 1349–1356.
[44] G. A. Jefrey, *An Introduction to Hydrogen Bonding*, Oxford University Press, Oxford, **1997**.
[45] WINEPR-Simphonia 1. 25 Bruker Analytic Gmbh, Kalrsruhe, Germany, **1994–96**.
[46] J. Liu, T. Zhang, L. Que, H. Zhou, Q. Zhang, J. Liangnian, *J. Inorg. Biochem.* **2002**, *91*, 269–276.
[47] A. Mazumder, C. L. Sutton, D. S. Sigman, *Inorg. Chem.* **1993**, *32*, 3516–3560.
[48] S. H. Chiou, N. Ohtsu, K. G. Bensch, in *Biological and Inorganic Copper Chemistry* (Eds.: D. Karlin, J. Zubieta), Adenine Press, New York, **1985**, pp. 119–123.
[49] C. A. Detmer III, F. V. Pamatong, J. R. Bocarsly, *Inorg. Chem.* **1996**, *35*, 6292–6298.
[50] C. A. Detmer III, F. V. Pamatong, J. R. Bocarsly, *Inorg. Chem.* **1997**, *36*, 3676–3682.
[51] C. J. Burrows, J. G. Muller, *Chem. Rev.* **1998**, *98*, 1109–1152.
[52] B. Haliwell, J. M. C. Gutteridge, in *CRC Handbook of Methods for Oxygen Radical Research* (Ed.: R. A. Greenwald), CRC Press, Boca Raton, FL, **1985**, p. 177.
[53] F. V. Pamatong, C. A. Detmer III, J. R. Bocarsly, *J. Am. Chem. Soc.* **1996**, *118*, 5339–5345.
[54] D. R. Graham, L. E. Marshall, K. A. Reich, D. S. Sigman, *J. Am. Chem. Soc.* **1980**, *102*, 5419–5421.
[55] D. S. Sigman, *Acc. Chem. Res.* **1986**, *19*, 180–186.
[56] COLLECT, Nonius BV, **1997–2000**.
[57] DENZO-SCALEPACK, Z. Otwinowski, W. Minor, *"Processing of X-ray Diffraction Data Collected in Oscillation Mode"*, Methods in Enzymology, Volume 276: Macromolecular Crystallography, part A, p. 307–326 (Eds.: C. W. Carter Jr, R. M. Sweet), Academic Press, **1997**.
[58] SIR97: A. Altomare, M. C. Burla, M. Camalli, G. L. Cascarano, C. Giacovazzo, A. Guagliardi, A. G. G. Moliterni, G. Polidori, R. Spagna, *J. Appl. Crystallogr.* **1999**, *32*, 115–119.

 © 2007 Wiley-VCH Verlag GmbH & Co. KGaA, Weinheim 

[59] SHELX97, G. M. Sheldrick, *SHELX97. Programs for Crystal Structure Analysis (Release 97-2)*, University of Göttingen, Germany, **1997**.
[60] PARST: a) M. Nardelli, *Comput. Chem.* **1983**, *7*, 95–97; b) M. Nardelli, *J. Appl. Crystallogr.* **1995**, *28*, 659.
[61] ORTEP3 for Windows: L. J. Farrugia, *J. Appl. Crystallogr.* **1997**, *30*, 565.
[62] B. Halliwell, J. M. C. Gutteridge, in CRC *Handbook of methods for Oxygen Radical Research* (Ed.: R. A. Greenwald), CRC Press, Boca Raton, FL, USA, **1985**, p. 177.
[63] R. M. Burger, A. R. Berkowith, J. Peisach, S. B. Horwitz, *J. Biol. Chem.* **1980**, *255*, 11832–11838.

Received: September 5, 2006
Published Online: January 12, 2007

 © 2007 Wiley-VCH Verlag GmbH & Co. KGaA, Weinheim 

DOI: 10.1002/ejic.200600878

# Isolation and Characterization of $Zn^{II}$ and $Hg^{II}$ Coordination Polymers with a Designed Azo-Aromatic Ligand: Identification of Micrometer- and Nanometer-Sized Particles

**Priyabrata Banerjee,[a] Soumitra Kar,[b] Asim Bhaumik,[b] Gene-Hsiang Lee,[c] Shie-Ming Peng,[c] and Sreebrata Goswami*[a]**

**Keywords:** Coordination polymers / Azo-aromatic ligands / $d^{10}$ metal ions / X-ray structures / Nanostructures / Fluorescence

Controlled layering of the deprotonated methanolic solution of the azo-aromatic ligand $[L^3]^-$ ($HL^3$ = 2-[3-(pyridylamino)-phenylazo]pyridine) over the aqueous/methanolic solutions of metal chlorides $MCl_2$ (M = Zn, Hg) afforded nano- and micrometer-sized particles of the metal–organic polymeric complexes of $[HgCl(C_{16}H_{12}N_5)]_\infty$ (**1**) and $[ZnCl(C_{16}H_{18}N_5O_3)]_\infty$ (**2**). Time-dependent growth of the above particles is followed by the SEM and TEM analyses of the samples at different time intervals. The X-ray structure of the mercury polymer reveals that two infinite 1D, *zigzag* chains composed of $[HgCl(L^3)]_\infty$ units run along the *a* axis antiparalelly. The polynuclear Zn compound, in contrast, agglomerates fast to form hemispherical microcrystals with a diamondoid surface morphology, and no suitable X-ray quality crystal of this complex could be isolated. Powder XRD analyses of the samples as well as thermogravimetric analysis (TGA) are used for their characterization. Unusually, these metal–organic polymers of the reference $d^{10}$ metal ions are green and absorb in the low-energy region of the visible spectrum, 660–675 nm. Semiempirical calculations on a representative complex **1** suggest that the transitions in the complexes involve ligand orbitals. These also show multiple emissions in the blue-green region. The Zn complex, which is microporous, shows reversible adsorption/desorption of $N_2$ and $H_2$ gasses. The mercury polymer, on the other hand, shows poor adsorption ability.
(© Wiley-VCH Verlag GmbH & Co. KGaA, 69451 Weinheim, Germany, 2007)

## Introduction

Inorganic as well as organic polymeric substances have attracted intensive attention during the recent years primarily because of their potential applications as functional materials.[1] In the past decade, several organic and inorganic materials[2] have been synthesized and investigated. In contrast, examples[3,4] of nano- or micrometer-scale particles of metal–organic coordination polymers are limited. Thus, their preparation is challenging owing to their ability to tailor their physical and chemical properties through deliberate selection[5] of metal and multifunctional ligands. Various types of bridging ligands[6–8] have been used for the construction of coordination polymers. However, such examples containing azo-aromatic bridging ligands are uncommon primarily because of the lack of availability of suitable ligands.[8] Azo-aromatic compounds, with the exception of their use in dyestuff industry, have extensively been studied in recent years owing to their novel optical[9] and redox properties. Low-lying vacant π*(azo) orbitals in metal–azo-aromatic compounds are responsible for low-energy transitions and the colour of the compounds. During recent years we have been working on the coordination chemistry of a new class of azo-aromatic ligands [HL]. Three different ligands $HL^1$, $HL^2$ and $HL^3$ have been isolated[10–12] following regioselective *ortho* fusion of suitable aromatic amines. The deprotonated ligand $[L^1]^-$ binds in a bischelating fashion to produce monometallic complexes, the other two ligands, $[L^2]^-$ and $[L^3]^-$, each containing an additional pyridyl donor, serve as bridges between two or more metal centres. Moreover, the coordination mode of the deprotonated ligand $[L^3]^-$ is different from that of its positional isomer $[L^2]^-$ and is found to be suitable[13] for the construction of one-dimensional polymeric material,[14,15] particularly with coordinately unsaturated metal ions.

The primary concern of this paper is to report our results on the isolation of one-dimensional $Hg^{II}$ and $Zn^{II}$ coordination polymers with the bridging ligand $[L^3]^-$. Unusually, the polymeric $d^{10}$ metal complexes are intensely coloured and absorb in the low-energy region of the visible spectrum.

[a] Department of Inorganic Chemistry, Indian Association for the Cultivation of Science,
Kolkata 700 032, India
Fax: +91-33-2473-2805
E-mail: icsg@iacs.res.in
[b] Department of Material Science, Indian Association for the Cultivation of Science,
Kolkata 700 032, India
[c] Department of Chemistry, National Taiwan University,
Taipei, Taiwan, Republic of China
Supporting information for this article is available on the WWW under http://www.eurjic.org or from the author.

 © 2007 Wiley-VCH Verlag GmbH & Co. KGaA, Weinheim 

These polymers form different-sized particles (micrometer to nanometer) at different time intervals under identical experimental conditions. Their growth processes have been followed by FESEM, TEM, HRTEM, XRPD, EDS and single-crystal X-ray data analysis of the frameworks.

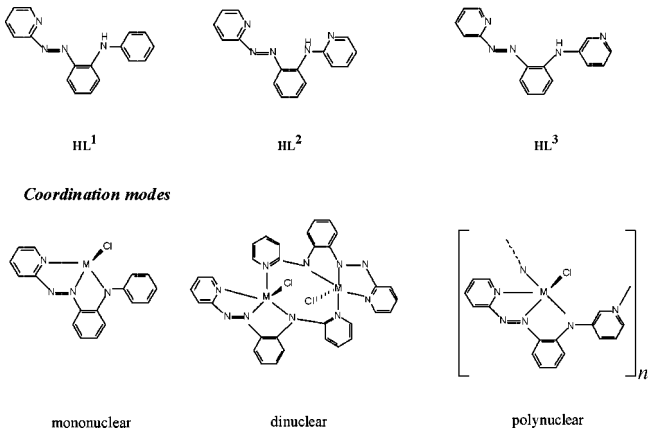


## Results and Discussion

The ligand $HL^3$ has been synthesized by regioselective C–N bond fusion of 3-aminopyridine to cobalt(II)-coordinated 2-(phenylazo)pyridine following the reaction strategy developed by us[10a] (Scheme 1).

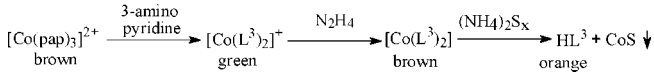


Scheme 1.

The green cobalt complex $[Co(L^3)_2]ClO_4$ was purified on a preparative TLC (silica gel) plate by using a chloroform/toluene (1:1) solvent mixture as eluent and was characterized spectroscopically. Its $^1H$ NMR spectrum is submitted as Figure S1 Supporting Information. Reduction of the cationic cobalt complex by dilute $N_2H_4$ followed by removal of $[Co]^{2+}$ as CoS led to the isolation of the ligand $[HL^3]$ in moderate yield. The pure ligand was obtained as a yellow crystalline solid, whose ESI-MS spectrum shows an intense peak at $m/z$ = 276 amu assigned to the $[H_2L^3]^+$ ion (Figure S2, Supporting Information). The $^1H$ and $^{13}C$ NMR spectra of the ligand $[HL^3]$ (Figures S3 and S4, Supporting Information) corroborate fully with its formulation. The deprotonated ligand $[L^3]^-$ (generated in situ by addition of $NEt_3$) reacts spontaneously with the methanolic/aqueous solutions of $MCl_2$ (M = Zn, Hg) at room temperature. The dark green compounds, thus produced, are rapidly precipitated. However, by controlled layering of the deprotonated ligand solution over the solutions of metal salts, we could achieve the synthesis of stable particles of the reference metal–organic polymers. It may be noted here that the salt $CdCl_2$ failed to produce any stable compound under identical experimental conditions. Chemical compositions of the polymers were established on the basis of their elemental analyses. Both are pentacoordinate and have identical repeating units $[MCl(L^3)]$. Notably, the morphology and the growth process of the mercury polymer are totally different from those of the zinc analogue. The growth processes of the two products are detailed separately.

### Hg–$L^3$ Polymer

For the evaluation of the crystalline mercury coordination polymer, the synthetic reactions were carried out in

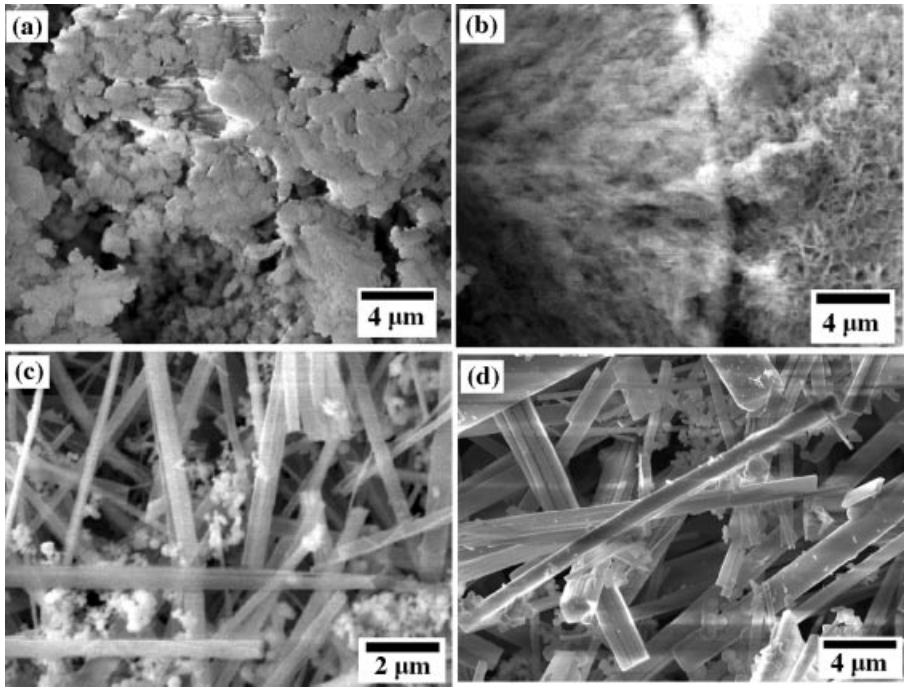


Figure 1. FESEM images of the $[HgClL^3]_\infty$ polymer at different time intervals: (a) 5 h, (b) 36 h, (c) 5 d, (d) 10 d.

 © 2007 Wiley-VCH Verlag GmbH & Co. KGaA, Weinheim 

five sealed glass tubes (A–E) under the same experimental conditions but with varying reaction times. A deprotonated methanolic solution of the ligand was layered over an aqueous solution of mercuric chloride and left undisturbed for diffusion (see Experimental Section). Figure 1a–d shows the SEM images of the as-synthesized products. It reveals the following features: (i) The product obtained from the tube A (after 5 h) is amorphous (Figure 1a); (ii) The SEM image (Figure 1b) of the second sample (tube B, after 36 h) reveals fine wirelike morphology; (iii) The SEM shown in Figure 1c is obtained from the third sample (tube C, after 5 d) and indicates the formation of nano-ribbonlike morphology. The width of these ribbons varies from a few nm to 500 nm, and their lengths lie within a few tens of micrometers. The facets of these ribbons are not well defined, which is an indication of their poor crystallinity; (iv) Interestingly, the fourth sample (tube D, after 10 d) is composed of well-defined microribbons (Figure 1d); and (v) X-ray-quality single crystals are obtained from tube E after 3 weeks and their X-ray structures are analyzed (vide infra).

For understanding the growth mechanism, we also investigated these samples by transmission electron microscopy (TEM). The first product is a featureless amorphous spherical compound, and the second is wirelike. The fourth sample (tube D) is quite thick for TEM measurement, and the electron beam failed to penetrate through it. Fairly interesting micrographs are obtained from the third sample (tube C). Figure 2a shows the TEM image of a single ribbonlike morphology. Closer observation of the image reveals the presence of large quantities of spherical particles embedded within the structure. Figure 2b shows the magnified TEM image of a ribbon, which indicates the presence of a large number of dark, spherical nanoparticles. The TEM image in Figure 2d reveals the presence of a large number of spherical nanoparticles of the polynuclear mercury sample **1** with diameters that vary between 10 and 30 nm. Some grain agglomeration is also observed in this image and is indicated by arrows. It is also interesting to note, from the TEM images, the layered nature of the agglomerated particles, which can perhaps explain the reason for the rapid increase in the dimension of the products. Thus, on the basis of the SEM and TEM observations we can conclude that the crystalline metal–organic framework (MOF) is produced in four steps. The first step is the formation of amorphous nucleation centres, followed by formation of the one-dimensional amorphous framework; the amorphous nature is also evident from its featureless powder XRD pattern (Figure S5, samples of Figure 1a and b). The nanocrystalline particles act as the nucleation sites (thus formed within the amorphous network), absorb more reactants from the solution and agglomerate with each other to grow in one-dimension to form fine wire- or ribbonlike products. In the final step these products crystallize to yield large whiskerlike single crystals. This is as expected since the amorphous products are high-energy systems[16] and have a natural tendency to minimize their energy by crystallization. Larger single-crystalline products are achieved if the reaction is allowed to take place for 3 weeks or more.

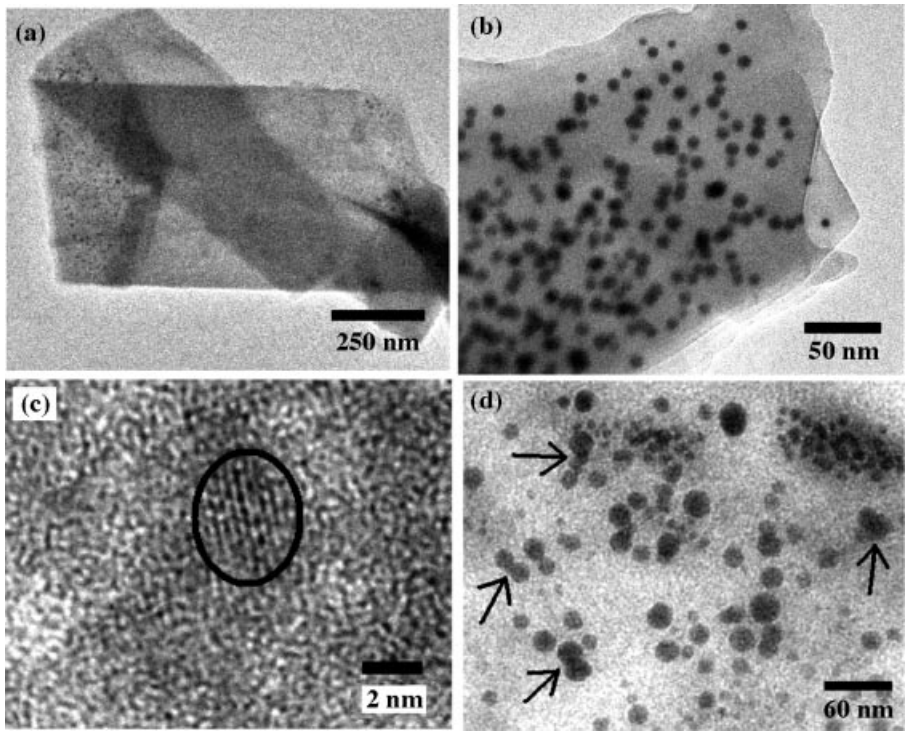


Figure 2. (a) TEM image of the single ribbonlike products of $[HgClL^3]_\infty$. (b) Zoomed TEM image showing spherical nanoparticles of Hg containing MOF. (c) Representative zoomed HRTEM image of a single metal–ligand nanoparticle. (d) Arrows indicating the agglomeration of the particles.

 © 2007 Wiley-VCH Verlag GmbH & Co. KGaA, Weinheim 

We examined the XRPD pattern for all the samples obtained from the aforementioned five tubes (A–E). The sample from tube A exhibits a featureless XRPD pattern, which implies that it is amorphous. However, experimental XRPD patterns of the samples from the three tubes (B–D) are similar and consistent with the simulated pattern derived from the single-crystal (tube E). Thus, we conclude that the bulk sample has the same structure as that of the single crystal. The experimental powder diffraction pattern of a representative sample (tube C), along with the simulated pattern, are shown in Figure 3 for comparison. Furthermore, microelemental analyses of the above mercury samples reveal that they have an identical composition, [HgCl($L^3$)], which was further supported by energy dispersive spectroscopy (EDS) (Figures S6 and S7).

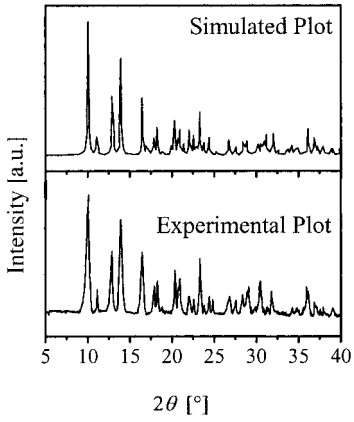


Figure 3. Experimental and simulated XRPD patterns of the as-synthesized mercury polymer $[HgClL^3]_\infty$.

### Zn–$L^3$ Polymer

The results obtained in this case were notably different from that of its mercury analogue. Here, two types of micrometer-sized particles are identified. The SEM image of the products obtained after 1 d reaction time shows the formation of large numbers of nanorods bundled together (Figure 4a). With time, these particles grow in one direction, and the basal region crystals penetrate through each other and agglomerate to form large microcrystals. As these particles grow on the tube walls they cannot form spheres, instead hemispherical particles are isolated (Figure 4b). The SEM image of a hemispherical single unit (after 6 d) is shown in Figure 4c, and a further magnified image of it is displayed in Figure 4d. This reveals that the individual basic units with pyramidal tips interpenetrate[16] to form the hemispherical particles. Figure 4e shows the broken basal region of a hemispherical crystal that indicates agglomeration[17] of closely packed individual units. No suitable single crystal of this sample could be isolated in this case, possibly because of fast agglomeration, although the powder diffraction pattern indicates a crystalline nature (Figure 5). The Zn samples are too thick for TEM measurements; however, high resolution transmission electron microscopy

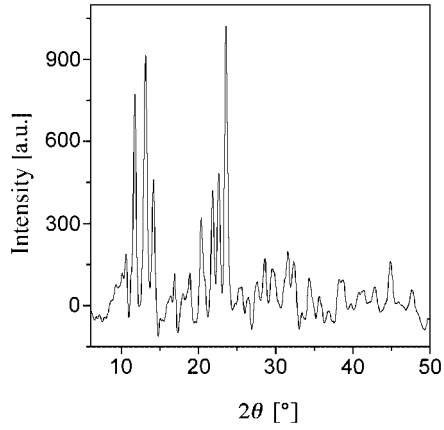


Figure 5. XRPD pattern of the polycrystalline polymer $[ZnClL^3{\cdot}3H_2O]_\infty$.

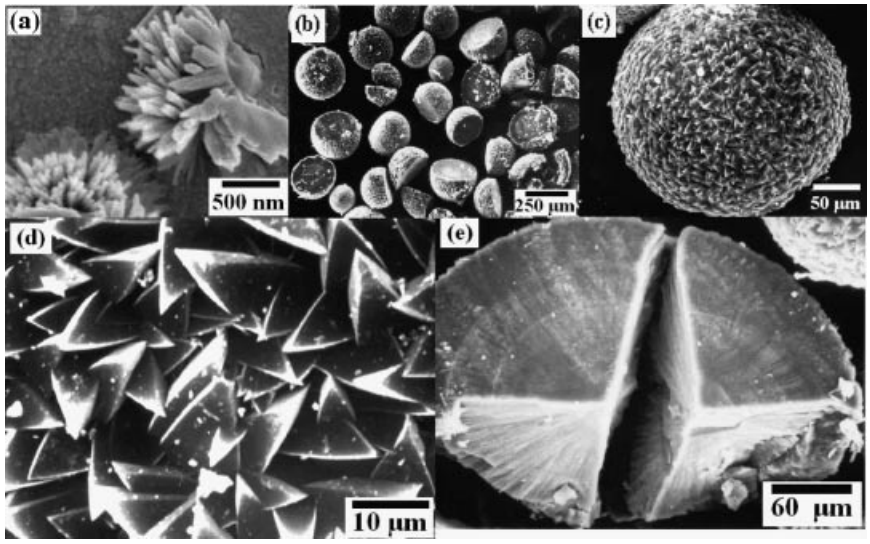


Figure 4. FESEM images of the $[ZnClL^3{\cdot}3H_2O]_\infty$ polymer at different time intervals: (a) 1 d, (b) 6 d. (c) Zoomed SEM image of one of the representative hemispheres. (d) Magnified surface image of (c). (e) Broken basal region of a hemisphere.

 © 2007 Wiley-VCH Verlag GmbH & Co. KGaA, Weinheim 

(HRTEM) on the crushed sample reveals that these particles are crystalline with a highly ordered arrangement of the micropores (Figure 6). Microelemental analyses on the Zn samples indicate that their compositions are similar to those of the mercury analogues, with the exception that the Zn polymer contains three $H_2O$ molecules of crystallization per formula weight ($[ZnCl(L^3)]\cdot 3H_2O$) of the repetitive building unit (TG analysis, vide infra). Energy dispersive spectra of these samples (Figures S8a and S8b) also corroborate the above formulation.

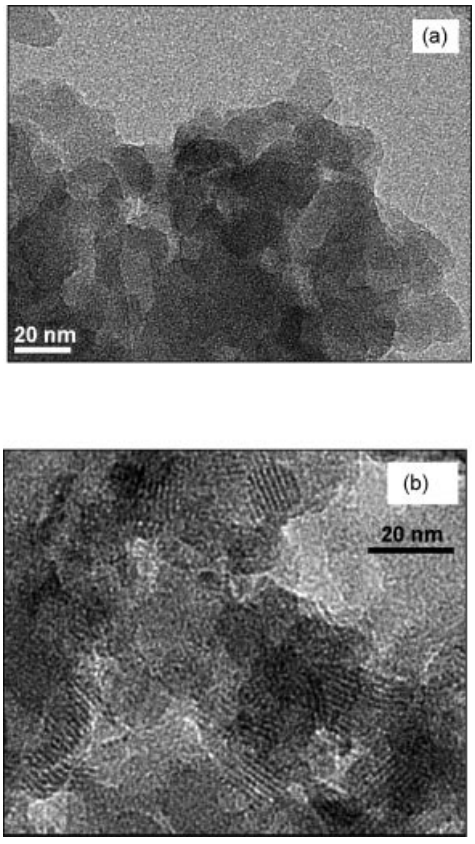


Figure 6. HRTEM images of the as-synthesized $[ZnClL^3\cdot 3H_2O]_\infty$ polymer: (a) low magnification, (b) high magnification.

### Crystal Structure of $[HgCl(L^3)]_\infty$ (1)

The three-dimensional structure of the mercury complex (sample obtained from tube E) was determined by single-crystal X-ray diffraction. In this structure, two 1D infinite polymeric chains made of $[HgCl(L^3)]_\infty$ units run antiparalelly along the *a* axis.[18] As shown in Figure 7, each mercury atom in this molecule is in a pentacoordinated $N_4Cl$ environment, and the geometry around each $Hg^{II}$ ion may be described as distorted square pyramidal[19] with a $\tau$ value of 0.21. In this context, we note that higher-coordination-number (>4) complexes of divalent mercury[20] are scarce in the literature. In the molecule **1**, Hg(1) sits above the plane formed by the three coordinating nitrogen atoms, N(1), N(3) and N(4), by 0.0464(1) Å; this pattern is repeated throughout the polymeric chain. The bending of the ligand and its coordination at the Hg centre result in *zigzag* chains that adopt a saw-tooth-like structure (Figure 8a). The two independent polymeric chains are closely packed/locked through metal–pi interactions[21a] along with face-to-face π–π ring interactions.[21b] Notably, the metal–pi interactions predominate over the π–π interactions. For example, the perpendicular distance between the centroids of the two interacting polymeric chains lies between 3.44 and 3.45 Å, whereas the distance between the Hg metal and centroid (Cg) lies in the range 3.37–3.41 Å. Selected bond lengths and angles, and the crystallographic data for the crystal $[HgCl(L^3)]_\infty$ are collected in Table 1 and Table 2, respectively. The secondary interactions in this structure (Figure 8b) work together to bring the two consecutive chains close together (Table 3 and Table 4). Notably, the closest distances between the two mercury atoms (both inter- and intramolecular) are quite long: intramolecular Hg(1)···Hg(1a) and Hg(2)···Hg(2a) distances are 6.243 Å and 6.307 Å, respectively, which are appreciably longer than the sum of the van der Waals radii[12c,22] between two consecutive mercury atoms (3.50 Å). The distance between two mercury atoms to complete one pitch [irrespective of Hg(1) or Hg(2)] is 10.145 Å. The Hg–π and π–π interactions are depicted in Figure 8b. For comparison, we wish to note that the ligand $HL^2$ reacts with $HgCl_2$ to produce the soluble dinuclear mercury(II) blue complex, in which the two $[L^2]^-$ ligands bridge the two mercury centres.[12c]

### Spectral Properties

Infrared spectra of the two polymeric complexes $[MClL^3]_\infty$ (M = Hg, Zn) are almost identical, and $\tilde{\nu}_{C=N}$ and $\tilde{\nu}_{N=N}$ appear[12] in the range 1585–1600 $cm^{-1}$ and 1305–1325 $cm^{-1}$, respectively. These complexes also show characteristic $\tilde{\nu}_{M-Cl}$ bands that appear[12] near 275 $cm^{-1}$. Both complexes are insoluble in common organic solvents, and their UV/Vis spectra in the solid state were studied. The lowest-energy transition in free $[L^3]^-$ (460 nm) is redshifted considerably by ca. 200 nm in the corresponding metal complexes. Whereas the mercury complex shows a broad transition at 660 nm, its zinc analogue absorbs at 675 nm. Notably, examples of $d^{10}$ metal ion complexes that absorb in such a low-energy part of the visible region are uncommon.[12] In order to gain some insight into the nature of the orbitals involved in electronic transitions of the above complexes, semiempirical EHMO calculations on the representative mercury complex $[HgClL^3]_\infty$ was performed with the program CACAO[23] created by Mealli and Proserpio. The calculations were made on the basis of atomic coordinates obtained from the single-crystal X-ray data analysis of compound **1**. The results reveal that HOMO–1, HOMO, LUMO and LUMO+1 all are essentially ligand orbitals with (>90% ligand contribution, see Figure S9). Thus the lowest-energy transitions in the present polymeric complexes are ascribed to electronic transitions within the ligand orbitals (π–π*). Modification of the properties of the ligand orbitals in the present examples is due to increased

 © 2007 Wiley-VCH Verlag GmbH & Co. KGaA, Weinheim 

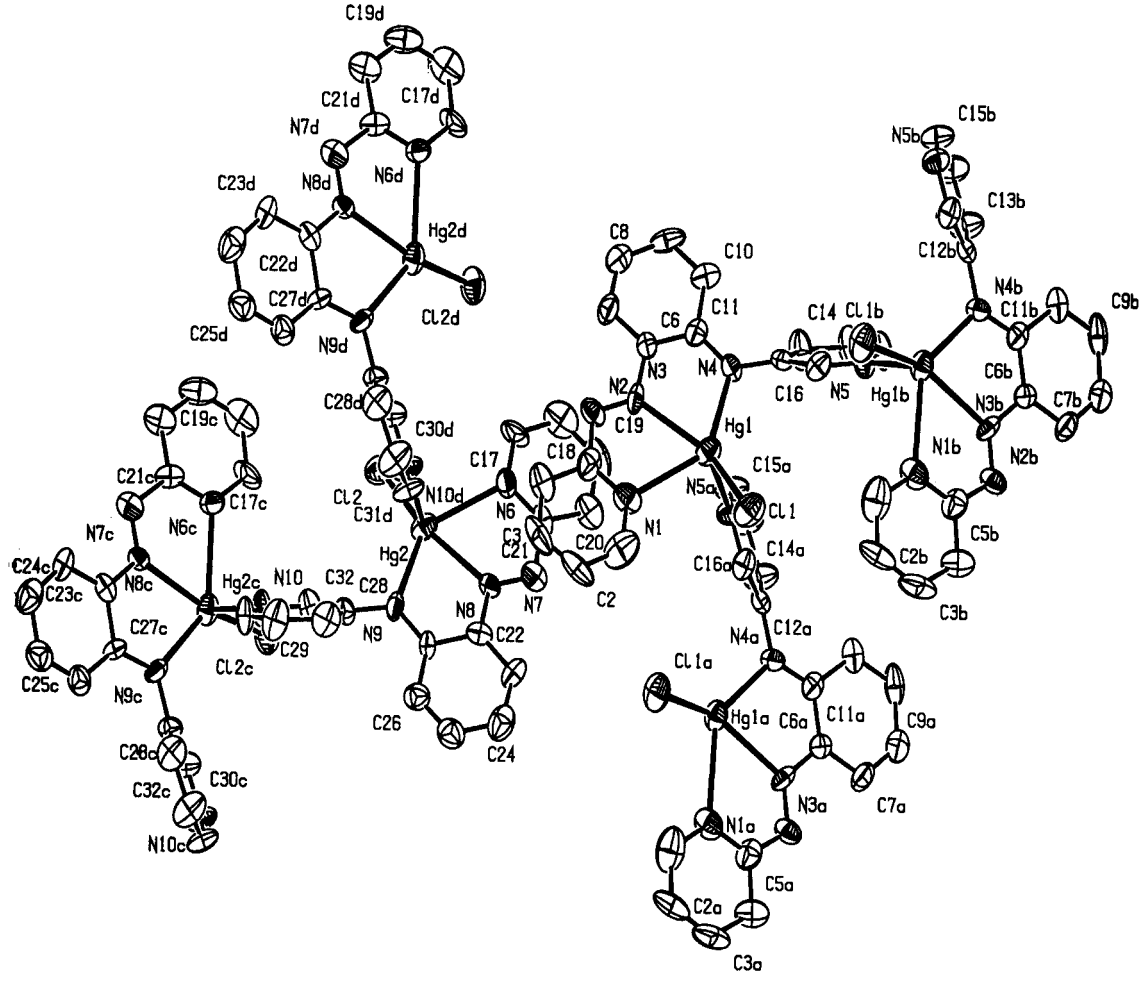


Figure 7. ORTEP and atom-numbering scheme for $[HgClL^3]_\infty$. Hydrogen atoms are omitted for clarity.

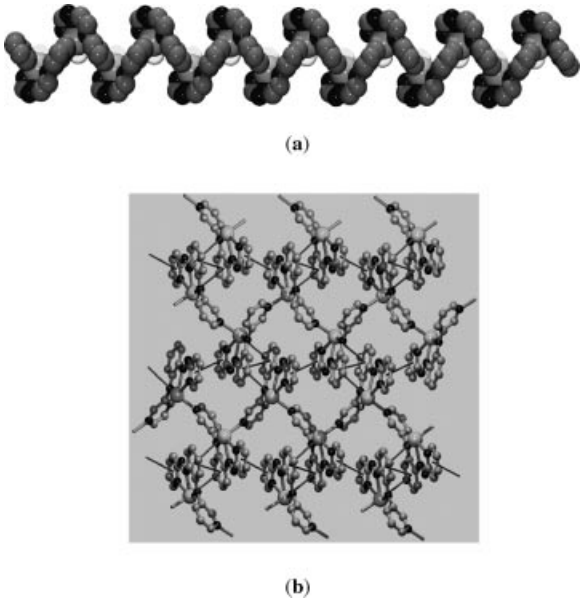


Figure 8. (a) Space-filling model for $[HgClL^3]_\infty$, showing the chain that adopts a saw-tooth-like backbone. (b) Different weak interactions constructed by π–π and (Hg) metal–π interactions between the adjacent polymer units running along the *a* axis.

Table 1. Selected bond lengths [Å] and bond angles [°] for $[HgClL^3]_\infty$ (**1**).

| Bond lengths | | | |
|---|---|---|---|
| Hg(1)–N(1) | 2.53(2) | Hg(2)–N(6) | 2.50(1) |
| Hg(1)–N(3) | 2.41(1) | Hg(2)–N(8) | 2.34(1) |
| Hg(1)–N(4) | 2.27(1) | Hg(2)–N(9) | 2.26(1) |
| Hg(1)–N(5) | 2.43(1) | Hg(2)–N(10) | 2.40(1) |
| Hg(1)–Cl(1) | 2.40(1) | Hg(2)–Cl(2) | 2.40(1) |
| N(2)–N(3) | 1.24(1) | N(7)–N(8) | 1.26(1) |
| N(3)–C(6) | 1.41(2) | N(8)–C(22) | 1.34(2) |
| C(6)–C(11) | 1.40(2) | C(22)–C(27) | 1.46(2) |
| C(11)–N(4) | 1.31(2) | C(27)–N(9) | 1.36(2) |
| N(4)–C(12) | 1.42(2) | N(9)–C(28) | 1.39(2) |
| **Bond angles** | | | |
| N(3)–Hg(1)–N(4) | 71.7(5) | N(1)–Hg(1)–N(3) | 63.0(5) |
| N(9)–Hg(2)–N(8) | 70.5(4) | N(8)–Hg(2)–N(6) | 66.2(4) |

planarity of the ligand and also to extensive charge delocalization along the ligand backbone. A similar type of finding was reported recently on the $Zn^{II}$ and $Cd^{II}$ complexes[24,25] of heterocyclic ligands. In such systems, heteroatoms decrease the π and π* orbital energies considerably, and as a result, the HOMO and LUMO lack contribution from the metal atoms. In addition, multiple electronic transitions are

 © 2007 Wiley-VCH Verlag GmbH & Co. KGaA, Weinheim 

Table 2. Crystallographic data for complex **1**.

| Complex | $[C_{16}H_{12}ClHgN_5]_\infty$ |
|---|---|
| Empirical formula | $C_{16}H_{12}ClHgN_5$ |
| Molecular mass | 510.35 |
| $T$ [K] | 295(2) |
| Crystal system | orthorhombic |
| Space group | $Pca2_1$ |
| Wavelengths [Å] | 0.71073 |
| $a$ [Å] | 10.1452(5) |
| $b$ [Å] | 18.1918(9) |
| $c$ [Å] | 17.3237(9) |
| $\alpha$ [°] | 90.00 |
| $\beta$ [°] | 90.00 |
| $\gamma$ [°] | 90.00 |
| $V$ [Å$^3$] | 3197.3(3) |
| $Z$ | 8 |
| $D_{calcd.}$ [g cm$^{-3}$] | 2.120 |
| Crystal dimension [mm] | $0.20 \times 0.10 \times 0.02$ |
| $\theta$ range for data collection [°] | 1.12–27.50 |
| GOF on $F^2$ | 1.042 |
| Reflections collected | 29113 |
| Unique reflections | 7341 |
| Final $R$ indices [$I>2\sigma$ ($I$)] | $R_1 = 0.0595$, $wR_2 = 0.0947$ |
| Largest diff. between peak and hole [e Å$^{-3}$] | 0.974, –1.466 |

Table 3. π–π interactions (face-to-face) in complex **1**.

| ring($i$) → ring($j$) | Dihedral angle between ring planes ($i$,$j$) [°] | Angle between first ring normal and the line joining ring Cgs ($i$,$j$) [°] | ⊥ distance of centroid($i$) from ring($j$) [Å] |
|---|---|---|---|
| R(1) → R(2)[a] | 4.16 | 39.02 | 3.441 |
| R(3) → R(4)[b] | 1.70 | 40.29 | 3.451 |

[a] Symmetry code: = 1 + $x$, $y$, $z$. [b]Symmetry code: = $x$, $y$, $z$.

Table 4. (Hg) metal–π ring interactions in complex **1**.[a]

| R($i$)–Hg($j$) | Metal-to-Cg distance [Å] | Angle between joining line and ring normal [°] |
|---|---|---|
| R(3)–Hg(2) | 3.373 | 24.08 |
| R(4)–Hg(1) | 3.412 | 26.63 |

[a] Where R(1) represents N1–C1–C2–C3–C4–C5; R(2) represents N6–C17–C18–C19–C20–C21; R(3) represents C6–C7–C8–C9–C10–C11; R(4) represents C22–C23–C24–C25–C26–C27.

also noted in the high-energy region. Spectral data of **1** and **2** are presented in the Experimental Section, and the spectra are shown in Figure 9.

The emission properties of the complexes were studied in the solid state at room temperature. The emission spectra are found to be dependent on the excitation wavelength. For example, the mercury complex **1** shows a relatively weak emission band at 690 nm upon excitation at 640 nm. Interestingly, multiple blue-green emission bands with maxima at 420, 450 and 485 nm are observed upon excitation at 335 nm, whereas emission bands with maxima at 425 nm and 460 nm are observed upon excitation with the very short wavelength of 235 nm. Multiple emission bands were reported[26] previously in other $d^{10}$ metal complexes. A similar behaviour in the emission spectrum of the corresponding zinc complex is also observed. The emission spectra of the mercury MOF are displayed in Figure 10, whereas the

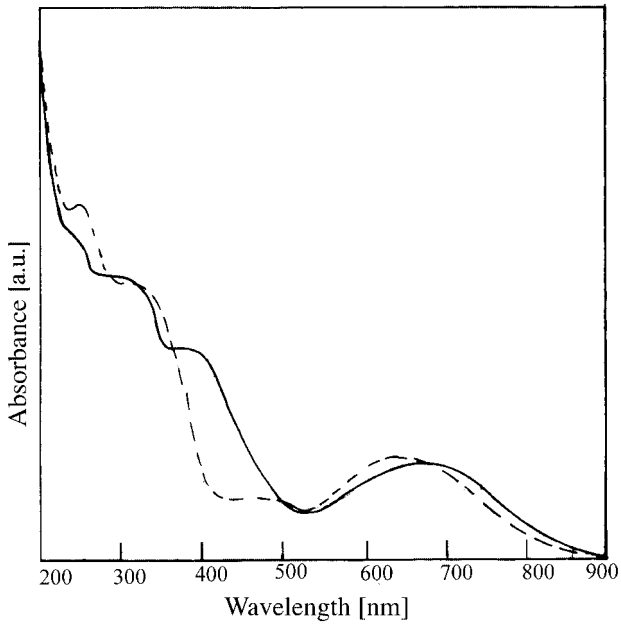


Figure 9. An overlay of UV/Vis spectra for the two MOFs in the solid state: (i) $[HgClL^3]_\infty$ (----), (ii) $[ZnClL^3 \cdot 3H_2O]_\infty$ (−).

emission spectra of its Zn analogue have been submitted as Supporting Information (Figure S10). It should be noted that the ligand [$HL^3$] shows very weak luminescence in the solid state upon excitation at 255 and 335 nm. The photophysical properties of complexes **1** and **2** are unique in the sense that no other reported compound of this and similar azo-aromatic ligands exhibit detectable luminescence. The luminescence properties in these examples thus may be attributed to the[27–28] polymeric nature of the complexes. This imparts rigidity in the ligand framework and thus reduces energy loss through a nonradiative relaxation pathway. In this context, it should be noted that blue-green luminescent coordination complexes have been studied intensively because of their possible applications in material science.[29]

## Sorption Properties

The presence of peaks at low $2\theta$ range in the XRPD pattern of the above polymers suggest that the possible ordering of the building units of these functional materials[30] is similar to that of microporous[31] systems. Whereas the Zn complex indeed shows the moderate ability of adsorption of small molecules like $N_2$ and $H_2$, its $Hg^{II}$ analogue shows poor adsorption ability.

The $N_2$ sorption experiment on the Zn polymer **2** at 77 K suggests a type I isotherm at low $P/P_0$ ratio of $N_2$ that corresponds to the presence of micropores with a BET surface area of 214 m$^2$ g$^{-1}$. Pore size distribution of the sample, obtained by using Horvath–Kawazoe method,[32] is shown in Figure 11. Two broad maxima can be seen at 9.2 and 14.1 Å in the micropore region.The average pore diameter of 9.2 Å can be explained from the low-range $2\theta$ peaks in the powder XRD pattern (Figure 5). The pore diameter of this sample

 © 2007 Wiley-VCH Verlag GmbH & Co. KGaA, Weinheim 

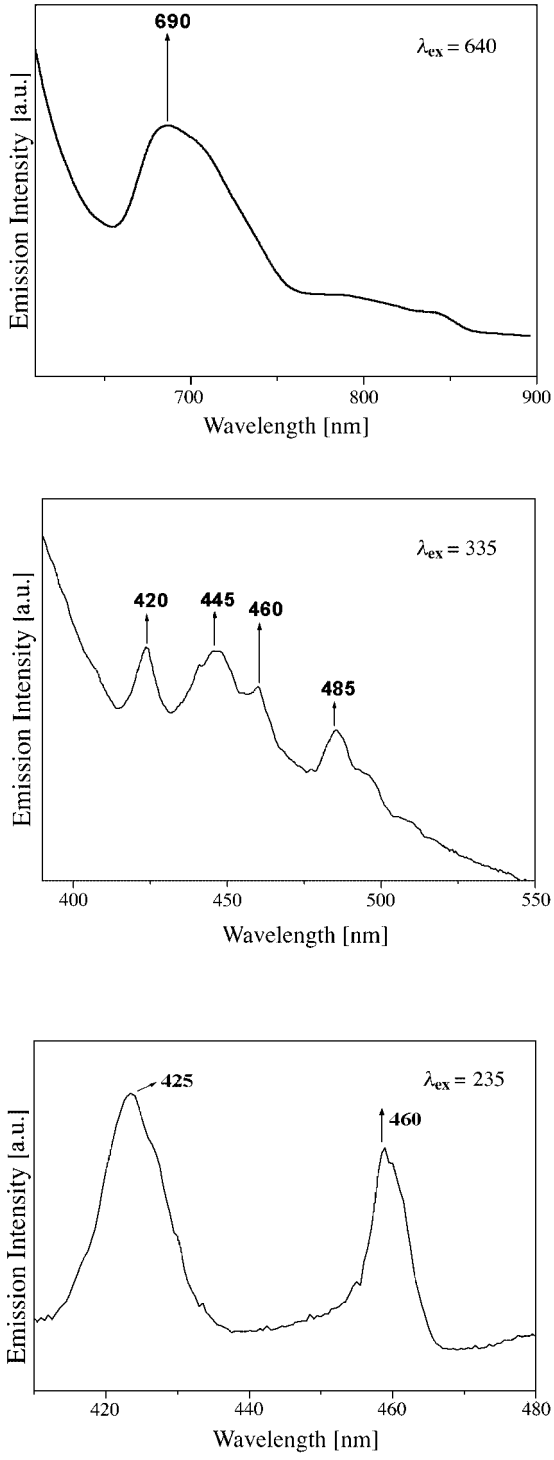


Figure 10. Multiple emission spectra for $[HgClL^3]_\infty$ at different excitation wavelengths.

estimated from the TEM analysis (vide supra) [Figure 6] agrees well with the $N_2$ sorption data. The presence of the peak at a pore diameter of 14.1 Å may be attributed to the large micropores generated at the interparticle cages. We have also carried out $H_2$ sorption on the reference Zn polymer. The $H_2$ adsorption/desorption isotherm at 77 K is shown in Figure 12. The nature of the isotherms suggests complete reversible adsorption and desorption for $H_2$, and a steady increment in the uptake of $H_2$ with increasing pressure.

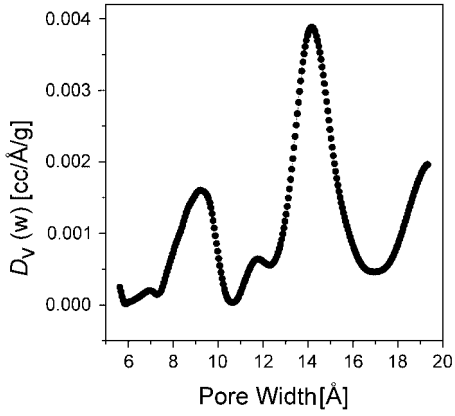


Figure 11. Pore size distribution curve for $[ZnClL^3{\cdot}3H_2O]_\infty$.

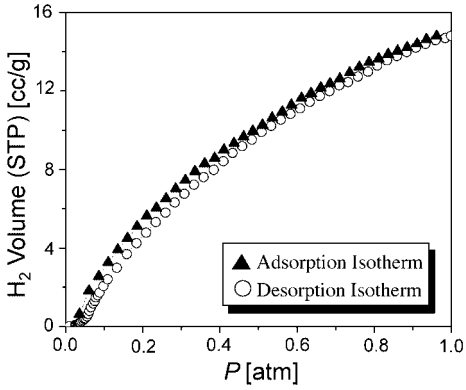


Figure 12. Isotherms for the adsorption and desorption of $H_2$ gas for $[ZnClL^3{\cdot}3H_2O]_\infty$.

The observed BET surface area of the mercury polymer is small, 13.5 $m^2g^{-1}$, and is quite low relative to that of the zinc sample. This indicates that nitrogen gas adsorption occurs primarily at the external surface of the mercury polymer and that the adsorbate nitrogen molecule cannot freely diffuse into the internal channels of this solid, as observed for other microporous solids.[33]

Thermogravimetric (TGA) analyses of samples **1** and **2** were performed to estimate the stability of the complexes at elevated temperatures. Figure S11 in the Supporting Information shows the TGA curves for samples **1** and **2**. The mercury sample **1** is stable only up to 97 °C. A continuous weight loss (>35%) followed by another massive weight loss of (> 50%) are noted in the temperature range 100–225 °C and 225–375 °C, respectively. The weight loss in the temperature range 100–225 °C may be attributed to the loss of the ligand, 2-(phenylazo)pyridine. In comparison, the Zn polymer **2** shows a slow weight loss of 7.2% in the range 25–275 °C, which is attributed to the loss of adsorbed water. Between 275 °C and 325 °C, there are multiple stages of

 © 2007 Wiley-VCH Verlag GmbH & Co. KGaA, Weinheim 

weight loss, which amount to 14.4%, presumably due to the loss of water present from the large micropore region. A weight loss of 11.1% in the range 325–370 °C and of 14.0% in the range 370–500 °C, as a result of the collapse of the metal–ligand framework, is observed. We wish to note here that the Zn–$L^3$ framework remains intact up to 325 °C, as evidenced by their near identical XRPD pattern; above this temperature, the network collapses.

## Conclusions

In this work we have described the isolation and characterization of a polymeric network of $Zn^{II}$ and $Hg^{II}$ with a designed azo-aromatic ligand. The gradual growth of the particles of the polymeric materials has been followed by successive product isolation at different time intervals. Unusually, the polymers are blue-green, have five-coordinate metal centres and display emission in the blue-green region of the visible spectrum. The Zn polymer is microporous and its sorption isotherm is reversible. Our work in the area of designing multifunctional azo-aromatic bridging ligands continues.

## Experimental Section

**Materials:** The starting complex $[Co(pap)_3](ClO_4)_2$ was prepared by a reported procedure.[34] The salts $ZnCl_2$ and $HgCl_2$ were obtained from Merck India Limited and Qualigens, respectively. 3-Aminopyridine was obtained from S.D. Fine-chemical Limited. Solvents and chemicals used for synthesis were of analytical grade.

**Physical Measurements:** A JASCO V-570 Spectrophotometer was used to record electronic spectra. The IR spectra were recorded with a Perkin–Elmer 783 spectrophotometer. $^1H$ NMR spectra were measured in $CDCl_3$ with a Bruker Avance DPX 300 spectrometer, and $SiMe_4$ (TMS) was used as the internal standard. A Perkin–Elmer 240C elemental analyzer was used to collect microanalytical data (C, H and N). The compositional analyses were evaluated by energy dispersive spectroscopy (EDS). Microstructures of the nano forms were studied by scanning electron microscopy (SEM, Hitachi S-3200), transmission electron microscopy (TEM) and high resolution transmission electron microscopy (HRTEM, JEOL JEM 2010 TEM at an accelerating voltage of 200 kV). Solid state emission spectra were recorded at room temperature at different excitation wavelengths with a Perkin–Elmer LS 55 Luminescence Spectrometer. ESI mass spectra were recorded on a micromass Q-TOF mass spectrometer (serial no. YA-263). Powder XRD data were recorded on a Seifert 3000P diffractometer, on which small- and wide-angle goniometers were mounted, at 40 kV and 20 mA by using Cu-$K_\alpha$ radiation ($\lambda$ = 1.5406 Å) with a scan speed of 2° $min^{-1}$. Sorption isotherm studies were performed by using a Quantachrome AUTOSORB 1C-TCD sorption instrument at 77 K. Prior to gas adsorption measurements, samples were degassed for 2 h at 100 °C for **1** and at 120 °C for **2** to remove all guest molecules. Thermogravimetric (TGA) analyses for the representative samples were conducted at a scan rate of 5.00 °C $min^{-1}$ by using a Perkin–Elmer DIAMOND TG/DTA thermogravimeter. Melting points were determined with the help of a capillary fitting Mel. Temp. II (Laboratory Devices Inc., USA) apparatus.

**Synthesis of Compounds**

**$HL^3$ Synthesis:** Two steps were involved: (i) *ortho*-amination on $[Co(pap)_3]^{2+}$ followed by (ii) ligand isolation from the cobalt complex.

**Isolation of $[Co(L^3)_2]ClO_4$ from $[Co(pap)_3](ClO_4)_2$:** A mixture of $[Co(pap)_3](ClO_4)_2$ (0.2 g, 0.25 mmol) and 3-aminopyridine (0.1 g, 1.06 mmol) was heated on a steam bath for 7 h. The initial brown colour gradually became intense green. The crude product, which contained mainly the compound $[Co(L^3)_2]ClO_4$, was further purified on a preparative TLC plate (silica gel) with a acetonitrile/chloroform mixture (1:4) as eluent. A yellowish band of unreacted 3-aminopyridine moved first, followed by a major green band of the cobalt compound $[Co(L^3)_2]ClO_4$. The major green band was collected and was thoroughly washed with diethyl ether. Crystalline pure green $[Co(L^3)_2]ClO_4$ was obtained from a dichloromethane/hexane mixture. Yield: 0.125 g, 70%. ESI-MS: $m/z$ = 607.15 [M – $ClO_4^-$]. $C_{32}H_{24}ClCoN_{10}O_4$ (706.93): calcd. C 54.36, H 3.42, N 19.81; found C 54.40, H 3.40, N, 19.75. IR (KBr): $\tilde{\nu}$ = 1600 (s) [C=N], 1325 (vs) [N=N], 1085 (s), 620 (s) [$ClO_4^-$] $cm^{-1}$. UV/Vis (in dichloromethane, $\lambda_{max}$): 315, 400, 720, 790, 880 nm.

**Isolation of [3-(2-Pyridylamino)phenyl]azopyridine ($HL^3$) from $[Co(L^3)_2]ClO_4$:** The cobalt complex $[Co(L^3)_2]ClO_4$ (0.15 g, 0.21 mmol) was dissolved in ethanol (30 mL), and hydrazine hydrate (5 mL) and yellow ammonium sulfide (5 mL) were added. The mixture was then stirred for 30 min at room temperature. The resulting orange-yellow solution was evaporated to dryness, and the product was extracted with dichloromethane and loaded on a preparative TLC plate (silica gel) for purification. An orange-yellow band was eluted with a toluene/chloroform mixture (2:1), which on evaporation yielded orange crystals of $HL^3$. Yield: 0.075 g, 65%. M.p. 98 °C. ESI-MS: $m/z$ = 276.10. p$K_a$ = 8.7±0.1. $C_{16}H_{13}N_5$ (275.28): calcd. C 69.81, H 4.75, N 25.44; found. C 69.75, H 4.80, N 25.40. IR (KBr): $\tilde{\nu}$ = 1585 (s) [C=N], 1315 (vs) [N=N) $cm^{-1}$. UV/Vis (solid, $\lambda_{max}$): 255, 335, 460 nm.

**Polynuclear Mercury(II) Complex $[HgClL^3]_\infty$ (1):** In a long neck crystal tube, an aqueous solution (5 mL) containing $HgCl_2$ (100 mg, 0.365 mmol), water (2 mL) and a methanolic solution of a mixture of $HL^3$ (100 mg, 0.365 mmol) and of $NEt_3$ (2 drops) were layered gradually in the above order. In between the water and methanol solvent layer, a green ring formed almost immediately. The tube was stoppered and left undisturbed at room temperature. Slow diffusion between the two solutions afforded dark green crystals of complex **1** after 3 weeks. Yield: 0.130 g, 70%. $C_{16}H_{12}ClHgN_5$ (510.32): calcd. C 37.66, H 2.37, N 13.72; found C 37.65, H 2.39, N 13.67. IR (KBr): $\tilde{\nu}$ = 1590 (s) [C=N], 1300 (vs) [N=N] $cm^{-1}$. UV/Vis (solid, $\lambda_{max}$): 245, 345, 500, 660 nm.

The growth process of the mercury particles was followed by carrying out the synthetic reaction in five sealed tubes (A–E) by using an identical reaction mixture as stated above but by varying the reaction time. The samples were collected after 5 h, 36 h, 5 d, 10 d and 21 d.

**Polynuclear Zinc(II) Complex $[ZnClL^3 \cdot 3H_2O]_\infty$ (2):** In a long neck crystal tube, the deprotonated methanolic ligand solution of $[L^3]^-$ (100 mg, 0.365 mmol) was layered over a methanolic solution of $ZnCl_2$ (50 mg, 0.365 mmol). The tube was stoppered and left undisturbed at room temperature. A dark polycrystalline complex of the zinc polymer was isolated from the tube after 6 d. Yield: 0.125 g, 80%. $C_{16}H_{18}ClN_5O_3Zn$ (429.16): calcd. C 44.77, H 4.22, N 16.31; found C 44.70, H 4.22, N 16.26. IR (KBr): $\tilde{\nu}$ = 1595 (s) [C=N], 1310 (vs) [N=N], 3440 (s) [$H_2O$] $cm^{-1}$. UV/Vis (solid, $\lambda_{max}$): 255, 335, 380, 675 nm.

 © 2007 Wiley-VCH Verlag GmbH & Co. KGaA, Weinheim 

**X-ray Crystallography:** Crystallographic data for compound **1** is collected in Table 2. Specific details are given below.

**$[HgClL^3]_\infty$ (1):** Suitable X-ray quality crystals ($0.20 \times 0.10 \times 0.02$ mm) of $[HgClL^3]_\infty$ (**1**) were obtained by layering an aqueous solution of $HgCl_2$ over an aqueous solution of the deprotonated ligand $[L^3]^-$ in a crystal tube, as described above. Suitable crystals were obtained after 3 weeks from the tube. X-ray data were collected on a Bruker SMART diffractometer equipped with Mo-$K_\alpha$ radiation ($\lambda$ = 0.71073 Å) and were corrected for Lorentz-polarisation effects. A total of 29113 reflections were collected, of which 7341 were unique ($R_{int}$ = 0.0990) and were used in subsequent analysis. The structure was solved by employing the SHELXS-97 program package[35a,35b] and refined by full-matrix least-squares based on $F^2$ (SHELXL-97).[35c] Crystallographic graphics were obtained by using the programs ORTEP[36] and PLATON.[37] CCDC-621241 (for **1**) contains the supplementary crystallographic data for this paper. These data can be obtained free of charge from The Cambridge Crystallographic Data Centre via www.ccdc.cam.ac.uk/data_request/cif.

**Supporting Information** (see footnote on the first page of this article): ESI-MS spectrum of ligand $[H_2L^3]^+$, $^1$H- and $^{13}$C NMR spectra for $HL^3$ and $[Co(L^3)_2]^+$, powder X-ray diffraction analysis for amorphous complex **1**, photoluminescence spectra for complex **2**, energy dispersive spectra for complexes **1** and **2**, semiempirical EHMO calculation of complex **1**, and TGA curve for complexes **1** and **2** are available.

## Acknowledgments

Financial support received from the Council of Scientific and Industrial Research (CSIR) and the Department of Science and Technology, New Delhi is gratefully acknowledged. P. B. is thankful to CSIR for his fellowship. We are also thankful to Dr. Golam Mostafa of Jadavpur University for his help.

[1] a) B. F. Hoskins, R. Robson, *J. Am. Chem. Soc.* **1990**, *112*, 1546–1554; b) A. J. Blake, N. R. Champness, P. Hubberstey, W.-S. Li, M. A. Withersby, M. Schröder, *Coord. Chem. Rev.* **1999**, *183*, 117–138; c) B. Moulton, M. J. Zawartko, *Chem. Rev.* **2001**, *101*, 1629–1658; d) R. Kitaura, K. Fujimoto, S. Noro, M. Kondo, S. Kitagawa, *Angew. Chem. Int. Ed.* **2002**, *41*, 133–135; e) C. Janiak, *Dalton Trans.* **2003**, 2781–2804; f) Y. Xiong, Yi. Xie, S. Chen, Z. Li, *Chem. Eur. J.* **2003**, *9*, 4991–4996; g) B. Liu, D.-J. Qian, H.-X. Huang, T. Wakayama, S. Hara, W. Huang, C. Nakamura, J. Miyake, *Langmuir* **2005**, *21*, 5079–5084; h) M. Oh, C. L. Stern, C. A. Mirkin, *Inorg. Chem.* **2005**, *44*, 2647–2653; i) M. Oh, C. A. Mirkin, *Nature* **2005**, *438*, 651–654.

[2] a) X. Peng, L. Manna, W. Yang, J. Wickham, E. Scher, A. Kadavanich, A. P. Alivisatos, *Nature* **2000**, *404*, 59–61; b) C. Ye, G. Meng, Y. Wang, Z. Jiang, L. Zhang, *J. Phys. Chem. B* **2002**, *106*, 10338–10341; c) Z.-X. Deng, C. Wang, X.-M. Sun, Y.-D. Li, *Inorg. Chem.* **2002**, *41*, 869–873; d) X. Chen, H. Xu, N. Xu, F. Zhao, W. Lin, G. Lin, Y. Fu, Z. Huang, H. Wang, M. Wu, *Inorg. Chem.* **2003**, *42*, 3100–3106; e) Q. Peng, S. Xu, Z. Zhuang, X. Wang, Y. Li, *Small* **2005**, *1*, 216–221; f) S. Biswas, S. Kar, S. Chaudhuri, *J. Phys. Chem. B* **2005**, *109*, 17526–17530; g) S. Kar, S. Chaudhuri, *J. Phys. Chem. B* **2005**, *109*, 3298–3302; h) S. Kar, B. N. Pal, S. Chaudhuri, D. Chakravorty, *J. Phys. Chem. B* **2006**, *110*, 4605–4611; i) S. Kar, S. Chaudhuri, *J. Phys. Chem. B* **2006**, *110*, 4542–4547.

[3] a) T. Uemura, S. Kitagawa, *J. Am. Chem. Soc.* **2003**, *125*, 7814–7815; b) X. Zhang, Y. Xie, W. Yu, Q. Zhao, M. Jiang, Y. Tian, *Inorg. Chem.* **2003**, *42*, 3734–3737; c) M. Yamada, M. Arai, M. Kurihara, M. Sakamoto, M. Miyake, *J. Am. Chem. Soc.* **2004**, *126*, 9482–9483.

[4] a) S. Vaucher, M. Li, S. Mann, *Angew. Chem. Int. Ed.* **2000**, *39*, 1793–1796; b) S. Vaucher, J. Fielden, M. Li, E. Dujardin, S. Mann, *Nano Lett.* **2002**, *2*, 225–229; c) G. Larsen, R. V. Ortiz, K. Minchow, A. Barrero, I. G. Loscertales, *J. Am. Chem. Soc.* **2003**, *125*, 1154–1155; d) E. Y. Lee, S. Y. Jang, M. P. Suh, *J. Am. Chem. Soc.* **2005**, *127*, 6374–6381.

[5] a) S. R. Batten, R. Robson, *Angew. Chem. Int. Ed.* **1998**, *37*, 1460–1494; b) A. K. Cheetham, G. Férey, T. Loiseau, *Angew. Chem. Int. Ed.* **1999**, *38*, 3268–3292; c) D. Hagrman, P. J. Hagrman, J. Zubieta, *Angew. Chem. Int. Ed.* **1999**, *38*, 3165–3168; d) S. S.-Y. Chui, S. M. F. Lo, J. P. H. Charmant, A. G. Orpen, I. D. Williams, *Science* **1999**, *283*, 1148–1150; e) J.-C. Dai, X.-T. Wu, Z.-Y. Fu, C.-P. Cui, S.-M. Hu, W.-X. Du, L.-M. Wu, H.-H. Zhang, R.-Q. Sun, *Inorg. Chem.* **2002**, *41*, 1391–1396.

[6] a) A. Mederos, S. Domínguez, R. Hernández-Molina, J. Sanchiz, F. Brito, *Coord. Chem. Rev.* **1999**, *193–195*, 913–939; b) A. Mederos, S. Domínguez, R. Hernández-Molina, J. Sanchiz, F. Brito, *Coord. Chem. Rev.* **1999**, *193–195*, 857–911; c) Md. B. Zaman, M. D. Smith, D. M. Ciurtin, H.-C. zur Loye, *Inorg. Chem.* **2002**, *41*, 4895–4903 and reference herein; d) X. Xue, X.-S. Wang, L.-Z. Wang, R.-G. Xiong, B. F. Abrahams, X.-Z. You, Z.-L. Xue, C.-M. Che, *Inorg. Chem.* **2002**, *41*, 6544–6546; e) D. M. Shin, I. S. Lee, Y.-A. Lee, Y. K. Chung, *Inorg. Chem.* **2003**, *42*, 2977–2982; f) Y.-B. Dong, X. Zhao, R.-Q. Huang, M. D. Smith, H. C. zur Loye, *Inorg. Chem.* **2004**, *43*, 5603–5612; g) A. Cingolani, S. Galli, N. Masciocchi, L. Pandolfo, C. Pettinari, A. Sironi, *J. Am. Chem. Soc.* **2005**, *127*, 6144–6145.

[7] a) Y. Cui, H. L. Ngo, W. Lin, *Inorg. Chem.* **2002**, *41*, 1033–1035; b) Z.-Y. Fu, X.-T. Wu, J.-C. Dai, S.-M. Hu, W.-X. Du, H.-H. Zhang, R.-Q. Sun, *Eur. J. Inorg. Chem.* **2002**, 2730–2735; c) S. L. James, *Chem. Soc. Rev.* **2003**, *32*, 276–288; d) G. Férey, M. Latroche, C. Serre, F. Millange, T. Loiseau, A. P. Guégan, *Chem. Commun.* **2003**, 2976–2977; e) X. Wang, C. Qin, E. Wang, Y. Li, N. Hao, C. Hu, L. Xu, *Inorg. Chem.* **2004**, *43*, 1850–1856.

[8] J. Otsuki, N. Omokawa, K. Yoshiba, I. Yoshikawa, T. Akasaka, T. Suenobu, T. Takido, K. Araki, S. Fukuzumi, *Inorg. Chem.* **2003**, *42*, 3057–3066.

[9] a) S. Hvilsted, F. Andruzzi, P. S. Ramanujam, *Opt. Lett.* **1992**, *17*, 1234–1236; b) P. S. Ramanujam, S. Hvilsted, I. Zebger, F. Andruzzi, *Appl. Phys. Lett.* **1993**, *62*, 1041–1043; c) P. S. Ramanujam, S. Hvilsted, I. Zebger, H. W. Siesler, *Macromol. Rapid Commun.* **1995**, *16*, 455–461; d) G. J. Lee, D. Kim, M. Lee, *Appl. Opt.* **1995**, *34*, 138–143; e) I. Willner, S. Rubin, *Angew. Chem. Int. Ed. Engl.* **1996**, *35*, 367–385; f) N. Zheng, X. Bu, P. Feng, *J. Am. Chem. Soc.* **2002**, *124*, 9688–9689.

[10] a) A. Saha, A. K. Ghosh, P. Majumdar, K. N. Mitra, S. Mondal, K. K. Rajak, L. R. Falvello, S. Goswami, *Organometallics* **1999**, *18*, 3772–3774; b) A. Saha, P. Majumdar, S.-M. Peng, S. Goswami, *Eur. J. Inorg. Chem.* **2000**, 2631–2639; c) A. Saha, P. Majumdar, S. Goswami, *J. Chem. Soc., Dalton Trans.* **2000**, 1703–1708; d) C. Das, A. K. Ghosh, C.-H. Hung, G.-H. Lee, S.-M. Peng, S. Goswami, *Inorg. Chem.* **2002**, *41*, 7125–7135; e) C. Das, A. Saha, C.-H. Hung, G.-H. Lee, S.-M. Peng, S. Goswami, *Inorg. Chem.* **2003**, *42*, 198–204.

[11] A. Sanyal, P. Banerjee, G.-H. Lee, S.-M. Peng, C.-H. Hung, S. Goswami, *Inorg. Chem.* **2004**, *43*, 7456–7462.

[12] a) K. K. Kamar, S. Das, C.-H. Hung, A. Castiñeiras, M. D. Kuzmin, C. Rillo, J. Bartolomé, S. Goswami, *Inorg. Chem.* **2003**, *42*, 5367–5375; b) S. Das, C.-H. Hung, S. Goswami, *Inorg. Chem.* **2003**, *42*, 5153–5157; c) S. Das, C.-H. Hung, S. Goswami, *Inorg. Chem.* **2003**, *42*, 8592–8597; d) S. Das, S.-M. Peng, G.-H. Lee, S. Goswami, *Ind. J. Chem. Sect. A* **2005**, *44A*, 1561–1564.

[13] S. Das, P. Banerjee, S.-M. Peng, G.-H. Lee, J. Kim, S. Goswami, *Inorg. Chem.* **2006**, *45*, 562–570.

[14] Metal ions that have a preference for hexacoordination, for example $Co^{III}$, $Ni^{II}$ etc., produce monometallic complexes of

 © 2007 Wiley-VCH Verlag GmbH & Co. KGaA, Weinheim 

the type $[M(L^3)_2]^{n+}$, where the 3-pyridyl nitrogen atom of the ligand remains[15] uncoordinated. There are strong indications that suggest that these complexes might be useful building blocks for the construction of heterometallic systems.

[15] P. Banerjee, S.-M. Peng, G.-H. Lee, S. Goswami, unpublished results.

[16] a) K. Kobashi, K. Nishimura, Y. Kawate, T. Horiuchi, *Phys. Rev. B* **1988**, *38*, 4067–4084; b) Ch. Wild, N. Herres, P. Koidl, *J. Appl. Phys.* **1990**, *68*, 973–978; c) M. A. Tamor, M. P. Everson, *J. Mater. Res.* **1994**, *9*, 1839–1848; d) C. Ye, G. Meng, Y. Wang, Z. Jiang, L. Zhang, *J. Phys. Chem. B* **2002**, *106*, 10338–10341.

[17] M. Eddaoudi, D. B. Moler, H. Li, B. Chen, T. M. Reinke, M. O'Keeffe, O. M. Yaghi, *Acc. Chem. Res.* **2001**, *34*, 319–330.

[18] a) L. Pauling, R. B. Corey, *Chemistry* **1953**, *39*, 253; b) M. L. Mansfield, *J. Phys. Chem.* **1989**, *93*, 6926–6928.

[19] A. W. Addison, T. N. Rao, J. Reedijk, J. V. Rijn, G. C. Verschoor, *J. Chem. Soc., Dalton Trans.* **1984**, 1349–1356.

[20] a) A. E. Mauro, S. H. Pulcinelli, R. H. A. Santos, M. T. P. Gambardella, *Polyhedron* **1992**, *11*, 799–803; b) D. C. Bebout, D. E. Ehmann, J. C. Trinidad, K. K. Crahan, M. E. Kastner, D. A. Parrish, *Inorg. Chem.* **1997**, *36*, 4257–4264; c) D. C. Bebout, M. M. Garland, G. S. Murphy, E. V. Bowers, C. J. Abelt, R. J. Butcher, *Dalton Trans.* **2003**, 2578–2584 and references cited therein.

[21] a) M. Enders, G. Ludwig, H. Pritzkow, *Eur. J. Inorg. Chem.* **2002**, 539–542 and references therein; b) Z. D. Tomic, V. M. Leovac, Ž. K. Jaćimović, C. Giester, S. D. Zarić, *Inorg. Chem. Commun.* **2006**, *9*, 833–835.

[22] a) P. Pyykkö, *Chem. Rev.* **1997**, *97*, 597–636; b) P. Pyykkö, M. Straka, *Phys. Chem. Chem. Phys.* **2000**, *2*, 2489–2494.

[23] C. Mealli, D. M. Proserpio, *J. Chem. Educ.* **1990**, *67*, 399–402.

[24] S.-L. Zheng, J.-H. Yang, X.-L. Y0u, X.-M. Chen, W.-T. Wong, *Inorg. Chem.* **2004**, *43*, 830–838.

[25] S.-L. Zheng, J.-P. Zhang, X.-M. Chen, Z.-L. Huang, Z.-Y. Lin, W.-T. Wong, *Chem. Eur. J.* **2003**, *9*, 3888–3896.

[26] a) M. A. Omary, M. A. Rawashdeh-Omary, H. V. K. Diyabalanage, H. V. R. Dias, *Inorg. Chem.* **2003**, *42*, 8612–8614; b) X. Shi, G. Zhu, X. Wang, G. Li, Q. Fang, G. Wu, G. Tian, M. Xue, X. Zhao, R. Wang, S. Qiu, *Cryst. Growth Des.* **2005**, *5*, 207–213; c) R.-Q. Fang, X.-M. Zhang, *Inorg. Chem.* **2006**, *45*, 4801–4810.

[27] S.-L. Zheng, M.-L. Tong, S.-D. Tan, Y. Wang, J.-X. Shi, Y.-X. Tong, H.-K. Lee, X.-M. Chen, *Organometallics* **2001**, *20*, 5319–5325.

[28] a) B. Valuer, *Molecular Fluorescence*: *Principle and Applications*, Wiley-VCH, Weinheim, **2002**; b) A. W. Adamson, P. D. Fleischauer, *Concept of Inorganic Photochemistry*, John Wiley & Sons, New York, **1975**; c) H. Yersin, A. Vogler (Eds.), *Photochemistry and Photophysics of Coordination Compounds*, Springer-Verlag, Berlin, **1987**.

[29] J. Tao, M.-L. Tong, J.-X. Shi, X.-M. Chen, S. W. Ng, *Chem. Commun.* **2000**, 2043–2044.

[30] B. Chen, M. Eddaoudi, S. T. Hyde, M. O'Keeffe, O. M. Yaghi, *Science* **2001**, *291*, 1021–1023.

[31] R. Szostak, *Molecular Sieves: Principles of Synthesis and Identification*, Van Nostrand Reinhold, New York, **1989**.

[32] G. Horvath, K. Kawazoe, *J. Chem. Eng. Jpn.* **1983**, *16*, 470–475.

[33] M. Du, Z.-H. Zhang, X.-J. Zhao, Q. Xu, *Inorg. Chem.* **2006**, *45*, 5785–5792.

[34] A. K. Mahapatra, Ph. D. Thesis, Jadavpur University, Calcutta, India, **1986**.

[35] a) G. M. Sheldrick, *Acta Crystallogr., Sect. A* **1990**, *46*, 467–473; b) G. M. Sheldrick, *SHELXS-97, Program for the Solution of the Crystal Structures*, University of Göttingen, Göttingen, Germany, **1997**; c) G. M. Sheldrick, *SHELXL-97*, *Program for the Refinement of Crystal Structures*, University of Göttingen, Göttingen, Germany, **1997**.

[36] C. K. Johnson, *ORTEP* II, Report *ORNL*-5138, Oak Ridge National Laboratory, TN, USA, **1976**.

[37] A. L. Spek, *PLATON, A Multipurpose Crystallographic Tool*, Ultrecht University, Ultrecht, The Netherlands, **1999**.

Received: September 19, 2006
Published Online: January 10, 2007

 © 2007 Wiley-VCH Verlag GmbH & Co. KGaA, Weinheim 

DOI: 10.1002/ejic.200600890

# A New Chloro-Bridged $Cu^{II}$ Schiff Base Complex with Ferromagnetic Exchange Interaction

**Shu-Lan Ma,[a] Xu-Xia Sun,[a] Song Gao,[b] Chuan-Min Qi,*[a] Hai-Bo Huang,[a] and Wen-Xiang Zhu[a]**

**Keywords:** Copper / Schiff bases / Dinuclear complex / Crystal structure / Magnetic properties

The synthesis and characterization of the μ-Cl-bridged dinuclear complex $[CuLCl]_2$ with the new Schiff-base ligand HL, 2-methyl-6-[(pyridine-2-ylmethylene)amino]phenol, is reported. The structural study shows the complex has the unusual distorted trigonal-bipyramidal geometry. Variable temperature susceptibility measurements in the range of 2.0–300 K reveal a novel ferromagnetic coupling, $2J = 1.52\ cm^{-1}$. A comparison for the magnetic coupling of $[CuLCl]_2$ with other reported $Cu(\mu\text{-}Cl)_2Cu$ compounds with square-pyramidal or trigonal-bipyramidal geometry is discussed in detail. The complex may provide useful information for the magneto-structural correlations of these compounds.
(© Wiley-VCH Verlag GmbH & Co. KGaA, 69451 Weinheim, Germany, 2007)

## Introduction

Recently, chemists as well as physicists have concentrated their efforts on the study of multinuclear molecular-based magnetic materials so as to understand the magnetic interactions between the paramagnetic metal ions and the bridging ligands to develop the magneto-structural correlations enabling the design of interesting magnetic materials.[1] The exchange coupling between the spins of unpaired electrons on metal atoms in polynuclear compounds is termed ferro- or antiferromagnetism, depending upon whether the individual spins in the ground state show a parallel or antiparallel alignment. The construction of molecular-based magnetic materials with ferromagnetic ordering is a major challenge. The relative simplicity of dinuclear systems has permitted the proposal of some magneto-structural correlations that are very useful for predicting magnetic properties of new compounds.

A good degree of success has been accomplished in correlating structure and magnetic properties for dihydroxo-bridged dinuclear copper complexes,[2] but no unique magneto-structural correlation has been found for dichloro-bridged dinuclear copper complexes. Different magnetic behavior has been found in these systems and great difficulties remain in establishing a magneto-structural correlation due to the much larger structural variety.[3] Further investigations into the magneto-structural correlation of dichloro-bridged $Cu^{II}$ dimers seem necessary.

We synthesize the tridentate Schiff-base ligand HL {2-methyl-6-[(pyridine-2-ylmethylene)amino]phenol} containing one pyridine ring and one phenolic ring, from which the dichloro-bridged copper dimer $[CuLCl]_2$ is obtained. The complex provides unique trigonal-bipyramidal geometry and exhibits unusual ferromagnetic interaction.

## Results and Discussion

### UV Spectra

The UV-visible spectroscopic data for the ligand and the complex were studied in MeOH. HL exhibits three maxima centered at 289, 361, and 442 nm while $[CuLCl]_2$ shows three maxima at 281, 357, and 506 nm. The absorption bands at 200–400 nm in $[CuLCl]_2$ may correspond to the ligand-centered π-π* transitions, and the band at 506 nm may correspond to the ligand-to-metal charge transfer transition. The shifts and the new absorptions may account for the coordination.

### Description of Structure

The crystal structure of $[CuLCl]_2$ is shown in Figure 1. Selected bond lengths and bond angles are listed in Table 1. Besides $Cl^-$ bridges, the coordination sites of $Cu^{II}$ are the $N_{imine}$, $N_{py}$, and the deprotonated phenolate oxygen $O_{pheno}$ from the Schiff-base ligand. The distortion parameter $\tau$[4] of 0.448 (near to 0.50) in $[CuLCl]_2$ indicates that the geometry may be described as either a distorted square-pyramid

[a] College of Chemistry, Beijing Normal University, Beijing 100875, China
Fax: +86-10-64463640
E-mail: qicmin@sohu.com
mashulan@263.net
[b] State Key Laboratory of Rare Earth Materials Chemistry and Application, College of Chemistry and Molecular Engineering, Peking University, Beijing 100871, China
Supporting information for this article is available on the WWW under http://www.eurjic.org or from the author.

 © 2007 Wiley-VCH Verlag GmbH & Co. KGaA, Weinheim 

(SP) or a trigonal-bipyramid (TBP), which resembles other dimers ($\tau$ is 0.487, 0.485, and 0.455, respectively).[3b,5] In the TBP geometry for $[CuLCl]_2$, the apical sites are occupied by O1 and N2, with Cl1, Cl1A, and N1 making up the equatorial plane. The $Cu^{II}$ ion sits 0.043 Å apart from the plane, and the apical O1 and N2 are located –1.954 and 1.955 Å on either side. If the geometry is viewed as a SP, the axial ligand is Cl1A and the basal ones consist of N1, N2, O1, and Cl1, with $Cu^{II}$ sitting 0.455 Å from the plane. The bond angles for two idealized five-coordinate geometries are listed in Table 1. The distortion from ideal TBP geometry is observed in equatorial bond angles of 90.77, 132.34, and 136.77°, showing deviation from ideal 120° angles. The distortion from an ideal SP is much more obvious in the angles of 136.77° for N1–Cu1–Cl1 and 132.34° for N1–Cu1–Cl1A, showing significant deviation from the ideal angles of 180 and 90°, respectively. So this system is much more readily described as a distorted TBP. The bridging $Cu_2Cl_2$ unit is constrained to be planar by the presence of the crystallographic center. The Cu–Cl–Cu angle of 89.23° is slightly shorter than the average 89.40° and the Cu–Cu distance of 3.424 Å is in agreement with the average value for 188 chloro-bridged copper(II) dimers (3.499 Å) in CSD. The two Cu–Cl bridging distances of 2.444 and 2.430 Å fall into the range between 2.309 Å (short)[6] and 2.554 Å (long)[7] for five-coordinate copper(II) complexes.

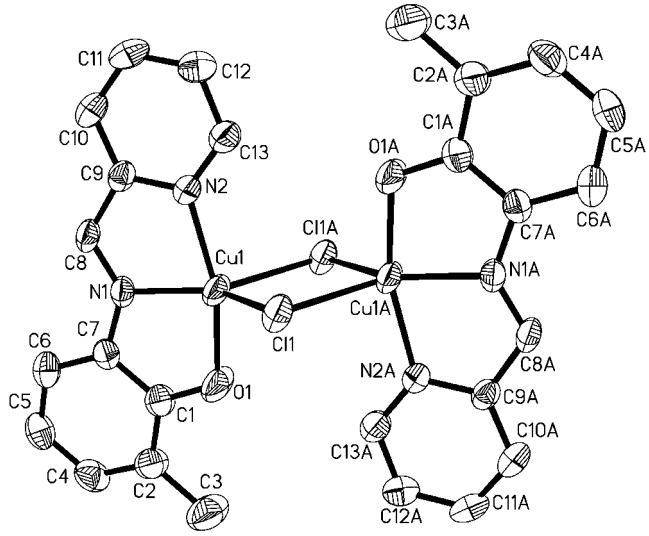


Figure 1. Molecular structure of the complex $[CuLCl]_2$ (thermal ellipsoids at 30% probability).

Table 1. Important bond lengths and angles for $[CuLCl]_2$ and corresponding angles for two idealized geometries.

| Atoms | Distance [Å] | Atoms | Angle [°] | TBP[b] [°] | SP[c] [°] |
|---|---|---|---|---|---|
| Cu1–O1 | 1.929(3) | O1–Cu1–N1 | 83.48(11) | 90 | 90 |
| Cu1–N1 | 1.961(3) | O1–Cu1–N2 | 163.66(11) | 180 | 180 |
| Cu1–N2 | 2.021(3) | O1–Cu1–Cl1 | 96.10(11) | 90 | 90 |
| Cu1–Cl1 | 2.4444(11) | O1–Cu1–Cl1A | 96.85(12) | 90 | 90 |
| Cu1–Cl1A[a] | 2.4302(11) | N1–Cu1–N2 | 80.18(12) | 90 | 90 |
| Cu1–Cu1A | 3.424 | N1–Cu1–Cl1 | 136.77(9) | 120 | 180 |
| C1–O1 | 1.313(4) | N1–Cu1–Cl1A | 132.34(9) | 120 | 90 |
| C7–N1 | 1.396(4) | N2–Cu1–Cl1 | 95.97(9) | 90 | 90 |
| C8–N1 | 1.282(4) | N2–Cu1–Cl1A | 93.95(9) | 90 | 90 |
| C9–N2 | 1.352(4) | Cl1–Cu1–Cl1A | 90.77(3) | 120 | 90 |

[a] Symmetry transformations used to generate equivalent atoms: #1 $-x + 1, -y, -z + 1$. [b] Angle for TBP geometry at Cu, with O1 and N2 axial and N1, C11 and C11A equatorial. [c] Angle for SP geometry at Cu, with C11A axial and O1, N1, N2 and C11 equatorial.

## Magnetic Properties

Variable temperature magnetic susceptibility on $[CuLCl]_2$ was measured in the range 2.0–300 K (Figure 2). At room temperature $\chi_m T$ is 0.88 $cm^3 mol^{-1} K$, which is slightly higher than the expected value 0.75 $cm^3 mol^{-1}$ K for two uncoupled spin-only $Cu^{II}$ ions ($S = 1/2$, $g = 2$). Upon cooling from room temperature, $\chi_m T$ increases very smoothly increasing continuously below 20 K, and reaching a value of 0.99 $cm^3 mol^{-1}$ K near to 2.0 K. The $\chi_m^{-1}$ vs. $T$ plot is essentially linear, and least-squares fitting of the data to the Curie–Weiss law gave $C = 0.88$ $cm^3 mol^{-1}$ K and $\theta = +0.52$ K. The increase of $\chi_m T$ upon cooling, and the small positive Weiss constant indicates that there exists a weak but unquestionably ferromagnetic coupling between two $Cu^{II}$ ions. The magnetization measured at 2.00 K increases with the field, and reaches 2.02 $N\beta$ per $Cu_2$ at 50 kOe, slightly higher than the expected saturation value of 2 $N\beta$ for two spin-only $Cu^{II}$ ions with $S = 1/2$, $g = 2.0$. The expression of the molar susceptibility $\chi_m$ is presented by the following Bleaney–Bowers equation:

$$\chi_m = 2Ng^2\beta^2/kT\cdot[3 + \exp(-2J/kT)]^{-1}$$

The best fitting for the experiment data leads to the parameters $g = 2.17$ and $2J = 1.52$ $cm^{-1}$. The agreement factor $R$, defined as $\Sigma(\chi_m T_{obs} - \chi_m T_{calc})^2/\Sigma(\chi_m T_{obs})^2$, is equal to $4.26\cdot10^{-4}$. The solid line in Figure 2 corresponds to the best theoretical fit.

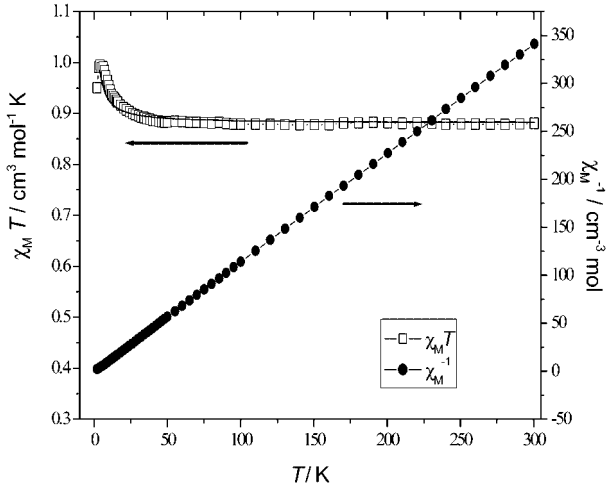


Figure 2. The plot of temperature dependence of $\chi_m^{-1}$ (●) and $\chi_m T$ (□) of complex $[CuLCl]_2$ measured at 1000 Oe. The solid line represents the best fit of the experimental data as discussed in the text.

 © 2007 Wiley-VCH Verlag GmbH & Co. KGaA, Weinheim 

The sign and magnitude of the coupling constant $2J$ for pentacoordinate $Cu(\mu\text{-}Cl)_2Cu$ dimers depend mainly on the Cu–Cl–Cu bridging angle $\varphi$, the Cu–Cl distance, the nature of the terminal ligands, and the distortions of the coordination geometry.[8] The SP geometry for these dimers is the usual one, but a distortion toward TBP can exist. Three different SP geometries have been experimentally characterized: square pyramids sharing a base-to-apex edge with parallel basal planes (SP I), square pyramids sharing a basal edge with coplanar basal planes (SP II), and square pyramids that also share a base-to-apex edge, but with perpendicular basal planes (SP III). For the less common TBP geometry, two types are formed: TBP I is formed by sharing an edge joining the axial and equatorial chloride atoms (axial-equatorial dimer) while TBP II is formed by sharing an edge joining two equatorial chloride ligands (equatorial-equatorial dimer). For reason of contrast, the SP I,[3c,9] SP II,[10] SP III[3d] compounds with ferromagnetic coupling, and the TBP I[3a,3b,5,11] and TBP II[12] compounds known so far with ferromagnetic or antiferromagnetic coupling, are listed in Table 2. The SP I compounds usually show small ferromagnetic[3c,9] or antiferromagnetic coupling constants,[13] and those of SP II show antiferromagnetic behavior when halide ions are present in the terminal ligands[14] and ferromagnetic behavior in the presence of N-donors.[10] The only SP III compound known so far presents ferromagnetic coupling ($2J$ = +85.88 $cm^{-1}$).[3d] The TBP I compounds usually exhibit antiferromagnetic behavior[3a,3b,5b,11] while TBP II compounds (only two examples) often show ferromagnetic behavior.[12]

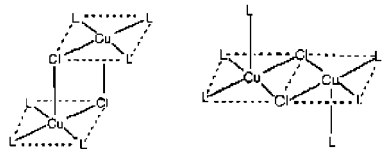


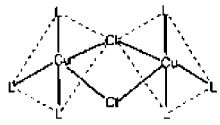


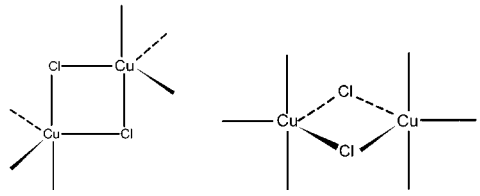


The values of Cu–Cl–Cu angle $\varphi$ in TBP I complexes are always obtuse and as shown in Table 2 (structures **10**–**15**) are close to 95° (from 94.8 to 97.9°). While the $\varphi$ values in TBP II geometries are always lower than 90°, and for the two compounds **16** and **17** they are in the range 81.8–89.3°.[12] The $2J$ obtained from the TBP complexes in

Table 2. The structural and magnetic properties for some $Cu(\mu\text{-}Cl)_2Cu$ dimers.[a]

| Complexes | Cu–Cu′ [Å] | Cu–Cl $R$ [Å] | Cu–Cl–Cu′ $\varphi$ [°] | $\varphi/R$ [°/Å] | $2J$ [$cm^{-1}$] | Geom. | Ref. |
|---|---|---|---|---|---|---|---|
| 1. $[Cu(dmgH)Cl_2]_2$ | 3.445 | 2.698 | 88.0 | 32.62 | +0.62 (Y) [b] | SP I | [9a] |
| 2. $[Cu(pfsa)Cl]_2$ | 3.825 | 2.846 | 95.27 | 33.6 | +0.30 (Y) | SP I | [3c] |
| 3. $[Cu(pmda)Cl]_2(ClO_4)_2$ | 3.396 | 2.581 | 88.2 | 34.17 | +2.24 (Y) | SP I | [9b] |
| 4. $[Cu(iyda)Cl]_2(ClO_4)_2$ | 3.494 | 2.657 | 88.81 | 33.42 | +1.16 (Y) | SP I | [9c] |
| 5. $[Cu(bpdio)Cl_2]_2$ | 3.842 | 2.844 | 96.68 | 33.99 | +4.87 (Y) | SP I | [9d] |
| 6. $[Cu_2(baamo)_2Cl_2]$ | 3.418 | 2.808 | 82.9 | 29.52 | +12.0 (N) [b] | SP I | [9e] |
| 7. $[CuCl_2(pytn)]_2$ | 3.612 | 2.906 | 88.60 | 30.49 | +27.46 (N) | SP I | [9f] |
| 8. $[CuCl(hpba)_3]_2$ | 3.394 | 2.316 | 94.51 | 40.81 | +33.70 (N) | SP II | [10] |
| 9. $[Cu_2(dpt)_2Cl_2](Cl)_2$ | 3.551 | 2.545 | 91.4 | 35.91 | +85.88 (N) | SP III | [3d] |
| 10. $[Cu(Et_3en)Cl_2]_2$ | 3.703 | 2.728 | 94.84 | 34.75 | +0.10 (Y) | TBP I | [3b] |
| 11. $[Cu(ampy)Cl_3]_2$ | – | 2.330 | 94.9 | 40.73 | +42.0 (N) | TBP I | [5a] |
| 12. $[Co(en)_3]_2[CuCl_8]Cl_2$ | 3.722 | 2.703 | 95.2 | 35.22 | –14.60 (Y) | TBP I | [5b,11a] |
| 13. $[Cu(dmtcp)Cl_2]_2$ | 3.570 | 2.543 | 95.34 | 37.49 | –38.80 (Y) | TBP I | [11b] |
| 14. $[Cu(guaH)Cl_3]_2$ | 3.575 | 2.447 | 97.9 | 40.01 | –82.6 (Y) | TBP I | [3a,11c] |
| 15. $[Cu(4\text{-}Metz)(DMF)Cl_2]_2$ | 3.721 | 2.724 | 95.3 | 34.99 | –3.60 (Y) | TBP I | [3b] |
| 16. $[Cu(btaH)_2Cl_2]_2 \cdot H_2O$ | 3.520 | 2.694 | 89.3 | 33.77 | +1.80 (Y) | TBP II | [12a,12b] |
| | 3.448 | 2.544 | 87.5 | (mean) | | | |
| 17. $[Cu_2Cl_3(bmdz)_5]Cl \cdot 4H_2O$ | 3.386 | 2.424 | 89.1 | 33.90 | +5.60 (Y) | TBP II | [12c] |
| | | 2.620 | 81.8 | (mean) | | | |
| $[CuLCl]_2$ | 3.424 | 2.444 | 89.23 | 36.51 | +1.52 (N) | TBP II | this work |

[a] Abbreviations: dmgH, dimethylglyoxime; pfsa, 3-[*N*-2-(pyridylethyl)formimidoyl]salicylic acid; pmda, 1-(2-pyridylmethyl)-1,5-diazacyclooctane; iyda, 1-(imidazol-4-ylmethyl)-1,5-diazacyclooctane; bpdio, 2,2-bis(2-pyridyl)-1,3-dioxolane; baamo, 8-amino-5-aza-4-methyl-3-octene-2-onate; pytn, 2-(pyrazol-1-yl)-2-thiazoline; hpba, hydrotris(1-pyrazolyl)borate anion; dpt, dipropylenetriamine; $Et_3en$, *N*,*N*,*N*′-triethylenediamine; ampy, 3-aminopyridinium; en, ethylenediamine; dmtcp, 3,5-dimethyl-1-thiocarboxamide pyrazole; guaH, guaninium; 4-Metz, 4-methylthiazole, DMF, *N*,*N*-dimethylformamide; btaH, benzotriazole; bmdz, benzimidazole; HL, 2-methyl-6-[(pyridine-2-ylmethylene)amino]phenol. [b] Y or N: obey or does not obey the empirical correlation between $2J$ and $\varphi/R$ described by Hatfield.

 © 2007 Wiley-VCH Verlag GmbH & Co. KGaA, Weinheim 

Table 2 including our present $[CuLCl]_2$ are consistent with the 90° angle rule[15] that the coupling is ferromagnetic for the $\varphi$ value near to 90° and antiferromagnetic for that diverging from 90°. The $\varphi$ values of 89.3 and 89.1° in **16** and **17**[12] and 89.23° in the present work are fairly close to 90°, and that induces their ferromagnetic coupling ($2J > 0$). TBP I compounds **12**–**15** have $\varphi$ values with a larger divergence from 90°, and hence antiferromagnetic interactions occur ($2J < 0$). Because the ferromagnetic coupling may increase when the Cu–Cl bridging distance decreases,[8b] the stronger ferromagnetic interaction in **11** may be thanks to its shorter Cu–Cl bridging bonds (2.330 Å) though with a large $\varphi$ value (94.9°). Another compound, $[(terpy)CuCl]_2[PF_6]_2$, has a $\varphi$ value near to 90° (89.9°)[13a] but shows antiferromagnetic coupling ($2J = -2.32$ cm$^{-1}$). The longer Cu–Cl bridging distance of 2.72 Å and the SP geometry may induce its antiferromagnetic behavior.

The bridge angle can determine the sign of the exchange-coupling constant, and the bond length in the superexchange pathway may inflect the magnitude of $2J$. Hatfield and co-workers have proposed an empirical correlation between $2J$ and the $\varphi/R_0$ ratio in $Cu(\mu\text{-}Cl)_2Cu$ complexes,[3b,16] where $R_0$ is the (longer) axial Cu–Cl bridging distance in the SP geometry while representing the equatorial distance in the TBP geometry.[3b] They found that for a value of $\varphi/R_0$ lower than 32.6 or higher than 34.8 [°/Å] the exchange interaction is antiferromagnetic and for values falling between these limits the interactions are ferromagnetic. Their analysis was predominantly for the SP I and TBP I systems involving the axial-equatorial dimers.[3b] From Table 2 we can see that most of the compounds with SP I and TBP I geometries are consistent with this correlation. The structures of TBP II complexes **16** and **17** are complicated by the presence of two crystallographically independent dimers in **16** and two nonequivalent Cu–Cl–Cu bridges in **17**, so we can only use the mean $\varphi/R_0$ ratios (33.77 for **16** and 33.90 for **17**). According to the mean $\varphi/R_0$ ratios, their magnetic coupling also fits the prediction of the correlation between $2J$ and $\varphi/R_0$. Our present complex $[CuLCl]_2$ has a relative simple and sterling structure and has an $\varphi/R_0$ value of 36.50, and it shows ferromagnetic coupling, which does not fit the trend of Hatfield's analysis. This may result from its unique geometry distortion. We can not substantiate the magneto-structural correlation due to the very sparse number of examples of this kind of TBP II complexes.

The unpaired spin should lie predominantly in the $d_{x^2-y^2}$ orbital in the SP geometry, and in the $d_{z^2}$ orbital in the TBP geometry.[3b,12c,17] But for the axial-equatorial SP I and TBP I dimers, this distinction is unnecessary, since they are interconvertible by a single angular deformation. Thus, they may be viewed as belonging to the same structural type and their magnetic properties can be compared directly as in the correlation between $2J$ and $\varphi/R_0$ by Hatfield.[3b] This statement is restricted to SP I and TBP I complexes, since the deformation would not transform SP I to the equatorial-equatorial TBP II dimer. An extended Hückel molecular orbital calculation for the TBP II compound **17** revealed that its occupied molecular orbitals were located mainly in the $d_{z^2}$ orbitals.[12c] Therefore, the relative orientation of the metallic part of the magnetic orbitals of our present complex may be represented as depicted in Figure 3. The distortion from SP to TBP induced a change in the $d_{Cu}$ metal orbital from $d_{x^2-y^2}$ to $d_{z^2}$, and an effective overlap occurs between two Cu centers, leading to the increase of the ferromagnetic contribution for $[CuLCl]_2$.[3a,8a,13a]

Another interesting structural feature for $[CuLCl]_2$ is that its $Cu_2Cl_2$ bridging unit is nearly a square (the two Cu–Cl bridging bonds are 2.444 and 2.430 Å, and the Cu–Cl–Cu′ and Cl–Cu–Cl′ angles are 89.23 and 90.77°, respectively), which is not observed in other known $Cu(\mu\text{-}Cl)_2Cu$ complexes. There are three complexes containing near Cu–Cl bridging bonds: $[KCuCl_3]_2$ (2.314, 2.322 Å),[18] $[(iPrNH_3)(CuCl_3)]_2$ (2.301, 2.315 Å),[14b] and $[CuCl(hpba_3)]_2$ (2.306, 2.316 Å).[10] But they all adopt the SP II geometries, have bridging angles diverging considerably from 90° (95.9, 95.4, and 94.51°), and exhibit divergent magnetic interaction ($2J$ = –38.23, –19.46, and +33.7 cm$^{-1}$, respectively). When $2J$ values of these complexes were plotted against $\varphi$, the points fell nearly in a straight line of slope –48.6 [cm$^{-1}$/°] and passed through $2J = 0$ at 95.1°.[8a,10] $[CuLCl]_2$ is not placed close to the line, which may be due to its unique TBP geometry.

Many chloro-bridged $Cu^{II}$ dimers use $Cl^-$ as terminal ligands, and a change from antiferromagnetic to ferromag-

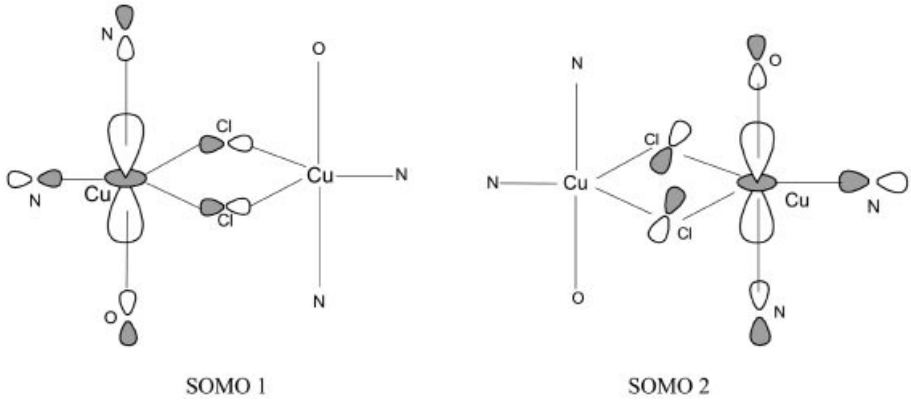


Figure 3. The two SOMOs of the complex $[CuLCl]_2$.

 © 2007 Wiley-VCH Verlag GmbH & Co. KGaA, Weinheim 

netic behavior may occur when $Cl^-$ is substituted by a N donor.[8b] Our present complex $[CuLCl]_2$ and **2**[3c] are two unique cases containing phenolate oxygen donors. The deprotonation of the phenolate group can provide one anion and cut down the number of $Cl^-$ anions thus featuring the unprecedented magnetic behavior.

$[CuLCl]_2$ represents a very rare example of the unique equatorial-equatorial TBP geometry. Its interesting structure and the novel ferromagnetic behavior might provide useful information for the magneto-structural correlations for this TBP system in the future. With continued research efforts designed to improve theoretical models and to obtain a greater number of experimental examples, the nature of the relationship between the structural properties and the exchange-coupling constant for TBP systems can be refined.

## Conclusions

In summary, we have prepared and characterized a novel equatorial–equatorial trigonal bipyramidal copper dimer with ferromagnetic exchange interaction. The complex has a Cu–Cl–Cu bridging angle close to 90° and two shorter and near Cu–Cl bridging bonds, and the deprotonation of the phenolate group can reduce the number of $Cl^-$ anions. The distortion from SP to TBP geometry may cause an effective overlap between two Cu centers. All these features of the complex may thus increase its ferromagnetic behavior.

## Experimental Section

**General Remarks:** All commercially available chemicals were of analytical grade and were used as received. C, H, and N were determined with an Elementar vario EL elemental analyzer. UV/Vis spectra were measured with a GBC Cintra 10e UV/Vis spectrophotometer in MeOH solution. The IR spectra were recorded with a Nicolet-AVATAR 360 FT-IR spectrometer using KBr pellets in the 4000–400 $cm^{-1}$ regions. $^1H$ NMR spectra were recorded with a Varian 500 Bruker spectrometer in DMSO. Variable-temperature magnetic susceptibility data for the crystalline sample were obtained in an external field of 1000 G on an Oxford Maglab 2000 system magnetometer in the 2–300 K temperature range. The susceptibilities were corrected for diamagnetism with Pascal's constants for all the constituent atoms.

**Synthesis of HL:** A mixture of pyridine-2-carbaldehyde (0.107 g, 1 mmol) and 2-amino-6-methylphenol (0.123 g, 1 mmol) was refluxed in anhydrous ethanolic solution (20 mL) for 2 h. After the solvent was removed, *n*-hexane was added (20 mL) and the mixture was refluxed for another 0.5 h. The reaction mixture was filtered and left to stand at room temperature and then brown crystals were obtained from the filtrate after 15 min. Yield: 0.172 g, 81%. M. p. 95–96 °C. $C_{13}H_{12}N_2O$ ($M_r$ = 212.10): calcd. C 73.56, H 5.70, N 13.20; found C 73.57, H 5.92, N 13.22. $^1H$ NMR (500 MHz, DMSO): $\delta$ = 8.76 (s, 1 H, phenol-OH), 8.74 (s, 1 H, imide-H), 8.70 (d, $J$ = 4.2 Hz, 1 H, pyridine-H), 8.58 (d, $J$ = 7.9 Hz, 1 H, pyridine-H), 7.96 (t, $J$ = 7.6 Hz, 1 H, pyridine-H), 7.50 (t, $J$ = 6.3 Hz, 1 H, pyridine-H), 7.28 (d, $J$ = 7.9 Hz, 1 H, Ar-H), 7.08 (d, $J$ = 7.3 Hz, 1 H, Ar-H), 6.78 (t, $J$ = 7.7 Hz, 1 H, Ar-H), 2.22 (s, 3 H, $-CH_3$) ppm. IR (KBr pellet): $\tilde{\nu}$ = 3402, 3061, 2918, 1627, 1600, 1582, 1566, 1476, 1433, 1344, 1235, 1205, 1163, 1079, 1013, 944, 834, 783, 742, 733, 598 $cm^{-1}$. UV/Vis ($\lambda_{max}$, MeOH): 289, 361, 442 nm.

**Synthesis of Complex $[CuLCl]_2$:** To a 10-mL $CH_2Cl_2$–$CH_3OH$ (1:1) yellow solution of HL (0.011 g, 0.05 mmol), a 5-mL $CH_3OH$ solution of $CuCl_2{\cdot}2H_2O$ (0.008 g, 0.05 mmol) was added dropwise with continuous stirring, and then the mixture was refluxed for 1 h. The reaction mixture was filtered and left to stand at room temperature. On slow evaporation of the solution for several days, the deep red crystals of $[CuLCl]_2$ suitable for X-ray analysis were collected. $C_{13}H_{11}ClCuN_2O$ ($M_r$ = 310.23): calcd. C 50.33, H 3.55, N 9.02; found C 50.43, H 3.45, N 9.27. IR (KBr pellet): $\tilde{\nu}$ = 3410, 3056, 3002, 1605, 1593, 1543, 1477, 1449, 1423, 1359, 1276, 1247, 1205, 1157, 1075, 922, 848, 782, 746 $cm^{-1}$. UV/Vis ($\lambda_{max}$, MeOH): 281, 357, 506 nm.

**X-ray Crystallographic Study:** The crystal with dimensions $0.30 \times 0.22 \times 0.10$ mm was selected for X-ray diffraction experiments. The measurements were performed with a Bruker SMART 1000 CCD diffractometer at room temperature (293 K) with graphite monochromatized Mo-$K_\alpha$ radiation ($\lambda$ = 0.71073 Å). Semi-empirical absorption corrections were applied using the SADABS program. The structures were solved by direct methods and refined by full-matrix least-squares on $F^2$ using the SHELXS-97 and SHELXL-97 programs.[19] All non-hydrogen atoms were refined with anisotropic displacement parameters and the hydrogen atoms were generated geometrically and treated by a mixture of independent and constrained refinements. A summary of the crystallographic data and details of the structure refinements are listed in Table 3. CCDC-285069 contains the supplementary crystallographic data for this paper. These data can be obtained free of charge from The Cambridge Crystallographic Data Centre via www.ccdc.cam.ac.uk/data_request/cif.

Table 3. Crystal data and structure refinement details for complex $[CuLCl]_2$.

| Empirical formula | $C_{26}H_{22}Cl_2Cu_2N_4O_2$ |
|---|---|
| Formula weight | 620.46 |
| Temperature [K] | 294(2) |
| Wavelength [Å] | 0.71073 |
| Crystal system | orthorhombic |
| Space group | *Pbca* |
| Unit cell dimensions | $a$ = 14.807(3) Å, $\alpha$ = 90° |
| | $b$ = 8.8132(16) Å, $\beta$ = 90° |
| | $c$ = 18.846(3) Å, $\gamma$ = 90° |
| Volume [Å$^3$] | 2459.4(8) |
| $Z$, calculated density [g/cm$^3$] | 8, 1.676 |
| Absorption coefficient [mm$^{-1}$] | 1.980 |
| $F$(000) | 1256 |
| Crystal size [mm] | $0.30 \times 0.22 \times 0.10$ |
| $\theta$ range for data collection | 2.16–26.47° |
| Reflections collected / unique | 12883 / 2524 [$R_{int}$ = 0.0599] |
| Data / restraints / parameters | 5444 / 39 / 381 |
| Goodness of fit on $F^2$ | 1.003 |
| Final $R$ indices [$I > 2\sigma(I)$] | $R_1$ = 0.0412, $wR_2$ = 0.0944 |
| $R$ indices (all data) | $R_1$ = 0.0700, $wR_2$ = 0.1114 |

## Acknowledgments

This work was supported by the National Natural Science Foundation of China (No. 20371009) and Key Laboratory of Radiopharmaceuticals of Beijing Normal University, Ministry of Education.

 © 2007 Wiley-VCH Verlag GmbH & Co. KGaA, Weinheim 

[1] a) J. S. Miller, A. J. Epstein, *Angew. Chem. Int. Ed. Engl.* **1994**, *33*, 385–415; b) J. S. Miller, A. J. Epstein, W. M. Reiff, *Science* **1988**, *240*, 40–47.
[2] a) P. J. Hay, J. C. Thibeault, R. Hoffmann, *J. Am. Chem. Soc.* **1975**, *97*, 4884–4899; b) V. H. Crawford, H. W. Richardson, J. R. Wasson, D. J. Hodgson, W. E. Hatfield, *Inorg. Chem.* **1976**, *15*, 2107–2110; c) M. F. Charlot, O. Kahn, S. Jeannin, Y. Jeannin, *Inorg. Chem.* **1980**, *19*, 1410–1411.
[3] a) R. F. Drake, V. H. Crawford, N. W. Laney, W. E. Hatfield, *Inorg. Chem.* **1974**, *13*, 1246–1250; b) W. E. Marsh, K. C. Patel, W. E. Hatfield, D. J. Hodgson, *Inorg. Chem.* **1983**, *22*, 511–515; c) F. Tuna, L. Patron, Y. Journaux, M. Andruh, W. Plass, J.-C. Trombe, *J. Chem. Soc., Dalton Trans.* **1999**, 539–545; d) M. Rodriguez, A. Llobet, M. Corbella, A. E. Martell, J. Reibenspies, *Inorg. Chem.* **1999**, *38*, 2328–2334.
[4] A. W. Addison, T. N. Rao, J. Reedijk, J. van Rijn, G. C. Verschoor, *J. Chem. Soc., Dalton Trans.* **1984**, 1349–1356.
[5] a) J. T. Blanchette, R. D. Willett, *Inorg. Chem.* **1988**, *27*, 843–849; b) D. J. Hodgson, P. K. Hale, W. E. Hatfield, *Inorg. Chem.* **1971**, *10*, 1061–1067.
[6] I. J. Bruno, J. C. Cole, P. R. Edgington, M. Kessler, C. F. Macrae, P. McCabe, J. Pearson, R. Taylor, *Acta Crystallogr., Sect. B* **2002**, *58*, 389–397.
[7] A. G. Orpen, L. Brammer, F. H. Allen, O. Kennard, D. G. Watson, R. Taylor, *J. Chem. Soc., Dalton Trans.* **1989**, 1–83.
[8] a) M. Rodríguez, A. Llobet, M. Corbella, *Polyhedron* **2000**, *19*, 2483–2491; b) A. Rodríguez-Fortea, P. Alemany, S. Alvarez, E. Ruis, *Inorg. Chem.* **2002**, *41*, 3769–3778.
[9] a) M. Mégnamisi-Bélombé, M. A. Novotny, *Inorg. Chem.* **1980**, *19*, 2470–2473; b) X.-H. Bu, M. Du, Z.-L. Shang, L. Zhang, Q.-H. Zhao, R.-H. Zhang, M. Shionoya, *Eur. J. Inorg. Chem.* **2001**, 1551–1558; c) X.-H. Bu, M. Du, L. Zhang, Z.-L. Shang, R.-H. Zhang, M. Shionoya, *J. Chem. Soc., Dalton Trans.* **2001**, 729–735; d) C. J. O'Connor, *Inorg. Chim. Acta* **1987**, *127*, 29–30; e) E. Kwiatkowski, M. Kwiatkowski, A. Olechnowicz, J. Mrozinski, D. M. Ho, E. Deutsch, *Inorg. Chim. Acta* **1989**, *158*, 37–42; f) A. Bernalte-García, A. M. Lozano-Vila, F. Luna-Giles, R. Pedrero-Marín, *Polyhedron* **2006**, *25*, 1399–1407.
[10] S. G. N. Roundhill, D. M. Roundhill, D. R. Bloomquist, C. Landee, R. D. Willett, D. M. Dooley, H. B. Gray, *Inorg. Chem.* **1979**, *18*, 831–835.
[11] a) K. T. McGregor, D. B. Losee, D. J. Hodgson, W. E. Hatfield, *Inorg. Chem.* **1974**, *13*, 756–759; b) I. R. Evans, J. A. K. Howard, L. E. M. Howard, J. S. O. Evans, Ž. K. Jaćimović, V. S. Jevtović, V. M. Leovac, *Inorg. Chim. Acta* **2004**, *357*, 4528–4536; c) J. A. Carrabirie, M. Sundaralingarn, *J. Am. Chem. Soc.* **1970**, *92*, 369–371.
[12] a) I. Søtofte, K. Nielsen, *Acta Chem. Scand. Ser. A* **1981**, *A35*, 733–738; b) D. J. Hodgson, E. Pedersen, *Acta Chem. Scand. Ser. A* **1982**, *A36*, 281–282; c) A. Tosik, W. Maniukievicz, M. Bukowska-Strzyzewska, J. Mrozinski, M. P. Sigalas, C. A. Tsipis, *Inorg. Chim. Acta* **1991**, *190*, 193–203.
[13] a) T. Rojo, M. I. Arriortua, J. Ruiz, J. Darriet, G. Villeneuve, D. Beltranporter, *J. Chem. Soc., Dalton Trans.* **1987**, 285–291; b) S. C. Lee, R. H. Holm, *Inorg. Chem.* **1993**, *32*, 4745–4753.
[14] a) C. P. Landee, A. Djili, D. F. Mudgett, M. Newhall, H. Place, B. Scott, R. D. Willett, *Inorg. Chem.* **1988**, *27*, 620–627; b) S. A. Roberts, D. R. Bloomquist, R. D. Willett, H. W. Dodgen, *J. Am. Chem. Soc.* **1981**, *103*, 2603–2610.
[15] a) P. J. Hay, J. C. Thiebeault, R. Hoffmann, *J. Am. Chem. Soc.* **1975**, *97*, 4884–4899; b) J. B. Goodenough, *Phys. Rev.* **1955**, *100*, 564–573.
[16] W. E. Marsh, W. E. Hatfield, D. J. Hodgson, *Inorg. Chem.* **1982**, *21*, 2679–2684.
[17] A. Benzekri, P. Dubourdeaux, J.-M. Latour, J. Laugier, P. Rey, *Inorg. Chem.* **1988**, *27*, 3710–3716.
[18] R. D. Willett, C. Dwiggins Jr, R. F. Kruh, R. E. Rundle, *J. Chem. Phys.* **1963**, *38*, 2429–2436.
[19] G. M. Sheldrick, *SHELXS-97* and *SHELXL-97*, programs for the solution and refinement of crystal structures, University of Göttingen, Göttingen, Germany, **1997**.

Received: September 23, 2006
Published Online: January 8, 2007

 © 2007 Wiley-VCH Verlag GmbH & Co. KGaA, Weinheim 

DOI: 10.1002/ejic.200600895

# The Active Intermediates of Non-Heme-Iron-Based Systems for Catalytic Alkene Epoxidation with $H_2O_2/CH_3COOH$

**Eduard A. Duban,[a] Konstantin P. Bryliakov,[a] and Evgenii P. Talsi*[a]**

**Keywords:** Oxidoiron(IV) complexes / Acylperoxido complexes / EPR spectroscopy / Paramagnetic NMR spectroscopy / Intermediates / Oxidation

Iron complexes with aminopyridine ligands $[Fe^{II}(BPMEN)(CH_3CN)_2](ClO_4)_2$ (**1**) [BPMEN = *N*,*N*′-dimethyl-*N*,*N*′-bis(2-pyridylmethyl)-1,2-diaminoethane] and $[Fe^{II}(TPA)(CH_3CN)_2](ClO_4)_2$ (**2**) [TPA = tris(2-pyridylmethyl)amine] are rare examples of iron-based catalysts for selective olefin epoxidation with $H_2O_2/CH_3COOH$ combination. Using $^{1,2}H$ NMR and EPR spectroscopy, it was shown that the active species of the catalytic systems **1**/$H_2O_2/CH_3COOH$ and **2**/$H_2O_2/CH_3COOH$ are mononuclear iron(IV)-oxido complexes $[(BPMEN)Fe^{IV}{=}O(S)]^{2+}$ and $[(TPA)Fe^{IV}{=}O(S)]^{2+}$, respectively (S = solvent molecule). These intermediates are formed via decomposition of the corresponding acylperoxido complexes $[(L)Fe^{III}(O_3CCH_3)]^{2+}$ (L = BPMEN or TPA). The acylperoxido complex $[(BPMEN)Fe^{III}(O_3CCD_3)]^{2+}$ was identified in the catalytic system **1**/$H_2O_2/CD_3COOD$ by $^2H$ NMR spectroscopy. The improved epoxidation activity and selectivity of the catalytic systems **1**/$H_2O_2/CH_3COOH$ and **2**/$H_2O_2/CH_3COOH$, with respect to **1**/$H_2O_2$ and **2**/$H_2O_2$, is caused by the effective formation of intermediates $[(L)Fe^{IV}{=}O(S)]^{2+}$ via decomposition of the acylperoxido complexes $[(L)Fe^{III}(O_3CCH_3)]^{2+}$.

(© Wiley-VCH Verlag GmbH & Co. KGaA, 69451 Weinheim, Germany, 2007)

## Introduction

Iron complexes with aminopyridine ligands are known to efficiently catalyze selective olefin oxidation using $H_2O_2$ or $CH_3CO_3H$ as terminal oxidants.[1–13] $[Fe^{II}(BPMEN)(CH_3CN)_2](ClO_4)_2$ (**1**) [BPMEN = *N*,*N*′-dimethyl-*N*,*N*′-bis(2-pyridylmethyl)-1,2-diaminoethane] and $[Fe^{II}(TPA)(CH_3CN)_2](ClO_4)_2$ (**2**) [TPA = tris(2-pyridylmethyl)amine] (Figure 1) represent the catalysts investigated thus far in the most detail.[1–3,10] Interestingly, the epoxidation of olefins by $H_2O_2$ catalyzed by **1** and **2** was improved by the addition of acetic acid,[2] and the in situ formation of peroxyacetic acid was later inferred in these systems.[4] The iron(IV)-oxido species $[LFe^{IV}{=}O(S)]^{2+}$ (L = BPMEN or TPA, S = solvent molecule) are considered as possible reactive intermediates of the catalytic systems **1**/$H_2O_2/CH_3COOH$ and **2**/$H_2O_2/CH_3COOH$. This postulate was derived from nearly identical product distribution obtained for olefin oxidations catalyzed by **1** and **2** with $CH_3CO_3H$ and $H_2O_2/CH_3OOH$ as oxidants.[12] However, whereas the $[(TPA)Fe^{IV}{=}O(S)]^{2+}$ intermediate active towards cyclooctene was trapped in the catalytic system **2**/$CH_3CO_3H$,[14] such type of species have never been detected in **2**/$H_2O_2/CH_3COOH$ and **1**/$H_2O_2/CH_3COOH$ combinations. Thus, the experimental proof is required for the proposed key role of an $Fe^{IV}{=}O$ oxidant in **1**/$H_2O_2/CH_3COOH$ and **2**/$H_2O_2/CH_3COOH$ systems.

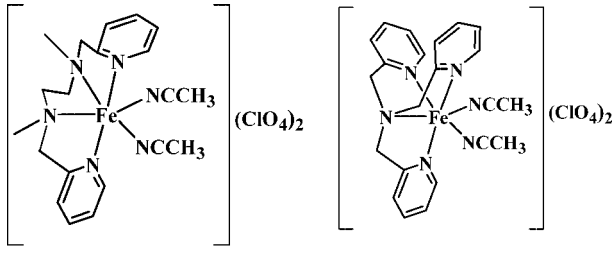


Figure 1. Structures of complexes **1** and **2**.

For **1**/$H_2O_2$ and **2**/$H_2O_2$ catalytic systems, the nature of active intermediates is even less clear. The low-spin ferric hydroperoxo species $[LFe^{III}(OOH)(S)]^{2+}$ were identified in **1**/$H_2O_2$[6] and **2**/$H_2O_2$.[15,16] Later, it was proposed that $[(TPA)Fe^{III}(OOH)(S)]^{2+}$ by itself is a sluggish oxidant but could be a precursor of more reactive species (e.g. $[(TPA)Fe^{IV}{=}O(S)]^{2+}$).[17] However, mononuclear $[LFe^{IV}{=}O(S)]^{2+}$ intermediates have never been detected in **1**/$H_2O_2$ and **2**/$H_2O_2$ systems.

In this work, we report $^{1,2}H$ NMR and EPR detection and reactivity studies of $[LFe^{IV}{=}O(S)]^{2+}$ and other intermediates formed in the catalytic systems **1**/$CH_3CO_3H$, **2**/$CH_3CO_3H$, **1**/$H_2O_2/CH_3COOH$, **2**/$H_2O_2/CH_3COOH$, and **1**/$H_2O_2$.

[a] Boreskov Institute of Catalysis, Siberian Branch of the Russian Academy of Sciences,
630090, Novosibirsk, Russian Federation
Fax: +7-383-3308056
E-mail: talsi@catalysis.ru


© 2007 Wiley-VCH Verlag GmbH & Co. KGaA, Weinheim

## Results and Discussion

### Catalytic Systems 1/$CH_3CO_3H$ and 1/$H_2O_2$/$CH_3COOH$

The $^1H$ NMR spectrum recorded 10 min after onset of the reaction of **1** with 2 equiv. of $CH_3CO_3H$ at –50 °C in a 1:1 $CD_2Cl_2/CD_3CN$ mixture displays broad peaks of $Fe^{III}$–O–$Fe^{III}$ dimers and additional sharp peaks (marked by points) of the new complex **3** (Figure 2, a). Most of the $^1H$ NMR peaks of **3** possess negative $^1H$ NMR chemical shifts, whereas mononuclear high-spin ferrous complex **1** and dinuclear $Fe^{III}$–O–$Fe^{III}$ species with BPMEN ligands exhibit mainly the $^1H$ NMR peaks with positive chemical shifts.[6,18] Such unusual negative $^1H$ NMR chemical shifts were previously observed for X-ray characterized low-spin mononuclear complex $[(N_4Py)Fe^{IV}=O]^{2+}$, where $N_4Py$ is the pentadentate ligand *N*,*N*′-bis(2-pyridylmethyl)-*N*-bis(2-pyridyl)methylamine.[19] Thus, complex **3** could be assigned to a mononuclear $Fe^{IV}$=O complex. In agreement with this assumption, complex **3** could also be obtained upon reaction of **1** with 1 equiv. of iodosylbenzene at –50 °C in a 1:1 $CD_2Cl_2/CD_3CN$ mixture (Figure 2, b). The reaction of a ferrous precursor with iodosylbenzene is the commonest method for the generation of $Fe^{IV}$=O species.[14] By analogy with X-ray characterized complex $[(TMC)Fe^{IV}=O(CH_3CN)]^{2+}$ (TMS is tetradentate ligand tetramethylcyclam, cyclam = 1,4,8,11-tetraazacyclotetradecene),[20] the following structure could be proposed for **3**: $[(BPMEN)Fe^{IV}=O(CH_3CN)]^{2+}$. A molecule of solvent ($CH_3CN$) occupies the sixth coordination site of **3**.

$[(BPMEN)Fe^{IV}=O(CH_3CN)]^{2+}$ **3**

$[(BPMEN)Fe^{III}(O_3CCH_3)]^{2+}$ **4**

$[(BPMEN)Fe^{III}–O–Fe^{IV}=O(BPMEN)(S)]^{3+}$ **5**

$[(TPA)Fe^{IV}=O(S)]^{2+}$ **6**

$[(OH)(BPMEN)Fe^{III}–O–Fe^{III}(BPMEN)(H_2O)](ClO_4)_3$ **7**

$[(BPMEN)Fe^{III}(OOH)]^{2+}$ **8**

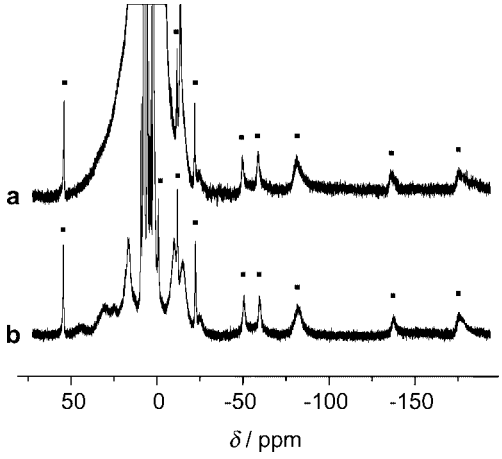


Figure 2. $^1H$ NMR spectra (–50 °C) of **1**/$CH_3CO_3H$ (a) and **1**/PhIO (b) systems recorded 10 min after mixing the reagents at –50 °C in a 1:1 $CD_2Cl_2/CD_3CN$ mixture ([**1**] = [PhIO] = 0.05 M, [$CH_3CO_3H$] = 0.1 M). Points denote peaks of **3**.

The number of the $^1H$ NMR peaks of **3** corresponds to the number of chemically nonequivalent protons of the BPMEN ligand.[21] The intensities of the $^1H$ NMR peaks of **3** correspond to the conversion of up to 30% of **1** into **3**. Complex **3** is stable in a 1:1 $CD_2Cl_2/CD_3CN$ mixture at –50 °C and decays at higher temperatures (the half-life time $\tau_{1/2}$ is 15 min at –10 °C). After the addition of 5 equiv. of cyclohexene to the solution containing **3** at –50 °C, the latter disappears within several minutes. This decay is accompanied by the rise of the $^1H$ NMR peaks of the 1,2-epoxycyclohexane. Thus, complex **3** is the key intermediate of epoxidation by the catalytic system **1**/$CH_3CO_3H$.

The same complex **3** was observed by $^1H$ NMR upon addition of $H_2O_2$ into the **1**/$CH_3COOH$ system ([**1**] = [$H_2O_2$] = [$CH_3COOH$] = 0.05 M, 1:1 $CD_2Cl_2/CD_3CN$ mixture, –50 °C). The concentration of **3** was close to that for the **1**/$CH_3O_3H$ system ([**1**] = [$CH_3CO_3H$] = 0.05 M, 1:1 $CD_2Cl_2/CD_3CN$ mixture, –50 °C). Thus, mononuclear ironoxido complex $[(BPMEN)Fe^{IV}=O(S)]^{2+}$ (**3**) is the active species of cyclohexene epoxidation by the catalytic systems **1**/$CH_3CO_3H$ and **1**/$H_2O_2$/$CH_3COOH$.

Apparently, it is the ferric acylperoxido complex $[(BPMEN)Fe^{III}(O_3CCH_3)]^{2+}$ (**4**) that is the precursor of **3**. We have undertaken the search for **4** by $^2H$ NMR using deuterated peroxo acetic acid ($CD_3CO_3H$). The $^2H$ NMR spectrum recorded 10 min after the addition of 1.5 equiv. of $CD_3CO_3H$ to **1** in a 1:1 $CH_2Cl_2/CH_3CN$ mixture at –50 °C exhibits a broad peak at $\delta$ = 102.7 ppm (the half height width $\Delta\nu_{1/2}$ = 230 Hz) (Figure 3). The same peak was observed after the addition of 1 equiv. of $H_2O_2$ to the sample containing **1** and 1 equiv. of $CD_3COOD$ in a 1:1 $CH_2Cl_2/CH_3CN$ mixture at –50 °C ([**1**] = 0.05 M). This peak disappeared upon warming ($\tau_{1/2}$ = 10 min at –30 °C). For the high-spin complex $(TPP)Fe^{III}–O–O–CD_2–CD_3$ (TPP = dianion of tetra-*p*-tolylporphyrin), a $CD_2$ peak was observed at $\delta$ = 180 ppm, and a $CD_3$- peak at 4 ppm.[22] On the basis of these data, the resonance at $\delta$ = 102.7 ppm could be assigned to the $OOCCD_3$ or $O_3CCD_3$ moiety bound to high-spin $Fe^{III}$. To rule out the assignment of the observed peak to the $OOCCD_3$ moiety, $CD_3COOD$ was added to the solution containing **1** at –50 °C. In this case, no $^2H$ NMR peaks near 100 ppm were observed. Thus, the $^2H$ NMR resonance at $\delta$ = 102.7 ppm belongs to the $O_3CCD_3$ moiety of the high-spin ferric acylperoxido complex **4**. The maximum

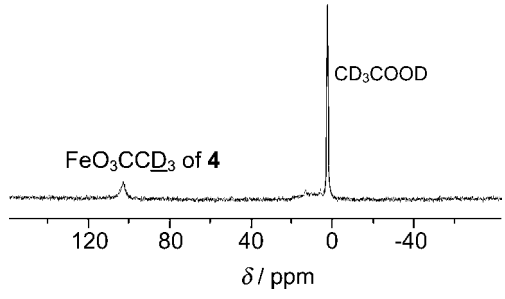


Figure 3. The $^2H$ NMR spectrum (–50 °C) of the system **1**/$CD_3CO_3D$ recorded 10 min after mixing the reagents at –50 °C in a 1:1 $CH_2Cl_2/CH_3CN$ mixture ([**1**] = 0.05 M, [$CD_3CO_3H$] = 0.075 M).

 © 2007 Wiley-VCH Verlag GmbH & Co. KGaA, Weinheim 

concentration of **4** was about 10% of the initial concentration of **1**.

The high-spin mononuclear ferric complex **4** should display an EPR signal at $g = 4.23$.[23,24] EPR spectra recorded in various moments of time after onset of the reaction of **1** with 2 equiv. of $CH_3CO_3H$ at –60 °C in a 2:1 $CH_2Cl_2$/$CH_3CN$ mixture show: (1) a signal at $g = 4.23$ (peak-to-peak width $\Delta H = 260$ G), (2) an axially anisotropic signal ($g_1 = g_2 = 2.42$, $g_3 = 2.67$), and (3) a very broad signal at $g \approx 2$ ($\Delta H = 1200$ G) (Figure 4, a and b). The signal at $g = 4.23$ ($\Delta H = 260$ G) was gone upon warming to room temperature, and another weaker and sharper signal ($\Delta H = 70$ G) with the same $g$-factor was observed. The latter signal persists after storing at room temperature for hours and thus belongs to a stable mononuclear high-spin ferric species. The broad signal near $g = 2$ disappeared upon warming (Figure 4, c).

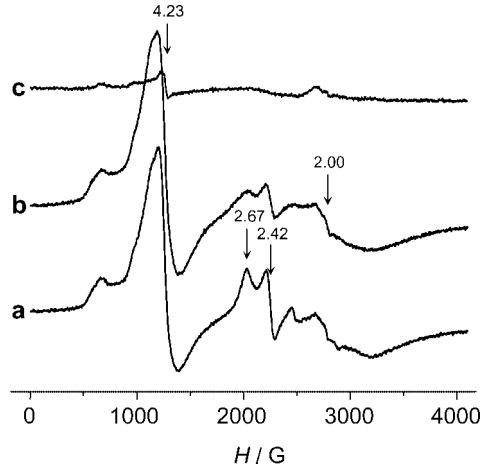


Figure 4. X-band EPR spectra (–196 °C) recorded 1 min (a) and 10 min (b) after mixing **1** and $CH_3CO_3H$ at –60 °C in a 2:1 $CH_2Cl_2$/$CH_3CN$ mixture. Sample (b) after warming to room temperature (c). ([**1**] = 0.05 M, [$CH_3CO_3H$] = 0.1 M).

It is tempting to assign the observed signal at $g = 4.23$ (Figure 4, a and b) to acylperoxido complex **4**. However, another high-spin ferric species (e.g., high-spin hydroxido complex [(BPMEN)$Fe^{III}$(OH)]$^{2+}$) could have an EPR signal in the same range. At present, it is difficult to determine the contribution of **4** to the observed signal at $g = 4.23$. The origin of a very broad signal near $g = 2$ (Figure 4, a and b) is also unclear.

The axial spectrum ($g_1 = g_2 = 2.42$, $g_3 = 2.67$) (Figure 4, a and b) belongs to the very unstable complex **5** ($\tau_{1/2}$ = 10 min at –60 °C). The same signal could be observed in the catalytic system **1**/$H_2O_2$ along with the rhombic spectra of the low-spin ferric hydroperoxido complexes [(BPMEN)-$Fe^{III}$(OOH)S]$^{2+}$ (see below).

EPR spectra of the low-spin ferric complexes (heme and non-heme) show a rhombic pattern ($g_x \neq g_y \neq g_z$) with $g$-values in the range ca. 1–4 (one of the $g$-values is less than $g_e = 2.0024$)[10,23–26] These spectra differ markedly from that of **5** ($g_1 = g_2 = 2.42$, $g_3 = 2.67$). The EPR spectra of high-spin ferric complexes with TPA- and BPMEN-type ligands display an EPR signal at $g_{eff} = 4.23$.[10,23–26] Therefore, complex **5** is not the low-spin, nor the high-spin ferric complex. EPR spectra of binuclear $Fe^{III}Fe^{II}$ moieties reported for some enzymes (methane monooxygenase, ribonucleotide reductase, Rieske-type dioxygenase, etc) and model compounds exhibit resonances in the range $g_1 = 1.93$–$2.01$, $g_2 = 1.85$–$1.92$, $g_3 = 1.64$–$1.80$,[24,25] and again are very different from that of **5**. Complexes with $Fe^{III}$–O–$Fe^{III}$, $Fe^{IV}$=O, and $Fe^{IV}$–O–$Fe^{IV}$ fragments are EPR silent.[13,14,24,27] Thus, it is reasonable to assume that **5** is a binuclear $Fe^{III}Fe^{IV}$ complex. Recently, Wieghardt et al. have identified iron species formed upon photooxidation of *trans*-[(cyclam)$Fe(N_3)_2$]$ClO_4$ in acetonitrile solution by Mössbauer and EPR spectroscopy. The major photolysis product in liquid solution at room temperature was nitrido-bridged binuclear ($Fe^{III}$, $Fe^{IV}$) complex with localized antiferromagnetically coupled $Fe^{III}$ ($S = 3/2$) and low-spin $Fe^{IV}$ ($S = 1$) units, the total spin being $S = 1/2$.[28] The EPR spectrum of this (μ-nitrido) diiron complex ($g$-values of 2.04, 2.06, and 2.20) resembles that of complex **5**. Both the spectra display almost axial symmetry and for both spectra all the $g$-values are larger than $g_e$. Thus, complex **5** can be tentatively assigned to a mixed-valence $Fe^{III}Fe^{IV}$ complex. The formation of $Fe^{III}$–O–$Fe^{III}$ binuclear complexes is highly characteristic for the catalytic systems studied.[18,29] Therefore, the existence of binuclear intermediates [(BPMEN)$Fe^{III}$–O–$Fe^{IV}$=O(BPMEN)(S)]$^{3+}$ (**5**) along with mononuclear species [(BPMEN)$Fe^{IV}$=O(S)]$^{2+}$(**3**) seems to be rather probable. The attempts to obtain additional spectroscopic evidences in favor of the proposed structure of **5** were unsuccessful due to the low concentration of **5** with respect to the concentrations of the other iron species present in the sample.

Intermediate **5** ($\tau_{1/2}$ = 10 min at –60 °C) is far less stable than **3** ($\tau_{1/2}$ = 15 min at –10 °C). As was mentioned, in the presence of cyclohexene, the decay of **3** at –50 °C is accompanied by the rise of concentration of the 1,2-epoxycyclohexane. Thus, despite the fact that intermediate **5** could also react with cycloxehene (see below), intermediate **3** is the active species of cyclohexene epoxidation by the catalytic systems **1**/$CH_3CO_3H$ and **1**/$H_2O_2$/$CH_3COOH$.

### Catalytic Systems 2/$CH_3CO_3H$ and 2/$H_2O_2$/$CH_3COOH$

By analogy with BPMEN-based systems, it is natural to assume that the active species of **2**/$CH_3CO_3H$ and **2**/$H_2O_2$/$CH_3COOH$ systems is the oxidoiron(IV) complex [(TPA)-$Fe^{IV}$=O(S)]$^{2+}$ (**6**). In full agreement with this assumption, peaks of **6** (marked by points) were observed in the $^1H$ NMR spectra of **2**/$H_2O_2$/$CH_3COOH$ and **2**/$CH_3CO_3H$ in 1:1 $CD_2Cl_2$/$CD_3CN$ at –50 °C (Figure 5). The remaining paramagnetically shifted signals belong to binuclear $Fe^{III}$–O–$Fe^{III}$ species.[29] Complex **6** is unstable ($\tau_{1/2}$ = 10 min at –10 °C). The most characteristic and easily assignable peaks of **6** belong to β,β′-protons of the picolinic rings [1:1 $CDCl_3$/$CD_2Cl_2$, –50 °C, $\delta$ = 58.8 (2 H), 49.8 (1 H), –24.9 (2 H), and –28.7 (1 H)]. The ratio between the four observed peaks (2:1:2:1) corresponds to two equivalent and one

 © 2007 Wiley-VCH Verlag GmbH & Co. KGaA, Weinheim 

unique picolinic rings of a coordinated TPA ligand. The observed pattern of β,β′-protons of **6** resembles that for X-ray characterized complex $[(N_4Py)Fe^{IV}=O]^{2+}$ [$\delta$ = 44.4 (2 H), 30.05 (2 H), –11.2 (2 H), –17.8 (2 H)].[19] The assignment of the other signals of **6** is more complicated and is still not completed, as in the case of $[(N_4Py)Fe^{IV}=O]^{2+}$. Complex **6** is stable at –50 °C and rapidly (within several minutes) disappears at this temperature in the presence of 5 equiv. of cyclohexene. The decay of **6** was accompanied by the rise of the $^1$H NMR peaks of 1,2-epoxycyclohexane. Fresh portions of $CH_3CO_3H$ or $H_2O_2/CH_3COOH$ restore the concentration of **6**. Apparently, it is the oxidoiron intermediate $[(TPA)Fe^{IV}=O(S)]^{2+}$ (**6**) that is the active species of the catalytic systems **2**/$H_2O_2$/$CH_3COOH$ and **2**/$CH_3CO_3H$. An intermediate similar to intermediate **5** in the BPMEN-based system was not detected in the TPA-based analogue.

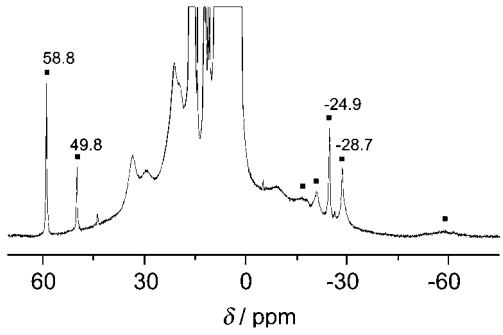


Figure 5. The $^1$H NMR spectrum (–50 °C) of the **2**/$H_2O_2$/$CH_3COOH$ system recorded 10 min after addition of $H_2O_2$ to **2**/$CH_3OOH$ in a 1:1 $CD_2Cl_2/CD_3CN$ mixture at –50 °C ([**2**] = [$CH_3COOH$] = 0.05 M, [$H_2O_2$] = 0.1 M). Points denote peaks of **6**.

### Catalytic System 1/$H_2O_2$

The $^1$H NMR spectrum of **1** in $CD_3CN$ at high temperature corresponds to a paramagnetic high-spin ferrous complex. Complex **1** decreases its spin state with decreasing temperature and displays the $^1$H NMR spectrum characteristic of diamagnetic low-spin ferrous species at –40 °C.[8,30] The addition of 2 equiv. of $H_2O_2$ to the 0.03 M solution of **1** in $CD_3CN$ at 20 °C gives rise to immediate conversion of the major part of **1** into a new complex with a $^1$H NMR spectrum very similar to that reported for binuclear complex $[(OH)(BPMEN)Fe^{III}–O–Fe^{III}(BPMEN)(H_2O)](ClO_4)_3$ (**7**).[18] Thus, the predominant iron-containing species in the **1**/$H_2O_2$ system is μ-oxo diferric complex **7**. To identify unstable intermediates, the reaction between **1** and $H_2O_2$ was studied at low temperatures.

Figure 6 shows the EPR spectrum recorded 1 min after onset of the reaction between **1** and 1.5 equiv. of $H_2O_2$ in a 2:1 $CH_2Cl_2/CH_3CN$ mixture at –60 °C. It is seen that besides the characteristic signals of the low-spin ferric hydroperoxo intermediates $[(BPMEN)Fe^{III}(OOH)(CH_3CN)]^{2+}$ (**8**-$CH_3CN$) ($g_1$ = 2.218, $g_2$ = 2.178, $g_3$ = 1.967) and $[(BPMEN)Fe^{III}(OOH)(H_2O)]^{2+}$ (**8**-$H_2O$) ($g_1$ = 2.195, $g_2$ = 2.128, $g_3$ = 1.970),[6] the axially symmetric signal of complex **5** ($g_1$ = $g_2$ = 2.42 and $g_3$ = 2.67) is observed. In the presence of 8 equiv. of cyclohexene, the decay of **5** at –60 °C increases at least by a factor of 5, whereas the rate of **8**-$CH_3CN$ and **8**-$H_2O$ decomposition remains unchanged (Figure 7 and Figure 8). These data are in agreement with

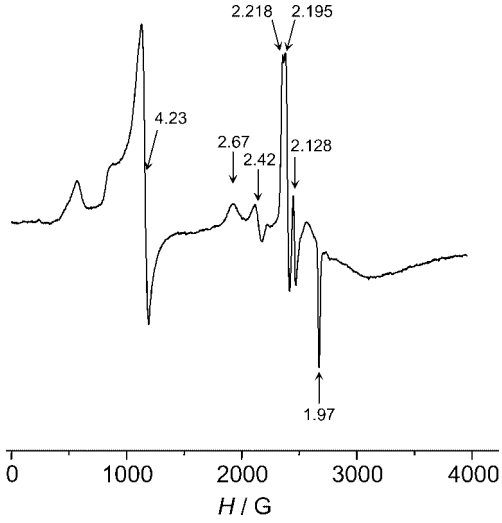


Figure 6. X-band EPR spectrum (–196 °C) recorded 1 min after mixing **1** and 1.5 equiv. of $H_2O_2$ at –60 °C in a 2:1 $CH_2Cl_2/CH_3CN$ mixture. ([**1**] = 0.05 M).

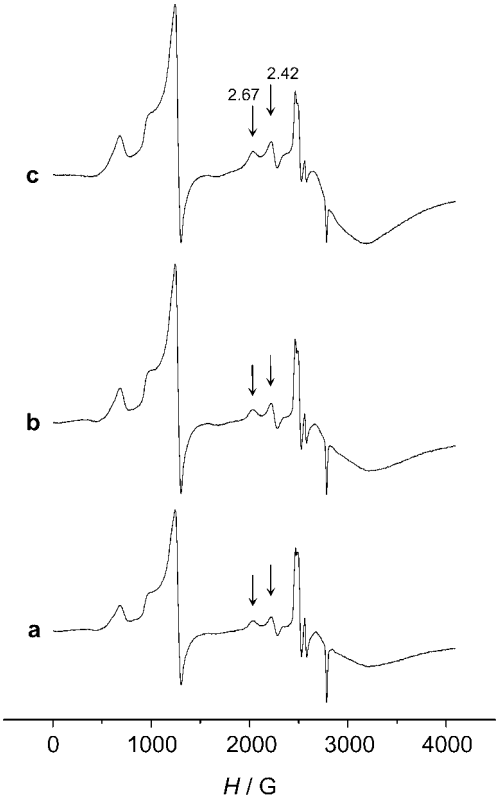


Figure 7. EPR spectra recorded 2 min (a), 5 min (b), and 7 min (c) after onset of reaction of **1** with 1.5 equiv. of $H_2O_2$ in a 2:1 $CH_2Cl_2/CH_3CN$ mixture at –60 °C.([**1**] = 0.05 M). Arrows denote signals of **5**.

 © 2007 Wiley-VCH Verlag GmbH & Co. KGaA, Weinheim 

our assumption that **5** contains the active $Fe^{IV}$=O moiety. The concentration of intermediates **5** and **8** does not exceed 5% of the concentration of **1**.

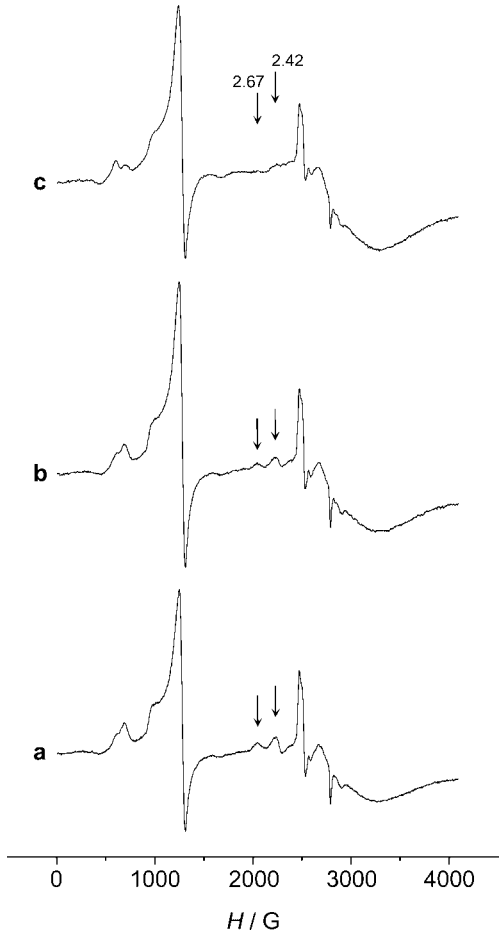


Figure 8. EPR spectra recorded 2 min (a), 3 min (b), and 6 min (c) after onset of reaction of **1** with 1.5 equiv. of $H_2O_2$ in a 2:1 $CH_2Cl_2$/$CH_3CN$ mixture containing cyclohexene at –60 °C ([**1**] = 0.05 M, [$C_6H_{10}$] = 0.4 M). Arrows denote signals of **5**.

In contrast to the **1**/$CH_3CO_3H$ and **1**/$H_2O_2$/$CH_3COOH$ catalytic systems, the mononuclear iron(IV) oxido intermediate **3** was not detected in the catalytic system **1**/$H_2O_2$. The only observable intermediate sensitive to the presence of substrate is complex **5** with the proposed structure [(BPMEN)$Fe^{III}$–O–$Fe^{IV}$=O(BPMEN)(S)]$^{3+}$. Thus, different intermediates operate in the catalytic systems **1**/$H_2O_2$ and **1**/$H_2O_2$/$CH_3COOH$. This result agrees with differing activities and selectivities of the catalytic systems **1**/$H_2O_2$ and **1**/$H_2O_2$/$CH_3COOH$ in epoxidation of olefins.[2,4,12] However, the actual role of intermediate **5** in epoxidation with **1**/$H_2O_2$ is far from being established. Very recently, it has been shown that binuclear iron(III)-BPMEN complexes are less active in epoxidation with $H_2O_2$ than mononuclear complex **1** under the same conditions.[31] This result argues against the involvement of a binuclear intermediate in the **1**/$H_2O_2$ system. On the other hand, the diiron complex with dinucleating, covalently linked TPA derivatives confirms the high reactivity of oxo-bridged diiron(III) species in olefin epoxidation.[32] Further studies are needed to elucidate the active species of the **1**/$H_2O_2$ and **2**/$H_2O_2$ catalytic systems.

Fortunately, for the most active and selective epoxidizing systems **1**/$H_2O_2$/$CH_3COOH$ and **2**/$H_2O_2$/$CH_3COOH$, the situation is more definite. On the basis of the results of our study, the active species of these catalytic systems are mononuclear $Fe^{IV}$ species [(L)$Fe^{IV}$=O(S)]$^{2+}$. The improved epoxidation activity and selectivity of the catalytic systems **1**/$H_2O_2$/$CH_3COOH$ and **2**/$H_2O_2$/$CH_3COOH$, with respect to **1**/$H_2O_2$ and **2**/$H_2O_2$, is caused by the effective formation of intermediates [(L)$Fe^{IV}$=O(S)]$^{2+}$ via decomposition of the acylperoxido complexes [(L)$Fe^{III}$($O_3CCH_3$)]$^{2+}$.

## Experimental Section

Acetonitrile, [$D_3$]acetonitrile, dichloromethane, [$D_2$]dichloromethane, [$D_4$]acetic acid, 2-picolyl chloride hydrochloride, and *N*,*N*′-dimethyl-1,2-ethanediamine were purchased from Aldrich and used without additional purification. Hydrogen peroxide (95 %) was obtained by concentration of commercial 30% $H_2O_2$ under reduced pressure. The concentrated $H_2O_2$ diluted ten times by a 1:1 $CH_2Cl_2$/$CH_3CN$ mixture was used for the preparation of samples. $CH_3CO_3H$ (or $CD_3CO_3D$) was prepared by mixing equivalent amounts of 95% $H_2O_2$ and $CH_3CO_3H$ (or $CD_3COOD$) in the presence of 1% $H_2SO_4$, and stirring the mixture overnight. [(TPA)$Fe^{II}$($CH_3CN$)$_2$]($ClO_4$)$_2$ and [(BPMEN)$Fe^{II}$($CH_3CN$)$_2$]($ClO_4$)$_2$ were synthesized following a method previously described[3,24] and satisfactorily characterized by $^1$H NMR spectroscopy. To start the reaction, 1.5–2 equiv. of $CH_3CO_3H$ or $H_2O_2$ was added to 0.5 mL of a 0.05 M solution of **1** or **2** in $CH_2Cl_2$/$CH_3CN$ or $CH_2Cl_2$/$CH_3CN$/$CH_3COOH$ mixtures at –60 to –50 °C directly in quartz EPR or glass NMR tubes ($d$ = 5 mm). For kinetic EPR studies, solutions containing unstable intermediates were placed in a thermostat at an appropriate temperature directly in an EPR tube. To stop the reaction, the tube was immersed in liquid nitrogen, followed by registration of the EPR spectrum at –196 °C. For kinetic NMR studies, $^1$H or $^2$H NMR spectra of intermediates were recorded at selected temperatures. If necessary, the appropriate amounts of cyclohexene were added to the reaction solutions. For evaluation of the concentration of **3** by $^1$H NMR, the integral intensity of the N–$CH_3$ peak of **3** was compared with the integral intensity of the residual peak of $CD_2HCN$ in $CD_3CN$. The concentration of residual $CD_2HCN$ in $CD_3CN$ was preliminarily determined by $^1$H NMR spectroscopy. For this goal the specified amount of $CHCl_3$ was added to $CD_3CN$. For evaluation of the concentration of **4**, the integral intensity of its $CD_3CO_3$ peak was compared with that of $CD_3COOD$.

EPR spectra (–196 °C) were recorded at 9.2–9.3 GHz with a Bruker ER-200D spectrometer. Measurements were made in a quartz Dewar vessel filled with liquid nitrogen. EPR signals near $g$ = 2 were quantified by double integration with copper(II) chloride as a standard at –196 °C. $^{1,2}$H NMR spectra were recorded at 400.13 and 61.425 MHz in 5-mm glass sample tubes, on a Bruker Avance 400 MHz NMR spectrometer. The following operating conditions were used for $^1$H NMR measurements: spectral width 125 kHz, spectrum accumulation frequency 10 Hz; number of scans 5000–10000; 45° pulse at 5 μs. The $^1$H and $^2$H chemical shifts were referenced to the residual peak of the solvent (C*H*$D_2$CN, and C*D*$H_2$CN, $\delta$ = 1.96 ppm). The typical operating conditions used for $^2$H NMR measurements were as follows: sweep width 125 kHz; spectrum accumulation frequency 2.5 Hz; number of transients 5000–10000; 45° pulse at 10 μs.

 © 2007 Wiley-VCH Verlag GmbH & Co. KGaA, Weinheim 

## Acknowledgments

We acknowledge the financial support from the Russian Foundation of Basic Research, grant 06–03–32214.

[1] K. Chen, L. Que Jr, *Chem. Commun.* **1999**, 1375–1376.
[2] M. C. White, A. G. Doyle, E. N. Jacobsen, *J. Am. Chem. Soc.* **2001**, *123*, 7194–7195.
[3] M. Costas, A. K. Tipton, K. Chen, D.-H. Jo, L. Que Jr, *J. Am. Chem. Soc.* **2001**, *123*, 6722–6723.
[4] M. Fujita, L. Que Jr, *Adv. Synth. Catal.* **2004**, *346*, 190–194.
[5] G. Dubois, A. Murphy, T. D. P. Stack, *Org. Lett.* **2003**, *5*, 2469–2472.
[6] E. A. Duban, K. P. Bryliakov, E. P. Talsi, *Mendeleev Commun.* **2005**, 12–13.
[7] J. Y. Ryu, J. Kim, M. Costas, K. Chen, W. Nam, L. Que Jr, *Chem. Commun.* **2002**, 1288–1289.
[8] K. Chen, M. Costas, J. Kim, A. K. Tipton, L. Que Jr, *J. Am. Chem. Soc.* **2002**, *124*, 3026–3035.
[9] M. Fujita, M. Costas, L. Que Jr, *J. Am. Chem. Soc.* **2003**, *125*, 9912–9913.
[10] M. Costas, M. P. Mehn, M. P. Jensen, L. Que Jr, *Chem. Rev.* **2004**, *104*, 939–986.
[11] S. V. Kryatov, E. V. Rybak-Akimova, S. Schindler, *Chem. Rev.* **2005**, *105*, 2175–2226.
[12] R. Mas-Ballesté, M. Fujita, C. Hemmila, L. Que Jr, *J. Mol. Catal. A: Chem.* **2006**, *251*, 45–50.
[13] M. R. Bukowski, P. Comba, A. Lienske, C. Limberg, C. L. de Laorden, R. Mas-Ballesté, M. Merz, L. Que Jr, *Angew. Chem. Int. Ed.* **2006**, *45*, 3446–3449.
[14] M. H. Lim, J.-U. Rohde, A. Stubna, M. R. Bukowski, M. Costas, R. Y. N. Ho, E. Münck, W. Nam, L. Que Jr, *Proc. Natl. Acad. Sci.* **2003**, *100*, 3665–3670.
[15] C. Kim, K. Chen, J. Kim, L. Que Jr, *J. Am. Chem. Soc.* **1997**, *119*, 5964–5965.
[16] M. V. Lobanova, K. P. Bryliakov, E. A. Duban, E. P. Talsi, *Mendeleev Commun.* **2003**, 175–177.
[17] M. J. Park, J. Lee, Y. Suh, J. Kim, W. Nam, *J. Am. Chem. Soc.* **2006**, *128*, 2630–2634.
[18] S. Taktak, S. V. Kryatov, E. V. Rybak-Akimova, *Inorg. Chem.* **2004**, *43*, 7196–7209.
[19] E. J. Klinker, J. Kajzer, W. W. Brennessel, N. L. Woodroom, C. J. Cramer, L. Que Jr, *Angew. Chem. Int. Ed.* **2005**, *44*, 3690–3694.
[20] J.-U. Rohde, J.-H. In, M. H. Lim, W. W. Brennessel, M. R. Bukowski, A. Stubna, E. Münck, W. Nam, L. Que Jr, *Science* **2003**, *229*, 1037–1039.
[21] $^1$H NMR spectrum of **3** (1:1 $CD_2Cl_2/CD_3CN$ mixture, –50 °C, $\delta$ values, ppm): –175.4 (s, 2 H, $\Delta\vartheta_{1/2}$ = 1500 Hz, CH*H*–CH*H*), –136.3 (s, 2 H, $\Delta\vartheta_{1/2}$ = 1100 Hz, CH*H*–N), –81.3 (s, 6 H, $\Delta\vartheta_{1/2}$ = 2100 Hz, $CH_3$), –58.9 (s, 2 H, $\Delta\vartheta_{1/2}$ = 740 Hz, C*H*H–C*H*H),–49.7 (s, 2 H, $\Delta\vartheta_{1/2}$ = 730 Hz, C*H*H–N), –22.0 (s, 2 H, $\Delta\vartheta_{1/2}$ = 240 Hz, picolinic H), –11.7 (s, 2 H, $\Delta\vartheta_{1/2}$ = 220 Hz, picolinic H), –0.81 (s, 2 H, $\Delta\vartheta_{1/2}$ = 230 Hz, picolinic H), 54 (s, 2 H, $\Delta\vartheta_{1/2}$ = 220 Hz, picolinic H).
[22] R. D. Arasasingham, A. L. Balch, C. R. Cornman, L. Latos-Grazynski, *J. Am. Chem. Soc.* **1989**, *111*, 4357–4363.
[23] M. Fontecave, S. Ménage, C. Duboc-Toia, *Coord. Chem. Rev.* **1998**, *178–180*, 1555–1572.
[24] E. I. Solomon, T. C. Brunold, M. I. Davis, J. N. Kemsley, S.-K. Lee, N. Lehnert, F. Neese, A. J. Skulan, Y.-S. Yang, J. Zhou, *Chem. Rev.* **2000**, *100*, 235–349.
[25] E. Y. Tshuva, S. J. Lippard, *Chem. Rev.* **2004**, *104*, 987–1012.
[26] L. Duelund, R. Hazell, C. J. McKenzie, L. P. Nielsen, H. Toftlund, *J. Chem. Soc., Dalton Trans.* **2001**, 152–156.
[27] A. Ghosh, F. Tiago de Oliveira, T. Yano, T. Nishioka, E. S. Beach, I. Kinoshita, E. Münck, A. D. Ryabov, C. P. Horwitz, T. J. Collins, *J. Am. Chem. Soc.* **2005**, *127*, 2505–2513.
[28] K. Meyer, E. Bill, B. Mienert, T. Weyhermüller, K. Wieghardt, *J. Am. Chem. Soc.* **1999**, *121*, 4859–4876.
[29] Y. Dong, H. Fujii, M. P. Hendrich, R. A. Leising, G. Pan, C. R. Randall, E. C. Wilkinson, Y. Zang, L. Que Jr, B. G. Fox, K. Kauffmann, E. Münck, *J. Am. Chem. Soc.* **1995**, *117*, 2778–2792.
[30] K. P. Bryliakov, E. A. Duban, E. P. Talsi, *Eur. J. Inorg. Chem.* **2005**, 72–76.
[31] S. Taktak, S. V. Kryatov, T. E. Haas, E. V. Rybak-Akimova, *J. Mol. Catal. A* **2006**, *259*, 24–34.
[32] M. Kodera, M. Itoh, K. Kano, T. Funabiki, M. Reglier, *Angew. Chem. Int. Ed.* **2005**, *44*, 7104–7106.

Received: September 25, 2006
Published Online: January 15, 2007

 © 2007 Wiley-VCH Verlag GmbH & Co. KGaA, Weinheim 

DOI: 10.1002/ejic.200600912

# Synthesis of Tin(II) Phosphate Open Frameworks Using Isomers of 1,2-Diaminocyclohexane as Template

Xuejun Yuan,[a,b] Yi-Zhi Li,[b] Yan Xu,[b] Xiaozeng You,*[b] and Robert J. Linhardt*[a]

**Keywords:** Tin(II) phosphate / Open framework / Templated hydrothermal synthesis / Leaching

A novel layered framework of tin(II) phosphate, $[Sn_4(PO_4)_3(OH)]^{2-}\cdot[trans\text{-}1,2\text{-}C_6H_{10}(NH_3)_2]^{2+}$, has been synthesized under hydrothermal conditions with tin(II) oxalate, phosphoric acid and a mixture of *trans*- and *cis*-1,2-diaminocyclohexane (1,2-DACH). The compound crystallizes in the monoclinic space group $P2_1/n$ (No. 14). The channels of the *trans*-1,2-DACH are occluded by hydrogen bonding in the doubly protonated form, which is leached out from the framework. Reaction using only *tran*-DACH gives the same compound. For comparison, when *cis*-DACH is used as template under the same conditions instead of the mixture of *trans* and *cis* isomers, the neutral inorganic phosphate framework $(Sn_3O)_2(Sn_2O)_2(PO_4)_4$ is formed. It crystallizes in the triclinic space group $P\bar{1}$ (No. 2). These results suggest that *trans*-1,2-DACH is selectively occluded in the framework $[Sn_4(PO_4)_3(OH)]^{2-}\cdot[trans\text{-}1,2\text{-}C_6H_{10}(NH_3)_2]^{2+}$.
(© Wiley-VCH Verlag GmbH & Co. KGaA, 69451 Weinheim, Germany, 2007)

## Introduction

During the past decade, preparation of open-framework metal phosphates has attracted much attention because of their potential applications, which take advantage of microporosity, thermal stability, appropriate acidity and their sturdiness with regard to solvent.[1] The use of structure-directing agents (SDA) or template agents in the synthesis of new solids exhibiting open-framework structures has gained prominence. It is now well established that for the synthesis of such new micro- and mesoporous materials, an organic template can be used to steer the process of crystallization to form open architectures.[2] An organic moiety is normally accommodated within the cavities or between neighboring sheets. In many cases, template can be removed by post-synthesis treatment such as calcination or chemical extraction (i.e. leaching).[3]

Open-framework tin(II) phosphate compounds can be synthesized with the aid of organic amines.[4] The building units in these compounds are commonly trigonal-pyramidal $SnO_3$, and/or square-pyramidal $SnO_4$ and tetrahedral $PO_4$ groups linked by sharing their vertices to form frameworks with channels and or cages.[5] The tin atoms are coordinated with oxygen atoms which occupy the vertex of pyramid, whereas the lone pair presumably occupies the fourth vertex of a polyhedron formed by oxygen atoms and the lone pair itself around the $Sn^{II}$ atom.[6] A single organic amine quite often affords several open framework phosphates with different structures.[7] The amine might act as a structure-directing agent or merely fill the available voids and stabilize the structure through hydrogen bonding and or other interactions.[8] Because the amine generally is protonated in reactions, it also helps in charge compensation of the inorganic framework. Recently, it has been suggested the formation of the amine phosphates may act as intermediates in the formation of the metal phosphates.[8,9]

We attempted to synthesize tin(II) phosphate framework under hydrothermal conditions using a mixture of *trans*- and *cis*-1,2-diaminocyclohexane(1,2-DACH), or only *trans*-1,2-DACH, or only *cis*-1,2-DACH as template. Interestingly, two tin(II) phosphate frameworks with unique structure characteristics, $[Sn_4(PO_4)_3(OH)]^{2-}\cdot[trans\text{-}1,2\text{-}C_6H_{10}(NH_3)_2]^{2+}$ (**1**) and $(Sn_3O)_2(Sn_2O)(PO_4)_4$ (**2**), were obtained. Here, we present the syntheses and structural determinations of them. In addition, the separation of the organic amine isomers of **1** is also described.

## Results and Discussion

### Synthesis

Dispersion of $SnC_2O_4$ in aqueous phosphoric acid followed by the addition of a mixture of *trans*- and *cis*-1,2-DACH and heating under pressure at 443 K affords colorless schistose single crystals of **1**. A reaction using only *trans*-1,2-DACH under the same conditions also gives compound **1**. Synthesis utilizing only *cis*-1,2-DACH affords colorless prismatic crystals of **2**.

[a] Department of Chemistry and Chemical Biology, Rensselaer Polytechnic Institute,
Troy, NY 12180, USA
Fax: +1-518-276-3405
E-mail: linhar@rpi.edu
[b] State Key Laboratory of Coordination Chemistry, School of Chemistry and Chemical Engineering, Nanjing University,
Nanjing 210093, China
Fax: +86-25-83314502
E-mail: youxz@nju.edu.cn

 InterScience © 2007 Wiley-VCH Verlag GmbH & Co. KGaA, Weinheim 

### Characterization

Inductively coupled plasma (ICP) analysis indicates that **1** contains 53.0 wt.-% Sn and 10.5 wt.-% P, in good agreement with the formula based on crystal-structure determination (calcd. 53.3 wt.-% Sn, 10.4 wt.-% P). This gives rise to an Sn/P ratio of 4:3. The elemental analysis showed that the C, H and N contents are 8.12, 1.70 and 3.16 wt.-% (calcd. 8.08 wt.-% C, 1.68 wt.-% H, 3.14 wt.-% N), respectively, corresponding to an empirical molar ratio of C/H/N = 6:17:2. These analysis results indicated that the solid sample of **1** was a pure phase.

The ICP analysis indicated that **2** contained 73.5 wt.-% Sn and 7.8 wt.-% P, in accordance with formula based on the single crystal structure analysis (calcd. 72.8 wt.-% Sn and 7.6 wt.-% P). The elemental analysis showed that it contained no C, H or N. These analytic results indicated that the solid sample of **2** was also a pure phase.

The FTIR spectrum of **1** was assigned as follows: The bands observed at 3505–3250 $cm^{-1}$ were attributed to H-bonded N–H groups. The band at 2920 $cm^{-1}$ was attributed to the $\delta_{C-H}$ vibration of 1,2-DACH. The bands 1109 and 965 $cm^{-1}$ were assigned as the asymmetric stretching vibration of $PO_4$ units. Absorptions at 624, 536 and 486 $cm^{-1}$ were due to bending vibration of $PO_4$ groups. The bands at 1624, 1559, 1540, 1446 and 1377 $cm^{-1}$ were attributed to $\delta_{N-H}$, $\nu_{C-H}$, $\nu_{C-C}$ and $\nu_{C-N}$ vibrations of the doubly protonated 1,2-DACH cation occluded in the framework. The FTIR of **2** showed vibrations corresponding to the $PO_4$ unit at 1065, 1009, 600, 553 and 442 $cm^{-1}$.

Thermogravimetric analysis (TGA) curve showed that the weight loss of **1** occurring between 310 °C and 400 °C is 13.6%, and was related to the loss of absorbed water and the decomposition of the occluded amine (calcd. 12.8%). Differential thermal analysis (DTA) curve afforded a single broad endothermic peak at approximately 345 °C, corresponding to this decomposition. Similar analysis of **2** showed only a small mass loss (ca. 1.0%) at < 200 °C, due to the loss of absorbed water.

### Description of the Structures

Detailed crystallographic data are listed in Table 1. and the selected bond lengths and angles are given in Table 2. The asymmetric unit of **1** is shown in Figure 1, (a). The structure of **1** shows the tin atom in a three-coordinate environment with respect to oxygen. The trigonal-pyramidal $SnO_3$ is alternatively linked to tetrahedral $PO_4$ units through bridging oxygen atoms. Of the eleven bridging oxygen atoms in the asymmetric unit, ten are bridged to a tin atom and a phosphorus atom. The remaining oxygen atom

Table 1. Crystallographic data and structure refinement parameters for $[Sn_4(PO_4)_3(OH)]^{2-}\cdot[trans\text{-}1,2\text{-}C_6H_{10}(NH_3)_2]^{2+}$ (**1**) and $(Sn_3O)_2(Sn_2O)(PO_4)_4$ (**2**).

| | Compound **1** | Compound **2** |
|---|---|---|
| Chemical formula | $C_6H_{17}N_2O_{13}P_3Sn_4$ | $O_{20}P_4Sn_{10}$ |
| Crystal system | monoclinic | triclinic |
| Space group | $P2_1/n$ (No.14) | $P\bar{1}$ (No.2) |
| $a$ [Å] | 7.02494(14) | 7.3400(15) |
| $b$ [Å] | 19.934(4) | 7.5700(15) |
| $c$ [Å] | 14.215(3) | 12.872(3) |
| $\alpha$ [°] | 90 | 87.59(3) |
| $\beta$ [°] | 99.02(3) | 85.77(3) |
| $\gamma$ [°] | 90 | 61.42(3) |
| $V$ [Å$^3$] | 2028.8(4) | 626.3(2) |
| $Z$ | 4 | 1 |
| $F$(000) | 1656 | 720 |
| $Fw$ | 892.87 | 1630.78 |
| $\rho_{calcd.}$ [g cm$^{-3}$] | 2.917 | 4.324 |
| $\lambda$ [Å] | 0.71073 | 0.71073 |
| $T$ [K] | 291(2) | 293(2) |
| $\mu$ [mm$^{-1}$] | 5.168 | 10.121 |
| $2\theta$ range | 3.54–55.00° | 3.18–49.6° |
| Total data collected | 7696 | 2196 |
| Index ranges | $0 \le h \le 9$ | $0 \le h \le 8$ |
| | $-25 \le k \le 25$ | $-7 \le k \le 8$ |
| | $-18 \le l \le 18$ | $-15 \le l \le 15$ |
| Unique data | 4354 | 1990 |
| Observed data [$I > 2\sigma(I)$] | 4075 | 1709 |
| Refinement method | full-matrix least squares on $F^2$ | full-matrix least squares on $F^2$ |
| $R$ Indexes [$I > 2\sigma(I)$] | $R$ = 0.0422 | $R$ = 0.0350 |
| | $R_w$ = 0.1056 | $R_w$ = 0.0885 |
| $R$ Indexes (all data) | $R$ = 0.0477 | $R$ = 0.0510 |
| | $R_w$ = 0.1087 | $R_w$ = 0.1297 |
| Goodness of fit ($S$) | 1.158 | 1.082 |
| No. of parameters | 264 | 155 |
| Largest difference map peak and hole [e Å$^{-3}$] | 0.988 and –1.221 | 2.211 and –1.911 |

 © 2007 Wiley-VCH Verlag GmbH & Co. KGaA, Weinheim 

bonds two tin atoms. From the Fourier map, we note that the oxygen atom forming the Sn–O–Sn units is protonated. Bond valence sum calculations performed on the framework confirm the presence of the proton on the oxygen involved in forming the Sn–O(H)–Sn linkages.[10] Bonding involved two tin atoms and a hydroxy group has been previously reported.[5,11]

Table 2. Selected bond lengths [Å] and angles [°] for $[Sn_4(PO_4)_3(OH)]^{2-}\cdot[trans\text{-}1,2\text{-}C_6H_{10}(NH_3)_2]^{2+}$ (**1**).[a]

| | | | |
|---|---|---|---|
| Sn(1)–O(5) | 2.122(3) | P(2)–O(7) | 1.520(4) |
| Sn(1)–O(10) | 2.133(3) | P(2)–O(8) | 1.541(3) |
| Sn(1)–O(4) | 2.165(3) | P(2)–O(6) | 1.553(3) |
| Sn(2)–O(13) | 2.139(4) | P(2)–O(5) | 1.560(3) |
| Sn(2)–O(1) | 2.160(3) | P(3)–O(11) | 1.518(4) |
| Sn(2)–O(6)[1] | 2.193(3) | P(3)–O(10) | 1.547(3) |
| Sn(3)–O(9) | 2.132(3) | P(3)–O(9) | 1.557(3) |
| Sn(3)–O(8) | 2.153(3) | P(3)–O(12) | 1.560(3) |
| Sn(3)–O(3)[2] | 2.188(3) | O(2)–Sn(4)[4] | 2.089(3) |
| Sn(4)–O(2)[3] | 2.089(3) | O(3)–Sn(3)[5] | 2.188(3) |
| Sn(4)–O(13) | 2.109(4) | O(6)–Sn(2)[6] | 2.193(3) |
| Sn(4)–O(12) | 2.156(3) | N(1)–C(1) | 1.504(6) |
| P(1)–O(2) | 1.519(3) | N(2)–C(2) | 1.501(6) |
| P(1)–O(4) | 1.541(3) | C(1)–C(2) | 1.506(9) |
| P(1)–O(3) | 1.542(3) | C(1)–C(6) | 1.521(8) |
| P(1)–O(1) | 1.546(3) | | |
| O(5)–Sn(1)–O(10) | 89.98(12) | O(11)–P(3)–O(10) | 113.9(2) |
| O(5)–Sn(1)–O(4) | 86.17(13) | O(11)–P(3)–O(9) | 106.6(2) |
| O(10)–Sn(1)–O(4) | 83.33(13) | O(10)–P(3)–O(9) | 110.49(19) |
| O(13)–Sn(2)–O(1) | 85.54(14) | O(11)–P(3)–O(12) | 110.9(2) |
| O(13)–Sn(2)–O(6)[1] | 89.20(15) | O(10)–P(3)–O(12) | 105.14(19) |
| O(1)–Sn(2)–O(6)[1] | 85.20(12) | O(9)–P(3)–O(12) | 110.7(2) |
| O(9)–Sn(3)–O(8) | 89.68(13) | P(1)–O(1)–Sn(2) | 135.12(18) |
| O(9)–Sn(3)–O(3)[2] | 86.18(13) | P(1)–O(2)–Sn(4)[4] | 140.43(2) |
| O(8)–Sn(3)–O(3)[2] | 83.50(15) | P(1)–O(3)–Sn(3)[5] | 127.6(2) |
| O(2)[3]–Sn(4)–O(13) | 88.60(16) | P(1)–O(4)–Sn(1) | 131.47(19) |
| O(2)[3]–Sn(4)–O(12) | 86.60(13) | P(2)–O(5)–Sn(1) | 109.94(18) |
| O(13)–Sn(4)–O(12) | 89.47(15) | P(2)–O(6)–Sn(2)[6] | 110.88(17) |
| O(2)–P(1)–O(4) | 111.24(19) | P(2)–O(8)–Sn(3) | 148.4(2) |
| O(2)–P(1)–O(3) | 112.1(2) | P(3)–O(9)–Sn(3) | 108.09(17) |
| O(4)–P(1)–O(3) | 106.3(2) | P(3)–O(10)–Sn(1) | 144.3(2) |
| O(2)–P(1)–O(1) | 106.98(18) | P(3)–O(12)–Sn(4) | 113.01(18) |
| O(4)–P(1)–O(1) | 110.29(18) | Sn(4)–O(13)–Sn(2) | 134.63(19) |
| O(3)–P(1)–O(1) | 110.03(18) | N(1)–C(1)–C(6) | 111.7(5) |
| O(7)–P(2)–O(8) | 114.1(2) | N(1)–C(1)–C(2) | 113.3(5) |
| O(7)–P(2)–O(6) | 111.9(2) | C(2)–C(1)–C(6) | 111.7(5) |
| O(8)–P(2)–O(6) | 103.88(19) | N(2)–C(2)–C(1) | 112.4(5) |
| O(7)–P(2)–O(5) | 106.09(2) | N(2)–C(2)–C(3) | 106.7(5) |
| O(8)–P(2)–O(5) | 110.7(2) | C(1)–C(2)–C(3) | 111.3(5) |
| O(6)–P(2)–O(5) | 110.18(18) | | |

[a] Symmetry transformations used to generate equivalent atoms: 1: $x-1/2, -y+3/2, z-1/2$; 2: $x-1/2, -y+3/2, z+1/2$; 3: $x-1, y, z$; 4: $x+1, y, z$; 5: $x+1/2, -y+3/2, z-1/2$; 6: $x+1/2, -y+3/2, z+1/2$.

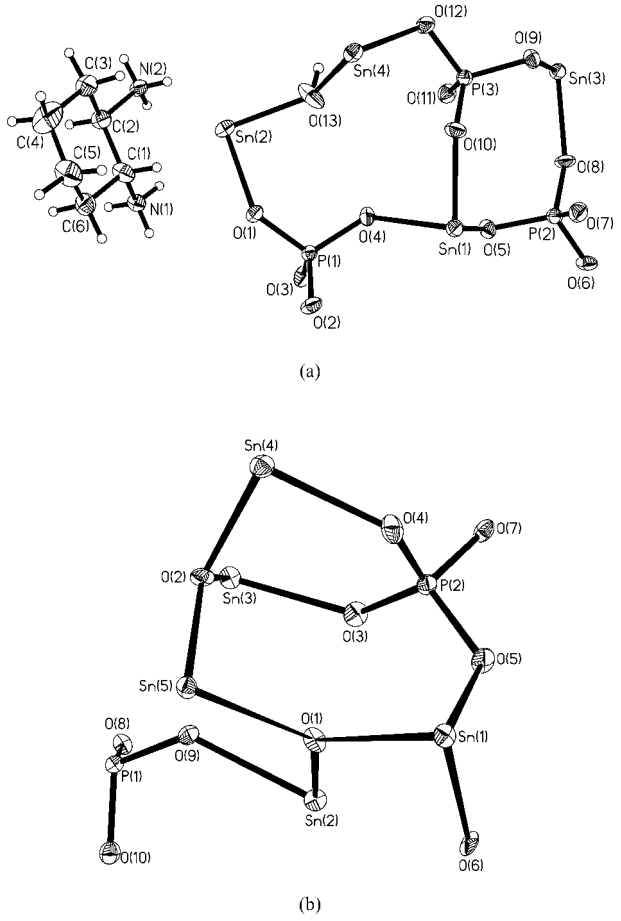


Figure 1. (a) ORTEP view of $[Sn_4(PO_4)_3(OH)]^{2-}\cdot[trans\text{-}1,2\text{-}C_6H_{10}(NH_3)_2]^{2+}$ structure showing the atom-labeling Scheme (30% thermal ellipsoids), with arbitrary radius of hydrogen atom. (b) ORTEP drawing of $(Sn_3O)_2(Sn_2O)(PO_4)_4$ structure showing the atom-labeling scheme (30% thermal ellipsoids).

There are two different phosphorus sites in the asymmetric unit of **1**. Of the three independent phosphorus atoms, P(1) atom is four-coordinate with respect to bridging oxygen (average P–O bond length 1.537 Å and average O–P–O bond angles 109.5°). P(2) and P(3) atoms are coordinated with three bridging oxygens and a double-bonded oxygen, respectively. The P(2)–O(7) distance of 1.520(4) Å and the P(3)–O(11) distance of 1.518(3) Å arise from the formal P=O double bond. The terminal P=O groups in $H_3PO_4\cdot0.5H_2O$, are generally between 1.485 and 1.495 Å in length.[12] The O–P–O bond angles are in the range 103.88–114.1° (av. 108.7°). The largest bond angle is observed for bonds involving the P=O linkage [114.1(1)° for P(2) and 113.7(2)° for P(3)], including the multiple-bond nature of P=O bonds. Each tin atom is triply coordinated to oxygen, resulting in average Sn–O bond length of 2.145 Å and average Sn–O bond angle of 86.93°. These values are in good agreement with other tin(II) phosphate open-framework structures.[5–7,13]

The connectivity of the $PO_4$ and $SnO_3$ units in **1** results in an anionic layer with the stoichiometry $[Sn_4(PO_4)_3(OH)]^{2-}$, which propagates along the *a*-axis. The structure is constructed entirely from a unit of double 5-rings.[14] Two 5-rings are joined each other through common edge of Sn–O–Sn to form the unit of two 5-rings. The units build up of zigzag chains through phosphorus bridges. These chains are related to one another by a center of inversion, and are linked in double-connected manner through oxygen bridges. The connection forms corrugated sheets along the *a* direction, resulting in 4-rings and 8-rings (Figure 2, a). The hydrogen atoms of the protonated *trans*-1,2-DACH molecules interact strongly with the framework oxygen atoms, espe-

 © 2007 Wiley-VCH Verlag GmbH & Co. KGaA, Weinheim 

cially the doubly bonded ones. The organic amine molecules balance the charges of the anionic layers. Major hydrogen bonding interactions are presented in Table 3.

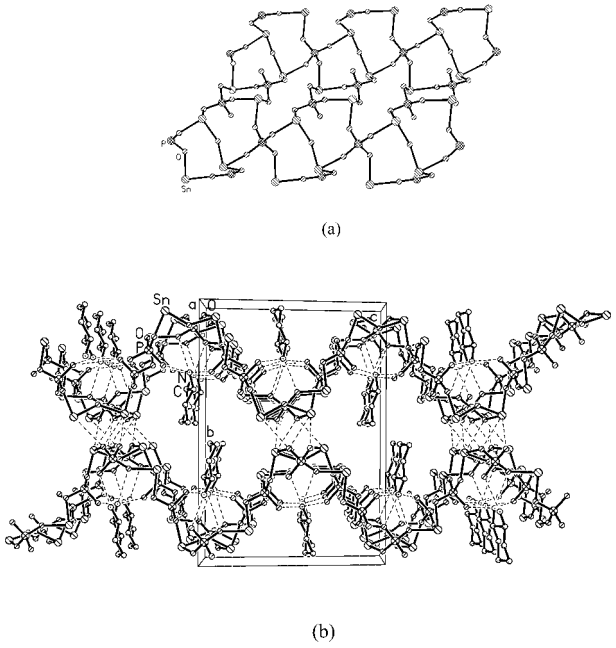


Figure 2. (a) Diagram of corrugated sheet along the *a*-axis, for compound **1**. (b) The structure of $[Sn_4(PO_4)_3(OH)]^{2-}$·[*trans*-1,2-$C_6H_{10}(NH_3)_2]^{2+}$ viewed along the *a*-axis, showing the pseudo 18-ring channels and the *trans*-1,2-diaminocyclohexane molecules (for clarity, hydrogen atoms are omitted).

Table 3. Important hydrogen bonds for $[Sn_4(PO_4)_3(OH)]^{2-}$·[*trans*-1,2-$C_6H_{10}(NH_3)_2]^{2+}$(**1**).

| D–H | A | *d*(D–H) | *d*(D···H) | *d*(H···A) | DHA [°] |
|---|---|---|---|---|---|
| N1–H91A | O11 | 0.89 | 1.92 | 2.749(6) | 154.1 |
| N1–H91B | O3 | 0.89 | 2.10 | 2.815(5) | 136.7 |
| N1–H91C | O7 | 0.89 | 2.19 | 2.758(5) | 121.0 |
| N1–H91C | O9 | 0.89 | 2.45 | 3.137(5) | 134.9 |
| N2–H92A | O4 | 0.89 | 2.37 | 2.931(5) | 121.6 |
| N2–H92B | O11 | 0.89 | 2.28 | 2.876(6) | 123.7 |
| N2–H92B | O5 | 0.89 | 2.30 | 3.044(6) | 141.4 |
| N2–H92C | O7 | 0.89 | 1.89 | 2.752(5) | 162.8 |

The bridging hydroxy groups in the framework are not involved in forming hydrogen bonds. The multipoint hydrogen-bonding interactions between amino groups and framework sheets cause the layers to bend. Presumably the two amino groups in *trans* configuration provide better access for hydrogen bond formation, compared to the *cis*-diamine. Thus, it afforded a more stable open-framework structure. This might be attributable to selective intercalation of *trans*-DACH with the exclusion of *cis*-DACH in compound **1**. This selectivity was confirmed by leaching experiments. The liquid residue obtained contained 98.9% *trans* diamine. The adjacent layers then are packed one over the other translated by approximately a one-half cell unit along the *c*-axis through the van der Waals interaction between tin atom and oxygen atom located in neighboring sheets (the distance between Sn and O is about 3.0 Å). This stacking leads to the formation of pseudo 18-ring channels along the *a*-axis (Figure 2, b). If van der Waals radii are taken into account, the width of 18-ring 1D channel is 1.62 nm × 1.26 nm (longest O–O distances and shortest O–O distances). The lone pair borne by the tin atom manifests itself in the lattice by creating open space in the channel. Repulsion between lone pairs associated with next tin atoms makes a small position shift between adjacent layers. At the same time, 8-ring channels are formed along the [011] direction.

An ORTEP representation of **2** is shown in part b of Figure 1 and the selected bond lengths and angles are given in Table 4. The tin atoms afford two different coordination environments with oxygen in this structure; the triply coordinated trigonal-pyramidal $SnO_3$ and the tetra-coordinated truncated square-pyramidal $SnO_4$. The $SnO_3$, $SnO_4$ and $PO_4$ moieties are vertex-linked forming the 3D neutral framework. The structure is dominated by a number of $Sn_2O_2$ 4-rings, resulting in a higher Sn/P ratio (2.5), in con-

Table 4. Selected bond lengths [Å] and angles [°] for $(Sn_3O)_2(Sn_2O)(PO_4)_4$ (**2**).[a]

| | | | |
|---|---|---|---|
| Sn(1)–O(5) | 2.134(12) | Sn(5)–O(8)$^3$ | 2.322(11) |
| Sn(1)–O(1) | 2.167(11) | P(1)–O(10) | 1.532(13) |
| Sn(1)–O(6) | 2.218(11) | P(1)–O(8) | 1.569(11) |
| Sn(2)–O(1) | 2.108(10) | P(1)–O(9) | 1.592(13) |
| Sn(2)–O(10)$^1$ | 2.130(12) | P(1)–O(6)$^4$ | 1.616(11) |
| Sn(2)–O(9) | 2.406(12) | P(2)–O(7) | 1.552(12) |
| Sn(3)–O(2) | 2.132(12) | P(2)–O(3) | 1.575(13) |
| Sn(3)–O(7)$^2$ | 2.252(12) | P(2)–O(4) | 1.584(13) |
| Sn(3)–O(3) | 2.293(12) | P(2)–O(5) | 1.598(12) |
| Sn(4)–O(2) | 2.154(11) | O(6)–P(1)$^5$ | 1.616(11) |
| Sn(4)–O(4) | 2.245(13) | O(7)–Sn(3)$^2$ | 2.252(12) |
| Sn(4)–O(7)$^2$ | 2.422(11) | O(7)–Sn(4)$^2$ | 2.422(11) |
| Sn(4)–O(8)$^3$ | 2.525(11) | O(8)–Sn(5)$^6$ | 2.322(11) |
| Sn(5)–O(2) | 2.088(11) | O(8)–Sn(4)$^6$ | 2.525(11) |
| Sn(5)–O(1) | 2.200(11) | O(10)–Sn(2)$^1$ | 2.130(12) |
| O(5)–Sn(1)–O(1) | 89.1(4) | O(7)–P(2)–O(3) | 110.4(7) |
| O(5)–Sn(1)–O(6) | 83.7(5) | O(7)–P(2)–O(4) | 108.0(7) |
| O(1)–Sn(1)–O(6) | 83.8(4) | O(3)–P(2)–O(4) | 110.3(7) |
| O(1)–Sn(2)–O(10)$^1$ | 84.2(4) | O(7)–P(2)–O(5) | 106.1(7) |
| O(1)–Sn(2)–O(9) | 80.1(4) | O(3)–P(2)–O(5) | 112.2(7) |
| O(10)$^1$–Sn(2)–O(9) | 85.4(4) | O(4)–P(2)–O(5) | 109.7(7) |
| O(2)–Sn(3)–O(7)$^2$ | 74.8(4) | Sn(2)–O(1)–Sn(1) | 114.9(5) |
| O(2)–Sn(3)–O(3) | 87.2(4) | Sn(2)–O(1)–Sn(5) | 117.6(5) |
| O(7)$^2$–Sn(3)–O(3) | 88.4(4) | Sn(1)–O(1)–Sn(5) | 127.4(5) |
| O(2)–Sn(4)–O(4) | 89.7(4) | Sn(5)–O(2)–Sn(3) | 127.4(6) |
| O(2)–Sn(4)–O(7)$^2$ | 71.0(4) | Sn(5)–O(2)–Sn(4) | 112.3(5) |
| O(4)–Sn(4)–O(7)$^2$ | 85.4(4) | Sn(3)–O(2)–Sn(4) | 111.5(5) |
| O(2)–Sn(4)–O(8)$^3$ | 74.3(4) | P(2)–O(3)–Sn(3) | 135.1(7) |
| O(4)–Sn(4)–O(8)$^3$ | 77.7(4) | P(2)–O(4)–Sn(4) | 137.0(7) |
| O(7)$^2$–Sn(4)–O(8)$^3$ | 141.3(4) | P(2)–O(5)–Sn(1) | 118.5(7) |
| O(2)–Sn(5)–O(1) | 94.6(4)) | P(1)$^5$–O(6)–Sn(1 | 141.2(7) |
| O(2)–Sn(5)–O(8)$^3$ | 80.0(4) | P(2)–O(7)–Sn(3)$^2$ | 122.9(7) |
| O(1)–Sn(5)–O(8)$^3$ | 86.7(4) | P(2)–O(7)–Sn(4)$^2$ | 122.8(7) |
| O(10)–P(1)–O(8) | 103.9(7) | Sn(3)$^2$–O(7)–Sn(4)$^2$ | 98.5(4) |
| O(10)–P(1)–O(9) | 110.0(7) | P(1)–O(8)–Sn(5)$^6$ | 122.2(6) |
| O(8)–P(1)–O(9) | 112.4(7) | P(1)–O(8)–Sn(4)$^6$ | 137.6(6) |
| O(10)–P(1)–O(6)$^4$ | 112.4(7) | Sn(5)$^6$–O(8)–Sn(4)$^6$ | 93.1(4) |
| O(8)–P(1)–O(6)$^4$ | 108.7(6) | P(1)–O(9)–Sn(2) | 129.4(7) |
| O(9)–P(1)–O(6)$^4$ | 109.4(7) | P(1)–O(10)–Sn(2)$^1$ | 138.5(8) |

[a] Symmetry transformations used to generate equivalent atoms: 1: $-x+1, -y+2, -z$; 2: $-x, -y+2, -z+1$; 3: $x-1, y, z$; 4: $x, y+1, z$; 5: $x, y-1, z$; 6: $x+1, y, z$.

 © 2007 Wiley-VCH Verlag GmbH & Co. KGaA, Weinheim 

trast to those reported previously.[5–7,13] The triply-coordinated oxygen atoms do not create a situation where P–O–P bonding occurs, in accordance with Loewenstein rule.[15] Of the five independent Sn atoms in the asymmetric unit, Sn(1), Sn(2), Sn(3) and Sn(5) are triply-coordinated with respect to oxygen and the remaining Sn(4) atom is tetra-coordinated. The Sn($x$)–O ($x$ = 1, 2, 3, 5) bond lengths are in the range 2.088–2.406 Å (av. 2.336 Å), and the O–Sn($x$)–O ($x$ = 1, 2, 3, 5) bond angle are in the range 74.8–94.6° (av. 85.2°); The Sn(4)–O distances are in the range of 2.154–2.525 Å (av. 2.336 Å), and O–Sn(4)–O bond angles are in the range 71.0–141.3° (av. 89.9°). The longest Sn–O distance (2.525 Å) in the present structure as well as the largest O–Sn–O bond angle (141.3°) are associated with the tetra-coordinated Sn(4). P(1) and P(2) are both tetra-coordinate with respect to bridging oxygen with average P–O bond length of 1.577 Å and average O–P–O bond angle of 109.4°. These values are in agreement with those reported earlier.[5–7,13]

In the neutral framework structure **2**, the trigonal-pyramidal $SnO_3$, square-pyramidal $SnO_4$ and tetrahedral $PO_4$ units are linked through bridging oxygen atoms. The second building unit (SBU) is a cage that is composed of eight Sn atoms and two P atoms (Figure 3, a). These cages are linked through 4-rings (2P + 2Sn) in three different ways (Figure 3, b), i.e. connections between an oxygen atom of the cage and a phosphorus atom of the 4-ring, or between a tin atom of the cage and a phosphorus atom of the 4-ring through bridging oxygen atom, or between an oxygen atom of the cage, and a tin atom of the 4-ring. A 4-ring is connected with six cages. Each phosphorus atom of the 4-ring is linked with two cages, while each tin atom linked only with one cage. These cages are related to each other by a center of inversion diagonally in the 4-ring. In contrast, each cage is connected with six 4-rings, four of them through phosphorus atom of the 4-ring and the rest two through a tin atom of the 4-ring. These connections result in formation of 3D framework with sequences of helical 6-ring and elliptical 12-ring channels in the b-direction (Figure 3, b). A 6-ring consists of three phosphorus and three tin atoms, and 12-membered ring consists of four phosphorus and eight tin atoms. The maximal width of the channel is 9.37 Å (P–P distance, not including van der Waals radii). However, the minimal width is merely 0.5 Å (Sn–Sn distance, not including van der Waals radii). Since the lone pair borne by tin atom occupies the channels, access by any molecule is prohibited. Experiments of $N_2$ adsorption and desorption also verify this conclusion affording an adsorbed volume is only 4.29 $cm^3 g^{-1}$ at pressure of 790 Torr.

The framework density (FD) for **1** and **2** are 13.8 and 22.35 T-atoms (T = Sn, P) per $nm^3$, respectively. Compound **2** shows dense packing morphology compared to other framework materials (FD < 20).[14,16]

In conclusion, although a mixture of isomers of 1,2-DACH was used in the synthesis, only the *trans* species were as templates occluded in **1** as confirmed through leaching experiments. The *trans* isomer has two chiral centers, corresponding to 1*S*,2*S* and 1*R*,2*R* enantiomers. Four [*trans*-1,2-

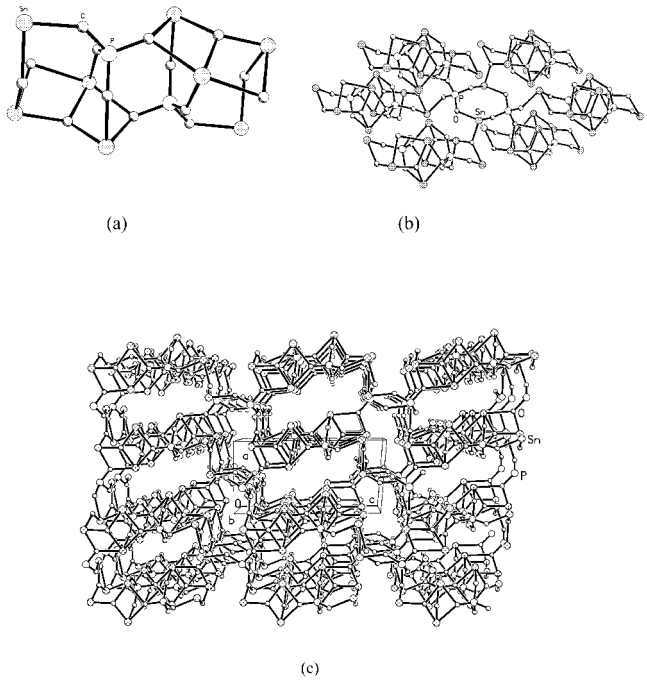


Figure 3. (a) Cage as a SUB for structure of compound **2**, $(Sn_3O)_2(Sn_2O)(PO_4)_4$. (b) The connections of cages with (2P + 2Sn) 4-ring. (c) The structure of $(Sn_3O)_2(Sn_2O)(PO_4)_4$ viewed along the *b*-axis, showing sequences of helical 6-rings and elliptical 12-rings channels in the same direction.

$C_6H_{10}(NH_3)_2]^{2+}$ cations are found in a unit cell and the nearest neighboring cations are symmetry related by a $2_1$-screw axis (Figure 2, b). The cation site is occupied by mirror plane related diastereoisomer with an occupancy factor of 50%. When only *cis* isomer was used as template in the synthesis of **2**, no template molecule is occluded in the inorganic framework (Figure 3, c). Only a *trans* orientation of the two amino groups provides the appropriate hydrogen bonding interaction to result in complex formation. This may afford some interesting insight in terms of role that templates play in hydrothermal synthesis.

## Experimental Section

**Synthesis:** All chemicals used were of analytical grade. Hydrothermal synthesis of **1** is described here. $SnC_2O_4$ (1.187 g, 5.74 mmol) was dispersed in 10 mL of water and 0.60 mL of 85 wt.-% aqueous $H_3PO_4$ was added to the mixture under continuous stirring. A mixture of *trans*- and *cis*-1,2-DACH (1.23 mL, 10 mmol) was added. The reaction mixture was stirred until it was homogeneous and the pH value was 7.4. The mixture ($SnC_2O_4$/1.5 $H_3PO_4$/1.8 DACH/58 $H_2O$) was transferred into a 23 mL Teflon™-lined stainless steel autoclave and heated at 443 K for 10 d under autogenous pressure. The pH value of the solution was 6.7. The solid product (in about 70% yield based on the Sn source) consisting of colorless schistose single crystals **1** was recovered by filtration, washed thoroughly with distilled water, and dried at room temperature. Compound **1** was also afforded with an approximate 60% yield when *trans*-1,2-DACH was used under the conditions. The pH values of the solution before and after reaction were 7.4 and 6.6, respectively. Colorless prismatic crystals of **2** were obtained hydrothermally using only

 © 2007 Wiley-VCH Verlag GmbH & Co. KGaA, Weinheim 

*cis*-1,2-DACH as template under the same reaction conditions to those for **1**. The pH value of solution was 7.5 and the yield was about 58%.

**Initial Characterization:** The element analysis of the product was performed with a Foss Heraeus CHN-O-RAPID elemental analyzer, and the ICP analysis was performed with a Jarell-Ash 1100+2000 ICP instrument. The IR spectra were recorded with a Bruker 410 FT-IR spectrometer using KBr pellets. TGA and DTA were conducted with V1.1B TA thermogravimetric analyzer under nitrogen in the range between 25 and 600 °C, with a heating rate of 10 °C min$^{-1}$. Assays of isomeric residue in leaching experiment were carried out with a Varain-5000 high-performance chromatograph with fixed-wavelength UV absorbance detector set at 254 nm under ambient temperatures, on a 150 mm × 4.6 mm reversed-phase Eclipse XDB-C8 LC Column (Agilent Technologies Corp., USA) with an eluting mobile phase consisting of acetonitrile/0.05% phosphoric acid (45:55).

**Single-Crystal X-ray Diffraction:** A plate-like crystal of approximate dimensions 0.30 × 0.30 × 0.20 mm for **1** was mounted on a glass fiber on a Siemens Smart-CCD diffractometer equipped with graphite-monochromated Mo-$K_\alpha$ ($\lambda$ = 0.71073 Å) radiation. A hemisphere of intensity data was collected at 291(2) K in the $2\theta$ range 3.54–55.00°. A total of 4354 reflection was collected, of which 4075 were considered to be observed with $I > 2\sigma(I)$. Data processing was accomplished with SAINT processing program.[17] The structure was solved by direct methods and refined by full-matrix least-squares on $F^2$ using SHELX97.[18] Each carbon attached to an amino group is disordered with a SOF (site occupation factor) of 0.5. All non-hydrogen atoms were refined anisotropically. The hydrogen atoms were placed geometrically and allowed to ride on the atoms to which they were attached with fixed isotropic thermal parameters by program.

CCDC-165851 contains the supplementary crystallographic data of **1** for this paper. These data can be obtained free of charge from Cambridge Crystallographic Data Center at www.ccdc.cam.ac.uk/data_request/cif.

A prismatic crystal with dimension of 0.3 × 0.2 × 0.2 mm for **2** was mounted on a glass fiber. Data were collected on FR590 CAD-4 diffractometer (Mo-$K_\alpha$ radiation, $\lambda$ = 0.71073 Å) at 293(2) K in the range $3.18 < 2\theta < 49.6°$ using the $\omega$ scan technique. A total of 1990 reflections were collected of which 1709 with $I > 2\sigma(I)$ were used. An empirical absorption correction was applied. The structure was solved by direct methods and refined using SHELX97 programs.[18] All atoms were refined anisotropically. Pertinent experimental details for the structure determination are listed in Table 1.

Further details of the crystal-structure investigation may be obtained from the Fachinformationszentrum Karlsruhe, 76344 Eggenstein-Leopoldshafen, Germany (http://www.fiz-karlsruhe.de), on quoting the depository number CSD-412358.

**Leaching Experiment:** Compound **1** (4.46 g, 5 mmol) was added to 50 mL of 0.2 N NaAc solution in THF. The mixture was continuously stirred under reflux for 10 h and cooled to room temperature. The solids were filtered off, washed with THF. Then 20 mL of 20% NaOH aqueous solution was added to the filtrate to liberate 1,2-DACH from the acetate salt. The mixture was continuously extracted with 40 mL of benzene for 5 h. The benzene extract was evaporated under vacuum, leaving a liquid residue (about 0.25 g, yield 44.0% based on the empirical formula of **1**). The liquid residue consisted of 98.9% *trans*-1,2-DACH and 1.1% *cis*-1,2-DACH.[19] After leaching, the crystal structure was lost and the resulting amorphous solid showed a different powder diffraction pattern from that of compound **1**.

## Acknowledgments

The authors acknowledge the financial support from the Ministry of Science and Technology of China (Major State Basic Research Development Program, G 200077500).

[1] a) P. Y. Feng, X. H. Bu, G. D. Stucky, *Nature* **1997**, *388*, 737–741; b) S. Ekambaram, S. C. Sevov, *Angew. Chem. Int. Ed.* **1999**, *38*, 372–375; c) A. K. Cheetham, G. Ferey, T. Loiseau, *Angew. Chem. Int. Ed.* **1999**, *38*, 3269–3292; d) A. Choudhry, S. Neeraj, S. Natarajan, N. R. C. Rao, *J. Mater. Chem.* **2001**, *11*, 1537–1540; e) W. T. A. Harrison, M. L. F. Phillips, J. Stanchfield, T. M. Nenoff, *Inorg. Chem.* **2001**, *40*, 895–899.
[2] a) S. Natarajan, M. P. Attfield, A. K. Cheetham, *Angew. Chem., Int. Ed. Engl.* **1997**, *36*, 978–980; b) R. K. Chiang, *Inorg. Chem.* **2000**, *39*, 4985–4988; c) C. N. R. Rao, S. Natarajan, S. Neeraj, *J. Am. Chem. Soc.* **2000**, *122*, 2810–2817; d) S. H. Feng, R. R. Xu, *Acc. Chem. Res.* **2001**, *34*, 239–247.
[3] a) S. Natarajan, A. K. M. Eswaramoorthy Cheetham, C. N. R. Rao, *Chem. Commun.* **1998**, 1561–1562; b) S. Natarajan, A. K. Cheetham, *Chem. Commun.* **1997**, 1089–1090; c) G. Y. Yang, S. C. Sevov, *J. Am. Chem. Soc.* **1999**, *121*, 8389–8390.
[4] a) S. Natarajan, A. K. Cheetham, *J. Solid State Chem.* **1997**, *134*, 207–210; b) N. Stock, G. D. Stucky, A. K. Cheetham, *Chem. Commun.* **2000**, *22*, 2277–2278.
[5] S. Natarajan, S. Ayyapan, A. K. Cheetham, C. N. R. Rao, *Chem. Mater.* **1998**, *10*, 1627–1631.
[6] Y. L. Liu, S. Zhu, J. S. Chen, L. Y. Na, J. Hua, W. Q. Pang, R. R. Xu, *Inorg. Chem.* **2000**, *39*, 1820–1822, and references herein.
[7] a) A. Choudhry, S. Natarajan, C. N. R. Rao, *Inorg. Chem.* **2000**, *39*, 4295–4304; b) C. N. R. Rao, S. Natarajan, S. Neeraj, *J. Am. Chem. Soc.* **2000**, *122*, 2810–2817; c) P. Ramaswamy, S. Natarajan, *Eur. J. Inorg. Chem.* **2006**, 3463–3471.
[8] C. N. R. Rao, S. Natarajan, A. Choudhury, S. Neeraj, A. A. Ayi, *Acc. Chem. Res.* **2001**, *34*, 80–87.
[9] a) C. N. R. Rao, S. Natarajan, S. Neeraj, *J. Solid State Chem.* **2000**, *152*, 302–321; b) S. Neeraj, S. Natarajan, C. N. R. Rao, *Angew. Chem. Int. Ed.* **1999**, *38*, 3480–3483.
[10] I. D. Brown, D. Aldermatt, *Acta Crystallogr., Sect. B* **1985**, *41*, 244–247.
[11] T. H. Jordan, L. W. Schroeder, B. Dickens, W. E. Brown, *Inorg. Chem.* **1976**, *15*, 1810–1814.
[12] B. Dickens, E. Prince, L. W. Schroeder, T. H. Jordan, *Acta Crystallogr., Sect. B* **1974**, *30*, 1470–1473.
[13] a) S. Natarajan, M. P. Attfield, A. K. Cheetham, *Angew. Chem. Int. Ed. Engl.* **1997**, *36*, 978–980; b) S. Natarajan, A. K. Cheetham, *Chem. Commun.* **1997**, 1089–10900; c) N. Stock, G. D. Stucky, A. K. Cheetham, *Chem. Commun.* **2000**, 2277–2278; d) S. Natarajan, *J. Mater. Chem.* **1998**, *8*, 2757–2760.
[14] L. B. McCusker, *Comprehensive Supramolecular Chemistry*, vol. 7 (Eds.: G. Alberti, T. Bein), Pergamon, Oxford, **1996**, p. 393–422.
[15] W. Loewenstein, *Am. Mineral.* **1954**, *39*, 92–96.
[16] a) W. T. A. Harrison, *Chem. Mater.* **1996**, *8*, 145–151; b) C. H. Lin, S. L. Wang, K. H. Lii, *J. Am. Chem. Soc.* **2001**, *123*, 4649–4650.
[17] Software package SMART and SAINT, Siemens Analytical X-ray Instruments Inc., Madison, WI, **1996**.
[18] SHELXS 97, Siemens Industrial Automation Inc., **1997**.
[19] Samples of the residue were assayed on Varain-5000 high performance chromatograph with fixed-wavelength UV absorbance detector set at 254 nm. Samples (5 μL injection) were chromatographed at ambient temperatures on a 150 mm × 4.6 mm reversed-phase Eclipse XDB-C8 LC Column

 © 2007 Wiley-VCH Verlag GmbH & Co. KGaA, Weinheim 

(Agilent Technologies Corp., USA) with an eluting mobile phase consisting of acetonitrile/0.05% phosphoric acid (45:55). Eluents were aspirated prior to use. At a flow-rate of 1.0 mL/min column equilibration with the mobile phase was achieved in approximately 30 min. The retention times are 8.6 min, 10.4 min, 11.9 min for *trans*-(1*S*,2*S*)-DACH, *cis*-1,2-DACH and *trans*-(1*R*,2*R*)-DACH, respectively. Samples preparation: 0.2 mL of 0.4% acetonitrile solution of 2,3,4,6-tetra-*O*-acetyl-D-glucopyranosyl isothiocyanate was added to 0.1 mL of 0.025% acetonitrile solution of 1,2-DACH. Ten minutes later, 0.1 mL of 0.2% acetonitrile solution of ethanolamine was added to the given mixture. And three minutes later, 2.0 mL of 0.05% phosphoric acid was added to dilute the above solution.

Received: September 27, 2006
Published Online: January 8, 2007

 © 2007 Wiley-VCH Verlag GmbH & Co. KGaA, Weinheim 

DOI: 10.1002/ejic.200600939

# Preparation, Structure and Reactivity of Polynuclear Gold(I) Phosphanyl Alkanethiolates

**Antonella Battisti,[a] Oliver Bellina,[a] Pietro Diversi,*[a] Serena Losi,[b] Fabio Marchetti,[a] and Piero Zanello[b]**

**Keywords:** Gold(I) complexes / Tertiary phosphane complexes / Thiolates / Aurophilicity / Redox behaviour

The homoleptic gold(I) thiolates of formula $[Au(SR)]_n$ (R = $CMe_3$, $CH_2CMe_3$, $CH_2CHMe_2$, $CPh_3$) have been converted into their phosphane derivatives of general formula [Au(SR)(L)] (L = $PMe_3$, $PMe_2Ph$, $PMePh_2$, $PPh_3$) and $[Au_2(SR)_2(dppe)]$ [dppe = 1,2-bis(diphenylphosphanyl)ethane], which have been characterized by elemental analysis, mass spectrometry, $^1H$ and $^{31}P$ NMR spectroscopy and cyclic voltammetry. Complexes $[Au(SCMe_3)(PMePh_2)]$ (**1c**), $[Au_2(SCMe_3)_2(dppe)]$ (**1e**) and $[Au(SCH_2CMe_3)(PPh_3)]$ (**3d**) have been characterized in the solid state by X-ray diffraction: no aurophilic interactions have been found. The electrochemical behaviour of these phosphane thiolato derivatives shows two irreversible oxidation processes, the first of which involves 0.5 electrons per Au–SR. Chemical oxidation by $[FeCp_2]BF_4$ produces disulfide and cationic gold(I) complexes of formula $[Au_2(SR)(L)_2][BF_4]$ and $[Au_2(SR)(dppe)][BF_4]$, characterized by elemental analysis, mass spectrometry and $^1H$ and $^{31}P$ NMR spectroscopy. All the complexes are presumably dimeric in the solid state as shown in the case of $[Au_4(SCMe_3)_2(dppe)_2][BF_4]_2$ (**5e**) and $[Au_4(SCH_2CMe_3)_2(PMe_3)_4][BF_4]_2$ (**7a**), which have been fully characterized by X-ray diffraction. The aurophilic interactions form a structure of four gold atoms with pairs of atoms bonded by bridging thiolato ligands, which are arranged in an almost perfect square in the case of **7a** and in an unprecedented zigzag sequence in the case of **5e**. Complex **4a** reacts with $HSCMe_3$ under basic conditions to give $[Au(SCMe_3)(PMe_3)]$ and with LiX (X = Me, $CH_2CMe_3$) to give a 1:1 mixture of $[AuX(PMe_3)]$ and $[Au(SCMe_3)(PMe_3)]$.

(© Wiley-VCH Verlag GmbH & Co. KGaA, 69451 Weinheim, Germany, 2007)

## Introduction

Research on gold(I) thiolate complexes has produced numerous reports over the past few decades, because of their various practical applications such as, i.a., in gilding technology,[1] in the treatment of rheumatoid arthritis and in cancer chemotherapy.[2] In fact some phosphane gold(I) thiolates are the active principles of Auranofin and other antiarthritic products,[3] whose therapeutic activity seems to be correlated to their oxidation products in vivo. In particular Bruce et al., by thoroughly investigating the oxidation of such thiolato-phosphane derivatives, have been able to show that the final products are cationic gold clusters stabilized in the solid state by aurophilic interactions.[3]

In spite of many literature reports on the synthesis and properties of gold thiolates,[4] complexes containing simple aliphatic groups have been limited to some scattered scientific reports[4a–4c,4g,4h] and some information deriving from patents.[5] So far attention has mostly been dedicated to the few homoleptic thiolates, which are soluble in organic solvents,[4k] and to the phosphane-thiolato derivatives carrying biologically interesting substrates.[3d]

In this paper we describe the synthesis, the characterization and the redox behaviour of a series of gold(I) thiolate complexes derived from simple sterically demanding alkanethiols, where the alkyl group is the *tert*-butyl, *sec*-butyl and neopentyl group. We have also studied triphenylmethanethiol derivatives for comparison purposes. We have prepared homoleptic, neutral derivatives with phosphanes, and the corresponding cationic products prepared according to the Bruce oxidative procedure[3] as a strategy for building gold–gold interactions in the solid state. We report also the structural characterization and a preliminary investigation on the reactivity of these polynuclear cations.

[a] Dipartimento di Chimica e Chimica Industriale dell'Università di Pisa,
Via Risorgimento 35, 56126 Pisa, Italy
Fax: +39-50-2219410
E-mail: div@dcci.unipi.it
[b] Dipartimento di Chimica, Università di Siena,
Via Aldo Moro, 53100 Siena, Italy

Supporting information for this article is available on the WWW under http://www.eurjic.org or from the author.

## Results and Discussion

### Syntheses

The homoleptic thiolates $[Au(SR)]_n$ (R = $CMe_3$, $CH_2CHMe_2$, $CH_2CMe_3$, $CPh_3$) have been prepared following essentially two literature methods: addition of an excess

 © 2007 Wiley-VCH Verlag GmbH & Co. KGaA, Weinheim 

(3:1) of the thiol to a solution of aqueous tetrachloroauric acid, or alternatively the use of bis(2-hydroxyethyl) sulfide as the auxiliary reducing agent before adding the thiol.[4c] The two methods give similar yields (almost quantitative), but the latter was preferred in the case of the neopentanethiolate, owing to the necessity of saving the starting thiol. In this case care must be used in controlling the temperature to avoid the formation of metallic gold. The thiolates have good stability either in the air or in the light and are generally insoluble at room temperature in the most common organic solvents, apart from the neopentanethiolate that is slightly soluble in benzene and dichloromethane after it has been kept for a while at 40–45 °C. Owing to their insolubility the complexes were characterized only by elemental analysis. They react easily with stoichiometric amounts of the appropriate phosphane to yield the corresponding gold(I) phosphane thiolates of formula [Au(SR)(L)] (R = *tert*-butyl, L = $PMe_3$ **1a**, $PMe_2Ph$ **1b**, $PMePh_2$ **1c**, $PPh_3$ **1d**; R = isobutyl, L = $PMe_3$ **2a**, $PMe_2Ph$ **2b**, $PMePh_2$ **2c**, $PPh_3$ **2d**; R = neopentyl, L = $PMe_3$ **3a**, $PMe_2Ph$ **3b**, $PMePh_2$ **3c**, $PPh_3$ **3d**; R = trityl, L = $PMe_3$ **4a**, $PMe_2Ph$ **4b**, $PMePh_2$ **4c**, $PPh_3$ **4d**).[4e,4h,4i] As far as we know, only [Au($SCMe_3$)($PPh_3$)] (**1d**) and [Au($SCH_2CHMe_2$)($PPh_3$)] (**2d**) have already been reported in the literature, **1d** having been prepared by the reaction of [AuCl($PPh_3$)] with [Pb($SCMe_3$)$_2$][4c] and **2d** by the reaction of [AuCl($PPh_3$)] with the thiol in the presence of a base.[4a]

The reactions were carried out in benzene at room temperature, the yields varying from 80 to 95%. The compounds are crystalline colourless solids, stable in the air and humidity, soluble in aromatic and chlorinated solvents and insoluble in aliphatic hydrocarbons.

The gold(I) dppe thiolates [$Au_2$($SR$)$_2$(dppe)] (R = $CMe_3$ **1e**; $CH_2CHMe_2$ **2e**; $CH_2CMe_3$ **3e**), have been prepared in the same way by using a phosphane/Au = 1/2 molar ratio. All the compounds have been characterized by elemental analysis and NMR spectroscopy.

Well-formed crystals suitable for X-ray determination have been obtained for [Au($SCMe_3$)($PMePh_2$)] (**1c**), [$Au_2$($SCMe_3$)$_2$(dppe)] (**1e**) and [Au($SCH_2CMe_3$)($PPh_3$)] (**3d**) by crystallization from toluene at low temperature. None of these complexes show the presence of aurophilic interactions. The molecular structure of **1c** is shown in Figure 1, the most relevant distances and angles are also listed in Table 1. The gold atom shows the expected linear coordination and Au–S and Au–P distances are very similar to those observed in many other structurally characterized gold(I) phosphanyl-thiolate complexes that are reported in the literature,[6] and closely correspond to those reported for other gold(I) methyldiphenylphosphane derivatives.[6c]

Figure 2 shows the centrosymmetric structure of compound **1e** whose geometrical parameters around the gold atom are listed in Table 1. The observed conformation of the dppe ligand is a normal feature in almost all the gold(I) diphosphanyl-thiolate complexes studied hitherto,[7] apart from the cases with bidentate thiolate ligands, which result in cyclic complexes.[8]

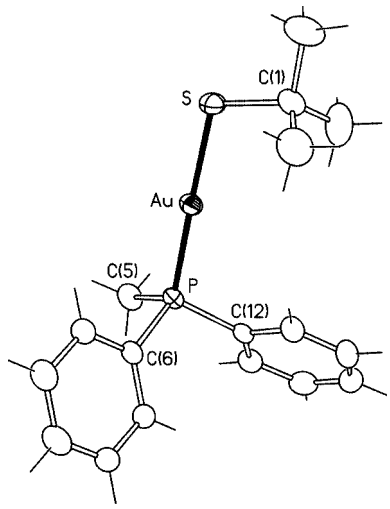


Figure 1. View of the molecular structure of **1c**. Ellipsoids are at 30% probability.

Table 1. Selected bond lenghts [Å] and angles [°] in **1c**, **1e** and **3d**.

| | | | |
|---|---|---|---|
| **1c** | | | |
| Au–P | 2.261(2) | Au–S | 2.288(2) |
| P–Au–S | 175.94(6) | C(5)–P–Au | 113.9(3) |
| C(6)–P–Au | 115.6(2) | C(12)–P–Au | 109.7(2) |
| C(1)–S–Au | 107.0(2) | | |
| **1e** | | | |
| Au–P | 2.264(2) | Au–S | 2.290(3) |
| P–Au–S | 176.9(1) | C(1)–P–Au | 109.9(3) |
| C(2)–P–Au | 116.2(3) | C(8)–P–Au | 115.6(3) |
| C(14)–S–Au | 107.3(4) | | |
| **3d** | | | |
| Au–P | 2.261(2) | Au–S | 2.285(3) |
| P–Au–S | 177.2(1) | C(1P)–P–Au | 112.1(4) |
| C(7P)–P–Au | 113.3(4) | C(13P)–P–Au | 114.7(3) |
| C(1)–S–Au | 107.0(4) | | |

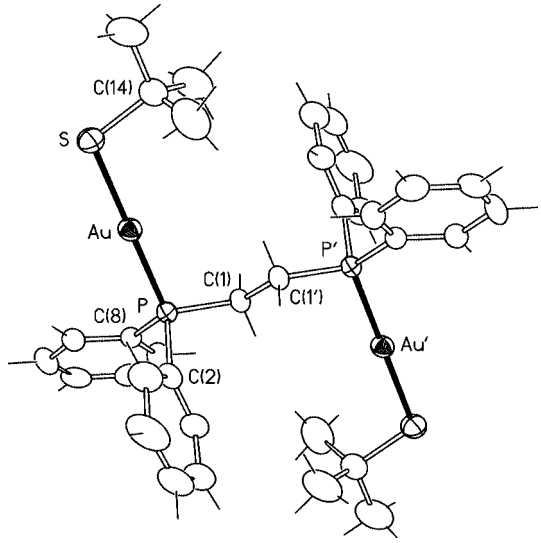


Figure 2. Projection of the molecular structure of **1e**. Thermal ellipsoids are at 30% probability. ′ = 1−*x*, 1−*y*, 1−*z*.

 © 2007 Wiley-VCH Verlag GmbH & Co. KGaA, Weinheim 

Finally, the most relevant distances and angles of **3d** (the molecular structure is shown in Figure S1 in the Supporting Information) are listed in Table 1. The gold coordination is very similar to that found in **1e** and **3d** and corresponds very closely to that which has been found in the neutral phosphanyl-thiolato complexes of gold(I) with triphenylphosphane.[7f,9]

### Oxidation of Gold Thiolates

In spite of the widespread use in several decomposition techniques and some applications in galvanic processes, the electrochemistry of gold complexes was until recently rather poorly explored. A review summarizes the results of the redox behaviour of gold and silver compounds.[11] In particular the Bruce group has found that gold phosphane thiolates undergo two irreversible oxidation processes, that, in agreement to theoretical studies, were assigned as sulfur- and gold-centred, respectively.[3] Chemical complications following oxidation have been elucidated by studying the reaction with ferrocenium tetrafluoroborate.[3] The oxidation process ultimately gives disulfide and a cationic cluster that in the solid state appears to be constituted by a dicationic tetragold system with gold–gold distances that are in the range of typical distances for aurophilic interactions.[3,10] Such reactivity has been observed in a variety of phosphane and diphosphane gold thiolates, and in particular in the case of those derivatives that are the active principles of Auranofin and of other antiarthritic drugs.[3]

The present study is aimed at elucidating the behaviour of our systems towards both electrochemical and chemical oxidation and exploiting the Bruce reaction in order to build up polynuclear structures, and possibly to understand how the structure and the geometry depend on the nature of the ligands.

### Electrochemical Studies

As representatively shown in Figure 3, which refers to [Au(SCH$_2$CMe$_3$)(PMe$_3$)], the gold thiolates with monophosphanes undergo two oxidation processes, both having features of chemical irreversibility.[12] Indeed, also limited to the first oxidation (peak **A**), it lacks the directly associated return peak even at high scan rates (2.0 V s$^{-1}$), thus indicating that the oxidized product undergoes rapid chemical complications.

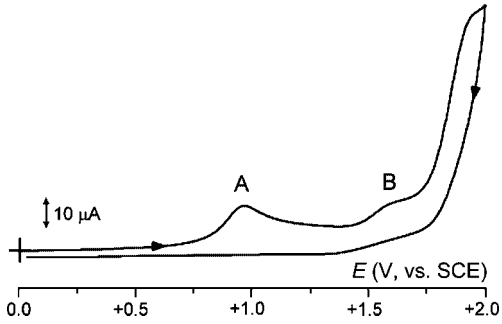


Figure 3. Cyclic voltammogram recorded at a platinum electrode in $CH_2Cl_2$ solution containing [Au(SCH$_2$CMe$_3$)(PMe$_3$)] ($1.8 \times 10^{-3}$ mol dm$^{-3}$) and [NBu$_4$][PF$_6$] (0.2 mol dm$^{-3}$). Scan rate: 0.2 V s$^{-1}$.

In agreement with the literature,[3] exhaustive oxidation that corresponds to the first oxidation ($E_w$ = +1.2 V) consumes ca. half an electron per molecule, confirming that the ligand centred[9] first process is coupled to fast chemical reactions. Because of the partial overlapping of the solvent discharge no attempts to identify the product arising from the second gold-centred process have been carried out (the standard reduction potential of the couple Au$^{I}$/Au$^{0}$ in water is +1.69 V).

Table 2 consists of the electrode potentials from the first oxidation of all the compounds studied: An attempt to account for the influence of the electronic effects from the different substituents present in the phosphane or the thiolate groups[12] on the location of the oxidation processes (Table S1 in the Supporting Information) suggests that the main contribution would arise from the inductive effects of the substituents of the phosphane moieties. In fact, they display the highest correlation coefficients, whereas the contribution of the thiolate substituents greatly departs from linearity. However, it has been considered that, given the irreversibility of the electron removals, the potentials for the first oxidation might have a thermodynamic meaning only under the assumption that the kinetics of the coupled chemical complications proceed with similar rates.[13]

In fact, as in the case of the mononuclear complexes, exhaustive oxidation at the first anodic process consumes half an electron per gold atom, which means one electron per molecule. The peak potentials for the first oxidation of the dinuclear derivatives are reported in Table 2.

Since in the mononuclear derivatives the SCMe$_3$ group seems to be a more efficient electron donor than the

Table 2. Peak potentials (V vs. SCE) for the first oxidation process exhibited by the present mono- and digold thiolates in $CH_2Cl_2$ solution.

| Complex | $E_p$[a] | Complex | $E_p$[a] | Complex | $E_p$[a] |
|---|---|---|---|---|---|
| [Au(SCMe$_3$)(PMe$_3$)] (**1a**) | +0.97 | [Au(SCH$_2$CHMe$_2$)(PMe$_3$)] (**2a**) | +0.97 | [Au(SCPh$_3$)(PMe$_3$)] (**4a**) | +0.91 |
| [Au(SCMe$_3$)($^{m}$e2Ph)] (**1b**) | +0.95 | [Au(SCH$_2$CHMe$_2$)(PPh$_3$)] (**2d**) | +1.09 | [Au(SCPh$_3$)(PMe$_2$Ph)] (**4b**) | +0.96 |
| [Au(SCMe$_3$)(PMePh$_2$)] (**1c**) | +1.03 | [Au(SCH$_2$CMe$_3$)(PMe$_3$)] (**3a**) | +1.00 | [Au(SCPh$_3$)(PMePh$_2$)] (**4c**) | +1.04 |
| [Au(SCMe$_3$)(PPh$_3$)] (**1d**) | +1.04 | [Au(SCH$_2$CMe$_3$)(PPh$_3$)] (**3d**) | +1.22 | [Au(SCPh$_3$)(PPh$_3$)] (**4d**) | +1.07 |
| [Au$_2$(SCMe$_3$)$_2$(dppe)] (**1e**) | +0.90 | | | | |
| [Au$_2$(SCH$_2$CHMe$_2$)$_2$(dppe)] (**2e**) | +1.10 | | | | |
| [Au$_2$(SCH$_2$CMe$_3$)$_2$(dppe)] (**3e**) | +0.75 | | | | |

[a] Measured at 0.2 V s$^{-1}$. In turn the dinuclear derivatives exhibit a voltammetric profile qualitatively similar to those of the mononuclear complexes {the cyclic voltammetric behaviour of [Au$_2$(SCH$_2$CMe$_3$)$_2$(dppe)] (**3e**) is illustrated in Figure S2 in the Supporting Information}.

 © 2007 Wiley-VCH Verlag GmbH & Co. KGaA, Weinheim 

$SCH_2CMe_3$ ligand, it is puzzling that $[Au_2(SCMe_3)_2(dppe)]$ is oxidized less easily than $[Au_2(SCH_2CMe_3)_2(dppe)]$, unless a different relative arrangement of the thiolato groups in the complexes with dppe might be operative.

### Chemical Oxidation

Following previous reaction conditions,[3] the phosphane gold thiolates **1**–**3** have been reacted with $[FeCp_2][BF_4]$ (Scheme 1). In all cases (apart from the thiolates **4**, which react giving uncharacterized products) the reaction proceeds by consuming one mol of ferrocenium salt per two mol of gold thiolate moiety, as shown by colour changes at the equivalence point (the persistence of the green colour of the ferrocenium ion indicates that the reaction is complete).

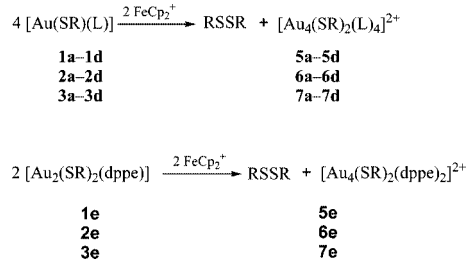


Scheme 1.

The solid residue, after evaporation of the solvent, is washed with diethyl ether in order to extract ferrocene and the disulfide (RSSR) (the oxidation product of the thiolato ligand), which were identified by NMR spectroscopy. The residue was crystallized from dichloromethane/hexane to give grey to pale yellow crystals of **5**–**7**, which are stable in the air and insoluble in aliphatic and aromatic hydrocarbons, and fairly soluble in acetone and dichloromethane. All the products present satisfactory elemental analyses and have been characterized by NMR spectroscopy and mass spectrometry. On the basis of the relative 2:1 ratio of the $^1H$ NMR signals from the phosphane and the thiolato groups we have attributed a general formula $[Au_2(SR)(L)_2][BF_4]$. Actually, for similar compounds, the literature reports[3] structures in the solid state that generally result from the aggregation of the monocations in dimers of the formula $[Au_4(SR)_2(phosphane)_4][BF_4]_2$, where the tetranuclear arrangement of the gold atoms is due to aurophilic interactions.

Well-formed crystals suitable for structural determination have been obtained in the case of **5e** and **7a** by crystallization from dichloromethane/hexane or dichloromethane/diethyl ether solutions.

The structure of the tetranuclear cation $[Au_4(SCH_2CMe_3)_2(PMe_3)_4]^{2+}$ is sketched in Figure 4 and the most significant bond lengths and angles are listed in Table 3. The four gold atoms make a square ring by means of four aurophilic interactions. Such an arrangement is very frequent in phosphanyl-thiolato complexes of gold(I), notably with the trimethylphosphane.[6e,14] The cation belongs to the point group 2/*m* ($C_{2h}$), possessing the inversion centre in the middle of the square of the four gold atoms, the twofold axis lying in the gold plane in the middle between the atoms Au and Au′ and the mirror perpendicular to the axis passing through the S and C(1) atoms. It is a common feature of the gold derivatives with this framework that the PSP plane makes a dihedral angle with the $Au_4$ plane acute from the side of the sulfur atom. Our cation conforms to this feature showing a torsion angle Au′–Au–Au′′–S of 85.2°. The methyl groups of the phosphanes do not comply with the high symmetry of the molecule, resulting in a statistical disorder between two limit conformations almost equally populated and corresponding to different torsion angles Au′–Au–P–C(5). For the sake of simplicity, only the A conformation of the methyl groups, as marked by the labels, has been drawn in the figure because of its slightly higher frequency.

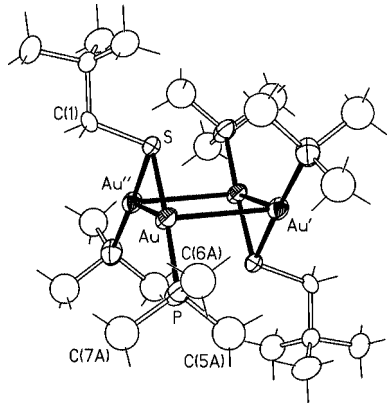


Figure 4. View of the structure of the cationic part of **7a**. Only the most populated positions of the disordered phosphanes have been represented. Thermal ellipsoids are at 30% probability. ′ = $1-x$, $1-y$, $z$; ′′ = $x$, $y$, $-z$.

Table 3. Selected bond lenghts [Å] and angles [°] in **7a**. The apexes in the atom labels have the same meaning as in Figure 4.

| | | | |
|---|---|---|---|
| Au–Au′ | 3.112(1) | Au–Au′′ | 3.138(1) |
| Au–P | 2.259(5) | Au–S | 2.332(4) |
| Au′–Au–Au′′ | 90.0 | S–Au–Au′ | 86.4(1) |
| S–Au–Au′′ | 47.72(9) | P–Au–Au′ | 96.1(1) |
| P–Au–Au′′ | 132.7(2) | Au–S–Au′′ | 84.6(2) |
| Au–S–C(1) | 104.3(5) | Au–P–C(5A) | 117(1) |
| Au–P–C(6A) | 113(1) | Au–P–C(7A) | 115(1) |

This structure is similar to those reported for $[Au_4(SMe)_2(PMe_3)_4]^{2+}$[6d] and $[Au_4(SCMe_3)_2(PPh_3)_4]^{2+}$,[15] prepared by different routes.

The structure of the tetranuclear cation present in the crystal of **5e**·$CH_2Cl_2$ is shown in Figure 5 and the bond lengths and angles around the metal are listed in Table 4. The projection has been done down the twofold axis, which relates the two moieties of the cation, point group 2 ($C_2$ in the Schoenflies notation). The gold atoms are arranged in a sort of zigzag chain. A similar metal arrangement has been found in Ag,[16a,16b] Ag–Pd[16c] Ni,[16d] Mo[16e] and Ta[16f] derivatives, but it has never been reported for gold. Different from almost all these examples, where the metal chain is lying on a plane, the chain of gold atoms is mark-

 © 2007 Wiley-VCH Verlag GmbH & Co. KGaA, Weinheim 

edly puckered so that it may be described as a tetrahedron heavily distorted by the stretching of some edges. The three shortest edges correspond to the drawn bonds Au(1)–Au(2), Au(2)–Au(2′) and Au(2′)–Au(1′), while the other three, Au(1)···Au(2′) and Au(2)···Au(1′), 3.717 Å, and Au(1)···Au(1′), 4.903 Å, correspond to non-bonding distances. The torsion angle Au(1)–Au(2)–Au(2′)–Au(1′), which in an undistorted tetrahedron is 70.5°, in our chain rises to 107.8° and only one of the twofold axes of the ideal tetrahedron is preserved.

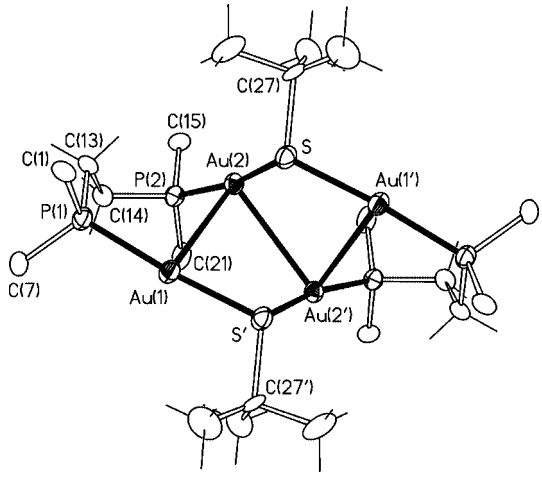


Figure 5. View of the structure of the cationic part of **5e** projected down the twofold axis. The phenyl groups of dppe have been omitted apart from the carbon atoms connected to the phosphorus atoms. Thermal ellipsoids are at 30% probability. ′ = –*x*, *y*, 1/2 – *z*.

Table 4. Selected bond lenghts [Å] and angles [°] in **3d**. The apexes in the atom labels have the same meaning as in Figure 4.

| | | | |
|---|---|---|---|
| Au(1)–Au(2) | 2.986(1) | Au(2)–Au(2′) | 3.152(1) |
| Au(1)–P(1) | 2.281(4) | Au(2)–P(2) | 2.285(5) |
| Au(1)–S′ | 2.320(4) | Au(2)–S | 2.346(5) |
| Au(2)–Au(1)–P(1) | 92.3(1) | Au(2)–Au(1)–S′ | 87.0(1) |
| P(1)–Au(1)–S′ | 172.8(2) | Au(1)–Au(2)–Au(2′) | 74.49(3) |
| P(2)–Au(2)–S | 168.4(2) | P(2)–Au(2)–Au(1) | 92.6(1) |
| S–Au(2)–Au(1) | 85.4(1) | S–Au(2)–Au(2′) | 82.7(1) |
| P(2)–Au(2)–Au(2′) | 107.8(1) | Au(1)–S′–Au(2′) | 105.6(2) |
| Au(1)–S′–C(27′) | 111.3(6) | Au(2)–S–C(27) | 107.3(7) |
| Au(1)–P(1)–C(1) | 111.2(7) | Au(1)–P(1)–C(7) | 113.8(6) |
| Au(1)–P(1)–C(13) | 112.5(6) | Au(2)–P(2)–C(14) | 110.3(6) |
| Au(2)–P(2)–C(15) | 112.2(7) | Au(2)–P(2)–C(21) | 118.0(6) |

Although both Au(1)–Au(2) and Au(2)–Au(2′) distances fall within the aurophilic bond range, the second one, 3.152 Å, suggests a rather weak interaction and being associated with a wide Au–S–Au angle, 105.6°, is in keeping with the suggested relationship between this angle and the strength of the gold–gold interaction.[15]

Hence, the corrected formulations for the complexes in the solid state are $[Au_4(SR)_2(L)_4][BF_4]_2$. On the basis of these results and on the literature reports we think that the other cationic compounds prepared have a similar structure, based on a core of four gold atoms associated by aurophilic interactions.

It is not clear if such structures will survive in solution (the literature is not conclusive in this regard). ESI-MS spectra of these complexes in methanol show peaks that can be attributed both to the corresponding dinuclear monocation and to the tetranuclear dication. However, in the case of $[Au_4(SCH_2CHMe_2)_2(PMe_3)_4][BF_4]_2$ (**6a**) and $[Au_4(SCH_2CHMe_2)_2(PPh_3)_4][BF_4]_2$ (**6d**), the spectra show, in addition to the peaks at *m*/*z* = 635 and 1007 for $[Au_2(SR)(PMe_3)_2]^+$ and $[Au_4(SR)_2(PMe_3)_4]^{2+}$, respectively, species at high molecular weights, e.g. $[Au_3(SR)_3(PMe_3)_2]^+$, $[Au_3(SR)_2(PMe_3)_2]^+$ and $[Au_3(SR)(PMe_3)_3]^+$, but it is not certain if those species derive from fragmentation of the tetranuclear species or from the aggregation of small fragments. Moreover, close inspection of the peak corresponding to $[Au_2(SR)(PMe_3)_2]^+$ shows that, in addition to the expected M, M + 1, M + 2 peaks, signals at M + 1/2 are present, which are assigned to the dicationic species $[Au_4(SR)_2(PMe_3)_4]^{2+}$. These observations suggest that tetranuclear species are present in solution (perhaps together with the dinuclear ones) although further experimental evidences are necessary in order to draw clear-cut conclusions.

## Reactions with Nucleophiles

### *Thiolate Anions*

The cationic gold clusters can be converted back to the neutral thiolates by reaction with the thiolato anion generated in situ: in fact reacting $[Au_4(SCMe_3)_2(PMe_3)_4][BF_4]_2$ (**4a**) with 2 equiv. of 2-methyl-2-propanethiol in the presence of a base (ethanolamine) produces almost quantitatively $[Au(SCMe_3)(PMe_3)]$ (**2a**). The reaction can easily be followed by $^1$H NMR spectroscopy. By adding a stoichiometric amount of 2-methyl-2-propanethiol and ethanolamine in a 1:1 molar ratio to a $CD_2Cl_2$ solution of the dication the signals from the initial cationic complex **4a** disappear immediately and the resonances from the protons of the neutral thiolate **2a** arise.

$$[Au_4(SCMe_3)_2(PMe_3)_4]^{2+} \xrightarrow[Me_3CSH/ethanolamine]{CH_2Cl_2} [Au_2(SCMe_3)_2(PMe_3)_4]$$

### *Lithium Alkyls*

We decided to study the reaction of $[Au_4(SCMe_3)_2(PMe_3)_4][BF_4]_2$ with LiMe and $LiCH_2CMe_3$ because of the spectral simplicity of the expected alkyl derivatives.

The reactions have been carried out with an excess of the alkylating agent in dichloromethane. When $[Au_4(SCMe_3)(PMe_3)_4][BF_4]_2$ was reacted with LiMe, after hydrolysis and extraction with benzene, a solid was obtained whose $^1$H NMR spectrum shows, in addition to the signals of $[Au(SCMe_3)(PMe_3)]$, two doublets at $\delta$ = 0.59 ppm ($J$ = 8.8 Hz) and 1.23 ppm ($J$ = 8.4 Hz). These signals, having a relative intensity of 3:1, could be attributed quite naturally to the $PMe_3$ and AuMe protons in $[Au(Me)(PMe_3)]$. Accordingly the $^{31}$P NMR spectrum of the reaction mixture shows the presence of signals at $\delta$ =

 © 2007 Wiley-VCH Verlag GmbH & Co. KGaA, Weinheim 

–3.51 ppm, corresponding to the gold phosphanyl thiolate $[Au(SCMe_3)(PMe_3)]$, and $\delta$ = 10.74 ppm, which seems logical to attribute to $[Au(Me)(PMe_3)]$.

Surprisingly our NMR spectroscopic data are not in agreement with those reported in the literature for $[Au(Me)(PMe_3)]$, prepared from $[Au(Cl)(PMe_3)]$ by alkylation with LiMe in diethyl ether ($\delta$ = 0.21 ppm, $J_{P,H}$ = 8.9 Hz and $\delta$ = 0.57 ppm, $J_{H,H}$ = 8.7 Hz).[17] We have prepared $[Au(Me)(PMe_3)]$ following the reported procedure,[18] and we found the same $^1H$ NMR signals as the methyl derivative formed by reacting $[Au_4(SCH_2CHMe_2)_2(PMe_3)_4][BF_4]_2$ with LiMe. The $^{31}P$ NMR spectrum showing a signal at $\delta$ = 12.35 ppm is rather consistent with the above value of $\delta$ = 10.74 ppm. The product reacts rapidly and quantitatively in deuterated benzene with an excess of trifluoroacetic acid, forming methane and $[Au(OOCF_3)(PMe_3)]$ as shown by the immediate appearance in the $^1H$ NMR spectrum of a singlet at $\delta$ = 0.14 ppm (methane) and in the $^{31}P$ NMR spectrum of a signal at $\delta$ = –16.14 ppm, to be attributed to $[Au(OOCF_3)(PMe_3)]$. This was unequivocally identified by purification and comparison of the $^1H$ NMR spectrum in $CDCl_3$ with that reported in the same solvent ($\delta$ = 1.68 ppm, d, $J_{P,H}$ = 11.36 Hz).[19]

Only an X-ray single-crystal determination could positively clarify this point but so far we have not been able to prepare suitable crystals.

$[Au_4(SCMe_3)_2(PMe_3)_4][BF_4]_2$ was similarly reacted with $LiCH_2CMe_3$ yielding an equimolar mixture of $[Au(SCMe_3)(PMe_3)]$ and $[Au(CH_2CMe_3)(PMe_3)]$. The neopentylgold derivative, which has not been reported in the literature thus far, was prepared by alkylation of the corresponding chloro derivative with $LiCH_2CMe_3$ in diethyl ether. The product was isolated as a white crystalline solid, which, even when stored under nitrogen at room temperature and out of light, becomes gradually grey after a few weeks. However, the complex shows well resolved NMR spectra in $CD_2Cl_2$. The $^1H$ NMR spectrum shows a singlet at $\delta$ = 1.01 ppm and a doublet at $\delta$ = 1.22 ppm ($J_{H,H}$ = 8.4 Hz) corresponding to the methyl and methylene protons, respectively, of the neopentyl group and a doublet at $\delta$ = 1.41 ppm ($J_{P,H}$ = 8.4 Hz) corresponding to the trimethylphosphane; accordingly the $^{31}P$ NMR spectrum shows a singlet at $\delta$ = 16.60 ppm. The reaction with trifluoroacetic acid in deuteriobenzene gave neopentane (singlet at $\delta$ = 0.89 ppm) and $[Au(OOCF_3)(PMe_3)]$, as expected.

These results show that, from the reaction of the above cationic gold thiolates with alkyllithium reagents, half of the metal centres undergo alkylation and the other half are released as a neutral phosphane thiolate:

$$[Au_4(SCMe_3)(PMe_3)_4]^{2+} \xrightarrow{LiR} [Au(SCMe_3)(PMe_3)] + 2\,[Au(R)(PMe_3)]$$

$R = Me, CH_2CMe_3$

## Conclusions

We report here the synthesis and characterization of a series of gold(I) thiolates, in which the thiolato ligands contain aliphatic $C_4$ and $C_5$ alkyls with different steric hindrance, or a trityl group. The aliphatic thiols give neutral gold thiolates that do not exhibit any Au–Au bonding interactions in the solid state, but upon oxidation afford cationic derivatives that at least in the solid state dimerize to dicationic tetranuclear species with pairs of gold atoms bonded by aurophilic interactions. As in the majority of the literature reports, the arrangement was found to be almost square in the case of **7a** but in the case of **5e**, where dppe is the phosphane supporting ligand, an unusual zigzag organization has been found. It is obviously premature to make a pertinent theory but we are attempting to attribute this peculiar structure to the presence of a chelating phosphane.

Apart from this dinuclear–tetranuclear issue, these cationic thiolates behave towards nucleophiles as $[Au(SR)(PMe_3)]$-stabilized $[Au(PMe_3)]^+$ cations losing the neutral complex and adding the nucleophile. This reactivity confirms that the aurophilic interactions and also the bridging thiolato ligands, which are responsible for the variety of structures in the solid state for gold(I), are easily disrupted in solution.

## Experimental Section

All manipulations and reactions were carried out under dinitrogen or argon using standard techniques. Diethyl ether and benzene were distilled prior to use, first over K/benzophenone and later over $LiAlH_4$. *n*-Pentane, $CH_2Cl_2$ and ethanol were dried under vacuum over molecular sieves. $^1H$ and $^{31}P$ NMR spectra were recorded with a Varian Gemini 200 instrument, working at 200 MHz. Centesimal analysis have been executed in the microanalysis laboratory of Dipartimento di Scienze Farmaceutiche dell'Università di Pisa. The mass spectra were obtained by an Ion Spray technique with the Perkin–Elmer instrument SCIEX API III, in methanol solution. Material and apparatus for electrochemistry have been described elsewhere.[20] All of the potential values refer to the Saturated Calomel Electrode (SCE). Under the present experimental conditions the one-electron oxidation of ferrocene occurs at +0.39 V. $[Au(SCMe_3)]_n$ was prepared according to the literature.[3a] $[Au(SCH_2CHMe_2)]_n$ was prepared in the same way (yield 93%). $C_4H_9AuS$ (286.15): calcd. C 16.79, H 3.17; found C 16.64, H 3.20. Neopentanethiol was prepared by a literature procedure[21] from the corresponding neopentyl tosylate, obtained from neopentyl alcohol and tosyl chloride in pyridine [yield 95%. $^1H$ NMR ($CDCl_3$): $\delta$ = 0.91 (s, 9 H, $CMe_3$), 2.46 (s, 3 H, MePh), 3.67 (s, 2 H, $CH_2S$) ppm] by treatment with NaSH in methoxyethanol [yield 21%. $^1H$ NMR ($CDCl_3$): $\delta$ = 0.96 (s, 9 H, Me), 1.20 (t, 1 H, $J_{H,H}$ = 8.8 Hz, SH), 2.41 (d, 2 H, $J_{H,H}$ = 8.8 Hz, $CH_2S$) ppm].

**Preparation of $[Au(SCH_2CMe_3)]_n$**

**Method A:** Neopentanethiol (0.327 g, 3.14 mmol) was added dropwise to an aqueous solution of $H[AuCl_4]$ (29.34 wt.-% Au) (0.676 g, 1 mmol Au) in EtOH (2.6 mL). An exothermic reaction occurred with the formation of a brown solid that turned white in 30 min. The mixture was heated at 50 °C for 10 min, and the white solid was then separated from the solvent by settling, washed first with

 © 2007 Wiley-VCH Verlag GmbH & Co. KGaA, Weinheim 

EtOH (2 × 10 mL) and then with $Et_2O$ (2 × 10 mL). The residual solvent was removed under vacuum to give a solid product (0.294 g, 98%), which is insoluble in the most common organic solvent. $C_5H_{11}AuS$ (300.17): calcd. C 20.01, H 3.69; found C 20.0, H 4.0.

**Method B:** An aqueous solution of bis(2-hydroxyethyl) sulfide (2 mL, 2.0 mmol) was added dropwise at 0 °C to a solution of $H[AuCl_4]\cdot xH_2O$ (1.05 mmol) in water (1 mL) and EtOH (2.6 mL). The stirring was maintained until the solution turned colourless. Neopentanethiol (0.109 g, 1.05 mmol) was added and a white solid began to precipitate immediately from the solution. After stirring for 30 min, the solid product was separated, washed as described above and dried under vacuum (0.234 g, 78%).

**Reaction of $[Au(SCMe_3)]_n$ with L (L = $PMe_3$, $PMe_2Ph$, $PMePh_2$, $PPh_3$, dppe). Formation of $[Au(SCMe_3)(L)]$ (1a, 1b, 1c, 1d, 1e):** The reaction of $[Au(SCMe_3)]_n$ with $PMe_3$ is reported as an example. Trimethylphosphane (0.6 mL of a 1 M solution in toluene, 0.6 mmol) was added to a suspension of $[Au(SCMe_3)]_n$ (0.152 g, 0.53 mmol) in toluene (10 mL) while stirring. The solid immediately dissolved to give a clear colourless solution, which was kept stirring for a further 30 min. The solution was concentrated under vacuum to ca 3 mL and pentane (15 mL) was added causing a white solid to precipitate. The solid was washed twice with pentane (15 mL) and recrystallized from toluene to give 0.187 g (98%) of **1a**. $C_7H_{18}AuPS$ (362.23): calcd. C 23.21, H 5.01; found C 23.3, H 5.3. $^1H$ NMR ($C_6D_6$): $\delta$ = 1.90 (s, 9 H, $CMe_3$), 0.55 (d, 9 H, $J_{H,P}$ = 9.5 Hz, $PMe_3$) ppm. $^{31}P$ NMR ($C_6D_6$): $\delta$ = 0.61 ppm.

The complexes **1b**–**1e** were prepared in a similar manner to that of $[Au(SCMe_3)]_n$ by reaction with the appropriate phosphane.

**Complex 1b:** Yield 90%. $C_{12}H_{20}AuPS$ (424.30): calcd. C 33.97, H 4.75; found C 33.52, H 4.95. $^1H$ NMR ($C_6D_6$): $\delta$ = 1.95 (s, 9 H, $CMe_3$), 0.81 (d, 6 H, $J_{H,P}$ = 9.5 Hz $PMe_2$), 7.02 (5 H, br. m, PPh) ppm. $^{31}P$ NMR ($C_6D_6$): $\delta$ = 13.01 ppm.

**Complex 1c:** Yield 97%. $C_{17}H_{22}AuPS$ (486.37): calcd. C 41.98, H 4.56; found C 41.79, H 4.45. $^1H$ NMR ($C_6D_6$): $\delta$ = 1.94 (s, 9 H, $CMe_3$), 1.21 (d, 3 H, $J_{H,P}$ = 8.8 Hz, PMe), 7.10 (10 H, br. m, $PPh_2$) ppm. $^{31}P$ NMR ($C_6D_6$): $\delta$ = 25.00 ppm.

**Complex 1d:** Yield 95%. $C_{22}H_{24}AuPS$ (548.44): calcd. C 48.18, H 4.41; found C 47.96, H 4.27. $^1H$ NMR ($C_6D_6$): $\delta$ = 1.92 (s, 9 H, $CMe_3$), 6.80–6.92 (9 H, br. m, $PPh_3$), 7.25–7.40 (6 H, br. m, $PPh_3$) ppm. $^{31}P$ NMR ($C_6D_6$): $\delta$ = 38.77 ppm.

**Complex 1e:** Yield 89%. $C_{34}H_{42}Au_2P_2S_2$ (970.72): calcd. C 42.07, H 4.36; found C 41.95, H 4.28. $^1H$ NMR ($C_6D_6$): $\delta$ = 1.90 (s, 9 H, $CMe_3$), 2.68 (s, 4 H, $PCH_2$), 6.8–7.0, 7.4–7.6 (20 H, br. m, $PPh_2$) ppm. $^{31}P$ NMR ($C_6D_6$): $\delta$ = 37.64 ppm.

**Reaction of $[Au(SCH_2CHMe_2)]_n$ with L (L = $PMe_3$, $PMe_2Ph$, $PMePh_2$, $PPh_3$, dppe). Formation of $[Au(SCH_2CHMe_2)(L)]$ (2a, 2b, 2c, 2d, 2e):** The following complexes were prepared as described before.

**Complex 2a:** White solid. Yield 79%. $C_7H_{18}AuPS$ (362.23): calcd. C 23.21, H 5.01; found C 22.97, H 4.88. $^1H$ NMR ($C_6D_6$): $\delta$ = 0.45 (d, 9 H, $J_{H,P}$ = 9.9 Hz, $PMe_3$), 1.23 (d, 6 H, $J_{H,H}$ = 6.6 Hz, $Me_2$), 2.10 (m, 1 H, $J_{H,H}$ = 6.6 Hz, CH), 3.32 (d, 2 H, $J_{H,H}$ = 6.6 Hz, $SCH_2$) ppm. $^{31}P$ NMR ($C_6D_6$): $\delta$ = –0.40 ppm.

**Complex 2b:** Grey oil. Yield 77%. $C_{12}H_{20}AuPS$ (424.30): calcd. C 33.97, H 4.75; found C 33.77, H 4.53. $^1H$ NMR ($C_6D_6$): $\delta$ = 0.86 (d, 6 H, $J_{H,P}$ = 9.9 Hz, $PMe_2$), 1.30 (d, 6 H, $J_{H,H}$ = 6.6 Hz, $Me_2$), 2.14 (m, 1 H, $J_{H,H}$ = 6.6 Hz, CH), 3.37 (d, 2 H, $J_{H,H}$ = 6.6 Hz, $SCH_2$), 6.8–7.3 (5 H, br. m, PPh) ppm. $^{31}P$ NMR ($C_6D_6$): $\delta$ = 11.31 ppm.

**Complex 2c:** Grey oil. Yield 81%. $C_{17}H_{22}AuPS$ (486.37): calcd. C 41.98, H 4.56; found C 41.78, H 4.25. $^1H$ NMR ($C_6D_6$): $\delta$ = 1.26 (d, 6 H, $J_{H,H}$ = 6.2 Hz, $Me_2$), 1.34 (d, 3 H, $J_{H,P}$ = 9.5 Hz, PMe), 2.11 (m, 1 H, $J_{H,H}$ = 6.4 Hz, CH), 3.38 (d, 2 H, $J_{H,H}$ = 6.2 Hz, $CH_2$), 6.8–7.4 (10 H, br. m, $PPh_2$) ppm. $^{31}P$ NMR ($C_6D_6$): $\delta$ = 23.53 ppm.

**Complex 2d:** White crystals. Yield 75%. $C_{22}H_{24}AuPS$ (548.44): calcd. C 48.18, H 4.41; found C 48.0, H 4.3. $^1H$ NMR ($C_6D_6$): $\delta$ = 1.27 (d, 6 H, $J_{H,H}$ = 6.6 Hz, $Me_2$), 2.10 (m, 1 H, $J_{H,H}$ = 6.6 Hz, CH), 3.37 (d, 2 H, $J_{H,H}$ = 6.6 Hz, $SCH_2$), 6.7–7.4 (15 H, br. m, $PPh_3$) ppm. $^{31}P$ NMR ($C_6D_6$): $\delta$ = 38.64 ppm.

**Complex 2e:** White solid. Yield 65%. $C_{34}H_{42}Au_2P_2S_2$ (970.72): calcd. C 42.07, H 4.36; found C 41.8, H 4.2. $^1H$ NMR ($C_6D_6$): $\delta$ = 1.25 (d, 12 H, $J_{H,H}$ = 6.6 Hz, $Me_2$), 2.09 (m, 2 H, $J_{H,H}$ = 6,6 Hz, CH), 2.57 (br. s, 4 H, $PCH_2$), 3.37 (d, 4 H, $J_{H,H}$ = 6.6 Hz, $CH_2$), 6.7–7.5 (20 H, br. m, $PPh_2$) ppm. $^{31}P$ NMR ($C_6D_6$): $\delta$ = 37.60 ppm.

**Reaction of $[Au(SCH_2CMe_3)]_n$ with L (L = $PMe_3$, $PMe_2Ph$, $PMePh_2$, $PPh_3$, dppe). Formation of $[Au(SCH_2CMe_3)(L)]$ (3a, 3b, 3c, 3d, 3e):** The following complexes were prepared as described above.

**Complex 3a:** White crystals. Yield 99%. $C_8H_{20}AuPS$ (376.25): calcd. C 25.5, H 5.4; found C 25.54, H 5.36. $^1H$ NMR ($CD_2Cl_2$): $\delta$ = 1.02 (s, 9 H, $CMe_3$), 1.56 (d, 9 H, $J_{H,P}$ = 10.3 Hz, $PMe_3$), 2.80 (s, 2 H, $SCH_2$) ppm. $^1H$ NMR ($C_6D_6$): $\delta$ = 0.62 (d, 9 H, $J_{H,P}$ = 10.3 Hz, $PMe_3$), 1.33 (s, 9 H, $CMe_3$), 3.37 (s, 2 H, $SCH_2$) ppm. $^{31}P$ NMR ($CDCl_3$): $\delta$ = 0.10 ppm. $^{31}P$ NMR ($C_6D_6$): $\delta$ = –1.03 ppm.

**Complex 3b:** Crystallized from $Et_2O$. Yield 85%. $C_{13}H_{22}AuPS$ (438.32): calcd. C 35.62, H 5.06; found C 35.52, H 5.4. $^1H$ NMR ($C_6D_6$): $\delta$ = 0.98 (d, 6 H, $J_{H,P}$ = 7.3 Hz 1.34, $PMe_2$), (s, 9 H, $CMe_3$); 3.42 (s, 2 H, $CH_2S$), 7.00 (3 H, br. m, PPh), 7.27 (2 H, br. m, PPh) ppm. $^{31}P$ NMR ($C_6D_6$): $\delta$ = 3.53 ppm.

**Complex 3c:** Crystallized from $Et_2O$. Yield 90%. $C_{18}H_{24}AuPS$ (500.39): calcd. C 43.21, H 4.83; found C 43.10; H 5.01. $^1H$ NMR ($C_6D_6$): $\delta$ = 1.29 (d, 3 H, PMe), 1.32 (s, 9 H, $CMe_3$); 3.41 (s, 2 H, $CH_2S$); 6.92 (6 H, br. m, PPh); 7.28 (m, 4 H, $PPh_2$) ppm. $^{31}P$ NMR ($C_6D_6$): $\delta$ = 16.64 ppm.

**Complex 3d:** White crystals from toluene at –5 °C. Yield 97%. $C_{23}H_{26}AuPS$ (562.47): calcd. C 49.11, H 4.66; found C 48.93, H 4.8. $^1H$ NMR ($CD_2Cl_2$): $\delta$ = 1.05 (s, 9 H, $CMe_3$), 2.92 (s, 2 H, $SCH_2$), 7.53–7.54 (15 H, br. m, $PPh_3$) ppm. $^1H$ NMR ($C_6D_6$): $\delta$ = 1.31 (s, 9 H, $CMe_3$), 3,40 (s, 2 H, $SCH_2$), 6.88 (m, 9 H, $PPh_3$), 7.29 (6 H, br. m, $PPh_3$) ppm. $^{31}P$ NMR ($CDCl_3$): $\delta$ = 39.26 ppm. $^{31}P$ NMR ($C_6D_6$): $\delta$ = 36.21 ppm.

**Complex 3e:** Crystallized from toluene at –5 °C. Yield 90%. $C_{36}H_{46}P_2S_2Au_2$ (998.77): calcd. C 43.29, H 4.64; found C 43.09, H 4.47. $^1H$ NMR ($CDCl_3$): $\delta$ = 1.07 (s, 18 H, $CMe_3$), 2.71 (s, 4 H, $CH_2S$), 3.02 (s, 4 H, $PCH_2$), 7.29–7.67 (20 H, br. m, $PPh_2$) ppm. $^1H$ NMR ($C_6D_6$): $\delta$ = 1.29 (s, 18 H, $CMe_3$), 2.68 (s, 4 H, $PCH_2$), 3.41(s, 4 H, $CH_2S$), 6.91 (12 H, br. m, $PPh_2$), 7.51 (8 H, br. m, $PPh_2$) ppm. $^{31}P$ NMR ($C_6D_6$): $\delta$ = 37.38 ppm.

**Preparation of $[Au(SCPh_3)]_n$. Method A:** Triphenylmethanethiol (1.076 g, 3.9 mmol) suspended in EtOH (10 mL) was added slowly to a solution of $H[AuCl_4]\cdot xH_2O$ (1.3 mmol) in water (1 mL) and EtOH (5 mL): the mixture was stirred for 3 h and a beige solid was formed. The solid was separated and washed with water (2 × 30 mL), EtOH (20 mL) and $Et_2O$ (20 mL). A beige solid was obtained (0.565 g, 92%). $C_{19}H_{15}AuS$ (472.36): calcd. C 48.31, H 3.20; found C 46.7, H 2.9. Mp: 128° (dec).

**Method B:** Bis(2-hydroxyethyl) sulfide (0.3 mL, 3 mmol) was added dropwise whilst stirring to 0.671 g of a solution of $H[AuCl_4]\cdot xH_2O$

 © 2007 Wiley-VCH Verlag GmbH & Co. KGaA, Weinheim 

(1.0 mmol) in water (10 mL) at 0 °C, causing a precipitate to form. Triphenylmethanethiol (0.276 g, 1 mmol) in $CHCl_3$ (20 mL) was added slowly in ca. 20 min and the reaction mixture stirred for 1 hour giving a grey precipitate. After addition of MeOH (40 mL), the solid was separated, washed with MeOH (2 × 40 mL) and dried (0.40 g, 85%).

**Reaction of $[Au(SCPh_3)]_n$ with L (L = $PMe_3$, $PMe_2Ph$, $PMePh_2$, $PPh_3$, dppe): Formation of $[Au(SCPh_3)(L)]$ (4a, 4b, 4c, 4d, 4e)**

**Complex 4a:** pale yellow crystals. Yield 61%. $C_{21}H_{24}AuPS$ (536.43): calcd. C 46.0, H 4.4; found C 45.7, H 4.2. Mp = 118 °C (dec). $^1H$ NMR ($C_6D_6$): $\delta$ = 0.37 (d, 9 H, $J_{PH}$ = 10.2 Hz, $PMe_3$), 6.8–7.4 (9 H, br. m, $CPh_3$), 8.06 (d, 6 H, $J_{H,H}$ = 7.3 Hz, $CPh_3$) ppm.$^{31}P$ NMR ($C_6D_6$): $\delta$ = 6.41 ppm.

**Complex 4b:** Pale yellow crystals. Yield 46%. $C_{26}H_{26}AuPS$ (598.50): calcd. C 51.1, H 4.3; found C 50.7, H 4.1. $^1H$ NMR ($C_6D_6$): $\delta$ = 0.69 (d, 6 H, $J_{H,P}$ = 9.9 Hz, $PMe_2$), 6.8–8.2 (m, 14 H, $CPh_3$ + PPh), 8.08 (d, 6 H, $J_{H,H}$ = 7.3 Hz, $CPh_3$) ppm. $^{31}P$ NMR ($C_6D_6$): $\delta$ = 40.18 ppm.

**Complex 4c:** Pale yellow microcrystals. Yield 52%. $C_{31}H_{28}AuPS$ (660.57): calcd. C 55.4, H 4.2; found C 55.2, H 4.1. $^1H$ NMR ($C_6D_6$): $\delta$ = 1.07 (d, 3 H, $J_{H,P}$ = 9.2 Hz, PMe), 6.8–8.2 (m, 19 H, $CPh_3$ + $PPh_2$), 8.09 (d, 6 H, $J_{H,H}$ = 7.7 Hz, $CPh_3$) ppm.$^{31}P$ NMR ($C_6D_6$): $\delta$ = 42.07 ppm.

**Complex 4d:** White solid. Yield 71%. $C_{36}H_{30}AuPS$ (722.64): calcd. C 59.0, H 4.1; found C 58.7, H 3.9. Mp = 140 °C (dec). $^1H$ NMR ($C_6D_6$): $\delta$ = 6.8–7.3 (m, 24 H, $PPh_3$ + $CPh_3$), 8.08 (d, 6 H, $J_{H,H}$ = 7.3 Hz, $CPh_3$) ppm. $^{31}P$ NMR ($C_6D_6$): $\delta$ = 48.22 ppm.

**Complex 4e:** Pale yellow microcrystals. Yield 87%. $C_{64}H_{54}Au_2P_2S_2$ (1343.14): calcd. C 57.2, H 4.0; found C 56.8, H 4.2. $^1H$ NMR ($C_6D_6$): $\delta$ = 2.0–2.5 (4 H, br. m, $PCH_2$), 6.8–7.4 (m, 50 H, $PPh_2$ + $CPh_3$), 8.05 (d, 12 H, $J_{H,H}$ = 7.7 Hz, $CPh_3$) ppm. $^{31}P$ NMR ($C_6D_6$): $\delta$ = 42.88 ppm.

**Reaction of $[Au(SCMe_3)(L)]$ (L = $PMe_3$, $PMe_2Ph$, $PMePh_2$, $PPh_3$) with $[FeCp_2][BF_4]$. Formation of $[Au_4(SCMe_3)_2(L)_4][BF_4]_2$ (L = 5a, 5b, 5c, 5d):** The reaction of $[Au(SCMe_3)(PMe_3)]$ with $[FeCp_2][BF_4]$ is reported as an example. $[FeCp_2][BF_4]$ (0.037 g, 0.136 mmol) was added to a solution of $[Au(SCMe_3)(PMe_3)]$ (0.100 g, 0.276 mmol) in dichloromethane (10 mL) and the mixture was stirred for 30 min giving a deep yellow solution. The solvent was evaporated and the solid residue was washed with $Et_2O$ (2 × 10 mL), followed by benzene (10 mL), dried under vacuum and crystallized from dichloromethane at –5 °C as colourless crystals (0.094 g, 94%). $C_{20}H_{54}Au_4B_2F_8P_4S_2$ (1444.15): calcd. C 16.6, H 3.8; found C 16.9, H 3.4. $^1H$ NMR ($CD_3COCD_3$): $\delta$ = 1.60 (s, 18 H, $CMe_3$), 1.83 (d, 36 H, $J_{H,P}$ = 11.7 Hz, $PMe_3$) ppm. $^1H$ NMR ($CD_2Cl_2$): $\delta$ = 1.60 (s, 18 H, $CMe_3$), 1.71 (d, 36 H, $J_{H,P}$ = 11.0 Hz, $PMe_3$) ppm. $^{31}P$ NMR ($CD_2Cl_2$): $\delta$ = 4.58 ppm. ESI-MS (methanol): *m/z* = 635 $[Au_2(SCMe_3)(PMe_3)_2]^+$, 579 $\{[Au_2(SCMe_3)(PMe_3)_2]^+ - C_4H_8\}$, 273 $[Au(PMe_3)]^+$, 87 $[BF_4]^-$. The organic phase was evaporated to dryness giving a solid from which ferrocene sublimates as yellow-orange crystals at 40 °C under high vacuum. $^1H$ NMR ($CD_2Cl_2$): $\delta$ = 4.18 ppm. The white residue was identified as $(SCMe_3)_2$. $^1H$ NMR($CD_2Cl_2$): $\delta$ = 1.31 ppm.

**Complex 5b:** Colourless crystals. Yield 92%. $C_{40}H_{62}Au_4B_2F_8P_4S_2$ (1692.43): calcd. C 28.4, H 3.7; found C 28.1, H 3.5. $^1H$ NMR ($CD_3COCD_3$): $\delta$ = 1.65 (s, 18 H, $CMe_3$); 7.60 (m, 12 H, PPh); 7.95 (m, 8 H, PPh) ppm. $^1H$ NMR ($CD_2Cl_2$): $\delta$ = 1.67 (s, 18 H, $CMe_3$), 1.93 (d, 24 H, $J_{H,P}$ = 11.0 Hz, $PMe_2$), 7.62 (m, 20 H, PPh) ppm. $^{31}P$ NMR ($CD_2Cl_2$): $\delta$ = 15.92 ppm. ESI-MS (methanol): *m/z* = 759 $[Au_2(SCMe_3)(PMe_2Ph)_2]^+$, 703 $\{[Au_2(SCMe_3)(PMe_2Ph)_2]^+ - C_4H_8\}$.

**Complex 5c:** Colourless crystals. Yield 95%. $C_{60}H_{70}Au_4B_2F_8P_4S_2$ (1940.72): calcd. C 37.1, H 3.6; found C 37.4, H 3.7. $^1H$ NMR ($CD_3COCD_3$): $\delta$ = 1.68 (s, 18 H, $CMe_3$), 2.42 (d, 12 H, $J_{H,P}$ = 10,3 Hz, PMe), 7.58 (m, 24 H, PPh), 7.84 (m, 16 H, PPh) ppm. $^1H$ NMR ($CD_2Cl_2$): $\delta$ = 1.67 (s, 18 H, $CMe_2Ph_3$), 2.20 (d, 12 H, $J_{H,P}$ = 10.3 Hz, PMe), 7.52 (40 H, br. m, PPh) ppm. $^{31}P$ NMR ($CD_2Cl_2$): $\delta$ = 27.51 ppm. ESI-MS (methanol): *m/z* = 883 $[Au_2(SCMe_3)(PMePh_2)_2]^+$, 817 $\{[Au_2(SCMe_3)(PMePh_2)_2]^+ - C_4H_8\}$.

**Complex 5d:** Colourless crystals. Yield 96%. $C_{80}H_{78}Au_4B_2F_8P_4S_2$ (2189.00): calcd. C 43.9, H 3.6; found C 43.6, H 3.4. $^1H$ NMR ($CD_3COCD_3$): $\delta$ = 1.70 (s, 9 H, $CMe_3$), 7.62 (15 H, br. m, $PPh_3$) ppm. $^1H$ NMR (200 MHz, $CD_2Cl_2$): $\delta$ = 1.75 (s, 9 H, $CMe_3$), 7.48 (15 H, br. m, $PPh_3$) ppm. $^1H$ NMR ($CD_3OD$): $\delta$ = 1.64 (s, 9 H, $CMe_3$), 7.49 (15 H, br. m, $PPh_3$) ppm. $^{31}P$ NMR ($CD_2Cl_2$): $\delta$ = 43.02 ppm. ESI-MS (methanol): *m/z* = 1007.3 $[Au_2(SCMe_3)(PPh_3)_2]^+$, 87 $[BF_4]^-$.

**Reaction of $[Au(SCH_2CHMe_2)(L)]$ (L = $PMe_3$, $PMe_2Ph$, $PMePh_2$, $PPh_3$) with $[FeCp_2][BF_4]$. Formation of $[Au_4(SCH_2CHMe_2)_2(L)_4][BF_4]_2$ (6a, 6b, 6c, 6d):** Following the above procedure $[Au(SCH_2CHMe_2)(PMe_3)]$ (0.130 g, 0.36 mmol) in $CH_2Cl_2$ (10 mL) was treated with $[FeCp_2][BF_4]$ (0.050 g, 0.18 mmol). The solvent was evaporated under vacuum and the residue was washed with pentane (2 × 30 mL) and benzene (2 × 30 mL). Crystallization from $CH_2Cl_2/Et_2O$ afforded a white solid (0.111 g, 86%). $C_{20}H_{54}Au_4B_2F_8P_4S_2$ (1444.15): calcd. C 16.6, H 3.7; found C 16.5, H 3.7. $^1H$ NMR ($CD_3COCD_3$): $\delta$ = 1.22 (d, 12 H, $J_{H,H}$ = 6.6 Hz, $Me_2$), 1.81 (d, 36 H, $J_{PH}$ = 11.7 Hz, $PMe_3$), 3.17 (d, 4 H, $J_{H,H}$ = 6,6 Hz, $CH_2$) ppm. $^{31}P$ NMR ($CD_3COCD_3$): $\delta$ = 2.80 ppm. ESI (MeOH): *m/z* = 635 $[Au_2(SCH_2CHMe_2)(PMe_3)_2]^+$, 349 $[Au(PMe_3)_2]^+$, 273 $[Au(PMe_3)]^+$. From the hydrocarbon extracts the solvent was evaporated leaving a solid residue, from which ferrocene [$^1H$ NMR ($CD_2Cl_2$): $\delta$ = 4.12 ppm] was obtained by sublimation under vacuum at 40 °C leaving a residue identified as $(SCH_2CHMe_2)_2$ [$^1H$ NMR (200 MHz, $CD_2Cl_2$): $\delta$ = 0.99 (d, 12 H, $J_{H,H}$ = 6.6 Hz, $Me_2$), 1.83 (m, 2 H, $J_{H,H}$ = 6.6 Hz, CH), 2.59 (d, 4 H, $J_{H,H}$ = 6.6 Hz, $CH_2$) ppm].

**Complex 6b:** Off-white crystals. Yield 55%. $C_{40}H_{62}Au_4B_2F_8P_4S_2$ (1692.43): calcd. C 28.4, H 3.7; found C 28.2, H 3.5. $^1H$ NMR ($CD_3COCD_3$): $\delta$ = 1.12 (d, 12 H, $J_{H,H}$ = 6.6 Hz, $Me_2$), 2.06 (d, 24 H, $J_{PH}$ = 11.0 Hz, $PMe_2$), 3.21 (d, 4 H, $J_{H,H}$ = 6.2 Hz, $CH_2$), 7.6–8.0 (20 H, br. m, PPh) ppm. $^{31}P$ NMR ($CD_3COCD_3$): $\delta$ = 14.83 ppm.

**Complex 6c:** Pale yellow solid. Yield 57%. $C_{60}H_{70}Au_4B_2F_8P_4S_2$ (1940.72): calcd. C 37.1, H 3.6; found C 36.8, H 3.4. $^1H$ NMR ($CD_3COCD_3$): $\delta$ = 1.16 (d, 12 H, $J_{H,H}$ = 6.6 Hz, $Me_2$); 3.26 (d, 4 H, $J_{H,H}$ = 6.2 Hz, $CH_2$), 2.39 (d, 12 H, $J_{PH}$ = 10.3 Hz, PMe), 7.2–8.0 (40 H, br. m, $PPh_2$) ppm. $^{31}P$ NMR ($CD_3COCD_3$): $\delta$ = 27.86 ppm.

**Complex 6d:** Grey solid. Yield 79%. $C_{80}H_{78}Au_4B_2F_8P_4S_2$ (2189.00): calcd. C 43.9, H 3.6; found C 43.8, H 3.3. $^1H$ NMR ($CD_3COCD_3$): $\delta$ = 1.06 (d, 12 H, $J_{H,H}$ = 6.2 Hz, $Me_2$), 1.86 (m, 2 H, $J_{H,H}$ = 6.4 Hz, CH), 3.13 (d, 4 H, $J_{H,H}$ = 6.2 Hz, $CH_2$), 7.3–7.8 (60 H, br. m, $PPh_3$) ppm. $^{31}P$ NMR ($CD_3COCD_3$): $\delta$ = 35.00 ppm. ESI-MS (MeOH): *m/z* = 1007 $[Au_2(SCH_2CHMe_2)(PPh_3)_2]^+$, 721 $[Au(PPh_3)_2]^+$, 459 $[Au(PPh_3)]^+$.

**Reaction of $[Au(SCH_2CMe_3)(L)]$ (L = $PMe_3$, $PMe_2Ph$, $PMePh_2$, $PPh_3$) with $[FeCp_2][BF_4]$. Formation of $[Au_4(SCH_2CMe_3)_2(L)_4][BF_4]_2$ (7a, 7b, 7c, 7d)**

**Complex 7a:** crystallized from dichloromethane/n-hexane to give a beige product. Yield 90%. $C_{22}H_{58}Au_4B_2F_8P_4S_2$ (1472.20): calcd. C 17.9, H 4.0; found C 17.7, H 3.8. $^1H$ NMR ($CD_2Cl_2$): $\delta$ = 1.11 (s,

 © 2007 Wiley-VCH Verlag GmbH & Co. KGaA, Weinheim 

18 H, $CMe_3$), 1.69 (d, 36 H, $J_{H,P}$ = 10,8 Hz, $PMe_3$), 3.10 (s, 4 H, $CH_2S$) ppm. $^1$H NMR ($CD_3COCD_3$): $\delta$ = 1.12 (s, 18 H, $CMe_3$), 1.82 (d, 36 H, $J_{H,P}$ = 11.3 Hz, $PMe_3$), 3.19 (s, 4 H, $CH_2S$) ppm. $^{31}$P NMR ($CD_2Cl_2$): $\delta$ = 2.96 ppm. ESI-MS (methanol): *m/z* 649 $[Au_2(SCH_2CMe_3)(PMe_3)_2]^+$, 349.1 $[Au(PMe_3)_2]^+$, 87 $[BF_4]^-$ ppm. From the ethereal phase ferrocene and $(SCH_2CMe_3)_2$ were isolated.

**Complex 7b:** Crystallized as off-white crystals from $CH_2Cl_2$. Yield 86%. $C_{42}H_{66}Au_4B_2F_8P_4S_2$ (1720.49): calcd. C 29.3, H 3.9; found C 29.5, H 4.2. $^1$H NMR ($CD_2Cl_2$): $\delta$ = 1.15 (s, 18 H, $CMe_3$), 1.93 (d, 6 H, $J_{H,P}$ = 12.8 Hz, $PMe_2$), 3.20 (s, 4 H, $CH_2S$), 7.67 (5 H, br. m, PPh) ppm. $^1$H NMR ($CD_3COCD_3$): $\delta$ = 1.12 (s, 18 H, $CMe_3$), 3.22 (s, 4 H, $CH_2S$), 7.63 (3 H, br. m, PPh), 7.94 (2 H, br. m, PPh) ppm. $^{31}$P NMR ($CD_2Cl_2$): $\delta$ = 15.23 ppm.

**Complex 7c:** Crystallized from $CH_2Cl_2$. Yield 82%. $C_{62}H_{74}Au_4B_2F_8P_4S_2$ (1968.77): calcd. C 37.8, H 3.8; found C 37.7, H 3.6. $^1$H NMR ($CD_2Cl_2$): $\delta$ = 1.17 (s, 18 H, $CMe_3$), 2.19 (d, 3 H, $J_{H,P}$ = 9.2 Hz, PMe), 3.26 (s, 4 H, $CH_2S$); 7.60 (10 H, br. m, $PPh_2$) ppm. $^1$H NMR ($CD_3COCD_3$): $\delta$ = 1.14 (s, 18 H, $CMe_3$); 2.41 (s, 3 H, PMe), 3.37 (s, 4 H, $CH_2S$), 7.58 (6 H, br. m, $PPh_2$), 7.84 (4 H, br. m, $PPh_2$) ppm. $^{31}$P NMR ($CD_2Cl_2$): $\delta$ = 28.32 ppm.

**Complex 7d:** Yellow crystals from dichloromethane/hexane. Yield 90%. $C_{82}H_{82}Au_4B_2F_8P_4S_2$ (2217.05): calcd. C 44.4, H 3.7; found C 44.5, H 3.9. $^1$H NMR ($CD_2Cl_2$): $\delta$ = 1.19 (s, 18 H, $CMe_3$), 3.32 (s, 4 H, $CH_2S$), 7.44 (m, 15 H, $PPh_3$) ppm.$^1$H NMR ($CD_3COCD_3$): $\delta$ = 1.16 (s, 18 H, $CMe_3$), 3.46 (s, 4 H, $CH_2S$), 7.51 (m, 15 H, $PPh_3$) ppm. $^{31}$P NMR ($CD_2Cl_2$): $\delta$ = 42.90 ppm.

**Reaction of $[Au_2(SR)_2(dppe)]$ (R = $CMe_3$, $CH_2CHMe_2$, $CH_2CMe_3$) with $[FeCp_2][BF_4]$. Formation of $[Au_4(SR)_2(dppe)_2][BF_4]_2$ (5e, 6e, 7e)**

**Complex 5e:** pale yellow crystals. Yield 93%. $C_{60}H_{66}Au_4B_2F_8P_4S_2$ (1936.69): calcd. C 37.2, H 3.4; found C 36.7, H 3.0. $^1$H NMR ($CD_3COCD_3$): $\delta$ = 1.65 (s, 18 H, $CMe_3$), 3.28 (d, 8 H, $J_{H,P}$ = 13.2 Hz, $PCH_2$), 7.72 (20 H, br. m, $PPh_2$) ppm. $^1$H NMR (200 MHz, $CD_2Cl_2$): $\delta$ = 1.58 (s, 18 H, $CMe_3$), 2.97 (d, 8 H, $J_{H,P}$ = 12.8 Hz, $PCH_2$), 7.60 (20 H, br. m, $PPh_2$) ppm. $^1$H NMR ($CD_3OD$): $\delta$ = 1.57 (s, 18 H, $CMe_3$), 3.04 (d, 8 H, $J_{H,P}$ = 13.2 Hz, $PCH_2$), 7.62 (15 H, br. m, $PPh_2$) ppm. $^{31}$P NMR ($CD_2Cl_2$): $\delta$ = 37.87 ppm. ESI-MS (methanol): *m/z* = 880.9 ($[Au_2(SCMe_3)$-$(dppe)]^+$), 1167 $[Au_3(SCMe_3)_2(dppe)]^+$, 87 $[BF_4]^-$.

**Complex 6e:** Pale grey solid. Yield 82%. $C_{60}H_{66}Au_4B_2F_8P_4S_2$ (1936.69): calcd. C 37.2, H 3.4; found C 36.8, H 3.3. $^1$H NMR ($CD_3COCD_3$): $\delta$ = 1.00 (d, 12 H, $J_{H,H}$ = 6.6 Hz, $Me_2$), 1.84 (m, 2 H, $J_{H,H}$ = 6.6 Hz, CH), 2.84 (d, 4 H, $J_{H,H}$ = 5.9 Hz, $CH_2$), 3.17 (m, 8 H, $PCH_2$), 7.2–8.0 (40 H, br. m, $PPh_2$) ppm. $^{31}$P NMR ($CD_3COCD_3$): $\delta$ = 37.91 ppm.

**Complex 7e:** Clear beige crystals. Yield 89%. $C_{62}H_{70}Au_4B_2F_8P_4S_2$ (1964.74): calcd. C 37.9, H 3.6; found C 38.0, H 4.0. $^1$H NMR ($CD_2Cl_2$): $\delta$ = 1.13 (s, 18 H, $CMe_3$), 2.94 (d, 8 H, $J_{H,P}$ = 12.5 Hz $CH_2P$), 3.36 (s, 4 H, $CH_2S$), 7.50 (20 H, br. m, $PPh_2$) ppm. $^1$H NMR ($CD_3COCD_3$): $\delta$ = 1.10 (s, 18 H, $CMe_3$), 3.15 (d, 8 H, $J_{H,P}$ = 13.2 Hz $CH_2P$), 3.60 (s, 4 H, $CH_2S$), 7.48 (m, 20 H, $PPh_2$) ppm. $^{31}$P NMR ($CD_2Cl_2$): $\delta$ = 39.11 ppm. ESI-MS (methanol): *m/z* = 895 $[Au_2(SCMe_3)(dppe)]^+$, 87 $[BF_4]^-$.

**Reaction of $[Au_4(SC_4H_9)_2(PMe_3)_4][BF_4]_2$ with 2-Methyl-2-propanethiol in the Presence of Ethanolamine:** The reaction was monitored by $^1$H NMR spectroscopy. Two NMR tubes were prepared containing a solution of $[Au_4(SC_4H_9)_2(PMe_3)_4][BF_4]_2$ (0.010 g, 0.0069 mmol) in $CD_2Cl_2$ (0.5 mL) and a solution of 2-methyl-2-propanethiol (0.0138 mmol) and ethanolamine (0.0138 mmol) in $CD_2Cl_2$ (0.5 mL). After recording the NMR spectra of the two samples as a blank the two solutions were added together and after a few minutes the resulting spectra showed the disappearance of the starting products and the presence of the signals of pure $[Au(SC_4H_9)(PMe_3)]$.

**[Au(Me)(PMe$_3$)]:** LiMe (0.3 mL of a 1.6 M solution in $Et_2O$, 0.5 mmol) was added to a suspension of $[Au(Cl)(PMe_3)]$ (0.150 g, 0.5 mmol) in $Et_2O$ (10 mL) and kept at –10 °C. The solution became yellow, then returned slowly to colourless. The reaction mixture was kept for 30 min at –10 °C and then for 2 h at room temperature. The mixture was cooled to 0 °C and was hydrolyzed with $H_2O$ (10 mL). The ethereal phase was separated, desiccated over anhydrous sodium sulfate and the solvents evaporated to dryness under vacuum. A light grey solid was recovered (0.094 g, 65%), which was stored away from the light. $C_4H_{12}AuP$ (288.08): calcd. C 16.68, H 4.20; found C 16.49, H 4.05. $^1$H NMR ($C_6D_6$): $\delta$ = 0.55 (9 H, d, $J_{H,P}$ = 8.4 Hz, $PMe_3$), 1.26 (3 H, d, $J_{H,H}$ = 8.4 Hz, $CH_3$) ppm. $^{31}$P NMR ($C_6D_6$): $\delta$ = 12.35 ppm.

**[Au(CH$_2$CMe$_3$)(PMe$_3$)]:** $Li(CH_2CMe_3)$ (0.038 g, 0.49 mmol) was added to a suspension of $[Au(Cl)(PMe_3)]$ (0.150 g, 0.49 mmol) in diethyl ether (15 mL) and the reaction was carried out as above. The mixture was then hydrolyzed with water (10 mL), the organic phase was dried with $Na_2SO_4$, concentrated and kept overnight at –20 °C. A white solid was obtained (0.149 g, 89%). $C_8H_{20}AuP$ (344.19): calcd. C 27.92, H 5.86; found C 27.65, H 5.90. $^1$H NMR ($C_6D_6$): $\delta$ = 0.53 (d, 9 H, $J_{H,P}$ = 8.8 Hz, $PMe_3$), 1.55 (s, 9 H, $CH_3$), 2.10 (d, 2 H, $J_{H,H}$ = 8.8 Hz, $CH_2$) ppm. $^1$H NMR ($CD_2Cl_2$): $\delta$ = 1.01 (s, 9 H, $CH_3$), 1.23 (d, 2 H, $J_{H,H}$ = 8.4 Hz, $CH_2$), 1.41 (d, 9 H, $J_{H,P}$ = 8.4 Hz, $PMe_3$) ppm. $^{31}$P NMR ($C_6D_6$): $\delta$ = 13.16 ppm.

**Reaction of $[Au_4(SCMe_3)_2(PMe_3)_4][BF_4]_2$ with Methyllithium. Formation of [Au(SCMe$_3$)(PMe$_3$)] and [Au(Me)(PMe$_3$)]:** A large excess of LiMe (0.5 mL of a 1.6 M solution in $Et_2O$, 0.8 mmol), was added to a solution of $[Au_4(SCH_2CHMe_2)_2(PMe_3)_4][BF_4]_2$ (0.052 g, 0.04 mmol) in $CH_2Cl_2$ (15 mL). A white precipitate formed immediately. The mixture was stirred for 2 h, and then water (10 mL) was added. The organic layer was separated, desiccated over anhydrous sodium sulfate, and was then evaporated to dryness to leave a light yellow solid showing NMR spectra that are the sum of of both the signals of $[Au(SCMe_3)(PMe_3)]$ and $[Au(Me)(PMe_3)]$. $^1$H NMR ($C_6D_6$): $\delta$ = 0.62 (d, 9 H, $J_{P,H}$ = 8.8 Hz, $[Au(Me)PMe_3]$, 1.20 (d, 3 H, $J_{H,H}$ = 8.4 Hz, $CH_3$) $[Au(Me)(PMe_3)]$, 1.48 (s, 9 H, $SCMe_3$), 1.57 (d, 9 H, $J_{H,P}$ = 10.3 Hz, $SAuPMe_3$) ppm. $^{31}$P NMR ($C_6D_6$): $\delta$ = 10.74 ($[Au(Me)(PMe_3)]$), 2.95 ($[Au(SCMe_3)(PMe_3)]$) ppm.

**Reaction of $[Au_4(SCMe_3)_2(PMe_3)_4][BF_4]_2$ with Neopentyllithium. Formation of [Au(SCMe$_3$)(PMe$_3$)] and [Au(CH$_2$CMe$_3$)(PMe$_3$)]:** Solid $LiCH_2CMe_3$ (0.004 g, 0.05 mmol) was added to a solution of $[Au_4(SCMe_3)_2(PMe_3)_4][BF_4]_2$ (0.034 g, 0.025 mmol) in $CH_2Cl_2$ (15 mL) kept at –20 °C. The mixture was warmed to room temperature. After stirring for 2 h water (10 mL) was added dropwise, the organic phase was separated, dried with anhydrous sodium sulfate and the solvents evaporated to dryness to give a light yellow solid whose NMR spectra show both the signals of $[Au(SCMe_3)(PMe_3)]$ and $[Au(CH_2CMe_3)(PMe_3)]$. $^1$H NMR ($CD_2Cl_2$): $\delta$ = 1.01 (s, 9 H, $CCMe_3$), 1.23 (d, 2 H, $J_{H,H}$ = 8.8 Hz, $CH_2$), 1.41 (d, 9 H, $J_{H,P}$ = 8.4 Hz, $CAuPMe_3$), 1.48 (s, 9 H, $SCMe_3$), 1.57 (d, 9 H, $J_{H,P}$ = 10.3 Hz, $SAuPMe_3$) ppm. $^{31}$P NMR ($CD_2Cl_2$): $\delta$ = 2.95 ($[Au(SCMe_3)(PMe_3)]$); 16.58 ($[Au(CH_2CMe_3)(PMe_3)]$) ppm.

**X-ray Diffraction:** Crystals of **1c**, **1e** and **3d** were obtained by cooling toluene solutions, and **5e** and **7a** were obtained from dichloromethane/pentane solutions. The X-ray diffraction experiments were carried out at room temperature ($T$ = 293 K) by means of a Bruker P4 diffractometer by operating with a graphite-monochromated Mo-$K_\alpha$ radiation. The samples were sealed in glass capillaries under an atmosphere of dinitrogen. The intensity data collection was car-

 © 2007 Wiley-VCH Verlag GmbH & Co. KGaA, Weinheim 

Table 5. Crystal data and structure refinements.

| | **1c** | **1e**·diethyl ether | **3d** | **5e**·$CH_2Cl_2$ | **7a** |
|---|---|---|---|---|---|
| Empirical formula | $C_{17}H_{22}AuPS$ | $C_{38}H_{52}Au_2OP_2S_2$ | $C_{23}H_{26}AuPS$ | $C_{61}H_{68}Au_4B_2Cl_2F_8P_4S_2$ | $C_{22}H_{58}Au_4B_2F_8P_4S_2$ |
| Formula mass [g mol$^{-1}$] | 486.34 | 1044.79 | 562.43 | 2021.54 | 1472.17 |
| Crystal system | triclinic | triclinic | monoclinic | monoclinic | orthorhombic |
| Space group | $P\bar{1}$ (No. 2) | $P\bar{1}$ (No. 2) | $P2_1/n$ (No. 14) | $C2/c$ (No. 15) | *Pnnm* (No. 58) |
| $a$ [Å] | 7.881(1) | 8.986(2) | 12.896(2) | 23.652(4) | 10.320(1) |
| $b$ [Å] | 11.149(1) | 10.837(1) | 14.001(3) | 17.030(2) | 10.511(1) |
| $c$ [Å] | 12.122(1) | 11.449(2) | 12.958(2) | 19.806(3) | 20.637(2) |
| $\alpha$ [°] | 106.701(7) | 94.423(9) | – | – | – |
| $\beta$ [°] | 105.168(9) | 90.51(1) | 109.43(1) | 121.96(1) | – |
| $\gamma$ [°] | 106.092(9) | 109.33(1) | – | – | – |
| $V$ [Å$^3$] | 910.3(2) | 1048.2(3) | 2206.4(7) | 6768.4(17) | 2238.6(4) |
| $Z$ | 2 | 1 | 4 | 4 | 2 |
| $D_{calc}$ [Mg m$^{-3}$] | 1.774 | 1.655 | 1.693 | 1.984 | 2.184 |
| $\mu$ [mm$^{-1}$] | 8.272 | 7.192 | 6.839 | 8.937 | 13.349 |
| No. measured | 4082 | 4700 | 4834 | 7672 | 3107 |
| No. unique [$R_{int}$] | 3306 [0.0431] | 3897 [0.0313] | 3982 [0.0496] | 6654 [0.0694] | 2382 [0.0570] |
| No. parameters | 185 | 195 | 236 | 343 | 73 |
| $R_1$, $wR_2$ [$I > 2\sigma(I)$][a] | 0.0305, 0.0696 | 0.0436, 0.1042 | 0.0510, 0.1077 | 0.0662, 0.1199 | 0.0565, 0.1196 |
| $R_1$, $wR_2$ [all data][a] | 0.0386, 0.0729 | 0.0687, 0.1147 | 0.0976, 0.1268 | 0.1619, 0.1533 | 0.1194, 0.1454 |
| Goodness of fit[a] on $F^2$ | 1.042 | 1.071 | 1.012 | 0.979 | 1.003 |

[a] $R(F_o) = \Sigma||F_o| - |F_c||/\Sigma|F_o|$; $Rw(F_o^2) = \{\Sigma[w(F_o^2 - F_c^2)^2]/\Sigma[w(F_o^2)^2]\}^{1/2}$; $w = 1/[\sigma^2(F_o^2) + (AQ)^2 + BQ]$ where $Q = [MAX(F_o^2,0) + 2F_c^2]/3$; GOF = $\{\Sigma[w(F_o^2 - F_c^2)^2]/(N - P)\}1/2$, where $N$, $P$ are the numbers of observations and parameters, respectively.

ried out with the $\omega/2\theta$ scan mode, collecting a redundant set of data. Three standard reflections were measured every 97 measurements to for check sample decay. The intensities were corrected for Lorentz and polarization effects and for absorption. In the case of **1e** and **7a** the absorption correction was made by means of an integration method based on the crystal habit.[22] For **1e**, **3d** and **5e**, the crystal fragments used in the data collection were rather irregular, therefore a precise numerical correction was impossible and a semi-empirical method was used.[22] The structure solutions were obtained by means of the automatic direct methods contained in the SHELXS97 program.[23] The refinement, based on full-matrix least-squares on $F^2$, were done by means of the SHELXL97 program.[22] Some other utilities contained in the WINGX suite were also used.[24] The more relevant crystal parameters are listed in Table 1.

The asymmetric unit of compound **1c** consists of one molecule [Au(S*t*Bu)($PMePh_2$)]. The hydrogen atoms were placed in calculated positions and during the refinement were allowed to "ride" on the connected carbon atoms. In the last of the refinement cycles all the heavy atoms were refined with anisotropic thermal parameters obtaining the reliability factors listed in Table 5.

The asymmetric unit of compound **1e** consists of one half of the molecule [$Au_2$(S*t*Bu)$_2$(dppe)] riding the inversion centre. A series of maxima around another inversion centre was interpreted as a disordered ethyl ether molecule. The maxima were fitted with the positional parameters of a well-refined ethyl ether molecule from the literature and were refined as a rigid group with isotropic thermal parameters. The hydrogen atoms were placed in calculated positions and anisotropic thermal parameters were used for the heavy atoms of the main molecule. The reliability factors obtained in the last refinement cycle are listed in Table 5.

The asymmetric unit of compound **3d** consists of one molecule [Au($SCH_2t$Bu)($PPh_3$)]. The hydrogen atoms were placed in calculated positions and during the refinement were allowed to "ride" on the connected carbon atoms. In the last of the refinement cycles all the heavy atoms were refined with anisotropic thermal parameters thus obtaining the reliability factors listed in Table 5.

The asymmetric unit of compound **5e** is made up of one half of the cation $[Au_4(StBu)_2(dppe)_2]^{2+}$ located on the twofold axis, one half of a dichloromethane molecule similarly located on the twofold axis and one $BF_4^-$ anion. The $BF_4^-$ anion presents a remarkable disorder and was refined as a rigid group distributed on two limit positions with variable occupancy, fixing the total occupancy to 1.0. The hydrogen atoms were placed in calculated positions and were allowed to "ride" on the connected carbon atoms. Anisotropic thermal parameters were used for all the heavy atoms, excluding those of the disordered anion. The reliability factors obtained in the last refinement cycle are listed in Table 5.

The asymmetric unit of compound **7a** is made up of one fourth of the cation $[Au_4(SCH_2tBu)_2(PMe_3)_4]^{2+}$, with 2/*m* symmetry and one $BF_4^-$ anion located on the twofold axis. Both the $-PMe_3$ group and the anion present a remarkable disorder. The $-PMe_3$ group was refined as a rigid group distributed, with different occupancy, on two positions related by rotation around the Au–P bond; the occupancies were refined fixing the total occupancy to 1.0. The disorder of the tetrahedral anion was instead due to a misalignment between the twofold axis of the crystal and the corresponding operator of the group. The $BF_4^-$ unit was therefore simply introduced in the model with occupancy 1/2. The hydrogen atoms were placed in calculated positions and were allowed to "ride" on the connected carbon atoms. Anisotropic thermal parameters were used for all the heavy atoms, excluding those of the disordered groups. The reliability factors obtained in the last refinement cycle are listed in Table 5.

CCDC-603883 (for **1c**), -603884 (for **1e**), -603885 (for **3d**), -603886 (for **5e**) and -603887 (for **7a**) contain the supplementary crystallographic data for this paper. These data can be obtained free of charge from The Cambridge Crystallographic Data Centre via www.ccdc.cam.ac.uk/data_request/cif.

**Supporting Information** (see also the footnote on the first page of this article): Additional figures for compounds **1c**, **1e**, **3d**, **5e** and **7a** (crystal structure, cyclic voltammogram) and a table relating electrochemical behaviour and the inductive electronic effects of the ligands are available.

 © 2007 Wiley-VCH Verlag GmbH & Co. KGaA, Weinheim 

## Acknowledgments

We thank Ceramvetro (Florence) for the generous gift of gold. P. Zanello gratefully acknowledges the financial support of the Università di Siena (PAR 2005).

[1] a) A. N. Papazian, *Gold. Bull. (London)* **1982**, *15*, 81; b) P. T. Bishop, *Gold Bull. (London)* **2002**, *35*, 89.
[2] a) D. T. Walz, M. J. DeMartin, L. W. Chakrin, B. M. Sutton, A. Misher, *J. Pharmacol. Exp. Ther.* **1976**, *197*, 1; b) C. F. Shaw III, *Chem. Rev.* **1999**, *99*, 2589; c) S. P. Fricker, in *The Chemistry of Organic Derivatives of Gold and Silver* (Eds.: S. Patai, Z. Rappoport), John Wiley & Sons: Chichester, **1999**; p. 641; d) E. R. T. Tiekink, *Gold Bull. (London)* **2003**, *36*, 117.
[3] a) J. Chen, T. Jiang, G. Wei, A. A. Mohamed, C. Homrighausen, J. A. Krause Bauer, A. E. Bruce, M. R. M. Bruce, *J. Am. Chem. Soc.* **1999**, *121*, 9225; b) A. A. Mohamed, A. E. Bruce, M. R. M. Bruce, *Met.-Based Drugs* **1999**, *6*, 233; c) A. A. Mohamed, H. E. Abdou, J. Chen, A. E. Bruce, M. R. M. Bruce, *Comments Inorg. Chem.* **2002**, *23*, 321; d) A. A. Mohamed, J. Chen, A. E. Bruce, M. R. M. Bruce, J. A. Krause Bauer, D. T. Hill, *Inorg. Chem.* **2003**, *42*, 2203; e) J. Chen, A. A. Mohamed, H. E. Abdou, J. A. Krause Bauer, J. P. Fackler Jr, A. E. Bruce, M. R. M. Bruce, *Chem. Commun.* **2005**, 1575.
[4] a) C. Kowala, J. M. Swan, *Aust. J. Chem.* **1966**, *19*, 547; b) G. A. Bowmaker, B. C. Dobson, *J. Chem. Soc.* **1981**, 267; c) A. K. Al-Sa′ady, K. Moss, C. A. McAuliffe, R. V. Parish, *J. Chem. Soc., Dalton Trans.* **1984**, 1609; d) E. Delgado, E. Hernandez, *Polyhedron* **1992**, *11*, 3135; e) R. Narayanaswamy, M. A. Young, E. Parkhurst, M. Ouellette, M. E. Kerr, D. M. Ho, R. C. Elder, A. E. Bruce, M. R. M. Bruce, *Inorg. Chem.* **1993**, *32*, 2506; f) P. J. Bonasia, D. E. Gindelberg, J. Arnold, *Inorg. Chem.* **1993**, *32*, 5126; g) J. M. Forward, D. Bohmann, J. P. Fackler Jr, R. Staples, *J. Inorg. Chem.* **1995**, *34*, 6330; h) W. B. Jones, J. Yuan, R. Narayanaswamy, M. A. Young, R. C. Elder, A. E. Bruce, M. R. M. Bruce, *Inorg. Chem.* **1995**, *34*, 1996; i) A. Sladek, H. Schmidbaur, *J. Chem. Soc., Chem. Commun.* **1995**, 907; j) P. Bishop, P. Marsh, A. K. Brisdon, B. J. Brisdon, M. F. Mahon, *J. Chem. Soc., Dalton Trans.* **1998**, 675; k) M. R. Wiseman, P. A. Marsh, P. T. Bishop, B. J. Brisdon, M. F. Mahon, *J. Am. Chem. Soc.* **2000**, *122*, 12598.
[5] a) H. M. Fitch US patent US 2,994,614 (**1961**); b) H. M. Fitch US patent US 2,984,575 (**1961**); c) H. M. Fitch, US patent US 3,163,665 (**1964**).
[6] a) E. Coates, C. Kowala, J. M. Swan, *Aust. J. Chem.* **1966**, *19*, 539; b) M. Nakamoto, W. Hiller, H. Schmidbaur, *Chem. Ber.* **1993**, *126*, 605; c) M. C. Gimeno, P. G. Jones, A. Laguna, M. Laguna, R. Terroba, *Inorg. Chem.* **1994**, *33*, 3932; d) J. M. Forward, D. Bohmann, J. P. Fackler Jr, R. J. Staples, *Inorg. Chem.* **1995**, *34*, 6330; e) A. Sladek, K. Angermaier, H. Schmidbaur, *Chem. Commun.* **1996**, 1959; f) L. S. Ahmed, W. Clegg, D. A. Davies, J. R. Dilworth, M. R. J. Elsegood, *Polyhedron* **1999**, *18*, 593.
[7] a) J. W. Faamau, E. R. T. Tiekink, *J. Coord. Chem.* **1994**, *31*, 93; b) M. Mar Artigas, O. Crespo, M. Concepcion Gimeno, P. G. Jones, A. Laguna, M. D. Villacampa, *J. Organomet. Chem.* **1998**, *561*, 1; c) B.-C. Tzeng, A. Schier, H. Schmidbaur, *Inorg. Chem.* **1999**, *38*, 3978; d) D. R. Smyth, B. R. Vincent, E. R. T. Tiekink, *CrystEngCommun.* **2000**, *2*, 115; e) D. R. Smyth, E. R. T. Tiekink, *Z. Kristallogr. - New Cryst. Struct.* **2002**, *217*, 361; f) S. Onaka, M. Yaguchi, R. Yamauchi, T. Ozeki, M. Ito, T. Sunahara, Y. Sugiura, M. Shiotsuka, K. Nunokawa, M. Horibe, K. Okazaki, A. Iida, H. Chiba, K. Inoue, H. Imai, K. Sako, *J. Organomet. Chem.* **2005**, *690*, 57.
[8] W. J. Hunks, M. C. Jennings, R. J. Puddephatt, *Inorg. Chem.* **2002**, *41*, 4590.
[9] a) P. Bishop, P. Marsh, A. K. Brisdon, B. J. Brisdon, M. F. Mahon, *J. Chem. Soc., Dalton Trans.* **1998**, 675; b) M. Bardaji, A. Laguna, M. R. Perez, P. G. Jones, *Organometallics* **2002**, *21*, 1877.
[10] a) F. Scherbaum, A. Grohmann, B. Huber, C. Krüger, H. Schmidbaur, *Angew. Chem. Int. Ed. Engl.* **1988**, *27*, 1602; b) H. Schmidbaur, *Gold Bull.* **1990**, *23*, 11; c) H. Schmidbaur, *Chem. Soc. Rev. (London)* **1995**, *24*, 391; d) H. Schmidbaur, *Gold Bull.* **2000**, *33*, 3.
[11] A. A. Mohamed, A. E. Bruce, M. R. M. Bruce, in *The Chemistry of Organic Derivatives of Gold and Silver* (Eds.: S. Patai, Z. Rappoport); John Wiley & Sons: Chichester, **1999**; p. 313.
[12] C. Hansch, A. Leo, R. W. Taft, *Chem. Rev.* **1991**, *91*, 165.
[13] a) E. R. Brown, J. R. Sandifer, in *Physical Methods of Chemistry: Electrochemical Methods*, vol. 2 (Eds.: B. W. Rossiter, J. F. Hamilton); John Wiley & Sons: New York, **1986**; (chap. 4); b) P. Zanello, *Inorganic Electrochemistry. Theory, Practice and Application* RSC: Cambridge, U. K., **2003**.
[14] A. Sladek, W. Schneider, K. Angermaier, A. Bauer, H. Schmidbaur, *Z. Naturforsch., B: Chem. Sci.* **1996**, *51b*, 765.
[15] A. Sladek, H. Schmidbaur, *Chem. Ber.* **1995**, *128*, 907.
[16] a) D. A. Edwards, R. M. Harker, M. F. Mahon, K. C. Molloy, *J. Chem. Soc., Dalton Trans.* **1997**, 3509; b) C. W. Liu, B.-J. Liaw, J.-C. Wang, T.-C. Keng, *Inorg. Chem.* **2000**, *39*, 1329; c) Y. Situ, S.-B. Huang, J.-G. Zhang, *Wuji Huaxue Xuebao (Chin.) (Chin. J. Inorg. Chem.)* **2003**, *19*, 983; d) J. Lisowski, P. Starynowicz, A. Jezierski, Z. Siatecki, *Polyhedron* **1996**, *15*, 3589; e) M. H. Chisholm, J. C. Huffman, C. C. Kirkpatrick, J. Leonelli, K. Folting, *J. Am. Chem. Soc.* **1981**, *103*, 6093; f) E. Babaian-Kibala, F. A. Cotton, *Inorg. Chim. Acta* **1991**, *182*, 77.
[17] a) H. Schmidbaur, A. Shiotani, *Chem. Ber.* **1971**, *104*, 2831; b) C. F. Shaw, R. S. Tobias, *Inorg. Chem.* **1973**, *12*, 965.
[18] H. Schmidbaur, A. Shiotani, *Chem. Ber.* **1971**, *104*, 2821.
[19] M. Preisenberger, A. Schier, H. Schmidbaur, *J. Chem. Soc., Dalton Trans.* **1999**, 1645.
[20] L. Messori, F. Abbate, G. Marcon, P. Orioli, M. Fontani, E. Mini, T. Mazzei, S. Carotti, T. O'Donnell, P. Zanello, *J. Med. Chem.* **2000**, *43*, 3541.
[21] A. Courtin, H.-R. von Tobel, G. Auerbach, *Helv. Chim. Acta* **1980**, *63*, 1412.
[22] G. M. Sheldrick, *SHELXTL-Plus*, Rel. 5.1, Bruker AXS Inc., Madison, Wisconsin, USA, **1997**.
[23] G. M. Sheldrick, *SHELX97, Programs for Crystal Structure Analysis* (Release 97-2), University of Göttingen, Göttingen, Germany, **1998**.
[24] L. J. Farrugia, *J. Appl. Crystallogr.* **1999**, *32*, 837.

Received: October 4, 2006
Published Online: January 12, 2007

 © 2007 Wiley-VCH Verlag GmbH & Co. KGaA, Weinheim 

DOI: 10.1002/ejic.200600947

# Bis(phosphinimino)methanides as Ligands in Divalent Samarium Chemistry: Synthesis, Structures and Catalysis

**Michal Wiecko,[a] Peter W. Roesky,*[a] Vladimir V. Burlakov,[b] and Anke Spannenberg*[b]**

**Keywords:** Catalysis / Caprolactone / N,P ligands / Polymerization / Samarium

The reaction of $K\{CH(PPh_2NSiMe_3)_2\}$ with samarium diiodide in a 1:1 molar ratio in thf affords the corresponding divalent samarium complex $[\{(Me_3SiNPPh_2)_2CH\}Sm(\mu\text{-}I)(thf)]_2$ (**1**), whereas treatment of $K\{CH(PPh_2NSiMe_3)_2\}$ with samarium diiodide in a 2:1 molar ratio in thf gives the homoleptic complex $[\{(Me_3SiNPPh_2)_2CH\}_2Sm]$ (**2**). When **1** is treated with $KNPh_2$ in toluene in a 2:1 molar ratio the mixed dimeric compound $[(\{(Me_3SiNPPh_2)CH\}_2Sm)_2(\mu\text{-}I)(\mu\text{-}NPh_2)]$ (**3**) is obtained. The single-crystal X-ray structures of all these complexes have been determined. $[\{(Me_3SiNPPh_2)_2CH\}Sm(\mu\text{-}I)(thf)]_2$ has also been successfully used as a catalyst for the polymerization of ε-caprolactone. Good activities and molecular masses are observed with this catalyst.

(© Wiley-VCH Verlag GmbH & Co. KGaA, 69451 Weinheim, Germany, 2007)

## Introduction

Over the past decade lanthanide reagents have become more and more recognized as useful reagents in organic synthesis.[1,2] Of the low-valent lanthanides, samarium has found the most widespread application.[3] In this context, the mild reducing agent $SmI_2$, introduced by Kagan and co-workers in the late 1970s, is still receiving much interest today.[4] Kagan showed that $SmI_2$ promotes the reduction of halides, aldehydes, ketones, and carboxylic acids, and reductive eliminations and deoxygenations. Although the use of other metals such as Yb, Eu, Tm, and Dy has been reported, $SmI_2$ has turned out to be the most versatile reagent with respect to the ease of preparation concomitant with a high redox potential. On the other hand, it is often necessary to enhance the reactivity by adding various salts and co-solvents such as the carcinogenic HMPTA. Other divalent samarium reagents such as $[(\eta^5\text{-}C_5H_5)_2Sm]$,[5] $SmBr_2$,[6] and $[Sm\{N(SiMe_3)_2\}_2(thf)_2]$[7] have also been used, although less frequently.

Beside $SmI_2$, the reactivity of the divalent samarocene $[(\eta^5\text{-}C_5Me_5)_2Sm(thf)_2]$[8] toward organic compounds has been extensively investigated by Evans and co-workers,[9,10] and it has also been shown that $[(\eta^5\text{-}C_5Me_5)_2Sm(thf)_2]$ is an active polymerization system for ε-caprolactone that maintains its activity after all of the initial batch of monomer is consumed.[11] An ε-caprolactone polymerization activity has also been observed for $[(\eta^5\text{-}C_5H_5)_2Sm]$,[12] $SmBr_2$, and $[(\eta^5\text{-indenyl})_2Yb(thf)_2]$.[13] In this context, Yasuda and co-workers have investigated the efficiency of divalent lanthanide complexes such as $[(\eta^5\text{-}C_5Me_5)_2Yb(thf)_2]$, $[(\eta^5\text{-}C_5Me_5)_2Sm(thf)_2]$, and $[(\eta^5\text{-indenyl})_2Yb(thf)_2]$ as catalysts for the polymerization of methyl methacrylate (MMA).[14] Although the living polymerization of MMA is initiated by these complexes, their initiator efficiencies are much smaller than those obtained by organolanthanide(III) complexes.

Based on these results, we became interested in the synthesis of new samarium(II) complexes and their application as catalysts in the polymerization of polar monomers. Recently, we introduced the monoanionic bis(phosphinimino)methanide $\{CH(PPh_2NSiMe_3)_2\}^-$ as a versatile ligand in di- and trivalent lanthanide chemistry. We have previously reported the synthesis of a series of bis(phosphinimino)methanide dichloride complexes of trivalent lanthanides, namely $[\{CH(PPh_2NSiMe_3)_2\}LnCl_2]_2$ (Ln = Y, Sm, Dy, Er, Yb, Lu).[15] These compounds were obtained by the reaction of $K\{CH(PPh_2NSiMe_3)_2\}$[16] with the corresponding yttrium or lanthanide trichloride. Further reactions of $[\{CH(PPh_2NSiMe_3)_2\}LnCl_2]_2$ have led to the corresponding amido complexes $[\{CH(PPh_2NSiMe_3)_2\}Ln(NPh_2)_2]$ (Ln = Y, Sm),[15] diphosphanylamido complexes $[\{CH(PPh_2NSiMe_3)_2\}Ln\{(Ph_2P)_2N\}Cl]$ (Ln = Y, La, Nd, Yb),[17] cyclopentadienido complexes $[\{CH(PPh_2NSiMe_3)_2\}Ln(\eta^5\text{-}C_5H_5)_2]$ (Ln = Y, Sm, Er),[18] and cyclooctatetraene complexes $[\{CH(PPh_2NSiMe_3)_2\}Ln(\eta^8\text{-}C_8H_8)]$ (Ln = Y, Sm, Er, Yb, Lu).[19] These derivatives have been used as homogeneous catalysts for a number of different catalytic applications. Thus, the complexes $[\{CH(PPh_2NSiMe_3)_2\}Ln\{(Ph_2P)_2N\}Cl]$ are active catalysts for the ring-opening polymerization of ε-caprolactone and the polymerization of MMA.[17]

In divalent lanthanide chemistry we have synthesized bis(phosphinimino)methanide complexes of composition $[\{(Me_3SiNPPh_2)_2CH\}Eu(\mu\text{-}I)(thf)]_2$ and $[\{(Me_3SiNPPh_2)_2$-

[a] Institut für Chemie und Biochemie, Freie Universität Berlin
Fabeckstraße 34-36, 14195 Berlin, Germany
[b] Leibniz-Institut für Katalyse e.V. an der Universität Rostock
Albert-Einstein-Straße 29a, 18059 Rostock, Germany

 InterScience © 2007 Wiley-VCH Verlag GmbH & Co. KGaA, Weinheim 

CH}YbI(thf)$_2$] by salt metathesis reactions from K{CH(PPh$_2$NSiMe$_3$)$_2$} and LnI$_2$.[20] Further reaction of these complexes with [K(thf)$_n$N(PPh$_2$)$_2$] has led selectively to the heteroleptic amido complexes [{(Me$_3$SiNPPh$_2$)$_2$CH}-Ln{(Ph$_2$P)$_2$N}(thf)] (Ln = Eu, Yb). The ytterbium complex can also be obtained by reduction of [{CH(PPh$_2$NSiMe$_3$)$_2$}-Yb{(Ph$_2$P)$_2$N}Cl]. So far the {CH(PPh$_2$NSiMe$_3$)$_2$}$^-$ ligand has not been used in the more redox-sensitive chemistry of samarium(II). Only the homoleptic samarium(II) complex [{CH(PPh$_2$NC$_6$H$_2$-2,4,6-Me$_3$)$_2$}$_2$Sm] of the related *N*-mesityl-substituted bis(phosphinimino)methanide has been reported recently by Hill and co-workers.[21] We report here on the synthesis of three bis(phosphinimino)methanide complexes of divalent samarium and their application in ε-caprolactone polymerization.

## Results and Discussion

### Synthesis and Structures

Reaction of K{CH(PPh$_2$NSiMe$_3$)$_2$} with samarium diiodide in a 1:1 molar ratio in thf afforded the corresponding divalent samarium complex [{(Me$_3$SiNPPh$_2$)$_2$CH}Sm(μ-I)(thf)]$_2$ (**1**) as crystals in good yields (Scheme 1).[22] The potassium reagent K{CH(PPh$_2$NSiMe$_3$)$_2$}, which was described earlier,[16] was used as starting material to avoid coordination of lighter alkali halides such as lithium chloride. The new complex was characterized by standard analytical and spectroscopic techniques, and its solid-state structure was established by single-crystal X-ray diffraction. The signals in the NMR spectra are broadened due to the presence of the paramagnetic metal. The signal of the SiMe$_3$ groups ($\delta$ = –0.16 ppm) is in the expected range. A similar shift is observed for the diamagnetic divalent complex [{(Me$_3$SiNPPh$_2$)$_2$CH}YbI(thf)$_2$] ($\delta$ = 0.44 ppm). The signal of the methine proton in the $^1$H NMR spectrum could not be clearly assigned, and those of the phenyl protons ($\delta$ = 7.05–7.70 ppm) are uncharacteristically broadened.

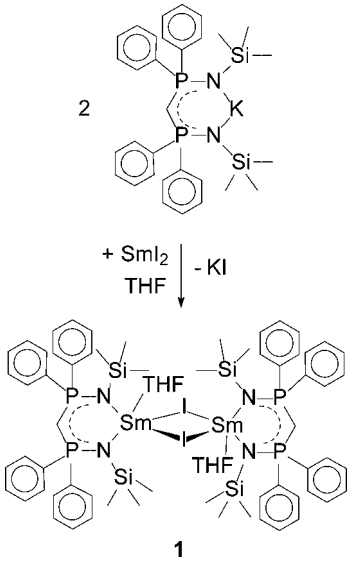


Scheme 1.

The solid-state structure of **1** is isostructural to the previously reported europium compound [{(Me$_3$SiNPPh$_2$)$_2$-CH}Eu(μ-I)(thf)]$_2$.[20] In **1**, which crystallizes in the monoclinic space group $P2_1/c$ the metal centers of the dimeric complexes are asymmetrically bridged by two iodine atoms [Sm–I 332.14(4) and Sm–I′ 335.74(4) pm; Figure 1]. A crystallographic inversion center is observed in the center of the Sm–I–Sm′–I′ plane. The bis(phosphinimino)methanide ligand forms a six-membered metallacycle (N1–P1–C1–P2–N2–Sm) by chelation of the two trimethylsilylimine groups to the lanthanide metal. The Sm–N distances [Sm–N1 259.2(3) and Sm–N2 256.3(3) pm] show an almost symmetrical attachment of the ligand to the metal center. The metallacycle adopts a twist-boat conformation in which the central carbon atom and the samarium atom are displaced from the N$_2$P$_2$ least-squares plane. As shown earlier, this displacement depends on the metal center and also on the packing in the solid state.[17]

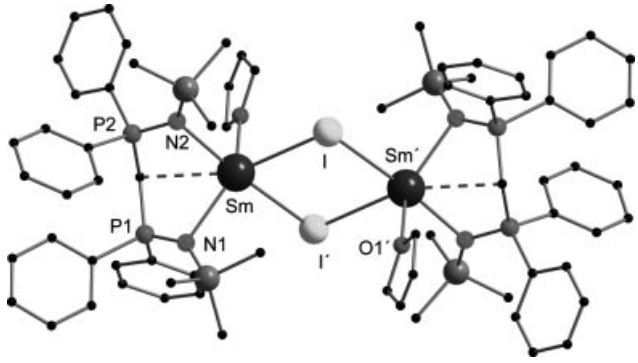


Figure 1. Solid-state structure of **1** showing the atom-labeling scheme. Hydrogen atoms have been omitted. Selected bond lengths [pm] and angles [°]: Sm–N1 259.2(3), Sm–N2 256.3(3), Sm–C1 297.7(4), Sm–I 332.14(4), Sm–I′ 335.74(4), Sm–O1 250.4(3), P1–N1 157.9(3), P2–N2 158.7(3); N1–Sm–N2 90.66(10), N1–Sm–C1 57.90(10), N2–Sm–C1 59.66(10), N1–Sm–I 133.19(8), N2–Sm–I 99.33(7), N1–Sm–I′ 95.02(7), N2–Sm–I′ 171.95(8), N1–Sm–O1 134.35(12), N2–Sm–O1 87.04(12), C1–Sm–I 158.36(6), C1–Sm–I′ 119.11(7), C1–Sm–O1 82.37(13), I–Sm–O1 92.01(9), I′–Sm–O1 84.92(9), I–Sm–I′ 80.896(10), Sm–I–Sm′ 99.104(10).

Reaction of **1** with a second equivalent of K{CH-(PPh$_2$NSiMe$_3$)$_2$} or treatment of K{CH(PPh$_2$NSiMe$_3$)$_2$} with samarium diiodide in a 2:1 molar ratio in thf gave the homoleptic complex [{(Me$_3$SiNPPh$_2$)$_2$CH}$_2$Sm] (**2**) as purple crystals (Scheme 2).[22] Compound **2** is similar to the *N*-mesityl-substituted bis(phosphinimino)methanide complex [{CH(PPh$_2$NC$_6$H$_2$-2,4,6-Me$_3$)$_2$}$_2$Sm].[21] Dark purple crystals suitable for X-ray crystallographic studies formed in concentrated *n*-pentane. Compound **2**, which crystallizes in the triclinic space group $P\bar{1}$ forms discrete homoleptic monomers in the solid state (Figure 2). As observed for **1**, six-membered metallacycles (N1–P1–C1–P2–N2–Sm), which adopt a twist-boat conformation, are formed by the {CH(PPh$_2$NSiMe$_3$)$_2$}$^-$ ligands and the samarium atom. The two {CH(PPh$_2$NSiMe$_3$)$_2$}$^-$ ligands act as tridentate donors. Thus, the samarium atom is six-coordinated. The distances

 © 2007 Wiley-VCH Verlag GmbH & Co. KGaA, Weinheim 

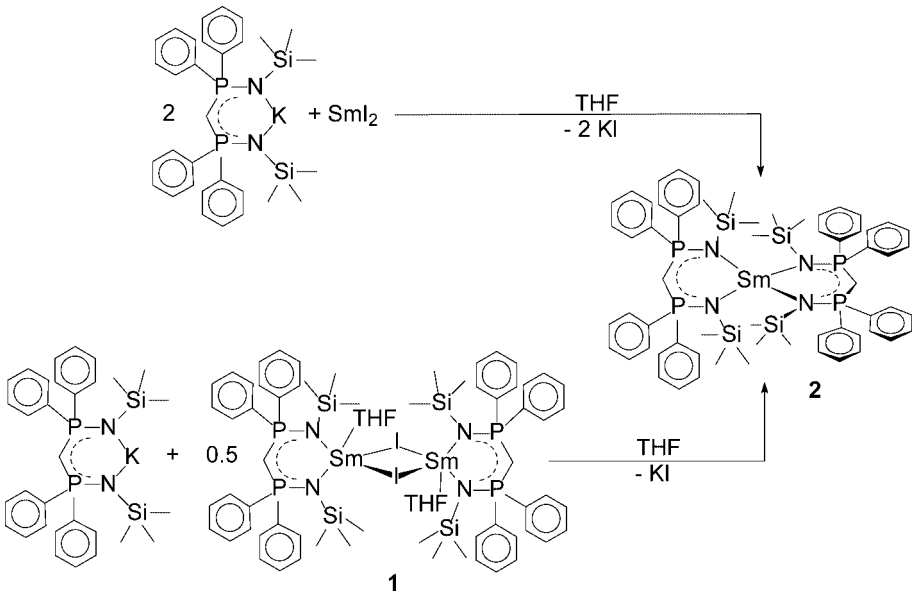


Scheme 2.

between the central carbon atom C1 and the samarium atom [Sm–C1 289.91(15) and Sm–C32 289.84(14) pm] are in the range of those for [{CH(PPh$_2$NC$_6$H$_2$-2,4,6-Me$_3$)$_2$}$_2$-Sm] [290.0(5) and 287.7(5) pm][21] and [Sm{C(SiMe$_3$)$_2$-(SiMe$_2$OMe)}$_2$(thf)] [278.7(5) and 284.5(5) pm][23] but significantly shorter than in **1** [297.7(4) pm]. On the other hand, the Sm–C$_{methine}$ bond lengths are significantly longer than in [($\eta^5$-C$_5$Me$_5$)Sm{CH$_2$(SiMe$_3$)$_2$}($\eta^5$-C$_5$Me$_5$)·K(thf)$_2$]$_n$ [265.2(9) pm].[24]

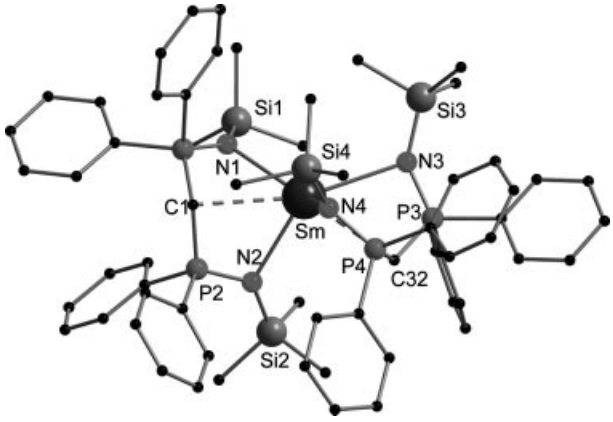


Figure 2. Solid-state structure of **2** showing the atom labeling scheme. Hydrogen atoms have been omitted. Selected bond lengths [pm] and angles [°]: Sm–N1 278.51(12), Sm–N2 260.70(10), Sm–N3 277.41(12), Sm–N4 261.25(11), Sm–C1 289.91(15), Sm–C32 289.84(14), N1–P1 157.81(15), N2–P2 158.30(14), N3–P3 157.86(13), N4–P4 158.13(14); N1–Sm–N2 85.34(3), N1–Sm–N3 116.48(4), N1–Sm–N4 136.31(4), N2–Sm–N3 135.46(4), N2–Sm–N4 105.16(4), N3–Sm–N4 85.69(4), N1–Sm–C32 163.78(4), N2–Sm–C32 90.27(4), N3–Sm–C32 57.63(4), N4–Sm–C32 59.90(4), N1–Sm–C1 57.09(4), N2–Sm–C1 59.97(4), N3–Sm–C1 164.50(4), N4–Sm–C1 91.23(4), C1–Sm–C32 132.66(4).

Earlier attempts to synthesize a heteroleptic complex of composition [{CH(PPh$_2$NC$_6$H$_2$-2,4,6-Me$_3$)$_2$}Sm{N(SiMe$_3$)$_2$}] did not succeed.[21] Therefore, to obtain another heteroleptic amido complex, **1** was treated with KNPh$_2$ in toluene in a 2:1 molar ratio. Surprisingly, we did not obtain the desired complex [{(Me$_3$SiNPPh$_2$)$_2$CH}Sm(NPh$_2$)$_2$] but instead repeatedly isolated the mixed dimeric compound [({(Me$_3$SiNPPh$_2$)$_2$CH}Sm)$_2$(μ-I)(μ-NPh$_2$)] (**3**) in high yields (Scheme 3).[22] Compound **3** was characterized by elemental analysis and Raman spectroscopy. The solid-state structure of **3** was also determined by single-crystal X-ray diffraction (Figure 3). It crystallizes in the monoclinic space group *C*2/*c* with one molecule of toluene and forms a dimer in the solid state in which the metal centers are symmetrically bridged by one iodine atom and the nitrogen atom of the

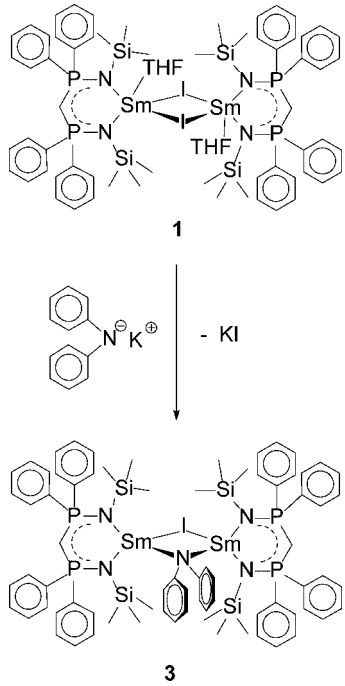


Scheme 3.

 © 2007 Wiley-VCH Verlag GmbH & Co. KGaA, Weinheim 

$Ph_2N^-$ group. A crystallographic $C_2$ axis is observed along I and N3. As a result of the bridging nature of the nitrogen atom, the Sm–N3 bond length [259.4(3) pm] is longer than in $[Sm\{N(SiMe_3)_2\}(thf)_2]$ [244.2(9) and 242.4(9) pm],[25] in which the $\{N(SiMe_3)_2\}^-$ groups are terminally bonded. The Sm–I bond length of 328.33(4) pm is a bit shorter than in $[Sm\{N(SiMe_3)_2\}(\mu\text{-}I)(DME)(thf)]_2$ [e.g. 334.14(9) and 335.53(9) pm].[25] As observed for **1** and **2**, the six-membered N1–P1–C1–P2–N2–Sm ring in **3**, which is formed by the $\{CH(PPh_2NSiMe_3)_2\}^-$ ligand and the samarium atom, adopts a twist-boat conformation. The distance between the central carbon atom C1 and the lanthanide atom [292.2(4) pm] lies between the values observed for **1** [297.7(4) pm] and **2** [Sm–C1 289.91(15) and Sm–C32 289.84(14) pm]. The Sm–N1 and Sm–N2 distances are 255.0(3) and 253.8(3) pm, respectively; and indicate an almost symmetrical attachment of the ligand at the metal center.

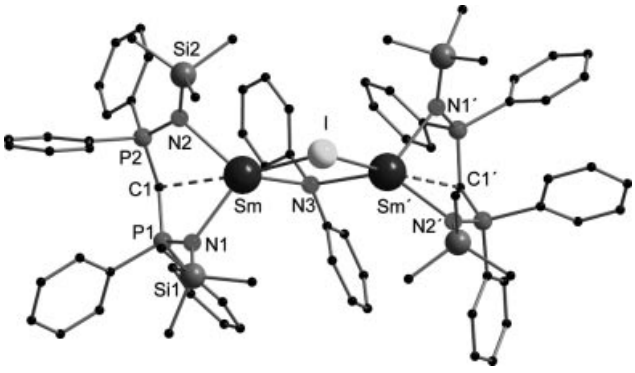


Figure 3. Solid-state structure of **3** showing the atom labeling scheme. Hydrogen atoms have been omitted. Selected bond lengths [pm] and angles [°]: Sm–N1 255.0(3), Sm–N2 253.8(3), Sm–N3 259.4(3), Sm–C1 292.2(4), Sm–I 328.33(4), N1–P1 159.1(3), N2–P2 158.4(3); N1–Sm–N2 94.24(10), N1–Sm–N3 118.45(8), N2–Sm–N3 135.65(8), N1–Sm–C1 59.33(9), N2–Sm–C1 60.46(10), N3–Sm–C1 109.64(11), N1–Sm–I 117.43(7), N2–Sm–I 109.95(7), N3–Sm–I 82.14(8), C1–Sm–I 168.06(7), Sm–N3–Sm 113.19(17), Sm–I–Sm 82.521(14).

### Catalysis

Since it is known that divalent lanthanide complexes such as $[(\eta^5\text{-}C_5H_5)_2Sm]$,[12] $[(\eta^5\text{-}C_5Me_5)_2Sm(thf)_2]$,[11] and $[(\eta^5\text{-indenyl})_2Yb(thf)_2]$[13] are efficient catalysts for the polymerization of ε-caprolactone (CL),[14] we were interested in using compound **1** as a precatalyst for this polymerization. Complex **1** showed high activity in polymerization of CL at room temperature. Monomer/initiator molar ratios of 1/2000 and 1/10000 afforded the corresponding poly(caprolactone)s with excellent yields (92–95%) within short reaction times. The molecular weights obtained depend strongly on the amount of initiator. Poly(caprolactone) with a $\bar{M}_n$ of 723000 was obtained in toluene with a [CL]/[**1**] ratio of 10000/1 in one hour with complete conversion at room temperature (Table 1, entry 2). The molecular weights decrease at elevated temperature (Table 1, entries 3 and 4). Moderate $\bar{M}_w/\bar{M}_n$ values (1.81–2.75) were observed.

## Conclusions

In summary, a series of bis(phosphinimino)methanide complexes of divalent samarium have been reported. Reaction of $K\{CH(PPh_2NSiMe_3)_2\}$ with samarium diiodide in a 1:1 molar ratio in thf affords the corresponding divalent samarium complex $[\{(Me_3SiNPPh_2)_2CH\}Sm(\mu\text{-}I)(thf)]_2$ (**1**). Reaction of **1** with a second equivalent of $K\{CH(PPh_2NSiMe_3)_2\}$ or treatment of $K\{CH(PPh_2NSiMe_3)_2\}$ with samarium diiodide in a 2:1 molar ratio in thf gives the homoleptic complex $[\{(Me_3SiNPPh_2)_2CH\}_2Sm]$ (**2**). When **1** is treated with $KNPh_2$ in toluene in a 2:1 molar ratio the mixed dimeric compound $[(\{(Me_3SiNPPh_2)_2CH\}_2Sm)_2(\mu\text{-}I)(\mu\text{-}NPh_2)]$ (**3**) is obtained. The single-crystal X-ray structures of all three complexes show that the $\{CH(PPh_2NSiMe_3)_2\}^-$ ligand is bound in an uncommon coordination mode to the metal atom. A six-membered N1–P1–C1–P2–N2–Sm metallacycle, which adopts a pseudo-boat conformation, is formed by chelation of the two trimethylsilylimine groups to the metal center. The heteroleptic complex **1** is an efficient catalyst for the polymerization of CL. Good polydispersity and molecular masses are obtained with this catalyst.

## Experimental Section

**General Considerations:** All manipulations of air-sensitive materials were performed with the rigorous exclusion of oxygen and moisture in flame-dried, Schlenk-type glassware either on a dual-manifold Schlenk line interfaced with a high vacuum ($10^{-3}$ Torr) line, or in an argon-filled MBraun glove box. Thf was pre-dried with Na wire and distilled under nitrogen from Na/K alloy benzophenone ketyl prior to use. Hydrocarbon solvents (toluene and *n*-pentane) were distilled under nitrogen from $LiAlH_4$. All solvents for vacuum line manipulations were stored in vacuo over $LiAlH_4$ in resealable flasks. Deuterated solvents were obtained from Chemotrade or Euriso-Top GmbH (99 atom% D). NMR spectra were recorded with

Table 1. Polymerization of ε-CL initiated by **1** in toluene.

| CL:**1**[a] | *T* [°C] | *t* [h] | Yield[b] [%] | $\bar{M}_{n(theor.)}$[c] [g mol$^{-1}$] | $\bar{M}_{n(obsd.)}$ [g mol$^{-1}$] | $\bar{M}_w/\bar{M}_n$[d] | $\bar{M}_{n(corr.)}$[e] [g mol$^{-1}$] |
|---|---|---|---|---|---|---|---|
| 2000:1 | room temp. | 1 | 93 | $2.12\cdot10^5$ | $1.07\cdot10^5$ | 2.47 | $0.6\cdot10^5$ |
| 10000:1 | room temp. | 1 | 95 | $10.8\cdot10^5$ | $7.23\cdot10^5$ | 2.52 | $4.05\cdot10^5$ |
| 2000:1 | 75 | 1 | 94 | $2.15\cdot10^5$ | $2.58\cdot10^4$ | 1.81 | $1.44\cdot10^4$ |
| 10000:1 | 75 | 1 | 92 | $10.5\cdot10^5$ | $3.85\cdot10^4$ | 2.75 | $2.16\cdot10^4$ |

[a] Initial molar CL/catalyst ratio. [b] Determined gravimetrically. [c] Calculated from $M_{monomer} \times [M]/[I] \times$ yield. [d] Measured by SEC. [e] SEC values multiplied by 0.56.[29]

 © 2007 Wiley-VCH Verlag GmbH & Co. KGaA, Weinheim 

a Jeol JNM-LA 400 FT-NMR spectrometer. Chemical shifts are referenced to internal solvent resonances and are reported relative to tetramethylsilane or 85% phosphoric acid ($^{31}$P). Raman spectra were recorded with a Bruker RFS 100. Elemental analyses were performed with an Elementar vario EL. $SmI_2(thf)_2$,[26] K{CH($PPh_2NSiMe_3$)$_2$},[16] and {$CH_2(PPh_2NSiMe_3)_2$}[27] were prepared according to literature procedures.

**[{($Me_3SiNPPh_2$)$_2$CH}Sm(μ-I)(thf)]$_2$ (1):** $SmI_2(thf)_2$ (1.20 g, 2.2 mmol) and K{CH($PPh_2NSiMe_3$)$_2$} (1.20 g, 2.0 mmol) were placed in a flask and 15 mL of thf was condensed onto the mixture. The mixture was stirred for 16 h at room temperature and filtered. The thf was removed from the resulting dark-purple solution in vacuo. The obtained dark solid was washed with 10 mL of cold toluene yielding 1.72 g (95%) of **1**. Crystals of **1** suitable for X-ray crystallographic studies were obtained by concentrating a hot thf/toluene (2:1) solution. $^1$H NMR ([D$_8$]THF, 400 MHz): $\delta$ = –0.16 (s, 36 H, $SiMe_3$), 4.97 (br. s), 6.75 (br. s) 7.05–7.70 (m, 40 H, Ph) ppm. $^{13}$C{H} NMR ([D$_8$]THF, 100.4 MHz): $\delta$ = 4.0 ($SiMe_3$), 128.5, 129.6, 130.4, 131.9 (Ph) ppm. Raman (solid): $\tilde{\nu}$ = 604 cm$^{-1}$ (s), 618 (m), 1000 (s), 1027 (m), 1104 (w), 1157 (w), 1573 (w), 1588 (m), 2889 (br), 3049 (s), 3059 (m). $C_{70}H_{92}I_2N_4O_2P_4Si_4Sm_2$ (1812.3): calcd. C 46.39, H 5.12, N 3.09; found C 46.77, H 4.47, N 2.67.

**[{($Me_3SiNPPh_2$)$_2$CH}$_2$Sm] (2):** $SmI_2(thf)_2$ (273 mg, 0.5 mmol) and K{CH($PPh_2NSiMe_3$)$_2$} (597 mg, 1.0 mmol) were placed in a flask and 15 mL of thf was condensed onto the mixture. The mixture was stirred for 16 h at room temperature. The solvent was removed in vacuo and the resulting residue was suspended in 15 mL of *n*-pentane and filtered. The obtained solution was concentrated at 35 °C. Dark crystals suitable for X-ray crystallographic studies formed after several hours. By further concentration of the mother liqueur an overall yield of 560 mg (89%) of **2** was obtained. Raman (solid): $\tilde{\nu}$ = 609 cm$^{-1}$ (m), 617 (w), 999 (s), 1027 (m), 1103 (w), 1156 (w), 1182 (w), 1572 (w), 1587 (m), 2897 (br), 2952 (br), 3055 (m). $C_{62}H_{78}N_4P_4Si_4Sm\cdot\frac{1}{2}C_5H_{12}$ (1265.91 + 36.08): calcd. C 59.50, H 6.50, N 4.30; found C 59.90, H 6.59, N 4.09.

**[({($Me_3SiNPPh_2$)$_2$CH}Sm)$_2$(μ-I)(μ-$NPh_2$)] (3):** Freshly prepared **1** (453 mg, 0.25 mmol) and $KNPh_2$ (104 mg, 0.50 mmol) were suspended in 15 mL of toluene. The dark mixture was stirred for 6 h at about 70 °C and another 10 h at room temperature. Filtration and concentration of the resulting solution yielded 676 mg (79%) of **3** as very dark purple crystals. $^{31}$P{$^1$H} NMR ($C_6D_6$, 161.7 MHz, 25 °C): $\delta$ = 341.7 ppm. Raman (solid): $\tilde{\nu}$ = 607 cm$^{-1}$ (s), 617 (m), 987 (m), 999 (s), 1026 (m), 1102 (w), 1157 (w), 1572 (w), 1588 (m), 2891 (br), 2944 (br), 3056 (m). $C_{74}H_{88}IN_5P_4Si_4Sm_2$ (1711.4): calcd. C 51.93, H 5.18, N 4.09; found C 52.10, H 5.14, N 3.73.

**Polymerization of ε-Caprolactone:** A 5 M solution of the ε-caprolactone in toluene (4 mL for 1:2000 or 20 mL for 1:10000) was added to **1** (0.018 g, 0.01 mmol). The mixture was stirred and left at room temperature or warmed to 75 °C. After one hour the reaction mixture was treated with an excess of methanol. After 2–3 h the polymer was separated from the mother liquor by decanting and dried in vacuo. The residue was dissolved in 20 mL (1:2000) or in 60 mL (1:10000) of toluene and the solution was transferred to a beaker and treated with an excess of methanol. The poly-ε-caprolactone was separated and dried in vacuo until the weight remained constant.

The molecular masses of poly(ε-caprolactone)s were measured by the GPC method on a Hewlett–Packard liquid chromatograph 1090 HP [SDV column $10^4 \times 10^3 \times 100$ Å (Polymer Standard Service); eluent: thf] and were corrected by calibration relative to polystyrene standards.

**X-ray Crystallographic Studies of 1–3:** Suitable crystals of **1**–**3** were covered in mineral oil (Aldrich) and mounted on a glass fiber. The crystal was transferred directly to the cold $N_2$ stream (–73 °C) of a Stoe IPDS 2T diffractometer. Subsequent computations were carried out with an Intel Pentium IV PC. Data collection and refinement were performed with SHELXS-97[28a] and SHELXL-97.[28b]

**[{($Me_3SiNPPh_2$)$_2$CH}Sm(μ-I)(thf)]$_2$ (1):** Monoclinic, space group $P2_1/c$ (no. 14); lattice constants $a$ = 1970.31(13), $b$ = 996.34(6), $c$ = 2366.4(2) pm, $\beta$ = 113.216(6)°, $V$ = 4269.3(5) × 10$^6$ pm$^3$, $Z$ = 2; $\mu$(Mo-$K_\alpha$) = 2.259 mm$^{-1}$; $2\theta_{max.}$ = 58.8°; 11260 ($R_{int}$ = 0.0423) independent reflections measured, of which 6555 were considered observed with $I > 2\sigma(I)$; max. residual electron density 0.946 and –1.140 e A$^{-3}$; 405 parameters (all non-hydrogen atoms except the thf molecules were calculated anisotropic; the positions of the H atoms were calculated for idealized positions) $R1$ = 0.0350; w$R2$ = 0.0750.

**[{($Me_3SiNPPh_2$)$_2$CH}$_2$Sm] (2):** Triclinic, space group $P\bar{1}$ (no. 2); lattice constants $a$ = 1182.45(6), $b$ = 1555.64(7), $c$ = 1994.55(10) pm, $\alpha$ = 75.270(4)°, $\beta$ = 81.858(4)°, $\gamma$ = 77.736(4)°, $V$ = 3452.4(3) × 10$^6$ pm$^3$, $Z$ = 1; $\mu$(Mo-$K_\alpha$) = 2.259 mm$^{-1}$; $2\theta_{max.}$ = 58.5°; 18523 ($R_{int}$ = 0.0803) independent reflections measured, of which 13118 were considered observed with $I > 2\sigma(I)$; max. residual electron density 1.072 and –1.361 e A$^{-3}$; 705 parameters (all non-hydrogen atoms except the pentane molecules were calculated anisotropic; the positions of the H atoms were calculated for idealized positions) $R1$ = 0.0491; w$R2$ = 0.1091.

**[({($Me_3SiNPPh_2$)$_2$CH}Sm)$_2$(μ-I)(μ-$NPh_2$)] (3):** Monoclinic, space group $C2/c$ (no. 15); lattice constants $a$ = 2144.9(3), $b$ = 1730.74(13), $c$ = 2445.1(3) pm, $\beta$ = 112.308(11)°, $V$ = 8397(2) × 10$^6$ pm$^3$, $Z$ = 4; $\mu$(Mo-$K_\alpha$) = 1.929 mm$^{-1}$; $2\theta_{max.}$ = 50.0°; 7408 ($R_{int}$ = 0.0490) independent reflections measured, of which 5877 were considered observed with $I > 2\sigma(I)$; max. residual electron density 1.490 and –0.726 e A$^{-3}$; 428 parameters (all non hydrogen atoms except the toluene molecules were calculated anisotropic; the positions of the H atoms were calculated for idealized positions) $R1$ = 0.0339; w$R2$ = 0.0779.

CCDC-622744 to -622746 (for **1**–**3**) contain the supplementary crystallographic data for this paper. These data can be obtained free of charge from The Cambridge Crystallographic Data Center via www.ccdc.cam.ac.uk/data_request/cif.

## Acknowledgments

This work was supported by the Deutsche Forschungsgemeinschaft (DFG Schwerpunktprogramm SPP 1166: Lanthanoidspezifische Funktionalitäten in Molekül und Material).

[1] T. Imamoto, *Lanthanides in Organic Synthesis*, Academic Press, London, **1994**.
[2] a) G. A. Molander, *Chem. Rev.* **1992**, *92*, 29–68; b) G. A. Molander, C. R. Harris, *Chem. Rev.* **1996**, *96*, 307–338.
[3] a) P. G. Steel, *J. Chem. Soc., Perkin Trans. 1* **2001**, 2727–2751; b) A. Dahlén, G. Hilmersson, *Eur. J. Inorg. Chem.* **2004**, 3393–3403.
[4] a) J. L. Namy, P. Girard, H. B. Kagan, *Nouv. J. Chim.* **1977**, *1*, 5–7; b) P. Girard, J. L. Namy, H. B. Kagan, *J. Am. Chem. Soc.* **1980**, *102*, 2693–2698; c) A. Krief, A.-M. Laval, *Acros Org. Acta* **1996**, *2*, 17–19; d) A. Krief, A.-M. Laval, *Chem. Rev.* **1999**, *99*, 745–777.
[5] J. L. Namy, J. Collin, J. Zhang, H. B. Kagan, *J. Organomet. Chem.* **1987**, *328*, 81–86.

 © 2007 Wiley-VCH Verlag GmbH & Co. KGaA, Weinheim 

[6] H. B. Kagan, J. Collin, J. L. Namy, C. Bied, F. Dallemer, A. Lebrun, *J. Alloys Compd.* **1993**, *192*, 191–196.
[7] E. Prasad, B. W. Knettle, R. A. Flowers II, *J. Am. Chem. Soc.* **2002**, *124*, 14663–14667.
[8] W. J. Evans, I. Bloom, W. E. Hunter, J. L. Atwood, *J. Am. Chem. Soc.* **1981**, *103*, 6507–6508.
[9] W. J. Evans, *Coord. Chem. Rev.* **2000**, *206*, 263–283.
[10] F. T. Edelmann, in *Comprehensive Organometallic Chemistry II* (Eds.: E. W. Abel, F. G. A. Stone, G. Wilkinson), Pergamon Press, Oxford, **1995**.
[11] W. J. Evans, H. Katsumata, *Macromolecules* **1994**, *27*, 2330–2332.
[12] S. Agarwal, N. E. Brandukova-Szmikowski, A. Greiner, *Macromol. Rapid Commun.* **1999**, *20*, 274–278.
[13] D. Cui, T. Tang, J. Cheng, N. Hu, W. Chen, B. Huang, *J. Organomet. Chem.* **2002**, *650*, 84–90.
[14] H. Yasuda, H. Yamamoto, M. Yamashita, K. Yokota, A. Nakamura, S. Miyake, Y. Kai, N. Kanehisa, *Macromolecules* **1993**, *26*, 7134–7143.
[15] M. T. Gamer, S. Dehnen, P. W. Roesky, *Organometallics* **2001**, *20*, 4230–4236.
[16] M. T. Gamer, P. W. Roesky, *Z. Anorg. Allg. Chem.* **2001**, *627*, 877–881.
[17] M. T. Gamer, P. W. Roesky, A. Steffens, M. Glanz, *Chem. Eur. J.* **2005**, *11*, 3165–3172.
[18] M. T. Gamer, P. W. Roesky, *J. Organomet. Chem.* **2002**, *647*, 123–127.
[19] a) A. Zulys, T. K. Panda, M. T. Gamer, P. W. Roesky, *Chem. Commun.* **2004**, 2584–2585; b) A. Zulys, T. K. Panda, M. T. Gamer, P. W. Roesky, *Organometallics* **2005**, *24*, 2197–2202.
[20] T. K. Panda, A. Zulys, M. T. Gamer, P. W. Roesky, *J. Organomet. Chem.* **2005**, *690*, 5078–5089.
[21] M. S. Hill, P. B. Hitchcock, *Dalton Trans.* **2003**, 4570–4571.
[22] The bonding situation in the drawings of the ligand system in all schemes has been simplified for clarity.
[23] W. Clegg, K. Izod, P. O'Shaughnessy, C. Eaborn, J. D. Smith, *Angew. Chem.* **1997**, *109*, 2925–2926; *Angew. Chem. Int. Ed. Engl.* **1997**, *36*, 2815–2817.
[24] a) Z. Hou, Y. Zhang, O. Tardif, Y. Wakatsuk, *J. Am. Chem. Soc.* **2001**, *123*, 9216–9217; b) Z. Hou, Y. Zhang, M. Nishiura, Y. Wakatsuki, *Organometallics* **2003**, *22*, 129–135.
[25] W. J. Evans, D. K. Drummond, H. Zhang, J. L. Atwood, *Inorg. Chem.* **1988**, *27*, 575–579.
[26] P. Girard, J. L. Namy, H. B. Kagan, *J. Am. Chem. Soc.* **1980**, *102*, 2693–2698.
[27] R. Appel, I. Ruppert, *Z. Anorg. Allg. Chem.* **1974**, *406*, 131–144.
[28] a) G. M. Sheldrick, *SHELXS-97, Program for Crystal Structure Solution*, University of Göttingen, Germany, **1997**; b) G. M. Sheldrick, *SHELXL-97, Program for Crystal Structure Solution*, University of Göttingen, Germany, **1997**.
[29] M. Save, M. Schappacher, A. Soum, *Macromol. Chem. Phys.* **2002**, *203*, 889–899.

Received: October 6, 2006
Published Online: January 5, 2007

 © 2007 Wiley-VCH Verlag GmbH & Co. KGaA, Weinheim 

DOI: 10.1002/ejic.200600975

# Thallium Halides – New Aspects of the Stereochemical Activity of Electron Lone Pairs of Heavier Main-Group Elements

**Anja-Verena Mudring*[a]**

*Dedicated to Prof. Dr. Josef Hahn on the occasion of his 65th birthday*

**Keywords:** Halides / Thallium / Electron lone pairs

Density functional theory studies in the linear muffin tin approximation on thallium halides (TlX; X = F, Cl, Br, I) show that structural distortions due to a stereochemically active lone pair of electrons depend crucially on cation–anion interactions. Such distortions do not originate from a 6s–6p hybridisation on the heavy metal as the Tl 6s and 6p states are energetically too far apart to mix directly. In the case of TlF, the Tl 6s and the F 2p states are located in the same energy region, which leads to an efficient interaction that produces strongly antibonding Tl–F states directly below the Fermi level that would destabilize the solid. Minimisation of these unfavourable covalent antibonding interactions is the driving force for structural distortion. In the case of the heavier thallium halides, the growing energetic mismatch between Tl 6s states and X *n*p states leads to weaker covalent interactions. Thus, the compounds become more ionic and high symmetry structures are adopted as covalent interactions play only a minor role. The low symmetry structure of TlI observed at low temperatures is stabilized by attractive metal–metal bonding.
(© Wiley-VCH Verlag GmbH & Co. KGaA, 69451 Weinheim, Germany, 2007)

## Introduction

Thallium shows a strong preference for the oxidation state +1, which has been attributed to the effect of the "inert electron pair", a term introduced by Sidgwick[1] to describe the tendency of the heavier main-group elements to adopt oxidation numbers that are two less than the respective group number.[2] Traditional considerations assume that this inert electron pair is generated by mixing of the 6s and 6p orbitals on the heavy metal cation. The hybrid orbital is therefore often considered to behave like an additional ligand in the coordination sphere.[3] The corresponding pair of electrons is thought to be chemically inert but stereochemically active. However, this would imply that the lone pair is stereochemically active in any environment, which is obviously not the case. Many thallium compounds are known where the lone pair is not stereochemically active, many of which even show interesting phase transitions between structures where the lone pair is active or not. So far, no comprehensive studies on the origin and nature of the lone pair in thallium compounds have appeared that can explain or even predict the stereochemistry of the $6s^2$ lone pair.

Thallium halides (TlX; X = F–I) offer a unique possibility to study the stereochemistry of the (chemically) inert electron pair since a large variety of TlX phases are known even though these compounds are simple 1:1 salts. Much work has been done over the years on the study of phase transitions of these simple compounds, mainly to investigate the temperature- and pressure-dependent behaviour of the $6s^2$ lone pair on the thallium atom.

Thallium(I) fluoride adopts an orthorhombic structure in the space group *Pbcm*, which can be regarded as a distorted rock-salt-type structure (Figure 1), under ambient conditions where both thallium and fluorine are coordinated by six counterions. However, the coordination polyhedron around the thallium cation deviates strongly from ideal octahedral symmetry. This fact has been ascribed to the presence of a stereochemically active lone pair. Although the orthorhombic structure of TlF is stable up to 3.5 GPa,[4] a structural phase transition apparently takes place at temperatures above 355 K to a higher symmetrical tetragonal structure, which still can be derived from a rock-salt-type structure.[5] The space group *I*4/*mmm* has been proposed for this structure. $^{205}$Tl and $^{19}$F NMR studies question this assumption, however, as they indicate different coordination polyhedra around Tl and F.[6] In contrast to TlF, the thallium halides with heavier halogens (TlCl and TlBr) adopt highly symmetrical cubic structures. Both compounds crystallise in the CsCl structure type under ambient conditions,[7] whereas at low temperatures a

[a] Anorganische Chemie I der Ruhr-Universität Bochum
Universitätsstraße 150, 44801 Köln, Germany
http://www.anjamudring.de
Supporting information for this article is available on the WWW under http://www.eurjic.org or from the author.

 © 2007 Wiley-VCH Verlag GmbH & Co. KGaA, Weinheim 

transition to the NaCl structure takes place.[8] TlI also crystallises in a CsCl-type structure under ambient conditions.[9] Interestingly it undergoes a phase transition, at low temperatures to a structure type in the space group *Cmcm*[10] (Figure 2) that is also found for indium monohalides.[11] Reliable crystallographic structure determinations are a requirement for further studies as wrong crystallographic studies, for example for TlF, have led to wrong interpretations of the lone pair effect[6] and even speculations about Tl–Tl interactions.[12]

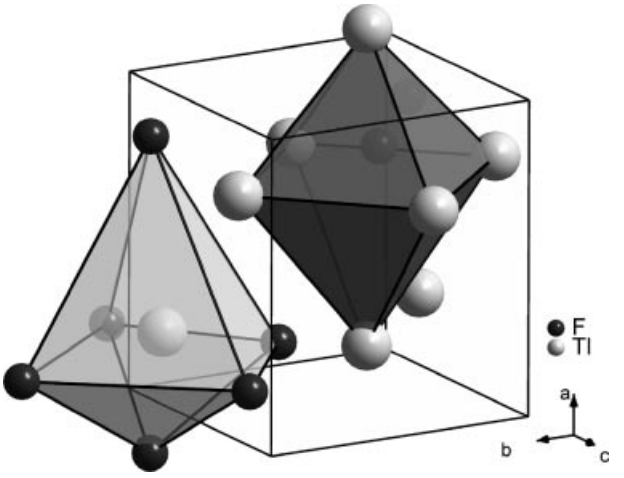


Figure 1. Crystal structure of TlF (*Pbcm*). The coordination polyhedra surrounding thallium and fluorine are shaded.

Recent studies on thallium(I) coordination compounds[13] show that s–p mixing on the heavy atom is neither the origin nor a necessity for a structural distortion that might otherwise be associated with a stereochemically active lone pair. Instead, antibonding Tl 6s/ligand-p interactions are the origin of these structural distortions. In order to investigate the lone pair effect in extended solid materials, calculations have been carried out on the different modifications of the thallium halides using density functional theory.[14]

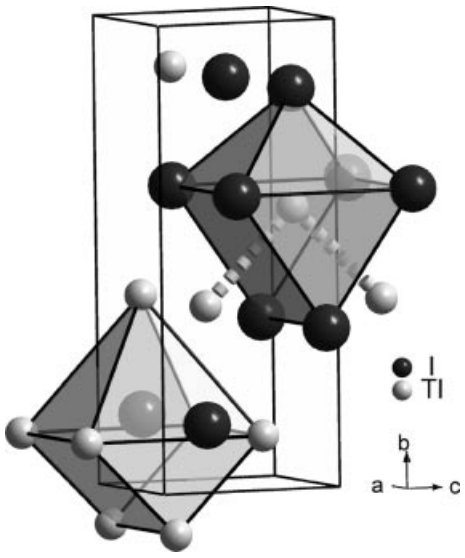


Figure 2. Crystal structure of TlI (*Cmcm*). The coordination polyhedra surrounding thallium and iodine are shaded. Closest Tl–Tl contacts indicated by broken bonds.

## Results and Discussion

The density of states for TlX (X = F, Cl, I) in the NaCl and CsCl structure types as well as for TlF and TlI in their own structure types are shown in Figures 3, 6 and 9, respec-

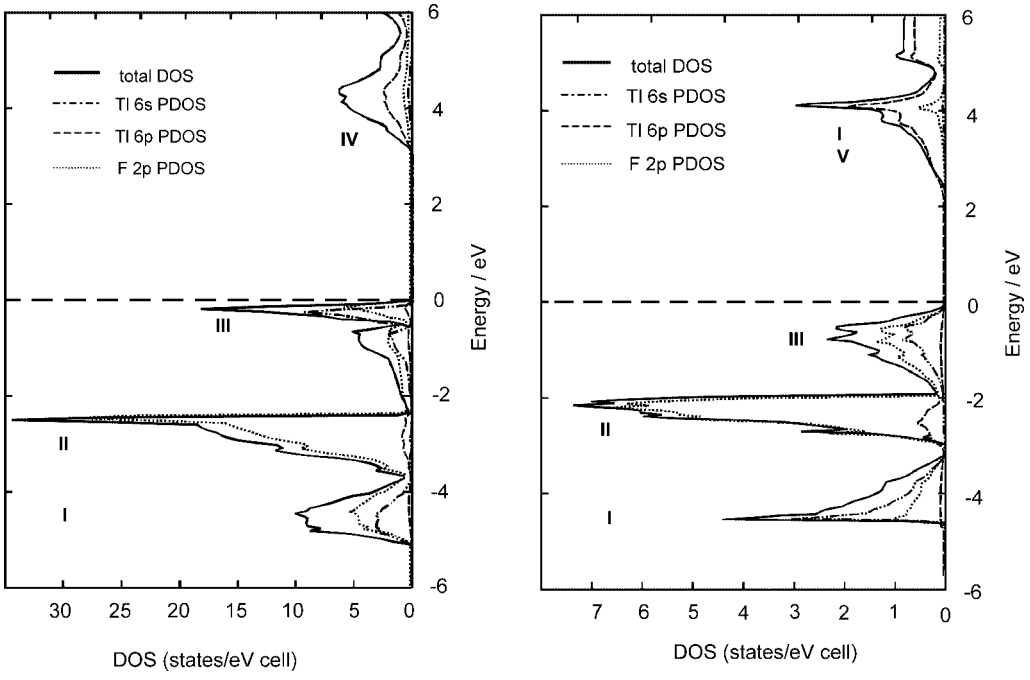


Figure 3. Total and partial densities of states for TlF (left: *Pbcm*; right: $Fm\bar{3}m$).

 © 2007 Wiley-VCH Verlag GmbH & Co. KGaA, Weinheim 

tively, between –6 and +6 eV (with respect to the highest occupied state). As both the halogen *n*s states and the Tl 5d states are located at energies significantly lower than –6 eV and have no impact on the chemical bonding, they are not shown.

### Thallium Fluoride (TlF)

The density of states (DOS) for TlF (Figure 3) in its room-temperature structure (space group *Pbcm*) and in the hypothetically idealised NaCl-type of structure (space group $Fm\bar{3}m$) can be partitioned into four significant sections, a region above the Fermi level which is mainly of Tl 6p character (IV) and a complex area below the Fermi level. This latter area shows three different segments (I–III). A region at lower energies around –4/–5 eV, which is of Tl 6s and F 2p character (I), is followed by a region of high DOS mainly made up by F 2p with small Tl 6p contributions (II). Then, up to the highest occupied states, a region is observed which again shows Tl 6s as well as F 2p contributions (III). The crystal orbital Hamiltonian population (COHP) curves for the Tl–F interactions (Figure 4) reveal that regions I and II are Tl–F bonding and region III right below the Fermi level is Tl–F antibonding. This clearly shows the ambivalent bonding situation in thallium halides: on the one hand there is a strong Coulombic attraction between cations and anions in the solid, whereas on the other unfavourable covalent antibonding Tl 6s/F 2p interactions take place right at the Fermi level. If these are reduced, the whole solid is energetically stabilized. A more thorough study of the DOS for TlF in both structures reveals some rather significant differences between the different structures (Table 1). The integrated DOSs show a higher F p and lower Tl s contribution for region I in the distorted NaCl structure compared to the undistorted (hypothetical) NaCl structure, whereas for region III the opposite is found. Furthermore, a significantly larger Tl p contribution is found for region II in the idealised NaCl structure. These observations can best be explained by a simple interaction

Table 1. Integrated projected density of states (IPDOS) and crystal orbital Hamiltonian populations (ICOHP) for TlX (X = F, Cl, I) in the different structure types.

| Compound | TlF | | TlCl | | TlI | |
|---|---|---|---|---|---|---|
| Space group | *Pbcm* | $Fm\bar{3}m$ | $Fm\bar{3}m$ | $Pm\bar{3}m$ | *Cmcm* | $Pm\bar{3}m$ |
| **I**[a] | | | | | | |
| IPDOS Tl s | 9.6% | 15.1% | 17.9% | 17.5% | 21.0% | 20.2% |
| IPDOS Tl p | 0.7% | 0.8% | 0.3% | 1.1% | 0.4% | 0.5% |
| IPDOS X p | 14.8% | 8.7% | 7.3% | 5.3% | 4.4% | 4.5% |
| ICOHP (Tl–X) | 1.58 | 1.38 | 1.83 | 1.79 | 1.17 | 1.61 |
| **II** | | | | | | |
| IPDOS Tl s | 0.7% | 0.4% | 0.7% | 2.6% | 1.5% | 2.6% |
| IPDOS Tl p | 0.1% | 3.6% | 4.8% | 5.0% | 5.6% | 6.4% |
| IPDOS X p | 49.2% | 46.2% | 45.7% | 38.1% | 35.1% | 36.5% |
| ICOHP (Tl–X) | 0.54 | 0.65 | 1.39 | 1.29 | 1.04 | 1.36 |
| **III** | | | | | | |
| IPDOS Tl s | 12.4% | 8.7% | 7.2% | 4.2% | 3.1% | 2.1% |
| IPDOS Tl p | 1.2% | 0.7% | 1.1% | 5.1% | 1.5% | 1.2% |
| IPDOS X p | 11.4% | 15.7% | 16.0% | 21.1% | 27.4% | 26.1% |
| ICOPH (Tl–X) | –1.13 | –1.18 | –1.63 | –1.20 | –0.58 | –0.62 |
| Total ICOHP (Tl–X) | 0.99 | 0.85 | 1.59 | 1.88 | 1.63 | 2.36 |

[a] The Roman numbers refer to the different segments of the DOS and COHP curves (see Figure 3).

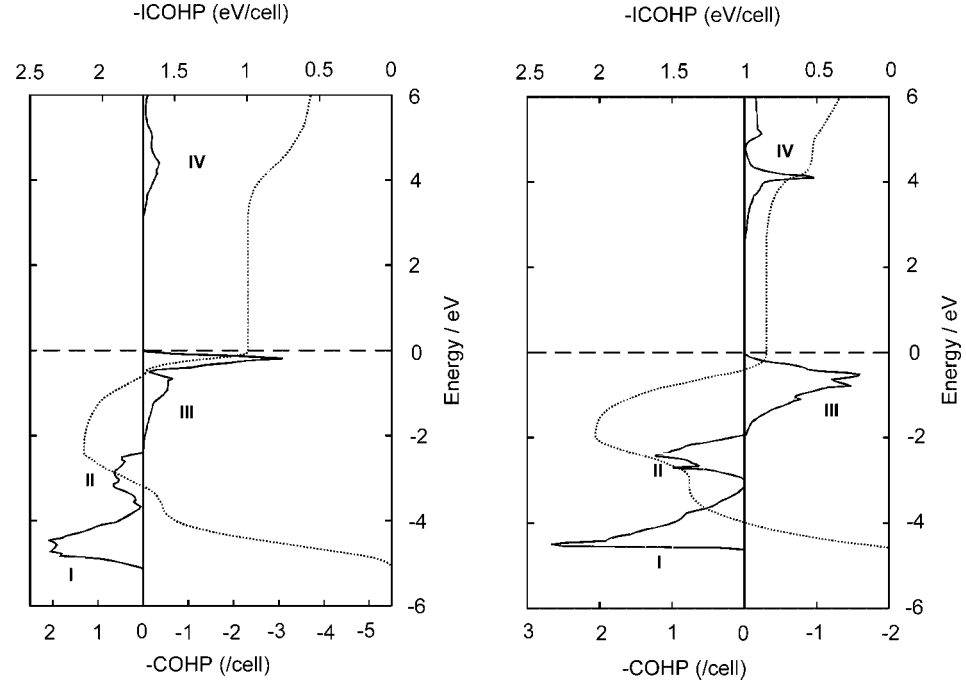


Figure 4. COHP and ICOHP of the Tl–F interaction (left: *Pbcm*; right: $Fm\bar{3}m$).

 © 2007 Wiley-VCH Verlag GmbH & Co. KGaA, Weinheim 

scheme (Figure 5). The Tl 6s and F 2p levels are found in a similar energy region and thus are able to interact efficiently which, however, leads to both strong bonding Tl 6s/F 2p combinations (region I) and antibonding Tl 6s/F 2p states right at the Fermi level (region III).

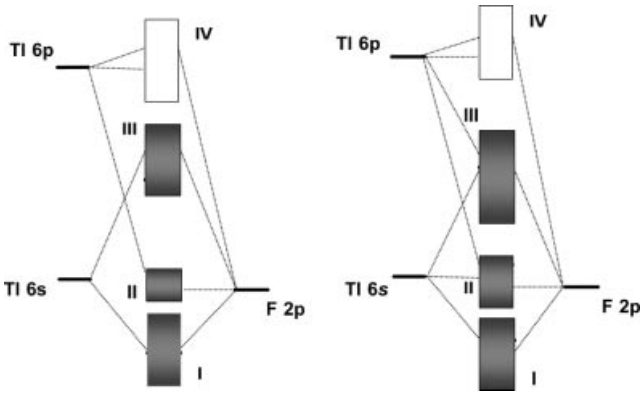


Figure 5. Schematic orbital interaction diagrams for TlF (a) in its actual distorted structure (*Pbcm*) and (b) in a hypothetical symmetrical structure ($Fm\bar{3}m$). Shaded blocks symbolize occupied levels, open blocks correspond to empty levels.

If the antibonding Tl 6s/F 2p interactions were reduced, an energetic stabilisation of the whole solid would be achieved. This can indeed be accomplished by a structural distortion [Figure 5(b)]. A comparison of the total energies per formula unit shows the distorted structure to be more stable than the undistorted NaCl type of structure. Upon distortion, the low-lying region I loses some of its Tl 6s character to region III right below the Fermi level. In exchange, region I gains F 2p character and region III loses F 2p character. Note also the high integrated crystal orbital Hamiltonian population (ICOHP) for region I (Table 1). Accordingly, the high lying antibonding Tl 6s/F 2p states in particular come closer in energy to the Tl 6p states, which now can mix into the antibonding region III. This introduces some additional Tl 6p/F 2p bonding, as noted earlier,[15] and, more importantly, moves the antibonding states partially above the Fermi level so that a net gain in bonding is achieved. Indeed, the ICOHP value for the Tl–F bond is higher for the distorted structure than for the symmetric structure (Table 1). In the distorted structure, the Tl–F contacts are unevenly distributed. Four shorter contacts at 243, 255 and 271 pm (2×) and two rather long Tl–F distances of 312 and 370 pm are observed. Closer inspection of the COHP curves (see Supporting Information) shows that the four shorter Tl–F distances essentially determine the whole Tl–F interaction, whereas the interactions at the two larger distances become essentially non-bonding.

It has been realized previously that the crystal orbital Hamiltonian population can be used as an indicator in trends of lone pair stereochemical activity.[16] This mixing cannot occur in highly symmetric (cubic) structures like the rock-salt-type structure, however, as it would be symmetry-forbidden. Note that for this gedankenexperiment the mean Tl–F distance is the same in all cases.

### Thallium Chloride and Bromide (TlCl and TlBr)

In contrast to TlF, no distortions associated with the stereochemistry of a lone pair have been observed so far for TlCl and TlBr. This becomes obvious by comparing the density of states and COHP curves for the thallium–halogen bond for hypothetically cubic TlF (Figures 3 and 4) with that for TlCl (Figures 6 and 7). As for TlF in the rock-salt structure, the density of states and COHP curves for

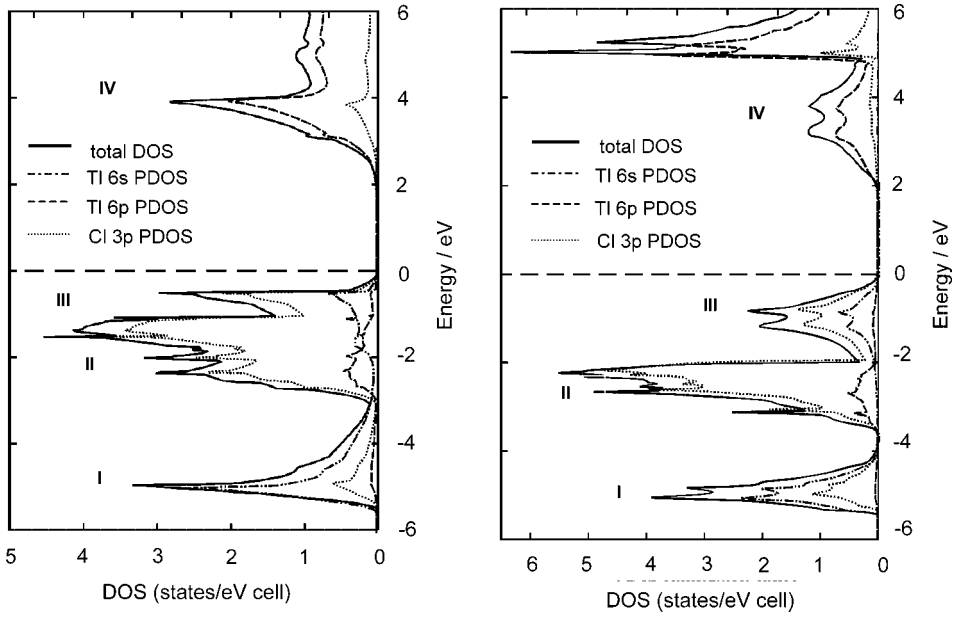


Figure 6. Total and partial densities of states for TlCl (left: *Pbcm*; right: $Fm\bar{3}m$).

 © 2007 Wiley-VCH Verlag GmbH & Co. KGaA, Weinheim 

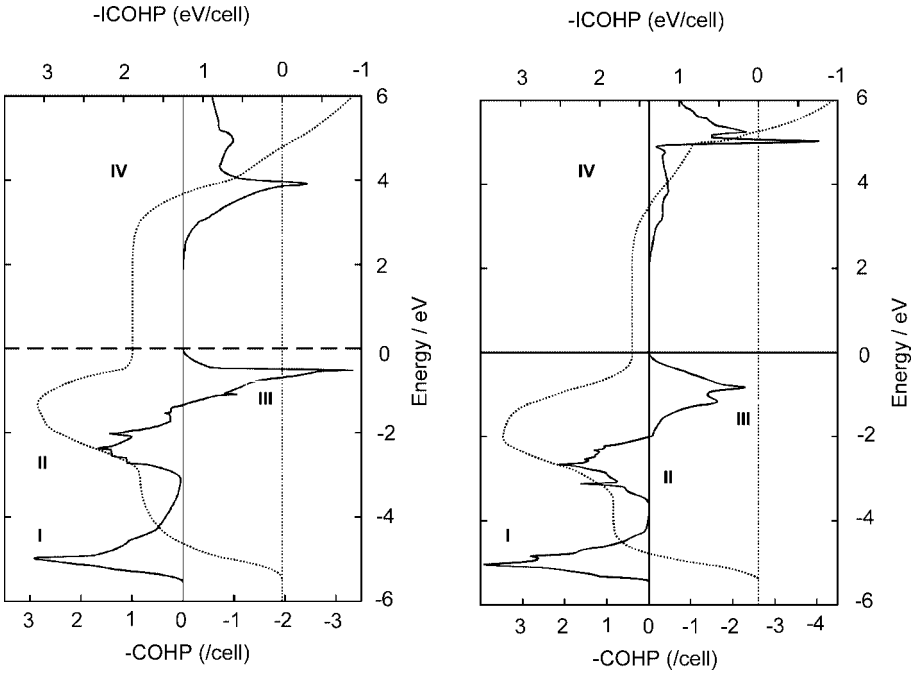


Figure 7. COHP and ICOHP of the Tl–Cl interaction (left: *Pbcm*; right: $Fm\bar{3}m$).

TlCl can be separated into four distinct regions. In the case of the CsCl-type structure, regions II and III have grown together when compared with the situation for TlF. However, it becomes clear that the principal features are still present, particularly when looking at the partial density of states and COHP curves. In the low energy region the states have predominantly Tl 6s/Cl 3p bonding character whereas the highest occupied states are Tl 6s/Cl 3p antibonding. the low lying states have substantially more Tl 6s character compared to TlF, and the states right below the Fermi level more Cl 3p character (Table 1). This can, again, be illustrated by a simple interaction scheme (Figure 8). As the Cl 3p states are located at higher energies than the F 2p states, they are farther apart from the Tl 6s states and thus the Tl 6s/Cl 3p interaction is less strong. This becomes particularly obvious when the band structures of TlF and TlCl in the CsCl-type structure are compared. The effects described for TlCl are even more pronounced for TlBr. The heavier the halogen atom, the larger the energy separation between Tl 6s and X-*n*p states and the weaker the covalent and the stronger the ionic interaction between $Tl^+$ and $X^-$. The energy separations between distorted and undistorted structures are reduced. Thus, in compounds with heavier halogens the necessity for a structural distortion from a highly symmetric structure with a large lattice energy (Madelung factor) to minimize unfavourable (antibonding) covalent interactions gradually vanishes.

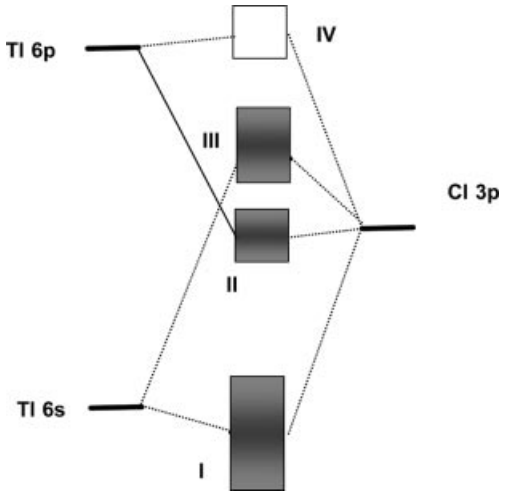


Figure 8. Schematic orbital interaction diagram for TlCl.

### Thallium Iodide (TlI)

The total and partial DOS diagrams for TlCl and TlI in the CsCl-type structure show similar features. The more ionic character of TlI becomes obvious by the fact that a pseudo gap opens up around about –3 eV due to the increasing ionic nature of the compound, this is in agreement with the trend observed for TlCl and TlBr (see above). However, the question remains as to why TlI adopts a comparatively low symmetry structure at low temperatures (Figure 2), which is also seen for the red monohalides of indium(I) (InX; X = Cl, Br, I).[17] This TlI type of structure (Figure 9) has the special property that the contraction of one sublattice (the cations) can be coupled with the dilatation of the other sublattice (the anions).[18] In the case of the low-temperature modification of TlI, the anions move apart from each other and the cations come closer. At the same time the mean cation–anion distance remains almost the same. Most importantly, short metal–metal contacts are created (two of about 371 pm and two of 457 pm). The

 © 2007 Wiley-VCH Verlag GmbH & Co. KGaA, Weinheim 

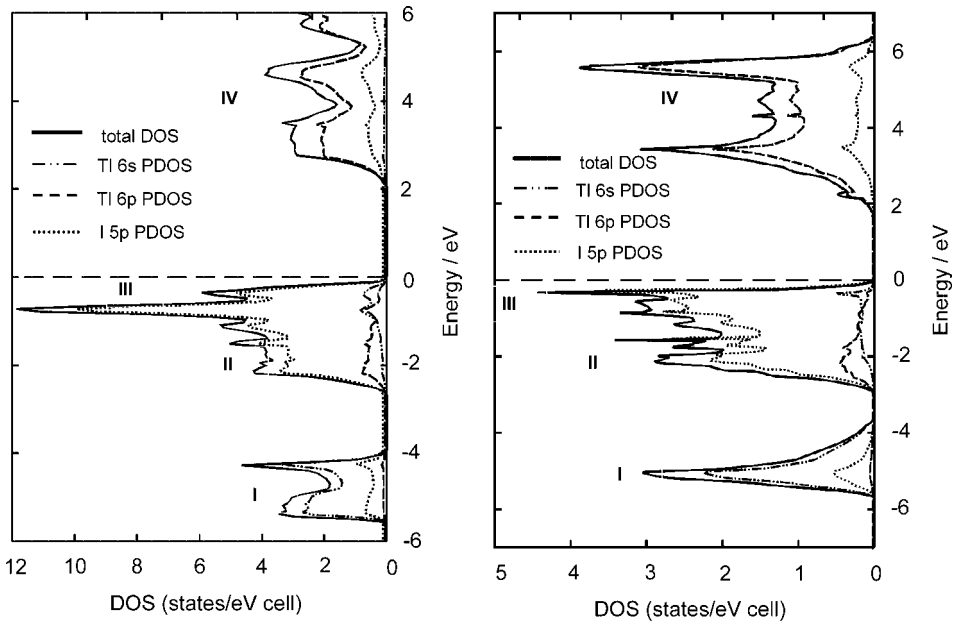


Figure 9. Total and partial densities of states for TlI (left: *Cmcm*; right: $Pm\bar{3}m$).

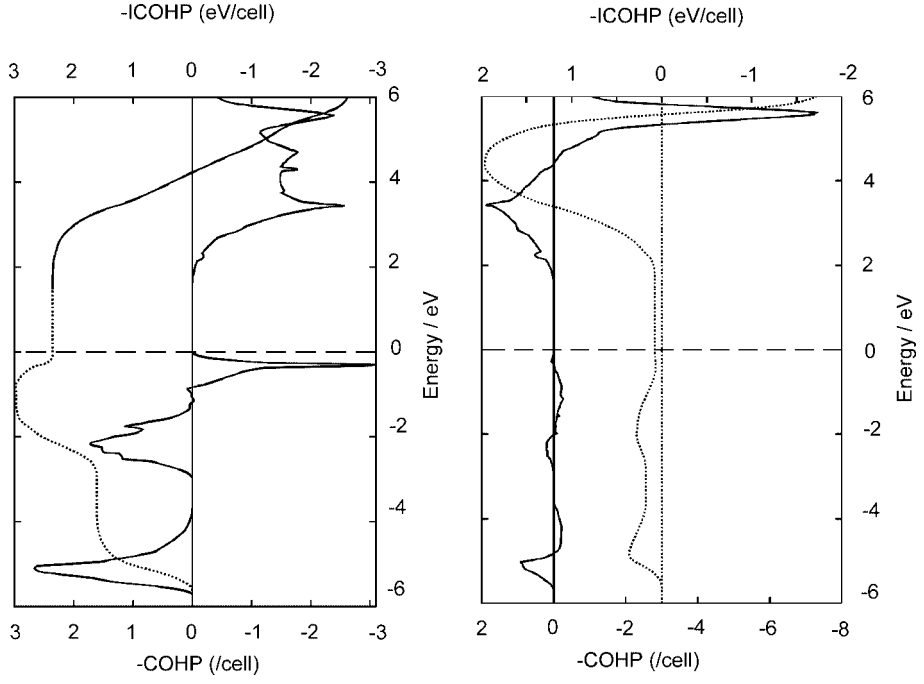


Figure 10. TlI ($Pm\bar{3}m$): COHP and ICOHP of the Tl–I (left) and Tl–Tl interactions.

COHP curves for the Tl–Tl interactions in TlI in the CsCl ($Pm\bar{3}m$; Figure 10, right) and InX (*Cmcm*; Figure 11, right) types of structure make it clear that Tl–Tl bonding becomes important in the case of the low-temperature (InX) structure whereas it is negligible for the room temperature structure (CsCl). Accordingly, the ICOPH values (Table 2) for the Tl–Tl interaction up to the Fermi level are higher for TlI in the InX type of structure than in the CsCl type of structure, which accounts for a stabilisation of the distorted structure at low temperatures through Tl–Tl bonding. Inter-

Table 2. ICOHP values of Tl–Tl interactions for TlI in the InX (*Cmcm*) and CsCl ($Pm\bar{3}m$) structure types.

| Region | Space group | |
|---|---|---|
| | *Cmcm* | $Pm\bar{3}m$ |
| I | 0.29 | 0.36 |
| II | –0.14 | –0.18 |
| III | 0.05 | 0.10 |
| IV | –0.08 | –0.21 |
| V | 0.05 | 0.01 |
| Total ICOHP | 0.17 | 0.07 |

 © 2007 Wiley-VCH Verlag GmbH & Co. KGaA, Weinheim 

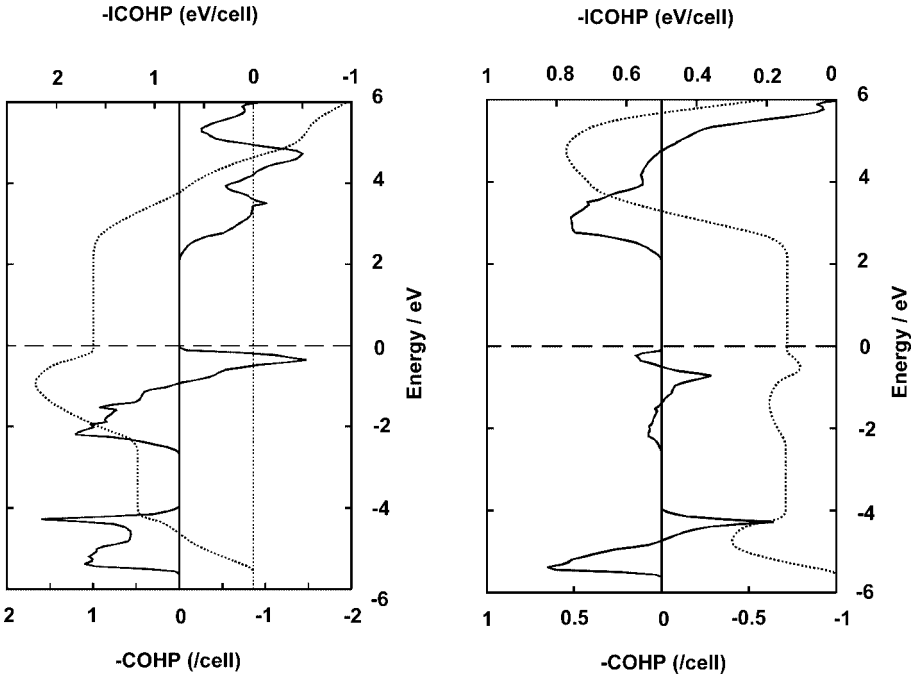


Figure 11. TlI (*Cmcm*): COHP and ICOHP of the Tl–I (left) and Tl–Tl interactions.

estingly, the shortest observed Tl–Tl distance of 371 pm in TlI is comparable to that found in pentabenzylcyclopentadienidothallium(I) (363 pm).[19]

## Conclusions

In summary, the calculations on thallium halides show, just like previous theoretical work on $Tl^{I}$ coordination compounds,[20] that structural distortions in $Tl^{I}$ compounds do not originate from a stereochemically active lone pair in the sense that Tl 6s and Tl 6p mix directly (or hybridize) to give the electron pair on thallium a directional character. The Tl 6s and Tl 6p states are energetically too far apart from each other to mix efficiently.[21,22] Instead, the minimisation of unfavourable covalent antibonding states, which originate from the interaction of the Tl 6s lone pair with lone pairs of the bonding partner, is the driving force for structural distortions. A comparison of TlF with the heavier thallium halides TlX (X = Cl, Br, I) shows that such lone pair distortions depend crucially on the relative energy levels of the valence states of the constituting elements and, in turn, on the number of occupied antibonding states within the crystal.

In the case of TlF, the Tl 6s and the F 2p states are located in the same energy region, which leads to a strong covalent interaction between both bonding partners that produces strongly antibonding Tl–F states just below the Fermi level that destabilize the solid. Due to the strong splitting, the highest states move closer in energy to the Tl 6p states. The admixture of empty Tl 6p states at the top of the valence band becomes allowed through a structural distortion (symmetry reduction). This leads to a decrease in energy of the antibonding states and thereby a net stabilisation of the structure. The large dispersion in the case of fluorine thus minimizes the energy gap between the Tl 6s and Tl 6p states such that the latter can participate in chemical bonding.

The heavier the anion the larger the energy mismatch between Tl 6s states and X *n*p states. This leads to weaker covalent interactions. The highest occupied valence states gain increasingly higher X p character while the lower valence states are mainly Tl 6s like. Thus, the compounds become more ionic and the gain of Coulombic energy outweighs the (decreasing) covalent antibonding forces at the Fermi level (note that this observation is in contrast to what would have been expected judging from relative electronegativities). Consequently, typical ionic structures like the rock-salt or cesium chloride types of structure are adopted. Similar observations have been made recently for lead chalcogenides.[23] That covalent forces may, under certain conditions, lead to unsymmetrical structures even in the case of heavier anions is exhibited by the example of TlI, which gains stability at low temperatures by attractive metal–metal bonding.

## Computational Details

Calculations of the electronic structure of the thallium halides were carried out using the tight-binding linear-muffin-tin orbital (LMTO) method in the local density (LDA) and atomic sphere (ASA) approximation within the framework of the density functional theory (DFT) method.[24,25] All major relativistic effects except spin-orbit coupling were taken into account using the scalar

 © 2007 Wiley-VCH Verlag GmbH & Co. KGaA, Weinheim 

relativistic approximation. The calculations include corrections for the neglect of the interstitial regions and the partial waves of higher order. To reduce the overlap of atomic spheres (AS), empty interstitial spheres were added to the crystal potential and the basis set. The construction of the atomic sphere radii was performed according to an automatic procedure of the program package until the empty space was sufficiently filled.[26] Reciprocal space integrations were carried out using the tetrahedron method.[27] The basis set of short-range, atom-centred TB-LMTOs contained 6s, 6p, 6d and 5f wave functions for Tl ($n$ = 5). The 6d and 5f partial waves were included only in the tails of the LMTOs according to the Löwdin downfolding procedure.[28] For fluorine, 3s and 2p were taken into account as valence orbitals and the 3s orbital was treated by the downfolding technique; for chlorine ($n$ = 4) and bromine ($n$ = 5), $n$s, ($n$ – 1)p and ($n$ – 1)d functions were treated as valence orbitals, with $n$s and ($n$ – 1)d being downfolded. For iodine, 6s, 5p, 5d and 4f orbitals were considered as valence orbitals and 6s and 5d were downfolded. The partial ($l$ and $m$ quantum number decomposed) electronic DOSs were calculated to examine the effect of the anion on the electronic density of states in detail. These were calculated by projecting the wave functions onto spherical harmonics centred on each atom. For bond analysis, the crystal orbital Hamiltonian population (COHP) method was used together with its integration, the ICOHP.[29] COHP gives the energy contributions for all electronic states for selected bonds by partitioning the band structure energy in terms of the respective orbital pair contributions. Note, however, that the values are negative for bonding and positive for antibonding interactions. Thus, the sign is inverted with respect to the crystal orbital overlap population (COOP) diagrams originally used in semi-empirical extended-Hückel calculations.[30]

For TlF[31] in space group *Pbnm*, TlCl[32] and TlBr[32] in the CsCl ($Pm\bar{3}m$) and NaCl ($Fm\bar{3}m$) structures as well as for TlI in the CsCl[8] structure and its low-temperature modification,[33] the structural data were employed as reported in the literature. Lattice constants for a hypothetical TlF in the rock-salt structure were estimated from the molar volume of room temperature TlF in space group *Pbcm*.

**Supporting Information** (see footnote on the first page of this article) contains COHP and ICOHP curves for the Tl–F interaction in TlF (*Pbcm*).

## Acknowledgments

A.-V. M. thanks the Bundesministerium für Bildung und Forschung (BMBF) and Fonds der Chemischen Industrie for support through a Liebig fellowship and the Deutsche Forschungsgemeinschaft for generous financial support. Prof. Dr. G. Meyer is acknowledged for his interest in this research, helpful discussions and for providing the infrastructure necessary to conduct this research.

[1] a) N. V. Sidgwick, *Some Physical Properties of the Covalent Link in Chemistry*, Cornell University Press, Ithaca, New York, **1933**; b) N. V. Sidgwick, *Annu. Rep.* **1933**, *30*, 120; c) N. V. Sidgwick, H. M. Powell, *Proc. R. Soc., London Ser. A* **1940**, *176*, 153; d) N. V. Sidgwick, *The Chemical Elements and their Compounds*, vol. 1, Clarendon Press, Oxford, **1950**.

[2] a) N. N. Greenwood, A. Earnshaw, *Chemistry of the Elements*, Pergamon, Oxford, **1997**; b) J. G. Huheey, E. A. Keiter, R. L. Keiter, *Inorganic Chemistry: Principles of Structure and Reactivity*, Pearson Education, New York, **1997**; c) F. A. Cotton, G. Wilkinson, C. A. Murillo, M. Bochmann, *Advanced Inorganic Chemistry*, 6th ed., Wiley, New York, **1999**.

[3] a) L. E. Orgel, *J. Chem. Soc.* **1959**, 3815; b) J. D. Dunitz, L. E. Orgel, *Adv. Inorg. Chem. Radiochem.* **1960**, *2*, 42.

[4] P. Berastegui, S. Hull, *J. Solid State Chem.* **2000**, *150*, 266. High-pressure DTA measurements indicate that a phase transition takes place at pressures of 1.3 GPa but no structural data are available (see ref.[5a]).

[5] a) C. W. F. T. Pistorius, J. B. Clark, *Phys. Rev.* **1968**, *173*, 692; b) M. Barlow, C. Meredith, *Z. Kristallogr.* **1968**, *130*, 304; c) D. Cubiccioti, H. Eding, *J. Chem. Eng. Data* **1965**, *10*, 343.

[6] S. P. Gabuda, S. G. Koziova, *J. Struct. Chem.* **1997**, *38*, 140.

[7] a) W. P. Davey, F. G. Wick, *Phys. Rev.* **1921**, *17*, 403; b) W. P. Davey, F. G. Wick, *Z. Phys. Chem.* **1925**, *117*, 51; c) A. E. van Arkel, *Physica* **1924**, *4*, 33; d) A. E. van Arkel, *Norsk Geologisk Tidsskrift* **1925**, *8*, 217.

[8] M. Blackman, I. H. Khan, *Proc. Phys. Soc.* **1961**, *77*, 471.

[9] T. Barth, G. Lunde, *Norsk Geologisk Tidsskrift* **1925**, *8*, 293.

[10] L. Helmholtz, *Z. Kristallographie, Kristallgeometrie, Kristallphysik, Kristallchemie* **1936**, *95*, 129.

[11] a) R. E. Jones, D. H. Templeton, *Acta Crystallogr.* **1955**, *8*, 847; b) C. P. J. M. van der Vorst, G. C. Verschoor, W. J. A. Maaskant, *Acta Crystallogr., Sect. B* **1978**, *34*, 3333c) G. Meyer, T. Staffel, *Z. Anorg. Allg. Chem.* **1989**, *574*, 114.

[12] S. P. Gabuda, S. G. Kozlova, R. L. Davidovich, *Chem. Phys. Lett.* **1996**, *263*, 253.

[13] F. Rieger, A.-V. Mudring, *Inorg. Chem.* **2005**, *44*, 6240.

[14] Comprehensive and state-of-the art calculations on thallium halides are available: a) P. Schwerdtfeger, G. A. Heath, M. Dolg, M. A. Bennett, *J. Am. Chem. Soc.* **1992**, *114*, 7518; b) P. Schwerdtfeger, J. Ischtwan, *J. Comput. Chem.* **1993**, *14*, 913.

[15] U. Häussermann, P. Berastegui, S. Carlson, J. Haines, J.-M. Léger, *Angew. Chem. Int. Ed.* **2001**, *40*, 4624.

[16] R. Seshadri, N. A. Hill, *Chem. Mater.* **2001**, *13*, 2892.

[17] G. Meyer, T. Staffel, *Z. Anorg. Allg. Chem.* **1989**, *574*, 114.

[18] D. Becker, H. P. Beck, *Z. Kristallogr.* **2004**, *219*, 348.

[19] a) H. Schumann, Ch. Janiak, J. Pickhardt, U. Börner, *Angew. Chem.* **1987**, *99*, 788; *Angew. Chem. Int. Ed. Engl.* **1987**, *26*, 115. For theoretical calculations see: b) C. Janiak, R. Hoffmann, *Angew. Chem.* **1989**, *101*, 1706; *Angew. Chem. Int. Ed. Engl.* **1989**, *28*, 1688; c) C. Janiak, R. Hoffmann, *J. Am. Chem. Soc.* **1990**, *112*, 5924; d) P. Schwerdtfeger, *Inorg. Chem.* **1991**, *30*, 1660.

[20] F. Rieger, A.-V. Mudring, *Inorg. Chem.* **2005**, *44*, 6240.

[21] If the $Tl^+$ cation lies on a centre of symmetry, mixing between occupied 6s and empty 6p states is forbidden. Lowering the internal energy by mixing can only be achieved by a second order Jahn–Teller effect that destroys the symmetry.

[22] R. Dronskowski, *Computational Chemistry of Solid State Materials*, Wiley-VCH, Weinheim, **2005**, Table 2.1 In the case of InBr a similar strong In s/p energy separation has been observed: R. Dronskowski, *Inorg. Chem.* **1994**, *33*, 6201.

[23] a) G. W. Watson, *J. Chem. Phys.* **2001**, *114*, 758; b) A. Walsh, G. W. Watson, *Phys. Rev. B* **2004**, *70*, 2535114; c) A. Walsh, W. Graeme, *J. Phys. Chem. B* **2005**, *109*, 18868; d) A. Walsh, G. W. Watson, *J. Solid State Chem.* **2005**, *178*, 1422.

[24] a) H. L. Shriver, *The LMTO Method*, Springer, Berlin, **1984**; b) O. Jepsen, M. Snob, O. K. Andersen, *Linearized Band-Structure Methods*, in *Electronic Band-Structure and its Applications*, Springer Lecture Note, Springer, Berlin, **1987**; c) O. K. Andersen, O. Jepsen, *Phys. Rev. Lett.* **1984**, *53*, 2571.

[25] R. W. Tank, O. Jepsen, A. Burckhardt, O. K. Andersen, *TB-LMTO-ASA Program*, ver. 4.7, Max-Planck-Institut für Festkörperforschung, Stuttgart, Germany, **1998**.

[26] O. Jepsen, O. K. Andersen, *Z. Phys. B* **1995**, *97*, 35.

[27] a) O. K. Andersen, O. Jespen, *Solid State Commun.* **1971**, *9*, 1763; b) P. Blöchl, O. Jepsen, O. K. Andersen, *Phys. Rev. B* **1994**, *34*, 16223.

[28] a) W. R. L. Lambrecht, O. K. Andersen, *Phys. Rev. B* **1986**, *34*, 2439; b) O. Jensen, O. K. Andersen, *Z. Phys. B* **1995**, *97*, 35;

 © 2007 Wiley-VCH Verlag GmbH & Co. KGaA, Weinheim 

c) G. Krier, O. Jepsen, O. K. Andersen, Max-Planck-Institute fur Festkörperforschung, Stuttgart, Germany, unpublished results.
[29] R. Dronskowski, P. E. Blöchl, *J. Phys. Chem.* **1993**, *97*, 8617.
[30] S. Wijeyesekera, R. Hoffmann, *Organometallics* **1984**, *3*, 949.
[31] P. Berastegui, S. Hull, *J. Solid State Chem.* **2000**, *150*, 266.
[32] See ref. [8] and M. A. Popova, T. J. Darvojd, M. A. Gurevich, *Zh. Neorg Khim.* **1966**, *11*, 1236.
[33] L. Helmholtz, *Z. Kristallographie, Kristallgeometrie, Kristallphysik, Kristallchemie* **1936**, *95*, 129.

Received: July 13, 2006
Published Online: January 16, 2007

 © 2007 Wiley-VCH Verlag GmbH & Co. KGaA, Weinheim 

DOI: 10.1002/ejic.200601066

# Synthesis of Novel Vinylic P–Se Heterocycles from Selenation of Alkynes by $[PhP(Se)(\mu\text{-}Se)]_2$

**Guoxiong Hua,[a] Yang Li,[a] Alexandra M. Z. Slawin,[a] and J. Derek Woollins*[a]**

**Keywords:** Selenium / Heterocycles / Alkynes / Woollins' reagent / Cycloaddition

Eleven novel five-membered $PSe_2C_2$ heterocycles have been synthesised from $[PhP(Se)(\mu\text{-}Se)]_2$ (Woollins' reagent) and alkynes (one or two C≡C triple bonds) by insertion of a Ph(Se)-$PSe_2$ fragment into alkyne triple bonds. An unusual diselenide formed by an intramolecular cycloaddition/rearrangement is also reported. All compounds have been characterised spectroscopically and four demonstrative X-ray crystal structures are reported.
(© Wiley-VCH Verlag GmbH & Co. KGaA, 69451 Weinheim, Germany, 2007)

## Introduction

Organoselenenium chemistry has attracted increasing attention in recent years. The interest in selenium-containing compound lies not only in their chemo-, regio-, and stereoselective reactions but also their useful biological activity.[1–7] However, the synthesis of selenium-containing organic heterocycles can be problematic involving use of toxic selenium reagents which are often difficult to handle. 2,4-Bis(phenyl)-1,3-diselenadiphosphetane 2,4-diselenide $[\{PhP(Se)(\mu\text{-}Se)\}_2]$ [**1**, Woollins' reagent (WR)], a selenium analogue of the well-known Lawesson's reagent, $[\{(p\text{-}MeOC_6H_4)P(S)(\mu\text{-}S)\}_2]$ has less unpleasant chemical properties than many systems and can be easily prepared and safely handled.[8,9]

WR has been shown to act as an efficient selenium transfer reagent for the synthesis of a range of selenoamides and selenoaldehydes by, for example, simple O/Se exchange reactions or reaction with ArCN followed by hydrolysis.[10–13] We have also reported the use of $FcP(S)S_2P(S)Fc$ (Fc = ferrocenyl) and WR in the preparation of novel metal complexes, C–P–S and C–P–Se heterocycles by reaction with a variety of reactive organic substrates/functionalities including $CS_2$, C=O, C=C double bond and C≡N triple bonds.[8,14–19]

To date, no general method for the synthesis of vinylic selenium-containing heterocycles has been established. We have focused our attention on the preparation of a series of novel vinylic heterocycles by reaction of WR with alkynes and here describe a series of new heterocycles. Four X-ray crystal structures have been determined.

[a] School of Chemistry, University of St Andrews, Fife, KY16 9ST, UK
E-mail: jdw3@st-and.ac.uk

## Results and Discussion

### Reaction of WR with Alkynes Containing one C≡C Triple Bond

WR reacts with one molar equivalent of phenylacetylene or diphenylacetylene in toluene at 130 °C over 12 h to give brown, air-stable crystals of $PhP(Se)Se_2(PhC{=}CH)$ (**2**) or $PhP(Se)Se_2(PhC{=}CPh)$ (**3**), respectively, in high yields (91% and 94%, based on WR) after column chromatographic purification (silica gel, toluene as eluent) and recrystallisation from dichloromethane/*n*-hexane (Scheme 1).

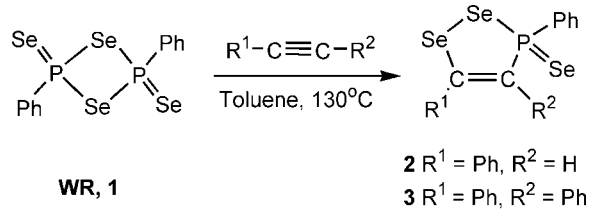


Scheme 1. Synthesis of **2** and **3**.

Although **2** was described previously by us no crystal structure has been published. The data obtained here from microanalysis and spectroscopic analysis match the literature data from our previous study of **2**[15] except that the yield was much improved by lengthening the reaction time and increasing the reaction scale. The $^{31}P\{^1H\}$ NMR spectrum of **3** consists of a sharp singlet at $\delta$ = 74.3 ppm, accompanied by a pattern of selenium satellites with $^{31}P$-$^{77}Se$ couplings of 357 and 779 Hz, respectively, similar to that observed in **2**. The $^{77}Se\{^1H\}$ NMR spectrum shows three distinct doublet signals at $\delta$ = 519.3 ppm [$^2J_{P,Se}$ 7 Hz], $\delta$ = 373.4 ppm [$^1J_{P,Se}$ 358 Hz] and $\delta$ = –28.6 ppm [$^1J_{P,Se}$ 777 Hz] assigned as C–Se, P–Se and P=Se, respectively. The $^1H$

 © 2007 Wiley-VCH Verlag GmbH & Co. KGaA, Weinheim InterScience 

NMR spectrum of **3** shows that only aryl protons are present.

The molecular structures of **2** and **3** (Figure 1 and Figure 2, Table 1 and Table 3) are composed of approximately planar five-membered $C_2PSe_2$ rings generated by the addition of $Ph(Se)PSe_2$ fragments from WR to the C≡C bond of alkynes. For **2**, the mean deviation of the Se(1)–C(7)–P(1)–C(8)–Se(2) plane is 0.13 Å, while in **3** the value is 0.25 Å, the extra deviation from planarity in **3** is also evident in a contraction of the P(1)–Se(2)–Se(3) and C(8)–P(1)–Se(2) internal angles on going from **2** to **3** [92.18(3)° and 101.02(12)° for **2**, 89.56(5)° and 98.6(2)° for **3**] and both effects probably reflect the steric influence of the phenyl group in **3** compared to a hydrogen atom in **2**. The majority of the other geometric parameters in these two compounds are similar, thus the exocyclic P(1)–Se(1) bond lengths in **2** and **3** [2.1137(11) and 2.0965(18) Å, respectively] are in good agreement with each other and consistent with the related selenides containing $P^V$=Se bonds [2.08–2.12 Å].[9,15–18] The P(1)–Se(2) distances [2.2616(10) Å for **2** and 2.2511(17) Å for **3**] are in the range for reported values of heterocycles containing $P^V$–Se single bonds.[8,9,15–18,20] The C(7)–C(8) bond lengths in **2** and **3** are not significantly different [1.339(4) and 1.345(9) Å, respectively], however, the P(1)–C(8) bond length in **2** is shorter than that in **3** [1.783(3) vs. 1.822(7) Å] which may reflect the different electronic effect of a hydrogen atom compared to a phenyl group. Finally, we note that the structure of **3** is chiral in the solid state, i.e. the crystal examined was a single enantiomer.

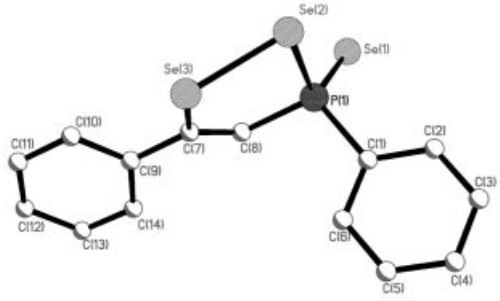


Figure 1. Molecular structure of **2** (C–H bonds omitted for clarity).

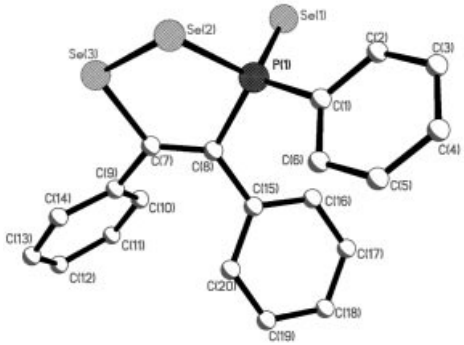


Figure 2. Molecular structure of **3** (C–H bonds omitted for clarity).

Table 1. Selected bond lengths [Å] and angles [°] for **2**, **3**, and **13**.

| | **2** | **3** | **13**[a] |
|---|---|---|---|
| Se(1)–P(1) | 2.1137(11) | 2.0965(18) | 2.1015(9) [2.1011(9)] |
| P(1)–Se(2) | 2.2616(10) | 2.2511(17) | 2.2432(9) [2.2612(8)] |
| P(1)–C(1) | 1.814(3) | 1.814(7) | 1.809(3) [1.812(3)] |
| P(1)–C(8) | 1.783(3) | 1.822(7) | 1.826(3) [1.822(3)] |
| Se(2)–Se(3) | 2.3735(7) | 2.3417(9) | 2.3484(5) [2.3473(5)] |
| Se(3)–C(7) | 1.901(3) | 1.927(6) | 1.929(3) [1.921(3)] |
| C(7)–C(8) | 1.339(4) | 1.345(9) | 1.334(4) |
| C(8)–P(1)–Se(2) | 101.02(12) | 98.6(2) | 100.06(10) [99.71(9)] |
| Se(1)–P(1)–Se(2) | 115.24(4) | 116.66(8) | 109.53(3) [117.80(3)] |
| P(1)–Se(2)–Se(3) | 92.18(3) | 89.56(5) | 90.96(2) [87.62 (2)] |
| Se(3)–C(7)–C(8) | 121.0(3) | 122.5(5) | 122.6(19) [120.9(2)] |
| Se(2)–Se(3)–C(7) | 96.41(10) | 94.3(2) | 94.11(9) [95.43(9)] |
| C(7)–C(8)–P(1) | 124.8(3) | 116.9(5) | 119.6(2) [118.8(2)] |

[a] Dimensions for second independent molecule in square parentheses.

### Reaction of WR with Alkynes Containing two C≡C Triple Bonds

The reaction between WR and bis(phenylethynyl)benzene or 9,10-bis(phenylethynyl)anthracene in refluxing toluene over 12 h gave two types of products, one involving cycloaddition at one C≡C triple bond (**4**, **6**, **8** and **10**) and the other involving cycloaddition at both C≡C triple bonds (**5**, **7**, **9** and **11**) (Scheme 2). In **4**–**11** the phosphorus atoms are potentially chiral but because there is no particular stereocontrol in the reaction we would expect to see racemic mixtures. Thus, **5, 7, 9** and **11** are diastereotopic with (*R*,*R*), (*R*,*S*), (*S*,*R*) and (*S*,*S*) isomers being possible. In the $^{31}P\{^1H\}$ NMR of **5** we observed two phosphorus signals with similar selenium satellites at $\delta_P$ = 73.3 and 73.0 ppm (intensity ratio 9:1) [$J_{P,Se}$ = 357/774 and 360/770 Hz, respectively] though we cannot assign them specifically to (*R*,*R*), (*S*,*S*) and (*R*,*S*), (*S*,*R*). Further purification of **5**, **7**, **9**, and **11** by recrystallisation from $CH_2Cl_2$/petroleum ether gave a single signal arising from one pair of enantiomers which are indistinguishable by NMR, [**5a** (11% yield), **7a** (18% yield), **9a** (15% yield) and **11a** (17% yield)].

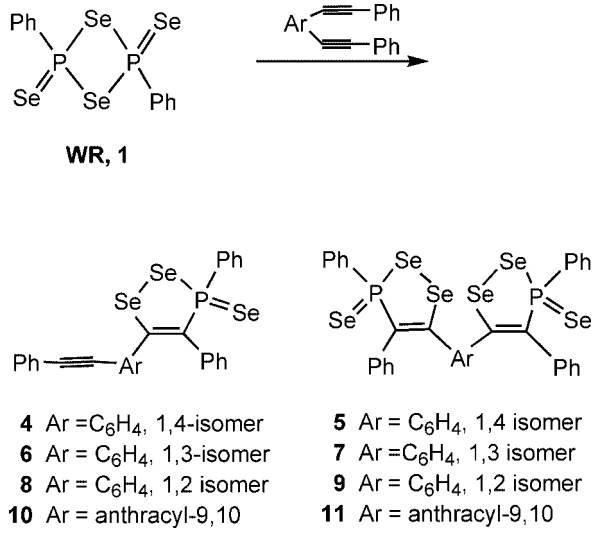


Scheme 2. Synthesis of **4**–**11**.

 © 2007 Wiley-VCH Verlag GmbH & Co. KGaA, Weinheim 

The reaction between WR and 1,8-bis(phenylethynyl)-naphthalene gave the expected compound **13** and a surprising diselenide **12**, which arises from an intramolecular cycloaddition, but no product with cycloaddition at two triple bonds (Scheme 3). Compound **12** has an analogue in sulfur chemistry, which was synthesised by Blum et al. from the reaction of 1,8-bis(phenylethynyl)naphthalene with elemental sulfur.[21] However, we failed to obtain **12** by the reaction of 1,8-bis(phenylethynyl)naphthalene with elemental selenium under identical conditions. This suggests that **12** was formed from the reaction of WR and 1,8-bis(phenylethynyl)-naphthalene. The mechanism of this reaction must be rather complex and to test if **13** is involved we heated pure **13** at reflux in toluene for 5 h and obtained **12** in 18% isolated yield.

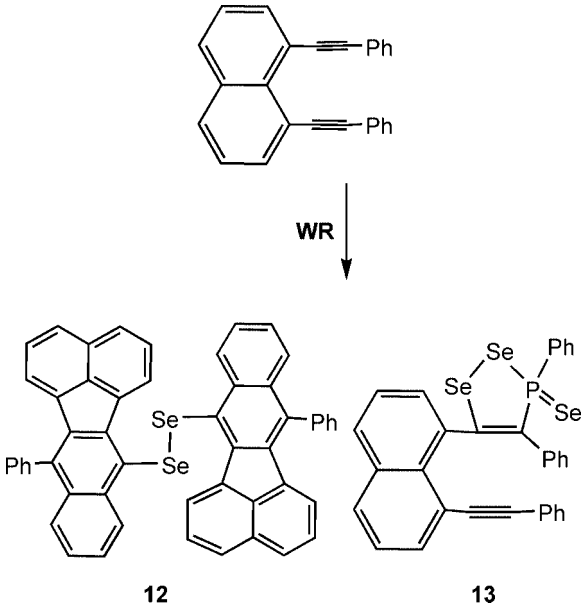


Scheme 3. Synthesis of **12** and **13**.

Heterocycles **4**–**13** are soluble in chlorinated solvents, toluene, methanol and diethyl ether, with lower solubility in hexane. They are air-stable in the solid state, however, their solutions are not stable at room temperature; red selenium crystals precipitated after a couple of days except for **12**. Characterisations of **4**–**13** were achieved by microanalysis, IR, $^{1}H$, $^{13}C$, $^{31}P\{^{1}H\}$ and $^{77}Se\{^{1}H\}$ NMR spectroscopy and mass spectrometry.

In the $^{31}P\{^{1}H\}$ NMR spectra for compounds **4**–**11** and **13** the magnitudes of $^{1}J_{P,Se}$ and $^{1}J_{P,Se}$ (348–380 Hz, 771–820 Hz, respectively) are normal.[15–18] For the products in which one C≡C triple bond has undergone P(Se)SeSe addition the $^{31}P\{^{1}H\}$ NMR spectra show singlets with similar patterns of $^{77}Se$ satellites. As mentioned above, in the crude products with two $C_2PSe_2$ rings the $^{31}P\{^{1}H\}$ NMR spectra are mixtures as a consequence of the chirality at phosphorus but after purification by crystallisation we were able to obtain spectrally pure samples which also display singlets with $^{77}Se$ satellites. Compounds **4**–**11** and **13** were further investigated by $^{77}Se\{^{1}H\}$ NMR which exhibit three signals, assigned as C–Se, P–Se and P=Se, respectively, indicating that in each compound there is one or more identical PhP(Se)–Se–Se fragment present and supporting the presence of both P–Se single and double bonds.[18]

The composition of **4**–**13** was confirmed by mass spectrometric data with a parent $M^+$, accompanied by major fragment ions. In their IR spectra the $\nu_{(P=Se)}$ vibration, observed in the range of 528–559 $cm^{-1}$ for **4**–**11** and **13**, are consistent with the published P–Se five-membered heterocycles.[8,15]

The $^{77}Se\{^{1}H\}$ NMR spectrum of **12** shows a singlet at $\delta_{Se}$ = 279.7 ppm and its $^{1}H$ NMR spectrum displays only aromatic protons present in a wide range at $\delta_{H}$ = 6.08–9.64 ppm. Several of the $^{1}H$ NMR peaks are broad at room temp. which we attribute to lack of free rotation of the two phenyl rings. The broadening is particularly pronounced for the low field signals of the more hindered protons (see experimental section). We did carry out VT-$^{1}H$ experiments and were able to sharpen the signals at 55 °C, whilst cooling to –61 °C gave considerable broadening, but no coalescence. The complexity of the overlapping peaks in the aromatic region precluded detailed analysis/extraction of activation barriers.

Attempts to grow single crystals of **4**–**13** for X-ray analysis have, to date, been successful for only **12** and **13**. The X-ray structure of **12** shows some interesting features (Figure 3, Table 2 and Table 3). The two diselenide-bound benzo[*k*]fluoranthene moieties are not parallel planes with a dihedral angle of 162.4°, which is markedly different from sulfur analogue [157°].[21] The two terminal phenyl rings, which are connected to C8 and C38, respectively, are twisted, so that the dihedral angles between them and the two benzo[*k*]fluoranthene planes are 103° and 92.4° [corresponding angles in the sulfur analogue 106° and 103°].[21]

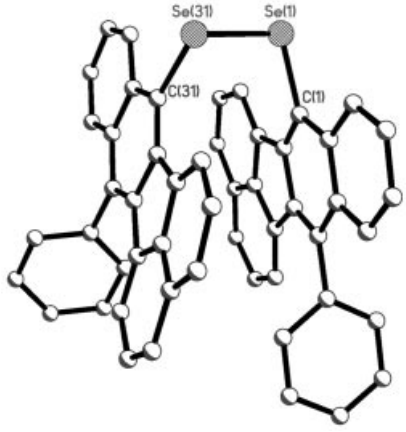


Figure 3. Molecular structure of **12** (C–H bonds omitted for clarity).

Table 2. Selected bond lengths [Å] and angles [°] for **12**.

| | | | |
|---|---|---|---|
| Se(1)–C(1) | 1.920(4) | C(31)–Se(31)–Se(1) | 97.76(9) |
| Se(1)–Se(31) | 2.3699(6) | C(2)–C(1)–Se(1) | 120.8(2) |
| Se(31)–C(31) | 1.921(3) | C(19)–C(1)–Se(1) | 119.2(2) |
| | | C(32)–C(31)–Se(31) | 120.8(2) |
| C(1)–Se(1)–Se(31) | 97.90(9) | C(49)–C(31)–Se(31) | 120.1(2) |

 © 2007 Wiley-VCH Verlag GmbH & Co. KGaA, Weinheim 

Table 3. Data collection and structural refinement parameters for **2**, **3**, **12** and **13**.

| | **2** | **3** | **12** | **13** |
|---|---|---|---|---|
| Formula | $C_{14}H_{11}PSe_3$ | $C_{20}H_{15}PSe_3$ | $C_{59}H_{38}Se_2$ | $C_{32}H_{21}PSe_3$ |
| *M* | 447.08 | 523.17 | 904.81 | 673.34 |
| Crystal system | triclinic | orthorhombic | triclinic | triclinic |
| Space group | $P\bar{1}$ | $P2(1)2(1)2(1)$ | $P\bar{1}$ | $P\bar{1}$ |
| *a* [Å] | 7.681(3) | 6.4664(5) | 11.3721(8) | 9.4900(17) |
| *b* [Å] | 8.950(3) | 11.6801(9) | 12.5182(9) | 14.217(2) |
| *c* [Å] | 10.713(3) | 24.8150(19) | 16.2458(13) | 19.639(4) |
| *α* | 96.644(7) | 90 | 74.019(14) | 95.628(5) |
| *β* | 94.434(7) | 90 | 76.960(15) | 93.245(3) |
| *γ* | 104.116(10) | 90 | 68.560(12) | 99.543(5) |
| $U/A^3$ | 705.2(4) | 1874.2(2) | 2049.2(3) | 2593.4(8) |
| *Z* | 2 | 4 | 2 | 4 |
| $\mu$ [$mm^{-1}$] | 7.915 | 5.971 | 1.840 | 4.337 |
| Reflections collected | 4519 | 13355 | 14315 | 17831 |
| Independent reflections ($R_{int}$) | 2444 (0.0243) | 3309 (0.0430) | 8163 (0.0343) | 9908 (0.0196) |
| $R_1$, $wR_2$ [$I > 2\sigma(I)$] | 0.0281, 0.0656 | 0.0381, 0.0868 | 0.0457, 0.0779 | 0.0324, 0.0675 |

The structure of **13** contains two independent molecules within the unit cell (Figure 4, Table 1 and Table 3), the rotation of aryl ring C(27)–C(32) leads to some steric interactions in the second independent molecule, which account for the differences in metric parameters in the two molecules. Like **2** and **3**, and triselenapentalenes with carbon- and nitrogen-containing backbones,[22,23] **13** is approximately planar; the mean deviation of $P(Se)Se_2C_2$ is 0.22 Å [0.26 Å for molecule 2], while Se(3) lies 0.26 Å [0.30 Å for molecule 2] out of this plane. The Se(2)–Se(3) bond length of 2.3483(5) Å [2.3474(5) Å for molecule 2] is identical to that in $PhP(Se)Se_2$-containing five membered ring.[15,18]

In order to gain some mechanistic insight, we examined the $^{31}P\{^1H\}$ and $^{77}Se$ NMR of a crude reaction mixture during the reaction of phenylacetylene with WR. Apart from the major product **2** [δ = 67.1 ppm] there are several smaller doublets centred at δ = 76.2, 58.1, 40.1, 9.2, –15.7 ppm indicating different phosphorus environments present in the reaction mixture. None of these values corres-

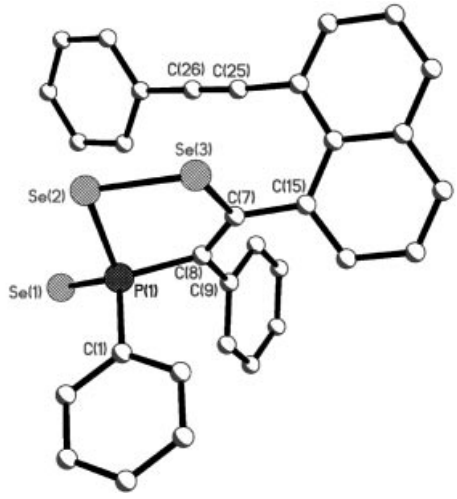


Figure 4. Molecular structure of one of the independent molecules in **13** (C–H bonds omitted for clarity).

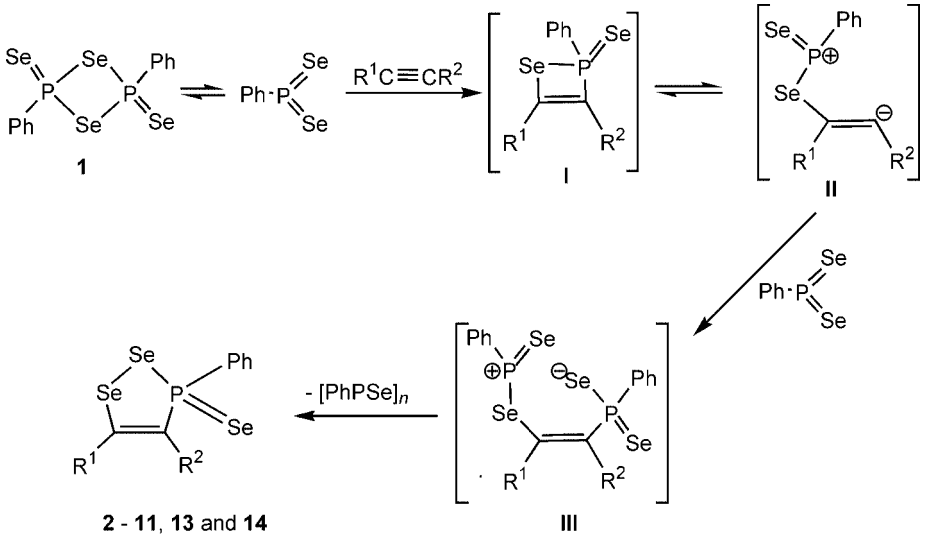


Scheme 4. Suggested mechanism for the formation of **2**–**11** and **13**.

 © 2007 Wiley-VCH Verlag GmbH & Co. KGaA, Weinheim 

pond to known Ph–P–Se rings[9] or WR [$\delta_P$ (solid state) = 18.7 ppm] The $^{31}$P-$^{31}$P coupling, typically ca. 270 Hz, along with $^{31}$P-$^{77}$Se coupling constant of ca. 220 Hz, suggest P–P–Se or P–Se–P linkages but does not provide any discriminatory evidence. The $^{77}$Se NMR showed >95% of the selenium present as the product **2** with only a very weak doublet at $\delta_{Se}$ = –308 ppm ($J$ = 765 Hz) and a singlet at $\delta_{Se}$ = 317 ppm. We can only speculate on a mechanism. At elevated temperatures **1** is believed to be in equilibrium with a diselenaphosphorane $PhPSe_2$, which is the true reactive species in refluxing solution. The first step in the reaction is a [2 + 2] cycloaddition of a P=Se bond from $PhPSe_2$ across the C≡C bond, giving an intermediate **I**, which exists in equilibrium in solution in two forms: the 1,2-selenaphosphacyclobutene **I** and the dipolar species **II**. We speculate that the latter species **II** can react with $PhPSe_2$ to give a second dipolar intermediate **III**, which rapidly eliminates $[PhPSe]_n$ to cyclise to subsequently afford **2**–**11** and **13** (Scheme 4).

In conclusion, we have successfully used Woollins' reagent for the syntheses of a series of novel vinylic P–Se heterocycles from alkyl C≡C triple bond organic substrates. Using $^1$H, $^{31}$P{$^1$H} and $^{77}$Se{$^1$H} NMR spectroscopy in conjunction with single-crystal X-ray crystallography we have elucidated the structures of the novel heterocycles.

## Experimental Section

Unless otherwise stated, all reactions were carried out under oxygen-free nitrogenusing pre-dried solvents and standard Schlenk techniques, subsequent chromatographic and work-up procedures were performed in air. Solvents were dried, purified, and stored according to common procedures.[24] 1,4-Bis(phenylethynyl)benzene,[25] 1,2-bis(phenylethynyl)benzene,[26] 1,3-bis(phenylethynyl)-benzene,[27] and 1,8-bis(phenylethynyl)naphthalene[28] were synthesised according to the literature methods.

$^1$H (270 Hz), $^{13}$C (67.9 Hz), $^{31}$P{$^1$H} (109 Hz) and $^{77}$Se{$^1$H} (51.4 Hz referenced to external $Me_2Se$) NMR spectra were recorded in $CDCl_3$ at 25 °C (unless stated otherwise) with a JEOL GSX 270. IR spectra were recorded as KBr pellets in the range of 4000–250 cm$^{-1}$ with a Perkin–Elmer 2000 FTIR/Raman spectrometer. Microanalysis was performed by the University of St Andrews microanalysis service. Mass spectrometry was performed by the EPSRC National Mass Spectrometry Service Centre, Swansea and the University of St Andrews Mass Spectrometry Service.

X-ray crystal data for **2**, **3**, **12** and **13** (Table 2 and Table 3) were collected at 93 K with a Rigaku MM007 High brilliance RA generator and Mercury CCD system. Intensities were corrected for Lorentz polarisation and for absorption. The structures were solved by direct methods. Hydrogen atoms bound to carbon were idealised. Structural refinements were obtained with full-matrix least squares based on $F^2$ by using the program SHELXTL.[29]

CCDC-6139164 to -613917 contain the supplementary crystallographic data for this paper. These data can be obtained free of charge from The Cambridge Crystallographic Data Centre via www.ccdc.cam.ac.uk/data_request/cif.

**3,5-Diphenyl-1,2,3-diselenaphosphole 3-Selenide (2):** A mixture of phenylacetylene (0.10 g, 1 mmol) and WR (0.54 g, 1 mmol) in 10 cm$^3$ of dry toluene was refluxed over 12 h to give a brown solution. Upon cooling to room temperature the solution was column-chromatographed (silica gel, toluene as eluent) to give a brown fraction of **2**, which was crystallised from dichloromethane/hexane. Yield 401 mg, 91%. $C_{14}H_{11}PSe_3$ (447.09): calcd. C 37.6, H 2.5; found C 37.7, H 2.6. IR (KBr): $\tilde{\nu}$ = 523 (s, $\nu_{P=Se}$) cm$^{-1}$. $^1$H NMR: $\delta$ = 8.29 (m, 2 H, Ph), 7.75 (m, 2 H, Ph), 7.65 (m, 3 H, Ph), 7.56 (m, 3 H, Ph), 7.26 (d, $^2J_{P,H}$ = 34 Hz, 1 H, =C–H) ppm. $^{13}$C NMR: $\delta$ = 132.7, 131.9, 131.7, 131.0, 129.3, 128.8, 128.6, 127.9, 121.9, 120.7 ppm. $^{31}$P NMR: $\delta$ = 67.1 (s, $^1J_{P,Se}$ = 350 Hz, $^1J_{P,Se}$ = 771 Hz) ppm. $^{77}$Se NMR: $\delta$ = 559.9 (d, $^2J_{P,Se}$ = 7 Hz), 411.7 (d, $^1J_{P,Se}$ = 350 Hz), –15.4 (d, $^1J_{P,Se}$ = 774 Hz) ppm. MS (CI): $m/z$ = 448 [M + H]$^+$.

**3,4,5-Triphenyl-3*H*-1,2,3-diselenaphosphole 3-Selenide (3):** A refluxing mixture of diphenylacetylene (0.18 g, 1 mmol) and WR (0.54 g, 1 mmol) in toluene was heated at 130 °C over 12 h to give a brown solution. Upon cooling to room temperature the solution was column-chromatographed (silica gel, toluene as eluent) to give an orange crystal of **3**, which was crystallised from dichloromethane/hexane. Yield 495 mg, 94 %. $C_{20}H_{15}PSe_3$ (523.19): calcd. C 45.9, H 2.9; found C 45.8, H 3.1. IR (KBr): $\tilde{\nu}$ = 539 (s, $\nu_{P=Se}$) cm$^{-1}$. $^1$H NMR: $\delta$ = 8.13 (m, 2 H, Ph), 7.45 (m, 3 H, Ph), 7.24 (m, 5 H, Ph), 7.01 (m, 5 H, Ph) ppm. $^1$H NMR: $\delta$ = 132.6, 132.4, 132.2, 130.7, 130.6, 129.8, 128.7, 128.6, 128.4, 128.2, 127.8 ppm. $^{31}$P NMR: $\delta$ = 74.3 (s, $^1J_{P,Se}$ = 357 Hz, $^1J_{P,Se}$ = 779 Hz) ppm. $^{77}$Se NMR: $\delta$ = 519.3 (d, $^2J_{P,Se}$ = 7 Hz), 373.4 (d, $^1J_{P,Se}$ = 358 Hz), –28.6 (d, $^1J_{P,Se}$ = 777 Hz) ppm. MS (ES$^+$): $m/z$ (%) = 546 [M + Na]$^+$.

**3,4-Diphenyl-5-[4-(phenylethynyl)phenyl]-3*H*-1,2,3-diselenaphosphole 3-Selenide (4) and 5,5′-(1,4-Phenylene)bis(3,4-diphenyl-3*H*-1,2,3-diselenaphosphole) 3,3′-Diselenide (5):** A solution of WR (1.08 g, 2 mmol) and 1,4-bis(phenylethynyl)benzene (0.28 g, 1 mmol) in toluene (10 cm$^3$) in a sealed tube was refluxed for 12 h, giving a yellow solution. Upon cooling to room temperature, the toluene solution was purified by column chromatography (silica gel, toluene as eluent) to afford a yellow fraction of **4** followed by another orange band, which was proved to be a mixture of conformational isomers by $^{31}$P NMR spectroscopy. Layering a dichloromethane solution of the mixture with hexane gave a major orange powder of **5a**.

**Compound 4:** Yield 180 mg, 29%. $C_{28}H_{19}PSe_3$ (623.30): calcd. C 54.0, H 3.1; found C 53.4, H 3.7. IR (KBr): $\tilde{\nu}$ = 539 (s, $\nu_{P=Se}$) cm$^{-1}$. $^1$H NMR: $\delta$ = 7.29–8.15 (m, 19 H, Ph) ppm. $^1$H NMR: $\delta$ = 140.6, 139.6, 134.8, 134.0, 133.0, 132.8, 132.6, 132.4, 132.2, 131.9, 129.8, 128.7, 128.6, 128.5, 128. 3, 125.4, 121.8, 121.4, 104.1, 83.6, 83.2, 81.7, 74.0 ppm. $^{31}$P NMR: $\delta$ = 73.9 (s, $^1J_{P,Se}$ = 357 Hz, $^1J_{P,Se}$ = 779 Hz) ppm. $^{77}$Se NMR: $\delta$ = 519.8 (d, $^2J_{P,Se}$ = 7 Hz), 382.3 (d, $^1J_{P,Se}$ = 355 Hz), –16.4 (d, $^1J_{P,Se}$ = 779 Hz) ppm. MS (EI): $m/z$ = 623 [M]$^+$, 278 [M – $PhPSe_3$]$^+$.

**Compound 5a:** Yield 105 mg, 11%. $C_{34}H_{24}P_2Se_6$ (968.26): calcd. C 42.2, H 2.5; found C 42.7, H 2.5. IR (KBr): $\tilde{\nu}$ = 559 (s, $\nu_{P=Se}$) cm$^{-1}$. $^1$H NMR: $\delta$ = 6.94–8.09 (m, 24 H, Ph) ppm. $^1$H NMR: $\delta$ = 132.4, 132.3, 132.2, 132.0, 130.5, 130.2, 130.1, 129.9, 129.6, 128.7, 128.5, 128.4, 128.2, 128.0, 127.6 ppm. $^{31}$P NMR: $\delta$ = 73.3 (s, $^1J_{P,Se}$ = 357 Hz, $^1J_{P,Se}$ = 774 Hz) ppm. $^{77}$Se NMR: $\delta$ = 522.9 (d, $^2J_{P,Se}$ = 7 Hz), 384.7 (d, $^1J_{P,Se}$ = 355 Hz), –16.3 (d, $^1J_{P,Se}$ = 773 Hz) ppm. MS (EI): $m/z$ = 968 [M]$^+$, 278 [M – 2$PhPSe_3$]$^+$.

**3,4-Diphenyl-5-[3-(phenylethynyl)phenyl]-3*H*-1,2,3-diselenaphosphole 3-Selenide (6) and 5,5′-(1,3-Phenylene)bis(3,4-diphenyl-3*H*-1,2,3-diselenaphosphole) 3,3′-Diselenide (7):** WR (1.08 g, 2 mmol) and 1,3-bisphenylethynylbenzene (0.28 g, 1 mmol) were stirred in 10 cm$^3$ of dry toluene at 130 °C in a sealed tube for 12 h, producing a dark yellow solution plus a tiny amount of black solid (selenium, resulted from the decomposition of WR). Column chromatography

 © 2007 Wiley-VCH Verlag GmbH & Co. KGaA, Weinheim 

(silica gel, toluene as eluent) produced a yellow fraction of **6** and subsequent another yellow band whose $^{31}P\{^{1}H\}$ NMR spectrum revealed a mixture of conformational isomers. Layering a dichloromethane solution of the mixture with hexane gave a yellow powder of **7a**.

**Compound 6:** Yield 360 mg, 58%. $C_{34}H_{24}P_2Se_6$ (968.26): calcd. C 54.0, H 3.1; found C 53.7, H 3.2. IR (KBr): $\tilde{\nu}$ = 532 (s, $\nu_{P=Se}$) $cm^{-1}$. $^{1}H$ NMR: $\delta$ = 6.95–8.18 (m, 19 H, Ph) ppm. $^{1}H$ NMR: $\delta$ = 135.5, 135.3, 134.6, 134.3, 133.5, 133.5, 132.7, 132.5, 132.2, 131.7, 131.6, 131.1, 130.7, 130.6, 130.0, 129.7, 129.3, 128.8, 128.4, 128.3, 122.8 ppm. $^{31}P$ NMR: $\delta$ = 74.3 (s, $^{1}J_{P,Se}$ = 356 Hz, $^{1}J_{P,Se}$ = 778 Hz) ppm. $^{77}Se$ NMR: $\delta$ = 520.7 (d, $^{2}J_{P,Se}$ = 7 Hz), 379.4 (d, $^{1}J_{P,Se}$ = 358 Hz), –25.3 (d, $^{1}J_{P,Se}$ = 777 Hz) ppm. MS (EI): *m*/*z* = 623 $[M]^+$, 278 $[M - PhPSe_3]^+$.

**Compound 7a:** Yield 175 mg, 18%. $C_{34}H_{24}P_2Se_6$ (968.26): calcd. C 42.2, H 2.5; found C 42.8, H 2.2. IR (KBr): $\tilde{\nu}$ = 538 (s, $\nu_{P=Se}$) $cm^{-1}$. $^{1}H$ NMR: $\delta$ = 7.13–8.06 (m, 24 H, Ph) ppm. $^{1}H$ NMR: $\delta$ = 132.0, 129.9, 129.7, 128.8, 128.7, 128.6, 128.5, 128.4 ppm. $^{31}P$ NMR: $\delta$ = 74.28 (s, $^{1}J_{P,Se}$ = 352 Hz, $^{1}J_{P,Se}$ = 771 Hz) ppm. $^{77}Se$ NMR: $\delta$ = 525.0 (d, $^{2}J_{P,Se}$ = 7 Hz), 381.9 (d, $^{1}J_{P,Se}$ = 354 Hz), –14.6 (d, $^{1}J_{P,Se}$ = 771 Hz) ppm. MS (EI): *m*/*z* = 968 $[M]^+$, 546 [M – Ph or Se – $PhPSe_3]^+$, 278 $[M - 2PhPSe_3]^+$.

**3,4-Diphenyl-5-[2-(phenylethynyl)phenyl]-3*H*-1,2,3-diselenaphosphole 3-Selenide (8) and 5,5′-(1,2-Phenylene)bis(3,4-diphenyl-3*H*-1,2,3-diselenaphosphole) 3,3′-Diselenide (9):** 1,2-Bis(phenylethynyl)-benzene (0.28 g, 1 mmol) and WR (1.08 g, 2 mmol) in toluene (10 $cm^3$) were refluxed for 12 h, giving a brownish yellow solution. Column chromatography (silica gel, toluene) gave a yellow fraction of **8** followed by a yellow band whose $^{31}P\{^{1}H\}$ NMR spectrum revealed a mixture of conformational isomers once again. Layering a dichloromethane solution of the mixture with hexane afforded a yellow powder of **9a**.

**Compound 8:** Yield 437 mg, 70%. $C_{34}H_{24}P_2Se_6$ (968.26): calcd. C 54.0, H 3.1; found C 54.2, H 3.8. IR (KBr): $\tilde{\nu}$ = 539 (s, $\nu_{P=Se}$) $cm^{-1}$. $^{1}H$ NMR: $\delta$ = 6.98–7.67 (m, 19 H, Ph) ppm. $^{1}H$ NMR: $\delta$ = 133.6, 133.3, 132.5, 132.3, 132.1, 132.0, 131.9, 131.4, 130.5, 129.7, 129.2, 129.0, 128.7, 128.5, 128.1, 128.0, 127.7 ppm. $^{31}P$ NMR: $\delta$ = 73.8 (s, $^{1}J_{P,Se}$ = 343 Hz, $^{1}J_{P,Se}$ = 779 Hz) ppm. $^{77}Se$ NMR: $\delta$ = 528.6 (d, $^{2}J_{P,Se}$ = 7 Hz), 409.8 (d, $^{1}J_{P,Se}$ = 346 Hz), –22.2 (d, $^{1}J_{P,Se}$ = 778 Hz) ppm. MS (EI): *m*/*z* = 623 $[M]^+$, 278 $[M - PhPSe_3]^+$.

**Compound 9a:** Yield 144 mg, 15%. $C_{34}H_{24}P_2Se_6$ (968.26): calcd. C 42.2, H 2.5; found C 42.7, H 2.6. IR (KBr): $\tilde{\nu}$ = 528 (s, $\nu_{P=Se}$) $cm^{-1}$. $^{1}H$ NMR: $\delta$ = 7.00–7.41 (m, 24 H, Ph) ppm. $^{1}H$ NMR: $\delta$ = 133.6, 133.4, 132.5, 132.3, 132.1, 131.9, 131.4, 130.6, 129.7, 129.2, 128.7, 128.5, 128.2, 128.1, 127.7 ppm. $^{31}P$ NMR: $\delta$ = 77.5 (s, $^{1}J_{P,Se}$ = 364 Hz, $^{1}J_{P,Se}$ = 822 Hz) ppm. $^{77}Se$ NMR: $\delta$ = 528.4 (d, $^{2}J_{P,Se}$ = 8 Hz), 409.8 (d, $^{1}J_{P,Se}$ = 365 Hz), –21.9 (d, $^{1}J_{P,Se}$ = 820 Hz) ppm. MS (EI): *m*/*z* = 968 $[M]^+$, 624 $[M - PhPSe_3]^+$, 278 $[M - 2PhPSe_3]^+$.

**3,4-Diphenyl-5-[10-(phenylethnyl)anthracen-9-yl]-3*H*-1,2,3-diselenaphosphole 3-Selenide (10) and 5,5′-Anthracene-9,10-diylbis(3,4-diphenyl-3*H*-1,2,3-diselenaphosphole) 3,3′-Diselenide (11):** A solution of WR (1.08 g, 2 mmol) and bis(phenylethynyl)anthracene (0.38 g, 1 mmol) in toluene (10 $cm^3$) in a sealed tube was refluxed for 12 h, giving a yellow solution. After cooling to room temperature the toluene solution was purified by column chromatography ($SiO_2$, toluene as eluent) to afford a yellow fraction of **10** followed by another orange band of the mixture. Layering a dichloromethane solution of the mixture with hexane gave orange powder of **11a**.

**Compound 10:** Yield 410 mg, 57%. $C_{36}H_{23}P_2Se_6$ (991.28): calcd. C 59.8, H 3.2; found C 59.9, H 3.4. IR (KBr): $\tilde{\nu}$ = 533 (s, $\nu_{P=Se}$) $cm^{-1}$. $^{1}H$ NMR: $\delta$ = 6.66–8.56 (m, 23 H, Ph) ppm. $^{1}H$ NMR: $\delta$ = 134.5, 134.3, 133.2, 133.0, 132.4, 132.1, 131.5, 130.1, 129.1, 128.8, 128.5, 128.2, 128.0, 127.1, 127.0, 126.7, 126.3, 126.0, 123.2, 119.8 ppm. $^{31}P$ NMR: $\delta$ = 73.3 (s, $^{1}J_{P,Se}$ = 352 Hz, $^{1}J_{P,Se}$ = 794 Hz) ppm. $^{77}Se$ NMR: $\delta$ = 529.3 (d, $^{2}J_{P,Se}$ = 7 Hz), 414.4 (d, $^{1}J_{P,Se}$ = 353 Hz), –19.6 (d, $^{1}J_{P,Se}$ = 792 Hz) ppm. MS (CI): *m*/*z* = 727 $[M + H]^+$, 378 $[M - PhPSe_3]^+$.

**Compound 11a:** Yield 183 mg, 17%. $C_{34}H_{24}P_2Se_6$ (968.26): calcd. C 47.2, H 2.6; found C 46.7, H 2.7. IR (KBr): $\tilde{\nu}$ = 533 (s, $\nu_{P=Se}$) $cm^{-1}$. $^{1}H$ NMR: $\delta$ = 6.63–8.26 (m, 28 H, Ph) ppm. $^{1}H$ NMR: $\delta$ = 133.2, 132.9, 132.8, 132.2, 132.0, 131.7, 129.9, 129.1, 128.7, 128.5, 127.9, 127.4, 127.0, 126.0 ppm. $^{31}P$ NMR: $\delta$ = 73.3 (s, $^{1}J_{P,Se}$ = 352 Hz, $^{1}J_{P,Se}$ = 779 Hz) ppm. $^{77}Se$ NMR: $\delta$ = 535.2 (d, $^{2}J_{P,Se}$ = 7 Hz), 404.0 (d, $^{1}J_{P,Se}$ = 355 Hz), –16.8 (d, $^{1}J_{P,Se}$ = 780 Hz) ppm. MS (CI): *m*/*z* = 1069 $[M + H]^+$, 726 $[M - PhPSe_3]^+$, 565 [M – $PhPSe_3$ – 2Se or 2Ph]$^+$, 378 $[M - 2PhPSe_3]^+$.

**Synthesis of Diselane 12 and 3,4-Diphenyl-5-[8-(phenylethynyl)-1-naphthyl]-3*H*-1,2,3-diselenaphosphole 3-Selenide (13):** A mixture of Woollins' reagent (1.08 g, 2 mmol) and 1,8-bis(phenylethynyl)naphthalene (0.45 g, 1 mmol) in toluene (20 $cm^3$) was heated at reflux for 12 h resulting in red solution. After cooling to room temperature, the solution was subjected to column chromatography ($SiO_2$, toluene as eluent) and afforded successively red **12** followed a pale yellow **13**.

**Compound 12:** Yield 57 mg, 14%. $C_{52}H_{30}Se_2$ (812.71): calcd. C 76.8, H 3.7; found C 76.1, H 3.9. IR (KBr): $\tilde{\nu}$ = 825 (w), 759 (m), 701 (w), 448 (w) $cm^{-1}$. $^{1}H$ NMR: $\delta$ = 6.08 (br., d, 1 H, Ph), 6.56–8.67 (br., m, 28 H, Ph), 9.64 (br., d, 1 H, Ph) ppm. $^{1}H$ NMR: $\delta$ = 135.7, 135.0, 134.2, 132.1, 131.7, 130.0, 129.9, 129.7, 129.3, 128.9, 128.0, 127.9, 125.7, 124.9, 124.8, 123.9, 122.3, 121.7, 120.9, 119.9, 119.1, 118.8 ppm. $^{77}Se$ NMR: $\delta$ = 279.7 (s, 2Se) ppm. MS (CI): *m*/*z* = 831 $[M + NH_4]^+$.

**Compound 13:** Yield 147 mg, 22%. $C_{32}H_{21}PSe_3$ (673.36): calcd. C 57.1, H 3.1; found C 57.7, H 3.3. IR (KBr): $\tilde{\nu}$ = 546 (s, $\nu_{P=Se}$) $cm^{-1}$. $^{1}H$ NMR: $\delta$ = 6.81–8.70 (m, 21 H, Ph) ppm. $^{1}H$ NMR: $\delta$ = 135.6, 134.0, 133.0, 132.4, 131.4, 131.0, 130.9, 130.0, 129.5, 129.4, 128.9, 128.7, 128.5, 127.3, 126.1, 125.8 ppm. $^{31}P$ NMR: $\delta$ = 66.5 (s, $^{1}J_{P,Se}$ = 380 Hz, $^{1}J_{P,Se}$ = 803 Hz) ppm. $^{77}Se$ NMR: $\delta$ = 564.9 (d, $^{2}J_{P,Se}$ = 11 Hz), 461.5 (d, $^{1}J_{P,Se}$ = 383 Hz), –14.7 (d, $^{1}J_{P,Se}$ = 802 Hz) ppm. MS ($CI^+$): *m*/*z* = 674 $[M + H]^+$, 436 [M – 3Se or 3Ph]$^+$, 328 $[M - PhPSe_3]^+$.

## Acknowledgments

We are grateful to the Engineering and Physical Sciences Research Council (EPSRC) (U. K.) for funding.

[1] G. L. Sommen, A. Linden, H. Heimgartner, *Helv. Chim. Acta* **2005**, *88*, 766–773.
[2] T. Wirth, *Tetrahedron* **1999**, *55*, 1–28; Y. Xu, E. T. Kool, *J. Am. Chem. Soc.* **2000**, *122*, 9040–9041.
[3] Y. Ogasawara, G. Lacourciere, T. C. Stadtman, *Proc. Natl. Acad. Sci. USA* **2001**, *98*, 9494–9498.
[4] H. E. Ganther, *Bioorg. Med. Chem.* **2001**, *9*, 1459–1466.
[5] G. Mugesh, W.-W. Du Mont, H. Sies, *Chem. Rev.* **2001**, *101*, 2125–2179.
[6] P. Ximenez-Embun, I. Alonso, Y. Madrid-Albarran, C. Camara, *J. Agric. Food Chem.* **2004**, *52*, 832–838.
[7] D. B. Vickerman, J. T. Trumble, G. N. George, I. J. Pickering, H. Nichol, *Environ. Sci. Technol.* **2004**, *38*, 3581–3586.
[8] I. P. Gray, P. Bhattacharyya, A. M. Z. Slawin, J. D. Woollins, *Chem. Eur. J.* **2005**, *11*, 6221–6227.

 © 2007 Wiley-VCH Verlag GmbH & Co. KGaA, Weinheim 

[9] J. C. Fitzmaurice, D. J. Williams, P. T. Wood, J. D. Woollins, *J. Chem. Soc., Chem. Commun.* **1988**, 741–743; P. T. Wood, J. D. Woollins, *J. Chem. Soc., Chem. Commun.* **1988**, 1190–1191; M. J. Pilkington, A. M. Z. Slawin, D. J. Williams, P. T. Wood, J. D. Woollins, *Heteroatom Chem.* **1990**, *1*, 351–355.
[10] I. Baxter, A. F. Hill, J. M. Malget, A. J. P. White, J. D. Williams, *Chem. Commun.* **1997**, 2049–2050.
[11] P. Bhattacharyya, J. D. Woollins, *Tetrahedron Lett.* **2001**, *42*, 5949–5951.
[12] J. Bethke, K. Karaghiosoff, L. A. Wessjohann, *Tetrahedron Lett.* **2003**, *44*, 6911–6913.
[13] G. Hua, Y. Li, A. M. Z. Slawin, J. D. Woollins, *Org. Lett*. **2006**, *8*, 5251–5254.
[14] I. P. Gray, H. L. Milton, A. M. Z. Slawin, J. D. Woollins, *Dalton Trans.* **2003**, 3450–3457; I. P. Gray, A. M. Z. Slawin, J. D. Woollins, *New J. Chem.* **2004**, *28*, 1383–1389; I. P. Gray, A. M. Z. Slawin, J. D. Woollins, *Dalton Trans.* **2004**, 2477–2486; I. P. Gray, A. M. Z. Slawin, J. D. Woollins, *Z. Anorg. Allg. Chem.* **2004**, *630*, 1851–1857; I. P. Gray, A. M. Z. Slawin, J. D. Woollins, *Dalton Trans.* **2005**, 2188–2194.
[15] P. Bhattacharyya, A. M. Z. Slawin, J. D. Woollins, *Chem. Eur. J.* **2002**, *8*, 2705–2711.
[16] P. Bhattacharyya, A. M. Z. Slawin, J. D. Woollins, *Angew. Chem. Int. Ed.* **2000**, *39*, 1973–1975.
[17] P. Bhattacharyya, A. M. Z. Slawin, J. D. Woollins, *J. Organomet. Chem.* **2001**, *623*, 116–119.
[18] P. Bhattacharyya, A. M. Z. Slawin, J. D. Woollins, *J. Chem. Soc., Dalton Trans.* **2001**, 300–303.
[19] P. Bhattacharyya, J. Novosad, J. R. Phillips, A. M. Z. Slawin, D. J. William, J. D. Woollins, *J. Chem. Soc., Dalton Trans.* **1995**, 1607–1613.
[20] D. L. An, N. Higeta, K. Toyota, M. Yoshifuji, *Chem. Lett.* **1998**, 17–18 and references cited therein.
[21] J. Blum, Y. Badrieh, O. Shaaya, L. Meltser, *Phosphorus Sulfur Silicon Relat. Elem.* **1993**, *79*, 87–96.
[22] R. Richter, J. Sieler, L. K. Hansen, R. Koehler, L. Beyer, E. Hoyer, *Acta Chem. Scand.* **1991**, *45*, 1–5.
[23] A. Hordvik, K. Julshamn, *Act Chem. Scand.* **1971**, *25*, 2507–2515.
[24] D. D. Perrin, W. L. F. Armarego, *Purification of Laboratory Chemicals*, 3rd ed., Pergamon Press, Oxford, **1988**.
[25] P. Nguyen, Z. Yuan, L. Agocs, G. Lesley, T. B. Marder, *Inorg. Chim. Acta* **1994**, *220*, 289–296.
[26] S. V. Kovalenko, S. Peabody, M. Manoharan, R. J. Clark, I. V. Alabugin, *Org. Lett.* **2004**, *6*, 2457; J. A. John, J. M. Tour, *Tetrahedron* **1997**, *53*, 15515–15534.
[27] T. Kawase, N. Ueda, H. R. Darab, M. Oda, *Angew. Chem. Int. Ed. Engl.* **1996**, *35*, 1556; C. J. F. Du, H. Hart, *J. Org. Chem.* **1987**, *52*, 4311–4314.
[28] B. Bossenbroek, D. C. Sanders, H. M. Curry, H. Shechter, *J. Am. Chem. Soc.* **1969**, *91*, 371–379.
[29] G. M. Sheldrick, *SHELXTL 6.10*, Bruker AXS, Madison, WI, **2002**.

Received: November 14, 2006
Published Online: January 10, 2007

 © 2007 Wiley-VCH Verlag GmbH & Co. KGaA, Weinheim

**The EUChemSoc Societies have taken the significant step into the future by merging their traditional journals, to form two leading chemistry journals, the *European Journal of Inorganic Chemistry* and the *European Journal of Organic Chemistry.* Three further EUChemSoc Societies (Austria, Czech Republic and Sweden) are Associates of the two journals.**

## COVER PICTURE

**The cover picture shows** the photograph of Robert Bunsen and the statue of Jöns Jakob Berzelius in the centre of Berzeli Park (Stockholm). Both famous chemists investigated the chemistry of tetramethyldiarsane $As_2Me_4$ (*kakodyl*), one of the first organometallic compounds that were initially prepared by Claude-Louis Cadet de Gassicourt (*Cadet's fuming liquid*) in 1757. Distibanes $Sb_2R_4$, the heavier congeners of diarsanes, exhibit much weaker metal−metal bonds and can be used for interesting bond-making and bond-breaking reactions with group 13 organometallic compounds. Details are discussed in the article by S. Schulz et al. on p. 931ff. The artwork was designed by Dr. Edgar Luttmann.

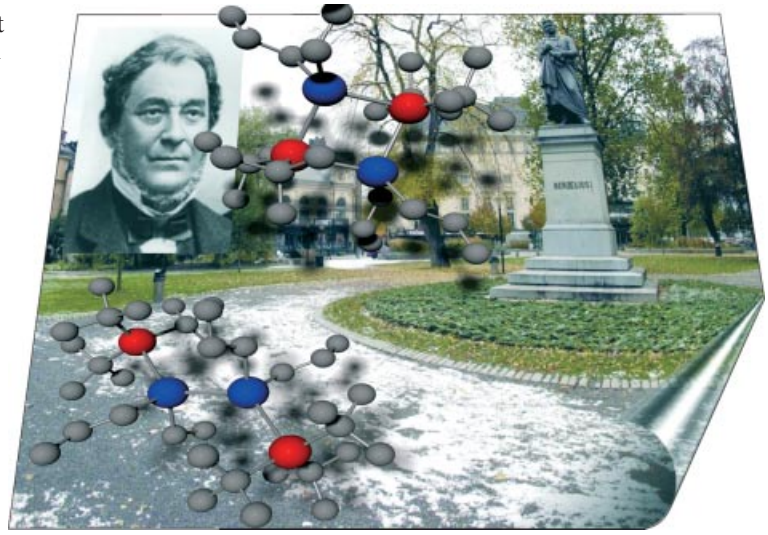

 © 2007 Wiley-VCH Verlag GmbH & Co. KGaA, Weinheim 

# CONTENTS

## MICROREVIEW

### Asymmetric Catalysis

**S. Dagorne,* S. Bellemin-Laponnaz,***
**A. Maisse-François ..... 913–925**

Metal Complexes Incorporating Monoanionic Bisoxazolinate Ligands: Synthesis, Structures, Reactivity and Applications in Asymmetric Catalysis

**Keywords:** Bisoxazolinate ligand / Asymmetric catalysis / Metal complex / Coordination chemistry

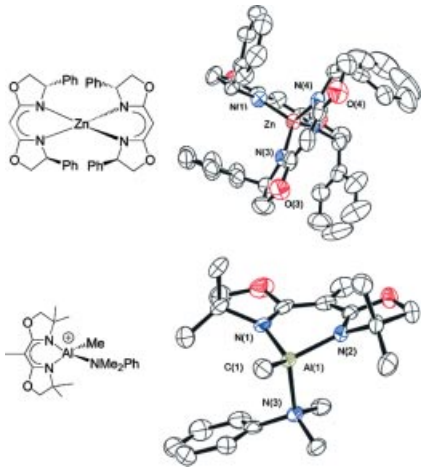


The anionic and bidentate bisoxazolinate ligand may be seen as an nitrogenated version of the acetylacetonate unit and as closely related to the diketiminate bidentate ligand; bisoxazolinate ligands exhibit a rich and versatile coordination chemistry with various metal centers. These excellent coordination properties combined with their ready accessibility in an enantiomerically pure form has opened the way to various applications in asymmetric catalysis involving this class of bidentate ligands.

## SHORT COMMUNICATION

### Corrosion Inhibitors

**V. Barba,* E. Vega, H. Höpfl,**
**L. S. Zamudio-Rivera,***
**M. A. Domínguez-Aguilar,**
**R. George-Tellez, F. Godínez-Salomon,**
**J. M. Hallen-Lopez,**
**H. I. Beltran ..... 927–930**

A Bis(di-*n*-butyltin)–Quinone Derivative as a Simultaneous Chemo- and Bioactive Corrosion Inhibitor

**Keywords:** Tin / Quinones / Corrosion / Biocide activity / X-ray structure

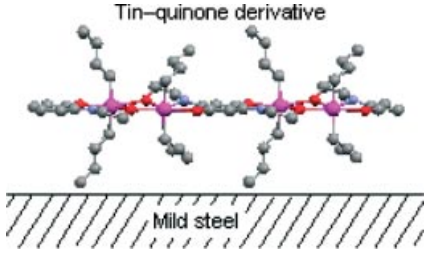


A bis(di-*n*-butyltin)–quinone derivative was synthesized and characterized; it was shown that the organometallic complex has a discrete structure in solution. In the solid state a coordination polymer is formed through Sn···O intermolecular bonds. The corrosion inhibition efficiency for steel and the inhibitory effect on aerobic and anaerobic bacteria were evaluated, showing that the title compound is a simultaneous chemo- and bioactive anticorrosion agent. Acute toxicity tests indicated a relatively low toxicity level for the environment.

## FULL PAPERS

### Distibanes

**D. Schuchmann, A. Kuczkowski,**
**S. Fahrenholz, S. Schulz,***
**U. Flörke ..... 931–935**

Reactions of Group 13 Organometallics $t$Bu$_3$M with Distibanes Sb$_2$R$_4$

**Keywords:** Main group elements / Lewis acids / Lewis bases / Solid-state structures

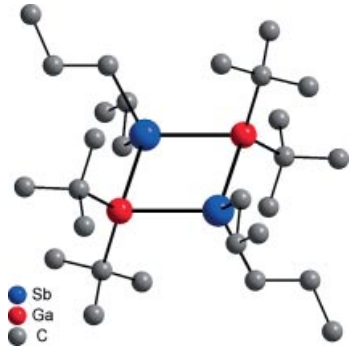


Reactions of tetraalkyldistibanes Sb$_2$R$_4$ with $t$Bu$_3$M (M = Al, Ga) initially yield Lewis acid–base adducts [$t$Bu$_3$M]$_2$[Sb$_2$R$_4$] [M = Al, R = $n$Pr (**1**), $i$Bu (**2**); M = Ga, R = $n$Pr (**3**), $i$Pr (**4**)], which in the case of the gallane adducts undergo Sb–Sb bond-breakage reactions with the subsequent formation of heterocyclic stibanylgallanes [$t$Bu$_2$GaSbR$_2$]$_2$ [R = $n$Pr (**5**), $i$Bu$_2$ (**6**)].

 © 2007 Wiley-VCH Verlag GmbH & Co. KGaA, Weinheim 

## $\eta^2$-Alkyne-1-thio Complexes

Not the steric demand but the σ-donor-π-acceptor behavior of solely one ligand L markedly determines the rate of the alkyne rotation. The influence of L on the preparation and on the electronic properties of $\eta^2$-*C*,*C*′-(BnS)alkyne complexes with a terminal sulfur atom has been investigated.

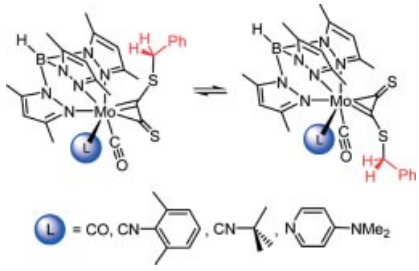


**W. W. Seidel,* B. L. Sánchez, M. J. Meel, A. Hepp, T. Pape ..... 936–943**

Electronic Control of the Rotational Barrier in $\eta^2$-Alkyne-1-thio Complexes

**Keywords:** (Alkylthio)alkyne ligands / Alkyne complexes / Molybdenum / Fluxionality / Ligand effects

## Is It Possible To Cleave Biphenyls?

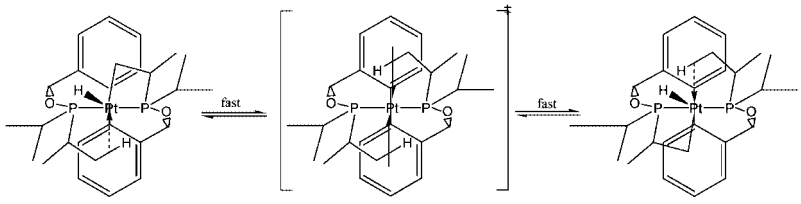


Dynamic C–H activation prevents an anticipated C–C single bond activation in a biphenyl fragment.

**K. Ruhland,* A. Brück, E. Herdtweck ..... 944–964**

Investigation of the Thermal Decomposition of [biphen(QP*i*Pr)Pt(alk)$_2$]: An Entry to C–C Single Bond Activation?

**Keywords:** Platinum / Reaction mechanisms / C–H activation / C–C activation / Agostic interactions

## Redox Properties of Ni Complexes

Electron-transfer (E) and follow-up chemical reactions (EC) of organometallic nickel complexes are studied in detail by various electrochemical and spectroelectrochemical (UV/Vis/NIR or EPR) methods. The metal oxidation states are discussed on the basis of the results of these experiments.

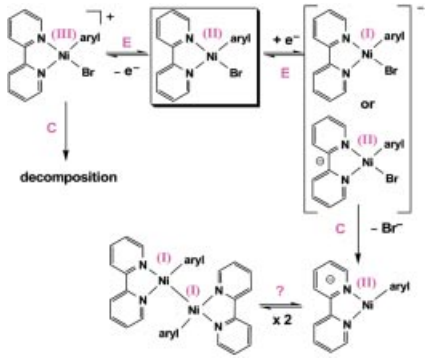


**A. Klein,* A. Kaiser, B. Sarkar, M. Wanner, J. Fiedler ..... 965–976**

The Electrochemical Behaviour of Organonickel Complexes: Mono-, Di- and Trivalent Nickel

**Keywords:** Electron transfer / Nickel / Electrochemistry / EPR spectroscopy / Spectroelectrochemistry

## Inorganic Supramolecular Chemistry

The supramolecular complexes $[Hg_6Z_4](MX_6)Hg_y$ (Z = As, Sb; M = Hg, Cd; X = Cl, Br, I; $y$ = 0, 0.5, 0.6) consist of discrete anion guests and a perovskite-like, 3D cationic framework composed of corner-sharing distorted $As_2Hg_6$ or $Sb_2Hg_6$ octahedra that possesses two types of closed cavities with different sizes. The octahedral anion guests $(MX_6)^{4-}$ are embedded in the larger cavities, while the smaller cavities trap the excess mercury atoms or remain empty. The electronic band structures and density of states (DOS) for these compounds are calculated by density functional methods.

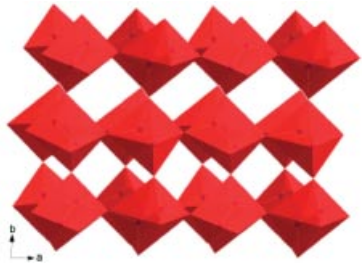

**J.-P. Zou, Y. Li, M.-L. Fu, G.-C. Guo,* G. Xu, X.-H. Liu, W.-W. Zhou, J.-S. Huang ..... 977–984**

The Synthesis, Crystal and Band Structures, and Properties of the Quaternary Supramolecular Complexes $[Hg_6Z_4](MX_6)Hg_y$ (Z = As, Sb; M = Hg, Cd; X = Cl, Br, I; $y$ = 0, 0.5, 0.6)

**Keywords:** Density functional calculations / Host–guest systems / Pnictides / Semiconductors / Supramolecular chemistry

 © 2007 Wiley-VCH Verlag GmbH & Co. KGaA, Weinheim 

# CONTENTS


## Cationic Zinc Thiolates

**J. Notni, W. Günther, E. Anders* ..... 985–993**

Zinc Thiolate Complexes $[ZnL_n(SR)]^+$ with Azamacrocyclic Ligands, Part III: The Influence of the Ligand $L_n$ on the Reactivity of Zinc-Bound Thiolate

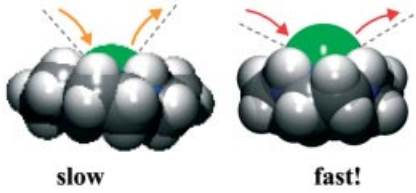


Reactions proceeding by an associated (metal-bound) mechanism are faster in cases of decreased obstruction of the zinc(II) ion by the macrocyclic ligand. This effect overrides electronic and/or orbital reaction control, as inferred from correlation plots of kinetic data against structural and electronic parameters obtained from density functional calculations.

**Keywords:** Zinc / Sulfur ligands / Kinetics / Density functional calculations / Enzyme models

## Tetratellurometallates

**M. Brandl, A. Ebner, M. M. Kubicki, Y. Mugnier, J. Wachter,* E. Vigier-Juteau, M. Zabel ..... 994–1003**

Syntheses, Properties and Structures of $[\{(C_5Me_5)_2Nb\}_2NiTe_4]$ and $[(t\text{BuC}_5H_4\text{-}Nb)_2Ni_5Te_7(Ph_2PCH_2PPh_2)_2]$: The Quest for Tetratelluronickelate Clusters

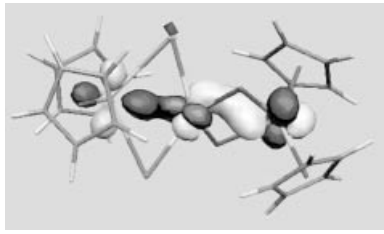

Two heterometallic telluride clusters have been obtained from $Ni(COD)_2$, $Cp_2NbTe_2H$, and $Ph_2PCH_2PPh_2$. The formation of a severely distorted $NiTe_4$ tetrahedron in $[\{(C_5Me_5)_2Nb\}_2NiTe_4]$ may be assisted by Nb–Ni (intraannular) and Te–Te (interannular) bonding interactions.

**Keywords:** Niobium / Nickel / Tellurium / Electrochemistry / Density functional calculations

## Coordination Polymer

**V. Chandrasekhar,* P. Thilagar, T. Senapati ..... 1004–1009**

Transition Metal-Assisted Hydrolysis of Pyrazole-Appended Organooxotin Carboxylates Accompanied by Ligand Transfer

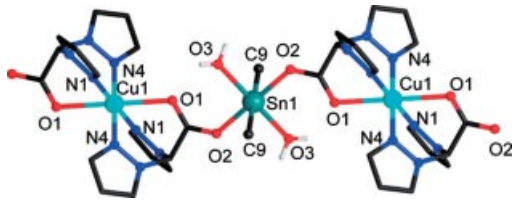


The reaction of $[\{n\text{Bu}_2\text{SnO}_2\text{CL}\}_2\text{O}]_2$ (**1**), $[\{n\text{Bu}_2\text{SnO}_2\text{CL}'\}_2\text{O}]_2$, (**2**) $[n\text{BuSn(O)O}_2\text{CL}]_6$ (**3**), and $[n\text{BuSn(O)O}_2\text{CL}']_6$ (**4**), (L = $(Pz)_2CH$-); L′ = $(3,5\text{-}Me_2Pz)_2CH$-; Pz = pyrazolyl) with hydrated metal salts leads to the hydrolysis of the organotin carboxylates and the formation of $[Cu(LCOO)_2(NO_3)_2(n\text{Bu}_2\text{Sn}((H_2O)_2)]_n$-$[Cu(LCOO)_2]$ (**5**), $[Mg(L'COO)_2]$ (**6**), $[Cu(LCOO)_2]$ (**7**), and $[\{(Cu(L'COO)_2\text{-}(Cu(MeOH))_3\}\{ClO_4\}_2]_n$ (**8**). The solid-state structure of **5** reveals that two independent molecules are present in the same asymmetric unit. One of these is a heterobimetallic coordination polymer containing inter-linked $[n\text{Bu}_2\text{Sn}(H_2O)_4]$ and $Cu(LCOO)_2$ sub-units.

**Keywords:** Organotin carboxylates / Organooxotin / Organostannoxane / Heterobimetallics / Supramolecular chemistry / Transition metals

## Coordination Polymers

**M. Bröring,* S. Prikhodovski, E. C. Tejero, S. Köhler ..... 1010–1019**

Tripyrrinatocadmium Complexes: Enforcing Supramolecular Aggregation by a Large Ion

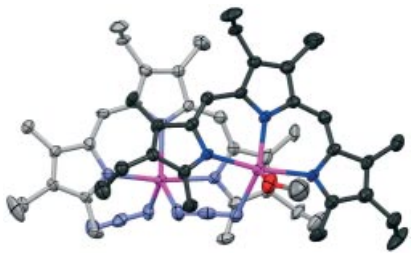

The employment of the large $Cd^{II}$ ion in an open-chain tripyrrolic ligand environment results in a simple, yet very effective approach for the construction of new supramolecular systems. The combination of either pseudohalide or *O*,*O*-chelate anions with cadmium(II)-tripyrrin complex fragments proved very successful and resulted in the formation of various 1D-chain structures.

**Keywords:** Tripyrrin / Cadmium / Porphyrinoids / Supramolecular chemistry


 © 2007 Wiley-VCH Verlag GmbH & Co. KGaA, Weinheim 

## Metalloenzyme Models

A truly functional model system for molybdenum oxotransferases provides evidence for all biologically realistic intermediates, namely mononuclear $Mo^{VI}$, $Mo^{V}$ and $Mo^{IV}$ species. Dinucleation to EPR-silent $[Mo^{V}_2O_3]$ species prevailing in homogeneous solution is suppressed by immobilising the active species to a polymeric support by two-point attachment.

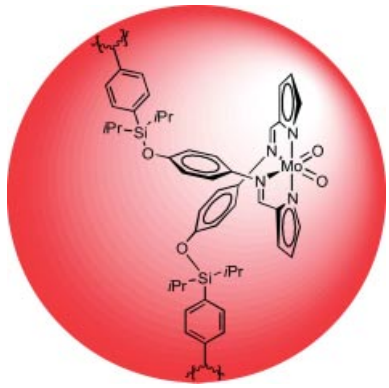


**K. Heinze,* A. Fischer ..... 1020–1026**

Polymer-Supported Dioxido-$Mo^{VI}$ Complexes as Truly Functional Molybdenum Oxotransferase Model Systems

**Keywords:** Enzyme models / Immobilised complexes / Molybdenum / Nitrogen ligands / Oxygen transfer

## Keggin-Type Polyoxotungstates

A systematic study of metal coordination in the Keggin-type anions $[PW_{12}O_{40}]^{3-}$, $[PW_{11}O_{39}]^{7-}$, $[PW_{11}M(H_2O)O_{39}]^{4-}$, M = Fe, Ru, and $[XW_{11}Mn^{III}(H_2O)O_{39}]^{n-}$, X = P, Si, B, was performed by EXAFS spectroscopy using multiple- and single-scattering analysis. This study allowed for the comparison of average inter-atomic distances in the different heteropolyanions of the same family in tetrabutylammonium salts and in acetonitrile solution.

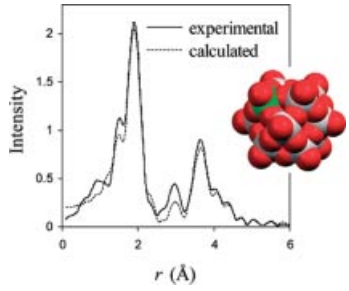


**M. S. S. Balula, I. C. M. S. Santos, J. A. F. Gamelas, A. M. V. Cavaleiro,* N. Binsted, W. Schlindwein .... 1027–1038**

Structural Studies of Keggin-Type Polyoxotungstates by Extended X-ray Absorption Fine Structure Spectroscopy

**Keywords:** Polyoxometalates / Keggin / EXAFS spectroscopy

**If not otherwise indicated in the article, papers in issue 6 were published online on February 13, 2007**

 © 2007 Wiley-VCH Verlag GmbH & Co. KGaA, Weinheim

**The EUChemSoc Societies have taken the significant step into the future by merging their traditional journals, to form two leading chemistry journals, the *European Journal of Inorganic Chemistry* and the *European Journal of Organic Chemistry.* Three further EUChemSoc Societies (Austria, Czech Republic and Sweden) are Associates of the two journals.**

## COVER PICTURE

**The cover picture shows** the photograph of Robert Bunsen and the statue of Jöns Jakob Berzelius in the centre of Berzeli Park (Stockholm). Both famous chemists investigated the chemistry of tetramethyldiarsane $As_2Me_4$ (*kakodyl*), one of the first organometallic compounds that were initially prepared by Claude-Louis Cadet de Gassicourt (*Cadet's fuming liquid*) in 1757. Distibanes $Sb_2R_4$, the heavier congeners of diarsanes, exhibit much weaker metal−metal bonds and can be used for interesting bond-making and bond-breaking reactions with group 13 organometallic compounds. Details are discussed in the article by S. Schulz et al. on p. 931ff. The artwork was designed by Dr. Edgar Luttmann.

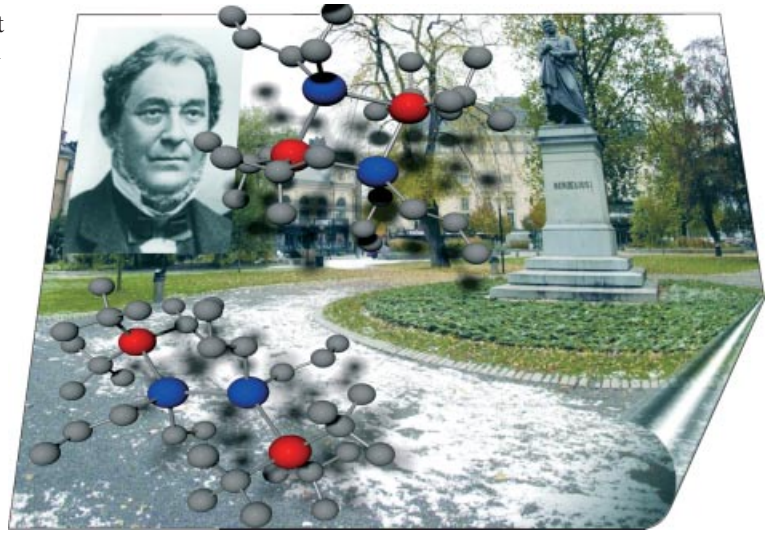

 © 2007 Wiley-VCH Verlag GmbH & Co. KGaA, Weinheim 

DOI: 10.1002/ejic.200601127

# Metal Complexes Incorporating Monoanionic Bisoxazolinate Ligands: Synthesis, Structures, Reactivity and Applications in Asymmetric Catalysis

**Samuel Dagorne,*[a] Stéphane Bellemin-Laponnaz,*[a] and Aline Maisse-François[a]**

**Keywords:** Bisoxazolinate ligand / Asymmetric catalysis / Metal complex / Coordination chemistry

The present contribution reviews the synthesis, structures, reactivity and applications in asymmetric catalysis of metal complexes containing monoanionic bisoxazolinate ligands. The anionic and bidentate bisoxazolinate ligand, which may be seen as a nitrogenated version of the acetylacetonate unit and may also be closely related to the diketiminate bidentate ligand, appears to exhibit a rich and versatile coordination chemistry with various metal centers. These excellent coordination properties, combined with the ready accessibility of chiral bisoxazolinate ligands in an enantiomerically pure form, has opened the way to various applications in asymmetric catalysis involving this class of bidentate ligands. Thus, the use of chiral bisoxazolinate ligands in asymmetric catalysis constitutes a central part of this review.
(© Wiley-VCH Verlag GmbH & Co. KGaA, 69451 Weinheim, Germany, 2007)

## Introduction

Chiral oxazolines are among the most widely used ligands in asymmetric catalysis.[1] The success of this "privileged" class of ligands in numerous metal-complex-catalyzed transformations may be related both to their ready accessibility and the possibility of using them as building blocks for the design of multidentate ligands, thereby allowing access to various chelating ligands with finely tuned coordination properties.[2] In addition to these attractive features, the intrinsic skeleton of the chiral oxazoline unit is expected to favor a high level of asymmetric induction as it incorporates a stereogenic center that is usually located on the carbon next to the metal-coordinated nitrogen. The latter feature, which is of obvious importance in asymmetric catalysis, is also largely responsible for the widespread use of these ligands in this field. Thus, since the earliest studies on the use of chiral oxazolines in catalysis, ligands incorporating an oxazoline with various donating groups include bisoxazolines,[3] trisoxazolines,[4] and oxazoline ligands with an additional chiral element attached to their skeleton or with a characteristic structure.[5]

[a] Université Louis Pasteur, Institut de Chimie, UMR CNRS 7177,
4 rue Blaise Pascal, 67000 Strasbourg, France
Fax: +33-3-90245001
E-mail: dagorne@chimie.u-strasbg.fr;
bellemin@chimie.u-strasbg.fr

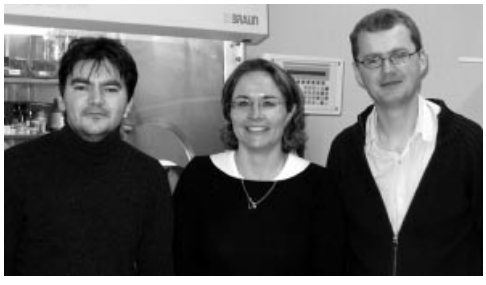

*Samuel Dagorne (left) obtained his undergraduate degree in chemistry at the Université de Rennes I (Rennes, France) in 1994. In 1995, he joined the group of Professor Richard F. Jordan at the University of Iowa (Iowa City, IA, USA) and graduated with a Ph.D in 1999 on the chemistry of chiral zirconocenes and group 13 compounds. In 1999, he became a member of the group of Professor Richard R. Schrock (Massachusetts Institute of Technology, Cambridge, MA, USA) as a postdoctoral fellow working on molydenum alkylidene chemistry. He joined the CNRS in october 2000 as a Chargé de recherche and is currently at Université Louis Pasteur. His research interests mainly concern the synthesis and reactivity studies of highly electrophilic group 13 species.*
*Stéphane Bellemin-Laponnaz (right) studied chemistry at the Université Joseph Fourier (Grenoble, France) and at the Université Louis Pasteur (Strasbourg, France). In 1994, he joined the group of Professor John A. Osborn at the Université Louis Pasteur to obtain his doctorate in 1998 studying the chemistry of rhenium oxo compounds. In 1999, he became a member of the group of Professor Gregory C. Fu (Massachusetts Institute of Technology, Cambridge, MA) as a postdoctoral fellow working on kinetic resolution and phosphametallocene chemistry. Since October 2000, he has been a Chargé de recherche CNRS at the Université Louis Pasteur. His research centres on asymmetric catalysis with highly symmetric ligands and N-heterocyclic carbenes.*
*Aline Maisse-François (middle) was born in 1974. She studied chemistry at the Université de Franche-Comté (Besançon, France) and Université Louis Pasteur (Strasbourg). In 1995 she joined the group of Dr. M. Pfeffer (ULP, Strasbourg) to obtain her doctorate in 1999 in organometallic chemistry. Then she became a member of the group of Pr. G. Suess-Fink (Université de Neuchâtel) as a postdoctoral associate working on catalysis with ruthenium clusters. Since September 2000, she has been Maître de Conférences at the Université Louis Pasteur.*

 © 2007 Wiley-VCH Verlag GmbH & Co. KGaA, Weinheim 

Among the above class of ligands, neutral $C_2$-symmetric bisoxazoline ligands have been the most studied as $C_2$-symmetric chelates have become landmark ligands for use in asymmetric catalysis since the pioneering work of Kagan in this area.[6] In general, bisoxazoline ligands in which one carbon atom links two oxazoline rings are the most frequently used (Scheme 1). Such entities, which can be structurally related to the semicorrin ligands **1** developed by Pfaltz and co-workers,[7] are neutral bidentate ligands of the type **2** and **3**. While derivatives **2** and **3** may be used as $L_2$ chelates, monoanionic bisoxazolinates **4** that act as $LX^-$ chelates may be obtained by deprotonation of **3**. Such anionic bidentate ligands may be seen as a chiral, nitrogenated version of the acetylacetonate (acac) unit, which is known to exhibit a rich and versatile coordination behavior with various metal centers.[8] Over the last few years, the use of chiral bisoxazolinate ligands of type **4** for coordination to metal centers has received a growing attention as the derived complexes may be of interest in asymmetric catalysis. In this regard, remarkable catalytic systems have already been developed based on this ligand structure. In addition, several recent reports on the coordination chemistry of bisoxazolinate to various metal centers have provided an insight into the structural trends that might be expected for this class of complexes.

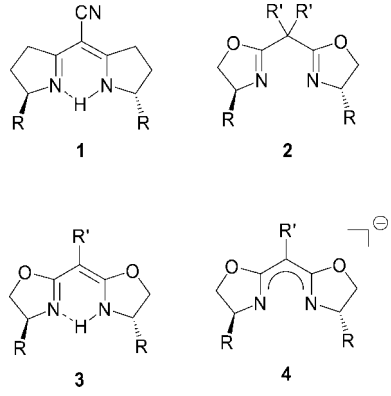


Scheme 1.

Although the coordination chemistry and the potential applications in catalysis of metal complexes bearing neutral bisoxazolines have been reviewed previously,[9] those of bisoxazolinato ligands has not been the subject of a similar survey despite the interesting results reported over the past few years with these monoanionic ligands. The present contribution thus reviews metal complexes incorporating monoanionic bisoxazolinate ligands of type **4** that have been prepared and structurally characterized thus far and the catalytic applications involving these metal complexes. A special emphasis will also be given to their use in asymmetric catalysis.

## Group 1 and 2 Metal Complexes

To date, coordination of the bisoxazolinate ligand to group 1 and 2 metals has been the subject of very few reports. Bisoxazolinatolithium salts, for example, which can be easily generated by reaction of neutral bisoxazolines of type **3** with Brönsted bases such as *n*BuLi and amidolithium salts, have been mainly used as convenient starting materials for subsequent salt metathesis reactions with various metal halides, thereby allowing access to the corresponding bisoxazolinate metal complexes. However, to date, no structural data are available on group 1 bisoxazolinate metal complexes.

As for group 2 derivatives, reports on these complexes have thus far been restricted to magnesium derivatives. An initial report by Singh concluded, on the basis of NMR, IR, and cryoscopic data, that bisoxazolines readily react with $R_2Mg$ or RMgCl to form the corresponding dinuclear magnesium complexes **5** by an alkane elimination (Scheme 2).[10] The use of two equivalents of bisoxazolines was reported to yield the homoleptic bis(bisoxazolinato)-magnesium complex **6** (Scheme 2).

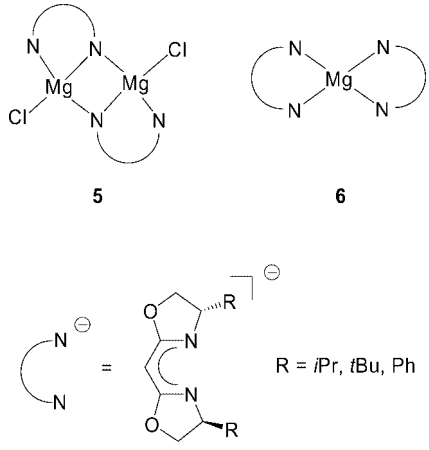


Scheme 2. Proposed structures of complexes **5** and **6**.

More recently, Hoffmann et al. have elegantly illustrated the potential use of chiral bisoxazolinatomagnesium complexes in enantioselective synthesis.[11] Thus, for example, the chiral alkylmagnesium complex **7**, which can be readily prepared by treatment of the corresponding chiral bisoxazoline with $iPr_2Mg$, can be used to differentiate the enantiotopic iodine atoms of 1,1-dihaloalkanes by a halogen/metal exchange reaction (Scheme 3).

The kinetically controlled iodine/magnesium exchange between **7** and a 1,1-dihaloalkane preferentially affords the diastereomer **8**, which was proposed to be configurationally stable at –78 °C on the basis of careful monitoring experiments and can be trapped by a combination of $AlMe_2Cl$ and benzaldehyde to afford the corresponding iodohydrins in good yield (73%) and with a reasonable *ee* (53%). The chiral bisoxazolinatomagnesium complex **7** was also used for an enantioselective halogen/metal exchange reaction of a racemic bromoiodo compound, thus providing access to an enantiomerically enriched bromohydrin, albeit in low *ee*, by a kinetic resolution process (33% yield, 18% *ee*, Scheme 4). The unreacted enantiomer of the racemic bromoiodo compound could be re-isolated in 62% yield with 8% *ee*.

 © 2007 Wiley-VCH Verlag GmbH & Co. KGaA, Weinheim 

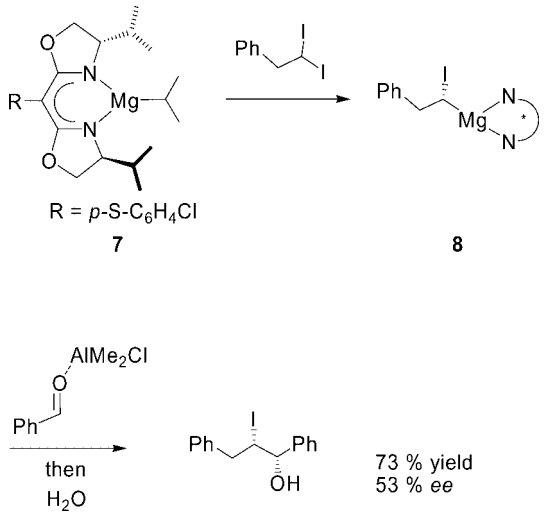


Scheme 3. Reaction of a 1,1-diiodoalkane with complex **7**.

From a reactivity point of view, these studies show that the basicity of the monoanionic bisoxazolinate ligand can greatly influence the outcome of the reaction between the neutral bisoxazoline and $i$Pr$_2$Mg. Thus, while the reaction of the simple bisoxazoline (BOX-$i$Pr$_2$)H with $i$Pr$_2$Mg yields a statistical mixture of $i$Pr$_2$Mg, the mono-bisoxazolinato, and the bis(bisoxazolinato)magnesium complexes (Scheme 5), that of the arylthio-substituted bisoxazoline yields the mono-bisoxazolinatomagnesium complex quantitatively (Scheme 5). This difference in reactivity may be ascribed to the less basic character of the arylthio-substituted bisoxazolinate with respect to (BOX-$i$Pr)$^-$.

### Group 3 Transition Metal Complexes

The use of nitrogen-based chelating ligands for coordination to rare earth metals (including scandium and yttrium) has been increasing over the last years, with the diketiminate bidentate ligand being a ligand of choice in this area.[12] It is therefore easily understood that bisoxazolinates have become of interest for coordination to group 3 metal complexes. In this regard, Anwander and collaborators first synthesized lanthanide complexes incorporating bisoxazolinate ligands.[13] The precursors Ln[N(SiHMe$_2$)$_2$]$_3$(thf)$_2$ (Ln = Y, La) were found to react smoothly with one or two equivalents of a lithium bisoxazolinate salt to give the corresponding chiral complexes **9** or **10** in good yields (Scheme 6). Yttrium and lanthanum were chosen for this study because

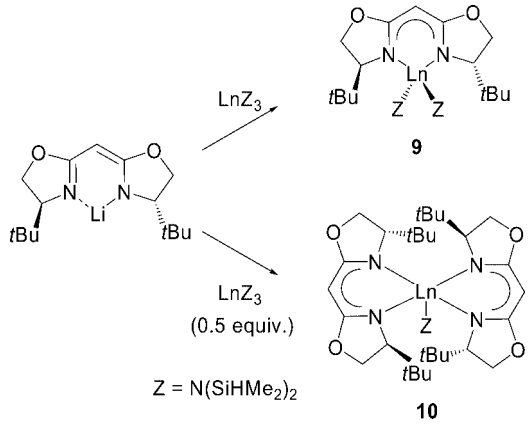


Scheme 6. Synthesis of lanthanide complexes **9** and **10** (Ln = Y, La).

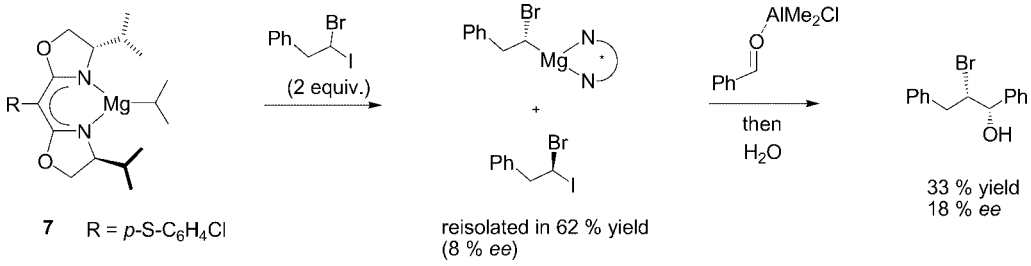


Scheme 4. Kinetic resolution of 1,1-bromoiodoalkane.

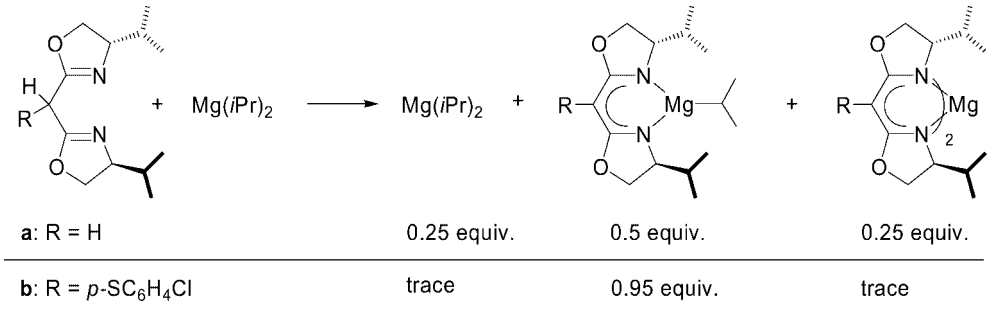


Scheme 5. Reaction of ligand **a** or **b** with Mg($i$Pr)$_2$.

 © 2007 Wiley-VCH Verlag GmbH & Co. KGaA, Weinheim 

they are representative of small and large lanthanides, respectively. The yttrium derivative **9** was characterized by an X-ray crystallographic study (Figure 1). The complex lies on a $C_2$-symmetric axis and the metal center adopts a distorted tetrahedral structure. The silylamide ligands are oriented away from the bulky *tert*-butyl groups, thereby minimizing the steric interactions. The bis(bisoxazolinato) complexes **10** were characterized by classical techniques, although no X-ray study was reported. Attempts to synthesize the homoleptic complexes $Ln(Box)_3$ failed, presumably for steric reasons.

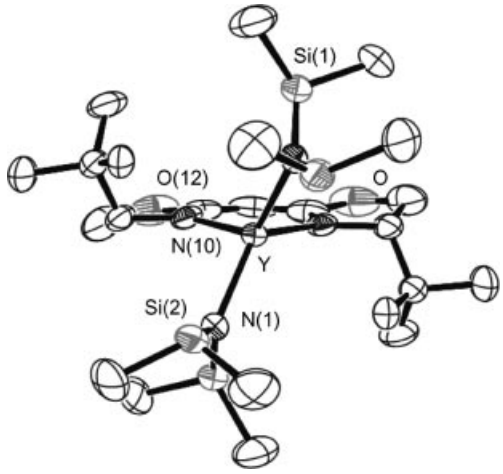


Figure 1. Molecular structure of **9**. Selected distances [Å] and angles [°]: Y–N(1) 2.222(6), Y–N(10) 2.288(5); N(10)–Y–N(10)′ 82.0(2), N(1)–Y–N(1)′ 126.4(2).

The ready and straightforward accessibility of chiral bisoxazolinato lanthanide complexes has prompted studies of their potential in enantioselective catalysis. In this area, Marks et al. have already thoroughly shown the usefulness of this new class of chiral complexes as catalysts for the enantioselective intramolecular hydroamination reaction − a formal addition of an N–H bond across a C=C double bond.[14] In the 1990s, chiral *ansa*-lanthanocenes were found to be efficient catalysts for this reaction, with *ee* values of up to 74% being reported for the formation of five-membered rings[15] and *ee* values of up to 67% for six-membered rings.[16] However, these chiral *ansa*-metallocene derivatives were found to racemize in the presence of amines, which lowers the enantioselectivity and also hampers accessibility to the substrate. In the search for a new catalyst class that may outperform chiral lanthanocenes, various lanthanide bisoxazolinate complexes were tested.[17]

Different screening experiments showed that lanthanide mono-bisoxazolinate complexes $(Box)Ln[N(TMS)_2]_2$ effectively catalyze the enantioselective intramolecular hydroamination with good rates and enantioselectivities (up to 67% *ee*; Scheme 7), which constitutes a rare example of an enantioselective hydroamination by non-Cp lanthanide complexes. Interestingly, and unlike the trend observed in metallocenes derivatives, the enantioselectivities were found to increase with the ionic radius of the metal, with the best results being observed for the chiral lanthanum derivatives. As for the bis(bisoxazolinato) lanthanide compounds, these were also found to catalyze the reaction, with similar enantioselectivities but lower activity.

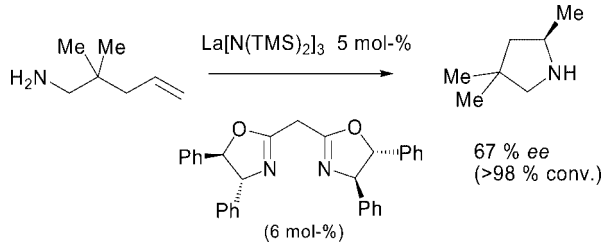


Scheme 7. Intramolecular hydroamination/cyclization with a chiral bis(oxazolinato)lanthanide catalyst generated in situ.

More recently, Carpentier et al. have reinvestigated the chemistry of bis(bisoxazolinato) lanthanide complexes such as **10** and synthesized new chiral and achiral bis(bisoxazolinato)yttrium and -lanthanum complexes.[18] The aim of their studies was to probe the potential of these complexes as initiators of the ring-opening polymerization (ROP) of (D,L)-lactide and (D,L)-β-butyrolactone. Along the way, the molecular structure of the achiral dimethylbisoxazolinate derivative **11** was established by X-ray crystallography; this is the first solid-state structure reported for a bis(bisoxazolinato) lanthanide compound (Figure 2). The geometry at the metal center in **11** is distorted trigonal bipyramidal, with the apical sites being occupied by two bisoxazolinate nitro-

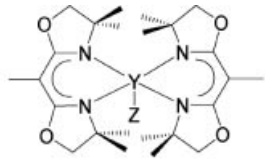


**11**
Z = N(SiHMe$_2$)$_2$

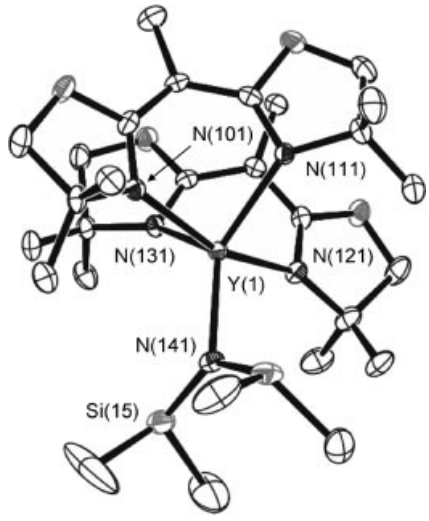


Figure 2. Molecular structure of **11**. Selected distances [Å] and angles [°]: Y(1)–N(111) 2.253(2), Y(1)–N(121) 2.389(2), Y(1)–N(131) 2.325(2), Y(1)–N(111) 2.336(2), Y(1)–N(101) 2.388(2); N(121)–Y(1)–N(141) 99.35(7).

 © 2007 Wiley-VCH Verlag GmbH & Co. KGaA, Weinheim 

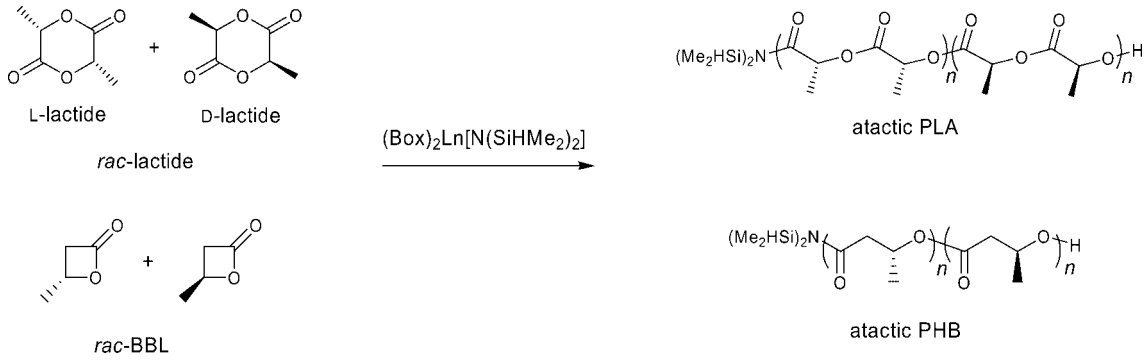


Scheme 8. Ring-opening polymerization of *rac*-lactide and *rac*-β-butyrolactone.

gens. As expected, a significant delocalization of the ligand's negative charge is indicated by an elongation of the N–C and a decrease of the C–C bond lengths of the bisoxazolinate chelating backbone with respect to those in the neutral bisoxazoline analogs.

The prepared complexes were found to be highly active and productive in the ROP of (D,L)-lactide and (D,L)-β-butyrolactone, with turnover frequencies of up to 31200 $h^{-1}$ and turnover numbers of up to 2400 (at room temperature; Scheme 8). These polymerizations proceed in a controlled manner and give polymers with relatively narrow polydispersities ($M_w/M_n$ = 1.08–1.44). However, in all cases, and regardless of the nature of the chelating bisoxazolinate ligand, the microstructure of the polymer exhibits no stereoregularity − only atactic polymers are produced.[19]

## Group 4–7 Transition Metal Complexes

### *Ti Complexes*

Taking advantage of the ready accessibility of enantiomerically pure bisoxazolines, an enantioselective reduction of ketones catalyzed by $Ti^{IV}$/chiral bisoxazolinate systems (using a silane as a stoichiometric hydride source) has recently been reported by Cozzi et al.[20] Once again, the main driving force for this work was the design and synthesis of alternative catalysts to the chiral Ti metallocenes originally developed by Buchwald, which were shown to be quite effective catalysts of the aforementioned reduction but whose isolation requires a tedious resolution process. The titanium(IV)/chiral bisoxazolinate catalytic systems were generated in situ by reaction of a chiral bisoxazoline with *n*BuLi followed by addition of a titanium(IV) ($TiX_4$) precursor. Since two equivalents of bisoxazolinates were used, the titanium complex was proposed to be an octahedral complex of the general formula [$(Box)_2TiX_2$] (**12**; Scheme 9).

According to their studies, the best results were obtained using ligand **13**, $TiF_4$, and $(EtO)_3SiH$ as the hydride source. Under these conditions, the reduction of various aryl alkyl ketones proceeds with enantiomeric excess of up to 85% (Scheme 10). However, in the present case, the *ee* values are, in general, lower than those observed with chiral titanium metallocenes.

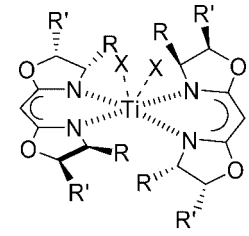

**12**

Scheme 9. Proposed structure of the titanium precatalyst.

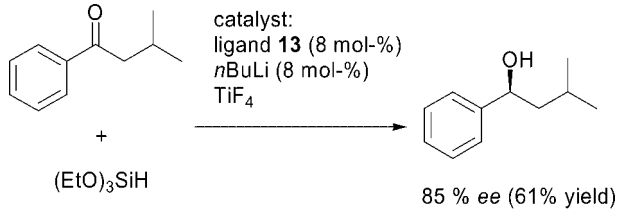


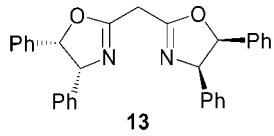

**13**

Scheme 10. Enantioselective reduction of isovalerophenone catalyzed by a chiral bisoxazolinatotitanium complex generated in situ.

Thorough theoretical investigations together with some NMR monitoring experiments were also carried out to gain insight into the mechanism of the $Ti^{IV}$/chiral bisoxazolinate-catalyzed reaction.[21] DFT calculations performed for two possible reaction pathways, one involving a $Ti^{IV}$ hydride as the active catalytic species and the other one a $Ti^{III}$ hydride species, concluded that the energetically favored mechanism involves a $Ti^{IV}$ hydride as the active species. These computational results apparently matched the experimental NMR spectroscopic data, since no formation of paramagnetic species could be detected. However, it is noteworthy that a titanium(III) hydride complex has been proposed as the active species in the case of chiral titanium metallocene catalysis.[45]

 © 2007 Wiley-VCH Verlag GmbH & Co. KGaA, Weinheim 

### *Re Complexes*

A chiral bisoxazolinato(oxido)rhenium(V) complex [(CN-BOX)($PPh_3O$)$ReOCl_2$] (**15**; Scheme 11 and Figure 3) that was found to catalyze the enantioselective hydrosilylation of ketones and imines has also been synthesized and structurally characterized recently. Initial studies by Toste et al. showed that the $Re^V$ complex [$(Ph_3P)_2Re(O)_2I$] efficiently catalyzes the hydrosilylation of ketones.[22] Based on mechanistic studies of the latter system, they anticipated that the use of a chiral and monoanionic bidentate ligand may open the way to an enantioselective catalytic system. While classical monoanionic bisoxazolinates do not react with [$(Ph_3P)_2Re(O)_2I$], the more acidic cyanobisoxazolines, first reported by Corey and Wang in 1993, do.[23] Thus, the reaction of cyanobisoxazoline **14** and [$(Me_2S)ReCl_3O(OPPh_3)$] affords complex **15** (Figure 3 and Scheme 11). The metal possesses a distorted octahedral geometry in which the oxido ligand is *trans* to the $Ph_3PO$ ligand.[24] This chiral $Re^V$ species is an active catalyst for the enantioselective phosphanyl imine reduction,[25] with good to excellent enantiomeric excesses (>99% *ee*) for aromatic imines (including heteroaromatic), α-imino esters, and α,β-unsaturated imines (Scheme 12). We also note that these reactions were carried out without the need for rigorous exclusion of air and moisture, thus rendering this catalytic system particularly attractive.

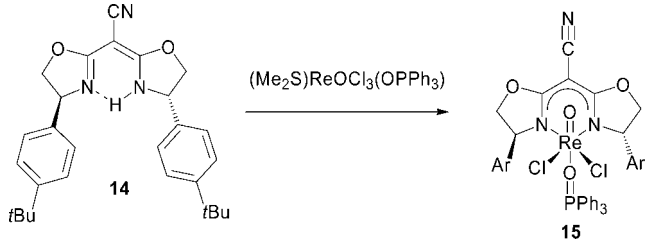


Scheme 11. Synthesis of the rhenium complex **15** from the cyanobisoxazoline **14**.

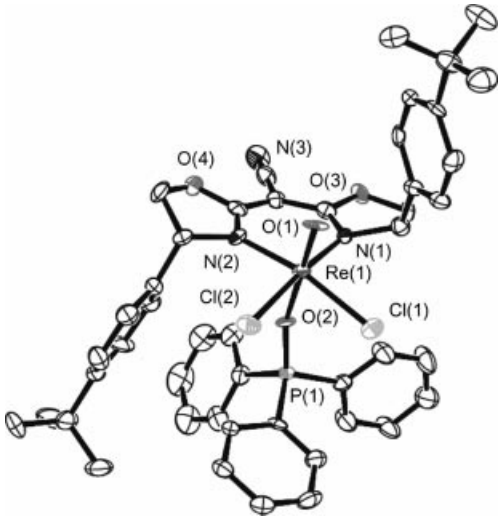


Figure 3. Molecular structure of **15**. Selected distances [Å] and angles [°]: Re(1)–O(1) 1.672(5), Re(1)–O(2) 2.131(6), Re(1)–N(1) 2.068(7), Re(1)–N(2) 2.045(7), Re(1)–Cl(1) 2.378(3), Re(1)–Cl(2) 2.368(2); N(1)–Re(1)–N(2) 90.1(3), O(1)–Re(1)–O(2) 174.7(3).

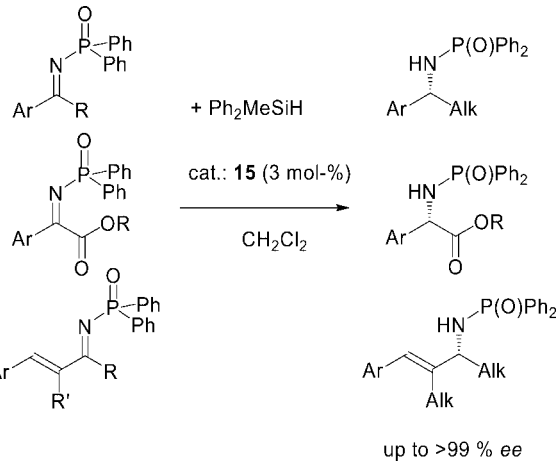


Scheme 12. Enantioselective imine reduction with rhenium precatalyst **15**.

## Group 9–12 Metal Complexes

### *Rh Complexes*

Bisoxazolinate ligands have also been found to be suitable for coordination to rhodium. In 1994, Brown et al. reported the synthesis and solid-state structure of the bisoxazolinato complex [(BOX-*i*Pr)$Rh^I(\eta^2\text{-ethene})_2$] (**16**; Figure 4).[26]

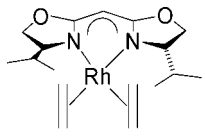


**16**

(BOX-Ph)$Rh^I$-(η-ethene)$_2$ (**17**)

(BOX-*t*Bu)$Rh^I$-(η-ethene)$_2$ (**18**)

Figure 4. Structure of the Rh complexes **16**–**18**.

The most interesting feature of **16** is that both ethenes are displaced from the ideal perpendicular geometry in a rotatory or "rolling" fashion by about 10°. This distortion occurs with little or no energetic cost according to theoretical calculations. More recently, the related $Rh^I$ complexes [(BOX-Ph)$Rh^I(\eta^2\text{-ethene})_2$] (**17**) and [(BOX-*t*Bu)$Rh^I(\eta^2\text{-ethene})_2$] (**18**) have also been characterized and found to exhibit similar distortions to those observed for **16**.[27] Interestingly, the $Rh^I$ complex **18** disproportionates to $Rh^0$ and the $Rh^{II}$ species [(BOX-*t*Bu)$_2Rh^{II}$] (**19**), whose identity was unambiguously established by X-ray crystallography (Figure 5).

 © 2007 Wiley-VCH Verlag GmbH & Co. KGaA, Weinheim 

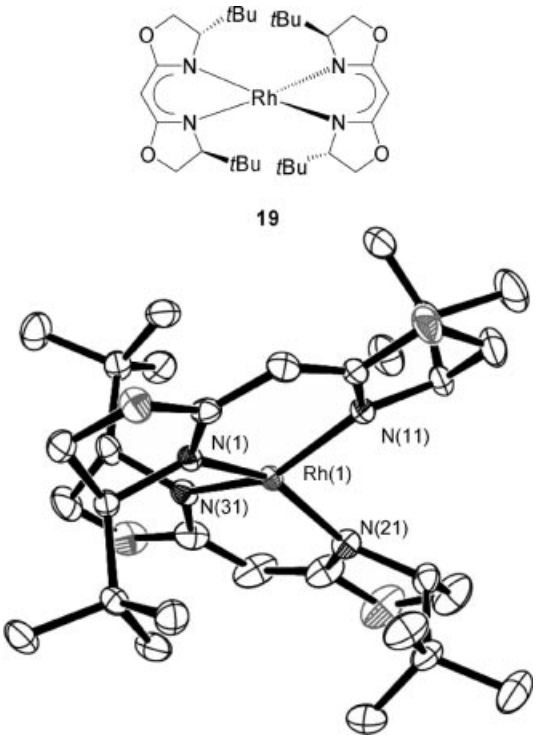


Figure 5. Molecular structure of **19**. Selected distances [Å] and angles [°]: Rh(1)–N(1) 2.041(2), Rh(1)–N(11) 2.0511(18), Rh(1)–N(21) 2.049(2), Rh(1)–N(31) 2.037(2); N(1)–Rh(1)–N(11) 90.14(10), N(21)–Rh(1)–N(31) 89.80(10).

$Rh^{II}$ complexes are especially rare owing to the relative instability of the +II oxidation state. In light of this, complex **19** is the first example of a fully characterized mononuclear $Rh^{II}$ complex obtained by disproportionation of a rhodium(I) complex species into $Rh^0$ and $Rh^{II}$, thus illustrating the excellent stabilizing properties of bidentate bisoxazolinate ligands. As shown in Figure 5, unlike other structurally characterized $Rh^{II}$ complexes, which are square planar, the coordination geometry of the Rh center in **19** is approximately halfway between square planar and tetrahedral. On the basis of DFT calculations, this unusual, distorted orientation of the ligands around $Rh^{II}$ apparently stems from an electronic preference rather than steric influences.

## Group 10–12 Metal Complexes

### *Ni Complexes*

The first example of an asymmetric conjugate addition of an alkynyl group to a cyclic α,β-enone was recently reported by Corey et al. using the well-defined chiral bisoxazolinatonickel complex **20** as a catalyst and an aluminum derivative as alkynyl source (Scheme 13).[28] This unprecedented $Ni^{II}$-catalyzed reaction proceeds with good yields (up to 86%) and *ee* values (up to 88%) under mild conditions.

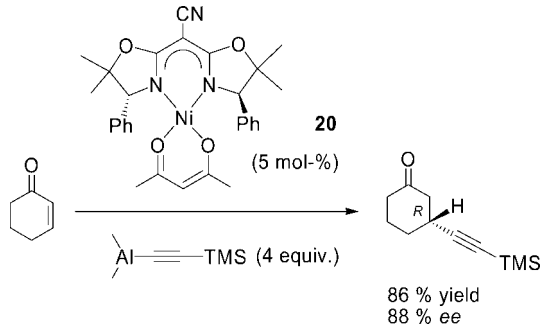


Scheme 13. Nickel-catalyzed asymmetric alkylynation of cyclohexenone.

To rationalize the observed results, the authors proposed a mechanism involving the carbometalation of the α,β-enone by an alkynylnickel intermediate (Scheme 14). Complex **20** constitutes the only reported example of a bisoxazolinatonickel complex. It is noteworthy that the outcome of this catalysis is quite different when performed with Ni(acac)$_2$ as the catalyst, where a coupled diacetylene, presumably derived from a bis(alkynyl)nickel(II) complex, was obtained as the major product. As conjectured by Corey et al., the fact that the bisoxazolinato ligand binds more tightly than the acac ligand most likely precludes the formation of this undesired bis(alkynyl)nickel(II) species.

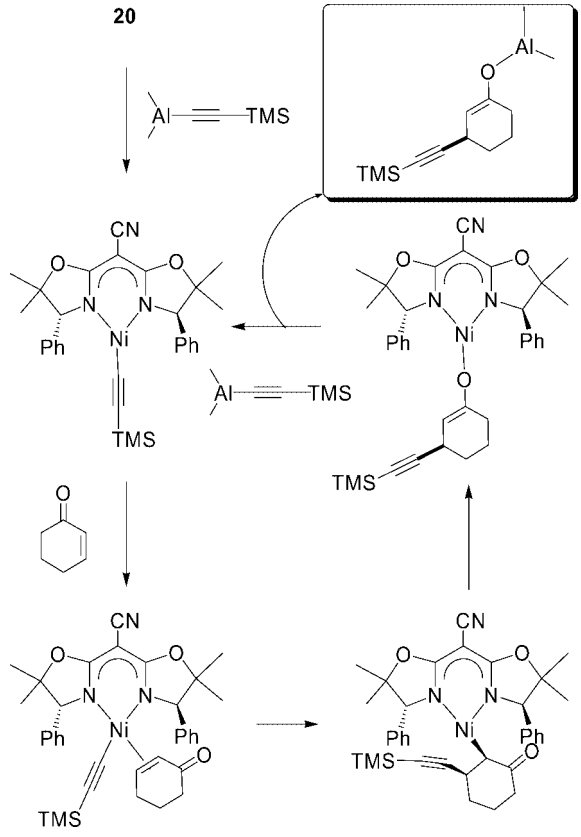


Scheme 14. Proposed mechanism for the Ni-catalyzed conjugate addition of TMS–C≡C–$AlMe_2$ to 2-cyclohexenone.

 © 2007 Wiley-VCH Verlag GmbH & Co. KGaA, Weinheim 

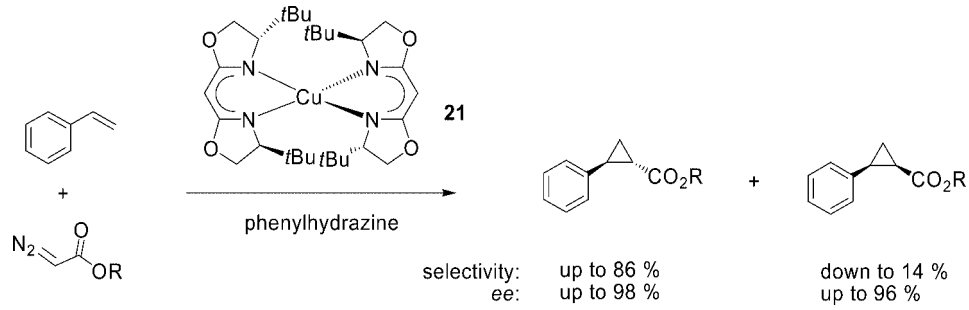


Scheme 15. Copper-catalyzed cyclopropanation of styrene.

### *Cu Complexes*

While numerous examples of neutral chiral bisoxazolines/Cu catalytic systems have been investigated since the late 1980s due to their great utility in asymmetric catalysis, the use of copper complexes incorporating monoanionic bisoxazolinate ligands is much less common and only a few derivatives have been fully characterized. In this area, Masamune et al. first reported in 1990 the synthesis of several chiral bisoxazolinatocopper(II) complexes of the type [(BOX-R)$_2$Cu] (**21**) that are able to catalyze the asymmetric cyclopropanation of olefins with *ee* values of up to 98% for the cyclopropanation of styrene with alkyl diazoacetate (Scheme 15).[3a] These cyclopropanation reactions, however, usually proceed with poor to moderate *cis*/*trans* diastereoselectivity.

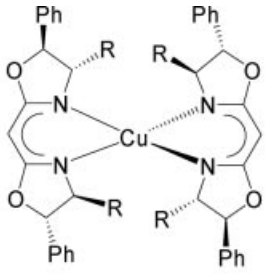

**22**
R = -CH$_2$OSi(Me$_2$)(*t*Bu)

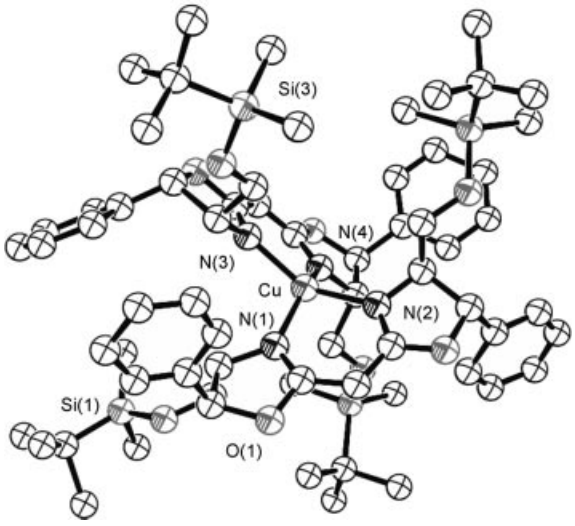


Figure 6. Molecular structure of **22**. Selected distances [Å] and angles [°]: Cu–N(1) 1.93, Cu–N(2) 1.96, Cu–N(3) 1.96, Cu–N(4) 1.91; N(1)–Cu–N(2) 91.6, N(3)–Cu–N(4) 90.8.

A little later, the first X-ray structure of a bisoxazolinatocopper(II) complex, namely [(BOX-CH$_2$OSi*t*BuMe$_2$)$_2$Cu] (**22**), was reported by Lehn et al. and showed the effective chelating ability of the bisoxazolinate unit toward Cu$^{II}$.[29] As illustrated in Figure 6, the copper atom in **22** adopts a distorted tetrahedral geometry, which may be ascribed to an increase of the ring strain between the R substituents of each bisoxazolinate ligand as they approach the Cu metal center. Precatalyst **22** was used in the asymmetric cyclopropanation of silyl enol ethers but gave poor yields and enantioselectivities.[30]

### *Zn Complexes*

While initial spectroscopic studies by Singh suggested that the bisoxazolinate ligand might be suitable for coordination to Zn$^{II}$, the potential interest and usefulness of bisoxazolinatozinc complexes have only been discovered quite recently.[31] Thus, bis(bisoxazolinato)zinc [(BOX)$_2$-Zn$^{II}$] complexes have been prepared in an elegant manner by Takacs et al. by chiral self-discrimination of enantiomeric bisoxazoline ligands. The reaction of a racemic mixture of phenyl-substituted BOX ligands (*R*,*R*)-**23** and (*S*,*S*)-**23** with Zn(OAc)$_2$ leads to the sole formation of the heteroleptic and tetrahedral Zn complex (*RR*,*SS*)-**24** (Scheme 16).[32]

This strong preference for (*RR*,*SS*)-**24** is most likely dictated by the steric interactions between the pendant aryl groups, as illustrated by its molecular structure (Figure 7).

This approach is an effective strategy for the development of modular metal complexes based upon self-assembly of subunits (such as bisoxazolinates) around a metal complex. Thus, using this modular approach, a library of chiral bidentate P,P-ligands **25** has been synthesized and the derived chiral diphosphane ligands found to be suitable for asymmetric palladium-catalyzed allylic amination reactions with excellent yields and *ee* values (Scheme 17).[33]

The most interesting feature in the above approach is that it is a remarkably flexible and effective strategy for catalyst design. In a similar strategy, the synthesis of single-enantiomer, chiral donor–acceptor zinc complexes incorporating bisoxazolinate pseudo racemates **26** has also been performed, thereby further illustrating the chiral self-dis-

 © 2007 Wiley-VCH Verlag GmbH & Co. KGaA, Weinheim 

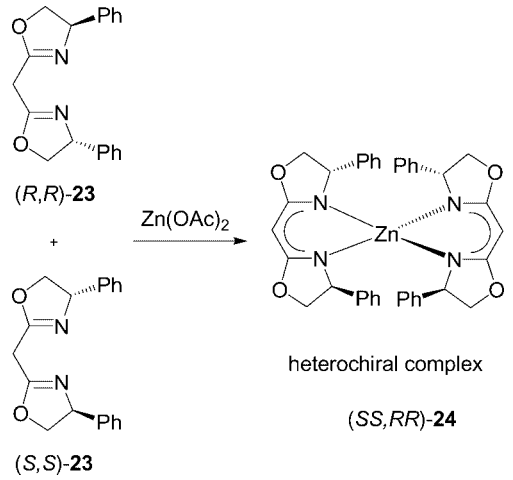


Scheme 16. Synthesis of the heterochiral complex **24**.

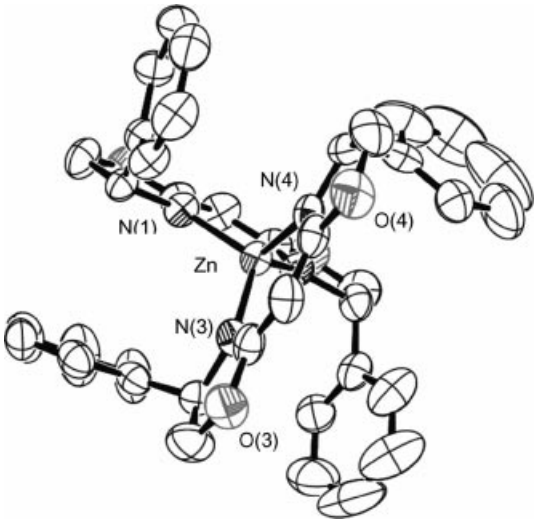


Figure 7. Molecular structure of **24**. Selected distances [Å] and angles [°]: Zn–N(1) 1.971(3), Zn–N(2) 1.973(3), Zn–N(3) 1.975(3), Zn–N(4) 1.976(3); N(1)–Zn–N(2) 94.21; N(3)–Zn–N(4) 93.56.

crimination approach (Scheme 18).[34] Such metal-organic complexes comprising electron donor, π-bridge, and acceptor (D-π-A) subunits are believed to be of potential interest for their nonlinear optical properties.

Apart from the above work, it is noteworthy that the chiral bisoxazolinate(allyl)zinc(II) complex **27**, which is readily accessible by reaction of an allylzinc bromide derivative with the corresponding bisoxazolinatolithium salt, has been shown to add in an enantioselective manner to various substrates such as olefins,[35] imines,[36] or ketones.[37] For example, addition of the allyl complex **27** to alkynyl ketones proceeds with excellent yields and *ee* values of up to 99.9% when the reaction is carried out at –100 °C (Scheme 19). This enantioselective allylic addition represents a rare example of a highly enantioselective addition to alkyl alkenyl ketones; in general, addition to ketone substrates other than alkyl aryl ketones occurs with a lower selectivity than that observed here.

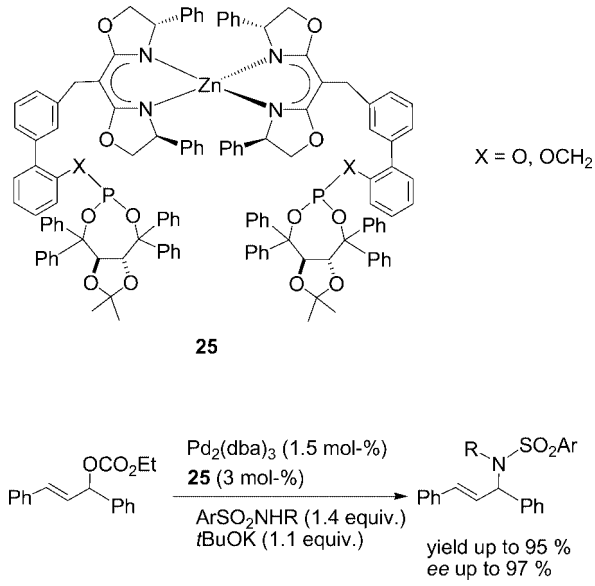


Scheme 17. Asymmetric allylic amination using self-assembled chiral bidentate P,P-ligands **25**.

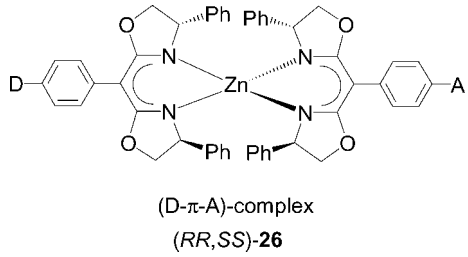


Scheme 18. Chiral self-assembly of bisoxazolinates containing an electron donor and acceptor.

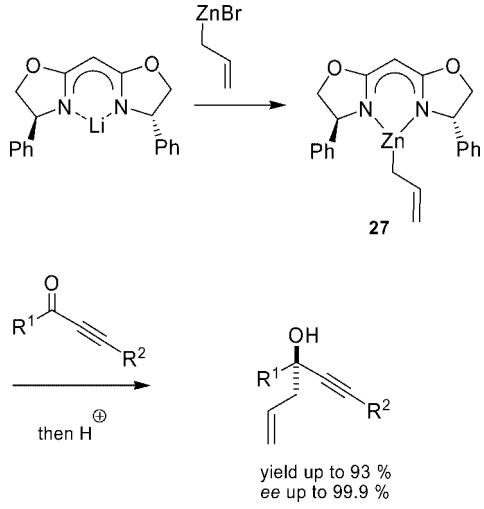


Scheme 19. Stoichiometric allylation of alkynyl ketones with **27**.

Nakamura further extended his studies on zinc complexes similar to **27** and briefly reported their use in the regioselective allylzincation of alkenyboronate; however, poor asymmetric inductions (up to 41% *ee*) as well as low yields were observed (Scheme 20).[38]

 © 2007 Wiley-VCH Verlag GmbH & Co. KGaA, Weinheim 

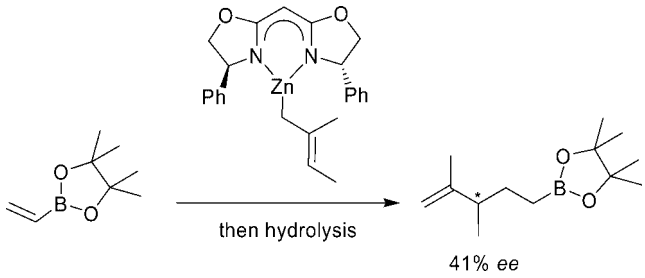


Scheme 20. Stoichiometric allylation of vinylboronate.

Coates et al. have probed the potential of the chiral bisoxazolinato(amido)zinc complex **28** (Scheme 22) as a catalyst for the copolymerization of $CO_2$ and cyclohexene oxide.[39] Surprisingly, complex **28** was found to be inactive in the aforementioned catalysis even though the structurally similar β-diketiminato(amido)zinc analogs exhibit an excellent activity. Finally, the chiral bis(bisoxazolinato)zinc(II) complex **29** (Scheme 21) has also been structurally characterized by Halcrow, Kee et al. and tested in for phospho-aldol catalysis, albeit with no success.[40]

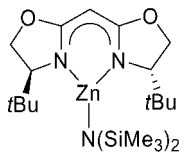


**28**

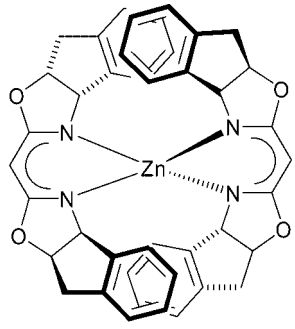


**29**

Scheme 21.

## Group 13 Metal Complexes

Boron bisoxazolinate complexes have also been structurally characterized and employed as chiral catalysts for the asymmetric reduction of various prochiral ketones. Thus, in 2001, Cozzi, Umani-Ronchi et al. reported that catecholborane readily reacts with neutral bisoxazolines to afford the corresponding four-coordinate bisoxazolinate boron complexes **30**, whose molecular structure was determined by X-ray crystallography, thereby confirming the formation of a four-coordinate coordinatively saturated boron complex and the effective chelation of one bisoxazolinate ligand to the boron center (Figure 8).[41]

Chiral versions of **30** were found to be effective catalysts in the enantioselective reduction of various ketones in the presence of catecholborane. This catalysis proceeds with *ee* values up to 86% and good yields when the bisoxazoline **31** is used as the supporting chiral ligand (Scheme 22).[42]

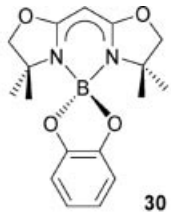

**30**

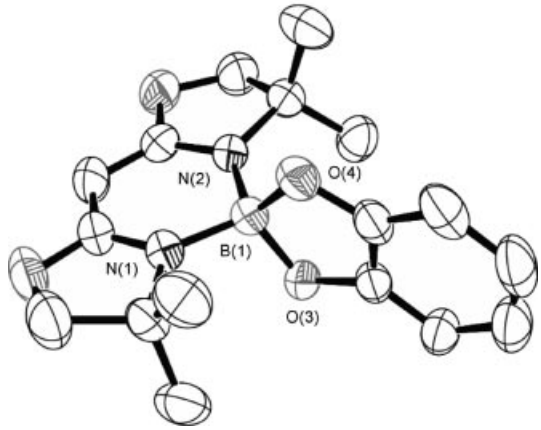


Figure 8. Molecular structure of **30**. Selected distances [Å] and angles [°]: B(1)–N(1) 1.541(2), B(1)–N(2) 1.548(2), B(1)–O(3) 1.481(2), B(1)–O(4) 1.479(2); N(1)–B(1)–N(2) 105.8(1), O(3)–B(1)–O(4) 104.5(1).

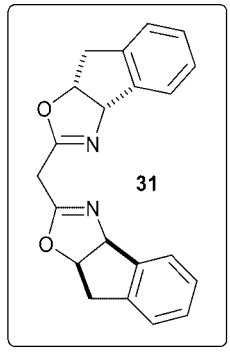

**31**

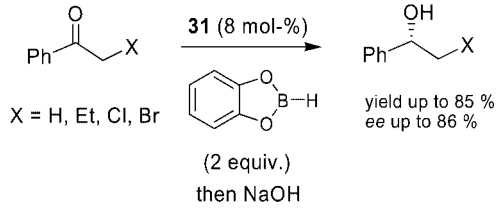


Scheme 22. Enantioselective reduction of ketones in the presence of **31**.

On the basis of detailed DFT calculations, the authors managed to gain insight into the mechanism of this reduction reaction and proposed that the transfer of the hydride ion from the boron atom of the catecholborane to the carbonyl of the prochiral ketone is the rate-determining step of the catalytic process. They also concluded that the origin of the enantioselectivity arises from a complex interplay involving, for the most part, steric repulsions between the ketone substituents and the boron-bisoxazolinate ring.

 © 2007 Wiley-VCH Verlag GmbH & Co. KGaA, Weinheim 

Monoanionic bisoxazolinate ligands are also suitable for coordination to aluminum and gallium, thus allowing the synthesis of the corresponding dimethyl and dichlorido mono-bisoxazolinate complexes **32** by either salt metathesis or an alkane elimination (Scheme 23).[43,44]

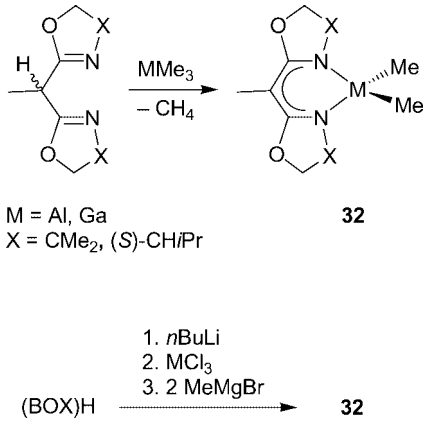


Scheme 23. Synthesis of aluminum and gallium bisoxazolinates **32**.

As illustrated in Figure 9, the molecular structure of the chiral bisoxazolinate aluminum derivative [{BOX-*i*Pr}-$AlMe_2$] exhibits a nearly perfectly planar six-membered Al metallacycle, with the Al metal center adopting a distorted tetrahedral geometry and being chelated by a π-delocalized bisoxazolinate ligand.

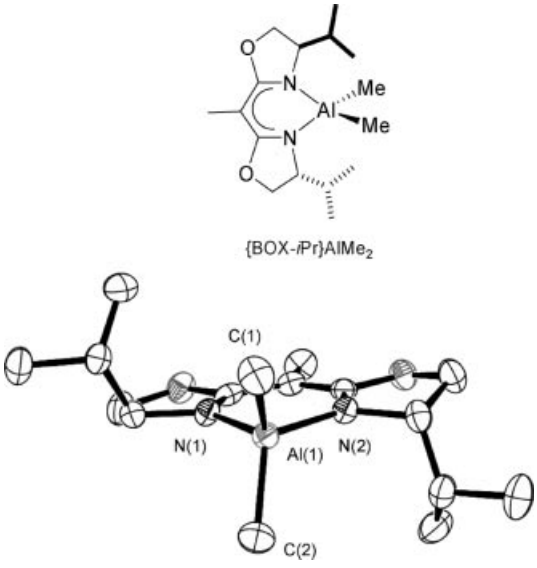


Figure 9. Molecular structure of **32** [M = Al]. Selected distances [Å] and angles [°]: Al(1)–N(1) 1.906(2), Al(1)–N(2) 1.899(2), Al(1)–C(1) 1.967(2), Al(1)–C(2) 1.968(3); N(1)–Al(1)–N(2) 93.13(7), C(1)–Al(1)–C(2) 111.8(1).

More importantly, the dimethylaluminum and -gallium mono-bisoxazolinato derivatives can be readily converted into four-coordinate metal cations **33** by a $Me^-$ abstraction reaction with $B(C_6F_5)_3$ in the presence of an external Lewis base such as an amine (Scheme 24). The excellent stability of the highly Lewis acidic cations **33** illustrates the suitability of the bisoxazolinate ligand for the generation of cationic chiral group 13 alkyl derivatives. The molecular structures of these complexes were unambiguously confirmed by X-ray crystallographic studies. The molecular structure of the aniline-stabilized, four-coordinate bisoxazolinate Al cation $[\{BOX\text{-}Me_2\}Al(Me)(NMe_2Ph)]^+$ is illustrated in Figure 10 as an example. Unlike [{BOX-*i*Pr}$AlMe_2$], the Al chelated six-membered ring is significantly distorted from planarity, with the Al center lying out of the plane of the bisoxazolinate backbone. In fact, the bidentate chelating ligand appears to be pushed away from the Al-$NMe_2Ph$ group, which may be to avoid significant steric interactions between the aniline and the bidentate ligand. Preliminary reactivity studies suggest that these cationic Lewis acids may be of interest as catalysts of hetero-Diels–Alder reactions and propylene oxide polymerizations.

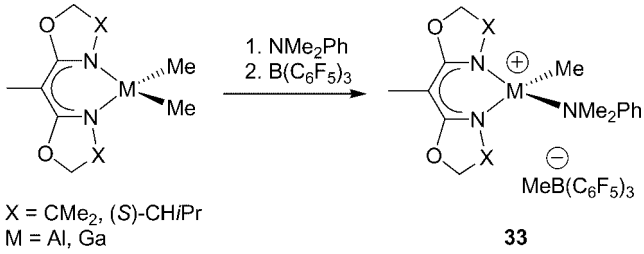


Scheme 24. Synthesis of the cationic species **33**.

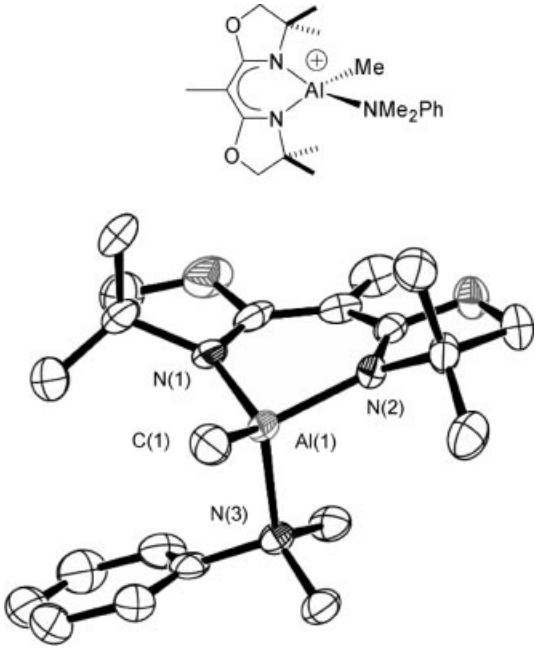


Figure 10. Molecular structure of **33** (M = Al; X = $CMe_2$). Selected distances [Å] and angles [°]: Al(1)–N(1) 1.852(5), Al(1)–N(2) 1.857(4), Al(1)–N(3) 2.018(4), Al(1)–C(1) 1.942(6); N(1)–Al(1)–N(2) 95.8(2), C(1)–Al(1)–N(3) 111.3(2).

Finally, from a reactivity point of view, it is interesting to note that, unlike $B(C_6F_5)_3$, $[Ph_3C][B(C_6F_5)_4]$ does not abstract a $Me^-$ from the Al or Ga metal center when treated with the dimethyl bisoxazolinate derivatives **32**; rather, it abstracts a hydride from the back of the bisoxazolinate ligand to afford the unexpected bisoxazoline metal complex

 © 2007 Wiley-VCH Verlag GmbH & Co. KGaA, Weinheim 

**34** (Scheme 25). This observed reactivity illustrates an unusual Lewis base character for a bisoxazolinate ligand incorporated in a metal complex.

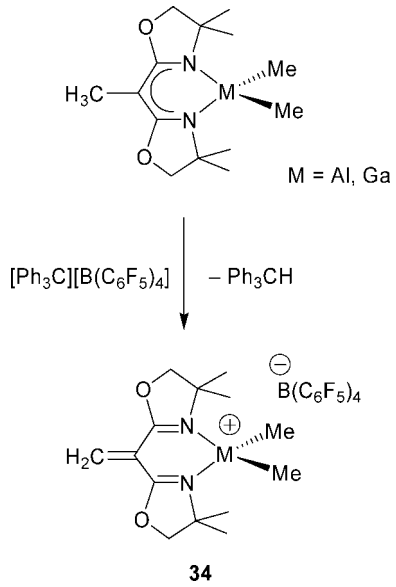


**34**

Scheme 25. Hydride abstraction reaction by $[Ph_3C]^+$ on **32**.

## Conclusions

Over the past few years, bisoxazolinate ligands have established themselves as a versatile class of monoanionic bidentate N,N-ligands that are able to effectively chelate various metal centers, with a coordination chemistry, for the most part, reminiscent of that of the β-diketiminate ligand. It is thus not surprising to find chiral $C_2$-symmetric bisoxazolinate ligands involved as supporting ligands in numerous metal-complex-catalyzed enantioselective reactions, as summarized in the present contribution. Overall, the excellent stability and robustness of this class of ligands, their good level of asymmetric induction in various enantioselective catalyses, and their frequent commercial availability at a moderate cost in an enantiomerically pure form are three major advantages that should promote the use of bisoxazolinato–metal complexes in the near future so as to extent their scope of applications.

[1] For recent reviews of nitrogen-based ligands in asymmetric catalysis, see: a) F. Fache, E. Schulz, M. Lorraine Tommasino, M. Lemaire, *Chem. Rev.* **2000**, *100*, 2159; b) A. Togni, L. M. Venanzi, *Angew. Chem. Int. Ed. Engl.* **1994**, *33*, 497.
[2] M. Gomez, G. Muller, M. Rocamora, *Coord. Chem. Rev.* **1999**, *193–195*, 769.
[3] a) R. E. Lowenthal, A. Abiko, S. Masamune, *Tetrahedron Lett.* **1990**, *31*, 6005; b) D. A. Evans, K. A. Woerpel, M. M. Hinman, M. M. Faul, *J. Am. Chem. Soc.* **1991**, *113*, 726; c) E. J. Corey, N. Imai, H. Y. Zhang, *J. Am. Chem. Soc.* **1991**, *113*, 728; d) D. Müller, G. Umbricht, B. Weber, A. Pfaltz, *Helv. Chim. Acta* **1991**, *74*, 232.
[4] a) K. Kawasaki, T. Katsuki, *Tetrahedron* **1997**, *53*, 6337; b) Y. Kohmura, T. Katsuki, *Tetrahedron Lett.* **2000**, *41*, 3941; c) S. Bellemin-Laponnaz, L. H. Gade, *Chem. Commun.* **2002**, 1286; d) S. Bellemin-Laponnaz, L. H. Gade, *Angew. Chem. Int. Ed.* **2002**, *41*, 3473; e) J. Zhou, Y. Tang, *J. Am. Chem. Soc.* **2002**, *124*, 9030; f) M.-C. Ye, J. Zhou, Y. Tang, *J. Org. Chem.* **2006**, *71*, 3576.
[5] Reviews: a) G. Helmchen, A. Pfaltz, *Acc. Chem. Res.* **2000**, *33*, 336; b) H. A. McManus, P. J. Guiry, *Chem. Rev.* **2004**, *104*, 4151.
[6] H. B. Kagan, T. P. Dang, *J. Am. Chem. Soc.* **1972**, *94*, 6429.
[7] a) A. Pfaltz, *Acc. Chem. Res.* **1993**, *26*, 339; b) H. Fritachi, U. Leutenegger, K. Siegmann, A. Pfaltz, W. Keller, C. Kratky, *Helv. Chim. Acta* **1988**, *71*, 1541..
[8] R. C. Mehrotra, R. Bohra, D. P. Gaur, *Metal β-Diketonates and Allied Derivatives*, Academic Press, New York, **1978**.
[9] a) A. K. Ghosh, P. Mathivanan, J. Cappiello, *Tetrahedron: Asymmetry* **1998**, *9*, 1; b) J. S. Johnson, D. A. Evans, *Acc. Chem. Res.* **2000**, *33*, 325; c) G. Desimoni, G. Faita, K. A. Jørgensen, *Chem. Rev.* **2006**, *106*, 3561.
[10] R. P. Singh, *Spectrochim. Acta A* **1997**, *53*, 1713.
[11] V. Schulze, R. W. Hoffmann, *Chem. Eur. J.* **1999**, *5*, 337.
[12] L. Bourget-Merle, M. F. Lappert, J. R. Severn, *Chem. Rev.* **2002**, *102*, 3031.
[13] H. W. Görlitzer, M. Spiegler, R. Anwander, *J. Chem. Soc., Dalton Trans.* **1999**, 4287.
[14] Organolanthanides are highly efficient catalysts for such transformations; thus, the development of chiral lanthanum catalysts is of growing interest, see: H. C. Aspinall, *Chem. Rev.* **2002**, *102*, 1807.
[15] M. R. Gagné, L. Brard, V. P. Conticello, M. A. Giardello, C. L. Stern, T. J. Marks, *Organometallics* **1992**, *11*, 2003.
[16] M. R. Douglass, M. Ogasawara, S. Hong, M. V. Metz, T. J. Marks, *Organometallics* **2002**, *21*, 283.
[17] a) S. Hong, S. Tian, M. V. Metz, T. J. Marks, *J. Am. Chem. Soc.* **2003**, *125*, 14768; b) S. Hong, A. M. Kawaoka, T. J. Marks, *J. Am. Chem. Soc.* **2003**, *125*, 15878.
[18] A. Alaaeddine, A. Amgoune, C. M. Thomas, S. Dagorne, S. Bellemin-Laponnaz, J.-F. Carpentier, *Eur. J. Inorg. Chem.* **2006**, 3652.
[19] For a review on ring-opening polymerization of lactides, see: O. Dechy-Cabaret, B. Martin-Vaca, D. Bourissou, *Chem. Rev.* **2004**, *104*, 6147.
[20] M. Bandini, P. G. Cozzi, L. Negro, A. Umani-Ronchi, *Chem. Commun.* **1999**, 39.
[21] M. Bandini, F. Bernardi, A. Bottoni, P. G. Cozzi, G. P. Miscione, A. Umani-Ronchi, *Eur. J. Inorg. Chem.* **2003**, 2972.
[22] J. J. Kennedy-Smith, K. A. Nolin, H. P. Gunterman, F. D. Toste, *J. Am. Chem. Soc.* **2003**, *125*, 4056.
[23] E. J. Corey, Z. Wang, *Tetrahedron Lett.* **1993**, *34*, 4001.
[24] K. A. Nolin, R. W. Ahn, F. D. Toste, *J. Am. Chem. Soc.* **2005**, *127*, 12462.
[25] These substrates are stable to air and moisture and the resulting phosphanylamine can be easily hydrolyzed into the corresponding amine.
[26] J. M. Brown, P. J. Guiry, D. W. Price, M. B. Hursthouse, S. Karalulov, *Tetrahedron: Asymmetry* **1994**, *5*, 561.
[27] S. T. H. Willems, J. C. Russcher, P. H. M. Budzelaar, B. de Bruin, R. de Gelder, J. M. M. Smits, A. W. Gal, *Chem. Commun.* **2002**, 148.
[28] Y.-S. Kwak, E. J. Corey, *Org. Lett.* **2004**, *6*, 3385.
[29] J. Hall, J.-M. Lehn, A. de Cian, J. Fischer, *Helv. Chim. Acta* **1991**, *74*, 1.
[30] R. Schumacher, F. Dammast, H.-U. Reiβig, *Chem. Eur. J.* **1997**, *3*, 614.
[31] R. P. Singh, *Bull. Soc. Chim. Fr.* **1997**, *134*, 765.
[32] J. M. Takacs, P. M. Hrvatin, J. M. Atkins, D. S. Reddy, J. L. Clark, *New J. Chem.* **2005**, *29*, 263.
[33] J. M. Takacs, D. S. Reddy, S. A. Moteki, D. Wu, H. Palencia, *J. Am. Chem. Soc.* **2004**, *126*, 4494.
[34] J. M. Atkins, S. A. Moteki, S. G. DiMagno, J. M. Takacs, *Org. Lett.* **2006**, *8*, 2759.

 © 2007 Wiley-VCH Verlag GmbH & Co. KGaA, Weinheim 

[35] M. Nakamura, M. Arai, E. Nakamura, *J. Am. Chem. Soc.* **1995**, *117*, 1179.
[36] M. Nakamura, A. Hirai, E. Nakamura, *J. Am. Chem. Soc.* **1996**, *118*, 8489.
[37] M. Nakamura, A. Hirai, M. Sogi, E. Nakamura, *J. Am. Chem. Soc.* **1998**, *120*, 5846.
[38] N. Nakamura, K. Ara, T. Hatakeyama, E. Nakamura, *Org. Lett.* **2001**, *3*, 3137.
[39] M. Cheng, N. A. Darling, E. B. Lobkovsky, G. W. Coates, *Chem. Commun.* **2000**, 2007.
[40] M. Jiang, S. Dalgarno, C. A. Kilner, M. A. Halcrow, T. P. Kee, *Polyhedron* **2001**, *20*, 2151.
[41] M. Bandini, P. G. Cozzi, M. Monari, R. Perciaccante, S. Selva, A. Umani-Ronchi, *Chem. Commun.* **2001**, 1318.
[42] M. Bandini, A. Bottoni, P. G. Cozzi, G. P. Miscione, M. Monari, R. Pierciaccante, A. Umani-Ronchi, *Eur. J. Inorg. Chem.* **2006**, 4596.
[43] S. Dagorne, S. Bellemin-Laponnaz, R. Welter, *Organometallics* **2004**, *23*, 3053.
[44] S. Dagorne, S. Bellemin-Laponnaz, A. Maisse-François, M.-N. Rager, L. Jugé, R. Welter, *Eur. J. Inorg. Chem.* **2005**, 4206.
[45] C. A. Willoughby, S. L. Buchwald, *J. Am. Chem. Soc.* **1994**, *116*, 11703.

Received: November 28, 2006
Published Online: February 2, 2007

 © 2007 Wiley-VCH Verlag GmbH & Co. KGaA, Weinheim 

DOI: 10.1002/ejic.200600953

# A Bis(di-*n*-butyltin)–Quinone Derivative as a Simultaneous Chemo- and Bioactive Corrosion Inhibitor

**Victor Barba,*[a] Edgar Vega,[a] Herbert Höpfl,[a] Luis S. Zamudio-Rivera,*[b] Marco A. Domínguez-Aguilar,[b] Rocío George-Tellez,[b] Fernando Godínez-Salomon,[b] José M. Hallen-Lopez,[c] and Hiram I. Beltran[d]**

**Keywords:** Tin / Quinones / Corrosion / Biocide activity / X-ray structure

The bis(di-*n*-butyltin) derivative of 2,5-bis(2-hydroxyethylamino)-1,4-benzoquinone was synthesized and characterized by common spectroscopic techniques. In solution, discrete molecules with pentacoordinate tin atoms were observed, whereas the X-ray diffraction analysis of the solid-state structure revealed polymeric chains that were due to intermolecular Sn···O bonds. In vitro tests demonstrated that the tin compound displays bactericidal activity against a wide range of aerobic and anaerobic bacteria. Acute toxicity tests indicated that the di-*n*-butyltin compound has a relatively low toxicity level. The corrosion inhibition efficiency of the ligand and the tin compound were evaluated by polarization scans of mild steel samples that had been exposed to a sour brine environment. The tin–quinone compound showed good inhibition efficiency (about 75 %) at relatively low concentrations (25–50 ppm) and at different testing times (0.25–20 h).

(© Wiley-VCH Verlag GmbH & Co. KGaA, 69451 Weinheim, Germany, 2007)

## Introduction

At present, organic compounds are widely used as corrosion inhibitors, since their structural features can be manipulated in order to improve properties such as solubility and chemical biodegradability. For that purpose, the formation of strong coordinative bonds with metallic surfaces is required, in particular in the very aggressive media present in oil manufacturing plants and pipelines. In this respect, nitrogen-based inhibitors have demonstrated excellent properties.[1]

It is well known that ligands based on quinones confer the ability to couple redox reactions, thus enabling the interaction with metallic ions and surfaces.[2] Earlier studies have shown that metal surfaces covered with poly(aminoquinones) (PAQs) form effective anticorrosive coatings because of their excellent corrosion resistance and adhesion to metal atoms.[3] Such films even displace water from rusted steel surfaces.[4] Hubbard and co-workers have attributed the high affinity of PAQs towards metal surfaces to a chemisorption process[5] in which the free electron pairs of the amine nitrogen and quinone oxygen atoms interact with the electron-deficient molecular orbital of the metal atom. Surprisingly, so far there is no reference related to the use of organometallic components containing benzoquinones as corrosion inhibitors for steel, and the manner in which coordination to metal atoms influences the corrosion inhibition properties has not been clarified yet.

Tin phthalocyanines were previously tested as corrosion inhibitors for carbon steel by using sour brine at pH 4.[6] The corrosion inhibition activity of these compounds provided efficiencies in the range 61–87% at concentrations of 500 ppm, and it was proposed that the concave π-electron-delocalized nanocap morphology of these compounds may induce an effective adsorption on the steel surface. In addition, tin compounds are capable of acting as biocides and have relatively low toxicities,[7] thus making them an attractive object of research for the development of chemicals having combined anticorrosive and antibacterial properties. This is because anaerobic bacteria are able to catalyze the corrosion processes in oil plants and pipelines.

Our interdisciplinary research group is interested in developing evironment-friendly multifunctional compounds, and, we describe herein the synthesis and properties of a new di-*n*-butyltin derivative of 2,5-bis(2-hydroxyethylamino)-1,4-benzoquinone (**1**). As far as we know, this is

[a] Centro de Investigaciones Químicas, Universidad Autónoma del Estado de Morelos,
Av. Universidad 1001, C.P. 62209 Cuernavaca, México
E-mail: vbarba@ciq.uaem.mx
[b] Programa de Ingeniería Molecular, Instituto Mexicano del Petróleo,
Eje Central L. Cárdenas 152, C.P. 07730, D.F., México
E-mail: lzamudio@imp.mx
[c] Departamento de Ingeniería Metalúrgica, E.S.I.Q.I.E. – Instituto Politecnico Nacional, Unidad Profesional A. López Mateos,
C. P. 07300, D. F., México
[d] Departamento de Ciencias Naturales, C. N. I., Universidad Autónoma Metropolitana – Cuajimalpa,
Av. Pedro A. de los Santos 84, Col. San Miguel Chapultepec, 11850, D. F., México

 © 2007 Wiley-VCH Verlag GmbH & Co. KGaA, Weinheim 

the first report on a tin compound that is able to protect steel simultaneously from electrochemical and microbiological corrosion.

## Results and Discussion

The 1,4-benzoquinone derivative **1** was prepared as described previously,[8] and its condensation reaction with di-*n*-butyltin oxide in methanol under reflux gave compound **2** in 80% yield (Scheme 1). Recrystallization of the product from methanol gave a deep red crystalline material. EI mass spectrometry revealed a peak at $m/z$ = 688 that corresponds to the molecular ion of compound **2**. The analysis of the $^1$H NMR spectroscopic data suggests that the structure of this compound is symmetric in solution, having a $C_2$ rotation axis. By using the equation developed by Holeček et al.,[9] the $^1J(^{119}Sn–^{13}C)$ coupling constant (628 Hz) was used to estimate the C–Sn–C angle, 127.4°, which is typical of pentacoordinate tin species. The $^{119}$Sn NMR chemical shift was observed at $\delta$ = –129 ppm, a value displaced to higher frequencies relative to parent diorganotin compounds derived from ONO Schiff base tridentate ligands (–150 to –180 ppm).[10] The difference can be attributed to the enhanced covalent character of the N–Sn bond that is mostly dative in analogous systems.

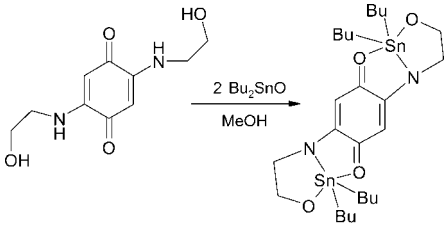


**1** **2**

Scheme 1. Synthesis of the tin–quinone compound **2**.

The X-ray analysis of compound **2** allowed to establish that in the solid state the point group of the tin molecules is $C_1$ (Figure 1). When the molecular packing was examined, intermolecular Sn···O interactions were found, providing hexacoordinate tin atoms that are surrounded by the ONO donor atoms of one ligand molecule (meridional distribution), two *n*Bu groups located in a *trans* orientation, and one additional oxygen atom from a neighboring molecule. The *n*-butyl groups attached to the tin atoms and the –$CH_2CH_2O$– fragments of the ligand are disordered over two different positions, indicating the presence of a low-density polymorphous arrangement. The N–Sn and O–Sn bond lengths are comparable to those already described for other ONO–tin compounds (for values see Figure 1).[10,11]

The formation of intermolecular Sn···O bonds, 2.488(6) (O2–Sn2) and 2.379(4) (Sn1–O3A) Å, situated at an equatorial position of the tin atom coordination sphere, gives rise to the formation of four-membered $Sn_2O_2$ rings that organize the individual molecules in linear 1D coordination polymers (Figure 2). This Sn···O intermolecular interaction

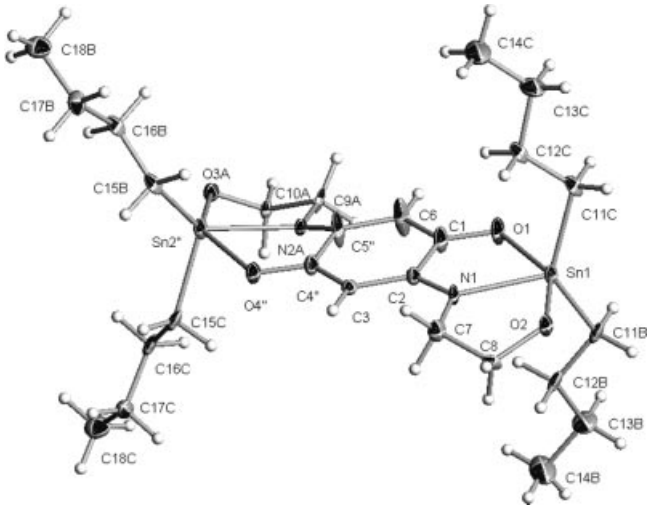


Figure 1. Fragment of the polymeric structure of compound **2** (50% thermal ellipsoids). Selected bond lengths [Å] and angles [°]: Sn1–O1 2.336(5), Sn1–O2 2.092(4), Sn1–N1 2.172(5), Sn1–C11B 2.1011(11), Sn1–C11C 2.1003(11), O1–Sn1–O2 147.17(16), O1–Sn1–N1 70.66(18), O2–Sn1–N1 76.51(19), C11C–Sn1–C11B 140.7(3).

has also been observed for other pentacoordinate di-*n*-butyltin complexes derived from ONO ligands.[12] The polymeric fragments are organized in layers, between which the *n*Bu moieties are located (Figure 2).

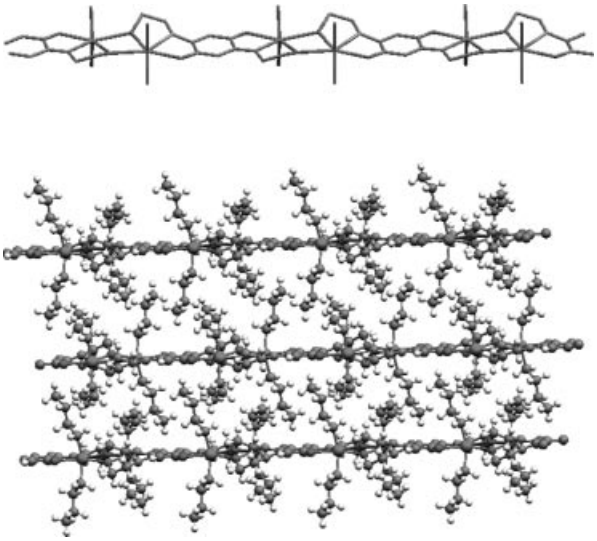

Figure 2. Schematic representation of the 1D coordination polymer formed through Sn···O intermolecular interactions (part of the *n*Bu groups are omitted, top). View of the parallel orientation for the polymeric chains, the *n*Bu groups are located in between (bottom).

The benzoquinone ligand **1** and the bis(di-*n*-butyltin)–quinone derivative **2** were screened in vitro for their antibacterial activity against three types of aerobic bacteria, *Bacillus subtilis* (Gram-positive, strain ATCC 6633), *Escherichia coli* (Gram-negative, strain DH5) and *Pseudomona fluorescens* (Gram-negative, strain BH3), and two types of anaerobic species (sulfate-reducing bacteria, SRB), *Desulfovibrio vulgaris* (strain DSM 644) and a bacteria con-

 © 2007 Wiley-VCH Verlag GmbH & Co. KGaA, Weinheim 

sortium (strain 82) isolated from a hydrocarbon pipeline of the Mexican oil industry (PEMEX). The agar well diffusion method[13] was used to determine the minimum inhibitory concentrations (MICs), showing that compound **2** has a higher biocide activity than the free quinone **1** (Table 1). The results also show that the presence of the di-*n*-butyl group confers selectivity in toxicity against certain bacterial species, which is important for the development of new prototypes of environmentally friendly biocides.

Table 1. Agar MICs of compounds **1** and **2** (ppm).[a]

| Compound | *B. subtilis* | *E. coli* | *P. fluorescens* | *D. vulgaris* | *Strain 82* |
|---|---|---|---|---|---|
| **1** | ≥ 200 | ≥ 200 | ≥ 200 | > 200 | > 200 |
| **2** | 10 | 100 | 10 | ≥ 100 | 150 |

[a] For *B. subtilis*, *E. coli*, and *P. fluorescens*, the MICs were measured after 16 h of incubation at 30 °C. For *D. vulgaris* and *Strain 82* the MICs were measured after 7 days of incubation at 32 °C.

The acute toxicity was determined by using luminescent bacteria toxicity (LBT) Mycrotox tests to record their environmental impact. The $EC_{50}$ values obtained from 5- and 15-min assays were very similar for the two compounds (Table 2), which permits their classification in the "slightly toxic" category.[14]

Table 2. Acute toxicity of compounds **1** and **2** against *P. phosphoreum*.[a]

| Compound | Toxicity $EC_{50}$ | | |
|---|---|---|---|
| | 5 min | 15 min | Category |
| **1** | 61 | 58 | slightly toxic |
| **2** | 62 | 60 | slightly toxic |

[a] Concentration range in ppm, classification, category 5: 0.01–0.10, extremely toxic; 4: 0.1–1.0, highly toxic; 3: 1–10, moderately toxic; 2: 10–100, slightly toxic; 1: 100–1000, particularly nontoxic; and 0: > 1000, nontoxic. See ref.[14] for further details.

The carbon steel corrosion inhibition properties of compounds **1** and **2** were tested in an aqueous hydrogen sulfide corrosive environment by electrochemical methods, which included the linear polarization resistance (LPR) technique and the Tafel extrapolation measurements. Upon electrode immersion for 15 minutes in sour brine at different inhibitor concentrations, the corrosion inhibition efficiencies of the benzoquinone ligand **1** were in the range 37–61%, whereas those of compound **2** were within 35–83%. The detailed analysis of the data shown in Table 3 shows that compound **2** is a better corrosion inhibitor than **1**, since a molar concentration of only one third of compound **2** is required to provide a higher inhibitive efficiency than that of compound **1**. After 20 h of electrode immersion, the results show that the inhibition efficiency of compound **1** tends to increase slightly, while that of compound **2** tends to decrease. There exists some evidence that planar compounds such as **1** give a parallel accommodation on the steel surface due to π-bonding interactions with the metal atoms.[2] In the case of compound **2**, the molecular volume is increased, which apparently improves the surface coverage.[15] The inhibition efficiencies of this new di-*n*-butyltin compound are in the order of those found for the tin phthalocyanines previously reported;[6a] however, the inhibitor concentration is five times lower.

Table 3. Corrosion inhibition efficiency (IE,%) for compounds **1** and **2**.

| Compound | Concentration | | IE (%) | |
|---|---|---|---|---|
| | ppm | mmol $L^{-1}$ | [a] | [b] |
| **1** | 10 | 0.0442 | 37 | 15 |
| | 25 | 0.1100 | 57 | 69 |
| | 50 | 0.2210 | 55 | 74 |
| | 100 | 0.4420 | 61 | 66 |
| **2** | 10 | 0.0145 | 35 | 8 |
| | 25 | 0.0363 | 82 | 66 |
| | 50 | 0.0726 | 87 | 70 |
| | 100 | 0.1453 | 83 | 72 |

[a] IE determined after 15 min. [b] IE after 20 h.

## Conclusion

The tin compound described herein can protect steel surfaces by serving as a chemo- and bioactive corrosion inhibitor. Further investigations considering similar tin–quinone derivatives are currently carried out in our laboratory.

## Experimental Section

**Synthesis and Spectroscopic Data for Compound 2:** Compound **2** was prepared from compound **1** (0.10 g, 0.442 mmol) and di-*n*-butyltin oxide (0.22 g, 0.884 mmol) in methanol under reflux (2 h). The product precipitated as a red solid in 80% yield (0.24 g). M.p. 247–250 °C. IR (KBr): $\tilde{\nu}_{max}$ = 2956, 2921, 2854, 1523 (C=O), 1433, 1398, 1329, 1288, 1066, 920, 872, 800, 680, 593 $cm^{-1}$. EI-MS: *m*/*z* (%) = 688 [$M^+$] (10), 661 (45), 632 [M – Bu]$^+$ (100), 604 (33), 543 (24), 513 (12), 486 (56), 400 (60), 371 (45), 280 (34), 203 (64), 174 (43), 123 (17), 91 (26). $^1$H NMR (200 MHz, $CDCl_3$): $\delta$ = 5.61 (s, 2 H, CH), 3.96 and 3.30 (AB, $J$ = 5.8 Hz, 8 H, $OCH_2CH_2N$), 1.60–1.16 (m, 24 H, $CH_{2Bu}$), 0.82 (t, $J$ = 6.9 Hz, 12 H, $CH_{3Bu}$) ppm. $^{13}$C NMR (50 MHz, $CDCl_3$), $\delta$: 181.0 (C=O), 151.1 ($C_{quin}$–N), 93.3 (C–H), 61.6 ($C_{aliph}$–O), 48.2 ($C_{aliph}$–N), 27.5 [$^2J$($^{119}$Sn–$^{13}$C) = 29 Hz, $C_{\beta\text{-Bu}}$], 26.9 [$^3J$($^{119}$Sn–$^{13}$C) = 87 Hz, $C_{\gamma\text{-Bu}}$], 19.7 [$^1J$($^{119}$Sn–$^{13}$C) = 628 Hz, $C_{\alpha\text{-Bu}}$], 13.8 ($C_{\delta\text{-Bu}}$) ppm. $^{119}$Sn NMR (75 MHz, $CDCl_3$): $\delta$ = –129 ppm. $C_{26}H_{46}N_2O_4Sn_2$ (688.07) calcd. C 45.38, H 6.73, N 4.07; found C 46.01, H 6.86, N 4.22.

**Antibacterial Activity Test:** The agar method was used to determine the minimum concentration of compound **1** and **2** capable of inhibiting the bacterial activity of the aerobic and anaerobic strains previously developed. The medium for the aerobic bacteria was prepared by cooling the molten agar to 40 °C and then adding the required amount of bacterial suspension ($8 \times 10^8$ bacteria per mL). The wells were dug in the media with the help of a sterile metallic borer of 24 mm diameter; into these wells the testing compounds were introduced (2.5, 10, 25, 50, 75, 100, 150 and 200 ppm). Additional wells were filled with ethanol to serve as a negative control, whereas the positive reference was a piperazine compound. The flat-bottomed, 90-mm Petri dishes were kept at 4 °C for 60 minutes and then stored in an incubator at a suitable growth temperature (30 ± 2 °C) for 16 hours. The strains prepared for the anaerobic bacteria were exposed to the testing compounds in the range 2.5–200 ppm, whereby the anaerobic strains were grown in 40-mL

 © 2007 Wiley-VCH Verlag GmbH & Co. KGaA, Weinheim 

flasks with a Postgate C modified medium. The bottles were inoculated with SRB (sulfate-reducing bacteria) cultures (1 mL) from the stock and incubated at 32 ± 2 °C for 7 d. Finally, the minimum inhibitor concentration (MIC) for each compound was determined by comparing positive (bottle without chemical) and negative (bottle not inoculated with culture) controls and recording the presence or absence of visible growth in the bottles.

**X-ray Crystallography:** X-ray diffraction studies were performed on a Bruker-APEX diffractometer with a CCD area detector, Mo-$K_\alpha$ radiation, $\lambda$ = 0.71073 Å, graphite monochromator. Frames were collected at $T$ = 100 K. The measured intensities were reduced to $F^2$ and corrected for absorption with SADABS (SAINT-NT).[16] Corrections were made for Lorentz and polarization effects. Structure solution, refinement and data output were carried out with the SHELXTL-NT program package.[16] Crystal system: Monoclinic, space group $P2_1/m$, $a$ = 6.9974(7), $b$ = 17.3487(17), $c$ = 11.7734(12) Å, $\beta$ = 91.799(2), $V$ = 1428.5(3) Å$^3$, $Z$ = 4, $D_{calcd.}$ = 1.604 g cm$^{-3}$, $\mu$ = 1.781 mm$^{-1}$, $F(000)$ = 700. For 2319 independent reflections and 245 parameters, final $R$ indices [$I > 2\sigma I$]: $R_1$ = 0.0370 and $wR_2$ = 0.0825. Non-hydrogen atoms were refined anisotropically. Hydrogen atoms were placed in geometrically calculated positions by using a riding model. The *n*Bu groups attached to the tin atoms and the –$CH_2CH_2O$– fragments of the ligand are disordered over two positions. CCDC-296858 contains the supplementary crystallographic data for this paper. These data can be obtained free of charge from The Cambridge Crystallographic Data Centre via www.ccdc.cam.ac.uk/data_request/cif.

## Acknowledgments

We thank Universidad Autónoma del Estado de Morelos (UAEM) and Instituto Mexicano del Petróleo (IMP) for the facilities and financial support provided.

[1] a) E. A. Noor, *Corros. Sci.* **2005**, *47*, 33–55; b) E. A. Flores-Oropeza, M. Lozada-Cassou, M. Galicia-Garcia, H. I. Beltran, R. George-Téllez, L. S. Zamudio-Rivera, A. Morales-Pacheco, A. Benavides-Lira, *Instituto Mexicano del Petróleo*, IMPI PA/a/**2004**/012908; c) P. Prince, *Baker Hughes Incorporated*, WO 98/51902, **1998** Nov.

[2] a) M. P. Soriaga, A. T. Hubbard, *J. Am. Chem. Soc.* **1982**, *104*, 2735–2742; b) A. K. Machocho, T. Win, S. Grinberg, S. Bittner, *Tetrahedron Lett.* **2003**, *44*, 5531–5534.

[3] a) V. S. Nithianandam, S. Erhan, *Polymer* **1998**, *39*, 4095–4098; b) V. S. Nithianandam, S. Erhan, *Polymer* **1991**, *32*, 1146–1149.

[4] K. Kaleem, F. Chertok, S. Erhan, *Prog. Org. Coat.* **1987**, *15*, 63–71.

[5] M. P. Soriaga, A. T. Hubbard, *J. Am. Chem. Soc.* **1982**, *104*, 2742–2747.

[6] a) H. I. Beltrán, R. Esquivel, M. Lozada-Cassou, M. A. Domínguez-Aguilar, A. Sosa-Sánchez, J. L. Sosa-Sánchez, H. Höpfl, V. Barba, R. Luna-García, N. Farfán, L. S. Zamudio-Rivera, *Chem. Eur. J.* **2005**, *11*, 2705–2715; b) H. I. Beltrán, R. Esquivel, A. Sosa-Sánchez, J. L. Sosa-Sánchez, H. Höpfl, V. Barba, N. Farfán, M. Galicia, O. Olivares-Xometl, L. S. Zamudio-Rivera, *Inorg. Chem.* **2004**, *43*, 3555–3557.

[7] L. S. Zamudio-Rivera, R. George-Tellez, G. López-Mendoza, A. Morales-Pacheco, E. Flores, H. Höpfl, V. Barba, F. J. Fernández, N. Cabirol, H. I. Beltrán, *Inorg. Chem.* **2005**, *44*, 5370–5378.

[8] a) S. Kulpe, *Tetrahedron* **1970**, *26*, 2899–2904; b) S. J. Rettig, J. Trotter, *Can. J. Chem.* **1975**, *53*, 777–783.

[9] J. Holeček, M. Nádvorník, K. Handlír, A. Lyčka, *J. Organomet. Chem.* **1986**, *315*, 299–308.

[10] a) H. I. Beltrán, L. S. Zamudio-Rivera, T. Mancilla, R. Santillan, N. Farfán, *Chem. Eur. J.* **2003**, *9*, 2291–2306; b) D. K. Dey, A. Lycka, S. Mitra, G. M. Rosair, *J. Organomet. Chem.* **2004**, *689*, 88–95; c) C. Pettinari, F. Marchetti, R. Pettinari, D. Martini, A. Drozdov, S. Troyanov, *Inorg. Chim. Acta* **2001**, *325*, 103–114.

[11] a) V. Chandrasekhar, S. Nagendran, V. Baskar, *Coord. Chem. Rev.* **2002**, *235*, 1–52; b) R. Willem, A. Bouhdid, A. Meddour, C. Camacho-Camacho, F. Mercier, M. Gielen, M. Biesemans, F. Ribot, C. Sanchez, E. R. T. Tiekink, *Organometallics* **1997**, *16*, 4377–4385; c) R. Willem, A. Bouhdid, F. Kayser, A. Delmotte, M. Gielen, J. C. Martins, M. Biesemans, B. Mahieu, E. R. T. Tiekink, *Organometallics* **1996**, *15*, 1920–1929.

[12] a) N. Farfán, T. Mancilla, R. Santillan, A. Gutierrez, L. S. Zamudio-Rivera, H. I. Beltran, *J. Organomet. Chem.* **2004**, *689*, 3481–3491; b) H. Reyes, C. García, N. Farfán, R. Santillan, P. G. Lacroix, C. Lepetit, K. Nakatani, *J. Organomet. Chem.* **2004**, *689*, 2303–2310.

[13] Atta-ur-Rahman, M. I. Choudhary, W. J. Thomsen, *Bioassay Techniques for Drug Development*, Harwood Academic OPA N. V. Amsterdam, **2001**, p. 16.

[14] G. F. Whale, T. S. Whitham in *SPE Health, Proceedings of the Safety and Environment in Oil and Gas Exploration and Production Conference, the Hague*, Netherlands, November 11–14, **1991**, Society of Petroleum Engineers **1991**, *23357*, 355.

[15] Y. Douda, R. Govea-Rueda, M. Galicia, H. I. Beltrán, L. S. Zamudio-Rivera, *J. Phys. Chem. B* **2005**, *109*, 22674–22684.

[16] Bruker Analytical X-ray Systems. SAINT-NT Version 6.04, **2001**; SHELXTL-NT Version 6.10, **2000**.

Received: October 10, 2006
Published Online: February 2, 2007

 © 2007 Wiley-VCH Verlag GmbH & Co. KGaA, Weinheim 

DOI: 10.1002/ejic.200600976

# Reactions of Group 13 Organometallics $t$Bu$_3$M with Distibanes Sb$_2$R$_4$

**Daniella Schuchmann,[a] Andreas Kuczkowski,[a] Sonja Fahrenholz,[a] Stephan Schulz,*[a] and Ulrich Flörke[a]**

**Keywords:** Main group elements / Lewis acids / Lewis bases / Solid-state structures

Tetraalkyldistibanes Sb$_2$R$_4$ (R = *n*Pr, *i*Bu) react with $t$Bu$_3$M (M = Al, Ga) at –30 °C with the formation of the Lewis acid–base adducts [$t$Bu$_3$M]$_2$[Sb$_2$R$_4$] [M = Al, R = *n*Pr (**1**), *i*Bu (**2**); M = Ga, R = *n*Pr (**3**), *i*Pr **4**)]. Compounds **1** and **2** are stable in solution whereas **3** undergoes a Sb–Sb bond-breakage reaction with the subsequent formation of [$t$Bu$_2$GaSb(*n*Pr)$_2$]$_2$ (**5**). The same trend was observed for the reaction of Sb$_2$(*i*Bu)$_4$ with $t$Bu$_3$Ga, which yielded the heterocyclic stibanylgallane [$t$Bu$_2$GaSb(*i*Bu)$_2$]$_2$ (**6**). In addition, the simple trialkylstibane adduct $t$Bu$_3$Al–Sb(*i*Bu)$_3$ (**7**) was obtained as a byproduct from the reaction of Sb$_2$(*i*Bu)$_4$ with $t$Bu$_3$Al. Compounds **1**–**7** were characterized by multinuclear NMR ($^1$H, $^{13}$C{$^1$H}) and mass spectroscopy and elemental analysis. Compounds **1**, **3**, **5**, and **7** were also investigated by single-crystal X-ray diffraction.
(© Wiley-VCH Verlag GmbH & Co. KGaA, 69451 Weinheim, Germany, 2007)

## Introduction

Lewis basic tetraalkyldipenteles R′$_2$E–ER′$_2$ (E = N to Bi) are capable of acting as monodentate[1] or bidentate ligands[2] as was shown in several reactions with transition metal complexes.[3] Surprisingly, reactions with main group Lewis acids such as group 13 organometallics MR$_3$ (M = B to Tl) have been studied to a far lesser extent even though Lewis acid–base adducts of trialkylpenteles ER′$_3$ are long known in group 13/15 chemistry. Only two diphosphane-borane adducts ([Me$_4$P$_2$][BH$_3$]$_2$ and [Me$_4$P$_2$][BH$_2$Br]$_2$)[4] have been structurally characterized prior to our studies. We started to investigate reactions of distibanes R′$_2$Sb–SbR′$_2$ and dibismuthines R′$_2$Bi–BiR′$_2$ with group 13 organometallics MR$_3$ (M = Al, Ga, In) because of our general interest in group 13/15 chemistry. These reactions typically yielded bisadducts of the type [R$_3$M]$_2$[E$_2$R′$_4$] (M = Al, Ga; E = Sb,[5] Bi[6]), with the dipenteles serving as bidentate ligands. Only tetraisopropyldistibane was found to form the monoadduct [$t$Bu$_3$Al][Sb$_2$(*i*Pr)$_4$] when reacted with $t$Bu$_3$Al, most likely because of the increased repulsive interactions caused by the bulky *i*Pr substituents.[7] The distibane alane adducts [R$_3$Al]$_2$[Sb$_2$R′$_4$] were found to be stable in their pure form and in solution,[8] whereas the corresponding gallane and indane adducts [R$_3$M]$_2$[Sb$_2$R′$_4$] (M = Ga, In) tended to undergo Sb–Sb bond-breakage reactions in solution with the subsequent formation of heterocyclic stibanylgallanes and -indanes [R$_2$MSbR′$_2$]$_x$ ($x$ = 2, 3). Comparable findings have previously been observed by Breunig et al. in reactions with main group[9] and transition metal complexes.[10]

[a] Department Chemie, Universität Paderborn
Warburger Strasse 100, 33098 Paderborn, Germany
Fax: +49-5251-603423
E-mail: stephan.schulz@upb.de

Because of our interest in completely alkyl-substituted heterocycles [R$_2$MSbR′$_2$]$_x$, which are promising candidates for the deposition of MSb thin films by the MOCVD process (metal organic chemical vapor deposition),[11] we extended our studies to the reaction of Sb$_2$R′$_4$ (R′ = *n*Pr, *i*Pr, *i*Bu) with trialkylalanes and gallanes MR$_3$. The influence of the organic ligand on the stability of the initially formed distibane adducts was of particular interest.

## Results and Discussion

In order to establish the distibane cleavage reaction as a general reaction type for the formation of completely alkyl-substituted heterocycles of the type [R$_2$MSbR′$_2$]$_x$ (M = Al, Ga) and to verify the influence of both the central group 13 metal and the organic ligands bound to the metal centers on the formation of the M–Sb heterocycles, reactions of three different distibanes Sb$_2$R$_4$ (R = *n*Pr, *i*Pr, *i*Bu) with $t$Bu$_3$Al and $t$Bu$_3$Ga, respectively, were investigated. The reaction of Sb$_2$(*i*Pr)$_4$ with $t$Bu$_3$Al was previously shown to yield [$t$Bu$_3$Al][Sb$_2$(*i*Pr)$_4$].[7]

Reactions of Sb$_2$R$_4$ (R′ = *n*Pr, *i*Pr, *i*Bu) with $t$Bu$_3$M (M = Al, Ga) yielded Lewis acid–base adducts [$t$Bu$_3$M]$_2$[Sb$_2$R$_4$] [M = Al, R = *n*Pr (**1**), *i*Bu (**2**); M = Ga, R = *n*Pr (**3**), *i*Pr (**4**)], which were isolated as light-yellow, crystalline solids after crystallization from solutions in pentane at –40 °C [Equation (1)].

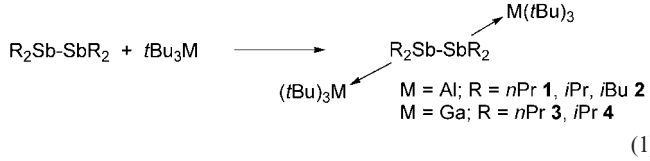


(1)

 © 2007 Wiley-VCH Verlag GmbH & Co. KGaA, Weinheim 

$^1$H NMR spectra of **1**–**4** show resonances from the organic ligands in a 2:3 molar ratio as was expected from the formation of the bisadducts $[t\mathrm{Bu_3M}]_2[\mathrm{Sb_2R_4}]$. The Sb centers in the distibane adducts are prochiral, leading to two separated sets of resonances of the diasterotropic α-$CH_2$ protons of the *n*Pr and *i*Bu groups in **1**, **2**, and **3**. Mass spectra of **1**–**4** only show signals arising from the dissociation into $Sb_2R_4$ and $t\mathrm{Bu_3M}$ as well as from typical fragmentation reactions. Single crystals of **1** suitable for an X-ray structure determination were obtained from a solution in pentane at –30 °C. In addition, the trialkylstibane adduct $t\mathrm{Bu_3Al–Sb}(i\mathrm{Bu})_3$ (**7**) was isolated from the reaction of $t\mathrm{Bu_3Al}$ with $\mathrm{Sb}_2(i\mathrm{Bu})_4$, which was contaminated with $\mathrm{Sb}(i\mathrm{Bu})_3$ (about 10%) as was shown by NMR spectroscopy. Figure 1, Figure 2 and Figure 3 show solid-state structures of **1**, **3**, and **7**, respectively [Equation (2)].

$$\mathrm{R_2Sb\text{-}SbR_2} + t\mathrm{Bu_3Ga} \xrightarrow[-t\mathrm{BuSbR_2}]{} 1/2\,[t\mathrm{Bu_2GaSbR_2}]_2 \quad \mathrm{R} = n\mathrm{Pr}\ \mathbf{5},\ i\mathrm{Bu}\ \mathbf{6} \tag{2}$$

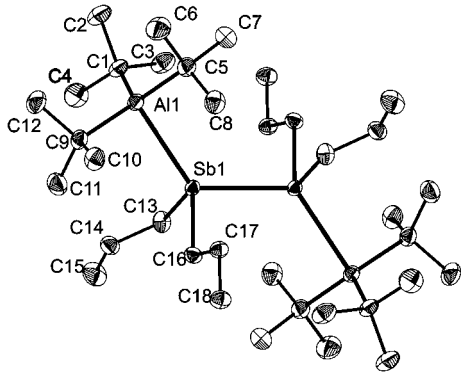


Figure 1. ORTEP plot (50% probability level; H omitted for clarity) showing the solid-state structure and atom-numbering scheme for **1**. Selected bond lengths [Å] and angles [°]: Sb1–Sb1a 2.839(1), Sb1–Al1 2.964(1), Al1–C1 2.009(2), Al1–C5 2.018(2), Al1–C9 2.038(2), Sb1–C13 2.158(2), Sb1–C16 2.153(2), C1–Al1–C5 116.5(1), C1–Al1–C9 117.1(1), C5–Al1–C9 116.6(1), C13–Sb1–C16 96.4(1), C13–Sb1–Sb1a 97.1(1), C16–Sb1–Sb1a 98.7(1), Sb1a–Sb1–Al1 126.8(2).

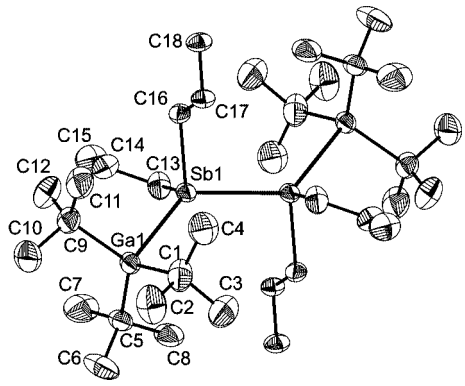


Figure 2. ORTEP plot (50% probability level; H omitted for clarity) showing the solid-state structure and atom-numbering scheme for **3**. Selected bond lengths [Å] and angles [°]: Sb1–Sb1a 2.822(1), Sb1–Ga1 2.988(1), Ga1–C1 2.056(5), Ga1–C5 2.030(4), Ga1–C9 2.033(4), Sb1–C13 2.172(4), Sb1–C16 2.160(3), C1–Ga1–C5 116.5(2), C1–Ga1–C9 116.7(2), C5–Ga1–C9 117.3(2), C13–Sb1–C16 96.2(2), C13–Sb1–Sb1a 97.1(1), C16–Sb1–Sb1a 97.4(1), Sb1a–Sb1–Ga1 127.5(2).

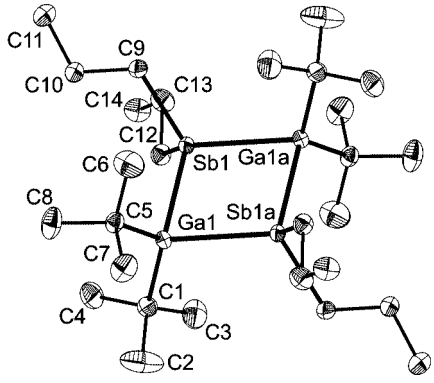


Figure 3. ORTEP plot (50% probability level; H omitted for clarity) showing the solid-state structure and atom-numbering scheme for **7**. Al1–Sb1 2.903(2), Sb1–C1 2.159(4), Sb1–C5 2.153(4), Sb1–C9 2.157(4), Al1–C13 2.028(4), Al1–C17 2.016(5), Al1–C21 2.013(4); C1–Sb1–C5 106.91(16), C1–Sb1–C9 95.84(15), C5–Sb1–C9 99.61(16), C13–Al1–C17 116.20(19), C13–Al1–C21 115.96(18), C17–Al1–C21 115.01(18).

Compounds **1** and **3** crystallize in the monoclinic space group $P2_1/n$ (No. 14) and **7** in $P2_1/c$ (No. 14), respectively. Compounds **1** and **3** possess crystallographic $C_i$ symmetry with the center of symmetry at the Sb–Sb bond. The central Sb–Sb bond lengths observed in **1** [2.839(1) Å] and **3** [2.822(5) Å] are almost identical to those of pure distibanes $Sb_2R_4$ {R = Me 2.862(2) Å,[12] 2.830(1), 2.838(1) Å;[13] *t*Bu 2.817(1) Å;[14] Ph 2.844(1) Å;[15] $SiMe_3$ 2.867(1) Å;[15] $SnMe_3$ 2.866(1) Å[16]}. There is no sign of any Sb–Sb bond weakening upon coordination to Lewis acidic $t\mathrm{Bu_3M}$. Comparable findings have been previously observed for other distibane adducts $[t\mathrm{Bu_3Al}]_x[\mathrm{Sb_2R_4}]$ [R = Me 2.811(1),[5] Et 2.838(1),[5] *i*Pr 2.855(1) Å[7]]. The most significant structural change of the distibane moiety due to the adduct formation is the increase of the degree of pyramidalization of the central Sb atoms. The sums of the C–Sb–C and C–Sb–Sb bond angles observed for **1** (292.2°) and **3** (290.6°) are significantly increased compared with uncomplexed distibanes such as $Me_4Sb_2$ (283.1°), resulting from an increase in p character of the former Sb electron lone pair and an increase in s character of the former Sb–C and Sb–Sb bonding electrons pairs. The Al–Sb bond length observed for **1** [2.964(1) Å] is elongated compared to that of $[t\mathrm{Bu_3Al}]_2[\mathrm{Sb_2Me_4}]$ [2.919(1) Å],[5] whereas $[t\mathrm{Bu_3Al}]_2[\mathrm{Sb_2Et_4}]$ [3.001(1) Å][5] and $[t\mathrm{Bu_3Al}][\mathrm{Sb}_2(i\mathrm{Pr})_4]$ [3.003(2) Å][7] exhibit slightly longer intermetallic Al–Sb distances. In particular the longer Al–Sb distance of $[t\mathrm{Bu_3Al}]_2[\mathrm{Sb_2Et_4}]$ is somehow surprising since repulsive interactions between the organic substituents were expected to be more pronounced for the *n*Pr substituents than the sterically slightly less demanding Et substituents. Comparable trends are observed for gallane adduct **3** [2.988(1) Å], which shows a slightly shorter inter-

 © 2007 Wiley-VCH Verlag GmbH & Co. KGaA, Weinheim 

metallic Ga–Sb bond length compared with $[t\mathrm{Bu_3Ga}]_2$-$[\mathrm{Sb_2Et_4}]$ [3.022(1) Å], whereas that observed for $[t\mathrm{Bu_3Ga}]_2$-$[\mathrm{Sb_2Me_4}]$ [2.919(1) Å] is significantly shorter. The Al–Sb bond length of **7** [2.903(2) Å] is slightly shorter than that of **1** and in between those observed for $t\mathrm{Bu_3Al–SbEt_3}$ [2.845(1)] and $t\mathrm{Bu_3Al–Sb}(i\mathrm{Pr})_3$ [2.927(1) Å]. The average Al–C bond lengths [average values of **1** (2.022) and **7** (2.019 Å)] and C–Al–C bond angles [**1** (116.7°) and **7** (115.7°)] are comparable to those of previously reported alane adducts of trialkylstibanes.[17]

Distibane adducts of trialkylgallanes and -indanes have been previously found to tend to undergo consecutive Sb–Sb bond-cleavage reactions in solution with subsequent formation of heterocyclic stibanylgallanes and -indanes $[\mathrm{R_2MSbR'_2}]_x$, whereas the corresponding Al–Sb heterocycles were not formed.[5,7] The same trends were observed for the distibane adducts **1**–**4**. Alane adducts **1** and **2** remained unchanged in solutions of pentane or hexane and can be stirred for days without any sign of decomposition whereas $t\mathrm{Bu_3Ga}$ reacts with $\mathrm{Sb_2R_4}$ (R = *i*Pr, *i*Bu) with almost quantitative formation of the corresponding Ga–Sb heterocycles $[t\mathrm{Bu_2GaSb}(n\mathrm{Pr})_2]_2$ (**5**) and $[t\mathrm{Bu_2GaSb}(i\mathrm{Bu})_2]_2$ (**6**) within four days.[18] In contrast, the reaction of $t\mathrm{Bu_3Ga}$ with $\mathrm{Sb_2}(i\mathrm{Pr})_4$ proceeds much slower. Even after the reaction mixture was stirred for 10 days there is still some distibane adduct **4** detectable in solution. Unfortunately, $[t\mathrm{Bu_2GaSb}(i\mathrm{Pr})_2]_2$ could not be isolated from byproducts, to date, but its formation is clearly indicated by NMR spectroscopy. Obviously, the steric demand of the organic substituents bound to the Sb centers plays the key role for the required reaction time. Sterically less hindered distibanes such as $\mathrm{Sb_2Me_4}$ and $\mathrm{Sb_2Et_4}$ react with $t\mathrm{Bu_3Ga}$ within two days with almost quantitative formation of the corresponding stibanylgallanes $[t\mathrm{Bu_2GaSbMe_2}]_3$ and $[t\mathrm{Bu_2GaSbEt_2}]_2$,[5] whereas the formation of **5** and **6** requires longer reaction times. Compounds **5** and **6** were obtained as colorless crystalline solids in almost quantitative yields, which were recrystallized from solutions in hexane.

$^1$H and $^{13}$C NMR spectra of **5** and **6** show resonances of the organic ligands in the expected 1:1 molar ratio. Since the Sb centers in the distibane adducts are no longer prochiral only a single resonance of the α-$CH_2$ protons of the *n*Pr and *i*Bu groups occurs. The mass spectra of **5** and **6** show typical fragmentation patterns of the heterocycles, whereas no molecular ion peak could be detected. Suitable crystals of **5** for a single-crystal X-ray diffraction study were obtained from a solution in hexane at –30 °C. (Figure 4).

Compound **5** crystallizes in the monoclinic space group $P2_1/c$ (No. 14) and adopts a planar four-membered ring. The metal atoms reside in distorted tetrahedral environments. The Ga–Sb bond lengths [2.736(1), 2.738(1) Å] are almost identical to those observed for $[t\mathrm{Bu_2GaSbEt_2}]_2$ [2.731(1)–2.735(1) Å] and $[\mathrm{Et_2GaSb(SiMe_3)_2}]_2$ [2.718(1), 2.729(1) Å],[19] whereas $[t\mathrm{Bu_2GaSb(SiMe_3)_2}]_2$ [2.768(1) Å][20] shows slightly longer Ga–Sb distances due to increased repulsive interactions between the sterically more demanding organic substituents. The C–Sb–C bond angles [97.3(2)°] are smaller than the C–Ga–C bond angles [122.2(2)°] as is typical for this type of compound and the Ga–C [2.016(4), 2.011(3) Å] and Sb–C bond lengths [2.161(3), 2.166(3) Å] are within typical ranges.

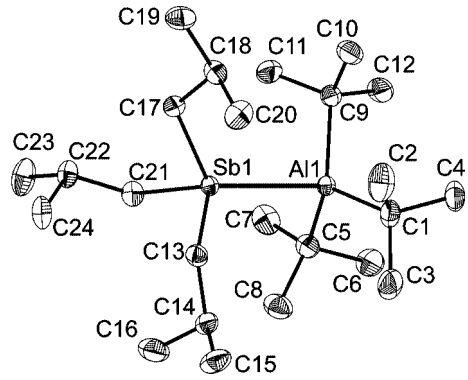


Figure 4. ORTEP plot (50% probability level; H omitted for clarity) showing the solid-state structure and atom-numbering scheme for **5**. Ga1–Sb1 2.736(1), Ga1a–Sb1 2.738(1), Sb1–C9 2.161(3), Sb1–C12 2.166(3), Ga1–C1 2.016(4), Ga1–C5 2.011(3), Sb1–Ga1–Sb1a 83.4(1), Ga1–Sb1–Ga1a 96.6(1), C9–Sb1–Ga1 117.1(1), C12–Sb1–Ga1 113.8(1), C1–Ga1–Sb1 108.8(1), C5–Ga1–Sb1 113.4(1), C1–Ga1–C5 122.2(2), C9–Sb1–C12 97.3(2).

## Conclusions

Distibanes $\mathrm{Sb_2R_4}$ (R = *n*Pr, *i*Pr, *i*Bu) react with trialkylalanes and -gallanes $t\mathrm{Bu_3M}$ with the initial formation of Lewis acid–base adducts $[t\mathrm{Bu_3M}]_2[\mathrm{Sb_2R_4}]$. The gallane adducts were found to tend to undergo Sb–Sb bond-cleavage reactions with the subsequent formation of heterocyclic stibanylgallanes $[t\mathrm{Bu_2GaSbR_2}]_2$, whereas the alane adducts remained unchanged in solution.

## Experimental Section

**General:** All manipulations were performed in a glovebox under an Ar atmosphere or by standard Schlenk techniques. $t\mathrm{Bu_3Al}$,[21] $t\mathrm{Bu_3Ga}$,[22] $\mathrm{Sb_2}(n\mathrm{Pr})_4$,[23] $\mathrm{Sb_2}(i\mathrm{Pr})_4$,[23] and $\mathrm{Sb_2}(i\mathrm{Bu})_4$[23] were prepared according to literature methods. $^1$H and $^{13}$C{$^1$H} spectra were recorded using a Bruker Avance 500 spectrometer and are referenced to internal $C_6D_5H$ ($^1$H NMR: $\delta$ = 7.154, $^{13}$C NMR: $\delta$ = 128.0 ppm). Melting points were measured in sealed capillaries and are not corrected. Mass spectra (EI) were recorded with a Finnigan MAT 8230 spectrometer. Melting points were measured in sealed capillaries and were not corrected. Elemental analyses were performed at the Elementaranalyse Labor of the University of Paderborn. Yields are given for the pure products after recrystallization.

**Synthesis of $[t\mathrm{Bu_3M}]_2[\mathrm{Sb_2R_4}]$:** $t\mathrm{Bu_3M}$ (1 mmol) and $\mathrm{Sb_2R_4}$ (0.5 mmol) were combined in the glovebox, and the resulting yellow oil was dissolved in *n*-pentane (5 mL) and stored at –40 °C. Light yellow crystals of **1**–**4** were formed within 2 d. Yields are given for isolated compounds after recrystallization.

**$[t\mathrm{Bu_3Al}]_2[\mathrm{Sb_2}(n\mathrm{Pr})_4]$ (1):** Yield 0.22 g, 0.35 mmol, 70%. M.p. 85 °C. $C_{36}H_{82}Al_2Sb_2$ (812.51): calcd. C 53.2, H 10.2; found C 54.2, H 9.5. $^1$H NMR (500 MHz; $C_6D_5H$, 25 °C): $\delta$ = 0.89 [t, $^3J_{H,H}$ = 7.2 Hz, 12 H, $CH_3CH_2CH_2Sb$], 1.22 [s, 54 H, $Me_3CAl$], 1.53–1.62 [m, 8 H, $CH_3CH_2CH_2Sb$], 1.75–1.81 [m, 4 H, $CH_3CH_2CH_2Sb$], 1.88–1.93

 © 2007 Wiley-VCH Verlag GmbH & Co. KGaA, Weinheim 

[m, 4 H, $CH_3CH_2CH_2Sb$] ppm. $^{13}C\{^1H\}$ NMR (125 MHz; $C_6D_5H$, 25 °C): $\delta$ = 13.4 (s, *Me*$CH_2CH_2Sb$), 17.8 [s, Me*CH*$_2CH_2Sb$], 19.5 [s, $Me_3CAl$], 23.1 [s, $MeCH_2CH_2Sb$], 31.9 [s, *Me*$_3$CAl] ppm. EI-MS (70 eV, 70 °C): *m*/*z* (%) = 416 (35) $[Sb_2(nPr)_4]^+$, 375 (5) $[Sb_2(nPr)_3]^+$, 331 (25) $[Sb_2(nPr)_2]^+$, 288 (40) $[Sb_2(nPr)H]^+$, 141 (35) $[tBu_2Al]^+$, 84 (5) $[tBuAl]^+$, 57 (100) $[tBu]^+$.

**[*t*Bu$_3$Al]$_2$[Sb$_2$(*i*Bu)$_4$] (2):** Yield 0.40 g, 0.46 mmol, 92%. M.p. < 0 °C. $C_{40}H_{90}Al_2Sb_2$ (868.61): calcd. C 55.3, H 10.4; found C 56.1, H 10.2. $^1H$ NMR (500 MHz; $C_6D_5H$, 25 °C): $\delta$ = 1.00 [d, $^3J_{H,H}$ = 7.2 Hz, 24 H, $(CH_3)_2CHCH_2Sb$], 1.14 [s, 54 H, *Me*$_3$CAl], 1.75–1.78 [m, $^3J_{H,H}$ = 6.7 Hz, 4 H, $(CH_3)_2CHCH_2Sb$], 1.93 [sept, $^3J_{H,H}$ = 6.7 Hz, 4 H, $(CH_3)_2CHCH_2Sb$], 2.01–2.05 [m, $^3J_{H,H}$ = 6.7 Hz, 4 H, $(CH_3)_2CHCH_2Sb$] ppm. $^{13}C\{^1H\}$ NMR (125 MHz; $C_6D_5H$, 25 °C): $\delta$ = 22.8 [s, $Me_2CHCH_2Sb$], 25.7 [s, *Me*$_2$CHCH$_2$Sb], 27.7 [s, Me$_3$*C*Al], 29.1 [s, $Me_2CHCH_2Sb$], 30.8 [s, *Me*$_3$CAl] ppm.

**[*t*Bu$_3$Ga]$_2$[Sb$_2$(*n*Pr)$_4$] (3):** Yield 0.28 g, 0.31 mmol, 62%. M.p. 37 °C. $C_{36}H_{82}Ga_2Sb_2$ (897.98) calcd. C 48.2, H 9.2; found C 47.1, H 8.8. $^1H$ NMR (500 MHz; $C_6D_5H$, 25 °C): $\delta$ = 0.93 [t, $^3J_{H,H}$ = 7.2 Hz, 12 H; $CH_3CH_2CH_2Sb$], 1.26 [s, 54 H, *Me*$_3$CGa], 1.62 [m, 8 H, $CH_3CH_2CH_2Sb$], 1.71–1.77 [m, 4 H, $CH_3CH_2CH_2Sb$], 1.84–1.88 [m, 4 H, $CH_3CH_2CH_2Sb$] ppm. $^{13}C\{^1H\}$ NMR (125 MHz; $C_6D_5H$, 25 °C): $\delta$ = 13.1 [s, Me*CH*$_2$CH$_2$Sb], 18.2 [s, *Me*CH$_2$CH$_2$Sb], 23.7 [s, $MeCH_2CH_2Sb$], 29.7 [s, Me$_3$*C*Ga], 31.9 [s, *Me*$_3$CGa] ppm.

**[*t*Bu$_3$Ga]$_2$[Sb$_2$(*i*Pr)$_4$] (4):** Yield 0.42 g, 0.47 mmol, 94%. M.p. < 0 °C. $C_{36}H_{82}Ga_2Sb_2$ (897.98) calcd. C 48.2, H 9.2; found C 47.1, H 8.9. $^1H$ NMR (500 MHz; $C_6D_5H$, 25 °C): $\delta$ = 1.18 [s, 54 H, *Me*$_3$CGa], 1.42 [d, $^3J_{H,H}$ = 7.3 Hz, 12 H, $(CH_3)_2CHSb$], 1.49 [d, $^3J_{H,H}$ = 7.3 Hz, 12 H, $(CH_3)_2CHSb$], 2.31 [sept, 4 H, $(CH_3)_2CHSb$] ppm. $^{13}C\{^1H\}$ NMR (125 MHz; $C_6D_5H$, 25 °C): $\delta$ = 13.9 [s, Me$_2$*CH*Sb], 24.7 [s, *Me*$_2$CHSb], 25.6 [s, *Me*$_2$CHSb], 30.7 [s, *Me*$_3$CGa] ppm.

**General Synthesis of [tBu$_2$GaSbR$_2$]$_2$:** $Sb_2R_4$ (1 mmol) was added to a solution of *t*Bu$_3$Ga (1.5 mmol, 0.35 g) dissolved in hexane (10 mL). The resulting yellow solution was stirred for 4 d at ambient temperature. Storage at –30 °C under the absence of light yielded colorless crystals of **5** and **6** within 12 h.

**[*t*Bu$_2$GaSb(*n*Pr)$_2$]$_2$ (5):** Yield 0.30 g, 0.39 mmol, 78%. M.p. 160 °C. $C_{28}H_{64}Ga_2Sb_2$ (783.75) calcd. C 42.9, H 8.2; found C 42.2, H 8.1. $^1H$ NMR (500 MHz; $C_6D_5H$, 25 °C): $\delta$ = 0.95 [t, $^3J_{H,H}$ = 7.3 Hz, 12 H, $CH_3CH_2CH_2Sb$], 1.34 [s, 36 H, *Me*$_3$CGa], 1.66–1.73 [m, 8 H, $CH_3CH_2CH_2Sb$], 2.05–2.08 [m, 8 H, $CH_3CH_2CH_2Sb$] ppm. $^{13}C\{^1H\}$ NMR (125 MHz; $C_6D_5H$, 25 °C): $\delta$ = 9.9 [s, $MeCH_2CH_2Sb$], 18.3 [s, *Me*CH$_2$CH$_2$Sb], 24.1 [s, Me*CH*$_2$CH$_2$Sb], 28.5 [s, Me$_3$*C*Ga], 32.2 [s, *Me*$_3$CGa] ppm. EI-MS (70 eV, 70 °C): *m*/*z* (%) = 527 (8) $[GaSb_2(nPr)tBu_3]^+$, 416 (30) $[Sb_2(nPr)_4]^+$, 345 (30) $[Sb_2(nPr)tBuH]^+$, 288 (40) $[Sb_2(nPr)H]^+$, 57 (100) $[tBu]^+$.

**[*t*Bu$_2$GaSb(*i*Bu)$_2$]$_2$ (6):** Yield 0.36 g, 0.43 mmol, 86%. M.p. 162 °C (dec.). $C_{32}H_{72}Ga_2Sb_2$ (839.86): calcd. C 45.8, H 8.6; found C 45.2; H, 8.5. $^1H$ NMR (500 MHz; $C_6D_5H$, 25 °C): $\delta$ = 1.06 [d, $^3J_{H,H}$ = 6.3 Hz, 24 H, $(CH_3)_2CHCH_2Sb$], 1.39 [s, 36 H, *Me*$_3$CGa], 2.15 [m, 4 H, $(CH_3)_2CHCH_2Sb$], 2.22 [d, $^2J_{H,H}$ = 7.2 Hz, 8 H, $(CH_3)_2CHCH_2Sb$] ppm. $^{13}C\{^1H\}$ NMR (125 MHz; $C_6D_5H$, 25 °C): $\delta$ = 19.7 [s, $(CH_3)_2CHCH_2Sb$], 25.3 [s, $(CH_3)_2CHCH_2Sb$], 29.2 [s, Me$_3$*C*Ga], 29.9 [s, $(CH_3)_2CHCH_2Sb$], 32.1 [s, *Me*$_3$CGa] ppm. EI-MS (70 eV, 100 °C): *m*/*z* (%) = 472 (20) $[Sb_2(iBu)]^+$, 420 (15) $[tBu_2GaSb(iBu)_2]^+$, 363 (40) $[GaSb(i/tBu)_3]^+$, 307 (35) $[GaSb(i/tBu)_2]^+$, 251 (15) $[GaSb(i/tBu)]^+$, 236 (5) $[iBu_2Sb]^+$, 183 (65) $[tBu_2Ga]^+$, 178 (15) $[iBuSb]^+$, 127 (25) $[tBuGa]^+$, 69 (55) $[Ga]^+$, 57 (100) $[i/tBu]^+$.

***t*Bu$_3$Al–Sb(*i*Bu)$_3$ (7):** Compound **7** was obtained in the form of colorless crystals as a byproduct from the reaction of *t*Bu$_3$Al with $Sb_2(iBu)_4$, which contained about 10% Sb(*i*Bu)$_3$ according to NMR spectroscopic studies. Compound **7** was also independently prepared by the reaction of *t*Bu$_3$Al (1.5 mmol, 0.18 g) with Sb(*i*Bu)$_3$ (1.5 mmol, 0.28 g). Yield 0.23 g, 0.5 mmol, 50%. M.p. 47 °C. $C_{24}H_{54}AlSb$ (491.42): calcd. C 58.7, H 11.1; found C 57.3, H 10.9. $^1H$ NMR (500 MHz; $C_6D_5H$, 25 °C): $\delta$ = 0.96 [d, $^3J_{H,H}$ = 6.6 Hz, 18 H, $(CH_3)_2CHCH_2Sb$], 1.18 [s, 27 H, *Me*$_3$CAl], 1.49 [d, $^3J_{H,H}$ = 6.7 Hz, 6 H, $(CH_3)_2CHCH_2Sb$], 1.90 [sept, $^3J_{H,H}$ = 6.6 Hz, 3 H, $(CH_3)_2CHCH_2Sb$] ppm. $^{13}C\{^1H\}$ NMR (125 MHz; $C_6D_5H$, 25 °C): $\delta$ = 20.4 [s, Me$_3$*C*Al], 26.0 [s, *Me*$_2$CHCH$_2$Sb], 27.6 [s, Me$_2$CH*CH*$_2$Sb], 27.8 [s, Me$_2$*CH*CH$_2$Sb], 31.4 [s, *Me*$_3$CAl] ppm.

Table 1. Crystallographic data for [*t*Bu$_3$Al]$_2$[Sb$_2$(*n*Pr)$_4$] (**1**), [*t*Bu$_3$Ga]$_2$[Sb$_2$(*n*Pr)$_4$] (**3**), [*t*Bu$_2$GaSb(*n*Pr)$_2$]$_2$ (**5**), and *t*Bu$_3$Al–Sb(*i*Bu)$_3$ (**7**).

| | [*t*Bu$_3$Al]$_2$[Sb$_2$(*n*Pr)$_4$] (**1**) | [*t*Bu$_3$Ga]$_2$[Sb$_2$(*n*Pr)$_4$] (**3**) | [*t*Bu$_2$GaSb(*n*Pr)$_2$]$_2$ (**5**) | *t*Bu$_3$Al–Sb(*i*Bu)$_3$ (**7**) |
|---|---|---|---|---|
| Molecular formula | $C_{36}H_{82}Al_2Sb_2$ | $C_{36}H_{82}Ga_2Sb_2$ | $C_{28}H_{64}Ga_2Sb_2$ | $C_{24}H_{54}AlSb$ |
| Formula mass [g mol$^{-1}$] | 812.48 | 897.96 | 783.73 | 491.40 |
| Crystal system | monoclinic | monoclinic | monoclinic | monoclinic |
| Space group | $P2_1/n$ (no. 14) | $P2_1/n$ (no. 14) | $P2_1/n$ (no. 14) | $P2_1/c$ (no. 14) |
| *a* [Å] | 12.916(5) | 12.8845(9) | 12.4726(8) | 10.2575(16) |
| *b* [Å] | 13.122(5) | 13.3124(9) | 8.9185(6) | 14.503(2) |
| *c* [Å] | 12.971(5) | 12.9979(9) | 15.8908(10) | 18.631(3) |
| $\beta$ [deg] | 90.103(2) | 91.633(1) | 92.574(1) | 96.590(3) |
| *V* [Å$^3$] | 2198.4(14) | 2228.5(3) | 1765.9(2) | 2753.3(7) |
| *Z* | 2 | 2 | 2 | 4 |
| $\mu$ [mm$^{-1}$] | 1.289 | 2.415 | 3.036 | 1.040 |
| $D_{calcd}$ [g cm$^{-3}$] | 1.227 | 1.338 | 1.474 | 1.185 |
| Crystal dim. [mm] | 0.39 × 0.24 × 0.21 | 0.48 × 0.43 × 0.39 | 0.43 × 0.09 × 0.08 | 0.40 × 0.32 × 0.27 |
| Reflections recorded | 18798 | 19346 | 15141 | 24588 |
| Nonequiv. reflections recorded | 5318 | 5315 | 4272 | 6689 |
| $R_{merg}$ | 0.0430 | 0.0448 | 0.0469 | 0.0714 |
| Parameters refined/restraints | 181 | 181 | 145 | 235 |
| $R_1$[a]; $wR_2$[b] | 0.0253; 0.0599 | 0.0379; 0.1032 | 0.0343; 0.0699 | 0.0506; 0.0844 |
| Goodness of fit[c] | 1.048 | 1.064 | 1.014 | 0.925 |
| Final max., min. $\Delta\rho$ (e Å$^{-3}$) | 1.063, –0.532 | 0.937, –0.905 | 0.898, –0.610 | 0.985, –0.960 |

[a] $R_1 = \Sigma(||F_o| - |F_c||) / \Sigma|F_o|$ [for $I > 2\sigma(I)$]. [b] $wR_2 = \{\Sigma[w(F_o^2 - F_c^2)^2] / \Sigma[w(F_o^2)^2]\}^{1/2}$. [c] Goodness of fit = $\{\Sigma[w(|F_o^2| - |F_c^2|)^2] / N_{obs} - N_{param})\}^{1/2}$.

 © 2007 Wiley-VCH Verlag GmbH & Co. KGaA, Weinheim 

**X-ray Structure Solution and Refinement:** Crystallographic data of **1**, **3**, **5**, and **7** are summarized in Table 1. Figures 1–4 show ORTEP diagrams of the solid-state structures of **1**, **3**, **5**, and **7**. Data were collected with a Bruker SMART APEX CCD diffractometer[24] using Mo-$K_\alpha$ radiation ($\lambda$ = 0.71073 Å) at $T$ = 120(2) K and the structures were solved by Direct and Fourier Methods (SHELXTL),[24] and refined by full-matrix least-squares on $F^2$. All non-hydrogen atoms in **1**, **3**, **5** and **7** were refined anisotropically and hydrogen atoms were located from $\Delta F$ maps and refined at idealized positions with a riding model (SHELXTL).

CCDC-623814 (for **1**), -623815 (for **3**), -623816 (for **5**), and -623813 (for **7**) contain the supplementary crystallographic data for this paper. These data can be obtained free of charge from The Cambridge Crystallographic Data Centre via www.ccdc.cam.ac.uk/data_request/cif.

## Acknowledgments

This work was financially supported by the Deutsche Forschungsgemeinschaft (DFG), Fonds der Chemischen Industrie (FCI), and the Bundesministerium für Bildung, Wissenschaft, Forschung und Technologie (BMBF).

[1] I.-P. Lorenz, S. Rudolph, H. Piotrowski, K. Polborn, *Eur. J. Inorg. Chem.* **2005**, 82.

[2] See the following and ref. cited therein: a) N. A. Bailey, P. D. Frisch, J. A. McCleverty, N. W. J. Walker, J. Williams, *J. Chem. Soc., Chem. Commun.* **1975**, 350; b) U. Weber, L. Zsolnai, G. Huttner, *Z. Naturforsch. B: Chem. Sci.* **1985**, *40*, 1430; c) J. Bultitude, L. F. Larkworthy, D. C. Povey, G. W. Smith, J. R. Dilworth, G. J. Leigh, *J. Chem. Soc., Chem. Commun.* **1986**, 174; d) S. Vogel, A. Barth, G. Huttner, T. Klein, L. Zsolnai, R. Kremer, *Angew. Chem. Int. Ed. Engl.* **1991**, *30*, 303; e) R. R. Schrock, T. E. Glassman, M. G. Vale, M. Kol, *J. Am. Chem. Soc.* **1993**, *115*, 1760; f) H. J. Breunig, J. Pawlik, *Z. Anorg. Allg. Chem.* **1995**, *621*, 817; g) P. Sharma, N. Rosas, S. Hernandez, A. Cabrera, *J. Chem. Soc., Chem. Commun.* **1995**, 1325; h) H. J. Breunig, I. Ghesner, M. E. Ghesner, E. Lork, *J. Organomet. Chem.* **2003**, *677*, 15; i) G. Balazs, H. J. Breunig, E. Lork, S. Mason, *Organometallics* **2003**, *22*, 576.

[3] For a recent review see: H. J. Breunig, *Adv. Organomet. Chem.* **2003**, *49*, 95.

[4] a) H. Nöth, *Z. Naturforsch., Teil B* **1960**, *15*, 327; b) A. B. Burg, R. I. Wagner, *J. Am. Chem. Soc.* **1953**, *75*, 3872; c) A. B. Burg, J. Brendel, *J. Am. Chem. Soc.* **1958**, *80*, 3198; d) A. B. Burg, *J. Am. Chem. Soc.* **1961**, *83*, 2226; e) H. L. Carrell, J. Donohue, *Acta Crystallogr., Sect. B* **1968**, *24*, 699; f) H. Schmidbaur, T. Wimmer, A. Grohmann, O. Steigelmann, G. Müller, *Chem. Ber.* **1989**, *122*, 1607.

[5] A. Kuczkowski, S. Schulz, M. Nieger, P. Saarenketo, *Organometallics* **2001**, *20*, 2000.

[6] A. Kuczkowski, S. Schulz, M. Nieger, *Angew. Chem. Int. Ed.* **2001**, *40*, 4222.

[7] A. Kuczkowski, S. Fahrenholz, S. Schulz, M. Nieger, *Organometallics* **2004**, *23*, 3615.

[8] Distibane adducts can be stored at –30 °C in the dark under an Ar atmosphere for months without any sign of decomposition.

[9] H. J. Breunig, M. Stanciu, R. Rösler, E. Lork, *Z. Anorg. Allg. Chem.* **1998**, *624*, 1965.

[10] H. J. Breunig, W. Fichtner, *Z. Anorg. Allg. Chem.* **1981**, *477*, 119.

[11] a) A. H. Cowley, R. A. Jones, C. M. Nunn, D. L. Westmoreland, *Chem. Mater.* **1990**, *2*, 221; b) H. S. Park, S. Schulz, H. Wessel, H. W. Roesky, *Chem. Vap. Deposition* **1999**, *5*, 179; c) S. Schulz, S. Fahrenholz, A. Kuczkowski, W. Assenmacher, A. Seemayer, K. Wandelt, *Chem. Mater.* **2005**, *17*, 1982. For a recent review article see: S. Schulz, in: *Top. Organomet. Chem.*, vol. 9 (Ed.: R. A. Fischer), **2005**, p. 101.

[12] A. J. Ashe III, E. G. Ludwig Jr., J. Oleksyszyn, J. C. Huffman, *Organometallics* **1984**, *3*, 337.

[13] O. Mundt, H. Riffel, G. Becker, A. Simon, *Z. Naturforsch., Teil B* **1984**, *39*, 317.

[14] O. Mundt, G. Becker, H.-J. Wessely, H. J. Breunig, H. Kischkel, *Z. Anorg. Allg. Chem.* **1982**, *486*, 70.

[15] G. Becker, H. Freudenblum, C. Witthauer, *Z. Anorg. Allg. Chem.* **1982**, *492*, 37.

[16] G. Becker, M. Meiser, O. Mundt, J. Weidlein, *Z. Anorg. Allg. Chem.* **1989**, *569*, 62.

[17] See the following and ref. cited therein: a) S. Schulz, A. Kuczkowski, M. Nieger, *J. Organomet. Chem.* **2000**, *604*, 202; b) S. Schulz, *Adv. Organomet. Chem.* **2003**, *49*, 225; c) S. Schulz, *Coord. Chem. Rev.* **2001**, *215*, 1.

[18] The initially formed distibane adduct [$t$Bu$_3$Ga][Sb$_2$($i$Bu)$_4$], whose formation was clearly indicated by NMR spectroscopy, remains liquid even at –40 °C and withstands any attempt of crystallization, to date.

[19] E. E. Foos, R. J. Jouet, R. L. Wells, A. L. Rheingold, L. M. Liable-Sands, *J. Organomet. Chem.* **1999**, *582*, 45.

[20] a) R. L. Wells, E. E. Foos, P. S. White, A. L. Rheingold, L. M. Liable-Sands, *Organometallics* **1997**, *16*, 4771; b) M. Nieger, S. Schulz, private communication **1999**, CCDC-133814.

[21] H. Lehmkuhl, O. Olbrysch, H. Nehl, *Justus Liebigs Ann. Chem.* **1973**, 708.

[22] R. A. Kovar, G. Loaris, H. Derr, J. O. Callaway, *Inorg. Chem.* **1974**, *13*, 1476.

[23] H. J. Breunig, W. Kanig, *J. Organomet. Chem.* **1980**, *186*, C5.

[24] *SMART (Version 5.62), SAINT (Version 6.02), SHELXTL (Version 6.10) and SADABS (Version 2.03)*, Bruker AXS Inc., Madison, Wisconsin, USA, 2002.

Received: October 16, 2006
Published Online: December 19, 2006

 © 2007 Wiley-VCH Verlag GmbH & Co. KGaA, Weinheim 

DOI: 10.1002/ejic.200600619

# Electronic Control of the Rotational Barrier in $\eta^2$-Alkyne-1-thio Complexes

**Wolfram W. Seidel,*[a] Beatriz López Sánchez,[a] Matthias J. Meel,[a] Alexander Hepp,[a] and Tania Pape[a]**

**Keywords:** (Alkylthio)alkyne ligands / Alkyne complexes / Molybdenum / Fluxionality / Ligand effects

A family of thio-alkyne complexes [Tp′Mo(CO)(L)($BnSC_2S$)] {Bn = benzyl, Tp′ = hydrotris(3,5-dimethylpyrazolyl)borate, L = carbonyl (**2**), 2,6-dimethylphenyl isocyanide (**7**), *tert*-butyl isocyanide (**8**), 4-(dimethylamino)pyridine (**9**)} was prepared by reductive removal of a benzyl group in the corresponding bis(benzylthio)acetylene complexes [Tp′Mo(CO)(L)-($BnSC_2SBn$)]($PF_6$) (**1**-$PF_6$, **4**-$PF_6$, **5**-$PF_6$ and **6**-$PF_6$). All complexes were characterized by IR, $^1H$, $^{13}C$ spectroscopy and cyclic voltammetry. X-ray diffraction studies of **5**-$PF_6$, **8** and **9** were carried out. The alkyne ligand is bound symmetrically to molybdenum in **5**-$PF_6$ and unsymmetrically in **8** and **9**. The trend in the π-acidity of ligand L is reflected in the spectroscopic and electrochemical data as well as in the molecular structures. Variable temperature $^1H$ NMR investigations with **7**, **8** and **9** disclosed that the barrier of the alkyne rotation at molybdenum decreases in the order of rising electron density at the metal center while the steric demand increases. Therefore, electronic control of the barrier by the specific character of the ligand L is evident.

(© Wiley-VCH Verlag GmbH & Co. KGaA, 69451 Weinheim, Germany, 2007)

## Introduction

Applying the terms of simple VB theory alkynes can act in their complexes as two-, three- or four-electron donor ligands. The possible interaction of two occupied π- and two unoccupied π*-alkyne orbitals with metal orbitals renders an appropriate description of the binding situation more complex compared to the Dewar–Chatt–Duncanson model for coordinated alkenes. However, the easy rotation of the side on bound ligand is of typical behaviour for both alkene and alkyne complexes. In asymmetric alkyne complexes this dynamic behaviour can regularly be studied by variable temperature NMR spectroscopy. In this context, the evaluation of both the alkyne-$\pi_\perp$-donation into the metal dπ manifold, and the alkyne-$\pi_\parallel$*-acceptance of metal dπ density seems feasible, because the activation barrier of the rotation should reflect the strength of the metal alkyne π-interaction. The dependence of the rotational barrier from electronic factors such as the π-acid-π-base properties of ancillary ligands[1] and the type of the alkyne[2] is evident in many examples. Electronic factors must be involved, when the observed trend within related complexes does not follow the varying steric demand.[1c] Large barrier differences in complexes with high electronic and steric similarity like [Mo($\eta^5$-$C_5H_5$)(dppe)($MeC_2Me$)]($BF_4$) and [Mo($\eta^5$-$C_5H_5$)($PPh_2Me$)$_2$($MeC_2Me$)]($BF_4$) emphasize the importance of the particular position of the ligand π-orbitals with respect to the metal dπ manifold.[1b] In contrast, the size of the alkyl substituents R predominantly accounts for barrier differences in [Nb($\eta^5$-$C_5H_4SiMe_3$)(R)$_2$($Me_3SiC_2SiMe_3$)] complexes.[3] However, frequently the differences in the activation enthalpies are small and the interfering steric and electronic factors can not be separated.[4] Thus, neutral $Mo^{II}$ and $W^{II}$ alkyne complexes with the hydrotris(3,5-dimethylpyrazolyl)borate (Tp′) ancillary ligand show distinctively higher barriers[5] compared to those with hydrotris(pyrazolyl)borate. However, the small differences within [TpM($RC_2R'$)(CO)I] complexes (M = Mo, W) upon variation of R/R′ can be attributed to both steric and electronic reasons.[6] In formal $Mo^{VI}$ complexes with a strong π-donating imido ligand the rotational barrier is even independent of the type of the alkyne.[7] Recently, in paramagnetic complexes [Mo($\eta^5$-$C_5H_5$){P(OMe)$_3$}$_2$($RC_2R$)] temperature-dependent EPR spectroscopy was used to determine much lower barriers of an approximately quarter-turn alkyne oscillation process at the metal.[8] Depending on the particular $d^8$-metal[9] or type of the ancillary ligand, observation of rotamers with respect to 90° rotation at the metal, that can be considered as the extreme of an "inverted" rotational barrier, emphasizes the delicate balance of steric and electronic influences.[10]

In the course of our studies on the coordination chemistry of sulfur-substituted alkynes[11] we isolated and characterized a number of closely related (R–S)-alkyne complexes, which allow a surprising insight into the problem discussed above. In the complexes [Tp′Mo(CO)(L)($\eta^2$-$BnSC_2S$)], in

[a] Institut für Anorganische und Analytische Chemie, Westfälische Wilhelms-Universität Münster,
Corrensstraße 30/36, 48149 Münster, Germany
Fax: +49-251-8333108
E-mail: seidelww@uni-muenster.de

Supporting information for this article is available on the WWW under http://www.eurjic.org or from the author.

 © 2007 Wiley-VCH Verlag GmbH & Co. KGaA, Weinheim 

which the ligand L represents either carbonyl, an isocyanide or a pyridine derivative, the electron density at the metal is increased in this order as can be concluded from IR spectroscopic and electrochemical evidence. The variable-temperature $^1$H NMR spectroscopic investigations of these complexes showed that the free activation enthalpy of the alkyne rotation is notably lowered, while the steric demand of the ligands rises, respectively. Therefore, the electronic determination of the rotational barrier in the complexes [Tp′Mo(CO)(L)(η²-BnSC$_2$S)], described in this contribution, is remarkably obvious.

## Results and Discussion

The (BnS)(S)-alkyne complex [Tp′Mo(CO)$_2$(η²-BnSC$_2$S)] (**2**) with a terminal sulfur atom is accessible by a single electron reduction of the corresponding cationic bis(benzylthio)acetylene complex [Tp′Mo(CO)$_2$(η²-BnSC$_2$SBn)](PF$_6$) **1**-PF$_6$ and the subsequent removal of a benzyl radical.[11] The desired substitution of one carbonyl ligand in **2** was preferably performed with **1**-PF$_6$, since the carbonyls are easier to remove in the electron-poorer cation **1**$^+$. Following a procedure described by Templeton,[5] complex **1**-PF$_6$ was transformed into the acetonitrile complex [Tp′Mo(CO)(CH$_3$CN)(η²-BnSC$_2$SBn)](PF$_6$) (**3**-PF$_6$), which served as a convenient starting material for the introduction of other neutral ligands. The substitution of acetonitrile in **3**-PF$_6$ by 2,6-dimethylphenyl isocyanide, *tert*-butyl isocyanide or 4-(dimethylamino)pyridine in boiling dichloromethane (Scheme 1) proceeds very clean, if **3**-PF$_6$ is analytically pure. A facile and fast purification of **3**-PF$_6$, which is unexpectedly stable, is possible by column chromatography using SiO$_2$ as solid phase and dichloromethane as eluent. The products of the substitution according to Scheme 1, [Tp′Mo(CO)(Me$_2$C$_6$H$_3$NC)(η²-BnSC$_2$SBn)](PF$_6$) (**4**-PF$_6$), [Tp′Mo(CO)(Me$_3$CNC)(η²-BnSC$_2$SBn)](PF$_6$) (**5**-PF$_6$) and [Tp′Mo(CO)(Me$_2$NC$_5$H$_4$N)(η²-BnSC$_2$SBn)](PF$_6$) (**6**-PF$_6$), were isolated by crystallization from dichloromethane solutions after layering with diethyl ether.

The preparation of [Tp′Mo(CO)(Me$_2$C$_6$H$_3$NC)(η²-BnSC$_2$S)] (**7**), [Tp′Mo(CO)(Me$_3$CNC)(η²-BnSC$_2$S)] (**8**) and [Tp′Mo(CO)(Me$_2$NC$_5$H$_4$N)(η²-BnSC$_2$S)] (**9**) was achieved by one-electron reduction of **4**-PF$_6$, **5**-PF$_6$ and **6**-PF$_6$ according to Scheme 1. The reduction at –78 °C resulted in all cases in intensely red molybdenum(I) species, which are characterized by low frequencies of the carbonyl and, in the case of **4** and **5**, isocyanide C–N vibrations. A color change to dark green at ambient temperature indicates the formation of the final products by cleavage of a benzyl radical. The dicarbonyl complex **2** is synthesized following the same procedure using **1**-PF$_6$ as starting material.[11] However, the removal of one benzyl group proceeds much faster with improved yields after reduction of **4**-PF$_6$, **5**-PF$_6$ and **6**-PF$_6$. We believe that this benefit can be attributed to both steric and electronic reasons. The higher steric demand of the ligands L compared to CO hamper the formation of undesired by-products, which were shown to involve attack of

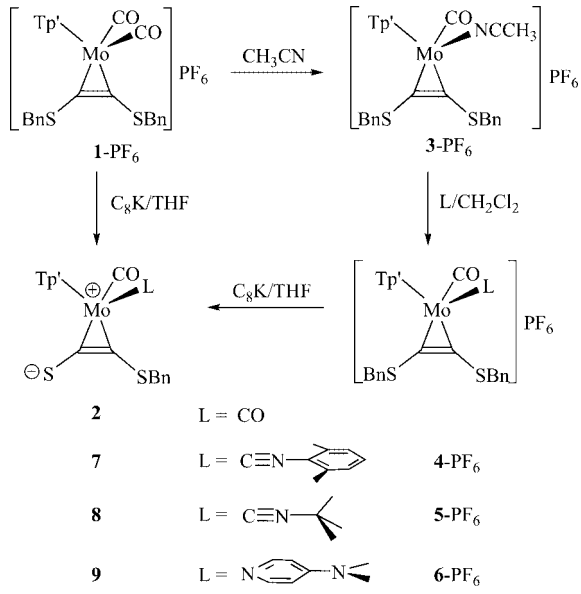


Scheme 1. Synthesis of complexes **2**–**9**, Tp′ = hydrotris(3,5-dimethylpyrazolyl)borate, Bn = benzyl.

benzyl radicals at the coordinated carbonyl.[11] In addition, delocalization of unpaired spin density into the alkyne has been shown to cause the homolytic C–S bond cleavage.[11] Therefore, the facilitated benzyl cleavage in the synthesis of **7**, **8** and **9** compared to that of **2** reflect the higher electron density at the Mo$^I$ species with L. While **7** and **8** can be purified by column chromatography with toluene as eluent, the (dimethylamino)pyridine complex **9** is not sufficiently stable. However, analytically pure **9**·CH$_2$Cl$_2$ was obtained by crystallization from a toluene/CH$_2$Cl$_2$ solution.

The molecular structures of cationic [**5**]$^+$ as well as neutral **8** and **9** (Figure 1 and Figure 2, Table 1) were determined by X-ray structure analysis in order to investigate the steric interference of ligand L with the rotational process of the alkyne ligand. The molecular structures are generally similar and show roughly octahedral polyhedrons considering the alkyne as occupying a single coordination site. The alkyne SCCS planes lie between the two σ-donor-π-acceptor ligands, but rather tilted to the Mo–CO vector to a varying extent. In consideration of the overall similarly complex structures, the removal of one benzyl group ensues one major difference between cationic [**5**]$^+$ and neutral **8** and **9**. While the bis(benzylthio)acetylene ligand is bound symmetrically to molybdenum in [**5**]$^+$, **8** and **9** show one short and one long molybdenum–carbon bond. This observation is reflected in the resonance structure **B** with a thioketo group and one metal carbon double bond (Figure 3). In addition, the SCCS alkyne plane in **8** and **9** is more clearly aligned with the remaining carbonyl ligand compared to [**5**]$^+$. The torsion angle C3–Mo–C2–C1 amounts to 11.6° in **8** and 11.9° in **9**. Despite the rather bulky isocyanides used, replacement of one carbonyl in **2** by an isocyanide does not seem to increase the hindrance of alkyne rotation due to the linear nature of the CNR unit and the longer Mo–CNR bond (compare Mo–C4 2.117(4) Å and Mo–C3 1.996(4) Å

 © 2007 Wiley-VCH Verlag GmbH & Co. KGaA, Weinheim 

in [**5**]$^+$). However, the steric demand in proximity to the alkyne unit clearly increases from **2** to the 4-(dimethylamino)pyridine complex **9**, in which a $sp^2$-hybridisized nitrogen atom as a part of an aromatic ring serves as donor. In addition, inspection of the molybdenum alkyne–carbon bond lengths reveals that the Mo–C1 bond is significantly shorter in the 4-(dimethylamino)pyridine complex **9** [2.104(4) Å] compared to the dicarbonyl complex **2** [2.143(3) Å].[11] Therefore, taking into account solely geometric factors the highest rotational barrier is expected for **9**.

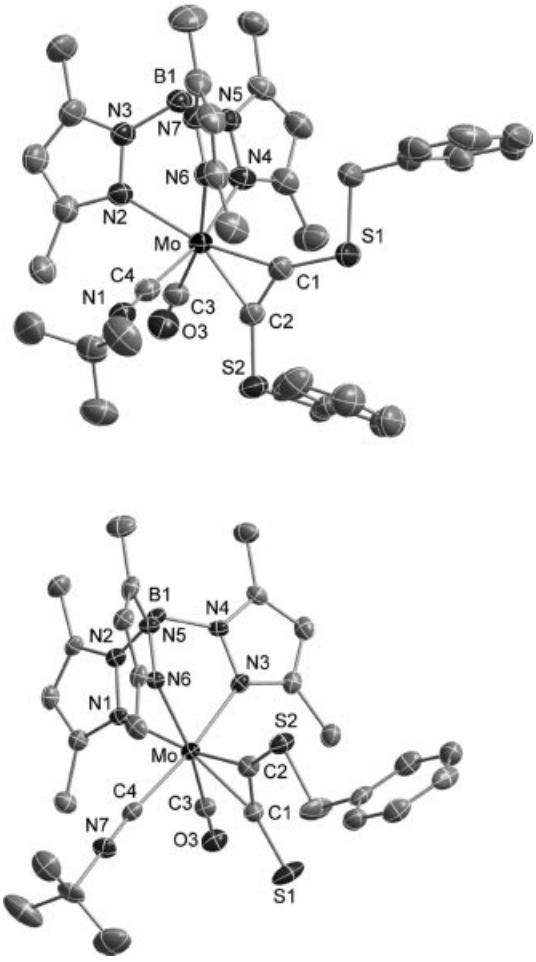


Figure 1. Molecular structures of [**5**]$^+$ (top) and **8** (bottom). Hydrogen atoms have been omitted for clarity.

The increase of the electron density at the molybdenum atom while substituting one carbonyl in **1**-$PF_6$ with isocyanides in **4**-$PF_6$ and **5**-$PF_6$ and 4-(dimethylamino)pyridine in **6**-$PF_6$ is evident by IR spectroscopy and cyclic voltammetry. Similar observations apply to the series **2**, **7**, **8** and **9**. The prototype complex **1**-$PF_6$ shows two reversible electron transfer waves at $E_{p,c}$ = –0.80 V and –1.65 V (cathodic peak potentials referenced vs. ferrocene/ferrocenium). The first one at moderate potential is shifted to lower potential, while going to **4**-$PF_6$ and finally to **6**-$PF_6$. In turn the CVs. of the more electron rich complexes **4**-$PF_6$ and **6**-$PF_6$ show an additional oxidation process (see supporting information). As a result, the second reduction could not even be recorded in the CV of **6**-$PF_6$. The neutral thio-alkyne complexes **2**, **7** and **8** show concordantly one quasi-reversible electron transfer wave at low potential, while the corresponding reduction process in **9** appears irreversible (Figure 4, Table 2). The cathodic peak potential estimated vs. ferrocene/ferrocenium at a scan rate of 100 mV s$^{-1}$ changes from –1.64 V for **2** to –1.91 V for **7**, –2.01 V for **8** and finally to –2.31 V for **9**. Consistently, in the same order the force constant of the CO stretching vibration decreases from 16.57 N cm$^{-1}$ in **2** to 15.10 N cm$^{-1}$ in **7**, 14.93 N cm$^{-1}$ in **8** and finally to 14.48 N cm$^{-1}$ in **9**. Additionally, the high π-backbonding capacity of molybdenum in **9** is reflected in the hindrance of the pyridine rotation about the Mo–N bond as indicated by $^1$H NMR spectroscopy.

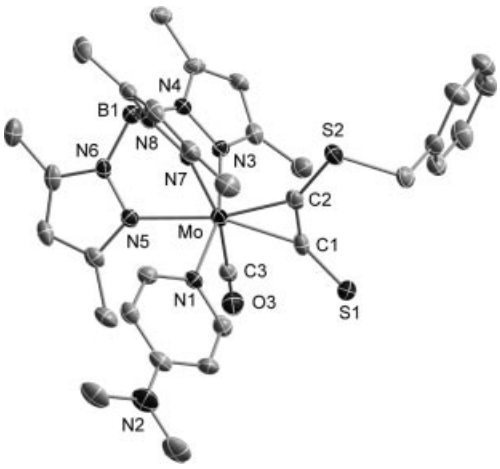


Figure 2. Molecular structure of **9**. Hydrogen atoms have been omitted for clarity.

Table 1. Bonding parameters in thio-alkyne complexes, selected bonds [Å] and angles [°].

| | **5**-$PF_6$ | **8** | **9** |
|---|---|---|---|
| Mo–C1 | 2.032(4) | 2.122(4) | 2.104(4) |
| Mo–C2 | 2.028(3) | 2.006(5) | 1.999(4) |
| Mo–C3 | 1.996(4) | 1.970(4) | 1.949(4) |
| Mo–C4 | 2.117(4) | 2.116(4) | – |
| Mo–N1 | – | – | 2.217(3) |
| C1–C2 | 1.320(5) | 1.345(6) | 1.333(6) |
| C1–S1 | 1.686(4) | 1.659(4) | 1.667(4) |
| C2–S2 | 1.692(4) | 1.700(5) | 1.699(4) |
| C1–C2–S2 | 145.5(3) | 136.2(4) | 139.0(4) |
| C2–C1–S1 | 137.2(3) | 143.8(4) | 144.1(4) |

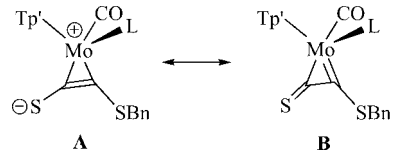


Figure 3. Resonance forms of thio-alkyne complexes.

 © 2007 Wiley-VCH Verlag GmbH & Co. KGaA, Weinheim 

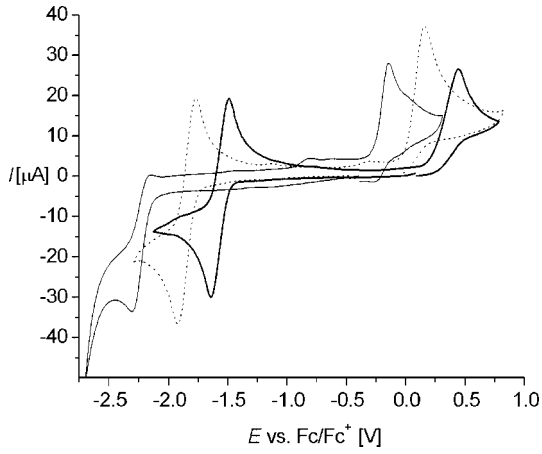


Figure 4. Cyclic voltammograms of **2** (bold line), **7** (dotted) and **9** (line) in $CH_2Cl_2$.

Table 2. CO force constants, cathodic peak potentials and free activation enthalpies.

| | $k$(CO) /N cm$^{-1}$ | $E_{p,c}$ vs. Fc/Fc$^+$ /V | $\Delta G^*_{298}$ ($\Delta G^*_{rev\ 298}$) /kJ mol$^{-1}$ |
|---|---|---|---|
| **2** | 16.57 | –1.64 | 60.5 |
| **7** | 15.10 | –1.91 | 53.1 (51.6) |
| **8** | 14.93 | –2.01 | 51.5 (51.3) |
| **9** | 14.48 | –2.31 | 45.5 (42.2) |

The room temperature $^1$H NMR spectra of **2** and **7**–**9** show fluxional behavior, which is particularly evident for the benzylic protons. The alkyne resonances in the $^{13}$C NMR spectra of **7** and **8** are in coalescence at ambient temperature. However, at 220 K a double set of signals with one carbonyl and two alkyne resonances for each isomer are found between $\delta$ = 220 and 250 ppm. Complex **9** is in fast exchange in the room temperature $^{13}$C NMR spectrum and three resonances at 227, 233 and 238 ppm are observed. These values are typical for four-electron donor alkyne complexes.[1a] The underlying dynamic behavior can be attributed to rotation of the unsymmetric thio-alkyne ligand at the metal center based on the following reasons. Alkyne rotation in complexes **2** and **7**–**9** implies an isomer interconversion and both rotamers for **2** and **7**–**9** were observed in the low temperature NMR spectra. The $^1$H NMR shifts of the benzylic $CH_2$ protons show a considerable difference of 2 ppm between the two isomers. The similarity of these chemical shifts to the shifts of the two benzyl groups in the cationic bis(benzylthio)acetylene complexes were considered a first hint that alkyne rotation accounts for the fluxional behavior. The resonances of the benzylic $CH_2$ groups in either *syn* or *anti* position to the carbonyl differ so much because of opposing anisotropy effects by the pyrazole rings and the triple bonds of carbonyl and isocyanide. Therefore, the low field shifted signal is assigned to the *syn* position with respect to the carbonyl ligand, while the high field shifted signal reflects the proximity of the $CH_2$ group to the pyrazolyl pocket. This perception is proven by 2D NMR spectroscopic experiments.

A gHMBC spectrum of **2** in the slow exchange at 210 K shows the correlation of the PhC$H_2$ resonance pair with the low field shifted alkyne carbon pair.[11] Accordingly, the gHMBC spectrum of **9** at 300 K in the fast exchange displays correlation of only one of the alkyne carbon atoms with the PhC*H*H resonances (Figure 5). These observations rule out a migration process of the benzyl group from one sulfur atom to the other as reason for the fluxionality because the benzylthio group remains attached to one of the alkyne carbon atoms. In addition, the protons in both isomers of **7**, **8** and **9** are diastereotopic because of the $C_1$ symmetry of the whole complex. The stereochemistry of the PhC*H*H group is generally retained in the fast exchange, which is evident in the spectrum of **9** at 300 K (Figure 6) and of **8** at 335 K (Figure S7). The difference between the high temperature signal of **9** in $CDCl_3$ (Figure 6) and in $CD_2Cl_2$ (Figure S9) indicates that the observation of a singlet in the latter case is coincidental. The identity of the isomers, which are not observed in the crystal structures, as *syn* isomer with respect to the benzyl group and the carbonyl ligand, and not as rotamer with respect to the $C_{sp}$–S bond, is confirmed by a low-temperature ROESY spectrum of **8**. At 210 K both isomers of **8** show proximity of one of the benzyl-CH*H* protons with one of the Tp′ methyl groups, while no correlation to the pyrazol-CH protons was found. In contrast, a weak correlation peak of one benzyl-CH*H* proton of the major isomer with the methyl groups of the isocyanide ligand was detected (see supporting information for details).[12] In addition, DFT calculations were performed in order to estimate the energy differences between four different isomers of the slightly reduced model complex [TpMo(CO)$_2$(MeSC$_2$S)]. Geometry optimizations resulted that the energy differences between the rotational isomers with respect to the $C_{sp}$–S bond are smaller (approximately 5 kJ/mol) compared to the differences between the isomers with respect to the alkyne rotation at the metal (approximately 10 kJ/mol, see supporting information for details). Finally, the observation of comparable rotational barriers in K[Tp′W(CO)$_2$($\eta^2$-C$_2$S$_2$)] and its complexes without any benzyl group strongly supports our isomer assignment.[13]

While the isomer ratio is largely balanced in **2**, the isomer with the benzyl group directed at the carbonyl is found at the low temperature limit in proportion of 64% in **7**, of 60% in **8** and of 83% in **9**. The primary crystallization of the minor isomers could be attributed to lower solubilities and crystal packing forces. Variable temperature $^1$H NMR spectra were measured with **7**, **8** and **9** (Figure 6). The coalescence temperature is about ambient temperature for complex **7** and **8**, while the very fast exchange area is out of range. In contrast, the rotational barrier in **9** is so low that the coalescence temperature is just reached at 220 K, while the exchange is fast at room temperature. The activation parameters of **7**–**9** were estimated by line-shape simulation performed with the MEXICO program package[14] (see supporting information for details). The corresponding values of **2** have already been published.[11] The activation parameters obtained are listed in Table 2. The differences are substantial in consideration of the fact that the complexes are very similar and that only one σ-donor/π-ac-

 © 2007 Wiley-VCH Verlag GmbH & Co. KGaA, Weinheim 

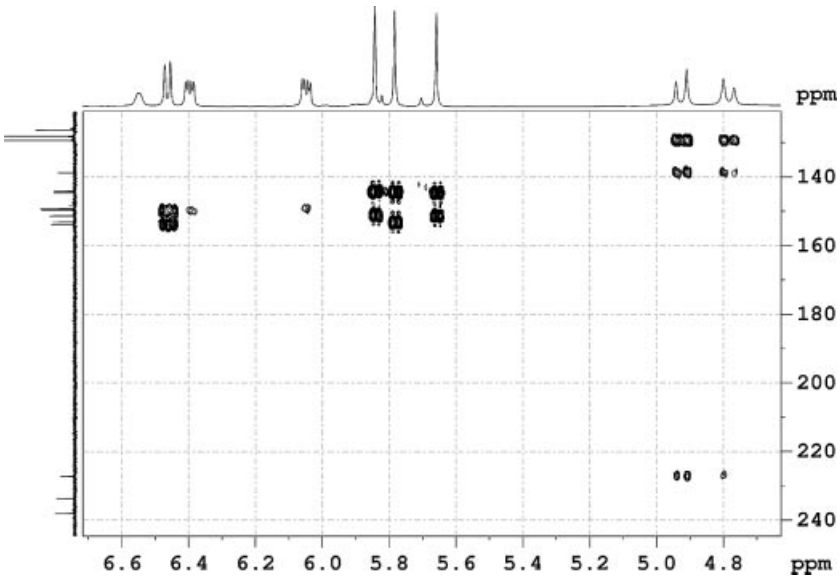


Figure 5. Part of the gHMBC spectrum of **9** at 300 K.

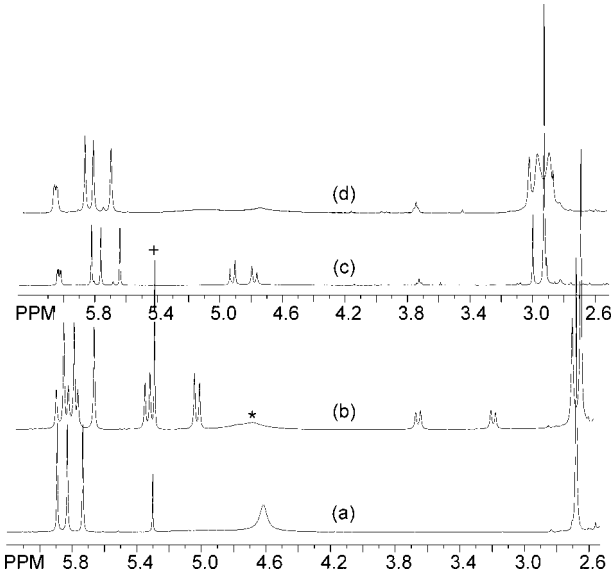


Figure 6. Variable-temperature $^1$H-NMR spectra in $CDCl_3$: **7** at 335 K (a), **7** at 220 K (b), **9** at 300 K (c) and **9** at 220 K (d), + $CH_2Cl_2$, * B*H*.

ceptor ligand is varied. The barrier decreases clearly with rising electron density at molybdenum despite increasing steric demand. Therefore the rate of the alkyne rotation must be determined electronically in complexes **2** and **7**–**9** and a crucial contribution of steric factors can be ruled out.

The facilitated rotation of the alkyne with increasing electron density at the metal is not easy to explain, because a stronger back-donation from the metal generally strengthens the π interaction, which is associated with a higher rotational barrier. However, according to a qualitative molecular orbital Scheme for octahedral alkyne d$^4$-metal complexes presented by Templeton[15,5] two of the frontier orbitals involve metal alkyne π interactions. The bonding combination of the $d_{yz}$ orbital and the $\pi^*_{\|}$ orbital, which represents the π back-donation from the metal, is considered occupied (Figure 7). In contrast, the antibonding combination of the $d_{xy}$ orbital with the $\pi_\perp$-orbital of the alkyne is accounted the LUMO. Templeton has pointed out[1a] that both $\pi_\perp$ and $\pi^*_{\|}$ interchange their partners on the metal, if the alkyne rotates away from the ground state orientation to the orthogonal position with respect to the CO ligand. The π-acidity of the ligand L is particularly important for the $d_{xy}$ orbital, which is considered populated in the excited rotational state.[1a] The perception that ligand L and the alkyne compete for the electron density of the $d_{xy}$ orbital in the excited rotational state reflects the strong influence of the ligand L on the barrier. The decreasing π-acceptor ability in the order CO, isocyanide and pyridine ensues an enhanced π-back bonding to the thio-alkyne ligand resulting in a stabilization of this state. Therefore, the decrease of the rotational barrier can predominantly be attributed to a stabilization of the excited rotational state. In addition, this interpretation explains the otherwise paradox trend of shorter metal–C(alkyne) bonds in the ground-state structure and a facilitated rotation of the alkyne in solution.

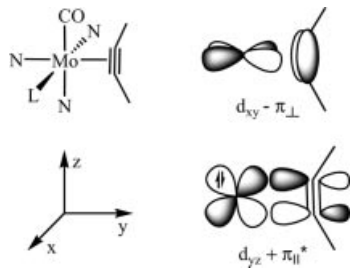


Figure 7. Qualitative molecular orbital Scheme of molybdenum–alkyne π interactions.

 © 2007 Wiley-VCH Verlag GmbH & Co. KGaA, Weinheim 

## Conclusions

Alkyne complexes with a terminal sulfur atom attached to the alkyne are accessible at the Tp′Mo(CO)(L) fragment by reductive cleavage of one benzyl group in the corresponding bis(benzylthio)acetylene complexes [Tp′Mo(CO)(L)(BnSC$_2$SBn)](PF$_6$). The resulting thio-alkyne complexes [Tp′Mo(CO)(L)(BnSC$_2$S)] are interesting as neutral sulfur ligands[16] and as starting materials for the preparation of η²-*C*,*C*′ complexes with acetylenedithiolate.[13] The variation of L with respect to a modified σ-donor-π-acceptor character leads to altered reaction rates in the benzyl cleavage and pronounced trends in the molecular structures, the electrochemical parameters and the solution dynamics. Decreasing π-acidity of L leads to a facilitated rotation of the alkyne at molybdenum. These observations substantiate our strategy to adjust the donor ability on the sulfur atoms in heterobimetallic complexes by slight variations in the coordination sphere of the alkyne complex moiety.

## Experimental Section

**General Procedures:** All operations were carried out under a dry argon atmosphere using standard Schlenk and glove box techniques. All solvents were dried and saturated with argon by standard methods and freshly distilled prior to use. [Tp′Mo(CO)$_2$(BnSC$_2$SBn)]PF$_6$ (**1**-PF$_6$) {Tp′ = hydrotris(3,5-dimethylpyrazolyl)borate}[11] and C$_8$K[17] were prepared according to literature methods. 2,6-dimethylphenyl isocyanide, *tert*-butyl isocyanide and 4-(dimethylamino)pyridine were purchased from Aldrich. $^1$H and $^{13}$C NMR spectra were recorded on a Bruker AC 200 and Bruker Avance 400 NMR spectrometer. Elemental analyses were performed on a Vario EL III CHNS elemental analyzer. ESI mass spectra were obtained using a QUATTRO LCZ (Waters-Micromass). Infrared spectra were recorded on a Bruker Vektor 22. Cyclic voltammetry data was acquired on a ECO/Metrohm PGSTAT 30 potentiostat using a glassy carbon working electrode, an Ag/0.01 M AgNO$_3$/CH$_3$CN reference electrode, (NBu$_4$)(PF$_6$) as supporting electrolyte and ferrocene as internal standard.

**[Tp′Mo(CO)(CH$_3$CN){η²-(BnS)CC(SBn)}](PF$_6$) (3-PF$_6$):** A solution of **1**-PF$_6$ (3.02 g, 3.50 mmol) in acetonitrile (50 mL) was heated to reflux. After two days the product was isolated by column chromatography at SiO$_2$ using CH$_2$Cl$_2$ as eluent (2.53 g, 83%). Recrystallization from CH$_2$Cl$_2$/Et$_2$O yielded dark green crystals. MS (ESI in CH$_2$Cl$_2$): *m*/*z* = 734 [M]$^+$ with the expected isotopic pattern. IR (KBr): $\tilde{\nu}_{CN}$ = 2179, $\tilde{\nu}_{CO}$ = 1956 cm$^{-1}$. $^1$H NMR (200 MHz, CDCl$_3$, 20 °C): $\delta$ = 7.46–7.26 (m, 8 H, Ph-*H*), 6.86 (m, 2 H, Ph-*H*), 6.01 (s, 2 H, Tp′-C*H*), 5.95 (s, 1 H, Tp′-C*H*), 5.00 (d, $^2J_{HH}$ = 12.9 Hz, 1 H, SCH*H*), 4.91 (d, $^2J_{HH}$ = 12.9 Hz, 1 H, SC*H*H), 3.49 (d, $^2J_{HH}$ = 12.0 Hz, 1 H, SCH*H*), 2.80 (d, $^2J_{HH}$ = 12.0 Hz, 1 H, SC*H*H), 2.62 (s, 3 H, Tp′-*Me*), 2.51 (s, 9 H, Tp′-*Me*), 2.44 (s, 3 H, Tp′-*Me*), 2.01 (s, 3 H, Tp′-*Me*), 1.42 ppm (s, 3 H, NCC*H*$_3$). $^{13}$C NMR (50 MHz, CDCl$_3$, 20 °C): $\delta$ = 230.4 (Mo*C*SCH$_2$), 216.5 (*C*O), 207.6 (Mo*C*SCH$_2$), 152.8, 152.1, 149.9, 146.8, 145.8, 142.9 (Tp′-*C*Me), 134.8, 134.0, 129.2, 128.9, 128.8, 128.7, 128.1, 128.0 (Ph-*C*), 108.2, 107.5, 107.3 (Tp′-*C*H), 43.1, 40.5 (S*C*H$_2$), 15.1, 14.2, 14.0, 12.7, 12.5, 7.0 (Tp′-*C*H$_3$), 3.9 ppm (NC*C*H$_3$).

**[Tp′Mo(CO)(CN-C$_6$H$_3$Me$_2$-2,6){η²-(BnS)CC(SBn)}](PF$_6$) (4-PF$_6$):** A solution of **3**-PF$_6$ (5 g, 5.7 mmol) in dichloromethane (80 mL) was treated with 2,6-dimethylphenyl isocyanide (0.75 g, 5.72 mmol) and heated under reflux for two days. The solution was cooled to ambient temperature and the formation of **4**-PF$_6$ was checked by IR spectroscopy. The solution was reduced in vacuo to 20 mL and layered with diethyl ether (80 mL). After 24 hours green crystals, which had formed, were collected by removing the mother liquor, washing with diethyl ether and drying in vacuo. Yield: 4.4 g (80%). IR (KBr): $\tilde{\nu}_{CN}$ = 2146, $\tilde{\nu}_{CO}$ = 1971 cm$^{-1}$. $^1$H NMR (200 MHz, CDCl$_3$, 20 °C): $\delta$ = 7.40–7.25 (m,10 H, Ph-*H*), 7.16 (m, 1 H, Ph-*H*), 6.85 (m, 2 H, Ph-*H*), 6.07 (s, 1 H, Tp′-C*H*), 5.97 (s, 1 H, Tp′-C*H*),5.96 (s, 1 H, Tp′-C*H*), 5.41 (br. s, 1 H, B*H*), 4.86 (d, $^2J$ = 19 Hz, 1 H, SCH*H*), 4.82 (d, $^2J$ = 19 Hz, 1 H, SC*H*H), 3.35 (d, $^2J$ = 12 Hz, 1 H, SCH*H*), 2.29 (d, $^2J$ = 12 Hz, 1 H, SC*H*H), 2.55 (s, 3 H, Tp′-*Me*), 2.53 (s, 3 H, Tp′-*Me*), 2.51 (s, 3 H, Tp′-*Me*), 2.43 (s, 3 H, Tp′-*Me*), 2.24 (s, 6 H, PhC*H*$_3$), 1.88 (s, 3 H, Tp′-*Me*), 1.52 ppm (s, 3 H, Tp′-*Me*). $^{13}$C NMR (200 MHz, CDCl$_3$, 20 °C): $\delta$ = 226.2 (Mo*C*SCH$_2$), 221.1 (*C*O), 205.1 (Mo*C*SCH$_2$), 168.9 (Mo*C*N), 152.7, 151.6, 150.1, 147.7, 146.4, 146.3 (Tp′-*C*Me), 134.5, 133.2, 130.6, 129.0, 128.9, 128.9, 128.8, 128.8, 129.7, 128.5, 128.3, 128.2 (Ph-*C*), 108.5, 107.4, 107.3 (Tp′-*C*H), 44.1, 41.4 (S*C*H$_2$), 18.5 (Ph-*C*H$_3$), 15.6, 14.6, 14.0, 13.0, 12.6, 12.5 ppm (Tp′-*C*H$_3$).

**[Tp′Mo(CO)(Me$_3$CNC){η²-(BnS)CC(SBn)}](PF$_6$) (5-PF$_6$):** The complex was synthesized analogously to **4**-PF$_6$ using **3**-PF$_6$ (2.58 g, 2.95 mmol) and *tert*-butyl isocyanide (0.34 mL, 2.95 mmol). Recrystallization from CH$_2$Cl$_2$/Et$_2$O yielded green crystals (2.58 g, 76%). MS (ESI in CH$_2$Cl$_2$): *m*/*z* = 776 [M]$^+$ with the expected isotopic pattern. IR (KBr): $\tilde{\nu}_{CN}$ = 2179, $\tilde{\nu}_{CO}$ = 1971 cm$^{-1}$. $^1$H NMR (200 MHz, CDCl$_3$, 20 °C): $\delta$ = 7.37–7.26 (m, 8 H, Ph-*H*), 6.89 (m, 2 H, Ph-*H*), 6.05 (s, 1 H, Tp′-C*H*), 5.99 (s, 1 H, Tp′-C*H*), 5.96 (s, 1 H, Tp′-C*H*), 4.88 (d, $^2J_{HH}$ = 13.5 Hz, 1 H, SCH*H*), 4.75 (d, $^2J_{HH}$ = 13.5 Hz, 1 H, SC*H*H), 3.28 (d, $^2J_{HH}$ = 12.0 Hz, 1 H, SCH*H*), 2.85 (d, $^2J_{HH}$ = 12.0 Hz, 1 H, SC*H*H), 2.63 (s, 3 H, Tp′-*Me*), 2.51 (s, 3 H, Tp′-*Me*), 2.50 (s, 3 H, Tp′-*Me*), 2.41 (s, 3 H, Tp′-*Me*), 1.84 (s, 3 H, Tp′-*Me*), 1.49 [s, 9 H, C(C*H*$_3$)$_3$], 1.48 ppm (s, 3 H, Tp′-*Me*). $^{13}$C NMR (100 MHz, CDCl$_3$, 20 °C): $\delta$ = 228.4 (Mo*C*SCH$_2$), 219.7 (*C*O), 204.0 (Mo*C*SCH$_2$), 152.8, 151.5, 150.0, 147.7, 146.3 (Tp′-*C*Me, two resonances are accidentally isochronic), 135.2, 133.4, 129.1, 129.0, 128.8, 128.7, 128.4, 128.3 (Ph-*C*), 108.5, 107.4, 107.3 (Tp′-*C*H), 60.0 [*C*(CH$_3$)$_3$], 44.0, 41.0 (S*C*H$_2$), 30.0 [C-(*C*H$_3$)$_3$], 15.6, 14.3, 14.1, 13.0, 12.6, 12.5 ppm (Tp′-*C*H$_3$).

**[Tp′Mo(CO)(NC$_5$H$_4$NMe$_2$){η²-(BnS)CC(SBn)}](PF$_6$) (6-PF$_6$):** The complex was synthesized analogously to **4**-PF$_6$ using **3**-PF$_6$ (3.24 g, 3.65 mmol) and 4-(dimethylamino)pyridine (668 mg, 5.48 mmol). Recrystallization from CH$_2$Cl$_2$/Et$_2$O yielded dark green crystals (2.75 g, 79%). MS (ESI in CH$_2$Cl$_2$): *m*/*z* = 815 [M]$^+$ with the expected isotopic pattern. IR (KBr): $\tilde{\nu}_{CO}$ = 1937 cm$^{-1}$. $^1$H NMR (200 MHz, CDCl$_3$, 20 °C): $\delta$ = 8.10 (d, $^3J$ = 6.1 Hz, 1 H, NC*H*), 7.40–7.26 (m, 8 H, Ph-*H*), 6.83 (m, 2 H, Ph-*H*), 6.40 (d, $^3J$ = 6.1 Hz, 1 H, NC*H*), 6.30 (m, 1 H, NCHC*H*), 6.25 (m, 1 H, NCHC*H*), 6.04 (s, 1 H, Tp′-C*H*), 5.93 (s, 1 H, Tp′-C*H*), 5.91 (s, 1 H, Tp′-C*H*), 4.98 (d, $^2J_{HH}$ = 12.8 Hz, 1 H, SCH*H*), 4.87 (d, $^2J_{HH}$ = 12.8 Hz, 1 H, SC*H*H), 3.48 (d, $^2J_{HH}$ = 11.7 Hz, 1 H, SCH*H*), 3.06 [s, 6 H, N(C*H*$_3$)$_2$], 2.65 (d, $^2J_{HH}$ = 11.7 Hz, 1 H, SC*H*H), 2.54 (s, 3 H, Tp′-*Me*), 2.48 (s, 3 H, Tp′-*Me*), 2.44 (s, 3 H, Tp′-*Me*), 1.92 (s, 3 H, Tp′-*Me*), 1.55 (s, 3 H, Tp′-*Me*), 1.39 ppm (s, 3 H, Tp′-*Me*). $^{13}$C NMR (100 MHz, CDCl$_3$, 20 °C): $\delta$ = 233.2 (Mo*C*SCH$_2$), 213.8 (*C*O), 205.4 (Mo*C*SCH$_2$), 154.5, 153.1, 152.6, 150.4, 149.7, 149.2 (Tp′-*C*Me), 146.8 (N*C*H), 146.5 (N*C*H), 146.2 [*C*N(CH$_3$)$_2$], 135.0, 134.4, 129.2, 129.1, 128.9, 128.8, 128.4, 128.1 (Ph-*C*), 108.6 (Tp′-*C*H), 108.3 (NCH*C*H), 108.2, 107.6 (Tp′-*C*H), 106.9

 © 2007 Wiley-VCH Verlag GmbH & Co. KGaA, Weinheim 

(NCH*C*H), 42.9 (S*C*H$_2$), 40.3 [N(*C*H$_3$)$_2$], 39.6 (S*C*H$_2$), 14.6, 14.4, 13.7, 13.0, 12.9, 12.8 ppm (Tp′-*C*H$_3$).

**[Tp′Mo(CO)(CN-C$_6$H$_3$Me$_2$-2,6){η$^2$-(BnS)CC(S)}] (7):** At –78 °C potassium graphite $C_8K$ (583 mg, 4.3 mmol) was added to a solution of **4**-$PF_6$ (3.5 g, 3.6 mmol) in THF (150 mL) leading to an intense red solution. The mixture was stirred for 12 h at room temperature while the solution turned olive-coloured. The product was isolated by column chromatography at $SiO_2$ using toluene as eluent (1.2 g, 45%). Evaporation of dichloromethane from a dichloromethane/*n*-hexane solution of **7** yielded dark green crystals. $C_{34}H_{38}BMoN_7OS_2$ (731.59): calcd. C 55.82, H 5.24, N 13.40, S 8.77; found C 55.67, H 5.26, N 13.28, S 8.69. IR (KBr): $\tilde{\nu}_{CN}$ = 2108, $\tilde{\nu}_{CO}$ = 1915 cm$^{-1}$. $^1$H NMR (200 MHz, $CDCl_3$, 57 °C): δ = 7.25–7.15 (m, 8 H, Ph-*H*), 5.87 (s, 1 H, Tp′-C*H*), 5.80 (s, 1 H, Tp′-C*H*), 5.71 (s, 1 H, Tp′-C*H*), 4.59 (s, 2 H, SCH$_2$), 2.65 (s, 3 H, Tp′-*Me*), 2.47 (s, 3 H, Tp′-*Me*), 2.42 (s, 3 H, Tp′-*Me*), 2.38 [s, 6 H, C$_6$H$_3$(C*H*$_3$)$_2$], 2.35 (s, 3 H, Tp′-*Me*), 2.03 (s, 3 H, Tp′-*Me*), 1.57 ppm (s, 3 H, Tp′-*Me*). $^1$H NMR (400 MHz, $CDCl_3$, –63 °C): δ = 5.25 (d, $^2J$ = 12.1 Hz, 64% 1 H, C*H*H), 5.13 (d, $^2J$ = 12.1 Hz, 64% 1 H, CH*H*), 3.55 (d, $^2J$ = 11.4 Hz, 36% 1 H, C*H*H), 3.09 (d, $^2J$ = 11.4 Hz, 36% 1 H, CH*H*). $^{13}$C NMR (50 MHz, $CDCl_3$, 20 °C): δ = 232.2, 231.1 (Mo*C*S, Mo*C*O), 179.9 (*C*N), 153.3, 151.4, 151.0, 145.3, 144.4, 144.2 (Tp′-*C*Me), 137.6, 134.3, 129.2, 128.6, 128.3, 127.9, 127.8, 126.8 (Ph-*C*), 107.3, 106.5, 106.5 (Tp′-*C*H), 37.7 (S*C*H$_2$), 19.2 [C$_6$H$_3$(*C*H$_3$)$_2$], 15.5, 15.1, 14.3, 12.9, 12.8, 12.6 ppm (Tp′-*C*H$_3$). $^{13}$C NMR (100 MHz, $CDCl_3$, –63 °C): δ = 246.2, 242.1, 232.3, 231.6, 231.2, 231.0 ppm (Mo*C*S, Mo*C*O), other signals have been omitted for clarity.

**[Tp′Mo(CO)(Me$_3$CNC){η$^2$-(BnS)CC(S)}] (8):** The complex was synthesized analogously to **7** using **5**-$PF_6$ (1.14 g, 1.24 mmol) and $C_8K$ (200 mg, 1.48 mmol) in THF (80 mL). Yield after chromatography: 730 mg (86%). Recrystallization from $CH_2Cl_2$/$Et_2O$ yielded dark green crystals. $C_{30}H_{38}BMoN_7OS_2$ (683.54): calcd. C 52.71, H 5.60, N 14.34, S 9.38; found C 52.56, H 5.76, N 14.18, S 9.21. IR (KBr): $\tilde{\nu}_{CN}$ = 2144, $\tilde{\nu}_{CO}$ = 1922 cm$^{-1}$. $^1$H NMR (200 MHz, $CDCl_3$, 20 °C): δ = 7.22 (m, 5 H, Ph-*H*), 5.91 (s, 1 H, Tp′-C*H*), 5.88 (s, 1 H, Tp′-C*H*), 5.75 (s, 1 H, Tp′-C*H*), 2.75 (s, 3 H, Tp′-*Me*), 2.48 (s, 3 H, Tp′-*Me*), 2.44 (s, 3 H, Tp′-*Me*), 2.37 (s, 3 H, Tp′-*Me*), 1.98 (s, 3 H, Tp′-*Me*), 1.55 (s, 3 H, Tp′-*Me*), 1.52 ppm [s, 9 H, C(C*H*$_3$)$_3$]. $^1$H NMR (400 MHz, $CDCl_3$, –63 °C): δ = 5.25 (d, $^2J$ = 12.5 Hz, 60% 1 H, C*H*H), 5.12 (d, $^2J$ = 12.5 Hz, 60% 1 H, CH*H*), 3.55 (d, $^2J$ = 12.0 Hz, 40% 1 H, C*H*H), 3.09 (d, $^2J$ = 12.0 Hz, 40% 1 H, CH*H*). $^{13}$C NMR (50 MHz, $CDCl_3$, 20 °C): δ = 232.9, 231.3 (Mo*C*S, Mo*C*O), 162.8 (*C*N), 153.1, 151.1, 150.4, 145.2, 144.2, 144.0 (Tp′-*C*Me), 137.6, 129.0, 128.1, 126.6 (*C*$_6$H$_5$), 107.2, 106.3, 106.1 (Tp′-*C*H), 57.5 [*C*(CH$_3$)$_3$], 37.7 (S*C*H$_2$), 30.5 [C(*C*H$_3$)$_3$], 15.2, 14.3, 14.1, 12.7, 12.5, 12.4 ppm (Tp′-*C*H$_3$). $^{13}$C NMR (100 MHz, $CDCl_3$, –63 °C): δ = 242.5, 238.0, 232.5, 232.3, 232.2, 231.7 ppm (Mo*C*S, Mo*C*O), other signals have been omitted for clarity.

**[Tp′Mo(CO)(NC$_5$H$_4$-4-NMe$_2$){η$^2$-(BnS)CC(S)}] (9):** At –78 °C $C_8K$ (111 mg, 0.82 mmol) was added to a solution of **6**-$PF_6$ (650 mg, 0.68 mmol) in THF (80 mL) leading to an intense red solution. The mixture was stirred for 18 h at room temperature while the solution turned green. The solution was filtered, subsequently reduced in volume to 10 mL in vacuo and finally layered with diethyl ether (30 mL). The green solid formed was washed with diethyl ether (2 × 10 mL) and dried in vacuo (345 mg, 70%). Recrystallization from dichloromethane/diethyl ether yielded dark green crystals. $C_{33}H_{41}BCl_2MoN_8OS_2$ (807.52): calcd. C 49.08, H 5.12, N 13.88, S 7.49; found C 49.26, H 5.23, N 13.73, S 7.38. IR (KBr): $\tilde{\nu}_{CO}$ = 1893 cm$^{-1}$. $^1$H NMR (400 MHz, $CDCl_3$, 20 °C): δ = 8.93 (d, $^3J$ = 6.8 Hz, 1 H, NC*H*), 7.25–7.10 (m, 5 H, Ph-*H*), 6.45 (d, $^3J$ = 6.8 Hz, 1 H, NC*H*), 6.38 (dd, $^3J$ = 6.8 Hz, $^2J$ = 3.0 Hz, 1 H, NCHC*H*), 6.03 (dd, $^3J$ = 6.8 Hz, $^2J$ = 3.0 Hz, 1 H, NCHC*H*), 5.82 (s, 1 H, Tp′-C*H*), 5.76 (s, 1 H, Tp′-C*H*), 5.64 (s, 1 H, Tp′-C*H*), 4.92 (d, $^2J_{HH}$ = 12.8 Hz, 1 H, SCH*H*), 4.78 (d, $^2J_{HH}$ = 12.8 Hz, 1 H, SC*H*H), 2.93 [s, 6 H, N(C*H*$_3$)$_2$], 2.47 (s, 3 H, Tp′-*Me*), 2.37 (s, 3 H, Tp′-*Me*), 2.36 (s, 3 H, Tp′-*Me*), 1.96 (s, 3 H, Tp′-*Me*), 1.52 (s, 3 H, Tp′-*Me*), 1.35 ppm (s, 3 H, Tp′-*Me*). $^1$H NMR (400 MHz, $CD_2Cl_2$, –93 °C): δ = 5.26 (d, $^2J$ = 12.3 Hz, 83% 1 H, C*H*H), 5.03 (d, $^2J$ = 12.3 Hz, 83% 1 H, CH*H*), 3.57 (broad, 17% 1 H, C*H*H), the forth CH*H* signal is obscured. $^{13}$C NMR (100 MHz, $CDCl_3$, 20 °C): δ = 237.9, 233.7 (Mo*C*S, Mo*C*O), 227.2 (Mo*C*SBn), 153.8, 153.1, 151.4, 151.2, 149.8, 149.2 (Tp′-*C*Me), 144.6 (N*C*H), 144.5 (N*C*H), 144.1 [*C*N(CH$_3$)$_2$], 138.7, 129.3, 128.1, 126.4 (Ph-*C*), 107.2 (Tp′-*C*H), 106.8 (NCH*C*H), 106.6 (Tp′-*C*H), 106.5 (NCH*C*H), 106.3 (Tp′-*C*H), 38.9 [N(*C*H$_3$)$_2$], 36.3 (S*C*H$_2$), 15.0, 14.0, 13.8, 12.8, 12.7, 12.6 ppm (Tp′-*C*H$_3$).

**Crystal Structure Determination:** Single crystals suitable for X-ray analysis were coated in perfluoropolyether oil and mounted on a glass fiber. The intensity data of the complexes were collected on a Bruker AXS Apex system equipped with a rotating anode. The data were measured using either graphite-monochromated Mo-$K_a$ radiation or Cu-$K_a$ radiation monochromated by a Goebel mirror. Data collection, cell refinement, data reduction and integration as well as absorption correction were performed with the Bruker AXS program packages SMART, SAINT and SADABS. Crystal and space group symmetries were determined using the XPREP program. All crystal structures were solved with SHELXS[18] by direct methods and were refined by full-matrix least-square techniques against $F_o^2$ with SHELXL.[19] All non-hydrogen atoms were refined anisotropically. The hydrogen atoms were included at calculated positions with fixed thermal parameters.

**Crystal Data for 5-PF$_6$:**[20] $C_{37}H_{45}BF_6MoN_7OPS_2$, $M_r$ = 919.64 g mol$^{-1}$, dark green prisms, size 0.23 × 0.19 × 0.14 mm$^3$, monoclinic, space group *P*2(1)/*n*, *a* = 10.695(2), *b* = 21.182(4), *c* = 18.879(4) Å, β = 102.883(4)°, *V* = 4169.1(14) Å$^3$, *T* = 153 K, *Z* = 4, $\rho_{calcd.}$ = 1.465 g cm$^{-1}$, μ(Mo-$K_a$) = 0.519 mm$^{-1}$, reflections: 40384 collected, 9563 unique, 8034 observed $F_o \geq 2\sigma(F_o)$, $1.47 \leq \Theta \leq 27.50$, $R_{int}$ = 0.0542, 514 parameter, 0 restrains, $R_1$(obs) = 0.0577, $wR_2$(obs) = 0.1406, $R_1$(all) = 0.0696, $wR_2$(all) = 0.1470, GOF = 1.089, largest difference peak/hole: 1.077/–0.766 eÅ$^3$.

**Crystal Data for 8:**[20] $C_{30}H_{38}BMoN_7OS_2$, $M_r$ = 683.54 g mol$^{-1}$, dark green plates, size 0.17 × 0.09 × 0.03 mm$^3$, monoclinic, space group *P*2(1), *a* = 8.409(4), *b* = 12.133(6), *c* = 16.017(8) Å, β = 95.369(9)°, *V* = 1626.9(14) Å$^3$, *T* = 153 K, *Z* = 2, $\rho_{calcd.}$ = 1.395 g cm$^{-1}$, μ(Mo-$K_a$) = 0.567 mm$^{-1}$, reflections: 15710 collected, 7391 unique, 6095 observed $F_o \geq 2\sigma(F_o)$, $1.28 \leq \Theta \leq 27.50$, $R_{int}$ = 0.0539, 388 parameter, 1 restrain, $R_1$(obs) = 0.0447, $wR_2$(obs) = 0.0834, $R_1$(all) = 0.0636, $wR_2$(all) = 0.0898, GOF = 0.986, largest difference peak/hole: 0.585/–0.567 eÅ$^3$.

**Crystal Data for 9·CH$_2$Cl$_2$:**[20] $C_{33}H_{41}BCl_2MoN_8OS_2$, $M_r$ = 807.51 g mol$^{-1}$, dark green prisms, size 0.14 × 0.11 × 0.07 mm$^3$, triclinic, space group $P\bar{1}$, *a* = 10.5994(2), *b* = 11.3942(2), *c* = 17.0769(4) Å, α = 100.314(2)°, β = 100.370(2)°, γ = 110.974(1), *V* = 1826.53(6) Å$^3$, *T* = 110 K, *Z* = 2, $\rho_{calcd.}$ = 1.468 g cm$^{-1}$, μ(Cu-$K_a$) = 5.666 mm$^{-1}$, reflections: 10829 collected, 6111 unique, 4468 observed $F_o \geq 2\sigma(F_o)$, $2.73 \leq \Theta \leq 70.10$, $R_{int}$ = 0.038, 451 parameter, 0 restrains, $R_1$(obs) = 0.0452, $wR_2$(obs) = 0.0959, $R_1$(all) = 0.0625, $wR_2$(all) = 0.0997, GOF = 0.922, largest difference peak/hole: 1.005/–0.877 eÅ$^3$.

**Calculations:** DFT calculations were performed with the Gaussian 03 package using the hybrid functional B3LYP[21] with a

 © 2007 Wiley-VCH Verlag GmbH & Co. KGaA, Weinheim 

6-311 g(d,p) basis function set for C, H, B, N, O, S and an energy-consistent pseudopotential for Mo from the Stuttgart group.[22]

**Supporting Information** (see also the footnote on the first page of this article): Cyclic voltammograms of **4**-$PF_6$, **5**-$PF_6$, **6**-$PF_6$, COSY and ROESY spectra of **7** and **8**, geometry optimized structures of isomers of $[TpMo(CO)_2(MeSC_2S)]$, comprehensive variable temperature $^1H$ and $^{13}C$ NMR spectroscopic data of **7**, **8** and **9**, Eyring plots for **7**, **8** and **9** obtained by line-shape analysis. This material is available on the www under http://www.eurjic.org or from the author.

## Acknowledgments

The Deutsche Forschungsgemeinschaft is gratefully acknowledged for financial support of this work W. W. S. thanks Prof. F. E. Hahn for generous support.

[1] a) J. L. Templeton, *Adv. Organomet. Chem.* **1989**, *29*, 1–100, and references herein; b) S. R. Allen, P. K. Baker, S. G. Barnes, M. Green, L. Trollope, L. Manojlovic-Muir, K. W. Muir, *J. Chem. Soc., Dalton Trans.* **1981**, 873–884; c) P. B. Winston, S. J. N. Burgmayer, T. L. Tonker, J. L. Templeton, *Organometallics* **1986**, *5*, 1707–1715; d) D. J. Wink, N. J. Cooper, *Organometallics* **1991**, *10*, 494–500; e) A. K. Powell, M. J. Went, *J. Chem. Soc., Dalton Trans.* **1992**, 439–445.
[2] P. Oulie, N. Brefuel, L. Vendier, C. Duhayon, M. Etienne, *Organometallics* **2005**, *24*, 4306–4314.
[3] A. Galindo, M. Gómez, P. Gómez-Sal, A. Martín, D. del Río, F. Sánchez, *Organometallics* **2002**, *21*, 293–304.
[4] H. G. Alt, H. E. Engelhardt, *Z. Naturforsch., Teil B* **1985**, *40*, 1134–1138.
[5] S. G. Feng, C. C. Philipp, A. S. Gamble, P. S. White, J. L. Templeton, *Organometallics* **1991**, *10*, 3504–3512.
[6] D. M. Schuster, J. L. Templeton, *Organometallics* **1998**, *17*, 2707–2715.
[7] E. A. Ison, T. M. Cameron, K. A. Abboud, J. M. Boncella, *Organometallics* **2004**, *23*, 4070–4076.
[8] C. J. Adams, N. G. Connelly, P. H. Rieger, *Chem. Commun.* **2001**, 2458–2459.
[9] G. Marinelli, W. E. Streib, J. C. Huffman, K. G. Caulton, M. R. Gagne, J. Takats, M. Dartiguenave, C. Chardon, S. A. Jackson, O. Eisenstein, *Polyhedron* **1990**, *9*, 1867–1881.
[10] a) M. Etienne, P. S. White, J. L. Templeton, *Organometallics* **1991**, *10*, 3801–3803; b) M. D. Curtis, J. Real, D. Kwon, *Organometallics* **1989**, *8*, 1644–1651; c) G. Smith, R. R. Schrock, M. R. Churchill, W. J. Youngs, *Inorg. Chem.* **1981**, *20*, 387–393; d) M. Etienne, B. Donnadieu, R. Mathieu, J. F. Baeza, F. Jalon, A. Otero, M. E. Rodrigo-Blanco, *Organometallics* **1996**, *15*, 4597–4603.
[11] W. W. Seidel, M. D. Ibarra Arias, M. Schaffrath, M. C. Jahnke, A. Hepp, T. Pape, *Inorg. Chem.* **2006**, *45*, 4791–4800.
[12] We are indebted to one of our reviewers for the inspiring objections in order to clarify the questions of isomer identity and interconversion in solution.
[13] W. W. Seidel, M. Schaffrath, T. Pape, *Angew. Chem.* **2005**, *117*, 7976–7979; *Angew. Chem. Int. Ed.* **2005**, *44*, 7798–7800.
[14] A. D. Bain, G. J. Duns, *Can. J. Chem.* **1996**, *74*, 819–824.
[15] J. L. Templeton, J. L. Caldarelli, S. Feng, C. C. Philipp, M. B. Wells, B. E. Woodworth, P. S. White, *J. Organomet. Chem.* **1994**, *478*, 103–110.
[16] W. W. Seidel, M. D. Ibarra Arias, M. Schaffrath, K. Bergander, *Dalton Trans.* **2004**, 2053–2054.
[17] F. A. Cotton, E. A. Hillard, C. A. Murillo, X. Wang, *Inorg. Chem.* **2003**, *42*, 6063–6070.
[18] G. M. Sheldrick, *SHELXS-97: Program for Crystal Structure Solution*, Universität Göttingen, Göttingen, Germany, **1986**–**1997**.
[19] G. M. Sheldrick, *SHELXL-97: Program for Crystal Structure Refinement*, University of Göttingen, Göttingen, Germany, **1997**.
[20] CCDC-612528 (for **5**-$PF_6$), -612530 (for **8**), and -612531 (for **9**) contain the supplementary crystallographic data for this paper. These data can be obtained free of charge from The Cambridge Crystallographic Data Centre via www.ccdc.cam.ac.uk/data_request/cif.
[21] A. D. Becke, *J. Chem. Phys.* **1993**, *98*, 5648–5652.
[22] D. Andrae, U. Haeussermann, M. Dolg, H. Stoll, H. Preuss, *Theor. Chim. Acta* **1990**, *77*, 123.

Received: June 30, 2006
Published Online: February 2, 2007

 © 2007 Wiley-VCH Verlag GmbH & Co. KGaA, Weinheim 

DOI: 10.1002/ejic.200600848

# Investigation of the Thermal Decomposition of [biphen(QP*i*Pr)Pt(alk)$_2$]: An Entry to C–C Single Bond Activation?

**Klaus Ruhland,*[a] Andreas Brück,[a] and Eberhardt Herdtweck[a]**

**Keywords:** Platinum / Reaction mechanisms / C–H activation / C–C activation / Agostic interactions

The reaction of [(COD)PtCl$_2$] with biphen(QP*i*Pr)(Q′P*i*Pr) (Q, Q′ = O, CH$_2$O) yields *cis*-[{biphen(QP*i*Pr)(Q′P*i*Pr)}PtCl$_2$]. Treatment of *trans*-[PtCl$_2$(ethene)(py)] with biphen(QP*i*Pr)-(Q′P*i*Pr) (Q, Q′ = O, CH$_2$O) gives *trans*-[{biphen(QP*i*Pr)-(Q′P*i*Pr)}PtCl$_2$] for Q or Q′ ≠ O. No *trans*/*cis* isomerization can be observed for these compounds after 24 h at 105 °C in [D$_8$]toluene. In the case of Q = Q′ = O a *trans*/*cis* isomerization takes place at room temperature. X-ray structures of a molecule in the solid state were determined for the compounds *cis*/*trans*-[{biphen(QP*i*Pr)(Q′P*i*Pr)}PtCl$_2$] with Q or Q′ ≠ O. In the case of Q = O and Q′ = CH$_2$O the closer of the two bridging C atoms in the biphenyl fragment of the ligand is only 3.42 Å away from the Pt center but does not show a coupling to it in the $^{13}$C NMR spectrum. Treatment of both *cis*- and *trans*-[{biphen(QP*i*Pr)(Q′P*i*Pr)}PtCl$_2$] with two equivalents of ethyl- or *n*-propylmagnesium chloride gives *cis*-[{biphen(QP*i*Pr)(Q′P*i*Pr)}PtAlk$_2$]; the X-ray structures of *cis*-[{biphen(CH$_2$OP*i*Pr)$_2$}PtEt$_2$] and *cis*-[{biphen(OP*i*Pr)$_2$}Pt-(*n*Pr)$_2$] are discussed. These complexes give the related alkene complexes as a result of β-H elimination/reductive elimination if heated to temperatures above 90 °C in [D$_8$]toluene, but none of the complexes with Q or Q′ ≠ O is stable at 95 °C. The thus-formed Pt(alkene) complex loses the alkene (ethene or propene) in a consecutive reaction. For [{biphen(CH$_2$OP*i*Pr)$_2$}PtEt$_2$], selective deuteration of the CH$_2$O group and the Pt-ethyl group proves that scrambling of deuterium into the *i*Pr methyl groups occurs (by a CH activation/insertion/β-H elimination/reductive elimination sequence) after the β-H elimination and before the loss of ethene, which at 95 °C is almost as fast as the loss of ethene. In the final alkene-free 14 e complex a fast dynamic C–H activation of the *i*Pr CH$_3$ protons by the Pt center (one H at a time) can be detected [an Isotopic Perturbation of Resonance (IPR) is found for the partially deuterated compound], which most probably prevents a further reaction of the complex (e.g. activation of the bridging C–C single bond in the biphenyl backbone or permanent coordination of PPh$_3$). H$_2$, however, is activated by the final complex, and the use of D$_2$ proves that deuterium is incorporated into the *i*Pr groups of the ligand. The reaction of [(COD)PtCl$_2$] with *o*-Br-phen(QP*i*Pr) gives *cis*-[PtCl$_2${*o*-Br-phen(QP*i*Pr)}$_2$] (X-ray structure reported), which forms *cis*-[Pt{phen(QP*i*Pr)}$_2$] upon treatment with *s*BuLi. The reaction of *trans*-[PtCl$_2$(ethene)-(py)] with *o*-I-phen(QP*i*Pr) gives *trans*-[PtCl$_2${*o*-I-phen-(QP*i*Pr)}$_2$] (X-ray structure reported), which also forms *cis*-[Pt{phen(QP*i*Pr)}$_2$] upon treatment with *s*BuLi. *cis*-[Pt{phen(CH$_2$OP*i*Pr)}$_2$] (X-ray structure reported) slowly isomerizes quantitatively at 95 °C in toluene to the *trans* complex. No product of reductive elimination can be detected up to 150 °C in mesitylene. *cis*-[Pt{phen(OP*i*Pr)}$_2$] (X-ray structure reported) forms two products − the *trans* isomer (X-ray structure reported) and most likely a dimeric *trans*-configured complex − upon heating to 95 °C. Again, no reductive elimination is observed regardless of whether the reaction is performed under argon or ethene atmosphere up to 150 °C in mesitylene. All materials were characterized by means of $^1$H, $^2$H, $^{13}$C, $^{31}$P, and $^{195}$Pt NMR spectroscopy, FAB mass spectrometry, FT-IR spectroscopy, elemental analysis, and X-ray crystallography. DFT calculations (B3PW91/LANL2DZ) are also included for the most important compounds.
(© Wiley-VCH Verlag GmbH & Co. KGaA, 69451 Weinheim, Germany, 2007)

## Introduction

We are currently searching for a way to activate and cleave the bridging C–C single bond in nonstrained biphenyl fragments, a reaction that is still without precedent, although the strained biphenylene has been successfully activated.[1] Other groups have reported their strategies, successes, and challenges in the area of C–C single bond activation.[2] Several advantages of focusing on the activation of the bridging C–C single bond in a biphenyl fragment have been discussed by us earlier,[3] and in light of this we decided to use the well-known principle of chelating assistance[4] to enhance the chance of observing the activation. Additionally, the ligand architecture is chosen in a way that in the course of the reaction a vibrational bending mode of the coordinated ligand forces the C–C single bond to approach the metal center in a promising orientation concerning an activation of it (compound **c** in Scheme 1).

Our former work[3] showed that Scheme 1 describes the behavior of [{biphen(OP*i*Pr)$_2$}PtEt$_2$] ([**1**]PtEt$_2$) well, except that the most decisive reaction (D) was not observed. Herein we report our progress with this strategy.

[a] TU München, Department Chemie, Lehrstuhl für Anorganische Chemie,
Lichtenbergstr. 4, 85748 Garching
E-mail: klaus.ruhland@ch.tum.de

 WILEY InterScience DISCOVER SOMETHING GREAT © 2007 Wiley-VCH Verlag GmbH & Co. KGaA, Weinheim 

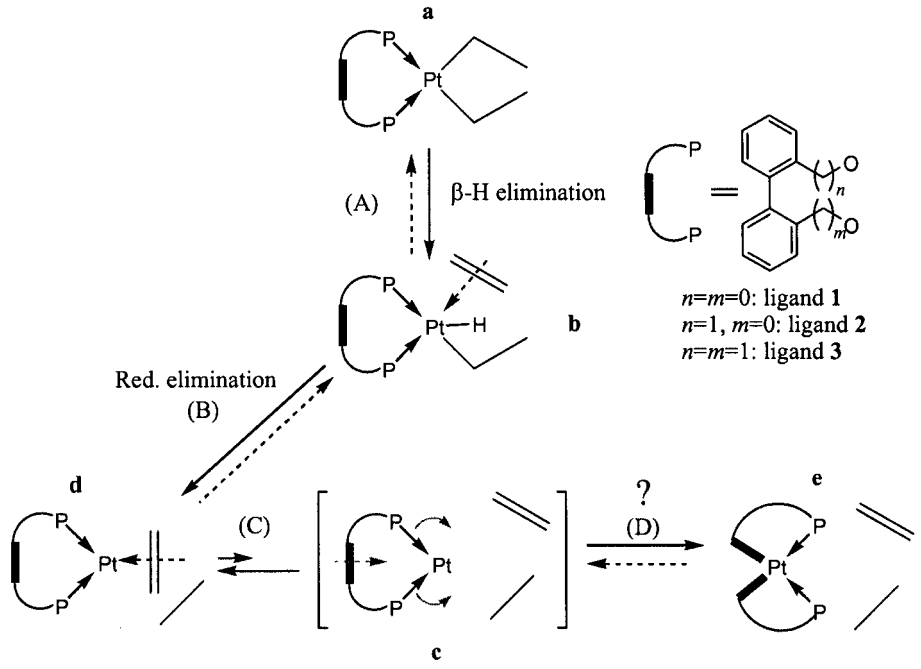


Scheme 1.

## Results and Discussion

### Calculations on the Reaction Path

One critical point about the strategy in Scheme 1 is that the ligand architecture used in intermediate **c** might be too strained to allow the desired movement along the reaction coordinate (bending vibration of P–Pt–P) if the biphenyl fragment and the coordinating phosphorus atoms are connected only by an oxo group. To gain more insight into this question, we calculated the energy profile of the P–Pt–P bending vibration mode with an oxo group (ligand **1**) and a $CH_2O$ group as connector (ligand **3**). This was done with Gaussian03[5] using density functional theory (functional: B3PW91; basis set: LANL2DZ) and employing the "frozen coordinate" function implemented in the program package. Table 1 contains the calculated data and Figure 1 shows the plot of $\Delta G$ as a function of the P–Pt–P angle.

Table 1. Calculated differences between $G$ and $G_{min}$ of the P–Pt–P bending vibration and its dependence on the bending angle, $\alpha$, for both [**1**]Pt and [**3**]Pt.

| P–Pt–P $\alpha$ [°] | $G - G_{min}$ for [**1**]Pt [kcal mol$^{-1}$] | $G - G_{min}$ for [**3**]Pt [kcal mol$^{-1}$] |
|---|---|---|
| 120 | 14.84 | 33.18 |
| 130 | 7.70 | 17.36 |
| 140 | 2.84 | 9.43 |
| 150 | 1.27 | 4.54 |
| 153 | 0 | – |
| 160 | – | 18.29 |
| 165 | 2.48 | – |
| 170 | 4.72 | 0.065 |
| 175 | 7.38 | – |
| 177 | – | 0 |

The following conclusions can be drawn from the calculated data:

> For ligand **1** the additional kinetic driving force concerning the C–C single bond activation is high and "downhill" at the beginning but, because of the small P–Pt–P equilibrium angle (153°), decisively "uphill" at the end of the reaction pathway. In the range $120° < \alpha < 180°$ no decisive gain in energy is predicted by the calculations because the two effects cancel each other out (energy gain of about 7 kcal mol$^{-1}$ at most). The angle determined for [**1**]Pt-(ethene) by X-ray analysis is 120°.[3]

> For ligand **3** the additional kinetic driving force is even greater than for **1** at the beginning of the C–C single bond approach, and the equilibrium P–Pt–P angle is larger (178°). Thus, the approach of the C–C single bond to be activated is less hindered at the end of the reaction pathway. The calculations predict an energy gain of about 33 kcal mol$^{-1}$ in the best case. Moreover, the force constant (determined using the harmonic potential approximation) in the case of ligand **3** is calculated to be 0.438 mdyn Å rad$^{-2}$ and is thus softer than for ligand **1** (0.636 mdyn Å rad$^{-2}$). As a consequence, ligand **3** enhances the flexibility of the bending vibration in the area of its minimum in comparison to ligand **1**.

It must be stated at this point that the calculations give no indication of any kind of agostic interaction between parts of the ligand and the Pt center, neither through geometric proximity (the nearest H atom is more than 3 Å away from Pt) nor through the calculated wavenumbers of the vibration modes. This fact will become important below. Figure 2 shows a plot of the calculated minimum structure of [**3**]Pt.

### Ligand Synthesis and Complexation

In light of the results of the calculations we synthesized the three biphen ligands **1**, **2**, and **3** (Scheme 2) to examine

 © 2007 Wiley-VCH Verlag GmbH & Co. KGaA, Weinheim 

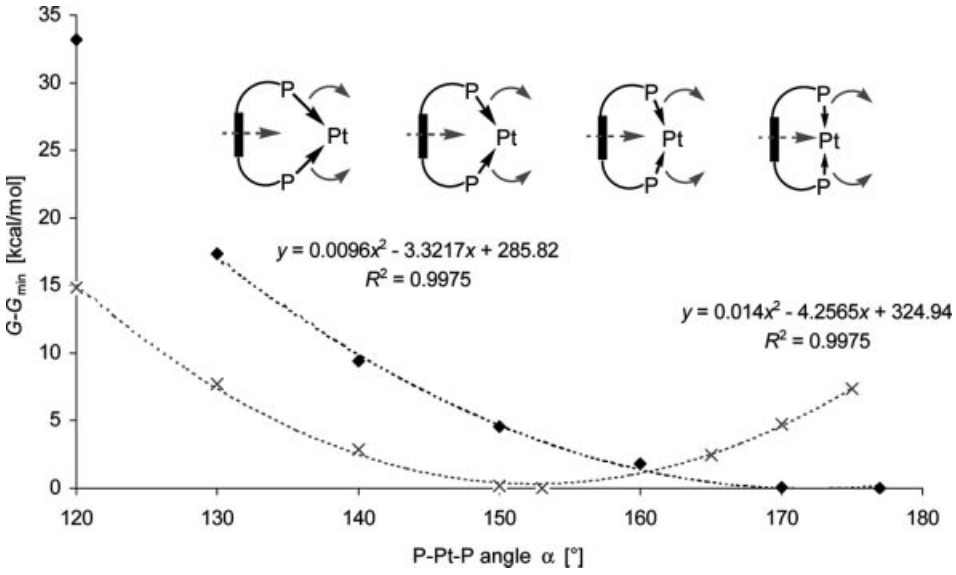


Figure 1. Potential of the P–Pt–P bending vibration for [**1**]Pt (×) and [**3**]Pt (♦) calculated using DFT theory (functional: B3PW91; basis set: LANL2DZ).

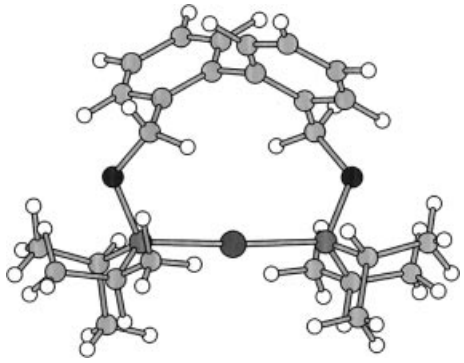

Figure 2. Plot of the calculated minimum structure of [**3**]Pt.

the influence of the ligand "arm" length on the basic strategy of Scheme 1.

The synthesis was performed analogously to our previously published procedures.[3] The precursor for **2** was synthesized from fluoren-9-one by a Baeyer–Villiger oxidation and reduction of the resulting lactone with $LiAlH_4$. We were interested in the corresponding *cis*- and *trans*-$PtCl_2$ complexes of the ligands as the *cis* compounds could serve as a precursor for the dialkyl complexes and the *trans* compounds as an experimentally available model for the transition state of the potential activation step in the thermolysis. In this context, the Cl ligands have two functions, namely they stabilize the potential transition state structure, thereby allowing us to do X-ray analysis, and because of the Cl ligands the Pt center is in the oxidation state +2, which is the oxidation state of the desired product.

In the transition state the oxidation number should, of course, be somewhere between 0 and +2. The complexes were also synthesized according to Scheme 2. The complexation reaction with ligands **2** and **3** is less clean than that with **1**, and thorough and repeated washing of the product with diethyl ether and recrystallization from dichloromethane is necessary to isolate analytically pure compounds. For **1**, which has the shortest backbone, the *trans* complex could not be isolated because it isomerizes to *cis*-[**1**]$PtCl_2$ too fast if the ligand-exchange reaction is performed at low concentrations (0.1 mmol $L^{-1}$) whereas a weakly soluble *trans*-configured coordination polymer is formed at higher concentrations. We propose that strain in the *trans*-[**1**]$PtCl_2$ complex is the reason for this behavior. All the other *cis*/*trans*-(ligand)$PtCl_2$ complexes show no isomerization upon heating to 105 °C in toluene for 24 h, thus demonstrating that the activation barrier for this process must be high and supporting the fact that no strain is to be expected in the transition state **c** for **2** and **3** (Scheme 1) in accordance with the results of the calculations. It should be mentioned that the synthesis of the complexes (ligand)$PtCl_2$ [*trans* (*cis*) precursor results in *trans* (*cis*) complex] is only stereoselective for $P(iPr)_2$ or $PCy_2$ ligand groups and not for $PPh_2$.

## Structural and Spectroscopic Comparison of the Dichlorido Complexes

The most confident parameter to distinguish between *cis* and *trans* (diphosphane)$PtCl_2$ complexes besides an X-ray structure is the $^1J_{Pt,P}$ coupling constant, which shows values of about 4000–4200 Hz for *cis* complexes and values of about 2650 Hz for *trans* complexes.[6] This is confirmed in our case (Table 2).

The fairly large value of the *trans*-[**1**]$PtCl_2$ coupling constant (2865.5 Hz) might be due to the strain present in this compound. Additionally, the $^2J_{P,P}$ coupling constant for **2**, which has two inequivalent phosphorus atoms, shows the expected small value for the *cis* configuration (5 Hz) and a much larger value for the *trans* configuration (488.5 Hz). As can be seen from Table 2, the chemical shift in the $^{195}Pt$ NMR spectrum can be used as a diagnostic criterion for the complex configuration (*cis*: $\delta \approx -4100$ ppm; *trans*: $\delta \approx$

 © 2007 Wiley-VCH Verlag GmbH & Co. KGaA, Weinheim 

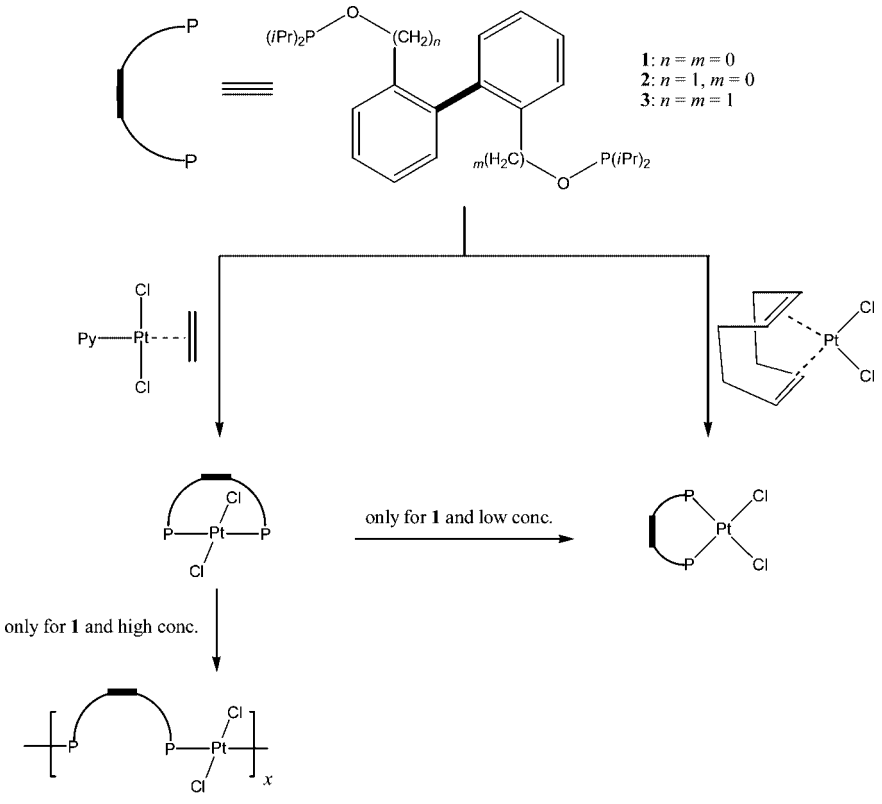


Scheme 2.

Table 2. A comparison of the NMR spectroscopic data for the compounds (ligand)$PtCl_2$.

| Compound | $\delta_{^{31}P}$ [ppm] | $^1J_{Pt,P}$ [Hz] | $\delta_{^{195}Pt}$ [ppm] | $^2J_{P,P}$ [Hz] |
|---|---|---|---|---|
| *cis*-[**1**]$PtCl_2$ | 123.4 | 4147.2 | –4122.8 | – |
| *trans*-[**1**]$PtCl_2$ | 117.0 | 2865.5 | n.d. | – |
| *cis*-[**2**]$PtCl_2$ | 112.5, 115.7 | 4099.0, 4149.6 | –4116.8 | 5.0 |
| *trans*-[**2**]$PtCl_2$ | 109.3, 118.8 | 2624.9, 2690.7 | –3805.7 | 488.5 |
| *cis*-[**3**]$PtCl_2$ | 115.7 | 4267.2 | –4223.4 | – |
| *trans*-[**3**]$PtCl_2$ | 118.4 | 2627.5 | –3763.1 | – |

–3800 ppm), in contrast to the chemical shift in the $^{31}P$ NMR spectrum. In the case of **2** and **3**, a $^3J_{H,P}$ coupling of about 8 Hz is found for the $CH_2$ group in the *trans* complexes, while no H–P coupling is resolved in the *cis* complexes for the $CH_2$ groups. This behavior can be explained by using the structural data of a molecule in the solid state determined by X-ray diffraction. The structures of *trans*-[**2**]$PtCl_2$ and *trans*-[**3**]$PtCl_2$ are shown in Figure 3 (Table 3). Details on the the X-ray structures of *cis*-[**2**]$PtCl_2$ and *cis*-[**3**]$PtCl_2$ can be obtained from the CCDC (for more information see Exp. Sect.; relevant quality parameters of the structure determination are given in the Exp. Sect. together with all other characterization data of the compounds).

A Karplus equation for the $^3J_{P,H}$(POCH) coupling has been reported for phosphites.[7] According to this equation, the coupling constant should be small for POCH torsional angles of about 60° and have maximum values for angles of about 150–180° and 0–30°. As can be seen from Table 3, the POCH torsional angles for the *cis* complexes are about 60° and no $^3J_{P,H}$ coupling is resolved in the $^1H$ NMR spectra, whereas for the *trans* complexes the torsional angles are in an area for which the $^3J_{P,H}$ coupling constants are expected be about 10 Hz, in accordance with what we find in the $^1H$ NMR spectra. Some other structural parameters in Table 3 can be compared and discussed as follows:

> Due to a canceling *trans* influence in the *trans* complexes, the Pt–P bond is significantly longer than those in the *cis* complexes (the Pt–Cl bond behaves in the opposite manner as it is longer in the *cis* complexes).

> In spite of the fact that the bridging C–C single bond of the biphenyl fragment in *trans*-[**2**]$PtCl_2$ is only about 3.42 Å

 © 2007 Wiley-VCH Verlag GmbH & Co. KGaA, Weinheim 

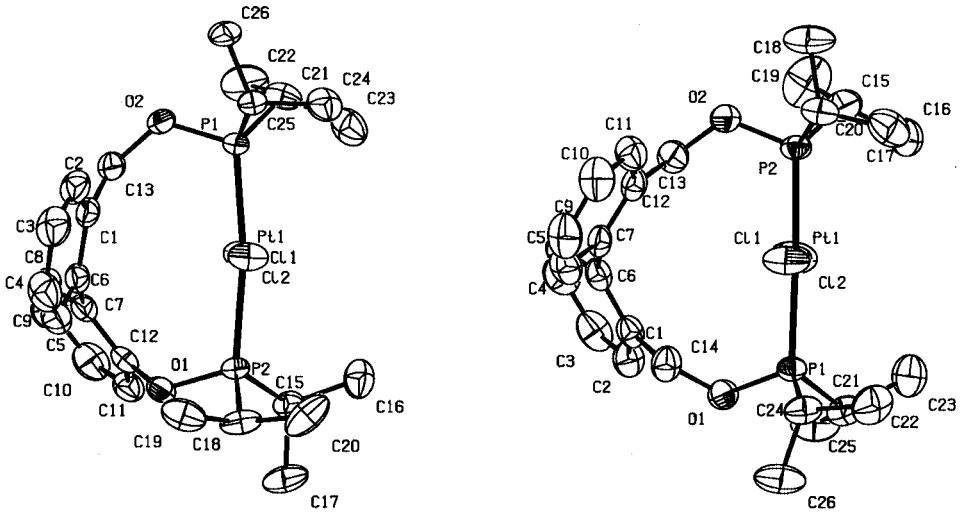


Figure 3. ORTEP style plot of the compounds *trans*-[**2**]$PtCl_2$ (left) and *trans*-[**3**]$PtCl_2$ (right) in the solid. Thermal ellipsoids are drawn at the 50% probability level. Hydrogen atoms have been omitted for clarity.

Table 3. A comparison of the geometric data for the compounds (ligand)$PtCl_2$ determined by X-ray analysis.

| | *cis*-[**1**]$PtCl_2$[3] | *cis*-[**2**]$PtCl_2$ | *cis*-[**3**]$PtCl_2$ | *trans*-[**2**]$PtCl_2$ | | *trans*-[**3**]$PtCl_2$ |
|---|---|---|---|---|---|---|
| Pt–P1 [Å] | 2.2321(12) | 2.2421(13) | 2.238(3) | 2.3103(15) | 2.3167(16) | 2.3169(12) |
| Pt–P2 [Å] | 2.2291(11) | 2.2527(15) | 2.236(3) | 2.3076(15) | 2.3110(15) | 2.3292(13) |
| Pt–Cl1 [Å] | 2.3671(12) | 2.3579(13) | 2.379(3) | 2.2993(15) | 2.3135(13) | 2.3017(12) |
| Pt–Cl2 [Å] | 2.3534(12) | 2.3591(13) | 2.374(3) | 2.3148(15) | 2.2992(15) | 2.3083(13) |
| C6–C7 (bridge) [Å] | 1.483(7) | 1.486(8) | 1.492(15) | 1.482(9) | 1.494(9) | 1.492(7) |
| Pt···C6 [Å] | 4.391(4) | 4.865(5) | 6.226(14) | 3.419(7) | 3.457(7) | 4.132(5) |
| Pt···C7 [Å] | 4.896(4) | 5.433(6) | 6.256(13) | 3.657(6) | 3.720(6) | 4.255(5) |
| P–Pt–P [°] | 95.52(4) | 95.90(5) | 96.61(11) | 171.50(6) | 170.29(6) | 177.91(4) |
| Cl–Pt–Cl [°] | 89.12(4) | 85.60(4) | 85.44(10) | 178.43(6) | 177.77(6) | 173.49(6) |
| Torsional angle HC13/14OP [°] | – | Hα 59<br>Hβ –61 | Hα –67<br>Hβ 52 | Hα –44<br>Hβ –162 | Hα 50<br>Hβ 167 | Hα –25<br>Hβ –5<br>Hα′ –143<br>Hβ′ –23 |

apart from the metal center, no $J_{Pt,C}$ coupling can be detected in the $^{13}C$ NMR spectrum and, thus, no evidence for an interaction between these two centers can be found.

> In accordance with this finding no significant elongation of the bridging C–C single bond in the biphenyl fragment is found in *trans*-[**2**]$PtCl_2$ or *trans*-[**3**]$PtCl_2$.

> The P–Pt–P bond angle of about 178° in *trans*-[**3**]$PtCl_2$ is in good agreement with the calculated data for [**3**]Pt, thereby showing that the theoretical results are fairly confident and a structural comparison of the two compounds is justified.

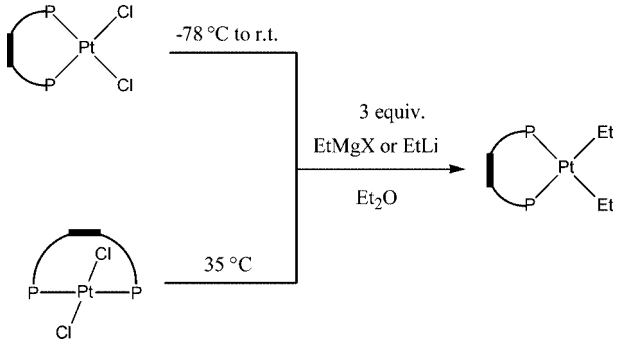


Scheme 3.

### Alkylation of the Dichlorido Complexes

Treatment of *cis*-[**2**]$PtCl_2$ and *cis*-[**3**]$PtCl_2$ with ethylmagnesium chloride at low temperatures in diethyl ether yielded the corresponding *cis*-(ligand)$PtEt_2$ complexes, which are the starting compounds **a** in Scheme 1. The analogous complexes *trans*-[**2**]$PtCl_2$ and *trans*-[**3**]$PtCl_2$ showed no reaction at low temperature, even with EtLi. Alkylation was possible, though, in refluxing diethyl ether with both ethylmagnesium chloride and EtLi to give *cis*-(ligand)$PtEt_2$ rather than the *trans* complexes (Scheme 3).

We propose the following mechanism to explain this behavior (Scheme 4). The slower reaction of the *trans*-(ligand)$PtCl_2$ complexes is explained by transition state **T1**, which is sterically crowded and is therefore formed slowly in comparison to transition state **C1**. It is proposed that a fast Berry pseudorotation transforms **T1** into the sterically and electronically preferred **C1**. It will be shown later in this publication that the chelating character of the phosphinite ligand is not the decisive factor in this mechanism. We propose that the combination of an alkyl substituent, a halide,

 © 2007 Wiley-VCH Verlag GmbH & Co. KGaA, Weinheim 

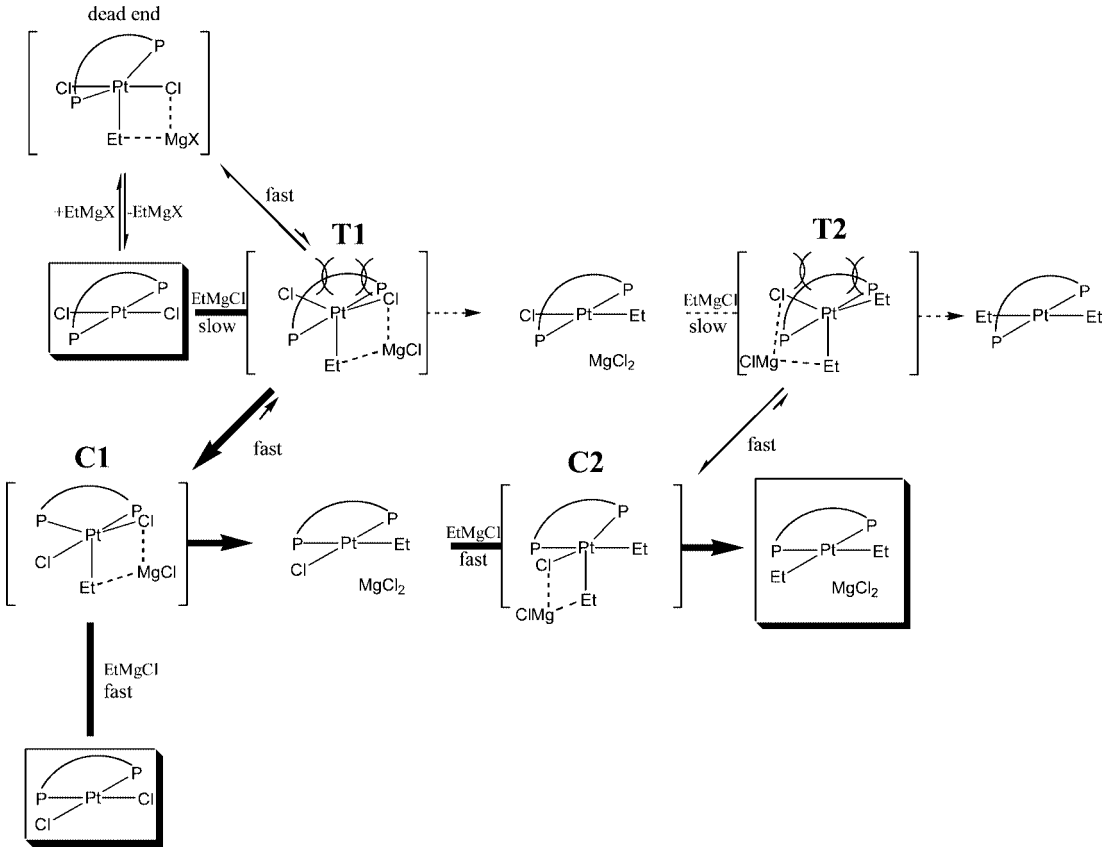


Scheme 4.

and a phosphinite in an equatorial position in **C1** and **C2** is electronically favored because of a synergistic cooperation of a strong σ-donor (alkyl) and a strong π-acceptor (phosphinite), both of which weaken the Pt–Cl bond and thus lower the activation energy. Even if the *trans*-(ligand)PtEtCl complex is partly formed, when generating **T2** there is a second chance for the reaction to switch into the *cis* pathway (**C2**), again by a Berry pseudorotation. This is the reason why *cis*-(ligand)PtEt$_2$ is formed exclusively from the *trans*-(ligand)PtCl$_2$ complex. The mechanism proposed in Scheme 4 is supported by the finding that the use of one equivalent of ethylmagnesium chloride results in the formation of a mixture of *cis*-(ligand)PtCl$_2$, *cis*-(ligand)PtEtCl, and *cis*-(ligand)PtEt$_2$ (3:2:1) if *cis*-(ligand)PtCl$_2$ is the starting material. In the case of *trans*-(ligand)PtCl$_2$, though, the product is a mixture of unchanged *trans*-(ligand)PtCl$_2$ and *cis*-(ligand)PtEt$_2$ only; no monoethyl complex is formed.

Relevant quality parameters of the crystal structure determinations of compounds *cis*-[**1**]Pt(*n*Pr)$_2$ and *cis*-[**3**]PtEt$_2$ are given in the Exp. Sect. together with all other characterization data of the compounds. Some key data are summarized in Table 4. The X-ray structures of *cis*-[**1**]PtEt$_2$ and *cis*-[**1′**]PtEt$_2$ (**1′** = **1**, but with phenyl substituents at the phosphorus atom instead of *i*Pr) have been published by us previously.[3]

Table 4. A comparison of the geometric data for two (ligand)-Pt(alk)$_2$ compounds, as determined by X-ray analysis.

| | [**1**]Pt(*n*Pr)$_2$ | [**3**]PtEt$_2$ |
|---|---|---|
| Pt–P [Å] | 2.2784(6) | 2.2657(14) |
| Pt–C [Å] | 2.152(3) | 2.124(4) |
| $C_a$–$C_b$(bridge) [Å] | 1.477(4) | 1.480(7) |
| Pt···$C_a$ [Å] | 4.377(3) | 6.316(5) |
| P–Pt–P [°] | 111.87(2) | 96.15(4) |
| alk–Pt–alk [°] | 86.56(10) | 82.72(17) |

The main difference in the structures of *cis*-[**1**]Pt(alk)$_2$ and *cis*-[**3**]PtEt$_2$ is that a decisive extension of the P–Pt–P angle in **1** to values larger than 90° is observed; this is much less pronounced in the case of **3**.

## Thermolysis Behavior

The thermolysis of *cis*-[**1**]PtEt$_2$ in the temperature range 60–110 °C has been reported by us in detail.[3] The major result concerning our strategy in Scheme 1 is that [**1**]Pt(ethene) is formed by β-H elimination and reductive elimination of ethane without the permanent loss of ethene. This means that the ethene is firmly bound. Its dissociation could be proven only indirectly by trapping reactions and kinetic analysis of the Pt(ethene)/(free ethene) exchange (Scheme 5).

 © 2007 Wiley-VCH Verlag GmbH & Co. KGaA, Weinheim 

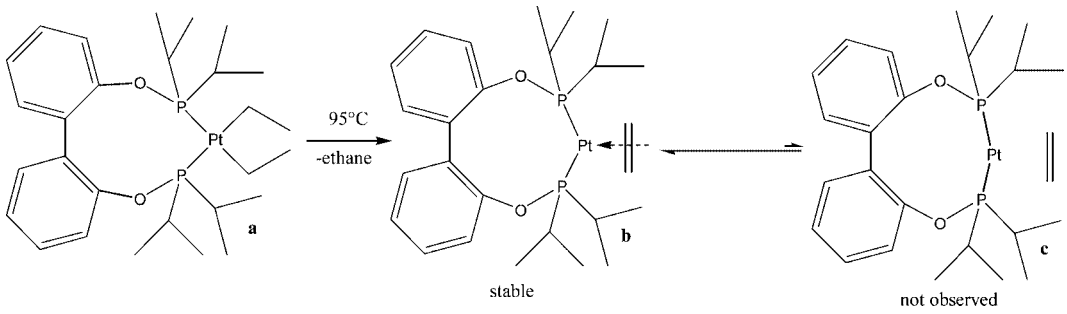


Scheme 5.

To labilize the alkene sterically we examined *cis*-[**1**]-Pt(*n*Pr)$_2$ in the thermolysis reaction. *cis*-[**1**]Pt(*n*Pr)$_2$ forms [**1**]Pt(propene) at 80 °C, which is not stable and decomposes in a not well defined manner while losing propene, further supporting the proposal that the ligand backbone architecture in **1** is too rigid to approach the metal center. The [**1**]-Pt thus formed can be trapped cleanly by treatment with $H_2SiEt_2$ to give the Si-H oxidative addition product. For *cis*-[**2**]PtEt$_2$ and *cis*-[**3**]PtEt$_2$ the (ligand)Pt(ethene) complex is clearly formed in the course of the thermolysis, but it is not stable at 95 °C and further reacts cleanly and completely to a final product with the formation of free ethene (which was not observed in the case of [**1**]PtEt$_2$) and ethane ($\delta$ = 5.3 and 0.8 ppm, respectively in the $^1$H NMR spectrum; ethene/ethane ratio of 1:1. This quantification is better performed by $^2$H NMR spectroscopy and [**3**]Pt(D$_5$-Et)$_2$ as starting material because in this case no peak overlaps with the *i*Pr groups are observed in the region around $\delta$ = 0.8 ppm). The compound thus formed could not be isolated but its assignment as a (ligand)Pt(ethene) complex due to its chemical shift in the $^{31}$P and $^{195}$Pt NMR spectra as well as the $^1J_{P,Pt}$ coupling constants (Table 5) is unequivocal. The small $^2J_{P,P}$ coupling constant in [**2**]Pt(ethene) suggests that the P–Pt–P bond angle is not much larger than 90° and it is similar to that found for [**1**]Pt(propene).

Table 5. NMR spectroscopic data for the compounds (ligand)Pt(alkene) and (ligand)Pt.

| Compound | $\delta_{^{31}P}$ [ppm] | $\delta_{^{195}Pt}$ [ppm] | $^1J_{P,Pt}$ [Hz] | $^2J_{P,P}$ [Hz] |
|---|---|---|---|---|
| [**1**]Pt(ethene)[3] | 186.3 | –5105.4 | 3999.7 | – |
| [**1**]Pt(propene) | 185.7, 185.5 | n.d. | 4181.5, 3658.9 | 16.2 |
| [**2**]Pt(ethene) | 172.1, 172.4 | –5002.7 | 3881.1, 3959.4 | 11.8 |
| [**3**]Pt(ethene) | 177.5 | –5077.9 | 4133.7 | – |
| [**2**]Pt | 144.8, 156.3 | –4770.7 | 3178.8, 3262.0 | 486.6 |
| [**3**]Pt | 160.1 | –4894.8 | 3158.8 | – |

Figure 4 shows the kinetic development of the thermolysis of [**3**]PtEt$_2$ followed by $^{31}$P NMR spectroscopy at 95 °C. The pseudo triplet at about $\delta$ = 145 ppm belongs to the starting material, the [**3**]Pt(ethene) intermediate shows up at about $\delta$ = 177 ppm, and the final product at 95 °C appears at about $\delta$ = 160 ppm quantitatively. The question now arises as to what is the nature of this final product.

In order to answer this question we examined the final product by means of FAB-MS and FT-IR, $^1$H, $^{13}$C, $^{31}$P, and $^{195}$Pt NMR spectroscopy. The FAB mass spectrum for [**3**]-PtEt$_2$ shows the mass peak at *m*/*z* 641.3 (M minus ethene and ethane with correct isotopic pattern). The mass peak for the final product [**3**]Pt shows up at *m*/*z* 642.3 and the

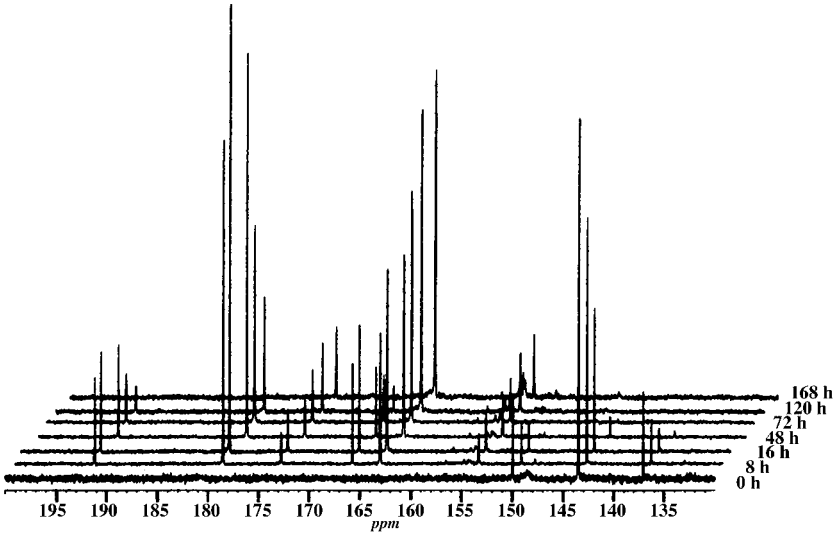


Figure 4. $^{31}$P NMR spectra recorded during the thermolysis of [**3**]PtEt$_2$ at 95 °C in [D$_8$]toluene.

 © 2007 Wiley-VCH Verlag GmbH & Co. KGaA, Weinheim 

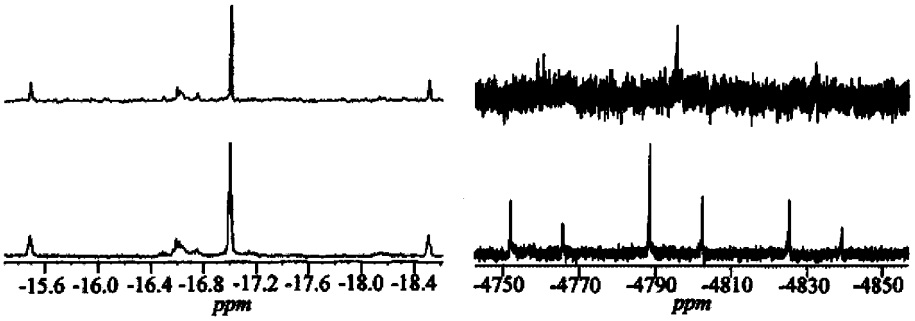


Figure 5. Portions of the $^1$H (left) and $^{195}$Pt (right) NMR spectra showing the Pt–H signals. Top: $^1$H{$^{31}$P} and $^{195}$Pt{$^1$H}.

isotopic pattern is correctly reproduced assuming the loss of both ethane and ethene during the course of the thermolysis (98% M + 1 and 2% M with M = $C_{26}H_{40}O_2P_2Pt$ = [**3**]Pt). That the final product contains only the ligand **3** and Pt is also supported by the fact that performing the thermolysis with [**3**]Pt(*n*Pr)$_2$ results in the same final product as is found with [**3**]PtEt$_2$, according to $^1$H, $^{13}$C, $^{31}$P, and $^{195}$Pt NMR spectroscopy as well as FT-IR spectroscopy and FAB-MS. In the case of [**3**]Pt(*n*Pr)$_2$ the intermediate [**3**]Pt(propene) was not observed and free propene instead of ethene was found ($^1$H NMR spectroscopy). However, $^1$H NMR spectroscopy shows a peculiarity concerning the final product [**3**]Pt: a triplet of pseudo triplets at $\delta$ = –17 ppm can be found which integrates to about 0.7 H atoms relative to the $CH_2$–O protons and the phenyl C–H protons as internal standard (Figure 5). In the FT-IR spectrum an unusual peak of low intensity appears at $\tilde{\nu}$ = 1945 cm$^{-1}$ (Figure 9).

The pseudo triplet (1208.5 Hz splitting) is unequivocally due to a $^1J_{Pt,H}$ coupling, while the triplet (4.9 Hz splitting) was proven to be a $^2J_{P,H}$ coupling from the $^1$H{$^{31}$P} NMR spectrum, in which this coupling disappears (Figure 5, top left). A doublet (1208.5 Hz) of triplets (3160 Hz) in the $^{195}$Pt NMR spectrum can be found using the default $^{195}$Pt{$^1$H} acquisition program with the $^1$H decoupler center at $\delta$ = 5 ppm (Figure 5, bottom right). If the decoupler center is changed to $\delta$ = –17 ppm the doublet splitting in the $^{195}$Pt NMR spectrum vanishes (Figure 5, top right). From this finding we conclude that one and only one H atom (at a time) is in strong electronic interaction with the Pt center. This H atom must be placed in such a manner that the complex (at least in average) has at least $C_2$ symmetry since only one signal (pseudo triplet) is found for the P atoms (Figure 4). The small $^2J_{P,H}$ coupling constant of about 5 Hz mentioned before suggests that the angle between the P atoms and the H atom is about 90°. The $^1J_{Pt,P}$ coupling constant of 3160 Hz is in accordance with the *trans* P–Pt–P orientation that would be expected for [**3**]Pt in light of the above calculations. Furthermore, the $^3J_{P,H}$ coupling constants of 7 and 12 Hz in the $POCH_2$ fragment indicate a *trans* configuration. This is further supported by the fact that a $^2J_{P,P}$ coupling constant of 485 Hz is found for [**2**]Pt, which shows similar peculiarities in the $^1$H and $^{195}$Pt NMR spectra but is not stable even at room temperature and decomposes into as-yet unknown products within a few hours. In the $^{13}$C{$^1$H} NMR spectrum of [**3**]Pt a coupling to the Pt center is observed for the $CH_2O$ carbons (83.7 Hz) and one $CH_3$ group (22.1 Hz), which is slightly separated from the other methyl groups to higher fields by about 1 ppm. The signals of the other $CH_3$ groups overlap but clearly show a structure different from simple singlets. For the P-CH carbons only a coupling to phosphorus is found. No coupling of Pt to any of the aromatic carbons could be detected.

### Deuteration Experiments

We wanted to get more insight into the peculiarity mentioned above. Thus, we first selectively deuterated the $CH_2O$ groups to examine whether they are the origin of the peak at $\delta$ = –17 ppm in the $^1$H NMR spectrum. This deuteration was achieved by reduction of biphenic acid with $LiAlD_4$. The [$D_4$-**3**]Pt formed in the course of thermolysis shows, analogously to [**3**]Pt, the expected peak at M + 1 (*m*/*z* 646.1) with the correct isotopic pattern in the FAB mass spectrum. In the $^2$H NMR spectrum the $CD_2O$ protons show up as two broad, unresolved peaks at the same chemical shift as was found for the $CH_2O$ groups of [**3**]Pt in the $^1$H NMR spectrum, while no peak is observed at $\delta$ = –17 ppm. In the $^1$H NMR spectrum the multiplets for the $CH_2O$ groups are missing and the peak at $\delta$ = –17 ppm is present with the same intensity as was observed for [**3**]Pt. In the $^{31}$P and $^{195}$Pt NMR spectra no difference with respect to the unlabeled complex can be seen. From these findings we conclude that the $CH_2O$ protons are not responsible for the observed interaction with the platinum center. We next selectively deuterated the ethyl groups in [**3**]-$PtEt_2$ by using commercial $CD_3CD_2Br$ in a Grignard reaction. The thermolysis of [**3**]Pt($D_5$-Et)$_2$ occurs slower than that of [**3**]PtEt$_2$, thus indicating a normal kinetic isotope effect for the reaction, which we did not quantify. The product of the thermolysis shows a peak pattern for the mass peak in the FAB mass spectrum that is best described as a superposition of 65% [**3**]Pt and 35% of [$D_1$-**3**]Pt, thus giving a first hint that the complete reaction is more complicated than we had anticipated initially. In the $^1$H NMR spectrum the most obvious difference is that besides the

 © 2007 Wiley-VCH Verlag GmbH & Co. KGaA, Weinheim 

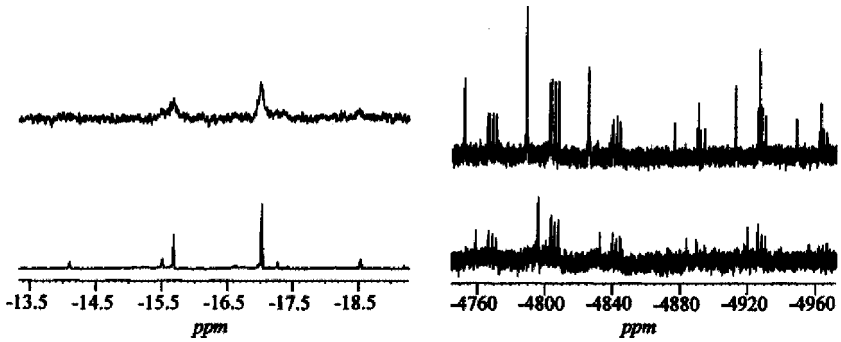


Figure 6. Excerpt of the $^{1}H$ (bottom left), $^{2}H$ (top left), $^{195}Pt$ (top right ), and $^{195}Pt\{^{1}H\}$ (bottom right ) NMR spectra showing the Pt–H(D) signals.

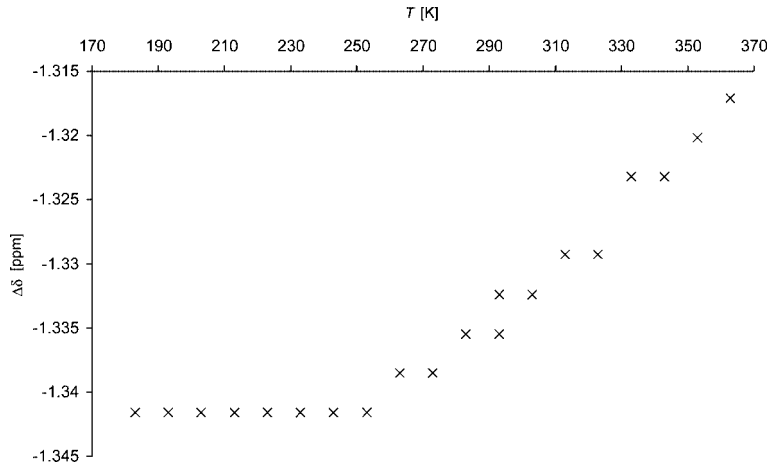


Figure 7. Temperature dependence of the chemical-shift difference, $\Delta\delta$, in the $^{1}H$ NMR spectrum between the two peaks at about $\delta$ = –15.5 and –17 ppm.

pseudo triplet of triplets at $\delta$ = –17 ppm an additional peak with the same multiplicity shows up (ratio 2:1) at about $\delta$ = –15.5 ppm ($^{1}J_{Pt,H}$ = 1266.1, $^{2}J_{P,H}$ = 3.7 Hz), which together integrate to 0.7 protons (Figure 6).

Since we expected that the origin of the second peak should be an isotopic perturbation of resonance (IPR[9]) we performed variable-temperature measurements in the temperature range –90 °C to +90 °C (Figure 7).

As can be seen from Figure 7, a small but significant temperature-dependent change in $\Delta\delta$ between the two peaks at about $\delta$ = –15.5 and –17 ppm is observed, which supports the existence of an IPR. In the temperature range in which $\Delta\delta$ remains constant (below 253 K), the signals in the $^{2}H$ NMR spectrum broaden significantly and almost disappear with decreasing temperature. We conclude from this that $^{1}H$ and not $^{2}H$ atoms are predominantly found at low temperatures in the "hydrido" position (responsible for the peaks at negative ppm), which is in accordance with theory.

In the $^{2}H$ NMR spectrum peaks for ethene and ethane appear along with the signals at $\delta$ = –15.5 and –17 ppm, and a peak group in the area of 1 ppm also shows up where the $CH_3$ groups are found in the $^{1}H$ NMR spectrum (Figure 8).

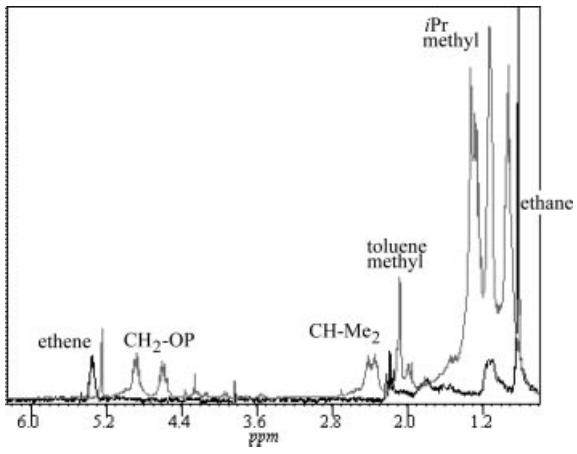


Figure 8. $^{1}H$ NMR spectrum (grey) of [**3**]Pt in [$D_8$]toluene and the $^{2}H$ NMR spectrum of [$D_m$-**3**]Pt (m: number of incorporated deuterium atoms into the ligand in the course of the thermolysis) in non-deuterated toluene (black) in the region between 0.7 and 6 ppm.

The FT-IR spectrum shows two new peaks (Figure 9), one at 2224 $cm^{-1}$, which in accordance with the $^{2}H$ NMR findings we assign to aliphatic C–D stretching vibrations,

 © 2007 Wiley-VCH Verlag GmbH & Co. KGaA, Weinheim 

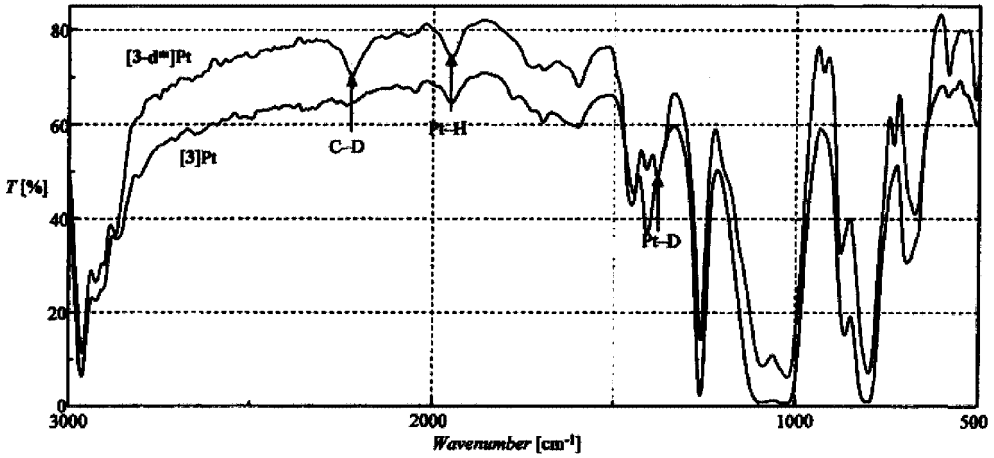


Figure 9. FT-IR spectra for [D$_m$-**3**]Pt and [**3**]Pt.

and one at 1383 cm$^{-1}$, which we assign to a Pt–D stretching vibration corresponding to the peak at 1945 cm$^{-1}$.

The $^{13}$C NMR spectrum, in accordance with the $^{1}$H NMR results, contains two very close sets of signals for each carbon ($\Delta\delta \approx -0.15$ ppm, ratio 2:1), with the more intense set being identical to the unlabeled case. A $J_{C,D}$ coupling could not be unequivocally detected for any of the carbons, although the methyl signals overlap and, thus, are not clearly resolved. A similar kind of experimental finding in the $^{13}$C NMR spectrum (desymmetrization by partial deuteration) has been used (among several other cases) to prove that the keto–enol tautomerization equilibrium in acetylacetone contains two energetic minima with asymmetric hydrogen bonds between the oxygens, the symmetric connectivity being a transition state rather than an intermediate.[9f] This supports our findings and conclusions concerning the $^{1}$H and $^{2}$H NMR spectra.

The $^{31}$P NMR spectrum shows two very close groups of signals ($\delta$ = 163.6 and 164.1 ppm, ratio 1:2; Figure 10), which correspond to the two signals at negative ppm in the $^{1}$H NMR spectrum, thus demonstrating that several different compounds are present at the end of the thermolysis that are very similar to each other (Figure 10). $^{195}$Pt NMR spectroscopy, which, in general, provides only limited information, is very powerful in this specific case. In accordance with the $^{1}$H and $^{2}$H NMR spectra four different compounds are detected at very similar chemical shifts, two of them have an almost identical chemical shift and can only be distinguished by the coupling pattern, which provides a $^{1}J_{Pt,H}$ coupling (doublet splitting, $^{1}J_{Pt,H}$ identical to that in the $^{1}$H NMR spectrum) in one case and a $^{1}J_{Pt,D}$ coupling (triplet splitting with about 1/7th of the magnitude of $^{1}J_{Pt,H}$) in the second case (Figure 6). This is further support for the desymmetrization by partial deuteration found by $^{1}$H, $^{2}$H, $^{13}$C, and $^{31}$P NMR spectroscopy.

A more detailed examination of the thermolysis was performed by $^{2}$H and $^{31}$P NMR spectroscopy (Figure 10).

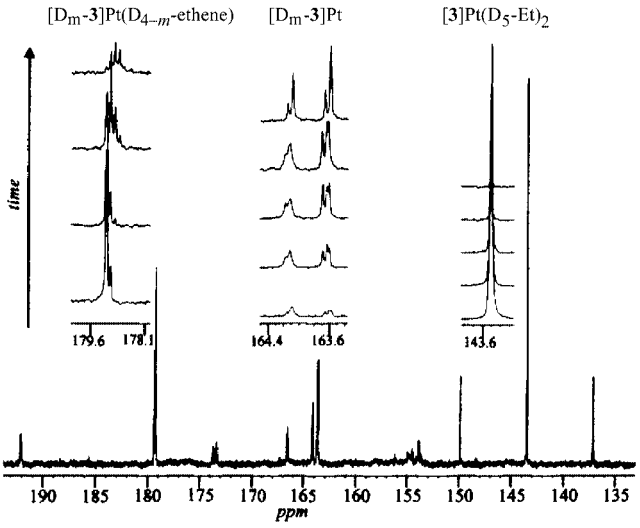


Figure 10. Time-dependent $^{31}$P NMR spectra for the thermolysis of [**3**]Pt(D$_5$-Et)$_2$ showing the scrambling of deuterium into the ligand during the reaction.

As can be seen from Figure 10, the signal of the intermediate [**3**]Pt(D$_4$-ethene) splits with time due to a scrambling of deuterium into the *i*Pr groups of the ligand, as proven by $^{2}$H NMR spectroscopy (Figure 8). This scrambling also leads to a peak splitting in the final product [**3**]Pt. The starting material does not show any splitting. Isolated [D$_m$-**3**]Pt does not change its peak pattern upon further heating. If the same experiment is performed with [**3**]Pt(D$_5$-Et)$_2$ under an atmosphere of unlabeled ethene the scrambling in both [D$_m$-**3**]Pt(D$_{4-m}$-ethene) and [D$_m$-**3**]Pt is still observed, thus proving that the scrambling process is faster than the loss or exchange of ethene. If the thermolysis of [**3**]PtEt$_2$ is performed under an atmosphere of H$_2$, no ethene can be detected. Instead, *trans*-PtH$_2$ shows up in small amounts in

 © 2007 Wiley-VCH Verlag GmbH & Co. KGaA, Weinheim 

the $^1$H NMR spectrum ($\delta$ = –2.45 ppm, $^2J_{P,H}$ = 21.2, $^1J_{Pt,H}$ = 799 Hz; cf. *cis*-[**1**]PtH$_2$: $\delta$ = –3.43 ppm, $^2J_{P,Hcis}$ = 31.8, $^1J_{Pt,H}$ = 1029.5 Hz[3]). [**3**]Pt is still the final product. If $D_2$ is used instead of $H_2$, the final product is [$D_m$-**3**]Pt, which shows the same splitting in the $^1$H and $^{31}$P NMR spectra due to deuterium scrambling into the ligand as is found with [**3**]Pt($D_5$-Et)$_2$ as starting material (although in different ratios), whereas this time no scrambling is found in the intermediate [**3**]Pt(ethene) (or in [**3**]PtEt$_2$). Additionally, when using $D_2$ a small peak for *trans*-[**3**]PtH$_2$ and an even smaller peak for *trans*-[**3**]PtHD ($\delta$ = –2.27 ppm, $^2J_{P,H}$ = 21.2, $^2J_{HD}$ ≈ 1 Hz) can be detected in the $^1$H NMR spectrum after some time. If the final product [**3**]Pt (without labelling) is heated under an atmosphere of $D_2$, incorporation of deuterium can again be detected, but this occurs more slowly than during the thermolysis starting from [**3**]PtEt$_2$.

Finally, if [**3**]Pt is treated with $PPh_3$ in excess in [$D_8$]toluene the signal for $PPh_3$ in the $^{31}$P NMR spectrum is broadened and appears almost at the same position as free $PPh_3$. This broadening cannot be frozen out even at –100 °C. For [**3**]Pt, the only peaks that broaden are those in the $^{195}$Pt NMR spectrum. We can therefore conclude from these findings that there is contact between the $PPh_3$ and the Pt center, but the interaction is only weak. [**1**]Pt(ethene), in contrast, quantitatively coordinates $PPh_3$ at room temperature (triplet at $\delta$ = 41 ppm with $^1J_{Pt,P(Ph)}$ = 3969.3, $^2J_{P,P}$ = 192.2 Hz and doublet at $\delta$ = 199.2 ppm with $^1J_{Pt,P(iPr)}$ = 4910.6, $^2J_{P,P}$ = 192.2 Hz).

### Explanation of the Behavior

Agostic interactions between the ligands' H atoms and the metal center are not uncommon, especially in 14-electron complexes.[8] There is precedence for this (at least) with group 8, group 9, and group 10 metals, for which agostic interactions to C–H bonds in P-Ph, P-*t*Bu, and P-Cy ligand fragments have been found. However, in all these cases the P-*i*Pr fragment turned out to be an exception and showed no such interaction, especially not in {P(*i*Pr)$_3$}$_2$Pt.[8a] However, in our case there is strong experimental evidence for an interaction between the *i*Pr methyl groups and the Pt$^0$ center.

We ascribe the second peak at $\delta$ = –15.5 ppm in the $^1$H NMR spectrum of the final product when performing the thermolysis with [**3**]Pt($D_5$-Et)$_2$ to a dynamic equilibrium concerning a C–H activation of the *i*Pr methyl groups by the Pt$^0$ center as shown in Scheme 6.

This peak at δ = –15.5 ppm proves that the symmetric structure with two agostic interactions shown in the center of Scheme 6 can only be a transition state. The ground states must therefore be asymmetric (IPR). This is supported by the $^{195}$Pt NMR spectrum, which shows only one Pt···H interaction at a time, and by the second set of signals in the $^{13}$C NMR spectrum upon partial deuteration, which is an additional indicator for an IPR.

We propose the behavior in Scheme 7 to explain the experimental results. [**3**]PtEt$_2$ irreversibly loses ethane by a β-H elimination/reductive elimination if heated to 95 °C. The [**3**]Pt(ethene) complex (**2**) intramolecularly C–H activates the *i*Pr methyl groups of the ligand and the coordinated ethene inserts reversibly into the Pt–H bond via compound **4b**. Indirect evidence for the existence of **4b** is given by the incorporation of deuterium into the *i*Pr methyl groups if the thermolysis is performed with [**3**]Pt($D_5$-Et)$_2$ (Figure 8 and Figure 10). Compounds **2** and **4a** in Scheme 7 lose ethene reversibly to form ethene-free [**3**]Pt, which must be thermodynamically more stable than **2** and **4** because if [$D_m$-**3**]Pt is heated to 95 °C under an atmosphere of unlabeled ethene instead of argon, **2** cannot be detected and the degree of labelling in [$D_m$-**3**]Pt slowly decreases (over days). The loss of ethene is compensated in [**3**]Pt by the dynamic interaction of two *i*Pr methyl groups of the ligand with the Pt center (one at a time, because an IPR was found).

That the interaction between the Pt center and the *i*Pr groups of the ligand (**3** in Scheme 7) must be strong is further supported by the finding that pyridine and $PPh_3$ are not permanently coordinated even at 100 °C in toluene.

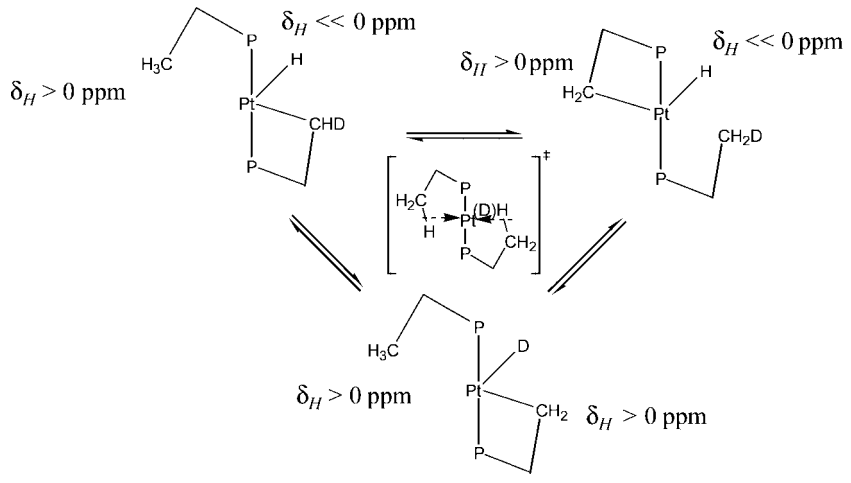


Scheme 6.

 © 2007 Wiley-VCH Verlag GmbH & Co. KGaA, Weinheim 

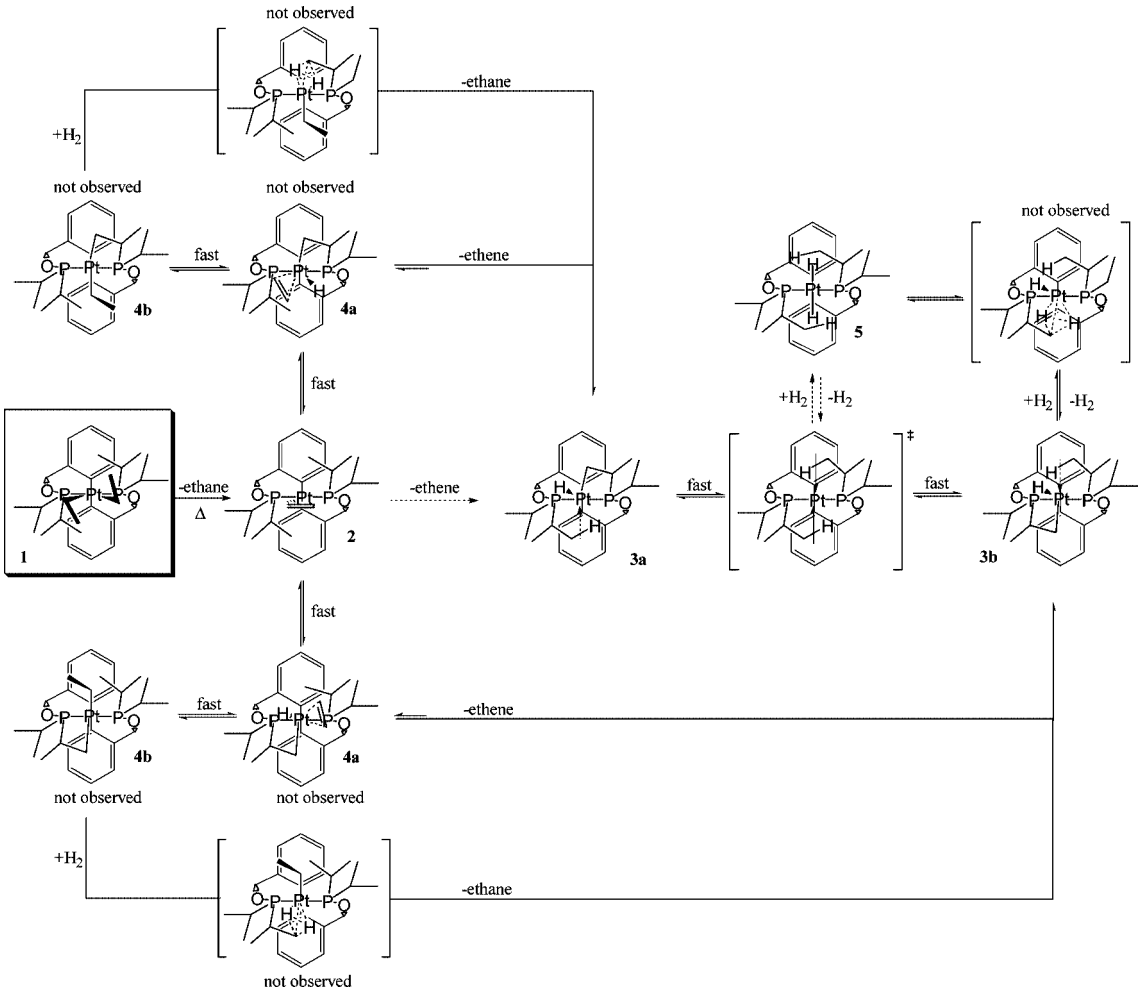


Scheme 7.

Since no incorporation of deuterium into **2** can be detected when doing the thermolysis under an atmosphere of $D_2$, neither **2** nor **4a** can be attacked by $D_2$ (nor can **1**). The finding that the incorporation of deuterium into **3** is faster during the thermolysis under $D_2$ atmosphere than when heating **3** under $D_2$ at the same temperature is further indirect evidence for the existence of **4b**. The reaction pathway via **4b** also explains why no ethene can be detected during the thermolysis under an atmosphere of $H_2$.

All these findings can be explained by the mechanism proposed in Scheme 7. Unfortunately, we have not yet been able to grow single crystals of [**3**]Pt suitable for X-ray analysis. The most similar kind of interaction to the one described here, that we are aware of, was reported by Crabtree et al. with an $Ir^{III}$ complex,[8l] where two *ortho*-phenyl C–H bonds are found to dynamically oxidatively add to the Ir center.

### Approach from the Product Side

In a previous publication we reported on the problems to synthesize the expected products of the anticipated activation process via orthometalated precursors because of a rearrangement taking place.[3] We have since overcome these problems by first coordinating the phosphinites to the platinum center and then performing the orthometalation followed by salt metathesis (the last two steps in a one-pot reaction) using *s*BuLi in toluene.

The complexes *trans*-(ligand)$^X$PtCl$_2$ can be synthesized from the *ortho*-iodophosphinite as precursor (relevant quality parameters of the crystal structure determination are given in the Exp. Sect. together with all other characterization data of the compounds). For the *cis* isomers the *ortho*-iodophosphinite precursor cannot be used, presumably because of an intramolecular oxidative addition. Only an unidentified mixture of products can be isolated if (COD)PtCl$_2$ is treated with *ortho*-iodophosphinite. Switching to the less reactive *ortho*-bromophosphinite solves this problem and leads to the desired product in good yield (relevant quality parameters of the crystal structure determination are given in the Exp. Sect. together with all other characterization data of the compounds).

The $^{31}$P NMR signal of *cis*-[**1***]$^{Br}$PtCl$_2$ broadens with decreasing temperature, thus indicating a dynamic process with an approximate activation enthalpy of about 6 kcal mol$^{-1}$ (line shape analysis), which we assign to a re-

 © 2007 Wiley-VCH Verlag GmbH & Co. KGaA, Weinheim 

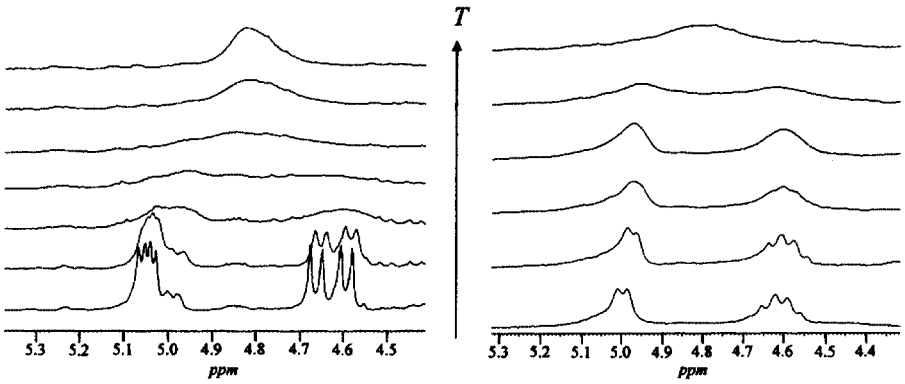


Figure 11. Results of the variable-temperature $^1$H NMR measurements for the $OCH_2$ protons in *cis*-[**3***]Pt (left) and *trans*-[**3***]Pt (right) between –90 and 100 °C.

stricted rotation about the P–Pt axis. This is supported by the crystal structure determination. Similar to the behavior described in Scheme 4, we find that both *cis*- and *trans*-(ligand)$^X$PtCl$_2$ form the *cis*-(ligand)Pt product upon treatment with four equivalents of *s*BuLi. The configuration of this product was deduced from the $^1J_{P,Pt}$ coupling constant of about 2000 Hz and the $^2J_{P,C}$ coupling constants of about 10 Hz for the *cis* coupling and about 105 Hz for the *trans* coupling (cf. *cis*-[**2**]PtEt$_2$: $^2J_{C,Pcis}$ = 8.1, $^2J_{C,Ptrans}$ = 110.5 Hz and *cis*-[**3**]PtEt$_2$: $^2J_{C,Pcis}$ = 10.7, $^2J_{C,Ptrans}$ = 113.4 Hz). The question to be examined for the *cis*-(ligand)Pt complexes was how they behave under the thermolysis conditions employed for *cis*-(ligand)PtEt$_2$ (80–100 °C, ethene present).

*cis*-[**3***]Pt isomerizes slowly and quantitatively at 95 °C in toluene (with and without ethene) to give *trans*-[**3***]Pt ($\delta_{trans}$ = 122.1 ppm, $^1J_{Pt,P}$ = 3038.1 Hz). Variable-temperature measurements by $^1$H NMR spectroscopy between –90 °C and 100 °C in toluene indicate a dynamic process in *cis*-[**3***]-Pt [broadening of the $OCH_2$ protons and the *i*Pr groups; line shape analysis: $\Delta H^{\neq}$ = 7.6 kcal mol$^{-1}$, $\Delta S^{\neq}$ = –14.6 cal mol$^{-1}$ K$^{-1}$, coalescence point 0 °C; Figure 11 (left)]. Since no line broadening is observed in the $^{31}$P NMR spectrum we can conclude that the phosphorus atoms remain coordinated during the dynamic process, which we assign to restricted conformational change of the chelating six-membered rings.

This is supported by the X-ray structure of a molecule in the solid state (Figure 12, Table 6). P1, P2, Pt1, C6, and C7 are almost in one plane in *cis*-[**3***]Pt and the P–Pt–P angle is 105° (larger than 90°). The distance between the "cleaved" C atoms C6 and C7 is 2.8 Å and the C6–Pt–C7 angle is 85°.

The same kind of broadening is observed in the $^1$H NMR spectrum of *trans*-[**3***]Pt [broadening of the $OCH_2$ protons and the *i*Pr groups; line shape analysis: $\Delta H^{\neq}$ = 6.1 kcal mol$^{-1}$, $\Delta S^{\neq}$ = –20.5 cal mol$^{-1}$ K$^{-1}$, coalescence point 0 °C; Figure 11 (right)]. These are the only changes taking place. No back reaction to [**3**]Pt(ethene) or [**3**]Pt is found up to 150 °C in mesitylene under ethene atmosphere either for the *cis*- or for the *trans* complex.

*cis*-[**1***]Pt is slowly and quantitatively transformed into two new products when heated to 95 °C. One of these has

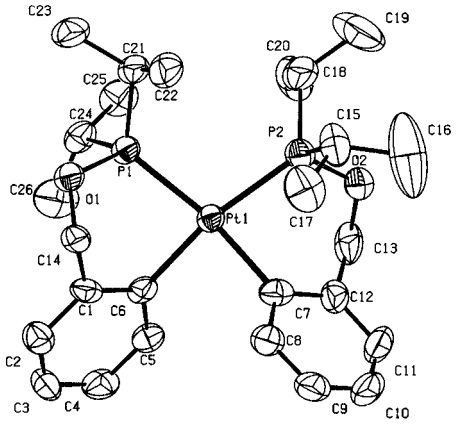


Figure 12. ORTEP style plot of the compound *cis*-[**3***]Pt in the solid. Thermal ellipsoids are drawn at the 50% probability level. Hydrogen atoms have been omitted for clarity.

Table 6. Geometric data for three (ligand)Pt compounds as determined by X-ray analysis.

| | *cis*-[**1***]Pt | *trans*-[**1***]Pt | *cis*-[**3***]Pt |
|---|---|---|---|
| Pt–P2 [Å] | 2.2756(7) | 2.2611(12) | 2.294(3) |
| Pt–P3 [Å] | 2.2726(7) | 2.2611(12) | 2.297(3) |
| Pt–C4 [Å] | 2.070(3) | 2.094(2) | 2.069(10) |
| Pt–C5 [Å] | 2.083(3) | 2.094(2) | 2.080(11) |
| $C_a$–$C_b$ (bridge) [Å] | 3.063(4) | – | 2.806(16) |
| P–Pt–P [°] | 108.44(3) | 180 | 105.0(1) |
| alk–Pt–alk [°] | 95.04(11) | 180 | 85.1(4) |

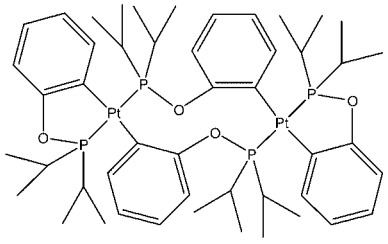


Figure 13. Proposed structure of the second product found in the course of *cis*/*trans* isomerization of *cis*-[**1***]Pt based on the $^{31}$P NMR results.

 © 2007 Wiley-VCH Verlag GmbH & Co. KGaA, Weinheim 

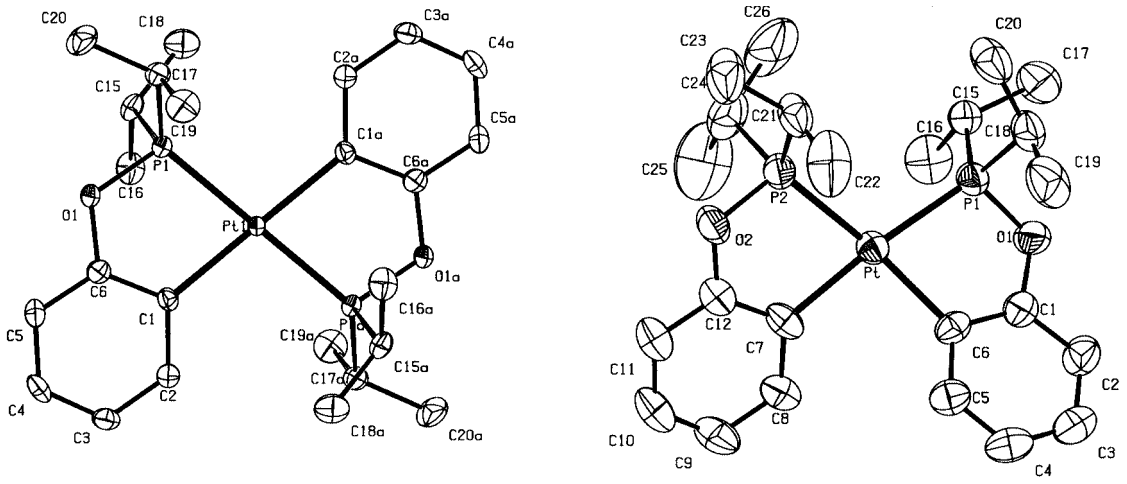


Figure 14. ORTEP style plot of the compounds *trans*-[**1***]Pt (left) and *cis*-[**1***]Pt (right) in the solid. Thermal ellipsoids are drawn at the 50% probability level. Hydrogen atoms have been omitted for clarity.

equivalent P atoms and the other one has inequivalent ones (all of them bound to Pt) and they are formed regardless of whether the reaction is performed under an atmosphere of argon or ethene. The product with equivalent P atoms is *trans*-[**1***]Pt, which was isolated and single crystals were grown from toluene solution. We assume the second product to be a *trans*-configured dimer (Figure 13), although we could not support this supposition by FAB mass spectrometry. A *trans* configuration would be in accordance with the $^1J_{P,Pt}$ coupling constants of 3073.6 and 2867.5 Hz and the $^2J_{P,P}$ coupling constant of 439.9 Hz. In this connectivity the two phenyl planes of one Pt center should be oriented perpendicular to each other and thus prevent close contacts with the *i*Pr groups.

X-ray structures of *cis*/*trans*-[**1***]Pt were determined and are shown in Figure 14 (Table 6). In contrast to *trans*-[**1***]-Pt, which is almost square planar, *cis*-[**1***]Pt is significantly distorted out of the square plane, most probably to avoid close contacts between the two *i*Pr groups and/or the two *ortho* protons in the phenyl groups. Compound **d** of Scheme 1 ([**1**]Pt(ethene)) is not observed in the course of the *cis*/*trans* isomerization, thus demonstrating that both the *cis*- and *trans*-[**1***]Pt complexes are stable or inert against a reductive elimination and should thus be observable if formed in the course of the reactions proposed in Scheme 1.

## Conclusions

We have been able to push our master plan to activate and cleave a C–C single bond in a non-strained biphenyl fragment one step further (loss of the alkene) by allowing the backbone of the chelating ligand to be more flexible, although we have still not been able to reach our final target. We have shown that loss of the alkene is not the limiting factor and we have found convincing evidence that a dynamic C–H activation of the methyl groups in the *i*Pr substituents of the chelating ligand prevents a further reaction of the 14e intermediate, especially a potential activation of the bridging C–C single bond in the biphenyl fragment of the chelating ligand. We have also proved that the potential C–C single bond activation products are stable (or inert) under the reaction conditions employed. The scrambling of deuterium into the methyl groups of the ligand in the course of thermolysis underlines the ability of the intermediate to activate less reactive bonds. Although the investigation of the dynamic C–H activation is an interesting exercise, this is not our main target. One solution to successfully finish our strategy might be to exchange the H atoms in the *i*Pr methyl groups by F atoms. Preliminary attempts in this direction have shown that the synthesis of the fluorinated ligand will be tedious and expensive. The exchange of our oxo group for a $CH_2$ might be advantageous too.[4m] Detailed DFT calculations in order to determine the C–C single bond activation barrier are also underway.

## Experimental Section

Manipulations and experiments were performed under argon using standard Schlenk techniques and/or in an argon-filled glove-box if not mentioned otherwise. Diethyl ether, pentane, acetonitrile, dichloromethane, toluene and thf were dried and degassed using a two-column drying system (MBraun) and stored under argon over molecular sieves. $CDCl_3$, [$D_8$]toluene, and [$D_5$]pyridine were stored under argon over molecular sieves. Ethene 2.7, $H_2$ 5.0, and $D_2$ 2.7 were purchased from Messer Grießheim and used as delivered. $K_2PtCl_4$ was purchased from Strem Chemicals and used without further manipulation. (1*Z*,5*Z*)-cyclooctadiene (COD), chlorodiphenylphosphane, chlorodiisopropylphosphane, 2,2′-dihydroxybiphenyl, 2,2′-biphenylmethanol, biphenic acid, *n*-propyl- and ethylmagnesium chloride (2 M in diethyl ether), $CD_3CD_2Br$, $LiAlH_4$, $LiAlD_4$, and chloroperoxobenzoic acid were purchased from Aldrich and used without further purification. [(COD)$PtCl_2$] and *trans*-[$PtCl_2$(ethene)(py)] were synthesized according to the literature.[10]

NMR spectra were recorded on a Bruker AMX400. $^1H$ ($\delta$ = 7.24 ppm, 400 MHz) and $^{13}C$ ($\delta$ = 77.0 ppm, 100 MHz) were referenced to the $CDCl_3/CHCl_3$ resonances, $^{31}P$ (161 MHz) to 85% $H_3PO_4$ as external standard, and $^{195}Pt$ ($\delta$ = –3329 ppm, 85.6 MHz) to [(COD)$PtCl_2$] as external standard. FTIR spectra were recorded

 © 2007 Wiley-VCH Verlag GmbH & Co. KGaA, Weinheim 

with a JASCO FI7IR-460plus machine using KBr pellets. Variable-temperature measurements were performed as reported previously.[3,11]

**Benzo[*c*]chromen-6-one:** Fluoren-9-one (1.0 g, 5.55 mmol) and of *m*-chloroperoxobenzoic acid (1.91 g, at least 77%/8.52 mmol) were dissolved in 12 mL of glacial acetic acid and 2 mL of conc. sulfuric acid and the mixture refluxed for 2 d. After cooling to room temperature, 200 mL of diethyl ether was added followed by a saturated sodium sulfite solution to destroy the unreacted peroxide until no more gas evolution was observed. The organic phase was then washed with a saturated sodium carbonate solution until the water phase was clear and slightly basic. The light yellow ether phase was washed with 100 mL of distilled water, dried with $MgSO_4$, and the solvent was removed in vacuo to give 0.86 g (4.38 mmol, 79%) of the pure product as a yellow solid. $^1$H NMR ($CDCl_3$): $\delta$ = 7.35 (t, $^3J_{H,H}$ = 9.8 Hz, 2 H, CH arom.), 7.49 (m, 1 H, CH arom.), 7.63 (m, 1 H, CH arom.), 7.87 (t, $^3J_{H,H}$ = 7.4 Hz, 1 H, CH arom.), 8.04 (d, $^3J_{H,H}$ = 7.4 Hz, 1 H, CH arom.), 8.11 (d, $^3J_{H,H}$ = 7.4 Hz, 1 H, CH arom.), 8.40 (d, $^3J_{H,H}$ = 9.8 Hz, 1 H, CH arom.) ppm. $^{13}$C{$^1$H} NMR ($CDCl_3$): $\delta$ = 117.8 (s, CH arom.), 118.1 (s, CH arom.), 121.3 (s, CH arom.), 121.7 (s, CH arom.), 122.8 (s, CH arom.), 124.5 (s, CH arom.), 128.9 (s, CH arom.), 130.4 (s, CH arom.), 130.6 (s, CH arom.), 134.8 (s, CH arom.), 135.6 (s, CH-arom.), 151.3 (s, CH arom.), 161.2 (s, -CO-) ppm.

**2-Hydroxy-2′-(hydroxymethyl)biphenyl:** Lithium aluminum hydride (0.58 g, 15.3 mmol) was suspended in 100 mL of diethyl ether in a 500-mL, two-necked vessel equipped with a condenser and dropping funnel and of benzo[*c*]chromen-6-one (1.0 g, 5.10 mmol) in 100 mL of diethyl ether was dropwise added while stirring. The mixture was then refluxed in a water bath for 3.5 h. After cooling to 0 °C the grey suspension was treated slowly with 100 mL of cold water, then 0.1 M aqueous HCl was added until the grey precipitate had dissolved completely. The yellow organic phase was separated and the water phase was extracted three times with 100 mL of diethyl ether. The combined organic phases were dried with $MgSO_4$ and the solvent was removed in vacuo. The light brownish solid was recrystallized from methanol. Yield: 94%. $^1$H NMR ($CDCl_3$): $\delta$ = 2.18 (br. s, 1 H, -$CH_2$-O*H*), 4.48 (s, 2 H, -C*H*$_2$-), 5.76 (br. s, 1 H, benzyl-OH), 6.97 (m, 2 H, CH arom.), 7.10 (m, 1 H, CH arom.), 7.26 (m, 2 H, CH arom.), 7.38–7.44 (m, 2 H, CH arom.), 7.53 (m, 1 H, CH arom.) ppm. $^{13}$C{$^1$H} NMR ($CDCl_3$): $\delta$ = 63.7 (s, CH arom.), 116.4 (s, CH arom.), 120.9 (s, CH arom.), 127.6 (s, CH arom.), 128.6 (s, CH arom.), 128.7 (s, CH arom.), 129.3 (s, CH arom.), 129.4 (s, CH arom.), 130.7 (s, CH arom.), 130.9 (s, CH arom.), 136.3 (s, CH arom.), 138.9 (s, CH arom.), 152.8 (s, -CO-) ppm.

**2-(Diisopropylphosphanyloxy)-2′-[(diisopropylphosphanyl)oxymethyl]biphenyl (2):** The synthesis was performed according to our previous published procedure.[3] Colorless oil, yield: 75%. $^1$H NMR ($CDCl_3$): $\delta$ = 0.71–1.33 (m, 28 H, CHC*H*$_3$), 1.57–1.76 (m, 4 H, C*H*CH$_3$), 4.46 (m, 2 H, $CH_2$), 7.00 (d, $^3J_{H,H}$ = 7.4 Hz, 1 H, CH arom.), 7.16 (m, 2 H, CH arom.), 7.26–7.36 (m, 4 H, CH arom.), 7.58 (d, $^3J_{H,H}$ = 7.4 Hz, 1 H, CH arom.) ppm. $^{13}$C{$^1$H} NMR ($CDCl_3$): $\delta$ = 17.9 (d, $^2J_{C,P}$ = 19.6 Hz, CH*C*H$_3$), 28.0 (d, $^1J_{C,P}$ = 16.8 Hz, *C*HCH$_3$), 72.0 (d, $^2J_{C,P}$ = 21.2 Hz, $CH_2$), 117.2 (s, CH arom.), 117.4 (s, CH arom.), 121.2 (s, CH arom.), 126.6 (s, CH arom.), 126.9 (s, CH arom.), 127.1 (s, CH arom.), 130.3 (s, CH arom.), 130.9 (s, CH arom.), 137.0 (s, CH arom.), 138.3 (d, $^3J_{C,P}$ = 8.8 Hz, *C*-$CH_2$OP), 155.8 (d, $^2J_{C,P}$ = 8.1 Hz, COP) ppm. $^{31}$P{$^1$H} NMR ($CDCl_3$): $\delta$ = 155.0 (s), 158.3 (s) ppm.

**2,2′-Bis[(diisopropylphosphanyl)oxymethyl]biphenyl (3):** The synthesis was performed according to our previous published procedure.[3] Clear oily liquid, yield: 70%. $^1$H NMR ($CDCl_3$): $\delta$ = 0.91–1.04 (m, 28 H, CHC*H*$_3$), 1.68 (sept, $^2J_{H,H}$ = 7.4 Hz, 4 H, CHCH$_3$), 4.42 (d, $^2J_{H,H}$ = 12.3 Hz, 1 H, -$CH_2$-), 4.47 (d, $^2J_{H,H}$ = 12.3 Hz, 1 H, -$CH_2$-), 7.14 (d, $^3J_{H,H}$ = 7.3 Hz, 2 H, 1 H, CH arom.), 7.29 (d, $^3J_{H,H}$ = 7.3 Hz, 1 H, CH-arom.), 7.31 (d, $^3J_{H,H}$ = 7.4 Hz, 1 H, CH arom.), 7.36 (d, $^3J_{H,H}$ = 7.3 Hz, 1 H, CH arom.), 7.38 (d, $^3J_{H,H}$ = 7.4 Hz, 1 H, CH arom.), 7.57 (d, $^3J_{H,H}$ = 7.3 Hz, 2 H, CH arom.) ppm. $^{13}$C{$^1$H} NMR ($CDCl_3$): $\delta$ = 16.9 (d, $^2J_{C,P}$ = 8.1 Hz, CH*C*H$_3$), 17.0 (d, $^2J_{C,P}$ = 8.8 Hz, CH*C*H$_3$), 17.7 (d, $^2J_{C,P}$ = 6.6 Hz, CH*C*H$_3$), 17.9 (d, $^2J_{C,P}$ = 6.6 Hz, CH*C*H$_3$), 27.9 (d, $^2J_{C,P}$ = 16.1 Hz, *C*HCH$_3$), 28.1 (d, $^2J_{C,P}$ = 16.1 Hz, *C*HCH$_3$), 71.9 (d, $^2J_{C,P}$ = 20.5 Hz, $CH_2$OP), 127.0 (s, CH arom.), 127.6 (s, CH arom.), 128.1 (s, CH arom.), 129.6 (s, CH arom.), 137.3 (d, $^3J_{C,P}$ = 8.8 Hz, *C*-$CH_2$-O), 138.8 (s, CH arom.) ppm. $^{31}$P{$^1$H} NMR ($CDCl_3$): $\delta$ = 154, 4 (s) ppm.

**Synthesis of the Dichloridodiphosphinite Complexes. General Procedure for the Synthesis of the Complexes [Y]PtCl$_2$ (Y = 2, 3):** A solution of 0.3 mmol of ligand Y in 5 mL of dichloromethane was added with a syringe to a suspension of 0.3 mmol of precursor in 20 mL of dichloromethane. The mixture was stirred overnight at room temperature and the solvent was then removed in vacuo. The white to light-yellow residue was washed with 10 mL of pentane (in some cases additionally with 4 mL of diethyl ether) and dried for 2 h in vacuo. Recrystallization from dichloromethane was necessary to give analytically pure material.

***cis*-[2]PtCl$_2$:** Light-yellow powder, yield: 70%. $^1$H NMR ($CDCl_3$): $\delta$ = 0.63 (d, $^3J_{H,H}$ = 7.8 Hz, 3 H, CHC*H*$_3$), 0.65 (d, $^3J_{H,H}$ = 6.9 Hz, 3 H, CHC*H*$_3$), 0.88 (d, $^3J_{H,H}$ = 7.8 Hz, 3 H, CHC*H*$_3$), 0.92 (d, $^3J_{H,H}$ = 6.8 Hz, 3 H, CHC*H*$_3$), 0.98 (d, $^3J_{H,H}$ = 6.9 Hz, 3 H, CHC*H*$_3$), 1.06 (d, $^3J_{H,H}$ = 7.8 Hz, 3 H, CHC*H*$_3$), 1.45 (d, $^3J_{H,H}$ = 6.9 Hz, 3 H, CHC*H*$_3$), 1.48 (d, $^3J_{H,H}$ = 7.8 Hz, 3 H, CHC*H*$_3$), 2.51 (m, 1 H, C*H*CH$_3$), 2.60 (m, 1 H, C*H*CH$_3$), 2.75 (m, 1 H, C*H*CH$_3$), 3.46 (m, 1 H, C*H*CH$_3$), 4.61 (d, $^3J_{H,H}$ = 8.8 Hz, 1 H, -$CH_2$-), 4.70 (d, $^3J_{H,H}$ = 6.9 Hz, 1 H, -$CH_2$-), 7.14–7.50 (m, 8 H, CH arom.) ppm. $^{13}$C{$^1$H} NMR ($CDCl_3$): $\delta$ = 16.4 (d, $^2J_{C,P}$ = 6.2 Hz, CH*C*H$_3$), 17.1 (d, $^2J_{C,P}$ = 6.2 Hz, CH*C*H$_3$), 17.8 (d, $^2J_{C,P}$ = 2.5 Hz, CH*C*H$_3$), 18.7 (br. d, $^2J_{C,P}$ = 13.3 Hz, CH*C*H$_3$), 19.5 (br.s, CH*C*H$_3$), 20.4 (d, $^2J_{C,P}$ = 3.7 Hz, CH*C*H$_3$), 28.6 (d, $^2J_{C,P}$ = 32.1 Hz, *C*HCH$_3$), 31.0 (d, $^2J_{C,P}$ = 35.7 Hz, *C*HCH$_3$), 31.8 (d, $^2J_{C,P}$ = 35.8 Hz, *C*HCH$_3$), 34.2 (d, $^2J_{C,P}$ = 43.2 Hz, *C*HCH$_3$), 69.2 (d, $^1J_{C,P}$ = 13.6 Hz, $CH_2$), 119.3 (d, $^4J_{C,P}$ = 6.2 Hz, *C*HCCH$_2$), 123.3 (s, CH arom.), 128.1 (s, CH arom.), 129.4 (s, CH arom.), 129.5 (s, CH arom.), 129.8 (s, CH arom.), 130.3 (s, CH arom.), 132.1 (d, $^3J_{C,P}$ = 6.2 Hz, *C*HCOP), 134.1 (d, $^4J_{C,P}$ = 6.2 Hz, *C*HCCH$_2$), 139.6 (s, CH arom.), 151.9 (d, $^3J_{C,P}$ = 8.6 Hz, C-O-P) ppm. $^{31}$P{$^1$H} NMR ($CDCl_3$): $\delta$ = 112.5 (pseudo t, $^1J_{P,Pt}$ = 4099.0, $^2J_{P,P}$ = 5.0 Hz), 110.5 (pseudo t, $^1J_{P,Pt}$ = 4149.6, $^2J_{P,P}$ = 5.0 Hz) ppm. $^{195}$Pt{$^1$H} NMR ($CDCl_3$): $\delta$ = –4116.8 (dd, $^1J_{P,Pt}$ = 4099.0, 4149.6 Hz) ppm. $C_{25}H_{38}Cl_2O_2P_2Pt$ (698.50): calcd. C 42.99, H 5.48, Cl 10.15, P 8.87; found C 43.07, H 5.55, Cl 9.78, P 8.05.

**Crystal-Structure Analysis of *cis*-[2]PtCl$_2$·2(CHCl$_3$):** $C_{27}H_{40}Cl_8O_2P_2Pt$, $M_r$ = 937.26, colorless fragment ($0.06 \times 0.18 \times 0.12$ mm$^3$), monoclinic, $P2_1/c$ (no. 14), $a$ = 9.9002(1), $b$ = 17.7053(2), $c$ = 21.2118(3) Å, $\beta$ = 100.9809(5)°, $V$ = 3650.06(8) Å$^3$, $Z$ = 4, $D_{calc}$ = 1.706 g cm$^{-3}$, $F(000)$ = 1848, $\mu$ = 4.542 mm$^{-1}$. Preliminary examination and data collection were carried out on a κ-CCD device (Nonius, Mach3) with an Oxford Cryosystems cooling system at the window of a rotating anode (Nonius FR591) with graphite-monochromated Mo-$K_\alpha$ radiation ($\lambda$ = 0.71073 Å). Data collection was performed at 173 K within the $\Theta$ range $1.51° < \Theta < 25.36°$. A total of 44141 intensities were integrated. Raw data were corrected for Lorentz, polarization, and

 © 2007 Wiley-VCH Verlag GmbH & Co. KGaA, Weinheim 

latent decay and absorption effects arising from the scaling procedure. After merging ($R_{int}$ = 0.0429), 6670 [5689: $I_0 > 2\sigma(I_0)$] independent reflections remained and all were used to refine 369 parameters. The structure was solved by a combination of direct methods and difference-Fourier syntheses. All non-hydrogen atoms were refined with anisotropic displacement parameters. All hydrogen atoms were placed in calculated positions and refined using a riding model. Full-matrix least-squares refinements were carried out by minimizing $\Sigma w(F_o^2 - F_c^2)^2$ and converged with $R1$ = 0.0380 [$I_0 > 2\sigma(I_0)$], $wR2$ = 0.0702 (all data), GOF = 1.162, and shift/error < 0.001. The final difference-Fourier map showed no striking features ($\Delta e_{min/max}$ = +1.01/–1.02 e Å$^{-3}$). CCDC-613907.

***cis*-[3]PtCl$_2$:** White powder, yield: 83%. $^1$H NMR ($CDCl_3$): $\delta$ = 0.91 (d, $^3J_{H,H}$ = 7.3 Hz, 3 H, CHC*H*$_3$), 0.95 (d, $^3J_{H,H}$ = 4.9 Hz, 3 H, CHC*H*$_3$), 1.22 (d, $^3J_{H,H}$ = 7.4 Hz, 3 H, CHC*H*$_3$), 1.26 (d, $^3J_{H,H}$ = 7.3 Hz, 3 H, CHC*H*$_3$), 1.32 (d, $^3J_{H,H}$ = 7.4 Hz, 3 H, CHC*H*$_3$), 1.35 (d, $^3J_{H,H}$ = 4.9 Hz, 3 H, CHC*H*$_3$), 1.57 (d, $^3J_{H,H}$ = 7.4 Hz, 3 H, CHC*H*$_3$), 1.62 (d, $^3J_{H,H}$ = 7.4 Hz, 3 H, CHC*H*$_3$), 2.27 (m, 2 H, C*H*CH$_3$), 3.48 (m, 2 H, C*H*CH$_3$), 4.37 (d, $^3J_{H,H}$ = 9.8 Hz, 2 H, CH$_2$), 4.81 (d, $^3J_{H,H}$ = 9.8 Hz, 2 H, CH$_2$), 7.14 (d, $^3J_{H,H}$ = 7.3 Hz, 2 H, CH arom.), 7.21–7.32 (m, 4 H, CH arom.), 7.35 (d, $^3J_{H,H}$ = 7.4 Hz, 2 H, CH arom.) ppm. $^{13}$C{$^1$H} NMR ($CDCl_3$): $\delta$ = 17.2 (br. s, CH*C*H$_3$), 17.8 (br. s, CH*C*H$_3$), 18.8 (s, CH*C*H$_3$), 19.2 (s, CH*C*H$_3$), 26.1 (d, $^1J_{C,P}$ = 30.7 Hz, *C*HCH$_3$), 30.2 (d, $^1J_{C,P}$ = 41.7 Hz, *C*HCH$_3$), 68.0 (d, $^2J_{C,P}$ = 13.2 Hz, -CH$_2$-), 128.6 (s, CH arom.), 129.1 (s, CH arom.), 130.4 (s, CH arom.), 134.2 (pseudo t, $^4J_{C,P}$ = 4.4 Hz, *C*CH$_2$OP), 140.2 (s, CH arom.) ppm. $^{31}$P{$^1$H} NMR ($CDCl_3$): $\delta$ = 115.7 (br. pseudo t, $^1J_{P,Pt}$ = 4267.2 Hz) ppm. $^{195}$Pt{$^1$H} NMR ($CDCl_3$): $\delta$ = –4223.4 (t, $^1J_{P,Pt}$ = 4267.2 Hz) ppm. $C_{26}H_{40}Cl_2O_2P_2Pt$ (712.52): calcd. C 43.83, H 5.66, Cl 8.69, P 9.95; found C 43.71, H 5.69, Cl 8.40, P 9.95.

**Crystal-Structure Analysis of *cis*-[3]PtCl$_2$·3(CHCl$_3$):** $C_{29}H_{43}Cl_{11}O_2P_2Pt$, $M_r$ = 1070.66, colorless fragment (0.18 × 0.21 × 0.33 mm$^3$), monoclinic, *C*2/*c* (no. 15), *a* = 32.6825(2), *b* = 19.3448(2), *c* = 21.0863(2) Å, $\beta$ = 120.9619(4)°, *V* = 11431.91(18) Å$^3$, *Z* = 8, $D_{calc}$ = 1.658 g cm$^{-3}$, *F*(000) = 5640, $\mu$ = 4.352 mm$^{-1}$. Preliminary examination and data collection were carried out on a κ-CCD device (Nonius, Mach3) with an Oxford Cryosystems cooling system at the window of a rotating anode (Nonius FR591) with graphite-monochromated Mo-$K_\alpha$ radiation ($\lambda$ = 0.71073 Å). Data collection was performed at 173 K within the $\Theta$ range 1.28° < $\Theta$ < 23.27°. A total of 37465 intensities were integrated. Raw data were corrected for Lorentz, polarization, and latent decay and absorption effects arising from the scaling procedure. After merging ($R_{int}$ = 0.0437), 8197 [6947: $I_0 > 2\sigma(I_0)$] independent reflections remained and all were used to refine 247 parameters. The structure was solved by a combination of direct methods and difference-Fourier syntheses. All non-hydrogen atoms were refined with anisotropic displacement parameters. All hydrogen atoms were placed in calculated positions and refined using a riding model. Full-matrix least-squares refinements were carried out by minimizing $\Sigma w(F_o^2 - F_c^2)^2$ and converged with $R1$ = 0.0405 [$I_0 > 2\sigma(I_0)$], $wR2$ = 0.0783 (all data), GOF = 1.089, and shift/error < 0.001. The final difference-Fourier map showed no striking features ($\Delta e_{min/max}$ = +0.85/–0.58 e Å$^{-3}$). CCDC-613913.

***trans*-[2]PtCl$_2$:** Light-yellow powder, yield: 59%. $^1$H NMR ($CDCl_3$): $\delta$ = 1.04 (d, $^3J_{H,H}$ = 7.4 Hz, 3 H, CHC*H*$_3$), 1.09 (d, $^3J_{H,H}$ = 7.4 Hz, 3 H, CHC*H*$_3$), 1.15–1.25 (m, 6 H, CHC*H*$_3$), 1.31 (pseudo t, $^3J_{H,H}$ = 7.4 Hz, 6 H, CHC*H*$_3$), 1.47 (d, $^3J_{H,H}$ = 7.4 Hz, 3 H, CHC*H*$_3$), 1.50 (d, $^3J_{H,H}$ = 12.3 Hz, 3 H, CHC*H*$_3$), 2.90 (m, 3 H, C*H*CH$_3$), 3.23 (s, $^3J_{H,H}$ = 7.4 Hz, 1 H, C*H*CH$_3$), 4.89 (dd, $^3J_{P,H}$ = 27.0, $^2J_{H,H}$ = 12.3 Hz, 1 H, CH$_2$), 5.35 (dd, $^3J_{P,H}$ = 7.4, $^2J_{H,H}$ = 12.3 Hz, 1 H, -CH$_2$-), 6.87 (d, $^3J_{H,H}$ = 7.4 Hz, 1 H, CH arom.), 7.00 (d, $^3J_{H,H}$ = 9.8 Hz, 1 H, CH arom.), 7.11 (pseudo t, $^3J_{H,H}$ = 7.4 Hz, 2 H, CHC*H*$_3$), 7.23 (m, 1 H, CH arom.), 7.33 (m, 2 H, CH arom.), 7.49 (d, $^3J_{H,H}$ = 7.4 Hz, 1 H, CH arom.) ppm. $^{13}$C{$^1$H} NMR ($CDCl_3$): $\delta$ = 15.8 (d, $^2J_{C,P}$ = 2.2 Hz, CH*C*H$_3$), 16.1 (s, CH*C*H$_3$), 16.3 (d, $^2J_{C,P}$ = 2.2 Hz, CH*C*H$_3$), 16.9 (d, $^2J_{C,P}$ = 5.1 Hz, CH*C*H$_3$) 17.3 (s, CH*C*H$_3$), 17.5 (s, CH*C*H$_3$), 17.6 (s, CH*C*H$_3$), 18.0 (d, $^2J_{C,P}$ = 4.4 Hz, CH*C*H$_3$), 24.6 (d, $^1J_{C,P}$ = 23.4 Hz, *C*HCH$_3$), 24.9 (d, $^1J_{C,P}$ = 31.5 Hz, *C*HCH$_3$), 25.1 (d, $^1J_{C,P}$ = 27.2 Hz, *C*HCH$_3$), 25.6 (d, $^1J_{C,P}$ = 30.7 Hz, *C*HCH$_3$), 67.7 (d, $^2J_{C,P}$ = 13.2 Hz, CH$_2$), 123.4 (s, CH arom.), 123.8 (s, CH arom.), 127.0 (s, CH arom.), 128.0 (s, CH arom.), 128.6 (s, CH arom.), 129.3 (s, CH arom.), 131.0 (s, CH arom.), 132.7 (s, CH arom.), 133.6 (s, CH arom.), 133.6 (s, CH arom.), 138.8 (s, CH arom.), 150.8 (d, $^3J_{C,P}$ = 7.3 Hz, C-O-P) ppm. $^{31}$P{$^1$H} NMR ($CDCl_3$): $\delta$ = 109.3 (d pseudo t, $^2J_{P,P}$ = 488.5 Hz, $^1J_{P,Pt}$ = 2624.9 Hz), 118.8 (d pseudo t, $^2J_{P,P}$ = 488.5, $^1J_{P,Pt}$ = 2690.7 Hz) ppm. $^{195}$Pt{$^1$H} NMR ($CDCl_3$): $\delta$ = –3805.7 ppm (dd, $^1J_{P,Pt}$ = 2624.9, $^1J_{P,Pt}$ = 2690.7 Hz). $C_{25}H_{38}Cl_2O_2P_2Pt$ (698.50): calcd. C 42.99, H 5.48, Cl 10.15, P 8.87; found C 43.15, H 5.61, Cl 9.48, P 8.10.

**Crystal-Structure Analysis of *trans*-[2]PtCl$_2$:** $C_{25}H_{38}Cl_2O_2P_2Pt$, $M_r$ = 698.50, pale-yellow plate (0.05 × 0.10 × 0.26 mm$^3$), triclinic, $P\bar{1}$ (no. 2), *a* = 10.4738(1), *b* = 16.4348(1), *c* = 17.7791(2) Å, $\alpha$ = 11.7991(5)°, $\beta$ = 100.3275(4)°, $\gamma$ = 97.7027(4)°, *V* = 2727.71(4) Å$^3$, *Z* = 4, $D_{calc}$ = 1.701 g cm$^{-3}$, *F*(000) = 1384, $\mu$ = 5.477 mm$^{-1}$. Preliminary examination and data collection were carried out on a κ-CCD device (Nonius, Mach3) with an Oxford Cryosystems cooling system at the window of a rotating anode (Nonius FR591) with graphite-monochromated Mo-$K_\alpha$ radiation ($\lambda$ = 0.71073 Å). Data collection was performed at 173 K within the $\Theta$ range 1.27° < $\Theta$ < 25.42°. A total of 62373 intensities were integrated. Raw data were corrected for Lorentz, polarization, and latent decay and absorption effects arising from the scaling procedure. After merging ($R_{int}$ = 0.0257), 10013 [8464: $I_0 > 2\sigma(I_0)$] independent reflections remained and all were used to refine 593 parameters. The structure was solved by a combination of direct methods and difference-Fourier syntheses. All non-hydrogen atoms were refined with anisotropic displacement parameters. All hydrogen atoms were placed in calculated positions and refined using a riding model. Full-matrix least-squares refinements were carried out by minimizing $\Sigma w(F_o^2 - F_c^2)^2$ and converged with $R1$ = 0.0336 [$I_0 > 2\sigma(I_0)$], $wR2$ = 0.0832 (all data), GOF = 1.132, and shift/error < 0.001. The final difference-Fourier map showed no striking features ($\Delta e_{min/max}$ = +1.32/–1.49 e Å$^{-3}$). CCDC-613904.

***trans*-[3]PtCl$_2$:** White powder, yield: 61%. $^1$H NMR ($CDCl_3$): $\delta$ = 1.18–1.27 (m, 18 H, CHC*H*$_3$), 1.36 (d, $^3J_{H,H}$ = 7.0 Hz, 3 H, CHC*H*$_3$), 1.41 (d, $^3J_{H,H}$ = 7.1 Hz, 3 H, CHC*H*$_3$), 2.90–3.05 (m, 4 H, C*H*CH$_3$), 4.83 (pseudo t, $^2J_{H,H}$ = $^3J_{P,H}$ = 8.3 Hz, 2 H, -CH$_2$-), 4.87 (pseudo t, $^2J_{H,H}$ = $^3J_{P,H}$ = 8.3 Hz, 2 H, -CH$_2$-), 5.59 (pseudo t, $^2J_{H,H}$ = $^3J_{P,H}$ = 8.3 Hz, 2 H, -CH$_2$-), 5.62 (pseudo t, $^2J_{H,H}$ = $^3J_{P,H}$ = 8.3 Hz, 2 H, -CH$_2$-), 6.96 (d, $^3J_{H,H}$ = 7.4 Hz, 2 H, CH arom.), 7.25 (m, 2 H, CH arom.), 7.38 (d, $^3J_{H,H}$ = 7.1 Hz, 1 H, CH arom.), 7.40 (d, $^3J_{H,H}$ = 7.6 Hz, 1 H, CH arom.), 7.58 (d, $^3J_{H,H}$ = 7.6 Hz, 2 H, CH arom.) ppm. $^{13}$C{$^1$H} NMR ($CDCl_3$): $\delta$ = 16.5 (s, CH*C*H$_3$), 16.9 (s, CH*C*H$_3$), 17.3 (s, CH*C*H$_3$), 17.4 (s, CH*C*H$_3$), 25.3 (d, $^1J_{C,P}$ = 35.5 Hz, *C*HCH$_3$), 25.5 (d, $^1J_{C,P}$ = 32.2 Hz, *C*HCH$_3$), 68.4 (s, -CH$_2$-), 122.7 (s, CH arom.), 126.6 (s, CH arom.), 127.7 (s, CH arom.), 129.7 (s, CH arom.), 136.9 (s, CH arom.), 137.5 (s, CH arom.) ppm. $^{31}$P{$^1$H} NMR ($CDCl_3$): $\delta$ = 118.4 (pseudo t, $^1J_{P,Pt}$ = 2627.5 Hz) ppm. $^{195}$Pt{$^1$H} NMR ($CDCl_3$): $\delta$ = –3763.1 (t, $^1J_{P,Pt}$ = 2627.5 Hz) ppm. $C_{26}H_{40}Cl_2O_2P_2Pt$ (712.53): calcd. C 43.83, H 5.66, Cl 9.95, P 8.69; found C 43.53, H 5.73, Cl 9.80, P 7.81.

 © 2007 Wiley-VCH Verlag GmbH & Co. KGaA, Weinheim 

**Crystal-Structure Analysis of *trans*-[3]PtCl$_2$:** $C_{26}H_{40}Cl_2O_2P_2Pt$, $M_r$ = 712.53, pale-yellow plate (0.15 × 0.21 × 0.46 mm$^3$), monoclinic, $P2_1/n$ (no. 14), $a$ = 14.8880(2), $b$ = 11.2034(2), $c$ = 17.3298(2) Å, $\beta$ = 94.4762(9)°, $V$ = 2881.73(7) Å$^3$, $Z$ = 4, $D_{calc}$ = 1.698 g cm$^{-3}$, $F(000)$ = 1464, $\mu$ = 5.190 mm$^{-1}$. Preliminary examination and data collection were carried out on a κ-CCD device (Nonius, Mach3) with an Oxford Cryosystems cooling system at the window of a rotating anode (Nonius FR591) with graphite-monochromated Mo-$K_\alpha$ radiation ($\lambda$ = 0.71073 Å). Data collection was performed at 173 K within the $\Theta$ range 1.74° < $\Theta$ < 25.34°. A total of 25293 intensities were integrated. Raw data were corrected for Lorentz, polarization, and latent decay and absorption effects arising from the scaling procedure. After merging ($R_{int}$ = 0.0286), 5265 [4430: $I_0 > 2\sigma(I_0)$] independent reflections remained and all were used to refine 306 parameters. The structure was solved by a combination of direct methods and difference-Fourier syntheses. All non-hydrogen atoms were refined with anisotropic displacement parameters. All hydrogen atoms were placed in calculated positions and refined using a riding model. Full-matrix least-squares refinements were carried out by minimizing $\Sigma w(F_o^2 - F_c^2)^2$ and converged with $R1$ = 0.0301 [$I_0 > 2\sigma(I_0)$], $wR2$ = 0.0750 (all data), GOF = 1.042, and shift/error < 0.001. The final difference-Fourier map showed no striking features ($\Delta e_{min/max}$ = +0.72/–1.39 e Å$^{-3}$). CCDC-613906.

**Synthesis of the Dialkyldiphosphinite Complexes. General Procedure for the Synthesis of the Complexes [Y]PtR′$_2$ (Y = 1, 1′, 2, 3; R′ = Alkyl):** The dichlorido complex (0.15 mmol) was suspended in 10 mL of diethyl ether and cooled to –78 °C. Then, 0.45 mmol of Alkyl-Grignard were added while stirring and it was warmed up to room temperature overnight. The next day, 0.45 mmol of 1,4-dioxane were added, the white residue was filtered through alumina and washed with 10 mL of diethyl ether. The solvent was removed from the ether extracts in vacuo and the resulting solid was dried in vacuo for two hours.

***cis*-[1]Pt(*n*Pr)$_2$:** White powder, yield: 62%. $^1$H NMR ($CDCl_3$): $\delta$ = 0.60 (d, $^2J_{H,H}$ = 7.4 Hz, 3 H, CHC$H_3$), 0.64 (d, $^2J_{H,H}$ = 7.3 Hz, 3 H, CHC$H_3$), 0.87 (d, $^2J_{H,H}$ = 7.4 Hz, 3 H, CHC$H_3$), 0.90 (d, $^2J_{H,H}$ = 4.9 Hz, 3 H, CHC$H_3$), 0.86–1.13 (m, 10 H, C$H_2$C$H_3$), 1.13–1.38 (m, 12 H, C$H_2$C$H_3$, CHC$H_3$), 2.06 (m, 2 H, C$H$CH$_3$), 2.66 (m, 2 H, C$H$CH$_3$), 7.01 (d, $^2J_{H,H}$ = 7.4 Hz, 2 H, CH arom.), 7.09 (t, $^2J_{H,H}$ = 7.4 Hz, 2 H, CH arom.), 7.21–7.26 (m, 4 H, CH arom.) ppm. $^{13}$C{$^1$H} NMR ($CDCl_3$): $\delta$ = 15.5 [s, Pt(CH$_2$)$_2$C$H_3$], 17.8 (s, $^2J_{C,Pt}$ = 11.7 Hz, PCH$_2$C$H_3$), 18.6 (s, $^2J_{C,Pt}$ = 11.7 Hz, PCH$_2$C$H_3$), 24.1 (dd, $^2J_{C,P\text{-}cis}$ = 10.3, $^2J_{C,P\text{-}trans}$ = 105.4, $^1J_{C,Pt}$ = 642.6 Hz, Pt$C$H$_2$), 25.7 (br. s, PtCH$_2$CH$_2$), 31.7 (d, $^1J_{C,P}$ = 9.5, $^1J_{C,Pt}$ = 36.6 Hz, P-$C$HCH$_3$), 31.9 (d, $^1J_{C,P}$ = 9.5, $^1J_{C,Pt}$ = 36.6 Hz, P$C$HCH$_3$), 32.2 (m, P$C$HCH$_3$), 121.3 (s, CH arom.), 123.5 (s, CH arom.), 131.5 (s, CH arom.), 132.4 (s, CH arom.), 153.3 (d, $^1J_{C,P}$ = 4.4 Hz, C-O-P), 153.3 (d, $^1J_{C,P}$ = 5.1 Hz, C-O-P) ppm. $^{31}$P{$^1$H} NMR ($CDCl_3$): $\delta$ = 153.2 (pseudo t, $^1J_{P,Pt}$ = 1983.1 Hz) ppm. $^{195}$Pt{$^1$H} NMR ([D$_8$]toluene): $\delta$ = –4561.3 (t, $^1J_{P,Pt}$ = 1983.1 Hz) ppm. $C_{30}H_{50}O_2P_2Pt$ (699.74): calcd. C 51.49, H 7.20; found C 52.05, H 7.12.

**Crystal-Structure Analysis of *cis*-[1]Pt(*n*Pr)$_2$:** $C_{30}H_{50}O_2P_2Pt$, $M_r$ = 699.74, colorless needle (0.06 × 0.08 × 0.18 mm$^3$), monoclinic, $C2/c$ (no. 15), $a$ = 14.5639(2), $b$ = 12.4757(3), $c$ = 17.4797(3) Å, $\beta$ = 108.1046(17)°, $V$ = 3018.73(10) Å$^3$, $Z$ = 4, $D_{calc}$ = 1.540 g cm$^{-3}$, $F(000)$ = 1416, $\mu$ = 4.778 mm$^{-1}$. Preliminary examination and data collection were carried out on a κ-CCD device (Nonius, Mach3) with an Oxford Cryosystems cooling system at the window of a rotating anode (Nonius FR591) with graphite-monochromated Mo-$K_\alpha$ radiation ($\lambda$ = 0.71073 Å). Data collection was performed at 173 K within the $\Theta$ range 1.00° < $\Theta$ < 25.35°. A total of 11634 intensities were integrated. Raw data were corrected for Lorentz, polarization, and latent decay and absorption effects arising from the scaling procedure. After merging ($R_{int}$ = 0.0190), 2468 [2437: $I_0 > 2\sigma(I_0)$] independent reflections remained and all were used to refine 164 parameters. The structure was solved by a combination of direct methods and difference-Fourier syntheses. All non-hydrogen atoms were refined with anisotropic displacement parameters. All hydrogen atoms were placed in calculated positions and refined using a riding model. Full-matrix least-squares refinements were carried out by minimizing $\Sigma w(F_o^2 - F_c^2)^2$ and converged with $R1$ = 0.0145 [$I_0 > 2\sigma(I_0)$], $wR2$ = 0.0364 (all data), GOF = 1.123, and shift/error < 0.001. The final difference-Fourier map showed no striking features ($\Delta e_{min/max}$ = +0.83/–0.50 e Å$^{-3}$). CCDC-613912.

***cis*-[2]PtEt$_2$:** Light-yellow powder, yield: 64%. $^1$H NMR ($CDCl_3$): $\delta$ = 0.63 (d, $^3J_{H,H}$ = 7.4 Hz, 3 H, PCHC$H_3$), 0.66 (d, $^3J_{H,H}$ = 7.4 Hz, 3 H, PCHC$H_3$), 0.77–1.51 (m, 28 H, PCHC$H_3$, PtC$H_2$C$H_3$), 2.01 (m, 1 H, C$H$CH$_3$), 2.26 (m, 1 H, C$H$CH$_3$), 2.41 (m, 1 H, C$H$CH$_3$), 2.71 (m, 1 H, C$H$CH$_3$), 4.40 (d, $^3J_{H,H}$ = 9.8 Hz, 1 H, -CH$_2$-), 4.54 (d, $^3J_{H,H}$ = 9.8 Hz, 1 H, -CH$_2$-), 6.95 (t, $^3J_{H,H}$ = 7.4 Hz, 1 H, CH arom.), 7.03 (d, $^3J_{H,H}$ = 7.4 Hz, 1 H CH arom.), 7.10 (d, $^3J_{H,H}$ = 7.4 Hz, 1 H, CH arom.), 7.14–7.28 (m, 4 H, CH arom.), 7.35 (t, $^3J_{H,H}$ = 7.4 Hz, 1 H, CH arom.) ppm. $^{13}$C{$^1$H} NMR ($CDCl_3$): $\delta$ = 10.1 (dd pseudo t, $^2J_{C,P\text{-}trans}$ = 8.1, $^2J_{C,P\text{-}cis}$ = 110.5, $^1J_{C,Pt}$ = 481.2 Hz, CH$C$H$_3$), 14.0 (dd pseudo t, $^2J_{C,P\text{-}trans}$ = 6.6, $^2J_{C,P\text{-}cis}$ = 110.5, $^1J_{C,Pt}$ = 553.9 Hz, CH$C$H$_3$), 15.5 (d pseudo t, $^3J_{C,P}$ = 6.6, $^2J_{C,Pt}$ = 36.9 Hz, PtCH$_2$C$H_3$), 15.5 (d pseudo t, $^3J_{C,P}$ = 6.6, $^2J_{C,Pt}$ = 38.0 Hz, PtCH$_2$C$H_3$), 16.7 (s, CH$C$H$_3$), 16.8 (s, CH$C$H$_3$), 17.8 (br. s, CH$C$H$_3$), 18.3 (br. s, CH$C$H$_3$), 18.7 (pseudo t, $^3J_{C,P}$ = 10.2 Hz, CH$C$H$_3$), 19.8 (pseudo t, $^3J_{C,P}$ = 9.8 Hz, CH$C$H$_3$), 27.1 (d, $^1J_{C,P}$ = 13.2 Hz, $C$HCH$_3$), 28.2 (d, $^1J_{C,P}$ = 15.4 Hz, $C$HCH$_3$), 29.4 (d, $^1J_{C,P}$ = 43.2 Hz, $C$HCH$_3$), 33.9 (d, $^1J_{C,P}$ = 28.5 Hz, $C$HCH$_3$), 67.1 (d, $^2J_{C,P}$ = 6.6 Hz,CH$_2$), 119.3 (d, $^3J_{C,P}$ = 6.6 Hz, $C$CCH$_2$OP.), 120.9 (s, CH arom.), 127.2 (s, CH arom.), 128.2 (s, CH arom.), 128.6 (s, CH arom.), 128.8 (s, CH arom.), 128.9 (s, CH arom.), 130.3 (s, CH arom.), 132.8 (d, $^3J_{C,P}$ = 3.7 Hz, $C$COP.), 136.4 (d, $^3J_{C,P}$ = 6.6 Hz, $C$CH$_2$OP), 140.7 (s, CH arom.), 154.2 (d, $^2J_{C,P}$ = 3.7 Hz, COP) ppm. $^{31}$P{$^1$H} NMR ($CDCl_3$): $\delta$ = 135.0 (d pseudo t, $^2J_{P,P}$ = 17.8, $^1J_{P,Pt}$ = 2008.0 Hz), 110.5 (d pseudo t, $^2J_{P,P}$ = 17.8, $^1J_{P,Pt}$ = 1894.2 Hz) ppm. $^{195}$Pt{$^1$H} NMR ([D$_8$]toluene): $\delta$ = –4456.0 (dd, $^1J_{P,Pt}$ = 1894.2, $^1J_{P,Pt}$ = 2008.0 Hz) ppm. $C_{29}H_{48}O_2P_2Pt$ (685.72): calcd. C 50.80, H 7.06; found C 50.94, H 7.20.

***cis*-[3]PtEt$_2$:** White powder, yield: 66%. $^1$H NMR ($CDCl_3$): $\delta$ = 0.71 (d, $^3J_{H,H}$ = 7.4 Hz, 3 H, CHC$H_3$), 0.75 (d, $^3J_{H,H}$ = 7.4 Hz, 3 H, CHC$H_3$), 0.80–1.12 (m, 14 H, CHC$H_3$, -C$H_2$-C$H_3$), 1.31 (d, $^3J_{H,H}$ = 7.3 Hz, 3 H, CHC$H_3$), 1.33 (d, $^3J_{H,H}$ = 4.9 Hz, 3 H, CHC$H_3$), 1.40 (d, $^3J_{H,H}$ = 4.9 Hz, 3 H, CHC$H_3$), 1.44 (d, $^3J_{H,H}$ = 7.4 Hz, 3 H, CHC$H_3$), 2.27 (m, 2 H, C$H$CH$_3$), 2.53 (m, 2 H, C$H$CH$_3$), 4.33 (d, $^3J_{H,H}$ = 9.8 Hz, 2 H, CH$_2$), 4.61 (d, $^3J_{H,H}$ = 9.8 Hz, 2 H, CH$_2$), 7.08 (d, $^3J_{H,H}$ = 9.8 Hz, 2 H, CH arom.), 7.32 (t, $^3J_{H,H}$ = 7.4 Hz, 2 H, CH arom.), 7.37 (t, $^3J_{H,H}$ = 7.4 Hz, 2 H, CH arom.), 7.50 (d, $^3J_{H,H}$ = 9.8 Hz, 2 H, CH arom.) ppm. $^{13}$C{$^1$H} NMR ($CDCl_3$): $\delta$ = 12.8 (dd pseudo t, $^2J_{C,P\text{-}cis}$ = 10.7, $^2J_{C,P\text{-}trans}$ = 113.4, $^1J_{C,Pt}$ = 626.4 Hz, Pt-$C$H$_2$CH$_3$), 15.3 (pseudo t, $^2J_{C,Pt}$ = 5.8 Hz, PtCH$C$H$_3$), 17.5 (pseudo t, $^2J_{C,Pt}$ = 5.8 Hz, PCH$C$H$_3$), 18.3 (pseudo t, $^3J_{C,Pt}$ = 5.8 Hz, PCH$C$H$_3$), 19.0 (d, $^2J_{C,Pt}$ = 7.4 Hz, PCH$C$H$_3$), 19.1 (d, $^2J_{C,Pt}$ = 6.6 Hz, PCH$C$H$_3$), 19.4 (br.s, PCH$_2$C$H_3$) 26.0 (pseudo t, $^1J_{C,P}$ = 7.3, $^2J_{C,Pt}$ = 36.1 Hz, $C$HCH$_3$), 26.9 (d pseudo t, $^1J_{C,P}$ = 10.0, $^2J_{C,Pt}$ = 47.2 Hz, $C$HCH$_3$), 27.0 (d pseudo t, $^1J_{C,P}$ = 9.5, $^2J_{C,Pt}$ = 47.3 Hz, $C$HCH$_3$), 68.3 (d, $^2J_{C,P}$ = 6.6 Hz, -CH$_2$-), 66.5 (d, $^2J_{C,P}$ = 7.3 Hz, -CH$_2$-), 127.9 (s, CH arom.), 128.0 (s, CH arom.), 129.6 (s, CH arom.), 130.6 (s, CH arom.), 136.4 (pseudo t, $^3J_{C,P}$ = 3.7 Hz, CH$_2$OP), 136.5 (pseudo t, $^3J_{C,P}$ = 2.9 Hz, CH$_2$OP), 140.6 (s) ppm.

 © 2007 Wiley-VCH Verlag GmbH & Co. KGaA, Weinheim 

$^{31}P\{^1H\}$ NMR ($CDCl_3$): $\delta$ = 133.6 (pseudo t, $^1J_{P,Pt}$ = 2099.9 Hz) ppm. $^{195}Pt\{^1H\}$ NMR ($CDCl_3$): $\delta$ = –4633.4 (t, $^1J_{P,Pt}$ = 2099.9 Hz) ppm. MS (FAB): *m*/*z* (%) 641.3 (100) [M – (ethane + ethene)] (with correct isotope pattern for $C_{26}H_{40}O_2P_2Pt$). $C_{30}H_{50}O_2P_2Pt$: calcd. C 51.49, H 7.20; found C 51.35, H 7.23.

**Crystal-Structure Analysis of *cis*-[3]PtEt$_2$:** $C_{30}H_{50}O_2P_2Pt$, $M_r$ = 699.74, colorless needle (0.10 × 0.12 × 0.33 mm$^3$), monoclinic, *P*2/c (no. 13), $a$ = 15.3987(1), $b$ = 12.8649(1), $c$ = 16.8436(2) Å, $\beta$ = 112.0657(4)°, $V$ = 3092.36(5) Å$^3$, $Z$ = 4, $D_{calc}$ = 1.503 g cm$^{-3}$, $F$(000) = 1416, $\mu$ = 4.665 mm$^{-1}$. Preliminary examination and data collection were carried out on a κ-CCD device (Nonius, Mach3) with an Oxford Cryosystems cooling system at the window of a rotating anode (Nonius FR591) with graphite-monochromated Mo-$K_\alpha$ radiation ($\lambda$ = 0.71073 Å). Data collection was performed at 173 K within the $\Theta$ range 1.43° < $\Theta$ < 23.35°. A total of 37465 intensities were integrated. Raw data were corrected for Lorentz, polarization, and latent decay and absorption effects arising from the scaling procedure. After merging ($R_{int}$ = 0.0167), 5676 [5124: $I_0 > 2\sigma(I_0)$] independent reflections remained and all were used to refine 322 parameters. The structure was solved by a combination of direct methods and difference-Fourier syntheses. All non-hydrogen atoms were refined with anisotropic displacement parameters. All hydrogen atoms were placed in calculated positions and refined using a riding model. Full-matrix least-squares refinements were carried out by minimizing $\Sigma w(F_o^2 - F_c^2)^2$ and converged with $R1$ = 0.0204 [$I_0 > 2\sigma(I_0)$], $wR2$ = 0.0451 (all data), GOF = 1.061, and shift/error < 0.001. The final difference-Fourier map showed no striking features ($\Delta e_{min/max}$ = +0.82/–1.14 e Å$^{-3}$). CCDC-613908.

***cis*-[1′]Pt(*n*Pr)$_2$:** White powder, yield: 64%. $^1H$ NMR ([D$_8$]toluene): $\delta$ = 0.63 (br. t, $^3J_{H,H}$ = 7.4 Hz, 6 H, $CH_3$), 0.97 (m, 4 H, C$H_2$CH$_3$), 1.18 (m, 4 H, PtC$H_2$), 6.69 (d, $^3J_{H,H}$ = 7.4 Hz, 2 H, biphenyl-CH), 6.83 (d, $^3J_{H,H}$ = 7.4 Hz, 2 H, biphenyl-CH), 6.89 (t, $^3J_{H,H}$ = 7.4 Hz, 2 H, biphenyl-CH), 7.12 (t, $^3J_{H,H}$ = 7.4 Hz, 6 H, CH arom.), 7.24-7.33 (m, 16 H, CH-arom.) ppm. $^{13}C\{^1H\}$ NMR ([D$_8$]toluene): $\delta$ = 4.6 (br. s, $CH_3$), 15.6 (s, $^3J_{C,P}$ = 2.9, $^2J_{C,Pt}$ = 41.7 Hz, *C*H$_2$CH$_3$), 23.9 (m pseudo t, $^1J_{C,Pt}$ = 501.3 Hz, PtCH$_2$), 130.9 (s), 131.1 (s), 131.2 (s), 131.3 (s), 131.3 (s), 131.4 (s), 131.7 (s), 131.8 (s), 131.9 (s), 132.0 (s), 132.3 (s), 132.3 (s), 132.6 (s), 132.7 (s), 132.8 (s), 133.5 (s), 140.7 (br. s), 153.3 (pseudo t, $^3J_{C,P}$ = 4.4 Hz, COP) ppm. $^{31}P\{^1H\}$ NMR ([D$_8$]toluene): $\delta$ = 111.8 (pseudo t, $^1J_{P,Pt}$ = 1970.5 Hz) ppm. $^{195}Pt\{^1H\}$ NMR ([D$_8$]toluene): $\delta$ = –4526.1 (t, $^1J_{P,Pt}$ = 1970.5 Hz) ppm.

**General Synthetic Procedure for the *trans*-[Ligand*]$^X$PtCl$_2$ Complexes:** *trans*-Dichlorido(η$^2$-ethylene)(pyridine)platinum(II) (0.27 mmol) and ligand (0.54 mmol) were dissolved in 10 mL of dichloromethane and stirred overnight at room temperature. After removing the solvent in vacuo the residue was washed with diethyl ether and dried in vacuo.

***trans*-[1*]$^I$PtCl$_2$:** Light-yellow powder. Yield: 92%. $^1H$ NMR ($CDCl_3$): $\delta$ = 1.35 (d, $^3J_{H,H}$ = 7.8 Hz, 3 H, CHC$H_3$), 1.37 (d, $^3J_{H,H}$ = 8.8 Hz, 6 H, CHC$H_3$), 1.39 (d, $^3J_{H,H}$ = 7.8 Hz, 6 H, CHC$H_3$), 1.41 (d, $^3J_{H,H}$ = 8.1 Hz, 6 H, CHC$H_3$), 1.43 (d, $^3J_{H,H}$ = 7.6 Hz, 3 H, CHC$H_3$), 2.92–3.01 (m, 4 H, C*H*CH$_3$), 6.74–6.78 (m, 2 H, CH arom.), 7.20–7.24 (m, 2 H, CH arom.), 7.70 (m, 2 H, CH arom.), 7.89 (d, $^3J_{H,H}$ = 8.1 Hz, 2 H, CH arom.) ppm. $^{13}C\{^1H\}$ NMR ($CDCl_3$): $\delta$ = 17.5 (s, CH*C*H$_3$), 18.3 (s, CH*C*H$_3$), 28.3 (pseudo t, $^1J_{C,P}$ = 16.8 Hz, *C*HCH$_3$), 89.0 (s, C–I), 120.1 (s, CH arom.), 124.8 (s, CH arom.), 128.7 (s, CH arom.), 139.6 (s, CH arom.), 154.4 (s, CH arom.) ppm. $^{31}P\{^1H\}$ NMR ($CDCl_3$): $\delta$ = 128.3 (s, $^1J_{P,Pt}$ = 2631.6 Hz) ppm. $^{195}Pt\{^1H\}$ NMR ($CDCl_3$): $\delta$ = –3796.8 (t, $^1J_{P,Pt}$ = 2631.6 Hz) ppm. $C_{24}H_{36}Cl_2I_2O_2P_2Pt$ (938.27): calcd. C 30.72, H 3.87, Cl 7.56, P 6.60; found C 30.85, H 3.95, Cl 7.92, P 6.62.

**Crystal-Structure Analysis of *trans*-[1*]$^I$PtCl$_2$:** $C_{24}H_{36}Cl_2I_2O_2P_2Pt$, $M_r$ = 938.27, colorless needle (0.11 × 0.12 × 0.19 mm$^3$), monoclinic, $P2_1/n$ (no. 14), $a$ = 8.0215(1), $b$ = 12.6774(2), $c$ = 16.6598(3) Å, $\beta$ = 94.9889(7)°, $V$ = 1687.8(18) Å$^3$, $Z$ = 4, $D_{calc}$ = 3.692 g cm$^{-3}$, $F$(000) = 1776, $\mu$ = 12.513 mm$^{-1}$. Preliminary examination and data collection were carried out on a κ-CCD device (Nonius, Mach3) with an Oxford Cryosystems cooling system at the window of a rotating anode (Nonius FR591) with graphite-monochromated Mo-$K_\alpha$ radiation ($\lambda$ = 0.71073 Å). Data collection was performed at 173 K within the $\Theta$ range 2.02° < $\Theta$ < 25.34°. A total of 14416 intensities were integrated. Raw data were corrected for Lorentz, polarization, and latent decay and absorption effects arising from the scaling procedure. After merging ($R_{int}$ = 0.0216), 3086 [2611: $I_0 > 2\sigma(I_0)$] independent reflections remained and all were used to refine 165 parameters. The structure was solved by a combination of direct methods and difference-Fourier syntheses. All non-hydrogen atoms were refined with anisotropic displacement parameters. All hydrogen atoms were placed in calculated positions and refined using a riding model. Full-matrix least-squares refinements were carried out by minimizing $\Sigma w(F_o^2 - F_c^2)^2$ and converged with $R1$ = 0.0279 [$I_0 > 2\sigma(I_0)$], $wR2$ = 0.0793 (all data), GOF = 1.077, and shift/error < 0.001. The final difference-Fourier map showed no striking features ($\Delta e_{min/max}$ = +1.09/–0.97 e Å$^{-3}$). CCDC-613910.

***trans*-[3*]$^I$PtCl$_2$:** Light-yellow powder, yield: 90%. *trans*-Dichlorido(η$^2$-ethylene)(pyridine)platinum(II) (0.1 g, 0.27 mmol) and (2-iodobenzoxy)diisopropylphosphane (0.18 g, 0.54 mmol) were dissolved in 10 mL of dichloromethane and stirred overnight at room temperature. After stripping off the solvent in vacuo the residue was washed with 3 mL of diethyl ether and dried in vacuo. Yellow powder: 0.24 g (90%). $^1H$ NMR ($CDCl_3$): $\delta$ = 1.33 (d, $^3J_{H,H}$ = 7.4 Hz, 3 H, CHC$H_3$), 1.37 (d, $^3J_{H,H}$ = 7.4 Hz, 6 H, CHC$H_3$), 1.41 (d, $^3J_{H,H}$ = 8.6 Hz, 6 H, CHC$H_3$), 1.45 (d, $^3J_{H,H}$ = 8.6 Hz, 6 H, CHC$H_3$), 2.67–2.73 (m, 4 H, C*H*CH$_3$), 5.26 (m, 4 H, CH arom.), 6.96 (m, 2 H, CH arom.), 7.32 (t, $^3J_{H,H}$ = 7.4 Hz, 2 H, CH arom.), 7.60 (d, $^3J_{H,H}$ = 7.4 Hz, 2 H, CH arom.), 7.76 (d, $^3J_{H,H}$ = 7.4 Hz, 2 H, CH arom.) ppm. $^{13}C\{^1H\}$ NMR ($CDCl_3$): $\delta$ = 16.7 (s, CH*C*H$_3$), 17.9 (s, CH*C*H$_3$), 26.9 (d, $^1J_{C,P}$ = 17.6 Hz, *C*HCH$_3$), 27.2 (d, $^1J_{C,P}$ = 18.3 Hz, *C*HCH$_3$), 74.8 (s, CH$_2$), 96.7 (s, C–I), 128.2 (s, CH arom.), 128.5 (s, CH arom.), 129.2 (s, CH arom.), 138.8 (s, CH arom.), 140.4 (d, $J_{C,P}$ = 3.7 Hz, CH$_2$*C*), 140.5 (d, $J_{C,P}$ = 4.4 Hz, CH$_2$*C*) ppm. $^{31}P\{^1H\}$ NMR ($CDCl_3$): $\delta$ = 129.9 (pseudo t, $^1J_{P,Pt}$ = 2603.7 Hz) ppm. $^{195}Pt\{^1H\}$ NMR ($CDCl_3$): $\delta$ = –3758.9 (t, $^1J_{P,Pt}$ = 2603.7 Hz) ppm. $C_{26}H_{40}Cl_2I_2O_2P_2Pt$ (966.32): calcd. C 32.31, H 4.17, P 6.61; found C 32.24, H 4.06, P 6.14.

**General Synthetic Procedure for the *cis*-[Ligand*]$^X$PtCl$_2$ Complexes:** [(COD)PtCl$_2$] 0.27 mmol and ligand 0.54 mmol were dissolved in 10 mL of dichloromethane and stirred overnight at room temperature. After removing the solvent in vacuo the residue was washed with diethyl ether and dried in vacuo.

***cis*-[1*]$^{Br}$PtCl$_2$:** Off-white powder. Yield: 97%. $^1H$ NMR ($CDCl_3$): $\delta$ = 1.37 (dd, $^3J_{H,H}$ = 7.4, $^3J_{P,H}$ = 6.1 Hz, 12 H, CHC$H_3$), 1.55 (d, $^3J_{H,H}$ = 7.4, $^3J_{P,H}$ = 6.1 Hz, 12 H, CHC$H_3$), 3.20 (dsept, $^3J_{H,H}$ = 7.4, $^1J_{P,H}$ = 6.1 Hz, 4 H, C*H*CH$_3$), 6.85 (t, $^3J_{H,H}$ = 7.4 Hz, 2 H, CH arom.), 7.07 (t, $^3J_{H,H}$ = 7.4 Hz, 2 H, CH arom.), 7.24 (d, $^3J_{H,H}$ = 7.4 Hz, 2 H, CH arom.), 7.38 (d, $^3J_{H,H}$ = 7.4 Hz, 2 H, CH arom.) ppm. $^{13}C\{^1H\}$ NMR ($CDCl_3$): $\delta$ = 18.2 (s, CH*C*H$_3$), 19.6 (s, CH*C*H$_3$), 31.3 (d, $^1J_{C,P}$ = 33.7 Hz, *C*HCH$_3$), 113.9 (s, CH arom.), 120.2 (s, CH arom.), 124.8 (s, CH arom.), 128.1 (s, CH arom.), 134.0 (s, CH arom.), 149.7 (d, $^2J_{C,P}$ = 13.2 Hz, CH arom.) ppm. $^{31}P\{^1H\}$ NMR ($CDCl_3$): $\delta$ = 124.3 (br. pseudo t, $^1J_{P,Pt}$ = 4191.1 Hz) ppm. $^{195}Pt\{^1H\}$ NMR ($CDCl_3$): $\delta$ = –4299.7 (t, $^1J_{P,Pt}$ = 4191.4 Hz) ppm. $C_{24}H_{36}Br_2Cl_2O_2P_2Pt$ (844.28): calcd. C 34.14, H 4.30; found C 34.07, H 4.33.

 © 2007 Wiley-VCH Verlag GmbH & Co. KGaA, Weinheim 

**Crystal-Structure Analysis of *cis*-[1*]$^{Br}$PtCl$_2$·(CH$_2$Cl$_2$):** $C_{25}H_{38}Br_2Cl_4O_2P_2Pt$, $M_r$ = 1014.13, colorless needle ($0.10 \times 0.15 \times 0.22$ mm$^3$), monoclinic, $C2/c$ (no. 15), $a$ = 18.2485(9), $b$ = 14.6811(9), $c$ = 15.6006(9) Å, $\beta$ = 119.725(2)°, $V$ = 3629.6(4) Å$^3$, $Z$ = 4, $D_{calc}$ = 1.856 g cm$^{-3}$, $F(000)$ = 1968, $\mu$ = 6.621 mm$^{-1}$. Preliminary examination and data collection were carried out on a κ-CCD device (Nonius, Mach3) with an Oxford Cryosystems cooling system at the window of a rotating anode (Nonius FR591) with graphite-monochromated Mo-$K_\alpha$ radiation ($\lambda$ = 0.71073 Å). Data collection was performed at 173 K within the $\Theta$ range 1.89° < $\Theta$ < 25.38°. A total of 17358 intensities were integrated. Raw data were corrected for Lorentz, polarization, and latent decay and absorption effects arising from the scaling procedure. After merging ($R_{int}$ = 0.061), 1891 [1551: $I_0 > 2\sigma(I_0)$] independent reflections remained and all were used to refine 175 parameters. The structure was solved by a combination of direct methods and difference-Fourier syntheses. All non-hydrogen atoms were refined with anisotropic displacement parameters. All hydrogen atoms were placed in calculated positions and refined using a riding model. Full-matrix least-squares refinements were carried out by minimizing $\Sigma w(F_o^2 - F_c^2)^2$ and converged with $R1$ = 0.0751 [$I_0 > 2\sigma(I_0)$], $wR2$ = 0.1761 (all data), GOF = 1.106, and shift/error < 0.001 ($\Delta e_{min/max}$ = +1.98/–1.54 e Å$^{-3}$). CCDC-613911.

***cis*-[3*]$^{Br}$PtCl$_2$:** Off-white powder. Yield: 89%. $^1$H NMR ($CDCl_3$): $\delta$ = 1.33 (dd, $^3J_{H,H}$ = 7.4, $^3J_{P,H}$ = 6.1 Hz, 12 H, CHC$H_3$), 1.57 (d, $^3J_{H,H}$ = 7.4, $^3J_{P,H}$ = 6.1 Hz, 12 H, CHC$H_3$), 3.05 (dsept, $^3J_{H,H}$ = 7.4, $^1J_{P,H}$ = 6.1 Hz, 4 H, C$H$CH$_3$), 4.76 (d, $^3J_{P,H}$ = 4.9 Hz, 4 H, O-C$H_2$), 7.04 (t, $^3J_{H,H}$ = 7.4 Hz, 2 H, CH arom.), 7.14 (t, $^3J_{H,H}$ = 7.4 Hz, 2 H, CH arom.), 7.29 (d, $^3J_{H,H}$ = 7.4 Hz, 2 H, CH arom.), 7.36 (d, $^3J_{H,H}$ = 7.4 Hz, 2 H, CH arom.) ppm. $^{13}$C{$^1$H} NMR ($CDCl_3$): $\delta$ = 18.2 (s, CH$C$H$_3$), 19.6 (s, CH$C$H$_3$), 29.6 (d, $^1J_{C,P}$ = 4.0 Hz, $C$HCH$_3$), 68.8 (d, $^2J_{C,P}$ = 11.0 Hz, C$H_2$), 121.0 (s, CH arom.), 127.2 (s, CH arom.), 127.4 (s, CH arom.), 129.3 (s, CH arom.), 132.5 (s, CH arom.), 135.1 (s, CH arom.) ppm. $^{31}$P{$^1$H} NMR ($CDCl_3$): $\delta$ = 123.1 (s, $^1J_{P,Pt}$ = 4191.4 Hz) ppm. $^{195}$Pt{$^1$H} NMR ($CDCl_3$): $\delta$ = –4299.7 (t, $^1J_{P,Pt}$ = 4191.4 Hz) ppm. $C_{26}H_{40}Br_2Cl_2O_2P_2Pt$ (872.33): calcd. C 35.80, H 4.62; found C 35.70, H 4.71.

**General Synthetic Procedure for the [Ligand*]Pt Complexes:** The complex (ligand)$^X$PtCl$_2$ (0.27 mol) was dissolved in 20 mL of toluene and the solution was cooled with dry ice. Then 0.54 mol of *s*BuLi (1.3 M solution in benzene/hexane) was added with a syringe and the solution was stirred overnight while warming up to room temperature. The next day it was filtered and the solvent removed in vacuo. The remaining white solid was washed with three 5-mL portions of pentane and dried in vacuo.

***cis*-[1*]Pt:** White powder, yield: 85%. $^1$H NMR ($CDCl_3$): $\delta$ = 1.10 (d, $^3J_{H,H}$ = 6.84 Hz, 6 H, CHC$H_3$), 1.15 (d, $^3J_{H,H}$ = 7.8 Hz, 6 H, CHC$H_3$), 1.19 (d, $^3J_{H,H}$ = 6.84 Hz, 6 H, CHC$H_3$), 1.22 (d, $^3J_{H,H}$ = 6.84 Hz, 6 H, CHC$H_3$), 2.36 (m, 4 H, C$H$CH$_3$), 6.91 (m, 2 H, CH arom.), 6.99–7.07 (m, 4 H, CH arom.), 7.74 (t, $^3J_{H,H}$ = 6.3, $J_{H,Pt}$ = 47.0 Hz, 2 H, CH arom.) ppm. $^{13}$C{$^1$H} NMR ($C_7D_8$): $\delta$ = 16.8 (pseudo t, $J_{C,Pt}$ = 15.4 Hz, P-CH-$C$H$_3$), 17.8 (m, P-CH-$C$H$_3$), 30.8 (d pseudo t, $^1J_{C,P}$ = 22.0, $^2J_{C,Pt}$ = 21.2 Hz, P-$C$H), 110.2 (d pseudo t, $^3J_{C,P}$ = 13.2, $^2J_{C,Pt}$ = 6.6 Hz, *C*-arom.), 122.4 (pseudo t, $^3J_{C,Pt}$ = 53.4 Hz, *C*-arom.), 126.6 (s, *C*-arom.), 141.2 (pseudo t, $^3J_{C,Pt}$ = 38.1 Hz, *C*-arom.), 150.0 (d pseudo t, $^1J_{C,Pt}$ = 850.4, $^2J_{C,P}$*cis* = 9.0, $^2J_{C,P}$*trans* = 104.7 Hz, *C*-Pt), 167.6 (d pseudo t, $^2J_{C,P}$ = 8.8, $^2J_{C,Pt}$ = 8.8 Hz, O-*C*) ppm. $^{31}$P{$^1$H} NMR ($CDCl_3$): $\delta$ = 179.0 (pseudo t, $^1J_{P,Pt}$ = 2147.2 Hz) ppm. $^{195}$Pt{$^1$H} NMR ($CDCl_3$): $\delta$ = –4583.9 (t, $^1J_{P,Pt}$ = 2147.2 Hz) ppm. MS (FAB): *m*/*z* (%) 613.1 (100) [M], with correct isotope pattern for $C_{24}H_{36}O_2P_2Pt$. $C_{24}H_{36}O_2P_2Pt$ (613.57): calcd. C 46.98, H 5.91; found C 46.76, H 5.82.

**Crystal-Structure Analysis of *cis*-[1*]Pt:** $C_{24}H_{36}O_2P_2Pt$, $M_r$ = 613.56, colorless fragment ($0.11 \times 0.14 \times 0.20$ mm$^3$), monoclinic, $P2_1/n$ (no. 14), $a$ = 12.5818(1), $b$ = 13.8769(1), $c$ = 15.2961(1) Å, $\beta$ = 106.9606(4)°, $V$ = 2554.49(3) Å$^3$, $Z$ = 4, $D_{calc}$ = 1.595 g cm$^{-3}$, $F(000)$ = 1216, $\mu$ = 5.635 mm$^{-1}$. Preliminary examination and data collection were carried out on a κ-CCD device (Nonius, Mach3) with an Oxford Cryosystems cooling system at the window of a rotating anode (Nonius FR591) with graphite-monochromated Mo-$K_\alpha$ radiation ($\lambda$ = 0.71073 Å). Data collection was performed at 173 K within the $\Theta$ range 1.85° < $\Theta$ < 25.35°. A total of 55295 intensities were integrated. Raw data were corrected for Lorentz, polarization, and latent decay and absorption effects arising from the scaling procedure. After merging ($R_{int}$ = 0.0789), 4739 [3137: $I_0 > 2\sigma(I_0)$] independent reflections remained and all were used to refine 270 parameters. The structure was solved by a combination of direct methods and difference-Fourier syntheses. All non-hydrogen atoms were refined with anisotropic displacement parameters. All hydrogen atoms were placed in calculated positions and refined using a riding model. Full-matrix least-squares refinements were carried out by minimizing $\Sigma w(F_o^2 - F_c^2)^2$ and converged with $R1$ = 0.0399 [$I_0 > 2\sigma(I_0)$], $wR2$ = 0.0709 (all data), GOF = 0.997, and shift/error < 0.001. The final difference-Fourier map showed no striking features ($\Delta e_{min/max}$ = +1.43/–1.16 e Å$^{-3}$). CCDC-613903.

***cis*-[3*]Pt:** White powder, yield: 91%. $^1$H NMR ($C_7D_8$, –80 °C): $\delta$ = 0.59 (dd, $^3J_{H,H}$ = 7.36, $^3J_{P,H}$ = 6.12 Hz, 3 H, C$H_3$), 0.79 (dd, $^3J_{H,H}$ = 7.36, $^3J_{P,H}$ = 11.00 Hz, 3 H, C$H_3$), 1.07 (dd, $^3J_{H,H}$ = 9.80, $^3J_{P,H}$ = 6.16 Hz, 3 H, C$H_3$), 1.60 (dsept, $^3J_{H,H}$ = 7.36, $^2J_{P,H}$ = 7.36 Hz, 2 H, P-C$H$), 1.80 (dsept, $^3J_{H,H}$ = 7.36, $^2J_{P,H}$ = 4.88 Hz, 2 H, P-C$H$), 4.62 (dd, $^2J_{H,H}$ = 9.8, $^4J_{P,H}$ = 27.59 Hz, 2 H, CH$H$-O), 5.04 (dd, $^2J_{H,H}$ = 9.8, $^4J_{P,H}$ = 10.42 Hz, 2 H, CH$H$-O), 7.31 (m, 2 H, arom. CH), 7.38 (m, 2 H, arom. CH), 8.04 (d, $^3J_{H,H}$ = 7.36 Hz, 2 H, arom. CH) ppm. $^{13}$C{$^1$H} NMR ($CDCl_3$): $\delta$ = 17.1 (br. s, $C$H$_3$), 18.9 (d pseudo t, $^2J_{C,P}$ = 5.6, $^3J_{C,Pt}$ = 5.4 Hz, $C$H$_3$), 31.7 (m, P-$C$H), 79.1 (pseudo t, $^3J_{C,Pt}$ = 101.0 Hz, $C$H$_2$-O), 122.6 (pseudo t, $J_{C,Pt}$ = 5.0 Hz, *C*-arom.), 125.4 (d pseudo t, $J_{C,P}$ = 5.1, $J_{C,Pt}$ = 34.4 Hz, *C*-arom.), 126.8 (d pseudo t, $J_{C,P}$ = 5.1, $J_{C,Pt}$ = 64.4 Hz, *C*-arom.), 140.4 (m, C-arom.), 140.7 (pseudo t, $J_{C,Pt}$ = 39.5 Hz, C-arom.), 158.2 (d pseudo t, $^1J_{C,Pt}$ = 808.0, $^2J_{C,P}$*cis* = 13.2, $^2J_{C,P}$*trans* = 103.2 Hz, *C*-Pt) ppm. $^{31}$P{$^1$H} NMR ($CDCl_3$): $\delta$ = 128.5 (pseudo t, $^1J_{P,Pt}$ = 2072.9 Hz) ppm. $^{195}$Pt{$^1$H} NMR ($CDCl_3$): $\delta$ = –4644.3 (t, $^1J_{P,Pt}$ = 2072.9 Hz) ppm. MS (FAB): *m*/*z* (%) 642.1 (100) [M], with correct isotope pattern for $C_{26}H_{40}O_2P_2Pt$.

**Crystal-Structure Analysis of *cis*-[3*]Pt:** $C_{26}H_{40}O_2P_2Pt$, $M_r$ = 712.53, colorless fragment ($0.05 \times 0.11 \times 0.21$ mm$^3$), monoclinic, $P2_1/n$ (no. 14), $a$ = 8.8313(1), $b$ = 25.0326(3), $c$ = 14.2562(2) Å, $\beta$ = 104.8610(6)°, $V$ = 3046.20(7) Å$^3$, $Z$ = 4, $D_{calc}$ = 1.399 g cm$^{-3}$, $F(000)$ = 1280, $\mu$ = 4.728 mm$^{-1}$. Preliminary examination and data collection were carried out on a κ-CCD device (Nonius, Mach3) with an Oxford Cryosystems cooling system at the window of a rotating anode (Nonius FR591) with graphite-monochromated Mo-$K_\alpha$ radiation ($\lambda$ = 0.71073 Å). Data collection was performed at 215 K within the $\Theta$ range 1.63° < $\Theta$ < 25.36°. A total of 64277 intensities were integrated. Raw data were corrected for Lorentz, polarization, and latent decay and absorption effects arising from the scaling procedure. After merging ($R_{int}$ = 0.0338), 3716 [3069: $I_0 > 2\sigma(I_0)$] independent reflections remained and all were used to refine 288 parameters. The structure was solved by a combination of direct methods and difference-Fourier syntheses. All non-hydrogen atoms were refined with anisotropic displacement parameters. All hydrogen atoms were placed in calculated positions and refined using a riding model. Full-matrix least-squares refinements were carried out by minimizing $\Sigma w(F_o^2 - F_c^2)^2$ and converged with $R1$ = 0.0361 [$I_0 > 2\sigma(I_0)$], $wR2$ = 0.0867 (all data), GOF = 1.053, and

 © 2007 Wiley-VCH Verlag GmbH & Co. KGaA, Weinheim 

shift/error < 0.001. The final difference-Fourier map showed no striking features ($\Delta e_{min/max}$ = +0.79/–0.61 e Å$^{-3}$). CCDC-613905.

***trans*-[1*]Pt:** White powder, yield: 87%. $^1$H NMR ($C_7D_8$): $\delta$ = 1.08 (dd, $^3J_{H,H}$ = 7.32, $^3J_{P,H}$ = 7.32 Hz, 12 H, C*H*$_3$), 1.12 (dd, $^3J_{H,H}$ = 8.80, $^3J_{P,H}$ = 8.80 Hz, 12 H, C*H*$_3$), 2.28 (sept, $^3J_{H,H}$ = 7.32 Hz, 4 H, C*H*CH$_3$), 6.87 (t, $^3J_{H,H}$ = 7.28 Hz, 2 H, arom. CH), 7.08 (t, $^3J_{H,H}$ = 7.32 Hz, 2 H, arom. CH), 7.28 (d, $^3J_{H,H}$ = 7.32 Hz, 2 H, arom. CH), 7.81 (d pseudo t, $^3J_{H,H}$ = 7.32, $^3J_{Pt,H}$ = 39.5 Hz, 2 H, arom. CH) ppm. $^{13}$C{$^1$H} NMR ($C_7D_8$): $\delta$ = 16.7 (br. s, *C*H$_3$), 18.2 (br. s, *C*H$_3$), 29.51 (pseudo t, $^1J_{C,P}$ = 35.85 Hz, P-*C*H), 111.3 (pseudo t, $^2J_{C,Pt}$ = 11.96 Hz), 121.8 (pseudo t, $^3J_{C,Pt}$ = 37.69 Hz), 125.9 (s), 143.6 (pseudo t, $^2J_{C,Pt}$ = 9.20 Hz, C-O), 168.4 (dd, $^2J_{C,P\,cis\,A}$ = 6.42, $^2J_{C,P\,cis\,B}$ = 7.35 Hz, C-Pt) ppm. $^{31}$P{$^1$H} NMR ($C_7D_8$): $\delta$ = 173.7 (pseudo t, $^1J_{P,Pt}$ = 2998.6 Hz) ppm. $^{195}$Pt{$^1$H} NMR ($C_7D_8$): $\delta$ = –4349.7 (pseudo t, $^1J_{P,Pt}$ = 2998.6 Hz) ppm. MS (FAB): *m*/*z* (%) 613.1 (100) [M], with correct isotope pattern for $C_{24}H_{36}O_2P_2Pt$.

**Crystal-Structure Analysis of *trans*-[1*]Pt:** $C_{24}H_{36}O_2P_2Pt$, $M_r$ = 613.56, colorless needle (0.09 × 0.12 × 0.25 mm$^3$), monoclinic, $P2_1/c$ (no. 14), $a$ = 7.8126(1), $b$ = 16.4322(3), $c$ = 9.9638(2) Å, $\beta$ = 109.5947(8)°, $V$ = 1205.1(3) Å$^3$, $Z$ = 4, $D_{calc}$ = 3.382 g cm$^{-3}$, $F$(000) = 1216, $\mu$ = 11.943 mm$^{-1}$. Preliminary examination and data collection were carried out on a κ-CCD device (Nonius, Mach3) with an Oxford Cryosystems cooling system at the window of a rotating anode (Nonius FR591) with graphite-monochromated Mo-$K_\alpha$ radiation ($\lambda$ = 0.71073 Å). Data collection was performed at 173 K within the $\Theta$ range 2.48° < $\Theta$ < 25.32°. A total of 11134 intensities were integrated. Raw data were corrected for Lorentz, polarization, and latent decay and absorption effects arising from the scaling procedure. After merging ($R_{int}$ = 0.0244), 2196 [1894: $I_0 > 2\sigma(I_0)$] independent reflections remained and all were used to refine 138 parameters. The structure was solved by a combination of direct methods and difference-Fourier syntheses. All non-hydrogen atoms were refined with anisotropic displacement parameters. All hydrogen atoms were placed in calculated positions and refined using a riding model. Full-matrix least-squares refinements were carried out by minimizing $\Sigma w(F_o^2 - F_c^2)^2$ and converged with $R1$ = 0.0171 [$I_0 > 2\sigma(I_0)$], $wR2$ = 0.0412 (all data), GOF = 1.052, and shift/error < 0.001. The final difference-Fourier map showed no striking features ($\Delta e_{min/max}$ = +0.88/–0.76 e Å$^{-3}$). CCDC-613909.

**[3]Pt:** Off-white powder, yield: quantitative. $^1$H NMR ($C_7D_8$): $\delta$ = –17 (t pseudo t, $^2J_{P,H}$ = 4.9 Hz $^1J_{Pt,H}$ = 1208.1 Hz, 0.7 H, agost. H), 0.95 (dd, $^3J_{H,H}$ = 7.4 Hz $^3J_{H,P}$ = 7.4 Hz, 6 H, CH$_3$), 1.10 (dd, $^3J_{H,H}$ = 7.4 Hz $^3J_{H,P}$ = 7.4 Hz, 6 H, CH$_3$), 1.16 (dd, $^3J_{H,H}$ = 7.3 Hz $^3J_{H,P}$ = 7.4 Hz, 6 H, CH$_3$), 1.26 (dd, $^3J_{H,H}$ = 7.4, $^3J_{H,P}$ = 9.8 Hz, 6 H, CH$_3$), 2.35 (hept., $^3J_{H,H}$ = 7.4 Hz, 2 H, C*H*-CH$_3$), 2.43 (hept., $^3J_{H,H}$ = 7.4 Hz, 2 H, C*H*-CH$_3$), 4.61 (dd, $^2J_{H,H}$ = 9.8 Hz $^3J_{P,H}$ = 12.24 Hz, 2 H, CH$_2$-O), 4.90 (dd, $^2J_{H,H}$ = 7.4 Hz $^3J_{P,H}$ = 7.4 Hz, 2 H, CH$_2$-O), 6.66 (d, $^3J_{H,H}$ = 7.4 Hz, 2 H, CH arom.), 6.95 (t, $^3J_{H,H}$ = 7.4 Hz, 2 H, CH arom.), 7.18 (t, $^3J_{H,H}$ = 7.4 Hz, 2 H, CH arom.), 7.61 (d, $^3J_{H,H}$ = 7.4 Hz, 2 H, CH arom.) ppm. $^{13}$C{$^1$H} NMR ($CDCl_3$): $\delta$ = 16.65 (pseudo t, $J_{C,Pt}$ = 21.9 Hz), 17.3–17.6 (several br. s, CH$_3$), 27.70 (t, $^1J_{P,C}$ = 20.1 Hz, *C*HCH$_3$), 29.50 (t, $^1J_{P,C}$ = 16.5 Hz, *C*HCH$_3$), 70.52 (pseudo t, $^3J_{C,Pt}$ = 83.1 Hz, CH$_2$), 122.89 (s, arom. C), 126.55 (s, arom. C), 130.14 (s, arom. C), 136.87 (s, arom. C), 138.49 (s, arom. C) ppm. $^{31}$P{$^1$H} NMR ($C_7D_8$): $\delta$ = 160.1 (pseudo t, $^1J_{P,Pt}$ = 3158.8 Hz) ppm. $^{195}$Pt{$^1$H} NMR ($C_7D_8$): $\delta$ = –4894.8 (t, $^1J_{P,Pt}$ = 3158.8 Hz) ppm. MS (FAB): *m*/*z* 642.3 [M + 1], with correct isotopic pattern. FT-IR (KBr): $\tilde{\nu}$ = 1945 cm$^{-1}$ (w, Pt–H).

**Calculations:** The DFT calculations were performed using the program suite Gaussian 03.[5] All molecular geometries were fully optimized. The DFT method used includes Becke's three parameter hybrid exchange functional in combination with the correlation functional of Perdew and Wang (B3PW91). Geometry optimizations and frequency calculations were performed using the valence double-zeta LANL2DZ basis set. The frozen-coordinate analysis was done using the program codes implemented in Gaussian 03.

**Single Crystal X-ray Structure Determination of Compounds *cis*-[2]PtCl$_2$·2(CHCl$_3$), *trans*-[2]PtCl$_2$, *cis*-[3]PtCl$_2$·3(CHCl$_3$), *trans*-[3]PtCl$_2$, *cis*-[1]Pt(*n*Pr)$_2$, *cis*-[3]PtEt$_2$, *trans*-[1*]$^1$PtCl$_2$, *cis*-[1*]$^{Br}$PtCl$_2$·(CH$_2$Cl$_2$), *trans*-[1*]Pt, *cis*-[1*]Pt, and *cis*-[3*]Pt:** The crystal was stored under perfluorinated ether, transferred into a Lindemann capillary, fixed, and sealed. Preliminary examination and data collection were carried out as described above for each complex. Neutral atom scattering factors for all atoms and anomalous dispersion corrections for the non-hydrogen atoms were taken from the International Tables for Crystallography.[12d] All calculations were performed on an Intel Pentium II PC, with the STRUX-V system, including the programs PLATON, SIR92, and SHELXL-97.[12]

CCDC-613903 to -613913 contain the supplementary crystallographic data for this paper. These data can be obtained free of charge from The Cambridge Crystallographic Data Centre via www.ccdc.cam.ac.uk/data_request/cif.

## Acknowledgments

K. R. thanks the Deutsche Forschungsgemeinschaft (DFG) for financial support (Ru519/3-2) and the Fonds der Chemischen Industrie for a Liebig grant. He is also grateful to Prof. Dr. mult. W. A. Herrmann for financial support.

[1] a) B. L. Edelbach, R. J. Lachicotte, W. D. Jones, *J. Am. Chem. Soc.* **1998**, *120*, 2843–2853; b) G. Ujaque, F. Maseras, O. Eisenstein, L. Liable-Sands, A. L. Rheingold, W. Yao, R. H. Crabtree, *New J. Chem.* **1998**, *22*, 1493–1498; c) Z. Lu, C. H. Jun, S. R. de Gala, M. P. Sigalas, O. Eisenstein, R. H. Crabtree, *Organometallics* **1995**, *14*, 1168–1175; d) C. N. Iverson, W. D. Jones, *Organometallics* **2001**, *20*, 5745–5750; e) X. Zhang, G. B. Carpenter, D. A. Sweigart, *Organometallics* **1999**, *18*, 4887–4888; f) H. Schwager, S. Spyroudis, K. P. C. Vollhardt, *J. Organomet. Chem.* **1990**, *382*, 191–200; g) J. J. Eisch, A. M. Piotrowski, K. I. Han, C. Krüger, Y. H. Tsay, *Organometallics* **1985**, *4*, 224–231; h) R. M. Shaltout, R. Sygula, A. Sygula, F. R. Fronczek, G. G. Stanley, P. W. Rabideau, *J. Am. Chem. Soc.* **1998**, *120*, 835–836; i) T. Schaub, U. Radius, *Chem. Eur. J.* **2005**, *11*, 5024–5030.

[2] a) A. E. Shilov, G. B. Shul'pin, *Chem. Rev.* **1997**, *97*, 2879–2932; b) R. H. Crabtree, *Chem. Rev.* **1985**, *85*, 245–269; c) J. Halpern, *Inorg. Chim. Acta* **1985**, *100*, 41–48; d) G. W. Parshall, *Acc. Chem. Res.* **1975**, *8*, 113–117; e) *Activation and Catalytic Reactions of Saturated Hydrocarbons in the Presence of Metal Complexes* (Eds.: A. E. Shilov, G. B. Shul'pin), Kluwer Academic Publishers **2000**, Dordrecht, The Netherlands; f) *Selective Hydrocarbon Activation* (Eds.: J. A. Davies, P. L. Watson, J. F. Liebman, A. Greenberg), VCH Publishers, New York/Weinheim, **1990**; g) *Theoretical Aspects of Homogeneous Catalysis* (Eds.: P. W. N. M. van Leeuwen, K. Morokuma, J. H. van Lenthe), Kluwer Academic Publishers, Dordrecht, The Netherlands, **1995**; h) A. D. Ryabov, *Chem. Rev.* **1990**, *90*, 403–424; i) W. D. Jones, F. J. Feher, *Acc. Chem. Res.* **1989**, *22*, 91–100; j) B. A. Arndtsen, R. G. Bergman, T. A. Mobley, T. H. Peterson, *Acc. Chem. Res.* **1995**, *28*, 154–162; k) B. Rybtchinski, D. Milstein, *Angew. Chem. Int. Ed.* **1999**, *38*, 870–883; l) C.-H. Jun, *Chem. Soc. Rev.* **2004**, *33*, 610–618.

[3] K. Ruhland, E. Herdtweck, *J. Organomet. Chem.* **2005**, *690*, 5215–5236.

 © 2007 Wiley-VCH Verlag GmbH & Co. KGaA, Weinheim 

[4] a) J. W. Suggs, C.-H. Jun, *J. Am. Chem. Soc.* **1984**, *106*, 3054; b) J. W. Suggs, C.-H. Jun, *J. Am. Chem. Soc.* **1986**, *108*, 4679; c) J. W. Suggs, C.-H. Jun, *J. Chem. Soc., Chem. Commun.* **1985**, 92; d) N. Chatani, Y. Ie, F. Kakiuchi, S. Murai, *J. Am. Chem. Soc.* **1999**, *121*, 8645; e) S.-Y. Liou, M. E. van der Boom, D. Milstein, *Chem. Commun.* **1998**, 687; f) B. Rybtchinski, S. Oevers, M. Montag, A. Vigalok, H. Rozenberg, J. M. L. Martin, D. Milstein, *J. Am. Chem. Soc.* **2001**, *123*, 9064–9077; g) A. Sundermann, O. Uzan, D. Milstein, J. M. L. Martin, *J. Am. Chem. Soc.* **2000**, *122*, 7095–7104; h) B. Rybtchinski, D. Milstein, *J. Am. Chem. Soc.* **1999**, *121*, 4528–4529; i) C.-H. Jun, C. W. Moon, D.-Y. Lee, *Chem. Eur. J.* **2002**, *8*, 2423; j) C.-H. Jun, H. Lee, *J. Am. Chem. Soc.* **1999**, *121*, 880; k) C.-H. Jun, D.-Y. Lee, H. Lee, J.-B. Hong, *Angew. Chem. Int. Ed.* **2000**, *39*, 3070; l) C.-H. Jun, H. Lee, S.-G. Lim, *J. Am. Chem. Soc.* **2001**, *123*, 751; m) H. Salem, Y. Ben-David, L. J. W. Shimon, D. Milstein, *Organometallics* **2006**, *25*, 2292–2300.

[5] Gaussian 03, Revision B.01, M. J. Frisch, G. W. Trucks, H. B. Schlegel, G. E. Scuseria, M. A. Robb, J. R. Cheeseman, J. A. Montgomery Jr, T. Vreven, K. N. Kudin, J. C. Burant, J. M. Millam, S. S. Iyengar, J. Tomasi, V. Barone, B. Mennucci, M. Cossi, G. Scalmani, N. Rega, G. A. Petersson, H. Nakatsuji, M. Hada, M. Ehara, K. Toyota, R. Fukuda, J. Hasegawa, M. Ishida, T. Nakajima, Y. Honda, O. Kitao, H. Nakai, M. Klene, X. Li, J. E. Knox, H. P. Hratchian, J. B. Cross, C. Adamo, J. Jaramillo, R. Gomperts, R. E. Stratmann, O. Yazyev, A. J. Austin, R. Cammi, C. Pomelli, J. W. Ochterski, P. Y. Ayala, K. Morokuma, G. A. Voth, P. Salvador, J. J. Dannenberg, V. G. Zakrzewski, S. Dapprich, A. D. Daniels, M. C. Strain, O. Farkas, D. K. Malick, A. D. Rabuck, K. Raghavachari, J. B. Foresman, J. V. Ortiz, Q. Cui, A. G. Baboul, S. Clifford, J. Cioslowski, B. B. Stefanov, G. Liu, A. Liashenko, P. Piskorz, I. Komaromi, R. L. Martin, D. J. Fox, T. Keith, M. A. Al-Laham, C. Y. Peng, A. Nanayakkara, M. Challacombe, P. M. W. Gill, B. Johnson, W. Chen, M. W. Wong, C. Gonzalez, and J. A. Pople, Gaussian, Inc., Pittsburgh, PA, **2003**.

[6] a) C. A. Tolman, *Chem. Rev.* **1977**, *77*, 313; b) R. Mason, D. W. Merck, *Angew. Chem.* **1978**, *90*, 195; *Angew. Chem. Int. Ed. Engl.* **1978**, *17*, 183; c) P. S. Pregosin, *Transition Metal Nuclear Magnetic Resonance*, Elsevier Science Publishers **1991**, Amsterdam, The Netherlands; d) C. Brevard, P. Granger, *Handbook of High Resolution Multinuclear NMR*, John Wiley & Sons Inc., Chichester, UK, **1981**.

[7] a) J. G. Verkade, L. D. Quin, *Phosphorus-31 NMR Spectroscopy in Stereochemical Analysis*, VCH Publishers, Weinheim, Germany, **1987**; b) D. W. White, J. G. Verkade, *J. Magn. Reson.* **1970**, *3*, 111–116; c) M. Kainosho, A. Nakamura, *Tetrahedron* **1969**, *25*, 4071–4081.

[8] a) S. Otsuka, T. Yoshida, M. Matsumoto, K. Nakatsu, *J. Am. Chem. Soc.* **1976**, *98*, 5850–5858; b) A. C. Cooper, E. Clot, J. C. Huffman, W. E. Streib, F. Maseras, O. Eisenstein, K. G. Caulton, *J. Am. Chem. Soc.* **1999**, *121*, 97–106; c) G. Ujaque, A. C. Cooper, F. Maseras, O. Eisenstein, K. G. Caulton, *J. Am. Chem. Soc.* **1998**, *120*, 361–365; d) A. Cooper, W. E. Streib, O. Eisenstein, K. G. Caulton, *J. Am. Chem. Soc.* **1997**, *119*, 9069–9070; e) W. Baratta, E. Herdtweck, *Angew. Chem. Int. Ed.* **1999**, *38*, 1629–1631; f) R. L. Harlow, D. L. Thorn, R. T. Baker, N. L. Jones, *Inorg. Chem.* **1992**, *31*, 993–997; g) J. Fawcett, J. H. Holloway, G. C. Saunders, *Inorg. Chim. Acta* **1992**, *202*, 111–113; h) R. Cini, A. Cavaglioni, *Inorg. Chem.* **1999**, *38*, 3751–3754; i) D. Huang, W. E. Streib, J. C. Bollinger, K. G. Caulton, R. F. Winter, T. J. Scheiring, *J. Am. Chem. Soc.* **1999**, *121*, 8087–8097; j) R. H. Heyn, S. A. Macgregor, T. T. Nadasdi, M. Ogasawara, O. Eisenstein, K. G. Caulton, *Inorg. Chim. Acta* **1997**, *259*, 5–26; k) A. C. Albeñiz, G. Schulte, R. H. Crabtree, *Organometallics* **1992**, *11*, 242–249; l) M. Brookhart, M. L. H. Green, L.-L. Wong, *Prog. Inorg. Chem.* **1988**, *36*, 1–124.

[9] a) X.-L. Luo, R. H. Crabtree, *J. Am. Chem. Soc.* **1990**, *112*, 6912–6918; b) E. Gutierrez-Puebla, A. Monge, M. Paneque, M. L. Poveda, S. Taboada, M. Trujillo, E. Carmona, *J. Am. Chem. Soc.* **1999**, *121*, 346–354; c) W. J. Oldham, A. S. Hinkle, D. M. Heinekey, *J. Am. Chem. Soc.* **1997**, *119*, 11028–11036; d) M. Saunders, L. Telkowski, M. R. Kates, *J. Am. Chem. Soc.* **1977**, *99*, 8070–8071; e) R. B. Calvert, J. R. Shapley, *J. Am. Chem. Soc.* **1978**, *100*, 7726–7727; f) H.-U. Siehl, *Adv. Phys. Org. Chem.* **1987**, *23*, 63–165.

[10] J. Chatt, L. M. Vallarino, L. M. Venanzi, *J. Chem. Soc.* **1957**, 2496–2505; b) L. E. Crascall, J. L. Spencer, *Inorg. Synth.* **1990**, *28*, 126–135; c) P. J. Buss, B. Greene, M. Orchin, *Inorg. Synth.* **1990**, *20*, 181–182.

[11] a) A. L. van Geet, *Anal. Chem.* **1970**, *42*, 679–680; b) H. Friebolin, G. Schilling, L. Pohl, *Org. Magn. Reson.* **1979**, *12*, 569–573; c) C. Piccinni-Leopardii, O. Fabre, J. Reisse, *Org. Magn. Reson.* **1976**, *8*, 233–236; d) F. H. Köhler, X. Xie, *Magn. Reson. Chem.* **1997**, *35*, 487–492; e) J. Bornais, S. Brownstein, *J. Magn. Reson.* **1978**, *29*, 207–211.

[12] a) Data Collection Software for Nonius κ-CCD devices, Delft (The Netherlands), **2001**; b) Z. Otwinowski, W. Minor, *Methods Enzymol.* **1997**, *276*, 307; c) *SIR92*: A. Altomare, G. Cascarano, C. Giacovazzo, A. Guagliardi, M. C. Burla, G. Polidori, M. Camalli, *J. Appl. Crystallogr.* **1994**, *27*, 435–436; d) *International Tables for Crystallography*, Vol. C, Tables 6.1.1.4, 4.2.6.8, and 4.2.4.2 (Ed.: A. J. C. Wilson), Kluwer Academic Publishers, Dordrecht (The Netherlands), **1992**; e) A. L. Spek, PLATON, *A Multipurpose Crystallographic Tool*, Utrecht University, Utrecht, The Netherlands, **2001**; f) G. M. Sheldrick, *SHELXL-97*, University of Göttingen, Germany, **1998**.

Received: September 12, 2006
Published Online: January 23, 2007

 © 2007 Wiley-VCH Verlag GmbH & Co. KGaA, Weinheim 

DOI: 10.1002/ejic.200600865

# The Electrochemical Behaviour of Organonickel Complexes: Mono-, Di- and Trivalent Nickel

**Axel Klein,*[a] André Kaiser,[a] Biprajit Sarkar,[b] Matthias Wanner,[b] and Jan Fiedler[c]**

**Keywords:** Electron transfer / Nickel / Electrochemistry / EPR spectroscopy / Spectroelectrochemistry

The redox properties of organometallic nickel complexes of the type [(α-diimine)Ni(Mes)Br], [(α-diimine)Ni(Mes)$_2$] and the complexes *trans*-[(PPh$_3$)$_2$Ni(Mes)Br] and *trans*-[(PPh$_3$)$_2$-Ni(Fmes)Br] [Mes = mesityl (2,4,6-trimethylphenyl); Fmes = tris(2,4,6-trifluoromethyl)phenyl] have been studied in detail by various electrochemical and spectroelectrochemical (UV/Vis/NIR and EPR) methods. Upon electrochemical reduction, the bromido mesityl derivatives undergo cleavage of the bromide ligand. The resulting reactive species and their products from follow-up reactions are investigated. Electrochemical oxidation leads to formally trivalent nickel species. The metal contribution to the unpaired electron for the formally monovalent and trivalent nickel species can be estimated from EPR spectroscopy.
(© Wiley-VCH Verlag GmbH & Co. KGaA, 69451 Weinheim, Germany, 2007)

## Introduction

Organonickel(II) complexes are widely used in organometallic catalysis. One of the first benchmarks in that field were the nickel phosphane complexes used in the Shell higher olefin process (SHOP).[1] In the last decade the interest in organonickel catalysts has mainly focused on nickel diimine complexes. Highly reactive catalysts for olefin polymerisation have been developed on the basis of methylnickel complexes of various diimine ligands, mainly by Brookhart.[2] The active catalyst species were found to be mainly cationic complexes of the type [(N^N)Ni(R)L]$^+$ (N^N = α-diimine; L = easily replaceable ligand). Furthermore, nickel diimine complexes have gained an enormous interest in electrocatalytic applications[3] such as electrocatalytic C–C or C–P coupling reactions with various aryl, vinyl or alkyl halides R–X (see Scheme 1),[4–7] homogeneous electromediated reduction (HEMR) of olefins, ketones or alkyl halides,[8–10] electrochemical carboxylation of bromostyrenes[11] or aziridines,[12] electroreductive carbonylation of organic halides[13] and electroreductive coupling of olefins and polyhalo compounds.[14]

A mechanism for the C–C coupling reactions was initially proposed by Amatore and Jutand[15] for the corresponding diphosphane (dppe) complexes and was subsequently established for 2,2′-bipyridine-containing systems

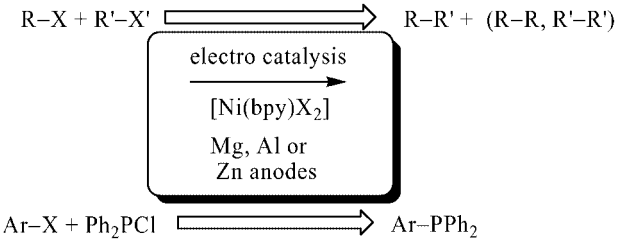


Scheme 1. Electrocatalytic C–C or C–P coupling reactions of aryl, vinyl or alkyl halides.

mainly based on kinetic investigations.[6,16,17] For a system starting from [(bpy)NiX$_2$] (X = halide) pre-catalysts it can be depicted as in Scheme 2.

In addition to these kinetic investigations, the oxidative addition reaction of ArBr to zero-valent nickel species formed in situ as the first part of the catalytic cycle has been proved by preparative electrochemistry. Thus, the oxidative addition of aryl halides to species formed upon electrochemical reduction of [(bpy)$_n$NiX$_2$] ($n$ = 1–3; X = Br, BF$_4$) leads to the nickel(II) complexes [(bpy)Ni$^{II}$(Ar)Br] in reasonably high yields.[18,19] The complex [(bpy)Ni(Mes)Br], which is an excellent catalyst precursor for the oligomerisation of ethylene, is obtained from [(bpy)NiBr$_2$] and MesBr in 87% yield.[18]

The subsequent steps of the proposed catalytic cycle comprise a single electron transfer and subsequent scission of the bromide ligand to give the monovalent species [(bpy)-Ni$^{I}$(Ar)]. Oxidative addition of RX then leads to trivalent pentacoordinate [(bpy)Ni$^{III}$(Ar)(R)X], which finally eliminates the coupling product ArR. The resulting nickel(I) species is then reduced to the aforementioned nickel(0) catalyst [(bpy)Ni$^0$]. So far very little preparative or spectroscopic

[a] Universität zu Köln, Institut für Anorganische Chemie, Greinstraße 6, 50969 Köln, Germany
E-mail: axel.klein@uni-koeln.de
[b] Universität Stuttgart, Institut für Anorganische Chemie, Pfaffenwaldring 55, 70569 Stuttgart, Germany
[c] J. Heyrovský Institute of Physical Chemistry, Academy of Sciences of the Czech Republic, Dolejškova 3, 18 000 Prague 8, Czech Republic

 © 2007 Wiley-VCH Verlag GmbH & Co. KGaA, Weinheim 

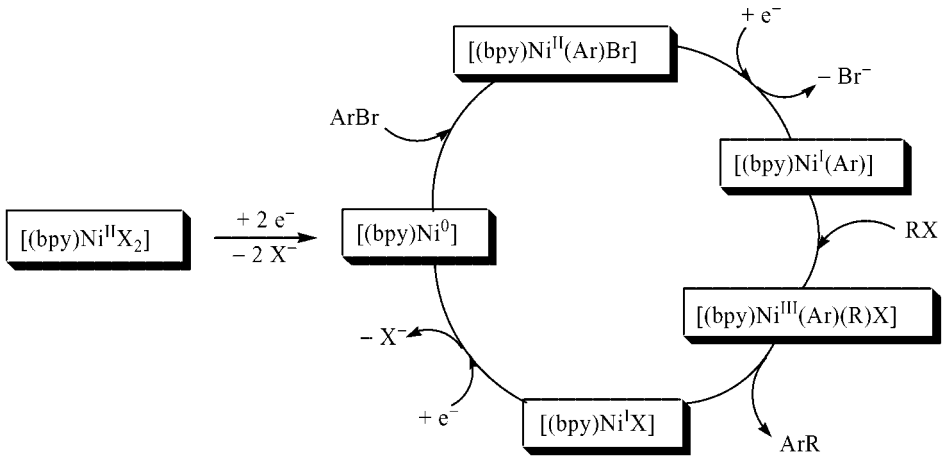


Scheme 2. Proposed mechanism for the C–C coupling reactions.

evidence has been published for this part. The NMR spectroscopic data of the proposed nickel(III) species [(bpy)-Ni(Mes)$_2$Br] have been reported,[19] but these data do not show any sign of paramagnetic shifts, and the characterisation of these species by EPR spectroscopy was not performed. No spectroscopic evidence has been found so far for the nickel(I) species in the next catalytic step.

To explore the mechanism of this interesting electrocatalytic reaction in further details we have started an investigation on the electrochemistry of a number of mesitylnickel complexes of various α-diimine ligands [(N^N)Ni(Mes)Br], thus starting at the point of the proposed cycle which has remained largely unclear so far. We have used spectroelectrochemical methods (UV/Vis/NIR and EPR) to characterise the resulting species as these techniques allow the in situ generation and spectroscopic characterisation of labile or even transient species.[20]

The complexes [(N^N)Ni(Mes)Br] used in this investigation, with the α-diimine ligands depicted in Scheme 3, have been described in preliminary detailed studies using optical spectroscopy, XRD and EXAFS spectroscopy in combination with quantum chemical calculations.[21–23] It was shown that the LUMOs were mainly localised in the diimine π* levels, which means that the diimine ligands should be largely involved in electrochemical reduction of these complexes. Since the splitting of the bromide ligand is presumed from the reduced states of these complexes, the related dimesityl complexes [(N^N)Ni(Mes)$_2$], which have been described recently,[21,23] were also included in this study. For further comparison we also incorporated the complex *trans*-[(PPh$_3$)$_2$Ni(Mes)Br], which usually serves as a precursor to the title complexes,[22,23] and the perfluorinated derivatives *trans*-[(PPh$_3$)$_2$Ni(Fmes)Br] and [(bpy)-Ni(Fmes)Br] [Fmes = nonafluoromesityl = 2,4,6-tris(trifluoromethyl)phenyl], the preparation and analytical data of which are given in the Experimental Section.

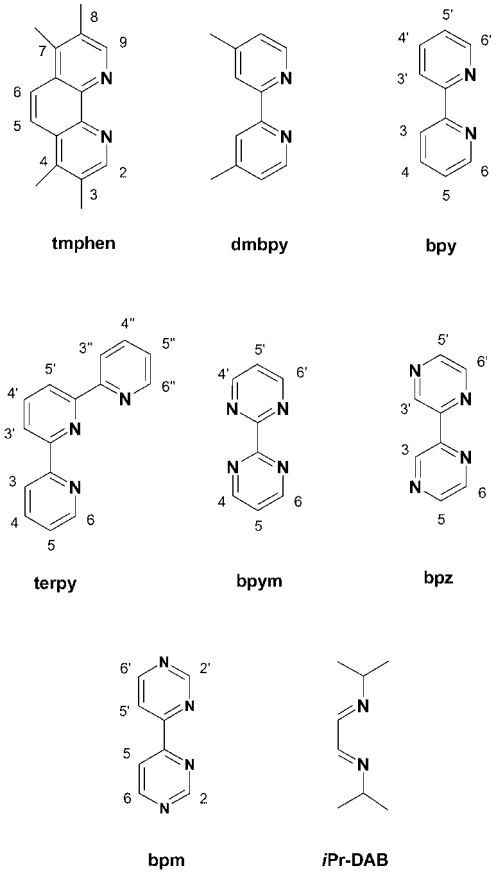


Scheme 3. Diimine ligands (N^N). tmphen = 3,4,7,8-tetramethyl-1,10-phenanthroline, dmbpy = 4,4′-dimethyl-2,2′-bipyridine, bpy = 2,2′-bipyridine, terpy = 2,2′,6′′-terpyridine, bpym = 2,2′-bipyrimidine, bpz = 2,2′-bipyrazine, bpm = 4,4′-bipyrimidine, *i*Pr-DAB = *N*,*N*′-diisopropyl-1,2-ethanediimine (*N*,*N*′-diisopropyl-1,4-diazabutadiene).

 © 2007 Wiley-VCH Verlag GmbH & Co. KGaA, Weinheim 

## Results and Discussion

### Electrochemistry

#### *Reduction Reactions*

The bromido mesityl complexes [(N^N)Ni(Mes)Br] exhibit rather complex electrochemical behaviour at 298 K, as shown in Figure 1 (data summarised in Table 1).

After a first irreversible reduction wave ($E_{R1}$) we observe a reversible wave $E_2$ ($E_{R2}/E_{O2}$) for the more basic ligands tmphen, dmbpy and bpy. The cathodic peak potentials $E_{R1}$ and $E_{R2}$ increase (shift positively) along the series tmphen > dmbpy > bpy > bpym > bpz > *i*Pr-DAB > bpm. Since the values for $E_{R2}$ increase more rapidly, $E_{R1}$ and $E_{R2}$ overlap partially at the lower end of the series, starting from bpym. Here, square-wave voltammetry helped to determine the individual values. This series represents the decreasing basicity or increasing π-accepting ability (in accordance with the low-lying π* LUMOs) of the diimine ligand. On the reverse scan a re-oxidation wave ($E_{O1'}$) is observed at around –1 V. The two reduction waves are followed by further waves that are partly reversible ($E_{R3}$) for the less basic ligands. An exception for this complex behaviour can be observed for the terpy complex $[(terpy)Ni(Mes)]^+$, for which two reversible reduction waves are found. The corresponding dimesityl complexes $[(N^N)Ni(Mes)_2]$ also exhibit full reversibility of the first two reduction processes (Figure 2, Table 2). Since no bromide co-ligand is present in these systems a first strong evidence emerges that the splitting of the bromide from the complexes [(N^N)Ni(Mes)Br] after the first reduction reaction is the reason for their complicated behaviour. This splitting reaction has been proposed before by others,[16,18,19] but no convincing proof was provided.

At low temperature (213 K) the situation is altered. For the dmbpy complex a re-oxidation $E_{O1}$ to the first electrochemical process (E) is observed. At normal scan rates the ratio $I_{pa}/I_{pc}$ is less than 1, although it reaches unity when scanned at rates above 500 mV s$^{-1}$. For the complexes with bpy (Figure 3), bpym, *i*Pr-DAB and bpm the process $E_1$ ($E_{R1}/E_{O1}$) is fully reversible even at normal scan rates. Com-

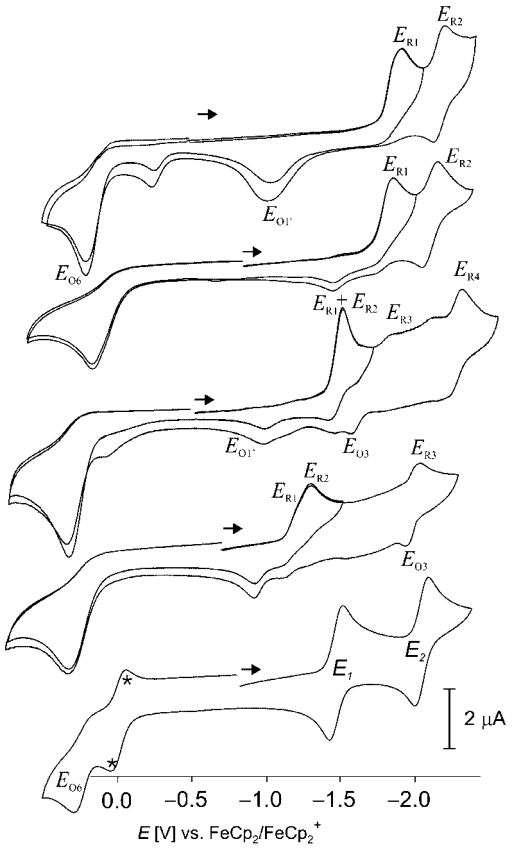


Figure 1. Cyclic voltammograms of [(tmphen)Ni(Mes)Br], [(dmbpy)Ni(Mes)Br], [(bpym)Ni(Mes)Br] (in thf), [(bpz)Ni(Mes)-Br] and $[(terpy)Ni(Mes)]^+$ (from top to bottom), in dmf/$Bu_4NPF_6$ solution at 298 K; * marks the redox waves of the ferrocene/ferrocenium standard.

Table 1. Electrochemical data of the bromido(mesityl)nickel complexes [(N^N)Ni(Mes)Br].[a]

| (N^N) | $E_{O6}$ | $E_{O1'}$ | $E_{R1\ (irr.)}$ or $E_1$ ($\Delta E_{pp}$) | $E_{R2\ (irr.)}$ or $E_2$ ($\Delta E_{pp}$) | $E_{R2'\ (irr.)}$ or $E_3$ ($\Delta E_{pp}$) | $E_{R3\ (irr.)}$ or $E_3$ ($\Delta E_{pp}$) | $E_{R1} - E_{R1(L)}$ | $T$ [K] |
|---|---|---|---|---|---|---|---|---|
| tmphen | 0.16 | –1.51 | –1.94 irr. | –2.18 (78) | – | –2.84 irr. | 0.72 | 298 |
| tmphen | 0.27 | –1.27 | –2.00 irr | –2.16 (64) | – | –2.90 irr. | 0.54 | 213 |
| dmbpy | 0.18 | –1.47 | –1.86 irr. | –2.08 (76) | – | –2.85 irr. | 0.80 | 298 |
| dmbpy | 0.42 | – | –1.87 (76) | –2.10 irr. | –2.58 irr. | –2.85 (91) | 0.79 | 213 |
| bpy | 0.25 | –1.45 | –1.85 irr. | –2.00 (71) | – | –2.61 irr. | 0.74 | 298 |
| bpy | 0.45 | – | –1.79 (73) | –1.94 irr. | –2.65 (91) | –2.83 irr. | 0.80 | 213 |
| bpym | 0.31 | –1.04 | –1.49 irr. | –1.58 irr. | – | –2.42 (96) | 0.77 | 298 |
| bpym | 0.52 | – | –1.47 (60) | –1.53 (81) | –2.22 (83) | –2.46 irr. | 0.79 | 213 |
| *i*Pr-DAB | 0.30 | –0.93 | –1.34 irr. | –1.46 irr. | – | –2.10 irr. | 1.30 | 298 |
| *i*Pr-DAB | 0.43 | – | –1.37 (74) | –1.56 irr. | – | –2.45 irr. | 1.27 | 213 |
| bpz | 0.29 | –0.87 | –1.31 irr. | –1.36 irr. | – | –2.02 irr. | 0.77 | 298 |
| bpz | 0.37 | – | –1.34 (75) | – | –1.88 (86) | –2.11 irr. | 0.74 | 213 |
| bpm | 0.30 | –0.67 | –1.25 irr. | – | – | –1.91 (88) | 0.61 | 298 |
| bpm | 0.29 | – | –1.20 (66) | – | –1.82 (92) | –1.92 (92) | 0.66 | 213 |
| terpy | 0.28 | – | –1.45 (78) | –2.03 (81) | – | –2.79 (99) | 1.04 | 298 |

[a] From cyclic voltammetry or square-wave voltammetry in 0.1 M dmf/$Bu_4NPF_6$ solutions. Scan rate: 100 mV s$^{-1}$. Potentials ($E$) in V vs. ferrocene/ferrocenium. Reduction potentials $E_{R1}$, $E_{R2}$ and $E_{R3}$ are cathodic peak potentials for irreversible waves. $E_1$ and $E_2$ are half-wave potentials for reversible waves, with the peak-to-peak separation $\Delta E_{pp}$ in mV given in parentheses. Oxidation potentials are given as anodic peak potentials.

 © 2007 Wiley-VCH Verlag GmbH & Co. KGaA, Weinheim 

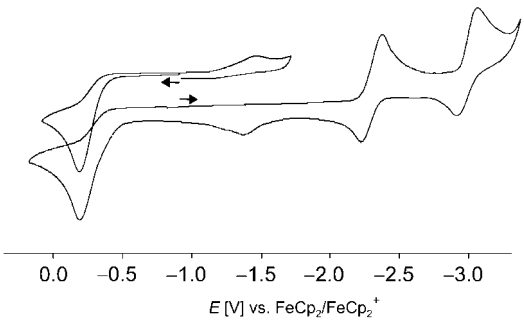


Figure 2. Cyclic voltammograms of [(bpy)Ni(Mes)$_2$] in thf/$Bu_4NPF_6$; scan rate: 100 mV s$^{-1}$ at 298 K.

pared to measurements at 298 K, the peaks $E_{R2}$ and $E_{R3}$ are much smaller and further small reduction waves, for example $E_{R2'}$, are observed. We can therefore conclude that $E_2$ and $E_3$ are processes that are due to products emerging from the first electrochemical reduction (E) followed by a chemical reaction (C; EC mechanism). Evidence that the C process is the cleavage of $Br^-$ thus comes from the reversible behaviour of the terpy complex, the dimesityl complexes (Figure 2, Table 2) and, as tested subsequently, from the increasing reversibility of the $E_1$ process upon addition of an excess of $Bu_4NBr$. Such an EC mechanism has been established for a number of diimine complexes of other transition metals such as Ru, Os, Rh, Ir or Re with halide coligands,[20b,24–26] and also for related phosphane complexes of Pd and Ni.[27]

If we examine the details further we find that in comparison to the dimesityl complexes the first reduction potentials of the bromido mesityl complexes are shifted to less negative values and that within the series of complexes the potentials depend strongly on the nature of the diimine ligand. Quantitative measurements using the Baranski method[28] revealed two successive one-electron reductions for the dimesityl complexes. Polarographic measurements on the bromido mesityl complexes also confirmed the uptake of one electron for the $E_{R1}$ process. Other studies have shown that in the presence of additional MesBr the first reduction wave of [(bpy)Ni(Mes)Br] comprises two electrons and the complex [(bpy)Ni(Mes)$_2$] is formed under these conditions.[16,18,19] Corresponding experiments by us confirm these results. However, without additional MesBr only small amounts of the dimesityl complexes are formed during the reduction, therefore these species cannot account for the reversible waves $E_2$.

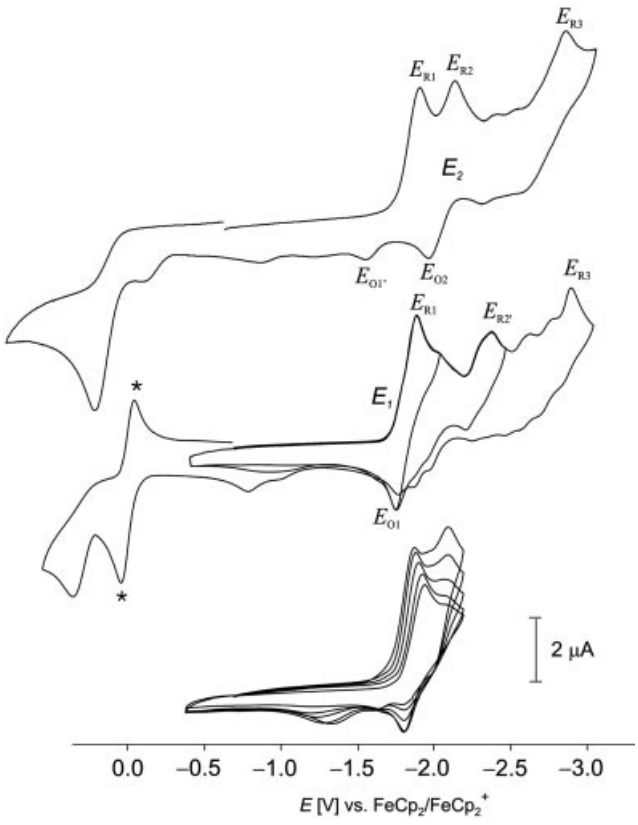


Figure 3. Cyclic voltammograms of [(bpy)Ni(Mes)Br] in thf/$Bu_4NPF_6$ solution at 298 K (top), in dmf/$Bu_4NPF_6$ solution at 238 K (middle), and dmf/$Bu_4NPF_6$ solution at temperatures varying between 238 and 278 K (bottom); * marks the redox waves of the ferrocene/ferrocenium standard.

The reductive electrochemistry of the perfluorinated derivative [(bpy)Ni(Fmes)Br] occurs at much less negative potential, as expected due to the presence of the electron-withdrawing F substituents (Table 3). Under normal experimental conditions (scan rate: 100 mV s$^{-1}$ at 298 K) the first wave appears almost reversible ($\Delta E_{pp}$ = 66 mV; peak-current ratio = 0.91). This is interesting, since the use of very poor bases like *i*Pr-DAB or bpz also increases the reduction potential but does not lead to reversible behaviour to the same extent. Obviously, the rate of bromide splitting depends on the net electron density on the nickel atom, which is not

Table 2. Electrochemical data of dimesitylnickel complexes [(N^N)Ni(Mes)$_2$].[a]

| (N^N) | $E_{O1}$ | $E_1$ ($\Delta E_{pp}$) | $E_2$ ($\Delta E_{pp}$) | $E_{R3}$ | $\Delta E_1 - E_2$ | $\Delta E_1 - E_1(L)$ | Solvent |
|---|---|---|---|---|---|---|---|
| tmphen | –0.23 | –2.42 (75) | –3.11 (105) | –3.40 | 0.69 | 0.26 | thf |
| tmphen | –0.25 | –2.22 (73) | –2.97 irr. | –3.33 | 0.75 | 0.46 | dmf |
| bpy | –0.14 | –2.19 (87) | –2.97 (99) | – | 0.78 | 0.58 | thf |
| bpy | –0.19 | –2.02 (71) | –2.89 (89) | –3.08 | 0.87 | 0.55 | dmf |
| bpz | 0.09 | –1.61 (72) | –2.53 (92) | –3.08 | 0.92 | 0.61 | thf |
| bpz | 0.05 | –1.48 (78) | –2.36 (81) | –2.83 | 0.88 | 0.60 | dmf |

[a] From cyclic voltammetry or square-wave voltammetry at 298 K in 0.1 M solvent/$Bu_4NPF_6$ solutions. Scan rate: 100 mV s$^{-1}$. Potentials ($E$) in V vs. ferrocene/ferrocenium. Reduction potentials are given as half-wave potentials ($E_1$ or $E_2$), with peak-to-peak separation $\Delta E_{pp}$ in mV given in parentheses, or cathodic peak potentials ($E_{R3}$). Oxidation potentials are given as anodic peak potentials ($E_{O1}$).

 © 2007 Wiley-VCH Verlag GmbH & Co. KGaA, Weinheim 

Table 3. Electrochemical data of nickel complexes with Fmes or $PPh_3$ ligands.[a]

| Compound | $E$ (oxII)[b] | $E_{1/2}$ (oxI) ($\Delta E_{pp}$)[c] | $E_{1/2}$ (redI) ($\Delta E_{pp}$)[c] | $E_{1/2}$ (redII) ($\Delta E_{pp}$)[c] | Solvent/$T$ [K] |
|---|---|---|---|---|---|
| [(bpy)Ni(Fmes)Br] | – | 0.86 irr.[b] | –1.68 (66) | –2.13 (85) | thf/298 |
| [(bpy)Ni(Fmes)Br] | 1.89 | 0.92 irr.[b] | – | – | $CH_2Cl_2$/298 |
| [(bpy)Ni(Fmes)Br] | 1.90 | 0.81 (83) | – | – | $CH_2Cl_2$/258 |
| $[(PPh_3)_2Ni(Mes)Br]$ | 1.62 | 0.58 irr.[b] | –2.55 irr.[d] | – | $CH_2Cl_2$/298 |
| $[(PPh_3)_2Ni(Fmes)Br]$ | 1.66 | 0.85 (79) | –2.18 irr.[d] | –2.44 irr.[d] | $CH_2Cl_2$/298 |
| $[(PPh_3)_2Ni(Fmes)Br]$ | – | 0.93 (76) | –1.99 irr.[d] | –2.92 irr.[d] | thf/298 |

[a] From cyclic voltammetry in 0.1 M solvent/$Bu_4NPF_6$ solutions at 100 mV $s^{-1}$ scan rate. Potentials ($E$) in V vs. ferrocene/ferrocenium couple. [b] Anodic peak potentials ($E_{pa}$) for irreversible oxidation steps. [c] Half-wave potentials $E_{1/2}$, with peak potential differences $\Delta E_{pp} = E_{pa} - E_{pc}$ in mV in parentheses. [d] Cathodic peak potentials ($E_{pa}$) for irreversible reduction steps.

adequately reflected by the reduction potential. For the phosphane complexes $[(PPh_3)_2Ni(Mes)Br]$ and $[(PPh_3)_2Ni(Fmes)Br]$ the reductions occur at rather negative potentials and are irreversible even at low temperatures and in the presence of excess bromide.

For the diimine complexes [(N^N)Ni(Mes)Br] we can now draw a reaction scheme (Scheme 4) to illustrate the proposed EC mechanism as well as further feasible electrochemical or chemical reactions.

The first reduction ($E_1$) is followed by a rapid cleavage of bromide ($C_1$). The transient 15 VE species can be stabilised by coordinating a solvent molecule ($C_2$) or by dimerisation ($C_{2'}$). Coordinatively unsaturated species have been observed for other late transition metal complexes[29] but can be ruled out for our investigation since thf or dmf should have sufficient donor capacity to act as a ligand. The solvent complexes can be described by two different canonical forms $[(N\hat{}N^{\cdot-})Ni^{II}(Mes)(solv)] \leftrightarrow [(N\hat{}N)Ni^{I}(Mes)(solv)]$, which have either a reduced diimine ligand or monovalent nickel. The dimerisation occurs upon formation of a nickel–nickel bond with a formal $Ni^{I}$–$Ni^{I}$ unit. Examples of this type of reaction have been found, for example, in the $Ru^{I}$–$Ru^{I}$ dimers that are formed after electrochemical reduction of the $Ru^{II}$ complexes $[(bpy)Ru(CO)_2X_2]$,[24] or in the formation of $Re^0$–$Re^0$ dimers $[(L)(CO)_3Re–Re(CO)_3(L)]$ from $[Re(CO)_3(L)X]$ (L = bpy or phen; X = Cl or CN).[26] Both are formal $d^7$–$d^7$ systems. Examples for related $d^9$–$d^9$ dimers are the $Pd^{I}$–$Pd^{I}$ systems [(phen)(MeCN)Pd–Pd(MeCN)(phen)]$^{2+}$, formed from a comproportionation reaction of $Pd^{II}$ and $Pd^0$ precursors,[30] and $[(L)(RNC)Pd–Pd(RNC)(L)]^{2+}$ (L = bpy, phen or dmphen; RNC = 2,4,6-$Me_3C_6H_2NC$).[31] A bpy-bridged $Pt^{I}$–$Pt^{I}$ dimer is present in $[Pt_2(bpy)_3]^{2+}$, which is formed upon electroreduction of $[Pt(bpy)_2]^{2+}$.[32]

The $E_{R2}$ and $E_{R3}$ processes might thus correspond to the reduction of the solvent complexes or dimers, respectively. From the observation that the reduction wave $E_{R2}$ is dominant in the case of the more basic ligands like bpy, whereas for the good acceptor ligands like bpz or bpm the second electron is accepted predominantly in the more negative

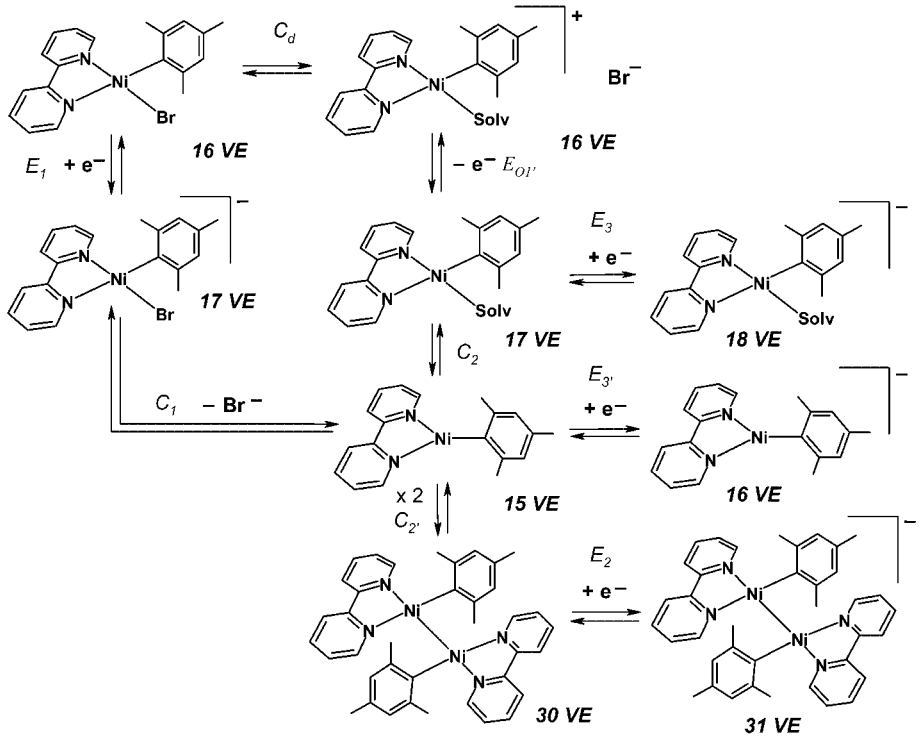


Scheme 4. Proposed mechanism for the electrochemical (E) and chemical reactions (C).

 © 2007 Wiley-VCH Verlag GmbH & Co. KGaA, Weinheim 

wave $E_{R3}$, we can assume a higher tendency of the complexes with basic diimine ligands to form dimeric species (30 VE) and a higher preference for the monomer radicals (17 VE) in the case of complexes with good acceptor ligands. Support for this assumption comes from the fact that using dmf instead of thf shifts the equilibrium between monomeric and dimeric species towards the monomeric solvent-stabilised species. At low temperatures the chemical processes are hampered and therefore we can partially observe the second reduction wave of the parent complexes $E_{R3'}$.

### *Oxidation Reactions*

When measured at 298 K the nickel diimine complexes all exhibit irreversible oxidation waves (Tables 1, 2 and 3), which can be attributed to $Ni^{II}/Ni^{III}$ couples. The potentials are quite low and vary according to the expected influence of the chelate ligand. For rather basic ligands like tmphen they occur at the least positive potentials. The bromido mesityl complexes generally show higher potentials than the dimesityl derivatives. The precursor complex $[(PPh_3)_2Ni(Mes)Br]$ exhibits a far higher potential than the corresponding diimine complexes and the Fmes co-ligand shifts the oxidation potentials to higher values. At lower temperatures the dimesitylnickel complexes exhibit some degree of reversibility for the first oxidation wave, which is in agreement with observations for related platinum(II)[33] or palladium(II)[34] complexes where sterically shielding mesityl ligands have allowed the observation of trivalent states. However, the latter exhibit reversible waves already at 298 K, whereas the nickel analogues are not fully reversible even at 213 K. The phosphane complex $[(PPh_3)_2Ni(Mes)Br]$ shows irreversible oxidation behaviour even at 213 K. A remarkable difference is observed for the oxidation waves of the Fmes derivatives. [(bpy)Ni(Fmes)Br] exhibits a fully reversible first oxidation at 243 K and $[(PPh_3)_2Ni(Fmes)Br]$ shows full reversibility at 298 K. Since a stabilisation of the trivalent nickel species for the non-fluorinated derivatives cannot be achieved even with two shielding mesityl groups, we assume that this enhancement is not only due to the better steric shielding by the $CF_3$ groups but also to the electron-withdrawing effect. Furthermore, we assume that C–H activation of the axial methyl groups plays an essential role in the decomposition of the corresponding mesityl derivatives. The superior stability of the $CF_3$ analogues might thus be due to the hampering of this pathway. Future investigations will therefore focus on the follow-up products of these oxidation reactions.

### *Bulk Reductive Electrolysis*

To support the assumptions depicted in Scheme 4 we tried to isolate defined products from solutions of [(bpy)Ni(Mes)Br] in thf/$Bu_4NPF_6$ that had been submitted to bulk electrolysis (see Experimental Section). When the electrolysis was not driven to completeness, the main species isolated was the starting material together with the free bpy ligand as by-product. After exhaustive electrolysis mainly free bpy ligand and traces of the dimesityl complex [(bpy)Ni(Mes)$_2$] were found, as already mentioned above.

### Spectroelectrochemistry

In order to support the above assignments we studied the products of the electrochemical or chemical reactions by controlled electrolyses combined with in situ spectroscopy (UV/Vis/NIR or EPR).

### *Reductive UV/Vis/NIR Spectroelectrochemistry*

Optical spectroscopy was used to study the products generated in situ from the reductive electrochemistry as this should allow us to answer the question whether the chelate ligand or the metal is hosting the odd electron in the reduced species and furthermore help to discriminate between the formation of solvent complexes [(N^N)Ni(Mes)(solv)] or dimers [(N^N)(Mes)Ni–Ni(Mes)(N^N)] and allow us to characterise them. Figures 4, 5 and 6 show some representative spectra, and Tables 4 and 5 summarise the obtained data.

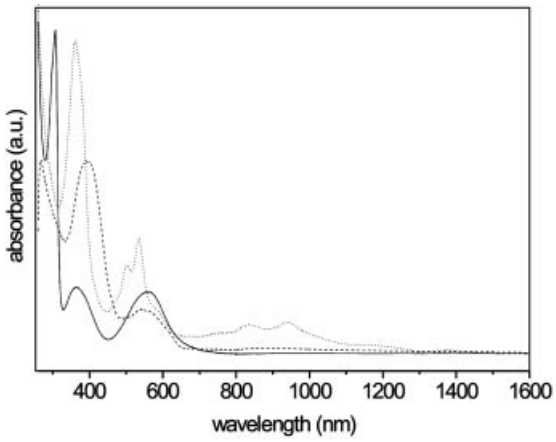


Figure 4. Absorption spectra of $[(bpy)Ni(Mes)_2]^n$ ($n$ = 0: solid line; –1: dotted; –2: dashed) from UV/Vis/NIR spectroelectrochemistry in dmf/$Bu_4NPF_6$ solution. Note that in the last spectrum there is some residual absorption around 900 nm, which is due to an incomplete second reduction.

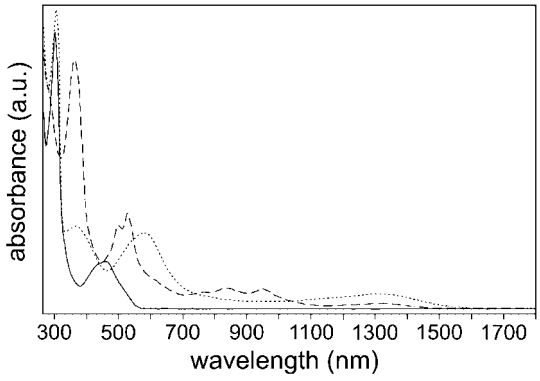


Figure 5. UV/Vis/NIR spectroelectrochemistry of [(bpy)Ni(Mes)Br] in dmf/$Bu_4NPF_6$ solution. Absorption spectra of the parent compound (solid) and after one-electron reduction, spectrum at higher concentration (about $5 \times 10^{-2}$ M, dotted) and dilute solution (about $10^{-4}$ M, dashed).

 © 2007 Wiley-VCH Verlag GmbH & Co. KGaA, Weinheim 

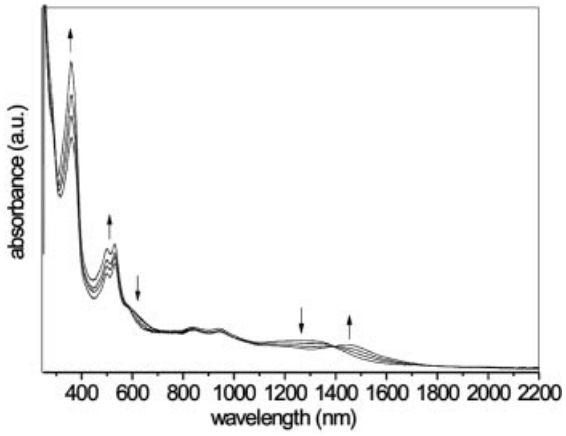


Figure 6. UV/Vis/NIR absorption spectra of [(bpy)Ni(Mes)Br] during the second reduction in dmf/$Bu_4NPF_6$ solution.

Table 4. Long-wavelength absorption maxima of reduced nickel complexes $[(N^{\wedge}N)Ni(Mes)_2]^{n-}$ (N^N = bpy, bpz or tmphen).[a]

| | $\lambda_1$ ($\varepsilon$) | $\lambda_2$ ($\varepsilon$) | $\lambda_3$ ($\varepsilon$) | $\lambda_4$ ($\varepsilon$) | $\lambda_5$ ($\varepsilon$) |
|---|---|---|---|---|---|
| bpy/$n$ = 0 | 298 (15.1) | 367 (3.2) | 564 (3.1) | – | – |
| $n$ = 1 | – | 355 (14.9) | 530 (6.0) | 940 (1.7) | – |
| $n$ = 2 | – | – | 392 (7.4) | 530 (2.6) | – |
| bpz/$n$ = 0 | – | 394 sh | 632 | – | – |
| $n$ = 1 | 449 sh | 493 sh | 642 | 1055 | 1200 |
| $n$ = 2 | 355 | 493 | 589 sh | 1070 sh | 1258 |
| tmphen/$n$ = 0 | 278 | 341 sh | 521 | – | – |
| $n$ = 1 | 345 sh | 369 sh | 534 | 617 sh | 820 sh |
| $n$ = 2 | 381 | 489 | 604 | 843 | 962 |

[a] Generated and measured in dmf/$Bu_4NPF_6$ solution, absorption maxima in nm with extinction coefficients $\varepsilon$ ($\times 1000\ M^{-1}cm^{-1}$) in parentheses.

Figure 4 shows the optical spectra of $[(bpy)Ni(Mes)_2]$ in the parent, singly reduced and doubly reduced state. The long-wavelength absorption bands of the reduced species can be assigned to intra-ligand transition from the singly (or doubly) occupied former LUMO,[23,31] which has been calculated recently to be 96% centred on the bpy ligand,[21] thus clearly showing the mainly bpy-centred character of the reductions. The same assignments can be made for the bpz and tmphen derivatives (see Table 4).

When performing the same spectroelectrochemical experiment for the bromido mesityl derivative (Figure 5 and Table 5) we found that the observed absorption bands of the one-electron-reduced complex were concentration dependent. At high concentrations (about $5 \times 10^{-2}$ M) the spectrum is characterised by a weak broad long-wavelength band around 1300 nm, two medium strong bands around 600 and 350 nm and a very strong band at 300 nm. In dilute solutions ($<10^{-4}$ M) two structured band systems around 900 and 500 nm are visible together with a UV band at around 350 nm. At 1300 nm there is only a very weak residual absorption. Medium concentrated solutions show all the above-described band systems simultaneously. In view of the dimesityl system (Figure 4) and the corresponding spectra of the free ligands,[35] we can ascribe the spectral features of dilute solutions to a species containing a reduced bipyridine ligand and we assume this to be the radical complex $[(bpy^{-})Ni(Mes)(solv)]^{\cdot}$. Apart from the 1300-nm band, the spectra of concentrated solutions resemble those of the starting complex. We tentatively assign this species to the dimer [(bpy)(Mes)Ni–Ni(Mes)(bpy)] since the observed species does not seem to contain a reduced bpy ligand. The 1300-nm band might be ascribed to a transition arising from the nickel–nickel bond (probably a σ–σ* transition).

Table 5. Long-wavelength absorption maxima of parent complexes and species resulting from reductive electrolysis of bromido mesityl complexes [(N^N)Ni(Mes)Br] + $n$ electrons.[a]

| (N^N) $n$ | Species | $\lambda$ ($\varepsilon$) | | | |
|---|---|---|---|---|---|
| tmphen | | | | | |
| $n$ = 0 | parent | 281 | 409 | – | – |
| $n$ = 1 | dimer | 285, 345 | 516 | 637 sh | – |
| $n$ = 2 | dimer | 292 | 385, 490, 608 | 852, 921 | – |
| dmbpy | | | | | |
| $n$ = 0 | parent | 301 | 439, 470 | – | – |
| $n$ = 1 | monomer | 363 | 518, 550 | 788 | – |
| $n$ = 1 | dimer | 300 | 524 | 779 | 1410 |
| $n$ = 2 | dimer | 352 | 352, 512, 527 | 794 | 1512 |
| bpy | | | | | |
| $n$ = 0 | parent | 308 (17.2) | 465 (2.3) | – | – |
| $n$ = 1 | monomer | 361 (14) | 500 (5.0), 532 (5.4) | 945 (1.2) | – |
| $n$ = 1 | dimer | 310 (17.8) | 370 (4.5) | 580 (4.4) | 1305 (1.0) |
| $n$ = 2 | dimer | 372 (15.5) | 500 (6.1), 530 (6.3) | 942 (1.3) | 1448 (1.0) |
| bpz | | | | | |
| $n$ = 0 | parent | 325 | 538 | – | – |
| $n$ = 1 | monomer | 333, 382 | 530 | 1092 | – |
| $n$ = 2 | monomer | 344, 385 | 780 | – | – |
| bpm | | | | | |
| $n$ = 0 | parent | 275 | 340 sh, 530 | – | – |
| $n$ = 1 | monomer | 355 | 460, 482 | 635 | – |
| $n$ = 2 | monomer | 345 | 585 | – | – |

[a] Generated and measured in dmf/$Bu_4NPF_6$ solution, absorption maxima in nm with the extinction coefficients $\varepsilon$ ($\times 1000\ M^{-1}cm^{-1}$) in parentheses.

 © 2007 Wiley-VCH Verlag GmbH & Co. KGaA, Weinheim 

Furthermore, the spectra exhibit two broad medium-strong bands in the visible and a strong band in the UV region. From comparison with the mononuclear dimesityl and bromido mesityl complexes[21] the first two are assigned to mixed MLCT/L′LCT and the latter to π–π* transitions. Careful inspection of the depicted spectra reveals that all spectra exhibit both of the species in varying amounts, which is in line with the assumed equilibrium in Scheme 4. Comparison of all the studied systems (Table 5) shows that after one-electron reduction the spectra of complexes with more basic diimine ligands preferably show the broad band systems indicative for dimeric species. In the extreme case of the tmphen derivative we assign the spectral features to solely the dimeric species. In contrast to this, for the good π-acceptor ligands bpz or bpm no dimer formation is observed, and instead only the monomeric radical complexes are detected (several structured band systems). Furthermore, in systems where both monomeric and dimeric species are observed we found an influence of the solvent on the equilibrium. In thf solution a higher tendency to form dimeric species is observed, whereas in dmf the monomeric radicals (solvent stabilised) are favoured; this is due to the better donor behaviour of the latter solvent.

Figure 6 shows the addition of a second electron to a solution of [(bpy)Ni(Mes)Br] in dmf. We assume that the starting spectrum represents a mixture of the mononuclear species [(bpy$^{-}$)Ni(Mes)Br]$^{\bullet}$ and the dimer [(bpy)(Mes)Ni–Ni(Mes)(bpy)]. At the potential applied behind the peak $E_{R2}$ the dimer is reduced to form the radical [(bpy$^{-}$)(Mes)-Ni–Ni(Mes)(bpy)]$^{\bullet-}$ whereas the monomeric species does not undergo any change. This consideration is based on the red-shift of the long-wavelength band and the increase of the structured band systems around 500 and 350 nm. The two latter bands are indicative of a mono-reduced bipyridine ligand (in the dimeric complex); no evidence is found for a doubly reduced ligand.

For the good π-acceptor ligands bpz and bpm all spectral features clearly represent the reduced ligand and no long-wavelength band indicative of the dimer formation can be detected. Therefore, we assign the two observed reduction processes to the sequence $E_1$–$C_1$–$C_2$–$E_3$.

### *Oxidative UV/Vis/NIR Spectroelectrochemistry*

Oxidation of the diimine nickel(II) complexes [(N^N)-Ni(Mes)Br] or [(N^N)Ni(Mes)$_2$] leads to rapid decomposition of the complexes at 298 K under the conditions of our spectroelectrochemical experiments, therefore we cannot present any spectroscopic data for the generated trivalent species. Spectroelectrochemical experiments at low temperature might help but are not possible for us at present.

### *EPR Spectroelectrochemistry*

Since many of the proposed species are radicals, EPR spectroscopy should give some evidence for the proposed mechanisms for the reductive electrochemistry. EPR data can also provide conclusive information on the metal or ligand contribution to the singly occupied molecular orbital (SOMO)[20] for species from both reductive and oxidative electrochemistry.

#### *Reductive EPR Spectroelectrochemistry*

The EPR spectra of the anion radicals of the dimesitylnickel complexes [(N^N)Ni(Mes)$_2$]$^{\bullet-}$ all exhibit relatively narrow resonances with hyperfine splitting (HFS) in the range of 0.1–0.5 mT. Such HFS constants are typical for couplings of the unpaired electron to the protons and nitrogen atoms of the diimine ligand. Together with the *g* values, which are close to the free-electron value of 2.0023, this is a strong indication for an almost pure π*(diimine) character of the singly occupied molecular orbital (SOMO). For bpy a simulation of the spectrum gave 0.335 mT for N, 0.408 mT for H5, 0.150 mT for H3, 0.081 mT for H4 and 0.065 mT for H6.[23]

At low temperatures in glassy frozen solutions a rhombic-type spectrum was obtained for [(bpy)Ni(Mes)$_2$]$^{\bullet-}$ with $g_1$ = 2.014, $g_2$ = 2.004 and $g_3$ = 1.996. The averaged value is in agreement with $g_{iso}$ = 2.0049. The small *g* anisotropy ($\Delta g$ = 0.018) is indicative of a quite small metal contribution to the radical anion, in agreement with the $g_{iso}$ and the HFS signal found at 298 K. Therefore, and in agreement with the findings from UV/Vis/NIR spectroelectrochemistry and from previous studies on the frontier orbitals of these complexes,[21] we can conclude that the first reduction of the dimesityl complexes occurs into orbitals with mainly π*(diimine) character. Very similar spectra were obtained for the tmphen and bpz derivatives (Table 6). The corresponding radicals are best described as reduced diimine ligands bound to a nickel(II) centre [(N^N$^{-}$)Ni$^{II}$(Mes)$_2$]$^{\bullet-}$.

The first signal observed during reductive electrolysis of [(bpy)Ni(Mes)Br] in thf/$Bu_4NPF_6$ solution at the first reduction wave is rather narrow, shows partial HFS and has a *g* value of 2.0016 (Figure 7, top). Electrolysis at more negative potential (second wave) first leads to an increase of the intensity of this signal and, after a few minutes, an additional, comparably broad signal appears (Figure 7, bottom left) which lies at far higher *g* (2.140) and does not show any HFS. Measurements of this solution at 110 K (glassy frozen solution) reveal that the high-*g* species now exhibits a rhombic-type spectrum, whereas the low-*g* species remains isotropic and narrow (Figure 8).

Table 6. EPR data from reductive spectroelectrochemistry of dimesitylnickel complexes.[a]

| Complex | *T* [K] | $g_{iso}/g_{av}$ | $g_1$ | $g_2$ | $g_3$ | $\Delta g$ [b] | $\Delta H$ [c] [mT] |
|---|---|---|---|---|---|---|---|
| [(tmphen)Ni(Mes)$_2$]$^{\bullet-}$ | 298 | 2.0067 | | | | | 2.8 |
| [(bpy)Ni(Mes)$_2$]$^{\bullet-}$ | 298 | 2.0049 | | | | | 3.1 |
| [(bpy)Ni(Mes)$_2$]$^{\bullet-}$ | 110 | 2.0047 | 2.014 | 2.004 | 1.996 | 0.018 | – |
| [(bpz)Ni(Mes)$_2$]$^{\bullet-}$ | 298 | 2.0063 | | | | | 4.0 |

[a] Generated and measured in thf/$Bu_4NPF_6$ solution. [b] *g* anisotropy $\Delta g = g_1 - g_3$. [c] Signal width.

 © 2007 Wiley-VCH Verlag GmbH & Co. KGaA, Weinheim 

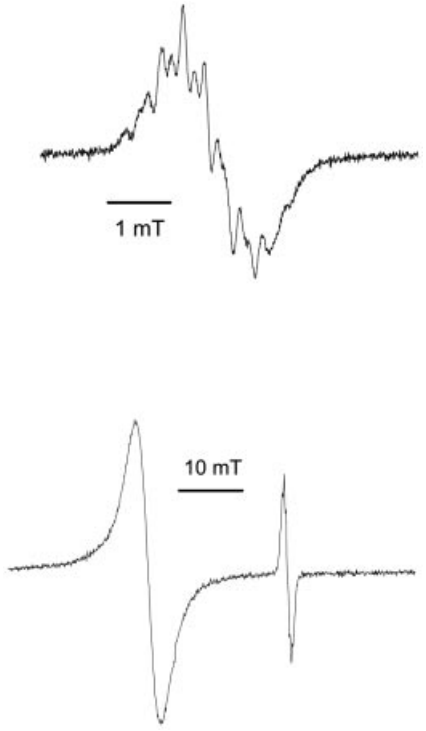


Figure 7. EPR spectra obtained during electrochemical reduction of [(bpy)Ni(Mes)Br] in thf/$Bu_4NPF_6$ at 298 K. Signals obtained upon first (top) and second reduction (bottom).

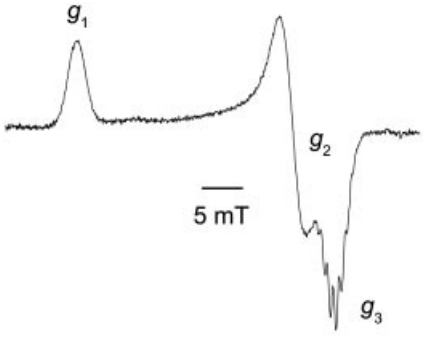


Figure 8. EPR spectrum of a solution obtained at the second reduction wave of [(bpy)Ni(Mes)Br] in thf/$Bu_4NPF_6$, measured at 110 K (glassy frozen solution). The isotropic spectrum (with HFS) of the monomeric complex is overlapping with the $g_3$ component of the main signal (see text and Table 7).

No signal was observed for tmphen at 298 K, although freezing the electrolysed solutions to 110 K allowed the observation of an unresolved narrow signal at $g = 1.9999$ that is comparable to the low-$g$ signal of the bpy derivative. For bpym, bpz, bpm and *i*Pr-DAB we obtained narrow signals with HFS and $g$ values of about 2. For the bpm derivative the solution frozen at 110 K yielded an axial signal with very small $g$ anisotropy. Summarising the data collected in Table 7 we can make the following assignments and conclusions. The signals with $g$ values around the value of the free electron (2.0023) and with detectable HFS were assigned to monomeric nickel(II) complexes containing reduced diimine ligands $[(N\text{^}N^{-})Ni^{II}(Mes)L]^{\cdot}$ (L = Br or solvent). These are the only signals obtained for most of the complexes, which is in line with the observation from UV/Vis/NIR absorption spectroscopy for the good acceptor ligands (vide supra). A second signal was observed for bpy after the reduction at more negative potential, with no HFS, a far higher isotropic $g$ value and a rather high $g$ anisotropy. The two latter parameters point to a far higher nickel contribution to the unpaired electron in this species, which is in line with the assumption that the corresponding species is the proposed dimer in its reduced state $[(bpy^{-})(Mes)Ni^{I}–Ni^{I}(Mes)(bpy)]^{\cdot-}$. For tmphen the observation of such dimeric species would be also expected from the trend of monomer–dimer equilibrium discussed in the electrochemistry section. So far we do not understand the reason why we did not observe any signal at 298 K. At low temperatures we observed only a narrow signal indicative of a monomeric radical.

It is also noteworthy that the EPR results did not give any evidence for the corresponding radicals $[(N\text{^}N^{-})Ni^{II}(Mes)_2]^{\cdot-}$. This confirms our conclusion from the electrochemistry that no large amounts of the dimesityl complexes are formed during reductive electrolysis on the first two reduction waves.

### *Oxidative EPR Spectroelectrochemistry*

As outlined above the UV/Vis/NIR spectroelectrochemical experiments did not allow the observation of nickel(III) species due to rapid decomposition at 298 K. Since the spectroelectrochemical cell used for EPR studies allows electrolysis at lower temperature we tried to study the oxi-

Table 7. EPR data from species observed during reductive spectroelectrochemistry of bromido(mesityl )nickel complexes [(N^N)Ni(Mes)Br].[a]

| (N^N) | Proposed species | Solvent | $T$ [K] | $g_{iso}/g_{av}$ | $g_1$ | $g_2$ | $g_3$ | $\Delta g$[b] | $\Delta H$[c] [mT] |
|---|---|---|---|---|---|---|---|---|---|
| tmphen | monomer | dmf | 110 | 1.9999 | | | | | 8.0 |
| bpy | monomer | thf | 298 | 2.0016 | | | | | 3.1 |
| | dimer | thf | 298 | 2.140 | | | | | 15.0 |
| | dimer | thf | 110 | 2.139 | 2.214 | 2.198 | 2.007 | 0.207 | – |
| | dimer | dmf | 110 | 2.1311 | 2.2635 | 2.0785 | 2.0449 | 0.2186 | – |
| bpym | monomer | thf | 298 | 2.0038 | | | | | 3.0 |
| | monomer | dmf | 298 | 2.0038 | | | | | 3.0 |
| bpz | monomer | thf | 298 | 2.0112 | | | | | 3.8 |
| bpm | monomer | thf | 298 | 2.0039 | | | | | 3.2 |
| | monomer | thf | 110 | 1.9969 | 2.0024 | 2.0024 | 1.9854 | 0.0165 | – |
| *i*Pr-DAB | monomer | thf | 298 | 2.0038 | | | | | 3.0 |

[a] Generated and measured in solvent/$Bu_4NPF_6$ solutions. [b] $g$ anisotropy $\Delta g = g_1 - g_3$. [c] Signal width.

 © 2007 Wiley-VCH Verlag GmbH & Co. KGaA, Weinheim 

dation process of selected nickel(II) complexes and the generated nickel(III) species by EPR spectroscopy. Although we examined a number of compounds, only the complex *trans*-[$(PPh_3)_2$Ni(Fmes)Br] gave a reasonable EPR signal (Figure 9). This is not unexpected in view of its promising reversible cyclic voltammetric behaviour (Table 3).

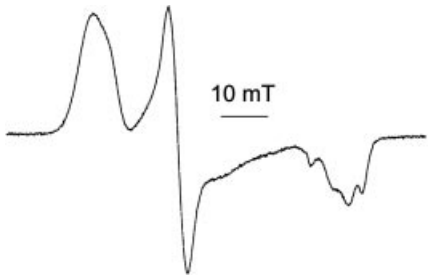


Figure 9. X-band EPR spectrum obtained during electrochemical oxidation of *trans*-[$(PPh_3)_2$Ni(Fmes)Br] in $CH_2Cl_2$/$Bu_4NPF_6$ at 258 K. Measured at 4 K in a glassy frozen solution.

No signal was observed at the corresponding electrolysis temperature of 258 K. At 4 K a rhombic signal (Figure 9) was obtained with very large anisotropy and high averaged $g$ value ($g_1$ = 2.825, $g_2$ = 2.453, $g_3$ = 1.947, $\Delta g$ = 0.878, $g_{av.}$ = 2.435). The $g_3$ component shows a partial HFS of about 5–6 mT and $g_1$ also shows some signs of HFS, whereas the $g_2$ component is sharp and unstructured. In view of the rather high $g$ anisotropy we assign this signal to a radical with a very high nickel contribution to the unpaired electron, and thus to a "real" nickel(III) complex [$(PPh_3)_2Ni^{III}$(Fmes)Br]$^{\cdot+}$ with square-planar geometry, a $d^7$ low-spin configuration and $S$ = 1/2 spin state. There are only very few comparable monomolecular organonickel(III) species reported so far. EPR measurements at low-temperature for the homoleptic complex [$Ni(C_6Cl_5)_4$]$^{\cdot-}$ gave an axial signal with $g_\perp$ = 2.84, $g_\parallel$ = 1.92 and a $g$ anisotropy of 0.92,[36] which is comparable to the value found for our species. For the arylnickel(III) species [(*NCN*)$NiCl_2$], which contains a bis(dimethylamino)phenyl pincer ligand, a $g$ anisotropy of 0.345 has been found.[37] For non-organometallic, formally nickel(III) species the $g$ anisotropy is usually much lower, for example $\Delta g$ = 0.486 for [Ni(emi)]$^-$ [$H_4$emi = *N*,*N*-ethylenebis(2-mercaptoisobutyramide)],[38] $\Delta g$ = 0.372 for the related tetramidonickel complex [Ni(L)]$^{\cdot-}$ ($H_4$L = 6,6-diethyl-3,3,9,9,12,12,14,14-octamethyl-1,4,8,11-tetraazacyclotetradecane-2,5,7,10,13-pentaone; see Scheme 5),[39] or $\Delta g$ = 0.247 for the oxamato complex [Ni(L′)]$^{\cdot-}$ ($H_4$L′ = *N*-[2-(oxalylamino)phenyl]oxalamic acid).[40] Whereas for many species formally described as nickel(III) an appropriate ligand contribution to the unpaired electron from non-innocent ligands such as imines, oxamates or thiolates must be assumed, the [Ni(L)]$^{\cdot-}$ system contains an innocent tetramido ligand, thus an almost pure metal-centred SOMO can be supposed.[39] Comparing its $g$ anisotropy with the values obtained for the two organonickel systems discussed above, it seems that organo ligands lead to distinctly higher $g$ anisotropy and thus highly metal-centred radical states. However, the very small number of examples allows only very tentative conclusions and it would be worthwhile to synthesise further examples of trivalent organonickel complexes.

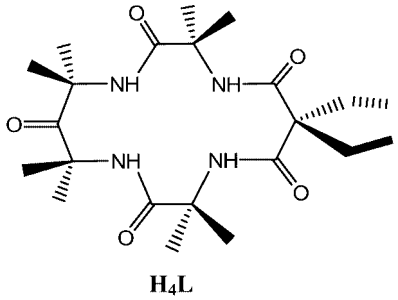


**$H_4$L**

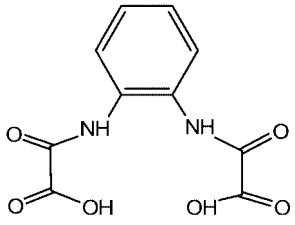


**$H_4$L'**

Scheme 5. Drawings of macrocyclic ligands $H_4$L and $H_4$L′.

## Conclusions

Electrochemical reduction of the organometallic nickel(II) complexes [(N^N)Ni(Mes)Br] leads to highly reactive radicals which undergo follow-up chemical reactions. The nature of the products could not be established unambiguously, but strong evidence was found from optical and EPR spectroelectrochemistry that radical solvent complexes [(N^N)NiMes(Solv)]$^{\cdot}$ with a mainly diimine ligand centred SOMO are formed in processes that start with a ligand-centred one-electron reduction, followed by a splitting of the bromide ligand (EC process). Strong evidence for this comes from various electrochemical experiments and comparison with UV/Vis/NIR absorption and EPR spectra of the corresponding dimesityl radical complexes [(N^N)-$Ni(Mes)_2$]$^{\cdot-}$. For both dimesityl and bromido mesityl complexes a description as monovalent nickel species is not appropriate.

In the case of the comparably basic ligands tmphen, dmbpy or bpy additional spectroscopic features were assigned to the formation of dimers [(N^N)(Mes)Ni–Ni-(Mes)(N^N)] with monovalent nickel after the splitting of the bromide ligand. Evidence comes from long-wavelength bands in the corresponding UV/Vis/NIR spectra and from the EPR signals of the corresponding reduced species at more negative potentials (second reduction) with comparably high $g$ values and $g$ anisotropy in the solid state. Unfortunately, attempts to isolate the proposed dimer complexes using preparative electrochemical reduction (bulk electrolysis) have failed so far, which is a pity in view of catalytic applications.

 © 2007 Wiley-VCH Verlag GmbH & Co. KGaA, Weinheim 

Oxidation of the nickel(II) complexes leads to very short-lived trivalent nickel species that have been characterised by EPR spectroscopy for the perfluorinated complex $[(PPh_3)_2Ni(Fmes)Br]^{\cdot+}$. An almost pure metal-centred character for the SOMO can be concluded from the very high *g* anisotropy of the rhombic signal obtained at 4 K.

Thus, we can add some new evidence to the proposed mechanism for the electrochemical C–C coupling reactions catalysed by nickel diimine complexes. The mechanism has so far been explored in detail up to the catalytically active species [(N^N)Ni(aryl)X]. We can conclude from our work that: i) the assumption of nickel(I) species after the first electrochemical reduction must be corrected towards a mainly diimine ligand centred reduction. Nevertheless, the splitting of the bromide occurs very rapidly, regardless of the character of the SOMO; ii) the diaryl complexes $[(N^N)Ni(aryl)_2]$ are formed in only very small quantities from decomposed material during reductive electrolysis; the formation of nickel(I)–nickel(I) dimers [(N^N)(aryl)Ni–Ni(aryl)(N^N)], which might have an impact on the catalysis, seems to be more important; iii) the proposed monomeric nickel(III) species after oxidative addition of aryl halides have gained some evidence as plausible transient states from our investigations. It seems that organo ligands favour nickel-centred radical states; although this has been demonstrated for a complex containing phosphane instead of diimine ligands. The trivalent diimine nickel species generated upon one-electron oxidation of [(N^N)Ni(Mes)(L)] (L = Mes or Br] are highly unstable even at low temperatures and could not be detected by us.

## Experimental Section

**Instrumentation:** $^1$H NMR spectra were recorded with Bruker Avance300 or AC250 spectrometers. UV/Vis/NIR absorption spectra were recorded with a Bruins Instruments Omega 10 photospectrometer. Cyclic voltammetry and square-wave voltammetry were carried out in 0.1 M $Bu_4NPF_6$ solutions using a three-electrode configuration (glassy-carbon working electrode, Pt counter electrode, Ag/AgCl reference) and a PAR 273 potentiostat and function generator. Half-wave ($E_{1/2}$), anionic ($E_{pa}$) or cationic peak potentials ($E_{pc}$) are given with respect to the ferrocene/ferrocenium couple, which also serves as internal reference. Polarographic measurements were carried out with a PAR Model 263A device. EPR spectra at X-band frequency (ca. 9.5 GHz) were obtained with a Bruker ESP300 spectrometer equipped with a Bruker ER035M gaussmeter and a HP 5350B microwave counter. Spectral simulations were performed with Bruker SimFonia V1.25. UV/Vis/NIR spectroelectrochemical measurements were performed with an optically transparent thin-layer electrode (OTTLE) cell.[41] EPR spectroelectrochemical studies were performed with a platinum two-electrode cell.

**Materials and Procedures:** The preparation of the complex $[(PPh_3)_2Ni(Mes)Br]$ and the diimine complexes [(N^N)Ni(Mes)Br] and $[(N^N)Ni(Mes)_2]$ has been reported recently.[21–23] All preparations and physical measurements in this work were carried out in dry solvents under argon, using Schlenk techniques.

**Preparation of *trans*-[$(PPh_3)_2$Ni(Fmes)Br]:** $NiBr_2$ (218 mg, 1 mmol) was suspended in 200 mL of thf. After addition of $PPh_3$ (524 mg, 2 mmol) the solution turned green. After refluxing for 2 h the reaction mixture was cooled to 298 K and Li(Fmes) (374 mg, 1.3 mmol) in 100 mL of diethyl ether was added. The mixture was stirred for 18 h then 10 mL of aqueous saturated $NH_4Cl$ solution was slowly added to give orange precipitate in the aqueous phase. After separation of the phases and washing the aqueous phase with three 10-mL portions of thf the combined thf solutions were dried with anhydrous $Na_2SO_4$ (1 h) then filtered and the solvents evaporated to dryness. The resulting orange material was recrystallised twice from thf to give red crystals. Yield: 651 mg (0.69 mmol, 69%). $C_{45}H_{32}BrF_9NiP_2$ (944.30): calcd. C 57.24, H 3.42; found C 57.28, H 3.46. $^1$H NMR ([D$_6$]acetone): $\delta$ = 7.9–7.3 (m, 30 H, Ph–P), 7.03 (s, 2 H, Fmes) ppm. $^1$H NMR ($CDCl_3$): $\delta$ = 8.2–7.1 (m, 30 H, Ph–P), 6.93 (s, 2 H, Fmes) ppm. $^{13}$C NMR ([D$_6$]acetone): $\delta$ = 137.1 ($C^1$–P), 136.4 ($C^1$Fmes), 133.6 ($C^{2,6}$P), 131.5 ($C^4$Fmes), 131.0 ($C^{2,6}$Fmes), 128.6 ($C^4$–P), 128.4 ($C^{3,5}$–P), 125.0 ($C^{3,5}$Fmes) ppm. $^{31}$P NMR ($CDCl_3$): $\delta$ = 15.55 ppm (s). $^{19}$F NMR ($CDCl_3$): $\delta$ = –56.59 (t, $^5J_{P,F}$ = 5.9 Hz, 3 F, *o*-$CF_3$), –63.13 (s, 3 F, *p*-$CF_3$) ppm.

**Preparation of [(bpy)Ni(Fmes)Br]:** The compound was prepared by stirring a solution of *trans*-[$(PPh_3)_2$Ni(Fmes)Br] (110 mg, 0.116 mmol) together with bpy (28 mg, 0.18 mmol) in diethyl ether overnight. After evaporation to dryness, the resulting orange-brown solid was washed with *n*-heptane to remove the $PPh_3$ and excess bpy. It was then recrystallised from acetone to give orange needles. Yield: 57 mg (0.1 mmol, 85%). $C_{19}H_{10}BrF_9N_2Ni$ (575.91): calcd. C 39.63, H 1.75, N 4.87; found C 39.61, H 1.78, N 4.88. $^1$H NMR ([D$_6$]acetone): $\delta$ = 9.07 (d, $^3J_{6,5}$ = 5.62 Hz, 2 H, bpy-H6), 8.42 (d, $^3J_{3,4}$ = 8.1 Hz, 2 H, bpy-H3), 8.40 (d, $^3J_{3',4'}$ = 7.86 Hz, 2 H, bpy-H3′), 8.28 (dd, $^3J_{4,5}$ = 6.23 Hz, 2 H, bpy-H4), 8.25 (dd, $^3J_{4',5'}$ = 5.62 Hz, 2 H, bpy-H4′), 7.80 (s, 2 H, Fmes), 7.75 (ddd, 2 H, bpy-H5), 7.40 (ddd, $^3J_{6',5'}$ = 5.72 Hz, 2 H, bpy-H5′), 7.18 (d, 2 H, bpy-H6′) ppm. $^{19}$F NMR ([D$_6$]acetone): $\delta$ = –58.1 (s, 6 F, *o*-$CF_3$), –62.97 (s, 3 F, *p*-$CF_3$) ppm.

**Bulk Reductive Electrolysis:** Electrolysis experiments were carried out with solutions of [(bpy)Ni(Mes)Br] in thf/$Bu_4NPF_6$ using a Pt grid working electrode (total surface are of about 10 cm$^2$), a Pt counter electrode in a separate compartment (separated by a G4 glass frit) and an Ag/AgCl reference electrode. A PAR 273 potentiostat and function generator served to perform the electrolysis and allowed the control of electrons passed into the solution. Cyclic voltammograms were taken from time to time during the electrolysis and after electrolysis the solutions were evaporated to dryness. $^1$H NMR spectra were either recorded for [D$_6$]acetone solutions of the obtained residues or recrystallised material (from thf/diethyl ether, 1:5).

## Acknowledgments

This work was supported by the Grant Agency of the Academy of Sciences of the Czech Republic (grant no. A400400505).

[1] *Applied Homogeneous Catalysis with Organometallic Compounds* (Eds.: B. Cornils, W. A. Herrmann), Wiley/VCH, Weinheim, 2nd edition, **2002**.
[2] a) S. D. Ittel, L. K. Johnson, M. Brookhart, *Chem. Rev.* **2000**, *100*, 1169–1203; b) A. Michalak, T. Ziegler, *Organometallics* **2001**, *20*, 1521–1532; c) S. Mecking, *Angew. Chem. Int. Ed.* **2001**, *40*, 534–540; d) V. C. Gibson, S. K. Spitzmesser, *Chem. Rev.* **2003**, *103*, 283–315.
[3] J.-Y. Nédélec, J. Périchon, M. Troupel, *Top. Curr. Chem.* **1997**, *185*, 141–173.
[4] a) K. W. R. de Franca, J. de Lira Oliveira, T. Florencio, A. P. Da Silva, M. Navarro, E. Léonel, J.-Y. Nédélec, *J. Org. Chem.*

 © 2007 Wiley-VCH Verlag GmbH & Co. KGaA, Weinheim 

**2005**, *70*, 10778–10781; b) M. Durandetti, J. Périchon, *Synthesis* **2004**, 3079–3083; c) F. Raynal, R. Barhdadi, J. Périchon, A. Savall, M. Troupel, *Adv. Synth. Catal.* **2002**, *344*, 45–49; d) K. W. R. de Franca, M. Navarro, E. Léonel, M. Durandetti, J.-Y. Nédélec, *J. Org. Chem.* **2002**, *67*, 1838–1842.
[5] a) D. G. Yakhvarov, Y. H. Budnikova, O. G. Sinyashin, *Russ. J. Electrochem.* **2003**, *39*, 1261–1269; b) Y. H. Budnikova, Y. M. Kargin, J.-Y. Nédélec, J. Périchon, *J. Organomet. Chem.* **1999**, *575*, 63–66.
[6] C. Amatore, A. Jutand, J. Périchon, Y. Rollin, *Monatsh. Chem.* **2000**, *131*, 1293–1304.
[7] a) C. Gosmini, J.-Y. Nédélec, J. Périchon, *Tetrahedron Lett.* **2000**, *41*, 5039–5042; b) dito, *Tetrahedron Lett.* **2000**, *41*, 201–203; c) G. Meyer, M. Troupel, J. Périchon, *J. Organomet. Chem.* **1990**, *393*, 137–142.
[8] a) A. P. Da Silva, S. D. C. Mota, L. W. Bieber, M. Navarro, *Tetrahedron* **2006**, *62*, 5435–5440; b) A. P. Da Silva, A. C. S. Maia, M. Navarro, *Tetrahedron Lett.* **2005**, *46*, 3233–3235.
[9] D. M. Goken, D. G. Peters, J. A. Karty, J. P. Reilly, *J. Electroanal. Chem.* **2004**, *564*, 123–132.
[10] a) D. Franco, K. Wenger, S. Antonczak, D. Cabrol-Bass, E. Dunach, M. Rocamora, M. Gomez, G. Muller, *Chem. Eur. J.* **2002**, *8*, 664–672; b) S. Olivero, D. Franco, J.-C. Clinet, E. Dunach, *Collect. Czech. Chem. Commun.* **2000**, *65*, 844–861.
[11] C. Kuang, Q. Yang, H. Senbuko, M. Tokuda, *Chem. Lett.* **2005**, *34*, 528–529.
[12] P. Tascedda, E. Dunach, *Chem. Commun.* **2000**, 449–450.
[13] M. Ocafrain, E. Dolhem, J.-Y. Nédélec, M. Troupel, *J. Organomet. Chem.* **1998**, *571*, 37–42.
[14] S. Sengmany, E. Léonel, J. P. Paugam, J.-Y. Nédélec, *Tetrahedron* **2002**, *58*, 271–277.
[15] C. Amatore, A. Jutand, *Organometallics* **1988**, *7*, 2203–2214.
[16] D. G. Yakhvarov, Y. H. Budnikova, O. G. Sinyashin, *Russ. Chem. Bull. Int. Ed.* **2003**, *52*, 567–569.
[17] M. Durandetti, M. Devaud, J. Périchon, *New J. Chem.* **1996**, *20*, 659–667.
[18] D. G. Yakhvarov, D. I. Tazeev, O. G. Sinyashin, G. Giambastiani, C. Bianchini, A. M. Segarra, P. Lönnecke, E. Hey-Hawkins, *Polyhedron* **2006**, *25*, 1607–1612.
[19] a) D. G. Yakhvarov, E. G. Samieva, D. I. Tazeev, Y. H. Budnikova, *Russ. Chem. Bull. Int. Ed.* **2002**, *51*, 796–804; b) Y. H. Budnikova, J. Périchon, D. G. Yakhvarov, Y. M. Kargin, O. G. Sinyashin, *J. Organomet. Chem.* **2001**, *630*, 185–192.
[20] a) E. Alessio, S. Daff, M. Elliot, E. Iengo, L. A. Jack, K. G. Macnamara, J. M. Pratt, L. J. Yellowlees, *Spectroelectrochemical Techniques*, in *Trends in Molecular Electrochemistry* (Eds.: A. J. L. Pombeiro, C. Amatore), FontisMedia S. A., Lausanne, **2004**, p. 339–381; b) W. Kaim, *From Electron Transfer to Chemistry: Electrochemical Analysis of Organometallic Reaction Centers and of Their Interaction Across Ligand Bridges*, in *Trends in Molecular Electrochemistry* (Eds.: A. J. L. Pombeiro, C. Amatore), FontisMedia S. A., Lausanne, **2004**, p. 127–151; c) J. A. McCleverty, M. D. Ward, *Mono- and Dinuclear Molybdenum and Tungsten Complexes: Electrochemistry, Optics and Magnetics*, in *Trends in Molecular Electrochemistry* (Eds.: A. J. L. Pombeiro, C. Amatore), FontisMedia S. A., Lausanne, **2004**, p. 71–96.
[21] A. Klein, M. P. Feth, H. Bertagnolli, S. Záliš, *Eur. J. Inorg. Chem.* **2004**, 2784–2796.
[22] M. P. Feth, A. Klein, H. Bertagnolli, *Eur. J. Inorg. Chem.* **2003**, 839–852.
[23] A. Klein, *Z. Anorg. Allg. Chem.* **2001**, *627*, 645–650.
[24] a) S. Chardon-Noblat, A. Deronzier, R. Ziessel, *Collect. Czech. Chem. Commun.* **2001**, *66*, 207–227; b) S. Chardon-Noblat, A. Deronzier, F. Hartl, J. van Slageren, T. Mahabiersing, *Eur. J. Inorg. Chem.* **2001**, 613–617; c) S. Chardon-Noblat, G. H. Cripps, A. Deronzier, J. S. Field, S. Gouws, R. Haines, F. Southway, *Organometallics* **2001**, *20*, 1668–1675; d) S. Chardon-Noblat, A. Deronzier, R. Ziessel, D. Zsoldos, *Inorg. Chem.* **1997**, *36*, 5384–5389.
[25] a) F. Baumann, W. Kaim, G. Denninger, H.-J. Kümmerer, J. Fiedler, *Organometallics* **2005**, *24*, 1966–1973; b) A. Dogan, B. Sarkar, A. Klein, F. Lissner, Th. Schleid, J. Fiedler, S. Záliš, V. K. Jain, W. Kaim, *Inorg. Chem.* **2004**, *43*, 5973–5980; c) S. Berger, J. Fiedler, R. Reinhardt, W. Kaim, *Inorg. Chem.* **2004**, *43*, 1530–1538.
[26] F. Paolucci, M. Marcaccio, C. Paradisi, S. Roffia, C. A. Bignozzi, C. Amatore, *J. Phys. Chem. B* **1998**, *102*, 4759–4769.
[27] a) C. Amatore, A. Jutand, *Acc. Chem. Res.* **2000**, *33*, 314–321; b) C. Amatore, A. Jutand, *J. Am. Chem. Soc.* **1991**, *113*, 2819–2825.
[28] A. S. Baranski, W. R. Fawcett, C. M. Gilbert, *Anal. Chem.* **1985**, *57*, 166–170.
[29] a) R. Poli, *Chem. Rev.* **1996**, *96*, 2135–2204; b) R. Poli, *Acc. Chem. Res.* **1997**, *30*, 494–501; c) H. Urtel, C. Meier, F. Eisenträger, F. Rominger, J. P. Joschek, P. Hofmann, *Angew. Chem. Int. Ed.* **2001**, *40*, 781–784; d) P. H. M. Budzelaar, N. N. P. Moonen, R. De Gelder, J. M. M. Smits, A. W. Gal, *Eur. J. Inorg. Chem.* **2000**, 753–769.
[30] T. Muruhashi, T. Nagai, T. Okuno, T. Matsutani, H. Kurosawa, *Chem. Commun.* **2000**, 1689–1690.
[31] T. Tanase, H. Ukaji, Y. Yamamoto, *J. Chem. Soc., Dalton Trans.* **1996**, 3059–3064.
[32] A. R. Brown, Z. Guo, F. W. J. Mosselmans, S. Parsons, M. Schröder, L. J. Yellowlees, *J. Am. Chem. Soc.* **1998**, *120*, 8805–8811.
[33] a) A. Klein, W. Kaim, F. M. Hornung, J. Fiedler, S. Záliš, *Inorg. Chim. Acta* **1997**, *264*, 269–278; b) W. Kaim, A. Klein, *Organometallics* **1995**, *14*, 1176–1186; c) A. Klein, W. Kaim, E. Waldhoer, H.-D. Hausen, *J. Chem. Soc., Perkin Trans. 2* **1995**, 2121–2126; d) A. Klein, E. J. L. McInnes, T. Scheiring, S. Záliš, *J. Chem. Soc., Faraday Trans.* **1998**, 2979–2984.
[34] A. Klein, M. Niemeyer, *Z. Anorg. Allg. Chem.* **2000**, *626*, 1191–1195.
[35] M. Krejčík, S. Záliš, M. Ladwig, W. Matheis, W. Kaim, *J. Chem. Soc., Perkin Trans. 2* **1992**, 2007–2010.
[36] P. J. Alonso, L. R. Falvello, J. Fornies, A. Martin, B. Menjon, G. Rodriguez, *Chem. Commun.* **1997**, 503–504.
[37] D. M. Grove, G. van Koten, P. Mul, R. Zoet, J. G. M. van der Linden, J. Legters, J. E. J. Schmitz, N. W. Murrall, A. J. Welch, *Inorg. Chem.* **1988**, *27*, 2466–2473.
[38] H.-J. Krüger, G. Peng, R. H. Holm, *Inorg. Chem.* **1991**, *30*, 734–742.
[39] T. J. Collins, T. R. Nichols, E. S. Uffelman, *J. Am. Chem. Soc.* **1991**, *113*, 4708–4709.
[40] X. Ottenwaelder, R. Ruiz-Garcia, G. Blondin, R. Carasco, J. Cano, D. Lexa, Y. Journaux, A. Aukauloo, *Chem. Commun.* **2004**, 504–505.
[41] M. Krejčík, M. Daňek, F. Hartl, *J. Electroanal. Chem.* **1991**, *317*, 179–187.

Received: September 15, 2006
Published Online: January 19, 2007

 © 2007 Wiley-VCH Verlag GmbH & Co. KGaA, Weinheim 

DOI: 10.1002/ejic.200600894

# The Synthesis, Crystal and Band Structures, and Properties of the Quaternary Supramolecular Complexes $[Hg_6Z_4](MX_6)Hg_y$ (Z = As, Sb; M = Hg, Cd; X = Cl, Br, I; $y$ = 0, 0.5, 0.6)

**Jian-Ping Zou,[a,b] Yan Li,[a] Ming-Lai Fu,[a] Guo-Cong Guo,*[a] Gang Xu,[a] Xue-Hui Liu,[a] Wei-Wei Zhou,[a] and Jin-Shun Huang[a]**

**Keywords:** Density functional calculations / Host–guest systems / Pnictides / Semiconductors / Supramolecular chemistry

The series of supramolecular complexes $(Hg_6As_4)(CdCl_6)Hg_{0.5}$ (**1**), $(Hg_6As_4)(HgCl_6)Hg_{0.5}$ (**2**), $(Hg_6As_4)(CdBr_6)$ (**3**), and $(Hg_6Sb_4)(CdI_6)Hg_{0.6}$ (**4**) has been prepared by a solid-state reaction and their crystal structures determined by single-crystal X-ray diffraction. All these compounds crystallize in the space group $Pa\bar{3}$ with four formula units in a cell: $a$ = 12.172(2) (**1**), 12.189(1) (**2**), 12.3738(5) (**3**), and 13.234(2) Å (**4**). Their structures feature a 3D cationic host framework that is built up of linearly coordinated mercury and tetrahedrally coordinated pnicogen atoms to form distorted $As_2Hg_6$ or $Sb_2Hg_6$ octahedra, and discrete guest anions. The distorted octahedra corner-share with each other to form a perovskite-like, 3D cationic framework that possess two types of closed cavities with different sizes. The octahedral guest anions $(MX_6)^{4-}$ are embedded in the larger cavities, whereas the smaller cavities trap the excess mercury atoms or remain empty. The optical properties were investigated by diffuse reflectance and FT IR spectroscopy. The electronic band structures and density of states (DOS) calculated by DFT methods indicate that the present compounds are semiconductors and that the optical absorption mainly originates from the charge transitions from the p orbital of the pnicogen (As or Sb) and halogen (Cl, Br or I) atoms states to the Hg1 6s states for **1**, **3**, and **4**, and to Hg1 6s and Hg3 6s states for **2**.

(© Wiley-VCH Verlag GmbH & Co. KGaA, 69451 Weinheim, Germany, 2007)

## Introduction

The field of inorganic supramolecular chemistry has attracted more and more attention and has experienced enormous growth because it covers a large diversity of compounds that possess a huge variety of crystal and electronic structures and physical and chemical properties.[1] For instance, a broad family of supramolecular assemblies based on mercury pnicogen cationic frameworks has been reported since the 1990s.[2] Among them, the three dimensional host frameworks with positive charges are ordinarily built up of linearly coordinated mercury and tetrahedrally coordinated pnicogen atoms, whereas the guest anions are usually composed of halometalate or monoatomic anions with different shapes and sizes.[3] Two principal types of networks can be distinguished in these compounds according to the dimensions of the voids. The first type are analogues of the well-known Millon's base salts,[4] which are composed of cationic frameworks with the formula $(Hg_2Z)^+$ (Z = P, As) and adopt a tridymite-like topology filled with different tetrahedral anions such as $ZnI_4^{2-}$[3c,3d] or $CdI_4^{2-}$.[3g] The second one is the topology with the formula $(Hg_6Z_4)^{4+}$ (Z = P, As, Sb),[3,5] among which the frameworks possess cavities of two different sizes in close proximity. These are capable of trapping guests of two different types: octahedral guests with the formula $(MX_6)^{4-}$ or $(M'X_6)^{3-}$ (M = divalent metal atoms; M′ = trivalent metal atoms; X = Cl, Br, I)[2b,2c,3] in the bigger cavities and monoatomic guests in the smaller ones. In most cases, the coordination centers of the octahedral guests are trivalent metal atoms rather than divalent metal atoms. Until now, two divalent metals, namely Hg[3b,6] and Fe,[2b] acting as the coordination centers of the octahedral guest anions have been reported, among which only one quaternary supramolecular mercury pnictide halide, $(Hg_4As_6)(FeBr_6)Hg_{0.6}$,[2b] has been characterized.

Recently, we have begun a systematic investigation of mercury pnictide-based mixed-framework compounds to further explore new self-assembly supramolecular materials. The idea is to exploit cationic host framework that have various structures together with different cavities for trapping different guest anions. Because the II–V group compounds have good semiconducting and thermoelectric properties,[7] we have chosen mercury and cadmium in combination with pnicogens in order to obtain new semicon-

[a] State Key Laboratory of Structural Chemistry, Fujian Institute of Research on the Structure of Matter, Chinese Academy of Sciences,
Fuzhou, Fujian 350002, P. R. China
Fax: +86-591-8371-4946
E-mail: gcguo@ms.fjirsm.ac.cn
[b] Graduate School, Chinese Academy of Sciences,
Beijing 100039, P. R. China
Supporting information for this article is available on the WWW under http://www.eurjic.org or from the authors.

 © 2007 Wiley-VCH Verlag GmbH & Co. KGaA, Weinheim 

ducting compounds with unique physical properties and abundant structural features. Our ongoing research in this field has resulted in some interesting compounds.[2e,3g]

In the present work, with the intention of preparing new quaternary host–guest compounds based on the mercury-pnicogen framework, we selected divalent cadmium cation as the coordination center of the octahedral guest anions and changed the halogen and pnicogen atoms from Cl to I, and P to Sb, respectively. We succeeded in synthesizing a new series of supramolecular complexes, $(Hg_6As_4)(CdCl_6)$-$Hg_{0.5}$ (**1**), $(Hg_6As_4)(HgCl_6)Hg_{0.5}$ (**2**), $(Hg_6As_4)(CdBr_6)$ (**3**), and $(Hg_6Sb_4)(CdI_6)Hg_{0.6}$ (**4**). Herein, we report the syntheses, crystal and band structures, and properties of these new supramolecular inorganic complexes. These band structure and optical and thermal studies are the first to be reported for supramolecular complexes based on mercury pnictide halides, which are also the major interest for us.

## Results and Discussion

The present compounds are all stable in air. Their crystal structures were determined by means of single-crystal X-ray diffraction. All these compounds have a similar structural organization. Their crystal structures feature a 3D cationic host framework and discrete different guest anions. The 3D cationic network is built up of linearly coordinated mercury and tetrahedrally coordinated pnicogen atoms to form distorted $As_2Hg_6$ or $Sb_2Hg_6$ octahedra. The distorted octahedra corner-share with each other to form a perovskite-like 3D cationic framework that possess two types of closed cavities with different sizes (Figure 1).

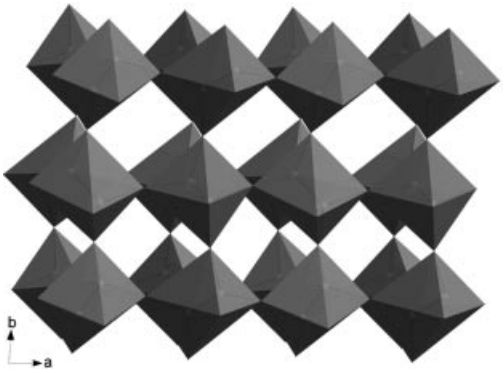


Figure 1. The perovskite-like 3D cationic framework built from corner-sharing distorted octahedra viewed along the *c* axis.

The octahedral guest anions $(CdCl_6)^{4-}$, $(HgCl_6)^{4-}$, and $(CdI_6)^{4-}$ are embedded in the larger cavities of the host framework in **1**, **2**, and **4**, respectively, whereas the smaller cavities trap the excess mercury atoms with 50%, 50%, and 60% site occupancy for **1**, **2**, and **4**, respectively (Figure 2). Partial occupancy of the smaller cavities by mercury atoms has been reported previously in the literature, particularly for $(Hg_6As_4)(HgCl_6)Hg_{0.4}$, which is nearly same as **2** except for the different occupancy of the discrete mercury atom.[2b,3b] Like the ternary compounds $(Hg_6P_4)(HgBr_6)$[3b] and $(Hg_6Sb_4)(HgBr_6)$,[6a] in which the larger cavities of the host framework are filled with the octahedral guest anions $(HgX_6)^{4-}$ with the smaller cavities remaining empty, compound **3** is the first quaternary compound with this structural feature in metal pnictide halides (see Figure S1 in the Supporting Information).

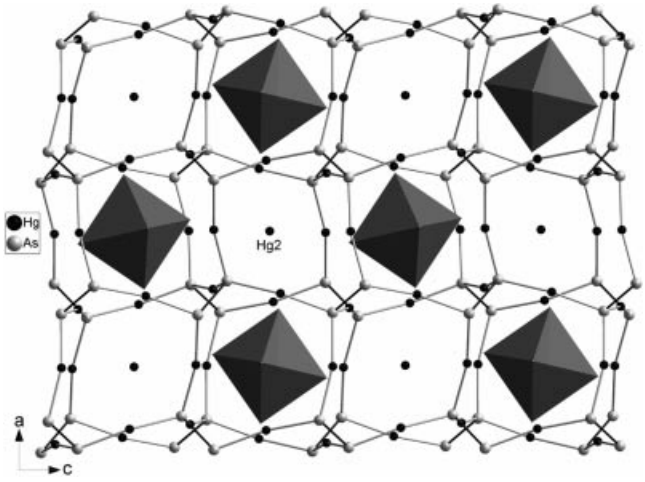


Figure 2. View of the structure of **1**, **2**, and **4** along the *b* axis. The $(CdCl_6)^{4-}$, $(HgCl_6)^{4-}$, and $(CdI_6)^{4-}$ octahedra are drawn in grey.

The Hg1–As, Hg1–Sb, and As–As bond lengths in the cationic moieties in the present compounds range from 2.496(2) to 2.531(2), 2.686(2) to 2.693(2), and 2.389(7) to 2.428(6) Å, respectively, all of which lie in the normal ranges for Hg–Z and As–As bond lengths in known mercury pnictide halides.[2–6] The Sb–Sb bond length of 2.790(5) Å is also in good agreement with those found in various mercury antimonide halides.[3f,6a] The Hg3–Cl [2.70(1) Å] and Cd–X [Cd–Cl 2.636(7), Cd–Br 2.806(3), Cd–I 3.006(2) Å] bond lengths in the guest anions are all close to the those in mercury and cadmium pnictide halides.[2e,2f]

The distances between the hosts and anionic guests in the present compounds are significantly longer than the expected values for covalent bonding, thus suggesting the typical supramolecular interactions between them.[1b] The interatomic distance between the chlorine atoms of the guest anions and the mercury atoms in the host framework range from 2.95 to 3.30, 2.93 to 3.30, 3.02 to 3.28, and 3.20 to 3.58 Å for **1**, **2**, **3**, and **4**, respectively, all of which are much longer than the Hg–X covalent bond lengths but shorter than the sum of the van der Waals radii of Hg and X. Therefore, host–guest supramolecular interactions are present in the crystal structures and these fix the octahedral guest anions to their specific positions so that no positional or rotational disorder is observed. This situation has also been reported in the literature.[2b,2d,2h]

As for the monatomic guests, the discrete mercury atoms have similar environments in **1**, **2**, and **4**. In the first coordination sphere, each Hg atom displays a coordination number of 14 [(6 Hg + 2 As + 6 Cl) in **1** and **2** and (6 Hg + 6 I + 2 Sb) in **4**]. The distances between the hosts and monatomic guests fall in the ranges 3.50–3.68 Å for **1**, 3.55–3.70 Å for **2**, and 3.68–3.92 Å for **4**. With such coordination, the monatomic guests can be regarded as being clath-

 © 2007 Wiley-VCH Verlag GmbH & Co. KGaA, Weinheim 

rated with an oxidation state of zero, similar to the case found in $(Hg_6As_4)(HgCl_6)Hg_{0.4}$[3b] and $(Hg_6As_4)(FeBr_6)$-$Hg_{0.6}$,[2b] where the zero oxidation state of the guest mercury was confirmed by means of solid-state $^{199}Hg$ NMR spectroscopy.

As shown in Figure 3, the diffuse reflectance spectra of the present compounds reveal the presence of an optical gap of 2.05, 2.01, 1.94, and 1.23 eV for **1**–**4**, respectively, which suggests that the compounds are semiconductors and is consistent with their colors. The bandgaps are shifted to lower energies in the order Cl > Br > I, which is similar to other cases reported in the literature.[8] The bandgap of **4** is close to those of CdTe (1.44 eV), GaAs (1.43 eV), and $CuInS_2$ (1.55 eV), all of which are highly efficient photovoltaic materials.[9] Thus, we suppose that this compound may find a use for the efficient absorption of solar radiation in solar cell applications. The IR spectra of the present compounds show no obvious absorptions in the range of 4000–400 $cm^{-1}$ (see Figures S2–S5 in the Supporting Information) which, in combination with their good thermal stability (see Figure S6–S9 in the Supporting Information), may make them useful as window materials for laser delivery media and infrared transmitters for optical fiber applications in telecommunications.[10]

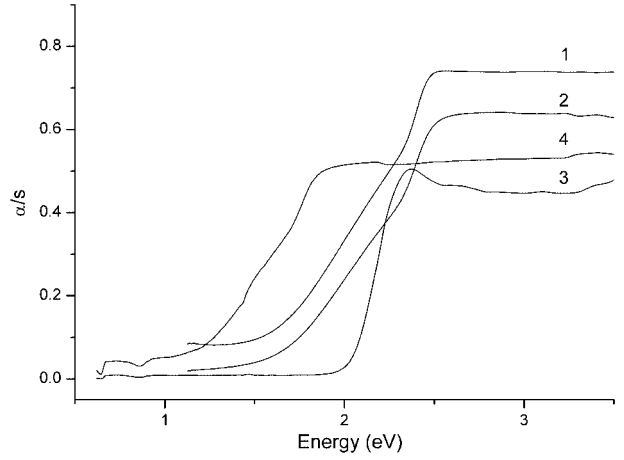


Figure 3. Diffuse reflectance spectra of **1**–**4**.

The calculated band structures of the present compounds along the high symmetry points of the first Brillouin zone are plotted in Figure 4a–d for **1**–**4**, respectively. It can be seen that the valence bands (VBs) and conduction bands (CBs) are both disperse. All four compounds show semiconductor character: the lowest *k*-point of the CBs and the highest *k*-point of the VBs are both localized at the G point and the direct bandgaps are about 1.86, 1.72, and 1.89 eV for **1**–**3**, respectively. For **4**, the lowest *k*-point of the CBs and the highest *k*-point of the VBs are not localized at the same point, which indicates that compound **4** has indirect semiconductor character, with a bandgap of 1.33 eV. The calculated energy gaps for the present compounds are similar to their experimental values. The bands can be assigned according to total and partial densities of states (DOS), as plotted in parts a–d of Figure 5 for **1**–**4**, respectively. In **1**

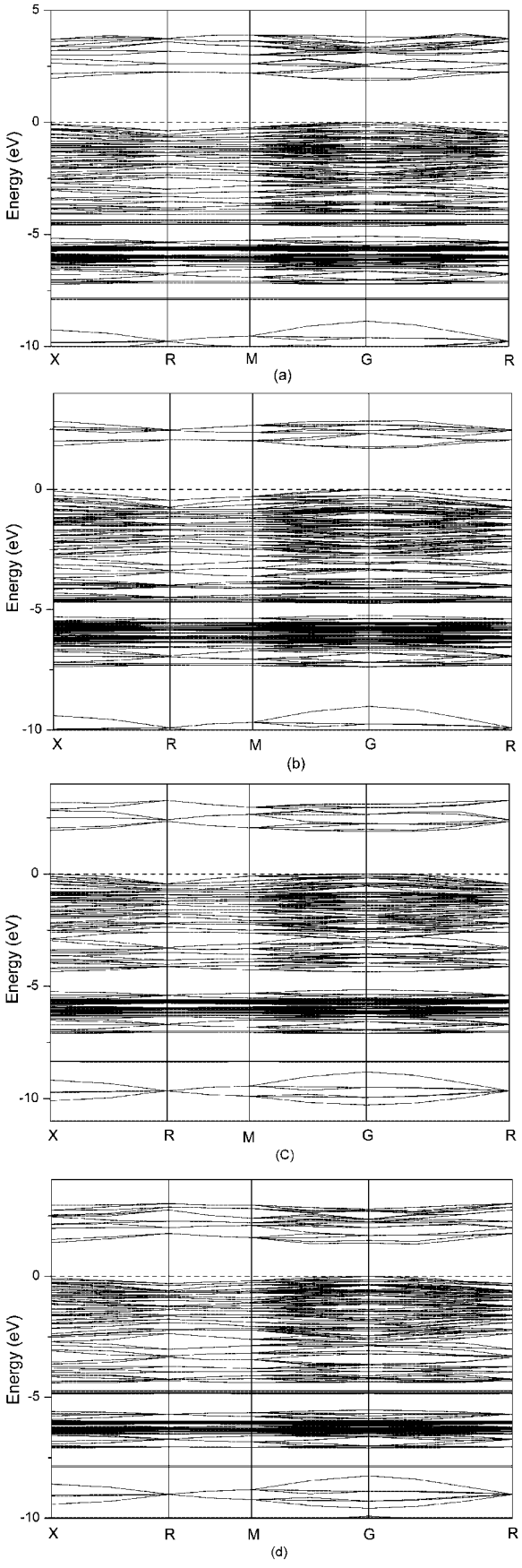


Figure 4. The band structures of **1** (a), **2** (b), **3** (c), and **4** (d). The Fermi level is set at 0 eV.

 © 2007 Wiley-VCH Verlag GmbH & Co. KGaA, Weinheim 

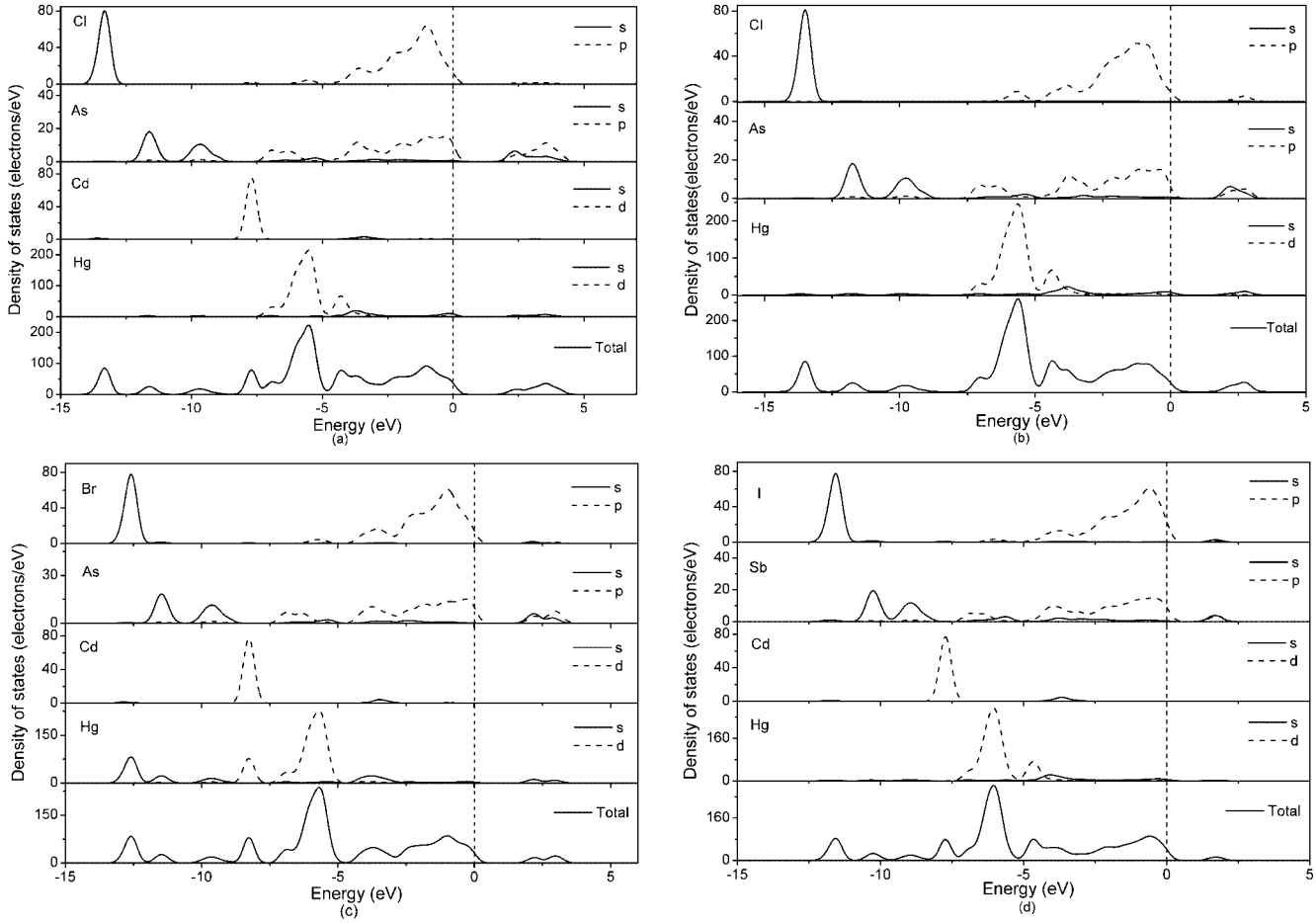


Figure 5. Total and partial density of states for **1** (a), **2** (b), **3** (c), and **4** (d). The Fermi level (vertical dotted line) is set at 0 eV.

and **2**, the VBs between –15.0 and –5.0 eV are mostly formed by the Hg 5d and Cd 4d states mixing with small Cl 3s and As 4s states, and the VBs lying about between –5.0 eV and the Fermi level (0.0 eV) are the main contributions from the Cl 3p and As 4p states mixing with a small amount of Hg 5d state, while the CBs between 1.7 and 5.0 eV are due to the Hg 6s, As 4s, and As 4p states. In addition, comparing the partial DOS of the different types of mercury atoms in **1** and **2** (parts a,b in Figure 6), the DOS of Hg1 6s state is seen to be much higher than that of the Hg2 6s state at the bottom of the CBs in **1**, and the DOS of the Hg1 6s and Hg3 6s states are much higher than that of the Hg2 6s state at the bottom of the CBs in **2**. This shows that electron transitions mostly come from the s orbital of the mercury atoms in the host framework or the octahedral guest anions rather than from the s orbital of the monoatomic mercury to Cl 3p and As 4p states. Therefore, the optical absorption is mainly ascribed to the charge transitions from Cl 3p and As 4p to Hg1 6s states for **1**, and Cl 3p and As 4p to Hg1 6s and Hg3 6s states for **2**.

Similarly, the VBs between –15.0 and –5.0 eV are mostly formed by the Hg 5d and Cd 4d states mixing with small Br 4s, As 4s, and Hg 6s, and I 5s and Sb-5s states for **3** and **4**, respectively. The VBs between –5.0 eV and the Fermi level (0.0 eV) are mostly formed by Br 4p and As 4p states for **3**, and I 5p and Sb 5p states for **4**, hybridized with a small amount of the s orbital of the transition metals, whereas the CBs between 1.3 and 5.0 eV are made from the Hg 6s state mixed with the s and p orbitals of the pnicogen atoms. Thus, it can be concluded that the optical absorption can be mainly assigned to the charge transitions from Br 4p and As 4p to Hg 6s states for **3**. As shown in Figure 6 (c), the partial DOS of the different type of mercury atoms in **4** shows that the DOS of the Hg1 6s state is much higher than that of the Hg2 6s state at the bottom of the CBs, which indicates that the electron transitions arise mostly from the Hg1 6s rather than Hg2 6s to I 5p and Sb 5p states. Therefore, the optical absorption is mainly ascribed to the charge transitions from I 5p and Sb 5p to Hg1 6s.

In addition, we calculated the atomic site and angular momentum projected DOS of the present compounds to elucidate the nature of the electronic band structures and chemical bonds. As shown in Figure 5, we observed that the density and shape of the p orbital of the pnicogen atoms states are similar to that of the Hg 6s state between –5.0 and –2.5 eV, while the DOS of the p orbital of the halogen atoms states are higher than that of the Cd 5s state (Hg 6s state for **2**) for each compound. Accordingly, we can conclude that there are strongly covalent Hg1–As and Hg1–Sb

 © 2007 Wiley-VCH Verlag GmbH & Co. KGaA, Weinheim 

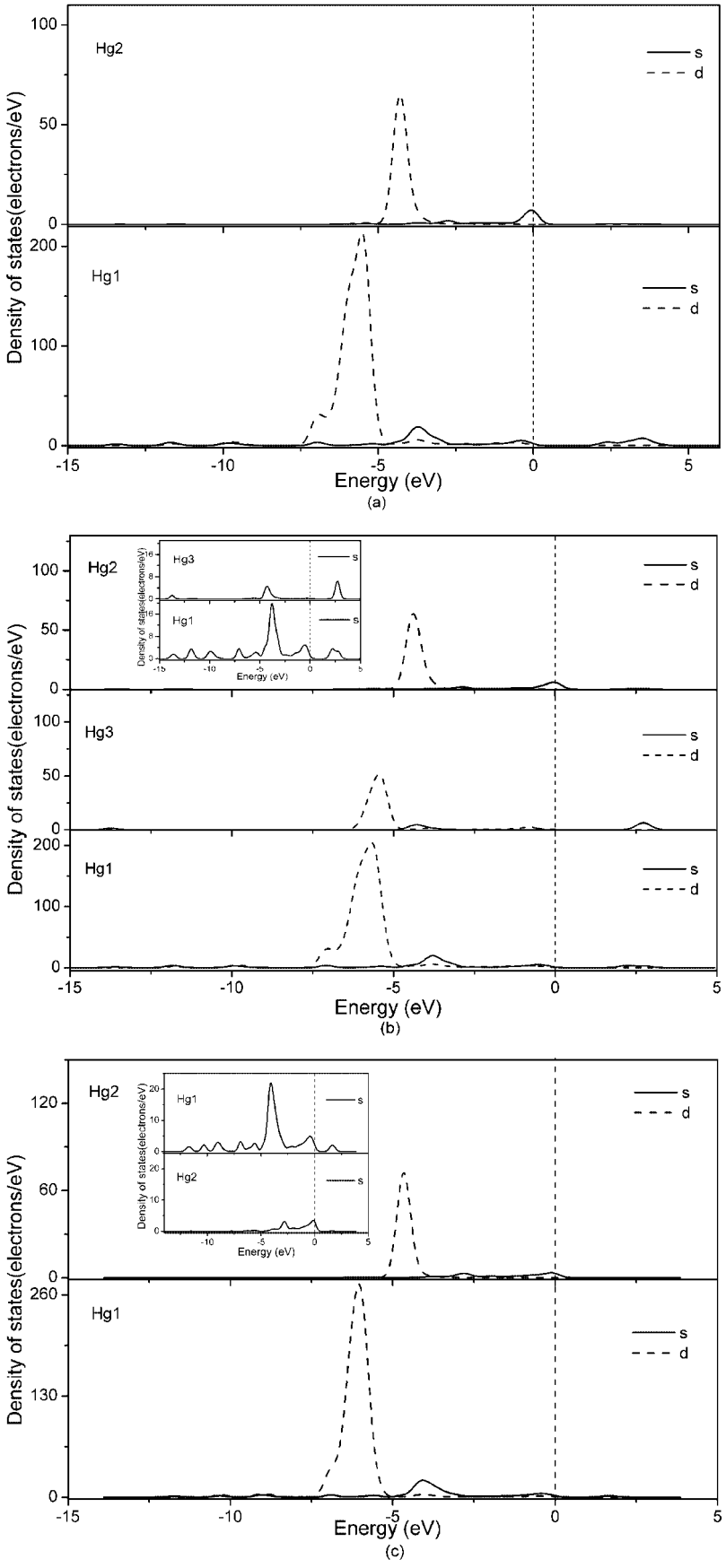


Figure 6. Partial density of states of the Hg atoms in **1** (a), **2** (b), and **4** (c). The Fermi level (vertical dotted line) is set at 0 eV. The insets show an expansion of the low-energy region for Hg1 and Hg3 in (b) and Hg1 and Hg2 in (c).

 © 2007 Wiley-VCH Verlag GmbH & Co. KGaA, Weinheim 

interactions in the host cations and weakly covalent Cd–Cl, Hg3–Cl, Cd–Br, and Cd–I interactions in the guest anions for **1**–**4**, respectively.

Semi-empirical population analyses allow for a more quantitative bond analyses. The calculated bond orders of **1**–**4** within a unit cell are listed in Table 1; the bond order of a purely covalent single bond is generally 1.0 e. As can be seen, except for the Z–Z bond in **4**, the covalent interactions of the bonds are in the order Hg1–X < M–X < Z–Z < Hg1–Z (M = Hg3 for **2** and Cd for **1**, **3**, **4**) for each compound. This indicates that the covalent interactions of the Hg–Z bonds are stronger than those of the M–X bonds, which is in agreement with the results from the DOS analyses. The Hg1–X bond is the weakest of all four types of bonds, which is consistent with the existence of supramolecular interactions between the host framework and guest anions.

Table 1. Calculated bond orders (e) of **1**–**4** within the unit cell.

| | Hg1–Z | Z–Z | M–X[a] | Hg1–X |
|---|---|---|---|---|
| **1** | 0.48 to 0.49 | 0.36 | 0.29 | 0.04 to 0.16 |
| **2** | 0.47 to 0.48 | 0.34 | 0.26 | 0.04 to 0.16 |
| **3** | 0.54 to 0.62 | 0.45 | 0.26 | –0.18 to –0.02 |
| **4** | 0.59 to 0.75 | 0.77 | 0.12 | –0.42 to –0.22 |

[a] M = Hg3 for **2** and Cd for **1**, **3**, and **4**.

## Conclusions

In summary, a series of quaternary supramolecular $[Hg_6Z_4](MX_6)Hg_y$ complexes has been synthesized and structurally characterized. Their main structural feature is that they all consist of discrete guest anions and a perovskite-like 3D cationic framework composed of corner-sharing distorted $As_2Hg_6$ or $Sb_2Hg_6$ octahedra that possesses two types of closed cavities with different sizes. The octahedral guest anions $(MX_6)^{4-}$ are embedded in the larger cavities, while the smaller cavities trap the excess mercury atoms or remain empty. The present compounds, which have a bandgap range of 1.2–2.1 eV and are transparent over a broad range of IR frequencies, may have applications as efficient photovoltaic materials and IR window materials. The calculations of the electronic band structures and density of states (DOS) indicate that their optical absorption mainly originates from the charge transitions from the p orbital of the pnicogen and halogen atoms to the Hg1 6s states for **1**, **3**, and **4**, and to Hg1 6s and Hg3 6s for **2**.

## Experimental Section

**Materials and Measurement:** All chemicals were analytically pure (>99.99%) and used without further purification. The powder X-ray diffraction patterns were collected with a Rigaku DMAX2500 diffractometer at 40 kV and 100 mA for Cu-$K_\alpha$ radiation ($\lambda$ = 1.5406 Å) with a scan speed of 5° per minute at room temperature. The simulated patterns were produced using the Mercury program and single-crystal reflection data. Thermogravimetric analysis (TGA) and differential scanning calorimetry were performed on a Netzsch Sta449C thermoanalyzer under a $N_2$ atmosphere in the range 30–800 °C at a heating rate of 10 °C min$^{-1}$. IR spectra were recorded with a Magna 750 FT-IR spectrometer as KBr pellets in the range 4000–400 cm$^{-1}$. Optical diffuse reflectance spectra were measured with a PE Lambda 35 UV/Vis spectrophotometer for **1** and **2**, and a 900 UV/Vis spectrophotometer for **3** and **4** equipped with an integrating sphere at 293 K, and the $BaSO_4$ plate was used as the reference. The absorption spectra were calculated from reflection spectra by the Kubelka–Munk function:[11] $\alpha/S = (1 - R)^2/2R$, where $\alpha$ is the absorption coefficient, $S$ is the scattering coefficient, which is practically wavelength independent when the particle size is larger than 5 μm, and $R$ is the reflectance. The energy gap was determined as the intersection point between the energy axis at the absorption offset and the line extrapolated from the linear portion of the absorption edge in the $\alpha/S$ vs. $E$ (eV) plot. Microprobe elemental analysis on Hg, Cd, Sb, As, Cl, Br, and I for the present compounds were performed with a field-emission scanning electron microscope (FESEM, JSM6700F) equipped with an energy dispersive X-ray spectroscope (EDS, Oxford INCA).

**Synthesis of $(Hg_6As_4)(CdCl_6)Hg_{0.5}$ (1):** Yellow crystals of **1** were initially prepared by the solid-state reaction of a mixture of $HgCl_2$ (1.5 mmol, 407 mg), Cd (0.5 mmol, 56 mg), $CdCl_2$ (0.5 mmol, 91 mg), and As (1.0 mmol, 75 mg) at 450 °C for 120 h. Microscope element analysis on several single crystals of **1** confirmed the presence of Hg, Cd, As, and Cl in the approximate molar ratio 6.5:1.0:3.9:6.1, which is in good agreement with that obtained from structural analysis. After structural analysis, a yellow crystalline sample of **1** was obtained quantitatively by the reaction of a mixture of $Hg_2Cl_2$, Hg, Cd, and As in a 6:1:2:8 molar ratio at 450 °C for 120 h. The TGA curve of **1** shows no weight change up to 310 °C (see Figure S6 in the Supporting Information). The purity of the yellow crystalline sample was confirmed by XRD powder diffraction (see Figure S10 in the Supporting Information). The powder diagram of **1** shows some splitting of the reflections, which indicates there is a lower symmetry in **1**.

**Synthesis of $(Hg_6As_4)(HgCl_6)Hg_{0.5}$ (2):** Yellow crystals of **2** were initially prepared by the reaction of a mixture of $Hg_2Cl_2$ (1.0 mmol, 472 mg), Cd (0.5 mmol, 56 mg), and As (1.0 mmol, 75 mg) at 320 °C for 120 h in an attempt to obtain the new phase $(Hg_6As_4)(CdCl_6)$. The results of the single-crystal X-ray diffraction analysis indicated the absence of Cd. Microscope element analysis on several single crystals of **2** confirmed the presence of Hg, As, and Cl in the approximate molar ratio 7.4:4.0:5.9, which is in good agreement with that obtained from structural analysis. After structural analysis, a yellow crystalline sample of **2** was then obtained quantitatively by the reaction of a mixture of $Hg_2Cl_2$, Hg, and As in a 6:3:8 molar ratio at 320 °C for 120 h. The TGA curve of **2** shows no weight change up to 320 °C (see Figure S7 in the Supporting Information). The purity of the yellow crystalline sample was confirmed by XRD powder diffraction (see Figure S11 in the Supporting Information). The powder diagram of **2** shows some splitting of the reflections, which indicates there is a lower symmetry in **2**.

**Synthesis of $(Hg_6As_4)(CdBr_6)$ (3):** Red crystals of **3** were prepared by the reaction of a mixture of $HgBr_2$ (1.0 mmol, 361 mg), Cd (0.5 mmol, 56 mg), and As (1.0 mmol, 75 mg) at 350 °C for 120 h. Microscope element analysis on several single crystals of **3** confirmed the presence of Hg, Cd, As, and Br in the approximate molar ratio 5.9:1.0:3.9:5.8, which is in good agreement with that obtained from structural analysis. After structural analysis, a red crystalline sample of **3** was then obtained quantitatively by the reaction of a mixture of $Hg_2Br_2$, Cd, and As in a 3:1:4 molar ratio at 350 °C for 120 h. The TGA curve of **3** shows no weight change up to

 © 2007 Wiley-VCH Verlag GmbH & Co. KGaA, Weinheim 

Table 2. Crystal data and structure refinement parameters for **1**, **2**, **3**, and **4**.

| | **1** | **2** | **3** | **4** |
|---|---|---|---|---|
| Empirical formula | $[Hg_6As_4](CdCl_6)Hg_{0.5}$ | $[Hg_6As_4](HgCl_6)Hg_{0.5}$ | $[Hg_6As_4](CdBr_6)$ | $[Hg_6Sb_4](CdI_6)Hg_{0.6}$ |
| Formula mass [g mol$^{-1}$] | 1928.61 | 2016.80 | 2095.08 | 2684.69 |
| Crystal color | yellow | yellow | red | black |
| Crystal habit | plate | plate | chip | block |
| Crystal system | cubic | cubic | cubic | cubic |
| Space group | $Pa\bar{3}$ | $Pa\bar{3}$ | $Pa\bar{3}$ | $Pa\bar{3}$ |
| $a$ [Å] | 12.172(2) | 12.189(1) | 12.3738(5) | 13.234(2) |
| Volume [Å$^3$] | 1803.2(5) | 1810.7(3) | 1894.6(1) | 2317.7(7) |
| Z | 4 | 4 | 4 | 4 |
| $\lambda$ (Mo-$K_\alpha$) [Å] | 0.71073 | 0.71073 | 0.71073 | 0.71073 |
| $D_{calcd.}$ [g cm$^{-3}$] | 7.104 | 7.398 | 7.345 | 7.694 |
| $\mu$ [mm$^{-1}$] | 64.427 | 71.452 | 69.095 | 56.981 |
| $F(000)$ | 3208 | 3336 | 3480 | 4392 |
| $\theta$ range [°] | 2.90–25.03 | 2.89–25.06 | 3.68–25.09 | 2.67–25.02 |
| Reflections collected | 604 | 628 | 11390 | 2174 |
| Observed reflections | 377 | 380 | 421 | 445 |
| Independent reflections | 534 | 546 | 554 | 683 |
| $R_1$,[a] $wR_2$[b] | 0.0499, 0.1052 | 0.0666, 0.1570 | 0.0565, 0.0963 | 0.0646, 0.1104 |
| Goodness-of-fit | 0.998 | 0.999 | 0.990 | 0.994 |
| $\Delta\rho_{max}$ and $\Delta\rho_{min}$ [e/Å$^3$] | 2.457, –2.905 | 3.959, –4.863 | 3.200, –2.611 | 3.295, –2.702 |

[a] $R = \Sigma||F_o| - |F_c||/\Sigma|F_o|$. [b] $R_w = \{\Sigma[w(F_o^2 - F_c^2)^2]/\Sigma[w(F_o^2)^2]\}^{1/2}$.

Table 3. Selected bond lengths [Å] and angles [°] for **1**–**4**.[a]

| | | | |
|---|---|---|---|
| Compound **1** | | | |
| Hg(1)–As(1) | 2.496(2) | Cd(1)–Cl(1) × 6 | 2.636(7) |
| Hg(1)–As(2) | 2.498(2) | As(1)–As(2) × 2 | 2.392(6) |
| Hg(1)–Cl(1) | 2.947(6) | | |
| As(1)–Hg(1)–As(2) | 164.3(1) | As(2)#3–As(1)–Hg(1) | 106.5(1) |
| As(1)–Hg(1)–Cl(1) | 106.3(2) | Hg(1)–As(1)–Hg(1)#4 | 112.24(9) |
| As(2)–Hg(1)–Cl(1) | 87.2(2) | As(1)#5–As(2)–Hg(1) | 110.47(9) |
| Cl(1)#1–Cd(1)–Cl(1)#2 | 93.1(2) | Hg(1)–As(2)–Hg(1)#6 | 108.5(1) |
| Cl(1)#1–Cd(1)–Cl(1) | 86.9(2) | Cd(1)–Cl(1)–Hg(1) | 100.2(2) |
| Cl(1)#2–Cd(1)–Cl(1) | 180.0(3) | | |
| Compound **2** | | | |
| Hg(1)–As(1) | 2.496(2) | Hg(3)–Cl(1) × 6 | 2.701(1) |
| Hg(1)–As(2) | 2.502(2) | As(1)–As(2) × 2 | 2.389(7) |
| Hg(1)–Cl(1) | 2.933(9) | | |
| As(1)–Hg(1)–As(2) | 164.4(1) | Cl(1)#1–Hg(3)–Cl(1)#4 | 180.0 |
| As(1)–Hg(1)–Cl(1) | 106.3(2) | As(2)#5–As(1)–Hg(1) | 106.8(1) |
| As(2)–Hg(1)–Cl(1) | 87.1(2) | Hg(1)#6–As(1)–Hg(1) | 111.98(11) |
| Cl(1)#1–Hg(3)–Cl(1)#2 | 86.6(2) | As(1)#7–As(2)–Hg(1) | 110.3(1) |
| Cl(1)#2–Hg(3)–Cl(1) | 93.4(2) | Hg(1)–As(2)–Hg(1)#8 | 108.6(1) |
| Cl(1)–Hg(3)–Cl(1)#3 | 180.0(4) | Hg(3)–Cl(1)–Hg(1) | 99.6(3) |
| Compound **3** | | | |
| Hg(1)–As(2) | 2.529(2) | Cd(1)–Br(1) × 6 | 2.806(3) |
| Hg(1)–As(1) | 2.531(2) | As(1)–As(2) × 2 | 2.428(6) |
| Hg(1)–Br(1) | 3.022(3) | | |
| As(2)–Hg(1)–As(1) | 165.5(1) | Br(1)#1–Cd(1)–Br(1) | 180.0(1) |
| As(2)–Hg(1)–Br(1) | 87.31(8) | Cd(1)–Br(1)–Hg(1) | 98.34(9) |
| As(1)–Hg(1)–Br(1) | 105.2(1) | As(2)#4–As(1)–Hg(1)#5 | 107.3(1) |
| Br(1)#1–Cd(1)–Br(1)#2 | 86.67(8) | Hg(1)#5–As(1)–Hg(1)#6 | 111.6(1) |
| Br(1)#1–Cd(1)–Br(1)#3 | 93.33(7) | As(1)#7–As(2)–Hg(1) | 110.5(1) |
| Br(1)#2–Cd(1)–Br(1)#3 | 86.67(7) | Hg(1)#8–As(2)–Hg(1) | 108.5(1) |
| Compound **4** | | | |
| Hg(1)–Sb(2) | 2.686(2) | Cd(1)–I(1) × 6 | 3.006(2) |
| Hg(1)–Sb(1) | 2.693(2) | Sb(1)–Sb(2) × 2 | 2.790(5) |
| Hg(1)–I(1) | 3.204(3) | | |
| Sb(2)–Hg(1)–Sb(1) | 161.92(9) | I(1)–Cd(1)–I(1)#2 | 180.0 |
| Sb(2)–Hg(1)–I(1) | 85.22(7) | Hg(1)#3–Sb(1)–Hg(1) | 112.75(7) |
| Sb(1)–Hg(1)–I(1) | 108.54(8) | Hg(1)#3–Sb(1)–Sb(2)#4 | 105.95(8) |
| I(1)#1–Cd(1)–I(1) | 87.33(5) | Hg(1)–Sb(2)–Hg(1)#5 | 110.79(7) |
| I(1)#1–Cd(1)–I(1)#2 | 92.67(5) | Hg(1)–Sb(2)–Sb(1)#6 | 108.11(7) |

[a] Symmetry transformations used to generate equivalent atoms. **1**: #1 –*y* + 1/2, *z* + 1/2, *x*; #2 –*x*, –*y* + 1, –*z*; #3 –*x* + 1/2, *y* + 1/2, *z*; #4 –*y* + 1, *z* + 1/2, –*x* + 1/2; #5 –*x* + 1/2, *y* – 1/2, *z*; #6 *z*, *x*, *y*. **2**: #1 –*y* + 1, –*z*, –*x* + 1; #2 *z* + 1, *x* – 1, *y*; #3 –*x* + 2, –*y*, –*z*; #4 *y* + 1, *z*, *x* – 1; #5 –*x* + 3/2, *y* – 1/2, *z*; #6 *z* + 1/2, –*x* + 1/2, –*y*; #7 –*x* + 3/2, *y* + 1/2, *z*; #8 –*z* + 1, *x* – 1/2, –*y* + 1/2. **3**: #1 –*x*, –*y* + 1, –*z* + 1; #2 –*y* + 1/2, –*z* + 1, *x* + 1/2; #3 –*z* + 1/2, *x* + 1/2, *y*; #4 *x* – 1/2, *y*, –*z* + 1/2; #5 –*z*, *x* + 1/2, –*y* + 1/2; #6 *y* – 1/2, –*z* + 1/2, –*x*; #7 *x* + 1/2, *y*, –*z* + 1/2; #8 *y*, *z*, *x*. **4**: #1 –*y* + 1, –*z* + 1, –*x* + 1; #2 –*x* + 1, –*y* + 1, –*z* + 1; #3 –*y* + 1/2, –*z* + 1, *x* + 1/2; #4 –*x* + 1/2, *y* – 1/2, *z*; #5 –*z* + 1, *x* + 1/2, –*y* + 3/2; #6 –*x* + 1/2, *y* + 1/2, *z*.

 © 2007 Wiley-VCH Verlag GmbH & Co. KGaA, Weinheim 

280 °C (see Figure S8 in the Supporting Information). The purity of the red crystalline sample was confirmed by XRD powder diffraction (see Figure S12 in the Supporting Information).

**Synthesis of $(Hg_6Sb_4)(CdI_6)Hg_{0.6}$ (4):** Black crystals of **4** were prepared by the reaction of a mixture of $Hg_2I_2$ (0.6 mmol, 393 mg), Cd (0.3 mmol, 34 mg), and Sb (0.9 mmol, 110 mg) at 350 °C for 120 h. Microscope element analysis on several single crystals of **4** confirmed the presence of Hg, Cd, Sb, and I in the approximate molar ratio 6.5:1.0:4.2:6.1, which is in good agreement with that obtained from structural analysis. After structural analysis, a mixture of liquid mercury and a black crystalline sample of **4** was then obtained quantitatively by the reaction of a mixture of $Hg_2I_2$, Hg, Cd, and Sb in a 3:1:1:4 molar ratio at 350 °C for 120 h. The TGA curve of **4** shows no weight change up tol 260 °C (see Figure S9 in the Supporting Information). The purity of the black crystalline sample was confirmed by XRD powder diffraction (see Figure S13 in the Supporting Information).

**X-ray Crystallographic Studies:** Single crystals of **1**–**4** suitable for X-ray analysis were mounted at the apex of a glass fiber for data collection. Data sets for **1**, **2**, and **4** were collected with a Rigaku AFC7R diffractometer, and that for **3** was collected with Rigaku Mercury CCD, both of which were equipped with a graphite-monochromated Mo-$K_\alpha$ radiation source ($\lambda$ = 0.71073 Å) from a rotating anode generator at 293 K. The intensity data were collected with the $\omega$-scan technique and corrected for Lorentz polarization factors. All the structures were solved by direct methods and difference Fourier synthesis and refined by full-matrix least-squares techniques using the Siemens SHELXTL™ version 5 crystallographic software package.[12] All atoms were refined anisotropically. Crystallographic data for **1**–**4** are listed in Table 2 and selected bond lengths and angles are given in Table 3. Further details of the crystal structure investigation can be obtained from the Fachinformationzentrum Karlsruhe, 76344 Eggenstein-Leopoldshafen, Germany, on quoting the depository number CSD-417040, -417038, -417039, and -417037 for **1**–**4**, respectively.

**Computational Details:** The X-ray crystallographic data of the present compounds were used to calculate their electronic band structures. The calculations of electronic band structures along with density of states (DOS) were carried out using density functional theory (DFT) with one of the three nonlocal gradient-corrected exchange-correlation functionals (GGA-PBE) and performed with the CASTEP code,[13] which uses a plane wave basis set for the valence electrons and norm-conserving pseudopotential[14] for the core electrons. The number of plane waves included in the basis was determined by a cutoff energy, $E_c$, of 450 eV for **1**, **3**, and **4**, and 400 eV for **2**. Pseudo-atomic calculations were performed for Cl $3s^23p^5$, Br $4s^24p^5$, I $5s^25p^5$, As $4s^24p^3$, Sb $5s^25p^3$, Cd $4d^{10}5s^2$, and Hg $5d^{10}6s^2$. The parameters used in the calculations and convergence criteria were set by the default values of the CASTEP code.[13]

**Supporting Information:** (see also the footnote on the first page of this article): Experimental and simulated powder X-ray diffraction patterns, TG and DTA curves, and IR spectra of compounds **1**–**4**.

## Acknowledgments

We gratefully acknowledge the financial support of the National Science Foundation of China (20571075 and 20521101), the National Science Foundation for Distinguished Young Scientists of China (20425104), and the National Science Foundation of CAS (KJCX2-SW-h05).

[1] a) G. R. Desiraju, *Angew. Chem. Int. Ed. Engl.* **1995**, *34*, 2311–2327; b) A. Müller, H. Reuter, S. Dillinger, *Angew. Chem. Int. Ed. Engl.* **1995**, *34*, 2328–2361.

[2] a) A. V. Olenev, A. I. Baranov, O. S. Oleneva, I. I. Vorontsov, M. Y. Antipin, A. V. Shevelkov, *Eur. J. Inorg. Chem.* **2003**, 1053–1057; b) A. V. Olenev, O. S. Oleneva, M. Lindsjö, L. A. Kloo, A. V. Shevelkov, *Chem. Eur. J.* **2003**, *9*, 3201–3208; c) O. S. Oleneva, A. V. Olenev, E. V. Dikarev, A. V. Shevelkov, *Eur. J. Inorg. Chem.* **2004**, 4006–4010; d) A. V. Olenev, A. I. Baranov, A. V. Shevelkov, B. A. Popovkin, *Eur. J. Inorg. Chem.* **2002**, 547–553; e) J.-P. Zou, G.-C. Guo, W.-T. Chen, X. Liu, M.-L. Fu, Z.-J. Zhang, J.-S. Huang, *Inorg. Chem.* **2006**, *45*, 6365–6369; f) A. V. Shevelkov, M. M. Shatruk, *Russ. Chem. Bull. Int. Ed.* **2001**, *50*, 337–362; g) A. V. Olenev, A. V. Shevelkov, *Angew. Chem. Int. Ed.* **2001**, *40*, 2353–2354; h) A. V. Olenev, A. I. Baranov, A. V. Shevelkov, B. A. Popovkin, *Eur. J. Inorg. Chem.* **2000**, 265–270.

[3] a) A. V. Shevelkov, E. V. Dikarev, M. Yu. Mustiakimov, B. A. Popovkin, *J. Chem. Soc., Dalton Trans.* **1996**, 147–148; b) A. V. Shevelkov, E. V. Dikarev, B. A. Popovkin, *J. Solid State Chem.* **1996**, *126*, 324–327; c) A. V. Olenev, A. V. Shevelkov, B. A. Popovkin, *Russ. J. Inorg. Chem.* **1999**, *44*, 1814–1816; d) A. V. Olenev, A. V. Shevelkov, B. A. Popovkin, *Russ. J. Inorg. Chem.* **1999**, *44*, 1853–1861; e) J. Beck, U. Neisel, *Z. Anorg. Allg. Chem.* **2000**, *626*, 1620–1626; f) J. Beck, S. Hedderich, U. Neisel, *J. Solid State Chem.* **2000**, *154*, 350–355; g) $(Hg_2As)_2(CdI_4)$: J.-P. Zou, D.-S. Wu, S.-P. Huang, J. Zhu, G.-C. Guo, J.-S. Huang, *J. Solid State Chem.*, DOI: 10.1016/j.jssc.2006.11.018.

[4] a) L. Nijssen, W. N. Lipscomb, *Acta Crystallogr.* **1954**, *7*, 103–106; b) W. R. Dorff, K. Brodersen, *Z. Anorg. Allg. Chem.* **1953**, *274*, 323–340; c) R. Airoldi, G. Magnano, *Rass. Chim.* **1967**, *5*, 181–189.

[5] a) H. Puff, M. Grönke, B. Kilger, P. Möltgen, *Z. Anorg. Allg. Chem.* **1984**, *518*, 120–124; b) A. V. Shevelkov, M. M. Shatruk, *Russ. Chem. Bull. Int. Ed.* **2001**, *50*, 337–362.

[6] a) A. V. Shevelkov, E. V. Dikarev, B. A. Popovkin, *J. Solid State Chem.* **1992**, *98*, 133–136; b) A. V. Shevelkov, E. V. Dikarev, B. A. Popovkin, *J. Solid State Chem.* **1993**, *104*, 177–180.

[7] a) R. Laiho, A. V. Lashkul, K. G. Lisunov, E. Lähderanta, M. O. Safonchik, M. A. Shakhov, *J. Phys. Condens. Matter* **2004**, *16*, 333–342; b) R. Laiho, A. V. Lashkul, K. G. Lisunov, E. Lähderanta, M. O. Safonchik, M. A. Shakhov, *Semicond. Sci. Technol.* **2004**, *19*, 602–609.

[8] a) G. A. Mousdis, V. Gionis, G. C. Papavassiliou, C. P. Raptopoulou, A. Terzis, *J. Mater. Chem.* **1998**, *8*, 2259–2262; b) M. Braum, W. Tuffentsammer, H. Wachtel, H. C. Wolf, *Chem. Phys. Lett.* **1999**, *307*, 373–378.

[9] a) C. H. Champness, *Phosphorus, Sulfur Relat. Elem.* **1988**, *38*, 385–397; b) R. H. Dube, *Photovoltaic Materials*, Imperial College Press, **1998**, p. 135; c) P. Dürichen, W. Bensch, *Eur. J. Solid State Inorg. Chem.* **1997**, *34*, 1187–1190.

[10] a) J. A. Harrington, *Infrared Fibers and Their Applications*, SPIE Press, Bellingham, WA, **2004**; b) D. Marchese, M. De Sario, A. Jha, A. K. Kar, E. C. Smith, *J. Opt. Soc. Am. B* **1998**, *15*, 2361–2370.

[11] a) W. W. Wendlandt, H. G. Hecht, *Reflectance Spectroscopy*, Interscience Publishers, New York, **1966**; b) G. Kortüm, *Reflectance Spectroscopy*, Springer-Verlag, New York, **1969**.

[12] *Siemens SHELXTL™ Version 5 Reference Manual*, Siemens Energy & Automation Inc., Madison, Wisconsin, U. S. A. **1994**.

[13] a) M. Segall, P. Linda, M. Probert, C. Pickard, P. Hasnip, S. Clark, M. Payne, *Materials Studio CASTEP version 2.2*, **2002**; b) M. Segall, P. Linda, M. Probert, C. Pickard, P. Hasnip, S. Clark, M. Payne, *J. Phys.: Condens. Matter* **2002**, *14*, 2717–2744.

[14] D. R. Hamann, M. Schluter, C. Chiang, *Phys. Rev. Lett.* **1979**, *43*, 1494–1797.

Received: September 25, 2006
Published Online: January 16, 2007

 © 2007 Wiley-VCH Verlag GmbH & Co. KGaA, Weinheim 

DOI: 10.1002/ejic.200600962

# Zinc Thiolate Complexes $[ZnL_n(SR)]^+$ with Azamacrocyclic Ligands, Part III: The Influence of the Ligand $L_n$ on the Reactivity of Zinc-Bound Thiolate[‡]

**Johannes Notni,[a] Wolfgang Günther,[a] and Ernst Anders*[a]**

**Keywords:** Zinc / Sulfur ligands / Kinetics / Density functional calculations / Enzyme models

In this study, we focus on the structure–reactivity relationship of cationic zinc thiolate complexes with the general formula $[Zn(L_n)(SR)]ClO_4$ ($L_n$: *n*-dentate azamacrocyclic ligand; R = phenylmethyl). The complexes feature macrocyclic ligands with ring sizes varying from 11 to 16 atoms and possess three or four nitrogen donors (three of them containing one tertiary nitrogen). Thiol methylations with methyl iodide have been performed in order to determine the relative reactivities, because this reaction has been used before to investigate zinc thiolate reactivity and therefore allows comparison of our results with literature data. The kinetic behaviour was investigated in nitromethane and dichloromethane and was found to be second order in all cases. The observed rate constants vary in the range of $k_2$ = 2.46–55.28×$10^{-3}$ $M^{-1}s^{-1}$ in nitromethane and $k_2$ = 0.23–7.35×$10^{-3}$ $M^{-1}s^{-1}$ in dichloromethane at 300 K. Furthermore, the structures of all thiolate complexes were optimised at the B3LYP/6-311+G(d) level of theory. Natural bond orbital (NBO) analyses were performed to obtain information on partial charges of the heteroatoms and energies of a lone pair in a p-type orbital at the zinc-bound sulfur. In order to elucidate which parameters determine reactivity, selected structural and electronic parameters were correlated with the experimental rate constants. As a result, we found that the reaction is controlled predominantly by frontier orbital energy in dichloromethane and by charge in nitromethane. However, we observed that electronic reactivity control can be overridden by the degree of steric obstruction of the zinc ion, which directly depends on ring size and configuration of the ring nitrogens. The complex $[Zn(cyclen)(SR)]ClO_4$ (**5**) can therefore not be included in any of the correlations; steric constraint imposed by the comparably small ring system causes an extraordinarily increased reactivity. In turn, this finding provides a new rationale for the high reactivity reported for the cyclen complex $[Zn(cyclen)(OH)]^+$, which has been used as a model for carbonic anhydrase in previous studies.
(© Wiley-VCH Verlag GmbH & Co. KGaA, 69451 Weinheim, Germany, 2007)

## Introduction

Methylation is of outstanding importance for biosystems.[2] Irregularities in this process are implicated in the development of the most severe diseases such as cancer, cardiac diseases and neural tube defects. Currently, about 150 methyl transferases (EC 2.1.1.*n*) are known, of which approximately 140 use *S*-adenosylmethionine (SAM) as a methyl donor.[3] As the SAM precursor methionine is produced (regenerated) by methylation of the thiol function of homocysteine, thiol-methylating enzymes such as the cobalamine-dependent/independent methionine synthases[4,5] play a crucial role for biological methylation in general. Both require zinc(II) as a cofactor. Other thiol-alkylating enzymes that also feature a zinc centre in their catalytic domain are the Ada DNA repair protein,[6] farnesyl transferase,[7] methanol-CoM-methyltransferase[8] and betaine-homocysteine *S*-methyltransferase.[9]

The biological importance of the reactions catalysed by these enzymes led to the development of a variety of zinc(II) complexes as functional model compounds in order to gain better understanding of the reaction mechanism. They all feature at least one zinc-thiolate linkage and one or more additional ligands that are responsible for the overall charge of the complex and the reactivity of the thiolate ligand. For a long time, the mechanism of methylation has been subject to debate. Two substantially different reaction modes have been proposed: an attack of free thiolate after prior dissociation of the complex, and an associative mechanism that includes a four-centre transition structure. The first path would show a first-order kinetic behaviour and the latter is expected to be second-order. However, the observed kinetic behaviour cannot finally prove a proposed mechanism because of possible perturbation effects, which could influence the observed reaction order. In the following, a brief survey of selected important studies on this subject is given.

Wilker and Lippard employed the dianionic tetrathiolate $[Zn(SPh)_4]^{2-}$ as a functional model for Ada.[10] They found that methylation of the complex by $(MeO)_3PO$ yielded

[‡] For further reference see: Zinc Thiolate Complexes $[ZnL_n(SR)]^+$ with Azamacrocyclic Ligands, Part I: Synthesis and Structural Properties[1]

[a] Friedrich-Schiller-Universität Jena, Institut für Organische Chemie und Makromolekulare Chemie,
Humboldtstr. 10, 07743 Jena, Germany
E-mail: ernst.anders@uni-jena.de

Supporting information for this article is available on the WWW under http://www.eurjic.org or from the author.

 © 2007 Wiley-VCH Verlag GmbH & Co. KGaA, Weinheim 

PhSMe and postulated a dissociative reaction mechanism. This seems particularly plausible as the reaction was carried out in a polar solvent, thus facilitating the dissociation of the thiolate from the highly charged complex anion. Vahrenkamp et al. studied the methylation of tris(pyrazolyl)-boratozinc(II) thiolates $Tp^{R,R}ZnSR$ in chloroform. Investigation of the kinetics provided strong evidence that these reactions occur intramolecularly, featuring a four-centre transition structure.[11–13] A similar conclusion has been drawn by Carrano et al., who investigated the methylation of a series of scorpionate zinc thiolates.[14–16] Darensbourg et al. studied alkylations of a zinc complex with a bis-thiolate $[N_2S_2]^{2-}$ chelate ligand.[17] They also obtained the thioether derivatives, but did not discuss the mechanism. Riordan and co-workers investigated the reactivity of zinc thiolates with a borato ligand,[18] focusing in particular on the influence of additional hydrogen bonds to the thiolate.[19] They found that hydrogen bonding considerably lowers the nucleophilicity of the thiolates. Similar to the results by Vahrenkamp et al., an associative mechanism is proposed because of the observed second-order kinetic behaviour of the reactions. However, in a recent contribution by Vahrenkamp and co-workers, which covers a comparison of methylation rates of zinc thiolates with $N_3$, $N_2S$, $NS_2$ and $S_3$ tripod ligands, evidence is given that a "sulfur-rich" coordination environment is likely to promote a dissociative mechanism.[20]

In all preceding studies of complexes $[ZnL_nSR]$, much attention is paid to the influence of the reactive thiolate ligand on alkylation mechanism and reactivity, or their dependence on different N/S ligations of the zinc ion. In contrast, we focus exclusively on *N*-ligated zinc thiolates. Our interest lies mainly in the coordination geometry and electronic properties of the complexes as reactivity-determining factors. Thus, we address the following questions: What is the actual contribution of $L_n$ to the nucleophilicity of a given thiolate ligand? Is it possible to derive a quantitative relation between structure and reactivity? Which, if any, structural and/or electronic parameters are suitable for the prediction of reactivity?

Recently, we introduced a series of novel zinc thiolate complexes[1] that are ideally suited for these investigations for several reasons: 11 different compounds meeting the experimental requirements are currently available; they feature both $N_3S$ and $N_4S$ coordination environments for zinc(II); all compounds are fully characterised by X-ray crystallography; they are insensitive to the influence of air and moisture; reactions with electrophiles (e.g., methyl iodide, benzyl bromide, acetyl and benzoyl chloride, and carbon disulfide[21]) were found to occur cleanly and on a convenient time scale; they comprise a sufficiently small number of non-hydrogen atoms to be suited for investigation by high-level density functional calculations. The latter instance offers the possibility to reveal the effect especially of electronic parameters that are only accessible by computation, for example, orbital energies and partial charges. This discloses a lot of new perspectives for the interpretation of the reactivity of such complexes.

## Results and Discussion

### Starting Materials

The alkylation experiments were performed using a series of 11 zinc(II) thiolate complexes with azamacrocyclic ligands of the general formula $[ZnL_n(S–CH_2–C_6H_5)]ClO_4$ (see Figure 1, Table 1). Their syntheses and structures have been reported in detail before.[1] They contain 11–16-membered azamacrocycles with three (**1**–**4**) and four (**5**–**11**) secondary nitrogen donors. In three of them, namely compounds **2**, **4** and **9**, one tertiary nitrogen is incorporated.

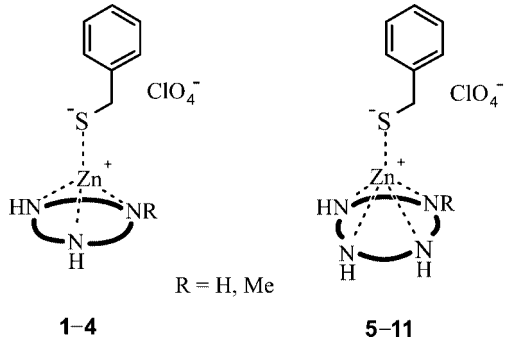


Figure 1. Generic structures of compounds **1**–**11**. Bold lines indicate alkyl bridges.

Table 1. Macrocyclic ligands of complexes **1**–**11**, with the general formula $[ZnL_n(S–CH_2–C_6H_5)]ClO_4$.

| Compound | $L_n$ abbreviated names | $L_n$ IUPAC names |
|---|---|---|
| **1** | [11]aneN$_3$ | 1,4,8-triazacycloundecane |
| **2** | methyl-[11]aneN$_3$ | 8-methyl-1,4,8-triazacycloundecane |
| **3** | [12]aneN$_3$ | 1,5,9-triazacyclododecane |
| **4** | methyl-[12]aneN$_3$ | 1-methyl-1,5,9-triazacyclododecane |
| **5** | [12]aneN$_4$ (cyclen) | 1,4,7,10-tetraazacyclododecane |
| **6** | [13]aneN$_4$ | 1,4,7,11-tetraazacyclotridecane |
| **7** | [14]aneN$_4$ (cyclam) | 1,4,8,11-tetraazacyclotetradecane |
| **8** | *i*[14]aneN$_4$ (*iso*-cyclam) | 1,4,7,11-tetraazacyclotetradecane |
| **9** | methyl-*i*[14]aneN$_4$ | 11-methyl-1,4,7,11-tetraazacyclotetradecane |
| **10** | [15]aneN$_4$ | 1,4,8,12-tetraazacyclopentadecane |
| **11** | [16]aneN$_4$ | 1,5,9,13-tetraazacyclohexadecane |

 © 2007 Wiley-VCH Verlag GmbH & Co. KGaA, Weinheim 

### Methylation Kinetics

For the determination of the reactivities we used the standard model reaction, methylation with methyl iodide, which yielded the corresponding iodide complexes and phenyl methyl sulfide [Equation (1)].

$$[ZnL_n(SCH_2Ph)]^+ + MeI \rightarrow [ZnL_nI]^+ + MeSCH_2Ph \quad (1)$$

At 300 K, the reactions come to completion within times of hours up to several days. No evidence for the formation of any byproducts was detected. Reaction monitoring could thus easily be performed using NMR spectroscopy. However, this required sufficiently concentrated solutions (0.02 M). In this respect, the varying solubilities of the model complexes proved to be a problem, as rate constants are only suited for direct comparison in case reactions are carried out in the same solvent. We initially intended to investigate the methylation in a nonpolar solvent in order to rule out a dissociative reaction mechanism. This was found to be unfeasible as only five compounds were soluble in chloroform and seven in dichloromethane. However, the semipolar solvent nitromethane could be used for all complexes. Second-order kinetic behaviour was observed in each case (with correlation coefficients of $R^2 > 0.99$ for all fit curves), thus indicating only associated reactions as proposed previously. In this work, we focus on kinetic data obtained from reactions in [$D_3$]nitromethane and [$D_2$]-dichloromethane solution.

Table 2 shows the experimentally determined second-order rate constants of methylation according to Equation 1. As expected, in the more polar solvent nitromethane the reactions proceed several times faster. The factor of acceleration by the solvent varies by about 3 for compound **11** and about 21 for **4**. We currently cannot give an explanation for this remarkable difference. However, the observed rate constants exhibit an even more pronounced dependence on the nature of the azamacrocycle. The fastest reaction in nitromethane was observed for complex **5**, which reacted more than 22 times faster than its slowest competitor, compound **2**. This effect is even more pronounced in dichloromethane; complex **11** reacts faster than **4** by a factor of 32. Because compound **5** is insoluble in this solvent, these data are of limited significance. Hence, a straightforward comparison of the two data sets is not possible in this way.

Table 2. Second-order rate constants of the methylation of compounds **1**–**11** at 300 K. Values are given in $10^{-3}$ $M^{-1}$ $s^{-1}$.

| Compound | In $CD_3NO_2$ | In $CD_2Cl_2$ |
|---|---|---|
| **1** | 4.71 | – |
| **2** | 2.46 | 0.28 |
| **3** | 7.05 | – |
| **4** | 4.92 | 0.23 |
| **5** | 55.28 | – |
| **6** | 29.03 | – |
| **7** | 21.60 | 1.52 |
| **8** | 13.93 | 1.00 |
| **9** | 8.66 | 0.53 |
| **10** | 16.69 | 2.81 |
| **11** | 23.12 | 7.35 |

A more expressive representation is given in Figure 2. It shows a comparison of the rate constants of all complexes that could be measured in both solvents. Again it is obvious that the absolute acceleration factor by a more polar solvent is not constant. Rather, a trend is reproduced, and compound **7** is the single exception. An explanation could be the following: The macrocycle cyclam ([14]aneN$_4$), which is featured in complex **7**, forms particularly stable tetracoordinate zinc complexes. The ring size of 14 atoms and the configuration of the *N*-bound hydrogen atoms in the complex enable the placement of the zinc ion in the plane of the four nitrogens[22] (a structural representation of **7** is given in the literature[1]). In the case of other ligands, a displacement is rather unavoidable. This renders the Zn–S bond of **7** less stable than in the other compounds regarded in this study. A similar conclusion can also be drawn from the mass spectra of the complexes.[1] In a polar solvent such as nitromethane, the Zn–S bond of **7** is weakened above average (without an actual dissociation taking place) and the reaction receives particular acceleration. Thus we conclude that the observed order of reaction rates obviously arises from a superposition of ligand and solvent control, but the macrocyclic ligand has the predominant influence on the reactivity of the thiolate. In addition, we found that the complexes with a tertiary nitrogen (**2**, **4** and **9**) exhibit a slightly reduced rate constant (by about 30–50%) compared to the analogue compounds without the methyl groups (**1**, **3** and **8**, respectively; see Table 2). The effect can be observed for both solvents.

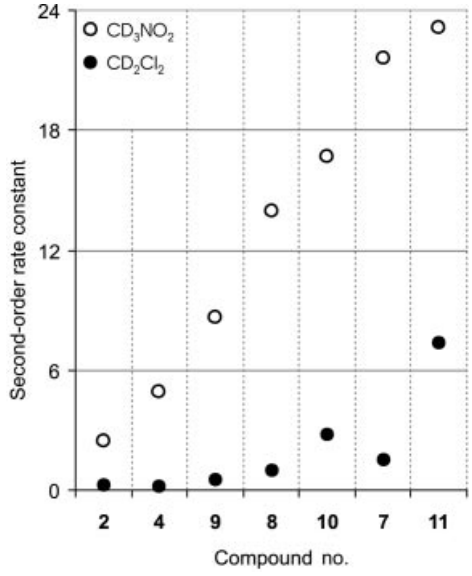


Figure 2. Comparison of second-order rate constants (given in $10^{-3}$ $M^{-1}$ $s^{-1}$) of the reactions with methyl iodide in $CD_2Cl_2$ and $CD_3NO_2$. Only the data of compounds that are soluble in both solvents are plotted.

### Density Functional Calculations

Different methods can be applied to obtain structural information, such as spectroscopy, computation or X-ray crystallography. However, the structural information pro-

 © 2007 Wiley-VCH Verlag GmbH & Co. KGaA, Weinheim 

vided by the latter is only of restricted use for the interpretation of processes in solution. In most cases, spectroscopical methods can be applied to solutions as well, but the structural information it provides is restricted to certain parameters and of limited generality. The search for parameters suitable to correlate to the experimentally determined reaction rates requires detailed information on the nature of the zinc–sulfur bond and the electronic properties of the sulfur atom that is not accessible by either spectroscopy or crystallography. Thus, quantum mechanical calculation is the method of choice to obtain structural and electronic data for correlation purposes. A comparable approach has been successfully applied by Halfen, Brunold et al., who investigated the electronic structure of 4-methylphenylthiolate and some transition-metal complexes thereof by density functional calculations in order to obtain an explanation for the observed nucleophilicities.[23]

An investigation that provided an accurate description of the observed reactivities would require more than gas-phase optimisations of the starting material complexes. Rather, a calculation of the transition state of the nucleophilic attack, including the modelling of solvent effects, had to be performed for the methylation reaction of every single compound. However, such calculations would by far push the boundary of the currently available computational resources. In addition, all our previous attempts to locate the transition states failed because of the extremely flat potential energy hypersurface. Thus, only gas-phase structures could be calculated at a sufficient level of theory, that is, one that includes polarised and diffuse functions, which are necessary for the correct description of coordination compounds. We were thus searching for a simple but effective means of characterising the observed reactivities using only the available structural and electronic data derived from gas-phase calculations. At least, we do not expect problems concerning the geometries obtained. According to our own experience, in the case of azamacrocycle-zinc(II) complexes, there are generally only minute differences between the structures obtained by calculations in the gas phase and in the presence of solvents.

We decided to use density functional theory because it is also applicable to larger molecules. All structures were optimised in the gas phase at the B3LYP/6-311+G(d) level of theory, with the molecular structures derived from X-ray diffraction[1] as starting geometries. The experimental and computational structures are in reasonable accordance. As expected, minor deviations in bond lengths and differences in the conformations (e.g., rotations about the Zn–S bond) were observed. Natural bond orbital (NBO)[24] analyses were performed for all structures to obtain information on orbital energies and partial charges on the metal and the heteroatoms. The energy of a specific lone pair orbital at the sulfur atom was determined, the reason for this being the following: In a previous study, it has been shown that a zinc-bound oxygen atom in complexes $[LZn–OH]^+$ possesses three lone pairs: two of sp hybridisation and one of pure p characteristic.[25] The latter one is the orbital with the highest energy, and because of its orientation, it is responsible for nucleophilic attack. A higher energy implicates a smaller energy gap between this orbital and the LUMO of an electrophilic substrate, thus facilitating orbital interaction and lowering transition-state energy. A comparable configuration was found for the zinc thiolate complexes. There are three localised orbitals at the zinc-bound sulfur atom, two with sp and one with a pure (>99%) p character, which also possesses the highest energy. Its strictly localised character has been proven for all structures regarded in this study. No significant overlap with other orbitals that would indicate multicentre bonding could be detected. It is thus reasonable to assume that the energy of this "localised HOMO" could be a controlling factor for the nucleophilic reactivity.

## Correlations

In the following consideration, we focus on possible correlations of computed parameters with the experimentally determined rate constants. We thus refer to three parameters based on gas-phase calculations that are likely to correlate with thiolate reactivity: the Zn–S bond length, the S atom partial charge and the above-mentioned S lone pair orbital energy.

As the Zn–S bond length reflects how tightly the thiolate is bound and how much its reactivity is lowered by zinc(II) complexation, one would expect it to be a good measure for reactivity. Figure 3 depicts the result, the rate constants of methylation plotted against the computed Zn–S bond lengths. There is apparently only a very loose correlation, which is certainly not sufficient for a quantitative description of reactivity. (Two points that correspond to compounds **5** and **6** are highlighted by means of square shaping in this and other charts; this is of importance and will be explained below.)

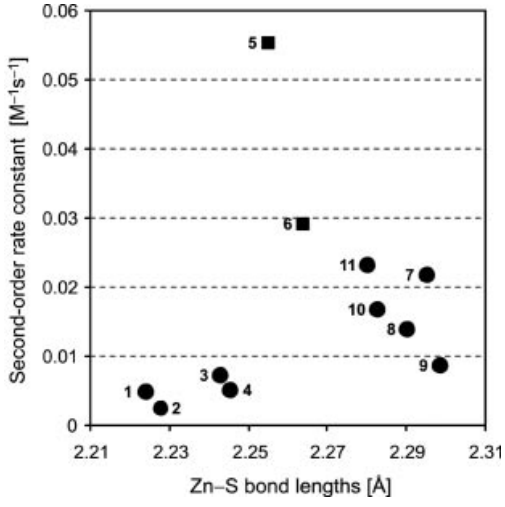


Figure 3. Second-order rate constants of thiolate methylation, plotted against the Zn–S bond lengths; solvent: nitromethane.

A much more promising situation is found for the plots of the sulfur's partial charge (see Figure 4). The data points for the reaction in nitromethane (with exception of **5** and

 © 2007 Wiley-VCH Verlag GmbH & Co. KGaA, Weinheim 

**6**) are found on a steady curve. In principle, this allows a prediction of reactivity: A larger absolute value of partial charge implicates an increased nucleophilic reactivity. The line that indicates this dependency is a spline curve, simply chosen by an obviously visible regularity of the data points. Of course, its existence does not permit any conclusions beyond the fact that there is a systematic relation between the two parameters regarded. It is also obvious that in the less polar solvent dichloromethane, such a correlation does not exist.

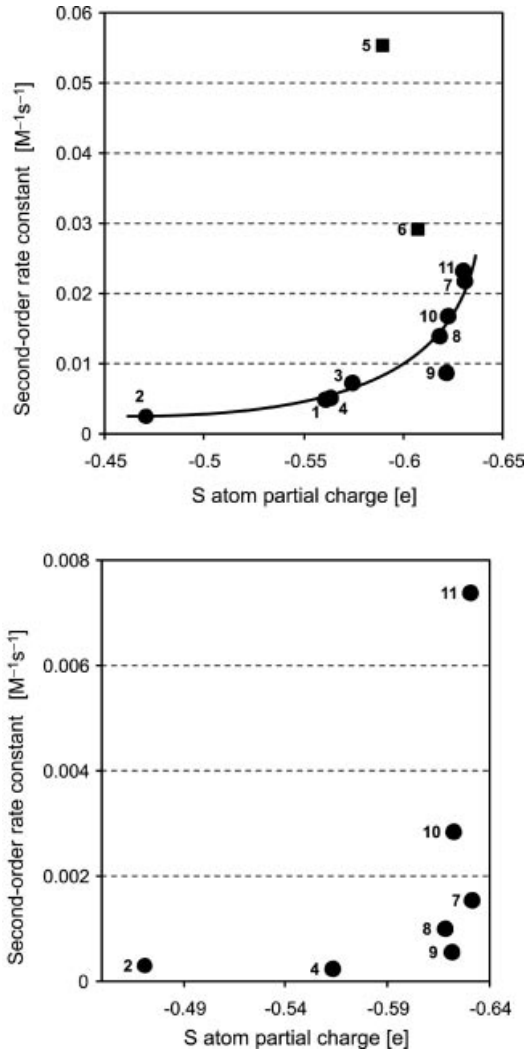


Figure 4. Second-order rate constants of thiolate methylation, plotted against partial charges of the sulfur atom. Upper diagram: solvent nitromethane; lower diagram: solvent dichloromethane.

The energy of the *p*-type lone pair seems to be a good measure for thiolate reactivity in both solvents (although again two exceptions, **5** and **6**, are encountered). As can be seen in Figure 5, the regularity is more pronounced in dichloromethane. The LP energy is the only parameter that allows a correlation with the rate constants for this solvent at all.

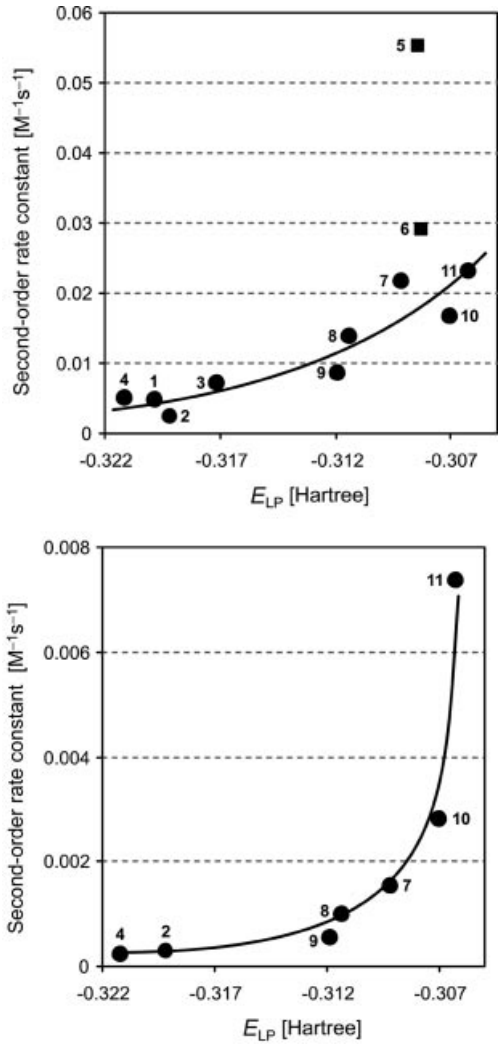


Figure 5. Second-order rate constants of thiolate methylation, plotted against energies of the sulfur's *p*-type lone pair. Upper diagram: solvent nitromethane; lower diagram: solvent dichloromethane.

All these findings allow some interesting conclusions: (1) Justifying solely from structural parameters (bond lengths), it is not possible to draw conclusions regarding the reactivity; one has to employ other sources of data, such as quantum mechanical calculation. (2) Obviously, the reaction can be biased towards charge or orbital control, depending on the polarity of the solvent. In nitromethane, both parameters (partial charge and orbital energy) are useful to describe the reactivity; in dichloromethane, the reaction is predominantly orbital-controlled. (3) The observed regularities include both $N_3S$ and $N_4S$ systems. The concept is obviously not restricted to a specific coordination environment of zinc(II) but is apparently valid for zinc thiolates in general.

However, we would like to emphasise that the correlations discussed herein are not supported by any equations or a stringent theory. This would of course not be permissible, as the results of gas-phase calculations are used in combination with data obtained from experiments in solu-

 © 2007 Wiley-VCH Verlag GmbH & Co. KGaA, Weinheim 

tion. Notwithstanding this background, some fundamental conclusions can be drawn, as will be demonstrated in the following.

### Steric Influences

Until now, we have not discussed the rate constants obtained for compounds **5** and **6**, which are indicated by squares in Figure 3, Figure 4 and Figure 5 (a structural representation of their calculated geometries is given in Figure 7, see below). Their reactivities differ significantly from those of the other complexes. They exhibit the largest rate constants whilst showing only average values for the structural and electronic parameters. Thus, we conclude that reactivity is also controlled by another important factor.

Regarding the reaction mechanism, we share the predominant viewpoint from the literature, the assumption that the methylation reaction involves an attack of the zinc-bound thiolate and features a four-centre intermediate (Scheme 1).[12–15,26,27] In this case, the methylation (as well as any other reaction) is restricted to occur at the thiolate side of the complex cation. As the coordination of the reacting molecules to $Zn^{II}$ implicates a steric demand, the degree of obstruction of the zinc(II) ion by the macrocycle should have a pivotal influence on the geometry of the transition state.

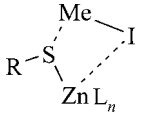


Scheme 1. Assumed four-centred transition state of the methylation of zinc-bound thiolate.

In case of planar chelate ligands, the degree of surface obstruction of a metal ion caused by complexation can easily be characterised by the bite angle; in case the ligand's donor atoms and the metal ion form a four-sided pyramid, one rather has to consider the solid angle at the Zn vertex. It is usually given in steradian [*sr*] and represents a measure for the extent to which the zinc ion is displaced out of the plane (or near-plane) of the four N atoms. In theory, values can vary between 0 *sr* (for infinite Zn–N distance) and 2π *sr* (for in-plane location of $Zn^{2+}$).[28] The results of these considerations are summarised in Figure 6, which also shows calotte model representations in order to illustrate the varying degree of steric demand of the macrocyclic ligands.

With regard to the comparably small solid angle of 0.95π *sr* associated to compound **5**, it is obvious that its coordination geometry can be assessed as being quite distorted in comparison to the other $N_4Zn$ systems (Figure 7). The calotte model drawings also show that the zinc ion in **5** is a lot more exposed. However, in the case of compound **6**, the solid angle is comparable to other $N_4$ complexes. As the corresponding calotte drawing still indicates a substantial degree of exposition of the metal ion, there is apparently another structural factor that affects the steric situation: the

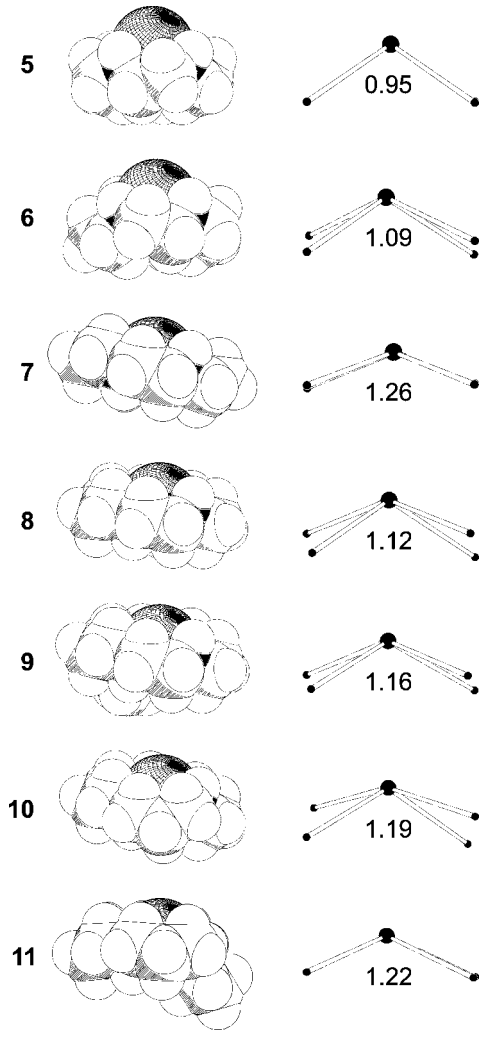


Figure 6. Left column: calotte model drawings of the cations of compounds **5**–**11**, thiolate ligands omitted. Right column: $N_4Zn$ coordination polyhedra and solid angles at the Zn vertex [π *sr*] of the same molecules; the perspective of vision corresponds to the drawings in the left column. All representations are derived from the calculated structures (see computational details).

configuration of the nitrogen atoms of the macrocycle. (In a previously published study, we discussed this aspect in detail, and structural representations of complexes **1**–**11** are given therein.[1]) Of the $N_4$ systems **5**–**11**, compounds **5** and **6** are the only examples in which all *N*-bound hydrogen atoms are located at the thiolate side [the (+)-side] of the molecule [the so-called (+ + + +)-configuration, see also Figure 7]. This characteristic accessorily accounts for a smaller degree of steric hindrance, as a hydrogen atom on the (+)-side obstructs the zinc(II) ion to a lesser extent than an alkyl bridge.

As a result of a superposition of both the ring size and configuration effects, complex **5** exhibits a markedly superior reactivity, while the just slightly increased reactivity of compound **6** is mainly based on the all-(+) configuration of the macrocycle. Moreover, a plausible mechanistic interpretation can be given for this acceleration: Given a more exposed zinc(II) ion, formation of a four-centred transition

 © 2007 Wiley-VCH Verlag GmbH & Co. KGaA, Weinheim 

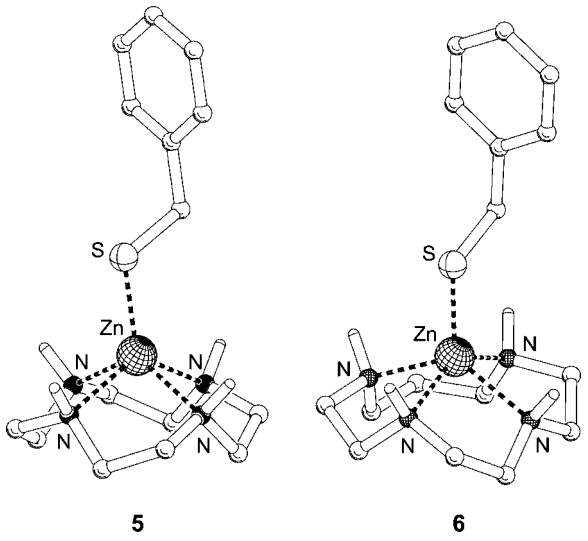


Figure 7. Structures of compounds **5** and **6**, calculated at the B3LYP/6-311+G(d) level of theory. Hydrogen atoms on carbon atoms are omitted for clarity of presentation. Note the good correlation of the values of the critical Zn–S bond lengths obtained by experimental and DFT calculation [for **5**: exp. 2.266(2) Å, calcd. 2.25 Å; for **6**: exp. 2.2853(9) Å, calcd. 2.26 Å].

state is facilitated rather than in the case of highly obstructed zinc(II), as illustrated in Figure 8. The latter would promote the formation of a more linear transition state that entails separation of the resulting iodide anion from the cationic centre, thus leading to a higher energy barrier for the overall reaction. Nevertheless, we do not expect this difference to amount to more than a couple of kilocalories per mole. However, as a small decrease of transition-state energy of 1.5 kcal mol$^{-1}$ already results in an increase of reaction velocity of about one order of magnitude, this allows for a sound explanation of the observed differences in reaction velocity.

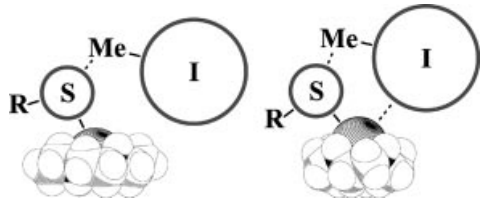


Figure 8. Illustration of possible differences in transition-state geometries for the nucleophilic attack of zinc-bound thiolate on methyl iodide. As examples, calotte model drawings of the $ZnL_n$ moieties of **7** (left) and **5** (right) were utilised. Ion radii of S and I are not exactly fitted to the ion radii of the calotte models.

## Conclusions

### General Remarks

The thiolate complexes have proven to be suitable functional models for thiolate-methylating enzymes. As expected, a clean second-order methylation reaction was found. The observed acceleration of the reaction in a polar environment comes as no surprise; neither do the general results concerning charge and orbital control in the different solvent systems. Similar observations have been reported by many other work groups (see above). However, an important improvement provided by our work is the presented way of analysing experimental reactivity data by correlation to electronic parameters obtained from gas-phase density functional calculations. It enabled us to elucidate to what extent certain geometry factors can influence reactivity and override electronic and/or orbital control. With regard to the rapidly increasing availability of computing power, this technique could generally prove to be a valuable tool in exploring structure–reactivity relationships and catalyst tailoring. However, we are aware that our procedure is only a coarse approximation. As mentioned above, an exact treatment of the subject would require DFT calculations of the transition states of the methyl iodide reactions for all investigated complexes, a task that we found to be unfeasible. We believe, however, that even though our approach is quite coarse, it provides interesting insight into the chemistry of nucleophilic cationic complexes.

### Implications Concerning CA Model Compounds

The unexpected reactivities of compounds **5** and **6** (Figure 7) allow some additional conclusions of high interest. Although it may not seem that this work relates to the enzyme carbonic anhydrase (CA), it nevertheless provides fundamentally enhanced insight into the chemistry of CA model compounds.

Carbonic anhydrases (CA) are a family of zinc enzymes that accelerate the reversible hydration of $CO_2$ by a factor of up to $10^7$ as compared to the uncatalysed reaction.[29,30] The catalytic domain consists of a zinc(II) ion that is bound to three histidine residues and bears an additional water molecule or hydroxide ligand (dependent from pH). The properties of this structural motif have been elucidated using a variety of monodentate zinc hydroxide complexes.[31–35] In addition, numerous experimental[36–38] and computational studies provided detailed insight into the reaction mechanism.[39–42]

In 1995, van Eldik and co-workers[43] published a study addressing the reaction rates of several functional CA model complexes of the general formula $[ZnL_n(OH)]^+$ with $CO_2$, according to Equation (2).

$$[ZnL_n(OH)]^+ + CO_2 \leftrightarrows [ZnL_n(OCO_2H)]^+ \quad (2)$$

They investigated complexes of various chelate ligands $L_n$, of which two macrocycles with four nitrogen donors are of particular interest. One is 14-membered (comparable to the ligand in compound **8**), and the other is cyclen as in compound **5**. They found that the $CO_2$ hydration velocity of the latter exceeds that observed for the first by a factor of approximately 15. However, no explanation for this remarkable variation is given. With regard to the results of the present work, we would like to propose a rationale for these observations, as, because of the close structural relationship of the ligands, we assume the steric situation for

 © 2007 Wiley-VCH Verlag GmbH & Co. KGaA, Weinheim 

those hydroxo complexes is comparable to compounds **8** and **5**, respectively.

In a previous study, some of us have shown that the aquation of zinc hydrogencarbonato complexes involves an intramolecular proton transfer as depicted in Scheme 2.[42] It involves the initial coordination of a water ligand to the zinc centre, which then protonates the hydrogen carbonate. Subsequently, carbonic acid is expelled (which, under normal conditions, will immediately be deprotonated in the reaction medium) and the hydroxo complex $[ZnL_n(OH)]^+$ is obtained. In the course of this mechanism, only uncharged molecules dissociate from the metal centre. However, with an increasing steric demand of the chelate ligand, the aquation may as well afford a preliminary dissociation of hydrogen carbonate, followed by addition of water, which is subsequently deprotonated. This dissociative reaction pathway necessarily includes a separation of electrical charges, which is very likely to result in an increased reaction barrier. In practice, one will normally encounter hybrid forms of both idealised mechanism types that are more or less biased to one side. We thus assume, by analogy with the results of the present work, that in the case of aquation of the two hydrogencarbonato complexes, the exposed placement of the zinc ion in the cyclen complex is much more likely to promote the associated reaction mechanism, thereby lowering the reaction barrier and increasing the aquation rate. We therefore conclude that the unique combination of properties united by the zinc(II) complexes of the ligand cyclen, that is, a small solid angle of the coordination polyhedron *and* the all-(+) configuration of the *N*-bound hydrogen atoms, results in an extraordinarily increased reactivity of additional monodentate ligands.

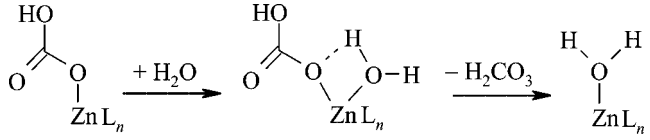


Scheme 2. Calculated mechanism of the aquation of zinc(II) hydrogencarbonato complexes.[41]

## Experimental Section

**General:** The thiolate complexes were prepared according to our published procedure.[1] Deuterated solvents were obtained from eurisotop. NMR spectra were recorded with a BRUKER AC 400 spectrometer at a temperature of 300 K.

**Methylation Kinetics:** The complex (0.1 mmol) was dissolved in deuterated solvent (5 mL) ($CD_2Cl_2$ or $CD_3NO_2$). Methyl iodide (0.1 mmol) was added with a microlitre syringe. After short stirring, a sample of the solution was placed in a sealable NMR tube and inserted into the spectrometer. $^1$H NMR spectra were recorded every 30 min for dichloromethane and every 15 min for nitromethane solutions. For determination of the rate constants of nitromethane solutions of **6**, **7** and **10**, the decreasing integral of the methyl peak of methyliodide was utilised. For all other measurements, the signals assigned to benzylic protons of the zinc-bound thiolate were used for integration. In all cases, the integral of all aromatic peaks was taken as a reference, as it was assumed to be constant. Thus, concentration data for kinetic analysis could be obtained directly from the standardised integral values. Under the condition that the reaction proceeds according to Equation (1) and the reactants are present in equal concentrations, a special case of a second-order kinetic law can be applied [Equation (3)].

$$1/c - 1/c_0 = k_2 t \quad (3)$$

In this equation, $c_0$ represents the initial concentration of any reactant and $c$ is the concentration of any reactant at a given time $t$. Accordingly, the obtained concentration data were plotted against $t$ and a linear function was obtained by regression analysis. Linear correlations were found in all cases, exhibiting correlation coefficients of $R > 0.995$. The second-order rate constants were obtained from the slopes of these fit functions.

**Computational Details:** Full geometry optimisations, that is, without constraints, were carried out using the Gaussian98[44] program package (Rev. A11/4). All optimisations were performed using the hybrid B3LYP[45] density functional method, which includes the use of a term that accounts for the effect of dynamic electron correlation (Coulomb hole).[46] Geometries were optimised in the gas phase using the standard 6-311+G(d) basis set. All structures were rigorously characterised as true minima. NBO analyses[24,47] were carried out using version 5.0 of the NBO program[48] as patched in Gaussian 98. A search for three-centre, four-electron hyperbonds using the keyword 3CHB yielded no evidence of nonlocalised orbitals. The partial charges of the heteroatoms were obtained by natural population analysis. Orbital energies were taken from the Natural Bond Orbital Summary Table.

**Supporting Information** (see also the footnote on the first page of this article): Mathematical details on calculation of the solid angle, a table with absolute energies (SCF energies, $\Delta U$, $\Delta G$) and cartesian coordinates in *xyz* format of all computed structures are given.

## Acknowledgments

Financial support of this work by the Deutsche Forschungsgemeinschaft, SFB 436 "Metal Mediated Reactions Modeled after Nature" is gratefully acknowledged. We particularly thank Prof. Dr. M. Westerhausen (FSU Jena) for an enlightening discussion, Dr. Stephan Schenk (ETH Zürich) for his advice concerning computational problems, and Steffen Kluge (FSU Jena) for his assistance in mathematics.

[1] J. Notni, H. Görls, E. Anders, *Eur. J. Inorg. Chem.* **2006**, 1444–1455.
[2] Z. S. Zhou, G. Zhao, W. Wan in *Frontiers of Biotechnology and Pharmaceuticals* (Eds.: H. Guo, R. Zhao), China Scientific Book Services, Beijing, China, **2001**, vol. 2, chapter 3, pp. 199–217.
[3] *Expasy Proteomics Server*, http://www.expasy.org.
[4] V. L. Schramm, *Curr. Opin. Chem. Biol.* **1997**, *1*, 323–331.
[5] K. Peariso, Z. S. Zhou, A. E. Smith, R. G. Matthews, J. E. Penner-Hahn, *Biochemistry* **2001**, *40*, 987–993.
[6] L. C. Myers, M. P. Terranova, A. E. Ferentz, G. Wagner, G. L. Verdine, *Science* **1993**, *261*, 1164–1167.
[7] H.-W. Park, S. R. Boduluri, J. F. Moomaw, P. J. Casey, L. S. Beese, *Science* **1997**, *275*, 1800–1805.
[8] K. Sauer, R. K. Thauer, *Eur. J. Biochem.* **1997**, *249*, 280–285.
[9] A. P. Breksa III, T. A. Garrow, *Biochemistry* **1999**, *38*, 13991–13998.
[10] J. J. Wilker, S. J. Lippard, *Inorg. Chem.* **1997**, *36*, 969–978.
[11] R. Burth, H. Vahrenkamp, *Z. Anorg. Allg. Chem.* **1998**, *624*, 381–385.

 © 2007 Wiley-VCH Verlag GmbH & Co. KGaA, Weinheim 

[12] U. Brand, M. Rombach, J. Seebacher, H. Vahrenkamp, *Inorg. Chem.* **2001**, *40*, 6151–6157.
[13] M. Ji, B. Benkmil, H. Vahrenkamp, *Inorg. Chem.* **2005**, *44*, 3518–3523.
[14] B. S. Hammes, C. J. Carrano, *Inorg. Chem.* **1999**, *38*, 4593–4600.
[15] B. S. Hammes, C. J. Carrano, *Inorg. Chem.* **2001**, *40*, 919–927.
[16] J. N. Smith, Z. Shirin, C. J. Carrano, *J. Am. Chem. Soc.* **2003**, *125*, 868–869.
[17] C. A. Grapperhaus, T. Tuntulani, J. H. Reibenspies, M. Y. Darensbourg, *Inorg. Chem.* **1998**, *37*, 4052–4058.
[18] S.-J. Chiou, J. Innocent, C. G. Riordan, K.-C. Lam, L. Liable-Sands, A. L. Rheingold, *Inorg. Chem.* **2000**, *39*, 4347–4353.
[19] S.-J. Chiou, C. G. Riordan, A. L. Rheingold, *Proc. Natl. Acad. Sci. USA* **2003**, *100*, 3695–3700.
[20] M. Rombach, J. Seebacher, M. Ji, G. Zhang, G. He, M. M. Ibrahim, B. Benkmil, H. Vahrenkamp, *Inorg. Chem.* **2006**, *45*, 4571–4575.
[21] J. Notni, S. Schenk, A. Roth, W. Plass, H. Görls, U. Uhlemann, A. Walter, M. Schmitt, J. Popp, S. Chatzipapadopoulos, T. Emmler, H. Breitzke, J. Leppert, G. Buntkowsky, K. Kempe, E. Anders, *Eur. J. Inorg. Chem.* **2006**, 2783–2791.
[22] A. W. Addison, E. Sinn, *Inorg. Chem.* **1983**, *22*, 1225–1228.
[23] D. C. Fox, A. Fiedler, H. L. Halfen, T. C. Brunold, J. A. Halfen, *J. Am. Chem. Soc.* **2004**, *126*, 7627–7638.
[24] A. E. Reed, R. B. Weinstock, F. Weinhold, *J. Chem. Phys.* **1985**, *83*, 735–746.
[25] M. Bräuer, J. L. Pérez-Lustres, J. Weston, E. Anders, *Inorg. Chem.* **2002**, *41*, 1454–1463.
[26] M. Rombach, H. Vahrenkamp, *Inorg. Chem.* **2001**, *40*, 6144–6150.
[27] H. Brombacher, H. Vahrenkamp, *Inorg. Chem.* **2004**, *43*, 6042–6049.
[28] For more detailed information on the mathematical background see Supporting Information.
[29] F. Botre, G. Gros, B. T. Storey (Eds.), *Carbonic Anhydrase*, VCH Publishers, New York, **1991**.
[30] I. Bertini, C. Luchinat, W. Maret, M. Zeppezauer (Eds.), *Zinc Enzymes*, Birkhäuser, Boston, **1986**.
[31] G. Parkin, *Chem. Rev.* **2004**, *104*, 699–767.
[32] E. Kimura, *Acc. Chem. Res.* **2001**, *34*, 171–179.
[33] X. Zhang, R. van Eldik, T. Koike, E. Kimura, *Inorg. Chem.* **1993**, *32*, 5749–5755.
[34] A. Looney, G. Parkin, R. Alsfasser, M. Ruf, H. Vahrenkamp, *Angew. Chem. Int. Ed. Engl.* **1992**, *31*, 92–93; *Angew. Chem.* **1992**, *104*, 57–58.
[35] A. Looney, R. Han, K. McNeill, G. Parkin, *J. Am. Chem. Soc.* **1993**, *115*, 4690–4697.
[36] D. W. Christianson, C. A. Fierke, *Acc. Chem. Res.* **1996**, *29*, 331–339.
[37] D. N. Silverman, S. Lindskog, *Acc. Chem. Res.* **1988**, *21*, 30–36.
[38] J.-Y. Liang, W. N. Lipscomb, *Biochemistry* **1988**, *27*, 8676–8682.
[39] A. Bottoni, C. Z. Lanza, G. P. Miscione, D. Spinelli, *J. Am. Chem. Soc.* **2004**, *126*, 1542–1550.
[40] C. S. Tautermann, M. J. Loferer, A. F. Voegele, K. R. Liedl, *J. Phys. Chem. B* **2003**, *107*, 12013–12020.
[41] Z. Smedarchina, W. Siebrand, A. Fernández-Ramos, Q. Cui, *J. Am. Chem. Soc.* **2003**, *125*, 243–251.
[42] M. Mauksch, M. Bräuer, J. Weston, E. Anders, *ChemBioChem* **2001**, *2*, 190–198.
[43] X. Zhang, R. van Eldik, *Inorg. Chem.* **1995**, *34*, 5606–5614.
[44] M. J. Frisch, G. W. Trucks, H. B. Schlegel, G. E. Scuseria, M. A. Robb, J. R. Cheeseman, V. G. Zakrzewski, J. A. Montgomery Jr, R. E. Stratmann, J. C. Burant, S. Dapprich, J. M. Millam, A. D. Daniels, K. N. Kudin, M. C. Strain, O. Farkas, J. Tomasi, V. Barone, M. Cossi, R. Cammi, B. Mennucci, C. Pomelli, C. Adamo, S. Clifford, J. Ochterski, G. A. Petersson, P. Y. Ayala, Q. Cui, K. Morokuma, N. Rega, P. Salvador, J. J. Dannenberg, D. K. Malick, A. D. Rabuck, K. Raghavachari, J. B. Foresman, J. Cioslowski, J. V. Ortiz, A. G. Baboul, B. B. Stefanov, G. Liu, A. Liashenko, P. Piskorz, I. Komaromi, R. Gomperts, R. L. Martin, D. J. Fox, T. Keith, M. A. Al-Laham, C. Y. Peng, A. Nanayakkara, M. Challacombe, P. M. W. Gill, B. Johnson, W. Chen, M. W. Wong, J. L. Andres, C. Gonzalez, M. Head-Gordon, E. S. Replogle, J. A. Pople, *Gaussian98*, revision A.11–4, **2002**, Gaussian, Inc., Pittsburgh, PA, http://www.gaussian.com.
[45] A. D. Becke, *J. Chem. Phys.* **1993**, *98*, 5648–5652.
[46] C. Lee, W. Yang, R. G. Parr, *Phys. Rev. B: Condens. Matter* **1988**, *37*, 785–789.
[47] A. E. Reed, L. A. Curtiss, F. Weinhold, *Chem. Rev.* **1988**, *88*, 899–926.
[48] F. Weinhold, *NBO*, version 5, http://www.chem.wisc.edu/~nbo5/.

Received: October 13, 2006
Published Online: January 16, 2007

 © 2007 Wiley-VCH Verlag GmbH & Co. KGaA, Weinheim 

DOI: 10.1002/ejic.200600690

# Syntheses, Properties and Structures of $[\{(C_5Me_5)_2Nb\}_2NiTe_4]$ and $[(tBuC_5H_4Nb)_2Ni_5Te_7(Ph_2PCH_2PPh_2)_2]$: The Quest for Tetratelluronickelate Clusters

**Martin Brandl,[a] Alexander Ebner,[a] Marek M. Kubicki,[b] Yves Mugnier,[b] Joachim Wachter,*[a] Estelle Vigier-Juteau,[b] and Manfred Zabel[a]**

**Keywords:** Niobium / Nickel / Tellurium / Electrochemistry / Density functional calculations

The reaction of $[Ni(COD)_2]$ with $[Cp^*_2NbTe_2H]$ (**1**; $Cp^*$ = $\eta$-$C_5Me_5$) in the presence of $Ph_2PCH_2PPh_2$ (dppm) in boiling toluene gives black-violet $[(Cp^*_2Nb)_2NiTe_4]$ (**3**). If $[Cp'_2NbTe_2H]$ (**2**; Cp′ = $tBuC_5H_4$) is used under similar conditions dark-brown $[(Cp'Nb)_2Ni_5Te_7(dppm)_2]$ (**4**) is formed. The structures of **3** and **4** have been determined crystallographically. Complex **3** contains a severely distorted $NiTe_4$ tetrahedron to which two niobocene groups are coordinated. Density functional analysis of the electronic structure of the $NiTe_4$ building block shows that it is best described as an $[Ni(\eta^2\text{-}Te_2)_2]^{2-}$ fragment. The structure of **4** reveals the presence of two $Ni_5$ and $Te_5$ tetragonal pyramids stacked into each other in an opposite way. Six of the Te bridges form two triangular faces, each of which is capped by a Cp′Nb fragment. Additionally, two dppm ligands bridge the long Ni–Ni edges of the $Ni_4$ bases. Oxidation of **3** with $[(C_5H_5)_2Fe]BPh_4$ gives paramagnetic $[(Cp^*_2Nb)_2NiTe_4]BPh_4$ (**6**), whereas oxidation with $[(C_5H_5)_2Fe]PF_6$ proceeds with fluoride transfer to give $[Cp^*_2NbF_2]PF_6$ (**5**). Electrochemical studies of **3** reveal the existence of the redox couples $[\mathbf{3}]^{2+}/[\mathbf{3}]^{+}/[\mathbf{3}]^{0}/[\mathbf{3}]^{-}/[\mathbf{3}]^{2-}$. Density functional calculations carried out on the different oxidation states of **3** reveal the following main features: the persistent presence of Nb–Ni bonds and the retention of Te–Te bonds in cationic and neutral species and their breaking off in reduced forms. Irrespective of the initial site of electrochemical attack, the Te atoms and Cp rings are principally affected in the final products.

(© Wiley-VCH Verlag GmbH & Co. KGaA, 69451 Weinheim, Germany, 2007)

## Introduction

The idea of employing tetrachalcogeno metallate anions $[MX_4]^{2-}$ as ligands for the synthesis of heterodimetallic chalcogenido clusters was first elaborated by Müller et al. with M = V, Mo, and W and X = S and Se.[1] Such compounds are of interest as building blocks in extended structures that possess nonlinear optical properties.[2] Little is known about telluro metallates with coordination number four, however.[3] Whereas bis(niobocene)tetrathio and -seleno metallates of formula $[(Cp^*_2Nb)_2MX_4]$ (M = Cr, Mo, Fe, Co; X = S, Se) are easily formed in the reaction between $[Cp^*_2NbE_2H]$ derivatives and the corresponding metal carbonyls,[4,5] $[\{(Cp'_2Nb)_2WTe_4\}W(CO)_4]$ has been synthesised only recently from $W(CO)_6$ and $[Cp'_2NbTe_2H]$ (**2**; Cp′ = $tBuC_5H_4$). This complex contains the hitherto unknown $[WTe_4]^{2-}$ moiety.[6] The versatile abilities of $[Cp^*_2NbTe_2H]$ (**1**) and **2** to serve as tellurium transfer reagents towards transition metal carbonyls has already been reviewed.[7] In this work, we report on the reactions of **1** and **2** with $[Ni(COD)_2]$ in the presence of $Ph_2PCH_2PPh_2$ (dppm). The structures and properties of the mixed early-late transition metal telluride clusters obtained are investigated and the electronic structure of the hitherto elusive $NiTe_4$ structural moiety is investigated in a theoretical study.

## Results and Discussion

### Syntheses, Properties and Structural Characterisation

Addition of **1** to a yellow solution of $[Ni(COD)_2]$ and half an equivalent of dppm in toluene at room temperature results in an immediate darkening. Attempts to isolate a well-defined product from this solution failed. After refluxing the solution for 18 h black-violet $[(Cp^*_2Nb)_2NiTe_4]$ (**3**) was isolated in 20% yield after chromatographic work-up. The analogous reaction of **2** with $[Ni(COD)_2]$/dppm in boiling toluene gave brown crystals of $[(Cp'Nb)_2Ni_5Te_7(dppm)_2]$ (**4**) after filtration and cooling to –24 °C in a total yield of 11%.

The field desorption (FD) mass spectrum of **3** exhibits the parent ion along with another peak at *m*/*z* 619 (intensity ratio 3:10), which may be attributed to the $[Cp^*_2NbTe_2]$ fragment. The composition of compound **3** is in agreement

[a] Institut für Anorganische Chemie der Universität Regensburg, 93040 Regensburg, Germany
[b] Laboratoire de Synthèse et d'Electrosynthèse Organométalliques, UMR 5188, Université de Bourgogne, 21078 Dijon, France

Supporting information for this article is available on the WWW under http://www.eurjic.org or from the author.

 © 2007 Wiley-VCH Verlag GmbH & Co. KGaA, Weinheim 

with the elemental analysis. The $^1$H NMR spectrum of **3** shows a singlet at $\delta$ = 1.89 ppm ($C_6D_6$) for the $C_5Me_5$ rings. Complex **4** was characterised by means of elemental analysis, FD-MS, and X-ray crystallography. The FD mass spectrum shows the molecular peak of **4** after focussing the scan range at 2380 ± 50 amu. This was necessary to avoid decomposition during routine registration and to increase the sensitivity of the detector (Figure 1). No satisfactory NMR spectra were obtained because of the low solubility of the cluster.

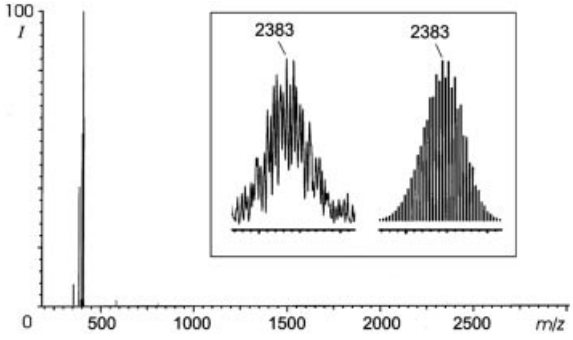


Figure 1. FD mass spectrum of **2** in $CH_2Cl_2$ (scan range up to 3000 amu). The inset shows the experimental (left) and simulated (right) spectra for a scan range of M ± 50 amu.

Oxidation of **3** with excess $[(C_5H_5)_2Fe]PF_6$ in thf gave yellow $[Cp^*_2NbF_2]PF_6$ (**5**) [Equation (1), path a] according to the FD mass spectrum and elemental analysis. The closely related salt $[(C_5Me_4Et)_2NbF_2]PF_6$ has been prepared previously from $[(C_5Me_4Et)_2NbCl_2]$ by reduction with Na/Hg and subsequent reaction with $HPF_6$.[8] Similar fluoride-transfer reactions from hexafluorophosphate anion to reactive niobocene derivatives are known.[8,9]

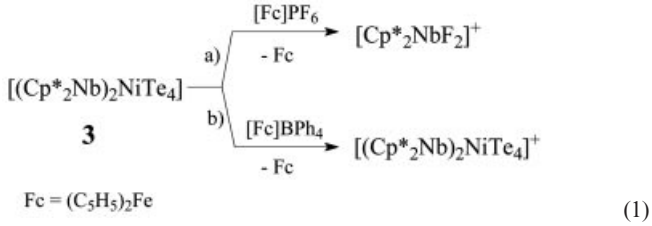


(1)

Reaction of **3** with $[(C_5H_5)_2Fe]BPh_4$, which contains the large and non-coordinating tetraphenylborate anion, was therefore attempted. Black-green $[(Cp^*_2Nb)_2NiTe_4]BPh_4$ (**6**) was formed in 37% yield in thf at room temperature [Equation (1), path b]. The composition was determined by elemental analysis and ESI-MS. The $^1$H NMR spectrum exhibits a broad singlet at $\delta$ = 11.15 ppm, which is in agreement with the expected paramagnetic nature of the new compound. Three multiplets at $\delta$ = 7.31, 7.03, and 6.88 ppm may be assigned to the tetraphenylborate anion. Attempts to measure an ESR signal were not successful due to a delocalisation of the unpaired electron over the trimetallic core including the telluride bridges (see below). Unfortunately, single crystals of **6** could not be obtained either.

In another experiment we tried to methylate the Te bridges of **3** with MeI, but $[Cp^*_2NbI_2]$ was obtained as the only product. This means that the lone pairs of the Te bridges are less accessible for methyl electrophilic attack than those in the dinuclear complex $[Cp'_4Nb_2(\mu\text{-}Te)_2]$, which gives $[Cp'_4Nb_2(\mu\text{-}CH_3Te)_2]^{2+}$ upon methylation.[10]

### *Structure of [Cp*$_4$Nb$_2$NiTe$_4$] (3)*

Compound **3** crystallises as monoclinic black rods. Its molecular structure contains a distorted $NiTe_4$ tetrahedron to which two mutually perpendicular niobocene units are coordinated (Figure 2). Thus, complex **3** is one of the extremely rare coordination compounds incorporating an $MTe_4$ structural unit and is the first tetratelluronickelate derivative. Another example of a tetratelluro metallate complex is $[(Cp'_2Nb)_2WTe_4{\cdot}W(CO)_4]$,[6] in which a central $WTe_4$ tetrahedron is surrounded by two niobocene fragments. Interestingly, tetrathionickelates like $[Ni(MoS_4)_2]$[11] and $[Ni(WS_4)_2]$[1] prefer a square-planar arrangement of the sulfur ligands around $Ni^{2+}$.

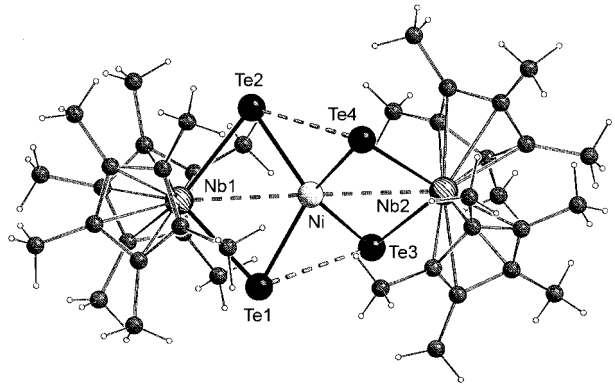


Figure 2. Structure of $[(Cp^*_2Nb)_2NiTe_4]$ (**3**). Selected bond lengths [Å] and angles [°]: Ni–Te 2.470(1)–2.481(1), Nb–Te 2.757(1)–2.766(1), Te1–Te3 3.122(1), Te2–Te4 3.201(1), Ni···Nb1 3.100(4), Ni···Nb2 3.147(4), Te1···Te2 4.212(1), Te3···Te4 4.169(1); Te1–Nb1–Te2 99.2(1), Te1–Ni–Te2 116.4(1), Te1–Ni–Te3 78.2(1), Te2–Ni–Te4 80.5(1), Te1–Ni–Te4 138.2(1), Nb1–Ni–Nb2 178.6(1).

The core of the molecule is characterised by a nearly linear Nb–Ni–Nb arrangement. The Ni–Te distances range from 2.467(1) to 2.481(1) Å and the Nb–Te distances are between 2.757(1) and 2.774(1) Å (see Table S1 in the Supporting Information). The Te–Te distances around Ni merit a more detailed discussion. Taking into account that two $NbTe_2Ni$ rings are linked together by nickel one may distinguish sets of two short and four long Te–Te distances. The latter range between 4.190 and 4.632 Å and are typical of nonbonding intra- and interannular interactions. However, it is striking that the short distances (mean: 3.161 Å) are found between (interannular) Te1 and Te3 and Te2 and Te4 of two different rings.

The geometrical parameters found in both $Cp'_2NbTe_2$ moieties of **3** differ considerably from those observed in $[Cp'_2Nb(Te_2)H{\cdot}Cr(CO)_5]$.[10] The Te–Nb–Te angle in this compound is contracted to 55.4(1)° and the distance of 2.695(1) Å corresponds well to those reported for side-on terminal $\eta^2$-$Te_2$ ligands in mononuclear complexes for which a Te–Te bond order of between 1 and 2 has been suggested.[12]

 © 2007 Wiley-VCH Verlag GmbH & Co. KGaA, Weinheim 

The Te–Te distances considered as bonding interactions in a series of complexes comprising the $NiTe_2Ni$ unit vary from 2.802(1) Å in $[\{(triphos)Ni\}_2(\mu\text{-}Te)_2]$[13] to 3.052(5) Å in $[\{(C_5H_iPr_4)Ni\}_2(\mu\text{-}Te)_2]$[14] and even up to 3.28 Å in $[\{CpNi\}_2(\mu_3\text{-}Te)_2\{Ni(PPh_3)Cp\}_2]$.[15] Consequently, the short interannular Te–Te distances observed close to 3.161 Å in the structure of **3** may be considered as long single Te–Te bonds. The question of coupling of two Te atoms coming from two different fragments (interannular) through $Ni^{2+}$ will be discussed in the calculations section below.

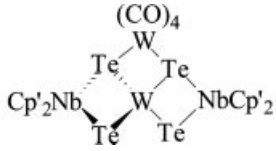


### *Structure of [(Cp′Nb)$_2$Ni$_5$Te$_7$(dppm)$_2$] (4)*

Compound **4** crystallises directly from the filtered reaction mixture as dark prisms. The molecular structure contains a tetragonal pyramid of five nickel atoms at its centre, the basal plane of which is formed by two short (av. 2.637 Å) and two long (av. 3.540 Å) Ni–Ni linkages (Figure 3, Table 1). Six edges of the nickel pyramid are bridged by Te ligands such that they form two triangular faces that serve as tridentate chelate ligands for the coordination of both niobium centres (Figure 4). Another tellurium ligand (Te1) bridges the nickel base in a $\mu_4$-fashion and thus serves as the top of a tetragonal $Te_5$ pyramid which is inverted with respect to the $Ni_5$ pyramid. The molecule is completed by two dppm ligands that bridge the long Ni–Ni edges of the rectangular nickel base. The axial phenyl rings of these ligands are arranged in two parallel pairs. The loss of one of the $t$BuC$_5$H$_4$ ligands from the niobocene unit in this reaction is not new as it has been observed previously during the thermal conversion of $[(Cp'_2NbS_2)_2(\mu\text{-}S_5)]$ into $[Cp'_3Nb_3S_{12}]$.[16]

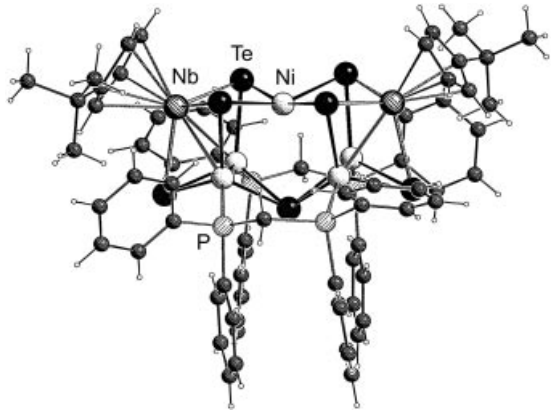


Figure 3. Structure of $[(Cp'Nb)_2Ni_5Te_7(dppm)_2]$ (**4**).

The combination of niobium and nickel atoms together in a polymetallic architecture such as that in **4** is, to the best of our knowledge, unique. The structural motif of the tetragonal d$^{10}$-metal pyramid is extremely rare; it has been realised previously only in $[Pd_5Se_5(PPh_3)_5]$[17] and $[Ni_5S_4(CH_3CO_2)(PPh_3)_5]^+$.[18]

Table 1. Selected bond lengths [Å] and angles [°] for $[(Cp'Nb)_2Ni_5Te_7{\cdot}2C_7H_8]$ (**4**).

| | | | |
|---|---|---|---|
| Ni1–Te2 | 2.563(6) | Ni5–Te1 | 2.482(5) |
| Ni1–Te3 | 2.700(6) | Ni5–Te6 | 2.551(5) |
| Ni1–Te5 | 2.551(6) | Ni5–Te7 | 2.436(5) |
| Ni1–Te6 | 2.634(6) | Ni5–P4 | 2.252(10) |
| Ni2–Ni3 | 2.631(7) | Nb1–Te2 | 2.640(4) |
| Ni2–Nb1 | 2.832(6) | Nb1–Te3 | 2.686(4) |
| Ni2–Te2 | 2.529(5) | Nb1–Te4 | 2.699(4) |
| Ni2–Te1 | 2.549(5) | Nb2–Te5 | 2.629(4) |
| Ni2–Te4 | 2.570(5) | Nb2–Te6 | 2.722(4) |
| Ni2–P1 | 2.120(10) | Nb2–Te7 | 2.676(5) |
| Ni3–Nb1 | 2.793(6) | Ni1–Ni2 | 2.948(6) |
| Ni3–Te1 | 2.457(5) | Ni1–Ni3 | 3.000(6) |
| Ni3–Te4 | 2.469(5) | Ni1–Ni4 | 2.988(6) |
| Ni3–Te3 | 2.527(5) | Ni1–Ni5 | 2.937(6) |
| Ni3–P3 | 2.224(10) | Ni2···Ni4 | 3.530(6) |
| Ni4–Ni5 | 2.644(7) | Ni3···Ni5 | 3.530(6) |
| Ni4–Nb2 | 2.820(5) | Ni1···Te1 | 3.184 |
| Ni4–Te1 | 2.559(5) | Te2···Te3 | 4.019 |
| Ni4–Te5 | 2.487(5) | Te2···Te5 | 3.213 |
| Ni4–Te7 | 2.519(5) | Te3···Te6 | 3.228 |
| Ni4–P2 | 2.079(10) | Te5···Te6 | 4.027 |
| Ni5–Nb2 | 2.806(6) | | |
| Ni2–Te1–Ni3 | 63.4(2) | Nb1–Te3–Ni1 | 76.2(2) |
| Ni2–Te1–Ni4 | 87.4(2) | Ni1–Te3–Ni3 | 70.0(2) |
| Ni2–Te1–Ni5 | 121.6(2) | Nb1–Te4–Ni2 | 65.0(2) |
| Nb1–Te2–Ni1 | 79.4(2) | Ni2–Te4–Ni3 | 62.9(2) |
| Nb1–Te2–Ni2 | 66.4(2) | Nb2–Te5–Ni1 | 78.6(2) |
| Nb2–Te5–Ni4 | 66.8(2) | Te2–Ni1–Te5 | 77.8(2) |
| Nb2–Te6–Ni1 | 75.5(2) | Te2–Ni1–Te6 | 158.1(2) |
| Nb2–Te6–Ni5 | 64.2(2) | Te2–Ni2–P1 | 107.1(3) |
| Nb2–Te7–Ni4 | 65.7(2) | Te4–Ni2–P1 | 113.2(3) |
| Te2–Nb1–Te3 | 97.9(2) | Nb1–Ni2–P1 | 145.1(3) |
| Te2–Nb1–Te4 | 108.2(2) | Te3–Ni3–P3 | 97.8(3) |
| Ni2–Nb1–Ni3 | 55.8(2) | P1–C1–P2 | 126.7(10) |
| Te2–Ni1–Te3 | 99.5(2) | P3–C2–P4 | 110.4(7) |

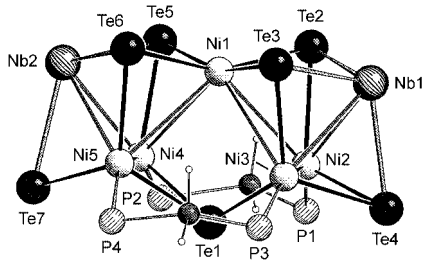


Figure 4. The $Nb_2Ni_5Te_7(P_2CH_2)_2$ core of **4** with labelling scheme.

The cluster core of **4** contains three different ranges of Ni–Ni distances around 2.64 (Ni2–Ni3, Ni4–Ni5), 2.80 (Ni1–Ni2–5), and 3.53 (Ni2–Ni4, Ni3–Ni5) Å. A wide range of Ni–Ni distances (2.49–2.87 Å) of more or less bonding character has been described in the literature, for example in $Ni_{10}$ and $Ni_{11}$ polyhedra.[19] Due to the small covalent radius of nickel (1.15 Å), no bonding interactions are to be expected between Ni2–Ni4 and Ni3–Ni5. On the other hand, the Ni–Nb distances (2.80 Å mean) may be short enough to exhibit a bonding character. Consequently, considering six Ni–Ni and four Ni–Nb metal–metal contacts, each metal centre formally fulfils the 18-electron rule,

 © 2007 Wiley-VCH Verlag GmbH & Co. KGaA, Weinheim 

although a delocalised bonding situation may be envisaged. Density functional calculations are planned in order to elucidate the electronic structure within the cluster core.

### Electrochemical Investigations

The trimetallic sulfido and selenido compounds $[(Cp^*_2Nb)_2MX_4]$ are distinguished by a pronounced redox activity.[4,5] Therefore, and in order to understand the chemical oxidation of **3** by ferricinium salts (see above), we examined the electrochemical behaviour of **3** and **6** in thf solution by rotating disk electrode (RDE) voltammetry, cyclic voltammetry and electrolysis.

The RDE voltammogram of **3** (thf/$NBu_4PF_6$) exhibits two oxidation waves E′ ($E_{1/2}$ = –0.22 V) and F′ ($E_{1/2}$ = +0.420 V) and three reduction waves A, B, and C (–1.61, –2.12 and –2.25 V, respectively). The heights of waves E′, F′, A and B are nearly equal, whereas wave C is twice as high as B (Figure 5).

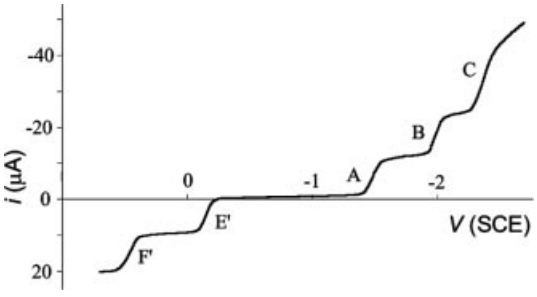


Figure 5. RDE voltammogram of **3** (thf/$NBu_4PF_6$) at a carbon electrode vs. SCE.

Three reversible systems A/A′, E/E′ and F/F′ are observed at room temperature by cyclic voltammetry (Figure 6). The current ratio $i_{p,a}/i_{p,c}$ for each system is equal to unity (or very close to it) for sweep rates $v$ between 20 and 200 mV s$^{-1}$ and the peak current increases linearly with $v^{1/2}$. The half-wave potential scan rate and the peak shape are characterised by $|E_{p,a} - E_{p,c}| \approx 60$ mV, in agreement with a one-electron transfer controlled by diffusion.[20,21]

Peak B is not reversible at room temperature and an oxidation peak appears at –1.74 V during the anodic scan. At 0 °C a low reversibility (system B/B′) is observed and the intensity of peak B′ increases with the scan rate. These results indicate that the species electrogenerated by one- ($[\mathbf{3}]^+$) or two-electron oxidation ($[\mathbf{3}]^{2+}$) and one-electron reduction ($[\mathbf{3}]^-$) are stable, whereas the product obtained by two-electron reduction ($[\mathbf{3}]^{2-}$) is relatively unstable.

Electrolysis at –1.8 V (plateau of wave A) consumes more than one electron equivalent. After reduction with two electrons the RDE voltammogram of the resulting solution shows the reduction waves A and B and the oxidation waves A′, E′ and F′ (Figure 7, b). After reduction with two and a half electrons wave A decreases and oxidation wave A′ increases (Figure 7, c). It is interesting to note that waves F′, A, A′ and B are nearly as high as the corresponding initial waves, whereas wave E′ is higher. No ESR signal is detected during the electrolysis. The solution shows a slow evolution towards partial regeneration of **3** from $[\mathbf{3}]^-$ upon standing under argon. This means that wave A increases while wave A′ decreases and the height of oxidation wave E′ grows considerably (Figure 7, d). It is still unclear why the formation of $[\mathbf{3}]^-$ consumes more than 1 F. It may well be that this reduction concerns one of the Nb atoms, which means that the anionic charge can be transferred by an intramolecular process to a ligand atom (probably tellurium). Consequently, subsequent oxidation at the potential of wave E′ may give rise to an increase of the height of the concerned oxidation wave.

When oxidative electrolysis is performed at –0.1 V (plateau of wave E′) the current drops to zero after a quantity of electricity of 0.2 F. The RDE voltammogram shows oxidation wave F′ and reduction waves E, A and B (Figure 8). Whereas these waves are in agreement with the formation of the cation $[\mathbf{3}]^+$, two additional reduction waves $E_1$ and $A_1$ are observed at –0.86 and –1.86 V, respectively. A similar result has been obtained in $CH_2Cl_2$/$NBu_4PF_6$ solution. Under these conditions, 0.2 F was consumed and a 0.2-V shift to more negative potentials is observed for all waves.

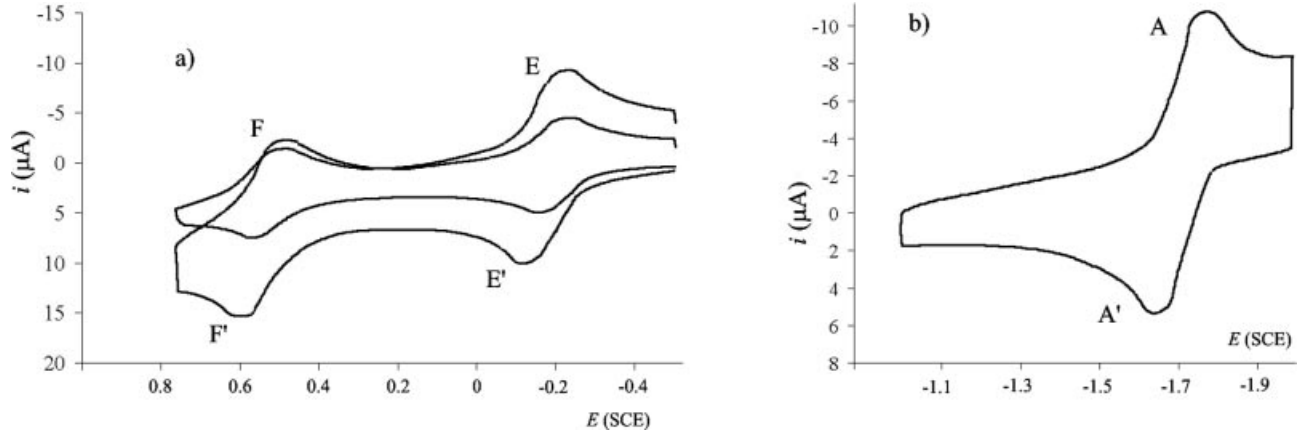


Figure 6. Cyclic voltammogram of **3** (thf/$NBu_4PF_6$): a) starting potential: –0.5 V; sweep rate: 20 and 100 mV s$^{-1}$; b) starting potential: –1 V; sweep rate: 50 mV s$^{-1}$.

 © 2007 Wiley-VCH Verlag GmbH & Co. KGaA, Weinheim 

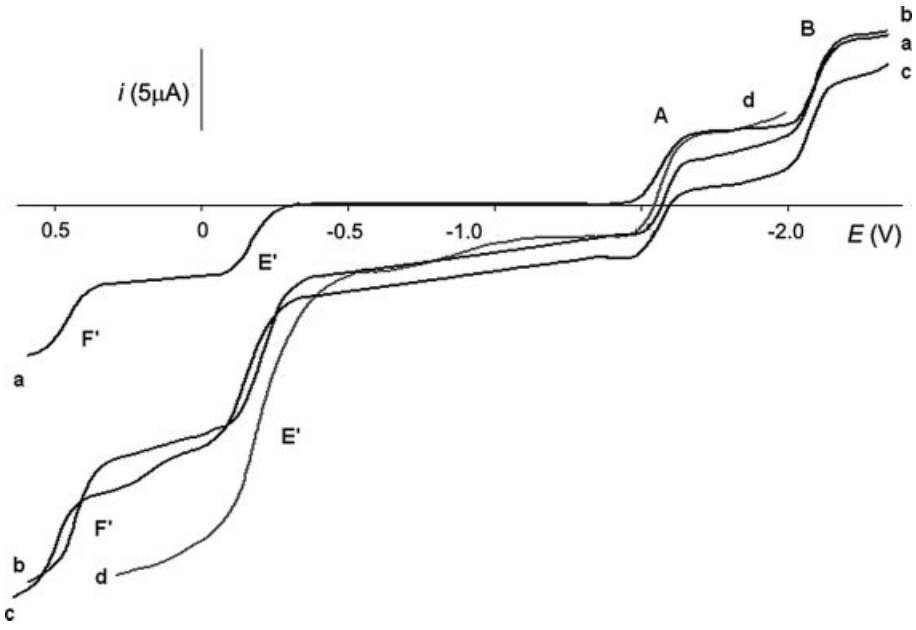


Figure 7. RDE voltammogram of **3** (thf/$NBu_4PF_6$): a) before electrolysis; b) after two-electron reduction at –1.8 V; c) after consumption of 2.5 F; d) evolution of the reduced solution at room temperature after 1 h.

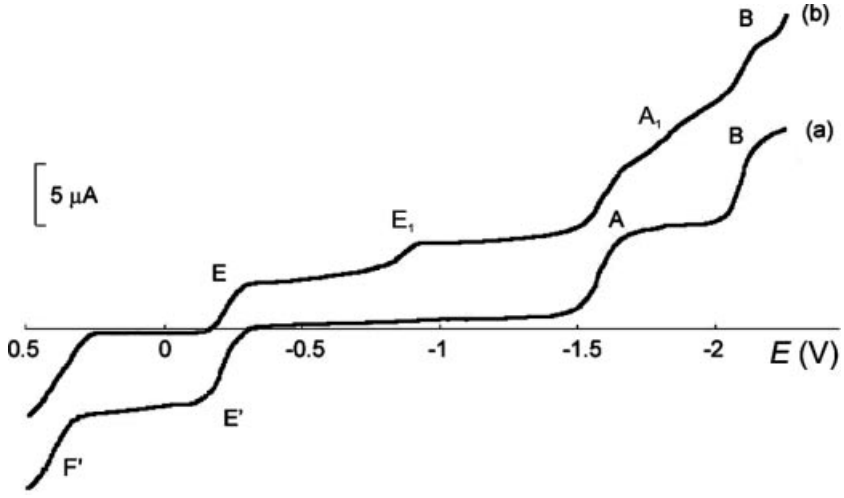


Figure 8. RDE voltammogram of **3** (thf/$NBu_4PF_6$): a) before electrolysis; b) after oxidation at –0.1 V and consumption of 0.2 F.

It is still unclear why the electrolysis of **3** at –0.1 V consumes 0.2 F instead of the required amount of 1 F for the formation of $[(Cp^*_2Nb)_2NiTe_4]^+$. However, if the oxidation is carried out at +0.35 V ($CH_2Cl_2$/$NBu_4PF_6$), 2 F are consumed and the subsequent cyclic voltammograms exhibit two new reversible systems $E_1/E_1'$ and $F_1/F_1'$ at 0.28 and –0.45 V, respectively. These systems may be assigned to the redox couples $[Cp^*_2NbF_2]/[Cp^*_2NbF_2]^+/[Cp^*_2NbF_2]^{2+}$. The first oxidation potential of $[(C_5Me_4Et)_2NbF_2]$ in $CH_2Cl_2$ has been determined to be $E_{1/2}$ = –0.38 V.[8]

The electrochemical behaviour of $[(Cp^*_2Nb)_2NiTe_4]BPh_4$ (**6**), which contains the cation [**3**]$^+$, was also studied. RDE voltammetry ($CH_2Cl_2$/$NBu_4PF_6$) gave the expected oxidation wave F′ at +0.28 V and the reduction wave E at –0.42 V. An additional reduction wave $E_1$ at –0.86 V is present, as in the case of the electrogenerated cation [**3**]$^+$. The heights of waves F′ and E are nearly equal and are twice as high as wave $E_1$ (see Figure S1 in the Supporting Information). Two reversible systems F′/F and E/E′ are observed in the cyclic voltammogram.

## Density Functional Calculations

The X-ray structure analysis of **3** shows that, contrary to the nearly tetrahedral $WTe_4^{2-}$ bridging fragment in $[\{(Cp'_2Nb)_2WTe_4\}W(CO)_4]$, the $NiTe_4$ moiety is highly distorted with short and long Te–Te distances. It is evident that the nickel atom is unable to reach the formal oxidation state +6 that is plausible for group 6 metals. In order to get an insight into the electronic structure of **3** and of its cationic and anionic species we have carried out DFT calcula-

 © 2007 Wiley-VCH Verlag GmbH & Co. KGaA, Weinheim 

tions with the Gaussian03 package by using the B3PW91/3-21G (SDD for Nb and Te) functional/basis set couple.[22] The molecular geometries of all systems studied were optimised first and then frequency calculations were performed to confirmation that the optimised geometries correspond well to energy minima. Cp ($C_5H_5$) replaces Cp* as a ligand in the models.

A preliminary analysis of the electronic properties of $[Cp_2NbTe_2]^-$ and the hypothetical $[NiTe_4]^{2-}$ anionic fragments derived from **3** will be useful for understanding the nature of **3**, and, in particular, why two pairs of Te atoms from two different niobocene ditelluride fragments form Te–Te bonds in the presence of $Ni^{2+}$.

Formally, complex **3** is built from $Ni^{2+}$ and two chelating $[Cp^*_2NbTe_2]^-$ anions. The electronic structures of bent metallocenes are well known.[23] We should recall, however, the main features of $[Cp_2NbTe_2]^-$ together with the shapes of the frontier molecular orbitals depicted in Figure 9. HOMO–5 to HOMO–3 are responsible for the σ and π Nb–Te bonds based on classical $1a_1$, $b_2$ and $2a_1$ bent metallocene molecular orbitals,[23] respectively, while HOMO–2 to HOMO are representative of Te lone pairs. Both LUMOs contain a large contribution from Nb atomic orbitals. All depicted orbitals may be involved in Te–Ni and Nb–Ni interactions upon formation of the trimetallic complex **3**. The optimised Nb–Te (2.722 Å), Te–Te (4.193 Å, labelled *intra*annular in **3**) and Te–Nb–Te (101.6°) parameters for $[Cp_2NbTe_2]^-$ are close to the corresponding values found in the crystal structure of **3**.

As shown above, the central $[NiTe_4]^{2-}$ moiety in the structure of **3** is severely distorted. In an attempt to clarify this feature we looked at the behaviour of the hypothetical $[NiTe_4]^{2-}$ anion in planar ($D_{4h}$ and $D_{2h}$), tetrahedral ($T_d$) and distorted tetrahedral ($D_{2d}$) symmetries in the singlet (s) and triplet (tr) spin states. The $D_{4h}$ initial geometry was ruled out because no convergence could be reached upon its optimisation. Remember that the $[NiX_4]^{n-}$ moiety (X = chalcogen) is extremely electron rich and is not known in classical mineral salts. Its stabilisation may occur with electron-withdrawing counterions like selected organometallic buffers. A niobocene seems to be a good candidate, as shown in this paper. $Ni^{2+}$ may exhibit its spin flexibility in distorted polyhedra, which is why both the singlet and triplet states were calculated. The geometry optimisations led to slightly $C_{3v}$ distorted (singlet) and to severely distorted $C_1$ (triplet) symmetries starting from tetrahedral $T_d$, and to approximately $D_2$-symmetric structures starting from $D_{2h}$ and $D_{2d}$ for both the singlet and triplet states. The total energies of the four main species obtained from geometry optimisations increase in the order $D_2$(tr) (0) < $C_1$(tr) (0.71) < $D_2$(s) (1.98) < $C_{3v}$(s) (2.84 eV). The triplet paramagnetic states are therefore more stable than the diamagnetic singlets. Due to the lack of experimental (e.g. magnetic) data for hypothetical $[NiTe_4]^{2-}$ we did not look at the nature of its singlet and triplet states and can therefore only state that the metal (Ni) must be responsible for them. In fact, in both the singlet and triplet $D_2$ optimised structures there are two short Te–Te bonding distances [mean: 2.970 (singlet) and 2.987 Å (triplet)] corresponding to the short *inter*annular ones in **3** and two sets of long separations (mean: 4.482/5.138 Å and 5.038/5.137 Å for singlet and triplet, respectively) that correspond to pairs of two long *inter*- and of two *intra*annular Te–Te distances in **3**. Thus, we can conclude that there are two ditelluride ($Te_2^{2-}$) ligands bound to the $Ni^{2+}$ centre in $[NiTe_4]^{2-}$.

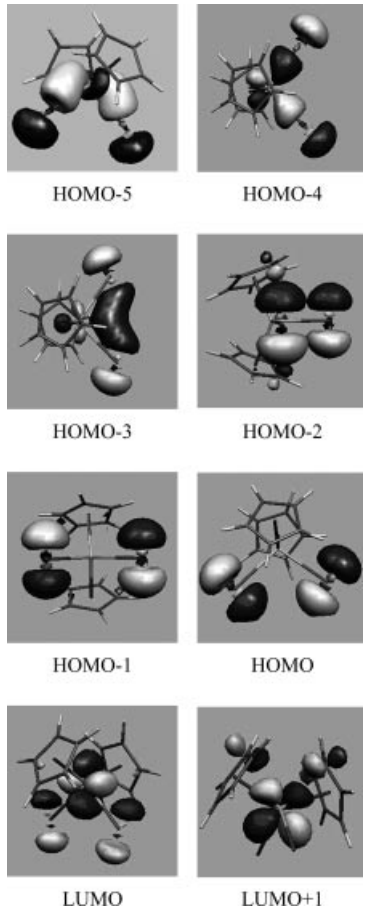


Figure 9. Shapes of significant molecular orbitals of the $[Cp_2NbTe_2]^-$ anion.

Such an intrinsic property of the $[NiTe_4]^{2-}$ anion, which is better described as bis(ditelluro)nickelate $[Ni(Te_2)_2]^{2-}$, in either the singlet or triplet spin state corroborates well the crystal structure of **3**. Selected molecular orbitals of $[Ni(Te_2)_2]^{2-}$ (singlet) are shown in Figure 10. The HOMO–11 and HOMO–3 are the Te–Te bonding orbitals, whereas the HOMO–7 and HOMO–2 may be considered as the non-bonding lone pairs of the Te atoms. Their shapes correspond to the HOMO–2 and HOMO–1 of the $[Cp_2NbTe_2]^-$ anion (Figure 9).

What do we know about the covalency of the Te–Te interaction in pertelluride ($Te_2^{2-}$)? X-ray data suggest a range of 2.67 to 3.05 Å for Te–Te bonds in $Te_2^{2-}$,[12–14,24] and covalent Te–Te bonds in the range of 2.74 to 2.93 Å have been reported from theoretical studies carried out on $H_2Te_2$ and $Me_2Te_2$.[25–27] We have calculated (B3WP91/SDD functional/basis set used in this paper) the Te–Te bond lengths for the singlet (2.946 Å) and triplet (3.364 Å) states of free

 © 2007 Wiley-VCH Verlag GmbH & Co. KGaA, Weinheim 

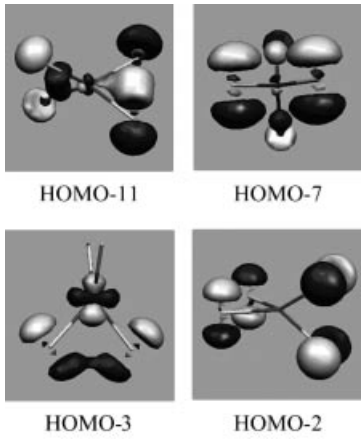


Figure 10. Shapes of selected molecular orbitals of $[Ni(Te_2)_2]^{2-}$.

ditelluride $Te_2^{2-}$. The triplet state consists of excitation of one electron from a π* antibonding to the high energy σ* orbital of $Te_2^{2-}$. The calculated Te–Te distance of 2.946 Å in the free diamagnetic molecule increases slightly to 2.970 Å in the diamagnetic complex $[Ni(Te_2)_2]^{2-}$ (vide supra) and up to 3.16 Å in trimetallic **3** (X-ray). In such a trimetallic environment of $Te_2^{2-}$ a lengthening and weakening of the Te–Te bond with retention of its covalent nature is acceptable for **3**. However, one may easily formulate a doubt about its existence at the distances (as long as 3.36 Å) calculated for the triplet state of free $Te_2^{2-}$ and the $[\mathbf{3}]^-$ anion (3.34 Å; vide infra). We checked this last question in the frame of Bader's AIM theory[28] for $Te_2^{2-}$ singlet and triplet states by using a full electron polarised 3-21G* basis set (needed for topological analysis of the wave function) coupled with the B3WP61 functional. The new optimised Te–Te distances are 2.865 (singlet) and 3.400 Å (triplet). Local topological properties such as electron density ($\rho$, e Å$^{-3}$), laplacian ($\nabla^2\rho$, e Å$^{-5}$), density of total energy $H$ ($H_a$, Å$^{-3}$) and derived "bond degree" $-H/\rho$ ($H_a$/e) at bond critical points (BCP) are useful for our purpose. In a simplified approach the covalent interaction needs accumulation of $\rho$ and a negative value of $H$ at the BCP. The $\nabla^2\rho$ may be negative (pure covalent shared–shared interaction) or positive [partially covalent shared–closed interaction; the closed–closed one (H positive) is of a van der Waals or ionic nature]. All considerations of atom–atom interactions need the detection of a BCP. This is the case for both the singlet and triplet states of $Te_2^{2-}$. The numerical values of $\rho$, $\nabla^2\rho$, $H$ and $-H/\rho$ at BCPs for the singlet/triplet are 0.37/0.17, –0.02/+0.72, –0.105/–0.012 and 0.28/0.07, respectively. These values also suggest a clearly covalent Te–Te bond in the singlet as some of its covalent nature is retained at a distance as long as 3.4 Å.

The initial geometry obtained from the DFT calculations on $[\mathbf{3}]^0$ is that of the X-ray structure of **3**. The optimisation of $[\mathbf{3}]^{2-}$ leads to one imaginary frequency (excited transition state) and will be only briefly mentioned below. The fact that we were not able to optimise the geometry of the ground state for $[\mathbf{3}]^{2-}$ agrees with the electrochemical evidence for its relative instability. Some metric, charge and energy data for the optimised structures of **3** in different oxidation states are given in Table S2 (see Supporting Information). On comparing the calculated and experimental metric parameters one can clearly see that the $NbTe_2Ni$ rings in $[\mathbf{3}]^0$ are compressed along the Nb–Ni vector by some 0.4 Å and stretched by 0.35 Å along the Te–Te *inter*annular vector with respect to **3** (X-ray). Thus, the direct Nb–Ni bonding interaction is favoured in the isolated molecule over the same molecule packed in the crystal. The shape of the HOMO–4 of **3**, which is clearly an Nb–Ni bonding orbital, is shown in Figure 11. The differences of other heavy atom distances between the calculated $[\mathbf{3}]^0$ and experimental **3** (X-ray) structures are close to 0.05 Å for mean values.

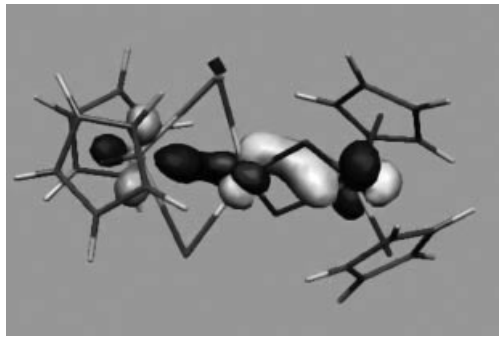

Figure 11. Shape of the HOMO–4 (Nb–Ni–Nb bonding) in the neutral complex **3**.

In the optimised $[\mathbf{3}]^n$ ($n$ = +2, +1, 0, –1) structures the calculated Nb–Ni, Nb–Te, Ni–Te, Te–Te (*intra*) and long Te–Te (*inter*) distances vary in an irregular manner, whereas the short Te–Te (*inter*) (ditelluride $Te_2^{2-}$) bonds increase regularly on going from $[\mathbf{3}]^{2+}$ to $[\mathbf{3}]^-$. A smooth increase is also observed for cationic and neutral species (mean values of 2.961, 3.040 and 3.105 Å), while a spectacular lengthening of the Te1–Te3 distance up to 3.908 Å is calculated for the anion. Note that the second *inter*annular (Te2–Te4) bond in $[\mathbf{3}]^-$ is also elongated, but "only" to 3.328 Å (Figure 12).

In all $[\mathbf{3}]^n$ species the Nb atoms bear a high positive charge, while the Ni atoms are negatively charged (except in $[\mathbf{3}]^+$). However, the variations of these charges (like those of metric parameters including Nb and Ni) do not correlate with the overall charges. It is, however, worth noting that the sums of metallic charges for all $[\mathbf{3}]^n$ ($n$ = +2, +1, 0, –1) species cover a narrow range of 2.38 ($[\mathbf{3}]^+$) to 2.08 Å ($[\mathbf{3}]^0$). On the other hand, the evolution of Mulliken charges on four Te atoms and four Cp rings follows the overall charges of $[\mathbf{3}]^{2+}$ to $[\mathbf{3}]^-$ species well. This is not surprising for the rings because of their well-known buffer properties. In the case of Te atoms, the observed trend strongly suggests that, whatever the first site of redox processes, the Te atoms are most affected in the final reduced or oxidised structure. Such an overview of the main metric and charge properties of $[\mathbf{3}]^n$ species argues well for the presence of two ditelluride $Te_2^{2-}$ ligands in complexes with $n$ = +2, +1 and 0, where

 © 2007 Wiley-VCH Verlag GmbH & Co. KGaA, Weinheim 

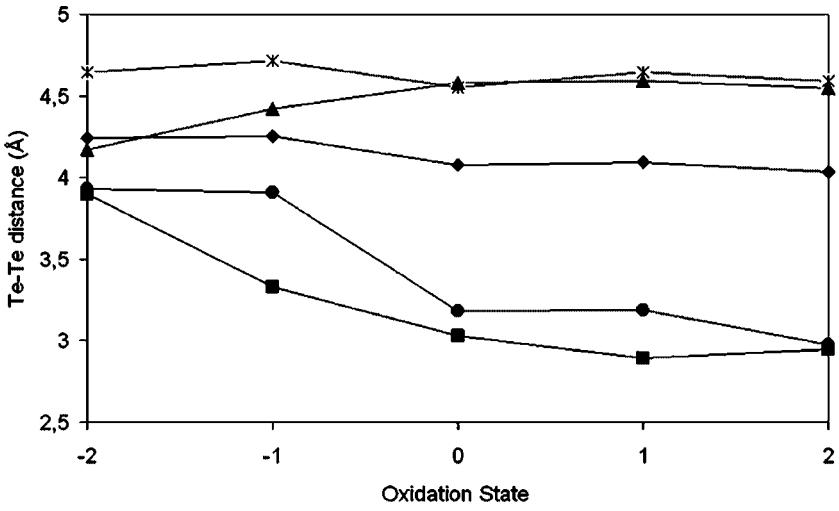


Figure 12. Evolution of the Te–Te distances in differently charged **3**: ■ Te2–Te4 *inter*annular short; ● Te1–Te3 *inter*annular short; ▲ mean of two *inter*annular long (Te1–Te4 and Te2–Te4); ♦ mean of all six Te–Te; × mean of two *intra*annular (Te1–Te2 and Te3–Te4).

the calculated Te–Te distances range between 2.894 and 3.186 Å. The presence of one ditelluride (calculated 3.328 Å) is also expected in the reduced $[\mathbf{3}]^-$ anion from both the tendencies observed in Figure 12 and from the AIM calculations. It is worth noting that the shortest Te–Te distances calculated for the transition state of doubly reduced $[\mathbf{3}]^{2-}$ are 3.896 and 3.929 Å, thus excluding any covalent Te–Te bonding interaction.

Electrochemical studies have revealed the presence of the redox-couples $[\mathbf{3}]^{2+}/[\mathbf{3}]^+$, $[\mathbf{3}]^+/[\mathbf{3}]$ and $[\mathbf{3}]/[\mathbf{3}]^-$ with $E_{1/2}$ potentials of +0.42, –0.22 and –1.61 V, respectively. These values should correlate with the energies (total, HOMO, LUMO) of the implied species. Taking the total energy of neutral $[\mathbf{3}]^0$ as the origin, those of $[\mathbf{3}]^{2+}$, $[\mathbf{3}]^+$ and $[\mathbf{3}]^-$ are equal to +13.979, +4.614 and –1.761 eV, respectively. There is a very good linear correlation between the total energy difference, $\Delta E_{tot}$, values (+9.365, +4.614 and –1.761 eV) and $E_{1/2}$ potentials (linear regression $R^2 = 0.997$) for the three redox systems. On the other hand, the linear correlation does not hold too well for $E_{1/2}$ or the energies of the HOMOs (oxidation, three points, $[\mathbf{3}]^+$, $[\mathbf{3}]^0$, $[\mathbf{3}]^-$, $R^2 = 0.927$) or the LUMOs {reduction, four points, $[\mathbf{3}]^{2+}$, $[\mathbf{3}]^+$, $[\mathbf{3}]^0$ and $[\mathbf{3}]^-$ (with $E_{1/2}$ $[\mathbf{3}]^-/[\mathbf{3}]^{2-} = -2.12$ V), $R^2 = 0.953$}. This may suggest that the one-electron oxidation of $[\mathbf{3}]^0$ does not necessarily operate on its HOMO similar to the one-electron reduction on its LUMO. Other occupied or empty orbitals may contribute to redox processes.

## Conclusions

The novel heterometallic telluride clusters $[(Cp^*_2Nb)_2NiTe_4]$ (**3**) and $[(Cp'Nb)_2Ni_5Te_7(dppm)_2]$ (**4**) have been obtained by the reaction of $[Ni(COD)]_2$ with $[Cp^*_2NbTe_2H]$ and $[Cp'_2NbTe_2H]$, respectively. Whereas the presence of the chelating phosphane dppm seems to increase the yields of **3**, it is essential for the formation of cluster **4**. The structure of the latter compound is characterised by two tetragonal $Ni_5$ and $Te_5$ pyramids stacked into each other.

Complex **3** is the first example of the trimetallic series $[(Cp^*_2Nb)_2MX_4]$ to contain a formally electron-rich tetratelluronickelate bridge. Contrary to some other experimentally observed tetrahedral $MX_4$ systems (M = Mo, W; X = S, Se, Te), the DFT calculations provide evidence for the presence of ditelluride ligands as an intrinsic property of the $[NiTe_4]^{2-}$ anion. The calculated Te–Te single bond lengths cover the range from 2.946 to 3.186 Å for $[\mathbf{3}]^{2+}$, $[\mathbf{3}]^+$ and $[\mathbf{3}]^0$, and are as high as 3.328 Å for the $[\mathbf{3}]^-$ anion. It follows from these calculations that the neutral complex **3** does not result from a simple chelation of two $[Cp^*_2NbTe_2]^-$ anions by $Ni^{2+}$. Instead, its formation is assisted by direct Nb–Ni interactions and bonding Te–Te interactions between both $[Cp^*_2NbTe_2]^-$ anions (*inter*annular bonds). A good linear correlation between the $E_{1/2}$ redox potentials and total energies of different oxidation states of **3** indicates that the electronically delocalised heavy atom core governs these reactions. However, the Te–Te bonding is most affected and thus plays a crucial role in redox processes involving **3**.

## Experimental Section

All manipulations were carried out under inert atmosphere using Schlenk line and/or glovebox techniques and dry solvents. Elemental analyses were performed at the Mikroanalytisches Laboratorium, University of Regensburg. IR spectra were obtained with a Mattson Genesis Series FTIR instrument; ESI mass spectra and FD mass spectra were measured with Finnigan TSQ 7000 and MAT 95 instruments, respectively. The $^1$H- NMR spectra were recorded with a Bruker ARX 250 instrument. $[Cp^*_2NbTe_2H]$ (**1**),[29] $[Cp'_2NbTe_2H]$ (**2**),[10] $[Ni(COD)_2]$[30] and $[(C_5H_5)_2Fe]BPh_4$[31] were prepared as described in the literature. Electrochemical experiments were carried out as described previously.[10]

**Synthesis of $[(Cp^*_2Nb)_2NiTe_4]$ (3):** $[Ni(COD)_2]$ (110 mg, 0.4 mmol) and dppm (80 mg, 0.2 mmol) were dissolved in toluene (120 mL) and a solution of **1** (250 mg, 0.4 mmol) in 15 mL of toluene, was added. The resulting mixture was stirred for 18 h at 110 °C. After cooling, the solvent was evaporated and the dark residue dissolved

 © 2007 Wiley-VCH Verlag GmbH & Co. KGaA, Weinheim 

in toluene/pentane (2:1, 15 mL). Chromatography on $SiO_2$ (column: 15 cm; diameter: 3 cm) gave an orange band containing some **1** upon elution with toluene/pentane (2:1) and then a broad black-violet band containing **3** (100 mg, 20% yield) with toluene. Recrystallisation from toluene/pentane (1:1) gave black crystals. Complex **3**: $C_{40}H_{60}Nb_2NiTe_4{\cdot}C_7H_8$ (1387.98): calcd. C 40.67, H 4.94; found C 40.94, H 4.96. FD-MS (from toluene): *m*/*z* 1296.7 (centre; $M^+$). $^1H$ NMR ($C_6D_6$): $\delta$ = 1.89 (s) ppm.

**Synthesis of $[(Cp'Nb)_2Ni_5Te_7(dppm)_2]$ (4):** A solution of **2** (160 mg, 0.27 mmol) in toluene (20 mL) was added to a yellow solution of $[Ni(COD)_2]$ (150 mg, 0.55 mmol) and dppm (104 mg, 0.27 mmol) in toluene (100 mL). The dark mixture was stirred for 18 h at 110 °C. After cooling, the solution was concentrated to 20 mL and filtered through a frit charged with dry kieselguhr. Then filtrate was then layered carefully with pentane (20 mL). Crystallisation at –20 °C gave several crops of black crystals with a total yield of 11%. Complex **4**: $C_{68}H_{70}Nb_2Ni_5P_4Te_7{\cdot}2C_7H_8$ (2567.94): calcd. C 38.35, H 3.38; found C 37.54, H 3.34. FD-MS (from $CH_2Cl_2$): *m*/*z* 2383.4 (centre; $M^+$).

**Reaction of 3 with $[Cp_2Fe]PF_6$:** A solution of **3** (200 mg, 0.15 mmol) in thf (20 mL) was mixed with a suspension of $[(C_5H_5)_2Fe]PF_6$ (100 mg, 0.30 mmol) in 15 mL of thf. After stirring for 2 h at room temperature a black precipitate separated from the yellow solution. After evaporation of the solvent the residue was suspended in toluene, transferred to a frit charged with Celite® and washed several times with toluene. Dissolving the residue in thf and evaporation of the solvent gave 40 mg (24%) of yellow $[Cp^*_2NbF_2]PF_6$ (**5**). The product is identical with a sample prepared from $[Cp^*_2NbCl_2]$ by reduction with Na/Hg and subsequent reaction with $HPF_6$.[8] Complex **5**: $C_{20}H_{30}F_8NbP$ (546.32): calcd. C 43.97, H 5.53; found C 43.83, H 5.43. FD-MS (from $CH_2Cl_2$): *m*/*z* 401.3 $[Cp^*_2NbF_2]^+$. $^1H$ NMR ($CD_2Cl_2$): $\delta$ = 2.13 (s) ppm.

**Synthesis of $[(Cp^*_2Nb)_2NiTe_4]BPh_4$ (6):** Complex **3** (250 mg, 0.24 mmol) was dissolved in thf (50 mL) and then added to a suspension of $[(C_5H_5)_2Fe]BPh_4$ (250 mg, 0.49 mmol) in 40 mL of thf. During the reaction the colour changed from black-violet to black-green. After stirring for 4 h at room temperature the solvent was removed. The residue was then washed with toluene (20 mL) to remove $[(C_5H_5)_2Fe]$ (50 mg, 0.27 mmol). The black residue was suspended in thf, filtered and the solvents evaporated to dryness to give 120 mg (37%) of **6**. Repeated recrystallisation from thf gave only microcrystalline material. Complex **6**: $C_{64}H_{80}BNb_2NiTe_4$ (1615.06): calcd. C 47.60, H 5.00; found C 47.31, H 4.84. ESI-MS (from $CH_2Cl_2$): Positive ion ESI: *m*/*z* 1295.7 $[\mathbf{6}]^+$; negative ion ESI: *m*/*z* 319.0 $[BPh_4]^-$. $^1H$ NMR ($CD_2Cl_2$): $\delta$ = 11.15 (br. s, 60 H, $C_5Me_5$), 7.31 (m, 8 H, $C_6H_5$), 7.03 (m, 8 H, $C_6H_5$), 6.88 (m, 4 H, $C_6H_5$) ppm.

### Crystal Structure Determination

**Complex 3:** Black rods were grown from a toluene solution at –24 °C. Data were collected at 173 K on a STOE imaging plate diffraction system (IPDS) using Mo-$K_\alpha$ radiation ($\lambda$ = 0.71073 Å). Crystallographic details are listed in Table 2. The structure was solved by direct methods and refined by full-matrix least-squares (SHELXL-97) with all reflections. All non-hydrogen atoms were refined with anisotropic displacement parameters. The H atoms were calculated geometrically and a riding model was used during the refinement process.

**Complex 4:** Crystal data were collected at 123 K on a STOE IPDS instrument using Mo-$K_\alpha$ radiation ($\lambda$ = 0.71073 Å). Crystallographic details are listed in Table 2. The space group determination following systematic extinction rules for the reflections together with the orthorhombic lattice constants led to space group *Pccn* (no. 56). First attempts to solve the structure by direct methods (SIR-97) immediately showed all heavy atoms. Searching for the carbon atoms by difference Fourier synthesis (SHELX-97) revealed that the chosen symmetry was too high. Inspection of the systematic absence violations of the reflections showed that all violations concern *h*0*l* reflections. Therefore, all following calculations were carried out in the acentric space group $Pc2_1n$, the unconventional setting of $Pna2_1$ (no. 33). In this space group there was no problem to locate all atoms by difference Fourier synthesis. Due to the high degree of pseudo-centrosymmetry and the fact that the crystal was an inversion twin with a ratio of 44:56, the correlation factors between a great number of atomic parameters made several constraints during the refinement calculations necessary. All carbon rings were fitted by the suitable AFIX instruction to a regular hexagon or pentagon, respectively. In particular, the C–C distances of one *tert*-butyl group had to be fixed. Despite including a damping factor during the least-squares refinements, all carbon atoms had to be refined with isotropic displacement factors. In addition, the solvent molecules showed severe positional disorder and could only be refined as a cloud of electron density. The shape of that cloud and the found electron numbers suggested that the solvent molecules are toluene. Despite these difficulties a reliable structure determination was obtained but with slightly increased estimated standard deviations for the interatomic distances.

Table 2. Crystal data for compounds **3** and **4**.

| | $[\mathbf{3}]{\cdot}C_7H_8$ | $[\mathbf{4}]{\cdot}2C_7H_8$ |
|---|---|---|
| Formula | $C_{40}H_{60}Nb_2NiTe_4{\cdot}C_7H_8$ | $C_{68}H_{70}Nb_2Ni_5P_4Te_7{\cdot}2C_7H_8$ |
| $M_w$ | 1387.9 | 2568.0 |
| Crystal system | monoclinic | orthorhombic |
| Crystal size [mm] | 0.30 × 0.13 × 0.12 | 0.24 × 0.12 × 0.08 |
| Space group | $P2_1/c$ | $Pc2_1n$ |
| *a* [Å] | 9.888(1) | 16.156(2) |
| *b* [Å] | 15.070(1) | 21.695(2) |
| *c* [Å] | 32.416(2) | 23.568(2) |
| $\beta$ [°] | 97.54(1) | |
| *V* [Å$^3$] | 4788.4(4) | 8260.6(2) |
| *Z* | 4 | 2 |
| $\rho_{calcd.}$ [g cm$^{-3}$] | 1.925 | 2.065 |
| $\lambda$ Mo-$K_\alpha$ [mm$^{-1}$] | 0.71073 | 0.71073 |
| *T* [K] | 173 | 123 |
| $\Theta$ range | 2.54–25.92 | 2.34–25.87 |
| Reflections collected | 43147 | 83476 |
| Unique reflections | 8839 [*R*(int) = 0.023] | 15897 [*R*(int) = 0.100] |
| Observed reflections [$I > 2\sigma(I)$] | 7469 | 6321 |
| Parameters refined | 487 | 416 |
| Absorption correction | numerical | analytical |
| Transmission | 0.649/0.588 | 0.613/0.445 |
| Max./min. residual density [e Å$^{-3}$] | 1.006/–0.624 | 1.548/–0.854 |
| *R*1 | 0.026 | 0.053 |
| *wR*2 | 0.067 | 0.110 |

CCDC-610345 (for **3**) and -610346 (for **4**) contain the supplementary crystallographic data for this paper. These data can be obtained free of charge from The Cambridge Crystallographic Data Centre via www.ccdc.cam.ac.uk/data_request/cif.

**Supporting Information** (see also the footnote on the first page of this article): Selected bond lengths, angles, interatomic distances and energies for redox species for **3**; RDE voltammogram of **6** on carbon electrode.

 © 2007 Wiley-VCH Verlag GmbH & Co. KGaA, Weinheim 

## Acknowledgments

We gratefully acknowledge continuous support over many years from Prof. Dr. H. Brunner and we are grateful to Dr. H. Cattey for her technical assistance. Parts of this work were supported by the Deutsche Forschungsgemeinschaft, the Deutscher Akademischer Auslandsdienst and the Ministère des Affaires Etrangères (program PROCOPE).

[1] A. Müller, E. Diemann, R. Jostes, H. Bögge, *Angew. Chem. Int. Ed. Engl.* **1981**, *20*, 934–955.
[2] a) Q.-F. Zhang, M.-T. Bao, M.-C. Hong, R. Cao, Y.-L. Song, X.-Q. Xin, *J. Chem. Soc., Dalton Trans.* **2000**, 605; b) Q.-F. Zhang, W.-H. Leung, X.-Q. Xin, H.-K. Fun, *Inorg. Chem.* **2000**, *39*, 417 and references cited therein; c) X. Chen, K. Wu, J. G. Snijders, C. Lin, *Inorg. Chem.* **2003**, *42*, 532–540.
[3] a) M. A. Ansari, J. C. Bollinger, J. A. Ibers, *J. Am. Chem. Soc.* **1993**, *115*, 3838–3839; b) M. A. Ansari, J. M. McConnachie, J. A. Ibers, *Acc. Chem. Res.* **1993**, *26*, 574–578.
[4] H. Brunner, M. M. Kubicki, G. Gehart, E. Lehrl, D. Lucas, W. Meier, Y. Mugnier, B. Nuber, B. Stubenhofer, J. Wachter, *J. Organomet. Chem.* **1996**, *510*, 291–295.
[5] O. Blacque, H. Brunner, M. M. Kubicki, D. Lucas, W. Meier, Y. Mugnier, B. Nuber, B. Stubenhofer, J. Wachter, *J. Organomet. Chem.* **1998**, *564*, 71–79.
[6] H. Brunner, J. Wachter, R. Wanninger, M. Zabel, *Eur. J. Inorg. Chem.* **2001**, 1151–1154.
[7] J. Wachter, *Eur. J. Inorg. Chem.* **2004**, 1367–1378.
[8] H. Brunner, G. Gehart, W. Meier, J. Wachter, A. Riedel, S. Elkrami, Y. Mugnier, B. Nuber, *Organometallics* **1994**, *13*, 134–140.
[9] H. Brunner, J.-C. Leblanc, D. Lucas, W. Meier, C. Moise, Y. Mugnier, B. Nuber, S. Rigny, A. Sadorge, J. Wachter, *J. Organomet. Chem.* **1998**, *566*, 203–210.
[10] H. Brunner, H. Cattey, D. Evrard, M. M. Kubicki, Y. Mugnier, E. Vigier, J. Wachter, R. Wanninger, M. Zabel, *Eur. J. Inorg. Chem.* **2002**, 1315–1325.
[11] I. Søtofte, *Acta Chem. Scand.* **1976**, *A30*, 157.
[12] a) V. J. Murphy, D. Rabinovich, S. Halkyard, G. Parkin, *J. Chem. Soc., Chem. Commun.* **1995**, 1099 and references cited therein; b) J. M. Fischer, W. E. Piers, L. R. MacGillivray, M. J. Zaworotko, *Inorg. Chem.* **1995**, *34*, 2499–2500.
[13] M. DiVaira, M. Peruzzini, P. Stoppioni, *J. Chem. Soc., Chem. Commun.* **1986**, 374.
[14] H. Sitzmann, D. Saurenz, G. Wolmershäuser, A. Klein, R. Boese, *Organometallics* **2001**, *20*, 700–705.
[15] D. Fenske, A. Hollnagel, K. Merzweiler, *Angew. Chem. Int. Ed. Engl.* **1988**, *27*, 965–966.
[16] H. Brunner, W. Meier, J. Wachter, B. Nuber, M. L. Ziegler, *J. Organomet. Chem.* **1990**, *381*, C7–C12.
[17] D. Fenske, H. Fleischer, H. Krautscheid, J. Magull, C. Oliver, S. Weisgerber, *Z. Naturforsch., Teil B* **1991**, *46*, 1384–1394.
[18] F. Cecconi, C. A. Ghilardi, S. Midollini, A. Orlandini, A. Vacca, *Inorg. Chem. Commun.* **2000**, *3*, 276–280.
[19] a) D. F. Rieck, J. A. Gavney Jr, R. L. Norman, R. K. Hayashi, L. F. Dahl, *J. Am. Chem. Soc.* **1992**, *114*, 10369–10379; b) D. F. Rieck, R. A. Montag, T. S. McKechnie, L. F. Dahl, *J. Chem. Soc., Chem. Commun.* **1986**, 1330–1331; c) P. D. Mlynek, L. F. Dahl, *Organometallics* **1997**, *16*, 1655–1667; d) A. Ceriotti, F. Demartin, B. T. Heaton, P. Ingallina, G. Longoni, M. Manassero, M. Marchionna, N. Masciocchi, *J. Chem. Soc., Chem. Commun.* **1989**, 786–787; e) A. J. Kahaian, J. B. Thoden, L. F. Dahl, *J. Chem. Soc., Chem. Commun.* **1992**, 353–355; f) V. G. Albano, F. Demartin, M. C. Iapalucci, G. Longoni, M. Monari, P. Zanello, *J. Chem. Soc., Dalton Trans.* **1992**, 497–502; g) J. P. Zebrowski, R. K. Hayashi, L. F. Dahl, *J. Am. Chem. Soc.* **1993**, *115*, 1142–1144; h) V. G. Albano, F. Demartin, C. Femoni, M. C. Iapalucci, G. Longoni, M. Monari, P. Zanello, *J. Organomet. Chem.* **2000**, *593–594*, 325–334.
[20] R. W. Murray, C. N. Reitley, *Electroanalytical Principles*, Interscience, New York, **1963**.
[21] R. S. Nicholson, *Anal. Chem.* **1965**, *37*, 1351–1355.
[22] *Gaussian 03, Revision B.05*, M. J. Frisch, G. W. Trucks, H. B. Schlegel, G. E. Scuseria, M. A. Robb, J. R. Cheeseman, J. A. Montgomery Jr, T. Vreven, K. N. Kudin, J. C. Burant, J. M. Millam, S. S. Iyengar, J. Tomasi, V. Barone, B. Mennucci, M. Cossi, G. Scalmani, N. Rega, G. A. Petersson, H. Nakatsuji, M. Hada, M. Ehara, K. Toyota, R. Fukuda, J. Hasegawa, M. Ishida, T. Nakajima, Y. Honda, O. Kitao, H. Nakai, M. Klene, X. Li, J. E. Knox, H. P. Hratchian, J. B. Cross, C. Adamo, J. Jaramillo, R. Gomperts, R. E. Stratmann, O. Yazyev, A. J. Austin, R. Cammi, C. Pomelli, J. W. Ochterski, P. Y. Ayala, K. Morokuma, G. A. Voth, P. Salvador, J. J. Dannenberg, V. G. Zakrzewski, S. Dapprich, A. D. Daniels, M. C. Strain, O. Farkas, D. K. Malick, A. D. Rabuck, K. Raghavachari, J. B. Foresman, J. V. Ortiz, Q. Cui, A. G. Baboul, S. Clifford, J. Cioslowski, B. B. Stefanov, G. Liu, A. Liashenko, P. Piskorz, I. Komaromi, R. L. Martin, D. J. Fox, T. Keith, M. A. Al-Laham, C. Y. Peng, A. Nanayakkara, M. Challacombe, P. M. W. Gill, B. Johnson, W. Chen, M. W. Wong, C. Gonzalez, and J. A. Pople, Gaussian, Inc., Pittsburgh PA, **2003**.
[23] J. W. Lauher, R. Hoffmann, *J. Am. Chem. Soc.* **1976**, *98*, 1729.
[24] P. Böttcher, J. Getzschmann, R. Keller, *Z. Allg. Anorg. Chem.* **1993**, *619*, 476–488.
[25] J. J. BelBruno, *Heteroat. Chem.* **1997**, *8*, 199–202.
[26] R. Berger, C. Van Wüllen, *J. Chem. Phys.* **2005**, *122*, 134316.
[27] J. M. Gonzales, D. G. Musaev, K. Morokuma, *Organometallics* **2005**, *24*, 4908–4914.
[28] R. F. W. Bader, *Atoms in Molecules: A Quantum Theory*, Clarendon Press, Oxford, U.K., **1990**.
[29] O. Blacque, H. Brunner, M. M. Kubicki, B. Nuber, B. Stubenhofer, J. Wachter, B. Wrackmeyer, *Angew. Chem. Int. Ed. Engl.* **1997**, *36*, 351–353.
[30] D. J. Krysan, P. B. Mackenzie, *J. Org. Chem.* **1990**, *55*, 4229–4230.
[31] T. Birchall, I. Drummond, *Inorg. Chem.* **1971**, *10*, 399–401.

Received: July 13, 2006
Published Online: January 16, 2007

 © 2007 Wiley-VCH Verlag GmbH & Co. KGaA, Weinheim 

DOI: 10.1002/ejic.200600978

# Transition Metal-Assisted Hydrolysis of Pyrazole-Appended Organooxotin Carboxylates Accompanied by Ligand Transfer

**Vadapalli Chandrasekhar,*[a] Pakkirisamy Thilagar,[a] and Tapas Senapati[a]**

**Keywords:** Organotin carboxylates / Organooxotin / Organostannoxane / Heterobimetallics / Supramolecular chemistry / Transition metals

The reaction of the potentially multi-site coordination ligands $[\{n\text{Bu}_2\text{SnO}_2\text{CL}\}_2\text{O}]_2$ (**1**), $[\{n\text{Bu}_2\text{SnO}_2\text{CL}'\}_2\text{O}]_2$ (**2**), $[n\text{BuSn(O)O}_2\text{CL}]_6$ (**3**), and $[n\text{BuSn(O)O}_2\text{CL}']_6$ (**4**), (L = $(\text{Pz})_2$CH-); L′ = $(3,5\text{-Me}_2\text{Pz})_2$CH-; Pz = pyrazolyl) with hydrated metal salts leads to the hydrolysis of the organotin carboxylates accompanied by the formation of insoluble organotinoxide/hydroxides and metal complexes. The in situ generated LCOO and L′COO ligands bind to the metal ions. The complexes $[\text{Cu(LCOO)}_2(\text{NO}_3)_2(n\text{Bu}_2\text{Sn}((\text{H}_2\text{O})_2)]_n[\text{Cu(LCOO)}_2]$ (**5**), $[\text{Mg(L′COO)}_2]$ (**6**), $[\text{Cu(LCOO)}_2]$ (**7**), and $[\{(\text{Cu(L′COO)}_2(\text{Cu(MeOH)})_3\}\{\text{ClO}_4\}_2]_n$ (**8**) were isolated and structurally characterized. The solid-state structure of **5** reveals that two discrete molecules are present in the same asymmetric unit; a heterobimetallic coordination polymer, $[\text{Cu(LCOO)}_2(\text{NO}_3)_2(n\text{Bu}_2\text{Sn}((\text{H}_2\text{O})_2)]_n$ and a discrete coordination complex, $[\text{Cu(LCOO)}_2]$. The cationic portion of the heterobimetallic compound contains alternate six-coordinate $\text{Sn}^{\text{IV}}$ and $\text{Cu}^{\text{II}}$ centers bridged by the carboxylate oxygen atoms of the LCOO ligand.

(© Wiley-VCH Verlag GmbH & Co. KGaA, 69451 Weinheim, Germany, 2007)

## Introduction

Synthetic polymers in spite of their many attractive features[1–2] suffer from a serious disadvantage.[1–2] Even in well-controlled polymerization pathways the chain lengths as well as the molecular structure of the various individual chains present in a given macromolecule are not the same. *Dendrimers* or *Star-burst* molecules are hyperbranched macromolecules with high surface area and structural symmetry which retain the advantages of the macromolecules while avoiding the structural imprecision found in the latter.[3–5] We and others have been pursuing the possibility of using inorganic cores for building star-burst-type molecules.[6–14] Thus, inorganic rings such as cyclophosphazenes,[6,8] cyclosiloxanes,[9] and borazines[10] have been used recently as supports for the preparation of novel compounds which contain a central inorganic core and a periphery of judiciously placed functional substituents. Other inorganic rings and cages that contain Al–N or Al–C units have been similarly investigated.[11]

We have been interested in organostannoxanes for some time now and have recently shown the utility of these compounds to support hexa-ferrocene[12] and hexa-porphyrin[13] architectures. Encouraged by the success in the use of stannoxanes as inert cores for supporting a functional periphery we have turned our attention to the possibility of building multi-site coordination ligands based on stannoxane cores. Accordingly we have recently reported a series of multi-site coordination ligands containing a central stannoxane core which is decorated by a periphery of bis-pyrazolyl groups.[14] By a one-step synthetic protocol involving the reaction of bis(pyrazol-1-yl)acetic acid, LCOOH, (L = $(\text{Pz})_2$CH-) or bis(3,5-dimethylpyrazol-1-yl)acetic acid, L′COOH (L′ = $(3,5\text{-Me}_2\text{Pz})_2$CH-) with various organooxotin precursors potentially multi-site coordination ligands $[\{n\text{Bu}_2\text{SnO}_2\text{CL}\}_2\text{O}]_2$ (**1**), $[\{n\text{Bu}_2\text{SnO}_2\text{CL}'\}_2\text{O}]_2$ (**2**), $[n\text{BuSn(O)O}_2\text{CL}]_6$ (**3**), and $[n\text{BuSn(O)O}_2\text{CL}']_6$ (**4**), were prepared.[14] The number of coordination units assembled on the stannoxane periphery depends on the type of stannoxane assembled. Metalation reactions of **1**–**4** with hydrated metal salts resulted, in all the cases, in the transfer of the bis(pyrazolyl)acetate unit from the tin to the transition/alkaline earth metal ion. In one instance involving the interaction between $[\{n\text{Bu}_2\text{SnO}_2\text{CL}\}_2\text{O}]_2$ (**1**) (L = $(\text{Pz})_2$CH-; Pz = pyrazolyl) and $\text{Cu(NO}_3)_2\cdot 3\text{H}_2\text{O}$ we isolated $[\text{Cu(LCOO)}_2(\text{NO}_3)_2(n\text{Bu}_2\text{Sn}(\text{H}_2\text{O})_2)]_n$ $[\text{Cu(LCOO)}_2]$ (**5**). The crystal structure of the latter reveals that its asymmetric unit contains two independent chemical entities viz., a heterobimetallic coordination polymer $[\{\text{Cu(LCOO)}_2\}\{n\text{Bu}_2\text{Sn}(\text{H}_2\text{O})_2\}]_n$ (**5a**) and a discrete six-coordinate copper complex $[\text{Cu(LCOO)}_2]$ **5b**. The structure of the heterobimetallic complex provides the clue that the transfer of the ligand from

[a] Department of Chemistry, Indian Institute of Technology, Kanpur,
Kanpur 208016, India
Fax: +91-512-2590007, -2597436
E-mail: vc@iitk.ac.in

Supporting information for this article is available on the WWW under http://www.eurjic.org or from the author.

 © 2007 Wiley-VCH Verlag GmbH & Co. KGaA, Weinheim 

the organotin compound to the transition metal ion is probably initiated and accompanied by a hydrolysis reaction.

## Results and Discussion

**Synthesis:** Compounds **5**–**8** were obtained in the reactions of the organotin precursors **1**–**4** with various hydrated metal salts (Scheme 1 and Supporting Information). In all these cases an insoluble colorless solid presumably a mixture of organotinoxide/hydroxides, was also isolated. For example, in the reaction of **3** with $Cu(ClO_4)_2 \cdot 6H_2O$ the insoluble material, **7b**, was obtained. The powder XRD of **7b** matches very closely that of *n*BuSn(O)OH based on its powder XRD (Figure S1, Supporting Information). Similarly the solid-state IR spectrum of **7b** also is in agreement with the spectrum of the authentic *n*BuSn(O)OH sample (Supporting Information, Figure S2). The insoluble product obtained in the reaction of metal salts with $Cu(NO_3)_2 \cdot 3H_2O$ and $Mg(NO_3)_2 \cdot 6H_2O$ has a powder XRD pattern similar to that of $nBu_2SnO$ (Supporting Information Figure S3–S4). These results imply that the organotin carboxylate cores of **1**–**4** decompose upon interaction with metal salts releasing hydrated organotin cations (Scheme 2) which can self-condense to afford organotin oxides/oxide hydroxides. In the process, the carboxylate ligand originally bound to the tin center is transferred to the interacting transition metal ion. Compound **5** is obtained in the reaction of **1** and Cu-

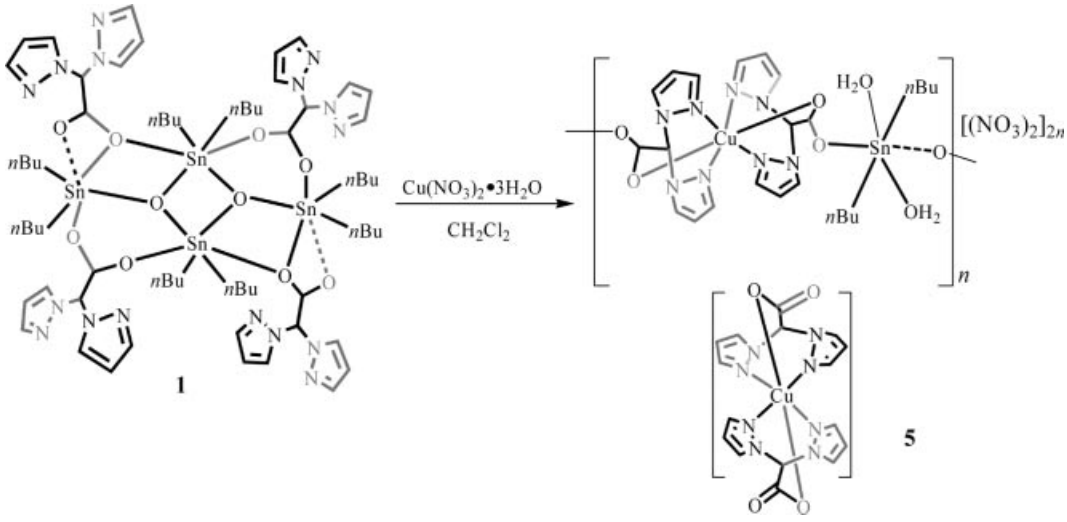


Scheme 1. Synthesis of **5**.

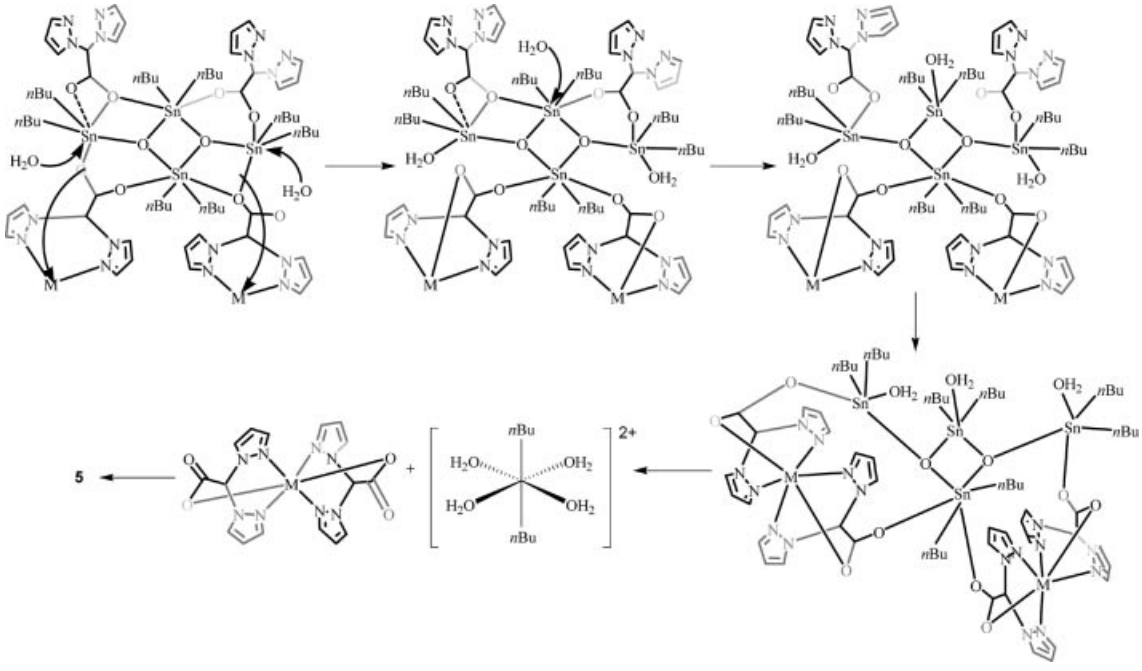


Scheme 2. Proposed mechanism for the hydrolysis of organotin carboxylates upon interaction with metal ions.

 © 2007 Wiley-VCH Verlag GmbH & Co. KGaA, Weinheim 

$(NO_3)_2 \cdot 3H_2O$ (Scheme 1) and is probably an intermediate on the way to the fully hydrolyzed products. One of the molecules present in the crystal structure of **5a** is a heterobimetallic coordination polymer containing both tin and copper atoms (Figure 1). We were unable to obtain a $^{119}Sn$ NMR for this compound because of the strong paramagnetic relaxation of $Cu^{II}$.

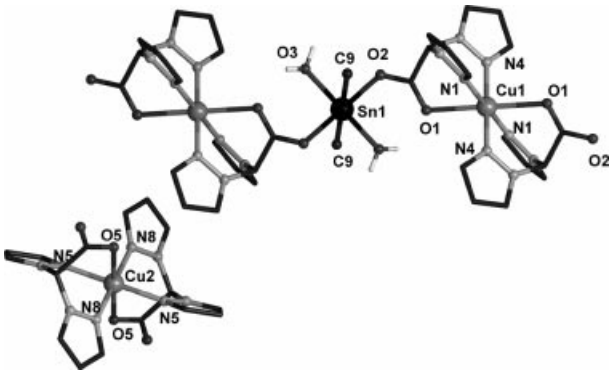


Figure 1. Independent crystallographic components of compound **5** with atom numbering. Heterobimetallic coordination polymer (top) and discrete mononuclear $Cu^{II}$ complex (bottom). Only the alpha carbon of the *n*-butyl group is shown. The other carbon atoms of the butyl group and the hydrogen atoms of the pyrazolyl rings are removed for the sake of clarity.

### X-ray Crystal Structure of 5

The X-ray structure of **5** is discussed herein. The structures of **6**–**8** along with their description and supramolecular structures are given in supporting information.

The crystal structure of **5** is quite unusual. Its asymmetric unit contains two independent chemical entities viz., a heterobimetallic coordination polymer $[\{Cu(LCOO)_2\}\{n Bu_2Sn(H_2O)_2\}]_n$ (**5a**) and a discrete six-coordinate copper complex $[Cu(LCOO)_2]$ **5b**. However, these two chemical entities are intimately related as discussed vide infra.

Complex **5a** is a coordination polymer containing alternately two sub-units. One of these is $Cu(LCOO)_2$ while the other is $[n Bu_2Sn(H_2O)_2]$. These are interlinked to each other to afford a one-dimensional helical polymer chain (Figure 1). Such a heterobimetallic coordination polymer is unprecedented among organotin compounds. The geometry around both of the metal ions found in **5a** can be described as distorted octahedral (Figure 2). The dihedral angle between the two square planes around $Cu^{II}$ and $Sn^{IV}$ is 16.322(5)°. The equatorial plane around $Cu^{II}$ is formed by four pyrazole nitrogen atoms derived from two LCOO moieties. The apical positions are occupied by two carboxylate oxygen atoms (O1 and O1′). The two uncoordinated oxygen atoms (O2 and O2′) of the $[Cu(LCOO)_2]$ unit assist in forming the coordination polymer by bridging two $[n Bu_2Sn(H_2O)_2]$ units (Figure 2). As a result the immediate coordination environment around $Sn^{IV}$ consists of two *n*-butyl groups (C9 and C9′), two water molecules (in the equatorial plane) and two oxygen atoms (O2 and O2′) in the axial sites. The two *n*-butyl groups are arranged in a *trans* manner with respect to each other. In spite of two different oxygen donors the Sn–O bond lengths in **5a** are nearly similar (Sn1–O2, 2.219(1); Sn1–O3, 2.207(1) Å). In the case of the copper sub unit of **5a** the Cu1–O1 distance is 2.381(1) Å. Interestingly, all the metric parameters found for the copper subunit in **5a** are very similar to that found in **5b**. The formation of **5a** can be readily rationalized as follows. Hydrolysis of the organotin carboxylate **1** leads to the formation of $[n Bu_2Sn(H_2O)_4]^{2+}$ and $Cu(LCOO)_2$. Interaction of these two entities results in the expulsion of two water molecules (that are *trans* to each other) from the former leading to the assembly of the heterobimetallic coordination polymer **5a** (Scheme 2). The presence of **5b**, fortuitously co-crystallizing with **5a**, strongly supports this supposition. Further, we have previously isolated $[n Bu_2Sn(H_2O)_4]^{2+}$, albeit in a different reaction.[15]

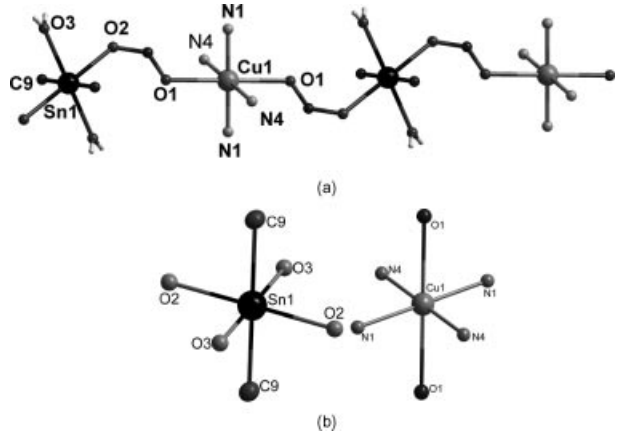


Figure 2. (a) Helical structure of compound **5** with atom numbering. The unlabeled atoms are generated by a symmetry relationship with the labeled atoms. (b) Coordination environment around Cu1 and Sn1. Important bond lengths [Å] and bond angles [°] in the monomer portion of the heterobimetallic polymer. Sn1–C9 2.133(2), Sn1–O3 2.207(1), Sn1–O2 2.219(1), Cu1–N4 1.995(1), Cu1–N1 2.013(1), Cu1–O1 2.381(1), C9–Sn1–C9 180, C9–Sn1–O3 86.137(7), O3–Sn1–O3 180, O2–Sn1–O2 180, N4–Cu1–N4 180, N4–Cu1–N1 91.355(6), N4–Cu1–O1 97.162(6), N1–Cu1–N1 180.0(6), N1–Cu1–O1 81.755(6), O1–Cu1–O1 180.

It must be mentioned that **1** itself does not undergo hydrolysis (Experimental Section). This means that the interaction of the metal ion with the coordination periphery of the organostannoxane ligand **1** accentuates the electrophilicity of the tin center and renders them susceptible to attack by water. Transfer of the bis(pyrazolylcarboxylate) ligand to the transition metal ion is also helped by the pincer-like coordination action of the released LCOO tripodal ligand resulting in the formation of two chelating five-membered rings arising from the coordination of the carboxylate oxygen atom to the metal center (Scheme 2).

**Supramolecular Structure of 5:** The crystal structures of **5**–**8** show rich supramolecular architectures mediated by intermolecular C-H---O, C-H---N, and O-H---O interactions. Only the case of **5** is discussed here. The remaining supramolecular structures are given in the Supporting Information (Figures S8–S12). The crystal structure of **5** shows interesting supramolecular interactions between **5a**

 © 2007 Wiley-VCH Verlag GmbH & Co. KGaA, Weinheim 

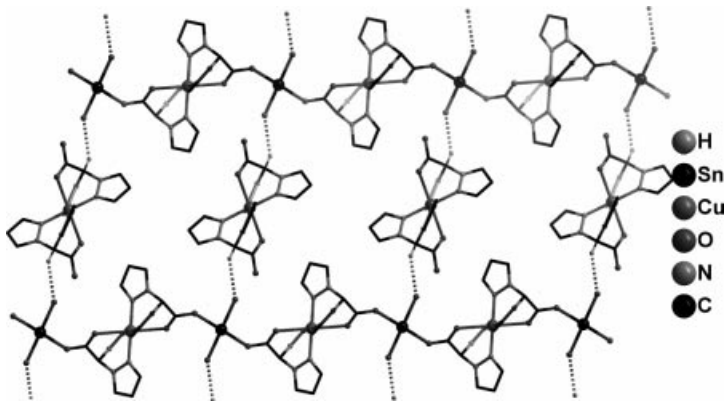


Figure 3. The 2D layer structure of compound **5** as a result of intermolecular C-H---O interactions [C19–H19···O13 2.673(1) Å and C19-H19---O13 134.747(11)°].

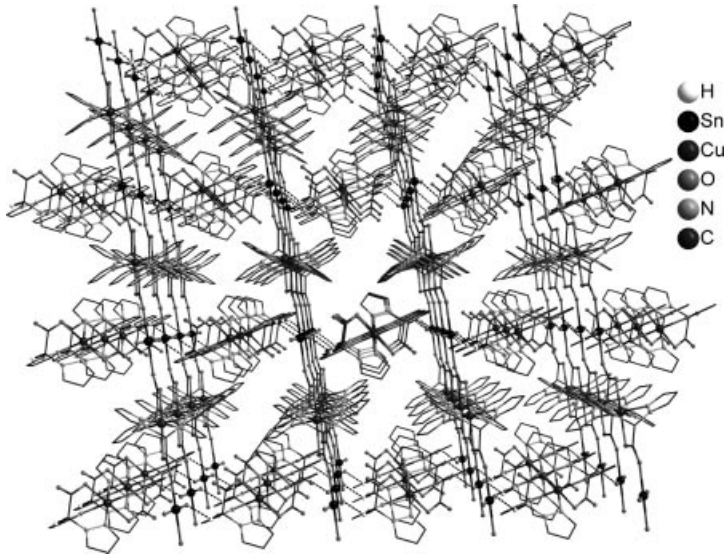


Figure 4. The 3D structure of **5**.

and **5b**. An intermolecular C-H---O interaction between the $Pz_2$-C-*H*-COO- of **5b** and an oxygen atom (belonging to a water molecule coordinated to tin) leads to the generation of a two-dimensional layer structure (Figure 3). Further intermolecular C-H---O interactions between the C-H′s of pyrazolyl ring of **5b** and the oxygen atoms of the nitrate anions leads to the elaboration of the supramolecular structure into a three-dimensional structure (Figure 4).

## Conclusions

In conclusion, we report in this contribution, the hydrolytic sensitivity of the organostannoxane cages $[\{n\mathrm{Bu_2SnO_2CL}\}_2\mathrm{O}]_2$ (**1**), $[\{n\mathrm{Bu_2SnO_2CL'}\}_2\mathrm{O}]_2$ (**2**), $[n\mathrm{BuSn(O)O_2CL}]_6$ (**3**), and $[n\mathrm{BuSn(O)O_2CL'}]_6$ (**4**), (L = $(Pz)_2$CH-); L′ = $(3,5\text{-}Me_2Pz)_2$CH-; Pz = pyrazolyl) upon interaction with hydrated metal salts. Interestingly, compounds **1**–**4** themselves do not hydrolyze in the absence of hydrated transition metal salts. This suggests that the coordination of the peripheral pyrazole arms of the organostannoxanes **1**–**4** renders the tin atoms electron deficient and therefore susceptible to nucleophilic attack by water leading to the collapse of the organostannoxane cores and the transfer of the ligands LCOO or L′COO to the metal ions. Another reason for the ligand transfer may be traced to the facile chelation that occurs *after* the ligand breaks off from the stannoxane and coordinates to the added metal ion. One of the ways of limiting this would be to insulate the tin atoms of the stannoxane core from the coordinating units by means of appropriate spacer groups. The delineation of this hypothesis is under progress.

## Experimental Section

**General:** All solvents were dried and purified by standard procedures. $Cu(NO_3)_2{\cdot}3H_2O$, $Cu(ClO_4)_2{\cdot}6H_2O$, and $Mg(NO_3)_2{\cdot}6H_2O$ were purchased from Aldrich and used without further purification. Melting points were measured with a JSGW melting point apparatus and are uncorrected. Elemental analyses were carried out by using a Thermo-quest CE instruments model EA/110 CHNS-O elemental analyzer. IR spectra were recorded as KBr pellets with a Bruker Vector 22 FT IR spectrophotometer operating from 400 to

 © 2007 Wiley-VCH Verlag GmbH & Co. KGaA, Weinheim 

4000 $cm^{-1}$. Compounds **1**–**4** were synthesized according to procedures published by us recently.[14]

**Synthesis of $[Cu(LCOO)_2(NO_3)_2(nBu_2Sn(H_2O)_2)]_n[Cu(LCOO)_2]$ (5):** To a solution of **1** (0.2 mmol, 345 mg) in dichloromethane (100 mL) was added $Cu(NO_3)_2{\cdot}3H_2O$ (0.4 mmol, 93 mg). The reaction mixture was stirred for 2 h at room temperature. An insoluble white solid (**5′**) was removed by filtration. The white solid **5′** has a powder XRD pattern similar to $[nBu_2SnO_2]_n$. The blue filtrate was concentrated to half of its volume and kept for crystallization. Blue crystals started to form after about a week. The crystals were collected, washed with diethyl ether, and dried. Total yield of the blue crystals: 34% (150 mg), m.p. 192–195 °C (d). IR (KBr): $\tilde{\nu}$ = 3341.0 (b), 3154.2–3124.7 (s, d), 2999.5 (w), 2959.2 (s), 2926.2 (s), 2863 (w), 1663.1 (s), 1515.1 (s) 1470.7 (s) 1410.4 (s), 1375.9 (s), 1291.6 (s), 1200.6 (w) 1102.2 (s), 1070.0 (w), 940.3 (w), 773.9 (s) and 749.9 (w) $cm^{-1}$.

A blank experiment was also performed to check if **1** underwent hydrolysis in the absence of the metal salt. Compound **1** (0.10 mmol, 0.18 g) was dissolved in methanol (35 mL), to this was added 2 mL of water. The reaction mixture was stirred for 3 h at room temperature. It was observed that **1** could be fully recovered. This was confirmed by the $^{119}Sn$ NMR [$CDCl_3$: δ = –172.1 (s), –195.5 (s) ppm] of **1** before and after performing the hydrolysis experiment.

Synthetic procedures for compounds **6**–**8**, IR and powder XRD traces for fully hydrolyzed products and their corresponding organooxotin precursors, molecular and supramolecular description for compounds **6**–**8** are given in the Supporting Information.

**X-ray Crystallography:** The crystal data for **5**–**8** were collected with a Bruker Smart diffractometer. All the structures were solved by direct methods using SHELXS-97[16] and refined by full-matrix least-squares on $F^2$ using SHELXL-97. All hydrogen atoms were included in idealized positions, and a riding model was used. Non-hydrogen atoms were refined with anisotropic displacement parameters. The asymmetric unit of compound **5** contains two independent structural entities. (1) A portion of a coordination polymeric chain with one copper (Cu1) and one tin (Sn1). (2) Half of the molecule of a mononuclear copper complex. All the metals in the asymmetric unit (Cu1, Sn1, and Cu2) have 0.5 occupancy. The asymmetric unit of compound **6** contains half of the molecule with two lattice water molecules (O3 and O4). The magnesium atom (Mg1) has 0.5 occupancy in the asymmetric unit and the oxygen atom (O4) of the lattice water molecule is disordered over two positions with 0.5 occupancies. The asymmetric unit of compound **7** contains half of the molecule with one copper center (Cu1) and the copper atom has 0.5 occupancy. The asymmetric unit of **8** contains two perchlorate molecules and a fraction of polymeric chain with three copper centers Cu1, Cu2, and Cu3. The atoms Cu1 and Cu3 have 0.5 occupancy in the asymmetric unit. Two of the perchlorate oxygen atoms (O11 and O14) are disordered. O11 is disordered over two positions with occupancies of 0.5 (O11a) and (O11b) and refined anisotropically. O14 is disordered over three positions with occupancies 0.4(O14a), 0.3 (O14b), and 0.3 (O14c), and are refined isotropically. Because of the inadequate quality of data we were unable to fix the hydrogen atoms on the oxygen atoms of the methanol molecules (O5, O6, and O7).

CCDC-608022, -608024, and -608027 contain the supplementary crystallographic data for this paper. These data can be obtained free of charge from The Cambridge Crystallographic Data Centre via www.ccdc.cam.ac.uk/data_request/cif. Figures 1–4 were obtained from the DIAMOND 3.0 software package.

## Acknowledgments

We are thankful to the Department of Science and Technology, New Delhi, for financial support. P. T. thanks IIT-K, for a Senior Research Fellowship. T. S is thankful to the Council of Scientific and Industrial Research, New Delhi, for a Junior Research Fellowship.

[1] a) B. G. Sumpter, P. Kumar, A. Mehta, M. D. Barnes, W. A. Shelton, R. J. Harrison, *J. Phys. Chem. B* **2005**, *109*, 7671–7685; b) H.-L. Cheng, K.-F. Lin, *Synth. Met.* **2001**, *122*, 387–393; c) M. M. Alam, S. A. Jenekhe, *Chem. Mater.* **2004**, *16*, 4647–4656; d) D. A. M. Egbe, L. H. Nguyen, B. Carbonnier, D. Mühlbacherd, N. S. Sariciftci, *Polymer* **2005**, *46*, 9585–9595; e) J. A. Mikroyannidis, *Synth. Metals* **2005**, *155*, 125–129; f) T. Kietzke, H.-H. Hörhold, D. Neher, *Chem. Mater.* **2005**, *17*, 6532–6537.

[2] a) J. M. Lupton, *Chem. Phys. Lett.* **2002**, *365*, 366–368; b) E. J. W. List, M. Gaal, R. Guentner, P. S. D. Freitas, U. Scherf, *Synth. Metals* **2003**, *139*, 759–763; c) C. F. Wang, J. D. White, T. L. Lim, J. H. Hsu, S. C. Yang, W. S. Fann, P. K. Y. Eng, S. A. Chen, *Phys. Rev. B* **2003**, *67*, 035202.

[3] a) H. P. Dijkstra, M. Albrecht, G. van Koten, *Chem. Commun.* **2002**, 126–127; b) R. M. Crooks, M. Zhao, L. Sun, V. Chechik, L. K. Yeung, *Acc. Chem. Res.* **2001**, *34*, 181–190; c) J. W. J. Knapen, A. W. van der Made, J. C. de Wilde, P. W. N. M. van Leeuwen, P. Wijkens, D. M. Grove, G. van Koten, *Nature* **1994**, *372*, 659–663; d) U. Kragl, C. Dreisbach, *Angew. Chem. Int. Ed. Engl.* **1996**, *35*, 642–645; e) M. T. Reetz, G. Lohmer, R. Schwickardi, *Angew. Chem. Int. Ed. Engl.* **1997**, *36*, 1526–1529; f) G. Giffels, J. Beliczey, M. Felder, U. Kragl, *Tetrahedron: Asymmetry* **1998**, *9*, 691–696.

[4] a) E. C. Constable, *Chem. Commun.* **1997**, 1073–1080; b) G. R. Newkome, E. He, C. N. Moorefield, *Chem. Rev.* **1999**, *99*, 1689–1746; c) M. A. Hearshaw, J. R. Moss, *Chem. Commun.* **1999**, 1–8; d) H.-J. van Maanen, F. C. J. M. van Veggel, D. N. Reinhoudt, *Top. Curr. Chem.* **2001**, *127*, 121–162; e) G. E. Oosterom, J. N. H. Reek, P. C. J. Kamer, P. W. N. M. van Leeuwen, *Angew. Chem. Int. Ed.* **2001**, *40*, 1828–1849; f) M. Q. Slagt, S.-E. Stiriba, R. J. M. K. Gebbink, H. Kautz, H. Frey, G. van Koten, *Macromolecules* **2002**, *35*, 5734–5737.

[5] a) N. Brinkmann, D. Giebel, G. Lohmer, M. T. Reetz, U. Kragl, *J. Catal.* **1999**, *183*, 163–168; b) N. J. Hovestad, E. B. Eggeling, H. J. Heidbüchel, J. T. B. H. Jastrzebski, U. Kragl, W. Keim, D. Vogt, G. van Koten, *Angew. Chem. Int. Ed.* **1999**, *38*, 1655–1658; c) D. De Groot, E. B. Eggeling, J. C. de Wilde, H. Kooijman, R. J. van Haaren, A. W. van der Made, A. L. Spek, D. Vogt, J. N. H. Reek, P. C. J. Kamer, P. W. N. M. van Leeuwen, *Chem. Commun.* **1999**, 1623–1624; d) H. P. Dijkstra, P. Steenwinkel, D. M. Grove, M. Lutz, A. L. Spek, G. van Koten, *Angew. Chem. Int. Ed.* **1999**, *38*, 2185–2188; e) M. Albrecht, N. J. Hovestad, J. Boersma, G. van Koten, *Chem. Eur. J.* **2001**, *7*, 1289–1294; f) A. W. Kleij, R. A. Gossage, R. J. M. Klein Gebbink, N. Brinkman, E. J. Reijerse, U. Kragl, M. Lutz, A. L. Spek, G. van Koten, *J. Am. Chem. Soc.* **2000**, *122*, 12112–121124.

[6] a) V. Chandrasekhar, A. Athimoolam, *Org. Lett.* **2002**, *4*, 2113–2116; b) V. Chandrasekhar, A. Athimoolam, S. G. Srivatsan, P. S. Sundaram, S. Verma, A. Steiner, S. Zacchini, R. Butcher, *Inorg. Chem.* **2005**, *44*, 4608–4615; c) V. Chandrasekhar, V. Krishnan, A. Steiner, J. F. Bickley, *Inorg. Chem.* **2004**, *43*, 166–172.

[7] a) Y. Kim, S. C. Zimmerman, *Curr. Opin. Chem. Biol.* **1998**, *2*, 733–740; b) D. A. Tomalia, A. M. Naylor, W. A. Goddard III, *Angew. Chem. Int. Ed. Engl.* **1990**, *29*, 138; c) F. Zeng, S. C. Zimmerman, *Chem. Rev.* **1997**, *97*, 1681–1712; d) D. Astruc, F. Chardac, *Chem. Rev.* **2001**, *101*, 2991–3024; e) S. M. Grayson, J. M. Frëchet, *Chem. Rev.* **2001**, *101*, 3819–3868; f) G. R. New-

 © 2007 Wiley-VCH Verlag GmbH & Co. KGaA, Weinheim 

kome, E. He, C. N. Moorefield, *Chem. Rev.* **1999**, *99*, 1689–1746.
[8] a) C. Galliot, C. Larre, A. M. Caminade, J. P. Majoral, *Science* **1997**, *277*, 1981–1984; b) S. Sengupta, *Tetrahedron Lett.* **2003**, *44*, 7281–7284; c) V. Balzani, P. Ceroni, A. Juris, M. Venturi, S. Campagna, F. Puntoriero, C. Serroni, *Coord. Chem. Rev.* **2001**, *219*, 545–572; d) S. Campagna, C. D. Pietro, F. Loiseau, B. Maubert, N. McClenaghan, R. Passalacqua, F. Puntoriero, V. Ricevuto, S. Serroni, *Coord. Chem. Rev.* **2002**, *229*, 67–74; e) N. D. McClenaghan, R. Passalacqua, F. Loiseau, S. Campagna, B. Verheyde, A. Hameurlaine, W. Dehaen, *J. Am. Chem. Soc.* **2003**, *125*, 5356–5365; f) J. P. Cross, M. Lauz, P. D. Badger, S. Petoud, *J. Am. Chem. Soc.* **2004**, *126*, 16278–16279.
[9] a) S. G. Kim, J. Choi, R. Tamaki, R. M. Laine, *Polymer* **2005**, *46*, 4514–4524; b) R. H. Baney, M. Itoh, A. Sakakibara, T. Suzuki, *Chem. Rev.* **1995**, *95*, 1409–1430; c) M. A. Sellinger, R. Tamaki, R. M. Laine, K. Ueno, H. Tanabe, E. W. Ghassan, E. Jabbour, *Chem. Commun.* **2005**, 3700–3702; d) C. M. Casado, I. Cuadrado, M. Moran, B. Alonso, M. Barranco Losada, *J. Appl. Organomet. Chem.* **1999**, *13*, 245–259; e) K. J. Haxton, D. J. Cole-Hamilton, R. E. Morris, *Dalton Trans.* **2004**, 1665–1669; f) J. M. Thomas, R. Raja, D. W. Lewis, *Angew. Chem. Int. Ed.* **2005**, *44*, 6456–6482.
[10] Q. Hua, M. F. Lo, I. D. Williams, N. Koda, Y. Uchimaru, G. Jia, *J. Organomet. Chem.* **2003**, *670*, 243–247.
[11] a) M. V. Russo, A. Furlani, S. Licoccia, R. C. Paolesse, A. Villa, C. Guastini, *J. Organomet. Chem.* **1994**, *469*, 245–252; b) A. Koridze, A. I. Yanovsky, T. Yu, *J. Organomet. Chem.* **1992**, *441*, 277–284; c) S. S. Kumar, J. Rong, S. Singh, H. W. Roesky, D. Vidovic, J. Magull, D. Neculai, *Organometallics* **2004**, *23*, 3496–3500; d) S. S. Kumar, N. D. Reddy, H. W. Roesky, D. Vidovic, J. Magull, R. F. Winter, *Organometallics* **2003**, *22*, 3348–3350.
[12] V. Chandrasekhar, S. Nagendran, S. Bansal, M. A. Kozee, D. R. Powell, *Angew. Chem. Int. Ed.* **2000**, *112*, 1833–1835.
[13] V. Chandrasekhar, S. Nagendran, R. Azhakar, M. R. Kumar, A. Srinivasan, K. Ray, T. K. Chandrashekar, C. Madhavaiah, S. Verma, U. D. Priyakumar, G. N. Sastry, *J. Am. Chem. Soc.* **2005**, *39*, 2410–2411.
[14] V. Chandrasekhar, P. Thilagar, P. Sasikumar, *J. Organomet. Chem.* **2006**, *691*, 1681–1692.
[15] V. Chandrasekhar, R. Boomishankar, S. Singh, A. Steiner, S. Zachini, *Organometallics* **2002**, *21*, 4575–4577.
[16] a) G. M. Sheldrick, *SHELXL-97*, software for crystal structure refinement, University of Göttingen, Göttingen, Germany, **1997**; b) G. M. Sheldrick, *SHELXTL*, Reference Manual: Version 5.1, Bruker AXS, Madison, WI, **1998**.

Received: October 17, 2006
Published Online: January 16, 2007

 © 2007 Wiley-VCH Verlag GmbH & Co. KGaA, Weinheim 

DOI: 10.1002/ejic.200601016

# Tripyrrinatocadmium Complexes: Enforcing Supramolecular Aggregation by a Large Ion

Martin Bröring,*[a] Serguei Prikhodovski,[a] Esther Cónsul Tejero,[a] and Silke Köhler[a]

**Keywords:** Tripyrrin / Cadmium / Porphyrinoids / Supramolecular chemistry

A newly developed method for the preparation of free base tripyrrin ligands HTrpy by cyanide-promoted demetalation of nickel chelates TrpyNiNCO was used in order to explore the chemistry of cadmium tripyrrins TrpyCdX with a variety of anionic co-ligands X. The introduction of the large $Cd^{II}$ ion into the tripyrrin $N_3$ coordination site was accomplished by the use of cadmium acetate as the metal precursor. Ligand exchange experiments using sodium salts of different anions disclose a marked tendency for pentacoordination, which is achieved either by the formation of chelates or of 1D coordination polymers that form as a consequence of the size of the central metal. The attempted introduction of chlorido, iodido, or cyanato ligands thus leads mainly to decomposed material, while the use of 1,1,1-trifluoracetylacetonate, salicylate, and acetate ligands results in stable, pentacoordinate and monomeric complexes with the external ligand bound as a four- or six-membered *O,O*-chelate ring. With the pseudohalogenido ligands thiocyanate, selenocyanate, and azide as well as with the weakly coordinating trifluoroacetate 1D coordination polymers with a variety of chain structures were obtained and investigated by X-ray diffraction studies. Interestingly $TrpyCdN_3$ is present in the crystal as a coordinatively and hydrogen-bonded methanol adduct with a dimeric repeating subunit.
(© Wiley-VCH Verlag GmbH & Co. KGaA, 69451 Weinheim, Germany, 2007)

## Introduction

The $Cd^{II}$ ion has only recently been recognized as a useful species in porphyrinoid chemistry. In a series of ring-exchanged porphyrinoids like *m*-benziporphyrin, *S*-confused thiaporphyrin and the like (Figure 1) the spin-active nuclei of $^{111}Cd$ and $^{113}Cd$ ($I = 1/2$) have been used to detect unusual metal–ligand interactions through the observation of $^{1}H$-Cd and $^{13}C$-Cd scalar couplings (so-called "through-space couplings") in the NMR spectra.[1] This approach makes the $Cd^{II}$ ion a unique probe, that allows the direct spectroscopic investigation of nonbonding metal–ligand interactions for diamagnetic ions. Cadmium complexes of porphyrins are also known,[2] but have only scarcely been used[3] due to their pronounced solvolytic lability. The problem appears to be the size of the $Cd^{II}$ ion, which is too large to allow a proper adaptation of the porphyrin macrocycle. This results in largely domed structures with open sites for solvent attack. As has been shown in 1998 flexible open-chain tetrapyrroles with more than four donor atoms are much more effective in providing a suitable coordination sphere for cadmium, which obviously prefers a coordination number of larger than four in a porphyrinoid environment (Figure 1).[4]

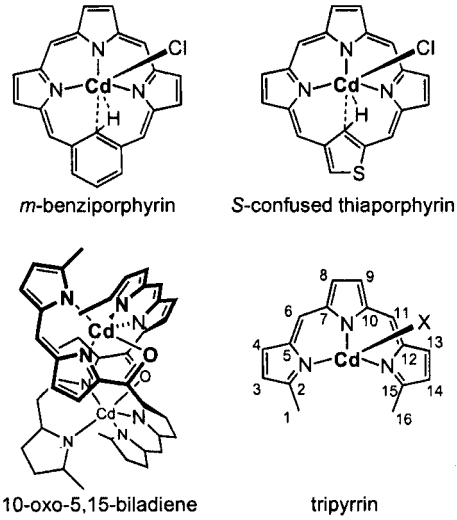


Figure 1. Selected tri- and tetrapyrrolic cadmium chelates.

The tripyrrin ligand HTrpy is formally derived from the macrocyclic parent porphyrin by the loss of one of the four $C_4N$ rings.[5] Chemically, however, the Trpy ligand differs largely from the porphyrin and from other macrocyclic porphyrinoids with respect to ligand stability and the open *cis*-situated coordination site at the central ion. The presence of two terminal methyl moieties, which is currently one of the synthetic limitations of tripyrrin ligand synthesis, leads to an effective shielding of the one coordination site situated in the $N_3M$-plane of a given complex.[6] Earlier studies

[a] Fachbereich Chemie, Philipps-Universität Marburg, Hans-Meerwein-Straße, 35032 Marburg, Germany
Fax: +49-6421-282-5356
E-mail: Martin.Broering@chemie.uni-marburg.de
Supporting information for this article is available on the WWW under http://www.eurjic.org or from the author.

 © 2007 Wiley-VCH Verlag GmbH & Co. KGaA, Weinheim 

have shown, that as a result of this steric constraint palladium(II) complexes of Trpy ligands are always distorted from a square-planar geometry[7] and that tetracoordinate tripyrrinatonickel(II) complexes display a sterically induced HS ground state despite an intermediately strong ligand field.[8]

The presence of two terminal methyl groups at the tripyrrin ligand framework limits the maximum coordination number of all metallotripyrrins described so far to five. The association of a fifth donor L to a four-coordinate compound TrpyMX can in principle occur from either side of the tripyrrin plane, resulting in two different coordination geometries **A** and **B** (Figure 2). In this regard tripyrrins differ largely from the structurally similar, but more flexible bis(arylimino)isoindolines (BAI), which have been shown in the recent past to adopt nonplanar conformations and nonmeridonal tridentate binding modes in several instances.[9] Complexes of type **A** are of particular interest due to their propensity to form 1D- and 3D coordination polymers with a large structural variety. However, the number of ions that have been shown to form five-coordinate metallotripyrrins is almost limited to one, i.e. $Ni^{II}$.[10] In addition, two examples of mononuclear pentacoordinate palladium(II)-tripyrrin complexes and one example for an extremely labile pentacoordinate cobalt(II)-tripyrrin complex have been unravelled.[11] In this contribution we describe our successful attempt to employ the large ion $Cd^{II}$ in order to enforce the formation of 1D coordination polymers from TrpyCd subunits.

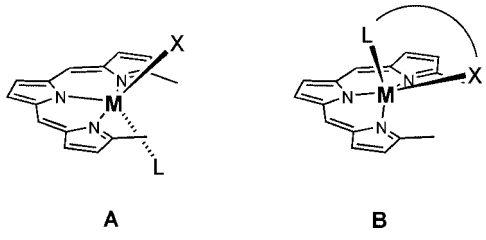


Figure 2. Generalized structures **A** and **B** for pentacoordinate metallotripyrrins.

## Results and Discussion

*Preparation and spectroscopic characterization*. During our studies on ligand exchange procedures of TrpyNi complexes we recently realized that the attempted ligand exchange of the isocyanates TrpyNiNCO **1** and **2**[10a] with excess cyanide results in the demetalation of the chelate complexes, which is indicated by an immediate color change from dark green to red. The red solutions of the putative free base tripyrrins **3** and **4**, which were obtained after washing with water and phase separation, proved very unstable over time. The advent of the free base ligands **3** and **4**, however, opens the desired possibility to obtain more sensitive tripyrrin complexes like TrpyCdX, which are unavailable by other means. For the metalation of the free base tripyrrins a two-phase system with the ligand in the ethereal phase and $Cd(OAc)_2$ in the aqueous one was applied. Some methanol was added to ensure the interpenetration of the two layers and thus to enhance the metalation rate. No additional base is necessary to drive the metalation to completion. Since the removal of the solvent often leads to the decomposition of sensitive metallotripyrrins the product solutions of **5** and **6** were used directly in ligand exchange reactions without further purification. Only for TrpyCdOAc **5** an attempt to isolate and characterize the compound was undertaken (Scheme 1).

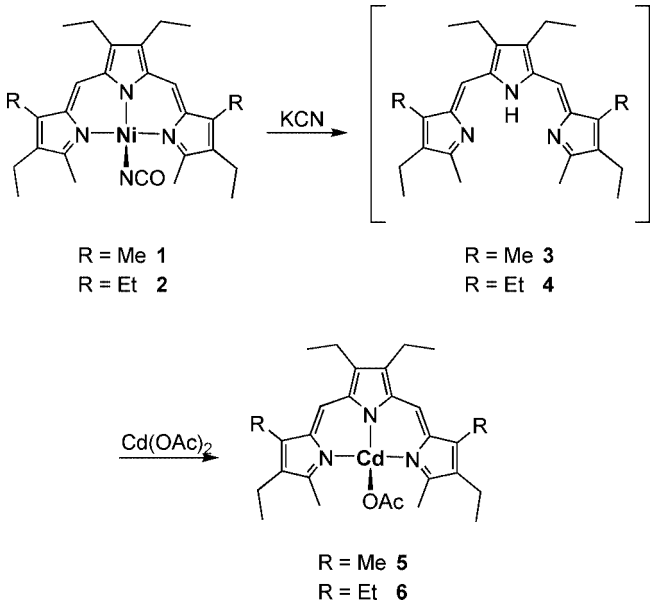


Scheme 1. Preparation of tripyrrinatocadmium complexes **5** and **6** via free base tripyrrins **3** and **4**.

The composition TrpyCdOAc was confirmed for the new complex **5** by elemental analysis and by EI mass spectrometry, which shows two peaks at $m/z$ = 561 and 501 for the $M^+$ and $[M - OAc]^+$ ion, respectively. The UV/Vis spectrum is dominated by two absorptions at 350 and 650 nm from ligand-based transitions and resembles those of other metallotripyrrins.[10,11] Spectroscopically, the new complex shows $A_2X_3$ systems for two chemically distinct ethyl substituents in addition to four singlets for the methyl groups at C-2,15 ($\delta$ = 2.50 ppm), C-4,13 ($\delta$ = 2.20 ppm) and at the acetate ($\delta$ = 1.87 ppm) as well as for the *meso* protons at C-6,11 ($\delta$ = 6.86 ppm). The spectrum is almost indistinguishable from those of TrpyZnX species[12] and contains no information for the coordination mode of the acetato ligand. From IR data the acetate coordination can be assigned to a bidentate binding mode. The $\nu_{CO}$ stretching band is found at 1553 $cm^{-1}$ and therefore below the value for the free acetate ion. For monodentate acetate ligands stretching frequencies of >1600 $cm^{-1}$ are typical.[13] TrpyCdOAc **5** can therefore be regarded as a pentacoordinate species, presumably of type **B**.

Ligand exchange reactions were carried out on **5** and **6** under biphasic standard conditions using different monoanionic halide, pseudohalide, and *O*,*O*-chelate ligands as their sodium salts (Scheme 2). The use of chlorido-, bromido-, iodido-, and cyanato ligands resulted in labile material which decomposed to a large extent upon the attempted

 © 2007 Wiley-VCH Verlag GmbH & Co. KGaA, Weinheim 

isolation. For X = NCS, NCSe, $N_3$, sal, 1,1,1-trifluoracetylacetonate ($acac^F$), and trifluoroacetate ($OAc^F$), however, pure complexes TrpyCdX **7**–**12** were obtained in good yield (the azido derivative **9** was obtained as a methanol adduct) and characterized by means of elemental analyses and mass spectra.

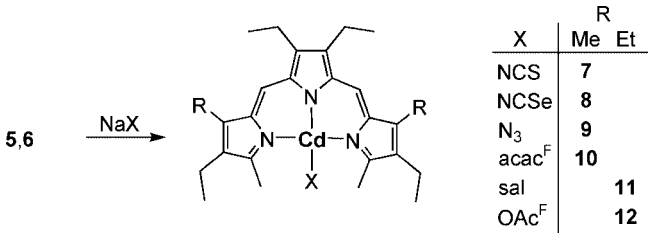


| X | R: Me | Et |
|---|---|---|
| NCS | **7** | |
| NCSe | **8** | |
| $N_3$ | **9** | |
| $acac^F$ | **10** | |
| sal | | **11** |
| $OAc^F$ | | **12** |

Scheme 2. Anion metathesis reactions on tripyrrinatocadmium complexes **5** and **6**.

All new complexes form violet crystals with a metallic sheen. In solution intense green colors are observed throughout. The solubility, however, differs strongly with the anionic ligand. The pseudohalide derivatives TrpyCdNCS **7**, TrpyCdNCSe **8**, and TrpyCd$N_3$(MeOH) **9** are almost insoluble in nondonor solvents, while the compounds with the *O*,*O*-chelate ligands TrpyCdacac$^F$ **10**, TrpyCdsal **11**, and TrpyCdOAc$^F$ **12** dissolve readily in, for example, dichloromethane. From UV/Vis data **7**–**12** can be divided into two groups. Thiocyanate **7** and selenocyanate **8** yield optical spectra with two major maxima at about 345 and 630 nm, while the *O*,*O*-chelated species **10**–**12** and the methanol-azido compound **9** yield spectra similar to that of the acetato complex **5** with maxima at about 350 and 650 nm. $^1$H and $^{13}$C NMR spectra of **7**–**12** are also very similar to the one discussed in detail for **5** and differ mainly by the signals for the respective anionic coligands. Characteristic shifts for the coordination number or type were not found for the diamagnetic cadmium chelates (Figure 3).

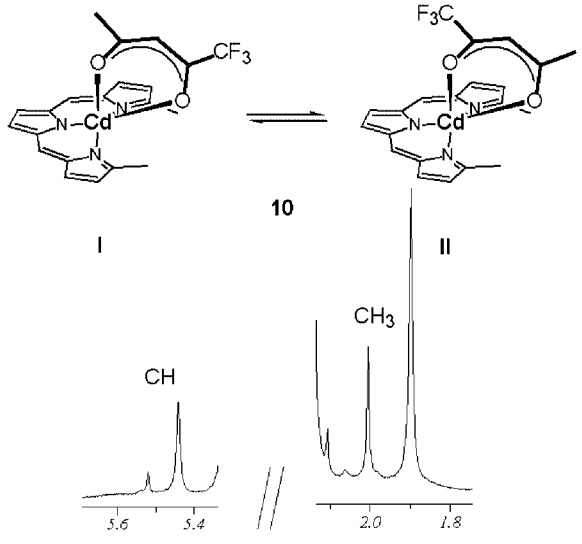


Figure 3. Details of the $^1$H NMR spectra of TrpyCdacac$^F$ (**10**) (230 K, $CD_2Cl_2$) and schematic representations of isomers I and II (β-alkyl groups omitted).

Dynamic behavior was observed in the proton NMR spectra of the 1,1,1-trifluoroacetoacetato derivative TrpyCdacac$^F$ **10**. At ambient temperature, the resonance signals of the $acac^F$ ligand appear extremely broadened and split into two pairs of singlets with a ratio of 5:2 at low temperature (Figure 3). At 230 K, the peaks for the major form are found at 1.90 ($CH_3$) and 5.44 (CH) ppm, while those for the minor form are recorded low field at $\delta$ = 2.00 and 5.52 ppm. This dynamic process of **10** can be interpreted in terms of the interconversion of two isomers I and II (Figure 3). The attempted assignment of I and II to major and minor form by a ROESY experiment, however, failed.

IR spectroscopy is a particularly well-suited tool in order to determine the binding mode (i.e. terminal or bridging) of the anion in complexes with pseudohalide ligands, and thus to assign the degree of complex association. Typical of monomeric omplexes with *N*-bound terminal NCS and NCSe ligands are $\nu_{as}$ vibrations with wavenumbers well below 2100 cm$^{-1}$.[13] For TrpyCdNCS (**7**) and TrpyCdNCSe (**8**), however, the band for this vibration is found at 2103 and 2115 cm$^{-1}$, respectively. In combination with the low solubility of these species this finding points to the presence of bridging pseudohalide ligands for **7** and **8** and thus of coordination polymers in the solid state. The thiocyanate ion has frequently been reported as a bridging ligand in coordination polymers,[14,15] as has been for the homologous selenocyanate, although reports about the use of this nonconventional pseudohalide are rather rare.[15,16]

In the IR spectra of the azido complex TrpyCd$N_3$(MeOH) (**9**) two equally intense bands are found in the region for the $N_3$ vibrations at 2090 and 2067 cm$^{-1}$. As before these values are higher than those expected for complexes with terminal monodentate azido ligands. In addition, the splitting into two bands indicates, that the azide is situated in a bridging coordination mode. From this data it remains open, whether an *end-on* ($\mu_{1,1}$) or an *end-to-end* ($\mu_{1,3}$) coordination is realized for **9**.[17] The $\nu_s$ bands at about 1300 cm$^{-1}$, which are characteristic for the distinction between these two binding modes, overlap severely with bands from the tripyrrin backbone and cannot be assigned unambiguously. For sterical reasons, however, the *end-to-end* ($\mu_{1,3}$) coordination is favored and thus the formation of a polymeric structure of TrpyCd$N_3$(MeOH) (**9**).

*X-ray crystallographic characterization*. Single crystal X-ray diffraction studies were undertaken on suitable crystals of the pseudohalide species TrpyCdNCS (**7**), TrpyCdNCSe (**8**), and TrpyCd$N_3$(MeOH) (**9**) as well as on the *O*,*O*-chelate complexes TrpyCdacac$^F$ (**10**), TrpyCdsal (**11**), and TrpyCdOAc$^F$ (**12**) and will be discussed below. Details for the structure solutions and refinements are summarized in Table 1.

TrpyCdNCS and TrpyCdNCSe crystallize isotypically by slow evaporation of respective solutions in toluene/methanol in the monoclinic system, space group *C*2/c, with *Z* = 4 and very similar unit cell metrics [**7**: *a* = 26.972(3), *b* = 11.7933(9), *c* = 18.827(2) Å, *β* = 95.564(13)°; **8**: *a* = 27.073(2), *b* = 11.9547(9), *c* = 18.7485(16) Å, *β* = 95.391(10)°]. In both cases one half molecule of a severely

 © 2007 Wiley-VCH Verlag GmbH & Co. KGaA, Weinheim 

Table 1. Crystal data and structure refinement for compounds **7**–**12**.

| | **7**·0.5 $C_7H_8$ | **8**·0.5 $C_7H_8$ | **9** | **10** | **11**·0.5 $CH_2Cl_2$ | **12** |
|---|---|---|---|---|---|---|
| Formula | $C_{61}H_{68}Cd_2N_8S_2$ | $C_{61}H_{68}Cd_2N_8Se_2$ | $C_{54}H_{76}Cd_2N_{12}O_2$ | $C_{31}H_{39}CdF_3N_3O_2$ | $C_{67}H_{80}Cd_2Cl_2N_6O_6$ | $C_{30}H_{38}CdF_3N_3O_2$ |
| $M_r$ | 1202.16 | 1295.96 | 1150.07 | 655.05 | 1361.09 | 642.03 |
| Crystal system | monoclinic | monoclinic | triclinic | triclinic | monoclinic | monoclinic |
| Space group | *C*2/*c* | *C*2/*c* | $P\bar{1}$ | $P\bar{1}$ | $P2_1/n$ | $P2_1/c$ |
| *a* [Å] | 26.972(3) | 27.073(2) | 11.2992(16) | 11.1577(8) | 11.3946(4) | 13.433(3) |
| *b* [Å] | 11.7933(9) | 11.9547(9) | 12.5623(15) | 11.9654(8) | 16.1260(5) | 10.076(2) |
| *c* [Å] | 18.827(2) | 18.7485(16) | 19.676(2) | 12.2531(8) | 17.7046(6) | 22.511(5) |
| $\alpha$ [°] | 90 | 90 | 95.312(14) | 101.419(6) | 90 | 90 |
| $\beta$ [°] | 95.564(13) | 95.391(10) | 93.744(15) | 107.581(5) | 106.589(3) | 99.16(3) |
| $\gamma$ [°] | 90 | 90 | 92.689(16) | 97.061(6) | 90 | 90 |
| *Z* | 4 | 4 | 2 | 2 | 2 | 4 |
| $\rho_{calcd.}$ [g cm$^{-3}$] | 1.340 | 1.425 | 1.378 | 1.451 | 1.448 | 1.418 |
| Radiation | Mo-$K_\alpha$ | Mo-$K_\alpha$ | Mo-$K_\alpha$ | Mo-$K_\alpha$ | Mo-$K_\alpha$ | Mo-$K_\alpha$ |
| Monochromator | graphite | graphite | graphite | graphite | graphite | graphite |
| Temperature [K] | 193(2) | 193(2) | 193(2) | 193(2) | 193(2) | 193(2) |
| Data collection | $\phi$-scan | $\phi$-scan | $\phi$-scan | $\omega$-scan | $\omega$-scan | $\phi$-scan |
| $\Theta$ range [°] | 2.14–25.35 | 1.86–26.06 | 1.81–25.35 | 1.80–26.19 | 1.70–26.13 | 1.83–26.11 |
| Measured reflections | 21904 | 23525 | 26093 | 21357 | 65693 | 23416 |
| Indep. reflections[a] | 3134 | 3207 | 4625 | 5656 | 5797 | 4333 |
| Absorption coefficient | 0.827 | 1.952 | 0.818 | 0.779 | 0.824 | 0.775 |
| Solution method[b] | direct | direct | direct | Patterson | direct | direct |
| Final $R_1$ value | 0.0281 | 0.0317 | 0.0605 | 0.0697 | 0.0640 | 0.0464 |

[a] $I > 2\sigma(I)$. [b] All structures were solved using "SHELXS, Program for Crystal Structure Determination"[18] and refined with "SHELXL, Program for Crystal Structure Refinement".[19]

disordered toluene molecule per formula unit is present in the cell. As expected from the IR spectroscopic results both compounds indeed form 1D coordination polymers (Figure 4; Table 2).

TrpyCdNCS (**7**) and TrpyCdNCSe (**8**) form type **A** metallotripyrrins in the solid state. The coordination environment of the $Cd^{II}$ ion in 7 and **8** can be assigned to distorted trigonal bipyramids with N1 and N3 in the apices and N2, N4, and S or Se, respectively, in the equatorial positions. The assignment is based mainly on the N–Cd–N and N–Cd–S/Se angles which deviate less than 11° from the ideal 90°, 120°, or 180° for this polyhedron. The combination of the large ionic radius of cadmium and the coordination number of 5 results in the longest M–$N_{Trpy}$ bonds of 2.217–2.274 Å observed so far in the chemistry of the tripyrrins. The typical relation, that the central M–N2 bond is shorter than the terminal N1–M and N3–M bonds, is found for type **A** cadmium tripyrrins, too. The tripyrrin backbones C2–C15 of both compounds display slight helical distortions, which appears necessary in order to accommodate the large cadmium atom in the ligand N,N,N planes [deviation ("doming") for **7**: 0.0799(2), for **8**: 0.1545(3) Å]. As a result the methyl termini C1 and C16 are as far apart from each other as 5.570(6) (**7**) and 5.596(6) Å (**8**) and leave much space for the binding of N4 and S/Se. In fact, despite the size of the S or Se donor the arrangement at the open sites of the TrpyCd moieties is almost unstrained, and the distance between the N4 and S/Se donor on one hand and the terminal methyl groups C1, C16 on the other undercuts the sum of the van der Waals distances by only 4.5 (**7**) and 5.8% (**8**). For comparison, this value is of the same magnitude as for most tetracoordinate metallotripyrrins, and is increased to almost 20%, if the metal enforces a square-planar coordination mode like in TrpyNiCN.[10a]

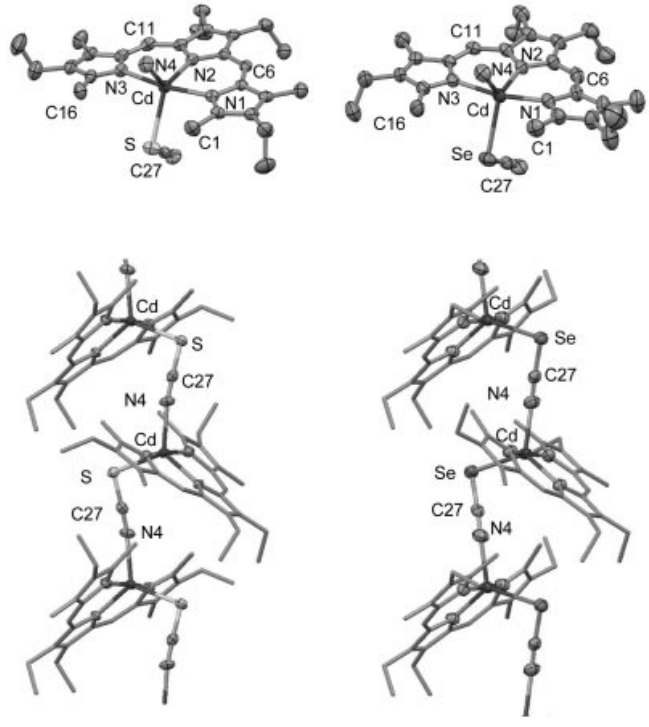


Figure 4. Repeating units of TrpyCdNCS (**7**) (top left) and TrpyCdNCSe (**8**) (top right) from X-ray crystallographic analyses, and representation of the isotypical single chain arrangements of **7** (left) and **8** (right; ellipsoids set at 50% probability; hydrogen atoms omitted for clarity).

As mentioned above, **7** and **8** form isotypical 1D coordination polymers that propagate in the direction of the crystallographic *b* axis. The TrpyCd plates are organized with a Cd···Cd distance of 6.184 (**7**) and 6.230 Å (**8**), and arrange

 © 2007 Wiley-VCH Verlag GmbH & Co. KGaA, Weinheim 

Table 2. Selected bond lengths [Å] and angles [°] for complexes TrpyCdNCS (**7**), TrpyCdNCSe (**8**), and $TrpyCdN_3(MeOH)$ (**9**).

| | **7**·0.5 $C_7H_8$ | **8**·0.5 $C_7H_8$ | **9** Subunit I (Cd1) | Subunit II (Cd2) |
|---|---|---|---|---|
| M–N1 | 2.266(3) | 2.270(3) | 2.259(7) | 2.248(7) |
| M–N2 | 2.220(3) | 2.217(3) | 2.250(6) | 2.219(6) |
| M–N3 | 2.274(3) | 2.268(3) | 2.239(7) | 2.277(7) |
| M–D1[a] | 2.309(2) | 2.323(4) | 2.357(8) | 2.295(7) |
| M–D2[a] | 2.6667(11) | 2.7369(6) | 2.295(7) | 2.346(7) |
| N1–M–N2 | 85.87(9) | 86.03(12) | 86.0(2) | 86.2(2) |
| N1–M–N3 | 171.16(9) | 169.16(11) | 171.7(2) | 168.9(2) |
| N1–M–D1[a] | 90.23(10) | 89.68(13) | 87.3(3) | 102.0(3) |
| N1–M–D2[a] | 93.52(7) | 95.42(8) | 90.5(3) | 89.2(3) |
| N2–M–N3 | 86.12(9) | 85.93(12) | 85.7(2) | 86.8(2) |
| N2–M–D1[a] | 123.49(10) | 122.47(12) | 125.3(2) | 133.5(3) |
| N2–M–D2[a] | 121.49(7) | 123.46(7) | 122.4(3) | 118.7(2) |
| N3–M–D1[a] | 91.06(10) | 88.51(13) | 96.9(3) | 89.1(3) |
| N3–M–D2[a] | 93.86(7) | 95.08(8) | 94.5(2) | 86.6(2) |
| D1–M–D2[a] | 115.01(8) | 114.06(9) | 111.9(3) | 107.2(3) |
| C1···C16 | 5.570(6) | 5.596(6) | 5.597(13) | 5.613(14) |
| C1···D1 | 3.454(5) | 3.362(5) | 3.498(13) | 3.595(13) |
| C1···D2 | 3.701(4) | 4.002(4) | 3.412(13) | 3.569(13) |
| C16···D1 | 3.380(5) | 3.430(6) | 3.508(12) | 3.342(11) |
| C16···D2 | 3.940(4) | 3.769(4) | 3.690(12) | 3.476(13) |
| ΔvdW/%[b] | –4.5 | –5.8 | –3.0 | –5.9 |
| M···Ct($N_3$)[c] | 0.0799(2) | 0.1545(3) | 0.0154(7) | 0.1807(7) |

[a] D1 = N4 for **7** and **8**, N9 for **9-I** or O1 for **9-II**; D2 = S for **7**, Se for **8**, N10 for **9-I**, or N7 for **9-II**. [b] Difference between the C1···D1/2 or C16···D1/2 distance and the sum of the van der Waals radii of D1/2 and the closest terminal methyl group. [c] Displacement of the metal ion from the *N*,*N*,*N* plane of the tripyrrin ligand (doming).

almost vertical with an angle of 97.2 (**7**) and 93.4° (**8**) towards each other. This arrangement is a result of the size (NCS: 2.805; NCSe: 2.948 Å) and binding angles Cd–N4–C27 and Cd–S/Se–C27 of the almost linear pseudohalide ligands (NCS: 177.86; NCSe: 176.84°). As depicted in Figure 4, the coordination of the pseudohalide ligand via the *N*-donor end is rather straight with 166.98 for **7** and 169.42° for **8**, while the chalcogeno donors coordinate at angles as steep as 98.61 (**7**) and 94.14° (**8**). This relaxed arrangement still allows a tight intrastrand packing of the monomers, with minimum distances between methyl carbon atoms of one unit and the $sp^2$ system of the next of 3.283 (7) and 3.254 Å, and without losing the rather weak Cd–S and Cd–Se coordination.

The pillars consisting of the 1D polymeric strands of **7** and **8** pack more tightly in the crystallographic *c* than in the *a* direction, forming layers of pillars with interdigitated alkyl groups in the solid state. These layers are glued together by disordered toluene molecules that occupy the clefts and thus stabilize the structures of **7** and **8** (Figure 5).

The azido ligand deviates from the above pseudohalides by a reduced size. This change in metrics leads to a different solid-state arrangement for **9** and to the necessity to introduce methanol into the coordination of the cadmium ion. After crystallization of freshly prepared $TrpyCdN_3$ from a toluene/methanol mixture the 1D coordination polymer **9** was obtained, which displays chains of methanol and H-bridge linked $TrpyCdN_3$ dimers. The chain structure of **9**, a detailed view of the dimeric building block and a representation of the layer-like structure formed by the individual chains are presented in Figure 6. Crystallographic data

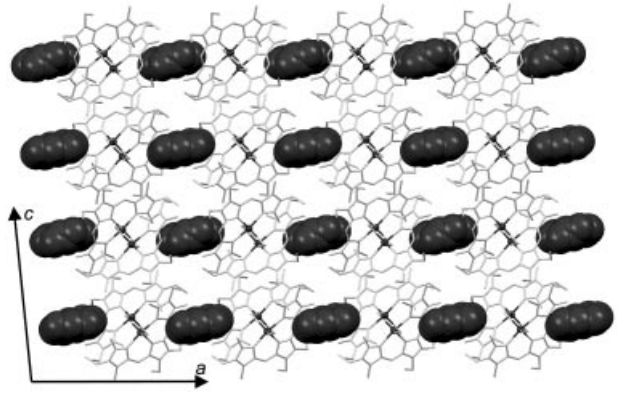


Figure 5. View down the polymeric chains (crystallographic *b* axis) of TrpyNCS (**7**) (capped sticks with balls for the $Cd^{II}$ ions, bright) and representation of the layered structure from alternating pillars of **7** and disordered toluene solvent molecules (space-fill, dark; hydrogen atoms omitted throughout).

for **9** and selected molecular parameters can be found in Table 1 and Table 2.

The dinuclear $(TrpyCd)_2N_3$ fragment of the coordination polymer **9** consists of two nonequivalent cadmium tripyrrin units TrpyCd1 and TrpyCd2. In order to adapt sterically to the voluminous $Cd^{II}$ ions the tripyrrin ligands of both TrpyCd units show a slight helical distortion known as "ruffling" in porphyrin chemistry[20] with mean deviations from planar $C_{14}N_3$ frameworks of 0.105 and 0.089 Å for TrpyCd1 and TrpyCd2, respectively. The coordination geometry at the cadmium ions can be described in both cases as distorted trigonal bipyramidal with N1,N2 and N4,N6

 © 2007 Wiley-VCH Verlag GmbH & Co. KGaA, Weinheim 

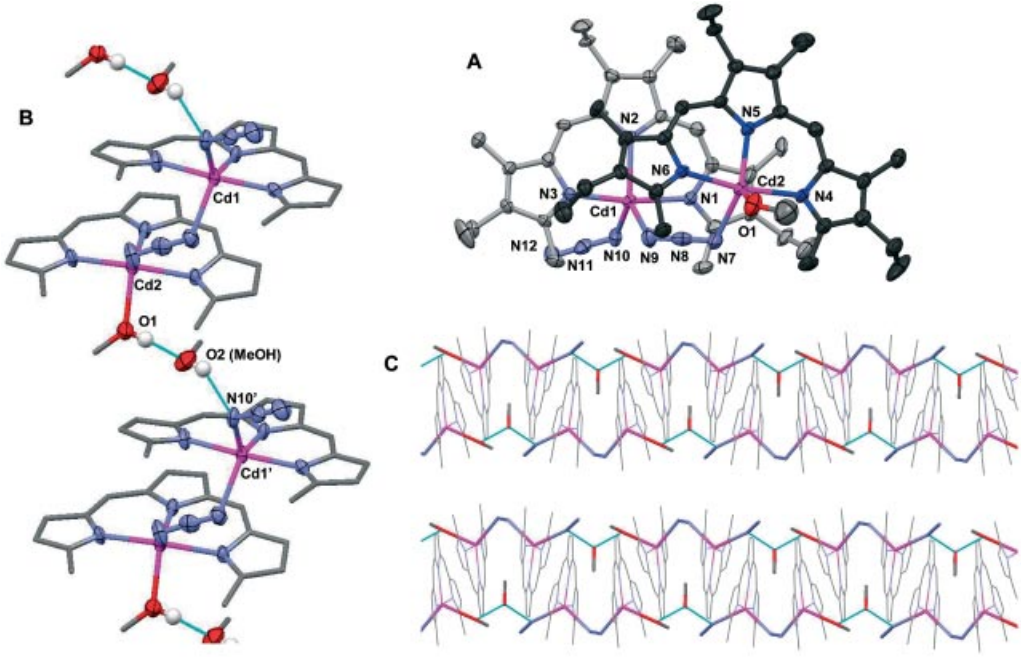


Figure 6. Presentation of the dimeric asymmetric unit (**A**, ellipsoids at 50% probability), the MeOH and H-bond initiated chain formation (**B**, ball-and-stick representation) and the sheet structure (**C**) of coordination polymer $[TrpyCdN_3(MeOH)]_n$ (**9**) [hydrogen atoms (A–C) and β-alkyl substituents (B,C) omitted for clarity].

in the apical positions, and with N2,N9,N10 and N5,N7,O1 in the equatorial ones. The deviation from an ideal geometry is particularly large for the TrpyCd2 subunit, where angles N7–Cd2–O1 and N4–Cd2–N6 are found at 107.2(3) and 168.9(2)° instead of the ideal 120 and 180°, respectively. Cd1 and Cd2 are bridged by a linear $\mu_{1,3}$ azido ligand [N7–N8–N9: 178.6(9)°], which coordinates to both metal ions in a bent fashion [Cd1–N9–N8: 118.2(6)°, Cd2–N7–N8: 116.2(5)°] and with a torsion Cd1–N9–N7–Cd2 of 75.2(5)°. The Cd–N bonds to the $\mu_{1,3}$ azido ligand are longer for Cd1–N9 than for Cd2–N7 [2.356(8) vs. 2.294(8) Å], which results in slightly asymmetric N–N bonds within the azide anion of N7–N8: 1.215(12) and N8–N9: 1.192(12) Å. The mean planes of the $C_{14}N_3$ frameworks of the tripyrrin subunits are arranged almost coplanar with an angle of 13.57(11)°, and are rotated against each other by 14.4(2)° as indicated by the N2–Cd1–Cd2–N5 torsion angle. The cadmium ions Cd1 and Cd2 of the dimeric unit are separated by 5.2139(12) Å.

A second azido ligand is coordinated to Cd1 with a Cd1–N10 distance of 2.296(8) Å and a Cd1–N10–N11 angle of 120.1(6)°. Cd2, on the other hand, is coordinated to the oxygen atom O1 of a methanol molecule as the fifth donor in a distance of 2.356(7) Å. The N10- and O1′ atoms of neighboring dimeric fragments are connected to each other by H-bonds to a second molecule of methanol at O1′–O2 and O2–N10 distances of 2.623(8) and 2.748(8) Å, respectively. This H-bond network results in the formation of a 1D-coordination polymer (**B** in Figure 6) with the Cd atoms of neighboring dimers Cd1 and Cd2′ situated 8.154(6) Å apart from each other. From a structural point-of-view the second azido anion N10N11N12 should be assigned as a $\mu_{1,1}$ bridging ligand rather than as a terminal azide. As for **7** and **8** before the single chains of the 1D coordination polymer **9** organize to 2D sheets in the crystal lattice, but in this case without interlayered solvent (**C** in Figure 6).

From a dichloromethane/*n*-hexane solution a single crystal of **10** was grown. The X-ray crystallographic analysis proofs the chelate character of the $acac^F$ ligand in the solid state (Figure 7). From the possible isomers only form I (see Figure 3) is present in the crystal. One of the six ethyl groups as well as the $CF_3$ group of the $acac^F$ ligand were found disordered and treated as such in the structure refinement. Selected molecular parameters of **10** are summarized in Table 3.

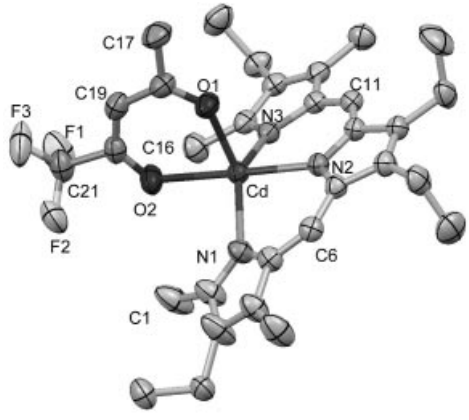


Figure 7. Molecular structure of $TrpyCdacac^F$ (**10**) (ellipsoids at 50% probability; hydrogen atoms omitted for clarity).

The crystallographic analysis identifies **10** as a monomeric molecule of type **B** with a $\kappa^2$ coordinated $acac^F$ li-

 © 2007 Wiley-VCH Verlag GmbH & Co. KGaA, Weinheim 

Table 3. Selected bond lengths [Å] and angles [°] for complexes TrpyCdacac$^F$ (**10**), TrpyCdsal (**11**), and TrpyCdOAc$^F$ (**12**).

| | **10** | **11** | **12** |
|---|---|---|---|
| M–N1 | 2.2592(18) | 2.221(4) | 2.263(3) |
| M–N2 | 2.2104(16) | 2.199(3) | 2.226(3) |
| M–N3 | 2.2427(17) | 2.213(4) | 2.260(3) |
| M–O1 | 2.2873(15) | 2.323(4) | 2.263(3) |
| M–O2 | 2.2613(16) | 2.418(4) | 2.346(3) |
| N1–M–N2 | 83.85(6) | 86.95(14) | 86.37(12) |
| N1–M–N3 | 140.13(6) | 142.94(14) | 171.85(12) |
| N1–M–O1 | 116.12(6) | 102.22(14) | 91.76(13) |
| N1–M–O2 | 92.75(7) | 98.80(14) | 91.70(11) |
| N2–M–N3 | 86.24(6) | 86.09(13) | 87.18(12) |
| N2–M–O1 | 92.63(6) | 104.25(13) | 133.86(13) |
| N2–M–O2 | 169.78(6) | 159.41(13) | 130.37(12) |
| N3–M–O1 | 102.82(6) | 114.77(14) | 96.30(13) |
| N3–M–O2 | 102.37(7) | 100.36(13) | 88.69(12) |
| O1–M–O2 | 80.18(6) | 55.26(12) | 95.76(11) |
| X–O1[a] | 1.243(3) | 1.253(6) | 1.255(5) |
| Y–O2[a] | 1.253(3) | 1.274(6) | 1.206(5) |
| X–Z[a] | 1.422(3) | 1.484(7) | 1.536(6) |
| Y–Z[a] | 1.364(3) | | |
| C1···C16 | 5.023(4) | 4.874(9) | 5.505(7) |
| C1···O1 | 5.289(5) | 4.645(8) | 3.242(6) |
| C1···O2 | 3.142(4) | 3.401(9) | 3.350(6) |
| C16···O1 | 4.802(3) | 4.839(6) | 3.475(6) |
| C16···O2 | 3.266(3) | 3.369(7) | 3.237(6) |
| ΔvdW/%[b] | –11.5 | –5.1 | –8.8 |
| M···Ct(N$_3$)[c] | 0.7639(1) | 0.6982(3) | 0.1042(3) |

[a] X = C28 (**10**), C27 (**11**), or C29 (**12**), Y = C30 (**10**) or X (**11**,**12**), Z = C29 (**10**), C28 (**11**), or C30 (**12**). [b] Difference between the C1···O1/2 or C16···O1/2 distance and the sum of the van der Waals radii of O1/2 and the closest terminal methyl group. [c] Displacement of the metal ion from the *N*,*N*,*N* plane of the tripyrrin ligand (doming).

gand. The coordination of the tripyrrin ligand to the voluminous cadmium atom demands a doming of 0.7639(1) Å and an additional distortion of the ligand backbone similar to the *saddling* conformation of the porphyrins.[20] The Cd$^{II}$ ion is bound to the three nitrogen donors at distances of 2.21–2.26 Å. Perpendicular to the TrpyCd subunit the anionic acac$^F$ ligand forms a six-membered chelate ring with an O1–Cd–O2 angle of 80.18(6)° and Cd–O1 and Cd–O2 distances of 2.2873(15) and 2.2613(16) Å, respectively. The $CdN_3O_3$ core forms a distorted trigonal bipyramidal structure with N2 and O2 in the apices. With respect to the ideal values the angle N1–Cd–N3 of 140.13(6)° shows the largest deviation. Surprisingly, the distance between O2 and the methyl termini C1 and C16 of **29** is found up to 11.5% below the sum of the van der Waals radii, producing a significant amount of intramolecular strain. A six-membered chelate ring thus appears too large for a strainless coordination of two donor centers from one side of a TrpyM subunit.

Single crystals from TrpyCdsal (**11**) were obtained from dichloromethane/*n*-hexane solutions. For **11** one half molecule of dichloromethane per formula unit is present in the crystal lattice. A disorder model with two orientations for the solvent was successfully applied in the solution and refinement of the structure. The results of the crystallographic determination proves the preferential formation of a four-membered over a possible six-membered ring chelate, as observed before in a related nickel(II)-tripyrrin.[10a] The molecular structure of **11** is shown in Figure 8. Table 3 contains selected molecular parameters.

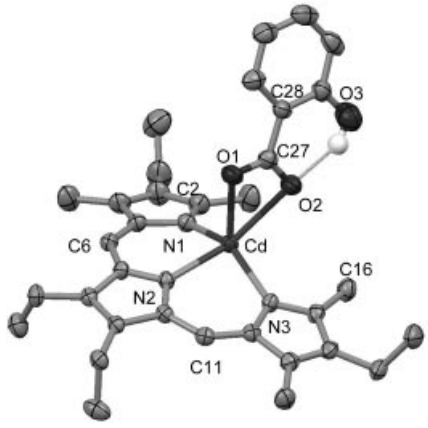


Figure 8. Molecular structure of the salicylato complex TrpyCdsal (**11**) (ellipsoids at 50% probability; CH hydrogen atoms omitted for clarity).

TrpyCdsal can be assigned to a pentacoordinate metallotripyrrin of type **B**. A noticeable feature of the molecular structure of **11** is the severely distorted $C_{14}N_3$ perimeter of the trpyrrin ligand which has a maximum deviation from the mean tripyrrin plane of 0.307(6) Å as compared to only 0.165(3) Å for the related nickel derivative.[10a] The Cd–N bonds of **11** are 2.199(3)–2.221(4) Å long and therefore at the short end of those observed in this series of cadmium complexes. The sal ligand of **11** is coordinated via both carboxylate oxygen atoms to the metal ions with M–O1 being the smaller distance. The aromatic ring of the salicylato ligands and the four-membered $CO_2M$ ring are oriented towards each other in a coplanar fashion, and the sal ligand of **11** is tilted by about 20° from a perpendicular arrangement with the tripyrrin. This finding is caused by an intermolecular π-stacking interaction of the sal group with a $C_4N$ subunit of a neighboring molecule of **11**. The sal complex shows an intramolecular H-bridge from the hydroxy functionality of the salicylato ligands, which binds to O2 with an O2–O3 distance of 2.564(6) Å. This is different from the above-mentioned nickel chelate, where the aryl group is rotated by 180° so as to form a H-bridge with O1. With respect to the O2–$C_{term}$ distance and the *out-of-plane* distortion of the tripyrrin ligand the structure of complex **11** with the four-membered *O*,*O* chelate appears to be more relaxed than that of the six-membered ring chelate TrpyCdacac$^F$ **10**. This finding emphasizes the preference of four- vs. six-membered ring chelate formation on sterically hindered TrpyM fragments.

A different scenario is provided by the structure of the trifluoroacetate **12** (Figure 9, Table 3). The donor strength of the weak OAc$^F$ ligand appears too small to compensate for the strain of a four-membered ring chelate. Therefore, this ring opens at the Cd–O2 bond up to a distance between these atoms of 3.333(3) Å. At the same time, the O2′ donor atom of an adjacent TrpyCdOAc$^F$ molecule coordinates to

 © 2007 Wiley-VCH Verlag GmbH & Co. KGaA, Weinheim 

the free site at the Cd central atom in a distance of 2.346(3) Å. Similar to the NCS/NCSe and the azido/methanol derivatives **7**–**9** a chain structure from coordinatively connected pentacoordinate TrpyCd fragments results. Complex **12** thus escapes the strained situation of a four-membered ring by the formation of a typical coordination polymer with type **A** metallotripyrrin fragments.

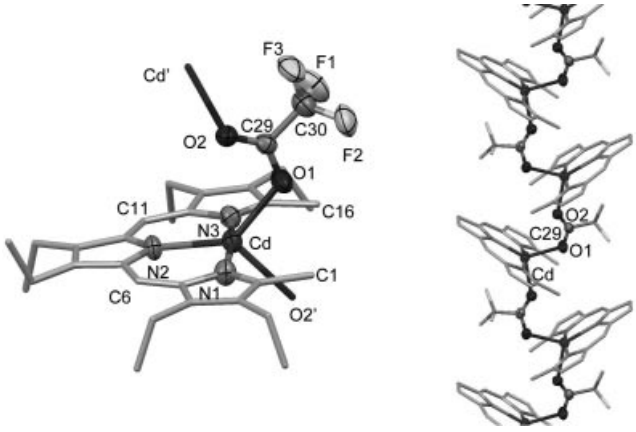


Figure 9. Crystallographically determined structure of the monomeric unit (left; ellipsoids at 50% probability) and the polymeric chain arrangement (right) of TrpyCdOAc$^F$ (**12**) (hydrogen atoms and ethyl groups omitted for clarity).

The trifluoroacetate in **12** functions as a nonsymmetrical bridging ligand. O1 is bound with greater strength to the central metal atom than O2 as indicated by a shorter Cd–O1 bond ($\Delta$ = 0.083 Å) and a longer O1–C29 bond ($\Delta$ = 0.049 Å). The coordination geometry at the cadmium atom can best be described as distorted trigonal bipyramidal with O1, O2, and N2 at the equatorial and N1, N3 at the apical positions. The distortion is particularly strong at the O1–Cd–O2 angle, which is found to be as narrow as 95.76(11)° instead of the ideal 120°. The monomeric units are organized with a Cd···Cd′ distance of 5.541(2) Å and thus further apart than for the dimeric unit of **9** although the O1···O2 distance is as short as 2.222(3) Å. Other than in the azido case **9** the TrpyCd fragments of **12** are not in a near-coplanar orientation but are found to be bent towards each other by 67.39(17)° and additionally rotated by 172.40(19)°, similar to that found for the pseudohalide species **7** and **8**. The markedly planarized tripyrrin ligand of **12** and the O–$C_{term}$ distances of only 8.8% or less below the sum of the van der Waals radii prove the polymeric form as a largely strain-free assembly and an alternative for cases with weakly bound *O*,*O* chelate ligands. The individual pillars are densely packed in all directions and leave no inner space between the isolated chains. The formation of layers, which was seen in **7**–**9**, is also not detected in this case.

## Conclusions

We have shown for a series of pseudohalide and *O*,*O*-chelate ligands that the size of the cadmium(II) ion leads to the formation of tripyrrinatocadmium(II) complexes TrpyCdX with a high propensity for pentacoordination. It appears, that complexes containing the TrpyCd fragment seem to be insufficiently shielded with only four donors at the metal ion and tend to form the desired larger associates. Most of the crystallographically determined molecular structures of these new complexes display coordination polyhedra, which deviate significantly from ideal geometries. The structures are determined by steric factors alone and can be understood on the basis of van der Waals radii and intramolecular interactions. The two limiting geometries **A** and **B** typically obtained for pentacoordinate metallotripyrrins have both also been observed in the case of $Cd^{II}$.

In all 1D-coordination polymers formed from the TrpyCd fragment the external donor atoms bind from opposite sites of the TrpyCd plane, i.e. in type **A**. Unstrained complexes with almost planar Trpy ligands result from this arrangement. *O*,*O*-Chelating co-ligands, however, usually bind with both oxygen donor atoms from the same side of the TrpyCd unit (type **B**). The presence of two donor atoms in the same segment of the coordination sphere results in additional intramolecular strain. The stresses are compensated for by a shortening of the $O_{donor}\cdots CH_{3term}$ distances and by nonplanar tripyrrin conformations. The weak donor ligand trifluoroacetate in the complex TrpyCdOAc$^F$ (**12**) is not capable of keeping up the strained situation of geometry **B**. In this case a strain-driven polymerization with transformation of the coordination environment to geometry **A** is observed.

To summarize, we have achieved the first general description of the syntheses, spectroscopic properties, and structures of sterically hindered tripyrrinatocadmium(II) complexes.

## Experimental Section

**General:** All reagents were purchased from commercial sources and used as received. Solvents were dried by standard protocols and distilled prior to use. TrpyNiNCO **1** and **2**[10a] and sodium 1,1,1-trifluoroacetylacetonate[21] were prepared according to literature procedures. NMR spectra were obtained with a Bruker AMX 400 spectrometer. Chemical shifts ($\delta$) are given in ppm relative to residual protio solvent resonances ($^1$H spectra), chloroform ($^{13}$C), or $CFCl_3$ ($^{19}$F). Mass spectra were recorded with a Finnigan 90 MAT (EI, FAB), Finnigan-MAT 95S (ESI), or the Bruker Biflex IV instrument (MALDI-TOF); *m*/*z* values are given for the most abundant isotopes only. IR spectra were recorded with a Bruker Vector 22 spectrometer in Nujol paste. UV data were collected with a Hitachi U-3200 spectrophotometer. For X-ray crystallographic measurements an IPDS-1 or IPDS-2 instrument from STOE was used.

**Preparation of Complexes**

**Acetato(tripyrrinato)cadmium Complexes 5 and 6 (TrpyCdOAc) from Free Base Tripyrrins. General Procedure:** Complexes **1** or **2** of type TrpyNiNCO (0.1 mmol) was dissolved in diethyl ether (40 mL) and treated with a saturated KCN solution (10 mL) at ambient temperature in an ultrasonic bath for 2 h. During this time the color of the mixture changes from green to red. After phase separation the organic layer was washed with water (2 × 20 mL) and dried with sodium sulfate, which resulted in a red ethereal solution of **3** or **4**. These solutions were treated with water (30 mL) and

 © 2007 Wiley-VCH Verlag GmbH & Co. KGaA, Weinheim 

a saturated solution of cadmium(II) acetate in methanol (5 mL). Upon stirring of this mixture for 30 min at ambient temperature the color changes to blue-green. The phases were separated and the organic layer was washed with water (2 × 10 mL) and dried with sodium sulfate. The resulting solution of cadmium complex **5** or **6** can directly be used for further reactions. For **5** an attempt to isolate the compound was performed by reducing the volume of the solution to 5 mL and adding ice-cold pentane. Violet microcrystals of **5** precipitated overnight. Yield: 43.1 mg (77%). $^1$H NMR (400 MHz, $CD_2Cl_2$): $\delta$ = 1.08 (t, $J$ = 7.6 Hz, 6 H, 2× $CH_2CH_3$), 1.19 (t, $J$ = 7.6 Hz, 6 H, 2× $CH_2CH_3$), 1.87 (s, 3 H, OAc), 2.20 (s, 6 H, 2× $CH_3$), 2.42 (q, $J$ = 7.6 Hz, 4 H, 2× $CH_2CH_3$), 2.50 (s, 6 H, 2× $CH_3$), 2.62 (q, $J$ = 7.6 Hz, 4 H, 2× $CH_2CH_3$), 6.86 (s, 2 H, 2× $H_{meso}$) ppm. $^{13}$C{$^1$H} NMR (100 MHz, $CD_2Cl_2$): $\delta$ = 10.0, 14.3, 17.4, 17.5, 17.9, 18.2, 21.5, 120.1, 136.0, 139.2, 143.3, 144.6, 145.4, 171.4, 180.3 ppm. MS (70 eV, EI): $m/z$ (%) = 561 ($M^+$), 501 ([M – OAc]$^+$). UV/Vis ($CH_2Cl_2$): $\lambda_{max}$ ($\varepsilon$) = 279 (18000), 350 (69000), 413 (11000), 610 sh (35000), 648 nm (60000 mol$^{-1}$ dm$^3$ cm$^{-1}$). IR (Nujol): $\nu$ = 1597 ($\nu_{C=C}$), 1553 ($\nu_{C=O}$) cm$^{-1}$. $C_{28}H_{37}CdN_3O_2$ (560.023): calcd. C 60.05, H 6.66, N 7.50; found C 59.82, H 6.79, N 7.60.

**Ligand Exchange by Treatment with Aqueous Salt Solutions. General Procedure:** The solution of acetato cadmium complex TrpyCdOAc **5** or **6** (0.1 mmol based on 100% yield) in diethyl ether (30 mL) was treated with a saturated NaY solution (15 mL; Y = anionic ligand) with intense stirring for 16 h. The ether was removed from the mixture in vacuo, and the product was filtered off the aqueous phase and washed with additional water. If the solubility was sufficiently low, the residue was washed with cold pentane or methanol and dried in vacuo.

**Thiocyanato-(3,8,9,14-tetraethyl-2,4,13,15-tetramethyltripyrrinato)-cadmium(II) (TrpyCdNCS, 7):** Yield: 48.1 mg (86%). $^1$H NMR (400 MHz, [D$_6$]acetone): $\delta$ = 1.07 (t, $J$ = 7.6 Hz, 6 H, 2× $CH_2CH_3$), 1.15 (t, $J$ = 7.6 Hz, 6 H, 2×$CH_2CH_3$), 2.19 (s, 6 H, 2× $CH_3$), 2.43 (q, $J$ = 7.6 Hz, 4 H, 2× $CH_2CH_3$), 2.56 (s, 6 H, 2× $CH_3$), 2.65 (q, $J$ = 7.6 Hz, 4 H, 2× $CH_2CH_3$), 6.92 (s, 2 H, 2× $H_{meso}$) ppm. $^{13}$C{$^1$H} NMR (100 MHz, [D$_6$]acetone): $\delta$ = 11.3, 16.2, 18.4, 19.3, 19.7, 20.0, 121.7, 138.6, 141.3, 144.6, 146.6, 147.7, 173.4 ppm. MS (70 eV, EI): $m/z$ (%) = 560 ($M^+$), 501 ([M – SCN]$^+$). UV/Vis (acetone): $\lambda_{max}$ ($\varepsilon$) = 345 (58000), 401 (9000), 600 sh (34700), 630 nm (61100 mol$^{-1}$ dm$^3$ cm$^{-1}$). IR (Nujol): $\nu$ = 2103 ($\nu_{NCS}$), 1595 cm$^{-1}$ ($\nu_{C=C}$). $C_{27}H_{34}CdN_4S$ (559.06): calcd. C 58.01, H 6.13, N 10.02; found C 58.36, H 6.46, N 9.69.

**Selenocyanato-(3,8,9,14-tetraethyl-2,4,13,15-tetramethyltripyrrinato)cadmium(II) (TrpyCdNCSe, 8):** Yield: 54.5 mg (90%). $^1$H NMR (400 MHz, [D$_6$]acetone): $\delta$ = 1.05 (t, $J$ = 7.6 Hz, 6 H, 2× $CH_2CH_3$), 1.16 (t, $J$ = 7.6 Hz, 6 H, 2× $CH_2CH_3$), 2.19 (s, 6 H, 2× $CH_3$), 2.42 (q, $J$ = 7.6 Hz, 4 H, 2× $CH_2CH_3$), 2.55 (s, 6 H, 2× $CH_3$), 2.66 (q, $J$ = 7.6 Hz, 4 H, 2× $CH_2CH_3$), 6.94 (s, 2 H, 2× $H_{meso}$) ppm. $^{13}$C{$^1$H} NMR (100 MHz, [D$_6$]acetone): $\delta$ = 10.2, 15.0, 17.8, 18.2, 18.6, 18.9, 120.6, 134.1, 137.3, 140.2, 145.4, 150.1, 172.1 ppm. MS (70 eV, EI): $m/z$ (%) = 606 ($M^+$), 501 ([M – SeCN]$^+$). UV/Vis (acetone): $\lambda_{max}$ ($\varepsilon$) = 345 (60000), 403 (9000), 595 sh (35000), 631 nm (62000 mol$^{-1}$ dm$^3$ cm$^{-1}$). IR (Nujol): $\nu$ = 2115 ($\nu_{NCSe}$), 1596 cm$^{-1}$ ($\nu_{C=C}$). $C_{27}H_{34}CdN_4Se$ (605.96): calcd. C 53.51, H 5.66, N 9.25; found C 53.33, H 5.91, N 8.86.

**Azido-(3,8,9,14-tetraethyl-2,4,13,15-tetramethyltripyrrinato)-cadmium(II)·MeOH (TrpyCdN$_3$·MeOH, 9):** Purified by recrystallization from methanol/toluene. Yield: 47.1 mg (82%). $^1$H NMR (400 MHz, $CD_3OD$): $\delta$ = 1.09 (t, $J$ = 7.6 Hz, 6 H, 2× $CH_2CH_3$), 1.18 (t, $J$ = 7.6 Hz, 6 H, 2× $CH_2CH_3$), 2.16 (s, 6 H, 2× $CH_3$), 2.43 (q, $J$ = 7.6 Hz, 4 H, 2× $CH_2CH_3$), 2.45 (s, 6 H, 2× $CH_3$), 2.64 (q, $J$ = 7.6 Hz, 4 H, 2× $CH_2CH_3$), 6.78 (s, 2 H, 2× $H_{meso}$) ppm. $^{13}$C{$^1$H} NMR (100 MHz, [D$_6$]DMSO): $\delta$ = 9.6, 14.4, 15.3, 16.2, 17.3, 17.6, 17.7, 119.1, 136.0, 138.6, 141.5, 143.7, 144.8, 170.8 ppm. MS (70 eV, EI): $m/z$ (%) = 501 ([M – MeOH – SeCN]$^+$). UV/Vis ($CH_2Cl_2$): $\lambda_{max}$ ($\varepsilon$) = 270 (14000), 335 sh (26000), 350 (51000), 413 (10000), 564 sh (14000), 610 sh (24000), 649 nm (41000 mol$^{-1}$ dm$^3$ cm$^{-1}$). IR (Nujol): $\nu$ = 2090, 2067 ($\nu_{NNN}$), 1594 cm$^{-1}$ ($\nu_{C=C}$). $C_{27}H_{38}CdN_6O$ (575.041): calcd. C 56.39, H 6.66, N 14.61; found C 56.67, H 6.53, N 14.35.

**Salicylato-(3,8,9,14-tetraethyl-2,4,13,15-tetramethyltripyrrinato)-cadmium(II) (TrpyCdsal, 10):** Yield: 42.1 mg (66%). $^1$H NMR (400 MHz, $CD_2Cl_2$): $\delta$ = 1.05 (t, $J$ = 7.5 Hz, 6 H, 2× $CH_2CH_3$), 1.20 (t, $J$ = 7.5 Hz, 6 H, 2× $CH_2CH_3$), 2.19 (s, 6 H, 2× $CH_3$), 2.39 (q, $J$ = 7.5 Hz, 4 H, 2× $CH_2CH_3$), 2.51 (s, 6 H, 2× $CH_3$), 2.62 (q, $J$ = 7.5 Hz, 4 H, 2× $CH_2CH_3$), 6.88 (s, 2 H, 2× $H_{meso}$), 6.73–6.78, 6.80–6.82, 7.27–7.33, 7.81–7.83 (4m, 4 H, $H_{Ar}$), 12.21 (br., 1 H, O$H$) ppm. $^{13}$C{$^1$H} NMR (100 MHz, $CD_2Cl_2$): $\delta$ = 10.0, 14.3, 17.4, 17.6, 18.0, 18.2, 116.5, 118.3, 120.0, 131.6, 133.8, 136.1, 139.3, 143.4, 144.5, 145.4, 161.4, 171.3 ppm. MS (70 eV, EI): $m/z$ (%) = 501 ([M – sal]$^+$). UV/Vis ($CH_2Cl_2$): $\lambda_{max}$ ($\varepsilon$) = 278 (18000), 350 (69000), 413 (12000), 600 sh (33000), 648 nm (60000 mol$^{-1}$ dm$^3$ cm$^{-1}$). IR (Nujol): $\nu$ = 3384 ($\nu_{OH}$), 1595 cm$^{-1}$ ($\nu_{C=C}$, $\nu_{C=O}$). $C_{33}H_{39}CdN_3O_3$ (638.092): calcd. C 62.12, H 6.16, N 6.59; found C 61.91, H 6.07, N 6.34.

**1,1,1-Trifluoroacetylacetonato-(3,8,9,14-tetraethyl-2,4,13,15-tetramethyltripyrrinato)cadmium(II) (TrpyCdacac$^F$, 11):** Yield: 39.2 mg (60%). $^1$H NMR (400 MHz, $CD_2Cl_2$): $\delta$ = 1.06 (t, $J$ = 7.6 Hz, 6 H, 2× $CH_2CH_3$), 1.20 (t, $J$ = 7.6 Hz, 6 H, 2× $CH_2CH_3$), 1.93 (br., 3 H, $CH_3$ [acac$^F$]), 2.18 (s, 6 H, 2× $CH_3$), 2.40 (q, $J$ = 7.6 Hz, 4 H, 2× $CH_2CH_3$), 2.47 (s, 6 H, 2× $CH_3$), 2.64 (q, $J$ = 7.6 Hz, 4 H, 2× $CH_2CH_3$), 5.46 (br., 1 H, C$H$ [acac$^F$]), 6.86 (s, 2 H, 2× $H_{meso}$) ppm. $^{13}$C{$^1$H} NMR (100 MHz, $CD_2Cl_2$): $\delta$ = 10.0, 14.3, 17.1, 17.3, 18.0, 18.2, 29.8, 120.0, 136.1, 138.9, 143.2, 144.5, 146.0, 172.3 ppm. $^{19}$F{$^1$H} NMR ($CD_2Cl_2$): $\delta$ = –76.2 ppm. MS (70 eV, EI): $m/z$ (%) = 501 ([M – acac$^F$]$^+$). UV/Vis ($CH_2Cl_2$): $\lambda_{max}$ ($\varepsilon$) = 276 (18000), 351 (69000), 410 (11000), 605 sh (30000), 652 nm (61000 mol$^{-1}$ dm$^3$ cm$^{-1}$). IR (Nujol): $\nu$ = 1636, 1612 ($\nu_{C=O}$), 1594 cm$^{-1}$ ($\nu_{C=C}$). $C_{31}H_{38}CdF_3N_3O_2$ (654.059): calcd. C 56.93, H 5.86, N 6.42; found C 56.59, H 5.81, N 6.25.

**Trifluoracetato-(3,4,8,9,13,14-hexaethyl-2,15-dimethyltripyrrinato)-cadmium(II) (TrpyCdOAc$^F$, 12):** Yield: 43.0 mg (67%). $^1$H NMR (400 MHz, $CD_2Cl_2$): $\delta$ = 1.10 (t, $J$ = 7.6 Hz, 6 H, 2× $CH_2CH_3$), 1.19 (t, $J$ = 7.6 Hz, 6 H, 2× $CH_2CH_3$), 1.20 (t, $J$ = 7.6 Hz, 6 H, 2× $CH_2CH_3$), 2.42 (q, $J$ = 7.6 Hz, 4 H, 2× $CH_2CH_3$), 2.51 (s, 6 H, 2× $CH_3$), 2.62 (q, $J$ = 7.6 Hz, 4 H, 2× $CH_2CH_3$), 2.63 (q, $J$ = 7.6 Hz, 4 H, 2× $CH_2CH_3$), 6.87 (s, 2 H, 2× $H_{meso}$) ppm. $^{13}$C{$^1$H} NMR (100 MHz, $CD_2Cl_2$): $\delta$ = 14.8, 17.0, 17.4, 17.8, 17.9, 18.2, 18.4, 120.2, 135.4, 139.5, 144.1, 144.6, 150.2, 171.5 ppm. $^{19}$F{$^1$H} NMR ($CD_2Cl_2$): $\delta$ = –74.1 ppm. MS (70 eV, EI): $m/z$ (%) = 529 ([M – OAc$^F$]$^+$). UV/Vis ($CH_2Cl_2$): $\lambda_{max}$ ($\varepsilon$) = 276 (16000), 350 (65000), 403 (12000), 596 sh (33000), 656 nm (59000 mol$^{-1}$ dm$^3$ cm$^{-1}$). IR (Nujol): $\nu$ = 1602, 1597 cm$^{-1}$ ($\nu_{C=C}$, $\nu_{C=O}$). $C_{30}H_{38}CdF_3N_3O_2$ (642.048): calcd. C 56.12, H 5.97, N 6.54; found C 55.93, H 6.02, N 6.29.

CCDC-625800 to -625805 contain the supplementary crystallographic data for this paper. These data can be obtained free of charge from The Cambridge Crystallographic Data Centre via www.ccdc.cam.ac.uk/data_request/cif.request/cif.

**Supporting Information** (see also the footnote on the first page of this article): UV/Vis spectra of **8** in acetone and in MeOH.

 © 2007 Wiley-VCH Verlag GmbH & Co. KGaA, Weinheim 

## Acknowledgments

We gratefully acknowledge financial support from the Deutsche Forschungsgemeinschaft (DFG).

[1] a) M. J. Chmielewski, M. P. Pawlicki, N. Sprutta, L. Szterenberg, L. Latos-Grażyński, *Inorg. Chem.* **2006**, *45*, 8664; b) M. Stępień, L. Latos-Grażyński, *Acc. Chem. Res.* **2005**, *38*, 88; c) M. Pawlicki, L. Latos-Grażyński, L. Szterenberg, *Inorg. Chem.* **2005**, *44*, 9779; d) M. Stępień, L. Latos-Grażyński, L. Szterenberg, J. Panek, Z. Latajka, *J. Am. Chem. Soc.* **2004**, *126*, 4566; e) M. Stępień, L. Latos-Grażyński, *J. Am. Chem. Soc.* **2002**, *124*, 3838.

[2] a) A. Shamim, P. Hambright, *J. Inorg. Nucl. Chem.* **1980**, *42*, 1645; b) A. Shamim, P. Hambright, *Inorg. Chem.* **1980**, *19*, 564.

[3] a) M. E. Milanesio, F. S. Moran, E. I. Yslas, M. G. Alvarez, V. Rivarola, E. N. Durantini, *Bioorg. Med. Chem.* **2001**, *9*, 1943; b) K. Takahashi, H. Katsurada, T. Komura, H. Imanaga, *Bull. Chem. Soc. Jpn.* **1990**, *63*, 3315.

[4] R. G. Khoury, L. Jaquinod, K. M. Smith, *Tetrahedron* **1998**, *54*, 2339.

[5] a) S. P. Rath, M. M. Olmstead, L. Latos-Grażyński, A. L. Balch, *J. Am. Chem. Soc.* **2003**, *125*, 12678; b) A. Krivokapic, A. R. Cowley, H. L. Anderson, *J. Org. Chem.* **2003**, *68*, 1089; c) H. Furuta, H. Maeda, A. Osuka, *Inorg. Chem. Commun.* **2003**, *6*, 162; d) J. L. Sessler, A. Gebauer, V. Král, V. Lynch, *Inorg. Chem.* **1996**, *35*, 6636; e) A. Jaumà, J.-A. Farrera, J. M. Ribó, *Monatsh. Chem.* **1996**, *127*, 935; f) R. G. Khoury, M. O. Senge, J. E. Colchester, K. M. Smith, *J. Chem. Soc., Dalton Trans.* **1996**, 3937; g) D. Eichinger, H. Falk, *Monatsh. Chem.* **1987**, *118*, 261; h) F.-P. Montforts, U. M. Schwartz, *Liebigs Ann. Chem.* **1985**, 1228; i) F.-P. Montforts, *Angew. Chem.* **1981**, *93*, 795; *Angew. Chem. Int. Ed. Engl.* **1981**, *20*, 778; j) H. von Dobeneck, U. Sommer, E. Brunner, E. Lippacher, F. Schnierle, *Justus Liebigs Ann. Chem.* **1973**, *11*, 1934.

[6] M. Bröring, C. D. Brandt, *Chem. Commun.* **2001**, 499.

[7] M. Bröring, C. D. Brandt, *J. Chem. Soc., Dalton Trans.* **2002**, 1391.

[8] M. Bröring, S. Prikhodovski, C. D. Brandt, *J. Chem. Soc., Dalton Trans.* **2002**, 4213.

[9] a) B. L. Dietrich, J. Egbert, A. M. Morris, M. Wicholas, O. P. Anderson, S. M. Miller, *Inorg. Chem.* **2005**, *44*, 6476; b) O. P. Anderson, A. La Cour, A. Berg, A. D. Garrett, M. Wicholas, *Inorg. Chem.* **2003**, *42*, 4513; c) O. P. Anderson, A. La Cour, A. Dodd, A. D. Garrett, M. Wicholas, *Inorg. Chem.* **2003**, *42*, 122; d) D. M. Baird, K. Y. Shih, J. H. Welch, R. D. Bereman, *Polyhedron* **1989**, *8*, 2359.

[10] a) M. Bröring, S. Prikhodovski, C. D. Brandt, E. Cónsul Tejero, *Chem. Eur. J. accepted*; b) M. Bröring, S. Prikhodovski, C. D. Brandt, *Inorg. Chim. Acta* **2004**, 1733.

[11] a) M. Bröring, C. D. Brandt, S. Link, *Inorg. Chim. Acta* **2005**, *358*, 3122; b) M. Bröring, C. D. Brandt, S. Köhler, M. Sieber, *J. Porphyrins Phthalocyanines* **2005**, *9*, 683; c) M. Bröring, C. D. Brandt, S. Stellwag, *Chem. Commun.* **2003**, 2344; d) M. Bröring, C. D. Brandt, *Chem. Commun.* **2003**, 2156.

[12] M. Bröring, C. D. Brandt, S. Prikhodovski, *J. Porphyrins Phthalocyanines* **2003**, *7*, 17.

[13] K. Nakamoto, *Infrared and Raman Spectra of Inorganic and Coordination Compounds*, part B, vol. 5, Wiley, New York, **1997**.

[14] a) T. Rojo, R. Cortés, L. Lezama, M. I. Arriortua, K. Urtiaga, G. Villeneuve, *J. Chem. Soc., Dalton Trans.* **1991**, 1779; b) R. Vicente, A. Escuer, J. Ribas, X. Solans, *J. Chem. Soc., Dalton Trans.* **1994**, 259; c) A. Escuer, R. Vicente, M. S. El Fallah, X. Solans, M. Font-Bardía, *J. Chem. Soc., Dalton Trans.* **1996**, 1013; d) M. Monfort, C. Bastos, C. Dias, J. Ribas, *Inorg. Chim. Acta* **1994**, *218*, 185; e) H. Grove, M. Julve, F. Lloret, P. E. Kruger, K. W. Törnroos, J. Sletten, *Inorg. Chim. Acta* **2001**, *325*, 115; f) T. K. Maji, I. R. Laskar, G. Mostafa, A. J. Welch, P. S. Mukherjee, N. R. Chaudhuri, *Polyhedron* **2001**, *20*, 651; g) L. Shen, Y.-Z. Xu, *J. Chem. Soc., Dalton Trans.* **2001**, 3413; h) R. Sekiya, S. Nishikiori, *Chem. Eur. J.* **2002**, *8*, 4803; i) A. Skorupa, B. Korybut-Daszkiewicz, J. Mroziński, *Inorg. Chim. Acta* **2002**, *336*, 65; j) B. Żurowska, J. Mroziński, M. Julve, F. Lloret, A. Maslejova, W. Sawka-Dobrowolska, *Inorg. Chem.* **2002**, *41*, 1771; k) J. Tercero, C. Diaz, J. Ribas, E. Ruiz, J. Mahía, M. Maestro, *Inorg. Chem.* **2002**, *41*, 6780; l) J. A. Real, A. B. Gaspar, V. Niel, M. C. Muñoz, *Coord. Chem. Rev.* **2003**, *236*, 121; m) S. Deoghoria, S. Sain, B. Moulton, M. J. Zaworotko, S. K. Bera, S. K. Chandra, *Polyhedron* **2002**, *21*, 2457.

[15] a) J. Ribas, C. Diaz, X. Solans, M. Font-Bardía, *J. Chem. Soc., Dalton Trans.* **1996**, 35; b) P. M. Secondo, J. M. Land, R. G. Baughman, H. L. Collier, *Inorg. Chim. Acta* **2000**, *309*, 13; c) J. Tercero, C. Diaz, J. Ribas, J. Mahía, M. Maestro, X. Solans, *J. Chem. Soc., Dalton Trans.* **2002**, 2040; d) A. B. Gaspar, M. C. Muños, N. Moliner, V. Ksenofontov, G. Levchenko, P. Gütlich, J. A. Real, *Monatsh. Chem.* **2003**, *134*, 285.

[16] a) U. Turpeinen, *Finn. Chem. Lett.* **1997**, *24*, 75; b) S. Sain, T. K. Maji, G. Mostafa, T.-H. Lu, M. Y. Chiang, N. R. Chaudhuri, *Polyhedron* **2002**, *21*, 2293.

[17] For some recent work on bridging azides in coordination polymers see: a) J. Ribas, A. Escuer, M. Monfort, R. Vicente, R. Cortés, L. Lezama, T. Rojo, *Coord. Chem. Rev.* **1999**, *193–195*, 1027; b) H. Grove, M. Julve, F. Lloret, P. E. Kruger, K. W. Törnroos, J. Sletten, *Inorg. Chim. Acta* **2001**, *325*, 115; c) E.-Q. Gao, S.-Q. Bai, C.-F. Wang, Y.-F. Yue, C.-H. Yan, *Inorg. Chem.* **2003**, *42*, 8456; d) J. Carranza, C. Brennan, J. Sletten, J. M. Clemente-Juan, F. Lloret, M. Julve, *Inorg. Chem.* **2003**, *42*, 8716; e) M. Monfort, I. Resino, J. Ribas, X. Solans, M. Font-Barbia, H. Stoeckli-Evans, *New J. Chem.* **2002**, *26*, 1601; f) A. Panja, N. Shaikh, P. Vojtíšek, S. Gao, P. Benerjee, *New J. Chem.* **2002**, *26*, 1025; g) R. Kurtaran, C. Arıcı, K. C. Emregül, D. Ülkü, O. Atakol, M. Taştekin, *Z. Anorg. Allg. Chem.* **2003**, *629*, 1617; h) U. Ray, B. Chand, G. Mostafa, J. Cheng, T.-H. Lu, C. Sinha, *Polyhedron* **2003**, *22*, 2587; i) M. Fujii, S. Goto, Y. Nakao, M. Shiro, T. Sato, W. Mori, *Chem. Lett.* **2003**, *32*, 868; j) J. Cabrero, C. de Graaf, E. Bordas, R. Caballol, J.-P. Malrieu, *Chem. Eur. J.* **2003**, *9*, 2307; k) M. S. Ray, A. Ghosh, R. Bhattacharya, G. Mukhopadhyay, M. G. B. Drew, J. Ribas, *Dalton Trans.* **2004**, 252.

[18] G. M. Sheldrick, *SHELXS-97*, Program for Crystal Structure Determination, University of Göttingen, **1997**.

[19] G. M. Sheldrick, *SHELXL-97*, Program for Crystal Structure Refinement, University of Göttingen, **1997**.

[20] W. R. Scheidt in *The Porphyrin Handbook* (Eds.: K. M. Kadish, K. M. Smith, R. Guilard), Academic Press, New York, **2000**, vol. 3, p. 55.

[21] H. K. Shin, K. M. Chi, J. Farkas, M. J. Hampden-Smith, T. T. Kodas, E. N. Duesler, *Inorg. Chem.* **1992**, *31*, 424.

Received: October 27, 2006
Published Online: January 23, 2007

 © 2007 Wiley-VCH Verlag GmbH & Co. KGaA, Weinheim 

DOI: 10.1002/ejic.200601120

# Polymer-Supported Dioxido-Mo$^{VI}$ Complexes as Truly Functional Molybdenum Oxotransferase Model Systems

**Katja Heinze*[a] and Andreas Fischer[a]**

**Keywords:** Enzyme models / Immobilised complexes / Molybdenum / Nitrogen ligands / Oxygen transfer

A truly functional model system for molybdenum oxotransferases provides evidence for all biologically realistic intermediates, namely mononuclear Mo$^{VI}$, Mo$^{V}$ and Mo$^{IV}$ species. Dinucleation to EPR-silent [Mo$^{V}_2$O$_3$] species prevailing in homogeneous solution is suppressed by immobilising the active species to a polymeric support by two-point attachment.

(© Wiley-VCH Verlag GmbH & Co. KGaA, 69451 Weinheim, Germany, 2007)

## Introduction

Currently there is a great interest in structural and functional biomimetic models for active sites of metalloenzymes which mimic the primary coordination sphere (number and nature of ligating atoms) as well as the secondary coordination sphere (protein environment, site isolation, substrate selectivity, entatic state, secondary interactions with substrates, etc.).[1] Mononuclear molybdenum enzymes catalyse the net transfer of an oxygen atom between substrate and water [Equation (1)] shuttling between Mo$^{VI}$, Mo$^{V}$ and Mo$^{IV}$ states.[2,3]

$$X + H_2O \Leftrightarrow XO + 2H^+ + 2e^- \quad (1)$$

$$XO + Y \rightarrow X + YO \quad (2)$$

$$L_nMo^{VI}O_2 + L_nMo^{IV}O \rightarrow L_{2n}Mo^{V}_2O_3 \quad (3)$$

$$2\,L_nMo^{V}(OH)O \rightarrow L_{2n}Mo^{V}_2O_3 + H_2O \quad (4)$$

The primary oxo atom transfer (OAT) from/to molybdenum model compounds to/from substrates [Equation (2)] has been extensively investigated by Holm, Wedd, Young, Enemark, Basu and many others and is well understood.[4–7] The most successful model systems are based on enedithiolate ligands mimicking the natural sulfur ligation,[8–12] multidentate N/S ligands[13–17] and substituted hydrotris(pyrazolyl)borate ligands (Tp*, Tp$^{iPr}$).[18–21] Especially the latter family, although bearing no structural resemblance to natural enzymes, has been exceptionally useful for identifying mononuclear Mo$^{V}$ species which are essential to the enzymatic catalytic cycle involving OAT and CEPT reactions (CEPT = coupled electron proton transfer). In these model systems the inherent tendency of molybdenum oxido complexes to form dinuclear species with a [Mo$_2$O$_3$] core via comproportionation [Equation (3)] or condensation [Equation (4)] is reduced due to steric hindrance. In molybdenum enzymes, the active site is located in the interior of the protein matrix and the substrate approaches the catalytic centre through a "funnel".[2,6] Of course dinucleation does not occur in natural systems.

[a] Anorganisch-Chemisches Institut der Universität Heidelberg, Im Neuenheimer Feld 270, 69120 Heidelberg, Germany
Fax: +49-6221-545707
E-mail: katja.heinze@urz.uni-heidelberg.de

Supporting information for this article is available on the WWW under http://www.eurjic.org or from the author.

## Results and Discussion

The present report describes a different solution to the dinucleation problem, namely immobilisation of an active complex on a polymer support. In order to improve site-isolation and minimise leaching, the Mo complexes are immobilised onto the support via two-point fixation with two chelating 2-imino-pyrrolato ligands. The twofold attachment to the support parallels the incorporation of molybdenum in oxotransferases by pterin dithiolene and cysteinato ligands (e.g. sulfite oxidase or DMSO reductase).[2–7] Different EPR-active states have been observed in natural systems depending on preparation and environment.[2,3] The artificial system described below also shows several EPR-active Mo$^{V}$ states during full biomimetic catalytic turnover [OAT and CEPT; Equation (1)]. First we introduce a sterically unencumbered model system, investigate the chemistry in homogeneous solution, and finally we describe our results for the immobilised system.

The soluble 2-imino-pyrrole ligand cleanly forms the bis(chelate) dioxido Mo$^{VI}$ complex **1a** with MoCl$_2$O$_2$(dme) (Scheme 1). **1a** was fully characterised by NMR, IR and UV/Vis spectroscopic methods as well as mass spectrometric and elemental analysis (see Exp. Sect.). Reduction of **1a** with tertiary phosphanes results in OAT from the Mo$^{VI}$ complex to the substrate giving the corresponding phosphane oxide (Scheme 2). Stoichiometric reaction with one

 © 2007 Wiley-VCH Verlag GmbH & Co. KGaA, Weinheim 

equivalent $PPh_3$ only produces 0.5 equiv. $OPPh_3$ even after prolonged reaction times as shown by time-dependent $^{31}P\{^1H\}$ NMR spectroscopy (Figure 1). Similar observations are made with $PMe_3$ as substrate albeit OAT proceeds faster in this case.[22] Thus comproportionation of $Mo^{VI}$ and initially formed $Mo^{IV}$ species to the diamagnetic μ-oxo species **2a** (Scheme 2) significantly slows down full conversion to $Mo^{IV}$. Complex **2a** has been analysed by mass spectrometry as well as NMR, IR and UV/Vis spectroscopy (see Exp. Sect.). The FAB and HR-FAB mass spectra confirm the dinuclear nature of the complex. A strong absorption band can be observed around 548 nm in the UV/Vis spectrum which is assigned the characteristic π-π* transition of the Mo–O–Mo unit. The antisymmetric Mo=O stretching vibration of the [O=Mo–O–Mo=O] core appears at 960 $cm^{-1}$.

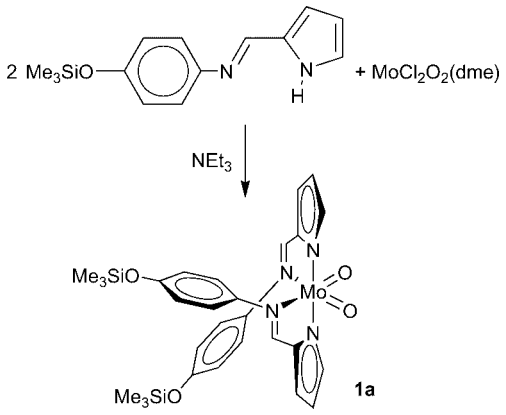


Scheme 1.

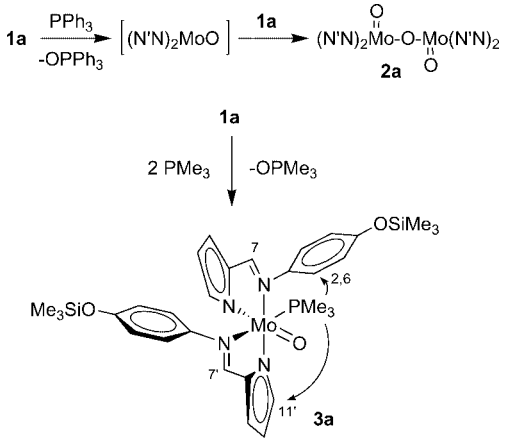


Scheme 2.

Full reduction of **1a** is achieved by using excess $PMe_3$ in THF at elevated temperature giving a green solution of the highly air-sensitive $PMe_3$ complex **3a** (Scheme 2). Coordination of $PMe_3$ to $Mo^{IV}$ is shown by multinuclear two-dimensional NMR spectroscopy [$\delta(^{31}P) = 2.4$; $^2J_{PH} = 8.5$ Hz to methyl protons and $^4J_{PH} = 2.8$, <2 Hz to protons $H^{7'}$ and $H^7$ of the chelate ligands; Figure 2] and LIFDI mass spectrometry (*m*/*z* = 704, molecular ion peak[23]). In the NOESY spectrum NOE cross peaks are observed between

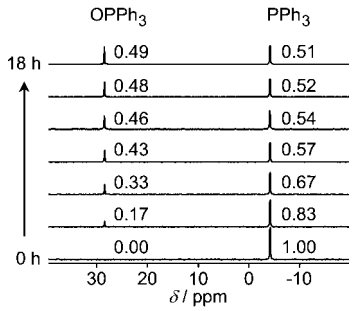


Figure 1. $^{31}P\{^1H\}$ NMR spectra of **1a** and 1 equiv. $PPh_3$ at 25 °C.

methyl protons of the $PMe_3$ ligand and protons of both chelate ligands ($H^{2,6}$ and $H^{11'}$) compatible with $PMe_3$ coordination *trans* to an imine nitrogen donor atom of one chelate ligand and *cis* to the imine nitrogen of the other (Scheme 2). Thus a second substrate can coordinate to molybdenum in the +IV state during OAT. Precedence for such a behaviour was only recently reported using a bis($\eta^2$-pyrazolate)$MoO_2$ complex.[24]

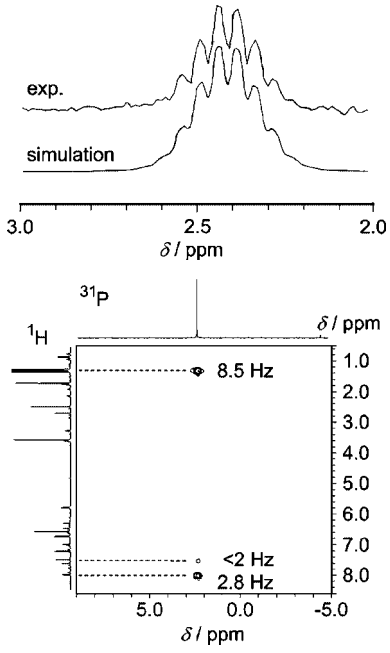


Figure 2. $^{31}P$ NMR spectrum and simulation (top) and PH-COSY spectrum of **3a** (bottom).

Re-oxidation of **3a** with DMSO as oxygen donor at 50 °C under single-turnover conditions yields dinuclear **2a** after 20 min and **1a** after 24 h. Thus a full OAT cycle [Equation (2)] from DMSO to $PMe_3$ has been accomplished with complex **1a**, however, with intermediate formation of dinuclear **2a** via comproportionation.

The reaction of **1a** with excess $PMe_3$ in THF (Scheme 2) was monitored UV-spectrophotometrically at 548 nm where **2a** possesses an absorption maximum (π-π* transition). Numerical simulation[25,26] of the data (Figure 3, top) yielded rate constants *k* for the rate-determining step (attack of $PMe_3$ at one oxido ligand of **1a**) and equilibrium constants *K* for the comproportionation [Equation (3)]. An Eyring

 © 2007 Wiley-VCH Verlag GmbH & Co. KGaA, Weinheim 

analysis yielded $\Delta H^{\neq}$ = 53 kJ mol$^{-1}$ and $\Delta S^{\neq}$ = –82 J mol$^{-1}$ K$^{-1}$ (Figure 3, bottom). The negative activation entropy agrees with the associative transition state in the bimolecular reaction between **1a** and $PMe_3$.[4–7]

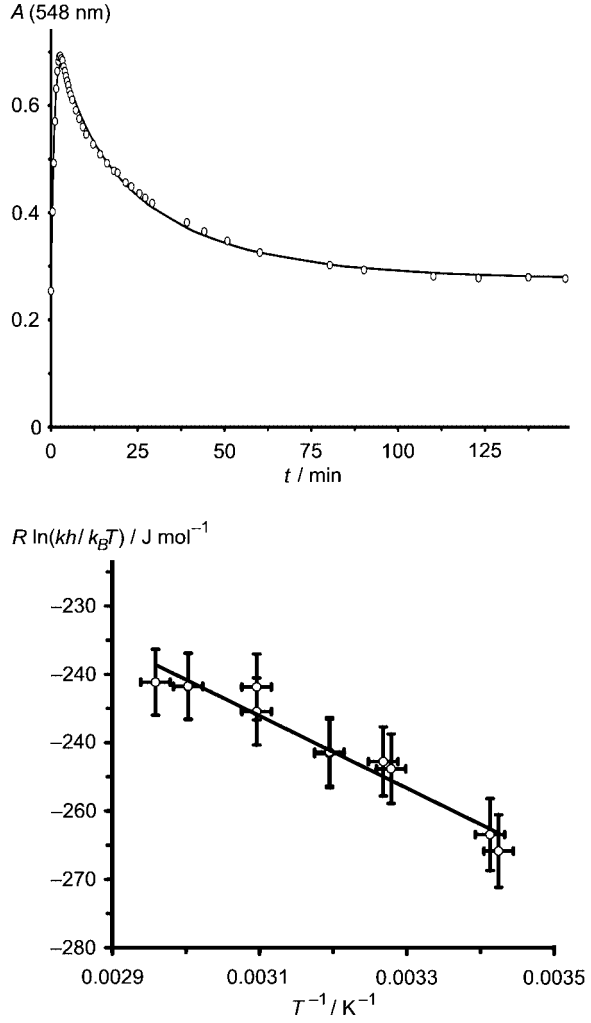


Figure 3. *A* vs. *t* plot of the reaction of **1a** and 100 eq $PMe_3$ at 60 °C (top) and Eyring plot (bottom).

So far it has been shown that oxo transfer chemistry (OAT) is possible with the system **1a/3a**. However, all attempts to observe mononuclear $Mo^V$ species in homogeneous solution by EPR spectroscopy failed due to the high stability of EPR-silent **2a** towards disproportionation ($K_{dis} \approx 5 \cdot 10^{-6}$) and hydrolysis. To suppress (or at least diminish) formation of dinuclear species the doubly anchored versions of **1a/3a** are investigated (Scheme 3).

The immobilised bis(chelate) complex **1b** is prepared analogously to **1a** employing polymer-supported chelate ligands (Scheme 1 and Scheme 3; ligand loading 0.6–0.8 mmol g$^{-1}$ polymer; polymer = polystyrene/2% divinylbenzene).[27–32] The amount of molybdenum incorporated by **1b** is compatible with the required 2:1 ligand/metal stoichiometry as shown by molybdenum uptake measurements.[23] Thus the molybdenum complexes are anchored to the polymeric backbone by two attachment points which should guarantee the desired site isolation effect (at least

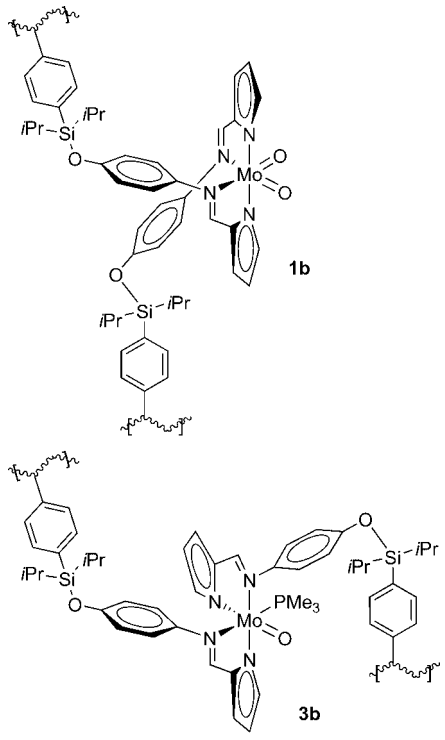


Scheme 3.

for some sites within the polymer). Cleaving the Si–O bonds of **1b** with fluoride ions releases the hydroxy analogue of **1a** into solution confirming the correct formation of **1b**.[27–32]

$PMe_3$ is oxidised by **1b** to $OPMe_3$ as shown by $^{31}P\{^1H\}$ NMR spectroscopic analysis of the solution. The reduction product of **1b** is the immobilised $PMe_3$ complex **3b** (Scheme 3) characterised by its CP MAS $^{31}P\{^1H\}$ NMR signal at $\delta$ = 2.4 which fits to that observed for the soluble complex **3a** (Figure 2 and Figure 4).

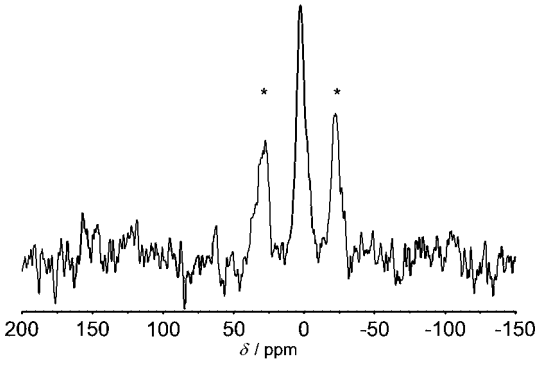


Figure 4. CP MAS $^{31}P\{^1H\}$ NMR spectrum (4 kHz) of **3b** (* denote rotational side bands).

The anchored $Mo^{VI}$ and $Mo^{IV}$ complexes **1b** and **3b** were subjected to one-electron reduction and oxidation, respectively (CEPT chemistry). Reaction of **1b** with cobaltocene $Co(C_5H_5)_2$[33] gave polymer **4b** which is EPR-active. Anisotropic EPR spectra ($g_1$ = 1.9544, $g_2$ = 1.9388, $g_3$ = 1.9111; **1b** and **3b** are EPR-silent) both in the solid and the THF gel-phase of the polymer are observed at room temperature (Figure 5). We have previously shown that singly polymer

 © 2007 Wiley-VCH Verlag GmbH & Co. KGaA, Weinheim 

attached $Cu^{II}$ complexes give isotropic EPR spectra under gel-phase conditions suggesting that a single-point attachment allows for sufficient mobility.[34] However, two-point fixation seems to decrease the mobility of the anchored complexes **4b** resulting in anisotropic EPR spectra even in the gel-phase at room temperature.[35] In addition this finding proves that the molybdenum species are still bound to the support as otherwise isotropic signals for soluble species would have been observed.

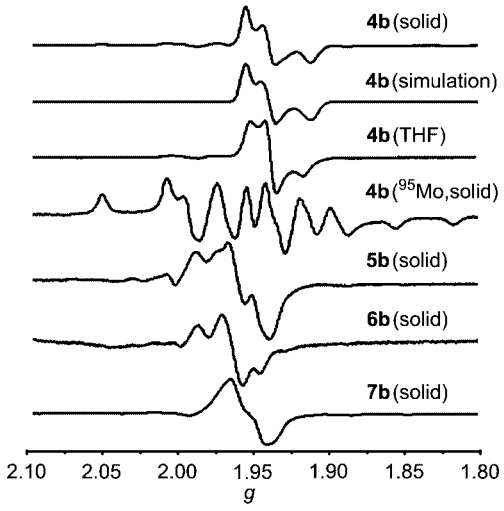


Figure 5. EPR spectra of **4b**–**7b** (295 K, 9.4 GHz).

All *g*-values observed for **4b** are well below 2.0 typical for $Mo^{V}$ species with non-thiolate donor atoms. Further confirmation of mononuclear $Mo^{V}$ present is provided by using $^{95}$Mo-enriched precursors (98%; $I = {}^{5}/_{2}$). The isotopically enriched polymer **4b** displays characteristic anisotropic hyperfine coupling to the $^{95}$Mo nucleus in the EPR spectrum (Figure 5). Upon one-electron reduction of **1b** an anionic dioxido-$Mo^{V}$ species should be formed initially. For $[MoO_2(NCS)Tp^*]^-$ an anisotropic spectrum (*g*-values of 1.9939, 1.9277, 1.8350) is observed at 77 K, while the corresponding protonated complex MoO(OH)(NCS)Tp* displays signals at $g = 1.966$, 1.944 and 1.922 much more similar to the values observed for **4b**.[21] Addition of a proton source ($HBF_4$) to the reduced polymer **4b** had no influence on the EPR spectrum, suggesting that **4b** has already captured a proton. However, if protonation to the hydroxo complex occurred during reduction split signals due to coupling to the hydroxo proton are expected which is not observed for **4b**.[21] The protonation state of **4b** remains ambiguous at the moment.

One-electron oxidation of the anchored $Mo^{IV}$ complex **3b** with $[Fe(C_5H_5)_2][PF_6]$[33] yields polymer **5b**. Again $^{95}$Mo labelling proves the presence of $Mo^{V}$ species.[23] The EPR pattern of **5b** differs from that of **4b** as additional coupling to an $I = {}^{1}/_{2}$ nucleus is observed ($g_1 = 1.9812$, $g_2 = 1.9528$, $g_3 = 1.9415$; $A_1 = 23$ G, $A_2 = 27$ G, $A_3 = 23$ G; Figure 5). Thus it is suggested that $PMe_3$ ($^{31}$P: $I = {}^{1}/_{2}$) is still bound to molybdenum in the +V state. $PMe_3$ coordinated to $Mo^{V}$ should only be weakly bound so that ligand displacement reactions should be possible.

Indeed, reaction of **4b** with water displaces the phosphane and generates the $Mo^{V}$-containing polymer **6b**. The EPR spectrum of **6b** could only be reasonably simulated with two equivalent $I = {}^{1}/_{2}$ nuclei present ($g_1 = 1.9868$, $g_2 = 1.9624$, $g_3 = 1.9440$; $A_1 = 30$ G, $A_2 = 7$ G, $A_3 = 28$ G; Figure 5).[23] We tentatively assign these nuclei to two protons of a coordinated water molecule (or less likely to two hydroxo ligands). Substitution of $PMe_3$ is also possible with chloride ions ($[nBu_4N]Cl$) giving polymer **7b**. The EPR spectrum of **7b** can be simulated with coupling to one Cl nucleus ($^{35,37}$Cl: $I = {}^{3}/_{2}$; $g_1 = 1.9680$, $g_2 = 1.9522$, $g_3 = 1.9362$; $A_1 = 7$ G, $A_2 = 10$ G, $A_3 = 8$ G; Figure 5).[39] Thus different ligands (substrate, water, chloride) can occupy the free coordination site at $Mo^{V}$ as suggested by the different EPR spectra – similar to the situation assumed in molybdenum enzymes.[2] Remarkably, no evidence for leaching was observed during all these operations (reduction, oxidation, ligand exchange).

A full catalytic cycle (OAT and CEPT) involving $PMe_3$ as oxygen acceptor, $[Fe(AcC_5H_4)_2][BF_4]$ as one-electron oxidant,[33] water as oxygen donor and phosphazene base $P_1$-*t*Bu[36] as proton acceptor is finally attempted. $[Fe(AcC_5H_4)_2][BF_4]$ is employed instead of $[Fe(C_5H_5)_2][BF_4]$ because of its higher oxidation potential.[33] A suggested mechanism is depicted in Scheme 4. In fact, under these conditions **1b** catalysed the production of 25 equiv. $OPMe_3$ from $PMe_3$, water and oxidant within 48 h as shown by $^{31}P\{^{1}H\}$ NMR spectroscopy (Figure 6). With $^{18}$O-enriched water the label is incorporated into $OPMe_3$ as shown by mass spectrometric analysis. This proves that water is the source of the oxygen atom in the phosphane oxide product as required [Equation (1)].[23]

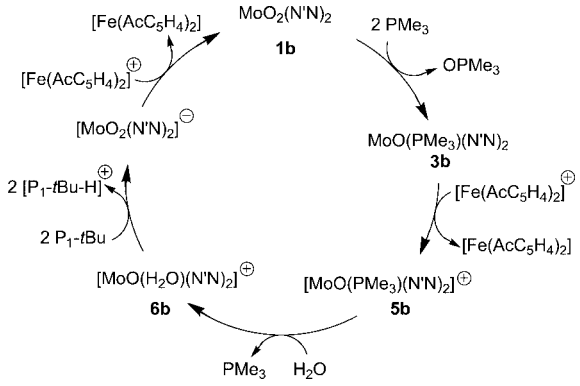


Scheme 4.

Although the present system definitely does not represent a structural model (Mo enzymes prefer sulfur coordination[2]) it is a truly functional model providing evidence for all biologically realistic mononuclear intermediates, namely $Mo^{VI}$, $Mo^{V}$ and $Mo^{IV}$ species. Dinucleation to EPR-silent $[Mo^{V}_2O_3]$ species prevailing in homogeneous solution and inhibiting CEPT chemistry is largely suppressed when the active species are doubly bound to a polymeric support. Double anchoring of active pre-catalysts to polymeric matrices with the aim to detect reactive interme-

 © 2007 Wiley-VCH Verlag GmbH & Co. KGaA, Weinheim 

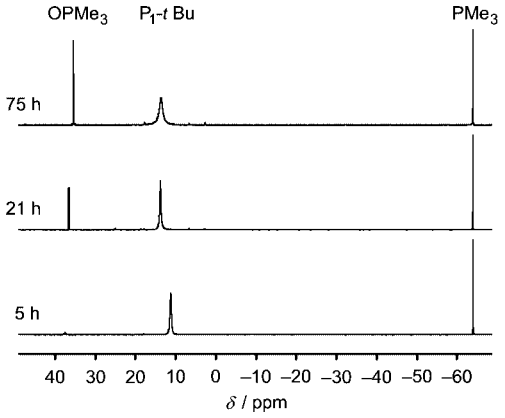


Figure 6. Selected $^{31}P\{^{1}H\}$ NMR spectra during catalysis.

diates of catalytic cycles will be further developed in our laboratories.

## Experimental Section

Unless noted otherwise, all manipulations were carried out under anaerobic conditions by means of standard Schlenk techniques. For the solid-phase reactions a flask with a nitrogen inlet and a fritted glass filter with large pores that allows addition and removal of reagents and solvents without exposure of the resin to the atmosphere was used. All solvents were dried by standard methods and distilled under anaerobic conditions prior to use.

NMR: Bruker Avance DPX 200 at 200.15 MHz and Varian Unity Plus 400 at 399.89 MHz ($^{1}H$); chemical shifts ($\delta$) in ppm with respect to residual solvent peaks as internal standard: $[D]_8THF$ ($^{1}H$: $\delta$ = 1.73, 3.58; $^{13}C$: $\delta$ = 25.5, 67.7) or with respect to external 85% $H_3PO_4$ ($^{31}P$: $\delta$ = 0 ppm). CP MAS NMR: Bruker Avance 400 NMR with a 4 mm MAS probe head. IR: BioRad Excalibur FTS 3000 spectrometer using CsI disks. EI-MS, FAB-MS: Finnigan MAT 8400 spectrometer. – LIFDI-MS: JEOL JMS-700 double-focusing magnetic sector mass spectrometer.[37] UV/Vis: Perkin–Elmer Lambda 19, 0.2-cm cells (Hellma, suprasil). – Melting points: Gallenkamp capillary melting point apparatus MFB 595 010. – Elemental analyses: Microanalytical Laboratory of the Organic Chemistry Department, University of Heidelberg. – EPR: Bruker ELEXSYS E500 spectrometer (X-band). Xsophe, version 1.0.2β was used for simulation of the spectra using the following parameters: isotope $^{98}Mo$ ($I$ = 0; 100%), $^{31}P$, $^{1}H$, $^{35,37}Cl$ natural isotope distribution; $g$- and $A$-strain Gaussian line shape model; matrix diagonalisation; 25 theta orientations; 5 field segments; orthorhombic symmetry. No attempts have been made for simulation of $^{95}Mo$ spectra or $^{95}Mo$ satellites.

**Synthesis of 1a:** The ligand (1.67 g, 6.5 mmol) dissolved in THF (10 mL) was added to a suspension of $MoCl_2O_2$(dme) (0.94 g, 3.24 mmol) in THF (40 mL) and triethylamine (0.9 mL, 6.5 mmol) was added. The red mixture was stirred at 25 °C for 1 h and heated under reflux for 2 h. After cooling to room temperature the mixture was filtered and the solvent was removed in vacuo. Toluene (40 mL) was added, covered with hexanes and the solution was cooled to 4 °C. The red precipitate was collected by filtration and dried. Yield 55% (2.31 g, 3.6 mmol); m.p. 168 °C; calcd. for $C_{28}H_{34}MoN_4O_4Si_2$ (642.7) C 52.33, H 5.33, N 8.72; found C 52.55, H 5.40, N 8.74. MS (EI): $m/z$ (%) = 644 (98) $[M]^+$, 387 (11) $[M - C_{14}H_{17}N_2OSi]^+$, 257 (100) $[C_{14}H_{17}N_2OSi]$. HR-MS (EI): calcd. for $^{98}Mo$ 644.1177, found 644.1217; calcd. for $^{96}Mo$ 642.1176, found 642.1129; calcd. for $^{95}Mo$ 641.1181, found 641.1144. IR (CsI): $\tilde{\nu}$ = 2961 $cm^{-1}$ (w), 1605 (m), 1585 (s), 1526 (m), 1499 (m), 1251 (s, C–O), 930 (m, Mo=O), 902 $cm^{-1}$ (m, Mo=O). UV (THF): $\lambda_{max}$ = 303 nm (43260 $M^{-1}cm^{-1}$), 440 nm (6130 $M^{-1}cm^{-1}$). $^{1}H$ NMR ($[D_8]$THF): $\delta$ = 7.94 (s, 1 H, $H^7$), 7.25 (s, 1 H, br. s, $H^{11}$), 6.97 (d, 2 H, $^{3}J$ = 8.5 Hz, $H^{2,6}$), 6.60 (d, 2 H, $^{3}J$ = 8.5 Hz, $H^{3,5}$), 6.39 (dvd, 1 H, $^{3}J$ = 3.4 Hz, 1.0 Hz, $H^9$), 6.11 (dvd, 1 H, $^{3}J$ = 3.4 Hz, 2.4 Hz, $H^{10}$), 0.23 (s, 9 H, $CH_3$); $^{13}C\{^{1}H\}$ NMR ($[D_8]$THF): $\delta$ = 158.1 (s, $C^7$), 153.8 (s, $C^4$), 148.6 (s, $C^1$), 142.9 (s, $C^{11}$), 139.4 (s, $C^8$), 123.1 (s, $C^{2,6}$), 120.3 (s, $C^{3,5}$), 119.6 (s, $C^9$), 114.8 (s, $C^{10}$), –0.35 (s, $CH_3$); assignments are based on 2D NMR spectra.

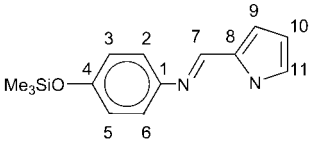


**Synthesis of 2a:** Complex **1a** (0.643 g, 1 mmol) was dissolved in THF (20 mL) and $PMe_3$ (1 M in THF, 0.6 mL, 0.6 mmol) was added. The reaction mixture was maintained at 50 °C for 12 h. The solvent was removed in vacuo and the residue was washed with diethyl ether giving a brown product. Yield 95% (0.60 g, 0.48 mmol). MS (FAB): $m/z$ (%) = 1268 (3) $[M]^+$, 1011 (2) $[M - C_{14}H_{17}N_2OSi]^+$, 628 (72) $[M - C_{28}H_{34}MoN_4O_4Si_2]^+$. HR-MS (FAB): calcd. for $^{98}Mo/^{98}Mo$ 1272.2396, found 1272.2418; calcd. for $^{96}Mo/^{98}Mo$ 1270.2389, found 1270.2380; calcd. for $^{96}Mo/^{96}Mo$ 1268.2414, found 1268.2393. IR (CsI): $\tilde{\nu}$ = 2960 $cm^{-1}$ (w), 1604 (s), 1581 (s), 1509 (s), 1493 (s), 1253 (s, C–O), 960 $cm^{-1}$ (m, Mo=O). UV (THF): $\lambda_{max}$ = 300 (81850 $M^{-1}cm^{-1}$), 468 (20990 $M^{-1}cm^{-1}$) 548 nm (11150 $M^{-1}cm^{-1}$). $^{1}H$ NMR ($[D_8]$THF): $\delta$ = 7.86 (s, 1 H, $H^7$), 7.73 (s, 1 H, $H^{7'}$), 7.63 (br. s, 1 H, $H^{11'}$), 7.12 (d, 2 H, $^{3}J$ = 8.5 Hz, $H^{2',6'}$), 6.98 (d, 2 H, $^{3}J$ = 8.5 Hz, $H^{2,6}$), 6.59 (d, 2 H, $^{3}J$ = 8.5 Hz, $H^{3,5}$), 6.54 (d, 2 H, $^{3}J$ = 8.5 Hz, $H^{3',5'}$), 6.43 (d, 1 H, $^{3}J$ = 3.1 Hz, $H^{9'}$), 6.37 (d, 1 H, $^{3}J$ = 3.1 Hz, $H^9$), 6.32 (dvd, 1 H, $H^{10'}$), 6.08 (br. s, 1 H, $H^{11}$), 5.80 (dvd, 1 H, $H^{10}$), 0.21 (s, 9 H, $CH_3$), 0.20 (s, 9 H, $CH_3$); assignments are based on 2D NMR spectra; low solubility prevented acquisition of $^{13}C$ NMR spectroscopic data.

**Synthesis of 3a:** Complex **1a** (0.643 g, 1 mmol) was dissolved in THF (20 mL) and $PMe_3$ (1 M in THF, 2 mL, 2 mmol) was added. The reaction mixture was maintained at 50 °C for 12 h. The solvent was removed in vacuo and the residue was washed with diethyl ether giving a green product. Yield 80% (0.562 g, 0.80 mmol); LIFDI-MS: $m/z$ (%) = 704 (100) $[M]^+$, 627 (30) $[M - PMe_3]^+$. IR (CsI): $\tilde{\nu}$ = 2961 $cm^{-1}$ (w), 2906 (w), 1604 (m), 1572 (s), 1506 (vs), 1266 (vs, C–O), 1253 (vs, C–O), 954 $cm^{-1}$ (m, Mo=O). UV (THF): $\lambda_{max}$ = 294 (26090 $M^{-1}cm^{-1}$), 345 (27970 $M^{-1}cm^{-1}$), 410 nm (sh, 9060 $M^{-1}cm^{-1}$), 478 (sh, 3170 $M^{-1}cm^{-1}$), 629 (1050 $M^{-1}cm^{-1}$). $^{1}H$ NMR ($[D_8]$THF): $\delta$ = 7.98 (d, 1 H, $^{4}J_{PH}$ = 2.8 Hz, $H^7$), 7.61 (br. s, 1 H, $H^{11}$), 7.50 (br. s, 1 H, $H^{7'}$), 7.22 (d, 2 H, $^{3}J$ = 8.8 Hz, $H^{3,5}$), 7.00 (d, 1 H, $^{3}J$ = 3.4 Hz, $H^9$), 6.73 (d, 2 H, $^{3}J$ = 8.8 Hz, $H^{2,6}$), 6.57 (s, 4 H, $H^{2',6',3',5'}$), 6.49 (dvd, 1 H, $H^{10}$), 6.30 (d, 1 H, $^{3}J$ = 3.4 Hz, $H^{9'}$), 5.80 (br. s, 1 H, $H^{11'}$), 5.78 (dvd, 1 H, $H^{10'}$), 1.29 (d, 9 H, $^{2}J_{PH}$ = 8.5 Hz, $PMe_3$), 0.29 (s, 9 H, $CH_3$), 0.24 (s, 9 H, $CH_3$); $^{13}C\{^{1}H\}$ NMR ($[D_8]$THF): $\delta$ = 158.0 (s, $C^7$), 150.6 (s, $C^{7'}$), 147.3 (s, $C^{11}$), 137.8 (s, $C^{11'}$), 158.0 (s, $C^7$), 125.0 (s, $C^{3,5}$), 124.1 (s, $C^{3',5'}$), 120.3 (s, $C^{2',6'}$), 119.9 (s, $C^{2,6}$), 118.9 (s, $C^9$), 115.2 (s, $C^{9'}$), 114.5 (s, $C^{10}$), 113.1 (s, $C^{10'}$), 16.2 (d, $^{1}J_{PC}$ = 23.3 Hz, $PCH_3$), 0.40 (s, $CH_3$), 0.39 (s, $CH_3$); assignments are based on 2D NMR spectra; low solubility prevented observation of $C^1$, $C^4$, $C^8$; $^{31}P\{^{1}H\}$ NMR ($[D_8]$THF): $\delta$ = 2.41 (s). $^{31}P$ NMR ($[D_8]$THF): $\delta$ = 2.41 (m, $^{2}J_{PH}$ = 8.5 Hz, $^{4}J_{PH}$ = 2.8 Hz).

 © 2007 Wiley-VCH Verlag GmbH & Co. KGaA, Weinheim 

**Determination of Activation Parameters for OAT between 1a and $PMe_3$:** In a typical experiment a UV cell containing a known amount of **1a** in THF was thermostatted at the desired temperature and 100 eq $PMe_3$ (1 M in THF) were added. The time dependence of the absorbance was measured at 548 nm.

**Synthesis of 1b:** The immobilised ligand (1.0 g, 0.8 mmol) was suspended in THF (30 mL) and $MoCl_2O_2$(dme) (116 mg, 0.4 mmol) was added as a solid. After 10 min triethylamine (0.28 mL, 2 mol) was added. The suspension was stirred at 25 °C for 1 h and heated under reflux for 2 h. After cooling to room temperature the mixture was filtered and washed successively with THF and diethyl ether giving a bright red resin. The isotopically enriched samples were prepared starting from $^{95}MoO_3$ (98% $^{95}$Mo) via $Na_2{}^{95}MoO_4$ and $^{95}MoCl_2O_2$(dme).

**Determination of Mo Uptake:** 1.0 g (0.80 mmol) of immobilised ligand was treated as above with $MoCl_2O_2$(dme) (103.8 mg, 0.36 mmol). All washing solutions were collected, evaporated to dryness and dissolved in ethanol (50 mL). 4 mL of this solution were treated with a $3.3\cdot10^{-3}$ M solution of 5,7-dibromo-8-hydroxyquinoline (1 mL), 0.5 M $H_2SO_4$ (1 mL) and ethanol (4 mL). The solution was diluted with $H_2O$ to 10 mL. Absorbance was measured at 400 nm and molybdenum content was determined using a calibration graph.[23] $A$(400 nm) = 1.432122 corresponds to 32.1 mg (0.11 mmol) $MoCl_2O_2$(dme), i.e. 0.25 mmol molybdenum was immobilised onto the polymer.[38]

**Cleavage with [$n$Bu$_4$N]F:** To resin **1b** (500 mg, 0.13 mmol Mo) suspended in THF (10 mL) was added [$n$Bu$_4$N]F·3H$_2$O (107 mg, 0.34 mol) dissolved in THF (10 mL). The solution immediately became coloured. The solution was collected by filtration and the solvents evaporated to dryness. The residue was washed with diethyl ether (to remove ammonium salts and free ligand) giving a red product. $^1$H NMR ([D$_8$]THF): $\delta$ = 11.0 (br. s, 1 H, OH), 8.05 (s, 1 H, H$^7$), 7.13 (s, 1 H, br. s, H$^{11}$), 7.10 (d, 2 H, $^3J$ = 8.5 Hz, H$^{2,6}$), 6.66 (d, 2 H, $^3J$ = 8.5 Hz, H$^{3,5}$), 6.45 (d, 1 H, $^3J$ = 2.5 Hz, H$^9$), 6.15 (pt, 1 H, H$^{10}$).

**Synthesis of 3b:** To resin **1b** (300 mg, 0.08 mmol Mo) suspended in THF (10 mL) was added $PMe_3$ (1 M in THF, 0.2 mL, 0.2 mmol) and the mixture was held at 40 °C for 4 h. The $OPMe_3$ formed was detected by $^{31}$P NMR spectroscopy. The resulting resin was washed with THF and diethyl ether giving a dark coloured resin. $^{31}$P{$^1$H} CP-MAS NMR: $\delta$ = 2.4.

**Reduction of 1b with Co($C_5H_5$)$_2$:** To resin **1b** (300 mg, 0.08 mmol Mo) suspended in THF (10 mL) was added Co($C_5H_5$)$_2$ (19 mg, 0.1 mmol) and the mixture was held at 40 °C for 5 h. The resulting resin was washed with THF and diethyl ether giving a dark coloured resin **4b**. EPR (solid, 295 K): $g_1$ = 1.9544, $g_2$ = 1.9388, $g_3$ = 1.9111.

**Oxidation of 3b with [Fe($C_5H_5$)$_2$][$BF_4$]:** To resin **3b** (300 mg, 0.08 mmol Mo) suspended in THF (10 mL) was added [Fe($C_5H_5$)$_2$][$PF_6$] (33 mg, 0.1 mmol) and the mixture was held at 40 °C for 5 h. The resulting resin was washed with THF and diethyl ether giving a dark coloured resin **5b**. EPR (solid, 295 K): $g_1$ = 1.9812, $g_2$ = 1.9528, $g_3$ = 1.9415; $A_1$($^{31}$P) = 23 G, $A_2$($^{31}$P) = 27 G, $A_3$($^{31}$P) = 23 G.

**Reaction of 5b with $H_2O$:** To resin **5b** (300 mg, 0.08 mmol Mo) suspended in THF (10 mL) was added $H_2O$ (0.1 mL, 5.6 mmol) and the mixture was held at 25 °C for 18 h. The resulting resin was washed with THF and diethyl ether giving a dark coloured resin **6b**. EPR (solid, 295 K): $g_1$ = 1.9868, $g_2$ = 1.9624, $g_3$ = 1.9440; $A_1(2\times{}^1H)$ = 30 G, $A_2(2\times{}^1H)$ = 7 G, $A_3(2\times{}^1H)$ = 28 G.

**Reaction of 5b with [$n$Bu$_4$N]Cl:** To resin **5b** (80 mg, 0.02 mmol Mo) suspended in THF (5 mL) was added [$n$Bu$_4$N]Cl (28 mg, 0.1 mmol) and the mixture was held at 25 °C for 18 h. The resulting resin was washed with THF and diethyl ether giving a dark coloured resin **7b**. EPR (solid, 295 K): $g_1$ = 1.9680, $g_2$ = 1.9522, $g_3$ = 1.9362; $A_1$($^{35,37}$Cl) = 7 G, $A_2$($^{35,37}$Cl) = 10 G, $A_3$($^{35,37}$Cl) = 8 G.[39]

**Catalytic Experiments with 1b:** To resin **1b** (50 mg, 0.013 mmol Mo) suspended in THF/$CH_3CN$ (5 mL, 1 mL) was added $PMe_3$ (1 M in THF, 1 mL, 1 mmol), $P_1$-$t$Bu (0.5 mL, 2 mmol), $H_2O$ (0.030 mL, 1.6 mmol) and [Fe($AcC_5H_4$)$_2$][$BF_4$] (714 mg, 2 mmol) and the mixture was held at 35 °C. $^{31}$P{$^1$H} NMR spectra of the solution indicated selective formation of $OPMe_3$. The $^1$H NMR spectrum of the solution after 126 h displays signals for $OPMe_3$ ($\delta$ = 1.35 ppm, d, $^2J_{PH}$ = 13.1 Hz), residual $PMe_3$ ($\delta$ = 0.90 ppm, d, $^2J_{PH}$ = 2.2 Hz), $P_1$-$t$Bu ($\delta$ = 2.63, 2.59, 1.17 ppm), $H_2O$ ($\delta$ = 2.80 ppm) and Fe($AcC_5H_4$)$_2$ ($\delta$ = 4.71, 4.46, 2.22 ppm).

The EI mass spectra of the dried residue show signals for Fe($AcC_5H_4$)$_2$ ($m/z$ = 270, 255, 227, 199, 163), $P_1$-$t$Bu ($m/z$ = 234, 219) and $OPMe_3$ ($m/z$ = 92, 77). Using $^{18}$O-labeled water (95% $^{18}$O) the EI mass spectra display peaks for $^{18}OPMe_3$ ($m/z$ = 94, 79). Additionally the mass spectra indicate incorporation of the $^{18}$O label into Fe($AcC_5H_4$)$_2$ ($m/z$ = 272 [single $^{18}$O; 36.10%], 274 [double $^{18}$O, 6.1%]), probably by hydrating the ketone groups and dehydrating the geminal diol. This reduces the fraction of $H_2{}^{18}O$ present during catalysis from 95% to 40 ± 12% as calculated from the amount of $^{16}$O released from Fe($AcC_5H_4$)$_2$, the amount of $^{16}$O present in the catalyst and in the water employed. The fraction of $^{18}OPMe_3$ was calculated as 33.1% from the mass spectroscopic analysis agreeing within error with the expected value.

**Supporting Information** (see also the footnote on the first page of this article): The Supporting Information contains the LIFDI-MS spectrum of **3a** and molecular ion peak, the UV/Vis absorption spectra of **1a** and 100 eq $PMe_3$ at 60 °C, the calibration graph for Mo uptake, the EPR spectrum of **5b** at 295 K and simulation, the EPR spectrum of **6b** at 295 K and simulation, the EPR spectrum of **7b** at 295 K and simulation, the conversion vs. time plot, the $^1$H NMR spectrum after 126 h and the partial EI mass spectra of the reaction products.

## Acknowledgments

This work was supported by the Deutsche Forschungsgemeinschaft (DFG, German Research Foundation) (Collaborative Research Center 623). K. H. gratefully acknowledges a Heisenberg fellowship from the German Science Foundation. We thank Prof. J. Blümel (Heidelberg) for measuring the CP MAS $^{31}$P{$^1$H} NMR spectrum and Dr. J. Gross (Heidelberg) for the LIFDI mass spectra.

[1] A complete issue of *Chemical Reviews* is devoted to the subject "*Biomimetic Inorganic Chemistry*": *Chem. Rev.* **2004**, *104*, 347–1200.
[2] R. Hille, *Chem. Rev.* **1996**, *96*, 2757–2816.
[3] J. H. Enemark, C. G. Young, *Adv. Inorg. Chem.* **1993**, *40*, 1–88.
[4] C. G. Young, in: *Biomimetic Oxidations Catalyzed by Transition Metals* (Ed.: B. Meunier), Imperial College Press, London, **2004**, pp. 415–459.
[5] J. H. Enemark, J. J. A. Cooney, J. J. Wang, R. H. Holm, *Chem. Rev.* **2004**, *104*, 1175–1200.
[6] J. M. Tunney, J. McMaster, D. C. Garner, in: *Comprehensive Coordination Chemistry II*, vol. 8 (Eds.: J. A. McCleverty, T. J. Meyer), Elsevier Pergamon, Amsterdam, **2004**, pp. 459–477.
[7] R. H. Holm, *Coord. Chem. Rev.* **1990**, *100*, 183–221.

 © 2007 Wiley-VCH Verlag GmbH & Co. KGaA, Weinheim 

[8] J. Jiang, R. H. Holm, *Inorg. Chem.* **2005**, *44*, 1068–1072.
[9] F. Jalilehvand, B. S. Lim, R. H. Holm, B. Hedman, K. O. Hodgson, *Inorg. Chem.* **2003**, *42*, 5531–5536.
[10] K.-M. Sung, R. H. Holm, *J. Am. Chem. Soc.* **2002**, *124*, 4312–4320.
[11] K.-M. Sung, R. H. Holm, *J. Am. Chem. Soc.* **2001**, *123*, 1931–1943.
[12] B. S. Lim, R. H. Holm, *J. Am. Chem. Soc.* **2001**, *123*, 1920–1930.
[13] C. J. Doonan, D. A. Slizys, C. G. Young, *J. Am. Chem. Soc.* **1999**, *121*, 6430–6436.
[14] J. A. Craig, R. H. Holm, *J. Am. Chem. Soc.* **1989**, *111*, 2111–2115.
[15] J. M. Berg, R. H. Holm, *J. Am. Chem. Soc.* **1985**, *107*, 925–932.
[16] S. F. Gheller, B. E. Schultz, M. J. Scott, R. H. Holm, *J. Am. Chem. Soc.* **1992**, *114*, 6934–6935.
[17] R. H. Holm, J. M. Berg, *Acc. Chem. Res.* **1986**, *19*, 363–370.
[18] V. N. Nemykin, P. Basu, *Inorg. Chem.* **2005**, *44*, 7494–7502.
[19] A. J. Millar, C. J. Doonan, P. D. Smith, V. N. Nemykin, P. Basu, C. G. Young, *Chem. Eur. J.* **2005**, *11*, 3255–3267.
[20] Z. Xiao, M. A. Bruck, J. H. Enemark, C. G. Young, A. G. Wedd, *Inorg. Chem.* **1996**, *35*, 7508–7515.
[21] Z. Xiao, M. A. Bruck, C. Doyle, J. H. Enemark, C. Grittini, R. W. Gable, A. G. Wedd, C. G. Young, *Inorg. Chem.* **1995**, *34*, 5950–5962.
[22] Probably due to the smaller cone angle of $PMe_3$ (118°) as compared to that of $PPh_3$ (145°): C. A. Tolman, *Chem. Rev.* **1977**, *77*, 313–348.
[23] See supporting information for details.
[24] K. Most, J. Hoßbach, D. Vidović, J. Magull, N. C. Mösch-Zanetti, *Adv. Synth. Catal.* **2005**, *347*, 463–472.
[25] M. S. Reynolds, J. M. Berg, R. H. Holm, *Inorg. Chem.* **1984**, *23*, 3057–3062.
[26] $K$ is strongly correlated to $\varepsilon_{548}$ of **2a** thus fits of similar quality are possible for different combinations of $\varepsilon_{548}$ and $K$[25] but reasonable combinations are $\varepsilon_{548} = 9000 \pm 3000$ $M^{-1}cm^{-1}$ and $K = 2 \pm 1\ 10^5$ $M^{-1}$. The rate constant $k$ is well defined by the time of maximum absorbance.
[27] S. Reinhardt, K. Heinze, *Z. Anorg. Allg. Chem.* **2006**, 1465–1470.
[28] K. Heinze, V. Jacob, C. Feige, *Eur. J. Inorg. Chem.* **2004**, 2053–2061.
[29] K. Heinze, J. B. Toro, *Eur. J. Inorg. Chem.* **2004**, 3498–3507.
[30] K. Heinze, J. B. Toro, *Angew. Chem.* **2003**, *115*, 4671–4674; *Angew. Chem. Int. Ed.* **2003**, *42*, 4533–4536.
[31] K. Heinze, *Chem. Eur. J.* **2001**, *7*, 2922–2932.
[32] K. Heinze, U. Winterhalter, T. Jannack, *Chem. Eur. J.* **2000**, *6*, 4203–4210.
[33] For redox potentials see: N. G. Connelly, W. E. Geiger, *Chem. Rev.* **1996**, *96*, 877–910.
[34] K. Heinze, A. Reinhardt, *Inorg. Chem.* **2006**, *45*, 2695–2703.
[35] Singly polymer attached $Mo^V$ complexes have been prepared directly from $Mo^V$ salts. As expected, anisotropic EPR spectra are obtained in the dry state: J. Topich, *Inorg. Chem.* **1982**, *21*, 2079–2082.
[36] R. Schwesinger, *Nachr. Chem. Tech. Lab.* **1990**, *38*, 1214–1226.
[37] J. H. Gross, N. Nieth, H. B. Linden, U. Blumbach, F. J. Richter, M. E. Tauchert, R. Tompers, P. Hofmann, *Anal. Bioanal. Chem.* **2006**, *386*, 52–58.
[38] M. J. Ahmed, M. E. Haque, *Anal. Sci.* **2002**, *18*, 433–439.
[39] We are aware that extraction of six parameters from a broad EPR signal is rather difficult and the values given should be taken with care. However, it was not possible to simulate the EPR signal without assumption of coupling to an $I = {}^3/_2$ nucleus ($^{35,37}Cl$).

Received: November 27, 2006
Published Online: January 15, 2007

 © 2007 Wiley-VCH Verlag GmbH & Co. KGaA, Weinheim 

DOI: 10.1002/ejic.200500681

# Structural Studies of Keggin-Type Polyoxotungstates by Extended X-ray Absorption Fine Structure Spectroscopy

**M. Salete S. Balula,[a] Isabel C. M. S. Santos,[a] José A. F. Gamelas,[a] Ana M. V. Cavaleiro,*[a] Norman Binsted,[b] and Walkiria Schlindwein[c]**

**Keywords:** Polyoxometalates / Keggin / EXAFS spectroscopy

Extended X-ray absorption fine structure spectroscopy (EXAFS) was used to characterize several Keggin-type polyoxotungstates (tetrabutylammonium salts) in the solid state and in acetonitrile solution. The polyoxometalates studied were $[PW_{12}O_{40}]^{3-}$ (the parent Keggin anion), $[PW_{11}O_{39}]^{7-}$ (a lacunary anion), $[PW_{11}M(H_2O)O_{39}]^{4-}$, M = Fe, Ru, and $[XW_{11}Mn^{III}(H_2O)O_{39}]^{n-}$, X = P, Si, B (transition-metal-substituted anions). The role of multiple-scattering contributions was evaluated for $[PW_{12}O_{40}]^{3-}$ for which an accurate structure determination was available. The results from the multiple-scattering analyses were compared with the single-scattering method. The average W-shell inter-atomic distances were determined in relation to a selected tungsten atom ($W_c$) by W $L_{III}$ edge transmission analysis. Several shells of up to 3.8–4.0 Å were identified. For the anion $[PW_{12}O_{40}]^{3-}$, the obtained inter-atomic distances in the solid sample and in acetonitrile were identical but for the lacunary anion the EXAFS spectrum of the solid was different from that in solution (the number of atoms coordinated to $W_c$ in $[PW_{11}O_{39}]^{7-}$ was the same in both cases, but the calculated distances for the shells were slightly different). Metal-substituted anions were studied by W $L_{III}$ edge transmission and by Fe, Mn, or Ru *K* edge fluorescence analysis. The average coordination sphere of tungsten was affected by the replacement of a W=O by a M–$OH_2$ group. The EXAFS results indicate that on average the $MnO_6$ octahedron is larger than $FeO_6$ or $RuO_6$ and also larger than the average of all $WO_6$ octahedra in $[PW_{11}M(H_2O)O_{39}]^{4-}$. This was attributed to the occurrence of the Jahn–Teller effect in the coordination sphere of $Mn^{III}$. A comparison of the W $L_{III}$ edge analysis EXAFS data for three $Mn^{III}$-substituted anions (X = P, Si, B) suggested that the average size of the $W_3O_{13}$ groups did not depend on X.
(© Wiley-VCH Verlag GmbH & Co. KGaA, 69451 Weinheim, Germany, 2007)

## Introduction

Keggin-type polyoxometalates[1–4] have been continuously studied in the last decade due to their interesting properties and possible applications in various fields, like catalysis,[5,6] materials science,[7] and medicine.[8] The Keggin-type polyoxotungstates include a large number of anions structurally related to the parent Keggin anions, α-$[XW_{12}O_{40}]^{n-}$, X = P, Si, B, etc., namely the lacunary, α-$[XW_{11}O_{39}]^{n-}$, and the metal-monosubstituted polyoxotungstates, α-$[XW_{11}M(H_2O)O_{39}]^{n-}$, M = transition or p-block metal, among others.[1,9]

The structure of the α isomer of $[PW_{12}O_{40}]^{3-}$ ($PW_{12}$) has been known since 1933[10] and is presented in Figure 1 (a). The twelve $WO_6$ octahedra, arranged in four corner shared $W_3O_{13}$ groups, surround a central tetrahedral $PO_4$ group, forming a tungsten–oxygen cluster with overall $T_d$ symmetry. Each $W_3O_{13}$ group comprises three edge-sharing $WO_6$ octahedra. This structure was found for a variety of other $[XMo_{12}O_{40}]^{n-}$ and $[XW_{12}O_{40}]^{n-}$ anions.[1] Only the α-isomers will be considered in this paper and the prefix will be omitted hereafter.

Only a few crystallographic studies are known for simple salts of the lacunary and monosubstituted Keggin-type polyoxotungstates.[1,9] The disorder observed for the $XO_4$ central group and also for the substituting $MO_6$ group (over twelve positions) usually precludes the determination of the structures with acceptable refinement parameters and no information can be given for the structural environment around M. Exceptions were found for a few compounds, namely $[Et_3NH]_5[XW_{11}Co^{II}O_{39}]\cdot 3H_2O$ (X = P, As),[11] $(ET)_8[PW_{11}Mn^{II}O_{39}]\cdot 2H_2O$,[12,13] and $(ET)_8[PW_{11}Ni^{II}(H_2O)O_{39}]\cdot 2H_2O$,[13] in which the metals M were disordered over two positions, $[Co(dpa)_2(H_2O)_2]_2[Hdpa][PW_{11}Co^{II}O_{39}]$,[14] $(Hpbpy)_5[PW_{11}Co^{II}(pbpy)O_{39}]\cdot 2H_2O$,[15] and $[Ni(DETA)_2]_3[SiW_{11}Ni^{II}O_{39}]\cdot 2.5H_2O$[16] [ET = bis(ethylenedithio)tetrathiafulvalene, dpa = di(2-pyridyl)amine, pbpy = 5-phenyl-2-(4-pyridinyl)pyridine, DETA = diethylenetriamine]. The formation of chains of linked heteropolyanions was observed for most of these compounds.

[a] Department of Chemistry, University of Aveiro, 3810-193 Aveiro, Portugal
Fax: +351-234-370084
E-mail: ana@dq.ua.pt
[b] CCLRC Daresbury Laboratory, Warrington, WA4 4AD, UK
[c] Leicester School of Pharmacy, De Montfort University, LE1 9BH, Leicester, UK

 © 2007 Wiley-VCH Verlag GmbH & Co. KGaA, Weinheim 

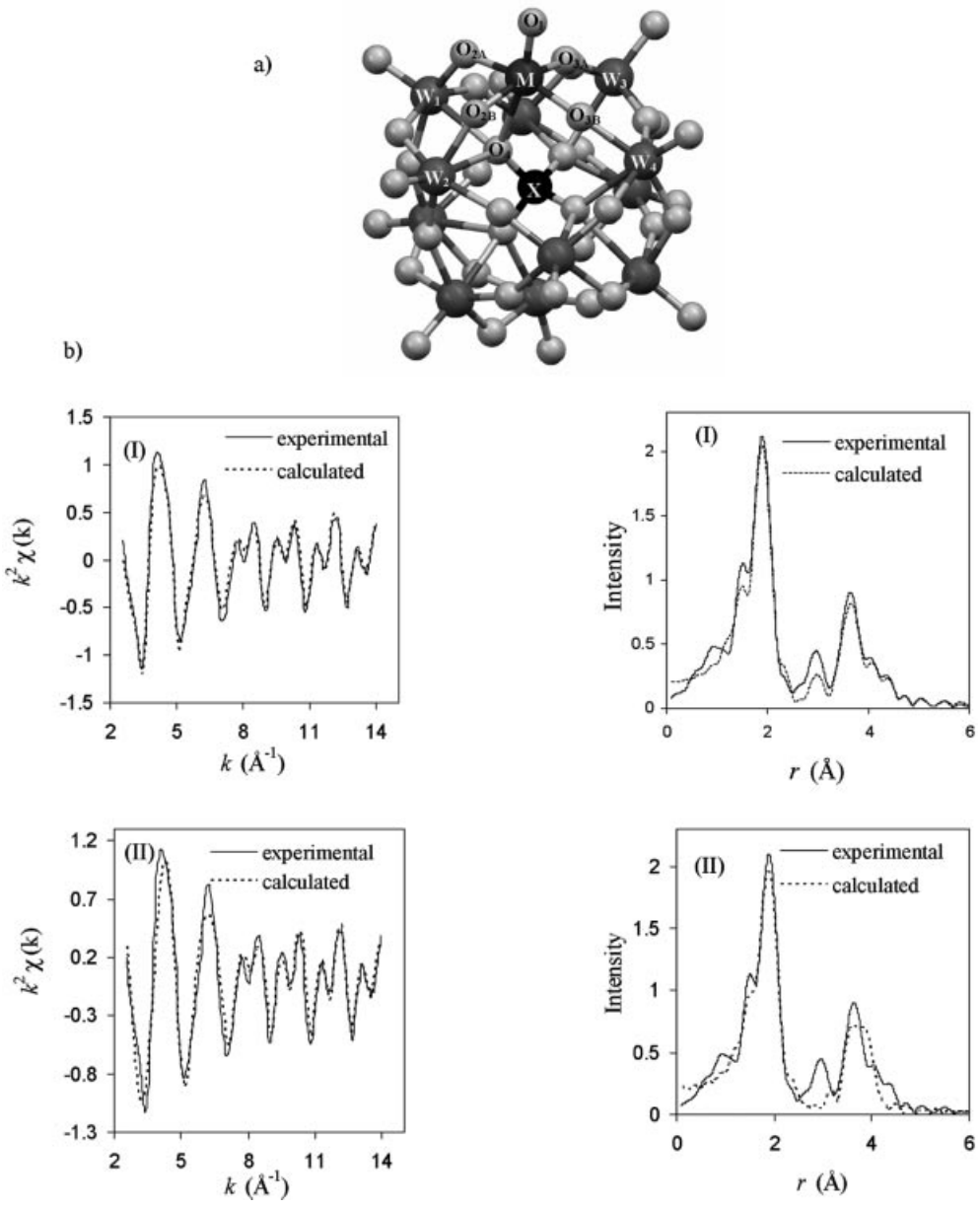


Figure 1. (a) The structure of the Keggin-type polyoxoanions (M = W, Fe, Mn, Ru). (b) EXAFS fit to $k^2\chi(k)$, and Fourier transform of $[PW_{12}O_{40}]^{3-}$: (I) multiple scattering calculation using crystallographic coordinates[25] with refined Debye–Waller factors, $E_f$ and AFAC; (II) using refined shell parameters.

An approach to the solution of the problem created by the disorder of X-ray crystal structures can be given by the use of extended X-ray absorption fine structure (EXAFS) spectroscopy. Information regarding the coordination sphere of W, the substituting metal M (first shell), and other longer-distance interactions (farther shells), up to about 4 Å, is, in many cases, possible. Besides, the EXAFS technique has the advantage that the measurements can be made in solids as well as in solution. Polyoxometalates have already been studied by EXAFS and related techniques. Particularly, studies on Keggin-type heteropolyanions, the majority performed in the solid state, have been published. Evans et al. used EXAFS to characterize the structure of $[PMo_{12}O_{40}]^{3-}$ and $[PW_{12}O_{40}]^{3-}$.[17] Previous studies in this area have been performed by Watanabe and coworkers.[18] Zhang and Pope investigated the nature of the ligand (L) coordinated to the Mn atom within the $[ZnW_{11}Mn^{IV}(L)O_{39}]^{6-}$ and $[ZnW_{11}Mn^{II}(L)O_{39}]^{8-}$ heteropolyanions.[19] EXAFS was used to determine the local structure of tetrahedral $Co^{III}$ in $[CoW_{12}O_{40}]^{5-}$.[20] Other published studies concerned supported $[PW_{12}O_{40}]^{3-}$ (mainly to confirm the presence of the anion) and vanadium-substituted tungstophosphates.[21] Studies of Keggin polyoxomolybdates that are related to their use in heterogeneous catalysis (e.g. formation of the anions on supports, thermal stability, environment of substituting metals) are also found.[22,23] Studies

 © 2007 Wiley-VCH Verlag GmbH & Co. KGaA, Weinheim 

referring to non-Keggin heteropolyanions were also reported.[24] In general, it can be summarized that EXAFS and related techniques were used to probe the coordination geometry or oxidation states of different metals encapsulated, coordinated, or supported by the polyoxometalates and the formation or stability of the heteropolyanions (mostly heteropolymolybdates) on heterogeneous catalysts. In spite of the importance of Keggin-type anions in homogeneous oxidative catalysis,[5] no studies in solution in conditions used in homogeneous catalysts have been reported so far.

In this work, EXAFS results are reported regarding the structural aspects of W and M in the tetrabutylammonium (TBA) salts of the Keggin-type anions $[PW_{11}O_{39}]^{7-}$ ($PW_{11}$), $[PW_{11}M(H_2O)O_{39}]^{4-}$ ($PW_{11}M$), M = Fe, Ru, and $[XW_{11}Mn^{III}(H_2O)O_{39}]^{n-}$ ($XW_{11}M$), X = P, Si, B. The role of multiple scattering contribution was evaluated for $[PW_{12}O_{40}]^{3-}$ ($PW_{12}$) for which an accurate structure was available that was determined by neutron diffraction.[25] The average inter-atomic distances in the series of anions formed when one tungsten atom of dodecatungstophosphate is removed to create a vacancy or is substituted isomorphically by a transition metal, $M^{III}$ = Fe, Mn, and Ru, are compared in the solid state and in acetonitrile solution. Structural data for the majority of these compounds are given for the first time. Some of these salts have been found to be good catalysts for the oxidation of cycloalkanes and other organic comounds with hydrogen peroxide in acetonitrile[26–28] and this prompted us to use this solvent in our studies with the aim of obtaining results that may be used in future studies on the stability of Keggin anions in homogeneous catalytic conditions.

## Results and Discussion

### The Keggin Heteropolyanion, $[PW_{12}O_{40}]^{3-}$ – Multiple versus Single Scattering Analysis

Multiple scattering (MS) generally makes a significant contribution to XAFS.[29] At low energy covalent clusters may give a massive contribution to the "white line", associated with resonant scattering of a photoelectron. The significance of these paths is such that unless the near edge region is entirely avoided the effect will be seen even in the Fourier transform of the first shell. At higher energies the paths will certainly make large contributions where the forward scattering path angles are 150° or more. Other paths may or may not give significant effects. Quite often, the main effect is a phase change over all or part of the spectrum, which may be especially conspicuous near a scattering minimum associated with an $l > 1$ final state. However, these are only general rules and for any specific structure it is necessary to compare results with and without multiple scattering before presuming to adopt the single-scattering approximation.

The role of MS was evaluated for $[PW_{12}O_{40}]^{3-}$, for which an accurate structure was available determined by neutron diffraction.[25] This allowed the EXAFS data to be fitted with no adjustable parameters other than a small number of Debye–Waller terms (for groups of shells of similar type and distance), the energy zero $E_f$, and the overall amplitude AFAC. The result, using a cluster of 6 Å radius, with 3796 MS paths to the fifth order, is shown in Figure 1 (b, I). The *R* factor obtained was 19%, which is considered good given that no structural variables were involved. Most of the error actually appears to be involved in residual low-frequency background contributions rather than any intrinsic inaccuracy in the technique. Multiple scattering makes an important contribution, but this is dominated by a small number of paths: principally the W–O–W second and third order paths with bond angles close to 120 or 150°. The number of structural parameters required to describe this cubic phase is small, but this is not the case for the lacunary or monosubstituted compounds, for which published structures show a low symmetry with several different metal sites, and oxygen polyhedra of $C_1$ or $C_2$ symmetry. For these, a simplified model is required using a reduced number of shells and without multiple scattering, which requires the addition of more parameters to describe the bond angles. To test the validity of this we repeated the analysis using only seven shells, and without multiple scattering. The fit, shown in Figure 1(b, II), gave an *R* factor of 26%, which is considered acceptable, and although the distances are different they differ by no more than 0.03 Å. The results are shown in Table 1. Given that this is only an approximate structural model, errors of this magnitude can be expected, and we believe that the results obtained are sufficient to draw the conclusions we do concerning the nature of the oxygen octahedra and metal–metal distances in the cluster. This approach was therefore used throughout this paper.

Table 1. Theoretical EXAFS best-fit parameters for $[PW_{12}O_{40}]^{3-}$ with and without multiple scattering. Data obtained from neutron diffraction.[25] $E_f$ is the edge position relative to the photoelectron wavevector (eV); $R_x$ refer to the distances (in angstroms) and *A* are the Debye–Waller Factor terms (in Å$^2$); the *R* factor gives a meaningful indication of the quality of the fit in *k* space (in%).

| | Multiple scattering (3796 paths) | Simplified single scattering |
|---|---|---|
| Shells | **33** | **7** |
| R1 (1 × O) | 1.715 | 1.737 (0.019) |
| R2 (2 × O) | 1.915 | 1.919 (0.007) |
| R3 (2 × O) | 1.921 | 1.919 |
| R4 (1 × O) | 2.445 | 2.459 (0.039) |
| R5 (2 × W) | 3.435 | 3.446 (0.019) |
| R6 (1 × O) | 3.574 | |
| R7 (1 × P) | 3.578 | 3.557 (0.061) |
| R8 (1 × O) | 3.645 | |
| R9 (2 × W) | 3.720 | 3.748 (0.016) |
| *A*[1] | 0.004 (0.002) | 0.004 |
| *A*[2–3] | 0.005 (0.001) | 0.004 (0.001) |
| *A*[4] | 0.014 (0.001) | 0.009 (0.011) |
| *A*[6,8] | 0.017 (0.013) | |
| *A*[7] | 0.004 (0.008) | 0.004 (0.008) |
| *A*[5,9] | 0.004 (0.001) | 0.005 (0.002) |
| $E_f$ (eV) | –11.6 | –12.3 |
| *R* (%) | 19.0 | 26.4 |

 © 2007 Wiley-VCH Verlag GmbH & Co. KGaA, Weinheim 

Data were collected for solid $TBA_3[PW_{12}O_{40}]$ as well as in acetonitrile solution. The fitted results of the EXAFS experimental data are presented in Table 2. The average W-shell inter-atomic distances are determined in relation to a selected tungsten atom referred here as $W_c$. Results for the solid sample are in good agreement with those of the previous EXAFS study by Evans et al.[17] and with the reported diffraction data.[25] They are presented here for comparison with results obtained for $[PW_{12}O_{40}]^{3-}$ in solution and for the other Keggin-type anions. From the results in Table 2 it can be seen that the structure of the $[PW_{12}O_{40}]^{3-}$ anion does not change when the compound is dissolved in acetonitrile. The differences in bond lengths and Debye–Waller factors for the shells fitted in both cases (solid and in acetonitrile solution) are within the standard deviation. These results parallel those observed previously for the related $[PMo_{12}O_{40}]^{3-}$ anion.[17]

Table 2. Experimental EXAFS best-fit parameters for the Keggin heteropolyanion in $TBA_3[PW_{12}O_{40}]$ (W $L_{III}$ edge transmission mode). Parameters as defined in Table 1.

| Shells | Solid state | $CH_3CN$ solution | Published data EXAFS[17] | Neutron diffraction[25] |
|---|---|---|---|---|
| R1 (1×O) | 1.697 (0.006) | 1.697 (0.008) | 1.710 | 1.715 |
| R2 (2×O) | 1.915 (0.002) | 1.917 (0.006) | 1.898 | 1.915 |
| R3 (2×O) | 1.915 (0.002) | 1.917 (0.006) | 1.898 | 1.921 |
| R4 (1×O) | 2.304 (0.017) | 2.318 (0.027) | | 2.445 |
| R5 (2×W) | 3.459 (0.008) | 3.461 (0.012) | 3.403 | 3.435 |
| R6 (1×O) | | | | 3.574 |
| R7 (1×P) | 3.545 (0.015) | 3.540 (0.020) | | 3.578 |
| R8 (1×O) | | | | 3.645 |
| R9 (2×W) | 3.733 (0.014) | 3.736 (0.013) | 3.680 | 3.720 |
| *A*[1] | 0.005 (0.001) | 0.004 (0.002) | 0.009 | |
| *A*[2–3] | 0.009 (0.001) | 0.010 (0.001) | 0.012 | |
| *A*[4] | 0.016 (0.006) | 0.017 (0.001) | | |
| *A*[7] | 0.005 (0.001) | 0.005 (0.002) | | |
| *A*[5,9] | 0.010 (0.002) | 0.010 (0.003) | 0.011 | |
| $E_f$ (eV) | –11.4 | –14.0 | | |
| *R* (%) | 20.8 | 30.5 | | |

In agreement with the known Keggin structure, six oxygen atoms were found around $W_c$ (only five had been detected by Evans et al.[17]). For the solid sample, the shortest observed bond length between tungsten and oxygen, attributed to the terminal oxygen atoms ($O_1$, Figure 1, a, M = $W_c$), was 1.697 Å. Four bridging oxygen atoms ($O_{2a}$, $O_{2b}$, $O_{3a}$, $O_{3b}$) were found at a distance of 1.915 Å from $W_c$ and the oxygen of the central $PO_4$ tetrahedron ($O_4$) at a distance of 2.304 Å. Each oxygen atom from the central $PO_4$ tetrahedron belongs to one of the four $W_3O_{13}$ groups. Two tungsten atoms at a distance of 3.459 Å probably belong to the same $W_3O_{13}$ group as $W_c$ ($W_1$ and $W_2$, Figure 1, a), whereas two tungsten atoms at a distance of 3.733 Å must be located in different $W_3O_{13}$ groups in relation to $W_c$ ($W_3$ and $W_4$, Figure 1, a). The distance between $W_c$ and the phosphorus atom of the central $PO_4$ tetrahedron is 3.545 Å. The inclusion of one phosphorus atom improved the *R* value; however, the improvement was even more significant when tungsten atoms were introduced at 3.733 Å. The results obtained for the dodecatungstophosphate in the solid state and in acetonitrile solution (Table 2) are very similar.

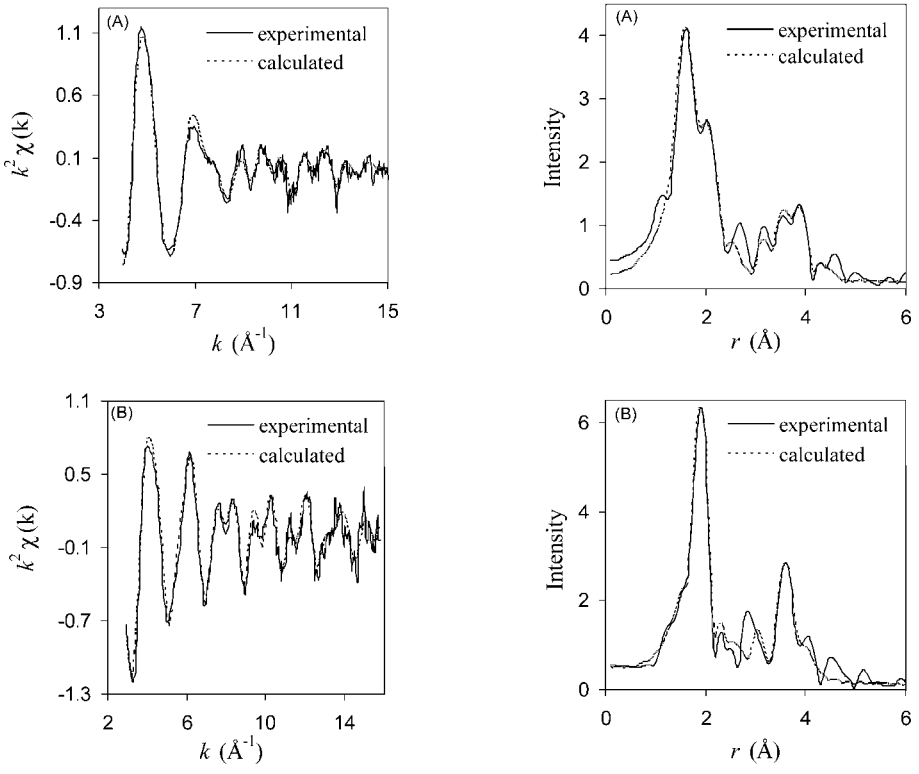


Figure 2. W $L_{III}$ edge EXAFS spectrum and Fourier transform for the $[PW_{11}O_{39}]^{7-}$ anion in $TBA_4H_3[PW_{11}O_{39}]$: (a) solid state; (b) $CH_3CN$ solution.

 © 2007 Wiley-VCH Verlag GmbH & Co. KGaA, Weinheim 

### The Lacunary Polyoxoanion, $[PW_{11}O_{39}]^{7-}$

The lacunary anion $[PW_{11}O_{39}]^{7-}$ has a Keggin structure from which one W=O group was removed. In this case not all W atoms are equivalent because four of the eleven W atoms have two terminal oxygen atoms. Figure 2 shows the EXAFS spectrum and the Fourier transform for the $PW_{11}$ anion. In this case the spectrum of the solid was different from that obtained in solution. The fit of the EXAFS results is presented in Table 3. The average number of atoms coordinated to $W_c$ (average of all tungsten atoms presented in the structure) was the same in both cases, but the calculated distances for the shells are slightly different. The structure of the lacunary anion is globally less rigid than that of the parent $PW_{12}$. This may be the reason that different distance values were observed for the anion in the solid state and in $CH_3CN$ solution, reflecting different environments in each case, contrary to what was observed for $PW_{12}$.

Table 3. EXAFS best-fit parameters for the lacunary heteropolyanion in $TBA_4H_3[PW_{11}O_{39}]$ (W $L_{III}$ edge transmission mode). Parameters as defined in Table 1.

| Shells | Solid state | $CH_3CN$ solution |
|---|---|---|
| R1 (1 × O) | 1.641 (0.004) | 1.782 (0.014) |
| R2 (2 × O) | 1.761 (0.005) | 1.937 (0.003) |
| R3 (2 × O) | 2.205 (0.007) | 2.121 (0.017) |
| R4 (1 × O) | 2.412 (0.022) | 2.436 (0.012) |
| R5 (2 × W) | 3.394 (0.009) | 3.457 (0.005) |
| R7 (1 × P) | 3.346 (0.028) | 3.220 (0.012) |
| R9 (2 × W) | 3.919 (0.029) | 3.765 (0.016) |
| *A*[1] | 0.008 (0.001) | 0.019 (0.004) |
| *A*[2–3] | 0.015 (0.002) | 0.010 (0.002) |
| *A*[4] | 0.015 (0.005) | 0.004 (0.002) |
| *A*[7] | 0.023 (0.008) | 0.005 (0.002) |
| *A*[5,9] | 0.023 (0.007) | 0.012 (0.004) |
| $E_f$ (eV) | 10.2 | 13.5 |
| *R* (%) | 22.5 | 21.8 |

From the EXAFS fit of the lacunary anion four shells of oxygen atoms were deduced in the first coordination sphere of $W_c$. In the solid state the shortest oxygen–tungsten bond length was 1.641 Å and corresponds to the average of the W–O distance to the oxygen atoms protruding from the anion. The value of 1.761 Å is possibly the average of terminal (oxygen atoms surrounding the lacuna) and bridging W–O bond lengths. This is a consequence of the fact that each of the W atoms surrounding the lacuna is bound to two monocoordinated oxygen atoms. Other bridging oxygen atoms are located at a distance of 2.205 Å. Finally, the W–O distance to the oxygen of the central $PO_4$ group was found to be 2.412 Å. These values are comparable to those reported for $[PW_{11}O_{39}]^{7-}$[30] and $[SiW_{11}O_{39}]^{8-}$,[31] obtained by X-ray crystallography. In these studies the position of the vacancy could not be located with certainty.[30,31]

### W $L_{III}$ Edge Analysis of Monosubstituted Polyoxoanions, $[PW_{11}M(H_2O)O_{39}]^{4-}$, M = Fe and Mn

It is commonly accepted that the Keggin structure is maintained when one W=O group from the anion $[PW_{12}O_{40}]^{3-}$ is substituted by $M^{III}–OH_2$, M = transition metal, to form $[PW_{11}M(H_2O)O_{39}]^{4-}$ and the results here presented for M = Fe, Mn are in agreement with this fact. Figure 3 shows the W $L_{III}$ edge EXAFS spectrum and the Fourier transform for the solid samples of TBA salts of $PW_{11}Mn$ and $PW_{11}Fe$. The results from the curve fitting are presented in Table 4. For these anions, the EXAFS data obtained from the W $L_{III}$ edge analysis are the average of the eleven tungsten atoms in an octahedral coordination.

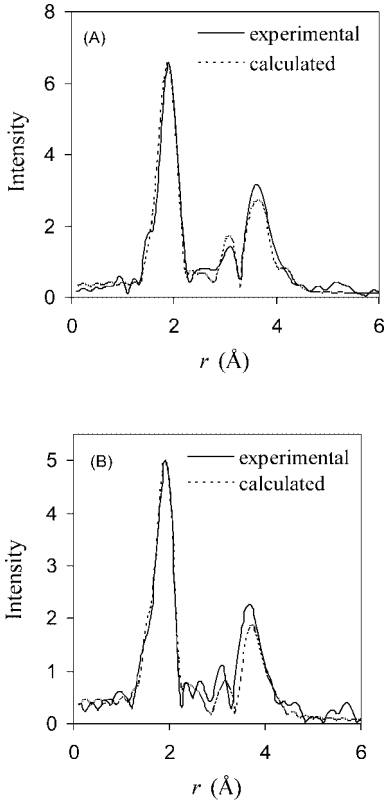


Figure 3. W $L_{III}$ edge Fourier transform for $[PW_{11}Fe(H_2O)O_{39}]^{4-}$ (a) and $[PW_{11}Mn(H_2O)O_{39}]^{4-}$ (b) in solid state TBA salts.

Table 4. EXAFS best-fit parameters for solid $TBA_4[PW_{11}Fe^{III}(H_2O)O_{39}]\cdot H_2O$ and $TBA_4[PW_{11}Mn^{III}(H_2O)O_{39}]$ (W $L_{III}$ edge transmission mode). Parameters as defined in Table 1.

| Shells | $PW_{11}Fe$ solid state | Shells | $PW_{11}Mn$ solid state |
|---|---|---|---|
| R1 (1 × O) | 1.628 (0.014) | R1 (2 × O) | 1.705 (0.016) |
| R2 (3 × O) | 1.944 (0.003) | R2 (2 × O) | 1.931 (0.007) |
| R3 (2 × O) | 2.131 (0.015) | R3 (2 × O) | 2.225 (0.028) |
| $R_{Fe}$ (1 × Fe) | 2.994 (0.016) | $R_{Mn}$ (1 × Mn) | 2.564 (0.040) |
| R5 (1 × W) | 3.234 (0.013) | R5 (1 × W) | 3.034 (0.031) |
| R7 (1 × P) | 3.583 (0.032) | R7 (1 × P) | 4.168 (0.061) |
| R9 (2 × W) | 3.767 (0.011) | R9 (2 × W) | 3.730 (0.035) |
| *A*[1] | 0.029 (0.004) | *A*[1] | 0.020 (0.005) |
| *A*[2–3] | 0.010 (0.002) | *A*[2–3] | 0.010 (0.002) |
| *A*[Fe] | 0.016 (0.004) | *A*[Mn] | 0.034 (0.005) |
| *A*[7] | 0.005 (0.004) | *A*[7] | 0.010 (0.006) |
| *A*[5,9] | 0.011 (0.002) | *A*[5,9] | 0.016 (0.004) |
| $E_f$ (eV) | 10.9 | $E_f$ (eV) | 12.1 |
| *R* (%) | 26.5 | *R* (%) | 29.9 |

 © 2007 Wiley-VCH Verlag GmbH & Co. KGaA, Weinheim 

As found for $PW_{12}$ and $PW_{11}$, the $W_c$ atom of $PW_{11}Fe$ has six oxygen atoms in the first coordination sphere with bond lengths of 1.628 Å, 1.944 Å, and 2.131 Å (Table 4). These average distances do not differ much from those of the $PW_{12}$ unit. The Fe atom was located at a distance of 2.994 Å from $W_c$ and the nearest W atom at a distance of 3.234 Å. These distances are close enough to suggest that the W is localized within a $W_cWFeO_{13}$ group. The shortest W–$W_c$ distance obtained for $PW_{12}$ was 3.459 Å (Table 2). These values seem to indicate that when Fe replaces one W atom from a $W_cW_2O_{13}$ unit (in $PW_{12}$) it stays closer to $W_c$ than the replaced W was in the $PW_{12}$ structure. Also, the distance from $W_c$ to the four coordinated oxygen atoms of the $W_c$–O–P bridge is shorter in the iron anion than in $PW_{12}$. Therefore, even if the structure of the polyoxoanion is not globally altered the coordination sphere of tungsten is affected by the change of the W atom (with its terminal oxygen) for Fe, possibly with a terminal water molecule as a ligand.

For the $[PW_{11}Mn(H_2O)O_{39}]^{4-}$ polyoxoanion, the $W_c$–O bond lengths within the $W_cO_6$ octahedron (Table 4) were similar to the analogous bond lengths for $PW_{12}$. The terminal oxygen is at a distance of 1.705 Å from $W_c$, and the bridging oxygen atoms are at distances in the range of 1.931–2.225 Å. One tungsten atom from a $W_cWMnO_{13}$ group ($W_2$, 3.034 Å) and two other from a different $W_3O_{13}$ group ($W_3$ and $W_4$, 3.730 Å) are also at a close distance to the $W_c$ atom.

In the case of the $PW_{12}$ anion the four equatorial $W_c$–O(–W) bond lengths have the same value. This is not the case for $PW_{11}Fe$ and $PW_{11}Mn$, for which one of these distances was found to be longer than the other three, reflecting the loss of symmetry associated with the replacement of tungsten by a different transition metal.

The average of the W–O bond lengths around $W_c$ in $PW_{12}$, $PW_{11}Fe$, and $PW_{11}Mn$ are 1.94, 1.95, and 1.95 Å, respectively. However, the Mn seems to be closer (2.564 Å) to the $W_c$ atom than the Fe (2.994 Å) in the structure of $PW_{11}Fe$. These differences may be related to a higher distortion of the $W_cWMO_{13}$ group in the case of Mn, possibly as a consequence of the Jahn–Teller effect of the $Mn^{III}$ ion.

### Fe *K* Edge Analysis of $[PW_{11}Fe(H_2O)O_{39}]^{4-}$

Polyoxoanions like $PW_{11}Fe$ and $PW_{11}Mn$, with two different transition metals in their structure, have the advantage of providing two different elements for EXAFS studies. Curve-fitting results for the Fe *K* edge fluorescence EXAFS data for $PW_{11}Fe$ in the solid state and in $CH_3CN$ solution are presented in Figure 4 and Table 5. It was assumed for all M substituted anions that no replacement of the coordinated water of the M–$OH_2$ group by acetonitrile occurred. The results indicate that the structures around Fe are very similar in both media. On comparing the distances of the six oxygen atoms to Fe in the $FeO_6$ octahedron (values for the solid state and in solution are in the range 1.943–2.512 and 1.976–2.522 Å, respectively, Table 5) with those of the six oxygen–tungsten bonds in the $WO_6$ octahedra of the parent Keggin anion (1.697–2.318 Å, first three shells in

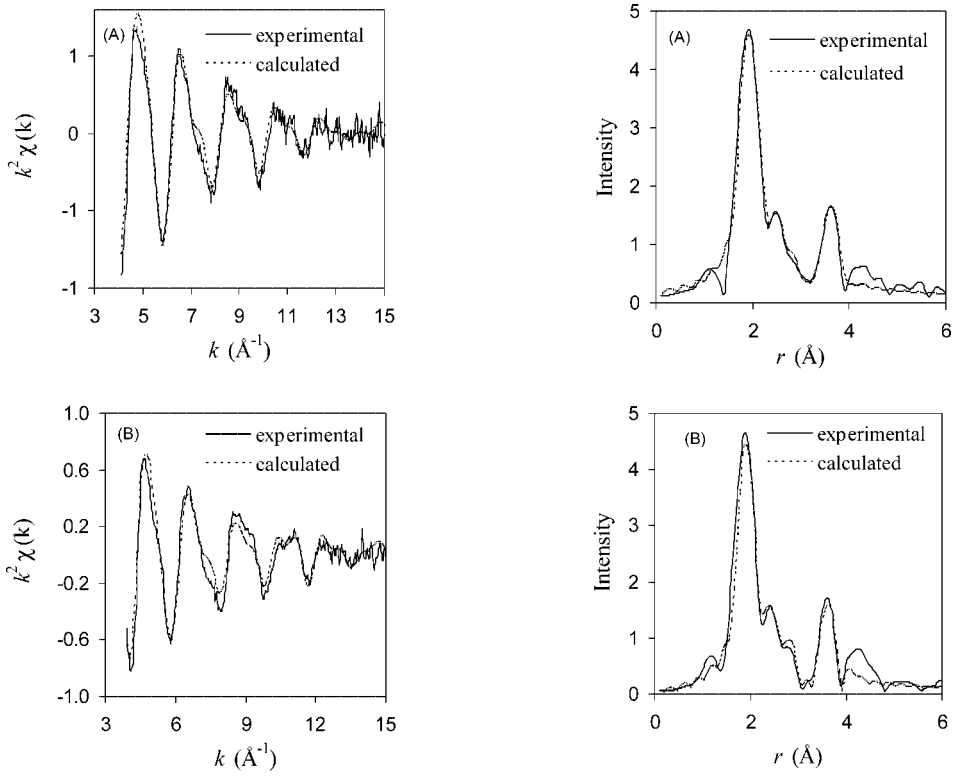


Figure 4. Fe *K* edge EXAFS spectrum and Fourier transform for $[PW_{11}Fe(H_2O)O_{39}]^{4-}$ in solid state TBA salt (a) and in $CH_3CN$ solution (b).

 © 2007 Wiley-VCH Verlag GmbH & Co. KGaA, Weinheim 

Table 2), it can be noticed that the $FeO_6$ octahedron is larger than the $WO_6$ that it has substituted. It is also larger than the nearest $WO_6$ octahedra (Table 4).

Table 5. EXAFS best-fit parameters for $TBA_4[PW_{11}Fe^{III}(H_2O)O_{39}]\cdot H_2O$ (Fe *K* edge fluorescence mode). Parameters as defined in Table 1.

| Shells | Solid state | $CH_3CN$ solution |
|---|---|---|
| R2 (2 × O) | 1.943 (0.040) | 1.976 (0.010) |
| R3 (2 × O) | 2.361 (0.031) | 2.390 (0.020) |
| R4 (2 × O) | 2.512 (0.025) | 2.522 (0.020) |
| R5 (2 × W) | 3.181 (0.045) | 3.247 (0.022) |
| R7 (1 × P) | 3.105 (0.041) | 3.156 (0.012) |
| R9 (2 × W) | 3.523 (0.097) | 3.547 (0.029) |
| *A*[2] | 0.010 (0.002) | 0.020 (0.005) |
| *A*[3] | 0.022 (0.008) | 0.026 (0.004) |
| *A*[4] | 0.010 (0.005) | 0.004 (0.002) |
| *A*[7] | 0.020 (0.010) | 0.016 (0.005) |
| *A*[5,9] | 0.018 (0.008) | 0.015 (0.004) |
| $E_f$ (eV) | 10.2 | 11.1 |
| *R* (%) | 30.0 | 30.1 |

Polyoxotungstophosphates with $Fe^{III}$ have been structurally characterized by Li et al.[32] and by Hill and collaborators.[33] The former determined the structure of the dimeric $[Fe_4(OH)_4(PW_{10}O_{37})_2]^{10-}$, whereas the latter studied the sandwich anions $[Fe_4(H_2O)_2(PW_9O_{34})_2]^{6-}$ and $[Fe_4(H_2O)_2(P_2W_{15}O_{56})_2]^{12-}$. Structures of multi-iron polyoxotungstates (tungstosilicates, tungstogermanates and others) and of the anion $[Fe_4(H_2O)_2(FeW_9O_{34})_2]^{10-}$ were also reported.[34,35] The Fe–$O(H_2)$ bond lengths in the sandwich-type iron polyoxotungstophosphates were found to be around 2.00 Å.[33] Other values reported, for polyoxometalates or iron complexes, fall in the range 2.02–2.19 Å.[34,36] The average value reported for hexaaquairon(III) countercations in Keggin-type molybdophosphate compounds, obtained from EXAFS data, was 1.98 Å.[23] Thus, the Fe–O bond length corresponding to the oxygen from the terminal water molecule for the $PW_{11}Fe$ anion is possibly 1.943 Å in the solid sample and 1.976 Å in the $CH_3CN$ solution. With this assumption the average value of the equatorial Fe–O distances is 2.29 Å. The iron–oxygen distances found for the sandwich and the dimeric anions with P were in the range 1.88–1.99 Å for Fe–O–W and 2.18–2.40 Å in the Fe–O–P bridges.[32,33] In all cases the iron was octahedrally coordinated, but the arrangements of atoms around the $FeO_6$ octahedra in those anions are different from that of the monosubstituted $PW_{11}Fe$. The results obtained by EXAFS reported in this paper seem to indicate a larger and more distorted $FeO_6$ for $PW_{11}Fe$ than for the dimeric or the sandwich anions, which is obviously related to the difference in the structural arrangements, in which the possibility of an increase in Fe–O distances is higher for the less rigid $PW_{11}Fe$ anion. It is interesting to note that the Fe in $PW_{11}Fe$ is at a closer distance from the phosphorus heteroatom (3.105 Å in the solid, 3.156 Å in solution) than the W in the Keggin, lacunary, and iron-monosubstituted structures (3.545, 3.346, and 3.583, respectively, for solid samples). The enlargement of the $FeO_6$ octahedron is possibly accompanied by a rearrangement of the whole $FeW_2O_{13}$ group. Nevertheless, results from infrared spectroscopy suggest that there is not a significant distortion of the central $PO_4$ group.[37] The infrared spectrum, between 1000–1100 $cm^{-1}$, of the TBA salt of the $PW_{11}Fe$ anion has only one band,[38] assigned to the $\nu_{as}$(P–O) at 1069 $cm^{-1}$. The corresponding value for the $PW_{12}$ anion is 1080 $cm^{-1}$. The splitting of the $\nu_{as}$(P–O) is usually less pronounced for TBA than for K salts,[38] with the possible exception of the TBA salt of the $PW_{11}$ anion, for which the infrared spectrum shows two bands in this region at 1107 $cm^{-1}$ and 1054 $cm^{-1}$.[39]

### Mn *K* Edge Analysis of $[PW_{11}Mn(H_2O)O_{39}]^{4-}$

The Mn *K* edge analysis of $PW_{11}Mn$ indicated that there are six oxygen atoms in the first coordination sphere of Mn (Figure 5) with distances in the range of 1.981–2.626 Å (Table 6). The two W atoms in the same $W_2MnO_{13}$ group are at an average distance of 3.243 Å from Mn. The longest bond length was attributed to the Mn–O in the Mn–O–P group. This long Mn–O(–P) distance was considered to be evidence of Jahn–Teller tetragonal distortion of the octahedron around the high spin $Mn^{III}$ ion. One oxygen atom at 2.140 Å was attributed to the Mn–$O(H_2)$ group from a comparison with values reported by Zhang et al.[40] The average Mn–O bond lengths found in the EXAFS spectroscopic study described here are larger than the usual $Mn^{III}$–O bond lengths reported in the literature either in polyoxometalates[40,41] or otherwise.[42] As a consequence of the

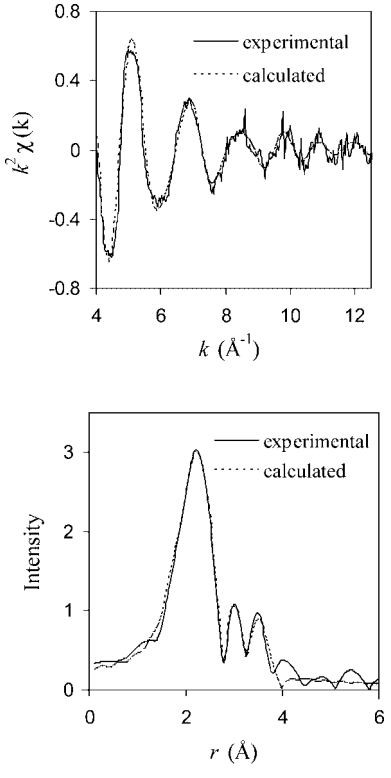


Figure 5. Mn *K* edge EXAFS spectrum and Fourier transform for $[PW_{11}Mn(H_2O)O_{39}]^{4-}$ in solid state TBA salt.

 © 2007 Wiley-VCH Verlag GmbH & Co. KGaA, Weinheim 

Jahn–Teller effect, the $Mn^{III}$ ion is possibly slightly out of the polyoxometalate vacancy of the $PW_{11}$ ligand, and this may be the reason for the long Mn–O bond length values found in this study. It may be noted, comparing the data in Table 4, Table 5, and Table 6, that the average of the M–O bond lengths in the $MO_6$ octahedra for M = Mn, Fe, (2.30 Å and 2.27 Å, respectively) are larger than the average W–O distances in $PW_{11}M$.

Table 6. EXAFS best-fit parameters for solid $TBA_4[PW_{11}Mn^{III}(H_2O)O_{39}]$ (Mn *K* edge fluorescence mode). Parameters as defined in Table 1.

| Shells | Solid state |
|---|---|
| R1 (1 × O) | 1.981 (0.007) |
| R2 (2 × O) | 2.140 (0.006) |
| R3 (2 × O) | 2.460 (0.008) |
| R4 (1 × O) | 2.626 (0.006) |
| R5 (2 × W) | 3.243 (0.016) |
| R7 (1 × P) | 3.128 (0.021) |
| *A*[1] | 0.020 (0.002) |
| *A*[2] | 0.012 (0.002) |
| *A*[3] | 0.007 (0.002) |
| *A*[4] | 0.010 (0.002) |
| *A*[5] | 0.028 (0.004) |
| *A*[7] | 0.024 (0.005) |
| $E_f$ (eV) | 8.2 |
| *R* (%) | 23.4 |

### $[PW_{11}Ru(H_2O)O_{39}]^{4-}$, Ru *K* Edge Analysis

Table 7 shows the distances from the shells to the Ru atom. The distance from the Ru atom to the first six oxygen atoms average 2.23 Å in the solid state (2.056–2.413 Å) and 2.35 Å in acetonitrile solution (2.106–2.603 Å). The two W atoms from the same $W_2RuO_{13}$ group ($W_1$ and $W_2$, Figure 1, a) are localized at 3.361 Å in the solid state and 3.410 Å in $CH_3CN$ solution (Table 7). Thus the structure of $PW_{11}Ru$ seems to be approximately the same in the solid compound and in solution. The phosphorus atom was found at a longer distance from ruthenium for the $PW_{11}Ru$ in acetonitrile than in the solid state (3.781 Å and 3.571 Å, respectively), and this is the only important difference when we compare these two environments (Table 7 and Figure 6).

Table 7. EXAFS best-fit parameters for $TBA_4[PW_{11}Ru^{III}(H_2O)O_{39}]\cdot H_2O$ (Ru *K* edge fluorescence mode). Parameters as defined in Table 1.

| Shells | Solid state | Shells | $CH_3CN$ solution |
|---|---|---|---|
| R2 (2 × O) | 2.056 (0.004) | R2 (2 × O) | 2.106 (0.004) |
| R3 (2 × O) | 2.234 (0.014) | R3 (2 × O) | 2.343 (0.010) |
| R4 (2 × O) | 2.413 (0.017) | R4 (2 × O) | 2.603 (0.010) |
| R5 (2 × W) | 3.361 (0.021) | R5 (2 × W) | 3.410(0.016) |
| R7 (1 × P) | 3.571 (0.049) | R7 (1 × P) | 3.781 (0.019) |
| R9 (2 × W) | 3.584 (0.046) | R9 (2 × W) | 3.564 (0.017) |
| *A*[2–3] | 0.010 (0.003) | *A*[2–3] | 0.020 (0.005) |
| *A*[4] | 0.003 (0.008) | *A*[4] | 0.014 (0.003) |
| *A*[7] | 0.009 (0.006) | *A*[7] | 0.023 (0.004) |
| *A*[5,9] | 0.020 (0.010) | *A*[5,9] | 0.008 (0.003) |
| $E_f$ (eV) | –4.8 | $E_f$ (eV) | –6.6 |
| *R* (%) | 26.5 | *R* (%) | 20.7 |

By comparing the EXAFS data of $PW_{11}Ru$ with $PW_{11}Fe$ it may be noted that the results suggested that the size of

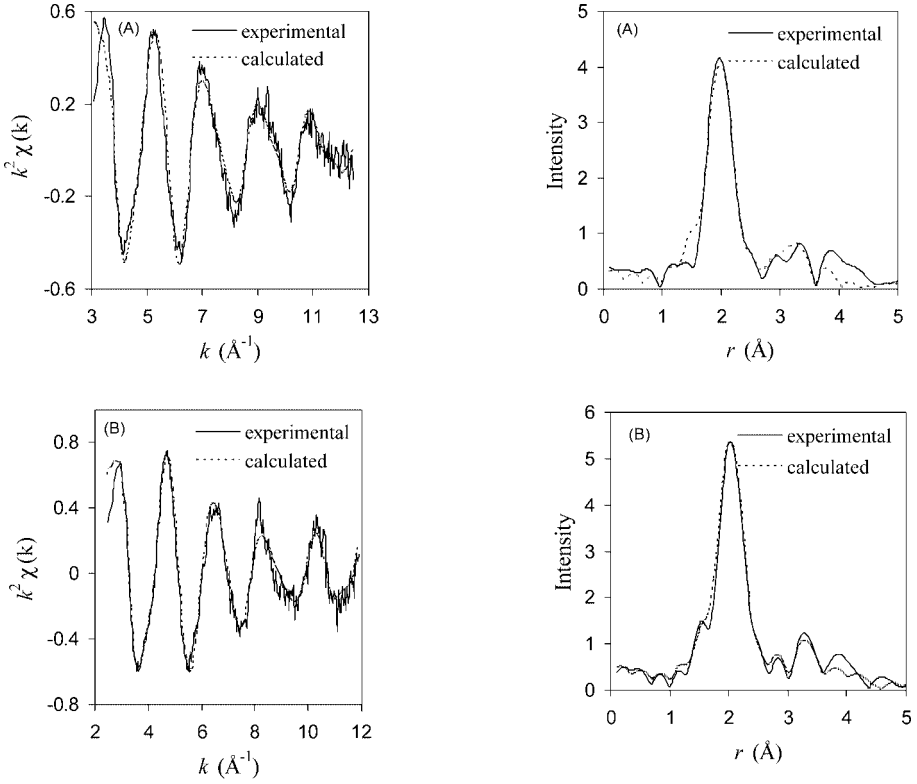


Figure 6. Ru *K* edge EXAFS spectrum and Fourier transform for $[PW_{11}Ru(H_2O)O_{39}]^{4-}$ in solid state TBA salt (a) and in $CH_3CN$ solution (b).

 © 2007 Wiley-VCH Verlag GmbH & Co. KGaA, Weinheim 

the $FeO_6$ and the $RuO_6$ octahedra were not very different. The Ru atom is at a longer distance from the heteroatom P than it is from Fe. Also, the size of the group $W_2RuO_{13}$ seems to be bigger than $W_2FeO_{13}$ because the distance from the Ru atom to the closest two W atoms, Ru–W, is larger than for Fe–W. The two other W atoms (outside the $W_2RuO_{13}$ unit) are at a distance from the Ru atom of 3.584 Å in the solid state and at 3.564 Å in the $CH_3CN$ solution.

The crystal structure of a salt of the anion $[SiW_{11}Ru^{III}(S\text{-}DMSO)O_{39}]^{5-}$ was reported recently.[43] This was the first Ru-monosubstituted Keggin ion in which the ruthenium center was not crystallographically disordered. The Ru–O bond lengths averaged 2.04 Å in this anion.[43];7

### Effect of Changing the Central Heteroatom X (P, Si, and B)

The effect of changing the central heteroatom (X) on the structure of polyoxotungstates was studied by comparing EXAFS data resulting from W $L_{III}$ edge analysis for $PW_{11}Mn^{III}$, $SiW_{11}Mn^{III}$, and $BW_{11}Mn^{III}$ (Figure 7 and Table 8). Because of the possible occurrence of the Jahn–Teller effect the environment of the Mn ion was expected to be more distorted than for other substituting metals. Thus, the ability of the $W_{11}Mn(H_2O)O_{39}$ unit to accommodate different heteroatom sizes of varying formal oxidation states could be studied in the solid compounds.

Table 8. EXAFS best-fit parameters for solid $TBA_4H[SiW_{11}Mn(H_2O)O_{39}]\cdot H_2O$ and $TBA_4H_2[BW_{11}Mn(H_2O)O_{39}]\cdot 2H_2O$ (W $L_{III}$ edge transmission mode). Parameters as defined in Table 1.

| Shells | $SiW_{11}Mn$ | Shells | $BW_{11}Mn$ |
|---|---|---|---|
| R1 (1 × O) | 1.717 (0.005) | R1 (1 × O) | 1.714 (0.007) |
| R2 (2 × O) | 1.883 (0.005) | R2 (2 × O) | 1.889 (0.006) |
| R3 (2 × O) | 2.010 (0.006) | R3 (2 × O) | 2.003 (0.008) |
| R4 (1 × O) | 2.277 (0.020) | R4 (1 × O) | 2.272 (0.012) |
| $R_{Mn}$ (1 × Mn) | 2.386 (0.024) | $R_{Mn}$ (1 × Mn) | 2.421 (0.016) |
| R5 (1 × W) | 3.388 (0.005) | R5 (1 × W) | 3.074 (0.019) |
| R9 (2 × W) | 3.744 (0.032) | R9 (2 × W) | 3.636 (0.009) |
| R10 (1 × Si) | 4.018 (0.030) | R10(1 × B) | 4.460 (0.057) |
| *A*[1] | 0.004 (0.001) | *A*[1] | 0.006 (0.001) |
| *A*[2–3] | 0.006 (0.001) | *A*[2–3] | 0.010 (0.002) |
| *A*[4] | 0.013 (0.004) | *A*[4] | 0.009 (0.003) |
| *A*[Mn] | 0.039 (0.005) | *A*[Mn] | 0.033 (0.003) |
| *A*[5,9] | 0.007 (0.004) | *A*[5,9] | 0.006 (0.004) |
| *A*[10] | 0.015 (0.008) | *A*[10] | 0.001 (0.002) |
| $E_f$ (eV) | 10.5 | $E_f$ (eV) | 10.8 |
| *R* (%) | 18.8 | *R* (%) | 20.1 |

The six oxygen atoms from the first coordination sphere $WO_6$ were localized in the range 1.717–2.277 Å for X = Si and 1.714–2.272 Å for X = B (Table 8). It can be noticed that the average W–$O_4$ distance (Figure 1, a) in the $WO_6$ octahedra are slightly smaller for the polyanion with X = P (Table 4). Contrary, the distance between the Mn atom and $W_c$ is bigger for X = P than for X = Si and B.

No relationship between the average bond lengths and the size of the central atom could be deduced (in line with published results for the parent Keggin anions[44,45]). Glob-

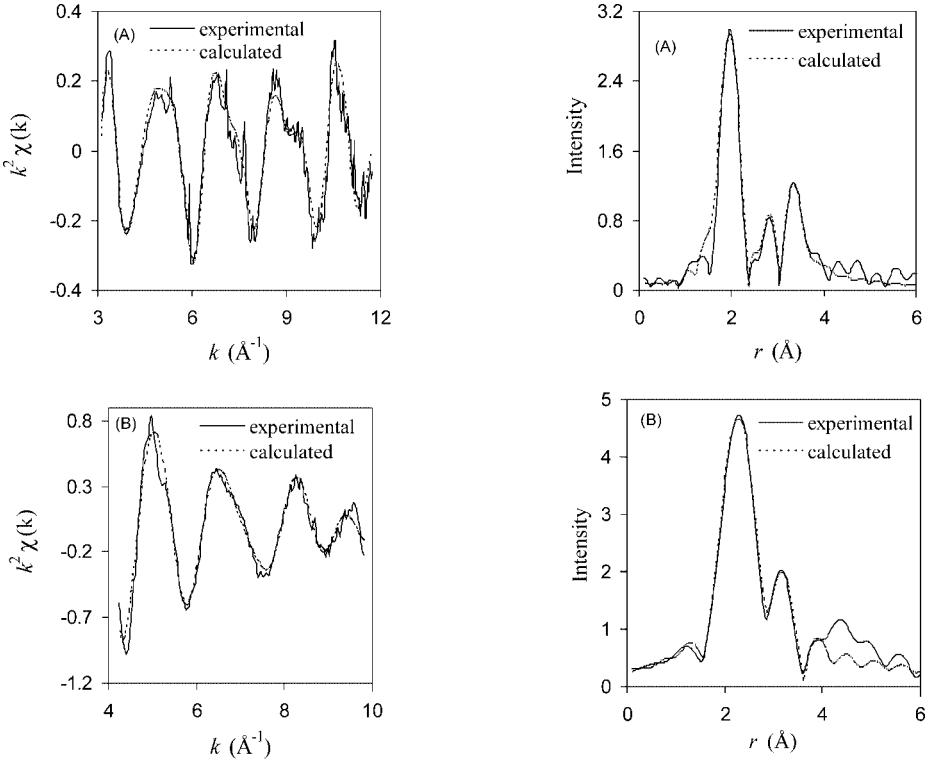


Figure 7. W $L_{III}$ edge EXAFS spectrum and Fourier transform for $[SiW_{11}Mn(H_2O)O_{39}]^{5-}$ (a) and $[BW_{11}Mn(H_2O)O_{39}]^{6-}$ (b) anions in solid state compounds.

 © 2007 Wiley-VCH Verlag GmbH & Co. KGaA, Weinheim 

ally, the size of the $W_3O_{13}$ groups seems to be independent of X because of the similarity between all X = P, Si, and B anions.

## Conclusions

EXAFS spectroscopy was used to characterize several tetrabutylammonium Keggin-type polyoxotungstates in the solid state and in acetonitrile solution. With this technique the local average environment around W and other substituting metals (Fe, Mn, Ru) was revealed in the lacunary and metal-substituted tungstophosphates $[PW_{11}O_{39}]^{7-}$ and $[PW_{11}M(H_2O)O_{39}]^{4-}$, M = Fe, Mn, Ru, and compared with that of the parent Keggin anion $[PW_{12}O_{40}]^{3-}$. These are compounds with interesting catalytic properties and the detailed knowledge of their structure, particularly around the lacunae or of the substituting metals, has unquestionable relevance. The average structure of W in the series $[XW_{11}Mn^{III}(H_2O)O_{39}]^{n-}$, X = P, Si, B was also obtained and compared. Of those anions, only the structure of $[PW_{12}O_{40}]^{3-}$ and $[PW_{11}O_{39}]^{7-}$ are known from crystallographic studies.[25,30] For the different anions EXAFS data allowed the determination of bond lengths and other interatomic distances in the vicinity of target atoms. The influence of the lacuna or of substituting metals on the W–O bond lengths was not, in general, very large, but could be noticed. The substituting metals (Fe, Mn, Ru) were coordinated by six oxygen atoms, but the coordination octahedron around Mn was found to be larger and more distorted than for the other metals. This was considered to be evidence of Jahn–Teller distortion.

For most cases little change in EXAFS and in the determined parameters occurred upon dissolution of the compounds in acetonitrile. The lacunary anion was, however, the most affected. EXAFS spectroscopy may be used to monitor the stability of the polyoxometalates in solution. The structure of the polyoxoanions in the presence of $H_2O_2$ will be described in a forthcoming paper. In this context, the results presented here may open a way of studying the fate of polyoxometalates in homogeneous catalysis in acetonitrile.

In conclusion, this EXAFS study allowed (1) the determination of structural information and details of metal coordination in these anions, not obtained to date by other techniques, in view of the natural difficulties introduced by the structural disorder, and (2) the comparison of the interatomic distances in different heteropolyanions of the same family in the solid state and in solution. This is the first systematic structural study using EXAFS of lacunary or metal-monosubstituted Keggin-type anions.

## Experimental Section

**Materials:** All reagents were used as received. Acetonitrile (Panreac, for instrumental analysis) and boron nitride (Aldrich) were used. The following compounds were prepared and purified as reported previously: $TBA_3[PW_{12}O_{40}]$,[46] $TBA_4H_3[PW_{11}O_{39}]$,[26] $TBA_4[PW_{11}M(H_2O)O_{39}]$, M = Fe[26] and Mn,[47] $TBA_4H[SiW_{11}Mn(H_2O)O_{39}]$,[47] and $TBA_4H_2[BW_{11}Mn(H_2O)O_{39}]\cdot H_2O$.[27] IR spectra of $PW_{11}Mn$ [$cm^{-1}$]: $\nu_{as}$(P–$O_a$) 1086, 1074 (s), $\nu_{as}$(W–$O_d$) 962 (vs), $\nu_{as}$(W–$O_b$–W) 881 (s), $\nu_{as}$(W–$O_c$–W), 804 (vs) ($O_d$, terminal oxygen, $O_b$, $O_c$, bridging oxygens, and $O_a$, central oxygen atom[46]). The general procedure used for the TBA salt of $PW_{11}Fe$[26] was adapted to prepare $TBA_4[PW_{11}Ru(H_2O)O_{39}]\cdot 4H_2O$:[48] aqueous solutions of $RuCl_3$ (Fluka) and $PW_{11}$, prepared in situ, were mixed at 90 °C; the solid obtained after the addition of aqueous TBABr was filtered and recrystallized in acetonitrile. Analytical data (%) with calculated values in parenthesis: C: 18.93 (20.03), H: 3.79 (4.05), N: 1.82 (1.46). The IR spectrum shows characteristic peaks attributed to $\nu_{as}$(W–$O_d$) at 945 $cm^{-1}$, $\nu_{as}$(W–$O_b$–W) at 892 $cm^{-1}$, $\nu_{as}$(W–$O_c$–W) at 820 $cm^{-1}$, and $\nu_{as}$(P–$O_a$) at 1080 and 1045 $cm^{-1}$.

**Data Collection and Analysis:** The extended X-ray absorption spectra associated with Fe (7.112 keV) or Mn (6.539 keV) *K* edges were collected in the fluorescence mode on stations 7.1 [double crystal Si (111) order-sorting monochromator] and with the Ru *K* edge (22.117 keV) on station 9.2 [double crystal Si (220) order-sorting monochromator]. W $L_{III}$ edge (10.207 keV) was collected in transmission mode on station 7.1. Both stations are located at Daresbury Laboratory (Synchrotron Radiation Source-SRS). The energy of the storage ring is 2 GeV and during the experiments the average current was 150 mA. Solid samples of polyoxotungstates were diluted when necessary with boron nitride and pressed into self supporting pellets with a typical thickness of 0.3 mm. Liquid samples of polyoxotungstates (10 mM) were prepared by direct dissolution of the compound in acetonitrile and placed in liquid cells that were 2 mm in thickness. The measurements were carried out at room temperature.

EXCALIB,[49] SPLINE,[50] and EXCURV98[51] were the programs used to process and analyze the EXAFS data. For each sample at least six scans were averaged. Curve-fitting analyses by least-squares refinement of the non-Fourier filtered $k^2$-weighted EXAFS data were carried out with the EXCURV98 program.[51] The calculations were performed using single scattering. The coordination number of each shell was fixed according to literature values. EXAFS refinements were performed in the *R* space. The number of parameters ($N_i$) was calculated for each refinement and this number indicates the number of parameters that can be refined. The number of shells that were fitted depended on the number of parameters determined. $N_i$ was quantified considering the distance range in the Fourier transform ($\Delta r$) and the energy range in EXAFS oscillations ($\Delta k$), $N_i = 2\Delta r\Delta k/\pi$. The number of parameters refined for each sample was smaller than $N_i$.

The analysis of the W $L_{III}$ edge structure of the Keggin anion $[PW_{12}O_{40}]^{3-}$ was done using as reference the published structural data.[25] For the lacunary $[PW_{11}O_{39}]^{7-}$ and for the substituted anions, $[XW_{11}M^{III}(H_2O)O_{39}]^{n-}$, X = P, M = Fe, Mn, Ru, and X = Si, B, M = Mn, this was done using the X-ray single crystal data of the similar lacunary anion $[SiW_{11}O_{39}]^{8-}$,[31] and of the $[PW_{11}Co(H_2O)O_{39}]^{5-}$ polyanion,[11] respectively.

## Acknowledgments

Thanks go to Daresbury Laboratory (synchrotron Radiation source-SRS) for the EXAFS analysis and to Fundação para Ciência e Tecnologia (FCT) and the University of Aveiro for the financial support of this work. M. S. B. is grateful to FCT and FEDER for her PhD grant.

 © 2007 Wiley-VCH Verlag GmbH & Co. KGaA, Weinheim 

[1] M. T. Pope, *Heteropoly and Isopoly Oxometalates*, Springer-Verlag, Berlin, **1983**.

[2] M. T. Pope, A. Muller, *Angew. Chem. Int. Ed. Engl.* **1991**, *30*, 34–48.

[3] M. T. Pope, A. Muller (Eds.), *Polyoxometalate Chemistry: From Topology via Self-assembly Applications*, Kluwer, Dordrecht, **2001**.

[4] M. T. Pope, A. Muller (Eds.), *Polyoxometalates: From Platonic Solids to Antirectroviral Activity*, Kluwer, Dordrecht, **1994**.

[5] a) R. Neumann in *Modern Oxidative Methods* (Ed.: J. E. Bäckvall), Wiley-VCH, Weinheim, **2004**, ch. 8; b) R. Neumann, *Prog. Inorg. Chem.* **1998**, *47*, 317–370; c) I. V. Kozhevnikov, *Chem. Rev.* **1998**, *98*, 171–198; d) C. L. Hill, C. M. Prosser-McCartha, *Coord. Chem. Rev.* **1995**, *143*, 407–455.

[6] a) T. Okuhara, N. Mizuno, M. Misono, *Appl. Catal. A* **2001**, *222*, 63–77; b) N. Mizuno, M. Misono, *Chem. Rev.* **1998**, *98*, 199–217.

[7] a) E. Coronado, P. Day, *Chem. Rev.* **2004**, *104*, 5419–5448; b) P. Gomez-Romero, *Adv. Mater.* **2001**, *13*, 163–174; c) J. M. Clemente-Juan, E. Coronado, *Coord. Chem. Rev.* **1999**, *193–195*, 361–394; d) E. Coronado, C. J. Gomez-Garcia, *Chem. Rev.* **1998**, *98*, 273–296; e) L. Ouahab, *Coord. Chem. Rev.* **1998**, *178–180*, 1501–1531.

[8] J. T. Rhule, C. L. Hill, D. A. Judd, *Chem. Rev.* **1998**, *98*, 327–357.

[9] A. M. V. Cavaleiro, J. D. Pedrosa de Jesus, H. I. S. Nogueira in *Metal Clusters in Chemistry* (Eds.: P. Braunstein, L. A. Oro, P. R. Raithby), Wiley-VCH, Weinheim, **1999**, vol. 1, p. 444–458.

[10] a) J. F. Keggin, *Proc. R. Soc.* **1934**, *A144*, 75–100; b) J. F. Keggin, *Nature* **1933**, *131*, 908–909.

[11] H. T. Evans, T. J. R. Weakley, G. B. Jameson, *J. Chem. Soc., Dalton Trans.* **1996**, 2537–2540.

[12] J. R. Galan-Mascaros, C. Gimenez-Saiz, S. Triki, C. J. Gomez-Garcia, E. Coronado, L. Ouahab, *Angew. Chem. Int. Ed. Engl.* **1995**, *34*, 1460–1462.

[13] E. Coronado, J. R. Galan-Mascaros, C. Gimenez-Saiz, C. J. Gomez-Garcia, S. Triki, *J. Am. Chem. Soc.* **1998**, *120*, 4671–4681.

[14] B. Yan, Y. Xu, X. Bu, N. K. Goh, L. S. Chia, G. D. Stucky, *J. Chem. Soc., Dalton Trans.* **2001**, 2009–2014.

[15] Z. Han, Y. Zhao, J. Peng, H. Ma, Q. Liu, E. Wang, *J. Mol. Stuct.* **2005**, *738*, 1–7.

[16] J. Niu, Z. Wang, J. Wang, *J. Solid State Chem.* **2004**, *177*, 3411–3417.

[17] J. Evans, M. Pillinger, J. M. Rummey, *J. Chem. Soc., Dalton Trans.* **1996**, 2951–2961.

[18] T. Miyanaga, T. Fujikawa, N. Matubayashi, T. Fukumoto, K. Yokoi, I. Watanabe, S. Ikeda, *Bull. Chem. Soc. Jpn.* **1989**, *62*, 1791–1796.

[19] X. Zhang, M. T. Pope, M. R. Chance, G. B. Jameson, *Polyhedron* **1995**, *14*, 1381–1392.

[20] G. Muncaster, G. Sankar, C. R. A. Catlow, J. M. Thomas, S. J. Coles, M. Hursthouse, *Chem. Mater.* **2000**, *12*, 16–18.

[21] a) A. D. Newman, D. R. Brown, P. Siril, A. F. Lee, K. Wilson, *Phys. Chem. Chem. Phys.* **2006**, *8*, 2893–2902; b) B. B. Bardin, R. J. Davis, *App. Catal. A* **2000**, *200*, 219–231; c) D. E. Clinton, D. A. Tryk, I. T. Bae, F. L. Urbach, M. R. Antonio, D. A. Scherson, *J. Phys. Chem.* **1996**, *100*, 18511–18514.

[22] a) T. Ressler, O. Timpe, F. Girgsdies, J. Wienold, T. Neisius, *J. Catal.* **2005**, *231*, 279–291; b) T. Ressler, O. Timpe, F. Girgsdies, *Z. Kristallogr.* **2005**, *220*, 295–305; c) M. H. Tran, H. Ohkita, T. Mizushima, N. Kakuta, *Appl. Catal. A: General* **2005**, *287*, 129–134; d) C. J. Dillon, J. H. Holles, R. J. Davis, J. A. Labinger, M. E. Davis, *J. Catal.* **2003**, *218*, 54–66; e) J. Wienold, O. Timpe, T. Ressler, *Chem. Eur. J.* **2003**, *9*, 6007–6017; f) F. C. Jentoft, S. Klokishner, J. Krohnert, J. Melsheimer, T. Ressler, O. Timpe, J. Wienold, R. Schlogl, *App. Catal. A* **2003**, *256*, 291–317; g) T. Sugino, A. Kido, N. Azuma, A. Ueno, Y. Udagawa, *J. Catal.* **2000**, *190*, 118–127; h) B. B. Bardin, R. J. Davis, *App. Catal. A* **1999**, *185*, 283–292.

[23] Q. Huynh, J. M. M. Millet, *J. Phys. Chem. Solids* **2005**, *66*, 887–894.

[24] a) H. Carabineiro, R. Villaneau, X. Carrier, P. Herson, F. Lemos, F. R. Ribeiro, A. Proust, M. Che, *Inorg. Chem.* **2006**, *45*, 1915–1923; b) C. Martin, C. Lamonier, M. Fournier, O. Mentré, V. Harlé, D. Guillaume, E. Payen, *Chem. Mater.* **2005**, *17*, 4438–4448 and references cited therein; c) M. Chiang, M. R. Antonio, C. W. Williams, L. Soderholm, *Dalton Trans.* **2004**, 801–806 and references cited therein; d) R. Villaneau, H. Carabineiro, X. Carrier, R. Thouvenot, P. Herson, F. Lemos, F. R. Ribeiro, M. Che, *J. Phys. Chem. B* **2004**, *108*, 12465–12471; e) R. Villaneau, A. Proust, F. Robert, F. Villain, M. Verdaguer, P. Gouzerth, *Polyhedron* **2003**, *22*, 1157–1165 and references cited therein; f) I. Pettiti, I. L. Botto, C. I. Cabello, S. Colonna, M. Faticanti, G. Minelli, P. Porta, H. J. Thomas, *Appl. Catal A: General* **2001**, *220*, 113–121.

[25] G. M. Brown, M. R. Noe-Spirlet, W. R. Busing, H. A. Levy, *Acta Crystallogr., Sect. B* **1977**, *33*, 1038–1046.

[26] M. M. Q. Simões, C. M. M. Conceição, J. A. F. Gamelas, P. M. D. N. Domingues, A. M. V. Cavaleiro, J. A. S. Cavaleiro, A. J. V. Ferrer-Correia, R. A. W. Johnstone, *J. Mol. Catal. A* **1999**, *144*, 461–468.

[27] I. C. M. S. Santos, M. M. Q. Simões, S. M. M. M. Pereira, R. R. L. Martins, M. G. P. M. S. Neves, J. A. S. Cavaleiro, A. M. V. Cavaleiro, *J. Mol. Catal. A* **2003**, *195*, 253–262.

[28] a) M. M. Q. Simões, I. C. M. S. Santos, M. S. S. Balula, J. A. F. Gamelas, A. M. V. Cavaleiro, M. G. P. M. S. Neves, J. A. S. Cavaleiro, *Catal. Today* **2004**, *91–92*, 211–214; b) M. S. S. Balula, I. C. M. S. Santos, M. M. Q. Simões, M. G. P. M. S. Neves, J. A. S. Cavaleiro, A. M. V. Cavaleiro, *J. Mol. Catal. A* **2004**, *222*, 159–165; c) I. M. S. Santos, M. S. S. Balula, M. M. Q. Simões, M. G. P. M. S. Neves, J. A. S. Cavaleiro, A. M. V. Cavaleiro, *Synlett* **2003**, 1643–1646.

[29] N. Binsted, D. Norman, *Jpn. J. Appl. Phys. 1* **1993**, *32*, 342–346, Suppl. 32–2.

[30] J. Fuchs, A. Thiele, R. Palm, *Z. Naturforsch., Teil B* **1981**, *36*, 544–550.

[31] K. Y. Matsumoto, Y. Sasaki, *Bull. Chem. Soc. Jpn.* **1976**, *49*, 156–158.

[32] M. Li, S. Jin, H. Liu, G. Xie, M. Chen, Z. Xu, X. You, *Polyhedron* **1998**, *17*, 3721–3725.

[33] a) X. Zhang, Q. Chen, D. C. Duncan, C. F. Campana, C. L. Hill, *Inorg. Chem.* **1997**, *36*, 4208–4215; b) X. Zhang, Q. Chen, D. C. Duncan, R. J. Lachicotte, C. L. Hill, *Inorg. Chem.* **1997**, *36*, 4381–4386.

[34] a) B. Botar, Y. V. Geletii, P. Kogerler, D. G. Musaev, K. Morokuma, I. A. Weinstock, C. L. Hill, *J. Am. Chem. Soc.* **2006**, *128*, 11268–11277; b) T. M. Anderson, W. A. Neiwert, K. I. Hardcastle, C. L. Hill, *Inorg. Chem.* **2004**, *43*, 7353–7358; c) E. M. Limanski, M. Piepenbrink, E. Droste, K. Burgemeister, B. Krebs, *J. Cluster Sci.* **2002**, *13*, 369–378; d) I. Loose, E. Droste, M. Bosing, H. Pohlmann, M. H. Dickman, C. Rosu, M. T. Pope, B. Krebs, *Inorg. Chem.* **1999**, *38*, 2688–2694.

[35] a) L. Bi, U. Kortz, S. Nellutla, A. C. Stowe, J. Tol, N. S. Dalal, B. Keita, L. Nadjo, *Inorg. Chem.* **2005**, *44*, 896–903; b) S. H. Wasfi, A. L. Reingold, G. F. Kokoszka, A. S. Golstein, *Inorg. Chem.* **1987**, *26*, 2934–2939.

[36] a) S. Poussereau, G. Blondin, G. Chottard, J. Guilhem, L. Tchertanov, E. Riviere, J. J. Girerd, *Eur. J. Inorg. Chem.* **2001**, 1057–1062; b) P. C. Junk, B. J. McCool, B. Moubaraki, K. S. Murray, L. Spiccia, *Angew. Chem. Int. Ed.* **1999**, *38*, 2224–2226.

[37] C. Rocchiccioli-Deltcheff, R. Thouvenot, *J. Chem. Res. (S)* **1977**, 46–47.

[38] J. A. F. Gamelas, F. A. Couto, M. C. Trovão, A. M. V. Cavaleiro, J. A. S. Cavaleiro, J. D. Pedrosa de Jesus, *Thermochim. Acta* **1999**, *326*, 165–173.

[39] E. Radkov, R. H. Beer, *Polyhedron* **1995**, *14*, 2139–2143.


 © 2007 Wiley-VCH Verlag GmbH & Co. KGaA, Weinheim 

[40] a) X. Zhang, C. J. O'Connor, G. B. Jameson, M. T. Pope, *Inorg. Chem.* **1996**, *35*, 30–34; b) X. Zhang, G. B. Jameson, C. J. O'Connor, M. T. Pope, *Polyhedron* **1996**, *15*, 917–922.
[41] D. Drewes, M. Piepenbrink, B. Krebs, *J. Clust. Sci.* **2006**, *17*, 361–374.
[42] B. Chiswell, E. D. McKenzie in *Comprehensive Coordination Chemistry* (Eds.: G. Wilkinson, R. D. Gillard, J. A. McCleverty), Pergamon Press, Oxford, **1987**, vol. 4, p. 1.
[43] M. Sadakane, D. Tsukuma, M. H. Dickman, B. Bassil, U. Kortz, M. Higashijima, W. Ueda, *Dalton Trans.* **2006**, 4271–4276.
[44] A. L. Nolan, C. C. Allen, R. C. Burns, D. C. Craig, G. A. Lawrance, *Aust. J. Chem.* **2000**, *53*, 59–66.
[45] H. Fletcher, C. C. Allen, R. C. Burns, D. C. Craig, *Acta Crystallogr., Sect. C* **2001**, *57*, 505–507.
[46] C. Rocchiccioli-Deltcheff, M. Fournier, R. Franck, R. Thouvenot, *Inorg. Chem.* **1983**, *22*, 207–216.
[47] M. S. Balula, J. A. Gamelas, H. M. Carapuça, A. M. V. Cavaleiro, W. Schlindwein, *Eur. J. Inorg. Chem.* **2004**, 619–628.
[48] C. Rong, M. T. Pope, *J. Am. Chem. Soc.* **1992**, *114*, 2932–2938.
[49] *EXCALIB*, CCLRC Daresbury Laboratory Computer Program, **1982**.
[50] *Exspline*, a program for EXAFS background subtraction, Daresbury Laboratory, **2000**, based on an original program, P. Ellis Spline, PhD Thesis, University of Sydney, **1995**.
[51] N. Binsted, *EXCURV98*, CCLRC Daresbury Laboratory computer program, **1998**.

Received: July 28, 2005
Extented Version Received: November 28, 2006
Published Online: February 2, 2007

 © 2007 Wiley-VCH Verlag GmbH & Co. KGaA, Weinheim

**The EUChemSoc Societies have taken the significant step into the future by merging their traditional journals, to form two leading chemistry journals, the *European Journal of Inorganic Chemistry* and the *European Journal of Organic Chemistry.* Three further EUChemSoc Societies (Austria, Czech Republic and Sweden) are Associates of the two journals.**

## COVER PICTURE

**The cover picture shows** the one-dimensional polymeric iron(II) spin crossover material, $Fe(NCX)_2$-(cddt)·*n*(guest) (X = S or Se) containing the ligand 2-chloro-4,6-bis(dipyrid-2-ylamino)-1,3,5-triazine. The thiocyanate analogue undergoes a "half" spin crossover, illustrated at the bottom, where at low temperatures there are alternating, crystallographically distinct, high spin (yellow) and low spin (red) iron(II) centres (as can be seen in the structural diagram). The selenocyanate material undergoes a full spin crossover illustrated at the base of the image. Further characterisation of the thiocyanate material has been carried out by powder X-ray diffraction using synchrotron radiation; a representative image is shown in the background of the picture. Details are discussed in the article by K. S. Murray et al. on p. 1073 ff.

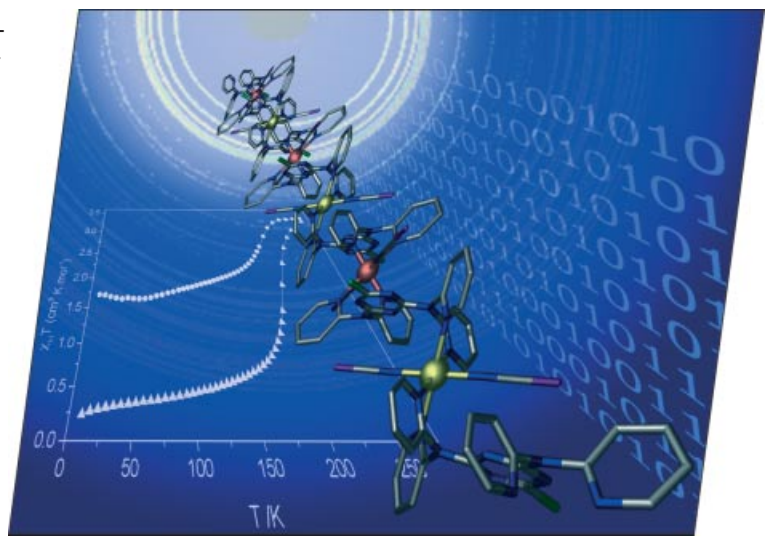


 © 2007 Wiley-VCH Verlag GmbH & Co. KGaA, Weinheim 

# CONTENTS

## MICROREVIEW


### Cluster-Based Materials

**H. Zhou, A. Lachgar* ..... 1053–1066**

Octahedral Metal Clusters $[Nb_6Cl_{12}(CN)_6]^{4-}$ as Molecular Building Blocks: From Supramolecular Assemblies to Coordination Polymers

**Keywords:** Metal clusters / Self-assembly / Supramolecular Chemistry / Coordination polymers


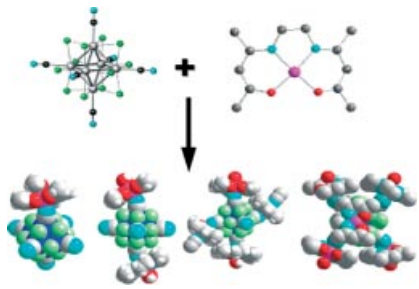


Reactions between octahedral niobium cyanochloride metal clusters and coordinatively unsaturated metal complexes in different solvents led to the formation of supramolecular moieties with different sizes and different charges. Judicious choice of the synthetic conditions led to the preparation of either supramolecules that are hydrogen bonded, or to coordination polymers with 1D, 2D, and 3D frameworks built from cluster anions and metal complexes linked by CN ligands.


## SHORT COMMUNICATION


### Zinc Siloxides

**C. Krempner,* H. Reinke, K. Weichert ..... 1067–1071**

Synthesis and Structure of Cyclic Trinuclear Zinc Disiloxides

**Keywords:** Oligosilanes / Zinc / Siloxides / Clusters


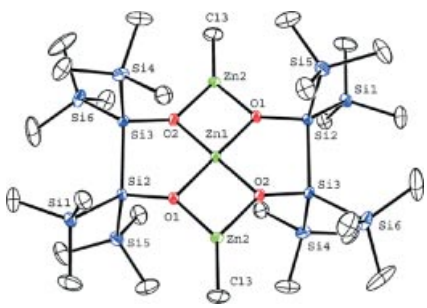



The synthesis of three new cyclic trinuclear zinc disiloxides has been reported from reactions of $ZnMe_2$ with various vicinal silanediols. The solid-state structure of one of the zinc siloxides (see Figure) reveals unusual square-planar coordination geometry of the inner $Zn^{2+}$ ion, which is enforced by steric interactions of the silyl groups.


## FULL PAPERS


### Iron(II) Spin Crossover

**S. M. Neville, B. A. Leita, D. A. Offermann, M. B. Duriska, B. Moubaraki, K. W. Chapman, G. J. Halder, K. S. Murray* ... 1073–1085**

Spin-Crossover Studies on a Series of 1D Chain and Dinuclear Iron(II) Triazine-Dipyridylamine Compounds

**Keywords:** Iron / N ligands / Spin crossover / 1D chains / Dinuclear / Magnetic properties


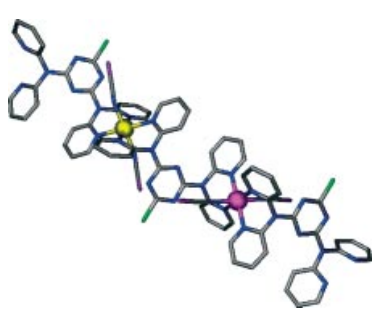


Detailed structural and magnetic studies on a series of polynuclear and dinuclear iron(II) materials, several of which show spin crossover.

## Silazane Complexes

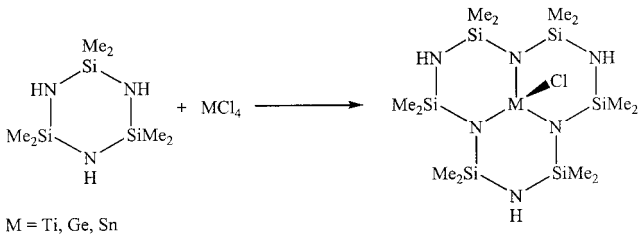


M = Ti, Ge, Sn

**C. Lehnert, J. Wagler, E. Kroke, G. Roewer* ..... 1086–1090**

Synthesis and Characterization of Novel Titanium, Germanium, and Tin Silazane Complexes Bearing a Cyclohexasilazane-triido Ligand

Novel titanium, germanium and tin silazane complexes can be synthesized by the reactions of 1,1,3,3,5,5-hexamethylcyclotrisilazane $H_3$(HMCTS) with the corresponding metal tetrachloride under various reaction conditions. The molecular structures of these complexes exhibit a new dodecamethylcyclohexasilazane system with the Ti, Ge, and Sn atom in the center. The metal atoms are coordinated by one chlorine atom and three nitrogen atoms that are part of three six-membered heterosilazane rings.

**Keywords:** Heterometallic complexes / N ligands / Titanium / Germanium / Tin / Cyclohexasilazane complexes

## Bridged Azido – Nickel(II) Complexes

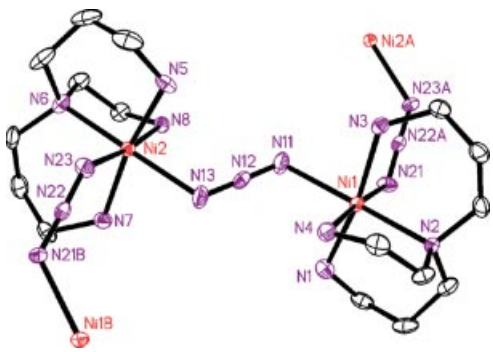


**S. S. Massoud,* F. A. Mautner, R. Vicente, A. A. Gallo, E. Ducasse ..... 1091–1102**

Dinuclear and Polynuclear Bridged Azido–Nickel(II) Complexes: Synthesis, Structure Determination, and Magnetic Properties

A new series of azido–$Ni^{II}$ complexes $[Ni_2(trpn)_2(\mu_{1,3}\text{-}N_3)_2](ClO_4)_2$ (**1**), 1D *cis*-$[Ni(abap)(\mu_{1,3}\text{-}N_3)]_n(ClO_4)_n$ (**2**), 1D *cis*-$[Ni(Me_6trien)(\mu_{1,3}\text{-}N_3)]_n(ClO_4)_n{\cdot}nH_2O$ (**3a**), and $[Ni(Me_6trien)(N_3)]ClO_4$ (**3b**) were synthesized and structurally characterized by spectroscopic techniques, X-ray crystallography, and magnetic measurements.

**Keywords:** Nickel / Azido bridges / Crystal structure / Magnetic properties

## Mo and W Metallocenes

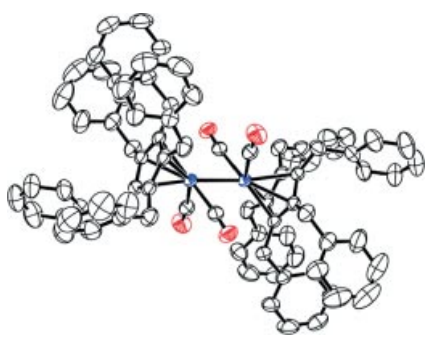

**S. Namorado, J. Cui, C. G. de Azevedo, M. A. Lemos, M. T. Duarte, J. R. Ascenso, A. R. Dias, A. M. Martins* .. 1103–1113**

(Pentabenzylcyclopentadienyl)molybdenum Complexes: Synthesis, Structures and Redox Properties

$[MoCpBz(CO)_2]_2$ (**5**) and $[MCpBz(CO)_3]_2$ (M = Mo, W; CpBz = pentabenzylcyclopentadienyl) are described. Hydrido complexes $[MH(CpBz)(CO)_3]$ have been obtained from reactions of $Li[MCpBz(CO)_3]$ with $H^+$. Cyclic voltammetry and controlled potential coulometry of **5** have been performed and mechanisms for the redox behaviour are proposed.

**Keywords:** Molybdenum / Tungsten / Cyclopentadienyl ligands / Half-sandwich complexes / Cyclic voltammetry

 © 2007 Wiley-VCH Verlag GmbH & Co. KGaA, Weinheim 

# CONTENTS

## C−H Activation

**J. Ito, H. Nishiyama* ..... 1114−1119**

Carbon−Hydrogen Bond Activation of Arenes by a [Bis(oxazolinyl)phenyl]rhodium(III) Acetate Complex

**Keywords:** C−H activation / Arenes / Rhodium / Substituent effects

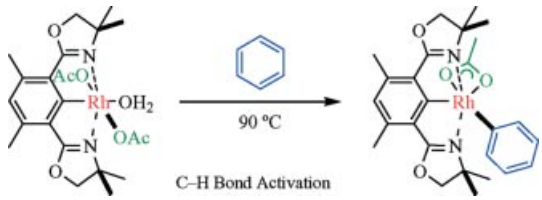


Thermolysis of a [bis(dimethyloxazolinyl)-phenyl]rhodium(III) acetate complex in the presence of various arenes results in the formation of the corresponding aryl complexes by intermolecular C−H bond activation assisted by the acetato ligand as a proton acceptor.

## Host−Guest Complexes

**R. Puchta,* R. van Eldik ..... 1120−1127**

Host−Guest Complexes of Oligopyridine Cryptands: Prediction of Ion Selectivity by Quantum Chemical Calculations

**Keywords:** Density functional calculations / Semiempirical calculations / Cryptands / Host−guest systems / Cation selectivity

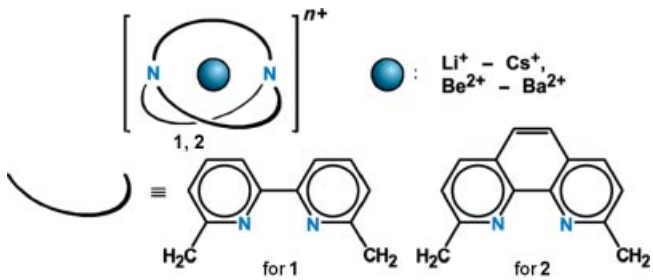


Quantum chemical investigations of endohedral ion complexation by the cryptands **1** and **2** predict a favourable binding of $K^+$, $Ca^{2+}$ and $Sr^{2+}$ by **1** and $Na^+$, $Ca^{2+}$ and $Sr^{2+}$ by **2**. To obtain the best coordination mode for each cation, the cryptands fold around the ions by twisting their torsion angles.

## Nanomaterials

**L. B. Yang, Y. H. Shen,* A. J. Xie, J. J. Liang, J. M. Zhu, L. Chen ..... 1128−1134**

Synthesis of Controllable-Size Core−Shell Se@Ag and Se@Au Nanoparticles in UV-Irradiated TSA Solution

**Keywords:** Nanostructures / Photochemistry / Core−shell structures / Selenium

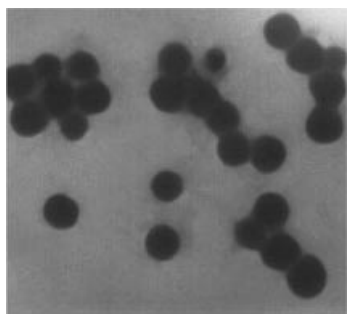

The formation of Se-core−Au-shell and Se-core−Ag-shell nanoparticles by using photochemically reduced tungstosilicate Keggin ions has been described. With this method, the core size and the shell thickness can be controlled by varying the conditions.

## A Volatile Iron Amidinate

**X.-G. Li,* Z. Li, H. Li, R. G. Gordon* ..... 1135−1142**

Synthesis and Sublimation Kinetics of a Highly Volatile Asymmetric Iron(II) Amidinate

**Keywords:** Asymmetric iron(II) amidinate / Bridging ligands / Metathesis / Sublimation kinetics / Thermochemistry

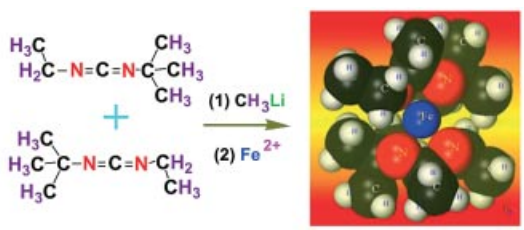


Iron(II) bis(*N*-*tert*-butyl-*N*′-ethylacetamidinate), was synthesized and characterized for the first time by NMR spectroscopy, MS, IR spectroscopy and TG techniques. The activation energy of the sublimation is 105 kJ $mol^{-1}$. The optimal starting iron (II) compound and reaction medium are iron (II) acetylacetonate and diethyl ether, respectively. The combination offers the highest yield, the greatest volatilizability of 98%, and thus the purest product.

 © 2007 Wiley-VCH Verlag GmbH & Co. KGaA, Weinheim 

## Copper Complexes

Thirteen crystal structures of copper(II) complexes with a series of dipicolylamine (DPA)-based ligands, namely *N*-(2-methoxyethyl)-*N*,*N*-bis(2-pyridylmethyl)amine (**L1**), *N*-[2-(2-hydroxyethyloxy)ethyl]-*N*,*N*-bis(2-pyridylmethyl)amine (**L2**) and *N*-(3-methoxypropyl)-*N*,*N*-bis(2-pyridylmethyl)-amine (**L3**), have been determined and the factors that control the coordination of the ether-oxygen atom of these ligands to the copper centre are discussed.

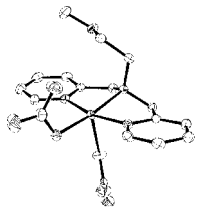

$[Cu(\mathbf{L1})(NO_3)_2]$

$[Cu(\mathbf{L1})Cl]^+$

**Y. Mikata,* T. Fujimoto, Y. Sugai, S. Yano ..... 1143–1149**

Control of Intramolecular Ether-Oxygen Coordination in the Crystal Structure of Copper(II) Complexes With Dipicolylamine-Based Ligands

**Keywords:** N,O ligands / Copper / Coordination modes / Ligand effects

## Coordination Polymers with Channels

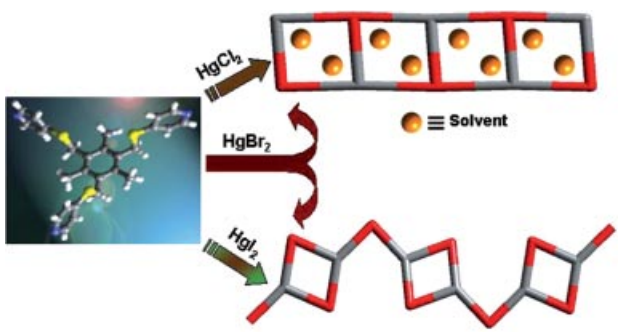


Coordination assemblies of conformationally flexible 1,3,5-tris(4-pyridylsulfanylmethyl)-2,4,6-trimethylbenzene with different mercuric halides have been shown to form significantly different complexes, which can be differentiated by composition and structural features (solvated and unsolvated structures).

**J. PrakashaReddy, V. R. Pedireddi* ..... 1150–1158**

Metal–Organic Hybrids of 1,3,5-Tris(4-pyridylsulfanylmethyl)-2,4,6-trimethylbenzene with Mercuric Halides

**Keywords:** Metal–organic hybrids / Supramolecular chemistry / Crystal engineering / Fluxional thio ligands / Mercuric halides

## Catalysis of Hydroaminations

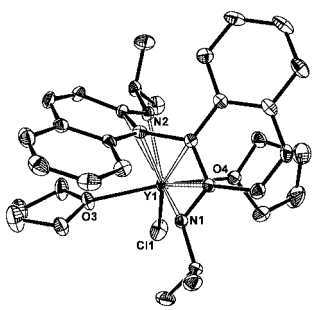


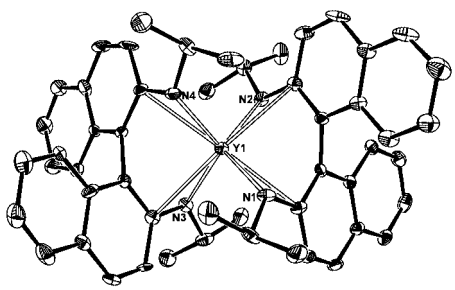


$[Y\{(R)\text{-}C_{20}H_{12}(NiPr)_2\}Cl(thf)_2]$ has been prepared and characterized by X ray analysis as well as the corresponding yttrium ate complex $[Li(thf)_4][Y\{(R)\text{-}C_{20}H_{12}(NiPr)_2\}_2]$. The neutral yttrium complex $[Y\{(R)\text{-}C_{20}H_{12}(NiPr)_2\}\{NiPr_2\}\{LiCl(thf)_2\}]$ and the ate complex catalyze the formation of several pyrrolidines and piperidines with different activities and enantioselectivities.

**D. Riegert, J. Collin,* J.-C. Daran, T. Fillebeen, E. Schulz, D. Lyubov, G. Fukin, A. Trifonov* ..... 1159–1168**

Neutral Yttrium Tris(amide) and Ate Complexes Coordinated by an (*R*)-*N*,*N*′-Diisopropyl-1,1′-binaphthyl-2,2′-diamido Ligand as Enantioselective Catalysts for Intramolecular Hydroamination

**Keywords:** Asymmetric catalysis / N ligands / Yttrium / Hydroamination / Nitrogen heterocycles

**If not otherwise indicated in the article, papers in issue 7 were published online on February 16, 2007**

 © 2007 Wiley-VCH Verlag GmbH & Co. KGaA, Weinheim

**The EUChemSoc Societies have taken the significant step into the future by merging their traditional journals, to form two leading chemistry journals, the *European Journal of Inorganic Chemistry* and the *European Journal of Organic Chemistry.* Three further EUChemSoc Societies (Austria, Czech Republic and Sweden) are Associates of the two journals.**

## COVER PICTURE

**The cover picture shows** the one-dimensional polymeric iron(II) spin crossover material, $Fe(NCX)_2$-(cddt)·*n*(guest) (X = S or Se) containing the ligand 2-chloro-4,6-bis(dipyrid-2-ylamino)-1,3,5-triazine. The thiocyanate analogue undergoes a "half" spin crossover, illustrated at the bottom, where at low temperatures there are alternating, crystallographically distinct, high spin (yellow) and low spin (red) iron(II) centres (as can be seen in the structural diagram). The selenocyanate material undergoes a full spin crossover illustrated at the base of the image. Further characterisation of the thiocyanate material has been carried out by powder X-ray diffraction using synchrotron radiation; a representative image is shown in the background of the picture. Details are discussed in the article by K. S. Murray et al. on p. 1073 ff.

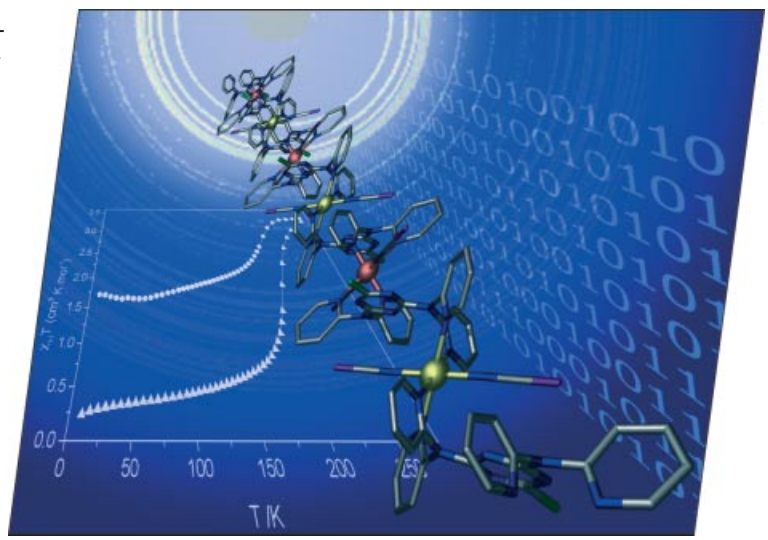


 © 2007 Wiley-VCH Verlag GmbH & Co. KGaA, Weinheim 

DOI: 10.1002/ejic.200600900

# Octahedral Metal Clusters $[Nb_6Cl_{12}(CN)_6]^{4-}$ as Molecular Building Blocks: From Supramolecular Assemblies to Coordination Polymers

**Huajun Zhou[a] and Abdessadek Lachgar*[a]**

*This microreview is dedicated to the memory of Ekatherina Anokhina*

**Keywords:** Metal clusters / Self-assembly / Supramolecular Chemistry / Coordination polymers

There are considerable advantages for using metal clusters as building units of supramolecular materials because of their unique structural, chemical, and physical properties, all of which fall in between normal valence compounds and the metals. In this microreview, we describe the synthetic methodology and structural properties of recent findings in the use of octahedral niobium hexacyanochloride anions as building units of assemblies of different size, charge, and dimensionality. We focus on the use of a metal-directed approach to prepare cluster-based supramolecular assemblies and coordination polymers with one-, two-, and three-dimensional frameworks. The materials described herein are all built from diamagnetic cyanochloride cluster anions $[Nb_6Cl_{12}(CN)_6]^{4-}$ and coordinatively unsaturated metal complexes such as $[Mn(salen)]^+$ and their derivatives. The overall structures are largely determined by the number of coordination sites available for linkage to the cluster unit and coordination preferences of the metal complexes.
(© Wiley-VCH Verlag GmbH & Co. KGaA, 69451 Weinheim, Germany, 2007)

## 1. Introduction

Supramolecular chemistry "chemistry beyond the molecule" focuses on the rational design and preparation of supramolecular structures through self-assembly processes in which building units are linked through noncovalent forces such as hydrogen bonding, coordination bonds, electrostatic and charge-transfer attractions, and aromatic π-π stacking interactions.[1,2] It is fundamentally related to the field of crystal engineering which focuses on the organization of molecular or ionic building units into functional crystalline materials with desired structures and properties.[3]

[a] Department of Chemistry, Wake Forest University, Winston-Salem, NC 27109, USA
Fax: +1-336-758-4656
E-mail: lachgar@wfu.edu

*Abdou Lachgar graduated from the University of Nantes, France in 1982 and obtained his Ph.D. degree in materials science and solid state chemistry from the Institute of Materials Jean Rouxel in Nantes in 1987. He joined the group of John Corbett at Iowa State University (1988–1990) to pursue his postdoctoral studies and investigated the chemistry of reduced zirconium and scandium iodides. In 1990, he joined the University of Washington in Seattle, as a research fellow with James Mayer. He concentrated on the synthesis of extended solids from molecular precursors by using electrochemical processes. In 1991, he joined the Department of Chemistry at Wake Forest University as an Assistant Professor. He was promoted to Associate Professor in 1996 and then to Professor in 2002. His teaching and research interests are in the area of materials chemistry with a focus on the use of the molecular building block approach for the rational preparation of hybrid inorganic–organic materials. He was awarded visiting faculty fellowships from the Japanese Government in 1997 and 1998, and he was a visiting Professor at the Institute of Materials Jean Rouxel in 2003 and the institute Gallile in Paris in 2006.*

*Huajun Zhou obtained his B.S in chemistry from Beijing University (China) in 1999. After conducting research on Li-ion batteries as a research scientist for two years at BYD Co. Ltd (China), he joined Professor Lachgar's group at Wake Forest University in 2002. His current research focuses on strategies used in crystal engineering for the preparation of supramolecular materials built from octahedral cyanochloride clusters and metal ions/metal complexes as building units and the correlation of their structures with their observed properties.*

 © 2007 Wiley-VCH Verlag GmbH & Co. KGaA, Weinheim 

Progress in supramolecular chemistry has led to the use of more complex molecular building units to prepare materials with novel structures and properties. Inspired by the success of using hexacyanometalate anions $[M(CN)_6]^{n-}$ as building units to construct functional solids with diverse structures,[4] several groups are actively exploring the use of their expanded analogues, such as octahedral transition metal clusters, as building units to investigate the effect of the metal–metal bonds on their physicochemical properties. Octahedral transition metal clusters based on an $M_6$ octahedron in which six metal atoms are linked to each other through metal–metal bonds and $\mu_2$ or $\mu_3$ ligands to give a $M_6L_{12}$ or $M_6L_8$ cluster core (Figure 1) have received considerable interest since the discovery of the Chevrel phases which consist of 3D frameworks based on the 6–8 type clusters.[5] Different synthetic methodologies have been developed to excise these clusters from their solid-state precursors through solution chemistry routes.[6] The cluster core $[M_6L_{12}]^{n+}$ or $[M_6L_8]^{n+}$ has an atom- or ion-like behavior. It is larger in size compared with mononuclear metal complexes, has versatile electronic structures, multiple coordination sites, and potential catalytic properties that make them promising candidates as building units of supramolecular structures.[7] Face-capped octahedral cluster units $[W_6S_8(CN)_6]^{6-}$ and $[Re_6Q_8(CN)_6]^{n-}$ (Q = S, Se and Te) have been used as building units of supramolecular structures, some of which show functional properties such as catalysis and molecular sieves.[8]

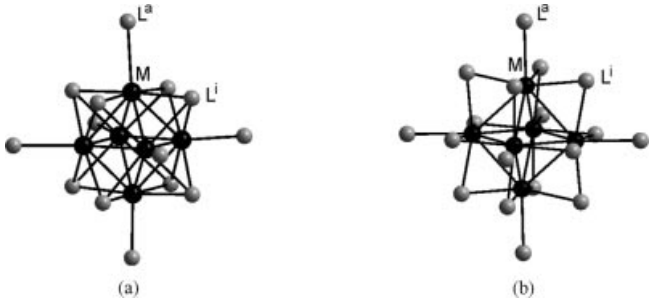


Figure 1. (a) The structure of the cluster $[(M_6L_8^i)L_6^a]$ common for M = Mo, W, Re; L = halides, S, Se, Te. (b) The structure of the cluster $[(M_6L_{12}^i)L_6^a]$ common for M = Nb, Ta; L = Cl, Br, O; and M = Zr; L = halides.

The use of edge-capped octahedral niobium halide clusters as building units remains largely unexplored compared with the extensive work that has been reported on octahedral face-capped rhenium and tungsten clusters. These two cluster types differ from each other not only in terms of the coordination mode of inner ligands, but also by the number of valence electrons available for metal–metal bonding (VEC). The use of the cyanochloride cluster $[Nb_6Cl_{12}(CN)_6]^{n-}$ as building units should, in principle, lead to the formation of supramolecular materials with new structures and properties. This microreview describes our recent results in the use of $[Nb_6Cl_{12}(CN)_6]^{4-}$ and metal complexes as building units of supramolecular structures by using the cyanide ditopic coordination ability and the coordination requirement of the metal complexes.

## 2. Synthetic Strategy

The cluster anion $[Nb_6Cl_{12}(CN)_6]^{4-}$ can be considered as an expanded analogue of $[Fe(CN)_6]^{4-}$ in which $Fe^{2+}$ is replaced by an $[Nb_6Cl_{12}]^{2+}$ cluster core. As in the case of $[Fe(CN)_6]^{4-}$, the cyanochloride cluster reacts with virtually all hydrated $[M(H_2O)_6]^{2+}$ ions to afford compounds that are expanded analogues of the iron-based Prussian-blue.[9] Their crystal structure is based on edge-bridged $[Nb_6Cl_{12}]^{2+}$ clusters and $M^{2+}$ ions bridged by cyanide ligands to form a cubic face centered anionic framework $[MNb_6Cl_{12}(CN)_6]^{2-}$ in which all tetrahedral sites are occupied by the cations $[Me_4N]^+$, which act as charge compensating templates.

After investigating the interaction between the cyanochloride cluster and simple metal ions, we focused on the use of the "directional-bonding" approach first cited by Stang and coworkers and systematized by coordination chemists to prepare supramolecular species.[10,11] The fundamental principle of this approach is the use of coordinatively unsaturated metal complexes as building units. These complexes have specific coordination sites available for ligands from other building units located at appropriate angles to "direct" the formation of desired supramolecular structures. For instance, *cis*-$[Ni(bpy)_2(\mu_{1,3}\text{-}N_3)](PF_6)$[12] and *trans*-$[Ni(N\text{-}Eten)_2(\mu_{1,3}\text{-}N_3)](PF_6)$[13] have been used to prepare 1D coordination polymers with different structural features because of different angles between the two coordination sites available for the incoming azide ligand. Similar strategies have been developed for metal clusters where site-differentiated clusters $[Re_6Se_8(PEt_3)_n(MeCN)_{6-n}]^{2+}$ have been used as building units of supramolecular assemblies.[14]

The reactivity between coordinatively unsaturated metal complexes and $[Nb_6Cl_{12}(CN)_6]^{4-}$ equipped with six cyanide ligands was studied. Two types of metal complexes have been investigated: 1) complexes with tetradentate salen-type ligands (*L1–L3*) (Figure 2) chosen for their potential catalytic properties,[15] and 2) complexes coordinated by one or two chelating diamine ligands (phen and en) that block two or four coordination sites, respectively. This leaves different numbers of coordination sites available depending on the nature of the metal ions. The structures of the compounds obtained can be, to a certain extent, predicted from the coordination requirements of the metal complexes. However, the competition between different geometries with similar stoichiometries does not allow complete predictability without considering the effect of solvent, counterions, and stability of the complexes.[16] This review intends to highlight some basic structures to illustrate the use of the concept of "metal complex directed assembly" to build supramolecular structures with versatile geometrical and topological features. Investigations into the combination of metal complexes such as $[Mn(salen)]^+$ with $Re_6$ clusters resulted in the synthesis of extended framework materials, whereas the use of metal porphyrins with $Re_6$ clusters led to discrete supramolecular units that have shown excellent catalytic activity toward the epoxidation of olefins.[17,8d]

 © 2007 Wiley-VCH Verlag GmbH & Co. KGaA, Weinheim 

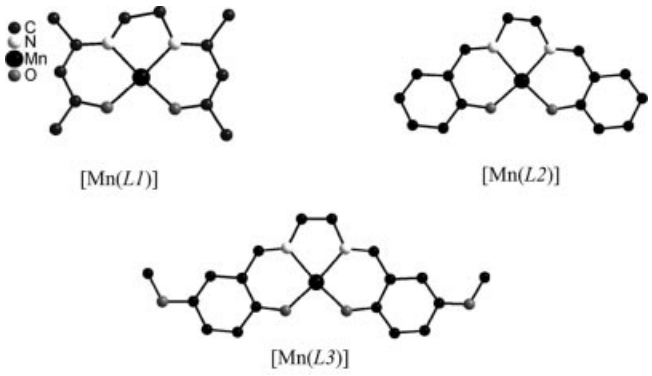


Figure 2. Molecular structures of $Mn^{III}$ complexes with tetradentate salen-type ligands used in the present study. $L1^{2-}$ = bis(acetylacetonato)ethylenediamine; $L2^{2-}$ = bis(salicylidene)ethylenediaminato; $L3^{2-}$ = bis(5-methoxysalicylidene)ethylenediaminato.

## 3. Synthesis of the $[Nb_6Cl_{12}(CN)_6]^{4-}$ Building Unit

The clusters are prepared following a three-step procedure. Firstly, solid-state precursors containing the chloride cluster $[Nb_6Cl_{12}]^{2+}$ are prepared from reactions between Nb metal, $NbCl_5$, and chloride salts that provide the cations as needed. The reactants are sealed in silica containers under vacuum and heated at 700–900 °C.[18] The second step involves dissolving the solid state precursor in a common polar solvent to excise the chloride cluster. In the third step, substitution of all outer chloride ligands by cyanides is performed. $Li_2Nb_6Cl_{16}$ was used as the solid-state precursor because of its ease of preparation, high yield, and ease of solubility in different solvents. The complete procedure is described by the chemical equations given in steps 1–3.

Scheme 1 shows the use of $Li_2Nb_6Cl_{16}$ as the solid state precursor for the preparation of $[Nb_6Cl_{12}(CN)_6]^{4-}$. $Li_2Nb_6Cl_{16}$ features a 2D framework in which each $[Nb_6Cl_{18}]^{4-}$ cluster is connected to four neighboring clusters by sharing four outer chloride ligands. $[Me_4N]_3[Nb_6Cl_{18}]$ (**1**), which contains the 15-electron cluster $[Nb_6Cl_{18}]^{3-}$, was obtained by dissolving $Li_2Nb_6Cl_{16}$ in EtOH and adding excess $Me_4NCl$.[9] The reaction time was substantially reduced to 30 min when these two steps were performed at 60 °C. Addition of excess KCN to a solution of **1** in $MeCN/H_2O$ followed by recrystallization from MeOH/ether results in the formation of $[Me_4N]_4[Nb_6Cl_{12}(CN)_6]$ (**2**).[19] The compounds were characterized by single-crystal XRD. The average Nb–Nb [2.983(5) Å], Nb–$Cl^i$ [2.441(6) Å], and Nb–$Cl^a$ [2.53(1) Å] bond lengths in **1** are close to those reported for compounds containing the 15-electron cluster $[Nb_6Cl_{18}]^{3-}$.[20] The average bond lengths of Nb–Nb [2.927(4) Å] and Nb–$Cl^i$ [2.464(7) Å] in **2** are the same as those observed in $Li_2Nb_6Cl_{16}$ [Nb–Nb: 2.919(6) Å; Nb–$Cl^i$: 2.46(2) Å], which contains the 16-electron cluster $[Nb_6Cl_{18}]^{4-}$. The bond lengths Nb–C [2.282(1) Å] and C≡N [1.131(6) Å] are close to those observed in other compounds containing $[Nb_6Cl_{12}(CN)_6]^{4-}$.[21,22] The stretching frequency for the C≡N group appears at 2126 $cm^{-1}$ in the IR spectrum, which is higher than that observed in $K_4[Fe(CN)_6]$ (2044 $cm^{-1}$) but close to that found in $K_3[Cr(CN)_6]$ (2129 $cm^{-1}$).[23] The Nb–C≡N linkages are almost linear [∠ Nb–C≡N = 178.3(6)°].

$[Et_4N]_4[Nb_6Cl_{12}(CN)_6]$ was prepared through a cation metathesis reaction in which an aqueous solution of $Et_4NBr$ was added to an aqueous solution of **2**.

$[Me_4N]_4[Nb_6Cl_{12}(CN)_6]$ (aq.) + $4Et_4NBr$ (aq.) → $[Et_4N]_4[Nb_6Cl_{12}(CN)_6]$ (s) + $4Me_4NBr$ (aq.)

## 4. Supramolecular Assemblies and Their Hydrogen-Bonded Frameworks

Supramolecular assemblies in which the cluster is coordinated by a different number of metal complexes have been isolated and investigated. For a clearer description, we con-

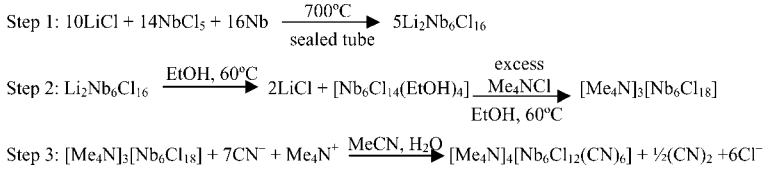


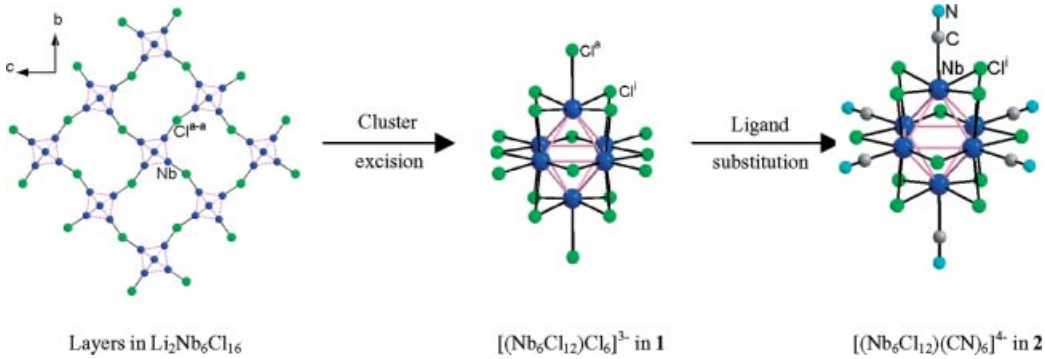


Scheme 1.

 © 2007 Wiley-VCH Verlag GmbH & Co. KGaA, Weinheim 

sider each cluster as an entity and follow the nomenclature that is widely used for assemblies built from hexacyanometalates and metal complexes.[24,25] For example, supramolecular assemblies with two metal complexes attached to one cluster will be referred to as heterotrimers.

In compounds **3**, **4**, and **6**, each cluster is coordinated by one, two, or four manganese complexes to give di-, tri-, and pentamers. Each cluster in **5** is coordinated by two $[Ca(phen)_2(H_2O)_3]^{2+}$ to give neutral trimeric units, whereas **7** is built from a combination of cationic heptamers and anionic trimers. In all these compounds, the supramolecular assemblies are held together through significant hydrogen bonding to form one-, two-, and three-dimensional frameworks.

### 4.1 Anionic Heterodimers

Reactions between methanolic solutions of **2** and [Mn(*L1*)]Cl afforded $[Me_4N][Mn(L1)(MeOH)_2]_2\{[Mn(L1)(MeOH)][Nb_6Cl_{12}(CN)_6]\}$ (**3**).[26] In **3**, each cluster is coordinated by one $[Mn(L1)(MeOH)]^+$ through a Nb–C≡N–Mn linkage to give anionic heterodimers $\{[Mn(L1)(MeOH)][Nb_6Cl_{12}(CN)_6]\}^{3-}$ (Figure 3a). Only one of the six CN ligands is bridging, whereas the other five are involved in extensive hydrogen bonding. The bond length of the bridging C≡N ligand [1.150(7) Å] is significantly longer than those for nonbridging CN ligands [1.133(7) Å]. IR spectra show a broad unsymmetrical absorption band at 2134 $cm^{-1}$, which corresponds to the CN bond stretching frequency. The Mn–C≡N linkage is significantly bent [∠Mn–N≡C = 150.3(4)°] because of the electronic structure of the metal complex. The heterodimers are connected to each other through strong hydrogen bonds between the $CN^-$ ligand and the coordinated MeOH molecule. The dimers are further connected to each other by two solvated metal complexes $[Mn(L1)(MeOH)_2]^+$ through hydrogen bonding between the $CN^-$ ligand and the coordinated MeOH to afford hybrid tubular-like chains (Figure 3b). The manganese adopts distorted octahedral coordination environments ($MnN_3O_3$ in the dimer and $MnN_2O_4$ in the cations). The chains lie on top of each other when viewed along the crystallographic *a* axis to form layers within which the chains are parallel to each other and separated by solvent molecules and cations. The layers are related to each other by an inversion center. Analogous dimers built from hexacyanometalates and $Mn^{III}$ Schiff-base complexes were found in $[Et_4N]_2\{[Mn(saldmen)(H_2O)][Fe(CN)_6]\}$ (**I**).[27]

The anionic charge of the heterodimer is balanced by two solvated Mn complex cations, which leads to an $Mn:Nb_6$ ratio of 3:1; however, **3** also formed even when the starting ratio $Mn:Nb_6$ was increased to 6:1. Interestingly, direct mixing of the two solutions followed by vigorous stirring led to slow formation of the Prussian-blue analogue $[Me_4N]_2[MnNb_6Cl_{12}(CN)_6]$[9] probably because of slow decomposition of the manganese complex in methanol followed by further hydrolysis to afford $Mn^{2+}$ ions.[28]

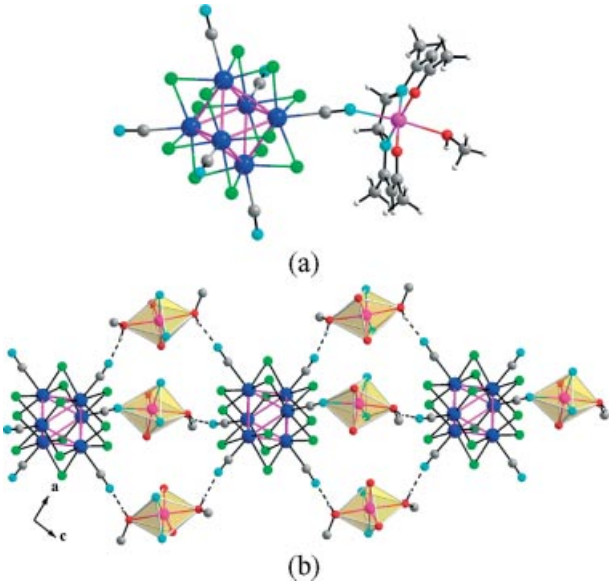


Figure 3. (a) The anionic heterodimeric unit $\{[Mn(L1)(MeOH)][Nb_6Cl_{12}(CN)_6]\}^{3-}$. (b) The anionic tubular-like chain built through extensive hydrogen bonding. *L1* ligands except $N_2O_2$ atoms, and all hydrogen atoms except those involved in hydrogen bonding are omitted for clarity. Hydrogen bonding is represented as dashed lines. The Mn complexes are shown as $\{MnN_3O_3\}$ and $\{MnN_2O_4\}$ octahedra.

### 4.2 Anionic Heterotrimers

Reactions between $[Et_4N]_4[Nb_6Cl_{12}(CN)_6]$ and $[Mn(L2)](ClO_4)\cdot 2H_2O$ in methanol led to precipitation of $[Et_4N]_2\{[Mn(L2)(MeOH)]_2[Nb_6Cl_{12}(CN)_6]\}$ (**4**).[19] In **4**, each cluster is *trans*-coordinated by two $[Mn(L2)(MeOH)]^+$ complexes to afford anionic heterotrimers $\{[Mn(L2)(MeOH)]_2[Nb_6Cl_{12}(CN)_6]\}^{2-}$ (Figure 4a). The cluster core $[Nb_6Cl_{12}]^{2+}$ in **4** is similar to that found in **3** in terms of its bond lengths and angles. Of the six CN ligands, two link the cluster to Mn complexes, and four have their N atom involved in hydrogen bonding. The bond lengths of the bridging C≡N ligand [1.143(5) Å] are not significantly different from those found for the nonbridging ones [1.146(5) Å]. Only one band at 2131 $cm^{-1}$ in the IR spectrum was observed for the C≡N stretching frequency. The bond angle Mn–C≡N [157.2(3)°] is slightly larger than that in **3** because of the differences between the salen-type ligands. The heterotrimers are connected to each other through hydrogen bonds between coordinated MeOH molecules and $CN^-$ ligands to afford chains along the crystallographic *a* axis (Figure 4b). The chains run parallel to each other and are separated by solvent molecules and ammonium ions.

Analogous trimeric units built from $[M(CN)_6]^{3-}$ (M = Fe, Cr) *trans*-coordinated by two Mn Schiff-base (SB) complexes have been previously reported.[29–31] For instance, in $K\{[Mn(5\text{-}Br\text{-}salen)(H_2O)]_2[Fe(CN)_6]\}\cdot 2H_2O$ (**II**) each $[Fe(CN)_6]^{3-}$ anion is coordinated by two solvated Mn complexes to afford the units $\{[Mn(5\text{-}Br\text{-}salen)(H_2O)]_2[Fe(CN)_6]\}^-$.

 © 2007 Wiley-VCH Verlag GmbH & Co. KGaA, Weinheim 

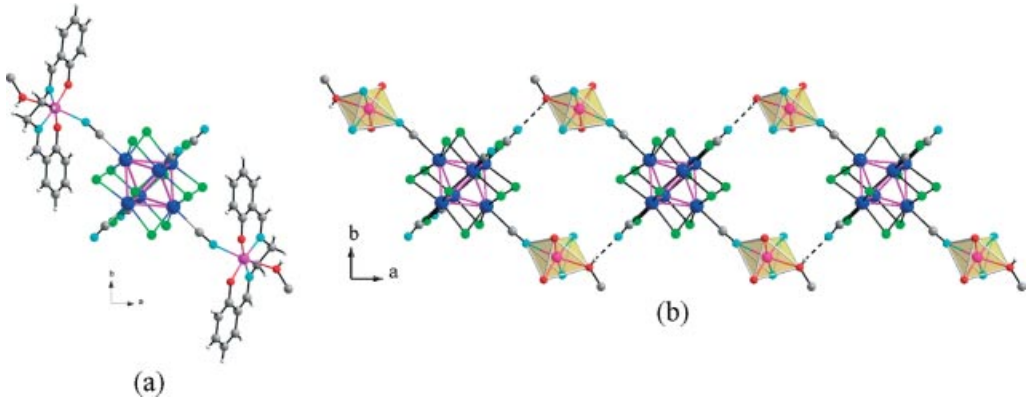


Figure 4. (a) The anionic heterotrimeric unit $\{[Mn(L2)(MeOH)]_2[Nb_6Cl_{12}(CN)_6]\}^{2-}$ in which each cluster is coordinated by two $[Mn(L2)(MeOH)]^+$ complexes in a *trans* fashion. (b) The anionic chain along the *a* axis in which the heterotrimeric units are connected to each other through hydrogen bonds. All hydrogen atoms except those involved in hydrogen bonding are omitted.

### 4.3 Neutral Heterotrimers

$\{[Ca(phen)_2(H_2O)_3]_2[Nb_6Cl_{12}(CN)_6]\}$ (**5**) was obtained by mixing a solution of $Ca(NO_3)_2$ and phen (mol ratio = 1:2) in $H_2O$/EtOH with an aqueous solution of $[Me_4N]_4[Nb_6Cl_{18}]$ and KCN.[32] In **5**, each cluster is *trans*-coordinated by two $[Ca(phen)_2(H_2O)_3]^{2+}$ complexes through Nb–C≡N–Ca linkages to form neutral trimeric units $\{[Ca(phen)_2(H_2O)_3]_2[Nb_6Cl_{12}(CN)_6]\}$ (Figure 5a). Each Ca ion is coordinated by four N atoms from two phen ligands, one N atom from the cyanide ligand, and three O atoms from water molecules to give an overall eight coordination environment (distorted square antiprism) that is common for calcium.[33–35] For the cyanide ligands coordinated to Ca ions, the C≡N bond length is 1.149(9) Å, whereas for nonbridging cyanide ligands the bond lengths range from 1.11(1) to 1.15(1) Å. Only one absorption band at

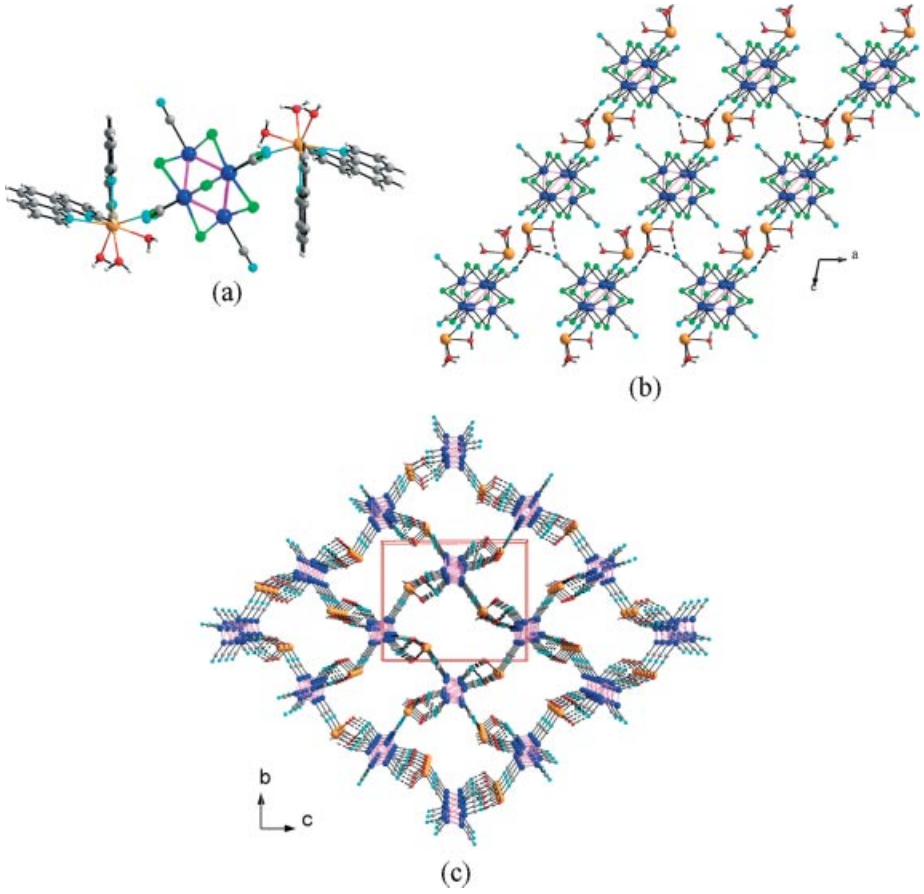


Figure 5. (a) The neutral trimeric unit $\{[Ca(phen)(H_2O)_3]_2[Nb_6Cl_{12}(CN)_6]\}$ in which each cluster is coordinated by two $[Ca(phen)(H_2O)_3]^{2+}$ complexes in a *trans* fashion. (b) Projection along the *b* axis of the neutral layer in which each trimeric unit links four trimeric units through hydrogen bonding. phen Ligand and all hydrogen atoms except those involved in hydrogen bonding are omitted. (c) Perspective view along the *a* axis, which shows the 3D framework of **5**. Inner chloride ligands are omitted.

 © 2007 Wiley-VCH Verlag GmbH & Co. KGaA, Weinheim 

2128 $cm^{-1}$ was observed for the C≡N stretching frequency. Each trimer is linked to four neighboring trimers by hydrogen bonds between the aqua ligand in $[Ca(phen)_2(H_2O)_3]^{2+}$ and the cyanide ligands to afford layers (Figure 5b). The layers are further connected by hydrogen bonds between calcium complexes and cluster units from neighboring layers to form a 3D framework (Figure 5c). Hydrogen-bonded frameworks built from similar trimeric units in which mononuclear hexacyanometalates such as $[Fe(CN)_6]^{3-}$ and Ca-phen complexes have been reported, as is the case in {$[Ca(phen)_2(H_2O)_2][Fe(CN)_6][Ca(phen)_2(H_2O)(NO_3)]$}- (**III**).[36,37]

### 4.4 Heteropentamers

Slow evaporation of a solution of $[Me_4N]_4[Nb_6Cl_{12}(CN)_6]$ and a sixfold excess of [Mn(*L1*)]Cl in partially dried acetonitrile resulted in crystals of {$[Mn(L1)(MeCN)]_2[Mn(L1)(H_2O)]_2[Nb_6Cl_{12}(CN)_6]$} (**6**).[26] In **6**, each cluster uses four CN ligands to connect to four solvated manganese complexes: two $[Mn(L1)(MeCN)]^+$ complexes and two $[Mn(L1)(H_2O)]^+$ complexes to form neutral heteropentamers (Figure 6a). The complexes are located opposite to each other across the cluster and are related by an inversion center. The average bond length of the bridging cyanide ligands is 1.148(4) Å, which is close to that of nonbridging cyanide ligands [1.145(5) Å]. In the IR spectrum, only one broad absorption band at 2142 $cm^{-1}$ is observed. The bond length $Mn–N_{CN}$ [2.26(2) Å] is slightly shorter than that found in **3** and **4**. The pentamers link to each other through hydrogen bonds between the cyanide and aqua ligands from adjacent assemblies and form chains (Figure 6b) that run parallel to each other and interact through acetonitrile solvent molecules.

Pentameric units of this type have been found in compounds built from hexacyanometalate and Mn Schiff-base complexes such as $\{[Mn(saltmen)(H_2O)]_4[Fe(CN)_6]\}(ClO_4)$[27] in which the pentamers are hydrogen bonded to each other, and $\{[Mn_2(saltmen)_2]_2[Fe(CN)_6]\}(ClO_4)\cdot H_2O$ (**IV**)[29] which is a 2D coordination polymer built from the pentamers $\{[Mn(saltmen)]_4[Fe(CN)_6]\}^+$ linked through phenoxo bridges between the manganese complexes.

In the synthesis of **6**, it was observed that a small amount of water in the acetonitrile plays an important role in its formation. When dry acetonitrile was used and extra care was taken to reduce inadvertent exposure to moisture, a 3D coordination polymer $[Me_4N]\{[Mn(L1)]_3[Nb_6Cl_{12}(CN)_6]\}$ (**12**) was obtained (vide infra).[38] Despite the availability of two cyanide ligands, attempts to increase the nuclearity of the supramolecular assemblies by using a tenfold excess of [Mn(*L1*)]Cl were not successful. Only when the reaction was performed in a $MeOH/H_2O$ mixture were heptameric assemblies containing a cluster connected to six manganese complexes isolated (vide infra).

### 4.5 Heteroheptameric and Heterodimeric Supramolecules

When **2** was mixed with [Mn(*L1*)]Cl in a $MeOH/H_2O$ mixture, $\{[Mn(L1)(H_2O)]_4[Mn(L1)]_2[Nb_6Cl_{12}(CN)_6]\}\{[Mn(L1)]_2[Nb_6Cl_{12}(CN)_6]\}$ (**7**) was isolated. Its structure consists of the heptamers $\{[Mn(L1)(H_2O)]_4[Mn(L1)]_2[Nb_6Cl_{12}(CN)_6]\}^{2+}$ (Figure 7a) and trimers $\{[Mn(L1)]_2[Nb_6Cl_{12}(CN)_6]\}^{2-}$ (Figure 7b). The cation assembly consists of $[Nb_6Cl_{12}(CN)_6]^{4-}$ linked to six Mn complexes by way of Nb–C≡N–Mn linkages. Two complexes are pentacoordinate, two oxygen atoms and two nitrogen atoms from the Schiff-base ligand and one nitrogen atom from the cyanide ligand, which leads to a distorted square-pyramidal coordination geometry. The complexes are related to each other by an inversion centre. The other four manganese ions are coordinated by two oxygen atoms and two nitrogen atoms from the tetradentate ligand, one nitrogen from the cyanide ligand, and one oxygen from the solvent molecule, which leads to the formation of a distorted octahedral environment. The overall shape of the heptameric cation can be described as a large flattened sphere with a diameter of about 2.1 nm. The anionic trimer is built from $[Nb_6Cl_{12}(CN)_6]^{4-}$ complexes coordinated by two pentacoordinate manganese complexes that are similar to those observed in the heptamer. The trimers are similar to those found in **4** except that the manganese ions in **4** are hexacoordinate because of the presence of a solvent molecule as a ligand. Hydrogen bonds between the $CN^-$ ligand from the

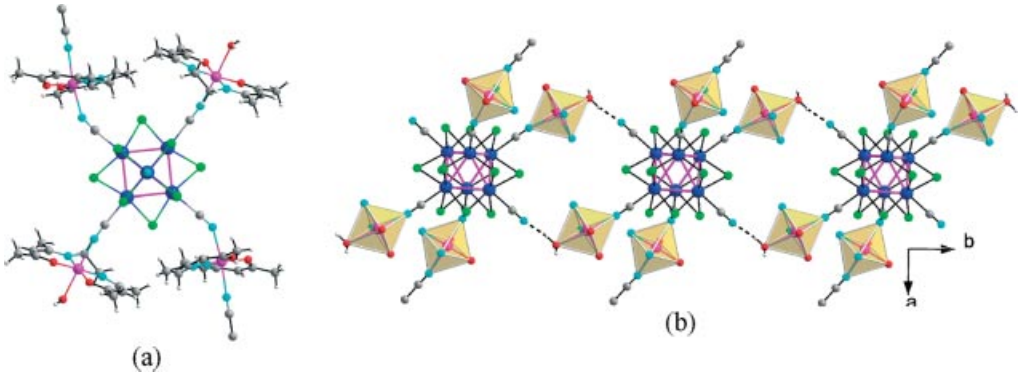


Figure 6. (a) The heteropentamers $\{[Mn(L1)(MeCN)]_2[Mn(L1)(H_2O)]_2[Nb_6Cl_{12}(CN)_6]\}$ in which each cluster is coordinated by two $[Mn(L1)(MeCN)]^+$ complexes and two $[Mn(L1)(H_2O)]^+$ complexes. (b) Neutral chains extending along the *b* axis in which heteropentameric units are connected to each other through hydrogen bonding.

 © 2007 Wiley-VCH Verlag GmbH & Co. KGaA, Weinheim 

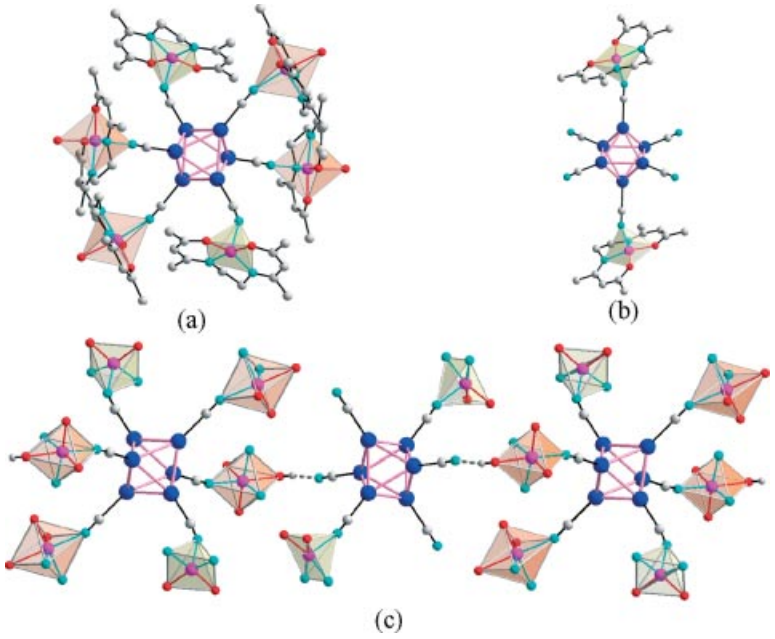


Figure 7. (a) The heteroheptamer $\{[Mn(L1)(H_2O)]_4[Mn(L1)]_2[Nb_6Cl_{12}(CN)_6]\}^{2+}$ complex where each cluster is coordinated by four $[Mn(L1)(H_2O)]^+$ complexes and two $[Mn(L1)]^+$ complexes. (b) The heterotrimer $\{[Mn(L1)]_2[Nb_6Cl_{12}(CN)_6]\}^{2-}$ where each cluster is linked to two $[Mn(L1)]^+$ complexes in the *trans* position. (c) Chains built from hydrogen bonding between coordinated water molecules from cations and cyanide ligands from anions.

anions and the coordinated $H_2O$ molecules from the cations lead to the formation of chains (Figure 7c). The C≡N bond length [1.146(4) Å] for the ligands coordinated to the hexacoordinate Mn complex is longer than that for the CN ligand coordinated to the pentacoordinate manganese [1.137(4) Å]. The average bond length of $Mn–N_{CN}$ for the pentacoordinate Mn complex [2.150(3) Å] is significantly shorter than that found in the hexacoordinate Mn complex [2.287(3) Å] as a result of the solvent coordination effect.

The structure of compound **7** is interesting in terms of the coexistence of the cationic heteroheptamers and anionic heterotrimers as well as penta- and hexacoordinate Mn ions. However, both penta- and hexacoordinate Mn ions have been observed in $[Mn(L2)]_4[Re_6Te_8(CN)_6]$[17a] in which two $[Mn(L2)]^+$ complexes bridge the cluster units to give a 2D framework whereas two other complexes are attached to one cluster unit only through the $N_{CN}$ atom. Similar cationic–anionic assemblies have been observed in compounds containing hexacyanometalates $[M(CN)_6]^{3-}$ (M = $Fe^{3+}$, $Cr^{3+}$) as building units.[39,40] For example, $\{[Mn(L2)(H_2O)]_6[Fe(CN)_6]\}[Fe(CN)_6]$ (**V**)[41] is built from $[Fe(CN)_6]^{3-}$ complex anions coordinated by six solvated $[Mn(L2)(H_2O)]^+$ complex cations to form the heptamer $\{[Mn(L2)(H_2O)]_6[Fe(CN)_6]\}^{3+}$.

## 5. Coordination Polymers Built from $[Nb_6Cl_{12}(CN)_6]^{4-}$ and Metal Complexes

The species described in Section 4 can be described as octahedral clusters ligated by one, two, four, and six metal complexes to form larger supramolecular assemblies. In most cases, the solvent completes the preferred octahedral coordination environment for $Mn^{III}$, which prevents the formation of coordination polymers. Judicious choice of the synthetic conditions such as cations, solvents, stoichiometries, metal complexes, and salen-type ligands led to the preparation of coordination polymers with 1D, 2D, and 3D frameworks. The framework dimension depends on the cluster/metal complex ratio and the connectivity mode between the two building units. The clusters in all the coordination polymers are similar to those found in supramolecular assemblies in terms of bond lengths and angles.

### 5.1 One-Dimensional Coordination Polymers

Two coordination polymers with one-dimensional frameworks built from $[Nb_6Cl_{12}(CN)_6]^{4-}$ and $[Mn(L)]^+$ connected by cyanide ligands have been characterized. The salen-type ligand and the solvent system determine which one of these two compounds forms.

$[Me_4N]_3\{[Mn(L1)][Nb_6Cl_{12}(CN)_6]\}$ (**8**) cocrystallized with $[Me_4N]_2[MnNb_6Cl_{12}(CN)_6]$ from the reaction of equimolar amounts of **2** and $[Mn(L1)]Cl$ in dry MeCN. It crystallizes in the tetragonal symmetry (space group: $I4_1/a$) and is formed from two sets of chains related to each other by a $4_1$ screw axis (Figure 8a). In **8**, each cluster is coordinated by two $[Mn(L1)]^+$ complex cations through Nb–C≡N–Mn linkages, and each $[Mn(L1)]^+$ complex connects two clusters to give anionic zigzag chains $\{[Mn(L1)][Nb_6Cl_{12}(CN)_6]\}_\infty^{3-}$ (Figure 8b) that extend along the crystallographic *a* and *b* axes. The chains are bent with ∠Mn–N≡C of 152.9(2)° and 156.5(3)°. The Nb–C bond length associated with the bridging cyanide ligands [2.301(3) Å] is larger than that of a nonbridging cyanide ligand [2.268(3) Å]. The bond length for a

 © 2007 Wiley-VCH Verlag GmbH & Co. KGaA, Weinheim 

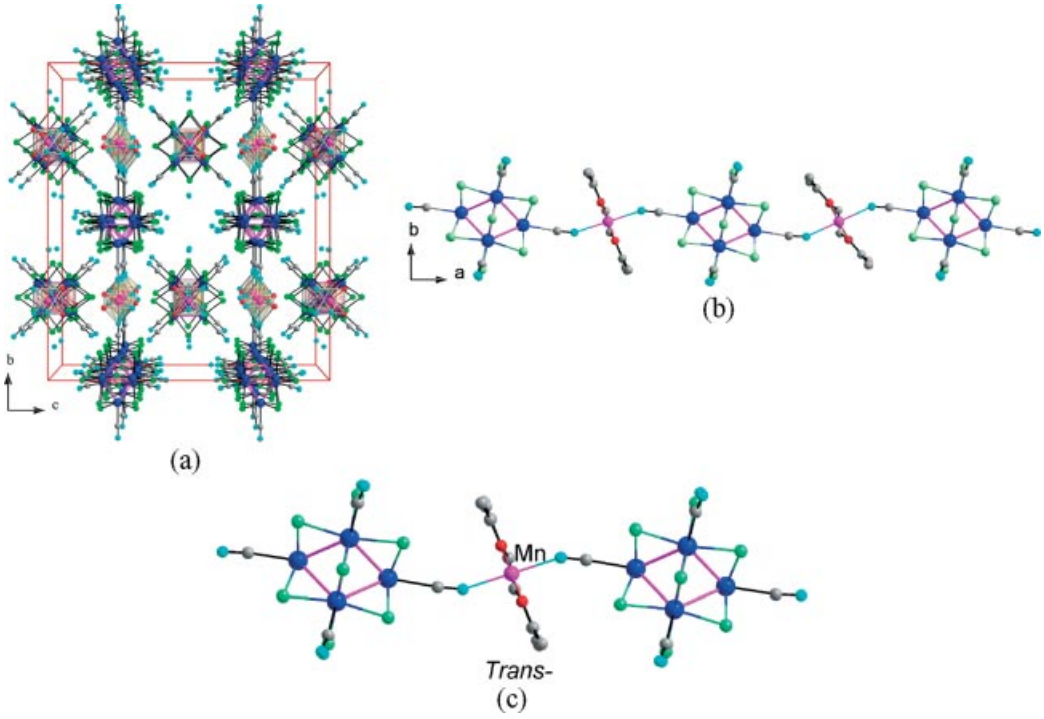


Figure 8. (a) Perspective view of the 1D coordination polymer $[Me_4N]_3\{[Mn(L1)]\ [Nb_6Cl_{12}(CN)_6]\}$ (**8**); (b) The anionic zigzag chain extending along the *a* axis. (c) Each Mn complex is coordinated by two cluster units in a *trans* conformation. The Mn complexes are shown as $\{MnN_4O_2\}$ octahedra.

bridging C≡N ligand [1.145(4) Å] is slightly longer than that for a nonbridging C≡N group [1.139(4) Å]. Two Mn–$N_{CN}$ bond lengths are observed [2.332(3) and 2.382(3) Å] and they are longer than those found in all supramolecular assemblies described above. The chains belong to the 2,2-TT type because each cluster is *trans* coordinated by two Mn complexes and each Mn complex is connected to two clusters in a *trans* conformation (Figure 8c).[42] The chains are stacked parallel to each other along the *ac* and *ab* planes and are separated by solvent molecules and ammonium ions (Figure 8a).

$[Me_4N]_3\{[Mn(L3)][Nb_6Cl_{12}(CN)_6]\}$ (**9**) was obtained from reaction of **2** with $[Mn(L3)(MeOH)](ClO_4)$ in methanol (mol ratio $[Nb_6Cl_{12}(CN)_6]^{4-}$:$[Mn(L3)]^+ \approx 1.0$).[38] It is a 1D coordination polymer with the same cluster complex connectivity as that observed for **8**. Each cluster is connected to two complexes through two cyanide ligands on opposite sides, and each complex connects two clusters to afford anionic zigzag chains $\{[Mn(L3)][Nb_6Cl_{12}(CN)_6]\}_\infty^{3-}$ that extend along the crystallographic *c* axis. The chains stack parallel to each other along the *a* axis (Figure 9a) to form layers parallel to the *ac* plane. Ammonium ions and solvent molecules are located between the chains. The Nb–C bond lengths for the bridging C≡N ligands are 2.278(8) and 2.288(8) Å, slightly larger than those for nonbridging CN ligands [2.25(1)–2.271(9) Å]. The bond lengths of the bridging C≡N ligand [1.129(9) and 1.126(9) Å] are significantly smaller than those for nonbridging cyanide ligands [1.15(1) Å]. Yet only one broad asymmetric band is observed in the IR spectrum at 2128 $cm^{-1}$. The Mn–N≡C

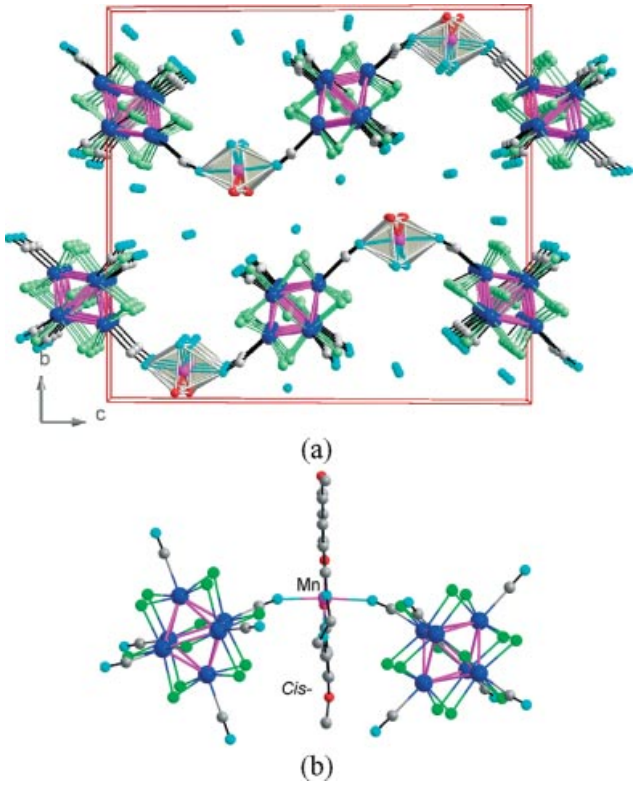


Figure 9. (a) Perspective view of the structure of 1D coordination polymer $[Me_4N]_3\{[Mn(L3)]\ [Nb_6Cl_{12}(CN)_6]\}$ (**9**) along the crystallographic *a* axis; (b) each Mn complex is coordinated by two cluster units in the *cis* conformation.

 © 2007 Wiley-VCH Verlag GmbH & Co. KGaA, Weinheim 

linkage [∠Mn–N≡C = 148.59(8)°] is bent to a greater extent than in **8**. The $N_{CN}$–Mn–$N_{CN}$ linkage [∠$N_{CN}$–Mn–$N_{CN}$ = 174.2(2)°] is also slightly more bent compared to that observed in **8**. The geometric conformation of the metal complex dictates the topology of the chains in **8** and **9**. In **8**, each manganese is linked to two clusters located on opposite sides of the $N_{CN}$–Mn–$N_{CN}$ axis (*trans* conformation), whereas in **9**, each Mn complex is linked to two clusters located on the same side of the $N_{CN}$–Mn–$N_{CN}$ axis (*cis* conformation) (Figure 9b). Complex **9** is an expanded analogue of $[Et_4N]_2\{[Mn(L1)][Fe(CN)_6]\}$ (**VI**) in which $[Mn(L1)]^+$ and $[Fe(CN)_6]^{3-}$ are linked by CN ligands to afford chains.[43]

Reactions between $[Et_4N]_3[Fe(CN)_6]$ and $[Mn(L3)(H_2O)]^+$ in methanol led to the formation of $[Et_4N]\{[Mn_2(L3)_2][Fe(CN)_6]\}$ built from phenoxo-bridged dimers $[Mn_2(L3)_2]^{2+}$ and $[Fe(CN)_6]^{3-}$ linked by the cyanide ligand to form one dimensional coordination polymers.[44] The formation of the dimeric Mn complexes is most likely due to the relative stability of the monomer versus the dimer, which depends on the solvent used.

### 5.2 Two-Dimensional Coordination Polymers

Direct mixing of dilute methanolic solutions of **2** and $[Mn(L2)](ClO_4)$ (mol ratio complex:cluster = 2) led to quantitative formation of $[Me_4N]_2\{[Mn(L2)]_2[Nb_6Cl_{12}(CN)_6]\}$ (**10**).[19] Polymer **10** can be obtained as a microcrystalline powder when the molar ratio $[Mn(L2)]^+$:$[Nb_6Cl_{12}(CN)_6]^{4-}$ ranges from 1.0 to 4.0. In **10**, each cluster is coordinated by four $[Mn(L2)]^+$ complexes through Nb–C≡N–Mn linkages and each $[Mn(L2)]^+$ complex connects two $[Nb_6Cl_{12}(CN)_6]^{4-}$ anionic complexes to generate anionic layers $\{[Mn(L2)]_2[Nb_6Cl_{12}(CN)_6]\}_\infty^{2-}$ that are parallel to the *bc* plane (Figure 10b). The Nb–C bond lengths associated with bridging cyanide ligands are about 2.29 Å and longer than those associated with nonbridging cyanides (2.27 Å). In contrast, the C≡N bond lengths are all about 1.13 Å, which is consistent with the observation of only one absorption band in the IR spectrum at 2134 $cm^{-1}$ for the C≡N stretch. The Mn–$N_{CN}$ bond lengths are significantly different from each other and vary between 2.23 and 2.36 Å owing to the bowl-shaped salen-type ligand *L2* with the longer Mn–$N_{CN}$ linkages on the concave side of the ligand. The Mn–N≡C bond angles are also significantly different, 144.2(3) and 155.0(3)°, respectively. The two phenyl groups of the *L2* ligand in **10** are located in a *cis* fashion with respect to the basal $N_2O_2$ plane; in contrast, the phenyl groups in $[Mn(L2)](ClO_4)$[45], which is used as a precursor, are located in a *trans* fashion.[46] The layers are stacked in a staggered fashion along the crystallographic *a* axis and are separated by ammonium ions that are found in the vicinity of the uncoordinated cyanide ligands (Figure 10a). Similar layers have been observed in $[Mn(L2)]_4[Re_6Te_8(CN)_6]$[17a] in which $Re_6$ clusters are coordinated by six [Mn(*L2*)], two of which are dangling. Polymer **10** represents a cluster-expanded analogue of the compound $[Et_4N]\{[Mn(L2)]_2[Fe(CN)_6]\}$ (**VII**)[47] in which each $[Fe(CN)_6]^{3-}$ is linked to four complexes and each complex links two ferricyanides to form anionic layers that stack perfectly on top of each other contrary to the stacking in **10**.

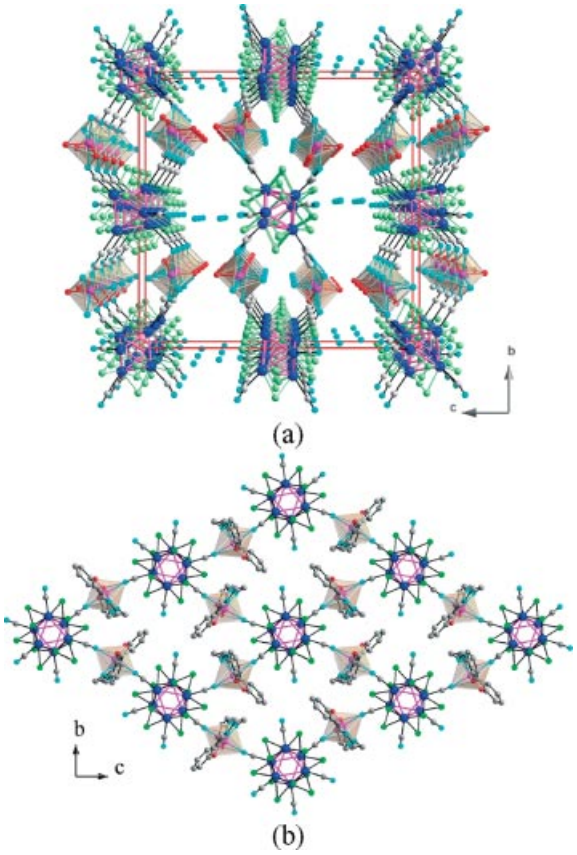


Figure 10. (a) Perspective view of the structure of 2D coordination polymer $[Me_4N]_2\{[Mn(L2)][Nb_6Cl_{12}(CN)_6]\}$ (**10**) along the crystallographic *a* axis; (b) A projection of the anionic layer parallel to the crystallographic *bc* plane along the *a* axis.

### 5.3 Effect of the Metal Complex Coordination Requirements: The Layered Framework of $[Zn(en)]_2[Nb_6Cl_{12}(CN)_6]$

The topology, dimension, and properties of frameworks built from clusters and metal complexes presumably depend on the metal complex and the coordination preferences of the metal ion. The use of $[Zn(en)]^{2+}$ and the cluster as building units led to the formation of $[Zn(en)]_2[Nb_6Cl_{12}(CN)_6]$ (**11**) which has a layered framework and was obtained from the reaction between an aqueous solution of $Na_4[Nb_6Cl_{12}(CN)_6]$ and an ethanolic solution containing equimolar amounts of $Zn(ClO_4)_2{\cdot}6H_2O$ and en.[48] The structure of **11** consists of neutral layers in which each cluster $[Nb_6Cl_{12}(CN)_6]^{4-}$ is coordinated by six $[Zn(en)]^{2+}$ complexes through Nb–C≡N–Zn linkages and each $[Zn(en)]^{2+}$ is connected to three cluster units to afford layers parallel to the *ab* plane (Figure 11a). Although the C≡N bond lengths are all found at ca. 1.15 Å, not much different

 © 2007 Wiley-VCH Verlag GmbH & Co. KGaA, Weinheim 

from that observed in **10**, the C≡N IR bond stretch frequency appears at 2167 $cm^{-1}$, which is much higher than that observed for **10**. The Zn–N bond length [2.051(8) Å] is shorter than that of the Mn–N bond found in compounds containing supramolecular assemblies and coordination polymers and reflects the smaller ionic radius of $Zn^{2+}$. The Zn–N≡C bond angle is 172.5(9)°, which is close to those found for Ca–N≡C in **5** [172.9(8)°] but larger than the Mn–N≡C bond angles in **3**, **4**, and **6**–**9** [144.2(3)–165.8(3)°]. The layers stack on top of each other along the *c* axis and are held together only through weak Van der Waals interactions. Projection along the crystallographic *b* axis indicates that [Zn(en)] complexes are alternatively located above and below the plane (Figure 11b).

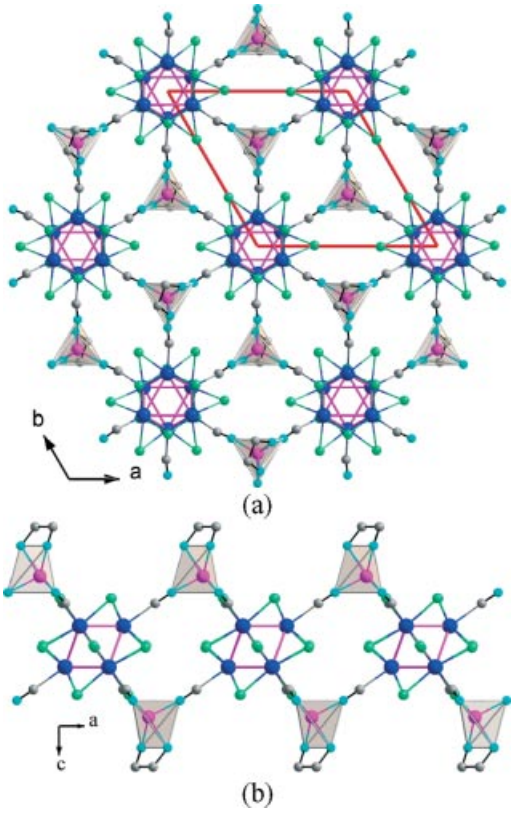


Figure 11. (a) A projection of the layer in $[Zn(en)]_2[Nb_6Cl_{12}(CN)_6]$ (**11**) along the *c* axis. (b) A projection of the layer along the crystallographic *b* axis, which shows that the [Zn(en)] complexes are alternatively located above and below the plane.

Similar layers have been observed in $[Zn(H_2O)]_2[Fe(CN)_6]$[49] and in $[Zn(H_2O)]_2[Re_6Se_8Fe(CN)_6]$.[8k] However, in contrast to **11** where $Zn^{2+}$ is coordinated by two N atoms from the chelating en ligand and three $N_{CN}$ atoms from three different clusters to form a distorted square pyramid $ZnN_5$, in the latter compounds $Zn^{2+}$ is coordinated by one oxygen atom from the aqua ligand and three $N_{CN}$ atoms, which leads to the formation of distorted $ZnN_3O$ tetrahedra. The layers in **11** can be considered as expanded layers of the $CdCl_2$ or $CdI_2$ structure types[50,51] in which the $[Nb_6Cl_{12}]^{2+}$ cluster core takes the place of $Cd^{2+}$, and the complex anion $[Zn(en)(CN)_3]^-$ takes the place of the halide; thus the chemical formula can be written as $[Nb_6Cl_{12}][Zn(en)(CN)_3]_2$. However, the layers are stacked on top of each other in **11**, whereas in $CdCl_2$ and $CdI_2$, the layers are staggered.

### 5.4 Three-Dimensional Coordination Polymers

$[Me_4N]\{[Mn(L1)]_3[Nb_6Cl_{12}(CN)_6]\}$ (**12**) was obtained from the reaction of **2** with [Mn(*L1*)]Cl (8 equiv.) in dry acetonitrile.[38] In the presence of even trace amounts of water in acetonitrile, compound **7** was obtained instead. In **12**, each cluster is coordinated by six $[Mn(L1)]^+$ complexes and each complex links two cluster units to give an overall 3D framework (Figure 12a). The structure consists of identical but symmetry independent layers parallel to the *bc* plane with the same cluster complex connectivity as that found in **10** (Figure 12b). The layers are linked to each other through manganese complexes, which leads to the formation of cavities where the cation and acetonitrile molecules are located. The C≡N bond lengths range between 1.14 and 1.16 Å and only one peak at 2142 $cm^{-1}$ was observed for the C≡N vibrational stretching frequency. This value is larger than that found in the starting materials (2126 $cm^{-1}$) and 2D coordination polymer **10** built from [Mn(*L2*)] (2134 $cm^{-1}$). Two symmetry independent manga-

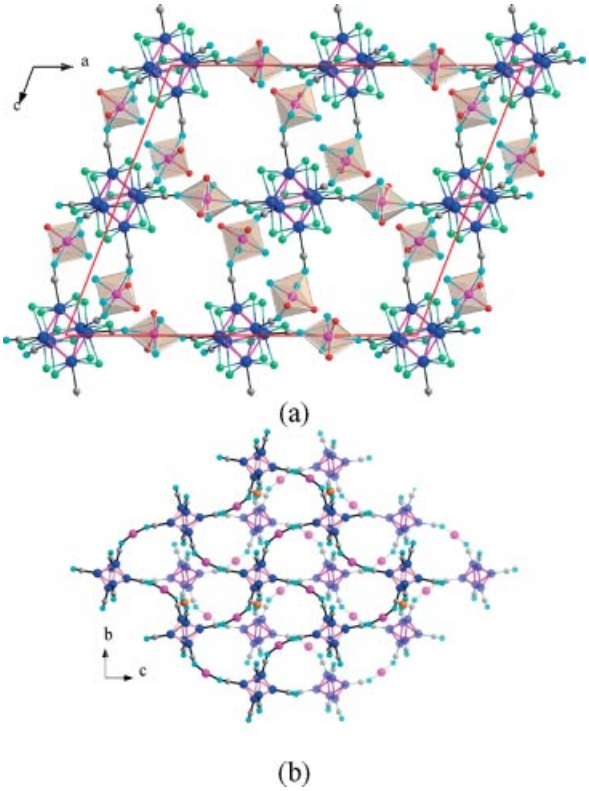


Figure 12. (a) Projection of the structure of the 3D coordination polymer $[Me_4N]\{[Mn(L1)][Nb_6Cl_{12}(CN)_6]\}$ (**12**) along the crystallographic *b* axis; (b) A projection along the *a* direction of two adjacent layers (one is bold and the other is faded), which shows the staggered packing of the layers along the *a* axis. The layers are further connected to each other through an additional set of Mn complexes.

 © 2007 Wiley-VCH Verlag GmbH & Co. KGaA, Weinheim 

nese complexes are used to connect the clusters within the layers with bond lengths $Mn–N_{CN}$ = 2.34 Å, whereas a third manganese complex links the layers together to form the 3D framework with an average bond length $Mn–N_{CN}$ = 2.296 Å. The compound $Na\{[Mn(L2)]_3[Re_6Se_8(CN)_6]\}$[17a] also features a 3D coordination polymer in which each $Re_6$ cluster is surrounded by six Mn complexes.

The overall structure can be considered a 3D framework in which layers found in **10** are connected to each other through additional Mn complexes by using the two remaining CN ligands. The compound has been shown to lose almost all solvent molecules after being washed or when evacuated at room temperature without loss of crystallinity. Careful structural analysis reveals that solvent molecules are not involved in hydrogen bonding.

### 5.5 Effect of the Metal Complex: The 3D Framework of $[Ba(phen)_2(H_2O)]_2[Nb_6Cl_{12}(CN)_6]$ (13)

This compound was synthesized in a one-pot reaction by mixing a solution of $BaCl_2$ and phen (mol ratio = 1:2) in $H_2O$/EtOH with an aqueous solution containing $[Me_4N]_4[Nb_6Cl_{18}]$ and KCN.[32] The cyanochloride cluster was generated in situ. The structure of **13** is a neutral 3D framework built from $[Nb_6Cl_{12}(CN)_6]^{4-}$ and $[Ba(phen)_2(H_2O)]^{2+}$ (Figure 13a). Each cluster unit is linked to six barium complexes through cyanide ligands and each Ba complex links three clusters. Two crystallographically independent Ba complexes are present and arranged in a *mer* conformation around the cluster. Each set of Ba complexes links the cluster units to form ladder-like chains along the *c* and *b* axis (Figure 13b); this generates channels along the crystallographic *a* axis in which the phen ligands are located. The bond length of C≡N is about 1.14 Å yet two C≡N stretches were observed in the IR spectrum (2122, 2131 $cm^{-1}$). In addition to three N atoms from the cyanide ligands, each barium is additionally coordinated by four N atoms from two phen ligands and one O atom from a water molecule. Extended frameworks containing Ba-phen complexes and hexacyanometalates as building units have been reported. For instance, $\{[Ba_2(phen)_4(H_2O)_6][Fe(CN)_6]\}Cl$ (**VIII**)[52] is built from dimeric unit $[Ba_2(phen)_4(H_2O)_6]^{4+}$ and $[Fe(CN)_6]^{3-}$ and they are connected to each other by CN ligands to form chains. The dimers $[Ba_2(phen)_4(H_2O)_6]^{4+}$ are built from monomers $[Ba(phen)_2(H_2O)_2]^{2+}$ that are connected to each other by two water molecules through Ba–O–Ba linkages. Ba ions are nine-coordinate by four N atoms from two phen ligands, four O atoms from water molecules, and one N atom from a cyanide ligand.

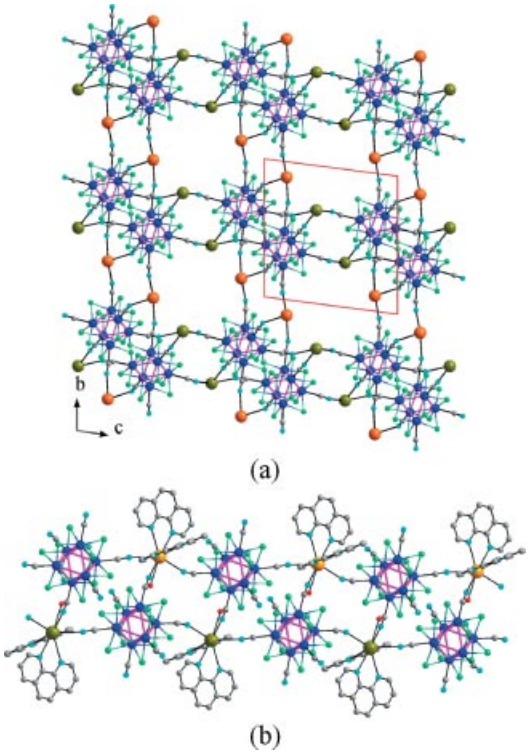


Figure 13. (a) Projection of the 3D framework found in $[Ba(phen)_2(H_2O)]_2[Nb_6Cl_{12}(CN)_6]$ (**13**) along the *a* direction. Water molecules and phen ligands located within the cavities have been omitted for clarity. (b) Ba complexes link cluster units to afford ladder chains along the *c* direction.

## 6. Properties

### 6.1 Thermal Stability

The thermal stability of compounds built from cluster units and Mn complexes depends on the nature of their framework. Thus, when heated to 200 °C in air-flow, materials built from supramolecular assemblies lose their crystallinity after losing all solvent molecules essential to the formation of the hydrogen-bonded frameworks. Figure 14 shows typical TGAs for materials based on supramolecular assemblies and coordination polymers. The stability of the

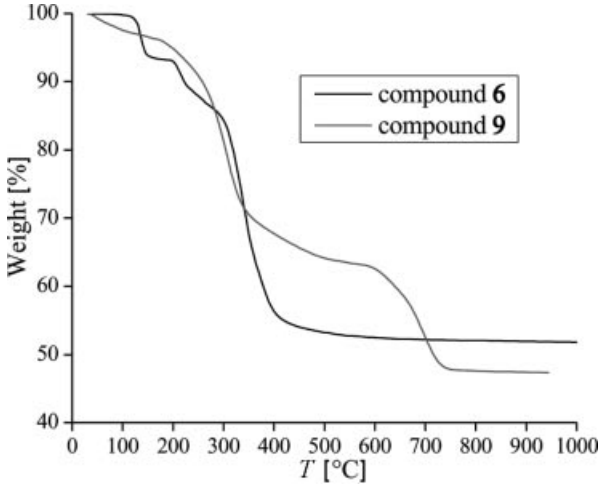


Figure 14. TGA of **6** built from supramolecular assemblies and **9** characteristic of coordination polymer heated from 30 °C to 950 °C at 5 °C /min under air-flow (40 mL/min).

 © 2007 Wiley-VCH Verlag GmbH & Co. KGaA, Weinheim 

coordination polymers is different because the solvent molecules are not involved in building the frameworks. When heated in air-flow, the product obtained after 700 °C is generally a mixture of metal oxides with compositions determined by the ratio of Mn:$Nb_6$ in the initial material. When the ratio Mn:$Nb_6$ = 1 or 2, the product is a mixture of $MnNb_2O_6$ and $Nb_2O_5$, and when Mn/$Nb_6$ = 3, only $MnNb_2O_6$ is observed. The thermal decomposition can be described by the following chemical equation:

$\{[Mn(L)]_n[Nb_6Cl_{12}(CN)_6]\} + [(15 + n)/2 + n]O_2 \rightarrow nMnNb_2O_6 + (3 - n)Nb_2O_5$ ($n$ = 1, 2, 3)

It is worth noting that the columbite $MnNb_2O_6$ forms in the temperature range 400–750 °C, much lower than the temperatures (800–1400 °C) at which $MnNb_2O_6$ is prepared through conventional mixed oxide route.[53]

### 6.2 Magnetic Properties

In all compounds described above, the Nb–Nb bond lengths are characteristic of diamagnetic 16-electron clusters.[18] The effective magnetic moment in **6**, **10**, and **12** are characteristic of high-spin $Mn^{III}$ ions. For example, for **12** the $\mu_{eff}$ value at 300 K is 5.17 $\mu_B$, close to the calculated value of the spin-only effective moment of the high-spin $Mn^{3+}$ ion (4.90 $\mu_B$). As the compound is cooled from 300 K to 20 K, the effective magnetic moment remains almost the same and then decreases slowly. The data were fitted with the Curie–Weiss relation $\chi(T) = \chi_0 + C/(T - \theta)$ to give C = 3.36 emu K $mol^{-1}$ and $\theta$ = –2.02 K (Figure 15). No evidence of magnetic exchange coupling between the $Mn^{III}$ centers was observed even for the 3D framework of **12**. This is different from the case of the Prussian-blue $Fe^{III}_4[Fe^{II}(CN)_6]_3 \cdot 14H_2O$ in which the $Fe^{III}$ ions are separated from each other by diamagnetic $Fe^{II}$ ions, yet ferromagnetic coupling ($T_c$ = 5.6 K) was observed.[54] Two reasons can account for this: 1) the large size of the cluster units, which separate two $Mn^{III}$ ions, results in a Mn interdistance of 15.1(2) Å for **12**, and 2) the electronic structure of the diamagnetic 16-electron cluster.

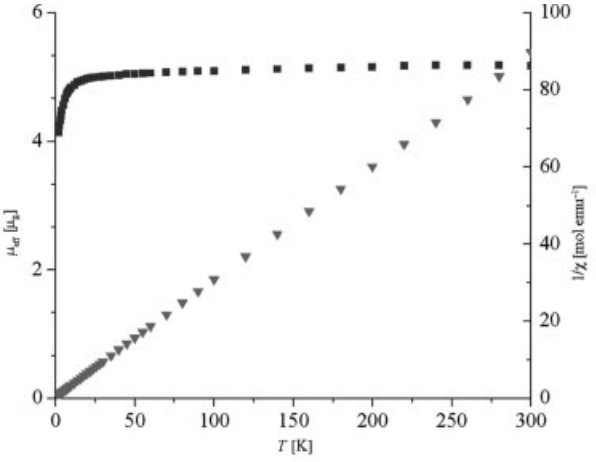


Figure 15. Plot of $\mu$ (left) and $1/\chi$ (right) versus $T$ of **12** measured under a 1 kG magnetic field.

## 7. Conclusion

Octahedral niobium cyanochloride clusters and coordinatively unsaturated metal complexes have been successfully used as components of larger assemblies. Two types of assemblies have been obtained depending on the metal complex chosen, the solvent system, and the molar ratios used. Table 1 summarizes the most important bond lengths and angles, as well as the $\nu$(C≡N) bond stretching frequency of the compounds described here and their analogues based on $[Fe(CN)_6]^{3-}$. The following observations can be made: 1) Supramolecular assemblies in which the cluster is progressively coordinated by one, two, four, and six metal complexes have been obtained. The size of these supramolecules increases from 1.5 to 2.4 nm as the number of metal complexes per cluster increases. The cluster-based supramolecules are about 0.5 to 0.8 nm larger than analogous species built from $[Fe(CN)_6]^{3-}$ and metal complexes, which is consistent with the fact that the size of $[Nb_6Cl_{12}(CN)_6]^{4-}$ is about 0.5 nm larger than $[Fe(CN)_6]^{3-}$. 2) The functionalization of the cluster unit by attaching a different number of metal complexes led to the formation of different species with different charges. 3) The dimension and topology of coordination polymers built from clusters and metal complexes are dictated by the coordination requirements of the metal complex and the connectivity mode between the metal complex and the cluster. Thus, $Mn^{III}$ Schiff-base complexes containing two free coordination sites are used to build 1D, 2D, and 3D coordination polymers as the cluster uses two, four, and six CN ligands to link to the metal complex and the Mn:$Nb_6$ ratio increases from 1 to 3. Both $[Zn(en)]^{2+}$ and $[Ba(phen)_2(H_2O)]^{2+}$ use three coordination sites to build either 2D and 3D coordination polymers because of the availability of three coordination sites. 4) Though similarities between the compounds reported here and their counterparts that are built from $[Fe(CN)_6]^{3-}$ or $Re_6$ clusters are observed, the compounds differ from each other in terms of their structural features and properties. The reactivity of $[Nb_6Cl_{12}(CN)_6]^{4-}$ towards metal complexes is also different from that of $[Fe(CN)_6]^{3-}$ and $Re_6$ clusters. 5) The formation of supramolecular assemblies results from the substitution of ammonium ions with coordinatively unsaturated metal complexes. Di-, tri-, and pentameric supramolecules are formed as the number of Mn complexes attached to the cluster increases. The process can be represented by the following chemical equation:

$[Me_4N]_4[Nb_6Cl_{12}(CN)_6] + n[Mn(L)]+ \rightarrow [Me_4N]_{4-n}\{[Mn(L)]_n[Nb_6Cl_{12}(CN)_6]\} + n[Me_4N]+ (0 \leq n \leq 4)$

6) The formation of 1D, 2D, and 3D coordination polymers is governed by the same chemical equation as above. As $n$ increases from 1 to 3, 1D, 2D, and 3D frameworks are obtained. These coordination polymers can be viewed as supramolecular units connected to each other by additional clusters. Thus, the 1D polymer can be described as being formed from heterotrimers connected to cluster units to form chains, the 2D material can be described as heteropen-

 © 2007 Wiley-VCH Verlag GmbH & Co. KGaA, Weinheim 

Table 1. Most important bond lengths [Å] and bond angles [°] and the $\nu$(C≡N) [$cm^{-1}$] for the compounds described in the present review and their iron(III) hexacyanide analogues.[a]

| | **3** | **I** | **4** | **II** | **5** | **III** | **6** | **IV** | **7** | **V** |
|---|---|---|---|---|---|---|---|---|---|---|
| Nb(Fe)–C | 2.279(7) | 1.94(4) | 2.286(14) | 1.933(5) | 2.288(7) | 1.943(6) | 2.286(6) | 1.97(8) | 2.282(8) | 1.941(2) |
| C≡N | 1.140(6) | 1.15(1) | 1.144(2) | 1.164(6) | 1.14(2) | 1.1531 | 1.147(2) | 1.13(3) | 1.142(3) | 1.149(2) |
| Nb(Fe)–C≡N | 175.7(13) | 177.6(8) | 176.7(5) | 178.8(4) | 177(2) | 177(2) | 176.7(18) | 177.7(17) | 177(2) | 177.7(2) |
| Mn–$N_{CN}$ | 2.280(5) | 2.198(9) | 2.295(3) | 2.332(3) | 2.54(1)[a] | 2.50(1)[a] | 2.26(2) | 2.193 | 2.150(3), 2.287(3) | 2.334(2) |
| Mn–$N_{CN}$≡C | 150.3(4) | 162.4(8) | 157.2(3) | 146.6(3) | 172.9(8)[a] | 149(2)[a] | 148.6(3), 165.8(3) | 156(1) | 150.3(3)–161.5(3) | 150.7(1) |
| $\nu_{CN}$ | 2134 | 2104 | 2131 | 2128, 2110 | 2128 | 2118 | 2143 | 2118 | 2140, 2128 | 2108, 2115 |
| | **8** | **9** | **VI** | **10** | **VII** | **11** | **12** | **13** | **VIII** | |
| Nb(Fe)–C | 2.28(1) | 2.27(1) | 1.958(6) | 2.279(7) | 1.941(5) | 2.260(8) | 2.28(1) | 2.286(8) | 1.94(1) | |
| C≡N | 1.144(5) | 1.13(1) | 1.147(2) | 1.133(4) | 1.162(8) | 1.15(1) | 1.149(8) | 1.140(5) | 1.150(3) | |
| Nb(Fe)–C≡N | 175.6(14) | 175(3) | 177.1(4) | 175.1(3) | 177(1) | 172.6(9) | 175.3(25) | 169.7(6)–177.4(7) | 176.9(8) | |
| Mn–$N_{CN}$ | 2.36(3) | 2.345(3) | 2.316(4) | 2.233(3), 2.365(3) | 2.266(3), 2.337(3) | 2.051(8)[b] | 2.31(3) | 2.803(6)–2.864(8)[c] | 2.835(7)[c] | |
| Mn–$N_{CN}$≡C | 152.9(2), 156.5(3) | 148.59(8) | 152.5(3) | 144.2(3), 155.0(3) | 146.2(2), 167.8(3) | 172.5(9)[b] | 145.3(7)–158.3(7) | 130.5–172.6[c] | 157.7(3), 165.8(2)[c] | |
| $N_{CN}$–Mn–$N_{CN}$ | 178.92(3) | 174.2(2) | 172.0(2) | 173.3(1) | 169.4(1) | 100.16(2)[b] | 168.3(2)–176.1(3) | 142.3(2)[c] | N/A | |
| $\nu_{CN}$ | 2127 | 2127 | 2124 | 2131 | 2106, 2131 | 2167 | 2132 | 2122, 2131 | 2100, 2104 | |

[a] Compounds **I**–**VIII** are based on $[Fe(CN)_6]^{3-}$ as building units and were used to compare compounds based on mononuclear hexacyanides to their cluster analogues.

tamers linked by way of cluster units, whereas the 3D framework consists of heteroheptamers connected by cluster units.

Further studies are necessary to advance our understanding of this system and to allow the preparation of materials with tailored structural features and properties. The stability of the supramolecular assemblies in solution is of interest in order to study their potential use as larger building units for the preparation of materials with more complex structures. More important are the opportunities these assemblies present in terms of their functionalization by use of different metal complexes and different ligands. The rate-limiting step of advances in this field, as in many other areas of synthesis, is the preparation of single-crystals suitable for structural characterization. The use of powder XRD to solve and refine the crystal structure is in most cases of little use as PXRD patterns are generally dominated by four or five peaks. For instance, in the case of the Prussian-blue analogues, the structure initially determined from PXRD was significantly different from that determined later from single-crystal XRD. Magnetic studies of supramolecular assemblies and coordination polymers show that no magnetic coupling was observed between the cluster units and the metal ions or between the metal ions through cluster units, possibly a result of the diamagnetism and large size of the metal cluster. Oxidation–reduction of the cluster and its use as a building unit may lead to modification of the physical properties of the materials obtained. Recently, the 15-electron cluster $[Nb_6Cl_{12}(CN)_6]^{3-}$ was isolated, and it is being investigated as a building unit in complexes to determine its effect on magnetic properties.

## Acknowledgments

This material is based upon work supported by the National Science Foundation under Grant No. DMR-0446763 and partial support through grant DMR-0305245.

[1] a) J. Rebek, *Angew. Chem. Int. Ed. Engl.* **1990**, *29*, 245–255; b) F. Vögtle, *Supramolecular Chemistry*, John Wiley & Sons, New York, **1991**; c) A. Harada, K. Li, M. Kamachi, *Nature* **1994**, *370*, 126–128.

[2] a) J. M. Lehn, *Science* **1993**, *260*, 1762–1763; b) J. M. Lehn, *Supramolecular Chemistry: Concepts and Perspectives*, VCH, Weinheim, **1995**; c) D. B. Amabilino, J. F. Stoddart, *Chem. Rev.* **1995**, *95*, 2725–2828; d) M. C. T. Fyfe, J. F. Stoddart, *Acc. Chem. Res.* **1997**, *30*, 393–401; e) A. Harada, J. Li, M. Kamachi, *Nature* **1992**, *356*, 325–327.

[3] a) G. M. J. Schmidt, *Pure Appl. Chem.* **1971**, *27*, 647–678; b) G. R. Desiraju, *Crystal Engineering: The Design of Organic Solids*, Elsevier, Amsterdam, **1989**; c) M. C. Etter, *Acc. Chem. Res.* **1990**, *23*, 120–126; d) G. R. Desiraju, *Nature* **2001**, *412*, 397–400.

[4] M. Verdaguer, A. Bleuzen, V. Marvaud, J. Vaissermann, M. Seuleiman, C. Desplanches, A. Scuiller, C. Train, R. Garde, G. Gelly, C. Lomenech, I. Rosenman, P. Veillet, C. Cartier, F. Villain, *Coord. Chem. Rev.* **1999**, *190–192*, 1023–1047 and references therein.

[5] R. Chevrel, M. Sergent, J. Prigent, *J. Solid State Chem.* **1971**, *3*, 515–519.

[6] a) S. C. Lee, R. H. Holm, *Angew. Chem. Int. Ed. Engl.* **1990**, *29*, 840–856; b) T. Saito in *Early Transition Metal Clusters with π-Donor Ligands* (Ed.: M. H. Chisholm), VCH, **1995**; c) T. Saito, *Adv. Inorg. Chem.* **1997**, *44*, 45–91; d) N. Prokopuk, D. F. Shriver, *Adv. Inorg. Chem.* **1998**, *46*, 1–49; e) T. Saito, *J. Chem. Soc., Dalton Trans.* **1999**, 97–106; f) J. C. P. Gabriel, K. Boubekeur, S. Uriel, P. Batail, *Chem. Rev.* **2001**, *101*, 2037–2066; g)

 © 2007 Wiley-VCH Verlag GmbH & Co. KGaA, Weinheim 

E. J. Welch, J. R. Long, *Prog. Inorg. Chem.* **2005**, *54*, 1–45 and references therein.

[7] a) T. J. Paskach, G. L. Schrader, R. E. McCarley, *J. Catal.* **2002**, *211*, 285–295; b) S. Kamiguchi, M. Watanabe, K. Kondo, M. Kodomari, T. Chihara, *J. Mol. Catal. A* **2003**, *203*, 153–163; c) S. Kamiguchi, M. Noda, Y. Miyagishi, S. Nishida, M. Kodomari, T. Chihara, *J. Mol. Catal. A* **2003**, *195*, 159–171; d) S. Kamiguchi, S. Iketani, M. Kodomari, T. Chihara, *J. Cluster Sci.* **2004**, *15*, 19–31; e) S. Kamiguchi, S. Nishida, M. Kodomari, T. Chihara, *J. Cluster Sci.* **2005**, *16*, 77–91; f) S. Kamiguchi, A. Nakamura, A. Suzuki, M. Kodomari, M. Nomura, Y. Iwasawa, T. Chihara, *J. Catal.* **2005**, *230*, 204–213.

[8] a) S. Jin, F. J. DiSalvo, *Chem. Commun.* **2001**, 1586; b) S. Jin, F. J. DiSalvo, *Chem. Mater.* **2002**, *14*, 3448; c) N. G. Naumov, A. V. Virovets, V. E. Fedorov, *J. Struct. Chem.* **2000**, *41*, 499–520; d) V. E. Fedorov, N. G. Naumov, Y. V. Mironov, A. V. Virovets, S. B. Artemkina, K. A. Brylev, S. S. Yarovoi, O. A. Efremova, U. H. Peak, *J. Struct. Chem.* **2002**, *43*, 669–684; e) Y. V. Mironov, V. E. Fedorov, I. Ijjaali, J. A. Ibers, *Inorg. Chem.* **2001**, *40*, 6320–6323; f) K. A. Brylev, Y. V. Mironov, N. G. Naumov, V. E. Fedorov, J. A. Ibers, *Inorg. Chem.* **2004**, *43*, 4833–4838; g) M. P. Shores, L. G. Beauvais, J. R. Long, *J. Am. Chem. Soc.* **1999**, *121*, 775–779; h) L. G. Beauvais, M. P. Shores, J. R. Long, *J. Am. Chem. Soc.* **2000**, *122*, 2763–2772; i) M. V. Bennett, M. P. Shores, L. G. Beauvais, J. R. Long, *J. Am. Chem. Soc.* **2000**, *122*, 6664–6668; j) Y. Kim, S. K. Choi, S. M. Park, W. Nam, S. J. Kim, *Inorg. Chem. Commun.* **2002**, *5*, 612–615, k) L. G. Beauvais, L. G. Shores, J. R. Long, *Chem. Mater.* **1998**, *10*, 3783.

[9] B. B. Yan, H. J. Zhou, A. Lachgar, *Inorg. Chem.* **2003**, *42*, 8818–8822.

[10] S. Leininger, B. Olenyuk, P. J. Stang, *Chem. Rev.* **2000**, *100*, 853–907.

[11] B. J. Holliday, C. A. Mirkin, *Angew. Chem. Int. Ed.* **2001**, *40*, 2022–2043 and references therein.

[12] R. Cortés, K. Urtiaga, L. Lezama, J. L. Pizarro, A. Goñi, M. I. Arriortua, T. Rojo, *Inorg. Chem.* **1994**, *33*, 4009–4015.

[13] M. Monfort, I. Resino, M. S. E. Fallah, J. Ribas, X. Solans, M. Font-Bardia, H. Stoeckli-Evans, *Chem. Eur. J.* **2001**, *7*, 280–287.

[14] H. D. Selby, B. K. Roland, Z. P. Zheng, *Acc. Chem. Res.* **2003**, *36*, 933–944 and references therein.

[15] E. N. Jacoben, *Acc. Chem. Res.* **2000**, *33*, 421–431.

[16] A. Vogler, H. Nikol, *Pure Appl. Chem.* **1992**, *64*, 1311–1317.

[17] a) Y. Kim, S. M. Park, W. Nam, S. J. Kim, *Chem. Commun.* **2001**, 1470–1471; b) Y. Kim, S. M. Park, W. Nam, S. J. Kim, *Inorg. Chem. Commun.* **2002**, *5*, 592–595.

[18] E. V. Anokhina, Ph. D. Thesis, Wake Forest University, **2001** and references therein.

[19] H. J. Zhou, C. S. Day, A. Lachgar, *Chem. Mater.* **2004**, *16*, 4870–4877.

[20] F. W. Koknat, R. E. McCarley, *Inorg. Chem.* **1974**, *13*, 295–300.

[21] N. G. Naumov, S. Cordier, C. Perrin, *Solid State Sci.* **2003**, *5*, 1359–1367.

[22] V. P. Fedin, I. V. Kalinina, A. V. Virovets, N. V. Podberezskaya, I. S. Neretin, Y. L. Slovokhotov, *Chem. Commun.* **1998**, 2579–2580.

[23] L. H. Jones, *Inorg. Chem.* **1963**, *2*, 777–780.

[24] V. Marvaud, C. Decroix, A. Scuiller, F. Tuyèras, C. Guyard-Duhayon, J. Vaissermann, J. Marrot, F. Gonnet, M. Verdaguer, *Chem. Eur. J.* **2003**, *9*, 1692–1705.

[25] V. Marvaud, C. Decroix, A. Scuiller, C. Guyard-Duhayon, J. Vaissermann, F. Gonnet, M. Verdaguer, *Chem. Eur. J.* **2003**, *9*, 1677–1691.

[26] H. J. Zhou, A. Lachgar, *Cryst. Growth Des.* **2006**, *6*, 2384–2391.

[27] H. Miyasaka, H. Ieda, N. Matsumoto, N. Re, R. Crescenzi, C. Florián, *Inorg. Chem.* **1998**, *37*, 255–263.

[28] M. I. Fernández, M. Fondo, A. M. García-Deibe, B. Fernández, M. J. Rodríguez, M. R. Bermejo, *Transition Met. Chem.* **2002**, *27*, 416–422.

[29] H. Miyasaka, N. Matsumoto, H. Ōkawa, N. Re, E. Gallo, C. Floriani, *J. Am. Chem. Soc.* **1996**, *118*, 981–994.

[30] H. J. Choi, J. J. Sokol, J. R. Long, *Inorg. Chem.* **2004**, *43*, 1606–1608.

[31] H. Miyasaka, N. Matsumoto, N. Re, E. Gallo, C. Floriani, *Inorg. Chem.* **1997**, *36*, 670–676.

[32] Z. H. Yan, C. S. Day, A. Lachgar, *Inorg. Chem.* **2005**, *44*, 4499–4505.

[33] G. Smith, E. J. O'Reilly, C. H. L. Kennard, A. H. White, *J. Chem. Soc., Dalton Trans.* **1985**, 243–251.

[34] X. M. Chen, T. C. W. Mak, *Polyhedron* **1994**, *13*, 1087–1090.

[35] X. M. Chen, T. C. W. Mak, *Inorg. Chem.* **1994**, *33*, 2444–2447.

[36] A. Datta, N. K. Karan, S. Mitra, E. R. Tiekink, *Polyhedron* **2002**, *21*, 2237–2241.

[37] A. Datta, G. M. Hossain, N. K. Karan, K. M. Malik, S. Mitra, *Inorg. Chem. Commun.* **2003**, *6*, 266–269.

[38] H. J. Zhou, B. Cloix, C. S. Day, A. Lachgar, *Chem. Mater.* **2006**, submitted.

[39] R. J. Parker, L. Spiccia, K. J. Berry, G. D. Fallon, B. Moubarakia, K. S. Murraya, *Chem. Commun.* **2001**, 333–334.

[40] R. J. Parker, L. Spiccia, S. R. Batten, J. D. Cashion, G. D. Fallon, *Inorg. Chem.* **2001**, *40*, 4696–4704.

[41] X. P. Shena, B. L. Lia, J. Z. Zou, H. M. Hu, Z. Xu, *J. Mol. Struct.* **2003**, *657*, 325–331.

[42] J. Černák, M. Orendáč, I. Potočňák, J. Chomič, A. Orendáčová, J. Skoršepa, A. Feher, *Coord. Chem. Rev.* **2003**, *224*, 51–66.

[43] N. Re, E. Gallo, C. Floriani, H. Miyasaka, M. Matsumoto, *Inorg. Chem.* **1996**, *35*, 6004–6008.

[44] M. Ferbinteanu, H. Miyasaka, W. Wernsdorfer, K. Nakata, K. I. Sugiura, M. Yamashita, C. Coulon, R. Clerac, *J. Am. Chem. Soc.* **2005**, *127*, 3090–3099.

[45] H. Li, Z. J. Zhong, C. Duan, X. You, T. C. W. Mak, B. Wu, *J. Coord. Chem.* **1997**, *41*, 183–189.

[46] A. Garcia-Deibe, A. Sousa, M. R. Bermejo, P. P. Macrory, C. A. McAuliffe, R. G. Pritchard, M. Hellwell, *J. Chem. Soc., Chem. Commun.* **1991**, 728–729.

[47] H. Miyasaka, H. Ieda, N. Matsumoto, K. I. Sugiura, M. Yamashita, *Inorg. Chem.* **2003**, *42*, 3509–3515.

[48] B. B. Yan, C. S. Day, A. Lachgar, *Chem. Commun.* **2004**, 2390–2391.

[49] H. Siebert, B. Nuber, W. Jentsch, *Z. Anorg. Allg. Chem.* **1981**, *474*, 96–104.

[50] D. E. Partin, M. O'Keeffe, *J. Solid State Chem.* **1991**, *95*, 176–183.

[51] G. K. Chadha, *Z. Kristallogr.* **1974**, *139*, 147–152.

[52] N. K. Karan, S. Mitra, G. Rosair, D. J. Jenkins, K. M. Abdul-Malik, *Inorg. Chem. Commun.* **2001**, *4*, 712–715.

[53] a) H. J. Lee, K. S. Hong, S. J. Kim, I. T. Kim, *Mater. Res. Bull.* **1997**, *32*, 847; b) R. C. Pullar, J. D. Breeze, N. M. Alford, *J. Am. Ceram. Soc.* **2005**, *88*, 2466.

[54] A. Ito, M. Suenaga, K. Ono, *J. Chem. Phys.* **1968**, *48*, 3597.

Received: September 25, 2006
Published Online: February 13, 2007

 © 2007 Wiley-VCH Verlag GmbH & Co. KGaA, Weinheim 

DOI: 10.1002/ejic.200600957

# Synthesis and Structure of Cyclic Trinuclear Zinc Disiloxides

Clemens Krempner,*[a] Helmut Reinke,[a] and Katja Weichert[a]

**Keywords:** Oligosilanes / Zinc / Siloxides / Clusters

The synthesis and structure of the new disilane-1,2-diol $[(Me_3Si)_2SiOH]_2$ (**2b**) and the trinuclear zinc disiloxides of the formula $[Me_2Si\{(Me_3Si)_2SiO\}_2]_2Zn_3Me_2$ (**3a**), $[\{(Me_3Si)_2SiO\}_2]_2Zn_3Me_2$ (**3b**) and $[E\text{-}\{Me(Me_3Si)_3SiSiO\}_2]_2Zn_3Me_2$ (**3c**) are reported. Compounds **3a**–**c** were prepared by reactions of the corresponding silanedioles **2a**–**c** with $ZnMe_2$. The results of an X-ray structure analysis of **3b** reveal an almost perfectly planar spirocyclic $Zn_3O_4$ core with a square-planar geometry of the inner $Zn^{2+}$ ion, whereas in **3a**,**c** the inner zinc ions are distorted tetrahedral. Upon treatment with $B(C_6F_5)_3$, compounds **3b**,**c** have been converted quantitatively into the complexes $[\{(Me_3Si)_2SiO\}_2]_2Zn_3(C_6F_5)_2$ (**4b**) and $[E\text{-}\{Me(Me_3Si)_3SiSiO\}_2]_2Zn_3(C_6F_5)_2$ (**4c**).

(© Wiley-VCH Verlag GmbH & Co. KGaA, 69451 Weinheim, Germany, 2007)

## Introduction

There has been a considerable interest in recent years in the chemistry and structures of zinc siloxides as the steric hindrance of the ligand ($R_3SiO^-$) in such compounds can lead to novel structural features and unusual reactivity.[1] For example, some structurally well-defined zinc compounds have been found application as soluble precursors for zinc oxides and silicates.[2] Significant synthetic and structural studies of a variety of mainly monodentate zinc siloxides are reported from the Driess group. They could demonstrate that the degree of aggregation of the central $(ZnO)_n$ core decreases as the bulkiness of the attached siloxide ligand increases.[3] Bidentate cyclic zinc siloxides, however, are rare and the only example has been reported from the reaction of $ZnMe_2$ with $Ph_2Si(OH)_2$, which under self-condensation of the silanol affords a remarkable polycyclic hexanuclear zinc complex with two $Zn_3O_4$ cores.[4]

We have a long-term interest in the synthesis and structural characterization of cyclic five- and six-membered metal disiloxides, as these highly strained cycles might be useful for the selective ring insertion of metal species, which may form novel hetero- and homobimetallic complexes as we have shown recently for a dinuclear titanium disiloxide derived from a mononuclear cyclic species.[5] In this contribution we describe the preparation of a new disilane-1,2-diol and we report on the synthesis of polycyclic trinuclear zinc disiloxides from reactions of $ZnMe_2$ with various sterically congested vicinal silanediols together with their solid-state structures.

## Results and Discussion

A rather straightforward strategy for the design of vicinal silanediols with an oligosilane backbone involves the use of phenyl-substituted metal silanides in salt metathesis reactions. In analogy to the synthesis of the trisilane-1,3-diol **2a** previously reported,[5] treatment of $Ph(Me_3Si)_2Si\text{-}K$ with $BrCH_2CH_2Br$ provides easy access to the diphenyl oligosilane **1b** in high yields.[6] This compound was treated with two equivalents of trifluoromethanesulfonic acid (TfOH) and subsequently hydrolyzed to give almost quantitatively the silanediol **2b** as a colorless solid (Scheme 1). The compound slowly decomposes at room temperature within several days and must be stored in a freezer at ca. –40 °C. However, the structure of **2b** was unambiguously established by standard spectroscopic methods and elemental analysis. The synthesis of the racemic disilane-1,2-diol **2c** has been reported elsewhere.[7]

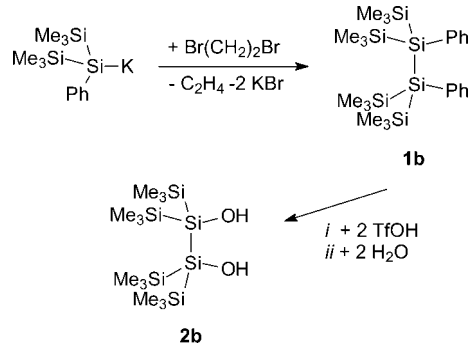


Scheme 1. Synthesis of **2b**.

As reported recently, differently aggregated zinc silanolates can be prepared by acid–base reactions of silanols $R_3SiOH$ (R = Me, Et, *i*Pr, Ph) with $ZnR_2$ (R = Me, Et).

[a] Institut für Chemie der Universität Rostock,
Albert-Einstein-Str. 3a, 18059 Rostock, Germany

 © 2007 Wiley-VCH Verlag GmbH & Co. KGaA, Weinheim 

Employing $ZnMe_2$ as the reagent the trinuclear zinc complexes **3a**–**c** have been synthesized in good yields as outlined in Scheme 2. The NMR and MS data and the results of elemental analysis have confirmed the proposed structures of **3a**–**c**. The NMR ($^1H$, $^{13}C$, $^{19}Si$) spectra of all complexes are rather straightforward and show roughly the same features as observed for the corresponding free ligands **2a**–**c**. For example, the $^1H$ and $^{13}C$ NMR spectra of **3a** exhibit only one signal for the $SiMe_3$ and $SiMe_2$ groups, respectively, and also the $^{29}Si$ NMR spectra showed only one signal for the $SiMe_3$ silicon atoms.

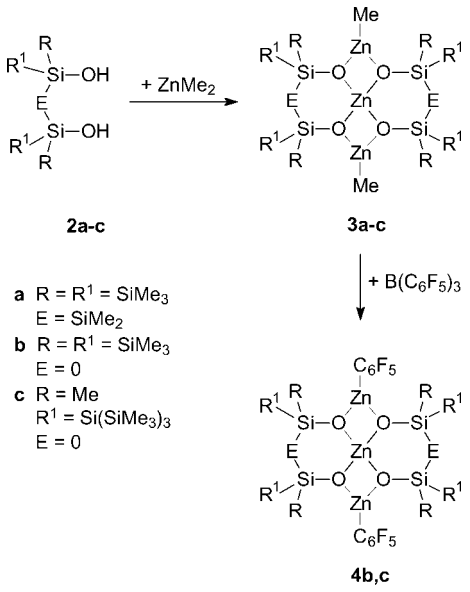


Scheme 2. Synthesis of **3a**–**c** and reaction behavior toward $B(C_6F_5)_3$.

In addition, the solid-state structures of **3a**–**c** have been determined by X-ray crystallography; suitable single crystals were grown from pentane solutions at room temperature. The molecular structures along with selected bond lengths and bond angles are shown in Figure 1, 2, 3, and 4. Compounds **3a**–**c** crystallize in the triclinic space group $P\bar{1}$. All structures consist of fused polycyclic ring systems with central trinuclear $Zn_3O_4$ cores, which are coordinated in a chelate fashion by two diolate ligands, respectively. The coordination of the ligand to the inner zinc ion in **3a** results in the formation of a six-membered ring system with a distorted chair conformation. In **3b** and **3c**, however, five-membered rings are formed, which are either strongly twisted [**3b**; dihedral angle O1–Si2–Si3–O2 32.05(6)°] or almost planar [**3c**; dihedral angle O1–Si3–Si4–O2 2.70(10)°]. The outer zinc atoms of **3a** and **3c** are three-coordinate with trigonal-planar ligand environments, while the inner $Zn^{2+}$ ions are four-coordinate with distorted tetrahedral geometries. Overall, the observed distorted geometries of the $Zn_3O_4$ cores are in good agreement with those of the monodentate zinc siloxides $[(iPr_3SiO)_4Zn_3Me_2]$ (**5**),[2a] $[(Ph_3SiO)_4Zn_3Me_2]$ (**6**)[4] and $[(OSiPh_2OSiPh_2O)(OSiPh_2)OZn_2Me_2 \cdot THF]_2$ (**7**)[4] (see Table 1).

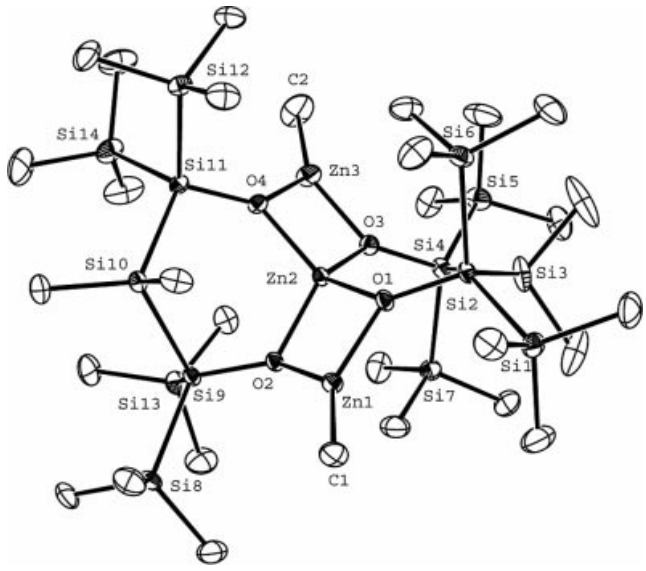


Figure 1. Molecular structure of **3a** in the crystal. The thermal ellipsoids correspond to 30% probability (hydrogen atoms are omitted for clarity). Selected bond lengths [Å] and angles [°]: Zn1–C1 1.942(4), Zn3–C2 1.934(5), Zn2–O1 1.975(2), Zn2–O2 1.968(2), Zn2–O3 1.959(2), Zn2–O4 1.973(2), Zn1–O1 1.952(2), Zn1–O2 1.954(2), Zn3–O3 1.953(2), Zn3–O4 1.959(2), Si2–O1 1.673(2), Si4–O3 1.673(2), Si9–O2 1.678(2), Si11-O4 1.679(2), Si2–Si3 2.3597(14), Si3–Si4 2.3775(14), O3–Zn2–O2 135.37(10), O3–Zn2–O4 85.50(9), O2–Zn2–O4 112.70(9), O3–Zn2–O1 110.92(9), O2–Zn2–O1 84.63(9), O4–Zn2–O1 135.80(10), O1–Zn1–O2 85.64(9), O3–Zn3–O4 86.03(9), C1–Zn1–O1 137.17(14), C2–Zn3–O3 140.12(19), Zn2–O3–Si4–Si3 45.43(18), O3–Si4–Si3–Si2 14.59(12), Si4–Si3–Si2–O1 23.79(12), Si3–Si2–O1–Zn2 43.74(19), Si2–O1–Zn2–O3 21.8(2), O1–Zn2–O3–Si4 34.34(19).

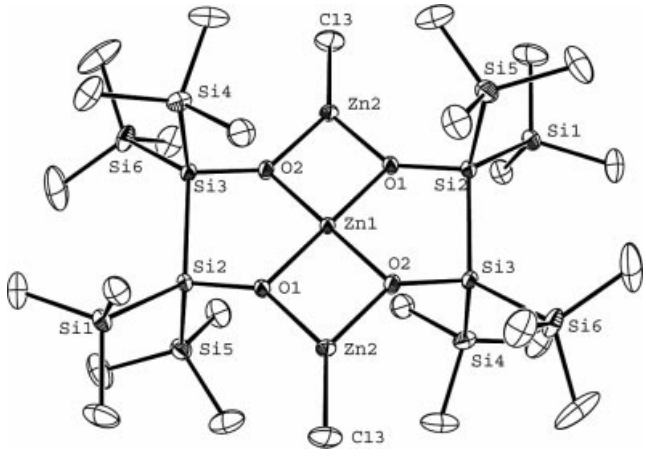


Figure 2. Molecular structure of **3b** in the crystal. The thermal ellipsoids correspond to 30% probability (hydrogen atoms are omitted for clarity). Selected bond lengths [Å] and angles [°]: Zn2–C13 1.9223(16), Zn1–O1 1.9721(9), Zn1–O2 1.9831(10), Zn2–O2 1.9438(10), Zn2–O1 1.9403(10), Si2–O1 1.6744(11), Si3–O2 1.6763(10), Si2–Si3 2.3832(5), O1–Zn1–O2 96.88(4), O1–Zn1–O1A 180.0, O1–Zn1–O2A 83.12(4), O2–Zn2–O1A 84.99(4), O1A–Zn2–C13 137.63(8).

The most remarkable feature of the zinc siloxide **3b**, however, is the unusual square-planar coordination geometry of the inner $Zn^{2+}$ ion. To the best of our knowledge, this is the first completely planar structure with a spirocyclic

 © 2007 Wiley-VCH Verlag GmbH & Co. KGaA, Weinheim 

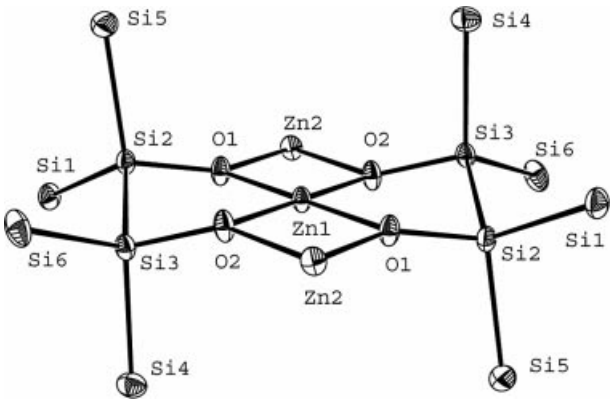


Figure 3. View along the Si2–Si3 axis of **3b**. Selected dihedral angles (all methyl groups are omitted for clarity): Si6–Si3–Si2–Si5 42.01(3)°, O1–Si2–Si3–O2 32.05(6), Si1–Si2–Si3–Si4 44.18(3), Si1–Si2–Si3–Si6 86.92(3), Si5–Si2–Si3–Si4 173.12(2).

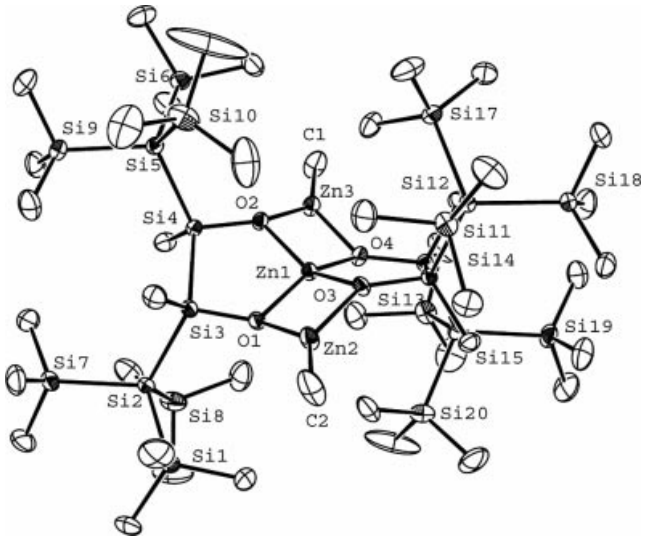


Figure 4. Molecular structure of **3c** in the crystal. The thermal ellipsoids correspond to 30% probability (hydrogen atoms are omitted for clarity). Selected bond lengths [Å] and angles [°]: Zn2–C2 1.934(3), Zn3–C1 1.933(3), Zn1–O1 1.9665(17), Zn1–O2 1.9650(16), Zn1–O3 1.9677(16), Zn1–O4 1.9650(16), Zn2–O1 1.9687(17), Zn2–O3 1.9588(16), Zn3–O2 1.9644(16), Zn3–O4 1.9664(16), Si3–O1 1.6672(17), Si4–O2 1.6650(17), Si13–O3 1.6653(17), Si14–O4 1.6685(17), Si3–Si4 2.4229(9), Si13–Si14 2.4003(9), Si2–Si3 2.3891(10), O2–Zn1–O4 86.64(7), O2–Zn1–O1 101.54(7), O4–Zn1–O1 151.34(8), O2–Zn1–O3 147.62(7), O4–Zn1–O3 100.93(7), O1–Zn1–O3 86.84(7), O3–Zn2–O1 87.02(7), O2–Zn3–O4 86.62(7), C2–Zn2–O3 135.32(12), C2–Zn2–O1 137.66(12), C1–Zn3–O4 134.97(11), O1–Si3–Si4–O2 2.70(10), O3–Si13–Si14–O4 10.53(10).

$Zn_3X_4$ core (X = S, O, N, P). Apart from three planar mononuclear zinc complexes with bidentate phenolate type ligands,[8] only in porphyrin complexes the zinc ion has an almost perfect square-planar coordination environment. A view along the Si2–Si3 axis in **3b** (Figure 3) clearly reveals this arrangement to be mainly enforced by the steric repulsion of the adjacent trimethylsilyl groups. In fact, the steric interactions of the trimethylsilyl groups can be significantly minimized by adopting a staggered conformation along the Si2–Si3 axis, which results in the formation of a planar spirocyclic $ZnO_2ZnO_2Zn$ core. This is not evident for **3a**, because the $SiMe_2$ spacer group, which reduces steric repulsions within the molecule, separates the vicinal trimethylsilyl groups. Consequently the bulky trimethylsilyl groups can adopt an eclipsed conformation, which enables the inner zinc ion to be coordinated in the energetically preferred tetrahedral geometry.

Table 1. Selected average bond lengths [Å] and angles [°] for trinuclear zinc disiloxides.

| Compound | **3a** | **3b** | **3c** | **5**[a] | **6**[b] | **7**[c] |
|---|---|---|---|---|---|---|
| Zn–C | 1.94 | 1.92 | 1.93 | 1.95 | 1.92 | 1.95 |
| Si–O | 1.68 | 1.68 | 1.67 | 1.65 | 1.64 | 1.61 |
| $Zn_{inner}$–O | 1.97 | 1.98 | 1.97 | 1.97 | 1.95 | 1.96 |
| $Zn_{outer}$–O | 1.95 | 1.94 | 1.97 | 1.98 | 1.96/2.01 | 2.02 |
| O–$Zn_{inner}$–O | 85/86 | 83 | 87/87 | 87/87 | 84/86 | 88/88 |
| | 86/111 | 97 | 101/102 | 117/120 | 112/120 | 114/104 |
| | 113/135 | 180 | 148/151 | 120/131 | 124/133 | 133/138 |
| O–$Zn_{outer}$–O | 86 | 85 | 87 | 86 | 84 | 84 |
| Zn–Zn–Zn | 177 | 180 | 177 | 166 | 159 | 176 |

[a] $[(iPr_3SiO)_4Zn_3Me_2]$. [b] $[(Ph_3SiO)_4Zn_3Me_2]$. [c] $[(OSiPh_2OSiPh_2O)(OSiPh_2)OZn_3Me_2{\cdot}THF]_2$.

For comparison, a summary of selected average distances and angles together with those of the complexes recently reported by Driess et al. is given in Table 1. As expected, the Zn–O distances and O–Zn–O angles of the inner zinc ions and also the Zn–C distances in all these complexes are rather similar to each other. It is worthy to note, however, that the Si–O distances in **3a**–**c** are markedly longer and the Zn–O distances for the outer zinc ions are shorter than those of the closely related complexes **5–7**. The longer Si–O distances can be attributed to the specific electronic situation in **3a**–**c**, in which the central silicon atoms possess electropositive silyl groups. These electron-donating groups clearly diminish the capability of silicon to act as strong π acceptor for oxygen, which gives rise to stronger electrostatic oxygen–zinc interactions and consequently to shorter Zn–O distances as compared to **5–7**.

Furthermore, we have investigated the reactivity of the highly strained trinuclear zinc complexes **3b**,**c** towards the Lewis acid $B(C_6F_5)_3$ that is known to abstract alkyl groups from the metal center to form cationic metal species. The reactions were performed at room temperature in a J-Young NMR tubes using [D$_6$]benzene as solvent, and the course of the reaction was monitored by $^1$H NMR spectroscopy. The complexes **3b**,**c** reacted cleanly with $B(C_6F_5)_3$ (molar ratio 1:1) within minutes, resulting in the formation of $[\{(Me_3Si)_2SiO\}_2]_2Zn_3(C_6F_5)_2$ (**4b**) and $[E\text{-}\{Me(Me_3Si)_3SiSiO\}_2]_2Zn_3(C_6F_5)_2$ (**4c**), the quantitative products of a rapid $C_6F_5$ group transfer, as evidenced by multinuclear NMR spectroscopic data. The compounds **4b**,**c** could be isolated in a larger scale and the spectroscopic data obtained were identical to those from the NMR experiments (Scheme 2). Solutions of **4b**,**c** in $C_6D_6$ proved to be fairly stable over a prolonged period of time, and even at higher temperature no substantial decomposition occurred. Similar $C_6F_5$ transfer reactions have been observed for the reaction of $ZnMe_2$.[9] The fact that the $C_6F_5$ groups have re-

 © 2007 Wiley-VCH Verlag GmbH & Co. KGaA, Weinheim 

placed both methyl groups rapidly is somewhat surprising; however, it indicates an increased electrophilicity of the zinc centers caused by the electron-withdrawing disiloxide ligands.

## Experimental Section

**General Remarks:** All manipulations of air- and/or moisture-sensitive compounds were carried out under argon using standard Schlenk and Glove Box techniques. THF, *n*-heptane and *n*-pentane were distilled under argon from alkali metals prior to use. $CH_2Cl_2$ was distilled from $CaH_2$ and stored over molecular sieves. [$D_6$]Benzene was dried with activated molecular sieves and stored in the glove box. $B(C_6F_5)_3$ was prepared as described previously.[10] NMR: Bruker AC 250, Bruker ARX 300. IR: Nicolet 205 FT-IR. MS: Intectra AMD 402, chemical ionization with isobutane as the reactant gas.

**2,3-Dihydroxy-1,1,1,4,4,4-hexamethyl-2,3-bis(trimethylsilyl)tetrasilane (2b):** Freshly distilled TfOH (0.97 mL, 0.011 mol) was added at –40 °C to a stirred solution of **1b** (2.51 g, 0.005 mol) in $CH_2Cl_2$ (25 mL) and the mixture was warmed to room temp. within 2 h. After changing the solvent from $CH_2Cl_2$ to diethyl ether, an aqueous solution of $NH_4COONH_2$ (10 mL, 1 M) was added dropwise and stirring was continued for 30 min. The organic phase was separated, dried with $MgSO_4$, and the solvent was evaporated. Drying under high vacuum afforded 1.76 g (92%) of the title compound, which was kept in a freezer. $^1$H NMR ($C_6D_6$, 250 MHz): $\delta$ = 0.72 (br. s, OH, 2 H), 0.29 [s, $Si(CH_3)_3$, 36 H] ppm. $^{13}$C NMR ($C_6D_6$, 62.9 MHz): $\delta$ = 0.1 [$Si(CH_3)_3$] ppm. $^{29}$Si-INEPT ($C_6D_6$, 59.6 MHz): $\delta$ = 8.1 (SiOH), –15.0 [$Si(CH_3)_3$] ppm. MS (70 eV): *m*/*z* (%) = 383 (8) [$M^+$], 279 (8) [$M^+$ – 2Me – $SiMe_3$], 205 (20) [$M^+$ – Me – 2$SiMe_3$ – OH], 131 (42) [$M^+$ – Me – 3$SiMe_3$ – OH]. $C_{12}H_{38}O_2Si_6$ (382.94): calcd. C 37.64, H 10.00; found C 37.49, H 9.98. IR (Nujol): $\tilde{\nu}_{OH}$ = 3394.4 cm$^{-1}$ (assoc.), 3641.6 cm$^{-1}$ (non-assoc.).

**[$Me_2Si${$(Me_3Si)_2SiO$}$_2$]$_2Zn_3Me_2$ (3a):** Solid **2a** (2.0 g, 4.5 mmol) was added to a vigorously stirred solution of $ZnMe_2$ (2 M, 3.6 mL, 7.2 mmol) in *n*-pentane (20 mL) at –78 °C. After stirring for 2 h at room temp., the solvent was removed under vacuum. Crystallization of a concentrated *n*-pentane solution in a freezer at –40 °C afforded the title compound as colorless crystals. Yield 1.75 g (65%). M.p. 115–117 °C. $^1$H NMR ($C_6D_6$, 250 MHz): $\delta$ = 0.43 [s, $Si(CH_3)_2$, 12 H], 0.34 [s, $Si(CH_3)_3$, 72 H], –0.04 (s, $ZnCH_3$, 6 H) ppm. $^{13}$C NMR ($C_6D_6$, 75.5 MHz): $\delta$ = 1.2 [$Si(CH_3)_3$], –0.4 [$Si(CH_3)_2$], –10.8 ($ZnCH_3$) ppm. $^{29}$Si NMR ($C_6D_6$, 59.6 MHz): $\delta$ = 14.8 (SiOZn), –16.1 [$Si(CH_3)_3$], –37.1 [$Si(CH_3)_2$] ppm. $C_{30}H_{90}O_4Si_{14}Zn_3$ (1104.40): calcd. C 32.63, H 8.21; found C 32.47, H 8.24.

**[{$(Me_3Si)_2SiO$}$_2$]$_2Zn_3Me_2$ (3b):** A heptane solution of **2b** (0.5 g, 1.31 mmol) was added to a vigorously stirred solution of $ZnMe_2$ (2 M, 0.8 mL, 1.6 mmol) in *n*-pentane (20 mL) at –78 °C. After stirring for 2 h at room temp., the solvent was removed under vacuum. Crystallization of a concentrated *n*-pentane solution in a freezer at –40 °C afforded the title compound as colorless crystals. Yield 0.41 g (63%). M.p. 169–171 °C. $^1$H NMR ($C_6D_6$, 250 MHz): $\delta$ = 0.30 [s, $Si(CH_3)_3$, 72 H], –0.13 (s, $ZnCH_3$, 6 H) ppm. $^{13}$C NMR ($C_6D_6$, 75.5 MHz): $\delta$ = 0.1 [$Si(CH_3)_3$], –15.1 ($ZnCH_3$) ppm. $^{29}$Si NMR ($C_6D_6$, 59.6 MHz): $\delta$ = 1.2 (SiOZn), –16.4 [$Si(CH_3)_3$] ppm. $C_{26}H_{78}O_4Si_{12}Zn_3$ (988.09): calcd. C 31.60, H 7.96; found C 31.42, H 7.84.

**[E-{$Me(Me_3Si)_3SiSiO$}$_2$]$_2Zn_3Me_2$ (3c):** A heptane solution of **2c** (0.5 g, 0.81 mmol) was added to a vigorously stirred solution of $ZnMe_2$ (2 M, 0.6 mL, 1.2 mmol) in *n*-heptane (15 mL) at –78 °C. After warming to room temp., the suspension was stirred overnight and refluxed until the colorless precipitate fully dissolved. Crystallization of the solution at room temp. afforded the title compound as colorless crystals. Yield 0.45 g (75%). M.p. 161–164 °C. $^1$H NMR ($C_6D_6$, 250 MHz): $\delta$ = 0.94 (s, $SiCH_3$, 12 H), 0.41 [s, $Si(CH_3)_3$, 108 H], 0.04 (s, $ZnCH_3$, 6 H) ppm. $^{13}$C NMR ($C_6D_6$, 75.5 MHz): $\delta$ = 11.0 ($SiCH_3$), 4.6 [$Si(CH_3)_3$], –10.3 ($ZnCH_3$) ppm. $^{29}$Si NMR ($C_6D_6$, 59.6 MHz): $\delta$ = 15.8 (SiOZn), –10.0 [$Si(CH_3)_3$], –127.1 ($Si$$Si_4$) ppm. MS (70eV): *m*/*z* (%) = 1438 (2) [$M^+$ – Me], 1207 (22) [$M^+$ – $Si(SiMe_3)_3$], 1110 (8) [$M^+$ – $Si(SiMe_3)_3$ – 2Me – Zn], 247 (35) [$Si(SiMe_3)_3$]. $C_{42}H_{126}O_4Si_{20}Zn_3$ (1453.33): calcd. C 34.71, H 8.74; found C 34.51, H 8.74.

Table 2. Crystal data collection, and refinement details for crystal structures.[a]

| Compound | **3a** | **3b** | **3c** |
|---|---|---|---|
| Formula | $C_{30}H_{90}O_4Si_{14}Zn_3$ | $C_{26}H_{78}O_4Si_{12}Zn_3$ | $C_{42}H_{126}O_4Si_{20}Zn_3{\cdot}C_6H_{14}$ |
| Molecular weight | 1104.39 | 988.07 | 1539.51 |
| Crystal size [mm] | 1.00 × 0.37 × 0.22 | 0.67 × 0.35 × 0.22 | 0.62 × 0.62 × 0.36 |
| Crystal system | triclinic | triclinic | triclinic |
| Space group | $P\bar{1}$ | $P\bar{1}$ | $P\bar{1}$ |
| *a* [Å] | 13.9735(4) | 9.8213(6) | 14.2317(6) |
| *b* [Å] | 14.1182(3) | 11.5149(7) | 17.3635(7) |
| *c* [Å] | 18.5569(5) | 13.5301(13) | 21.2325(8) |
| $\alpha$ [°] | 81.7090(10) | 102.830(4) | 68.0030(10) |
| $\beta$ [°] | 68.8770(10) | 97.107(4) | 78.540(2) |
| $\gamma$ [°] | 65.2840(10) | 111.836(3) | 71.779(2) |
| *V* [Å]$^3$ | 3102.01(14) | 1348.43(17) | 4601.1(3) |
| *Z* | 2 | 1 | 2 |
| $\rho$ [g/cm$^3$] | 1.182 | 1.217 | 1.111 |
| $\mu$ [mm$^{-1}$] | 1.448 | 1.615 | 1.067 |
| 2$\Theta$ limit [°] | 2.97–25.00 | 1.99–27.50 | 2.21–25.00 |
| Measured reflections | 56017 | 53729 | 82788 |
| Independent reflections | 10852 [*R*(int) = 0.0696] | 6125 [*R*(int) = 0.0304] | 15934 [*R*(int) = 0.0246] |
| Data/restraints/parameter | 10852/0/491 | 6125/0/218 | 15934/0/678 |
| Final R$^1$/$wR_2$[b] | 0.0661/0.1812 | 0.0210/0.0558 | 0.0367/0.1030 |

[a] All data sets were collected with a Bruker X8Apex diffractometer system with Mo-$K_\alpha$ radiation [$\lambda$ = 0.71073 Å at 173(2) K]. [b] The value of $R_1$ is based on selected data with $F > 4\sigma(F)$; the value of $wR_2$ is based on all data.

 © 2007 Wiley-VCH Verlag GmbH & Co. KGaA, Weinheim 

**Reaction of 3b,c with $B(C_6F_5)_3$ in $C_6D_6$:** An NMR tube (equipped with J. Young valve) was charged in the glove box with **3b** or **3c** and $B(C_6F_5)_3$ (molar ratio 1:1) and dissolved in $C_6D_6$ (0.5 mL). The progress of the reaction was monitored by $^1H$ NMR spectroscopy and complete conversion of the starting materials into **4b** and **4c** and a mixture of the boranes $MeB(C_6F_5)_2$ ($\delta$ = 1.35 ppm), $Me_2BC_6F_5$ ($\delta$ = 0.98 ppm) and $BMe_3$ ($\delta$ = 0.74 ppm) was observed within 2 h at room temperature, according to the $^1H$ , $^{29}Si$ , $^{11}B$ and $^{19}F$ NMR spectra.

**Isolation of 4b,c:** A stirred mixture of $B(C_6F_5)_3$ and **3b** or **3c** (molar ratio 1:1) was dissolved in *n*-pentane at ca. –20 °C and stirring was continued for 2 h at room temperature. Crystallizations of concentrated solutions in a freezer afforded colorless crystals of the title compounds.

**$[\{(Me_3Si)_2SiO\}_2]_2Zn_3(C_6F_5)_2$ (4b):** Compound **3b** (0.15 g, 0.15 mmol), $B(C_6F_5)_3$ (0.08 g, 0.15 mmol) and *n*-pentane (10 mL). Yield 0.1 g (67%). $^1H$ NMR ($C_6D_6$, 250 MHz): $\delta$ = 0.24 [s, $Si(CH_3)_3$, 72 H] ppm. $^{13}C$ NMR ($C_6D_6$, 75.6 MHz): $\delta$ = –0.1 [$Si(CH_3)_3$], 135.4–150.6 ($C_6F_5$) ppm. $^{29}Si$ NMR ($C_6D_6$, 59.6 MHz): $\delta$ = 7.9 (SiO), –16.0 [$Si(CH_3)_3$] ppm. $^{19}F$ NMR ($C_6D_6$, 235.4 MHz): $\delta$ = –169.5, –140.2, –116.2 (*o*-, *p*-, *m*-F, $C_6F_5$) ppm. $C_{36}H_{72}F_{10}O_4Si_{12}Zn_3$ (1292.11): calcd. C 33.46, H 5.62; found C 33.09, H 5.44.

**$[E\text{-}\{Me(Me_3Si)_3SiSiO\}_2]_2Zn_3(C_6F_5)_2$ (4c):** Compound **3c** (0.15 g, 0.1 mmol), $B(C_6F_5)_3$ (0.05 g, 0.1 mmol) and *n*-pentane (10 mL). Yield 0.09 g (61%). $^1H$ NMR ($C_6D_6$, 250 MHz): $\delta$ = 1.00 (s, $SiCH_3$, 12 H), 0.31 [s, $Si(CH_3)_3$, 72 H] ppm. $^{13}C$ NMR ($C_6D_6$, 75.6 MHz): $\delta$ = 4.5 [$Si(CH_3)_3$], 10.9 ($SiCH_3$), 136.1–151.2 ($C_6F_5$) ppm. $^{29}Si$ NMR ($C_6D_6$, 59.6 MHz): $\delta$ = 21.0 (SiO), –9.9 [$Si(CH_3)_3$], –125.4 ($SiSi_4$) ppm. $C_{52}H_{120}F_{10}O_4Si_{20}Zn_3$ (1757.35): calcd. C 35.54, H 6.88; found C 35.18, H 6.79.

Crystal data collection see Table 2 for **3a**, **3b** and **3c** are deposited in the Cambridge Crystallographic Data Centre. CCDC-622651 (for **3a**), -622650 (for **3b**) and -622649 (for **3c**) contain the supplementary crystallographic data for this paper. These data can be obtained free of charge from The Cambridge Crystallographic Data Centre via www.ccdc.cam.ac.uk/data_request/cif.


[1] a) F. Schindler, H. Schmidbaur, U. Krüger, *Angew. Chem.* **1965**, *77*, 865; *Angew. Chem. Int. Ed. Engl.* **1965**, *4*, 876; b) F. Schindler, H. Schmidbaur, *Angew. Chem.* **1967**, *79*, 697–708; *Angew. Chem. Int. Ed. Engl.* **1967**, *6*, 683–694; c) G. Anantharaman, H. W. Roesky, J. Magull, *Angew. Chem.* **2002**, *114*, 1525; *Angew. Chem. Int. Ed.* **2002**, *41*, 1226–1229.

[2] a) K. Su, T. D. Tilley, M. J. Sailor, *J. Am. Chem. Soc.* **1996**, *118*, 3459–3468; b) A. Fina, H. C. L. Abbenhuis, D. Tabuani, A. Frache, G. Camino, *Polym. Degrad. Stab.* **2006**, *91*, 1064–1070; c) J. Hambrock, M. Rabe, K. Merz, A. Birkner, A. Wohlfart, R. A. Fischer, M. Driess, *J. Mater. Chem.* **2003**, *13*, 1731–1736.

[3] a) M. Driess, K. Merz, S. Rell, *Eur. J. Inorg. Chem.* **2000**, 2517–2522; K. Merz, S. Block, R. Schoenen, M. Driess, *Dalton Trans.* **2003**, 3365–3369.

[4] K. Merz, H. M. Hu, S. Rell, M. Driess, *J. Inorg. Chem.* **2003**, 51–53.

[5] C. Krempner, M. Köckerling, H. Reinke, K. Weichert, *Inorg. Chem.* **2006**, *45*, 3203–3211.

[6] C. Krempner, U. Jäger-Fiedler, K. Mamat, A. Spannenberg, K. Weichert, *New J. Chem.* **2005**, *29*, 1581–1584.

[7] D. Hoffmann, H. Reinke, C. Krempner, *J. Organomet. Chem.* **2002**, *662*, 1–8.

[8] a) H. N. Hou, *Acta Crystallogr., Sect. E* **2005**, *61*, 1197–1198; b) Z. Y. Xiong, L. J. Liu, *Acta Crystallogr., Sect. E* **2005**, *61*, 863–864; c) Q. Chen, *Acta Crystallogr., Sect. E* **2006**, *62*, 56–57.

[9] D. A. Walker, T. J. Woodmann, D. L. Hughes, M. Bochmann, *Organometallics* **2001**, *20*, 3772–3776.

[10] A. N. Chernega, A. J. Graham, M. L. H. Green, J. Haggitt, J. Lloyd, C. P. Mehnert, N. Metzler, J. Souter, *J. Chem. Soc., Dalton Trans.* **1997**, *13*, 2293–2303.


Received: October 12, 2006
Published Online: February 2, 2007

 © 2007 Wiley-VCH Verlag GmbH & Co. KGaA, Weinheim 

DOI: 10.1002/ejic.200601034

# Spin-Crossover Studies on a Series of 1D Chain and Dinuclear Iron(II) Triazine-Dipyridylamine Compounds

**Suzanne M. Neville,[a] Ben A. Leita,[a] Daniel A. Offermann,[a] Martin B. Duriska,[a] Boujemaa Moubaraki,[a] Karena W. Chapman,[b] Gregory J. Halder,[c] and Keith S. Murray*[a]**

**Keywords:** Iron / N ligands / Spin crossover / 1D chains / Dinuclear / Magnetic properties

Four isostructural one-dimensional polymeric iron(II) spin crossover materials containing the ligand 2-chloro-4,6-bis(dipyrid-2-ylamino)-1,3,5-triazine (cddt) have been synthesised and magnetically and structurally characterised. The polymeric material $Fe(NCS)_2(cddt)\cdot n(guest)$ (**1**), self assembles into three crystallographically distinct phases; the compounds **1b** and **1c**, $[Fe(NCS)_2(cddt)]\cdot 2(CH_3OH)$, are polymorphs, however, **1a**, $[Fe(NCS)_2(cddt)]\cdot 1/2(CHCl_3)\cdot(H_2O)$ contains a different solvent system. Each phase shows very different magnetic behaviour; phases **1a** and **1b** remain high spin over all temperatures, whilst phase **1c** undergoes a "half" spin crossover between 225 and 125 K. The structural consequences of the spin transition in **1c** have been followed using variable temperature synchrotron powder X-ray diffraction techniques. Variation of the chalcogenide ligand in the complex $[Fe(NCSe)_2(cddt)]\cdot 2(CH_3OH)$, **2**, leads to a full one-step spin crossover with a $T_{1/2}$ of 200 K. Structural analysis of **1c** below the transition temperature reveals alternating, crystallographically distinct, HS and LS iron(II) centres (HS: high spin, LS: low spin) along the chain, and structural analysis of **2** below the transition temperature reveals all LS iron(II) centres. Also reported are the structural characterisations of two dinuclear materials, containing the ligand 2,4,6-tris(dipyridin-2-ylamino)-1,3,5-triazine (tdt), of the formula $[Fe(tdt)(X)_2]_2\cdot(ClO_4)\cdot$(solvent) (X = $H_2O$, $Cl^-$ for **3a**, **3b**) which are analogous to those recently reported by Gamez et al. In addition, the structural characterisations are described for dinuclear materials, containing the ligand cddt, of the formula $[Fe(cddt)(Cl)(X)]_2\cdot(Y)_2\cdot n$(solvent) (X: $H_2O$ or $NCCH_3$, Y: $ClO_4^-$, $BF_4^-$ **4a**, **4b** and **4d**) and for a cobalt(II) analogue, $[Co(cddt)(Cl)(H_2O)]_2\cdot(BF_4)_2\cdot n$(solvent) (**4c**).

(© Wiley-VCH Verlag GmbH & Co. KGaA, 69451 Weinheim, Germany, 2007)

## Introduction

The recent papers of Gamez, Roubeau and coworkers[1,2] dealing with exchange coupling and spin crossover (SCO) in dinuclear iron(II) complexes of triazine-based bridging ligands prompts us to report our contemporaneous studies using the same ligand, and a related one. Similarities and differences in the two studies are emphasised, with a series of 1D (one-dimensional) chain SCO species being reported here for the first time. Our work forms part of a wide investigation into the synthesis, structures and magnetism of dinuclear,[3–7] and higher nuclearity,[8–14,19] iron(II) SCO compounds. We[15] and others[16] are interested in probing fundamental questions dealing with, for example, the synergy, if any, between exchange coupling and SCO, and the possible increase in cooperativity [e.g. thermal hysteresis of the spin transition(s)] in dinuclear and polynuclear SCO materials when compared to mononuclear. A range of structural designs of the bridging geometry and of the chemical nature of the bridging ligands has been employed in order to attempt to answer some of these questions.[17] The ligand common to both studies is 2,4,6-tris(dipyrid-2-ylamino)-1,3,5-triazine (labelled dpyatriz by Gamez et al.[1–2] and tdt herein, Figure 1) while the other ligand is 2-chloro-4,6-bis(dipyridin-2-ylamino)-1,3,5-triazine (labelled cddt, Figure 1).

There have been several reports recently of ligands based on dipyrid-2-ylamine (dpa) being incorporated into mono- and dinuclear systems.[1–2,4,18] The mononuclear complex $Fe(dpa)_2(NCS)_2$ containing *cis*-coordinated thiocyanate ligands, recently reported by Real et al., undergoes an incomplete one-step spin crossover with a $T_{1/2}$ of 88 K.[18] The mononuclear complex *trans*-$Fe(tdt)_2(NCS)_2$ recently reported by Gamez et al.,[2] undergoes a complete one-step spin crossover with a $T_{1/2}$ of 200 K. This was the first report for an iron(II) dpa-style material containing *trans*-thiocyanate ligands.[2] We recently reported the dinuclear complex

[a] School of Chemistry, Building 23, Monash University, Clayton, Victoria 3800, Australia
Fax: +61-3-99054597
E-mail: keith.murray@sci.monash.edu.au
[b] X-ray Science Division, Advanced Photon Source, Argonne National Laboratory, Argonne, Illinois 60439, USA
[c] School of Chemistry, University of Sydney, NSW 2006, Australia

Supporting information for this article is available on the WWW under http://www.eurjic.org or from the author.

 © 2007 Wiley-VCH Verlag GmbH & Co. KGaA, Weinheim 

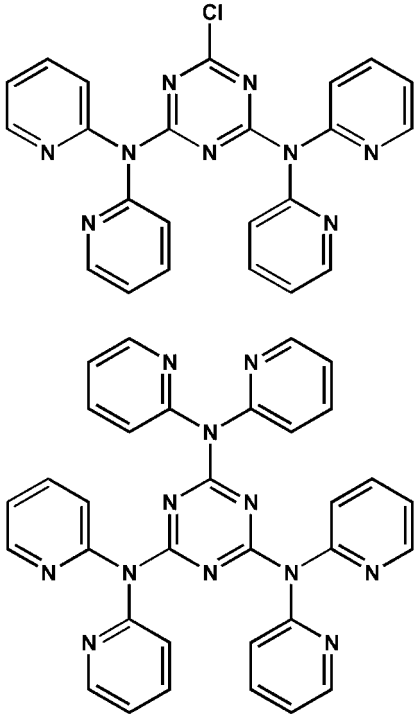

Figure 1. The ligands 2-chloro-4,6-bis(dipyrid-2-ylamino)-1,3,5-triazine (cddt) and 2,4,6-tris(dipyrid-2-ylamino)-1,3,5-triazine (tdt).

[*cis*-Fe(ddpp)$(NCS)_2$]$_2$·4$(CH_2Cl_2)$ [ddpp = 2,5-bis(dipyrid-2-ylamino)pyridine], which undergoes a two-step spin crossover influenced by the number and type of solvent molecules present.[4] This material uniquely shows structural resolution of a "trapped" [HS-LS] state dinuclear complex (HS = high spin, LS = low spin). Here, we present a new series of 1D polymeric species containing the ligand cddt, $[Fe(NCS)_2(cddt)]\cdot 1/2(CHCl_3)\cdot(H_2O)$ (**1a**), the polymorphs $[Fe(NCS)_2(cddt)]\cdot 2(CH_3OH)$ (**1b** and **1c**) and $[Fe(NCSe)_2(cddt)]\cdot 2(CH_3OH)$ (**2**). **1c** undergoes a half spin crossover and **2** undergoes a complete spin crossover. We also report a series of dinuclear materials similar to those reported by Gamez et al.[1–2] containing the ligand tdt, $[Fe(tdt)(Cl)]_2(ClO_4)_2\cdot(C_2H_5OH)\cdot 2(CHCl_3)$ (**3a**) and $[Fe(tdt)(H_2O)]_2(ClO_4)_4\cdot 6(H_2O)$ (**3b**), and a series of dinuclear complexes containing the ligand cddt, $[Fe(cddt)(H_2O)Cl]_2(ClO_4)_2\cdot 2(C_2H_5OH)\cdot(H_2O)$ (**4a**), $[Fe(cddt)(H_2O)Cl]_2(BF_4)_2\cdot 2(C_2H_5OH)\cdot 2(H_2O)$ (**4b**), $[Co(cddt)(H_2O)Cl]_2(BF_4)_2\cdot 2(C_2H_5OH)\cdot 2(H_2O)$ (**4c**) and $[Fe(cddt)(NCCH_3)(H_2O)]_2(ClO_4)_4\cdot(NCCH_3)$ (**4d**). All attempts to incorporate the tdt ligand into polymeric iron(II) systems have thus far resulted in the formation of the monomeric spin crossover material reported by Gamez et al.[1–2]

Structural analysis on two-step/half spin crossover materials reveal that there are two ways which the octahedral environments of the iron(II) centres can be observed at the plateau temperature below the transition temperature. Firstly, it can be observed as an average Fe–N bond length between HS and LS where there is no ordering (trapping) of the LS and HS states, and secondly, as two crystallographically distinct iron(II) centres where 50% are HS and 50% LS (indeed these are the same possibilities for systems where a half spin crossover is observed). The former is by far the most commonly observed and much effort is currently being invested in understanding the two modes of crossover, in particular for dinuclear systems where two-step and half crossovers are commonly observed.[3–7] In the case of polynuclear systems, there have been relatively few examples where two-step spin crossovers are observed[8,19] and few have shown ordering of HS and LS iron(II) at the plateau region of the temperature between the two spin transitions. Here, the polymeric material $[Fe(cddt)(NCS)_2]\cdot 2(CH_3OH)$ (**1c**) undergoes a spin crossover and, at low temperatures, alternating HS and LS iron(II) centres have been observed for the first time in a 1D chain.

Initially, the present polynuclear iron(II) systems were synthesised with the intention of observing the magnetic influence of incorporating dpa style ligands into extended materials. However, the unexpected synthesis of three different crystalline phases of **1**, $[Fe(cddt)(NCS)_2]\cdot 1/2(CHCl_3)\cdot(H_2O)$ (**1a**) and $[Fe(cddt)(NCS)_2]\cdot 2(CH_3OH)$ (**1b** and **1c**), of which two are polymorphs, presents one of the first cases of polymorphism in a polymeric SCO species and as such offers a valuable opportunity to directly compare intra- and intermolecular structural effects on materials where metal centres are linked. There have been two previous reports of polymorphism in polymeric spin crossover materials, namely, $\{Fe(pmd)_2[Ag(CN)_2]_2\}$ (pmd = pyrimidine) and $\{Fe(3\text{-}CNpy)[Au(CN)_2]_2\}\cdot n(H_2O)$ (3-CNpy = 3-cyanopyridine).[20,21] The majority of reports of polymorphism have been in mononuclear iron(II) species,[22–26] in particular, the compounds [*cis*-$Fe(phen)_2(NCS)_2$][22] and [*cis*-$Fe(bipy)_2(NCS)_2$][23] (phen = 1,10-phenanthroline, bipy = 2,2-bipyridyine) exist as polymorphs and have received a large amount of interest over many years. More recently, the material $[Fe(dppa)_2(NCS)_2]$ [dppa = (3-aminopropyl)bis(pyrid-2-ylmethyl)amine] was reported[25] which forms as three crystallographically distinct polymorphs; **A**: triclinic, **B**: monoclinic and **C**: orthorhombic. The **A** phase displayed a gradual SCO, the **B** phase remained high spin and the **C** phase had an abrupt SCO with hysteresis and structurally it was tentatively explained in terms of the presence of an array of intermolecular contacts in **C** that led to more cooperativity. Guionneau et al.[26] have further investigated the structural features between two polymorphs of the compound $[Fe(PM\text{-}BiA)_2(NCS)_2]$ (PM = *N*-pyrid-2-ylmethylene and BiA = 4-aminobiphenyl) that crystallised in the same symmetry, however, they displayed gradual and abrupt spin transitions, respectively. They found a direct correlation between the abruptness of a transition and a set of structural parameters that reflected the inter- and intramolecular interactions. While it is now clearly established that intermolecular interactions, such as hydrogen bonding and π-π interactions influence spin transitions, it appears that, from one chemical example to the next, little correlation exists. Certainly, for spin crossover materials to become useful in devices, understanding the governing factors that drive cooperativity is very important. In this context, the present study compares the structural features of a series of poly-

 © 2007 Wiley-VCH Verlag GmbH & Co. KGaA, Weinheim 

meric spin crossover materials which reveal the presence of π-π interactions to be the primary characteristic influencing the spin transition.

## Results and Discussion

### Syntheses

In synthesising the 1D complexes $[Fe(NCS)_2(cddt)]\cdot n(guest)$ (**1**) [guest: $1/2(CHCl_3)(H_2O)$ for **1a**, $2(CH_3OH)$ for **1b** and **1c**] direct addition of $Fe(NCS)_2$ to cddt in the relevant solvent systems, resulted in immediate precipitation of yellow powders. In order to obtain structural information, single crystals of each phase were grown by slow diffusion techniques by using a vial for multiple solvent systems and a H-shaped tube for single solvent systems. For the materials **1b** and **1c** it was found that by using 2:4:1 ratios of Fe:NCS:cddt crystals of both phases grew together. By altering the Fe:NCS:cddt ratio to 1:2:1 it was found that that crystals of the spin crossover material **1c** could be grown with only a ca. 10% impurity of the **1b** phase. Furthermore, allowing the slow diffusion of **1c** to proceed at <5 °C the **1c** phase formed in isolation. Crystals of **1b** formed as light yellow blocks whereas crystals of **1c** formed as dark yellow-orange clumps of inter-grown crystals.

The synthesis of the dinuclear complex $[Fe(tdt)(Cl)]_2(ClO_4)_2\cdot(C_2H_5OH)\cdot 2(CHCl_3)$ (**3a**) containing the ligand tdt was carried out by slow diffusion methods in a H-tube. Single crystals of **3a** contain bound $Cl^-$, however, the synthesis was not carried out in the presence of chloride ions. Three possible chloride ion sources are; trace amounts from the tdt ligand synthesis, $Fe(ClO_4)_2\cdot 6(H_2O)$ and chloroform solvent. Gamez et al.[2] commented, in their synthesis of the analogous material, that the addition of stoichiometric amounts of chloride salt reduced the product yield compared to limited amounts, here whichever the chloride source is, it would be in small amounts and potentially drive the formation of the observed dinuclear. In addition, the synthesis of **3a** was carried out in the presence of $NaNCBH_3$, intended to be bound to the metal via the terminal nitrogen group, but has not been incorporated in the dinuclear material. Microanalysis of **3a** revealed a hydrated product.

The synthesis of the dinuclear complex $[Fe(tdt)(H_2O)]_2(ClO_4)_4\cdot 6(H_2O)$ (**3b**) was carried out in a mixed solvent system of methanol and acetonitrile, in air. Structural analysis revealed water molecules to be both bound to the metal, and as a solvate, and would originate from the solvent methanol and the metal salt.

The syntheses of dinuclear complexes containing the ligand cddt, $[Fe(cddt)(Cl)(X)]_2\cdot(Y)_2\cdot n(solvent)$ (X: $H_2O$ or $NCCH_3$, Y: $ClO_4^-$, $BF_4^-$ **4a**, **4b** and **4d**) and $[Co(cddt)(Cl)(H_2O)]_2\cdot(BF_4)_2\cdot n(solvent)$ (**4c**), as with **3a** did not contain any free $Cl^-$. The possible chloride ion sources are; trace amounts from the cddt ligand synthesis, from decomposition of the ligand and, for **4a**, from $Fe(ClO_4)_2\cdot 6(H_2O)$. While it is unclear where the chloride salt arises from it is likely from the cddt ligand. Microanalysis revealed hydrated species for each of these materials.

### Magnetic Studies

The complex **1a** remains high spin over all temperatures and the $\chi_M T$ vs. temperature plot is shown in Figure S11 (see Supporting Information). The $\chi_M T$ values remain constant at 3.29 $cm^3 mol^{-1}$ K down to ca. 15 K, followed by a small decrease due to a combination of weak antiferromagnetic coupling and zero field splitting. A sufficient amount of sample of **1b** for carrying out magnetism studies was unfortunately not obtained, as it grows as an impurity in the synthesis of **1c**, and, as such, no magnetic measurements were made on this phase. However, the crystal structure of **1b** at 123(2) K revealed all iron(II) centres to be in the high spin state, and upon quench cooling of the sample in liquid nitrogen, no colour change occurred in the yellow crystals, indicating that a spin transition probably did not occur.

Plots of $\chi_M T$ vs. temperature for polycrystalline samples of **1c** and **2** are shown in Figure 2. Compound **1c** undergoes an incomplete spin crossover with what appears to be a subtle, two-step nature. At temperatures above 240 K the material is in the fully high spin state with a maximum $\chi_M T$ of 3.38 $cm^3 mol^{-1}$ K. Between 240 and 200 K there is a gradual drop in $\chi_M T$ to ca. 2.66 $cm^3 mol^{-1}$ K. Below 200 K the transition becomes even more gradual with a lowest $\chi_M T$ of 1.64 $cm^3 mol^{-1}$ K attained below 70 K, which corresponds to 50% of the iron(II) centres being in the high spin state. From 200 K to low temperatures, slow kinetics or a structural effect may prevent the completion of the spin transition.

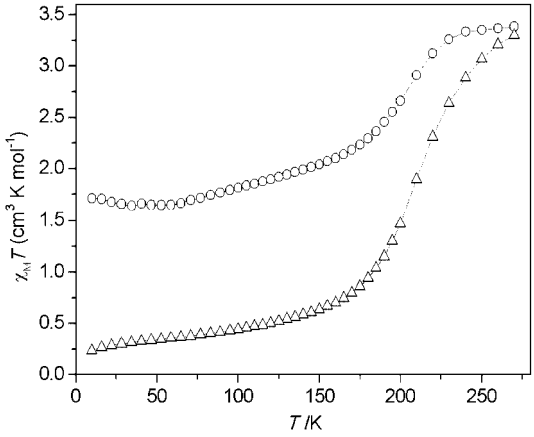


Figure 2. $\chi_M T$ vs. temperature for $[Fe(NCS)_2(cddt)]\cdot 2(CH_3OH)$ (**1c**) (o) and $[Fe(NCSe)_2(cddt)]\cdot 2(CH_3OH)$ (**2**) (Δ).

The selenocyanate analogue **2**, undergoes a full one-step spin crossover with a $T_{1/2}$ of ca. 220 K. At 270 K, a $\chi_M T$ value of 3.29 $cm^3 mol^{-1}$ K is attained corresponding to the majority of iron(II) centres being in the high spin state. The $\chi_M T$ values have not reached the LS plateau as between 270 and 170 K there is a gradual decrease in $\chi_M T$. Below 170 K

 © 2007 Wiley-VCH Verlag GmbH & Co. KGaA, Weinheim 

a plateau $\chi_M T$ value of 0.23 $cm^3 mol^{-1}$ K is observed corresponding to all the iron(II) centres being in the low spin $t_{2g}^6$ state. The non-zero magnitude of $\chi_M T$ at low temperature is a common occurrence in iron(II) spin crossover LS states and is due to second order Zeeman effects. No thermal hysteresis occurred in either **1c** or **2**.

The $T_{1/2}$ values observed for **1c** and **2** are similar in size to that observed by Gamez et al.[1,2] for Fe(dpyatriz)$_2$(NCS)$_2$, ca. 200 K. Each of these materials contains the *trans*-Fe(DPA)$_2$(NCS)$_2$ coordination environment and the similar $T_{1/2}$ values and lack of abrupt transitions and thermal hysteresis suggest that incorporation into a polymeric, covalently linked species does not increase the communication between spin crossover centres. Further detailed structural comparisons of the materials are discussed below.

The dinuclear compounds **3a**, **3b**, **4a**, **4b**, **4c** and **4d** contain iron(II) and cobalt(II) coordination environments that involve $Cl^-$ and $H_2O$ groups and are thus expected to be HS-HS. Some interesting magnetic results were reported, however, for dinuclear systems by Gamez et al.[1] For example, [Fe(tdt)(NCCH$_3$)(H$_2$O)]$_2$(ClO$_4$)$_4$ displayed a gradual, partial spin crossover with a $T_{1/2}$ of ca. 280 K. This is unusual for iron(II) [FeN$_5$O] coordination environments. The replacement of acetonitrile by $H_2O$ by exposure to air led to HS-HS magnetic behaviour, as expected, and similar to that noted for [Fe(tdt)(H$_2$O)(CH$_3$OH)]$_2$(BF$_4$)$_4$, also having [$Fe^{II}N_4O_2$] coordination.[1] A very small $J$ value of –0.37 $cm^{-1}$ was obtained for the latter, possibly with a zero-field splitting parameter of ca. 4 $cm^{-1}$, rather than $J$, being responsible for the rapid decrease in $\mu_{eff}$ being observed below 50 K.

Interestingly, the triazine *N*-bonded example [Fe(tdt)(Cl)]$_2$(CF$_3$SO$_3$)$_2$ was reported to show weak ferromagnetic coupling between the $S$ = 2 $Fe^{II}$ centres.[1] However, care has to be taken to exclude crystallite torquing effects as being the cause of increases in $\mu_{eff}$ in such $^5T_{2g}$ (parent) single-ion states and dispersal of the powder in Vaseline is the way to check for such effects. The magnetic behaviour of the present analogue [Fe(tdt)(Cl)]$_2$(ClO$_4$)$_2$·(C$_2$H$_5$OH)·2(CHCl$_3$) (**3a**) unfortunately could not be measured due to insufficient and impure amounts of bulk sample.

The cddt analogue [Fe(cddt)(NCCH$_3$)(H$_2$O)]$_2$(ClO$_4$)$_4$·(CH$_3$CN) (**4d**) contains the same iron(II) [FeN$_5$O] coordination environment as [Fe(tdt)(NCCH$_3$)(H$_2$O)]$_2$(ClO$_4$)$_4$ which, as discussed above, undergoes a gradual SCO. Here, the complex **4d** remains HS over all temperatures and the $\chi_M T$ vs. temperature plot is shown in Figure S12. The $\chi_M T$ values remain constant at 3.49 $cm^3 mol^{-1}$ K down to ca. 15 K, followed by a small decrease due to a combination of weak antiferromagnetic coupling and zero field splitting.

## One-Dimensional Chain Complexes

### *General. [Fe(NCS)$_2$(cddt)]·n(guest) (1)*

Crystal data and refinement details for the complexes **1a**, **1b** and **1c** can be found in Table 2. Three crystallographically distinct materials of the general formula [Fe(NCS)$_2$(cddt)]·*n*(guest) (**1**) have been synthesised and crystallised by slow diffusion techniques. All three phases are composed of one-dimensional (1D) chains which differ in their crystal packing and the number and type of solvent molecules. The general structures of **1a**, **1b** and **1c** are the same. However, as seen above, these three phases display vastly different magnetic properties [see part (a) of Figure 2 and Figure S11 in the Supporting Information]; **1a** and **1b** are HS and **1c**

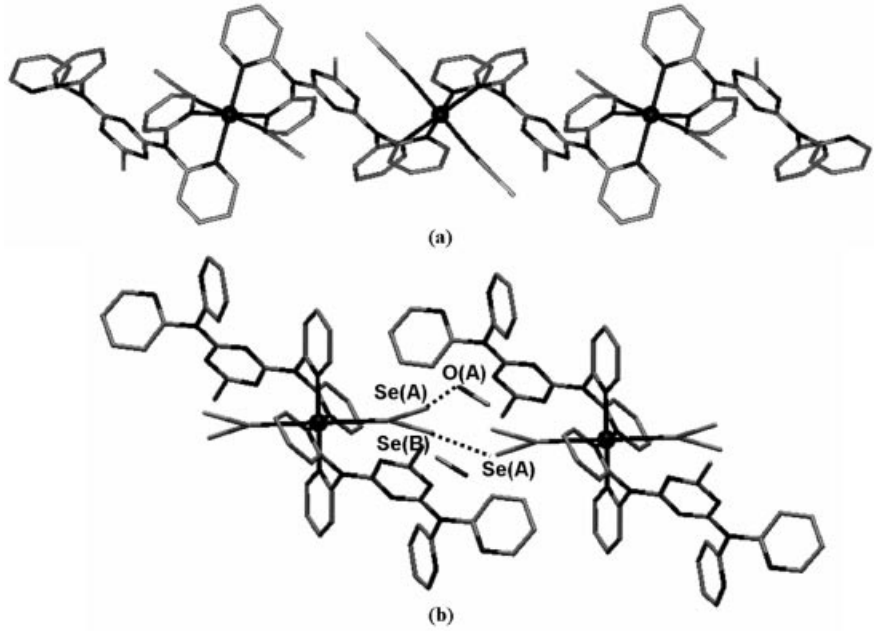


Figure 3. The general polymeric 1D chain structure observed in the materials (a) **1a**, **1b**, **1c** and (b) **2** illustrating the A and B positions of the disordered selenium atoms, the Se(A)···Se(B) interactions between adjacent chains and the Se(A)···O interactions are shown with dotted lines. Iron(II) centres are shown as black spheres, hydrogen atoms have been omitted.

 © 2007 Wiley-VCH Verlag GmbH & Co. KGaA, Weinheim 

undergoes a spin transition. The iron(II) environments and extended structure of these materials are, nevertheless, isostructural. These systems are highly relevant for making structural comparisons in order to attempt to determine both the intra- and inter-chain structural influence on the magnetism.

$[Fe(NCS)_2(cddt)]\cdot 1/2(CHCl_3)\cdot(H_2O)$ (**1a**) is grown as a pure crystalline phase by slow diffusion in methanol and chloroform. The two phases **1b** and **1c** are polymorphs, $[Fe(NCS)_2(cddt)]\cdot 2(CH_3OH)$, and grow simultaneously but they differ in their crystal symmetries (**1b**: monoclinic and **1c**: triclinic); **1c** is the major product. By subtle variation in the stoichiometry of reactants, **1c** can be grown in isolation, as indicated above. There have previously been in-depth studies into understanding the differences in spin crossover behaviours observed in polymorphic species;[20–24] here we will continue this, further, through detailed structural comparisons between each of the materials **1b** and **1c**.

All three phases, **1a**, **1b** and **1c** consist of iron(II) coordinated by *trans*-thiocyanate ligands bound through the terminal nitrogen and two half cddt ligands, the full ligands generated by symmetry [Figure 3 (a)]. The cddt ligands bridge two metal centres, binding via the terminal pyridyl groups of the bis(2-pyridyl)amine moiety. Each alternate ligand is rotated *ca*. 180° such that the triazine chlorine atom is directed up or down. This extends to form infinite 1D chains. Following are detailed structural descriptions of each of the three phases of **1**. The octahedral distortion parameter $\Sigma$ has been calculated for each of the materials **1a**, **1b** and **1c**, smaller $\Sigma$ values are associated with stronger crystal fields and stabilisation of the LS state.[27]

### *[Fe(NCS)$_2$(cddt)]·1/2(CHCl$_3$)·(H$_2$O) (1a)*

Structural analysis of **1a** revealed a tetragonal symmetry with all iron(II) centres equivalent and with Fe–N distances typical of the HS iron(II) state (Table 1). The 1D chains are stacked parallel and run along the *c*-axis [Figure 4 (a)]. In the *ac*- and *bc*-planes the adjacent 1D chains are rotated by 90° [Figure 5 (a)]. Located between the chains are two types of alternating 1D channels along the *c*-axis which account for 23.4% of the unit cell volume [Figure 4 (a)]. The first type of channel is lined by the chlorine atoms from the cddt ligand and is filled with chloroform molecules. The second type of channel is lined by aromatic ligand rings and is filled by a 1D chain of water molecules. Neither the water or chloroform molecules interact with the 1D chains. It was surprising that since this material was synhesised in a mixed solvent system consisting of methanol and chloroform, no

Table 1. Selected bond lengths for **1a**, **1b**, **1c** and **2** obtained at 123 K.

| Bond [Å] | **1a** | **1b** | **1c** | **2** |
|---|---|---|---|---|
| Fe(1)–N(CS) | 2.083(9) | 2.082(9) | 1.953(5) | 1.969(5) |
| Fe(1)–N(py) | 2.223(9) | 2.232(7) | 1.995(4) | 2.007(4) |
| Fe(1)–N(py) | 2.237(8) | 2.216(7) | 2.002(4) | 2.011(4) |
| Fe(2)–N(CS) | – | 2.108(8) | 2.084(5) | 1.933(5) |
| Fe(2)–N(py) | – | 2.198(6) | 2.203(4) | 2.016(4) |
| Fe(2)–N(py) | – | 2.201(7) | 2.226(4) | 2.017(4) |

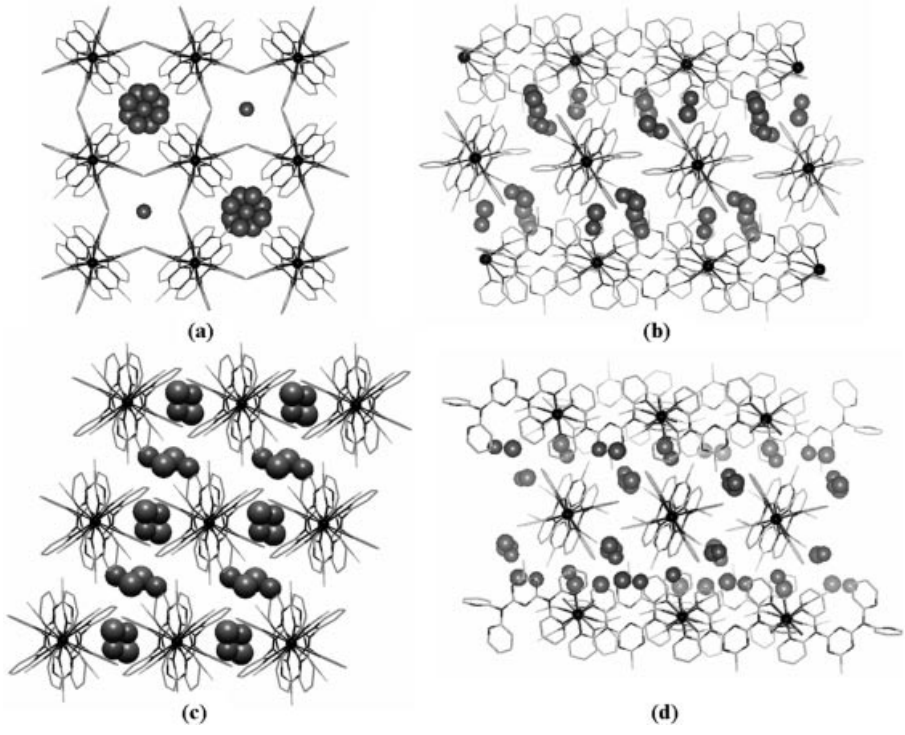


Figure 4. Illustration of the crystal packing of 1D chains and solvent in (a) **1a**, tetragonal, (b) **1b**, monoclinic, (c) **1c**, triclinic and (d) **2**, monoclinic. Hydrogen atoms have been omitted. Solvent molecules are represented by space-filling, iron(II) atoms as black spheres and 1D chains as sticks.

 © 2007 Wiley-VCH Verlag GmbH & Co. KGaA, Weinheim 

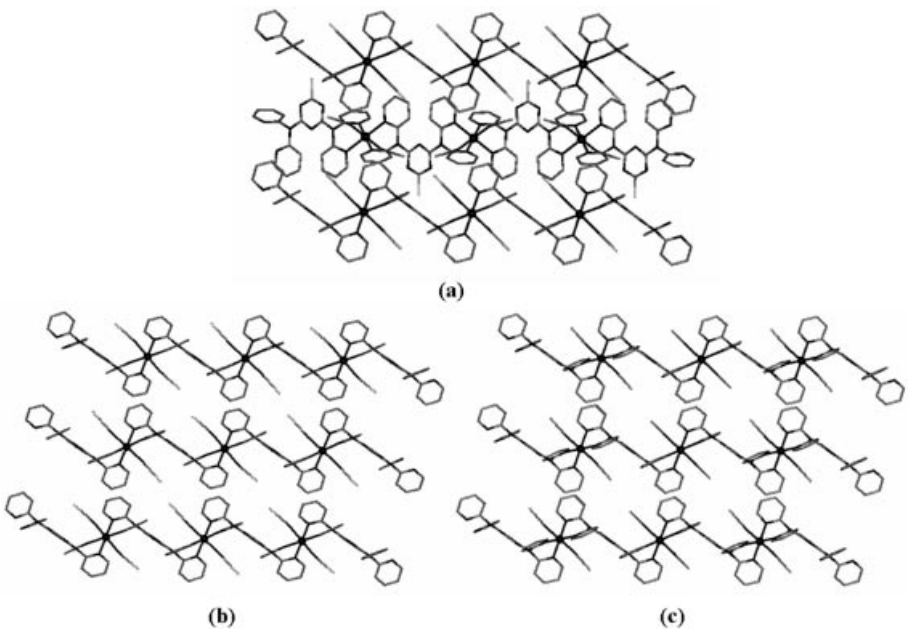


Figure 5. Illustration of the crystal packing of adjacent 1D chains in the *ab*-plane (a) **1a** (b) **1b** and (c) **1c**. Hydrogen atoms and solvent molecules have been omitted. Iron(II) atoms as black spheres and 1D chains as sticks.

methanol has been incorporated into the crystalline material. The chlorine atoms on the cddt ligand are involved in Cl···Cl interactions with adjacent chains [Cl···Cl: 3.204(10) Å]. Analysis of the geometry of the iron(II) centre revealed an octahedral distortion parameter $\Sigma$ of 45.6° which is comparable to other $[Fe(N)_4(NCS)_2]$ centres in the HS state.[4,18,27] The Fe···Fe separation within each chain is 9.345(3) Å and this is similar to that between chains 9.258(2) Å.

### *[Fe(NCS)$_2$(cddt)]·2(CH$_3$OH) (1b)*

The complex **1b** has different stacking of the 1D chains to that seen in both **1a** and **1c** [Figure 4 (b)]. Structural analysis of **1b** revealed a monoclinic symmetry with two iron(II) centres in the asymmetric unit which are both in the HS state at 123(2) K with average Fe–N bond lengths for Fe1 and Fe2 of 2.176(6) and 2.169(5) Å, respectively (Table 1). There are two crystallographically distinct thiocyanate ligands in the asymmetric unit; the sulfur atom of the thiocyanate ligand bound to Fe1 is disordered over two sites, **A** and **B** (Figure S2). The 1D chains are parallel packed in the *ab*-plane, where adjacent chains within the same *ab*-plane are generated by a translation along either the *a*- or *b*-axis [Figure 5 (b)]. The chains in the next *ab*-plane are rotated by 90° [Figure 4 (b)]. The Fe···Fe separation within each chain is 9.584(6) Å and smaller between chains, 8.717(6) Å. There are two solvent methanol molecules present in the asymmetric unit; one of the methanol molecules is hydrogen bonded to a sulfur atom of the **A** component of the disordered thiocyanate ligand [O2···S2A: 3.193(3) Å, Figure 5]. This thiocyanate ligand is also involved in a S···S interaction with its symmetry equivalent atom on an adjacent chain [S2A···S2A: 3.029(11) Å]. Neither the **B** component of the other thiocyanate ligand are involved in any significant O···S or S···S interactions. The most obvious distinction between the two iron(II) centres in the asymmetric unit is their hydrogen bonding interactions. However, further analysis of the metal centre geometries revealed that the iron(II) centre involved in the hydrogen bonding interaction, Fe1, is in a less distorted octahedral environment than is the other iron(II) centre, Fe2, thus, $\Sigma$(Fe1): 34.4 and $\Sigma$(Fe2): 44.8°.[27] The distortion parameter of Fe1 is considerably lower than Fe2 which is often indicative of the LS state being stabilised. However, while we do not have magnetic data, both iron(II) centres are in the HS state down to 123 K. The average Fe–N bond lengths for both Fe1 and Fe2 are indicative of high spin iron(II). Notably, the Fe2–N(CS) bond length is 2.108(8) Å, which is longer than the ca. 2.0 Å usually observed for iron(II). It is well known that weak intermolecular interactions can strongly influence the observed spin crossover features,[26] comparison of such features with **1c** will be discussed in the following section.

### *[Fe(NCS)$_2$(cddt)]·2(CH$_3$OH) (1c)*

Structural analysis of **1c** at 123(2) K revealed a triclinic symmetry with two iron(II) centres in the asymmetric unit [Figure 4 (c)]. At 123(2) K, Fe1 is in the LS state and Fe2 is in the HS state with average Fe–N bond lengths of 1.983(3) and 2.171(4) Å, respectively (Table 1). This is a most unusual situation to have alternating HS and LS centres along the chains. In contrast, a recent iron(III) 1D system has been reported which contains isolated alternating HS and LS chains.[29]

The 1D chains in **1c** run along the *c*-axis, where adjacent chains are generated by a translation along either the *a*- or

 © 2007 Wiley-VCH Verlag GmbH & Co. KGaA, Weinheim 

*b*-axis as seen in **1b** [Figure 5 (c)]. In contrast to **1b**, all of the 1D polymer chains in **1c** run in the same direction, i.e., along the *c*-axis [Figure 4 (c)]. The Fe···Fe separation within each chain is 9.512(3) Å and between chains is 8.818(4) Å, which is similar to that observed for **1b**. There are two solvent methanol molecules present per metal centre and one of these molecules is hydrogen bonded to a sulfur atom of a thiocyanate [O2···S1: 3.267(5) Å]. In addition, there is a π-π interaction between a pyridyl ring coordinated to Fe1 and its symmetry generated ring on an adjacent chain, 3.699(2) Å. One of the pyridyl rings attached to Fe2 is also in the correct orientation for a π-π interaction with its symmetry equivalent however the distance of 4.699(2) Å is too long to be a significant interaction. It is well known that intramolecular π-π interactions influence spin transitions[28] and indeed the presence of such interactions in **1c**, but not in **1b**, is likely to determine whether spin crossover behaviour will be observed.

As discussed above, smaller octahedral distortion parameters generally suggest a more stabilised LS state.[27] Further analysis of the geometries of the two metal centres in **1c** revealed that the iron(II) centre involved in this hydrogen bonding interaction is in a less distorted octahedral environment than the other iron centre, $\Sigma$(Fe1): 32.28 and $\Sigma$(Fe2): 42.76° which has been observed previously for materials in an intermediate [HS-LS] state.[4,18,27] Interestingly, $\Sigma$ is comparable for Fe1 and Fe2 in **1b** and **1c**, where only **1c** undergoes a spin transition. This suggests that the interplay between intermolecular interactions, as discussed above and metal coordination environments are influencing these systems greatly.

### *Variable-Temperature Powder X-ray Diffraction of 1c*

Some difficulties were encountered in preparing phase pure bulk sample of **1c**, such as required for SQUID magnetometry, with up to ca. 10% impurity of **1b** typically observed. Consequently, it was necessary to confirm the nature of the (two-step) spin transition identified in this way. This was achieved using variable-temperature diffraction methods whereby the structural perturbations accompanying the changes in Fe–N bond length associated with the spin transition are evident as pronounced changes in the lattice dimensions. Typically a contraction in unit cell volume of 10% is observed for a full transition from high to low spin. While this approach can be applied to both single crystal[4,8,26] and powdered samples,[30] the latter probes bulk samples allowing the temperature dependence of lattice parameters of individual phases to be monitored and the component(s) undergoing structural transitions to be identified. Moreover, crystals of **1c** are typically twinned which would complicate single-crystal studies.

Here, variable temperature powder diffraction methods have been applied to study the structural and spin transition in **1c**. Powder diffraction data were collected at 3 K intervals upon cooling of the sample from 250 to 85 K, the temperature region in which the spin transition was observed. The lattice parameter of the majority phase was refined using a single phase Le Bail fit to the data (Figure S13) based on the crystal symmetry and lattice parameters determined in single crystal structural studies of **1c**.[40] The adequacy of the single phase refinement confirms the phase purity of the bulk sample used here.

The relative changes in the refined lattice parameters for **1c** upon cooling from 250 to 85 K are shown in Figure 6. Two sets of non-linear features evident in the temperature dependence of the lattice parameters for **1c** (at 250–200 K and ca. 125 K) support the two-step nature of the spin transition in this phase. The sharp contraction in the unit cell volume (ca. 2%) in the range 250–200 K correlates directly with the sharp decrease observed in the magnetic susceptibility at 250–200 K associated with a partial spin transition. This contraction was highly anisotropic, with different temperature dependent behaviour observed along the *a*-, *b*- and *c*-axes (Figure 6). A more gradual contraction in the unit cell volume (ca. 1.5%) occurs upon further cooling between 200 and 100 K, which corresponds to the second more gradual spin transition observed in the magnetic susceptibility. The magnitude of the volume contraction observed over the entire temperature range studied (ca. 3.5%), and those attributed to each step are consistent with the degree of spin transition indicated by the magnetic susceptibility measurements with a total volume contraction of 3–5% anticipated for this "half" spin-crossover phase. Although the intrinsic thermal expansion of the framework would also contribute to a contraction of the lattice with decreasing temperature, the non-linearity of the observed behaviour supports the existence of additional phenomena. This non-linearity is most evident for the individual cell axes. In particular, the *c*-axis, along which the 1D chains are oriented, is most directly sensitive to the spin transition and associated changes in the Fe–N bond length. This axis shows pronounced non-linear behaviour (a minimum) at ca.

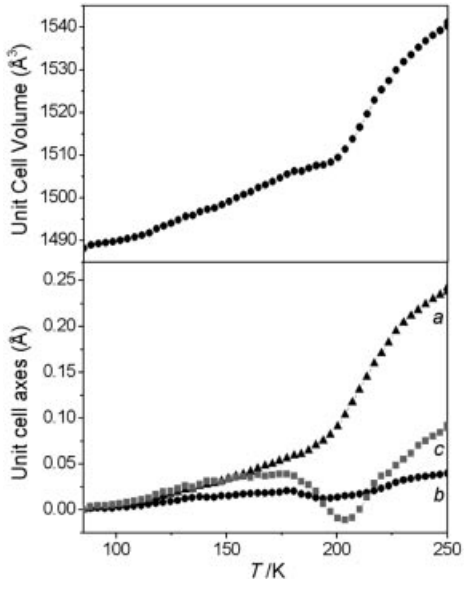


Figure 6. Unit cell volume (top) and axes (bottom) evolution vs. temperature for the spin transition in **1c** over the range 85–250 K obtained by synchrotron powder diffraction.

 © 2007 Wiley-VCH Verlag GmbH & Co. KGaA, Weinheim 

200 K and a more subtle non-linearity at ca. 125 K. Non-linear thermal expansion behaviour was also evident along the *a*- and *b*-axes which is associated with the contraction of Fe–N bonds oriented in the *ab*-plane, and structural perturbations which propagate via intermolecular interactions including the π-π interactions present in this phase.

### *[Fe(NCSe)$_2$(cddt)]·2(CH$_3$OH) (2)*

Crystal data and refinement details of complex **2** can be found in Table 2. Structural analysis of **2** revealed a monoclinic symmetry, isomorphous to **1b**, with two iron(II) centres in the asymmetric unit. The selenocyanate sulfur atom attached to Fe2 is disordered over two crystallographically distinct sites, **A** and **B** (50:50 site occupancies). There is a Se···Se interaction between adjacent chains from the part **A** of the disordered selenocyanate to part **B** [Se···Se: 3.369(2), Figure 3 (b)]. The Se atoms associated with Fe1 are not involved in any interactions. There are two solvent molecules in the asymmetric unit, however one is only present 50% of the time and is associated with the **B** part of the disordered selenocyanate [Figure 3 (b)]. There are no π-π interactions present in this compound which is converse to the case in the thiocyanate analogue **1c**. The Fe···Fe separation within each chain is 9.330(2) Å and between chains is 8.988(2) Å, similar to that of **1b** and **1c**. Further analysis of the geometries of the two metal centres revealed octahedral distortion parameters for Fe1 and Fe2 of $\Sigma$: 30 and 26.04°, respectively.[27] Firstly, it can be seen that Fe1 is slightly more distorted than Fe2 in agreement with the presence of two crystallographically distinct metal centres in the asymmetric unit. Secondly, the distortion parameters for Fe1 and Fe2 are of the same magnitude and similar to the distortion parameter observed in **1c** for Fe1, i.e. 32.28°. Of great interest, here, is the large difference in octahedral distortion of the iron(II) centres between the isomorphous materials **1b** and **2**, which highlights the influence of the stronger ligand field of the $NCSe^-$ ligand. As discussed above, the π-π interactions observed in **1c** are thought to play a major role in influencing the spin transition, no such interactions are observed in **2**, however, the stronger ligand field strength of the $NCSe^-$ ligand compared to the $NCS^-$ ligand would contribute towards the spin state of iron(II) and the observed crossover in **2**.

## Dinuclear Fe$^{II}$ and Co$^{II}$ Complexes of tdt and cddt

### *General*

Crystal data and refinement details for the dinuclear complexes **3a**, **3b**, **4a**, **4b**, **4c** and **4d** are summarised in Table 3. **3a** and **3b** contain the ligand tdt and their two kinds of dinuclear structures have been reported recently by Gamez et al.,[1] differing only in the anion and solvent present and so will not be discussed here in detail. **4a**, **4b**, **4c** and **4d** contain the ligand cddt and consist of isostructural dinuclear moieties that differ in their metals, associated anions and solvents.

### *[Fe(tdt)(Cl)]$_2$(ClO$_4$)$_2$·(C$_2$H$_5$OH)·2(CHCl$_3$) (3a)*

The dinuclear complex **3a** consist of two iron(II) centres coordinated by two tdt ligand and two chloride ligands (Figure S5). The metal centres are in a distorted octahedral environment consisting of five Fe–N bonds from two tdt ligands, including a triazine N donor, and one terminal Fe–Cl bond. The average Fe–Cl and Fe–N bond lengths are 2.3386(18) and 2.2114(5) Å, respectively (Table S1), and correlated well with those of HS iron(II) and those reported by Gamez et al. for [Fe(tdt)(Cl)]$_2$·($CF_3SO_3$).[1] The iron(II) centres are in an extremely distorted octahedral environment illustrated by the octahedral distortion parameters of 66.65°.[27] The Fe···Fe separation within the dinuclear moiety is 8.384(2) Å.

### *[Fe(tdt)(H$_2$O)$_2$]$_2$(ClO$_4$)$_4$·6(H$_2$O) (3b)*

The dinuclear complex **3b** consists of two iron(II) centres coordinated by two tdt ligands and four terminal water molecules. The triazine nitrogen atoms do not coordinate. The average Fe–O and Fe–N bond lengths are 2.161(3) and 2.174(4) Å, respectively (Table S1), and correlated well with those of HS iron(II) and those reported by Gamez et al. for [Fe(tdt)($H_2O$)($CH_3OH$)]$_2$($BF_4$)$_4$.[1] Here, however, we observed the coordination of two water molecules rather than one water and one methanol by Gamez et al.[1] The Fe···Fe separation within the dinuclear molecule is 9.215(2) Å.

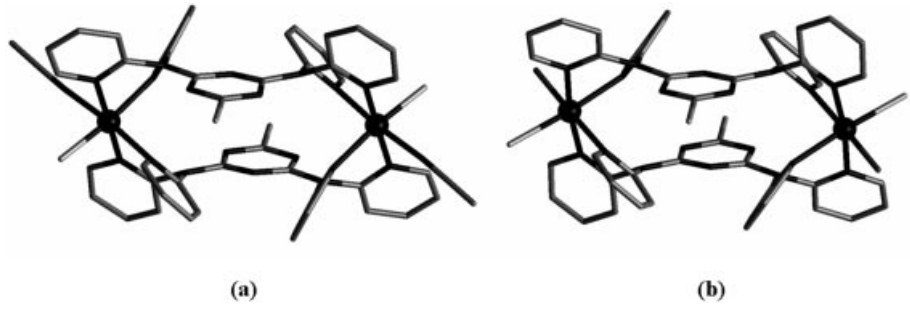


Figure 7. Structural representations of the dinuclear complexes containing the ligand cddt (a) **4a**, **4b**, **4c** and (b) **4d**.

 © 2007 Wiley-VCH Verlag GmbH & Co. KGaA, Weinheim 

### *[M(cddt)(H$_2$O)Cl]$_2$(X)$_2$·n(C$_2$H$_5$OH, H$_2$O) [M: Fe, X: ClO$_4$ (4a), M: Fe, X: BF$_4$ (4b), M: Co, X: BF$_4$ (4c)]*

The dinuclear structures of **4a**, **4b** and **4c** generally consists of two metal(II) centres each in a distorted octahedral environment, two cddt ligands and terminal water and chlorine atoms [Figure 7 (a)]. Each cddt ligand is bound to two metal centres through both pyridyl groups of each di(pyrid-2-yl)amine, as seen in **3b**. The chlorine atoms of the cddt ligand are not involved in any interactions within the metal coordination sphere or any hydrogen bonding interactions. However, hydrogen bonding interactions are present between the metal coordinated chlorine atoms and the solvent water molecule [Cl···O: 3.149(4) (**4a**), 3.150(6) (**4b**) and F···O: 3.331(13) Å (**4c**)] and between the metal coordinated water molecules and the solvent ethanol [O···O: 2.703(5) Å (**4a**), 2.688(7) (**4b**) and 2.704(9) Å (**4c**)]. The Fe–N or Co–N bond lengths for each of these compounds are indicative of HS iron(II) or cobalt(II) (Table S1). The average Fe–Cl, Fe–O and Fe–N bond lengths for **4a** are 2.3954(13), 2.174(3) and 2.207(4) Å, respectively. The average Fe–Cl, Fe–O and Fe–N bond lengths for **4b** are 2.389(2), 2.164(5) and 2.206(5) Å, respectively. The average Co–Cl, Co–O and Co–N bond lengths for **4c** are 2.400(2), 2.136(5) and 2.160(6) Å, respectively. The Fe···Fe separations for **4a**, **4b** and **4c** within the dinuclears are 9.479(7), 9.459(9) and 9.351(5) Å, respectively.

### *[Fe(cddt)(NCCH$_3$)(H$_2$O)]$_2$(ClO$_4$)$_4$·(CH$_3$CN) (4d)*

The general structure of **4d** is a dinuclear complex that is isostructural to **4a**, **4b** and **4c**, however, the coordinated chloride atoms are replaced here by acetonitrile molecules bound through the terminal nitrogen [Figure 7 (b)]. **4d** crystallises in the monoclinic space group $P2_1/n$ whereas **4a**, **4b** and **4c** crystallise in the monoclinic space group $C2/c$ (Table 3), resulting in a different packing of the dinuclear units within their respective unit cells. The average Fe–O and Fe–N bond lengths are 2.123(2) and 2.173(2) Å, respectively, and are indicative of HS iron(II) (Table S1). This same coordination environment was observed for the dinuclear complex [Fe(tdt)(NCCH$_3$)(H$_2$O)]$_2$(BF$_4$)$_4$·(CH$_3$CN) reported by Gamez et al.[1] and was observed to undergo a one step spin transition. Here the Fe–N and Fe–O bond lengths are comparable, but we observed no spin crossover. The Fe···Fe separation within the dinuclear is 9.068(2) Å, this distance is shorter both to that observed in **4a** and **4b** and in [Fe(tdt)(NCCH$_3$)(H$_2$O)]$_2$(BF$_4$)$_4$·(CH$_3$CN).[1]

## Conclusions

Structural and magnetic studies of a range of polynuclear compounds using the dipyrid-2-ylamine containing ligands tdt and cddt have been carried out on a series of 1D polymers of the type [Fe(NCS)$_2$(cddt)$_2$]·*n*(guest) (**1a**, **1b**, and **1c**) and [Fe(NCSe)$_2$(cddt)$_2$]·*n*(guest) (**2**). A combination of such measurements has revealed the role of crystal packing and symmetry on the observed magnetic properties. Three crystal phases of **1** were obtained and exist in tetragonal (**1a**), monoclinic (**1b**) and triclinic (**1c**) symmetries, with only the triclinic phase displaying a thermally induced spin transition. Full structural comparisons of **1a**, **1b**, **1c** and **2** revealed very similar iron(II) coordination environments and extended 1D chain structures. Each of the compounds **1a**, **1b**, **1c** and **2** contain S···S or Se···Se interactions and solvent···S or Se hydrogen bonds, respectively. However, **1c** contains additional π-π interactions which are thought to be the major influence on the observed spin transition. The complex **2** does not contain any π-π interactions but undergoes a spin transition that is probably due to the increase ligand field strength of the NCSe$^-$ ligand compared to the NCS$^-$ ligand in **1c**.

**1c** displays a one-step half spin crossover with a slight two-step character at low temperatures. To differentiate between the presence of a second step or the possibility of sample impurity (due the possibly presence of three crystal phases), further structural characterisation was carried out by monitoring the unit cell evolution of **1c** at temperatures over the spin transition. All the crystals of **1c** grow twinned, hence single crystal techniques for this experiment were not viable so powder diffraction using synchrotron radiation was utilised. This technique has scope to be used, in future, to desolvate and resolvated powder samples, in situ, and monitor such influences on any spin transition observed.

The most celebrated iron(II) SCO chains are the triply-bridged 1,2,4-triazole complexes of type [Fe(4-R-1,2-triazole)$_3$](anion)$_2$.[31] These materials display abrupt spin transitions near to room temperature, with wide hysteresis widths, the $T_{1/2}$ and $\Delta T$ values varying with R and anion. No crystal structures have been obtained but they are assumed similar to the structurally characterised Cu$^{II}$ 1D species.[32] They would possibly benefit from synchrotron powder XRD measurements of the kind given in Figure 6 to ascertain their phase purity and to see if hysteresis occurred in the structural data. In comparison to the present 1D compounds [Fe(NCS)$_2$(cddt)$_2$]·*n*(guest), **1c** and [Fe(NCSe)$_2$(cddt)$_2$]·*n*(guest), **2**, the tris-triazole complexes form more rigid *facially* bridging motifs, with Fe···Fe separations less than in the cddt systems. On this basis, it would appear that such rigidity would favour the strong cooperativity noted, compared to the weak cooperativity observed here in the more flexibly-bridged cddt species. This still begs the question of how, as the HS to LS transition occurs, all the Fe$^{II}$ centres along the tris-$\mu$-triazole chains are able to structurally adjust to accommodate the smaller coordination spheres existing in the LS state, be it in "an all at once" or a sequential process. Such readjustment should be more facile in the present systems. The inter-chain effects upon the Fe$^{II}$ sites, modulated by anions or solvate molecules are, of course, very difficult to define.

Two dinuclear materials containing the ligand tdt have been structurally characterised that are isostructural to those recently reported by Gamez et al.[1] but with different counter anions and solvent molecules. Complex **3a** involves triazine N–Fe coordination, while complex **3b** does not. A similar series of dinuclear materials **4a**, **4b**, **4c** and **4d** containing the ligand cddt, of the **3b** structure type, have been

 © 2007 Wiley-VCH Verlag GmbH & Co. KGaA, Weinheim 

structurally characterised and shown to contain the same general dinuclear structure but differ in their counter anions and solvent molecules. Each of the dinuclear compounds containing either tdt or cddt ligands were intended to have both a $FeN_6$ coordination sphere through incorporation of the *N*-donor ligand thiocyanate, and display spin transitions. However, even though such a situation is sterically possible it is apparent that coordination of chloride atoms and/or water molecules is much more favourable. In the paper by Gamez et al.[1] it was suggested that extended framework materials incorporating the ligand tdt were possible, however all attempts, here, to synthesise such materials, using $NCS^-$ as co-ligand, have resulted in the formation of the mononuclear spin crossover complex $Fe(NCS)_2(tdt)_2$ already reported.[2] The present direct synthesis contrasts with the report that it could only be made from dinuclear precursors.[2]

There are some interesting similarities and differences noted between the present dinuclear iron(II) compounds and the analogues described by Gamez et al.[1] If the effects of intermoleculear interactions in crystals are ignored, and the ligand-field around each iron(II) is assumed dominant, then the following conclusions can be made about the ligand-field and the spin state on the iron(II) centres. The complexes possessing a triazine N-donor $[Fe(tdt)(Cl)]_2(ClO_4)_2{\cdot}(C_2H_5OH){\cdot}2(CHCl_3)$ (**3a**) here, and the complex $[Fe(tdt)(Cl)]_2(CF_3SO_3)_2$ in Gamez et al.,[1] have a $[FeN_5Cl]$ coordination set and are both HS-HS. The other dinuclear type, not displaying triazine coordination are $[Fe(cddt)(NCCH_3)(H_2O)]_2(ClO_4)_4{\cdot}(CH_3CN)$ (**4d**) and the complex $[Fe(tdt)(NCCH_3)(H_2O)]_2(ClO_4)_4$ in Gamez et al.,[1] both with $[Fe_5NO]$ coordination. The SCO behaviours observed in the tdt system contrasts with the HS-HS behaviour in **4d** and, thus, tdt provides a stronger ligand-field contribution than does cddt.

## Experimental Section

**General:** All the reagents and solvents were used as commercially available and used as received. The ligands tdt and cddt were prepared by literature methods.[33] Infrared spectra were recorded on single crystals mounted on a Low-e microscope slide using a Varian FTS7000 FT-IR spectrometer with a VMA600 microscope in reflectance mode. CHN analyses were performed by Campbell Microanalytical Laboratory, Department of Chemistry, University of Otago, Dunedin, New Zealand.

**Magnetic Susceptibility Measurements:** Magnetic susceptibility data were collected using a Quantum Design MPMS 5 SQUID magnetometer under an applied field of 1 T. The powder samples were placed in a quartz tube and great care was taken to avoid any solvent loss and/or torquing of crystallites of these potentially anisotropic HS iron(II) species, the latter by dispersal of the powder in a Vaseline mull. Care was also taken to allow long thermal equilibration times at each temperature point.

**Crystallographic Data Collection and Refinement (Tables 2 and 3):** Crystallographic data and parameters for all materials are summarised in Tables 2 and 3. Single crystal diffraction data for all structures were collected on a Bruker APEX X8 diffractometer using Mo-$K_\alpha$ ($\lambda$ = 0.71073 Å) radiation and equipped with an Oxford Instruments nitrogen gas cryostream. Crystals were mounted on a MiTeGen MicroMounts fibre in a small amount of oil. Crystals were quench-cooled to 123(2) K for all data sets.

Diffraction data analysis was performed using SAINT+ within the APEX2 software package.[34] Empirical absorption corrections were applied to all data using SADABS.[35] The structures were solved using SHELXS and refined using SHELXL-97 within WINGX.[34,36] All non–hydrogen atoms in the structures were refined anisotropically and hydrogen atoms were generated using the riding model. The data set for the material **1c** was merohedrally twinned over two orientations related by a 179.9° rotation about the reciprocal axis 010. Initial indexing for the two components was carried out using CELL NOW within the APEX2 software package.[34] Multi-component integration was carried out using SAINT+.[34] Scaling and empirical absorption corrections were then applied using TWINABS.[34] The structure was solved as above using a HKLF 5 command with a resulting BASF parameter of 0.3477.

CCDC-625487 to -625496 contain the supplementary crystallographic data for this paper. These data can be obtained free of charge from The Cambridge Crystallographic Data Centre via www.ccdc.cam.ac.uk/datarequest/cif.

Table 2. Crystal data and refinement details for compounds **1a**, **1b**, **1c** and **2**.

| | **1a** | **1b** | **1c** | **2** |
|---|---|---|---|---|
| Spin states | HS | HS | HS-LS | LS |
| $T$ [K] | 123(2) | 123(2) | 123(2) | 123(2) |
| Empirical formula | $C_{51}H_{32}Cl_5Fe_2N_{22}O_2S_4$ | $C_{27}H_{24}ClFeN_{11}O_2S_2$ | $C_{27}H_{24}ClFeN_{11}O_2S_2$ | $C_{27}H_{24}ClFeN_{11}O_2Se_2$ |
| Formula mass/g mol$^{-1}$ | 1402.22 | 689.99 | 689.99 | 767.77 |
| Crystal system (space group) | tetragonal (*P4/ncc*) | monoclinic ($P2_1/n$) | triclinic ($P\bar{1}$) | monoclinic ($P2_1/n$) |
| $Z$ | 4 | 4 | 2 | 2 |
| $a$/Å | 18.5157(6) | 14.6590(4) | 8.8106(5) | 14.0888(7) |
| $b$/Å | 18.5157(6) | 12.3486(4) | 9.4825(5) | 12.2342(6) |
| $c$/Å | 18.7076(10) | 17.4349(6) | 19.0242(11) | 17.9765(9) |
| $\alpha$/° | 90.00 | 90.00 | 78.458(5) | 90.00 |
| $\beta$/° | 90.00 | 102.0530(10) | 77.652(3) | 100.798(3) |
| $\gamma$/° | 90.00 | 90.00 | 73.638(4) | 90.00 |
| $V$/Å$^3$ | 6413.5(5) | 3086.46(17) | 1473.08(14) | 3043.7(3) |
| $\rho_{calcd.}$/Mg·m$^{-3}$ | 1.452 | 1.485 | 1.556 | 1.676 |
| $\mu$/mm$^{-1}$ | 0.848 | 0.757 | 0.793 | 3.019 |
| $R(F)$/% [$I > 2\sigma(I)$, all] | 0.1156 [0.1887] | 0.0785 [0.0966] | 0.0860 [0.0916] | 0.0616 [0.1082] |
| $R_w(F^2)$/% [$I > 2\sigma(I)$, all] | 0.3251 [0.3972] | 0.2007 [0.2162] | 0.1903 [0.1934] | 0.1257 [0.1426] |
| GoF | 1.009 | 1.050 | 1.210 | 1.034 |

 © 2007 Wiley-VCH Verlag GmbH & Co. KGaA, Weinheim 

Table 3. Crystal data and refinement details for compounds **3a**, **3b**, **4a**, **4b**, **4c** and **4d**.

| | **3a** | **3b** | **4a** |
|---|---|---|---|
| $T$ [K] | 123(2) | 123(2) | 123(2) |
| Empirical formula | $C_{70}H_{56}Cl_{10}Fe_2N_{24}O_9$ | $C_{66}H_{48}Cl_4Fe_2N_{24}O_{26}$ | $C_{50}H_{46}Cl_6Fe_2N_{18}O_{13}$ |
| Formula mass/g mol$^{-1}$ | 1843.59 | 1846.78 | 1431.45 |
| Crystal system (space group) | triclinic ($P\bar{1}$) | monoclinic ($P2_1/n$) | monoclinic ($C2/c$) |
| $Z$ | 1 | 2 | 4 |
| $a$/Å | 12.9071(9) | 13.430(3) | 19.4533(3) |
| $b$/Å | 13.1087(17) | 14.303(3) | 16.1016(2) |
| $c$/Å | 13.2276(10) | 20.390(4) | 20.3064(3) |
| $\alpha$/° | 104.345(4) | 90.00 | 90.00 |
| $\beta$/° | 115.873(2) | 101.11(3) | 110.6570(10) |
| $\gamma$/° | 95.102(4) | 90.00 | 90.00 |
| $V$/Å$^3$ | 1900.4(3) | 3843.2(13) | 5951.63(15) |
| $\rho_{calcd.}$/Mg·m$^{-3}$ | 1.611 | 1.596 | 1.598 |
| $\mu$/mm$^{-1}$ | 0.808 | 0.614 | 0.835 |
| $R(F)$/% [$I > 2\sigma(I)$, all] | 0.1069 [0.1661] | 0.0642 [0.1493] | 0.0670 [0.1101] |
| $R_w(F^2)$/% [$I > 2\sigma(I)$, all] | 0.2601 [0.3043] | 0.1695 [0.2413] | 0.1825 [0.2325] |
| GoF | 1.062 | 1.063 | 1.158 |
| | **4b** | **4c** | **4d** |
| $T$ [K] | 123(2) | 123(2) | 123(2) |
| Empirical formula | $C_{50}H_{46}B_2Cl_4F_8Fe_2N_{18}O_6$ | $C_{50}H_{46}B_2Cl_4Co_2F_8N_{18}O_6$ | $C_{52}H_{42}Cl_6Fe_2N_{21}O_{18}$ |
| Formula mass/g mol$^{-1}$ | 1422.17 | 1428.33 | 1573.47 |
| Crystal system (space group) | monoclinic ($C2/c$) | monoclinic ($C2/c$) | monoclinic ($P2_1/n$) |
| $Z$ | 4 | 4 | 2 |
| $a$/Å | 19.466(4) | 19.4162(3) | 12.6006(3) |
| $b$/Å | 16.055(3) | 15.9960(3) | 14.6048(4) |
| $c$/Å | 20.511(4) | 20.4328(4) | 18.1261(5) |
| $\alpha$/° | 90.00 | 90.00 | 90.00 |
| $\beta$/° | 112.24(3) | 112.550(5) | 106.6940(10) |
| $\gamma$/° | 90.00 | 90.00 | 90.00 |
| $V$/Å$^3$ | 5934(2) | 5860.9(3) | 3195.14(15) |
| $\rho_{calcd.}$/Mg·m$^{-3}$ | 1.592 | 1.619 | 1.635 |
| $\mu$/mm$^{-1}$ | 0.760 | 0.840 | 0.793 |
| $R(F)$/% [$I > 2\sigma(I)$, all] | 0.0790 [0.1799] | 0.0979 [0.2111] | 0.0577 [0.0626] |
| $R_w(F^2)$/% [$I > 2\sigma(I)$, all] | 0.2000 [0.2968] | 0.2198 [0.3061] | 0.1395 [0.1424] |
| GoF | 0.998 | 1.122 | 1.085 |

**Powder Synchrotron X-ray Diffraction:** A pulverised sample of $[Fe(NCS)_2(cddt)]\cdot 2(CH_3OH)$ (**1c**) was loaded in a polyimide capillary of 0.8 mm diameter and kept in an inert helium atmosphere for the duration of the experiments.[37] The X-rays (20.02 keV, 0.61915 Å) available at the 1-BM beamline at the Advanced Photon Source at Argonne National Laboratory were used in combination with a MAR-345 imaging plate (IP) detector to record diffraction patterns. The sample temperature was controlled using an Oxford Cryosystems Cryostream 700 and data were collected in 1 s exposures upon continuous cooling from 250 K to 85 K at 100 Kh$^{-1}$. This corresponds to the collection of diffraction images at 3 K intervals. The raw images were processed using Fit-2D.[38–39] The sample-to-detector distance and tilt of the IP relative to the beam were refined using a $LaB_6$ standard. Le Bail analyses of the variable-temperature diffraction data were performed within GSAS.[40] Details of the refinements are included in the Supporting Information.

**$[Fe(cddt)(NCS)_2]\cdot 1/2(CHCl_3)\cdot(H_2O)$ (1a):** A 5 mL solution of cddt (45 mg, 0.1 mmol) in chloroform was placed at the base of a test tube onto which an 8 mL 50:50 mixture of methanol/chloroform was carefully layered. A 5 mL solution of $Fe(ClO_4)_2\cdot 6(H_2O)$ (25 mg, 0.1 mmol) and NaNCS (16 mg, 0.2 mmol) in methanol was then layered on-top and the test tube stoppered. After two weeks bright yellow needle shaped crystals formed (61 mg, 88%). IR: ν = 3445 (br), 2062 (s), 1604 (m), 1554 (m), 1466 (s), 1261 (m), 658 (w). $C_{51}H_{32}Cl_5Fe_2N_{22}O_2S_4$ (1402): calcd. C 39.97, H 2.71, N 19.72; found C 39.69, H 3.15, N 17.85.

**$[Fe(cddt)(NCS)_2]\cdot 2(CH_3OH)$ (1b):** A 2 mL solution of cddt (22 mg, 0.05 mmol) in methanol was placed at the base of one arm of an H-shaped tube. A 2 mL solution of $Fe(ClO_4)_2\cdot 6(H_2O)$ (25 mg, 0.1 mmol) and NaNCS (16 mg, 0.2 mmol) was placed in the other arm of the H-shaped tube. Solvent methanol was carefully layered to fill the tube, which was then stoppered. After one week yellow block shaped crystals formed (yield: unknown forms as a mixed product with **1c** ca. 10%). IR: ν = 3440 (br), 2063 (s), 1598 (m), 1550 (m), 1465 (m), 1264 (m), 668 (w).

**$[Fe(cddt)(NCS)_2]\cdot 2(CH_3OH)$ (1c):** A 2 mL solution of cddt (45 mg, 0.1 mmol) in methanol was placed at the base of one arm of an H-shaped tube. A 2 mL solution of $Fe(ClO_4)_2\cdot 6(H_2O)$ (25 mg, 0.1 mmol) and NaNCS (16 mg, 0.2 mmol) was placed in the other arm of the H-shaped tube. Solvent methanol was carefully layered to fill the rest of the tube, which was then stoppered. After one week yellow block shaped crystals formed (60 mg, 87%). IR: ν = 3440 (br), 2057 (s), 1603 (m), 1552 (m), 1399 (s), 1229 (m), 670 (w). $C_{27}H_{24}ClFeN_{11}O_2S_2$ (689): calcd. C 47.9, H 2.58, N 24.62; found C 47.6 H 2.73, N 24.48.

**$[Fe(cddt)(NCSe)_2]\cdot 2(CH_3OH)$ (2):** A 5 mL solution of cddt (45 mg, 0.1 mmol) in methanol was placed at the base of one arm of an H-tube. A 2 mL solution of $Fe(ClO_4)_2\cdot 6(H_2O)$ (25 mg, 0.1 mmol) and

 © 2007 Wiley-VCH Verlag GmbH & Co. KGaA, Weinheim 

KNCSe (28 mg, 0.2 mmol) in methanol was placed in the other arm of the H-shaped tube. Solvent methanol was carefully layered to fill the rest of the H-tube, which was then stoppered. After two weeks bright yellow needle shaped crystals formed (58 mg, 74%). IR: ν = 3400 (br), 2061 (s), 1603 (m), 1552 (m), 1398 (m), 1230 (m), 656 (m). $C_{27}H_{24}ClFeN_{11}O_2Se_2$ (768): calcd. C 41.72, H 2.24, N 21.41; found C 43.70 H 2.93 N 21.54.

**$[Fe(tdt)(Cl)]_2(ClO_4)_2\cdot(C_2H_5OH)\cdot2(CHCl_3)$ (3a):** A 2 mL solution of tdt (59 mg, 0.1 mmol) in chloroform was placed at the base of one arm of an H-shaped tube. A 2 mL solution of $Fe(ClO_4)_2\cdot6(H_2O)$ (25 mg, 0.1 mmol) and $NaNCBH_3$ (12 mg, 0.2 mmol) in ethanol was placed in the other arm of the H-shaped tube. Solvent ethanol was carefully layered to fill the rest of the H-tube, which was then stoppered. After two weeks yellow block shaped crystals formed (120 mg, 32%). IR: ν = 3385 (br), 1601 (w), 1547 (m), 1466 (m), 1368 (s), 1008 (br). $C_{70}H_{56}Cl_{10}Fe_2N_{24}O_9$ (1843): calcd. C 40.93, H 3.64, N 16.84; found C 39.93, H 3.08, N 18.67.

**$[Fe(tdt)(H_2O)]_2(ClO_4)_4\cdot6(H_2O)$ (3b):** A 2 mL solution of tdt (59 mg, 0.1 mmol) in methanol and a 2 mL solution of $Fe(ClO_4)_2\cdot6H_2O$ (25 mg, 0.1 mmol) in acetonitrile were mixed in a vial. Over a period of 2 weeks yellow block crystals formed (125 mg, 36%). IR: ν = 3386 (br), 1602 (w), 1547 (m), 1466 (m), 1368 (s), 1001 (br). $C_{66}H_{48}Cl_4Fe_2N_{24}O_{26}$ (1743): calcd. C 41.68, H 3.39, N 17.68; found C 42.53, H 3.78, N 17.75.

**$[Fe(cddt)(H_2O)Cl]_2(ClO_4)_2\cdot2(C_2H_5OH)\cdot(H_2O)$ (4a):** A 2 mL solution of cddt (45 mg, 0.1 mmol) in ethanol and a 2 mL solution of $Fe(ClO_4)_2\cdot6H_2O$ (25 mg, 0.1 mmol) in ethanol were mixed in a vial. Over a period of 2 weeks yellow block crystals formed (150 mg, 52%). IR: ν = 3198 (br), 1601 (m), 1548 (m), 1466 (m), 1371 (s), 1050 (br). $C_{50}H_{46}Cl_6Fe_2N_{18}O_{13}$ (1431): calcd. C 36.27, H 3.84, N 16.55; found C 35.97, H 3.84, N 16.55.

**$[Fe(cddt)(H_2O)Cl]_2(BF_4)_2\cdot2(C_2H_5OH)\cdot2(H_2O)$ (4b):** A 2 mL solution of cddt (45 mg, 0.1 mmol) in ethanol and a 2 mL solution of $Fe(BF_4)_2\cdot6H_2O$ (34 mg, 0.1 mmol) in acetonitrile were mixed in a vial. Over a period of 2 weeks yellow block crystals formed (160 mg, 56%). IR: ν = 3199 (br), 1601 (m), 1548 (m), 1465 (m) 1368 (s), 1052 (br).

**$[Co(cddt)(H_2O)Cl]_2(BF_4)_2\cdot2(C_2H_5OH)\cdot2(H_2O)$ (4c):** A 2 mL solution of cddt (45 mg, 0.1 mmol) in ethanol and a 2 mL solution of $Co(BF_4)_2\cdot6H_2O$ (34 mg, 0.1 mmol) in acetonitrile were mixed in a vial. Over a period of 2 weeks orange block crystals formed (175 mg, 61%). IR: ν = 3358 (br), 1602 (m), 1546 (m), 1467 (m), 1371 (s), 1053 (br). $C_{50}H_{46}B_2Cl_4Co_2F_8N_{18}O_6$ (1428): calcd. C 43.34, H 3.64, N 17.84; found C 44.55, H 3.89, N 18.78.

**$[Fe(cddt)(NCCH_3)(H_2O)]_2(ClO_4)_4\cdot(CH_3CN)$ (4d):** A 2 mL solution of cddt (45 mg, 0.1 mmol) in acetonitrile was placed at the base of one arm of an H-shaped tube. A 2 mL solution of $Fe(ClO_4)_2$ (25 mg, 0.1 mmol) in acetonitrile was placed in the other arm of the H-shaped tube. Neat acetonitrile was carefully layered to fill the rest of the H-tube, which was then stoppered. After two weeks yellow block shaped crystals formed. (200 mg, 63%). IR: ν = 2130 (w), 2138 (w), 1607 (m), 1550 (m), 1387 (s), 1260 (w), 1229 (w), 1118 (br), 623 (m). $C_{52}H_{42}Cl_6Fe_2N_{21}O_{18}$ (1573): calcd. C 39.62, H 2.88, N 18.04; found C 39.13, H 3.02, N 18.04.

**Supporting Information** (see also the footnote on the first page of this article): Thermal ellipsoid diagrams, including numbering schemes for all materials discussed here are included. Table of selected bond lengths of the dinuclear materials are included. Additional magnetic susceptibility plots for selected materials are also included. Detailed refinement and processing of powder diffraction data, including tables of $\chi^2$ values.

## Acknowledgments

This work was supported by an ARC Discovery Grant (KSM) and the Australian Synchrotron Research Program, which is funded by the Commonwealth of Australia under the Major National Research Facilities Program. Use of the Advanced Photon Source was supported by the U.S. Department of Energy, Office of Science, Basic Energy Sciences, under Contract No. DE-AC02-06CH11357.

[1] M. Quesada, P. de Hoog, P. Gamez, O. Roubeau, G. Aromí, B. Donnadieu, C. Massera, M. Lutz, A. L. Spek, J. Reedijk, *Eur. J. Inorg. Chem.* **2006**, *7*, 1353–1361.
[2] M. Quesada, M. Monrabal, G. Aromí, V. de la Peña-O'Shea, M. Gich, E. Molins, O. Roubeau, S. Teat, E. MacLean, P. Gamez, J. Reedijk, *J. Mater. Chem.* **2006**, *26*, 2669–2676.
[3] B. A. Leita, B. Moubaraki, K. S. Murray, J. P. Smith, J. D. Cashion, *Chem. Commun.* **2004**, 156–157.
[4] J. J. M. Amoore, C. J. Kepert, J. D. Cashion, B. Moubaraki, S. M. Neville, K. S. Murray, *Chem. Eur. J.* **2006**, *12*, 8220–8227.
[5] C. Schneider, J. D. Cashion, B. Moubaraki, S. M. Neville, S. R. Batten, D. R. Turner, K. S. Murray, *Polyhedron* **2006**, doi:10.1016/j.poly.2006.09.003.
[6] K. Nakano, S. Kawata, K. Yoneda, A. Fuyuhiro, T. Yagi, S. Nasu, S. Morimoto, S. Kaizaki, *Chem. Commun.* **2004**, *24*, 2892–2893.
[7] K. Yoneda, K. Nakano, J. Fujioka, K. Yamada, T. Suzuki, A. Fuyuhiro, S. Kawata, S. Kaizaki, *Polyhedron* **2005**, *24*, 2437–2442.
[8] G. J. Halder, C. J. Kepert, B. Moubaraki, K. S. Murray, J. D. Cashion, *Science* **2002**, *298*, 1762–1765.
[9] C. J. Kepert, *Chem. Commun.* **2006**, 695–700.
[10] S. M. Neville, B. Moubaraki, K. S. Murray and C. J. Kepert, *Angew. Chemie. Int. Ed.*, **2006**, submitted.
[11] O. Kahn, C. J. Martinez, *Science* **1998**, *279*, 44.
[12] J. A. Real, E. Andres, M. C. Muñoz, M. Julve, T. Granier, A. Bousseksou, F. Varret, *Science* **1995**, *268*, 265–267.
[13] V. Niel, A. L. Thompson, M. C. Muñoz, A. Galet, A. S. E. Goeta, J. A. Real, *Angew. Chem. Int. Ed.* **2003**, *42*, 3760–3763.
[14] K. Yoneda, K. Adachi, S. Hayami, Y. Maeda, M. Katada, A. Fuyuhiro, S. Kawata, S. Kaizaki, *Chem. Commun.* **2006**, *1*, 45–47.
[15] K. S. Murray, C. J. Kepert, *Top. Curr. Chem.* **2004**, *233*, 195.
[16] A. B. Gaspar, M. C. Muñoz, J. A. Real, *J. Mater. Chem.* **2006**, *16*, 2522–2533.
[17] S. R. Batten, J. Bjernemose, P. Jensen, B. A. Leita, K. S. Murray, B. Moubaraki, J. Smith, H. Toftlund, *Dalton Trans.* **2004**, 3370–3375.
[18] A. B. Gaspar, G. Agustí, V. Martínez, M. C. Muñoz, G. Levchenko, J. A. Real, *Inorg. Chim. Acta* **2005**, 4089–4094.
[19] Y. Garcia, O. Kahn, L. Rabardel, B. Chansou, L. Salmon, J. P. Tuchagues, *Inorg. Chem.* **1999**, *38*, 4663.
[20] A. Galet, M. C. Muñoz, A. B. Gaspar, J. A. Real, *Inorg. Chem.* **2005**, *44*, 8749–8755.
[21] A. Galet, M. C. Muñoz, V. Martínez, J. A. Real, *Chem. Commun.* **2004**, 2268–2269.
[22] E. König, K. Madeja, *Inorg. Chem.* **1967**, *6*, 48.
[23] E. König, K. Madeja, K. J. Watson, *J. Am. Chem. Soc.* **1968**, *90*, 1146.
[24] A. Ozarowski, B. R. McGarvey, A. B. Sarkar, J. E. Drake, *Inorg. Chem.* **1988**, *27*, 628.
[25] S. Matouzenko, A. Bousseksou, S. Lecoca, P. J. van Koningsbruggen, M. Perrin, O. Kahn, A. Kollet, *Inorg. Chem.* **1997**, *36*, 5869.
[26] M. Marchivie, P. Guionneau, J.-F. Letard, D. Chasseau, *Acta Crystallogr., Sect. B* **2003**, *59*, 479–486.

 © 2007 Wiley-VCH Verlag GmbH & Co. KGaA, Weinheim 

[27] P. Guionneau, C. Brigouleix, Y. Barrans, A. E. Goeta, J.-F. Létard, J. A. Howard, J. Gaultier, D. C. Chasseau, *R. Acad. Sci. Ser. IIc* **2001**, *4*, 161–171.
[28] P. Guionneau, M. Marchivie, G. Bravic, J.-F. Letard, D. Chasseau, *Top. Curr. Chem.* **2004**, *234*, 97–128.
[29] S. Imatomi, R. Kitashima, T. Hamamatsu, M. Okeda, Y. Ogawa, N. Matsumoto, *Chem. Lett.* **2006**, *35*, 502.
[30] K. W. Chapman, P. J. Chupas, C. J. Kepert, *J. Am. Chem. Soc.* **2006**, *128*, 7009–7014.
[31] Y. Garcia, V. Niel, C. Muñoz, J. A. Real, *Top. Curr. Chem.* **2004**, *233*, 229–257.
[32] A. Michalowicz, G. L. Moscovici, Y. Garcia, O. Kahn, *J. Synchrotron Radiat.* **1999**, *6*, 231.
[33] P. De Hoog, P. Gamez, W. L. Driessen, J. Reedijk, *Tetrahedron Lett.* **2002**, *43*, 6783.
[34] *APEX2 Software Package v 1.27*. Bruker AXS Inc., Madison, WI, **2005**.
[35] G. M Sheldrick, *SADABS, Empirical adsorption correction program for area detector data*, University of Göttingen, Germany, **1996**.
[36] L. J. Farugia, *J. Appl. Chem.* **1999**, *32*, 837–838.
[37] P. J. Chupas, M. F. Ciraolo, J. C. Hanson, C. P. Grey, *J. Am. Chem. Soc.* **2001**, *123*, 1694–1702.
[38] A. P. Hammersley, *ESRF Internal Report*, **1997**, ESRF97HA02T.
[39] A. P. Hammersley, S. O. Svensson, M. Hanfland, A. N. Fitch, D. Hausermann, *High-Pressure Res.* **1996**, *14*, 235–248.
[40] A. C. Larson, R. B. V. Dreele, *General Structure Analysis System (GSAS)*, **2000**, Los Alamos National Laboratory Report, LAUR 86–748.

Received: November 3, 2006
Published Online: January 25, 2007

 © 2007 Wiley-VCH Verlag GmbH & Co. KGaA, Weinheim 

DOI: 10.1002/ejic.200601007

# Synthesis and Characterization of Novel Titanium, Germanium, and Tin Silazane Complexes Bearing a Cyclohexasilazanetriido Ligand

Christian Lehnert,[a] Jörg Wagler,[a] Edwin Kroke,[a] and Gerhard Roewer*[a]

**Keywords:** Heterometallic complexes / N ligands / Titanium / Germanium / Tin / Cyclohexasilazane complexes

Novel heterometallic silazane complexes were synthesized by the reaction of 1-lithio-2,2,4,4,6,6-hexamethylcyclotrisilazane Li(HMCTS)$H_2$ with the tetrachloride salts of titanium and germanium as well as by the reaction of 1,1,3,3,5,5-hexamethylcyclotrisilazane $H_3$(HMCTS) with tin tetrachloride and excess triethylamine. The products [$H_3$(DMCHS)TiCl] (**1**), [$H_3$(DMCHS)GeCl] (**2**), and [$H_3$(DMCHS)SnCl] (**3**) {$H_3$(DMCHS) = 2,2,4,4,6,6,8,8,10,10,12,12-dodecamethylcyclohexasilazane-1,5,9-triido} were characterized by $^1$H-, $^{13}$C-, $^{14}$N-, and $^{29}$Si NMR spectroscopy, elemental analyses and single-crystal X-ray structure analyses. The complexes have a surprising and interesting structure, that of a new dodecamethylcyclohexasilazane system with the Ti, Ge, or Sn atom in the center. These metal atoms are coordinated by one chlorine atom and three nitrogen atoms. The metal centers are part of three six-membered hetero-silazane rings.
(© Wiley-VCH Verlag GmbH & Co. KGaA, 69451 Weinheim, Germany, 2007)

## Introduction

Silazanes offer promising ligand properties in reactions with metal chlorides because of their reactive N–H and Si–N bonds.[1–3] Especially, the cyclic silazane 1,1,3,3,5,5-hexamethylcyclotrisilazane $H_3$(HMCTS) shows striking reactivity patterns. In addition to substitution reactions, isomerizations of the cyclotrisilazane system into cyclodisilazanes and ring coupling reactions were observed, which led to an assortment of structurally diverse compounds.[4–10]

Silazanes are widely used as precursors for silicon-based non-oxide ceramic materials with outstanding thermal, mechanical, and chemical properties, which make them uniquely applicable under extreme conditions.[11–13] Furthermore, silazane derivatives of Ti, Zr, Fe, B, Al, and Ge are used for the synthesis of multinary ceramics. The incorporation of these elements provides access to new classes of ceramic materials and to the development of new applications. For example, the integration of boron can improve the thermal stability of silicon-based ceramic materials up to 2000 °C because of the suppression of recrystallization processes.[14] The incorporation of iron leads to magnetic ceramics.[15] The germanium(II) precursor, Ge[N(SiMe$_3$)$_2$]$_2$, has been employed to obtain germanium nanocrystals by thermal decomposition of the complex.[16]

These developments encouraged us to examine reactions between $H_3$(HMCTS) and $TiCl_4$, $GeCl_4$, and $SnCl_4$ in order to combine the interesting chemistry of cyclic silzanes and the synthesis of metal-atom-containing Si–C–N molecules. In this paper, we report the ring-isomerization of $H_3$(HMCTS) with formation of novel Ti-, Ge-, and Sn-centered tricyclic silazane frameworks.

## Results and Discussion

1-Lithio-2,2,4,4,6,6-hexamethylcyclotrisilzane [Li(HMCTS)$H_2$] was prepared by treating a toluene solution of $H_3$(HMCTS) with an equimolar amount of a solution of *n*-butyllithium in hexane. The subsequent reaction of Li(HMCTS)$H_2$ with $TiCl_4$ or $GeCl_4$ in a molar ratio of 2:1 should produce Ti- or Ge-containing silazane compounds and LiCl as by-product (Scheme 1, route A). Surprisingly, the $^{29}$Si NMR spectra of the products exhibit only one resonance signal. This fact and also the result of the elemental analyses were not in accord with any structures derived from simple substitutions or ring contractions of the cyclotrisilazane system. Fortunately, we were able to obtain crystals of both products, and the nature of the new complexes **1** and **2** could easily be clarified by crystal structure analysis (Scheme 1, route B).

Both complexes **1** and **2** exhibit the same cyclohexasilazane ring system with the titanium or germanium atom in the center of the ring system. When the reaction conditions were varied and $H_3$(HMCTS), titanium tetrachloride, and excess triethylamine were used, the same titanium complex **1** formed, with only a small difference in the yield. Furthermore, the reaction pathway was almost unaffected by the type of solvent used. The reaction of Li(HMCTS)$H_2$ with tin tetrachloride in a ratio of 2:1 yields the substitution product dichlorobis(2,2,4,4,6,6-hexamethylcyclotrisilazano)-stannane, as we reported recently (Scheme 2, route A),[17] but a complex analogous to **1** or **2** was not found. Complex

[a] TU Bergakademie Freiberg, Institut für Anorganische Chemie, Leipziger Strasse 29, 09596 Freiberg, Germany
Fax: +49-3731-39-4058
E-mail: Gerhard.Roewer@chemie.tu-freiberg.de

 © 2007 Wiley-VCH Verlag GmbH & Co. KGaA, Weinheim 

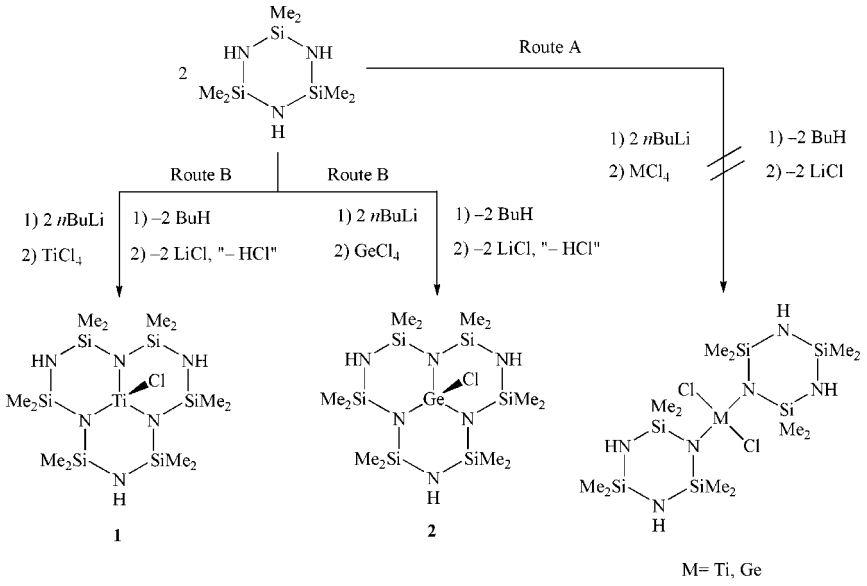


Scheme 1. Synthesis of titanium and germanium cyclohexasilazane complexes by reaction of lithiated $H_3$(HMCTS) with $TiCl_4$ and $GeCl_4$.

**3**, which exhibits the same molecular structure as **1** and **2**, was synthesized by reacting $H_3$(HMCTS) with 3 equiv. $SnCl_4$ and excess triethylamine (Scheme 2, route B).

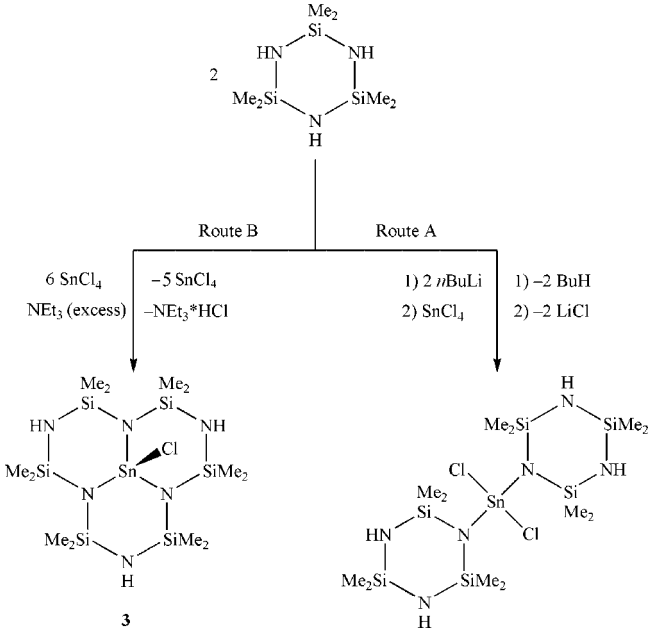


Scheme 2. Formation of the tin cyclohexasilazane complex **3** by reaction of $H_3$(HMCTS) with $SnCl_4$ and $Et_3N$.

The formation of **3** deserves specific attention because of the different starting material molar ratios from those used in the reactions of Li(HMCTS)$H_2$ with $TiCl_4$ and $GeCl_4$. The NMR spectroscopic data of **1**, **2**, and **3** are presented in Table 1.

Table 1. $^1$H, $^{13}$C, $^{14}$N, $^{29}$Si, $^{49}$ Ti, and $^{119}$Sn NMR spectroscopic data for the new complexes **1**, **2**, and **3**.

| Compound | $^1$H Si–Me | N–H | $^{13}$C | $^{14}$N M–N | N–H | $^{29}$Si | $^{49}$Ti, $^{73}$Ge or $^{119}$Sn |
|---|---|---|---|---|---|---|---|
| **1** | 0.20, 0.26 | 0.56 | 1.9, 4.5 | –85 | –343 | –7.0 | –137 |
| **2** | 0.28, 0.35 | 0.61 | 2.5, 5.3 | –83 | –349 | –3.8 | not obtained |
| **3** | 0.21, 0.33 | 0.58 | 3.3, 4.6 | –71 | –350 | –3.9 | –169 |

The $^{29}$Si NMR spectra of the heterometallic complexes exhibit one resonance signal each, which is located at –7 ppm for **1** and at ca. –4 ppm for **2** and **3**. Therefore, the chemical shifts are nearly identical with that of $H_3$(HMCTS) [$\delta$($^{29}$Si) = –4.3 ppm].

Time-dependent $^{29}$Si NMR studies of the reaction between $H_3$(HMCTS) and $TiCl_4$ provided valuable data from which a possible reaction pathway can be proposed, although the overall reaction mechanism is not clear so far. The $^{29}$Si resonance of the silazane starting material quickly disappears after the start of the reaction, and new resonance signals ranging from 10 to 15 ppm arise in the spectra. They can be assigned to silicon atoms of $(Si–N)_2$ rings[17] and indicate cyclodisilazanes as intermediates in the formation of the dodecamethylcyclohexasilazane ring, which is found in complexes **1**–**3**. During the reaction, the intensities of the resonance signals between 10 and 15 ppm decrease, and simultaneously, the $^{29}$Si resonance of the titanium complex **1** appears at $\delta$ = –7 ppm.

Compound **1** has a $^{49}$Ti NMR signal at $\delta$ = –137 ppm, and compound **3** a $^{119}$Sn resonance at $\delta$ = –169 ppm, but no $^{73}$Ge signal was measured for compound **2** because of the quadrupolar momentum of this nucleus and the unsym-

 © 2007 Wiley-VCH Verlag GmbH & Co. KGaA, Weinheim 

metrical substitution pattern of the germanium atom in **2**. The methyl moieties at each silicon atom are diastereotopic as indicated by two signals for the methyl groups in both the $^{1}H$- and $^{13}C$ NMR spectra of complexes **1**–**3**. The $^{14}N$ NMR spectra exhibit a broad resonance signal at around –350 ppm, which results from the nitrogen atoms bearing one hydrogen atom. The location of this signal is similar to that of the chemical shift of the silazane starting material [$\delta(^{14}N)$ = –360 ppm]. Additionally, a sharp signal is detected between –85 and –70 ppm, which indicates the deprotonated nitrogen atom that is bonded to the titanium, germanium, and tin atoms.

Crystals suitable for X-ray diffraction analysis were easily obtained in the case of compound **1** by crystallization from hexane. The reaction of $GeCl_4$ with $Li(HMCTS)H_2$ primarily gave a clear, colorless oil. However, storage of this oil at –20 °C for several days produced white crystals. In case of the tin complex **3**, crystals were obtained by sublimation ($T$ = 120 °C, $p$ = 5 Torr) of the crude product. The molecular structures of compounds **1**, **2**, and **3** are illustrated in Figures 1, 2, and 3, respectively. Crystal data collection parameters and structure refinement details are given in the Experimental Section (Table 2).

The single-crystal X-ray structure analysis of **1** shows that the titanium complex crystallizes in two different modifications (trigonal $P31c$; hexagonal $P6_3$) with two molecules in each unit cell. Both modifications exhibit analogous molecular conformations and similar cell dimensions. The corresponding bond lengths and angles of **1** in the two modifications are identical within the range of standard error. The titanium atom is coordinated by three nitrogen atoms and one chlorine substituent. Thus, the coordination sphere exhibits a tetrahedral geometry (Figure 1). The angles N1–Ti–N1* [109.6(1)°] and N1–Ti–Cl [109.3(1)°] in **1** ($P6_3$) perfectly match this coordination pattern. Si–N bond lengths in **1** are in the typical range 1.72–1.75 Å. In both modifications, the Ti–Cl bond is situated on a threefold axis of rotation. Therefore, the asymmetric unit consists of one third of a molecule of **1**.

The germanium complex **2** crystallizes in the same trigonal space group $P31c$ as found for one modification of **1** with two molecules in the unit cell. The germanium atom in **2** has a slightly distorted tetrahedral coordination sphere with a N1–Ge–N1* angle of 111.6(1)° and a N1–Ge–Cl angle of 107.3(1)° (Figure 2).

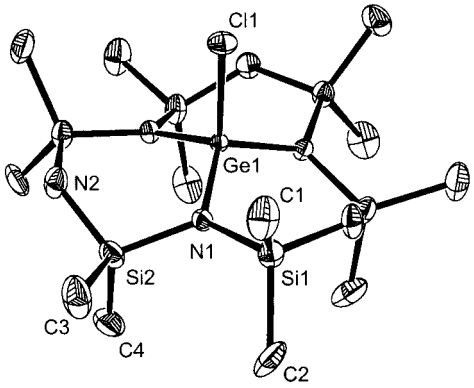


Figure 2. ORTEP plot of one molecule of **2** (thermal ellipsoids at the 50% probability level). Selected bond lengths [Å] and angles [°]: **2**: Ge–N1 1.823(4), Ge–Cl 2.192(2), Si1–N1 1.735(4), Si2–N1 1.761(5), Si1–N2 1.720(5), Si2–N2 1.722(5), N1–Ge–N1* 111.6(1), N1–Ge–Cl 107.3(1), N1–Si1–N2 105.0(2), N1–Si2–N2 107.4(2), Si1–N1–Si2 122.0(3), Si1–N2–Si2 125.8(3).

The tin complex **3** crystallizes in the hexagonal space group $P6_3$ with two molecules in the unit cell and is isomorphic with one modification of **1**. The tin atom in the center of the complex is almost tetrahedrally coordinated by the ligands, with bond angles of 110.1° and 108.8° for N1–Sn–N1* and N1–Sn–Cl, respectively (Figure 3). Despite the different metal atoms, the corresponding bond lengths and angles in **2** and **3** are similar to those in **1** with only minor differences that can arise as a result of the different atomic radii of Ti, Ge, and Sn.

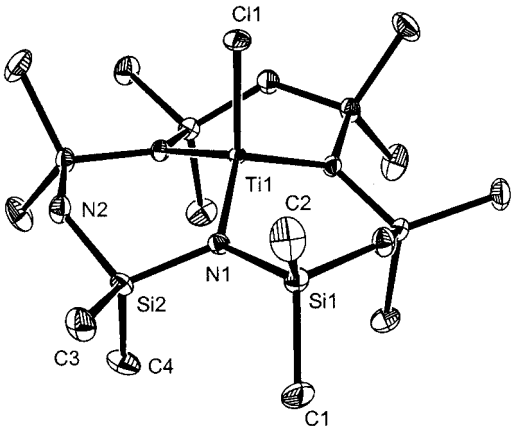


Figure 1. ORTEP plot of one molecule of **1** in space group $P6_3$ (thermal ellipsoids at the 50% probability level). Selected bond lengths [Å] and angles [°]: **1** ($P6_3$): Ti–N1 1.899(1), Ti–Cl 2.276(1), Si1–N1 1.740(1), Si2–N1 1.751(1), Si2–N2 1.717(1), N1–Ti–N1* 109.6(1), N1–Ti–Cl 109.3(1), N1–Si1–N2 105.8(1), N1–Si2–N2 107.4(1), Si1–N1–Si2 123.0(1), Si1–N2–Si2 127.7(1).

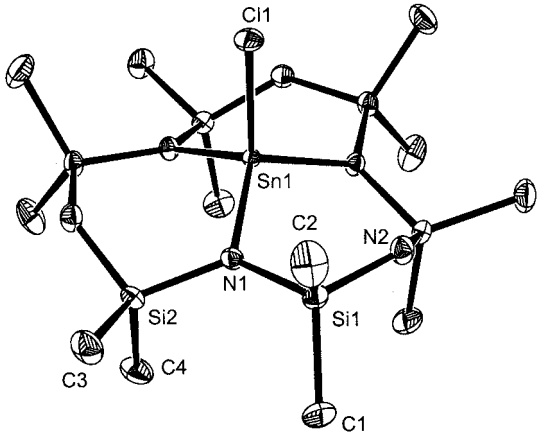


Figure 3. ORTEP plot of one molecule of **3** (thermal ellipsoids at the 50% probability level). Selected bond lengths [Å] and angles [°]: **3**: Sn–N1 2.016(1), Sn–Cl 2.351(1), Si1–N1 1.731(1), Si2–N1 1.741(1), Si1–N2 1.720(1), Si2–N2 1.721(1), N1–Sn–N1* 110.1(1), N1–Sn–Cl 108.8(1), N1–Si1–N2 106.0(1), N1–Si2–N2 107.5(1), Si1–N1–Si2 127.9(1), Si1–N2–Si2 130.7(1).

 © 2007 Wiley-VCH Verlag GmbH & Co. KGaA, Weinheim 

## Conclusions

For the first time, titanium, germanium, and tin complexes exhibiting a dodecamethylcyclohexasilazano ligand have been synthesized by reactions starting from $H_3$(HMCTS) and $MCl_4$ (M = Ti, Ge, Sn). In contrast to conversions of $TiCl_4$ and $GeCl_4$ with Li(HMCTS)$H_2$ to the new compounds **1** and **2**, respectively, the analogous reaction with $SnCl_4$ leads to the substitution product $Cl_2Sn[(HMCTS)H_2]_2$. However, the tin complex **3** that features the same molecular structure of **1** and **2** is obtained by using $NEt_3$/$H_3$(HMCTS) instead of Li(HMCTS)$H_2$ as starting materials. The formation of the novel cyclohexasilazane framework in **1**–**3** emphasizes the striking reactivity patterns of $H_3$(HMCTS) in reactions with metal chlorides to mark a new reaction pathway in addition to the well-known ring-contraction reactions and substitution reactions of the cyclotrisilazane system. The titanium and germanium complexes **1** and **2** are potentially good candidates to act as single-source precursors for ceramic materials of the quaternary SiCNTi and SiCNGe systems, respectively. All new compounds represent valuable synthons for further reactions because of their reactive M–Cl bonds. Further investigation of derivatization reactions of **1**–**3** and of the reaction mechanism of the overall formation reaction are to be undertaken now.

## Experimental Section

All manipulations were carried out under an inert atmosphere of argon by using a standard Schlenk line, a glovebox, and syringe techniques. $H_3$(HMCTS) was purchased from ABCR GmbH, and *n*BuLi, $SiCl_4$, $GeCl_4$, and $SnCl_4$ from Acros Organics. Toluene and hexane were distilled from over sodium/benzophenone and stored over sodium wire. NMR spectra were recorded at 400.13 MHz ($^1$H NMR), 100.62 MHz ($^{13}$C NMR), 28.91 MHz ($^{14}$N NMR), 79.49 MHz ($^{29}$Si NMR), 22.56 MHz ($^{49}$Ti NMR), and 149.21 MHz ($^{119}$Sn NMR) with a BRUKER DPX 400 instrument. Elemental analyses were performed on a Foss Heraeus CHN-O-Rapid apparatus. X-ray structure data were recorded with a Bruker-Nonius-X8-APEX2-CCD diffractometer with Mo-$K_\alpha$ radiation ($\lambda$ = 0.71073 Å), and semi-empirical correction (SADABS) was applied. The structures were solved with direct methods (SHELXS-97) and refined by full-matrix least-squares methods (refinement of $F^2$ against all reflections with SHELXS-97). All non-hydrogen atoms were refined anisotropically. Hydrogen atoms were placed in idealized positions and refined isotropically. Merohedral twinning was found for **1** in both modifications as well as for **2** (about 50:50 ratio in each case). The crystal of **3** exhibited neither merohedral nor racemic twinning. Selected data for the structure determination and refinement are summarized in Table 2. CCDC-621166 (**1** *P*31*c*), CCDC-621165 (**1** $P6_3$), CCDC-621164 (**2**), and CCDC-621163 (**3**) contain the supplementary crystallographic data for this paper. These data can be obtained free of charge from The Cambridge Crystallographic Data Centre via www.ccdc.cam.ac.uk/data_request/cif.

**Chlorido-2,2,4,4,6,6,8,8,10,10,12,12-dodecamethylcyclohexasilazane-1,5,9-triidotitanium (1):** A solution of *n*-butyllithium (3.7 mL of a 2.5-M solution, 9.2 mmol) in hexane was slowly added to an ice-cooled solution of 1,1,3,3,5,5-hexamethylcyclotrisilazane (2.0 g, 9.1 mmol) in toluene (25 mL). The resulting clear, colorless solution was allowed to reach room temperature and was stirred for 1 h. A solution of $TiCl_4$ (0.86 g, 4.5 mmol) in toluene (25 mL) was then added dropwise to the resulting solution of 1-lithio-2,2,4,4,6,6-hexamethylcyclotrisilazane. This procedure led to a

Table 2. Crystallographic data for complexes **1**, **2**, and **3**.

| Compound | **1a** | **1b** | **2** | **3** |
|---|---|---|---|---|
| Empirical formula | $C_{12}H_{39}ClN_6Si_6Ti$ | $C_{12}H_{39}ClN_6Si_6Ti$ | $C_{12}H_{39}ClGeN_6Si_6$ | $C_{12}H_{39}ClN_6Si_6Sn$ |
| $F_w$ | 519.38 | 519.38 | 544.07 | 590.17 |
| Crystal system | trigonal | hexagonal | trigonal | hexagonal |
| Space group | *P*31*c* | $P6_3$ | *P*31*c* | $P6_3$ |
| *a* [Å] | 11.368(1) | 11.343(1) | 11.285(1) | 11.475(1) |
| *b* [Å] | 11.368(1) | 11.343(1) | 11.285(1) | 11.475(1) |
| *c* [Å] | 12.320(1) | 12.205(1) | 12.211(1) | 12.257(1) |
| $\alpha$ [°] | 90 | 90 | 90 | 90 |
| $\beta$ [°] | 90 | 90 | 90 | 90 |
| $\gamma$ [°] | 120 | 120 | 120 | 120 |
| *V* [Å$^3$] | 1378.8(1) | 1360.0(1) | 1346.8(2) | 1397.8(1) |
| *Z* | 2 | 2 | 2 | 2 |
| $\lambda$ [Å] | 0.71073 | 0.71073 | 0.71073 | 0.71073 |
| $\rho_{calcd.}$ [g cm$^{-3}$] | 1.251 | 1.268 | 1.342 | 1.402 |
| Crystal size [mm] | 0.50 × 0.40 × 0.30 | 0.60 × 0.40 × 0.20 | 0.40 × 0.05 × 0.03 | 0.30 × 0.14 × 0.10 |
| *T* [K] | 203(2) | 90(2) | 93(2) | 90(2) |
| Limiting indices | $-20 \le h \le 19$ | $-11 \le h \le 17$ | $-13 \le h \le 13$ | $-24 \le h \le 24$ |
| | $-20 \le k \le 19$ | $-23 \le k \le 20$ | $-13 \le k \le 12$ | $-24 \le k \le 24$ |
| | $-21 \le l \le 14$ | $-25 \le l \le 25$ | $-14 \le l \le 14$ | $-24 \le l \le 25$ |
| R(int) | 0.0303 | 0.0405 | 0.0738 | 0.0300 |
| $\Theta_{max}$ [°]/compl. [%] | 39.23/99.6 | 47.99/99.9 | 25.00/100.0 | 48.99/100.0 |
| Max. transmission | 0.8223 | 0.8747 | 0.9560 | 0.8829 |
| Min. transmission | 0.7278 | 0.7458 | 0.5956 | 0.8022 |
| Data/parameters | 4778/81 | 8686/80 | 1601/81 | 9081/82 |
| $R_1/wR_2$ [$I > 2\sigma(I)$] | 0.0286/0.0702 | 0.0266/0.0518 | 0.0338/0.0653 | 0.0213/0.0447 |
| $R_1/wR_2$ (all data) | 0.0330/0.0722 | 0.0353/0.0546 | 0.0416/0.0679 | 0.0263/0.0458 |
| GOF | 1.024 | 1.039 | 1.054 | 1.041 |

 © 2007 Wiley-VCH Verlag GmbH & Co. KGaA, Weinheim 

slight warming of the reaction mixture. After 24 h of stirring at room temperature, the color of the solution became yellow-orange. The solvents were removed under reduced pressure, and the residue was dissolved in hexane and filtered to give a clear yellow solution. After reducing the filtrate volume by evaporation of the solvent, yellow crystals were obtained, which were filtered off and dried in vacuo. Yield: 2.94 g (62%). $C_{12}H_{39}ClN_6Si_6Ti$ (519.38): calcd. C 27.74, H 7.57, N 16.18; found C 27.37, H 7.38, N 16.03. $^1$H NMR (400.13 MHz, $CDCl_3$, 25 °C): $\delta$ = 0.20 (s, 12 H, Si–Me), 0.26 (s, 12 H, Si–Me), 0.56 (s, 3 H, N–H) ppm. $^{13}$C NMR (100.62 MHz, $CDCl_3$, 25 °C): $\delta$ = 1.9 (Si–Me), 4.5 (Si–Me) ppm. $^{14}$N NMR (28.91 MHz, $CDCl_3$, 25 °C): $\delta$ = –85 (Ti–N), –343 (N–H) ppm. $^{29}$Si NMR (79.49 MHz, $CDCl_3$, 25 °C): $\delta$ = –7.0 ppm. $^{49}$Ti NMR (22.56 MHz, $CDCl_3$, 25 °C): $\delta$ = –137 ppm.

**Chlorido-2,2,4,4,6,6,8,8,10,10,12,12-dodecamethylcyclohexasilazane-1,5,9-triidogermanium (2):** The synthesis was carried out as described for **1** with a solution of *n*-butyllithium (5.5 mL of a 2.5-M solution, 13.8 mmol) in hexane, 1,1,3,3,5,5-hexamethylcyclotrisilazane (3.0 g, 13.7 mmol) in toluene (25 mL), and $GeCl_4$ (1.46 g, 6.8 mmol) in toluene (25 mL) as reagents. After removal of the solvents, dissolution of the residue in hexane, and filtration, the hexane was removed from the filtrate under vacuum to give a clear, colorless oil. Storage of the oil at –20 °C for several days led to the formation of white crystals, which were dried in vacuo. Yield: 2.56 g (69%). $C_{12}H_{39}ClGeN_6Si_6$ (544.05): calcd. C 26.49, H 7.22, N 15.45; found C 26.52, H 7.37, N 15.37. $^1$H NMR (400.13 MHz, $CDCl_3$, 25 °C): $\delta$ = 0.28 (s, 12 H, Si–Me), 0.35 (s, 12 H, Si–Me), 0.61 (s, 3 H, N–H) ppm. $^{13}$C NMR (100.62 MHz, $CDCl_3$, 25 °C): $\delta$ = 2.5 (Si–Me), 5.3 (Si–Me) ppm. $^{14}$N NMR (28.91 MHz, $CDCl_3$, 25 °C): $\delta$ = –83 (Ti–N), –349 (N–H) ppm. $^{29}$Si NMR (79.49 MHz, $CDCl_3$, 25 °C): $\delta$ = –3.8 ppm.

**Chlorido-2,2,4,4,6,6,8,8,10,10,12,12-dodecamethylcyclohexasilazane-1,5,9-triidotin (3):** At room temperature, a solution of $SnCl_4$ (7.04 g, 27.0 mmol) in toluene (20 mL) was added dropwise to a solution of 1,1,3,3,5,5-hexamethycyclotrisilazane (2.0 g, 9.1 mmol) and triethylamine (3.0 g, 29.7 mmol) in toluene (40 mL). The resulting yellow reaction mixture was stirred for 24 h. Precipitated $NEt_3$·HCl was filtered off, and the solvent as well as the excess triethylamine were removed from the filtrate under reduced pressure to give a brownish solid product. Subsequent sublimation ($T$ = 120 °C, $p$ = 5 Torr) yielded white crystals of compound **3**. Yield: 1.47 g (54.7%). $C_{12}H_{39}ClN_6Si_6Sn$ (590.17): calcd. C 24.42, H 6.66, N 14.24; found C 24.28, H 6.58, N 14.11. $^1$H NMR (400 MHz, $CDCl_3$, 25 °C): $\delta$ = 0.21 (s, 12 H, Si–Me), 0.33 (s, 12 H, Si–Me), 0.58 (s, 3 H, N–H) ppm. $^{13}$C NMR (100.62 MHz, $CDCl_3$, 25 °C): $\delta$ = 3.3 (Si–Me), 4.6 (Si–Me) ppm. $^{14}$N NMR (28.91 MHz, $CDCl_3$, 25 °C): $\delta$ = –71 (Ti–N), –350 (N–H) ppm. $^{29}$Si NMR (79.49 MHz, $CDCl_3$, 25 °C): $\delta$ = –3.9 ppm. $^{119}$Sn NMR (149.21 MHz, $CDCl_3$, 25 °C): $\delta$ = –169 ppm.

[1] D. C. Bradley, R. G. Copperthwaite, *Inorg. Synth.* **1978**, *18*, 112–120.
[2] E. C. Alyea, D. C. Bradley, R. G. Copperthwaite, *J. Chem. Soc., Dalton Trans.* **1972**, *14*, 1580–1584.
[3] M. F. Lappert, P. P. Power, *J. Chem. Soc., Dalton Trans.* **1985**, *1*, 51–57.
[4] W. Fink, *Angew. Chem.* **1961**, *73*, 467.
[5] L. W. Breed, R. L. Elliott, J. C. Wiley, *J. Organomet. Chem.* **1970**, *24*, 315–325.
[6] U. Klingebiel, D. Enterling, A. Meller, *Chem. Ber.* **1977**, *110*, 1277–1283.
[7] U. Klingebiel, D. Enterling, A. Meller, *Z. Naturforsch., Teil B* **1978**, *33*, 527–532.
[8] E. Egert, U. Klingebiel, D. Schmidt, *Z. Anorg. Allg. Chem.* **1987**, *548*, 89–96.
[9] B. Jaschke, N. Helmold, I. Müller, T. Pape, M. Noltemeyer, R. Herbst-Irmer, U. Klingebiel, *Z. Anorg. Allg. Chem.* **2002**, *628*, 2071–2085.
[10] U. Klingebiel, M. Noltemeyer, H.-J. Rakebrandt, *Z. Anorg. Allg. Chem.* **1997**, *623*, 281–287.
[11] E. Kroke, Y. Li, C. Konetschny, E. Lecomte, C. Fasel, R. Riedel, *Mater. Sci. Eng.* **2000**, *26*, 97–199.
[12] J. Luecke, J. Hacker, D. Suttor, G. Ziegler, *Appl. Organomet. Chem.* **1997**, *11*, 181–194.
[13] J. Wan, M. J. Gasch, A. K. Mukherjee, *J. Mater. Res.* **2001**, *16*, 3274–3286.
[14] R. Riedel, A. Kienzle, V. Szabo, J. Mayer, *J. Mater. Sci.* **1993**, *28*, 3931–3938.
[15] Y. Li, Z. Zheng, C. Xu, C. Ren, Z. Zhang, Z. Xie, *J. Appl. Polym. Sci.* **2003**, *90*, 306–309.
[16] H. Gerung, S. D. Bunge, T. J. Boyle, C. J. Brinker, S. M. Han, *Chem. Commun.* **2005**, 1914–1916.
[17] C. Lehnert, J. Wagler, E. Kroke, G. Roewer, *Chem. Heterocycl. Compd.* **2006**, *12*, 1845–1856.

Received: October 25, 2006
Published Online: February 9, 2007

 © 2007 Wiley-VCH Verlag GmbH & Co. KGaA, Weinheim 

DOI: 10.1002/ejic.200600725

# Dinuclear and Polynuclear Bridged Azido–Nickel(II) Complexes: Synthesis, Structure Determination, and Magnetic Properties

**Salah S. Massoud,*[a] Franz A. Mautner,[b] Ramon Vicente,[c] August A. Gallo,[a] and Elodie Ducasse[a]**

**Keywords:** Nickel / Azido bridges / Crystal structure / Magnetic properties

Azido–$Ni^{II}$ complexes of dinuclear, $[Ni_2(trpn)_2(\mu_{1,3}\text{-}N_3)_2](ClO_4)_2$ (**1**), and monodimensional structures *cis*-$[Ni(abap)(\mu_{1,3}\text{-}N_3)]_n(ClO_4)_n$ (**2**) and *cis*-$[Ni(Me_6trien)(\mu_{1,3}\text{-}N_3)]_n(ClO_4)_n \cdot nH_2O$ (**3a**) as well as the monomer $[Ni(Me_6trien)(N_3)]ClO_4$ (**3b**) {trpn = tris(3-aminopropyl)amine; abap = *N*-(2-aminoethyl)-*N*,*N*-bis(3-aminopropyl)amine; $Me_6$trien = 1,1,4,7,10,10-hexamethyltriethylene tetramine} were synthesized and structurally characterized by spectroscopic techniques, X-ray crystallography, and variable-temperature magnetic measurements. In the complexes **1**–**3a**, the $ClO_4^-$ groups are counterions and the $Ni^{2+}$ centers are bridged by the azido ligands in an end-to-end bonding fashion. The coordination geometry around the $Ni^{II}$ ions is six-coordinate with a distorted octahedral environment achieved by the four N atoms of the tetradentate amines and two terminal N atoms of the azide groups. Complex **1** consists of dinuclear units with doubly bridged azido groups whereas in **2** and **3a**, a polymeric 1D chain is formed in which the adjacent azido groups link the $Ni^{II}$ centers in a *cis* arrangement. In complex **2**, the structural parameters of the two adjacent azido bridging ligands are different and an alternating 1D system with two different end-to-end azido bridges is produced. Complex **3a** is a uniform 1D system where the strong steric hindrance imposed by the methyl groups of the $Me_6$trien ligand [diagonal N(azide)–Ni–N(amine) bond angles] causes pronounced deviation from the ideal octahedral geometry. Complex **3b** exhibits a distorted square pyramidal geometry. The complexes **1**–**3a** show antiferromagnetic coupling. In complex **1**, the exchange coupling constant was $J = -64(1)$ cm$^{-1}$, whereas in the polynuclear species **2** and **3a**, the calculated values were $J_1 = -63.7(2)$ ($\alpha = 0.52$) and $J = -26.8(1)$ cm$^{-1}$, respectively. The magnetic parameters have been correlated to the structural data.

(© Wiley-VCH Verlag GmbH & Co. KGaA, 69451 Weinheim, Germany, 2007)

## Introduction

The pseudohalides and especially the azido bridging ligands have been reported to be efficient transmitters for propagating magnetic interaction between paramagnetic divalent metal centers ($Mn^{2+}$, $Co^{2+}$, $Cu^{2+}$, $Ni^{2+}$)[1] This property makes the metal complexes derived from these ligands an attractive topic for materials scientists and for physicists,[2] and for the same reason this class of compounds was considered to be one of the most extensively studied systems in the last three decades.[3–28] This was attributed to the distinct possibilities of magnetic coupling interactions through the azide bridge and the versatility of the ligand when it binds metal ions.[4–28] In general, two different coordination modes were established in the azido/$M^{2+}$ systems: end-to-end coordination ($\mu_{1,3}$-$N_3$) and end-on coordination ($\mu_{1,1}$-$N_3$).[4–24] Restricting our discussion to azido $Ni^{II}$ complexes derived from amines and/or amine derivatives as blocking ligands, the azido ligand generates a variety of bonding modes ranging from discrete molecules,[4–6] dinuclear ($\mu_2$-1,3-$N_3$ and $\mu_2$-1,1-$N_3$)[7–18] and even polynuclear species ($\mu_3$-1,1,1-$N_3$, $\mu_3$-1,1,3-$N_3$, $\mu_4$-1,1,1,1-$N_3$ and $\mu_4$-1,1,3,3-$N_3$)[19–21] to polymeric molecules with different dimensionality ranging from 1D[22–26] to 2D[27] networks. Moreover, many 1D polymers containing alternate chains with the same or two different bonding modes (end-to-end: $\mu_{1,3}$-$N_3$ and end-on: $\mu_{1,1}$-$N_3$) were also reported.[1,26] Azido compounds with 3D network structures were separated out and characterized in the case of $Mn^{II}$ systems.[28] The different modes of coordination of the azide group to $Ni^{2+}$ are illustrated in Scheme 1.

In general, the end-to-end coordination mode results in antiferromagnetically coupled compounds,[1,8–13] whereas the end-on coordination gives ferromagnetically coupled compounds.[1,14,16,17] However, deviation may exist in certain cases for example in the single end-to-end bridged azido 1D compound $[Ni(5\text{-methylpyrazole})_4(\mu_{1,3}\text{-}N_3)]_n(ClO_4)_n$ ferromagnetic coupling with an exchange coupling constant $J = 6.5$ cm$^{-1}$ was reported.[15] In alternating 1D

[a] Department of Chemistry, University of Louisiana at Lafayette, P. O. Box 44370, Lafayette, LA 70504-4370, USA
Fax: +1-337-482-5676
E-mail: ssmassoud@louisiana.edu
[b] Institut für Physikalische and Theoretische Chemie, Technische Universität Graz,
8010 Graz, Austria
E-mail: mautner@ ptc.tu-graz.ac.at
[c] Departament de Química Inorgànica, Universitat de Barcelona, Diagonal 647, 08028 Barcelona, Spain
E-mail: ramon.vicente@qi.ub.es

 © 2007 Wiley-VCH Verlag GmbH & Co. KGaA, Weinheim 

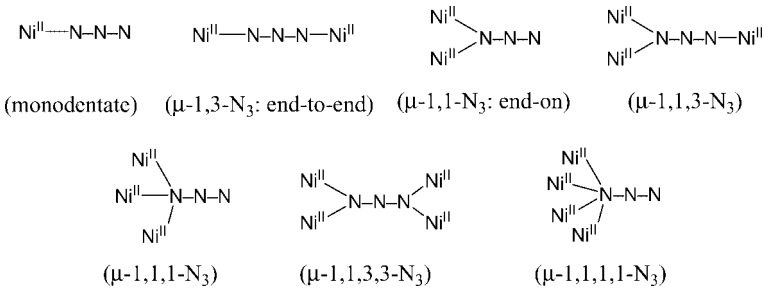


Scheme 1.

systems containing double azido bridging ligands in end-to-end and end-on coordination alternatively, two *J* values were obtained; ferromagnetic coupling with a positive *J* value corresponding to end-on azido bridging and an antiferromagnetic coupling with a negative *J* value for the end-to-end coordination.[1,26] Moreover there exists also alternating 1D systems containing single azido bridging ligands in the same end-to-end coordination mode due to the alternation in the structural parameters associated with the bridging azido environment.[1] A number of factors were addressed to correlate the magnetic behavior of the metal–azido complexes to their structural parameters. These include the intradimer M···M and M···N(azido) distances and, in the end-to-end coordination mode, the M–N–N(azido) angle and the dihedral angle, $\tau$ (the angle between the mean planes M–N1–N2–N3 and N1′–N2′–N3′–M′), in the singly bridged azido complexes or the dihedral angle, $\delta$ (the angle between the plane defined by the six *N*-azido atoms and the N1–M–N3′ plane), in the doubly bridged complexes, and also the M–($N_3$)–M angle in the end-on bonding mode.[1]

The 1D *trans*-Ni($\mu_{1,3}$-$N_3$) systems containing one azido bridging ligand between the two nickel atoms have been widely studied from the point of view of the magnetostructural correlations.[1] However, a few studies have been reported on the corresponding *cis*-Ni($\mu_{1,3}$-$N_3$) systems.[1] Therefore, in an effort to shed light on the 1D *cis*-Ni($\mu_{1,3}$-$N_3$) systems, we have selected the tripod tetradentate amines tris(3-aminopropyl)amine (trpn), *N*-(2-aminoethyl)-*N*,*N*-bis(3-aminopropyl)amine (abap), and the sterically hindered linear tetradentate amine 1,1,4,7,10,10-hexamethyltriethylenetetramine ($Me_6$trien) as blocking ligands to enforce the formation of complexes of *cis*-Ni($\mu_{1,3}$-$N_3$) geometry. With abap and $Me_6$trien amines, the reactions afforded the desired 1D compounds *cis*-[Ni(abap)($\mu_{1,3}$-$N_3$)]$_n$($ClO_4$)$_n$ (**2**) and *cis*-[Ni($Me_6$trien)($\mu_{1,3}$-$N_3$)]$_n$($ClO_4$)$_n$·*n*$H_2O$ (**3a**), but with the trpn ligand, the dinuclear compound [$Ni_2$(trpn)$_2$($\mu_{1,3}$-$N_3$)$_2$]($ClO_4$)$_2$ (**1**) was produced. The magnetic properties of these complexes were measured and correlated to their structural parameters.

## Results and Discussion

### Synthesis and IR Spectra

The blue azido bridged dinuclear complexes [$Ni_2$(trpn)$_2$($\mu_{1,3}$-$N_3$)$_2$]($ClO_4$)$_2$ (**1**), and the 1D polymeric chain *cis*-[Ni(abap)($\mu_{1,3}$-$N_3$)]$_n$($ClO_4$)$_n$ (**2**), and the anhydrous green complex [Ni($Me_6$trien)($N_3$)]$ClO_4$ (**3b**) were prepared in a reasonably good yield (74–81%) by dropwise addition of $NaN_3$ dissolved in $H_2O$ to a hot aqueous solution containing equimolar amounts of Ni($ClO_4$)$_2$·6$H_2O$ and the polyamine ligand. Crystals suitable for X-ray analysis were obtained by slow evaporation of dilute aqueous solutions of the complexes at room temperature or in the refrigerator. However, it should be noted that a solid sample of the monomer [Ni($Me_6$trien)($N_3$)]$ClO_4$ (**3b**) slowly absorbs water at ambient temperature to form the polymeric species [Ni($Me_6$trien)($\mu_{1,3}$-$N_3$)]$_n$($ClO_4$)$_n$·*n*$H_2O$ (**3a**) without losing its crystallinity (see the X-ray section). The synthesized complexes were characterized by elemental analysis and IR and UV/Vis spectroscopy.

The IR spectra of the two bridged azido complexes **1** and **2** displayed a single very strong absorption band over the range 2075–2094 $cm^{-1}$, whereas the fresh anhydrous [Ni($Me_6$trien)($N_3$)]$ClO_4$ revealed the band at a relatively lower frequency, 2060 $cm^{-1}$. The strong absorption observed in this region is attributable to the asymmetric stretching of the coordinated azido group, $\nu(N_3^-)$. The strong stretching absorption of $\nu$(Cl–O) assigned to the noncoordinated $ClO_4^-$ group was observed over the 1082–1092 $cm^{-1}$ region. Interestingly, the IR spectrum of the **3b** sample which was used for the X-ray analysis and was measured after about two months of the synthesis displayed a new broad band of medium intensity centered at 3449 $cm^{-1}$ due to the $\nu$(O–H) of lattice water. Moreover, the azido band which was located at 2060 $cm^{-1}$ in the parent complex disappeared, two strong bands at 2125 and 2092 $cm^{-1}$ were detected instead, and the strong $\nu$(Cl–O) of the perchlorate ion was slightly shifted from 1082 to 1090 $cm^{-1}$. On the basis of these data and the X-ray structural determination (see next section), the formula [Ni($M_6$trien)($\mu_{1,3}$-$N_3$)]$_n$($ClO_4$)$_n$·*n*$H_2O$ (**3a**) was proposed.

### Description of the Structures

#### *[Ni(trpn)(μ$_{1,3}$-N$_3$)]$_2$(ClO$_4$)$_2$ (1)*

A labeled ORTEP plot for compound **1** is shown in Figure 1 and selected bond parameters are given in Table 1. The structure of the compound consists of centrosymmetric [$C_{18}H_{48}N_{14}Ni_2$]$^{2+}$ dinuclear units in which the nickel atoms are bridged by two azide ions in a $\mu_2$-1,3 end-to-end (EE)

 © 2007 Wiley-VCH Verlag GmbH & Co. KGaA, Weinheim 

fashion and $ClO_4^-$ counterions. Each nickel atom has distorted octahedral coordination geometry. The octahedron around the $Ni^{2+}$ center is achieved by the four N atoms of the tetradentate amine, trpn, and the two terminal N atoms of the azide groups. The Ni–N(trpn) bond lengths are in the range 2.072(4)–2.162(4) Å, and the Ni–N($N_3$) bond lengths are Ni(1)–N(11) = 2.180(4) and Ni(1)–N(13) = 2.169(5) Å. The largest deviation of *cisoid* and *transoid* N–Ni–N bond angles from the ideal geometry is 8.6(2)°, whereas the N(11)–Ni(1)–N(13) bond angle is 87.3(2)°. The bond lengths of the EE-bridging azide group are N(11)–N(12) = 1.182(6) and N(12)–N(13A) = 1.163(6) Å. The Ni(1)–N(11)–N(12), Ni(1)–N(13)–N(12A), and N(11)–N(12)–N(13A) bond angles in the bridge are 119.9(3), 149.3(4), and 177.5(5)°, respectively. The Ni(1)–N(11)···N(13A)–Ni(1A) torsion angle is –19.2(7)°. The six atoms of the $N_3^-$ bridging ligands are in one plane, and the dihedral angle between this plane and the N(11)–Ni(1)–N(13) plane is 8.3(3)°; i.e. the eight-membered $Ni_2(N_3)_2$ ring adapts a flat "chair conformation". The Ni(1)···Ni(1A) intradinuclear distance is 5.4310(16) Å, and the shortest Ni(1)···Ni(1B) interdimer distance is 5.9657(17) Å. The shortest hydrogen bond of type N–H···O (Table 4) is observed between N(3) and the perchlorate oxygen atom O(1) [2 – *x*, 1 – *y*, –*z*], with a separation of 3.121(6) Å.

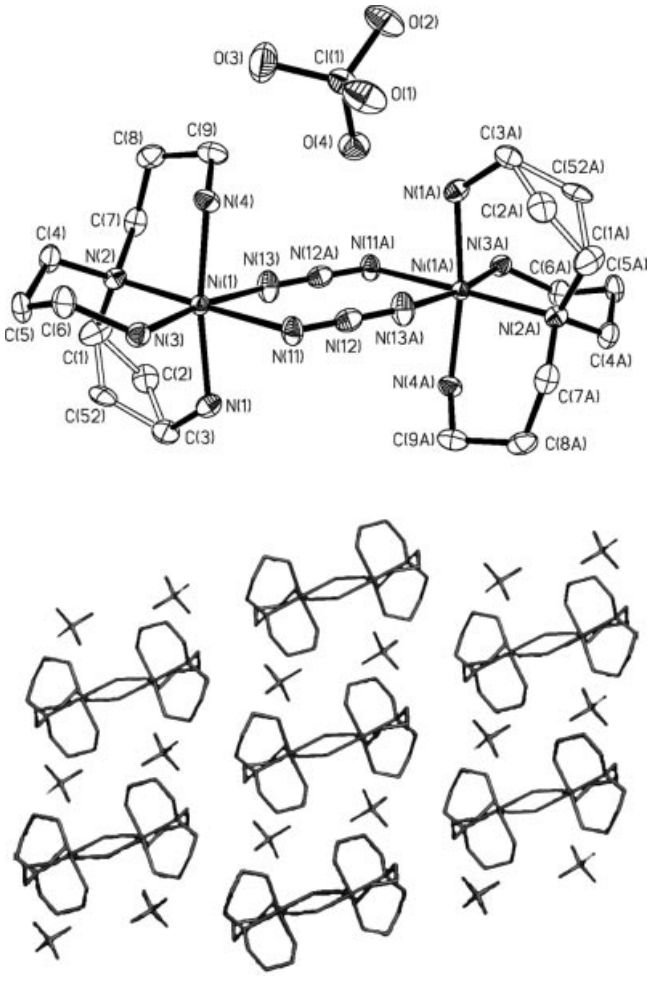


Figure 1. (top) ORTEP drawing (50% ellipsoids) and atom labeling scheme of the dinuclear complex $[Ni_2(trpn)_2(\mu_{1,3}\text{-}N_3)_2](ClO_4)_2$ (**1**). (bottom) Packing view of **1**.

Table 1. Selected bond lengths [Å] and angles [°] for $[Ni_2(trpn)_2(\mu_{1,3}\text{-}N_3)_2](ClO_4)_2$ (**1**).[a]

| | | | |
|---|---|---|---|
| Ni(1)–N(3) | 2.072(4) | Ni(1)–N(4) | 2.085(4) |
| Ni(1)–N(1) | 2.096(4) | Ni(1)–N(2) | 2.162(4) |
| Ni(1)–N(13) | 2.169(5) | Ni(1)–N(11) | 2.180(4) |
| N(11)–N(12) | 1.182(6) | N(12)–N(13A) | 1.163(6) |
| Ni(1)···Ni(1A) | 5.4310(16) | Ni(1)···Ni(1B) | 5.9657(17) |
| N(3)–Ni(1)–N(4) | 92.2(2) | N(3)–Ni(1)–N(1) | 92.3(2) |
| N(4)–Ni(1)–N(1) | 171.4(2) | N(3)–Ni(1)–N(2) | 95.0(2) |
| N(4)–Ni(1)–N(2) | 89.6(2) | N(1)–Ni(1)–N(2) | 97.2(2) |
| N(3)–Ni(1)–N(13) | 172.0(2) | N(4)–Ni(1)–N(13) | 91.5(2) |
| N(1)–Ni(1)–N(13) | 83.2(2) | N(2)–Ni(1)–N(13) | 92.1(2) |
| N(3)–Ni(1)–N(11) | 85.6(2) | N(4)–Ni(1)–N(11) | 89.4(2) |
| N(1)–Ni(1)–N(11) | 83.7(2) | N(2)–Ni(1)–N(11) | 178.8(2) |
| N(13)–Ni(1)–N(11) | 87.3(2) | N(12)–N(11)–Ni(1) | 119.9(3) |
| N(13A)–N(12)–N(11) | 177.5(5) | N(12A)–N(13)–Ni(1) | 149.3(4) |

[a] Symmetry code: (A) $-x + 2, -y, -z$; (B) $-x + 2, -y + 1, -z$.

### *cis*-[Ni(abap)($\mu_{1,3}$-$N_3$)]$_n$($ClO_4$)$_n$ (2)

A labeled ORTEP drawing of compound **2** is shown in Figure 2 (top) and selected bond parameters are given in Table 2. The structure of the compound consists of cationic

Table 2. Selected bond lengths [Å] and angles [°] for *cis*-[Ni(abap)($\mu_{1,3}$-$N_3$)]$_n$($ClO_4$)$_n$ (**2**).[a]

| | | | |
|---|---|---|---|
| Ni(1)–N(1) | 2.099(4) | Ni(1)–N(4) | 2.102(4) |
| Ni(1)–N(21) | 2.103(4) | Ni(1)–N(3) | 2.105(4) |
| Ni(1)–N(2) | 2.131(4) | Ni(1)–N(11) | 2.199(4) |
| N(11)–N(12) | 1.181(6) | N(12)–N(13) | 1.182(6) |
| N(13)–Ni(2) | 2.178(4) | N(21)–N(22A) | 1.177(5) |
| N(22)–N(23) | 1.176(5) | N(22)–N(21B) | 1.177(5) |
| N(23)–Ni(2) | 2.109(4) | Ni(2)–N(5) | 2.082(4) |
| Ni(2)–N(7) | 2.102(4) | Ni(2)–N(8) | 2.114(4) |
| Ni(2)–N(6) | 2.135(4) | Ni(1)···Ni(2) | 5.820(2) |
| Ni(1)···Ni(2A) | 5.340(2) | Ni(1)···Ni(1B) | 7.714(3) |
| Ni(2)···Ni(2B) | 7.603(3) | | |
| N(1)–Ni(1)–N(4) | 92.7(2) | N(1)–Ni(1)–N(21) | 85.3(2) |
| N(4)–Ni(1)–N(21) | 175.5(2) | N(1)–Ni(1)–N(3) | 169.6(2) |
| N(4)–Ni(1)–N(3) | 91.3(2) | N(21)–Ni(1)–N(3) | 91.4(2) |
| N(1)–Ni(1)–N(2) | 95.1(2) | N(4)–Ni(1)–N(2) | 83.6(2) |
| N(21)–Ni(1)–N(2) | 92.5(2) | N(3)–Ni(1)–N(2) | 94.9(2) |
| N(1)–Ni(1)–N(11) | 86.8(2) | N(4)–Ni(1)–N(11) | 91.1(2) |
| N(21)–Ni(1)–N(11) | 92.8(2) | N(3)–Ni(1)–N(11) | 83.6(2) |
| N(2)–Ni(1)–N(11) | 174.5(2) | N(12)–N(11)–Ni(1) | 116.0(3) |
| N(13)–N(12)–N(11) | 179.1(5) | N(12)–N(13)–Ni(2) | 117.0(3) |
| N(22A)–N(21)–Ni(1) | 126.4(3) | N(23)–N(22)–N(21B) | 177.9(5) |
| N(22)–N(23)–Ni(2) | 131.9(3) | N(5)–Ni(2)–N(7) | 169.0(2) |
| N(5)–Ni(2)–N(23) | 85.9(2) | N(7)–Ni(2)–N(23) | 92.2(2) |
| N(5)–Ni(2)–N(8) | 91.1(2) | N(7)–Ni(2)–N(8) | 91.8(2) |
| N(23)–Ni(2)–N(8) | 173.6(2) | N(5)–Ni(2)–N(6) | 96.1(2) |
| N(7)–Ni(2)–N(6) | 94.7(2) | N(23)–Ni(2)–N(6) | 91.1(2) |
| N(8)–Ni(2)–N(6) | 83.6(2) | N(5)–Ni(2)–N(13) | 85.7(2) |
| N(7)–Ni(2)–N(13) | 83.7(2) | N(23)–Ni(2)–N(13) | 93.4(2) |
| N(8)–Ni(2)–N(13) | 92.0(2) | N(6)–Ni(2)–N(13) | 175.3(2) |

[a] Symmetry codes: (A) $x - 1/2, y, -z + 3/2$; (B) $x + 1/2, y, -z + 3/2$.

 © 2007 Wiley-VCH Verlag GmbH & Co. KGaA, Weinheim 

$[Ni(abap)(N_3)]_n^{n+}$ chains in which the nickel atoms are bridged by means of single $\mu_2$-1,3 EE azide groups in *cis* arrangement, and $ClO_4^-$ counterions. Within the chains two different crystallographic nickel(II) centers exist with similar distorted octahedral coordination geometry. Each $NiN_6$ chromophore is achieved by the four N atoms of the tetradentate abap blocking ligand, and two terminal N atoms of azide groups adopting the *cis* arrangement. The Ni–N(abap) bond lengths are in the range 2.082(4)–2.135(4) Å, and the Ni–N($N_3$) bond lengths are in the range 2.103(4)–2.199(4) Å. The largest deviation of *cisoid* and *transoid* N–Ni–N bond angles from the ideal geometry is 11.0(2)°, whereas the N(11)–Ni(1)–N(21) and N(13)–Ni(2)–N(23) bond angles are 92.8(2) and 93.4(2)°, respectively. The bond lengths of the EE-bridging azide groups vary from 1.176(5) to 1.181(6) Å and the Ni–N–N bond angles from 116.0(3) to 131.9(3)°. The N(11)–N(12)–N(13) and N(23)–N(22)–N(21B) bond angles are 179.1(5) and 177.9(5)°, respectively. The Ni(1)–N(11)···N(13A)–Ni(1A) and Ni(1)–N(21)···N(23A)–Ni(2A) torsion angles are 171.0(2) and –64.3(4)°, respectively. The Ni(1)···Ni(2) and Ni(1)···Ni(2A) intrachain distances are 5.820(2) and 5.340(2) Å, whereas the shortest Ni···Ni interchain distance is 8.088(3) Å. The arrangement of the Ni–azido chain may be described as a compressed helix (Figure 2, bottom), extended along the *a* axis of the orthorhombic unit cell. Hydrogen bonds of type N–H···O and N–H···N (Table 4) form a supramolecular network.

### *cis-[Ni(Me$_6$trien)($\mu_{1,3}$-N$_3$)]$_n$(ClO$_4$)$_n$·nH$_2$O (3a)*

An ORTEP drawing for **3a** together with the atom labeling scheme is illustrated in Figure 3 (top), and selected bond parameters are given in Table 3. The structure of **3a** consists of cationic $[Ni(Me_6trien)(N_3)]_n^{n+}$ chains in which the nickel atoms are bridged by means of single $\mu_2$-1,3 EE azide groups in *cis* arrangement, $ClO_4^-$ counterions, and lattice water molecules. The nickel atoms have distorted octahedral coordination geometry. Similar as in **2**, each $NiN_6$ chromophore is achieved by the four N atoms of the $Me_6$-trien ligand and two terminal N atoms of azide groups adopting *cis* arrangement. The Ni–N(Me$_6$trien) bond lengths are in the range 2.183(3)–2.234(3) Å, and the corresponding Ni–N(azide) bond lengths, Ni(1)–N(11) and Ni(1)–N(21) are 2.088(3) and 2.101(3) Å, respectively. As a

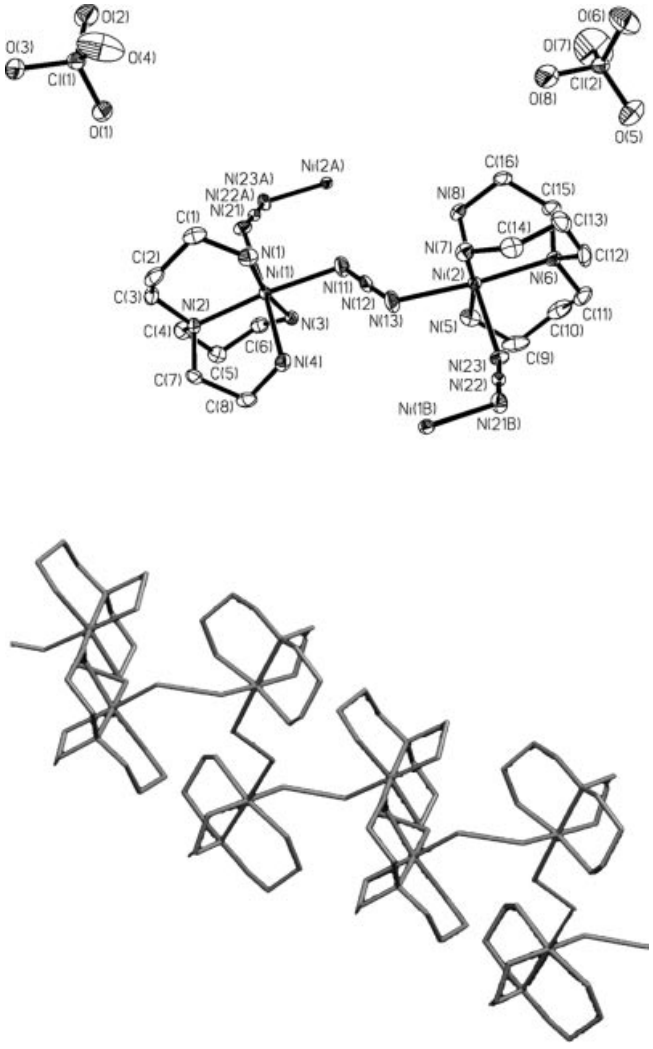




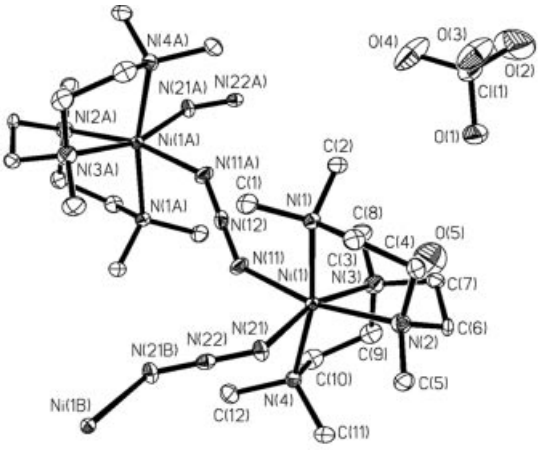


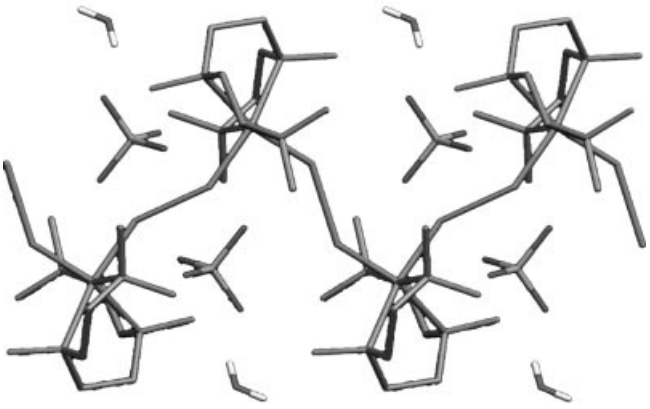

Figure 2. (top) ORTEP view (50% ellipsoids) and atom labeling scheme of *cis*-[Ni(abap)($\mu_{1,3}$-$N_3$)]$_n$($ClO_4$)$_n$ (**2**). (bottom) The *cis*-[Ni(abap)($\mu_{1,3}$-$N_3$)]$_n^{n+}$ 1D chain of **2**.

Figure 3. (top) ORTEP drawing (50% ellipsoids) and atom labeling scheme of *cis*-[Ni(Me$_6$trien)($\mu_{1,3}$-$N_3$)]$_n$($ClO_4$)$_n$·n$H_2O$ (**3a**). (bottom) Crystal packing of **3a**.

 © 2007 Wiley-VCH Verlag GmbH & Co. KGaA, Weinheim 

consequence of the bulky $Me_6$trien blocking ligand, the N–Ni–N bond angles deviate up to 17.3(2)° from the ideal octahedral geometry, the N(11)–Ni(1)–N(21) bond angle is 96.90(13)°. The central nitrogen atoms of the two EE-bridging azide groups are located at inversion centers where the azide groups are symmetric [N(11)–N(12) = 1.174(3), N(21)–N(22) = 1.175(3) Å] and linear [N–N–N = 180°]. The Ni(1)–N(11)–N(12) and Ni(1)–N(21)–N(22) bond angles are 138.8(2) and 135.8(2)°, respectively. The Ni(1)–N(11)···N(11A)–Ni(1A) and Ni(1)–N(21)···N(21B)–Ni(1B) torsion angles both are 180°. The Ni(1)···Ni(1A) and Ni(1)···Ni(1B) intrachain distances are 6.1412(16) and 6.1110(15) Å, respectively, whereas the shortest Ni···Ni interchain distance is 8.619(2) Å. The Ni–azide "zigzag" chain extends along the *a* axis of the orthorhombic unit cell (Figure 3 bottom). Lattice water molecules form hydrogen bonds (Table 4) of the type O–H···O to oxygen atoms O(3) of perchlorate counterions [with O···O distances of 2.956(6) and 3.337(6) Å].

Table 4. Selected hydrogen bonds in $[Ni_2(trpn)_2(\mu_{1,3}\text{-}N_3)_2](ClO_4)_2$ (**1**), *cis*-$[Ni(abap)\text{-}(\mu_{1,3}\text{-}N_3)]_n(ClO_4)_n$ (**2**), and *cis*-$[Ni(Me_6trien)(\mu_{1,3}\text{-}N_3)]_n(ClO_4)_n{\cdot}nH_2O$ (**3a**).

| Comp. | D–H···A[a] | D···A [Å] | DHA [°] | Symmetry code of A |
|---|---|---|---|---|
| **1** | N(1)–H(1B)···O(1) | 3.155(6) | 148.1 | 2 – *x*, 1 – *y*, –*z* |
| | N(3)–H(3A)···O(1) | 3.121(6) | 175.1 | 2 – *x*, 1 – *y*, –*z* |
| | N(3)–H(3B)···N(11) | 3.166(6) | 154.0 | 2 – *x*, 1 – *y*, –*z* |
| | N(4)–H(4A)···O(3) | 3.289(7) | 152.0 | 1 – *x*, 1 – *y*, –*z* |
| | N(4)–H(4B)···O(4) | 3.142(7) | 156.7 | |
| **2** | N(1)–H(1A)···O(6) | 3.003(6) | 172.3 | 1 – *x*, 1/2 + *y*, 3/2 – *z* |
| | N(1)–H(1B)···O(4) | 3.144(6) | 172.7 | 1 – *x*, –*y*, 1 – *z* |
| | N(3)–H(3C)···N(13) | 3.408(6) | 151.9 | –1/2 + *x*, *y*, 3/2 + *z* |
| | N(3)–H(3D)···O(8) | 3.178(6) | 161.2 | 1/2 – *x*, 1/2 + *y*, *z* |
| | N(4)–H(4C)···O(7) | 3.267(8) | 166.8 | 1/2 – *x*, 1/2 + *y*, *z* |
| | N(4)–H(4D)···O(6) | 3.256(6) | 163.2 | 1 – *x*, 1/2 + *y*, 3/2 – *z* |
| | N(5)–H(5C)···O(7) | 2.387(8) | 170.1 | 1/2 – *x*, 1/2 + *y*, *z* |
| | N(5)–H(5D)···O(2) | 3.072(6) | 168.2 | 1/2 – *x*, –*y*, 1/2 + *z* |
| | N(7)–H(7C)···O(3) | 3.270(7) | 167.7 | 1 – *x*, –*y*, 1 – *z* |
| | N(8)–H(8C)···O(2) | 3.217(5) | 164.9 | 1/2 – *x*, –*y*, 1/2 + *z* |
| | N(8)–H(8D)···O(3) | 3.047(7) | 139.7 | 1 – *x*, –*y*, 1 – *z* |
| **3a** | O(5)–H(51)···O(3) | 3.337(6) | 155.2 | 1/2 – *x*, –1/2 + *y*, 3/2 – *z* |
| | O(5)–H(52)···O(3) | 2.956(6) | 168.0 | –1/2 + *x*, 1/2 – *y*, –1/2 + *z* |

[a] D = donor, A = acceptor.

Table 3. Selected bond lengths [Å] and angles [°] for *cis*-$[Ni(Me_6trien)(\mu_{1,3}\text{-}N_3)]_n(ClO_4)_n{\cdot}nH_2O$ (**3a**).[a]

| | | | |
|---|---|---|---|
| Ni(1)–N(11) | 2.088(3) | Ni(1)–N(21) | 2.101(3) |
| Ni(1)–N(2) | 2.183(3) | Ni(1)–N(3) | 2.193(3) |
| Ni(1)–N(4) | 2.203(3) | Ni(1)–N(1) | 2.234(3) |
| N(11)–N(12) | 1.174(3) | N(12)–N(11A) | 1.174(3) |
| N(21)–N(22) | 1.175(3) | N(22)–N(21B) | 1.175(3) |
| Ni(1)···Ni(1A) | 6.1412(16) | Ni(1)···Ni(1B) | 6.1110(15) |
| N(11)–Ni(1)–N(21) | 96.90(13) | N(11)–Ni(1)–N(2) | 166.86(13) |
| N(21)–Ni(1)–N(2) | 90.25(12) | N(11)–Ni(1)–N(3) | 94.43(13) |
| N(21)–Ni(1)–N(3) | 162.74(13) | N(2)–Ni(1)–N(3) | 81.32(13) |
| N(11)–Ni(1)–N(4) | 84.64(12) | N(21)–Ni(1)–N(4) | 86.41(12) |
| N(2)–Ni(1)–N(4) | 106.88(12) | N(3)–Ni(1)–N(4) | 81.72(13) |
| N(11)–Ni(1)–N(1) | 87.04(13) | N(21)–Ni(1)–N(1) | 86.90(12) |
| N(2)–Ni(1)–N(1) | 82.35(12) | N(3)–Ni(1)–N(1) | 106.70(12) |
| N(4)–Ni(1)–N(1) | 168.62(12) | N(12)–N(11)–Ni(1) | 138.8(2) |
| N(11)–N(12)–N(11A) | 180.0 | N(22)–N(21)–Ni(1) | 135.8(2) |
| N(21)–N(22)–N(21B) | 180.0 | | |

[a] Symmetry codes: (A) –*x* + 1, –*y*, –*z* + 2; (B) –*x* + 2, –*y*, –*z* + 2.

### *[Ni(Me$_6$trien)(N$_3$)]ClO$_4$ (3b)*

An ORTEP drawing for **3b** together with the atom labeling scheme is illustrated in Figure 4, and selected bond parameters are given in Table 5. The structure of **3b** consists of monomeric $[Ni(Me_6trien)(N_3)]^+$ complex cations and $ClO_4^-$ counterions. The $NiN_5$ chromophore may be described as a distorted square pyramid ($\tau$ = 0.117)[29] with N(11) of the azide group, N(1), N(2), and N(3) of the $Me_6$-trien ligand in basal sites and N(4) or N(5) of the partially disordered tetramine ligand at the apical site. The Ni(1)–N bond lengths range from 1.997(2) to 2.135(2) Å. In contrast to the symmetric EE azide bridges in **3a**, the monodentate azido group has asymmetric bond parameters [N(1)–N(2) = 1.189(3), N(2)–N(3) = 1.159(3) Å, N(11)–N(12)–N(13) =

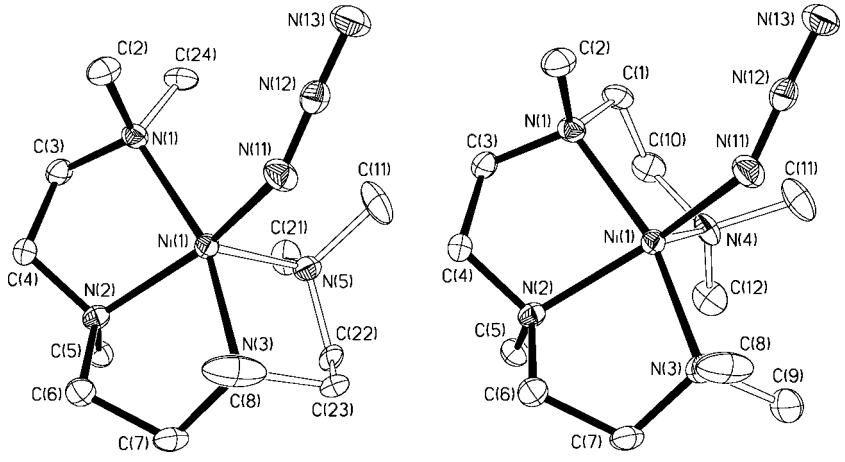


Figure 4. $[Ni(Me_6trien)(N_3)]ClO_4$ (**3b**): ORTEP drawing (50% ellipsoids) and atom labeling scheme of the two split orientations of complex cation. Open stick bonds indicate disordered parts of the $Me_6$trien ligand with 50% occupancy.

 © 2007 Wiley-VCH Verlag GmbH & Co. KGaA, Weinheim 

176.7(3)°]. The shortest Ni···Ni and N(13)···Ni distances to adjacent monomeric units are 7.584(3) and 5.403(5) Å, respectively.

Table 5. Selected bond lengths [Å] and angles [°] for [Ni($Me_6$trien)($N_3$)]$ClO_4$ (**3b**).

| | | | |
|---|---|---|---|
| Ni(1)–N(11) | 1.997(2) | Ni(1)–N(1) | 2.122(2) |
| Ni(1)–N(2) | 2.135(2) | Ni(1)–N(3) | 2.105(3) |
| Ni(1)–N(4) | 2.049(7) | Ni(1)–N(5) | 2.119(7) |
| N(11)–N(12) | 1.189(3) | N(12)–N(13) | 1.159(3) |
| N(11)–Ni(1)–N(4) | 99.3(2) | N(11)–Ni(1)–N(3) | 89.12(10) |
| N(4)–Ni(1)–N(3) | 108.1(2) | N(11)–Ni(1)–N(5) | 98.0(2) |
| N(3)–Ni(1)–N(5) | 89.7(2) | N(11)–Ni(1)–N(1) | 95.13(10) |
| N(4)–Ni(1)–N(1) | 90.4(2) | N(3)–Ni(1)–N(1) | 160.13(10) |
| N(5)–Ni(1)–N(1) | 108.8(2) | N(11)–Ni(1)–N(2) | 153.13(10) |
| N(4)–Ni(1)–N(2) | 107.5(2) | N(3)–Ni(1)–N(2) | 83.63(10) |
| N(5)–Ni(1)–N(2) | 107.7(2) | N(1)–Ni(1)–N(2) | 83.88(9) |
| N(11)–N(12)–N(13) | 176.7(3) | N(12)–N(11)–Ni(1) | 137.8(2) |

### Electronic Spectra

The UV/Vis spectra of the azido–nickel(II) complexes under investigation were recorded in the solid state and in $H_2O$. In addition the polymer [Ni($Me_6$trien)($\mu_{1,3}$-$N_3$)]$_n$-($ClO_4$)$_n$·$n$$H_2O$ (**3a**) and its monomer (**3b**) were also measured in different organic solvents, and the data are collected in Table 6. The solid and the aqueous solution spectra of [$Ni_2$(trpn)$_2$($\mu_{1,3}$-$N_3$)$_2$]$^{2+}$ and [Ni(abap)$_2$($\mu_{1,3}$-$N_3$)]$_n^{n+}$ display two bands over 360–370 and 570–590 nm, and a shoulder or broad band over 770–1000 nm range. Similarly, the electronic diffuse reflectance spectrum of **3a**, [Ni($Me_6$-trien)($\mu_{1,3}$-$N_3$)]$_n$($ClO_4$)$_n$·$n$$H_2O$ reveals the presence of the three absorption bands at 367, 655, and ca. 900 nm. These spectral features are consistent with six-coordinate octahedral geometry for $Ni^{II}$ complexes and the spectrum of the complex ions of **1**, **2**, or **3a** is adequately explained by d-d transitions in the $Ni^{2+}$ ion in a distorted octahedral environment where the last two maxima observed in the visible region result from $^3A_{2g}$→$^3T_{1g}$(F) and $^3A_{2g}$→$^3T_{2g}$(F) transitions, respectively, and the high energy band from the $^3A_{2g}$→$^3T_{1g}$(P) transition. When the spectra of **1** were measured in organic solvents ($CH_3CN$, $CH_3NO_2$, dmso, dmf), the positions of $\lambda_{max}$ did not show any significant change and were almost independent of the nature of the solvent used. The insolubility and/or the very low solubility of complex **2** prohibit measuring its spectrum in organic solvents. The reflectance spectra of the complexes **1**–**3a** showed low resolution and the fact that the low energy broad band was detected at higher wavelengths ($\lambda_{max} \geq 900$ nm) compared to that observed in $H_2O$ or other solvent may be attributed to the contribution of the vibrational transitions in this region. Interestingly, these findings in solutions and in the solid state were consistent with the distorted octahedral geometry around the $Ni^{2+}$ ion as determined by X-ray.

The electronic diffuse reflectance spectrum of the complex [Ni($Me_6$trien)($N_3$)]$ClO_4$ (**3b**) displays two bands at 659 nm and a shoulder at 477 nm besides a very broad band at ca. 960 nm (Table 6). Although this spectrum was not completely conclusive, it is most likely consistent with the presence of a five-coordinate environment around the $Ni^{2+}$ center where the first two bands could be assigned to $^3B_1$ (F)→$^3E$ (F) and $^3B_1$ (F)→$^3A_2$, $^3E$ (P) transitions, respectively.[30] When the spectra of the complex were measured in different coordinated solvents, the dissolution was associated with color change and the visible spectrum exhibits strong dependence on the nature of the solvent used. The spectra reveal the presence of the three bands typical for distorted octahedral $Ni^{II}$ complexes as indicated above. The six-coordinate geometry in **3b** was achieved by the addition of a solvent molecule to the coordinatively unsaturated nickel(II) center to form [Ni($Me_6$trien)($N_3$)(solv)]$^+$ where the ligand field strength increases in the order: $CH_3NO_2$ < dmf < $H_2O$ < $CH_3CN$ < dmso. Similar spectral dependence was also observed for the corresponding polymer [Ni-($Me_6$trien)($\mu_{1,3}$-$N_3$)]$_n$($ClO_4$)$_n$·$n$$H_2O$ (**3a**) in $CH_3CN$ and in dmso (Table 6) which clearly demonstrates the octahedral geometry for the central $Ni^{2+}$ ion. The fact that in the same solvent, the monomer **3b** and the polymer **3a** gave absorption bands which are different in position and intensity might rule out the formation of the same six-coordinate species and instead a different octahedral $Ni^{II}$ species is

Table 6. Electronic spectroscopic data for the azido–nickel(II) complexes.

| Complex | Solvent | $\lambda_{max}$ [nm] ($\varepsilon_{max}$, $M^{-1}cm^{-1}$) |
|---|---|---|
| [$Ni_2$(trpn)$_2$($\mu_{1,3}$-$N_3$)$_2$]($ClO_4$)$_2$ (**1**) | solid[a] | 360 (sh), 578, 980 (br) |
| | $H_2O$ | 369 (49), 592 (29), 840 (5.0, br) |
| *cis*-[Ni(abap)($\mu_{1,3}$-$N_3$)]$_n$($ClO_4$)$_n$ (**2**) | solid[a] | 360 (sh), 570, 995 (br) |
| | $H_2O$/$CH_3CN$[b] | 356 (29), 570 (18), 770 (sh) |
| *cis*-[Ni($Me_6$trien)($\mu_{1,3}$-$N_3$)]$_n$($ClO_4$)$_n$·$n$$H_2O$ (**3a**) | solid[a] | 367, 655, ca. 900 (br) |
| | $H_2O$ | 393 (38), 662 (27), 750 (27) |
| | $CH_3CN$ | ca. 390 (sh, 85), 659 (29), 745 (29) |
| | dmso | ca. 408 (sh, 71), 671 (28), 747 (26) |
| [Ni($Me_6$trien)($N_3$)]$ClO_4$ (**3b**) | solid[a] | 477 (sh), 659, ca. 960 (vbr) |
| | $H_2O$[c] | 394, 656, 749 |
| | $CH_3CN$ | 392 (82), 643 (23), 737 (18) |
| | dmso | ca. 364 (ca. 191), 415 (75), 676 (23) |
| | $CH_3NO_2$ | ca. 489 (ca. 31), 669 (39), 862 (29) |
| | dmf | 404 (57), 656 (25), 739 (18) |

[a] Reflectance spectra for solid samples were diluted with $BaSO_4$ and measured against $BaSO_4$ standard. [b] Fifty percent by volume $H_2O$/$CH_3CN$. [c] Saturated solution.

 © 2007 Wiley-VCH Verlag GmbH & Co. KGaA, Weinheim 

produced in solution from the polymer **3a**. Upon dissolution, the complex $[Ni(Me_6trien)(\mu_{1,3}\text{-}N_3)]_n(ClO_4)_n{\cdot}nH_2O$ undergoes solvolysis via bond rupture of the bridged Ni–N(azido) bonds and displacement of one of the azido ligands with a solvent molecule to form the dimeric six-coordinate species, $[(solv)(Me_6trien)Ni(\mu_{1,3}\text{-}N_3)Ni(Me_6trien)(solv)]^{3+}$. The interaction of the solvent molecules with $[Ni(Me_6trien)(\mu_{1,3}\text{-}N_3)]_n^{n+}$ is not surprising in terms of the strong steric hindrance imposed by the methyl groups of $Me_6$trien in $[Ni(Me_6trien)(\mu_{1,3}\text{-}N_3)]_n^{n+}$ where the two diagonal N(azido)–Ni–N(amine) bond angles namely N(21)–Ni(1)–N(3) and N(11)–Ni(1)–N(2) deviate from the ideal octahedral geometry by 17.3 and 13.1°, respectively. Therefore, the Ni–N(azido) bond rupture and an azide displacement with solvent molecule seems to reduce the magnitude of crowding. A similar solvent effect was also observed in the dinuclear doubly bridged end-to-end azido complex $[Cu(Et_2dien)(\mu_{1,3}\text{-}N_3)]_2(ClO_4)_2$, where $Et_2$dien = *N*,*N*-diethyldiethylenetriamine.[3a] However, it is difficult to propose with certainty any nuclearity for the species in solution without measuring the electrical conductivity.

## Magnetic Properties

The molar magnetic susceptibility, $\chi_M$, for polycrystalline samples of **1**, **2**, and **3a** were measured as a function of temperature and the plots of $\chi_M$ vs. $T$ are illustrated in Figure 5, Figure 6, and Figure 7, respectively. At room temperature compound **1** exhibits a $\chi_M$ value of $7.6\times10^{-3}$ cm$^3$mol$^{-1}$. This value increases as the temperature decreases, reaching a broad maximum of $14.2\times10^{-3}$ cm$^3$mol$^{-1}$ at ca. 70 K. Below this temperature, the molar magnetic susceptibility decreases continuously and reaches a minimum value of $6.77\times10^{-3}$ cm$^3$mol$^{-1}$ at 2 K. Careful inspection of the graph in Figure 5 clearly indicates a small change in the slope of the curve around 25 K which can be attributed to a little structural change. The susceptibility data in the range 25–300 K for **1** were fitted to the expression [Equation (1)] for the magnetic susceptibility of isotropically coupled S = 1 dinuclear compounds, derived from the Hamiltonian $H = -JS_1S_2$:

$$\chi_M = [0.375g^2/(T-\theta)]\{[2\exp(x) + 10\exp(3x)]/[1 + 3\exp(x) + 5\exp(3x)]\} \quad (1)$$

A Weiss $\theta$ parameter was introduced in the formula to take into consideration the possible antiferromagnetic interactions between the dinuclear molecules. The results of the best fit, shown as the solid line in Figure 5, were $J$ = –64(1) cm$^{-1}$, $g$ = 2.34(1), and $\theta$ = 14(1) K. Dinuclear complexes with core formula $[Ni_2(\mu_{1,3}\text{-}N_3)_2]^{2+}$ are known to develop a magnetostructural relationship between the exchange coupling constant, $J$, and the structural parameters.[1,9a] The main factor determining the $|J|$ value is the [Ni–$(\mu_{1,3}\text{-}N_3)_2$–Ni] dihedral angle, $\delta$; the more planar the structure ($\delta$ is close to 0°) the more antiferromagnetic the interaction and hence the higher $|J|$.[1,9a] In this compound, the small dihedral angle $\delta$ (8.3°) should account for the relatively high observed $|J|$ value (64 cm$^{-1}$).

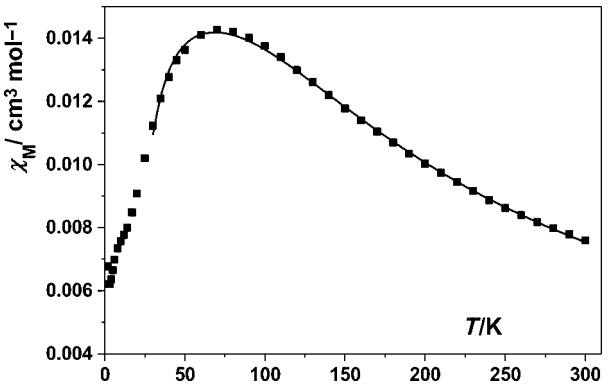


Figure 5. Plot of $\chi_M$ vs. $T$ in the 300–2 K temperature range for $[Ni_2(trpn)_2(\mu_{1,3}\text{-}N_3)_2](ClO_4)_2$ (**1**) measured on cooling under an external magnetic field of 0.7 T. The solid line shows the best fit as a dinuclear compound (see text).

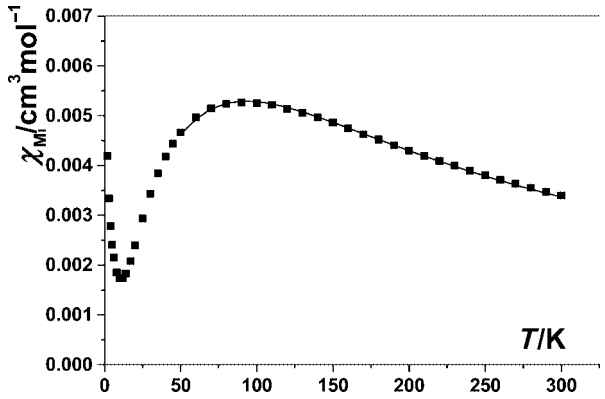


Figure 6. Plot of $\chi_M$ vs. $T$ in the 300–2 K temperature range for *cis*-$[Ni(abap)(\mu_{1,3}\text{-}N_3)]_n(ClO_4)_n$ (**2**) measured on cooling under an external magnetic field of 0.7 T. The solid line shows the best fit as an alternating antiferromagnetic chain (see text).

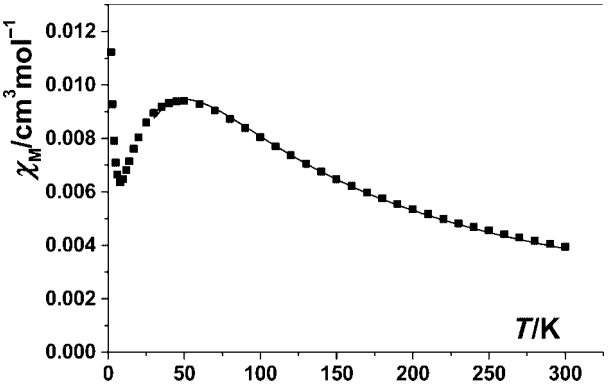


Figure 7. Plot of $\chi_M$ vs. $T$ in the 300–2 K temperature range for *cis*-$[Ni(Me_6trien)(\mu_{1,3}\text{-}N_3)]_n(ClO_4)_n{\cdot}nH_2O$ (**3a**) measured on cooling under external magnetic field of 0.7 T. The solid line shows the best fit as a uniform antiferromagnetic chain (see text).

For compound **2**, the $\chi_M$ value at room temperature ($3.48\times10^{-3}$ cm$^3$mol$^{-1}$) increases as the temperature decreases, reaching a broad maximum of $5.35\times10^{-3}$ cm$^3$mol$^{-1}$ at ca. 90 K (Figure 6). This high temperature maximum clearly indicates strong antiferromagnetic coupling between the $Ni^{II}$ ions through the azido brid-

 © 2007 Wiley-VCH Verlag GmbH & Co. KGaA, Weinheim 

ges. Below this temperature, the molar magnetic susceptibility decreases continuously and reaches a minimum value of $1.82 \times 10^{-3}$ cm$^3$ mol$^{-1}$ at 10 K. Beyond this temperature, $\chi_M$ increases sharply to a value of $4.28 \times 10^{-3}$ cm$^3$ mol$^{-1}$ at 2 K, most likely due to the presence of paramagnetic impurities.

In a first approach, experimental data were fitted up to near the maximum to the Weng equation[31] for uniform chains based on the Hamiltonian $H = -J\sum_i S_i \cdot S_{i+1}$, where the nickel ion and the exchange interaction are isotropic. The fitting is only possible up to near the maximum (in our case up to 90 K) because neither the zero-field splitting nor the Haldane gap are taken into account.[32] The best parameters so obtained were $J = -49.4(1)$ cm$^{-1}$ and $g = 2.40(2)$. The high $J$ value indicates a good superexchange pathway. When the alternating chain structure of compound **2** was taken into account, the coupling parameters were optimized up to 50 K by using Equation (1) for an alternating chain[33] based on the Hamiltonian $H = -J_1[\Sigma^N_{i=1} S_{2i}S_{2i+1} + \alpha\Sigma^N_{i=1} S_{2i}S_{2i-1}]$ [Equation (2)]:

$$\chi_M = (2Ng^2\mu_B^2/3kT)/(X_r T_r) \quad (2)$$

in which [Equation (3)]:

$$X_r T_r = (AT_r^2 + BT_r + C)/(T_r^3 + DT_r^2 + ET_r + F) \quad (3)$$

with $T_r = kT/|J_1|$, $X_r = 3\chi_M|J_1|/2N_A g^2\mu_B$, and $\alpha = |J_2|/|J_1|$. A–F are polynomial expressions of the $\alpha$ alternance parameter. There are two sets of polynomial expressions in the regions of $\alpha \leq 0.5$ and $\alpha \geq 0.5$. This equation can reproduce the experimental data up to the value of $kT/J \approx 0.4$. The values corresponding to minimum in the regression are $J_1 = -63.7(2)$ cm$^{-1}$, $J_2 = -33.4(2)$ cm$^{-1}$ ($\alpha = 0.52$), and $g = 2.35(1)$ in the $\alpha \leq 0.5$ region. This result with $\alpha > 0.5$ indicates that the set of polynomial expressions to be used in the regression are those corresponding to $\alpha \geq 0.5$. But in the region where $\alpha \geq 0.5$ the values corresponding to the minimum in the regression are $J_1 = -49(2)$ cm$^{-1}$, $J_2 = -48(2)$ cm$^{-1}$ ($\alpha = 0.97$), and $g = 2.37(1)$, which means to a practically uniform 1D $\mu_{1,3}$-azido chain with a similar $J$ value to that obtained by using the Weng equation.[31] In fact, this was not the case because of the presence of two sets of alternating $\mu_{1,3}$-azido bridging ligands. One of them is associated with Ni–N–N angles of 116.0 and 117.0°, and a Ni–N···N–Ni torsion angle of 171.02° and the second set with Ni–N–N angles of 131.9 and 126.4°, and a Ni–N···N–Ni torsion angle of –64.3°. By taking this into consideration and the fact that the value of $\alpha = 0.52$ is very close to the upper limit of the region, we believe physically more coherent are the parameters $J_1 = -63.7(2)$ cm$^{-1}$, $J_2 = -33.4(2)$ cm$^{-1}$ ($\alpha = 0.52$), and $g = 2.35(1)$ in the $\alpha \leq 0.5$ region.

The second point is the assignment of the $J$ values of –63.7(2) and –33.4(2) cm$^{-1}$ to the two sets of structurally different alternating $\mu_{1,3}$-azido bridging ligands. To do so, we checked the literature for magnetostructural correlations in closely related monobridged 1D *cis*-Ni-($\mu_{1,3}$-$N_3$)–Ni systems[1,9b,34–37] and the data are collected in Table 7. These systems have been fairly well studied and it can be concluded[1,34] that in a correlation between the $|J|$ coupling values and the structural parameters in the bridging region, the bond parameters that must be taken into account are in the order: the bond angles Ni–N–N, the Ni–N···N–Ni torsion angle, and finally the bond lengths Ni–N(azido bridging).[1,33] Maximum coupling was found for a Ni–N–N angle of 108° and decreases when Ni–N–N increases. Also, for fixed Ni–N–N angles $|J|$ is maximum for a Ni–N···N–Ni torsion angle of 180° (or 0°) and decreases when Ni–N···N–Ni increases from 0 to 90°. On the basis of this experimental finding, the highest $|J|$ value of –63.7(2) cm$^{-1}$ calculated for compound **2** is assigned to the superexchange pathway created by the $\mu_{1,3}$-azido bridging ligands with the set of parameters Ni–N–N angles of 116.0 and 117.0°, and a Ni–N···N–Ni torsion angle of 171.02° whereas the lowest $|J|$ value of –33.4 cm$^{-1}$ is assigned to the superexchange pathway created by the $\mu_{1,3}$-azido bridging ligands with the set of parameters Ni–N–N angles of 131.9 and 126.4°, and a Ni–N···N–Ni torsion angle of –64.3°. Also, it should be

Table 7. Structural and magnetic parameters for 1D *cis*-Ni-($\mu_{1,3}$-$N_3$)–Ni systems: Ni–Nα–Nβ and Ni′–Nγ–Nβ angles, $\tau$ dihedral angles [°]; $J$ [cm$^{-1}$]; $\tau'$ = interplanar angle Ni–Nα···Nγ and Ni′–Nγ···Nα.

| Compound[a] | Ni–N–N | Ni–N–N | $\tau'$ | $\tau$ | $J$ | Ref. |
|---|---|---|---|---|---|---|
| $[Ni(3,3,3\text{-tet})_2(\mu_{1,3}\text{-}N_3)]_n(PF_6)_n$ | 151.8 | 151.3 | 37.2 | –37.2 | –18.5 | [34] |
| $[Ni(2\text{-methyl})_2(\mu_{1,3}\text{-}N_3)]_n(ClO_4)_n$ | 131.8 | 125.9 | 53.9 | –53.9 | –16.8 | [35] |
| $[Ni(2\text{-methyl})_2(\mu_{1,3}\text{-}N_3)]_n(PF_6)_n$ | 135.0 | 122.6 | 51.4 | –51.4 | –3.2 | [35] |
| $[Ni(bipy)_2(\mu_{1,3}\text{-}N_3)]_n(ClO_4)_n$ | 123.7 | 120.1 | 46.2 | 133.8 | –33.0 | [36] |
| | 126.6 | 121.3 | 41.0 | 139.0 | | |
| $[Ni(bipy)_2(\mu_{1,3}\text{-}N_3)]_n(PF_6)_n$ | 122.6 | 122.6 | 45.1 | 134.9 | –22.4 | [36] |
| | 120.6 | 127.4 | 42.0 | 138.0 | | |
| $[Ni(aep)_2(\mu_{1,3}\text{-}N_3)]_n(ClO_4)_n$ | 127.8 | 126.2 | 123.4 | 123.4 | <1 | [9b] |
| $[Ni(abap)(\mu_{1,3}\text{-}N_3)]_n(ClO_4)_n$ (**2**) | 116.0 | 117.0 | 171.0 | 171.0 | –63.7 | this work |
| | 131.9 | 126.4 | 64.3 | 64.3 | –33.4 | |
| $[Ni(Me_6trien)(\mu_{1,3}\text{-}N_3)]_n(ClO_4)_n \cdot nH_2O$ (**3a**) | 138.8 | 135.8 | 0.0 | 180 | –26.8 | this work |
| $[Ni(L)(N_3)(\mu_{1,3}\text{-}N_3)]_n$ | 133.4 | 124.5 | 73.2 | 106.8 | 13.5 | [37] |

[a] Ligand abbreviations: 3,3,3-tet = *N*,*N*′-bis(3-aminopropyl)-1,3-diaminopropane; 2-methyl = 1,2-diamino-2-methylpropane; bipy = 2,2′-bipyridyl; aep = 2-(2-aminoethyl)pyridine; abap = *N*-(2-aminoethyl)-*N*,*N*-bis(3-aminopropyl)amine; $Me_6$trien = 1,1,4,7,10,10-hexamethyltriethylenetetramine; L = the Schiff base of the condensation reaction of pyridine-2-carbaldehyde and *N*,*N*,2,2-tetramethylpropane-1,3-diamine.

 © 2007 Wiley-VCH Verlag GmbH & Co. KGaA, Weinheim 

noted that for one of the two sets of the structural parameters compound **2** reveals the highest reported $|J|$ value (Table 7). This high $J$ value, as has been stated above, is in accordance with the nearest Ni–N–N angles to 108° and Ni–N···N–Ni torsion angle to 180°.

For compound **3a**, the $\chi_M$ value at room temperature ($3.94 \times 10^{-3}$ cm$^3$ mol$^{-1}$) increases as the temperature decreases, reaching a broad maximum of $9.40 \times 10^{-3}$ cm$^3$ mol$^{-1}$ at ca. 50 K (Figure 7). This temperature maximum clearly indicates moderate antiferromagnetic coupling between the Ni$^{II}$ ions through the azido bridges. Below this temperature, the molar magnetic susceptibility decreases continuously and reaches a minimum value of $6.51 \times 10^{-3}$ cm$^3$ mol$^{-1}$ at 8 K. After this temperature, $\chi_M$ increases rapidly to a value of $11.38 \times 10^{-3}$ cm$^3$ mol$^{-1}$ at 2 K due to the presence of paramagnetic impurities.

Thus, taking into account that compound **3a** is structurally a uniform chain, experimental data were fitted up to near the maximum (50 K) to the Weng equation for uniform chains.[31] The best parameters so obtained were $J$ = –26.8(1) cm$^{-1}$ and $g$ = 2.36(1). The $J$ value indicates a moderate superexchange pathway. The set of parameters related with the antiferromagnetic superexchange pathway in **3a** are Ni–N–N angles of 138.8 and 135.8° and a Ni–N···N–Ni torsion angle of 180°.

Finally, it should be mentioned that the *cis* 1D Ni$^{II}$–azido complexes **2** and **3a** can be used as examples of low-dimensional magnetic systems to calculate the Haldane gap: for 1D systems containing integer values of the spin, $S$, Haldane predicted that they will exhibit a singlet ground state separated from the first triplet excited state by an energy gap $E_g$ (Haldane gap), whereas for half-odd integer spin, this gap would not exist.[38] As a consequence in the 1D compounds at $T$ = 0 K, $\chi_M$ has a zero value for integer spin systems and finite values for half-odd integer spin systems.[38] Thus, the integer $S$ 1D systems with low interchain coupling are considered to be good candidates to measure the Haldane gap[39] and several well-isolated *trans* 1D azido-bridged Ni$^{II}$ systems have been studied to demonstrate this phenomenon.[40,41] The two *cis* 1D azido-bridged Ni$^{II}$ complexes **2** and **3a** should add further examples that potentially can serve to calculate the Haldane gap.

For the monomer compound [Ni(Me$_6$trien)(N$_3$)]ClO$_4$ (**3b**), the $\chi_M T$ vs. $T$ plot is illustrated in Figure 8. The calculated room temperature $\chi_M T$ value of 1.29 cm$^3$ mol$^{-1}$ K was found to be larger than the spin only value of 0.99 cm$^3$ mol$^{-1}$ K for $S$ = 1 in mononuclear compounds. The $\chi_M T$ value decreases slowly with decreasing temperature and at ca. 50 K the decrease is becoming too fast, reaching a $\chi_M T$ value of 0.20 cm$^3$ mol$^{-1}$ K at 2 K. The experimental susceptibility data were fitted using Equation (4):[42]

$$\chi_M = (2Ng^2\beta^2/3kT)[2x^{-1} - 2\exp(-x)x^{-1} + \exp(-x)]/[1 + 2\exp(-x)] \quad (4)$$

where $x = D/kT$ and $D$ is the Zero field splitting parameter. This equation considers only noninteracting $S$ = 1 ions in the presence of single ion anisotropy. The best fit is given by the parameters $D$ = 19 cm$^{-1}$, $g$ = 2.22. The $D$ value is related to the geometry around the nickel(II) ion; the high anisotropy for the pentacoordinate nickel(II) ions implies high $D$ values.[43] The high value reported here for **3b** (19 cm$^{-1}$) is comparable with the high $D$ values of 14.7 and 14.8 cm$^{-1}$ found in similar pentacoordinate Ni$^{II}$ compounds [Ni(Me$_5$dien)(NCS)$_2$] and [Ni(Me$_4$Etdien)(NCS)$_2$], respectively where Me$_5$dien = 1,1,4,7,7-pentamethyldiethylenetriamine and Me$_4$Etdien = 4-ethyl-1,1,7,7-tetramethyldiethylenetriamine.[43]

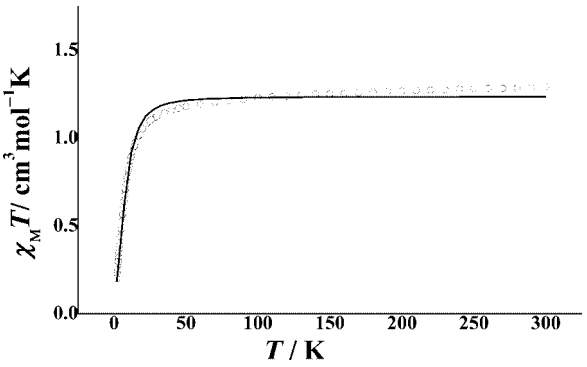


Figure 8. Plot of $\chi_M T$ vs. $T$ in the 300–2 K temperature range for [Ni(Me$_6$trien)(N$_3$)]ClO$_4$ (**3b**) measured on cooling under an external magnetic field of 0.7 T. The solid line shows the best fit as a uniform antiferromagnetic chain (see text).

## Conclusions

Bridged azido–Ni$^{II}$ complexes have been synthesized by using tetradentate amine ligands where the Ni$^{2+}$ centers are linked by the azido ligands in end-to-end-bond fashion. With the tripod amine trpn = N(CH$_2$CH$_2$CH$_2$NH$_2$)$_3$, dinuclear doubly bridged azido complex, [Ni$_2$(trpn)$_2$($\mu_{1,3}$-N$_3$)$_2$](ClO$_4$)$_2$ (**1**) was obtained. A small alteration in the trpn ligand skeleton to produce the corresponding tripod abap = N(CH$_2$CH$_2$CH$_2$NH$_2$)$_2$(CH$_2$CH$_2$NH$_2$), afforded the polynuclear 1D chain *cis*-[Ni(abap)($\mu_{1,3}$-N$_3$)]$_n$(ClO$_4$)$_n$ (**2**) in which the two azido groups adopt a *cis* arrangement. Surprisingly, when the tripod ligands were replaced with the linear tetradentate amine Me$_6$trien = [Me$_2$NCH$_2$CH$_2$N(Me)CH$_2$-CH$_2$N(Me)CH$_2$CH$_2$NMe$_2$], a 1D polynuclear species *cis*-[Ni(M$_6$trien)($\mu_{1,3}$-N$_3$)]$_n$(ClO$_4$)$_n$·$n$H$_2$O (**3a**) was also obtained with a distorted octahedral structure similar to **2**, in which the Ni–azide is extended in a zigzag chain. In complex **3a** strong steric hindrance imposed by the methyl groups of Me$_6$trien causes pronounced deviations for the two diagonal N(azide)–Ni–N(amine) bond angles from the ideal octahedral geometry. The magnetic behavior of **1**–**3a** is consistent with antiferromagnetic coupling. Compound **2** is a magnetically alternating 1D *cis* Ni($\mu_{1,3}$-N$_3$) compound, and one set of the structural parameters shows the high reported $|J|$ value. Complex **3a** is a magnetically uniform 1D *cis* Ni($\mu_{1,3}$-N$_3$) compound.

 © 2007 Wiley-VCH Verlag GmbH & Co. KGaA, Weinheim 

## Experimental Section

**Materials and Physical Measurements:** 1,1,4,7,10,10-hexamethyltriethylenetetramine ($Me_6$trien) and *N*-(2-*b*romoethyl)phthalimide were purchased from Aldrich Chem. Co., whereas tris(3-aminopropyl)amine (trpn) was obtained from TCI-America. All other materials were reagent grade quality. Infrared spectra were recorded with a JASCO FT/IR-480 plus spectrometer as KBr pellets. Electronic spectra of the complexes in solutions were recorded with the JASCO V-550 UV/Vis. spectrophotometer and the solid spectra (diluted with $BaSO_4$) were measured by the BECKMAN DK 2A spectrophotometer using $BaSO_4$ as a standard. Elemental analyses were carried out by Atlantic Microlaboratory, Norcross, Georgia, U.S.A. Magnetic susceptibility measurements under several magnetic fields in the range 2–300 K and magnetization measurements in the field range 0.4–1 T were performed with a Quantum Design MPMS-XL SQUID magnetometer at the Magnetochemistry Service of the University of Barcelona. All measurements were performed on polycrystalline samples. Pascal's constants were used to estimate the diamagnetic corrections, which were subtracted from the experimental susceptibilities to give the corrected molar magnetic susceptibilities.

***Caution:*** *Salts of perchlorate and azide as well as their metal complexes are potentially explosive and should be handled with great care and in small quantities.*

**Synthesis of the Compounds**

***N*-(2-Aminoethyl)-*N*,*N*-bis(3-aminopropyl)amine Tetrahydrochloride Trihydrate (abap·4HCl·3$H_2O$):** This ligand was prepared according to the literature method[44] by fusing 3,3-diphthalimidodipropylamine (observed m.p. 136–138 °C, lit. m.p. 136–137 °C) with *N*-(2-bromoethyl)phthalimide and the product, *N*-(2-phthalimidoethyl)-*N*,*N*-bis(3-phthalimidopropyl)amine, was hydrolyzed in HCl (8 M). $C_8H_{32}Cl_4N_4O_3$ (374.18): calcd. C 25.68, H 8.62, N 14.97; found C 25.54, H 8.49, N 14.55.

**[$Ni_2$(trpn)$_2$($\mu_{1,3}$-$N_3$)$_2$]($ClO_4$)$_2$ (1):** Nickel(II) perchlorate hexahydrate (0.365 g, 1.0 mmol) dissolved in $H_2O$ (5 mL) was added to tris(3-aminopropyl)amine (0.190 g, 1.0 mmol) in $H_2O$ (10 mL). The mixture was then heated on a steam bath for 5 min, followed by dropwise addition of an aqueous solution of $NaN_3$ (10 mL, 0.130 g, 2 mmol). The resulting solution was heated for another 10 min and then filtered through Celite. Slow evaporation at ambient temperature afforded mauve-blue crystals suitable for X-ray analysis. These crystals were collected by filtration, washed with cold ethanol (10 mL), ether, and air dried (yield: 0.286 g, 74%). $C_9H_{24}ClNiN_7O_4$ (388.50): calcd. C 27.82, H 6.23, N 25.24; found C 28.11, H 6.24, N 24.88. Selected IR bands (KBr): ν($N_3^-$) stretching 2092 (vs); ν(Cl–O) ($ClO_4^-$) centered at 1092 (vs); ν(N–H) stretching at 3328 (m) and 3288 (m) $cm^{-1}$.

***cis*-[Ni(abap)($\mu_{1,3}$-$N_3$)]$_n$($ClO_4$)$_n$ (2):** To abap·4HCl·3$H_2O$ (0.372 g, 1 mmol) dissolved in $H_2O$ (10 mL) and four equivalents of NaOH (0.160 g) was added $Ni(ClO_4)_2$·6$H_2O$ (0.375 g, 1.0 mmol) in $H_2O$ (10 mL). The solution was heated for 15 min and then an aqueous solution of $NaN_3$ (0.0720 g, 1.1 mmol in 10 mL $H_2O$) was added, drop by drop. The resulting blue solution was heated on a steam bath for 15 min, followed by filtration through Celite and allowed to crystallize at room temperature. After one week, the blue crystals which separated out were collected by filtration, washed with ethanol and ether and air dried (overall yield: 0.29 g, 77%). Crystals of X-ray quality were obtained from a dilute solution that was kept at room temperature. $C_8H_{22}ClNiN_7O_4$ (370.02): calcd. C 25.62, H 5.96, N 26.14; found C 25.78, H 6.00, N 26.32. Selected IR bands (KBr): ν($N_3$), 2075 (vs); ν(Cl–O) ($ClO_4^-$), 1091 (vs); ν(N–H) stretching, 3334 (m) and 3288 (m) $cm^{-1}$.

**[Ni($Me_6$trien)($N_3$)]$ClO_4$ (3b):** The complex was prepared by a procedure similar to that described for **1** and then allowed to crystallize in the refrigerator. After two weeks, the complex was separated out as green crystals (yield: 0.348 g, 81%). Single crystals were obtained from dilute solutions. $C_{12}H_{30}ClNiN_7O_4$ (430.57): calcd. C 33.47, H 7.02, N 22.71; found C 33.48, H 7.22, N 22.77. Selected IR bands (KBr): ν($N_3^-$) stretching 2060 (vs); ν(Cl–O) ($ClO_4^-$) 1082 (vs) $cm^{-1}$.

***cis*-[Ni($Me_6$trien)($\mu_{1,3}$-$N_3$)]$_n$($ClO_4$)$_n$·*n*$H_2O$ (3a):** When the solid sample of [Ni($Me_6$trien)($N_3$)]$ClO_4$ (**3b**) was allowed to stand at room temperature for about two months, it absorbed water without losing its crystallization shape. $C_{12}H_{32}ClNiN_7O_5$ (448.59): calcd. C 32.13, H 7.19, N 21.86; found C 32.55, H 7.16, N 21.79. The IR spectrum of the hydrated sample, which was then used for single-crystal X-ray structure determination, exhibited a new band centered at 3449 $cm^{-1}$ (mb) attributable to the ν(O–H) of lattice water and two strong bands for the azido groups at 2125 and 2092 $cm^{-1}$. The strong ν(Cl–O) of the perchlorate ion was detected at 1090 $cm^{-1}$.

**Crystal Structure Analyses:** The single-crystal X-ray data of compounds **1**, **2**, and **3b** were collected with a modified STOE four-circle diffractometer and that of compound **3a** with a Bruker-AXS SMART APEX CCD diffractometer. The crystallographic data, conditions retained for the intensity data collection, and some features of the structure refinements are listed in Table 8. Crystal size: 0.30 × 0.20 × 0.06 mm for **1**, 0.42 × 0.32 × 0.20 mm for **2**, 0.42 × 0.34 × 0.22 mm for **3a**, and 0.36 × 0.27 × 0.14 mm for **3b**. Intensities were collected with graphite-monochromated Mo-$K_\alpha$ radiation ($\lambda$ = 0.7107 Å). Total of 3117 (**1**), 5926 (**2**), 3788 (**3a**), and 4069 (**3b**) reflections were nonequivalent by symmetry, and observed reflections by applying the condition $I > 2\sigma(I)$ were 2278 for **1**, 4288 for **2**, 3498 for **3a**, and 3153 for **3b**. Lorentz polarization and absorption corrections using the SADABS computer program[45] were made for **3a**, and DIFABS program[46] for **1**, **2**, and **3b**. The structures were solved by direct methods using the SHELXS-86 computer program,[47] and refined by full-matrix least-squares methods on $F^2$, using the SHELXL-93 program[48] incorporated in the SHELXTL/PC V 5.03 program package.[49] All non-hydrogen atoms were refined anisotropically. The hydrogen atoms were assigned with isotropic displacement factors and included in the final refinement cycles by use of geometrical restraints ($C_{ar}$–H = 0.93 Å; $C_{Me}$–H = 0.96 Å; N–H = 0.90 Å; O–H = 0.82 Å). In the case of **1**, split occupancy of 0.79(2) and 0.21(2), was applied to the disordered methylene group with atoms C(2) and C(52), respectively. In the case of **3b**, split occupancy of 0.50 was applied to atoms N(4), N(5),C(1), C(2), C(9), C(10), C(12), and C(21)–C(24) of disordered $Me_6$trien, respectively. The final *R* (on *F*) factors were 0.0589, 0.0572, 0.0592, and 0.0430 for the four compounds, respectively, whereas the corresponding *wR* (on $F^2$) were 0.1468 for **1**, 0.1504 for **2**, 0.1267 for **3a**, and 0.0986 for **3b**. Numbers of refined parameters were 210, 379, 250, and 278 for **1**, **2**, **3a**, and **3b**, respectively. Maximum and minimum peaks in the final difference Fourier syntheses were 0.556 and –0.628 e Å$^{-3}$, respectively, for **1**, 1.074 and –0.733 e Å$^{-3}$, respectively, for **2**, 0.721 and –0.593 e Å$^{-3}$, respectively, for **3a**, and 0.347 and –0.413 e Å$^{-3}$, respectively, for **3b**. The molecular plots were obtained by using the ORTEP-32 program.[50] CCDC-609516–CCDC-609518 for **1**–**3a** and CCDC-628117 for **3b** contains the supplementary crystallographic data for this paper. These data can be obtained free of charge from The Cambridge Crystallographic Data Centre via www.ccdc.cam.ac.uk/data_request/cif.

 © 2007 Wiley-VCH Verlag GmbH & Co. KGaA, Weinheim 

Table 8. Crystal data and structure refinement for $[Ni_2(trpn)_2(\mu_{1,3}\text{-}N_3)_2](ClO_4)_2$ (**1**), *cis*-$[Ni(abap)(\mu_{1,3}\text{-}N_3)]_n(ClO_4)_n$ (**2**), *cis*-$[Ni(Me_6trien)(\mu_{1,3}\text{-}N_3)]_n(ClO_4)_n{\cdot}nH_2O$ (**3a**), and $[Ni(Me_6trien)(N_3)]ClO_4$ (**3b**).

| Compound | **1** | **2** | **3a** | **3b** |
|---|---|---|---|---|
| Empirical formula | $C_9H_{24}ClN_7NiO$ | $C_{16}H_{44}Cl_2N_{14}Ni_2O_8$ | $C_{12}H_{32}ClN_7NiO_5$ | $C_{12}H_{30}ClN_7NiO_4$ |
| Formula mass | 388.49 | 748.93 | 448.59 | 430.57 |
| Crystal system | monoclinic | orthorhombic | monoclinic | monoclinic |
| Space group | $P2_1/n$ | $Pbca$ | $P2_1/n$ | $P2_1/n$ |
| $a$ [Å] | 8.643(2) | 12.251(4) | 8.619(2) | 8.723(3) |
| $b$ [Å] | 7.944(2) | 22.144(7) | 17.297(4) | 15.073(4) |
| $c$ [Å] | 23.662(5) | 22.416(7) | 13.213(3) | 14.569(4) |
| $\alpha$ [°] | 90 | 90 | 90 | 90 |
| $\beta$ [°] | 100.06(2) | 90 | 90.85(3) | 103.44(2) |
| $\gamma$ [°] | 90 | 90 | 90 | 90 |
| $V$ [Å$^3$] | 1599.7(6) | 6081.2(34) | 1969.6(7) | 1863.1(10) |
| $Z$ | 4 | 8 | 4 | 4 |
| $T$ [K] | 100(2) | 100(2) | 100(2) | 100(2) |
| $\mu$ [mm$^{-1}$] | 1.409 | 1.479 | 1.159 | 1.218 |
| $D_{calcd.}$ [Mg/m$^3$] | 1.613 | 1.636 | 1.513 | 1.535 |
| $R$ [$I>2\sigma(I)$] | 0.0589 | 0.0572 | 0.0592 | 0.0430 |
| $wR_2$ (all data) | 0.1468 | 0.1504 | 0.1267 | 0.0986 |

## Acknowledgments

S. S. M. acknowledges the Summer Research Award (2005) and the financial support from the Department of Chemistry, University of Louisiana at Lafayette, and also thanks Dean B. Clark and Dr. R. B. Braun (ULL). F. A. M. thanks Prof. Kratky, Prof. Belaj (Univ. Graz), and Dr. Baumgartner (TU-Graz) for assistance.

[1] J. Ribas, A. Escuer, M. Monfort, R. Vicente, R. Cortés, L. Lezama, T. Rojo, *Coord. Chem. Rev.* **1999**, *193–195*, 1027–1068.

[2] a) M. M. Turnbull, T. Sugimoto, L. K. Thompson (Eds.), *Molecular-Based Magnetic Materials: Theory, Techniques and Applications*, ACS Symposium Series, 664, ACS, Washington, DC, **1996**; b) A. Caneschi; D. Gatteschi, L. Pardi, R. Sessoli, "Clusters, Chain and Layered Molecules: The Chemists way to Magnetic Materials" in A. F. Williams (Ed.), *Perspectives in Coordination Chemistry*, VCH, Weinheim, **1992**.

[3] a) S. S. Massoud, F. A. Mautner, *Inorg. Chim. Acta* **2005**, *358*, 3334–3340; b) A. Escuer, M. Font-Bardia, S. S. Massoud, F. A. Mautner, E. Peñalba, X. Solans, R. Vicente, *New J. Chem.* **2004**, *28*, 681–686; c) F. A. Mautner, R. Vicente, S. S. Massoud, *Polyhedron* **2006**, *25*, 1673–1680.

[4] a) A. Escuer, R. Vicente, M. S. El-Fallah, X. Solans, M. Font-Bardia, *Inorg. Chim. Acta* **1996**, *247*, 85–91; b) M. H. D'Aniello Jr, M. T. Mocella, F. Wagner, E. K. Barefield, I. C. Paul, *J. Am. Chem. Soc.* **1975**, *97*, 192–194; c) D. Sellmann, R. Prakash, F. Geipel, F. W. Heinemann, *Eur. J. Inorg. Chem.* **2002**, 2138–2146; d) N. Mondal, S. Mitra, V. Gramilich, S. K. Ghodsi, K. M. A. Malik, *Polyhedron* **2001**, *20*, 135–141; e) J.-P. Costes, F. Dahan, J. M. Dominguez-Vera, J.-P. Laurent, J. Ruiz, J. Sotiropoulos, *Inorg. Chem.* **1994**, *33*, 3908–3913.

[5] a) A. J. Blake, F. A. Devillanova, A. Garau, A. Harrison, F. Isaia, V. Lippolis, S. K. Tiwary, M. Schroder, G. Verani, G. Whittaker, *J. Chem. Soc., Dalton Trans.* **2002**, 4389–4394; b) A. McAuley, D. G. Fortier, D. H. Macartney, T. W. Whitcombe, C. Xu, *J. Chem. Soc., Dalton Trans.* **1994**, 2071–2079; c) C. Dietz, F. W. Heinemann, J. Kuhnigk, C. Kruger, M. Gerdan, A. X. Trautwein, A. Grohmann, *Eur. J. Inorg. Chem.* **1998**, 1041–1049.

[6] a) L. Li, D. Liao, Z. Jiang, S. Yin, *J. Mol. Struct.* **2003**, *649*, 37–42; b) K.-Y. Choi, K.-M. Chun, K.-C. Lee, J. Kim, *Polyhedron* **2002**, *21*, 1913–1920; c) K.-Y. Choi, H. Ryu, I.-H. Suh, *Polyhedron* **1998**, *17*, 1241–1246; d) M. K. Urtiaga, M. I. Arriortua, I. G. De Muro, R. Cortés, *Acta Crystallogr., Sect. C: Cryst. Struct. Commun.* **1995**, *51*, 62–65.

[7] M. Monfort, I. Resino, J. Ribas, X. Solans, M. Font-Bardia, H. Stoeckli-Evans, *New J. Chem.* **2002**, *26*, 1601–1606.

[8] J. Hausmann, M. H. Klingele, V. Lozan, G. Steinfeld, D. Siebert, Y. Journaux, J. J. Girerd, B. Kersting, *Chem. Eur. J.* **2004**, *10*, 1716–1728.

[9] a) J. Ribas, M. Monfort, C. Diaz, C. Bastos, X. Solans, *Inorg. Chem.* **1993**, *32*, 3557–3561; b) J. Ribas, M. Monfort, B. K. Ghosh, R. Cortés, X. Solans, M. Font-Bardia, *Inorg. Chem.* **1996**, *35*, 864–868.

[10] F. Fabrizi de Biani, E. Ruiz, J. Cano, J. J. Novoa, S. Alvarez, *Inorg. Chem.* **2000**, *39*, 3221–3229.

[11] B. Kersting, G. Steinfeld, D. Siebert, *Chem. Eur. J.* **2001**, *7*, 4253–4258.

[12] C. G. Pierpont, D. N. Hendrickson, D. M. Duggan, F. Wagner, E. K. Barefield, *Inorg. Chem.* **1975**, *14*, 604–610.

[13] P. Chaudhuri, M. Guttmann, D. Ventur, K. Wieghardt, B. Nuber, J. Weiss, *J. Chem. Soc., Chem. Commun.* **1985**, 1618–1620.

[14] Q.-L. Wang, X.-Q. Jia, D.-Z. Liao, S.-P. Yan, P. Cheng, G.-M. Yang, H.-X. Ren, Z.-H. Jiang, *Transition Met. Chem.* **2006**, *31*, 434–440.

[15] C. S. Hong, Y. Do, *Angew. Chem. Int. Ed.* **1999**, *38*, 193–195.

[16] R. Vicente, A. Escuer, J. Ribas, M. S. El-Fallah, X. Solans, M. Font-Bardia, *Inorg. Chem.* **1993**, *32*, 1920–1924.

[17] a) S. Sarkar, A. Mondal, M. S. El-Fallah, J. Ribas, D. Chopra, H. Stoeckli-Evans, K. K. Rajak, *Polyhedron* **2006**, *25*, 25–30; b) S. Deoghoria, S. Sain, M. Soler, W. T. Wong, G. Christou, S. K. Bera, S. K. Chandra, *Polyhedron* **2003**, *22*, 257–262; c) X.-J. Liu, Z. Shen, Y. Song, H.-J. Xu, Y.-Z. Li, X.-Z. You, *Inorg. Chim. Acta* **2005**, *358*, 1963–1969.

[18] G. Leibeling, S. Demeshko, B. Bauer-Siebenlist, F. Meyer, H. Pritzkow, *Eur. J. Inorg. Chem.* **2004**, 2413–2420.

[19] F. Meyer, P. Kircher, H. Pritzkow, *Chem. Commun.* **2003**, 774–775.

[20] F. Meyer, S. Demeshko, G. Leibeling, B. Keresting, E. Kaifer, H. Pritzkow, *Chem. Eur. J.* **2005**, *11*, 1518–1526.

[21] a) S. Demeshko, G. Leibeling, W. Maringgele, F. Meyer, C. Mennerich, H.-H. Klauss, H. Pritzkow, *Inorg. Chem.* **2005**, *44*, 519–528; b) T. K. Karmakar, S. K. Chandra, J. Ribas, G. Mostafa, T. H. Lu, B. K. Ghosh, *Chem. Commun.* **2002**, 2364–2365.

[22] a) J. Ribas, M. Monfort, B. K. Ghosh, R. Cortés, X. Solans, M. Font-Bardia, *Inorg. Chem.* **1996**, *35*, 864–868; b) M. Monfort, J. Ribas, X. Solans, M. Font-Bardia, *Inorg. Chem.* **1996**, *35*, 7633–7638.

[23] M. S. El-Fallah, A. Escuer, R. Vicente, X. Solans, M. Font-Bardia, M. Verdaguer, *Inorg. Chim. Acta* **2003**, *344*, 133–142.

[24] M. A. S. Goher, A. Escuer, F. A. Mautner, N. A. Al-Salem, *Polyhedron* **2002**, *21*, 1871–1876.

 © 2007 Wiley-VCH Verlag GmbH & Co. KGaA, Weinheim 

[25] a) A. Escuer, R. Vicente, M. S. El-Fallah, S. B. Kumar, F. A. Mautner, D. Gatteschi, *J. Chem. Soc., Dalton Trans.* **1998**, 3905–3909; b) R. Vicente, A. Escuer, *Polyhedron* **1995**, *14*, 2133–2138; c) R. Vicente, A. Escuer, J. Ribas, X. Solans, *Inorg. Chem.* **1992**, *31*, 1726–1728; d) F. Meyer, H. Pritzkow, *Inorg. Chem. Commun.* **2001**, *4*, 305–307.

[26] a) M. Monfort, I. Resino, J. Ribas, X. Solans, M. Font-Bardia, *New J. Chem.* **2001**, *25*, 1577–1582; b) M. Monfort, I. Resino, X. Solans, M. Font-Bardia, P. Rabu, M. Drillon, *Inorg. Chem.* **2000**, *39*, 2572–2576; c) L. Li, D. Liao, Z. Jiang, S. Yan, *Polyhedron* **2000**, *19*, 1575–1578; d) P. Chaudhuri, T. Weyhermuller, E. Bill, K. Wieghardt, *Inorg. Chim. Acta* **1996**, *252*, 195–202.

[27] a) M. Monfort, I. Resino, J. Ribas, H. Stoeckli-Evans, *Angew. Chem. Int. Ed.* **2000**, *39*, 191–193; b) M. L. Hernández, M. G. Barandika, M. K. Urtiaga, R. Cortés, L. Lezama, M. I. Arriortua, *J. Chem. Soc., Dalton Trans.* **2000**, 79–84.

[28] a) A. Escuer, R. Vicente, F. A. Mautner, M. A. S. Goher, M. A. M. Abu-Youssef, *Chem. Commun.* **2002**, 64–65; b) F. A. Mautner, R. Cortés, L. Lezama, T. Rojo, *Angew. Chem. Int. Ed. Engl.* **1996**, *35*, 78–80.

[29] A. W. Addison, T. N. Rao, J. Reedijk, J. van Rijn, G. C. Verschoor, *J. Chem. Soc., Dalton Trans.* **1984**, 1349–1356.

[30] a) A. P. B. Lever, *Inorganic Electronic Spectroscopy*, Elsevier, Amsterdam, **1984**, pp. 513–520; b) M. D. Santana, G. Garcia, M. Julve, F. Lloret, J. Pérez, M. Liu, F. Sanz, J. Cano, G. López, *Inorg. Chem.* **2004**, *43*, 2132–2140; c) M. D. Santana, A. A. Lozano, G. Garcia, G. López, J. Pérez, *Dalton Trans.* **2005**, 104–109.

[31] C. Y. Weng, Ph. D. Thesis, Carnegie Institute of Technology, **1968**.

[32] a) A. Escuer, R. Vicente, J. Ribas, M. S. El Fallah, X. Solans, *Inorg. Chem.* **1993**, *32*, 1033–1035; b) A. Escuer, R. Vicente, J. Ribas, M. S. El Fallah, X. Solans, M. Font-Bardía, *Inorg. Chem.* **1993**, *32*, 3727–3732.

[33] J. J. Borrás Almenar, E. Coronado, J. Curely, R. Georges, *Inorg. Chem.* **1995**, *34*, 2699–2704.

[34] A. Escuer, R. Vicente, J. Ribas, M. S. El-Fallah, X. Solans, M. Font-Bardía, *Inorg. Chem.* **1994**, *33*, 1842–1847.

[35] J. Ribas, M. Monfort, C. Diaz, C. Bastos, C. Mer, X. Solans, *Inorg. Chem.* **1995**, *34*, 4986–4990.

[36] R. Cortes, K. Urtiaga, L. Lezama, J. L. Pizarro, A. Goñi, M. I. Arriortua, T. Rojo, *Inorg. Chem.* **1994**, *33*, 4009–4015.

[37] P. S. Mukherjee, S. Dalai, E. Zangrando, F. Lloret, N. R. Chaudhuri, *Chem. Commun.* **2001**, 1444–1445.

[38] a) F. D. Haldane, *Phys. Lett.* **1983**, *93A*, 464–468; b) J. P. Renard, M. Verdaguer, L. P. Regnault, W. A. K. Erkelens, J. Rossat-Mignod, W. G. Stirling, *Europhys. Lett.* **1987**, *3*, 945–952; c) I. Affleck, T. Kennedy, E. H. Lieb, H. Tasaki, *Phys. Rev. Lett.* **1987**, *59*, 799–802.

[39] a) T. Ishii, N. Aizawa, H. Hara, M. Yamashita, H. Matsuzaka, *Polyhedron* **2001**, *20*, 1297–1304; b) T. Takeuchi, M. Ono, H. Hori, T. Yosida, A. Yamagishi, M. Date, *J. Phys. Soc. Jpn.* **1992**, *61*, 3255–3261.

[40] a) M. S. El Fallah, A. Escuer, R. Vicente, X. Solans, M. Font-Bardia, M. Verdaguer, *Inorg. Chim. Acta* **2003**, *344*, 133–142; b) M. Kohno, M. Takahashi, M. Hagiwara, *Phys. Rev. B* **1998**, *57*, 1046–1051; c) L. K. Chou, D. R. Talham, W. W. Kim, P.-J. C. Signore, M. W. Meisel, *Physica B* **1994**, *194*, 313–314; d) T. Takeuchi, H. Hori, M. Date, T. Yosida, K. Katsumata, J. P. Renard, V. Gadet, M. Verdaguer, *J. Magn. Magn. Mater.* **1992**, *194*, 813–814.

[41] a) T. Manabe, M. Yamashita, T. Ohishi, T. Takeuchi, T. Yosida, Y. Yu, Z. Honda, K. Katsumata, *Synth. Met.* **1997**, *85*, 1717–1718; b) M. Yamashita, K. Inoue, T. Ohishi, H. Miyamae, T. Takeuchi, T. Yosida, *Synth. Met.* **1995**, *71*, 1961–1964.

[42] C. P. Landee, D. M. Mudgett, B. M. Foxman, *Inorg. Chim. Acta* **1991**, *186*, 45–49.

[43] R. Vicente, A. Escuer, X. Solans, M. Font-Bardía, *Inorg. Chim. Acta* **1996**, *248*, 59–65.

[44] a) R. L. Fanshawe, A. G. Blackman, *Inorg. Chem.* **1995**, *34*, 421–423; b) R. L. Fanshawe, A. G. Blackman, C. R. Clark, *Inorg. Chim. Acta* **2003**, *342*, 114–124.

[45] R. H. Blessing, *Acta Crystallogr. Sect. A* **1995**, *51*, 33–38; SADABS, Bruker AXS, **1998**.

[46] N. Walker, D. Stuart, *Acta Crystallogr., Sect. A* **1983**, *39*, 158–166.

[47] G. M. Sheldrick, *SHELXS-86, Program for the solution of crystal structures*, University of Göttingen, Göttingen, Germany, **1986**.

[48] G. M. Sheldrick, *SHELXL-93, Program for the refinement of crystal structures*, University of Göttingen, Göttingen, Germany, **1993**.

[49] *SHELXTL 5.03 (PC-Version), Program library for the solution and molecular graphics*, Siemens Analytical Instruments Division, Madison, WI, **1995**.

[50] *ORTEP-32 for Windows*: L. J. Farrugia, *J. Appl. Crystallogr.* **1997**, *30*, 565.

Received: August 3, 2006
Published Online: February 9, 2007

 © 2007 Wiley-VCH Verlag GmbH & Co. KGaA, Weinheim 

DOI: 10.1002/ejic.200600777

# (Pentabenzylcyclopentadienyl)molybdenum Complexes: Synthesis, Structures and Redox Properties

Sónia Namorado,[a] Jinlan Cui,[a] Cristina G. de Azevedo,[a] M. Amélia Lemos,[b] M. Teresa Duarte,[a] José R. Ascenso,[a] Alberto R. Dias,[a] and Ana M. Martins*[a]

**Keywords:** Molybdenum / Tungsten / Cyclopentadienyl ligands / Half-sandwich complexes / Cyclic voltammetry

[MCpBz(CO)$_3$]$_2$ (M = Mo **3**, W **4**; CpBz = pentabenzylcyclopentadienyl) complexes were prepared by reaction of Li[MCpBz(CO)$_3$] [M = Mo (**1**), W (**2**)] with Fe$^{III}$. [MoCpBz(CO)$_2$]$_2$ (**5**) can be prepared by thermal elimination of CO from **3** and also by reaction of **1** with C$_3$H$_5$Br. The steric bulk of the CpBz ligands causes all the dimers to exist either in the solid state or in solution as the *trans* isomers. The hydrido complexes [MH(CpBz)(CO)$_3$] [M = Mo (**6**), W (**7**)] were prepared by reactions of **1** and **2** with H$^+$. Cyclic voltammetry and controlled potential coulometry of **5** in CH$_2$Cl$_2$, thf and CH$_3$CN were performed and mechanisms for the redox behaviour are proposed.
(© Wiley-VCH Verlag GmbH & Co. KGaA, 69451 Weinheim, Germany, 2007)

## Introduction

The thermodynamic and kinetic properties of transition metal complexes are strongly dependent on the interplay of the ligands' stereochemical and electronic features. For metallocene complexes, the importance of cyclopentadienyl (Cp) substituents is extensively documented, with current practice being to tune the metal centres' reactivity through the choice of appropriate Cp ligands. In this context, we recently became interested in pentabenzylcyclopentadienyl (CpBz) derivatives with the aim of assessing the influence of the five bulky benzyl groups on the structures and properties of half-sandwich Mo and W complexes. Preliminary studies with [MoCpBz(O)$_2$Cl] have shown an enhanced performance in the catalytic epoxidation of cyclooctene. A comparison of [MoCp′(O)$_2$Cl] (Cp′ = Cp, Cp*, Cp*i*Pr$_4$, CpBz) complexes showed that the CpBz derivative leads to the most active and stable catalyst system when activated with *t*BuOOH.[1] Moreover, chlorination reactions of low oxidation-state (CpBz)carbonylmolybdenum and -tungsten complexes also differ from those of their Cp and Cp* analogues. In particular, the reactions of [MoCpBz(CO)$_3$(CH$_3$)] with PCl$_5$ or PhICl$_2$ have been observed to proceed by different routes leading to the formation of [MoCpBz{$\eta^2$-C(O)CH$_3$}Cl$_3$] or [MoCpBzCl$_4$], respectively.[2] Among the extremely varied reactivity of half-sandwich molybdenocene and tungstocene complexes, the application of hydrido complexes of general formula [MCp(CO)$_2$L(H)] (M = Mo, W; L = CO, PR$_3$) as hydrogenation catalysts of ketones and aldehydes has recently been reported.[3,4]

The results presented here are part of our ongoing interest in (pentabenzylcyclopentadienyl)molybdenum and -tungsten reactivity. To determine the influence of the benzyl substituents on the metal electronic features, we performed electrochemical studies of the dimer [MoCpBz(CO)$_2$]$_2$.

## Results and Discussion

All new complexes are represented in Scheme 1. Li[MCpBz(CO)$_3$] [M = Mo (**1**), W (**2**)] are readily prepared in thf or dmf solution, respectively, by treating M(CO)$_6$ with LiCpBz.[5] Treatment of **1** and **2** with Fe$^{III}$ in CH$_3$COOH at 0 °C leads to the formation of [MCpBz(CO)$_3$]$_2$ [M = Mo (**3**), W (**4**)], which precipitate from their solution as red and orange solids, respectively.

The IR spectrum of **3** in KBr pellets shows three bands at 1932, 1901 and 1876 cm$^{-1}$ for the carbonyl ligands. In **4**, the three carbonyl bands appear at 1928, 1897 and 1868 cm$^{-1}$. These values are lower than those reported for similar [MCp(CO)$_3$]$_2$ complexes (Mo: 1966, 1922, 1914 cm$^{-1}$; W: 2012, 1952, 1905 cm$^{-1}$).[6,7]

The $^1$H NMR spectra of [MCpBz(CO)$_3$]$_2$ in CD$_2$Cl$_2$ display only one resonance for the benzyl protons at $\delta$ = 3.88 ppm for **3** and $\delta$ = 3.92 ppm for **4**. This means that there are no constraints on the free rotation of the pentabenzylcyclopentadienyl ligands around the metal–C$_{5ring}$ and the C$_{5ring}$–CH$_2$Ph bonds and, considering the arrangement of the CpBz ligands in relation to the metal–metal bonds,

[a] Centro de Química Estrutural, Instituto Superior Técnico, Av. Rovisco Pais, 1, 1049-001 Lisboa, Portugal
E-mail: ana.martins@ist.utl.pt
[b] IBB – Institute for Biotechnology and Bioengineering, CEBQ, Instituto Superior Técnico, Av. Rovisco Pais, 1, 1049-001 Lisboa, Portugal
Supporting information for this article is available on the WWW under http://www.eurjic.org or from the author.

 © 2007 Wiley-VCH Verlag GmbH & Co. KGaA, Weinheim 

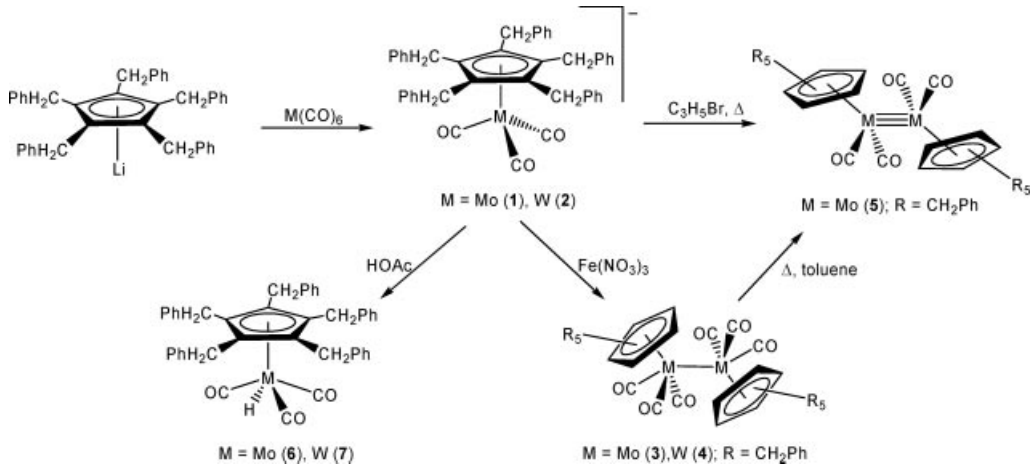


Scheme 1.

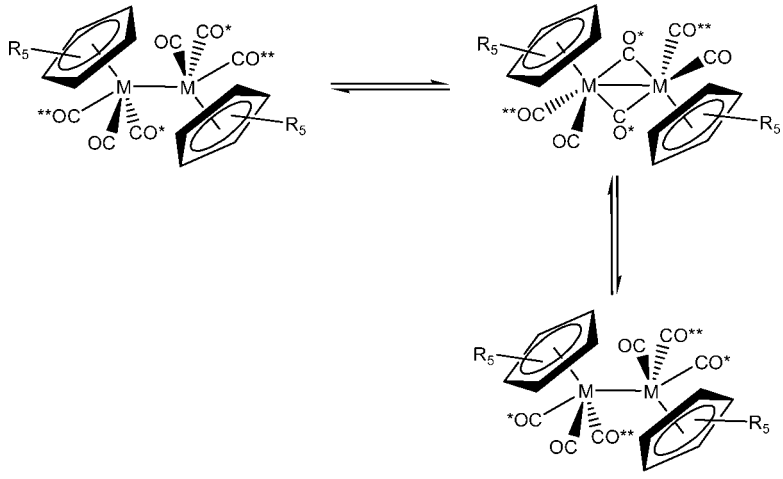

Scheme 2. The asterisks on the CO groups denote inequivalent carbonyl ligands.

is indicative of the presence of only one isomer in solution. The $^{13}C$ NMR spectra of **3** and **4** corroborate this result and also show that there is a fluxional process in solution that renders the six carbonyl groups equivalent, which gives rise to only one resonance at $\delta$ = 234.7 ppm (Mo) and $\delta$ = 224.3 ppm (W). The mechanism that accounts for this process is a rapid scrambling of the CO ligands among the six positions available at the two metal centres that involves CO-bridged intermediates, as represented in Scheme 2.[8]

Attempts to block the CO scrambling process by lowering the temperature did not produce any modifications in the NMR spectra down to –80 °C. This behaviour also indicates that *cis*/*trans* isomerisation is not operative, which might be expected on stereochemical arguments, and that the unique isomers in solution are *trans*-$[MCpBz(CO)_3]_2$ for both molybdenum and tungsten complexes. Thus, in contrast to their Cp analogues, *cis*/*trans* isomerisation processes in **3** and **4** are hampered.[6,9]

Treatment of $Li[MoCpBz(CO)_3]$ with an excess of $C_3H_5Br$ led to the dimer $[MoCpBz(CO)_2]_2$ (**5**; Scheme 1). This complex was isolated in 76% yield upon recrystallisation from diethyl ether as orange-red single crystals that were suitable for X-ray diffraction. It is clear that the reaction of $C_3H_5Br$ with **1** is not an elementary process. The formation of $[MoCpBz(CO)_2]_2$ probably results from an outer-sphere redox reaction between the anion $[MoCpBz(CO)_3]^-$ and $C_3H_5Br$, leading to the radical $[MoCpBz(CO)_3]$, which, upon dimerisation and a thermally induced Mo–CO bond cleavage,[10] finally gives $[MoCpBz(CO)_2]_2$. By analogy with the formation of $[MoCpBz(CO)_3Me]$ from **1** and MeI, $[MoCpBz(CO)_3(\sigma\text{-}C_3H_5)]$ would be the expected product. An allyl radical elimination from the putative $Mo^{II}$ intermediate $[MoCpBz(CO)_3(\sigma\text{-}C_3H_5)]$ may, however, be excluded, as it goes against the usual reactivity trend that affords π-allyl coordination by thermal or photochemical activation of σ-allyl precursors.[11,12] The formation of $[MoCpBz(CO)_3]_2$ as an intermediate in the synthesis of **5** was confirmed by the quantitative formation of the latter from a toluene solution of **3** under reflux (Scheme 1).

The IR spectrum of **5** shows characteristic peaks due to CpBz and peaks ascribed to the carbonyl ligands at 1878 and 1821 $cm^{-1}$. These values, which are notably lower than those reported for the Cp ($\nu_{CO}$: 1900 and 1850 $cm^{-1}$) and

 © 2007 Wiley-VCH Verlag GmbH & Co. KGaA, Weinheim 

Cp* ($\nu_{CO}$: 1940, 1907, 1874 and 1846 $cm^{-1}$) analogues,[10,13] should reflect extensive Mo–CO backbonding. The $^1H$ and $^{13}C$ NMR spectra display one set of CpBz resonances, consistent with the free rotation of the ligand in solution. The magnetically equivalent CO ligands give rise to a resonance at $\delta$ = 239.3 ppm.

Li[Mo(CpBz)$(CO)_3$] does not react with other electrophiles like $Me_3CCH_2Br$, as attested by the essentially quantitative recovery of the starting material. This result is probably dictated by stereochemical constraints that prevent the coordination of the neopentyl ligand.

The hydrido complexes [MH(CpBz)$(CO)_3$] [M = Mo (**6**), W (**7**)] were obtained upon treatment of **1** with $CH_3COOH$ in 90% and 95% yield for **6** and **7**, respectively. The IR spectrum of **6** displays carbonyl stretching vibrations at 2008 (vs), 1928 (vs) and 1822 $cm^{-1}$ (m) and that of **7** shows carbonyl peaks at 2008 (vs) and 1901 $cm^{-1}$ (vs). The lower CO vibration values displayed by **6** and **7** with respect to their Cp and Cp* counterparts are, once more, indicative of a more extensive metal–carbonyl backbonding in the CpBz derivatives.[14,15] The hydrido resonances in **6** appear at $\delta$ = –4.85 ppm and in **7** at $\delta$ = –6.31 ppm.

Crystals suitable for X-ray analysis of compound **4** were grown from a toluene solution at –20 °C. The molecular structure is shown in Figure 1 and selected bond lengths and angles are listed in Table 1.

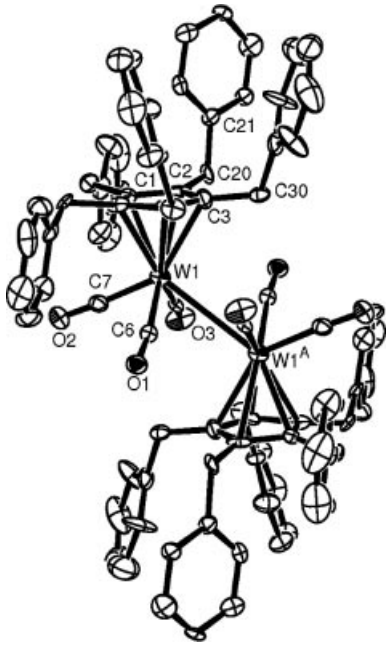


Figure 1. Molecular structure of complex **4**. H atoms have been excluded for clarity. Thermal ellipsoids are shown at the 50% probability level.

The tungsten coordination geometry is best described as a distorted four-legged piano-stool with a CpBz(CT)–W(1)–W(1A) angle of 125.06(19)° and CpBz(CT)–W(1)–C(*n*) angles of 125.5(4), 114.2(4) and 124.2(4) for C(6), C(7) and C(8), respectively [CpBz(CT) = centroid of the cyclopentadienyl ring]. The spatial arrangement of the cyclopentadienyl substituents displays three benzyl groups directed opposite to the metal atom and the other two slightly bent towards it. The relative conformation of the phenyl rings is characterised by the torsion angles of the pendent benzyl arms, defined as M–C(CpBz)–C($CH_2$)–$C_{ipso}$ in Table 1. As a whole, the molecular structure of **4** parallels those previously reported for related dimers.[9,16–19] Two carbonyl ligands of each tungsten atom bend over the metal–metal bond, whereas the remaining carbonyl groups are mutually *trans* in relation to the metal–metal bond and their structural features are typical of linear terminal CO ligands. These carbonyl groups point towards the middle region between the two CpBz benzyl groups that point down towards the tungsten centres. The steric bulk requirements of the CpBz ligands are responsible for elongated metal–metal and metal–CpBz(CT) bond lengths, when compared with analogous complexes [3.215 < W–W < 3.287 Å; 1.995 < W–Cp′(CT) < 2.029 Å].[9,16–19] Short-contact distances have been found between carbonyl oxygen atoms and the methylenic protons of the benzyl groups pointing down and belonging to the other half of the molecule [O(1)···H(20) 2.383, O(3)···H(40) 2.489 Å]. The most peculiar feature of

Table 1. Selected bond lengths [Å] and bond and torsion angles [°] for **4** and **5**.

| | [WCpBz$(CO)_3]_2$ (**4**) | [MoCpBz$(CO)_2]_2$ (**5**) |
|---|---|---|
| M–C(6) | 1.976(16) | 1.950(3) |
| M–C(7) | 1.913(16) | 1.948(3) |
| M–C(8) | 1.992(16) | – |
| C(6)–O(1) | 1.160(16) | 1.158(3) |
| C(7)–O(2) | 1.195(16) | 1.157(3) |
| C(8)–O(3) | 1.165(17) | – |
| M–M | 3.331(19) | 2.5198(8) |
| M–CpBz(CT) | 2.0441(8) | 1.9978(6) |
| M–C(1) | 2.342(13) | 2.321(3) |
| M–C(2) | 2.402(14) | 2.358(2) |
| M–C(3) | 2.427(14) | 2.372(3) |
| M–C(4) | 2.387(13) | 2.333(2) |
| M–C(5) | 2.349(13) | 2.314(2) |
| C(1)–C(2) | 1.424(19) | 1.432(3) |
| C(2)–C(3) | 1.49(2) | 1.421(4) |
| C(3)–C(4) | 1.410(19) | 1.425(3) |
| C(4)–C(5) | 1.46(2) | 1.439(4) |
| C(5)–C(1) | 1.401(18) | 1.439(3) |
| M–C(6)–O(1) | 171.7(12) | 173.1(2) |
| M–C(7)–O(2) | 176.5(12) | 171.8(2) |
| M–C(8)–O(3) | 172.6(13) | – |
| C(6)–M–C(7) | 78.1(6) | 87.93(11) |
| C(6)–M–C(8) | 110.2(5) | – |
| C(6)–M–M | 67.53(19) | 76.58(8) |
| C(7)–M–C(8) | 77.5(6) | – |
| C(7)–M–M | 120.65(19) | 71.43(8) |
| C(8)–M–M | 71.62(19) | – |
| CpBz(CT)–M–C(6) | 125.5(4) | 116.95(8) |
| CpBz(CT)–M–C(7) | 114.2(4) | 119.31(8) |
| CpBz(CT)–M–C(8) | 124.2(4) | – |
| CpBz(CT)–M–M | 125.06(19) | 161.54(8) |
| M–C(1)–C(10)–C(11) | –69.98(19) | –148.2(2) |
| M–C(2)–C(20)–C(21) | 179.45(19) | –162.69(19) |
| M–C(3)–C(30)–C(31) | –167.43(19) | 172.4(2) |
| M–C(4)–C(40)–C(41) | –161.34(19) | 154.8(2) |
| M–C(5)–C(50)–C(51) | 63.41(19) | –176.37(18) |

 © 2007 Wiley-VCH Verlag GmbH & Co. KGaA, Weinheim 

the structure of $[WCpBz(CO)_3]_2$ is related to the cyclopentadienyl ring. The C–C bond lengths deserve a comment as two are longer (1.46 and 1.49 Å) than the other three, which are in accordance with the usual average C–C distances in $\eta^5$-Cp ligands (1.41 Å).[16] This difference reflects an asymmetry in the metal–ring bonding that is reminiscent of an $\eta^3+\eta^2$ coordination.[20–23]

The molecular structure of $[Mo(CpBz)(CO)_2]_2$ is depicted in Figure 2 and some selected distances and angles are listed in Table 1.

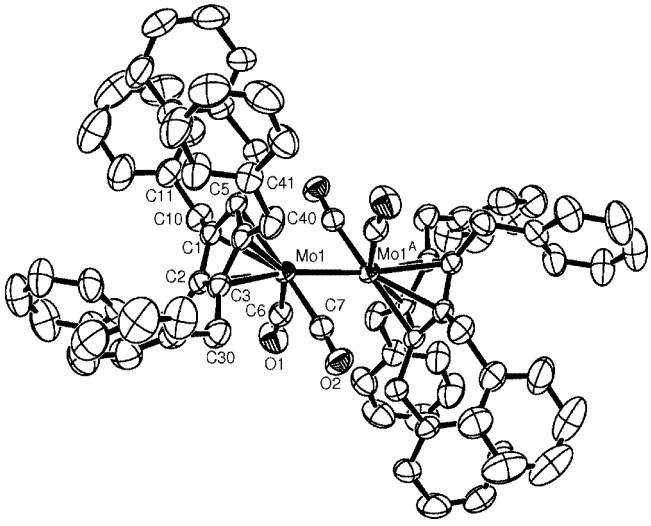


Figure 2. Molecular structure of complex **5**. H atoms have been excluded for clarity. Thermal ellipsoids are shown at the 50% probability level.

The molybdenum coordination is best described as a distorted piano-stool geometry with basal angles ranging between 71.43(8) and 87.93(11)° and CpBz(CT)–Mo(1)–X angles [X = C(6), C(7), Mo(1A)] varying from 116.95(8) to 119.31(8)°. The CpBz(CT)–Mo(1)–Mo(1A) angle [161.54(8)°] is more acute than that reported for $[MoCp(CO)_2]_2$, which displays a linear Cp–Mo–Mo arrangement,[13] but close to the values reported for the majority of $[MCp'(CO)_2]_2$ complexes [M = Cr, Mo, W; Cp′ = $C_5H_5$, $C_5Me_5$, Ind, $C_5H_4COOEt$, $C_5H_3tBu_2$, $C_5Me_4(CH_2)_2NMe_2$].[13,24–28] The Mo(1)–Mo(1A) distance [2.5198(8) Å] is compatible with a metal–metal triple bond, although it is longer than in $[MoCp'(CO)_2]_2$ [Cp′ = $C_5H_5$ 2.448(1) Å, $C_5Me_5$ 2.488(3) Å].[13,28] As generally observed for $[MoCp'(CO)_2]_2$ complexes, the carbonyl ligands in **5** are linear semi-bridging.[24,25] The Mo(1)–C(6) [1.950(3) Å] and Mo(1)–C(7) [1.948(3) Å] bond lengths are thus identical to those of similar compounds,[13,25–28] and much shorter than in $[MoCp(CO)_2]_2$ [2.14(2) and 2.52(2) Å]. All the CpBz phenyl rings in **5** point away from the metal atom and define torsion angles of between 148.2(2) and 176.37(18)°.

The relative orientation of the cyclopentadienyl rings towards the metal–metal bonds in $[Cp'M(CO)_2]_2$ complexes (M = Cr, Mo; Cp′ = $C_5H_5$, $C_5Me_5$), which results in linear or bent arrangements, has been attributed to electronic rather than stereochemical reasons. The combination of ring orbitals with σ or π* metal–metal orbitals was taken as the determining factor for the Cp(CT)–M–M angle values whilst pointing out that the metal–ring and metal–metal bonds are strongly interdependent, that is, the Cp rings may be thought of as conjugated with the M≡M system.[26] In the case of bent Cp(CT)–M–M arrangements, since σ* metal–metal orbitals are involved, the weakening (and thus the lengthening) of the metal–metal bond is more pronounced.

The molecular structures of **6** and **7** are represented in Figures 3 and 4, respectively, and selected bond lengths and angles are listed in Table 2.

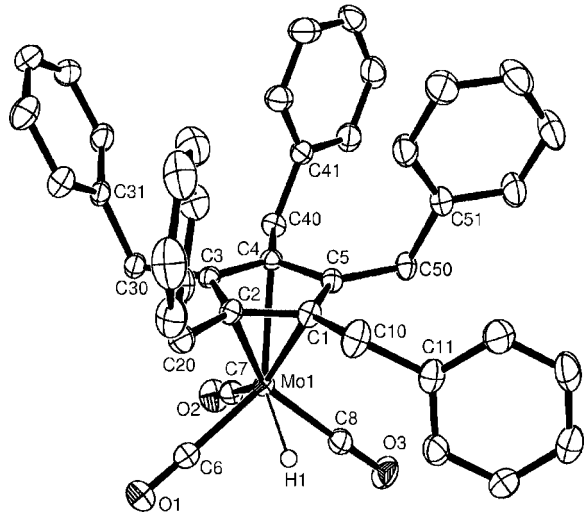


Figure 3. Molecular structure of complex **6**. H atoms have been excluded for clarity, except the hydride ion. Thermal ellipsoids are shown at the 50% probability level.

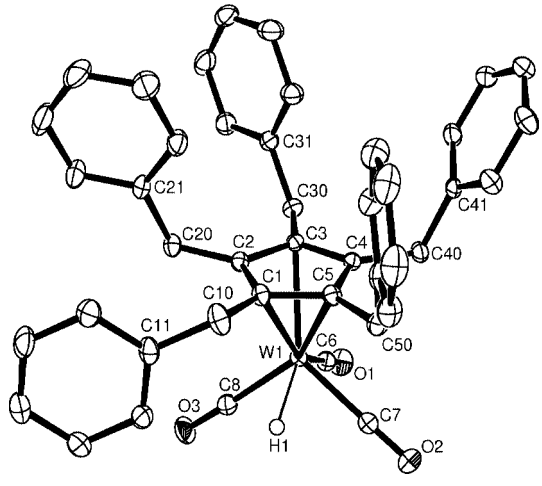


Figure 4. Molecular structure of complex **7**. H atoms have been excluded for clarity, except the hydride ion. Thermal ellipsoids are shown at the 50% probability level.

 © 2007 Wiley-VCH Verlag GmbH & Co. KGaA, Weinheim 

Table 2. Selected bond lengths [Å] and bond and torsion angles [°] for **6** and **7**.

| | [MoH(CpBz)(CO)$_3$] (**6**) | [WH(CpBz)(CO)$_3$] (**7**) |
|---|---|---|
| M–C(6) | 1.9737(19) | 1.9948(15) |
| M–C(7) | 1.9938(18) | 1.9771(16) |
| M–C(8) | 1.9815(18) | 1.9861(15) |
| C(6)–O(1) | 1.147(2) | 1.1522(18) |
| C(7)–O(2) | 1.142(2) | 1.1522(19) |
| C(8)–O(3) | 1.146(2) | 1.1492(18) |
| M–H | 1.6058(268) | 1.7045(216) |
| M–CpBz(CT) | 1.99902(16) | 2.00093(11) |
| M–C(6)–O(1) | 175.65(18) | 178.82(13) |
| M–C(7)–O(2) | 179.55(17) | 175.58(14) |
| M–C(8)–O(3) | 177.44(17) | 176.94(14) |
| C(6)–M–C(7) | 81.60(8) | 81.14(6) |
| C(6)–M–C(8) | 105.88(7) | 81.13(6) |
| C(7)–M–C(8) | 81.74(7) | 106.32(6) |
| CpBz(CT)–M–C(6) | 122.85(6) | 122.11(4) |
| CpBz(CT)–M–C(7) | 122.19(5) | 123.00(5) |
| CpBz(CT)–M–C(8) | 126.94(5) | 126.87(4) |
| CpBz(CT)–M–H | 115.91(98) | 114.69(72) |
| M–C(1)–C(10)–C(11) | 61.23(22) | –61.65(18) |
| M–C(2)–C(20)–C(21) | 162.94(12) | 166.85(9) |
| M–C(3)–C(30)–C(31) | 178.41(11) | 159.82(9) |
| M–C(4)–C(40)–C(41) | –159.78(11) | –178.19(9) |
| M–C(5)–C(50)–C(51) | –167.15(11) | –163.07(9) |

Complexes **6** and **7** have similar four-legged piano-stool metal coordination geometries, as also reported for analogous metal hydride complexes.[29–32] The structural parameters displayed are consistent with the data found in the literature for this class of compounds and will not be discussed further. The M–CpBz(CT)–C($CH_2$)–$C_{ipso}$ torsion angles are similar to those observed for complex **4**, although in **6** and **7** only one phenyl ring approaches the metal atoms.

## Electrochemical Studies

The electrochemical behaviour of [Mo(CpBz)(CO)$_2$]$_2$ (**5**) was investigated by means of cyclic voltammetry (CV) and controlled-potential coulometry (CPC). The CV results in thf, $CH_2Cl_2$ and $CH_3CN$, using $Bu_4NBF_4$ or $Bu_4NPF_6$ as electrolyte, measured at 200 mV s$^{-1}$, are summarised in Table 3 (Figures S1–S3 in the Supporting Information show the voltammograms of **5** in the three solvents with different electrolytes at different scan rates).

Table 3. Electrochemical data [$E_p^{ox}$(V) vs. FcH] for **5**.

| Solvent | $CH_2Cl_2$ | THF | $CH_3CN$ |
|---|---|---|---|
| $Bu_4NPF_6$ | 0.49 | – | 0.26 (I)<br>0.52 (II) |
| $Bu_4NBF_4$ | – | 0.56 | 0.26 (I)<br>0.54 (II) |

In thf and $CH_2Cl_2$, **5** exhibits one irreversible oxidation process at $E_p^{ox}$ = 0.56 and 0.49 V, respectively (Figure S1, Supporting Information). A different behaviour was observed in $CH_3CN$ (Figure 5), where a new irreversible anodic wave appears at a significantly lower oxidation potential of $E_p^{ox}$(I) = 0.26 V. A second oxidation process occurs in $CH_3CN$ at $E_p^{ox}$(II) = 0.52 V or $E_p^{ox}$(II) = 0.54 V, depending on the electrolyte. The relative intensity of the two waves varies with the scan rates. Thus, the ratio between the intensity of the second and first oxidation waves increases when the scan rate decreases from 200 to 20 mV s$^{-1}$ (Figure S2, Supporting Information). This behaviour suggests that the oxidation process taking place at the higher potential is related to the product formed at the first oxidation potential by an ECE-type mechanism (ECE = heterogeneous electron transfer, homogeneous chemical reaction and heterogeneous electron transfer, in sequence). Furthermore, the second wave is much higher when $Bu_4NPF_6$ is used instead of $Bu_4NBF_4$ (Figure S3, Supporting Information). This dependence on the electrolyte is suggestive of a chemical reaction that requires its participation and, assuming that the two oxidation waves are linked by an ECE-type mechanism, the rate of the intermediate chemical reaction must be much higher in the case of $PF_6^-$ than in the case of $BF_4^-$. Moreover, the lower potential at which the first redox process occurs in $CH_3CN$, in comparison with the other solvents, indicates that the first oxidation process should be supported somehow by the solvent.

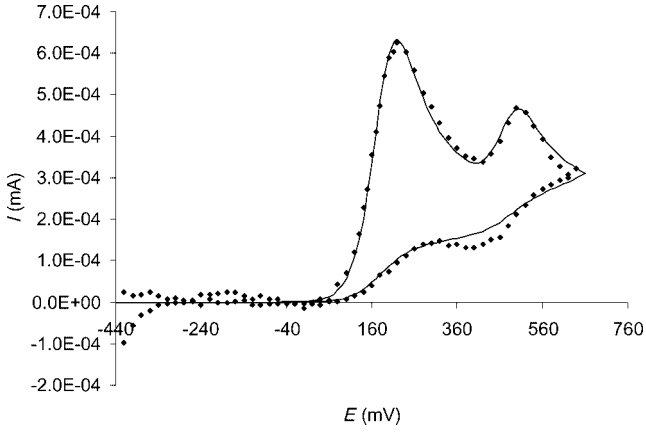


Figure 5. Voltammogram of a solution of **5**, at a Pt disc electrode, at a scan rate of 20 mV s$^{-1}$ in $CH_3CN$ with $Bu_4NBF_4$ as supporting electrolyte. The line corresponds to simulation using Scheme 3 with the parameters shown in Table 4.

Controlled-potential coulometry of **5** in $Bu_4NPF_6$/$CH_2Cl_2$, at a potential of 0.56 V, reveals a complex pattern of current vs. time (Figure S5, Supporting Information) that is compatible with the concomitant occurrence of a redox process involving the exchange of four electrons per molecule and a chemical reaction. On the other hand, coulometry of **5** in $CH_3CN$, performed at the first wave potential (0.26 V), reveals an exchange of two electrons independently of the electrolyte used (Figure S4, Supporting Information).

The experimental results described above may be interpreted as follows. The much lower potential observed for the transfer of the first two electrons in $CH_3CN$ suggests the participation of the solvent, which, as it is a better donor than $CH_2Cl_2$ and thf, makes the metal centre more electron-rich. Based on literature reports, it would be plausible

 © 2007 Wiley-VCH Verlag GmbH & Co. KGaA, Weinheim 

to consider acetonitrile coordination to **5**, leading to the formation of an adduct. This type of compound has been described by Curtis et al., who have reported the addition of soft nucleophiles to $[MoCp(CO)_2]_2$ to give products in which the metal–metal π bonds have been displaced.[33] On the other hand, studies on the oxidation of $[MoCp(CO)_3]_2$ and $[MoCp(CO)_3]^-$ have shown that the cleavage of the dimer occurs with $CH_3CN$ coordination to afford the 19-electron species $[MoCp(CO)_3(CH_3CN)]^{\cdot}$, which are oxidized to $[MoCp(CO)_3(CH_3CN)]^+$ at a lower potential than would be observed for non-stabilized 17-electron species.[34–36] However, efforts to identify a solvent adduct by NMR and IR spectroscopy have proved unsuccessful, and the nature of the interaction with the solvent remains unclear, although it is probable that the oxidation of **5** results in metal–metal bond cleavage and the formation of the cation $[MoCpBz(CO)_2(CH_3CN)_2]^+$.

The intensity of the second oxidation wave observed in $CH_3CN$ depends on the electrolyte counterion. Thus, it is likely that, despite the high dielectric constant of the solvent, ion pairs are formed between the cation $[MoCpBz(CO)_2(CH_3CN)_2]^+$ and the anions $BF_4^-$ or $PF_6^-$, which are present in a large excess in solution. The rate of formation of these species, which are oxidized at the higher potentials (0.52 or 0.54 V), is reflected in the different peaks' intensity (Figure S3, Supporting Information). Considering the molar amount of **5**, the number of electrons involved in this process is two, which corresponds to one electron per molybdenum centre.

In $CH_2Cl_2$ and thf a global transfer of four electrons occurs at a unique potential (0.54 or 0.56 V). Taking into consideration this higher potential, it can be assumed that the first oxidation process is not assisted by solvent coordination. This assumption is consistent with the poorer donor ability of these solvents in comparison with $CH_3CN$. The oxidative cleavage of the metal–metal bond would afford 2 equiv. of $[MoCpBz(CO)_2(L)_2]^+$ (L = $CH_2Cl_2$, thf). At this potential, two electrons are exchanged in succession. As proposed to occur in $CH_3CN$, ion-pair formation and subsequent oxidation attest for the exchange of the remaining two electrons of the overall transfer. Ruiz et al. have reported that the two-electron oxidation of $[M_2Cp_2(CO)_4(\mu\text{-}PPh_2CH_2PPh_2)]$ (M = Mo, W) with $[FeCp_2]X$ (X = $BF_4$, $PF_6$) is followed by reactions with the counterions, which lead to different reaction pathways.[37] Further support for this interpretation is provided by Bullock and co-workers, who reported the formation of M–$FBF_3$ complexes in their mechanistic studies of hydride-transfer reactions of transition metal hydrides,[38] and by our own results on the analogous CpBz systems for which $[MoCpBz(CO)_3(CH_2Cl_2)]^+$ and $[MoCpBz(CO)_3(FBF_3)]$ have been identified and by the CV of $[MoCpBz(CO)_3(FBF_3)]$ in $NBu_4BF_4$/THF, which shows an irreversible anodic wave at 0.54 V.[39]

Simulation of the controlled-potential coulometry results in $CH_2Cl_2$ and $CH_3CN$ and of the voltammograms obtained in $CH_3CN$, using $Bu_4NBF_4$ as electrolyte, has been performed according to Scheme 3. The fittings obtained for the potential coulometry results are presented in the Supporting Information (Figures S4 and S5) and the estimated kinetic parameters in $Bu_4NBF_4$/$CH_3CN$ are listed in Table 4. Figures 5 and S6 (Supporting Information) depict the fittings obtained for this system at three different scan rates.

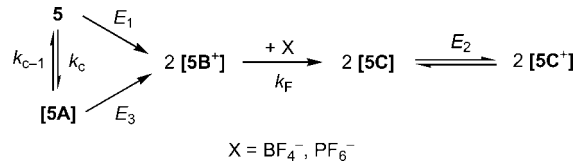


Scheme 3.

Table 4. Kinetic rate constants for the electrochemical behaviour of **5** in $Bu_4NBF_4$/$CH_3CN$, at a Pt disc electrode, based on Scheme 3.

| Electron transfer | Heterogeneous standard rate constant $k_{het}$ [cm s$^{-1}$] | Formal potential $E^{0\prime}$ [V] | Transfer coefficient $\alpha$ |
|---|---|---|---|
| $E_1$ | $1 \times 10^{-2}$ | 0.38 | 0.5 |
| $E_2$ | $1 \times 10^{-2}$ | 0.49 | 0.5 |
| $E_3$ | $1 \times 10^{-2}$ | 0.23 | 0.5 |
| Homogeneous rate constants [s$^{-1}$] | | | |
| $k_{c1}$ | 2 | $k_{c-1}$ | 0.2 |
| $k_F$ | 5.8 | | |

The first issue to be addressed is the difference in behaviour between the voltammograms obtained in $CH_3CN$ and those displayed in $CH_2Cl_2$ and thf. It is clear that the performance in the two latter solvents is similar, thus indicating that a series of electron transfers occurs, followed by some sort of chemical reaction that generates a non-electroactive species since the oxidation wave is irreversible for all scan rates studied. Although the second wave in $CH_3CN$ is significantly coincident with the wave observed in the other two solvents, another wave at lower potential is observed. The best fittings of the simulation to the experimental results obtained in $CH_3CN$ require the acceptance of an equilibrium that converts complex **5** into a new species (**5A**) that undergoes oxidation in the first wave. As discussed above, this species should result from an unidentified interaction with the solvent. The apparent first-order rate constant (the solvent concentration is incorporated in the rate constant value) was estimated as $k_{c1} = 2$ s$^{-1}$, a much lower value than those found for the coordination of acetonitrile to the $[CpMo(CO)_3]^{\cdot}$ radical[35] (ranging from $6.3 \times 10^5$ to $6.0 \times 10^8$ s$^{-1}$) and to the iron centre in $[Fe(\eta^5\text{-}C_6H_7)(CO)_3]^+$[40] ($8.0 \times 10^2$ s$^{-1}$). This first wave involves the sequential exchange of two electrons. It was simulated by an ECE sequence and a homogeneous rate constant for the chemical step in-between the two electron-transfer processes of more than 500 s$^{-1}$ was estimated. In $CH_2Cl_2$ and thf, although it is likely that a similar ECE pattern involving the transfer of two electrons is taking place, the available data is not good enough to estimate the rate constant for the chemical step. However, due to the shape of the voltammetric wave, it is not possible to consider that the two electrons are exchanged in a single step.

 © 2007 Wiley-VCH Verlag GmbH & Co. KGaA, Weinheim 

The voltammograms obtained in $CH_3CN$ also reveal some additional aspects. During the voltammetric experiment, if the scan rate is sufficiently low, all **5A** is oxidised and, during this period, the equilibrium between **5** and **5A** is displaced towards the latter, which is oxidised in a typical CE mechanism (CE = homogeneous chemical reaction preceding heterogeneous electron transfer). At higher scan rates this interconversion has no time to occur and thus, after oxidation of the initial amount of **5A** present, compound **5** is oxidised at the second wave in the same way as in dichloromethane or thf. This explains why the second wave does not disappear, although it remains relatively small, even at very high scan rates. This second wave has, then, two components that result from the oxidation of **5** and from the oxidation of the ion pair formed by the interaction with the electrolyte counterions, as explained above.

The simulation of the voltammograms obtained in $Bu_4NPF_6/CH_3CN$ may be explained using the same set of parameters listed in Table 4, with the exception of the reaction rate constant for the anion. In this case the value obtained is $k_F = 30\ s^{-1}$, which is significantly higher than that obtained in $Bu_4NBF_4/CH_3CN$ (only $5.8\ s^{-1}$). The cationic species $\mathbf{5B}^+$ and $\mathbf{5C}^+$ are considered to decompose through a first-order chemical reaction with estimated constants of $k_{d1} = 12$ and $k_{d2} = 1.5\ s^{-1}$ ($Bu_4NBF_4/CH_3CN$) and $k_{d2} = 10\ s^{-1}$ ($Bu_4NPF_6/CH_3CN$). The simulation results are depicted in Figures 5 and S6 (see Supporting Information).

Previous electrochemical studies on related carbonyl group 6 metal dimers have been dominated by complexes of general formula $[MCp'(CO)_3]_2$, where Cp′ = Cp,[41–43] Cp*,[44] CpR (CpR = $\eta^5$-$C_5H_4R$),[41,45] Fv [Fv = ($\eta^5$:$\eta^5$-$C_5H_4)_2$][45,46] and M = Mo and W. Even though the electron-transfer processes in the hexacarbonyl dimers involve the disruption of the dinuclear unit,[35,41–43,45,46] as proposed for **5**, and the anodic wave at around 0.5 V compares well with those reported for $[MoCp'(CO)_3]_2$, the cathodic shift observed for the first oxidation wave at 0.26 V in $CH_3CN$ has no parallel in the hexacarbonyl dimers' oxidation, and the irreversibility of the redox process for **5** contrasts with the reversible processes reported for $[MoCp'(CO)_3]_2$.

## Conclusion

As a final comment, we conclude that the set of reactions depicted in Scheme 3 explains all the available CV and CPC data, as can be seen from the good fittings obtained at several scan rates. It should be noted, however, that, although this may not be the only possible combination of reaction steps, it is probably the simplest one that fulfils all the experimental observations in agreement with the reported studies found in the literature for analogous systems.

## Experimental Section

**General Procedures and Starting Materials:** All manipulations were carried out under dry nitrogen using standard Schlenk techniques. Solvents were dried and distilled by the usual methods prior to use. Deuteriated solvents were dried with molecular sieves (4 Å), degassed and stored under nitrogen. NMR spectra were recorded at room temperature with a Varian Unity 300 and referenced to the proton and carbon resonances of the residual protonated solvents. Infrared spectra were obtained with a Perkin–Elmer 577 spectrophotometer. Elemental analyses were performed by the Laboratório de Análises do I.S.T., Lisbon, with a Fisons Instruments 1108. The compound HCpBz was prepared according to the described procedure.[5] All other reagents were of commercial grade and used without further purification, except $Bu_4NBF_4$ and $Bu_4NPF_6$, which were of electrochemical grade.

**$[Mo(CpBz)(CO)_3]_2$:** HCpBz (1.01 g, 1.96 mmol) was dissolved in thf (20 mL) and a 1.6 M solution of BuLi in hexanes (1.30 mL, 2.08 mmol) was slowly added at –5 °C. The resulting light-yellow solution was stirred for 1 h and then added to a suspension of $Mo(CO)_6$ (0.88 g, 3.34 mmol) in thf (10 mL) and the yellow solution obtained was refluxed overnight. The red mixture formed was cooled to room temperature and a solution of $Fe(NO_3)_3{\cdot}9H_2O$ (3.00 g) and acetic acid (2 mL) in water (10 mL) was added dropwise. By the end of the addition, a red precipitate had formed and the mixture was stirred at –5 °C for 2 h. The solution was filtered off and the red precipitate was washed with diethyl ether (10 mL). Yield: 95% (1.29 g, 0.93 mmol). $^1H$ NMR ($CD_2Cl_2$, 25 °C): $\delta$ = 7.03–6.89 (m, 15 H, *p*-$C_6H_5$, *m*-$C_6H_5$), 6.78–6.71 (m, 10 H, *o*-$C_6H_5$), 3.88 (s, 10 H, C$H_2$Ph) ppm. $^{13}C\{^1H\}$ NMR ($CD_2Cl_2$, –80 °C): $\delta$ = 234.7 (*C*O), 138.6 (*i*-$C_6H_5$), 128.1 (*o*-$C_6H_5$), 127.7 (*m*-$C_6H_5$), 125.6 (*p*-$C_6H_5$), 109.5 [$C_5(CH_2Ph)_5$], 31.3 (*C*$H_2$Ph) ppm. IR (KBr pellet): $\nu_{C\equiv O}$ = 1932, 1901, 1876 $cm^{-1}$. $C_{86}H_{70}Mo_2O_6$ (1391.4): calcd. C 74.24, H 5.07; found C 74.13, H 5.35.

**$[WCpBz(CO)_3]_2$:** HCpBz (1.07 g, 2.07 mmol) was dissolved in thf (25 mL) and a 1.6 M solution of BuLi in hexanes (1.30 mL, 2.08 mmol) was slowly added at –5 °C. The resulting light yellow solution was stirred for 1 h and was then added to a suspension of $W(CO)_6$ (0.78 g, 2.19 mmol) in thf (10 mL). The yellow solution obtained was refluxed overnight and then cooled to room temperature. A solution of $Fe(NO_3)_3{\cdot}9H_2O$ (3.55 g) and acetic acid (2 mL) in water (10 mL) was added dropwise at –10 °C. The mixture was stirred for 3 h and a precipitate formed. The solution was filtered off and the precipitate washed with diethyl ether (10 mL). The orange solid obtained was separated by filtration and dried. Yield: 31% (0.50 g, 0.32 mmol). Crystals suitable for X-ray diffraction were obtained from a toluene solution. $^1H$ NMR ($CD_2Cl_2$, 25 °C): $\delta$ = 7.01–6.99 (m, 15 H, *p*-$C_6H_5$, *m*-$C_6H_5$), 6.71–6.70 (m, 10 H, *o*-$C_6H_5$), 3.92 (s, 10 H, C$H_2$Ph) ppm. $^{13}C\{^1H\}$ NMR ($CD_2Cl_2$, 25 °C): $\delta$ = 224.3 (*C*O), 139.3 (*i*-$C_6H_5$), 129.3 (*o*-$C_6H_5$), 128.4 (*m*-$C_6H_5$), 126.5 (*p*-$C_6H_5$), 109.2 [$C_5(CH_2Ph)_5$], 32.8 (*C*$H_2$Ph) ppm. IR (KBr pellet): $\nu_{C\equiv O}$ = 1928, 1897, 1868 $cm^{-1}$. $C_{86}H_{70}O_6W_2$ (1567.2): calcd. C 65.91, H 4.50; found C 65.89, H 4.76.

**$[MoCpBz(CO)_2]_2$:** A solution of $Li[MoCpBz(CO)_3]$ (1.81 g, 2.57 mmol) in thf was treated with $CH_2{=}CHCH_2Br$ (0.27 mL, 3.08 mmol) and heated overnight at 50 °C, whereupon the initial red-brown solution turned red. The volatiles were removed in vacuo to give an oily material, which was extracted with $Et_2O$. The solution was concentrated and cooled to –20 °C, which led to the formation of orange-red crystals in 76% yield (1.30 g, 0.97 mmol). In an alternative procedure, $[Mo(CpBz)(CO)_3]_2$ (1.76 g, 1.26 mmol) was refluxed overnight in toluene (40 mL) and the solution was then cooled to room temperature and filtered. Solvent removal afforded a red microcrystalline solid in 91% yield (1.54 g, 1.15 mmol). $^1H$ NMR ($C_6D_6$): $\delta$ = 6.85–6.84 (m, 15 H, *p*-$C_6H_5$, *m*-$C_6H_5$), 6.70–6.69 (m, 10 H, *o*-$C_6H_5$), 4.16 (s, 10 H, C$H_2$ Ph) ppm.

 © 2007 Wiley-VCH Verlag GmbH & Co. KGaA, Weinheim 

$^{13}C\{^1H\}$ NMR ($C_6D_6$, 25 °C): $\delta$ = 239.3 (*C*O), 139.4 (*i*-$C_6H_5$), 129.3 (*o*-$C_6H_5$), 128.3 (*m*-$C_6H_5$), 126.3 (*p*-$C_6H_5$), 109.3 [$C_5(CH_2Ph)_5$], 32.2 ($CH_2Ph$) ppm. $^1H$ NMR ($CDCl_3$): $\delta$ = 6.95–6.92 (m, 15 H, *p*-$C_6H_5$, *m*-$C_6H_5$), 6.63–6.60 (m, 10 H, *o*-$C_6H_5$), 3.87 (s, 10 H, $CH_2Ph$) ppm. $^{13}C\{^1H\}$ NMR ($CDCl_3$, 25 °C): $\delta$ = 238.6 (*C*O), 138.9 (*i*-$C_6H_5$), 128.8 (*o*-$C_6H_5$), 128.0 (*m*-$C_6H_5$), 126.0 (*p*-$C_6H_5$), 108.6 ($C_5\{CH_2Ph\}_5$), 31.5 ($CH_2Ph$) ppm. IR (KBr pellet): $\nu_{C\equiv O}$ = 1878 (s), 1821 (s) $cm^{-1}$. $C_{84}H_{70}Mo_2O_4$ (1335.3): calcd. C 75.55, H 5.28; found C 75.05, H 5.44.

**[MoH(CpBz)(CO)$_3$]:** A 1.6 M solution of BuLi in hexanes (1.4 mL, 2.24 mmol) was added dropwise, at –5 °C, to a solution of HCpBz (1.10 g, 2.13 mmol) in thf (25 mL). The reaction mixture was stirred for 1 h and added to a suspension of $[Mo(CO)_6]$ (0.68 g, 2.57 mmol) in thf (10 mL) and the mixture was refluxed for 24 h. After cooling to room temperature, glacial acetic acid (1 mL; 11 mmol) was added and the solution was stirred for 12 h. The solvent was removed under vacuum and the brown solid obtained extracted with diethyl ether and filtered. Concentration and cooling to 4 °C yielded yellow crystals. Yield: 98% (1.47 g). $^1H$ NMR ([$D_8$]-toluene): $\delta$ = 6.90 (m, 15 H, *p*-$C_6H_5$, *m*-$C_6H_5$), 6.72 (m, 10 H, *o*-$C_6H_5$), 3.66 (s, 10 H, $CH_2Ph$), –4.85 (s, 1 H, Mo-*H*) ppm. $^{13}C\{^1H\}$ NMR ([$D_8$]toluene): $\delta$ = 228.5 (*C*O), 140.1 (*i*-$C_6H_5$), 128.9 (*o*-$C_6H_5$), 128.3 (*m*-$C_6H_5$), 126.4 (*p*-$C_6H_5$), 111.4 [$C_5(CH_2Ph)_5$], 32.6 ($CH_2Ph$) ppm. IR (KBr pellet): $\nu_{C\equiv O}$ = 2008 (s), 1928 (s) $cm^{-1}$. $C_{43}H_{36}MoO_3$ (696.7): calcd. C 74.13, H 5.21; found C 74.11, H 5.82.

**[WH(CpBz)(CO)$_3$]:** A 1.6 M solution of BuLi in hexanes (1.2 mL; 1.92 mmol) was added dropwise, at –5 °C, to a solution of HCpBz (1.00 g, 1.94 mmol) in thf (20 mL). The reaction mixture was then stirred for 1 h and the solvent was removed. After the addition of dmf (20 mL), the resulting solution was added to a suspension of $[W(CO)_6]$ (0.71 g, 2.00 mmol) in dmf (10 mL). The mixture was then heated at 80 °C for 24 h and cooled to room temperature. Glacial acetic acid (1 mL, 11 mmol) was then added and the solution stirred overnight. The volatiles were removed under vacuum and the brown solid obtained extracted with diethyl ether to give a yellowish solution, which was filtered and the solvents were evaporated to dryness. Yield: 95% (1.47 g). $^1H$ NMR ([$D_8$]toluene): $\delta$ = 6.88 (m, 15 H, *p*-$C_6H_5$, *m*-$C_6H_5$), 6.68 (m, 10 H, *o*-$C_6H_5$), 3.69 (s, 10 H, $CH_2Ph$), –6.31 (s, 1 H, W-*H*) ppm. $^{13}C\{^1H\}$ NMR ([$D_8$]-toluene): $\delta$ = 219.4 (*C*O), 139.9 (*i*-$C_6H_5$), 128.9 (*o*-$C_6H_5$), 128.3 (*m*-$C_6H_5$), 126.5 (*p*-$C_6H_5$), 109.9 [$C_5(CH_2Ph)_5$], 32.7 ($CH_2Ph$) ppm. IR (KBr pellet): $\nu_{C\equiv O}$ = 2008 (s), 1901 (s) $cm^{-1}$. $C_{43}H_{36}O_3W$ (784.6): calcd. C 65.82, H 4.62; found C 65.92, H 4.80.

**General Procedures for X-ray Crystallography:** Pertinent details for the individual compounds can be found in Tables 5 and 6. Crystallographic data for compounds **4**, **6** and **7** were collected using graphite-monochromated Mo-$K_\alpha$ radiation ($\lambda$ = 0.71069 Å) with a Bruker AXS-KAPPA APEX II area detector diffractometer equipped with an Oxford Cryosystem open-flow nitrogen cryostat; data were collected at 150 K for compounds **4** and **6** and at 130 K for compound **7**. Cell parameters were retrieved using the Bruker

Table 5. Crystallographic data for **4** and **5**.

| | **4** | **5** |
|---|---|---|
| Empirical formula | $C_{86}H_{70}O_6W_2$ | $C_{84}H_{68}Mo_2O_4$ |
| Formula mass | 1567.12 | 1335.28 |
| Temperature [K] | 130(2) | 293(2) |
| Wavelength [Å] | 0.71069 | 0.71069 |
| Crystal system | triclinic | monoclinic |
| Space group | $P\bar{1}$ | $P2_1/c$ |
| *a* [Å] | 12.131(3) | 11.322(5) |
| *b* [Å] | 12.154(2) | 13.817(5) |
| *c* [Å] | 12.587(3) | 21.630(7) |
| $\alpha$ [°] | 86.157(9) | 90 |
| $\beta$ [°] | 79.061(10) | 102.36(2) |
| $\gamma$ [°] | 63.143(9) | 90 |
| Volume [Å$^3$] | 1625.2(7) | 3305(2) |
| *Z* | 2 (half molecule) | 4 (half molecule) |
| $D_{calcd.}$ [g cm$^{-3}$] | 1.601 | 1.342 |
| Absorption coefficient | 3.595 mm$^{-1}$ | 0.432 mm$^{-1}$ |
| *F*(000) | 782 | 1380 |
| Crystal size [mm] | 0.2 × 0.2 × 0.2 | – |
| Crystal morphology | cube | needle |
| Colour | orange | red |
| $\theta$ range for data collection [°] | 1.9–24.2 | 1.76–25.99 |
| Limiting indices | $-12 \le h \le 12$ | $0 \le h \le 13$ |
| | $-12 \le k \le 12$ | $0 \le k \le 17$ |
| | $-12 \le l \le 13$ | $-26 \le l \le 26$ |
| Reflections collected/unique | 9012/3749 | 6779/6442 |
| | [*R*(int) = 0.1110] | [*R*(int) = 0.0231] |
| Completeness to $\theta$ | 71.9% ($\theta$ = 24.2°) | 99.4% ($\theta$ = 25.99°) |
| Refinement method | full-matrix least-squares on $F^2$ | |
| Data/restraints/parameters | 3749/6/355 | 6442/0/406 |
| Goodness of fit on $F^2$ | 1.020 | 1.017 |
| Final *R* indices [$I > 2\sigma(I)$] | *R*1 = 0.0780, *wR*2 = 0.1796 | *R*1 = 0.0340, *wR*2 = 0.0787 |
| *R* indices (all data) | *R*1 = 0.1224, *wR*2 = 0.2087 | *R*1 = 0.0564, *wR*2 = 0.0856 |
| Extinct. coefficient | 0.0133(2) | none |
| Absorption correction | multiscan | none |
| Largest difference peak/hole [e Å$^{-3}$] | 3.75/–3.59 | 0.526/–0.491 |

 © 2007 Wiley-VCH Verlag GmbH & Co. KGaA, Weinheim 

Table 6. Crystallographic data for **6** and **7**.

| | **6** | **7** |
|---|---|---|
| Empirical formula | $C_{43}H_{36}MoO_3$ | $C_{43}H_{36}O_3W$ |
| Formula mass | 696.66 | 784.57 |
| Temperature [K] | 150(2) | 130(2) |
| Wavelength [Å] | 0.71069 | 0.71069 |
| Crystal system | monoclinic | monoclinic |
| Space group | $P2_1/n$ | $P2_1/n$ |
| $a$ [Å] | 13.1690(9) | 13.1880(9) |
| $b$ [Å] | 15.2930(10) | 15.2970(10) |
| $c$ [Å] | 16.9420(10) | 16.9500(12) |
| $\beta$ [°] | 95.396(3) | 95.302(3) |
| Volume [Å$^3$] | 3396.9(4) | 3404.8(4) |
| $Z$ | 4 | 4 |
| $D_{calcd.}$ [g cm$^{-3}$] | 1.362 | 1.531 |
| Absorption coefficient | 0.426 mm$^{-1}$ | 3.432 mm$^{-1}$ |
| $F$(000) | 1440 | 1568 |
| Crystal size [mm] | $0.40 \times 0.20 \times 0.05$ | $0.20 \times 0.10 \times 0.10$ |
| Crystal morphology | prism | prism |
| Colour | yellow | yellow |
| $\theta$ range for data collection [°] | 1.80–30.49 | 1.80–39.94 |
| Limiting indices | $-18 \le h \le 18$ | $-23 \le h \le 23$ |
| | $-21 \le k \le 21$ | $-24 \le k \le 27$ |
| | $-24 \le l \le 24$ | $-30 \le l \le 28$ |
| Reflections collected/unique | 94559/10331 | 101111/20943 |
| | [$R$(int) = 0.0620] | [$R$(int) = 0.0366] |
| Completeness to $\theta$ | 99.7% | 99.6% |
| Refinement method | full-matrix least-squares on $F^2$ | |
| Data/restraints/parameters | 10331/0/428 | 20943/0/428 |
| Goodness of fit on $F^2$ | 1.088 | 1.018 |
| Final $R$ indices [$I > 2\sigma(I)$] | $R1$ = 0.0303, $wR2$ = 0.0814 | $R1$ = 0.0285, $wR2$ = 0.0595 |
| $R$ indices (all data) | $R1$ = 0.0472, $wR2$ = 0.0950 | $R1$ = 0.0506, $wR2$ = 0.0667 |
| Absorption correction | none | none |
| Largest difference peak/hole [e Å$^{-3}$] | 0.447/–0.417 | 1.062/–0.903 |

SMART software and refined using SAINT with all observed reflections. Absorption corrections were applied using SADABS. Data for compound **5** were collected at room temperature with a MACH3-Bruker Nonius diffractometer equipped with an Mo-$K_\alpha$ radiation ($\lambda$ = 0.71069 Å) source. Data were corrected for Lorentz and polarisation effects but not for absorption. Cell dimensions were determined from the setting angles of 25 reflections, within $\theta$ values of 15–17°. The structures were solved by direct methods using either SHELXS-97[47] or SIR 97[48] and refined using full-matrix least-squares refinement against $F^2$ using SHELXL-97.[47] All programs are included in the package of programs WINGX, version 1.64.05.[49] All non-hydrogen atoms were refined anisotropically and all hydrogen atoms except the hydride ions were inserted in idealised positions and allowed to refine as riding on the parent carbon atom. The molecular structures were produced with ORTEP3 for Windows,[50] included in the software package. CCDC-616390, -617703, -616388 and -616389 for complexes **4**, **5**, **6** and **7**, respectively, contain the supplementary crystallographic data for this paper. These data can be obtained free of charge from The Cambridge Crystallographic Data Centre via www.ccdc.cam.ac.uk/data_request/cif.

**General Procedures for Electrochemistry:** Cyclic voltammetric and controlled-potential coulometry measurements were carried out using a Radiometer DEA 101 Digital Electrochemical Analyser interfaced with an IMT 102 Electrochemical Interface. For cyclic voltammetry measurements, a three-electrode cell with a total volume of around 5 mL was used. A platinum disc electrode was used as working electrode, the counter-electrode was a Pt wire and a silver wire was used as a pseudo-reference electrode; this electrode was kept in a separate compartment and connected to the main compartment by a Luggin capillary. The ferrocene/ferrocenium couple was used as internal standard to measure wave potentials, according to IUPAC recommendations.[51] The controlled-potential coulometry electrochemical cell had a three-compartment design. A large platinum gauze electrode was employed as working electrode, the pseudo-reference electrode was similar to the one used for cyclic voltammetry measurements and it was also connected to the main compartment by a Luggin capillary. The counter electrode was also a platinum gauze electrode and it was kept in a different compartment which was connected to the main compartment by a sintered-glass separation disk. Concentrations of around 0.2 M were used for cyclic voltammetry and 0.3 M for electrolysis experiments. Concentrations in the range $1.1–1.3 \times 10^{-3}$ M were used for the complexes studied. All experiments were carried out at 25 °C in the absence of oxygen. Dry nitrogen was bubbled through the solution in the cell before measurements.

**Cyclic Voltammetry Simulation:** Digital simulation of cyclic voltammograms was carried out using a custom-made program, developed in Turbo Pascal 6 (© Borland Inc.) and run on a Pentium IV computer at 2.4 GHz. The solution of the partial differential equations describing the reaction ion-diffusion processes of all the species involved in the mechanism was performed by the method of lines, using a non-uniform space grid.[52] Space discretisation was performed upon a diffusion layer ($\delta$) computed according to the formula $\partial = \sqrt{(\pi D \tau)}$, where D is the diffusion coefficient and $\tau$ is the duration of each scan.[53] The time-course integration of the

 © 2007 Wiley-VCH Verlag GmbH & Co. KGaA, Weinheim 

differential equations resulting from the semi-discretisation process of the space coordinate was carried out using a fourth-order Runge–Kutte method. Parameter estimation was performed by visual fitting of simulated data to a series of base-line-corrected experimental voltammograms, using a single set of model parameters. In this procedure, the parameters involved in the model were systematically varied so as to obtain the best possible agreement between the simulated and the experimental values. Various mechanisms were tried, starting from a simple ECE scheme, which was refined so that the most relevant features of the voltammetric response were explained, resulting in the proposed scheme.

**Controlled-Potential Coulometry:** Digital simulation of the experiments was carried out in Excel (© Microsoft Corporation). The relevant differential equations were solved using the Euler method and the parameters were estimated by least-squares regression using the Solver utility to minimize the sum of the square of the residuals.

**Supporting Information** (see footnote on the first page of this article): Voltammograms of **5** in different solvents (thf, $CH_2Cl_2$ and $CH_3CN$) at different scan rates and with $Bu_4NBF_4$ or $Bu_4NPF_6$ as supporting electrolyte; graphics of current vs. time for controlled potential coulometry of **5**; simulation curves of CV and CPC results.

## Acknowledgments

The authors would like to thank the Fundação para a Ciência e a Tecnologia, Portugal for funding this work (research project POCI/QUI/55744/2004 and research grant SFRH/BD/13374/2003).

[1] A. M. Martins, C. C. Romão, M. Abrantes, M. C. Azevedo, J. L. Cui, A. R. Dias, M. T. Duarte, M. A. Lemos, T. Lourenco, R. Poli, *Organometallics* **2005**, *24*, 2582–2589.
[2] A. M. Martins, R. Branquinho, J. L. Cui, A. R. Dias, M. T. Duarte, J. Fernandes, S. S. Rodrigues, *J. Organomet. Chem.* **2004**, *689*, 2368–2376.
[3] R. M. Bullock, M. H. Voges, *J. Am. Chem. Soc.* **2000**, *122*, 12594–12595.
[4] B. F. M. Kimmich, P. J. Fagan, E. Hauptman, W. J. Marshall, R. M. Bullock, *Organometallics* **2005**, *24*, 6220–6229.
[5] L. C. Song, L. Y. Zhang, Q. M. Hu, X. Y. Huang, *Inorg. Chim. Acta* **1995**, *230*, 127–131.
[6] R. D. Adams, F. A. Cotton, *Inorg. Chim. Acta* **1973**, *7*, 153–156.
[7] A. S. Goldman, D. R. Tyler, *J. Am. Chem. Soc.* **1986**, *108*, 89–94.
[8] R. D. Adams, M. Brice, F. A. Cotton, *J. Am. Chem. Soc.* **1973**, *95*, 6594–6602.
[9] A. L. Rheingol, J. Harper, *Acta Crystallogr., Sect. C* **1991**, *47*, 184–186.
[10] R. B. King, M. B. Bisnette, *J. Organomet. Chem.* **1967**, *8*, 287–297.
[11] M. Cousins, M. L. H. Green, *J. Chem. Soc.* **1963**, 889.
[12] M. L. H. Green, A. N. Stear, *J. Organomet. Chem.* **1964**, *1*, 230–234.
[13] L.-C. Song, J.-Q. Wang, W.-J. Zhao, Q.-M. Hu, Y.-Q. Fang, S.-J. Zhang, R.-J. Wang, H.-G. Wang, *J. Organomet. Chem.* **1993**, *453*, 105–109.
[14] R. B. King, A. Fronzaglia, *Inorg. Chem.* **1966**, *5*, 1837–1846.
[15] S. P. Nolan, C. D. Hoff, J. T. Landrum, *J. Organomet. Chem.* **1985**, *282*, 357–362.
[16] R. D. Adams, D. M. Collins, F. A. Cotton, *Inorg. Chem.* **1974**, *13*, 1086–1090.
[17] A. Avey, S. C. Tenhaeff, T. J. R. Weakley, D. R. Tyler, *Organometallics* **1991**, *10*, 3607–3613.
[18] H. G. Alt, J. S. Han, R. D. Rogers, *J. Organomet. Chem.* **1993**, *454*, 165–172.
[19] T. J. R. Weakley, A. A. Avey Jr, D. R. Tyler, *Acta Crystallogr., Sect. C* **1992**, *48*, 154–155.
[20] H. Sitzmann, G. Wolmershauser, *Chem. Ber.* **1994**, *127*, 1335–1342.
[21] A. M. Martins, M. M. Marques, J. R. Ascenso, A. R. Dias, M. T. Duarte, A. C. Fernandes, S. Fernandes, M. J. Ferreira, I. Matos, M. C. Oliveira, S. S. Rodrigues, C. Wilson, *J. Organomet. Chem.* **2005**, *690*, 874–884.
[22] G. Huttner, H. H. Brintzinger, L. G. Bell, P. Friedrich, V. Bejenke, D. Neugebauer, *J. Organomet. Chem.* **1978**, *145*, 329–333.
[23] J. R. Ascenso, C. G. de Azevedo, I. S. Goncalves, E. Herdtweck, D. S. Moreno, M. Pessanha, C. C. Romão, *Organometallics* **1995**, *14*, 3901–3919.
[24] R. J. Klingler, W. M. Butler, M. D. Curtis, *J. Am. Chem. Soc.* **1978**, *100*, 5034–5039.
[25] J. Potenza, P. Giordano, D. Mastropa, A. Efraty, *Inorg. Chem.* **1974**, *13*, 2540–2544.
[26] M. D. Curtis, W. M. Butler, *J. Organomet. Chem.* **1978**, *155*, 131–145.
[27] M. A. Greaney, J. S. Merola, T. R. Halbert, *Organometallics* **1985**, *4*, 2057–2058.
[28] J. S. Huang, L. F. Dahl, *J. Organomet. Chem.* **1983**, *243*, 57–68.
[29] F. Shafiq, D. J. Szalda, C. Creutz, R. M. Bullock, *Organometallics* **2000**, *19*, 824–833.
[30] M. Calvo, P. Gomez-Sal, A. Manzanero, P. Royo, *Polyhedron* **1998**, *17*, 1081–1089.
[31] L. Brammer, D. Zhao, R. M. Bullock, R. K. Mcmullan, *Inorg. Chem.* **1993**, *32*, 4819–4824.
[32] P. Leoni, E. Grilli, M. Pasquali, M. Tomassini, *J. Chem. Soc., Dalton Trans.* **1986**, 1041–1043.
[33] R. J. Klingler, W. Butler, M. D. Curtis, *J. Am. Chem. Soc.* **1975**, *97*, 3535–3536.
[34] K. M. Kadish, D. A. Lacombe, J. E. Anderson, *Inorg. Chem.* **1986**, *25*, 2246–2250.
[35] M. Tilset, *Inorg. Chem.* **1994**, *33*, 3121–3126.
[36] J. R. Pugh, T. J. Meyer, *J. Am. Chem. Soc.* **1992**, *114*, 3784–3792.
[37] M. A. Alvarez, G. Garcia, M. E. Garcia, V. Riera, M. A. Ruiz, M. Lanfranchi, A. Tiripicchio, *Organometallics* **1999**, *18*, 4509–4517.
[38] T. Y. Cheng, B. S. Brunschwig, R. M. Bullock, *J. Am. Chem. Soc.* **1998**, *120*, 13121–13137.
[39] S. Namorado, J. R. Ascenso, A. M. Martins, unpublished work.
[40] M. F. N. N. Carvalho, M. A. N. D. A. Lemos, L. F. Veiros, G. R. Stephenson, *J. Organomet. Chem.* **2001**, *632*, 49–57.
[41] D. C. Barbini, P. S. Tanner, T. D. Francone, K. B. Furst, W. E. Jones, *Inorg. Chem.* **1996**, *35*, 4017–4022.
[42] K. M. Kadish, D. A. Lacombe, J. E. Anderson, *Inorg. Chem.* **1986**, *25*, 2246–2250.
[43] J. R. Pugh, T. J. Meyer, *J. Am. Chem. Soc.* **1992**, *114*, 3784–3792.
[44] A. Asdar, M. J. Tudoret, C. Lapinte, *J. Organomet. Chem.* **1988**, *349*, 353–366.
[45] M. L. Marcos, C. Moreno, R. M. Medina, M. J. Macazaga, S. Delgado, J. Gonzalez-Velasco, *J. Organomet. Chem.* **1998**, *568*, 185–196.
[46] R. Moulton, T. W. Weidman, K. P. C. Vollhardt, A. J. Bard, *Inorg. Chem.* **1986**, *25*, 1846–1851.
[47] G. M. Sheldrick, *SHELXL-97, A program for refining crystal structures*, University of Göttingen, Germany, **1998**.
[48] A. Altomare, M. C. Burla, M. Camalli, G. Cascarano, C. Giacovazzo, A. Guagliardi, A. G. G. Moliterni, G. Polidori, R. Sparna, *J. Appl. Crystallogr.* **1999**, *32*, 115–119.

 © 2007 Wiley-VCH Verlag GmbH & Co. KGaA, Weinheim 

[49] L. J. Farrugia, *J. Appl. Crystallogr.* **1999**, *32*, 837–838.
[50] L. J. Farrugia, *J. Appl. Crystallogr.* **1997**, *30*, 565.
[51] G. Gritzner, J. Kuta, *J. Electrochim. Acta* **1984**, *29*, 869–873.
[52] M. A. N. D. A. Lemos, A. J. L. Pombeiro, in *Molecular Electrochemistry of Inorganic, Bioinorganic and Organometallic Compounds*, vol. 385 (Eds.: A. J. L. Pombeiro, J. A. McCleverty), Kluwer Academic Publishers, Dordrecht, **1993**, p. 477.
[53] D. Britz, *Digital Simulation in Electrochemistry*, 2nd ed., Springer-Verlag, Berlin, **1988**.

Received: August 21, 2006
Published Online: February 9, 2007

 © 2007 Wiley-VCH Verlag GmbH & Co. KGaA, Weinheim 

DOI: 10.1002/ejic.200601085

# Carbon–Hydrogen Bond Activation of Arenes by a [Bis(oxazolinyl)phenyl]-rhodium(III) Acetate Complex

**Jun-ichi Ito[a] and Hisao Nishiyama*[a]**

**Keywords:** C–H activation / Arenes / Rhodium / Substituent effects

Thermolysis of the rhodium(III) complex [(*dm*-Phebox-*dm*)-$Rh(OAc)_2(H_2O)$] [**1**; *dm*-Phebox-*dm* = 2,6-bis(4,4-dimethyloxazolinyl)phenyl] in various arenes results in the formation of the corresponding aryl complexes [(*dm*-Phebox-*dm*)Rh(Ar)($\kappa^2$-OAc)] [Ar = $C_6H_5$ (**2**), 3,5-$Me_2C_6H_3$ (**3**), 3,4-$Me_2C_6H_3$ (**4**), $C_6H_4Me$ (**5**), $C_6H_4CF_3$ (**6**), $C_6H_4OMe$ (**7**), $C_6H_4COMe$ (**8**), $C_6H_4Cl$ (**9**)]. The reaction of **1** with monosubstituted benzenes such as toluene, anisole, acetophenone, trifluorotoluene, and chlorobenzene produces a mixture of *meta*- and *para*-activated complexes, the ratio of which depends on the substituents on the benzene ring. The relative rate of the reaction of **1** with monosubstituted benzenes $C_6H_5X$ was determined to be: X = OMe (1.8) > COMe (1.6) > $CF_3$ (1.2), Cl (1.2) > $CH_3$ (1). The acetato ligand of **1** appears to be essential for C–H bond activation of arenes as no reaction of the $Rh^{III}$ complex [(*dm*-Phebox-*dm*)$RhCl_2(H_2O)$] is observed in chlorobenzene at 120 °C. The first-order rate constants obtained by thermolysis of **1** in [$D_8$]toluene at 97.1–116.5 °C yielded the following activation parameters: $\Delta H^{\ddagger}$ = 22(2) kcal mol$^{-1}$, $\Delta S^{\ddagger}$ = –24(5) cal mol$^{-1}$ K$^{-1}$. The kinetic isotope effect for the C–H bond activation of toluene by **1** was determined to be $k_H/k_D$ = 5.4 at 100 °C. These data suggest that the rate-determining step involves the C–H bond cleavage with a rigid, cyclic transition structure.
(© Wiley-VCH Verlag GmbH & Co. KGaA, 69451 Weinheim, Germany, 2007)

## Introduction

Intermolecular C–H bond activation has been considered to be an essential step for functionalization of unreactive hydrocarbons due to their relatively high dissociation energies.[1] Such transformations are attractive from a synthetic point of view due to the possibility of using simple and naturally abundant compounds to provide more useful and complex products.[2] Thus far, a number of studies have focused on the mechanism involving oxidative addition, σ-bond metathesis, 1,2-addition, and electrophilic activation.[3] Recently, electron-deficient Pd complexes bearing acetato ligands have been found to be reactive for inter- and intramolecular C–H bond activation and have been applied to a suitable precursor for catalytic reactions.[4] Furthermore, computational studies of the C–H bond activation by $Pd(OAc)_2$ and related complexes have suggested a mechanism whereby the acetato ligand assists the heterolytic cleavage through a six-membered cyclic transition state, as shown in Scheme 1.[5] Although Rh and Ir complexes have been known to undergo oxidative addition to the electron-rich metal center for some time,[3] only very recently have Periana and co-workers reported the C–H bond cleavage of arenes by the action of the alkoxy ligands of the $Ir^{III}$ complexes [$Ir(acac)_2(OR)L$].[6] Similarly, Davies and co-workers have reported the intramolecular C–H bond activation of {Cp*M} (M = Rh, Ir) species.[7] Such base-assisted C–H bond activation is very attractive as an alternative mechanism to oxidative addition. In this context, the $Rh^{III}$ complexes [(Phebox)$Rh(OAc)_2(H_2O)$] [Phebox = 2,6-bis(oxazolinyl)phenyl],[8] which possess an $Rh^{III}$ center and meridional stereochemistry, could be expected to combine the functions of a Lewis acid for coordination of the substrate and a base to act as a proton acceptor during the C–H bond cleavage step (Scheme 2). The $Rh^{III}$ acetate complex would therefore provide different information regarding the coordination chemistry in the meridional reaction field compared with the structurally related Rh and Ir complexes having a phosphane-based ligand (PCP- and PNP-type li-

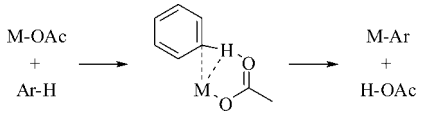


Scheme 1.

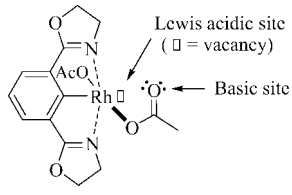


Scheme 2.

[a] Department of Applied Chemistry, Graduate School of Engineering, Nagoya University,
Chikusa, Nagoya 464-8603, Japan
Fax: +81-52-789-3209
E-mail: hnishi@apchem.nagoya-u.ac.jp


© 2007 Wiley-VCH Verlag GmbH & Co. KGaA, Weinheim

gands).[9] We report herein an intermolecular C–H bond activation reaction of simple arenes to a (Phebox)$Rh^{III}$ acetate complex.

## Results and Discussion

When a solution of the $Rh^{III}$ acetate complex [(*dm*-Phebox-*dm*)$Rh(OAc)_2(H_2O)$] [**1**; *dm*-Phebox-*dm* = 2,6-bis(4,4-dimethyloxazolinyl)phenyl][8b] in benzene was heated at 90 °C for 144 h, C–H bond activation took place to produce the novel phenylrhodium(III) complex [(*dm*-Phebox-*dm*)-Rh(Ph)($\kappa^2$-OAc)] (**2**) in 60% isolated yield (Scheme 3). Thermolysis of **1** in *m*- and *o*-xylenes also gave the corresponding arylRh$^{III}$ complexes [(*dm*-Phebox-*dm*)Rh(Ar)($\kappa^2$-OAc)] [Ar = 3,5-$Me_2C_6H_3$ (**3**), 3,4-$Me_2C_6H_3$ (**4**)] in 56% and 64% yields, respectively (Scheme 3). Since products arising from *ortho*-C–H bond activation of xylenes were not detected, the regioselectivity of the reactions must be strongly affected by the steric hindrance in the coordination environment of the Phebox ligand. The authentic phenyl complex **2** could be synthesized in 82% yield by treating **1** with $PhB(OH)_2$.

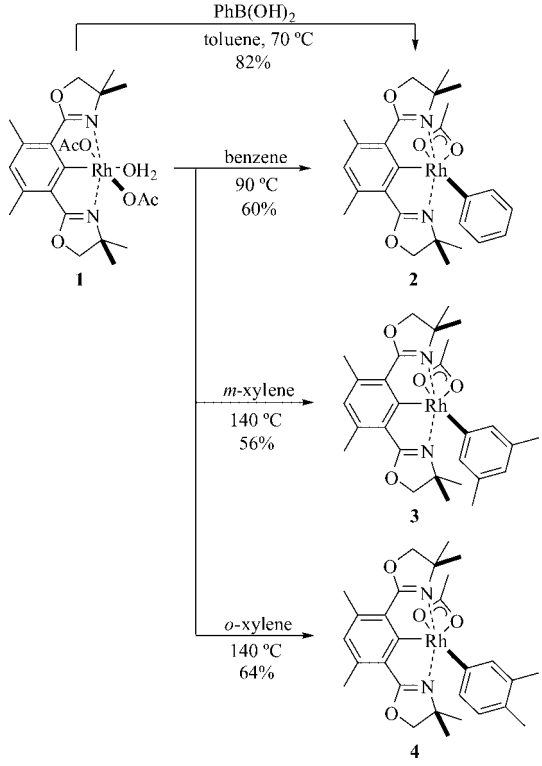


Scheme 3.

An X-ray analysis of **3** confirmed its structure as an arylRh$^{III}$ complex (Figure 1). The orientation of the aryl ligand is perpendicular to the Phebox plane [C(1)–Rh(1)–C(19) 91.81(9)°]. The difference in angles around the *ipso*-carbon atom of the aryl ligand [C(20)–C(19)–Rh(1) 128.83(17), C(24)–C(19)–Rh(1) 113.55(17)°] indicates that the aryl ring is bent slightly towards the acetato ligand, probably due to steric repulsion with the Phebox ligand. The Rh(1)–C(19) bond length of 1.993(2) Å is comparable to those in other arylRh$^{III}$ complexes.[10] The $\kappa^2$-acetato ligand makes the Rh center saturated.

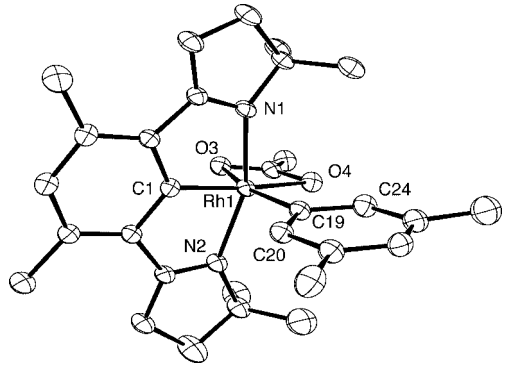


Figure 1. Molecular structure of **3** with ellipsoids at the 40% probability level (one of the molecules in the unit cell has been omitted for clarity). Selected bond lengths [Å] and angles [°]: Rh(1)–C(1) 1.919(2), Rh(1)–C(19) 1.993(2), Rh(1)–O(3) 2.2687(16), Rh(1)–O(4) 2.2673(16), Rh(1)–N(1) 2.0753(18), Rh(1)–N(2) 2.0580(18); N(2)–Rh(1)–N(1) 158.72(7), C(20)–C(19)–Rh(1) 128.83(17), C(24)–C(19)–Rh(1) 113.55(17).

Since the substituent on the benzene ring has been shown to affect the selectivity of C–H bond activation, we examined the reactivity of **1** toward the monosubstituted benzenes $C_6H_5X$ (X = Me, $CF_3$, OMe, COMe, Cl; Scheme 4). Thermolysis of **1** in toluene resulted in the formation of *para*- and *meta*-tolyl complexes **5p** and **5m** in 64% isolated yield in a 1:1.4 ratio, respectively. We did not detect the *ortho*-C–H activated product, as observed in the reaction of xylenes. We also prepared the authentic tolyl complex **5p** as a single isomer by the reaction of **1** with *p*-tolylboronic acid (Figure 2). A similar C–H bond activation of electron-deficient $C_6H_5CF_3$ took place to produce a 1:7.8 mixture of **6p** and **6m**, respectively, in 76% yield. In the cases of anisole and acetophenone, the formation of *para*- and *meta*-activated complexes was observed. This suggests that precoor-

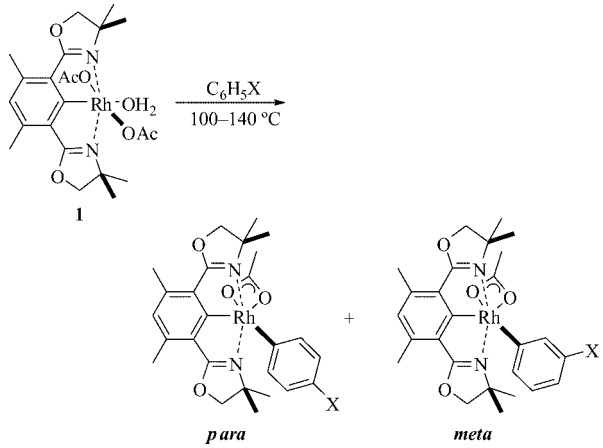


Scheme 4.

 © 2007 Wiley-VCH Verlag GmbH & Co. KGaA, Weinheim 

dination of the carbonyl and methoxy groups to the Rh center is not important for the selectivity of the C–H bond activation.[11] Reaction of **1** with $C_6H_5Cl$ produced the *para*- and *meta*-activated complexes **9p** and **9m**. The C–Cl bond-activated complex was not detected in the (Phebox)-Rh system.[12] Selectivity for the *para* position in preference to the *meta* position was observed for electron-rich toluene and anisole, whereas the inverse selectivity was observed for electron-deficient trifluorotoluene and acetophenone. This tendency is due to electrophilic aromatic substitution reactions. It is noteworthy that interconversion between **5p** and **5m** is inhibited, as shown by no observation of isomerization of **5p** in toluene at 120 °C for 24 h.

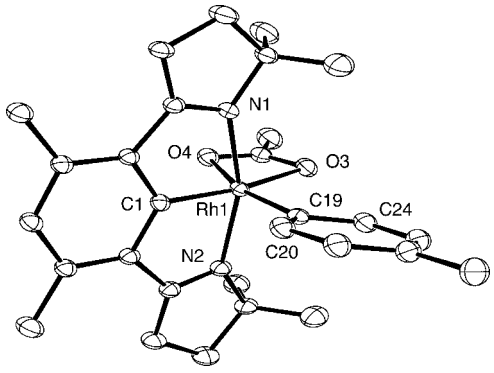


Figure 2. Molecular structure of **5p** with ellipsoids at the 40% probability level (one of the molecules in the unit cell has been omitted for clarity). Selected bond lengths [Å] and angles [°]: Rh(1)–C(1) 1.912(2), Rh(1)–C(19) 2.005(2), Rh(1)–O(3) 2.2843(17), Rh(1)–O(4) 2.2328(18), Rh(1)–N(1) 2.0526(19), Rh(1)–N(2) 2.0592(19); N(1)–Rh(1)–N(2) 159.00(8), C(20)–C(19)–Rh(1) 128.69(19), C(24)–C(19)–Rh(1) 113.81(19).

The substituent effect for C–H bond activation of monosubstituted benzenes was determined by competition reactions between two different aromatic compounds. The relative rate of reaction of **1** with $C_6H_5X$ decreased in the following sequence: OMe (1.8) > COMe (1.6) > $CF_3$ (1.2), Cl (1.2) > $CH_3$ (1); no correlation with Hammett's σ values was observed. This result is inconsistent with electrophilic C–H bond activation, where the $\rho$ values have been determined in the cases of $PtCl_6^{2-}$ and [(OEP)RhCl] (OEP = octaethylporphyrinato).[13,14]

Thermolysis of **1** in a 1:1 mixture of toluene and [$D_8$]-toluene at 100 °C resulted in formation of the C–H- and C–D-activated complexes **5** and [$D_7$]**5**. $^1$H NMR analysis revealed that the kinetic isotope effect is 5.4. This large value suggests that the C–H bond cleavage is the rate-determining step. Additionally, the rate constants obtained in the range of 97.1–116.5 °C yielded the following activation parameters: $\Delta H^{\ddagger} = 22 \pm 2$ kcal mol$^{-1}$ and $\Delta S^{\ddagger} = -24 \pm 5$ cal mol$^{-1}$ K$^{-1}$. The relatively large and negative value of the activation entropy suggests a rigid transition state.[15]

We also checked the reaction of the $Rh^{III}$ complex [(*dm*-Phebox-*dm*)$RhCl_2(H_2O)$] with chlorobenzene. When a solution of the complex in chlorobenzene was heated at 120 °C for 40 h, no reaction was observed. This result clearly indicates that the acetato ligand in **1** is essential for C–H bond activation.

The proposed mechanism for C–H bond activation of arenes by **1** is illustrated in Scheme 5. We have demonstrated previously that the coordination site of $H_2O$ in [(Phebox)$RhCl_2(H_2O)$] plays the role as the Lewis acidic position.[16] We therefore presume that a coordinatively unsaturated intermediate **A** with a vacant site can be formed by dissociation of $H_2O$. According to the final geometry of the aryl complexes, isomerization to **B** might be important to accept the arene molecule. The negative activation entropy suggests that the C–H bond of arenes is cleaved though a rate-determining six-centered transition state **C**.[5,7b] However, we cannot rule out mechanisms involving σ-bond metathesis and oxidative hydrogen migration, which require the four-centered transition state **D**.[3,17]

## Conclusion

We have found intermolecular C–H bond activation of various arenes by the structurally well-defined $Rh^{III}$ acetate complex **1**, where the acetato ligand acts as a proton acceptor. A large kinetic isotope effect and negative entropy were found in this system. X-ray analysis of **3** has revealed a molecular structure with the aryl ligand at the apical position and a $\kappa^2$-acetato ligand. Further detailed mechanistic and derivatization studies of arenes are in progress.

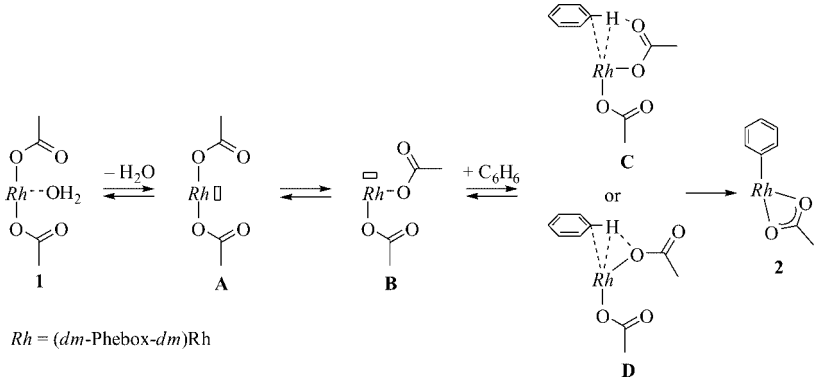


Scheme 5.

 © 2007 Wiley-VCH Verlag GmbH & Co. KGaA, Weinheim 

## Experimental Section

**General Procedures:** $^1$H and $^{13}$C NMR spectra were obtained at 25 °C with a Varian Mercury 300 spectrometer. $^1$H NMR chemical shifts are reported relative to the singlet at $\delta$ = 7.26 ppm for chloroform or $\delta$ = 7.16 ppm for benzene. $^{13}$C NMR spectra are reported in terms of chemical shifts relative to the triplet at $\delta$ = 77.0 ppm for $CDCl_3$ or $\delta$ = 128.0 ppm for $C_6D_6$ as an internal standard. IR spectra were recorded with a JASCO FT/IR-230 spectrometer. Elemental analysis was performed with a Perkin–Elmer 2400II. [(*dm*-Phebox-*dm*)Rh(OAc)$_2$(H$_2$O)] (**1**) and [(*dm*-Phebox-*dm*)Rh(Cl)$_2$(H$_2$O)] were prepared according to a literature procedure.[8b]

**Reaction of 1 with Benzene:** Complex **1** (27 mg, 0.050 mmol) was dissolved in benzene (5 mL) in a 20-mL Schlenk tube under argon and the solution was stirred at 90 °C for 144 h. After removal of the solvent, the yellow residue was purified by column chromatography on silica gel with ethyl acetate/MeOH (10:1) as eluent to give [(*dm*-Phebox-*dm*)Rh(Ph)($\kappa^2$-OAc)] (**2**; 17 mg, 62%) as a yellow solid. Complex **2** was alternatively synthesized by treatment of **1** (54 mg, 0.10 mmol) with PhB(OH)$_2$ (27 mg, 0.22 mmol) in toluene (2 mL) at 70 °C for 46 h. Workup as described above gave **2** (44 mg, 0.082 mmol, 82%). $^1$H NMR (300 MHz, $CDCl_3$, room temp.): $\delta$ = 0.97 (s, 6 H, Phebox-*Me*), 1.39 (s, 6 H, Phebox-*Me*), 2.07 (s, 3 H, O*Ac*), 2.56 (d, $J_{H,H}$ = 0.6 Hz, 6 H, 3,5-*Me*), 4.23 (d, $J_{H,H}$ = 8.2 Hz, 2 H, Phebox-C$H_2$), 4.33 (d, $J_{H,H}$ = 8.2 Hz, 2 H, Phebox-C$H_2$), 6.69–6.79 (m, 6 H, $C_6H_5$ and 4-*H*) ppm. $^{13}$C NMR (75 MHz, $CDCl_3$, room temp.): $\delta$ = 19.08, 24.45 (OAc), 27.01, 27.19, 65.18, 81.87, 121.5, 125.3, 126.1, 126.7, 134.1, 139.7, 146.0 (d, $J_{Rh,C}$ = 31.9 Hz, $C_{ipso}$), 171.0 (d, $J_{Rh,C}$ = 5.2 Hz), 183.5 (OAc), 196.5 (d, $J_{Rh,C}$ = 29.6 Hz) ppm. $C_{26}H_{31}N_2O_4Rh$ (538.44): calcd. C 58.00, H 5.80, N 5.20; found C 58.11, H 5.67, N 5.07.

**Reaction of 1 with *m*-Xylene:** Complex **1** (54 mg 0.10 mmol) was dissolved in *m*-xylene (10 mL) in a 20-mL Schlenk tube under argon and the solution was stirred at 140 °C for 60 h. The reaction mixture was purified by column chromatography on silica gel with ethyl acetate as eluent to give [(*dm*-Phebox-*dm*)Rh(3,5-Me$_2$C$_6$H$_3$)($\kappa^2$-OAc)] (**3**; 32 mg, 56%) as a yellow solid. $^1$H NMR (300 MHz, $CDCl_3$, room temp.): $\delta$ = 1.00 (s, 6 H, Phebox-*Me*), 1.38 (s, 6 H, Phebox-*Me*), 2.05 (s, 3 H, OAc), 2.06 (s, 6 H), 2.55 (s, 6 H), 4.24 (d, $J_{H,H}$ = 8.1 Hz, 2 H, Phebox-C$H_2$), 4.33 (d, $J_{H,H}$ = 8.4 Hz, 2 H, Phebox-C$H_2$), 6.32 (s, 1 H, $C_6H_3Me_2$), 6.38 (s, 2 H, $C_6H_3Me_2$), 6.68 (s, 1 H, 4-*H*) ppm. $^{13}$C NMR (75 MHz, $CDCl_3$, room temp.): $\delta$ = 19.08, 21.52, 24.47 (OAc), 27.06, 27.14, 65.23, 81.84, 123.6, 126.0, 126.7, 131.6, 131.6, 133.9, 139.5, 145.6 (d, $J_{Rh,C}$ = 31.4 Hz, $C_{ipso}$), 170.9 (d, $J_{Rh,C}$ = 5.7 Hz), 183.3 (OAc), 196.7 (d, $J_{Rh,C}$ = 29.6 Hz) ppm. $C_{28}H_{35}N_2O_4Rh$ (566.49): calcd. C 59.37, H 6.23, N 4.95; found C 59.34, H 6.33, N 4.46.

**Reaction of 1 with *o*-Xylene:** Complex **1** (27 mg 0.050 mmol) was dissolved in *o*-xylene (2 mL) in a 20-mL Schlenk tube under argon and the solution was stirred at 140 °C for 36 h. The reaction mixture was purified by column chromatography on silica gel with ethyl acetate as eluent to give [(*dm*-Phebox-*dm*)Rh(3,4-Me$_2$C$_6$H$_3$)($\kappa^2$-OAc)] (**4**; 24 mg, 86%) as a yellow solid. $^1$H NMR (300 MHz, $CDCl_3$, room temp.): $\delta$ = 1.01 (s, 6 H, Phebox-*Me*), 1.38 (s, 6 H, Phebox-*Me*), 2.06 (m, 9 H, OAc and $C_6H_3Me_2$), 2.55 (d, $J_{H,H}$ = 0.6 Hz, 6 H), 4.23 (d, $J_{H,H}$ = 8.1 Hz, 2 H, Phebox-C$H_2$), 4.33 (d, $J_{H,H}$ = 8.1 Hz, 2 H, Phebox-C$H_2$), 6.17 (d, $J_{H,H}$ = 7.8 Hz, 1 H, $C_6H_3Me_2$), 6.48 (d, $J_{H,H}$ = 7.8 Hz, 1 H, $C_6H_3Me_2$), 6.68 (m, 1 H, 4-*H*), 6.76 (s, 1 H, $C_6H_3Me_2$) ppm. $^{13}$C NMR (75 MHz, $CDCl_3$, room temp.): $\delta$ = 19.05, 19.08, 19.90, 24.52 (OAc), 27.17, 65.19, 81.84, 125.9, 126.7, 126.8 (d, $J_{Rh,H}$ = 1.1 Hz), 129.1, 131.4, 133.0, 134.9 (d, $J_{Rh,C}$ = 1.1 Hz), 139.5 (d, $J_{Rh,C}$ = 1.1 Hz), 141.2 (d, $J_{Rh,C}$ = 32.0 Hz, $C_{ipso}$), 170.9 (d, $J_{Rh,C}$ = 5.7 Hz), 183.4 (OAc), 196.8 (d, $J_{Rh,C}$ = 29.6 Hz) ppm. $C_{28}H_{35}N_2O_4Rh$ (566.49): calcd. C 59.37, H 6.23, N 4.95; found C 58.75, H 6.19, N 4.28.

**Reaction of 1 with Toluene:** Complex **1** (27 mg 0.050 mmol) was dissolved in toluene (10 mL) in a 20-mL Schlenk tube under argon and the solution was stirred at 115 °C for 144 h. The reaction mixture was purified by column chromatography on silica gel with ethyl acetate as eluent to give [(*dm*-Phebox-*dm*)Rh($C_6H_4Me$)($\kappa^2$-OAc)] (**5**; 22 mg, 78%) as a yellow solid. The $^1$H NMR spectrum of the crude product revealed the formation of **5p** and **5m** in a 1.0:1.4 ratio. Complex **5p** was alternatively synthesized by treatment of **1** (54 mg, 0.10 mmol) with (*p*-$C_6H_4Me$)B(OH)$_2$ (30 mg, 0.20 mmol) in toluene (2 mL) at 90 °C for 16 h. Workup as described above gave complex **5p** (36 mg, 65%). **5p:** $^1$H NMR (300 MHz, $CDCl_3$, room temp.): $\delta$ = 0.99 (s, 6 H, Phebox-*Me*), 1.37 (s, 6 H, Phebox-*Me*), 2.06 (s, 3 H, O*Ac*), 2.14, (s, 3 H, $C_6H_4Me$), 2.55 (s, 3,5-*Me*), 4.23 (d, $J_{H,H}$ = 8.4 Hz, 2 H, Phebox-C$H_2$), 4.33 (d, $J_{H,H}$ = 8.4 Hz, 2 H, Phebox-C$H_2$), 6.57 (d, $J_{H,H}$ = 8.0 Hz, 2 H, $C_6H_4$Me), 6.61 (d, $J_{H,H}$ = 8.0 Hz, 2 H, $C_6H_4$Me), 6.69 (s, 1 H,4-*H*) ppm. $^{13}$C NMR (75 MHz, $CDCl_3$, room temp.): $\delta$ = 19.09, 20.67 ($C_6H_4Me$), 24.48 (OAc), 27.11, 27.23, 65.18, 81.87, 122.4–139.6, 140.8 (d, $J_{Rh,H}$ = 31.9 Hz, $C_{ipso}$), 170.9 ($J_{Rh,C}$ = 5.2 Hz), 183.5 (O*Ac*), 196.7 ($J_{Rh,C}$ = 29.6 Hz) ppm. **5m:** $^1$H NMR (300 MHz, $CDCl_3$, room temp.): $\delta$ = 0.99 (s, 6 H, Phebox-*Me*), 1.38 (s, 6 H, Phebox-*Me*), 2.06 (s, 3 H, *OAc*), 2.13, (s, 3 H, $C_6H_4Me$), 2.55 (s, 3,5-Me), 4.23 (d, $J_{H,H}$ = 8.1 Hz, 2 H, Phebox-C$H_2$), 4.33 (d, $J_{H,H}$ = 8.1 Hz, 2 H, Phebox-C$H_2$), 6.27 (d, $J_{H,H}$ = 7.6 Hz, 1 H, $C_6H_4$Me), 6.50 (d, $J_{H,H}$ = 7.6 Hz, 1 H, $C_6H_4$Me), 6.60 (t, $J_{H,H}$ = 7.6 Hz, 1 H, $C_6H_4$Me), 6.69 (s, 1 H), 6.87 (s, 1 H, $C_6H_4$Me) ppm. $^{13}$C NMR (75 MHz, $CDCl_3$, room temp.): $\delta$ = 19.09, 21.67 ($C_6H_4Me$), 24.48 (OAc), 27.05, 27.17, 65.21, 81.87, 122.4–139.60, 145.8 (d, $J_{Rh,C}$ = 31.4 Hz, $C_{ipso}$), 170.9 (d, $J_{Rh,C}$ = 5.2 Hz), 183.5 (OAc), 196.6 (d, $J_{Rh,C}$ = 29.6 Hz) ppm. $C_{27}H_{33}N_2O_4Rh$ (552.47): calcd. C 58.70, H 6.02, N 5.07; found C 58.83, H 5.98, N 4.96.

**Reaction of 1 with α,α,α-Trifluorotoluene:** Complex **1** (27 mg 0.050 mmol) was dissolved in α,α,α-trifluorotoluene (3 mL) in a 20-mL Schlenk tube under argon and the solution was stirred at 100 °C for 140 h. The reaction mixture was purified by column chromatography on silica gel with ethyl acetate as eluent to give [(*dm*-Phebox-*dm*)Rh($C_6H_4CF_3$)($\kappa^2$-OAc)] (**6**; 23 mg, 76%) as a yellow solid. The $^1$H NMR spectrum of the crude products revealed the formation of **6p** and **6m** in a ratio of 1:7.8. **6p:** $^1$H NMR (300 MHz, $CDCl_3$, room temp.): $\delta$ = 0.94 (s, 6 H, Phebox-*Me*), 1.39 (s, 6 H, Phebox-*Me*), 2.06 (s, 3 H, O*Ac*), 2.57 (s, 3,5-*Me*), 4.25 (d, $J_{H,H}$ = 8.4 Hz, 2 H, Phebox-C$H_2$), 4.35 (d, $J_{H,H}$ = 8.4 Hz, 2 H, Phebox-C$H_2$), 6.74 (s, 1 H, 4-*H*), 6.77–6.97 (4 H, $C_6H_4CF_3$) ppm. **6m:** $^1$H NMR (300 MHz, $CDCl_3$, room temp.): $\delta$ = 0.94 (s, 6 H, Phebox-*Me*), 1.39 (s, 6 H, Phebox-*Me*), 2.06 (s, 3 H, O*Ac*), 2.57 (s, 3,5-*Me*), 4.25 (d, $J_{H,H}$ = 8.4 Hz, 2 H, Phebox-C$H_2$), 4.35 (d, $J_{H,H}$ = 8.4 Hz, 2 H, Phebox-C$H_2$), 6.74 (s, 1 H, 4-*H*), 6.77–6.97 (3 H, $C_6H_4CF_3$), 7.18 (s, 1 H, $C_6H_4CF_3$) ppm. $^{13}$C NMR (75 MHz, $CDCl_3$, room temp.): $\delta$ = 19.11, 24.45 (OAc), 26.99, 27.23, 65.23, 81.94, 118.5 (q, $J_{C,F}$ = 4.1 Hz), 124.4 (q, $J_{C,F}$ = 269.9 Hz), 127.0 (q, $J_{C,F}$ = 31.4 Hz), 130.4 (q, $J_{C,F}$ = 2.9 Hz), 134.3, 140.1, 147.4 (d, $J_{Rh,C}$ = 31.9 Hz, $C_{ipso}$), 171.1 (d, $J_{Rh,C}$ = 5.1 Hz), 184.1 (OAc), 195.6 (d, $J_{Rh,C}$ = 29.1 Hz) ppm. $C_{27}H_{30}F_3N_2O_4Rh$ (606.44): calcd. C 53.47, H 4.99, N 4.62; found C 54.13, H 5.27, N 3.85.

**Reaction of 1 with Anisole:** Complex **1** (27 mg 0.050 mmol) was dissolved in anisole (3 mL) in a 20-mL Schlenk tube under argon and the solution was stirred at 120 °C for 44 h. The reaction mixture was purified by column chromatography on silica gel with ethyl acetate as eluent to give [(*dm*-Phebox-*dm*)Rh($C_6H_4OMe$)($\kappa^2$-OAc)] (**7**; 20 mg, 70%) as a yellow solid. The $^1$H NMR spectrum

 © 2007 Wiley-VCH Verlag GmbH & Co. KGaA, Weinheim 

of the crude products revealed the formation of **7p** and **7m** in a 1:1 ratio. **7p:** $^1$H NMR (300 MHz, $CDCl_3$, room temp.): $\delta$ = 0.98 (s, 6 H, Phebox-*Me*), 1.38 (s, 6 H, Phebox-*Me*), 2.05 (s, 3 H, OAc), 2.55 (s, 3,5-Me), 3.64 (s, 3 H, OMe), 4.23 (d, $J_{H,H}$ = 8.1 Hz, 2 H, Phebox-C$H_2$), 4.33 (d, $J_{H,H}$ = 8.1 Hz, 2 H, Phebox-C$H_2$), 6.42 (d, $J_{H,H}$ = 7.8 Hz, 2 H, $C_6H_4$OMe), 6.60 (d, $J_{H,H}$ = 7.8 Hz, 2 H, $C_6H_4$OMe), 6.69 (s, 1 H, 4-*H*) ppm. $^{13}$C NMR (75 MHz, $CDCl_3$, room temp.): $\delta$ = 19.10, 24.47 (OAc), 27.03, 27.23, 55.07 (O*Me*), 65.16, 81.88, 111.5, 126.0, 126.7, 133.3 (d, $J_{Rh,C}$ = 33.1 Hz, $C_{ipso}$), 133.9, 139.6, 155.6, 170.9 (d, $J_{Rh,C}$ = 5.3 Hz), 183.6 (O*Ac*), 196.6 (d, $J_{Rh,C}$ = 29.0 Hz) ppm. **7m:** $^1$H NMR (300 MHz, $CDCl_3$, room temp.): $\delta$ = 0.99 (s, 6 H, Phebox-*Me*), 1.38 (s, 6 H, Phebox-*Me*), 2.05 (s, 3 H, OAc), 2.54 (s, 3,5-*Me*), 3.61 (s, 3 H, O*Me*), 4.23 (d, $J_{H,H}$ = 8.1 Hz, 2 H, Phebox-C$H_2$), 4.33 (d, $J_{H,H}$ = 8.1 Hz, 2 H, Phebox-C$H_2$), 6.01 (m, 1 H, $C_6H_4$OMe), 6.27 (d, $J_{H,H}$ = 7.8 Hz, 1 H, $C_6H_4$OMe), 6.69 (t, $J_{H,H}$ = 7.8 Hz, 1 H, $C_6H_4$OMe), 6.69 (s, 1 H, 4-*H*), 6.77 (d, $J_{H,H}$ = 7.8 Hz, 1 H, $C_6H_4$OMe) ppm. $^{13}$C NMR (75 MHz, $CDCl_3$, room temp.): $\delta$ = 19.10, 24.47 (OAc), 27.03, 27.23, 54.82 (O*Me*), 65.21, 81.88, 106.5, 120.0, 124.8, 126.2, 126.6, 127.0, 139.7, 148.0 (d, $J_{Rh,C}$ = 31.4 Hz, $C_{ipso}$), 156.4, 170.9 (d, $J_{Rh,C}$ = 5.2 Hz), 183.6 (O*Ac*), 196.3 (d, $J_{Rh,C}$ = 29.7 Hz) ppm. $C_{27}H_{33}N_2O_5Rh$ (568.47): calcd. C 57.05, H 5.85, N 4.93; found C 56.85, H 5.76, N 4.72.

**Reaction of 1 with Acetophenone:** Complex **1** (27 mg 0.050 mmol) was dissolved in acetophenone (3 mL) in a 20-mL Schlenk tube under argon and the solution was stirred at 140 °C for 24 h. The reaction mixture was purified by column chromatography on silica gel with ethyl acetate as eluent to give [(*dm*-Phebox-*dm*)-Rh($C_6H_4$COMe)($\kappa^2$-OAc)] (**8**; 23 mg, 78%) as a yellow solid. The $^1$H NMR spectrum of the crude products revealed the formation of **8p** and **8m** in a 1:4.5 ratio. **8p:** $^1$H NMR (300 MHz, $CDCl_3$, room temp.): $\delta$ = 0.95 (s, 6 H, Phebox-*Me*), 1.39 (s, 6 H, Phebox-*Me*), 2.07 (s, 3 H, OAc), 2.44 (s, 3 H, -CO*Me*), 2.57 (s, 3,5-*Me*), 4.24 (d, $J_{H,H}$ = 8.5 Hz, 2 H, Phebox-C$H_2$), 4.35 (d, $J_{H,H}$ = 8.5 Hz, 2 H, Phebox-C$H_2$), 6.74 (s, 1 H, 4-*H*), 6.96 (d, $J_{H,H}$ = 8.0 Hz, 2 H), 7.31 (d, $J_{H,H}$ = 8.0 Hz, 2 H) ppm. **8m:** $^1$H NMR (300 MHz, $CDCl_3$, room temp.): $\delta$ = 0.95 (s, 6 H, Phebox-*Me*), 1.39 (s, 6 H, Phebox-*Me*), 2.07 (s, 3 H, OAc), 2.39 (s, 3 H, -CO*Me*), 2.57 (s, 3,5-*Me*), 4.24 (d, $J_{H,H}$ = 8.5 Hz, 2 H, Phebox-C$H_2$), 4.35 (d, $J_{H,H}$ = 8.5 Hz, 2 H, Phebox-C$H_2$), 6.74 (s, 1 H, 4-*H*), 6.84 (t, $J_{H,H}$ = 7.8 Hz, 1 H, $C_6H_4$COMe), 7.15 (d, $J_{H,H}$ = 7.8 Hz, 1 H, $C_6H_4$COMe), 7.23 (s, 1 H, $C_6H_4$COMe), 7.31 (d, $J_{H,H}$ = 7.8 Hz, 1 H, $C_6H_4$COMe) ppm. $^{13}$C NMR (75 MHz, $CDCl_3$, room temp.): $\delta$ = 19.11, 24.52 (OAc), 26.70 (CO*Me*), 27.06, 27.33, 65.20, 81.92, 121.8, 125.1, 126.5, 126.6, 133.3, 139.5, 140.1, 146.7 (d, $J_{Rh,C}$ = 31.9 Hz, $C_{ipso}$), 171.1 (d, $J_{Rh,C}$ = 5.7 Hz), 184.0 (OAc), 195.9 (d, $J_{Rh,C}$ = 29.7 Hz), 199.0 (*C*OMe) ppm. $C_{28}H_{33}N_2O_5Rh$ (580.48): calcd. C 57.93, H 5.73, N 4.83; found C 57.68, H 5.60, N 4.64.

**Reaction of 1 with Chlorobenzene:** Complex **1** (27 mg 0.050 mmol) was dissolved in chlorobenzene (5 mL) in a 20-mL Schlenk tube under argon and the solution was stirred at 120 °C for 50 h. The reaction mixture was purified by column chromatography on silica gel with ethyl acetate as eluent to give [(*dm*-Phebox-*dm*)-Rh($C_6H_4$Cl)($\kappa^2$-OAc)] (**9**; 23 mg, 80%) as a yellow solid. The $^1$H NMR spectrum of the crude products revealed the formation of **9p** and **9m** in a 1:2.2 ratio. **9p:** $^1$H NMR (300 MHz, $C_6D_6$, room temp.): $\delta$ = 0.78 (s, 6 H, Phebox-*Me*), 1.17 (s, 6 H, Phebox-*Me*), 2.16 (s, 3 H, OAc), 2.48 (s, 6 H, 3,5-*Me*), 3.43 (d, $J_{H,H}$ = 8.7 Hz, Phebox-C$H_2$), 3.55 (d, $J_{H,H}$ = 8.7 Hz, Phebox-C$H_2$), 6.49 (s, 1 H, 4-*H*), 6.91 (d, $J_{H,H}$ = 8.3 Hz, 2 H, $C_6H_4$Cl), 7.08 (d, $J_{H,H}$ = 8.3 Hz, 2 H, $C_6H_4$Cl) ppm. $^{13}$C NMR (75 MHz, $C_6D_6$, room temp.): $\delta$ = 19.35, 25.04 (OAc), 27.10, 27.34, 65.45, 81.90, 122.5–140.0, 145.2 (d, $J_{Rh,C}$ = 32.5 Hz, $C_{ipso}$), 171.4 (d, $J_{Rh,C}$ = 4.5 Hz), 184.1, 198.3 (d, $J_{Rh,C}$ = 28.0 Hz) ppm. **9m:** $^1$H NMR (300 MHz, $C_6D_6$, room temp.): $\delta$ = 0.81 (s, 6 H, Phebox-*Me*), 1.16 (s, 6 H, Phebox-*Me*), 2.16 (s, 3 H, OAc), 2.45 (s, 6 H, 3,5-*Me*), 3.40 (d, $J_{H,H}$ = 8.1 Hz, Phebox-C$H_2$), 3.52 (d, $J_{H,H}$ = 8.1 Hz, Phebox-C$H_2$), 6.47 (s, 1 H, 4-*H*), 6.61 (t, $J_{H,H}$ = 7.8 Hz, 2 H, $C_6H_4$Cl), 6.84 (d, $J_{H,H}$ = 7.8 Hz, 2 H, $C_6H_4$Cl), 6.97 (d, $J_{H,H}$ = 7.8 Hz, 2 H, $C_6H_4$Cl), 7.46 (s, 1 H, $C_6H_4$Cl) ppm. $^{13}$C NMR (75 MHz, $C_6D_6$, room temp.): $\delta$ = 19.35, 25.04 (OAc), 27.04, 27.34, 65.45, 81.90, 122.5–140.1, 150.4 (d, $J_{Rh,C}$ = 32.6 Hz, $C_{ipso}$), 171.5 (d, $J_{Rh,C}$ = 5.2 Hz), 184.1, 198.1 (d, $J_{Rh,C}$ = 28.0 Hz) ppm. $C_{26}H_{30}ClN_2O_4Rh$ (572.89): calcd. C 54.51, H 5.28, N 4.89; found C 54.66, H 5.18, N 4.72.

**Competition Reaction:** Complex **1** (16 mg, 0.030 mmol) was dissolved in a 1:1 molar mixture (4 mL) of toluene and $C_6H_5X$ (X = OMe, COMe, $CF_3$, or Cl) under argon. The solution was stirred at 100 °C for 24 h and then passed through a short column. The relative ratio of products was determined on the basis of the $^1$H NMR spectra in $CDCl_3$.

**Reaction of 1 with [D$_8$]Toluene/Toluene:** Complex **1** (11 mg 0.020 mmol) was dissolved in a 1:1 mixture of [$D_8$]toluene and toluene (1 mL) in a 20-mL Schlenk tube under argon. The solution was stirred at 100 °C for 40 h and then the solvent was removed under reduced pressure. The $^1$H NMR spectrum of the resulting residue revealed the formation of [$D_7$]**3** and **3** in a 5.4:1 ratio.

**Monitoring the Reaction of 1 with [D$_8$]Toluene:** Complex **1** (16.0 mg, 0.030 mmol) was dissolved in [$D_8$]toluene (3 mL) under argon. The solution (0.6 mL) was placed into an NMR tube and then the tube was flame-sealed. The four samples were maintained in oil baths at 97.1, 105.0, 111.3, and 116.5 °C. The reaction was monitored by $^1$H NMR spectroscopy by recording the signal of the methyl group. The rate constants were estimated as $2.48(5)\times10^{-6}$ (97.1 °C), $4.13(5)\times10^{-6}$ (105.0 °C), $7.12(9)\times10^{-6}$ (111.3 °C), and $1.21(1)\times10^{-5}$ s$^{-1}$ (116.5 °C). The Eyring plot gave the following activation parameters: $\Delta H^{\ddagger}$ = 22 ± 2 kcal mol$^{-1}$ and $\Delta S^{\ddagger}$ = –24 ± 5 cal mol$^{-1}$ K$^{-1}$.

**X-ray Diffraction Study:** Single crystals of **3** and **5p** suitable for an X-ray diffraction study were obtained from hexane/$CH_2Cl_2$ solutions at room temperature. The diffraction data were collected with a Bruker SMART APEX CCD diffractometer with graphite-monochromated Mo-$K_\alpha$ radiation ($\lambda$ = 0.71073 Å). An empirical absorption correction was applied with SADABS. The structure was solved by direct methods and refined by full-matrix least squares on $F^2$ using SHELXTL. All non-hydrogen atoms of the rhodium complex were refined with anisotropic displacement parameters. All hydrogen atoms were located at calculated positions and refined as rigid groups. Refinement details for **3**: empirical formula: $C_{29.50}H_{38.50}N_2O_4Rh$; $M_r$ = 588.03; temperature: 153(2) K; crystal system: triclinic; space group: $P\bar{1}$; $a$ = 11.2915(5), $b$ = 13.4972(7), $c$ = 19.5574(9) Å, $\alpha$ = 96.8790(10), $\beta$ = 103.3450(10), $\gamma$ = 101.8940(10)°, $V$ = 2793.7(2) Å$^3$, $Z$ = 4, $\rho_{calcd.}$ = 1.398 Mg m$^{-3}$, $\mu$ = 0.648 mm$^{-1}$, $F$(000) = 1226, crystal size = 0.40 × 0.40 × 0.30 mm, $\theta$ range = 1.74–27.53°; index ranges: $-14 \le h \le 14$, $-16 \le k \le 17$, $-25 \le l \le 21$; reflections collected: 19914; independent reflections: 12803 [$R$(int) = 0.0187], completeness to $\theta$ = 27.53°: 99.2%; max/min transmission: 1.000000/0.788581; data/restraints/parameters: 12803/0/673; goodness-of-fit on $F^2$: 1.030; final $R$ indices [$I > 2\sigma(I)$]: $R1$ = 0.0343, $wR2$ = 0.0844; $R$ indices (all data): $R1$ = 0.0438, $wR2$ = 0.0895; largest diff. peak/hole: 0.946/–0.363 e Å$^{-3}$. Refinement details for **5p**: empirical formula: $C_{27}H_{33}N_2O_4Rh$; $M_r$ = 552.46; temperature: 173(2) K; crystal system: triclinic; space group: $P\bar{1}$; $a$ = 11.3424(5), $b$ = 13.1787(6), $c$ = 17.4623(8) Å, $\alpha$ = 94.8920(10), $\beta$ = 94.7150(10), $\gamma$ = 102.4740(10)°, $V$ = 2525.7(2) Å$^3$, $Z$ = 4, $\rho_{calcd.}$ = 1.453 Mg m$^{-3}$, $\mu$ = 0.711 mm$^{-1}$, $F$(000) = 1144, crystal size = 0.30 × 0.20 × 0.10 mm, $\theta$ range = 1.18–27.51°; index ran-

 © 2007 Wiley-VCH Verlag GmbH & Co. KGaA, Weinheim 

ges: $-14 \leq h \leq 14$, $-17 \leq k \leq 16$, $-14 \leq l \leq 22$; reflections collected: 18003, independent reflections: 11516 [$R$(int) = 0.0353], completeness to $\theta$ = 27.51°: 99.3%; max/min transmission: 1.000000/0.735363; data/restraints/parameters: 11516/0/629; goodness-of-fit on $F^2$: 0.983; final $R$ indices [$I > 2\sigma(I)$]: $R1$ = 0.0320, $wR2$ = 0.0788; $R$ indices (all data): $R1$ = 0.0407, $wR2$ = 0.0872; largest diff. peak/hole: 0.901 and –0.661 e Å$^{-3}$. CCDC-623906 and -623907 contain the supplementary crystallographic data for complexes **3** and **5p**, respectively. These data can be obtained free of charge from The Cambridge Crystallographic Data Center via www.ccdc.cam.ac.uk/datarequest/cif.

## Acknowledgments

This research was financially supported by a Grant-in-Aid for Scientific Research from the Ministry of Education, Culture, Sports, Science, and Technology, Japan.

[1] S. J. Blanksby, G. B. Ellison, *Acc. Chem. Res.* **2003**, *36*, 255–263.
[2] a) V. Ritleng, C. Sirlin, M. Pfeffer, *Chem. Rev.* **2002**, *102*, 1731–1770; b) F. Kakiuchi, S. Murai, *Acc. Chem. Res.* **2002**, *35*, 826–834; c) K. Godula, D. Sames, *Science* **2006**, *312*, 67–72; d) G. Dyker, *Angew. Chem. Int. Ed.* **1999**, *38*, 1698–1712; e) T. Ishiyama, N. Miyaura, *J. Organomet. Chem.* **2003**, *680*, 3–11.
[3] a) B. A. Arndtsen, R. G. Bergman, T. A. Mobley, T. H. Peterson, *Acc. Chem. Res.* **1995**, *28*, 154–162; b) J. A. Labinger, J. E. Bercaw, *Nature* **2002**, *417*, 507–514; c) W. D. Jones, *Acc. Chem. Res.* **2003**, *36*, 140–146.
[4] a) C. Jia, T. Kitamura, Y. Fujiwara, *Acc. Chem. Res.* **2001**, *34*, 633–639; b) L. V. Desai, K. L. Hull, M. S. Sanford, *J. Am. Chem. Soc.* **2004**, *126*, 9542–9543; c) M. D. K. Boele, F. P. F. Van Strijdonck, A. H. M. De Vries, P. C. J. Kamer, J. G. De Vries, P. W. N. M. Van Leeuwen, *J. Am. Chem. Soc.* **2002**, *124*, 1586–1587.
[5] a) B. Biswas, M. Sugimoto, S. Sakaki, *Organometallics* **2000**, *19*, 3895–3908; b) D. L. Davies, S. M. A. Donald, S. A. Macgregor, *J. Am. Chem. Soc.* **2005**, *127*, 13754–13755; c) V. R. Ziatdinov, J. Oxgaard, O. A. Mironov, K. J. H. Young, W. A. Goddard III, R. A. Periana, *J. Am. Chem. Soc.* **2006**, *128*, 7404–7405.
[6] a) W. J. Tenn III, K. J. H. Young, G. Bhalla, J. Oxgaard, W. A. Goddard III, R. A. Periana, *J. Am. Chem. Soc.* **2005**, *127*, 14172–14173; b) W. J. Tenn III, K. J. H. Young, J. Oxgaard, R. J. Nielsen, W. A. Goddard III, R. A. Periana, *Organometallics* **2006**, *25*, 5173–5175.
[7] a) D. L. Davies, O. Al-Duaij, J. Fawcett, M. Giardiello, S. T. Hilton, D. R. Russell, *Dalton Trans.* **2003**, 4132–4139; b) D. L. Davies, S. M. A. Donald, O. Al-Duaij, S. A. Macgregor, M. Polleth, *J. Am. Chem. Soc.* **2006**, *128*, 4210–4211.
[8] a) Y. Kanazawa, Y. Tsuchiya, K. Kobayashi, T. Shiomi, J. Itoh, M. Kikuchi, Y. Yamamoto, H. Nishiyama, *Chem. Eur. J.* **2006**, *12*, 63–71; b) J. Ito, T. Shiomi, H. Nishiyama, *Adv. Synth. Catal.* **2006**, *348*, 1235–1240.
[9] a) M. E. van der Boom, D. Milstein, *Chem. Rev.* **2003**, *103*, 1759–1792; b) M. Kanzelberger, B. Singh, M. Czerw, K. Krogh-Jespersen, A. S. Goldman, *J. Am. Chem. Soc.* **2000**, *122*, 11017–11018.
[10] a) S. Gatard, R. Çelenligil-Çetin, C. Guo, B. M. Foxman, O. V. Ozerov, *J. Am. Chem. Soc.* **2006**, *128*, 2808–2809; b) W. D. Jones, F. J. Feher, *Inorg. Chem.* **1984**, *23*, 2376–2388; c) R. Cohen, M. E. van der Boom, L. J. W. Shimon, H. Rozenberg, D. Milstein, *J. Am. Chem. Soc.* **2000**, *122*, 7723–7734.
[11] A. D. Ryabov, *Chem. Rev.* **1990**, *90*, 403–424.
[12] For examples of C–H bond activation in preference to C–Cl bond activation, see: a) Y. Fuchita, Y. Utsunomiya, M. Yasutake, *J. Chem. Soc., Dalton Trans.* **2001**, 2330–2334; b) E. Ben-Ari, M. Gandelman, H. Rozenberg, L. J. W. Shimon, D. Milstein, *J. Am. Chem. Soc.* **2003**, *125*, 4714–4715; c) E. Ben-Ari, R. Cohen, M. Gandelman, L. J. W. Shimon, J. M. L. Martin, D. Milstein, *Organometallics* **2006**, *25*, 3190–3210; d) L. Fan, S. Parkin, O. V. Ozerov, *J. Am. Chem. Soc.* **2005**, *127*, 16772–16773; e) T. Ishiyama, J. Takagi, K. Ishida, N. Miyaura, N. R. Anastasi, J. F. Hartwig, *J. Am. Chem. Soc.* **2002**, *124*, 390–391; f) G. A. Chotana, M. A. Rak, M. R. Smith III, *J. Am. Chem. Soc.* **2005**, *127*, 10539–10544; g) J. Y. K. Tsang, M. S. A. Buschhaus, P. Legzdins, B. O. Patrick, *Organometallics* **2006**, *25*, 4215–4225.
[13] G. B. Shul'pin, G. V. Nizova, A. T. Nikitaev, *J. Organomet. Chem.* **1984**, *276*, 115–153.
[14] Y. Aoyama, T. Yoshida, K. Sakurai, H. Ogoshi, *Organometallics* **1986**, *5*, 168–173.
[15] a) A. D. Ryabov, I. K. Sakodinskaya, A. K. Yatsimirsky, *J. Chem. Soc., Dalton Trans.* **1985**, 2629–2638; b) M. Gómez, J. Granell, M. Martinez, *Organometallics* **1997**, *16*, 2539–2546.
[16] Y. Motoyama, M. Okano, H. Narusawa, N. Makihara, K. Aoki, H. Nishiyama, *Organometallics* **2001**, *20*, 1580–1591.
[17] J. Oxgaard, R. P. Muller, W. A. Goddard III, R. A. Periana, *J. Am. Chem. Soc.* **2004**, *126*, 352–363.

Received: November 6, 2006
Published Online: February 2, 2007

 © 2007 Wiley-VCH Verlag GmbH & Co. KGaA, Weinheim 

DOI: 10.1002/ejic.200600715

# Host–Guest Complexes of Oligopyridine Cryptands: Prediction of Ion Selectivity by Quantum Chemical Calculations[‡]

**Ralph Puchta*[a,b] and Rudi van Eldik[b]**

**Keywords:** Density functional calculations / Semiempirical calculations / Cryptands / Host–guest systems / Cation selectivity

The structures and complex-formation energies for the cryptands 6,6′,6′′,6′′′,6′′′′,6′′′′′-bis[nitrilotri(methylene)]tris(2,2′-bipyridine) (**1**) and 2,2′,2′′,9,9′,9′′-bis[nitrilotri(methylene)]tris(1,10-phenanthroline) (**2**) with alkali and alkaline-earth cations are obtained by PM3/SPASS and density functional (B3LYP/LANL2DZp) calculations and the results used to predict the ion selectivity. Both cryptands **1** and **2** have a cavity size similar to [2.2.2] and prefer $Ca^{2+}$ and $Sr^{2+}$, while **1** has a preference for $K^+$ and **2** favours $Na^+$ and $K^+$. The cryptand flexibility for **1** is attributed mainly to the bipyridine building block and that for **2** to the groups neighbouring the bridgehead nitrogen atoms.
(© Wiley-VCH Verlag GmbH & Co. KGaA, 69451 Weinheim, Germany, 2007)

## Introduction

The selective complexation of guest molecules and ions is an essential prerequisite for the proper functioning of enzymes and receptors in biological and technical systems, and it has therefore been investigated over several decades.[1,2] In order to mimic the geometric and electronic requirements necessary for selective complexation as observed in nature, many different model compounds with cavities of variable size and structure have been studied experimentally and computationally.[3–5] Examples are the well-known calixarenes,[6,7] crown ethers,[8] cryptands,[9,10] and their inclusion complexes, along with the corresponding metallatopomers, which are easily accessible by self-organisation.[11]

The synthesis of 4,7,13,16,21,24-hexaoxa-1,10-diazabicyclo[8.8.8]hexacosane, which was reported by Dietrich, Lehn and Sauvage in 1969, today well known as [2.2.2] and traded as Kryptofix 222, led to a wide range of applications, although other cryptands with similar topology have hardly been explored. It was immediately recognized that [2.2.2] and its derivatives have an outstanding potential to selectively bind guests, in particular alkali and alkaline-earth metal ions. Today, cryptands and cryptates like [2.2.2] and their different derivatives are widely applied, for example in phase-transfer catalysis,[12,13] studies on Zintl phases,[14] selective complexation of radioactive or toxic ions in medicine[15] and elsewhere,[16,17] as chelates for MRI contrast agents,[18] and as models for carrier-antibiotics such as Valinomycin and enzyme inhibitors.[19] In contrast, the cryptands 6,6′,6′′,6′′′,6′′′′,6′′′′′-bis[nitrilotri(methylene)]tris-(2,2′-bipyridine) (**1**) and 2,2′,2′′,9,9′,9′′-bis[nitrilotri(methylene)]tris(1,10-phenanthroline) (**2**) are systems that have only been partially investigated (see Figure 1).

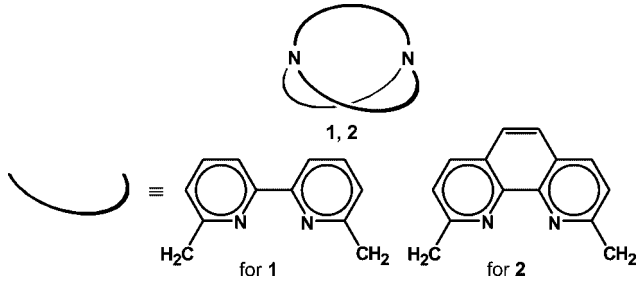


Figure 1. 6,6′,6′′,6′′′,6′′′′,6′′′′′-Bis[nitrilotri(methylene)]tris(2,2′-bipyridine) (**1**) and 2,2′,2′′,9,9′,9′′-bis[nitrilotri(methylene)]-tris(1,10-phenanthroline) (**2**).

In the 1984 report on the first synthesis of cryptands, two project aims for these newly designed polypyridine cryptands were expressed: (i) as ligand systems with novel metal-ion binding properties and (ii) special photophysical/photochemical properties for electron-transfer processes.[20] In the following years much research has been focused on their photophysics and photochemistry,[21] and the lanthanide complexes $[Ln\subset\mathbf{1}]^{3+}$ and $[Ln\subset\mathbf{2}]^{3+}$ were found to be efficient luminophores for converting UV light into visible light.[22,23] These properties can be utilized in fluorescent markers,[24] for example for detecting or locating nucleic acids,[25] or in other labelling techniques.[26] With the help of NMR techniques, the water exchange of $[Gd(H_2O)_3\subset\mathbf{1}]^{3+}$ has been investigated by Merbach et al., who tested $[Gd(H_2O)_3\subset\mathbf{1}]^{3+}$ as a potential contrast agent for magnetic

[‡] Part II; for part I see ref.[38]

[a] Computer Chemistry Center, University of Erlangen-Nürnberg, Nägelsbachstrasse 25, 91052 Erlangen, Germany
E-mail: ralph.puchta@chemie.uni-erlangen.de
[b] Institute for Inorganic Chemistry, University of Erlangen-Nürnberg,
Egerlandstrasse 1, 91058 Erlangen, Germany


© 2007 Wiley-VCH Verlag GmbH & Co. KGaA, Weinheim

resonance imaging.[27] However, for the first proposed aim and application involving the selective ion binding of **1** and **2**, only two studies on the separation of $Am^{3+}$ and $Eu^{3+}$ have appeared.[28,29] This is surprising since different cryptand/cryptate or crown ether-solvent combinations have been investigated,[30–34] especially with respect to their transport properties[35] or ion conductivity and potential applications in batteries and capacitors,[36] while parallel alkali and alkaline-earth ion complexes with phenanthroline and bipyridine moieties have also been studied.[37]

In a recent report we demonstrated that ion selectivity can be studied by quantum chemical methods for [2.2.2] and smaller homologues. The calculated complex-formation energy is a reliable value to conclude which ion fits best.[38] In this study we will tie up with the first report by Lehn et al., where **1** and **2** were synthesised as $[Na\subset\mathbf{1}]^+$ and $[Na\subset\mathbf{2}]^+$ (see Figures 2 and 3).[20] We have calculated the complex-formation energies for the alkali and alkaline-earth metal ions to determine which ions fit best into **1** and **2**. In addition, we have investigated how the host responds to the different guest ions.

## Quantum Chemical Methods

We performed B3LYP/LANL2DZp hybrid density functional calculations, with pseudo-potentials on the heavy elements and the valence basis set augmented with polarisation functions.[39,40] During the optimisation of the structures no constraints other than symmetry were applied. In addition, the resulting structures were characterised as minima, transition structures, etc., by computation of their vibrational frequencies. The relative energies were corrected for zero-point vibrational energies (ZPE). The Gaussian suite of programs was used for all calculations.[41]

Semiempirical PM3 calculations[42] for $Li^+$[43], $K^+$[44] and $Ca^{2+}$[45] were performed using VAMP.[46] The PM3/

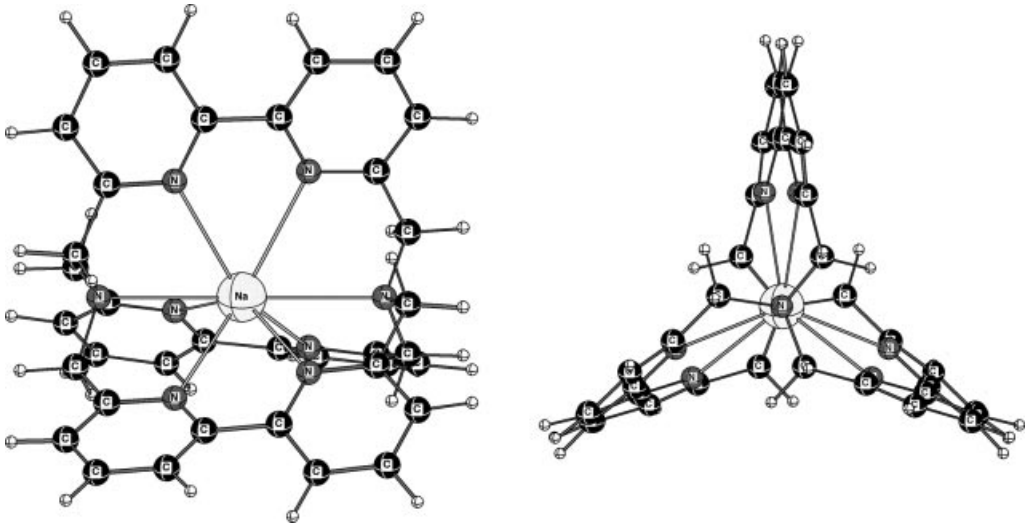

Figure 2. Calculated (RB3LYP/LANL2DZp) structure ($D_3$) of $[Na\subset\mathbf{1}]^+$.

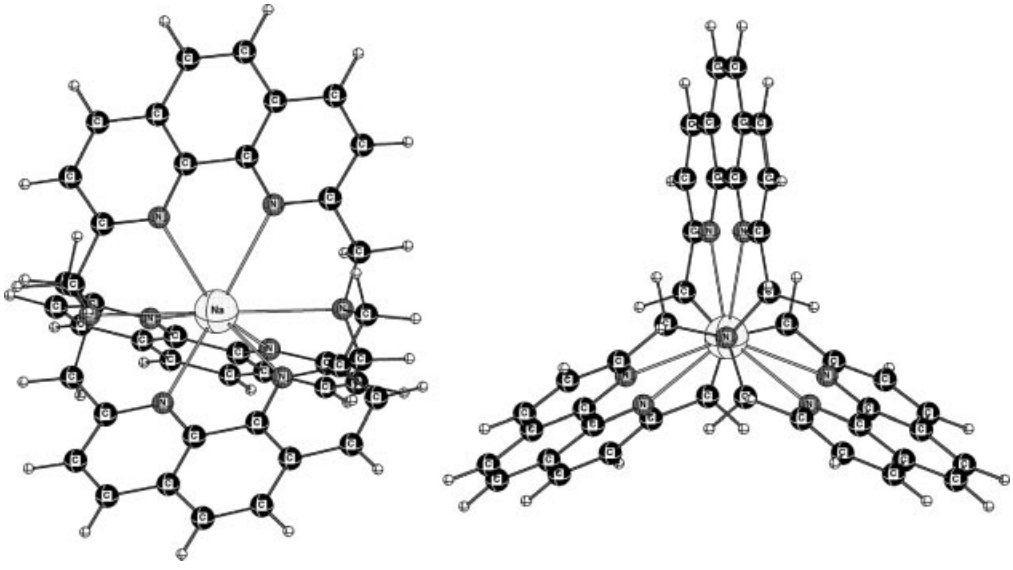

Figure 3. Calculated (RB3LYP/LANL2DZp) ($D_3$) and X-ray structure of $[Na\subset\mathbf{2}]^+$ (X-ray: $Na–N_{sp^2}$ = 2.70, $Na–N_{sp^3}$ = 2.79 Å[50]).

 © 2007 Wiley-VCH Verlag GmbH & Co. KGaA, Weinheim 

SPASS[38,47] calculations for all other alkali and alkaline-earth ions not included in PM3 were performed using MOPAC 6.0.[48]

## Results and Discussion

In contrast to [2.2.2], for which X-ray structures of all alkali and alkaline-earth metal cryptate complexes have been published, only the structures of [Na **1**]$^+$e$^-$[49] and [Na⊂**2**]Br[50] have been published for **1** and **2**. The cryptatium species [Na⊂**1**]$^+$e$^-$ is an electride[49] and therefore cannot be taken into consideration. The structural parameters for the calculated (Table 2) and published X-ray structure of [Na⊂**2**]$^+$ are in satisfactory agreement (the mean X-ray bond length between Na and the sp$^2$-hybridized pyridine nitrogen (Na–$N_{sp^2}$) is 2.70 Å, and that between Na and the amine nitrogen ($N_{sp^3}$) is 2.79 Å),[50] as expected. Further selected data for the calculated structures (metal–$N_{sp^2}$ and metal–$N_{sp^3}$ distances and the twist angle) are summarised in Tables 1 and 2.

The $Li^+$ and $Be^{2+}$ ions seem to be too small for **1** and **2** as the calculated $D_3$ structures of [Li⊂**1**]$^+$ and [Li⊂**2**]$^+$ as well as [Be⊂**1**]$^{2+}$ and [Be⊂**1**]$^{2+}$ are not local minima on the potential hypersurface. The $D_3$ structures of all endohedral complexed $Li^+$ and $Be^{2+}$ are transition states for the movement of the metal ion inside the cavity of **1** and **2**. This motion leads from one $N_{sp^3}$ to the other. Whereas [Li⊂**1**]$^+$ shows a clear barrier of 3.3 kcal mol$^{-1}$ for this movement, the $C_3$ and $D_3$ conformers of [Li⊂**2**]$^+$ have no barrier, indeed $D_3$ is even slightly negative (–0.1 kcal mol$^{-1}$). The $Be^{2+}$ ion is significantly smaller than $Li^+$ and therefore the barriers are higher: [Be⊂**1**]$^{2+}$ 22.4 kcal mol$^{-1}$ and [Be⊂**2**]$^{2+}$

Table 1. Distances [Å] and angles [°] of the metal–donor interactions in **1** (calculated structures: $D_3$ symmetry).[a]

| | $Li^+$ (C3) | $Li^+$ (t.s.) | $Na^+$ | $K^+$ | $Rb^+$ | $Cs^+$ | $Be^{2+}$ (C3) | $Be^{2+}$ (t.s.) | $Mg^{2+}$ | $Ca^{2+}$ | $Sr^{2+}$ | $Ba^{2+}$ |
|---|---|---|---|---|---|---|---|---|---|---|---|---|
| M–$N_{sp^2}$ (DFT) | 2.45/ 2.91 | 2.65 | 2.82 | 2.90 | 2.96 | 3.04 | 1.78/ 3.54 | 2.09 | 2.47 | 2.71 | 2.82 | 2.91 |
| M–$N_{sp^2}$ (PM3/SPASS) | 2.54/ 2.53 | – | 2.79 | 2.78 | 2.86 | 2.88 | 1.71/ 4.15 | – | 1.89/ 4.15(C3) | 2.67 | 2.69 | 2.81 |
| M–$N_{sp^3}$ (DFT) | 2.35/ 5.15 | 2.81 | 2.82 | 2.94 | 3.01 | 3.09 | 1.76/ 5.07 | 3.26 | 2.82 | 2.75 | 2.82 | 2.93 |
| M–$N_{sp^3}$ (PM3/SPASS) | 3.04/ 3.01 | – | 2.89 | 2.85 | 2.99 | 3.02 | 1.69/ 6.33 | – | 1.83/ 6.18(C3) | 2.78 | 2.88 | 2.95 |
| $N_{sp^2}$–C···C–$N_{sp^2}$ (DFT) | –26.1 | –23.4 | 21.5 | 34.0 | 41.3 | 54.4 | –68.2 | –32.7 | –24.4 | –14.2 | 15.06 | 26.4 |
| $N_{sp^2}$–C···C–$N_{sp^2}$ (PM3/SPASS) | –21.3 | – | 8.3 | 6.9 | 16.6 | 23.4 | –100.9 | – | –88.1(C3) | –8.7 | –6.9 | 9.2 |
| $CH_2$–$N_{sp^3}$···$N_{sp^3}$–$CH_2$ (DFT) | –99.4 | –100.3 | –78.4 | –62.1 | –53.3 | –42.7 | –109.0 | –138.3 | –113.9 | –95.5 | –78.2 | –61.9 |
| $CH_2$–$N_{sp^3}$···$N_{sp^3}$–$CH_2$ (PM3/SPASS) | –100.0 | – | –82.5 | –86.6 | –67.9 | –63.3 | –50.3 | – | –32.1(C3) | –100.8 | –90.3 | –73.7 |

[a] C3: the cryptate complex has only $C_3$ symmetry; t.s.: transition state.

Table 2. Distances [Å] and angles [°] of the metal–donor interactions in **2** (calculated structures: $D_3$ symmetry).[a]

| | $Li^+$ (C3) | $Li^+$ (t.s.) | $Na^+$ | $K^+$ | $Rb^+$ | $Cs^+$ | $Be^{2+}$ (C3) | $Be^{2+}$ (t.s.) | $Mg^{2+}$ | $Ca^{2+}$ | $Sr^{2+}$ | $Ba^{2+}$ |
|---|---|---|---|---|---|---|---|---|---|---|---|---|
| M–$N_{sp^2}$ (DFT) | 2.60/ 2.91 | 2.69 | 2.75 | 2.84 | 2.90 | 2.97 | 1.92/ 3.16 | 2.11 | 2.51 | 2.71 | 2.78 | 2.87 |
| M–$N_{sp^2}$ (PM3/SPASS) | 2.61/ 2.62 | – | 2.75 | 2.78 | 2.83 | 2.85 | 1.78/ 3.49 | – | 1.93/ 3.60 (C3) | 2.67 | 2.69 | 2.77 |
| M–$N_{sp^3}$ (DFT) | 2.41/ 3.25 | 2.82 | 2.84 | 2.90 | 2.96 | 3.03 | 1.79/ 4.28 | 3.22 | 2.78 | 2.80 | 2.85 | 2.92 |
| M–$N_{sp^3}$ (PM3/SPASS) | 2.96/ 2.94 | – | 2.93 | 2.85 | 2.98 | 3.00 | 1.70/ 5.32 | – | 1.84/ 5.27 (C3) | 2.82 | 2.92 | 2.96 |
| $N_{sp^2}$–C···C–$N_{sp^2}$ (DFT) | –2.1 | –2.1 | –0.2 | 2.8 | 5.1 | 7.7 | –16.7 | –16.2 | –7.2 | –1.6 | 0.4 | 3.0 |
| $N_{sp^2}$–C···C–$N_{sp^2}$ (PM3/SPASS) | –4.8 | – | 0.3 | 1.2 | 3.5 | 4.4 | –22.4 | – | –16.3(C3) | –2.2 | –2.2 | 0.6 |
| $CH_2$–$N_{sp^3}$···$N_{sp^3}$–$CH_2$ (DFT) | –86.8 | –92.3 | –85.4 | –73.8 | –64.9 | –55.1 | –119.5 | –138.3 | –109.9 | –89.6 | –80.5 | –68.8 |
| $CH_2$–$N_{sp^3}$···$N_{sp^3}$–$CH_2$ (PM3/SPASS) | –95.7 | – | –83.8 | –85.3 | –72.4 | –68.9 | –122.6 | – | –110.2 (C3) | –97.8 | –87.5 | –77.1 |

[a] C3: the cryptate complex has only $C_3$ symmetry; t.s.: transition state.

 © 2007 Wiley-VCH Verlag GmbH & Co. KGaA, Weinheim 

11.6 kcal mol$^{-1}$. The lower barriers in both cryptates based on **2** can be attributed to the rigidity of the phenanthroline moieties.

Interestingly, the quality of the structures calculated applying the simple PM3/SPASS method, in which the metal cation is modelled by a "sparkle" (a charged pseudo-atom), is very satisfactory, although the metal–sp$^2$-nitrogen distances are somewhat too short and the metal–sp$^3$-nitrogen interactions are somewhat too long compared to the DFT data.

The main goal of this work was to investigate the selective complexation of alkali and alkaline-earth metal ions by the cryptands **1** and **2**. As demonstrated in our earlier contributions,[11d,38] one can inspect two properties in order to predict whether or not an ion will be complexed. The bond length between the metal ion and the donor atoms in the cryptate can be compared with those computed for a metal ion complexed by solvent molecules like acetonitrile or ammonia. This method only seems to be of value if the donor atoms coordinating to the metal ions are the same in the cryptand and have the same hybridisation as in the solvent, and was therefore not followed further in this work. Alternatively, the energy of the model reactions shown in Equations (1) and (2) can be evaluated. Note that, for the sake of consistency, sixfold coordination is adopted for all cations. The lithium[51] and sodium cations prefer four- and fivefold coordination, respectively, with additional water molecules hydrogen-bonded in the second coordination sphere instead of being coordinated to the cation. However, in the gas phase $[Li(OH_2)_6]^+$ and $[Na(OH_2)_6]^+$ are local minima.

$$[M(H_2O)_6]^{n+} + \mathbf{1} \rightarrow [M\subset\mathbf{1}]^{n+} + 6H_2O \quad (1)$$

$$[M(H_2O)_6]^{n+} + \mathbf{2} \rightarrow [M\subset\mathbf{2}]^{n+} + 6H_2O \quad (2)$$

The complexation energies computed in this way are plotted against the ionic radii in Figures 4, 5, 6 and 7. The most stable endohedral complexes of **1** with the alkali-metal ions are formed for $K^+$ followed by $Na^+$ and with the alkaline-earth ions $Ca^{2+}$ and $Sr^{2+}$, followed by $Ba^{2+}$. Cryptand **2** prefers to bind $Na^+$ followed by $K^+$ of the alkali-metal ions, and $Ca^{2+}$ and $Sr^{2+}$ followed by $Ba^{2+}$ of the alkaline-earth ions. Therefore, we conclude that the cavity sizes of **1** and **2** are of the same order as the cavity size of [2.2.2], and that the cavity of **1** is slightly larger than that of **2**.

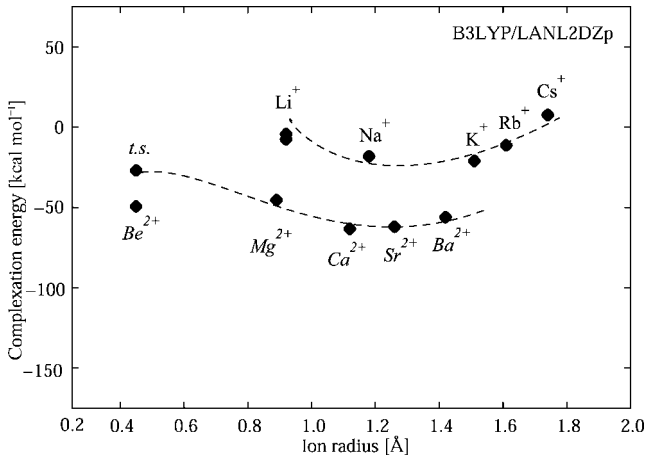


Figure 4. RB3LYP/LANL2DZp complexation energies for $[M\subset\mathbf{1}]^{n+}$ according to reaction (1), plotted against the ionic radius of $M^{n+}$ (dashed line represents observed trend; for the data see Table 3).

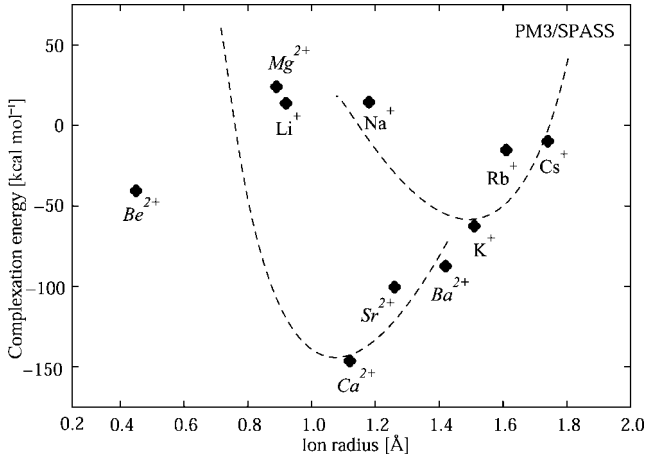


Figure 5. PM3/SPASS complexation energies for $[M\subset\mathbf{1}]^{n+}$ according to reaction (1), plotted against the ionic radius of $M^{n+}$ (dashed line represents observed trend; for the data see Table 4).

Table 3. Energy contributions[a] to the complexation energy for $[M\subset\mathbf{1}]^{n+}$ (RB3LYP/LANL2DZp).[b]

| | $Li^+$ (C3) | $Li^+$ (t.s.) | $Na^+$ | $K^+$ | $Rb^+$ | $Cs^+$ | $Be^{2+}$ (C3) | $Be^{2+}$ (t.s.) | $Mg^{2+}$ | $Ca^{2+}$ | $Sr^{2+}$ | $Ba^{2+}$ |
|---|---|---|---|---|---|---|---|---|---|---|---|---|
| $\Delta E_{tot}$ | –3.0 | –2.7 | –16.3 | –15.2 | –1.4 | 23.0 | –23.1 | –10.1 | –38.0 | –60.2 | –60.1 | –52.4 |
| ΔZPE | –5.9 | –6.3 | –5.0 | –5.2 | –5.2 | –5.1 | –10.8 | –12.2 | –9.6 | –8.5 | –8.1 | –6.9 |
| Complexation energy | –8.9 | –9.0 | –21.2 | –20.4 | –6.6 | 17.9 | –33.9 | –22.3 | –47.7 | –68.8 | –68.2 | –59.4 |

[a] In kcal mol$^{-1}$. [b] C3: the cryptate complex has only $C_3$ symmetry; t.s.: transition state.

Table 4. Complexation energy [kcal mol$^{-1}$] for $[M\subset\mathbf{1}]^{n+}$ (PM3/SPASS).[a]

| | $Li^+$ (C3) | $Na^+$ | $K^+$ | $Rb^+$ | $Cs^+$ | $Be^{2+}$ (C3) | $Mg^{2+}$ | $Ca^{2+}$ | $Sr^{2+}$ | $Ba^{2+}$ |
|---|---|---|---|---|---|---|---|---|---|---|
| Complexation energy | –2.5 | –8.2 | –40.8 | 4.4 | 12.5 | 19.7 | 73.3 | –125.9 | –822 | –69.4 |

[a] C3: the cryptate complex has only $C_3$ symmetry.

 © 2007 Wiley-VCH Verlag GmbH & Co. KGaA, Weinheim 

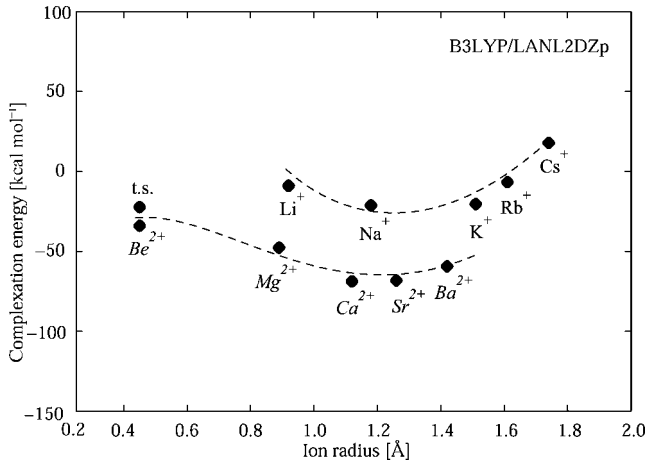


Figure 6. RB3LYP/LANL2DZp complexation energies for $[M\subset\mathbf{2}]^{n+}$ according to reaction (2), plotted against the ionic radius of $M^{n+}$ (dashed line represents observed trend; for the data see Table 5).

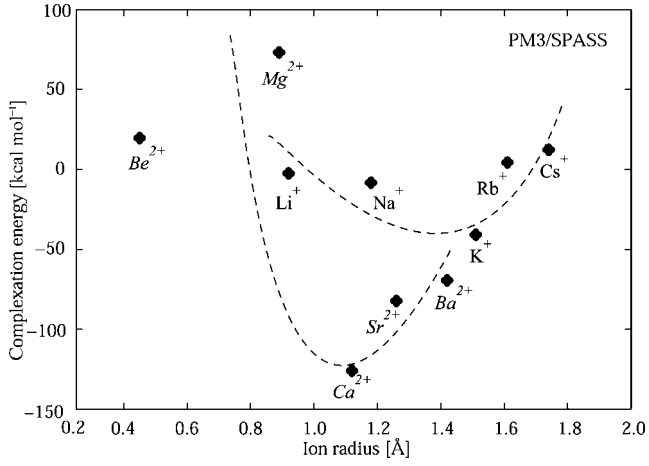


Figure 7. PM3/SPASS complexation energies for $[M\subset\mathbf{2}]^{n+}$ according to reaction (2), plotted against the ionic radius of $M^{n+}$ (dashed line represents observed trend; for the data see Table 6).

The same trend can be qualitatively found by application of semiempirical methods, in this case PM3/SPASS. (see Figures 5 and 7) In the semiempirical series, $[Ca\subset\mathbf{1}]^{2+}$ and $[Ca\subset\mathbf{2}]^{2+}$ and, to a lesser extent, $[K\subset\mathbf{2}]^{+}$ and $[K\subset\mathbf{2}]^{+}$, are computed to be too stable. Previous studies on the endohedral complexation of $Ca^{2+}$[38] and calculations on $[Ca(H_2O)_n]^{2+}$ and $[Ca(NH_3)_n]^{2+}$ confirm that the calcium PM3 parameters do not describe Ca–N and Ca–O interactions correctly. The semiempirical structures of $[Mg\subset\mathbf{1}]^{2+}$ and $[Mg\subset\mathbf{2}]^{2+}$ lead to a clear fourfold-coordinated $C_3$ structure and therefore show a larger energy gap than in the DFT case, although the qualitative result is not affected.

A comparison of the M–N distances (Tables 1 and 2) shows an increase in the metal–donor bond lengths with increasing size of the guest ion. This behaviour is clearly attributed to the different contributions of the guest ions, but it is also a distinct hint that the investigated cryptands show some flexibility. An essential prerequisite for flexibility is that the molecular moieties can undergo twisting and tilting. While in $[M\subset\mathbf{1}]^{n+}$ every molecular bar has two N–$CH_2$(pyridine) motifs adjacent to the N bridgehead and a conformationally nearly unhampered C–C bond bridging the two pyridine rings, $[M\subset\mathbf{2}]^{n+}$ has only two such pyridine motifs adjacent to the N bridgehead, and the two pyridine rings in phenanthroline are stiffened by a third, weaker aromatic[52] six-membered ring. A descriptor for the twist and tilt of these moieties is the torsion angle $N_{sp^2}$–C···C–$N_{sp^2}$ between the aromatic pyridine groups and the $CH_2$–$N_{sp^3}$···$N_{sp^3}$–$CH_2$ angle between the aliphatic methylene building blocks (see Tables 1 and 2).

Both sorts of torsion angles show a qualitative linear behaviour that mainly depends on the ion size (see Figures 8, 9, 10 and 11). The $CH_2$–$N_{sp^3}$···$N_{sp^3}$–$CH_2$ angle covers a wide range in both host–guest systems [96° for $[M\subset\mathbf{1}]^{n+}$ (see Figure 8)[53] and 83° for $[M\subset\mathbf{2}]^{n+}$ (see Figure 10)[53]]. Throughout the series, all cryptates show the same stereochemistry, which is easily derivable from the algebraic sign (here minus, and therefore λ). As expected, there are more drastic differences in the series of $N_{sp^2}$–C···C–$N_{sp^2}$ angles. Whereas the bipyridine building block shows a 1/3 higher value for the twist (123°)[53] (see Figure 9) compared to $CH_2$–$N_{sp^3}$···$N_{sp^3}$–$CH_2$, the phenanthroline moiety is inflexible and only shows a three times lower angle (25°)[53] (see Figure 11) than $CH_2$–$N_{sp^3}$···$N_{sp^3}$–$CH_2$. Interestingly, both coordinating systems use the same principle to improve the

Table 5. Energy contributions[a] to the complexation energy for $[M\subset\mathbf{2}]^{n+}$ (RB3LYP/LANL2DZp).[b]

| | $Li^+$ (C3) | $Li^+$ (t.s.) | $Na^+$ | $K^+$ | $Rb^+$ | $Cs^+$ | $Be^{2+}$ (C3) | $Be^{2+}$ (t.s.) | $Mg^{2+}$ | $Ca^{2+}$ | $Sr^{2+}$ | $Ba^{2+}$ |
|---|---|---|---|---|---|---|---|---|---|---|---|---|
| $\Delta E_{tot}$ | 1.5 | –1.5 | –13.71 | –16.59 | –6.5 | 11.8 | –38.7 | –15.12 | –36.2 | –55.27 | –54.46 | –49.78 |
| ΔZPE | –5.8 | –6.1 | –4.4 | –4.5 | –4.7 | –4.2 | –10.6 | –11.8 | –9.3 | –8.1 | –7.5 | –6.3 |
| Complexation energy | –4.3 | –7.6 | –18.1 | –21.1 | –11.3 | 7.5 | –49.3 | –26.9 | –45.5 | –63.4 | –62.0 | –56.1 |

[a] In kcal mol$^{-1}$. [b] C3: the cryptate complex has only $C_3$ symmetry; t.s.: transition state.

Table 6. Complexation energy [kcal mol$^{-1}$] for $[M\subset\mathbf{2}]^{n+}$ (PM3/SPASS).[a]

| | $Li^+$ (C3) | $Na^+$ | $K^+$ | $Rb^+$ | $Cs^+$ | $Be^{2+}$ (C3) | $Mg^{2+}$ | $Ca^{2+}$ | $Sr^{2+}$ | $Ba^{2+}$ |
|---|---|---|---|---|---|---|---|---|---|---|
| Complexation energy | 13.8 | 14.4 | –62.6 | –15.3 | –9.8 | –40.6 | 24.0 | –146.4 | –100.5 | –87.4 |

[a] C3: the cryptate complex has only $C_3$ symmetry.

 © 2007 Wiley-VCH Verlag GmbH & Co. KGaA, Weinheim 

interactions between donor and guest ion: in order to get more tilted and closer to the ion, the puckered ring formed by the pyridine moieties and guest ions interconvert their stereochemistry. Therefore, small ions like $Li^+$, $Be^{2+}$ and $Ca^{2+}$ have a λλ arrangement as both torsion angles show negative algebraic signs, whereas the larger ions $K^+$, $Rb^+$, $Cs^+$, $Sr^{2+}$ and $Ba^{2+}$ have a λδ arrangement since $CH_2$–$N_{sp^3}$···$N_{sp^3}$–$CH_2$ is negative and $N_{sp^2}$–C···C–$N_{sp^2}$ is positive. The sodium cation is a special case. Thus, whereas $[Na\subset\mathbf{1}]^+$ is clearly λλ, the stiffened cryptand $[Na\subset\mathbf{2}]^+$ is only just λλ since the $N_{sp^2}$–C···C–$N_{sp^2}$ angle is only –0.2°.

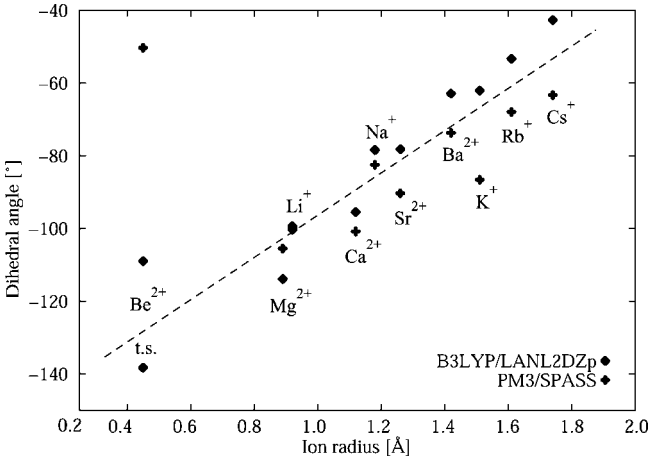


Figure 8. RB3LYP/LANL2DZp and PM3/SPASS torsion angle $CH_2$–$N_{sp^3}$···$N_{sp^3}$–$CH_2$ of $[M\subset\mathbf{1}]^{n+}$ plotted against the ionic radius of $M^{n+}$ (dashed line represents observed trend).

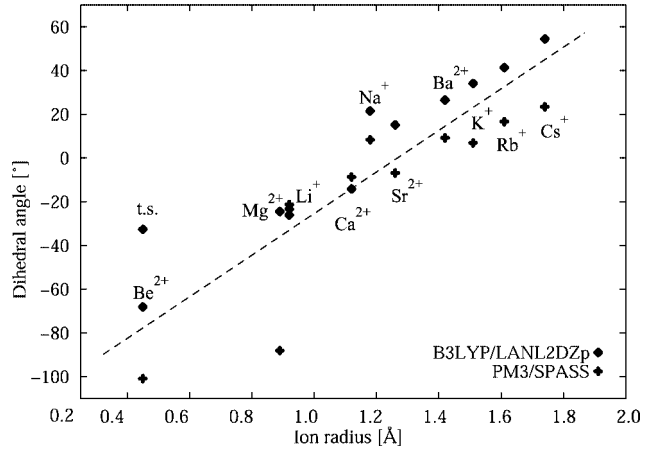


Figure 9. RB3LYP/LANL2DZp and PM3/SPASS torsion angle $N_{sp^2}$–C···C–$N_{sp^2}$ of $[M\subset\mathbf{1}]^{n+}$ plotted against the ionic radius of $M^{n+}$ (dashed line represents observed trend).

## Conclusions

Density functional theory and PM3/SPASS suggest that **1** and **2** have similar-sized cavities to [2.2.2]. According to our calculations and introduced model reactions, the investigated cryptands prefer $Ca^{2+}$ and $Sr^{2+}$ as alkaline-earth ions, whereas $K^+$ is preferred by **1** and **2** binds $Na^+$ and $K^+$ equally well. The flexibility, which is important for selective

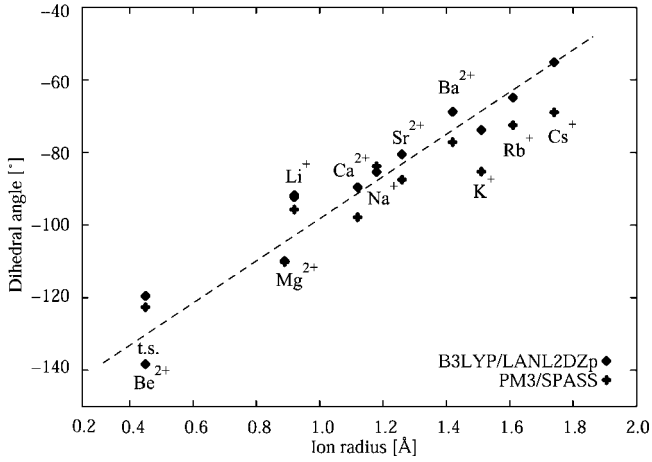


Figure 10. RB3LYP/LANL2DZp and PM3/SPASS torsion angle $CH_2$–$N_{sp^3}$···$N_{sp^3}$–$CH_2$ of $[M\subset\mathbf{2}]^{n+}$ plotted against the ionic radius of $M^{n+}$ (dashed line represents observed trend).

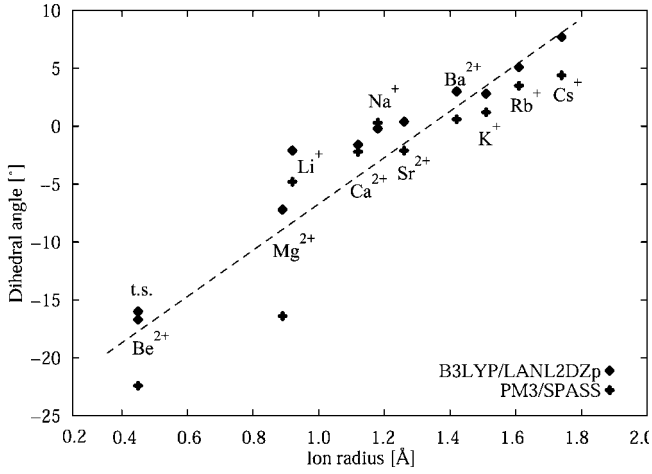


Figure 11. RB3LYP/LANL2DZp and PM3/SPASS torsion angle $N_{sp^2}$–C···C–$N_{sp^2}$ of $[M\subset\mathbf{2}]^{n+}$ plotted against the ionic radius of $M^{n+}$ (dashed line represents observed trend).

host binding, is dominated in **1** by the flexibility of the pyridine–pyridine connection, whereas in the more rigid **2** the $CH_2$–$N_{sp^3}$···$N_{sp^3}$–$CH_2$ motif contributes the main part. The stereo-arrangement of the molecular cage axis fixed at the bridgehead nitrogen is identical in all host–guest systems investigated and does not change during the calculations. On the contrary, the stereochemistry of the coordinating bipyridine and phenanthroline moieties can change depending on the size of the guest ion.

## Acknowledgments

The authors gratefully acknowledge financial support from the Deutsche Forschungsgemeinschaft as part of the SFB 583 "Redox-Active Metal Complexes" and the Fonds der Chemischen Industrie. We thank Prof. Tim Clark for hosting this work at the CCC, Nico van Eikema Hommes and Roland Meier for helpful discussions, and the Regionales Rechenzentrum Erlangen (RRZE) for a generous allotment of computer time.

 © 2007 Wiley-VCH Verlag GmbH & Co. KGaA, Weinheim 

[1] F. Haber, *Angew. Chem.* **1927**, *40*, 303–314.
[2] E. Bayer, H. Fiedler, K.-L. Hock, D. Otterbach, G. Schenk, W. Voelter, *Angew. Chem.* **1964**, *76*, 76–83; *Angew. Chem. Int. Ed. Engl.* **1964**, *3*, 325–332 and the literature cited therein.
[3] J.-M. Lehn, *Supramolecular Chemistry*, VCH, Weinheim **1995**.
[4] F. Vögtle, *Supramolekulare Chemie*, Teubner, Stuttgart **1992**.
[5] G. Jaouen, *Bioorganometallics*, Wiley-VCH, Weinheim **2005**.
[6] See, for example: a) J. Schatz, *Collect Czech. Chem. Commun.* **2004**, *69*, 1169–1194; b) R. Puchta, T. Clark, W. Bauer, *J. Mol. Model.* **2006**, *12*, 739–747.
[7] W. Śliwa, *Pol. J. Chem.* **2001**, *75*, 921–940.
[8] See, for example, a) C. J. Pedersen, *Angew. Chem.* **1988**, *100*, 1053–1059; *Angew. Chem. Int. Ed. Engl.* **1988**, *27*, 1021–1027; b) D. J. Cram, *Angew. Chem.* **1988**, *100*, 1041–1052; *Angew. Chem. Int. Ed. Engl.* **1988**, *27*, 1009–1020; c) J.-M. Lehn, *Angew. Chem.* **1988**, *100*, 91–116; *Angew. Chem. Int. Ed. Engl.* **1988**, *27*, 89–112 and the literature cited therein; d) J. Ellermann, W. Bauer, M. Schütz, F. W. Heinemann, M. Moll, *Monatsh. Chem.* **1998**, *129*, 547–566; e) S. H. Hausner, C. A. F. Striley, J. A. Krause-Bauer, H. Zimmer, *J. Org. Chem.* **2005**, *70*, 5804–5817.
[9] See, for example: J.-M. Lehn, *Acc. Chem. Res.* **1978**, *11*, 49–57.
[10] B. Dietrich, P. Viout, J-M. Lehn, *Macrocyclic Chemistry*, VCH, Weinheim **1993**.
[11] See, for example: a) R. W. Saalfrank, A. Dresel, V. Seitz, S. Trummer, F. Hampel, M. Teichert, D. Stalke, C. Stadler, J. Daub, V. Schünemann, A. X. Trautwein, *Chem. Eur. J.* **1997**, *3*, 2058–2061; b) R. W. Saalfrank, N. Löw, S. Kareth, V. Seitz, F. Hampel, D. Stalke, M. Teichert, *Angew. Chem.* **1998**, *110*, 182–184; *Angew. Chem. Int. Ed.* **1998**, *37*, 172–174; c) R. W. Saalfrank, V. Seitz, D. L. Caulder, K. N. Raymond, M. Teichert, D. Stalke, *Eur. J. Inorg. Chem.* **1998**, 1313–1317; d) R. Puchta, V. Seitz, N. J. R. van Eikema Hommes, R. W. Saalfrank, *J. Mol. Model.* **2000**, *6*, 126–132; e) R. W. Saalfrank, V. Seitz, F. W. Heinemann, C. Göbel, R. Herbst-Irmer, *J. Chem. Soc., Dalton Trans.* **2001**, 599–603; f) R. W. Saalfrank, I. Bernt, E. Uller, F. Hampel, *Angew. Chem.* **1997**, *109*, 2596–2599; *Angew. Chem. Int. Ed. Engl.* **1997**, *36*, 2482–2485; g) O. Waldmann, J. Schülein, R. Koch, P. Müller, I. Bernt, R. W. Saalfrank, H.-P. Andres, H. U. Güdel, *Inorg. Chem.* **1999**, *38*, 5879–5886; h) R. W. Saalfrank, Ch. Deutscher, H. Maid, A. M. Ako, S. Sperner, T. Nakajima, W. Bauer, F. Hampel, B. A. Heß, N. J. R. van Eikema Hommes, R. Puchta, F. W. Heinemann, *Chem. Eur. J.* **2004**, *10*, 1899–1905; i) R. W. Saalfrank, T. Nakajima, N. Mooren, A. Scheurer, H. Maid, F. Hampel, Ch. Trieflinger, J. Daub, *Eur. J. Inorg. Chem.* **2005**, 1149–1153 and the literature cited therein.
[12] See, for example: E. V. Demlov, *Phase Transfer Catalysts*, MERCK-Schuchardt, Darmstadt.
[13] See, for example: J.-H. Li, J. S. Shih, *J. Chin. Chem. Soc.* **1999**, *46*, 885–888.
[14] See, for example: C. E. Housecroft, *Clusterverbindungen von Hauptgruppenelementen*, VCH, Weinheim, **1994**.
[15] See, for example: W. H. Müller, *Naturwissenschaften* **1970**, *57*, 248; J.-M. Lehn, F. Montavon, *Helv. Chim. Acta* **1978**, *61*, 67–82; J.-M. Lehn, M. Kirch, *Angew. Chem.* **1975**, *87*, 542–543; *Angew. Chem. Int. Ed. Engl.* **1975**, *14*, 555–556.
[16] See, for example: H. S. Ajgaonkar, S. M. Khopkar, *Chem. Anal.* **1999**, *44*, 61–66.
[17] D. Tait, G. Haase, A. Wiechen, *Kieler Milchwirtschaftliche Forschungsberichte* **1998**, *50*, 211–223.
[18] L. Burai, R. Scopelliti, E. Tóth, *Chem. Commun.* **2002**, 2366–2367.
[19] M. Farahbakhsh, H. Schmidt, D. Rehder, *Chem. Ber./Recueil* **1997**, *130*, 1123–1127.
[20] J.-C. Rodriguez-Urbi, B. Alpha, D. Plancherel, J.-M. Lehn, *Helv. Chim. Acta* **1984**, *67*, 2264–2269.
[21] H. Dürr, K. Zengerle, H. P. Trierweiler, *Z. Naturforsch. Teil B* **1988**, *43*, 361–367.
[22] B. Alpha, J.-M. Lehn, G. Mathis, *Angew. Chem.* **1987**, *99*, 259–261; *Angew. Chem. Int. Ed. Engl.* **1987**, *26*, 266–267.
[23] B. Alpha, V. Balzani, J.-M. Lehn, S. Perathoner, N. Sabbatini, *Angew. Chem.* **1987**, *99*, 1310–1311; *Angew. Chem. Int. Ed. Engl.* **1987**, *26*, 1266–1267.
[24] G. Mathis, J.-M. Lehn, FR 2570703, **1986**.
[25] H. Bazin, G. Mathis, WO 9918114, **1999**.
[26] M. A. Billadeau, J. K. Leland, L. Shen, WO 9641177, **1996**.
[27] L. Burai, E. Tóth, H. Bazin, M. Benmelouka, Z. Jászberényi, L. Helm, A. E. Merbach, *Dalton Trans.* **2006**, 629.
[28] V. K. Manchana, P. K. Mohapatra, *J. Incl. Phenom.* **1993**, *15*, 121–130.
[29] V. K. Manchana, P. K. Mohapatra, *Polyhedron* **1993**, *12*, 1115–1117.
[30] E. Karkhaneei, M. H. Zebarjadian, M. Shamsipur, *J. Solution Chem.* **2001**, *30*, 323–333.
[31] T. Madrakian, M. Shamsipur, *J. Coord. Chem.* **2000**, *52*, 139–149.
[32] M. Hojo, I. Hisatsune, H. Tsurui, S. Minami, *Anal. Sci.* **2000**, *16*, 1277–1284.
[33] T. Madrakian, M. Shamsipur, *Polyhedron* **1996**, *15*, 1681–1685.
[34] M. Shamsipur, E. Karkhaneei, A. Afkhami, *J. Coord. Chem.* **1998**, *44*, 23–32.
[35] A. D′Aprano, B. Sesta, A. Capalbi, M. Immarino, V. Mauro, *J. Electroanal. Chem.* **1996**, *403*, 257–260.
[36] E. Pasgreta, R. Puchta, M. Galle, N. J. R. van Eikema Hommes, A. Zahl, R. van Eldik, *J. Incl. Phenom.*; DOI: 10.1007/s10847-006-9125-y.
[37] T. Madrakian, A. Afkhami, J. Ghasemi, M. Shamsipur, *Polyhedron* **1996**, *15*, 3647–3652.
[38] M. Galle, R. Puchta, N. J. R. van Eikema Hommes, R. van Eldik, *Z. Phys. Chem.* **2006**, *220*, 511–523.
[39] a) A. D. Becke, *J. Phys. Chem.* **1993**, *97*, 5648–5652; b) C. Lee, W. Yang, R. G. Parr, *Phys. Rev. B* **1988**, *37*, 785–789; c) P. J. Stephens, F. J. Devlin, C. F. Chabalowski, M. J. Frisch, *J. Phys. Chem.* **1994**, *98*, 11623–11627; d) T. H. Dunning Jr, P. J. Hay, *Mod. Theor. Chem.* **1976**, *3*, 1–28; e) P. J. Hay, W. R. Wadt, *J. Chem. Phys.* **1985**, *82*, 270–283; f) P. J. Hay, W. R. Wadt, *J. Chem. Phys.* **1985**, *82*, 284–298; g) P. J. Hay, W. R. Wadt, *J. Chem. Phys.* **1985**, *82*, 299–310; h) *Gaussian Basis Sets for Molecular Calculations* (Ed.: ), S. Huzinaga, Elsevier, Amsterdam **1984**.
[40] The performance of the computational level employed in this study is well documented. See for example: a) R. Puchta, R. Meier, N. J. R. van Eikema Hommes, R. van Eldik, *Eur. J. Inorg. Chem.* **2006**, 4063–4067; b) A. Scheurer, H. Maid, F. Hampel, R. W. Saalfrank, L. Toupet, P. Mosset, R. Puchta, N. J. R. van Eikema Hommes, *Eur. J. Org. Chem.* **2005**, 2566–2574; c) P. Illner, A. Zahl, R. Puchta, N. van Eikema Hommes, P. Wasserscheid, R. van Eldik, *J. Organomet. Chem.* **2005**, *690*, 3567–3576; d) Ch. F. Weber, R. Puchta, N. van Eikema Hommes, P. Wasserscheid, R. van Eldik, *Angew. Chem.* **2005**, *117*, 6187–6192; *Angew. Chem. Int. Ed.* **2005**, *44*, 6033–6038.
[41] *Gaussian 03*, Revision C.02, M. J. Frisch, G. W. Trucks, H. B. Schlegel, G. E. Scuseria, M. A. Robb, J. R. Cheeseman, J. A. Montgomery Jr, T. Vreven, K. N. Kudin, J. C. Burant, J. M. Millam, S. S. Iyengar, J. Tomasi, V. Barone, B. Mennucci, M. Cossi, G. Scalmani, N. Rega, G. A. Petersson, H. Nakatsuji, M. Hada, M. Ehara, K. Toyota, R. Fukuda, J. Hasegawa, M. Ishida, T. Nakajima, Y. Honda, O. Kitao, H. Nakai, M. Klene, X. Li, J. E. Knox, H. P. Hratchian, J. B. Cross, C. Adamo, J. Jaramillo, R. Gomperts, R. E. Stratmann, O. Yazyev, A. J. Austin, R. Cammi, C. Pomelli, J. W. Ochterski, P. Y. Ayala, K. Morokuma, G. A. Voth, P. Salvador, J. J. Dannenberg, V. G. Zakrzewski, S. Dapprich, A. D. Daniels, M. C. Strain, O. Farkas, D. K. Malick, A. D. Rabuck, K. Raghavachari, J. B. Foresman, J. V. Ortiz, Q. Cui, A. G. Baboul, S. Clifford, J. Cioslowski, B. B. Stefanov, G. Liu, A. Liashenko, P. Piskorz, I. Komaromi, R. L. Martin, D. J. Fox, T. Keith, M. A. Al-Laham, C. Y. Peng, A. Nanayakkara, M. Challacombe, P. M. W. Gill,


 © 2007 Wiley-VCH Verlag GmbH & Co. KGaA, Weinheim 

B. Johnson, W. Chen, M. W. Wong, C. Gonzalez, and J. A. Pople, Gaussian, Inc., Wallingford CT, **2004**.
[42] J. J. P. Stewart, *J. Comput. Chem.* **1989**, *10*, 209–220; J. J. P. Stewart, *J. Comput. Chem.* **1991**, *12*, 320–341.
[43] E. Anders, R. Koch, P. Freunscht, *J. Comput. Chem.* **1993**, *14*, 1301–1312.
[44] Z. Havlas, S. Nick, H. Bock, *Int. J. Quantum Chem.* **1992**, *44*, 449–467.
[45] J. Yu, W. J. Hehre, to be published (implemented in Spartan, Version 4.1 and higher).
[46] VAMP 7.5a, T. Clark, A. Alex, B. Beck, J. Chandrasekhar, P. Gedeck, A. Horn, M. Hutter, B. Martin, G. Rauhut, W. Sauer, T. Schindler, T. Steinke, Erlangen **1999**.
[47] PM3 augmented with a Sparkle parameter for $Na^+$, $Rb^+$, $Cs^+$, $Sr^{2+}$ and $Ba^{2+}$, R. Puchta, PhD Thesis, Erlangen, **2003**.
[48] MOPAC 6.0: J. J. P. Stewart, *QCPE 455*.
[49] L. Echegoyen, A. DeCian, J. Fischer, J.-M. Lehn, *Angew. Chem.* **1991**, *103*, 884–886; *Angew. Chem. Int. Ed. Engl.* **1991**, *30*, 838–840.
[50] A. Caron, J. Guilhem, C. Rieche, C. Pascard, B. Alpha, J.-M. Lehn, J.-C. Rodriguez-Urbis, *Helv. Chim. Acta* **1985**, *68*, 1577–1582.
[51] R. Puchta, M. Galle, N. van Eikema Hommes, E. Pasgreta, R. van Eldik, *Inorg. Chem.* **2004**, *43*, 8227–8229 and the literature cited therein.
[52] Z. Chen, Ch. S. Wannere, C. Corminboeuf, R. Puchta, P. von Ragué Schleyer, *Chem. Rev.* **2005**, *105*, 3842–3888.
[53] Values taken from the DFT calculations.

Received: August 1, 2006
Published Online: February 9, 2007

 © 2007 Wiley-VCH Verlag GmbH & Co. KGaA, Weinheim 

DOI: 10.1002/ejic.200600850

# Synthesis of Controllable-Size Core–Shell Se@Ag and Se@Au Nanoparticles in UV-Irradiated TSA Solution

**Liangbao Yang,[a] Yuhua Shen,*[a,b] Anjian Xie,[a,b] Jianjun Liang,[a] Jinmiao Zhu,[a] and Long Chen[a]**

**Keywords:** Nanostructures / Photochemistry / Core–shell structures / Selenium

The formation of Se-core–Au-shell and Se-core–Ag-shell nanoparticles by using photochemically reduced tungstosilicate Keggin ions has been described. The Se core structure serves both as a chemical and a physical template for the coating of Au and Ag. With this method, the core size and the shell thickness can be controlled by varying the conditions. With this strategy, it is possible to realize a large combination of core–shell nanostructures with potential application in engineered nanomaterials and catalysis by using Keggin ions.

(© Wiley-VCH Verlag GmbH & Co. KGaA, 69451 Weinheim, Germany, 2007)

## Introduction

For many years, considerable effort has been made to design, fabricate and manipulate nanostructured systems with functional properties.[1] This knowledge, together with effective strategies towards the fabrication of nanostructures, has inspired the design and development of new composites for advanced applications. Core–shell structures provide a useful means to modify the properties of nanoparticles.[2] Such core–shell nanoparticles have become attractive because of the advantages offered by the combination of the properties of different compositions and of the shelled structures. They are used as building blocks for photonic crystals,[3] as heterogeneous catalysts,[4] in multienzyme biocatalysis,[5] and in surface-enhanced Raman scattering[6] and drug-delivery applications.[7] Most studies on the core–shell particles have focused on composites that are typically composed of solid or liquid cores surrounded by shells of polymers, inorganic compounds, or biomacromolecules. They provide the possibility of enhanced functionality and multifunctional properties, which is in contrast with their more-limited, single-component counterparts.

Semiconductor-metal core–shell structures are most interesting because of the bifunctional properties of the metal and the semiconductor.[8–10] In this work, we report a facile, one-pot synthesis of Se@Au and Se@Ag composite colloids in UV-irradiated TSA solution. Such Se@Au(Ag) nanocomposite colloids are expected to be useful in biotechnology, as Se is an essential trace element for humans. Further, Se is an important elemental semiconductor, because of its many intriguing photoelectrical properties as well as its applications in semiconductor rectifiers, solar cells, photographic exposure meters, and xerography.[11] Silver or gold exhibits high-temperature and high-pressure stability and resistance to acids, bases, and solvents.[12] Combination of the two nanomaterials of Se and Au or of Se and Ag provides a model structure for the further understanding of the core–shell heterostructures and their properties. The composite colloids produced are also expected to have potential applications in electronics, photonics, catalysis, and sensors. Metal-based materials with nanoscale hollow interiors exhibit promising properties for diverse applications.[13] As reported previously,[14] the Se-core composites can be used as precursors to yield hollow capsules by subsequent removal of the sacrificial Se cores; this is because Se exhibits high solubility in various solvents (e.g. $CS_2$ and $N_2H_4$) and a relatively low melting point (≈ 217 °C).[11]

Experimental procedures for the synthesis of core–shell nanostructures are rather cumbersome and involve several steps. Generally, growth of core–shell structures can be accomplished by the successive reduction of one metal ion over the core of another.[15–18] Keggin ions have a special structure, which may be reduced photochemically.[19,20] Sastry and co-workers have demonstrated that bimetallic nanoparticles can be synthesized by using Keggin ions as a UV-switchable reducing agent.[21,22] In this paper, we use a strategy that involves the immobilization of a reducing agent such as tungstosilicate acid (TSA) in the solution of the core, which, when exposed to the second metal ions, can selectively reduce them on the surface to lead to phase-pure

[a] School of Chemistry and Chemical Engineering, Anhui University,
Hefei 230039, P. R. China
Fax: +86-551-5107342
E-mail: s_yuhua@163.com
[b] State Key Laboratory of Coordination Chemistry, Nanjing University,
Nanjing 210093, P. R. China
[c] Chuzhou Vocational Technology College,
Chuzhou 239000, P. R. China

 © 2007 Wiley-VCH Verlag GmbH & Co. KGaA, Weinheim 

core–shell structures. An advantageous feature of this approach for obtaining phase-pure core–shell nanoparticle structures could be a reducing agent bound to the surface of the core nanoparticle that can be selectively activated (i.e. whose reducing capability can be switched off and on at will). The mechanism is also discussed. Presented below are details of the investigation.

## Results and Discussion

Figures 1A and B show the UV/Vis spectra of the Se-core–Au-shell and Se-core–Ag-shell nanoparticle solutions, respectively, at different stages of preparation. Curve 1 in Figure 1 corresponds to the spectrum of a 1 mM TSA/1 mM $H_2SeO_3$ aqueous solution. It can be observed that there is no absorption in the visible region of the electromagnetic spectrum. The UV/Vis absorption spectrum recorded after UV irradiation of the TSA/$H_2SeO_3$ solution for 5 h is shown as curve 2 in Figure 1. It can be clearly seen that an absorption band starts to form from ca. 655 nm. This absorption band may arise as a result of excitation of the surface plasmon vibrations in the Se nanoparticles.[23] The TSA/Se nanoparticle solution was further irradiated with UV light for 3 h; this UV/Vis spectrum is shown as curve 3 in Figure 1. At this stage, the color of the solution changed from orange to bluish-red; these changes are reflected as an increase in absorption at 760 nm in the spectrum. This increase in absorption at long wavelengths clearly indicates that the TSA ions have been reduced.[20] Curve 4 in Figure 1 corresponds to the UV/Vis spectra of the UV-irradiated TSA/Se nanoparticle solution after addition of $HAuCl_4$ (Figure 1A) and $AgNO_3$ solutions (Figure 1B). Strong absorption bands at ca. 540 nm and ca.410 nm are observed. These absorption bands arise from excitation of the surface plasmon vibrations in the Au[20,21,24] and Ag[20,21] nanoparticles. Curve 5 in Figure 1 corresponds to the TSA/Se solution without further UV irradiation (sample 2) with the addition of $10^{-3}$ M aqueous solutions of $HAuCl_4$ (Figure 1A) and $AgNO_3$ (Figure 1B). When curves 4 and 5 in Figures 1A and B are compared, large changes in both the UV/Vis absorption spectra of the gold and silver nanoparticle solutions are observed. Thus, the photochemical charging of the TSA molecules is the most crucial step in the protocol, which sets this protocol apart from other bimetallic nanoparticle core–shell synthesis protocols that employ reducing agents present uniformly in the reaction media. That the reducing capability of the TSA ions can be switched on by irradiation with UV light is an additional feature that enhances the versatility of this technique.

The XRD pattern recorded from a drop-coated film of the UV-irradiated TSA solution after addition of $H_2SeO_3$ on a glass substrate is shown in Figure 2, curve 1. All of the strong and sharp reflection peaks can readily be indexed to a single phase of trigonal-structured selenium (indicated by "*", JCPDS Cards No. 86-2246). Curve 2 in Figure 2 shows the XRD pattern recorded from a drop-coated film of the UV-irradiated TSA/Se solution after addition of $HAuCl_4$ (Figure 2A) and $AgNO_3$ (Figure 2B) solutions. The (111), (200), and (220) Bragg reflections of face-centered cubic gold and silver are clearly observed. The background is most likely caused by Brownian motion of the particles during the scan, solvent scattering, or the short-range order of the solvation cage around the particles. The results, obtained from XRD, indicate that the products of Se and Au/Ag are crystalline and have a high purity.

To confirm the presence of Se, Au, and Ag in Se–Au- and Se–Ag-core–shell nanoparticles, a chemical analysis of these samples was performed by using XPS. The Se 3d core level spectra recorded from the Se-core–Au-shell and Se-core–Ag-shell nanoparticles at various stages of preparation are shown in Figure 3A and Figure 3B, respectively, while the Au 4f core level spectrum from the Se-core–Au-shell sample and the Ag 3d core level spectrum from the Se-core–Ag-shell nanoparticles are shown in Figure 3C and Figure 3D, respectively. The binding energy at 53.61 eV (Figure 3A) or 54.32eV (Figure 3B), corresponding to Se 3d, is the characteristic peak for elemental selenium,[25,26] which

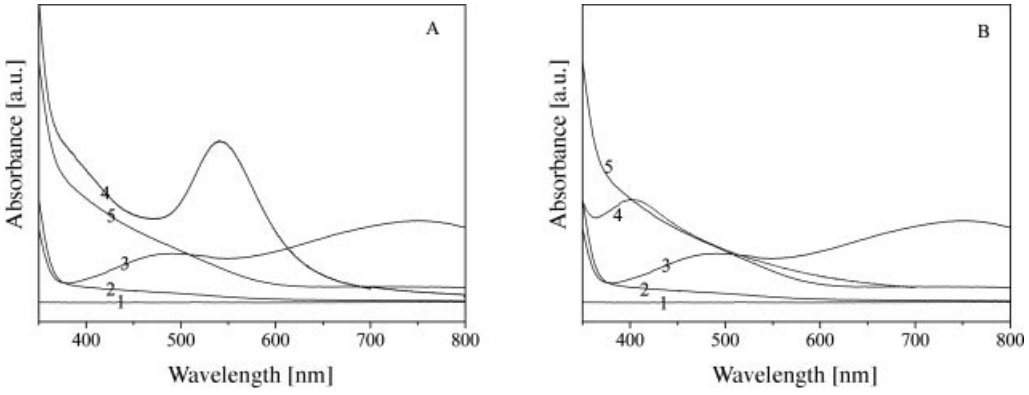


Figure 1. (A) and (B) show the UV/Vis spectra of the Se-core–Au/Ag-shell nanoparticle solutions at different stages of reaction. Curve 1 in (A) and (B): $10^{-3}$ M TSA/$10^{-3}$ M $H_2SeO_3$ aqueous solution before UV irradiation; curve 2 in (A) and (B): TSA/$H_2SeO_3$ solution (sample 1) after UV irradiation for 5 h.; curve 3 in (A) and (B): further UV irradiation of sample 2 (for 3 h); curve 4: addition of $10^{-3}$ M $HAuCl_4$ (A) and $AgNO_3$ (B) solutions to sample 3; curve 5: addition of $10^{-3}$ M aqueous solutions of $HAuCl_4$ (A) and $AgNO_3$ (B) to sample 2 (no further UV irradiation).

 © 2007 Wiley-VCH Verlag GmbH & Co. KGaA, Weinheim 

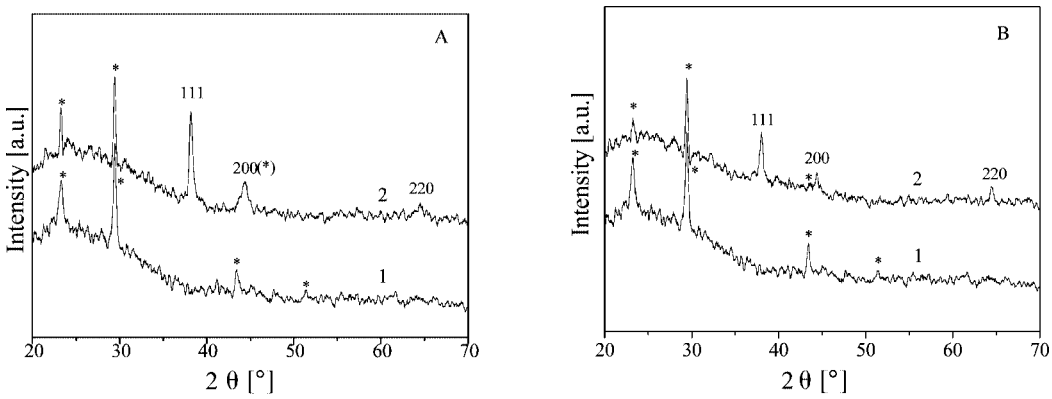


Figure 2. (A) and (B) show the XRD patterns recorded from drop-coated films on glass substrates of the Se-core–Au/Ag-shell nanoparticle solutions at different stages of reaction. Curve 1 in (A) and (B): UV-irradiated TSA solution after addition of $10^{-3}$ M $H_2SeO_3$; Curve 2: UV-irradiated TSA/Se solution after addition of $10^{-3}$ M $HAuCl_4$ (A) and $AgNO_3$ (B) solutions. The Bragg reflections marked * correspond to Se.

implies that the valence of selenium in the core is zero. The Au 4f core level spectrum recorded from the Se–Au-core–shell nanoparticle sample could be resolved into a single spin-orbit pair (spin-orbit splitting ≈ 3.71 eV) with a $4f_{7/2}$ binding energy (BE) of 83.68 eV (Figure 3C). This BE is characteristic of Au in the fully reduced state.[27] The Ag 3d spectrum (Figure 3D) resolves into two spin-orbit components. The Ag $3d_{5/2}$ and $3d_{3/2}$ peaks occur at a BE of 367.8 and 373.8 eV, respectively, and correspond to metallic silver.[28] This result demonstrates that only one form of Ag is present in solution, in the form of $Ag^0$.

Figure 4 shows a representative TEM image of the Se nanoparticle solution. From the TEM image, it can clearly be seen that the nanoparticles, with an average size in diameter of 40 nm, are spherical colloids. Figure 5A and Figure 6A display the SEM images of Se@Au- and Se@Ag-

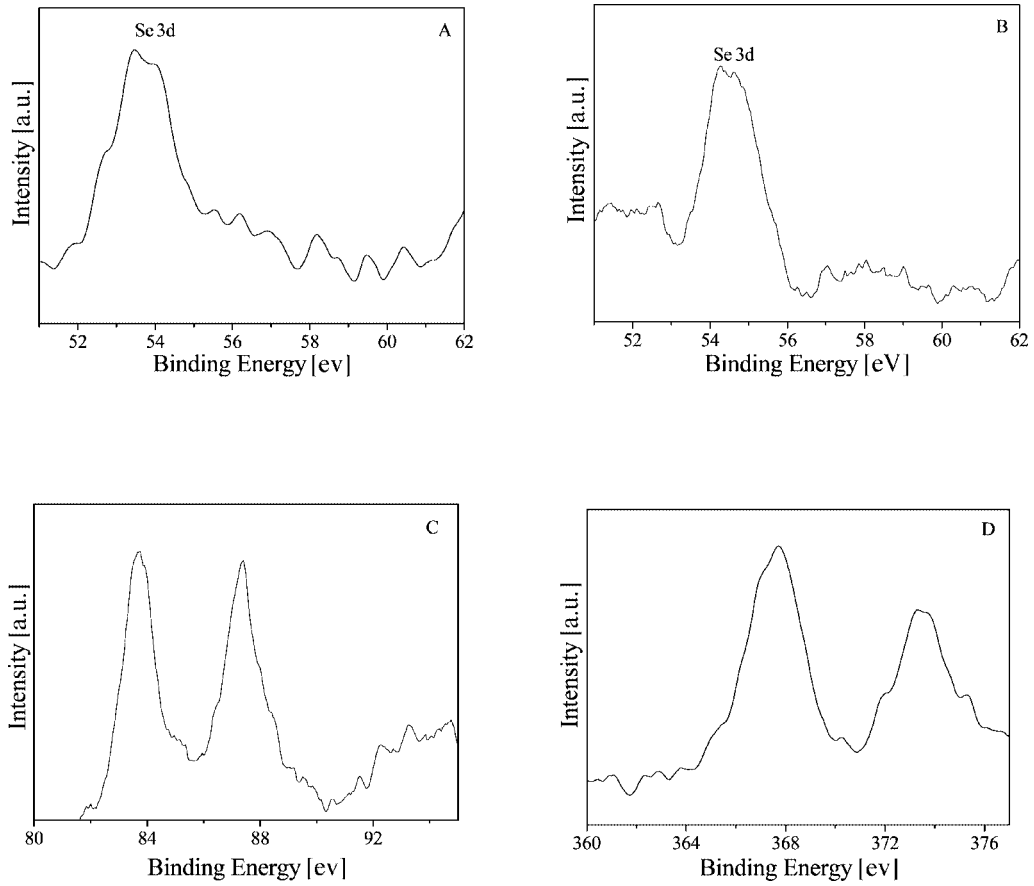


Figure 3. Se 3d core level spectra recorded from Se–Au- (A) and Se–Ag-core–shell nanoparticles (B). Au 4f (C) and Ag 3d (D) core level spectrum recorded from Se–Au- and Se–Ag-core–shell nanoparticles, respectively.

 © 2007 Wiley-VCH Verlag GmbH & Co. KGaA, Weinheim 

core–shell colloids formed by sequential reduction by a UV-irradiated TSA solution. Such core–shell colloids were quite uniform and could be obtained in copious quantities. Figure 5B and Figure 6B show the TEM images of the same samples of Figure 5A and Figure 6A, respectively, which reveal the smoothness and uniformity of these spheres with sizes in diameter of 51 nm and 99 nm, respectively. Again, the Se cores could selectively be removed by chemical or thermal means.[14] When the Se@Au and Se@Ag nanoparticles (Figures 5A,B and 6A,B) are compared with the Se nanoparticles (Figure 4), it can be seen that the particles are quite monodisperse and show a small increase in size (ranging from 40 nm to 51 nm and to 99 nm, respectively).

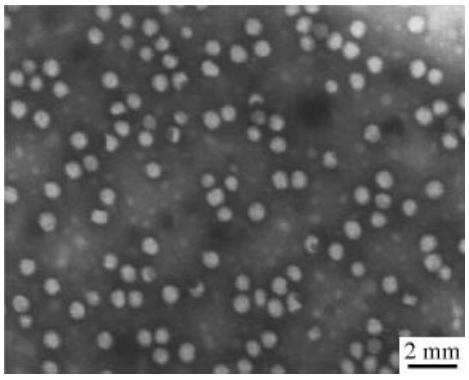


Figure 4. TEM image of Se nanoparticles reduced by UV-irradiated TSA solution.

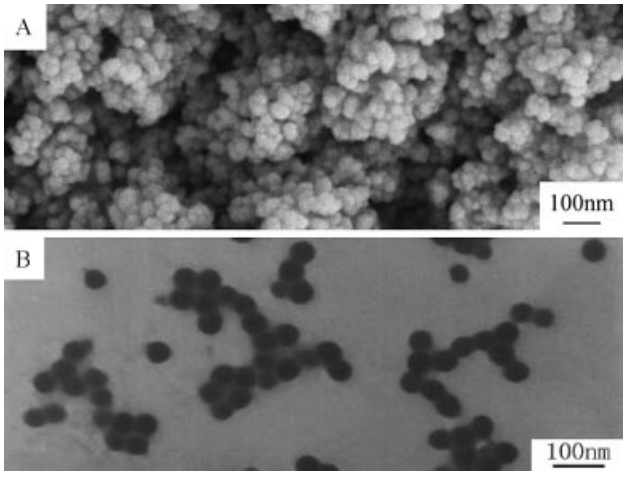


Figure 5. (A) SEM of Se@Au-core–shell colloids formed by sequential reduction of selenium and gold ions by UV-irradiated TSA solution. (B) TEM of the same sample.

Figure 7 shows the TEM image of Au nanoparticles reduced by a UV-irradiated TSA solution. From Figure 7, it can clearly be seen that the gold nanoparticles are very different from those covering the templates of Se. This control experiment thus clearly shows that the template in the nucleation step facilitates the formation of the coating on the template. From Figures 5 and 6, we notice that the t-Se templates are well coated by the Au and Ag nanoshells. In our study, we believe that the Se structures serve as both chemical and physical templates.[14a] The coating of Se templates

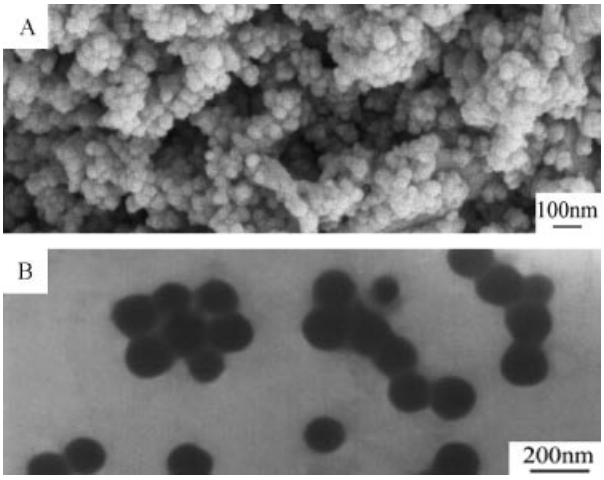


Figure 6. (A) SEM of Se@Ag-core–shell colloids formed by sequential reduction of selenium and gold ions by UV-irradiated TSA solution. (B) TEM of the same sample.

with Au and Ag is believed to occur through two distinct reduction reactions: (i) the initial reduction of the $Au^{III}$ or $Ag^{I}$ salt by the Se template itself at the interface, which is similar to the method described in the literature[29], and (ii) the reduction of the $Au^{III}$ or $Ag^{I}$ salt by the UV-irradiated TSA solution. The galvanic reduction of $Au^{III}$ or $Ag^{I}$ by a Se template can continue until the surface is completely covered. Subsequent deposition of the Au- or Ag coating is dominated by the UV-irradiated TSA solution. The engagement of the template in the nucleation step facilitates the formation of homogeneous, uniform coating on the template. This is also the major reason why Se is such a good template for the coating by metals relative to inert structures such as polystyrene beads or silica spheres. On the other hand, we believe that such spontaneous "landing" of the small nanoparticles of Au or Ag on the backbone of the Se nanoparticles followed by self aggregation rather than aggregation with the Se nanoparticles can be related to the "contact epitaxy" mechanism proposed by Averback et al.[30,31] The driving force for this spontaneous, oriented attachment is substantial reduction in the surface free energy (from a thermodynamic viewpoint) that arises as a result of the elimination of pairs of high energy surfaces.[32,33] The

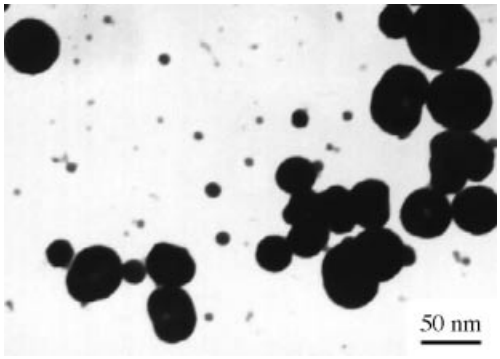


Figure 7. TEM image of Au nanoparticles reduced by UV-irradiated TSA solution.

 © 2007 Wiley-VCH Verlag GmbH & Co. KGaA, Weinheim 

initial randomly oriented nanocrystals can align epitaxially with the substrate (the Se nanoparticles in this case), which can be explained by the rotation of the nanoparticles within the aggregates that is driven by short-range interactions between adjacent surfaces.[30,31]

Figures 8A and B show the dependence of the diameters of the Se–Au- and Se–Ag-core–shell nanoparticles, respectively, on pH. In Figure 8 a, b, c, and d four samples with pH of 1.5, 2.5, 3.5, and 4.5, respectively, are represented. In Figure 8A, the mean diameters of the four samples of the Se-core–Au-shell are 59.5 nm, 51.1 nm, 48 nm, and 47.4 nm, respectively. From Figure 8A, it can clearly be seen that the diameter of the particles continuously decreases with increasing pH from 1.5 to 4.5. However, the rate at which the diameter decreases diminishes gradually, and when the pH is >4, the decrease in the diameter of the Se-core–Au-shell nanoparticles is minimal. In Figure 8B, the mean diameters of the four samples of the Se-core–Ag-shell are 95.6 nm, 99.3 nm, 125.5 nm, and 128 nm. From Figure 8B, it can clearly be seen that the diameter of the particles continuously increases with increasing pH from 1.5 to 4.5. In the regions between 1.5 and 2.5 and between 3.5 and 4.5, the increase in the diameter of the Se-core–Ag-shell nanoparticles is slight; however, there is a great increase in the region between pH 2.5 and 3.5. Comparing Figures 8A and B, we notice that the diameter of the Se-core–Au-shell nanoparticles decreases with increasing pH, while that of the Se-core–Ag-shell nanoparticles increases.

We also study the relationship between the diameter of the core shell nanoparticles and temperature, which is shown in Figures 9A (Se–Au) and B (Se–Ag). In Figure 9 a, b, c, and d four samples the- core–shell nanoparticles having different diameters at 20, 40, 60, and 80 °C, respectively, are represented. The mean diameters of the four typical samples of the Se-core–Au-shell are 52.3 nm, 60.3 nm, 66.3 nm, and 69.1 nm, respectively. As demonstrated in Figure 9A, the size of these colloids can conveniently be controlled by simply varying the reaction temperature, i.e. the diameter continuously increases with an increase in the temperature. In Figure 9B, the mean diameters of the four samples of the Se-core–Ag-shell are 105 nm, 99 nm, 69.2 nm, and 47.2 nm. It can clearly be seen from Figures 9A and B that the diameter of Se-core–Au-shell nanoparticles increases with increasing temperature, while that of Se-core–Ag-shell nanoparticles decreases. The reasons for the above phenomena are not clear yet.

Since the size of these core–shell nanoparticles can conveniently be controlled by simply varying the pH of the reaction solution and the reaction temperatures, it is believed that the procedure described here should provide an effective route to produce Se@Au and Se@Ag nanoparticles with controllable size. In this current investigation in which

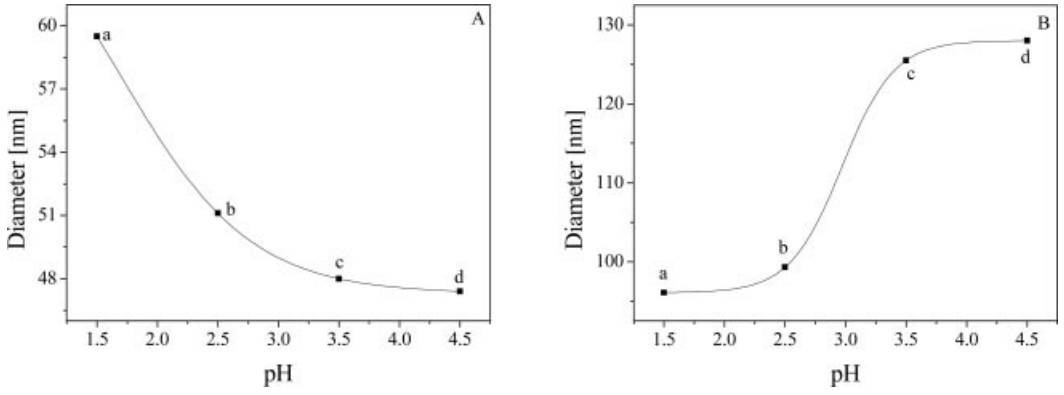


Figure 8. (The dependence of the diameter of the Se–Au- (A) and Se–Ag-core–shell nanoparticles (B) on pH. a, b, c, and d correspond to a pH value of 1.5, 2.5, 3.5, and 4.5, respectively. (Conditions: temperature, ca. 25 °C; the diameter of the Se core, ca.40 nm).

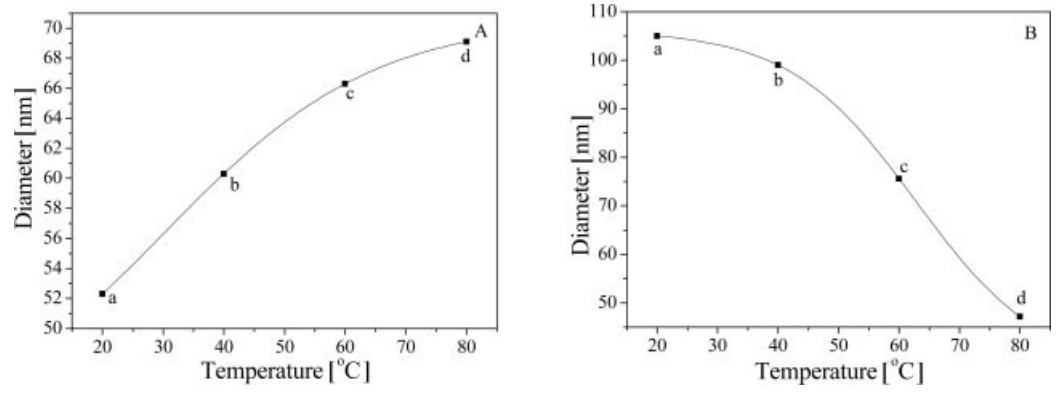


Figure 9. The dependence of the diameter of the Se–Au- (A) and Se–Ag-core–shell nanoparticles (B) on temperature. a, b, c, and d correspond to 20, 40, 60, and 80 °C. (Conditions: pH, ca. 2.5; the diameter of the Se core, ca.40 nm).

 © 2007 Wiley-VCH Verlag GmbH & Co. KGaA, Weinheim 

we studied the formation of the nanoparticles as a function of temperature, the size of the t-Se colloids could conveniently be controlled by simply varying the reaction temperature, which ranged from 20 to 80 °C; the diameter increased from about 44.7 to about 83.3 nm. We can therefore control the size of the core and the thickness of the shell. In principle, this procedure can be extended to several other noble metal shells that have been prepared as nanocomplexes by reduction with TSA-ion particles.

## Conclusions

In summary, we have demonstrated the use of t-Se colloids as templates in forming controllable-size Se-core–Au/Ag-shell nanoparticle structures. It is also worth mentioning that the Se templates are not limited to the randomly dispersed nanostructures shown in this work. It has been demonstrated that the Se nanowires and colloids could be organized into ordered structures such as networks (or meshes) and crystalline lattices.[34] These templates are expected to play an increasingly important role in fabricating metal nanostructures with complex (yet controllable) morphologies. In addition, the monodisperse shells of Au/Ag will be suitable as a new class of building blocks to fabricate colloidal crystals that are expected to exhibit improved photonic bandgap properties.[35]

## Experimental Section

Tungstosilicate acid [$H_4(SiW_{12}O_{40})$, TSA], selenious acid ($H_2SeO_3$), silver nitrate ($AgNO_3$), chloroauric acid ($HAuCl_4$), and 2-propanol [$CH_3CH(OH)CH_3$] were all A.R. grade and obtained from Shanghai reagent Co. All the reagents in the experiment were used as received. Doubly distilled water was used throughout to prepare the solutions.

In a typical experiment, an aqueous, deaerated solution of tungstosilicate acid (30 mL of a 1 mM solution), an aqueous, deaerated solution of $H_2SeO_3$ (30 mL of a 1 mM solution), and propan-2-ol (2 mL) were placed in a test tube. This mixture was irradiated with UV light (Pyrex filter, >280 nm, 450 W Hanovia medium pressure lamp) for 5 h. UV irradiation leads to the in situ reduction of $H_2SeO_3$ by the electron-rich $[SiW_{12}O_{40}]^{5-}$ ions {formed by the photochemical reduction of $[SiW_{12}O_{40}]^{4-}$ ions}, which can clearly be seen by the appearance of an orange solution. The above solution was further irradiated with UV light for 3 h, and the color of the solution changed from orange to bluish-red. To this solution (15 mL) were added aqueous solutions of $HAuCl_4$ and $AgNO_3$ (15 mL of 1 mM solution, each) separately whilst stirring. The color of the solutions changed from bluish-red to pink and light brown, which indicates the formation of gold and silver nanoparticles, respectively.

UV/Vis spectroscopic measurements of the samples were carried out with a TU-1901 model UV/Vis double beam spectrophotometer (Beijing Purkinje General Instrument Co., Ltd, China) operated at a resolution of 2 nm. XRD analyses of drop-coated films of the Se solution and Se@Ag and Se@Au on glass substrates were carried out with a MAP18AHF instrument (Japan MAC Science Co.). XPS measurements of the Se nanoparticles were carried out with a VG ESCALAB MKII instrument at a pressure $>10^{-6}$ Pa. The general scan and Se core-level spectra were recorded with non-monochromatized Mg–$K_\alpha$ radiation (photon energy = 1253.6 eV). The core-level binding energies (BEs) were aligned with respect to the $C_{1s}$ BE of 285 eV. Samples for TEM analysis were prepared by drop-coating films of the Se solution and Se@Ag and Se@Au solutions on carbon-coated copper TEM grids and allowing the grid to stand for 2 min following which the extra solution was removed using blotting paper. The above TEM analysis was carried out with a JEM model 100SX electron microscope instrument (Japan Electron Co.) operated at an accelerating voltage at 80 kV. SEM measurements were carried out with a Leica Stereoscan-440 instrument equipped with a Phoenix energy dispersive analysis of X-rays (EDAX) attachment. The size distribution of the nanoparticles was measured by PCS on the Zetasizer $3000HS_A$ instrument (Malvern Instruments Limited).

## Acknowledgments

This work is supported by the National Science Foundation of China (20471001, 20371001), the Specific Project for Talents of Science and Technology of Universities of Anhui Province (2005hbz03), the Key Laboratory of Environment-friendly Polymer Materials of Anhui Province, and Science Foundation of Anhui Province (2006KJ155B).

[1] a) Y. W. Cao, R. Jin, C. A. Mirkin, *J. Am. Chem. Soc.* **2001**, *123*, 7961–7962; b) W. Schartl, *Adv. Mater.* **2000**, *12*, 1899–1908; c) L. X. Cao, J. H. Zhang, S. L. Ren, S. H. Huang, *Appl. Phys. Lett.* **2002**, *80*, 4300–4302; d) J. C. Yu, X. C. Wang, L. Wu, W. K. Ho, L. Z. Zhang, G. T. Zhou, *Adv. Funct. Mater.* **2004**, *14*, 1178–1183; e) X. C. Wang, J. C. Yu, H. Y. Yip, L. Wu, P. K. Wang, S. Y. Lai, *Chem. Eur. J.* **2005**, *11*, 2997–3004; f) Y. J. Kang, T. A. Taton, *Angew. Chem.* **2005**, *117*, 413–416; *Angew. Chem. Int. Ed.* **2005**, *44*, 409–412.

[2] a) X. G. Peng, M. C. Schlamp, A. V. Kadavanich, A. P. Alivisatos, *J. Am. Chem. Soc.* **1997**, *119*, 7019–7029; b) S. U. Son, Y. Jang, J. Park, H. B. Na, H. M. Park, H. J. Yun, J. Lee, T. Hyeon, *J. Am. Chem. Soc.* **2004**, *126*, 5026–5027; c) X. W. Teng, D. Black, N. J. Watkins, Y. L. Gao, H. Yang, *Nano Lett.* **2003**, *3*, 261–264; d) H. Zeng, J. Li, Z. L. Wang, J. P. Liu, S. H. Sun, *Nano Lett.* **2004**, *4*, 187–190.

[3] A. Rogach, A. Susha, F. Caruso, G. Sukhorukov, A. Kornowski, S. Kershaw, H. Mohwald, A. Eychmuller, H. Weller, *Adv. Mater.* **2000**, *12*, 333–337.

[4] a) C. W. Chen, M. Q. Chen, T. Serizawa, M. Akashi, *Chem. Commun.* **1998**, 831–832; b) C. W. Chen, T. Serizawa, M. Akashi, *Chem. Mater.* **1999**, *11*, 1381–1389.

[5] a) C. Schuler, F. Caruso, *Macromol. Rapid Commun.* **2000**, *21*, 750–753; b) F. Caruso, H. Fiedler, K. Haage, *Colloids Surf. A* **2000**, *169*, 287–293.

[6] S. J. Oldenburg, S. L. Westcott, R. D. Averitt, N. J. Halas, *J. Chem. Phys.* **1999**, *111*, 4729–4739.

[7] a) K. S. Oh, K. E. Lee, S. S. Han, S. U. H. Cho, D. Kim, S. H. Yuk, *Biomacromolecules* **2005**, *6*, 1062–1067; b) K. S. Soppimath, D. C. W. Tan, Y. Y. Yang, *Adv. Mater.* **2005**, *17*, 318–323; c) T. Riley, C. R. Heald, S. Stolnik, M. C. Garnett, L. Illum, S. S. Davis, S. M. King, R. K. Heenan, S. C. Purkiss, R. J. Barlow, P. R. Gellert, C. Washington, *Langmuir* **2003**, *19*, 8428–8435.

[8] P. V. Kamat, B. Shanghavi, *J. Phys. Chem. B* **1997**, *101*, 7675–7679.

[9] I. Honma, T. Sano, H. Komiyama, *J. Phys. Chem.* **1993**, *97*, 6692–6695.

[10] Y. Lu, Y. D. Yin, Z. Y. Li, Y. A. Xia, *Nano Lett.* **2002**, *2*, 785–788.

[11] a) L. I. Berger, *Semiconductor Materials*, CRC, Boca Raton, FL, **1997**; b) D. M. Chizhikov, V. P. Schastlivy, *Selenium and*

 © 2007 Wiley-VCH Verlag GmbH & Co. KGaA, Weinheim 

*Selenides*, Collet's, London, Wellingborough, **1968**; c) R. A. Zingaro, W. C. Cooper, *Selenium*, Van Nostrand Reinhold, New York, **1974**.
[12] A. H. Lu, W. C. Li, N. Matoussevitch, B. Spliethoff, H. Bonnemann, F. Schuth, *Chem. Commun.* **2005**, 98–100.
[13] a) G. S. Chai, S. B. Yoon, J. H. Kim, J. S. Yu, *Chem. Commun.* **2004**, 2766–2767; b) S. Han, Y. Yun, K. W. Park, Y. E. Sung, T. Hyeon, *Adv. Mater.* **2003**, *15*, 1922–1925; c) Y. D. Xia, R. Mokaya, *Adv. Mater.* **2004**, *16*, 886–891.
[14] a) B. Mayer, X. C. Jiang, D. Sunderland, B. Cattle, Y. N. Xia, *J. Am. Chem. Soc.* **2003**, *125*, 13364–13365; b) U. Y. Jeong, Y. N. Xia, *Adv. Mater.* **2005**, *17*, 102–106; c) X. C. Jiang, B. Mayers, Y. L. Wang, B. Cattle, Y. N. Xia, *Chem. Phys. Lett.* **2004**, *385*, 472–476.
[15] G. Schmid, A. Lehnert, J.-O. Malm, J.-O. Bovin, *Angew. Chem. Int. Ed. Engl.* **1991**, *30*, 874–876.
[16] X. Teng, D. Black, N. J. Watkins, Y. Gao, H. Yang, *Nano Lett.* **2003**, *3*, 261–264.
[17] C. S. Ah, S. D. Hong, D. J. Jang, *J. Phys. Chem. B* **2001**, *105*, 7871–7873.
[18] I. Srnova-Sloufova, F. Lednicky, A. Gemperle, J. Gemperlova, *Langmuir* **2000**, *16*, 9928–9935.
[19] E. Papaconstantinou, *Chem. Soc. Rev.* **1989**, *18*, 1–31.
[20] A. Troupis, A. Hiskia, E. Papaconstantinou, *Angew. Chem. Int. Ed.* **2002**, *41*, 1911–1914.
[21] S. Mandal, P. R. Selvakannan, R. Pasricha, M. Sastry, *J. Am. Chem. Soc.* **2003**, *125*, 8440–8441.
[22] S. Mandal, A. B. Mandale, M. Sastry, *J. Mater. Chem.* **2004**, *14*, 2868–2871.
[23] Y. R. Ma, L. M. Qi, W. Shen, J. M. Ma, *Langmuir* **2005**, *21*, 6161–6164.
[24] S. Link, Z. L. Wang, M. A. El-Sayed, *J. Phys. Chem. B* **1999**, *103*, 3529–3533.
[25] Ch. H. An, K. B. Tang, X. M. Liu, Y. T. Qian, *Eur. J. Inorg. Chem.* **2003**, 3250–3255.
[26] S. Zhang, H. L. Wang, Y. P. Bao, L. D. Zhang, *Life Sci.* **2004**, *75*, 237–244.
[27] A. Sanyal, S. Mandal, M. Sastry, *Adv. Funct. Mater.* **2005**, *15*, 273–280.
[28] C. S. Fadley, D. A. Shirley, *J. Res. Natl. Bur. Stand.* **1970**, *74 A*, 543.
[29] D. M. Chizhikov, V. P. Shchastlivyi, *Selenium and Selenides* (translated from Russian by E. M. Elkin), Collet's Ltd., London and Wellingborough, **1968**, p. 40.
[30] H. L. Zhu, R. S. Averback, *Philos. Magn. Lett.* **1996**, *73*, 27–33.
[31] M. Yeadon, M. Ghaly, J. C. Yang, R. S. Averback, J. M. Gibson, *Appl. Phys. Lett.* **1998**, *73*, 3208–3210.
[32] F. Banfield, S. A. Welch, H. Zhang, T. T. Ebert, R. L. Penn, *Science* **2000**, *289*, 751–754.
[33] A. P. Alivisatos, *Science* **2000**, *289*, 736–737.
[34] a) B. Mayers, K. Liu, D. Sunderland, Y. Xia, *Chem. Mater.* **2003**, *15*, 3852–3858; b) B. Gates, B. T. Mayers, A. Grossman, Y. Xia, *Adv. Mater.* **2002**, *14*, 1749–1752.
[35] Y. Xia, B. Gates, Y. Yin, Y. Lu, *Adv. Mater.* **2000**, *12*, 693–713.
Received: September 12, 2006
Published Online: February 2, 2007

 © 2007 Wiley-VCH Verlag GmbH & Co. KGaA, Weinheim 

DOI: 10.1002/ejic.200600960

# Synthesis and Sublimation Kinetics of a Highly Volatile Asymmetric Iron(II) Amidinate

Xin-Gui Li,*[a,b] Zhengwen Li,[a] Huazhi Li,[a] and Roy G. Gordon*[a]

**Keywords:** Asymmetric iron(II) amidinate / Bridging ligands / Metathesis / Sublimation kinetics / Thermochemistry

A highly volatile asymmetric iron(II) amidinate, iron(II) bis(*N*-*tert*-butyl-*N*′-ethylacetamidinate), was synthesized for the first time by systematically changing starting iron(II) compounds such as acetylacetonate, acetate, and chloride, in different media such as diethyl ether, toluene, and tetrahydrofuran. The amidinate has been characterized and compared with the symmetric iron(II) bis(*N*,*N*′-diisopropylacetamidinate) by NMR spectroscopy, MS, IR spectroscopy, and dynamic and isothermal thermogravimetric techniques. Different amidinates from three starting compounds exhibit almost the same NMR, MS, and IR spectra, a melting point of 85 °C, and the same solution color in the same solvents, but quite different synthetic yields, volatilities, and colors in different solvents. This implies that the amidinates show an interesting solvatochromism. In particular, the asymmetric iron(II) amidinates obtained should be a mixture of paramagnetic and diamagnetic compounds. The thermostability and sublimation kinetics of the iron(II) amidinates have been investigated in detail. It is found that the average activation energy of 106 kJ mol$^{-1}$ for the nonisothermal sublimation is slightly higher than the average activation energy of 104 kJ mol$^{-1}$ determined from the isothermal thermogravimetric experiments. The sublimation is a diffusion-controlled process because the temperature and the rate of the sublimation depend strongly on the sublimation level and the sample size. The optimal iron(II) starting compound and reaction medium should be iron(II) acetylacetonate and diethyl ether, respectively, because the combination offers the highest yield, the greatest volatilizability of 98 %, and thus the purest product.
(© Wiley-VCH Verlag GmbH & Co. KGaA, 69451 Weinheim, Germany, 2007)

## Introduction

Metal amidinate complexes with intriguing structural diversity and novel properties have been the subject of intense investigations in chemistry, electronics, optics, energy, and materials science.[1–4] Great interest has been focused on the applicability of the complexes as single-source precursors of advanced functional materials,[5] efficient homogeneous catalysts in olefin and caprolactone polymerizations,[6–7] initiators for the stereospecific and degenerative transfer living Ziegler–Natta polymerization of alpha-olefins with an extremely high level of stereoselectivity,[8] and activators for the polymerization of *rac*-lactide to produce heterobiased polylactides.[9] Metal-based amidinate complexes that are of particular relevance to this paper have been used as highly volatile precursors for atomic layer deposition of films with novel multifunctionalities and a wide variety of applications in modern high technology, including semiconductor microelectronics, high-resolution displays, optical filters, magnetic information storage, and catalysis.[10–12]

The precursors need to be designed in such a way that the compounds are volatile and thermally stable at growth temperatures.[10,13] Generally, the more volatile the better the precursors are. The synthesis and characterization of numerous metal compounds with amidinate ligands have been reported in the literature.[10,12–14] The volatility and thermal stability of symmetric amidinates of transition metals and lanthanum with oxidation states of one (Cu, Ag, Au),[15] two (Mg, Mn, Fe, Co, Ni),[16] three (Ti, V, Y, Al, Ga, La),[17] and four (Ru, Hf)[8] have been reported. Note that the symmetric metal amidinates usually exhibit a lower volatility than asymmetric metal amidinates with the same molar mass because there is relatively disordered molecular aggregation and hence a lower molecular interaction among the asymmetric amidinates. However, no studies on the synthesis, characterization, and volatility of asymmetric iron(II) amidinates were found to the best of our knowledge.

Herein we describe a facile synthesis of a highly volatile asymmetric iron(II) amidinate, iron(II) bis(*N*-*tert*-butyl-*N*′-ethylacetamidinate). The effect of starting iron(II) compounds and amidination solvents on the synthetic yield, molecular structure, and properties of the iron(II) amidinate was studied. The NMR spectral characteristics of various iron(II) amidinates obtained under different synthetic

[a] Department of Chemistry and Chemical Biology, Harvard University,
12 Oxford Street, Cambridge, MA 02138, USA
Fax: +1-617-495-4723
E-mail: adamxgli@yahoo.com
gordon@chemistry.harvard.edu
[b] Institute of Materials Chemistry, College of Materials Science & Engineering, Tongji University,
1239 Siping Road, Shanghai 200092, China
Fax: +86-21-6598-0524
E-mail: adamxgli@yahoo.com

 © 2007 Wiley-VCH Verlag GmbH & Co. KGaA, Weinheim 

conditions were carefully compared. In particular, the thermostability, volatility, and sublimation kinetics were investigated in detail for the first time.

## Results and Discussion

### Synthesis of Iron(II) Amidinates

All iron amidinate compounds listed in Table 1 were synthesized by the metathesis reactions of starting iron compounds with corresponding equivalents of the lithium amidinates [*N*-*tert*-butyl-*N*′-ethylacetamidinate (*t*Bu-Et-MeAMD) and *N*,*N*′-diisopropylacetamidinate (*i*Pr-MeAMD)] in various solvents. Lithium amidinates were prepared in situ from the corresponding carbodiimide with methyllithium and not isolated. Compounds **1**–**3** and **6**–**7** are all solids at room temperature but compounds **4**–**5** look like semisolids at room temperature. The synthetic yield and physical properties are summarized in Table 1. It appears that the starting iron(II) compounds and acetamidination solvents influence the synthesis and properties of the final iron complexes.

In the solvent diethyl ether it is found that the yield increases and product color darkens when changing the starting iron(II) materials from iron(II) acetate to iron(II) chloride to iron(II) acetylacetonate. This phenomenon should be attributed to the solubility difference of the three iron compounds in diethyl ether. Iron(II) acetate is almost insoluble in diethyl ether and iron(II) chloride is slightly soluble in diethyl ether. However, iron(II) acetylacetonate is nearly completely soluble in diethyl ether. As a result the highest yield achieved with iron(II) acetylacetonate as the starting material should be ascribed to its best solubility in diethyl ether. Note that the three iron amidinate products obtained have similar melting points and sublimation temperatures.

In addition, the synthetic yield increases steadily when changing the acetamidination solvent from toluene to THF to diethyl ether by using a fixed starting iron(II) material of iron(II) acetylacetonate, which could result from an increased solubility of iron(II) acetylacetonate in toluene to THF to diethyl ether. The product obtained in THF has the lowest melting point. A similar variation of the yield and melting point with changing solvent from THF to diethyl ether is observed with a fixed starting iron(II) material of iron(II) chloride. It can then be concluded that a combination of iron(II) acetylacetonate and diethyl ether is better for the synthesis of the asymmetric iron(II) bis(*N*-*tert*-butyl-*N*′-ethylacetamidinate)s giving a higher yield. On the contrary, this combination produces a symmetric iron(II) bis(*N*,*N*′-diisopropylacetamidinate) with a lower yield but higher melting point than the asymmetric iron(II) bis(*N*-*tert*-butyl-*N*′-ethylacetamidinate)s. The different colors of the final solid products could be ascribed to different spatial arrangements of atoms from different starting materials or acetamidination solvents regardless of their same molecular structure.

### Molecular Structure of the Iron(II) Amidinates

The asymmetric iron(II) amidinates were systematically characterized by $^1$H NMR, IR and MS methods. It seems that the NMR spectra of the compounds do not display a high resolution, possibly because of the presence of a very small amount of impurity resulting from their light sensitivity. Just like other paramagnetic iron(II) amidinates,[18,19] however, the $^1$H NMR spectra of the asymmetric iron(II) amidinates in $CDCl_3$ show two series of resonance peaks over a very wide chemical shift range from –10 to +200 ppm. The first series of resonance peaks at 8.6 ppm (sharp, $NCH_2CH_3$), 3.5 ppm (sharp, $N_2CCH_3$), 1.5 ppm [broad, $NC(CH_3)_3$], and 0.3 ppm (sharp triplet, $NCH_2CH_3$) are typically attributed to the diamagnetic fraction. The second series of resonance peaks at $\delta$ = 199.5 ppm (broad, $NCH_2CH_3$), 56.7–111 ppm (sharp, $N_2CCH_3$), 29.7 ppm [broad, $NC(CH_3)_3$], and –6.1 ppm (sharp triplet, $NCH_2CH_3$) are ascribed to the paramagnetic fraction because of their much higher chemical shift. Therefore, the area ratio, calculated from the resonance peaks at 29.7 over 1.5 ppm, could be used to estimate the paramagnetic percentage, as listed in Table 1. As shown in Figure 1, $^1$H NMR spectra of the iron(II) bis(*N*-*tert*-butyl-*N*′-ethylacetamidinate) in $CDCl_3$ look almost the same regardless of the change of starting iron(II) materials from iron(II) acetate and $FeCl_2$ to iron(II) acetylacetonate for the synthesis of the asymmetric iron(II) amidinate. This implies that the three iron(II) amidinates that were obtained should have

Table 1. The synthesis and principal parameters of the iron(II) bis(*N*-*tert*-butyl-*N*′-ethylacetamidinate)s and bis(*N*,*N*′-diisopropylacetamidinate).

| No. | Acetamidination conditions Starting materials | | | Solvent | Iron(II) bis(*N*-*tert*-butyl-*N*′-ethylacetamidinate)s Yield | Color of the solid obtained | M.p. | Paramagnetic fraction in $CDCl_3$ | Subl. temp. at 10 °C min$^{-1}$ |
|---|---|---|---|---|---|---|---|---|---|
| | | | | | [%] | | [°C] | [mol.-%] | [°C] |
| **1** | [a] | MeLi | iron(II) acetate | diethyl ether | 22 | purplish blue | 85 | 60 | 141 |
| **2** | [a] | MeLi | iron(II) chloride | diethyl ether | 25 | dark blue | 85 | 58 | 140 |
| **3** | [a] | MeLi | iron(II) acetylacetonate | diethyl ether | 42 | black | 85 | 55 | 147 |
| **4** | [a] | MeLi | iron(II) acetylacetonate | THF | 22 | reddish black | 30 | 47 | 141 |
| **5** | [a] | MeLi | iron(II) chloride | THF | 7 | dark black | 30 | 54 | – |
| **6** | [a] | MeLi | iron(II) acetylacetonate | toluene | 11 | purplish black | 85 | 37 | 177 |
| **7** | [b] | MeLi | iron(II) acetylacetonate | diethyl ether | 22 | dark blue | 95 | – | 130 |

[a] 1-*tert*-Butyl-3-ethylcarbodiimide. [b] 1,3-Diisopropylcarbodiimide.

 © 2007 Wiley-VCH Verlag GmbH & Co. KGaA, Weinheim 

the same molecular structure. Note that their paramagnetic percentages and sublimation behavior (as discussed below) are slightly different. It is seen from Table 1 that the highest paramagnetic percentage, up to 60%, could be found in the amidinate made from iron(II) acetate.

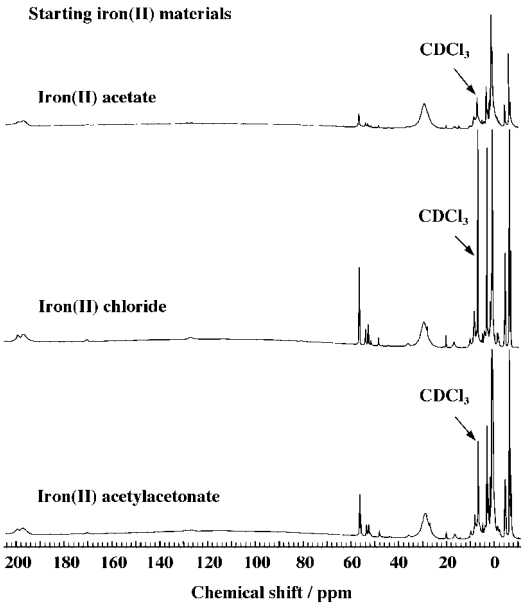


Figure 1. The $^1$H NMR spectra of the resulting iron(II) bis(*N*-*tert*-butyl-*N*′-ethylacetamidinate)s obtained with iron(II) acetate, chloride, and acetylacetonate as starting iron(II) materials, respectively.

However, the $^1$H NMR spectra of the iron(II) bis(*N*-*tert*-butyl-*N*′-ethylacetamidinate) vary significantly with the amidination media and NMR testing solvent used in the synthesis of the iron(II) amidinates, regardless of whether the other conditions are kept constant, as shown in Figure 2 and Figure 3. It is found from Figure 2 that the iron(II) bis(*N*-*tert*-butyl-*N*′-ethylacetamidinate) obtained in diethyl ether exhibits nearly the same $^1$H NMR spectral characteristics as that obtained in THF, signifying that the molecular structure of the iron(II) bis(*N*-*tert*-butyl-*N*′-ethylacetamidinate)s obtained in diethyl ether and THF should be very similar. Note that the iron(II) bis(*N*-*tert*-butyl-*N*′-ethylacetamidinate) obtained in toluene displays quite a different spectrum with a chemical shift range of 10–205 ppm compared with those obtained in diethyl ether and THF. In addition, their paramagnetic percentages and sublimation behavior (as discussed below) are distinctly different. Table 1 reveals that the paramagnetic percentage in the iron(II) bis(*N*-*tert*-butyl-*N*′-ethylacetamidinate) obtained from the same iron(II) acetylacetonate consistently increases from 37 to 47 to 55% when changing the amidination solvent from toluene to THF to diethyl ether. A similar situation is also discovered for the iron(II) bis(*N*-*tert*-butyl-*N*′-ethylacetamidinate) obtained from the same $FeCl_2$. This structure difference might be attributable to the different structural characteristics of the solvents used. Toluene is an aromatic hydrocarbon with a low dielectric constant (2.3), whereas diethyl ether and THF are aliphatic ether solvents with relatively high dielectric constants (4.2 and 7.4, respectively). That is to say, acetamidination solvents will significantly influence the synthesis of the target iron(II) bis(*N*-*tert*-butyl-*N*′-ethylacetamidinate), notwithstanding the other conditions. Hence, the acetamidination solvents should be carefully selected for the synthesis of an ideal asymmetric iron(II) amidinate. The ether could be an optimal acetamidination solvent for the synthesis of the iron(II) bis(*N*-*tert*-butyl-*N*′-ethylacetamidinate).

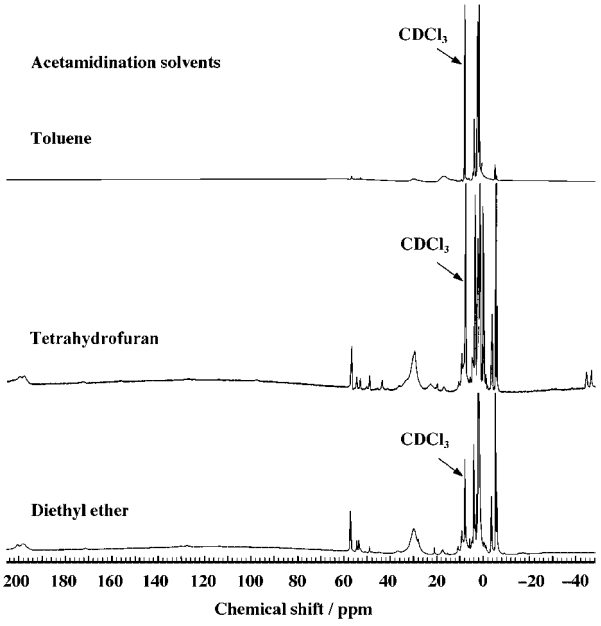


Figure 2. The effect of the acetamidination solvent on the $^1$H NMR spectra of the iron(II) bis(*N*-*tert*-butyl-*N*′-ethylacetamidinate)s with iron(II) acetylacetonate as the same starting iron(II) material.

Figure 3 reveals that the same iron(II) bis(*N*-*tert*-butyl-*N*′-ethylacetamidinate) obtained in diethyl ether exhibits totally different NMR spectra if NMR testing solvents were changed from $C_6D_6$ to $CDCl_3$ to $C_5D_5N$ with dielectric constants of 2.3, 4.8, and 13.3, respectively. This should result from different interactions between the iron amidinate and solvent molecules with different characteristics. In particular, the NMR spectrum obtained in $C_6D_6$ suggests the lowest paramagnetism, whereas the NMR spectrum in $C_5D_5N$ suggests the highest paramagnetic content of up to 60%, implying that the paramagnetism of the iron(II) amidinates depends on the solvent characteristics. It appears that the paramagnetism of the complexes in the solvent with the highest dielectric constant is higher. The diversification of the NMR spectra with changing NMR testing solvents from $CDCl_3$ to $C_6D_6$ to $C_5D_5N$ is also observed for the same iron(II) bis(*N*,*N*′-diisopropylacetamidinate) in this study. Therefore, NMR testing solvents should be carefully chosen for the obtainment of an ideal NMR spectrum of the paramagnetic materials. The deuterated solvent with a high dielectric constant could be optimal for the NMR spectroscopic analysis.

IR spectra of iron(II) complexes obtained show the expected and very strong absorptions at 1651–1653 and 548 cm$^{-1}$ attributable to the delocalized –N⋯C⋯N– and Fe–

 © 2007 Wiley-VCH Verlag GmbH & Co. KGaA, Weinheim 

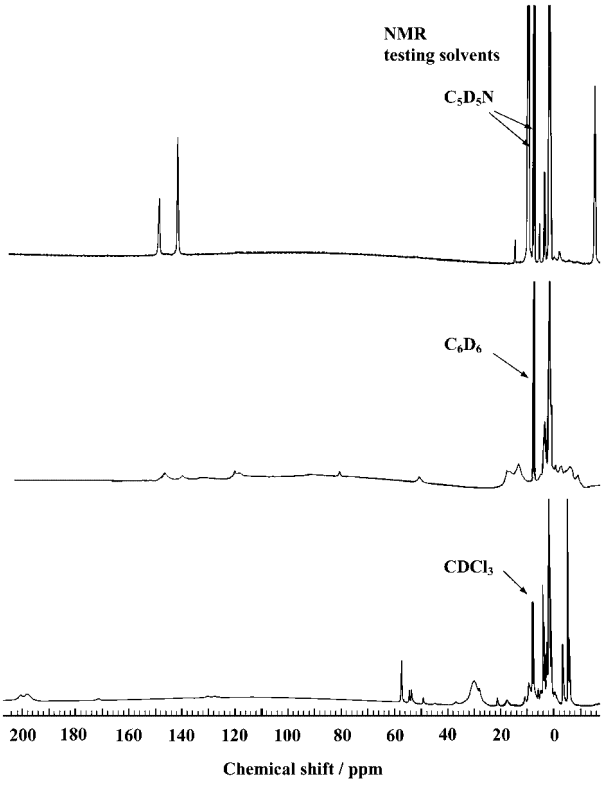


Figure 3. The effect of the NMR testing solvent on the $^1$H NMR spectra of the same iron(II) bis(*N*-*tert*-butyl-*N*′-ethylacetamidinate) with iron(II) acetylacetonate as a starting iron(II) material in diethyl ether.

N stretching modes, respectively, but no characteristic absorptions at 3436 and 2100 cm$^{-1}$ due to the amidine $\phi_{NH}$ and free carbodiimide $\upsilon_{N=C=N}$ stretching modes are observed.[20,21] These results strongly suggest the formation of the iron(II) bis(*N*-*tert*-butyl-*N*′-ethylacetamidinate).

In the mass spectra, all the amidinate complexes are characterized by a loss of the methyl and *tert*-butyl groups from the ions.[18] The ligand bonds between N and Fe break the most easily. It seems that the breaking mode of the complexes does not change with elevating MS testing temperatures from 120, 150, to 300 °C. However, the MS spectra indeed vary if 10% water is added to MCN or when changing starting iron(II) materials from acetylacetonate to acetate to chloride. These results also significantly indicate a successful synthesis of the iron(II) bis(*N*-*tert*-butyl-*N*′-ethylacetamidinate).

### Sublimation and Volatility of the Iron(II) Amidinates

TG and derivative thermogravimetry (DTG) curves of the iron(II) bis(*N*-*tert*-butyl-*N*′-ethylacetamidinate)s obtained from three starting iron(II) compounds in diethyl ether are given in Figure 4. Sublimation or thermal decomposition occurs clearly in one step at a lower temperature (110–170 °C)[10,13] with a lower residual mass of 3%, that is, a higher volatility of 97%. The low sublimation temperature of iron(II) bis(*N*-*tert*-butyl-*N*′-ethylacetamidinate) might be ascribed to the weak intermolecular forces, which are due to its spherical shape (Scheme 1). The weaker intermolecular forces of iron(II) bis(*N*,*N*′-diisopropylacetamidinate) can also be used to explain the fact that its sublimation temperature (Table 1) is lower than that of the iron(II) bis(*N*-*tert*-butyl-*N*′-ethylacetamidinate), which has the same molecular mass, because the iron(II) bis(*N*,*N*′-diisopropylacetamidinate) molecule should be more spherical and more symmetric. The iron(II) bis(*N*-*tert*-butyl-*N*′-ethylacetamidinate)s obtained with iron(II) acetate and chloride as starting iron(II) materials exhibit the same sublimation or volatile characteristics, which are different from that of the iron(II) bis(*N*-*tert*-butyl-*N*′-ethylacetamidinate) obtained with iron(II) acetylacetonate. The iron(II) bis(*N*-*tert*-butyl-*N*′-ethylacetamidinate) obtained with iron(II) acetylacetonate begins to sublimate at a higher temperature with a further residual weight of 2% lower than the other two. In other words, the iron(II) bis(*N*-*tert*-butyl-*N*′-ethylacetamidinate) obtained with iron(II) acetylacetonate possesses the highest volatilizability of 98%.

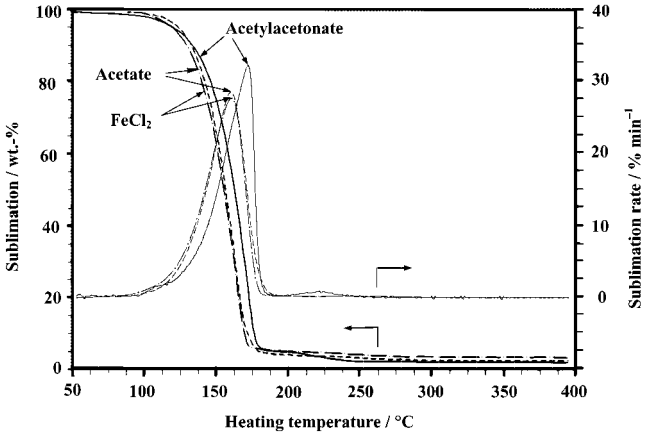


Figure 4. The effect of the starting iron(II) compounds on the sublimation of the iron(II) bis(*N*-*tert*-butyl-*N*′-ethylacetamidinate) obtained in diethyl ether at a heating rate of 10 °C/min.

The TG sublimation thermograms of the iron(II) bis(*N*-*tert*-butyl-*N*′-ethylacetamidinate)s vary significantly with iron(II) amidination solvents despite the same synthetic conditions being used, as shown in Figure 5. It is found that the iron(II) bis(*N*-*tert*-butyl-*N*′-ethylacetamidinate) obtained in diethyl ether exhibits nearly the same major sublimation characteristics as that obtained in THF, suggesting that the two iron(II) bis(*N*-*tert*-butyl-*N*′-ethylacetamidinate)s obtained in diethyl ether and THF should be very similar. However, the iron(II) bis(*N*-*tert*-butyl-*N*′-ethylacetamidinate) obtained in THF displays a much higher residual weight percentage or lower volatilizability than that obtained in diethyl ether, implying that the latter is much purer in composition. Note that the iron(II) bis(*N*-*tert*-butyl-*N*′-ethylacetamidinate) obtained in toluene displays quite a different TG thermogram as compared with those obtained in diethyl ether and THF, indicative of the iron(II) amidinates having different molecular structures. This is corroborated by the NMR results discussed above. The

 © 2007 Wiley-VCH Verlag GmbH & Co. KGaA, Weinheim 

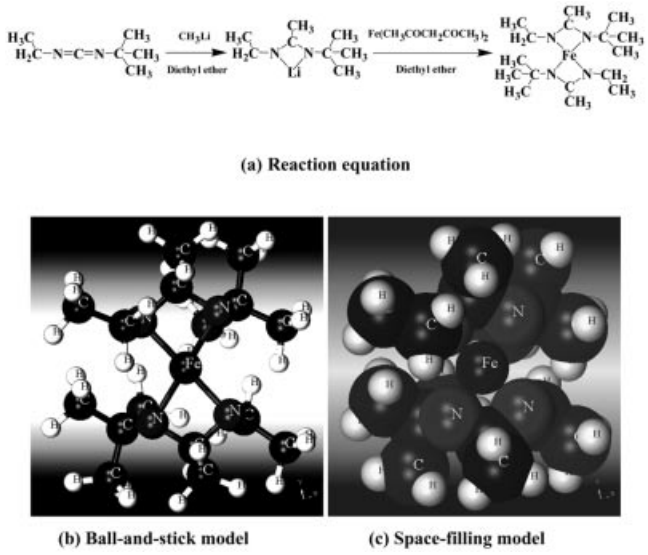


Scheme 1. The synthesis of the iron(II) bis(*N*-*tert*-butyl-*N*′-ethylacetamidinate) and its structural models at the minimum energy.

iron(II) bis(*N*,*N*′-diisopropylacetamidinate) obtained with iron(II) acetylacetonate as the iron(II) source exhibits a much lower sublimation temperature (150 °C) at the maximal-sublimation rate than that (225 °C) of the iron(II) bis(*N*,*N*′-diisopropylacetamidinate) obtained with $FeCl_2$ as the iron(II) source.[10] This suggests that iron(II) acetylacetonate could be a better starting iron(II) material for the synthesis of the iron(II) amidinates with higher volatility at a much lower temperature than $FeCl_2$.

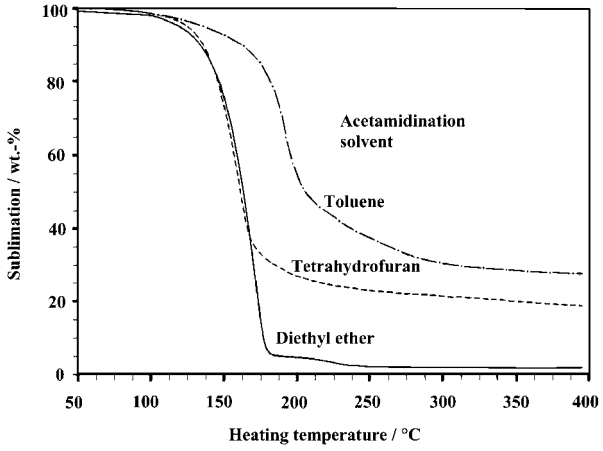


Figure 5. The effect of the amidination solvent on the sublimation of the iron(II) amidinate complex from iron(II) acetylacetonate at a heating rate of 10 °C/min.

## Sublimation Kinetics of the Iron(II) Amidinates

A strong and regular effect of the heating rate on the nonisothermal TG and DTG curves of the iron(II) bis(*N*-*tert*-butyl-*N*′-ethylacetamidinate) obtained with iron(II) acetylacetonate as a starting iron(II) source in diethyl ether is shown in Figure 6. The isothermal TG and DTG curves of the iron(II) bis(*N*-*tert*-butyl-*N*′-ethylacetamidinate) obtained with iron(II) acetylacetonate and acetate as the starting iron(II) sources in diethyl ether are shown in Figure 7. According to Equations (1)–(3) of the Flynn–Wall technique the activation energy of sublimation for iron(II) bis(*N*-*tert*-butyl-*N*′-ethylacetamidinate)s and bis(*N*,*N*′-di-

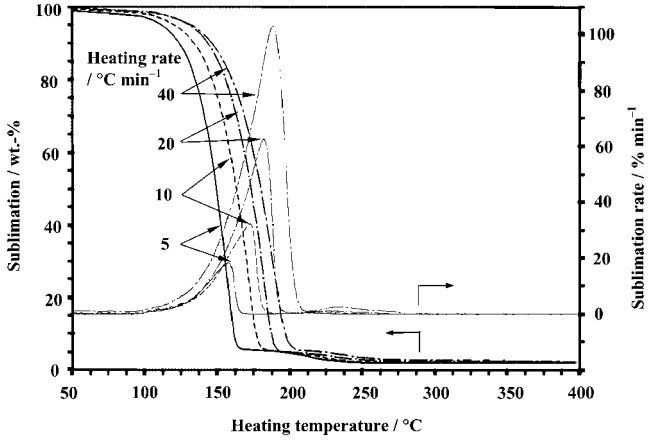


Figure 6. The effect of the heating rate on the the TG and DTG curves of the iron(II) bis(*N*-*tert*-butyl-*N*′-ethylacetamidinate) obtained with iron(II) acetylacetonate as a starting iron(II) source in diethyl ether.

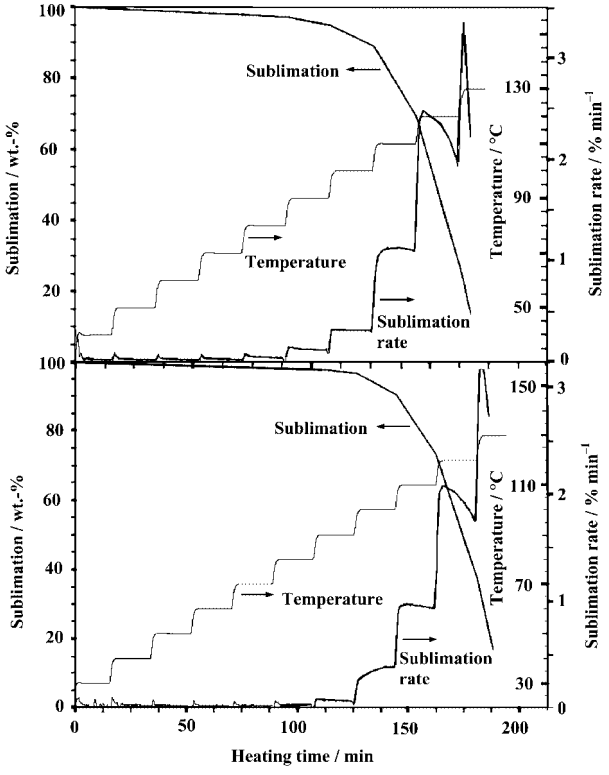


Figure 7. Multiple-stage isothermal TG and DTG curves of the iron(II) bis(*N*-*tert*-butyl-*N*′-ethylacetamidinate) obtained with iron(II) acetylacetonate (top) and iron(II) acetate (bottom) as starting iron(II) sources in diethyl ether.

 © 2007 Wiley-VCH Verlag GmbH & Co. KGaA, Weinheim 

isopropylacetamidinate) is summarized in Figure 8 and Table 2. Figure 8 discloses that the activation energy decreases with an increase in the sublimation level, indicating that a variation in the thermal sublimation kinetics, from diffusion-controlled kinetics to sublimation-controlled kinetics, is occurring. Under a large sample size at an early sublimation step the heat diffusion across the whole sample may be slow, leading to a diffusion control. As listed in Table 2, a larger sample size will result in a higher activation energy of the isothermal sublimation for sample No. **4**. It is also seen from Table 2 that two kinds of nonisothermal techniques, Flynn–Wall and Kissinger, afford similar activation energies of sublimation for the five iron(II) amidinates. However, the activation energy of the isothermal sublimation is different from that of the nonisothermal sublimation. In particular, the activation energy of the isothermal sublimation over a lower temperature range between 40 and 80 °C is much lower. In addition, the variation of the sublimation activation energy calculated by nonisothermal techniques for the iron(II) amidinates **1** to **7** is different from that calculated by isothermal techniques. These signify that the sublimation characteristics could vary with the heating method and temperature range. Nevertheless, it is interesting that the average activation energy (106 kJ mol$^{-1}$) for the nonisothermal sublimation at 127–198 °C is almost the same as the average activation energy (104 kJ mol$^{-1}$) determined from the isothermal thermogravimetric experiments at 80–130 °C.

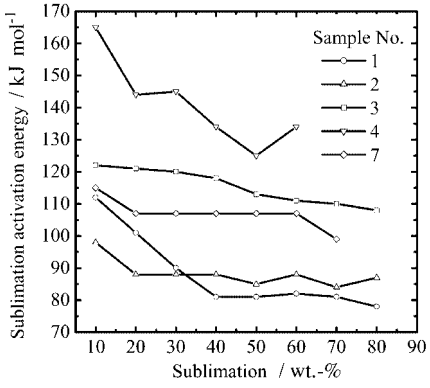


Figure 8. The variation of the sublimation activation energy with sublimation level based on the Flynn–Wall plot of ln (heating rate) against the reciprocal temperature for the iron(II) bis(*N*-*tert*-butyl-*N*′-ethylacetamidinate) and bis(*N*,*N*′-diisopropylacetamidinate).

### Solubility and Solvatochromism of the Iron(II) Amidinates

All dark solid iron(II) amidinates will immediately become red upon exposure in air or water because of their fast decomposition over several seconds. That is to say, the iron(II) amidinates are highly air and moisture sensitive. Solubility of the iron(II) amidinates is investigated in several representative solvents with different dielectric constants in a nitrogen atmosphere. It is found that almost all the iron(II) bis(*N*-*tert*-butyl-*N*′-ethylacetamidinate)s and bis(*N*,*N*′-diisopropylacetamidinate) are readily soluble in most organic solvents like chloroform, benzene, pyridine, toluene, hexane, pentane, diethyl ether, and THF with dielectric constants between 1.9 and 13.3 but except for methanol with a high dielectric constant of 32.4. It is of interest that a variation of the amidinate solution color with the solvents is observed, i.e., a novel solvatochromism. The solution of the same amidinate exhibits different colors within various solvents. The black solid iron(II) bis(*N*-*tert*-butyl-*N*′-ethylacetamidinate) becomes blue in chloroform, purple in pyridine, and brown in benzene, toluene, hexane, pentane, diethyl ether, and THF. Similarly, dark-blue solid iron(II) bis(*N*,*N*′-diisopropylacetamidinate) becomes blue in chloroform, bluish black in benzene, and brown in pyridine. This indicates that the amidinate molecules may have different conformations and hence different solvates in different solvents, induced by the different interactions between the amidinate and the solvent molecules with different dielectric constants and polarity. In other words, the solvatochromism might be adjusted by changing the amidinate structure and choosing the solvent. However, there is no regular variation of the amidinate solvatochromism with the solvent dielectric constant. Similar solvatochromism has also been observed for the intrinsically conducting copolymers from orthanilic acid and aniline.[22]

## Conclusions

A highly volatile and paramagnetic asymmetric iron(II) amidinate, iron(II) bis(*N*-*tert*-butyl-*N*′-ethylacetamidinate), was successfully synthesized. The optimal starting iron(II) compound and reaction solvent should be iron(II) acetylacetonate and diethyl ether, respectively, because the combination offers the highest yield, the strongest volatilizability of 98%, and the purest product. The NMR spectra of the iron(II) amidinates depend strongly on the deuterated sol-

Table 2. The activation energy (kJ mol$^{-1}$) of the sublimation of the iron bis(*N*-*tert*-butyl-*N*′-ethylacetamidinate) and bis(*N*,*N*′-diisopropylacetamidinate).

| No. | Nonisothermal sublimation activation energy | | Isothermal sublimation activation energy at a sample size of 2.1–3.0 mg | |
|---|---|---|---|---|
| | Flynn–Wall (average) | Kissinger | 80–130 °C | 40–80 °C |
| **1** | 88 | 90 | 114 | 25 |
| **2** | 88 | 91 | 111 | 37 |
| **3** | 115 | 107 | 104 | 11 |
| **4** | 141 | 127 | 87(90)[a] | 25(41)[a] |
| **7** | 107 | 97 | 79 | 48 |

[a] The sample size is 3.9 mg.

 © 2007 Wiley-VCH Verlag GmbH & Co. KGaA, Weinheim 

vent used. It seems that deuterated chloroform is the optimal solvent for the structure characterization of the paramagnetic iron(II) amidinates. The different iron(II) amidinates from various starting iron(II) compounds exhibit almost the same NMR, MS, and IR spectra, a melting point of 85 °C (with an exception in THF around 25 °C), and solution color in the same solvents but different synthetic yields, paramagnetic fractions, volatilizabilities, and colors in different solvents. This implies that the iron(II) amidinates exhibit interesting variable paramagnetism and solvatochromism. The iron(II) bis(*N*-*tert*-butyl-*N*′-ethylacetamidinate) demonstrates an average activation energy of 106 kJ mol$^{-1}$ for the nonisothermal sublimation, which is very close to the average activation energy of 104 kJ mol$^{-1}$ calculated on the basis of the isothermal sublimation. The sublimation is a diffusion-controlled process because the temperature and rate of the sublimation depend strongly on the sublimation level and sample size. Great volatilizability at a lower temperature is a special feature of the asymmetric iron(II) amidinates compared with other related compounds.

## Experimental Section

**General:** All reactions, manipulations, and characterizations were conducted under a nitrogen atmosphere using an inert atmosphere box. Tetrahydrofuran (THF), diethyl ether, toluene, and hexane were dried by using an innovative solvent purification system and stored over 0.4-nm molecular sieves. Methyllithium, 1-*tert*-butyl-3-ethyl-carbodiimide, 1,3-diisopropylcarbodiimide, anhydrous $FeCl_2$, iron(II) acetylacetonate[$Fe(CH_3COCH_2COCH_3)_2$], and iron(II) acetate (Aldrich) were used after vacuum treatment in nitrogen.

**Iron(II) Bis(*N*-*tert*-butyl-*N*′-ethylacetamidinate) ([Fe(*t*Bu-Et-Me-AMD)$_2$]):** A solution of methyllithium (1.6 M in diethyl ether, 3.8 mL, 6 mmol) in diethyl ether was added dropwise to a solution of 1-*tert*-butyl-3-ethyl-carbodiimide (0.9 g, 7 mmol) in diethyl ether (20 mL) at –30 °C. The mixture was warmed to room temperature and stirred for 4 h. This colorless mixture solution was then added to a solution of iron(II) acetylacetonate (0.9 g, 35 mmol) in diethyl ether (10 mL). The reaction mixture was stirred for 24 h. After all the volatiles were removed under reduced pressure the resulting solid was extracted with hexane (30 mL). The hexane extract was filtered through a pad of Celite on a glass frit to afford a dark solution. Subsequent sublimation afforded pure dark products (42%). Sublimation: 80 °C at 30 mTorr. The whole reaction procedure for the synthesis of the iron(II) complex is depicted in Scheme 1. The iron(II) bis(*N*,*N*′-diisopropylacetamidinate) was prepared in the same manner as described above. The iron(II) amidinate synthesized from iron(II) acetylacetonate in diethyl ether exhibits the following spectra: $^1$H NMR ($CDCl_3$, 25 °C): 199.5 (broad, N$CH_2$CH$_3$), 56.7–111 (very broad, $N_2CCH_3$), 29.7 [broad, NC($CH_3$)$_3$], –6.1 (sharp triplet, $NCH_2CH_3$) ppm for paramagnetic iron(II) amidinate; 8.6 (sharp, N$CH_2$CH$_3$), 3.5 (sharp, $N_2CCH_3$), 1.5 [broad, NC($CH_3$)$_3$], 0.3 (sharp triplet, $NCH_2CH_3$) ppm for non-paramagnetic (diamagnetic) iron(II) amidinate. On the basis of the area ratio of the resonance peaks at 29.7 over 1.5 ppm it could be estimated that 55% of the product is paramagnetic. $^1$H NMR ($C_5D_5N$, ([D$_5$]pyridine), 25 °C): 147.5 (sharp, N$CH_2$CH$_3$), 140.6 (sharp, $N_2CCH_3$), 9.1 (broad, NC($CH_3$)$_3$), –15.9 (sharp, $NCH_2CH_3$) ppm for paramagnetic iron(II) amidinate; 4.7 (sharp, N$CH_2$CH$_3$), 2.8 (sharp, $N_2CCH_3$), 1.1 [broad, NC($CH_3$)$_3$], 0.79 (sharp, $NCH_2CH_3$) ppm for diamagnetic iron(II) amidinate. The product could be 60% paramagnetic on the basis of the area ratio of the resonance peaks at 9.1 over 1.1 ppm. IR absorbances: 3268 (vw), 2968 (s), 2922 (s), 2854 (m), 1651 (vs), 1543 (m), 1457 (m), 1374 (m), 1288 (w), 1220 (m), 1157 (vw), 1031 (vw), 686 (s), and 548 (s) cm$^{-1}$. ES-MS at 120 °C: *m*/*z* [fragment, relative intensity (%)] = 331 [M – $(CH_3)_2$ + Na$^+$, 16], 321 [M – $(CH_3)_2$ + acetonitrile(MCN)$^+$, 7], 297 [M – $(CH_3)_2$–$C_2H_5$ + $NH_4^+$, 6], 269 [M – $(CH_3)_2$–$C(CH_3)_3$ + $NH_4^+$, 42], 207 [$FeNC(CH_3)NC(CH_3)_3$ + K$^+$, 6], 143 [$C_2H_5NC(CH_3)NC(CH_3)_3$ + 2H$^+$, 100]. The iron(II) amidinate from iron(II) acetate displays the following $^1$H NMR ($CDCl_3$, 25 °C): 196.8 (broad, N$CH_2$CH$_3$), 56.3–114.5 (very broad, $N_2CCH_3$), 29.4 [broad, NC($CH_3$)$_3$], –5.6 (sharp, $NCH_2CH_3$) ppm for paramagnetic iron(II) amidinate; 8.8 (sharp, N$CH_2$CH$_3$), 3.6 (sharp, $N_2CCH_3$), 1.2 [broad, NC($CH_3$)$_3$], 0.4 (broad, $NCH_2CH_3$) ppm for diamagnetic iron(II) amidinate. On the basis of the area ratio of the resonance peaks at 29.4 over 1.2 ppm it could be calculated that 60% of the product should be paramagnetic. IR absorbances: 3250 (vw), 3043 (vw), 2962 (s), 2922 (s), 2856 (m), 1653 (vs), 1559 (m), 1510 (m), 1457 (m), 1374 (m), 1288 (w), 1220 (m), 1157 (vw), 1030 (vw), 687 (s), and 548(s) cm$^{-1}$. ES-MS at 120 °C: *m*/*z* [fragment, relative intensity (%)] = 350[M – $C_2H_5$ + MCN$^+$, 4], 331 [M – $(CH_3)_2$ + Na$^+$, 21], 321[M – $(CH_3)_2$ + MCN$^+$, 9], 281 [M – $C(CH_3)_3$, 4], 269 [M – $(CH_3)_2$–$C(CH_3)_3$ + $NH_4^+$, 8], 143 [$C_2H_5NC(CH_3)NC(CH_3)_3$] + 2H$^+$, 100]. The iron(II) amidinate synthesized from $FeCl_2$ in diethyl ether demonstrates the following: $^1$H NMR ($CDCl_3$, 25 °C): 196.8 (broad, N$CH_2$CH$_3$), 56.3–115 (very broad, $N_2CCH_3$), 29.8 [broad, NC($CH_3$)$_3$], –5.8 (sharp, $NCH_2CH_3$) ppm for paramagnetic iron(II) amidinate; 8.8 (sharp, N$CH_2$CH$_3$), 3.6 (sharp, $N_2CCH_3$), 1.4 [broad, NC($CH_3$)$_3$], 0.6 (broad, $NCH_2CH_3$) ppm for diamagnetic iron(II) amidinate. It is evaluated based on the area ratio of the resonance peaks at 29.8 over 1.4 ppm that 58% of the product could be paramagnetic. ES-MS at 120 °C: *m*/*z* [fragment, relative intensity (%)] = 350 [M – $C_2H_5$ + MCN$^+$, 50], 349 [M – $C_2H_5$ + H$^+$ + K$^+$, 25], 348 [M – $(CH_3)_2$ + H$^+$ + K$^+$, 100], 339 [M + H$^+$, 16], 338 [M, 55], 331 [M – $(CH_3)_2$ + Na$^+$, 13], 324 [M – $CH_3$ + H$^+$, 17], 323 [M – $CH_3$, 87], 322 [M – $(C_2H_5)_2$ + MCN$^+$, 53]. The iron(II) amidinate synthesized from iron(II) acetylacetonate in toluene shows the following: $^1$H NMR ($CDCl_3$, 25 °C): 56 (N$CH_2$CH$_3$), 29.2 (broad, $N_2CCH_3$), 16.2 [broad, NC($CH_3$)$_3$], –5.8 (sharp, $NCH_2CH_3$) ppm for paramagnetic iron(II) amidinate; 8.6 (N$CH_2$CH$_3$), 3.2 (sharp, $N_2CCH_3$), 1.4 [broad, NC($CH_3$)$_3$], 1.1 (broad, $NCH_2CH_3$) ppm for diamagnetic iron(II) amidinate. The paramagnetic fraction calculated based on the area ratio of the resonance peaks at 16.2 over 1.4 ppm is 37%.

**Measurements:** $^1$H NMR spectra of the iron(II) amidinate solutions in test tubes filled with nitrogen were recorded with a Bruker AM-500 spectrometer. Melting points were obtained in a sealed capillary using optical microscopy. Infrared spectra were obtained with a Nicolet FT-IR 7000 spectrometer with sample solutions in diethyl ether in a nitrogen atmosphere. Mass spectra of the sample in THF were recorded with a Micromass LCT time-of-flight Mass Spectrometer operating in electrospray mode. Solution samples of the respective complexes in diethyl ether or THF were rapidly introduced by a direct inlet technique with acetonitrile as a mobile phase at a source temperature of 120–300 °C. Thermogravimetry (TG) was performed with a TGA Q50 V6.2 Build 187 thermogravimetric analyzer. Conventional constant heating-rate TG measurements were run at 5 °C, 10 °C, 20 °C, and 40 °C min$^{-1}$ in nitrogen with a sample size of 1–3 mg to provide a control set of values for thermal sublimation parameters. Isothermally programmed TG analyses

 © 2007 Wiley-VCH Verlag GmbH & Co. KGaA, Weinheim 

were carried out at 40, 50, 60, 70, 80, 90, 100, 110, 120, and 130 °C in nitrogen at a flow rate of 40 mL min$^{-1}$ with a sample size of 2–3 mg. The furnace was quickly heated at a heating rate of 60 °C min$^{-1}$ to the selected temperature after the sample was inserted in the furnace. There are several techniques for the kinetic evaluation of the TG thermal weight-loss data, and they have been discussed in an earlier publication.[23] The thermal sublimation kinetics were examined by the following three evaluating techniques [Equation (1)], [Equation (2)], and [Equation (3)].

**Flynn–Wall Technique**[24]

$$\ln(\text{Heating rate}) = \ln(ZE/R) - \ln[F(a)] - E/(RT) \quad (1)$$

$$\ln(\text{Heating rate}/T_{sm}^2) = \ln[n(1-\alpha_m)^{n-1}ZR/E] - E/(RT_{sm}) \quad (2)$$

$$\ln(d\alpha/dt)_m = \ln Z + n\ln(1-\alpha_m) - E/(RT) \quad (3)$$

The activation energy, $E$, can be calculated from a plot of ln (heating rate) against $1/T$ (absolute temperature) at a fixed weight loss since the slope of such a line is given by $E/R$ (gas constant 8.314 J mol$^{-1}$K$^{-1}$).

**Kissinger Technique**[25]

Where $T_{sm}$ and $\alpha_m$ are the absolute temperature and sublimation, respectively, at the maximum sublimation rate $(d\alpha/dt)_m$. The slope of ln (Heating rate/$T_{sm}^2$) vs. $1/T_{sm}$ is equal to $-E/R$.

**For an Isothermal TG Measurement at Several Isothermal Temperatures**[23]

The $E$ value of isothermal degradation was calculated from the slope of the plot of the maximum weight-loss rate ln $(d\alpha/dt)_m$ vs. the reciprocals of the several isothermal temperatures ($1/T$).

## Acknowledgments

This work was supported in part by the National Science Foundation (grant ECS-0354213). We thank Leonard N. J. Rodriguez, Dr. Venkateswara Rao Pallem, Dr. Jin-Seong Park, and Dawen Pang from Harvard University, as well as Prof. Dr. Charles Musgrave from Stanford University for their valuable help.

[1] A. R. Sadique, M. J. Heeg, C. H. Winter, *J. Am. Chem. Soc.* **2003**, *125*, 7774–7775.
[2] J. R. Hagadorn, J. Arnold, *Angew. Chem. Int. Ed.* **1998**, *37*, 1729–1731; *Angew. Chem.* **1998**, *110*, 1813–1815.
[3] H. Kondo, K. Matsubara, H. Nagashima, *J. Am. Chem. Soc.* **2002**, *124*, 534–535.
[4] X. Jiang, J. C. Bollinger, M. H. Baik, D. Lee, *Chem. Commun.* **2005**, *8*, 1043–1045.
[5] J. Barker, N. C. Blacker, P. R. Phillips, N. W. Alcock, W. Errington, M. G. H. Wallbridge, *J. Chem. Soc., Dalton Trans.* **1996**, 431–437.
[6] D. Abeysekera, K. N. Robertson, T. S. Cameron, J. A. C. Clyburne, *Organometallics* **2001**, *20*, 5532–5536.
[7] C. Villiers, P. Thuery, M. Ephritikhine, *Eur. J. Inorg. Chem.* **2004**, *23*, 4624–4632.
[8] D. A. Kissounko, Y. H. Zhang, M. B. Harney, L. R. Sita, *Adv. Synth. Catal.* **2005**, *347*, 426–432.
[9] T. Chivers, C. Fedorchuk, M. Parvez, *Organometallics* **2005**, *24*, 580–586.
[10] B. S. Lim, A. Rahtu, J.-S. Park, R. G. Gordon, *Inorg. Chem.* **2003**, *42*, 7951–7958.
[11] a) D. Hausmann, J. Becker, S. Wang, R. G. Gordon, *Science* **2002**, *298*, 402–406; b) B. S. Lim, A. Rahtu, R. G. Gordon, *Nat. Mater.* **2003**, *2*, 749–754; c) R. G. Gordon, S. Barry, R. N. R. Broomhall-Dillard, D. J. Teff, *Adv. Mater. Optics Electron.* **2000**, *10*, 201–211.
[12] A. I. Kingon, J. P. Maria, S. K. Streiffer, *Nature* **2000**, *406*, 1032–1038.
[13] Z. Li, S. T. Barry, R. G. Gordon, *Inorg. Chem.* **2005**, *44*, 1728–1735.
[14] F. T. Edelmann, D. M. M. Freckmann, H. Schumann, *Chem. Rev.* **2002**, *102*, 1851–1896.
[15] H. E. Abdou, A. A. Mohamed, J. M. Lopez-de-Luzuriaga, J. P. Fackler, *J. Cluster Sci.* **2004**, *15*, 397–411.
[16] a) R. T. Boere, M. L. Cole, P. C. Junk, *New J. Chem.* **2005**, *29*, 128–134; b) F. A. Cotton, N. S. Dalal, C. Y. Liu, C. A. Murillo, J. M. North, X. P. Wang, *J. Am. Chem. Soc.* **2003**, *125*, 12945–12952.
[17] a) M. J. McNevin, J. R. Hagadorn, *Inorg. Chem.* **2004**, *43*, 8547–8554; b) P. de Rouffignac, J. S. Park, R. G. Gordon, *Chem. Mater.* **2005**, *17*, 4808–4814; c) W. X. Zhang, M. Nishiura, Z. M. Hou, *J. Am. Chem. Soc.* **2005**, *127*, 16788–16789; d) M. L. Cole, C. Jones, P. C. Junk, M. Kloth, A. Stasch, *Chem. Eur. J.* **2005**, *11*, 4482–4491.
[18] H. Kawaguchi, T. Matsuo, *Chem. Commun.* **2002**, *9*, 958–959.
[19] B. Vendemiati, G. Prini, A. Meetsma, B. Hessen, J. H. Teuben, O. Traverso, *Eur. J. Inorg. Chem.* **2001**, *3*, 707–711.
[20] J. Zhang, R. Ruan, Z. Shao, R. Cai, L. Weng, X. Zhou, *Organometallics* **2002**, *21*, 1420–1424.
[21] a) B. Clare, N. Sarker, R. Shoemaker, J. R. Hagadorn, *Inorg. Chem.* **2004**, *43*, 1159–1166; b) V. K. K. Praneeth, C. Näther, G. Peters, N. Lehnert, *Inorg. Chem.* **2006**, *45*, 2795–2811.
[22] X.-G. Li, R.-R. Zhang, M.-R. Huang, *J. Comb. Chem.* **2006**, *8*, 174–183.
[23] X.-G. Li, M.-R. Huang, *Polym. Degrad. Stabil.* **1999**, *64*, 81–90.
[24] J. H. Flynn, L. A. Wall, *J. Polym. Sci. B* **1966**, *4*, 323–328.
[25] H. E. Kissinger, *Anal. Chem.* **1957**, *29*, 1702–1706.

Received: August 18, 2006
Published Online: February 9, 2007

 © 2007 Wiley-VCH Verlag GmbH & Co. KGaA, Weinheim 

DOI: 10.1002/ejic.200600801

# Control of Intramolecular Ether-Oxygen Coordination in the Crystal Structure of Copper(II) Complexes With Dipicolylamine-Based Ligands

**Yuji Mikata,*[a] Tomomi Fujimoto,[b] Yuko Sugai,[b] and Shigenobu Yano[b]**

**Keywords:** N,O ligands / Copper / Coordination modes / Ligand effects

Thirteen crystal structures of copper(II) complexes with a series of dipicolylamine (DPA)-derived ligands, *N*-(2-methoxyethyl)-*N*,*N*-bis(2-pyridylmethyl)amine (**L1**), *N*-[2-(2-hydroxyethyloxy)ethyl]-*N*,*N*-bis(2-pyridylmethyl)amine (**L2**) and *N*-(3-methoxypropyl)-*N*,*N*-bis(2-pyridylmethyl)amine (**L3**), have been determined and the factors that control the coordination of the ether-oxygen atom of these ligands to the copper centre are discussed. Complexes that have +1 or +2 charges exhibit coordination of the ether-oxygen atom, whereas neutral complexes in which two anions are bound to the copper(II) centre tend to lose the oxygen coordination. Upon chelation of the oxygen atom, **L3** forms a six-membered chelate ring with respect to the 3-aminopropyl ether moiety whereas **L1** and **L2** form a five-membered chelate. This difference, especially in the nitrate and bromide complexes, determines whether the ether-oxygen atom chelates to the metal centre to give a monocationic complex, or the second anion coordinates to the metal centre to form the ether-free, neutral complex. The terminal anchor hydroxy group of **L2** facilitates the ether-oxygen coordination via a hydrogen bond interaction to the donor atom located *trans* to the aliphatic nitrogen atom in the basal plane.
(© Wiley-VCH Verlag GmbH & Co. KGaA, 69451 Weinheim, Germany, 2007)

## Introduction

Weak interatomic interactions with noncovalent bonds, including hydrogen bonds and electrostatic and van der Waals interactions, are essential elements not only in life sciences but also in chemistry in general.[1–3] Cooperative binding by multipoint interactions, which are often called cluster effects in glycoscience, makes weak interactions strong and specific.[3–5] On/off switching of such noncovalent interactions is another important process, and triggers of such switching include conformational changes induced by remote sites as well as redox changes in the metal centre.[6] It is therefore important to regulate these weak interatomic interactions both in solution and in the solid state.

In this report, we will focus on the coordination of ether-oxygen atoms to metal ions. Although multipoint coordination of ether-oxygen atoms, such as those found in crown ethers, can exhibit strong metal-binding, an isolated oxygen atom has only a moderate to weak binding ability to the metal centre.[7–9] Sigel et al. have been extensively studying the solution chemistry of intramolecular ether-oxygen coordination to metal centres using phosphate-pendant alkyl ether derivatives.[10,11] Recently, by employing the sugar-pendant dipicolylamine (DPA) ligand, we reported that the oxygen atom in an asymmetric ether is capable of becoming a stereogenic centre upon coordination to a copper(II) ion.[12,13] Strong binding of the DPA unit to the copper(II)[14–19] assists the asymmetric coordination of the anomeric oxygen atom of the sugar unit to the metal centre in the crystal and in solution.

In this study, in order to gain general information about intramolecular ether-oxygen chelation, the factors that promote the oxygen atom coordination to the copper(II) centre in the solid state are investigated by means of X-ray crystallography with a series of DPA-derived ligands, namely *N*-(2-methoxyethyl)-*N*,*N*-bis(2-pyridylmethyl)amine (**L1**),[20–24] *N*-[2-(2-hydroxyethyloxy)ethyl]-*N*,*N*-bis(2-pyridylmethyl)amine (**L2**)[25] and *N*-(3-methoxypropyl)-*N*,*N*-bis(2-pyridylmethyl)amine (**L3**).[21] The anion of the metal salt as well as the ligand structure control the ether-oxygen coordination to the copper(II) centre in these complexes.

## Results and Discussion

### Preparation and Structure Determination of the Complexes

Single crystals of complexes of **L1** with $Cu(NO_3)_2$ {$[Cu(\mathbf{L1})(NO_3)_2]$ (**1**) and $[Cu(\mathbf{L1})(NO_3)](ClO_4)$ (**2**)}, **L3** with $Cu(NO_3)_2$ {$[Cu(\mathbf{L3})(NO_3)_2]$ (**3**) and $[Cu(\mathbf{L3})(NO_3)(ClO_4)]$ (**4**)}, **L1** with $Cu(ClO_4)_2$ {$[Cu(\mathbf{L1})(ClO_4)(CH_3OH)](ClO_4)$ (**5**) and $[Cu(\mathbf{L1})(CH_3CN)(H_2O)](ClO_4)_2$ (**6**)}, **L2** with $Cu(ClO_4)_2$ ($[Cu(\mathbf{L2})(ClO_4)(CH_3OH)](ClO_4)$ (**7**)], **L1** with $CuCl_2$ {$[Cu(\mathbf{L1})Cl](ClO_4)$ (**8**)}, **L2** with $CuCl_2$

[a] KYOUSEI Science Center, Nara Women's University, Nara 630-8506, Japan
Fax: +81-742-20-3095
E-mail: mikata@cc.nara-wu.ac.jp
[b] Division of Materials Science, Nara Women's University, Nara 630-8506, Japan
Supporting information for this article is available on the WWW under http://www.eurjic.org or from the author.

 © 2007 Wiley-VCH Verlag GmbH & Co. KGaA, Weinheim 

{[Cu(**L2**)Cl]($ClO_4$) (**9**)}, **L3** with $CuCl_2$ {[Cu(**L3**)Cl]($ClO_4$) (**10**)}, **L1** with $CuBr_2$ {[Cu(**L1**)Br]($ClO_4$) (**11**)}, **L2** with $CuBr_2$ {[Cu(**L2**)Br]($ClO_4$) (**12**)} and **L3** with $CuBr_2$ {[Cu(**L3**)$Br_2$] (**13**)} were prepared from methanol solutions of the ligand and metal salt by slow diffusion of diethyl ether into these solutions; in some cases sodium perchlorate was added. The complex numbers and metal salt/ligand combinations are summarised in Table 1. Complexes **3** and **10** afforded crystals from methanol/diethyl ether of insufficient quality for X-ray analysis and were therefore recrystallised from acetonitrile/diethyl ether, which resulted in good quality crystals. Complex **6** was prepared in acetonitrile and crystals were grown by ether diffusion. The crystallographic data and X-ray diffraction conditions for complexes **1**–**13** are summarised in Tables S1–S4 (see Supporting Information). ORTEP diagrams of these complexes with 50% probability ellipsoids are shown in Figures 1 (**1**), 2 (**2**), 3 (**3**), 4 (cation of **6**), 5 (cation of **7**), 6 (cation of **9**) and 7 (cation of **10**). The remainder are given as Supporting Information (Figures S1–S6). Selected bond lengths and the coordination geometries, including $\tau$ values,[26] ether oxygen atom coordination, complex charges and hydrogen-bond interactions, for the copper centres in complexes **1**–**13** are summarised in Tables 2 and 3.

Table 1. Preparation of copper(II) complexes **1**–**13**.[a]

| | Ligand | | |
|---|---|---|---|
| Metal salt | **L1** | **L2** | **L3** |
| $Cu(NO_3)_2$ | **1**, **2**[b] | _[c] | **3***, **4**[b] |
| $Cu(ClO_4)_2$ | **5**, **6*** | **7** | _[d] |
| $CuCl_2$ + $NaClO_4$ | **8*** | **9** | **10** |
| $CuBr_2$ + $NaClO_4$ | **11** | **12** | **13** |

[a] Crystals were grown from the reaction mixture in methanol by diffusion of diethyl ether vapour except for those indicated with asterisks (*), which were obtained by recrystallisation from $CH_3CN$/diethyl ether. [b] In the presence of one equivalent of $NaClO_4$. [c] Reported in ref.[25] [d] No single crystals suitable for X-ray analysis were obtained.

The crystal structure for the complex of **L2** with $Cu(NO_3)_2$ has already been reported.[25] In spite of extensive crystallisation trials, the mixture of **L3** and $Cu(ClO_4)_2$ in methanol did not afford single crystals suitable for X-ray crystallography, although the formation of a metal–ligand complex was confirmed by UV/Vis spectral changes and ESI mass spectrometry (data not shown). All structures exhibit meridional coordination geometries for the DPA unit.[14–20,23–25] Among them, [Cu(**L1**)($NO_3$)]($ClO_4$) (**2**),

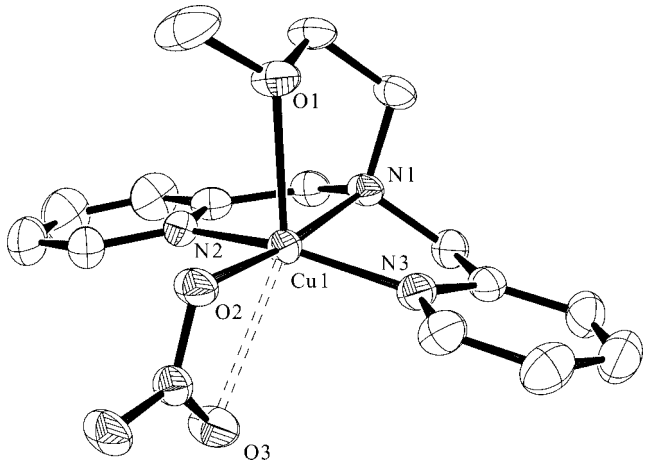


Figure 2. ORTEP plot of the cation of [Cu(**L1**)($NO_3$)]($ClO_4$) (**2**).

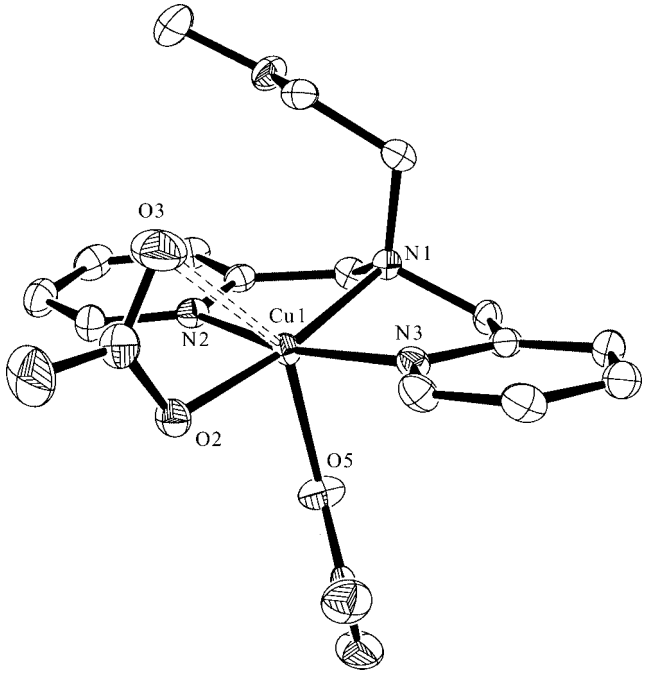


Figure 1. ORTEP plot of [Cu(**L1**)($NO_3$)$_2$] (**1**).

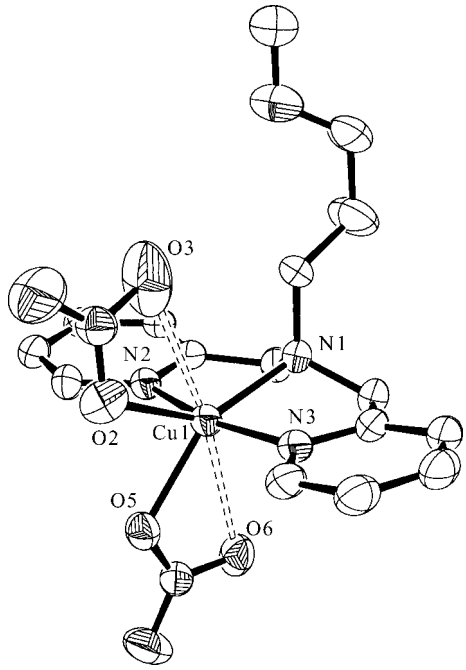


Figure 3. ORTEP plot of [Cu(**L3**)($NO_3$)$_2$] (**3**).

 © 2007 Wiley-VCH Verlag GmbH & Co. KGaA, Weinheim 

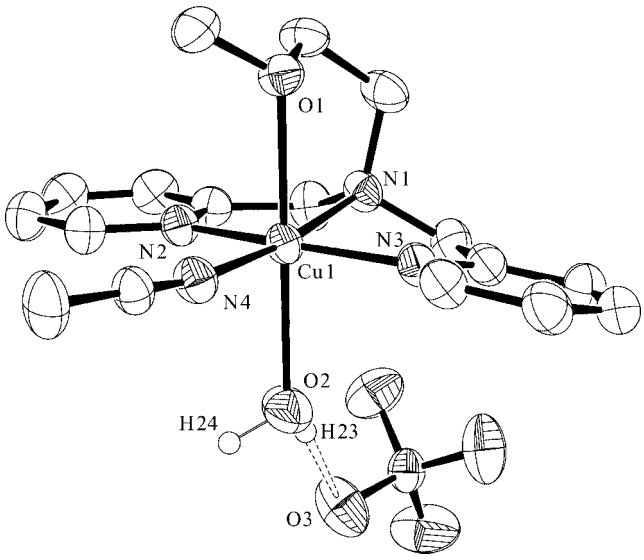


Figure 4. ORTEP plot of the cation of [Cu(**L1**)($CH_3CN$)($H_2O$)]-($ClO_4$)$_2$ (**6**). Both hydrogen atoms of the coordinated water molecule (H23 and H24) are hydrogen bonded to the oxygen atoms of perchlorate ion (O3 and O4).

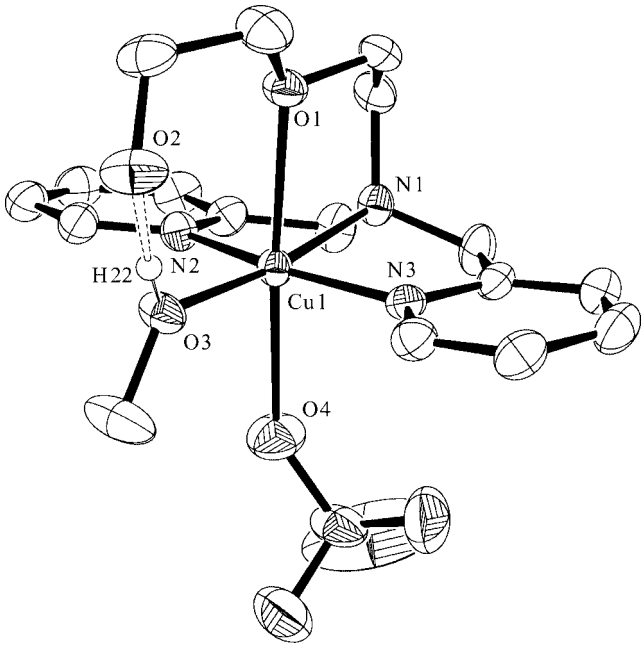


Figure 5. ORTEP plot of the cation of [Cu(**L2**)($ClO_4$)($CH_3OH$)]-($ClO_4$) (**7**).

[Cu(**L1**)($ClO_4$)($CH_3OH$)]($ClO_4$) (**5**), [Cu(**L1**)($CH_3CN$)-($H_2O$)]($ClO_4$)$_2$ (**6**), [Cu(**L2**)($ClO_4$)($CH_3OH$)]($ClO_4$) (**7**), [Cu(**L1**)Cl]($ClO_4$) (**8**), [Cu(**L2**)Cl]($ClO_4$) (**9**), [Cu(**L3**)Cl]-($ClO_4$) (**10**), [Cu(**L1**)Br]($ClO_4$) (**11**) and [Cu(**L2**)Br]($ClO_4$) (**12**) are mono- or dicationic complexes with coordination of the ether-oxygen atom to the copper centre. The ether-oxygen atom in these structures occupies the apical position of a Jahn–Teller-distorted copper(II) centre with Cu–O bond lengths of between 2.329 and 2.453 Å.

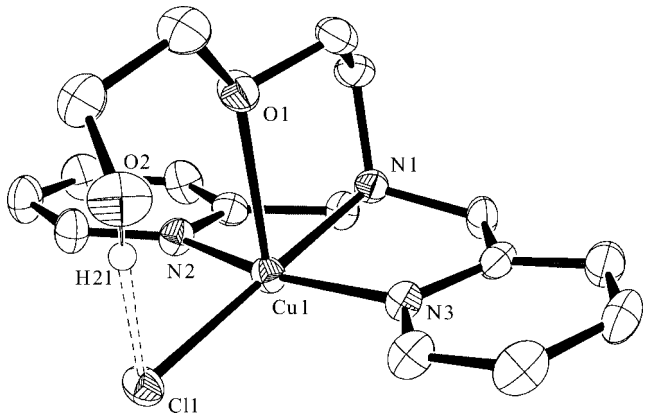


Figure 6. ORTEP plot of the cation of [Cu(**L2**)Cl]($ClO_4$) (**9**).

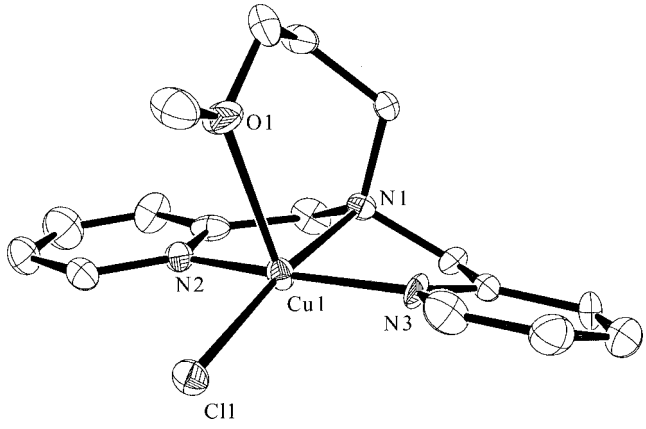


Figure 7. ORTEP plot of the cation of [Cu(**L3**)Cl]($ClO_4$) (**10**).

### Nitrate Complexes

Metzler-Nolte and co-workers have already reported the structures of $Ni^{II}$, $Cu^{II}$, $Co^{II}$ and $Zn^{II}$ nitrate complexes of **L2**.[25] In all cases, the ether-oxygen atom in **L2** coordinates to the metal centre. In contrast to the Ni, Co and Zn complexes in which the hydroxy group of **L2** is directly coordinated to the metal centre, the hydroxy group in the Cu-**L2** complex no longer binds to the metal centre. This is due to the elongated Cu–$O_{ether}$ distance (2.562 Å) resulting from the Jahn–Teller effect of the $d^9$ copper(II) centre. As a consequence, the hydroxy group of **L2** in the complex is separated from the metal coordination sphere and hydrogen-bonded to the metal-coordinated water molecule located in the basal plane containing copper and three DPA nitrogen atoms.

The present study shows that the absence of the hydroxy anchor group results in the dissociation of the ether-oxygen atom from the copper(II) centre in the nitrate complexes (see Figures 1 and 3). Complex **1** adopts a five-coordinate, slightly distorted square-pyramidal geometry ($\tau$ = 0.11) and is ligated by DPA and two nitrate anions. Weak chelation to the sixth site by the oxygen atom of the coordinated nitrate ion [Cu–O3 = 2.721(2) Å] is also observed. The coor-

 © 2007 Wiley-VCH Verlag GmbH & Co. KGaA, Weinheim 

Table 2. Bond lengths around the copper centre in complexes **1**–**13**.[a]

| Complex | Cu–N1 | Cu–N2 | Cu–N3 | Cu–$X_{basal}$ | Cu–O1 | Cu–$X_{ap}$ | Figure |
|---|---|---|---|---|---|---|---|
| **1** [Cu(**L1**)$(NO_3)_2$] | 2.035(2) | 1.991(2) | 1.982(2) | 1.983(1)[b] | | 2.237(2)[b]<br>*2.721(2)*[b] | 1 |
| **2** [Cu(**L1**)$(NO_3)$]$ClO_4$ | 2.026(2) | 1.970(2) | 1.968(2) | 2.000(2)[b] | 2.329(2) | | 2 |
| **3** [Cu(**L3**)$(NO_3)_2$] | 2.077(3) | 1.969(3) | 1.967(3) | 2.086(3)[b] | | 2.321(4)[b]<br>*2.646(3)*[b]<br>*2.805(6)*[b] | 3 |
| **4** [Cu(**L3**)$(NO_3)(ClO_4)$] | 2.042(6) | 1.949(6) | 1.957(6) | 2.012(5)[b] | | 2.408(5)[b]<br>*2.721(2)*[b] | S1 |
| **5** [Cu(**L1**)$(ClO_4)(CH_3OH)$]$(ClO_4)$ | 1.997(5) | 1.974(5) | 1.991(5) | 1.952(6)[c] | 2.427(5) | *2.672(5)*[b] | S2 |
| **6** [Cu(**L1**)$(CH_3CN)(H_2O)$]$(ClO_4)_2$ | 2.033(2) | 1.997(2) | 1.982(2) | 1.999(2)[d] | 2.367(2) | 2.385(3)[c] | 4 |
| **7** [Cu(**L2**)$(ClO_4)(CH_3OH)$]$(ClO_4)$ | 2.013(3) | 1.981(3) | 1.985(3) | 1.954(3)[c] | 2.453(3) | 2.478(3)[b] | 5 |
| **8** [Cu(**L1**)Cl]$(ClO_4)$ | 2.059(1) | 1.988(1) | 1.991(1) | 2.2357(4)[e] | 2.381(1) | | S3 |
| **9** [Cu(**L2**)Cl]$(ClO_4)$ | 2.026(3) | 2.000(3) | 2.013(3) | 2.2471(8)[e] | 2.451(2) | | 6 |
| **10** [Cu(**L3**)Cl]$(ClO_4)$ | 2.029(7) | 1.961(6) | 1.989(6) | 2.271(2)[e] | 2.398(6) | | 7 |
| **11** [Cu(**L1**)Br]$(ClO_4)$ | 2.061(2) | 1.994(2) | 1.982(2) | 2.3900(4)[f] | 2.452(2) | | S4 |
| **12** [Cu(**L2**)Br]$(ClO_4)$ | 2.051(2) | 1.988(2) | 2.007(2) | 2.3725(4)[f] | 2.4221(18) | | S5 |
| **13** [Cu(**L3**)$Br_2$] | 2.124(3) | 1.986(4) | 1.977(4) | 2.5119(7)[f] | | 2.5282(6)[f] | S6 |

[a] Bond lengths in italics indicate semi-coordination (Cu–X = 2.5–2.9 Å). [b] X = O (anion: $NO_3^-$ or $ClO_4^-$). [c] X = O (solvent: $H_2O$ or $CH_3OH$). [d] X = N. [e] X = Cl. [f] X = Br.

Table 3. Summary of the coordination geometries, ether-oxygen coordination, complex charges and hydrogen-bond interactions for complexes **1**–**13**.

| Complex | Coordination[a] geometry | $\tau$ | O1-coordination | Complex charge | Hydrogen bond |
|---|---|---|---|---|---|
| [Cu(**L1**)$(NO_3)_2$] (**1**) | sqp | 0.11 | no | 0 | – |
| [Cu(**L1**)$(NO_3)$]$(ClO_4)$ (**2**) | sqp | 0.18 | yes | 1 | – |
| [Cu(**L3**)$(NO_3)_2$] (**3**) | sqp-tbp | 0.28 | no | 0 | – |
| [Cu(**L3**)$(NO_3)(ClO_4)$] (**4**) | sqp | 0.08 | no | 0 | – |
| [Cu(**L1**)$(ClO_4)(CH_3OH)$]$(ClO_4)$ (**5**) | sqp/oh | 0.14 | yes | 1 | – |
| [Cu(**L1**)$(CH_3CN)(H_2O)$]$(ClO_4)_2$ (**6**) | oh | – | yes | 2 | coordinated water/perchlorate |
| [Cu(**L2**)$(ClO_4)(CH_3OH)$]$(ClO_4)$ (**7**) | oh | – | yes | 1 | O2-coordinated methanol |
| [Cu(**L1**)Cl]$(ClO_4)$ (**8**) | sqp | 0.24 | yes | 1 | – |
| [Cu(**L2**)Cl]$(ClO_4)$ (**9**) | sqp | 0.22 | yes | 1 | O2-coordinated chloride |
| [Cu(**L3**)Cl]$(ClO_4)$ (**10**) | sqp | 0.14 | yes | 1 | – |
| [Cu(**L1**)Br]$(ClO_4)$ (**11**) | sqp | 0.19 | yes | 1 | – |
| [Cu(**L2**)Br]$(ClO_4)$ (**12**) | sqp | 0.28 | yes | 1 | – |
| [Cu(**L3**)$Br_2$] (**13**) | tbp | 0.59 | no | 0 | – |

[a] sqp: square pyramidal; oh: octahedral; tbp: trigonal bipyramidal.

dination geometry of pentacoordinate complex **3** is more distorted ($\tau$ = 0.28) and is close to a trigonal-bipyramidal geometry. For complex **3**, taking the weak intramolecular chelations [Cu–O6 = 2.646(3), Cu–O3 = 2.805(6) Å] into account, this structure can be regarded as seven-coordinate with a pentagonal bipyramidal geometry. This steric hindrance of chelated nitrate may remain during the crystallisation process, and, in combination with the neutral nature of the complexes, prevent the coordination of the ether side chain in **L1** and **L3** in the crystal structures.

In contrast, the addition of sodium perchlorate to the reaction solution of **L1** with $Cu(NO_3)_2$ affords the ether-bound complex **2** (Figure 2). Perchlorate ion is considered to promote crystallisation of monocationic complexes, giving rise to the oxygen-coordinated complex. On the other hand, for the **L3**/$Cu(NO_3)_2$/$NaClO_4$ system, a perchlorate anion coordinates to the copper centre together with a nitrate ion to give the neutral, ether-free complex **4** (Figure S1 in the Supporting Information). This difference could originate from the preferred formation of a five-membered chelate ring over a six-membered ring by the aminoalkyl ether system.

## Perchlorate Complexes

Copper(II) perchlorate complexes were subsequently examined. Unfortunately, single crystals of the Cu/**L3** complex could not be obtained but the other two ligands afforded crystals suitable for X-ray analysis, resulting in the structures of the cationic portions of [Cu(**L1**)$(ClO_4)$-$(CH_3OH)$]$(ClO_4)$ (**5**), [Cu(**L1**)$(CH_3CN)(H_2O)$]$(ClO_4)_2$ (**6**) and [Cu(**L2**)$(ClO_4)(CH_3OH)$]$(ClO_4)$ (**7**) shown in Figures S2 (see Supporting Information), 4 and 5, respectively.

In complexes **5** and **7**, which were crystallised from methanol, the copper centre adopts an $N_3O_3$ hexacoordinate, slightly distorted octahedral geometry ligated by the tridentate DPA, methanol, perchlorate and the ether-oxygen atom

 © 2007 Wiley-VCH Verlag GmbH & Co. KGaA, Weinheim 

in the ligand. Since the bond length for the sixth site of complex **5** occupied by the perchlorate oxygen atom is very long [Cu–O = 2.672(5) Å], the geometry of this complex could also be described as a distorted square-pyramid ($\tau$ = 0.14). The Cu–$O_{ether}$ bond lengths of these two complexes are similar [2.427(5) Å for **5** and 2.453(3) Å for **7**] and are significantly different from that in the $Cu(NO_3)_2$/**L2** complex (2.562 Å).[25]

For complex **6**, which was crystallised from acetonitrile, the perchlorate anion is no longer coordinated to the copper centre; instead, acetonitrile and water molecules occupy the basal and apical positions, respectively. The weak coordination ability and superior crystallising ability of the perchlorate complex promotes the formation of a dicationic complex that facilitates the ether-oxygen coordination to the copper centre. The bond length between copper and the ether-oxygen atom (O1) in this six-coordinate complex is very short (2.367 Å) but slightly longer than that of the five-coordinate, monocationic complex **2** (2.329 Å). Both hydrogen atoms of the copper-bound water molecule in complex **6** are hydrogen-bonded to perchlorate anions, which increases the donor ability of this metal-coordinated water oxygen atom. Thus, the Cu–$O_{water}$ bond length [2.385(3) Å] is very short and is close to those seen for anion coordination distances in the apical position [2.237(2) Å for **1**, 2.321(4) Å for **3** and 2.408(5) Å for **4**]. This strong water coordination to the copper centre makes the Cu–O1 bond relatively weak for dicationic complex **6** compared to that in monocationic complex **2**.

### Chloride Complexes

Chloride anion, in combination with sodium perchlorate, is found to facilitate ether-oxygen coordination to the copper centre for all ligands (see Figure S3 in the Supporting Information and Figures 6 and 7). Complexes **8**–**10** comprise one copper(II) ion, one ligand molecule and one chloride ion in five-coordinate complexes with distorted square-pyramidal geometries ($\tau$ = 0.14–0.24). The copper-bound chloride ions occupy the site *trans* to the aliphatic nitrogen atom of DPA, which reduces the steric hindrance around the metal centre. For the perchlorate-bound, ether-coordinated complexes **5** and **7**, the weakly coordinating perchlorate anion occupies the Jahn–Teller-elongated apical position that allows solvent methanol to coordinate to the metal centre from the basal plane, which satisfies the steric requirements for ether-oxygen binding. For the ether-free neutral complexes **1**, **3** and **4**, the moderate coordination strength and steric hindrance of the nitrate anion located at the equatorial site prevent ether-oxygen binding to the metal centre. Chloride anion has enough coordination ability to occupy the equatorial ordinate and less steric bulk, which gives rise to ether-coordinated complexes for all ligands. In complex **9**, the hydroxy group is hydrogen-bonded to the metal-coordinated chloride atom.

In the absence of sodium perchlorate, the reaction mixture of **L1** and $CuCl_2$ afforded a complex formulated as $[Cu(\mathbf{L1})Cl]_2[CuCl_4]$ (data not shown). The structure of the cationic portion of this complex is almost the same as complex **8**. Ligands **L2** and **L3** did not afford any precipitates in the absence of sodium perchlorate.

### Bromide Complexes

Bromide ion as the counterion also has an effect on the coordination sphere (see Figures S4–S6 in the Supporting Information). Complex **13** crystallises directly from the ligand/metal solution mixture, but addition of sodium perchlorate was found to be effective for crystallisation of complexes **11** and **12**. Even in the presence of perchlorate anion, the reaction mixture of **L3** with $CuBr_2$ in methanol affords the dibromide complex **13**. From these results, **L3** seems to exhibit weaker ether-oxygen coordination than **L1** and **L2**, thus forming an ether-free, neutral complex. This difference again highlights the preferred formation of a five-membered chelate over a six-membered ring, although the superior crystallising ability of complex **13** might be important. This complex adopts a distorted trigonal-bipyramidal geometry ($\tau$ = 0.59) due to the bulkiness of two copper-bound bromide ions. Complexes **11** and **12** exhibit five-coordinate, distorted square-pyramidal geometries ($\tau$ = 0.19 and 0.28) similar to the chloride complexes, but for **12**, the hydroxy group of the ligand is no longer hydrogen-bonded to the copper-bound bromide atom.

### Solution Studies

The electronic absorption spectra, cyclic voltammetry and EPR spectra were examined for complexes **1**–**13** to investigate the solution structure. In methanol solution, all complexes exhibit a copper d–d transition band around 640–710 nm ($\varepsilon$ = 80–200). No specific relationship between absorption maxima and ligand/complex structure was observed. For cyclic voltammetry in acetonitrile, the reduction potentials were significantly altered by ligand structure. Thus, the complexes ligated by **L3** exhibit positive-shifted reduction potentials that indicate a strong electron requirement for the copper centre. The EPR spectra in acetonitrile at room temperature exhibit well-resolved $^{63/65}$Cu hyperfine splitting in the range of 7–8 mT, except for complexes **7** and **13**, which show broad signals. $^{79/81}$Br hyperfine splitting in the range of 3 mT was also observed for complexes **11**–**13**, and this could be responsible for broadness of the signals for the dibromide complex **13**. Further studies of the solution structures of these complexes are in progress in our laboratory.

## Conclusions

As summarised in Table 3, the ligand structure and the anion of the starting metal salt play crucial roles in the ether-oxygen coordination in metal complexes in the crystal structure. The difference in chelate ring size determines the ether-oxygen coordination to the metal centre. The steric

 © 2007 Wiley-VCH Verlag GmbH & Co. KGaA, Weinheim 

bulk of the chelating nitrate ion prevents ether-oxygen coordination whereas chloride ion promotes it. As a consequence, complexes that have +1 or +2 charges exhibit coordination of the ether-oxygen atom, whereas neutral complexes in which two anions are bound to the copper(II) centre tend to dissociate the ether-oxygen atom. The strong electron-withdrawing character of the metal centre in cationic complexes requires ether-oxygen coordination. However, stronger electron demand would require more efficient coordination by anion binding. Compensating balance between enthalpy gain and entropy loss caused by the coordination of the external anion, as well as crystallising ability of the complex, controls the choice of formation of intramolecular ether-oxygen binding to afford cationic complexes or intermolecular anion binding leading to neutral complexes. The hydroxy group of **L2** does not coordinate to the copper centre but promotes the ether-oxygen coordination by hydrogen bonding to the oxygen or chloride atom located *trans* to the aliphatic nitrogen in the basal plane. The present information provides an important strategy to regulate the coordination of an oxygen atom to the metal centre in the solid state.

## Experimental Section

**Materials:** *N*-(2-Methoxyethyl)-*N*,*N*-bis(2-pyridylmethyl)amine (**L1**),[21] *N*-[2-(2-hydroxyethyloxy)ethyl]-*N*,*N*-bis(2-pyridylmethyl)-amine (**L2**)[25] and *N*-(3-methoxypropyl)-*N*,*N*-bis(2-pyridylmethyl)-amine (**L3**)[21] were prepared from the corresponding amine by refluxing with two equivalents of 2-chloromethylpyridine hydrochloride in the presence of potassium carbonate in acetonitrile (75–84% yield). The spectroscopic data of **L1**–**L3** are in good agreement with those reported in the literature. Copper(II) nitrate trihydrate, copper(II) perchlorate hexahydrate (Wako Pure Chemical Industries, Ltd.), copper(II) chloride dihydrate, copper(II) bromide (Nacalai Tesque), sodium perchlorate monohydrate and all solvents (Wako Pure Chemical Industries, Ltd.) were used as received.

**Preparation of Complexes:** A methanolic solution of the ligands (0.03–0.25 mmol) was mixed with 1 equiv. of copper(II) salt in the same solvent at room temperature (total methanol volume: 0.4–2.0 mL), then diethyl ether vapour was introduced at 4 °C. In case crystallisation or precipitation did not occur, 1 equiv. of sodium perchlorate was added to the reaction mixture before ether diffusion. In most cases, single crystals suitable for X-ray crystallography were obtained directly from the reaction mixture. Complexes **3** and **8** precipitated from the reaction mixture and were recrystallised from acetonitrile/diethyl ether to obtain satisfactory single crystals. Single crystals of complex **6** were prepared from the ligand/metal mixture in acetonitrile under ether diffusion conditions. Table 1 summarises the preparation conditions, metal salt/ligand combinations and complex numbers.

***CAUTION:*** *Perchlorate salts of metal complexes with organic ligands are potentially explosive. All due precautions should be taken.*

**[Cu(L1)(NO$_3$)$_2$] (1):** Starting from **L1** (64.3 mg, 0.25 mmol), 72.5 mg of complex was obtained (65% yield). $C_{15}H_{19}CuN_5O_7$ (**1**) (444.89): calcd. C 40.50, H 4.30, N 15.74; found C 40.52, H 4.40, N 15.66.

**[Cu(L1)(NO$_3$)](ClO$_4$) (2):** Starting from **L1** (12.9 mg, 0.05 mmol), 14.9 mg of complex **2** was obtained (62% yield). $C_{15}H_{19}ClCuN_4O_8$ (482.34): calcd. C 37.35, H 3.97, N 11.62; found C 37.57, H 4.07, N 11.66.

**[Cu(L3)(NO$_3$)$_2$] (3):** Starting from **L3** (40.7 mg, 0.15 mmol), 29.3 mg of complex **3** was obtained (41% yield). $C_{16}H_{23}CuN_5O_8$ (**3**·$H_2O$; 476.93): calcd. C 40.29, H 4.86, N 14.68; found C 40.48, H 4.77, N 14.83.

**[Cu(L3)(NO$_3$)(ClO$_4$)] (4):** Starting from **L3** (8.1 mg, 0.03 mmol), 10.3 mg of complex **4** was obtained (69% yield). $C_{16}H_{21}ClCuN_4O_8$ (496.36): calcd. C 38.72, H 4.26, N 11.29; found C 38.22, H 4.52, N 11.37.

**[Cu(L1)(ClO$_4$)(CH$_3$OH)](ClO$_4$) (5):** Starting from **L1** (18.0 mg, 0.07 mmol), 27.6 mg of complex **5** was obtained (69% yield). $C_{16}H_{25}Cl_2CuN_3O_{11}$ (**5**·$H_2O$; 569.84): calcd. C 33.72, H 4.42, N 7.37; found C 33.94, H 4.39, N 7.56.

**[Cu(L1)(CH$_3$CN)(H$_2$O)](ClO$_4$)$_2$ (6):** Starting from **L1** (12.9 mg, 0.05 mmol), 17.8 mg of complex **6** was obtained (62% yield). $C_{17}H_{24}Cl_2CuN_4O_{10}$ (578.85): calcd. C 35.27, H 4.18, N 9.68; found C 34.77, H 4.36, N 9.25.

**[Cu(L2)(ClO$_4$)(CH$_3$OH)](ClO$_4$) (7):** Starting from **L2** (14.4 mg, 0.05 mmol), 15.6 mg of complex **7** was obtained (52% yield). $C_{17}H_{27}Cl_2CuN_3O_{12}$ (**7**·$H_2O$; 599.87): calcd. C 34.04, H 4.54, N 7.00; found C 34.28, H 4.23, N 7.27.

**[Cu(L1)Cl](ClO$_4$) (8):** Starting from **L1** (7.7 mg, 0.03 mmol), 5.0 mg of complex **8** was obtained (34% yield). $C_{16}H_{23}Cl_2CuN_3O_6$ (**8**·$CH_3OH$; 487.83): calcd. C 39.39, H 4.75, N 8.61; found C 39.02, H 4.34, N 8.90.

**[Cu(L2)Cl](ClO$_4$) (9):** Starting from **L2** (14.4 mg, 0.05 mmol), 15.5 mg of complex **9** was obtained (62% yield). $C_{16}H_{23}Cl_2CuN_3O_7$ (**9**·$H_2O$; 503.83): calcd. C 38.14, H 4.60, N 8.34; found C 38.09, H 4.43, N 8.47.

**[Cu(L3)Cl](ClO$_4$) (10):** Starting from **L3** (21.7 mg, 0.08 mmol), 27.9 mg of complex **10** was obtained (71% yield). $C_{16}H_{23}Cl_2CuN_3O_6$ (**10**·$H_2O$; 487.83): calcd. C 39.39, H 4.75, N 8.61; found C 39.60, H 4.53, N 8.34.

**[Cu(L1)Br](ClO$_4$) (11):** Starting from **L1** (12.9 mg, 0.05 mmol), 17.9 mg of complex **11** was obtained (71% yield). $C_{15}H_{19}BrClCuN_3O_5$ (500.24): calcd. C 36.02, H 3.83, N 8.40; found C 36.04, H 3.78, N 8.34.

**[Cu(L2)Br](ClO$_4$) (12):** Starting from **L2** (8.6 mg, 0.03 mmol), 11.2 mg of complex **12** was obtained (71% yield). $C_{16}H_{21}BrClCuN_3O_6$ (530.26): calcd. C 36.24, H 3.99, N 7.92; found C 36.37, H 4.09, N 7.88.

**[Cu(L3)Br$_2$] (13):** Starting from **L3** (8.1 mg, 0.03 mmol), 10.3 mg of complex **13** was obtained (65% yield). $C_{17}H_{25}Br_2CuN_3O_2$ (**13**·$CH_3OH$; 526.76): calcd. C 38.76, H 4.78, N 7.98; found C 38.45, H 4.36, N 7.97.

**X-ray Crystallography:** Single crystals of **1**–**13** were covered by paraffin oil and mounted on a glass fibre. All data were collected at 173 K on a Rigaku Mercury CCD detector, with monochromatic Mo-$K_\alpha$ radiation, operating at 50 kV/40 mA. Data were processed with a PC using CrystalClear Software (Rigaku). Structures were solved by direct methods (SIR-97, SIR-92 or SHELXS-97) and refined by full-matrix least-squares methods on $F^2$ (SHELXS-97).

CCDC-612373 to -612385 contain the supplementary crystallographic data for this paper. These data can be obtained free of charge from The Cambridge Crystallographic Data Centre via www.ccdc.cam.ac.uk/data_request/cif.request/cif.

 © 2007 Wiley-VCH Verlag GmbH & Co. KGaA, Weinheim 

**Supporting Information** (see also the footnote on the first page of this article): Crystallographic data for all complexes and ORTEP drawings for complexes **4**, **5**, **8**, **11**, **12** and **13**.

## Acknowledgments

The authors would like to thank Prof. Isamu Kinoshita and Dr. Riichi Miyamoto for performing the EPR measurements. This work was supported by the Asahi-Glass Foundation, a Nara Women's University (Intramural Grant for Project Research), and a Grant-in Aid for Scientific Research from the MEXT, Japan (16350032, 18550059).

[1] L. M. Berreau, *Eur. J. Inorg. Chem.* **2006**, 273–283.
[2] M. S. Taylor, E. N. Jacobsen, *Angew. Chem. Int. Ed.* **2006**, *45*, 1520–1543.
[3] D. H. Williams, E. Stephens, D. P. O'Brien, M. Zhou, *Angew. Chem. Int. Ed.* **2004**, *43*, 6596–6616.
[4] R. Roy, *Trends Glycosci. Glycotechnol.* **2003**, *15*, 291–310.
[5] Y. C. Lee, R. T. Lee, *Acc. Chem. Res.* **1995**, *28*, 321–327.
[6] V. Amendola, L. Fabbrizzi, M. Licchelli, C. Mangano, P. Pallavicini, L. Parodi, A. Poggi, *Coord. Chem. Rev.* **1999**, *190–192*, 649–669.
[7] M. R. A. Al-Mandhary, P. J. Steel, *Inorg. Chim. Acta* **2003**, *351*, 7–11.
[8] M. R. A. Al-Mandhary, P. J. Steel, *Eur. J. Inorg. Chem.* **2004**, 329–334.
[9] L. Tei, A. J. Blake, A. Bencini, B. Valtancoli, C. Wilson, M. Schröder, *Inorg. Chim. Acta* **2002**, *337*, 59–69.
[10] H. Sigel, L. E. Kapinos, *Coord. Chem. Rev.* **2000**, *200–202*, 563–594.
[11] H. Sigel, *Chem. Soc. Rev.* **2004**, *33*, 191–200.
[12] Y. Mikata, Y. Sugai, S. Yano, *Inorg. Chem.* **2004**, *43*, 4778–4780.
[13] Y. Mikata, Y. Sugai, M. Obata, M. Harada, S. Yano, *Inorg. Chem.* **2006**, *45*, 1543–1551.
[14] M. Palaniandavar, S. Mahadevan, M. Köckerling, G. Henkel, *J. Chem. Soc., Dalton Trans.* **2000**, 1151–1154.
[15] M. Palaniandavar, R. J. Butcher, A. W. Addison, *Inorg. Chem.* **1996**, *35*, 467–471.
[16] F. Ugozzoli, C. Massera, A. M. M. Lanfredi, N. Marsich, A. Camus, *Inorg. Chim. Acta* **2002**, *340*, 97–104.
[17] M. J. Young, D. Wahnon, R. C. Hynes, J. Chin, *J. Am. Chem. Soc.* **1995**, *117*, 9441–9447.
[18] T. Murakami, S. Hatakeyama, S. Igarashi, Y. Yukawa, *Inorg. Chim. Acta* **2000**, *310*, 96–102.
[19] S. I. Kirin, P. Dübon, T. Weyhermüller, E. Bill, N. Metzler-Nolte, *Inorg. Chem.* **2005**, *44*, 5405–5415.
[20] S. Tanase, C. Foltz, R. de Gelder, R. Hage, E. Bouwman, J. Reedijk, *J. Mol. Catal. A* **2005**, *225*, 161–167.
[21] J.-Z. Wu, E. Bouwman, A. M. Mills, A. L. Spek, J. Reedijk, *Inorg. Chim. Acta* **2004**, *357*, 2694–2702.
[22] S. Ito, T. Okuno, H. Matsushima, T. Tokii, Y. Nishida, *J. Chem. Soc., Dalton Trans.* **1996**, 4037–4039.
[23] Y. Ishikawa, S. Ito, S. Nishino, S. Ohba, Y. Nishida, *Z. Naturforsch., C: Biosci.* **1998**, *53*, 378–381.
[24] Y. Nishida, T. Okuno, S. Ito, A. Harada, S. Ohba, H. Matsushima, T. Tokii, *Chem. Lett.* **1995**, 885–886.
[25] S. I. Kirin, C. M. Happel, S. Hrubanova, T. Weyhermüller, C. Klein, N. Metzler-Nolte, *Dalton Trans.* **2004**, 1201–1207.
[26] A. W. Addison, T. N. Rao, J. Reedijk, J. van Rijn, G. C. Verschoor, *J. Chem. Soc., Dalton Trans.* **1984**, 1349–1356.

Received: August 30, 2006
Published Online: February 9, 2007

 © 2007 Wiley-VCH Verlag GmbH & Co. KGaA, Weinheim 

DOI: 10.1002/ejic.200600867

# Metal–Organic Hybrids of 1,3,5-Tris(4-pyridylsulfanylmethyl)-2,4,6-trimethylbenzene with Mercuric Halides

**Jayarama PrakashaReddy[a] and Venkateswara Rao Pedireddi*[a]**

**Keywords:** Metal–organic hybrids / Supramolecular chemistry / Crystal engineering / Fluxional thio ligands / Mercuric halides

Synthesis and solid-state structure elucidation of metal–organic hybrids of 1,3,5-tris(4-pyridylsulfanylmethyl)-2,4,6-trimethylbenzene with $Hg^{II}$ halides ($HgCl_2$, $HgBr_2$, and $HgI_2$) are reported. In the metal-hybrids of **L¹**, a reaction with $HgCl_2$ in dmso as well as in dmf gave host–guest complexes, **1a** and **1b**, respectively, with the corresponding solvent of crystallization as the guests, while a reaction with $HgI_2$ gave open-frame network structures without any solvent of crystallization from both dmso and dmf (**1c**). However, reaction with $HgBr_2$ gave crystals of two different morphologies from each solvent dmso and dmf (**1d**–**1f**), which corresponds to the structures with and without solvent of crystallization that resemble the related structures formed by $HgCl_2$ and $HgI_2$, respectively. Three-dimensional structures of all the compounds were characterized by single-crystal X-ray diffraction methods. While **1a** and **1b** crystallize in triclinic $P\bar{1}$ space groups **1a**: $a$ = 9.049(2), $b$ = 13.646(4), $c$ = 16.298(4) Å, $\alpha$ = 111.99(1), $\beta$ = 90.43(1), $\gamma$ = 101.57(1)°, $Z$ = 2, $V$ = 1820.6(8) Å$^3$; **1b**: $a$ = 8.979(3), $b$ = 13.611(5), $c$ = 16.355(5) Å, $\alpha$ = 111.57(1), $\beta$ = 92.37(1), $\gamma$ = 101.07(1)°, $Z$ = 2, $V$ = 1810.05(11) Å$^3$, complexes **1c**–**1f** crystallize into monoclinic space groups [**1c**: $C2/c$, $a$ = 27.661(7), $b$ = 18.821(4), $c$ = 15.786(4) Å, $\beta$ = 113.13(1), $Z$ = 4, $V$ = 7558(3) Å$^3$, **1d**: $P2_1/c$, $a$ = 17.950(5), $b$ = 9.031(2), $c$ = 22.200(6) Å, $\beta$ = 113.62(1), $Z$ = 4, $V$ = 3297.3(15) Å$^3$, **1e**: $C2/c$, $a$ = 26.753(15), $b$ = 18.415(10), $c$ = 14.940(7) Å, $\beta$ = 109.50(1), $Z$ = 4, $V$ = 6938(6) Å$^3$, **1f**: $P2_1/n$, $a$ = 17.697(10), $b$ = 9.224(5), $c$ = 21.933(12) Å, $\beta$ = 112.50(1), $Z$ = 4, $V$ = 3308(3) Å$^3$].
(© Wiley-VCH Verlag GmbH & Co. KGaA, 69451 Weinheim, Germany, 2007)

## Introduction

Design and synthesis of coordination polymers with exotic supramolecular architectures in the solid state are of current research interest because of the potential applications of the assemblies in the areas of separation technology, catalysis, gas storage devices, etc.[1–5] Thus, there are numerous reports of a myriad of supramolecular assemblies of coordination polymers utilizing different types of organic ligands possessing varied functionalities like carboxylates, aza-donor groups, etc., in recent literature.[6,7] In general, most of the assemblies known in the literature, however, were synthesized by utilizing organic moieties as rigid, spacer entities.[8] Thus, the crucial role of organic ligands with respect to the geometry and position of the functional groups was demonstrated in the formation of the desired topology. Also, another important feature of organic ligands is their conformational flexibility, which has been utilized in metal–organic framework structures in recent studies.[9] In this process, taking into account the well-established synthetic routes for the preparation of the required fluxional organic molecules, novel thio-based ligands with multi-armed, tripodal geometry, such as pyridylsulfanylmethyl derivatives, were synthesized, and these ligands demonstrated their significance in the supramolecular studies.[10]

Because of our continued interest in both molecular and supramolecular synthesis,[11] we were motivated to study the influence of such thio-based, flexible-armed molecules in the creation of assemblies with tailor-made geometries that possess cavities, channels, etc., and subsequently to evaluate possible applications. Thus, we have synthesized a pyridylsulfanyl compound 1,3,5-tris(4-pyridylsulfanylmethyl)-2,4,6-trimethylbenzene (**L¹**) and prepared its host–guest complexes in the form of metal–organic hybrid assemblies in which solvents are incorporated in the channels. Thus, in this manuscript, we report on coordination polymers of **L¹** with different halides of $Hg^{II}$ obtained by carrying out supramolecular synthesis from different solvents as illustrated in Scheme 1.

## Results and Discussion

### Solid-State Structure of Complex $[Hg(L^1)Cl_2]\cdot(dmso)_2$ (1a)

Crystallization of a precipitate of **L¹** and $HgCl_2$ from dmso gave single crystals that were suitable for analysis by

[a] Solid State and Supramolecular Structural Chemistry Laboratory, Division of Organic Chemistry National Chemical Laboratory,
Pune 411008, India
Fax: +91-2025902624
E-mail: vr.pedireddi@ncl.res.in
Supporting information for this article is available on the WWW under http://www.eurjic.org or from the author.

 © 2007 Wiley-VCH Verlag GmbH & Co. KGaA, Weinheim 

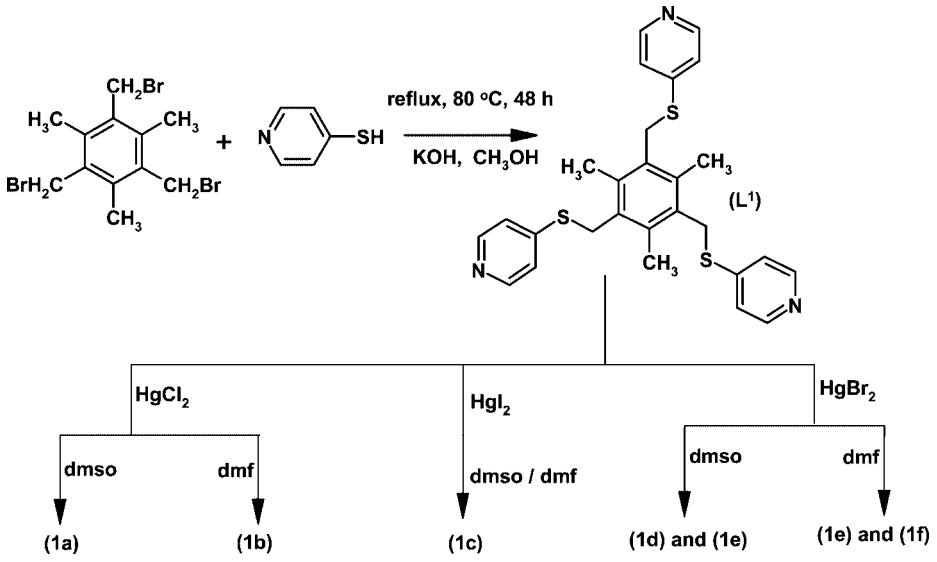


Scheme 1.

X-ray diffraction methods. The crystal structure determination reveals that, as expected, the pyridyl N atoms of $\mathbf{L^1}$ form coordination bonds with $Hg^{II}$ (Figure 1). The observed Hg–N bond distances (2.457–2.479 Å) are in agreement with distances presented in the literature.[12] Further, each $Hg^{II}$ is connected to two halide ions to form Hg–Cl bonds with distances of 2.458 and 2.491 Å. The pertinent coordination bonds and angles are given in Table 1. Thus, each $Hg^{II}$ with pentacoordination has a square-pyramidal geometry. This interaction results in the formation of a cavity of dimension $9 \times 12$ Å$^2$ and each cavity is created by two molecules of $\mathbf{L^1}$ and $Hg^{II}$ as shown in Figure 2a. The cavities are further aligned in a three-dimensional arrangement to yield channels (see Figure 2b), which are occupied by dmso molecules (solvent of crystallization) that exist in both ordered and disordered forms. Furthermore, both types of dmso molecules exist as dimers independently through the formation of C–H···O hydrogen bonds (see insets in Figure 2a).

### Solid-State Structure of Complex $[Hg(L^1)Cl_2]\cdot(dmf)_2$ (1b)

A precipitate of ligand $\mathbf{L^1}$ with $HgCl_2$ from dmf gave solvent-incorporated crystals as confirmed by X-ray diffraction methods, and each $Hg^{II}$ is connected to ligand $\mathbf{L^1}$ in exactly the same mode as that observed in **1a** (Figure 3a). The Hg–N distances are in the range 2.464–2.515 Å, and the Hg–Cl distances are 2.430 and 2.451 Å.

Thus, in the crystals of **1b**, dmf molecules are present in the cavities like the dmso molecules in **1a**, but both the dmf molecules are disordered in **1b**. Further, the symmetry-independent dmf molecules interact with each other through C–H···O hydrogen bonds with C···O distances of 3.07 and 3.13 Å. A typical hydrogen-bonding network between the dmf molecules is shown in the inset of Figure 3b. However, unlike in **1a**, no interaction exists between symmetry-dependent molecules.

### Supramolecular Structure of $[Hg(L^1)I_2]$ (1c)

A precipitate of ligand $\mathbf{L^1}$ and $HgI_2$ (used in a ratio of 2:3) from dmso gave **1c**. Crystallographic details of **1c** are given in Table 2. In this structure, ligand $\mathbf{L^1}$ forms coordination bonds with $Hg^{II}$ with Hg–N distances of 2.353–2.440 Å. Furthermore, $Hg^{II}$ forms Hg–I coordination bonds with distances in the range 2.623–2.661 Å (Figure 4).

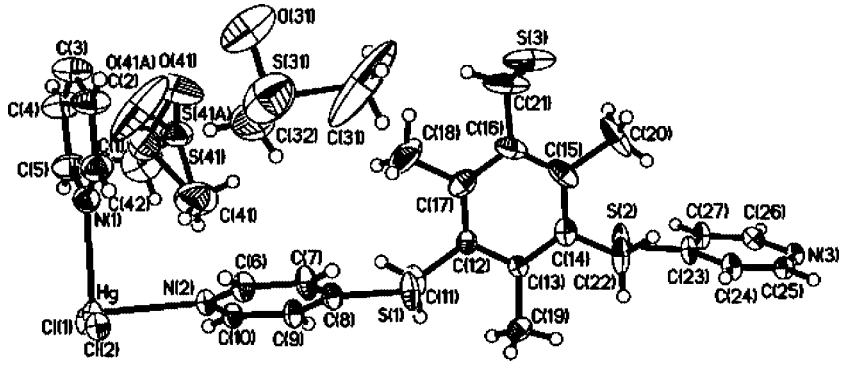


Figure 1. ORTEP drawing of the asymmetric unit in the coordination complex **1a**, along with dmso molecules.

 © 2007 Wiley-VCH Verlag GmbH & Co. KGaA, Weinheim 

Table 1. Selected bond lengths [Å] and bond angles [°] around the coordination sphere in complexes **1a**–**1f**.

| **1a** | | | | **1b** | | | |
|---|---|---|---|---|---|---|---|
| Hg–N(1) | 2.457(7) | N(1)–Hg–N(2) | 88.1(2) | Hg–N(1) | 2.464(4) | N(1)–Hg–N(2) | 90.2(1) |
| Hg–N(2) | 2.462(6) | N(1)–Hg–N(3) | 86.5(2) | Hg–N(2) | 2.493(4) | N(1)–Hg–N(3) | 178.3(1) |
| Hg–N(3) | 2.479(6) | N(2)–Hg–N(3) | 174.5(2) | Hg–N(3) | 2.515(4) | N(2)–Hg–N(3) | 88.7(1) |
| Hg–Cl(1) | 2.491(2) | N(1)–Hg–Cl(1) | 92.0(2) | Hg–Cl(1) | 2.430(1) | Cl(1)–Hg–N(2) | 99.4(1) |
| Hg–Cl(2) | 2.458(2) | N(1)–Hg–Cl(2) | 97.2(2) | Hg–Cl(2) | 2.451(1) | Cl(1)–Hg–N(1) | 91.3(9) |
| | | N(2)–Hg–Cl(1) | 89.8(2) | | | Cl(1)–Hg–N(3) | 87.5(9) |
| | | N(3)–Hg–Cl(1) | 90.9(2) | | | Cl(1)–Hg–Cl(2) | 167.9(4) |
| | | Cl(2)–Hg–Cl(1) | 170.7(7) | | | Cl(2)–Hg–N(3) | 91.3(9) |
| | | Cl(2)–Hg–N(2) | 91.3(2) | | | Cl(2)–Hg–N(1) | 90.1(9) |
| | | Cl(2)–Hg–N(3) | 88.8(2) | | | Cl(2)–Hg–N(2) | 92.7(1) |
| **1c** | | | | **1d** | | | |
| Hg(1)–N(1) | 2.353(1) | N(1)–Hg(1)–N(1) | 83.0(7) | Hg–N(2) | 2.342(1) | N(2)–Hg–N(3) | 119.6(4) |
| Hg(1)–I(1) | 2.634(2) | N(1)–Hg(1)–I(1) | 104.7(4) | Hg–N(3) | 2.348(1) | N(2)–Hg–Br(1) | 103.0(3) |
| Hg(2)–N(2) | 2.440(2) | N(1)–Hg(1)–I(1) | 105.0(4) | Hg–Br(1) | 2.520(2) | N(2)–Hg–Br(2) | 101.2(3) |
| Hg(2)–N(3) | 2.406(2) | I(1)–Hg(1)–I(1) | 140.0(9) | Hg–Br(2) | 2.515(2) | N(3)–Hg–Br(1) | 98.8(3) |
| Hg(2)–I(2) | 2.623(2) | N(3)–Hg(2)–N(2) | 85.6(6) | | | N(3)–Hg–Br(2) | 101.0(3) |
| Hg(2)–I(3) | 2.653(2) | N(2)–Hg(2)–I(2) | 102.2(4) | | | Br(2)–Hg–Br(1) | 135.3(7) |
| | | N(3)–Hg(2)–I(3) | 101.1(4) | | | | |
| | | N(3)–Hg(2)–I(2) | 107.8(4) | | | | |
| | | N(2)–Hg(2)–I(3) | 101.3(4) | | | | |
| | | I(2)–Hg(2)–I(3) | 143.8(7) | | | | |
| **1e** | | | | **1f** | | | |
| Hg(1)–N(1) | 2.421(2) | N(1)–Hg(1)–N(1) | 81.9(9) | Hg–N(1) | 2.310(2) | N(1)–Hg–N(2) | 116.7(9) |
| Hg(1)–Br(1) | 2.455(3) | N(1)–Hg(1)–Br(1) | 102.0(4) | Hg–N(2) | 2.380(2) | N(1)–Hg–Br(1) | 100.8(6) |
| Hg(2)–N(2) | 2.346(2) | N(2)–Hg(2)–N(3) | 88.1(7) | Hg–Br(1) | 2.486(4) | N(1)–Hg–Br(2) | 103.5(6) |
| Hg(2)–N(3) | 2.370(2) | N(2)–Hg(2)–Br(2) | 99.9(4) | Hg–Br(2) | 2.509(3) | N(2)–Hg–Br(2) | 98.6(7) |
| Hg(2)–Br(2) | 2.485(3) | N(2)–Hg(2)–Br(3) | 105.4(4) | | | N(2)–Hg–Br(1) | 98.6(8) |
| Hg(2)–Br(3) | 2.448(3) | N(3)–Hg(2)–Br(2) | 100.5(4) | | | Br(1)–Hg–Br(2) | 139.7(1) |
| | | N(3)–Hg(2)–Br(3) | 99.6(3) | | | | |
| | | Br(1)–Hg(1)–Br(1) | 148.1(1) | | | | |
| | | Br(3)–Hg(2)–Br(2) | 148.0(1) | | | | |

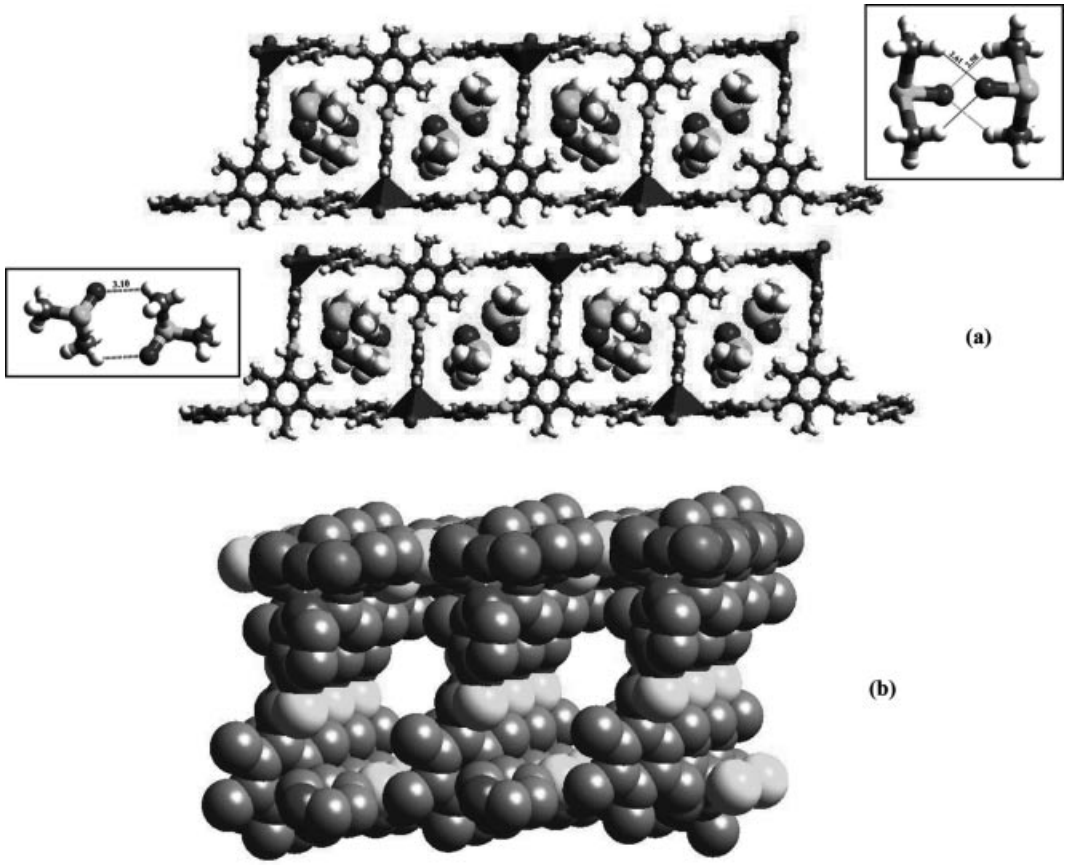


Figure 2. (a) Presentation of the cavities occupied by dmso molecules in the crystal structure of **1a**. The different types of interaction between the dmso molecules are shown in the insets. Disorder in dmso is omitted for purposes of clarity. (b) Three –dimensional formation of the channels; the alignment of the cavities is shown in (a).

 © 2007 Wiley-VCH Verlag GmbH & Co. KGaA, Weinheim 

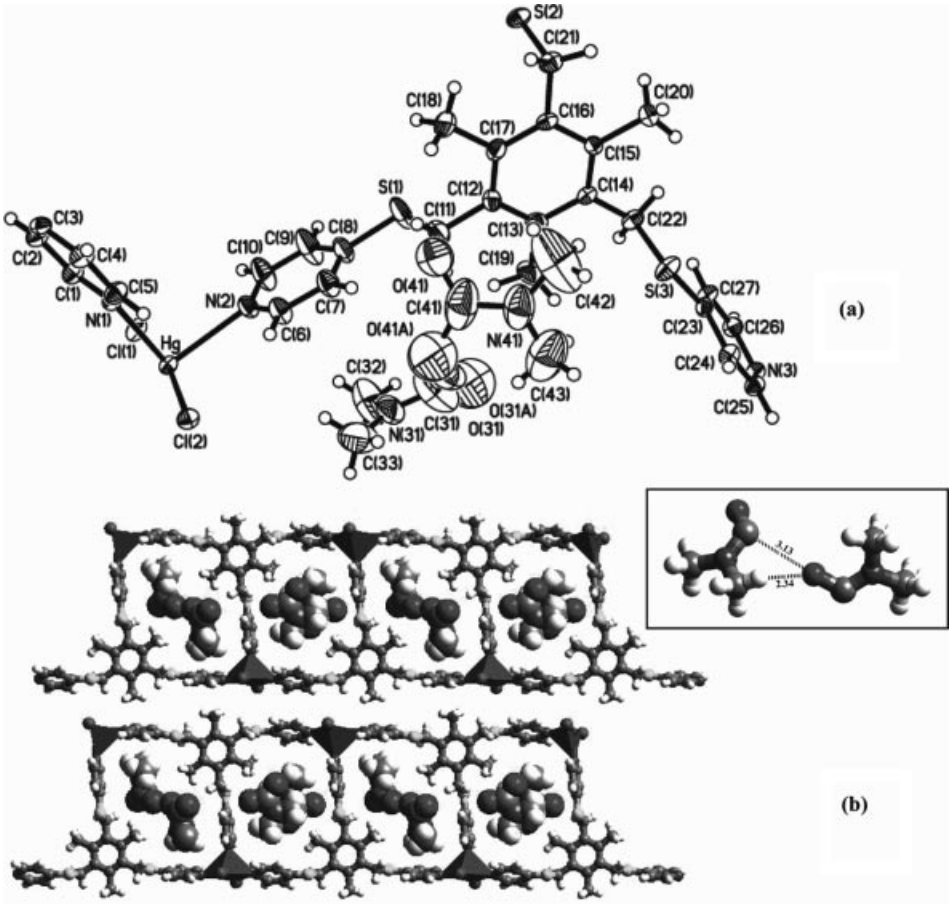


Figure 3. (a) ORTEP drawing of the asymmetric unit in the crystal structure of **1b** along with the solvent of crystallization, dmf. (b) Arrangement of dmf molecules in the cavities, and the intermolecular interactions between the adjacent molecules are shown in the inset.

Table 2. Crystallographic data of metal complexes of $\mathbf{L}^1$, **1a**–**1f**.

| | **1a** | **1b** | **1c** | **1d** | **1e** | **1f** |
|---|---|---|---|---|---|---|
| Empirical formula | $(HgCl_2)(C_{27}H_{27}N_3S_3)\cdot 2C_2H_6SO$ | $(HgCl_2)(C_{27}H_{27}N_3S_3)\cdot 2C_3H_7NO$ | $(HgI_2)_3(C_{27}H_{27}N_3S_3)_2$ | $(HgBr_2)(C_{27}H_{27}N_3S_3)\cdot C_2H_6SO$ | $(HgBr_2)_3(C_{27}H_{27}N_3S_3)_2$ | $(HgBr_2)(C_{27}H_{27}N_3S_3)\cdot C_3H_7NO$ |
| Formula mass | 917.44 | 905.36 | 2342.56 | 928.23 | 2060.62 | 922.19 |
| Crystal shape | blocks | blocks | blocks | thin plates | blocks | thin plates |
| Crystal color | colorless | colorless | colorless | colorless | colorless | colorless |
| Crystal system | triclinic | triclinic | monoclinic | monoclinic | monoclinic | monoclinic |
| Space group | $P\bar{1}$ | $P\bar{1}$ | $C2/c$ | $P2_1/c$ | $C2/c$ | $P2_1/n$ |
| $a$ [Å] | 9.049(2) | 8.979(3) | 27.661(7) | 17.950(5) | 26.753(15) | 17.697(10) |
| $b$ [Å] | 13.646(4) | 13.611(5) | 18.821(4) | 9.031(2) | 18.415(10) | 9.224(5) |
| $c$ [Å] | 16.298(4) | 16.355(5) | 15.786(4) | 22.200(6) | 14.940(7) | 21.933(12) |
| $\alpha$ [°] | 111.99(1) | 111.57(1) | 90 | 90 | 90 | 90 |
| $\beta$ [°] | 90.43(1) | 92.37(1) | 113.13(1) | 113.62(1) | 109.50(1) | 112.50(1) |
| $\gamma$ [°] | 101.57(1) | 101.07(1) | 90 | 90 | 90 | 90 |
| $V$ [Å$^3$] | 1820.6(8) | 1810.5(11) | 7558(3) | 3297.3(15) | 6938(6) | 3308(3) |
| $Z$ | 2 | 2 | 4 | 4 | 4 | 4 |
| $D_{calcd.}$ [g cm$^{-3}$] | 1.674 | 1.661 | 2.059 | 1.870 | 1.973 | 1.852 |
| $T$ [K] | 133 | 133 | 133 | 133 | 133 | 133 |
| Mo-$K_\alpha$ | 0.71073 | 0.71073 | 0.71073 | 0.71073 | 0.71073 | 0.71073 |
| $\mu$ [mm$^{-1}$] | 4.693 | 4.609 | 8.730 | 7.373 | 10.295 | 7.289 |
| $2\theta$ range [°] | 46.54 | 52.12 | 46.66 | 46.62 | 46.82 | 46.62 |
| $F$(000) | 912 | 900 | 4296 | 1800 | 3864 | 1788 |
| Total reflections | 15091 | 18822 | 15672 | 13942 | 4747 | 13554 |
| Unique reflns. | 5225 | 7103 | 5451 | 4755 | 4002 | 4758 |
| [$R$ (int)] | [0.0469] | [0.0468] | [0.1232] | [0.0543] | [0.0255] | [0.1469] |
| No. reflns. used | 4931 | 6481 | 2929 | 4411 | 2542 | 3305 |
| No. parameters | 403 | 425 | 339 | 356 | 339 | 320 |
| GOF on $F^2$ | 1.512 | 0.747 | 0.927 | 1.380 | 1.265 | 1.142 |
| $R_1$ [$I > 2\sigma(I)$] | 0.0532 | 0.0354 | 0.0570 | 0.0729 | 0.0517 | 0.1079 |
| $wR_2$ | 0.1486 | 0.0928 | 0.1374 | 0.1558 | 0.1493 | 0.3029 |

 © 2007 Wiley-VCH Verlag GmbH & Co. KGaA, Weinheim 

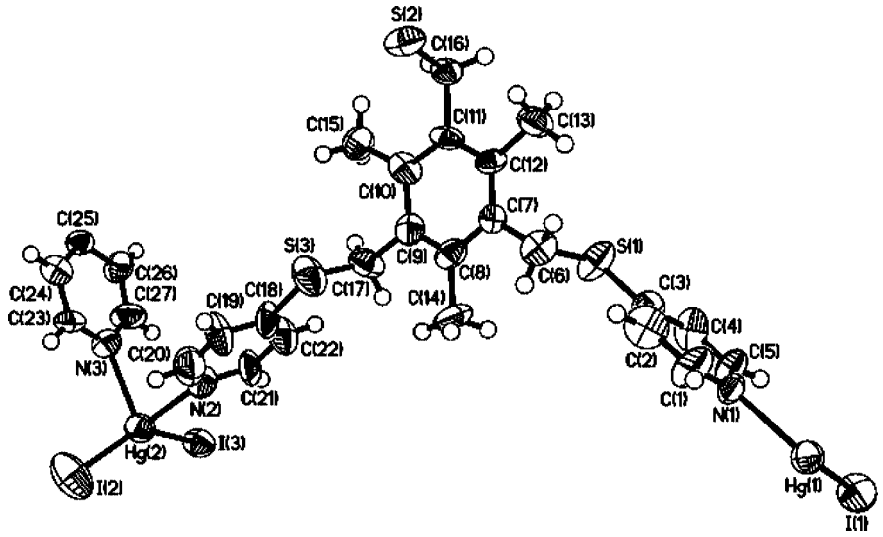


Figure 4. ORTEP drawing of the coordination geometry in the crystal structure of **1c**.

Further, the coordination geometry around $Hg^{II}$ in **1c** is distorted tetrahedral and differs from the square pyrimidal geometry observed in **1a** and **1b**. Thus, the coordination moieties in **1c** yield a polymer network comprising interconnected square grids with cavities (Figure 5a, b). However, the cavities could not be translated into channels in a three-dimensional arrangement as the void space is filled by moieties from adjacent chains as shown in Figure 5c.

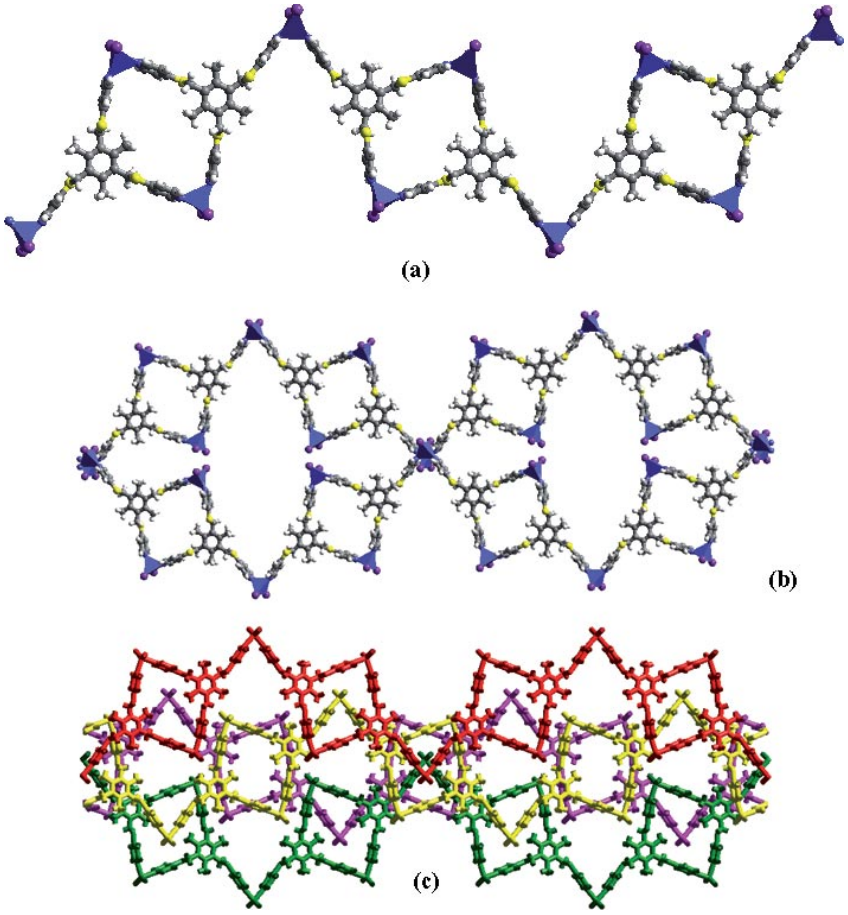


Figure 5. (a) Square-grid network mediated coordination polymers in the crystal structure of **1c**. (b) Arrangement of two adjacent polymer networks. (c) The three-dimensional arrangement of the coordination polymers. Each polymer network is shown in different colors.

 © 2007 Wiley-VCH Verlag GmbH & Co. KGaA, Weinheim 

### Solid-State Structures of Complexes of $L^1$ with $HgBr_2$ (1d–1f)

The complexes formed by $HgBr_2$ are quite intriguing and in fact further reinforce the systematic changes generally observed in the halogen series. Crystallization of a solid mixture of $\mathbf{L^1}$ and $HgBr_2$ from dmso and dmf gave concomitant crystals of two different morphologies from each solvent. Structure analysis reveals that, while one of the morphologies from each solvent [**1d** (dmso) and **1f** (dmf)] corresponds to a solvated structure such as for $HgCl_2$ (**1a** and **1b**, respectively), the other morphologies gave structures without a solvent of crystallization (**1e**) like **1c** formed by $HgI_2$.

Although **1d** and **1f** have similar unit cell parameters, they are not isomorphous, as they crystallize in different space groups, $P2_1/c$ and $P2_1/n$, respectively. The full crystallographic details are given in Table 2. However, structure analysis reveals that both **1d** and **1f** are isostructural with the formation of identical three-dimensional arrangements. In a typical interaction, as shown in Figure 6, the ligand $\mathbf{L^1}$ interacts with $Hg^{II}$ by forming Hg–N bonds (Table 1) to yield an infinite coordination polymer chain.

Figure 6. Coordination polymer formed between $\mathbf{L^1}$ and $HgBr_2$ yielding a chain.

Thus, out of the available three pyridyl moieties only two interact with $Hg^{II}$. Also, each $Hg^{II}$ is bonded to two Br atoms (Table 1). Thus, in **1d** and **1f**, the coordination geometry around each $Hg^{II}$ atom is also distorted tetrahedral as shown in Figure 6. Such adjacent chains are held together by C–H···N hydrogen bonds with H···N distances of 2.66–2.89 Å, as observed in the structure of the free ligand (Supporting Information) and form cavities of dimension $11 \times 16$ Å$^2$ (Figure 7), which are aligned in a three-dimensional arrangement to yield channels. The channels are occupied by the solvent molecules dmso and dmf in **1d** and **1f**, respectively. Thus, **1d** and **1f** show some similarities with **1a** and **1b** in the formation of an open-frame network. However, the metal coordination and geometry around each $Hg^{II}$ in **1d** and **1f** has a close resemblance to that of **1c**. Further, the solvent molecules present in the channels of the structures **1d** and **1f** do not interact with each other but are bound to the host lattice through numerous intermolecular interactions.

However, complex **1e**, obtained as concomitant crystals along with **1d** and **1f**, crystallizes in the monoclinic space group $C2/c$. Further, packing analysis reveals that the structure of **1e** is identical to that formed by $HgI_2$ (**1c**) in all respects except for the difference of the halogen atoms. A typical structural arrangement in complex **1e** is shown in Figure 8 for purposes of comparison with the structure of **1c**.

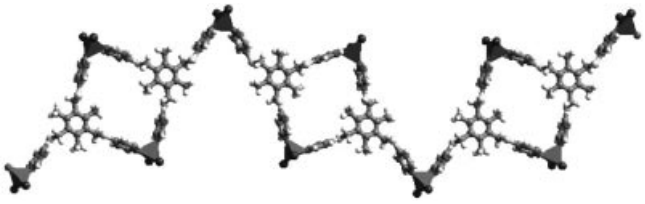

Figure 8. Square-grid network found in the solid-state structure of complex **1e**.

By comparing the crystal structures of the metal complexes described herein, it is clearly evident that the structures obtained are in agreement with the proposition of

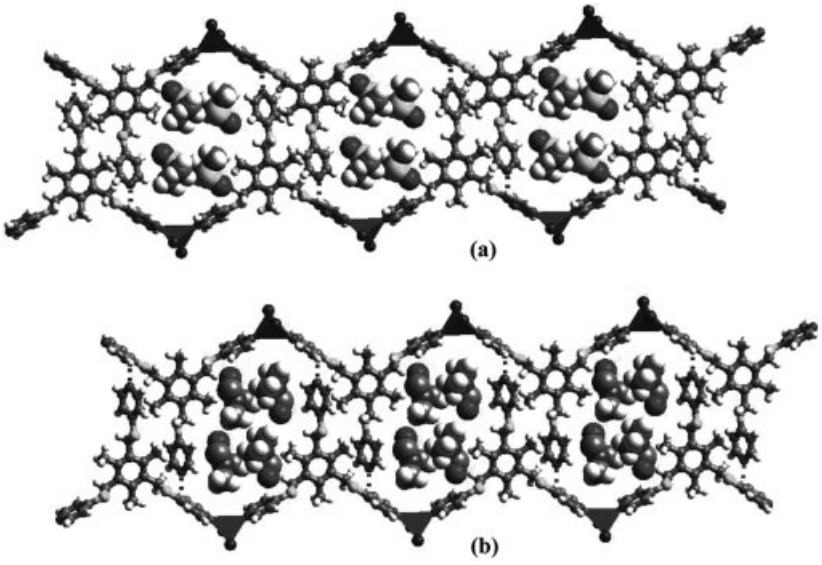


Figure 7. Representation of cavities formed by the interaction of the adjacent polymeric chains through C–H···N hydrogen bonds in the crystal structures (a) **1d** and (b) **1f**, along with the solvent molecules dmso and dmf, respectively.

 © 2007 Wiley-VCH Verlag GmbH & Co. KGaA, Weinheim 

utilization of pyridylsulfanyl ligands in the supramolecular synthesis through either dative bonds (**1a**–**1c**, **1e**) or a combination of dative bonds and hydrogen bonds (**1d** and **1f**). Another intriguing feature of these metal complexes is the systematic variation with the change in halogen. While $HgCl_2$ forms solvated structures, $HgI_2$ forms structures exclusively without solvents of crystallization.

One more interesting feature is the conformational changes in ligand $\mathbf{L^1}$ that occur when the ligand is uncoordinated and when it is in the different complexes (Figure 9). It is apparent that all the metal complexes, except **1d** and **1f**, adopt the same conformation (*cis*, *trans*, *trans*), which is different from that of the conformation observed in the pure structure of $\mathbf{L^1}$ (*cis*, *cis*, *cis*). It is well known from the literature that tripodal ligands like $\mathbf{L^1}$ show both types of conformation observed in this study, but often the conformation was attributed to the nature of the anion present in the structures.

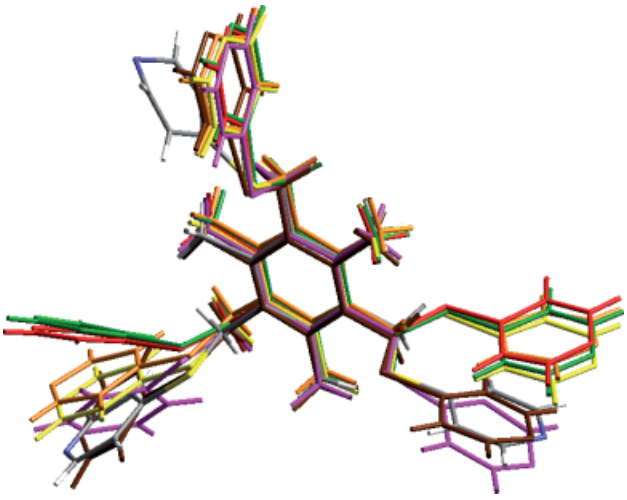

Figure 9. An overlay diagram of the molecular conformation of ligand $\mathbf{L^1}$ in its crystal structure (gray) and also in the complexes **1a**–**1f**. Brown and pink correspond to **1d** and **1f**.

However, it is apparent from this study that the coordination environment of the metal species as well as denticity of the ligands also may play a significant role in determining the conformation. In particular, the complexes formed by $HgBr_2$ are quite significant in this respect. Since, the same halogen (Br) gave structures of both conformations, which can be differentiated by the number of metal coordination centers, it may be understood that interaction with three metal ions like $Hg^{II}$ leads to strained crowding in a *cis*, *cis*, *cis* geometry, which might have forced the transformation of the conformation to *cis*, *trans*, *trans* in **1e**, whereas in **1d** and **1f**, with only two $Hg^{II}$ involved in complex formation, the conformation is retained as such, as in $\mathbf{L^1}$.

## Conclusions

In conclusion, we have reported the solid-state structures of metal–organic hybrids of conformationally flexible thio ligand $\mathbf{L^1}$ with different mercuric halides. Complexes **1a**–**1f** were prepared and the supramolecular assembly networks have been analyzed, and it is understood that all the complexes have open-frame networks with void space. In complexes **1a**, **1b**, **1d**, and **1f**, solvent of crystallization occupies the void space, while in other structures (**1c** and **1e**), the void space was filled by the self-protrusion of functional groups from adjacent molecules. In particular, the variations observed in the conformations of the ligand $\mathbf{L^1}$ are intriguing and may provide further insight in modeling experiments, especially for the evaluation of metal-hybrids as catalysts, which has increased demands under the current research themes.

## Experimental Section

**Synthesis of 1,3,5-Tris(4-pyridylsulfanylmethyl)-2,4,6-trimethylbenzene ($\mathbf{L^1}$):** 1,3,5-tris-(bromomethyl)-2,4,6-trimethylbenzene (399 mg, 1 mmol) was added to an ice-cooled solution of pyridine-4-thiol (333 mg, 3 mmol) and KOH (560 mg, 10 mmol, slight excess) in methanol whilst stirring. The mixture was heated at reflux for 48 h at 80 °C. The solution was poured into ice-cold water, the crude product was filtered and separated by column chromatography, and a colorless microcrystalline solid was obtained ($\mathbf{L^1}$) in 72% yield (m.p. 228–230 °C). Single crystals of $\mathbf{L^1}$ suitable for X-ray diffraction were obtained from methanol solution after 2–3 d.

**Preparation of Complex $[Hg(L^1)Cl_2]\cdot(dmso)_2$ (1a):** A white precipitate obtained by dissolving $HgCl_2$ (81 mg, 0.3 mmol) and $\mathbf{L^1}$ (49 mg, 0.1 mmol) in methanol was filtered and dissolved in dmso and allowed to slowly evaporate at room temperature. Within 48 h, well-grown colorless single crystals of **1a** were obtained in 36% yield (m.p. 204–206 °C).

**Preparation of Complex $[Hg(L^1)Cl_2]\cdot(dmf)_2$ (1b):** A white precipitate was obtained as described for **1a**; however dmf was used instead of dmso. After slow evaporation under ambient conditions, gave colorless single crystals of **1b** were obtained in 42% yield (m.p. 213–215 °C).

**Preparation of Complex $[Hg(L^1)I_2]$ (1c):** A solution of $HgI_2$ (135 mg, 0.3 mmol) in methanol was added to a solution of $\mathbf{L^1}$ (49 mg, 0.1 mmol) in methanol, and a white precipitate was obtained. The precipitate was filtered and dissolved in dmso to obtain colorless crystals of **1c** in 31% yield (m.p. 208–210 °C). The complex **1c** was also obtained by dissolving the precipitate in dmf and by evaporating the solution under ambient conditions.

**Preparation of Complexes $[Hg(L^1)Br_2]\cdot(dmso)$ (1d) and $[Hg(L^1)Br_2]$ (1e):** A solution of $HgBr_2$ (108 mg, 0.3 mmol) in methanol was added to a solution of $\mathbf{L^1}$ (49 mg, 0.1 mmol) in methanol. The resulting white precipitate was filtered and dissolved in dmso. Colorless crystals of two morphologies (plates **1d** and blocks **1e**) were obtained in 21 and 11% yields, respectively [m.p. 177–179 (**1d**) and 197–199 °C (**1e**)].

**Preparation of Complex $[Hg(L^1)Br_2]\cdot(dmf)$ (1f):** A solution of $HgBr_2$ (108 mg, 0.3 mmol) in methanol was added to a solution of $\mathbf{L^1}$ (49 mg, 0.1 mmol) in methanol. The white precipitate obtained

 © 2007 Wiley-VCH Verlag GmbH & Co. KGaA, Weinheim 

was filtered and dissolved in dmf. Colorless crystals of two morphologies (blocks **1e**; plates **1f**) were obtained in 28 and 14% yields, respectively, (**1f**: m.p. 184–186 °C).

**Crystal Structure Determination:** Good quality, single crystals of $\mathbf{L^1}$ and **1a**–**1f**, grown as described above, were carefully chosen with the aid of a polarized optical microscope and glued to glass fiber to mount on a X-ray diffractometer goniometer equipped with a CCD area detector.[13] The data collection proceeded without any complication and was processed using the Bruker suite of software. The structures were determined and refined by using the SHELXTL suite of programs, and absorption corrections were made on all the crystals with SADABS.[14] All the non-hydrogen atoms were refined anisotropically except a few atoms in **1d** (one atom) and **1f** (nine atoms). All hydrogen atoms were placed in the calculated positions.

The structural parameters are given in Table 2. All the intra- and intermolecular distances were computed with PLATON software.[15] The packing drawings were generated either by an XP package of SHELXTL or Cerius$^2$ of Accelrys, Inc. CCDC-625087–625093 for $\mathbf{L^1}$ and **1a**–**1f**, respectively, contain the supplementary crystallographic data for this paper. These data can be obtained free of charge from The Cambridge Crystallographic Data Centre via www.ccdc.cam.ac.uk/data_request/cif.

**Supporting Information** (see footnote on the first page of this article): Discussion of the structure of $\mathbf{L^1}$ and corresponding figures, its crystallographic information and powder X-ray diffraction patterns (both experimental and simulated from crystal data) are given.

## Acknowledgments

We thank Dr. S. Sivaram (Director, NCL) and Dr. K. N. Ganesh (Head of Organic Division, NCL) for their constant support and encouragement. Also, we acknowledge the financial assistance of DST and BRNS for the ongoing projects. One of us (J. P.) thanks the Council of Scientific and Industrial Research (CSIR), New Delhi for a research fellowship.

[1] a) F. A. Cotton, G. Wilkinson, *Advanced Inorganic Chemistry: A Comprehensive Text*, Wiley, New York, **1979**; b) B. Moulton, M. J. Zaworotko, *Chem. Rev.* **2001**, *101*, 1629–1658; c) M. Eddaoudi, D. B. Moler, H. Li, B. Chen, T. M. Reineke, M. O'Keeffe, O. M. Yaghi, *Acc. Chem. Res.* **2001**, *34*, 319–330; d) O. M. Yaghi, G. Li, H. Li, *Nature* **1995**, *378*, 703–706; e) S. R. Seidel, P. J. Stang, *Acc. Chem. Res.* **2002**, *35*, 972–983; f) M. Dan, C. N. R. Rao, *Angew. Chem. Int. Ed.* **2006**, *45*, 281–285; g) M. Yaghi, H. Li, C. Davis, D. Richardson, T. L. Groy, *Acc. Chem. Res.* **1998**, *31*, 474–484; h) P. J. Hagrman, D. Hagrman, J. Zubieta, *Angew. Chem. Int. Ed.* **1999**, *38*, 2638–2684; i) N. Seethalekshmi, V. R. Pedireddi, *Inorg. Chem.* **2006**, *45*, 2400–2402.

[2] a) V. R. Pedireddi, S. Varughese, *Inorg. Chem.* **2004**, *43*, 450–457; b) O. M. Tominaga, K. Suzuki, M. Kawano, T. Kusukawa, T. Ozeki, S. Sakamoto, K. Yamaguchi, M. Fujita, *Angew. Chem. Int. Ed.* **2004**, *43*, 5621–5625; c) S. Leininger, B. Olenyuk, P. J. Stang, *Chem. Rev.* **2000**, *100*, 853–907; d) M. J. Zaworotko, *Chem. Commun.* **2001**, 1–9; e) S. L. James, *Chem. Soc. Rev.* **2003**, *32*, 276–288; f) S. R. Batten, R. Robson, *Angew. Chem. Int. Ed.* **1998**, *37*, 1460–1494; g) G. Ferey, *Chem. Commun.* **2003**, 2976–2977; h) G. S. Papaefstathiou, L. R. MacGillivray, *Coord. Chem. Rev.* **2003**, *246*, 169–184; i) A. M. Beatty, *Coord. Chem. Rev.* **2003**, *246*, 131–143; j) D. Braga, L. Brammer, N. R. Champness, *CrystEngComm* **2005**, *7*, 1–19; k) B. J. Holliday, C. A. Mirkin, *Angew. Chem. Int. Ed.* **2001**, *40*, 2023–2043.

[3] a) M. Eddaoudi, J. Kim, N. Rosi, D. Vodak, J. Wachter, M. O'Keeffe, O. M. Yaghi, *Science* **2002**, *295*, 469–472; b) O. M. Yaghi, M. O'Keeffe, N. W. Ockwig, H. K. Chae, M. Eddaoudi, J. Kim, *Nature* **2003**, *423*, 705–714; c) R. Matsuda, R. Kitaura, S. Kitagawa, Y. Kubota, R. V. Belosludov, T. C. Kobayashi, H. Sakamoto, T. Chiba, M. Takata, Y. Kawazoe, Y. Mita, *Nature* **2005**, *436*, 238–241; d) M. J. Rosseinsky, *Microporous Mesoporous Mater.* **2004**, *73*, 15–30; e) B. Gomez-Lor, E. Gutierrez-Puebla, M. Iglesias, M. A. Monge, C. Ruiz-Valero, N. Snejko, *Chem. Mater.* **2005**, *17*, 2568–2573.

[4] a) P. N. W. Baxter in *Comprehensive Supramolecular Chemistry* (Ed.: J.-M. Lehn), Pergamon. Oxford, **1996**, vol. 9, ch. 5; b) S. Kitagawa, R. Kitaura, S. I. Noro, *Angew. Chem. Int. Ed.* **2004**, *43*, 2334–2375; c) X. M. Ouyang, Z. W. Li, T. A. Okamura, Y. Z. Li, W. Y. Sun, W. X. Tang, N. Ueyama, *J. Solid State Chem.* **2004**, *177*, 350–360.

[5] a) C. Janiak, *Dalton Trans.* **2003**, 2781; b) B. Gomez-Lor, E. Gutierrez-Puebla, M. Iglesias, M. A. Monge, C. Ruiz-Valero, N. Snejko, *Inorg. Chem.* **2002**, *41*, 2429–2432; c) S. R. Batten, K. S. Murray, *Coord. Chem. Rev.* **2003**, *246*, 103–130; d) M. Ruben, U. Ziener, J. M. Lehn, V. Ksenofontov, P. Gutlich, G. B. M. Vaughan, *Chem. Eur. J.* **2005**, *11*, 94–100.

[6] a) S. Varughese, V. R. Pedireddi, *Chem. Commun.* **2005**, 1824–1826; b) M. Tominaga, K. Suzuki, T. Murase, M. Fujita, *J. Am. Chem. Soc.* **2005**, *127*, 11950–11951; c) C. Addicott, I. Oesterling, T. Yamamoto, K. Llen, P. J. Stang, *J. Org. Chem.* **2005**, *70*, 797–801; d) Z. Wang, V. C. Kravtsov, M. J. Zaworotko, *Angew. Chem. Int. Ed.* **2005**, *44*, 2877–2880.

[7] a) W. Mori, S. Takamizawa, C. N. Kato, T. Ohmura, T. Sato, *Microporous Mesoporous Mater.* **2004**, *73*, 31–46; b) C. N. R. Rao, S. Natarajan, R. Vaidhyanathan, *Angew. Chem. Int. Ed.* **2004**, *43*, 1466–1496; c) P. J. Steel, *Acc. Chem. Res.* **2005**, *38*, 243–250; d) B. H. Ye, M. L. Tong, X. M. Chen, *Coord. Chem. Rev.* **2005**, *249*, 545–565.

[8] a) M. Schweiger, T. Yamamoto, P. J. Stang, D. Ser, R. Boese, *J. Org. Chem.* **2005**, *70*, 4861–4864; b) S. Noro, R. Kitaura, M. Kondo, S. Kitagawa, T. Ishii, H. Matsuzaka, M. Yamashita, *J. Am. Chem. Soc.* **2002**, *124*, 2568–2583; c) C. Ma, C. Chen, Q. Liu, D. Liao, L. Li, L. Sun, *New J. Chem.* **2003**, *27*, 890–894.

[9] a) M. Du, X.-J. Zhao, Y. Wang, *Dalton Trans.* **2004**, 2065–2072; b) D. L. Reger, R. F. Semeniuc, C. A. Little, M. D. Smith, *Inorg. Chem.* **2006**, *45*, 7758–7769; c) G. K. H. Shimizu, *J. Solid State Chem.* **2005**, *178*, 2519–2526; d) Y.-B. Dong, M. D. Smith, H.-C. zur Loye, *Angew. Chem. Int. Ed.* **2000**, *39*, 4271–4273; e) C.-Y. Su, M. D. Smith, H.-C. zur Loye, *Angew. Chem. Int. Ed.* **2003**, *42*, 4085–4089; f) M. Du, X.-J. Zhao, Y. Wang, *Dalton Trans.* **2004**, 2065–2972; g) D. L. Reger, R. F. Semeniuc, C. A. Little, M. D. Smith, *Inorg. Chem.* **2006**, *45*, 7758–7769; h) H. Miyaji, M. Dudic, J. H. R. Tucker, I. Prokes, M. E. Light, T. Gelbrich, M. B. Hursthouse, I. Stibor, P. Lhotak, L. Brammer, *Supramol. Chem.* **2003**, *15*, 385–390; i) L. Brammer, C. S. Rodger, A. J. Blake, N. R. Brooks, N. R. Champness, J. W. Cunningham, P. Hubberstey, S. J. Teat, C. Wilson, M. Schroder, *J. Chem. Soc., Dalton Trans.* **2002**, 4134–4142; j) G. K. H. Shimizu, *J. Solid State Chem.* **2005**, *178*, 2519–2526; k) M. Oh, C. L. Stern, C. A. Mirkin, *Inorg. Chem.* **2005**, *44*, 2647–2653; l) H. Ohi, Y. Tachi, S. Itoh, *Inorg. Chem.* **2004**, *43*, 4561–4563; m) W. Zhao, Y. Song, T. A. Okamura, J. Fan, W. Y. Sun, N. Ueyama, *Inorg. Chem.* **2005**, *44*, 3330–3336; n) Z. H. Zhang, Y. Song, T. A. Okamura, Y. Hasegawa, W. Y. Sun, N. Ueyama, *Inorg. Chem.* **2006**, *45*, 2896–2902.

[10] a) D. A. McMorran, P. J. Steel, *Tetrahedron* **2003**, *59*, 3701–3707; b) D. J. Bray, L.-L. Liao, B. Antonioli, K. Gloe, L. Lindoy, J. C. McMurtrie, G. Wei, X.-Y. Zhang, *Dalton Trans.* **2005**, 2082–2083; c) M. Hong, W. Su, R. Cao, M. Fujita, J. Lu, *Chem. Eur. J.* **2000**, *6*, 427–431; d) R. Peng, D. Li, T. Wu, X.-P. Zhou, S. W. Ng, *Inorg. Chem.* **2006**, *45*, 4035–4046; e) C. M. Hartshorn, P. J. Steel, *J. Chem. Soc., Dalton Trans.* **1998**, 3935–3940.

 © 2007 Wiley-VCH Verlag GmbH & Co. KGaA, Weinheim 

[11] a) K. K. Arora, V. R. Pedireddi, *J. Org. Chem.* **2003**, *68*, 9177–9185; b) S. Varughese, V. R. Pedireddi, *Chem. Eur. J.* **2006**, *12*, 1597–1609; c) V. R. Pedireddi, N. Seethalekshmi, *Tetrahedron Lett.* **2004**, *45*, 1903–1906.
[12] a) T. J. Burchell, D. T. Eisler, R. J. Puddephatt, *Inorg. Chem.* **2004**, *43*, 5550–5557; b) P. Grasshans, A. Jouaiti, V. Bulach, J.-M. Planeix, M. W. Hosseini, J.-F. Nicoud, *Chem. Commun.* **2003**, 1336–1337.
[13] Bruker, *SMART*, version V 5.060, Bruker Analytical X-ray Systems, Madison, WI.
[14] a) G. M. Sheldrick, *SHELXTL-PLUS, Program for Crystal Structure Solution and Refinement*, University of Göttingen, Germany; b) G. M. Sheldrick, *SADABS, Siemens Area Detector Absorption Correction Program*, University of Göttingen, Germany.
[15] A. L. Spek, *PLATON, Molecular Geometry Program*, University of Utrecht, Utrecht, The Netherlands, **1995**.

Received: September 16, 2006
Published Online: February 2, 2007

 © 2007 Wiley-VCH Verlag GmbH & Co. KGaA, Weinheim 

DOI: 10.1002/ejic.200600872

# Neutral Yttrium Tris(amide) and Ate Complexes Coordinated by an (*R*)-*N*,*N*′-Diisopropyl-1,1′-binaphthyl-2,2′-diamido Ligand as Enantioselective Catalysts for Intramolecular Hydroamination

**David Riegert,[a] Jacqueline Collin,*[a] Jean-Claude Daran,[b] Tauqir Fillebeen,[a] Emmanuelle Schulz,[a] Dmitrii Lyubov,[c] Georgy Fukin,[c] and Alexander Trifonov*[c]**

**Keywords:** Asymmetric catalysis / N ligands / Yttrium / Hydroamination / Nitrogen heterocycles

A bis(amido)yttrium chloride coordinated by (*R*)-*N*,*N*′-diisopropyl-1,1′-binaphthyl-2,2′-diamide [Y{(*R*)-$C_{20}H_{12}$(N*i*Pr)$_2$}-Cl(thf)$_2$] has been prepared and characterized by X-ray analysis along with the corresponding yttrium ate complex [Li(thf)$_4$][Y{(*R*)-$C_{20}H_{12}$(N*i*Pr)$_2$}$_2$]. The reaction of [(*R*)-*N*,*N*′-diisopropyl-1,1′-binaphthyl-2,2′-diamido]yttrium chloride with lithium diisopropylamine leads to the formation of a neutral tris(amido)yttrium complex which was characterized by NMR spectroscopy. The new complexes [Y{(*R*)-$C_{20}H_{12}$(N*i*Pr)$_2$}-{N*i*Pr$_2$}] and [{Li(thf)$_4$}(Y{(*R*)-$C_{20}H_{12}$(N*i*Pr)$_2$}$_2$)], which contain the same enantiopure binaphthyldiamido ligand, are compared for the catalysis of several intramolecular hydroamination reactions. Both complexes provide pyrrolidines and piperidines with moderate to high enantioselectivities.
(© Wiley-VCH Verlag GmbH & Co. KGaA, 69451 Weinheim, Germany, 2007)

## Introduction

The intramolecular hydroamination of alkenes is an atom-economic process that leads to the formation of nitrogen heterocycles that are found in numerous biologically active compounds.[1] The pioneering work of Marks and coworkers has shown the ability of lanthanocenes to perform hydroamination/cyclization reactions.[2] More recently non-cyclopentadienido rare-earth complexes[3] as well as transition metal complexes and others[4] have been reported to catalyze the intramolecular hydroamination of alkenes. However, enantioselective hydroamination reactions have been less studied and only a few chiral asymmetric catalysts have been reported to date.[5]

Chiral catalysts that are efficient for the asymmetric cyclization of aminoalkenes are almost all prepared from lanthanides with different types of ligands and are either isolated or used in situ. The first enantioselective catalysts reported for hydroamination/cyclization were the *ansa*-lanthanocene complexes substituted by a menthyl or neomenthyl group synthesized by Marks et al. that possess two stereogenic centers (backbone and lanthanide chirality, see **A** in Figure 1).[6] Diastereomeric mixtures and diastereomerically pure precatalysts yielded the formation of pyrrolidines with identical enantiomeric excesses of up to 74% *ee*. Similar rare-earth metal complexes with an octahydrofluorenido group instead of a tetramethylcyclopentadienido group (structure **B** in Figure 1) have been isolated and have been found to be more efficient for the preparation of piperidines (up to 67% *ee*).[7] Both series of complexes were prepared in a two-step synthesis that includes the formation of a metal chloride followed by its transformation into the amido or alkyl complex. Chiral lanthanide bis(aryloxide)s and bis(naphthoxide)s have been prepared by a different route and studied for the catalysis of aminoalkene cyclization. Scott et al. have thus synthesized chiral rare-earth metal bis(aryloxide) complexes by the reaction of the ligand [a bis(phenol) with a bis(arylamine) providing the chirality, structure **C**] with the tris(amide) precursors [Ln{N(SiHMe$_2$)$_2$}$_3$(thf)$_2$].[8] The lanthanum complex was found to cyclize an aminopentene, albeit with low activity (reaction performed at 70 °C), with 61% *ee*. A similar chiral cationic zirconium complex has also been characterized and tested for the hydroamination/cyclization of secondary amines; it affords 82% *ee* for a piperidine.[9] Hultzsch et al. have synthesized various lanthanide bis(phenolate)s and bis(naphtholate)s.[10] They isolated dimeric alkyllanthanum bis(phenolate) complexes from the reaction of 3,3′-substituted bis(phenol) with [La{CH(SiMe$_3$)$_2$}$_3$] which exhibited only low enantioselectivity for hydroamination reactions.[10a] The amidoyttrium biphenolate and binaphtholate

[a] Equipe de Catalyse Moléculaire, ICMMO, UMR 8182, Université Paris-Sud,
91405 Orsay, France
Fax: +33-1-69154680
E-mail: jacollin@icmo.u-psud.fr
[b] Laboratoire de Chimie de Coordination,
205 route de Narbonne, 31077 Toulouse, France
[c] G. A. Razuvaev Institute of Organometallic Chemistry of Russian Academy of Sciences,
Tropinia 49, 603600 Nizhny Novgorod GSP-445, Russia
Fax: +7-8312-127497
E-mail: trif@imoc.sinn.ru

 © 2007 Wiley-VCH Verlag GmbH & Co. KGaA, Weinheim 

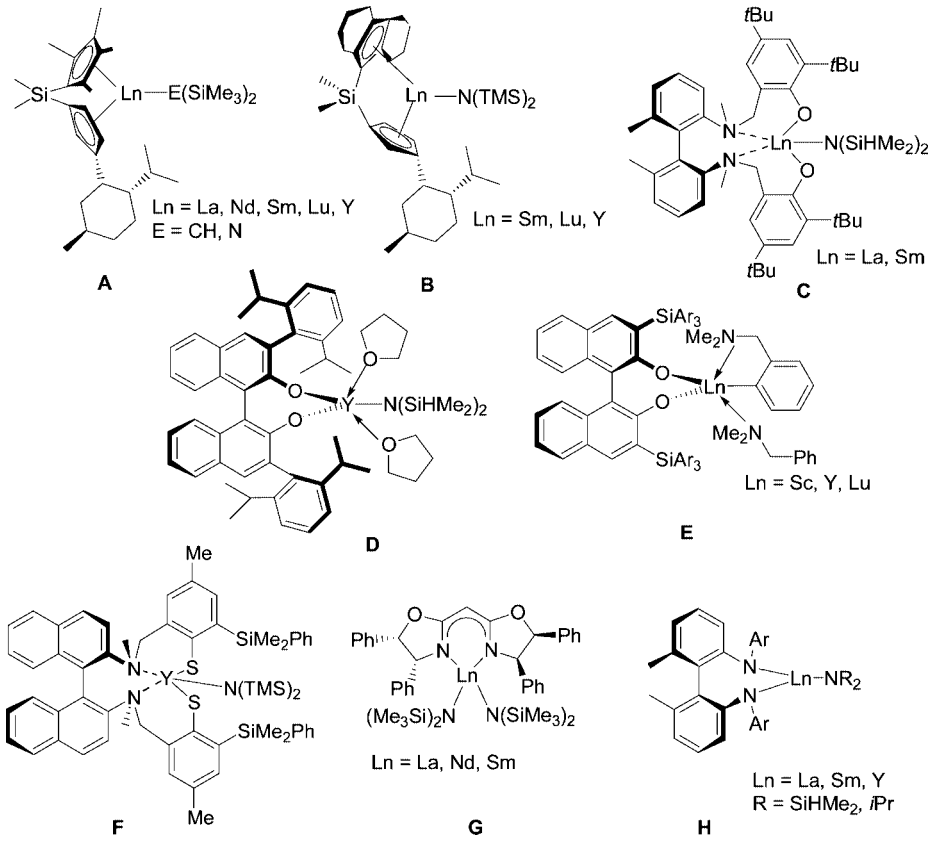


Figure 1. Complexes for intramolecular hydroamination reactions.

complexes synthesized according to a similar procedure (complex **D** in Figure 1) afforded moderate activities in these transformations, with enantiomeric excesses of up to 57%.[10b] To the best of our knowledge, the highest enantioselectivities obtained for intramolecular hydroamination are provided by chiral lanthanide 3,3′-tris(arylsilyl)binaphtholates prepared by arene, alkane or amine elimination and used in situ. The yttrium,[10c] lutetium, and scandium binaphtholates prepared from [Ln{*o*-$C_6H_4CH_2NMe_2$}$_3$] and 3,3′-bis(triarylsilyl)binaphthol (structure **E**) allow the cyclization of aminopentenes to be performed at room temperature with high turnovers and with enantiomeric excesses of up to 95%.[10d] Other enantioselective catalysts have also been prepared by the same procedure and used in situ. The amidoyttrium compounds synthesized by Livinghouse et al. from [Y{$N(TMS)_2$}$_3$] and chiral bis(thiolate) ligands (complex **F**) catalyze the cyclization of aminoalkenes at 60 °C and with enantiomeric excesses above 80% for several substrates.[11] Similarly, by the reaction of lanthanide amides with commercially available $C_2$-symmetric bis(oxazoline)s, Marks et al. have prepared enantioselective catalysts (structure **G** in Figure 1) that are active at room temperature (up to 67% *ee*).[12] A chiral, bridged aminotroponiminate complex of lutetium was very recently synthesized by Roesky[13] that shows moderate enantioselectivities for intramolecular hydroamination.

Since the pioneering work of Livinghouse et al. that showed that lanthanide tris(amide)s are active hydroamination catalysts and that the stereoselectivity and the rate of the reaction can be tuned by varying the diamine ligands,[3b,3d] the preparation of chiral lanthanide tris(amide)s for the enantioselective catalysis of hydroamination reactions has been a challenge. Interesting results have been reported by the group of Scott, who prepared precatalysts by the reaction of bis(arylamine)s possessing axial chirality with lanthanide tris(amide)s. These complexes (structure **H** in Figure 1) catalyze the cyclization of 2,2-dimethylpent-4-enylamine at 60 °C, albeit with only moderate asymmetric inductions.[14]

We have previously reported the preparation of lanthanide catalysts coordinated by chiral amido ligands for intramolecular hydroamination.[15] A new family of lanthanide ate complexes [Li(thf)$_4$][Ln{(*R*)-$C_{20}H_{12}(NR)_2$}$_2$] (Ln = Yb, Sm, Nd, Lu; **1** in Scheme 1) derived from chiral, disubstituted (*R*)-binaphthylamido ligands was studied. These compounds consist of a complex anion resulting from coordination of two (*R*)-binaphthylamine ligands to the lanthanide atom and a discrete [Li(thf)$_4$]$^+$ counterion. Both the influence of the lanthanide and of the alkyl substituent on the nitrogen groups was examined in a hydroamination test reaction. The activity and enantioselectivity of these catalysts were evaluated for the cyclization of *C*-(1-allylcyclohexyl)-methylamine. The ytterbium and lutetium complexes with bulky substituents (isopropyl, cyclohexyl) on the nitrogen atom led to the highest enantioselectivities (up to 76% *ee* for the spiropyrrolidine).

 © 2007 Wiley-VCH Verlag GmbH & Co. KGaA, Weinheim 

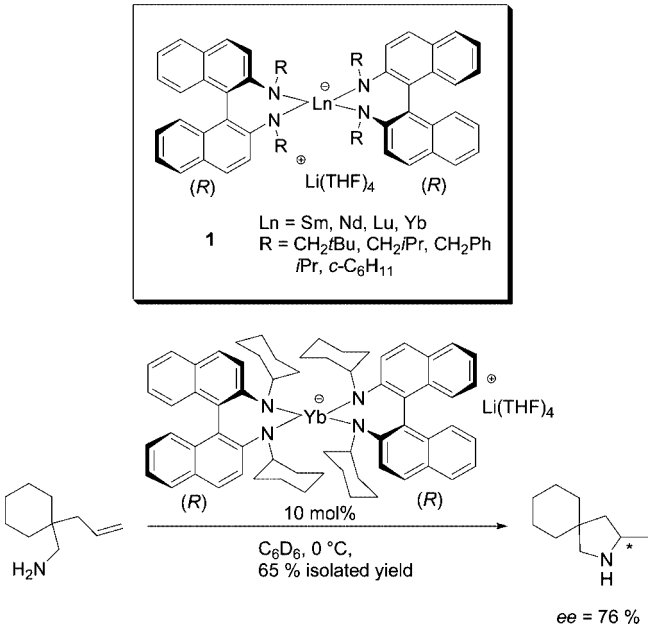


Scheme 1. Intramolecular hydroamination catalyzed by chiral lanthanide ate complexes.

In order to gain insight into the nature of the active catalytic species for the hydroamination reaction mediated by the ionic compounds $[Li(thf)_4][Ln\{(R)\text{-}C_{20}H_{12}(NR)_2\}_2]$, we considered the synthesis of both neutral and ate complexes of the same metal coordinated with the same chiral ligand and compared their catalytic properties.

## Results and Discussion

### Preparation and Characterization of Complexes

With the aim of preparing neutral tris(amido)lanthanide complexes $[Ln\{(R)\text{-}C_{20}H_{12}(NR)_2\}\{NR'_2\}]$ with binaphthylamino ligands, we focused on the synthesis of yttrium derivatives since yttrium tris(amide)s have been already synthesized and characterized by X-ray analysis. Several lanthanide tris(amide)s have been prepared by metathesis reactions,[16] and yttrium complexes coordinated by a chiral bis(arylamido) ligand have been used as enantioselective hydrosilylation catalysts.[17]

Initially, we attempted to use the amine elimination reaction as a synthetic approach to the neutral complexes $[Ln\{(R)\text{-}C_{20}H_{12}(NR)_2\}\{NR'_2\}]$ (Ln = Y, La, Sm; R = $CH_2CMe_3$, *i*Pr; R′ = $SiMe_3$). Thus, reactions of $[Ln\{N(SiMe_3)_2\}_3]$ (Ln = Y, La, Sm) with chiral diamines $(R)\text{-}C_{20}H_{12}(NHR)_2$ (R = $CH_2CMe_3$, *i*Pr) in a 1:1 molar ratio were carried out in toluene at 70 °C. However, these reactions were found to occur with complete substitution of the $N(SiMe_3)_2$ groups in the parent tris(amido) complexes since the $^1H$ NMR spectra of the solid products indicated the absence of the corresponding signals. The salt metathesis reaction of anhydrous $YCl_3$ with 1 equiv. of $Li_2\{(R)\text{-}C_{20}H_{12}(NiPr)_2\}$[18] in thf at ambient temperature allowed the isolation of the chiral diamidoyttrium chloride complex **2** in 81% yield (Scheme 2).

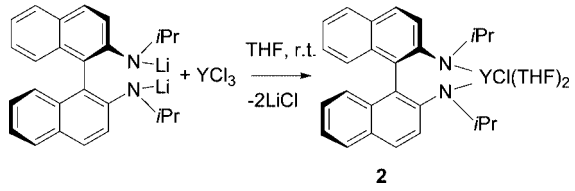


Scheme 2. Synthesis of the neutral yttrium complex $[Y\{(R)\text{-}C_{20}H_{12}(NiPr)_2\}Cl(thf)_2]$ (**2**).

Complex **2** was purified by extraction of the solid residue with toluene after evaporation of thf and subsequent recrystallization from thf/hexane mixtures. The $^1H$ and $^{13}C$ NMR spectra of complex **2** in $C_6D_6$ at 20 °C show the expected sets of resonances due to the (*R*)-*N*,*N*′-diisopropyl-1,1′-binaphthyl-2,2′-diamido ligand and the coordinated thf molecules.

This salt metathesis reaction turned out to be highly sensitive to the substituent on the nitrogen atom of the starting (*R*)-1,1′-binaphthyl-2,2′-diamine. Thus, the reaction of equimolar amounts of $YCl_3$ and the dilithium derivative of (*R*)-*N*,*N*′-diphenyl-1,1′-binaphthyl-2,2′-diamine under analogous conditions afforded the ate complex $[Li(thf)_4]\text{-}[Y\{(R)\text{-}C_{20}H_{12}(NPh)_2\}_2]$ (**3**) in 42% yield instead of the expected complex $[Y\{(R)\text{-}C_{20}H_{12}(NPh)_2\}Cl(thf)_n]$ (Scheme 3).

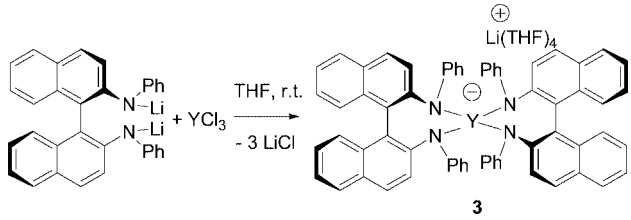


Scheme 3. Synthesis of the yttrium ate complex $[Li(thf)_4][Y\{(R)\text{-}C_{20}H_{12}(NPh)_2\}_2]$ (**3**).

Complex **3** was purified by extraction of the solid residue obtained after evaporation of thf with hot toluene. Slow cooling of hot solutions of **3** in toluene afforded crystalline samples. The $^1H$ and $^{13}C$ NMR spectra of complex **3** in $C_6D_6$ at 20 °C show the expected sets of signals corresponding to the aromatic protons of the diamido ligand and the coordinated thf molecules.

In order to synthesize the amidoyttrium complex containing a chiral ancillary ligand, we carried out the reaction of complex **2** with $LiNiPr_2$ in thf at room temperature (Scheme 4). After evaporation of thf, the crude complex $[Y\{(R)\text{-}C_{20}H_{12}(NiPr)_2\}\{NiPr_2\}\{LiCl(thf)_2\}]$ (**4**) was characterized by $^1H$ and $^{13}C$ NMR spectroscopy. According to the $^1H$ NMR spectrum, complex **4** contains two molecules of thf. Unfortunately, the experimental data did not allow us to conclude with certainty whether these thf molecules are coordinated to Y or Li. Extraction of the complex with toluene and recrystallization from thf/hexane resulted in the products of ligand-redistribution reactions. All attempts to isolate individual compounds to obtain samples suitable for

 © 2007 Wiley-VCH Verlag GmbH & Co. KGaA, Weinheim 

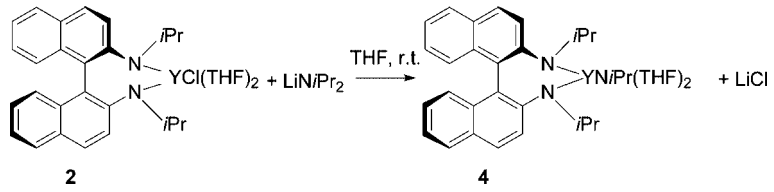


2 4

Scheme 4. Synthesis of [Y{(*R*)-$C_{20}H_{12}$(N*i*Pr)$_2$}{N*i*Pr$_2$}{LiCl(thf)$_2$}] (**4**).

X-ray analysis failed. We also tried to prepare alkylyttrium derivatives containing the (*R*)-*N*,*N*′-diisopropyl-1,1′-binaphthyl-2,2′-diamido ligand. However, reactions of **2** with the alkyllithium reagents $LiCH_2SiMe_3$ (toluene 0 °C) and MeLi ($Et_2O$, 0 °C, in the presence of a twofold molar excess of TMEDA) did not afford any tractable organoyttrium compounds.

The ate complex [Li(thf)$_4$][Y{(*R*)-$C_{20}H_{12}$(N*i*Pr)$_2$}$_2$] (**5**) was synthesized by the metathesis reaction of anhydrous $YCl_3$ with 2 equiv. of Li$_2${(*R*)-$C_{20}H_{12}$(N*i*Pr)$_2$} in thf at ambient temperature (Scheme 5).

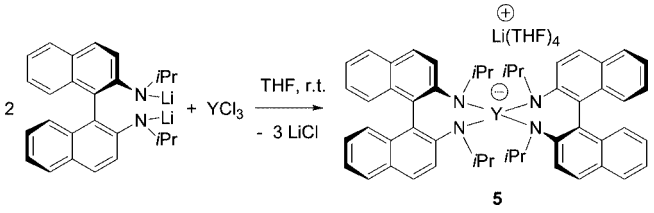


5

Scheme 5. Synthesis of the ate complex [Li(thf)$_4$][Y{(*R*)-$C_{20}H_{12}$(N*i*Pr)$_2$}$_2$] (**5**).

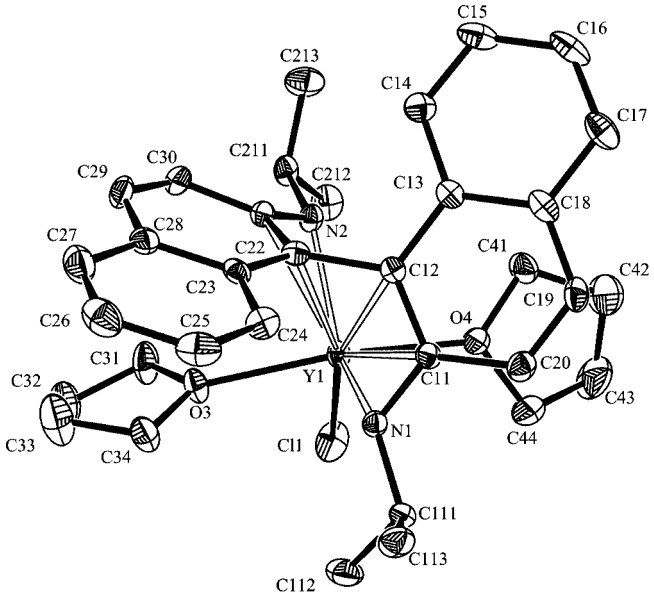


Figure 2. ORTEP drawing of complex **2** with the atom labeling scheme. Ellipsoids are drawn at the 30% probability level. The hydrogen atoms have been omitted for clarity. Selected bond lengths [Å] and angles [°]: Y1–N1 2.254(3), Y1–N2 2.257(4), Y1–Cl1 2.5835(14), Y1–C11 2.700(4), Y1–C12 2.756(4), Y1–C21 2.717(4), Y1–C22 2.746(4); N1–Y1–N2 123.36(15), N1–Y1–Cl1 115.78(12), N2–Y1–Cl1 120.86(10).

Complex **5** was purified by extraction of the solid residue remaining after evaporation of thf with toluene and subsequent recrystallization from thf/hexane mixtures; it was isolated in 71% yield. Complexes **2**–**5** were obtained as yellow, highly air- and moisture-sensitive crystalline solids. Complexes **2**, **4**, and **5** are soluble in thf and toluene and insoluble in hexane. Complex **3** is soluble in thf and hot toluene. Clear single-crystalline samples of complex **2** suitable for X-ray investigation were obtained by slow condensation of hexane into the concentrated thf solution at room temperature. Complex **2** crystallizes in the monoclinic space group $P2_1$ with four molecules in the unit cell. The molecular structure of **2** is depicted in Figure 2, and the crystal and structural refinement data are listed in the Experimental Section. The X-ray single-crystal structure analysis showed that complex **2** adopts a monomeric structure, thus indicating a considerable steric demand of the diamido ligand.

The coordination sphere of the yttrium atom in **2** contains the two nitrogen atoms of the (*R*)-*N*,*N*′-diisopropyl-1,1′-binaphthyl-2,2′-diamido ligand, one chlorido ligand, and two oxygen atoms of two thf molecules. The formal coordination number of the metal atom is five, which is rather low for yttrium. The presence in complex **2** of short contacts between the metal atom and the carbon atoms in the *ipso* and *ortho* positions to the amido groups [Y(1)–C(211) 2.708(4), Y(1)–C(111) 2.719(5), Y(1)–C(112) 2.745(4), Y(1)–C(212) 2.758(4) Å] comparable to those reported for the yttrium π-complexes [({PhP(CH$_2$SiMe$_2$NSiMe$_2$CH$_2$)$_2$PPh}Y)$_2${η$^6$:η$^6$-($C_6H_5$)$_2$}] [2.699(1)–2.738(4) Å][19] and [Y(*o*-2,6-Ph$_2$$C_6H_3$)$_3$] [2.84(1)–3.38(1) Å][20] probably reflects an η$^2$-interaction of the yttrium atom with the aromatic rings of the binaphthyl ligand, which leads to a saturation of the coordination sphere of the yttrium atom. The Y–N bond lengths in **2** [2.254(3) and 2.257(4) Å] are very close to the length of the covalent bond reported for the amidoyttrium complexes [{[6,6′-Me$_2$-($C_6H_3$)$_2$](2,2′-NSiMe$_2$*t*Bu)$_2$}YCl(thf)$_2$] [2.247(7) and 2.252(7) Å][21] and [Cp*$_2$Y{N(SiMe$_3$)$_2$}] [2.274(1) and 2.253(1) Å].[22] The Y–Cl bond length in **2** [2.5835(14) Å] is comparable to those in [{[6,6′-Me$_2$-($C_6H_3$)$_2$](2,2′-NSiMe$_2$*t*Bu)$_2$}YCl(thf)$_2$] [2.574(2) Å][21] and [Cp*$_2$YCl(thf)] (2.579 and 2.577 Å).[23]

Clear single-crystal samples of complex **3** suitable for X-ray investigation were obtained by slow cooling of its hot toluene solution from 70 °C to room temperature. Complex **3** crystallizes in the orthorhombic space group $P2_12_12_1$ with four molecules in the unit cell. Complex **3** was isolated as a solvate containing three molecules of toluene per molecule

 © 2007 Wiley-VCH Verlag GmbH & Co. KGaA, Weinheim 

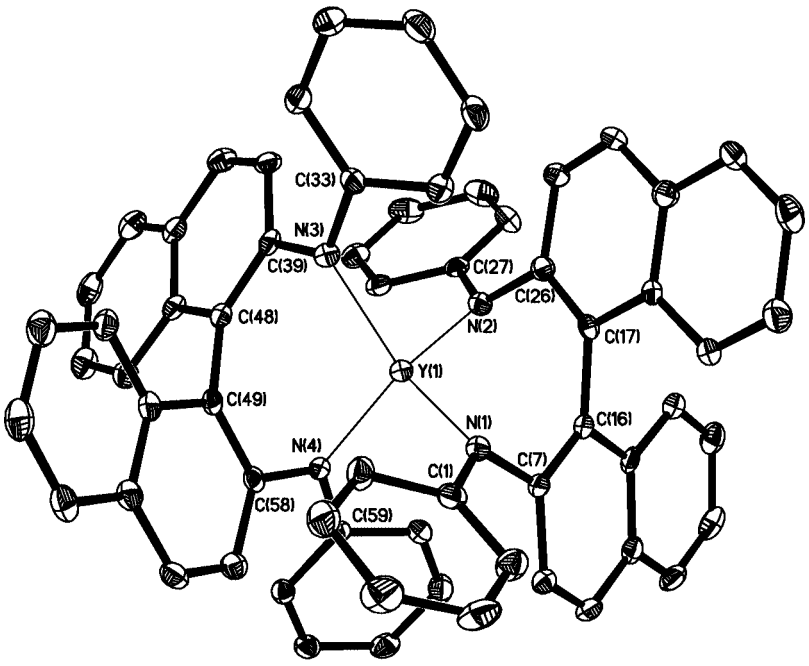


Figure 3. ORTEP drawing of complex **3** with the atom labeling scheme. Ellipsoids are drawn at the 30% probability level. The $Li(thf)_4^+$ cation and the hydrogen atoms have been omitted for clarity. Selected bond lengths [Å] and angles [°]: Y1–N1 2.275(2), Y1–N2 2.267(2), Y1–N3 2.270(2), Y1–N4 2.288(2), Y1–C26 2.747(2), Y1–C16 2.849(3), Y1–C7 2.727(3), Y1–C39 2.743(3), Y1–C58 2.746(3); N1–Y1–N2 118.47(8), N1–Y1–N3 103.74(8), N2–Y1–N3 104.69(9), N1–Y1–N4 108.65(8), N2–Y1–N4 103.84(8), N3–Y1–N4 118.15(8).

of complex, i.e., $[\{Li(thf)_4\}(Y\{(R)\text{-}C_{20}H_{12}(NPh)_2\}_2)\text{-}(C_7H_8)_3]$. The molecular structure of **3** is depicted in Figure 3 and the crystal and structural refinement data are listed in the Experimental Section.

The X-ray single-crystal structure analysis revealed that compound **3** is an ionic complex containing a discrete $Li(thf)_4^+$ cation and a discrete $[Y\{(R)\text{-}C_{20}H_{12}(NPh)_2\}_2]^-$ complex anion resulting from the coordination of two diamido ligands to the trivalent yttrium atom. The Y–N bonds within the complex anion of **3** [2.267(2), 2.270(2), 2.275(2), and 2.288(2) Å] are slightly longer than the same distances in neutral complex **2** and are comparable to those in ionic $[Li(thf)_4][Y(NPh_2)_4]$ [2.244(2)–2.271(2) Å].[24] Short contacts between the yttrium atom and the carbon atoms in the *ipso* and *ortho* positions [Y(1)–C(39) 2.743(3), Y(1)–C(58) 2.746(3), Y(1)–C(26) 2.747(2), Y(1)–C(16) 2.849(3) Å] to the amido groups are also observed in complex **3**.

Crystals of **5** suitable for X-ray diffraction studies were obtained by slow condensation of hexane into concentrated thf solutions at room temperature. Complex **5** crystallizes as a thf solvate containing one molecule of thf per molecule

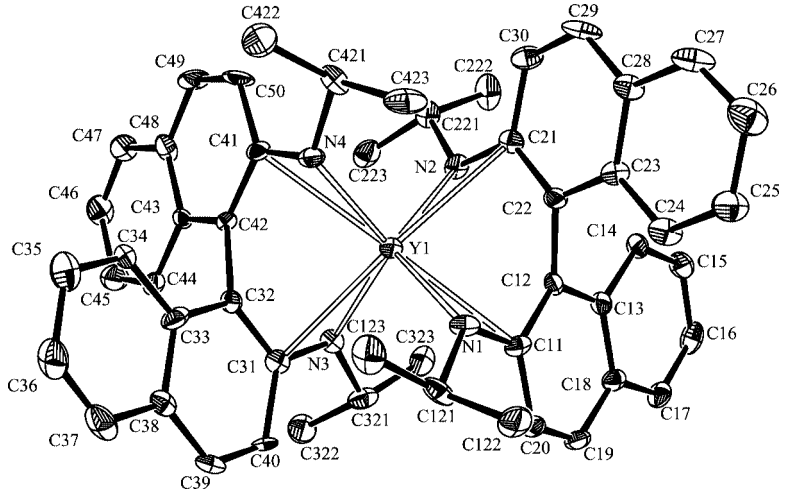


Figure 4. ORTEP drawing of complex **5** with the atom labeling scheme. Ellipsoids are drawn at the 30% probability level. The $Li(thf)_4^+$ cation and the hydrogen atoms have been omitted for clarity. Selected bond lengths [Å] and angles [°]: Y1–N1 2.297(5), Y1–N2 2.284(5), Y1–N3 2.290(5), Y1–N4 2.265(6), Y1–C11 2.712(6), Y1–C21 2.767(6), Y1–C31 2.733(7), Y1–C41 2.753(7); N1–Y1–N2 118.50(2), N1–Y1–N3 102.07(18), N2–Y1–N3 109.1(2), N1–Y1–N4 108.7(2), N2–Y1–N4 100.8(2), N3–Y1–N4 118.5(2).

 © 2007 Wiley-VCH Verlag GmbH & Co. KGaA, Weinheim 

of complex, i.e., $[Li(thf)_4][Y\{(R)\text{-}C_{20}H_{12}(NiPr)_2\}_2](C_4H_8O)$. The molecular structure of **5** is shown in Figure 4, and the structure refinement data are listed in the Experimental Section. Complex **5** crystallizes in the orthorhombic space group $P2_12_12_1$ with four molecules in the unit cell. The X-ray diffraction study shows that complex **5**, similarly to **3**, is an ionic complex consisting of a discrete $Li(thf)_4^+$ cation and a complex $\{Y[(R)\text{-}C_{20}H_{12}(NiPr)_2]_2\}^-$ anion. The yttrium is coordinated by the four nitrogen atoms of the two (*R*)-1,1′-binaphthyl-2,2′-diamido ligands. The Y–N bond lengths in **5** are 2.297(5), 2.284(5), 2.290(5), and 2.265(6) Å. The average value of the Y–N bond lengths in **5** [2.284(5) Å] is very similar to that found for complex **3** [2.275(2) Å].

## Catalytic Tests

We have previously reported the efficiency of an ytterbium ate complex $[Li(thf)_4][Yb\{(R)\text{-}C_{20}H_{12}(NiPr)_2\}_2]$ for the cyclization of various aminopentene derivatives to the corresponding pyrrolidines with high enantioselectivities (up to 70% *ee*).[15b] This complex requires several days of reaction at room temperature, however, to reach complete conversion. The new amidoyttrium complexes **3**, **4**, and **5** have been tested for their ability to perform enantioselective intramolecular hydroamination reactions. Complex **3** is not active for the cyclization of *C*-(1-allylcyclohexyl)methylamine (**6**), whereas **4** and **5** are efficient catalysts for several intramolecular hydroaminations (see Table 1).

The hydroamination/cyclization of **6** was initially investigated with both complexes at room temperature; the expected spiropyrrolidine (**7**) was obtained with a similar enantioselectivity (68% *ee*). It should be noted that catalyst **4** is much more active since it cyclized substrate **6** in 4 h, whereas a reaction time of 20 h was necessary for catalyst **5** to achieve the same transformation (Entries 1 and 2, Table 1). Similarly, in the cyclization of *C*-(1-allylcyclopentyl)methylamine (**8**) both catalysts afforded the spiropyrrolidine **9** with the same enantiomeric excess (Entries 3 and 4). With other substrates, however, the enantioselectivity depended on the catalyst employed. For the cyclization of 2,2-dimethylpent-4-enylamine (**10**) and 2,2-diphenylpent-4-enylamine (**12**), for example, complex **4** proved to be both more active and enantioselective than **5** – catalysts **4** and **5** afforded the pyrrolidine **11** with 68% *ee* and 40% *ee*, respectively (Entries 5 and 6), and the pyrrolidine **13** with 65% *ee* and 50% *ee* (Entries 7 and 8).

The cyclization of aminohexene derivatives into piperidines is a more difficult process, and substrate **14** could only be partially transformed into the corresponding spiropiperidine **15** within 12 d in the presence of catalyst **4** (Entry 9). This transformation was greatly accelerated at 60 °C, however, and the piperidine was obtained after only 8 h with 18% *ee* (Entry 10). Under the same reaction conditions, the aminohexene was cyclized in 17 h in the presence of complex **5**. Surprisingly, and only for this substrate, catalyst **5** gave a better enantioselectivity and product **15** was isolated with 29% *ee* (Entry 11).

The yttrium complex **4** is more stable than the ate lanthanide complexes that we prepared earlier as we performed catalytic hydroamination reactions with samples of **4** prepared two months previously with no loss of enantioselectivity. We thus investigated the possibility of reusing catalyst **4** in successive reactions. The results are given in Table 2.

Table 2. Reuse of catalyst **4** for the cyclization of aminopentene **6**.

| Reuse | Cat. ratio (mol-%) | *t* (h) | Conv. (%) | *ee* (%) |
|---|---|---|---|---|
| 0 | 8 | 4 | 100 | 69 |
| 1 | 4 | 17 | 100 | 67 |
| 2 | 3 | 14 | 100 | 65 |
| 3 | 2 | 14 | 79 | 65 |
| 4 | 1.5 | 23 | 59[a] | 62 |

[a] New substrate was added in the fourth reuse before complete consumption of the substrate in the preceding run.

The experiments were performed in an NMR tube. After the first reaction, an aliquot of the reaction mixture was separated to determine the enantiomeric excess and additional substrate in solution in $C_6D_6$ was added to the NMR tube. This procedure was repeated three times without loss of enantioselectivity. For the fourth reuse, a slight

Table 1. Intramolecular hydroamination reactions with **4** and **5**.

| Entry | Substrate | *T* (°C) | Cat. (ratio, mol-%) | *t* (h) | Product | Conv. (%) | *ee* (%) |
|---|---|---|---|---|---|---|---|
| 1 | 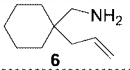 | 25 | **4** (4) | 4 | 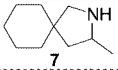 | 100 | 68 |
| 2 | **6** | 25 | **5** (7) | 20 | **7** | 100 | 67 |
| 3 | 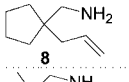 | 25 | **4** (10) | 72 | 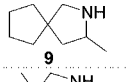 | > 95 | 50 |
| 4 | **8** | 25 | **5** (8) | 20 | **9** | 49 | 51 |
| 5 | 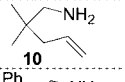 | 25 | **4** (11) | 23 | 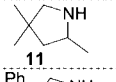 | 77 | 68 |
| 6 | **10** | 25 | **5** (10) | 44 | **11** | 73 | 40 |
| 7 | 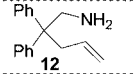 | 25 | **4** (6) | 12 | 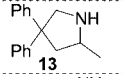 | 100 | 65 |
| 8 | **12** | 25 | **5** (5) | 43 | **13** | 100 | 50 |
| 9 | 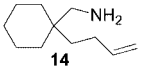 | 25 | **4** (10) | 288 | 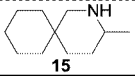 | 50 | 19 |
| 10 | | 60 | **4** (14) | 8 | | 100 | 18 |
| 11 | **14** | 60 | **5** (10) | 17 | **15** | > 90 | 29 |

 © 2007 Wiley-VCH Verlag GmbH & Co. KGaA, Weinheim 

decrease of enantioselectivity was observed together with a lower rate of reaction due to the decrease in the catalytic ratio or inhibition by the reaction product.[10d,25] Nevertheless, these results indicate that this neutral, chiral yttrium complex is highly stable and active for performing enantioselective hydroamination reactions. While this work was going on, Marks et al. reported a new procedure for the reuse of nonchiral organolanthanide hydroamination catalysts.[26] Their homogeneous lanthanocene precatalyst was recycled three times in the presence of amino-derived polystyrene resins.

The reactions catalyzed by the neutral yttrium complex **4** and the yttrium ate complex **5** coordinated with the same binaphthylamine ligand do not afford the same rates and/or enantiomeric excesses for the various hydroamination reactions studied. Shibasaki has demonstrated that for enantioselective carbon–carbon bond formation promoted by heterodimetallic catalysts both lanthanide and alkali metals are involved in the reaction mechanism.[27] Hence, these results suggest that the catalytically active species are not the same in the reactions involving precatalysts **4** and **5**. A mechanism for hydroamination reactions catalyzed by lanthanocenes has been proposed by Marks.[2] In the first step, the lanthanide–carbon or lanthanide–nitrogen bond of the precatalyst is cleaved by the amino olefin to form an amidolanthanide intermediate. This proton transfer is then followed by the insertion of the double bond in the lanthanide–nitrogen bond, which is the rate-determining step. Release of the cyclized product is favored by reaction of another amino olefin. For hydroamination reactions catalyzed by *ansa*-lanthanocenes[2] or lanthanide binaphtholates,[10d] several species with different coordination numbers that are in equilibrium have been proposed to be formed after the reaction of the amino olefin with the precatalyst.

Reaction of neutral complex **4** with an amino olefin may indeed form the tris(amide) species **4a** with selective replacement of the diisopropylamido group by the unsaturated substrate as the amido ligand. One or two amino ligands arising from the substrate or the cyclized product may then coordinate to the lanthanide center to give species **4b**. As for the yttrium ate complex **5**, at least two different structures can be considered for the active species formed by reaction with the amino olefin: after the proton transfer, a binaphthylamine ligand is transformed into the corresponding monolithium salt, which can coordinate (**5a**), or not (**4a**), to the yttrium atom.[28] In the case of the complete decoordination of one binaphthlyamine ligand, the structures of the active species for the catalysis by neutral complex **4** or ate complex **5** should be identical (**4a** and **4b**, Scheme 6). Furthermore, additional amino ligands from the substrate or the product may coordinate to the yttrium atom to form species **5b**.

For reactions involving substrates **6** or **8** the same catalytic species could be involved during catalysis by complexes **4** or **5**. This is probably not the case for hydroamination reactions involving the other substrates, although further studies are required to gain insight into the mechanism of hydroamination catalyzed by lanthanide ate complexes for more precise explanations concerning the role of the second chiral ligand.

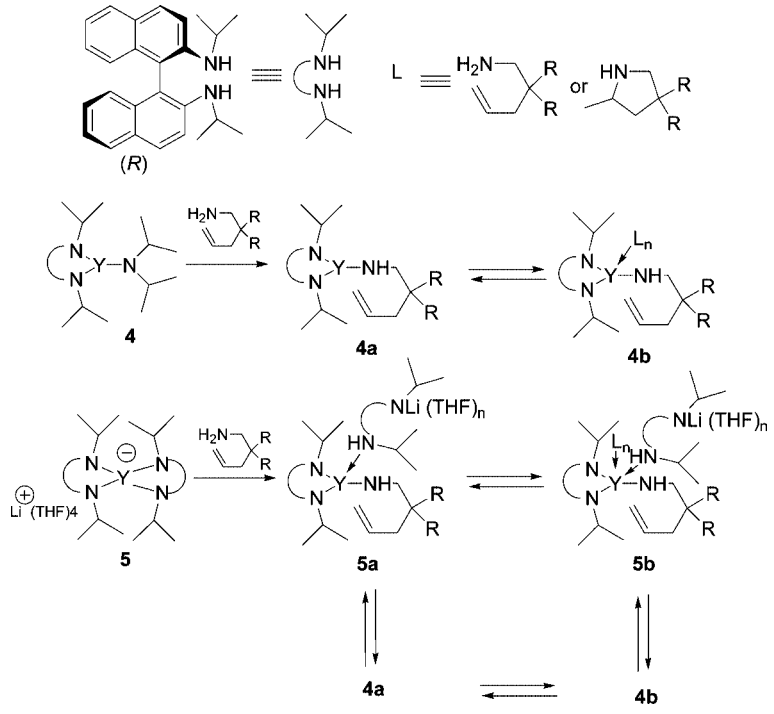


Scheme 6. Proposed structures for the intermediate catalytic species.

 © 2007 Wiley-VCH Verlag GmbH & Co. KGaA, Weinheim 

## Conclusion

We have prepared new asymmetric yttrium ate complexes and an asymmetric yttrium tris(amide) coordinated by *N*-substituted binaphthylamine ligands. An ate and a neutral complex coordinated with the same ligand are active catalysts for intramolecular hydroamination reactions. Comparison of the hydroamination reactions with different substrates catalyzed by both complexes has shown differences in activity and/or enantioselectivity, thus indicating that different active species are involved. Higher reaction rates and/or higher asymmetric inductions are generally observed for the formation of several pyrrolidines with the neutral yttrium tris(amide).

## Experimental Section

**General:** All procedures were performed under argon using standard Schlenk and glove-box techniques. Tetrahydrofuran (thf) was distilled from sodium benzophenone ketyl prior to use. Hexane and toluene were purified by distillation from sodium/triglyme benzophenone ketyl or $CaH_2$. Deuterated benzene was dried with sodium benzophenone ketyl and vacuum-transferred. Anhydrous $LnCl_3$ was purchased from Aldrich. The *N*,*N*′-diisopropylbinaphthyldiamine ligand and its lithium salt were prepared according to ref.[15b] The *N*,*N*′-diphenylbinaphthyldiamine ligand was prepared according to ref.[29] The substrates for the hydroamination/cyclization reactions were prepared as reported in ref.[15c] All other commercially available chemicals were used after the appropriate purification. Bruker AM 250, and Bruker DRX 400 NMR spectrometers (operating at 250 and 400 MHz, respectively) were used to record the NMR spectra. Chemical shifts for $^1H$ and $^{13}C$ NMR spectra were referenced internally with respect to the residual solvent resonances. IR spectra were recorded with a Perkin–Elmer FT-IR spectrometer as Nujol mulls. Elemental analyses were performed by the Microanalytical laboratory of the Institute of Organometallic Chemistry of RAS.

**Synthesis of [Y{(*R*)-$C_{20}H_{12}$(N*i*Pr)$_2$}Cl(thf)$_2$] (2):** $Li_2${(*R*)-$C_{20}H_{12}$(N*i*Pr)$_2$} (0.303 g, 0.799 mmol) was slowly added to a suspension of $YCl_3$ (0.156 g, 0.799 mmol) in thf (25 mL) at 20 °C with vigorous stirring. The reaction mixture was stirred for 3 h, then the thf was evaporated in vacuo and the resulting solid extracted with toluene (15 mL). The extracts were filtered, the toluene was evaporated off, and the solid residue was dissolved in thf (5 mL). Slow condensation of hexane into the thf solution at 20 °C resulted in yellow crystals of **1** (0.410 g, 81%). $C_{34}H_{42}ClN_2O_2Y$ (634.77): calcd. C 64.33, H 6.61, Y 14.00; found C 63.81, H 6.20, Y 14.11. $^1H$ NMR ($C_6D_6$): $\delta$ = 1.07 (br. s, 8 H, β-$CH_2$, thf), 1.35 (d, $^3J_{H,H}$ = 5.8 Hz, 6 H, CHC$H_3$), 1.62 (d, $^3J_{H,H}$ = 5.8 Hz, 6 H, CHC$H_3$), 3.28, 3.40 (2 br. s, 8 H, α-$CH_2$, thf), 4.04 (br. m, 4 H, C*H*CH$_3$) 7.07–7.34 (m, 8 H, Ar), 7.64–7.74 (m, 4 H, Ar) ppm. $^{13}C$ NMR ($C_6D_6$): $\delta$ = 24.7 (β-$CH_2$, thf), 25.4, 25.2 (CH*C*H$_3$), 46.6 (*C*HCH$_3$), 70.7 (α-$CH_2$, thf), 112.7, 116.4, 121.2, 124.7, 126.7, 127.6, 128.1, 131.6, 136.4, 150.2 (Ar) ppm. IR (Nujol, KBr): $\tilde{\nu}$ = 3048 (w), 1610 (s), 1591 (s), 1541 (s), 1364 (s), 1301 (s), 1286 (s), 1249 (s), 1209 (s), 1146 (m), 1118 (w), 1036 (m), 1016 (m), 976 (w), 940 (w), 918 (m), 870 (m), 836 (w), 808 (w), 745 (s) cm$^{-1}$.

**Synthesis of [Li(thf)$_4$][Y{(*R*)-$C_{20}H_{12}$(NPh)$_2$}$_2$] (3):** $Li_2${(*R*)-$C_{20}H_{12}$(NPh)$_2$} (0.338 g, 0.756 mmol) was slowly added to a suspension of $YCl_3$ (0.147 g, 0.756 mmol) in thf (25 mL) at 20 °C with vigorous stirring. The reaction mixture was stirred for 5 h, then the thf was evaporated in vacuo and the resulting solid extracted with hot toluene (15 mL). Slow cooling of the toluene extract from 70 to 20 °C resulted in yellow crystals of **3** (0.480 g, 42%). $C_{101}H_{100}LiN_4O_4Y$ (1529.7): calcd. C 79.30, H 6.53, Y 5.81; found C 78.86, H 6.17, Y 6.00. $^1H$ NMR ($C_6D_6$): $\delta$ = 1.08 (br. s, 16 H, β-$CH_2$, thf), 2.09 (s, 9 H, C$H_3C_6H_5$), 3.10 (br. s, 16 H, α-$CH_2$, thf), 6.58–7.99 (m, 59 H, Ar) ppm. $^{13}C$ NMR ($C_6D_6$): $\delta$ = 21.1 (C$H_3$), 24.8 (β-$CH_2$, thf), 67.9 (α-$CH_2$, thf), 117.0, 117.5, 118.3, 120.0, 122.1, 123.1, 123.7, 124.7, 125.2, 125.4, 125.6, 126.6, 127.6, 128.0, 129.0, 129.2, 129.5, 129.7, 129.9, 130.2, 130.5, 134.4, 136.1, 137.6, 140.8, 142.7, 154.7 (Ar) ppm. IR (Nujol, KBr): $\tilde{\nu}$ = 3050 (w), 1587 (m), 1348 (s), 1297 (s), 1173 (m), 1148 (m), 1079 (m), 1015 (m), 965 (m), 859 (m), 726 (s), 696 (s) cm$^{-1}$.

**Synthesis of [Y{(*R*)-$C_{20}H_{12}$(N*i*Pr)$_2$}{N*i*Pr$_2$}{LiCl(thf)$_2$}] (4):** [Y{(*R*)-$C_{20}H_{12}$(N*i*Pr)$_2$}Cl(thf)$_2$] (0.039 g, 0.061 mmol) was slowly added to a solution of LiN*i*Pr$_2$ (0.007 g, 0.061 mmol) in thf (1.5 mL) at 20 °C with vigorous stirring. The reaction mixture was then stirred for 20 h and the thf evaporated in vacuo. The complex was used without further purification as a crude yellow powder. $^1H$ NMR ($C_6D_6$): $\delta$ = 1.06–1.14 (m, 12 H, CHC$H_3$), 1.20–1.27 (m, 6 H, CHC$H_3$), 1.28 (br. s, 8 H, β-$CH_2$, thf), 1.48–1.62 (m, 6 H, CHC$H_3$), 3.02–3.15 (m, 2 H, C*H*CH$_3$), 3.35 (br. s, 8 H, α-$CH_2$, thf), 3.88–4.13 (m, 2 H, C*H*CH$_3$), 6.62–7.84 (m, 12 H, Ar) ppm. $^{13}C$ NMR ($C_6D_6$): $\delta$ = 25.1, 25.3, 25.4, 25.52, 25.60, 25.64, 25.7, 26.0 (C$H_3$), 25.2 (β-$CH_2$, thf), 47.1, 48.3, 48.5, 67.9 (α-$CH_2$, thf), 116.0, 116.4, 117.2, 118.0, 118.8, 120.8, 121.0, 121.1, 122.7, 124.7, 126.6, 126.7, 128.9, 131.5, 131.9, 132.5, 133.2, 135.4, 150.5, 154.9 (Ar) ppm. IR (Nujol, KBr): $\tilde{\nu}$ = 3047 (m), 1610 (s), 1593 (s), 1540 (m), 1496 (s), 1421 (s), 1377 (s), 1310 (s), 1246 (s), 1171 (s), 1038 (s), 916 (m), 810 (s), 746 (s) cm$^{-1}$.

**Synthesis of [Li(thf)$_4$][Y{(*R*)-$C_{20}H_{12}$(N*i*Pr)$_2$}$_2$] (5):** $YCl_3$ (0.061 g, 0.313 mmol) was slowly added to a solution of $Li_2${(*R*)-$C_{20}H_{12}$(N*i*Pr)$_2$} (0.238 g, 0.626 mmol) in thf (15 mL) at 20 °C with vigorous stirring. The reaction mixture was stirred for 3 h, then the thf was evaporated in vacuo and the resulting solid extracted with toluene (20 mL). The extracts were filtered, the toluene was evaporated off, and the solid residue was dissolved in thf (2 mL). Slow condensation of hexane into the thf solution at 20 °C resulted in yellow crystals of **5** (0.276 g, 71%). $C_{72}H_{92}LiN_4O_5Y$ (1189.35): calcd. C 72.75, H 7.73, Y 7.47; found C 72.28, H 7.30, Y 7.81. $^1H$ NMR ($C_6D_6$): $\delta$ = 1.29–1.35 (m, 20 H, β-$CH_2$, thf), 1.37 (d, $^3J_{H,H}$ = 6.1 Hz, 12 H, CHC$H_3$), 1.41 (d, $^3J_{H,H}$ = 6.1 Hz, 12 H, CHC$H_3$), 3.30–3.50 (m, 20 H, α-$CH_2$, thf), 3.90–4.10 (m, 4 H, C*H*CH$_3$), 6.90–7.85 (m, 24 H, Ar) ppm. $^{13}C$ NMR ($C_6D_6$): $\delta$ = 24.7 (C$H_3$), 25.1 (β-$CH_2$, thf), 26.9 (C$H_3$), 45.9, 67.7 (α-$CH_2$, thf), 113.5, 115.3, 117.9, 124.9, 125.2, 125.8, 127.1, 129.1, 138.5, 155.0 (Ar) ppm. IR (Nujol, KBr): $\tilde{\nu}$ = 3036 (w), 2802 (w), 2578 (w), 1609 (s), 1590 (s), 1540 (m), 1496 (m), 1420 (s), 1364 (s), 1304 (m), 1286 (s), 1247 (m), 1208 (w), 1168 (m), 1145 (m), 1115 (w), 1043 (s), 1015 (w), 916 (m), 886 (m), 851 (w), 835 (w), 808 (s), 745 (s) cm$^{-1}$.

**General Procedure for NMR-Scale Hydroamination/Cyclization of Aminoalkenes:** In an argon-filled glove box, the appropriate aminoalkene (0.176 mmol) was dissolved in $C_6D_6$ (0.1 mL) and dried with molecular sieves (4 Å) for 2 h. Complex **4** or **5** (see Tables 1 and 2 for the corresponding catalytic ratio) was introduced into an NMR tube equipped with a Teflon screw cap, dissolved in $C_6D_6$ (0.5 mL), and the aminoalkene solution was then introduced. The hydroamination reaction was monitored by $^1H$ NMR spectroscopy by observing the decrease of the signals of the olefinic protons. After the reaction time mentioned in the tables, the reaction was quenched with $CH_2Cl_2$. Determination of the enantiomeric excesses of the products was performed as described in ref.[15c]

 © 2007 Wiley-VCH Verlag GmbH & Co. KGaA, Weinheim 

Table 3. Crystal data and structure refinement for complexes **2**, **3** and **5**.

| | **2** | **3** | **5** |
|---|---|---|---|
| Empirical formula | $C_{34}H_{42}ClN_2O_2Y$ | $C_{101}H_{100}LiN_4O_4Y$ | $C_{72}H_{92}LiN_4O_5Y$ |
| Formula mass | 635.06 | 1529.70 | 1189.35 |
| Temperature [K] | 180(2) | 180(2) | 180(2) |
| Wavelength [Å] | 0.71073 | 0.71073 | 0.71073 |
| Crystal system | monoclinic | orthorhombic | orthorhombic |
| Space group | $P2_1$ | $P2_12_12_1$ | $P2_12_12_1$ |
| $a$ [Å] | 9.8722(7) | 17.8673(5) | 10.5453(10) |
| $b$ [Å] | 10.3133(8) | 19.9247(6) | 17.7356(16) |
| $c$ [Å] | 15.9820(11) | 23.1695(7) | 35.465(3) |
| $\alpha$ [°] | 90 | 90 | 90 |
| $\beta$ [°] | 99.829(6)° | 90 | 90 |
| $\gamma$ [°] | 90 | 90 | 90 |
| $V$ [Å$^3$] | 1603.3(2) | 8248.4(4) | 6632.9(11) |
| $Z$ | 2 | 4 | 4 |
| $D_{calcd.}$ [Mg m$^{-3}$] | 1.315 | 1.232 | 1.191 |
| $\mu$ [mm$^{-1}$] | 1.933 | 0.763 | 0.930 |
| $F(000)$ | 664 | 3232 | 2536 |
| Crystal size [mm] | $0.43 \times 0.37 \times 0.15$ | $0.30 \times 0.27 \times 0.25$ | $0.44 \times 0.17 \times 0.06$ |
| $\theta$ range [°] | 3.26 to 26.37 | 1.76 to 24.50 | 3.00 to 24.97 |
| Reflections collected | 11197 | 63151 | 45105 |
| Independent reflections [$R_{int}$] | 5691 [0.0489] | 13688 [0.0888] | 11698 [0.1777] |
| Absorption correction | multi-scan | sadabs | multi-scan |
| Refinement method | $F^2$ | $F^2$ | $F^2$ |
| Data/restraints/parameters | 5691/1/365 | 13688/27/1006 | 11698/144/801 |
| GOF on $F^2$ | 0.985 | 1.000 | 1.000 |
| $R1$, $wR2$ [$I > 2\sigma(I)$] | 0.0474, 0.1029 | 0.0486, 0.0961 | 0.0915, 0.1210 |
| $R1$, $wR2$ (all data) | 0.0585, 0.1089 | 0.0743, 0.1035 | 0.1475, 0.1421 |
| Flack parameter | –0.002(6) | 0.022(4) | 0.000(8) |
| Largest diff. peak/hole | 0.593/–0.533 | 0.450/–0.320 | 0.615/–0.499 |

**X-ray Structure Determination:** A single crystal of each compound was mounted under inert perfluoropolyether at the tip of a glass fiber and cooled in the cryostream of an Oxford Diffraction XCALIBUR CCD diffractometer for **2**, **3**, and **5**. Data were collected using monochromatic Mo-$K_\alpha$ radiation ($\lambda$ = 0.71073). Further details are provided in Table 3. The structures were solved by direct methods (SIR97)[30] and refined by least-squares procedures on $F^2$ using SHELXL-97.[31] All hydrogen atoms attached to carbon atoms were introduced in the calculation in idealized positions and treated as riding models. In compound **5**, there is one thf solvate molecule disordered over two positions. The disordered moieties were refined applying the restraints available within SHELXL-97.[32] The absolute configuration was determined by refining the Flack parameter[32] using a large number of Friedel pairs. The drawings of the molecules were produced with ORTEP32.[33] CCDC-615714, -615715 and -625520 (**2**, **3**, and **5**, respectively) contain the supplementary crystallographic data for this paper. These data can be obtained free of charge from The Cambridge Crystallographic Data Centre via www.ccdc.cam.ac.uk/data_request/cif.

## Acknowledgments

The CNRS is acknowledged for giving financial support and a postdoctoral grant to D. R. A. T. thanks the Russian Foundation for Basic Research (grant no. 05-03-32390), the Russian Foundation for Science Support, the Federal Agency for Science and Innovation (contract 02.445.11.7365), and a Grant of the President of the RF for leading scientific schools (grant no. 8017.2006.3).

[1] For general reviews on hydroamination reactions, see: a) T. E. Müller, M. Beller, *Chem. Rev.* **1998**, *98*, 675–704; b) M. Nobis, B. Driessen-Hölscher, *Angew. Chem. Int. Ed.* **2001**, *40*, 3983–3985; c) J. J. Brunet, D. Neibecker, in *Catalytic Heterofunctionalization: From Hydroamination to Hydrozirconation* (Eds.: A. Togni, H. Grützmacher), Wiley-VCH, Weinheim, **2001**, pp. 91–141; d) F. Pohlki, S. Doye, *Chem. Soc. Rev.* **2003**, *32*, 104–114; e) M. Beller, A. Tillack, J. Seayad, in *Transition Metals for Organic Synthesis*, 2nd ed. (Eds.: M. Beller, C. Bolm), Wiley-VCH, Weinheim, **2004**, vol. 2, pp. 403–414; f) S. Hong, T. J. Marks, *Acc. Chem. Res.* **2004**, *37*, 673–686.

[2] M. R. Gagné, C. L. Stern, T. J. Marks, *J. Am. Chem. Soc.* **1992**, *114*, 275–294 and references cited therein.

[3] a) Y. K. Kim, T. Livinghouse, J. E. Bercaw, *Tetrahedron Lett.* **2001**, *42*, 2933–2935; b) Y. K. Kim, T. Livinghouse, *Angew. Chem. Int. Ed.* **2002**, *41*, 3645–3647; c) Y. K. Kim, T. Livinghouse, Y. Horino, *J. Am. Chem. Soc.* **2003**, *125*, 9560–9561; d) J. Y. Kim, T. Livinghouse, *Org. Lett.* **2005**, *7*, 4391–4393; e) K. C. Hultzsch, F. Hampel, T. Wagner, *Organometallics* **2004**, *23*, 2601–2612; f) A. Zulys, T. K. Panda, M. T. Gamer, P. W. Roesky, *Chem. Commun.* **2004**, 2584–2585; g) T. K. Panda, A. Zulys, M. T. Gamer, P. W. Roesky, *J. Organomet. Chem.* **2005**, *690*, 5078–5089; h) M. Rastätter, A. Zulys, P. W. Roesky, *Chem. Commun.* **2006**, 874–876; i) S. Bambirra, H. Tsurugi, D. van Leusen, B. Hessen, *Dalton Trans.* **2006**, 1157–1161; j) F. Lauterwasser, P. G. Hayes, S. Bräse, W. E. Piers, L. L. Schafer, *Organometallics* **2004**, *23*, 2234–2237.

[4] a) A. Ates, C. Quinet, *Eur. J. Org. Chem.* **2003**, 1623–1626; b) P. Horillo Martinez, K. C. Hultzsch, F. Hampel, *Chem. Commun.* **2006**, 2221–2223; c) M. R. Crimmin, I. J. Casely, M. S. Hill, *J. Am. Chem. Soc.* **2005**, *127*, 2042–2043; d) A. Zulys, M. Dochnahl, D. Hollmann, K. Löhnwitz, J.-S. Herrmann, P. W. Roesky, S. Blechert, *Angew. Chem. Int. Ed.* **2005**, *44*, 7794–7798; e) N. Meyer, K. Löhnwitz, A. Zulys, P. W. Roesky, M. Dochnahl, S. Blechert, *Organometallics* **2006**, *25*, 3730–3734; f) J. A. Bexrud, J. D. Beard, D. C. Leitch, L. L. Schafer, *Org. Lett.* **2005**, *7*, 1959–1962; g) C. Müller, C. Loos, N. Schulenberg, S. Doye, *Eur. J. Org. Chem.* **2006**, 2499–2503; h) R. K. Thomson, J. A. Bexrud, L. L. Schafer, *Organometallics* **2006**, *25*, 4069–4071; i)

 © 2007 Wiley-VCH Verlag GmbH & Co. KGaA, Weinheim 

C. F. Bender, R. A. Widenhoefer, *J. Am. Chem. Soc.* **2005**, *127*, 1070–1071; j) A. Takemiya, J. F. Hartwig, *J. Am. Chem. Soc.* **2006**, *128*, 6042–6043.
[5] For reviews on enantioselective hydroamination reactions, see: a) P. W. Roesky, T. E. Müller, *Angew. Chem. Int. Ed.* **2003**, *42*, 2708–2710; b) K. C. Hultzsch, *Adv. Synth. Catal.* **2005**, *347*, 367–391; c) K. C. Hultzsch, *Org. Biomol. Chem.* **2005**, *3*, 1819–1824.
[6] a) M. R. Gagné, L. Brard, V. P. Conticello, M. A. Giardello, C. L. Stern, T. J. Marks, *Organometallics* **1992**, *11*, 2003–2005; b) M. A. Giardello, V. P. Conticello, L. Brard, M. Sabat, A. L. Rheingold, A. L. Stern, T. J. Marks, *J. Am. Chem. Soc.* **1994**, *116*, 10212–10240; c) M. A. Giardello, V. P. Conticello, L. Brard, M. R. Gagné, T. J. Marks, *J. Am. Chem. Soc.* **1994**, *116*, 10241–10254.
[7] M. R. Douglass, M. Ogasawara, S. Hong, M. V. Metz, T. J. Marks, *Organometallics* **2002**, *21*, 283–292.
[8] P. N. O'Shaughnessy, P. D. Knight, C. Morton, K. M. Gillespie, P. Scott, *Chem. Commun.* **2003**, 1770–1771.
[9] P. D. Knight, I. Munslow, P. N. O'Shaughnessy, P. Scott, *Chem. Commun.* **2004**, 894–895.
[10] a) D. V. Gribkov, F. Hampel, K. C. Hultzsch, *Eur. J. Inorg. Chem.* **2004**, 4091–4101; b) D. V. Gribkov, K. C. Hultzsch, F. Hampel, *Chem. Eur. J.* **2003**, *9*, 4796–4810; c) D. V. Gribkov, K. C. Hultzsch, *Chem. Commun.* **2004**, 730–731; d) D. V. Gribkov, K. C. Hultzsch, F. Hampel, *J. Am. Chem. Soc.* **2006**, *128*, 3748–3759.
[11] J. Y. Kim, T. Livinghouse, *Org. Lett.* **2005**, *7*, 1737–1739.
[12] S. Hong, S. Tian, M. V. Metz, T. J. Marks, *J. Am. Chem. Soc.* **2003**, *125*, 14768–14783.
[13] N. Meyer, A. Zulys, P. W. Roesky, *Organometallics* **2006**, *25*, 4179–4182.
[14] a) P. N. O'Shaughnessy, P. Scott, *Tetrahedron: Asymmetry* **2003**, *14*, 1979–1983; b) P. N. O'Shaughnessy, K. M. Gillespie, P. D. Knight, I. Munslow, P. Scott, *Dalton Trans.* **2004**, 2251–2256.
[15] a) J. Collin, J. C. Daran, E. Schulz, A. Trifonov, *Chem. Commun.* **2003**, 3048–3049; b) J. Collin, J.-C. Daran, O. Jacquet, E. Schulz, A. Trifonov, *Chem. Eur. J.* **2005**, *11*, 3455–3462; c) D. Riegert, J. Collin, A. Meddour, E. Schulz, A. Trifonov, *J. Org. Chem.* **2006**, *71*, 2514–2517.
[16] a) F. G. N. Cloke, B. R. Elvidge, P. B. Hitchcock, V. M. E. Lamarche, *J. Chem. Soc., Dalton Trans.* **2002**, 2413–2414; b) A. G. Avent, F. G. N. Cloke, B. R. Elvidge, P. B. Hitchcock, *Dalton Trans.* **2004**, 1083–1096.
[17] T. I. Gountchev, T. D. Tilley, *Organometallics* **1999**, *18*, 5661–5667.
[18] C. Drost, P. B. Hitchcock, M. F. Lappert, *J. Chem. Soc., Dalton Trans.* **1996**, 3595–3601.
[19] a) M. D. Fryzuk, J. B. Love, S. J. Rettig, *J. Am. Chem. Soc.* **1997**, *119*, 9071–9072; b) M. D. Fryzuk, L. Jafarpour, F. M. Kerton, J. B. Love, B. O. Patrick, S. J. Rettig, *Organometallics* **2001**, *20*, 1387–1396.
[20] G. B. Deacon, T. Feng, C. M. Forsyth, A. Gitlits, D. Hockless, Q. Slien, B. W. Skelton, A. H. White, *J. Chem. Soc., Dalton Trans.* **2000**, 961–966.
[21] T. I. Gountchev, T. D. Tilley, *Organometallics* **1999**, *18*, 2896–2905.
[22] K. H. Den Haan, J. L. De Boer, J. H. Teuben, A. L. Speak, B. Kojic-Prodic, G. R. Hays, R. Huis, *Organometallics* **1986**, *5*, 1726–1733.
[23] W. J. Evans, J. W. Grate, K. R. Levan, I. Bloom, T. T. Petersen, R. J. Doedens, H. Zhang, J. L. Atwood, *Inorg. Chem.* **1986**, *25*, 3614–3619.
[24] Y. Yao, X. Lu, Q. Shen, K. Yu, *J. Chem. Crystallogr.* **2004**, *34*, 275–279.
[25] S. Hong, A. M. Kawaoka, T. J. Marks, *J. Am. Chem. Soc.* **2003**, *125*, 15878–15892.
[26] J. Zhao, T. J. Marks, *Organometallics* **2006**, *25*, 4763–4772.
[27] M. Shibasaki, N. Yoshikawa, *Chem. Rev.* **2002**, *102*, 2187–2209.
[28] We have checked that the mono- and dilithium salts of the (*R*)-*N*,*N*′-diisopropyl-1,1′-binaphthyl-2,2′-diamido ligand are not active catalysts for the hydroamination reactions even at higher temperatures (see ref.[4b]).
[29] S. Vyskocil, S. Jaracz, M. Smrcina, M. Sticha, V. Hanus, M. Polasek, P. Kocovsky, *J. Org. Chem.* **1998**, *63*, 7727–7737.
[30] *SIR97, a program for automatic solution of crystal structures by direct methods*: A. Altomare, M. C. Burla, M. Camalli, G. L. Cascarano, C. Giacovazzo, A. Guagliardi, A. G. G. Moliterni, G. Polidori, R. Spagn, *J. Appl. Crystallogr.* **1999**, *32*, 115.
[31] G. M. Sheldrick, *SHELXL97, a program for crystal structure refinement*, University of Göttingen, Germany, **1997**.
[32] a) H. D. Flack, *Acta Crystallogr., Sect. A* **1983**, *39*, 876–881; b) G. Bernardinelli, H. D. Flack, *Acta Crystallogr., Sect. A* **1985**, *41*, 500–511.
[33] *ORTEP3* for Windows: L. J. Farrugia, *J. Appl. Crystallogr.* **1997**, *30*, 565.

Received: September 19, 2006
Published Online: February 9, 2007

 © 2007 Wiley-VCH Verlag GmbH & Co. KGaA, Weinheim 

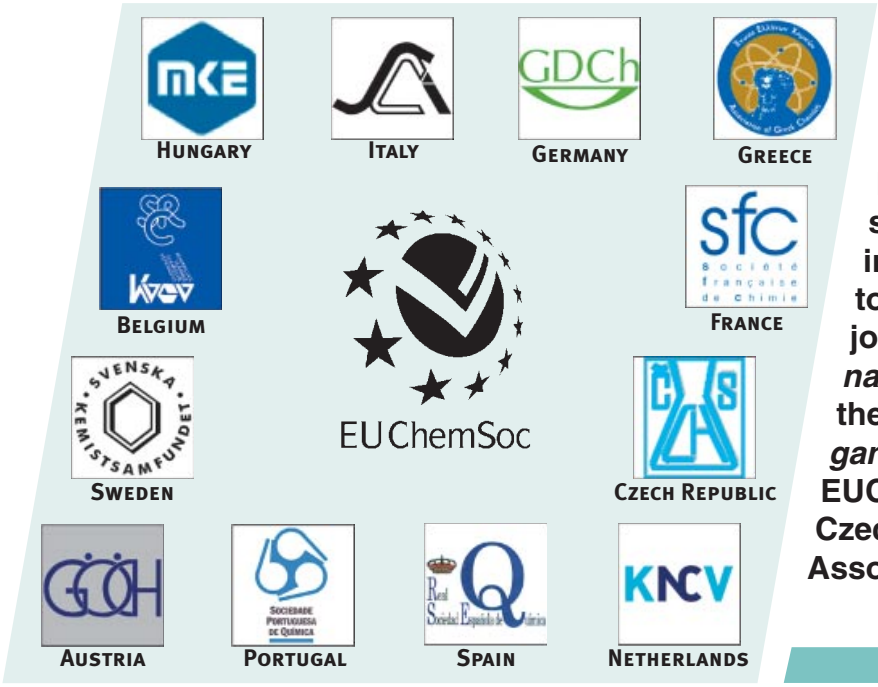


**The EUChemSoc Societies have taken the significant step into the future by merging their traditional journals, to form two leading chemistry journals, the *European Journal of Inorganic Chemistry* and the *European Journal of Organic Chemistry.* Three further EUChemSoc Societies (Austria, Czech Republic and Sweden) are Associates of the two journals.**

## COVER PICTURE

**The cover picture shows** the disruption of amido- and alkoxo-to-metal π-donation because of a filled dπ manifold, which occurs for metal centers in low oxidation states and which renders the anionic amido, alkoxo and related ligands highly reactive. The low oxidation states decrease the predilection toward metal-center reduction and, as a result, tend to promote "even-electron" chemistry over odd-electron radical chemistry that is based on net single-electron reduction of the metal. For $Ru^{II}$ and $Cu^{I}$ complexes, evidence for the enhanced reactivity of the heteroatomic ligands is derived from acid/base reactions as well as from nucleophilic additions. The combination of a Lewis acid metal center and a basic/nucleophilic heteroatomic ligand (amido, hydroxo, alkoxo, etc.) can be exploited for the activation of substrates that possess polar and nonpolar bonds, for example for metal-mediated C−H activation and for catalytic hydroamination and hydroalkoxylation of activated olefins. Details are presented in the Microreview by T. B. Gunnoe on p. 1185 ff.

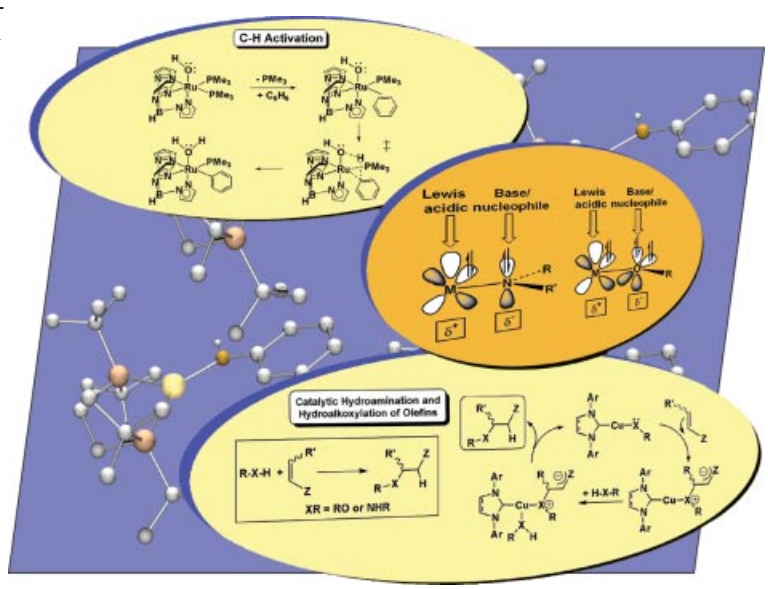


 © 2007 Wiley-VCH Verlag GmbH & Co. KGaA, Weinheim 

# CONTENTS

## MICROREVIEW

### Organometallic Chemistry

**T. B. Gunnoe* ..... 1185–1203**

Reactivity of Ruthenium(II) and Copper(I) Complexes that Possess Anionic Heteroatomic Ligands: Synthetic Exploitation of Nucleophilicity and Basicity of Amido, Hydroxo, Alkoxo, and Aryloxo Ligands for the Activation of Substrates that Possess Polar Bonds as well as Nonpolar C–H and H–H Bonds

**Keywords:** Nondative heteroatomic ligands / Ruthenium / Copper / C–H Activation

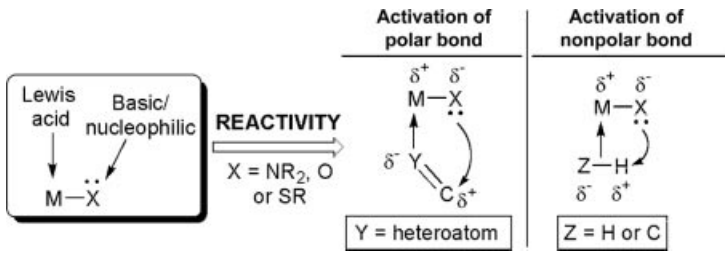


The coordination of amido, sulfido alkoxo, aryloxo, and hydroxo ligands to late transition-metal complexes in low oxidation states can disrupt ligand-to-metal π bonding. As a result, anionic and heteroatomic ligands coordinated to metals with high d-electron counts often exhibit highly basic and nucleophilic reactivity. The microreview summarizes the preparation, characterization, and reactivity of a series of Ru and Cu complexes with these and related ligands.

## SHORT COMMUNICATIONS

### Diaminocarbene Ligands

**A. Labande,* J.-C. Daran, E. Manoury, R. Poli* ..... 1205–1209**

New (1-Phosphanylferrocen-1′- and -2-yl)-methyl-Linked Diaminocarbene Ligands: Synthesis and Rhodium(I) Complexes

**Keywords:** Carbene ligands / Phosphane ligands / Ferrocenes / Rhodium

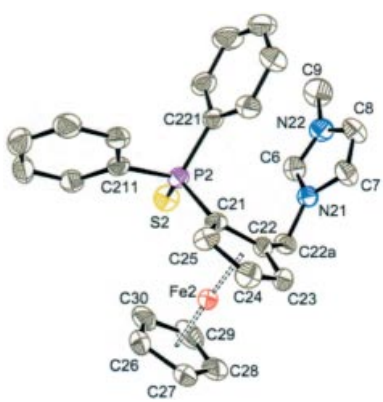


New, bifunctional (1-phosphanylferrocen-1′- and -2-yl)methyl-linked NHC ligands have been accessed by a general and simple method from the corresponding [1-(thiophosphanyl)ferrocen-1′- and -2-yl]methanols and used to prepare rhodium(I) complexes.

### NH,NR-Stabilized NHC Ligands

**N. Meier, F. E. Hahn,* T. Pape, C. Siering, S. R. Waldvogel* ..... 1210–1214**

Molecular Recognition Utilizing Complexes with NH,NR-Stabilized Carbene Ligands

**Keywords:** Carbene ligands / Supramolecular chemistry / Hydrogen bonds / Homogeneous catalysis / N-Heterocyclic carbenes

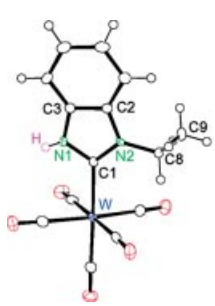


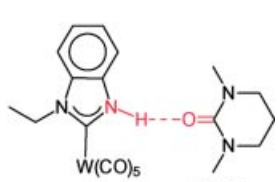


**1** DMPU

The NH group in tungsten complex **1** with an NH,NR-stabilized N-heterocyclic carbene ligand can act as a recognition unit by forming hydrogen bonds to carbonyl compounds.

 © 2007 Wiley-VCH Verlag GmbH & Co. KGaA, Weinheim 

## Hydrogen-Bond Network

A new hybrid inorganic–organic $Mo^{VI}$ polymer with a two-dimensional layer structure has been synthesized and crystallographically characterized. This complex is an efficient catalyst, with $H_2O_2$ as the oxygen-source oxidant and $NaHCO_3$ as the cocatalyst, in the epoxidation of olefinic compounds under ambient conditions.

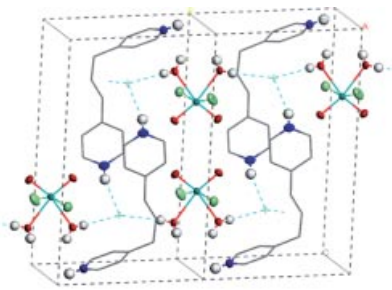

**Y. Luan, G. Wang,* R. L. Luck, M. Yang ..... 1215–1218**

A Two-Dimensional, Hydrogen-Bond-Cross-Linked Molybdenum(VI) Network Polymer with Catalytic Activity

**Keywords:** Hydrogen bonds / Crystal engineering / Hydrogen peroxide / Epoxidation / Molybdenum

## Nanotubes

Silver(I) chloride reacts with 2-mercapto-3,4,5,6-tetrahydropyrimidine ($StpmH_2$, $C_4H_8N_2S$) in DMSO with excess triethylamine to give a complex of formula $\{[Ag_4Cl_4(\mu_3\text{-}StpmH_2)_4]_n\}$ (**1**). The structure consists of octagonal $Ag_4S_4$ cores where $\mu_3$-S bonding interactions lead to an infinite nanotube assembly which exhibits quasi-aromaticity.

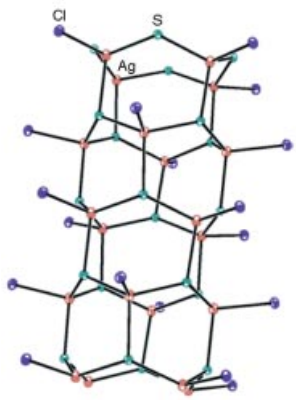


**S. Zartilas, N. Kourkoumelis, S. K. Hadjikakou,* N. Hadjiliadis,* P. Zachariadis, M. Kubicki, A. Yu. Denisov, I. S. Butler ..... 1219–1224**

A New Silver(I) Aggregate Having an Octagonal $Ag_4S_4$ Core Where $\mu_3$-S Bonding Interactions Lead to a Nanotube Assembly that Exhibits Quasiaromaticity

**Keywords:** Bioinorganic chemistry / Silver / Aromaticity / Nanotubes

## Silanedithiol

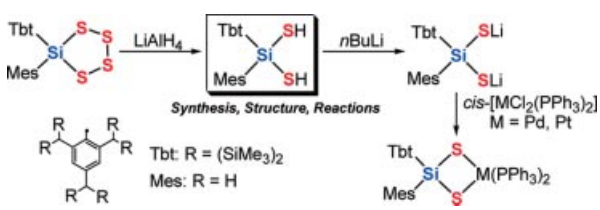


An overcrowded silanedithiol was synthesized as an air- and moisture-stable crystalline compound by the reaction of the corresponding tetrathiasilolane with $LiAlH_4$. The reaction of dilithium silanedithiolate, which was generated by the reaction of silanedithiol with *n*-butyllithium, with *cis*-$[MCl_2(PPh_3)_2]$ (M = Pd, Pt) afforded the corresponding silanedithiolato complexes quantitatively.

**T. Tanabe, N. Takeda, N. Tokitoh* ..... 1225–1228**

First Structural Characterization of Silanedithiol and Its Application toward the Synthesis of Silanedithiolato Complexes

**Keywords:** Silanedithiol / Silanedithiolato complexes / Silaneselenol / Group 10 transition metal complexes / X-ray crystallography

## Water Clusters

Adamantanoid water clusters H-bonded to bromide ions and other water molecules form a cage-like structure. Bromide-encapsulated aza cryptands reside within this cage to form a host-within-a-host-like structure. This adamantanoid water decamer is remarkably similar to that of cubic ice ($I_c$).

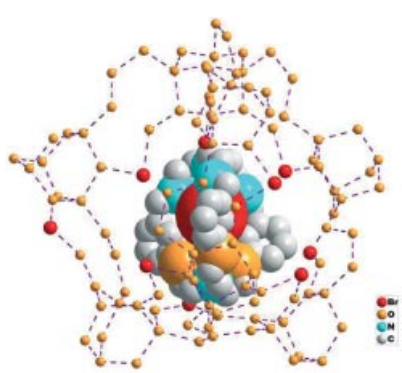

**M. C. Das, P. K. Bharadwaj* ..... 1229–1232**

Molecular Ice with Hybrid Water–Bromide Network around a Cryptand with a Bromide Ion Included in the Cavity to Form a Host-within-a-Host-Like Structure

**Keywords:** Anion binding / Cryptands / Hydrogen bonds / Water chemistry / X-ray diffraction

 © 2007 Wiley-VCH Verlag GmbH & Co. KGaA, Weinheim 

# CONTENTS

## FULL PAPERS


### Hydrogen Bonding

**F.-M. Nie, G. Leibeling, S. Demeshko, S. Dechert, F. Meyer* ..... 1233–1239**

Intra- and Intermolecular H···Cl–Ni Bonding Patterns in a Series of Highly Pre-organized Dinuclear Nickel(II) Complexes

**Keywords:** Nickel / Dimetallic complexes / Hydrogen bonds / Pyrazolate ligands / Magnetic properties

Various Cl···H–O hydrogen-bonding motifs are identified in a series of pyrazolato-based dinickel complexes, where either the H-donor (MeOH or $H_2O$) or the H-acceptor (chlorido) or both are bound to a nickel ion.

### Heterodimetallic Complexes

**Z.-H. Ni, L. Zheng, L.-F. Zhang, A.-L. Cui, W.-W. Ni, C.-C. Zhao, H.-Z. Kou* ..... 1240–1250**

Cyanido-Bridged Dimetallic Complexes Derived from Manganese(III) Schiff Bases and Pentacyanidonitrosylchromate(I): Synthesis, Crystal Structure and Magnetic Properties

**Keywords:** Cyanide ligands / Bridging ligands / Magnetic properties / Manganese / Schiff-base ligands

Four types of cyanido-bridged complexes derived from the $[Cr(CN)_5(NO)]^{3-}$ anion and $Mn^{III}$ Schiff-base cations have been synthesized with trinuclear, 1D chain or 2D layered molecular structures. Antiferromagnetic $Mn^{III}$–$Cr^{I}$ coupling has been exclusively observed in these complexes.

### Ruthenium Complexes

**S. Nag, R. J. Butcher, S. Bhattacharya* ..... 1251–1260**

*N*-(Aryl)picolinamide Complexes of Ruthenium: Usual Coordination and Strategic Cyclometalation

**Keywords:** Picolinamide ligands / Ruthenium complexes / Cyclometalation

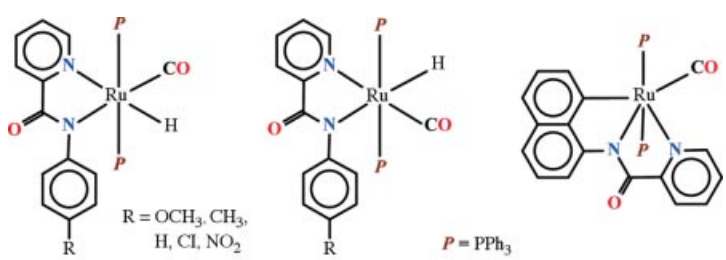


**1-R** **2-R** **3**

Reaction of $[Ru(PPh_3)_2(CO)_2Cl_2]$ with five *N*-(4-*R*-phenyl)picolinamides in the presence of a base affords two geometrical isomers (**1-R** and **2-R**) on N–H activation. A similar reaction with *N*-(naphthyl)-picolinamide affords complex **3** on additional C–H activation.

### Single-Molecule Studies

**Y.-Q. Zhang,* C.-L. Luo ..... 1261–1267**

A Theoretical Study of the Nearest Cu···Cu Antiferromagnetic Exchange Coupling Interactions in $[LaCu_6]$ and $[YCu_6]$

**Keywords:** Magnetic properties / Density functional calculations / Broken symmetry / Single-molecule studies

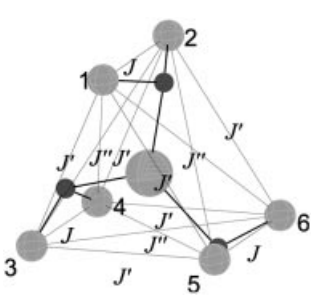


Calculation of the exchange coupling interactions between the nearest $Cu^{II}$ centers in complexes $[LaCu_6]$ and $[YCu_6]$ show that the Cu···Cu antiferromagnetic interactions increase with a decrease of the ionic radius of the central $La^{III}$ and $Y^{III}$ and the stronger antiferromagnetic interactions between the nearest $Cu^{II}$ centers in $[LaCu_6]$ than in $[YCu_6]$ are not due to the central $La^{III}$ but the structure.


 © 2007 Wiley-VCH Verlag GmbH & Co. KGaA, Weinheim 

## Modified Keggin Polyoxometalates

**J. Sha, J. Peng,* H. Liu, J. Chen, B. Dong, A. Tian, Z. Su ..... 1268–1274**

Keggin POMs Modified by Bonding to Multitrack Cu(bipy) Chains through Linearly Arrayed Terminal and Bridging Oxygen Atoms of the $M_3O_{13}$ Triad

**Keywords:** Polyoxometalates / N ligands / Copper / Organic–inorganic hybrids

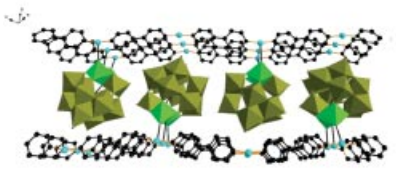

**1**

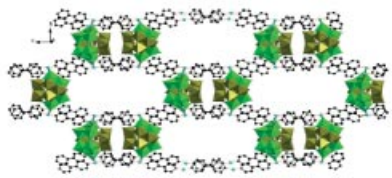

**2**

Fully oxidized Keggin $SiMo_{12}$ and $SiW_{12}$ anions as polydentate pendant ligands covalently bonded to a multitrack Cu(bipy) chain(s) through linearly arrayed terminal and bridging oxygen atoms of the $M_3O_{13}$ triad(s) are reported for the first time. Compound **1** has a tri-chain 1D "zipper" structure, and **2** a di-chain 2D net-texture structure.

## Organic–Inorganic Nanoparticles

**T. Antoun, R. Brayner, S. Al terary, F. Fiévet, M. Chehimi, A. Yassar* ..... 1275–1284**

Facile Synthesis of Oligothiophene-Capped CdS Nanoparticles

**Keywords:** Nanoparticle synthesis / Oligothiophenes / Photovoltaics / Conjugated polymers / Nanostructures

To improve the electronic communication between nanocrystal semiconductors and conjugated molecules, we have prepared CdS-bound oligothiophenes. In such a design, the two components are in intimate contact and electron transfer is not altered by the presence of insulating surfactants.

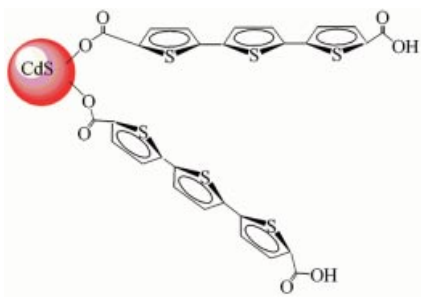


## Magneto-Structural Correlations

**G. Fernández, M. Corbella*, G. Aullón, M. A. Maestro, J. Mahía ..... 1285–1296**

New Dinuclear $Mn^{III}$ Compounds with 2-$MeC_6H_4COO$ and 2-$FC_6H_4COO$ Bridges – Effect of Terminal Monodentate Ligands ($H_2O$, $ClO_4^-$ and $NO_3^-$) on the Magnetic Properties

**Keywords:** Manganese / Magnetic properties / Ligand effects

The magnetic properties of dinuclear $Mn^{III}$ complexes with a $[Mn_2O(RCOO)_2]^{2+}$ core could be sensitive to the type and orientation of the monodentate ligand coordinated to the manganese ions.

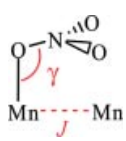


## Stannole Anions

**R. Haga, M. Saito,* M. Yoshioka ..... 1297–1306**

Synthesis and Reactions of Stannole Anions

**Keywords:** Anions / Aromaticity / Lithium / Metallacycles / Tin

Methods for the preparation of stannole anions are described: (i) the reduction of hexaphenylstannole with the proper amount of lithium, and (ii) the reaction of the stannole dianion with various halogen reagents. NMR studies on the stannole anions and their reactions are also reported.

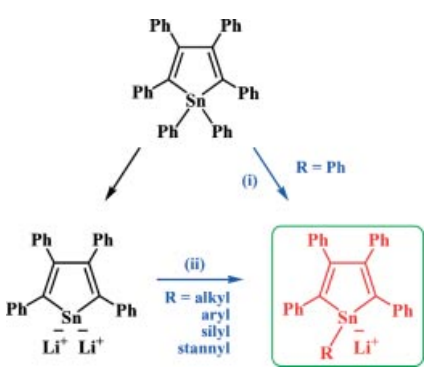


**If not otherwise indicated in the article, papers in issue 8 were published online on March 2, 2007**

 © 2007 Wiley-VCH Verlag GmbH & Co. KGaA, Weinheim 

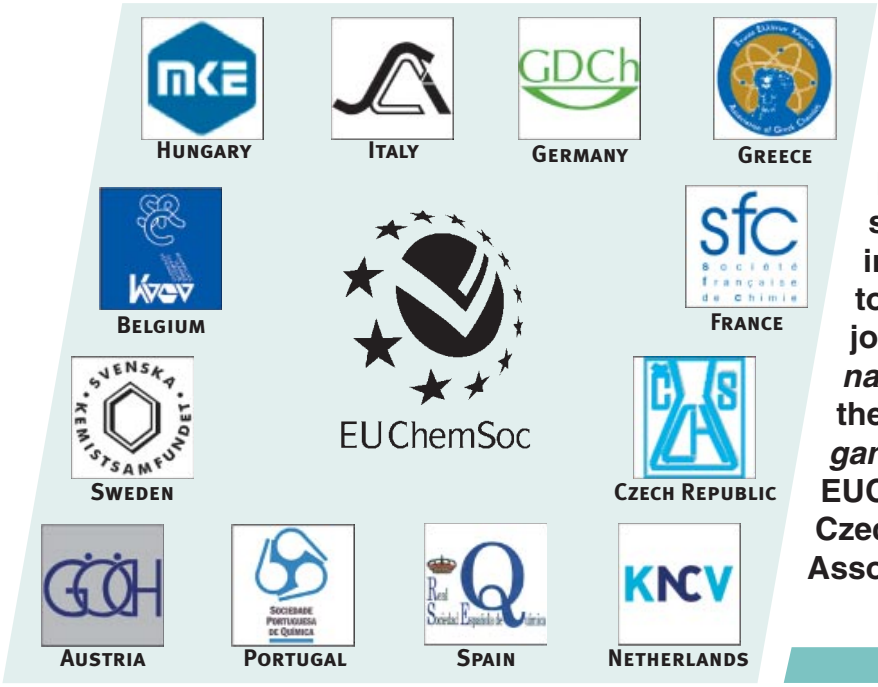


**The EUChemSoc Societies have taken the significant step into the future by merging their traditional journals, to form two leading chemistry journals, the *European Journal of Inorganic Chemistry* and the *European Journal of Organic Chemistry.* Three further EUChemSoc Societies (Austria, Czech Republic and Sweden) are Associates of the two journals.**

## COVER PICTURE

**The cover picture shows** the disruption of amido- and alkoxo-to-metal π-donation because of a filled dπ manifold, which occurs for metal centers in low oxidation states and which renders the anionic amido, alkoxo and related ligands highly reactive. The low oxidation states decrease the predilection toward metal-center reduction and, as a result, tend to promote "even-electron" chemistry over odd-electron radical chemistry that is based on net single-electron reduction of the metal. For $Ru^{II}$ and $Cu^{I}$ complexes, evidence for the enhanced reactivity of the heteroatomic ligands is derived from acid/base reactions as well as from nucleophilic additions. The combination of a Lewis acid metal center and a basic/nucleophilic heteroatomic ligand (amido, hydroxo, alkoxo, etc.) can be exploited for the activation of substrates that possess polar and nonpolar bonds, for example for metal-mediated C−H activation and for catalytic hydroamination and hydroalkoxylation of activated olefins. Details are presented in the Microreview by T. B. Gunnoe on p. 1185 ff.

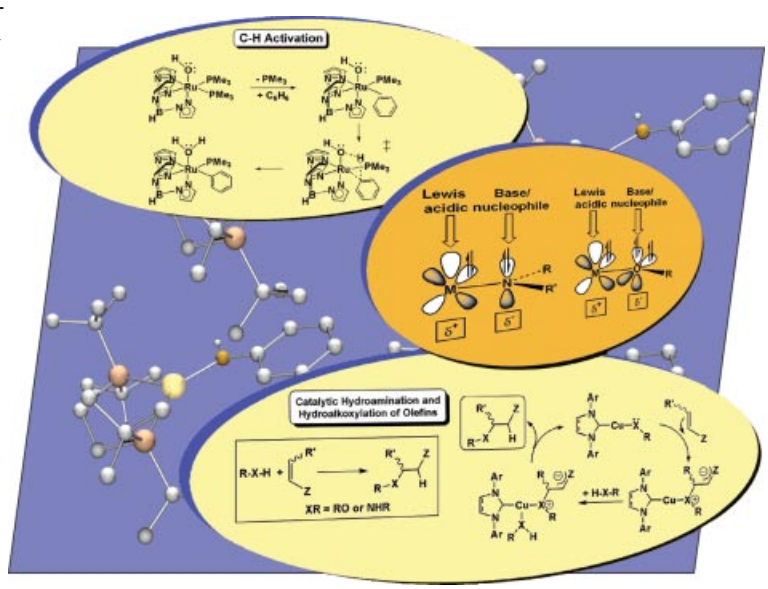


 © 2007 Wiley-VCH Verlag GmbH & Co. KGaA, Weinheim 

DOI: 10.1002/ejic.200601072

# Reactivity of Ruthenium(II) and Copper(I) Complexes that Possess Anionic Heteroatomic Ligands: Synthetic Exploitation of Nucleophilicity and Basicity of Amido, Hydroxo, Alkoxo, and Aryloxo Ligands for the Activation of Substrates that Possess Polar Bonds as well as Nonpolar C–H and H–H Bonds

**T. Brent Gunnoe*[a]**

**Keywords:** Nondative heteroatomic ligands / Ruthenium / Copper / C–H Activation

The preparation and reactivity of late transition-metal complexes in low oxidation states with nondative-heteroatomic ligands (e.g., amido, hydroxo, alkoxo, and aryloxo ligands) are described. For such complexes the disruption of ligand-to-metal π-donation because of a filled dπ manifold can enhance the nucleophilic and/or basic reactivity at the nondative-heteroatomic ligand relative to transition-metal complexes in high oxidation states. The chemistry of five- and six-coordinate Ru complexes with amido, hydroxo, methoxo, and aryloxo ligands is described including Brønsted acid/base reactions, coordination, and activation of polar substrates toward N–C bond forming reactions and metal-mediated activation of dihydrogen and C–H bonds. The impact of ancillary ligands and Ru oxidation states ($Ru^{II}$ versus $Ru^{III}$) are discussed. In addition, the preparation and reactivity of well-defined monomeric two- and three-coordinate Cu complexes with amido, alkoxo, hydroxo, and aryloxo ligands are presented including examples of reactions to probe fundamental reactivity patterns as well as catalytic addition of N–H and O–H bonds across C=C bonds of olefins.
(© Wiley-VCH Verlag GmbH & Co. KGaA, 69451 Weinheim, Germany, 2007)

## Introduction

Nondative-heteroatomic fragments are a common class of ligand that formally bear anionic, dianionic, or trianionic charge. Such ligands based on nitrogen, oxygen, or sulfur, including amido, alk-/aryl-/hydr-oxo, alkyl-/aryl-/hydro-sulfido, oxide, sulfide, imido, and nitrido, have been utilized as nonreactive ancillary supports for reactive transition-metal systems as well as for *active participation* in "group transfer" and other catalytic processes. Prominent examples of the latter include olefin epoxidation and aziridination, olefin dihydroxylation, and polymerization sequences.[1–9] As part of our efforts to understand and develop the reactivity of late transition-metal complexes in low oxidation states with formally anionic heteroatomic ligands, our group has been studying the synthesis and reactivity of $Ru^{II}$ and $Cu^{I}$ systems. Herein, the scope of complexes accessed and their reactivity are reviewed with a focus on the development of new stoichiometric and catalytic reactions that are based on the nucleophilic/basic character of the nondative ligands.

Bonding between a transition metal and an anionic heteroatomic ligand results from a metal–ligand σ bond and one ligand–metal π-interaction. Thus, when the metal center possesses one or more empty orbitals of π-symmetry metal–ligand multiple bonds result.[10] On the basis of metal–X (X = OR, $NR_2$ or SR ligand) bond polarity it is anticipated that nondative-heteroatomic ligands should exhibit inherent nucleophilicity and basicity; however, ligand-to-metal π-donation can serve to delocalize electron density from the heteroatomic ligand to the metal center. As a result, the electron density centered on the heteroat-

[a] Department of Chemistry,
North Carolina State University, Raleigh, NC 27695-8204, USA
Fax: +1-919-515-8909
E-mail: brent_gunnoe@ncsu.edu

*T. Brent Gunnoe was born in Charleston, West Virginia, USA in 1971. He received his B. A. in chemistry from West Virginia University in 1993 where he worked on early transition-metal aryloxo chemistry with Dr. Jeffrey Petersen. Under the supervision of Dr. Joseph L. Templeton, he received a PhD in 1997 from the University of North Carolina at Chapel Hill with research efforts focused on chiral group VI organometallic complexes. After working with Dr. W. Dean Harman as a postdoctoral researcher at the University of Virginia on the development of metal-mediated dearomatization sequences based on chiral $Re^{I}$ systems, he began as Assistant Professor at North Carolina State University in 1999. His current title is Associate Professor of Chemistry with research interests that include organometallic and inorganic chemistry especially applied to homogeneous catalysis.*

 © 2007 Wiley-VCH Verlag GmbH & Co. KGaA, Weinheim 

omic ligand can be attenuated and, in some cases, the heteroatomic ligand is rendered relatively inert. Schrock-type carbene complexes supported by alkoxo and imido ligands represent classic examples of unreactive anionic heteroatomic ligands. For these complexes, the formally anionic and dianionic heteroatomic ligands are reaction inert relative to the carbene moiety.[11] High oxidation states for metal centers tend to facilitate the ligand-to-metal π-bonding and, hence, serve to decrease the impact of M–X bond polarity and ligand-centered electron density and, consequently, to decrease nucleophilic and/or basic reactivity at the heteroatomic ligand. The lack of reaction of $TpOs^{IV}(Cl)_2NHPh$ with HCl (a thermodynamic effect) serves as a striking example that potentially illustrates the effect on reactivity of reduced charge density at the anionic heteroatomic ligand (due to increased ligand-to-metal π-donation).[12]

The majority of anionic heteroatomic ligands of early or middle transition elements are coordinated to relatively high oxidation state systems. In contrast, late(r) transition metals, which are more predisposed toward low oxidation states, often have high d-electron counts that disrupt ligand-to-metal π-bonding (Scheme 1). Until relatively recently, examples of anionic heteroatomic ligands coordinated to late transition-metal systems in low oxidation states were scant compared with high oxidation state complexes of the early and middle transition elements.[13–15] Recent efforts have substantially increased the number of late transition-metal complexes and revealed a wealth of interesting reactivity.[15–22] Careful studies of thermodynamic trends and reactivity indicate that the bond dissociation energies (BDEs) between heteroatom-based ligands and late transition-metal centers can be substantial, and recent bonding models suggest that these M–L bonds are relatively strong; however, the disruption of metal-to-ligand π-bonding can afford enhanced reactivity by decreasing electron delocalization from the ligand to the metal.[17]

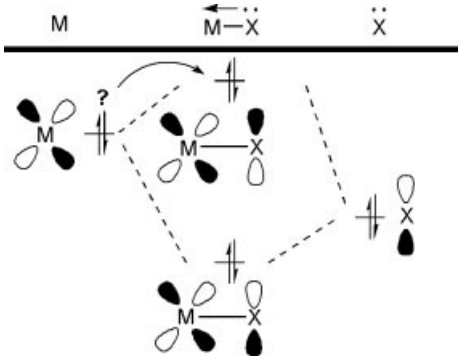


Scheme 1. M–X (M = transition metal, X = $NR_2$, OR, SR, etc.) multiple bonding occurs if dπ orbital(s) is vacant. Filled dπ manifold results in no net π-bond.

Our group has been interested in understanding and exploiting the reactivity of late transition-metal systems with highly nucleophilic/basic heteroatom-based ligands including amido and alk-/aryl-/hydroxo ligands coordinated to $Ru^{II}$ and $Cu^{I}$.[23–38] From the perspective of catalyst development, the positioning of a nucleophilic/basic heteroatomic ligand adjacent to a Lewis acidic metal center provides opportunities for the coordination and activation of external organic substrates toward controlled bond-breaking and bond-forming reactions (Scheme 2). From a fundamental perspective, we have been studying the impact of metal identity, ancillary ligand identity, and the heteroatomic ligand identity and substituents on reactivity. Herein, we summarize results over the past five years and comment on future prospects.

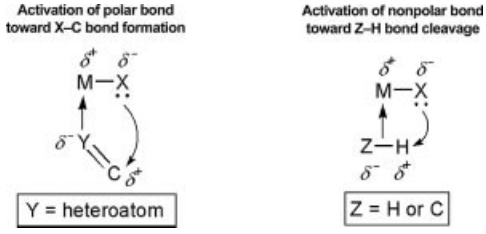


Scheme 2. Potential use of Lewis acidic metal centers with the basic anionic ligand "X" (X = $NR_2$, OR, SR, etc.) to activate substrates with polar and nonpolar bonds.

## Octahedral $TpRu^{II}$ Systems

### Preparation and Characterization

We have used the monoanionic hydridotris(pyrazolyl)borate (Tp) ligand[39] as a foundation to build octahedral Ru complexes with anionic heteroatom-based ligands.[24,26,31–36] Our strategy has been to utilize the template $[TpRu(L)(L')X]^{n+}$ (L, L′ = neutral, two-electron donor ligands, X = anionic heteroatomic ligand; $n$ = 0 or 1) to access systems with variable ancillary ligands (L/L′), heteroatomic ligands (X), and oxidation states. Two strategies have been used for syntheses: (1) coordination of amine or alcohols followed by deprotonation and (2) metathesis of the anionic heteroatomic moiety with Ru–halide or Ru–triflate linkages (Scheme 3).

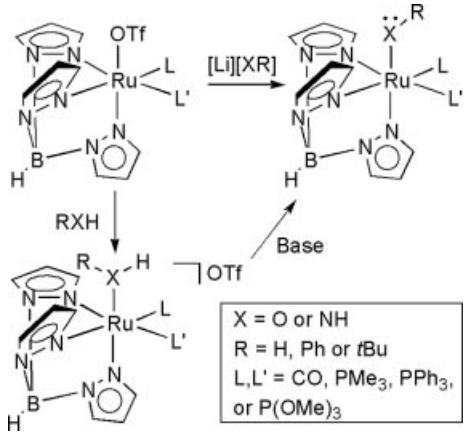


Scheme 3. Two general routes used for the preparation of TpRu(L)(L′)NHR and TpRu(L)(L′)OR systems.

For the $Ru^{II}$ oxidation state, the hydroxo and parent amido complexes exhibit upfield chemical shifts between –1 and –4 ppm for the N–H/O–H resonances ($^1$H NMR spec-

 © 2007 Wiley-VCH Verlag GmbH & Co. KGaA, Weinheim 

troscopy), which is indicative of electron-rich nondative-heteroatomic ligands (a hallmark of the disruption of ligand-to-metal π-donation for amido and hydroxo ligands). Upfield chemical shifts have been observed for related $Ru^{II}$ systems.[26,31,34] For the anilido complexes [TpRu(L)(L′)-NHPh], variable-temperature $^1H$ NMR spectroscopy provides a convenient means to determine the Gibbs free energy of activation for rotation around the Ru–$N_{amido}$ and the $C_{ipso}$–$N_{amido}$ bonds (Scheme 4).[33] Although the data set is limited there is an inverse correlation between the magnitudes of these two rotational barriers, a result that is consistent with anticipated Ru–N multiple-bond character in response to metal-electron density. That is, the presence of strongly electron-donating and poorly π-acidic ancillary L/L′ reduces anilido-to-Ru multiple bonding (via three-center, four-electron interactions), which most likely increases the extent of anilido-to-phenyl π* back-bonding and hence increases the $N_{amido}$–$C_{ipso}$ multiple-bond character. Using this rationale, an inverse correlation between Ru–$N_{amido}$ and $C_{ipso}$–$N_{amido}$ bond lengths is anticipated. In fact, comparing structural data for the series of octahedral $Ru^{II}$–anilido complexes [TpRu(CO)($PPh_3$)NHPh],[35] [TpRu{P-$(OMe)_3$}$_2$NHPh],[33] [($\eta^6$-$C_6Me_6$)Ru(Ph)($PMe_3$)NHPh],[40] and [$(PMe_3)_4$Ru(H)NHPh][41] reveals such a trend (Figure 1). In addition, the equilibrium constants for a series of reactions of [TpRu($PMe_3$)$_2$NHPh] with *p*-substituted anilines ($NH_2Ar$) to form [TpRu($PMe_3$)$_2$(NHAr)] (Ar = *p*-substituted phenyl) and aniline afforded a Hammett plot (using $\sigma_p^-$) with $\rho = 4.1$, which is consistent with the delocalization

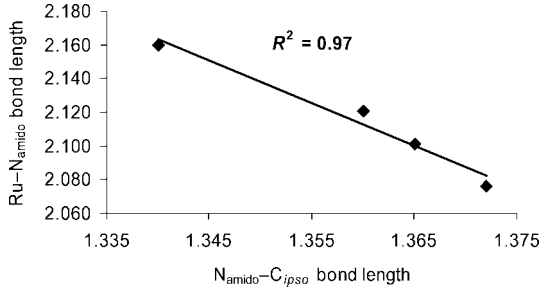


Figure 1. Plot of Ru–$N_{amido}$ and $N_{amido}$–$C_{ipso}$ bond lengths (Å), which illustrates an inverse relationship for the series of Ru–anilido complexes [TpRu(CO)($PPh_3$)NHPh],[35] [TpRu{P($OMe)_3$}$_2$-NHPh],[33] [($\eta^6$-$C_6Me_6$)Ru(Ph)($PMe_3$)NHPh],[40] and [$(PMe_3)_4$Ru-(H)NHPh].[41]

of electron density from the amido ligand to the aryl substituent.[31] This $\rho$ value is similar to the value of 3.4 obtained for Cp*Ni($PEt_3$)(NHPh)/$NH_2Ar$ reactions.[42] In contrast, a study of equilibria for four-coordinate $Re^{III}$–aryloxo complexes revealed a correlation with Hammett $\sigma$ parameters with a much smaller $\rho$ value of 0.7.[43]

## Acid–Base Reactions

The coordination of anionic heteroatomic ligands to late transition-metal complexes in low oxidation states can impart substantial basicity/nucleophilicity to the ligand, a feature that has been attributed to polar metal–ligand bonds and the disruption of ligand-to-metal π-donation. For example, Bergman et al. have demonstrated that *trans*-[$(DMPE)_2$Ru(H)$NH_2$] {DMPE = 1,2-bis(dimethylphosphanyl)ethane} forms an acid–base equilibrium upon reaction with triphenylmethane (p$K_a \approx 31.5$ in THF) to form *trans*-[$(DMPE)_2$Ru(H)$NH_3$][$Ph_3C$],[44] and related octahedral $Ru^{II}$ and $Fe^{II}$ parent amido complexes exhibit analogous reactivity.[45,46] Similarly, [TpRu(L)(L′)NHR] (R = Ph, H or *t*Bu) complexes react with weakly acidic C–H bonds. For example, the anilido complexes [TpRu(L)(L′)NHPh] form acid–base equilibria with malononitrile (p$K_a \approx 24$ in THF),[47] which is the least acidic substrate that we have found to react at room temperature with the anilido complexes (Scheme 5).[33] For [TpRu(L)(L′)NHR] (R = H or *t*Bu), the combination with phenylacetylene (p$K_a \approx 28.7$ in DMSO)[48] results in the formation of ion pairs [TpRu(L)(L′)$NH_2$R][$PhC_2$] at room temperature (Scheme 5).[31] Thus, the formal substitution of H or *t*Bu for phenyl as the amido substituent likely increases basicity by several orders of magnitude. For [TpRu($PMe_3$)$_2$-($NH_2t$Bu)][$PhC_2$], heating to 80 °C cleanly forms free $t$BuNH$_2$ and [TpRu($PMe_3$)$_2$(C≡CPh)].

Although no reaction is observed at room temperature, heating solutions of [TpRu(L)(L′)NHPh] and phenylacetylene to 80 °C forms free aniline and [TpRu(L)(L′)(C≡CPh)]; however, detailed mechanistic studies have revealed that these transformations do not likely proceed through the formation of ion pairs [TpRu(L)(L′)($NH_2$Ph)][$PhC_2$] (as do the parent amido and *t*Bu-amido systems, see above).[31] Rather, small and undetectable quantities of [TpRu(L)(L′)-

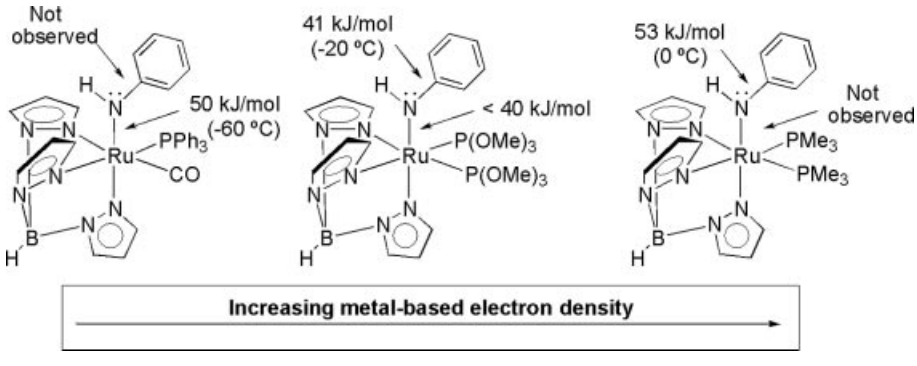


Scheme 4. Impact of ancillary ligands on Ru–N and $N_{amido}$–$C_{ipso}$ bond rotational barriers.

 © 2007 Wiley-VCH Verlag GmbH & Co. KGaA, Weinheim 

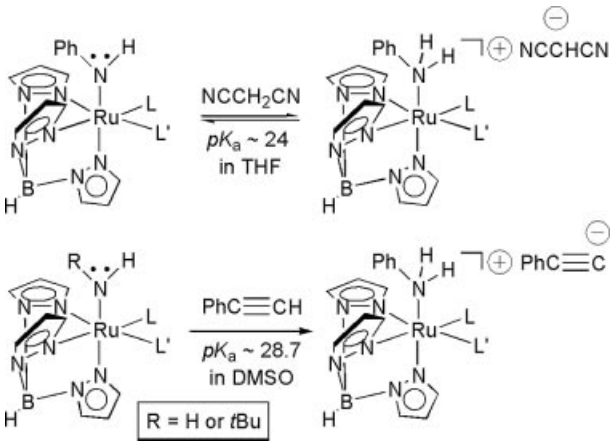


Scheme 5. Acid/base equilibria observed for [TpRu(L)(L′)NHR] (R = H, *t*Bu or Ph) systems upon treatment with malononitrile or phenylacetylene.

OTf] likely catalyze the reaction as shown in Scheme 6. For the $PMe_3$ system, late in the reaction the putative vinylidene intermediate is trapped by free aniline to form the Fischer carbene complex [$Tp(PMe_3)_2Ru{=}C(CH_2Ph)(NHPh)$], a reaction that is confirmed by independent conversion of [$Tp(PMe_3)_2Ru{=}C{=}C(H)Ph$] and aniline to [$Tp(PMe_3)_2Ru{=}C(CH_2Ph)(NHPh)$].

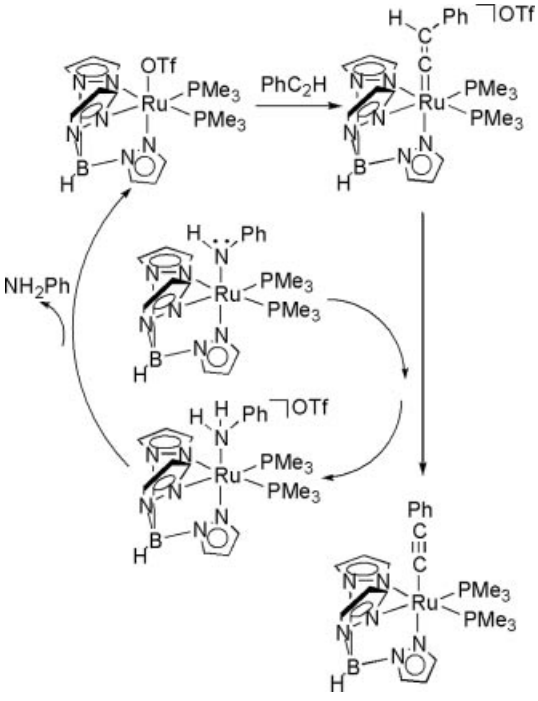


Scheme 6. Proposed pathway for the conversion of [$TpRu(PMe_3)_2$-NHPh] and phenylacetylene to [$TpRu(PMe_3)_2C{\equiv}CPh$], which is catalyzed by [$TpRu(PMe_3)_2OTf$].

At 80 °C, [$TpRu(PMe_3)_2NHR$] (R = H or *t*Bu) complexes react with 1,4-cyclohexadiene to ultimately form benzene, free amine, and [$TpRu(PMe_3)_2H$] with a 1:1 molar ratio of benzene and Ru–hydride.[31] Preceding the formation of benzene and Ru–hydride, the isomerization of 1,4-cyclohexadiene to 1,3-hexadiene is observed ($k_{obs}$ = $2.0 \times 10^{-5}$ $s^{-1}$ at 80 °C). The addition of free $PMe_3$ does not influence the rate of isomerization of the 1,4-cyclohexadiene. We have proposed that these reactions occur by the acid–base pathway shown in Scheme 7. Although hydrogen atom abstraction pathways are also possible and have been observed for late transition-metal complexes with heteroatomic ligands in which the metal centers are in relatively high oxidation states,[49–57] the failure of [$TpRu(PMe_3)_2$-NHPh], which is much less basic than the parent or *t*Bu-amido complexes, to react with 1,4-cyclohexadiene is consistent with the proposed acid–base pathway. Furthermore, initial hydrogen atom abstraction would form a cyclohexadienyl radical and [$TpRu^{I}(PMe_3)_2NH_2R$], which is a 19-electron $Ru^{I}$ complex that is likely to be a high-energy species. For [$TpRu(PMe_3)_2NHR$] systems, the Ru(II/I) potential is negative of –2.0 V (vs. NHE), which supports the suggestion that access to [$TpRu^{I}(PMe_3)_2NH_2R$] is most likely a high-energy process. In comparison, an octahedral $Fe^{III}$–methoxo complex that converts 1,4-cyclohexadiene to benzene by a proposed hydrogen atom abstraction pathway exhibits an Fe(III/II) potential of 0.73 V.[52,53]

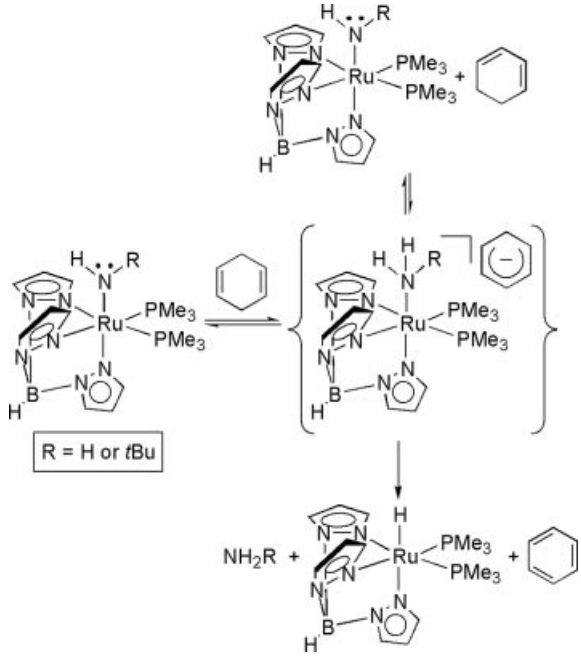


Scheme 7. Proposed pathway for isomerization of 1,4-cyclohexadiene to 1,3-cyclohexadiene by [$TpRu(PMe_3)_2NHR$] and ultimate conversion to benzene, [$TpRu(PMe_3)_2H$], and amine.

We have recently extended our studies of octahedral $Ru^{II}$ complexes to [$TpRu(PMe_3)_2OH$].[24,26,36] Similar to the amido complexes, the $Ru^{II}$–hydroxo complex is basic. For example, reactions with MeOH, EtOH, or *t*BuOH result in the formation of species whose NMR spectra are consistent with the ion pairs [$TpRu(PMe_3)_2OH_2$][OR] [R = Me, Et, or *t*Bu; Equation (1)].[36] In contrast to the parent amido complexes, [$TpRu(PMe_3)_2OH$] does not react with phenylacetylene at room temperature; however, at an elevated temperature (80 °C) [$TpRu(PMe_3)_2OH$] and phenylacetylene are converted to water and [$TpRu(PMe_3)_2(C{\equiv}CPh)$]. Sim-

 © 2007 Wiley-VCH Verlag GmbH & Co. KGaA, Weinheim 

ilar to the amido complexes, at 85 °C [TpRu(PMe$_3$)$_2$OH] and 1,4-cyclohexadiene are converted to benzene, water, and [TpRu(PMe$_3$)$_2$H] with a 1:1 molar ratio of benzene to Ru–H [Equation (2)]. Consistent with an acid–base pathway (see Scheme 7) and the reduced basicity of the hydroxo complex relative to the parent and *t*Bu-amido complexes, the reaction of [TpRu(PMe$_3$)$_2$OH] and 1,4-cyclohexadiene is only 33% complete after 9 days at 85 °C. In comparison, [TpRu(PMe$_3$)$_2$NH$_2$] and 1,4-cyclohexadiene produce benzene and [TpRu(PMe$_3$)$_2$H] in about 50% conversion after 3 days at 75 °C.

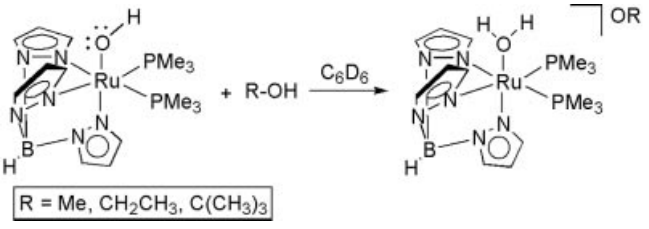


(1)

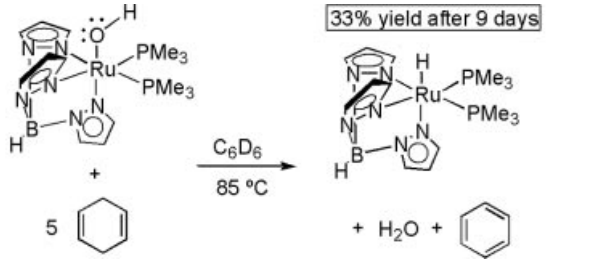


(2)

Single-electron oxidation of [TpRu(PMe$_3$)$_2$OH] yields the paramagnetic and NMR spectroscopic silent $Ru^{III}$ system [TpRu(PMe$_3$)$_2$OH]$^+$.[36] For the cationic $Ru^{III}$–hydroxo complex, Evans NMR spectroscopic experiments reveal $\mu_{eff}$ = 1.78 $\mu_B$ (room temperature), which is consistent with a single unpaired electron and close to the spin-only value of 1.73 $\mu_B$. Similar to the $Ru^{II}$–hydroxo complex [TpRu(PMe$_3$)$_2$-OH], the $Ru^{III}$ system [TpRu(PMe$_3$)$_2$OH]$^+$ converts 1,4-cyclohexadiene to benzene; however, experimental evidence points to a pathway that involves net hydrogen atom abstraction rather than even-electron acid–base chemistry (Scheme 8). In the absence of an external radical trap, [TpRu(PMe$_3$)$_2$OH]$^+$ most likely reacts with 1,4-cyclohexadiene to produce [TpRu(PMe$_3$)$_2$(OH$_2$)]$^+$ and a cyclohexadienyl radical, the latter is probably consumed rapidly by a second equivalent [TpRu(PMe$_3$)$_2$OH]$^+$ to form benzene and a second equivalent of [TpRu(PMe$_3$)$_2$(OH$_2$)]$^+$. The observed stoichiometry of products (2:1 molar ratio of [TpRu(PMe$_3$)$_2$(OH$_2$)]$^+$ and benzene) is consistent with the proposed mechanism. When the radical trap TEMPO (TEMPO = 2,2,6,6-tetramethylpiperidinyloxy) is added the cyclohexadienyl radical is trapped by TEMPO to give benzene and hence a 1:1 ratio of [TpRu(PMe$_3$)$_2$(OH$_2$)]$^+$ and benzene in the products. [TpRu(PMe$_3$)$_2$OH]$^+$ reacts with substrates that possess C–H bonds with bond dissociation energies up to ca. 335 kJ/mol. Using the approximate p$K_a$ of [TpRu(PMe$_3$)$_2$(OH$_2$)]$^+$ and the Ru(III/II) potential of [TpRu(PMe$_3$)$_2$OH] a thermodynamic cycle has been used to estimate the O–H BDE of [TpRu(PMe$_3$)$_2$OH$_2$]$^+$ to be between 343 and 356 kJ/mol, which is consistent with the experimental reactivity of the [TpRu$^{III}$(PMe$_3$)$_2$OH]$^+$ complex. Furthermore, DFT calculations of the model [(Tab)Ru(PH$_3$)$_2$(OH$_2$)]$^+$ [Tab = tris(azo)borate] reveal that the O–H BDE is 351 kJ/mol.

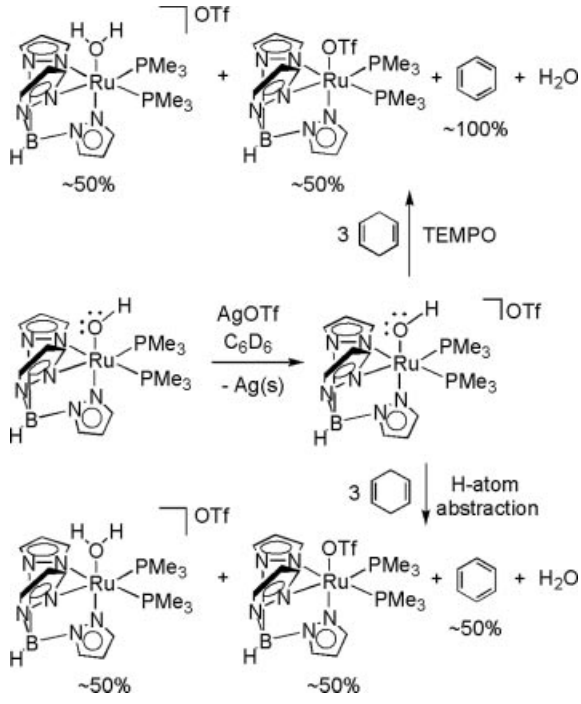


Scheme 8. The conversion of 1,4-cyclohexadiene to benzene by [TpRu(PMe$_3$)$_2$OH]$^+$ most likely proceeds by hydrogen-atom abstraction.

From a synthetic perspective, our interest in anionic heteroatomic ligands coordinated to late transition metals is derived predominantly from the positioning of a basic/nucleophilic moiety adjacent to a Lewis acidic metal center (Scheme 2). Hence, opportunities exist to coordinate substrates to the Lewis acidic metal and to activate them toward reactions with the heteroatomic ligands. For example, metal-mediated C–H activation by σ-bond metathesis pathways involve the conversion of M–R and R′–H to M–R′ and R–H via a transition state in which net $H^+$ is transferred to a basic alkyl or aryl ligand "R" (Scheme 9). We have considered that related reactions of late transition metals with nondative-heteroatomic ligands might provide facile and controlled C–H activation/functionalization. In this case, the net C–H activation might be best viewed as an intramolecular proton transfer to the basic heteroatomic ligand. In related examples, the net 1,2-additions of dihydrogen across Ru amido ligands have been implicated in enantioselective ketone hydrogenation as well as Rh and Ir catalysts.[58–62] Morris et al. have demonstrated that the reaction of a $Ru^{II}$ amido complex with dihydrogen yields a complex

 © 2007 Wiley-VCH Verlag GmbH & Co. KGaA, Weinheim 

in which the H–H bond is intermediate between protic-hydridic and dihydrogen,[63] dihydrogen adds across an $Ir^{III}$–amido bond,[64] and the chelating amido ligand of $\{Ru(Cl)(PPh_3)[N(SiMe_2CH_2PPh_2)_2]\}$ deprotonates dihydrogen to yield $\{Ru(Cl)(H)(PPh_3)[NH(SiMe_2CH_2PPh_2)_2]\}$.[65] In addition, early transition-metal imido complexes have been demonstrated to activate C–H bonds for 1,2-addition across the M = NR moiety to yield amido and alkyl or aryl ligands (Scheme 9).[66–74] Studies have demonstrated that key factors in the imido-based C–H activation include coordination of the C–H bond to the metal center and the polar nature of the metal–imido bond.[75–77] We have been pursuing the utilization of $Ru^{II}$ systems for the activation of nonpolar bonds such as dihydrogen and carbon–hydrogen bonds.

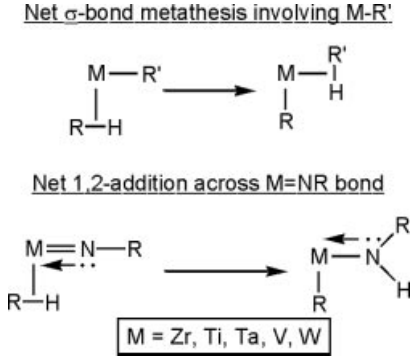


Scheme 9. Net 1,2-addition of C–H bonds across early transition-metal imido fragments has been observed.

Several strategies exist for oxygen or nitrogen functionalization of C–H bonds via metal-mediated activation, and the net 1,2-addition of C–H bonds across metal heteroatom bonds is a potentially viable step in catalytic sequences. For example, Scheme 10 depicts two possible catalytic cycles for C–H functionalization involving the 1,2-addition of C–H bonds across M–X bonds (X = amido, imido, oxide, alkoxo, etc.). Route A illustrates C–H functionalization with three key steps: (1) 1,2-addition of a C–H bond across a metal–oxide or metal–imido bond, (2) O–C or N–C reductive elimination, and (3) formal oxidation of the metal to reform the oxide or imido complex. Although the 1,2-addition of C–H bonds across M–X bonds has been demonstrated for early transition-metal–imido complexes (see above),[66–77]

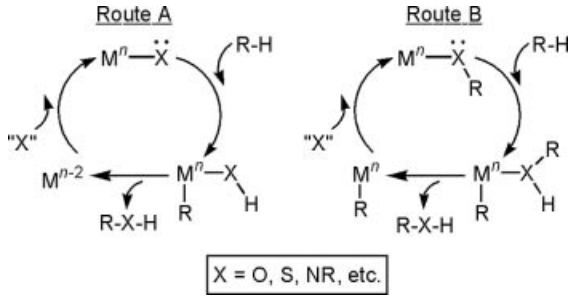


Scheme 10. Two possible routes to incorporate the net 1,2-addition of C–H bonds across transition-metal–heteroatom bonds (e.g., imido, oxide, amido, alkoxo, etc. ligands) into catalytic cycles.

the product forming reductive elimination from electropositive early transition metals is likely to be substantially unfavorable. In contrast, N–C and O–C reductive elimination reactions have been successfully incorporated into catalytic cycles involving late transition-metal systems (e.g., catalytic arylamine or aryl ether preparation).[78–82] Thus, *catalytic cycles* by Route A are potentially more viable with late transition-metal systems; however, the 1,2-addition of C–H bonds across late transition-metal–oxide or –imido bonds remains, to the best of our knowledge, unknown.

Route B (Scheme 10) illustrates an alternative catalytic cycle with three key steps: (1) the 1,2-addition of a C–H bond occurs across a metal–amido or metal–alkoxo (or aryloxo) bond, (2) dissociation of the alcohol or amine, and (3) net oxygen atom or nitrene insertion into the newly formed M–R or M–Ar bond.[83] To the best of our knowledge, prior to our work and efforts by Periana et al., evidence for the 1,2-addition of C–H bonds across the bonds of late transition metals and amido, alkoxo, and related ligands was unknown.[24,26,84] Macgregor et al. have suggested a related pathway for a C–H cyclometalation by Pd–acetate and Ir complexes.[85,86] Addition of a C–H bond across a Pt–Cl bond has been proposed as a possibility in the Shilov reaction.[87] Establishing the viability of these potential catalytic cycles requires an understanding of the metal-mediated C–H activation by late transition-metal amido, alkoxo, and related systems.

In addition to the C–H activation step, oxo or nitrogen functionalization of the M–R or M–Ar bond is a substantial challenge to the development of catalytic cycles shown in Route B. For example, insertions of metal–oxo ligands into metal–alkyl (or aryl) bonds are extremely rare, especially under nonphotolytic conditions.[88,89] However, Periana et al. have recently reported kinetically facile conversions of a $Re^{VII}$–methyl ligand and external oxidants to a Re–OMe linkage, and they have proposed that the key to the relatively low activation barriers is a mechanism that does not involve a rhenium–oxo ligand but rather resembles the classic organic Baeyer–Villiger reaction.[83] *Thus, both of the reaction steps for catalytic oxy functionalization of C–H bonds by Route B in* Scheme 10 *have been observed to be kinetically accessible under reasonably mild reaction conditions using late transition-metal systems.* With a better understanding of both reactions, it might be possible to merge the two steps with a single catalyst.

$[TpRu(PMe_3)_2OH]$ and $[TpRu(PMe_3)_2NHPh]$ provide kinetic access to aromatic C–H activation sequences that involve the net 1,2-addition of C–H(D) bonds across the Ru–OH and Ru–NHPh bonds.[24,26] For example, heating these systems in $C_6D_6$ results in H/D exchange between the deuterated benzene and the hydroxo and anilido ligands, which has been observed by both $^1H$ and $^2H$ NMR spectroscopy. In addition to the incorporation of deuterium at the heteroatomic ligand, highly regioselective H/D exchange is observed at the Tp 4-position (Scheme 11). On the basis of several experimental results including detailed kinetic studies and complementary computational studies,[24] the mechanism in Scheme 12 has been proposed. Initial dissoci-

 © 2007 Wiley-VCH Verlag GmbH & Co. KGaA, Weinheim 

ation of $PMe_3$ provides a pathway to coordinate and activate the aromatic substrate (benzene in Scheme 12). Activation of the aromatic C–H(D) bond imparts acidic character, which results in the transfer of the "protic" hydrogen to the basic hydroxo or anilido site (intramolecular transfer) or transfer to the most basic pyrazolyl position (the 4-position, intermolecular transfer). The proposed mechanism suggests that the C–H(D) activations are thermally disfavored, and consistent with this notion heating $[TpRu(PMe_3)_2Ph]$ and aniline in $C_6D_6$ initially results in the conversion to benzene and $[TpRu(PMe_3)_2NHPh]$. In closely related work, Periana et al. have directly observed the conversion of an octahedral $Ir^{III}$–methoxo complex, which is isoelectronic to the $[TpRu(PMe_3)_2X]$ systems, and benzene to the corresponding $Ir^{III}$–phenyl and methanol.[84]

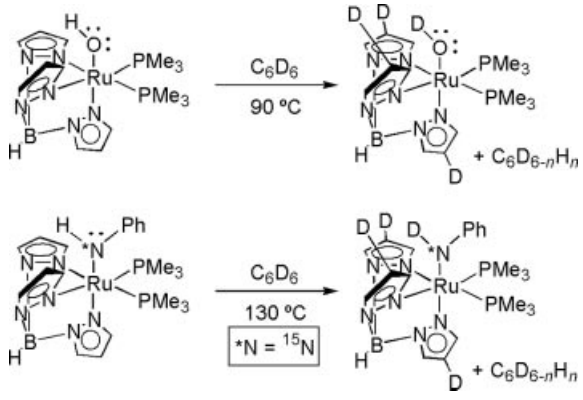


Scheme 11. Observed H/D exchange from heating $[TpRu(PMe_3)_2X]$ (X = OH or NHPh) in $C_6D_6$ (N* = isotopically labeled $^{15}N$).

DFT calculations performed by Cundari et al. using the Tp model "Tab" [Tab = tris(azo)borate] and $PH_3$ reveal the energetics for the conversion of $[(Tab)Ru(PH_3)_2OH]$ and benzene to $[(Tab)Ru(PH_3)_2Ph]$ and $H_2O$ (Scheme 13). Consistent with the experimental evidence suggesting that the 1,2-additions of the benzene C–H(D) bonds are thermally disfavored, the conversion of $[(Tab)Ru(PH_3)_2OH]$ and benzene to $[(Tab)Ru(PH_3)(OH_2)Ph]$ and free $PH_3$ is calculated to be endergonic by 77 kJ/mol, and conversion to $[(Tab)Ru(PH_3)_2Ph]$ and free $H_2O$ is calculated to be endergonic by 38 kJ/mol relative to starting materials. Similar to calculations for C–H activation by isoelectronic [TpRu(L)R] (R = alkyl) systems,[90,91] the calculated pathway for benzene C–H activation by $[(Tab)Ru(PH_3)OH]$ does not involve oxidative addition but rather more closely resembles a σ-bond metathesis reaction that is typically observed with $d^0$ metal systems (i.e., the C–H and O–H bonds are simultaneously broken and formed). The intramolecular C–H activations with Ru–X (X = OH or NHPh) are perhaps best considered as intramolecular deprotonations (see below).

While examples of C–H activation by late transition-metal complexes that involve the overall conversion of M–R + R′H to M–R′ and RH or oxidative addition of C–H bonds are relatively common,[90–110] related examples involving M–X + R–H to M–R + X–H (X = amido, alkoxo, etc.) are rare. Thus, an important fundamental aspect of the latter transformations is the relative predilection toward C–H activation for systems that possess nondative-heteroatomic ligands. *That is, what features of the metal center and ligand "X" decrease the activation barrier for the C–H activation?* Part of our efforts with late transition-metal nondative-heteroatomic complexes is directed toward elucidating such features. For example, *our preliminary results and calculations suggest that the net 1,2-addition of C–H bonds across M–X (X = anionic heteroatomic ligand) may be more facile than related reactions involving M–R bonds, which may be explained by considering the C–H activation as an intramolecular proton transfer that is facilitated by the lone pair on the hydroxo and related ligands* (Scheme 14). For example, Scheme 15 depicts benzene C–H activation by [TpRu(PMe$_3$)X] (X = OH, NHPh, or Me) fragments. The activated benzene C–H bond can either produce a net transfer of $H^+$ to the pyrazolyl ring of another Ru system ($k_{inter}$ in Scheme 15) or the intramolecular transfer of $H^+$ to X ($k_{intra}$) in Scheme 15. For X = OH and NHPh, $k_{intra}$ is more rapid than $k_{inter}$; however, for X = Me, $k_{inter}$ is more rapid that $k_{intra}$, ***results which are consistent with the presence of a lone pair on ligand X facilitating the intramolecular transfer of a proton from the activated benzene C–H(D) bond***. The

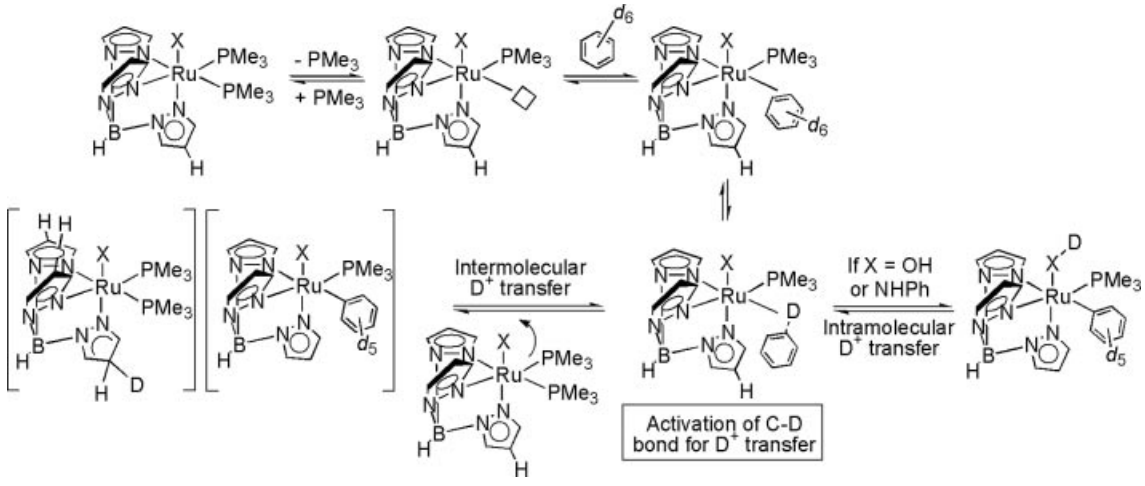


Scheme 12. Proposed mechanism for H/D exchange with $[TpRu(PMe_3)_2X]$ (X = OH or NHPh) and deuterated arene solvents.

 © 2007 Wiley-VCH Verlag GmbH & Co. KGaA, Weinheim 

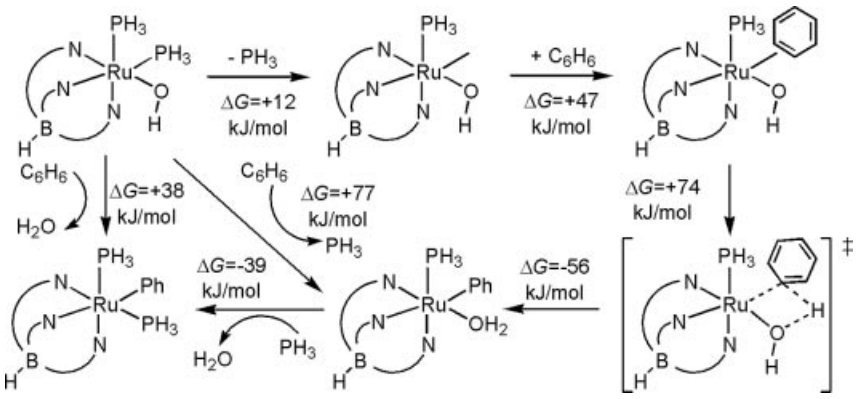


Scheme 13. Calculated energetics for benzene C–H activation using a model complex [(Tab)Ru($PH_3$)$_2$OH].

$k_{inter}$ for X = Me is an estimate based on an approximate half-life acquired in an NMR tube reaction of [TpRu($PMe_3$)$_2$Me] in $C_6D_6$ to produce [TpRu($PMe_3$)$_2$(Ph-$d_5$)] and $CH_3D$ at 130 °C.

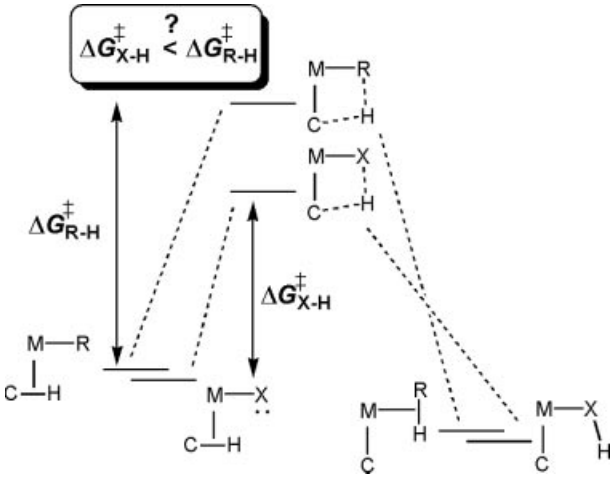


Scheme 14. For late transition-metal systems in low oxidation states the net 1,2-addition of C–H bonds across M–X (X = anionic heteroatomic ligand such as hydroxo, amido, etc.) may possess inherently lower activation barriers than analogous reactions of M–R (R = alkyl or aryl) bonds.

Clearly, more work is needed to substantiate (or disprove) this possibility as well as to understand the influence of the metal oxidation state, metal identity, identity of the nondative-heteroatomic ligand, identity of substituents on the nondative ligand, and the donating ability of the ancillary ligands. We are currently studying such details both experimentally and computationally. However, these preliminary experimental and computational results suggest that 1,2-additions of C–H bonds across M–X (X = anionic heteroatomic ligand) bonds with late transition metals in low oxidation states might be viable reactions for catalytic C–H functionalization.

## Five- and Six-Coordinate (PCP)Ru$^{II}$ Systems

### Preparation and Characterization of (PCP)Ru$^{II}$ Systems

In order to access coordinatively unsaturated Ru$^{II}$ amido complexes we employed the sterically bulky PCP ligand 2,6-($CH_2P$-$t$Bu$_2$)$_2$C$_6$H$_3$, which is strongly donating and coordinates in a meridonal fashion.[111] The addition of ammonia to the previously reported complex [(PCP)Ru(CO)Cl] results in reversible coordination of the amine to form [(PCP)Ru(CO)($NH_3$)Cl], and reactions of the Ru$^{II}$–amine complex with strong bases produce the parent amido complex [(PCP)Ru(CO)$NH_2$] (Scheme 16).[29] In contrast to the octahedral 18-electron [TpRu(L)(L′)$NH_2$] parent amido complexes (see above), the resonance arising from the amido protons appears downfield at $\delta$ = 4.36 ppm. The

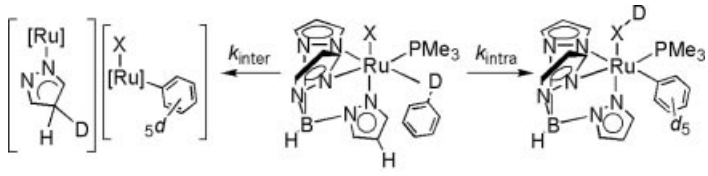


| X | $k_{intra}$ | $k_{inter}$ | $k_{intra}/k_{inter}$ |
|---|---|---|---|
| OH[a] | $2.4 \times 10^{-4}$[b] | $5.2 \times 10^{-6}$ | 46 |
| NHPh[c] | $1.4 \times 10^{-5}$ | $5.6 \times 10^{-6}$ | 2.5 |
| Me[c] | $1.1 \times 10^{-6}$ | $1.1 \times 10^{-5}$ | 0.1 |

Scheme 15. Comparison of rates of inter- versus intramolecular transfer of the proton ($D^+$) from the activated benzene C–D bond for a series of complexes [TpRu($PMe_3$)($C_6D_6$)X] (X = OH, NHPh or Me) {[a] Data at 90 °C, [b] calculated at 90 °C from the value acquired at 80 °C (assuming constant $\Delta G^{\ddagger}$), [c] Data at 130 °C}.

 © 2007 Wiley-VCH Verlag GmbH & Co. KGaA, Weinheim 

downfield chemical shift most likely reflects amido-to-Ru π-donation as a result of the metal's coordinative and electronic unsaturation.

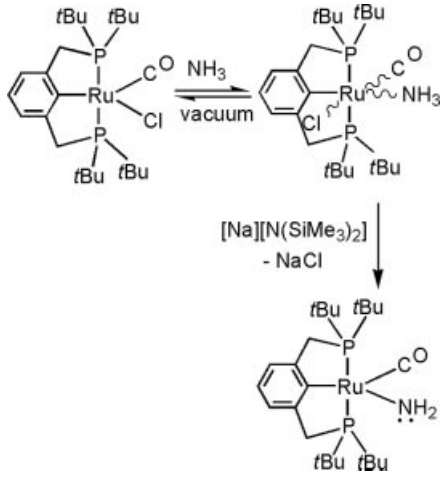


Scheme 16. Preparation of five-coordinate [(PCP)Ru(CO)$NH_2$].

The anilido complex [(PCP)Ru(CO)NHPh] has been prepared via transformation of [(PCP)Ru(CO)Cl] and TMSOTf to [(PCP)Ru(CO)OTf] followed by reaction with [Li][NHPh].[27,28] The addition of $PMe_3$ to [(PCP)Ru(CO)-NHPh] allows the isolation of the octahedral complex [(PCP)Ru(CO)($PMe_3$)NHPh] (Scheme 17). Variable-temperature $^1H$ and $^{31}P$ NMR spectroscopy of [(PCP)Ru(C-O)($PMe_3$)NHPh] reveals three fluxional processes including

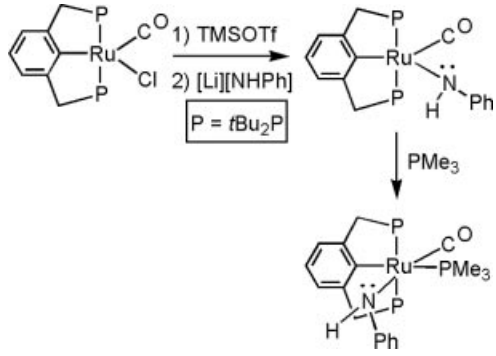


Scheme 17. Preparation of [(PCP)Ru(CO)NHPh] and [(PCP)Ru(C-O)($PMe_3$)NHPh].

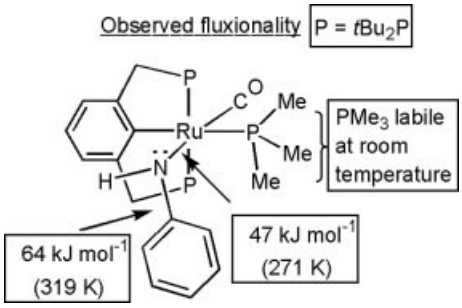


Scheme 18. Fluxional processes observed for [(PCP)Ru(CO)-($PMe_3$)NHPh] using variable-temperature NMR spectroscopy.

facile dissociation of $PMe_3$ and hindered rotation about the Ru–$N_{anilido}$ ($\Delta G^{\ddagger}$ = 47 kJ/mol at 271 K) and $N_{anilido}$–$C_{ipso}$ ($\Delta G^{\ddagger}$ = 64 kJ/mol at 319 K) bonds (Scheme 18).

### Reactivity of (PCP)$Ru^{II}$ Systems

The (PCP)$Ru^{II}$ amido complexes undergo reactions similar to the Tp$Ru^{II}$ amido complexes, but also afford access to transformations not observed with the Tp systems. For example, similar to the TpRu parent amido complexes, [(PCP)Ru(CO)$NH_2$] reacts with phenylacetylene to produce free ammonia and [(PCP)Ru(CO)(C≡CPh)]; however, in contrast to the Tp systems, the putative intermediate(s) [(PCP)Ru(CO)$NH_3$][$PhC_2$] or [(PCP)Ru(CO)($NH_3$)-(C≡CPh)] are not observed (even at –78 °C) as they apparently undergo rapid conversion to the five-coordinate acetylide complex [(PCP)Ru(CO)(C≡CPh)] (Scheme 19).

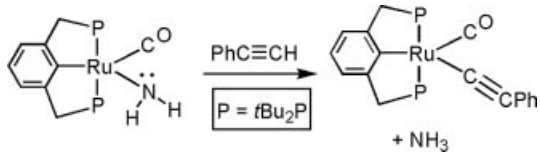


Scheme 19. Reaction of [(PCP)Ru(CO)$NH_2$] and phenylacetylene to produce [(PCP)Ru(CO)C≡CPh] and free ammonia.

The failure of the TpRu parent amido complexes to react with dihydrogen is potentially attributable to the lack of an open coordination site to bind and activate the dihydrogen. Consistent with this notion, the five-coordinate complex [(PCP)Ru(CO)$NH_2$] rapidly reacts with dihydrogen at room temperature to produce [(PCP)Ru(CO)H], and mechanistic studies suggest the pathway displayed in Scheme 20.[29] In related chemistry, Morris et al. demonstrated that the reaction of a $Ru^{II}$ amido complex with dihydrogen yields a complex in which the H–H bond is intermediate between protic-hydridic and dihydrogen bonding.[63] Fryzuk et al. have reported the 1,2-addition across a Ru–amido bond in which the amido is part of a chelated PNP ligand.[65] Rauchfuss has recently reported the addition of dihydrogen across an $Ir^{III}$–amido bond.[64] Also, the 1,2-addition of dihydrogen across Ru–amido linkages has been implicated for asymmetric hydrogenation reactions.[58,59] The conversion of [(PCP)Ru(CO)$NH_2$] and dihydrogen to [(PCP)Ru(CO)H] and ammonia suggests that nonpolar bonds can be activated with late transition metals in low oxidation states that possess anionic heteroatomic ligands.

Despite the facile activation of dihydrogen by [(PCP)-Ru(CO)$NH_2$], this system does not mediate the 1,2-addition of C–H bonds of benzene or methane across the Ru–$NH_2$ bond. Rather, intramolecular C–H activation of a *t*Bu group of the PCP ligand kinetically competes with intermolecular C–H activation (Scheme 21). Fryzuk et al. have recently reported a related intramolecular cyclometalation of a triphenylphosphane ligand that involves the conversion of an amido moiety to amine coordinated to $Ru^{II}$.[112] The intramolecular C–H activation occurs for [(PCP)Ru(CO)X] (X = $NH_2$ or Me) with the rate of reaction approximately

 © 2007 Wiley-VCH Verlag GmbH & Co. KGaA, Weinheim 

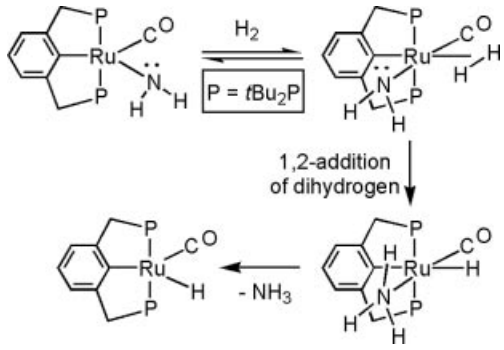


Scheme 20. Proposed pathway for the conversion of [(PCP)Ru(CO)$NH_2$] and dihydrogen to free ammonia and [(PCP)Ru(CO)H].

five times faster for the methyl complex at 50 °C. Eyring plots for both complexes over a temperature range of 30 °C revealed identical $\Delta H^{\ddagger}$ values of 75(4) kJ/mol with a $\Delta S^{\ddagger}$ value of –23(4) eu for [(PCP)Ru(CO)$NH_2$] and –18(4) eu for [(PCP)Ru(CO)Me]. Thus, the difference in the reaction rate for intramolecular 1,2-addition of C–H bonds across $Ru^{II}$–X (X = $NH_2$ or Me) bonds for these systems is predominantly due to a more ordered transition state for X = $NH_2$ than X = Me. Interestingly, the comparative rates of intramolecular C–H activation for the PCP systems with X = $NH_2$ or Me are in contrast to the more rapid 1,2-addition of benzene C–D bonds by [TpRu($PMe_3$)$_2$OH] versus [TpRu($PMe_3$)$_2$Me] (see above).

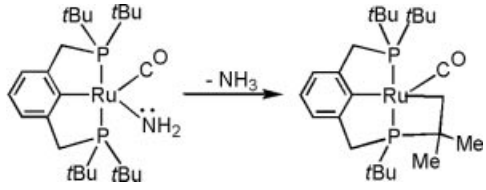


Scheme 21. Intramolecular C–H activation via 1,2-addition of the C–H bond across the Ru–$NH_2$ bond.

Consistent with experimental observations, DFT calculations {B3LYP/SBK(d)} by Cundari et al. suggest that the conversion of [(PCP′)Ru(CO)$NH_2$] (PCP′ = model PCP ligand with *t*Bu groups replaced with hydrogen) and dihydrogen to [(PCP′)Ru(CO)($NH_3$)H] is exothermic ($\Delta H$ = –71 kJ/mol) and exergonic ($\Delta G$ = –39 kJ/mol; Scheme 22). In contrast, the 1,2-addition of a C–H bond of methane to [(PCP′)Ru(CO)$NH_2$] to form [(PCP′)Ru(CO)($NH_3$)Me] is calculated to be both endothermic ($\Delta H$ = +17 kJ/mol) and endergonic ($\Delta G$ = +59 kJ/mol). While the calculated endergonic nature of the methane conversion is not entirely unexpected (due to consumption of gaseous methane), the endothermic nature is perhaps more difficult to rationalize. For example, the enthalpic change from the cleavage of a C–H bond of methane in combination with Ru–$C_{Me}$ and N–H bond formation is calculated to be ca. 134 kJ/mol; however, calculations also reveal that the conversion of the Ru–$NH_2$ moiety to the dative Ru←$NH_3$ bond comes at the expense of approximately 167 kJ/mol (Scheme 22)! Thus, in addition to intramolecular competition with the *t*Bu groups, the calculations reveal that the desired intermolecular C–H activation is thermally disfavored, and these results are consistent with both calculations and experimental observations for [TpRu$L_2$X] (X = amido or hydroxo) systems (see above). These results suggest that *direct observation* of the 1,2-addition of C–H bonds across the bonds of late transition-metal–heteroatomic ligands requires a more favorable change in M–X BDE. Interestingly, Periana et al. have reported that benzene C–H activation by an $Ir^{III}$–methoxo complex, which is isoelectronic to our $Ru^{II}$ systems, to form methanol and an Ir–phenyl complex is thermally favored.[84]

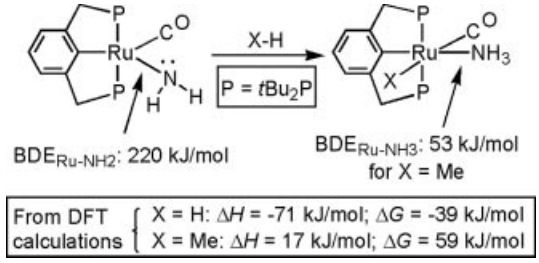


Scheme 22. Calculations for 1,2-addition of H–H and C–H (methane) across the Ru–$NH_2$ bond of [(PCP)Ru(CO)$NH_2$].

In addition to reactivity with nonpolar H–H and C–H bonds the combination of a Lewis acidic metal center and nucleophilic amido ligand of [(PCP)Ru(CO)NHPh] can be utilized to coordinate and activate polar bonds.[27,28] These transformations are of potential relevance to transition-metal-catalyzed polymerization of heterofunctionalized monomers such as carbodiimides, carbon dioxide, lactams, lactones, lactides, isocyanates, epoxides, and aziridines,[6,8,9,113–124] catalytic hydration of nitriles,[125] catalytic transamidation and transesterification,[126–135] and related transformations.

[(PCP)Ru(CO)($PMe_3$)NHPh] reacts with nitriles to form the amidinate complexes. Detailed kinetic studies for the reaction with NCMe are consistent with the rate law from the mechanism shown in Scheme 23, which involves dissociation of $PMe_3$, coordination of acetonitrile, and intramolecular C–N bond formation. For reactions with 10 equiv. of

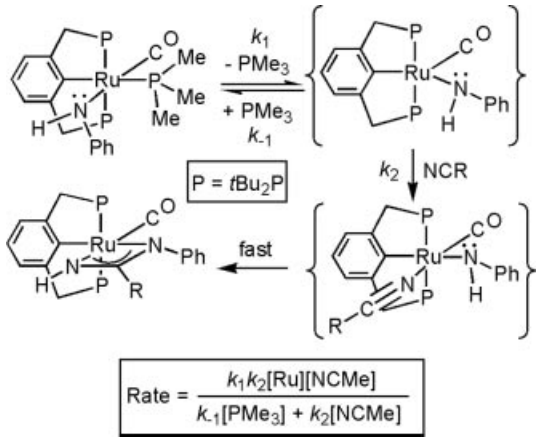


Scheme 23. Proposed pathway for the conversion of [(PCP)Ru(CO)($PMe_3$)NHPh] and nitriles to amidinate complexes, and the corresponding rate law.

 © 2007 Wiley-VCH Verlag GmbH & Co. KGaA, Weinheim 

acetonitrile and 10 to 25 equiv. of $PMe_3$, the rate of conversion of complex **1** and acetonitrile to the amidinate complex **2** is inverse first order in concentration of $PMe_3$, which is consistent with the term in the denominator "$k_{-1}$[$PMe_3$]" dominating the term "$k_2$[NCMe]" *under the specific conditions of these experiments* with $k_{obs}$ under pseudo-first-order conditions being equal to $k_1k_2$[NCMe]/$k_{-1}$[$PMe_3$]. A plot of $k_{obs}$ versus the concentration of NCMe for reactions with 10 equiv. of $PMe_3$ and between 10 and 50 equiv. of NCMe reveals a first-order dependence on the concentration of NCMe at low concentrations of NCMe while saturation kinetics are apparent at higher concentrations. Thus, in agreement with the observation of an inverse dependence of reaction rate on the concentration of $PMe_3$ at lower concentrations of NCMe, the term "$k_{-1}$[$PMe_3$]" is greater than "$k_2$[NCMe]" with the pseudo-first-order rate constant equal to $k_1k_2$[NCMe]/$k_2$[$PMe_3$]. At elevated concentrations of NCMe the term "$k_2$[NCMe]" becomes greater than "$k_{-1}$[$PMe_3$]" with $k_{obs}$ independent of the concentration of NCMe. Monitoring the rate of disappearance of [(PCP)Ru(CO)($PMe_3$)NHPh] in the presence of 100 equiv. of acetonitrile with 10, 15, or 20 equiv. of $PMe_3$ reveals that $k_{obs}$ is independent of the $PMe_3$ concentration and is equal to $1.29(7) \times 10^{-5}$ $s^{-1}$. For reactions that are pseudo-first order in concentration of [(PCP)Ru(CO)($PMe_3$)NHPh], rearrangement of the rate law shown in Scheme 23 indicates that a plot of $1/k_{obs}$ versus [$PMe_3$]/[NCMe] should be linear with the slope equal to $k_{-1}/k_1k_2$ and the $y$ intercept equal to $1/k_1$ [Equation (3)]. From the plot shown in Figure 2, $k_1$ was estimated to be $1.8 \times 10^{-5}$ $s^{-1}$, and using the value of $k_1$ and the slope from the plot in Figure 2, the ratio of $k_{-1}/k_2$ was calculated to be 3; however, small deviations in the slope can result in substantial deviations for the $y$ intercept.

$$1/k_{obs} = \frac{k_{-1}[PMe_3]}{k_1k_2[NCR]} + \frac{1}{k_1} \quad (3)$$

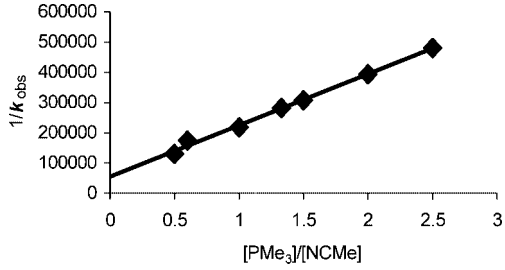


Figure 2. Plot of $1/k_{obs}$ versus [$PMe_3$]/[NCMe] for the conversion of [(PCP)Ru(CO)($PMe_3$)NHPh] and NCMe to the amidinate complex ($R^2$ = 0.99).

[(PCP)Ru(CO)($PMe_3$)NHPh] also reacts with carboxamides, isocyanates, carbodiimides, benzaldehyde, and water (Scheme 24). The reactions with carbodiimides, isocyanates, and benzaldehyde follow similar pathways to the reaction of [(PCP)Ru(CO)($PMe_3$)NHPh] with nitriles to form $\kappa^2$-ligands, which most likely result from intramolecular C–N bond formation. Thus, coordination of polar substrates with Lewis basic sites by the $Ru^{II}$ fragment activates the

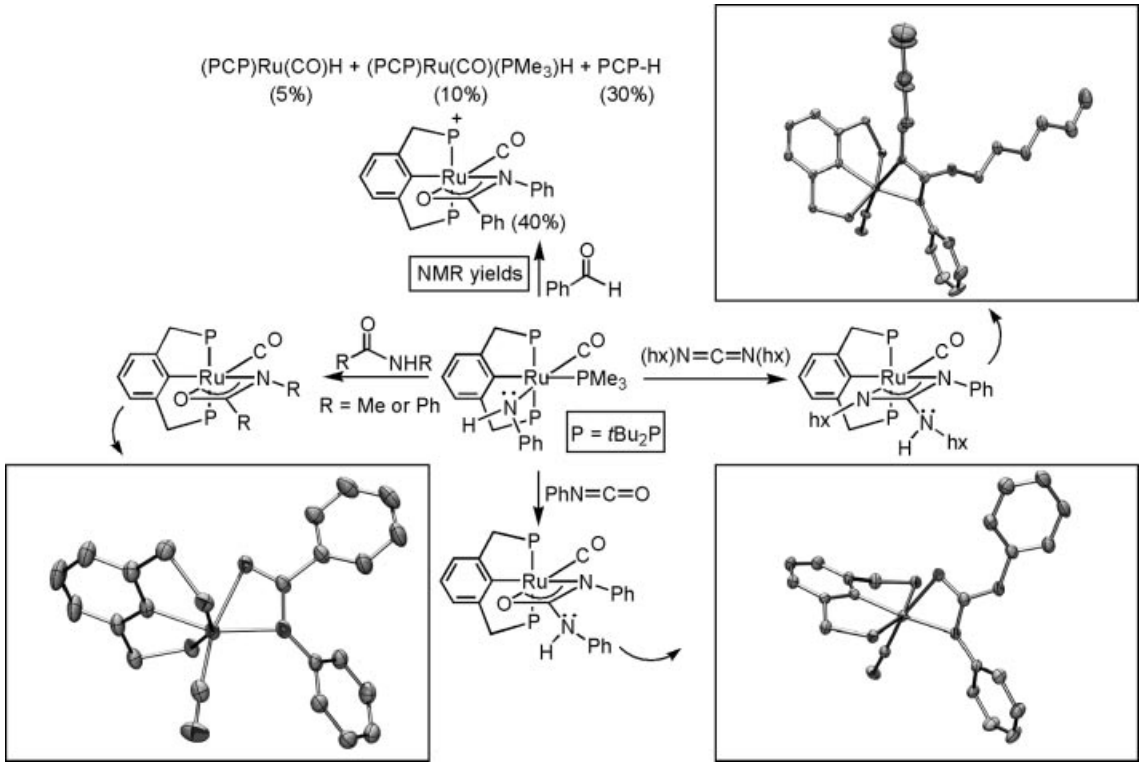


Scheme 24. Reactions of [(PCP)Ru(CO)($PMe_3$)NHPh] including ORTEPs (30% probability) of three products (with hydrogen atoms and *t*Bu groups omitted).

 © 2007 Wiley-VCH Verlag GmbH & Co. KGaA, Weinheim 

unsaturated molecules toward intramolecular nucleophilic addition by the amido ligand. For benzaldehyde, the amidate complex is isolated in only 40% yield because of side reactions that produce [(PCP)Ru(CO)H] (5%), [(PCP)-Ru(CO)($PMe_3$)H] (10%), and free PCPH (30%).

## Two- and Three-Coordinate $Cu^I$ Systems

### Preparation and Characterization of $Cu^I$ Systems

Copper has played an important role in the development of metal-mediated organic synthesis. However, despite the prevalence of anionic heteroatomic ligands with early and middle transition metals, increasing evidence for the highly reactive nature of late transition-metal complexes with anionic heteroatomic ligands and the possibility that Cu–imido complexes are intermediates in Cu-catalyzed olefin aziridination,[3,136–140] the isolation and full characterization of *monomeric* Cu amido complexes was, to the best of our knowledge, unknown prior to our efforts. Multinuclear systems with bridging-amido ligands have been reported,[141–146] including an example of a nonbridging amido that is part of a chelated ligand.[147] In addition, reports of monomeric Cu–alkoxo and Cu–aryloxo complexes are relatively scant.[148–154] Thus, we sought ligand platforms and synthetic routes that would allow the isolation of well-defined *monomeric* $Cu^I$ systems with amido, alkoxo, and related ligands. Sterically bulky ancillary ligands have been incorporated in an effort to inhibit the formation of dimeric or multinuclear Cu systems bridged by the heteroatomic ligands.

Chloride/amido metathesis between [(dtbpe)Cu(μ-Cl)]$_2$ {dtbpe = 1,2-bis(di-*tert*-butylphosphanyl)ethane} and [Li][NHPh] allows the isolation of monomeric [(dtbpe)-Cu(NHPh)] (**1**) (Scheme 25).[30] The bulky dtbpe most likely prevents the dimerization of **1** via bridging-anilido ligands, and the strongly donating nature probably prevents reduction of $Cu^I$ to $Cu^0$ by the lithium amide salt (as is observed for $Cu^I$ systems with more weakly donating aryl–phosphane ligands). The Cu–$N_{amido}$ bond length {1.890(6) Å} of **1** is shorter than that of the corresponding aniline complex [(dtbpe)Cu($NH_2$Ph)][OTf] by ca. 0.12 Å. Recently, Johnson et al. have reported a multinuclear $Cu_9$ system that possesses Cu–amido linkages.[147] The three-coordinate $d^{10}$ $Cu^I$ complex **1** has a vacant p orbital of π-symmetry with respect to the Cu–$N_{amido}$ bond, and the amido ligand is oriented for overlap with the Cu-based p orbital. For example, the P–Cu–N–$C_{ipso}$ torsion angle is about 13°, while a torsion angle of 0° would provide an orientation optimized for π-overlap (see Figure 4 below). This amido orientation is approximately perpendicular to that observed by Hillhouse and Mindiola for the closely related $d^9$ $Ni^I$ complex (dtbpe)Ni{NH(2,6-$CHMe_2$)$C_6H_3$}.[155] The phenyl substituent of **1** is also oriented for π-overlap with the amido lone pair (see Figure 4 below).

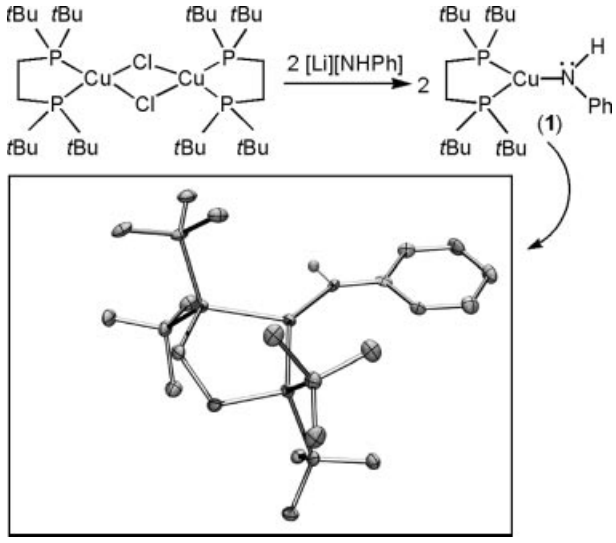


Scheme 25. Preparation of the monomeric $Cu^I$–anilido complex [(dtbpe)Cu(NHPh)] (**1**) and its ORTEP diagram (30%).

Similar to the preparation of Cu–methyl complexes by Sadighi et al,[156] we have employed NHC (NHC = N-heterocyclic carbene) ligands to stabilize monomeric two-coordinate $Cu^I$ systems with anionic heteroatomic ligands.[23,25,38] The NHC ligand has been varied between IMes {1,3-bis-(2,4,6-trimethylphenyl)imidazol-2-ylidene}, IPr {1,3-bis(2,6-diisopropylphenyl)imidazol-2-ylidene}, and SIPr {1,3-bis(2,6-diisopropylphenyl)imidazolin-2-ylidene}. Complexes with amido, alkoxo, and aryloxo ligands can be prepared upon reaction of amines or alcohols with [(NHC)-Cu(R)] (R = Me or Et) complexes or via metathesis using [(NHC)Cu(Cl)] and lithium salts of the anionic heteroatomic ligand (Scheme 26). For the conversion of [(IPr)-Cu(Me)] and aniline to methane and [(IPr)Cu(NHPh)] (**2**) studies suggest that the reaction involves the initial coordination of aniline followed by protonation of the methyl ligand.[25]

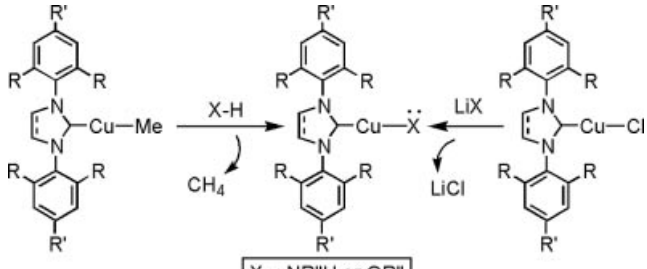


| NHC | X | NHC | X |
|---|---|---|---|
| IPr | NHPh (**2**) | IPr | OPh (**8**) |
| SIPr | NHPh (**3**) | SIPr | OPh (**9**) |
| IMes | NHPh (**4**) | IMes | OPh (**10**) |
| IPr | OEt (**5**) | IPr | SPh (**11**) |
| SIPr | OEt (**6**) | SIPr | SPh (**12**) |
| IMes | OEt (**7**) | IMes | SPh (**13**) |

Scheme 26. Two routes for the preparation of [(NHC)Cu(X)] complexes (X = NHPh, OEt or OPh).

 © 2007 Wiley-VCH Verlag GmbH & Co. KGaA, Weinheim 

Several of these complexes have been characterized by single-crystal X-ray diffraction. In all cases the structures reveal approximately linear two-coordinate monomeric systems (Figure 3). We have structurally characterized three Cu–NHPh complexes: [(dtbpe)Cu(NHPh)], [(IPr)Cu(NHPh)], and [(SIPr)Cu(NHPh)]. In all three systems, the plane of the anilido–phenyl group is approximately coplanar with the H–N–$C_{phenyl}$ plane, which optimizes delocalization of the amido lone pair into the phenyl π* system (Figure 4). Consistent with the amido-to-phenyl electron delocalization, the $N_{amido}$–$C_{phenyl}$ bond lengths {1.351(4) Å to 1.359(3) Å} are shorter than a typical N–C single bond (1.47 Å) and shorter than the corresponding N–C bond of the aniline complex [(dtbpe)Cu($NH_2$Ph)][$PF_6$], which is 1.444(4) Å.[23,30]

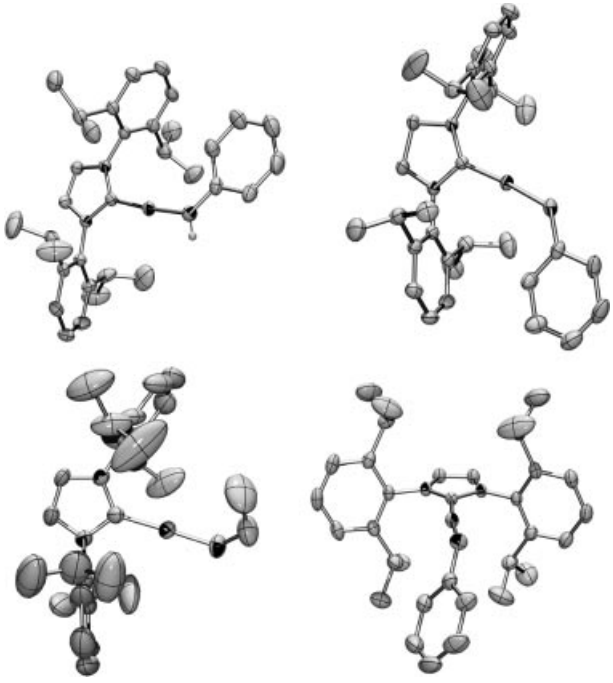

Figure 3. ORTEPs (30%) of representative examples of [(NHC)Cu(X)] (X = nondative heteroatomic ligand) complexes including [(IPr)Cu(NHPh)] (**2**), [(SIPr)Cu(NHPh)] (**3**), [(IPr)Cu(OEt)] (**5**), and [(IPr)Cu(OPh)] (**8**) (presented from left to right and top to bottom).

Consistent with the solid-state structures that suggest a negligible Cu–$N_{amido}$ π-interaction for the $Cu^{I}$ anilido complexes **1**–**4**, the calculated Kohn–Sham (KS) HOMO of these systems has little Cu character, and that which is present is Cu 3d ($p_{amido}$–$d_{Cu}$ π*) rather than 4p (Figure 5).[23] However, the KS HOMOs possess a substantial contribution from the phenyl π-system.

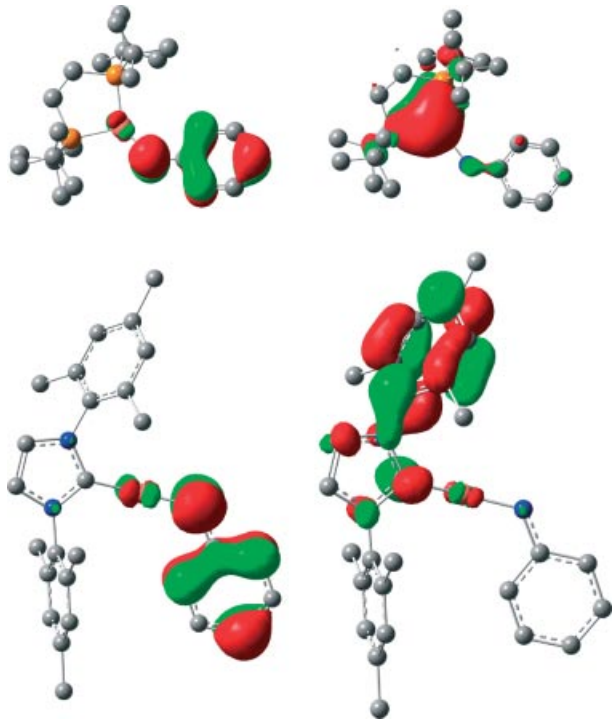

Figure 5. Highest occupied (left) and lowest unoccupied (right) Kohn–Sham orbitals for [(dtbpe)Cu(NHPh)] (**1**) (top pair) and [(IMes)Cu(NHPh)] (**4**) (bottom pair). Orbitals for other NHC $Cu^{I}$–anilido complexes are similar.

### Reactivity of $Cu^{I}$ Systems

As a straight-forward probe of nucleophilic reactivity, the rates of net $S_N2$ reactions of $Ru^{II}$– and $Cu^{I}$–anilido complexes with bromoethane to produce the corresponding metal–bromide and ethyl aniline were compared.[23] The complexes [TpRu($PMe_3$)$_2$NHPh], [(dtbpe)Cu(NHPh)] (**1**), [(IPr)Cu(NHPh)] (**2**), [(SIPr)Cu(NHPh)] (**3**), and [(IMes)Cu(NHPh)] (**4**) all react with bromoethane with the rate of reaction for Ru being considerably slower than Cu (Scheme 27 and Table 1). Using $\Delta G^{\ddagger}$ values calculated at variable temperatures and calculating rate constants at 298 K, which assumes a constant $\Delta G^{\ddagger}$, reveals that the reactions with the Cu complexes are 55000 to 250000 times more rapid than for the TpRu system. These results suggest

Figure 4. Depiction of the orientation of phenyl substituents of anilido ligands of [(SIPr)Cu(NHPh)] (**3**) (left), [(IPr)Cu(NHPh)] (**2**) (middle), and [(dtbpe)Cu(NHPh)] (**1**) (right) with most atoms removed.

 © 2007 Wiley-VCH Verlag GmbH & Co. KGaA, Weinheim 

that the $L_nCu–X$ (X = anionic heteroatomic ligand) are highly reactive and indicate that they may be useful for the development of Cu-mediated catalytic organic syntheses.

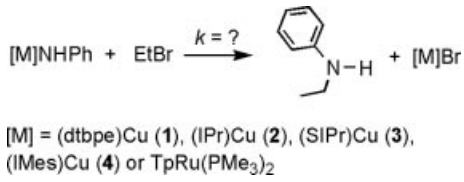


Scheme 27. Nucleophilic substitution reaction of amido complexes with bromoethane.

Table 1. Kinetic data for the reaction of bromoethane with [(IPr)-Cu(NHPh)] (**2**), [(SIPr)Cu(NHPh)] (**3**), [(IMes)Cu(NHPh)] (**4**), [(dtbpe)Cu(NHPh)] (**1**), and [TpRu($PMe_3$)$_2$(NHPh)] (see Scheme 27). All reactions were carried out at room temperature except [TpRu($PMe_3$)$_2$NHPh], which was performed at 80 °C.

| Complex | $k_{obs}$ [$s^{-1}$] | $t_{1/2}$[a] | $\Delta G^{\ddagger}$[b] |
|---|---|---|---|
| [(dtbpe)Cu(NHPh)] | $5.5(2)\times10^{-4}$ | 21.0(6) | 91 |
| [(IMes)Cu(NHPh)] | $3.3(3)\times10^{-4}$ | 35(3) | 92 |
| [(IPr)Cu(NHPh)] | $2.4(2)\times10^{-4}$ | 49(4) | 93 |
| [(SIPr)Cu(NHPh)] | $1.1(1)\times10^{-4}$ | 109(8) | 94 |
| [TpRu($PMe_3$)$_2$(NHPh)] | $8.6(3)\times10^{-6}$ | 22[c] | 121 |

[a] Minutes. [b] kJ/mol. [c] Hours.

In general, the thermodynamics of reactions between transition-metal amido (and related) complexes and dihydrogen to form metal–hydride complexes and free amines appear to be dependent upon the identity of the metal center. Early and middle transition-metal systems in relatively high oxidation states tend to favor metal–amido/dihydrogen while late transition-metal systems in low oxidation states exhibit a trend toward the metal–hydride/free amine (Scheme 28 and see below for examples). This trend can be rationalized by increased metal–amido bond energies due to amido-to-metal π-donation for metal centers in relatively high oxidation states. For late transition-metal centers in low oxidation states the π-bonding is disrupted and the M–$N_{amido}$ BDE is presumably decreased relative to systems in which π-bonding is present. The [(NHC)Cu(NHPh)] systems exhibit reactivity that contrasts these general trends. For example, [(IPr)Cu(NHPh)] (**2**) does not react with dihydrogen, while [[(IPr)Cu(μ-H)]$_2$] rapidly reacts with aniline to form dihydrogen and complex **2** (Scheme 29), reactivity which is consistent with an *early* transition-metal system. Furthermore, [(IPr)Cu(Ph)] reacts with aniline to produce benzene and [(IPr)Cu(NHPh)] with an equilibrium constant > 1000 (Scheme 30).

Examples of systems that follow the relative thermodynamics for reactions of amido complexes and dihydrogen (see paragraph above) include the conversion of [Cp*Ru($PMe_3$)$_2$($NPh_2$)] (Cp* = pentamethylcyclopentadienyl) and dihydrogen to free amine and Ru–hydride complexes,[157] reaction of [(PCP)Ru(CO)$NH_2$] and dihydrogen to produce free ammonia and Ru–hydride complexes,[29] release of aniline and formation of a Pt–dihydride

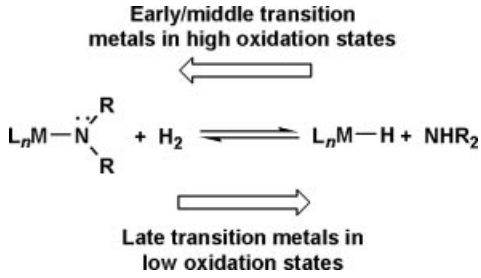


Scheme 28. Equilibrium trends between metal–amido/dihydrogen and metal–hydride/amine based on the identity and oxidation state of the transition metal.

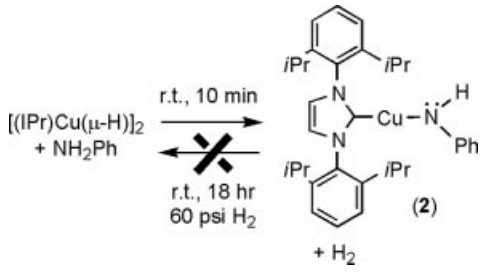


Scheme 29. Observed equilibrium for Cu–hydride/aniline and Cu–anilido/dihydrogen.

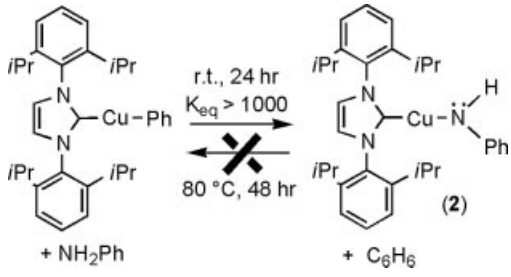


Scheme 30. Observed equilibrium for Cu–phenyl/aniline and Cu–anilido/benzene.

upon combination of *trans*-[($PEt_3$)$_2$Pt(H)NHPh] and dihydrogen,[158] and reaction of Cp*$_2$M(H)$_2$ (M = Zr or Hf) with ammonia to produce dihydrogen and the corresponding parent amido complexes.[159] In contrast to the late transition metal and low oxidation state $Ru^{II}$ and $Pt^{II}$ systems, complex **2** favors the Cu–amido and dihydrogen. The conversion of [(IPr)Cu(Ph)] and aniline to [(IPr)Cu(NHPh)] (**2**) and benzene also contrasts reactivity observed with another late transition-metal anilido complex. [(PCP)Ir(H)(Ph)] and free $NH_2Ph$ are thermally favored over [(PCP)-Ir(H)(NHPh)] and free $C_6H_6$ with $K_{eq}$ = 105.[160] In contrast, the [(IPr)$Cu^{I}$] fragment demonstrates a thermodynamic propensity for the formation of a Cu–NHPh bond and free benzene, which seems to suggest a shift in the relative magnitude of M–H/M–$N_{anilido}$ and M–$C_{phenyl}$/M–$N_{anilido}$ BDEs from established norms.

Analysis of the Cu–$N_{amido}$ BDE using B3LYP/CEP-31G(d) calculations provides a rationale for the observed equilibria. For [(IPr)Cu(NHPh)], the Cu–$N_{amido}$ BDE is

 © 2007 Wiley-VCH Verlag GmbH & Co. KGaA, Weinheim 

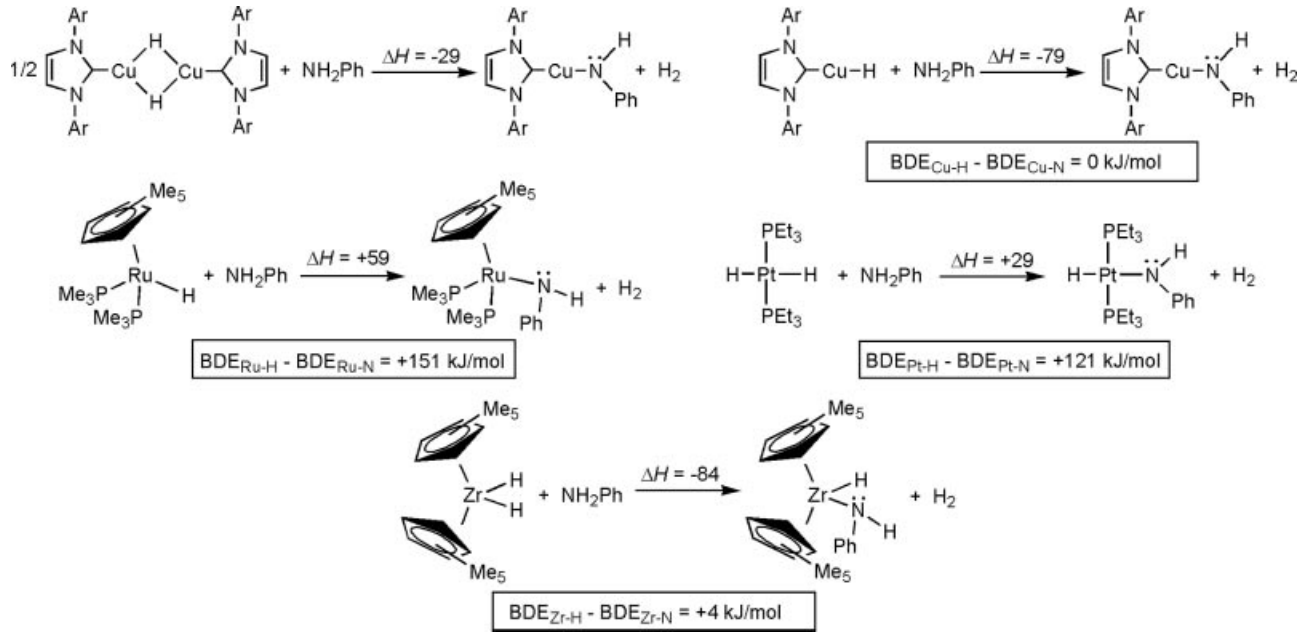


Scheme 31. DFT calculated changes in enthalpy (kJ/mol) for conversion of transition-metal–hydride complexes and aniline to transition-metal–anilido complexes and dihydrogen.

calculated to be 364 kJ/mol. In comparison, the calculated M–$N_{amido}$ BDEs of [Cp*$_2$Zr(NHPh)(H)] (284 kJ/mol; Cp* = pentamethylcyclopentadienyl), *trans*-[$(Et_3P)_2$Pt(H)(NHPh)] (180 kJ/mol), and [Cp*Ru$(PMe_3)_2$NHPh] (146 kJ/mol) are substantially weaker (Scheme 31).[23] The difference in M–$N_{amido}$ BDE for the Zr and Pt/Ru systems is easily rationalized by, at least in part, the π-bonding component of the Zr–$N_{amido}$ bond, which is likely to be negligible for $Pt^{II}$ and octahedral $Ru^{II}$. The large BDE for the Cu–$N_{amido}$ is more difficult to rationalize, and future studies will address whether this is an anomaly or a central feature of $Cu^{I}$ systems with anionic heteroatomic ligands. *At this point it can be stated that in terms of ground-state energetics the Cu–NHPh systems appear similar to early/middle transition-metal systems in high oxidation states. In contrast, the reactivity of Cu–NHPh related systems is more reminiscent of highly nucleophilic complexes in low oxidation states.*

The hydroamination or hydroalkoxylation of electron-deficient olefins under acidic or basic conditions is known; however, such reactions typically require relatively harsh conditions, including high temperatures that are often incompatible with functional groups and do not allow the control of regio-, chemo- or stereoselectivity.[161] In contrast, transition-metal-catalyzed reactions offer the promise of more ambient conditions and greater control over product selectivity. For example, both early and late transition-metal complexes as well as lanthanide systems have been developed for olefin hydroamination, with many of these systems limited to specific substrates or more facile intramolecular reactions.[162–167]

Copper catalysts for the enantioselective conjugate addition of carbon-based nucleophiles have been reported,[168] and we have become interested in related reactions for hetero-conjugate additions. $Cu(OTf)_2$ systems have been recently reported to catalyze the hydroamination of olefins.[169] The [(NHC)Cu(X)] and [(dtbpe)Cu(X)] (X = anionic heteroatomic ligand) complexes catalyze the conjugate

Table 2. Hydroamination of electron-deficient olefins catalyzed by [(IPr)Cu(NHPh)] (**2**) and uncatalyzed control experiments.

| Olefin | Nucleophile | Time[a] | % Conv.[b] | Product | Control expt.[c] |
|---|---|---|---|---|---|
| | $PhNH_2$ | 12 h | >95 | 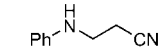 | 0 |
| | $PhNH_2$ | 5 min | >95 | 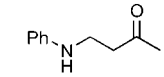 | 0 |
| 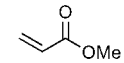 | $PhNH_2$ | 19 h | 55 | 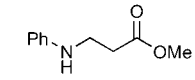 | 0 |
| 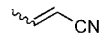 | $PhNH_2$ | 40 h[d] | 54 | 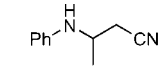 | 0[d] |
| 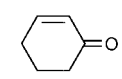 | $PhNH_2$ | 3 h | 85 | 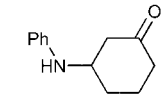 | 0 |
| | $tBuNH_2$ | 22 h | 57 | 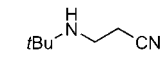 | 0 |
| | $nPrNH_2$ | 1 h | >95 | 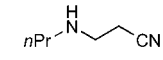 | 0 |
| | $Et_2NH$ | 9 h | >95 | 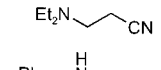 | 14 |
| | $PhCH_2NH_2$ | 5 min | >95 | 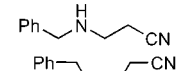 | 0 |
| | $(PhCH_2)_2NH$ | 90 h | 60 | 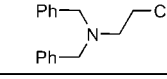 | 0 |

[a] All reactions performed with 5 mol-% catalyst at room temperature in $C_6D_6$. [b] % Conversions determined by $^1H$ NMR spectroscopy. [c] Control experiments reported after similar reaction times and given in % conversion. [d] Reaction conducted at 80 °C.

 © 2007 Wiley-VCH Verlag GmbH & Co. KGaA, Weinheim 

addition of N–H and O–H bonds across the C=C bonds of electron-deficient olefins (Table 2 and Table 3).[37] In all examples studied the reactions are regioselective for the "anti-Markovnikov" product (Scheme 32). Under conditions identical to catalysis some of the substrates undergo transformation in the absence of a Cu catalyst; however, comparison of reaction rates clearly indicates that the Cu complexes are serving as catalysts. For comparison, Table 2 and Table 3 depict results from control experiments under identical reaction conditions and times for the Cu-catalyzed transformations.

Table 3. Hydroalkoxylation and hydroaryloxylation of olefins and uncatalyzed control reactions.

| [Cu] | Olefin | Nucleophile | Temp (°C) | Time[a] | % Conv.[b] | Products | Control expt.[c] |
|---|---|---|---|---|---|---|---|
| 5 | | EtOH | r.t. | 20 h | 93 | 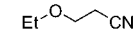 | 0% |
| 5 | | EtOH | r.t. | 7 h | >95 | 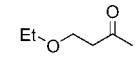 | 0% |
| 5, 6 | 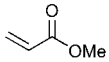 | EtOH | r.t. | -- | 0[d] | 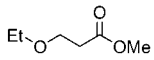 | 0% |
| 5 | 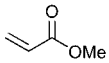 | EtOH | r.t. | 1 h | >95[e] | 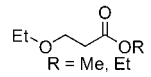 R = Me, Et | 0% |
| 6 | 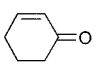 | EtOH | r.t. | 4.5 h | 25 | 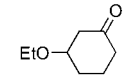 | 0% |
| 8 | | PhOH | 80 | 40 h | 64 | 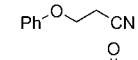 | 0% |
| 8 | | PhOH | 80 | 52 h | 60 | 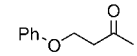 | 0% |
| 8 | 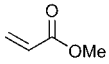 | PhOH | 120 | 235 h | 40[f] | 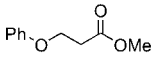 | 0% |

[a] All reactions performed with 5 mol-% catalyst in $C_6D_6$. [b] % Conversions determined by $^1H$ NMR spectroscopy. [c] Control experiments are reported after similar reaction times to catalyzed variants and are given in % conversion. [d] Transesterification observed. [e] Addition of *t*BuNC (1 equiv. based on EtOH) allows observation of hydroalkoxylation. [f] Approximately 10% transesterification also observed.

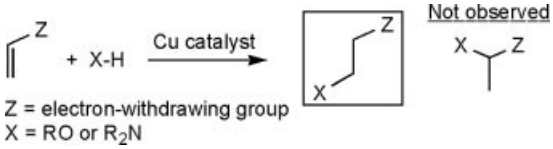


Scheme 32. Cu-catalyzed additions of N–H and O–H across C=C bonds of electron-deficient olefins are selective for the "anti-Markovnikov" products.

In general, reactions that incorporate stronger nucleophiles react more rapidly. For example, among amines and alcohols, catalysis is generally slower and less broad in scope for alcohols than for amines. Amongst a series of amines, alkylamines react more rapidly than arylamines. Table 2 shows comparative reactions for aniline and alkylamines with acrylonitrile. The exception to this generalization is the sterically bulky *t*BuNH$_2$, which reacts more slowly with acrylonitrile than aniline.

We have recently proposed a reaction mechanism for the copper-catalyzed hydroamination (and related reactions) of electron-deficient olefins in which initial intermolecular nucleophilic addition of the amido ligand to the olefin produces an unobserved zwitterionic intermediate.[38] Subsequent proton transfer yields a new copper amido complex and reaction with aniline (presumably via coordination to Cu) yields a free organic product and regenerates the original Cu system (Scheme 33). The hydroalkoxylation reactions are proposed to proceed through a similar mechanism with the exception that product formation likely originates from the zwitterionic intermediate or a linkage isomer Cu–alkyl complex. The relative rate of catalysis is consistent with a nucleophilic addition pathway. For example, reactivity decreases in the order N(H)*n*Pr > N(H)Ph > OEt > OPh for reactions with acrylonitrile. It is also possible that olefin coordination precedes N–C or O–C bond formation; however, this pathway seems unlikely as it does not necessarily account for the observed anti-Markovnikov regioselectivity. Furthermore, the addition of coordinating *t*BuNC slightly accelerates the rate of catalysis for the addition of aniline to acrylonitrile. If olefin coordination precedes N–C bond formation, competition for coordination between acrylonitrile and the isocyanide would be anticipated to re-

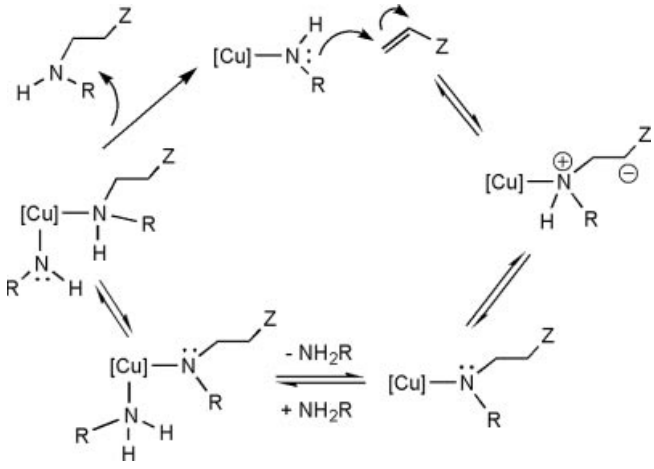


Scheme 33. Proposed catalytic cycle for Cu–amido catalytic hydroamination reactions.

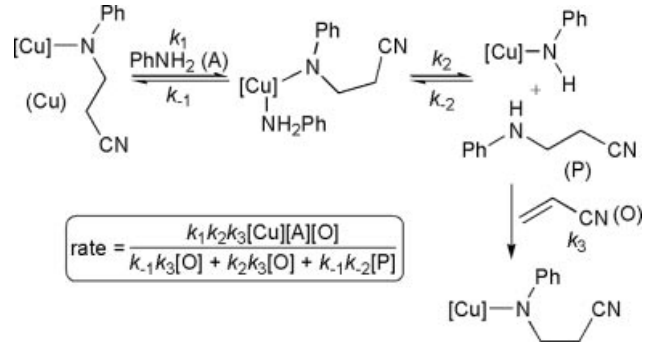


Scheme 34. Proposed mechanism and derived rate law for addition of aniline to acrylonitrile catalyzed by [(IPr)Cu(NHPh)] {[Cu] = (IPr)Cu in scheme, A = aniline, O = acrylonitrile, P = product}.

 © 2007 Wiley-VCH Verlag GmbH & Co. KGaA, Weinheim 

duce the rate of catalysis. In addition, reaction of [(IPr)Cu(NHPh)] and acrylonitrile produces [(IPr)CuN(Ph)($CH_2CH_2CN$)]. Finally, kinetic studies (using initial rates) for the addition of aniline to acrylonitrile reveal that the catalysis is first order in Cu catalyst and aniline, 0.7 order in acrylonitrile, and inhibited by the presence of organic product. These results are consistent with the proposed mechanism and derived rate law shown in Scheme 34 in which the rate-determining step is the reaction with acrylonitrile.[37]

## Summary and Future Outlook

Work presented herein and reported by others have demonstrated that anionic heteroatomic ligands coordinated to metal centers in low oxidation states results in highly reactive heteroatomic ligands. Such substrates are potentially useful for catalytic polymerizations as well as transformations of small molecules. Using well-defined $Ru^{II}$ and $Cu^{I}$ systems, we have demonstrated controlled stoichiometric and catalytic N–C bond formation using polar substrates, N–C and O–C bond formation using olefins as well as metal-mediated activation of dihydrogen and carbon–hydrogen bonds. Mechanistic studies indicate that, in some cases, the combination of a Lewis acidic metal center and nucleophilic/basic heteroatomic ligand form the foundation of these transformations.

Future efforts will be directed toward continued development of catalysts using these, and related, complexes. For example, we are presently pursuing strategies to extend the scope and selectivity of Cu-catalyzed hydroamination and hydroalkoxylation reactions as well as to develop other methods of N–C and O–C bond formation using these reactive Cu systems. Furthermore, efforts toward using the 1,2-addition of C–H bonds across metal–heteroatom bonds as a key step for C–H functionalization sequences are continuing. In terms of the reactivity of anionic heteroatomic ligands, future work will be directed toward an increased understanding of the impact of ancillary ligands, metal identity, and metal oxidation state on accessible reactions.

## Acknowledgments

The National Science Foundation, the Alfred P. Sloan Foundation, the Office of Basic Energy Sciences, United States Department of Energy, and the Petroleum Research Fund administered by the American Chemical Society are gratefully acknowledged for support of this work. T. B. G. also gratefully acknowledges the efforts and dedication of the students, postdocs and collaborators who have worked on these projects.

[1] K. A. Jørgensen, *Chem. Rev.* **1989**, *89*, 431.
[2] J. P. Collman, X. Zhang, V. J. Lee, E. S. Uffelman, J. I. Brauman, *Science* **1993**, *261*, 1404.
[3] P. Müller, C. Fruit, *Chem. Rev.* **2003**, *103*, 2905.
[4] H. C. Kolb, M. S. VanNieuwenhze, K. B. Sharpless, *Chem. Rev.* **1994**, *94*, 2483.
[5] Q.-H. Xia, H.-Q. Ge, C.-P. Ye, Z.-M. Liu, K.-X. Su, *Chem. Rev.* **2005**, *105*, 1603.
[6] K. Shibayama, S. W. Seidel, B. M. Novak, *Macromolecules* **1997**, *30*, 3159.
[7] H.-Z. Tang, Y. Lu, G. Tian, M. D. Capracotta, B. M. Novak, *J. Am. Chem. Soc.* **2004**, *126*, 3722.
[8] J. Cheng, T. J. Deming, *J. Am. Chem. Soc.* **2001**, *123*, 9457.
[9] D. R. Moore, M. Cheng, E. B. Lobkovsky, G. W. Coates, *J. Am. Chem. Soc.* **2003**, *125*, 11911.
[10] W. A. Nugent, J. M. Mayer, *Metal-Ligand Multiple Bonds*, John Wiley & Sons, New York, **1988**.
[11] R. R. Schrock, A. H. Hoveyda, *Angew. Chem. Int. Ed.* **2003**, *42*, 4592.
[12] J. D. Soper, B. K. Bennett, S. Lovell, J. M. Mayer, *Inorg. Chem.* **2001**, *40*, 1888.
[13] J. M. Mayer, *Comments Inorg. Chem.* **1988**, *8*, 125.
[14] K. G. Caulton, *New J. Chem.* **1994**, *18*, 25.
[15] R. G. Bergman, *Polyhedron* **1995**, *14*, 3227.
[16] J. R. Fulton, A. W. Holland, D. J. Fox, R. G. Bergman, *Acc. Chem. Res.* **2002**, *35*, 44.
[17] P. L. Holland, R. A. Andersen, R. G. Bergman, *Comments Inorg. Chem.* **1999**, *21*, 115.
[18] H. E. Bryndza, W. Tam, *Chem. Rev.* **1988**, *88*, 1163.
[19] M. D. Fryzuk, C. D. Montgomery, *Coord. Chem. Rev.* **1989**, *95*, 1.
[20] P. R. Sharp, *Comments Inorg. Chem.* **1999**, *21*, 85.
[21] P. R. Sharp, *J. Chem. Soc., Dalton Trans.* **2000**, 2647.
[22] D. M. Roundhill, *Chem. Rev.* **1992**, *92*, 1.
[23] L. A. Goj, E. D. Blue, S. A. Delp, T. B. Gunnoe, T. R. Cundari, A. W. Pierpont, J. L. Petersen, P. D. Boyle, *Inorg. Chem.* **2006**, *45*, 9032.
[24] Y. Feng, M. Lail, N. A. Foley, T. B. Gunnoe, K. A. Barakat, T. R. Cundari, J. L. Petersen, *J. Am. Chem. Soc.* **2006**, *128*, 7982.
[25] L. A. Goj, E. D. Blue, C. Munro-Leighton, T. B. Gunnoe, J. L. Petersen, *Inorg. Chem.* **2005**, *44*, 8647.
[26] Y. Feng, M. Lail, K. A. Barakat, T. R. Cundari, T. B. Gunnoe, J. L. Petersen, *J. Am. Chem. Soc.* **2005**, *127*, 14174.
[27] J. Zhang, T. B. Gunnoe, J. L. Petersen, *Inorg. Chem.* **2005**, *44*, 2895.
[28] J. Zhang, T. B. Gunnoe, P. D. Boyle, *Organometallics* **2004**, *23*, 3094.
[29] D. Conner, K. N. Jayaprakash, T. R. Cundari, T. B. Gunnoe, *Organometallics* **2004**, *23*, 2724.
[30] E. D. Blue, A. Davis, D. Conner, T. B. Gunnoe, P. D. Boyle, P. S. White, *J. Am. Chem. Soc.* **2003**, *125*, 9435.
[31] D. Conner, K. N. Jayaprakash, M. B. Wells, S. Manzer, T. B. Gunnoe, P. D. Boyle, *Inorg. Chem.* **2003**, *42*, 4759.
[32] D. Conner, K. N. Jayaprakash, T. B. Gunnoe, P. D. Boyle, *Organometallics* **2002**, *21*, 5265.
[33] D. Conner, K. N. Jayaprakash, T. B. Gunnoe, P. D. Boyle, *Inorg. Chem.* **2002**, *41*, 3042.
[34] K. N. Jayaprakash, D. Conner, T. B. Gunnoe, *Organometallics* **2001**, *20*, 5254.
[35] K. N. Jayaprakash, T. B. Gunnoe, P. D. Boyle, *Inorg. Chem.* **2001**, *40*, 6481.
[36] Y. Feng, T. B. Gunnoe, T. V. Grimes, T. R. Cundari, *Organometallics* **2006**, *25*, 5456.
[37] C. Munro-Leighton, S. A. Delp, E. D. Blue, T. B. Gunnoe, *Organometallics* **2007**, ASAP.
[38] C. Munro-Leighton, E. D. Blue, T. B. Gunnoe, *J. Am. Chem. Soc.* **2006**, *128*, 1446.
[39] S. Trofimenko, *Scorpionates: The Coordination Chemistry of Polypyrazolylborate Ligands*, Imperial College Press, London, **1999**.
[40] J. M. Boncella, T. M. Eve, B. Rickman, K. A. Abboud, *Polyhedron* **1998**, *17*, 725.
[41] J. F. Hartwig, R. A. Andersen, R. G. Bergman, *Organometallics* **1991**, *10*, 1875.
[42] P. L. Holland, R. A. Andersen, R. G. Bergman, J. Huang, S. P. Nolan, *J. Am. Chem. Soc.* **1997**, *119*, 12800.

 © 2007 Wiley-VCH Verlag GmbH & Co. KGaA, Weinheim 

[43] T. K. G. Erikson, J. C. Bryan, J. M. Mayer, *Organometallics* **1988**, *7*, 1930.
[44] J. R. Fulton, S. Sklenak, M. W. Bouwkamp, R. G. Bergman, *J. Am. Chem. Soc.* **2002**, *124*, 4722.
[45] A. W. Holland, R. G. Bergman, *J. Am. Chem. Soc.* **2002**, *124*, 14684.
[46] D. J. Fox, R. G. Bergman, *Organometallics* **2004**, *23*, 1656.
[47] K. Abdur-Rashid, T. P. Fong, B. Greaves, D. G. Gusev, J. G. Hinman, S. E. Landau, A. J. Lough, R. J. Morris, *J. Am. Chem. Soc.* **2000**, *122*, 9155.
[48] F. G. Bordwell, *Acc. Chem. Res.* **1988**, *21*, 456.
[49] J. M. Mayer, *Acc. Chem. Res.* **1998**, *31*, 441.
[50] J. R. Bryant, J. E. Taves, J. M. Mayer, *Inorg. Chem.* **2002**, *41*, 2769.
[51] A. S. Larsen, K. Wang, M. A. Lockwood, G. L. Rice, T.-J. Won, S. Lovell, M. Sadílek, F. Turecek, J. M. Mayer, *J. Am. Chem. Soc.* **2002**, *124*, 10112.
[52] C. R. Goldsmith, R. T. Jonas, T. D. P. Stack, *J. Am. Chem. Soc.* **2002**, *124*, 83.
[53] R. T. Jonas, T. D. P. Stack, *J. Am. Chem. Soc.* **1997**, *119*, 8566.
[54] M. J. Baldwin, V. L. Pecoraro, *J. Am. Chem. Soc.* **1996**, *118*, 11325.
[55] M. Taki, S. Itoh, S. Fukuzumi, *J. Am. Chem. Soc.* **2001**, *123*, 6203.
[56] S. Ogo, S. Wada, Y. Watanabe, M. Iwase, A. Wada, M. Harata, K. Jitsukawa, H. Masuda, H. Einaga, *Angew. Chem. Int. Ed.* **1998**, *37*, 2102.
[57] H. V. Obias, Y. Lin, N. N. Murthy, E. Pidcock, E. I. Solomon, M. Ralle, N. J. Blackburn, Y.-M. Neuhold, A. D. Zuberbühler, K. D. Karlin, *J. Am. Chem. Soc.* **1998**, *120*, 12960.
[58] C. A. Sandoval, T. Ohkuma, K. Muñiz, R. Noyori, *J. Am. Chem. Soc.* **2003**, *125*, 13490.
[59] K. Murata, H. Konishi, M. Ito, T. Ikariya, *Organometallics* **2002**, *21*, 253.
[60] R. Guo, R. H. Morris, D. Song, *J. Am. Chem. Soc.* **2005**, *127*, 516.
[61] S. E. Clapham, A. Hadzovic, R. H. Morris, *Coord. Chem. Rev.* **2004**, *248*, 2201.
[62] K. Abdur-Rashid, S. E. Clapham, A. Hadzovic, J. N. Harvey, A. J. Lough, R. H. Morris, *J. Am. Chem. Soc.* **2002**, *124*, 15104.
[63] K. Abdur-Rashid, M. Faatz, A. J. Lough, R. H. Morris, *J. Am. Chem. Soc.* **2001**, *123*, 7473.
[64] Z. M. Heiden, T. B. Rauchfuss, *J. Am. Chem. Soc.* **2006**, *128*, 13048.
[65] M. D. Fryzuk, C. D. Montgomery, S. J. Rettig, *Organometallics* **1991**, *10*, 467.
[66] P. J. Walsh, F. J. Hollander, R. G. Bergman, *J. Am. Chem. Soc.* **1988**, *110*, 8729.
[67] H. M. Hoyt, F. E. Michael, R. G. Bergman, *J. Am. Chem. Soc.* **2004**, *126*, 1018.
[68] J. L. Bennett, P. T. Wolczanski, *J. Am. Chem. Soc.* **1997**, *119*, 10696.
[69] C. C. Cummins, S. M. Baxter, P. T. Wolczanski, *J. Am. Chem. Soc.* **1988**, *110*, 8731.
[70] J. D. With, A. D. Horton, *Angew. Chem. Int. Ed. Engl.* **1993**, *32*, 903.
[71] C. P. Schaller, P. T. Wolczanski, *Inorg. Chem.* **1993**, *32*, 131.
[72] C. P. Schaller, J. B. Bonanno, P. T. Wolczanski, *J. Am. Chem. Soc.* **1994**, *116*, 4133.
[73] C. P. Schaller, C. C. Cummins, P. T. Wolczanski, *J. Am. Chem. Soc.* **1996**, *118*, 591.
[74] D. F. Schafer II, P. T. Wolczanski, *J. Am. Chem. Soc.* **1998**, *120*, 4881.
[75] T. R. Cundari, *J. Am. Chem. Soc.* **1992**, *114*, 10557.
[76] T. R. Cundari, T. R. Klinckman, P. T. Wolczanski, *J. Am. Chem. Soc.* **2002**, *124*, 1481.
[77] L. M. Slaughter, P. T. Wolczanski, T. R. Klinckman, T. R. Cundari, *J. Am. Chem. Soc.* **2000**, *122*, 7953.
[78] S. L. Buchwald, A. R. Muci, in *Topics in Current Chemistry* (Ed.: N. Miyaura), vol. 219, *Cross-Coupling Reactions: A Practical Guide*, chapter *Practical Palladium Catalysts for C–N and C–O Bond Formation*, Springer, Berlin, **2002**, pp. 131–209.
[79] J. F. Hartwig, in *Modern Amination Methods* (Ed.: A. Ricci), Wiley-VCH, Weinheim, **2000**, pp. 195.
[80] J. P. Wolfe, S. Wagaw, J.-F. Marcoux, S. L. Buchwald, *Acc. Chem. Res.* **1998**, *31*, 805.
[81] S. L. Buchwald, J. P. Wolfe, M. Palucki, Massachusetts Institute of Technology, USA, US Patent 6,166,226, Dec. 26, **2000**, p. 1.
[82] J. F. Hartwig, *Angew. Chem. Int. Ed.* **1998**, *37*, 2046.
[83] B. L. Conley, S. K. Ganesh, J. M. Gonzales, W. J. Tenn, K. J. H. Young, J. Oxgaard, W. A. Goddard III, R. A. Periana, *J. Am. Chem. Soc.* **2006**, *128*, 9018.
[84] W. J. Tenn III, K. J. H. Young, G. Bhalla, J. Oxgaard, W. A. Goddard III, R. A. Periana, *J. Am. Chem. Soc.* **2005**, *127*, 14172.
[85] D. L. Davies, S. M. A. Donald, S. A. Macgregor, *J. Am. Chem. Soc.* **2005**, *127*, 13754.
[86] D. L. Davies, S. M. A. Donald, O. Al-Duaij, S. A. Macgregor, M. Pölleth, *J. Am. Chem. Soc.* **2006**, *128*, 4210.
[87] P. E. M. Siegbahn, R. H. Crabtree, *J. Am. Chem. Soc.* **1996**, *118*, 4442.
[88] S. N. Brown, J. M. Mayer, *Organometallics* **1995**, *14*, 2951.
[89] S. N. Brown, J. M. Mayer, *J. Am. Chem. Soc.* **1996**, *118*, 12119.
[90] M. Lail, C. M. Bell, D. Conner, T. R. Cundari, T. B. Gunnoe, J. L. Petersen, *Organometallics* **2004**, *23*, 5007.
[91] K. A. Pittard, J. P. Lee, T. R. Cundari, T. B. Gunnoe, J. L. Petersen, *Organometallics* **2004**, *23*, 5514.
[92] B. A. Arndtsen, R. G. Bergman, *Science* **1995**, *270*, 1970.
[93] A. G. Wong-Foy, G. Bhalla, X. Y. Liu, R. A. Periana, *J. Am. Chem. Soc.* **2003**, *125*, 14292.
[94] C. N. Iverson, C. A. G. Carter, R. T. Baker, J. D. Scollard, J. A. Labinger, J. E. Bercaw, *J. Am. Chem. Soc.* **2003**, *125*, 12674.
[95] D. M. Tellers, R. G. Bergman, *J. Am. Chem. Soc.* **2000**, *122*, 954.
[96] A. A. Bengali, B. A. Arndtsen, P. M. Burger, R. H. Schultz, B. H. Weiller, K. R. Kyle, C. B. Moore, R. G. Bergman, *Pure App. Chem.* **1995**, *67*, 281.
[97] R. G. Bergman, *Science* **1984**, *223*, 902.
[98] T. O. Northcutt, D. D. Wick, A. J. Vetter, W. D. Jones, *J. Am. Chem. Soc.* **2001**, *123*, 7257.
[99] W. D. Jones, F. J. Feher, *Acc. Chem. Res.* **1989**, *22*, 91.
[100] U. Fekl, K. I. Goldberg, *J. Am. Chem. Soc.* **2002**, *124*, 6804.
[101] U. Fekl, W. Kaminsky, K. I. Goldberg, *J. Am. Chem. Soc.* **2003**, *125*, 15286.
[102] D. D. Wick, K. I. Goldberg, *J. Am. Chem. Soc.* **1997**, *119*, 10235.
[103] K. I. Goldberg, A. S. Goldman, in *ACS Symposium Series*, vol. 885, American Chemical Society, Washington, DC, **2004**.
[104] K. Krogh-Jespersen, M. Czerw, K. Zhu, B. Singh, M. Kanzelberger, N. Darji, P. D. Achord, K. B. Renkema, A. S. Goldman, *J. Am. Chem. Soc.* **2002**, *124*, 10797.
[105] S. Reinartz, P. S. White, M. Brookhart, J. L. Templeton, *Organometallics* **2000**, *19*, 3854.
[106] C. N. Kostelansky, M. G. MacDonald, P. S. White, J. L. Templeton, *Organometallics* **2006**, *25*, 2993.
[107] M. Lail, B. N. Arrowood, T. B. Gunnoe, *J. Am. Chem. Soc.* **2003**, *125*, 7506.
[108] W. H. Lam, G. Jia, Z. Lin, C. P. Lau, O. Eisenstein, *Chem. Eur. J.* **2003**, *9*, 2775.
[109] T. C. Flood, K. E. Janak, M. Iimura, H. Zhen, *J. Am. Chem. Soc.* **2000**, *122*, 6783.
[110] S. M. Ng, W. H. Lam, C. C. Mak, C. W. Tsang, G. Jia, Z. Lin, C. P. Lau, *Organometallics* **2003**, *22*, 641.
[111] M. van der Boom, D. Milstein, *Chem. Rev.* **2003**, *103*, 1759.
[112] M. D. Fryzuk, M. J. Petrella, B. O. Patrick, *Organometallics* **2005**, *24*, 5440.
[113] H.-Z. Tang, P. D. Boyle, B. M. Novak, *J. Am. Chem. Soc.* **2005**, *127*, 2136.

 © 2007 Wiley-VCH Verlag GmbH & Co. KGaA, Weinheim 

[114] T. J. Deming, B. M. Novak, *J. Am. Chem. Soc.* **1993**, *115*, 9101.
[115] T. E. Patten, B. M. Novak, *Macromolecules* **1993**, *26*, 436.
[116] L. Jia, H. Sun, J. T. Shay, A. M. Allgeier, S. D. Hanton, *J. Am. Chem. Soc.* **2002**, *124*, 7282.
[117] J. N. Cha, G. D. Stucky, D. E. Morse, T. J. Deming, *Nature* **2000**, *403*, 289.
[118] S. W. Seidel, T. J. Deming, *Macromolecules* **2003**, *36*, 969.
[119] D. J. Darensbourg, M. W. Holtcamp, *Coord. Chem. Rev.* **1996**, *153*, 155.
[120] I. C. Stewart, C. C. Lee, R. G. Bergman, F. D. Toste, *J. Am. Chem. Soc.* **2005**, *127*, 17616.
[121] L. R. Rieth, D. R. Moore, E. B. Lobkovsky, G. W. Coates, *J. Am. Chem. Soc.* **2002**, *124*, 15239.
[122] R. Bizzarri, F. Chiellini, R. Solaro, E. Chiellini, S. Cammas-Marion, P. Guerin, *Macromolecules* **2002**, *35*, 1215.
[123] S. Bloembergen, D. A. Holden, T. L. Bluhm, G. K. Hamer, R. H. Marchessault, *Macromolecules* **1989**, *22*, 1663.
[124] E. Chiellini, R. Solaro, *Adv. Mater.* **1996**, *8*, 305.
[125] K. L. Breno, M. D. Pluth, D. R. Tyler, *Organometallics* **2003**, *22*, 1203.
[126] J. Otera, *Chem. Rev.* **1993**, *93*, 1449.
[127] M. G. Stanton, M. R. Gagné, *J. Am. Chem. Soc.* **1997**, *119*, 5075.
[128] M. G. Stanton, M. R. Gagné, *J. Org. Chem.* **1997**, *62*, 8240.
[129] M. G. Stanton, C. B. Allen, R. M. Kissling, A. L. Lincoln, M. R. Gagné, *J. Am. Chem. Soc.* **1998**, *120*, 5981.
[130] R. M. Kissling, M. R. Gagné, *J. Org. Chem.* **2001**, *66*, 9005.
[131] W. Y. Mills, R. M. Kissling, M. R. Gagné, *Chem. Commun.* **1999**, 1713.
[132] S. E. Eldred, D. A. Stone, S. H. Gellman, S. S. Stahl, *J. Am. Chem. Soc.* **2003**, *125*, 3422.
[133] D. A. Kissounko, I. A. Guzei, S. H. Gellman, S. S. Stahl, *Organometallics* **2005**, *24*, 5208.
[134] J. M. Hoerter, K. M. Otte, S. H. Gellman, S. S. Stahl, *J. Am. Chem. Soc.* **2006**, *128*, 5177.
[135] C. Han, J. P. Lee, E. Lobkovsky, J. A. Porco Jr, *J. Am. Chem. Soc.* **2005**, *127*, 10039.
[136] D. A. Evans, M. M. Faul, M. T. Bilodeau, *J. Org. Chem.* **1991**, *56*, 6744.
[137] D. A. Evans, M. M. Faul, M. T. Bilodeau, B. A. Anderson, D. M. Barnes, *J. Am. Chem. Soc.* **1993**, *115*, 5328.
[138] Z. Li, K. R. Conser, E. N. Jacobsen, *J. Am. Chem. Soc.* **1993**, *115*, 5326.
[139] P. Brandt, M. J. Södergren, P. G. Andersson, P.-O. Norrby, *J. Am. Chem. Soc.* **2000**, *122*, 8013.
[140] Y. M. Badiei, A. Krishnaswamy, M. M. Melzer, T. H. Warren, *J. Am. Chem. Soc.* **2006**, *128*, 15056.
[141] H. Chen, M. M. Olmstead, S. C. Shoner, P. P. Power, *J. Chem. Soc., Dalton Trans.* **1992**, 451.
[142] H. Hope, P. P. Power, *Inorg. Chem.* **1984**, *23*, 936.
[143] P. P. Power, *Prog. Inorg. Chem.* **1991**, *39*, 75.
[144] S. Gambarotta, M. Bracci, C. Floriani, A. Chiesi-Villa, C. Guastini, *J. Chem. Soc., Dalton Trans.* **1987**, 1883.
[145] T. Tsuda, M. Miwa, T. Saegusa, *J. Org. Chem.* **1979**, *44*, 3734.
[146] T. Tsuda, K. Watanabe, K. Miyata, H. Yamamoto, T. Saegusa, *Inorg. Chem.* **1981**, *20*, 2728.
[147] A. L. Keen, M. Doster, H. Han, S. A. Johnson, *Chem. Commun.* **2006**, 1221.
[148] N. P. Mankad, D. S. Laitar, J. P. Sadighi, *Organometallics* **2004**, *23*, 3369.
[149] P. M. Jeffries, S. R. Wilson, G. S. Girolami, *Inorg. Chem.* **1992**, *31*, 4503.
[150] A. P. Purdy, C. F. George, J. H. Callahan, *Inorg. Chem.* **1991**, *30*, 2812.
[151] K. Osakada, T. Takizawa, M. Tanaka, T. Yamamoto, *J. Organomet. Chem.* **1994**, *473*, 359.
[152] B. A. Jazdzewski, P. L. Holland, M. Pink, J. Young Jr, D. J. E. Spencer, W. B. Tolman, *Inorg. Chem.* **2001**, *40*, 6097.
[153] N. Kitajima, K. Fujisawa, M. Tanaka, Y. Moro-oka, *J. Am. Chem. Soc.* **1992**, *114*, 9232.
[154] A. F. Stange, T. Sixt, W. Kaim, *Chem. Commun.* **1998**, 469.
[155] D. J. Mindiola, G. L. Hillhouse, *J. Am. Chem. Soc.* **2001**, *123*, 4623.
[156] N. P. Mankad, T. G. Gray, D. S. Laitar, J. P. Sadighi, *Organometallics* **2004**, *23*, 1191.
[157] H. E. Bryndza, L. K. Fong, R. A. Paciello, W. Tam, J. E. Bercaw, *J. Am. Chem. Soc.* **1987**, *109*, 1444.
[158] R. L. Cowan, W. C. Trogler, *J. Am. Chem. Soc.* **1989**, *111*, 4750.
[159] G. L. Hillhouse, J. E. Bercaw, *J. Am. Chem. Soc.* **1984**, *106*, 5472.
[160] M. Kanzelberger, X. W. Zhang, T. J. Emge, A. S. Goldman, J. Zhao, C. Incarvito, J. F. Hartwig, *J. Am. Chem. Soc.* **2003**, *125*, 13644.
[161] P. Perlmutter, *Conjugate Addition Reactions in Organic Synthesis*, vol. 9, Pergamon Press, Oxford, **1992**.
[162] J. J. Brunet, D. Neibecker, in *Catalytic Heterofunctionalization: From Hydroamination to Hydrozirconation* (Eds.: A. Togni, H. Grützmacher), Wiley-VCH, Weinheim, **2001**, pp. 91.
[163] T. E. Müller, M. Beller, *Chem. Rev.* **1998**, *98*, 675.
[164] M. Beller, J. Seayad, A. Tillack, H. Jiao, *Angew. Chem. Int. Ed.* **2004**, *43*, 3368.
[165] S. Hong, T. J. Marks, *Acc. Chem. Res.* **2004**, *37*, 673.
[166] J. F. Hartwig, *Pure Appl. Chem.* **2004**, *76*, 507.
[167] K. C. Hultzsch, *Adv. Synth. Catal.* **2005**, *347*, 367.
[168] A. Alexakis, C. Benhaim, *Eur. J. Org. Chem.* **2002**, 3221.
[169] J. G. Taylor, N. Whittall, K. K. Hii, *Org. Lett.* **2006**, *8*, 3561.

Received: November 15, 2006
Published Online: February 22, 2007

 © 2007 Wiley-VCH Verlag GmbH & Co. KGaA, Weinheim 

DOI: 10.1002/ejic.200601193

# New (1-Phosphanylferrocen-1′- and -2-yl)methyl-Linked Diaminocarbene Ligands: Synthesis and Rhodium(I) Complexes

**Agnès Labande,*[a] Jean-Claude Daran,[a] Eric Manoury,[a] and Rinaldo Poli*[a]**

**Keywords:** Carbene ligands / Phosphane ligands / Ferrocenes / Rhodium

Two ferrocenylmethanols, [1′-(diphenylthiophosphanyl)-ferrocen-1-yl]methanol (**3**) and [2-(diphenylthiophosphanyl)-ferrocen-1-yl]methanol (**6**), have been converted in one step into the 1,1′- and 1,2-ferrocenediyl-linked thiophosphane/*N*-R-imidazolium salts **4a**,**b** and **7a**,**b** (**a**: R = Me; **b**: R = 2,4,6-$Me_3C_6H_2$ or Mes). This straightforward method allows the linkage of an imidazolium group to a ferrocene unit with a nonsubstituted methylene bridge. After desulfurisation of the phosphane group, the ligands reacted with an $Rh^I$ precursor, in the presence of *t*BuOK, to give cationic complexes **9a**,**b** and **10a**,**b**. All compounds were characterised by elemental analysis, NMR spectroscopy and mass spectrometry. The molecular structures of compounds **4a**, **7a** and **9a** were determined by X-ray crystallography.
(© Wiley-VCH Verlag GmbH & Co. KGaA, 69451 Weinheim, Germany, 2007)

The chemistry of N-heterocyclic carbenes (NHCs) has experienced a very rapid development over the past ten years.[1] They have found many applications in catalysis, since the corresponding transition metal complexes have proven to be very active, robust and generally air-stable.[2] Ligands associating an NHC and a phosphane have also shown very interesting properties,[3] in particular for C–C coupling reactions catalysed by palladium or nickel.[4]

To date, there are only two synthetic methods allowing the preparation of ferrocenediyl-linked phosphane/NHC ligands with an aryl (or ferrocenyl) substituent on the imidazole moiety.[5,6] However, the carbon atom situated in α-position to the Cp ring has a methyl substituent in both cases. To the best of our knowledge, there is no precedent in the literature for 1,1′-disubstituted ferrocenediyl phosphane/imidazolium ligands. On the other hand, the fundamental difference between our 1,2-disubstituted ligands and previously reported ligands is that the former possess only planar chirality, whereas the latter have both planar and central chirality.[5,6] Thus, it becomes possible to study the specific effect of planar chirality in asymmetric catalytic reactions. We present here a new synthetic method for 1,1′- and racemic 1,2-disubstituted ferrocenediyl phosphane/imidazolium ligands, which are precursors of phosphane/NHCs.

The precursors for the introduction of the imidazolium moiety are alcohols **3** (Scheme 1) and **6** (Scheme 2). The synthesis of racemic (as well as enantiomerically pure) alcohol **6** is already well known.[7,8] We have adapted this method to prepare the new alcohol **3**. It was successfully obtained in two steps from known 1-bromo-1′-(diphenylphosphanyl)ferrocene,[9] with satisfactory yields.

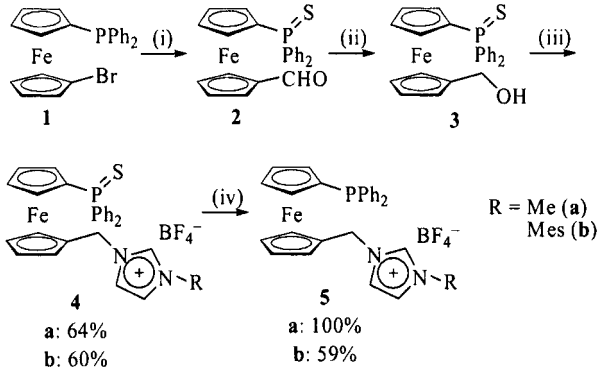


Scheme 1. Synthesis of 1,1′-ferrocenediyl ligands. i. a) *n*BuLi, THF, –25 °C, b) dmf, –25 °C, c) $S_8$, $CH_2Cl_2$, 40 °C (70%); ii. $NaBH_4$, toluene/NaOH, 0 °C (88%); iii. a) $HBF_4$, $CH_2Cl_2$, room temp., b) *N*-R-imidazole; iv) Raney Ni, MeCN, room temp. or 80 °C.

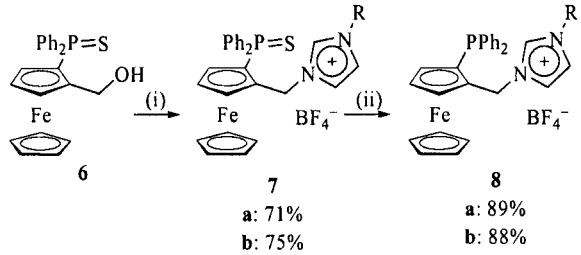


Scheme 2. Synthesis of 1,2-ferrocenediyl ligands. i. a) $HBF_4$, $CH_2Cl_2$, room temp., b) *N*-R-imidazole; ii) Raney Ni, MeCN, room temp. or 80 °C.

[a] Laboratoire de Chimie de Coordination, UPR CNRS 8241 (lié par convention à l'Université Paul Sabatier et à l'Institut National Polytechnique de Toulouse),
205 route de Narbonne, 31077 Toulouse Cedex 4, France
E-mail: agnes.labande@lcc-toulouse.fr
Supporting information for this article is available on the WWW under http://www.eurjic.org or from the author.

 © 2007 Wiley-VCH Verlag GmbH & Co. KGaA, Weinheim 

Procedures for introducing an *N*-substituted imidazole ring on a ferrocenyl unit can involve the displacement of a chloride,[10] an acetate,[6,11] or a dimethylamino group.[5] Bolm et al. described the efficient conversion of ferrocenyl alcohols into corresponding imidazolium compounds by a two-step procedure.[12,13] However, this method has not been applied so far to introduce aryl or tertiary alkyl groups. Here, the imidazolium functionality has been introduced in one-pot procedure from the alcohol, according to a protocol developed earlier in our group for the introduction of various nucleophiles on 1,2-disubstituted ferrocenediyl phosphanes.[14] The α-carbocation is generated with a strong acid and reacts with the *N*-R-imidazole (**a**: R = Me; **b**: R = 2,4,6-$Me_3C_6H_2$ or Mes). This method allowed us to introduce equally well imidazolium groups bearing a primary alkyl or an aryl substituent. The reactions are clean, very rapid and high-yielding (Schemes 1 and 2).[15] The structure of the intermediates **4a** and **7a** was confirmed by X-ray diffraction methods (Figure 1). The bond lengths and angles in both compounds are all within the expected range. The imidazolium moiety is *exo* with respect to the ferrocene unit, and slightly tilted towards the diphenylphosphanyl group in the case of **7a**. In **4a**, the packing is governed by C–H···π interactions involving the H(64) atom of the imidazolium group and the centroid of the symmetry-related Cp ring bearing the imidazolium group [C(64)–H(64)···Cg2$^{i}$: C(64)–H(64) 0.95 Å; H(64)···Cg2$^{i}$ 2.74 Å; C(64)···Cg2$^{i}$ 3.562(5) Å; C(64)–H(64)···Cg2$^{i}$ 144.8°; symmetry code (i): $-x + 1, -y + 1, -z + 1$], leading to the formation of a centrosymmetric pseudo dimer. The two molecules within the asymmetric unit in **7a** are also connected through weak C–H···π interactions involving the H(14) atom of the substituted Cp ring of one molecule and the centroid of the C(211)–C(216) phenyl ring of the other one [C(14)–H(14)···Cg3: C(14)–H(14) 0.93 Å; H(14)···Cg3 3.13 Å; C(14)···Cg3 3.755(3) Å; C(14)–H(14)···Cg3 126.5°]. In **7a**, the imidazolium ring and one of the phenyl rings [C(121)–C(126); C(221)–C(226)] interact through an offset π–π stacking with a plane-to-plane distance of 3.566(2) Å [3.438(2) Å], a centroid-to-centroid distance of 3.9217(3) Å [3.6301(3) Å] and an offset angle of 24.6° [18.7°]. The sulfur atom in **7a** is pointing towards the iron atom, as has been seen with similar 1,2-disubstituted ferrocenediyl ligands.[8]

Mild reaction conditions were then required for the phosphane deprotection, compatible with the imidazolium moiety. After several attempts, we found that the use of Raney nickel in acetonitrile gave the best results.[16]

(Carbene)rhodium(I) complexes were obtained by deprotonation of the imidazolium salts in the presence of potassium *tert*-butoxide and $[RhCl(cod)]_2$ in THF, followed by chloride abstraction (Scheme 3). The latter step could be carried out with either $NaBF_4$ in $CH_2Cl_2/H_2O$, or $AgBF_4$ in $CH_2Cl_2$. The silver reagent results in a faster abstraction process while it does not oxidize the ferrocene unit. Room-temperature conditions for the deprotonation step resulted in good yields (75%) for product **9a**, but less satisfactory results were obtained in other cases (i.e. 32% for **10b**). However, carrying out the deprotonation at –78 °C raised the yield of **10b** to 77%. This shows that the bulky imidazolium substituent does not negatively affect the coordination process. Good yields (81%) were also obtained for **9b** when using the low temperature deprotonation protocol, whereas the yield of **9a** was lowered (62%). While the products with the 1,1′-disubstituted ligands, **9a**,**b**, were obtained selec-

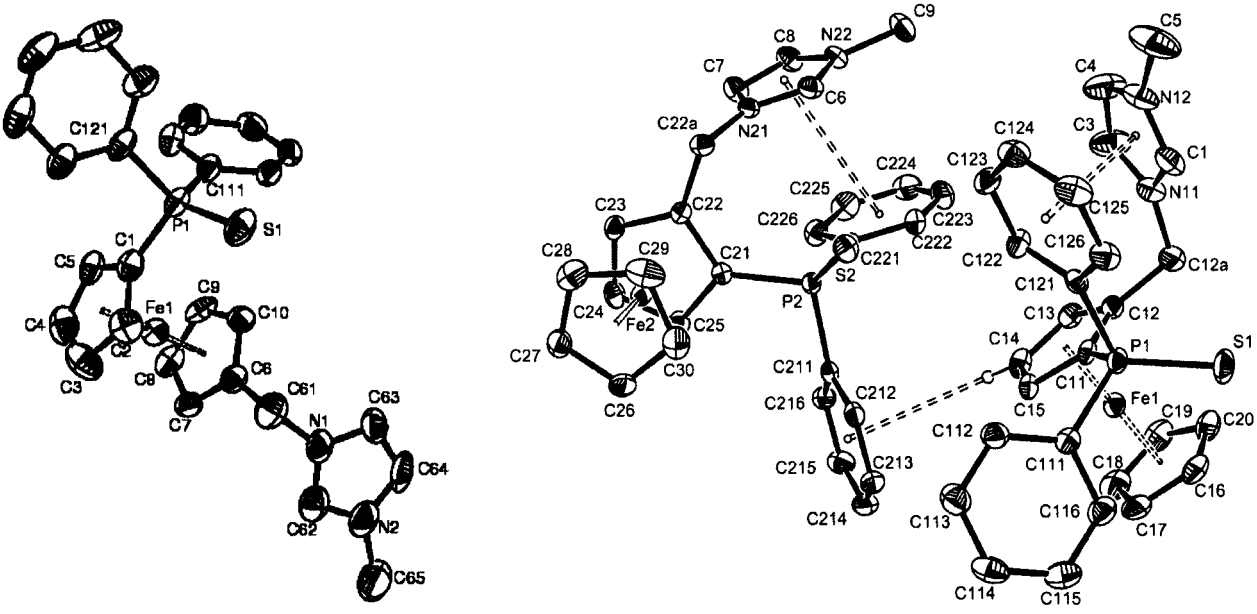


Figure 1. Molecular views of compounds **4a** (left) and **7a** (right) with atom labelling scheme. Ellipsoids are plotted at the 50% level. H atoms have been omitted for clarity. Selected bond lengths [Å] and bond angles [°]: **4a**: C(1)–P(1) 1.790(3), C(62)–N(1) 1.324(5), C(62)–N(2) 1.313(5), C(63)–C(64) 1.330(6); N(2)–C(62)–N(1) 108.6(3); **7a**: C(11)–P(1) 1.792(3), C(1)–N(11) 1.317(3), C(1)–N(12) 1.309(4), C(3)–C(4) 1.333(5); N(11)–C(1)–N(12) 109.7(3); C(21)–P(2) 1.801(3), C(6)–N(21) 1.316(3), C(6)–N(22) 1.323(3), C(7)–C(8) 1.344(4); N(21)–C(6)–N(22) 109.4(3).

 © 2007 Wiley-VCH Verlag GmbH & Co. KGaA, Weinheim 

tively, the reactions with the 1,2-disubstituted ligands yielded by-products. The selectivity for **10b** was almost total,[17] however, complex **10a** was obtained along with another carbene/phosphane complex in a 85:15 ratio.[18,19] It is reasonable to think that, in the case of 1,2-disubstituted ligands, the selectivity is affected by the steric encumbrance of the imidazolium substituent. All complexes are stable in air and could be purified by filtration through silica gel. The structure of complex **9a** was confirmed by X-ray diffraction methods (see Figure 2). The structure shows a square-planar geometry with the carbene and phosphane donors in a *cis* arrangement. The bond lengths and angles are again within the expected range for this kind of complexes. The Rh–carbene distance is in accordance with what Seo obtained with a very similar complex, although the Rh–P distance is slightly longer in our case [2.3345(8) Å instead of 2.2935(10) Å in Seo's $Rh^I$ complex, which has two NHC/phosphane ligands coordinated to the metal centre].[5] However, we do not observe any significant lenghtening of the Rh–C bonds *trans* to the carbene [Rh(1)–CG1], with respect to the other Rh–C bonds [Rh(1)–CG2], as is commonly observed for bifunctional NHC ligands.[5,13] Finally, no tilting of the Cp rings can be observed upon complexation of the ligand to the rhodium centre [the angles between the two least-squares Cp planes are 4.66(29)° for **4a** and 3.15(24)° for **9a**].

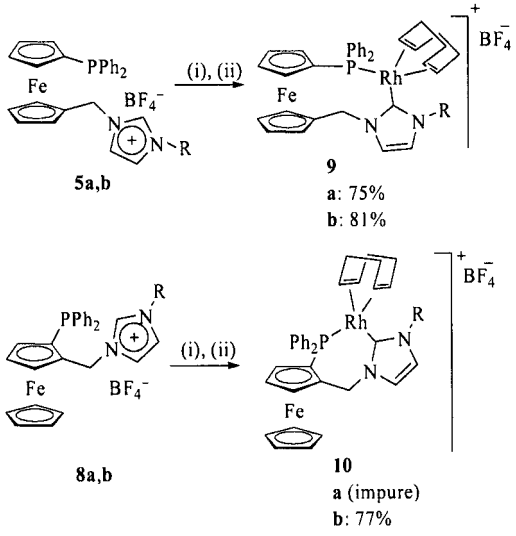


Scheme 3. Synthesis of Rh complexes. i. *t*BuOK, $[Rh(cod)Cl]_2$, THF; ii. $NaBF_4$, $CH_2Cl_2/H_2O$, room temp. or $AgBF_4$, $CH_2Cl_2$, room temp.

Preliminary tests have been carried out to evaluate the activity of complexes **9a**, **9b** and **10b** (racemic mixture) for the hydrosilylation of ketones. The reaction of diphenylsilane with acetophenone was carried out in dichloromethane or THF at room temperature, with 2 mol-% of catalyst (Table 1). The first results show that THF is a better solvent, despite the low solubility of complexes **9a** and **9b**, and that the complex bearing a 1,2-disubstituted ligand is more active. All complexes show a moderate activity, compared with other literature benchmarks.[13,20]

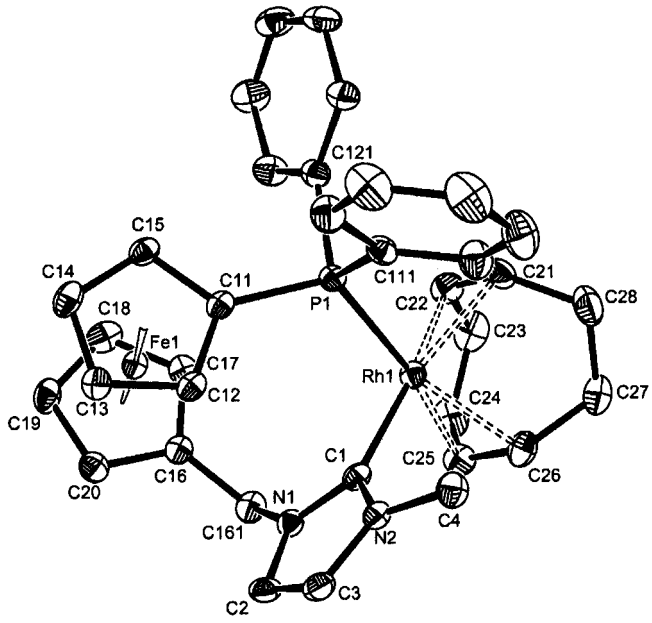


Figure 2. Molecular view of compound **9a** with atom labelling scheme. Ellipsoids are plotted at the 50% level. H atoms have been omitted for clarity. Selected bond lengths [Å] and bond angles [°]: Rh(1)–C(1) 2.047(3), Rh(1)–P(1) 2.3345(8), Rh(1)–C(21) 2.215(3), Rh(1)–C(22) 2.231(3), Rh(1)–C(25) 2.220(3), Rh(1)–C(26) 2.217(3), Rh(1)–CG1 2.1140(3), Rh(1)–CG2 2.1091(3), N(1)–C(1) 1.359(4), N(2)–C(1) 1.357(4), C(2)–C(3) 1.338(4); C(1)–Rh(1)–P(1) 90.83(8), C(1)–Rh(1)–CG1 175.91(8), C(1)–Rh(1)–CG2 90.46(8), CG1–Rh(1)–P(1) 93.26(2), CG2–Rh(1)–P(1) 174.69(2), CG2–Rh(1)–CG1 85.450(10), N(1)–C(2)–N(2) 104.5(2). CG1 and CG2 denote the C(21)–C(22) centroid and the C(25)–C(26) centroid, respectively.

Table 1. Hydrosilylation of acetophenone with diphenylsilane. Conditions: 1 equiv. of acetophenone, 1.1 equiv. of diphenylsilane, 2 mol-% of catalyst, room temperature.

| Entry | Complex | Solvent | *t* (d) | Conversion (%)[a] |
|---|---|---|---|---|
| 1 | **9a** | $CH_2Cl_2$ | 7 | 17 |
| 2 | **9a** | THF | 3 | 46 |
| 3 | **9b** | THF | 3 | 49 |
| 4 | **10b** | THF | 3 | 67 |

[a] Determined by $^1H$ NMR spectroscopy after hydrolysis of the silylated intermediate.

In conclusion, we have prepared new ferrocenediyl phosphane/imidazolium ligands by a general and effective method. Further tests will be carried out to evaluate the activity of the $Rh^I$ complexes in various catalytic reactions. Enantiomerically pure 1,2-disubstituted ligands will also be prepared and tested in the asymmetric version of the reactions. Results will be published in due course.

## Experimental Section

**General:** All reactions were carried out under dry argon using Schlenk glassware and vacuum-line techniques. Solvents for syntheses were dried and degassed by standard methods before use. *N*,*N*-Dimethylformamide (dmf) was purified by distillation from $CaH_2$. Spectra were recorded with a Bruker AM250, a Bruker AV300 or a Bruker AV500 spectrometer. All spectra were recorded in $CDCl_3$,

 © 2007 Wiley-VCH Verlag GmbH & Co. KGaA, Weinheim 

unless otherwise stated. Mass spectra were obtained from acetonitrile solutions with a TSQ7000 instrument from ThermoElectron. All new compounds described were fully characterised by $^{1}H$, $^{13}C$, and $^{31}P$ NMR spectroscopy, elemental analysis and mass spectrometry. 1,1′-dibromoferrocene and 1-bromo-1′-(diphenylphosphanyl)-ferrocene were prepared according to literature procedures.[9]

**General Procedures for the Preparation of Imidazolium Salts:** To a solution of **3** (100 mg, 0.23 mmol) in degassed dichloromethane (5 mL) was quickly added $HBF_4$ (35 μL, 54 wt-% in $Et_2O$), immediately followed by an *N*-substituted imidazole (0.35 mmol). The mixture was washed with 2 M aq. HCl, water, satd. aq. $NaHCO_3$ and water again. The organic phase was dried ($MgSO_4$), filtered and concentrated in vacuo. Methyl-substituted salts: the residue was taken up in dichloromethane (1 mL), diethyl ether was added and the orange precipitate was filtered, washed with diethyl ether and dried in vacuo to give a yellow-orange solid. Mesityl-substituted salts: the residue was purified by column chromatography on silica gel (eluent: $CH_2Cl_2$/acetone, 9:1) to give a yellow-orange solid. Similar yields were obtained starting from 500 mg of **3**.

**Imidazolium Salt 4a:** 86 mg, 64% yield. Single crystals suitable for X-ray diffraction studies were obtained by slow concentration of a dichloromethane solution. $C_{27}H_{26}BF_4FeN_2PS$ (584.21): calcd. C 55.51, H 4.49, N 4.80; found C 54.98, H 4.16, N 4.55. $^{1}H$ NMR (300 MHz, $CD_2Cl_2$, 25 °C): $\delta$ = 8.65 (s, 1 H, NC*H*N$^+$), 7.79–7.72 (m, 4 H, $PPh_2$), 7.59–7.47 (m, 6 H, $PPh_2$), 7.29 (s, 1 H, HC=C Im$^+$), 7.27 (s, 1 H, HC=C Im$^+$), 5.09 (s, 2 H, Cp), 4.69 (s, 2 H, Cp), 4.54 (s, 2 H, Cp or C$H_2$Im$^+$), 4.50 (s, 2 H, Cp or C$H_2$Im$^+$), 4.16 (s, 2 H, Cp), 3.88 (s, 3 H, C$H_3$Im$^+$) ppm. $^{13}C\{^{1}H\}$ NMR (75.5 MHz, $CD_2Cl_2$, 25 °C): $\delta$ = 135.5 (NCN$^+$), 134.2 (d, $J_{P,C}$ = 87.0 Hz, 2× quat. $PPh_2$), 131.55 (2× $PPh_2$), 131.53 (d, $J_{P,C}$ = 10.6 Hz, 4× $PPh_2$), 128.4 (d, $J_{P,C}$ = 12.5 Hz, 4× $PPh_2$), 123.6 (C=C Im$^+$), 121.8 (C=C Im$^+$), 80.4 (quat. Cp$^C$), 76.2 (d, $J_{P,C}$ = 96.9 Hz, quat. Cp$^P$), 74.1 (d, $J_{P,C}$ = 12.4 Hz, 2× Cp$^P$), 73.1 (d, $J_{P,C}$ = 10.0 Hz, 2× Cp$^P$), 71.7 (2× Cp$^C$), 71.3 (2× Cp$^C$), 49.1 (*C*$H_2$Im$^+$), 36.3 (*C*$H_3$Im$^+$) ppm. $^{31}P\{^{1}H\}$ NMR (81.0 MHz, $CD_2Cl_2$, 25 °C): $\delta$ = 41.0 ppm. MS (ESI): *m*/*z* (%) = 497 (70) [M$^+$], 415 (100) [M$^+$ – $C_4H_6N_2$].

**Imidazolium Salt 4b:** 96 mg, 60% yield. $C_{35}H_{34}BF_4FeN_2PS$ (688.36): calcd. C 61.07, H 4.98, N 4.07; found C 60.31, H 4.71, N 3.91. $^{1}H$ NMR (300 MHz, $CD_3CN$, 25 °C): $\delta$ = 8.54 (s, 1 H, NC*H*N$^+$), 7.80–7.73 (m, 4 H, $PPh_2$), 7.60–7.50 (m, 7 H, $PPh_2$ + HC=C Im$^+$), 7.40 (s, 1 H, HC=C Im$^+$), 7.11 (s, 2 H, Mes), 5.15 (br. s, 2 H, C$H_2$Im$^+$), 4.71 (br. s, 2 H, Cp), 4.55 (br. s, 2 H, Cp), 4.51 (br. s, 2 H, Cp), 4.18 (br. s, 2 H, Cp), 2.36 (s, 3 H, *p*-$CH_3$ Mes), 2.00 (s, 6 H, *o*-$CH_3$ Mes) ppm. $^{13}C\{^{1}H\}$ NMR (75.5 MHz, $CD_3CN$, 25 °C): $\delta$ = 141.2 (quat. Mes), 135.8 (NCN$^+$), 134.7 (2× quat. Mes), 134.4 (d, $J_{P,C}$ = 87.0 Hz, 2× quat. $PPh_2$), 131.7 (d, $J_{P,C}$ = 2.9 Hz, 2× $PPh_2$), 131.4 (d, $J_{P,C}$ = 10.7 Hz, 4× $PPh_2$), 131.0 (quat. Mes), 129.5 (2× C-H Mes), 128.5 (d, $J_{P,C}$ = 12.5 Hz, 4× $PPh_2$), 124.2 (C=C Im$^+$), 122.7 (C=C Im$^+$), 80.7 (quat. Cp$^C$), 76.1 (d, $J_{P,C}$ = 97.3 Hz, quat. Cp$^P$), 74.0 (d, $J_{P,C}$ = 12.4 Hz, 2× Cp$^P$), 73.2 (d, $J_{P,C}$ = 10.1 Hz, 2× Cp$^P$), 71.6 (2× Cp$^C$), 71.2 (2× Cp$^C$), 49.2 (*C*$H_2$Im$^+$), 20.2 (*p*-$CH_3$ Mes), 16.6 (2× *o*-$CH_3$ Mes) ppm. $^{31}P\{^{1}H\}$ NMR (121.5 MHz, $CD_3CN$, 25 °C): $\delta$ = 40.6 ppm. MS (ESI): *m*/*z* (%) = 601 (100) [M$^+$], 415 (100) [M$^+$ – $C_{12}H_{14}N_2$].

**Imidazolium Salt 7a:** 96 mg, 71% yield. Single crystals suitable for X-ray diffraction studies were obtained by slow diffusion of diethyl ether into a THF solution. $C_{27}H_{26}BF_4FeN_2PS$ (584.21): calcd. C 55.51, H 4.49, N 4.80; found C 51.53, H 3.90, N 4.32. $^{1}H$ NMR (500 MHz, $CDCl_3$, 25 °C): $\delta$ = 8.33 (s, 1 H, NC*H*N$^+$), 7.73–7.33 (m, 10 H, $PPh_2$), 6.98 (br. s, 1 H, HC=C Im$^+$), 6.87 (br. s, 1 H, HC=C Im$^+$), 6.41 (br. s, 1 H, C$H_2$Im$^+$), 5.15–5.04 (m, 2 H, C$H_2$Im$^+$ + Cp), 4.52 (br. s, 1 H, Cp), 4.41 (br. s, 5 H, Cp′), 3.81 (br. s, 1 H, Cp), 3.52 (br. s, 3 H, C$H_3$Im$^+$) ppm. $^{13}C\{^{1}H\}$ NMR (125.8 MHz, $CDCl_3$, 25 °C): $\delta$ = 135.9 (NCN$^+$), 134.0 (d, $J_{P,C}$ = 85.6 Hz, 2× quat. $PPh_2$), 132.2–131.8 (m, 5× $PPh_2$), 131.4 (d, $J_{P,C}$ = 10.1 Hz, 2× $PPh_2$), 128.7 (d, $J_{P,C}$ = 12.6 Hz, $PPh_2$), 128.45 (d, $J_{P,C}$ = 12.6 Hz, 2× $PPh_2$), 123.6 (C=C, Im$^+$), 122.4 (C=C, Im$^+$), 83.4 (d, $J_{P,C}$ = 11.3 Hz, quat. Cp), 77.5–77.0 (Cp + $CDCl_3$), 76.3 (d, $J_{P,C}$ = 11.3 Hz, Cp), 74.3 (d, $J_{P,C}$ = 94.4 Hz, quat. Cp), 71.4 (Cp′), 71.3 (Cp), 48.2 (*C*$H_2$Im$^+$), 37.0 (*C*$H_3$Im$^+$) ppm. $^{31}P\{^{1}H\}$ NMR (202.5 MHz, $CDCl_3$, 25 °C): $\delta$ = 40.7 ppm. MS (ESI): *m*/*z* (%) = 497 (37) [M$^+$], 415 (100) [M$^+$ – $C_4H_6N_2$].

**Imidazolium Salt 7b:** 121 mg, 76% yield. $C_{35}H_{34}BF_4FeN_2PS$ (688.36): calcd. C 61.07, H 4.98, N 4.07; found C 60.34, H 4.93, N 3.98. $^{1}H$ NMR (300 MHz, $CDCl_3$, 25 °C): $\delta$ = 8.67 (s, 1 H, NC*H*N$^+$), 7.84–7.77 (m, 2 H, $PPh_2$), 7.58–7.28 (m, 9 H, $PPh_2$ + HC=C Im$^+$), 6.92 (s, 2 H, Mes), 6.71 (s, 1 H, HC=C Im$^+$), 6.66 (d, $J_{H,H}$ = 14.3 Hz, 1 H, C$H_2$Im$^+$), 5.58 (d, $J_{H,H}$ = 14.3 Hz, 1 H, C$H_2$Im$^+$), 5.31 (br. s, 1 H, Cp), 4.56 (br. s, 1 H, Cp), 4.35 (s, 5 H, Cp′), 3.96 (br. s, 1 H, Cp), 2.30 (s, 3 H, *p*-$CH_3$ Mes), 1.84 (br. s, 3 H, *o*-$CH_3$ Mes), 1.68 (br. s, 3 H, *o*-$CH_3$ Mes) ppm. $^{13}C\{^{1}H\}$ NMR (75.5 MHz, $CDCl_3$, 25 °C): $\delta$ = 141.2 (quat. Mes), 136.2 (NCN$^+$), 135.0 (d, $J_{P,C}$ = 86.0 Hz, quat. $PPh_2$), 134.2 (quat. Mes), 132.3 (d, $J_{P,C}$ = 87.3 Hz, quat. $PPh_2$), 132.0 (d, $J_{P,C}$ = 11.0 Hz, 2× $PPh_2$ + d, $J_{P,C}$ = 3.1 Hz, $PPh_2$), 131.7 (d, $J_{P,C}$ = 2.9 Hz, $PPh_2$), 131.4 (d, $J_{P,C}$ = 10.5 Hz, 2× $PPh_2$), 130.5 (quat. Mes), 129.7 (C-H Mes), 128.6 (d, $J_{P,C}$ = 12.4 Hz, 2× $PPh_2$), 128.3 (d, $J_{P,C}$ = 12.7 Hz, 2× $PPh_2$), 122.9 (C=C Im$^+$), 122.2 (C=C Im$^+$), 83.6 (d, $J_{P,C}$ = 12.3 Hz, quat. Cp$^C$), 76.9 (d, $J_{P,C}$ = 8.6 Hz, Cp), 75.7 (d, $J_{P,C}$ = 11.4 Hz, Cp), 72.9 (d, $J_{P,C}$ = 94.5 Hz, quat. Cp$^P$), 71.8 (d, $J_{P,C}$ = 10.1 Hz, Cp), 71.4 (Cp′), 48.0 (*C*$H_2$Im$^+$), 21.0 (*p*-$CH_3$ Mes), 17.2 (2× *o*-$CH_3$ Mes) ppm. $^{31}P\{^{1}H\}$ NMR (121.5 MHz, $CDCl_3$, 25 °C): $\delta$ = 40.4 ppm. MS (ESI): *m*/*z* (%) = 601 (100) [M$^+$], 415 (27) [M$^+$ – $C_{12}H_{14}N_2$], 187 (20).

**Supporting Information** (see footnote on the first page of this article): Full experimental details, $^{1}H$, $^{13}C$ and $^{31}P$ NMR spectroscopic data, mass spectrometric data and elemental analyses for all new compounds. Crystal data for **4a**, **7a** and **9a** (CCDC-616649 to -616651 contain the supplementary crystallographic data for this paper; these data can be obtained free of charge from The Cambridge Crystallographic Data Centre via www.ccdc.cam.ac.uk/datarequest/cif).

## Acknowledgments

We thank the CNRS for support of this work and Yannick Coppel for NMR analysis of the rhodium complexes.

[1] D. Bourissou, O. Guerret, F. P. Gabbai, G. Bertrand, *Chem. Rev.* **2000**, *100*, 39.
[2] W. A. Herrmann, *Angew. Chem. Int. Ed.* **2002**, *41*, 1290–1309; N. M. Scott, S. P. Nolan, *Eur. J. Inorg. Chem.* **2005**, 1815–1828.
[3] N. Stylianides, A. A. Danopoulos, N. Tsoureas, *J. Organomet. Chem.* **2005**, *690*, 5948–5958; L. D. Field, B. A. Messerle, K. Q. Vuong, P. Turner, *Organometallics* **2005**, *24*, 4241–4250.
[4] C. Yang, H. M. Lee, S. P. Nolan, *Org. Lett.* **2001**, *3*, 1511–1514; J. Wolf, A. Labande, J.-C. Daran, R. Poli, *J. Organomet. Chem.* **2006**, *691*, 433–443; J. Wolf, A. Labande, M. Natella, J.-C. Daran, R. Poli, *J. Mol. Catal. A* **2006**, *259*, 205–212.
[5] H. Seo, H.-J. Park, B. Y. Kim, J. H. Lee, S. U. Son, Y. K. Chung, *Organometallics* **2003**, *22*, 618–620.
[6] S. Gischig, A. Togni, *Organometallics* **2004**, *23*, 2479–2487.
[7] T. Hayashi, T. Mise, M. Fukushima, M. Kagotani, N. Nagashima, Y. Hamada, A. Matsumoto, S. Kawakami, M. Konishi,

 © 2007 Wiley-VCH Verlag GmbH & Co. KGaA, Weinheim 

K. Yamamoto, M. Kumada, *Bull. Chem. Soc. Jpn.* **1980**, *53*, 1138–1151.
[8] N. Mateus, L. Routaboul, J.-C. Daran, E. Manoury, *J. Organomet. Chem.* **2006**, *691*, 2297–2310.
[9] T.-Y. Dong, L.-L. Lai, *J. Organomet. Chem.* **1996**, *509*, 131–134; T.-Y. Dong, P.-H. Ho, C.-K. Chang, *J. Chin. Chem. Soc.* **2000**, *47*, 421–424.
[10] K. S. Coleman, S. Turberville, S. I. Pascu, M. L. H. Green, *J. Organomet. Chem.* **2005**, *690*, 653–658.
[11] H. Seo, B. Y. Kim, J. H. Lee, H.-J. Park, S. U. Son, Y. K. Chung, *Organometallics* **2003**, *22*, 4783–4791.
[12] C. Bolm, M. Kesselgruber, G. Raabe, *Organometallics* **2002**, *21*, 707–710.
[13] Y. Yuan, G. Raabe, C. Bolm, *J. Organomet. Chem.* **2005**, *690*, 5747–5752.
[14] L. Routaboul, S. Vincendeau, J.-C. Daran, E. Manoury, *Tetrahedron: Asymmetry* **2005**, *16*, 2685–2690.
[15] Any attempt to prepare the imidazolium salts by other methods (generation of chloride, bromide or acetate leaving groups from alcohol **3**) failed to give the expected compound, or the reactions were neither selective nor effective.
[16] D. Liu, W. Tang, X. Zhang, *Org. Lett.* **2004**, *6*, 513–516.
[17] Along with the doublet attributed to **10b** in the $^{31}$P NMR spectrum, a second, weak doublet can be observed. However, no other compound can be detected apart from **10b** in the $^{1}$H NMR spectrum.
[18] The yield of **10a** is not given, as we obtained an inseparable mixture of two compounds.
[19] The $^{1}$H NMR signals of the minor compound indicate that it might be a rhodium complex bearing two carbene/phosphane ligands and no cod ligand.
[20] V. César, S. Bellemin-Laponnaz, H. Wadepohl, L. H. Gade, *Chem. Eur. J.* **2005**, *11*, 2862–2873.

Received: December 15, 2006
Published Online: February 14, 2007

 © 2007 Wiley-VCH Verlag GmbH & Co. KGaA, Weinheim 

DOI: 10.1002/ejic.200601258

# Molecular Recognition Utilizing Complexes with NH,NR-Stabilized Carbene Ligands

Nicole Meier,[a] F. Ekkehardt Hahn,*[a] Tania Pape,[a] Carsten Siering,[b] and Siegfried R. Waldvogel*[b]

**Keywords:** Carbene ligands / Supramolecular chemistry / Hydrogen bonds / Homogeneous catalysis / N-Heterocyclic carbenes

Tungsten complex [W(NHC)(CO)$_5$] (**1**) (NHC=NH,N-ethyl-substituted benzimidazolin-2-ylidene ligand) was prepared by transmetallation of lithiated 1-ethylbenzimidazole with the pentacarbonyltungsten complex fragment. The hydrogen-bonding ability of the carbene-NH group to substrates with carbonyl groups was investigated by NMR titration. Structural analogues to **1** with a catalytically active rhodium center show a distinct substrate-selective hydrogenation behaviour.

(© Wiley-VCH Verlag GmbH & Co. KGaA, 69451 Weinheim, Germany, 2007)

## Introduction

Complexes with NR,NR-substituted N-heterocyclic carbene ligands are important catalysts for various transformations. However, much less is known about complexes with NH,NR-substituted carbene ligands, which thus have been disregarded for catalytic applications.[1] We became interested in complexes with NH,NR-substituted carbene ligands because the NH function could act as a hydrogen-bonding donor. In a catalytically active complex bearing an NH,NR-functionalized carbene ligand this could lead to recognition and temporary binding of a substrate with a hydrogen-bonding acceptor moiety like carbonyl compounds. We report here a new one-pot synthesis of a tungsten complex with an NH,NR-stabilized carbene ligand and the observation of hydrogen bonding between the carbene-NH group and carbonyl compounds in solution.

Aminocarbenes with an NH group are obtained, when protic nucleophiles like alcohols or primary or secondary amines attack a coordinated isocyanide ligand (Scheme 1). Unintentionally and most likely unrecognized, this method was first applied as early as 1915 when Tschugajeff and Skanawy-Grigorjewa treated tetrakis(methyl isocyanide)-platinum(II) with hydrazine and isolated a red salt[2] which was very likely the first carbene complex to be synthesized in pure form, predating Fischer's seminal carbene synthesis from carbonylmetal compounds[3] by 49 years. Tschugajeff's red salt was unambiguously established as a carbene complex in 1970[4] and a number of derivatives, partially forming higher associates through hydrogen bonds, have been described recently.[5]

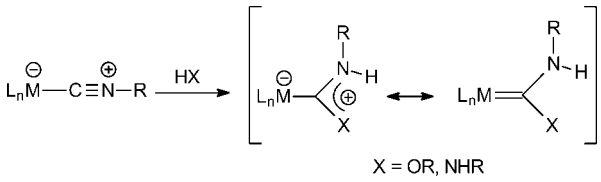


Scheme 1. Nucleophilic attack of a proton base HX at a coordinated isocyanide ligand.

The use of β-functionalized isocyanides, which contain both the isocyanide und the nucleophile in the same molecule, gives access to complexes with N-heterocyclic carbenes through an intramolecular 1,2-addition across the C≡N triple bond (Scheme 2). This method has been used for the preparation of a large number of complexes with NH,O-[6] and NH,NH-heterocyclic carbenes derived from aliphatic[7] and aromatic[8] isocyanides. The NH,NH-stabilized carbene ligands in **A** are easily and stepwise alkylated to give the *N*-alkyl derivatives **B** and **C** by reaction with a base and an alkyl halide.[7,8] However, the preparation of the β-functionalized isocyanides is tedious as are alternative methods for the preparation of complexes with NH,NR-stabilized carbene ligands like the metalla Ugi reaction[9] and others.[10]

[a] Institut für Anorganische und Analytische Chemie, Westfälische Wilhelms-Universität Münster, Corrensstraße 36, 48149 Münster, Germany
Fax: +49-251-8333108
E-mail: fehahn@uni-muenster.de
[b] Kekulé-Institut für Organische Chemie und Biochemie, Rheinische Friedrich-Wilhelms-Universität Bonn, Gerhard-Domagk-Straße 1, 53121 Bonn, Germany
Fax: +49-228-739608
E-mail: waldvogel@uni-bonn.de

 InterScience © 2007 Wiley-VCH Verlag GmbH & Co. KGaA, Weinheim 

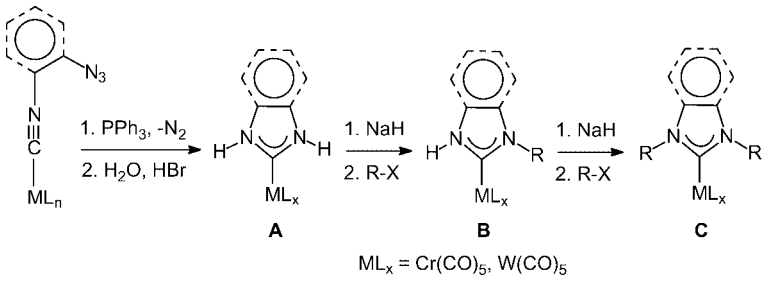


Scheme 2. Template-controlled cyclization of β-functionalized isocyanides.

## Results and Discussion

We have now found an easy one-pot synthesis leading to complexes with NH,NR-stabilized benzimidazolin-2-ylidenes which avoids the use of functionalized isocyanides. If benzimidazole is deprotonated with *n*BuLi and treated with $[W(CO)_5(THF)]$ followed by protonation, only the complex with an *N*-coordinated benzimidazole was obtained.[11] However, the reaction of 1-ethylbenzimidazole with *n*BuLi in THF yields the lithium 1-ethylbenzimidazolate which reacts exclusively under C2 metallation with freshly prepared $[W(CO)_5(THF)]$ (Scheme 3). Complex **1** was formed by protonation of the initially obtained anionic complex with $HCl/Et_2O$. The air- and moisture-stable complex **1** was obtained after column chromatography in 69% yield. The method depicted in Scheme 3 constitutes an alternative and time-saving approach to complexes with NH,NR-substituted N-heterocyclic carbene ligands compared to the intramolecular cyclization of coordinated isocyanide ligands followed by *N*-alkylation.

Complex **1** was investigated by $^1H$ NMR spectroscopy where a broad singlet at $\delta$ = 8.65 ppm was observed for the NH proton and by IR spectroscopy showing a strong absorption for the NH stretching mode at $\tilde{\nu}$ = 3422 $cm^{-1}$. The $^{13}C$ NMR spectrum shows the resonance for the carbene carbon atom at $\delta$ = 191.1 ppm which is a typical value for pentacarbonyltungsten complexes containing a benzannulated N-heterocyclic carbene.[8] The molecular structure of **1** was determined by X-ray diffraction (Figure 1) confirming the connectivity within the complex. Bond lengths and angles in **1** show no unusual features and are within the range observed previously for pentacarbonyltungsten complexes with saturated[7] or benzannulated[9] N-heterocyclic carbene ligands.

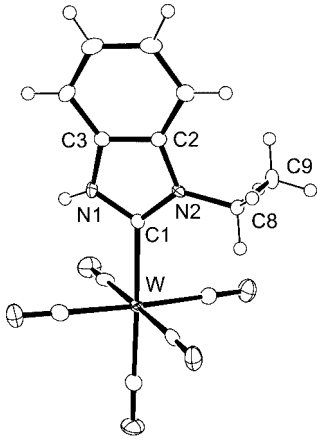


Figure 1. Molecular structure of one of the two independent, essentially identical molecules of **1** in the asymmetric unit. Selected bond lengths [Å] and angles [°] for molecule 1 [molecule 2]: W–C1 2.244(3) [2.242(3)], C1–N1 1.350(4) [1.353(4)], C1–N2 1.351(4) [1.357(4)]; W–C1–N1 123.4(2) [124.2(2)], W–C1–N2 131.1(2) [131.5(2)], N1–C1–N2 105.2(3) [104.2(3)].

Only little is known about the hydrogen-bonding properties of complexes with N-heterocyclic carbenes exhibiting free NH functions. Hydrogen bonding between the NH group of an NH,O-stabilized carbene ligand and triphenylphosphane oxide has been described (Scheme 4).[12] We became interested in the hydrogen-bonding properties of **1**.

$^1H$ NMR techniques allowed a detailed insight into the hydrogen bonding involving the NH proton of the N-heterocyclic carbene. Complex **1** was titrated with the strong hydrogen-bond acceptor DMPU (Scheme 4) as a model for carbonyl compounds in $CDCl_3$ and the reaction was monitored by $^1H$ NMR spectroscopy (Figure 2). Since **1** involves

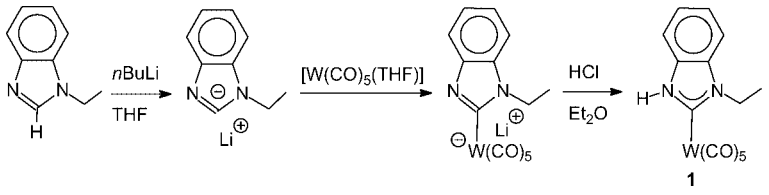


Scheme 3. Preparation of **1** by transmetallation of lithium 1-ethylbenzimidazolate.

 © 2007 Wiley-VCH Verlag GmbH & Co. KGaA, Weinheim 

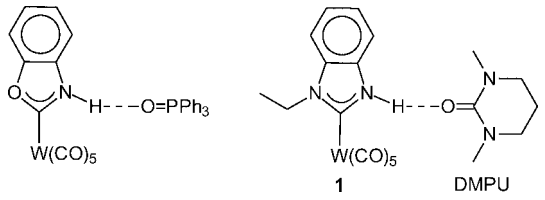


Scheme 4. Hydrogen bonds involving NH,O- and NH,NR-stabilized cyclic carbene ligands.

both a hydrogen-bond donor (NH) and acceptor ($NR_3$), self-assembly to supramolecular aggregates seemed possible. Self-aggregation of the carbene complex as well as the formation of higher aggregates could be excluded by dilution experiments. The investigated concentration range covered several orders of magnitude.[13]

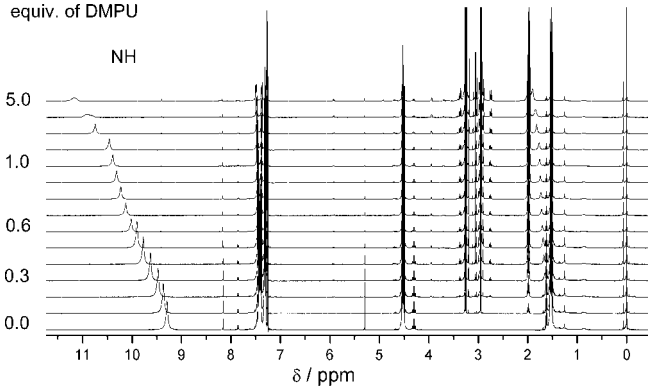


Figure 2. $^1$H NMR titration of **1** with DMPU (up to 5 equiv.).

The NMR titration was carried out at 27 °C in $CD_2Cl_2$ and demonstrated a significant downfield shift of the resonance for the NH proton upon addition of DMPU, while the chemical shifts for all other protons remained essentially unchanged. Only broadening of the NH signal was observed after addition of more than 1 equiv. of DMPU (up to 5 equiv.).

The chemical shifts were fitted using standard tools.[14] Multiple experiments revealed a binding constant of about $40 \pm 10$ M$^{-1}$ for the single hydrogen bond which corresponds to $\Delta G_{ass} = 2.2$ kcal mol$^{-1}$. Investigations of the secondary interaction using optical spectroscopy failed since the high dilution required does not favour the hydrogen bonding. The hydrogen bonding is supported by chlorinated solvents and THF, whereas protic media like alcohols impede the supramolecular interaction.

The NH group of an NH,NR-stabilized carbene ligand is able to function as a supramolecular recognition site. Its close proximity to the metal center is unusual. In most described cases the supramolecular host moieties are connected to the metal center by a flexible spacer causing entropic problems.[15] Secondary interactions of the NH group with selected substrates should be suitable to direct metal-mediated conversions. In the rhodium(I)-catalyzed hydrogenation reaction of a suitably carbonyl-functionalized olefin, for example, the substrate will interact initially by multiple contacts while some attractive interactions will disappear after the catalytic transformation at the metal center (Scheme 5), which generates an interesting motif for directed transition metal catalysis.

Preliminary studies of the catalytic properties of the (carbene)rhodium(I) complex **2** (Scheme 6) yielded proof of our concept. Complex **2** is equipped with an NH,NR-stabilized carbene ligand.[16] The use of triphenylphosphane in the preparation of **2**, however, gave a mixture of complexes. Together with complex **2** (major), the complex with an *N*-coordinated methylbenzimidazole ligand (minor) were obtained, which appeared to interconvert in solution.

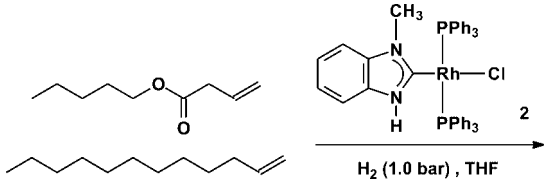


Scheme 6. Competitive hydrogenation experiment utilizing the substrate selectivity of the NH,NR-stabilized carbene ligand in **2**.

In the hydrogenation of 1-octene the mixture of **2** and its isomer turned out to be catalytically more active than Wilkinson's catalyst. When the mixture was treated in a

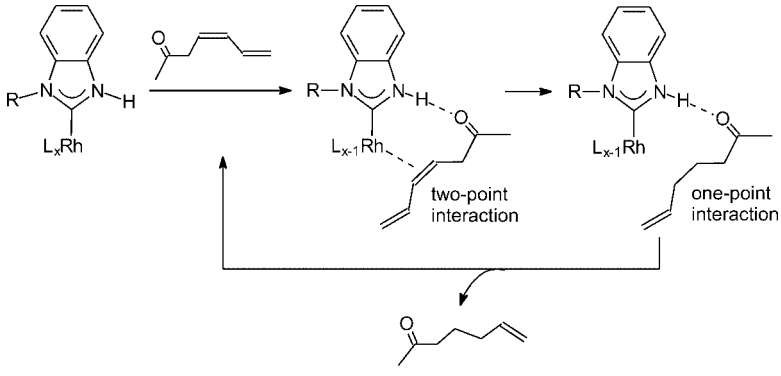


Scheme 5. Concept of two-point interaction/recognition of substrates with complexes bearing NH,NR-stabilized N-heterocyclic carbene ligands.

 © 2007 Wiley-VCH Verlag GmbH & Co. KGaA, Weinheim 

competitive hydrogenation experiment with 1-dodecene and a 3-butenoic acid ester (Figure 3), the substrate with the supramolecular recognition unit is clearly preferred. Up to a conversion of 80% a significant preference for the substrate bearing the supramolecular key was observed. Control experiments with Wilkinson's catalyst clearly eliminate the Lewis acidic properties of rhodium(I) as source for this selectivity since only a very slight preference for the oxygenated substrate was found in this case.

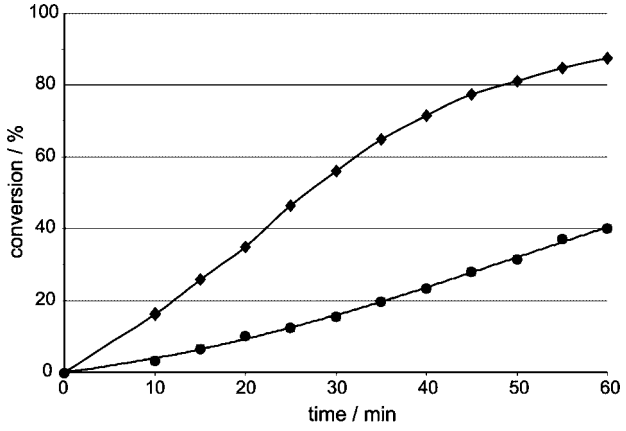


Figure 3. Competitive hydrogenation of 1-dodecene (dots) and a 3-butenoic acid ester (diamonds) using catalyst **2**.

## Conclusions

We have described a straightforward one-pot synthesis of complex **1** bearing an N-heterocyclic carbene ligand which exhibits a free NH function. The NH group is able to act as a hydrogen-bond donor. However, hydrogen bonding does not lead to self-aggregation in the case of **1**. The NH group of an NH,NR-stabilized N-heterocyclic carbene ligands can act as a supramolecular key in the vicinity of a catalytically active rhodium center which enabled a substrate-selective hydrogenation. Currently, we are studying complexes with NH,NR-stabilized N-heterocyclic carbene ligands bound to various catalytically active metal centers with the intention of employing the supramolecular recognition of suitable substrates for selective catalytic transformations, e.g. for regioselective C–C coupling reactions.

## Experimental Section

**Analytical Data for Complex 1**: $^1$H NMR (200.1 MHz, $CDCl_3$): $\delta$ = 8.65 (br. s, 1 H, NH), 7.46–7.26 (m, 4 H, Ar-H), 4.52 (q, 2 H, $CH_2$), 1.50 (t, 3 H, $CH_3$) ppm. $^{13}$C NMR (50.3 MHz, $CDCl_3$): $\delta$ = 201.0 ($CO_{trans}$), 197.6 ($CO_{cis}$), 191.1 (NCN), 133.9, 132.9, 123.7, 123.3, 110.6, 110.3 (Ar-C), 44.5 ($CH_2$), 14.9 ($CH_3$) ppm. IR (KBr): $\tilde{\nu}$ = 3422 (s, NH), 3087–3008 (w, CH aliphatic), 3001–2877 (w, CH aromatic), 2063 (vs, CO), 1910 (vs, CO), 1859 (vs, CO) cm$^{-1}$. MS (EI): *m/z* (%) = 470 (100) $[M]^+$, 442 (50.0) $[M - CO]^+$, 414 (90.0) $[M - 2\,CO]^+$, 386 (15) $[M - 3\,CO]^+$. $C_{14}H_{10}N_2O_5W$ (470.09): calcd. C 35.77, H 2.14, N 5.96; found C 35.50, H 2.53, N 5.87.

**Crystal Data for Complex 1**: $C_{14}H_{10}N_2O_5W$, $M$ = 470.09, $T$ = 123(2) K, $\lambda$ = 0.71073 Å, monoclinic, $P2_1/c$, $Z$ = 8, $a$ = 13.257(2), $b$ = 17.566(2), $c$ = 12.853(2) Å, $\beta$ = 96.744(3)°, $V$ = 2972.4(7) Å$^3$, 33820 measured reflections, 8650 unique reflections ($R_{int}$ = 0.0481), $R$ = 0.0279, $wR$ = 0.0567 for 7446 contributing reflections [$I \geq 2\sigma(I)$], refinement against $|F^2|$with anisotropic thermal parameters for all non-hydrogen atoms and hydrogen atoms on calculated positions. CCDC-618744 contains the supplementary crystallographic data for this paper. These data can be obtained free of charge from The Cambridge Crystallographic Data Centre via www.ccdc.cam.ac.uk./data/request/cif.

## Acknowledgments

Financial support by the DFG (SPP 1118, "Activation of less reactive substrates by secondary interactions" and IRTG 673) is acknowledged.

[1] a) W. A. Herrmann, *Angew. Chem. Int. Ed.* **2002**, *41*, 1290–1309; b) F. E. Hahn, *Angew. Chem. Int. Ed.* **2006**, *45*, 1348–1352.
[2] a) L. Tschugajeff, M. Skanawy-Grigorjewa, *J. Russ. Chem. Soc.* **1915**, *47*, 776; b) L. Tschugajeff, M. Skanawy-Grigorjewa, A. Posnjak, *Z. Anorg. Allg. Chem.* **1925**, *148*, 37–42.
[3] E. O. Fischer, A. Maasböl, *Angew. Chem. Int. Ed. Engl.* **1964**, *3*, 580–581.
[4] a) G. Rouschias, B. Shaw, *J. Chem. Soc. D* **1970**, 183; b) A. Burke, A. L. Balch, J. H. Enemark, *J. Am. Chem. Soc.* **1970**, *92*, 2555–2557.
[5] a) A. I. Moncada, S. Manne, J. M. Tanski, L. M. Slaughter, *Organometallics* **2006**, *25*, 491–505; b) J. R. Stork, M. M. Olmstead, J. C. Fettinger, A. L. Balch, *Inorg. Chem.* **2006**, *45*, 849–857; c) J. R. Stork, M. M. Olmstead, A. L. Balch, *Inorg. Chem.* **2004**, *43*, 7508–7515.
[6] a) M. Tamm, F. E. Hahn, *Coord. Chem. Rev.* **1999**, *182*, 175–209; b) M. Basato, R. A. Michelin, M. Mozzon, P. Sgarbossa, A. Tassan, *J. Organomet. Chem.* **2005**, *690*, 5414–5420.
[7] a) F. E. Hahn, V. Langenhahn, T. Pape, *Chem. Commun.* **2005**, 5390–5392; b) M. Basato, F. Benetollo, G. Faccin, R. A. Michelin, M. Mozzon, S. Pugliese, P. Sgarbossa, S. M. Sbovata, A. Tassan, *J. Organomet. Chem.* **2004**, *689*, 454–462.
[8] a) F. E. Hahn, V. Langenhahn, N. Meier, T. Lügger, W. P. Fehlhammer, *Chem. Eur. J.* **2003**, *9*, 704–712; b) F. E. Hahn, C. Garcia Plumed, M. Münder, T. Lügger, *Chem. Eur. J.* **2004**, *10*, 6285–6293; c) F. E. Hahn, V. Langenhahn, T. Lügger, T. Pape, D. Le Van, *Angew. Chem. Int. Ed.* **2005**, *44*, 3759–3763.
[9] D. Rieger, S. D. Lotz, U. Kernbach, C. André, J. Bertran-Nadal, W. P. Fehlhammer, *J. Organomet. Chem.* **1995**, *491*, 135–152.
[10] a) H. G. Raubenheimer, G. J. Kruger, A. van A. Lombard, L. Linford, J. C. Viljoen, *Organometallics* **1985**, *4*, 275–284; b) F. Bonati, A. Burini, B. R. Pietrosi, B. Bovio, *J. Organomet. Chem.* **1989**, *375*, 147–160; c) S.-T. Liu, T.-Y. Hsieh, G.-H. Lee, S.-M. Peng, *Organometallics* **1996**, *15*, 1055–1061.
[11] F. E. Hahn, C. Radloff, unpublished results.
[12] F. E. Hahn, L. Imhof, *Organometallics* **1997**, *16*, 763–769.
[13] Dilution experiments were performed in $CD_2Cl_2$. No changes in the $^1$H NMR chemical shifts were observed in the range of $10^{-5}$ to $5 \times 10^{-1}$ M.
[14] Fitting of the data was performed with *SPECFIT*, version 2.12, Spectrum Software Associates, Chapel Hill, NC, USA; H. Gampp, M. Maeder, C. J. Meyer, A. D. Zuberbühler, *Talanta* **1986**, *33*, 943 and references cited therein. The given error is based on the applied method. Multiple determinations gave a good reproducibilty. Prolonged exposure of **1** to ambient conditions lead to some decomposition. Employed conditions: $2 \times 10^{-2}$ M **1** in $CD_2Cl_2$ treated with DMPU.

 © 2007 Wiley-VCH Verlag GmbH & Co. KGaA, Weinheim 

[15] a) H. K. A. C. Coolen, P. W. N. M. van Leeuwen, R. J. M. Nolte, *Angew. Chem. Int. Ed. Engl.* **1992**, *31*, 905–907; b) M. T. Reetz, S. R. Waldvogel, *Angew. Chem. Int. Ed. Engl.* **1997**, *36*, 865–867.

[16] An analogue of complex **2**, namely [RhCl($PCy_3$)$_2$(*N*-methylbenzimidazolin-2-ylidene)], was obtained as an intermediate in the [RhCl(coe)$_2$]-catalyzed arylation of *N*-methylbenzimidazole. This complex could also be obtained from the stoichiometric reaction of *N*-methylbenzimidazole with [RhCl(coe)$_2$] and $PCy_3$. The mechanism for this reaction is currently unknown. The stoichometric reaction of *N*-methylbenzimidazole with [RhCl(coe)$_2$] and $PPh_3$ yields complex **2** (major) and its isomer with an *N3*-coordinated *N1*-methylbenzimidazole ligand (minor). See: J. C. Lewis, S. H. Wiedemann, R. G. Bergman, J. A. Ellman, *Org. Lett.* **2004**, *6*, 35–38.

Received: December 31, 2006
Published Online: February 15, 2007

 © 2007 Wiley-VCH Verlag GmbH & Co. KGaA, Weinheim 

DOI: 10.1002/ejic.200601054

# A Two-Dimensional, Hydrogen-Bond-Cross-Linked Molybdenum(VI) Network Polymer with Catalytic Activity

**Yi Luan,[a] Ge Wang,*[b] Rudy L. Luck,[c] and Mu Yang[b]**

**Keywords:** Hydrogen bonds / Crystal engineering / Hydrogen peroxide / Epoxidation / Molybdenum

The new hybrid inorganic–organic polymer $[MoO_2Cl_2(H_2O)_2]\cdot(H_2dipy\text{-}pra)Cl_2$ (**1**), where dipy-pra = 1,3-bis(4-pyridyl)propane, has been synthesized and crystallographically characterized. $MoO_2Cl_2(H_2O)_2$ and the $[H_2dipy\text{-}pra]^{2+}$ cation are cross-linked by Mo–$H_2O$···Cl and $H_2$dipy-pra···Cl hydrogen bonds to form a two-dimensional layer structure. Complex **1** is an efficient catalyst, with $H_2O_2$ as the oxygen-source oxidant and $NaHCO_3$ as the cocatalyst, in the epoxidation of olefinic compounds under ambient conditions.

(© Wiley-VCH Verlag GmbH & Co. KGaA, 69451 Weinheim, Germany, 2007)

The design and synthesis of metal–organic coordination polymers that is based on the strategy of crystal engineering is an emerging area, and a variety of novel supramolecular architectures have been obtained. Moreover, coordination polymers are used in areas such as magnetism,[1,2] optoelectronics,[3] guest exchangeability,[4,5] and catalysis.[6] The concept of crystal engineering was first introduced as an approach to more efficient topochemical reactions in the early 1960s.[7] However, the synthesis of coordination polymers following the principles of crystal engineering was not achieved until 1995.[8,9] Several recent reviews have described how coordination polymers ranging from one-dimensional to three dimensional can be attributed to the rapid development of crystal engineering research.[10,11] Molybdenum- and tungsten-based supramolecular networks have also been investigated.[12] Zubieta described a molybdenum-based network that employed protonated 4,4′-bipyridine as a ligand serving to buttress the inorganic layers.[13] In light of recent successes in the construction of potentially useful coordination polymers, we wanted to utilize a bidentate ligand and a dioxidomolybdenum(VI) center to yield this type of metal–organic hydrogen-bond network by crystal engineering.

Organomolybdenum reagents have been used in a variety of oxidation reactions such as epoxidation and the oxidation of alcohols and sulfides. In the past few years, dioxidomolybdenum(VI) halide complexes have been found to be efficient epoxidation catalysts.[14] We reported a series of dioxidomolybdenum(VI) halide complexes that catalyze the epoxidation of olefins with *tert*-butyl hydroperoxide (TBHP).[15,16] From both an economic and an environmental viewpoint, there is a definite need for catalytic oxidations employing hydrogen peroxide as the stoichiometric oxidant, because hydrogen peroxide is environmentally friendly, cheap, and readily available.[17] To the best of our knowledge, there is no report regarding efficient epoxidations with $H_2O_2$ by using dioxidomolybdenum(VI) halide complexes. In the present work, the synthesis, crystal structure, and characterization of $[MoO_2Cl_2(H_2O)_2]\cdot(H_2dipy\text{-}pra)Cl_2$ is reported, as well as the potential of this complex as an epoxidation catalyst with hydrogen peroxide as the oxidant.

The key to our approach was the utilization of aromatic amines such as 1,3-bis(4-pyridyl)propane. It is known that under more acidic reaction conditions protonation of the aromatic amine provides an aromatic ammonium cation. Thus, the aromatic ammonium cations of a linear bidentate ligand can serve as a structure-directing template by virtue of multipoint hydrogen bonding between the cation and the metal complex to form a new hydrogen-bond network structure. Compound **1** was synthesized by the reaction of $MoO_2Cl_2(H_2O)_2$ and protonated dipy-pra.[18] Single-crystal X-ray diffraction studies on the sample obtained from the reaction revealed its composition, $[MoO_2Cl_2(H_2O)_2]\cdot(H_2dipy\text{-}pra)Cl_2$, and an extended structure composed of the building units shown in Figure 1.

The supramolecular structure of complex **1** is shown in Figure 2. Each dipy-pra molecule is linked by H-bonds to a $H_2O$ molecule of two uncharged $MoO_2Cl_2(H_2O)_2$ units through external chloride anions. The two-dimensional polymeric structure was formed by H-bonded linkages (O2W···Cl4 = 3.087, N2···Cl4 = 3.100, O1W···Cl4 = 3.059, O2W···Cl3 = 3.125, O1W···Cl3 = 3.047, N1···Cl3 = 3.038 Å). The Mo–O(oxido) and Mo–Cl distances, and the *cis*-$MoO(oxido)_2$ and *trans*-$MoCl_2$ angles, are comparable

[a] Beijing University of Chemical Technology, Beijing 100029, P. R. China
[b] School of Materials Science and Engineering, University of Science and Technology Beijing, Beijing 100083, P. R. China
E-mail: gewang@mater.ustb.edu.cn
[c] Department of Chemistry, Michigan Technological University, Houghton, MI 49931, USA

 © 2007 Wiley-VCH Verlag GmbH & Co. KGaA, Weinheim 

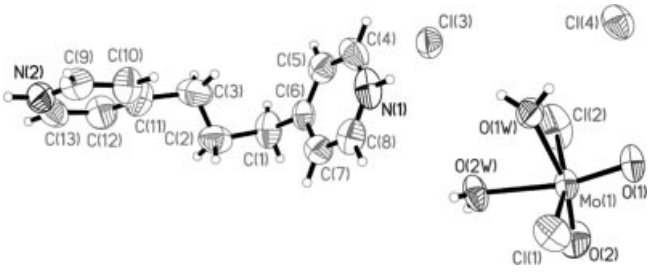


Figure 1. The building-block unit present in crystalline **1**. Thermal ellipsoids are drawn at the 50% probability level. Selected bond lengths [Å] and angles [°]: Mo(1)–O(2) 1.671(3), Mo(1)–O(1) 1.683(3), Mo(1)–O(1W) 2.217(3), Mo(1)–O(2W) 2.244(3), Mo(1)–Cl(1) 2.3739(13), Mo(1)–Cl(2) 2.3754(15), O(2)–Mo(1)–O(1) 105.12(16), O(1W)–Mo(1)–O(2W) 75.33(12), Cl(1)–Mo(1)–Cl(2) 162.13(6).

to those reported for other related $MoO_2Cl_2L_2$ complexes.[19] There are slight differences in the Mo–O(W) distances, and the shorter distance, i.e. Mo–O(1W) = 2.217(3) Å, correlates with a smaller O(1W)–Mo–O(2) angle of 164.07(14)° and the longer Mo–O(2W) distance of 2.244(3) Å with a larger O(2W)–Mo–O(1) angle of 166.08(14)°. This significant difference in Mo–O(W) bond lengths would appear to be related to the *trans* effect of the oxido ligand.

The catalytic property of compound **1** was then studied. With complex **1** as the catalyst, $NaHCO_3$ as the cocatalyst, and $H_2O_2$ as the oxygen source, we were able to catalyze the epoxidation of olefinic compounds. Cyclooctene was selected as a standard substrate for the optimization process with $H_2O_2$ in acetonitrile. A good yield (99%) of the epoxide was achieved with a catalytic amount of **1** (1 mol-%) and $NaHCO_3$ as cocatalyst (25 mol-%) after 1 h at room temperature (25 °C).

To evaluate the scope of this procedure, the oxidation of other alkenes was also studied (Table 1). As shown, carbocyclic alkenes were oxidized to produce the corresponding epoxy compounds in high yields (entries 1 and 2, Table 1). However, oxidation of the aromatic and linear alkenes required longer reaction times than that of the carbocyclic alkenes (entries 3 and 4, Table 1), especially 1-octene. Similarly, the allylic alcohols underwent oxidation without affecting the hydroxy group (entry 5, Table 1). Kuhn reported that dioxidomolybdenum derivatives are able to catalyze the olefin epoxidation reaction with TBHP but not with $H_2O_2$.[14]

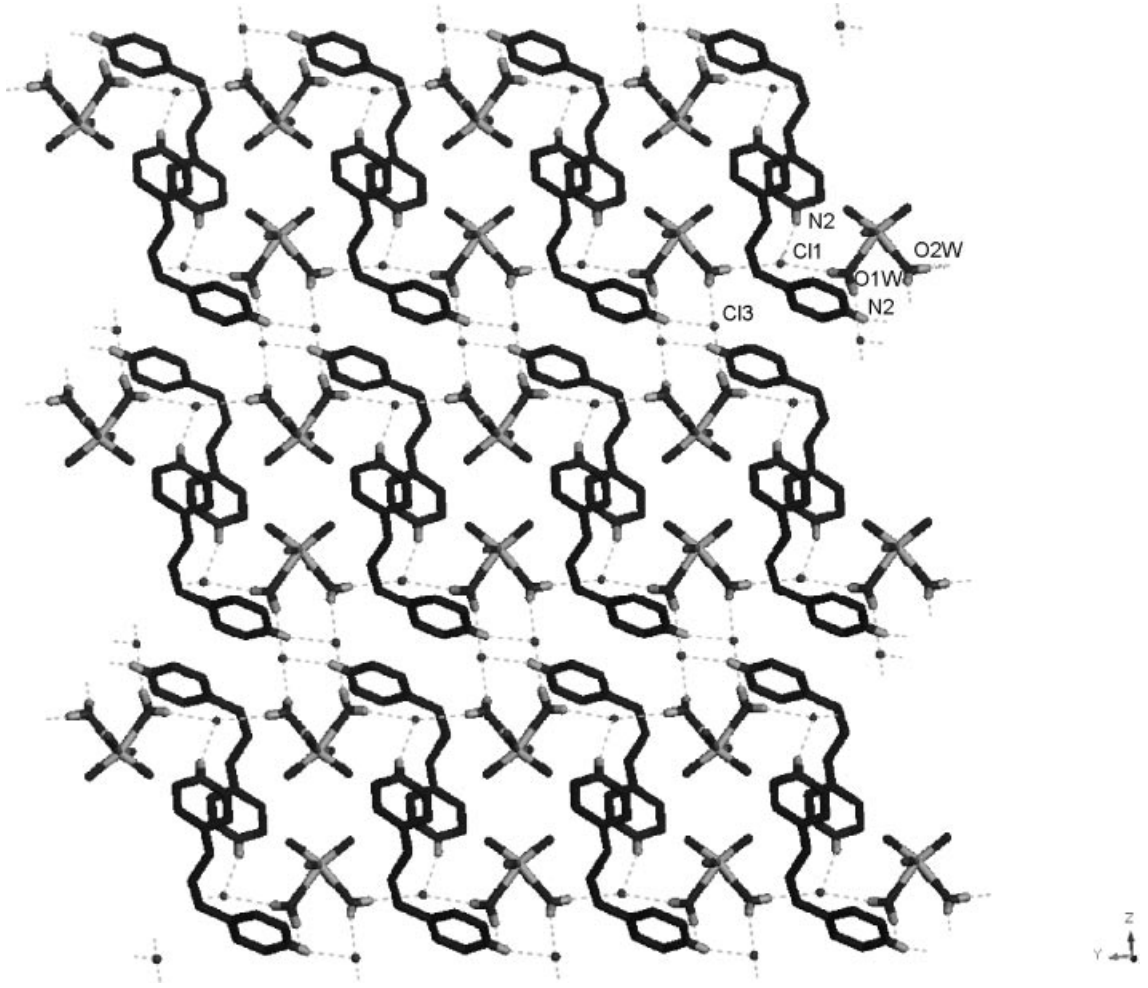


Figure 2. The two-dimensional layer structure of complex **1**. For clarity, part of the H atoms have been omitted.

 © 2007 Wiley-VCH Verlag GmbH & Co. KGaA, Weinheim 

Table 1. Epoxidation of selected olefins catalyzed by molybdenum(VI) complex **1**, with $H_2O_2$ as oxidant and hydrogencarbonate as cocatalyst.[a]

| Entry | Substrate | Time [h] | Product | Yield[b] [%] | Selectivity [%] |
|---|---|---|---|---|---|
| 1 | | 1 | | 99[c] | 99 |
| 2 | | 1.5 | | 99[c] | 99 |
| 3 | 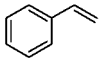 | 4 | 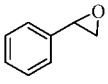 | 86[c] | 99 |
| 4 | 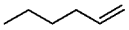 | 4 | 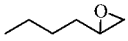 | 92 | 99 |
| 5 | | 2 | | 95 | 99 |

[a] Reaction conditions: the substrate (10 mmol), catalyst **1** (0.1 mmol, 1 mol-%), $NaHCO_3$ (2.5 mmol, 25 mol-%) and 30% aqueous $H_2O_2$ (40 mmol) dissolved in acetonitrile (10 mL) at 25 °C. [b] Determined by GC by using an internal standard technique. [c] Isolated yield.

Notably, the chemoselectivity was reduced at higher temperatures. In the epoxidation of cyclic alkenes (such as cyclohexene) at 50 °C, 2,3-epoxycyclohexanone and 2-cyclohexen-1-one were obtained in addition to the desired epoxide product. When the reaction was carried out at reflux temperature, i.e. 75 °C, the efficiency was significantly reduced. To confirm whether this reduction in efficiency was due to the conversion of $NaHCO_3$ (which acts as a cocatalyst) into $Na_2CO_3$, $NaHCO_3$ was replaced by $Na_2CO_3$; this resulted in almost no oxidation products, even after 24 h.[20]

Besides our system, Burgess and Bhattacharyya demonstrated that $MnSO_4$ and $[MoO(O_2)_2(saloxH)]$ can catalyze epoxidation reactions efficiently with $NaHCO_3/H_2O_2$.[21,22] The epoxidation of alkenes in the presence of hydrogencarbonate alone was also investigated.[20,23] Interestingly, the use of complex **1** or hydrogencarbonate alone gave much lower yields of epoxides than when they were used together.[21,22] Richardson showed that a key aspect of such reactions is that hydrogen peroxide and hydrogencarbonate combine in an equilibrium process to produce peroxymonocarbonate, $HCO_4^-$.[24,25] $HCO_4^-$ may be more reactive than hydrogen peroxide and can be expected to attack the metal center or other more potent, activated groups at a much faster rate.[21] The mechanism for our epoxidation reaction is under investigation.

In conclusion, a novel 2D network material with the general formula $[MoO_2Cl_2(H_2O)_2]\cdot(dipy\text{-}praH_2)Cl_2$ has been synthesized and successfully applied to epoxidation reactions. Our current observations suggest that, under acidic conditions, the protonated $[H_2dipy\text{-}pra]^{2+}$ cation serves as a structure-directing template by using multipoint hydrogen bonding in the formation of infinite frameworks. The epoxidation of alkenes was studied with hydrogen peroxide in the presence of complex **1** to give products in high yields. This reaction provides a new environmentally friendly route for the conversion of a variety of alkenes to their respective epoxides.

## Acknowledgments

We thank the NSFC (Grant no. 2220406003) and the Program for New Century Excellent Talents in University (NCET-05–0103) for support. We also thank Dr. Zhan Shi at Jilin University for the determination of the X-ray structure.

[1] X. Y. Wang, B. L. Li, X. Zhu, S. Gao, *Eur. J. Inorg. Chem.* **2005**, *16*, 3277–3286.
[2] K. Inoue, T. Hayamizu, H. Iwamura, D. Hashizume, Y. Ohashi, *J. Am. Chem. Soc.* **1996**, *118*, 1803–1804.
[3] O. R. Evans, W. B. Lin, *Chem. Mater.* **2001**, *13*, 2705–2712.
[4] O. M. Yaghi, C. E. Davis, G. M. Li, H. L. Li, *J. Am. Chem. Soc.* **1997**, *119*, 2861–2868.
[5] S. Kawata, S. Kitagawa, H. Kumagai, C. Kudo, H. Kamesaki, T. Ishiyama, R. Suzuki, M. Kondo, M. Katada, *Inorg. Chem.* **1996**, *35*, 4449–4461.
[6] K. Endo, T. Kake, T. Sawaki, O. Hayashida, H. Masuda, H. Aoyama, *J. Am. Chem. Soc.* **1997**, *119*, 4117–4122.
[7] B. F. Hoskins, R. Robson, *J. Am. Chem. Soc.* **1990**, *112*, 1546–1554.
[8] S. Mann, *J. Chem. Soc., Dalton Trans.* **1993**, 1–9.
[9] L. R. MacGillivray, S. Subramanian, M. J. Zaworotko, *J. Chem. Soc., Chem. Commun.* **1994**, 1325–1326.
[10] K. Biradha, M. Sarkar, L. Rajput, *Chem. Commun.* **2006**, 4169–4179.
[11] N. W. Ockwig, O. Delgado-Friedrichs, M. O'Keeffe, O. M. Yaghi, *Acc. Chem. Res.* **2005**, *38*, 176–182.
[12] B. Sieklucka, R. Podgajny, T. Korzeniak, P. Przychodzen, R. Kania, *Cr. Chim.* **2002**, *5*, 639–649.
[13] P. J. Zapf, R. C. Haushalter, J. Zubieta, *Chem. Commun.* **1997**, 321–322.
[14] F. E. Kuhn, A. M. Santos, A. D. Lopes, I. S. Goncalves, E. Herdtweck, C. C. Ramao, *J. Mol. Catal. A* **2000**, *164*, 25–38.
[15] G. Wang, G. Chen, R. L. Luck, Z. Q. Wang, Z. C. Mu, D. G. Evans, X. Duan, *Inorg. Chim. Acta* **2004**, *357*, 3223–3229.
[16] G. Wang, L. S. Feng, R. L. Luck, D. G. Evans, Z. Q. Wang, X. Duan, *J. Mol. Catal. A* **2005**, *241*, 8–14.
[17] R. Noyori, M. Aoki, K. Sato, *Chem. Commun.* **2003**, 1977–1986.
[18] Experimental details: $MoO_3$ (0.826 g, 5.74 mmol) was dissolved in excess concentrated HCl by stirring at 40 °C for 4 h; a pale yellow solution was obtained. The solution was cooled in an ice bath, and a solution of a dipy-pra (1.138 g, 5.74 mmol) in ethanol (10 mL) was then added in portions. After stirring for 6 h, a yellow solution was obtained, which when left overnight at ca. 4 °C afforded the lemon yellow crystalline complex **1** in 1.48 g, 51% yield. The characterization results are as follows: $C_{13}H_{20}Cl_4MoN_2O_4$ (506.66): calcd. C 30.85, H 3.98, Mo 18.96, N 5.54, $O_2^{2-}$ 12.65; found C 30.71, H 4.11, Mo 18.91, N 5.46, $O_2^{2-}$ 12.87. IR (KBr disc; selected bands): 952, 936 ($MoO_2$, asym.), 906 ($MoO_2$, sym.) $cm^{-1}$. Crystal data for **1** at 293 K: $C_{13}H_{20}N_2O_4Cl_4Mo$, $M$ = 506.05, triclinic, space group $P\bar{1}$, yellow plate crystal (0.32 mm × 0.28 mm × 0.24 mm), $a$ = 8.6398(17), $b$ = 8.6481(17), $c$ = 13.944(3) Å, $\alpha$ = 85.33(3), $\beta$ = 83.03(3), $\gamma$ = 82.44(3)°, $V$ = 1022.9(4) Å$^3$, $Z$ = 2, $D_{calcd.}$ = 1.643 Mg/m$^3$, $\mu$ = 1.182 mm$^{-1}$, $F$(000)= 508, 10144 reflections measured, 4632 unique. CCDC-614792 contains the supplementary crystallographic data for this paper. These data can be obtained free of charge from The Cambridge Crystallographic Data Centre via www.ccdc.cam.ac.uk/data_request/cif.
[19] M. J. Taylor, J. R. Wang, C. E. F. Rickard, *Polyhedron* **1993**, *12*, 1433–1435.

 © 2007 Wiley-VCH Verlag GmbH & Co. KGaA, Weinheim 

[20] H. R. Yao, D. E. Richardson, *J. Am. Chem. Soc.* **2000**, *122*, 3220–3221.
[21] B. S. Lane, M. Vogt, V. J. DeRose, K. Burgess, *J. Am. Chem. Soc.* **2002**, *124*, 11946–11954.
[22] S. K. Maiti, S. Dinda, N. Gharah, R. Bhattacharyya, *New J. Chem.* **2006**, *30*, 479–489.
[23] W. C. Frank, *Tetrahedron: Asymmetry* **1998**, *9*, 3745–3749.
[24] J. Flanagan, D. P. Jones, W. P. Griffith, A. C. Skapski, A. P. West, *J. Chem. Soc., Chem. Commun.* **1986**, 20–21.
[25] A. Adam, M. Mehta, *Angew. Chem. Int. Ed.* **1998**, *37*, 1387–1388.

Received: November 10, 2006
Published Online: February 14, 2007

 © 2007 Wiley-VCH Verlag GmbH & Co. KGaA, Weinheim 

DOI: 10.1002/ejic.200601187

# A New Silver(I) Aggregate Having an Octagonal $Ag_4S_4$ Core Where $\mu_3$-S Bonding Interactions Lead to a Nanotube Assembly that Exhibits Quasiaromaticity

**Sotiris Zartilas,[a] Nikolaos Kourkoumelis,[a] Sotiris K. Hadjikakou,*[a] Nick Hadjiliadis,*[a] Panagiotis Zachariadis,[a] Maciej Kubicki,[b] Alexey Yu. Denisov,[c] and Ian S. Butler[c]**

**Keywords:** Bioinorganic chemistry / Silver / Aromaticity / Nanotubes

Silver(I) chloride reacts with 2-mercapto-3,4,5,6-tetrahydropyrimidine ($StpmH_2$, $C_4H_8N_2S$) in DMSO with excess triethylamine to give a complex of formula $\{[Ag_4Cl_4(\mu_3\text{-}StpmH_2)_4]_n\}$ (**1**). The product was characterized by elemental analyses, FTIR far-IR, UV/Vis, and $^1H$ and $^{109}Ag$ NMR spectroscopic techniques. The $^{109}Ag$ NMR spectroscopic data of the complexes $\{[Ag_6(\mu_2\text{-}Br)_6(\mu_2\text{-}StpmH_2)_4(\mu_3\text{-}StpmH_2)_2]_n\}$ (**2**) and $\{[Ag_4(\mu_2\text{-}StpmH_2)_6](NO_3)_4\}_n$ (**3**) are also reported here for comparison. Crystal structure of complex **1** was determined by X-ray diffraction at 100(1) K. Complex **1**, $C_4H_8AgClN_2S$, crystallized in the tetragonal system, space group *P4cc*, $a$ = 15.7761(9) Å, $b$ = 15.7761(9) Å, $c$ = 6.9624(8) Å, $V$ = 1732.8(2) Å$^3$, $Z$ = 2. Each metal ion is bonded to one terminal Cl atom and three $\mu_3$-S atoms from three $StpmH_2$ ligands. Four silver ions are bridged by four sulfur atoms forming an octagonal $Ag_4S_4$ core. Each $Ag^I$ ion of one core is also bridged to an $Ag^I$ ion of another core through a sulfur atom, which forms an infinite nanotube structure. A computational study utilizing the method of nucleus-independent chemical shifts (NICS) showed that the $Ag_4S_4$ core exhibits strong quasiaromaticity at the geometric cage center. To the best of our knowledge, this is the first example of an $Ag^I$ cluster that presents quasiaromaticity and stacking interactions.

(© Wiley-VCH Verlag GmbH & Co. KGaA, 69451 Weinheim, Germany, 2007)

## Introduction

The research in designing infinite molecular components with specific chains and networks is a matter of current interest.[1] This self-assembly process between metal ions and ligands is known to depend on steric and interactive information stored in the ligand and governed by the metal ions through their coordination geometry demands.[1b,1c] Recently, a new type of aromaticity that results from the cyclical delocalization of electron density of d- as well as (d–p)π-type orbitals instead of the usual p orbitals on metal–ligand rings has been reported;[2] this may introduce greater stability to the higher-order structures. From this point of view, the ability of silver(I) thiolate or thionate complexes to adopt geometries with variable nuclearities and structural diversity makes the study of silver(I) chemistry very attractive.[3–4] Such silver(I) complexes with sulfur-containing ligands exhibit a wide range of applications in medicine, analytical chemistry, or the industrial preparation of polymers.[3,4] Biomedical applications and uses of silver(I) complexes are related to their antibacterial action,[5a,5b] which appears to involve interactions with DNA.[5c] The molecular design and structural characterization of silver(I) complexes is therefore an intriguing aspect of bioinorganic chemistry and metal-based drugs.[6]

A great deal of work has been devoted to the study of thioamides because of their tendency to bridge metal centers to form oligo- and polynuclear species with potential usage as functional solid materials.[7] Furthermore, 2-mercapto-3,4,5,6-tetrahydropyrimidine can coordinate up to three metal centers at short distances, which offers the possibility of studying the metal–metal interaction of $d^{10}$ systems which have attracted considerable attention.[8] Such well-defined higher-order structures of 2-mercapto-3,4,5,6-tetrahydropyrimidine have already been reported for complexes **2** and **3**.[9]

In this paper, we report the structural and spectroscopic characterization of a new silver complex with the heterocyclic thioamide 2-mercapto-3,4,5,6-tetrahydropyrimidine (Scheme 1) of formula $\{[Ag_4Cl_4(\mu_3\text{-}StpmH_2)_4]_n\}$ (**1**). Also, a computational study of the aromaticity aimed at the rationalization of the stability of this structure and its $^{109}Ag$ NMR spectroscopic data in relation to the corresponding known complexes $\{[Ag_6(\mu_2\text{-}Br)_6(\mu_2\text{-}StpmH_2)_4(\mu_3\text{-}StpmH_2)_2]_n\}$ (**2**) and $\{[Ag_4(\mu_2\text{-}StpmH_2)_6](NO_3)_4\}_n$ (**3**) is de-

[a] Section of Inorganic and Analytical Chemistry, Department of Chemistry, University of Ioannina,
45110 Ioannina, Greece
Fax: +30-26510-44831
E-mail: nhadjis@uoi.gr
[b] Department of Chemistry, A. Mickiewicz, University,
ul. Grunwaldzka 6, 60-780 Poznan, Poland
[c] Department of Chemistry, McGill University,
801 Sherbrooke Street West, Montreal, Quebec H2A 2K6, Canada

 © 2007 Wiley-VCH Verlag GmbH & Co. KGaA, Weinheim 

tailed. To the best of our knowledge, this is the first example of an experimentally isolated silver(I) cluster that possesses (d-p)π-type quasiaromaticity.

## Results and Discussion

### General Aspects

The synthesis of complex **1** was carried out in DMSO with excess triethylamine according to the reaction shown in Equation (1).

$$4n\ AgCl + 4n\ StpmtH_2 \xrightarrow[DMSO]{Et_3N} \{[Ag_4Cl_4(\mu_3\text{-}StpmtH_2)_4]_n\} \quad (1)$$

No deprotonation of the thioamide ligand was observed in this case even though excess triethylamine was used. When 2-mercaptonicotinic acid reacted with silver(I) chloride under the same reaction conditions, a hexanuclear, water-soluble aggregate of formula $\{[Ag_6(\mu_3\text{-Hmna})_4(\mu_3\text{-mna})_2]^{2-}\cdot[(Et_3NH)^+]_2\cdot(DMSO)_2\cdot(H_2O)\}$ formed.[8d] Complex **1** has an infinite nanotube structure (vide infra) that consists of an octagonal $Ag_4S_4$ core. Four silver ions bridged by four sulfur atoms form an octagonal $Ag_4S_4$ core. Each $Ag^I$ ion of a core is also bridged to a $Ag^I$ ion of another core through a sulfur atom. Notably, the geometry around the silver(I) ions in **1** is tetrahedral.

The formula of synthesized compound **1** was first deduced from elemental analysis and spectroscopic data. Complex **1** is soluble in DMSO and DMF. The crystals of the complex were stable in air but were stored in darkness.

With the use of 3-(*tert*-butyldimethylsilyl)pyridine-2-thione, and 3,6-bis(*tert*-butyldimethylsilyl)pyridine-2-thione,[10a] 2-(triorganosilyl)thiophenols, 2,6-bis(triorganosilyl)thiophenols,[10b] and 2-(triorganosilyl)methanethione[10c] as ligands for the silver(I) ions, Zubieta et al.[10] established that the extent of the association in silver(I) ions in their clusters intimately depends on the nature of the thioamide. Thus, silver(I) ions with unbranched-chain thiolate ligands are highly polymeric as silver(I) is unprotected from the approach of additional bridging thiolate groups, whereas bulky ligands such as substituted thiolates increase the aggregation degree of the class of $[Ag(LS)]_n$ compounds.[10] In accordance with the above findings, the aggregate of formula $\{[Ag_6(\mu_3\text{-Hmna})_4(\mu_3\text{-mna})_2]^{2-}\cdot[(Et_3NH)^+]_2\cdot(DMSO)_2\cdot(H_2O)\}$[8d] was recently synthesized by using the branched substituted 2-mercaptonicotinic acid. When the unbranched, nonaromatic 2-mercapto-3,4,5,6-tetrahydropyrimidine was used for the synthesis of complexes **1**, $\{[Ag_6(\mu_2\text{-Br})_6(\mu_2\text{-StpmH}_2)_4(\mu_3\text{-StpmH}_2)_2]_n\}$ (**2**),[9] and $\{[Ag_4(\mu_2\text{-StpmH}_2)_6](NO_3)_4\}_n$ (**3**),[9] highly polymeric structures, were obtained.

### Spectroscopy

*Infrared*: The infrared spectra of complex **1** show distinct vibrational bands at 1572 and 1235 $cm^{-1}$, which were assigned as vibrations of the C–N bond (thioamide I and II bands), and at 1017 and 621 $cm^{-1}$, which were attributed to the C–S bond vibrations (thioamide III and IV bands). The corresponding thioamide bands of the free 2-mercapto-3,4,5,6-tetrahydropyrimidine ligand are given at 1557, 1206, 1067, and 644 $cm^{-1}$. The new band at 142 $cm^{-1}$ in the far-IR spectrum of complex **1** was assigned to the vibration of the Ag–S bond,[11] whereas a band appearing at 149 $cm^{-1}$ was attributed to the vibration of the Ag–Cl bond.

*NMR:* The $^1H$ NMR spectrum of a $[D_6]$DMSO solution of free ligand $StpmH_2$ shows resonance signals at $\delta$ = 7.86 ppm for the amide proton and at $\delta$ = 3.20 and 1.75 ppm for the $CH_2$ a and b protons. The band for the amide protons is shifted to 8.80 ppm in the $^1H$ NMR spectrum of complex **1**, obtained from a $[D_6]$DMSO solution, which confirms the N,S–metal coordination.

The $^{109}Ag$ NMR spectrum of complex **1** shows a signal at $\delta$ = +852 ppm. The corresponding signals for **2** and **3** are found at $\delta$ = 753 and 709 ppm, respectively. The significantly higher value of the chemical shift in the case of complex **1** relative to that of **2** and **3** could be due to the calculated aromaticity of complex **1** (see Computational Study). When the silver(I) ion is coordinated to the imine nitrogen atoms of a neutral $N_4$ donor system, as in the case of $[Ag_2\{\mu\text{-(R,S)-1,2-(6-R-py-2-CH=N)}_2Cy_2\}](OSCF_3)_2$ {where (R,S) = 1,2-(6-R-py-2-CH=N)$_2$Cy and R = H (a) or Me (b), and Cy = cyclohexane}, the chemical shift value for (a) is $\delta$ = 580 ppm and for (b) $\delta$ = 612 ppm.[12]

### Crystal and Molecular Structures of Complex $\{[Ag_4Cl_4(\mu_3\text{-}StpmH_2)_4]_n\}$ (1)

In complex **1** (Figure 1), four $\mu_3$-S atoms from the thione ligands bridge four silver(I) ions, which forms an eight-membered ring. The four $Ag^I$ ions define an $Ag_4$ plane that rises 0.826 Å from the corresponding $S_4$ plane defined by the sulfur atoms. Strong $\mu_3$-S intramolecular interactions bridge two eight-membered rings through silver(I) ions, whereas the coordination sphere of each silver ion is completed by a terminal Cl atom. The distance between two $Ag_4$ planes is 3.481 Å, which shows a stacking interaction. The same distance between two subsequent $S_4$ planes is also observed. Thus, an infinite nanotube structure is formed with strong interatomic interactions (Figure 2). A disordered solvent molecule (not identified) is also trapped inside the voids that are formed between the nanotubes.

The Ag–S bond lengths are Ag1–S2 = 2.5117(11) Å, Ag1–S2B = 2.5421(11) Å (symmetry code to equivalent position B: $1-y, -1+x, z$) and Ag1–S2A = 2.6627(13) Å (symmetry code to equivalent position A: $x, -y, z+1/2$). These values are in the range of those measured in complexes with infinite ribbon structures as in $\{[Ag_6(\mu_3\text{-pyS})_4(\mu_4\text{-pyS})_2]_n\}$[1a] [Ag–S = 2.456(5) to 2.959(5) Å], $\{[Ag_5(pyS)_4(pySH)BF_4]_n\}$[7] (Ag–S = 2.45 to 2.90 Å), $\{[Ag_6(SPh)_8](Me_4N)_2\}$[11] [Ag–S = 2.431(3) to 2.878(2) Å], and $\{[Ag(\mu_2\text{-pyS})]_n\}$[1a] [Ag–S = 2.587(4) and Ag–S(a) = 2.502 Å] (pySH = 2-mercaptopyridine).

 © 2007 Wiley-VCH Verlag GmbH & Co. KGaA, Weinheim 

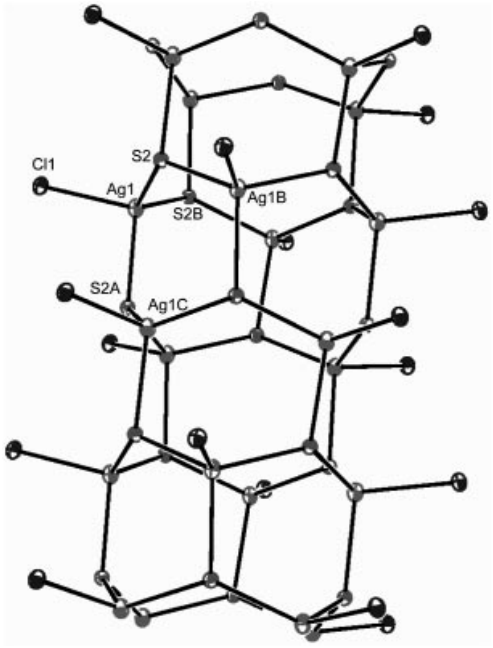


Figure 1. Molecular diagram of compound **1** together with the atomic numbering scheme (C, H, and N atoms were omitted for clarity). Symmetry codes to equivalent positions: A: 1 –*y*, –1 + *x*, *z*, B: *x*, –*y*, 1/2 + *z*, C: 1 –*y*, –1 + *x*, *z*. The displacement ellipsoids are drawn at the 50% probability level. Selected bond lengths [Å]: Ag1–S2 = 2.5117(11), Ag1–S2B = 2.5421(11), Ag1–S2A = 2.6627(13), Ag1–Cl1 = 2.6627(13), Ag1···Ag1B = 4.4614(5). Contact across ring [Å]: S2···S2A = 4.119(1), Ag1···Ag1C = 4.3487(5). Selected angles [°]; Cl1–Ag1–S2 = 109.04(4), Cl1–Ag1–S2B = 108.82(4), Cl1–Ag1–S2A = 101.41(4), S2–Ag1–S2B = 119.26(5), S2–Ag1–S2A = 112.18(3), S2B–Ag1–S2A = 104.61(3).

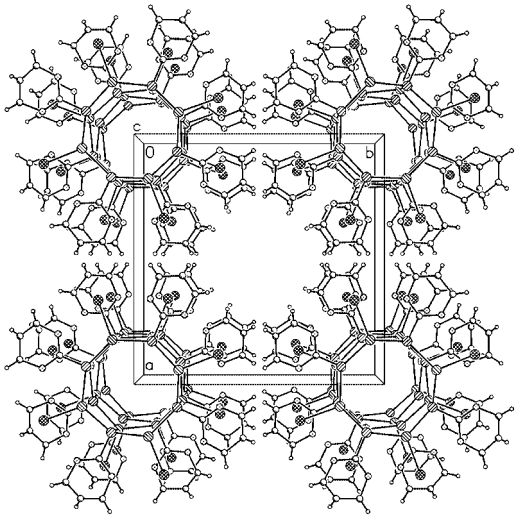


Figure 2. Unit cell of complex **1**. Strong $\mu_3$-S bonding interaction between $Ag^I$ ions of octagonal $Ag_4S_4$ cores lead to an infinite nanotube structure. The disordered guest molecule was omitted for clarity.

The Ag···Ag distance in the $Ag_4S_4$ ring in complex **1** is Ag1···Ag1B = 4.4614(5) Å, whereas the Ag···Ag distance between two subsequent rings is Ag1···Ag1C = 4.3487(5) Å (symmetry code to equivalent position C: 1 –*y*, –1 + *x*, *z*) and this is longer than twice the van der Waals radius for silver (3.44 Å),[6b] which indicates that there is no Ag···Ag interaction. The corresponding Ag···Ag distances in $\{[Ag_6(\mu_2\text{-}Br)_6(\mu_2\text{-}StpmH_2)_4(\mu_3\text{-}StpmH_2)_2]_n\}$ (**2**) are 3.063(1) Å and 2.963(2) Å, and they are shorter than twice the van der Waals radius for silver, which indicates that there is a strong Ag···Ag interaction, whereas in the case of complex $\{[Ag_4(\mu_2\text{-}StpmH_2)_6](NO_3)_4\}_n$ (**3**), no Ag···Ag interaction was observed because Ag1–Ag1B = 3.666(5) Å and Ag1–Ag1C = 3.954(5) Å. Other compounds presenting Ag···Ag interactions include $\{[Ag_6(\mu_3\text{-}pyS)_4(\mu_4\text{-}pyS)_2]_n\}$,[1a] with Ag···Ag = 2.959(2) Å, the neutral cluster $\{[Ag_6(\mu_3\text{-}Hmna)_6]\cdot 8DMSO\}$ ($H_2$mna = 2-mercaptonicotinic acid)[6b] with Ag···Ag = 2.911(1) Å, $\{[Ag_5(pyS)_4(pySH)BF_4]_n\}$[7] with Ag···Ag = 2.995 Å, $\{[Ag_6(\mu_3\text{-}Hmna)_4(\mu_3\text{-}mna)_2]^{2-}\cdot[(Et_3NH)^+]_2\cdot(DMSO)_2\cdot(H_2O)\}$[9] with Ag···Ag = 2.916 Å, and $\{[Ag_6(SPh)_8](Me_4N)_2\}$[11] with Ag···Ag = 2.959(1) Å. It is noteworthy that in all complexes with a short silver(I)–silver(I) distance (shorter than twice the van der Waals radius for silver) there is no halogen atom in the coordination sphere of the metal center. Complex **2** is still the only example of a silver(I) cluster containing a bromide ion in the coordination sphere of the metal center and presenting a Ag···Ag interaction.

The C–S bond length found in complex **1** is S2–C2 = 1.755(5) Å, which shows single bond character, whereas the C–N bond lengths are C2–N1 = 1.323(6) Å, C2–N3 = 1.328(5) Å, C6–N1 = 1.453(5) Å, and C4–N3 = 1.480(5) Å. Thus, in this case there are two equivalent short C–N bonds and a single C–S bond upon coordination to the silver(I) ion. These bond lengths, as well as all bond angles C–N–C and N–C–S that are around 122° [C2–N1–C6 = 123.7(4) and C2–N3–C4 = 121.8(4)°] and 119° [N1–C2–S2 = 119.9(3)° and N3–C2–S2 = 119.0(4)°], indicate that the ligand coordinates to silver(I) ion through zwitterionic form IIIc (Scheme 1).

The Ag–S–Ag bond angle in the $Ag_4S_4$ octagonal ring of complex **1** is S2–Ag1–S2B = 119.25(4)°, which is far from the ideal value of 135° of the normal octagon because of the nonplanar arrangements of the atoms, whereas the corresponding Ag–S–Ag angles formed between the octagonal

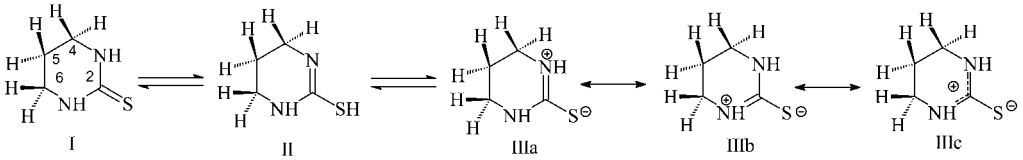


Scheme 1.

 © 2007 Wiley-VCH Verlag GmbH & Co. KGaA, Weinheim 

rings are S2–Ag1–S2A = 112.18(4)° and S2B–Ag1–S2A = 104.57(4)°.

### Computational Study

Theoretical as well as experimental evidence of aromaticity in all-metal systems[13a] has introduced a novel category of compounds containing either an aromatic cycle completely composed of metal atoms[2c,2e,2f] or ligand-stabilized aromatic molecules with the ligands being either terminal or bridging adjacent metal atoms.[13b,13c] Furthermore, aromatic clusters involving d orbitals in pseudooctahedral and in tetrahedral three-dimensional metal cages were extensively studied by density functional methods.[2b,2e] Despite that, experimentally structurally characterized compounds containing aromatic metalloid and metal clusters play a significant role in the *metallaromaticity* concept because they verify results obtained computationally.[13d–13f] We evaluated the aromaticity of compound **1** by means of magnetic criteria and by utilizing the nucleus-independent chemical shifts (NICS) method proposed by Schleyer et al. in 1996[2a] as a precept to estimate the aromatic character of cyclic structures.

NICS indexes are defined as the negative isotropic values of the absolute magnetic shieldings calculated at the geometric ring centers (nonweighted mean of the heavy atom coordinates) and at the cage metal centers. In general, negative and positive NICS values are associated with aromatic and antiaromatic character, respectively, whereas values near zero are indicative of nonaromaticity. The use of the NICS method in 3D structures has been recently evaluated comprehensively[13g] showing the successful estimation of aromaticity. Here, the core of compound **1** adopts a $D_4$ symmetry and to assess its aromaticity we have calculated NICS values at the geometric cage center, NICS(0), and at various equal distances along the $C_4$ symmetry axis (Figure 3).

The calculated results are illustrated in Figure 4, and they should be compared with the corresponding value of –6.9 ppm obtained for benzene at the same level of theory. The NICS data of –9.7 ppm at the cage barycenter confirms the aromatic character of the structure. The shielding influence reaches its minimum value of –13.1 ppm at NICS(1.7), which is the geometric center of one of the two $D_{4h}$ four-membered metal rings, whereas NICS(–1.7) is –6.4 ppm. Both results suggest the presence of induced diatropic ring current at each of the molecular planes that is set up by four Ag and four S atoms,[13e] and it is this (d-p)π bonding that accounts for the equalization of the Ag–S bonds in the homometallic clusters. Also, induced diatropic ring current is characteristic of cyclic electron delocalization of d or (d-p)π-type orbital electron density,[13e] which causes the strong chemical shifts of the $^{109}$Ag NMR signals in the spectrum of complex **1** (see NMR Study). Consistent with the literature,[13h] the sensitivity of NICS falls considerably with distance and the values are shifted downfield as the distance from the centre is increased, which eventually is proven as a suitable position for the evaluation of aromaticity.

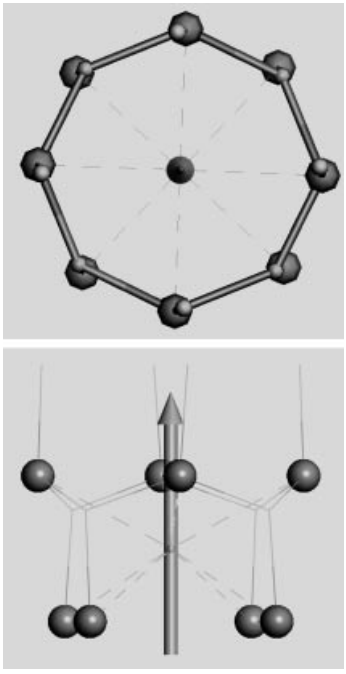

Figure 3. Geometrical representation for the core structure along and alongside the main symmetry axis.

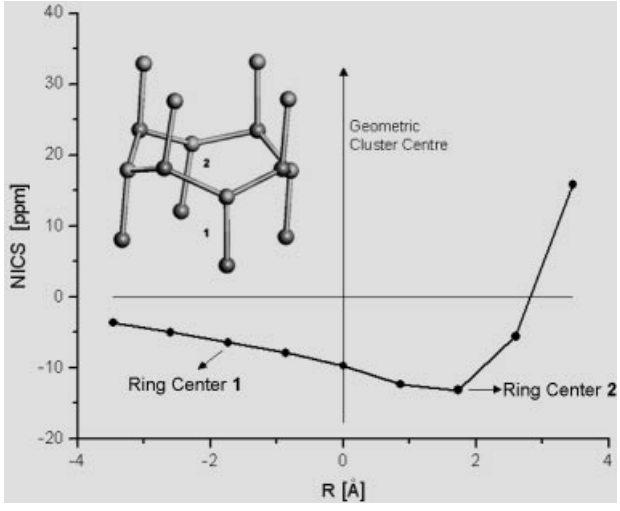


Figure 4. A plot of B3LYP/LANL2DZ NICS calculated along the $C_4$ axis for the asymmetric unit.

## Conclusions

One new $Ag^I$ aggregate was synthesized by the reaction of silver chloride and 2-mercapto-3,4,5,6-tetrahydropyrimidine. The crystal structure of complex **1** reveals that the formed $Ag_4S_4$ core exhibits strong (d-p)π-type quasiaromaticity. Stacking interactions between sequential rings are also observed. As a result, the $^{109}$Ag NMR resonance signal of complex **1** is observed at a higher positive value relative to that observed for complexes **2** and **3**. Thus, the delocal-

 © 2007 Wiley-VCH Verlag GmbH & Co. KGaA, Weinheim 

ization of the electron density in the (d-p)π-type orbitals, which results from quasiaromaticity, leads to deshielding of the electron density at the silver atoms.

## Experimental Section

**Materials and Instruments:** All solvents were of reagent grade. 2-Mercapto-3,4,5,6-tetrahydropyrimidine (Aldrich) was used with no further purification. Elemental analyses for C, H, N, and S were carried out with a Carlo Erba EA model 1108 elemental analyzer. Infrared were recorded with a Perkin–Elmer Spectrum GX FTIR spectrophotometer. A Jasco UV/Vis/NIR V 570 series spectrophotometer was used to obtain the electronic absorption spectra. The $^1H$ and $^{13}C$ NMR spectra were recorded with a Bruker AC 250 FTNMR instrument. Chemical shifts are given relative to internal tetramethylsilane. The $^{109}Ag$ NMR spectra were recorded with a Bruker DRX-600 spectrometer with Ag-109 resonance at 27.93 MHz at 30 °C, and $AgNO_3$ was used as a reference standard.

**Synthesis and Crystallization of $\{[Ag_4Cl_4(\mu_3\text{-}StpmH_2)_4]_n\}$ (1):** A clear DMSO solution (7 mL) of 2-mercapto-3,4,5,6-tetrahydropyrimidine (0.234 g, 2 mmol) was treated with silver(I) chloride (0.143 g, 1 mmol). After stirring for 30 min, triethylamine (0.5 mL, 3.6 mmol) was added. The resulting clear solution was then filtered, and the filtrate was kept in the dark at room temp. After a few days, colorless crystals ($0.10 \times 0.20 \times 0.30$ mm) of complex **1** that were suitable for single-crystal X-ray analysis were obtained. M.p. 190–195 °C. $^1H$ NMR (250 MHz, [D$_6$]DMSO): $\delta$ = 8.80 (s, 1 H, NH), 3.40 (t, 2 H, $J$ = 7 Hz, $C^4H_2$), 1.81 (q, $J$ = 7 Hz, 2 H, $C^5H_2$) ppm. IR (KBr): $\tilde{\nu}$ = 3199, 1572, 1235, 1017, 621 cm$^{-1}$. Far-IR (polyethylene): $\tilde{\nu}$ = 142, 149 cm$^{-1}$. UV/Vis (DMSO): $\lambda$ = 258.0 nm. $C_4H_8AgClN_2S$: calcd. C 18.51, H 3.11, N 10.79, S 12.36; found C 18.89, H 2.97, N 10.95, S 12.22.

**Computational Details:** Calculations were based on the molecular geometry acquired by X-ray diffraction methods. Magnetic shielding tensors for a ghost atom placed at different interior and near exterior positions of the metal–ligand cluster (asymmetric unit) were computed by using the gauge-independent atomic orbital (GIAO) DFT method[14a–14c] within the B3LYP level of theory. Nucleus independent chemical shift (NICS) values were estimated with the B3LYP functional by using the Los Alamos effective core potentials plus double zeta (LANL2DZ).[14d] All theoretical results reported were carried out with the Gaussian03W program package.[14e]

**X-ray Structure Determination:** Data were collected by the ω scan technique in the range $3.9° < 2\theta < 29.1°$ with a KUMA KM4CCD four-circle diffractometer[15a] equipped with a CCD detector with the use of graphite-monochromated Mo-$K_\alpha$ ($\lambda$ = 0.71073 Å) at 100(1) K. Cell parameters were determined by a least-squares fit method.[15b] All data were corrected for Lorentz-polarization effects and absorption.[15b,15c] The structure was solved with direct methods with SHELXS97[15d] and refined by full-matrix least-squares procedure on $F^2$ with SHELXL97.[15e] All non-hydrogen atoms were refined anisotropically, hydrogen atoms were located at calculated positions and refined as a "riding model" with isotropic thermal parameters fixed at 1.2 times the $U_{eq}$'s of the appropriate carrier atom.

**1**: $C_4H_8AgN_2S$, tetragonal in $P4cc$, $a$ = 15.7761(9) Å, $b$ = 15.7761(9) Å, $c$ = 6.9624(8) Å, $V$ = 1732.8(2) Å$^3$, $Z$ = 2, $T$ = 100(1) K, $\rho_{calcd.}$ = 2.166 g cm$^{-3}$, $\mu$ = 2.8 mm$^{-1}$, reflections collected: total, unique data, $R$(int) = 9927, 1824, 0.043, index range: $-21 < h < 20$, $-21 < k < 20$, $-9 < l < 7$, observed data [$I > 2.0$ sigma($I$)]: 1445, final $R$[a], $wR2$[b] [$I > 2\sigma(I)$] indices: 0.0289 and 0.0605, respectively. ([a] $R = \Sigma||F_o| - |F_c||/\Sigma|F_o|$; [b] $wR2 = [\Sigma w(F_o^2 - F_c^2)^2/\Sigma w(F_o^2)^2]^{1/2}$, goodness of fit: 1.032.

CCDC-624697 (for **1**) contains the supplementary crystallographic data for this paper. These data can be obtained free of charge from The Cambridge Crystallographic Data Centre via www.ccdc.cam.ac.uk/data_request/cif.

## Acknowledgments

The graduate program in Bioinorganic Chemistry financed by the Ministry of Education of Greece and coordinated by Professor N. Hadjiliadis is acknowledged. N. H. and I. S. also thank a NATO grant for exchange of scientists that they were awarded.

[1] a) M. Hong, W. Su, R. Cao, W. Zhang, J. Lu, *Inorg. Chem.* **1999**, *38*, 600–602; b) J.-M. Lehn, *Supramolecular Chemistry: Concepts and Perspectives*, VCH, Weinheim, **1995**; c) M. Hong, W. Su, R. Cao, M. Fujita, J. Lu, *Chem. Eur. J.* **2000**, *6*, 427–431.

[2] a) P. v. R. Schleyer, C. Maerker, A. Dransfeld, H. Jiao, N. J. R. v. E. Hommes, *J. Am. Chem. Soc.* **1996**, *118*, 6317; b) C. Corminboeuf, C. S. Wannere, D. Roy, R. B. King, P. v. R. Schleyer, *Inorg. Chem.* **2006**, *45*, 214–219; c) C. S. Wannere, C. Corminboeuf, Z.-X. Wang, M. D. Wodrich, R. B. King, P. v. R. Schleyer, *J. Am. Chem. Soc.* **2005**, *127*, 5701–5705; d) A. C. Tsipis, C. A. Tsipis, *J. Am. Chem. Soc.* **2005**, *127*, 10623–10638; e) C. A. Tsipis, E. E. Karagiannis, P. F. Kladou, A. C. Tsipis, *J. Am. Chem. Soc.* **2004**, *126*, 12916–12929; f) A. C. Tsipis, C. A. Tsipis, *J. Am. Chem. Soc.* **2003**, *125*, 1136–1137; g) C. A. Tsipis, *Coord. Chem. Rev.* **2005**, *249*, 2740–2762; h) J. Li, C.-W. Liu, J.-X. Lu, *J. Cluster Sci.* **1996**, *7*, 469–500; i) Z. Chen, *J. Cluster Sci.* **1995**, *6*, 357–377.

[3] a) B. Krebs, G. Hengel, *Angew. Chem. Int. Ed. Engl.* **1991**, *30*, 769–788; b) P. G. Blower, J. R. Dilworth, *Coord. Chem. Rev.* **1987**, *76*, 121–185.

[4] a) E. S. Raper, *Coord. Chem.* **1985**, *61*, 115–184; b) E. S. Raper, *Coord. Chem. Rev.* **1994**, *129*, 91–156; c) E. S. Raper, *Coord. Chem. Rev.* **1996**, *153*, 199–255.

[5] a) *Martindale: The Extra Pharmacopoeia* (Ed.: J. E. F. Reynolds), 28th ed., Pharmaceutical Press, London, **1982**; b) M. Wruble, *J. Am. Pharm. Assoc. Sci. Ed.* **1943**, *32*, 80–88; c) H. S. Rosenkranz, S. Rosenkranz, *Antimicrob. Agents Chemother.* **1972**, *2*, 373–379.

[6] a) K. Nomiya, Y. Kondoh, H. Nagano, M. Oda, *J. Chem. Soc., Chem. Commun.* **1995**, 1679–1680; b) K. Nomiya, S. Takahashi, R. Noguchi, *J. Chem. Soc., Dalton Trans.* **2000**, 2091–2097.

[7] W. Su, M. Hong, J. Weng, R. Cao, S. Lu, *Angew. Chem. Int. Ed.* **2000**, *39*, 2911–2914.

[8] a) J. Vicente, M. T. Chicote, C. Rubio, *Chem. Ber.* **1996**, *129*, 327–330; b) J. Vicente, M. T. Chicote, M. C. Lagunas, *Inorg. Chem.* **1993**, *32*, 3748–3754; c) O. Steigelmann, P. Bissinger, H. Schmidbaur, *Angew. Chem. Int. Ed. Engl.* **1990**, *29*, 1399–1400; *Angew. Chem.* **1990**, *102*, 1473–1474; d) P. C. Zachariadis, S. K. Hadjikakou, N. Hadjiliadis, A. Michaelides, S. Skoulika, Y. Ming, Y. Xiaolin, *Inorg. Chim. Acta* **2003**, *343*, 361–365.

[9] P. C. Zachariadis, S. K. Hadjikakou, N. Hadjiliadis, A. Michaelides, S. Skoulika, J. Balzarini, E. De Clercq, *Eur. J. Inorg. Chem.* **2004**, 1420–1426.

[10] a) A. A. Perez-Lourido, J. A. Garcia-Vazquez, J. Romero, M. S. Louro, A. Sousa, Q. Chen, Y. Chang, J. Zubieta, *J. Chem. Soc., Dalton Trans.* **1996**, 2047–2054; b) E. Block, M. Gernon, H. Kang, G. Ofori-Okai, J. Zubieta, *Inorg. Chem.* **1989**, *28*, 1263–1271; c) K. Tang, M. Aslam, E. Block, T. Nicholson, J. Zubieta, *Inorg. Chem.* **1987**, *26*, 1488–1497.

[11] I. G. Dance, *Inorg. Chem.* **1981**, *20*, 1487–1492.

 © 2007 Wiley-VCH Verlag GmbH & Co. KGaA, Weinheim 

[12] G. C. van Stein, G. van Koten, K. Vrieze, C. Brevard, A. L. Speks, *J. Am. Chem. Soc.* **1984**, *106*, 4486–4492.
[13] a) X. Li, A. E. Kuznetsov, H. Zhang, A. I. Boldyrev, L. Wang, *Science* **2001**, *291*, 859–861; b) E. Janssens, S. Neukemans, F. Vanhoutte, R. E. Silverans, P. Lievens, A. Navaro-Vasquez, P. v. R. Schleyer, *J. Chem. Phys.* **2003**, *118*, 5862–5871; c) R. B. King, *Inorg. Chem.* **2003**, *42*, 8755–8761; d) A. I. Boldyrev, L. S. Wang, *Chem. Rev.* **2005**, *105*, 3716–3757; e) C. A. Tsipis, *Coord. Chem. Rev.* **2005**, *249*, 2740–2762; f) X. Huang, H. Zhai, B. Kiran, L. Wang, *Angew. Chem. Int. Ed.* **2005**, *44*, 7251–7254; g) Z. Chen, R. B. King, *Chem. Rev.* **2005**, *105*, 3613–3642; h) P. v. R. Schleyer, M. Manoharan, Z. Wang, B. Kiran, H. Jiao, R. Puchta, N. J. R. v. E. Hommes, *Org. Lett.* **2001**, *3*, 2465–2468.
[14] a) R. McWeeny, *Phys. Rev.* **1962**, *126*, 1028; b) J. L. Dodds, R. McWeeny, A. Sadlej, *J. Mol. Phys.* **1980**, *41*, 1419; c) R. Ditchfield, *Mol. Phys.* **1974**, *27*, 789; d) P. J. Hay, W. R. Wadt, *J. Chem. Phys.* **1985**, *82*, 299–310; e) M. J. Frisch, G. W. Trucks, H. B. Schlegel, G. E. Scuseria, M. A. Robb, J. R. Cheeseman, J. A. Montgomery Jr, T. Vreven, K. N. Kudin, J. C. Burant, J. M. Millam, S. S. Iyengar, J. Tomasi, V. Barone, B. Mennucci, M. Cossi, G. Scalmani, N. Rega, G. A. Petersson, H. Nakatsuji, M. Hada, M. Ehara, K. Toyota, R. Fukuda, J. Hasegawa, M. Ishida, T. Nakajima, Y. Honda, O. Kitao, H. Nakai, M. Klene, X. Li, J. E. Knox, H. P. Hratchian, J. B. Cross, V. Bakken, C. Adamo, J. Jaramillo, R. Gomperts, R. E. Stratmann, O. Yazyev, A. J. Austin, R. Cammi, C. Pomelli, J. W. Ochterski, P. Y. Ayala, K. Morokuma, G. A. Voth, P. Salvador, J. J. Dannenberg, V. G. Zakrzewski, S. Dapprich, A. D. Daniels, M. C. Strain, O. Farkas, D. K. Malick, A. D. Rabuck, K. Raghavachari, J. B. Foresman, J. V. Ortiz, Q. Cui, A. G. Baboul, S. Clifford, J. Cioslowski, B. B. Stefanov, G. Liu, A. Liashenko, P. Piskorz, I. Komaromi, R. L. Martin, D. J. Fox, T. Keith, M. A. Al-Laham, C. Y. Peng, A. Nanayakkara, M. Challacombe, P. M. W. Gill, B. Johnson, W. Chen, M. W. Wong, C. Gonzalez, J. A. Pople, *Gaussian 03, Revision C.02*, Gaussian, Inc., Wallingford, **2004**.
[15] a) *KUMA KM-4CCD User Manual*, KUMA Diffraction, Wroclaw, Poland **1999**; b) *CrysAlis: Program for Reduction of the Data from KUMA CCD Diffractometer*, KUMA Diffraction, Wroclaw, Poland, **1999**; c) R. H. Blessing, *J. Appl. Crystallogr.* **1989**, *22*, 396; d) G. M. Sheldrick, *Acta Crystallogr., Sect. A* **1990**, *46*, 467; e) G. M. Sheldrick, *SHELXL-97: Program for the Refinement of Crystal Structures*, University of Göttingen, Göttingen, **1997**.

Received: December 13, 2006
Published Online: February 16, 2007

 © 2007 Wiley-VCH Verlag GmbH & Co. KGaA, Weinheim 

DOI: 10.1002/ejic.200601226

# First Structural Characterization of Silanedithiol and Its Application toward the Synthesis of Silanedithiolato Complexes

Taro Tanabe,[a] Nobuhiro Takeda,[a] and Norihiro Tokitoh*[a]

**Keywords:** Silanedithiol / Silanedithiolato complexes / Silaneselenol / Group 10 transition metal complexes / X-ray crystallography

In this paper, we report the synthesis and the structural characterization of stable examples of silanedithiol [Tbt(Mes)Si(SH)$_2$ (**1**)], hydroxysilanethiol [Tbt(Mes)Si(OH)(SH) (**3**)], and hydroxysilaneselenol [Tbt(Mes)Si(OH)(SeH) (**7**)], which are kinetically stabilized by an effective combination of steric protection groups, Tbt (2,4,6-tris[bis(trimethylsilyl)methyl]phenyl) and Mes (2,4,6-trimethylphenyl). Silanedichalcogenols **1**, **3**, and **7** are suggested to exist as a monomer without any intermolecular contact such as hydrogen bonds both in the solid state and in solution as judged by X-ray structural analysis and IR spectroscopy. Treatment of **1** with 2 equiv. of butyllithium resulted in the quantitative formation of the corresponding dilithium silanedithiolate, Tbt(Mes)Si(SLi)$_2$ (**8**), the generation of which was confirmed by a trapping experiment using MeI. Furthermore, the addition of *cis*-[MCl$_2$(PPh$_3$)$_2$] (M = Pd, Pt) to a THF solution of **8** afforded the corresponding silanedithiolato complexes, [Tbt(Mes)Si(μ-S)$_2$M(PPh$_3$)$_2$] (**9a**: M = Pd; **9b**: M = Pt), respectively.
(© Wiley-VCH Verlag GmbH & Co. KGaA, 69451 Weinheim, Germany, 2007)

## Introduction

Controlled synthesis of (chalcogenido)metal clusters has been one of the most attractive subjects in organometallic chemistry.[1] Recently, silanethiolato or silanedithiolato complexes of late transition metals have been shown to be good precursors of (sulfido)mixed-metal clusters prepared by ligand exchange involving Si–S bond cleavage.[2,3] However, chelating silanedithiolato complexes are less common due to the limitation of appropriate synthetic methodology. That is, an excess amount of 1,3,5,2,4,6-trithiatrisilinane (SSiMe$_2$)$_3$ should be required as a sulfur transfer reagent for the synthesis of such silanedithiolato complexes.[4] On the other hand, silanedithiols, which should be a good precursor of silanedithiolato complexes, have attracted much interest from the viewpoint of their structure and properties. However, it is very difficult to isolate silanedithiols due to their high sensitivity toward moisture, and the properties remained little understood.[5] As for the analogues of main group elements having two geminal SH groups, three examples are structurally characterized, i.e., TbtB(SH)$_2$,[6] AlL(SH)$_2$,[7] and Dep(Dip)Ge(SH)$_2$[8] {Tbt = 2,4,6-tris[bis(trimethylsilyl)methyl]phenyl, L (β-diketiminato) = [N(Dip)C(Me)]$_2$CH, Dip = 2,6-diisopropylphenyl, Dep = 2,6-diethylphenyl}, where the reactive M–SH moieties are protected by bulky substituents. All of these compounds could be easily converted into the heterodimetallic sulfido clusters.[9] Thus, kinetic stabilization should be an appropriate method for the stabilization of M(SH)$_2$ species. In this paper, we present the synthesis and the first structural characterization of a silanedithiol, which is kinetically stabilized by an effective steric protection group, Tbt. In addition, its application as a building block toward the synthesis of silanedithiolato complexes will also be presented.

## Results and Discussion

Silanedithiol **1** was synthesized by the reaction of the corresponding sterically hindered tetrathiasilolane **2**[10] with 1.5 equiv. of LiAlH$_4$ at 0 °C as air- and moisture-stable crystals in 83% isolated yield (Scheme 1). When the reaction was carried out at room temperature, further reduction occurred to give a mixture of **1**, Tbt(Mes)Si(H)SH and Tbt(Mes)SiH$_2$.

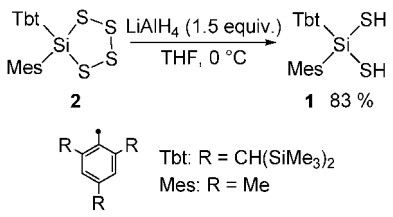


Scheme 1. Synthesis of **1**.

[a] Institute for Chemical Research, Kyoto University
Gokasho, Uji, Kyoto 611-0011, Japan
Fax: +81-774-38-3200
E-mail: tokitoh@boc.kuicr.kyoto-u.ac.jp
Supporting information for this article is available on the WWW under http://www.eurjic.org or from the author.

 © 2007 Wiley-VCH Verlag GmbH & Co. KGaA, Weinheim 

Silanedithiol **1** is stable in [$D_6$]benzene solution even in the presence of $H_2O$ for 1 d, reflecting the extreme bulkiness of the combination of Tbt and Mes groups. However, **1** underwent ready hydrolysis during preparative thin layer chromatography ($SiO_2$) to afford the corresponding hydroxysilanethiol **3** quantitatively (Scheme 2).

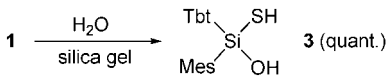


Scheme 2. Synthesis of **3** by hydrolysis of **1**.

The successful isolation of silanedithiol **1** prompted us to attempt the synthesis of the selenium analogue, silanediselenol, a stable example of which has been unknown. Unfortunately, tetraselenasilolane, the selenium analogue of **2**, is known to be not available.[10] Another synthetic route is required to obtain the heavier analogue. We focused our attention on the (silanedichalcogenolato)zirconium complexes, which possess reactive Zr–E (E = S, Se) bonds. When disilene **5**[10] was treated with $Cp_2ZrE_5$ at 60 °C, the corresponding silanedichalcogenolato complexes **6a**,**b** were obtained.[11] Treatment of **6a** with $H_2O$ followed by the separation afforded **1**, where the hydrolysis of the Zr–S bonds should occur selectively. Thus, the $SiS_2Zr$ ring system (**6a**) was found to be another precursor for silanedithiol **1**. The selenium analogue **6b** should be a good precursor for silanediselenol. However, the reaction of **6b** with $H_2O$ gave hydroxysilaneselenol **7**, which was probably formed by further hydrolysis of the initially generated silanediselenol **4** (Scheme 3).

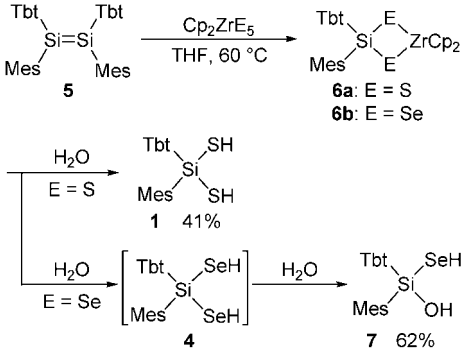


Scheme 3. Reaction of **5** with $Cp_2ZrE_5$ (E = S, Se).

The molecular structures of the newly isolated silanedichalcogenols, **1**, **3**, and **7**, were fully determined by X-ray crystallographic analysis (Figure 1).[12] To the best of our knowledge, these are the first examples of the X-ray structural analyses of a silanedithiol, a hydroxysilanethiol, and a hydroxysilaneselenol.[13] The Si–E (E = O, S, Se) bond lengths of **1**, **3**, and **7** are within the range of those reported for the corresponding single bonds between silicon and chalcogen atoms. Absence of intermolecular hydrogen bonding in the solid state was suggested by the packing view, where the observed intermolecular distances between chalcogen atoms are apparently longer than the sum of the van der Waals radii.[14]

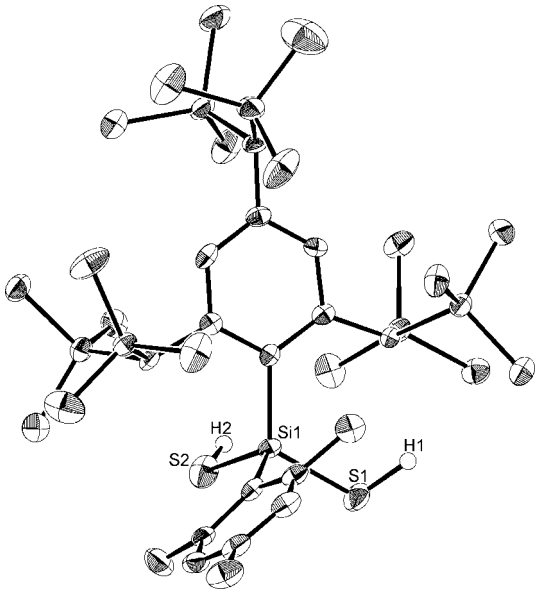


Figure 1. Crystal structure of **1** (ORTEP plot; thermal ellipsoids are shown at 50% probability; hydrogen atoms except for the S–H hydrogen atoms are omitted for clarity). Selected bond lengths [Å] and angles [°]: Si(1)–S(1) 2.1576(16), Si(1)–S(2) 2.1436(15); S(1)–Si(1)–S(2) 101.73(6).

The IR spectra in the solid state for **1**, **3**, and **7** show sharp absorptions assigned to the E–H stretching vibrations [**1**: 2572 $cm^{-1}$; **3**: 2661 $cm^{-1}$, 3646 $cm^{-1}$; **7**: 2479 $cm^{-1}$, 3656 $cm^{-1}$], suggesting the absence of intra- and intermolecular interactions through hydrogen bonds.[15] No change of the IR spectra in $CCl_4$ with several concentrations indicated their monomeric structure and almost no intermolecular contact even in solution.

The generation of dilithium silanedithiolate **8** in the reaction of **1** with 2 equiv. of *n*BuLi was confirmed by a trapping experiment with MeI. Compound **8** should be applicable toward the development of a new synthetic strategy for (silanedithiolato)transition-metal complexes. Addition of *cis*-[$MCl_2(PPh_3)_2$] (M = Pd, Pt) to a THF solution of **8** resulted in the almost quantitative formation of the corresponding silanedithiolato complexes **9a**,**b**, respectively (Scheme 4).[16] The $^{29}Si$ NMR signals of the central silicon atoms in the silanedithiolato complexes **9a** ($\delta_{Si}$ = 15.3 ppm) and **9b** ($\delta_{Si}$ = 14.2 ppm), which appear in the characteristic region of silanedithiolato complex signals,[4c] are in a lower-field region than that of **1** ($\delta_{Si}$ = –1.8 ppm). The structures of **9a**,**b** were revealed by X-ray crystallography. Both of the four-membered rings consisting of Si, S, and Pd or Pt atoms have puckered structures, though the $SiS_2Pd$ ring of the reported (silanedithiolato)palladium complex, [$Me_2Si(\mu\text{-}S)_2Pd(PEt_3)_2$],[4c] has an almost planar structure. This is probably due to the steric repulsion between the extremely bulky

 © 2007 Wiley-VCH Verlag GmbH & Co. KGaA, Weinheim 

Tbt group and the triphenylphosphane groups. The X-ray structural analysis of **9b**[17] is the first example of a silanedithiolato complexes of platinum (Figure 2, Scheme 4).

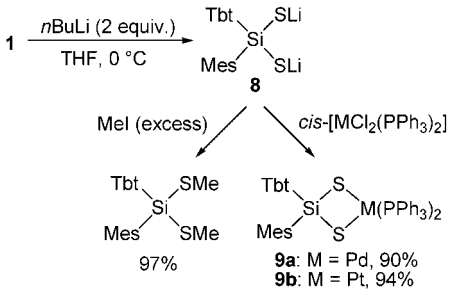


Scheme 4. Synthesis of silanedithiolato complexes **9**.

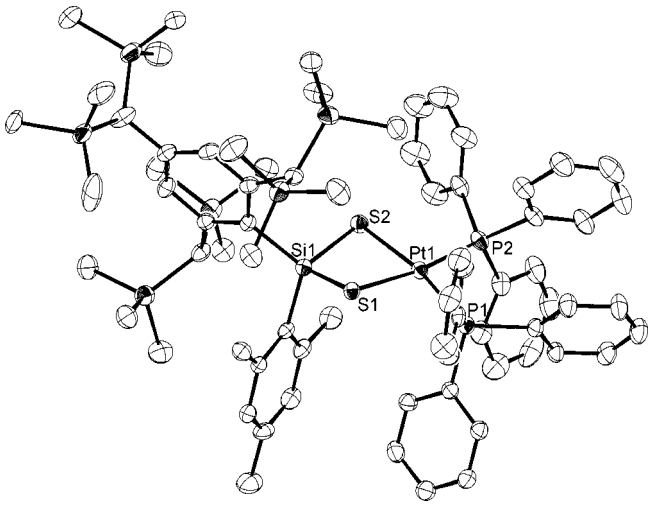


Figure 2. Crystal structure of **9b·hexane** (ORTEP plot; thermal ellipsoids are shown at 30% probability; hexane and hydrogen atoms are omitted for clarity). Selected bond lengths [Å] and angles [°]: Si(1)–S(1) 2.157(2), Si(1)–S(2) 2.115(2), Pt–S(1) 2.3667(15), Pt–S(2) 2.3333(17); S(1)–Si(1)–S(2) 94.92(9), S(1)–Pt–S(2) 84.09(6).

## Conclusions

We have succeeded in the synthesis and characterization of a stable silanedithiol **1** and its application toward the synthesis of the silanedithiolato complexes of palladium and platinum. The stable silanedithiol should be a key species as a building block for several types of (sulfido)mixed-metal clusters. Further investigation on the reactivity of **8** and related compounds are currently in progress.

## Experimental Section

**General Procedure**. All experiments were performed under anhydrous conditions under argon unless otherwise noted. All solvents used in the reactions were purified prior to use by standard methods and/or by an Ultimate Solvent System (Glass Contour Company).[18] $C_6D_6$ used as a solvent was dried with Na, then with a K mirror. $^1$H NMR (300 or 400 MHz) spectra were measured in $CDCl_3$ or $C_6D_6$ with a JEOL AL-400 or AL-300 spectrometer using residual $CHCl_3$ ($\delta$ = 7.25 ppm) or $C_6D_5H$ ($\delta$ = 7.15 ppm) as an internal standard. $^{13}$C NMR (75 MHz) spectra were recorded with a JEOL JNM AL-300 spectrometer. $^{13}$C chemical shifts are reported in ppm downfield from tetramethylsilane and referenced to the carbon signal of $CDCl_3$ ($\delta$ = 77.0 ppm) or $C_6D_6$ ($\delta$ = 128.0 ppm). The multiplicity of signals in the $^{13}$C NMR spectra was determined by the DEPT technique. The $^{29}$Si (59 MHz), $^{31}$P (120 MHz), $^{77}$Se (95 MHz), and $^{195}$Pt (64 MHz) NMR spectra were recorded with a JEOL JNM AL-300 spectrometer. IR spectra were recorded with a JASCO FT/IR-5300 spectrometer. High- and low-resolution mass spectrometric data were obtained with a JEOL JMS-700 spectrometer. Elemental analyses were carried out at the Microanalytical Laboratory of the Institute for Chemical Research, Kyoto University. All melting points were measured with a Yanaco micro melting point apparatus and are uncorrected. Wet column chromatography (WCC) and preparative thin-layer chromatography (PTLC) were performed using Wakogel C-200 and Merk Kieselgel 60 PF254, respectively. GPLC (gel permeation liquid chromatography) was performed on LC-908, LC-918 (Japan Analytical Industry Co., Ltd. Systems) equipped with JAIGEL 1H and 2H columns (eluent: toluene).

**1**: To a solution of **2** (165 mg, 238 μmol) in THF (15 mL) was added $LiAlH_4$ (13.5 mg, 356 μmol) at 0 °C. After the mixture was stirred at 0 °C for 1 h, ethyl acetate (5 mL) was added. After removal of the solvent, hexane was added to the residue. The suspension was filtered through Celite®, and the solvent was removed. The residue was separated by silica gel chromatography (*n*-hexane) to afford **1** (149.7 mg, 195.5 μmol, 83%); colorless crystals, m.p. 177–178 °C. $^1$H NMR (300 MHz, $CDCl_3$): $\delta$ = –0.02 (s, 18 H), 0.00 (s, 18 H), 0.04 (s, 18 H), 1.18 (s, 2 H, S–H), 1.31 (s, 1 H), 2.22 (s, 3 H), 2.49 (s, 1 H), 2.57 (s, 6 H), 2.63 (s, 1 H), 6.24 (s, 1 H), 6.38 (s, 1 H), 6.76 (s, 2 H) ppm. $^{13}$C NMR (75 MHz, $CDCl_3$): $\delta$ = 0.9 (q), 1.6 (q), 1.9 (q), 20.9 (q), 26.4 (q), 28.0 (d), 28.3 (d), 30.6 (d), 123.3 (d), 126.3 (s),128.5 (d), 130.5 (d), 134.9 (s), 139.7 (s), 142.8 (s), 145.5 (s), 151.9 (s), 152.2 (s) ppm. $^{29}$Si NMR (59 MHz, $CDCl_3$): $\delta$ = –1.8, 1.9, 2.9, 3.0 ppm. IR (KBr): $\tilde{\nu}$ = 2572 [ν(S–H)] cm$^{-1}$. HRMS (FAB$^+$): calcd. for $C_{36}H_{72}S_2Si_7$ $[M]^+$ 764.3460, found 764.3472. $C_{36}H_{72}S_2Si_7$ (765.69): calcd. C 56.47, H 9.48, S 8.38; found C 56.51, H 9.57, S, 8.81.

**9b**: To a solution of **1** (27.8 mg, 36.3 μmol) in THF (3 mL) was added *n*BuLi (1.64 N hexane solution, 51 μL, 82.1 μmol) at 0 °C. After the mixture was stirred at 0 °C for 30 min, a THF solution (15 mL) of *cis*-bis(triphenylphosphane)platinum dichloride (43.1 mg, 54.4 μmol) was added. After removal of the solvent, benzene (3 mL) was added to the residue. The mixture was filtered through Celite®, and the solvent was removed. The residue was separated with HPLC (toluene) to afford **9b** (50.5 mg, 34.1 μmol, 94%) as a pale yellow solid. Pale yellow crystals suitable for X-ray structural analysis were grown from hexane at –20 °C; pale yellow crystals, m.p. 250–252 °C (dec.). $^1$H NMR (300 MHz, $C_6D_6$): $\delta$ = 0.21 (s, 18 H), 0.29 (s, 18 H), 0.34 (s, 18 H), 1.49 (s, 1 H), 2.11 (s, 1 H), 2.31 (s, 3 H), 2.53 (s, 1 H), 2.93 (s, 6 H), 6.50 (s, 1 H), 6.62 (s, 1 H), 6.83 (s, 2 H), 6.85–6.94 (m, 18 H, $Ph_3P$), 7.49–7.55 (m, 12 H, $Ph_3P$) ppm. $^{13}$C{$^1$H} NMR (75 MHz, $C_6D_6$): $\delta$ = 1.2 ($CH_3$), 2.1 ($CH_3$), 2.5 ($CH_3$), 21.1 ($CH_3$), 25.3 (CH), 25.6 (CH), 26.9 ($CH_3$), 30.5 (CH), 127.8 (CH), 128.3 (CH), 128.5 (CH), 128.6 [d, $^4J_{CP}$ = 1.2 Hz, CH, *p*-Ph($PPh_3$)], 131.41 [*d*, $^3J_{CP}$ = 1.9 Hz. CH, *m*-Ph($PPh_3$)], 131.42 [dd, $^1J_{CP}$ = 54.9 Hz, $^3J_{CP}$ = 6.8 Hz, C, *ipso*-Ph

 © 2007 Wiley-VCH Verlag GmbH & Co. KGaA, Weinheim 

($PPh_3$)], 135.3 [AA′X pattern, $1/2(^2J_{CP} + {}^4J_{CP})$ = 5.5 Hz, CH, *o*-Ph ($PPh_3$)], 136.6 (C), 137.9 (C), 141.9 (C), 143.1 (C), 143.3 (C), 151.3 (C), 151.6 (C) ppm. $^{29}$Si NMR (59 MHz, $C_6D_6$): $\delta$ = 1.6, 2.5, 14.1 ppm. $^{31}$P NMR (120 MHz, $C_6D_6$): $\delta$ = 21.2 (s, with platinum satellites, $^1J_{PPt}$ = 3047 Hz) ppm. $^{195}$Pt NMR (64 MHz, $C_6D_6$, $Na_2PtCl_4$): $\delta$ = –4527.7 (t, $^1J_{PtP}$ = 3047 Hz) ppm. UV/Vis (*n*-hexane): $\lambda_{max}$ = 290 (br., $\varepsilon = 4\times10^4$), 269 (br., $\varepsilon = 6\times10^4$), 232 (br., $\varepsilon = 1\times10^5$), 209 ($\varepsilon = 2\times10^5$) nm. HRMS (FAB$^+$): calcd. for $C_{72}H_{100}P_2{}^{195}PtS_2Si_7$ $[M]^+$ 1481.4774, found 1481.4771. $C_{72}H_{100}P_2PtS_2Si_7$ (1483.32): calcd. C 58.30, H 6.80, S 4.32; found C 58.39, H 6.89, S 4.31.

**Supporting Information** (see footnote on the first page of this article): Experimental procedures, spectroscopic data, and crystal data of **3**, **7**, **9a** and **9b**.

## Acknowledgments

This work was supported in part by Grants-in-Aid for Creative Scientific Research (17GS0207), Scientific Research on Priority Area (No. 14078213), COE Research on Elements Science (No. 12CE2005), and the 21st Century COE Program, Kyoto University Alliance for Chemistry, from the Ministry of Education, Culture, Sports, Science and Technology, Japan. We are grateful to Dr. Takahiro Sasamori, Institute for Chemical Research, Kyoto University, for the valuable discussions.

[1] For reviews, see; a) D. Coucouvanis, *Acc. Chem. Res.* **1991**, *24*, 1–8; b) H. Weller, *Angew. Chem. Int. Ed. Engl.* **1993**, *32*, 41–53; c) M. Hidai, S. Kuwata, Y. Mizobe, *Acc. Chem. Res.* **2000**, *33*, 46–52.

[2] a) L. Cai, R. H. Holm, *J. Am. Chem. Soc.* **1994**, *116*, 7177–7178; b) D. T. T. Tran, N. J. Taylor, J. F. Corrigan, *Angew. Chem. Int. Ed.* **2000**, *39*, 935–937; c) P. A. Shapely, H.-C. Liang, N. C. Dopke, *Organometallics* **2001**, *20*, 4700–4704; d) T. Komuro, T. Matsuo, H. Kawaguchi, K. Tatsumi, *Angew. Chem. Int. Ed.* **2003**, *42*, 465–468.

[3] T. Komuro, T. Matsuo, H. Kawaguchi, K. Tatsumi, *Chem. Commun.* **2002**, 988–989.

[4] a) D. M. Giolando, T. B. Rauchfuss, G. M. Clark, *Inorg. Chem.* **1987**, *26*, 3080–3082; b) J. Albertsen, R. Steudel, *J. Organomet. Chem.* **1992**, *424*, 153–158; c) T. Komuro, T. Matsuo, H. Kawaguchi, K. Tatsumi, *Inorg. Chem.* **2003**, *42*, 5340–5347.

[5] There are only few reports on dialkyl- or diarylsilanedithiols. Dimethylsilanedithiol has been characterized only by IR spectroscopy due to its extreme instability: G. Gattow, H. P. Dewald, *Z. Anorg. Allg. Chem.* **1991**, *604*, 63–67. As for diphenylsilanedithiol, only the boiling point has been reported: Y. Cai, B. P. Roberts, *Tetrahedron Lett.* **2001**, *42*, 763–766. Syntheses and some reactions of several dialkoxysilanedithiols have been reported: a) W. Wojnowski, M. Wojnowska, *Z. Anorg. Allg. Chem.* **1972**, *389*, 302–306; b) W. Wojnowski, M. Wojnowska, *Z. Anorg. Allg. Chem.* **1973**, *398*, 167–172; c) W. Wojnowski, A. Herman, *Z. Anorg. Allg. Chem.* **1976**, *425*, 91–96; d) W. Wojnowski, E. W. Felcyn, *Z. Anorg. Allg. Chem.* **1987**, *546*, 229–234.

[6] a) N. Tokitoh, M. Ito, R. Okazaki, *Organometallics* **1995**, *14*, 4460–4462; b) M. Ito, N. Tokitoh, R. Okazaki, *Organometallics* **1997**, *16*, 4314–4319.

[7] a) V. Jancik, Y. Peng, H. W. Roesky, J. Li, D. Neculai, A. M. Neculai, R. Herbst-Irmer, *J. Am. Chem. Soc.* **2003**, *125*, 1452–1453; b) V. Jancik, H. W. Roesky, D. Neculai, A. M. Neculai, R. Herbst-Irmer, *Angew. Chem. Int. Ed.* **2004**, *43*, 6192–6196.

[8] a) T. Matsumoto, K. Tatsumi, *Chem. Lett.* **2001**, 964–965; b) T. Matsumoto, Y. Nakaya, K. Tatsumi, *Organometallics* **2006**, *25*, 4835–4845.

[9] Such as TbtB(μ-S)$_2$TiCp$_2$, AlL(μ-S)$_2$MCp$_2$, and Dep(Dip)Ge(μ-S)$_2$Ru(η$^6$-benzene) (Cp = $C_5H_5$, M = Ti, Zr), see refs.[6–8]

[10] a) N. Tokitoh, H. Suzuki, R. Okazaki, *J. Am. Chem. Soc.* **1993**, *115*, 10428–10429; b) H. Suzuki, N. Tokitoh, R. Okazaki, *Bull. Chem. Soc. Jpn.* **1995**, *68*, 2471–2481.

[11] Recently, we reported the synthesis of (silanedichalcogenolato)-titanium complexes by the reaction of a disilene **4** with $Cp_2TiE_5$: N. Takeda, T. Tanabe, N. Tokitoh, *Bull. Chem. Soc. Jpn.* **2006**, *79*, 1573–1579.

[12] Crystal data for **1**: The intensity data were collected with a Rigaku/MSC Mercury CCD diffractometer with graphite-monochromated Mo-$K_\alpha$ radiation ($\lambda$ = 0.71070 Å). The structures were solved by direct methods (SIR-97) and refined by full-matrix least-squares procedures on $F^2$ for all reflections (SHELXL-97). Formula $C_{36}H_{72}S_2Si_7$, $MW$ = 765.69; triclinic; space group $P\bar{1}$ (#2); $a$ = 9.2535(4), $b$ = 15.9925(5), $c$ = 15.8055(7) Å; $\alpha$ = 82.9726(15), $\beta$ = 81.7950(17), $\gamma$ = 81.365(4)°; $V$ = 2276.62(16) Å$^3$; $Z$ = 2; $\mu$ = 0.324 mm$^{-1}$; $D_{calcd.}$ = 1.117 g cm$^{-3}$; $2\theta_{max}$ = 51.0°; $T$ = 103(2) K; $R_1$ [$I > 2\sigma(I)$] = 0.0563; $wR_2$ (all data) = 0.1350; GOF = 1.049 for 8315 reflections and 427 parameters. CCDC-627421 (**1**) contains the supplementary crystallographic data for this paper. These data can be obtained free of charge from The Cambridge Crystallographic Data Center via www.ccdc.cam.ac.uk/data_request/cif. Crystal data for **3** and **7** are given in the Supporting Information. CCDC-627422 (**3**) and -627425 (**7**) contain the supplementary crystallographic data for this paper. These data can be obtained free of charge from The Cambridge Crystallographic Data Center via www.ccdc.cam.ac.uk/data_request/cif.

[13] We have already reported the synthesis of the stable silanethione and silaneselone, Tbt(Tip)Si=Ch (Ch = S, Se; Tip = 2,4,6-triisopropylphenyl). They should be related compounds to compounds **1**, **3**, and **7**, since the hydrolyzed products of the silanethione and silaneselone are Tbt(Tip)Si(OH)(SH) and Tbt(Tip)Si(OH)(SeH), which have already been reported. For reviews on heavy ketones, see: R. Okazaki, N. Tokitoh, *Acc. Chem. Res.* **2000**, *33*, 625–630.

[14] A. Bondi, *J. Phys. Chem.* **1964**, *68*, 441–451.

[15] The absorptions assignable to the E–H (E = O, S, Se) vibrations with E–H–E hydrogen bonding should be broadened and shifted to lower wavenumbers. For example, [Ru(SH$_2$)(PPh$_3$)'S$_4$'] shows one broad band for ν(S–H···S) at 2300 cm$^{-1}$(KBr): D. Sellmann, P. Lechner, F. Knoch, M. Moll, *J. Am. Chem. Soc.* **1992**, *114*, 922–930.

[16] For the experimental procedure, spectral and crystal data for **9a**, see the Supporting Information. CCDC-627423 (**9a**) contains the supplementary crystallographic data for this paper. These data can be obtained free of charge from The Cambridge Crystallographic Data Center via www.ccdc.cam.ac.uk/data_request/cif.

[17] Crystal data for **9b** (**9b·hexane**): Formula $C_{78}H_{114}P_2PtS_2Si_7$, $MW$ = 1569.47; triclinic; space group $P\bar{1}$ (#2); $a$ = 13.7853(8), $b$ = 16.8910(9), $c$ = 21.0444(17) Å; $\alpha$ = 113.276(7), $\beta$ = 102.504(4), $\gamma$ = 92.842(3)°; $V$ = 4344.4(5) Å$^3$; $Z$ = 2; $\mu$ = 1.833 mm$^{-1}$; $D_{calcd.}$ = 1.200 Mg/m$^3$; $2\theta_{max}$ = 50.0°; $T$ = 173(2) K; $R_1$ [$I > 2\sigma(I)$] = 0.0511; $wR_2$ (all data) = 0.1272; GOF = 1.078 for 15211 reflections and 870 parameters. CCDC-627424 (**9b**) contains the supplementary crystallographic data for this paper. These data can be obtained free of charge from The Cambridge Crystallographic Data Center via www.ccdc.cam.ac.uk/data_request/cif.

[18] A. B. Pangborn, M. A. Giardello, R. H. Grubbs, R. K. Rosen, F. J. Timmers, *Organometallics* **1996**, *15*, 1518–1520.

Received: December 22, 2006
Published Online: February 13, 2007

 © 2007 Wiley-VCH Verlag GmbH & Co. KGaA, Weinheim 

DOI: 10.1002/ejic.200601082

# Molecular Ice with Hybrid Water–Bromide Network around a Cryptand with a Bromide Ion Included in the Cavity to Form a Host-within-a-Host-Like Structure

**Madhab C. Das[a] and Parimal K. Bharadwaj*[a]**

**Keywords:** Anion binding / Cryptands / Hydrogen bonds / Water chemistry / X-ray diffraction

A new mode of association of water molecules is described. Adamantanoid water clusters bonded to bromide ions as well as other water molecules form a cage within which bromide-encapsulated aza cryptands reside to form a host-within-a-host-like structure. The structure of this adamantanoid water decamer is remarkably similar to that of cubic ice ($I_c$). The average O···O distance is 2.78 Å, which is close to 2.75 Å present in $I_c$, and the average O···O···O angle of 109.40° is also close to the tetrahedral angle in ice $I_c$.

(© Wiley-VCH Verlag GmbH & Co. KGaA, 69451 Weinheim, Germany, 2007)

## Introduction

Complexation of anions by different host molecules has become an area of intense research[1] because the function of anions is essential in biological systems and in diverse enzymatic reactions. Anions are also implicated[2] in several diseases such as cystic fibrosis, Alzheimer's disease, etc. In addition, different environmental problems are associated with anions. Herein, we report the supramolecular association of ten water molecules into "molecular ice", which further connects other such units and a cluster of water and bromide ions to form a 3D cage within which lies a cryptand that encapsulates a bromide ion in its cavity. There are other cryptands also present with empty cavities.

The importance of water and its well-discussed anomalies have resulted in a large number of theoretical as well as experimental studies[3–6] that cover a broad range of topics on the structure of water. For ice, there are several crystalline[7] and amorphous[8] phases known. Phases $I_h$ and $I_c$ are the two most common forms[7a] of ice and are strikingly similar in structure. They differ only in the stacking sequence of the puckered layers relative to one another such that the interconnecting rings are in the boat conformation in ice $I_h$ whereas they assume a chair conformation in ice $I_c$. This form of ice is also called cubic ice and its formation is of utmost importance in cryobiology where formation of ice upon cooling the sample is the primary cause of cell damage. Biological samples are better preserved in $I_c$ which form tiny crystals all around and do not lead to extensive solute segregation,[9] whereas $I_h$ causes massive cell damage. Cubic ice is also likely to be present[10] in the outer spheres of some of the planets of our solar system, including earth.

## Results and Discussion

Complex **1** was isolated as colorless crystals[11] from an aqueous methanolic solution of **L**[12] (Scheme 1) in the presence of HBr in 65% yield. The asymmetric unit of **1** consists of two bridges from two different cryptand units, seven water molecules, and three bromides, where one of the bromides (Br1) sits on a crystallographic threefold symmetry axis. The atom Br1, included in the cryptand cavity, pulls the two bridgehead N atoms towards itself thereby decreasing their interatomic distance to 8.452 Å from the observed value of 9.904 Å [12] in **L**. This bromide is H-bonded with the three protonated secondary amines in the three bridges (N6···Br1, 3.278 Å; N6–H2···Br1, 148.55°) and three aromatic CH protons (C20···Br1, 3.439 Å; C20–H20···Br1, 127.73°) to complete a distorted octahedral coordination (Figure 1) geometry. The second bromide (Br2), which occupies a position outside the cryptand cavity, forms one strong N–H···Br hydrogen bond (N6···Br2, 3.286 Å; N6–

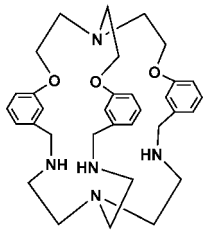


**L**

Scheme 1. Illustration of aza cryptand **L**.

[a] Department of Chemistry, Indian Institute of Technology Kanpur,
Kanpur 208016, India
E-mail: pkb@iitk.ac.in

Supporting information for this article is available on the WWW under http://www.eurjic.org or from the author.

 © 2007 Wiley-VCH Verlag GmbH & Co. KGaA, Weinheim 

H1···Br2, 119.59°) with the bromide-encapsulated cryptand and two strong N–H···Br hydrogen bonds (N3···Br2, 3.262 Å; N3–H2···Br2, 127.55°, and N3···Br2, 3.262 Å; N3–H1···Br2, 141.85°) with the bromide-free cryptand, thereby acting as a linker among the cryptand units. Thus, each of the protonated secondary amines of the "tren" end of the bromide-encapsulated cryptand makes two contacts: one N–H···Br1 and one N–H···Br2. Each of the protonated secondary amines of the bromide-free cryptand also makes two different N–H···Br2 intermolecular contacts (Figure 2).

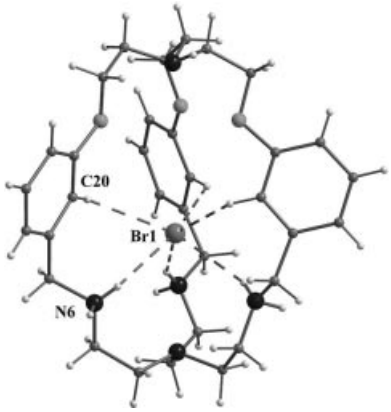


Figure 1. A perspective view showing a bromide ion (Br1) encapsulated inside the cryptand cavity.

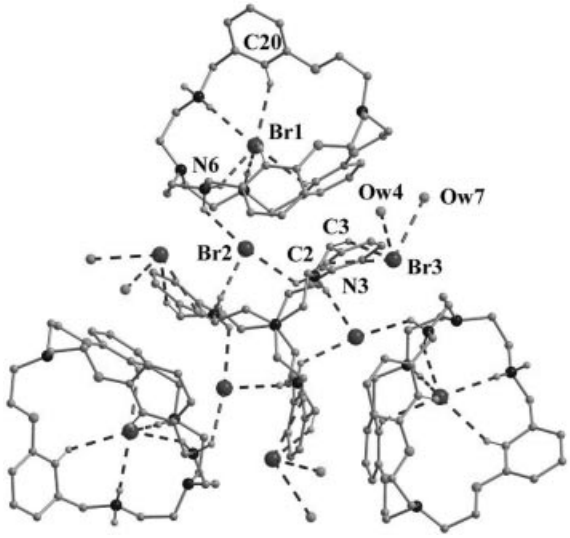


Figure 2. A view showing different hydrogen bonding interactions of the three bromide ions. Only those H atoms that are involved in H-bonding are shown.

Out of the seven water molecules present in the asymmetric unit, four are involved with other symmetry related $H_2O$ molecules to form an adamatanoid $(H_2O)_{10}$ cluster whereas the rest join these $(H_2O)_{10}$ clusters to form a layer of supramolecularly assembled water molecules. Br3 ions are H-bonded to the layer of water molecules that reinforce the structure. Overall, there are three different types of H-bonding networks associated with the adamantanoid water cluster (three Ow2···Ow7···Br3, three Ow3···Ow5···Ow6, and three Ow4···Br3···Ow7 networks). Six adamantanoid units form a 3D cage-like supramolecular network through connections with the remaining $H_2O$ molecules and Br3 ions. The bromide-encapsulated cryptand lies within this cage and assumes a host-within-a-host-like structure (Figure 3), which resembles the Russian nesting doll.[13]

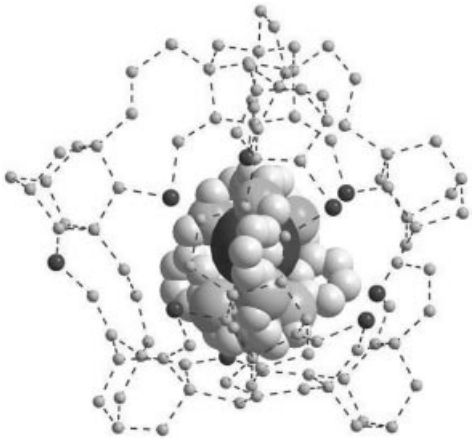

Figure 3. A view of the host within a host structure. Bromide encapsulated cryptand moiety is shown in space-filling model. Hydrogen atoms are omitted for clarity. Color code: C light grey, N medium grey, O dark grey, Br black.

Figure 4 represents the coordination environment of the adamantanoid water cluster, which consists of four different types of water molecules with respect to their noncovalent interactions. The $(H_2O)_{10}$ cluster is termed "molecular ice" because this is the smallest unit of naturally occurring cubic ice. The structure of this adamantanoid water decamer in **1** is remarkably similar to that of ice $I_c$.[14] The average O···O distance in **1** is 2.78 Å, which is close to 2.75 Å, present in $I_c$.[14] The average O···O···O angle of 109.40° in the structure is also close to the tetrahedral angle in ice $I_c$.[14] The distance across the water decamer from Ow2 to Ow4 is slightly lower [6.282(2) Å] than the value (6.35 Å) observed in $I_c$.[15] Adamantanoid $(H_2O)_{10}$ clusters detected in the voids of a

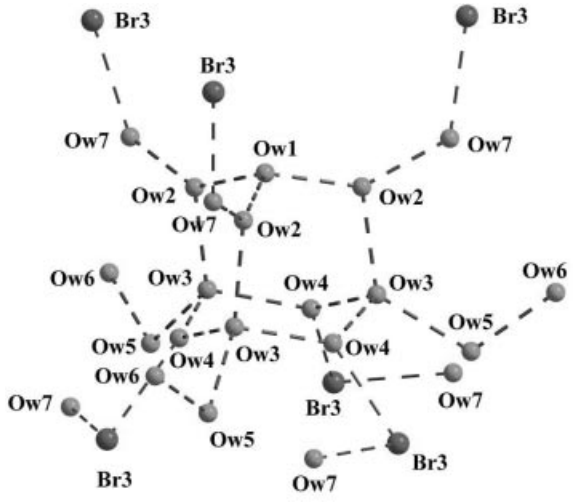


Figure 4. A close view of the adamantanoid water cluster and its environment.

 © 2007 Wiley-VCH Verlag GmbH & Co. KGaA, Weinheim 

cupric complex[16] or within a hydrophobic self-assembled cage[17] have comparable noncovalent parameters. Notably, the Ow6 makes three H-bonded contacts with three Ow5 and creates three fused nonameric units;[18] each nonamer contains two water molecules of one adamantanoid unit (Ow2, Ow3), two water molecules of another adamantanoid unit (Ow3, Ow4), two Ow5, and one Br3 ion. Figure 5 shows the packing diagram of the different constituent units present in **1**.

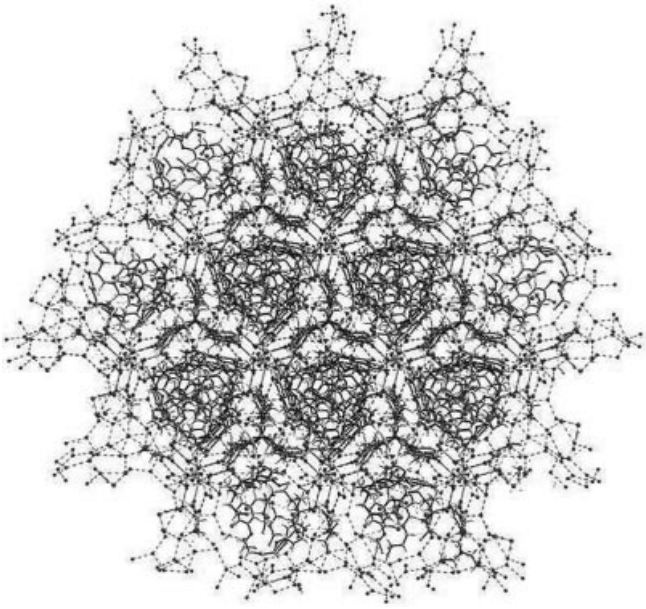

Figure 5. Packing diagram of **1** viewed along the two bridgehead N atoms of the bromide encapsulated cryptand.

Compound **1** exhibits a strong broad peak at about 3404 $cm^{-1}$ in the IR spectrum, and this peak is attributed[18] to O–H stretching pertaining to the water cluster. The O–H stretching vibration for $I_c$ appears[14] as a broad band centered around 3200 $cm^{-1}$. The difference in the stretching vibrations of **1** in comparison to $I_c$ is due to its different environment. Thermal gravimetric analysis[18] reveals that **1** loses 9.55% of weight at 120 °C, which corresponds to ca. 10 molecules of water. The rest of the water molecules are lost along with decomposition of the compound after only 250 °C, which signifies that the remaining water molecules are tightly held in the crystal lattice. After heating[18] the compound at 120 °C to remove ten molecules of water, the IR spectrum shows the broad peak characteristic of the remaining association of water molecules. Powder X-ray data taken[18] before and after heating the sample in vacuo at 120 °C for 2 h show that once the bulk of the water molecules are removed, the lattice breaks down.

## Conclusions

In conclusion, we have shown that a bromide-encapsulated cryptand is surrounded by a cage formed by connecting molecular ice-like water clusters with other water molecules and bromide ions. Thus, the structure looks like a Russian nesting doll. The understanding of three-dimensional structures of this and similar systems have profound effects in several areas, from molecular self-assembly,[19] gas clathrate hydrates,[20] to cryobiology.[9] We are presently working along these lines.

## Experimental Section

Cryptand **L** was synthesized as reported[12] previously from our lab. Complex **1** was synthesized by allowing a solution of the cryptand (84 mg, 0.15 mmol) in aqueous methanol (6 mL, 1:1, v/v) in the presence of HBr to concentrate. After a few days, crystals of $\{[H_3\mathbf{L}][H_4\mathbf{L}]\cdot(Br)_7\cdot 15H_2O\}_n$ (**1**) appeared as colorless rectangular plates in 65% yield. $C_{66}H_{127}Br_7N_{10}O_{21}$ (1956.10): calcd. C 40.52, H 6.54, N 7.16; found C 40.46, H 6.59, N 7.08.

**Supporting Information** (see footnote on the first page of this article): FTIR spectrum, TGA curve, and PXRD analysis of **1**. Additional figures that show the structure of the cryptand cage-like structure.

## Acknowledgments

Financial support received from the Department of Science and Technology, New Delhi, India (grant No. SR/S5/NM-38/2003 to P. K. B.) and a JRF grant (CSIR) to M. C. D. are gratefully acknowledged.

[1] a) T. Mizuno, W. H. Wei, L. R. Eller, J. L. Sessler, *J. Am. Chem. Soc.* **2002**, *124*, 1134; b) R. M. Begum, D. Powell, K. Bowman-James, *Inorg. Chem.* **2006**, *45*, 964; c) P. D. Beer, P. A. Gale, *Angew. Chem. Int. Ed.* **2001**, *40*, 486; d) C. A. IIioudis, D. A. Tocher, J. W. Steed, *J. Am. Chem. Soc.* **2004**, *126*, 12395; e) S. O. Kang, D. Powell, V. W. Day, K. Bowman-James, *Angew. Chem. Int. Ed.* **2006**, *45*, 1921; f) S. O. Kang, D. Powell, K. Bowman-James, *J. Am. Chem. Soc.* **2005**, *127*, 13478.

[2] a) N. Kartner, J. W. Hanraha, T. J. Jensen, A. L. Nalsmith, S. Sun, C. A. Ackerley, E. F. Reyes, L. C. Tsui, J. M. Rommens, C. E. Bear, J. R. Riordan, *Cell* **1991**, *64*, 681; b) D. P. Rich, R. J. Gregory, M. P. Anderson, P. Manavalan, A. E. Smith, M. J. Welsh, *Science* **1991**, *253*, 205; c) K. Renkawck, G. J. C. G. M. Bosman, *Neuroreport* **1995**, *6*, 929.

[3] a) F. N. Keutsch, R. J. Saykally, *Proc. Natl. Acad. Sci. (USA)* **2001**, *98*, 10533; b) D. R. Alfonso, K. Karapetian, D. C. Sorescu, K. D. Jordan, *J. Phys. Chem. B* **2004**, *108*, 3431; c) M. F. Chaplin, *Biophys. Chem.* **1999**, *83*, 211; d) S. Vaitheeswaran, H. Yin, J. C. Rasaiah, G. Hummer, *Proc. Natl. Acad. Sci. (USA)* **2004**, *101*, 17002; e) M. Matsumoto, S. Saito, I. Ohmine, *Nature* **2002**, *416*, 409; f) T. Koddermann, F. Schulte, M. Huelsekopf, R. Ludwig, *Angew. Chem. Int. Ed.* **2003**, *42*, 4904.

[4] a) M. Miyazaki, A. Fujii, T. Ebata, N. Mikami, *Science* **2004**, *304*, 1134; b) T. S. Zwier, *Science* **2004**, *304*, 1119; c) Y. Zubavicus, M. Grunze, *Science* **2004**, *304*, 974; d) C. Ruan, V. A. Lobastov, F. Vigliotti, S. Chen, A. H. Zewail, *Science* **2004**, *304*, 80; e) P. Wernet, D. Nordlund, U. Bergmann, M. Cavalleri, M. Odelius, H. Ogasawara, T. K. Hirsch, P. Glatzel, L. G. M. Pettersson, A. Nilsson, *Science* **2004**, *304*, 995; f) G. W. Robinson, *Water in Biology, Chemistry, and Physics: Experimental Overviews and Computational Methodologies*, World Scientific, Singapore, River Edge, NJ, **1996**.

[5] a) P. K. Thallapally, G. O. Lloyd, J. L. Atwood, L. J. Barbour, *Angew. Chem. Int. Ed.* **2005**, *44*, 3848; b) P. S. Lakshminarayanan, E. Suresh, P. Ghosh, *Angew. Chem. Int. Ed.* **2006**, *45*, 3807; c) S. K. Ghosh, P. K. Bharadwaj, *Angew. Chem. Int. Ed.*

 © 2007 Wiley-VCH Verlag GmbH & Co. KGaA, Weinheim 

**2004**, *43*, 3577; d) J. L. Sessler, D. E. Gross, W. S. Cho, V. M. Lynch, F. P. Schmidtchen, G. W. Bates, M. E. Light, P. A. Gale, *J. Am. Chem. Soc.* **2006**, *128*, 12281.
[6] a) R. Ludwig, *Angew. Chem. Int. Ed.* **2001**, *40*, 1808; b) L. Infantes, S. Motherwell, *CrystEngComm* **2002**, *4*, 454; c) L. Infantes, J. Chisholm, S. Motherwell, *CrystEngComm* **2003**, *5*, 480; d) P. G. Sennikov, S. K. Ignatov, O. Schrems, *ChemPhysChem* **2005**, *6*, 392; e) N. S. Oxtoby, A. J. Blake, N. R. Champness, C. Wilson, *Chem. Eur. J.* **2005**, *11*, 1.
[7] a) N. H. Fletcher, *The Chemical Physics of Ice*, Cambridge University Press, Cambridge, **1970**; b) C. Loban, J. J. Finney, W. F. Kuhs, *Nature* **1998**, *391*, 268; c) M. Koza, H. Schober, A. Tölle, F. Fujara, T. Hansen, *Nature* **1999**, *397*, 660.
[8] O. Mishima, H. E. Stanley, *Nature* **1998**, *396*, 329.
[9] a) L. Bachmann, E. Mayer, *Physics of Water and Ice: Implications for Cryofixation* (Eds.: R. A. Steinbrecht, K. Zierold), Springer, Berlin, **1987**; b) J. Dubochet, M. A. Kohl, E. Mayer, A. Hallbrucker, *Phys. Chem. Chem. Phys.* **2000**, *2*, 1579.
[10] a) E. Whalley, *Science* **1981**, *211*, 389; b) P. G. Sennikov, S. K. Ignatov, O. Schrems, *ChemPhysChem* **2005**, *6*, 392.
[11] Crystal data for **1**: Colorless, hexagonal, crystal dimensions $0.16 \times 0.12 \times 0.11$ mm, cubic, P $2_13$, $Z = 12$, $a = 20.880(5)$, $b = 20.880(5)$, $c = 20.880(5)$ Å, $V = 9103(4)$ Å$^3$, $\rho_{calcd.} = 1.454$ g cm$^{-3}$, $T = 100(1)$ K, $\mu = 3.154$ mm$^{-1}$, $\theta_{max} = 28.23°$, 7554 reflections collected of which 5483 were unique. $R_1 = 0.0767$, $wR_2 = 0.1975$ with a GOF of 1.062 for $I > 2\sigma(I)$; residual electron density: 2.465 and –1.349 e Å$^{-3}$. The X-ray data were collected with a Bruker SMART APEX CCD diffractometer by using graphite monochromated Mo-$K_\alpha$ radiation (0.71069 Å). The following programs were used during data collection and refinement: SMART (version 5.628 to acquire frame data), SAINT (version 6.45 to determine final unit parameters and integrate frame data). The structure was solved by the direct methods and refined on $F^2$ using SHELX-97 (G. M. Sheldrick, *SHELX-97: Program for the Solution and Refinement of Crystal Structures*, University of Göttingen, Germany, **1997**). The hydrogen atoms of the water molecules could not be located in the difference Fourier maps with certainty although other H atoms could be located. The non-hydrogen atoms were refined anisotropically. CCDC-616374 contains the supplementary crystallographic data for this paper. This data can be obtained from The Cambridge Crystallographic Data Centre via www.ccdc.cam.ac.uk/data_request/cif.
[12] D. K. Chand, P. K. Bharadwaj, *Inorg. Chem.* **1996**, *35*, 3380.
[13] a) J. L. Atwood, L. J. Barbour, S. J. Dalgarno, M. J. Hardie, C. L. Raston, H. R. Webb, *J. Am. Chem. Soc.* **2004**, *126*, 13170; b) M. J. Hardie, C. L. Raston, *J. Chem. Soc., Dalton Trans.* **2000**, 2483; c) B. R. Bhogala, A. Nangia, *Cryst. Growth Des.* **2006**, *6*, 32.
[14] D. Eisenberg, W. Kauzmann, *The Structure and Properties of Water*, Oxford University Press, Oxford, UK, **1969**.
[15] H. König, *Z. Kristallogr.* **1994**, *105*, 279.
[16] L. J. Barbour, G. W. Orr, J. L. Atwood, *Nature* **1998**, *393*, 671.
[17] M. Yoshizawa, T. Kusukawa, M. Kawano, T. Ohhara, I. Tanaka, K. Kurihara, N. Niimura, M. Fujita, *J. Am. Chem. Soc.* **2005**, *127*, 2798.
[18] See Supporting Information.
[19] J. D. Joannopoulous, *Nature* **2001**, *414*, 257.
[20] a) M. T. Kirchner, R. Boese, W. E. Billups, L. R. Norman, *J. Am. Chem. Soc.* **2004**, *126*, 9407; b) C. A. Koh, *Chem. Soc. Rev.* **2002**, *31*, 157; c) D. K. Staykova, W. F. Kuhs, A. N. Salamatin, T. Hansen, *J. Phys. Chem. B* **2003**, *107*, 10299.

Received: November 18, 2006
Published Online: February 20, 2007

 © 2007 Wiley-VCH Verlag GmbH & Co. KGaA, Weinheim 

DOI: 10.1002/ejic.200600889

# Intra- and Intermolecular H···Cl–Ni Bonding Patterns in a Series of Highly Preorganized Dinuclear Nickel(II) Complexes

**Feng-Mei Nie,[a][‡] Guido Leibeling,[a] Serhiy Demeshko,[a] Sebastian Dechert,[a] and Franc Meyer*[a]**

**Keywords:** Nickel / Dimetallic complexes / Hydrogen bonds / Pyrazolate ligands / Magnetic properties

Four dinickel complexes $[L^1Ni_2(\mu\text{-}Cl)(Cl)_2]\cdot 2CH_3OH$ (**1a**), $[L^1Ni_2(\mu\text{-}Cl)(CH_3OH)](ClO_4)_2$ (**1b**), $[L^2Ni_2(\mu\text{-}Cl)Cl_2(H_2O)_2]\cdot H_2O$ (**2**) and $[L^3Ni_2Cl_2(CH_3OH)_2]Cl\cdot 2CH_3OH$ (**3**) were synthesized and structurally characterized. The ligand scaffolds have a central pyrazolato bridge and N-donor chelate arms that provide two proximate binding pockets for the nickel ions. While the longer ligand side arms in **1a**, **1b** and **2** induce Ni···Ni distances of around 4.0 Å and favour incorporation of a chlorido bridge within the dimetallic pocket, a stretched Ni···Ni separation of 4.6 Å with an unusual intramolecular Cl···H–O linkage is observed in **3**. Various Cl···H–O hydrogen-bonding motifs are identified in the solid-state structures of **1**–**3**, where either the H-donor (MeOH or $H_2O$) or the H-acceptor (chlorido) or both are bound to a nickel ion, and their relative donor–acceptor distances are discussed. Magnetic coupling mediated through the pyrazolato and chlorido bridges is rather weak and antiferromagnetic, but it is even weaker for the Cl···H–O linkage.
(© Wiley-VCH Verlag GmbH & Co. KGaA, 69451 Weinheim, Germany, 2007)

## Introduction

Hydrogen bonding to metal-bound ligands can have profound effects on fundamental properties of the metal complex, such as the metal–ligand bond lengths, redox potentials and reactivity.[1–3] Metal-bound chlorido ligands have been identified as a very good hydrogen-bond acceptor (in contrast to its organochlorine counterpart), having the potential to interact with hydrogen-bond donors in both a strong (i.e., short) and anisotropic fashion.[4,5] While hydrogen bonds to metal-bound fluorido ligands are even stronger, they also exhibit a distinct angular preference for larger H···F–M angles.[6] Intermolecular D–H···X–M (D = N, O; X = F, Cl, Br, I) interactions are increasingly applied in molecular recognition, crystal engineering and the noncovalent assembly of metallosupramolecules,[7,8] while intramolecular D–H···X–M motifs involving pendant nonligating hydrogen-bonding groups allow the stabilization of unusual ligands, such as HF, at a metal ion.[9] A particular situation arises if the hydrogen-bond donor D is itself acting as a ligand towards a second metal ion. This may enhance the acidity of the D–H unit and may induce particularly strong intramolecular D–H···X–M interactions, as was observed in some Cu–(H)O–H···F–Cu motifs with extremely short H···F distances.[10,11] In order to enforce the formation of such hydrogen bonds, the use of dinucleating ligand scaffolds that constrain the metal–metal separation appears most promising. Here we report the structural characterization of a series of pyrazolato-based dinickel chloride complexes that exhibit various hydrogen-bonding arrangements. These involve the nickel-bound chlorido ligand and water or methanol solvent molecules, comprising an unusual intramolecular Ni–(Me)O–H···Cl–Ni interaction. The set of compartmental ligands used in this work is depicted in Scheme 1.

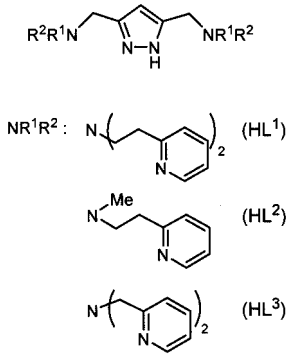


Scheme 1. Ligands used in this work.[10]

The ligands differ by the number of side arm donor sites ($HL^1$ versus $HL^2$) or by the side arm chain length ($HL^1$ versus $HL^3$). The latter variation was previously shown to determine the preferred metal–metal distance in the resulting dimetallic complexes, with the shorter side arms in

[a] Institut für Anorganische Chemie, Georg-August-Universität Göttingen
Tammannstrasse 4, 37077 Göttingen, Germany
Fax: +49-551-393063
E-mail: franc.meyer@chemie.uni-goettingen.de
[‡] New address: Department of Chemistry, Capital Normal University,
Beijing 100037, P. R. China
Supporting information for this article is available on the WWW under http://www.eurjic.org or from the author.

 © 2007 Wiley-VCH Verlag GmbH & Co. KGaA, Weinheim 

$HL^3$ enforcing larger metal–metal distances of >4 Å.[12,13] With 3d transition-metal ions such as copper(II) and zinc(II), $\{L^1M_2\}$ scaffolds (M = Cu, Zn) allow small bridges such as a hydroxido group to span the two metal ions, while the shorter ligand side arms in $\{L^3M_2\}$ pull the metal ions back and apart. The latter situation induces incorporation of an additional solvent molecule, giving functionalities such as (H)O–H–O(H) or F–H–O(H) within the dimetallic pocket.[10,14] Similar effects are now anticipated in nickel complexes of the current pyrazolato ligands and are investigated in order to probe hydrogen-bonding patterns to nickel-bound chlorido ligands.

## Results and Discussion

### Synthesis and Structural Characterization

Dinickel complexes of $[L^1]^-$, $[L^2]^-$ and $[L^3]^-$ were readily prepared from the respective pyrazole derivative $HL^1$, $HL^2$ and $HL^3$, 2 equiv. of $NiCl_2{\cdot}6H_2O$ and a base (usually $NEt_3$). Crystalline material of the resulting complexes **1a**, **2** and **3** was obtained from methanol/diethyl ether solutions. In order to gain some insight into the structural consequences that result from the presence of fewer chlorido ligands, complex **1b** was prepared by a similar procedure starting from $HL^1$, but using 2 equiv. of $Ni(ClO_4)_2{\cdot}6H_2O$ and 1 equiv. of NaCl. FAB mass spectra of **1a**, **2** and **3** feature dominant signals for the respective $[LNi_2Cl_2]^+$ ions, while the FAB mass spectrum of **1b** shows a signal for $[L^1Ni_2Cl(ClO_4)]^+$.

The molecular structures of all four complexes are depicted in Figures 1, 2, 3 and 4, along with selected interatomic distances and bond angles. In all cases the two nickel ions are hosted within the binding pockets of the ligand scaffold, spanned by the pyrazolato ligand and coordinated by the side arm nitrogen atoms. In $[L^1Ni_2Cl_3]$ (**1a**), both nickel(II) ions are six-coordinate; the coordination environment of each nickel ion consists of four nitrogen atoms from the pyrazolato, a bridging chlorido and a terminal chlorido ligand (Figure 1). Interestingly, the chlorido ligand at Ni1 is located *trans* to the pyrazolato N1 atom, while the chlorido ligand at Ni2 is found *trans* to the pyridyl N8 atom. When only a single chlorido ligand is present per dimetallic entity in $[L^1Ni_2(Cl)(CH_3OH)](ClO_4)_2$ (**1b**), it occupies the bridging position, leaving Ni2 five-coordinate while a methanol solvent molecule fills the remaining site at Ni1 (Figure 2). Fewer ligand side arms in $[L^2Ni_2Cl_3(H_2O)_2]$ (**2**) allow for the binding of a water solvent molecule to each of the metal ions, with one of the chlorido ligands in the bridging position and the others terminally bound *trans* to the pyrazolato N atom (Figure 3). The Ni–O distances in **1b** and **2** (2.16 and 2.14 Å) are comparable to those found in other six-coordinate nickel complexes with three or four nitrogen donor atoms and one or two chlorido ligands, as for example in $[(phen)_2NiCl(H_2O)]Cl{\cdot}EtOH{\cdot}H_2O$ (2.03 Å, phen = 1,10-phenanthroline)[15] or [(1,4,8,11-tetraazaundecane)$NiCl(H_2O)$]Cl (2.18 Å).[16] Metal···metal separations in all three complexes are very similar and quite short at 4.09 (**1a**), 4.00 (**1b**) and 4.11 (**2**) Å. It should be noted that related nickel(II) chloride complexes of some pyrazolato-derived ligands bearing aliphatic N-donor side arms usually feature five-coordinate nickel atoms,[17] in contrast to the systems studied here. However, close inspection reveals that the Ni–Cl–Ni bridge in **1a** is highly asymmetric with a long Ni1–Cl2 distance (2.82 Å) and a much shorter Ni2–Cl2 bond (2.50 Å). All other Ni–Cl distances ranging from 2.36 to 2.57 Å for Ni–Cl and from 2.46 to 2.65 Å for Ni–(μ-Cl) are in agreement with expectations.[17] The slight asymmetry of the Ni–Cl–Ni bridge in **1b** [*d*(Ni1–Cl1) = 2.61 Å, *d*(Ni2–Cl1) = 2.46 Å] reflects the different coordination numbers of the metal ions. The methanol molecule bound to Ni1 in **1b** is hydrogen-bonded to one of the perchlorate counteranions [*d*(O1···O21) = 2.80 Å].

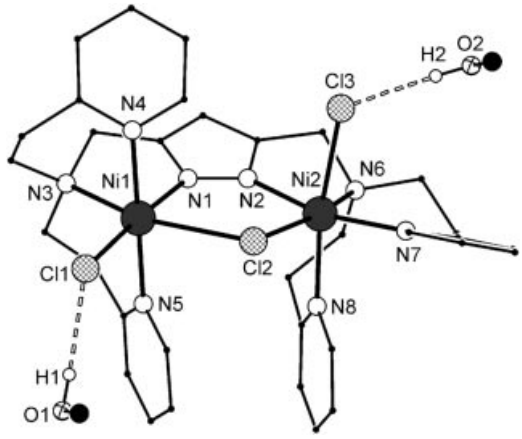


Figure 1. Plot of the molecular structure of **1a**. All hydrogen atoms except the O–H protons have been omitted for clarity. Selected interatomic distances [Å] and angles [°]: Ni1–Cl1 2.3632(6), Ni1–Cl2 2.8251(6), Ni1–N1 1.982(2), Ni1–N3 2.180(2), Ni1–N4 2.142(2), Ni1–N5 2.117(2), Ni2–Cl2 2.4947(5), Ni2–Cl3 2.5723(6), Ni2–N2 1.984(2), Ni2–N6 2.205(2), Ni2–N7 2.105(2), Ni2–N8 2.118(2), Ni1···Ni2 4.0917(6), O1–H1 0.86(3), O1···Cl1 3.184(2), O2–H2 0.82(3), O2···Cl3 3.062(2); Ni1–Cl2–Ni2 100.37(2), N1–Ni1–Cl1 175.94(4), N1–Ni1–Cl2 82.25(4), Cl2–Ni1–N3 162.44(4), N4–Ni1–N5 178.30(6), N2–Ni2–N7 166.14(6), N2–Ni2–Cl2 87.73(4), Cl3–Ni2–N8 169.42(4), O1–H1···Cl1 162(3), O2–H2···Cl3 170(3).

The terminal chlorido ligands in **1a** are involved in hydrogen bonding with methanol molecules included in the crystal lattice (Figure 1), where the Cl···O distances correlate with the Ni–Cl bond lengths; the chlorido ligand Cl1 with a short *d*(Ni1–Cl1) = 2.36 Å forms a relatively long hydrogen bond [*d*(Cl1···O1) = 3.18 Å], while the hydrogen bond of the more loosely bound Cl3 [*d*(Ni2–Cl3) = 2.57 Å] is significantly shorter at *d*(Cl3···O2) = 3.06 Å. The pyrazolato-based dinickel entities in **2** are strongly dimerized in the solid state through a series of O–H···Cl hydrogen bonds (Figure 3). In this closed hydrogen-bonding motif each nickel-bound water molecule forms two hydrogen bonds to chlorido ligands of the opposite dinickel array, giving rise to a zig-zag sequence of O–H···Cl linkages. The dimerized

 © 2007 Wiley-VCH Verlag GmbH & Co. KGaA, Weinheim 

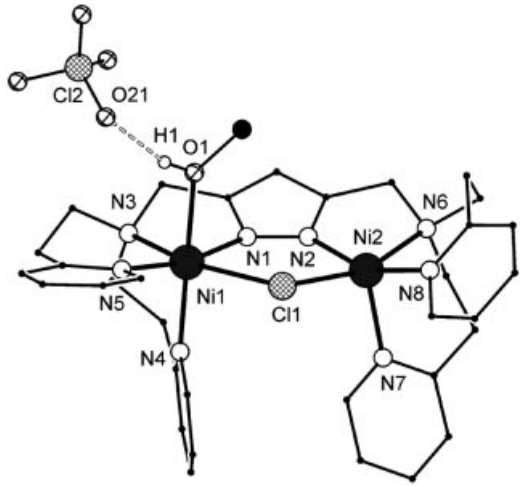


Figure 2. Plot of the molecular structure of **1b**. All hydrogen atoms except the O–H protons and the second $ClO_4^-$ ion have been omitted for clarity. Selected interatomic distances [Å] and angles [°]: Ni1–Cl1 2.610(1), Ni1–O1 2.162(3), Ni1–N1 1.975(3), Ni1–N3 2.138(3), Ni1–N4 2.095(3), Ni1–N5 2.084(3), Ni2–Cl1 2.455(1), Ni2–N2 1.944(3), Ni2–N6 2.157(4), Ni2–N7 2.043(3), Ni2–N8 2.039(4), Ni1···Ni2 4.0038(8), O1–H1 0.82(1), O1···O21 2.803(4); Ni1–Cl1–Ni2 104.43(4), N1–Ni1–N5 167.7(1), N1–Ni1–Cl1 82.9(1), Cl1–Ni1–N3 162.97(9), O1–Ni1–N4 175.3(1), N2–Ni2–N8 156.8(2), N2–Ni2–Cl1 87.0(1), Cl1–Ni2–N6 161.2(1), Cl1–Ni2–N7 99.3(1), O1–H1···O21 164(5).

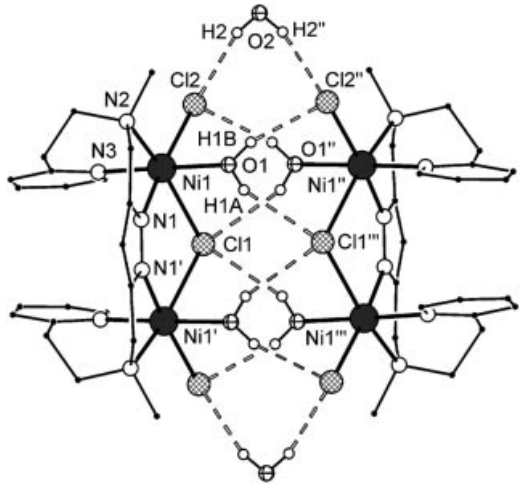


Figure 3. Plot of the molecular structure of **2**. All hydrogen atoms except the O–H protons have been omitted for clarity. Selected interatomic distances [Å] and angles [°]: Ni1–Cl1 2.6447(5), Ni1–Cl2 2.4013(5), Ni1–O1 2.143(1), Ni1–N1 1.996(2), Ni1–N2 2.148(2), Ni1–N3 2.080(2), Ni1···Ni1′ 4.1119(5), Ni1···Ni1′′ 5.4022(6), Ni1···Ni1′′′ 6.7890(5), O1–H1A 0.80(3), O1···Cl1′′′ 3.286(2), O1–H1B 0.86(3), O1···Cl2′′ 3.145(2); O2–H2 0.87(2), O2···Cl2 3.249(2), Ni1–Cl1–Ni1′ 102.04(2), N1–Ni1–Cl2 173.35(5), N1–Ni1–Cl1 83.96(5), Cl1–Ni1–N2 163.41(4), O1–Ni1–N3 177.98(6), O1–H1A···Cl1′′′ 155(3), O1–H1B···Cl2′′ 161(2), O2–H2···Cl2 163(4). Symmetry transformations used to generate equivalent atoms: ′: $x$, $1-y$, $z$; ′′: $1-x$, $y$, $2-z$; ′′′: $1-x$, $1-y$, $2-z$.

arrangement is capped by hydrogen bonds to two additional water molecules included in the crystal lattice, thus preventing the formation of chains or 3D hydrogen-bonded

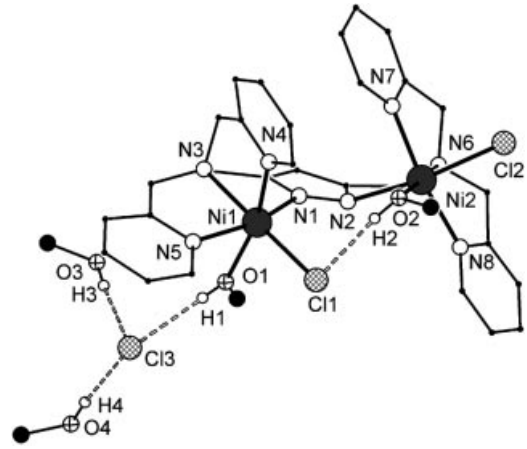


Figure 4. Plot of the molecular structure of **3**. All hydrogen atoms except the O–H protons have been omitted for clarity. Selected interatomic distances [Å] and angles [°]: Ni1–Cl1 2.3641(6), Ni1–O1 2.184(2), Ni1–N1 2.052(2), Ni1–N3 2.121(2), Ni1–N4 2.092(2), Ni1–N5 2.082(2), Ni2–Cl2 2.4522(7), Ni2–O2 2.070(2), Ni2–N2 2.144(2), Ni2–N6 2.106(2), Ni2–N7 2.066(2), Ni2–N8 2.070(2), Ni1···Ni2 4.6007(7), O1–H1 0.77(3), O1···Cl3 3.054(2), O2–H2 0.83(3), O2···Cl1 3.052(2), O3–H3 0.80(3), O3···Cl3 3.150(2), O4–H4 0.85(4), O4···Cl3 3.133(2); N1–Ni1–N5 159.32(6), N1–Ni1–Cl1 101.35(4), Cl1–Ni1–N3 177.81(5), O1–Ni1–N4 166.58(6), N2–Ni2–Cl2 171.67(4), N2–Ni2–O2 91.82(6), O2–Ni2–N6 174.73(6), N7–Ni2–N8 161.91(7), O1–H1···Cl3 167(3), O2–H2···Cl1 172(3), O3–H3···Cl3 174(3), O4–H4···Cl3 174(3).

networks. Overall, each chlorido ligand and each water molecule is involved in two hydrogen-bonding contacts. The resulting dimer of dinickel subunits in **2** is located on a centre of inversion, with each dinickel molecule having crystallographically imposed $C_s$ symmetry. As expected, O–H···Cl interactions to the bridging chlorido ligands are the longest at $d$(Cl1···O1) = 3.29 Å, but they are well within the range expected for HOH···Cl or $RCH_2OH$···Cl hydrogen bonds.[5,8]

The molecular structure of **3** that incorporates the pyrazolato ligand $[L^3]^-$ with shorter side arms differs fundamentally from those of **1a**, **1b** and **2**, since the chlorido atom Cl1 does not occupy a bridging position within the dimetallic pocket (Figure 4). Instead, a methanol molecule is inserted at Ni2 to give an unusual intramolecular Ni–Cl···H–O(Me)–Ni bridge with a short hydrogen bond [$d$(Cl1···O2) = 3.05 Å]. As a consequence, the Ni···Ni separation in **3** (4.60 Å) is considerably longer than in **1a**, **1b** and **2** (4.09, 4.00 and 4.11 Å, respectively). Ligand $[L^3]^-$ has previously been shown to favour longer metal–metal separations of around 4.5 Å because of the shorter chelate arms than those of $[L^1]^-$.[12] Observation of $[L^3Ni_2Cl_2]^+$ as the dominant ion in the FAB mass spectrum of **3** suggests, however, that the inserted methanol molecule is readily lost under reduced pressure.

Both nickel(II) ions in **3** are six-coordinate, but a major difference to the analogous complex of ligand $[L^1]^-$ (i.e., complex **1a**) is the coordination isomerism of some chlorido

 © 2007 Wiley-VCH Verlag GmbH & Co. KGaA, Weinheim 

ligands. In **1a** a chlorido ligand (Cl1) is terminally bound to Ni1 and forms a hydrogen bond to a lattice methanol molecule, while an inverse situation is found for **3** where the methanol molecule acts as a ligand to Ni1 and is hydrogen-bonded to the chlorido ligand Cl3 that is dissociated from the metal ion. The distance Cl3···O1 in **3** is very short and comparable to the short intramolecular Cl···H–O linkage (3.05 Å), in accordance with the idea that a dissociated chloride ion should be a better H-bond acceptor because of its larger negative charge compared with a metal-bound chlorido ligand such as in **1a** and **2**.[5] Interestingly, the "free" Cl3 in **3** forms two further hydrogen-bonding interactions to lattice methanol molecules which are significantly longer (3.13 and 3.15 Å; Figure 4) than the hydrogen bond to nickel-bound O1, thus supporting the assumption that the hydrogen-bond strength is enhanced by coordination and acidification of the H-donor methanol.

## Magnetic Properties

In order to evaluate the effect of the different structural features and bridging units of the dimetallic scaffolds on the magnetic coupling between the proximate nickel(II) ($S$ = 1) ions, magnetic susceptibility measurements were carried out for all four complexes at two different magnetic fields in a temperature range from 2.0 to 295 K. No significant field dependence was observed for any of the complexes. The temperature dependence of the magnetic susceptibility $\chi_M$ and the product $\chi_M T$ is shown in Figure 5. In all cases, the observed $\chi_M T$ values of around 2.5 $cm^3 K mol^{-1}$ (≈ 4.5 $\mu_B$) at room temperature are close to the value expected for two uncoupled nickel(II) ions ($\chi_M T$ = 2.42 $cm^3 K mol^{-1}$ for $g$ = 2.2). The $\chi_M T$ curves gradually but steadily drop with decreasing temperature and finally tend to zero, indicating an $S$ = 0 ground state. $\chi_M$ accordingly goes through a maximum, but only at very low temperatures, suggesting that the coupling is weak.

Magnetic parameters were determined using a fitting procedure to the appropriate Heisenberg spin Hamiltonian for isotropic exchange coupling. Simulation of the experimental magnetic data was performed with full-matrix diagonalization of exchange coupling and Zeeman splitting according to the Hamiltonian in Equation (1).[18]

$$H = -2J\vec{S}_1\vec{S}_2 + g\mu_B(\vec{S}_1 + \vec{S}_2)\vec{B} \quad (1)$$

Before simulation the experimental data were corrected for the underlying diamagnetism by using tabulated Pascal constants (incremental method) and for temperature-independent paramagnetism (*TIP*; included in the data representation in Figure 5). A Curie-behaved paramagnetic impurity (*PI*) with spin $S$ = 1 was included according to $\chi = (1 - PI)\chi + PI\chi_{mono}$. Satisfactory fits were obtained for all four systems, and values for $g$, $J$, *PI* and *TIP* are listed in Table 1.

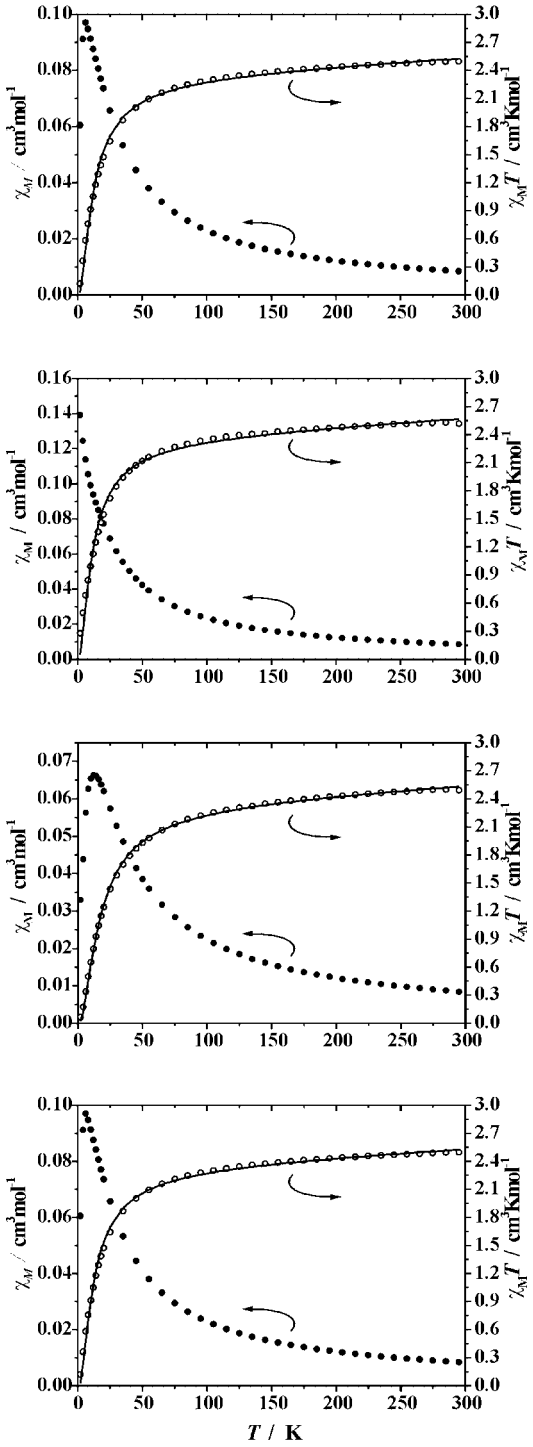


Figure 5. $\chi_M$ (solid circles) and $\chi_M T$ (open circles) vs. $T$ plot for **1a** (top), **1b** (second from top), **2** (second from bottom) and **3** (bottom) at 5000 G; the solid line represents the calculated curve fit (see text).

Table 1. Magnetic parameters for complexes **1a**, **1b**, **2** and **3** according to Equation (1).

| | **1a** | **1b** | **2** | **3** |
|---|---|---|---|---|
| $g$ | 2.18 | 2.20 | 2.22 | 2.20 |
| $J$ [$cm^{-1}$] | –3.6 | –3.4 | –5.1 | –1.7 |
| *PI* [%] | 0.7 | 2.0 (fixed) | 2.0 (fixed) | 1.5 |
| *TIP* [$10^{-4}$ $cm^3 mol^{-1}$] | 7.2 | 7.8 | 7.8 | 4.3 |

 © 2007 Wiley-VCH Verlag GmbH & Co. KGaA, Weinheim 

Since nickel(II) may exhibit significant zero-field splitting that can be similar in magnitude to the *J* values determined, data analysis was also probed with an additional term $2D[S_z^2 - 1/3S(S + 1)]$ included in Equation (1) that accounts for a local zero-field splitting parameter *D*. However, with reasonable values for *D* and *PI* this analysis did not lead to any substantial changes in the *J* values, while the decrease of $\chi_M T$ at low temperatures could not be described by considering *D* only (i.e., without exchange Hamiltonian, $J = 0$).[19]

In view of the aggregation of **2** in the solid state as described earlier, an alternative "dimer of dimer" model according to Scheme 2 has also been applied to the magnetic data analysis of this complex. This model gives a similarly good fit with $g = 2.25$, $J_1 = -3.9\ cm^{-1}$, $J_2 = -2.6\ cm^{-1}$, $PI = 2\%$ and $TIP = 8.8 \times 10^{-4}\ cm^3 mol^{-1}$. Note that assignment of $J_1$ and $J_2$ to the *intra*dimer and *inter*dimer coupling is arbitrary because of the symmetry of the Hamiltonian.

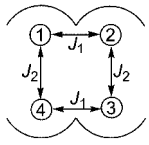


Scheme 2. Alternative coupling scheme for **2**.

Rather small negative *J* values confirm relatively weak antiferromagnetic coupling between the adjacent nickel ions in all cases, but subtle differences are discernible. The coupling is clearly weakest in **3**, while it appears to be strongest in **2**. Although the multitude of structural variations among the four complexes (coordination numbers and geometries, distortion of the nickel ions out of the pyrazolato plane, etc.) prevents any definite interpretation in terms of magnetostructural correlations, one may attribute the much lower *J* value for **3** to the lack of a chlorido bridge and to the much weaker coupling efficiency of the intramolecular Cl···H–O linkage. This also corroborates the assignment of $J_1$ and $J_2$ in the "dimer of dimer" model for **2**, since any interaction through the hydrogen bonds should be weak. The somewhat weaker coupling in **1a** and **1b** relative to the coupling within the pyrazolato-based dinickel entities of **2** may be a result of the pronounced asymmetry of the Ni–Cl–Ni bridge and the presence of a very long Ni–Cl bond in the two former systems [*d*(Ni1–Cl2) = 2.83 Å in **1a**; *d*(Ni1–Cl1) = 2.61 Å in **1b**], as such long distances provide no efficient exchange pathway. It should be emphasized, though, that additional factors such as the canting between the basal planes of the two nickel ions and the plane of the pyrazolato bridge will also play a substantial role and should contribute to the diminished coupling in **3**.

## Conclusions

The compartmental pyrazolato-based ligands $HL^1$, $HL^2$ and $HL^3$ with pyridyl side arms are obviously well suited to form dinuclear nickel(II) complexes, similar to related pyrazolato ligands with aliphatic chelate arms. Since the latter have provided useful scaffolds for synthetic models of the active site of the dinickel enzyme urease, a likewise rich chemistry is now expected for $HL^1$, $HL^2$ and $HL^3$. The current set of complexes confirms that different Ni···Ni distances and distinct coordination spheres can be obtained by proper modifications of the ligand side arms attached to the central pyrazolato bridge. Various O–H···Cl hydrogen-bonding motifs were characterized crystallographically in **1**–**3**, where either the H-donor (MeOH or $H_2O$) or the H-acceptor (chlorido) or both are bound to a metal ion, that is, nickel(II). The structural trends are in line with the following ranking of such interactions: (1) the hydrogen bond is shortened by coordination and acidification of the H-donor, *d*[Cl⁻···H(Me)O–Ni] < *d*[Cl⁻···H(Me)O]; (2) free chloride ions are better H-acceptors than metal-bound chlorido ligands, *d*[Cl⁻···H(Me)O–Ni] < *d*[Ni–Cl···H(Me)-O–Ni]; and (3) a terminal chlorido ligand is a better H-acceptor than a bridging one, *d*[Ni–Cl···H(H)O–Ni] < *d*[Ni(μ-Cl)···H(H)O–Ni]. Magnetic couplings through the chlorido and pyrazolato bridges are rather weak, but are even weaker through a Cl···H–O linkage or when the metal ions are displaced out of the plane of the pyrazolato ligand. These comparisons may prove useful for the assessment of hydrogen-bonding interactions in molecular recognition, crystal engineering and related fields.

## Experimental Section

***Caution!*** Although no problems were encountered in this work, transition metal perchlorates are potentially explosive and should be handled with care and with proper precautions.

**General:** Ligands $HL^1$, $HL^2$ and $HL^3$ were prepared as described previously.[10] All other chemicals were purchased from commercial sources and used as received. Microanalyses were performed by the Analytical Laboratory of the Inorganic Chemistry Institute at Georg-August-University Göttingen. Infrared spectra: Digilab Excalibur, recorded as KBr pellets. Mass spectra (FAB MS): Finnigan MAT 95 with nitrobenzylalcohol as the matrix.

**Synthesis of $[L^1Ni_2(\mu\text{-}Cl)(Cl)_2]\cdot 2CH_3OH$ (1a):** A solution of $HL^1$ (0.273 g, 0.5 mmol) in methanol (40 mL) was treated with 1 equiv. of $NEt_3$ (0.051 g, 0.5 mmol) and stirred for 10 min. To the reaction mixture was then added a solution of $NiCl_2\cdot 6H_2O$ (0.291 g, 1.0 mmol) in methanol (40 mL), and stirring was continued for a further 2 h. All volatile material was then evaporated under reduced pressure, the residue was taken up in methanol (10 mL) and this solution was filtered. The filtrate was layered with diethyl ether to gradually yield green crystals (203 mg, 49%) of **1a**. $C_{33}H_{37}Cl_3N_8Ni_2\cdot 2CH_3OH$ (833.5): calcd. C 50.43, H 5.44, N 13.44; found C 49.61, H 5.47, N 13.22. FAB MS: *m/z* (%) = 733 (100) $[L^1Ni_2Cl_2]^+$, 698 (60) $[L^1Ni_2Cl]^+$. IR (KBr): $\tilde{\nu}$ = 3474 (s), 3415 (s), 3267 (s), 2853 (m), 1637 (m), 1606 (s), 1567 (m), 1485 (s), 1443 (s), 1330 (s), 1314 (s), 1161 (w), 1108 (w), 1066 (w), 1045 (w), 1021 (m), 939 (w), 785 (s), 758 (s), 582 (w), 422 (w) $cm^{-1}$.

**Synthesis of $[L^1Ni_2(\mu\text{-}Cl)(CH_3OH)](ClO_4)_2$ (1b):** A solution of $HL^1$ (0.273 g, 0.5 mmol) in methanol (40 mL) was treated with 1 equiv. of $NEt_3$ (0.051 g, 0.5 mmol) and stirred for 10 min. The reaction mixture was then transferred to a solution containing 2 equiv. of $Ni(ClO_4)_2\cdot 6H_2O$ (0.365 g, 1.0 mmol) in methanol (40 mL). The re-

 © 2007 Wiley-VCH Verlag GmbH & Co. KGaA, Weinheim 

action mixture was stirred for 1 h before 1 equiv. of NaCl (0.027 g, 0.5 mmol) was added, and stirring was continued overnight. All volatile material was then evaporated under reduced pressure, the residue was taken up in methanol (10 mL) and the solution was filtered. The filtrate was layered with diethyl ether to gradually yield green crystals (139 mg, 29%) of **1b**. $C_{34}H_{41}Cl_3N_8Ni_2O_9$ (929.5): calcd. C 43.94, H 4.45, N 12.06; found C 43.81, H 4.57, N 11.93. FAB MS: *m*/*z* (%) = 797 (100) $[L^1Ni_2Cl(ClO_4)]^+$, 696 (30) $[L^1Ni_2Cl]^+$. IR (KBr): $\tilde{\nu}$ = 3410 (m), 3074 (w), 2939 (w), 2902 (w), 2858 (w), 1609 (s), 1568 (m), 1488 (s), 1443 (s), 1383 (w), 1336 (w), 1310 (m), 1296 (w), 1162 (m), 1088 (vs), 1020 (s), 981 (m), 933 (m), 831 (w), 781 (m), 765 (m), 646 (w), 623 (s), 587 (w), 462 (w), 424 (m) $cm^{-1}$.

**Synthesis of $[L^2Ni_2(\mu\text{-}Cl)Cl_2(H_2O)_2]\cdot H_2O$ (2):** A solution of $HL^2$ (0.181 g, 0.5 mmol) in methanol (40 mL) was treated with 1 equiv. of $NEt_3$ (0.051 g, 0.5 mmol) and stirred for 10 min. The reaction mixture was then transferred to a solution containing 2 equiv. of $NiCl_2\cdot 6H_2O$ (0.291 g, 1.0 mmol) in methanol (40 mL) and stirred for a further 2 h. All volatile material was then evaporated under reduced pressure, the residue was taken up in methanol (10 mL) and the solution was filtered. The filtrate was layered with diethyl ether to gradually yield green crystals (0.103 g, 40%) of **2**. $C_{21}H_{33}Cl_3N_6Ni_2O_3$ (641.3): calcd. C 39.33, H 5.19, N 13.10; found C 38.99, H 5.28, N 12.69. FAB MS: *m*/*z* (%) = 551 (100) $[L^2Ni_2Cl_2]^+$. IR (KBr): $\tilde{\nu}$ = 3379 (br s), 2914 (w), 2859 (w), 2814 (w), 1632 (m), 1607 (s), 1571 (m), 1485 (m), 1444 (s), 1376 (w), 1322 (s), 1287 (w), 1246 (w), 1156 (w), 1099 (w), 1042 (m), 988 (m), 926 (w), 863 (w), 766 (s), 642 (m), 593 (m), 426 (m) $cm^{-1}$.

**Synthesis of $[L^3Ni_2Cl_2(CH_3OH)_2]Cl\cdot 2CH_3OH$ (3):** To a solution of $NiCl_2\cdot 6H_2O$ (0.291 g, 1.0 mmol) in methanol (40 mL) was added a solution of $HL^3$ (0.245 g, 0.5 mmol) and $NEt_3$ (0.051 g, 0.5 mmol) in methanol (40 mL), and the reaction mixture stirred at room temp. for 2 h. All volatile material was then evaporated under reduced pressure, the residue was taken up in methanol (10 mL) and this solution was filtered. The filtrate was layered with diethyl ether to gradually yield blue needle-like crystals (268 mg, 64%) of **3**. Upon storage in air, the methanol solvent molecules appear to be partly replaced by water, and the compound appears to be somewhat hygroscopic according to elemental analysis. $C_{31}H_{37}Cl_3N_8Ni_2O_2\cdot 4H_2O$ (849.49): calcd. C 43.83, H 5.34, N 13.19; found C 43.32, H 5.08, N 13.02. FAB MS: *m*/*z* (%) = 677 (100) $[L^3Ni_2Cl_2]^+$, 642 (20) $[L^3Ni_2Cl]^+$. IR (KBr): $\tilde{\nu}$ = 3344 (vs), 2920 (w), 1625 (m), 1605 (vs), 1573 (w), 1480 (m), 1441 (s), 1322 (m), 1287 (m), 1259 (w), 1154 (w), 1098 (m), 1052 (w), 1022 (m), 903 (w), 959 (w), 876 (w), 767 (s), 642 (w), 493 (w), 428 (w) $cm^{-1}$.

**X-ray Crystallographic Study:** X-ray data for **1a** and **3** were collected with a Bruker P4 diffractometer (graphite-monochromated Mo-$K_\alpha$ radiation, $\lambda$ = 0.71073 Å) by use of $\omega$ scans at –140 °C and –100 °C, respectively (Table 2). Data for **1b** and **2** were collected with a STOE IPDS II diffractometer (graphite-monochromated Mo-$K_\alpha$ radiation, $\lambda$ = 0.71073 Å) by use of $\omega$ scans at –140 °C (Table 2). The structures were solved by direct methods and refined on $F^2$ using all reflections with SHELX-97.[20] The non-hydrogen atoms were refined anisotropically. Hydrogen atoms which were not involved in hydrogen bonding were placed in calculated positions and assigned to an isotropic displacement parameter of 0.08 $Å^2$. The positional and isotropic thermal parameters of the oxygen-bound hydrogen atoms H1 and H2 in **1a**, H1A/B in **2** and H1 to H4 in **3** were refined without any restraints or constraints. A DFIX restraint ($d_{O-H}$ = 0.82 Å) was applied for the O2–H2 distance in **2**. All other positional and isotropic thermal parameters of the hydrogen atom H2 were refined without restraints or constraints. SADABS was used to perform area-detector scaling and absorption corrections for **1a** and **3**.[21] Face-indexed absorption corrections were performed numerically with the program X-RED for **1b** and **2**.[22] Three oxygen atoms of one $ClO_4^-$ ion in **1b** are disordered about two positions [occupancy factors: 0.852(4)/0.148(4)]. SADI ($d_{Cl-O}$ and $d_{O\cdots O}$) restraints and EADP constraints were used to model the disorder and for anisotropic refinement. CCDC-616755 (**1a**), -616756 (**1b**), -616757 (**2**) and -616758 (**3**) contain the supplemen-

Table 2. Crystal data and refinement details for the complexes.

| | **1a** | **1b** | **2** | **3** |
|---|---|---|---|---|
| Empirical formula | $C_{33}H_{37}Cl_3Ni_2N_8$, 2 $CH_3OH$ | $C_{34}H_{41}ClNi_2N_8O^{2+}$, 2 $ClO_4^-$ | $C_{21}H_{31}Cl_3Ni_2N_6O_2$, $H_2O$ | $C_{31}H_{37}Cl_2Ni_2N_8O_2^+$, $Cl^-$, 2 $CH_3OH$ |
| Formula mass | 833.56 | 929.52 | 641.30 | 841.54 |
| Crystal size [mm] | 0.45 × 0.35 × 0.29 | 0.34 × 0.22 × 0.18 | 0.31 × 0.25 × 0.19 | 0.44 × 0.28 × 0.15 |
| Crystal system | monoclinic | monoclinic | monoclinic | monoclinic |
| Space group | $P2_1/n$ (No. 14) | $P2_1/c$ (No. 14) | $C2/m$ (No. 12) | $P2_1/n$ (No. 14) |
| *a* [Å] | 14.345(2) | 17.8241(14) | 14.6945(9) | 8.5936(15) |
| *b* [Å] | 8.4514(14) | 9.4017(4) | 19.1109(8) | 27.578(5) |
| *c* [Å] | 29.544(5) | 24.1439(18) | 9.8611(6) | 15.743(3) |
| $\beta$ [°] | 96.637(4) | 109.459(6) | 112.408(4) | 95.329(4) |
| *V* [$Å^3$] | 3557.7(10) | 3814.9(4) | 2560.1(2) | 3715.0(11) |
| $\rho_{calcd.}$ [g $cm^{-3}$] | 1.556 | 1.618 | 1.664 | 1.505 |
| *Z* | 4 | 4 | 4 | 4 |
| *F*(000) | 1736 | 1920 | 1328 | 1752 |
| $\mu$ [$mm^{-1}$] | 1.330 | 1.262 | 1.820 | 1.278 |
| $T_{max}/T_{min}$ | 0.6991/0.5860 | 0.8078/0.6673 | 0.7611/0.5666 | 0.8314/0.6032 |
| *hkl* range | ±18, ±10, –36–38 | ±20, –9–11, ±28 | ±17, ±22, –10–11 | –9–11, ±35, –12–20 |
| $\theta$ range [°] | 2.39–27.50 | 1.79–24.80 | 1.84–24.83 | 1.97–27.50 |
| Measured refl. | 35288 | 28730 | 25635 | 27111 |
| Unique refl. [$R_{int}$] | 8159 [0.0210] | 6502 [0.0776] | 2293 [0.0581] | 8499 [0.0211] |
| Observed refl. [$I > 2\sigma(I)$] | 7205 | 4376 | 2087 | 7258 |
| Data/restraints/param. | 8159–0–461 | 6502–22–520 | 2293–1–175 | 8499–0–471 |
| Goodness-of-fit | 1.042 | 1.008 | 1.075 | 1.049 |
| $R_1/wR_2$ [$I > 2\sigma(I)$] | 0.0275–0.0672 | 0.0439–0.0903 | 0.0229–0.0620 | 0.0298–0.0714 |
| $R_1/wR_2$ (all data) | 0.0330–0.0704 | 0.0740–0.0970 | 0.0256–0.0631 | 0.0386–0.0768 |
| Resid. el. dens. [e $Å^{-3}$] | 0.466/–0.229 | 0.813/–0.544 | 0.407/–0.384 | 0.682/–0.298 |

 © 2007 Wiley-VCH Verlag GmbH & Co. KGaA, Weinheim 

tary crystallographic data for this paper. These data can be obtained free of charge from The Cambridge Crystallographic Data Centre via www.ccdc.cam.ac.uk/data_request/cif.

**Supporting Information** (see footnote on the first page of this article): ORTEP plots of the molecular structures in Figures S1–S4.

## Acknowledgments

We sincerely thank the China Scholarship Council for a postdoctoral fellowship (to F.-M. N.) and Prof. Peter Roesky (FU Berlin) for collecting some of the X-ray data.

[1] A. S. Borovik, *Acc. Chem. Res.* **2005**, *38*, 54–61.
[2] J. C. Mareque Rivas, S. L. Hinchley, L. Metteau, S. Parsons, *Dalton Trans.* **2006**, 2316–2322.
[3] L. Brammer, *Dalton Trans.* **2003**, 3145–3157.
[4] G. P. A. Yap, A. L. Rheingold, P. Das, R. H. Crabtree, *Inorg. Chem.* **1995**, *34*, 3474–3476.
[5] G. Aullón, D. Bellamy, L. Brammer, E. A. Bruton, A. G. Orpen, *Chem. Commun.* **1998**, 653–654.
[6] L. Brammer, E. A. Bruton, P. Sherwood, *New J. Chem.* **1999**, *23*, 965–968.
[7] a) J. C. Mareque Rivas, L. Brammer, *Inorg. Chem.* **1998**, *37*, 4756–4757; b) A. Angeloni, P. C. Craword, A. G. Orpen, T. J. Podesta, B. J. Shore, *Chem. Eur. J.* **2004**, *10*, 3783–3791; c) Y. J. Park, J.-S. Kim, K.-T. Youm, N.-K. Lee, J. Ko, H.-S. Park, M.-J. Jun, *Angew. Chem.* **2006**, *118*, 4396–4400; *Angew. Chem. Int. Ed.* **2006**, *45*, 4290–4294.
[8] a) T. Steiner, *Acta Crystallogr., Sect. B* **1998**, *54*, 456–463; b) T. Steiner, *Angew. Chem.* **2002**, *114*, 50–80.
[9] D.-H. Lee, H. J. Kwon, B. P. Patel, L. M. Liable-Sands, A. L. Rheingold, R. H. Crabtree, *Organometallics* **1999**, *18*, 1615–1621.
[10] J. Ackermann, F. Meyer, H. Pritzkow, *Inorg. Chim. Acta* **2004**, *357*, 3703–3711.
[11] S.-J. Barlow, S. J. Hill, J. E. Hocking, P. Hubberstey, W.-S. Li, *J. Chem. Soc., Dalton Trans.* **1997**, 4701–4703.
[12] B. Bauer-Siebenlist, F. Meyer, E. Farkas, D. Vidovic, S. Dechert, *Chem. Eur. J.* **2005**, *11*, 4349–4360.
[13] J. Ackermann, S. Buchler, F. Meyer, *C. R. Chim.*, in press.
[14] a) F. Meyer, S. Beyreuther, K. Heinze, L. Zsolnai, *Chem. Ber./Recueil* **1997**, *130*, 605–613; b) F. Meyer, K. Heinze, B. Nuber, L. Zsolnai, *J. Chem. Soc., Dalton Trans.* **1998**, 207–213; c) F. Meyer, P. Rutsch, *Chem. Commun.* **1998**, 1037–1038; d) F. Meyer, E. Kaifer, P. Kircher, K. Heinze, H. Pritzkow, *Chem. Eur. J.* **1999**, *5*, 1617–1630; e) J. Ackermann, F. Meyer, E. Kaifer, H. Pritzkow, *Chem. Eur. J.* **2002**, *8*, 247–258; f) S. Buchler, F. Meyer, E. Kaifer, H. Pritzkow, *Inorg. Chim. Acta* **2002**, *337*, 371–386; g) B. Bauer-Siebenlist, F. Meyer, E. Farkas, D. Vidovic, J. A. C. Seijo, R. Herbst-Irmer, H. Pritzkow, *Inorg. Chem.* **2004**, *43*, 4189–4202.
[15] B. Brewer, N. R. Brooks, S. Abdul-Halim, A. G. Sykes, *J. Chem. Crystallogr.* **2003**, *33*, 651–662.
[16] A. E. Oblezov, D. R. Talham, K. A. Abboud, *Acta Crystallogr., Sect. E* **2003**, *59*, m1070–m1071.
[17] a) F. Meyer, U. Ruschewitz, P. Schober, B. Antelmann, L. Zsolnai, *J. Chem. Soc., Dalton Trans.* **1998**, 1181–1186; b) S. Buchler, F. Meyer, A. Jacobi, P. Kirchner, L. Zsolnai, *Z. Naturforsch., B: Chem. Sci.* **1999**, *54b*, 1295–1306.
[18] Simulation of the experimental magnetic data with a full-matrix diagonalization of exchange coupling and Zeeman splitting was performed with the julX program (E. Bill, Max Planck Institute for Bioinorganic Chemistry, Mülheim/Ruhr, Germany).
[19] When the term for zero-field splitting was included in Equation (1), the best fit gave $g = 2.18$, $J = -3.7\ cm^{-1}$, $D = -0.05\ cm^{-1}$, $PI = 1\%$ and $TIP = 7.3 \times 10^{-4}\ cm^3 mol^{-1}$ for **1a** and $g = 2.21$, $J = -1.7\ cm^{-1}$, $D = -0.51\ cm^{-1}$, $PI = 2\%$ and $TIP = 4.3 \times 10^{-4}\ cm^3 mol^{-1}$ for **3**.
[20] G. M. Sheldrick, *SHELXL-97*, *Program for Crystal Structure Refinement*, University of Göttingen, **1997**; G. M. Sheldrick, *SHELXS-97*, *Program for Crystal Structure Solution*, University of Göttingen, **1997**.
[21] G. M. Sheldrick, *SADABS*, *Program for Empirical Absorption Correction of Area Detector Data*, University of Göttingen, **1997**.
[22] STOE & CIE GmbH, *X-RED*, Darmstadt, **2002**.

Received: September 22, 2006
Published Online: February 13, 2007

 © 2007 Wiley-VCH Verlag GmbH & Co. KGaA, Weinheim 

DOI: 10.1002/ejic.200600958

# Cyanido-Bridged Dimetallic Complexes Derived from Manganese(III) Schiff Bases and Pentacyanidonitrosylchromate(I): Synthesis, Crystal Structure and Magnetic Properties

Zhong-Hai Ni,[a] Lei Zheng,[a] Li-Fang Zhang,[a] Ai-Li Cui,[a] Wei-Wei Ni,[a] Chong-Chao Zhao,[a] and Hui-Zhong Kou*[a]

**Keywords:** Cyanide ligands / Bridging ligands / Magnetic properties / Manganese / Schiff-base ligands

Four cyanido-bridged $Mn^{III}$–$Cr^{I}$ heterodimetallic complexes have been synthesized by the reactions of $Mn^{III}$ Schiff-base complexes with the $[Cr(CN)_5(NO)]^{3-}$ building block. X-ray diffraction analysis reveals that $[Mn(5\text{-Cl-salen})(H_2O)_2][Mn_2(5\text{-Cl-salen})_2(H_2O)_{1.5}Cr(CN)_5(NO)]$ (**1**) has a trinuclear structure, and $[Mn_3(salen)_3(H_2O)(CH_3CN)Cr(CN)_5(NO)]\cdot 0.5CH_3CN\cdot 0.5MeOH\cdot 2H_2O$ (**2**) and $[Mn(5\text{-Br-salen})(H_2O)(CH_3OH)][Mn_2(5\text{-Br-salen})_2(CH_3OH)Cr(CN)_5(NO)]\cdot 2H_2O$ (**3**) have novel 1D chain topological structures, whereas $[\{Mn(saltmen)\}_4Cr(CN)_5(NO)]ClO_4\cdot 3H_2O$ (**4**) displays a 2D layered network structure. Magnetic measurements show that the magnetic interaction between the $Mn^{III}$ and $Cr^{I}$ ions bridged by a cyanido group is antiferromagnetic for complexes **1**–**4**. The magnetic fitting for the trinuclear complex **1** gives the magnetic coupling constant $J = -10.4(1)$ cm$^{-1}$ and $J' = -1.29(2)$ cm$^{-1}$ based on the isotropic Hamiltonian $\hat{H} = -2J\hat{S}_{Cr}[\hat{S}_{Mn(1)} + \hat{S}_{Mn(2)}] - 2J'\hat{S}_{Mn(1)}\hat{S}_{Mn(2)}$. Complex **2** exhibits 3D antiferromagnetic ordering ($T_N = 3.5$ K) with a metamagnetic character below $T_N$. Complex **3** exhibits an obvious frequency-dependent AC magnetic susceptibility below 4.0 K, which is due to the spin-glass behavior. The layered complex **4** displays 3D ferromagnetic ordering with $T_c = 6.4$ K due to the ferromagnetic interaction between the ferrimagnetic layers.

(© Wiley-VCH Verlag GmbH & Co. KGaA, 69451 Weinheim, Germany, 2007)

## Introduction

In the past two decades, the design and synthesis of cyanido-bridged molecule-based magnetic materials with high-$T_c$, single-molecule magnets (SMMs), single-chain magnets (SCMs), and those that exhibit spin crossover (SCO) or photomagnetic behavior has become one of the most important fields in coordination chemistry and magnetochemistry.[1–10] (Schiff base)$Mn^{III}$ complexes and hexacyanidometalate building blocks have been shown to be two intriguing precursors for the above purpose. Indeed, their combinations have successfully yielded a variety of structures, including polynuclear[3b,11–18] 1D chains[19,20] and 2D networks,[11,12,21–23] by tuning the Schiff-base ligands and the coordination numbers around the $Mn^{III}$ ion. However, much attention has been paid to the investigation of $Mn^{III}$–$Fe^{III}$ complexes derived from (Schiff base)$Mn^{III}$ complexes and $[Fe(CN)_6]^{3-}$, and only limited examples have been obtained based on (Schiff base)$Mn^{III}$ complexes and other cyanido-containing building blocks.[7,17,18,24–30] In particular, to the best of our knowledge, there is still no report on cyanido-bridged $Mn^{III}$–$Cr^{I}$ or $Mn^{III}$–$Cr^{III}$ 1D chain-like complexes and only three known $Mn^{III}$–$Fe^{III}$ 1D assemblies,[19,20,25] one $Mn^{III}$–$Mn^{III}$, and one $Mn^{III}$–$Mo^{IV}$ 1D chain complex[24,26] derived from (Schiff base)$Mn^{III}$ complexes and $[Fe(CN)_6]^{3-}$, $[Fe(bpb)(CN)_2]^{-}$, $[Mn(salen)(CN)_2]^{-}$, or $[Mo(CN)_8]^{4-}$ building blocks.

In light of our continuing interest in cyanido-bridged dimetallic complexes, we are interested in extending this system to the paramagnetic $[Cr(CN)_5(NO)]^{3-}$ building block, which has the same negative charge as $[M^{III}(CN)_6]^{3-}$ (M = Fe, Cr, Co or Mn). In addition, the unpaired electron ($d^5$, low-spin) in $Cr^{I}$ means that it has the same low spin as the $Fe^{III}$ ion ($S = 1/2$), and is different from the $Cr^{III}$ ion ($S = 3/2$). Therefore, special interest lies in comparing the magnetic properties of $[Cr(CN)_5(NO)]^{3-}$ with $[Fe(CN)_6]^{3-}$ and in the search for a new family of molecule-based magnets. To this end, we decided to investigate complexes based on $[Cr(CN)_5(NO)]^{3-}$ and (Schiff base)$Mn^{III}$ building blocks. Herein, we report the synthesis, crystal structures, and magnetic properties of four such complexes, including the trinuclear complex $[Mn(5\text{-Cl-salen})(H_2O)_2][Mn_2(5\text{-Cl-salen})_2(H_2O)_{1.5}Cr(CN)_5(NO)]$ (**1**) and two novel 1D chain complexes $[Mn_3(salen)_3(H_2O)(CH_3CN)Cr(CN)_5(NO)]\cdot 0.5CH_3CN\cdot 0.5MeOH\cdot 2H_2O$ (**2**), and $[Mn(5\text{-Br-salen})(H_2O)(CH_3OH)][Mn_2(5\text{-Br-salen})_2(CH_3OH)Cr(CN)_5(NO)]\cdot 2H_2O$ (**3**), as well as one 2D layered compound $[\{Mn(saltmen)\}_4Cr(CN)_5(NO)]ClO_4\cdot 3H_2O$ (**4**), [salen$^{2-}$ = *N*,*N*′-ethylenebis(salicylideneaminato) dianion, 5-Br-salen$^{2-}$

[a] Department of Chemistry, Tsinghua University, Beijing, Beijing 100084, China
Fax: +86-10-62771748
E-mail: kouhz@mail.tsinghua.edu.cn

Supporting information for this article is available on the WWW under http://www.eurjic.org or from the author.

 InterScience © 2007 Wiley-VCH Verlag GmbH & Co. KGaA, Weinheim 

= *N*,*N*′-ethylenebis(5-bromosalicylideneaminato) dianion, 5-Cl-salen$^{2-}$ = *N*,*N*′-ethylenebis(5-chlorosalicylideneaminato) dianion, and saltmen$^{2-}$ = *N*,*N*′-(1,1,2,2-tetramethylethylene)bis(salicylideneaminato) dianion].

## Results and Discussion

### Synthesis and General Characterization

The reaction between the different (Schiff base)Mn$^{III}$ complexes {[Mn(salen)]$ClO_4$, [Mn(5-Cl-salen)]$ClO_4$, [Mn(5-Br-salen)]$ClO_4$, or [Mn(saltmen)]$ClO_4$} and $K_3Cr(CN)_5(NO)$ gave entirely different molecular structures under similar conditions. Complex **1**, for example, has an $Mn_2Cr$ trinuclear structure with a monomer (Schiff base)Mn$^{III}$ complex as the balanced cation, whereas complexes **2** and **3** have 1D topological structures (Scheme 1) with a 3:1 alternating arrangement of Mn$^{III}$ and Cr$^{I}$. Complex **4** is a 2D network in which the (Schiff base)Mn$^{III}$ complex forms an out-of-plane dimeric motif with a biphenolate bridge, which is similar to that of the previously reported complexes [{Mn(saltmen)}$_4${Fe(CN)$_6$}]$ClO_4$·$H_2O$,[12] $(Et_4N)[Mn_2(5\text{-}MeOsalen)_2Fe(CN)_6]$[20] [5-MeOsalen$^{2-}$ = *N*,*N*′-ethylenebis(5-methoxysalicylideneiminate)] and [Mn(salen)($H_2O$)$_2$]$_2$[{Mn(salen)($H_2O$)}{Mn(salen)}$_2${Mo(CN)$_8$}]·0.5$ClO_4$·0.5OH·4.5$H_2O$.[26] It is intriguing to note that the formation of different cyanido-bridged Mn$^{III}$–Cr$^{I}$ complexes is a very subtle process, which further shows that the steric effects of the Schiff-base ligands play an important role in the self-assembly of Mn$^{III}$–M (M = Fe$^{III}$, Cr$^{III}$ and Cr$^{I}$) complexes.

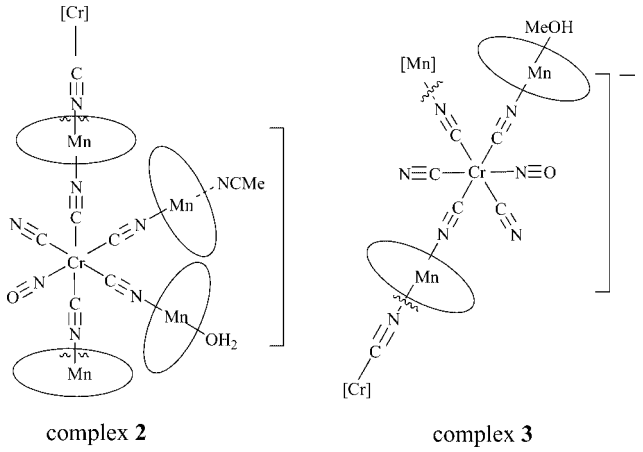


Scheme 1. Schematic representation of the chain-like structures in **2** and **3**. The circles represent salen$^{2-}$ and 5-Br-salen$^{2-}$ for **2** and **3**, respectively.

The IR spectra in the range 2100–2140 cm$^{-1}$ exhibit moderately sharp peaks assigned to cyanido stretching absorptions. The weak peaks at 1677–1712 cm$^{-1}$ can be attributed to the N=O stretching vibration in these complexes. For complex **4**, the strong broad peaks centered at around 1090 cm$^{-1}$ suggest the presence of $ClO_4^-$ anions in the complex.

### Crystal Structures

Complex **1** consists of two crystallographically independent trinuclear [{Mn(5-Cl-salen)}$_2$Cr(CN)$_5$(NO)]$^-$ units with two free [Mn(5-Cl-salen)($H_2O$)$_2$]$^+$ units as charge-balancing cations. The two [Mn(5-Cl-salen)]$^+$ segments are bound at the *cis* positions of the central Cr$^{I}$ ion through two *cis* cyanido groups (see Figure 1 and Table 1).

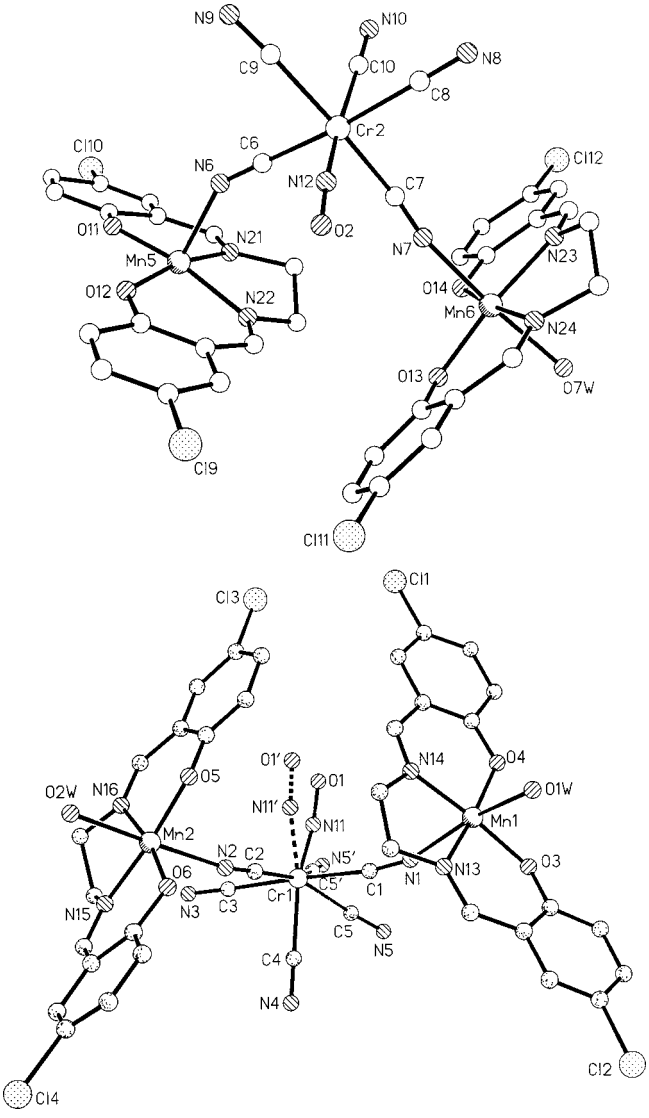


Figure 1. Structure of two $Mn_2Cr$ trinuclear anionic units in compound **1**.

Three Mn$^{III}$ ions in the trinuclear units are ligated by three nitrogen atoms from the 5-Cl-salen$^{2-}$ ligand and the cyanido bridge and three oxygen atoms from the Schiff-base ligand and the coordinated water molecule to give a distorted $MnN_3O_3$ octahedral environment. One Mn$^{III}$ ion is pentacoordinated by two Schiff-base nitrogen and two Schiff-base oxygen atoms as well as one cyanido nitrogen atom to yield a square-pyramidal $MnN_3O_2$ environment, which weakly interacts with a phenoxy oxygen atom [O(7)$^{\#}$] from an adjacent free (Schiff base)Mn$^{III}$ unit (symmetry operation: $^{\#}$ –2/3 + *x*, –1/3 + *y*, 2/3 + *z*) with an

 © 2007 Wiley-VCH Verlag GmbH & Co. KGaA, Weinheim 

Table 1. Selected bond lengths [Å] and angles [°] for complex **1**.[a]

| | | | | | |
|---|---|---|---|---|---|
| Mn(1)–N(1) | 2.264(6) | Mn(2)–N(2) | 2.229(11) | Mn(3)–N(17) | 1.985(6) |
| Mn(1)–N(13) | 1.980(7) | Mn(2)–N(15) | 1.975(11) | Mn(3)–N(18) | 1.964(6) |
| Mn(1)–N(14) | 1.952(8) | Mn(2)–N(16) | 2.017(10) | Mn(3)–O(7) | 1.890(5) |
| Mn(1)–O(3) | 1.886(6) | Mn(2)–O(5) | 1.861(11) | Mn(3)–O(8) | 1.876(5) |
| Mn(1)–O(4) | 1.893(5) | Mn(2)–O(6) | 1.916(9) | Mn(3)–O(3w) | 2.267(5) |
| Mn(1)–O(1w) | 2.291(5) | Mn(2)–O(2w) | 2.236(6) | Mn(3)–O(4w) | 2.306(5) |
| Mn(4)–N(19) | 1.980(7) | Mn(5)–N(6) | 2.131(6) | Mn(6)–N(7) | 2.214(7) |
| Mn(4)–N(20) | 1.983(6) | Mn(5)–N(21) | 1.952(6) | Mn(6)–N(23) | 1.993(7) |
| Mn(4)–O(9) | 1.873(5) | Mn(5)–N(22) | 1.982(6) | Mn(6)–N(24) | 1.990(7) |
| Mn(4)–O(10) | 1.888(5) | Mn(5)–O(11) | 1.873(5) | Mn(6)–O(13) | 1.904(6) |
| Mn(4)–O(5w) | 2.226(5) | Mn(5)–O(12) | 1.952(6) | Mn(6)–O(14) | 1.881(6) |
| Mn(4)–O(6w) | 2.240(5) | Mn(5)–O(7)$^{\#1}$ | 3.369(5) | Mn(6)–O(7w) | 2.235(7) |
| Mn(1)–N(1)–C(1) | 156.5(6) | Mn(2)–N(2)–C(2) | 161.9(11) | Mn(5)–N(6)–C(6) | 147.4(6) |
| Mn(6)–N(7)–C(7) | 169.3(6) | | | | |

[a] Symmetry operation: $^{\#1}$ –2/3 + *x*, –1/3 + *y*, 2/3 + *z*.

Mn(5)–O(7)$^{\#}$ bond length of 3.369(5) Å. The two discrete $Mn^{III}$ ions are coordinated by the Schiff-base ligand and two water molecules to form a distorted octahedral $MnN_2O_4$ environment. The Mn–$N_{cyanido}$ bond lengths vary from 2.131(6) to 2.264(6) Å. The Mn–N≡C bonds are bent [147.4(6)–168.3(6)°], with an average bond angle of 158.7(6)°. The shortest intramolecular Mn···Cr separation through the bridging cyanido ligand is 5.125 Å, and the shortest intermolecular metal–metal distance is 6.388 Å for Mn···Cr.

The cell-packing diagram of complex **1** (see Supporting Information) shows an H-bonding interaction between the two O atoms of one 5-Cl-salen$^{2-}$ ligand and a coordinated water molecule as well as between a cyanido nitrogen atom and a coordinated water molecule. Interestingly, the cell packing along the *c* axis is highly ordered, with many honeycomb holes in which all the chlorine atoms from the Schiff-base ligands face the center of the holes.

The structure of complex **2** consists of a neutral chain which is formed by a $[Cr(CN)_5(NO)]^{3-}$ and three $[Mn(salen)]^+$ units connected by cyanido ligands (Figure 2). Four cyanido ligands of $[Cr(CN)_5(NO)]^{3-}$ coordinate axially to the $[Mn(salen)]^+$ units. The primary chain is composed of alternate Cr(1) and Mn(1) units bridged by two *trans*-cyanido groups in $[Cr(CN)_5(NO)]^{3-}$. Two $[Mn(salen)]^+$ units [Mn(2) and Mn(3)] dangle outside the primary $Mn^{III}Cr^{I}$ chain. One dangling $[Mn(salen)]^+$ unit has a distorted octahedral environment with an acetonitrile nitrogen atom hemicoordinated [Mn(2)–N(13) 2.605(5) Å]. Each $Mn^{III}$ ion is hexacoordinate and has a distorted octahedral surrounding [$MnN_3O_3$ for Mn(2) and Mn(3), and $MnN_4O_2$ for Mn(1)] due to the Jahn–Teller effect for a high-spin $d^4$ $Mn^{III}$ ion. The Mn–$N_{cyanido}$ bonds are comparatively long, ranging from 2.206(3) to 2.333(3) Å. The $Cr^{I}$ ion lies in a compressed $CrC_5N$ octahedral geometry, as evidenced by the shorter Cr–N bond [1.695(3) Å for Cr(1)–N(6)] than the Cr–C distance [2.049(4)–2.111(3) Å], which is very different from those of the $Fe^{III}$ and $Cr^{III}$ ions in $[Fe(CN)_6]^{3-}$ and $[Cr(CN)_6]^{3-}$ building blocks, which have a standard octahedral geometry. The Cr–C≡N and Cr–N≡O bond angles are essentially linear [172.1(3)–176.7(3)°], whereas the Mn–N≡C bond angles deviate markedly from linearity [147.8(2)° for Mn(1)–N(5)–C(5), 148.0(2)° for Mn(1)$^{\#}$–N(3)–C(3) (symmetry operation: $^{\#}$ –*x* + 1/2, *y* + 1/2, –*z* + 3/2), 148.2(3)° for Mn(2)–N(2)–C(2), and 157.5(3)° for Mn(3)–N(4)–C(4)], and give rise to a wave-like chain structure (Table 2).

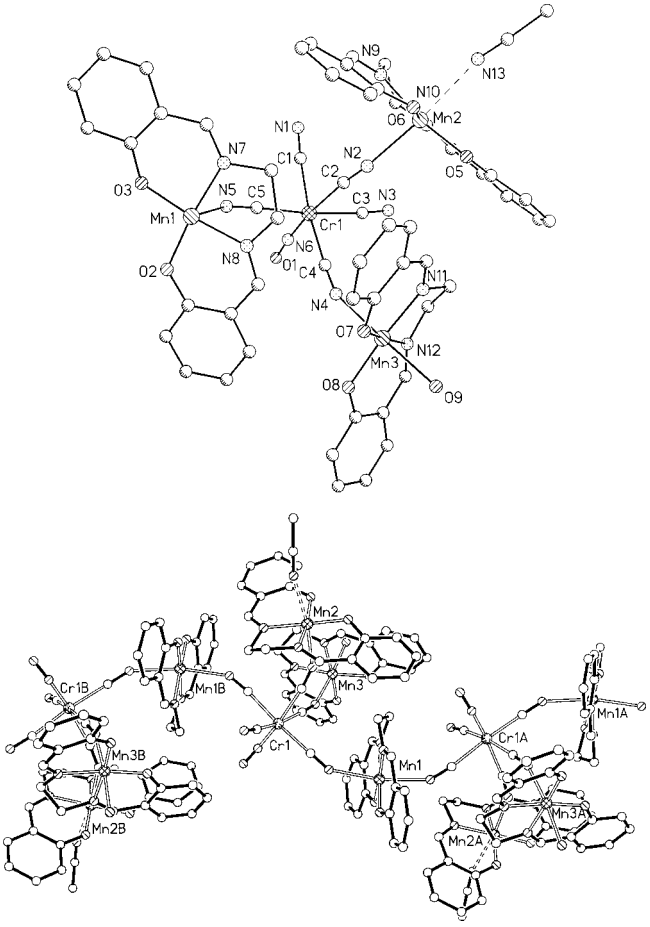


Figure 2. Tetrameric building unit (top) and the one-dimensional chain-like structure (bottom) in complex **2**.

Interestingly, two adjacent chains along the *a* axis arrange oppositely and form relatively broad cavities where the dangling $[Mn(salen)]^+$ units [Mn(2) and Mn(3)] are ac-

 © 2007 Wiley-VCH Verlag GmbH & Co. KGaA, Weinheim 

Table 2. Selected bond lengths [Å] and angles [°] for **2**.[a]

| | | | | | |
|---|---|---|---|---|---|
| Mn(1)–N(5) | 2.333(3) | Mn(2)–N(2) | 2.206(3) | Mn(3)–N(4) | 2.240(3) |
| Mn(1)–N(3)$^{\#1}$ | 2.296(3) | Mn(2)–N(9) | 1.981(3) | Mn(3)–N(11) | 1.979(3) |
| Mn(1)–N(7) | 1.987(3) | Mn(2)–N(10) | 1.974(3) | Mn(3)–N(12) | 1.977(3) |
| Mn(1)–N(8) | 1.991(3) | Mn(2)–O(5) | 1.866(2) | Mn(3)–O(7) | 1.861(2) |
| Mn(1)–O(2) | 1.885(2) | Mn(2)–O(6) | 1.871(2) | Mn(3)–O(8) | 1.888(2) |
| Mn(1)–O(3) | 1.879(2) | Mn(2)–N(13) | 2.605(5) | Mn(3)–O(9) | 2.331(3) |
| Cr(1)–C(1) | 2.049(4) | Cr(1)–C(2) | 2.111(3) | Cr(1)–C(3) | 2.068(3) |
| Cr(1)–C(4) | 2.052(3) | Cr(1)–C(5) | 2.066(3) | Cr(1)–N(6) | 1.695(3) |
| C(1)–N(1) | 1.149(4) | C(2)–N(2) | 1.147(4) | C(3)–N(3) | 1.138(4) |
| C(4)–N(4) | 1.151(4) | C(5)–N(5) | 1.151(4) | N(6)–O(1) | 1.188(4) |
| Mn(1)–N(5)–C(5) | 147.8(2) | Mn(2)–N(2)–C(2) | 148.2(3) | Mn(3)–N(4)–C(4) | 157.5(3) |
| Mn(1)$^{\#2}$–N(3)–C(3) | 148.0(3) | Cr(1)–C(1)–N(1) | 175.8(3) | Cr(1)–C(2)–N(2) | 172.5(3) |
| Cr(1)–C(3)–N(3) | 172.1(3) | Cr(1)–C(4)–N(4) | 176.1(3) | Cr(1)–C(5)–N(5) | 176.7(3) |
| Cr(1)–N(6)–O(1) | 176.1(3) | | | | |

[a] Symmetry operations: $^{\#1}$ $-x + 1/2$, $y - 1/2$, $-z + 3/2$; $^{\#2}$ $-x + 1/2$, $y + 1/2$, $-z + 3/2$.

commodated, whereas the Mn(1) units are situated in the formed narrow cavities and afford the shortest interchain metal–metal distance of 8.040 Å (Figure 3).

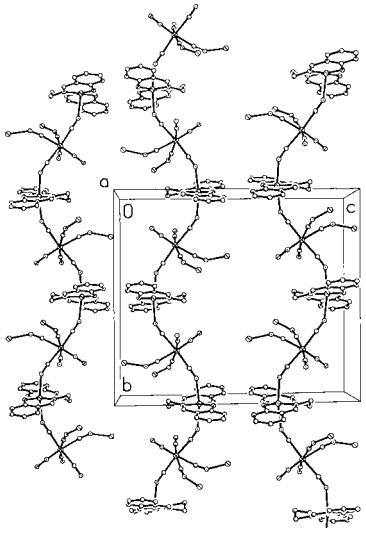


Figure 3. Cell-packing diagram of complex **2** showing the wave-like chain structure along the *a* axis [only the $Mn^{III}$ ions of the dangling Mn(salen) units are shown].

Unlike complex **2**, the structure of **3** consists of an anionic chain formed by a $[Cr(CN)_5(NO)]^{3-}$ and two $[Mn(5\text{-Br-salen})]^+$ units (see Figure 4 and Supporting Information), with a free $[Mn(5\text{-Br-salen})(H_2O)(MeOH)]^+$ moiety as the countercation. Three *mer*-cyanido groups of $[Cr(CN)_5(NO)]^{3-}$ in the chain are linked to the $[Mn(5\text{-Br-salen})]^+$ units. One $[Mn(5\text{-Br-salen})]^+$ and one $[Cr(CN)_5(NO)]^{3-}$ unit connect alternately through two *cis*-cyanido groups in $[Cr(CN)_5(NO)]^{3-}$ to give rise to a zigzag primary chain; another $[Mn(5\text{-Br-salen})(MeOH)]^+$ unit dangles outside the $Mn^{III}Cr^{I}$ chain. The free $[Mn(5\text{-Br-salen})(H_2O)(MeOH)]^+$ countercations are in the vicinity of the anionic chains. The Mn–$N_{cyanido}$ bond lengths are 2.230(11) Å for Mn(1)–N(1), 2.251(12) Å for Mn(2)–N(2), and 2.281(11) Å for Mn(2)–N(3)$^{\#}$ (symmetry operation: $^{\#}$ $-x + 1/2$, $y - 1/2$, $-z + 1/2$). The Mn–N≡C bond angles are 138.1(10)° for Mn(1)–N(1)–C(1), 160.7(12)° for Mn(2)–N(2)–C(2), and 145.6(11)° for Mn(2)$^{\#}$–C(3)–N(3) (symmetry operation: $^{\#}$ $-x + 1/2$, $y + 1/2$, $-z + 1/2$), with an average value of 148.1(11)° (Table 3).

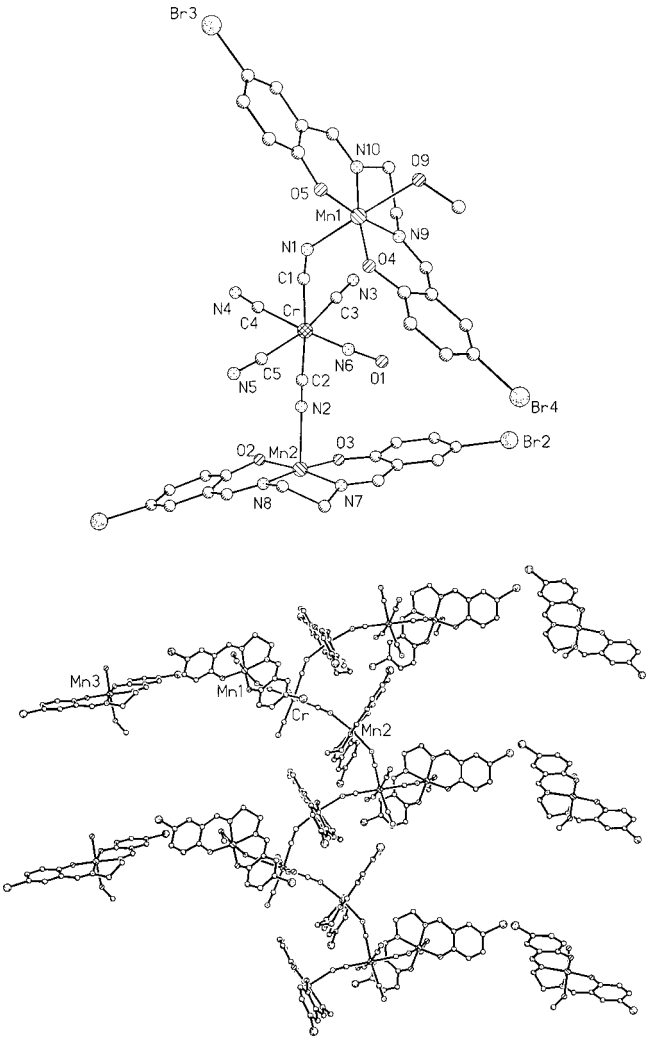


Figure 4. Top: one unit of the chain {the free $[Mn(5\text{-Br-salen})(H_2O)(CH_3OH)]^+$ block is omitted for clarity}; bottom: one-dimensional zigzag chain structure in complex **3**.

 © 2007 Wiley-VCH Verlag GmbH & Co. KGaA, Weinheim 

Table 3. Selected bond lengths [Å] and angles [°] for **3**.[a]

| | | | | | |
|---|---|---|---|---|---|
| Mn(1)–N(1) | 2.230(11) | Mn(2)–N(2) | 2.251(12) | Mn(3)–N(11) | 2.006(11) |
| Mn(1)–N(9) | 1.971(10) | Mn(2)–N(3)$^{\#1}$ | 2.281(11) | Mn(3)–N(12) | 1.988(10) |
| Mn(1)–N(10) | 1.971(9) | Mn(2)–N(7) | 2.007(9) | Mn(3)–O(6) | 1.881(8) |
| Mn(1)–O(4) | 1.890(7) | Mn(2)–N(8) | 1.995(9) | Mn(3)–O(7) | 1.878(9) |
| Mn(1)–O(5) | 1.881(9) | Mn(2)–O(2) | 1.892(7) | Mn(3)–O(8) | 2.310(11) |
| Mn(1)–O(9) | 2.332(8) | Mn(2)–O(3) | 1.888(7) | Mn(3)–O(2w) | 2.241(9) |
| Cr(1)–C(1) | 2.084(15) | Cr(1)–C(2) | 2.098(14) | Cr(1)–C(3) | 2.040(13) |
| Cr(1)–C(4) | 2.087(13) | Cr(1)–C(5) | 2.064(13) | Cr(1)–N(6) | 1.687(10) |
| C(1)–N(1) | 1.152(14) | C(2)–N(2) | 1.106(14) | C(3)–N(3) | 1.155(14) |
| C(4)–N(4) | 1.143(14) | C(5)–N(5) | 1.152(14) | N(6)–O(1) | 1.178(11) |
| Cr(1)···Mn(1) | 5.324 | Cr(1)···Mn(2) | 5.213 | Cr(1)···Mn(2)$^{\#2}$ | 5.228 |
| Mn(1)–N(1)–C(1) | 138.1(10) | Mn(2)–N(2)–C(2) | 160.7(12) | Mn(2)$^{\#2}$–N(3)–C(3) | 145.6(11) |
| Cr(1)–C(1)–N(1) | 173.0(11) | Cr(1)–C(2)–N(2) | 176.0(13) | Cr(1)–C(3)–N(3) | 178.8(12) |
| Cr(1)–C(4)–N(4) | 174.6(12) | Cr(1)–C(5)–N(5) | 175.2(11) | Cr(1)–N(6)–O(1) | 168.2(11) |

[a] Symmetry operations: $^{\#1}$ $-x + 1/2, y - 1/2, -z + 1/2$; $^{\#2}$ $-x + 1/2, y + 1/2, -z + 1/2$.

The zigzag chains form a 2D structure with alternating saddle-like squares through H-bonds between the free cyanido nitrogen atoms and the coordinated methanol oxygen atoms (see Supporting Information). This 2D layered structure is further linked by the free (Schiff base)$Mn^{III}$ units through H-bonds involving cyanido nitrogen, phenoxy oxygen, and coordinated water to form a 3D network structure. Since the adjacent chains are linked together by N···H–O H-bonds (N···O = 2.775 Å), the closest interchain metal–metal distance is only 6.722 Å for Mn–Cr, which is much shorter than that in complex **2** (8.040 Å).

The out-of-plane phenoxido-bridged dimeric $[Mn(saltmen)]_2^{2+}$ cations found in complex **4** connect $[Cr(CN)_5(NO)]^{3-}$ in a *trans* fashion to give rise to a 2D network structure with free $ClO_4^-$ as counteranion. The layered structure of **4** is very similar to that of the complex $[\{Mn(saltmen)\}_4\{Fe(CN)_6\}]ClO_4\cdot H_2O$[12] reported by Miyasaka et al. It is worth noting that a cyclic dodecanuclear square unit is formed through alternating dimeric $[Mn(saltmen)]_2^{2+}$ and $[Cr(CN)_5(NO)]^{3-}$ groups. Figure 5 shows the pentanuclear $[\{Mn(saltmen)\}_4\{Cr(CN)_5(NO)\}]^+$ moiety and the 2D network structure along the *c* axis (Table 4).

The $Mn^{III}$ ion in the complex has a distorted octahedral geometry in which the equatorial plane is occupied by $N_2O_2$ donor atoms from the saltmen$^{2-}$ ligand while the two *trans* positions are taken up by the cyanido nitrogen and the phenoxy oxygen atom [O(2)$^{\#}$] of the adjacent (Schiff base) $Mn^{III}$ unit (symmetry operation: $^{\#}$ $1/2 + x, 1/2 + y, z$). The $Mn–N_{cyanido}$ bond length is 2.166(9) Å for Mn(1)–N(1) and the corresponding Mn–N≡C bond angle is 154.6(8)° for Mn(1)–N(1)–C(1). The Mn(1)–O(2)$^{\#}$ bond length is 2.629(11) Å, comparable to those of $[\{Mn(saltmen)\}_4\{Fe(CN)_6\}]ClO_4\cdot H_2O$ [2.847(9) Å] and the dimeric precursor $[Mn(saltmen)(H_2O)]_2(ClO_4)_2$ [2.434(2) Å]. The Mn···Mn distance in the dimeric unit is 3.474(8) Å. The Mn···Cr distance through the cyanido ligand is 5.231(8) Å and the shortest interlayer metal–metal separation is 11.879(8) Å.

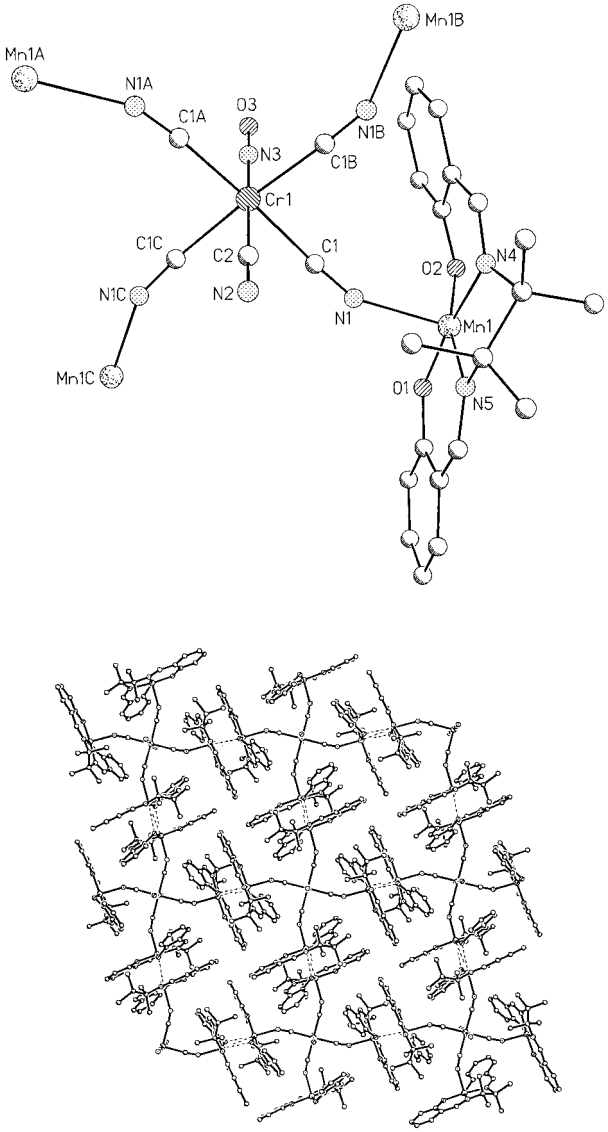


Figure 5. Pentanuclear $Mn_4Cr$ unit (top) and the two-dimensional network structure (bottom) in complex **4** (broken lines represent the weak axial phenoxido–$Mn^{III}$ coordination).

 © 2007 Wiley-VCH Verlag GmbH & Co. KGaA, Weinheim 

Table 4. Selected bond lengths [Å] and angles [°] for **4**.

| | | | | | |
|---|---|---|---|---|---|
| Mn(1)–N(1) | 2.166(9) | Mn(1)–N(4) | 1.987(9) | Mn(1)–N(5) | 1.967(10) |
| Mn(1)–O(1) | 1.883(6) | Mn(1)–O(2) | 1.892(8) | Cr(1)–C(1) | 2.061(11) |
| Cr(1)–C(2) | 2.06(3) | Cr(1)–N(3) | 1.74(2) | N(1)–C(1) | 1.160(12) |
| C(2)–N(2) | 1.17(3) | O(3)–N(3) | 1.19(2) | Cr(1)···Mn(1) | 5.230 |
| Mn(1)–N(1)–C(1) | 154.6(8) | Cr(1)–C(1)–N(1) | 175.2(9) | Cr(1)–C(2)–N(2) | 180.000(2) |
| O(3)–N(3)–Cr(1) | 180.0 | | | | |

## Magnetic Properties

The temperature-dependence of $\chi_m T$ for **1** is shown in Figure 6. Upon cooling, the $\chi_m T$ value decreases smoothly from 300 to 40 K before increasing again. The maximum of the curve is at 20 K, with a $\chi_m T$ value of 8.380 emu K mol$^{-1}$. The origin of the decrease in $\chi_m T$ (below 20 K) may be due to the saturation effect and the zero-field-splitting (ZFS) effect of $Mn^{III}$. The magnetic susceptibilities (25–300 K) obey the Curie–Weiss law with a negative Weiss constant, $\theta$, of –8.8 K and a Curie constant, $C$, of 9.425(1) emu K mol$^{-1}$, which also confirms the presence of an overall antiferromagnetic interaction in **1**.

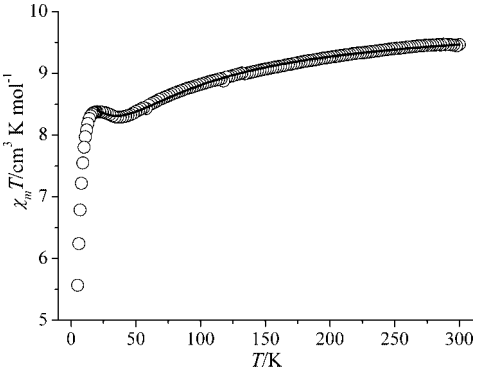


Figure 6. Temperature dependence of $\chi_m T$ for **1**. The solid line represents the theoretical results based on the parameters described in the text.

On the basis of the trinuclear model, the magnetic susceptibilities can be fitted by the expression given in Equation (1) derived from the isotropic exchange spin Hamiltonian $\hat{H} = -2J\hat{S}_{Cr}[\hat{S}_{Mn(1)} + \hat{S}_{Mn(2)}] - 2J'\hat{S}_{Mn(1)}\hat{S}_{Mn(2)}$ for an $Mn_2Cr$ trinuclear unit ($S_{Mn} = 2$, $S_{Cr} = 1/2$) by neglecting the bond-angle difference of Mn–N≡C for simplicity, where $A = 165 + 84\exp(-9J/kT) + 84\exp(-J/kT - 8J'/kT) + 35\exp(-8J/kT - 14J'/kT) + 35\exp(-2J/kT - 14J'/kT) + 10\exp(-7J/kT - 14J'/kT) + 10\exp(-3J/kT - 18J'/kT) + \exp(-6J/kT - 18J'/kT) + \exp(-4J/kT - 10J'/kT)$, and $B = 20 + 16\exp(-9J/kT) + 16\exp(-J/kT - 8J'/kT) + 12\exp(-8J/kT - 14J'/kT) + 12\exp(-2J/kT - 14J'/kT) + 8\exp(-7J/kT - 14J'/kT) + 8\exp(-3J/kT - 18J'/kT) + 4\exp(-6J/kT - 18J'/kT) + 4\exp(-4J/kT - 20J'/kT)$.

$$\chi_t = \frac{Ng^2\beta^2}{kT}\left[\frac{A}{B}\right] \quad (1)$$

The final molar magnetic susceptibility ($\chi_m/Mn_3Cr$) takes the form of Equation (2).

$$\chi_m = \chi_t + \frac{Ng_{Mn}^2\beta^2}{3kT} S_{Mn}(S_{Mn}+1) \quad (2)$$

The best-fit parameters obtained are $J = -10.4$ cm$^{-1}$, $g = g_{Mn} = 2.06$, $J' = -1.29$ cm$^{-1}$ and $R = \sum(\chi_{obsd}T - \chi_{calcd}T)^2/\sum(\chi_{obsd}T)^2 = 3.75 \times 10^{-5}$ in the temperature range 20–300 K. We note that the absolute $J$ value is much larger than that (ca. –2 cm$^{-1}$) for the antiferromagnetically coupled $Mn^{III}$–$Fe^{III}$ analogues,[11] which is indicative of the presence of a stronger magnetic interaction between $Mn^{III}$ and $Cr^{I}$.

The temperature dependence of the $\chi_m T$ product per $Mn_3Cr$ unit in the range 2–300 K for **2** is shown in Figure 7. The room-temperature $\chi_m T$ values are in good agreement with the expected value of 9.375 emu K mol$^{-1}$ (calculated by assuming $g = 2.0$) for one low-spin $Cr^{I}$ and three high-spin $Mn^{III}$ ions. Upon cooling, the $\chi_m T$ value of **2** decreases smoothly from 300 to 70 K and then increases, with a maximum value of 27.5 emu K mol$^{-1}$ at 4.3 K. The negative Weiss constant of –8.78(10) K and a Curie constant of 9.385(1) emu K mol$^{-1}$ can be obtained from the data between 5 and 300 K. These indicate that the $Mn^{III}$–$Cr^{I}$ magnetic coupling through the cyanido bridges is antiferromagnetic. The decrease in $\chi_m T$ below 4.3 K suggests the presence of interchain antiferromagnetic coupling (see below).

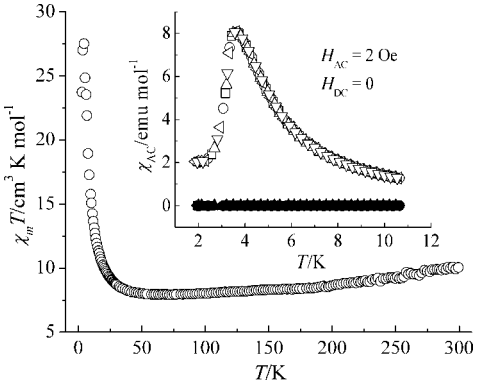


Figure 7. Temperature dependence of $\chi_m T$ for **2**. Inset: temperature dependence of the AC magnetization for **2** in zero static field and an AC field of 2 Oe at 111, 199, 355, 633 and 1111 Hz.

The field-cooled magnetization (FCM) and zero-field-cooled magnetization (ZFCM) plots for **2** (see Supporting Information) at an applied field, $H$, of 100 Oe show a maximum at around 3.6 K, which demonstrates that there is an antiferromagnetic phase transition at this temperature. The real part of the AC magnetic susceptibility displayed in the

 © 2007 Wiley-VCH Verlag GmbH & Co. KGaA, Weinheim 

inset of Figure 7 also has a maximum at around 3.6 K, and the imaginary part is zero, which suggests that the critical temperature ($T_N$) is approximately 3.6 K.

The field-dependence of the magnetization and the hysteresis loop measured at 1.83 K (see Supporting Information) show a spin transition from antiferromagnetic to ferromagnetic. A critical field of 500 Oe is observed. This metamagnetic behavior is commonly observed for 2D layered antiferromagnets with short-range, intralayer ferri- or ferromagnetic ordering.[31–35]

The temperature-dependence of the $\chi_m T$ magnetic behavior of **3** is similar to that of **1** and **2**, as shown in Figure 8. Upon cooling, $\chi_m T$ decreases smoothly, reaching a minimum at 80 K, and then increases. The maximum of the curve is at 9.2 K, with a $\chi_m T$ value of 12.1 emu K mol$^{-1}$. The magnetic susceptibilities above 10 K obey the Curie–Weiss law with a negative Weiss constant of –4.98(6) K and a Curie constant of 9.257(1) emu K mol$^{-1}$, which also confirms the presence of overall antiferromagnetic interactions in **3**.

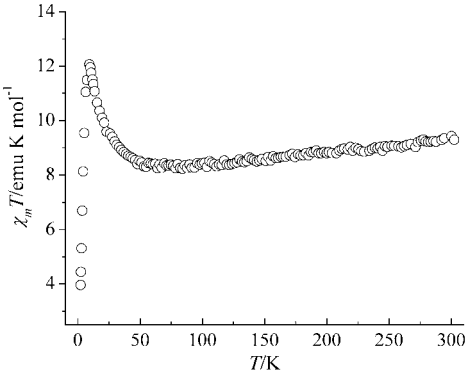


Figure 8. Temperature dependence of $\chi_m T$ for **3**.

The temperature dependence of the magnetic susceptibility in a zero DC and 3-Oe AC magnetic field for complex **3** is displayed in Figure 9. The out-of-phase AC magnetic susceptibility has nonzero values below 4.0 K and is strongly frequency-dependent. The shift of the peak temperature ($T_P$) of $\chi''$ is evaluated by the parameter $\Phi = (\Delta T_P/T_P)/\Delta(\log\omega) = 0.17$, which is larger than that for a canonical spin-glass but smaller than the normal value for a superparamagnet.[36–39] The hysteresis loop at 1.8 K shows noticeable magnetic hysteresis (Figure 10), which indicates the presence of magnetic ordering in complex **3**.

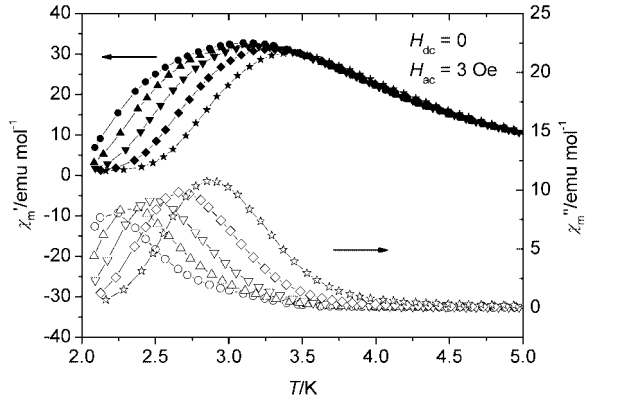


Figure 9. Temperature dependence of the AC magnetization for **3** in a zero static field and an AC field of 3 Oe at frequencies of 277 (circles), 666 (triangles tip up), 1633 (tringles tip down), 4111 (diamonds), and 9999 (stars) Hz.

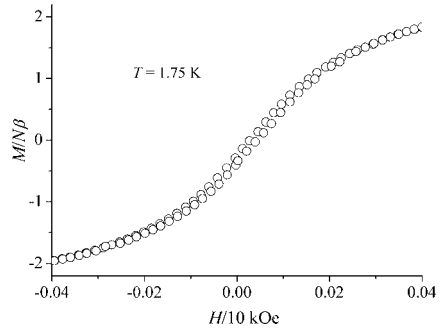


Figure 10. Magnetic hysteresis loop for **3** at 1.75 K.

The crystal data show that there is a large number of strong H-bonds in complex **3** which form a 3D network structure and that the metal···metal distance is 6.722 Å. This suggests the presence of a significant intermolecular magnetic interaction. Therefore, we tentatively attribute the slow relaxation of magnetization in **3** to a spin-glass behavior.[39] The origin of this spin-glass behavior may be due to the presence of competitive ferro- and antiferromagnetic coupling within the chains considering the presence of a wide range of cyanido bridging bond angles [138.1(10)–160.7(12)°].

The magnetic susceptibilities of complex **4** were measured in the temperature range 2–300 K in an applied magnetic field of 2000 Oe. The plot of $\chi_m T$ vs. $T$ for **4** is shown in Figure 11, where $\chi_m$ is the magnetic susceptibility per $Mn_4Cr$ unit. The room-temperature $\chi_m T$ value of 12.541 emu K mol$^{-1}$ is nearly equal to the spin-only value of 12.375 emu K mol$^{-1}$ for five uncoupled spins [four $S_{Mn}$ ($S$ = 2) and one $S_{Cr}$ ($S$ = 1/2)]. On lowering the temperature, $\chi_m T$ decreases gradually to 11.82 emu K mol$^{-1}$ at 150 K, then increases smoothly until about 50 K before rapidly reaching a maximum value of 166 emu K mol$^{-1}$ at 8 K, and then sharply decreases to 56.5 emu K mol$^{-1}$ at 2 K, which

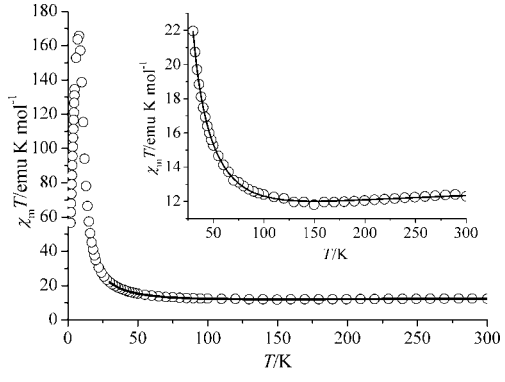


Figure 11. Temperature dependence of $\chi_m T$ for **4**. Inset: enlarged view in the temperature range 25–300 K. The solid line shows the best fit based on the parameters discussed in the text.

 © 2007 Wiley-VCH Verlag GmbH & Co. KGaA, Weinheim 

suggests the presence of global antiferromagnetic interactions and three-dimensional magnetic ordering in the complex. The plot of $1/\chi_m$ vs. $T$ above 150 K obeys the Curie–Weiss law with a negative Weiss constant of –12.5 K and a Curie constant of 12.4 emu K mol$^{-1}$, which suggest that antiferromagnetic coupling between $Mn^{III}$ and $Cr^{I}$ through a cyanido bridge is dominant in the high-temperature range with the $Mn^{III}$–$Mn^{III}$ ferromagnetic coupling through the phenoxido bridges superimposed. The higher temperature shift of the minimum in $\chi_m T$ for **4** (150 K) than those of complexes **1**–**3** (40 K for **1**, and 70 for **2**, and 80 K for **3**) may be due to the presence of ferromagnetic $Mn^{III}$–$Mn^{III}$ interactions through the phenoxy oxygen atoms.

To evaluate the magnitude of the intramolecular magnetic coupling, we tried to fit the magnetic susceptibilities to the model previously employed for coordination polymers.[20] The structural information shows that in complex **4** there are two different magnetic coupling pathways, namely cyanido bridges and phenoxido bridges. The layers are illustrated schematically in Scheme 2, where $J$ is for the cyanido bridges and $J'$ for the phenoxido ones. We can see from the $\chi_m T$ vs. $T$ plot that $J$ is dominant, i.e. $|J| >> |J'|$. The 2D layer can be accordingly described as weakly interacting $Mn_4Cr$ pentanuclear units in which an antiferromagnetic coupling ($J < 0$) is present.

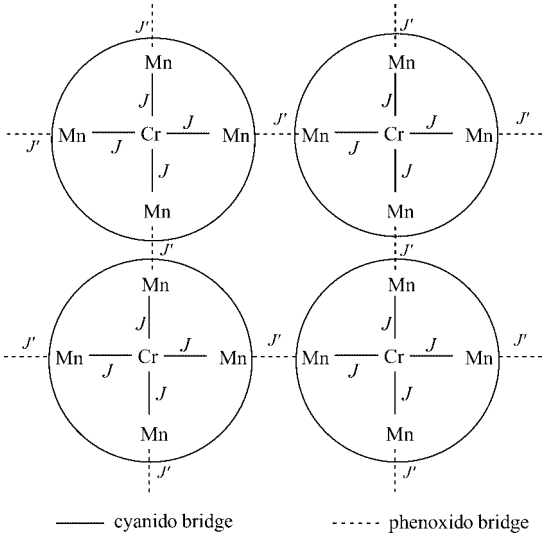


Scheme 2. Schematic view of the layer structure of **4** showing the magnetic coupling pathways.

Based on the above considerations, the magnetic data were fitted to the Van Vleck equation for the pentanuclear unit derived from the exchange Hamiltonian $\hat{H} = -2J\hat{S}_{Cr}(\hat{S}_{Mn1} + \hat{S}_{Mn2} + \hat{S}_{Mn3} + \hat{S}_{Mn4})$.[11,15] The magnetic coupling through the phenoxido bridges was treated as an intermolecular term using the mean-field method. The final molar magnetic susceptibility ($\chi_m$) is in the form of Equation (3), where $\chi_p$ is for the $Mn_4Cr$ pentanuclear unit, $J'$ is the coupling constant between the pentanuclear units, and $z$, the number of nearest $Mn_4Cr$ neighbors, is 4. Other symbols have their usual meanings.

$$\chi_m = \chi_p/[1 - \chi_p(2zJ'/Ng^2\beta^2)] \quad (3)$$

The best-fit parameters based on the data above 30 K are $J = -17.2$ cm$^{-1}$, $zJ' = 0.17$ cm$^{-1}$, $g_{Mn} = 1.97$, and $g_{Cr} = 3.70$. The calculated solid line shown in Figure 11 agrees well with the experimental values. The calculated $J$ value is comparable to that [–10.4(1) cm$^{-1}$] for the trinuclear $Mn_2Cr$ compound **1**. The positive $J'$ value suggests a ferromagnetic $Mn^{III}$–$Mn^{III}$ coupling through the phenoxido bridges. However, this value is smaller than that for the similar $Mn_2$ complexes according to the equation $J' = 4.5724 - 1.1868x$ ($x$ is the Mn–$O_{phenoxido}$ distance [Å] in the range of 2.4–3.7 Å) proposed by Miyasaka et al.[40] This may be due to the rough approximation of the fit. Furthermore, the $g_{Cr}$ value is too large, although the use of a value less than 3.0 did not give a satisfactory fit. Nevertheless, the $g_{Cr}$ value is not reasonable, and should be considered with care.

To further confirm the magnetic phase transition, the temperature dependence of the AC magnetic susceptibility was measured at a zero DC and a 5-Oe AC field, as shown in Figure 12. The real part of the AC magnetic susceptibility has a maximum peak at about 6.4 K which is accompanied by the occurrence of a nonzero $\chi_{AC}''$, thereby suggesting that the $T_c$ of complex **4** is about 6.4 K, similar to that of the 2D analogue [{Mn(saltmen)}$_4${Fe(CN)$_6$}]-$ClO_4 \cdot H_2O$[12] (4.5 K). The hysteresis loop at 2.0 K (see Supporting Information) displays a characteristic behavior for a soft ferromagnet, with a small coercive field of 10 Oe and a remnant magnetization of about 4.0 $N\beta$.

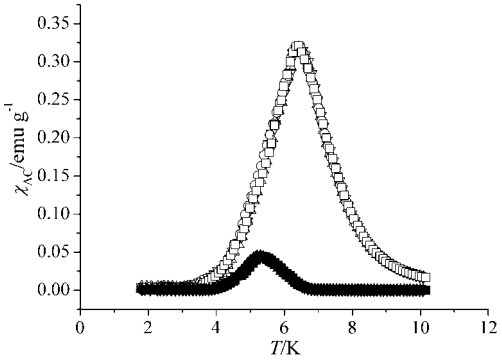


Figure 12. Temperature dependence of the AC magnetization for **4** in a zero static field and an AC field of 2 Oe at 277, 666, 1633, and 4111 Hz.

The nature of the magnetic coupling between the high-spin $Mn^{III}$ ion ($d^4$, $t_{2g}^3$, $e_g^1$) and the low-spin $Cr^{I}$ ion ($d^5$, $t_{2g}^5$) through the cyanido bridge should be similar to those of cyanido-bridged $Mn^{III}$–$Fe^{III}(CN)_6$ systems.[11,12,14] According to the GK rule,[41] ferromagnetic and antiferromagnetic contributions coexist, and the antiferromagnetic contributions that originate from the overlap of magnetic orbitals of $t_{2g}$ symmetry between $Mn^{III}$–$Fe^{III}$ and $Mn^{III}$–$Cr^{I}$ are dominant in these systems. Therefore, overall antiferromagnetic interactions between $Mn^{III}$ and $Cr^{I}$ through cyanido groups are expected for complexes **1**–**4** in this work, as is also observed in the 3D Prussian blue analogue $Mn^{III}$-$[Cr(CN)_5(NO)] \cdot H_2O$ recently reported by Liao et al.[42] In

 © 2007 Wiley-VCH Verlag GmbH & Co. KGaA, Weinheim 

addition, the bending of the Mn–N≡C angle is an important factor that affects the magnetic coupling in these systems because it diminishes the overlap of $t_{2g}$-type magnetic orbitals on adjacent metal ions and therefore weakens the antiferromagnetic contributions. It has been concluded empirically that an Mn–N≡C angle close to 150° tends to favor ferromagnetic coupling in cyanido-bridged $Mn^{III}$–$Fe^{III}$ systems.[14] However, the magnetic couplings for the cyanido-bridged $Mn^{III}$–$Cr^{I}$ systems in this work are all antiferromagnetic, with average Mn–N≡C angles in the range 148.1(11)–158.7(6)°, therefore further work needs to be done to fully elucidate the nature of the magnetic interactions in cyanido-bridged $Mn^{III}$–$Cr^{I}$ systems.

## Conclusions

Polynuclear 1D and 2D $Mn^{III}$–$Cr^{I}$ complexes have been synthesized by tuning the Schiff-base ligands around $Mn^{III}$. The complexes in the present work all show antiferromagnetic $Mn^{III}$–$Cr^{I}$ coupling, which is in contrast to the $[Fe(CN)_6]^{3-}$ analogues, which usually exhibit intermetallic ferromagnetic interactions.[11–16,19–23] In this regard, $[Cr(CN)_5(NO)]^{3-}$ is much like $[Cr(CN)_6]^{3-}$, as no ferromagnetic cyanido-bridged $Mn^{III}$–$Cr^{III}$ complexes have been found so far.[43] The present study further demonstrates that this is a good strategy for designing and assembling molecule-based magnetic materials based on (Schiff base)$Mn^{III}$ precursors and cyanido-bearing paramagnetic building blocks.

## Experimental Section

**General Remarks:** Elemental analyses for carbon, hydrogen, and nitrogen were carried out with an Elementar Vario EL. The IR spectra were recorded with a Magna-IR 750 spectrophotometer in the region 4000–650 $cm^{-1}$. Variable-temperature magnetic susceptibility measurements of **1**–**4** were performed with a Quantum Design MPMS SQUID magnetometer. The zero-field AC magnetic susceptibilities of **1**, **3**, and **4** were recorded with a MagLab 2000 magnetometer. The experimental susceptibilities were corrected for the diamagnetism of the constituent atoms (Pascal's tables).

**General Procedures for the Synthesis of (Schiff Base)$Mn^{III}$ Complexes:** The precursors [Mn(salen)]$ClO_4$, [Mn(5-Br-salen)]$ClO_4$, [Mn(5-Cl-salen)]$ClO_4$, and [Mn(saltmen)]$ClO_4$ were synthesized according to the following procedure. Solid $[Mn(ClO_4)_2]\cdot 6H_2O$ (1.8 g, 5 mmol) was added to an MeOH and EtOH solution (40 mL, MeOH/EtOH = 1:1, v/v) of the Schiff base $H_2$salen (1.34 g, 5 mmol), $H_2$-5-Cl-salen (1.7 g, 5 mmol), $H_2$-5-Br-salen (2.1 g, 5 mmol), or $H_2$saltmen (1.6 g, 5 mmol), then solid NaOH (5 mmol) was added directly to the above mixture whilst stirring at room temperature. The mixture was then warmed to about 60–70 °C and kept at this temperature for about 1–3 h until the solid Schiff base had completely dissolved and the solution had become dark red/brown. After cooling and filtering, the solution was kept at room temperature for several days, which gave rise to red/brown crystals in high yield (80%).

**Synthesis of Complexes 1–3:** Red/brown crystals of **1**, **2**, and **3** were obtained at room temperature by the slow diffusion of a yellow aqueous solution (5 mL) of $K_3[Cr(CN)_5(NO)]\cdot H_2O$ (0.1 mmol, 32.9 mg) into a reddish brown mixture of [Mn(5-Cl-salen)]$ClO_4$ (0.2 mol, 98.4 mg), [Mn(salen)]$ClO_4$ (0.2 mol, 84.4 mg), or [Mn(5-Br-salen)]$ClO_4$ (0.2 mol, 116 mg) in MeOH and MeCN (5 mL) over about one week. These crystals were collected carefully and air-dried. Yield: 10–15%. IR: **1**: ν(C≡N) 2114 m, ν(N≡O) 1687 m, ν(C=N) 1628 $cm^{-1}$ vs; **2**: ν(C≡N) 2113 m, 2246 w ($CH_3CN$), ν(N≡O) 1677 s, ν(C=N) 1625 $cm^{-1}$ vs; **3**: ν(C≡N) 2009 m, ν(N≡O) 1684 s, ν(C=N), 1627 $cm^{-1}$ vs. **1**: $C_{53}H_{43}Cl_6CrMn_3N_{12}O_{10.50}$ (1445.5): calcd. C 44.04, H 3.00, N 11.63; found C 44.79, H 2.96, N 11.35; **2**: $C_{56.50}H_{54}CrMn_3N_{13.50}O_{10.50}$ (1307.0): calcd. C 51.92, H 4.16, N 14.47; found C 51.37, H 4.13, N 14.22; **3**: $Mn_3CrC_{55}H_{50}Br_6N_{12}O_{12}$ (1767.4): calcd. C 37.38, H 2.85, N 9.51; found C 37.30, H 2.86, N 8.98.

**Synthesis of Complex 4:** Thin lamellar brown single crystals of **4** suitable for X-ray structure analysis were grown at room temperature by slow evaporation of an MeOH/MeCN/$H_2O$ solution of [Mn(saltmen)]$ClO_4$ (64.9 mg, 0.2 mmol) and $K_3[Cr(CN)_5(NO)]\cdot H_2O$ (32.0 mg, 0.1 mmol) for several days. Yield: 28 mg (30% based on Mn). IR: ν(C≡N) 2114 m, ν(N≡O) 1712 s, ν(C=N) 1602 $cm^{-1}$

Table 5. Crystal data for complexes **1**–**4**.

| | **1** | **2** | **3** | **4** |
|---|---|---|---|---|
| Empirical formula | $C_{53}H_{43}Cl_6CrMn_3N_{12}O_{10.50}$ | $C_{56.50}H_{54}CrMn_3N_{13.50}O_{10.50}$ | $C_{55}H_{50}CrBr_6Mn_3N_{12}O_{12}$ | $C_{85}H_{88}ClCrMn_4N_{14}O_{16}$ |
| Fomula mass | 1445.51 | 1306.95 | 1767.35 | 1868.90 |
| $T$ [K] | 123 | 293 | 293 | 123 |
| Crystal system | rhombohedral | monoclinic | monoclinic | tetragonal |
| Space group | $R\bar{3}$ | $P2_1/n$ | $P2_1/n$ | $I4/m$ |
| $a$ [Å] | 35.000(5) | 11.822(2) | 15.770(4) | 18.613(3) |
| $b$ [Å] | 35.000(5) | 19.0635(8) | 13.486(3) | 18.613(3) |
| $c$ [Å] | 27.442(6) | 22.1293(9) | 31.048(8) | 27.738(6) |
| $\alpha$ [°] | 90 | 90 | 90 | 90 |
| $\beta$ [°] | 90 | 96.777(1) | 97.77(2) | 90 |
| $\gamma$ [°] | 120 | 90 | 90 | 90 |
| $V$ [Å$^3$] | 29112(8) | 6085.3(4) | 6542(3) | 9610(3) |
| Z | 18 | 4 | 4 | 4 |
| $\rho_{calcd.}$ [g cm$^{-3}$] | 1.484 | 1.427 | 1.794 | 1.292 |
| $F$(000) | 13140 | 2682 | 3476 | 3860 |
| Data/restraints/parameters | 22777/1/1481 | 10676/0/802 | 9102/6/800 | 3847/3/287 |
| GOF on $F^2$ | 0.956 | 1.003 | 0.998 | 1.078 |
| $R_1$ [$I > 2\sigma(I)$] | 0.0741 | 0.0494 | 0.0744 | 0.1429 |
| $wR_2$ (all data) | 0.1859 | 0.1482 | 0.2134 | 0.2771 |

 © 2007 Wiley-VCH Verlag GmbH & Co. KGaA, Weinheim 

vs. $C_{85}H_{88}ClCrMn_4N_{14}O_{16}$ (1868.9): calcd. C 54.63, H 4.75, N 10.49; found C 54.25, H 4.68, N 10.26.

**X-ray Structure Determination:** Data collection for **2** was performed with a Simens Bruker P4 diffractometer, that for **3** with a Bruker Smart CCD, and that for **1** and **4** with a Rigaku Saturn70 CCD diffractometer (123 K). The structures were solved by direct methods with SHELXS-97 and refined by full-matrix least squares (SHELXL-97) on $F^2$. Hydrogen atoms were added geometrically and refined using a riding model. One free MeCN molecule in complex **2** and one $CN^-$ and one $NO^-$ group from one $[Cr(CN)_5(NO)]^{3-}$ unit in complex **1** are disordered over two sets of positions. Single crystals of **4** are thin, weakly diffracting, and give high final $R$ values: $R_1 = 0.1429$, $wR_2 = 0.2771$ (all data). Its molecular structure was further confirmed by elemental analysis and magnetism studies. Crystallographic data for complexes **1**–**4** are summarized in Table 5. CCDC-623479 to -623482 (**1**–**4**, respectively) contain the supplementary crystallographic data for this paper. These data can be obtained free of charge from The Cambridge Crystallographic Data Center via www.ccdc.cam.ac.uk/data_request/cif.

**Supporting Information** (see footnote on the first page of this article): Schematic view of the structures of **1** and **4**; cell packing diagrams for **1**–**4**; FCM and ZFCM plots, hysteresis loop, and magnetization data at 1.83 K for **2**; hysteresis loop at 2.0 K for **4**; powder XRD plot for complex **4**.

## Acknowledgments

This work was supported by the Ministry of Science Technology, China through a 973 Project (no. 2002CB613301) and the Fok Ying Tong Education Foundation.

[1] a) S. Ferlay, T. Mallah, R. Ouahès, P. Veillet, M. Verdaguer, *Nature* **1995**, *378*, 701–703; b) W. R. Entley, G. S. Girolami, *Science* **1995**, *268*, 397–400; c) S. M. Holmes, G. S. Girolami, *J. Am. Chem. Soc.* **1999**, *121*, 5593–5594; d) O. Hatlevik, W. E. Buschmann, J. L. Manson, J. S. Miller, *Adv. Mater.* **1999**, *11*, 914–918; e) H.-Z. Kou, S. Gao, J. Zhang, G.-H. Wen, G. Su, R. K. Zheng, X. X. Zhang, *J. Am. Chem. Soc.* **2001**, *123*, 11809–11810.

[2] a) M. Ohba, H. Ōkawa, *Coord. Chem. Rev.* **2000**, *198*, 313–328; b) K. Inoue, H. Imai, P. S. Ghalsasi, K. Kikuchi, M. Ohba, H. Okawa, J. V. Yakhmi, *Angew. Chem. Int. Ed.* **2001**, *40*, 4242–4245; c) T. Kashiwagi, S.-I. Ohkoshi, H. Seino, Y. Mizobe, K. Hashimoto, *J. Am. Chem. Soc.* **2004**, *126*, 5024–5025.

[3] a) T. E. Vos, J. S. Miller, *Angew. Chem. Int. Ed.* **2005**, *44*, 2416–2419; b) T. Glaser, M. Heidemeier, T. Weyhermüller, R.-D. Hoffmann, H. Rupp, P. Müller, *Angew. Chem. Int. Ed.* **2006**, *45*, 2416–2419.

[4] M. Verdaguer, A. Bleuzen, V. Marvaud, J. Vaissermann, M. Seuleiman, C. Desplanches, A. Scuiller, C. Train, R. Garde, G. Gelly, C. Lomenech, I. Rosenman, P. Veillet, C. Cartier, F. Villain, *Coord. Chem. Rev.* **1999**, *190–192*, 1023–1047.

[5] B. Sieklucka, R. Podgajny, T. Korzeniak, P. Przychodzeń, R. Kania, *C. R. Chimie* **2002**, *5*, 639–649.

[6] L. M. C. Beltran, J. R. Long, *Acc. Chem. Res.* **2005**, *38*, 325–334.

[7] R. Lescouëzec, L. Marilena Toma, J. Vaissermann, M. Verdaguer, F. S. Delgado, C. Ruiz-Pérez, F. Lloret, M. Julve, *Coord. Chem. Rev.* **2005**, *249*, 2691–2729.

[8] a) C. P. Berlinguette, D. Vaughn, C. Cañada-Vilalta, J. R. Galán-Mascarós, K. R. Dunbar, *Angew. Chem. Int. Ed.* **2003**, *42*, 1523–1526; b) Y. Song, P. Zhang, X.-M. Ren, X.-F. Shen, Y.-Z. Li, X.-Z. You, *J. Am. Chem. Soc.* **2005**, *127*, 3708–3709; c) E. J. Schelter, A. V. Prosvirin, K. R. Dunbar, *J. Am. Chem. Soc.* **2004**, *126*, 15004–15005; d) S. Wang, J.-L. Zuo, H.-C. Zhou, H. J. Choi, Y. Ke, J. R. Long, X.-Z. You, *Angew. Chem. Int. Ed.* **2004**, *43*, 5940–5943; e) D. F. Li, S. Parkin, G. Wang, G. T. Yee, A. V. Prosvirin, S. M. Holmes, *Inorg. Chem.* **2005**, *44*, 4903–4905; f) A. V. Palii, S. M. Ostrovsky, S. I. Klokishner, B. S. Tsukertlat, C. P. Berlinguette, K. R. Dunbar, J. R. Galán-Mascarós, *J. Am. Chem. Soc.* **2004**, *126*, 16860–16867.

[9] a) C. P. Berlinguette, A. Dragulescu-Andrasi, A. Sieber, H.-U. Güudel, C. Achim, K. R. Dunbar, *J. Am. Chem. Soc.* **2005**, *127*, 6766–6779; b) S. Bonhommeau, G. Molnár, A. Galet, A. Zwick, J.-A. Real, J. J. McGarvey, A. Bousseksou, *Angew. Chem. Int. Ed.* **2005**, *44*, 4069–4073; c) M. Nihei, M. Ui, M. Yokota, L. Han, A. Maeda, H. Kishida, H. Okamoto, H. Oshio, *Angew. Chem. Int. Ed.* **2005**, *44*, 6484–6487.

[10] a) O. Sato, T. Iyoda, A. Fujishima, K. Hashimoto, *Science* **1996**, *272*, 704–705; b) O. Sato, T. Kawakami, M. Kimura, S. Hishiya, S. Kubo, Y. Einaga, *J. Am. Chem. Soc.* **2004**, *126*, 13176–13177; c) V. Escax, G. Champion, M.-A. Arrio, M. Zacchigna, C. C. D. Moulin, A. Bleuzen, *Angew. Chem. Int. Ed.* **2005**, *44*, 4798–4801; d) T. Yamamoto, Y. Umemura, O. Sato, Y. Einaga, *J. Am. Chem. Soc.* **2005**, *127*, 16065–16073; e) J. G. Moore, E. J. Lochner, C. Ramsey, N. S. Dalal, A. E. Stiegman, *Angew. Chem. Int. Ed.* **2003**, *42*, 2741–2743.

[11] H. Miyasaka, H. Ieda, N. Matsumoto, N. Re, R. Crescenzi, C. Floriani, *Inorg. Chem.* **1998**, *37*, 255–263.

[12] H. Miyasaka, N. Matsumoto, H. Ōkawa, N. Re, E. Gallo, C. Floriani, *J. Am. Chem. Soc.* **1996**, *118*, 981–994.

[13] H. J. Choi, J. J. Sokol, J. R. Long, *Inorg. Chem.* **2004**, *43*, 1606–1608.

[14] H. Miyasaka, H. Takahashi, T. Madanbashi, K.-I. Sugiura, R. Clérac, H. Nojiri, *Inorg. Chem.* **2005**, *43*, 5969–5971.

[15] S.-F. Si, J.-K. Tang, Z.-Q. Liu, D.-Z. Liao, Z.-H. Jiang, S.-P. Yan, P. Cheng, *Inorg. Chem. Commun.* **2003**, *6*, 1109–1112.

[16] H. J. Choi, J. J. Sokol, J. R. Long, *J. Phys. Chem. Solids* **2004**, *65*, 839–844; T. Glaser, M. Heidemeier, T. Weyhermuller, R.-D. Hoffmann, H. Rupp, P. Muller, *Angew. Chem. Int. Ed.* **2006**, *45*, 6033–6037.

[17] X. Shen, B. Li, J. Zou, Z. Xu, Y. Yu, S. Liu, *Transition Met. Chem.* **2002**, *27*, 372–376.

[18] X. Shen, B. Li, J. Zou, H. Hu, Z. Xu, *J. Mol. Struct.* **2003**, *657*, 325–331.

[19] a) N. Re, E. Gallo, C. Floriani, H. Miyasaka, N. Matsumoto, *Inorg. Chem.* **1996**, *35*, 6004–6008; b) H.-R. Wen, C.-F. Wang, Y.-Z. Li, J.-L. Zuo, X.-Z. You, *Inorg. Chem.* **2006**, *45*, 7032–7034.

[20] M. Ferbinteanu, H. Miyasaka, W. Wernsdorfer, K. Nakata, K. Sugiura, M. Yamashita, C. Coulon, R. Clérac, *J. Am. Chem. Soc.* **2005**, *127*, 3090–3099.

[21] H. Miyasaka, H. Ieda, N. Matsumoto, K.-I. Sugiura, M. Yamashita, *Inorg. Chem.* **2003**, *42*, 3509–3515.

[22] H. Miyasaka, N. Matsumoto, N. Re, E. Gallo, C. Floriani, *Inorg. Chem.* **1997**, *36*, 670–676.

[23] H. Miyasaka, H. Okawa, A. Miyazaka, T. Enoki, *Inorg. Chem.* **1998**, *37*, 4878–4883.

[24] N. Matsumoto, Y. Sunatsuki, H. Miyasaka, Y. Hashimoto, D. Luneau, J.-P. Tuchagues, *Angew. Chem. Int. Ed.* **1999**, *38*, 171–173.

[25] Z.-H. Ni, H.-Z. Kou, L.-F. Zhang, C. Ge, A.-L. Cui, R.-J. Wang, Y. Li, O. Sato, *Angew. Chem. Int. Ed.* **2005**, *44*, 7742–7745.

[26] P. Przychodzeń, K. Lewinski, M. Balanda, R. Pełka, M. Rams, T. Wasiutynshi, C. Guyard-Duhayon, B. Sieklucka, *Inorg. Chem.* **2004**, *43*, 2967–2974.

[27] P. Przychodzeń, M. Rams, C. Guyard-Duhayon, B. Sieklucka, *Inorg. Chem. Commun.* **2005**, *8*, 350–354.

[28] H.-Z. Kou, Z.-H. Ni, B. C. Zhou, R.-J. Wang, *Inorg. Chem. Commun.* **2004**, *7*, 1150–1153.

[29] Y. Kim, S.-M. Park, S.-J. Kim, *Inorg. Chem. Commun.* **2002**, *5*, 592–595.

 © 2007 Wiley-VCH Verlag GmbH & Co. KGaA, Weinheim 

[30] M. Clemente-León, E. Coronado, J. R. Galán-Mascarós, C. J. Gómez-García, Th. Woike, J. M. Clemente-Juan, *Inorg. Chem.* **2001**, *40*, 87–94.
[31] a) E. Colacio, J. M. Dominguez-Vera, M. Ghazi, R. Kivekas, F. Lloret, J. M. Moreno, H. Stoeckli-Evans, *Chem. Commun.* **1999**, 987–988; b) E. Colacio, M. Ghazi, H. Stoeckli-Evans, F. Lloret, J.-M. Moreno, C. Perez, *Inorg. Chem.* **2001**, *40*, 4876–4883; c) Z. Shen, J.-L. Zuo, F.-N. Shi, Y. Xu, Y. Song, X.-Z. You, S. S. S. Raj, H. K. Fun, Z.-Y. Zhou, C. M. Che, *Transition Met. Chem.* **2001**, *26*, 345–350.
[32] H. Xiang, S. Gao, T. B. Lu, R. L. Luck, Z. W. Mao, X. M. Chen, L. N. Ji, *New J. Chem.* **2001**, *25*, 875–878.
[33] a) H.-Z. Kou, S. Gao, W.-M. Bu, D.-Z. Liao, B.-Q. Ma, Z.-H. Jiang, S.-P. Yan, Y.-G. Fan, G.-L. Wang, *J. Chem. Soc., Dalton Trans.* **1999**, 2477–2480; b) H.-Z. Kou, W.-M. Bu, S. Gao, D.-Z. Liao, Z.-H. Jiang, S.-P. Yan, Y.-G. Fan, G.-L. Wang, *J. Chem. Soc., Dalton Trans.* **2000**, 2996–2999.
[34] A. Marvilliers, S. Parsons, E. Riviere, J. P. Audiere, M. Kurmoo, T. Mallah, *Eur. J. Inorg. Chem.* **2001**, 1287–1293.
[35] H.-Z. Kou, S. Gao, O. Bai, Z.-M. Wang, *Inorg. Chem.* **2001**, *40*, 6287–6294.
[36] H. Miyasaka, R. Clerac, K. Mizushima, K.-i. Sugiura, M. Yamashita, W. Wernsdorfer, C. Coulon, *Inorg. Chem.* **2003**, *42*, 8203–8213.
[37] R. Lescouezec, J. Vaissermann, C. Ruiz-Perez, F. Lloret, R. Carrasco, M. Julve, M. Verdaguer, Y. Dromzee, D. Gatteschi, W. Wernsdorfer, *Angew. Chem. Int. Ed.* **2003**, *42*, 1483–1485.
[38] T.-F. Liu, D. Fu, S. Gao, Y.-Z. Zhang, H.-L. Sun, G. Su, Y.-J. Liu, *J. Am. Chem. Soc.* **2004**, *125*, 13976–13977.
[39] J. Kim, S. Han, K. I. Pokhodnya, J. M. Migliori, J. S. Miller, *Inorg. Chem.* **2005**, *44*, 6983–6988.
[40] H. Miyasaka, R. Clerac, T. Ishii, H.-C. Chang, S. Kitagawa, M. Yamashita, *J. Chem. Soc., Dalton Trans.* **2002**, 1528–1534.
[41] a) J. B. Goodenough, *Phys. Rev.* **1955**, *100*, 564–573; b) J. Kanamori, *J. Phys. Chem. Solids* **1959**, *10*, 87–98.
[42] H.-B. Zhou, W. Zhang, K. Yoshimura, Y. Ouyang, D.-Z. Liao, Z.-H. Jiang, S.-P. Yan, P. Cheng, *Chem. Commun.* **2005**, 4979–4981.
[43] An argument has been made to assign the oxidation state of Cr in $[Cr(CN)_5(NO)]^{3-}$ as +3: M. Ardon, S. Cohen, *Inorg. Chem.* **1993**, *32*, 3241–3243.

Received: October 13, 2006
Published Online: February 14, 2007

 © 2007 Wiley-VCH Verlag GmbH & Co. KGaA, Weinheim 

DOI: 10.1002/ejic.200600964

# *N*-(Aryl)picolinamide Complexes of Ruthenium: Usual Coordination and Strategic Cyclometalation

**Sumon Nag,[a] Ray J. Butcher,[b] and Samaresh Bhattacharya*[a]**

**Keywords:** Picolinamide ligands / Ruthenium complexes / Cyclometalation

Reaction of five *N*-(4-*R*-phenyl)picolinamides (R = $OCH_3$, $CH_3$, H, Cl, and $NO_2$) with $[Ru(PPh_3)_2(CO)_2Cl_2]$ in refluxing 2-methoxyethanol in the presence of a base ($NEt_3$) affords two geometrical isomers of a group of complexes (**1-R** and **2-R**), each of which contains an amide ligand coordinated to the metal center as a monoanionic bidentate *N*,*N* donor along with two triphenylphosphanes, a carbonyl, and a hydride. Similar reaction of *N*-(naphthyl)picolinamide with $[Ru(PPh_3)_2(CO)_2Cl_2]$ affords an organometallic complex, **3**, in which the amide ligand is coordinated to the metal center, by C–H activation of the naphthyl ring at the 8-position, as a dianionic tridentate *N*,*N*,*C* donor along with two triphenylphosphanes and one carbonyl. Structures of the **1-$OCH_3$**, **2-$CH_3$**, and **3** complexes have been determined by X-ray crystallography. In all the complexes the two triphenylphosphanes are *trans*. In the **1-R** complexes the hydride is *trans* to the pyridine nitrogen and in the **2-R** complexes it is *trans* to the amide-nitrogen. All the complexes are diamagnetic, and show characteristic $^1H$ NMR signals and intense MLCT transitions in the visible region. Cyclic voltammetry on all the complexes shows a $Ru^{II}$–$Ru^{III}$ oxidation within 0.71–0.93 V versus SCE. An oxidation and a reduction of the coordinated amide ligand are also observed within 1.29–1.69 V versus SCE and –1.02 to –1.21 V versus SCE respectively.

(© Wiley-VCH Verlag GmbH & Co. KGaA, 69451 Weinheim, Germany, 2007)

## Introduction

There has been considerable current interest in the chemistry of ruthenium complexes, largely because of their fascinating redox, photophysical, and photochemical properties.[1] As all these properties are directed primarily by the coordination environment around the metal center, complexation of ruthenium by ligands of selected types is of significant importance. In the present study, which has originated from our continued interest in the chemistry of ruthenium in different coordination environments,[2] we have selected a group of amide ligands (**$L^1$**) derived from picolinic acid and anilines with five different *para*-substituents in order to study their influence, if any, on the redox properties of the resulting ruthenium complexes.

Chemistry of the amide ligands is of particular interest with reference to their role in biological processes.[3] For example, the amide linkage plays a key role in the formation and maintenance of protein architectures, which are crucial for their performance in biological systems.[4] The selected amide ligands (**$L^1$**) are known to bind to metal ions either as neutral *N*,*O* donors (amide form, **I**) or as monoanionic *N*,*N* donors (amidate form, **II**) by loss of the amide pro-

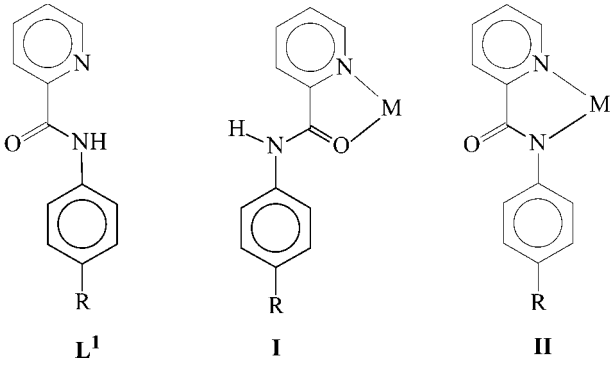


**$L^1$** **I** **II**

R = $OCH_3$, $CH_3$, H, Cl, $NO_2$

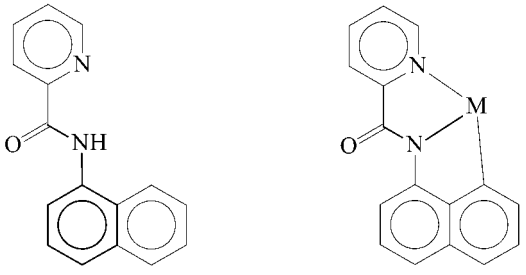


**$L^2$** **III**

[a] Department of Chemistry, Inorganic Chemistry Section, Jadavpur University,
Kolkata 700032, India
[b] Department of Chemistry, Howard University,
Washington, DC 20059, USA

Supporting information for this article is available on the WWW under http://www.eurjic.org or from the author.

 © 2007 Wiley-VCH Verlag GmbH & Co. KGaA, Weinheim 

ton.[5] Chelation in the amidate mode is known to stabilize metal ions in their high oxidation states, while that in the amide mode is reported to favor relatively lower oxidation states of a metal.[5] Interconversion between the amide (**I**) and amidate (**II**) modes of binding has been utilized to chemically manipulate redox properties of the metal center.[6] It may be mentioned here that though the chemistry of amide complexes of many transition metals has been extensively studied,[7] that of ruthenium appears to have received much less attention.[2j,8] As the source of ruthenium we have selected the $[Ru(PPh_3)_2(CO)_2Cl_2]$ complex, because of its demonstrated ability to accommodate bidentate ligands through displacement of carbonyl and chloride.[2f,2m] Reaction of the selected amides ($\mathbf{L^1}$) as well as a related ligand, viz. *N*-(naphthyl)picolinamide ($\mathbf{L^2}$), with $[Ru(PPh_3)_2(CO)_2Cl_2]$ has been found to afford interesting complexes where the amides ($\mathbf{L^1}$ and $\mathbf{L^2}$) are bound to ruthenium, as in **II** and **III** respectively. An account of the chemistry of all these complexes is presented in this report, with special reference to their formation, characterization, and spectral and electrochemical properties.

## Results and Discussion

Reactions of the *N*-(4-*R*-phenyl)picolinamides ($\mathbf{L^1}$) with $[Ru(PPh_3)_2(CO)_2Cl_2]$ proceed smoothly in refluxing 2-methoxyethanol in the presence of triethylamine. From each of these reactions two complexes were obtained, viz. a golden yellow complex and a yellow complex (**1-R** and **2-R**). The combined yield of these two complexes was reasonable.

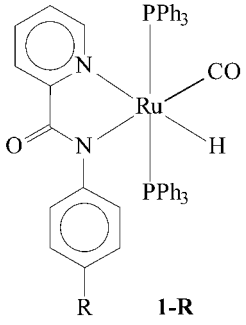


**1-R**

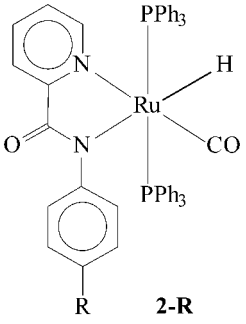


**2-R**

R = $OCH_3$, $CH_3$, H, Cl, $NO_2$

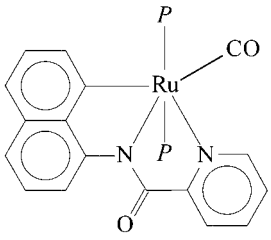


*P* = $PPh_3$

**3**

Preliminary (microanalytical, spectroscopic, magnetic, etc.) characterizations on these complexes (vide infra) indicate the presence of an amide ligand, two triphenylphosphanes, a carbonyl, and a hydride in the coordination sphere. In order to find the stereochemistries of these complexes as well as the coordination mode of the *N*-(4-*R*-phenyl)picolinamides in them, the structure of one representative complex from each family, viz. **1-$OCH_3$** and **2-$CH_3$**, has been determined by X-ray crystallography. The structure of the **1-$OCH_3$** is shown in Figure 1 and selected bond parameters are listed in Table 1.

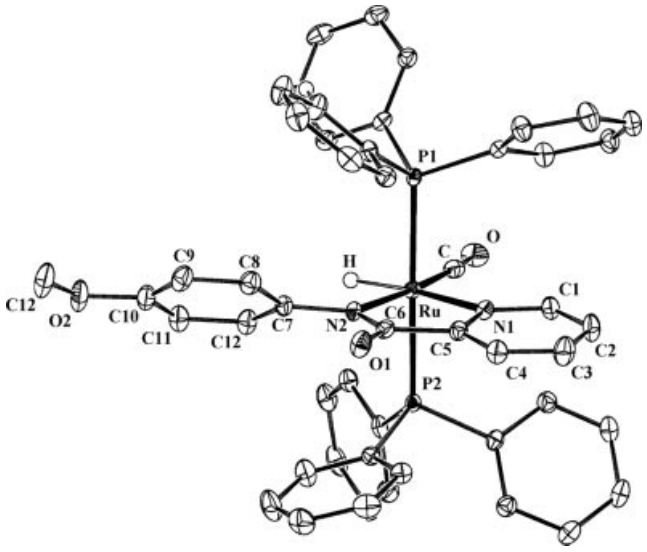


Figure 1. View of the **1-$OCH_3$** complex.

The structure shows that the *N*-(4-methoxyphenyl)picolinamide is coordinated to ruthenium, by dissociation of the acidic proton, as a monoanionic *N*,*N* donor (**II**). Two triphenylphosphanes, a hydride, and a carbonyl are also coordinated to the metal center. Ruthenium is therefore sitting in a $C_1H_1N_2P_2$ coordination environment, which is distorted octahedral in nature, as reflected in all the bond parameters around ruthenium. The coordinated picolinamide, hydride, and carbonyl constitute one equatorial plane with the metal at the center, where the hydride is *trans* to the pyridine nitrogen and the carbonyl is *trans* to the amide-nitrogen. The $PPh_3$ ligands occupy the remaining two axial positions and hence they are mutually *trans*. The observed Ru–P, Ru–C, and Ru–H distances are all quite normal,[9] and so are the bond lengths in the Ru(amide) fragment.[8b,8c] In the crystal lattice of the **1-$OCH_3$** complex, there are two water molecules present per molecule of the complex. In order to find out the link between these water molecules and the complex molecule, the packing pattern in the lattice has been scrutinized (Figure 2), which shows that a layer of water molecules lies in between two layers of complex molecules and thereby holds them together. A closer inspection into the network reveals that the methoxy-oxygen in each complex molecule is hydrogen-bonded to a phenyl hydrogen of a coordinated $PPh_3$ of an adjacent complex molecule and two such hydrogen bonds result in the formation of a dimeric unit. Four water molecules, which are interlinked by hydrogen bonds, bridge two such dimeric units by hydrogen bond formation involving the amide oxygen and a phenyl hydrogen of a $PPh_3$. These hydrogen-

 © 2007 Wiley-VCH Verlag GmbH & Co. KGaA, Weinheim 

Table 1. Selected bond lengths and bond angles for **1-OCH$_3$**, **2-CH$_3$**, and **3**.

| | | | |
|---|---|---|---|
| **1-OCH$_3$** | | | |
| Bond lengths [Å] | | | |
| Ru–C | 1.839(2) | C–O | 1.164(2) |
| Ru–N(2) | 2.1567(16) | N(2)–C(6) | 1.329(3) |
| Ru–N(1) | 2.1792(17) | C(5)–N(1) | 1.358(2) |
| Ru–H | 1.5475 | C(6)–O(1) | 1.253(2) |
| Ru–P(1) | 2.3636(5) | | |
| Ru–P(2) | 2.3689(5) | | |
| Bond angles [°] | | | |
| P(1)–Ru–P(2) | 178.495(17) | N(2)–Ru–N(1) | 76.50(6) |
| C–Ru–N(2) | 173.76(8) | Ru–C–O | 173.63(19) |
| N(1)–Ru–H | 168.3 | | |
| **2-CH$_3$** | | | |
| Bond lengths [Å] | | | |
| Ru–C | 1.844(3) | C–O | 1.162(3) |
| Ru–N(2) | 2.203(2) | N(2)–C(7) | 1.334(3) |
| Ru–N(1) | 2.152(2) | C(6)–N(1) | 1.352(3) |
| Ru–H | 1.58(3) | C(7)–O(1) | 1.249(3) |
| Ru–P(1) | 2.3687(7) | | |
| Ru–P(2) | 2.3569(7) | | |
| Bond angles [°] | | | |
| P(1)–Ru–P(2) | 172.61(2) | N(2)–Ru–N(1) | 75.46(8) |
| C–Ru–N(1) | 175.20(9) | Ru–C–O | 175.1(2) |
| N(2)–Ru–H | 170.2(9) | | |
| **3** | | | |
| Bond lengths [Å] | | | |
| Ru–C | 1.853(2) | C–O | 1.157(3) |
| Ru–N(1) | 2.1588(13) | N(2)–C(6) | 1.340(2) |
| Ru–N(2) | 2.0882(18) | C(5)–N(1) | 1.351(2) |
| Ru–C(15) | 2.0883(16) | C(6)–O(1) | 1.238(2) |
| Ru–P(1) | 2.3691(5) | | |
| Ru–P(2) | 2.3825(5) | | |
| Bond angles [°] | | | |
| P(1)–Ru–P(2) | 174.40(2) | N(1)–Ru–N(2) | 76.97(5) |
| N(2)–Ru–C | 176.48(8) | N(2)–Ru–C(15) | 80.31(6) |
| N(1)–Ru–C(15) | 157.04(6) | Ru–C–O | 176.57(17) |

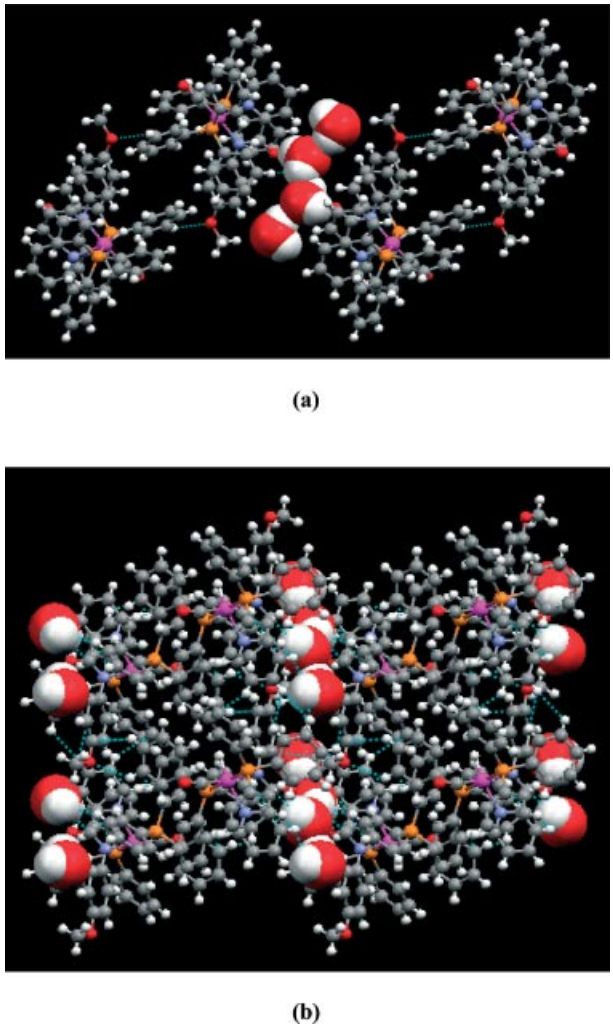


Figure 2. (a) Hydrogen bonding and (b) packing diagram (down the *b* axis) of the **1-OCH$_3$** complex.

bonding interactions in the crystal lattice appear to contribute a lot to its stability. As all the **1-R** complexes have been synthesized similarly and they show similar properties (vide infra), the other four **1-R** (R ≠ $OCH_3$) complexes are assumed to have a similar structure to the **1-OCH$_3$** complex.

The structure of the **2-CH$_3$** complex (Figure 3) shows that it is very similar to the **1-OCH$_3$** complex; the only differences are in the disposition of coordinated carbonyl and hydride with respect to the coordinated picolinamide. The hydride is *trans* to the amide-nitrogen and the carbonyl is *trans* to the pyridine nitrogen. All the bond parameters in this **2-CH$_3$** complex compare well with those observed in the **1-OCH$_3$** complex (Table 1). In the crystal lattice of **2-CH$_3$** there is one molecule of methanol per molecule of the complex. The packing pattern in the lattice shows (Figure S1, supporting information) that this methanol molecule is involved in three hydrogen-bonding interactions, two with the amide oxygen and a phenyl hydrogen of a $PPh_3$ of one

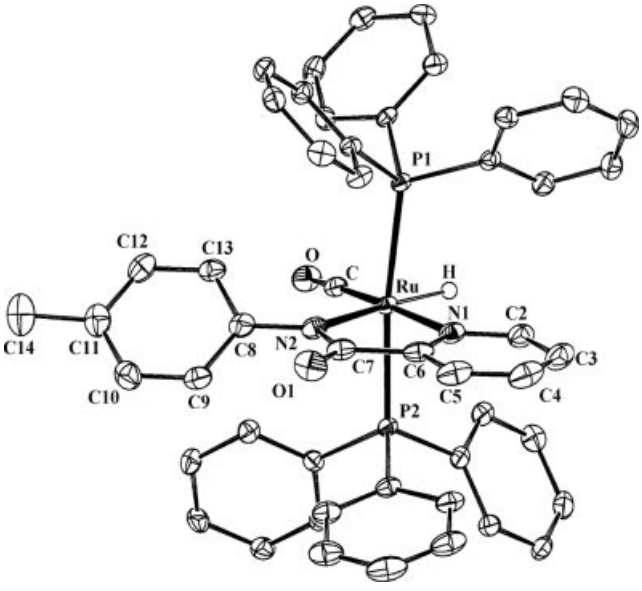


Figure 3. View of the **2-CH$_3$** complex.

 © 2007 Wiley-VCH Verlag GmbH & Co. KGaA, Weinheim 

complex molecule, and the third with the phenyl hydrogen of a $PPh_3$ of a second complex molecule. The methanol molecules thus bridge the individual complex molecules through hydrogen bonding. Based on the similarity in their synthesis and properties (vide infra), the other four **2-R** (R $\neq$ $CH_3$) complexes are assumed to have similar structures to **2-CH$_3$**. Each **2-R** complex is therefore a geometrical isomer of the corresponding **1-R** complex. The observed elemental (C, H, N) analytical data of the **1-R** and **2-R** complexes agree well with their compositions.

Formation of the two stereoisomers (**1-R** and **2-R**) from the same reaction may be rationalized in terms of Scheme 1. Upon reaction with $[Ru(PPh_3)_2(CO)_2Cl_2]$ the amide ligands (**L$^1$**) bind to the metal center, through dissociation of the acidic N-H proton, as monoanionic *N*,*N* donors with simultaneous dissociation of a CO and a chloride from the ruthenium starting complex to generate two stereoisomers (**A** and **B**) of an intermediate. These two stereoisomers, which are believed to remain in equilibrium, are probably formed by different kinetic routes. The Ru–Cl bond in these intermediates is then converted into a Ru–H bond under the prevailing reaction condition affording the **1-R** and **2-R** complexes respectively. Such conversion of a Ru–Cl bond into a Ru–H bond in alcoholic solvent in the presence of base is well documented in the literature.[10]

Disposition of the Ru–H bond with respect to the pendent phenyl ring in **1-R** points to the possibility of a C–H activation of the aryl ring. Such an activation could not take place in the **1-R** complexes, because in them the phenyl ring is not close enough to the metal center, and had the phenyl ring undergone an orthometalation it would have resulted in the formation of a sterically unstable four-membered metallacycle. In order to undergo C–H activation the aryl fragment should be so chosen that one of its C–H bonds should come in close proximity to the Ru–H bond. With this simple strategy in mind, *N*-(naphthyl)picolinamide (**L$^2$**) has been chosen as the target ligand for the C–H activation. Reaction of *N*-(naphthyl)picolinamide with $[Ru(PPh_3)_2(CO)_2Cl_2]$ has been carried out similarly as before, which has afforded an orange complex (**3**) in good yield. Preliminary characterizations on this complex indicate the presence of an amide ligand, two triphenylphosphanes, and a carbonyl in the coordination sphere, as well as the absence of any hydride. The identity of complex **3** has been revealed by its structure determination by X-ray crystallography. The structure (Figure 4) shows that *N*-(naphthyl)picolinamide is indeed coordinated to ruthenium in the expected *N*,*N*,*C* fashion (**III**). The Ru–C(naphthyl) bond is found to be normal[2m] and the other bond parameters compare well with those observed in the earlier structures (Table 1). The absence of any solvent of crystallization in the crystal lattice of complex **3** indicates the possible existence of some noncovalent interaction(s) between the individual complex molecules. A careful inspection of the packing pattern in the lattice shows that noncovalent interactions of two different types, viz. C–H···O and C–H···π interactions, are active in the lattice (Figure S2, Supporting Information). Two phenyl protons of two $PPh_3$ ligands belonging to two adjacent complex molecules are found to be hydrogen bonded to the π-cloud of two other phenyl rings of the same two $PPh_3$ ligands. However, this hydrogen-bonding interaction is directed to an edge of the phenyl ring in an $\eta^2$ fashion. The amide oxygen of a third complex molecule is also hydrogen-bonded to two phenyl hydrogen atoms of two $PPh_3$ ligands of the first two complex molecules. These C–H···O and C–H···π interactions are extended throughout the entire lattice of **3**. The noncovalent interactions, observed in all three crystals, play a key role in the packing of the molecules in the crystals, and it may be relevant to note here that such interactions are of significant importance in molecular recognition processes as well as in crystal engineering.[11]

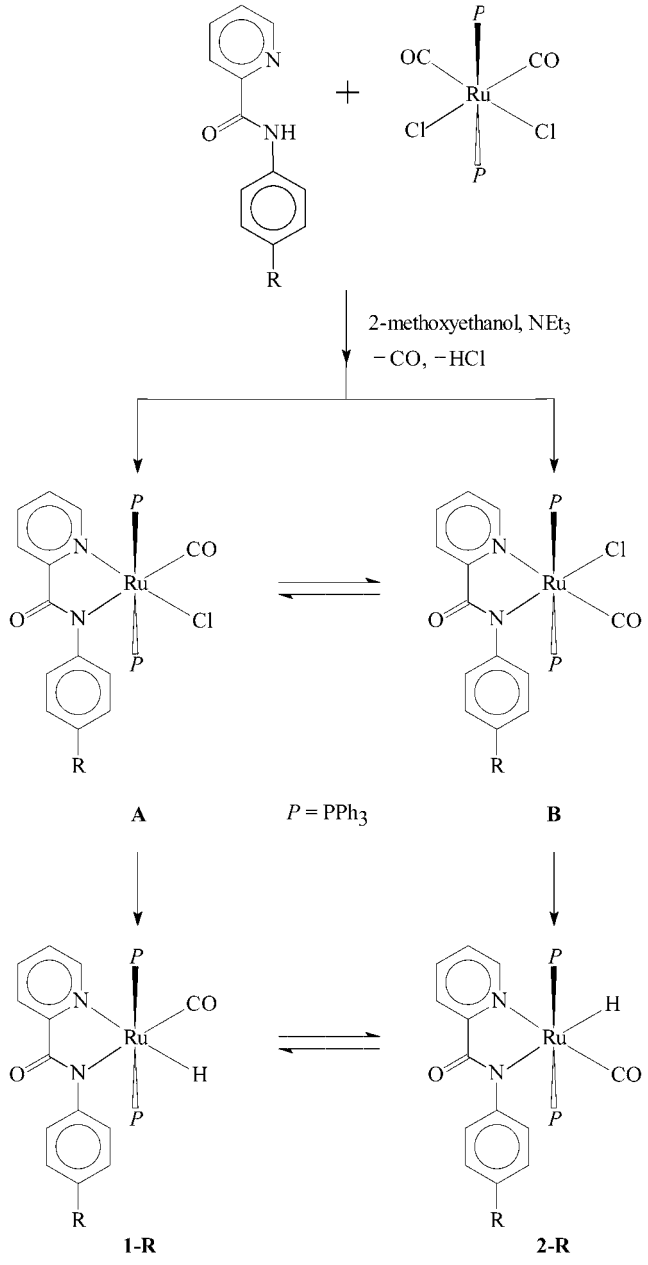


Scheme 1.

 © 2007 Wiley-VCH Verlag GmbH & Co. KGaA, Weinheim 

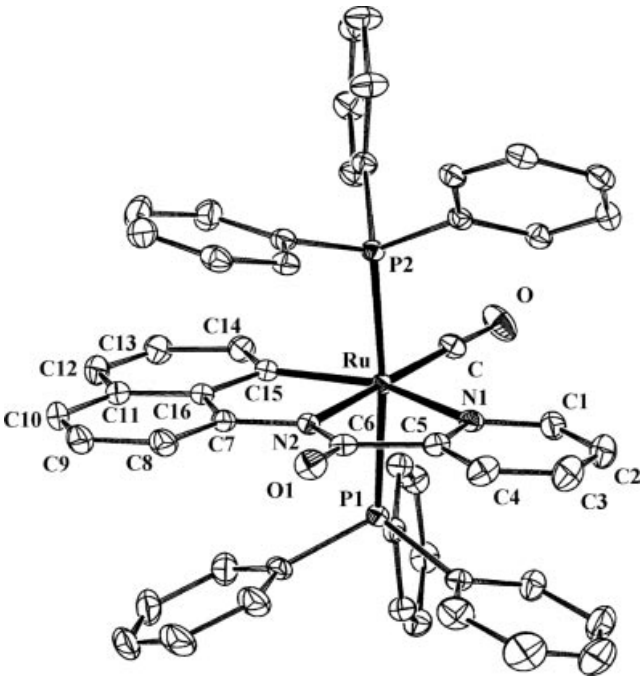


Figure 4. View of complex **3**.

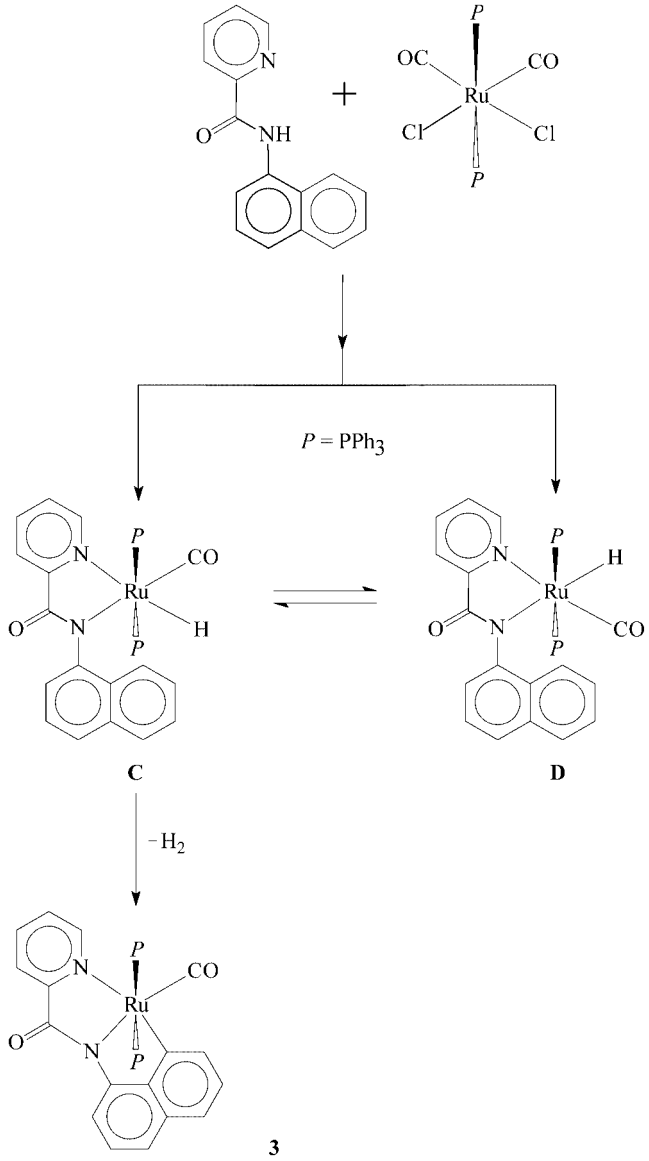


Scheme 2.

Probable sequences behind formation of the cyclometalated complex **3** are illustrated in Scheme 2. In the early stage of the synthetic reaction an equilibrium mixture of two stereoisomers (**C** and **D**) of a hydride intermediate (as shown in Scheme 1) are believed to be formed, in both of which ligand $\mathbf{L^2}$ is coordinated as a *N*,*N* donor. Isomer **C** of the intermediate then undergoes the C–H activation at the 8-position of the naphthyl ring affording the cyclometalated species **3** through elimination of molecular hydrogen.[12] As isomer **C** is irreversibly transformed into the cyclometalated species **3**, the equilibrium between the two isomers gradually shifts towards **C**, and thus only the cyclometalated species **3** is obtained as the sole product from this reaction and none of the two intermediates can be isolated.

Magnetic susceptibility measurements show that the **1-R**, **2-R**, and **3** complexes are diamagnetic, which corresponds to the +2 oxidation state of ruthenium (low-spin $d^6$, $S = 0$) in these complexes. $^1$H NMR spectra of the **1-R** complexes show broad signals within 7.1–7.7 ppm for the coordinated $PPh_3$ ligands. The hydride signal is observed as a distinct triplet, because of coupling with two magnetically equivalent phosphorus nuclei, near δ = –10.6 ppm. Most of the aromatic proton signals from the coordinated amide ligand are clearly observed in the expected region, while a few could not be detected because of their overlap with other signals in the same region. Signals for the methoxy and methyl groups in the **1-OCH$_3$** and **1-CH$_3$** complexes are observed respectively at $\delta$ = 3.67 and 2.11 ppm. In the $^1$H NMR spectra of the **2-R** complexes, the hydride signal (triplet) is observed at around δ = –12.1 ppm, and this significant shift in position, compared to the **1-R** complexes, has been useful as a diagnostic property in distinguishing this group of **2-R** complexes from their **1-R** isomers. Besides small shifts in the signal positions, the rest of the $^1$H NMR spectrum of each **2-R** complex is qualitatively similar to that of the corresponding **1-R** complex. It may be mentioned here that in $CDCl_3$ solution, each **1-R** (or **2-R**) complex is slowly and partially converted into the corresponding **2-R** (or **1-R**) isomer, which is easily recognized by the appearance of the characteristic hydride signal of the generated isomer. It may also be noted that conversion of **1-R** to **2-R** is relatively faster (takes about 6 d to reach equilibrium, where concentration ratio of **1-R** and **2-R** becomes approximately 2:1), while that of **2-R** to **1-R** is much slower (takes about 8 d to reach a concentration ratio of **1-R** and **2-R** of approximately 1:8). Except for the absence of the hydride signal and the presence of a few additional signals in the aromatic region, $^1$H NMR spectral features of complex **3** are similar to those of the **1-H** complex. $^{31}$P NMR spectra of all the **1-R** and **2-R** complexes show a single resonance

 © 2007 Wiley-VCH Verlag GmbH & Co. KGaA, Weinheim 

near 41.7 and 44.0 ppm respectively. In complex **3**, the $^{31}P$ signal is observed at $\delta$ = 31.42 ppm.

The infrared spectrum of each **1-R** complex shows many bands of different intensities in the 400–4000 $cm^{-1}$ region. Assignment of each individual band to a specific vibration has not been attempted. However, comparison with the spectra of the corresponding uncoordinated ligands shows that the N–H stretch, observed near 3140 $cm^{-1}$ in the uncoordinated ligands, is absent in the complexes. The amide C=O stretch, observed at around 1680 $cm^{-1}$ in the uncoordinated ligands, is also found to be shifted to around 1578 $cm^{-1}$ in the complexes. A strong band observed near 1900 $cm^{-1}$ in all the **1-R** complexes is due to the coordinated carbon monoxide, and three strong bands have been observed near 517, 692, and 746 $cm^{-1}$ in **1-R** complexes, indicating the presence of the coordinated $PPh_3$ ligands.[2m] Sharp bands are also observed near 1092, 1433, 1479, and 1557 $cm^{-1}$ in the **1-R** complexes, which are found to be absent in the spectrum of $[Ru(PPh_3)_2(CO)_2Cl_2]$, and hence these are attributed to the coordinated *N*-(aryl)picolinamide. Infrared spectra of the **2-R** and **3** complexes are similar to those of the **1-R** complexes. The $^1H$ NMR and IR spectroscopic data of the **1-R**, **2-R**, and **3** complexes are therefore consistent with their compositions.

The **1-R**, **2-R**, and **3** complexes are soluble in acetone, dichloromethane, chloroform, and so forth, producing bright yellow solutions. Electronic spectra of the complexes have been recorded in dichloromethane solution. All the complexes show several intense absorptions in the visible and ultraviolet regions (Table 2). The absorptions in the ultraviolet region are attributable to transitions within the ligand orbitals and those in the visible region are probably due to charge-transfer transitions. To have a better insight into the nature of the absorptions in the visible region, qualitative EHMO calculations have been performed[13] on computer-generated models of the complexes where phenyl rings of the triphenylphosphanes have been replaced by hydrogen. Partial MO diagrams of a selected **1-R** complex are shown in Figure 5 and those of a representative **2-R** and **3** complexes are deposited as supporting information (Figures S3 and S4). Compositions of selected molecular orbitals are given in Table S1 (supporting information). In the **1-R** complexes, the highest occupied molecular orbital (HOMO) and the next two filled orbitals (HOMO-1 and HOMO-2) have major contributions from the ruthenium $d_{xy}$, $d_{yz}$, and $d_{xz}$ orbitals.[14] These three occupied orbitals may therefore be regarded as the ruthenium $t_2$ orbitals. The lowest unoccupied molecular orbital (LUMO) has more than 90% contribution from the *N*-(aryl)picolinamide and is concentrated largely on the pyridine ring and the amido fragment. Among the next few vacant orbitals (LUMO+1, LUMO+2 etc.), LUMO+1 is primarily centered on the pyridine ring, while LUMO+2 is delocalized over both the pyridine ring and the pendent phenyl ring of the *N*-(aryl)picolinamide. The lowest energy absorption in the 392–420 nm region may therefore be assigned to the charge-transfer transition taking place from the highest filled ruthenium $t_2$ orbital (HOMO) to the vacant orbital delocalized over the *N*-(aryl)picolinamide (LUMO). The other intense absorptions in the visible region may be assigned to charge-transfer transitions from the ruthenium $t_2$ orbitals to the higher-energy vacant orbitals. The nature of the molecular orbitals in the **2-R** complexes is very similar to that in the **1-R** complexes, and the electronic spectral features of these two groups of complexes are also very similar. In complex **3**, however, the HOMO, HOMO-1, and HOMO-2 are found to have large contributions from the *N*-(naphthyl)picolinamide besides having significant contributions from the ruthenium $d_{xy}$, $d_{yz}$, and $d_{xz}$ orbitals. The LUMO of complex **3** is concentrated largely on the pyridine ring and the carbonamide functionality. The next two vacant orbitals (LUMO+1 and LUMO+2) are close in energy; LUMO+1 is primarily centered on the pyridine ring, while LUMO+2 is delocalized over both the naphthyl and pyridine ring of the *N*-(naphthyl)picolinamide. The absorption at 472 nm may therefore be assigned to a HOMO-to-LUMO charge-transfer transition and the other absorptions in the visible region to charge-transfer transitions from the filled orbitals to the higher-energy vacant orbitals.

Table 2. Electronic spectral and cyclic voltammetric data.

| | Electronic spectroscopic data[a] | Cyclic voltammetric data[b] | |
|---|---|---|---|
| | $\lambda_{max}$ [nm] ($\varepsilon$ [$M^{-1}cm^{-1}$]) | $E_{pa}$ [V] | $E_{pc}$ [V] |
| **1-$OCH_3$** | 230 (55300), 254[c] (32400), 348 (7800), 400 (3800) | 0.71, 1.29 | –1.19 |
| **1-$CH_3$** | 230 (34900), 254[c] (21600), 338 (5300), 396 (1800) | 0.77, 1.31 | –1.21 |
| **1-H** | 230 (35500), 254[c] (25300), 336 (6800), 392 (2500) | 0.80, 1.47 | –1.19 |
| **1-Cl** | 230 (32700), 256[c] (22800), 340 (7400), 394 (4100) | 0.83, 1.56 | –1.13 |
| **1-$NO_2$** | 230 (37800), 254[c] (25400), 322 (9400), 420 (1500) | 0.93, 1.69 | –1.12 |
| **2-$OCH_3$** | 230 (50300), 272[c] (19700), 354 (5600), 430 (2250) | 0.54, 1.26 | –1.05 |
| **2-$CH_3$** | 230 (95900), 272[c] (31250), 362 (7580), 432 (3000) | 0.55, 1.28 | –1.03 |
| **2-H** | 230 (47900), 274[c] (15100), 368 (3600), 424 (1700) | 0.60, 1.32 | –1.11 |
| **2-Cl** | 230 (36000), 274[c] (13480), 356 (3800), 440 (980) | 0.64, 1.35 | –1.10 |
| **2-$NO_2$** | 230 (15500), 278[c] (4800), 348 (3000), 448 (2600) | 0.69, 1.42 | –1.09 |
| **3** | 246 (28900), 348 (11800), 472 (2000) | 0.49, 1.34 | –1.02 |

[a] In dichloromethane. [b] Solvent: dichloromethane/acetonitrile, 1:9; supporting electrolyte, TBAP; reference electrode, SCE; $E_{pa}$ and $E_{pc}$ are anodic and cathodic peak potentials; scan rate, 50 $mV s^{-1}$. [c] Shoulder.

Electrochemical properties of the **1-R**, **2-R**, and **3** complexes have been studied by cyclic voltammetry in 1:9 dichloromethane/acetonitrile solution (0.1 M TBAP).[15] Each complex shows two anodic waves at positive potentials of the SCE reference electrode and a cathodic one at negative potential (Table 2). All the responses are irreversible in nature. In view of the composition of the HOMO, the first oxidation is assigned to $Ru^{II}$–$Ru^{III}$ oxidation. Simi-

 © 2007 Wiley-VCH Verlag GmbH & Co. KGaA, Weinheim 

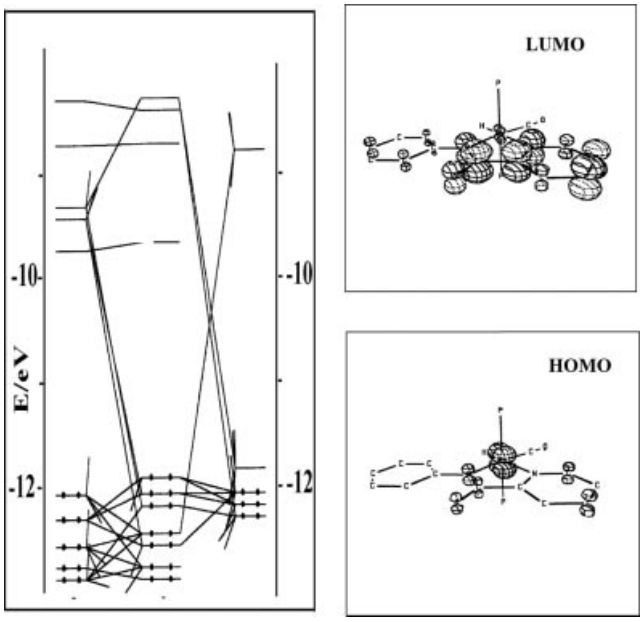


Figure 5. Partial molecular orbital diagram of the **1-H** complex.

larly based on composition of the LUMO, the reduction is assigned to reduction of the coordinated amide ligand. The second oxidation is attributed tentatively to oxidation of the coordinated amide ligand. Comparison of the potential of the $Ru^{II}$–$Ru^{III}$ couple in the **1-R** and **2-R** complexes shows that the bivalent state of ruthenium is much more stabilized in the former group of complexes, which may be attributed to the presence of carbonyl ligand *cis* to the pyridine nitrogen in the coordination sphere of ruthenium in the **1-R** complexes, favoring the back donation from the metal center to these two π-acidic ligands, rendering the ruthenium(II) state much more stable than the **2-R** complexes. In these **1-R** and **2-R** complexes, the potential of the $Ru^{II}$–$Ru^{III}$ oxidation has been observed to be sensitive to the nature of the substituent R in the *N*-(aryl)picolinamide. The potential ($E_{pa}$) increases with increasing electron-withdrawing character of the substituent R. The plots of $E_{pa}$ versus $\sigma$ [$\sigma$ = Hammett constant of R;[16] for $OCH_3$: –0.27, $CH_3$: –0.17, H: 0.00, Cl: 0.23, $NO_2$: 0.78] are linear for both the **1-R** and **2-R** complexes (see Figures S5 and S6 in the supporting information) with slopes ($\rho$) of 0.19 and 0.15 V ($\rho$ = reaction constant of this oxidation[17]) respectively. For both **1-R** and **2-R** complexes, the potential of the second oxidative response also shows linear correlation with the electron-withdrawing nature of substituent R (Figures S7 and S8, supporting information), with slopes ($\rho$) of 0.39 and 0.15 V, respectively. Potentials of the irreversible reductive response do not show any systematic variation with the nature of the substituent R.

## Conclusions

The present study shows that upon reaction with $[Ru(PPh_3)_2(CO)_2Cl_2]$ the *N*-(aryl)picolinamides (**$L^1$**) can bind to ruthenium as monoanionic *N*,*N*-donors by displacing a carbonyl and a chloride, as well as turning a Ru–Cl bond into a Ru–H bond. This study also demonstrates that the Ru–H bond can be utilized for inducing C–H activation of selective amides, such as *N*-(naphthyl)picolinamide. Utilization of the Ru–H bond for other useful reactions is currently under exploration.

## Experimental Section

**General Procedure:** Commercial ruthenium trichloride was purchased from Arora Matthey, Kolkata, India and was converted to $[Ru(PPh_3)_2(CO)_2Cl_2]$ by following a reported procedure.[18] The *N*-(aryl)picolinamides were prepared by condensing picolinic acid with *para*-substituted anilines or α-naphthylamine.[8a] Purification of dichloromethane and acetonitrile, and preparation of tetrabutylammonium perchlorate (TBAP) for electrochemical work were performed as reported in the literature.[19] All other chemicals and solvents were reagent grade commercial materials and were used as received. Microanalyses (C, H, N) were performed using a Heraeus Carlo Erba 1108 elemental analyzer. Magnetic susceptibilities were measured using a PAR 155 vibrating sample magnetometer fitted with a Walker scientific L75FBAL magnet. $^1$H NMR spectra were recorded in $CDCl_3$ solution with a Bruker Avance DPX 300 NMR spectrometer using TMS as the internal standard. IR spectra were obtained with a Shimadzu FTIR-8300 spectrometer with samples prepared as KBr pellets. Electronic spectra were recorded with a JASCO V-570 spectrophotometer. Electrochemical measurements were made using a CH Instruments model 600A electrochemical analyzer. A platinum disc working electrode, a platinum wire auxiliary electrode, and an aqueous saturated calomel reference electrode (SCE) were used in the cyclic voltammetry experiments. All electrochemical experiments were performed under dinitrogen. All electrochemical data were collected at 298 K and are uncorrected for junction potentials.

### Preparations of Complexes

The **1-R** and **2-R** complexes were obtained by following a general procedure. Specific details are given below for a particular pair of complexes.

**1-$OCH_3$ and 2-$OCH_3$:** *N*-(4-Methoxyphenyl)picolinamide (**$L^1$**, R = $OCH_3$) (30 mg, 0.13 mmol) was dissolved in warm 2-methoxyethanol (50 mL) and triethylamine (13 mg, 0.13 mmol) was added to it followed by $[Ru(PPh_3)_2(CO)_2Cl_2]$ (100 mg, 0.13 mmol). The mixture was refluxed for 24 h, whereby a yellow solution was obtained. Evaporation of this solution afforded a dark yellow solid, which was subjected to purification by thin layer chromatography on a silica plate. With 1:3 acetonitrile/benzene as the eluent, a distinct golden yellow band separated first followed by an orangish-yellow band, both of which were extracted separately with 1:3 dichloromethane/acetonitrile. Evaporation of these extracts respectively gave **1-$OCH_3$** as a crystalline golden yellow solid and **2-$OCH_3$** as a yellow crystalline solid.

**1-$OCH_3$:** Yield: 35 mg, 30%. $C_{50}H_{42}N_2O_3P_2Ru$ (881): calcd. C 68.10, H 4.76, N 3.17; found C 67.47, H 4.80, N 3.19. $^1$H NMR:[20] $\delta$ = –10.64 (t, $J$ = 19.5 Hz, 1 H); 3.67 ($OCH_3$); 6.20 (d, $J$ = 9.0 Hz, 2 H); 6.65 (t, $J$ = 5.7 Hz, 1 H); 6.84 (d, $J$ = 9.0 Hz, 2 H); 7.14–7.72 ($2PPh_3$+d)*; 7.92 (d, $J$ = 5.0 Hz, 1 H) ppm. $^{31}$P NMR: $\delta$ = 41.72 ppm. **1-$CH_3$:** Yield: 38 mg, 33%. $C_{50}H_{42}N_2O_2P_2Ru$ (865): calcd. C 69.36, H 4.85, N 3.23; found C 69.07, H 4.88, N 3.25. $^1$H NMR: $\delta$ = –10.59 (t, $J$ = 19.4 Hz, 1 H); 2.11 ($CH_3$); 6.41 (d, $J$ = 8.2 Hz, 2 H); 6.65 (t, $J$ = 6.2 Hz, 1 H); 6.73 (d, $J$ = 8.2 Hz, 2 H); 7.12–7.46 ($2PPh_3$); 7.69 (d, $J$ = 7.8 Hz, 1 H); 7.93 (d, $J$ = 5.0 Hz, 1 H) ppm.

 © 2007 Wiley-VCH Verlag GmbH & Co. KGaA, Weinheim 

$^{31}$P NMR: $\delta$ = 41.74 ppm. **1-H:** Yield: 34 mg, 30%. $C_{49}H_{40}N_2O_2P_2Ru$ (851): calcd. C 69.09, H 4.93, N 3.29; found C 68.67, H 4.92, N 3.26. $^1$H NMR: $\delta$ = –10.54 (t, $J$ = 19.4 Hz, 1 H); 6.60–6.68 (t + t + t, 3 H)*; 6.92 (d, $J$ = 6.1 Hz, 2 H); 7.13–7.49 (2PPh$_3$); 7.73 (d, $J$ = 7.8 Hz, 1 H); 7.92 (d, $J$ = 5.0 Hz, 1 H) ppm. $^{31}$P NMR: $\delta$ = 41.71 ppm. **1-Cl:** Yield: 38 mg, 32%. $C_{49}H_{39}ClN_2O_2P_2Ru$ (885.5): calcd. C 66.40, H 4.40, N 3.16; found C 66.07, H 4.46, N 3.14. $^1$H NMR: $\delta$ = –10.64 (t, $J$ = 19.4 Hz, 1 H); 6.54 (d, $J$ = 8.9 Hz, 2 H); 6.64 (t, $J$ = 6.1 Hz, 1 H); 6.87 (d, $J$ = 8.8 Hz, 2 H); 7.13–7.43 (2PPh$_3$); 7.731 (d, $J$ = 7.8 Hz, 1 H); 7.90 (d, $J$ = 5.0 Hz, 1 H) ppm. $^{31}$P NMR: $\delta$ = 41.72 ppm. **1-NO$_2$:** Yield: 40 mg, 34%. $C_{49}H_{39}N_3O_4P_2Ru$ (896): calcd. C 65.62, H 4.35, N 3.12; found C 65.30, H 4.30, N 3.14. $^1$H NMR: $\delta$ = –10.64 (t, $J$ = 19.4 Hz, 1 H); 6.72 (t, $J$ = 6.3 Hz, 1 H); 7.13–7.43 (2PPh$_3$); 7.48 (d, $J$ = 6.0 Hz, 2 H); 7.79 (d, $J$ = 7.8 Hz, 1 H), 7.95 (d, $J$ = 5.1 Hz, 1 H) ppm. $^{31}$P NMR: $\delta$ = 41.73 ppm.

**2-OCH$_3$:** Yield: 40 mg, 35%. $C_{50}H_{42}N_2O_3P_2Ru$ (881): calcd. C 68.10, H 4.76, N 3.17; found C 67.80, H 4.80, N 3.21. $^1$H NMR: $\delta$ = –12.16 (t, $J$ = 20.5 Hz, 1 H); 3.77 (OCH$_3$); 6.20 (t, $J$ = 6.4 Hz, 1 H); 6.46 (d, $J$ = 8.9 Hz, 2 H); 6.82 (d, $J$ = 8.9 Hz, 2 H); 7.10–7.40 (2PPh$_3$); 7.47 (d, $J$ = 5.3 Hz, 1 H); 7.62 (d, $J$ = 7.6 Hz, 1 H) ppm. $^{31}$P NMR: $\delta$ = 44.09 ppm. **2-CH$_3$:** Yield: 37 mg, 32%. $C_{50}H_{42}N_2O_2P_2Ru$ (865): calcd. C 69.36, H 4.85, N 3.23; found C 69.24, H 4.82, N 3.19. $^1$H NMR: $\delta$ = –12.05 (t, $J$ = 20.7 Hz, 1 H); 2.24 (CH$_3$); 6.21 (t, $J$ = 6.3 Hz, 1 H); 6.69 (d, $J$ = 8.1 Hz, 2 H); 6.78 (d, $J$ = 8.1 Hz, 2 H); 7.11–7.48 (2PPh$_3$); 7.48–7.70 (t + d + d, 3 H)* ppm. $^{31}$P NMR: $\delta$ = 44.04 ppm. **2-H:** Yield: 37 mg, 33%. $C_{49}H_{40}N_2O_2P_2Ru$ (851): calcd. C 69.09, H 4.93, N 3.29; found C 68.87, H 4.92, N 3.26. $^1$H NMR: $\delta$ = –12.09 (t, $J$ = 20.7 Hz, 1 H); 6.21 (t, $J$ = 6.2 Hz, 1 H); 6.85–6.89 (2d + 2t, 4 H)*; 7.11–7.48 (2PPh$_3$); 7.53–7.60 (t + d, 2 H)*; 7.69 (d, $J$ = 7.0 Hz, 1 H) ppm. $^{31}$P NMR: $\delta$ = 44.06 ppm. **2-Cl:** Yield: 40 mg, 34%. $C_{49}H_{39}ClN_2O_2P_2Ru$ (885.5): calcd. C 66.40, H 4.40, N 3.16; found C 66.17, H 4.35, N 3.12. $^1$H NMR: $\delta$ = –12.16 (t, $J$ = 20.5 Hz, 1 H); 6.20 (t, $J$ = 6.3 Hz, 1 H); 6.52–6.80 (d + d, 4 H)*; 7.11–7.63 (2PPh$_3$); 7.82 (d, $J$ = 5.1 Hz, 1 H) ppm. $^{31}$P NMR: $\delta$ = 44.10 ppm. **2-NO$_2$:** Yield: 40 mg, 34%. $C_{49}H_{39}N_3O_4P_2Ru$ (896): calcd. C 65.62, H 4.35, N 3.12; found C 65.38, H 4.31, N 3.11. $^1$H NMR: $\delta$ = –12.36 (t, $J$ = 20.1 Hz, 1 H); 6.24 (t, $J$ = 6.2 Hz, 1 H); 6.93 (d, $J$ = 9.0 Hz, 2 H); 7.11–7.36 (2PPh$_3$); 7.51 (d, $J$ = 8.1 Hz, 1 H); 7.66 (d, $J$ = 8.3 Hz, 1 H); 7.70 (d, $J$ = 9.3 Hz, 2 H) ppm. $^{31}$P NMR: $\delta$ = 44.14 ppm.

**3:** *N*-(1-Naphthyl)picolinamide (**L$^2$**) (32 mg, 0.13 mmol) was dissolved in warm 2-methoxyethanol (50 mL) and triethylamine (13 mg, 0.13 mmol) was added to it followed by [Ru(PPh$_3$)$_2$(CO)$_2$Cl$_2$] (100 mg, 0.13 mmol). The mixture was refluxed for 24 h, whereby a yellow solution was obtained. Evaporation of this solution afforded an orange solid, which was subjected to purification by thin layer chromatography on a silica plate. With 1:3 acetonitrile/benzene as the eluent, a distinct orange band separated, which was extracted with 1:3 dichloromethane/acetonitrile. Evaporation of this extract gave **3** as a crystalline orange solid. Yield: 84 mg, 70%. $C_{53}H_{40}N_2O_2P_2Ru$ (899): calcd. C 71.54, H 4.49, N 3.14; found C 72.23, H 4.46, N 3.11. $^1$H NMR: $\delta$ = 6.62 (t, $J$ = 6.2 Hz, 1 H); 6.76 (t, $J$ = 7.5 Hz, 1 H); 6.82–6.90 (t + 2d, 3 H)*, 6.99–7.15 (2PPh$_3$); 7.36 (t, $J$ = 7.8 Hz, 1 H); 7.48 (d, $J$ = 6.3 Hz, 1 H); 7.69 (d, $J$ = 7.9 Hz, 1 H), 8.05–8.07 (d + d, 2 H)* ppm. $^{31}$P NMR: $\delta$ = 31.42 ppm.

**X-ray Crystallography:** Single crystals of the **1-OCH$_3$** and **3** complexes were obtained by slow evaporation of acetonitrile solutions of the respective complexes. Single crystals of the **2-CH$_3$** complex were obtained by slow evaporation of a solution of the complex in a 1:1 mixture of methanol and dichloromethane. Selected crystal data and data collection parameters are given in Table 3. Data were collected on a Bruker CCD diffractometer using graphite-monochromated Mo-$K_\alpha$ radiation. X-ray data reduction, and structure solution and refinement were done using SHELXS-97 and SHELXL-97 programs.[21] The structures were solved by the direct methods.

CCDC-623582, -623583, and -623584 contain the supplementary crystallographic data for this paper. These data can be obtained free of charge from The Cambridge Crystallographic Data Centre via www.ccdc.cam.ac.uk/data_request/cif.

**Supporting Information** (see also the footnote on the first page of this article): Packing diagram showing hydrogen bonding in complexes **2-CH$_3$** (Figure S1) and **3** (Figure S2), partial molecular orbital diagrams of complexes **2-H** (Figure S3) and **3** (Figure S4), least-squares plots of $E_{pa}$ values of $Ru^{II}$–$Ru^{III}$ couple versus Ham-

Table 3. Crystallographic data for **1-OCH$_3$**, **2-CH$_3$** and **3**.

| | **1-OCH$_3$·2H$_2$O** | **2-CH$_3$·CH$_3$OH** | **3** |
|---|---|---|---|
| Empirical formula | $C_{50}H_{46}N_2O_5P_2Ru$ | $C_{51}H_{46}N_2O_3P_2Ru$ | $C_{53}H_{40}N_2O_2P_2Ru$ |
| Formula mass | 917.90 | 897.91 | 899.88 |
| Space group | triclinic, $P\bar{1}$ | monoclinic, $P2_1/c$ | monoclinic, $Cc$ |
| $a$ [Å] | 10.1885(10) | 19.958(3) | 11.6130(7) |
| $b$ [Å] | 13.7277(13) | 10.8273(18) | 22.0267(14) |
| $c$ [Å] | 15.0590(14) | 19.795(3) | 16.7471(11) |
| $\alpha$ [°] | 87.675(2) | 90 | 90 |
| $\beta$ [°] | 89.174(2) | 103.234(3) | 109.2660(10) |
| $\gamma$ [°] | 82.557(2) | 90 | 90 |
| $V$ [Å$^3$] | 2086.7(3) | 4164.1(12) | 4043.9(4) |
| $Z$ | 2 | 4 | 4 |
| $\lambda$ [Å] | 0.71073 | 0.71073 | 0.71073 |
| Crystal size [mm] | 0.66 × 0.45 × 0.15 | 0.44 × 0.35 × 0.15 | 0.17 × 0.36 × 0.67 |
| $T$ [K] | 293(2) | 293(2) | 103(2) |
| $\mu$ [mm$^{-1}$] | 0.505 | 0.501 | 0.514 |
| $R1$[a] | 0.0337 | 0.0372 | 0.0211 |
| $wR2$[b] | 0.0847 | 0.0880 | 0.0517 |
| Gof[c] | 1.029 | 1.022 | 1.039 |

[a] $R1 = \Sigma||F_o| - |F_c||/\Sigma|F_o|$. [b] $wR2 = [\Sigma\{w(F_o^2 - F_c^2)^2\}/\Sigma\{w(F_o^2)\}]^{1/2}$. [c] Gof = $\{\Sigma[w(F_o^2 - F_c^2)^2]/(M - N)\}^{1/2}$, where $M$ is the number of reflections and $N$ is the number of parameters refined.

 © 2007 Wiley-VCH Verlag GmbH & Co. KGaA, Weinheim 

mett substituent constant ($\sigma$) for the **1-R** and **2-R** complexes (Figure S5 and Figure S6), least-squares plots of $E_{pa}$ values of ligand-centered oxidation versus Hammett substituent constant ($\sigma$) for the **1-R** and **2-R** complexes (Figure S7 and Figure S8), composition of selected molecular orbitals for all the complexes (Table S1), and X-ray crystallographic data in CIF format.

## Acknowledgments

Financial assistance received from the Department of Science and Technology [Grant No. SR/S1/IC-15/2004] is gratefully acknowledged. S. N. thanks the Council of Scientific and Industrial Research, New Delhi, for his fellowship [Grant No. 9/96(401)2003-EMR-I].

[1] a) M. Turki, C. Daniel, *Coord. Chem. Rev.* **2001**, *216–217*, 31; b) V. Balzani, A. Juris, *Coord. Chem. Rev.* **2001**, *211*, 97; c) B.-Z. Shan, Q. Zhao, N. Goswami, D. M. Eichhom, D. P. Rillema, *Coord. Chem. Rev.* **2001**, *211*, 117; d) N. A. P. Kane-Maguire, J. F. Wheeler, *Coord. Chem. Rev.* **2001**, *211*, 145; e) L.-N. Ji, X.-H. Zou, J.-G. Liu, *Coord. Chem. Rev.* **2001**, *216–217*, 513; f) G. Simonneaux, P. Le Maux, *Coord. Chem. Rev.* **2002**, *228*, 43; g) H. Yersin, C. Kratzer, *Coord. Chem. Rev.* **2002**, *229*, 75; h) J. F. Endicott, H. B. Schlegel, M. J. Uddin, D. S. Seniveratne, *Coord. Chem. Rev.* **2002**, *229*, 95; i) S. I. Gorelsky, A. B. P. Lever, M. Ebadi, *Coord. Chem. Rev.* **2002**, *230*, 97; j) F. Hartl, M. P. Aarnts, H. A. Nieuwenhuis, J. van Slageren, *Coord. Chem. Rev.* **2002**, *230*, 106; k) C.-M. Che, J.-S. Huang, *Coord. Chem. Rev.* **2002**, *231*, 151; l) M. J. Clarke, *Coord. Chem. Rev.* **2002**, *232*, 69; m) E. Tfouni, M. Krieger, B. R. McGarvey, D. W. Franco, *Coord. Chem. Rev.* **2003**, *236*, 57; n) B. Serli, E. Zangrando, T. Gianferrara, L. Yellowless, E. Alessio, *Coord. Chem. Rev.* **2003**, *245*, 73; o) I. Ando, *Coord. Chem. Rev.* **2004**, *248*, 185; p) M. J. Clarke, *Coord. Chem. Rev.* **2003**, *236*, 209; q) M. A. S. Aquino, *Coord. Chem. Rev.* **2004**, *248*, 1025; r) R. F. Winter, S. Záli, *Coord. Chem. Rev.* **2004**, *248*, 1565; s) S. Rigaut, D. Touchard, P. H. Dixneuf, *Coord. Chem. Rev.* **2004**, *248*, 1585; t) M. K. Nazeeruddin, S. M. Zakeeruddin, J.-J. Lagref, P. Liska, P. Comte, C. Barolo, G. Viscardi, K. Schenk, M. Graetzel, *Coord. Chem. Rev.* **2004**, *248*, 1317; u) L. Spiccia, G. B. Deacon, C. M. Kepert, *Coord. Chem. Rev.* **2004**, *248*, 1329; v) Y. Saito, T. Azechi, T. Kitamura, Y. Hasegawa, Y. Wada, S. Yanagida, *Coord. Chem. Rev.* **2004**, *248*, 1469; w) Md. K. Nazeeruddin, C. Klein, P. Liska, M. Grätzel, *Coord. Chem. Rev.* **2005**, *249*, 1460.

[2] a) F. Basuli, S. M. Peng, S. Bhattacharya, *Inorg. Chem.* **1997**, *36*, 5645; b) F. Basuli, M. Ruf, C. G. Pierpont, S. Bhattacharya, *Inorg. Chem.* **1998**, *37*, 6113; c) A. K. Das, A. Rueda, L. R. Falvello, S. M. Peng, S. Bhattacharya, *Inorg. Chem.* **1999**, *38*, 4365; d) A. K. Das, S. M. Peng, S. Bhattacharya, *J. Chem. Soc., Dalton Trans.* **2000**, 181; e) F. Basuli, S. M. Peng, S. Bhattacharya, *Inorg. Chem.* **2000**, *39*, 1120; f) F. Basuli, S. M. Peng, S. Bhattacharya, *Inorg. Chem.* **2001**, *40*, 1126; g) I. Pal, F. Basuli, T. C. W. Mak, S. Bhattacharya, *Angew. Chem. Int. Ed.* **2001**, *40*, 2923; h) K. Majumder, R. J. Butcher, S. Bhattacharya, *Inorg. Chem.* **2002**, *41*, 4605; i) R. Acharyya, S. M. Peng, G. H. Lee, S. Bhattacharya, *Inorg. Chem.* **2003**, *42*, 7378; j) A. Das, S. M. Peng, G. H. Lee, S. Bhattacharya, *New. J. Chem.* **2004**, *28*, 712; k) S. Nag, P. Gupta, R. J. Butcher, S. Bhattacharya, *Inorg. Chem.* **2004**, *43*, 4814; l) P. K. Sinha, L. R. Falvello, S. Bhattacharya, *Indian J. Chem.* **2004**, *43A*, 1846; m) P. Gupta, S. Dutta, F. Basuli, S. M. Peng, G.-H. Lee, S. Bhattacharya, *Inorg. Chem.* **2006**, *45*, 460.

[3] a) P. Ford, D. E. P. Rudd, R. G. Gaunder, H. Taube, *J. Am. Chem. Soc.* **1968**, *90*, 1187; b) A. W. Zanella, P. C. Ford, *Inorg. Chem.* **1975**, *14*, 42; c) T. Matsubara, P. C. Ford, *Inorg. Chem.* **1976**, *15*, 1107; d) Y. Ilan, H. Taube, *Inorg. Chem.* **1983**, *22*, 1655; e) Y. Ilan, M. Kapon, *Inorg. Chem.* **1986**, *25*, 2350; f) H. Y. Huang, W. J. Chen, C. C. Yang, A. Yeh, *Inorg. Chem.* **1991**, *30*, 1862; g) M. H. Chou, C. Creutz, N. Sutin, *Inorg. Chem.* **1992**, *31*, 2318; h) M. H. Chou, B. S. Brunschwig, C. Creutz, N. Sutin, A. Yeh, R. C. Chang, C.-T. Lin, *Inorg. Chem.* **1992**, *31*, 5347; i) M. H. Chou, D. J. Szalda, C. Creutz, N. Sutin, *Inorg. Chem.* **1994**, *33*, 1674; j) S. M. Redmore, C. D. F. Rickard, S. J. Webb, L. J. Wright, *Inorg. Chem.* **1997**, *36*, 4743.

[4] B. Albert, D. Bray, J. Lewis, M. Raff, K. Roberts, J. D. Watson, *Molecular Biology of the Cell*, 3rd ed., Garland Publishing, New York, **1994**, ch. 3.

[5] a) H. Sigel, C. F. Naumann, B. Prijs, D. B. McCormick, M. C. Falk, *Inorg. Chem.* **1977**, *16*, 790; b) H. Sigel, *Inorg. Chem.* **1975**, *14*, 1535; c) M. F. El-Shazly, A. El-Dissowky, T. Salem, M. Osman, *Inorg. Chim. Acta* **1980**, *40*, 1; d) D. W. Margerum, *Pure Appl. Chem.* **1983**, *55*, 23; e) A. S. Borovik, T. M. Dewey, K. N. Raymond, *Inorg. Chem.* **1993**, *32*, 413; f) T. J. Collins, *Acc. Chem. Res.* **1994**, *27*, 279; g) M. J. Bartos, S. W. Gordon-Wylie, B. G. Fox, L. J. Wright, S. T. Weintraub, K. E. Kauffmann, E. Münck, K. L. Koskta, E. S. Uffelman, C. E. F. Rickard, K. R. Noon, T. J. Collins, *Coord. Chem. Rev.* **1998**, *174*, 361; h) A. White, X. Ding, J. C. vanderSpek, J. R. Murphy, D. Ringe, *Nature* **1998**, *394*, 502; i) E. Pohl, R. K. Holmes, W. G. J. Hol, *J. Mol. Biol.* **1999**, *292*, 653; j) B. M. Trost, C. B. Lee, *J. Am. Chem. Soc.* **2001**, *123*, 3671; k) M. D. Feese, B. P. Ingason, J. Goranson-Siekierke, R. K. Holmes, W. G. J. Hol, *J. Biol. Chem.* **2001**, *276*, 5959; l) T. J. Collins, *Acc. Chem. Res.* **2002**, *35*, 782; m) B. M. Trost, K. Dogra, I. Hachiya, T. Emura, D. L. Hughes, S. Krska, R. A. Reamer, M. Palucki, N. Yasuda, P. J. Reider, *Angew. Chem. Int. Ed.* **2002**, *41*, 1929; n) B. M. Trost, M. Crawley, *J. Am. Chem. Soc.* **2002**, *124*, 9328.

[6] T. Kojima, K. Hayashi, Y. Matsuda, *Inorg. Chem.* **2004**, *43*, 6793.

[7] a) H. Sigel, R. B. Martin, *Chem. Rev.* **1982**, *82*, 385; b) H. E. Bryndza, W. Tam, *Chem. Rev.* **1988**, *88*, 1163; c) K. Severin, R. Bergs, W. Beck, *Angew. Chem. Int. Ed.* **1998**, *37*, 1634; d) J. R. Fulton, A. W. Holland, D. J. Fox, R. G. Bergman, *Acc. Chem. Res.* **2002**, *35*, 44.

[8] a) S. Dutta, S. Pal, P. K. Bhattacharya, *Polyhedron* **1999**, *18*, 2157; b) S. Dutta, P. K. Bhattacharya, E. Horn, E. R. T. Tiekink, *Polyhedron* **2001**, *20*, 1815; c) S. Dutta, P. K. Bhattacharya, E. R. T. Tiekink, *Polyhedron* **2001**, *20*, 2027; d) A. K. Singh, V. Balamurugan, R. Mukherjee, *Inorg. Chem.* **2003**, *42*, 6497.

[9] a) F. Basuli, A. K. Das, G. Mostafa, S. M. Peng, S. Bhattacharya, *Polyhedron* **2000**, *19*, 1663; b) M. Menon, A. Pramanik, S. Chattopadhyay, N. Bag, A. Chakravorty, *Inorg. Chem.* **1995**, *34*, 1361; c) M. C. Barral, R. J. Aparicio, E. C. Royer, M. J. Saucedo, F. A. Urbanos, E. G. Puebla, C. R. Valero, *J. Chem. Soc., Dalton Trans.* **1991**, 1609.

[10] a) C. S. Yi, S. Y. Yun, I. A. Guzei, *Organometallics* **2004**, *23*, 5392; b) T. Li, R. Churlaud, A. J. Lough, K. Abdur-Rashid, R. H. Morris, *Organometallics* **2004**, *23*, 6239; c) R. Çelenligil-Çetin, L. A. Watson, C. Guo, B. M. Foxman, O. V. Ozerov, *Organometallics* **2005**, *24*, 186.

[11] a) S. K. Burley, G. A. Petsko, *Science* **1985**, *229*, 23; b) H. C. Weiss, D. Blaser, R. Boese, B. M. Doughan, M. M. Haley, *Chem. Commun.* **1997**, 1703; c) N. N. L. Madhavi, A. K. Katz, H. L. Carrell, A. Nangia, G. R. Desiraju, *Chem. Commun.* **1997**, 1953; d) S. K. Burley, G. A. Petsko, *Adv. Protein Chem.* **1988**, *39*, 125; e) M. Nishio, M. Hirota, Y. Umezawa, *The CH···π Interactions (Evidence, Nature and Consequences)*, Wiley-VCH, New York, **1998**; f) Y. Umezawa, S. Tsuboyama, K. Honda, J. Uzawa, M. Nishio, *Bull. Chem. Soc. Jpn.* **1998**, *71*, 1207; g) G. R. Desiraju, T. Steiner, *The Weak Hydrogen Bond (IUCr Monograph on Crystallography 9)*, Oxford Science Pub., USA, **1999**; h) M. J. Hannon, C. L. Painting, N. W. Alcock, *Chem. Commun.* **1999**, 2023; i) B. J. Mcnelis, L. C. Nathan, C. J. Clark, *J. Chem. Soc., Dalton Trans.* **1999**, 1831; j) K. Biradha, C. Seward, M. J. Zaworotko, *Angew. Chem. Int. Ed.* **1999**, *38*, 492; k) M. J. Calhorda, *Chem. Commun.* **2000**, 801; l) C. Janiak, S. Temizdemir, S. Dechert, *Inorg. Chem. Com-*

 © 2007 Wiley-VCH Verlag GmbH & Co. KGaA, Weinheim 

*mun.* **2000**, *3*, 271; m) C. Janiak, S. Temizdemir, S. Dechert, W. Deck, F. Girgsdies, J. Heinze, M. J. Kolm, T. G. Scarmann, O. M. Zipffel, *Eur. J. Inorg. Chem.* **2000**, 1229.
[12] The evolved hydrogen could not be detected experimentally.
[13] a) C. Mealli, D. M. Proserpio, *CACAO* Version 4.0, Italy, **1994**; b) C. Mealli, D. M. Proserpio, *J. Chem. Educ.* **1990**, *67*, 399.
[14] The HOMO of the **1-OCH$_3$** complex has little less contribution from ruthenium.
[15] A little dichloromethane was necessary to take the complex into solution. Addition of large excess of acetonitrile was necessary to record the redox responses in proper shape.
[16] L. P. Hammett, *Physical Organic Chemistry*, 2nd ed., McGraw Hill, New York, **1970**.
[17] R. N. Mukherjee, O. A. Rajan, A. Chakravorty, *Inorg. Chem.* **1982**, *21*, 785.
[18] N. Ahmad, S. D. Robinson, M. F. Uttley, *J. Chem. Soc., Dalton Trans.* **1972**, 843.
[19] a) D. T. Sawyer, J. L. Roberts Jr, *Experimental Electrochemistry for Chemists*, Wiley, New York, **1974**, pp. 167–215; b) M. Walter, L. Ramaley, *Anal. Chem.* **1973**, *45*, 165.
[20] Chemical shifts are given in ppm and multiplicity of the signals along with the associated coupling constants (*J* in Hz) are given in parentheses. Overlapping signals are marked with an asterisk.
[21] G. M. Sheldrick, *SHELXS-97* and *SHELXL-97*, Fortran programs for crystal structure solution and refinement, University of Göttingen, Göttingen, Germany, **1997**.

Received: October 13, 2006
Published Online: February 14, 2007

 © 2007 Wiley-VCH Verlag GmbH & Co. KGaA, Weinheim 

DOI: 10.1002/ejic.200600965

# A Theoretical Study of the Nearest Cu···Cu Antiferromagnetic Exchange Coupling Interactions in [$LaCu_6$] and [$YCu_6$]

**Yi-Quan Zhang*[a] and Cheng-Lin Luo[a]**

**Keywords:** Magnetic properties / Density functional calculations / Broken symmetry / Single-molecule studies

A density functional study of the exchange coupling interactions between the two nearest $Cu^{II}$ centers in [$LaCu_6$] and [$YCu_6$] is presented. Two approaches show that the Cu···Cu antiferromagnetic interactions increase with a decrease of the ionic radius of the diamagnetic central $La^{III}$ and $Y^{III}$ ions. However, the influence of the central ions on the Cu···Cu interactions is small compared to that of their structures according to our calculations. We therefore conclude that the stronger antiferromagnetic interactions between the two nearest $Cu^{II}$ centers in [$LaCu_6$] than in [$YCu_6$] are not a result of the central $La^{III}$ ion but the structure. The antiferromagnetic contributions of the direct overlap between the two nearest $Cu^{II}$ magnetic orbitals also play a major role according to the calculations of the overlap integral $S_{ij}$ based on Kahn's theory.

(© Wiley-VCH Verlag GmbH & Co. KGaA, 69451 Weinheim, Germany, 2007)

## Introduction

In recent years, the synthesis and study of single-molecule magnets with high total spin that can be used to store data has received much attention.[1–15] Among these single-molecule magnets, heteropolynuclear transition-metal and rare-earth mixed complexes are of great interest due to their interesting structures and magnetic properties.[14,15] In a recent experimental study, Liu et al.[10] considered that the substitution of the central $La^{III}$ ion with $Y^{III}$ will decrease the antiferromagnetic exchange coupling interactions between the two nearest $Cu^{II}$ ions in [$LaCu_6(\mu\text{-}OH)_3(HL)_2(L)_4$]($ClO_4$)$_2$·25$H_2O$[15] and [$YCu_6(\mu\text{-}OH)_3(HL)_2(L)_4$]($ClO_4$)$_2$·25$H_2O$[14] ($H_2L$ = iminodiacetic acid) clusters and that the direct overlap of Cu orbitals plays a minor role since this would enhance the antiferromagnetic coupling at shorter Cu···Cu separations. However, the above conclusions are not correct according to our calculations. Herein, we investigate the influence of the diamagnetic central ions $La^{III}$ and $Y^{III}$ and the effects of the direct overlap of Cu orbitals on the exchange coupling interactions between the two nearest $Cu^{II}$ ions in the clusters [$LaCu_6$] and [$YCu_6$] by density functional theory (DFT).

## Computational Methodology

### Description of the Complexes and Models

Complex **1-La**[15] [$LaCu_6(\mu\text{-}OH)_3(HL)_2(L)_4$] ($H_2L$ = iminodiacetic acid) contains two parallel layers, each of which is composed of three $Cu^{II}$ ions and three ligands. Six $Cu^{II}$ ions form a trigonal prism with the $La^{III}$ ion located in the center (see Figure 1). Each two nearest $Cu^{II}$ centers are connected by bridging hydroxides. The Cu–O–Cu angles are 120.7°. The nearest Cu···Cu distance is 3.383 Å and the La···Cu distance is 3.509 Å. The structure of model **1-Y** is the same as that of complex **1-La** except that its central ion is $Y^{III}$ not $La^{III}$. Complex **2-Y**[14] [$YCu_6(u\text{-}OH)_3(HL)_2(L)_4$] has a similar structure to that of **1-La** (see Figure 2). The Cu–O–Cu angles are 118.3°, the nearest Cu···Cu distance is 3.323 Å, and the Y···Cu distance is 3.447 Å. The structure of model **2-La** is the same as that of complex **2-Y** except

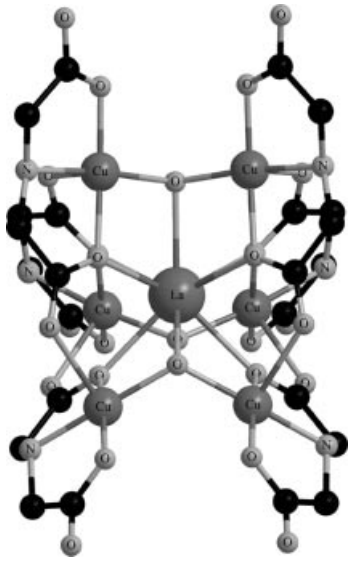

Figure 1. Structure of complex **1-La** ($LaCu_6$).

[a] School of Physical Science and Technology, Nanjing Normal University,
Nanjing 210097, China
E-mail: zhangyiquan@pine.njnu.edu.cn

 © 2007 Wiley-VCH Verlag GmbH & Co. KGaA, Weinheim 

that the central ion is $La^{III}$ not $Y^{III}$. In all the complexes and models, the six $Cu^{II}$ centers are symmetry equivalent. A thorough description of the above complexes can be found in the literature.[14,15] To be able to compare our calculated coupling constants for complete structures with the experimental values, we used the experimentally determined molecular structure rather than an optimized one in our calculations because small changes to the experimental structure could result in significant deviations of the coupling constant.

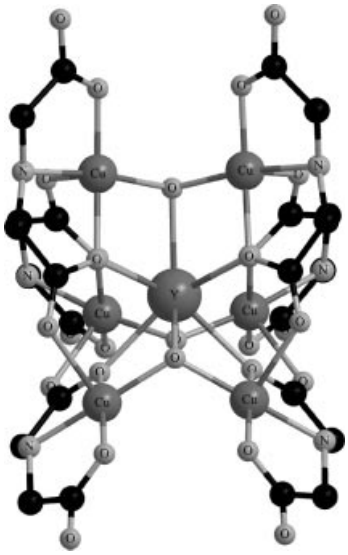

Figure 2. Structure of complex **2-Y** ($YCu_6$).

### Calculation of the Exchange Coupling Constants

There are two different approaches to calculate the exchange coupling constants for polynuclear complexes.[3–5] In all calculations, the spin-orbit coupling is not considered, so the magnetic anisotropy needs not be considered. The first approach consists of evaluating the exchange coupling constant, $J_{ij}$, between two paramagnetic metal centers *i* and *j* in the hexanuclear molecule by calculating the energy difference between the highest and broken-symmetry spin states of a model molecule in which the metal atoms, except for *i* and *j*, are substituted by diamagnetic $Zn^{II}$ cations. This approach has been used to calculate the exchange coupling interactions of hexanuclear complexes many times and has proven to give good results compared to the experimental ones.[3–5,16] The second approach is to calculate the different spin-state energies of hexanuclear complexes and use the Heisenberg Hamiltonian to obtain the exchange coupling constants between different metal centers.[3–5,16,17] This is a more rigorous approach for evaluating *J* for polynuclear complexes than the first one. How to use these two approaches will be discussed thoroughly below.

First of all we will discuss the first approach. The magnetic interactions between $Cu^{II}$ metal ions were studied on the basis of density functional theory (DFT) coupled with the broken-symmetry approach (BS).[18–20] The exchange coupling constants *J* were evaluated by calculating the energy difference between the high-spin state ($E_{HS}$) and the broken-symmetry state ($E_{BS}$) by assuming that the spin Hamiltonian is defined as shown in Equation (1).

$$\hat{H} = -2J\hat{S}_1\cdot\hat{S}_2 \quad (1)$$

If the spin-projected approach is used, the equation proposed by Noodleman[18–20] to extract the *J* value for a binuclear transition-metal complex becomes

$$J = \frac{E_{BS} - E_{HS}}{4S_1S_2} \quad (2)$$

For all the models, where $S_1 = 1/2$, $S_2 = 1/2$ for $Cu^{II}$, we derive Equation (3) from (2),

$$J = E_{BS} - E_{HS} \quad (3)$$

while with the non-projected approach[21]

$$2J = \frac{E_{BS} - E_{HS}}{2S_1S_2 + S_2} \quad (4)$$

where $S_1$ and $S_2$ are the total spins of the two interacting paramagnetic centers and $S_1$ is assumed to be greater than $S_2$ for heterodinuclear complexes.

For all the models, we derive Equation (5) from (4).

$$J = (E_{BS} - E_{HS})/2 \quad (5)$$

There are a lot of discussions as to whether Equation (4) can be used to calculate *J*.[21–27] Adamo and co-workers consider that Equation (4) corresponds strictly to the limit of complete overlap between the magnetic orbitals and such a hypothesis is not sustained,[22,23] although it can give good *J* results compared to experiment.[21,24,25] Ruiz and co-workers[26,27] think that the spin-projected approach [Equation (2)] introduces a double counting of the static correlation contributions due to the multi-determinant character of the broken symmetry solution obtained with the common functional that includes a self-interaction error. However, the non-projected approach [Equation (4)] can remove the self-interaction correction (SIC)[28] error and give better *J* values. A detailed discussion of the two approaches can be found in the literature.[21–27] In this paper, Equations (2) and (4) are both used to calculate the *J* values. The differences in the calculated *J* values using the two approaches will be discussed below.

Now we interpret the more rigorous second approach. If one neglects spin-orbit coupling effects, the Hamiltonian for a general extended structure is given by Equation (6).

$$\hat{H} = \sum_{i>j}(-2J_{ij}\hat{S}_i\hat{S}_j) \quad (6)$$

where $\hat{S}_i$ and $\hat{S}_j$ are the spin operators of the different paramagnetic centers and the $J_{ij}$ values are the coupling constants between all the paramagnetic centers. Here, we only consider the exchange interactions between nearest neighbors. This fact, together with the presence of additional symmetry elements in the structure, normally results in a reduced set of $J_{ij}$ values.

 © 2007 Wiley-VCH Verlag GmbH & Co. KGaA, Weinheim 

For complexes **1-La** and **2-Y**, 15 pair-wise coupling constants can in principle be calculated (see Figure 3), but these are reduced by symmetry to yield only three independent coupling constants for a symmetric structure:

$$J = J_{12} = J_{34} = J_{56};\ J' = J_{15} = J_{26} = J_{35} = J_{46} = J_{13} = J_{24};\ J'' = J_{16} = J_{25} = J_{36} = J_{45} = J_{14} = J_{23} \quad (7)$$

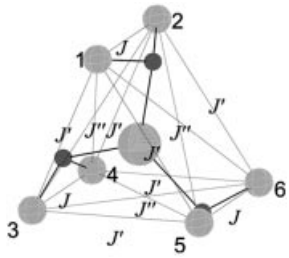


Figure 3. A sketch of the interactions between each $Cu^{II}$ center.

For the systems studied here, we only need to calculate four different spin configurations for each of the models **1-La**, **1-Y**, **2-Y**, and **2-La**, namely **A** ($S = 0$), **B** ($S = 0$), **C** ($S = 1$), and **F** ($S = 3$; see Figure 4). From the calculated relative energies of these spin configurations, we can extract exchange coupling constants by associating them to energy expressions obtained as a sum of pair-wise interactions, as introduced in the Heisenberg Hamiltonian. Given the energy differences between the four spin states, we can evaluate the exchange coupling constants *J*.

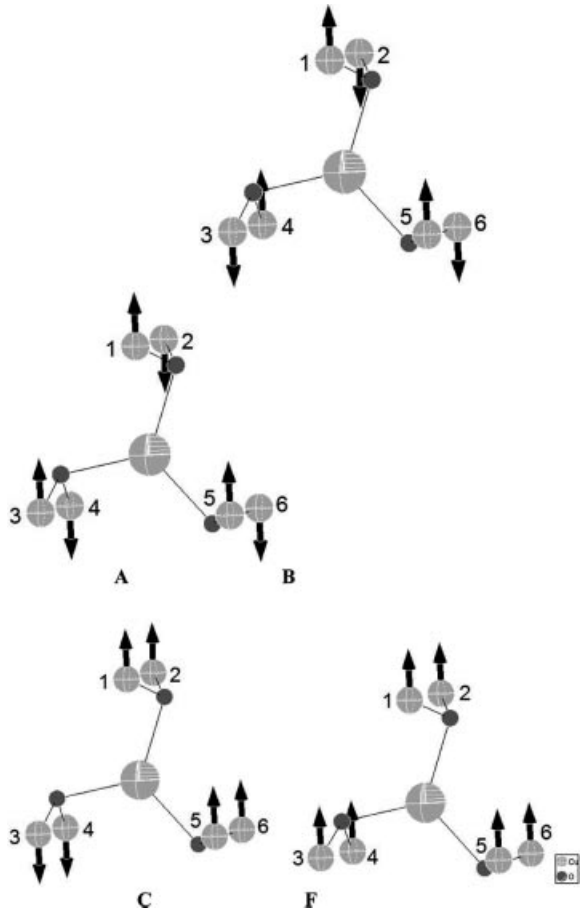


Figure 4. Four spin states: **A** ($S = 0$), **B** ($S = 0$), **C** ($S = 1$), and **F** ($S = 3$) for all the models.

$$E_A - E_F = 6J + 2(J' - J'') \quad (8)$$

$$E_A - E_B = 8(J' - J'') \quad (9)$$

$$J = \frac{(E_A - E_F)}{6} - \frac{(E_A - E_B)}{24} \quad (10)$$

Although the $J'$ and $J''$ values are very small and have no corresponding experimental equivalents, we also calculated these values using the second approach. The equations to extract $J'$ and $J''$ are:

$$J' = \frac{(E_C - E_F)}{4} + \frac{(E_A - E_B)}{16} \quad (11)$$

$$J'' = \frac{(E_C - E_F)}{4} - \frac{(E_A - E_B)}{16} \quad (12)$$

Density functional calculations were performed using the Amsterdam Density Functional (ADF, version 2004.01[29–31]) package for the four model clusters. Illas et al.[32] have shown the strong dependence of the calculated *J* with respect to the exchange-correlation functionals chosen, therefore several exchange-correlation functionals were used to evaluate *J*. In the calculations of *J* using ADF, the local density approximation (LDA) made use of the Vosko, Wilk, and Musair[33] (VWN) local correlation functional. A series of generalized gradient approximations (GGAs), namely the Perdew–Wang 1991 (PW91),[34] the Perdew–Burke–Ernzerhof (PBE),[35] and the recently developed OPTX-Perdew (OP86)[36,37] and OPTX-Perdew–Burke–Ernzerhof (OPBE)[35–37] functionals were examined. The tau-dependent meta-GGAs such as VSXC[38] and tau-HCTH[39] were also examined. For Cu and Zn, the TZV2P basis set (a basis set of triple-ξ quality[40] with two polarization functions) was applied. For La and Y, the TZV2P basis set (a basis set of triple-ξ quality[40] with one polarization function) was applied. The DZP basis set (a basis set of double-ξ quality[40] supplemented with one polarization function) was used for the other atoms (C, N, O and H). The inner core shells of C (1s), N (1s), O (1s), Cu (1s,2s,2p), Zn (1s,2s,2p), Y (1s,2s,2p,3s,3p,3d), and La (1s,2s,2p,3s,3p,3d,4s,4p,4d) were treated with the frozen core approximation. The accuracy parameter (accint) for the numerical integration grid was set to 4.0 for all complexes. The convergence standard of the system energy was set to be smaller than $10^{-6}$ eV in order to reach the precision required for the evaluation of *J*.

## Results and Discussion

### Evaluation of *J* for Each Model

The calculated and experimental values are shown in Table 1. The *J* values calculated using the first approach with Equation (2) for all the models show larger differences

 © 2007 Wiley-VCH Verlag GmbH & Co. KGaA, Weinheim 

with respect to the experimental values. However, there is a good improvement in the calculated ones obtained using Equation (4). The reason for this has been mentioned above. However, we obtain the same qualitative description of the magnetostructural correlations from the *J* values calculated using both Equation (2) and Equation (4). For models **1** (**1-La** and **1-Y**), the *J* values calculated using the two approaches with all the functionals are consistent with the experimental values. However, for models **2** (**2-Y** and **2-La**), the calculated *J* values using the first approach (BS-DFT) with all functionals except for the meta-GGA tau-HCTH show a large difference from the experimental values. In the BS-DFT approach we used $Zn^{II}$ to replace the $Cu^{II}$ to calculate the *J* values and did not consider the influence of the other $Cu^{II}$ center. This approximation is acceptable for models **1** because the *J′* and *J″* values are very small compared to *J*. However, the *J′* and *J″* values for models **2** are similar to that of *J* and so the influence of the other $Cu^{II}$ cannot be ignored. The BS-DFT approach therefore gives inaccurate *J* values for models **2**, although the second approach, which considers the influence of all the $Cu^{II}$ centers, gives better ones. The second approach is therefore a more rigorous one for evaluating Cu···Cu interactions irrespective of whether they are strong or weak, as we reported in our previous papers.[41,42]

For **1-La**, the *J* values calculated with the meta-GGA VSXC are the closest to the experimental value[15] (–12.0 $cm^{-1}$). However, the VSXC functional gives poor *J* values for **2-Y**. Although the first approach gives the opposite sign for complex **2-Y**, both approaches with all the functionals show that the antiferromagnetic interactions between the two nearest $Cu^{II}$ centers in complex **1-La** are stronger than those in complex **2-Y**, which is consistent with the experimental results. It can be seen that the calculated *J* values are qualitatively correct (indeed, some are in good agreement with the experimental ones) and empirically scale the *J* with respect to experiments.

In their studies, Liu et al.[14] considered that the strength of the antiferromagnetic interactions between the two nearest $Cu^{II}$ centers for the above two complexes is due to the central ions. They concluded that the stronger antiferromagnetic interactions in complex **1-La** are because its central ion is $La^{III}$, which has a greater ionic radius, and the direct overlap of metal orbitals plays a minor role. Whether the central ions have a dominant effect on the interactions between the two nearest $Cu^{II}$ ions will be discussed in the following section.

## Effects of the Central Ions on the Interactions Between the Two Nearest $Cu^{II}$ Ions

To investigate the effects of the central ions on the interactions between the two nearest $Cu^{II}$ ions, we replaced the $La^{III}$ in complex **1-La** with $Y^{III}$ to obtain the model **1-Y** and also substituted $Y^{III}$ with $La^{III}$ in complex **2-Y** to obtain the model **2-La**. From the calculated *J* values of **1-La** and **1-Y** (Table 1), we can see that substituting $La^{III}$ with $Y^{III}$ enhances the interactions between the two nearest $Cu^{II}$ centers, which is opposite to the conclusion reached by Liu et al.[14] From the calculated *J* values of **2-Y** and **2-La**, we find that replacing $Y^{III}$ with $La^{III}$ weakens the interactions, although the first approach with the GGAs PW91, PBE, OP86, and OPBE gives almost the same *J* values for **2-Y**

Table 1. Experimental *J* and calculated *J*, *J′*, and *J″* values [$cm^{-1}$] for models **1** (**1-La** and **1-Y**) and **2** (**2-La** and **2-Y**) obtained from the two approaches (one is the BS-DFT approach and the other approach is to obtain the $J_{ij}$ by calculating the energies of several pure spin states) with several LDA, GGA, and meta-GGA functionals.

| | **1-La** | | | | | **1-Y** | | | | |
|---|---|---|---|---|---|---|---|---|---|---|
| | Dinuclear model | | Full structure | | | Dinuclear model | | Full structure | | |
| | *J* [$cm^{-1}$] | | *J* [$cm^{-1}$] | *J′* [$cm^{-1}$] | *J″* [$cm^{-1}$] | *J*($cm^{-1}$) | | *J* [$cm^{-1}$] | *J′* [$cm^{-1}$] | J″ [$cm^{-1}$] |
| | Equation (2) | Equation (4) | | | | Equation (2) | Equation (4) | | | |
| VWN | –68.0 | –34.0 | –33.7 | 5.1 | 6.0 | –91.0 | –45.5 | –40.1 | 7.2 | 7.8 |
| PW91 | –49.2 | –24.6 | –22.5 | 6.1 | 8.3 | –65.4 | –32.7 | –26.8 | 6.9 | 8.9 |
| PBE | –49.2 | –24.6 | –22.4 | 6.4 | 8.4 | –65.2 | –32.6 | –26.7 | 7.0 | 9.0 |
| OP86 | –34.4 | –17.2 | –16.0 | 6.7 | 8.4 | –54.0 | –27.0 | –21.3 | 7.7 | 9.2 |
| OPBE | –33.4 | –16.7 | –15.2 | 7.3 | 9.0 | –53.0 | –26.5 | –20.1 | 8.2 | 9.8 |
| VSXC | –26.3 | –13.2 | –10.5 | 7.3 | 9.4 | –47.1 | –23.6 | –16.4 | 8.6 | 10.5 |
| tau-HCTH | –33.9 | –17.0 | –15.9 | 7.5 | 7.7 | –61.9 | –30.9 | –23.1 | 9.2 | 9.4 |
| Exp. | | | –12.0[11] | | | | | | | |
| | **2-Y** | | | | | **2-La** | | | | |
| | Dinuclear model | | Full structure | | | Dinuclear model | | Full structure | | |
| | *J* [$cm^{-1}$] | | *J* [$cm^{-1}$] | *J′* [$cm^{-1}$] | *J″* [$cm^{-1}$] | *J* [$cm^{-1}$] | | *J* [$cm^{-1}$] | *J′* [$cm^{-1}$] | *J″* [$cm^{-1}$] |
| | Equation (2) | Equation (4) | | | | Equation (2) | Equation (4) | | | |
| VWN | 15.0 | 7.5 | –12.3 | 3.0 | 0.4 | 23.6 | 11.8 | –6.8 | 2.9 | 0.7 |
| PW91 | 38.6 | 19.3 | –4.5 | 3.3 | 1.7 | 39.8 | 19.9 | –1.0 | 3.1 | 1.7 |
| PBE | 40.2 | 20.1 | –4.2 | 3.4 | 1.8 | 41.4 | 20.7 | –0.7 | 3.3 | 1.9 |
| OP86 | 32.8 | 16.4 | 1.8 | 5.8 | 4.3 | 33.8 | 16.9 | 5.5 | 5.6 | 5.0 |
| OPBE | 34.2 | 17.1 | 2.6 | 6.6 | 5.1 | 36.0 | 18.0 | 6.2 | 6.4 | 5.1 |
| VSXC | 67.2 | 33.6 | 9.4 | 7.1 | 5.4 | 66.6 | 33.3 | 13.9 | 7.0 | 5.7 |
| tau-HCTH | 1.2 | 0.6 | 2.6 | 10.4 | 8.4 | 7.4 | 3.7 | 8.3 | 10.2 | 8.5 |
| Exp. | | | –3.5[10] | | | | | | | |

 © 2007 Wiley-VCH Verlag GmbH & Co. KGaA, Weinheim 

and **2-La**. In conclusion, substituting $La^{III}$ with $Y^{III}$ enhances the antiferromagnetic interactions between the two nearest $Cu^{II}$ centers and these interactions in models **1** (**1-La** and **1-Y**) are always stronger than those in models **2** (**2-Y** and **2-La**), irrespective of whether the central ions are $La^{III}$ or $Y^{III}$. Moreover, we find that the central ions $La^{III}$ and $Y^{III}$ have only a very small influence on the values of $J'$ and $J''$ and can be ignored for models **1** (**1-La** and **1-Y**) and **2** (**2-Y** and **2-La**).

From the above results, we conclude that the antiferromagnetic Cu···Cu interactions increase with a decrease of the ionic radius of the diamagnetic central ion. Irrespective of whether the central ions are $La^{III}$ or $Y^{III}$, the nearest Cu···Cu interactions in models **1** (**1-La** and **1-Y**) are all stronger than those in models **2** (**2-Y** and **2-La**), therefore their structures have a larger influence on the nearest Cu···Cu interactions. In the next section we will investigate the effects of the structural parameters on the nearest Cu···Cu interactions.

### Effects of the Structural Parameters on the Interactions Between the Two Nearest $Cu^{II}$ Ions

The nearest Cu···Cu distance decreases from 3.383 to 3.323 Å, the Ln···Cu distance decreases from 3.509 to 3.447 Å, and the Cu···O···Cu angle decreases from 120.7° to 118.4° on going from complex **1-La** to complex **2-Y**. In a recent paper,[43] Ruiz et al. calculated the value of $J$ between $Cu^{II}$ with several different Cu···O···Cu angles and Cu···Cu distances and concluded that a decrease of the Cu···O···Cu angle weakens the antiferromagnetic Cu···Cu interactions when such angles are larger than about 100° in spite of the antiferromagnetic contributions due to the decrease of the Cu···Cu distance. We can see the same from Table 2, which only gives the results calculated using the PW91 functional, namely that the decrease of the Cu···O···Cu angle weakens the antiferromagnetic Cu···Cu interactions in spite of the decrease of the Cu···Cu distance when the diamagnetic central ions are $La^{III}$. The same results are also obtained using the other functionals. When the central ions are $Y^{III}$, we obtain the same trend. The above results can also be obtained from the book written by Kahn.[44] Therefore, we can see from the calculated and experimental results in Table 1 that the absolute $J$ values in models **1** (**1-La** and **1-Y**) are all larger than those in models **2** (**2-Y** and **2-La**).

From the calculated $J'$ and $J''$ values in Table 2, the weaker Cu···Cu ferromagnetic interactions in **2-La** appear to be due to its shorter Cu···Cu distances, which enhance the antiferromagnetic interactions and therefore decrease $J'$ and $J''$. The same results can also be found for **1-Y** and **2-Y**.

That the differences between the $J$ values calculated for **1-La** and **1-Y** or **2-Y** and **2-La** are small shows that the antiferromagnetic exchange interactions between the two nearest $Cu^{II}$ centers occur mostly through the nearest exchange pathway (Cu···O···Cu) and that the long exchange pathways via $Y^{III}$ or $La^{III}$ could possibly give rise to a weak antiferromagnetic component similar to the results reported in ref.[45]

Table 2. Dependence of $J_{ij}$ values between each two $Cu^{II}$ on $d$(Cu···Cu) and Cu···O···Cu for complexes **1-La** and **2-Y** using the second approach (this approach gives $J_{ij}$ by calculating the energies of several pure spin states) with the PW91 functional.

| | | $d$(Cu···Cu) [Å] | Cu···O···Cu [°] | $J_{ij}$ [$cm^{-1}$] |
|---|---|---|---|---|
| $J$ | **1-La** | 3.383 | 120.7 | –22.5 |
| | **2-La** | 3.323 | 118.3 | –1.0 |
| $J'$ | **1-La** | 5.326 | | 6.1 |
| | **2-La** | 5.230 | | 3.1 |
| $J''$ | **1-La** | 6.310 | | 8.3 |
| | **2-La** | 6.197 | | 1.7 |

### Qualitative Analysis of the Exchange Interaction

According to the Kahn–Briatt[46,47] (KB) and Hay–Thibeault–Hoffmann[48] (HTH) models, see Equations (13) and (14), respectively.

$$(\hat{H} = -2J\hat{S}_1\cdot\hat{S}_2)$$

$$J_{ab} = K_{ab} - S_{ab}(\Delta^2 - \delta^2)^{1/2} \quad (13)$$

$$J_{ab} = K_{ab} - \frac{(\varepsilon_1 - \varepsilon_2)^2}{2(J_{aa} - J_{ab})} \quad (14)$$

Some authors[49,50] have recently shown that magnetic orbitals **a** and **b** are well represented by the localized orbitals of the broken-symmetry solution (called the BS-OMSO[51]). As usual, the changes in the $J_{AF}$ term are more important and these contributions will usually control the magnetostructural correlations, especially those whose intramolecular interactions are antiferromagnetic. Hence, we have only considered the changes in the $J_{AF}$ term. The $J_{AF}$ term is associated with the overlap integral $S_{ab}$ in the broken-symmetry spin solution between the two $e_g$ magnetic orbitals ($d_{x^2-y^2}$) (KB model) or the square of the energy gap $(\varepsilon_1 - \varepsilon_2)^2$ in the high-spin solution between the orbitals bearing the unpaired electrons (HTH model). The $S_{ab}$ and $(\varepsilon_1 - \varepsilon_2)^2$ values calculated using the first approach with the PW91 functional are shown in Table 3, where it can be seen that the values for models **1-La** and **1-Y** are almost the same, but larger than those of models **2-La** and **2-Y**. The above results show that the different diamagnetic central ions essentially do not influence the overlap integrals $S_{ab}$ and the $(\varepsilon_1 - \varepsilon_2)^2$ values, although the structures of models **1** (**1-La** and **1-Y**) and **2** (**2-La** and **2-Y**) do have an influence on them. On going from the structures of models **1** to those of **2**, the Cu···O···Cu angles decrease from 120.7° to 118.4°. According to Kahn's investigations,[44] a decrease of the Cu···O···Cu angle will bring the magnetic orbitals closer to orthogonality and so the $S_{ab}$ values for models **1** are larger than those for **2**. The stronger antiferromagnetic interactions in models **1** corresponding to the larger $S_{ab}$ values show that the direct overlap between $Cu^{II}$ orbitals also plays a major role.

 © 2007 Wiley-VCH Verlag GmbH & Co. KGaA, Weinheim 

Table 3. Calculated $S_{ab}$ (a and b denote the magnetic orbitals occupied by the unpaired electrons on two $Cu^{II}$ centers in the broken-symmetry spin solutions), $(\varepsilon_1 - \varepsilon_2)^2$ ($eV^2$) ($\varepsilon_1$ and $\varepsilon_2$ denote the energies of the orbitals bearing the unpaired electrons in the high-spin solutions), and $-(\rho^2_{HS} - \rho^2_{BS})$ values for models **1** (**1-La** and **1-Y**) and **2** (**2-La** and **2-Y**) obtained using the first approach (BS-DFT) with the PW91 functional.

| | 1-La | 1-Y | 2-Y | 2-La |
|---|---|---|---|---|
| $S_{ab}$ | 0.021 | 0.023 | 0.008 | 0.008 |
| $(\varepsilon_1 - \varepsilon_2)^2$ [$eV^2$] | 0.6464 | 0.6544 | 0.1764 | 0.1789 |
| $\rho^2_{HS} - \rho^2_{BS}$ | 0.0092 | 0.0089 | 0.0027 | 0.0028 |

Blanchet-Boiteux and Mouesca[50,52] have proposed that the antiferromagnetic part of the exchange coupling constant in di-μ-oxo-bridged binuclear $Cu^{II}$ complexes can be split into two terms, one associated with the metal d orbitals, which is always positive, and the other representing the contribution of the bridging ligand. The second term can be related to the copper spin population through the analytical expression given in Equation (15), derived from a Mulliken population analysis.[53]

$$J \propto -(\rho^2_{HS} - \rho^2_{BS}) \quad (15)$$

Bi et al.[54] have found that the $J$ values are almost linearly related to $-(\rho^2_{HS} - \rho^2_{BS})$ for a series of oxamidocopper complexes. We have also used Equation (15) to evaluate binuclear $Mo^{III}$ complexes and also found that the $J$ values are almost linearly related to $-(\rho^2_{HS} - \rho^2_{BS})$.[55] The spin populations were obtained by PW91 calculations on the basis of a Mulliken population analysis[53] using the first approach. Due to the symmetry of the structures, we only give the results for one of the $Cu^{II}$ ions (Table 3). The stronger antiferromagnetic interactions in models **1** (**1-La** and **1-Y**), which correspond to larger $(\rho^2_{HS} - \rho^2_{BS})$ values, show that Equation (15) is also valid for the systems studied here, although it cannot differentiate the relative strengths of **1-La** and **1-Y** or **2-La** and **2-Y**.

## Conclusions

From the above calculations, we conclude that the strength of the nearest Cu···Cu antiferromagnetic interactions increase with a decrease of the ionic radius of the diamagnetic central ion. However, this influence of the central ion on the exchange coupling interactions is small compared to the influence of the variation of the Cu···O···Cu angle. The weaker Cu···Cu antiferromagnetic interactions in models **2** (**2-La** and **2-Y**) compared to those in models **1** (**1-La** and **1-Y**) are because of the smaller Cu···O···Cu angles corresponding to the smaller $S_{ab}$ and $(\varepsilon_1 - \varepsilon_2)^2$ values in models **2**. KB and HTH models have been used to demonstrate that the antiferromagnetic contributions of the direct overlap between the two nearest $Cu^{II}$ centers also plays a major role and that the influence of the diamagnetic central ion on the direct overlap can be ignored.

## Acknowledgments

This project was supported by the Natural Science Foundation of the University of Jiangsu Province, China (grant no. 05KJB150055) and the Natural Science Foundation of the Nanjing Normal University, China (grant no. 111080B142).

[1] O. Kahn, C. J. Martinez, *Science* **1998**, *279*, 44–48.
[2] R. Sessoli, D. Gatteschi, A. Caneschi, M. A. Novak, *Nature* **1993**, *365*, 141–143.
[3] E. Ruiz, J. Cano, S. Alvarez, A. Caneschi, D. Gatteschi, *J. Am. Chem. Soc.* **2003**, *125*, 6791–6794.
[4] E. Ruiz, A. Rodríguez-Fortea, P. Alemany, S. Alvarez, *Polyhedron* **2001**, *20*, 1323–1327.
[5] E. Ruiz, M. Llunell, P. Alemany, *J. Solid State Chem.* **2003**, *176*, 400–411.
[6] Y. Q. Zhang, C. L. Luo, Z. Yu, *New J. Chem.* **2005**, *29*, 1285–1290.
[7] Y. Q. Zhang, C. L. Luo, Z. Yu, *Int. J. Modern Phys. B* **2005**, *15–17*, 2538–2543.
[8] Y. Q. Zhang, C. L. Luo, *Int. J. Quantum Chem.* **2006**, *106*, 1551–1560.
[9] H. J. Choi, J. J. Sokol, J. R. Long, *J. Phys. Chem. Solids* **2004**, *65*, 839–844.
[10] X. Shen, B. Li, J. Zou, Z. Xu, *Transition Met. Chem.* **2002**, *27*, 372–376.
[11] J. J. Sokol, A. G. Hee, J. R. Long, *J. Am. Chem. Soc.* **2002**, *124*, 7656–7657.
[12] J. L. Heinrich, J. J. Sokol, A. G. Hee, J. R. Long, *J. Solid State Chem.* **2001**, *159*, 293–301.
[13] M. P. Shores, J. J. Sokol, J. R. Long, *J. Am. Chem. Soc.* **2002**, *124*, 2279–2292.
[14] Q. D. Liu, J. R. Li, S. Gao, B. Q. Ma, H. Z. Kou, O. Y. Liang, R. L. Huang, X. X. Zhang, K. B. Yu, *Eur. J. Inorg. Chem.* **2003**, 731–736.
[15] Q. D. Liu, S. Gao, J. R. Li, Q. Z. Zhou, K. B. Yu, B. Q. Ma, S. W. Zhang, X. X. Zhang, T. Z. Jin, *Inorg. Chem.* **2000**, *39*, 2488–2492.
[16] E. Ruiz, A. Rodríguez-Fortea, J. Cano, S. Alvarez, P. Alemany, *J. Comput. Chem.* **2003**, *24*, 982–989.
[17] O. Kahn, *Molecular Magnetism*, VCH Publishers, New York, **1993**, pp. 211–236.
[18] L. Noodleman, *J. Chem. Phys.* **1981**, *74*, 5737–5743.
[19] L. Noodleman, E. J. Baerends, *J. Am. Chem. Soc.* **1984**, *106*, 2316–2327.
[20] L. Noodleman, D. A. Case, *Adv. Inorg. Chem.* **1992**, *38*, 423–432.
[21] E. Ruiz, J. Cano, S. Awarez, P. Alemany, *J. Comput. Chem.* **1999**, *20*, 1391–1400.
[22] R. Caballol, O. Castell, F. Illas, I. de P. R. Moreira, J. P. Malrieu, *J. Phys. Chem. A* **1997**, *101*, 7860–7866.
[23] C. Adamo, V. Barone, A. Bencini, R. Broer, M. Filatov, N. M. Harrison, F. Illas, J. P. Malrieu, I. de P. R. Moreira, *J. Chem. Phys.* **2006**, *124*, 107101.
[24] E. Ruiz, P. Alemany, S. Alvarez, J. Cano, *Inorg. Chem.* **1997**, *36*, 3683–3688.
[25] A. Rodríguez-Fortea, P. Alemany, S. Alvarez, E. Ruiz, *Chem. Eur. J.* **2001**, *7*, 627–637.
[26] E. Ruiz, S. Alvarez, J. Cano, V. Polo, *J. Chem. Phys.* **2005**, *123*, 164110.
[27] E. Ruiz, J. Cano, S. Alvarez, V. Polo, *J. Chem. Phys.* **2006**, *124*, 107102.
[28] V. Polo, J. Gräfenstein, E. Kraka, D. Cremer, *Theor. Chem. Acc.* **2003**, *109*, 22–35.
[29] G. te Velde, F. M. Bickelhaupt, E. J. Baerends, C. Fonseca Guerra, S. J. A. van Gisbergen, J. G. Snijders, T. Ziegler, *J. Comput. Chem.* **2001**, *22*, 931–967.
[30] C. Fonseca Guerra, G. J. Snijders, G. te Velde, E. J. Baerends, *Theor. Chem. Acc.* **1998**, *99*, 391–403.

 © 2007 Wiley-VCH Verlag GmbH & Co. KGaA, Weinheim 

[31] ADF2004.01, SCM, Theoretical Chemistry, Vrije Universiteit, Amsterdam, The Netherlands, http://www.scm.com.
[32] F. Illas, I. de P. R. Moreira, J. M. Bofill, M. Filatov, *Phys. Rev. B* **2004**, *70*, 132414.
[33] S. H. Vosko, L. Wilk, M. Nusair, *Can. J. Phys.* **1980**, *58*, 1200.
[34] J. P. Perdew, J. A. Chevary, S. H. Vosko, K. A. Jackson, M. R. Pederson, D. J. Singh, C. Fiolhais, *Phys. Rev. B* **1992**, *46*, 6671–6687.
[35] J. P. Perdew, K. Burke, M. Ernzerhof, *Phys. Rev. Lett.* **1996**, *77*, 3865–3868.
[36] N. C. Handy, A. J. Cohen, *Mol. Phys.* **2001**, *99*, 403–412.
[37] J. P. Perdew, *Phys. Rev. B* **1986**, *33*, 8822–8824.
[38] T. van Voorhis, G. E. Scuseria, *J. Chem. Phys.* **1998**, *109*, 400–410.
[39] A. D. Boese, N. C. Handy, *J. Chem. Phys.* **2002**, *116*, 9559–9569.
[40] A. Schaefer, C. Huber, R. Ahlrichs, *J. Chem. Phys.* **1994**, *100*, 5829–5835.
[41] Y. Q. Zhang, C. L. Luo, *J. Phys. Chem. A* **2006**, *110*, 5096–5101.
[42] Y. Q. Zhang, C. L. Luo, *Eur. J. Inorg. Chem.* **2006**, 2292–2298.
[43] E. Ruiz, M. Llunell, J. Cano, P. Rabu, M. Drillon, C. Massobrio, *J. Phys. Chem. B* **2006**, *110*, 115–118.
[44] See ref. 17, pp. 159–163.
[45] Z. Q. Xu, L. K. Thompson, D. O. Miller, E. Ruiz, S. Alvarez, *Inorg. Chem.* **2003**, *42*, 1107–1111.
[46] O. Kahn, B. J. Briat, *J. Chem. Soc., Faraday Trans.* **1976**, *72*, 268–281.
[47] J. J. Girerd, Y. Journaux, O. Kahn, *Chem. Phys. Lett.* **1981**, *82*, 534–538.
[48] P. J. Hay, J. C. Thibeault, R. Hoffmann, *J. Am. Chem. Soc.* **1975**, *97*, 4884–4899.
[49] F. Fabrizi de Biani, E. Ruiz, J. Cano, J. J. Novoa, S. Alvarez, *Inorg. Chem.* **2000**, *39*, 3221–3229.
[50] C. Blanchet-Boiteux, J. M. Mouesca, *Theor. Chem. Acc.* **2000**, *104*, 257–264.
[51] C. Desplanches, E. Ruiz, A. Rodríguez-Fortea, *J. Am. Chem. Soc.* **2002**, *124*, 5197–5205.
[52] C. Blanchet-Boiteux, J. M. Mouesca, *J. Phys. Chem. A* **2000**, *104*, 2091–2097.
[53] A. Szabo, N. S. Ostlund, *Modern Quantum Chemistry*, McGraw-Hill, New York, **1989**.
[54] S. W. Bi, C. B. Liu, H. Q. Hu, *J. Phys. Chem. B* **2002**, *106*, 10786–10792.
[55] Y. Q. Zhang, C. L. Luo, Z. Yu, *Int. J. Quantum Chem.* **2005**, *102*, 165–173.

Received: October 13, 2006
Published Online: February 14, 2007

 © 2007 Wiley-VCH Verlag GmbH & Co. KGaA, Weinheim 

DOI: 10.1002/ejic.200601017

# Keggin POMs Modified by Bonding to Multitrack Cu(bipy) Chains through Linearly Arrayed Terminal and Bridging Oxygen Atoms of the $M_3O_{13}$ Triad

**Jingquan Sha,[a,b] Jun Peng,*[a] Hongsheng Liu,[a] Jing Chen,[a] Baoxia Dong,[a] Aixiang Tian,[a] and Zhongmin Su[a]**

**Keywords:** Polyoxometalates / N ligands / Copper / Organic–inorganic hybrids

Two novel complexes based on the Keggin POMs modified by the Cu(4,4′-bipy) moiety, $\{[Cu(4,4'\text{-bipy})]_3[HSiMo_{12}O_{40}]\}\cdot 1.5H_2O$ (**1**) and $\{[Cu(4,4'\text{-bipy})]_4[SiW_{12}O_{40}]\}\cdot 3H_2O$ (**2**) (bipy = bipyridine), have been hydrothermally synthesized and characterized by routine physical methods and single-crystal X-ray diffraction. Complexes **1** and **2** represent the first examples of fully oxidized Keggin POM anions as pendant polydentate ligands covalently bonded to a multitrack Cu(bipy) polymer chain(s) through linearly arrayed $O_d\cdots O_c\cdots O_d$ ($O_d$, terminal oxygen; $O_c$, bridging oxygen) atoms of single $M_3O_{13}$ triad(s). In the crystalline lattice of **1**, the 1D chain is constructed from a α-$[SiMo_{12}O_{40}]^{4-}$ ($SiMo_{12}$) cluster as a pendant tridentate ligand covalently bonded to three $Cu^I$(4,4′-bipy) subunits, and the neighbouring polymer strands interconnect with the Keggin fragments geared like the teeth of a zipper. In compound **2**, the 2D extended layer structure is composed of a α-$[SiW_{12}O_{40}]^{4-}$ ($SiW_{12}$) cluster as a pendant hexadentate ligand covalently bonded to four $Cu^I$(4,4′-bipy) subunits and forms a 2D net-texture structure with a large vacancy ($30.9\times 10.6$ Å), and the 2D layers are arranged in a parallel staggering fashion to form a 3D framework.

(© Wiley-VCH Verlag GmbH & Co. KGaA, 69451 Weinheim, Germany, 2007)

## Introduction

Polyoxometalates (POMs) composed of early transition metals (V, Nb, Ta, Mo, W) have been investigated for over a century because of their intriguing structural chemistry, unexpected reactivities, and potential applications.[1] Among a wide variety of POMs, the Keggin species $[XM_{12}O_{40}]^{n-}$ (X = B, P, Si, etc.; M = Mo and W) are one of the most important research topics, especially the modified Keggin derivatives. This reflects a current interest for the following reasons: the Keggin species are viewed as soluble metal oxide analogues and can therefore be used for the modeling of catalytic reactions taking place at metal oxide surfaces; they are valuable building blocks for tailor-made inorganic and organic or metal–organic hybrid materials with attractive structures and properties.[2] The increasing attention is currently devoted to their organometallic derivatives, and their multigraft modification could prove interesting in the context of the development of multidimensional framework structures.[3] Recently, a number of Keggin POMs covalently modified by transition-metal complexes have been reported, such as the mixed-valent compounds $[\{Cu_4(terpy)_4(PO_4)(H_2O)_2\}\{W^{VI}_{10}W^{V}_{2}O_{36}(PO_4)\}]\cdot 5H_2O$ described by Zubieta et al.,[4] $[PW_{12}O_{40}\cdot Ni(2,2\text{-bipy})_2(H_2O)]^{3-}$ by Xu et al.,[5] and $(NH_4)[Cu_{24}I_{10}L_{12}][PMo^{V}_{2}Mo^{VI}_{10}O_{40}]_3$ by Wang et al.;[6] the controlled assembly from lacunary Keggin POMs has also been reported by Pope et al.[7] and Gutiérrez-Zorrilla et al.[8] All these compounds featured sufficient charge density on the Keggin anion surface atoms to coordinate the transition-metal complexes. It is believed that surface activation is achieved by reducing the metal centres or by replacing metal centre(s) with a high oxidation state by other lower-valence metal(s). However, there are only a few examples of fully oxidized Keggin POMs modified by transition-metal complexes. These examples include the unsymmetrical discrete complex $[\{Cu_2(O_2CMe)_2(5,5\text{-dimethyl-2,2-bipy})_2\}\{Cu(5,5'\text{-dimethyl-2,2'-bipy})_2\}SiW_{12}O_{40}]$,[9] the 1D framework $[Ag_3(2,4'\text{-bipy})_3PMo_{12}O_{40}]$,[10] the 3D framework complexes $[Cu_3(pz)_3(PW_{12}O_{40})]$,[11] $[Ag_3(pz)_3(PW_{12}O_{40})]$,[11] $[Ag(4,4\text{-bipy})](OH)[\{Ag(4,4\text{-bipy})\}_2\{PAgW_{12}O_{40}\}]$,[12] and $KH_2[(D\text{-}C_5H_8NO_2)_4(H_2O)Cu_3][BW_{12}O_{40}]$.[13] In the last framework, chirality was designed into the helical motif. The coordination fashions of the Keggin POMs as polydentate ligands in these complexes are graphically summarized in Scheme 1: Keggin POMs provide only a terminal oxygen atom (see Scheme 1a, e and f) or both terminal and bridging oxygen atoms (see Scheme 1b–d).

[a] Key Laboratory of Polyoxometalate Science of Ministry of Education, Faculty of Chemistry, Northeast Normal University,
Changchun, Jilin 130024, P. R. China
E-mail: jpeng@nenu.edu.cn
pjun56@yahoo.com
[b] Faculty of Chemistry and Pharmacy, Jiamusi University, Jiamusi, HeilongJiang 154007, P.R. China

Supporting information for this article is available on the WWW under http://www.eurjic.org or from the author.


© 2007 Wiley-VCH Verlag GmbH & Co. KGaA, Weinheim

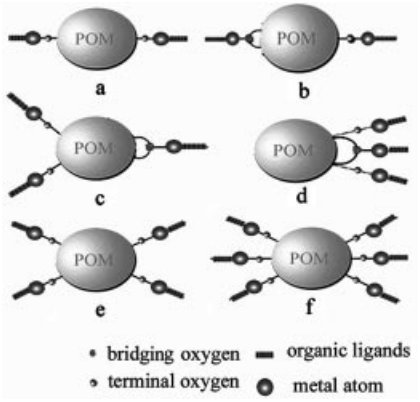


Scheme 1. Schematic representation of the coordination fashions of Keggin POMs as polydentate ligands.

It is noteworthy that most of these coordination fashions are prone to barycentre distribution of their oxo ligands, presumably because of steric crowding, with the exception of that shown in Scheme 1d, in which all the oxo ligands belong to a single $M_3O_{13}$ triad. To the best of our knowledge, the title compounds are unique examples with the coordination fashion represented in Scheme 1d. The ligand 4,4′-bipy is a rod-like molecule and is commonly used as a rigid ligand. The $d^{10}$ ions, the soft Lewis acid metal ions, generally show variable coordination numbers and tunable coordination spheres. Especially, Cu–bipy complex units have been widely used in magnetic and catalytic materials,[14] and some POM-based Cu–bipy polymers with interesting structures have been reported quite recently.[15] Hydrothermal synthesis represents a fast and excellent method to afford new POM structures. Although the hydrothermal synthesis employing the usual mixture of polyoxometalate, transition-metal salt, and nitrogen-containing ligand has been intensively extended, there is still abundant scope for the construction of intricate structures for new materials. The challenge is really to demonstrate control and expendability, to optimise the physical properties, etc. In this paper, we select the ligand 4,4′-bipy and the Cu ion to build metal–organic complex subunits in the hope of forming an extended structure of Keggin POMs modified by transition-metal complex moieties with little steric crowding, and we report the hydrothermal syntheses and crystal structures of two novel Cu(4,4′-bipy) modified Keggin derivatives, $[\{Cu(4,4'\text{-bipy})\}_3\{\alpha\text{-}HSiMo_{12}O_{40}\}]\cdot 1.5H_2O$ (**1**) and $[\{Cu(4,4'\text{-bipy})\}_4\{\alpha\text{-}SiW_{12}O_{40}\}]\cdot 3H_2O$ (**2**). They are the first examples of fully oxidized Keggin POM anions as pendant polydentate ligands covalently bonded to colinear multitrack Cu(bipy) chain(s) through $O_d\cdots O_c\cdots O_d$ atoms of $M_3O_{13}$ triad(s).

## Results and Discussion

The isolation of compounds **1** and **2** depends on the use of hydrothermal techniques. Hydrothermal reactions in the presence of organic ligand molecules have been established as a versatile method for the isolation of new materials with diverse structural architectures. Therefore, the introduction of hydrothermal techniques and the direct use of saturated Keggin POM as building blocks may produce a large number of novel organic–inorganic hybrid materials. By many parallel experiments, we found that the choice of starting materials is vital for the success of these reactions among other factors such as stoichiometry, temperature, pH and fill volume.[10,11] Transition-metal ions can greatly influence the structural formation of materials. We found that when $Cu(NO_3)_2\cdot 3H_2O$ was replaced by $Zn(NO_3)_2\cdot 6H_2O$, $NiCl_2\cdot 6H_2O$ or $MnCl_2\cdot 4H_2O$ in parallel experiments, we could not obtain the expected homologies but rather POM–4,4′-bipy supramolecular compounds. The oxidation states of the copper atoms in **1** and **2** are assigned as +1 on the basis of charge neutrality, coordination environments, valence sum calculations and XPS. A similar case of $Cu^{II}\rightarrow Cu^{I}$ was also observed in other polyoxometalates bridged by organonitrogen ligands coordinated to copper ions.[16] Additionally, the organic reductant species was also crucial for maintaining the intact skeleton of presynthesized saturated Keggin POMs. If the reducibility of the organic reductant were high, the skeleton of the saturated Keggin cluster may be inclined to decompose and reassemble into a new cluster.[17] We found that triethylamine was a good candidate.

### Structural Description of 1

Single-crystal X-ray diffraction analysis reveals that **1** consists of one $[SiMo_{12}O_{40}]^{4-}$ anion, three $[Cu(4,4'\text{-bipy})]^{+}$ moieties and one and a half water molecules (Figure 1). The heteropolyanion $[SiMo_{12}O_{40}]^{4-}$ possesses the classical α-Keggin-type structure without disorder.[18] The tetrahedrally coordinated Si is surrounded by four oxygen atoms with Si–O bonds ranging from 1.624(7) to 1.631(8) Å (mean 1.627 Å). All Mo atoms have $\{MoO_6\}$ octahedral environments. The distances of Mo–O bonds are divided into three groups: Mo–$O_a$ (centre oxygen atom), 2.316(7)–2.386(8) Å; Mo–$O_{b/c}$ (bridging oxygen atom), 1.821(8)–2.015(8) Å; Mo–$O_d$ (terminal oxygen atom), 1.660(9)–1.714(8) Å.

Each $\alpha\text{-}SiMo_{12}O_{40}$ cluster as a tridentate pendant ligand covalently bonds to three $Cu^{I}(4,4'\text{-bipy})$ complexes through

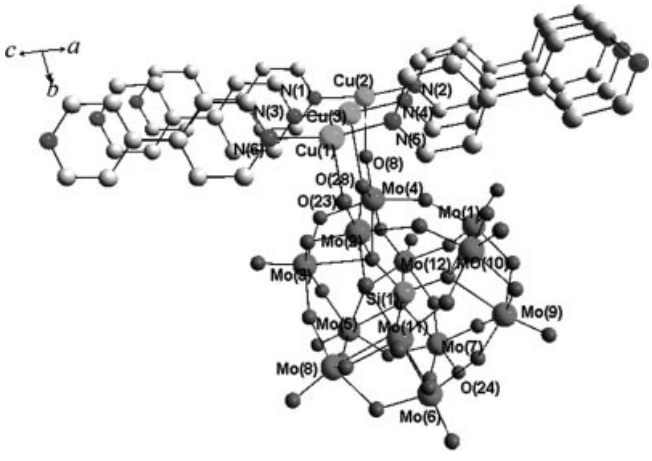


Figure 1. Representation of the molecular structure unit of **1**. The hydrogen atoms and crystal water molecules are omitted for clarity.

 © 2007 Wiley-VCH Verlag GmbH & Co. KGaA, Weinheim 

linearly arrayed O23, O28 and O8 atoms of the $Mo_3O_{13}$ triad (Mo2, Mo3 and Mo4). The bond lengths around the three $Cu^I$ ions are 2.298(8) Å (Cu1–O23), 2.383(8) Å (Cu2–O8), 2.493(8) Å (Cu3–O28), 1.888–1.898 Å (Cu1–N), 1.905–1.915 Å (Cu2–N) and 1.897–1.902 Å (Cu3–N), while the N–Cu–N angles are in the range 165.4–170.2° and the N–Cu–O angles are in the range 93.9–100.3°. There are three crystallographically independent $Cu^I$ atoms, and each $Cu^I$ atom adopts a "T-type" coordination geometry established by two nitrogen atoms of two 4,4′-bipy ligands and one oxygen atom of the $[SiMo_{12}O_{40}]^{4-}$ anion, which is similar to the coordination mode of $\{Cu_3(4,4'\text{-bpy})_3(H_2O)\}[PMo_{12}O_{40}(VO)_2]\cdot 5H_2O$.[19] In this way, each 4,4′-bipy ligand links two symmetrical $Cu^I$ atoms into a one-dimensional $Cu^I$(4,4′-bipy) complex chain. Because each α-$SiMo_{12}O_{40}$ cluster bonds to three parallel $Cu^I$(4,4′-bipy) subunits, the Keggin clusters become pendants of tri-track Cu(bipy) chains, projecting towards two sides (Figure 2).

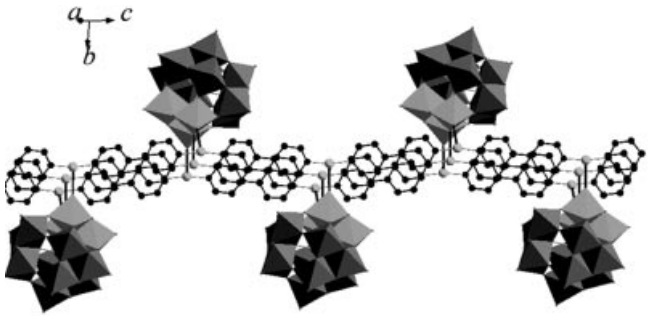


Figure 2. Combined polyhedral/wire representation of the 1D chain structure in **1**. The dark grey polyhedra represent the molybdenum polyhedra and the light grey polyhedra the $Mo_3O_{13}$ triad bound to Cu(bipy).

The tri-track chains with POM pendants are positioned relative to each other so that the POM clusters from different chains are alternatively arranged; each POM cluster joins other neighbouring clusters through hydrogen-bonding interactions. The shortest $O_d$(Mo9–O18)···$O_c$(Mo1–O16–Mo11) distance is 2.907 Å, and the distance between Cu2 and $O_d$ (O24) of the α-$SiMo_{12}O_{40}$ cluster of the neighbouring chain is 2.873 Å (Figure 3a), which is in the van der Waals interaction range. In this way, an interesting 2D structure is established in the manner of a "zipper" (Figure 3b).

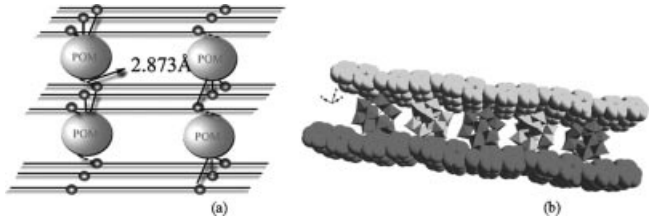


Figure 3. (a) Schematic view of part of the 2D structure in **1** with a dotted line representing the shortest distances between two adjacent chains (Cu2–O24); (b) Combined polyhedral/space filling representation of the "zipper" fashion in compound **1**. Selected bond lengths and angles for **1** are presented in Table S1.

**Structural Description of 2**

In the cell unit of complex **2**, there are four $Cu^I$ ions, four 4,4′-bipy ligands and one Keggin anion $[SiW_{12}O_{40}]^{4-}$ (Figure S1). The fully oxidized Keggin structure of $[SiW_{12}O_{40}]^{4-}$ contains four $W_3O_{13}$ units and one ordered $[SiO_4]^{4-}$ in the centre; the Si–O bonds range from 1.594(13) to 1.627(9) Å (mean 1.611 Å). The lengths of the W–O bonds can be divided into three groups: W–$O_a$ 2.320(12)–2.387(9) Å, W–$O_{b/c}$ 1.873(8)–1.908(12) Å and W–$O_d$ 1.691(12)–1.698(17) Å. Notably, the coordination fashion of the $Cu^I$(4,4′-bipy) chains to the Keggin cluster is very similar to that in complex **1** – they connect the Keggin cluster through the linearly arranged $O_d$···$O_c$···$O_d$ atoms of the $M_3O_{13}$ (W1, W2 and W6) triads. As shown in Figure 4a, there are three sets of linearly arranged $O_d$···$O_c$···$O_d$ atoms at the equatorial position that can be used as coordination atoms. We can see that the significant difference between the two compounds is that in **1** only one set of $O_d$···$O_c$···$O_d$ atoms is used (Figure 4b), while two sets of $O_d$···$O_c$···$O_d$ atoms are used in **2**. For **2**, this means that the Keggin cluster covalently bonds to four $Cu^I$(4,4′-bipy) moieties through six bridging and terminal oxygen atoms of two adjacent $W_3O_{13}$ triads at the equatorial position, which results in a rare hexadentate coordination mode in the Keggin-based coordination polymer (Figure 4c).

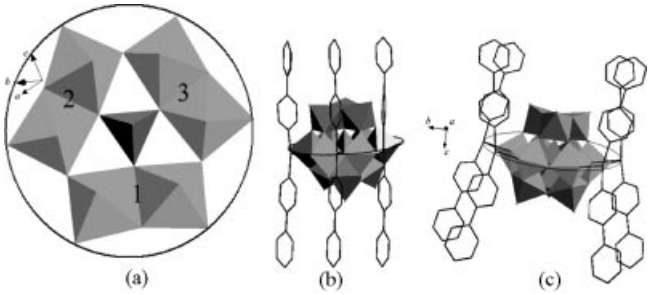


Figure 4. (a) The top view of the MO octahedra at the equatorial position; (b) Combined polyhedral/wire representation of the connection of Cu(bipy) with $SiM_{12}$ through one set of $O_d$···$O_c$···$O_d$ atoms in **1**, and (c) through two sets of $O_d$···$O_c$···$O_d$ atoms in **2**. Molybdenum octahedra of the $M_3O_{13}$ triad bound to Cu(bipy) are in light grey.

Crystal-structure analysis reveals that there are two independent $Cu^I$ centres in **2**, in which one copper centre (Cu1) is tricoordinated by two nitrogen atoms of two 4,4′-bipy ligands and one terminal oxygen atom of the $[SiW_{12}O_{40}]^{4-}$ anion, and the other (Cu2) is tetracoordinated by two nitrogen atoms of two 4,4′-bipy ligands and two oxygen atoms (terminal and bridging oxygen) of the $[SiW_{12}O_{40}]^{4-}$ anion. The bond lengths around the $Cu^I$ ions are 2.190 Å (Cu1–O11), 2.469(8) Å (Cu2–O10), 2.716(12) Å (Cu2–O3), 1.915–1.943 Å (Cu1–N) and 1.894–1.917 Å (Cu2–N), and the N–Cu–N bond angles are in the range 157.0–169.5° and the N–Cu–O angles in the range 97.2–105.3°. It is interesting that Cu1 and Cu2 are arrayed alternately in the 1D $Cu^I$ chain. In this way, each 4,4′-bpy ligand links two asymmetrical $Cu^I$ atoms into a one-dimensional $Cu^I$(4,4′-bipy) complex chain along the *c* axis direction. In contrast to compound **1**, each pair of adjacent α-$SiW_{12}O_{40}$ clusters covalently bonds to four

 © 2007 Wiley-VCH Verlag GmbH & Co. KGaA, Weinheim 

$Cu^{I}$ chains from opposite directions to form pendants of tetra-track Cu(bipy) chains. The two adjacent POM clusters (including the bonded Cu) present an inversed relation. Owing to POM groups linked to the $Cu^{I}$ chain with two opposite directions on the *b* axis and the inversed subunits alternately arrayed on the two sides of each pair of chains in the direction of the *c* axis, a 2D layer is extended in the [010] plane. In the 2D layer, the POM clusters and metal–organic complex chains are alternatively arranged to form a net texture with large vacancies (about $30.9 \times 10.6$ Å) (Figure 5a). The 2D layers are then stacked in a parallel staggering fashion and linked through supramolecular interactions, which lead to a 3D network frame, as shown in Figure 5b. Selected bond lengths and angles for **2** are presented in Table S2.

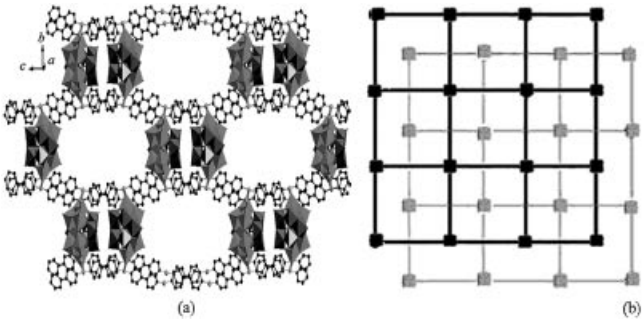


Figure 5. (a) Combined polyhedral/ball-and-stick representation of 2D layer structure in **2**. The dark grey polyhedra represent the tungsten polyhedra and the light grey polyhedra the $W_3O_{13}$ triad bound to Cu(bipy); (b) Schematic representation of the 3D network frame in **2**.

It is noteworthy that the $Cu^{I}$ ions show variable coordination numbers and present a nearly linear coordination with the nitrogen atoms in the bipyridine cationic chains, so they can easily accommodate one or two surface oxygen atoms of the POM to give a 2(N) + 1(O) T-type geometry (Cu1, Cu2 and Cu3 for **1**, and Cu1 for **2**), or a 2(N) + 2(O) distorted square-planar geometry (Cu2 for compound **2**), as shown in Figure 6. The O23, O28 and O8 atoms are coordinated to Cu1, Cu3 and Cu2 in **1** (Figure 6a) and the O11, and O10 and O3 atoms are coordinated to Cu1 and Cu2 in **2** (Figure 6b), respectively. The far distance between adjacent Cu atoms (Cu···Cu) make it possible that a Keggin POM is modified by bonding to co-parallel multichains of Cu(bipy) polymers through linearly arrayed $O_d$···$O_c$···$O_d$ atoms of the $M_3O_{13}$ triad(s). Such an unusual coordination mode has not hitherto been found in POM chemistry.

Also noteworthy are the differences in the dimension and in the number of co-parallel multichains of Cu(bipy) polymers in the two compounds, namely a tri-chain 1D structure for **1** and a di-chain 2D structure for **2**. This is perhaps due to the effect of the different volumes of the Keggin POMs. The volume of the $SiMo_{12}$ cluster is smaller than that of the $SiW_{12}$ cluster, and in compound **1**, the unit length of a Cu(bipy) chain can just accommodate a $SiMo_{12}$ cluster, which results in an array of $SiMo_{12}$ clusters side by side. Whereas, in compound **2**, the bigger $SiW_{12}$ clusters adopt an inversed face-to-face array, alternately arranged in pairs to form a 2D

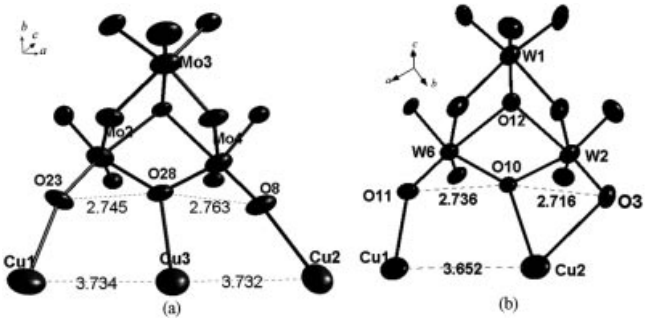


Figure 6. The view of the triad bound to multi-Cu(4,4′-bipy) with the Cu···**Cu** and $O_d$···$O_b$···$O_d$ distances [Å] for (a) **1** and (b) **2**.

net structure with large vacancies (about $30.9 \times 10.6$ Å). The micropores are occupied by water molecules, and the solvent-accessible volume of the unit cell is estimated to be 1451.1 $Å^3$ (PLATON program[20]), which is approximately 18.5% of the unit-cell volume (7844.0 $Å^3$). The contribution of the remaining solvent-accessible voids to the unit-cell volume after the guest water molecules are taken into account is 12.9% (1010.1 per unit cell). All these parameters are greater than those of **1**, in which the solvent-accessible volume of the unit cell is 224.0 $Å^3$, which is approximately 7.30% of the unit-cell volume (3068.1 $Å^3$), and the contribution of the remaining solvent-accessible voids to the unit-cell volume after the guest water molecules are taken into account is 3.7% (114.4 per unit cell).

### FTIR, XPS Spectra and TG Analyses

The IR spectra (Figure S2) exhibit prominent characteristic peaks for the α-Keggin structure at 947, 898 and 785 $cm^{-1}$ for compound **1**, and 956, 906 and 786 $cm^{-1}$ for compound **2**, which can be attributed to the $\nu_{as}$(M–$O_d$), $\nu_{as}$(Si–O) and $\nu_{as}$(M–$O_c$–M) bands (M = Mo, W), respectively.[21] The peaks in the 1410–1610 $cm^{-1}$ range are characteristic of the 4,4′-bipy ligands.

The bond valence sum calculations (BVS)[22] indicate that all the molybdenum and tungsten atoms are in the highest oxidation state (+6), while all the copper atoms are in the +1 oxidation state. Direct evidence for this is also provided by XPS measurements. The XPS spectra for both **1** and **2** (Figure S3) exhibit two peaks at 933.6 and 953.5 eV attributed to $Cu^{+}(2p_{3/2})$ and $Cu^{+}(2p_{5/2})$, respectively.[23] Two peaks at 232.1 and 235.7 eV can be attributed to $Mo^{+6}(3d_{5/2})$ and $Mo^{+6}$-$(3d_{3/2})$, respectively, for compound **1**, and a peak at 35.8 eV to $W^{+6}$ for compound **2**.[24] Hence, addition of a proton is necessary to balance the charge of **1** in the molecular formula. Calculation of the bond strength sums was used to predict the hydrogen atom positions. Possible protonation sites are the unshared oxygen atoms ($O_d$) or corner- and edge-sharing oxygen atoms ($O_{b/c}$). The calculated bond strength sums indicate that the basicity of $O_{b/c}$ is stronger than that of $O_d$. We therefore deduce that the corner- and edge-sharing oxygen atoms ($O_{b/c}$) are protonated.

Thermogravimetric analysis (TGA) also supports the chemical composition. The TGA curves show two steps of

 © 2007 Wiley-VCH Verlag GmbH & Co. KGaA, Weinheim 

weight loss for compounds **1** and **2** (Figure S4). In compound **1**, the initial weight loss of 1.40% (calcd. 1.08%) from 43 °C to 236 °C corresponds to the removal of lattice water molecules, and the second weight loss of 18.1% (calcd. 18.61%) in the range 236–461 °C is ascribed to decomposition of the 4,4′-bipy ligands. The whole weight loss (19.5%) is in good agreement with the calculated value (19.73%). For compound **2**, the first weight loss of 1.60% (calcd. 1.42%) from 50 °C to 290 °C is also assigned to the removal of lattice water molecules, and the second weight loss of 15.9% (calcd. 16.4%) in the range 290–760 °C is also ascribed to decomposition of the 4,4′-bipy ligands.

### Cyclic Voltammetry

To study the redox properties of compounds **1** and **2**, we used them as modifiers to fabricate chemically modified carbon paste electrode (CPE), owing to their insolubility in water and most organic solvents. As the intact Keggin skeletons in compounds **1** and **2** are still maintained, the electrochemical properties of **1** and **2** are expected to be similar to those of the parent compounds α-$H_4[SiM_{12}O_{40}]\cdot xH_2O$ (M = Mo or W).

The cyclic voltammogram of **1**-CPE was measured in 0.1 M $Na_2SO_4$ + 0.5 M $H_2SO_4$ aqueous solution in the potential range from +800 to –150 mV. There are three pairs of reversible redox peaks at +326, +217 and +8 mV [$E_{1/2} = (E_{pc} + E_{pa})/2$] (Figure 7), which correspond to three consecutive two-electron processes for Mo.[25] The values for the peak-to-peak separation between the corresponding anodic and cathodic peaks ($\Delta E_p$) are 29 (I–I′), 38 (II–II′) and 40 mV (III–III′). These values deviate from zero, the value expected for a reversible surface redox process, perhaps because of non-ideal behaviour. It is noteworthy that the expected redox peak in the range 100–200 mV attributed to $Cu^{II}/Cu^{I}$ was not observed, perhaps because of the overlap of the $Mo^{VI}/Mo^{V}$ redox peak.

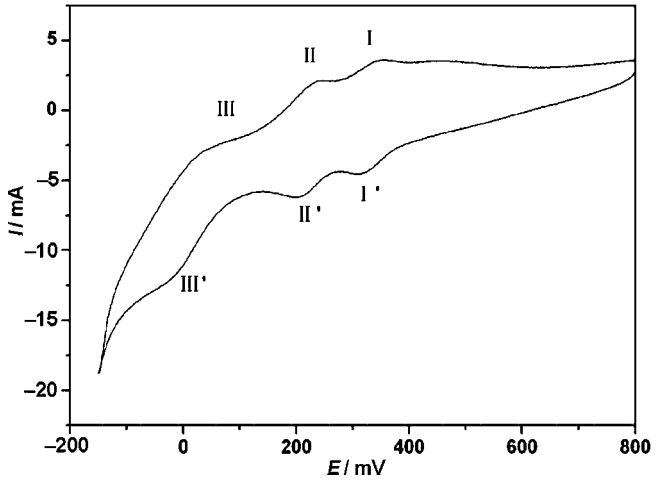


Figure 7. Cyclic voltammogram of **1**-CPE in 0.1 M $Na_2SO_4$ + 0.5 M $H_2SO_4$ aqueous solution at a scan rate of 100 mV/s.

Cyclic voltammetry on **2**-CPE was carried out in 0.1 M $Na_2SO_4$ + 0.5 M $H_2SO_4$ aqueous solution in the potential range from –700 to +300 mV. There are two pairs of reversible redox peaks at $E_{1/2}$ = –585 and –429 mV, and one irreversible peak at +131 mV (Figure 8). The values for the peak-to-peak separations between the corresponding anodic and cathodic peaks ($\Delta E_p$) are 74 (I–I′) and 80 mV (II–II′) which shows a one-electron process. The third irreversible anodic peak is assigned to the oxidation of $Cu^{I}$.

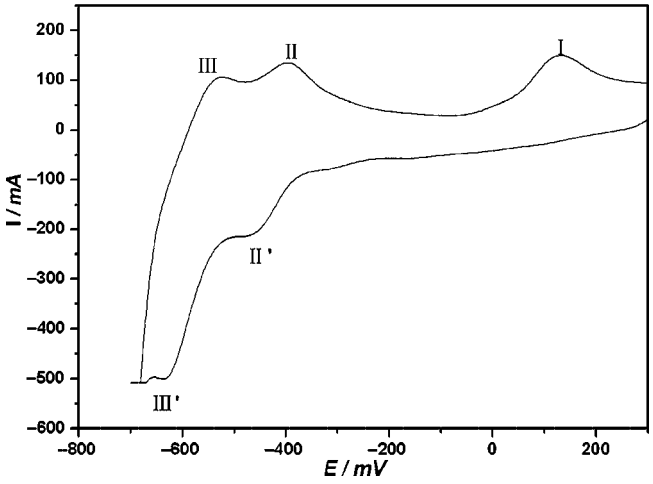


Figure 8. Cyclic voltammogram of **2**-CPE in 0.1 M $Na_2SO_4$ + 0.5 M $H_2SO_4$ aqueous solution at a scan rate of 100 mV/s.

The cyclic voltammetric behaviour of **1**-CPE as a function of scan rate (from 20 to 200 mV/s) was studied. The peak currents are proportional to the scan rates − the increase in the anodic and cathodic peak currents is almost the same, which indicates that the redox process is surface-controlled − and the exchange rate of the electrons becomes faster as the scan rate increases (Figure S5).[25b,26] The peak potentials change gradually: the cathodic peak potentials shift towards the negative direction and the corresponding anodic peak potentials towards the positive direction. The peak-to-peak separation between the corresponding cathodic and anodic peaks increases with the increasing scan rate, but the mean peak potentials do not change on the whole. In the experiment, **1**-CPE showed a higher stability than the conventional POM gel film electrode. The as-prepared electrode was stable over 300 cycle at a scan rate of 100 mV/s, and the current responses remained almost unchanged. The higher stability shows the merit of the robust POM derivatives as electrochemical active materials.

## Conclusions

We have isolated two novel Keggin derivatives by using presynthesized Keggin POMs, soft Lewis acid metal Cu ions and 4,4′-bipy ligands. In **1** and **2**, the fully oxidized Keggin clusters as pendants bond to multi-Cu(4,4′-bipy) metal–organic subunits in a unique coordination fashion: Cu(4,4′-bipy) moieties are parallelly arrayed and covalently linked to the Keggin clusters through linearly arranged $O_d\cdots O_c\cdots O_d$ atoms of single $M_3O_{13}$ triad(s). In this manner, the Keggin cluster is modified by bonding to a tri-track Cu(bipy) chain

 © 2007 Wiley-VCH Verlag GmbH & Co. KGaA, Weinheim 

through a set of linearly arrayed $O_d\cdots O_c\cdots O_d$ atoms of a single $Mo_3O_{13}$ triad in compound **1**, while the Keggin cluster is modified by bonding to di-track Cu(bipy) chains through two sets of linearly arrayed $O_d\cdots O_c\cdots O_d$ atoms of two $W_3O_{13}$ triads in compound **2**. It can be expected that there should be a Keggin POM that can be modified by bonding to multitrack Cu(bipy) chains through three sets of linearly arranged $O_d\cdots O_c\cdots O_d$ atoms from three $M_3O_{13}$ triads. The different volumes of the Keggin POMs may have a significant influence on the dimension and on the number of co-parallel multichains of Cu(bipy) polymers in the two compounds. A tri-chain 1D "zipper" structure is seen for **1** and a di-chain 2D net-texture structure for **2**, which again highlights the effect of POM units on the self-assembly of POM-based metal–organic polymer solid materials. The successful isolation of the two novel compounds shows the possibility of extending the POM family through reasonable modification of the POM clusters by selecting suitable second metals and organic ligands. The structures of these compounds should also be helpful for understanding catalytic reactions taking place at metal oxide surfaces. Design and synthesis of other Keggin POM derivatives with such coordination modes, perhaps with a higher dimension, are currently underway to obtain novel architectures and topologies and to satisfy functional demands for inorganic–organic hybrid materials.

## Experimental Section

**Materials and Methods:** All reagents were purchased commercially and used without further purification. Elemental analyses (C, H and N) were performed on a Perkin–Elmer 2400 CHN Elemental Analyzer, Cu, Mo and W analyses were determined by a Leaman inductively coupled plasma (ICP) spectrometer. The IR spectra were obtained on an Alpha Centaurt FTIR spectrometer in the 400–4000 $cm^{-1}$ region with a KBr pellet. XPS analyses were performed on a VGESCALABMKII spectrometer with a Mg-$K_\alpha$ (1253.6 eV) achromatic X-ray source. The vacuum inside the analysis chamber was maintained at $6.2\times10^{-6}$ Pa during analysis. The TG analyses were performed on a Perkin–Elmer TGA7 instrument under flowing $N_2$ with a heating rate of 10 °C/min. Cyclic voltammograms were obtained with a CHI 660 electrochemical workstation at room temperature. Platinum gauze was used as a counter electrode and Ag/AgCl electrode was used as the reference electrode. Chemically bulk-modified carbon paste electrodes were used as working electrodes.

**Synthesis**

**{[Cu(4,4′-bipy)]$_3$[α-HSiMo$_{12}$O$_{40}$]}·1.5H$_2$O (1):** The starting materials, α-$H_4[SiMo_{12}O_{40}]\cdot XH_2O$,[27] 4,4-bipy, $Cu(NO_3)_2\cdot3H_2O$, triethylamine and distilled water in a molar ratio of about 1:1:2:0.5:555, were mixed. The resulting suspension was stirred for 1 h, and the pH was adjusted to 4.3 by 1 M NaOH. The suspension was then sealed in an 18-mL Teflon-lined reactor and filled to a 60-% volume. After heating the mixture for 6 d at 160 °C, the reactor was slowly cooled to room temperature over a period of 16 h; the final pH was 4.6. Blocklike black-brown crystals of **1** were filtered, washed with water and dried at room temperature. Yield: 32% (80 mg). $C_{30}H_{28}Cu_3Mo_{12}N_6O_{42}Si$ (2507.9): calcd. C 14.36, H 1.12, Cu 7.66, Mo 45.92, N 3.35, ; found C 14.24, H 1.23, Cu 7.79, Mo 45.76, N 3.21.

**{[Cu(4,4′-bipy)]$_4$[SiW$_{12}$O$_{40}$]}·3H$_2$O (2):** Compound **2** was obtained in a manner similar to that illustrated for **1**, but the pH was adjusted to 5.26. Prismlike brown crystals of **2** were collected. Yield: 60% (228 mg). $C_{40}H_{38}Cu_4N_8O_{43}SiW_{12}$ (3807.19): calcd. C 12.61, H 0.99, Cu 6.67, N 2.94, W 58.00; found C 12.32, H 1.03, Cu 6.45, N 2.86, W 57.87.

**X-ray Crystallographic Study:** Crystal data for compounds **1** and **2** were collected on Rigaku RAXIS RAPID IP with Mo-$K_\alpha$ monochromatic radiation ($\lambda$ = 0.71073 Å) at 293 K. The structures were solved by direct methods and refined by full-matrix least-squares on $F^2$ by using the SHELXTL crystallographic software package.[28] All non-hydrogen atoms were refined anisotropically. The positions of the hydrogen atoms on carbon atoms were calculated theoretically. Crystallographic data are given in Table 1. CCDC-611115 (for **1**) and

Table 1. Crystal data and structure refinements for **1** and **2**.

| | **1** | **2** |
|---|---|---|
| Empirical formula | $C_{30}H_{28}Cu_3Mo_{12}N_6O_{41.5}Si$ | $C_{40}H_{38}Cu_4N_8O_{43}SiW_{12}$ |
| Formula mass | 2507.9 | 3807.19 |
| $T$ [K] | 293(2) | 293(2) |
| Wavelength [Å] | 0.71073 | 0.71073 |
| Crystal system | triclinic | monoclinic |
| Space group | $P\bar{1}$ | $C2/m$ |
| $a$ [Å] | 12.963(3) | 15.909(5) |
| $b$ [Å] | 13.571(3) | 23.537(5) |
| $c$ [Å] | 18.034(4) | 21.310(5) |
| $\alpha$ [°] | 88.78 | 90 |
| $\beta$ [°] | 87.08 | 100.580(5) |
| $\gamma$ [°] | 75.55 | 90 |
| $V$ [Å$^3$] | 3068.1(13) | 7844(4) |
| $Z$ | 1 | 4 |
| $D_{calcd.}$ [mg/m$^3$] | 2.709 | 3.219 |
| Absorption coefficient [mm$^{-1}$] | 3.499 | 18.678 |
| $F$(000) | 2358 | 6760 |
| Goodness-of-fit on $F^2$ | 0.931 | 1.039 |
| Final $R$ indices[a] | $R_1$ = 0.0657 | $R_1$ = 0.0570 |
| [$I > 2\sigma(I)$][b] | $wR_2$ = 0.1838 | $wR_2$ = 0.1397 |
| $R$ indices (all data) | $R_1$ = 0.0839 | $R_1$ = 0.0828 |
| | $wR_2$ = 0.1946 | $wR_2$ = 0.1514 |

[a] $R_1 = \Sigma||F_o| - |F_c||/\Sigma|F_o|$. [b] $wR_2 = \Sigma[w(F_o^2 - F_c^2)^2]/\Sigma[w(F_o^2)^2]^{1/2}$.

 © 2007 Wiley-VCH Verlag GmbH & Co. KGaA, Weinheim 

-620041 (for **2**) contain the supplementary crystallographic data for this paper. These data can be obtained free of charge from The Cambridge Crystallographic Data Centre via www.ccdc.cam.ac.uk/data_request/cif.

**Preparation of 1- and 2-CPE: 1-/2**-modified carbon paste electrode [**1**-/**2**-CPE] was prepared as follows: graphite powder (48 mg) and **1**/**2** (8 mg) were mixed and ground together by an agate mortar and pestle to achieve a uniform mixture, and nujol (0.6 mL) was then added with stirring. The homogenized mixture was packed into a glass tube with a 1.2-mm inner diameter, and the tube surface was wiped with paper. Electrical contact was established with a copper rod through the back of the electrode.

**Supporting Information** (see footnote on the first page of this article): Tables for selected bond lengths and bond angles for compounds **1** and **2**, representation of the molecular structure unit of **2**, and XPS, IR and TG data of complexes **1** and **2**.

## Acknowledgments

This work was financially supported by the National Natural Science Foundation of China (20671016). We would like to thank the referees for their comments.

[1] a) M. T. Pope, A. Müller (Eds.), *Polyoxometalate Chemistry from Topology via Self-Assembly to Applications*, Kluwer Academic Publishers, Dordrecht, **2001**; b) E. Coronado, L. Kazansky, A Müller, M. T. Pope (Eds.), *Polyoxometalate Molecular Science*, Kluwer Academic Publishers, Plenum Publishers, New York and Dordrecht, **2001**; c) M. T. Pope, *Heteropoly and Isopoly Oxometalates*, Springer-Verlag, Berlin, **1983**.
[2] a) C. L. Hill, *Chem. Rev.* **1998**, *98*, 1–2; b) A. Proust, P. Gouzerh, *Chem. Rev.* **1998**, *98*, 77.
[3] M. Pohl, Y. Lin, T. J. R. Weakley, K. Nomiya, M. Kaneko, H. Weiner, R. G. Finke, *Inorg. Chem.* **1995**, *34*, 767–777.
[4] E. Burkholder, V. Golub, C. J. O'Connor, J. Zubieta, *Inorg. Chem. Commun.* **2004**, *7*, 363–366.
[5] Y. Xu, J. Q. Xu, K. L. Zhang, Y. Zhang, X. Z. You, *Chem. Commun.* **2000**, *6*, 153–154.
[6] X. L. Wang, C. Qin, E. B. Wang, Z. M. Su, Y. G. Li, L. Xu, *Angew. Chem. Int. Ed.* **2006**, *45*, 7411–7414.
[7] S. Masahiro, M. H. Dickman, M. T. Pope, *Angew. Chem. Int. Ed.* **2000**, *39*, 2914–2916.
[8] a) L. S. Felices, P. Vitoria, J. M. Gutiérrez-Zorrilla, S. Reinoso, P. Vitoria, L. Lezama, *Chem. Eur. J.* **2004**, *10*, 5138–5146; b) S. Reinoso, P. Vitoria, J. M. Gutiérrez-Zorrilla, L. Lezama, J. I. Beitia, *Inorg. Chem.* **2005**, *44*, 9731–9741; c) S. Reinoso, P. Vitoria, L. S. Felices, J. M. Gutiérrez-Zorrilla, *Chem. Eur. J.* **2005**, *11*, 1538–1548.
[9] C. Ritchie, E. Burkholder, P. Kögerler, L. Cronin, *Dalton Trans.* **2006**, *14*, 1712–1714.
[10] Y. P. Ren, X. J. Kong, L. S. Long, R. B. Huang, L. S. Zheng, *Cryst. Growth Des.* **2006**, *6*, 572–576.
[11] Y. P. Ren, X. J. Kong, X. Y. Hu, M. Sun, L. S. Long, *Inorg. Chem.* **2006**, *45*, 4016–4024.
[12] J. X. Chen, T. Y. Lan, Y. B. Huang, C. X. Wei, Z. S. Li, *J. Solid State Chem.* **2006**, *179*, 1904–1911.
[13] H. Y. An, D. R. Xiao, E. B. Wang, Y. G. Li, Z. M. Su, L. Xu, *Angew. Chem. Int. Ed.* **2006**, *45*, 904–908.
[14] a) D. Ghosh, R. Mukherjee, *Inorg. Chem.* **1998**, *37*, 6597–6605; b) D. A. Rochcliffe, A. E. Martelldummy Martell, *J. Mol. Catal. A* **1995**, *99*, 101–105.
[15] a) L. S. Felices, P. Vitoria, J. M. Gutiérrez-Zorrilla, L. Lezama, S. Reinoso, *Inorg. Chem.* **2006**, *45*, 7748; b) C. Z. Lu, C. D. Wu, H. H. Zhuang, J. S. Huang, *Chem. Mater.* **2002**, *14*, 2649–2655; c) H. Jin, C. Qin, Y. G. Li, E. B. Wang, *Inorg. Chem. Commun.* **2006**, *9*, 482–485.
[16] a) C. D. Wu, C. Z. Lu, H. H. Zhuang, J. S. Huang, *Inorg. Chem.* **2002**, *41*, 5636–5637; b) C. M. Liu, D. Q. Zhang, D. B. Zhu, *Cryst. Growth Des.* **2005**, *5*, 1639–1642.
[17] C. M. Liu, D. Q. Zhang, M. Xiong, D. B. Zhu, *Chem. Commun.* **2002**, 1416–1417.
[18] A. S. J. Wery, J. M. Gutierrez-Zorrilla, A. Luque, P. Vitoria, P. Roman, M. Martinez-Ripoll, *Polyhedron* **1998**, *17*, 1247–1251.
[19] Z. Y. Shi, X. J. Gu, J. Peng, X. Yu, E. B. Wang, *Eur. J. Inorg. Chem.* **2006**, 385–388.
[20] A. L. Spek, *PLATON, A Multipurpose Crystallographic Tool*, Utrecht University, Utrecht, The Netherlands, **1998**.
[21] R. Thouvenot, M. Fournier, R. Franck, G. Rocchiccioli-Deltche, *Inorg. Chem.* **1984**, *23*, 598–605.
[22] I. D. Brown, D. Altermatt, *Acta Crystallogr., Sect. B: Struct. Sci.* **1985**, *41*, 244–247.
[23] Y. H. Feng, Z. G. Han, J. Peng, X.-R. Hao, *J. Mol. Struct.* **2005**, *734*, 171–176.
[24] Z. G. Han, Y. L. Zhao, J. Peng, A. X. Tian, Q. Liu, J. F. Ma, E. B. Wang, N. H. Hu, *CrystEngComm* **2005**, *7*, 380–387.
[25] a) M. Sadakane, E. Steckhan, *Chem. Rev.* **1998**, *98*, 219–237; b) Z. G. Han, Y. L. Zhao, J. Peng, Y. H. Feng, J. N. Yin, Q. Liu, *Electroanalysis* **2005**, *17*, 1097–1102; c) Z. G. Han, Y. L. Zhao, J. Peng, Q. Liu, E. B,Wang, *Electrochim. Acta* **2005**, *51*, 218–224.
[26] M. T. Pope, E. Papaconstantinou, *Inorg. Chem.* **1967**, *6*, 1147–1152.
[27] C. R. Deltcheff, M. Fournier, R. Franck, R. Thouvenot, *Inorg. Chem.* **1983**, *22*, 207–216.
[28] a) G. M. Sheldrick, *SHELX-97, Program for Crystal Structure Refinement*, University of Göttingen, Germany, **1997**; b) G. M. Sheldrick, *SHELXL-97, Program for Crystal Structure Solution*, University of Göttingen, Germany, **1997**.

Received: October 29, 2006
Published Online: February 16, 2007

 © 2007 Wiley-VCH Verlag GmbH & Co. KGaA, Weinheim 

DOI: 10.1002/ejic.200600641

# Facile Synthesis of Oligothiophene-Capped CdS Nanoparticles

**Tarek Antoun,[a] Roberta Brayner,[a] Seham Al terary,[a] Fernand Fiévet,[a] Mohamed Chehimi,[a] and Abderrahim Yassar*[a]**

**Keywords:** Nanoparticle synthesis / Oligothiophenes / Photovoltaics / Conjugated polymers / Nanostructures

CdS nanoparticles functionalized by electroactive oligothiophenes, with narrow size distribution, have been prepared and characterized. The structure of the hybrid product was investigated by TEM, XRD, optical and FTIR spectroscopy. The modified nanoparticles consist of a few tens of oligothiophene units attached to the CdS core. The grafting of conjugated oligomers to nanoparticles was made possible by complexing the dangling cadmium ion on the nanoparticle surface.

(© Wiley-VCH Verlag GmbH & Co. KGaA, 69451 Weinheim, Germany, 2007)

## Introduction

The design of nanostructured hybrid materials, with novel physical properties, has emerged as one of the most exciting areas of scientific endeavour in this decade, in which material and chemical research are playing a dominant role.[1] Nanocrystals (NCs) have a well-documented array of properties that differ from those of the corresponding bulk materials. Surface modification was shown to optimize the intrinsic optical properties, producing highly luminescent NCs, and also serves as a means of tuning their solubility. On the other hand, π-conjugated oligomers and polymers are a relatively new class of electronic materials that are revolutionizing important technological applications including large-area electronics, owing to their compatibility with low-temperature processing, the simplicity of thin-film device fabrication and the tunability of their electronic properties.[2] The richness of the synthetic organic chemistry allows the fabrication of π-conjugated materials with a degree of control unattainable with conventional inorganic semiconductors. Grafting conjugated polymers and oligomers onto the surface of nanoparticles provides a means of controlling not only the final surface functionality of the material, as one could do also with ligands, but also of introducing new optoelectronic and enhancing charge-transport properties.[3] Such physical properties have motivated many studies on π-conjugated systems and NC composites.

The encapsulation of inorganic nanoparticles by conjugated polymers has its origin in work by Greenham et al. which dates back over one decade.[4] Although much attention has been devoted to the study of the photovoltaic properties of these materials, there have been studies reporting the elaboration and the characterization of well-organized NCs embedded in conjugated polymers, as can be seen from reports of the Lahav group who studied the organization of $(Pb_{1-x}Cd_x)S$ nanoparticles within an oligo(*p*-phenyleneethylene)dicarboxylate matrix.[5] In optoelectronic devices, inorganic semiconductor NCs have been combined with π-conjugated systems in order to take advantage of the ease of processing, characteristic of many π-conjugated polymers, and their complementary properties. The inorganic semiconductor NCs have high electron affinities and the organic semiconductors show high hole mobilities, so charge transfer occurs rapidly in such systems. Photoinduced charge transfer can result in enhancement of the photoconductivity and photovoltaic effects. A major problem which arises in the fabrication of these composites is the immiscibility of the two materials due to differences in their polarities. In composites heavily loaded with NCs, phase segregation occurs even when the NCs are stabilized by hydrophilic ligands.[4]

To overcome this problem and to obtain a three-dimensional interpenetrating network of nanocomposites, many approaches have been used, in which NCs and conjugated polymers are intimately associated. In these approaches the conjugated systems are directly connected to the quantum dot surface. Milliron et al. reported the preparation of novel soluble oligothiophene-CdSe NCs, wherein electronic interaction between functional components was facilitated by attaching the binding group directly to the conjugated backbone.[6] Mutual fluorescence quenching of oligothiophenes and CdSe NCs indicates photoinduced charge transfer, which is essential for their potential utility as an active component in photovoltaic devices. Similarly, Sun et al. have

[a] Interfaces, Traitements, Organisation et Dynamique des Systèmes, CNRS, UMR 7086, Université Diderot (Paris 7), 1 rue Guy de la Brosse, 75005 Paris, France

 © 2007 Wiley-VCH Verlag GmbH & Co. KGaA, Weinheim 

demonstrated that devices fabricated from blends of tetrapod CdSe nanoparticles and a conjugated polymer perform better than devices made from nanorod/polymer blends.[7] The authors believe that the control of the NC shape provides an additional tool to control morphology and facilitate the charge transfer process. Nanocomposites based on $TiO_2$ nanoparticles functionalized by conjugated terthiophenecarboxylic acid have been prepared and characterized by Beek et al.[8] The fluorescence of the terthiophene moiety was completely quenched due to photoinduced electron transfer from terthiophene to titanium dioxide. The quenching is believed to be predominantly static rather than dynamic.

The role of organic surfactants and morphology control have been pointed out by Liu et al.[9] In their work, they showed that an end-functional poly(3-hexylthiophene) (P3HT) enhances the performance of P3HT/CdSe nanocrystal solar cells by increasing the dispersion of CdSe without introducing insulating surfactants. Despite several reports of various NC post-functionalization procedures, much development is still needed to elaborate NC-π-conjugated systems, in which the two components are in intimate contact and electron transfer is not altered by the presence of insulating surfactants. On the basis of a survey of published accounts, CdSe and CdS quantum dots are II–VI semiconductor nanoparticles. There is no distinction that separates the two nanoparticles in terms of desirable properties for applications. CdSe nanoparticles and π-conjugated polymers have to date been the most-studied nanocomposite materials; however, one of the limitations of CdSe nanoparticle synthesis is the use of hazardous and pyrophoric compounds such as dimethylcadmium, $(CH_3)_2CdSe$, TOPO and, especially, the high temperatures (300 °C) that are required. In contrast the synthesis of CdS is safer. These reasons motivated our choice of CdS nanoparticles as models to develop a versatile one-pot method for preparing CdS NC-bound conjugated materials.

In this work we report a one-pot method for preparing CdS NC-bound oligothiophenes. Transmission electron microscopy (TEM) and X-ray diffraction powder (XRD) show that the CdS nanoparticles are monodisperse. The amount of oligothiophene and the nature of surface binding are studied in detail using X-ray photoelectron spectroscopy (XPS), IR, UV/Vis and fluorescence spectroscopy. The major advantage of this method is that we use functionalized π-conjugated electroactive systems as ligands to control NC growth. The electroactive ligand binds to the NC surface, and allows intimate contact between the NC and the conjugated oligomer backbone leading to better electronic communication between the two components. The bonding of the oligomers to the NC surface was made possible by complexing the dangling cadmium ion on the NC surface by the lone-pair electrons of the carboxylate group in the oligomer. We have also found the carboxylate function to be a versatile and stable ligating group that can be easily attached to II–VI semiconductor nanoparticle surfaces.

## Results and Discussion

Scheme 1 depicts the chemical structures of the α,ω-oligothiophene dicarboxylic acids used in this study. 2,2′-Bithiophene-5,5′-dicarboxylic acid (**I**), 2,2′;5′,2′′-terthiophene-5,5′′-dicarboxylic acid (**II**), and 2,2′;5′,2′′;5′′,2′′′-quaterthiophene-5,5′′′-dicarboxylic acid (**III**) were prepared as described in detail elsewhere.[10] CdS NCs capped with **I**, **II** and **III** (**CdS-2T**, **CdS-3T**, **CdS-4T**, respectively) were then prepared in ethylene glycol (EG) according to the polyol process;[11] see Scheme 2.

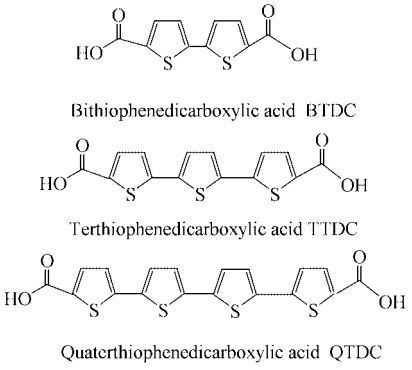


Scheme 1. Oligothiophenes used for the functionalization of CdS nanocrystals.

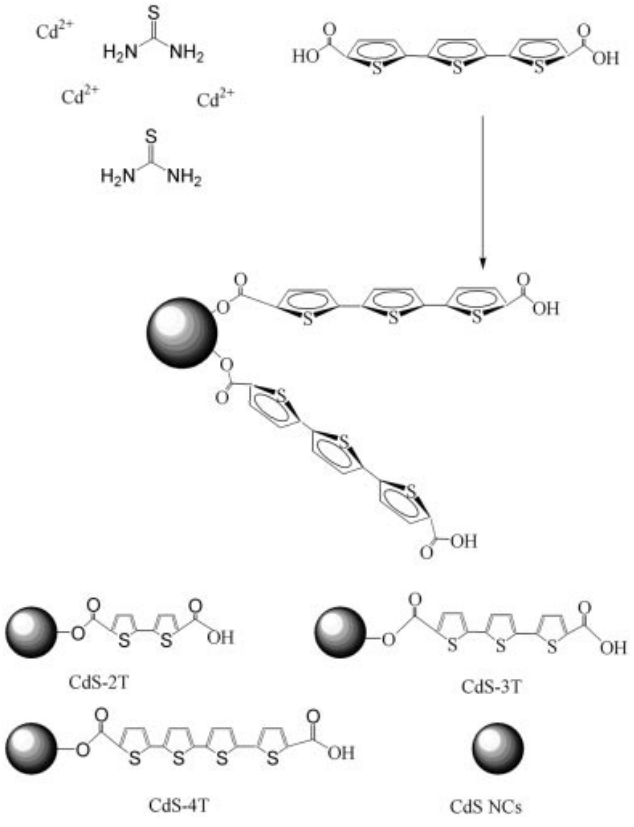


Scheme 2. Schematic representation of the preparation of CdS–oligothiophene by a one-pot procedure.

 © 2007 Wiley-VCH Verlag GmbH & Co. KGaA, Weinheim 

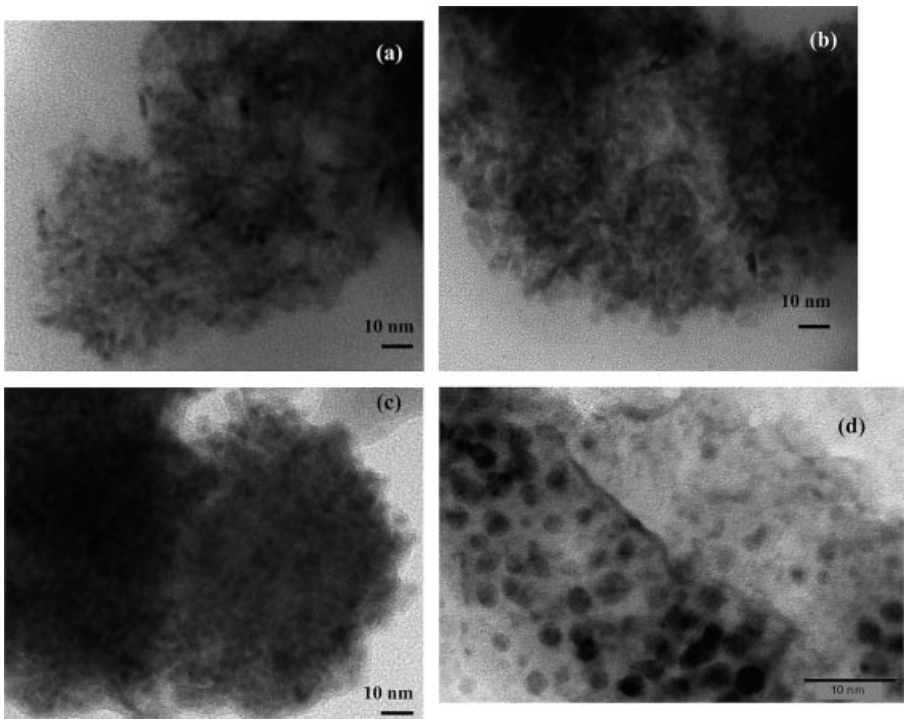


Figure 1. TEM micrographs of CdS–oligothiophene nanoparticles (a) **CdS-2T**; (b) **CdS-3T**; (c) **CdS-4T**; (d) **CdS-3T** prepared at pH = 9. The scale bar represents 10 nm in each case.

The general procedure involves addition of cadmium acetate and thiourea to a given volume of EG to obtain a concentration between $10^{-2}$ and $10^{-3}$ mol $L^{-1}$. To form CdS–oligothiophene hybrids, oligothiophenes were added to the reaction mixture in EG. The mixture was then heated with vigorous stirring to a temperature between 100 and 150 °C.

Transmission electron microscopy reveals that the oligothiophene molecules act as mediator templates towards the preparation of size-controlled spherical assemblies (50–200 nm) (Figure 1). The average individual CdS particle sizes are on the nanometer scale, 2–4 nm, depending on the conjugation length of the organic chain. In deionized water at pH = 9 CdS–oligothiophene nanoparticles are generally isolated from one another (Figure 1d). The assembly of CdS nanoparticles into nanospheres is believed to be a result of π–π interactions between conjugated systems.[12] The crystallinity of the **CdS-*n*T** samples was investigated by X-ray diffraction, as shown in Figure 2. At equilibrium reaction conditions, CdS nanoparticles present the thermodynamically stable hexagonal (wurtzite) structure. In this work, all samples can be indexed as cubic (sphalerite) in structure, showing (111), (220) and (311) peaks. This behaviour is perhaps due to the presence of oligothiophene molecules on the CdS surface. The same phase was observed by McPherson et al. for CdS synthesized in water-in-oil microemulsions using a combination of bis(2-ethylhexyl) sulfosuccinate (AOT) and the zwitterionic phospholipid L-α-phosphatidylcholine (lecithin).[13] An average size was estimated by applying Scherrer's formula. Crystallite sizes decrease with an increase in the conjugation length of the organic molecule, from 4 nm for **CdS-2T** to 2 nm for **CdS-4T**.

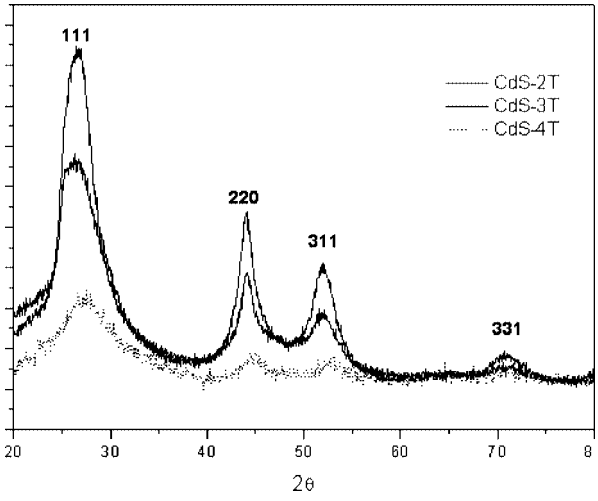


Figure 2. Powder X-ray diffraction patterns of three samples of **CdS-*n*T** nanoparticles.

The reduction of particle size with an increase in the conjugation length of the adsorbate can be understood as a passivation effect on the NC surface with longer oligomers. This result is somewhat surprising, that the steric effects are similar for the three oligomers, assuming they lie perpendicular to the NC surface. The HOMO–LUMO energy and carboxylate reactivity is an alternative explanation. In general, the smaller the HOMO–LUMO energy gap of an aromatic acid, the softer the anions. A soft base with smaller HOMO–LUMO energy will adsorb more readily on a surface. DFT calculations on the oligothiophenecarboxylates

 © 2007 Wiley-VCH Verlag GmbH & Co. KGaA, Weinheim 

show that changing the carboxylate from thiophene to bithiophene or terthiophene reduces the energy gap considerably.[14] The HOMO rises and the LUMO falls. In the light of these facts, we assume that the longer oligomers, i.e. **QTDC** and **TTDC** bind more strongly to the NC surface than **BTDC**; therefore, the longer oligomer straightforwardly passivates the NC surface and stops particle growth at an early stage of growth resulting in small nanoparticles.

FTIR spectroscopy was used to study CdS–oligothiophene core-shell structures and to reveal also the bonding mode of the organic molecule adsorbed on the NC. In the frequency region where C=C, C–C and C–S stretching vibrations are active, the infrared spectra of α,ω-oligothiophene diacids and **CdS-*n*T** show many similarities. These spectra exhibit characteristic bands of oligothiophenes that are centred at 1520, 1436, 890, 812 $cm^{-1}$, and 750 $cm^{-1}$, assigned to antisymmetric C=C, symmetric C=C, antisymmetric C–S, symmetric C–S stretching modes, and out-of-plane C–H deformation, respectively. However, we observe a slight vibration shift of the π-conjugated system upon adsorption of the oligomer on the NC surface. The $\nu_{ant}$ (C–C) and symmetric C–S modes are redshifted by 7 and 13 $cm^{-1}$, respectively. The out-of-plane deformation of C–H is blueshifted by 17 $cm^{-1}$. The change in the thiophene vibration can be attributed to the new electronic distribution of the bonded oligomers. Figure 3a, b represents typical FTIR spectra of the carboxylate region, for **BTDC**, **CdS-2T**, **TTDC** and **CdS-3T**.

The stretching band of the carbonyl group C=O, which appears at 1669 $cm^{-1}$ for **BTDC** and 1663 $cm^{-1}$ for **TTDC**, is no longer identified in the IR spectra of **CdS-*n*T**. Instead, the symmetric and asymmetric stretching vibrations of the $COO^-$ group appear distinctly at 1386 and 1560 $cm^{-1}$, respectively. The shoulder at 1617 $cm^{-1}$, observed for **CdS-2T** indicates the existence of a second coordination mode of the carboxylate group. The intensity of the latter increases and becomes a distinct band for **CdS-3T**. The presence of the $\nu_s(COO^-)$ band in the **CdS-*n*T** spectra clearly indicates that the oligothiophene binds to the CdS surface through the carboxylate group. Also, observing two types of carboxylate stretches indicates that the carboxylate group of the oligomers function in different coordination fashions, two at least. The binding mode can be determined from the carboxylate band splitting. Hence, it was established that the mode of carboxylic acid coordination in complexes or adsorbed on a surface can be determined using infrared spectroscopy. There are four common carboxylate coordination modes: monodentate, chelating bidentate, bridging bidentate and ionic interaction. The coordination mode can be distinguished by the different separations between the antisymmetric and symmetric stretching adsorption bands ($\Delta\nu$).[15] Bidentate coordination modes of the carboxylate group show a separation less than 200 $cm^{-1}$, whereas monodentate modes show a larger separation. In the present work band separations of $\Delta\nu$ = 180 and 240 $cm^{-1}$ were obtained for **CdS-3T**, indicating bidentate and monodentate coordination modes. The similarity of the **CdS-2T** spectrum and its band separations, $\Delta\nu$ = 180 and 230 $cm^{-1}$, indicates

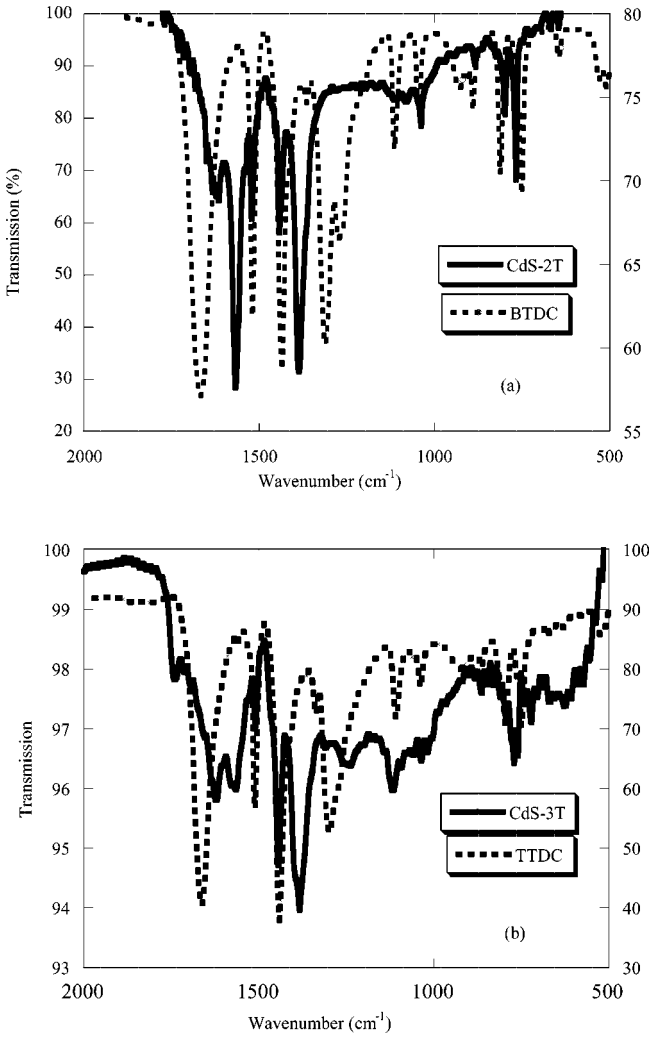


Figure 3. FT-IR spectra of (a) **BTDC** and **CdS-2T**, (b) **TTDC** and **CdS-3T**.

that a similar mode of binding occurs. The FTIR data show clearly that the final composition of the **CdS-*n*T** core shell includes both a thiophene oligomer shell and a CdS core. On the other hand, the complexation of oligothiophenecarboxylate with CdS nanoparticles occurs through strong ionic/covalent bonds. Also, the bonding of the oligomer on the NC surface deeply influences the electronic distribution of the π-conjugated system.

The elemental composition of the CdS–oligothiophene nanoparticles was analyzed by XPS. The XPS survey scan of **CdS-4T** is depicted in Figure 4, as a representative example. The main features, S2p, C1s, $Cd3d_{5/2}$ and O1s, are centred at 162, 285, 405 and 532 eV, respectively. The O1s/$Cd3d_{5/2}$ and C1s/$Cd3d_{5/2}$ intensity ratios differ markedly depending on the chemical structure of the oligomer, i.e. chain length. The high-resolution Cd3d region from **CdS-4T**, shown as an insert in Figure 4, exhibits $Cd3d_{5/2}$ and $Cd3d_{3/2}$ peaks (spin-orbit doublet) centred at 405.8 and 412.4 eV, respectively.

 © 2007 Wiley-VCH Verlag GmbH & Co. KGaA, Weinheim 

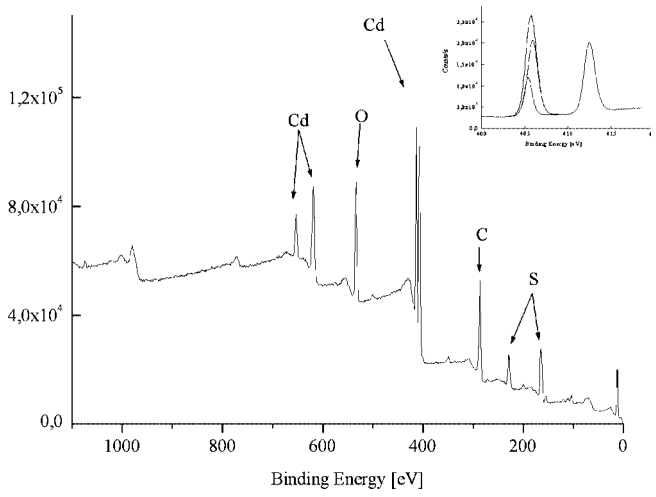


Figure 4. XPS survey scan of **CdS-4T**; the insert shows core level of $Cd3d_{5/2}$.

The $Cd3d_{5/2}$ binding energy is in line with the published data for CdS.[16] When care was taken to closely analyze the $Cd3d_{5/2}$ spectra, they were fitted with two peaks using Gaussian line shapes, which can be assigned to the bulk of Cd atoms, the second one at high binding energy, which should be attributed to surface cadmium atoms complexed to the oligomer through the carboxylate group. The surface contribution is about 20% of the total signal for **CdS-4T** and drops to 10% for **CdS-2T**. This is expected and is in agreement with literature data, which show that the surface contribution is larger for smaller NCs; the sizes of the nanoparticles are 4 and 2 nm for **CdS-2T** and **CdS-4T**, respectively.

Figure 5 compares the S2p regions of **CdS-2T** and **CdS-4T**. The spectra are fitted with three different spin-orbit split S2p doublets. The spin-orbit energy shift (ca. 1.2 eV) and the intensity ratio of 2:1 for the $S2p_{3/2}/S2p_{1/2}$ components has been taken to fit. The S2p peak-fitting parameters are reported in Table 1 for the three samples analyzed. The three components identified are attributed to sulfur in the bulk of CdS (161.9 eV), sulfur atoms from the oligothiophene (164.1 eV), the organic stabilizer bound to the nanoparticle, and a very small amount of oxidized sulfur (168.4 eV), from the oxidation of the particle surface. Table 2 reports the surface chemical composition (in percent) of the nanoparticles. Similarly, as previously observed for CdS and CdSe nanocrystals, the $Cd^{2+}/S^{2-}$ atomic ratio is nonstoichiometric,[17] showing a significant excess of cadmium atoms on the surface, with the atomic ratio of Cd/S = 1.54, 1.52 and 1.43 for **CdS-2T**, **CdS-3T** and **CdS-4T**, respectively. It is reasonable to assume that the lack of sulfur in the outermost layers of the nanoparticles is compensated by the carboxylate groups from the oligothiophene capping ligands.

The production of highly monodisperse semiconductor nanocrystals requires stabilizers such as amines, phosphanes, phosphane oxides and phosphonic acids as capping ligands. However, a few recent reports have examined in detail the binding of long-chain carboxylic capping ligands

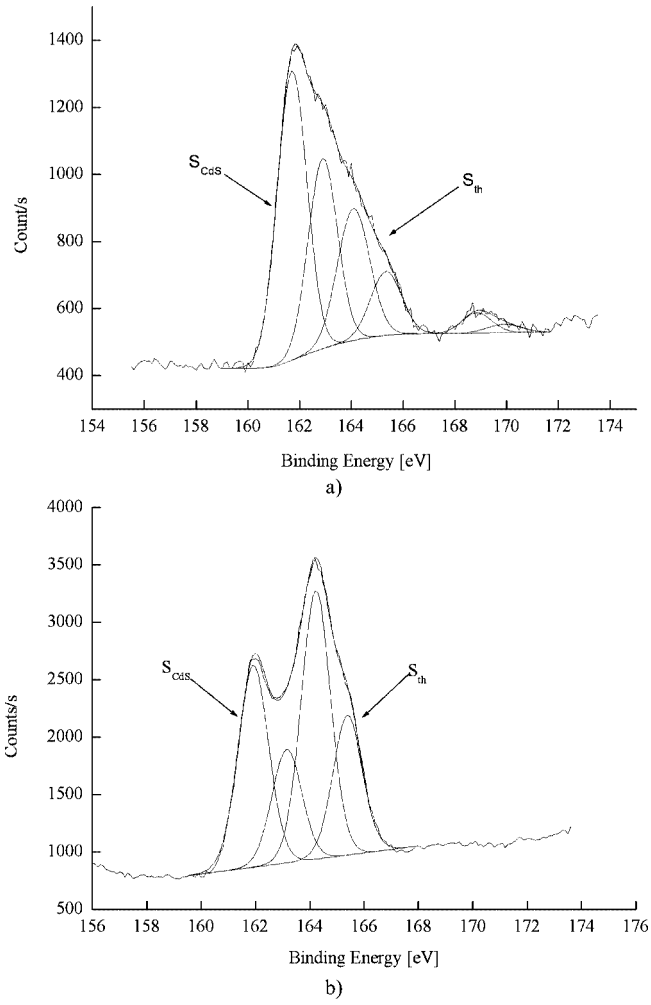


Figure 5. Core level of S2p for **CdS-4T** (top) and **CdS-2T**.

Table 1. Characteristic S2p binding energies (eV) for sulfur within different materials.[a]

| Materials | $S_{CdS}$ | | $S_{Th}$ | | $S_{ox}$ | |
|---|---|---|---|---|---|---|
| | S2p3/2 | S2p1/2 | S2p3/2 | S2p1/2 | S2p3/2 | S2p1/2 |
| **CdS-2T** | 161.7 | 162.9 | 164.1 | 165.3 | 168.4 | 169.9 |
| | 40.4 | 26.3 | 19.9 | 9.3 | 2.83 | 1.3 |
| **CdS-3T** | 161.6 | 162.9 | 164.0 | 165.2 | 168.7[b] | |
| | 48.9 | 25.8 | 15.4 | 7.9 | 1.9 | |
| **CdS-4T** | 161.9 | 163.2 | 164.2 | 165.4 | – | – |
| | 28.5 | 15.7 | 36.7 | 19.1 | – | – |

[a] For each specimen, each sulfur type has an $S2p_{3/2}$-$S2p_{1/2}$ doublet. The binding energy positions are in eV (top line) and the contribution to the total S2p peak area is given in % (bottom line). [b] The S2p peak was very poorly resolved, so $S2p_{3/2}$ and $S2p_{1/2}$ were combined.

Table 2. Apparent surface chemical composition of surface-modified CdS nanoparticles.

| Materials | Cd | $S_{CdS}$ | $S_T$ | $S_{ox}$ | C | O | Na |
|---|---|---|---|---|---|---|---|
| **CdS-2T** | 16.5 | 10.1 | 4.39 | 0.61 | 49.8 | 18.6 | – |
| **CdS-3T** | 26.3 | 16.9 | 5.19 | 0.44 | 36.0 | 15.2 | – |
| **CdS-4T** | 10.6 | 7.42 | 9.33 | – | 49.4 | 22.6 | 0.67 |

 © 2007 Wiley-VCH Verlag GmbH & Co. KGaA, Weinheim 

at the CdS and CdSe NC surface. Mulvany et al.[18] and Dushkin et al.[19] reported a version of the hot-matrix method for the synthesis of CdSe nanoparticles using a noncoordinating solvent and a carboxylic acid as the coordinating ligand. This new method is an adaptation of widely reported methods that use cadmium carboxylate salts as precursors for these NCs. Their synthetic approach allows one to tune the nucleation and growth of CdSe by altering the reactivities of selenium and cadmium and to probe more clearly the role of the chalcogenide and cadmium precursors on CdSe nanocrystal synthesis, as well as the role of TOPO on surface passivation. In these systems, it was shown that the usual stabilizing agent, TOPO, can be eliminated completely in favour of a fatty acid without effects on the particle size distribution or their optical properties. They claim that CdSe terminated with a long-chain carboxylate is one of the cleanest colloidal CdSe systems to date, with oleic acid as the sole stabilizer. Peng et al.[20] have developed a successful approach to synthesizing CdS in a noncoordinating solvent. Oleic acid, a natural surfactant, was chosen as the ligand for stabilizing the nanocrystals and the cationic precursors. The ability to use long-chain carboxylic acids as stabilizers was later extended to InP and InAs nanocrystals.[21]

Therefore, it is necessary to estimate the contribution of the carboxylate capping ligands to the total carbon content of the nanoparticles. Figure 6 displays a typical C1s region for **CdS-2T** fitted with five components centred at 285.0, 286.0, 287.4, 288.7 and 290.2 eV. The component centred at 288.7 eV is assigned to the carboxylate group from the oligothiophenes.[22] The contribution of the carboxylate groups to the C1s peak areas of the **CdS-2T**, **CdS-3T** and **CdS-4T** nanoparticles is 11.8, 12.1 and 9.9%, respectively, corresponding to 5.78, 4.35 and 4.88% carboxylate carbon atoms. Note that the contributions of the carboxylates to the C1s region differ slightly from those expected, due to unavoidable adventitious hydrocarbon contamination and the presence of carbonates (peak centred at ca. 290.5 eV).

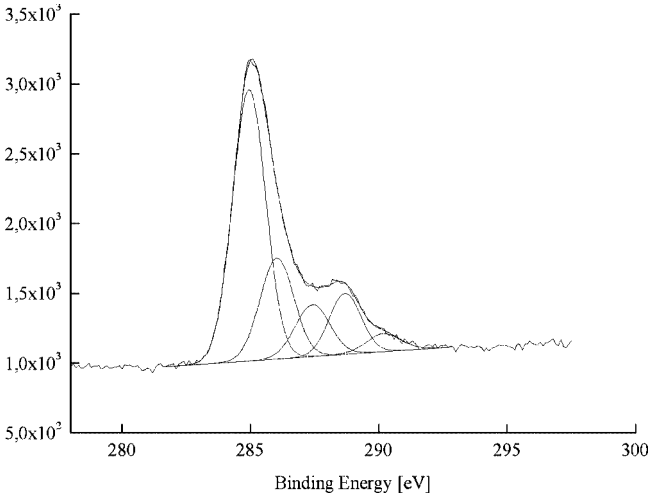


Figure 6. Narrow-scan XPS spectrum of C1s region for **CdS-2T**.

With the contribution of the carboxylates to the surface composition in hand, the $Cd/(S_{CdS}+1/2C_{COO^-})$ atomic ratio, assuming that only one carboxylate group per oligothiophene is coordinated with $Cd^{2+}$ on the particle surface, is 1.26, 1.31 and 1.07, which is in agreement with the stoichiometry of CdS. The contribution of the carboxylates to the surface chemical composition can further be related to the sulfur content due to the oligothiophenes, and the experimental $COO^-/S_T$ molar ratio compared to that expected from microanalysis. Figure 7 shows a plot of the experimental $COO^-/S_T$ molar ratio, as determined by XPS, vs. microanalysis data. The results reflect reasonably well the progressive relative concentration of the carboxylate groups within the oligothiophenes.

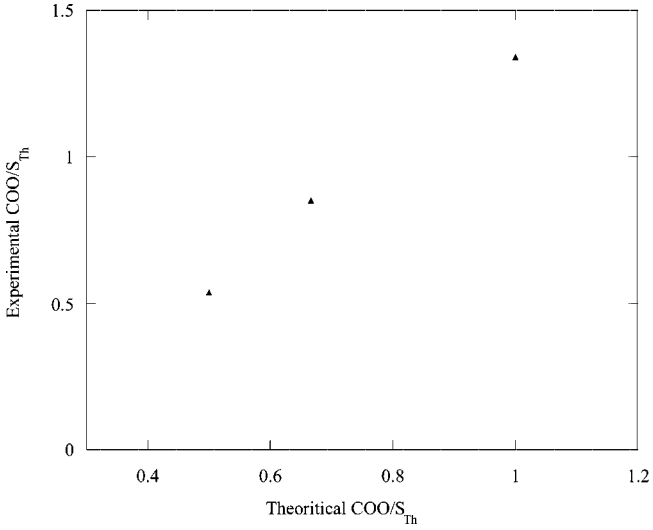


Figure 7. Plot of $COO^-/S_T$ molar ratio, as determined by XPS vs. microanalysis results.

From the surface chemical composition reported in Table 1, one can estimate the number of molecules bound per CdS particle. In this case, only the sulfur of the organic component is considered for the oligothiophenes, and the CdS nanoparticles are, to a first approximation, assumed to be stoichiometric. Because the nanoparticles have also diameters lower than the sampling depth probed by XPS, it is reasonable to assume that the apparent surface composition reflects that of the whole coated nanoparticle. For **Cd-3T** and **CdS-4T** the diameters are estimated to be 3.8 and 2 nm, respectively. Taking into account the density of CdS, and thus the number of Cd atoms per particle, one can estimate the number of bound oligothiophenes per nanoparticle using the ratio $(\%S_T/n_S)/(\%Cd/n_{Cd})$ where $\%S_T$ and %Cd are the atom percents reported in Table 2, $n_{Cd}$ the number of Cd atoms per CdS nanoparticle, and $n_S$ the number of thiophene repeat units per oligothiophene. For **CdS-3T** and **CdS-4T**, we find ca. 19 molecules of terthiophene and 18 molecules of quaterthiophene per nanoparticle.

The hybrid structures of **CdS-*n*T**, with two, three and four rings were characterized by means of absorption and emission spectroscopy. In the UV/Vis studies the structures

 © 2007 Wiley-VCH Verlag GmbH & Co. KGaA, Weinheim 

were investigated in EG and dimethyl sulfoxide. No marked differences were observed in the absorption spectra of these compounds in either solvent, the resulting spectra being essentially the additive combination of those of the two constituent parts, with slight modification. Figure 8 shows the typical spectra recorded for the CdS–oligothiophene series as well as CdS stabilized by acetate in EG. The NCs stabilized by acetate have an absorption shoulder at 440 nm corresponding to the first excitonic peak. Note that in our studies variation of the synthesis conditions was found to have no significant effect on the excitonic peak energy.

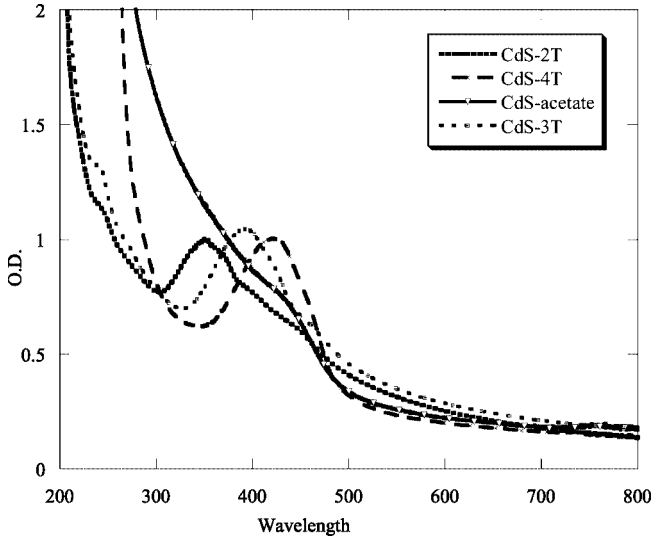


Figure 8. UV/Vis spectra of three samples of **CdS-*n*T** and **CdS-acetate**.

The spectrum of **CdS-*n*T** shows a main peak, in the visible region, due to the π–π* transition, and a weaker but well-defined shoulder at low energy attributed to NC excitonic absorption. The main peak exhibits a perfect correlation with the conjugation length, i.e. the maximum is significantly redshifted as the conjugation length of the corresponding oligothiophene shell increases. Hence, UV/Vis absorption spectra of **CdS-*n*T** show a maximum centred at 350, 395 and 428 nm for **CdS-2T**, **CdS-3T** and **CdS-4T**, respectively. All these maxima were found to be close to those observed for solutions of the oligothiophene dicarboxylates. However, when the spectra of the CdS-bound oligomers are examined carefully the absorption seems not to be a simple superposition of the two components, as can be seen in Figure 9. The easiest case is **CdS-2T**, where the two bands are separate. Additional shoulders appear at the low-energy side of the bithiophene absorption (367 and 400 nm), indicating a ground-state interaction between CdS NCs and the conjugated system. For longer oligomers, the absorption of the organic shell overlaps that of CdS, which makes discussion difficult. The structureless broad absorption observed indicates that the oligomers bound to the nanoparticle surface are relatively flexible for the formation of different conformers in the ground state.

The number of oligomers attached to the nanoparticle is fundamental to fully characterizing the **CdS-*n*T** hybrid core-shell materials. This can be calculated using the absorbance at the oligomer absorption maximum ($\lambda_{max}$), that at the CdS excitonic peak (450 nm) and their extinction coefficients. Although the determination of the NC extinction coefficient has been largely debated in the literature, recent work, has established for CdS NCs capped with oleic acid show a strong dependence of the extinction coefficient on the size of the NCs, while the nature of the ligands and the solution refractive index were shown not to have a significant effect.[23] Given the average particle size (4 nm for **CdS-2T**), $\varepsilon$ = 552820 L mol$^{-1}$ cm$^{-1}$ for the extinction coefficient of CdS NCs, and 26100 L mol$^{-1}$ cm$^{-1}$ for the extinction co-

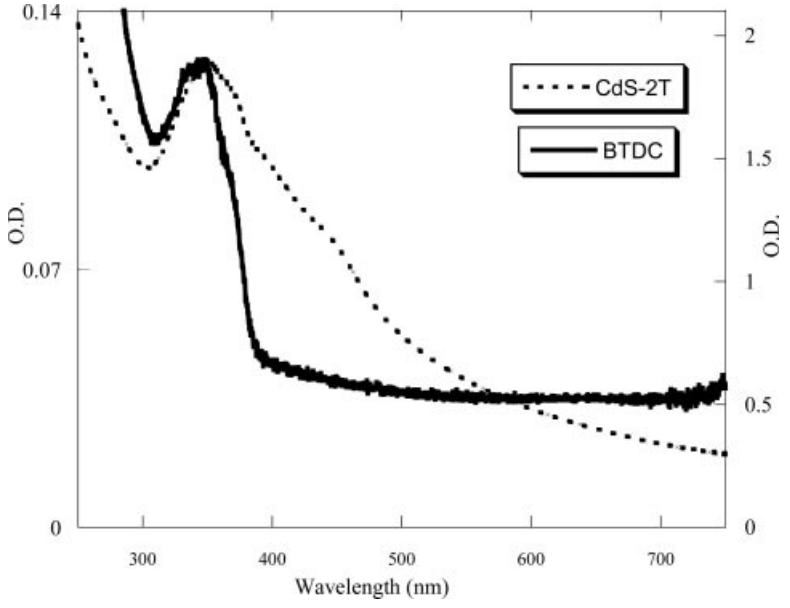


Figure 9. UV/Vis spectra of **CdS-2T** and **BTDC**.

 © 2007 Wiley-VCH Verlag GmbH & Co. KGaA, Weinheim 

efficient of **BTDC**, the maximum absorbance is 1.88 for **BTDC** and that for the CdS excitonic peak is 1.035. We found that each NC is embedded in 40 **BTDC** molecules. This result is consistent with the work of Milliron et al., who report 50 molecules of pentathiophene per CdSe nanocrystal.[6] Note that the value obtained is relatively low compared to the theoretical one. In fact, 200 molecules were expected to form a close-packed monolayer in a 4-nm diameter sphere. The area occupied per molecule was estimated using the following approximations. The molecule binds perpendicularly to the surface; the area occupied is the projection of the oligomer on the NC. From the known bond lengths, van der Waals atomic radii and the thickness of the oligomers, the area occupied per molecule is estimated to be 24 $Å^2$. Using the same UV/Vis procedure, an average of 18 molecules per NC was found for **CdS-3T**; this value is in good agreement with that estimated from the XPS measurements.

It is well known that the fluorescence properties of CdS NCs depend strongly on their surface states, surface passivation and size distributions. Fluorescence quench or changes in the quantum yield indicate also differences in the branching ratio between radiative and nonradiative decay and therefore might serve as a powerful probe of NC-conjugated polymer interactions. To determine the degree of electronic communication between CdS NCs and oligothiophene, we performed fluorescence measurements. Figure 10 illustrates the room-temperature fluorescence spectra of **CdS-*n*T**. The general trends observed are that the emission of CdS-bound oligothiophenes is weak and exhibits a weak Stokes shift. The intensity drops by a factor of two relative to their homologues, i.e. sodium dicarboxylates. We note also that the emission spectra of **CdS-*n*T** are redshifted relative to the oligothiophenedicarboxylates. This shift is more pronounced for the longer oligomers, i.e. **CdS-3T** and **CdS-4T**. Hence, the emission spectra of **CdS-2T** and its free ligand are similar in energy and shape, except for the low-energy side. **CdS-2T** has a long emission tail in the low-energy part of the spectrum. Quite different emission spectra were obtained for **CdS-3T** and **CdS-4T**, as seen in Figure 10b, c. Those of **TTDC** and **QTDC** sodium salts show two clearly resolved bands at 450 and 465 nm and at 480 and 500 nm, respectively, which have been identified as the vibronic replicas of the O–O transition. These emission maxima are redshifted to 490 and 530 nm for **CdS-3T** and **CdS-4T**, respectively. The intensity of the first band observed for the precursors decreases and becomes a shoulder in **CdS-*n*T**. The similarity in the appearance of the emission spectra of the precursors and CdS-bound oligothiophenes suggests that the origin of this emission is π*–π emission; no CdS NC emission is observed. Selective excitations have been undertaken to analyze the CdS NC emission. Upon excitation into the CdS excitonic absorption band (461 nm), the emission spectrum is similar to that when exciting into the main oligothiophene band, indicating a complete quench of CdS NC fluorescence. The **CdS-*n*T** excitation spectra are similar to the absorption spectra of the oligothiophene precursors.

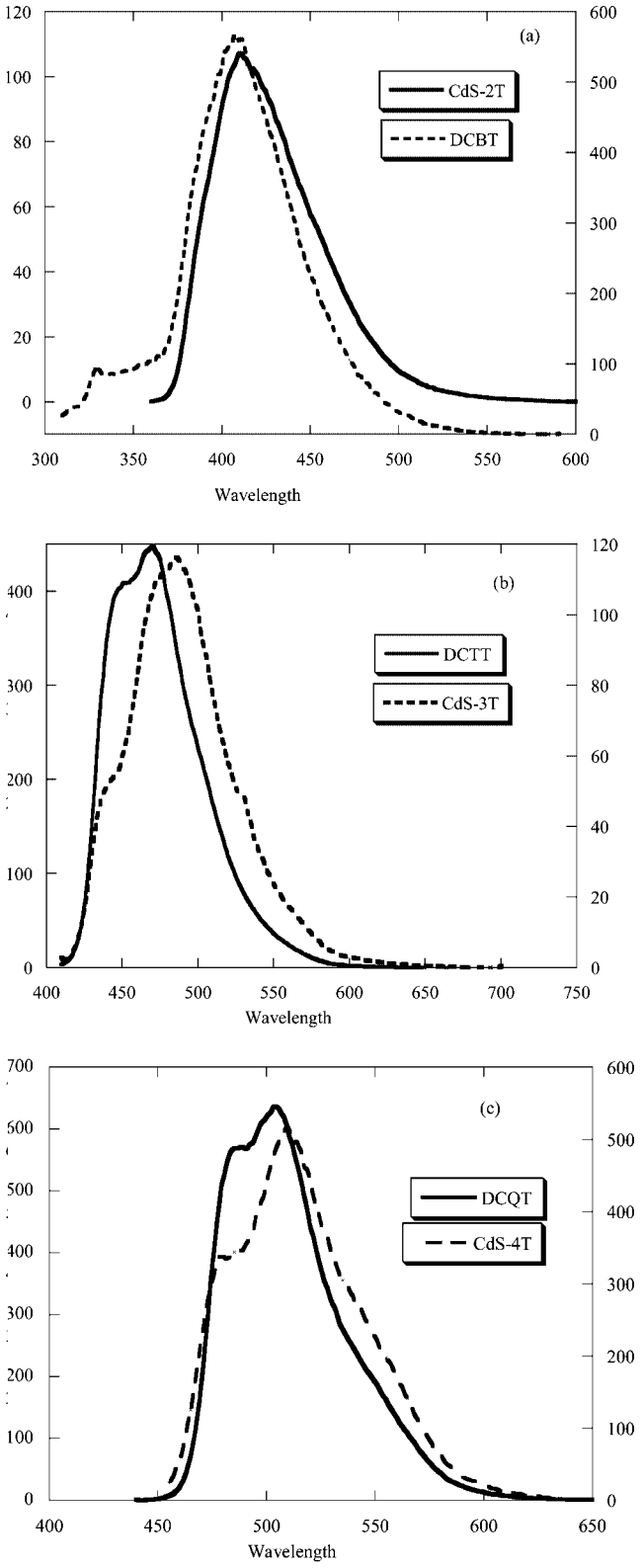


Figure 10. Fluorescence spectra of (a) **CdS-2T** and **BTDC**, (b) **CdS-3T** and **TTDC**, (c) **CdS-4T** and **QTDC**.

The fluorescence changes in the **CdS-*n*T** are in good agreement with the **ZnO-(Th)$_n$** fluorescence observed by Jiu et al. who reported a strong redshift in the precursor emis-

 © 2007 Wiley-VCH Verlag GmbH & Co. KGaA, Weinheim 

sion, when they were adsorbed on ZnO NC.[24] They found a 100-nm redshift emission of **ZnO-(Th)$_n$** and free precursors. Similar significant modification in the spectral distribution of fluorescence of the CdSe conjugated oligophenylene–vinylene surfactants, relative to blended films of the inorganic and organic components was recently observed by Emrick et al.[3] They attributed this effect to enhanced energy transfer between the conjugated ligand and the quantum dot facilitated by connecting the conjugated backbone directly to the quantum dot.

To help understand the fluorescence results, NC emission properties must be taken into account. Indeed, it has been established that the emission properties of NCs are very sensitive to their surface environment. In general, as-synthesized NCs have high fluorescence quantum yields approaching unity. Decrease in the quantum yield and/or change in the fluorescence shape are considered to be the result of the surface states located in the bandgap of the NCs, which act as trapping states for the photogenerated charges. These surface trapping states originate from the dangling bonds of some of the surface atoms. It has been speculated that in III–V semiconductor NCs, the nanoparticle surfaces are terminated by either cadmium or chalcogen sites. On the other hand, it is well established that an aromatic acid can be bound to a metal surface through the oxygen lone-pair electrons and aromatic carboxylates are also common O-donor ligands in cadmium coordination chemistry. In light of this evidence, and based on published reports showing that carboxylates can act as capping ligands,[18–21] we assume that the oligomer binds to a dangling cadmium ion on the NC surface through the lone-pair electrons of the carboxylate function. In this way, a monolayer of cadmium oligomer complex is formed on the surface of the CdS nanoparticles. This novel supramolecular structure composed of dangling cadmium and conjugated oligomer has more electronic delocalization, which profoundly influences the emission properties of the π-conjugated system of the oligomers. This assumption corroborates well with ab initio calculations made by Puzder et al. The authors calculated the binding energy of different organic functions to a range of the CdSe NC facets.[25] The dominant binding carboxylate interaction found is between oxygen atoms in the ligands and the dangling cadmium atoms on the NC surfaces.

## Conclusion

We have prepared a new organic–inorganic structure consisting of oligothiophenes grafted onto the surface of CdS nanocrystals, with narrow size distribution, using a one-pot reaction. The number of bound molecules and the grafting of the oligomers on the surface of the nanocrystals were investigated using XPS, IR, UV/Vis and fluorescence spectroscopy. The bonding of the oligomers to the nanocrystal surface is made possible by complexing the dangling cadmium ion on the surface with the lone-pair electrons of the carboxylate group at the end of the oligomers, leading to better electronic interaction between the two components. On the basis of the observed properties, these hybrid nanoparticles should have potential applications in optoelectronic and photovoltaic devices.

## Experimental Section

**Materials:** All chemicals used in the syntheses and the analytical grade solvents used for UV/Vis studies were purchased from Aldrich and used as received.

**Organic Synthesis:** 2,2′-Bithiophene-5,5′-dicarboxylic acid (**I**), 2,2′;5′,2″-terthiophene-5,5″-dicarboxylic acid (**II**), and 2,2′;5′,2″;5″,2‴-quaterthiophene-5,5‴-dicarboxylic acid (**III**) were prepared as described in detail elsewhere.[10] All the oligothiophenes were fully characterized by $^1$H and $^{13}$C NMR spectroscopy and elemental analysis.

**Synthesis of Oligothiophene-Functionalized CdS Nanoparticles:** CdS–oligothiophene hybrid nanoparticles were synthesized in ethylene glycol by the Polyol process.[11] Briefly, the general procedure involves addition of cadmium acetate and thiourea to a given volume of polyol to obtain a concentration between $10^{-2}$ and $10^{-3}$ mol L$^{-1}$. To form CdS–oligothiophene hybrids, oligothiophene with different conjugation lengths was added to the solution. The final oligothiophene concentration was also between $10^{-2}$ and $10^{-3}$ mol L$^{-1}$. The mixture was then heated with vigorous stirring to a temperature varying between 100 and 150 °C. Purification was achieved by adding excess methanol. The precipitate formed was centrifuged and the upper liquid layer decanted, and the isolated solid then dispersed in an appropriate solvent. The above centrifugation and isolation procedure was repeated several times.

**General Experimental Procedures:** UV/Vis spectroscopy. UV/Vis absorbance spectra were acquired with a Cary 50 spectrometer. Fluorescence spectra were recorded with a Perkin–Elmer LS50 spectrofluorometer. IR spectra were recorded on KBr pellets using a Nicolet IRTF-Magma 860. Transmission electron microscopy (TEM) observations were performed with a JEOL 100 kV JEM-100CX II microscope. The CdS-functionalized nanoparticles were deposited on the amorphous carbon membrane of the transmission electron microscope grid and the solvent then evaporated off at room temperature. The mean diameter was estimated from image analysis of a hundred particles. X-ray powder diffraction (XRD) patterns were recorded with a Philips PW1050/25 using Cu-$K_\alpha$ radiation. The diffractometer was calibrated using a standard Si sample. The counting time was 30 s per $2\theta$ step of 0.05°. The mean crystallite size was estimated using the Scherrer equation. X-ray photoelectron spectroscopy signals were recorded using a Thermo VG Scientific ESCALAB 250 system equipped with a micro-focused, monochromatic Al-$K_\alpha$ X-ray source (1486.6 eV) and a magnetic lens which increases the electron acceptance angle and hence the sensitivity. The specimens were pressed against double-sided adhesive tapes mounted on sample holders, and then pumped overnight in the fast-entry lock at ca. $5 \times 10^{-8}$ mbar before introduction into the analysis chamber. A 650-μm X-ray beam was used at a power of 13.7 mA × 15 kV. The spectra were acquired in the constant analyzer energy mode, with pass energies of 150 and 40 eV for the survey and the narrow regions, respectively. Charge compensation was achieved with an electron flood gun operated under argon flow at a partial pressure of $2 \times 10^{-8}$ mbar in the analysis chamber. Under these conditions, the surface charge was negative but perfectly uniform. Avantage software, version 2.2 (Thermo Electron), was used for digital acquisition and data processing.

 © 2007 Wiley-VCH Verlag GmbH & Co. KGaA, Weinheim 

Spectra were calibrated by setting the C1s peak maximum at 285.0 eV. The apparent surface compositions (in atom%) were determined by considering the integrated peak areas of the C1s, O1s, S2p and $Cd3d_{5/2}$ peaks and the manufacturer's sensitivity factors.

## Acknowledgments

The authors wish to thank the Conseil Régional d'Ile-de-France for financial support through the SESAME 2000 Scheme, and Ms. Carole Connan for her assistance with the XPS measurements, Marie-Josèphe Vaulay and Frédéric Herbst for TEM and XRD characterizations.

[1] a) Y. Xia, P. Yang, Y. Sun, Y. Wu, B. Mayer, B. Gates, Y. Yin, F. Kim, H. Yan, *Adv. Mater.* **2003**, *15*, 353–389; b) M. A. El-Sayed, *Acc. Chem. Res.* **2004**, *37*, 326–333.
[2] a) F. Garnier, *Acc. Chem. Res.* **1999**, *32*, 209–215; b) H. E. Katz, Z. Bao, S. L. Gilat, *Acc. Chem. Res.* **2001**, *34*, 359–369.
[3] a) M. Y. Odoi, N. I. Hammer, K. Sill, T. Emrick, M. D. Barnes, *J. Am. Chem. Soc.* **2006**, *128*, 3506–3507; b) H. Skaff, K. Still, T. Emrick, *J. Am. Chem. Soc.* **2004**, *126*, 11322–11325; c) J. Locklin, D. Patton, S. Deng, A. Baba, M. Millan, R. C. Advincula, *Chem. Mater.* **2004**, *16*, 5187–5193.
[4] N. C. Greenham, X. Peng, A. P. Alivisatos, *Phys. Rev. B* **1996**, *54*, 17628–17637.
[5] R. Buller, H. Cohen, E. Minkin, R. Popovitz-Biro, E. Lifshitz, M. Lahav, *Adv. Funct. Mater.* **2002**, *12*, 713–718.
[6] D. J. Miliron, A. P. Alivisatos, C. Pitois, C. Edder, J. M. J. Fréchet, *Adv. Mater.* **2003**, *15*, 58–61.
[7] B. Sun, E. Marx, N. C. Greenham, *Nano Lett.* **2003**, *3*, 961–963.
[8] W. J. E. Beek, R. A. J. Janssen, *Adv. Funct. Mater.* **2002**, *12*, 519–525.
[9] J. Liu, T. Tanaka, K. Sivula, A. P. Alivisatos, J. M. J. Frechet, *J. Am. Chem. Soc.* **2004**, *126*, 6550–6551.
[10] J. Kagan, S. K. Arora, A. Usunol, *J. Org. Chem.* **1983**, *48*, 4076–4078.
[11] a) G. Viau, R. Brayner, L. Poul, N. Chakroune, E. Lacaze, F. Fiévet-Vincent, F. Fiévet, *Chem. Mater.* **2003**, *15*, 486–494; b) C. Feldmann, Ch. Metzmacher, *J. Mater. Chem.* **2001**, *11*, 2603–2606.
[12] T. Matrab, A. Yassar, G. Viau, N. Chakroune, F. Fievet, P. C. Lacaze, *J. Colloid Interface Sci.* **2006**, *296*, 95–101.
[13] B. Simmons, S. Li, V. T. John, G. L. McPherson, A. Bose, W. Zhou, J. He, *Nano Lett.* **2002**, *2*, 263–268.
[14] M. J. Byrnes, M. H. Chisholm, R. J. H. Clark, J. C. Gallucci, C. M. Hadad, N. J. Patmore, *Inorg. Chem.* **2004**, *43*, 6334–6344.
[15] R. C. Mehrotra, R. Bohra, *Metal Carboxylate*, Academic Press, New York, **1983**.
[16] a) U. Winkler, D. Eich, Z. H. Chen, R. Fink, S. K. Kulkarni, E. Umbach, *Phys. Stat. Sol. A* **1999**, *173*, 253–259; b) J. E. Bowen Katari, V. L. Colvin, A. P. Alivisatos, *J. Phys. Chem.* **1994**, *98*, 4109–4117.
[17] a) H. Encai, S. Haiping, Z. Zheng, L. Junqiu, Y. Bai, S. Jiacong, *Chem. Mater.* **1999**, *11*, 3096–3102; b) B. Schreder, T. Schmidt, V. Ptatschek, U. Winkler, A. Materny, E. Umbach, M. Lerch, G. Müller, W. Kiefer, L. Spanhel, *J. Phys. Chem. B* **2000**, *104*, 1677–1685.
[18] A. Jasieniak, C. Bullen, J. Embden, P. Mulvaney, *J. Phys. Chem. B* **2005**, *109*, 20665–20668.
[19] G. G. Yordanov, G. D. Gicheva, B. H. Bochev, C. D. Dushkin, E. Adachi, *Colloids Surf. A* **2006**, *273*, 10–15.
[20] W. W. Yu, X. Peng, *Angew. Chem. Int. Ed.* **2002**, *41*, 2368–2371.
[21] D. Battaglia, X. Peng, *Nano Lett.* **2002**, *2*, 1027–1030.
[22] http://srdata.nist.gov/xps
[23] W. W. Yu, L. Qu, W. Guo, X. Peng, *Chem. Mater.* **2003**, *15*, 2854–2860.
[24] T. Jiu, H. Liu, H. Gan, Y. Li, S. Xiao, H. Li, Y. Liu, F. Lu, L. Jiang, D. Zhu, *Synth. Met.* **2005**, *148*, 313–319.
[25] A. Puzder, A. J. Williamson, N. Zaitseva, G. Galli, L. Manna, A. P. Alivisatos, *Nano Lett.* **2004**, *4*, 2361–2361.

Received: July 7, 2006
Published Online: February 9, 2007

 © 2007 Wiley-VCH Verlag GmbH & Co. KGaA, Weinheim 

DOI: 10.1002/ejic.200600708

# New Dinuclear $Mn^{III}$ Compounds with 2-$MeC_6H_4COO$ and 2-$FC_6H_4COO$ Bridges – Effect of Terminal Monodentate Ligands ($H_2O$, $ClO_4^-$ and $NO_3^-$) on the Magnetic Properties

**Gema Fernández,[a] Montserrat Corbella,*[a] Gabriel Aullón,[a] Miguel A. Maestro,[b] and José Mahía[c]**

**Keywords:** Manganese / Magnetic properties / Ligand effects

Four new dinuclear $Mn^{III}$ complexes with the general formula $[\{Mn(bpy)L\}(\mu\text{-}RCOO)_2(\mu\text{-}O)\{Mn(bpy)L'\}]^{n+}$ (bpy = 2,2′-bipyridine) have been synthesized with RCOO = 2-$MeC_6H_4COO$ (**1**, **2**) and 2-$FC_6H_4COO$ (**3**, **4**); the counteranion could be $NO_3^-$ (**1**, **3**) or $ClO_4^-$ (**2**, **4**), and a monodentate ligand (L, L′) completes the octahedral environment of the manganese ions. For compound **1** L = $H_2O$ and L′ = $H_2O$ or $NO_3^-$; compound **2** shows two different dinuclear complexes, one of them with L = L′ = $H_2O$ and the other one with L = L′ = $ClO_4^-$; for compound **3**, L and L′ = $H_2O$ or $NO_3^-$ and for compound **4**, L = $H_2O$ and L′ = $ClO_4^-$. The characterization by X-ray diffraction shows an important disorder in the crystal for the nitrate compounds, principally for compound **3**, where each monodentate ligand could be a water molecule or a nitrate anion. The antiferromagnetic contribution to the magnetic coupling constant *J* is weaker for the nitrate compounds (**1** and **3**) than for the perchlorate compounds (**2** and **4**), and a ferromagnetic behaviour is found for compound **3**, with $J = +1.4\ cm^{-1}$. The magnetic coupling constant found for compound **1** is $J = -0.5\ cm^{-1}$ and for compounds **2** and **4** it is $-5.6\ cm^{-1}$ and $-3.5\ cm^{-1}$, respectively. Extended Hückel calculations were carried out and there is evidence that the nitrate anions coordinated to the manganese atoms act as π-acid ligands providing a means to diminish the antiferromagnetic contribution.

(© Wiley-VCH Verlag GmbH & Co. KGaA, 69451 Weinheim, Germany, 2007)

## Introduction

Interest in dinuclear $Mn^{III}$ complexes with a carboxylate ligand is due to their presence in some metalloenzymes such as the Mn-catalase. With the aim of obtaining good model compounds of this enzyme several dinuclear $Mn^{III}$ complexes with the $[Mn_2(\mu\text{-}RCOO)_2(\mu\text{-}O)]^{2+}$ core have been reported in the literature,[1–15] but only 11 of them are characterized by X-ray diffraction and magnetic studies.[5–15]

It is well known that the magnetic interaction for this kind of complex is weak and could be antiferro- or ferromagnetic[16] with *J* values between +18 and –8 $cm^{-1}$. Three possible distortions of the coordination octahedron can be observed due to the Jahn–Teller effect: (a) compression in the direction of the oxo-bridge, (b) elongation in the direction of one of the blocking ligands or (c) rhombic distortion. In general, compounds with a compressed octahedron in the direction of the oxo-bridging ligand show a ferromagnetic coupling, while complexes with an elongated octahedron (*z*) show antiferromagnetic coupling (Scheme 1). When the distortion is rhombic the magnetic interaction can be ferro- or antiferromagnetic.[5,6,16]

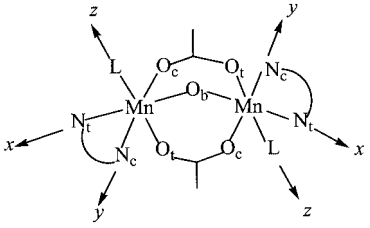


Scheme 1.

Tridentate amines $Me_3tacn$ (*N*,*N*′,*N*′′-trimethyl-1,4,7-triazacyclononane) and tp-tacn (trispyrrolidine-1,4,7-triazacyclononane) favour a compressed octahedron, and a significant ferromagnetic interaction was reported for $[\{Mn(Me_3tacn)\}_2(\mu\text{-}CH_3COO)_2(\mu\text{-}O)](ClO_4)_2$[11,12] ($J = +18.0\ cm^{-1}$) and $[\{Mn(tp\text{-}tacn)\}_2(\mu\text{-}CH_3COO)_2(\mu\text{-}O)](PF_6)_2$[13] ($J = +9.2\ cm^{-1}$). However, tridentate amines TMIP (tris(*N*-methylimidazol-2-yl)phosphane) and HB(pz)$_3$ (hidrotris(1-pyrazolyl)borate) lead to a rhombic distortion, (antiferromagnetic and ferromagnetic contributions are similar) and a small antiferromagnetic interaction was

[a] Departament de Química Inorgànica, Universitat de Barcelona, Martí i Franquès 1–11, 08028 Barcelona, Spain
E-mail: montse.corbella@ub.edu
[b] Departamento de Química Fundamental, Universidade da Coruña,
15071 A Coruña, Spain
[c] Servicios Xerais de Apoio a Investigación, Universidade da Coruña,
15071 A Coruña, Spain

 © 2007 Wiley-VCH Verlag GmbH & Co. KGaA, Weinheim 

found for compounds $[\{Mn(HBpz_3)\}_2(\mu\text{-}CH_3COO)_2(\mu\text{-}O)]$[14] ($J \approx -1$ cm$^{-1}$) and $[\{Mn(TMIP)\}_2(\mu\text{-}CH_3COO)_2(\mu\text{-}O)](ClO_4)_2$ ($J \approx -0.4$ cm$^{-1}$).[15]

When the blocking ligand is bpy (2,2′-bipyridine) the sixth position of the octahedron is occupied by a monodentate ligand; this situation provides a major flexibility to the coordination polyhedron and different types and degrees of distortion can be found. In this work we focused our attention on these kinds of compounds, with the aim of studying the effect of the carboxylate bridge and the monodentate ligand on the magnetic properties. We report here on four new complexes with a general formula $[\{Mn(bpy)L\}(\mu\text{-}RCOO)_2(\mu\text{-}O)\{Mn(bpy)L'\}]^{n+}$ with RCOO = 2-$MeC_6H_4COO$ (**1**, **2**) and 2-$FC_6H_4COO$ (**3**, **4**); the counteranion could be $NO_3^-$ (**1**, **3**) or $ClO_4^-$ (**2**, **4**). A monodentate ligand (L, L′) completes the octahedral environment of the manganese ions and could be $H_2O$, $NO_3^-$ or $ClO_4^-$. The coordination of the counteranion to the manganese ion enables us to study the effect of these ligands on the magnetic properties. Extended Hückel calculations were performed with the aim of clarifying the role of these ligands on the magnetic behaviour.

## Results and Discussion

### Syntheses

The synthetic method used to obtain the dinuclear $Mn^{III}$ complexes is a comproportionation reaction between $Mn^{II}$ and $MnO_4^-$ in the presence of carboxylic acid and a bidentate ligand (2,2′-bipyridine, bpy). The stoichiometry of this reaction is

$$1.6\ MnX_2 + 2\ RCOOH + 0.4\ Bu_4NMnO_4 + 2\ bpy \rightarrow [\{Mn(bpy)L\}(\mu\text{-}RCOO)_2(\mu\text{-}O)\{Mn(bpy)L'\}]X_{2-m} + 0.4\ Bu_4NX + 0.8\ HX + n\ H_2O$$

where RCOOH = 2-$MeC_6H_4COOH$, 2-$FC_6H_4COOH$, X = $NO_3$, $ClO_4$. These compounds show ionization isomerism, and the monodentate ligand (L and L′) could be $H_2O$ or the counteranion X. When both positions (L and L′) are occupied by X, a neutral complex is obtained ($m = 2$), while if L = $H_2O$ and L′ = X or $H_2O$ the complex is anionic (with $m = 1$ or 0).

The most significant difference between the four compounds synthesized here is their solubility. The perchlorate complexes **2** and **4** are very soluble in MeCN, so it is necessary to add $CH_2Cl_2$ (for **4**) or $CH_2Cl_2$ and hexanes (for **2**) to obtain good crystals. In contrast, the nitrate complexes **1** and **3** are less soluble, and subsequently it is necessary to work with dilute solutions to obtain crystalline products. In this case good crystals for X-ray diffraction are obtained directly from the mother liquor.

Infrared spectra of these compounds show two characteristics bands of the carboxylate bridging group at about 1600 and 1380 cm$^{-1}$. For compounds **1** and **3** the intense band of $NO_3^-$ appears overlapped with the carboxylate one (ca. 1380 cm$^{-1}$) and it is not possible to distinguish between the coordinated and free ion. Compounds **2** and **4** show three characteristic bands of the $ClO_4^-$ ion at ca. 1100 cm$^{-1}$. Several weak bands appear in the region between 800–400 cm$^{-1}$ corresponding to the counteranion, the Mn–O–Mn motive and the bpy ligand. The bipyridine ligand shows several bands, some of them in the range 1600–1440 cm$^{-1}$ and 780–635 cm$^{-1}$.

### Description of the Structures

The four compounds reported here display a similar structure. The cationic complex of each compound consists of a dinuclear unit with two carboxylates and one oxo group bridging the two manganese ions. The carboxylate bridging ligand is 2-$MeC_6H_4COO^-$, for **1** and **2**, and 2-$FC_6H_4COO^-$, for **3** and **4**. Each manganese ion is chelated by a bipyridine ligand (bpy), and the coordination sphere can be completed by a molecule of water or by an anion, i.e., nitrate or perchlorate. In all cases the carboxylate group and the aromatic ring of the $RCOO^-$ ligand are not in the same plane. The torsion angle $\delta(O\text{–}C_{carb}\text{–}C_{ar}\text{–}C'_{ar})$ is in the range 15.8–52.4°, however, the compounds with the 2-$FC_6H_4COO^-$ ligand (**3** and **4**) show smaller $\delta$ values than the compounds with the 2-$MeC_6H_4COO^-$ ligand (**1** and **2**). The relative orientation of the two coordination octahedrals is quite perpendicular, with the torsion angle $\tau$(L–Mn–Mn–L′) between 84.7–98.1°.

The Mn–$O_b$ distance for the compounds reported here is ca. 1.79 Å, similar to the values found for analogous compounds described in the literature.[5–15] The Mn–$O_b$–Mn angles for compounds **1**–**4** are between 121° and 125°; these values are also characteristic of these kinds of compounds. An important asymmetry in the carboxylate bridges is observed. In all these compounds, the Mn–O bond length is larger for the carboxylate oxygen atoms *trans* to the monodentate ligand than for the oxygen atoms placed in a *cis* position: $d$(Mn–$O_t$) > $d$(Mn–$O_c$). The bond lengths $d$(Mn–$O_t$) (ca. 2.16 Å) and $d$(Mn–$O_N$) (ca. 2.17 Å) are similar, while the distances $d$(Mn–$O_W$) and $d$(Mn–$O_{Cl}$) are longer (ca. 2.27 Å and ca. 2.36 Å, respectively). [$O_N$, $O_W$ and $O_{Cl}$ correspond to the oxygen atom of the L ligand coordinated to the manganese ions: nitrate, water and perchlorate, respectively.] Therefore, the monodentate ligand in these kinds of complexes produces an important effect on the coordination polyhedra of the manganese ions.

#### *[{Mn(bpy)($H_2O$)}(μ-2-$MeC_6H_4COO$)$_2$(μ-O){Mn($NO_3$)(bpy)}]$NO_3$·2$CH_3CN$·2$H_2O$ (1)*

This compound shows a certain disorder in the crystal structure between one water molecule and one nitrate anion. The labile position in Mn(2) is always occupied by a water ligand, O(1s). However, in Mn(1) only in 57% of the cases is this position occupied by a water ligand, O(5s), while in the rest of the cases it is occupied by one nitrate anion, O(6). In Figure 1 it is possible to see both ligands near to Mn(1), although only one of them is present in each dinuclear unit. The most relevant distances and angles are listed in Table 1. The nitrate ligand is situated approxi-

 © 2007 Wiley-VCH Verlag GmbH & Co. KGaA, Weinheim 

Table 1. Selected interatomic distances [Å] and angles [°] for compound [{Mn(bpy)($H_2O$)}(μ-2-$CH_3C_6H_4COO$)$_2$(μ-O){Mn($NO_3$)-(bpy)}]($NO_3$)·2$CH_3CN$·2$H_2O$ (**1**) with estimated standard deviations (Esd's) in parentheses.

| | | | |
|---|---|---|---|
| Mn(1)–O(1) | 1.796(3) | Mn(2)–O(1) | 1.784(2) |
| Mn(1)–O(2) | 1.959(3) | Mn(2)–O(5) | 1.958(3) |
| Mn(1)–N(1) | 2.075(3) | Mn(2)–N(3) | 2.069(3) |
| Mn(1)–N(2) | 2.076(3) | Mn(2)–N(4) | 2.083(3) |
| Mn(1)–O(4) | 2.151(3) | Mn(2)–O(3) | 2.123(3) |
| Mn(1)–O(6) | 2.258(3) | Mn(2)–O(1s) | 2.211(3) |
| Mn(1)–Mn(2) | 3.1480(7) | Mn(1)–O(1)–Mn(2) | 123.13(14) |
| O(6)–Mn(1)–Mn(2)–O(1s) | 97.20(13) | | |
| O(3)–C(11)–C(12)–C(17) | –15.78(60) | | |
| O(4)–C(18)–C(19)–C(24) | 41.83(59) | | |
| O(7)–N(5)–O(6)–Mn(1) | –101.27(82) | | |
| O(8)–N(5)–O(6)–Mn(1) | 79.21(78) | | |

mately perpendicular to the *z* axis, (defined in the L ligand direction as indicated above) with γ(O–*N*–O–Mn) angles of ca. 98°.

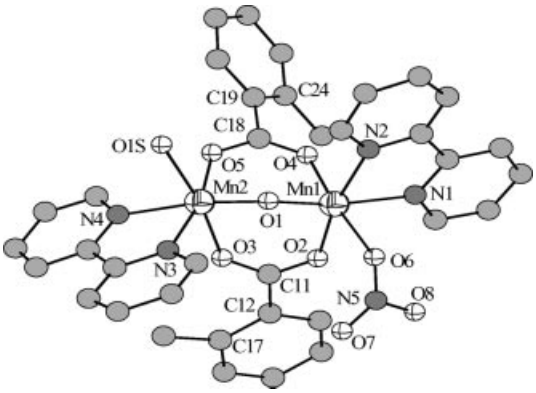


Figure 1. Drawing of the cation [{Mn(bpy)($H_2O$)}(μ-2-$CH_3C_6H_4COO$)$_2$(μ-O){Mn($NO_3$)(bpy)}]$^+$ in compound **1** showing two ligands coordinated in the same position for Mn(1): nitrate and water, corresponding to the two forms of the dinuclear unit present in the crystal.

There are hydrogen bonds between the nitrate anions and the coordinated water molecule generating a one-dimensional system. On one side, two Mn(2) ions of different dinuclear entities are bridged through the ionic nitrate anions and the coordinated water ligand, Mn(2)–O(1s)···O(10)–N–O(11)···O(1s)–Mn(2). On the other side, two Mn(1) ions of neighbour dinuclear complexes are bridged through the nitrate ion coordinated to one Mn(1) ion and the water molecule coordinated to the other Mn(1) ion, Mn(1)–O(6)–N–O(7)···O(5s)–Mn(1) (Figure 2).

### *[{Mn(bpy)($H_2O$)}$_2$(μ-2-$MeC_6H_4COO$)$_2$(μ-O)]-[{Mn($ClO_4$)(bpy)}$_2$(μ-2-$MeC_6H_4COO$)$_2$(μ-O)]($ClO_4$)$_2$·$CH_2Cl_2$ (2)*

The crystal structure of this compound shows two different dinuclear complexes. One of them is cationic, with the labile position on each manganese occupied by one water molecule, and the other one is neutral, with a perchlorate coordinated to each manganese in the labile position. Figure 3 shows the two dinuclear entities and the most important distances and angles are reported in Table 2. The cationic and neutral dinuclear complexes are bridged through hydrogen bonds between the water ligand of one entity and the perchlorate ligand of the other: Mn(3)–$O_W$···$O_{Cl}$–Mn(2). The same water ligand is also hydrogen bonded to one of the perchlorate anions.

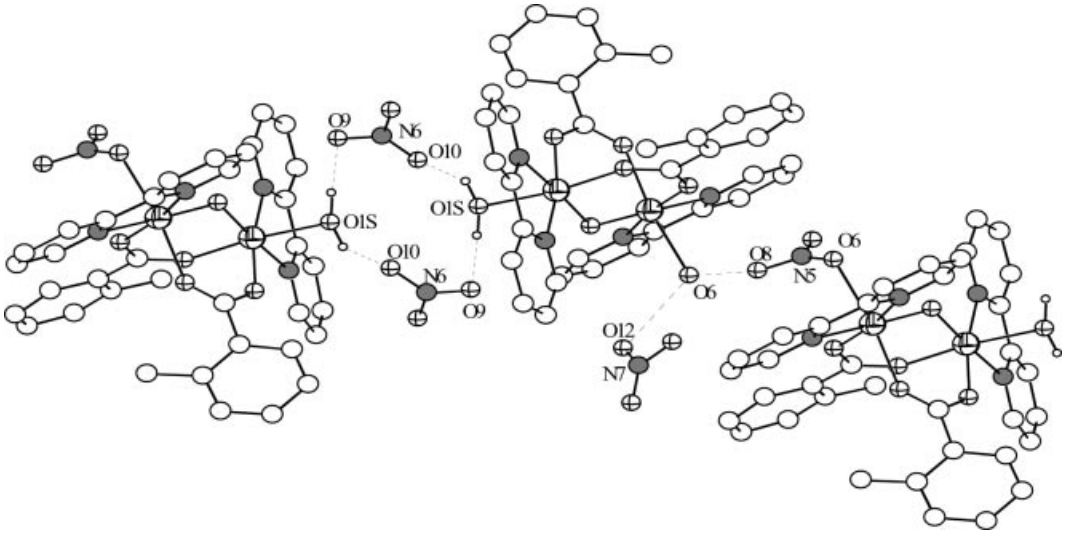


Figure 2. Plot of the hydrogen bonds present in the crystal of compound **1** between the nitrate ions and the water ligand on Mn(2), and between the nitrate ligand and water ligand on Mn(1).

 © 2007 Wiley-VCH Verlag GmbH & Co. KGaA, Weinheim 

Table 2. Selected interatomic distances [Å] and angles [°] for compound $[\{Mn(bpy)(H_2O)\}_2(\mu\text{-}2\text{-}CH_3C_6H_4COO)_2(\mu\text{-}O)][\{Mn(ClO_4)(bpy)\}_2(\mu\text{-}2\text{-}CH_3C_6H_4COO)_2(\mu\text{-}O)](ClO_4)_2\cdot 0.5CH_2Cl_2$ (**2**).

| | | | |
|---|---|---|---|
| Mn(1)–O(1) | 1.787(4) | Mn(3)–O(14) | 1.805(6) |
| Mn(1)–O(2) | 1.933(4) | Mn(3)–O(15) | 1.962(5) |
| Mn(1)–N(1) | 2.049(5) | Mn(3)–N(5) | 2.060(6) |
| Mn(1)–N(2) | 2.050(5) | Mn(3)–N(6) | 2.072(6) |
| Mn(1)–O(4) | 2.160(4) | Mn(3)–O(17) | 2.145(6) |
| Mn(1)–O(6) | 2.410(4) | Mn(3)–O(19) | 2.214(7) |
| Mn(2)–O(1) | 1.783(4) | Mn(4)–O(14) | 1.780(5) |
| Mn(2)–O(5) | 1.916(5) | Mn(4)–O(18) | 1.959(5) |
| Mn(2)–N(3) | 2.032(5) | Mn(4)–N(7) | 2.072(5) |
| Mn(2)–N(4) | 2.051(5) | Mn(4)–N(8) | 2.087(6) |
| Mn(2)–O(3) | 2.131(4) | Mn(4)–O(16) | 2.152(4) |
| Mn(2)–O(10) | 2.407(4) | Mn(4)–O(20) | 2.246(6) |
| Mn(1)–Mn(2) | 3.1182(13) | Mn(3)–Mn(4) | 3.149(3) |
| Mn(1)–O(1)–Mn(2) | 121.66(22) | Mn(3)–O(14)–Mn(4) | 122.90(28) |
| O(6)–Mn(1)–Mn(2)–O(10) | 112.15(13) | O(19)–Mn(3)–Mn(4)–O(20) | –90.00(21) |
| O(3)–C(1)–C(2)–C(3) | 52.39(94) | O(16)–C(37)–C(38)–C(39) | 45.75(97) |
| O(4)–C(9)–C(10)–C(11) | –45.97(95) | O(17)–C(45)–C(46)–C(47) | –43.32(96) |

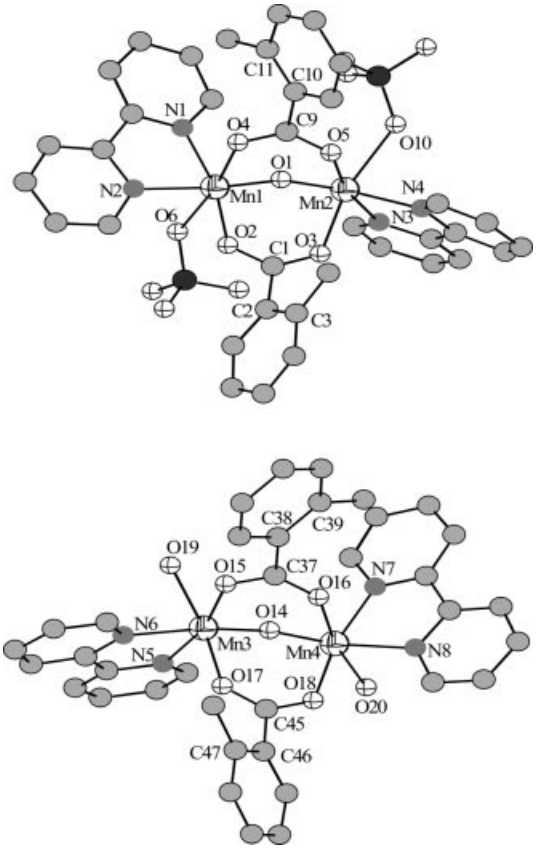


Figure 3. Drawing of the dinuclear complexes $[\{Mn(bpy)(H_2O)\}_2(\mu\text{-}2\text{-}CH_3C_6H_4COO)_2(\mu\text{-}O)]^{2+}$ (bottom) and $[\{Mn(ClO_4)(bpy)\}_2(\mu\text{-}2\text{-}CH_3C_6H_4COO)_2(\mu\text{-}O)]$ (top) present in the crystal of compound **2**.

### *[{Mn(bpy)(H$_2$O)}(μ-2-FC$_6$H$_4$COO)$_2$(μ-O){Mn(NO$_3$)(bpy)}]NO$_3$·H$_2$O (3)*

Similarly to compound **1**, a certain delocalization between the water and nitrate ligands is observed. In this case both manganese ions show disorder: in 31% of the dinuclear complexes both manganese ions present a coordinated water molecule, another 20% have one nitrate anion coordinated to each manganese and the last 49% show an asymmetric coordination (in one manganese ion the monodentate ligand is a nitrate ion, while in the other one it is a water molecule). Figure 4 shows the dinuclear complex with both possible ligands in the labile position. In comparison to compound **1**, the orientation of the nitrate ligand is different; in this case the ligand is placed quite parallel to the *z* axis, with $\gamma$(O–N–O–Mn) angles of ca. 20°. Selected interatomic bond lengths and angles are listed in Table 3. This compound shows disorder in the position of the F atoms of the carboxylate bridges: F(1) bonded to C(17) and F(1′) bonded to C(13) with an occupancy of 86% and 14%, respectively. And for the other carboxylate there is F(2) bonded to C(24) and F(2′) bonded to C(20) with an occupancy of 82% and 18%, respectively. Mn(1) and Mn(2) of neighbour complexes are bridged by hydrogen bonds between a water ligand of one dinuclear complex and a nitrate ligand of another complex, generating a 1D system.

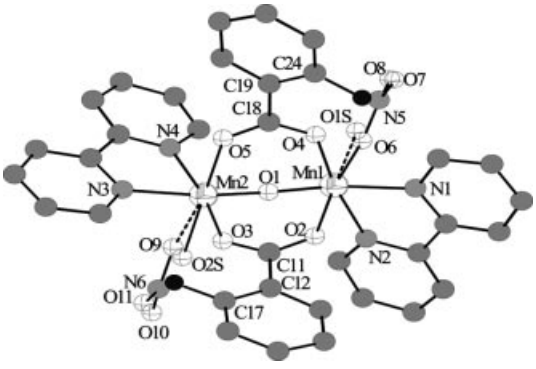


Figure 4. Drawing of the dinuclear complex of compound **3**. In the crystal the monodentate ligand attached to each manganese atom could be either nitrate or water. In the picture, both ligands are shown in each position.

### *[{Mn(bpy)(H$_2$O)}(μ-2-FC$_6$H$_4$COO)$_2$(μ-O){Mn(ClO$_4$)(bpy)}]ClO$_4$·2CH$_2$Cl$_2$ (4)*

Figure 5 show the dinuclear cationic complex of compound **4**. In this compound the labile position is occupied by one water ligand in Mn(1) and one perchlorate anion in

 © 2007 Wiley-VCH Verlag GmbH & Co. KGaA, Weinheim 

Table 3. Selected interatomic distances [Å] and angles [°] for compound [{Mn(bpy)($H_2O$)}(μ-2-$FC_6H_4COO$)$_2$(μ-O){Mn($NO_3$)(bpy)}]-$NO_3$·$H_2O$ (**3**).

| | | | |
|---|---|---|---|
| Mn(1)–O(1) | 1.791(3) | Mn(2)–O(1) | 1.791(3) |
| Mn(1)–O(4) | 1.987(3) | Mn(2)–O(3) | 1.986(3) |
| Mn(1)–N(2) | 2.075(3) | Mn(2)–N(3) | 2.087(4) |
| Mn(1)–N(1) | 2.081(4) | Mn(2)–N(4) | 2.087(3) |
| Mn(1)–O(6) | 2.15(2) | Mn(2)–O(9) | 2.14(3) |
| Mn(1)–O(2) | 2.187(3) | Mn(2)–O(5) | 2.187(3) |
| Mn(1)–O(1S) | 2.33(2) | Mn(2)–O(2S) | 2.34(3) |
| Mn(1)–Mn(2) | 3.179(13) | Mn(1)–O(1)–Mn(2) | 125.08(17) |
| O(1S)–Mn(1)–Mn(2)–O(9) | 89.6(11) | | |
| O(1S)–Mn(1)–Mn(2)–O(2S) | 93.6(10) | | |
| O(6)–Mn(1)–Mn(2)–O(2S) | 88.8(10) | | |
| O(6)–Mn(1)–Mn(2)–O(9) | 84.7(11) | | |
| O(4)–C(18)–C(19)–C(24) | –23.4(6) | | |
| O(3)–C(11)–C(12)–C(17) | –16.2(6) | | |
| O(7)–N(5)–O(6)–Mn(1) | –174.5(14) | | |
| O(8)–N(5)–O(6)–Mn(1) | 16.3(27) | | |
| O(10)–N(6)–O(9)–Mn(2) | –165.8(22) | | |
| O(11)–N(6)–O(9)–Mn(2) | 23.0(39) | | |

Mn(2). Selected interatomic bond lengths and angles are listed in Table 4. The water ligand bonds, through hydrogen atoms, the ionic perchlorate and the perchlorate ligand of the neighbour dinuclear entity. These bonds create a one-dimensional system depicted in Figure 6.

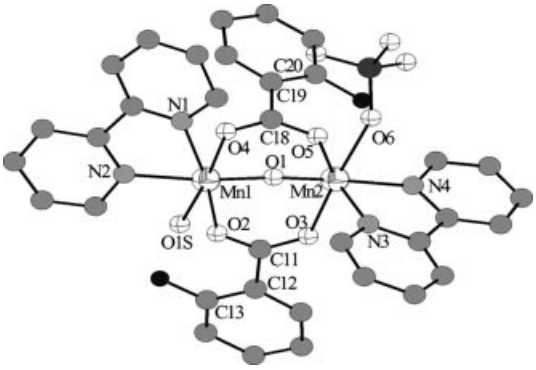


Figure 5. Drawing of the cationic complex [{Mn(bpy)($H_2O$)}(μ-2-$FC_6H_4COO$)$_2$(μ-O){Mn($ClO_4$)(bpy)}]$^+$ of compound **4**.

Table 4. Selected interatomic distances [Å] and angles [°] for compound [{Mn(bpy)($H_2O$)}(μ-2-$FC_6H_4COO$)$_2$(μ-O){Mn($ClO_4$)(bpy)}]-$ClO_4$·$2CH_2Cl_2$ (**4**).

| | | | |
|---|---|---|---|
| Mn(1)–O(1) | 1.787(6) | Mn(2)–O(1) | 1.778(5) |
| Mn(1)–O(2) | 1.978(5) | Mn(2)–O(5) | 1.949(7) |
| Mn(1)–N(1) | 2.070(6) | Mn(2)–N(3) | 2.037(8) |
| Mn(1)–N(2) | 2.068(9) | Mn(2)–N(4) | 2.031(8) |
| Mn(1)–O(4) | 2.185(6) | Mn(2)–O(3) | 2.142(5) |
| Mn(1)–O(1S) | 2.204(6) | Mn(2)–O(6) | 2.312(5) |
| Mn(1)–Mn(2) | 3.1543(19) | | |
| Mn(1)–O(1)–Mn(2) | 124.4(3) | | |
| O(1s)–Mn(1)–Mn(2)–O(6) | –93.6(2) | | |
| O(5)–C(18)–C(19)–C(20) | 19.9(11) | | |
| O(2)–C(11)–C(12)–C(13) | 19.1(12) | | |

Compounds **1**–**4** show intramolecular hydrogen bonds between the groups (or atoms) in the *ortho* position on the aromatic ring, the oxygen atoms of the carboxylate groups and the hydrogen atom of the bpy ligand (Figure 7). In compounds **3** and **4** the fluorine atom on the aromatic ring shows a preference for the position closest to the $O_c$ atom and the hydrogen bonds present in these compounds are F···$H_{bpy}$, $H_{Ph}$···$O_t$ and $O_c$···$H_{bpy}$. In contrast, the methyl group on the aromatic ring is placed closest to the $O_t$ atom

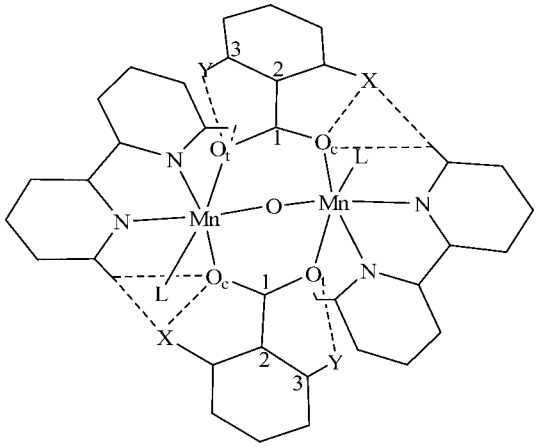


Figure 7. Drawing depicting the intramolecular H bonds presents in the dinuclear complexes. For compounds **1** and **2**, X = $H_{Ph}$ and Y = Me, and for compounds **3** and **4**, X = F and Y = $H_{Ph}$.

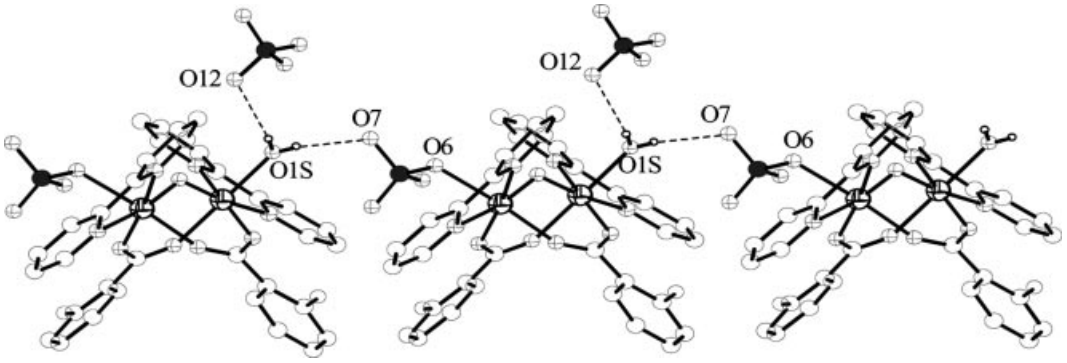


Figure 6. Plot of the hydrogen bonds present in the crystal of compound **4** between the coordinated perchlorate anion and the water ligand, giving a one-dimensional system, and between the water ligand and the ionic perchlorate.

 © 2007 Wiley-VCH Verlag GmbH & Co. KGaA, Weinheim 

and in these cases the observed hydrogen bonds are $H_{Ph}\cdots O_c$, $O_c\cdots H_{bpy}$ and $O_t\cdots H_{Me}$, and these bonds are weaker than in the fluoro complexes (Table 5).

Table 5. Intramolecular hydrogen bonds and torsion angles, $\delta(O_tC_1C_2C_3)$ and $\tau$(LMnMnL).

| | $O_c\cdots H_{Ph}$ [Å] | $O_c\cdots H_{bpy}$ [Å] | $O_t\cdots H_{Me}$ [Å] | $\delta$ [°] | $\tau$ [°] |
|---|---|---|---|---|---|
| **1** | 2.43/2.57 | 2.48/2.45 | 2.45/2.63 | 15.8/–41.7 | 97.3 |
| **2** ($ClO_4$) | 2.77/2.63 | 2.38/2.45 | 2.72/2.64 | 52.4/–46.1 | 97.8 |
| **2** ($H_2O$) | 2.64/2.65 | 2.55/2.43 | 2.66/2.52 | 45.8/–43.4 | 89.6 |
| | $O_c\cdots H_{bpy}$ | $F\cdots H_{bpy}$ | $O_t\cdots H_{Ph}$ | | |
| **3** | 2.54/2.55 | 2.37/2.34 | 2.51/2.49 | –21.6/–15.6 | 89.1 |
| **4** | 2.47/2.54 | 2.24/2.32 | 2.43/2.38 | 16.0/11.7 | 93.6 |

## Magnetic Properties

Magnetic susceptibility data were recorded for all complexes from room temperature to 4 K (or 2 K for **1** and **3**). The $\chi_M T$ product is ca. 5.6–5.9 $cm^3 mol^{-1}$ K at room temperature, which is close to the expected value for two uncoupled $Mn^{III}$ ions (6.0 $cm^3 mol^{-1}$ K). For compounds **1**, **2** and **4**, the $\chi_M T$ decreases with the temperature (very slowly for compound **1**) reaching a value of 0.4–0.8 $cm^3 mol^{-1}$ K at 4 K for compounds **2** and **4** and 4.4 $cm^3 mol^{-1}$ K for compound **1** (Figure 8). This behaviour is typical of an antiferromagnetic coupling between two $Mn^{III}$ ions. In contrast, for compound **3**, the $\chi_M T$ values increase when the temperature descends, reaching a maximum value of 6.43 $cm^3 mol^{-1}$ K at 16.5 K; at lower temperatures $\chi_M T$ decreases until 4.94 $cm^3 mol^{-1}$ K at 2 K. This behaviour is characteristic of ferromagnetic coupling. The expected value of $\chi_M T$ for a system with a ground state $S = 4$ must be 10 $cm^3 mol^{-1}$ K; the lower value found at 16.5 K and a decreasing of $\chi_M T$ below this temperature could be explained by the presence of zero-field splitting in the ground state and/or the intermolecular interactions. Magnetization measurements at 2 K, for compound **3**, show a $M/N\beta$ value of 5.5 at 50000 G, in agreement with the weak ferromagnetic interaction. For compounds **2** and **4** the $\chi_M$ vs. $T$ plot (Figure 8, inset) shows a maximum at 16.8 K ($\chi_M$ = 0.11 $cm^3 mol^{-1}$) and at 10.2 K ($\chi_M$ = 0.18 $cm^3 mol^{-1}$), respectively, indicating a major antiferromagnetic coupling for the former compound.

The spin Hamiltonian $H = -J\, S_1 \cdot S_2$ was used to fit the experimental data assuming that the two $Mn^{III}$ ions present the same $g$ value. The parameters $J$ and $g$ obtained from a least-squares fitting of the $\chi_M$ vs. $T$ data to the theoretical equation are listed below. Similar results are obtained by fitting the $\chi_M T$ vs. $T$ data. For the ferromagnetic compound (**3**), the theoretical equation was modified including the parameter of axial zero-field splitting, $D$, in the ground state $S = 4$. The Hamiltonian describing the ZFS was: $H_D = D[S_z^2 - S(S+1)/3]$. The best fits correspond to: $J = -0.5$ $cm^{-1}$ and $g = 1.98$, with $R = 5.5 \times 10^{-5}$ for **1**; $J = -5.6$ $cm^{-1}$ and $g = 1.98$, with $R = 4.1 \times 10^{-4}$ for **2**; $J = +1.4$ $cm^{-1}$, $|D| = 0.4$ $cm^{-1}$ and $g = 1.98$, with $R = 5.8 \times 10^{-5}$ for **3** and $J = -3.5$ $cm^{-1}$ and $g = 1.98$, with $R = 2.6 \times 10^{-5}$ for **4**.

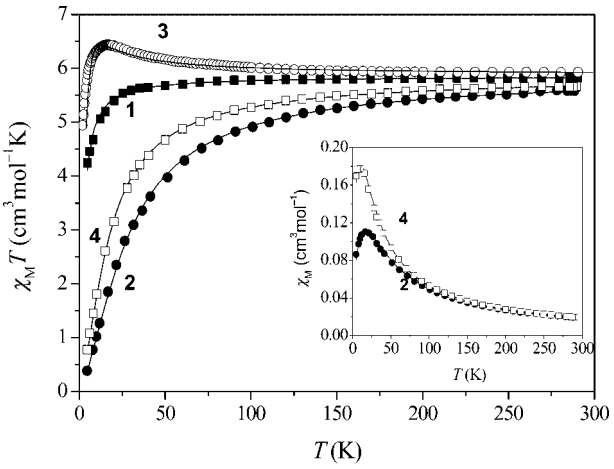


Figure 8. $\chi_M T$ vs. temperature plot for compounds **1**–**4**. The inset is the $\chi_M$ vs. $T$ plot for compounds with a perchlorate anion (**2** and **4**). The solid line is the best fit of the experimental data.

The four compounds show a moderate magnetic coupling. The strongest antiferromagnetic coupling was found for compound **2** while a ferromagnetic coupling was observed for compound **3**. As indicated in the previous section, in all cases the counteranion could be coordinated to the manganese ions. For compounds **2** and **4** the perchlorate anion is coordinated in 50% of the manganese ions, while for compounds **1** and **3**, the coordination of the nitrate anion is lower: only ca. 21% of the manganese ions show a nitrate ligand for compound **1**, while for compound **3** ca. 45% of the manganese ions show a coordinated nitrate anion. A comparison of the magnetic coupling constant of the four compounds indicates that, with the same carboxylate bridges, the perchlorate complexes show greater antiferromagnetic coupling than the nitrate complexes, with a difference of ca. 5 $cm^{-1}$. On the other hand, with the same anion, complexes with 2-$MeC_6H_4COO$ bridges show a stronger antiferromagnetic interaction than do complexes with 2-$FC_6H_4COO$ bridges, with a difference of ca. 2 $cm^{-1}$. The magnitude of the magnetic exchange interaction between the two $Mn^{III}$ ions found in compounds **1**–**4** may be compared with those reported for other dinuclear $Mn^{III}$ complexes with the general formula $[\{Mn(bpy)L\}_2(\mu\text{-}RCOO)_2(\mu\text{-}O)]^{n+}$ ($n = 2$ for neutral L ligands and $n = 0$ for anionic L ligands). Table 6 summarizes the most important structural parameters and the magnetic coupling constants for these compounds. As an example, the $Mn\text{–}O_b\text{–}Mn$ angle is in the range 122–125° and the $Mn\text{–}O_b$ distances are very similar for all compounds, since the d-orbital pointing to the oxo bridge is empty the magnitude of the magnetic interaction will not be very sensitive to this parameter.

Considering the $x$ axis in the oxo-bridge direction and the $z$ axis in the L direction (Scheme 1) we can find approximate values of the octahedron axes lengths by the addition of the Mn–ligand distances: $d(Mn\text{–}O_b) + d(Mn\text{–}N_t)$ ($x$ axis), $d(Mn\text{–}O_c) + d(Mn\text{–}N_c)$ ($y$ axis) and $d(Mn\text{–}L) + d(Mn\text{–}O_t)$ ($z$ axis). When the distance values for the $x$ and $y$ axis are similar, and smaller than the distance value found for the $z$ axis [$d(O_b\cdots N_t) \approx d(O_c\cdots N_c) < d(L\cdots O_t)$], the coordination

 © 2007 Wiley-VCH Verlag GmbH & Co. KGaA, Weinheim 

Table 6. Magnetic coupling constants[a] and selected structural parameters for $[\{Mn(bpy)L\}_2(\mu\text{-}RCOO)_2(\mu\text{-}O)]^{n+}$ complexes with the 2,2′-bipyridine (bpy) and monodentate L ligand as blocking ligands.[b]

| | L | Mn–O–Mn $\alpha$ [°] | Mn–$O_b$ [Å] | Mn–$O_c$ [Å] | Mn–$O_t$ [Å] | Mn–L [Å] | $x$[c] [Å] | $y$[c] [Å] | $z$[c] [Å] | $\gamma$[d] [°] | $J$ [$cm^{-1}$] |
|---|---|---|---|---|---|---|---|---|---|---|---|
| **1** | $H_2O$ $H_2O/NO_3$ | 123.1 | 1.79 | 1.96 | 2.14 | 2.23 | 3.86 | 4.04 | 4.37 | 98 | –0.5 |
| **2** | $H_2O$ $ClO_4$ | 122.3 | 1.79 | 1.94 | 2.15 | 2.32 | 3.86 | 3.99 | 4.47 | | –5.6 |
| **3** | $H_2O$ $NO_3$ | 125.1 | 1.79 | 1.99 | 2.19 | 2.24 | 3.87 | 4.07 | 4.43 | 20 | +1.4 |
| **4** | $H_2O$ $ClO_4$ | 124.4 | 1.78 | 1.96 | 2.16 | 2.26 | 3.83 | 4.01 | 4.42 | | –3.5 |
| **5** | OH $NO_3$ | 124.1 | 1.78 | 1.97 | 2.16 | 2.21 | 3.85 | 4.05 | 4.37 | 177 | +2.0 |
| **6** | $N_3$ | 122.0 | 1.80 | 2.04 | 2.13 | 2.12 | 3.89 | 4.19 | 4.25 | | +17.6 |
| **7** | $H_2O$ | 124.7 | 1.79 | 1.95 | 2.19 | 2.25 | 3.85 | 4.01 | 4.44 | | –2.9 |
| **8** | $H_2O$ | 124.6 | 1.79 | 1.96 | 2.24 | 2.20 | 3.86 | 4.02 | 4.44 | | –0.7 |
| **9** | $H_2O$ | 122.9 | 1.78 | 1.94 | 2.16 | 2.31 | 3.85 | 3.99 | 4.47 | | –6.8 |
| **10** | Cl | 124.3 | 1.78 | 1.94 | 2.20 | 2.56 | 3.87 | 4.01 | 4.76 | | –8.2 |
| **11** | $H_2O$ | 125.2 | 1.77 | 2.00 | 2.17 | 2.21 | 3.85 | 4.06 | 4.38 | | +4.7 |
| **11** | $H_2O$ $NO_3$ | 121.8 | 1.81 | 1.93 | 2.13 | 2.25 | 3.84 | 3.98 | 4.38 | 114 | +4.7 |

[a] Values using the $H = -J\ S_1 \cdot S_2$ convention. [b] See Scheme 1 for the terminology $O_c$, $O_b$, $N_t$ and $N_c$. [c] $x$, $y$ and $z$ symbolize the distances between ligands in the *trans* position, e.g., $x = O_b \cdots N_t$ is the addition of both manganese–ligand distances, $d(O_b \cdots N_t) = d(Mn\text{–}O_b) + d(Mn\text{–}N_t)$, $y = d(O_c \cdots N_c)$ and $z = d(O_t \cdots L)$. [d] $\gamma$ = ONOMn angle. All distances and angle values are the average of the two manganese centres, and for **2** it is also the average for the two complexes present in the crystal. **5** = $[\{Mn(OH)(bpy)\}(\mu\text{-}PhCOO)_2(\mu\text{-}O)\{Mn(NO_3)(bpy)\}]$;[5] **6** = $[\{Mn(N_3)(bpy)\}_2(\mu\text{-}PhCOO)_2(\mu\text{-}O)]$;[6] **7** = $[\{Mn(bpy)(H_2O)\}_2(\mu\text{-}ClCH_2COO)_2(\mu\text{-}O)](ClO_4)_2$;[8] **8** = $[\{Mn(bpy)(H_2O)\}_2(\mu\text{-}ClCH_2COO)_2(\mu\text{-}O)](NO_3)_2$.[8] **9** = $[\{Mn(bpy)(H_2O)\}_2(\mu\text{-}CH_3COO)_2(\mu\text{-}O)](PF_6)_2$;[9] **10** = $[\{Mn(Cl)(bpy)\}_2(\mu\text{-}CH_3COO)_2(\mu\text{-}O)]$;[6] **11** = $[\{Mn(bpy)(H_2O)\}_2(\mu\text{-phtha})_2(\mu\text{-}O)]$ $[\{Mn(bpy)(H_2O)\}(\mu\text{-phtha})_2(\mu\text{-}O\{Mn(bpy)(NO_3)\}](NO_3)_3$ (phtha = phthalate).[10]

polyhedron is considered elongated, while if the distance for the $x$ axis is shorter than the distances for the $z$ and $y$ axis $[d(O_b \cdots N_t) < d(O_c \cdots N_c) \approx d(L \cdots O_t)]$, the octahedron is compressed. Finally, if the distances of the three axes are different the octahedron presents a rhombic distortion. Then, we can define the distortion parameter as $(z - y)/(y - x)$, where $z = d(L \cdots O_t)$, $y = d(O_c \cdots N_c)$ and $x = d(O_b \cdots N_t)$, and the greater values of this parameter correspond to the compounds with a major antiferromagnetic coupling. For the four compounds reported here the major distortion parameter value corresponds to the complexes with perchlorate as the monodentate ligand. Figure 9 shows the distortion parameter for the compounds reported in Table 6, in front of the magnetic coupling constant. The two extreme values of the distortion parameter are found for compound **6**, with a distortion parameter close to zero, and for compound **10**, with a distortion parameter of 5.36.

Only one of the compounds collected in Table 6 shows compressed octahedra; this is the case for compound **6** $[\{Mn(N_3)(bpy)\}_2(\mu\text{-}C_6H_4COO)_2(\mu\text{-}O)]$.[6,7] As in the case of the complexes with tridentate amines[11–13] a ferromagnetic interaction is also observed for this compound. Compound **10** $[\{MnCl(bpy)\}_2(\mu\text{-}CH_3COO)_2(\mu\text{-}O)]$[7] is the compound with the most elongated octahedra and shows major antiferromagnetic coupling. The other compounds show closest distortion parameters between 1.5 and 3.5. Two compounds reported here, **2** and **4**, in which the perchlorate anion is coordinated to the manganese ions, also show elongated octahedra, and in general the magnitude of the antiferromagnetic coupling agrees with the values found for compounds **9**[9] and **10**.[7]

When the nitrate anion is coordinated to the manganese ion the Mn–L distances are shorter. Consequently, the elongation in the $z$ axis is moderate, and the distortion is intermediate between elongated and rhombic. The first

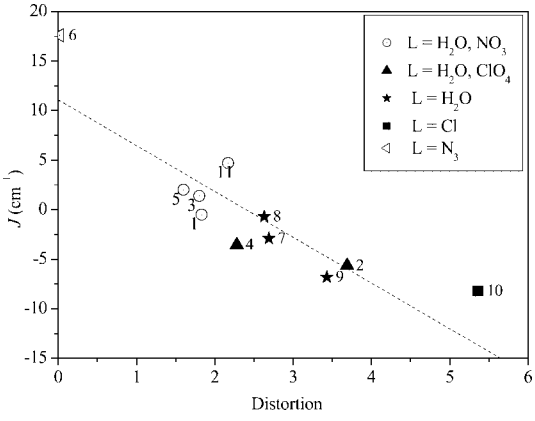


Figure 9. Correlation between the distortion around the $Mn^{III}$ ions and the magnetic interaction. The degree of distortion was measured as $(z - y)/(y - x)$, where $z = d(L \cdots O_t)$, $y = d(O_c \cdots N_c)$ and $x = d(O_b \cdots N_t)$ (See Scheme 1). The dashed line is the plot of the function $J = 11.1 - (4.6 \times \text{distortion})$, and the symbols are the experimental data.

compound of this kind described in the literature, $[\{Mn(OH)(bpy)\}(\mu\text{-}C_6H_4COO)_2(\mu\text{-}O\{Mn(NO_3)(bpy)\}]$ (**5**),[5] presents a rhombic distortion, and a ferromagnetic interaction was found. Compound **3** also shows a ferromagnetic coupling, while compound **1** is weakly antiferromagnetic. Another analogous compound reported in the literature has two different dinuclear complexes in the crystal, $[\{Mn(bpy)(H_2O)\}_2(\mu\text{-phtha})_2(\mu\text{-}O)][\{Mn(bpy)(H_2O)\}(\mu\text{-phtha})_2(\mu\text{-}O)\{Mn(bpy)(NO_3)\}](NO_3)_3$ (**11**) (phtha = phthalate),[10] one of them with two water molecules and the other with one water and one nitrate ligand. A net ferromagnetic interaction was reported for this compound, where we could expect a different degree of magnetic interaction in each dinuclear complex.

 © 2007 Wiley-VCH Verlag GmbH & Co. KGaA, Weinheim 

For dinuclear $Mn^{III}$ compounds with four electrons in each manganese ion ($i$ and $j$) the magnetic coupling constant is $J = 1/16\ \Sigma\ J_{ij}$.[17] Because of the presence of one empty orbital in each manganese ion there are eight crossing interactions between each single occupied orbital and the empty orbital ($x^2$–$y^2$), and this kind of interaction is postulated as ferromagnetic.[17] The most important antiferromagnetic contribution to the magnetic behaviour is due to the $xz(1)/xy(2)$ interaction (Figure 10). The other $\pi^*$ interaction through the oxo-bridging ligand, the $xy(1)/xz(2)$ interaction, could be sensitive to the Mn–$O_b$–Mn angle. For these kinds of complexes, with $\alpha \approx 124°$, an antiferromagnetic interaction can be expected. The same occurs with the $z^2(1)/z^2(2)$ interaction: for Mn–$O_b$–Mn angles far from 90° an antiferromagnetic interaction can be expected. Other antiferromagnetic contributions are the $z^2(1)/xz(2)$ and the $xy(1)/z^2(2)$ interactions. Subsequently, there are an important number of interactions of both signs, ferro- and antiferromagnetic, and the resultant magnetic behaviour of a compound is because of the balance of these contributions.

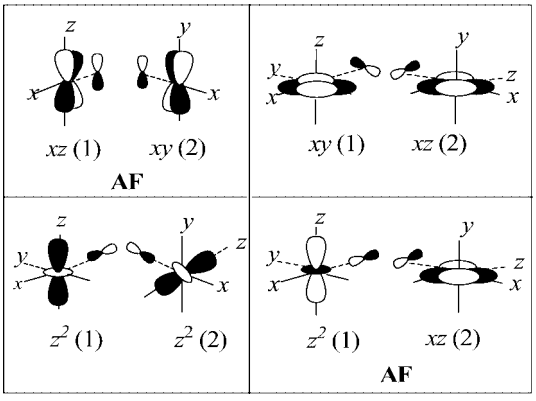


Figure 10. Schematic representation of the magnetic exchange pathway.

## Extended Hückel Calculations

In an attempt to rationalize the magnetic properties of the compounds **1**–**4**, we found that their molecular geometries can be differentiated by the following factors:

(a) the nature of the substituent of the benzoate bridge, with a $CH_3$ group for compounds **1** and **2** and an electron-withdrawing F atom for compounds **3** and **4**;

(b) the position of the F atom or the $CH_3$ group in the aromatic ring: the $CH_3$ group is on the side of the $O_t$ atom, while the F atom is placed on the side of the $O_c$ atom; (Figure 7)

(c) the nature of the monodentate ligand, which could be $H_2O$, $NO_3$ or $ClO_4$;

(d) the dihedral angle between the carboxylate group and the phenylic ring, defined by the $\delta(O_tC_1C_2C_3)$ angle (Figure 7);

(e) the relative orientation of the nitrate ligand in the environment of manganese, defined by the $\gamma$(ONOMn) angle.

With the aim of determining the effect of these factors on the magnetic properties, Extended Hückel calculations were carried out on the crystallographic coordinates of compounds **1**–**4** using the CACAO program.[18] Taking into consideration that in compounds **1** and **3** the monodentate ligand $H_2O$ could be replaced by the $NO_3$ anion, the different complexes present in the crystal, in each case, have been studied. Other calculations carried out were:

– the dihedral angle between the COO group and the aromatic ring, $\delta$, was modified from the original crystallographic coordinates and two values are considered: $\delta = 17°$ and 45°;

– the substituent on the aromatic ring, $CH_3$ or F was replaced by the other group (F or $CH_3$, respectively), in the same position as the original compound, and also, in the opposite position;

– for compounds **1** and **3** the crystallographic coordinates of the nitrate group have been modified, with $\gamma$ angles between 0–180°;

– with the aim of making comparisons with other compounds with nitrate ligands calculations with the crystallographic coordinates of compounds **5**[5] and **11**[10] have been also carried out. And the position of the nitrate ligand was also modified with $\gamma$ angles between 0–180°.

Considering the axis depicted in Scheme 1, the $x^2$–$y^2$ orbital of each manganese atom points to the $O_b$, $O_c$ of the carboxylate group and both N atoms of the bidentate ligand, and the $z^2$ orbital points to the monodentate ligand L and the $O_t$ atom. The energy diagram and the shape of the MO's are similar for all the studied compounds except for the MO with contributions from the $z^2$ orbital of the manganese ions. In all cases, the $z^2$ orbitals of the manganese ions contribute significantly to the first single occupied orbitals. The $z^2$ orbital of each manganese ion could overlap with the orbitals of the ligands in the $z$ axis (L and $O_t$), and to a lesser degree with the ligands in the equatorial plane ($O_b$, $N_t$, $N_c$ and $O_c$). The two resultant molecular orbitals are each considerably localized on one of the manganese atoms, even if a small contribution of the bridging ligands is present.

The analysis of the results shows a very small effect in the energy and composition of the MO by modification of the torsion angle between the carboxylate group and the aromatic ring, and the last with its substituent group. However, both factors modify the positive charge on the manganese ions. The clearest effect is due to the substituent in the aromatic ring: with the same crystallographic parameters the exchange $CH_3$/F slightly modifies the positive charge on the manganese ions (the methyl group, with a donor effect, decreases the positive charge on the manganese ions while the F atom, with a withdrawing effect, increases the positive charge).

The dinuclear complexes listed in Table 6 show different kinds of monodentate ligands: $H_2O$, $OH^-$, $ClO_4^-$, $Cl^-$, $NO_3^-$ and $N_3^-$. The $H_2O$, $ClO_4^-$ and $Cl^-$ ligands act as σ-donor ligands, and their HOMO's are low in energy. On the other hand, the $NO_3^-$ and $N_3^-$ ligands show two orbitals with similar energies to the d-orbitals of the manganese ions: a

 © 2007 Wiley-VCH Verlag GmbH & Co. KGaA, Weinheim 

filled nonbonding orbital with a σ-donor character and an empty π* orbital.

For the nitrate complexes with 2-$MeC_6H_4COO$ (**1**), 2-$FC_6H_4COO$ (**3**) and 2-$OOCC_6H_4COO$ (**11**) an important overlap between the empty π* orbital of the nitrate ligand and the $z^2$ of the $Mn^{III}$ ion is observed. Then, two molecular orbitals $\pi_L^* \pm z^2_{Mn}$ were found for each metallic centre. In contrast, for compound **5** [{Mn(OH)(bpy)}(μ-PhCOO)$_2$-(μ-O){Mn($NO_3$)(bpy)}][5] no contribution of the π* orbital of the nitrate ligand was found in the $z^2$ orbital. For this compound the nitrate ligand acts only as a σ-donor ligand. The energy of the $\pi_L^*$ orbital is very sensitive to the distortions in the nitrate anion. For compound **5**, the N–O distances are quite a bit shorter than those for complexes **1**, **3** and **11** (average of 1.19 Å for **5** and average of 1.25 Å for **1**, **3** and **11**) therefore the $\pi_L^*$ was found at a higher energy and no appreciable interaction with the $z^2$ of the metal was observed.

Another factor to consider is the orientation of the nitrate group. The combination $\pi_L^* \pm z^2_{Mn}$ must be sensitive to the orientation of the nitrate group in front of the $z$ axis. This orientation is related to the torsion angle $\gamma$(ONOMn). When the nitrate group is perpendicular to the $z$ axis ($\gamma$ = 90°) (Figure 11) a good overlap between the $\pi_L^*$ and the $z^2_{Mn}$ orbital can be found, while for the other extreme when the nitrate ligand is aligned to the $z$ axis ($\gamma$ = 0° or 180°) the overlap vanishes.

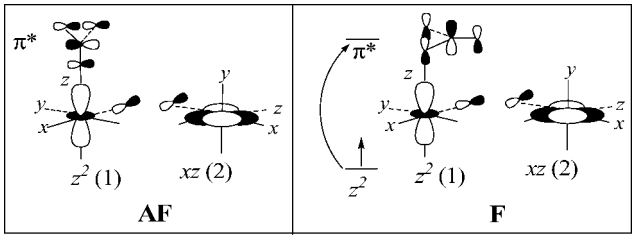


Figure 11. Schematic representation of the effect of the $NO_3^-$ ligand in the $z^2$–$xz$ antiferromagnetic contribution.

Then, for compound **5**, the small $\gamma$ angle and short N–O distances could explain that the $\pi_L^*$ orbital does not contribute to the $z^2$ orbital. In compound **1**, with 2-$MeC_6H_4$-COO bridges, the nitrate ligand shows a good overlap between the $\pi_L^*$ orbital and the $z^2_{Mn}$ orbital. The two combinations, $\pi_L^* \pm z^2_{Mn}$ show an important contribution of the nitrate and the manganese orbitals (39% Mn and 42% nitrate and 29% Mn and 63% nitrate). For compound **3**, with 2-$FC_6H_4COO$ bridges, the nitrate ligand is placed more parallel to the $z$ axis and the two MO's are more localized, one of them with a major contribution from the manganese ion (61% Mn and 23% nitrate) and the other one with a major contribution from the nitrate group (12% Mn and 82% nitrate). For the nitrate complex of compound **11** the higher energy orbital shows a major contribution from the π* of the nitrate ligand (60% of nitrate and 19% of $z^2_{Mn}$)

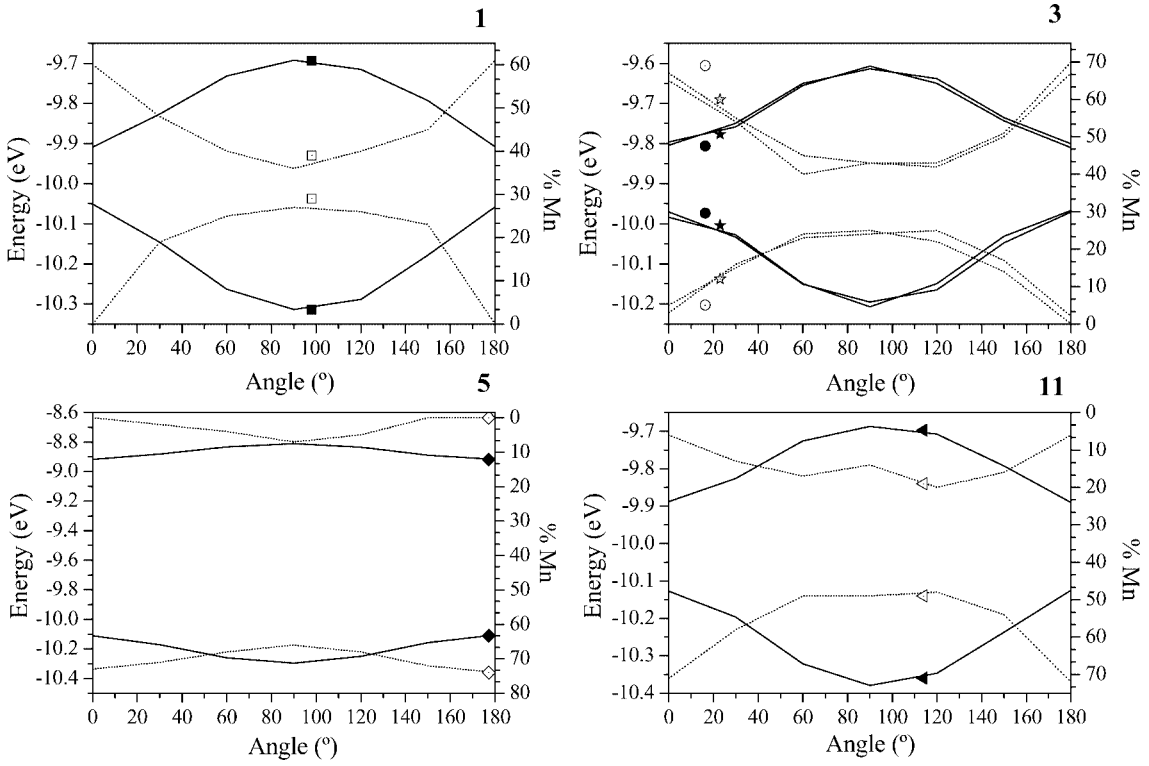


Figure 12. Energy of the $z^2 \pm \pi^*$ orbitals (solid line), and contribution of the Mn ions (%) to the MO (dotted line) as a function of the Mn–O–N–O angle ($\gamma$ angle) for compounds **1** (top, left), **3** (top, right), **5** (bottom, left) and **11** (bottom, right). The filled symbols show the energy and the dotted symbols show the composition (% Mn) of the orbitals found for the real compounds (experimental values of $\gamma$, Table 6). For compound **3** the coordination of the two nitrates is considered.

 © 2007 Wiley-VCH Verlag GmbH & Co. KGaA, Weinheim 

while the lower energy orbital shows a major contribution from the $z^2_{Mn}$ orbital (49%) and 31% of the π* orbital of the monodentate ligand.

Figure 12 shows the effect in the energy and composition of the $\pi_L^* \pm z^2_{Mn}$ orbitals by the variation of the Mn–O–N–O angle ($\gamma$), between 0–180°. This variation is not appreciable for compound **5**. For compounds **1**, **3** and **11** the modification of this torsion angle has an important effect. The major energy gap between the MO $\pi_L^*+z^2_{Mn}$ and $\pi_L^*-z^2_{Mn}$ orbitals was found for $\gamma \approx 90°$, and with this orientation a similar contribution of the $\pi_L^*$ and $z^2_{Mn}$ was found in all cases. Consequently, the nitrate ligand could act as a π-acid ligand, providing a means for the delocalization of the electronic density of the manganese $z^2$ orbital onto the ligand. This situation is enhanced if the nitrate ligand is placed perpendicular to the $z$ axis. Then, the antiferromagnetic interactions $z^2(1)/xz(2)$ and $xy(1)/z^2(2)$ could diminish, and when the delocalization to the empty π* orbital of the nitrate ligand is important the ferromagnetic contribution could be increased. This could explain the minor antiferromagnetic interaction observed for the nitrate complexes **1** and **3** in comparison to their analogous compounds with perchlorate ligands.

On the other hand, the energy of the $z^2$ orbital decreases considerably by increasing the elongation in the $z$ direction, therefore the antiferromagnetic interaction $z^2(1)/xz(2)$ and $xy(1)/z^2(2)$ could be more efficient; increases the antiferromagnetic contribution resulting in a more negative value for the overall coupling, as is observed for compounds **2**, **4**, **7**, **9** and **10**.

## Conclusions

In this paper we reported the synthesis of four dinuclear $Mn^{III}$ complexes with the general formula [{Mn(bpy)L}(μ-RCOO)$_2$(μ-O){Mn(bpy)L′}]$X_{2-m}$ (RCOO = 2-$MeC_6H_4$COO and 2-$FC_6H_4$COO); these compounds show a labile position on each manganese ion, which could be occupied by different ligands: $H_2O$, $NO_3^-$ or $ClO_4^-$. The magnetic properties are sensitive to the carboxylate bridges and the counteranion/monondentate ligand: compounds with 2-$MeC_6H_4$COO show much more antiferromagnetic coupling than compounds with 2-$FC_6H_4$COO, and perchlorate complexes show more of an antiferromagnetic interaction than the nitrate complexes. Several factors are being evaluated by Extended Hückel calculations and show that that the most important effect is the coordination of the nitrate ligand and their orientation, parallel to the $z$ axis (small values of $\gamma$) or perpendicular to the $z$ axis ($\gamma$ close to 90°). This ligand could act as a π-acid ligand and then provide a new ferromagnetic means of interaction.

## Experimental Section

**Synthesis:** All manipulations were performed under aerobic conditions. Organic reagents were used as received. $Bu_4NMnO_4$ was prepared as described in the literature.[19] The yield was calculated from the total available Mn.

***Caution!*** Perchlorate salts of compounds containing organic ligands are potentially explosive. Only small quantities of these compounds should be prepared and handled behind protective shields.

**[{Mn(bpy)L}(μ-2-RC$_6$H$_4$COO)$_2$(μ-O) {Mn(bpy)L′}]X$_{2-m}$, with R = CH$_3$ and X = NO$_3^-$ (1), ClO$_4^-$ (2), R = F and X = NO$_3^-$ (3), ClO$_4^-$ (4); L and L′ = H$_2$O or X:** The four compounds were synthesized using the same procedure: 1.6 mmol of the benzoic derivative acid (0.22 g of 2-$MeC_6H_4COOH$ or 0.23 g of 2-$FC_6H_4COOH$) was added to a solution containing the $Mn^{II}$ salt (1.28 mmol) in MeCN, $Mn(NO_3)_2{\cdot}4H_2O$ (0.32 g) or $Mn(ClO_4)_2{\cdot}6H_2O$ (0.45 g). $Bu_4NMnO_4$ (0.11 g, 0.32 mmol) dissolved in MeCN was then added to the solution, which immediately turned dark brown. Finally, a MeCN solution of 2,2′-bipyridine (0.25 g, 1.6 mmol) was added and the resulting solution was stirred for some minutes. The total volume for the nitrate compounds (**1** and **3**) was 100 mL, and was 30 mL for the perchlorate compounds (**2** and **4**). Small dark crystals were obtained from the nitrate solutions when they were left undisturbed in the refrigerator for several days (compounds **1** and **3**). For the compounds with perchlorate anions suitable X-ray diffraction crystals were obtained in the presence of $CH_2Cl_2$. The compound with the 2-$MeC_6H_4COO^-$ bridging ligand crystallized from the mother MeCN solution mixed with $CH_2Cl_2$ (1:1), which was layered with hexanes and left undisturbed at room temperature. While for the compound with 2-$FC_6H_4COO^-$ bridges, the mother MeCN solution was kept inside a container with an atmosphere of $CH_2Cl_2$ and after several days at room temperature crystals of compound **4** were obtained.

**Compound 1, [{Mn(bpy)(H$_2$O)}(μ-2-MeC$_6$H$_4$COO)$_2$(μ-O){Mn(NO$_3$)(bpy)}]NO$_3$·H$_2$O:** Yield 0.38 g (ca. 56%). $C_{36}H_{32}Mn_2N_6O_{12}{\cdot}H_2O$ (868.56): calcd. C 49.78, H 3.95, N 9.68; found C 49.9, H 3.8, N 9.7. IR (KBr): $\tilde{\nu}_{max}$ = 1609 (m, COO), 1384 (vs., COO + $NO_3$), 730 (m, $Mn_2O$) cm$^{-1}$.

**Compound 2, [{Mn(bpy)(H$_2$O)}$_2$(μ-2-MeC$_6$H$_4$COO)$_2$(μ-O)][{Mn(ClO$_4$)(bpy)}$_2$(μ-2-MeC$_6$H$_4$COO)$_2$(μ-O)](ClO$_4$)$_2$·CH$_2$Cl$_2$:** Yield 0.44 g (ca. 58%). $C_{72}H_{64}Cl_4Mn_4N_8O_{28}{\cdot}CH_2Cl_2{\cdot}$(1935.81): calcd. C 45.29, H 3.44, N 5.79; found C 45.5, H 3.4, N 5.9. IR (KBr): $\tilde{\nu}_{max}$ = 1604 (m COO), 1384 (vs., COO), 1156 (vs., $ClO_4$) 1150 (vs., $ClO_4$), 1031 (vs. $ClO_4$), 730 (m, $Mn_2O$) cm$^{-1}$.

**Compound 3, [{Mn(bpy)(H$_2$O)}(μ-2-FC$_6$H$_4$COO)$_2$(μ-O){Mn(NO$_3$)(bpy)}]NO$_3$·H$_2$O:** Yield 0.44 g (ca. 63%). $C_{34}H_{26}F_2Mn_2N_6O_{12}{\cdot}2H_2O$ (894.51): calcd. C 45.65, H 3.38, F 4.25, N 9.40; found C 45.6, H 3.2, F 4.2, N 9.6. IR (KBr): $\tilde{\nu}_{max}$ = 1610 (s, COO), 1384 (vs., COO + $NO_3$), 730 (w, $Mn_2O$) cm$^{-1}$.

**Compound 4, [{Mn(bpy)(H$_2$O)}(μ-2-FC$_6$H$_4$COO)$_2$(μ-O){Mn(ClO$_4$)(bpy)}]ClO$_4$:** Yield 0.42 g (ca. 57%). $C_{34}H_{26}Cl_2F_2Mn_2N_4O_{14}{\cdot}H_2O$ (951.38): calcd. C 42.92, H 2.97, Cl 7.45, F 3.99, N 5.89; found C 43.0, H 2.7, Cl 7.5, F 4.0, N 5.8. IR (KBr): $\tilde{\nu}_{max}$ = 1611 (vs., COO), 1383 (vs., COO), 1146 (vs., $ClO_4$), 1119 (vs., $ClO_4$), 1089 (vs., $ClO_4$), 725 (m, $Mn_2O$) cm$^{-1}$.

**Physical Measurements:** Elemental analyses of C, H, Cl, F and N were carried out by the "Serveis Científico-Tècnics" of the Universitat de Barcelona. Infrared spectra (4000–400 cm$^{-1}$) were recorded from KBr pellets with a Nicolet Impact 400 FT-IR spectrometer. Magnetic susceptibility measurements were performed with a Manics-DSM8 susceptometer equipped with an Oxford Instruments helium cryostat, working down to 4.2 K, and carried out at the "Servei de Magnetoquímica" (Universitat de Barcelona). The field used was in the interval 6000–8000 G. For the ferromagnetic compound the magnetic susceptibility (between 300–2 K, at

 © 2007 Wiley-VCH Verlag GmbH & Co. KGaA, Weinheim 

Table 7. Crystallographic data for **1**–**4**.

| | **1** | **2** | **3** | **4** |
|---|---|---|---|---|
| Formula | $C_{40}H_{44}Mn_2N_8O_{15}$ | $C_{73}H_{66}Cl_6Mn_4N_8O_{28}$ | $C_{34}H_{28}F_2Mn_2N_6O_{13}$ | $C_{36}H_{30}Cl_6F_2Mn_2N_4O_{14}$ |
| Formula mass [g mol$^{-1}$] | 986.70 | 1935.80 | 876.50 | 1103.22 |
| Crystal system | triclinic | triclinic | monoclinic | triclinic |
| Space group | $P\bar{1}$ | $P\bar{1}$ | $P2_1/n$ | $P\bar{1}$ |
| $a$ [Å] | 9.9202(1) | 15.7038(16) | 9.9948(1) | 10.096(2) |
| $b$ [Å] | 15.663 | 17.2438(17) | 25.2891(2) | 14.229(3) |
| $c$ [Å] | 17.0380(2) | 17.9876(17) | 16.5490(2) | 16.496(3) |
| $\alpha$ [°] | 108.401(1) | 109.245(2) | 90 | 66.66(3) |
| $\beta$ [°] | 105.429(1) | 107.223(2) | 100.19 | 89.652(16) |
| $\gamma$ [°] | 103.829(1) | 107.016(2) | 90 | 84.490(16) |
| $V$ [Å$^3$] | 2265.45(4) | 3959.9(7) | 4116.99(7) | 2164(8) |
| $Z$ | 2 | 2 | 4 | 2 |
| $T$ [K] | 173(2) | 173(2) | 298(2) | 173(2) |
| $\rho_{calcd.}$ [g cm$^{-3}$] | 1.444 | 1.623 | 1.414 | 1.693 |
| $\mu_{calcd.}$ [mm$^{-1}$] | 0.633 | 0.914 | 0.689 | 1.033 |
| $F(000)$ | 978 | 1972 | 1784 | 1112 |
| Transmission factors (max., min.) | 0.9117, 0.7238 | 0.8751, 0.7839 | 0.7701, 0.7245 | 0.8201, 0.6262 |
| $\Theta$ range for data collection [°] | 1.36 to 28.28 | 1.33 to 26.37 | 1.49 to 28.32 | 1.35 to 28.41 |
| Total reflections measured | 15735 | 23472 | 27341 | 11907 |
| Independent reflections, $R_{int}$ | 10819, 0.0318 | 15845, 0.0612 | 9902, 0.0766 | 9461, 0.1019 |
| Completeness to $\Theta_{max}$ | 96.2% | 97.8% | 96.4% | 86.9% |
| Parameters refined, restrains | 571, 21 | 1099, 0 | 616, 31 | 577, 0 |
| $R_1$[a] [$I > 2\sigma(I)$] | 0.0672 | 0.0687 | 0.0769 | 0.1170 |
| $wR_2$[b] [$I > 2\sigma(I)$] | 0.1937 | 0.1223 | 0.2152 | 0.2795 |
| $R_1$[a] [all data] | 0.0970 | 0.1765 | 0.1284 | 0.1971 |
| $wR_2$[b] [all data] | 0.2170 | 0.1592 | 0.2382 | 0.3287 |
| Goodness of fit on $F^2$ | 1.044 | 0.977 | 1.025 | 0.890 |
| Largest diff. peak and hole [e A$^{-3}$] | 1.350 and –0.735 | 0.747 and –0.860 | 0.784 and –0.640 | 1.177 and –2.046 |

[a] $R_1 = \Sigma||F_o| - |F_c|| / \Sigma|F_o|$. [b] $wR_2 = \{\Sigma[w(F_o^2 - F_c^2)^2] / \Sigma[w(F_o^2)^2]\}^{1/2}$.

1000 G) and the magnetization (at 2 K between 0–50000 G) were measured with a SQUID magnetometer, Quantum Design Magnetometer, model MPMP. Pascal's constants were used to estimate the diamagnetic corrections for each compound. The fits were performed by minimizing the function $R = \Sigma(\chi_M \cdot T_{exp} - \chi_M \cdot T_{calcd})^2 / \Sigma(\chi_M \cdot T_{exp})^2$. All the samples were prepared by crushing the crystalline products.

**Crystallographic Measurements:** A green plate crystal ($0.50 \times 0.50 \times 0.15$ mm) of [{Mn(bpy)($H_2O$)}(μ-2-$MeC_6H_4COO)_2$(μ-O){Mn($NO_3$)(bpy)}]$NO_3 \cdot 1.5CH_3CN \cdot 2H_2O$ (**1**), a brown block crystal ($0.28 \times 0.15 \times 0.15$ mm) of [{Mn(bpy)($H_2O$)}$_2$-(μ-2-$MeC_6H_4COO)_2$(μ-O)][{Mn($ClO_4$)(bpy)}$_2$(μ-2-$MeC_6H_4COO)_2$-(μ-O)]$(ClO_4)_2 \cdot 0.5CH_2Cl_2$ (**2**), a black block crystal ($0.50 \times 0.50 \times 0.40$ mm) of [{Mn(bpy)($H_2O$)}(μ-2-$FC_6H_4COO)_2$(μ-O){Mn($NO_3$)(bpy)}]-$NO_3 \cdot H_2O$ (**3**) and a dark green block crystal ($0.50 \times 0.25 \times 0.20$ mm) of [{Mn(bpy)($H_2O$)}(μ-2-$FC_6H_4COO)_2$(μ-O){Mn($ClO_4$)(bpy)}]-$ClO_4 \cdot 2CH_2Cl_2$ (**4**) were chosen for X-ray diffraction experiments. The unit cell and intensity data were measured with a Bruker SMART CCD area detector single-crystal diffractometer with graphite monochromated Mo-$K_\alpha$ radiation ($\lambda$ = 0.71073 Å) operating at 50 kV and 30 mA. A total of 1271 frames of intensity data were collected over a hemisphere of the reciprocal space by a combination of three exposure sets. Each frame covered 0.3° in $\omega$ and the first 50 frames were recollected at the end of the data collection to monitor crystal decay. Absorption corrections were applied using the SADABS program.[20] The structures were solved using the Bruker SHELXTL-PC software[21] by direct methods and refined by full-matrix least-squares methods on $F^2$. Hydrogen atoms were included in calculated positions and refined in the riding mode except those of the water molecules that were located on residual density maps, and their positions were then fixed and refined in the riding mode. All non-hydrogen atoms were refined anisotropically. Crystal data collection and refinement parameters are given in Table 7. Further details, concerning disorder for example, are given in the crystallographic CIF files. CCDC-288243 to -288246 contain the supplementary crystallographic data for this paper. These data can be obtained free of charge from The Cambridge Crystallographic Data Centre via www.ccdc.cam.ac.uk/datarequest/cif.

## Acknowledgments

The authors thank the Ministerio de Educación y Ciencia for financial support (Ramon y Cajal research contract and grants BQ 2003-00538 and CTQ 2005-08123-C02-02/BQU). Thanks also go to X. Solans for help with the crystallographic ressolution.

[1] B. C. Dave, R. S. Czernuszewickz, *Inorg. Chim. Acta* **1998**, *281*, 25.
[2] R. Ruiz, C. Sangregorio, A. Caneschi, P. Rossi, A. B. Gaspar, J. A. Real, M. C. Muñoz, *Inorg. Chem. Commun.* **2000**, *3*, 361.
[3] K. R. Reddy, M. V. Rajasekharan, S. Sukumar, *Polyhedron* **1996**, *15*, 4161.
[4] B. Albela, M. Corbella, J. Ribas, *Polyhedron* **1996**, *15*, 91.
[5] M. Corbella, R. Costa, J. Ribas, P. H. Fries, J. M. Latour, L. Ohrstrom, X. Solans, V. Rodríguez, *Inorg. Chem.* **1996**, *35*, 1857.
[6] J. B. Vincent, K. Folting, C. J. Huffman, G. Christou, *BioChem. Soc. Trans.* **1988**, *16*, 822.
[7] J. B. Vincent, H. L. Tsai, A. G. Blackman, S. Wang, P. D. Boyd, K. Folting, J. C. Huffman, E. B. Lobkovsky, D. N. Hendrickson, G. Christou, *J. Am. Chem. Soc.* **1993**, *115*, 12353.
[8] G. Fernández, M. Corbella, M. Alfonso, H. Stoeckli-Evans, I. Castro, *Inorg. Chem.* **2004**, *43*, 6684.
[9] S. Ménage, J.-J. Girerd, A. Gleizes, *J. Chem. Soc., Chem. Commun.* **1988**, 431.

 © 2007 Wiley-VCH Verlag GmbH & Co. KGaA, Weinheim 

[10] C. Chen, H. Zhu, D. Huang, T. Wen, Q. Liu, D. Liao, J. Cui, *Inorg. Chim. Acta* **2001**, *320*, 159.
[11] K. Wieghardt, U. Bossek, D. Ventur, J. Weiss, *J. Chem. Soc., Chem. Commun.* **1985**, 347.
[12] K. Wieghardt, U. Bossek, B. Nuber, J. Weiss, J. Bonvoisin, M. Corbella, S. E. Vitols, J. J. Girerd, *J. Am. Chem. Soc.* **1988**, *110*, 7398.
[13] C. Bolm, N. Meyer, G. Raabe, T. Weyhermüller, E. Bothe, *Chem. Commun.* **2000**, 2435.
[14] J. E. Sheats, R. S. Czernuszewicz, G. C. Dismukes, A. L. Rheingold, V. Petrouleas, J. A. Stubbe, W. H. Armstrong, R. H. Beer, S. J. Lippard, *J. Am. Chem. Soc.* **1987**, *109*, 1435.
[15] F. J. Wu, D. M. Kurtz Jr, K. S. Hagen, P. D. Nyman, P. G. Debrunner, V. A. Vankai, *Inorg. Chem.* **1990**, *29*, 5174.
[16] R. Hotzelmann, K. Wieghardt, U. Flörke, H.-J. Haupt, D. C. Weatherburn, J. Bonvoisin, G. Blondin, J.-J. Girerd, *J. Am. Chem. Soc.* **1992**, *114*, 1681.
[17] O. Kahn, *Molecular Magnetism*, Wiley-VCH, **1993**.
[18] C. Mealli, D. Proserpio, *J. Chem. Educ.* **1990**, *67*, 399.
[19] T. Sala, M. V. Sargent, *J. Chem. Soc., Chem. Commun.* **1978**, 253.
[20] G. M. Sheldrick, *SADABS, Program for Empirical Absorption Correction of Area Detector Data*, University of Göttingen, Germany, **1996**. On the basis of the method by Robert Blessing: R. H. Blessing, *Acta Crystallogr., Sect. A* **1995**, *51*, 33.
[21] M. Sheldrick, *SHELXTL-PC, Program for Crystal Structure Solution*, University of Göttingen: Göttingen, Germany, **1997**.

Received: July 28, 2006
Published Online: February 13, 2007

 © 2007 Wiley-VCH Verlag GmbH & Co. KGaA, Weinheim 

DOI: 10.1002/ejic.200600629

# Synthesis and Reactions of Stannole Anions

Ryuta Haga,[a] Masaichi Saito,*[a] and Michikazu Yoshioka[a]

**Keywords:** Anions / Aromaticity / Lithium / Metallacycles / Tin

The synthesis of stannole anions bearing various substituents on the tin atom is described. The reduction of hexaphenylstannole by the proper amount of lithium gave 1,2,3,4,5-pentaphenylstannole anion **1**. The reaction of **1** with 1,*n*-dihaloalkanes (*n* = 1, 3, 4, 5, 6) gave the corresponding 1,*n*-bis(1-stannacyclopentadien-1-yl)alkanes. In contrast, the reaction of **1** with 1,2-dihaloalkanes gave the 1,1′-bistannole. The reactions of stannole dianion **3** with an equimolar amount of bulky alkyl, aryl, silyl, and stannyl halides gave the corresponding stannole anions.
(© Wiley-VCH Verlag GmbH & Co. KGaA, 69451 Weinheim, Germany, 2007)

## Introduction

Metalolyl anions of heavier group 14 elements have received considerable attention in view of their potential aromatic character as heavier congeners of the cyclopentadienyl anion,[1] since the first report on the generation of a silole anion in 1958.[2] Over the past few decades, silole and germole anions have already been synthesized by deprotonation, dehalogenation, or transmetallation of the corresponding metaloles, and their structures have been discussed extensively by NMR, or X-ray structural analysis.[3–6] Boudjouk reported the first NMR characterization of a silole anion.[5] The negative charge was concluded to delocalize in the silole ring. In contrast to Boudjouk's silole anion, in some silole and germole anions, the negative charge localizes on the central atom, as evidenced by NMR[4] and/or X-ray structural analyses.[6] Although remarkable progress has been made on silicon and germanium analogues, no stannole anion had been reported before we undertook a study on such species a few years ago.[7] First, we reported the synthesis of 1,2,3,4,5-pentaphenylstannole anion **1** by the reaction of 1,1′-bistannole **2** with lithium (Scheme 1).[8] However, it was difficult to manipulate the stoichiometry or reaction conditions to produce stannole anion **1** without stannole dianion **3** from the 1,1′-bistannole **2** because no sufficient amount of **2** could be obtained in several steps from diphenylacetylene.[7–9] To investigate the chemistry of stannole anions, alternative methods for the synthesis of stannole anions using an easily accessible starting material were required. Very recently, we reported an efficient synthesis of the first tin-containing carbocyclic aromatic stannole dianion **3** by the reaction of hexaphenylstannole (**4**) with excess lithium and discussed its aromaticity by the aid of NMR studies, X-ray analysis and theoretical calculations (Scheme 2).[10,11] Furthermore, we reported the oxidation of the stannole dianion **3** to the 1,1′-bistannole dianion **5** as a novel method for the synthesis of a stannole anion.[12]

Herein we describe novel methods for the preparation of stannole anions: (i) the reduction of hexaphenylstannole (**4**) with the proper amount of lithium, and (ii) the reaction of the stannole dianion **3** with various halogen reagents. NMR studies on stannole anions and their reactions are also reported.

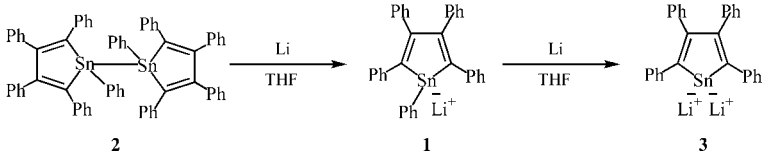


**2** **1** **3**

Scheme 1.

## Results and Discussion

### Synthesis and Reactions of 1,2,3,4,5-Pentaphenylstannole Anion (1)

#### *Synthesis of Stannole Anion 1 from Hexaphenylstannole 4*

Treatment of hexaphenylstannole (**4**) with 3 equiv. of lithium[13] in THF at room temperature gave a dark-red solu-

[a] Department of Chemistry, Graduate School of Science and Engineering, Saitama University
Shimo-okubo, Sakura-ku, Saitama-City, Saitama, 338-8570 Japan
Fax: +81-48-858-3698
E-mail: masaichi@chem.saitama-u.ac.jp
Supporting information for this article is available on the WWW under http://www.eurjic.org or from the author.

 © 2007 Wiley-VCH Verlag GmbH & Co. KGaA, Weinheim 

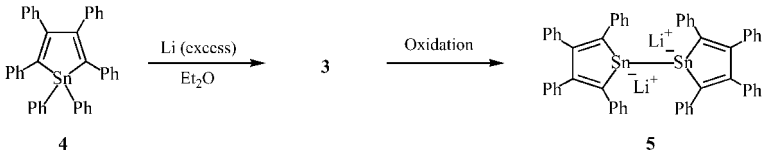


Scheme 2.

tion, suggesting the formation of an anion species. After stirring the reaction mixture for 6 h, addition of excess methyl iodide to this reaction mixture gave 1-methyl-1,2,3,4,5-pentaphenylstannole (**6**)[8] in 55% yield, indicating the effective formation of pentaphenylstannole anion **1** from **4** (Scheme 3). Treatment of **1** thus obtained with 1.8 equiv. of chlorotriphenylstannane at –100 °C gave 1-triphenylstannyl-1,2,3,4,5-pentaphenylstannole (**7**) in 66% yield.

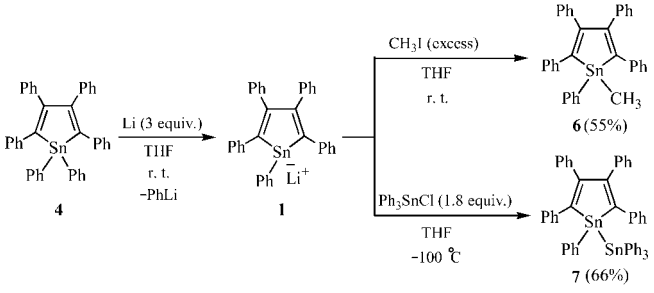


Scheme 3.

The reaction of **4** with 3 equiv. of lithium was monitored by NMR spectroscopy. In the $^{119}$Sn NMR spectrum, only one signal was observed at $\delta$ = –28.6 ppm in the same region as that in the previous synthesis from the 1,1′-bistannole **2**,[8,9] suggesting the formation of **1**. In contrast to the reduction of 1,1′-bistannole **2** to form both stannole anion **1** and the stannole dianion **3**, the $^{13}$C NMR spectrum revealed the clean formation of the stannole anion **1**. Although some unidentifiable signals were observed, the signals due to the stannole anion **1** could be completely assigned by the comparison of the chart of the mixture of the stannole anion **1** and the stannole dianion **3** obtained by the reduction of the 1,1′-bistannole **2**.[14] A phenyl group of hexaphenylstannole (**4**) was eliminated probably as phenyllithium, as in the reduction of hexaphenylstannole (**4**) to form the stannole dianion **3**,[10] although the signals due to phenyllithium were not observed in the reaction mixture. The signal assignable to the α-carbon atom in the five-membered ring was observed at $\delta$ = 176.5 ppm, judging from the large tin–carbon coupling constant of about 171 Hz. The low-field resonance of the α-carbon atom could be explained by paramagnetic contribution of a tin–carbon bond as was observed in the stannole dianion **3**.[10] In the $^{7}$Li NMR spectrum, a single resonance was observed at $\delta$ = –0.64 ppm. In contrast to the successful isolation of the stannole dianion **3**, recrystallization of the reaction mixture to purify the stannole anion **1** was not successful. Thus, the degree of aromaticity of **1** using the $^{7}$Li chemical shift could not be estimated because intermolecular exchange of lithium cations between **1** and phenyllithium could not be suppressed. Although the yield of **1** could not be estimated, the yields of the trapping products **6** and **7**, and the NMR spectra of **1**, especially the $^{119}$Sn NMR spectrum, suggest that the generation efficiency should be very high.

### *Reaction of Stannole Anion 1 with Dihaloalkanes*

Connecting two stannole skeletons with a hydrocarbon chain is a subject of interest because two stannole rings could face each other to reveal unique electronic properties resulting from through-space π-facial interactions.[15]

Reaction of **1** with excess dichloromethane gave bis(1,2,3,4,5-pentaphenyl-1-stannacyclopentadien-1-yl)methane (**8**) in 79% yield (Scheme 4). Compound **8** was proved to have a symmetrical structure having an Sn–C–Sn skeleton by $^{2}J$(Sn–Sn) of 284 Hz in the $^{119}$Sn NMR spectrum. The bis(stannoles) **9**–**12**, whose two stannole rings are connected by a saturated hydrocarbon chain were also synthesized by the reaction of **1** with 0.5 equiv. of the corresponding 1,*n*-dibromoalkanes (*n* = 3–6) in moderate yields (Scheme 4). The structures of all the bis(stannoles) thus obtained were determined by NMR spectroscopy and elemental analysis. These results are similar to the formation of 1,3-bis(triphenylstannyl)propane from triphenylstannyl anion and 1,3-dibromopropane.[16]

On the other hand, reactions of the stannole anion **1** with 1,2-dihaloethanes gave bi(1,2,3,4,5-pentaphenyl-1-stannacyclopentadien-1-yl) (**2**)[8,9] in about 70% yields. Oxidation

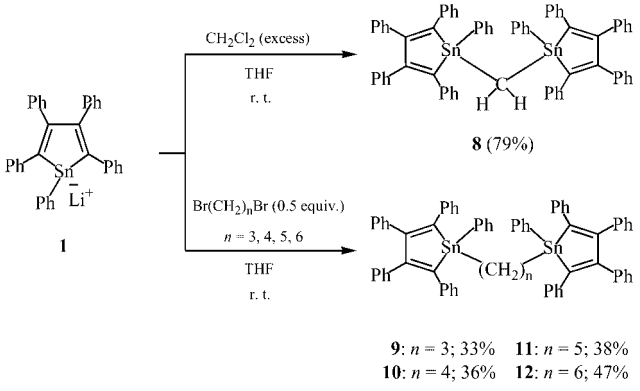


Scheme 4.

 © 2007 Wiley-VCH Verlag GmbH & Co. KGaA, Weinheim 

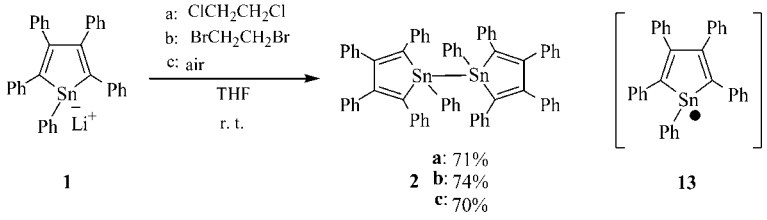


Scheme 5.

of the stannole anion **1** by air also gave **2** in high yield (Scheme 5). The formation of **2** can be reasonably interpreted in terms of the dimerization of stannole radical **13** resulting from oxidation of **1** by air or dihaloethanes. Evidently, dihaloethanes function as one-electron oxidants in these reactions.[17]

### *Reaction of Stannole Anion 1 with Di-tert-butyldichlorostannane*

Reaction of the stannole anion **1** with di-*tert*-butyldichlorostannane at –100 °C gave di-*tert*-butylbis(1,2,3,4,5-pentaphenyl-1-stannacyclopentadien-1-yl)stannane (**14**) in 49% yield (Scheme 6). In the $^{119}Sn$ NMR spectrum, two signals are observed with an intensity ratio of 2:1, resulting from the two equivalent terminal and one central tin atoms, respectively.

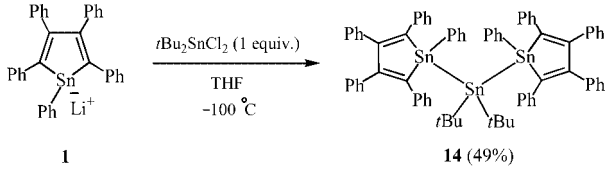


Scheme 6.

### *Photophysical Properties of Bis(stannoles) 8–12 and 14*

We examined the photophysical properties of the newly obtained bis(stannoles) **8**–**12** and **14** whose two stannole rings are connected by a saturated hydrocarbon or a stannyl chain. UV/Vis absorption spectra for **4**,[16] **8**–**12**, and **14** are listed in Table 1. The absorption maxima of **8**–**12** appear at almost the same wavelength as that of **4**, reflecting the same chromophore. Namely, the absorption is derived from the π–π* transition of the stannole ring.[18] The π–π* transitions of group 14 metaloles are observed in the same region at about 360 nm because the contribution of the diene moiety to both HOMO and LUMO is more predominant than that of the metal moiety.[18] This spectral feature suggests no significant through-space interaction between the two stannole rings in solution. Compound **14** displays two shoulder absorption bands at about 310 and 370 nm. The latter band can be assigned to π–π* transition of the stannole ring. The shorter band can be assigned to the transition of σ(Sn–Sn) to π* of the diene moiety because the corresponding band is absent in other bis(stannoles), **8**–**12** with no tin–tin bond.[9]

Table 1. UV/Vis absorptions of stannole **4** and bis(stannoles) **8**–**12**, **14** in $CH_2Cl_2$.

| Compound | $\lambda_{max}$/nm ($\varepsilon$) |
|---|---|
| **4** | 355 (12000) |
| **8** ($n$ = 1) | 359 (20000) |
| **9** ($n$ = 3) | 353 (10600) |
| **10** ($n$ = 4) | 353 (8800) |
| **11** ($n$ = 5) | 353 (16500) |
| **12** ($n$ = 6) | 349 (4100) |
| **14** | 315 (12000) 373 (6800) |

## Synthesis of Stannole Monoanions from Stannole Dianion 3

### *Alkylation of Stannole Dianion 3*

Because the reaction of **3** with methyl iodide gave 1,1-dimethylstannole,[8] *tert*-butyl chloride was chosen as a bulkier alkylating reagent than methyl iodide.[19] When

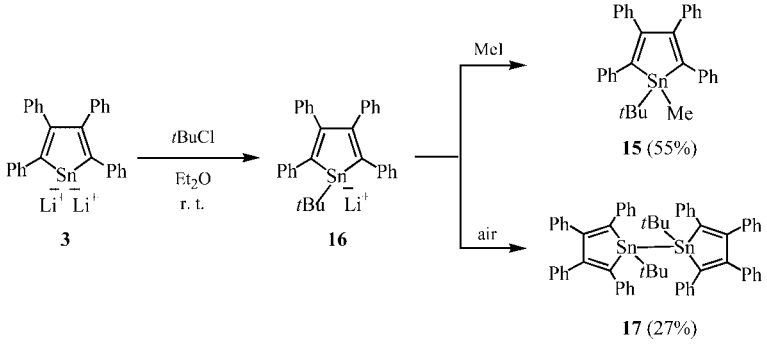


Scheme 7.

 © 2007 Wiley-VCH Verlag GmbH & Co. KGaA, Weinheim 

1 equiv. of *tert*-butyl chloride was added to a diethyl ether solution of the stannole dianion **3**, the color of the reaction mixture changed from deep red to bright red. By treatment of the reaction mixture with methyl iodide, the 1-*tert*-butyl-1-methylstannole **15**[19] was obtained in 55% yield, suggesting the formation of the stannole anion **16** bearing a *tert*-butyl group on the tin atom (Scheme 7). The formation of **16** from **3** is reasonably explained by an electron-transfer mechanism, as observed in the reaction of the tributylstannyl anion with *tert*-butyl halides.[20] The reaction of **3** with *tert*-butyl chloride followed by exposure of the reaction mixture to air gave the 1,1′-bistannole **17**[8,9] in 27% yield. The formation of **17** is interpreted in terms of the dimerization of the 1-*tert*-butylstannole radical resulting from the oxidation of **16**, as was observed in the oxidation of pentaphenylstannole anion **1** (Scheme 5).

### *Arylation of Stannole Dianion 3*

Next we examined the synthesis of 1-arylstannole anions by the reaction of the stannole dianion **3** with aryl halides. Reactions with small aryl halides, however, became complicated because of the formation of mono- and disubstituted products. Thus, bromo-2,4,6-triisopropylbenzene was chosen as a bulky aryl halide. On treatment of the stannole dianion **3** with 1 equiv. of 1-bromo-2,4,6-triisopropylbenzene in diethyl ether at room temperature, the color of the reaction mixture remained deep red, indicating the existence of an anion species. After addition of methyl iodide to the reaction solution, the color of the reaction mixture changed to green. After usual workup, the 1-methyl-1-(2,4,6-triisopropylphenyl)stannole **18** was obtained in 29% yield, indicating the formation of the intermediary stannole anion **19** bearing a 2,4,6-triisopropylphenyl group on the tin atom (Scheme 8). Treatment of **3** with 1-bromo-2,4,6-triisopropylbenzene followed by exposure of the reaction mixture to air gave a complex mixture without the formation of the expected 1,1′-bistannole **20**. The dimerization of the intermediary stannole radical generated by oxidation of **19** is suppressed due to the steric congestion around the tin atom, preventing the formation of **20**.

We examined the synthesis of the stannole anions **21** and **22** having an *m*-terphenyl group, Ar′ = $C_6H_3$-2,6-$Mes_2$ (Mes = $C_6H_3$-2,4,6-$Me_3$) and Ar″ = $C_6H_3$-2,6-$Tip_2$ (Tip = $C_6H_3$-2,4,6-*i*$Pr_3$), respectively, as a more bulky group than a Tip group on the tin atom (Scheme 9). The NMR spectra of these reaction mixtures suggest the formation of **21** or **22** (vide infra), although trapping of **21** and **22** with appropriate reagents was not successful.

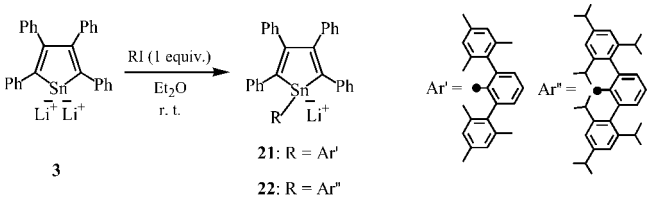


Scheme 9.

The formation of **19** from **3** can be also explained by an electron-transfer mechanism, as observed in the reaction of **3** with *tert*-butyl chloride (Scheme 7) because electrophilic substitution reactions rarely occur in simple aryl halides.

### *Silylation or Stannylation of Stannole Dianion 3*

On treatment of the stannole dianion **3** with 1 equiv. of chlorotriisopropylsilane in diethyl ether at room temperature, the color of the reaction mixture remained deep red. The NMR spectra of the reaction mixture reveal the presence of only one species which can be assigned to the 1-silyl-substituted stannole anion **23** (Scheme 10). Trapping of **23** by methyl iodide, however, gave a complex mixture. The reaction of the stannole dianion **3** with 1 equiv. of chlorotriphenylstannane in diethyl ether at room temperature gave a dark-brown solution. The formation of the 1-stannyl-substituted stannole anion **24** was evidenced by a chemical trapping reaction. Addition of methyl iodide or chlorotriphenylstannane to the solution of **24** gave the 1-methyl-1-(triphenylstannyl)stannole **25** and the 1,1-bis(triphenylstannyl)stannole **26** in 47 and 39% yields, respectively (Scheme 10).

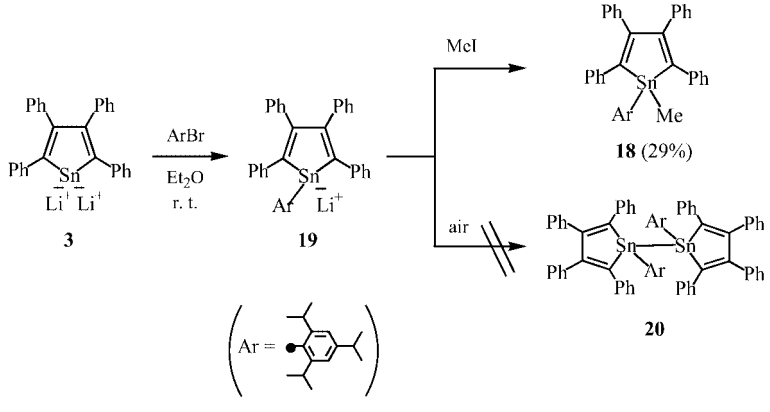


Scheme 8.

 © 2007 Wiley-VCH Verlag GmbH & Co. KGaA, Weinheim 

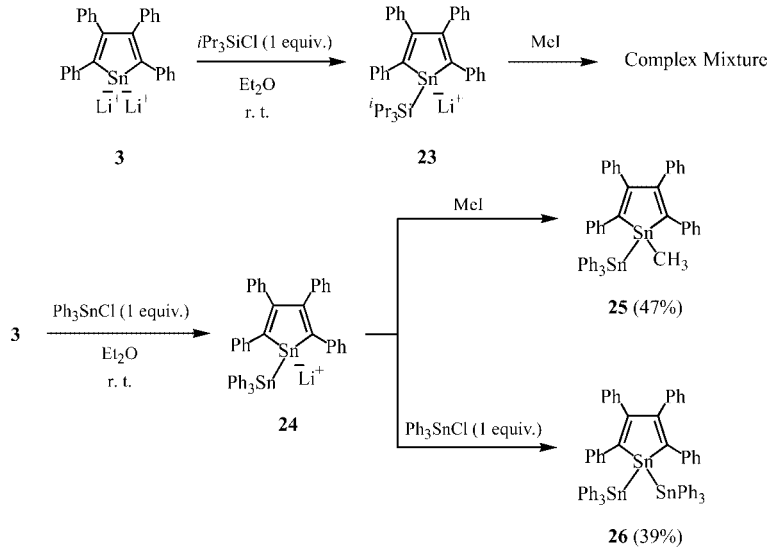


Scheme 10.

### *NMR Studies of the Newly Obtained Stannole Anions*

The structure in solution of the stannole anions was characterized by $^{1}H$, $^{13}C$, $^{119}Sn$ and $^{7}Li$ NMR spectroscopy (Table 2). In the $^{119}Sn$ NMR spectra, there appears only one signal assignable to the 1-*tert*-butyl-substituted stannole anion **16** at δ = 30.4 ppm, suggesting that the generation efficiency of **16** is relatively high, although the isolation of **16** by recrystallization was not successful. The resonance is at lower field than that of hexaphenylstannole (**4**) (δ = –88 ppm) or pentaphenylstannole anion **1** (δ = –28.6 ppm). The $^{119}Sn$ NMR signal of the stannyl anion ($t$Bu$_2$HSn–Sn$t$Bu$_2$Li) appears at low field (δ = 107.8 ppm in $D_2O$/THF).[21] Thus, the low-field shift of the stannole anion **16**

Table 2. Selected $^{13}C$, $^{119}Sn$ and $^{7}Li$ NMR chemical shifts of stannole anions (ppm).

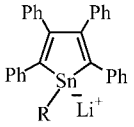


| Compounds | δ($^{13}C_\alpha$) | δ($^{13}C_\beta$) | δ($^{7}Li$) | δ($^{119}Sn$) |
|---|---|---|---|---|
| **1** (R = Ph) | 176.47 ($J_{C, Sn}$ = 171 Hz) | 150.24 | -0.64 | -28.6 |
| **16** (R = *t*Bu) | 170.66 ($J_{C, Sn}$ = 113 Hz) | 151.78 | 0.92 | 30.4 |
| **19** (R = Tip) | 170.39 ($J_{C, Sn}$ = 90 Hz) | 148.97 | 0.95 | -49.6 |
| **21** (R = $Mes_2C_6H_3$) | 170.34 | [a] | 0.15 | –50.2 (br) |
| **22** (R = $Tip_2C_6H_3$) | 170.33 | [a] | 0.61 | –47.1 |
| **23** (R = Si*i*Pr$_3$) | 156.01 ($J_{C, Sn}$ = 190 Hz) | 145.50 | 0.48 | –218.5 ($J_{Sn, Si}$ = 380 Hz) |
| **24** (R = $SnPh_3$) | 172.03 ($J_{C, Sn}$ = 150 Hz) | 148.85 | -0.74, 0.62 | –240.5 (ring) ($J_{Sn, Sn}$ = 3800 Hz) |

[a] Not identified.

 © 2007 Wiley-VCH Verlag GmbH & Co. KGaA, Weinheim 

can be explained by the substituent effect of the *tert*-butyl group on the tin atom. On the other hand, the $^{119}$Sn NMR signals of the stannole anions **19**, **21** and **22**, bearing an aryl group on the tin atom are observed at δ = –49.6 (Ar = Tip), –50.2 (Ar′ = $C_6H_3$-2,6-$Mes_2$) and –47.1 (Ar′′ = $C_6H_3$-2,6-$Tip_2$) ppm in the region similar to that of pentaphenylstannole anion **1**. Although the isolation of **19**, **21** and **22** by recrystallization was not successful, the $^{119}$Sn NMR signals due to **19**, **21** and **22** were major in each reaction mixture. Thus, the generation efficiency of **19**, **21** and **22** was estimated to be relatively high. The signal assignable to 1-silyl-substituted stannole anion **23** was observed at δ = –218 ppm with a coupling constant of 380 Hz resulting from a tin–silicon bond. The high-field resonance is characteristic of silyl-substituted stannanes.[22] Although the isolation of **23** by recrystallization was not successful, the generation efficiency of **23** was estimated to be very high, judging from the clean $^{119}$Sn, $^{13}$C, and $^{1}$H NMR spectra of the reaction mixture. The $^{119}$Sn NMR spectrum of the 1-stannyl-substituted stannole anion **24** reveals two signals at δ = –98.7 and –240.5 ppm, assignable to the triphenylstannyl and the stannole moieties, respectively. Each signal has a coupling constant of about 3800 Hz resulting from a tin–tin bond. Although hexaphenyldistannane was also generated in the reaction mixture as a minor product, probably because stannole dianion **3** functions as a reductant for triphenylstannyl chloride, the generation efficiency of **24** was estimated to be relatively high.

The $^{13}$C NMR signals due to **16**, **19**, **23** and **24** could be assigned completely. In particular, a characteristic low-field signal assignable to the α-carbon atom in **16**, **19** and **24** was observed at δ ≈ 170 ppm with a large tin–carbon coupling constant of about 90–150 Hz, as was observed in the stannole dianion **3** and pentaphenylstannole anion **1**. Interestingly, the α-carbon atom of **23** (δ = 156.0 ppm), assigned by a large tin–carbon coupling constant of about 190 Hz, appears at higher field than those of other stannole anions, probably due to the effect of the silyl group on the tin atom. The $^{13}$C NMR signals due to the α-carbon atom of **21** and **22** could be observed at δ = 170.34 ppm for **21** and δ = 170.33 ppm for **22**. Other signals in the $^{13}$C NMR spectra, however, are too complicated to be assigned, probably due to steric congestion around the tin atom. The $^{7}$Li NMR signals of all the stannole anions are observed at δ ≈ 0 ppm.

## Conclusions

We have succeeded in an efficient synthesis of pentaphenylstannole anion **1** by the reaction of hexaphenylstannole (**4**) with 3 equiv. of lithium. The stannole anion **1** reacted with 1,*n*-dihaloalkanes (*n* = 1, 3, 4, 5 and 6) to give the corresponding adducts, as do common organostannyl anions. On the other hand, 1,2-dihaloethanes reacted with **1** as one-electron oxidants. The UV/Vis spectra of the newly obtained bis(stannoles) reveal no significant interaction between the two stannole rings in solution. The synthesis of a variety of stannole anions from stannole dianion **3** could be also achieved. The formation of the anions was clearly evidenced by NMR analysis and chemical trapping reactions. The $^{7}$Li NMR signals of these stannole anions are observed at δ ≈ 0 ppm. The aromaticity of the newly obtained stannole anions can not be presently discussed by using $^{7}$Li NMR spectroscopy because of the involvement of exchange of lithium cations as well as a small possibility of $\eta^5$-coordination of a lithium cation to the stannole anion.

## Experimental Section

**General Procedures:** All experiments were performed under argon using a usual glass apparatus or a glovebox. THF, diethyl ether and [$D_6$]benzene were distilled from sodium/benzophenone or a potassium mirror. $^{1}$H (400 MHz) and $^{13}$C (101 MHz) NMR spectra were recorded with a Bruker AM-400 or a Bruker DRX-400 spectrometer in $CDCl_3$ or a mixture of THF or diethyl ether and [$D_6$]benzene. $^{119}$Sn (149 MHz) and $^{7}$Li (156 MHz) NMR spectra were recorded with a Bruker DRX-400 spectrometer in $CDCl_3$ or a mixture of THF or diethyl ether and [$D_6$]benzene. Wet column chromatography (WCC) was carried out with Kanto silica gel 60N. Preparative gel permeation chromatography (GPC) was carried out with an LC-918 (Japan Analytical Ind. Co., Ltd.) with JAIGEL-1H and -2H columns with chloroform as the eluent. All melting points were determined with a Mitamura Riken Kogyo MEL-TEMP apparatus and are uncorrected. Elemental analyses were carried out at the Microanalytical Laboratry of Molecular Analysis and Life Science Center, Saitama University.

**Synthesis of 1,2,3,4,5-Pentaphenylstannole Anion (1) from 1,1,2,3,4,5-Hexaphenylstannole (4):** A THF (4 mL) solution of hexaphenylstannole (**4**) (370 mg, 0.59 mmol) was treated with lithium (10 mg, 1.45 mmol) at room temperature. After the reaction mixture was stirred for 6 h, an aliquot (1.0 mL) of the reaction mixture was placed in an NMR tube with [$D_6$]benzene (0.2 mL) and the tube was degassed by freeze-pump-thaw cycles and sealed. **1:** $^{1}$H NMR (THF/$C_6D_6$): $\delta$ = 6.45–6.49 (m, 2 H), 6.55–6.58 (m, 2 H), 6.61–6.67 (m, 7 H), 6.70–6.74 (m, 4 H), 6.75–6.78 (m, 6 H), 6.86–6.90 (m, 3 H), 7.71–7.74 (m, 1 H) ppm. $^{13}$C NMR (THF/$C_6D_6$): $\delta$ = 121.36 (d), 123.51 (d), 124.10 (d), 126.44 (d), 126.56 (d), 126.59 (d), 128.54 (d), 131.58 (d), 138.66 (d), 145.59 (s), 150.24 (s), 150.66 (s, $J_{C,Sn}$ = 33 Hz), 161.96 (s), 176.47 (s, $J_{C,Sn}$ = 171 Hz) ppm. $^{119}$Sn NMR (THF/$C_6D_6$): $\delta$ = –28.6 ppm. $^{7}$Li NMR (THF/$C_6D_6$): $\delta$ = –0.64 ppm.

**Reaction of Pentaphenylstannole Anion 1 with Methyl Iodide:** To a THF (5 mL) solution of **1** prepared from **4** (148 mg, 0.235 mmol) and lithium (4 mg, 0.61 mmol) was added an excess amount of methyl iodide (1.0 mL, 1.61 mmol) at room temperature. After removal of volatile substances, the residue was subjected to column chromatography (hexane/ethyl acetate, 10:1) to afford 1-methyl-1,2,3,4,5-pentaphenylstannole (**6**) (80 mg, 0.13 mmol, 55%). **6:** M.p. 139–140 °C (decomp.) ($CH_2Cl_2$ + MeOH). $^{1}$H NMR ($CDCl_3$): $\delta$ = 0.86 (s, $J_{H,Sn}$ = 56 Hz, 3 H), 6.79–6.88 (m, 8 H), 6.94–7.06 (m, 12 H), 7.34–7.41 (m, 3 H), 7.51–7.67 (m, 2 H) ppm. $^{13}$C NMR ($CDCl_3$): $\delta$ = –9.06 (q), 125.19 (d), 125.77 (d), 127.30 (d), 127.80 (d), 128.76 (d), 129.15 (d), 129.20 (d), 130.29 (d), 136.45 (d), 139.50 (s), 140.71 (s), 142.55 (s), 143.62 (s), 154.59 (s) ppm. $^{119}$Sn NMR ($CDCl_3$): $\delta$ = –38.8 ppm. $C_{38}H_{34}Sn$ (609.42): calcd. C 74.10, H 4.97; found C 73.84, H 4.96.

**Reaction of Pentaphenylstannole Anion 1 with Chlorotriphenylstannane:** To a THF (4 mL) solution of **1** prepared from **4** (178 mg, 0.28 mmol) and lithium (6 mg, 0.85 mmol) was added chlorotri-

 © 2007 Wiley-VCH Verlag GmbH & Co. KGaA, Weinheim 

phenylstannane (202 mg, 0.52 mmol) at –100 °C. After being warmed to room temperature, the reaction mixture was stirred overnight. After removal of volatile substances, the residue was chromatographed (hexane/ethyl acetate, 10:1) to give 1,2,3,4,5-pentaphenyl-1-(triphenylstannyl)stannole (**7**) (169 mg, 0.19 mmol, 66%). **7:** M.p. 189 °C (decomp.). $^1$H NMR ($CDCl_3$): $\delta$ = 6.73–6.84 (m, 8 H), 6.85–6.92 (m, 6 H), 6.94–7.00 (m, 6 H), 7.25–7.38 (m, 12 H), 7.40–7.53 (m, 8 H) ppm. $^{13}$C NMR ($CDCl_3$): $\delta$ = 125.18 (d), 125.79 (d), 127.30 (d), 127.77 (d), 128.76 (d), 128.92 (d), 128.96 (d), 129.00 (d), 129.15 (d), 129.54 (d, $J_{C,Sn}$ = 21 Hz), 130.35 (d), 137.38 (d, $J_{C,Sn}$ = 9, 41 Hz), 136.15 (s), 140.80 (s), 142.57 (s), 146.97 (s), 154.23 (s) ppm. $^{119}$Sn NMR ($CDCl_3$): $\delta$ = –125.0 ($^1J_{Sn,Sn}$ = 3573 Hz), –111.5 ($^1J_{Sn,Sn}$ = 3573 Hz) ppm. $C_{52}H_{40}Sn_2$ (902.32): calcd. C 69.22, H 4.47; found C 68.81, H 4.36.

**Reaction of Pentaphenylstannole Anion 1 with Dichloromethane:** To a THF (5 mL) solution of **1** prepared from **4** (250 mg, 0.40 mmol) and lithium (7 mg, 1.05 mmol) was added excess dichloromethane (5 mL, 79 mmol) at room temperature. After removal of volatile substances, the residue was chromatographed (hexane/ethyl acetate, 10:1) to give bis(1,2,3,4,5-pentaphenyl-1-stannacyclopentadienyl)-methane (**8**) (88 mg, 0.079 mmol, conv. 79%). The starting **4** was recovered in 50% yield. **8:** M.p. 226–228 °C (decomp.) ($CH_2Cl_2$ + EtOH). $^1$H NMR ($CDCl_3$): $\delta$ = 1.14 (s, $J_{H,Sn}$ = 64 Hz, 2 H), 6.71–6.77 (m, 16 H), 6.90–6.95 (m, 24 H), 7.28–7.33 (m, 6 H), 7.42–7.52 (m, 4 H) ppm. $^{13}$C NMR ($CDCl_3$): $\delta$ = –15.37 (t, $J_{C,Sn}$ = 253, 256 Hz), 125.30 (d), 125.82 (d), 127.25 (d), 127.90 (d), 128.82 (d, $J_{C,Sn}$ = 39 Hz), 129.15 (d), 129.35 (d, $J_{C,Sn}$ = 22 Hz), 130.38 (d), 136.28 (d, $J_{C,Sn}$ = 41 Hz), 140.36 (s, $J_{C,Sn}$ = 18 Hz), 140.68 (s, $J_{C,Sn}$ = 70 Hz), 142.05 (s, $J_{C,Sn}$ = 47 Hz), 143.47 (s), 154.53 (s, $J_{C,Sn}$ = 89 Hz) ppm. $^{119}$Sn NMR ($CDCl_3$): $\delta$ = –29.5 ($^2J_{Sn,Sn}$ = 284 Hz) ppm. $C_{69}H_{52}Sn_2$(1118.61): calcd. C 74.09, H 4.69; found C 74.20, H 4.57.

**Reaction of Pentaphenylstannole Anion 1 with 1,3-Dibromopropane:** 1,3-Dibromopropane (0.03 mL, 0.30 mmol) was added to a THF (5 mL) solution of **1** prepared from **4** (350 mg, 0.56 mmol) and lithium (11 mg, 1.64 mmol) at room temperature. After removal of volatile substances, the residue was subjected to GPC to afford 1,3-bis(1,2,3,4,5-pentaphenyl-1-stannacyclopentadienyl)propane (**9**) (104 mg, 0.091 mmol, 33%). **9:** M.p. 90–95 °C (decomp.). $^1$H NMR ($CDCl_3$): $\delta$ = 1.65–1.86 (m, 4 H), 2.10–2.35 (m, 2 H), 6.73–6.85 (m, 16 H), 6.85–7.00 (m, 24 H), 7.27–2.36 (m, 6 H), 7.40–7.60 (m, 4 H) ppm. $^{13}$C NMR ($CDCl_3$): $\delta$ = 13.13 (t, $^1J_{C,Sn}$ = 340, 356 Hz, $^3J_{C,Sn}$ = 70 Hz), 24.63 (t, $^2J_{C,Sn}$ = 21 Hz), 125.14 (d), 125.72 (d), 127.26 (d), 127.83 (d), 128.78 (d), 129.05 (d, $J_{C,Sn}$ = 21 Hz), 129.09 (d), 130.30 (d), 136.75 (d, $J_{C,Sn}$ = 38 Hz), 139.26 (s), 140.66 (s, $J_{C,Sn}$ = 63 Hz), 142.72 (s, $J_{C,Sn}$ = 45 Hz), 144.02 (s, $J_{C,Sn}$ = 391, 409 Hz), 154.75 (s, $J_{C,Sn}$ = 79 Hz) ppm. $^{119}$Sn NMR ($CDCl_3$): $\delta$ = –49.9 ppm. $C_{71}H_{56}Sn_2$ (1146.67): calcd. C, 74.37, H 4.92; found C 74.07, H 4.92.

**Reaction of Pentaphenylstannole Anion 1 with 1,4-Dibromobutane:** 1,4-Dibromobutane (0.019 mL, 0.16 mmol) was added to a THF (3 mL) solution of **1** prepared from **4** (200 mg, 0.32 mmol) and lithium (6 mg, 0.89 mmol) at room temperature. After removal of volatile substances, the residue was subjected to GPC to afford 1,4-bis(1,2,3,4,5-pentaphenyl-1-stannacyclopentadienyl)butane (**10**) (66 mg, 0.057 mmol, 36%). **10:** M.p. 190 °C (decomp.). $^1$H NMR ($CDCl_3$): $\delta$ = 1.45–1.63 (m, 4 H), 1.68–1.86 (m, 4 H), 6.77–6.83 (m, 16 H), 6.90–7.01 (m, 24 H), 7.30–7.36 (m, 6 H), 7.46–7.58 (m, 4 H) ppm. $^{13}$C NMR ($CDCl_3$): $\delta$ = 12.71 (t, $^1J_{C,Sn}$ = 369 Hz), 30.92 (t, $^2J_{C,Sn}$ = 56 Hz, $^3J_{C,Sn}$ = 24 Hz), 125.13 (d), 125.73 (d), 127.27 (d), 127.81 (d), 128.77 (d), 129.09 (d, $J_{C,Sn}$ = 20 Hz), 129.09 (d), 130.32 (d), 136.71 (d, $J_{C,Sn}$ = 38 Hz), 139.58 (s), 140.73 (s, $J_{C,Sn}$ = 63 Hz), 142.84 (s, $J_{C,Sn}$ = 45 Hz), 144.21 (s, $J_{C,Sn}$ = 390, 408 Hz), 154.69 (s, $J_{C,Sn}$ = 81 Hz) ppm. $^{119}$Sn NMR ($CDCl_3$): $\delta$ = –47.3 ppm. $C_{72}H_{58}Sn_2$ (1160.70): calcd. C 74.51, H 5.04; found C 74.00, H 5.09.

**Reaction of Pentaphenylstannole Anion 1 with 1,5-Dibromopentane:** 1,5-Dibromopentane (0.046 mL, 0.35 mmol) was added to a THF (5 mL) solution of **1** prepared from **4** (430 mg, 0.68 mmol) and lithium (14 mg, 2.0 mmol) at room temperature. After removal of volatile substances, the residue was subjected to GPC to afford 1,5-bis(1,2,3,4,5-pentaphenyl-1-stannacyclopentadienyl)pentane (**11**) (152 mg, 0.13 mmol, 38%). **11:** M.p. 85–87 °C (decomp.). $^1$H NMR ($CDCl_3$): $\delta$ = 1.31–1.43 (m, 2 H), 1.43–1.58 (m, 4 H), 1.58–1.77 (m, 4 H), 6.63–6.84 (m, 16 H), 6.84–7.00 (m, 24 H), 7.29–7.42 (m, 6 H), 7.42–7.63 (m, 4 H) ppm. $^{13}$C NMR ($CDCl_3$): $\delta$ = 13.27 (t, $^1J_{C,Sn}$ = 355, 372 Hz), 26.26 (t, $^3J_{C,Sn}$ = 24 Hz), 37.98 (t, $^2J_{C,Sn}$ = 54 Hz), 125.10 (d), 125.71 (d), 127.28 (d), 127.79 (d), 128.74 (d), 129.14 (d, $J_{C,Sn}$ = 20 Hz), 129.14 (d), 130.29 (d), 136.72 (d, $J_{C,Sn}$ = 44 Hz), 139.63 (s), 140.75 (s, $J_{C,Sn}$ = 63 Hz), 142.90 (s, $J_{C,Sn}$ = 44 Hz), 144.32 (s, $J_{C,Sn}$ = 389, 406 Hz), 154.63 (s, $J_{C,Sn}$ = 79 Hz) ppm. $^{119}$Sn NMR ($CDCl_3$): $\delta$ = –46.5 ppm. $C_{73}H_{60}Sn_2$ (1174.73): calcd.C 74.64, H 5.15; found C 74.59, H 5.15.

**Reaction of Pentaphenylstannole Anion 1 with 1,6-Dibromohexane:** 1,6-Dibromohexane (0.04 mL, 0.27 mmol) was added to a THF (4 mL) solution of **1** prepared from **4** (338 mg, 0.54 mmol) and lithium (11 mg, 1.59 mmol) at room temperature. After removal of volatile substances, the residue was subjected to GPC to afford 1,6-bis(1,2,3,4,5-pentaphenyl-1-stannacyclopentadienyl)hexane (**12**) (151 mg, 0.13 mmol, 47%). **12:** M.p. 75–80 °C (decomp.). $^1$H NMR ($CDCl_3$): $\delta$ = 1.15–1.30 (m, 4 H), 1.51–1.75 (m, 8 H), 6.70–6.86 (m, 16 H), 6.86–7.05 (m, 24 H), 7.26–7.35 (m, 6 H), 7.45–7.63 (m, 4 H) ppm. $^{13}$C NMR ($CDCl_3$): $\delta$ = 13.63 (t, $^1J_{C,Sn}$ = 358, 373 Hz), 26.78 (t, $^3J_{C,Sn}$ = 24 Hz), 33.45 (t, $^2J_{C,Sn}$ = 50 Hz), 125.08 (d), 125.70 (d), 127.28 (d), 127.78 (d), 128.74 (d), 129.05 (d, $J_{C,Sn}$ = 20 Hz), 129.05 (d), 130.29 (d), 136.71 (d, $J_{C,Sn}$ = 45 Hz), 139.71 (s), 140.77 (s, $J_{C,Sn}$ = 63 Hz), 142.89 (s, $J_{C,Sn}$ = 45 Hz), 144.41 (s, $J_{C,Sn}$ = 388, 407 Hz), 154.61 (s, $J_{C,Sn}$ = 78 Hz) ppm. $^{119}$Sn NMR ($CDCl_3$): $\delta$ = –46.6 ppm. $C_{74}H_{62}Sn_2$ (1188.76): calcd. C 74.77, H 5.26; found C 75.01, H 5.39.

**Reaction of Pentaphenylstannole Anion 1 with 1,2-Dichloroethane:** Excess 1,2-dichloroethane (2 mL, 32 mmol) was added to a THF (4 mL) solution of **1** prepared from **4** (252 mg, 0.40 mmol) and lithium (9 mg, 1.30 mmol) at room temperature. After volatile substances were removed, the residue was washed with hexane to give 1,1′-bistannole **2**[8,9] (298 mg, 0.27 mmol, 71%).

**Reaction of Pentaphenylstannole Anion 1 with 1,2-Dibromoethane:** Excess 1,2-dibromoethane (0.5 mL, 5.8 mmol) was added to a THF (5 mL) solution of **1** prepared from **4** (303 mg, 0.48 mmol) and lithium (11 mg, 1.59 mmol) at room temperature. After volatile substances were removed, the residue was washed with hexane to give 1,1′-bistannole **2**[8,9] (196 mg, 0.18 mmol, 74%).

**Formation of 2 by Oxidation of Pentaphenylstannole Anion 1:** A THF (7 mL) solution of **1** prepared from **4** (408 mg, 0.65 mmol) and lithium (12 mg, 1.69 mmol) was exposed to air for a few minutes. After volatile substances were removed, the residue was washed with hexane to give 1,1′-bistannole **2**[8,9] (120 mg, 0.11 mmol, conv. 70%). The starting **4** was recovered in 20% yield.

**Reaction of Pentaphenylstannole Anion 1 with Di-*tert*-butyldichlorostannane:** A THF (4 mL) solution of **1** prepared from **4** (250 mg, 0.40 mmol) and lithium (8 mg, 1.16 mmol) was added to a THF (2 mL) solution of di-*tert*-butyldichlorostannane (121 mg, 0.40 mmol) at –100 °C. The reaction mixture was warmed to room

 © 2007 Wiley-VCH Verlag GmbH & Co. KGaA, Weinheim 

temperature and stirred overnight. After removal of volatile substances, the residue was subjected to GPC to afford di-*tert*-butylbis(1,2,3,4,5-pentaphenyl-1-stannacyclopentadienyl)stannane (**14**) (109 mg, 0.08 mmol, conv. 49%). The starting **4** was recovered in 16% yield. **14:** M.p. 138–140 °C (decomp.). $^1$H NMR ($CDCl_3$): $\delta$ = 1.15 (s, $J_{H,Sn}$ = 7, 77 Hz, 18 H), 6.72–6.83 (m, 24 H), 6.91–6.94 (m, 16 H), 7.25–7.34 (m, 6 H), 7.52–7.66 (m, 4 H) ppm. $^{13}$C NMR ($CDCl_3$): $\delta$ = 33.33 (q, $J_{C,Sn}$ = 10 Hz), 35.31 (s, $J_{C,Sn}$ = 31 Hz), 125.10 (d), 125.64 (d), 127.19 (d), 127.60 (d), 128.68 (d, $J_{C,Sn}$ = 11 Hz), 128.96 (d, $J_{C,Sn}$ = 44 Hz), 129.59 (d, $J_{C,Sn}$ = 20 Hz), 130.93 (d), 137.40 (d, $J_{C,Sn}$ = 41 Hz), 140.99 (s), 141.16 (s, $J_{C,Sn}$ = 54 Hz), 142.73 (s, $J_{C,Sn}$ = 47 Hz), 148.60 (s, $J_{C,Sn}$ = 16 Hz), 154.25 (s, $J_{C,Sn}$ = 71 Hz) ppm. $^{119}$Sn NMR ($CDCl_3$): $\delta$ = –103.2 ($^1J_{Sn,Sn}$ = 329 Hz), –44.8 ($^1J_{Sn,Sn}$ = 329 Hz) ppm. $C_{76}H_{68}Sn_3$ (1337.54): calcd. C 68.25, H 5.12; found C 68.23, H 5.11.

**Reaction of 1-*tert*-Butylstannole Anion 16 with Methyl Iodide:** A diethyl ether (5 mL) solution of stannole dianion **3** prepared from hexaphenylstannole **4** (270 mg, 0.43 mmol) and lithium (15 mg, 2.18 mmol) was added to a diethyl ether (2 mL) solution of *tert*-butyl chloride (0.05 mL, 0.46 mmol) was added at room temperature. After being stirred for 30 min, the mixture was treated with methyl iodide (0.03 mL, 0.07 mmol). After filtration of materials insoluble in dichloromethane, the filtrate was recrystallized from dichloromethane and methanol to give 1-*tert*-butyl-1-methyl-2,3,4,5-tetraphenylstannole (**15**)[17] (130 mg, 0.24 mmol, 55%). **15:** M.p. 75–80 °C (decomp.) ($CH_2Cl_2$ + MeOH). $^1$H NMR ($CDCl_3$): $\delta$ = 0.60 (s, $J_{H,Sn}$ = 51 Hz, 3 H), 1.22 (s, $J_{H,Sn}$ = 74 Hz, 9 H), 6.77–6.79 (m, 4 H), 6.83–6.85 (m, 4 H), 6.93–6.98 (m, 8 H), 7.04–7.08 (m, 4 H) ppm. $^{13}$C NMR ($CDCl_3$): $\delta$ = –10.57 (q), 29.90 (s), 30.68 (q), 124.86 (d), 125.58 (d), 127.18 (d), 127.74 (d), 129.09 (d), 130.44 (d), 141.01 (s), 143.62 (s), 145.41 (s), 154.47 (s) ppm. $^{119}$Sn NMR ($CDCl_3$): $\delta$ = 5.1 ppm. $C_{33}H_{32}Sn$ (547.35): calcd. C 72.42, H 5.89; found C 72.43, H 5.51.

**Preparation of 1-*tert*-Butylstannole Anion 16:** A diethyl ether (0.7 mL) solution of stannole dianion **3** prepared from hexaphenylstannole **4** (58 mg, 0.09 mmol) with lithium (5 mg, 0.72 mmol) was added to a diethyl ether (2 mL) solution of *tert*-butyl chloride (0.01 mL, 0.09 mmol) at room temperature. The resulting bright-red solution was degassed by freeze-pump-thaw cycles and sealed. **16:** $^1$H NMR ($Et_2O/C_6D_6$): $\delta$ = 1.25 (s, 9 H), 6.61–6.78 (m, 12 H), 6.80–6.83 (m, 4 H), 6.88–6.90 (m, 4 H) ppm. $^{13}$C NMR ($Et_2O/C_6D_6$): $\delta$ = 28.64 (s), 33.71 (q), 122.22 (d), 124.04 (d), 126.80 (d), 127.07 (d), 129.35 (d), 131.59 (d), 145.05 (s), 150.35 (s), 151.78 (s), 170.66 (s, $J_{C,Sn}$ = 113 Hz) ppm. $^{119}$Sn NMR ($Et_2O/C_6D_6$): $\delta$ = 30.4 ppm. $^7$Li NMR ($Et_2O/C_6D_6$): $\delta$ = 0.92 ppm.

**Formation of 17 by Oxidation of 1-*tert*-Butylstannole Anion 16:** A diethyl ether (4 mL) solution of stannole dianion **3** prepared from hexaphenylstannole **4** (197 mg, 0.31 mmol) with lithium (21 mg, 3.03 mmol) was added to a diethyl ether (2 mL) solution of *tert*-butyl chloride (0.04 mL, 0.34 mmol) at room temperature. After being stirred for 30 min, the resulting bright-red solution was exposed to air for a few minutes. After filtration of materials insoluble in dichloromethane, the filtrate was recrystallized from dichloromethane and methanol to give bi(1-*tert*-butyl-2,3,4,5-tetraphenyl-1-stannacyclopentadienyl) (**17**)[9] (45 mg, 0.042 mmol, 27%).

**Reaction of Stannole Dianion 3 with Bromobenzene:** A diethyl ether (7 mL) solution of stannole dianion **3** prepared from hexaphenylstannole **4** (404 mg, 0.64 mmol) and lithium (53 mg, 7.57 mmol) was added to a diethyl ether (2 mL) solution of bromobenzene (0.067 mL, 0.64 mmol) at room temperature. After being stirred for 5 h, the resulting solution was exposed to air for a few minutes. After filtration of materials insoluble in dichloromethane, a complex mixture (293 mg) was obtained.

**Preparation of 1-(2,4,6-Triisopropylphenyl)stannole Anion 19:** A diethyl ether (10 mL) solution of stannole dianion **3** prepared from hexaphenylstannole **4** (707 mg, 1.12 mmol) with lithium (77 mg, 11.1 mmol) was added to a diethyl ether (3 mL) solution of 1-bromo-2,4,6-triisopropylbenzene (317 mg, 1.12 mmol) at room temperature. After being stirred overnight, the resulting deep-red solution was degassed by freeze-pump-thaw cycles and sealed. In a glovebox, after filtration of insoluble materials, the filtrate was concentrated. The residue was washed with hexane to give 1-lithio-1-(2,4,6-triisopropylphenyl)-2,3,4,5-tetraphenylstannole (**19**). **19:** $^1$H NMR ($Et_2O/C_6D_6$): $\delta$ = 1.12–1.17 (m, 18 H), 2.66–2.80 (sept, $J_{H,H}$ = 7 Hz, 2 H), 2.88–2.98 (sept, $J_{H,H}$ = 7 Hz, 1 H), 6.55–6.61 (m, 2 H), 6.61–6.67 (m, 2 H), 6.67–6.77 (m, 8 H), 6.77–6.85 (m, 10 H) ppm. $^{13}$C NMR ($Et_2O/C_6D_6$): $\delta$ = 24.25 (q), 25.84 (q), 34.82 (d), 40.93 (d), 122.24 (d), 122.43 (d), 124.22 (d), 124.45 (d), 126.80 (d), 127.04 (d), 127.39 (d, $J_{C,Sn}$ = 14 Hz), 128.53 (d), 128.74 (d, $J_{C,Sn}$ = 14 Hz), 131.47 (d), 138.60 (d, $J_{C,Sn}$ = 47 Hz), 144.74 (s), 148.97 (s), 149.69 (s, $J_{C,Sn}$ = 35 Hz), 152.23 (s, $J_{C,Sn}$ = 15 Hz), 156.47 (s, $J_{C,Sn}$ = 150 Hz), 161.61 (s), 170.39 (s, $J_{C,Sn}$ = 90 Hz) ppm. $^{119}$Sn NMR ($Et_2O/C_6D_6$): $\delta$ = –49.6 ppm. $^7$Li NMR ($Et_2O/C_6D_6$): $\delta$ = 0.95 ppm. The elemental analysis of **19** could not be carried out because of its extremely high reactivity toward water and oxygen.

**Reaction of Stannole Anion 19 with Methyl Iodide:** A diethyl ether (4 mL) solution of stannole dianion **3** prepared from hexaphenylstannole **4** (150 mg, 0.24 mmol) and lithium (16 mg, 2.29 mmol) was added to a diethyl ether (2 mL) solution of 1-bromo-2,4,6-triisopropylbenzene (66 mg, 0.23 mmol) at room temperature. After being stirred for 4 h, the mixture was treated with methyl iodide (0.1 mL, 1.61 mol). After removal of volatile substances, materials insoluble in dichloromethane were removed by filtration. The residue was subjected to GPC to afford 1-methyl-2,3,4,5-tetraphenyl-1-(2,4,6-triisopropylphenyl)stannole (**18**) (48 mg, 0.07 mmol, 29%). **18:** M.p. 188 °C (decomp.). $^1$H NMR ($CDCl_3$): $\delta$ = 0.96 (s, $J_{H,Sn}$ = 55 Hz, 3 H), 1.05 (d, $J_{H,H}$ = 7 Hz, 12 H), 1.24 (d, $J_{H,H}$ = 7 Hz, 6 H), 2.86 (sept, $J_{H,H}$ = 7 Hz, 1 H), 2.97 (sept, $J_{H,H}$ = 7 Hz, 2 H), 6.73–6.84 (m, 4 H), 6.84–6.95 (m, 12 H), 6.95–7.05 (m, 6 H) ppm. $^{13}$C NMR ($CDCl_3$): $\delta$ = –3.04 (q, $J_{C,Sn}$ = 323 Hz), 23.88 (q), 24.93 (q), 34.14 (d), 38.13 (d, $J_{C,Sn}$ = 33 Hz), 121.50 (d, $J_{C,Sn}$ = 49 Hz), 124.90 (d), 125.49 (d), 127.07 (d), 127.62 (d), 128.93 (d, $J_{C,Sn}$ = 20 Hz), 130.30 (d), 137.17 (s), 140.93 (s, $J_{C,Sn}$ = 63 Hz), 143.12 (s, $J_{C,Sn}$ = 45 Hz), 147.09 (s, $J_{C,Sn}$ = 406 Hz), 150.12 (s, $J_{C,Sn}$ = 10 Hz), 153.08 (s, $J_{C,Sn}$ = 84 Hz), 155.92 (s, $J_{C,Sn}$ = 43 Hz) ppm. $^{119}$Sn NMR ($CDCl_3$): $\delta$ = –66.0 ppm. $C_{44}H_{46}Sn$ (693.60): calcd. C 76.20, H 6.69; found C 76.19, H 6.71.

**Oxidation of Stannole Anion 19:** A diethyl ether (4 mL) solution of stannole dianion **3** prepared from hexaphenylstannole **4** (310 mg, 0.49 mmol) and lithium (32 mg, 4.61 mmol) was added to 1-bromo-2,4,6-triisopropylbenzene (139 mg, 0.49 mmol) at room temperature. After being stirred for 8 h, the resulting solution was exposed to air for a few minutes. After filtration of materials insoluble in diethyl ether, a complex mixture (410 mg) was obtained.

**Preparation of 1-[2,6-Bis(2,4,6-trimethylphenyl)phenyl]stannole Anion 21:** A diethyl ether (7 mL) solution of stannole dianion **3** prepared from hexaphenylstannole **4** (770 mg, 1.22 mmol) and lithium (86 mg, 12.3 mmol) was added to a diethyl ether (3 mL) solution of 1-iodo-2,6-bis(2,4,6-trimethylphenyl)benzene[23] (450 mg, 1.09 mmol) at room temperature. After being stirred for 3 d, the resulting deep-red solution was degassed by freeze-pump-thaw cycles and sealed. After removal of insoluble materials by filtration,

 © 2007 Wiley-VCH Verlag GmbH & Co. KGaA, Weinheim 

the filtrate was concentrated in a glovebox to give 1-[2,6-bis(2,4,6-trimethylphenyl)phenyl]-1-lithio-2,3,4,5-tetraphenylstannole (**21**). The $^1$H and $^{13}$C NMR signals due to **21** are too complicated to be assigned probably because of steric congestion. However, in the $^{13}$C NMR spectrum, the signal assignable to the α-carbon atom was observed at $\delta$ = 170.34ppm. **21:** $^{119}$Sn NMR ($Et_2O/C_6D_6$): $\delta$ = –50.2 ppm. $^7$Li NMR ($Et_2O/C_6D_6$): $\delta$ = 0.15 ppm. The elemental analysis of **21** could not be carried out because of its extremely high reactivity toward water and oxygen.

**Preparation of 1-[2,6-Bis(2,4,6-triisopropylphenyl)phenyl]stannole Anion 22:** A diethyl ether (5 mL) solution of stannole dianion **3** from hexaphenylstannole **4** (319 mg, 0.50 mmol) and lithium (35 mg, 5.07 mmol) was added to a diethyl ether (2 mL) solution of 1-iodo-2,6-bis(2,4,6-triisopropylphenyl)benzene[24] (230 mg, 0.48 mmol) at room temperature. After being stirred for 3 d, the resulting deep-red solution was degassed by freeze-pump-thaw cycles and sealed. After removal of insoluble materials by filtration, the filtrate was concentrated in a glovebox to give 1-[2,6-bis(2,4,6-triisopropylphenyl)phenyl]-1-lithio-2,3,4,5-tetraphenylstannole (**22**). The $^1$H and $^{13}$C NMR signals for **22** are too complicated to be assigned probably because of steric congestion. However, in the $^{13}$C NMR spectrum, the signal assignable to the α-carbon atom was observed at $\delta$ = 170.33ppm. **22:** $^{119}$Sn NMR ($Et_2O/C_6D_6$): $\delta$ = –47.1 ppm. $^7$Li NMR ($Et_2O/C_6D_6$): $\delta$ = 0.61 ppm. The elemental analysis of **22** could not be carried out because of its extremely high reactivity toward water and oxygen.

**Preraration of 1-Triisopropylsilylstannole Anion 23:** Chlorotriisopropylsilane (0.025 mL, 0.12 mmol) was added to a diethyl ether (1 mL) solution of stannole dianion **3** (54 mg, 0.11 mmol) at room temperature in a glovebox. After being stirred overnight, the reaction mixture was concentrated in a glovebox to give 1-lithio-2,3,4,5-tetraphenyl-1-(triisopropylsilyl)stannole (**23**). **23:** $^1$H NMR ($Et_2O/C_6D_6$): $\delta$ = 1.20–1.46 (m, 3 H), 6.61–6.64 (m, 4 H), 6.64–6.75 (m, 6 H), 6.81–6.89 (m, 10 H) ppm. The signals due to the methyl protons of the triisopropylsilyl groups are overlapped with those of the methyl protons of diethyl ether. $^{13}$C NMR ($Et_2O/C_6D_6$): $\delta$ = 15.52 (q), 20.29 (d, $J_{C,Sn}$ = 13 Hz), 124.78 (d), 125.47 (d), 127.35 (d), 127.59 (d), 130.59 (d), 130.94 (d), 142.77 (s, $J_{C,Sn}$ = 37 Hz), 145.50 (s, $J_{C,Sn}$ = 40 Hz), 155.04 (s, $J_{C,Sn}$ = 46 Hz), 156.01 (s, $J_{C,Sn}$ = 190 Hz) ppm. $^{119}$Sn NMR ($Et_2O/C_6D_6$): $\delta$ = –218.5 ($^1J_{Sn,Si}$ = 380 Hz) ppm. $^7$Li NMR ($Et_2O/C_6D_6$): $\delta$ = 0.48 ppm. The elemental analysis of **23** could not be carried out because of its extremely high reactivity toward water and oxygen.

**Reaction of the 1-Triisopropylsilylstannole Anion 23 with Methyl Iodide:** In a glovebox, a diethyl ether (3 mL) solution of stannole dianion **3** (94 mg, 0.19 mmol) and chlorotriisopropylsilane (0.041 mL, 0.19 mmol) was stirred at room temperature overnight and the resulting mixture was treated with methyl iodide (0.1 mL, 1.61 mmol). After removal of materials insoluble in diethyl ether, a complex mixture (101 mg) was obtained.

**Preparation of 1-Triphenylstannylstannole Anion 24:** Chlorotriphenylstannane (55 mg, 0.16 mmol) was added to a diethyl ether (2 mL) solution of stannole dianion **3** (70 mg, 0.14 mmol) at room temperature in a glovebox. After being stirred overnight, the reaction mixture was concentrated in a glovebox to give 1-lithio-2,3,4,5-tetraphenyl-1-(triphenylstannyl)stannole (**24**). **24:** $^1$H NMR ($Et_2O/C_6D_6$): $\delta$ = 6.55–6.80 (m, 16 H), 6.80–6.94 (m, 4 H), 6.94–7.06 (m, 9 H), 7.35–7.46 (m, 6 H) ppm. $^{13}$C NMR ($Et_2O/C_6D_6$): $\delta$ = 122.48 (d), 124.10 (d), 126.73 (d), 126.82 (d), 127.09 (d), 127.71 (d), 129.58 (d), 131.76 (d), 138.51 (d, $J_{C,Sn}$ = 37, 188 Hz), 144.83 (s), 148.85 (s), 149.70 (s), 151.99 (s), 172.03 (s, $J_{C,Sn}$ = 148 Hz) ppm. $^{119}$Sn NMR ($Et_2O/C_6D_6$): $\delta$ = –98.7 ($^1J_{Sn,Sn}$ = 3801 Hz), –240.5 ($^1J_{Sn,Sn}$ = 3801 Hz) ppm. $^7$Li NMR ($Et_2O/C_6D_6$): $\delta$ = –0.74, 0.62 ppm. The elemental analysis of **24** could not be carried out because of its extremely high reactivity toward water and oxygen.

**Reaction of 1-(Triphenylstannyl)stannole Anion 24 with Methyl Iodide:** A diethyl ether (2 mL) solution of the stannole dianion **3** (102 mg, 0.21 mmol) and chlorotriphenylstannane (80 mg, 0.21 mmol) was stirred in a glovebox at room temperature for 2 h, and the resulting mixture was treated with methyl iodide (0.1 mL, 1.61 mmol). After removal of volatile substances, insoluble inorganic salts were filtered off. The residue was subjected to GPC to afford 1-methyl-2,3,4,5-tetraphenyl1-(triphenylstannyl)-stannole (**25**) (80 mg, 0.097 mmol, 47%). **25:** M.p. 143 °C (decomp.). $^1$H NMR ($CDCl_3$): $\delta$ = 0.89 (s, $J_{H,Sn}$ = 15, 53 Hz, 3 H), 6.70–6.80 (m, 8 H), 6.88–6.97 (m, 12 H), 7.25–7.34 (m, 9 H), 7.34–7.49 (m, 6 H) ppm. $^{13}$C NMR ($CDCl_3$): $\delta$ = –7.59 (q, $J_{C,Sn}$ = 59 Hz), 125.08 (d), 125.70 (d), 127.26 (d), 127.78 (d), 128.67 (d), 128.79 (d, $J_{C,Sn}$ = 11 Hz), 129.39 (d, $J_{C,Sn}$ = 21 Hz), 130.34 (d), 137.34 (d, $J_{C,Sn}$ = 8, 41 Hz), 139.13 (s, $J_{C,Sn}$ = 55 Hz), 140.86 (s, $J_{C,Sn}$ = 5, 58 Hz), 142.77 (s, $J_{C,Sn}$ = 47 Hz), 147.78 (s), 153.50 (s, $J_{C,Sn}$ = 21 Hz) ppm. $^{119}$Sn NMR ($CDCl_3$): $\delta$ = –87.3 (s, $^1J_{Sn,Sn}$ = 3532 Hz), –127.4 (s, $^1J_{Sn,Sn}$ = 3532 Hz) ppm. $C_{47}H_{38}Sn_2$ (840.25): calcd. C 67.18, H 4.56; found C 66.90, H 4.49.

**Reaction of the 1-(Triphenylstannyl)stannole Anion 24 with Chlorotriphenylstannane:** A diethyl ether (2 mL) solution of the stannole dianion **3** (107 mg, 0.22 mmol) and chlorotriphenylstannane (168 mg, 0.44 mmol) was stirred in a glovebox at room temperature for 30 min. The color of the reaction mixture changed from dark-red to yellow. After removal of volatile substances, insoluble inorganic salts were filtered off. The residue was subjected to GPC to afford 2,3,4,5-tetraphenyl-1,1-bis(triphenylstannyl)stannole (**26**) (100 mg, 0.085 mmol, 39%). **26:** M.p. 175–177 °C (decomp.). $^1$H NMR ($CDCl_3$): $\delta$ = 6.48–6.56 (m, 4 H), 6.66–6.75 (m, 8 H), 6.80–6.88 (m, 2 H), 6.88–7.00 (m, 6 H), 7.11–7.35 (m, 30 H) ppm. $^{13}$C NMR ($CDCl_3$): $\delta$ = 124.91 (d), 125.64 (d), 127.21 (d), 127.62 (d), 128.65 (d), 127.86 (d), 128.78 (d, $J_{C,Sn}$ = 11 Hz), 129.59 (d, $J_{C,Sn}$ = 15 Hz), 137.33 (d, $J_{C,Sn}$ = 8, 42 Hz), 139.06 (s, $J_{C,Sn}$ = 11, 54 Hz), 141.05 (s, $J_{C,Sn}$ = 50 Hz), 142.93 (s, $J_{C,Sn}$ = 45 Hz), 150.22 (s, $J_{C,Sn}$ = 12 Hz), 153.74 (s, $J_{C,Sn}$ = 19, 63 Hz) ppm. $^{119}$Sn NMR ($CDCl_3$): $\delta$ = –115.7 ($^1J_{Sn,Sn}$ = 2159 Hz, $^2J_{Sn,Sn}$ = 615 Hz), –219.8 ($^1J_{Sn,Sn}$ = 2159 Hz) ppm. The elemental analysis of **26** could not be carried out because of its instability. For the $^1$H, $^{13}$C, and $^{119}$Sn NMR spectra of **26**, see Supporting Information.

**Supporting Information** (see footnote on the first page of this article): All NMR spectroscopic data of compounds, **1**, **16**, **19**, **21**, **22**, **23**, **24**, and **26**. Experimental details for control experiment of the reduction of 1,1′-bistannole **1** with lithium to give stannole anion **1** and dianion **3**.

## Acknowledgments

This work was partially supported by a Grant-in-Aid for Young Scientists (B), No. 17750032 (M. S.) from the Ministry of Education, Culture, Sports, Science and Technology of Japan. M. S. acknowledges a research grant from Toray Science Foundation. R. H. thanks Research Fellowships of the Japan Society for the Promotion of Science for Young Scientists.

[1] For examples of reviews, see: a) E. Colomer, R. J. P. Corriu, M. Lheureux, *Chem. Rev.* **1990**, *90*, 265–282; b) J. Dubac, C. Guérin, P. Meunier, in: S. Patai, Z. Rappoport (Eds.), *The Chemistry of Organosilicon Compounds*, vol. 2, Wiley-Interscience,

 © 2007 Wiley-VCH Verlag GmbH & Co. KGaA, Weinheim 

Chichester, **1998**, p. 1961; c) M. Saito, M. Yoshioka, *Coord. Chem. Rev.* **2005**, *249*, 765–780.
[2] H. Gilman, R. D. Gorsich, *J. Am. Chem. Soc.* **1958**, *80*, 3243–3246.
[3] a) M. D. Curtis, *J. Am. Chem. Soc.* **1967**, *89*, 4241–4242; b) M. D. Curtis, *J. Am. Chem. Soc.* **1969**, *91*, 6011–6018; c) P. Jutzi, A. Karl, *J. Organomet. Chem.* **1981**, *215*, 19–25.
[4] a) W.-C. Joo, J.-H. Hong, S.-B. Choi, H.-E. C. H. Son, C. H. Kim, *J. Organomet. Chem.* **1990**, *391*, 27–36; b) P. Dufour, J. Dubac, M. Dartiguenave, Y. Dartiguenave, *Organometallics* **1990**, *9*, 3001–3003; c) J.-H. Hong, P. Boudjouk, I. Stoenescu, *Organometallics* **1996**, *15*, 2179–2181.
[5] J.-H. Hong, P. Boudjouk, *J. Am. Chem. Soc.* **1993**, *115*, 5883–5884.
[6] a) W. P. Freeman, T. D. Tilley, G. P. A. Yap, A. L. Rheingold, *Angew. Chem. Int. Ed. Engl.* **1996**, *35*, 882–884; b) W. P. Freeman, T. D. Tilley, L. M. Liable-Sands, A. L. Rheingold, *J. Am. Chem. Soc.* **1996**, *118*, 10457–10468.
[7] M. Saito, R. Haga, M. Yoshioka, *Heteroat. Chem.* **2001**, *12*, 349–353.
[8] M. Saito, R. Haga, M. Yoshioka, *Chem. Commun.* **2002**, 1002–1003.
[9] M. Saito, R. Haga, M. Yoshioka, *Eur. J. Inorg. Chem.* **2005**, 3750–3755.
[10] M. Saito, R. Haga, M. Yoshioka, K. Ishimura, S. Nagase, *Angew. Chem. Int. Ed.* **2005**, *44*, 6553–6556.
[11] Recent progress in the dianions of group 14 metaloles, see: M. Saito, M. Yoshioka, *Coord. Chem. Rev.* **2005**, *249*, 765–780 and references cited therein.
[12] R. Haga, M. Saito, M. Yoshioka, *J. Am. Chem. Soc.* **2006**, *128*, 4934–4935.
[13] The conversion of **4** to **1** using a stoichiometric amount (2 equiv.) of lithium was lower than that using 3 equiv. of lithium.
[14] For NMR spectra of a mixture of stannole anion **1** and dianion **3** which were obtained by reduction of 1,1′-bistannole **2**, see Supporting Information.
[15] H. Murata, Z. H. Kafafi, M. Uchida, *Appl. Phys. Lett.* **2002**, *80*, 189–191.
[16] Y. Ducharme, S. Latour, J. D. Wuest, *Organometallics* **1984**, *3*, 208–211.
[17] H. Grützmacher, *Angew. Chem. Int. Ed. Engl.* **1995**, *34*, 295–298, and references therein.
[18] J. Ferman, J. P. Kakareka, W. T. Klooster, J. L. Mullin, J. Quattrucci, J. S. Ricci, H. J. Tracy, W. J. Vining, S. Wallace, *Inorg. Chem.* **1999**, *38*, 2464–2472.
[19] For a preliminary report, see: M. Saito, R. Haga, M. Yoshioka, *Chem. Lett.* **2003**, 912–913.
[20] M. Wakasa, T. Kugita, *Organometallics* **1998**, *17*, 1913–1915.
[21] U. Englich, U. Hermann, I. Prass, Y. Schollmeier, K. Ruhlandt-Senga, F. Uhlig, *J. Organomet. Chem.* **2002**, *646*, 271–276.
[22] For examples of silyl-substituted stannyl anions, see: R. Fischer, J. Baumgartner, C. Marschner, F. Uhlig, *Inorg. Chim. Acta* **2005**, *358*, 3174–3182 and references cited therein.
[23] a) C. F. Du, H. Hart, K. D. Ng, *J. Org. Chem.* **1986**, *51*, 3162; b) K. Ruhlandt-Senge, J. J. Ellison, R. J. Wehmschulte, F. Pauer, P. P. Power, *J. Am. Chem. Soc.* **1993**, *115*, 11353–11357.
[24] B. Schiemenz, P. P. Power, *Organometallics* **1996**, *15*, 958–964.

Received: May 17, 2006
Published Online: February 20, 2007

 © 2007 Wiley-VCH Verlag GmbH & Co. KGaA, Weinheim

**The EUChemSoc Societies have taken the significant step into the future by merging their traditional journals, to form two leading chemistry journals, the *European Journal of Inorganic Chemistry* and the *European Journal of Organic Chemistry.* Three further EUChemSoc Societies (Austria, Czech Republic and Sweden) are Associates of the two journals.**

## COVER PICTURE

**The cover picture shows** the concept of selective anion separation using metal−organic frameworks. Functionalization of the coordination polymers with hydrogen-bonding groups for specific anion binding and recognition results in highly selective separations by direct anion exchange or competitive crystallization processes. The diagram in the lower-left corner depicts a qualitative model for anion separation selectivity, captured in three orthogonal concepts: *complementarity* (strength and number of anion-binding interactions), *organizational rigidity* of the framework, and *softness* (or degree of covalency for anion binding). The solvation-controlled (Hofmeister) selectivity that is normally observed in anion separations can be reversed (anti-Hofmeister) or completely replaced by peak selectivity (non-Hofmeister) when rigid, structurally constrained frameworks having a sufficient number of complementary anion-binding groups are employed, or when the anion is bound with a strong degree of covalency (soft−soft interactions). The background shows a structurally rigid metal−organic framework functionalized with −COOH anion-binding groups that exhibit peak selectivity for the $Cl(H_2O)_4^-$ anionic cluster. Details are presented in the Microreview oyer on p. 1321 ff.

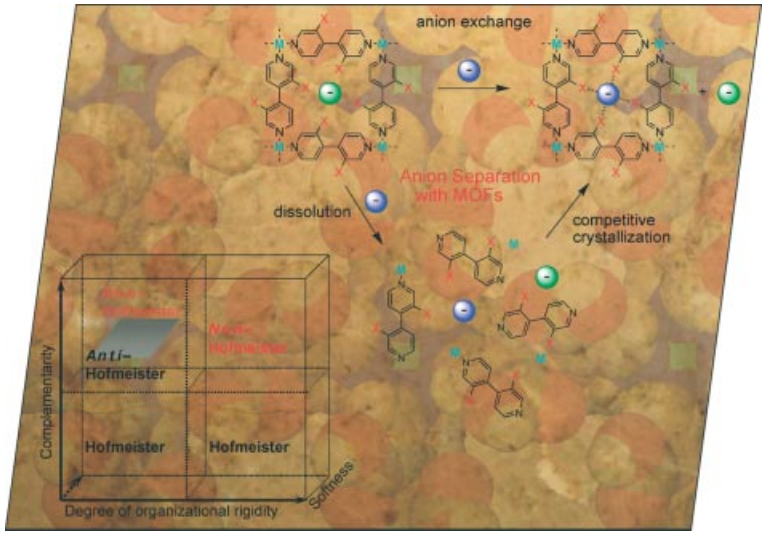


 © 2007 Wiley-VCH Verlag GmbH & Co. KGaA, Weinheim

**The EUChemSoc Societies have taken the significant step into the future by merging their traditional journals, to form two leading chemistry journals, the *European Journal of Inorganic Chemistry* and the *European Journal of Organic Chemistry.* Three further EUChemSoc Societies (Austria, Czech Republic and Sweden) are Associates of the two journals.**

## COVER PICTURE

**The cover picture shows** the concept of selective anion separation using metal−organic frameworks. Functionalization of the coordination polymers with hydrogen-bonding groups for specific anion binding and recognition results in highly selective separations by direct anion exchange or competitive crystallization processes. The diagram in the lower-left corner depicts a qualitative model for anion separation selectivity, captured in three orthogonal concepts: *complementarity* (strength and number of anion-binding interactions), *organizational rigidity* of the framework, and *softness* (or degree of covalency for anion binding). The solvation-controlled (Hofmeister) selectivity that is normally observed in anion separations can be reversed (anti-Hofmeister) or completely replaced by peak selectivity (non-Hofmeister) when rigid, structurally constrained frameworks having a sufficient number of complementary anion-binding groups are employed, or when the anion is bound with a strong degree of covalency (soft−soft interactions). The background shows a structurally rigid metal−organic framework functionalized with −COOH anion-binding groups that exhibit peak selectivity for the $Cl(H_2O)_4^-$ anionic cluster. Details are presented in the Microreview oyer on p. 1321 ff.

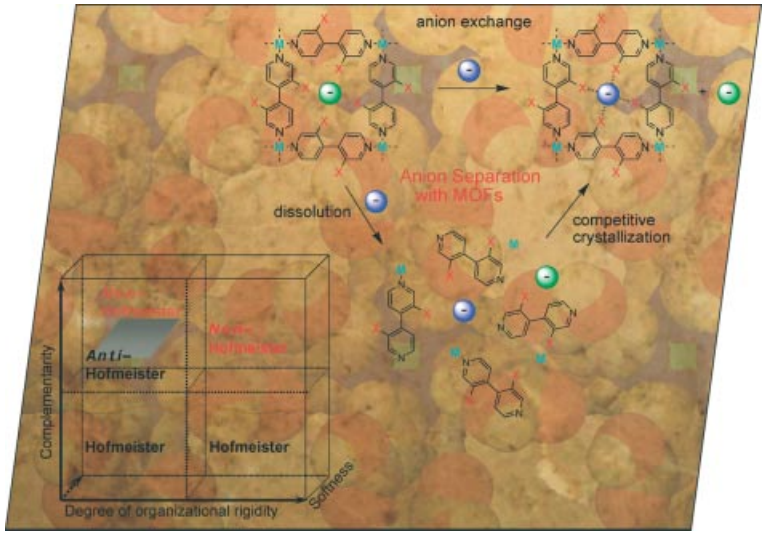


 © 2007 Wiley-VCH Verlag GmbH & Co. KGaA, Weinheim 

# CONTENTS

## MICROREVIEW

### Coordination Polymers

**R. Custelcean,***
**B. A. Moyer* ..... 1321–1340**

Anion Separation with Metal–Organic Frameworks

**Keywords:** Anions / Crystal engineering / Host-guest systems / Molecular recognition

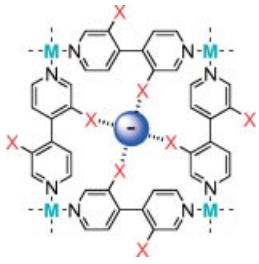

The application of metal-organic frameworks (MOFs) to anion separations with a special emphasis on anion selectivity is reviewed. Non-Hofmeister selectivity and shape recognition are observed in structurally constrained MOFs functionalized with hydrogen-bonding groups.

## SHORT COMMUNICATIONS

### Magnetic Relaxation

**D. Li, R. Clérac, G. Wang, G. T. Yee, S. M. Holmes* ..... 1341–1346**

Structural Distortion and Magnetic Behavior in Cyanide-Bridged $Fe^{III}_2Ni^{II}_2$ Complexes

**Keywords:** Cyanometalate / Magnetism / Single-molecule magnets / Pyrazolylborate / Magnetic relaxation

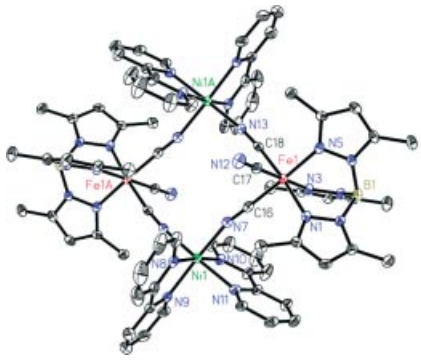

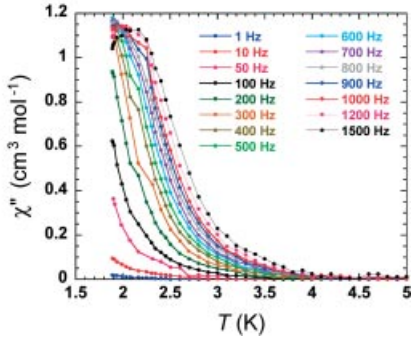


Magnetostructural comparisons between $\{[(Tp^*)Fe^{III}(CN)_3]_2[Ni^{II}(DMF)_4]_2[OTf]_2\}\cdot 2DMF$ (**1**) and the less symmetrical analog, an $S = 3$ cyanide-bridged complex, $\{[(Tp^*)Fe^{III}(CN)_3]_2[Ni^{II}(bipy)_2]_2[OTf]_2\}\cdot 2H_2O$ (**2**) show that, despite a non-planar $\{Fe^{III}_2Ni^{II}_2(\mu\text{-}CN)_4\}$ core and severely distorted $Ni^{II}$ coordination environment in **2**, the magnetic properties of **1** and **2** are similar. This similarity suggests that the $Ni^{II}$ centers play a minor role in determining the magnetization relaxation behavior of the clusters.

### Metallacrown Hosts

**C.-S. Lim, A. C. Van Noord, J. W. Kampf, V. L. Pecoraro* ..... 1347–1350**

Assessing Guest Selectivity within Metallacrown Host Compartments

**Keywords:** Molecular compartment / Metallacrown / Selective recognition / Host–guest chemistry

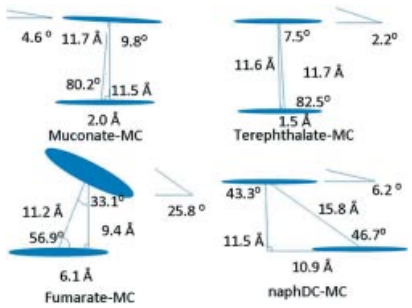


The impact of the chemical properties and lengths of dicarboxylate guests that can be sequestered within chiral $\{Gd[15\text{-}MC\text{-}5]\}_2^{6+}$ compartments in the solid state was assessed.

 © 2007 Wiley-VCH Verlag GmbH & Co. KGaA, Weinheim 

# FULL PAPERS

## Molecular Orbital Calculations

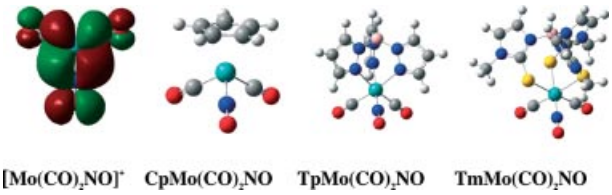


By investigating the hierarchical relationship between facially capping ligands (Cp/Tp/Tm) we can properly appreciate the qualities that a sulfur-donor system brings to the area of chemistry.

**M. Schwalbe, P. C. Andrikopoulos, D. R. Armstrong, J. Reglinski,* M. D. Spicer* ..... 1351–1360**

Structural and Theoretical Insights into Metal–Scorpionate Ligand Complexes

**Keywords:** Nitric oxide / Soft scorpionates / Molybdenum / Tungsten / Molecular orbital calculations

## Understanding Self-Assembly

Chiral tripodal tris(iminocatecholato) ligands form mononuclear gallium(III) or titanium(IV) complexes. Electrostatic repulsion within the complex is compensated by protonation and by adopting an enaminone/chinomethine structure.

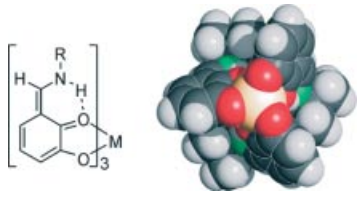

**M. Albrecht,* S. Burk, R. Stoffel, A. Lüchow, R. Fröhlich, M. Kogej, C. A. Schalley ..... 1361–1372**

Protonation of Tris(iminocatecholato) Complexes of Gallium(III) and Titanium(IV)

**Keywords:** Coordination compounds / Helicates / Protonation / Self-assembly / Computational chemistry

## Metal Pyridinehydroxamates

A series of metal pyridinehydroxamates all contain free N-donor atoms that endow them with the potential for use in the construction of pyridinehydroxamato-bridged supramolecular assemblies. The crystal structures of two iron(III) tris(pyridinehydroxamate) building blocks are found to have different packing systems.

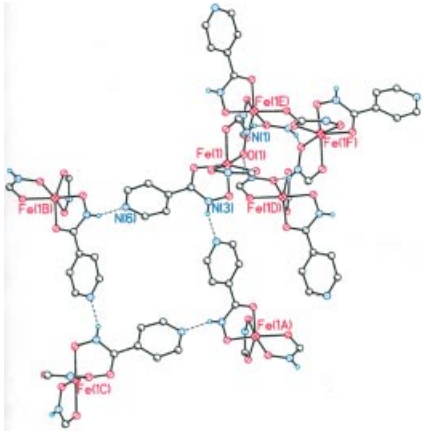


**C. Mulcahy, K. A. Krot, D. M. Griffith, K. Yu. Suponitsky, Z. A. Starikova, C. J. Marmion* ..... 1373–1380**

Iron(III) Tris(pyridinehydroxamate)s and Related Nickel(II) and Zinc(II) Complexes: Potential Platforms for the Design of Novel Heterodimetallic Supramolecular Assemblies

**Keywords:** Iron / Hydroxamic acids / Speciation / Supramolecular chemistry / Crystal packing

## Vibrational Properties

$CF_3SO_2OCF_3$ has been synthesised and its gas-phase structure determined from gas electron diffraction data. The infrared and the Raman spectra were obtained, and the observed bands were assigned. The experimental work was supported by theoretical calculations. The vibrational data along with the calculated theoretical force constants were used to define a scaled quantum mechanical force field for the studied molecule.

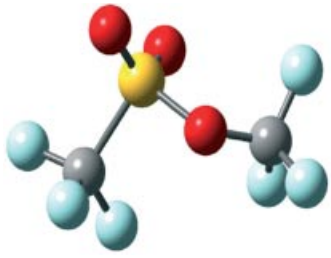

**M. E. Tuttolomondo, P. E. Argañaraz, E. L. Varetti, S. A. Hayes, D. A. Wann, H. E. Robertson, D. W. H. Rankin, A. Ben Altabef* ..... 1381–1389**

Gas-Phase Structure and Vibrational Properties of Trifluoromethyl Trifluoromethanesulfonate, $CF_3SO_2OCF_3$

**Keywords:** Electron diffraction / IR spectroscopy / Raman spectroscopy / Structure elucidation / Ab initio calculations

 © 2007 Wiley-VCH Verlag GmbH & Co. KGaA, Weinheim 

# CONTENTS

## Structural Tuning

**W. Schiessl, R. Puchta, Ž. D. Bugarčić, F. W. Heinemann, R. van Eldik* ..... 1390–1404**

Systematic Counterion Tuning of the Solid-State Structure of $[Pt(thiourea)_4]^{2+}$

**Keywords:** Counter ion / Conformers / Crystal engineering

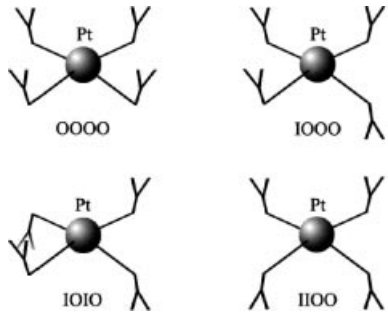


Seven $[Pt(TU)_4]X_n$ [X = $Cl^-$, $I^-$, $CF_3SO_3^-$, $BPh_4^-$ and $ClO_4^-$ ($n$ = 2), and $S_2O_8^{2-}$ and $SiF_6^{2-}$ ($n$ = 1)] complexes were synthesized and their crystal structures determined. DFT calculations show that the possible limiting conformations have only moderate energy differences. The four limiting conformations for the $[Pt(TU)_4]^{2+}$ cation (OOOO, IOOO, IIOO, IOIO) could be experimentally realized solely by the use of the different counterions.

## Ditertiary Phosphane Complexes

**G. M. Brown, M. R. J. Elsegood, A. J. Lake, N. M. Sanchez-Ballester, M. B. Smith,* T. S. Varley, K. Blann* ..... 1405–1414**

Mononuclear and Heterodinuclear Metal Complexes of Nonsymmetric Ditertiary Phosphanes Derived from $R_2PCH_2OH$

**Keywords:** Late-transition metals / P ligands / Heterobimetallics / Coordination modes

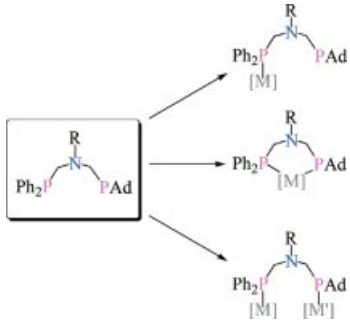


The synthesis of two new nonsymmetric ditertiary phosphanes and a study of their coordination chemistry at various late transition-metal centres are reported. All new compounds have been characterised by a combination of techniques including multinuclear NMR spectroscopy and single-crystal X-ray crystallography.

## Thin Films

**U. Qureshi, C. Blackman, G. Hyett, I. P. Parkin* ..... 1415–1421**

Tungsten Oxide and Tungsten Oxide-Titania Thin Films Prepared by Aerosol-Assisted Deposition – Use of Preformed Solid Nanoparticles

**Keywords:** Tungsten oxide / Aerosol-assisted CVD / Thin films

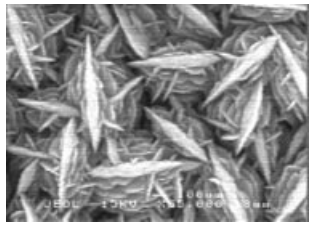

Aerosol-assisted deposition of an adhesive continuous $WO_3$ film was obtained from a solid nanoparticulate starting material suspended in toluene.

## Pincer $Pt^{II}$ Complexes

**G. D. Batema, K. T. L. van de Westelaken, J. Guerra, M. Lutz, A. L. Spek, C. A. van Walree, C. de Mello Donegá, A. Meijerink, G. P. M. van Klink, G. van Koten* ..... 1422–1435**

Luminescent and Electronic Properties of Stilbenoid NCN-Pincer $Pt^{II}$ Compounds

**Keywords:** Donor-acceptor systems / Luminescence / N-ligands / Platinum

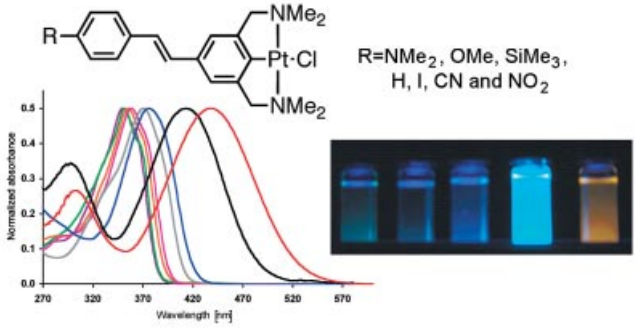


Tune in! A series of electronically tunable organometallic stilbenoid pincer platinum compounds were synthesized by a Horner–Wadsworth–Emmons reaction. By variation of the R substituent (see picture) the donor-acceptor properties of the molecule can be studied, which also changes the electronic density at the *para* situated platinum centre. By tuning the compounds, fluorescent metal complexes can be obtained.

 © 2007 Wiley-VCH Verlag GmbH & Co. KGaA, Weinheim 

## Anion Recognition

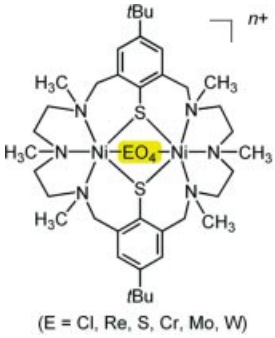


(E = Cl, Re, S, Cr, Mo, W)

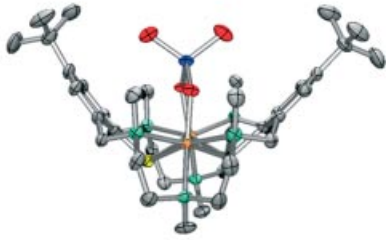

The macrocyclic $[(LMe)Ni_2]^{2+}$ complex binds doubly charged $EO_4^{2-}$ ions (E = S, Cr, Mo, W) more strongly than uninegative $EO_4^-$ species (E = Cl, Re).

**V. Lozan, B. Kersting* ..... 1436–1443**

Preparation and Characterization of Dinuclear $Ni^{II}$ Amine-Thiophenolate Complexes Coligated by $EO_4^-$ (E = Cl, Re) and $EO_4^{2-}$ Oxoanions (E = S, Cr, Mo, W)

**Keywords:** Dinuclear complexes / Macrocyclic ligands / Oxoanions

## Heterocyclic Thione Ligands

The preparation and structures of diorganotin(IV) and diphenyllead(IV) compounds with pyrimidine-2-thionate ligands are described. All the complexes synthesised have a distorted octahedral structure.

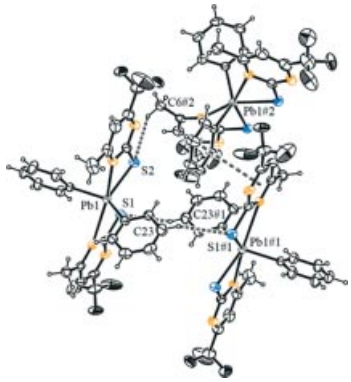


**A. Rodríguez, A. Sousa-Pedrares, J. A. García-Vázquez,* J. Romero, A. Sousa, U. Russo ..... 1444–1456**

Synthesis and Structural Characterisation of Diorganotin(IV) and Diphenyllead(IV) Complexes of Pyrimidine-2-thionate Derivatives

**Keywords:** Tin / Lead / N,S ligands / NMR spectroscopy / Moessbauer spectroscopy

**If not otherwise indicated in the article, papers in issue 9 were published online on March 9, 2007**

 © 2007 Wiley-VCH Verlag GmbH & Co. KGaA, Weinheim 

DOI: 10.1002/ejic.200700018

# Anion Separation with Metal–Organic Frameworks

**Radu Custelcean*[a] and Bruce A. Moyer*[a]**

**Keywords:** Anions / Crystal engineering / Host–guest systems / Molecular recognition

The application of metal–organic frameworks (MOFs) to anion separations with a special emphasis on anion selectivity is reviewed. The coordination frameworks are classified on the basis of the main interactions to the included anion, from weak and non-specific van der Waals forces to more specific interactions such as coordination to Lewis acid metal centers or hydrogen bonding. The importance of anion solvation phenomena to the observed anion selectivities is highlighted, and strategies for reversing the Hofmeister bias that favors large, less hydrophilic anions, and for obtaining peak selectivities based on shape recognition are delineated. Functionalization of the anion-binding sites in MOFs with strong and directional hydrogen-bonding groups that are complementary to the included anion, combined with organizational rigidity of the coordination framework, appears to be the most promising approach for achieving non-Hofmeister selectivity.

(© Wiley-VCH Verlag GmbH & Co. KGaA, 69451 Weinheim, Germany, 2007)

## 1. Introduction

Metal–organic frameworks (MOFs), also called coordination polymers, or coordination networks, have developed into one of the most prolific areas of research in materials chemistry.[1] The extraordinary popularity of MOFs could be explained by the ease of their synthesis based on the self-assembly of metal cations with organic linkers possessing divergent coordinating groups. Another appealing feature characteristic to this class of materials is their crystallinity, which allows for their precise structural characterization by diffraction methods, thus facilitating their rational design and the formulation of structure/property relationships. Furthermore, the ability to readily modify the linkers by employing the power of organic synthesis is another great advantage over purely inorganic materials. While the initial focus in this area was the synthesis and structural characterization, an increasing number of MOFs is now being explored for many potentially useful properties, which may very soon lead to commercial applications.[2] One of the early recognized functionalities in MOFs was their anion-exchange ability, particularly for cationic frameworks made from neutral organic linkers, which intrinsically include charge-balancing anions. Since the first reported example

[a] Chemical Sciences Division, Oak Ridge National Laboratory, Oak Ridge, TN 37831-6119, USA
E-mail: custelceanr@ornl.gov
moyerba@ornl.gov

*Radu Custelcean was born in 1972 in Transylvania, Romania, and studied Chemistry at Babes-Bolyai University, where he graduated with an MS degree in 1996. He then moved to Michigan State University, where he received his PhD in Chemistry under the supervision of James E. Jackson, for work on structure and reactivity of hydrogen-bonded crystals. In 2000 he joined the research group of Michael D. Ward at the University of Minnesota as a postoctoral fellow, where he worked on crystal design using hydrogen bonds. Since 2003 he has been working as a research scientist in the Chemical Separations Group at Oak Ridge National Laboratory. His main research interests are in crystal engineering of hydrogen-bonded and coordination frameworks, crystalline organic materials, and chemical separations.*

*Bruce A. Moyer received his PhD in Inorganic Chemistry in 1979 working with Thomas J. Meyer at the University of North Carolina at Chapel Hill. He then joined the staff at Oak Ridge National Laboratory, where he now leads the Chemical Separations Group. Since 2001, he has served as Co-Editor of the journal Solvent Extraction and Ion Exchange. His research interests have focused on use of molecular recognition principles in effecting selective extraction of inorganic ions and how the resulting understanding can be applied to problems in waste treatment, environmental remediation, and nuclear separations.*

 © 2007 Wiley-VCH Verlag GmbH & Co. KGaA, Weinheim 

of anion exchange in an MOF,[3] further examples of coordination frameworks with anion-exchange properties have been studied, revealing that the environment around the bound anions can vary considerably. It occurred to us to ask whether it was possible to identify systematic structural features that could in turn be related to selectivity in anion exchange. As selectivity is essential to any chemical separation process, a detailed understanding of the factors governing anion selectivity in MOFs is of paramount importance if this class of materials is to be successfully utilized in anion-separation applications. The primary scope of this review article is therefore to provide a concise summary of the progress in this area, including recent contributions from our own research, with a special emphasis on factors relating to anion selectivity. Toward this end, we found it helpful to draw comparisons to selectivity principles applicable to anion separation in molecular separation systems, where the basis for selectivity is better understood and somewhat simpler. Accordingly, in the following section on fundamentals of anion selectivity and separation, a general strategy is proposed for obtaining selectivity by design to overcome the dominant solvation-based Hofmeister bias that otherwise favors hydrophobic, charge-diffuse anions. Specific examples of anion exchange and separations with MOFs are then presented, which are organized around the main interactions between the anions and the coordination frameworks. Finally, the current status of the field is summarized at the end of the paper, emphasizing its outstanding challenges and suggesting future research directions.

## 2. Fundamentals of Anion Separations

### Selectivity Patterns in Separations

Selectivity may be classified as monotonic, step, peak, or some combination thereof in the separation of a related group of species. Within the unified theory of separations,[4] a separation is effected by a driving force acting unequally on species having different properties. Monotonic selectivity, which has been referred to as bias,[5] simply follows a steadily increasing or decreasing trend according to some varying property within the family of interest. Step or threshold phenomena occur when a limit or discontinuity is reached. Peak selectivity follows from recognition due to complementary bonding interactions. Each of these selectivity types has its uses, and one is better than another only in the context of the economics of the intended use. Hence, inferior selectivity is often tolerated in practice except under demanding circumstances where, for example, one is faced with high concentrations of competing species, high purity requirements, or very expensive footprint costs. Given that separation problems from such arenas as pharmaceuticals, metal recycling, electronics materials, environmental cleanup, nuclear-waste treatment, or nuclear reprocessing are increasingly demanding, the need for new separation systems exhibiting peak selectivity is growing.

Toward understanding principles of anion selectivity in MOFs, we focus in this section on origins of selectivity in molecular systems. This approach presupposes that bonding interactions underlie selectivity generally, and thus, the interactions found in molecular systems should be discernible in MOFs, subject to additional lattice considerations present in the solid state. Although the growing literature on anion recognition[6] has emphasized complexation in homogeneous media, it is of greatest interest in separations to examine partitioning processes, wherein interactions in the receiving phase are played-off against the strong energy requirement of the initial step of anion dehydration. By extension, an MOF would be the receiving phase of interest in the latter part of this review. The present section will begin with the examination of solvation-based selectivity, in which the receiving phase is a fluid environment that may freely reoptimize interactions about any given extracted anion. The discussion will then turn to the effects of single-point interactions in the receiving phase and finally to the effects of multi-point interactions presented by structured host environments. In a broad sense, interactions in the receiving phase may be controlled in their degree of electrostatic or covalent character and associated degree of structural constraint. The net effect is to control the steepness and sign of monotonic selectivity or, more interestingly, to effect sharp departures giving rise to step or peak selectivity.

### Hofmeister Effects on Selectivity

Almost 12 decades ago, Franz Hofmeister noted a particular ordering of anions in the ability of salts of a common cation to precipitate egg-white globulin.[7,8] The original ordering from this work was:

Sulfate > Phosphate* > Acetate > Citrate > Tartrate > Hydrogen carbonate > Chromate ≈ Chloride > Nitrate > Chlorate

(*tabulated by Hofmeister as phosphate but considered by him to be the monohydrogen phosphate dianion)

Hofmeister's key conclusion was that the effectiveness of the salts in precipitating the egg-white globulin increases with "their water attracting capacity." Because ion hydration is so strong and dominates in many chemical phenomena, it is not surprising that the "Hofmeister order" or variations of it have been broadly observed.[9–11] Indeed, a recent conference has been devoted to Hofmeister effects.[12] These phenomena have been divided into those that deal with bulk hydration or activity coefficients (Hofmeister's water-attracting capacity) and those involved with specific ion adsorption or surface effects (binding, partitioning, electrical double-layer, Donnan, etc.).[10] Because Hofmeister effects generally operate in complex systems, where the net observable properties arise from a combination of effects, there are often exceptions to the original order, as even noted immediately by Hofmeister himself.[13] Not surprisingly, the literature gives many variants of the Hofmeister order that include other anions, reversals of positions of certain anions in the order, and even complete reversal of the entire order. However, references to the "Hofmeister order" most often mirror the order of decreasing anion hydration energy or charge density.

 © 2007 Wiley-VCH Verlag GmbH & Co. KGaA, Weinheim 

Remarkably, the original observations of Hofmeister provide a useful starting point in interpreting the properties of MOFs that ultimately give rise to anion selectivity in crystallization. Given that the Hofmeister order is rather ubiquitous as a selectivity pattern in separations,[5] our premise is that controlling the binding environment of the anion within the MOF leads ultimately to controlled selectivity, especially selectivity that violates the Hofmeister order. We shall approach this question further below. At the outset, however, we recognize the importance of salting-out on solubility, expecting that the first role of Hofmeister effects on MOF solubility is to determine the solution-phase activity coefficients of dissolved MOF precursor components. By changing the anion in the solution phase, one in essence performs the classical Hofmeister experiment. The Hofmeister order would thus be expected on this basis. However, to the extent that one can control the aqueous-phase composition, one has some control over the salting effect in a given experiment. For example, one may employ low salt concentrations, where specific ion effects are minor. We will not concern ourselves further with this aspect of anion selectivity.

## Solvation-Based Selectivity: Normal and Anti-Hofmeister Bias

Hofmeister effects have long been known in ion-partitioning processes, although not named as such until recently. The order of anion exchange in liquid/liquid systems typically obtained is:[5]

$$PO_4^{3-} < CO_3^{2-} < SO_4^{2-} << Cl^- < Br^- < NO_3^- < SCN^- < I^- < ClO_4^-$$

This order is preserved over many systems in which the receiving phase does not possess strong hydrogen-bond (H-bond) donors or other specific anion-binding sites, and for practical purposes, it is the Hofmeister order to which we will refer for anion partitioning. Its similarity with Hofmeister's original order[7] is evident. Many more anions can be added to this list according to criteria discussed below and in more detail elsewhere,[5] but such fine-tuning invariably produces exceptions from system to system. It may be noted that the order above is preserved in certain related anion-partitioning systems, such as anion-exchange resins[14] and liquid-membrane potentiometric sensors.[15] The literature on anion sensing by membrane electrodes is particularly abundant, explicitly recognizing the Hofmeister order as the order of potentiometric selectivity typically observed if no recognition agents are added.

In general, the Hofmeister order in liquid/liquid systems can be understood in straightforward manner as the dehydration of the anion and resolvation in the receiving phase.[5] In terms of standard Gibbs energies, we have $\Delta G_p° = \Delta G_S° - \Delta G_h°$, where subscripts p, S, and h refer to partitioning, solvation, and hydration, respectively. Table 1 gives a listing of selected $\Delta G_h°$ values and other data for a few anions of interest here,[16] presented in order of decreasing $\Delta G_h°$ and extractability.

Table 1. Ionic radii ($r_-$) and standard Gibbs energies of hydration ($\Delta G_h°$) and transfer ($\Delta G_{tr}°$) for representative anions.[a]

| Anion | $r_-$ | $\Delta G_h°$ | $\Delta G_{tr}°$ 1,2-DCE | $\Delta G_{tr}°$ TFE | $\Delta G_{tr}°$ MeOH | $\Delta G_{tr}°$ $PhNO_2$ | $\Delta G_{tr}°$ FA |
|---|---|---|---|---|---|---|---|
| | [nm] | [kJ/mol] | [kJ/mol] | [kJ/mol] | [kJ/mol] | [kJ/mol] | [kJ/mol] |
| $Ph_4B^-$ | 0.421 | 42 | –33 | | –24 | –36 | –24 |
| $Pic^-$ | 0.329 | –197 | 4 | | –6 | –3 | –7 |
| $ClO_4^-$ | 0.225 | –214 | 17 | –3 | 6 | 10 | –12 |
| $TcO_4^-$ | 0.250 | –251 | 15 | | 6 | 5 | –2 |
| $CF_3SO_3^-$ | 0.230 | | 20 | | | | |
| $I^-$ | 0.220 | –275 | 25 | –2 | 7 | 18 | 7 |
| $SCN^-$ | 0.209 | –280 | 19 | | 6 | 16 | 7 |
| $ClO_3^-$ | 0.208 | –287 | 37 | | | 26 | |
| $N_3^-$ | 0.180 | –287 | | | 9 | | 11 |
| $CN^-$ | 0.187 | –305 | 41 | | 9 | 38 | 13 |
| $NO_3^-$ | 0.200 | –306 | 32 | | 13 | 24 | |
| $Br^-$ | 0.196 | –321 | 38 | –3 | 11 | 29 | 11 |
| $NO_2^-$ | 0.187 | –339 | | | | | |
| $Cl^-$ | 0.181 | –347 | 52 | –6 | 13 | 35 | 14 |
| $HCO_3^-$ | 0.207 | –368 | | | | | |
| $OAc^-$ | 0.194 | –373 | 58 | | 16 | | 20 |
| $OH^-$ | 0.152 | –439 | | | | | |
| $F^-$ | 0.126 | –472 | 65 | | 16 | 70 | 25 |
| $HPO_4^{2-}$ | 0.200 | | | | | | |
| $CrO_4^{2-}$ | 0.229 | –958 | | | | | |
| $SO_4^{2-}$ | 0.218 | –1090 | | | 31 | | |
| $CO_3^{2-}$ | 0.189 | –1315 | | | | | |
| $PO_4^{3-}$ | 0.230 | –2773 | | | | | |

[a] Values of $\Delta G_{tr}°$ are given in kJ/mol relative to the tetraphenylarsonium tetraphenylborate extrathermodynamic assumption at 25 °C. Abbreviations: 1,2-DCE: 1,2-dichloroethane; $PhNO_2$: nitrobenzene; $CH_3CN$: acetonitrile; FA: formamide; MeOH: methanol; TFE: 2,2,2-trifluoroethanol. Data taken from compilations[16–18] and published results.[19]

It may be seen at once that the $\Delta G_h°$ values approximately follow Hofmeister's original order, the greater hydration corresponding to the greater protein precipitation ability. Further, the $\Delta G_h°$ values decrease with increasing charge density, as the $\Delta G_h°$ values are nearly proportional to $-Z^2/r_-$ (where $Z$ is the charge and $r_-$ is the thermochemical radius). Further, except for tetraphenylborate, $\Delta G_h°$ values are negative and large. In the present context of anion extraction, anion hydration thus resists extraction, and for anions smaller than perchlorate, the Gibbs energy of hydration is typically not fully recovered in transfer to other solvents (positive $\Delta G_{tr}°$, where transfer refers to pure solvents, as opposed to mutually saturated in the case of partitioning). Thus, transfer for these ions is not favorable and requires an additional driving force to occur (e.g., cation co-extraction, binding, or ion-pairing). However, the values of $\Delta G_{tr}°$ approximately follow the same order as the values of $\Delta G_h°$, implying that hydration and solvation roughly follow the same order. The obtained Hofmeister behavior in partitioning thus corresponds to extraction strength increasing in order of decreasing anion hydration Gibbs energy. We have referred to such behavior as "Hofmeister bias"[20] or *normal Hofmeister* selectivity. As shown below,

 © 2007 Wiley-VCH Verlag GmbH & Co. KGaA, Weinheim 

it is in principle (if not in the exceptional actual example) possible to reverse Hofmeister bias in anion extraction if the solvent is capable of exceeding the solvation of the ion in water. In this case, we may expect *anti-Hofmeister* behavior. By contrast, an ordering in which certain anions are displaced from Hofmeister bias or its reverse would be referred to as *non-Hofmeister* behavior.

To illustrate the major factors underlying anion selectivity in anion transfer, Figure 1 shows several plots of $\Delta G_{tr}°$ for a series of anions vs. $1/r_-$ for a range of solvents. Over a fairly substantial range of anion radii (0.133 nm for $F^-$ to 0.421 nm for $Ph_4B^-$), it may be seen that, within some degree of scatter, extractability approximately increases with increasing anion radius for a given solvent. The scatter may be attributed in part to the nonspherical geometries for the eight nonhalide anions and overall varied nature of their properties (e.g., polarizability). As the anion radius increases, cavity formation begins to play a dominant role, because of the high cohesive energy density of water compared with organic solvents.[21] Cavity formation is an energetic cost or repulsive effect that has been related to the enthalpy of vaporization as the measure of difficulty in breaking solvent intermolecular interactions. In an extraction system with water as the starting phase, the effect is to repel the species into the receiving phase according to the molar volume of the species. Hence, as anion radii become larger than approximately perchlorate ($r_-$ = 0.240 nm), the transfer apparently becomes favorable owing to the increasing dominance of the cavity-formation term of the ion-transfer process. In general, the plots are not linear, as they bend over to varying degrees, though they are often treated as linear, when the hydrophobic (significant cavity-formation term) anions like picrate and $Ph_4B^-$ are omitted. It may be noted that acetonitrile, nitrobenzene, and 1,2-dichloroethylene have closely overlapping plots. In fact, one may find that analogous plots for other chemically diverse polar solvents fall about this band, provided that they do not have a strong H-bond donor ability ($\alpha < 0.5$, where $\alpha$ is the Kamlet–Taft solvatochromic H-bond parameter[22]). One may see that the exceptions are small-molecule solvents that are strong H-bond donors (formamide: $\alpha$ = 0.71; methanol: $\alpha$ = 0.93; 2,2,2-trifluoroethanol: $\alpha$ = 1.51). In other words, these are solvents that can efficiently replace the H-bonds lost in the dehydration part of the transfer process. The H-bond donor ability clearly plays a dominant role. In fact, in a statistical analysis of ion transfer Gibbs energies, it was noted that the solvent H-bond donor ability is the major solvent property governing the magnitude of $\Delta G_{tr}°$.[23] Remarkably, the loss of bias with increasing $\alpha$ reaches such a degree with 2,2,2-trifluoroethanol that the trend apparently reverses, fluoride ion being transferred slightly more favorably than the other halides. Thus, where anion hydration for anions smaller than perchlorate is generally not fully recovered on resolvation, in the case of the very strong H-bond donor solvents like 2,2,2-trifluoroethanol, the resolvation slightly overcompensates the loss of hydration. An example of this principle at work in favoring fluoride over the larger halides using a phenol as solvent has been reported.[24]

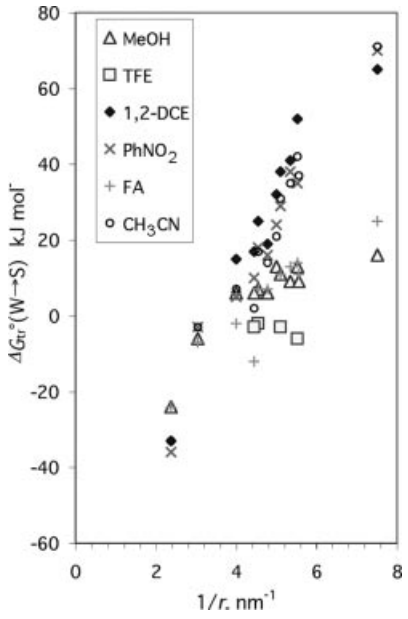


Figure 1. Standard Gibbs energies of transfer for univalent anions from water to organic solvents as a function of reciprocal anion thermochemical radius. Values of $\Delta G_{tr}°$ are given in kJ/mol relative to the tetraphenylarsonium tetraphenylborate extrathermodynamic assumption at 25 °C. Abbreviations: 1,2-DCE: 1,2-dichloroethane; $PhNO_2$: nitrobenzene; $CH_3CN$: acetonitrile; FA: formamide; MeOH: methanol; TFE: 2,2,2-trifluoroethanol. Data taken from compilations.[16–18]

To summarize monotonic anion selectivity, the process of anion transfer is strongly biased toward larger, charge-diffuse anions. This Hofmeister bias may be manipulated by varying the H-bond donor ability of the solvent and to a lesser extent by varying the size of the H-bond donor molecules, that is, the presumed number of H-bonds that the solvent can provide to a given anion based on packing considerations. The smaller the anion, the larger the effect. The trend can be reversed in principle by employing small, very strong H-bond donors as solvent molecules. For anions larger than perchlorate, cavity formation (lipophilicity) becomes dominant, and anion selectivity in this class becomes insensitive to H-bond donor ability. We will henceforth in this review interest ourselves in anions smaller than perchlorate as a class and refer to them without further distinction.

## Overcoming the Hofmeister Bias

### *A Qualitative Model*

Now that the Hofmeister bias has been seen to arise in solvation phenomena, we can begin to devise strategies to overcome it toward obtaining selectivity patterns of our own design. To organize our thinking in this regard, we have devized a qualitative model based on established foundational concepts in supramolecular chemistry[25] and bonding in coordination chemistry.[26] The model is shown

 © 2007 Wiley-VCH Verlag GmbH & Co. KGaA, Weinheim 

in Figure 2. The diagram shows regions corresponding to normal-Hofmeister, anti-Hofmeister, and non-Hofmeister selectivity.

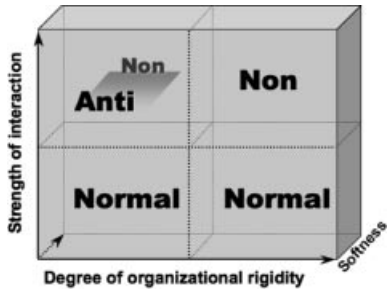


Figure 2. Selectivity in anion separation. The descriptors in the boxes refer to whether normal-Hofmeister, anti-Hofmeister, or non-Hofmeister selectivity is obtained.

It was seen above that the steepness and sign of the Hofmeister bias was controlled mainly by the strength of a primarily electrostatic interaction, H-bonding. Accordingly, as the *number* and *strength* of these individual interactions[25d] between solvent molecules and a given anion increase, normal Hofmeister bias decreases and then, in principle, reverses. Focusing for the moment only on H-bonding interactions, it is clear that the *total* strength of the interaction of the anion with its environment increases with increasing *complementarity*[25a,25c] between the arrangement of H-bonds donated by surrounding molecules and the receptor sites of the anion. However, solvent molecules are at best weakly constrained in their ability to assemble about the anion. Within their own steric constraints and thermal motion, they are free to maximize the net interaction with the anion and with themselves to come to a minimum Gibbs energy condition. If the anion is replaced with another anion, the solvent molecules will be able to move about to accommodate the new anion, again maximizing the total interaction. Thus, we have captured the concept of total interaction strength in the vertical axis in Figure 2, where H-bonding and other interactions can be manipulated subject to our own design. If the interactions are electrostatic and unconstrained, as in fluid systems, the effect is to produce either normal- or anti-Hofmeister selectivity.

To obtain non-Hofmeister selectivity, it is logical either to employ non-electrostatic interactions or to constrain the spatial arrangement of interacting groups or atoms about the anion. In any case, no strategy can succeed in this regard using only weak interactions, because of the steepness of the $Z^2/r_$ dependence. Thus, the lower regions of Figure 2 are the domain of normal Hofmeister selectivity. Most strategies for anion binding today employ H-bonding or other electrostatic interactions as the basis for recognition, and normal Hofmeister bias still tends to be commonly observed, leading us to conclude that systems so far investigated for separations often lack sufficiently strong and structurally constrained H-bond donor groups. The *affinity/selectivity* principle recently put forth[27] leads to the expectation that the greatest selectivity will occur with stronger interactions, which will magnify differences in the ability of a given host to accommodate anions of different size or structure. With a sufficiently strong total interaction with a given anion, implying strong individual interactions and with high overall complementarity, it is expected that peak selectivity for that anion will arise when the structure of the host environment is unable to rearrange to accommodate other anions. For molecular hosts, the familiar term *preorganization*[25b] embodies this concept, but this term loses meaning for self-assembled hosts that form in situ in the presence of the guests. Instead, we chose the term *organizational rigidity* for the horizontal axis in Figure 2, to capture both the concept of rigidity, meaning that the crystal lattice is unable to expand or contract, and structural uniqueness, meaning there is only one favorable way to assemble the subunits of the host framework.

The third axis in Figure 2 allows the introduction of a degree of softness or covalency into the interaction of donor groups with the anion. Given that the Hofmeister bias rests on the strength of electrostatic interactions, primarily H-bonding, then soft Lewis acid/base interactions[26] should lead to peak selectivity for soft or polarizable anions. This should be true even if the soft Lewis acid sites are not constrained in space.

In section 3 of this article, we try to make some comparisons of the above-presented model with literature observations as a way to test our thinking and to look for ways to escape the Hofmeister bias in anion separations. We believe the model is useful in describing three orthogonal concepts, that of total binding strength (embodying the concept of complementarity), organizational rigidity, and softness. However, the model is meant only to be a qualitative guide, with no fixed divisions between resultant selectivity patterns. Moreover, there are obvious limits to be encountered. For example, H-bond donor groups should not be so strong that proton-transfer processes occur, leading to considerations beyond this discussion. In addition, one does not desire to employ covalent interactions to the degree that the guest anion is chemically transformed or that the binding becomes irreversible. Host/guest chemistry and separation chemistry share the general approach of using reversible, non-covalent interactions.

### *Single-Point Interactions*

Toward ultimate shape selectivity that violates the Hofmeister bias in a separation, one must assemble groups in space that interact with an anion along defined vectors. Solid-state host assemblies like MOFs are well suited for this task, though most of the insight obtained thus far on anion recognition has emerged from studies of molecular systems in solution. From the literature on anion coordination chemistry, one can make use of H-bonding, coulombic, Lewis acid/base, van der Waals, hydrophobic, and other interactions.[28,29] Let us first examine selectivity inherent in certain single-point interactions that must ultimately be assembled in the complete host/guest supramolecular structure.

Coulombic interactions are anti-Hofmeister and will therefore influence bias. Whereas solvation involves the ide-

 © 2007 Wiley-VCH Verlag GmbH & Co. KGaA, Weinheim 

alized lone ion surrounded by solvent molecules, real separation systems involve interactions with counterions. These can be incorporated into receptor design itself[25a,28,29] but otherwise must still be allowed for as one of the governing factors in the resultant selectivity obtained. Viewing extraction as a step-wise process, the first step can be taken as ion partitioning followed by other interactions, which include ion-pairing or coordination. Ion-pairing usually favors small anions for a given cation, and this interaction opposes Hofmeister bias.[5] However, for univalent ions, ion-pairing is generally a weaker influence on selectivity as compared with solvation, and thus, Hofmeister bias persists, albeit attenuated. A prime example is the use of lipophilic quaternary ammonium salts as liquid/liquid anion exchangers, and the selectivity is also seen in strong-base anion-exchange resins.[5,14] It has been seen that the size of the cation determines the steepness of the bias, smaller quaternary ammonium cations possessing smaller alkyl chains, giving larger attenuation of Hofmeister bias.

More generally, coordination of anions with Lewis acid sites allows wide latitude in obtaining desired selectivity, leading to potential departures from Hofmeister bias selectivity. Such interactions may be treated as coordination or ion-pairing phenomena as appropriate, but in general the effect on selectivity derives from the bonding interaction with the Lewis acid site. Accordingly, the hard/soft acid/base concept[26] lends itself well in manipulating selectivity. Because the origin of Hofmeister behavior is so strongly influenced by the H-bonding ability of the solvating environment and because H-bonding is largely electrostatic, it may be expected that, constraining steric or multi-point (chelating) effects being absent, hard Lewis acid sites may tend to give rise to normal- or anti-Hofmeister bias. The hard/hard interaction itself tends to be anti-Hofmeister, the question being whether this effect is sufficiently strong to overcome the Hofmeister bias of the ion-partitioning step. If the charge on the hard Lewis acid site is not high, the strength of the coordination interaction is usually insufficient to reverse the Hofmeister bias of ion partitioning but only to attenuate it. This is typically the case with extraction of alkali and alkaline earth cations by crown ethers, which has been long known to follow the normal Hofmeister bias.[5,19,20,30] Accordingly, salts with charge-diffuse anions are easier to extract, implying that such anions (like perchlorate) would exchange for more hydrophilic ones (like nitrate or chloride) associated with the organic-phase crown ether complex of the extracted metal cation. This bias has been used to advantage to extract sodium pertechnetate from nuclear waste (high in nitrate), for example.[31,32] It should be pointed out that the actual coordination of the anion to Lewis acid centers in solution in most cases is not confirmed, and it is possible that the anion interacts through a mediating water molecule or outer-sphere ion-pairing.

As the charge of the Lewis acid site increases, it is indeed found that the Hofmeister bias can be disturbed or reversed in accordance with a strong hard/hard interaction, though steric influences are typically present. Thus, an enhanced fluoride selectivity is often observed, and the selectivity may overall be non- vs. anti-Hofmeister. Examples are known in which sorbent materials containing higher-charged metals like $Fe^{III}$ and $Zr^{IV}$ prefer small, hydrophilic anions.[33,34] In liquid/liquid extraction and transport, a (salen)$Mn^{III}$-type complex and a neutral tetraaza-macrocyclic $Ni^{II}$ complex were observed to have enhanced fluoride selectivity.[35] In transport using these respective carriers, the following orders were found: $F^- > Br^- > Cl^- > NO_3^-$ and $Cl^- > F^- > NO_3^- > Br^-$, while in extraction, the $Mn^{III}$ complex gave the order $Br^- > NO_3^- > F^-$ and the $Ni^{II}$ complex detectably extracted only $F^-$. Neutral tris(β-diketonato) complexes of lanthanides transport $Cl^-$ faster than $Br^-$, $I^-$, and even $ClO_4^-$.[36]

The use of Lewis acid sites for selective anion binding has been under investigation for development of potentiometric anion sensors, providing insight into anion-binding selectivity in ion partitioning. Typical membrane electrodes employ a polymer membrane, such as poly(vinyl chloride), containing a plasticizer, solvating additives, quaternary ammonium anion exchanger, and possibly an ion receptor. Without an anion receptor, the normal Hofmeister order of electrode selectivity is obtained in accordance with a governing solvation principle.[15,37] Added Lewis acid anion receptors yield selectivity patterns violating the normal Hofmeister order. Metalloporphyrins[38] and phthalocyanates[39] yield varied responses depending on the bound metal ion. With hard metal ions like $Zr^{IV}$,[38b] $Lu^{III}$,[38c] and $Al^{III}$,[39] it is typical for the $F^-$ response to be enhanced relative to the other anions, which still tend to follow the Hofmeister order. Fluoride and thiocyanate are even selected in preference to perchlorate using (octaethylporphyrin)$Zr^{IV}$.[38b] With (octaethylporphyrin)$In^{III}$, a striking rejection of nitrate and perchlorate in favor of thiocyanate and iodide was obtained in electrodes designed for salicylate response.[38a] Other types of Lewis acid receptors have also yielded non-Hofmeister selectivity in membrane electrodes. Thiocyanate selectivity has been obtained using a (Schiff base)Cd complex[40] and triphenyltin chloride.[41] Iodide selectivity was achieved with a lipophilic $Hg^{II}$ complex.[42] A remarkable non-Hofmeister selectivity was obtained with certain organodifluorotin(IV) compounds, giving the order: $F^- > CH_3COO^- > Cl^- > I^- \approx Br^- > ClO_4^- > NO_2^- > NO_3^- > SCN^-$.[43]

### *Multipoint Recognition*

Researchers have taken an active interest in finding synthetic molecular receptors that violate Hofmeister behavior in separations by use of constrained multipoint binding interactions. Despite the considerable challenge posed by the steep bias in ion partitioning ($Z^2/r_-$ dependence),[44] the progress made so far indicates that a combination of sufficiently strong and structurally constrained binding sites on the host can succeed in this regard. Starting with less effective systems, the bidentate H-bond donors that have been examined appear to be too weak with respect to H-bond strength or rigidity to effect significant departures from Hofmeister bias. In that the anions are still largely open to

 © 2007 Wiley-VCH Verlag GmbH & Co. KGaA, Weinheim 

the influence of solvation, overall complementarity is low, and the affinity/selectivity principle[27] would imply only perturbation or attenuation of Hofmeister bias. These near-normal Hofmeister systems thus lie in the lower left box in the selectivity model shown in Figure 2. Examples in liquid/liquid extraction include diphenylurea[45] and *m*-diphenyldisulfonamides,[20,46] though peak selectivity for iodide has been claimed for monothiouronium receptors.[47] Receptors offering four or more H-bonds on flexible arms show greater signs of disrupting the expected Hofmeister order. However, typically the charge-diffuse anions like $ClO_4^-$, $I^-$, and $SCN^-$ are still favored, and non-Hofmeister behavior tends to take the form of enhancements for certain anions or switched preferences within the series. Even with a rigid steroidal platform supporting two or three arms, "cholapod" receptors with varied H-bond donor functionalities (imide, amide, carbamate, urea, thiourea, and sulfonamide) still basically follow near-normal Hofmeister behavior in liquid/liquid extraction.[27,48] Tris- and tetrakis(amide) receptors employing polyaza-macrocycle platforms exhibited normal Hofmeister bias in transport.[34] Evaluated in ion-selective electrodes, this group also includes iodide-selective bis(thiouronium) receptors,[47] tripodal tris(ureas) with enhanced sulfate sensitivity,[49] and bis(thiourea) receptors employing a rigid steroidal platform also with enhanced sulfate sensitivity.[50]

The greatest degree of success in achieving non-Hofmeister behavior (upper right box in Figure 2) has involved macrocyclic geometries in which H-bond donor functionalities are constrained as part of the ring structure and also systems employing Lewis acid binding sites. An elegant demonstration of the macrocyclic effect on extraction selectivity was obtained by cyclization of two urea arms on a steroid platform, whereupon the nearly normal Hofmeister behavior of the uncyclized analog was transformed in the most striking case to the non-Hofmeister ordering: $Br^- > I^- \approx Cl^- > NO_3^- > PF_6^- > CH_3COO^- \approx EtSO_3^-$.[51] The selectivity order depended upon the link used in the cyclization. Fluorinated calixpyrroles featuring strong H-bond donation and the constraints of macrocyclic geometry exhibit non-Hofmeister behavior in liquid/liquid extraction.[52] Orders observed for the octafluorocalix[4]pyrrole and the decafluorocalix[5]pyrrole differed as follows: $ClO_4^- > I^- \approx Br^- \approx Cl^- > NO_3^- > F^-$ and $ClO_4^- > I^- \approx NO_3^- > F^- > Br^- > Cl^-$, respectively. Interestingly, the selectivity order for calix[4]pyrrole is anti-Hofmeister: $HPO_4^{2-} \approx F^- \approx OH^- > Cl^- > Br^-$.[53]

Receptors containing metal cations as well as H-bond donor groups offer the potential for anion/metal interaction and greater encapsulation of the anion, and the metal complexation can also serve to organize the anion-binding groups. Only a limited number of systems have been studied in extractive separations; (salophene)uranyl receptors bearing two sulfonamide sidearms were shown to be selective carriers for $H_2PO_4^-$ vs. $Cl^-$, the latter being the anion preferred by solvation effects alone.[54] A salicylaldoxime complex of $Ni^{II}$ exhibits the normal Hofmeister $Cl^-/SO_4^{2-}$ selectivity in transport experiments in which protonation of amine-containing sidearms provides both cationic and H-bond donor sites.[55] The metal ion serves only to organize the sidearms rather than serve as an anion-coordination site. Normal Hofmeister selectivity ($I^- > Br^- > Cl^-$) was also observed in transport of alkali metal salts by macrobicyclic receptors in which the two N atoms of the crown ether diaza-18-crown-6 are bridged by isophthalamide-type bridges capable of donating two H-bonds.[56] In this case, mild cation/anion interaction and structural constraints suffice only to attenuate the normal Hofmeister order. Selective transport of $Cl^-$ over other halide ions was observed with transition-metal-containing resorcinarenes bearing bis(pyridylmethyl)amine sidearms for metal-ion binding.[57]

## 3. Anion Separation with Metal–Organic Frameworks

Conceptually, we pose the question as to whether a strategy can be devized for obtaining separation selectivity by design in MOFs by taking some lessons learned from the study of molecular systems as discussed above and as illustrated in Figure 2. Quite simply, we are led to expect that normal Hofmeister selectivity will arise from H-bonding or other interactions involving the anion in the receiving-phase (MOF) environment that are weaker than those in water. Stronger H-bonding or other interactions that could compensate for anion dehydration would lead to anti- or non-Hofmeister behavior depending on the softness of the host binding sites and the degree of organizational rigidity of the MOF. In particular, MOFs offer the potential to achieve the extreme organizational rigidity that has been so elusive in molecular hosts. Provided that the included anions interact sufficiently strongly with surrounding groups within the MOF, which requires a high degree of complementarity between the binding sites of the guest anion and the host MOF, it should therefore be possible to approach perfect peak selectivity with total exclusion of all but the target anion. This ideal condition leads to non-Hofmeister selectivity in the upper right quadrant of Figure 2. If there are multiple ways to assemble the MOF to accommodate different anions or if the unit-cell parameters are adjustable, then the resulting lower degree of organizational rigidity would lead leftward in the diagram in Figure 2 toward anti- or non-Hofmeister behavior depending on the softness of the individual binding interactions. Regarding the lower right quadrant of the diagram, a question remains as to whether a rigid MOF with little or no ability to donate H-bonds would exhibit step or threshold selectivity. This may be true, as we suspect it is for molecular systems, but among the anions below the size threshold that could fit inside the MOF cavities, the larger, poorly hydrated anions would still be preferred, which is in effect Hofmeister behavior. The size cut-off effect may also apply to less rigid frameworks, as the crystal lattice can only expand to the point that the intermolecular interactions that insure the crystal cohesion become too weak relative to the solvation of the MOF components, which would lead to crystal dis-

 © 2007 Wiley-VCH Verlag GmbH & Co. KGaA, Weinheim 

solution. Alternatively, if anion binding represents a significant portion of the total lattice energy, the MOF crystal may only form with those anions whose interaction energies exceed a certain threshold, which would also lead to step selectivity.

An important issue with direct implications on how one can best approach the anion separation with MOFs is the anion-exchange mechanism in this class of materials. Figure 3 depicts the two mechanisms generally expected for anion exchange in MOFs. The early studies almost universally assumed a solid-state exchange mechanism, similar to those found in ion-exchange resins or zeolites, which occurs by diffusion of the ions in and out of the crystals with preservation of the structural integrity of the coordination network. This assumption was generally based on the observation that MOFs have very low solubility in most solvents, and, in some cases, on the structural similarities between the initial and final frameworks. However, a recent study by the groups of Champness and Schröder challenged this commonly accepted view, and demonstrated without equivoque that, at least in certain one-dimensional coordination polymers, the apparent anion exchange from water is solvent-mediated, involving dissolution and recrystallization of the MOF crystals.[58,59] This process is driven by the difference in solubility between the initial and final MOF phases, and does not require substantial water solubilities. In fact, anion exchange by dissolution/recrystallization has long been known in simple inorganic salts. For example, silver chloride, which for all practical purposes is considered water-insoluble, exchanges 90% of $Cl^-$ by $I^-$ within minutes, a process that is driven by the even smaller solubility of AgI in water. This process was exploited for the recovery of radioactive iodide from fission products.[60]

Although the dissolution/recrystallization appears the most likely mechanism for anion exchange from water, we cannot completely rule out the possibility that the anion exchange may occur by a solid-state exchange mechanism in some cases, or a combination of the two mechanisms. Such a scenario, however, requires that the anion diffusion through the coordination network be fast enough to compete with the dissolution/recrystallization process. To the best of our knowledge, no solid-state anion-exchange mechanism has been unequivocally demonstrated for any MOF to date.[61]

We have recently articulated an alternative approach to anion separation that involves competitive crystallization of the coordination networks.[62] This strategy differs from the traditional anion-exchange approach with the MOFs treated as separation agents, in that the crystallization process involved in the MOF synthesis is in itself exploited as a separation tool. More specifically, the MOF is competitively crystallized from a mixture of anions, which may result in the selective inclusion of certain anions depending on their size, shape, or specific interactions with the network. Such an approach avoids the common problem of slow ion-exchange kinetics in the solid state and broadens the applicability of MOFs to one of the commercially most important and economical separation technology, namely crystallization.

Whether the anion separation is realized by ion exchange, similarly to zeolites or ion-exchange resins, or by competitive crystallization, anion selectivity in MOFs is ultimately determined by the intermolecular interactions between the anion and the crystalline MOF matrix. It is therefore instructive to classify the MOFs that have relevance to anion exchange or separation based on the nature and

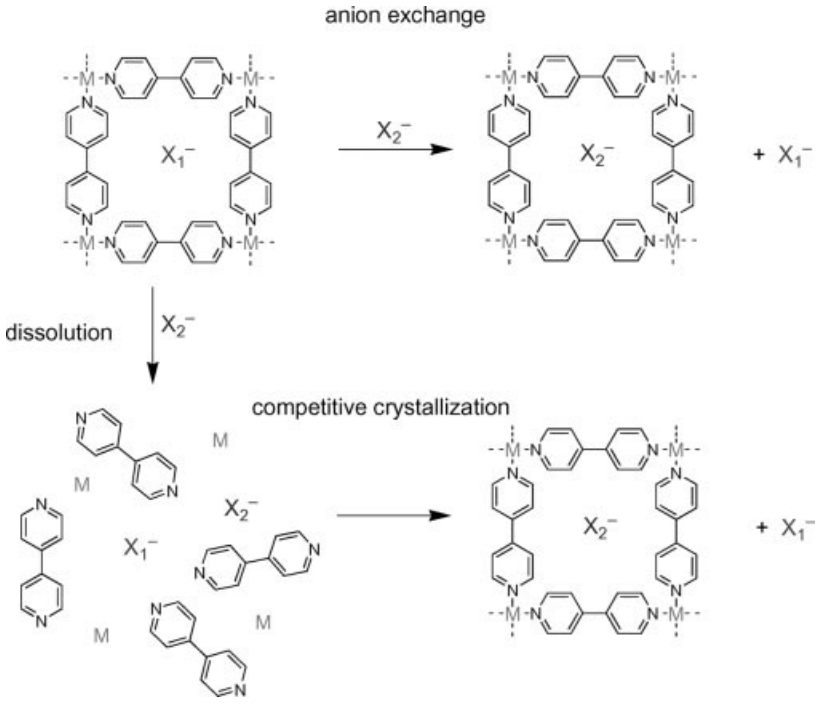


Figure 3. Generic representation of the two main mechanisms expected for anion exchange in MOFs.

 © 2007 Wiley-VCH Verlag GmbH & Co. KGaA, Weinheim 

strength of anion/framework interactions, and try to correlate these with the observed anion selectivities. Figure 4 illustrates the main types of interactions involving anions inside MOF crystals. The most common situation (case a) involves van der Waals interactions between the anion and the coordination network, with long-range coulombic interactions with the cationic framework additionally present.

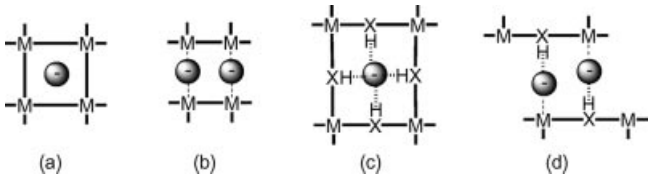


Figure 4. Typical intermolecular interactions involving anions inside MOFs. (a) van der Waals and coulombic; (b) metal coordination; (c) hydrogen bonding; (d) hydrogen bonding and metal coordination.

These interactions are typically too weak to overcome the solvation bias and thus lead to normal Hofmeister selectivity. A step (threshold) selectivity based on the anion size may nevertheless be expected, as too-large anions may not fit inside the MOF lattice and could therefore be excluded. The next case involves direct anion coordination to the metal centers in the network (case b). These Lewis acid/base interactions may partly compensate for the anion dehydration and thus attenuate the Hofmeister bias, or, if they are sufficiently strong, they may even reverse it (anti-Hofmeister selectivity). However, unless the MOF is organizationally rigid or unless the metal coordination sites are soft, peak selectivity (non-Hofmeister) is unlikely to be observed. Cases c and d involve specific hydrogen bonding or combinations of hydrogen bonding and metal coordination between the anion and the framework. These interactions may be very specific, and, as a function of their number and strength, may overcome the solvation bias resulting in

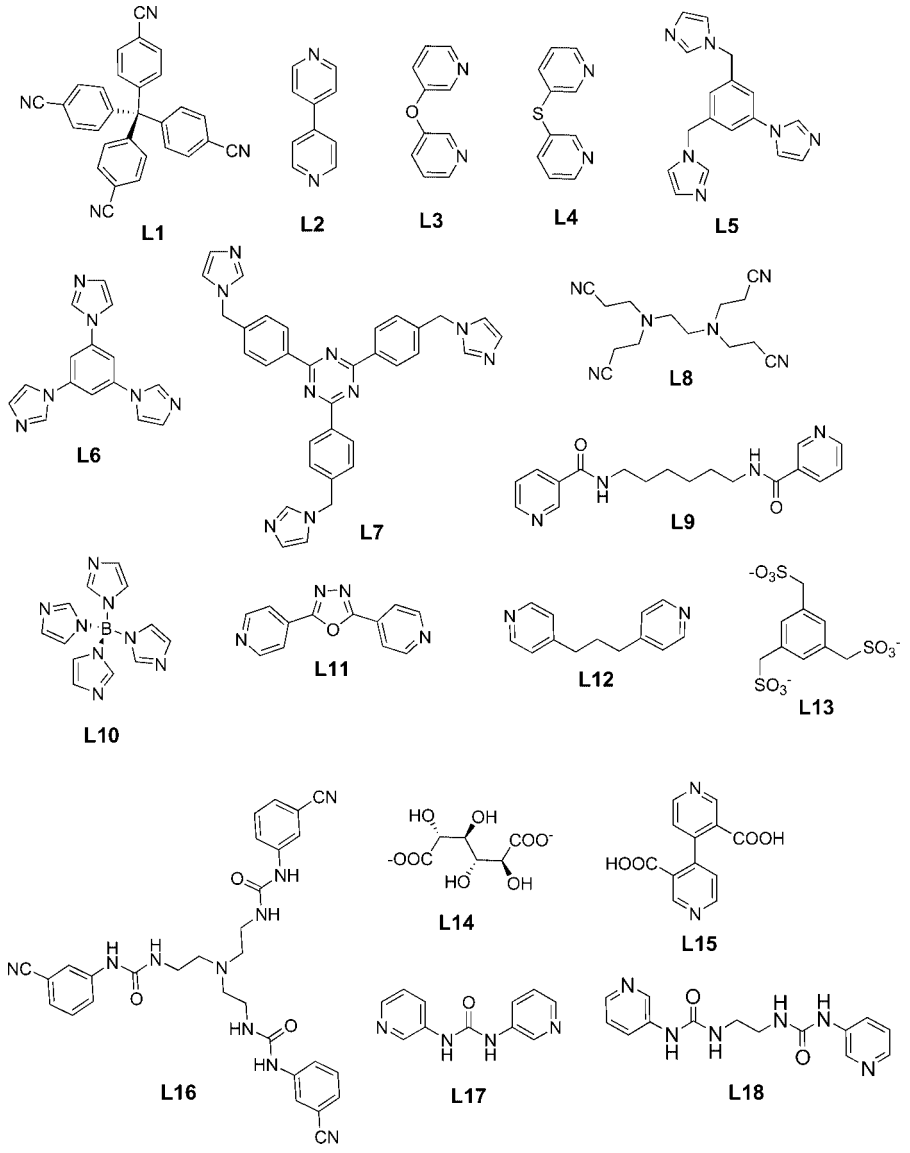


Figure 5. MOF linkers employed for anion exchange or separation.

 © 2007 Wiley-VCH Verlag GmbH & Co. KGaA, Weinheim 

either anti-Hofmeister or non-Hofmeister selectivities, depending on the rigidity of the framework.

In the following pages, specific examples of each class of anion interactions will be presented in the order of increasing binding strength, starting with nonspecific van der Waals interactions and moving towards more selective metal coordination and hydrogen-bonding interactions. Figure 5 lists the organic linkers involved in the MOFs discussed in this review.

### Anion Inclusion by van der Waals and Coulombic Interactions

As most coordination solids reported in the literature are built from relatively large and nonpolar organic linkers (Figure 5), the resulting anion-binding sites are fairly hydrophobic, an environment not very different from those found in nonpolar organic solvents or ion-exchange resins. Anion inclusion selectivity in these solids is thus typically dominated by solvation effects, which results in Hofmeister bias, favoring larger, less hydrophilic anions such as $ClO_4^-$ or $PF_6^-$.

One of the first deliberately designed coordination networks, reported by Robson et al. in 1990,[3] was built from linker **L1** and $Cu^I$ cations, which resulted in a 3D coordination framework with a diamondoid topology containing large pores filled with disordered solvent and $BF_4^-$ counteranions. The $BF_4^-$ anions could be easily exchanged with $PF_6^-$, but the reversibility and selectivity of the exchange was not reported. Five years later, Yaghi et al. reported another 3D coordination framework of $Cu^I$ with **L2**, which included hydrated $NO_3^-$ as counteranion. The disordered nitrate anions were loosely bound inside the channels, and could be easily exchanged in aqueous media by either hydrophobic $BF_4^-$, or hydrophilic $SO_4^{2-}$. The anion-exchange selectivity was, however, not addressed in this study.[63] When $NiClO_4$ was used with the same linker, a different coordination framework was obtained, which displayed a 1D railroad topology that included large channels filled with additional linker molecules, water solvent, and perchlorate anions. The anions were once again disordered, indicating weak interaction with the channel walls. Removal of the water solvent from the channels further increased the mobility of the perchlorate anions, which could be easily exchanged with $PF_6^-$.[64]

An interesting series of coordination polymers was reported by Jung et al., who used linker **L3** with various silver salts AgX (X = $NO_3^-$, $BF_4^-$, $ClO_4^-$, and $PF_6^-$) to assemble 1D helical coordination frameworks that included the anions inside the cationic cylindrical channels created inside the helices (Figure 6).[65] The coordination helices showed remarkable flexibility, adjusting their helical pitch to the size of the anion, from 7.4 to 9.6 Å. The anions could be readily exchanged with each other, which can be explained by their nonspecific interactions with the hydrophobic channels, and the high flexibility of the helices. However, no anion-selectivity information was provided. When the analogous linker **L4** was used instead, similar coordination polymers with helical topology were obtained, which also displayed anion exchange abilities, with the large $ClO_4^-$ and $PF_6^-$ being preferred over the smaller $NO_3^-$ or $BF_4^-$ anions (Hofmeister selectivity).[66]

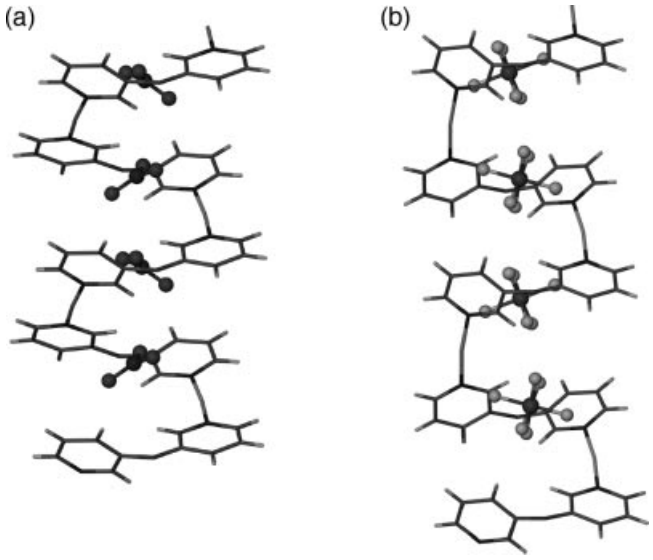


Figure 6. Crystal structures of [Ag(**L3**)]X showing helical coordination polymers (stick) with anions (ball-and-stick) included in the cylindrical channels inside helices: (a) X = $NO_3^-$; (b) X = $PF_6^-$.

A number of MOFs intercalating anions between hydrophobic 2D coordination layers have been reported. For example, Suh et al. described a series of Ag coordination polymers containing linker **L8**, and $NO_3^-$, $ClO_4^-$, and $CF_3SO_3^-$ anions, and reported their anion exchange properties.[67] The structures containing perchlorate or triflate displayed 2D coordination networks with the anions intercalated between the hydrophobic layers, while the structure containing the nitrate displayed 1D coordination chains, with the $NO_3^-$ coordinating the silver cations (Figure 7). Pairwise anion exchange experiments showed Hofmeister selectivity with $ClO_4^-$ being the most favored anion. Nitrate, on the other hand was favored over $CF_3SO_3^-$, which is a perturbation from the Hofmeister series, a fact that may be attributed to $NO_3^-$ coordination to the Lewis acid $Ag^+$.

Sun et al. reported a series of layered cationic frameworks with anion exchange properties, containing linkers **L5**–**L7** coordinating various transition metals.[68] Figure 8 illustrates a typical example involving linker **L5** and $Cd(NO_3)_2$, with the nitrate anions and solvent water molecules occupying the space between the cationic $Cd(\mathbf{L5})_2$ layers.[68b] The nitrate anions could be completely exchanged by $ClO_4^-$ with the formation of an isostructural coordination network, as found by powder X-ray diffraction and FTIR. The anion exchange was not completely reversible, as only about 50% of $ClO_4^-$ could be exchanged with $NO_3^-$, indicating Hofmeister selectivity. The $NO_2^-$ anion, on the other hand, could be reversibly exchanged with $NO_3^-$, apparently due to the more similar free energies of hydration of these two anions compared with the less hydrophilic $ClO_4^-$.

 © 2007 Wiley-VCH Verlag GmbH & Co. KGaA, Weinheim 

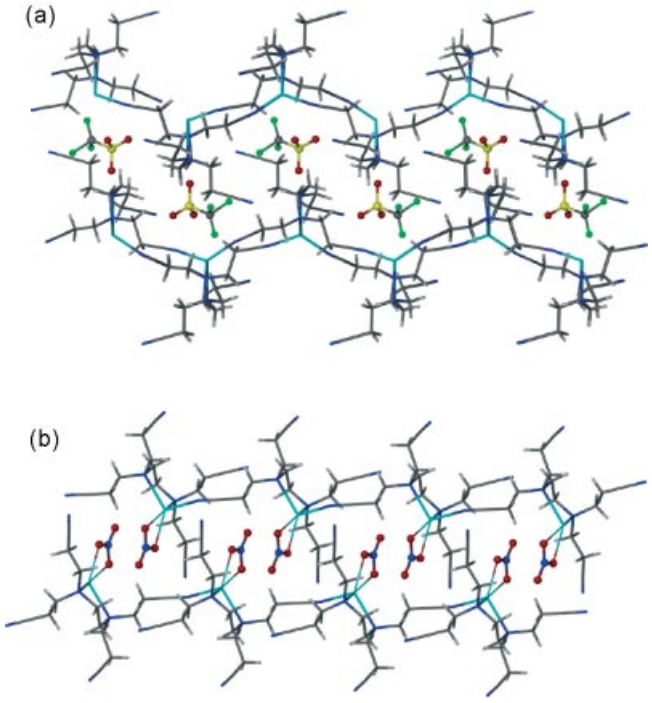


Figure 7. X-ray crystal structures of [Ag(**L8**)]X [X = $CF_3SO_3^-$ (a), $NO_3^-$ (b)], showing the intercalation of the anions between hydrophobic layers (a) or chains (b). Coordination frameworks and anions are shown as stick and ball-and-stick models, respectively.

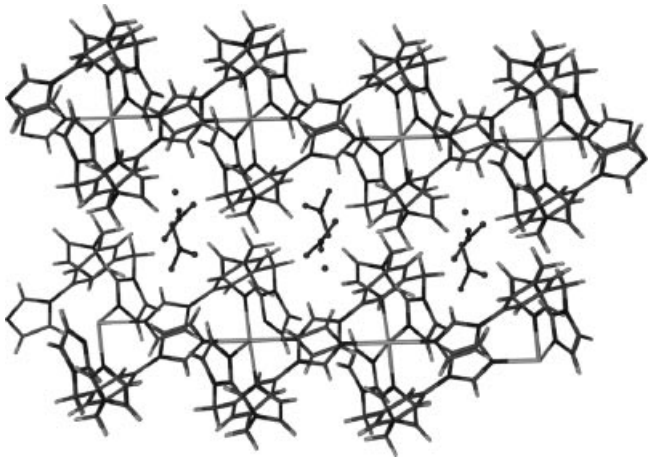

Figure 8. Crystal structure of [Cd(**L5**)$_2$]$(NO_3)_2(H_2O)$ with the nitrate and water intercalated between coordination layers. Coordination framework and anions are shown as stick and ball-and-stick models, respectively.

An interesting case of anion selectivity was found by Kitagawa et al. in a coordination polymer obtained from **L2** and $Cu^{2+}$ in the presence of an equimolar mixture of $PF_6^-$ and $ClO_4^-$ anions, which resulted in a 2D layered structure containing two types of channels, with the two anions included separately in each channel.[69] It is remarkable that despite the absence of any specific interactions between the anions and the coordination framework, the two anions were individually recognized by the two slightly different channels, which resulted in the separation of $PF_6^-$ and $ClO_4^-$, albeit only on a molecular scale (Figure 9).

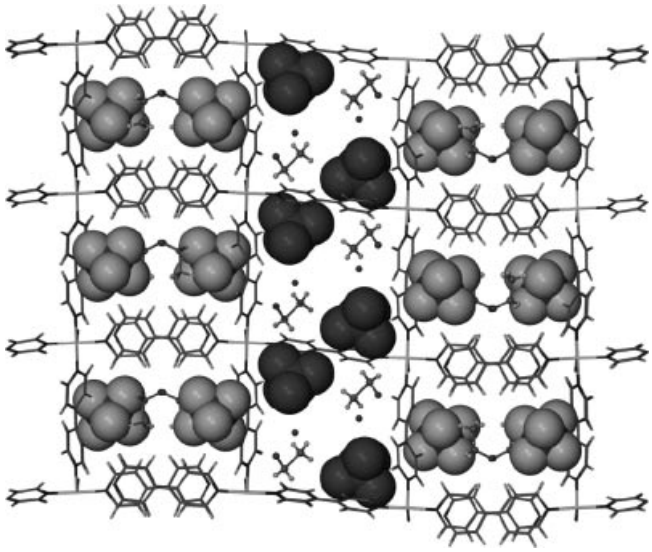

Figure 9. Crystal structure of $[Cu_2(\mathbf{L2})_5(H_2O)_4](ClO_4)_2(PF_6)_2(H_2O)_2(EtOH)_4$ showing the segregation of $ClO_4^-$ and $PF_6^-$ in alternating channels. Coordination framework, anions, and solvent are depicted as stick, space-filling, and ball-and-stick models, respectively.

### Anion Inclusion by Metal Coordination

Because most metal cations in MOFs have significant Lewis acidity, it is not uncommon for the metal nodes to serve as binding sites for the anions. Considering that these interactions may be relatively strong and directional, it can be anticipated that the presence of anion–metal coordination bonds could reverse the Hofmeister bias otherwise expected for anion exchange in hydrophobic MOFs. It should be kept in mind, however, that anion–metal coordination interactions do not operate alone in the crystal, and the ubiquitous van der Waals forces may remain in many cases the overall dominant interactions between the anion and the coordination framework, thus leading to Hofmeister selectivity. The same result should be expected if the anion is exposed to a significant degree to the water solvent present in the channels (poor complementarity).

An early example of exchange of an anion associated with a metal center in an MOF was reported by Yaghi et al.[70] Nitrate anions in [Ag(**L2**)]$(NO_3)$ interact weakly with the silver nodes in this 3D coordination network, and can be exchanged reversibly by $PF_6^-$, $MoO_4^-$, $BF_4^-$, or $SO_4^{2-}$. However, since the structures of the resulting exchanged solids have not been elucidated, and competition experiments have not been reported, it is difficult to evaluate the anion selectivity of these MOFs.

An extensive anion exchange study in a series of coordination polymers with the general formula [Ag(**L9**)]X (X = $ClO_4^-$, $NO_3^-$, $CF_3SO_3^-$) was reported by Yip et al.[71] The linker connects the silver nodes into 1D coordination

 © 2007 Wiley-VCH Verlag GmbH & Co. KGaA, Weinheim 

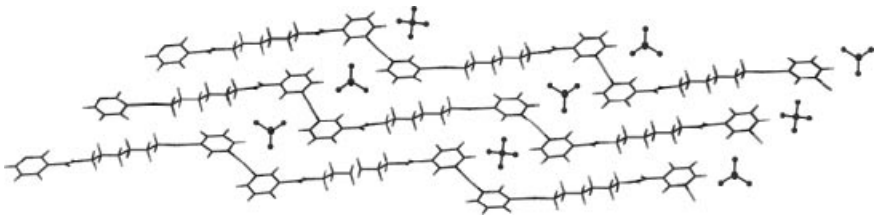

Figure 10. Crystal structure of [Ag(**L9**)]($ClO_4$) showing perchlorate anions intercalated between coordination layers and positioned within close proximity to the silver nodes. $ClO_4^-$ anions are disordered, and only one orientation is depicted for clarity. Coordination framework and anions are shown as stick and ball-and-stick models, respectively.

chains, which are further associated into layers by NH···O hydrogen bonds among the amide groups. The anions are weakly coordinated to the Ag cations and are located between the layers, with the perchlorate and nitrate anions displaying significant disorder (Figure 10). Despite the anions being coordinated to the Ag Lewis acid centers, these interactions were apparently not strong enough to completely overcome the anion solvation bias in this series of coordination polymers, as pairwise anion exchange experiments indicated the following selectivity: $ClO_4^- > NO_3^- > CF_3SO_3^-$. While the preference for perchlorate indicates Hofmeister behavior, the selectivity of $NO_3^-$ over $CF_3SO_3^-$ represents a perturbation from the Hofmeister series, which may be the result of the stronger nitrate coordination to the Ag nodes.

Crystallization of **L2** and $Cu^{2+}$ from an equimolar mixture of $NO_3^-$ and $PF_6^-$ resulted in the inclusion of both anions in a 1:3 ratio. The 2D square grids of the resulting coordination network are further linked in the third dimension by alternating $NO_3^-$ and $PF_6^-$, with two additional $PF_6^-$ anions being included inside the hydrophobic channels of the crystal (Figure 11). Attempts to co-include other anions such as $BF_4^-$ or $SO_4^{2-}$ failed, and only $PF_6^-$ was included in the presence of these two anions. Thus, the more hydrophobic $PF_6^-$ seems to be preferred by this coordination network, although the inclusion of $NO_3^-$ but not of $BF_4^-$ or $SO_4^{2-}$ indicates peak selectivity.[69]

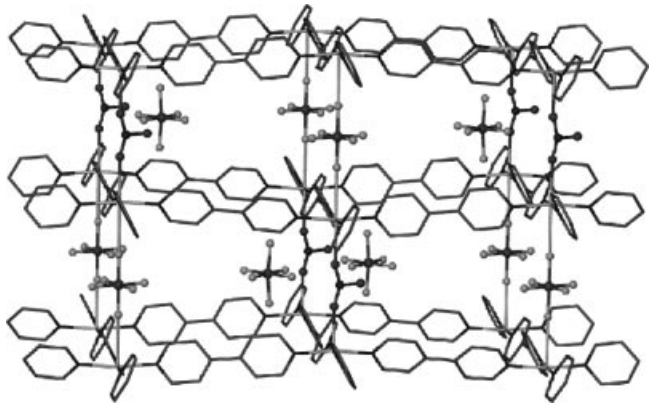

Figure 11. Crystal structure of $[Cu_2(PF_6)(NO_3)(\mathbf{L2})_4](PF_6)_2(H_2O)_2$ showing 2D $Cu^{II}$ coordination grids connected by bridging $NO_3^-$ and $PF_6^-$ anions, and the inclusion of additional $PF_6^-$ anions inside the channels. Included water solvent is not shown. Anions are depicted as ball-and-stick models and the framework as a stick model.

The anion selectivity in MOFs containing metal-binding sites can also be controlled by the match between the hardness or softness of the anion (Lewis base) and metal center (Lewis acid). For example, the 2D coordination network made from **L10** and soft $Pb^{2+}$ Lewis acid metal centers can easily exchange nitrate with the softer iodide. The nitrate anions do not coordinate the metal nodes and occupy the interlayer space together with solvating water molecules. Upon exposure to an aqueous solution containing 1 molequiv. of KI, the nitrate could be completely exchanged with iodide, with the latter coordinating the $Pb^{2+}$ Lewis acid centers (Figure 12).[72]

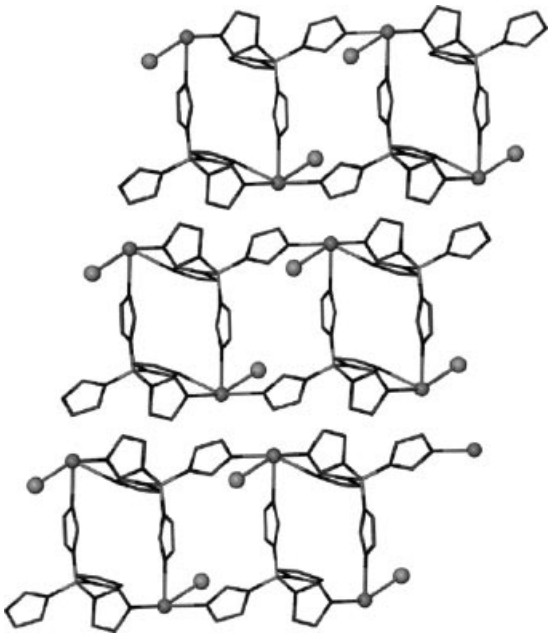

Figure 12. Crystal structure of [Pb(**L10**)]I showing a layered framework with the iodide anions coordinating the lead metal centers. The $I^-$ and $Pb^{2+}$ are depicted as balls and **L10** is shown as a stick model.

A clear example of anti-Hofmeister selectivity was observed in the anion exchange in a series of MOFs built from **L11** and $Cu^{2+}$.[73] When $PF_6^-$ and $ClO_4^-$ were used as anions, two isostructural coordination networks with interpenetrated 3D diamondoid topologies were obtained, with the non-coordinating hexafluorophosphate or perchlorate anions and water solvent molecules occupying the pores. These anions could be irreversibly exchanged with the more hydrophilic $N_3^-$ or $SO_4^{2-}$ anions, with complete reorganiza-

 © 2007 Wiley-VCH Verlag GmbH & Co. KGaA, Weinheim 

tion of the coordination networks. Figure 13 depicts the crystal structure of the sulfate-exchanged framework, which consists of layers of $Cu^{2+}$ coordinated by $\mu_3$-bridging sulfate anions, with the organic linkers connecting the inorganic layers. Apparently, the strong and specific coordinating bonds to the copper centers resulted in the sulfate anions being preferred against the weaker Lewis bases $PF_6^-$ or $ClO_4^-$. However, since the two structures have completely different architectures (and therefore different stabilities), it is not clear to what extent the preference for sulfate can be attributed to its stronger Lewis basicity or to the inherent difference in stability between the two coordination networks.

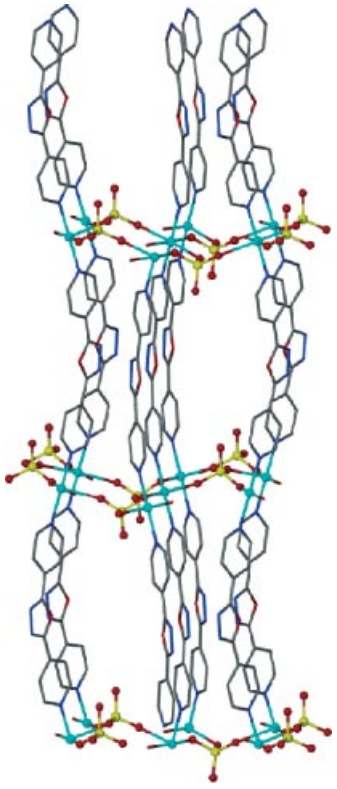

Figure 13. Structure of [Cu(**L11**)($H_2O$)($SO_4$)]($H_2O$)$_2$ showing $Cu^{II}$–$SO_4$ coordination layers connected by **L11** linkers into a 3D framework. The sulfate anions and the copper centers are depicted as ball-and-stick models and the linker is shown as a stick model. Water molecules included in the channels are not shown.

That the framework stability can decisively influence the anion exchange selectivity in MOFs was clearly demonstrated in the coordination networks [Ag(**L12**)(X)] (X = $ClO_4^-$, $PF_6^-$).[74] The two solids have similar coordination structures consisting of 1D coordination chains, with the anions weakly coordinating the silver centers. The two structures differ though in the number and strength of the inter-chain Ag–Ag interactions. The perchlorate anion was irreversibly exchanged with hexafluorophosphate, a process that was driven by the argentophilic interactions that were stronger and more numerous in the $PF_6^-$ structure. This example is a clear illustration of how other types of intermolecular forces in MOF crystals can override the anion-framework interactions, and thus control the anion selectivity.

### Anion Inclusion by Hydrogen Bonding

Among the intermolecular interactions involving anions, hydrogen bonding appears to have the greatest potential for inducing non-Hofmeister selectivity. In this regard, the ready availability of chelating hydrogen-bonding groups that can establish multiple contacts with the targeting anions, and the possibility of appending multiple such groups to organic linkers by using the power of organic synthesis, offer great prospects for the design of MOFs with shape recognition and non-Hofmeister selectivities. One of the remaining challenges associated with the utilization of hydrogen-bonding groups, though, is their tendency to self-associate, which diminishes or completely eliminates their ability to bind anions. The elaboration of functional MOFs for anion recognition and separation needs therefore to incorporate effective molecular- and crystal-design strategies that prevent such self-neutralizing "reactions" among the hydrogen-bonding groups from occurring.

The most common situation of anion hydrogen bonding in MOFs involves coordinating water as a proton donor. An example of coordination network in this category that was explored as an anion exchanger is [$Ba_2$(**L13**)($H_2O$)$_5$]Cl, reported by Shimizu et al.[75] This structure can be described as consisting of cationic barium sulfonate layers pillared by the mesitylene linkers into a 3D coordination network containing channels occupied by chloride anions (Figure 14). The $Ba^{2+}$ centers are further coordinated by water molecules, which act as hydrogen-bond donors to $Cl^-$. Most chloride anions (75–85%) could be exchanged by fluoride when the crystals were suspended in MeCN containing 1 equiv. of $F^-$. However, since the anion exchange was effected from a relatively nonpolar solvent, the inclusion of the more hydrophilic fluoride inside the polar channels of this coordination framework is not surprising, and may be considered normal Hofmeister behavior.

The microporous coordination polymer made from the hydrophilic linker **L14** and $Tb^{3+}$ was recently reported to selectively sense anions (Figure 15).[76] Despite its neutral charge, this coordination network can absorb different anions (as sodium salts) into its hydrophilic channels functionalized with free –OH groups. The anion inclusion was detected by the luminescence enhancement caused by the interactions of the anions with the network, presumably through hydrogen bonding. The response to various anions was found to follow the order: $CO_3^{2-} > CN^- > I^- > Br^- > Cl^- >> F^- \approx SO_4^{2-} \approx PO_4^{3-}$. One may easily notice that except for carbonate and cyanide the other anions conform to the Hofmeister behavior, indicating that the presence of the –OH hydrogen-bonding groups is not sufficient to reverse the solvation bias in this MOF. The strikingly different selectivity for carbonate and cyanide, which are both relatively strong bases, suggests to us a different mechanism

 © 2007 Wiley-VCH Verlag GmbH & Co. KGaA, Weinheim 

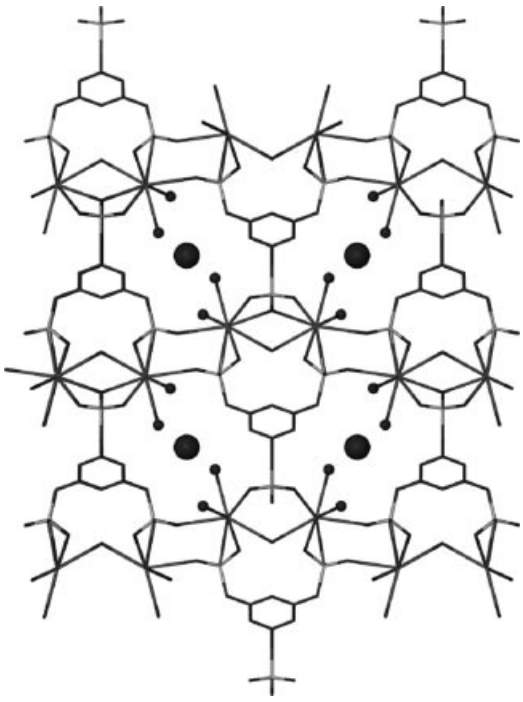

Figure 14. Structure of the $[Ba_2(\mathbf{L13})(H_2O)_5]Cl$ coordination network showing chloride anions (large balls) included in polar channels decorated with water molecules (small balls) acting as hydrogen-bond donors. The water protonscould not be located from the X-ray structure.

for their binding, possibly involving deprotonation of the OH groups. Unfortunately, no structural information about the binding of the anions (and the sodium countercation) inside the channels of this material is available, which makes the interpretation of the observed selectivity difficult.

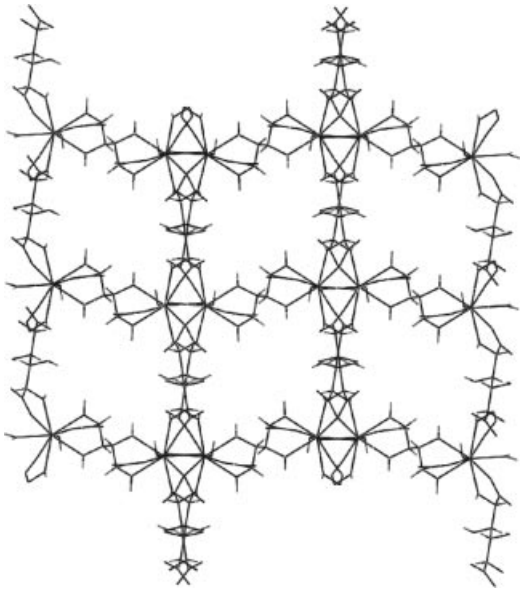

Figure 15. Crystal structure of $[Tb(\mathbf{L14})_{1.5}(H_2O)_2](H_2O)_5$, with the water included in the channels removed.

Work in our group has involved the design and synthesis of coordination frameworks functionalized with hydrogen-bonding groups for anion recognition and separation. Along this line, we synthesized a cationic square-grid coordination network assembled from $Cu^{2+}$ and linker **L15**, which contained 1D channels functionalized with free –COOH binding groups (Figure 16).[77] The availability of free carboxylic groups in a coordination network is remarkable, as these groups typically become involved in the network assembly through coordination to the metal centers or hydrogen bonding. The key factors for the formation of this functional MOF appear to be the low pH (1.6) involved in its synthesis, which kept the carboxylic groups protonated and thus unavailable for metal coordination, and the aqueous solvent, which prevented the –COOH groups from self-associating by hydrogen bonding. The carboxylic groups remained thus available to bind anionic guests included in the channels of this MOF. Competitive crystallization experiments found that this coordination network preferentially includes halides against $NO_3^-$, $SO_4^{2-}$, or $ClO_4^-$ oxo anions, with a slight preference for chloride. Single-crystal X-ray structural analysis showed the inclusion of $Cl(H_2O)_4^-$ clusters hydrogen-bonded by the carboxylic groups inside the 1D channels. The clusters assume a square-pyramidal geometry, which is the most stable structure of $Cl(H_2O)_4^-$, as predicted by theoretical calculations. The observed peak selectivity for halides can be rationalized by the good complementarity (size, symmetry, and hydrogen-bond functionality) between the channels of the MOF host and the $Cl(H_2O)_4^-$ guest. The larger oxo anions, by comparison, would have to lose most of their solvating water to fit inside the channels, which would be energetically unfavorable. On the other hand, $Br^-$ and $F^-$ are known to form water clusters that are similar in size and shape with the $Cl(H_2O)_4^-$, which may account for the reduced selectivity observed within the halide series. This system provides an example of non-Hofmeister anion selectivity in an MOF (upper-right quadrant in Figure 2), that results from the combination of high complementarity (insured by functionalization with H-bonding groups) with structural rigidity. Furthermore, this example inspires an alternative approach to anion separation with MOFs, where the coordination framework host can be designed to selectively include anion/water clusters of different sizes and geometries, which may result in selectivities that are different from those normally associated with "naked" anions.

Looking to improve anion recognition and selectivity in MOFs, we turned our attention to urea proton donors. Urea is a particularly effective anion-binding group, as it is capable of chelating the targeted anion with its two preorganized NH protons, which may result in enhanced binding strength and recognition abilities.[78] We and others have demonstrated that ureas can be easily incorporated as functional units into coordination frameworks, wherein they can specifically chelate various oxo anions.[79] Although ureas are prone to self-association into hydrogen-bonded tapes, we found that substitution with the electron-withdrawing pyridine groups, such as in linkers **L17** and **L18**, greatly

 © 2007 Wiley-VCH Verlag GmbH & Co. KGaA, Weinheim 

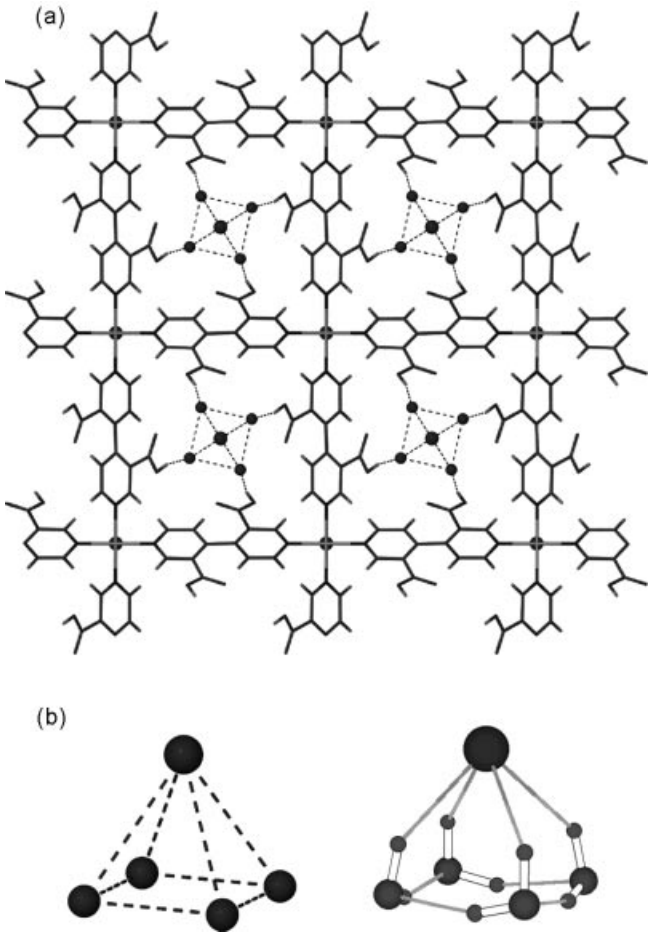


Figure 16. Structure of $[CuCl(\mathbf{L15})_2]Cl(H_2O)_4$. (a) Square-grid coordination network (stick) functionalized with –COOH groups that bind $Cl(H_2O)_4^-$ clusters (balls) included in the channels. (b) Structure of $Cl(H_2O)_4^-$ as found in the crystal (left) and as calculated in the gas-phase (right).

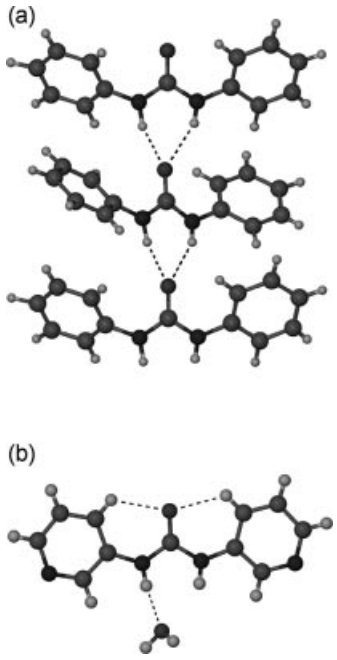


Figure 17. (a) Typical self-association of ureas in hydrogen-bonded tapes, as found in the crystals of diphenylurea. (b) Intramolecular CH···O hydrogen bonds in the crystals of bis(*m*-pyridyl)urea hydrate showing intramolecular CH···O interactions and intermolecular hydrogen bonding to the included water.

diminishes this tendency as a result of stronger intramolecular CH···O hydrogen bonds, which decreases the ability of the C=O group to engage in intermolecular hydrogen bonds (Figure 17).[79a,80]

The urea-functionalized linker **L17** forms 1D coordination polymers with $ZnCl_2$, $ZnBr_2$, $ZnI_2$, and $ZnSO_4$ from water/ethanol mixtures, with the coordination chains further linked by urea···anion hydrogen bonds and anion–Zn coordination bonds (Figure 18).[62] In direct contrast, $Zn(NO_3)_2$ and $Zn(ClO_4)_2$ do not form coordination networks under the same conditions, which prompted us to investigate the possibility of anion separation by selective crystallization of Zn(**L17**) coordination networks. Addition of an ethanolic solution of **L17** to an aqueous solution containing 1 equiv. of $Zn(NO_3)_2$ and 1 equiv. of each NaCl, NaBr, NaI, $NaClO_4$, and $Na_2SO_4$ resulted in selective crystallization of the halides as a solid solution with the composition $Zn(\mathbf{L17})(Cl)_x(Br)_y(I)_z$ ($x + y + z = 2$), and total exclusion of the oxo anions, as demonstrated by FTIR spectroscopy and X-ray diffraction. Although sulfate can form a coordination polymer under these conditions, this anion proved uncompetitive against the halides, as the formation of the $[Zn(\mathbf{L17})(SO_4)(H_2O)_3](EtOH)$ phase that would otherwise be observed is apparently inhibited by the presence of the competing anions. Furthermore, the size and charge mismatch of $SO_4^{2-}$ apparently prohibits its inclusion in the Zn(**L17**) halide phase. The composition of the precipitated solid from the competitive crystallization experiment was found to be time-dependent (Figure 19). Thus, after 30 min, the kinetically controlled crystalline product consisted of mainly the $Zn(\mathbf{L17})Cl_2$ phase, with a small amount of the $Zn(\mathbf{L17})Br_2$ phase also present. Elemental analysis indicated that chloride was the major halide found in this solid, followed by bromide and iodide, which corresponds to an anti-Hofmeister selectivity. The preference for the smaller, more densely charged $Cl^-$ against the more hydrophobic $Br^-$ and $I^-$ in the $Zn(\mathbf{L17})Cl_2$ phase can be rationalized on the basis of the strong interactions of the halides with the $Zn^{2+}$ Lewis acid centers and hydrogen bonding to the urea groups, which apparently provide a more stabilizing environment than that found in water. This solid, however, slowly redissolved, and, after 5 d, the thermodynamically more stable $Zn(\mathbf{L17})Br_2$ was the only phase observed. This phase also included chloride and iodide in a solid solution form, with the relative amounts of the halides still corresponding to an anti-Hofmeister selectivity. The relative halide content continued to change if the precipitated solid was left in the supernatant solution for up to 2 weeks, when the dominant halide in the solid became $Br^-$, followed by $Cl^-$ and $I^-$ (Figure 19). A crystal structure of the $Zn(\mathbf{L17})Br_2$ phase showed that it contained two different halide sites, with only one of them participating to hydrogen bonding with the urea groups (Figure 18), which

 © 2007 Wiley-VCH Verlag GmbH & Co. KGaA, Weinheim 

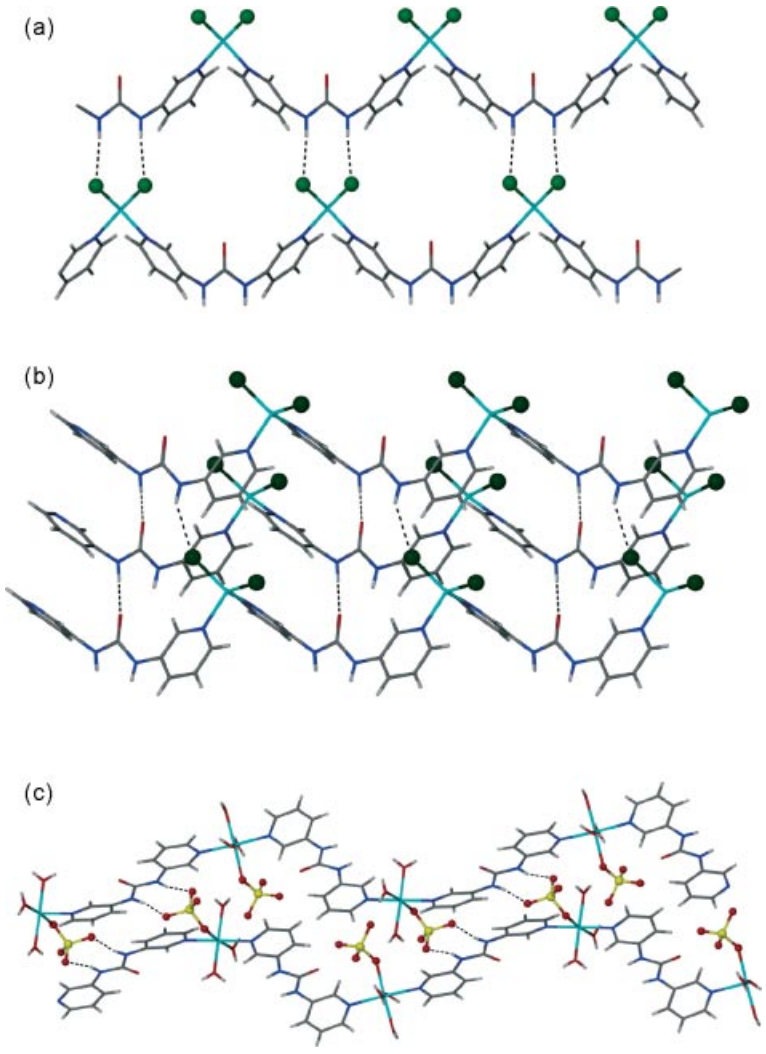


Figure 18. Crystal structures of the 1D Zn(**L17**) coordination polymers. (a) Structure of Zn(**L17**)$Cl_2$ showing the binding of the $Cl^-$ to the $Zn^{2+}$ centers and urea groups. (b) Structure of Zn(**L17**)$Br_2$ [isostructural with Zn(**L17**)$I_2$] showing two binding sites for the $Br^-$. (c) Structure of [Zn(**L17**)$(SO_4)(H_2O)_3$](EtOH) showing the sulfate anions coordinated to the $Zn^{2+}$ and hydrogen-bonded to urea groups. Coordination chains are shown as stick models and anions are shown as ball-and-stick models.

explains the lower discrimination among halides found in the final solid. Nevertheless, the Zn(**L17**)$Br_2$ phase is thermodynamically more stable than the Zn(**L17**)$Cl_2$ one, apparently due to its more efficient crystal packing. This observation points to another important factor in anion selectivity in MOF crystallizations, which is the overall lattice stabilities of the competing coordination networks, which ultimately dictate their solubilities.

The concomitant inclusion of different halides in the same structural frameworks simplifies the interpretation of the observed selectivity by careful examination of the coordination environments around the included anions. This was conveniently done by structural analysis of single crystals grown from 1:1 mixtures of different zinc halide salt pairs. For example, crystallization of a 1:1 mixture of $ZnCl_2$ and $ZnBr_2$ with a stoichiometric amount of **L17** resulted in concomitant formation of both the Zn(**L17**)$Br_2$ (major) and Zn(**L17**)$Cl_2$ (minor) single-crystalline phases. X-ray diffraction analysis of the major phase showed segregation of the

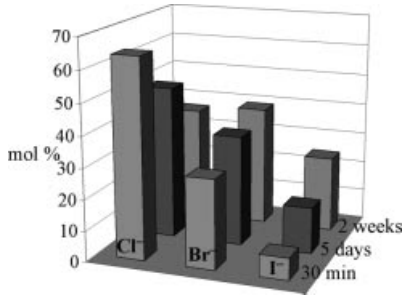


Figure 19. Halide compositions of the solids obtained from the competitive crystallizations of [Zn(**L17**)]$X_2$ coordination networks.

two halides between the two different halide sites. Thus, the site hydrogen-bonded to urea contained 66% $Cl^-$, while the non-hydrogen-bonded site contained only 40% $Cl^-$ (with the $Br^-$ occupying the remaining 34% and 60%, respectively, of the two sites), which corresponded to the $ZnCl_{1.06}Br_{0.94}$(**L17**) overall crystal composition. On the

 © 2007 Wiley-VCH Verlag GmbH & Co. KGaA, Weinheim 

other hand, the two equivalent halide sites in the Zn(**L17**)-$Cl_2$ minor crystal phase are both hydrogen-bonded by NH protons from an urea group, which translated into a higher chloride content of 71% [corresponding to the $ZnCl_{1.42}Br_{0.58}$(**L17**) crystal composition]. Analogous crystallization of a 1:1 mixture of $ZnBr_2$ and $ZnI_2$ with a stoichiometric amount of **L17** resulted in exclusive formation of the $ZnBr_2$(**L17**) phase, which, however, contained both bromide and iodide in different proportions depending on the crystal site. Thus, the urea-hydrogen-bonded site contained 59% $Br^-$, whereas the non-hydrogen-bonded site contained only 33% $Br^-$, corresponding to a crystal composition of $ZnBr_{0.92}I_{1.08}$(**L17**). An even more dramatic segregation of halides was found in the mixed crystals obtained from a 1:1 mixture of $ZnCl_2$ and $ZnI_2$, which contained 85% $Cl^-$ on the hydrogen-bonded site and only 26% $Cl^-$ on the non-hydrogen-bonded site [corresponding to the $ZnCl_{1.11}I_{0.89}$(**L17**) crystal composition]. These mixed structures allowed us to formulate some simple structure/selectivity principles for halide inclusion in these coordination frameworks. Thus, in the Zn(**L17**)$Cl_2$ phase, with all halide sites equivalent and consisting of strong coordination to the $Zn^{2+}$ centers and hydrogen bonding to urea, the more densely charged and stronger base $Cl^-$ was preferred against the larger, less basic $Br^-$. In the Zn(**L17**)$Br_2$ phase, on the other hand, the more acidic site hydrogen-bonded to urea included significantly larger proportions of the more basic halide, whereas the larger, less basic halides preferred the non-hydrogen-bonded site, where van der Waals forces were dominant. All these observations strongly indicate an anti-Hofmeister selectivity within the halide series. However, it should also be noted here that the total exclusion of the oxo anions could be considered as a non-Hofmeister behavior, or peak selectivity for the halide group.

In order to achieve higher selectivity for oxo anions, we reasoned that the design of more elaborate linkers, containing multiple urea groups positioned optimally around the anion, should result in superior shape recognition and peak selectivity. Towards this end, we have been interested in the design of coordination polymers with exclusive sulfate selectivity. Molecular models suggested that sulfate ideally accommodates 6 urea groups, each binding to one of the 6 O–S–O edges of the tetrahedral $SO_4^{2-}$ in a total of 12 hydrogen bonds (Figure 20a).[78a] Linker **L16**, built from TREN, seemed ideal for this purpose, as indicated by molecular modeling, which showed that sulfate can accommodate two such TREN-based linkers. Indeed, crystal-structure analysis showed that the coordination framework obtained from **L16** and $Ag_2SO_4$ encapsulates the sulfate (Figure 20), with 6 urea groups saturating the anion by 12 hydrogen bonds (three to each O atom).[81] For comparison, proteins are known to bind sulfate by only 7 hydrogen bonds, and the highest sulfate coordination number previously observed in a synthetic host was 8.[82] Other anions of various shapes and basicities, such as $BF_4^-$, $NO_3^-$, $MeSO_3^-$, or $CH_3COO^-$ did not form a coordination polymer with **L16** under similar conditions due to their negligible interactions with this linker, as indicated by NMR spectroscopy. Instead, crystallization of the free linker through urea···urea hydrogen bonding was observed in the presence

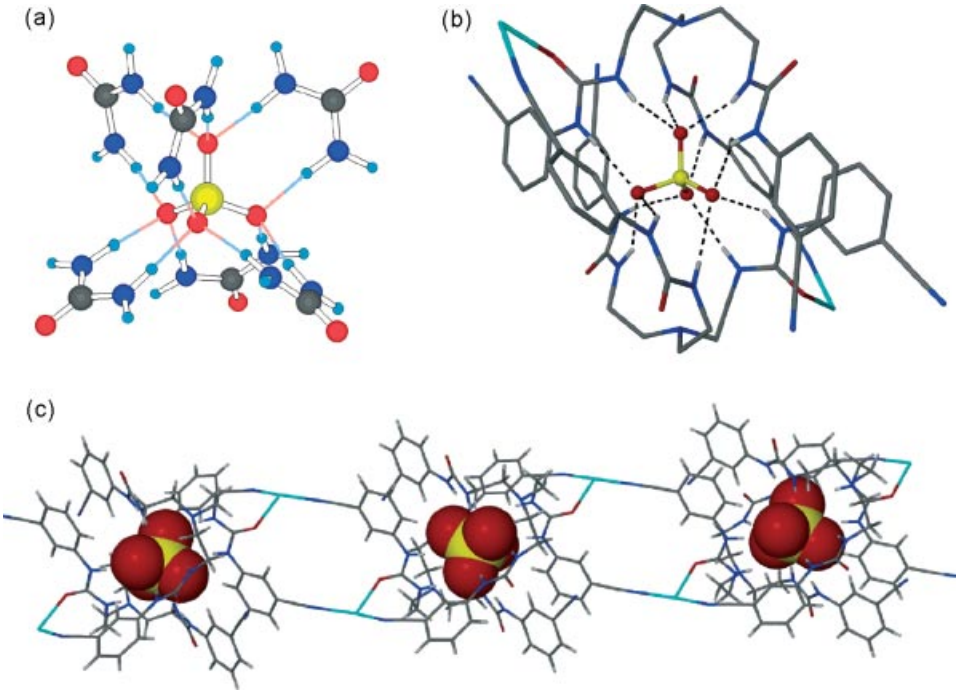


Figure 20. Encapsulation of $SO_4^{2-}$ in an urea-functionalized coordination polymer. (a) Molecular model showing optimal sulfate binding by 12 hydrogen bonds from 6 urea groups. (b) Sulfate encapsulation in the coordination cage obtained from **L16** and $Ag_2SO_4$. (c) 1D chain obtained by linking the cages through CN···Ag coordination bonds. The coordination framework and the sulfate anions are shown as stick and space-filling models, respectively.

 © 2007 Wiley-VCH Verlag GmbH & Co. KGaA, Weinheim 

of these anions, which indicates threshold selectivity, with only the strongly interacting sulfate anion being able to compete against linker self-association.[83]

## 4. Conclusions and Future Prospects

With their great structural diversity and ease of synthesis, MOFs are versatile materials for anion separations. However, without proper crystal structure control, this architectural variety may appear in the same time daunting to someone who wants to design an anion receptor with predictable anion selectivity. Like with any other potential applications of MOFs, further progress in crystal engineering of these materials is needed before they can be predictably used for anion separations. Towards this end, it is important to find new MOFs that preserve a common structural framework in the presence of various anions, to allow for unambiguous interpretation of the observed anion selectivity based on the interactions of the anions with the coordination frameworks. MOF functionalization with strong and specific anion-binding groups such as Lewis acid metal centers or hydrogen-bonding groups for complementary anion coordination is typically needed for selectivities that depart from the solvation bias. Like with discrete anion receptors in solution, the best peak selectivity is observed in MOFs that combine structural constraints and rigidity with a sufficient number of strong binding groups that are optimally positioned around the anion for shape recognition. To date, however, there is a very limited number of coordination frameworks that satisfy these conditions, which can be explained by the fact that most of these solids have not been specifically designed for anion recognition and separation. As a result, the vast majority of MOFs studied to date show typical solvation-controlled Hofmeister selectivities. More systematic structure/properties studies need to be done to better understand the principles governing anion selectivities inside the MOF cavities, with the ultimate goal to obtain peak selectivities for targeted anions by deliberate design. Sorely needed at this time are more quantitative studies of anion exchange and separations, including competition experiments, anion-exchange isotherms, thermodynamic and kinetic measurements, and mechanistic investigations of anion transport. Computational studies could also offer valuable information about the energetics of anion binding inside the coordination frameworks, as well as the electronic and steric requirements for optimal anion selectivity. Such fundamental inquiries may eventually reward us with new materials with unprecedented efficiencies in real-world separations.

## Acknowledgments

This research was sponsored by the Division of Chemical Sciences, Geosciences, and Biosciences, Office of Basic Energy Sciences, U. S. Department of Energy, under contract number DE-AC05-00OR22725 with Oak Ridge National Laboratory managed by UT-Battelle, LLC.

[1] For recent reviews, see: a) N. R. Champness, *Dalton Trans.* **2006**, 877–880; b) C. J. Kepert, *Chem. Commun.* **2006**, 695–700; c) N. W. Ockwig, O. Delgado-Friedrichs, M. O'Keeffe, O. M. Yaghi, *Acc. Chem. Res.* **2005**, *38*, 176–182; d) G. Férey, C. Mellot-Draznieks, C. Serre, F. Millange, *Acc. Chem. Res.* **2005**, *38*, 217–225; e) D. Bradshaw, J. B. Claridge, E. J. Cussen, T. J. Prior, M. J. Rosseinsky, *Acc. Chem. Res.* **2005**, *38*, 273–282; f) S. Kitagawa, R. Kitaura, S. Noro, *Angew. Chem. Int. Ed.* **2004**, *43*, 2334–2375; g) C. Janiak, *Dalton Trans.* **2003**, 2781–2804; h) S. L. James, *Chem. Soc. Rev.* **2003**, *32*, 276–288.
[2] U. Mueller, M. Schubert, F. Teich, H. Puetter, K. Schierle-Arndt, J. Pastré, *J. Mater. Chem.* **2006**, *16*, 626–636.
[3] B. F. Hoskins, B. R. Robson, *J. Am. Chem. Soc.* **1990**, *112*, 1546–1554.
[4] J. C. Giddings, *Unified Separation Science*, Wiley-Interscience, New York, **1991**.
[5] B. A. Moyer, P. V. Bonnesen, "Physical Factors in Anion Separations", in *Supramolecular Chemistry of Anions* (Eds.: A. Bianchi, K. Bowman-James, E. García-España), VCH, Weinheim, **1997**, p. 1–44.
[6] a) J. L. Sessler, P. A. Gale, W.-S. Cho, "Anion Receptor Chemistry", in *Monographs in Supramolecular Chemistry* (Ed.: F. Stoddart), Royal Society of Chemistry, Cambridge, **2006**; b) P. D. Beer, P. A. Gale, *Angew. Chem. Int. Ed.* **2001**, *40*, 486–516; c) F. P. Schmidtchen, M. Berger, *Chem. Rev.* **1997**, *97*, 1609–1646.
[7] F. Hofmeister, *Arch. Exp. Pathol. Pharmakol.* **1888**, *24*, 247–260.
[8] W. Kunz, J. Henle, B. W. Ninham, *Curr. Opin. Colloid Interface Sci.* **2004**, *9*, 19–37.
[9] K. D. Collins, M. W. Washabaugh, *Q. Rev. Biophys.* **1985**, *18*, 323–422.
[10] W. Kunz, P. Lo Nostro, B. W. Ninham, *Curr. Opin. Colloid Interface Sci.* **2004**, *9*, 1–18.
[11] W. Kunz, *Pure Appl. Chem.* **2006**, *78*, 1611–1617.
[12] W. Kunz, P. Lo Nostro, B. W. Ninham, *Curr. Opin. Colloid Interface Sci.* **2004**, *9*, VII.
[13] F. Hofmeister, *Arch. Exp. Pathol. Pharmakol.* **1888**, *25*, 1–30.
[14] R. M. Diamond and D. C. Whitney, *Resin Selectivity in Dilute to Concentrated Aqueous Solutions*, vol. 1 (Ed.: J. Marinsky), Marcel Dekker, New York, **1966**, 277–302.
[15] Z. Brzózka, *Potentiometric Sensors*, vol. 10 (Ed.: D. N. Reinhoudt), in *Comprehensive Supramolecular Chemistry* (Eds.: J. L. Atwood, J. E. D. Davies, D. D. MacNicol, F. Vögtle, J.-M. Lehn), Pergamon Press, Oxford, **1996**, p, 187–212.
[16] Y. Marcus, *Ion Properties*, Marcel Dekker, New York, **1997**.
[17] Y. Marcus, *J. Chem. Soc., Faraday Trans.* **1991**, *87*, 2995–2999.
[18] H. K. Roobottom, H. D. B. Jenkins, J. Passmore, L. Glasser, *J. Chem. Educ.* **1999**, *76*, 1570–1573.
[19] T. G. Levitskaia, L. Maya, G. J. Van Berkel, B. A. Moyer, *Inorg. Chem.* **2006**, *46*, 261–272.
[20] K. Kavallieratos, B. A. Moyer, *Chem. Commun.* **2001**, 1620–1621.
[21] Y. Marcus, *Ion Solvation*, Wiley, Chichester, **1985**.
[22] M. J. Kamlet, J.-L. M. Abboud, M. H. Abraham, R. W. Taft, *J. Org. Chem.* **1983**, *48*, 2877–2887.
[23] Y. Marcus, M. J. Kamlet, R. W. Taft, *J. Phys. Chem.* **1988**, *92*, 3613–3622.
[24] Y. Marcus, L. E. Asher, *J. Phys. Chem.* **1978**, *82*, 1246–1254.
[25] a) J.-M. Lehn, *Supramolecular Chemistry: Concepts and Perspectives*, VCH, Weinheim, **1995**; b) D. J. Cram, *J. Incl. Phenom.* **1988**, *6*, 397–413; c) D. H. Busch, *Chem. Rev.* **1993**, *93*, 847–860; d) H.-J. Schneider, A. Yatsimirsky, *Principles and Methods in Supramolecular Chemistry*, John Wiley, New York, **2000**.
[26] R. G. Pearson, *Chemical Hardness*, Wiley-VCH, New York, **1997**.

 © 2007 Wiley-VCH Verlag GmbH & Co. KGaA, Weinheim 

[27] J. P. Clare, A. J. Ayling, J. B. Joos, A. L. Sisson, G. Magro, M. N. Perez-Payan, T. N. Lambert, R. Shukla, B. D. Smith, A. P. Davis, *J. Am. Chem. Soc.* **2005**, *127*, 10739–10746.

[28] F. P. Schmidtchen, "Concepts for Structure and Guest Binding", in *Artificial Anion Hosts* (Eds.: A. Bianchi, K. Bowman-James, E. García-España), VCH, Weinheim, **1997**, p. 79–146.

[29] H.-J. Schneider, *Mechanisms of Anion Recognition* in *Fundamentals and Applications of Anion Separations* (Eds.: B. A. Moyer, R. P. Singh), Kluwer Academic/Plenum, New York, **2004**, p. 31–42.

[30] a) Y. Marcus, E. Pross, J. Hormadaly, *Proc. International Solvent Extraction Conference ISEC '80*, Liege, Belgium, **1980**, Paper 80–117; b) Y. Takeda, *The Solvent Extraction of Metal Ions by Crown Compounds*, vol. 121 (Eds.: F. Vögtle, E. Weber), Springer-Verlag, Berlin, **1984**, p. 1–38; c) B. A. Moyer, "Molecular Recognition: Receptors for Cationic Guests", in *Comprehensive Supramolecular Chemistry* (Ed.:J.-M. Lehn), vol. 1 (Ed.: G. W. Gokel), Pergamon Press, Oxford, **1996**, p. 377–416.

[31] R. A. Leonard, C. Conner, M. W. Liberatore, P. V. Bonnesen, D. J. Presley, B. A. Moyer, G. J. Lumetta, *Sep. Sci. Technol.* **1999**, *34*, 1043–1068.

[32] M. Takeuchi, S. Tanaka, M. Yamawaki, S. Tachimori, *J. Radioanal. Nucl. Chem.* **1995**, *191*, 189–199.

[33] A. Jyo, R. Weber, H. Egawa, *Anal. Sci.* **1993**, *9*, 599–603.

[34] K. Inoue, K. N. Ghimire, R. P. Dhakal, K. Makino, T. Miyajima, in *Fundamentals and Applications of Anion Separations* (Eds.: B. A. Moyer, R. P. Singh), Kluwer Academic/Plenum, New York, **2004**, p. 263–275.

[35] T. Fricke, J. Hamann, M. Bahadir, B. König, *Anal. Bioanal. Chem.* **2002**, *374*, 148–154.

[36] H. Tsukube, J. Uenishi, H. Shiba, O. Yonemitsu, *J. Membr. Sci.* **1996**, *114*, 187–191.

[37] a) H. Hara, H. Ohkubo, K. Sawai, *Analyst* **1993**, *118*, 549–552; b) D. Gao, J. Z. Li, R. Q. Yu, G. D. Zheng, *Anal. Chem.* **1994**, *66*, 2245–2249.

[38] a) E. Bakker, E. Malinowska, R. D. Schiller, M. E. Meyerhoff, *Talanta* **1994**, *41*, 881–890; b) L. Górski, M. E. Meyerhoff, E. Malinowska, *Talanta* **2004**, *63*, 101–107; c) M. S. Messick, S. K. Krishnan, M. K. Hulvey, E. D. Steinle, *Anal. Chim. Acta* **2005**, *539*, 223–228.

[39] N. N. Leyzerovich, N. V. Shvedene, Y. N. Blikova, L. G. Tomilova, I. V. Pletnev, *Electroanalysis* **2001**, *13*, 246–252.

[40] M. R. Ganjali, T. Poursaberi, F. Basiripour, M. Salavati-Niassari, M. Yousefi, M. Shamsipur, *Fresenius J. Anal. Chem.* **2001**, *370*, 1091–1095.

[41] S. Koizumi, T. Imato, N. Ishibashi, *Fresenius J. Anal. Chem.* **1997**, *357*, 37–43.

[42] S. Sasaki, T. Amano, S. Ozawa, T. Masuyama, D. Citterio, H. Hisamoto, H. Hori, K. Suzuki, *J. Chem. Soc., Perkin Trans. 1* **2001**, 1366–1371.

[43] S. Chandra, A. Ruzicka, P. Svec, H. Lang, *Anal. Chim. Acta* **2006**, *577*, 91–97.

[44] B. A. Moyer, P. V. Bonnesen, R. Custelcean, L. H. Delmau, B. P. Hay, *Kem. Ind.* **2005**, *54*, 65–87.

[45] M. M. Murad, T. Hayashita, K. Shigemori, S. Nishizawa, N. Teramae, *Anal. Sci.* **1999**, *15*, 1185–1189.

[46] K. Kavallieratos, J. C. Bryan, R. A. Sachleben, G. J. Van Berkel, O. D. Espetia, M. A. Kelly, A. Danby, K. Bowman-James, B. A. Moyer in *Fundamentals and Applications of Anion Separations* (Eds.: B. A. Moyer, R. P. Singh), Kluwer Academic/Plenum, New York, **2004**, p. 125–150.

[47] S. Sasaki, A. Hashizume, S. Ozawa, D. Citterio, N. Iwasawa, K. Suzuki, *Chem. Lett.* **2001**, 382–383.

[48] A. L. Sisson, J. P. Clare, L. H. Taylor, J. P. H. Charmant, A. P. Davis, *Chem. Commun.* **2003**, 2246–2247.

[49] M. J. Berrocal, A. Cruz, I. H. A. Badr, L. G. Bachas, *Anal. Chem.* **2000**, *72*, 5295–5299.

[50] J. H. Shim, I. S. Jeong, M. H. Lee, H. P. Hong, J. H. On, K. S. Kim, H. S. Kim, B. H. Kim, G. S. Cha, H. Nam, *Talanta* **2004**, *63*, 61–71.

[51] A. L. Sisson, J. P. Clare, A. P. Davis, *Chem. Commun.* **2005**, 5263–5265.

[52] T. G. Levitskaia, M. Marquez, J. L. Sessler, J. A. Shriver, T. Vercouter, B. A. Moyer, *Chem. Commun.* **2003**, 2248–2249.

[53] V. Kral, J. L. Sessler, T. V. Shishkanova, P. A. Gale, R. Volf, *J. Am. Chem. Soc.* **1999**, *121*, 8771–8775.

[54] L. A. J. Chrisstoffels, F. de Jong, D. N. Reinhoudt, *Chem. Eur. J.* **2000**, *6*, 1376–1385.

[55] S. G. Galbraith, L. F. Lindoy, P. A. Tasker, P. G. Plieger, *Dalton Trans.* **2006**, 1134–1136.

[56] J. M. Mahoney, G. U. Nawaratna, A. M. Beatty, P. J. Duggan, B. D. Smith, *Inorg. Chem.* **2004**, *43*, 5902–5907.

[57] J. S. Gardner, Q. P. Peterson, J. O. Walker, B. D. Jensen, B. Adhikary, R. G. Harrison, J. D. Lamb, *J. Membr. Sci.* **2006**, *277*, 165–176.

[58] A. N. Khlobystov, N. R. Champness, C. J. Roberts, S. J. B. Tendler, C. Thompson, M. Schröder, *CrystEngComm* **2002**, *4*, 426–431.

[59] C. Thompson, N. R. Champness, A. N. Khlobystov, C. J. Roberts, M. Schröder, S. J. B. Tendler, M. J. Wilkinson, *J. Microsc.* **2004**, *214*, 261–271.

[60] K. H. Von Lieser, W. Hild, *Radiochim. Acta* **1967**, *7*, 74–77.

[61] A recent paper described some examples of anion exchange by single-crystal-to-single-crystal transformations; however, the dissolution/recrystallization mechanism was not unambiguously ruled out: S. R. Halper, L. Do, J. R. Stork, S. M. Cohen, *J. Am. Chem. Soc.* **2006**, *128*, 15255–15268.

[62] R. Custelcean, T. J. Haverlock, B. A. Moyer, *Inorg. Chem.* **2006**, *45*, 6446–6452.

[63] O. M. Yaghi, H. Li, *J. Am. Chem. Soc.* **1995**, *117*, 10401–10402.

[64] O. M. Yaghi, H. Li, T. L. Groy, *Inorg. Chem.* **1997**, *36*, 4292–4293.

[65] O.-S. Jung, Y. J. Kim, Y.-A. Lee, J. K. Park, H. K. Chae, *J. Am. Chem. Soc.* **2000**, *122*, 9921–9925.

[66] O.-S. Jung, Y. J. Kim, Y.-A. Lee, H. K. Chae, H. G. Jang, J. Hong, *Inorg. Chem.* **2001**, *40*, 2105–2110.

[67] K. S. Min, M. P. Suh, *J. Am. Chem. Soc.* **2000**, *122*, 6834–6840.

[68] a) J. Fan, L. Gan, H. Kawaguchi, W.-Y. Sun, K.-B. Yu, W.-X. Tang, *Chem. Eur. J.* **2003**, *9*, 3965–3973; b) W. Zhao, J. Fan, T. Okamura, W.-Y. Sun, N. Ueyama, *New J. Chem.* **2004**, *28*, 1142–1150; c) S.-Y. Wan, Y.-T. Huang, Y.-Z. Li, W.-Y. Sun, *Microporous Mesoporous Mater.* **2004**, *73*, 101–108; d) W. Zhao, J. Fan, Y. Song, H. Kawaguchi, T. Okamura, W.-Y. Sun, N. Ueyama, *Dalton Trans.* **2005**, 1509–1517.

[69] S. Noro, R. Kitaura, M. Kondo, S. Kitagawa, T. Ishii, H. Matsuzaka, M. Yamashita, *J. Am. Chem. Soc.* **2002**, *124*, 2568–2583.

[70] O. M. Yaghi, H. Li, *J. Am. Chem. Soc.* **1996**, *118*, 295–296.

[71] S. Muthu, J. H. K. Yip, J. J. Vital, *J. Chem. Soc., Dalton Trans.* **2002**, 4561–4568.

[72] B. H. Hamilton, K. A. Kelly, T. A. Wagler, M. P. Espe, C. J. Ziegler, *Inorg. Chem.* **2004**, *43*, 50–56.

[73] M. Du, Y.-M. Guo, S.-T. Chen, X.-H. Bu, S. R. Batten, J. Ribas, S. Kitagawa, *Inorg. Chem.* **2004**, *43*, 1287–1293.

[74] L. Pan, E. B. Woodlock, X. Wang, K.-C. Lam, A. L. Rheingold, *Chem. Commun.* **2001**, 1762–1763.

[75] S. A. Dalrymple, G. K. H. Shimizu, *Chem. Eur. J.* **2002**, *8*, 3010–3015.

[76] K.-L. Wong, G.-L. Law, Y.-Y. Yang, W.-T. Wong, *Adv. Mater.* **2006**, *18*, 1051–1054.

[77] R. Custelcean, M. G. Gorbunova, *J. Am. Chem. Soc.* **2005**, *127*, 16362–16363.

[78] a) B. P. Hay, T. K. Firman, B. A. Moyer, *J. Am. Chem. Soc.* **2005**, *127*, 1810; b) V. Amendola, M. Bonizzoni, D. Esteban-Gómez, L. Fabbrizzi, M. Licchelli, F. Sancenón, A. Taglietti, *Coord. Chem. Rev.* **2006**, *250*, 1451–1470.

[79] a) R. Custelcean, B. A. Moyer, V. S. Bryantsev, B. P. Hay, *Cryst. Growth Des.* **2006**, *6*, 555–563; b) L. Applegarth, A. E. Goeta, J. W. Steed, *Chem. Commun.* **2005**, 2405–2406; c) D. K. Kumar, A. Das, P. Dastidar, *New J. Chem.* **2006**, *30*, 1267.


 © 2007 Wiley-VCH Verlag GmbH & Co. KGaA, Weinheim 

[80] a) M. C. Etter, Z. Urbanczyk-Lipkowska, M. Zia-Ebrahimi, T. W. Panunto, *J. Am. Chem. Soc.* **1990**, *112*, 8415–8426; b) L. S. Reddy, S. Basavoju, V. R. Vangala, A. Nangia, *Cryst. Growth Des.* **2006**, *6*, 161–173; c) A. M. Todd, K. M. Anderson, P. Byrne, A. E. Goeta, J. W. Steed, *Cryst. Growth Des.* **2006**, *6*, 1750–1752.
[81] R. Custelcean, B. A. Moyer, B. P. Hay, *Chem. Commun.* **2005**, 5971–5973.
[82] K. Bowman-James, *Acc. Chem. Res.* **2005**, *38*, 671–678.
[83] Exclusive selectivity for sulfate was recently achieved in the competitive crystallization of an $Ni^{II}$ coordination framework made from **L18**: R. Custelcean, V. Sellin, B. A. Moyer, *Chem. Commun.*, DOI:10.1039/b616761f.

Received: January 6, 2007
Published Online: February 23, 2007

 © 2007 Wiley-VCH Verlag GmbH & Co. KGaA, Weinheim 

DOI: 10.1002/ejic.200600819

# Structural Distortion and Magnetic Behavior in Cyanide-Bridged $Fe^{III}_2Ni^{II}_2$ Complexes

**Dongfeng Li,[a] Rodolphe Clérac,[b] Guangbin Wang,[c] Gordon T. Yee,[c] and Stephen M. Holmes*[a]**

**Keywords:** Cyanometalate / Magnetism / Single-molecule magnets / Pyrazolylborate / Magnetic relaxation

The X-ray structure, spectroscopic, and magnetic properties of a cyanide-bridged complex, $\{[(Tp^*)Fe^{III}(CN)_3]_2[Ni^{II}(bipy)_2]_2[OTf]_2\}\cdot 2H_2O$ (**2**) are described [Tp* = hydridotris(3,5-dimethylpyrazol-1-yl)borate; bipy = 2,2′-bipyridine; OTf = trifluromethanesulfonate]. Magnetic measurements indicate that **2** exhibits an $S = 3$ ground state and slow relaxation of the magnetization. Magnetostructural comparisons to the more symmetrical analog $\{[(Tp^*)Fe^{III}(CN)_3]_2[Ni^{II}(DMF)_4]_2[OTf]_2\}\cdot 2DMF$ (**1**) are also described. Surprisingly, the magnetic properties of **1** and **2** are similar despite the presence of a non-planar $\{Fe^{III}_2Ni^{II}_2(\mu\text{-}CN)_4\}$ core and severely distorted $Ni^{II}$ coordination sphere in **2**, suggesting that the $Ni^{II}$ centers play a minor role in the slow magnetization relaxation behavior of the clusters.
(© Wiley-VCH Verlag GmbH & Co. KGaA, 69451 Weinheim, Germany, 2007)

## Introduction

Single-molecule magnets (SMMs) have remained an active area of research over the last decade due to their unusual magnetic properties and potential use in molecule-based information storage devices.[1–5] The largest family of SMMs contain anisotropic metal centers linked by oxo- and carboxylate ligands, with $Mn_{12}O_{12}(O_2CMe)_{16}(OH_2)_4$ being the best characterized example. The complex exhibits superparamagnetic-like behavior owing to the large spin ground state and Ising-type anisotropy derived from the anisotropic metal centers present.[1–5]

Several polynuclear cyanide-bridged complexes that exhibit slow relaxation of the magnetization containing $[fac\text{-}LM(CN)_3]^{n-}$ units have been described over the last few years, where L = 1,4,7-trimethyltriazacyclononane, 1,1,1-tris(diphenylphosphanomethyl)ethane, tris(3,5-dimethylpyrazolyl)borate, and tris(pyrazolyl)borate.[5–15] Among these, we previously reported that $\{[(Tp^*)Fe^{III}(CN)_3Ni^{II}(DMF)_4]_2[OTf]_2\}\cdot 2DMF$ (**1**) exhibits slow relaxation of the magnetization with an apparent blocking temperature near 1.8 K [Tp* = hydridotris(3,5-dimethylpyrazol-1-yl)borate, OTf = trifluoromethanesulfonate, DMF = dimethylformamide].[7]

Recently, Rogez et al. reported that distorted six-coordinate nickel(II) complexes can exhibit very large and negative $D$ values ($D = -10.1$ cm$^{-1}$),[16] while Accorsi et al. demonstrated that anisotropy barriers in tetrairon(III) single-molecule magnets can be systematically tuned by ligand substitution; Brechin et al. has demonstrated that $[Mn^{III}]_6$ clusters can also be tuned by this strategy.[17] We rationalized that replacement of DMF ligands present in **1** for rigid, sterically demanding ancillary ligands such as 2,2′-bipryidine (bipy), would significantly distort the $Ni^{II}$ coordination sphere and afford greater single-ion anisotropy. If greater single-ion anisotropy of the $Ni^{II}$ centers translates into greater molecular anisotropy, then the energy barrier and the blocking temperature of the $\{Fe^{III}_2Ni^{II}_2\}$ complexes may also be systematically tuned. In the present Communication, we compare the structures and spectroscopic and magnetic properties of two rectangular complexes, $\{[(Tp^*)Fe^{III}(CN)_3]_2[Ni^{II}(L_n)]_2[OTf]_2\}$ ($L_n$ = 4 DMF, **1**; 2 bipy, **2**), that exhibit $S = 3$ ground states and slow relaxation of the magnetization.[7,18]

## Results and Discussion

### Synthesis and Characterization

Treatment of $\{[(Tp^*)Fe^{III}(CN)_3]_2[Ni^{II}(DMF)_4]_2[OTf]_2\}\cdot 2DMF$ (**1**)[7] with 2,2′-bipyridine (bipy) in MeCN/MeOH (v/v, 1:1) mixtures cleanly affords $\{[(Tp^*)Fe^{III}(CN)_3]_2[Ni^{II}(bipy)_2]_2[OTf]_2\}\cdot 2H_2O$ (**2**) as a red crystalline solid.[18] The infrared spectrum of **2** exhibits intense $\nu_{BH}$ and $\nu_{CN}$ stretching absorptions at 2553, 2158 and 2128 cm$^{-1}$, respectively, that are shifted to higher energies relative to those seen for $[NEt_4][(Tp^*)Fe^{III}(CN)_3]$ (2549 and

[a] University of Kentucky, Department of Chemistry, Lexington, Kentucky 40506-0055, USA
Fax: +1-859-323-1069
E-mail: smholm2@uky.edu
[b] Centre de Recherche Paul Pascal, UPR-CNRS 8641, 33600 Pessac, France
[c] Virginia Polytechnic and State University, Department of Chemistry, Blacksburg, Virginia 24061, USA
Supporting information for this article is available on the WWW under http://www.eurjic.org or from the author.

 © 2007 Wiley-VCH Verlag GmbH & Co. KGaA, Weinheim 

2115 $cm^{-1}$); the $\nu_{CN}$ stretches are tentatively assigned as bridging and terminal cyanides, respectively.[6–9,19–22] In comparison the energies of the $\nu_{BH}$ (2547 $cm^{-1}$) and $\nu_{CN}$ (2170, 2163, and 2120 $cm^{-1}$) stretching absorptions[7] for **1** are found at higher energies than those in **2**, suggesting that either depopulation of the 5σ cyanide orbital is less efficient, and/or more efficient π back-bonding occurs in **2**.[29]

Compound **2** crystallizes in the triclinic $P\bar{1}$ space group and is structurally related to **1**.[23] The cationic rectangular complex consists of two octahedral [*cis*-$Ni^{II}(bipy)_2]^{2+}$ centers that are linked to two adjacent $[(Tp^*)Fe^{III}(CN)_3]^-$ anions (Figure 1) through bridging cyanides. The Fe–C≡N bond angles and Fe–C and Ni–N bond lengths are comparable in **1** and **2**, respectively (Table 1). The structural details of **1** have been previously reported.[7]

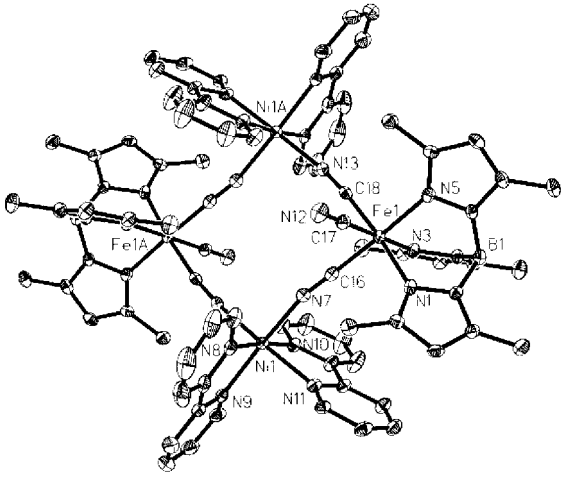


Figure 1. X-ray structure of **2**. Thermal ellipsoids are at the 50% level and all anions, lattice solvent, and hydrogen atoms are omitted for clarity.

Table 1. Selected bond lengths [Å] and angles (°) for **1** and **2**.

| | | | |
|---|---|---|---|
| Compound **1** | | | |
| Fe1–C16 | 1.928(5) | C16–Fe1–C18 | 85.4(2) |
| Fe1–C18 | 1.927(5) | N9–Ni1–N7A | 92.3(1) |
| Ni1–N9 | 2.039(4) | Ni1–N9–C18 | 176.9(4) |
| | | Fe1–C16–N7 | 177.3(4) |
| Compound **2** | | | |
| Fe1–C16 | 1.920(5) | C16–Fe1–C18 | 83.8(2) |
| Fe1–C17 | 1.932(5) | N7–Ni1–N13A | 95.1(2) |
| Ni1–N7 | 2.063(4) | Ni1–N7–C16 | 167.1(4) |
| | | Fe1–C16–N7 | 178.0(4) |

In **2**, the Ni1–N bond lengths for the *cis* cyanides are 2.042(4) (Ni1–N7) and 2.063(4) Å (Ni1–N13A), while those for the bipyridine, range from 2.074(4) (Ni1–N8) to 2.112(4) Å (Ni1–N11), respectively (Table 1). The bridging cyanide Fe1–C bond lengths, 1.916(5) and 1.920(5) Å, are nearly equivalent, while the longest distance [1.932(5) Å] is found for the terminal cyanide (Fe1–C17).[18] The bridging Fe–C≡N bond angles range from 173.4(4)° (Fe1–C18–N13) to 178.0(4)° (Fe1–C16–N7), while the terminal cyanide (Fe–C17–N12) is nearly linear [178.1(4)°]. The Ni–N≡C bond angles are significantly bent, ranging from 167.1(4)° (Ni1–N7–C16) to 171.9(3)° (Ni1–N13A–C18A), respectively; the N–Ni–N bond angles of the [*cis*-$Ni^{II}(bipy)_2(\mu\text{-}NC)_2$] fragments range from 78.5(2) to 98.8(2)°. We presume that significant steric congestion, between the Tp* and bipy ligands, afford dissimilar N7–Ni1–N13A [95.1(2) Å] and C16–Fe1–C18 [83.8(2) Å] bond angles, and a distorted nonplanar $\{Fe^{III}_2Ni^{II}_2(CN)_4\}$ framework. The intramolecular Fe1···Fe1A, Fe1···Ni1, and Ni1···Ni1A contacts are 7.628(1), 5.097(1), and 6.733(1) Å, respectively, while the closest intermolecular contacts between terminal cyanides and bipy rings are 3.297(1) Å (Figure 1).[18] In comparison the closest intercluster contacts for **1** are 4.363(3) Å.[7]

The structural distortions of **1** and **2** can be further described by the torsion angles present in each complex.[18] Looking down the Ni1(μ-CN)Fe1 axis and considering only the inner-sphere atoms coordinated to each metal center in **1** for clarity, the N7A–Ni1–Fe1–N7, O1A–Ni1–Fe1–N3, O1B–Ni1–Fe1–N5, and O1D–Ni1–Fe1–N8 torsion angles are ca. 3.6, 7.7, 11.3, and 8.4°, respectively, suggesting that **1** adopts a rather flat rectangular structure (Figure 2). In comparison, **2** exhibits a very distorted $\{Fe^{III}_2Ni^{II}_2(\mu\text{-}CN)_4\}$ core, as indicated by the nonlinear μ-CN bridges and large angular deviations from an eclipsed configuration of coordinated heteroatoms present on the Fe and Ni centers; the N11–Ni1–Fe1–N1, N8–Ni1–Fe1–N12, N13–Ni1–Fe1–N13A, and N10–Ni1–Fe1–N3 angles are 24.5, 18.4, 5.5, and 10.6°, respectively (Figure 1).[18]

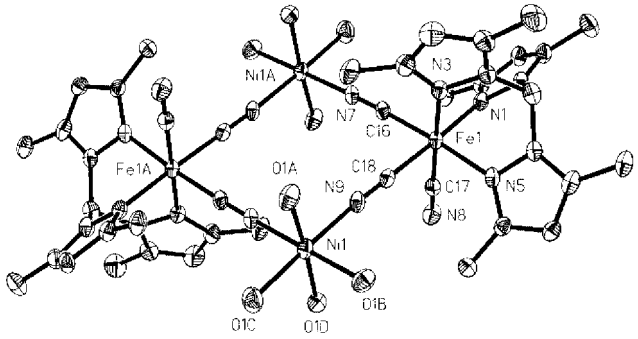


Figure 2. X-ray structure of **1**. Thermal ellipsoids are at the 50% level and all anions, lattice solvent, and hydrogen atoms are omitted for clarity.

## Magnetic Characterization

The $\chi T$ vs. $T$ data suggests that the $Fe^{III}$ ($S$ = 1/2) and $Ni^{II}$ ($S$ = 1) centers in **2** are ferromagnetically coupled (Figure 3), because the $\chi T$ product gradually increases from 3.8 $cm^3\,K\,mol^{-1}$ (300 K), reaching a maximum value of 7.7 $cm^3\,K\,mol^{-1}$ at 7 K. Below 7 K, $\chi T$ decreases towards a minimum value of 6.6 $cm^3\,K\,mol^{-1}$ at 1.83 K.[6–9,21,22] Based on the tetranuclear structure of **2**, the magnetic data has been modeled using an isotropic Heisenberg model in the weak field approximation.[24–26] The theoretical susceptibility has been deduced from application of the van Vleck equation to the Kambe method, by the following spin Ham-

 © 2007 Wiley-VCH Verlag GmbH & Co. KGaA, Weinheim 

iltonian: $H = -2J\{(S_1 + S_2)\cdot(S_3 + S_4)\}$,[27,28] where $J$ is the isotropic exchange interaction between $Fe^{III}$ and $Ni^{II}$ sites and $S_i$ is the spin operator for each metal center ($S_i$ = 1, $Ni^{II}$, with $i$ = 1–2; $S_i$ = 1/2, $Fe^{III}$, with $i$ = 3–4). The best set of parameters obtained are $J/k_B$ = +9.4(3) K and $g_{iso}$ = 2.29(1) using the data above 20 K, in order to minimize anisotropy effects or intermolecular antiferromagnetic exchange interactions (Figure 3).[8,11,18,22]

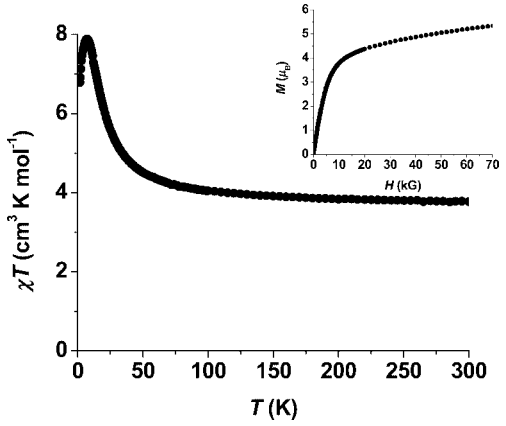


Figure 3. Temperature dependence of the $\chi T$ product for **2** at $H$ = 0.1 T. Inset: Field dependence of the magnetization at 1.8 K.

When non-zero inter complex exchange interactions ($J'$) are also taken into consideration using a mean field approximation,[24–26] the data can not be adequately reproduced between 300 and 1.8 K (Figure S2; supporting information; for supporting information see also the footnote on the first page of this paper),[18] indicating that additional factors (e.g. anisotropy, second-neighbor Fe···Fe or Ni···Ni magnetic interactions) may also be relevant. The magnitude of the magnetic Ni–Fe exchange coupling constant calculated for **2** is slightly larger than that determined for **1** [7.6 K],[8,18] being comparable to values found for other tri- and tetranuclear complexes containing $Ni^{II}$ and $[(Tp^{R,R})Fe^{III}(CN)_3]^-$ (R = H, Me) and centers.[6–9,24–26] Confirmation of an $S$ = 3 ground state is obtained in the $M$ vs. $H_{dc}$ data at 1.85 K because the magnetization is nearly saturated at 7 T, approaching a maximum value of 6 $\mu_B$ (see inset in Figure 3).[18]

The temperature dependence of the ac susceptibility for **2** was measured at several different frequencies at $H_{dc}$ = 0 Oe (Figure 4). The ac susceptibility is frequency-dependent suggesting that the **2** exhibits slow relaxation of the magnetization. From the data shown in Figure 3, the relaxation time $\tau$, can be determined from the maximum of $\chi''(T)$.[4] The relaxation time for **2** follows an Arrhenius law with an energy gap of 20.4 K and $\tau_0 = 5.4 \times 10^{-9}$ s (see inset in Figure S5 in the supporting information). As in many complexes that exhibit slow relaxation of the magnetization, it is likely that the observed energy barrier takes an effective value, resulting from a "short-cut" of the thermal barrier by quantum tunnelling of the magnetization (QTM). In zero field, the $\pm m_S$ states have the same energy and QTM between these pairs of levels is possible. When a magnetic field is applied, the $m_S < 0$ and $m_S > 0$ levels decrease and increase respectively in energy, preventing quantum tunneling between the $\pm m_S$ states.[4]

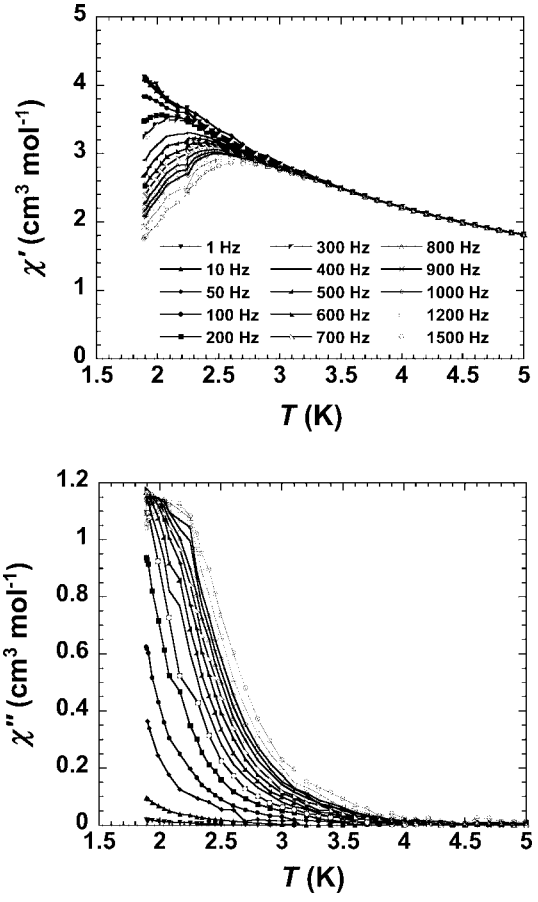


Figure 4. Temperature dependence of the real ($\chi'$, top) and imaginary ($\chi''$, bottom) components of the ac susceptibility for **2** ($H_{dc}$ = 0 Oe; $H_{ac}$ = 3 Oe) between 1 and 1500 Hz.

To further investigate the activated behavior of **2**, we performed ac susceptibility measurements under several applied dc magnetic fields (Figures 5, 6, and S3, S4 in the supporting information).[18] At 1.85 K, the characteristic frequency (maximum of the $\chi''$ vs. ν plot) decreases rapidly from 600 Hz at 0 Oe, approaches a nearly constant value of 2 Hz at 4000 Oe, and disappears when $H_{dc}$ ca. 14000 Oe, as expected when the magnetization is almost saturated (Figure 5). As shown by this result, the QTM relaxation pathway remains efficient even at 1.85 K in zero-field. As expected for a SMM that exhibits fast quantum tunneling of the magnetization (for $H_{dc}$ = 0), the application of non-zero magnetic fields increases the magnetization relaxation time (i.e. relaxation mode frequency decreases with increasing $H_{dc}$). For **2**, the relaxation time can be estimated using the ac measurements under 4000 Oe, which follow Arrhenius behavior with $\tau_0 = 8.4 \times 10^{-8}$ s and an effective energy gap of 25.7 K (Figure 6). This value allows for a rough estimation of the uniaxial anisotropy and affords $D/k_B \approx -2.9$ K.[18]

 © 2007 Wiley-VCH Verlag GmbH & Co. KGaA, Weinheim 

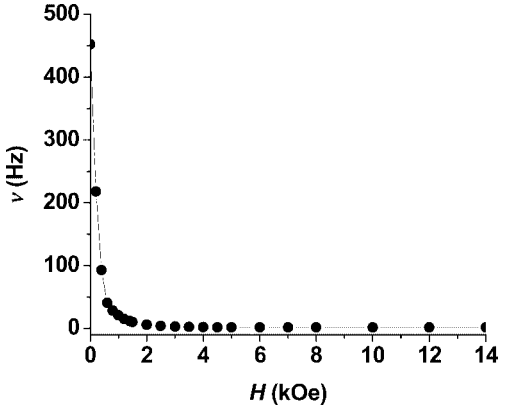


Figure 5. Field dependence of the characteristic frequency at 1.85 K.

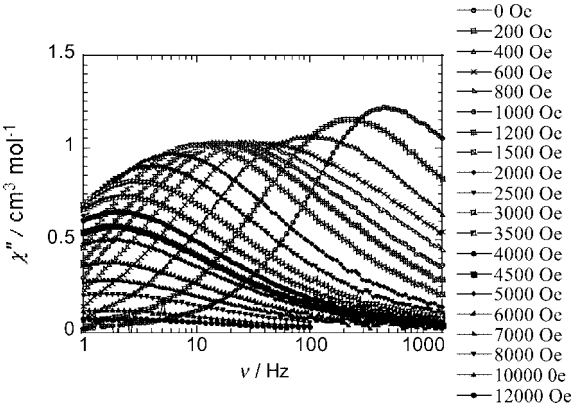


Figure 6. Frequency dependence of $\chi''$ at 1.85 K under various applied $H_{dc}$ for **2**.

To date, few systematic studies of cyanide-bridged polynuclear complexes that exhibit slow relaxation of the magnetization have been described for a given structural archetype. We previously reported that in $\{Fe^{III}_2Ni^{II}\}$ complexes bending of the M–C≡N–M′ bridges significantly impacts the superexchange efficiency ($J$) and anisotropy energy barrier ($\Delta$): nonlinear cyanide bridges usually afford smaller $J$ and $\Delta$ values.[24–26,30] We had anticipated that structural distortion of the $\{Fe^{III}_2Ni^{II}_2(\mu\text{-}CN)_4\}$ core and concomitant coordination spheres of the metal ions present would afford similar changes in exchange coupling ($J$), zero-field splitting ($D$), and effective barrier heights ($\Delta_{eff}$) of the tetranuclear complexes.

However, we were surprized to find that despite having bent Fe–C≡N–Ni units, **2** exhibits ferromagnetic superexchange interactions ($J > 0$) that are slightly larger than those in **1**.[7] Recent DFT calculations for $\{Fe^{III}_2M^{II}_2(\mu\text{-}CN)_4\}$ complexes ($M^{II}$ = Mn, Co, Ni) suggest that the total magnetic anisotropy of the ground state is largely dependent on transverse anisotropy contributions (ca. 15–36%) to the total longitudinal anisotropy, originating from the orbital contributions of the $S = 1/2$ $Fe^{II}$ centers.[31] In comparison to $Mn_{12}O_{12}(O_2CMe)_{16}(OH_2)_4$ faster quantum tunneling rates, larger $D$ parameters, and angular-momentum contributions to the magnetic ground state (ca. 4 times) are found for **1** and **2**. The ac susceptibility measurements ($H_{dc}$ = 0) indicate **1** and **2** exhibit similar behavior suggesting that both exhibit slow relaxation of the magnetization. We postulate that the single-ion anisotropy contributions of the $Ni^{II}$ centers are of minor importance in tuning the magnetic relaxation behavior of the these tetranuclear complexes.

## Conclusions

In summary, we have described the preparation, structures, and magnetic properties of two rectangular cyanide-bridged $\{Fe^{III}_2Ni^{II}_2\}$ complexes that exhibit slow relaxation of the magnetization. We propose that steric repulsion between the $[(Tp^*)Fe^{III}(CN)_3]^-$ and $[Ni^{II}(bipy)_2]^{2+}$ units affords bent cyanide bridges that are *cis* to each other affording a distorted-octahedral $Ni^{II}$ coordination environment in **2**. Surprisingly, despite severe structural distortion of the $\{Fe^{III}_2Ni^{II}_2(CN)_4\}$ core, **2** exhibits slow frequency-dependent magnetization relaxation behavior that is comparable to **1**, a more symmetrical analog. We tentatively propose that for **1** and **2** the height of the magnetization reversal barrier is largely dependent on the single-ion anisotropy contributions of the low-spin $Fe^{III}$ centers, while the $Ni^{II}$ centers appear to be of minor importance. A future report will describe how spin-orbit coupling and orbital contributions of the magnetic ions contribute to the overall magnetic anisotropy and relaxation behavior of several polynuclear cyanide-bridged complexes.[31]

## Experimental Section

**General:** All operations were conducted while dark in a vacuum or under argon using standard Schlenk and drybox techniques. Transfers of solutions containing cyanides were carried out through stainless steel cannulas. The salts $[NEt_4][(Tp^*)Fe^{III}(CN)_3]$,[7] $Ni(OTs)_2$,[32] and **1**[21] were prepared according to modified literature methods. Diethyl ether was distilled from sodium/benzophenone and sparged with argon prior to use. DMF (Baker) was dried with activated Linde 13-X molecular sieves and sparged with argon prior to use. 2,2′-Bipyridine (Aldrich) was used as received.

**Physical Methods:** The IR spectra were recorded as Nujol mulls between KBr plates with a Mattson Galaxy 5200 FTIR instrument. The dc magnetic measurements were obtained using crushed, single crystals of **2**, on a Quantum Design MPMS-XL SQUID magnetometer, operating between 1.8 and 300 K, in a 0.1 T static magnetic field. Initial ac measurements were obtained over 1.8 to 5 K ($H_{dc}$ = 0 Oe and $H_{ac}$ = 3 Oe) and between 1 and 1500 Hz; additional measurements were obtained at temperatures between 1.8 and 5 K ($H_{dc}$ = 0, 1000 and 4000 Oe; $H_{ac}$ = 3 Oe). Magnetic data were corrected for the sample holder diamagnetism, while diamagnetic contributions from the samples were estimated using Pascal's constants.[36] Microanalyses were performed by Robertson Microlit Laboratory.

**X-ray Structural Studies:** Crystals of **2** were grown from DMF/$Et_2O$ solutions of **1**[7] treated with 4 equiv. of 2,2′-bipyridine. X-ray diffraction data were collected at 90.0(2) K with a Bruker X8 Proteum rotating-anode CCD diffractometer with graphite-monochromated Cu-$K_\alpha$ ($\lambda$ = 1.54178 Å) radiation from irregular shaped crystals, mounted in Paratone-N oil on glass fibers. Initial cell parameters

 © 2007 Wiley-VCH Verlag GmbH & Co. KGaA, Weinheim 

were obtained (DENZO)[33] from ten 1° frames and were refined via a least-squares scheme using all data-collection frames (SCALEPACK).[33] Lorentz/polarization corrections were applied during data reduction. The structures were solved by direct methods (SHELXS97) and completed by difference Fourier methods (SHELXL97).[34] Refinement was performed against $F^2$ by weighted full-matrix least-squares (SHELXL97)[34] and empirical absorption corrections (either SCALEPACK[33] or SADABS[34]) were applied. Hydrogen atoms were found in difference maps and subsequently placed at calculated positions using suitable riding models with isotropic displacement parameters derived from their carrier atoms. Non-hydrogen atoms were refined with anisotropic displacement parameters. Atomic scattering factors were taken from the International Tables for Crystallography vol. C.3.[35] Crystal data, relevant details of the structure determinations, and selected geometrical parameters are provided in the supporting information.[18]

**Synthesis of 2:** Treatment of $\{[(Tp^*)Fe^{III}(CN)_3]_2[Ni^{II}(DMF)_4]_2[OTf]_2\}\cdot 2DMF$ (**1**) (0.949 g, 0.50 mmol) in MeOH/$CH_3CN$ [30 mL, 1:1 (v/v) ] with 2,2′-bipyridine (0.312 g, 2.00 mmol) afforded a red solution that was layered with $Et_2O$ (20 mL) and allowed to stand for 3 d. The red needles were collected by filtration, washed with $CH_3CN$ (5 mL) and $Et_2O$ (3 × 5 mL), and dried in air overnight. Yield: 0.546 g (55.3%). $C_{78}H_{84}B_2F_6Fe_2N_{26}Ni_2O_{10}S_2$ (1974.53): calcd. C 47.40, H 4.30, N 18.43; found C 47.43, H 4.10, N 18.76. IR (Nujol): $\tilde{\nu}$ = 3460 (br., m), 2952 (vs), 2926 (vs), 2854 (vs), 2553 (m), 2158 (vs), 2128 (m), 1634 (m), 1598 (s), 1575 (m), 1567 (m), 1543 (vs), 1489 (s), 1447 (vs), 1417 (vs), 1375 (vs), 1310 (m), 1285 (vs), 1256 (vs), 1227 (vs), 1203 (vs), 1162 (vs), 1108 (m), 1062 (vs), 1031 (vs), 988 (m), 867 (m), 815 (m), 806 (m), 775 (vs), 738 (s), 722 (m), 692 (m), 641 (vs), 575 (m), 544 (w), 517 (m), 440 (m), 429 (m), 410 (m) $cm^{-1}$.

**Supporting Information** (see also the footnote on the first page of this article): Crystallographic data (CIF format) and additional magnetic data for **2**.

CCDC-634744 contains the supplementary crystallographic data for this paper. These data can be obtained free of charge from The Cambridge Crystallographic Data Centre via www.ccdc.cam.ac.uk/data_request/cif.

## Acknowledgments

S. M. H. gratefully acknowledges the Kentucky Science and Engineering Foundation (Grants KSEF-621-RDE-006 and KSEF-992-RDE-008) and the National Science Foundation (CAREER CHE-0645414) for financial support. R. C. thanks MAGMANet (NMP3-CT-2005-515767), the French Centre National de Recherches Scientifique (CNRS), the University of Bordeaux 1, and the Conseil Régional d'Aquitaine for financial support. G. T. Y. thanks the National Science Foundation (CHE-0210395) for partial financial support. S. M. H. and R. C. are also grateful to Eugenio Coronado and Jeffery R. Long for providing the MAGPACK and ANISOFIT programs, respectively.

[1] M. N. Leuenberger, D. Loss, *Nature* **2001**, *410*, 789–793.
[2] W. Wernsdorfer, N. Aliaga-Alcalde, D. N. Hendrickson, G. Christou, *Nature* **2002**, *416*, 406–409.
[3] S. Hill, R. S. Edwards, N. Aliaga-Alcalde, G. Christou, *Science* **2003**, *302*, 1015–1018.
[4] R. Sessoli, D. Gatteschi, *Angew. Chem. Int. Ed.* **2003**, *42*, 268–297, and references therein.
[5] L. M. C. Beltran, J. R. Long, *Acc. Chem. Res.* **2005**, *38*, 325–334, and references therein.
[6] D. Li, S. Parkin, G. Wang, G. T. Yee, R. Clérac, W. Wernsdorfer, S. M. Holmes, *J. Am. Chem. Soc.* **2006**, *128*, 4214–4215.
[7] D. Li, S. Parkin, G. Wang, G. T. Yee, A. V. Prosvirin, S. M. Holmes, *Inorg. Chem.* **2005**, *44*, 4903–4905.
[8] D. Li, R. Clérac, S. Parkin, G. T. Yee, S. M. Holmes, *Inorg. Chem.* **2006**, *46*, 5251–5253.
[9] D. Li, R. Clérac, S. Parkin, G. Wang, G. T. Yee, S. M. Holmes, *Inorg. Chem.* **2006**, *46*, 7569–7571.
[10] E. J. Schelter, A. V. Prosvirin, K. R. Dunbar, *J. Am. Chem. Soc.* **2004**, *126*, 15004–15005.
[11] S. Wang, J.-L. Zou, H.-C. Zhou, H. J. Choi, Y. Ke, J. R. Long, X.-Z. You, *Angew. Chem. Int. Ed.* **2004**, *43*, 5940–5943.
[12] C. P. Berlinguette, D. Vaughn, C. Cañada-Vilalta, J. R. Galán-Mascarós, K. R. Dunbar, *Angew. Chem. Int. Ed.* **2003**, *42*, 1523–1526.
[13] A. V. Palii, S. M. Ostrovsky, S. I. Klokishner, B. S. Tsukerblat, K. R. Dunbar, J. R. Galán-Mascarós, *J. Am. Chem. Soc.* **2004**, *126*, 16860–16867.
[14] E. J. Schelter, A. V. Prosvirin, W. M. Reiff, K. R. Dunbar, *Angew. Chem. Int. Ed.* **2004**, *43*, 4912–4915.
[15] J. J. Sokol, A. G. Hee, J. R. Long, *J. Am. Chem. Soc.* **2002**, *124*, 7656–7657.
[16] G. Rogez, J.-N. Rebilly, A.-L. Barra, L. Sorace, G. Blondin, N. Kirchner, M. Duran, J. van Slageren, S. Parsons, L. Ricard, A. Marvilliers, T. Mallah, *Angew. Chem. Int. Ed.* **2005**, *44*, 1876–1879.
[17] a) S. Accorsi, A.-L. Barra, A. Caneschi, G. Chastanet, A. Cornia, A. C. Fabretti, D. Gatteschi, C. Mortalò, E. Olivieri, F. Parenti, P. Rosa, R. Sessoli, L. Sorace, W. Wernsdorfer, L. Zobbi, *J. Am. Chem. Soc.* **2006**, *128*, 4742–4755; b) C. J. Milios, A. Vinslava, P. A. Wood, S. Parsons, W. Wernsdorfer, G. Christou, S. P. Perepes, E. K. Brechin, *J. Am. Chem. Soc.* **2007**, *129*, 8–9.
[18] See the Supporting Information.
[19] J. Y. Yang, M. P. Shores, J. J. Sokol, J. R. Long, *Inorg. Chem.* **2003**, *42*, 1403–1419.
[20] J. Kim, S. Han, I.-K. Cho, K. Y. Choi, M. Heu, S. Yoon, B. J. Suh, *Polyhedron* **2004**, *23*, 1333–1339.
[21] D. Li, S. Parkin, G. Wang, G. T. Yee, S. M. Holmes, *Inorg. Chem.* **2006**, *45*, 1951–1959.
[22] D. Li, S. Parkin, G. Wang, G. T. Yee, S. M. Holmes, *Inorg. Chem.* **2006**, *45*, 2773–2775.
[23] Crystal and structure refinement parameters: **2**, $C_{78}H_{84}B_2F_6Fe_2N_{26}Ni_2O_{10}S_2$, $P\bar{1}$, $Z$ = 8, $a$ = 11.3573(3) Å, $b$ = 13.5093(3) Å, $c$ = 14.7470(4), $\alpha$ = 96.713(1)°, $\beta$ = 98.668(1)°, $\gamma$ = 99.237(1)°, $V$ = 2184.6(1) Å$^3$, $R_1$ = 0.0662, $wR_2$ = 0.1823.
[24] Y. Nakamura, M. Yonemura, K. Arimura, N. Usuki, M. Ohba, H. Okawa, *Inorg. Chem.* **2001**, *40*, 3739–3744.
[25] S. Wang, J.-L. Zuo, H.-C. Zhou, Y. Song, X.-Z. You, *Inorg. Chim. Acta* **2005**, *358*, 2101–2106.
[26] S. Wang, J.-L. Zuo, H.-C. Zhou, Y. Song, S. Gao, X.-Z. You, *Eur. J. Inorg. Chem.* **2004**, 3681–3687.
[27] J. H. van Vleck, *The Theory of Electric and Magnetic Susceptibility*, Oxford University Press, New York, **1932**.
[28] K. Kambe, *J. Phys. Soc. Jpn.* **1950**, *5*, 48–51.
[29] K. Nakamoto, *Infrared and Raman Spectra of Inorganic and Coordination Compounds*, 5th ed., Part B, Wiley, New York, **1997**.
[30] M. P. Shores, J. J. Sokol, J. R. Long, *J. Am. Chem. Soc.* **2002**, *124*, 2279–2292.
[31] K. Park, S. M. Holmes, *Phys. Rev. B* **2006**, *74*, 224440-1–224440-10.
[32] S. M. Holmes, S. G. McKinley, G. S. Girolami, *Inorg. Synth.* **2002**, *33*, 91–103.
[33] Z. Otwinowski, W. Minor, *Methods Enzymol.* **1997**, *276*, 307–326.

 © 2007 Wiley-VCH Verlag GmbH & Co. KGaA, Weinheim 

[34] G. M. Sheldrick, *SADABS, An empirical absorption correction program*, Bruker Analytical X-ray Systems, Madison, Wisconsin, **1996**; G. M. Sheldrick, *SHELX-97, Programs for Crystal Structure Solution and Refinement*, University of Göttingen, Germany, **1997**.
[35] International Tables for Crystallography, vol. C, Kluwer Academic Publishers, Dordrecht, The Netherlands, **1992**.
[36] O. Kahn, *Molecular Magnetism*, VCH Publishers, New York, **1993**.

Received: September 5, 2006
Published Online: February 22, 2007

 © 2007 Wiley-VCH Verlag GmbH & Co. KGaA, Weinheim 

DOI: 10.1002/ejic.200700054

# Assessing Guest Selectivity within Metallacrown Host Compartments

**Choong-Sun Lim,[a] Annabel Cutland Van Noord,[a] Jeff W. Kampf,[a] and Vincent L. Pecoraro*[a]**

**Keywords:** Molecular compartment / Metallacrown / Selective recognition / Host–guest chemistry

15-MC-5 complexes associate in the solid state to form chiral compartments capable of binding guests. Using small molecular yardsticks, we are able to assess the size restrictions of these structures. Dicarboxylate guests that are too short to span the $Gd^{III}$ ions are stabilized by solvates that hydrogen bond to the uncoordinated carboxylate, while guests that are too long destroy the weakly associated structure. We also demonstrate that all that is required for guest encapsulation is unsaturation of the chain connection carboxylates rather than necessitating the presence of aromaticity.
(© Wiley-VCH Verlag GmbH & Co. KGaA, 69451 Weinheim, Germany, 2007)

## Introduction

In 1989, we described the concept of building metallamacrocycles[1–3] using the metallacrown analogy.[4] These early analogs of crown ethers,[5,6] which have M–N–O connectivity instead of the O–C–C repeat unit of a crown ether, were often planar, containing a site for cation binding in a central cavity and a surface upon which anions could be appended.[7,8] Subsequently, chiral 15-MC-5 complexes,[9] adorned with aromatic groups, were shown to form molecular compartments[10–13] in the solid state. These compartments are reminiscient of the cryptatoclathrates described by Saalfrank.[14] Metallacrowns made exclusively with (*R*)- or (*S*)-phenylalaninehydroxamic acid form metallamacrocycles having a hydrophobic face surrounded by five benzyl groups that generate a cavity for a guest and a much less sterically encumbered hydrophilic face.[15] Previous solution studies have demonstrated that these 15-MC-5 structures are stable in solution when $Ln^{III}$ ions are present.[7,9,16] When crystals are grown from water, the phenyl groups from the two metallacrowns contact one another like two folded hands, hence we call this form the hands structure. In contrast, crystals prepared from methanol/water mixtures lead to a different "polymorph" in which the metallacrowns form helices with microporous channels rather than compartments.[17] In the hands polymorph, the hydrophobic faces of two metallacrowns associate, forming a compartment in which a guest is sequestered.[11,13] Of significant interest, aliphatic carboxylates are generally excluded from this compartment and bind solely to the hydrophilic face of the metallacrowns while, in contrast, aromatic carboxylic acids can be confined within this aromatic rich environment.[11,13] Thus, succinate or adipate have never been observed within the compartment, whereas terephthalate binds to this site preferentially.

[a] Department of Chemistry and Biophysics Research Division, The University of Michigan,
Ann Arbor, Michigan 48109-1055, USA
Fax: +1-17349367628
E-mail: vlpec@umich.edu

## Discussion and Results

The ability to exploit the size and chemical nature of organic dicarboxylates to discriminate guest binding is a desirable design concept. We have been interested in assessing whether an aromatic ring is an essential feature allowing access of the guest into the compartments hydrophobic cavity or whether simple unsaturation within the backbone is sufficient for cavity recognition.

Furthermore, we felt that it was prudent to use rigid molecules of varying length as molecular yardsticks that would determine to what extent the cylinder's long axis could be stretched in order to accommodate a dicarboxylate guest. In this report, we demonstrate that the presence of even one double bond allows the guest to insert within the compartment. We also show that when phenylalaninehydroxamic acid is used to form the host, there is a narrow range of acceptable lengths for guests to span the compartment.

We have chosen the well characterized $Gd(NO_3)_3$[15-$MC_{L\text{-pheHA}}$-5][11] as our host for these studies and we selected four different guest molecules (Scheme 1) to determine which physical properties of guests are required for a good fit within the compartments. Because carboxylates may bind to metals in an *endo*,*exo* or bidentate manner,[18] we have provided lengths for these molecules which are measured between the carboxylate carbon atoms rather than to the oxygen atoms. All four compounds have double bonds as well as carboxylate moieties at each end resulting in their binding to the gadolinium of each metallacrown toward the hydrophobic face.[19–22]

 © 2007 Wiley-VCH Verlag GmbH & Co. KGaA, Weinheim 

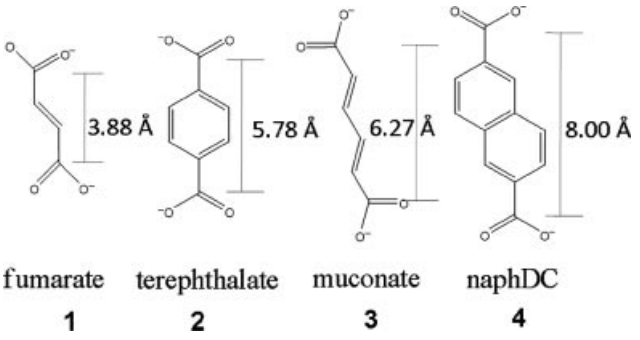


Scheme 1. Guest molecules bound to hydrophobic site of metallacrown (**3**: *trans*,*trans*-muconate, **4**: 2,6-naphthalenedicarboxylate).

By using X-ray diffraction studies, we observed that the terephthalate and *trans*,*trans*-muconate guests (with C–C bond lengths of 5.8 Å and 6.3 Å, respectively) connect two metallacrowns across the hydrophobic faces.[23] Each of the carboxylate groups bind to the $Gd^{III}$ in an *endo*,*endo*-1,3-bidentate fashion. These structures are shown in Figure 1. The Gd–Gd distances between the two metallacrowns are ca. 11.6 Å for both the muconate and terephthalate structures (Figure 2 and Table 1). Furthermore, the two metallacrowns are stacked nearly on top of one another with only a 2–5° tilt angle and are slipped to one side by only 7–10°. This observation suggests that the metallacrowns are ideally oriented, and that there are strong interactions between the phenyl groups of the two metallacrowns composing the compartment. In addition, two phenyl groups of the metallacrowns make hydrophobic contacts with the phenyl ring of the guest. Because both the terephthalate metallacrown and muconate metallacrown have similar structures, the formation of compartments is not affected by the difference in steric bulk of the two guests. *The fact that muconate is found within the hydrophobic cavity demonstrates that aromaticity is not an essential feature for guest recognition as the two double bonds of this molecule apparently are sufficient to drive it into the interior of the capsule.*

The shorter and longer dicarboxylates that were examined illustrate the length restriction for guests within the capsule. Fumarate has the shortest length (3.88 Å) between the two α-carbon atoms of the dicarboxylates. As shown in Figure 1, fumarate with a single double bond is still able to insert within the compartment; however, it is too short to span the two central Gd ions. This is even true given that fumarate adopts a monodentate, *endo* coordination mode which acts to extend the length of the molecule as compared to the bidentate geometries observed for muconate and terephthalate.

The fumarate is stabilized within the compartment by forming a hydrogen bond to a water molecule that is bound to the $Gd^{III}$ of the second metallacrown. Clearly, the compartment with bound fumarate is highly distorted. While the Gd–Gd distance shortens to 11.2 Å, the orientation of the two metallacrown rings is greatly perturbed. In particular, the $Gd^{III}$ of the top metallacrown is shifted over 6 Å with respect to the $Gd^{III}$ of the bottom metallacrown, whereas the corresponding orientation for muconate and

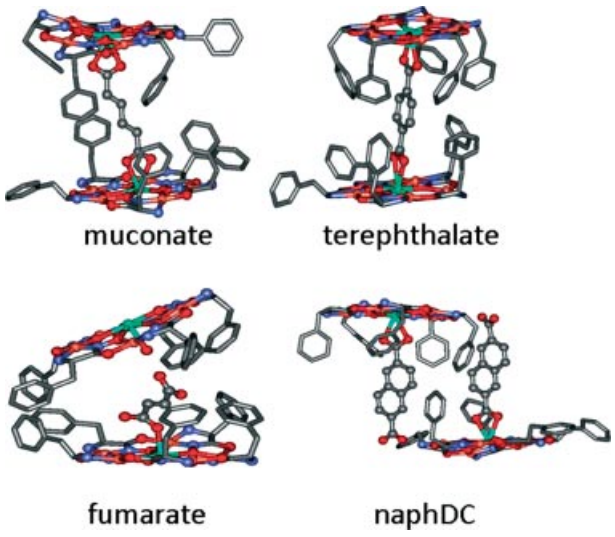


Figure 1. Structure of muconate-MC and terephthalate-MC show molecular compartments. However, fumarate-MC and 2,6-naphthalenedicarboxylate-MC do not form compartments. Guests on the hydrophilic sites of both metallacrowns of all compartments were omitted.[23]

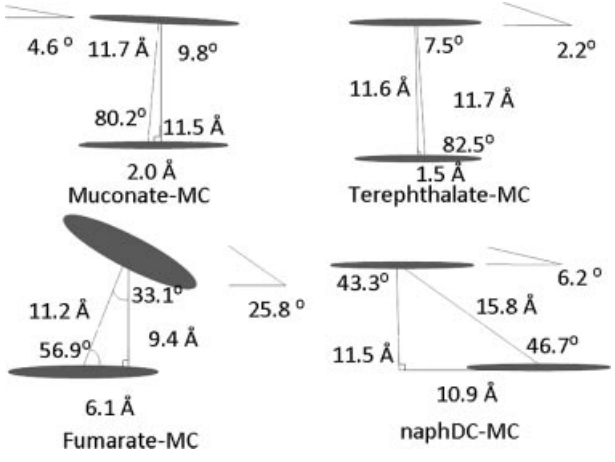


Figure 2. Diagram which shows bonding distance and angles between metallacrown and each guest compound in the crystal structure.

Table 1. Distances and angles of each guest to metallacrowns.

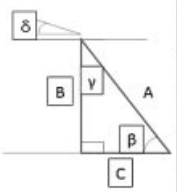


| | fumarate | Terephth-alate | Muconate | NaphDC |
|---|---|---|---|---|
| A | 11.2 Å | 11.7 Å | 11.7 Å | 15.8 Å |
| B | 9.4 Å | 11.6 Å | 11.5 Å | 11.5 Å |
| C | 6.1 Å | 1.5 Å | 2.0 Å | 10.9 Å |
| β | 56.9° | 82.5° | 80.2° | 46.7° |
| γ | 33.1° | 7.5° | 9.8° | 43.3° |
| δ | 25.8° | 2.2° | 4.6° | 6.2° |

A: distance between two centers of the planes
B: the closest distance between a center of one plane to the other plane
C: shifted distance of a metallacrown to the other one
δ: angle between two planes

 © 2007 Wiley-VCH Verlag GmbH & Co. KGaA, Weinheim 

terephthalate structures is 2 Å or less. This shift of the metallacrown centroids cause a marked slippage (33°) and tilting (26°) of the metallacrown rings as shown in Figure 2. All of these changes lead to a distorted and opened compartment.

While shortening the guest length causes major reorientation of the $[Gd(15\text{-}MC\text{-}5)]_2$ compartment, inclusion of naphthalenedicarboxylate as a guest, which has the longest distance (8 Å) between two α-carbon atoms, completely destroys the compartment structure. The distance between the two α-carbon atoms of naphthalenedicarboxylate is sufficient to connect the two metallacrowns. However, doing so prevents the phenyl groups of the hosts from interacting well with one another by pushing the two metallacrowns far away. The absence of the π–π interactions between these rings diminishes the stability of the compartment leading to a solid with individual naphthalenedicarboxylates bound to metallacrowns rather than forming compartments using the hands structure. Figure 1 illustrates that the naphthalenedicarboxylate binds to $Gd^{III}$ as an *endo*,*endo*-1,3-bidentate chelate; however, another metallacrown is unavailable to bind the second carboxylate group. The result is that the closest Gd–Gd distance is over 15 Å and the metallacrown rings are slid almost 11 Å with respect to one another. Interestingly, because the two metallacrowns are no longer constrained to form a compartment, the tilt angle between adjacent, noninteracting metallacrowns at 6.2° is more similar to muconate and terephthalate systems then the fumarate complex.

## Conclusion

A structural analysis of $[Gd(15\text{-}MC\text{-}5)]_2^{6+}$ compartments demonstrates that there is a narrow cylinder length that will accommodate a guest. For rigid ligands containing two carboxylates the length appears to be ca. 11.5 Å. Significantly shorter or longer guests perturb the compartment integrity and, in the case of guests that are too long, will completely disrupt the compartment from forming. These observations are useful for designing a second generation of metallacrown based compartments that will be able to bind longer guests with the ultimate objective of carrying out regio- or stereoselective transformations within the cavity of these supramolecular complexes. We conclude that longer guests such as 2,6-naphthalenedicarboxylate would be better able to fit into the hydrophobic site using extended aromatic side chains rather than the L-phenylalaninehydroxamic acid to form metallacrown compartments. In contrast, $Gd(NO_3)_3[15\text{-}MC_{L\text{-}pheHA}\text{-}5]$ complex appears perfect for guests such as muconate or terephthalate.

## Experimental Section

All reagents were purchased from Aldrich and used without further purification. $Gd(NO_3)_3[15\text{-}MC_{L\text{-}pheHA}\text{-}5]$ was prepared by the method published in ref.[11]

**Reaction of 1 with $Gd(NO_3)_3$[15-$MC_{L\text{-}pheHA}$-5]:** $Gd(NO_3)_3[15\text{-}MC_{L\text{-}pheHA}\text{-}5]$ (30 mg, 0.019 mol) and **1** (9.1 mg, 0.057 mol) reacted in water, and enough methanol was added to dissolve all products that formed yielding a water/methanol mixture of ratio 1:2. The solution was slowly evaporated to get single crystal for X-ray diffraction.

**Reaction of 2 with $Gd(NO_3)_3$[15-$MC_{L\text{-}pheHA}$-5]:** $Gd(NO_3)_3[15\text{-}MC_{L\text{-}pheHA}\text{-}5]$ (30 mg, 0.019 mol) and **2** (12 mg, 0.057 mol) reacted in water/methanol (1:2). Crystals were grown by slow evaporation.

**Reaction of 3 with $Gd(NO_3)_3$[15-$MC_{L\text{-}pheHA}$-5]:** $Gd(NO_3)_3[15\text{-}MC_{L\text{-}pheHA}\text{-}5]$ (30 mg, 0.019 mol) and **3** (8.1 mg, 0.057 mol), which had been neutralized with 1 N NaOH, reacted in water/methanol (1:2). Crystals were grown by slow evaporation.

**Reaction of 4 with $Gd(NO_3)_3$[15-$MC_{L\text{-}pheHA}$-5]:** $Gd(NO_3)_3[15\text{-}_{L\text{-}pheHA}\text{-}5]$ (30 mg, 0.019 mol) and **4** (17 mg, 0.057 mol) reacted in water/methanol (1:2). Crystals were grown by slow evaporation.

CCDC-635552 to -635554 contain the supplementary crystallographic data for this paper. These data can be obtained free of charge from The Cambridge Crystallographic Data Centre via www.ccdc.cam.ac.uk/data_request/cif.

## Acknowledgments

We thank the National Science Foundation for supporting this research (CHE-0111428).

[1] M. S. Lah, M. L. Kirk, W. Hatfield, V. L. Pecoraro, *J. Chem. Soc., Chem. Commun.* **1989**, 1606–1608.
[2] M. S. Lah, V. L. Pecoraro, *J. Am. Chem. Soc.* **1989**, *111*, 7258–7259.
[3] V. L. Pecoraro, *Inorg. Chim. Acta* **1989**, *155*, 171–173.
[4] V. L. Pecoraro, A. J. Stemmler, B. R. Gibney, J. J. Bodwin, H. Wang, J. W. Kampf, A. Barwinski, in *Progress in Inorganic Chemistry*, vol. 45 (Ed.: K. D. Karlin), John Wiley and Sons, Inc., New York, **1997**, pp. 83–177.
[5] C. J. Pedersen, *J. Am. Chem. Soc.* **1967**, *89*, 2495–2496.
[6] C. J. Pedersen, *J. Am. Chem. Soc.* **1967**, *89*, 7017–7036.
[7] A. J. Stemmler, J. W. Kampf, M. L. Kirk, B. H. Atasi, V. L. Pecoraro, *Inorg. Chem.* **1999**, *38*, 2807–2817.
[8] B. R. Gibney, D. P. Kessissoglou, J. W. Kampf, V. L. Pecoraro, *Inorg. Chem.* **1994**, *33*, 4840–4849.
[9] A. J. Stemmler, A. Barwinski, M. J. Baldwin, V. Young, V. L. Pecoraro, *J. Am. Chem. Soc.* **1996**, *118*, 11962–11963.
[10] J. Rebek, *Angew. Chem. Int. Ed.* **2005**, *44*, 2068–2078.
[11] A. D. Cutland, J. A. Halfen, J. W. Kampf, V. L. Pecoraro, *J. Am. Chem. Soc.* **2001**, *123*, 6211–6212.
[12] D. J. Cram, *Angew. Chem. Int. Ed. Engl.* **1991**, *30*, 1024–1027.
[13] G. Mezei, J. W. Kampf, V. L. Pecoraro, *Chem. Commun.* **2006**, in press.
[14] R. W. Saalfrank, R. Harbig, J. Nachtrab, W. Bauer, K.-P. Zeller, D. Stalke, M. Teichert, *Chem. Eur. J.* **1996**, *2*, 1363–1367.
[15] A. D. Cutland, R. G. Malkani, J. W. Kampf, V. L. Pecoraro, *Angew. Chem. Int. Ed.* **2000**, *39*, 2689–2691.
[16] M. Careri, F. Dallavalle, M. Tegoni, I. Zagnoni, *J. Inorg. Biochem.* **2003**, *93*, 174–180.
[17] A. C. Cutland-Van Noord, J. W. Kampf, V. L. Pecoraro, *Angew. Chem. Int. Ed.* **2002**, *41*, 4667–4670.
[18] R. L. Rardin, W. B. Tolman, S. J. Lippard, *New J. Chem.* **1991**, *15*, 417–430.
[19] Crystal data for [**1**–$Gd(NO_3)_3$[15-$MC_{L\text{-}pheHA}$-5]: $[C_{102}H_{155}Cu_{10}Gd_2N_{20}O_{58}]$, $M$ = 3521.34, Monoclinic, space group $P2(1)$ (no. 4), $a$ = 14.756(2), $b$ = 33.580(5), $c$ = 15.403(2), $\alpha$ = 90, $\beta$ = 118.573(2), $\gamma$ = 90, $V$ = 6702.8(16) Å$^3$, $Z$ = 2; $\rho_{calcd.}$ = 1.754 g/cm$^3$; crystal dimensions, 0.42 × 0.22 × 0.20 mm$^3$; $\mu$ = 2.624 mm$^{-1}$; $T$ = 113(2) K; 86931 reflections ($R_{int}$ = 0.0385), 32862 independent reflections and 31839 reflections [$I > 2\sigma(I)$],

 © 2007 Wiley-VCH Verlag GmbH & Co. KGaA, Weinheim 

for all data $R_1$ = 0.0510, $wR_2$ = 0.1149, for observed data [$I > 2\sigma(I)$] $R_1$ = 0.0487, $wR_2$ = 0.1137.

[20] Crystal data for **2**–$Gd(NO_3)_3$[15-$MC_{L\text{-}pheHA}$-5]: See ref.[11].

[21] Crystal data for **3**–$Gd(NO_3)_3$[15-$MC_{L\text{-}pheHA}$-5]: [$C_{108}H_{164.82}Cu_{10}Gd_2N_{22}O_{63.41}$], $M$ = 3735.90, triclinic, space group $P\bar{1}$ (no. 1), $a$ = 14.828(4), $b$ = 15.730(4), $c$ = 16.535(5), $\alpha$ = 102.277(5), $\beta$ = 101.471(5), $\gamma$ = 96.683(5), $V$ = 3642.3(17) Å$^3$, $Z$ = 1; $\rho_{calcd.}$ = 1.703 g/cm$^3$; crystal dimensions, 0.40 × 0.20 × 0.10 mm$^3$; $\mu$ = 2.423 mm$^{-1}$; $T$ = 123(2) K; 38960 reflections ($R_{int}$ = 0.0187), 31446 independent reflections and 30606 reflections [$I > 2\sigma(I)$], for all data $R_1$ = 0.0306, $wR_2$ = 0.0772, for observed data [$I > 2\sigma(I)$] $R_1$ = 0.0295, $wR_2$ = 0.0764.

[22] Crystal data for **4**–$Gd(NO_3)_3$[15-$MC_{L\text{-}pheHA}$-5]: [$C_{135}H_{184}Cu_{10}Gd_2N_{20}O_{56}$], $M$ = 3932.92, monoclinic, space group $P2(1)$ (no. 4), $a$ = 17.110(2), $b$ = 29.032(4), $c$ = 17.202(2), $\alpha$ = 90, $\beta$ 103.673(6), $\gamma$ = 90, $V$ = 8303(2) Å$^3$, $Z$ = 2; $\rho_{calcd.}$ = 1.573 g/cm$^3$; crystal dimensions, 0.50 × 0.40 × 0.32 mm$^3$; $\mu$ = 2.127 mm$^{-1}$; $T$ = 118(2) K; 88356 reflections ($R_{int}$ = 0.0375), 40705 independent reflections and 36609 reflections [$I > 2\sigma(I)$], for all data $R_1$ = 0.0568, $wR_2$ = 0.1369, for observed data [$I > 2\sigma(I)$] $R_1$ = 0.0497, $wR_2$ = 0.1333.

[23] In all structures, solvent waters and/or monodentate bound guests occupy the $Gd^{III}$ sites on the hydrophilic face.

Received: December 12, 2006
Published Online: February 26, 2007

 © 2007 Wiley-VCH Verlag GmbH & Co. KGaA, Weinheim 

DOI: 10.1002/ejic.200601175

# Structural and Theoretical Insights into Metal–Scorpionate Ligand Complexes

Matthias Schwalbe,[a] Prokopis C. Andrikopoulos,[a] David R. Armstrong,[a] John Reglinski,*[a] and Mark D. Spicer*[a]

**Keywords:** Nitric oxide / Soft scorpionates / Molybdenum / Tungsten / Molecular orbital calculations

The syntheses of the complexes $[M(Tm^{Me})(CO)_2(NO)]$ (M = Mo, W) by reaction of $NOBF_4$ with $[M(Tm^{Me})(CO)_3]^-$ are reported and their spectroscopic characterisation and crystal structures are described. The analogous Cr complex could not be prepared by this methodology. The complexes adopt the expected pseudo-octahedral geometry. Complexes $[M(L)(CO)_2(NO)]$ (M = Cr, Mo, W; L = Cp, Tp and $Tm^{Me}$) together with the hypothetical $[Mo(CO)_2(NO)]^+$ cation were subjected to DFT calculations. Geometry-optimised structures closely parallel the crystallographic determinations and indicate that the complex $[Cr(Tm^{Me})(CO)_2(NO)]$ is not inherently unstable. The DFT calculations allow the assignment of the C–O and N–O stretches in the IR spectrum and give insight into both the M–NO bonding and the metal to tripodal ligand bonding. The electron-donor strengths are confirmed to lie in the order $Tm^{Me} > Tp > Cp$. A side reaction of the B–H moiety of the $Tm^{Me}$ anion with $NO^+$ results in the isolation of the dimethylformamide adduct of (trismethimazolyl)borane, providing further evidence that the reaction pathways of the $Tm^R$ ligands are more varied and less passive than in the chemistry of the nitrogen-based scorpionates.

(© Wiley-VCH Verlag GmbH & Co. KGaA, 69451 Weinheim, Germany, 2007)

## Introduction

While a ligand may grow in popularity on the basis of a straightforward, high-yield preparation, and the ready synthesis of a suite of interesting complexes, its full utility can only be realised when a deeper understanding of the metal–ligand interaction is attained. Such an understanding leads in turn to an ability to predict the influence on a given metal centre, the chemistry it will support and the chemical frontiers which can be challenged by its use. Ground-breaking discoveries in chemistry, such as the first dihydrogen species, $[W(CO)_3(P\mathit{i}Pr_3)_2(H_2)]$,[1] and the unexpectedly stable alkyne complexes (e.g. $[CpMo(CO)(RC{\equiv}CR')_2]^+$)[2] are more easily rationalised in retrospect, when the various supporting ligand–metal interactions are understood.

The character of the ligand is usually described in terms of steric and electronic influences. Steric bulk can be readily altered, and demands only that the modified ligand does not preclude the formation of the principal metal–ligand bond. The result is to constrain the remaining coordination sites. Thus, with $PEt_3$, the complex $[Pt^0(PEt_3)_4]$ can be formed, while with the bulkier phosphane $PCy_3$, only three phosphanes are able to coordinate to the metal centre and $[Pt^0(PCy_3)_3]$ is formed.[3] Electronic properties are more complex, although ultimately the main concern is usually the donor strength. This can be influenced by inductive effects (basicity) and by the donor/acceptor properties of the ligand. Furthermore, terms such as hardness and softness and ligand-field strength can also be used in this context to explain aspects of ligand behaviour. However, what is clear is that these various steric and electronic factors rarely act in isolation, but rather a complex inter-relationship exists between them.

Many popular ligand systems are designed in such a way that the user can tailor both effects. Foremost amongst these ligand systems are the poly(azolyl)borate anions commonly known as the scorpionates.[4] Since their introduction in 1966 there has been a steady evolution of these systems. The introduction of steric bulk was quickly achieved, and latterly more limited attention has been given to their electronic properties.[5] We have sought to extend the scope of the scorpionate ligands by developing "soft" tripodal systems such as the hydrotris(methimazolyl)borate anion ($Tm^{Me}$)[6,7] (Scheme 1), replacing the heterocyclic nitrogen donors of hydrotris(pyrazolyl)borate anion (Tp) with thione sulfur donors. Initially, studies using these ligands produced results which were qualitatively in accordance with accepted hard and soft acid/base concepts. For example, it was found to be relatively simple to form soft scorpionate complexes of copper(I),[6,8] but much more difficult to generate the analogous copper(II) species and to this day the simple complexes of copper(II) remain elusive.[9] Furthermore, unlike the nominally hard pyrazole based ligands, our thione

[a] Department of Pure & Applied Chemistry,
University of Strathclyde,
295 Cathedral St., Glasgow G1 1XL, UK
Fax: +44-141-552-0876
E-mail: j.reglinski@strath.ac.uk
m.d.spicer@strath.ac.uk

Supporting information for this article is available on the WWW under http://www.eurjic.org or from the author.

 © 2007 Wiley-VCH Verlag GmbH & Co. KGaA, Weinheim 

donor ligands readily form a range of stable complexes of the lower main group elements (e.g. Sb, Te and Bi).[10] In the face of these predictable observations, a number of intriguing anomalies began to appear in the behaviour of these soft scorpionates, which did not support the view that their chemistry could be explained purely on the basis of hard and soft acid/base properties.

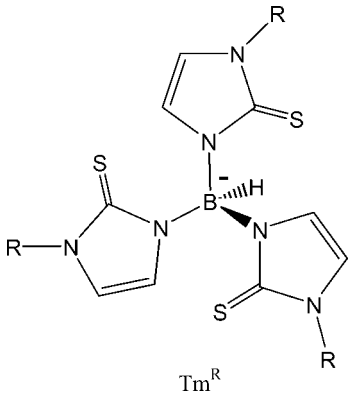

$Tm^R$

Scheme 1.

It is of interest to compare the three 6e⁻ face capping ligands, Tm, Tp and Cp. While the relative hardness of these ligands would be expected to lie in the order Tp > Cp > $Tm^{Me}$, most quantitative results obtained placed the ligands in a different order. Thus, in the complexes [$Fe^{II}(L)_2$], there is a transition from low spin (Cp) to spin-crossover (Tp) to high spin ($Tm^{Me}$) magnetic behaviour, suggesting that the spectrochemical series for these ligands lies in the order Cp > Tp > $Tm^{Me}$.[11] This is further supported by the cobalt chemistry of these ligands,[12] in which a tetrahedral (weak field) complex [$Co^{II}(Tm^{Me})X$] is obtained with $Tm^{Me}$, while the stronger field ligands Cp and Tp both form sandwich complexes [$Co^{II}(L)_2$].

Additionally, in our study of the group 6 species ([$Mo(Tm^{Me})(CO)_2(\eta^3\text{-}C_3H_5)$] and [$W(Tm^{Me})(CO)_3I$])[13a] we observed that the carbonyl stretching frequencies of the iodo and $\eta^3$-allyl species also lie in the order Cp > Tp > $Tm^{Me}$, suggesting that Tm is in fact the strongest electron donor of the three tripodal ligands and Cp the weakest. It is notable that Tp, as the moiety which relies on σ interactions, is found in the middle of this short series and not at either of its termini. This has been further supported by other observations. For instance, the reduction potentials of the complexes $[Co^{III}(L)_2]^+$ confirm that the $Tm^{Me}$ complex is the most difficult to reduce, consistent with $Tm^{Me}$ being the strongest electron donor.[12] Furthermore, we found that we were unable to stabilise tin(II) complexes with the $Tm^{Me}$ ligand, obtaining only the tin(IV) adducts. In this situation oxidation occurred even under anaerobic conditions,[10m] thus supporting the idea that the $Tm^{Me}$ ligand is an unusually strong electron donor.

It is clear that our appreciation of the $Tm^R$ ligand system is as yet incomplete. We therefore decided to undertake DFT calculations on an appropriate series of complexes in an effort to extend our understanding of both the ligand and the metal–ligand bonding interaction. The previously studied group 6 (Mo, W) carbonyl complexes seemed ideal for this purpose. However, the unusual geometries of the [$M(Tm^{Me})(CO)_3I$] and [$M(Tm^{Me})(CO)_2(\eta^3\text{-allyl})$] complexes seemed less than ideal and since the more regular octahedral complexes [$M(L)(CO)_2(NO)$] (L = Cp, Tp) are well known and several are structurally characterised, these were chosen. Helpfully, both the CO and NO ligands report (by their C–O and N–O stretching frequencies) on the electronic properties of the complexes. We have prepared the $Tm^{Me}$ analogues, characterised them crystallographically and spectroscopically and have undertaken DFT calculations on each of the complexes. We report here the results of this study.

## Results and Discussion

Initially the study set out to produce the complete series of group 6 species, [$M(Tm^{Me})(CO)_2(NO)$] (where M = Cr, Mo or W), using established methods (Scheme 2). The molybdenum and tungsten complexes were isolated and crystallised straightforwardly, albeit in poor yield. The reactions were not optimised, and as discussed below, there is at least one other product from the reaction, which is formed via a competing reaction pathway. In contrast, we were unable to isolate the chromium complex.[14] In retrospect this result is not particularly surprising, as the early reports of the preparation of the group 6 cyclopentadienyl complexes clearly show that a unified synthetic strategy for these compounds does not exist either.[15]

### Structural Analysis

The complexes [$M(Tm^{Me})(CO)_2(NO)$] (M = Mo, W) were characterised by X-ray crystallography to reveal the expected structural motifs (Figure 1) in which the $Tm^{Me}$ ligand caps one face of the coordination polyhedron, in keeping with the known Tp and Cp analogues. The metals adopt slightly distorted octahedral coordination geometries (Table 1) and, as previously observed, the ligand bite angles (S–M–S) are on average slightly greater than 90°, while the adjacent angles range from 85.53° to 93.27° for molybdenum and 86.25° to 94.28° for tungsten. Due to the lanthanide contraction and the more efficient overlap of the tungsten d-orbitals with those on sulfur, the M–S distances in

$$M(CO)_6 \xrightarrow{DMF/\Delta} M(CO)_3(DMF)_3 \xrightarrow{NaTm^{Me}} Na[M(Tm^{Me})(CO)_3] \xrightarrow{[NO]BF_4} [M(Tm^{Me})(CO)_2NO]$$

DMF = dimethylformamide, M = Mo, W

Scheme 2.

 © 2007 Wiley-VCH Verlag GmbH & Co. KGaA, Weinheim 

Table 1. Selected bond lengths [Å] and bond angles [°] for $[Tm^{Me}M(CO)_2NO]$ (where M = Mo or W) obtained by crystallographic and DFT methods.

| Bond or angle | $[Mo(Tm^{Me})(CO)_2NO]$ Exp. | Calcd. | $[W(Tm^{Me})(CO)_2NO]$ Exp. | Calcd. | $[Mo(Tp)(CO)_2NO]$ Exp. | Calcd. | $[Mo(Cp)(CO)_2NO]$ Exp. | Calcd. | $[Mo(CO)_2NO]^+$ Calcd. |
|---|---|---|---|---|---|---|---|---|---|
| M–S3 | 2.5865(7) | 2.680 | 2.5708(7) | 2.671 | | | | | |
| M–S4 | 2.5594(6) | 2.652 | 2.5480(7) | 2.654 | | | | | |
| M–S5 | 2.5767(7) | 2.693 | 2.5637(8) | 2.697 | | | | | |
| M–N42 | 1.901(2) | 1.837 | 1.892(3) | 1.851 | | 1.845 | 1.899 | 1.848 | 1.817 |
| M–C40 | 1.957(3) | 2.010 | 1.920(3) | 2.014 | | 2.022 | 1.957 | 2.004 | |
| M–C41 | 1.979(3) | 2.007 | 1.973(3) | 2.011 | | 2.022 | 1.941 | 2.004 | |
| < M–N–O | 176.8(2) | 179.2 | 177.7(2) | 179.5 | | 179.1 | 177.85 | 175.8 | |
| N–O | 1.163(3) | 1.193 | 1.185(3) | 1.198 | | 1.190 | 1.167 | 1.189 | 1.166 |
| < M–C–O | 176.8(2) | 179.5 | 177.3(3) | 179.0 | | 179.5 | 178.21 | 177.1 | |
| | 177.4(2) | 178.5 | 177.5(3) | 179.6 | | 179.5 | 176.80 | 177.2 | |
| C–O | 1.086(3) | 1.167 | 1.157(3) | 1.170 | | 1.165 | 1.143 | 1.164 | 1.150 |
| | 1.136(3) | 1.166 | 1.148(4) | 1.169 | | 1.165 | 1.154 | 1.164 | |
| < S3–M–S5 | 92.18(2) | 91.1 | 91.66(2) | 90.4 | N/A | | | | |
| < S3–M–S4 | 90.56(2) | 90.1 | 90.24(2) | 89.6 | | | | | |
| < S4–M–S5 | 89.29(2) | 90.0 | 88.79(2) | 89.7 | | | | | |
| < N42–M–C41 | 93.24(10) | 91.8 | 92.71(12) | 91.9 | | 90.8 | 91.35 | 93.0 | |
| < N42–M–C40 | 90.07(10) | 90.9 | 89.43(11) | 90.9 | | 90.8 | 91.79 | 93.1 | |
| < N42–M–S3 | 176.03(7) | 175.2 | 176.00(8) | 175.9 | | | | | |
| < C41–M–S4 | 86.47(7) | 88.4 | 86.93(8) | 88.7 | | | | | |
| < C40–M–S5 | 93.34(7) | 90.2 | 94.27(9) | 90.8 | | | | | |

the two complexes are similar, with the Mo–S distances in the molybdenum complex being slightly longer than the equivalent W–S distances. Consistent with the other structures obtained from the metal complexes of this ligand,[6–13] the methimazolyl rings of the $Tm^{Me}$ ligand lie at a mean angle of 33.5° to the imaginary H–B–M axis. This has the effect of reducing the symmetry of the $M(Tm^{Me})$ fragment from $C_{3v}$ to approximately $C_3$ thus minimising the steric strain in the eight-membered chelate rings.

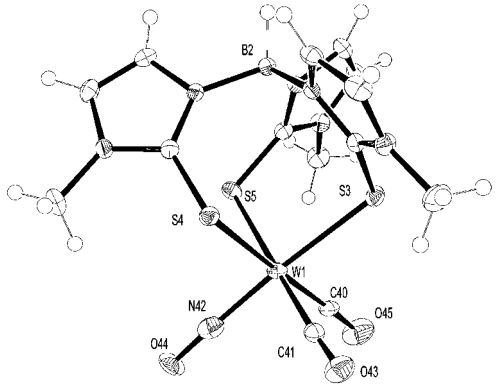


Figure 1. The X-ray crystal structure of $[W(Tm^{Me})(CO)_2(NO)]$. The molybdenum complex (not shown) is isostructural with its heavier congener. The atoms are labelled in a manner consistent with the output from the DFT studies. Thermal ellipsoids are at 50%.

Due to the difficulty in identifying the occupants of the positions associated with the carbonyl carbon atoms and nitrosyl nitrogen in the X-ray structure, the nitrosyl nitrogen was placed in accordance with the results of the DFT calculations (vide infra), i.e. *cis* to the shortest M–S bond. This problem obviates any meaningful comparison with the analogous Tp and Cp systems, which are beset by similar, but irresolvable, problems. Metrical parameters for $[W(Tp)(CO)_2NO]$ and $[W(Cp)(CO)_2NO]$ and the esds for $[Mo(Cp)(CO)_2NO]$ are not available. Values for the $[Mo(CO)_2NO]^+$ ion have been calculated in an attempt to provide information that is independent of the facial ligand.

Although the X-ray crystal structures clearly confirm the identity of the two species, ambiguity remains in that it was not possible to distinguish crystallographically between the C and N atoms of CO and NO. Consequently, the relative positions of the π acid ligands cannot be established beyond doubt. The problem of distinguishing between CO and NO is also evident in the structures of the analogous CpMo[16] and TpMo[17] complexes. Inspection of our structures revealed in each case one of the M–S distances to be shorter than the other two. Intuitively, the unique nitrosyl ligand might be expected to occupy the site *trans* to this bond with the two carbonyl ligands being placed *trans* to the two slightly longer M–S distances, reflecting the relative *trans*-effects of the M–CO and M–NO fragments.

In view of this ambiguity we were interested to apply DFT methods in an attempt to resolve the dilemma. Furthermore, calculations were expected to give insights into a number of aspects of these complexes, including (i) assignment of the CO and NO stretching frequencies in the IR spectrum, (ii) the nature of the M–NO bonding, and (iii) the nature of the metal to tripodal ligand bonds.

## DFT Molecular Orbital Calculations

Thus, we have subjected $[M(Tm^{Me})(CO)_2(NO)]$ (M = Cr, Mo, W) and their Tp and Cp analogues to DFT analysis, using the atomic coordinates retrieved from the respective X-ray crystal structures (where available) as a starting point for geometry optimisation (see Supporting Information). While calculations were performed for all nine possible complexes $[M(L)(CO)_2(NO)]$ (M = Cr, Mo, W; L = $Tm^{Me}$, Tp, Cp) only the data for molybdenum are presented in

 © 2007 Wiley-VCH Verlag GmbH & Co. KGaA, Weinheim

Figure 2. Calculated structures of $[Mo(L)(CO)_2NO]$ (from left to right, L absent, i.e. $[Mo(CO)_2NO]^+$, L = Cp, Tp, and $Tm^{Me}$).

detail here, together with the $Tm^{Me}$ complexes of Cr and W. The remaining data for the chromium and tungsten species are deposited as electronic supporting information, and show remarkably similar structural features and trends (for supporting information see also the footnote on the first page of this paper). Although we have been unable to prepare the complex $[Cr(Tm^{Me})(CO)_2(NO)]$ the calculations suggest there is no inherent instability of the complex provided an appropriate synthetic route can be devised. In addition, calculations on the fragment $[Mo(CO)_2(NO)]^+$, without the face capping ligand, were performed for comparative purposes.

The three calculated structures for the molybdenum complexes $[Mo(L)(CO)_2(NO)]$ (Figure 2) are found to maintain the same gross features as the crystallographic structures presented in Figure 1 and Table 1. It is interesting that for the $Tm^{Me}$ complexes they indicate that the NO ligand should lie *cis*- to the shortest M–S bond (rather than *trans*). We have subsequently refined the X-ray data in light of this observation to give acceptable convergence and structural parameters. However, as expected there are some deviations (up to 4% difference) between the crystallographically determined and calculated bond lengths and angles in all three species. These differences are seen most markedly in the metal-coordination sphere, where calculated M–S distances are ca. 0.1 Å longer than those observed experimentally, and in the π acid ligands, where the M–C, M–N, C–O and N–O distances do not exactly correlate. These differences presumably arise from a combination of factors not least the uncertainty of placing the key atoms in the X-ray structures (NO vs. CO), the approximations in the potentials used for the heavier transition metals, and because the calculations pertain to a gas-phase species in contrast to the solid state structural data. Nevertheless, consistent trends are observed giving confidence in the validity of the results.

One interesting feature of the DFT calculations is the infrared frequencies obtained (Table 2), which clearly identify the single NO and two CO stretches observed in these species. Correction factors are often applied to band frequencies in order to obtain acceptable agreement between experiment and theory. In this case no such correction was deemed necessary, as the agreement between the observed and calculated band frequencies is good. Indeed the discrepancies are not appreciably worse than those observed between the infra-red data obtained in the liquid and solid phase. The major divergence between experiment and theory is in the relative intensities of the bands (Table 2). The calculations suggest that the intensities of the three bands should be similar, but experimentally the νNO is significantly (×2) more intense than the νCO.

The hypothetical $[M(CO)_2(NO)]^+$ fragment was generated to allow us to better inspect the influence of the facially capping ligand. The fragment itself is calculated to have an ν(NO) = 1804 $cm^{-1}$ and ν(CO) = 2006 and 2062 $cm^{-1}$, which reflects the cationic nature of the species. The effect of adding a tripodal ligand to this fragment is to

Table 3. Mulliken Charge Distribution on the nitric oxide ligand in the series of compounds $[ML(CO)_2NO]$ (where M = Mo or W; L = Tm, Tp and Cp).

| | Molybdenum | | |
|---|---|---|---|
| | Cp | Tp | Tm |
| Nitrogen | –0.082 | –0.102 | –0.108 |
| Oxygen | –0.148 | –0.156 | –0.166 |
| Nitric oxide (sum) | –0.230 | –0.258 | –0.274 |
| | Tungsten | | |
| Nitrogen | –0.155 | –0.155 | –0.159 |
| Oxygen | –0.158 | –0.167 | –0.180 |
| Nitric oxide (sum) | –0.313 | –0.322 | –0.339 |

Table 2. The experimental ($CH_2Cl_2$) and calculated CO and NO stretching frequencies (calculated intensities in parentheses) for the nitrosyl complexes $[M(L)(CO)_2NO]$ (M = Mo or W; L = Tm, Tp and Cp) and for the hypothetical $[Mo(CO)_2NO]^+$ ion. All calculated frequencies (1600–2200 $cm^{-1}$) are reported.

| | | $[M(Tm^{Me})(CO)_2NO]$ | | $[M(Tp)(CO)_2NO]$ | | $[M(Cp)(CO)_2NO]$ | | $[Mo(CO)_2NO]^+$ |
|---|---|---|---|---|---|---|---|---|
| | | Obsd. | Calcd. | Obsd. | Calcd. | Obsd. | Calcd. | Calcd. |
| Mo | νNO | 1636 | 1682 (877) | 1666 | 1702 (912) | 1663 | 1702 (932) | 1804 |
| | νCO | 1915 | 1897 (863) | 1933 | 1914 (970) | 1937 | 1920 (1008) | 2006 |
| | νCO | 2006 | 1962 (787) | 2025 | 1978 (678) | 2020 | 1978 (613) | 2062 |
| | | obsd. | calcd. | obsd. | calcd. | obsd. | calcd. | |
| W | νNO | 1614 | 1669 (877) | 1651 | 1688 (920) | 1665 | 1693 (932) | |
| | νCO | 1886 | 1855 (912) | 1910 | 1902 (1028) | 1925 | 1913 (1055) | |
| | νCO | 1986 | 1954 (795) | 2010 | 1968 (723) | 2010 | 1971 (624) | |

 © 2007 Wiley-VCH Verlag GmbH & Co. KGaA, Weinheim 

lower the calculated stretching frequencies by ca. 100 $cm^{-1}$. This is consistent with the increased electron density at the metal centre, transmitted through classical back-bonding to the NO and CO π* orbitals. The fine detail reveals the relative effects of the individual tripodal ligands. On average, the complexes with the Cp ligand have slightly higher stretching frequencies than those with Tp, while the $Tm^{Me}$ complexes consistently have the lowest stretching frequencies by some 20–30 $cm^{-1}$. This implies that $Tm^{Me}$ is the most electron-releasing of the three ligands. The trend in IR stretching frequencies is mirrored by the changes in the calculated structural parameters. The N–O and C–O distances show an increase in the order Cp < Tp < $Tm^{Me}$, while the M–C and M–N distances decrease from Cp through to $Tm^{Me}$. The Mulliken charge distributions also support this view (Table 3). In each case the negative charge on the nitrosyl oxygen is found to increase Cp < Tp < Tm for molybdenum and tungsten, respectively, indicative of the expected decrease in overall cationic character of the nitrosyl ligand. Thus the calculations, combined with the experimental vibrational spectra, confirm Tm to be the most electron-donating of the three face-capping ligands.

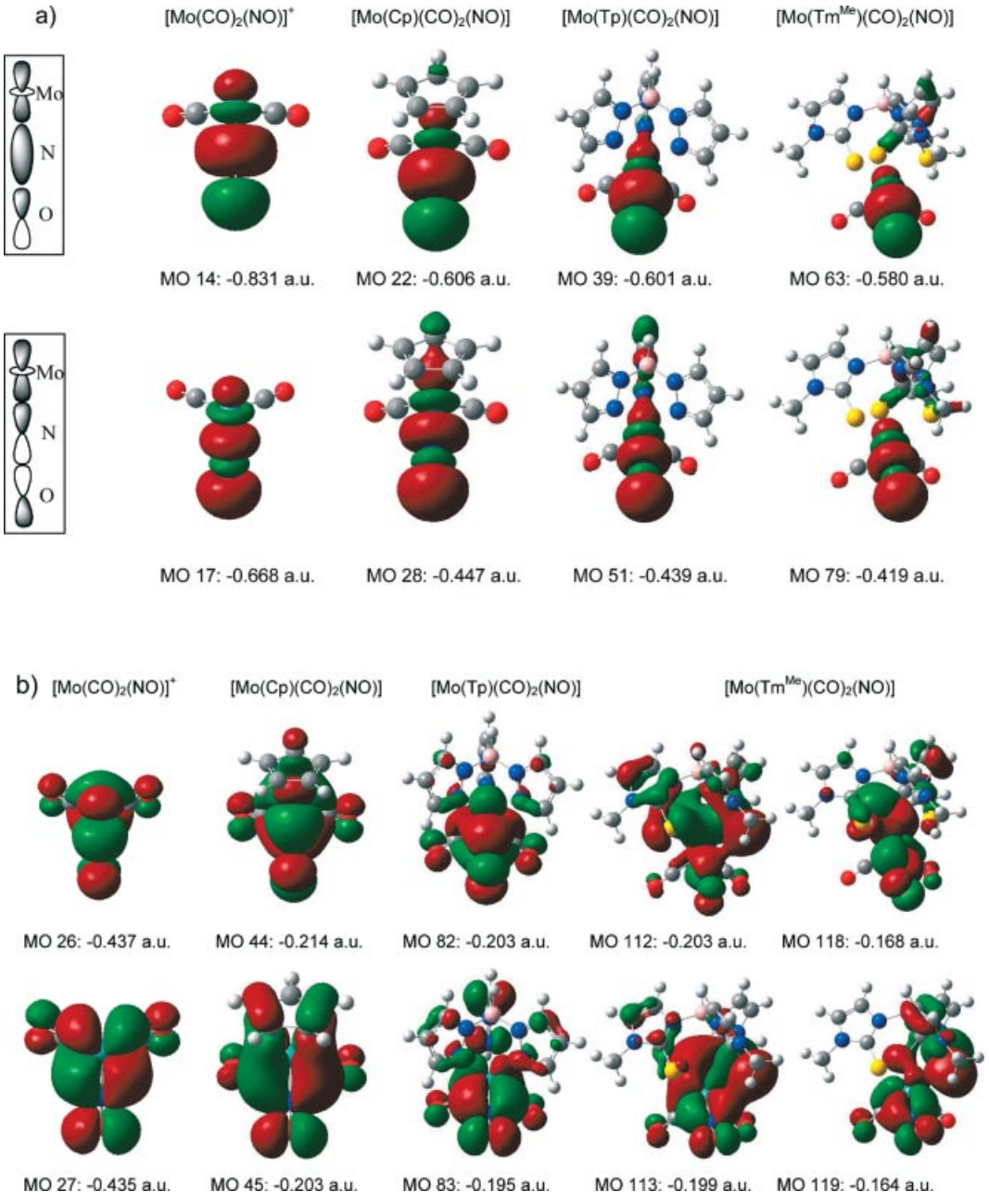


Figure 3. Calculated MOs describing a) the metal to NO σ bonding and b) the metal to NO π back-bonding in $[Mo(CO)_2(NO)]^+$, and $[Mo(L)(CO)_2(NO)]$ (L = Cp, Tp and $Tm^{Me}$). The symmetry of the $Tm^{Me}$ adducts are lower than the corresponding Tp and Cp species. Consequently the calculations reveal that $Tm^{Me}$ has two π* molecular orbitals of suitable energy for each of those identified for Tp and Cp.

 © 2007 Wiley-VCH Verlag GmbH & Co. KGaA, Weinheim 

Although the nitrosyl stretching frequencies of $[M(L)(CO)_2(NO)]$ (M = Mo, W; L = $Tm^{Me}$, Tp, Cp) place them within the range observed for bent nitrosyl ligands (1525–1690 $cm^{-1}$), it is evident from the DFT calculations and crystallographic studies, that the M–N–O moiety remains linear (<M–N–O 179° calcd.). The observed NO stretching frequency in $[W(Tm^{Me})(CO)_2(NO)]$ at 1614 $cm^{-1}$ is amongst the lowest values yet recorded for a linear NO ligand (1600 $cm^{-1}$).[18,19] This prompted us to examine the metal-nitrosyl bonding in more detail (Figure 3). In the absence of tripodal ligands, the description of the M–NO bonding derived from the DFT calculations confirms the accepted σ donor, π acceptor model. The NO ligand lies on the *z* axis and the $d_{z^2}$ orbital overlaps with nitrogen s and p orbitals to form the σ bond. The π component of the bonding involves interaction of $d_{xz}$ and $d_{yz}$ orbitals with the orthogonal sets of π* orbitals on NO. Furthermore, there appears to be significant overlap of the CO π* orbitals with the $d_{xy}$ orbital. The calculated ν(NO) is 1804 $cm^{-1}$, clearly in the region normally associated with linear NO ligands.

On addition of the facially capping ligands to the $[Mo(CO)_2(NO)]^+$ fragment, the bonding picture is largely maintained. However, in the cases of Cp and $Tm^{Me}$ there are significant interactions between the M–NO bonding orbitals and orbitals on the tripodal ligands. Furthermore, the loss of the plane of symmetry in the case of the $Tm^{Me}$ ligand, further complicates the picture. We have selected the major metal–ligand bonding orbitals in the $[M(CO)_2(NO)]^+$ fragment, identified the most closely corresponding orbitals in the $[M(L)(CO)_2(NO)]$ complexes and plotted their energies (Figure 4). On complexation of the face-capping ligand the species becomes electrically neutral and thus there is an increase in the orbital energies relative to the positively charged $[M(CO)_2(NO)]^+$ fragment. It must be argued that the overall effect of complexation of the ligand will be to stabilise this fragment via the bond energies associated with the formation of three extra M–S bonds. However, the rise in orbital energies reflects a destabilisation of the metal/π acid bonding. This is consistent with the weakening of C–O and N–O bonds in the accepted σ-donor π-(acceptor) bonding model. The DFT calculations also allow us an intriguing view of the key molecular orbital interactions in the three metal fragments CpM, TpM and TmM (Figure 3). Consistent with the work of Bergman et al.,[20] Joshi et al.,[21] and Nemykin & Basu,[22] the interactions between Tp and the metal seem to be predominantly directed through nitrogen-based σ donor interactions only and that the influence of the ligand on the ancillary π acid ligands is through these remote interactions. On the other hand, the CpMo fragment indicates significant, direct π overlap between the facially capping ligand and orbitals on

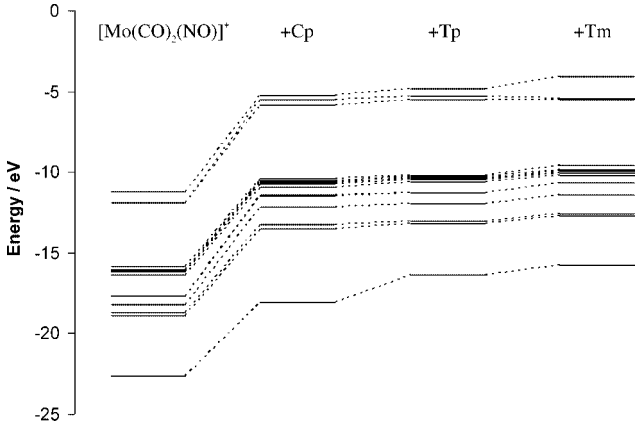


Figure 4. Perturbation of the Mo–π acid ligand bonding on addition of tripodal ligands to the $[Mo(CO)_2(NO)]^+$ fragment.

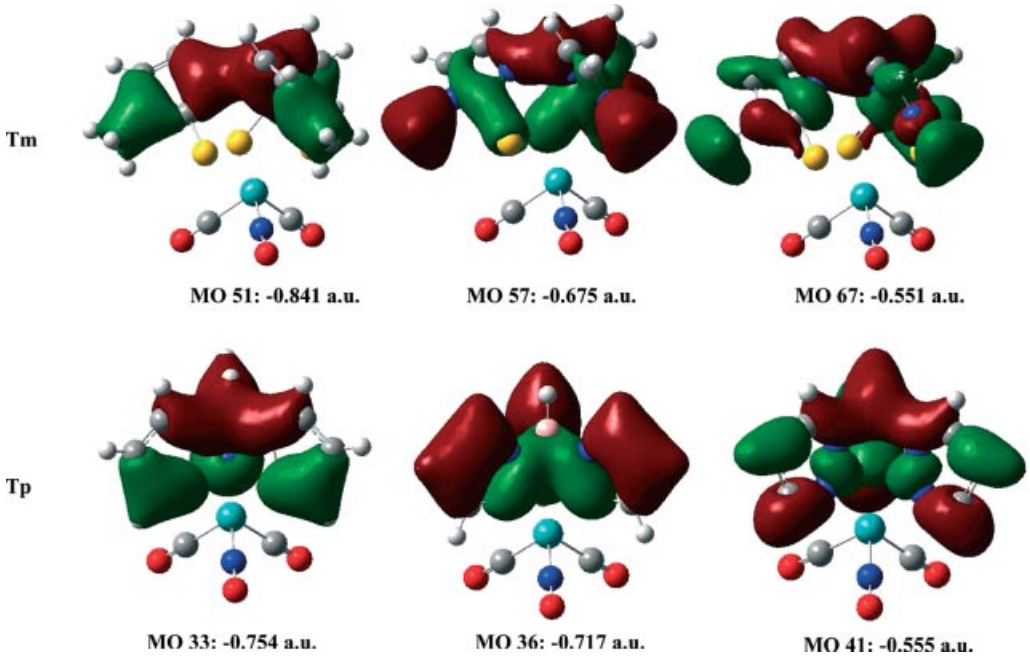


Figure 5. A selection of DFT derived orbitals depicting delocalisation through the $Tm^{Me}$ and Tp Ligands.

 © 2007 Wiley-VCH Verlag GmbH & Co. KGaA, Weinheim 

the π acid ligands (NO, CO) indicating that strong synergistic bonding operates through the metal centre. The molecular orbitals generated for Tm are more complex than both Cp and Tp, in part because of the lower symmetry and in part because there are significantly more atoms. The sulfur–metal interaction is also considerably more complex than the corresponding nitrogen–metal interaction in Tp complexes. This arises from the presence of predominantly p orbital lone pairs based on sulfur. The π interaction of the sulfur p orbitals with the metal to π acid backbonding orbitals (e.g. MO 113, Figure 3) suggests that the sulfur donor has a direct influence on the nitric oxide ligand. This observation may go some way to explaining why the M–NO fragment remains linear but has a very low stretching frequency.

The DFT calculations also give us an insight into the behaviour of the B–H and the heterocyclic moieties in Tm and Tp. As reported by Joshi et al. for Tp systems,[21] the Tm ligand also shows extensive delocalisation of the heterocyclic rings through boron (Figure 5). In effect each of these ligands has an extended π system which allows electronic communication throughout the ligand. Thus the calculations suggest that the substituents placed on the methimazolyl nitrogen (methyl in $Tm^{Me}$), and on the bridgehead boron atom, will have a significant influence on the donor properties of the ligand, perhaps greater than has hitherto been recognised.

Thus the DFT calculations confirm that the electron-donor properties ($Tm^{Me} > Tp > Cp$) of these three face-capping ligands are dominated by their bonding mode. The σ donor, π donor bonding of Tm is consistent with the lowest CO and NO stretching frequencies in these complexes, but also with the weak field behaviour observed in other systems.[11,12] Likewise, the simple σ donor Tp to metal interactions and the weak π acceptor properties of Cp are also consistent with the ordering of their properties. It is clear that the term "soft" in relation to the $Tm^R$ ligands is useful. However, this label effectively disguises the view that these ligands can be exceptionally strong electron donors.

### An Alternative Reaction Pathway

The overall yields of the reactions conducted in this work were low. This was in part due to the lack of priority in optimising them. However, it was also evident that the nitrosonium cation was not restricted to reacting at the metal centre alone. As a small oxidising agent it is also capable of reacting at the reducing borohydride group, producing a simple borane (Scheme 3), which is trapped by the DMF to produce the novel, neutral DMF adduct of tris(methimazolyl)borane (Figure 6). Although this species was only a minor by-product from the reaction containing molybdenum, it was a significant proportion of the product from the tungsten reaction. The boron-centred molecule maintains many of the structural features of the Tm anion. The three sulfur atoms revert to a position above the $BN_3$ plane, with the methimazoles adopting a $C_3$-symmetric propeller conformation around the B–O axis reminiscent of the orientation in the crystal structure of the free parent $Tm^{Me}$ anion.[7] The presence of the large DMF unit does however somewhat reduce the angle that the heterocyclic rings adopt to the main B–O axis. Oxidation of the anion and removal of the small negatively charged hydride leaves the borane with less electron density to distribute around the $B(mt)_3$ moiety, an effect which is evident in the C=S bond lengths, which are much shorter (i.e. have greater double-bond character) than those in the parent $Tm^{Me}$. If the parent $Tm^{Me}$ anion is considered to be a facially capping six electron donor analogous to Cp and Tp, then this new DMF adduct, being neutral, can be considered as an arene analogue.

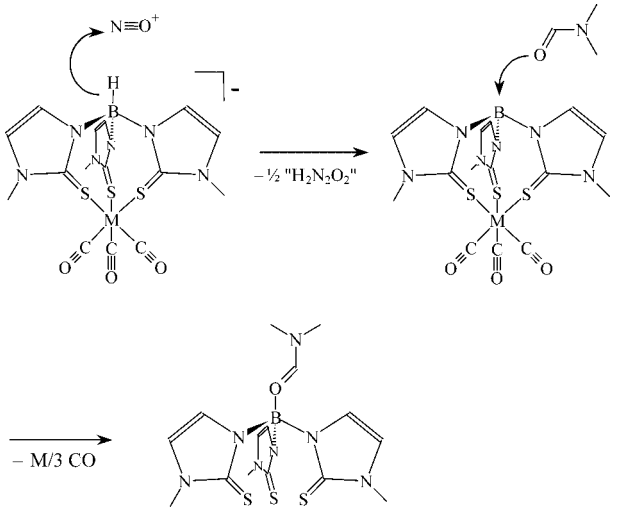


Scheme 3.

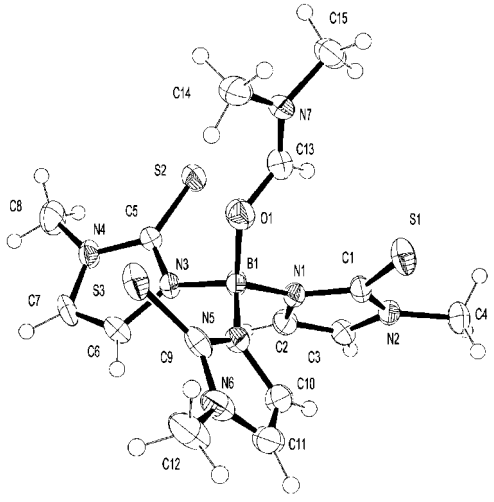


Figure 6. X-ray crystal structure of the dimethylformamide adduct of tris(methimazolyl)borane. Thermal ellipsoids are at 50%.

While the B–H moiety rarely reacts in Tp chemistry, it is not uncommon for it to do so in $Tm^R$ chemistry. Hill has identified two related products which stem from the same reaction profile, namely a cyclic species and an elegant series of metal boratranes.[23] We have observed additional species in these reactions and, because these "degradative"

 © 2007 Wiley-VCH Verlag GmbH & Co. KGaA, Weinheim 

pathways are of interest in themselves, they will be discussed in greater detail in a subsequent report. In conclusion the data supports the view that $Tm^{Me}$ is a strong π donor and that its character, i.e. its softness, is tempered by the nature of the bonding in the complex. This observation sets it apart from the anionic tripodal phosphanyl borate[24] and thioalkyl borates[5,8a–8c] and as such we can expect to continue seeing greater diversity within this sub grouping of the scorpionate species.

## Experimental Section

Unless otherwise stated all experiments were carried out using standard Schlenk techniques and commercially available chemicals. Hexane, THF and diethyl ether were dried and distilled from potassium under dinitrogen. Dichloromethane was dried and distilled from calcium hydride under dinitrogen. Dimethylformamide was dried with molecular sieves (4 Å) prior to distillation at reduced pressure. NMR analysis was carried out with a Bruker AMX 400 operating at 400 MHz for proton and 100 MHz for carbon. Infrared spectra were recorded as potassium bromide discs or in solution (dichloromethane) with a Nicolet Avatar 360 FT-IR spectrometer. Sodium hydrotris(methimazolyl)borate ($NaTm^{Me}$) was prepared using published methods.[6,7]

**Preparation of [Dicarbonyl(nitrosyl)hydrotris(methimazolyl)borato]-molybdenum:** Hexacarbonylmolybdenum (0.26 g, 1.0 mmol) was dissolved in dimethylformamide (20 mL) under dinitrogen. The reaction mixture was refluxed gently for 20 h whereupon the solution became very dark in colour. The solution was cooled to room temperature and $NaTm^{Me}$ (0.40 g, 1.1 mmol) added. The solution was stirred for 24 h after which time an equimolar amount of nitrosonium tetrafluoroborate (0.12 g, 1.0 mmol) was added. The solution was stirred for a further 2 h during which time gas evolution (CO) was evident. The DMF was removed by vacuum distillation and the product extracted into THF (3 × 40 mL), filtered through celite and stored at –20 °C overnight. The solution separated into a black tar and an orange liquor. The liquors were refiltered and reduced in volume and returned to the freezer at –20 °C. Over a 48-h period a crop of red crystals formed. These were collected by aspirating the liquors from the Schlenk tube thus leaving the desired material in the flask. Crystals suitable for X-ray analysis were removed from the sample prior to drying at reduced pressure overnight. Yield: 0.08 g, 15%. $C_{14}H_{16}BMoN_7O_3S_3$ (533.26): calcd. C 31.53, H 3.02, N 18.39; found C 32.13, H 3.87, N 18.57. $^1$H NMR (400 MHz, [D$_6$]DMSO): $\delta$ = 7.34 (dd, 2 H, –CH=), 7.30 (d, $J$ = 2.1 Hz, 1 H, CH), 7.04 (d, $J$ = 2.1 Hz, 1 H, CH), 7.02 (d, $J$ = 2.1 Hz, 1 H, CH), 6.97 (d, $J$ = 2.1 Hz, 1 H, CH), 3.61 (s, 3 H, $CH_3$), 3.56 (s, 3 H, $CH_3$), 3.50 (s, 3 H, $CH_3$) ppm. IR (KBr disc): $\tilde{\nu}$ = 2468 (weak, BH), 1995 (strong, CO), 1898 (strong, CO), 1630 (strong, NO), 736 (m, C=S), ($CH_2Cl_2$): $\tilde{\nu}$ = 2006 (strong, CO), 1915 (strong, CO), 1636 (strong, NO) cm$^{-1}$.

**Preparation of Dimethylformamido(trismethimazolyl)borane and [Dicarbonyl(nitrosyl)hydrotris(methimazolyl)borato]tungsten:** Hexacarbonyltungsten (0.70 g, 2.0 mmol) was dissolved in dimethylformamide (20 mL) under dinitrogen. The reaction mixture was refluxed gently for 20 h whereupon the solution became very dark green. The solution was cooled to room temperature and $NaTm^{Me}$ (0.75 g, 2.0 mmol) added. The solution was stirred for 48 h after which time an equimolar amount of nitrosonium tetrafluoroborate (0.24 g, 2.0 mmol) was added. The solution was stirred for a further 4 h during which time gas evolution (CO) was evident. The DMF was removed by vacuum distillation and the product extracted into THF (3 × 40 mL), filtered through celite, reduced in volume by 60% and stored at –20 °C overnight whereupon a crop of pale orange crystals formed. These were collected by aspirating the liquors from the Schlenk tube. Crystals for X-ray analysis were removed from the sample prior to drying at reduced pressure overnight. These were found to be an intriguing and significant side product. Yield: 70 mg, 8%. $C_{15}H_{22}BN_7OS_3$ (423.38): calcd. C 42.54, H 5.24, N 23.16; found C 41.22, H 3.90, N 23.46. $^1$H NMR (400 MHz, $CDCl_3$): $\delta$ = 8.70 (s, 1 H, –CHO), 6.68 (d, $J$ = 2.3 Hz, 3 H, CH), 6.46 (br. s, 3 H, CH), 3.59 (s, 9 H, $CH_3$), 3.32 (s, 3 H,

Table 4. Crystallographic data.

| | [Mo(Tm$^{Me}$)(CO)$_2$(NO)]·2THF | [W(Tm$^{Me}$)(CO)$_2$(NO)]·2THF | [B(mt)$_3$(DMF)][a] |
|---|---|---|---|
| Empirical formula | $C_{22}H_{32}B_1MoN_7O_5S_3$ | $C_{22}H_{32}B_1N_7O_5S_3W$ | $C_{15}H_{22}B_1N_7O_1S_3$ |
| $M_w$ | 677.48 | 765.39 | 423.40 |
| $T$ [K] | 123 | 123 | 123 |
| Crystal system | monoclinic | monoclinic | monoclinic |
| Space group | $P2_1/n$ | $P2_1/c$ | $P2_1/c$ |
| $a$ [Å] | 9.23550(10) | 9.2298(2) | 7.5076(1) |
| $b$ [Å] | 17.4571(2) | 17.4031(3) | 12.6102(2) |
| $c$ [Å] | 17.8692(3) | 17.8360(4) | 25.2145(5) |
| $a$ [deg] | 90 | 90 | 90 |
| $\beta$ [deg] | 85.3340(10) | 94.6830(10) | 92.976(1) |
| $\gamma$ [deg] | 90 | 90 | 90 |
| $Z$ | 4 | 4 | 4 |
| $V$ [Å$^3$] | 2871.41(7) | 2855.38(10) | 2384.35(17) |
| $\mu_{calcd.}$ [mm$^{-1}$] | 0.721 | 4.311 | 0.329 |
| $F$(000) | 1392 | 1520 | 888 |
| Crystal size [mm] | 0.38 × 0.3 × 0.24 | 0.5 × 0.4 × 0.04 | 0.4 × 0.4 × 0.3 |
| Radiations | Mo-$K_\alpha$ | Mo-$K_\alpha$ | Mo-$K_\alpha$ |
| Reflections measured | 12788 | 12008 | 8960 |
| Unique reflections | 6532 ($R_{int}$ = 0.0415) | 6468 ($R_{int}$ = 0.0224) | 5255 ($R_{int}$ = 0.0267) |
| Parameters | 359 | 351 | 249 |
| $R$[b] [$I > 2\sigma(I)$] | 0.0356 | 0.0252 | 0.0483 |
| $R_w$[c] (all reflections) | 0.0708 | 0.0480 | 0.1388 |
| GOF | 1.037 | 1.074 | 1.050 |

[a] mtH = 1-methylimidazole-2-thione (methimazole). [b] $R = \Sigma||F_o| - |F_c||/\Sigma |F_o|$. [c] $R_w = \{\Sigma[w(F_o^2 - F_c^2)^2]/\Sigma[w(F_o^2)^2]\}^{1/2}$.

 © 2007 Wiley-VCH Verlag GmbH & Co. KGaA, Weinheim 

$CH_3$), 3.25 (s, 3 H, $CH_3$) ppm. $^{13}C$ NMR (100.6 MHz, $CDCl_3$): $\delta$ = 165.1 (–CHO), 164.5 (C=S), 121.1 (CH), 118.3 (CH), 40.4 ($CH_3$), 36.4 ($CH_3$), 34.8 ($CH_3$) ppm. IR (KBr disc): $\tilde{\nu}$ = 1679 (strong, C=O), 736 (m, C=S) $cm^{-1}$.

The aspirated coloured liquors were placed in a clean vessel and the solvent reduced to a minimum and the vessel returned to the freezer. Overnight a crop of red crystals formed which were identified as the desired product. Yield 0.21 g, 17%. $C_{14}H_{16}BN_7O_3S_3W{\cdot}0.25THF$ (621.17): calcd. C 28.18, H 2.84, N 15.34; found C 28.17, H 2.55, N 15.64. $^1H$ NMR (400 MHz, [$D_6$]-DMSO): $\delta$ = 6.89 (dd, 2 H, –CH=), 6.86 (s, 2 H, CH), 6.85 (d, $J$ = 2.1 Hz, 1 H, CH), 6.82 (d, $J$ = 2.1 Hz, 1 H, CH), 3.75 (s, 3 H, $CH_3$), 3.72 (s, 3 H, $CH_3$), 3.69 (s, 3 H, $CH_3$) ppm. IR (KBr disc): $\tilde{\nu}$ = 2475 (weak, BH), 1975 (strong, CO), 1871 (strong, CO), 1612 (strong, NO), 739, (m, C=S), ($CH_2Cl_2$): $\tilde{\nu}$ = 1986 (strong, CO), 1886 (strong, CO), 1614 (strong, NO) $cm^{-1}$.

**X-ray Crystallography:** Crystals were coated in mineral oil and mounted on glass fibres. Data were collected at 123 K with a Nonius Kappa CCD diffractometer using graphite-monochromated Mo-$K_\alpha$ radiation. The heavy atom positions were determined by Patterson methods and the remaining atoms located in difference electron density maps. Full matrix least-squares refinement was based on $F^2$, with all non-hydrogen atoms anisotropic. While hydrogen atoms were mostly observed in the difference maps, they were placed in calculated positions riding on the parent atoms. The structure solution and refinement used the program SHELX-97[25] and the graphical interface WinGX.[26] The structure of $B(mt)_3{\cdot}$dmf contained severely disordered solvent molecule (THF), which was compensated for by use of the SQUEEZE algorithm.[27] A summary of the crystallographic parameters is given in Table 4.

**Density Functional Theory (DFT) Molecular Orbital Calculations:** Calculations were performed using the Gaussian 98 program.[28] The molecular species were subjected to geometry optimisation at the DFT[29] level and the 6-311G** basis set[30] for the atoms C, N, O, S, B and H. For molybdenum and tungsten, the Stuttgart RSC 1997 ECP basis set, augmented by a diffuse s and p functions with a common exponent of 0.005, was used.[31] Preliminary calculations were carried out on [Mo(Cp)$(CO)_2$(NO)] using four different DFT functionals namely BLYP,[32] B3LYP, BP86,[33] and MPW1PW91.[34] The best agreement with respect to the experimental carbonyl and nitrosyl infra-red frequencies was obtained using the BLYP functionals and hence these were used for the rest of the molecules.

**Supporting Information** (see also the footnote on the first page of this article): X-ray crystallographic data in CIF format and results of DFT calculations (calculated MO orbitals).

CCDC-625101 (for [$B(mt)_3$(DMF)]), -625102 (for [Mo($Tm^{Me}$)$(CO)_2$NO]) and -625103 (for [W($Tm^{Me}$)$(CO)_2$NO]) contain the supplementary crystallographic data for this paper. These data can be obtained free of charge from The Cambridge Crystallographic Data Centre via www.ccdc.cam.ac.uk/data_request/cif.

## Acknowledgments

We thank the European Union for funding.

[1] a) G. J. Kubas, *J. Chem. Soc., Chem. Commun.* **1980**, 61; b) G. J. Kubas, R. R. Ryan, B. I. Swanson, P. J. Vergamini, H. J. Wasserman, *J. Am. Chem. Soc.* **1984**, *106*, 451; c) G. J. Kubas, *J. Organomet. Chem.* **2001**, *635*, 37.

[2] J. L. Templeton, *Adv. Organomet. Chem.* **1989**, *29*, 1.

[3] C. A. Tolman, *Chem. Rev.* **1977**, *77*, 314.

[4] a) S. Trofimenko, *J. Am. Chem. Soc.* **1966**, *88*, 1842; b) S. Trofimenko, *Scorpionates: The Coordination Chemistry of Polypyrazolylborate Ligands*; Imperial College Press, London, **1999**.

[5] P. H. Ge, B. S. Haggerty, A. L. Rheingold, C. G. Riordan, *J. Am. Chem. Soc.* **1994**, *116*, 8406.

[6] M. Garner, J. Reglinski, I. Cassidy, M. D. Spicer, A. R. Kennedy, *Chem. Commun.* **1996**, 1975.

[7] J. Reglinski, M. Garner, I. D. Cassidy, P. A. Slavin, M. D. Spicer, D. R. Armstrong, *J. Chem. Soc., Dalton Trans.* **1999**, 2119.

[8] a) P. J. Schebler, C. G. Riordan, L. M. Liable-Sands, A. L. Rheingold, *Inorg. Chim. Acta* **1988**, *270*, 543; b) C. Ohrenberg, M. M. Saleem, C. G. Riordan, G. P. A. Yap, A. K. Verma, A. L. Rheingold, *Chem. Commun.* **1996**, 1081; c) C. Ohrenberg, L. M. Liable-Sands, A. L. Rheingold, C. G. Riordan, *Inorg. Chem.* **2001**, *40*, 4276; d) G. G. Lobbia, C. Pettinari, C. Santini, N. Somers, B. W. Skelton, A. W. White, *Inorg. Chim. Acta* **2001**, *319*, 15; e) M. Carei, L. Elviri, M. Lanfranchi, L. Marchio, C. Mora, M. A. Pellinghelli, *Inorg. Chem.* **2003**, *42*, 2109.

[9] C. A. Dodds, M. Garner, J. Reglinski, M. D. Spicer, *Inorg. Chem.* **2006**, *45*, 2733.

[10] a) P. J. Schlebler, C. G. Riordan, I. A. Guzel, A. L. Rheingold, *Inorg. Chem.* **1998**, *37*, 4754; b) J. Reglinski, M. D. Spicer, M. Garner, A. R. Kennedy, *J. Am. Chem. Soc.* **1999**, *121*, 2317; c) B. M. Bridgewater, G. Parkin, *J. Am. Chem. Soc.* **2000**, *122*, 7140; d) P. A. Slavin, J. Reglinski, M. D. Spicer, A. R. Kennedy, *J. Chem. Soc., Dalton Trans.* **2000**, 239; e) C. Kimblin, B. M. Bridgewater, G. Parkin, *J. Chem. Soc., Dalton Trans.* **2000**, 891; f) C. Kimblin, B. M. Bridgewater, T. Hascall, G. Parkin, *J. Chem. Soc., Dalton Trans.* **2000**, 1267; g) P. J. Bailey, M. Lanfranchi, L. Marchio, S. Parsons, *Inorg. Chem.* **2001**, *40*, 5030; h) J. F. Ojo, P. A. Slavin, J. Reglinski, M. Garner, M. D. Spicer, A. R. Kennedy, S. J. Teat, *Inorg. Chim. Acta* **2001**, *313*, 15; i) C. Santini, M. Pellei, G. G. Lobbia, C. Pettinari, A. Drozdov, S. Troyanov, *Inorg. Chim. Acta* **2001**, *325*, 20; j) M. Cammi, M. Lanfranchi, L. Marchio, C. Mora, C. Paiola, M. A. Pellinghelli, *Inorg. Chem.* **2003**, *42*, 1769; k) K. Fujita, A. L. Rheingold, C. G. Riordan, *Dalton Trans.* **2003**, 2004; l) C. A. Dodds, A. R. Kennedy, J. Reglinski, M. D. Spicer, *Inorg. Chem.* **2004**, *43*, 394; m) C. A. Dodds, M. Jagoda, J. Reglinski, M. D. Spicer, *Polyhedron* **2004**, *23*, 445; n) C. A. Dodds, J. Reglinski, M. D. Spicer, *Chem. Eur. J.* **2006**, *12*, 933.

[11] M. Garner, K. Lewinski, A. Pattek-Janczyk, J. Reglinski, B. Sieklucka, M. D. Spicer, M. Szaleniec, *Dalton Trans.* **2003**, 1181.

[12] C. A. Dodds, M. A. Lehmann, J. F. Ojo, J. Reglinski, M. D. Spicer, *Inorg. Chem.* **2004**, *43*, 4297.

[13] a) M. Garner, M.-A. Lehmann, J. Reglinski, M. D. Spicer, *Organometallics* **2001**, *20*, 5233; b) H. P. Kim, S. Kim, R. A. Jacobsen, R. J. Angelici, *Organometallics* **1986**, *5*, 2481; c) R. H. Hill, A. Becalska, N. Chiem, *Organometallics* **1991**, *10*, 2104.

[14] The species isolated from this reaction were organic in nature. These will be discussed elsewhere in a separate report.

[15] a) E. O. Fischer, O. Beckert, W. Hafner, H. O. Stahl, *Z. Naturforsch., Teil B* **1955**, *10*, 598; b) S. Trofimenko, *Inorg. Chem.* **1969**, *8*, 2675.

[16] S.-Y. Yang, W.-H. Sun, Y.-Q. Yin, K.-B. Yu, Z.-Y. Zhou, *Sci. China, Ser. B* **1991**, *34*, 1304.

[17] E. M. Holt, S. L. Holt, F. Cavalito, K. J. Watson, *Acta Chem. Scand. A* **1976**, *30*, 225.

[18] C. A. Reed, W. R. Roper, *J. Chem. Soc. A* **1970**, 3054.

[19] V. G. Albano, P. Bellon, M. Sansoni, *J. Chem. Soc. A* **1971**, 2420.

[20] R. G. Bergman, T. R. Cundari, A. M. Gillespie, T. B. Gunnoe, W. D. Harman, T. R. Klinckmam, M. D. Temple, D. P. White, *Organometallics* **2003**, *22*, 2331.

 © 2007 Wiley-VCH Verlag GmbH & Co. KGaA, Weinheim 

[21] H. K. Joshi, M. E. Arvin, J. C. Durivage, N. E. Gruhn, M. D. Carducci, B. L. Westcott, D. L. Lichtenberger, J. H. Enemark, *Polyhedron* **2004**, *23*, 429.
[22] V. N. Nemykin, P. Basu, *Inorg. Chem.* **2005**, *44*, 7494.
[23] a) A. F. Hill, G. R. Owen, A. J. P. White, D. J. Williams, *Angew. Chem. Int. Ed.* **1999**, *38*, 2759; b) I. R. Crossley, A. F. Hill, E. R. Humphrey, M. K. Smith, N. Tshabang, A. C. Willis, *Chem. Commun.* **2004**, 1878; c) I. R. Crossley, M. R. S. Foreman, A. F. Hill, A. J. P. White, D. J. Williams, *Chem. Commun.* **2005**, 221.
[24] a) A. A. Barney, A. F. Heyduk, D. G. Nocera, *Chem. Commun.* **1999**, 2379; b) J. C. Peters, J. D. Feldman, T. D. Tilley, *J. Am. Chem. Soc.* **1999**, *121*, 9871; c) T. A. Betley, J. C. Peters, *Inorg. Chem.* **2003**, *42*, 5074.
[25] G. M. Sheldrick, SHELX97 - Programs for Crystal Structure Analysis (Release 97–2). University of Göttingen, institute of inorganic chemistry, Tammanstrasse 4, 37077 Göttingen, Germany, **1998**.
[26] L. J. Farrugia, *J. Appl. Crystallogr.* **1999**, *32*, 837.
[27] P. van der Sluis, A. L. Spek, *Acta Crystallogr., Sect. A* **1990**, *46*, 194.
[28] Gaussian 98, Revision A.9, M. J. Frisch, G. W. Trucks, H. B. Schlegel, G. E. Scuseria, M. A. Robb, J. R. Cheeseman, V. G. Zakrzewski, J. A. Montgomery Jr, R. E. Stratmann, J. C. Burant, S. Dapprich, J. M. Millam, A. D. Daniels, K. Kudin, M. C. Strain, O. Farkas, J. Tomasi, V. Barone, M. Cossi, R. Cammi, B. Mennucci, C. Pomelli, C. Adamo, S. Clifford, J. Ochterski, G. A. Petersson, P. Y. Ayala, Q. Cui, K. Morokuma, D. K. Malick, A. D. Rabuck, K. Raghavachari, J. B. Foresman, J. Cioslowski, J. V. Ortiz, A. G. Baboul, B. B. Stefanov, G. Liu, A. Liashenko, P. Piskorz, I. Komaromi, R. Gomperts, R. L. Martin, D. J. Fox, T. Keith, M. A. Al-Laham, C. Y. Peng, A. Nanayakkara, M. Challacombe, P. M. W. Gill, B. Johnson, W. M. Chen, W. Wong, J. L. Andres, C. Gonzalez, M. Head-Gordon, E. S. Replogle, J. A. Pople, Gaussian, Inc., Pittsburgh PA, **1998**.
[29] W. Kohn, A. D. Becke, R. G. Parr, *J. Phys. Chem.* **1996**, *100*, 12974.
[30] a) A. D. McLean, G. S. Chandler, *J. Chem. Phys.* **1980**, *72*, 5639; b) R. Krishnan, J. S. Binkley, R. Seeger, J. A. Pople, *J. Chem. Phys.* **1980**, *72*, 650.
[31] a) M. Dolg, H. Stoll, H. Preuss, R. M. Pitzer, *J. Phys. Chem.* **1993**, *97*, 5852; b) Basis sets were obtained from the Extensible Computational Chemistry Environment Basis Set Database, Version 02/25/04, as developed and distributed by the Molecular Science Computing Facility, Environmental and Molecular Sciences Laboratory which is part of the Pacific Northwest Laboratory, P. O. Box 999, Richland, Washington 99352, USA, and funded by the U. S. Department of Energy. The Pacific Northwest Laboratory is a multi-program laboratory operated by Battelle Memorial Institute for the U. S. Department of Energy under contract DE-AC06-76RLO 1830. Contact David Feller or Karen Schuchardt for further information. http://www.emsl.pnl.gov/forms/basisform.html.
[32] a) A. D. Becke, *Phys. Rev. A* **1988**, *38*, 3098; b) C. T. Lee, W. T. Yang, R. G. Parr, *Phys. Rev. B* **1998**, *37*, 785.
[33] J. P. Perdew, *Phys. Rev. B* **1986**, *33*, 8822.
[34] a) C. Adamo, V. Barone, *J. Chem. Phys.* **1998**, *108*, 664; b) J. P. Perdew, J. A. Chevary, S. H. Vosko, K. A. Jackson, M. R. Pederson, D. J. Singh, C. Fiolhais, *Phys. Rev. B* **1992**, 46.

Received: November 8, 2006
Published Online: February 22, 2007

 © 2007 Wiley-VCH Verlag GmbH & Co. KGaA, Weinheim 

DOI: 10.1002/ejic.200601206

# Protonation of Tris(iminocatecholato) Complexes of Gallium(III) and Titanium(IV)

**Markus Albrecht,*[a] Simon Burk,[a] Ralf Stoffel,[b] Arne Lüchow,[b] Roland Fröhlich,[c] Michael Kogej,[d][‡] and Christoph A. Schalley[d]**

*Dedicated to Professor Dr. H. G. Thomas on the occasion of his 70th birthday*

**Keywords:** Coordination compounds / Helicates / Protonation / Self-assembly / Computational chemistry

The coordination behaviour of the chiral tren-type tripodal ligand **3**-$H_6$ with gallium(III) and titanium(IV) ions was investigated and it was found that only mononuclear complexes are formed. In the presence of $Na^+$, one of the cations acts as a template and is bound inside the "cap" of $[Na(\mathbf{3})M]^{n-}$ (M = Ga, $n$ = 2; M = Ti, $n$ = 1). If no such cation is present, three protons are bound to the iminocatechol units in order to prevent repulsion between lone pairs at nitrogen and oxygen. To minimize the charge repulsion between the protonated imines of $[H_3(\mathbf{3})M]^{n+}$ (M = Ga, $n$ = 0; M = Ti, $n$ = 1), an enamine/chinomethine mesomeric structure becomes important. The adoption of this unusual mesomeric form by the iminocatecholates was supported by computational methods. In further investigations, we found, that the addition of protons ($H_2SO_4$) to the dinuclear (catecholimine)titanium helicate $K_4[(\mathbf{4})_3Ti_2]$ leads to protonation of the imine part of the iminocatechol. An excess of acid results in the hydrolysis of the complexes as well as of the imine units.
(© Wiley-VCH Verlag GmbH & Co. KGaA, 69451 Weinheim, Germany, 2007)

## Introduction

Self-assembly processes depend strongly on the geometry of molecular building blocks, which are able to form well-defined aggregates by non-covalent or coordinative interactions.[1] The outcome is often predictable, if rigid moieties are used.[2] However, with flexible units, prediction is still challenging, because many different steric, electronic, and entropic aspects need to be taken into account, which may counterbalance each other to some extent and thus make it difficult to estimate their final net effect.

During the last couple of years we and others have been investigating the coordination chemistry of tris(catechol) ligands which have been able to form supramolecular tetrahedra of the $M_4L_4$ type.[3] Starting with rigid ligand systems like **1**-$H_6$, we easily obtained the desired container molecule $[Ti_4\mathbf{1}_4]^{8-}$, which shows interesting host–guest chemistry.[4]

[a] Institut für Organische Chemie, RWTH Aachen, Landoltweg 1, 52074 Aachen, Germany
E-mail: markus.albrecht@oc.rwth-aachen.de
[b] Institut für Physikalische Chemie, RWTH Aachen, Landoltweg 2, 52074 Aachen
[c] Organisch-Chemisches Institut, Universität Münster, Corrensstrasse 40, 48149 Münster, Germany
[d] Institut für Chemie und Biochemie – Organische Chemie der FU Berlin
Takustrasse 3, 14195 Berlin, Germany
[‡] Present address: Kekulé-Institut für Organische Chemie und Biochemie der Universität,
Gerhard-Domagk-Str. 1, 53121 Bonn, Germany

Ligand **2**-$H_6$ (Figure 1), on the other hand, is more flexible. Therefore, it either can form a mononuclear

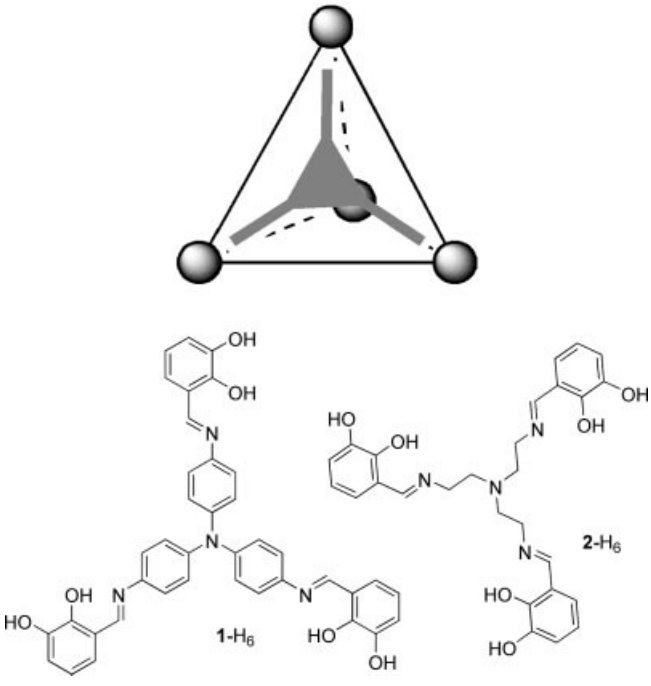


Figure 1. Schematic representation of a metallosupramolecular tetrahedon and appropriate triangular ligands.

 © 2007 Wiley-VCH Verlag GmbH & Co. KGaA, Weinheim 

"[Ti(**2**)]$^{2-}$" complex or a tetrahedron [Ti$_4$**2**$_4$]$^{8-}$ depending on the templating cation which is present. The smaller sodium cation nicely fits into the cavity formed when all catecholato units coordinate to the same metal center and thus template the formation of mononuclear complexes, while the potassium ion, whose size exceeds that of this cavity, favours the formation of the tetrahedron in dmso.[5]

Although a simple tetrahedron is not chiral, the self-assembled $M_4L_4$ tetrahedra possess twisted chiral complex units as cornerstones. In order to generate chiral enantiomerically pure tetrahedra, we now investigated triangular ligands **3**-$H_6$ based on the chiral tren-type platform, developed by Moberg et al.,[6] which can be considered to be a chiral variant of **2**-$H_6$. However, coordination studies with titanium(IV) and gallium(III) cations show the bulkiness of the isopropyl substituents at the ligand to be so high that the ligand cannot adopt the appropriate extended conformation with the triangular geometry required to occupy a face of the tetrahedron. Consequently, the ligand forms only mononuclear complexes. If no appropriate template cation is present to fill the cavity, the mononuclear complex is highly basic and takes up three protons in order to compensate the repulsion between electron pairs at the imine nitrogen atom and the internal catecholato oxygen atom. Similar hydrogen bonding can be observed in the complexes of catecholamides.[7]

This protonation behaviour cannot only be observed for the tritopic ligand **3**-$H_6$, but also in the case of a titanium helicate formed from the ditopic ligand **4**-$H_4$.[8] A gallium(III) complex of the monotopic **5**-$H_2$ seems to show a similar behaviour, but protonation is accompanied by decomposition (Figure 2).[9]

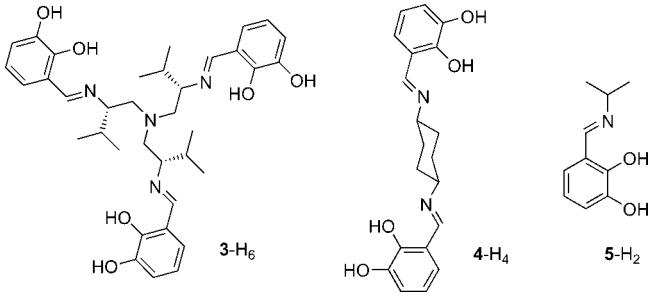


Figure 2. Ligands discussed in this study.

## Results and Discussion

### Coordination Chemistry of Ligand 3-$H_6$ with Titanium(IV) and Gallium(III)

The chiral tritopic ligand **3**-$H_6$ was prepared by utilizing Moberg's procedure[6] for the synthesis of the tetraamine precursor followed by imine condensation with 3 equiv. of 2,3-dihydroxybenzaldehyde (Scheme 1).[10]

Reaction of ligand **3**-$H_6$ with 1 equiv. of gallium(III) acetylacetonate in the presence of 1.5 equiv. of sodium carbonate does not only yield the desired mononuclear complex $Na_2$[Na⊂{(**3**)Ga}]. Instead, the $^1$H NMR spectrum in [$D_6$]-dmso indicates the presence of two different species. One set of low-field signals at $\delta$ = 7.89 (s, $CH_{imine}$), 6.06 (d, $J$ = 7.7 Hz, $H_{cat}$), 6.02 (d, $J$ = 7.7 Hz, $H_{cat}$) and 5.91 (t, $J$ = 7.7 Hz, $H_{cat}$) ppm can be assigned to $Na_2$[Na⊂{(**3**)Ga}] by comparison with the chemical shifts observed for the already known compound Na[Na⊂{(**2**)Ti}].[5] The second set of signals for catechol protons appears at $\delta$ = 6.40 (m, 6 H) and 6.33 (m, 3 H) ppm. The most intriguing feature is the appearance of the imine CH resonance at $\delta$ = 8.62 ppm as a doublet with $J$ = 13.5 Hz and of an additional doublet of doublets at $\delta$ = 12.5 ($J$ = 13.5, 11.1 Hz) ppm. According to the coupling pattern and the far low-field shift of this signal, we assign it to a proton at the imine nitrogen atom. As shown in Figure 4, both species can also be obtained in pure form. Use of the stronger base NaOH allows the formation of $Na_2$[Na⊂{(**3**)Ga}], while in the absence of base only the protonated species is obtained.

Using titanium(IV) as the central metal ion, we obtained similar results. With NaOH, the complex Na[Na⊂{(**3**)Ti}] is formed, while use of the weaker base sodium carbonate leads to the formation of only the species showing the protonated imine signals at $\delta$ = 12.0 (m, =NH) and 9.05 (d, $J$ = 14.6 Hz, =CH) ppm.[11]

According to those results, we propose, that both gallium and both titanium compounds are mononuclear complexes of ligand **3**. According to earlier crystal structure investigations of iminocatecholato complexes,[12] conformation **I** (Figure 3) is preferred over structure **II** due to electron-pair repulsion. However, molecular models suggest conformation **I** not to be achievable for the mononuclear complexes studied here due to the restrictions imposed by the tren subunit connecting the catecholate units. Consequently, the

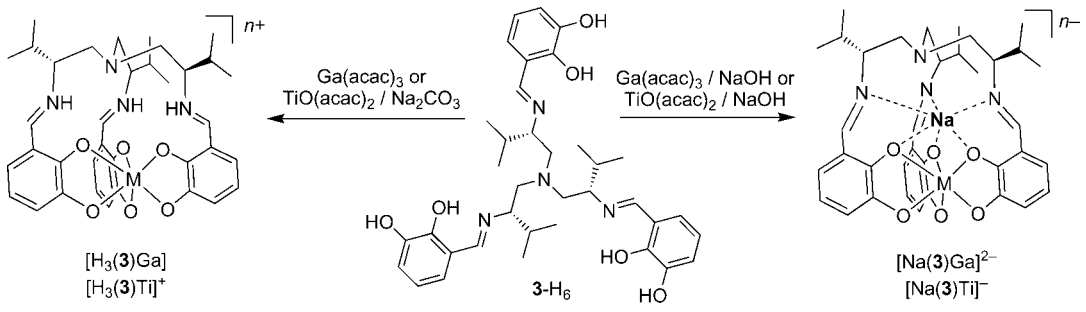


Scheme 1.

 © 2007 Wiley-VCH Verlag GmbH & Co. KGaA, Weinheim 

parent compounds $[(\mathbf{3})Ga]^{3-}$ and $[(\mathbf{3})Ti]^{2-}$ should significantly suffer from the repulsion of the electron pairs at the imine nitrogen atoms and at the internal catecholato oxygen atoms.

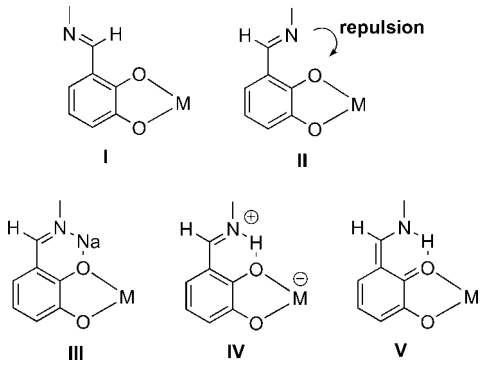


Figure 3. Different binding modes of the catecholimine ligand.

The formation of the mononuclear complexes is nevertheless possible, when the repulsion is taken care of by a cation (sodium) chelated by the imine group and the internal catecholato oxygen atom as in **III** or by protonation of the imine group, thus creating a hydrogen bond to the adjacent oxygen atom as shown in the two mesomeric structures **IV** and **V**.

According to the $^1H$ NMR spectra as shown in Figure 4 (d–f), a situation like that described by structures **IV** and **V** is present in our complexes.[13] The resonances at low field are due to the hydrogen bonds between N and O, which show a coupling with the imine CH group as well as with the CH group of the spacer. Complexes of similarly protonated salicylimines are frequently found, e.g. in the work by Binnemans et al. on mesogenic lanthanide complexes.[14] In the present case, this protonation needs to occur three times within the cavity of the complex in order to waive all three unfavorable N/O interactions in $[(\mathbf{3})M]^{n-}$ (M = Ga, $n$ = 3; M = Ti, $n$ = 2). This should lead to a high accumulation of positive charge in the triply protonated counterparts $[H_3(\mathbf{3})M]^{n+}$ (M = Ga, $n$ = 0; M = Ti, $n$ = 1), which is, however, at least to some extent compensated by the negatively charged metal complex units. In addition, the charges can be distributed over the respective aromatic system with the enaminone **V** as a "neutral" mesomeric structure.[15] These factors make the imine nitrogen atoms rather basic sites which are not fully deprotonated during complex formation with carbonate.

The gallium complex $[H_3(\mathbf{3})Ga]$ is soluble in $D_2O$. Hereby the acidic protons are exchanged by deuterium resulting in the disappearance of the corresponding signal and the appearance of a singlet for the imine proton.

The triply protonated compound $[H_3(\mathbf{3})Ga]$ is neutral and thus not directly detectable by mass spectrometry without attaching an additional – and potentially interfering – charge. The corresponding sodium complex $[Na(\mathbf{3})Ga]^{2-}$ on the other hand is a dianion, which again may cause problems due to charge repulsion in the gas phase. Therefore, we focused on the corresponding titanium(IV) species $[H_3(\mathbf{3})Ti]^+$ and $[Na(\mathbf{3})Ti]^-$ which should both be easily detected by electrospray ionization Fourier-transform ion-cy-

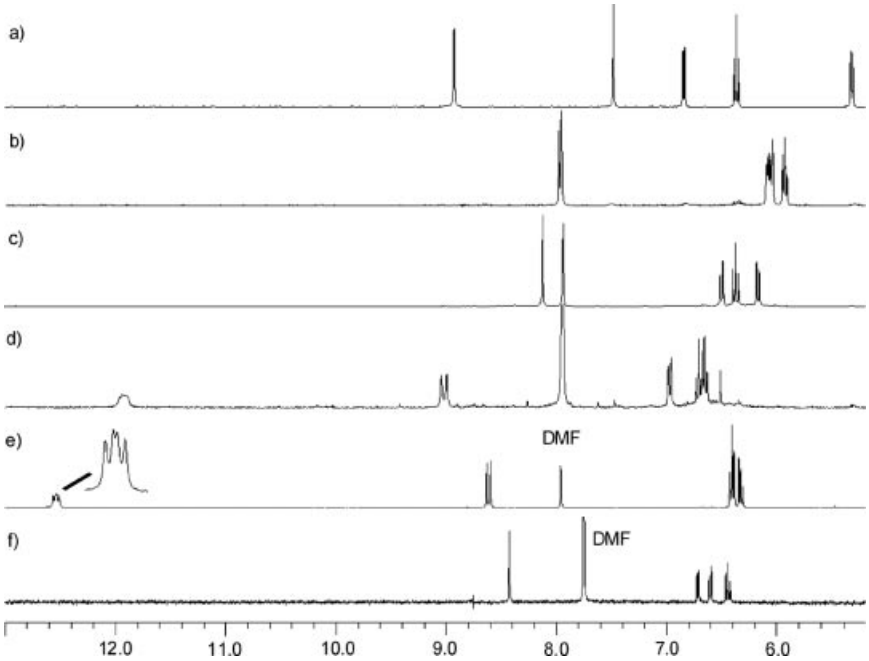


Figure 4. $^1H$ NMR spectra of the low-field region of **3**-$H_6$ (a), $Na_2[Na(\mathbf{3})Ga]$ (b), Na $[Na(\mathbf{3})Ti]$ (c), $[H_3(\mathbf{3})Ti]^+$ (d), and $[H_3(\mathbf{3})Ga]$ (e) in $[D_6]$dmso and of $[D_3(\mathbf{3})Ga]$ in $D_2O$ (f).

 © 2007 Wiley-VCH Verlag GmbH & Co. KGaA, Weinheim 

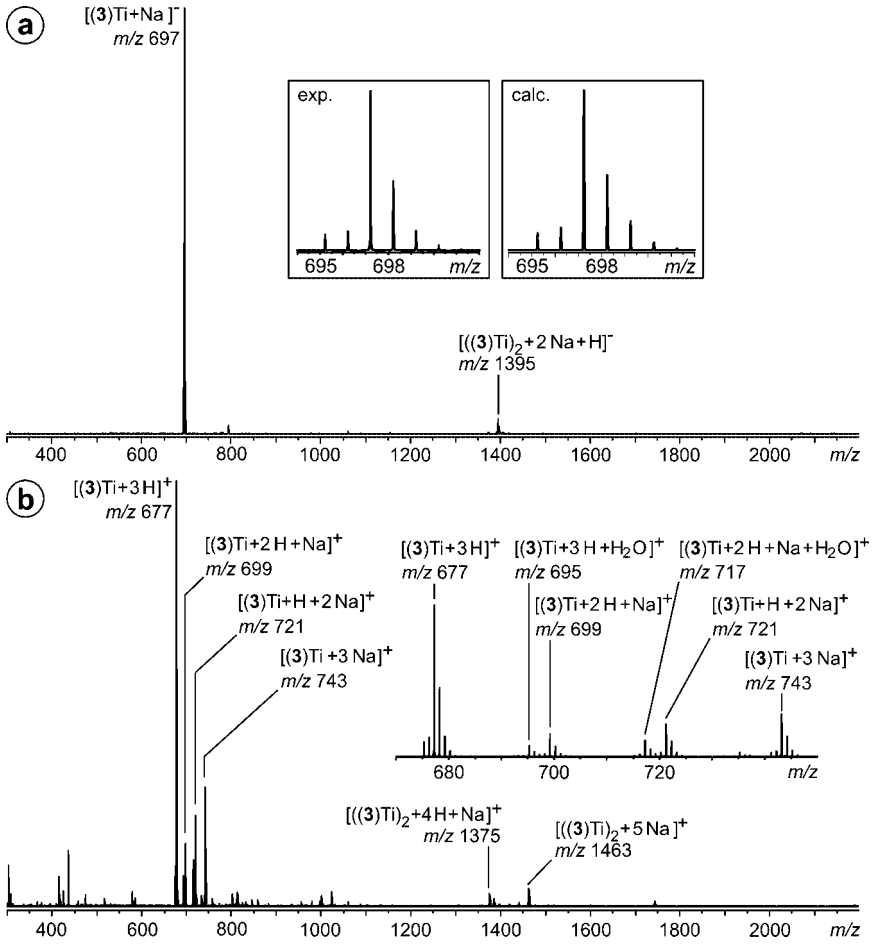


Figure 5. a) ESI FT-ICR mass spectrum of a 100 μM solution of Na[Na(**3**)Ti] in thf (negative mode). The insets show the observed and calculated isotope patterns. b) ESI FT-ICR mass spectrum of a 100 μM solution of Na[Na(**3**)Ti] in thf (positive mode). The region *m/z* = 670–750 is expanded. The water adducts and sodium/proton exchange products can be traced back to some residual water in the solvent.

clotron-resonance (ESI FT-ICR) mass spectrometric experiments (Figure 5).[16]

In the negative mode, a 100 μM solution of Na[Na(**3**)Ti] in thf gives rise to a signal corresponding to the anion [Na(**3**)Ti]⁻ as the by far dominating peak. The only other signal is due to {[Na(**3**)Ti]$_2$H}⁻ at *m/z* = 1395, which we attribute to an unspecific proton-bonded dimer. In the positive detection mode, a more complex spectrum is obtained, which exhibits signals for ions that underwent $Na^+/H^+$ exchange reactions up to the $[H_3(\mathbf{3})Ti]^+$ cation, where all sodium ions have been replaced. Although the source of the protons can only be residual water contained in the thf used as the spray solvent, the $[H_3(\mathbf{3})Ti]^+$ cation is the most prominent ion observed in the spectrum indicating a high tendency for protonation of the imine groups.

In a neutral, doubly protonated species [H$_2$(**3**)Ti], one imine site still suffers from a repulsion between N and O electron pairs, thus leading to a highly basic position within the complex (see Scheme 2). This site is able to deprotonate slightly acidic compounds like alcohols or water. In order to study this aspect further, *negative*-mode mass spectra of Na$_2$[(**3**)Ti] in thf were recorded in the presence of differently substituted alcohols (Figure 6). Besides the signal of the expected [Na(**3**)Ti]⁻ anion, several signals for anions appear

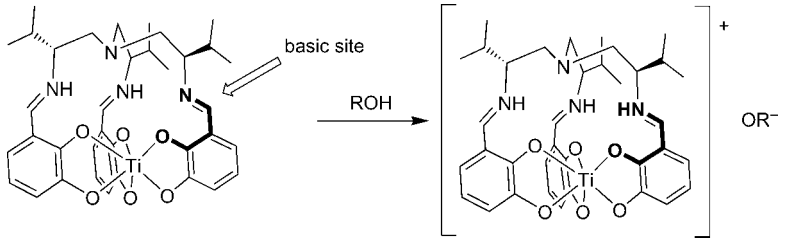


Scheme 2.

 © 2007 Wiley-VCH Verlag GmbH & Co. KGaA, Weinheim 

in which the sodium cation has been replaced by a proton: $[H(\mathbf{3})Ti]^-$, $[H_2(\mathbf{3})Ti]\cdot RO^-$, $[H_2(\mathbf{3})Ti]\cdot Cl^-$, and $[H_3(\mathbf{3})Ti]^+\cdot RO^-\cdot Cl^-$ (likely, the chloride is background chloride as often found in the negative-mode mass spectra). The latter three anions correspond to doubly protonated neutral or triply protonated cationic complexes in which an appropriate number of anions provides the overall negative charge necessary for the experiment in the negative mode. It is intri-

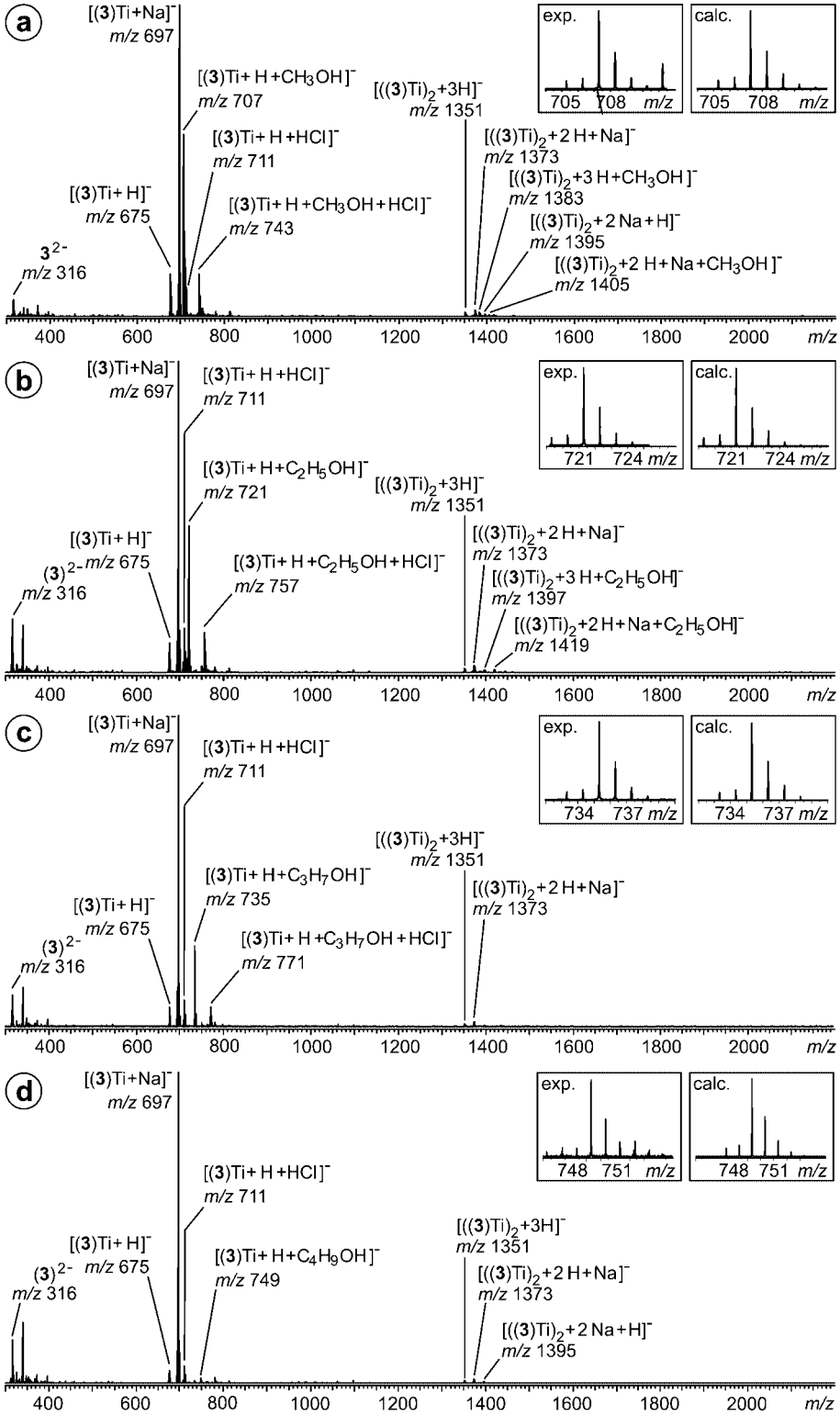


Figure 6. ESI FT-ICR mass spectrum of a 100 μM solution of $Na_2[(\mathbf{3})Ti]$ in thf (negative mode) in the presence of the same amount of different alcohols: (a) methanol, (b) ethanol, (c) 2-propanol, (d) *tert*-butyl alcohol. The observed and calculated isotopic patterns of the species with alcohol are shown. All spectra were measured under exactly the same conditions.

 © 2007 Wiley-VCH Verlag GmbH & Co. KGaA, Weinheim 

guing to see that the intensity ratios among these four complexes do not change much irrespective of the nature of the alcohol, while the ratio of the sum of all protonated complexes relative to the sodiated complexes undergoes a drastic change with increasing size of the substituent R on the alcohol. This trend follows the solution acidities of the alcohols ($pK_a$ values for alcohols determined in water: MeOH: 15.49; EtOH: 15.90; *i*PrOH: 16.57; *t*BuOH: 16.84).[17] Methanol as the most acidic one in this series yields the most intense signals for the protonated complexes; *tert*-butyl alcohol as the least acidic one gives rise only to signals of very low intensities for the protonated complexes relative to the sodiated ones. The observed trend, however, does not follow the gas-phase proton affinities ($MeO^-$: 1596 kJ/mol; $EtO^-$: 1583 kJ/mol; $iPrO^-$: 1569 kJ/mol; $tBuO^-$: 1568 kJ/mol),[18] which would – in contrast to the experiment – lead to the expectation that methanol protonates the complex less easily and thus does not form complexes such as [$H_2$(**3**)Ti]·$RO^-$ with higher abundance than *tert*-butyl alcohol. Consequently, we conclude that the mass spectrometric experiments provide some insight into the solution-phase protonation equilibria.

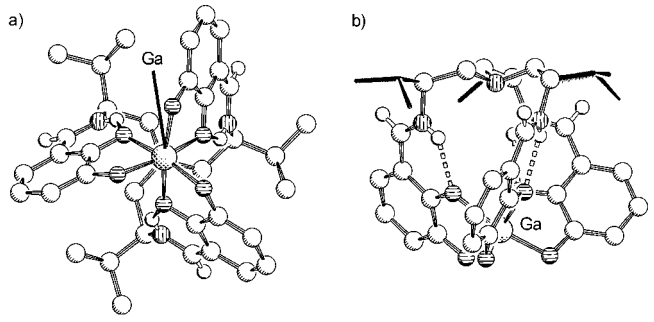


Figure 7. Molecular structure of [$H_3$(**3**)Ga] in the crystal. (a) View along the Ga–$N_{amine}$ $C_3$ axis. (b) Side view (isopropyl groups are only indicated). Hydrogen atoms other than imine CH and N–H···O are omitted for clarity.

Fortunately, we were able to obtain X-ray quality crystals of [$H_3$(**3**)Ga] from dmf/diethyl ether. The structure is shown in Figure 7. The compound crystallizes in the hexagonal space group $P6_3$ (No. 173) and was refined to $R = 0.051$. The molecule is located on an axis of threefold symmetry.

Figure 7 shows the molecular structure of [$H_3$(**3**)Ga]. The chiral tripodal ligand **3** is coordinating the gallium(III) ions and induces the Δ-configuration at the tris(catecholato) complex unit. The chiral "tren analogue" spacer is forming a close-to-planar platform with the isopropyl groups located in this plane, pointing to the outside. In this way, the sterically least crowded conformation is adopted. The imine units are protonated (the proton positions could be refined) forming hydrogen bonds to the internal oxygen atoms of the catecholato unit, as it was discussed in Figure 3 (**IV**/**V**).

A deeper insight into the structural features of this compound can be given by comparing the bond lengths with those of the related compounds **2**-$H_6$[19] and Na[Na(**2**)Ti],[5] as it is done in detail in Table 1.

For the catecholimine **A** of **2**-$H_6$, the bond lengths are in the expected range. The imine bond (**a**) is a typical C=N bond with a length of 1.280 Å. The distance $C(sp^2)_{imine}$–$C(sp^2)_{aromatic}$ is 1.450 Å (**b**). Within the aromatic system typical C–C bond lengths of approximately 1.38 Å (**c**–**h**) are found and the C–$O_{catechol}$ distances are about 1.36 Å (**i**, **j**). A similar situation is observed for the complex Na[Na(**2**)-Ti]. However, in the units **B** and **C** of **2**-$H_6$, a significant alternation of bond lengths can be observed for the aromatic units (**c**–**h**), while the C–O bond lengths are different, e.g. **B**: C–OH 1.360 Å (**i**), C=O 1.299 Å (**j**). The alternation of the aromatic bond lengths is even more pronounced in [$H_3$(**3**)Ga] so that the mesomeric structure **V** in Figure 3 significantly contributes to an accurate description of this

Table 1. Comparison of the bond lengths (Å) of the iminocatechol units of [$H_3$(**3**)Ga], Na[Na(**2**)Ti] and **2**-$H_6$ in the crystal. In Na[Na(**2**)Ti], the moieties are crystallographically independent and therefore the shortest and longest values are given. In **2**-$H_6$ one "normal" iminocatechol unit is observed (**A**) while the two others (**B**, **C**) show proton transfer from the catechol OH group to the imine nitrogen atom. Data for Na[Na(**2**)Ti][5] and **2**-$H_6$[19] were taken from the literature.

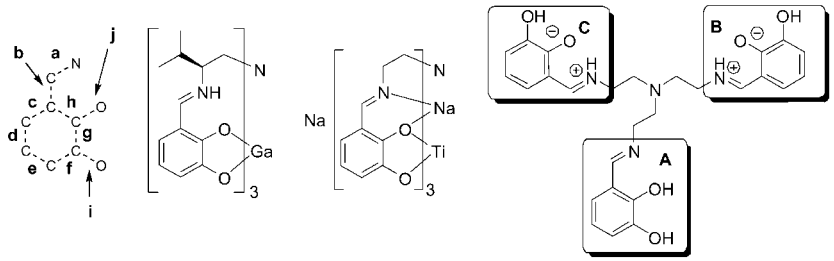


| | [$H_3$(**3**)Ga] | Na[Na(**2**)Ti] | **2**-$H_6$ (**A**) | **2**-$H_6$ (**B**) | **2**-$H_6$ (**C**) |
|---|---|---|---|---|---|
| **a** | 1.298 | 1.263–1.272 | 1.280 | 1.287 | 1.295 |
| **b** | 1.425 | 1.442–1.478 | 1.450 | 1.420 | 1.424 |
| **c** | 1.426 | 1.375–1.412 | 1.398 | 1.416 | 1.411 |
| **d** | 1.358 | 1.377–1.405 | 1.377 | 1.360 | 1.365 |
| **e** | 1.408 | 1.361–1.405 | 1.390 | 1.400 | 1.402 |
| **f** | 1.383 | 1.350–1.385 | 1.375 | 1.366 | 1.365 |
| **g** | 1.439 | 1.398–1.424 | 1.393 | 1.428 | 1.428 |
| **h** | 1.419 | 1.387–1.405 | 1.399 | 1.424 | 1.424 |
| **i** | 1.333 | 1.348–1.371 | 1.373 | 1.360 | 1.367 |
| **j** | 1.296 | 1.316–1.344 | 1.355 | 1.299 | 1.291 |

 © 2007 Wiley-VCH Verlag GmbH & Co. KGaA, Weinheim 

complex. Here, we observe four relatively long C–C distances of 1.408–1.439 Å and two short ones with 1.358 and 1.383 Å. A remarkable difference can be also observed for the $C_{catecholate}$–O bonds. The internal one is relatively short with 1.296 Å due to its increased double-bond character, while the other one is significantly longer (1.334 Å).

### The Protonation Behaviour of $K_4[(4)_3Ti_2]$

Attempts to obtain analogous protonated helicates of iminocatecholates by reaction of either gallium(III) acetylacetonate or titanoyl(IV) acetylacetonate with ligand **4**-$H_4$ in the absence of base were not successful. Therefore, we used the preformed helicate $K_4[(4)_3Ti_2]$[8] [the corresponding dinuclear gallium(III) helicate can unfortunately not be obtained] and protonated it by stepwise addition of sulfuric acid in [$D_6$]dmso.

The $^1$H NMR resonances (Figure 8) of the catechol protons of $K_4[(4)_3Ti_2]$ (**A**) appear at $\delta$ = 6.86, 6.29, and 6.07 ppm and that of the imine group at $\delta$ = 8.58 (s) ppm. Upon addition of sulfuric acid in steps of 1 equiv. $H^+$ (0.5 equiv. $H_2SO_4$), the spectrum changes drastically. This is best monitored by the shift of the imine CH signal (Figure 9). Initially a partial protonation occurs, which leads to a dynamic species (protonation ↔ deprotonation). Upon addition of 5–8 equiv. of protons, a final spectrum is obtained which corresponds to **B** in Figure 8.

The catechol signals of **B** are observed at $\delta$ = 7.04, 6.67, and 6.57 ppm and the imine resonance is found as a doublet at $\delta$ = 7.40 ($J$ = 15.7 Hz)ppm which couples with a signal at $\delta$ = 11.95 (dd, $J$ = 15.7, 5.2 Hz) ppm. The observed spectrum is in accordance with a protonated species $[H_6(4)_3Ti_2]^{2+}$, in which the six protons are fixed in the interior of the triple-stranded helicate in the same way as dis-

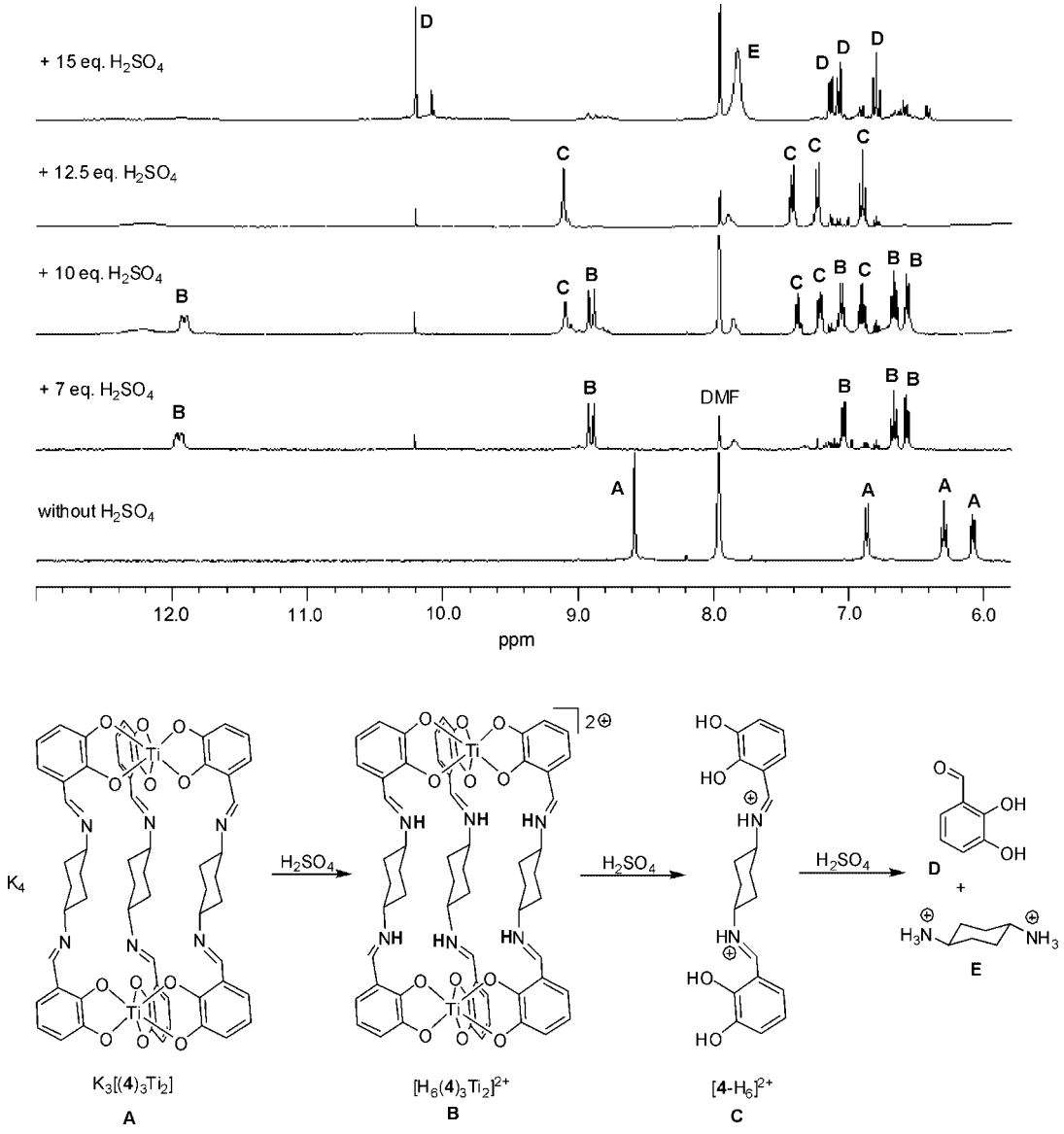


Figure 8. Change of the low-field region of the $^1$H NMR spectrum of $K_4[(4)_3Ti_2]$ in [$D_6$]dmso upon controlled addition of $H_2SO_4$ in [$D_6$]-dmso.

 © 2007 Wiley-VCH Verlag GmbH & Co. KGaA, Weinheim 

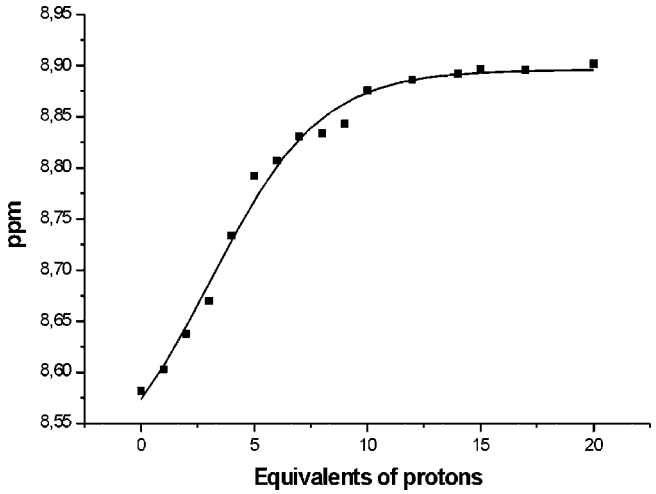


Figure 9. Change of the chemical shift of the imine CH resonance of $[(\mathbf{4})_3Ti_2]^{4-}$ in $[D_6]$dmso upon successive addition of protons ($H_2SO_4$).

cussed for the mononuclear complexes above. This compound can be observed by ESI MS at *m*/*z* = 1151.6 ($[\mathbf{4}_3Ti_2H_5]^+$), 1256.1 ($[\mathbf{4}_3Ti_2H_6SO_4Li]^+$), and 1452.5 ($[\mathbf{4}_3Ti_2H_6SO_4(H_2SO_4)_2Li]^+$).

Further addition of sulfuric acid generates a new species which – at 12.5 equiv. – becomes the major one (**C**). Here, the complex is decomposed and the free protonated ligand $[\mathbf{4}\text{-}H_6]^{2+}$ is liberated. The same spectrum is obtained by protonation of **4**-$H_4$ in $[D_6]$dmso in the absence of any metal ions. Further addition of acid leads to the hydrolysis of the imine groups by residual water in the solvent, and 2,3-dihydroxybenzaldehyde (**D**) and protonated *trans*-1,4-diaminocyclohexane (**E**) are formed.

The protonation of corresponding mononuclear complexes[20] is rather difficult, due to the lability of the complexes in the presence of protons. For $K_2[(\mathbf{5})_3Ti]$ and $K_3[(\mathbf{5})_3Ga]$, no reliable results were obtained. However, we were able to observe NMR resonances for $K_3[(\mathbf{5})_3Ga]$ with the characteristic pattern of an imine species. Unfortunately, we could not obtain pure compounds due to decomposition of the complex simultaneous to protonation.

## Computational Considerations

In order to obtain a deeper insight into the bonding behaviour of the iminocatecholates, we performed a computational study. The most simple model for the ligand we considered is the iminocatechol **6**. We calculated **6** and its enaminone tautomer **7** using the hybrid B3LYP density functional method (DFT) with the TZVP basis set[21] and the second-order Moller-Plesset perturbation theory (MP2) employing the 6-311G(d,p) basis set.[22] The imine is found to be more stable than the enaminone by 25 kJ/mol at the MP2 level of theory. The same result is obtained for the mono-deprotonated species. The X-ray data are more consistent with the enaminone structure **7** rather than with the iminocatechol **6**. The bond lengths are listed in Table 2. We analysed computationally the stability of both tautomeric forms in various metal complexes and found in those with gallium(III) ions no stable imine structure at all but only the enaminone. This can be understood in terms of a weakening of the O–H bond when the complex with the metal ion is formed. The most simple complex we considered was **8** for which the calculated bond lengths show very good agreement with the X-ray data of $[H_3(\mathbf{3})Ga]$. The largest complex we calculated on the B3LYP/TZVP level was the tren derivate $[H_3(\mathbf{2})Ga]$. The Ga atom was treated with a scalar relativistic effective core potential (ECP). For the small complexes such as **8** we employed the MDF10 ECP[23] with the corresponding cc-pVTZ-PP basis set.[24] In all complexes with three catecholato units the simpler ECP SDF28 was used with the corresponding basis set.[25] The

Table 2. Comparison of the bond lengths (Å) of the iminocatechol units of $[H_3(\mathbf{3})Ga]$ as found by X-ray crystallography and of **6**, **7**, **8**, and $[H_3(\mathbf{2})Ga]$ as obtained by computational methods.

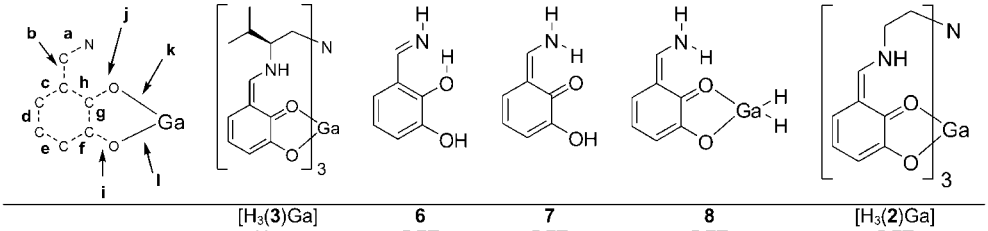

| | $[H_3(\mathbf{3})Ga]$ X-ray | **6** DFT | **7** DFT | **8** DFT | $[H_3(\mathbf{2})Ga]$ DFT |
|---|---|---|---|---|---|
| **a** | 1.298 | 1.282 | 1.324 | 1.320 | 1.326 |
| **b** | 1.425 | 1.451 | 1.390 | 1.397 | 1.395 |
| **c** | 1.426 | 1.406 | 1.433 | 1.434 | 1.435 |
| **d** | 1.358 | 1.381 | 1.360 | 1.365 | 1.365 |
| **e** | 1.408 | 1.398 | 1.426 | 1.418 | 1.422 |
| **f** | 1.383 | 1.384 | 1.363 | 1.385 | 1.383 |
| **g** | 1.439 | 1.403 | 1.448 | 1.444 | 1.444 |
| **h** | 1.419 | 1.406 | 1.448 | 1.430 | 1.432 |
| **i** | 1.333 | 1.359 | 1.352 | 1.309 | 1.311 |
| **j** | 1.296 | 1.348 | 1.264 | 1.296 | 1.289 |
| **k** | 2.020 | n/a | n/a | 2.070 | 2.080 |
| **l** | 1.947 | n/a | n/a | 1.920 | 1.916 |

 © 2007 Wiley-VCH Verlag GmbH & Co. KGaA, Weinheim 

bond lengths of $[H_3(\mathbf{2})Ga]$ do not deviate significantly from the simpler model complex **8** demonstrating that interactions of the three catecholato units do not change the bonding in this case. Very similar results were also obtained for gallium tris(catecholate)s with three simple imine-type ligands.

A closer inspection of Table 2 reveals a deviation of the computed and measured distances for the imine group. The X-ray $C_{aromatic}$–$C_{imine}$ and $C_{imine}$–N distances are about halfway between the imine structure **6** and the enamine structure **7**. The existence of the enamine tautomer rather than the imine form has been established computationally. As a tautomeric form of the enamine the protonated imine has to be considered. With the computational methods used here we can only predict that the enamine form dominates the protonated imine by analysing the order of the molecular orbitals, but more elaborate methods would be required to assess the contribution of the second mesomer.

The results of the computational chemistry strongly support the interpretations of our experimental findings. In the (iminocatecholato)gallium complexes an enamine/quinomethine-type structure is the dominating mesomeric form.

## Conclusions

Our earlier results on the formation of the molecular tetrahedron $[(\mathbf{2})_4Ti_4]^{8-}$ from the flexible ligand **2** made us believe, that we have an easy entry for the preparation of related derivatives, to which we can attach substituents, e.g. in order to introduce chiral information. However, the conformation of ligand **2** is controlled by electronic influences: the repulsion between the free imine nitrogen and catecholato oxygen electron pairs or by the ability of this unit to chelate a metal cation. On the other hand, for ligand **3** additional steric effects become dominant (Figure 10).

For the formation of a tetrahedron vs. a mononuclear complex, two different conformations of the ligand have to be considered. The tetrahedron is formed, if the ligand can spread out to form a triangle with the catechol units located at the corners. This is possible with ligand **2**-$H_6$. In case of **3**-$H_6$ this conformation is "sterically encumbered" due to the bulky isopropyl groups (see Figure 10). The most relaxed conformation is the "cap-type" structure, in which the three catechol moieties are predisposed for tripodal binding of one metal ion. In a 1:1 complex between **3** and a metal ion [e.g. gallium(III)] repulsion between the free electron pairs occurs. This can be overcome either by addition of sodium cations as templates or by proton extraction from solvent (alcohol or water). In the latter case, a high positive charge is now accumulated in the "cap" of the compound which is compensated by adopting an enaminone/chinomethine mesomeric structure.

In dinuclear helicate-type (and mononuclear noncapped) complexes, it is possible to obtain similar protonated structures by addition of mineral acids. However, addition of an excess of acid leads to the decomposition of the complex and finally to the hydrolysis of the imine ligands.

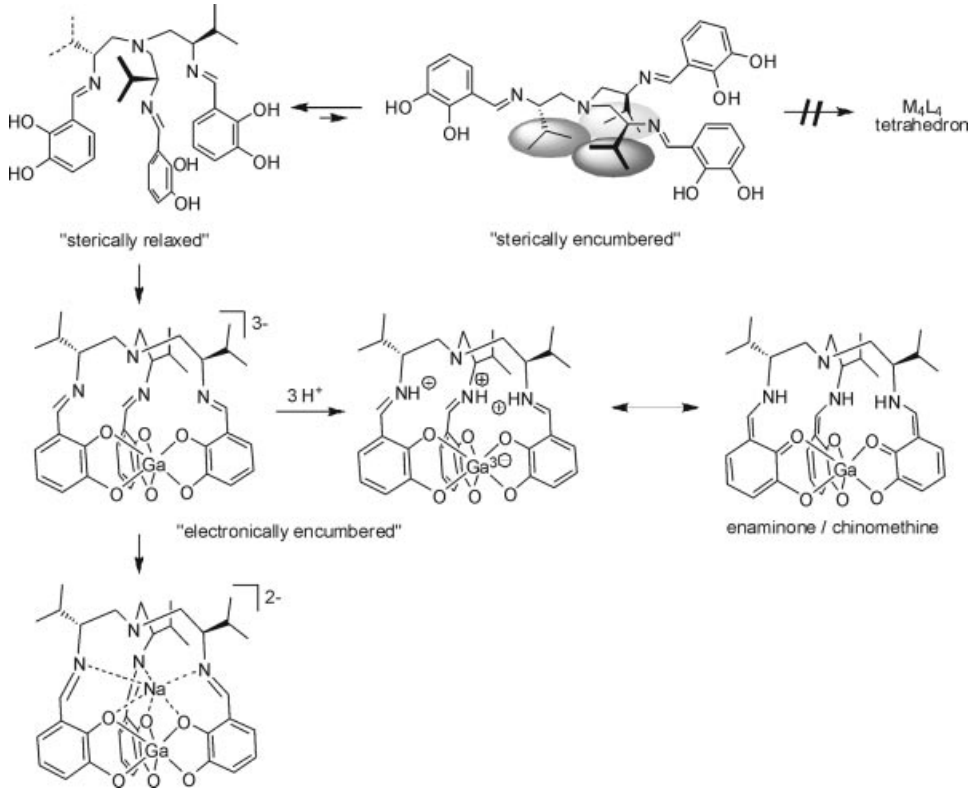


Figure 10. Stabilizing and destabilizing influences that control the sodium- or proton-templated formation of mononuclear gallium(III) complexes.

 © 2007 Wiley-VCH Verlag GmbH & Co. KGaA, Weinheim 

The experimental findings of this study were supported by high-level ab initio and density functional calculations on the simple mesomeric catechol structures **6** and **7**, and the complexes **8** and [$H_3$(**2**)Ga].

This study shows that subtle influences can control the outcome of a metallosupramolecular coordination study. Steric constraints at ligands, geometry of metal coordination, influence of templates, solvent effects, pH, electronic effects, steric effects are only few aspects, which have to be considered in order to rationally control the self-assembly of sophisticated supramolecular aggregates. The present study is only a small step in order to achieve this goal, but it demonstrates the power of several of the mentioned aspects to interfere in the assembly process.

## Experimental Section

**General:** NMR spectra were recorded with a Varian Mercury 300 or Inova 400 spectrometer. FT-IR spectra were recorded with a Bruker IFS spectrometer. Mass spectra were taken with a Thermo Deca XP mass spectrometer. Elemental analyses were obtained with a Heraeus CHN-O-Rapid analyser. ESI MS spectra were measured in thf using a Bruker APEX IV fourier-transform ion cyclotron resonance (FT-ICR) mass spectrometer with an Apollo electrospray ion source described in detail earlier.[26] The chiral tren derivative was prepared as described by Moberg et al.[6]

**3-$H_6$:** The (2*S*)-$N^1$,$N^1$-bis[(*S*)-2-amino-3-methylbutyl]-3-methylbutane-1,2-diamine (0.118 g, 0.43 mmol) and 2,3-dihydroxybenzaldehyde (0.185 g, 1.34 mmol, 3.1 equiv.) were dissolved in distilled methanol (10 mL), and the mixture was stirred overnight. The tris(catechol) **3**-$H_6$ precipitated as yellow solid. It was collected by filtration and was washed with cold methanol. Yield: 0.126 g (0.20 mmol, 46.4%). M.p. 259 °C. $^1$H NMR (400 MHz, [$D_6$]dmso): $\delta$ = 14.06 (s, 3 H, OH), 8.92 (s, 3 H, OH), 7.47 (s, 3 H, $CH_{aldehyde}$), 6.84 (dd, *J* = 1.4, 7.8 Hz, 3 H, $CH_{arom}$), 6.36 (t, *J* = 7.8 Hz, 3 H, $CH_{arom}$), 5.33 (dd, *J* = 1.4, 7.8 Hz, 3 H, $CH_{arom}$), 2.84 (m, 3 H, $CH_{alkyl}$), 2.70 (dd, *J* = 13.5, 8.5 Hz, 3 H, $CH_{alkyl}$), 2.57 (d, *J* = 13.5 Hz, 3 H, $CH_{alkyl}$), 1.79 (m, 3 H, $CH_{alkyl}$), 0.85 (d, *J* = 6.9 Hz, 9 H, $CH_{alkyl}$), 0.80 (d, *J* = 6.6 Hz, 9 H, $CH_{alkyl}$). IR (KBr): $\tilde{\nu}$ = 3392, 3290, 2961, 2877, 1636, 1544, 1522, 1465, 1395, 1230, 1055, 1016, 856, 780, 736, 490, 465 cm$^{-1}$. MS (EI, 70 eV): *m*/*z* = 632.3 [$M^+$], 440.2 [$C_{25}H_{35}N_3O_4^+$], 303.1 [$C_{17}H_{25}N_3O_2^+$], 318.1 [$C_{18}H_{28}N_3O_2^+$], 192.1 [$C_{11}H_{11}NO_2^+$], 123.0 [$C_7H_7O_2^+$]. $C_{36}H_{48}N_4O_6$ (632.79) calcd. C 68.33, H 7.65, N 8.85; found C 67.68, H 7.43, N 8.38.

**$Na_3$[(3)Ga]:** The ligand **3**-$H_6$ (30 mg, 0.0474 mmol), gallium(III) acetonylacetonate (170 mg, 0.0474 mmol) and sodium hydroxide (0.0057 g, 0.142 mmol) were dissolved in dimethylformamide (40 mL), and the mixture was stirred overnight. Then, the solvent was removed and the red-orange solid was dried under high vacuum. Yield: 0.042 g (0.0474 mmol, >99%). $^1$H NMR (400 MHz, [$D_6$]dmso): $\delta$ = 7.89 (s, 3 H, $NCH_{imine}$), 6.06 (d, *J* = 7.7 Hz, 3 H, $CH_{arom}$), 6.02 (d, *J* = 7.7 Hz, 3 H, $CH_{arom}$), 5.91 (t, *J* = 7.7 Hz, 3 H, $CH_{arom}$), 2.90 (m, 3 H, $CH_{alkyl}$), 2.77 (t, *J* = 11.5 Hz, 3 H, $CH_{alkyl}$), 1.91 (m, 3 H, $CH_{alkyl}$), 1.43 (m, 3 H, $CH_{alkyl}$), 0.76 (d, *J* = 6.6 Hz, 9 H, $CH_{alkyl}$), 0.69 (d, *J* = 6.9 Hz, 9 H, $CH_{alkyl}$). IR (KBr): $\tilde{\nu}$ = 3428, 2956, 2872, 2826, 2298, 1664, 1622, 1458, 1386, 1247, 1055, 867, 738 cm$^{-1}$. MS: positive ESI (dmf/MeOH): *m*/*z* = 721.5 [**3**$GaH_3Na^+$], 743.4 [**3**$GaNa_2H_2^+$], 1421.2 [$\mathbf{3}_2Ga_2H_6Na^+$], 1465.2 [$\mathbf{3}_2Ga_2H_4Na_3^+$]; negative ESI (dmf/MeOH): *m*/*z* = 632.1 [**3**$H^-$], 697.8 [**3**$GaH_2^-$], 719.8 [**3**$GaNaH^-$], 1395.2 [$\mathbf{3}_2Ga_2H_5^-$], 1419.2 [$\mathbf{3}_2Ga_2H_4Na^-$]. $C_{36}H_{42}GaN_4Na_3O_6$·dmf·5$H_2O$ (928.62): calcd. C 50.44, H 6.40, N 7.54, found C 50.21, H 6.41, N 7.49.

**$H_3$[(3)Ga]:** The ligand **3**-$H_6$ (30 mg, 0.0474 mmol) and gallium(III) acetonylacetonate (17 mg, 0.0474 mmol) were dissolved in dimethylformamide (40 mL), and the mixture was stirred overnight. Then, the solvent was removed and the red-orange solid was dried under high vacuum. Yield: 0.045 g (0.0474 mmol, >99%). $^1$H NMR (400 MHz, [$D_6$]dmso): $\delta$ = 12.53 (dd, *J* = 13.5, 11.1 Hz, 3 H, $CNH_{imine}$), 8.62 (d, *J* = 13.5 Hz, 3 H, $NCH_{imine}$), 6.40 (m, 6 H, $CH_{arom}$), 6.33 (m, 3 H, $CH_{arom}$), 4.05 (m, 3 H, $CH_{alkyl}$), 2.65 (dd, *J* = 13.5, 11.1 Hz, 3 H, $CH_{alkyl}$), 2.11 (m, 3 H, $CH_{alkyl}$), 1.78 (m, 3 H, $CH_{alkyl}$), 0.80 (d, *J* = 6.6 Hz, 9 H, $CH_{alkyl}$), 0.68 (d, *J* = 6.6 Hz, 9 H, $CH_{alkyl}$). $^1$H NMR (400 MHz, $D_2O$): $\delta$ = 8.43 (s, 3 H, $CNH_{imine}$), 6.40 (d, *J* = 7.2 Hz, 3 H, $CH_{arom}$), 6.33 (d, *J* = 7.7 Hz, 3 H, $CH_{arom}$), 6.44 (apt, *J* = 7.7 Hz, 3 H, $CH_{arom}$), 3.85 (m, 3 H, $CH_{alkyl}$), 2.62 (apt, *J* = 12.2 Hz, 3 H, $CH_{alkyl}$), 2.25 (m, 3 H, $CH_{alkyl}$), 1.65 (m, 3 H, $CH_{alkyl}$), 0.68 (d, *J* = 6.9 Hz, 9 H, $CH_{alkyl}$), 0.53 (d, *J* = 6.9 Hz, 9 H, $CH_{alkyl}$). $^1$H NMR (400 MHz, $CD_3OD$): $\delta$ = 8.46 (s, 3 H, $NCH_{imine}$), 6.74 (dd, *J* = 7.4, 1.1 Hz, 3 H, $CH_{arom}$), 6.54 (dd, *J* = 8.2, 0.9 Hz, 3 H, $CH_{arom}$), 6.44 (apt, *J* = 7.8 Hz, 3 H, $CH_{arom}$), 3.95 (m, 3 H, $CH_{alkyl}$), 2.86 (apt, *J* = 12.1 Hz, 3 H, $CH_{alkyl}$), 2.31 (dd, *J* = 12.5, 5.6 Hz, 3 H, $CH_{alkyl}$), 1.84 (m, 3 H, $CH_{alkyl}$), 0.89 (d, *J* = 6.9 Hz, 9 H, $CH_{alkyl}$), 0.76 (d, *J* = 6.9 Hz, 9 H, $CH_{alkyl}$). IR (KBr): $\tilde{\nu}$ = 3431, 2957, 2868, 1665, 1631, 1496, 1383, 1325, 1249, 1089, 1021, 873, 733, 593, 555 cm$^{-1}$. MS: positive ESI (dmf/MeOH): *m*/*z* = 699.6 [**3**$GaH_3H^+$], 721.5 [**3**$GaH_3Na^+$], 1399.5 [$\mathbf{3}_2Ga_2H_6H^+$], 1421.4 [$\mathbf{3}_2Ga_2H_6Na^+$]; negative ESI (dmf/MeOH): *m*/*z* = 697.9 [**3**$GaH_2^-$]. $C_{36}H_{45}GaN_4O_6$·3dmf·$H_2O$ (936.80): calcd. C 57.70, H 7.32, N 10.47; found C 57.94, H 7.15, N 10.21.

**X-ray Crystal Structure Analysis of $H_3$[(3)Ga]:** $C_{36}H_{45}GaN_4O_6$·3$C_3H_7NO$, *M* = 918.77, orange crystal 0.40 × 0.04 × 0.03 mm, *a* = 12.216(1), *c* = 19.119(1) Å, $\gamma$ = 120°, *V* = 2470.9(3) Å$^3$, $\rho_{calcd.}$ = 1.235 g cm$^{-3}$, $\mu$ = 0.614 mm$^{-1}$, empirical absorption correction (0.791 ≤ *T* ≤ 0.982), *Z* = 2, hexagonal, space group $P6_3$ (No. 173), $\lambda$ = 0.71073 Å, *T* = 198 K, $\omega$ and $\phi$ scans, 10869 reflections collected (±*h*, ±*k*, ±*l*), [(sin$\theta$)/$\lambda$] = 0.62 Å$^{-1}$, 3070 independent ($R_{int}$ = 0.039) and 2581 observed reflections [$I \geq 2\sigma(I)$], 194 refined parameters, *R* = 0.051, $wR^2$ = 0.082, Flack parameter 0.01(2), max. residual electron density 0.44/–0.30 e·Å$^{-3}$, hydrogen atom at N18 from difference Fourier map, others calculated and refined as riding atoms. Data set was collected with a Nonius KappaCCD diffractometer, equipped with a rotating anode generator. Programs used: data collection COLLECT (Nonius B.V., 1998), data reduction Denzo-SMN,[27] absorption correction Denzo,[28] structure solution SHELXS-97,[29] structure refinement SHELXL-97 (G. M. Sheldrick, Universität Göttingen, 1997), graphics SCHAKAL (E. Keller, 1997). CCDC-628295 contains the supplementary crystallographic data for this paper. These data can be obtained free of charge at www.ccdc.cam.ac.uk/conts/retrieving.html [or from the Cambridge Crystallographic Data Centre, 12 Union Road, Cambridge CB2 1EZ, UK; Fax: +44(1223)336-033, E-mail: deposit@ccdc.cam.ac.uk].

**$Na_2$[(3)Ti]:** The ligand **3**-$H_6$ (30 mg, 0.0474 mmol), TiO(acac)$_2$ (12 mg, 0.0474 mmol) and sodium carbonate (5.1 mg, 0.0481 mmol) were dissolved in dimethylformamide (40 mL), and the mixture was stirred overnight. Then, the solvent was removed and the red-orange solid was dried under high vacuum. Yield: 0.041 g (0.0474 mmol, quant.). $^1$H NMR (300 MHz, [$D_6$]dmso): $\delta$ = 8.14 (s, 3 H, $NCH_{imine}$), 6.51 (dd, *J* = 7.7, 1.1 Hz, 3 H, $CH_{arom}$), 6.38 (t, *J* = 7.7 Hz, 3 H, $CH_{arom}$), 6.18 (dd, *J* = 7.7, 1.1 Hz, 3 H, $CH_{arom}$), 3.10 (m, 3 H, $CH_{alkyl}$), 2.89 (m, 3 H, $CH_{alkyl}$), 2.08 (dd,

 © 2007 Wiley-VCH Verlag GmbH & Co. KGaA, Weinheim 

$J$ = 11.5, 3.6 Hz, 3 H, $CH_{alkyl}$), 1.57 (m, 3 H, $CH_{alkyl}$), 0.78 (d, $J$ = 6.7 Hz, 9 H, $CH_{alkyl}$), 0.75 (d, $J$ = 6.9 Hz, 9 H, 3 H, $CH_{alkyl}$) ppm. IR (KBr): $\tilde{\nu}$ = 3433, 2956, 2868, 1663, 1622, 1552, 1449, 1383, 1244, 1095, 1073, 865, 743, 655, 565, 523 $cm^{-1}$. MS: positive ESI (dmf/MeOH): $m/z$ = 700.7 [**3**$TiH_2Na^+$], 677.7 [**3**$TiH_3^+$]; negative ESI (dmf/MeOH): $m/z$ = 676.8 [**3**$TiH_2^-$]. $C_{36}H_{42}N_4Na_2O_6Ti$·dmf·$4H_2O$ (865.79): calcd. C 54.11, H 6.64, N 8.09, found C 54.17, H 6.42, N 8.88.

**$H_3$[(3)Ti]OH:** The ligand **3**-$H_6$ (25 mg, 0.0395 mmol), $TiO(acac)_2$ (10 mg, 0.0395 mmol) and potassium carbonate (5.5 mg, 0.0395 mmol) were dissolved in dimethylformamide (40 mL), and the mixture was stirred overnight. Then, the solvent was removed and the red-orange solid was dried under high vacuum. Yield: 0.040 g (quant.). $^1$H NMR (400 MHz, [$D_6$]dmso): $\delta$ = 11.95 (m, 3 H, NH), 9.04 (d, $J$ = 14.6 Hz, 3 H, $CH_{imine}$), 6.98 (d, $J$ = 7.7 Hz, 3 H, $CH_{arom}$), 6.72 (t, $J$ = 7.7 Hz, 3 H, $CH_{arom}$), 6.66 (d, $J$ = 7.7 Hz, 3 H, $CH_{arom}$), 4.30 (m, 3 H, $CH_{alkyl}$), 2.85 (m, 3 H, $CH_{alky}$), 2.40 (m, 3 H, $CH_{alkyl}$), 2.00 (m, 3 H, $CH_{alkyl}$), 0.81 (d, $J$ = 6.3 Hz, 18 H, $CH_{alkyl}$) ppm. IR (KBr): $\tilde{\nu}$ = 3425, 2956, 2873, 1648, 1549, 1486, 1385, 1250, 1216, 1084, 1053, 966, 782, 742, 668, 611, 504 $cm^{-1}$. MS: positive ESI (dmf/MeOH): $m/z$ = 697.2 [**3**$TiNa^+$], 715.2 [**3**$TiH_2ONa^+$], 1392.1 [$\mathbf{3}_2Ti_2H_4ONa^+$]; negative ESI (dmf/MeOH): $m/z$ = 675.6 [**3**$TiH^-$], 1351.6 [$\mathbf{3}_2Ti_2H_3^-$]. No correct elemental analysis was obtained.

**5-$H_2$:** 2,3-Dihydroxybenzaldehyde (0.5 g, 3.6 mmol) was dissolved in isopropylamine (5 mL). The solvent was distilled off to obtain the imine as a yellow-brown solid. Yield: 0.646 g (3.6 mmol, quant.). $^1$H NMR (300 MHz, $CDCl_3$): $\delta$ = 8.08 (s, 1 H, NCH), 6.86 (d, $J$ = 7.4 Hz, 1 H, $CH_{arom}$), 6.64 (d, $J$ = 7.9 Hz, 1 H, $CH_{arom}$), 6.49 (dd, $J$ = 7.9, 7.4 Hz, 1 H, $CH_{arom}$), 3.64 (sept, $J$ = 6.4 Hz, 1 H, $CH_{alkyl}$), 1.31 (d, $J$ = 6.4 Hz, 6 H, $CH_{alkyl}$). IR (KBr): $\tilde{\nu}$ = 3214, 3038, 2972, 2925, 1642, 1543, 1518, 1465, 1402, 1362, 1230, 1127, 1021, 900, 862, 749, 718, 490 $cm^{-1}$. MS (EI, 70eV): $m/z$ = 179.0 [**5**-$H_2^+$], 137.0 [$C_7H_7NO_2^+$], 136.0 [$C_7H_6NO_2^+$], 109.0 [$C_6H_5O_2^+$]. $C_{10}H_{13}NO_2$ (179.22): calcd. C 67.02, H 7.31, N 7.82; found C 67.29, H 7.00, N 7.89.

## Acknowledgments

Financial support by the Deutsche Forschungsgemeinschaft (SPP 1118 and SFB 624) is gratefully acknowledged. C. A. S. thanks the Fonds der Chemischen Industrie for a Dozentenstipendium.

[1] B. J. Holliday, C. A. Mirkin, *Angew. Chem.* **2001**, *113*, 2076–2097; *Angew. Chem. Int. Ed.* **2001**, *40*, 2022–2043.
[2] D. Caulder, K. N. Raymond, *J. Chem. Soc., Dalton Trans.* **1999**, 1185–1200.
[3] R. M. Yeh, J. Xu, G. Seeber, K. N. Raymond, *Inorg. Chem.* **2005**, *44*, 6228–6239.
[4] a) M. Albrecht, I. Janser, S. Meyer, P. Weis, R. Fröhlich, *Chem. Commun.* **2003**, 2854–2855; b) M. Albrecht, I. Janser, S. Burk, P. Weis, *Dalton Trans.* **2006**, 2875–2880; see also; c) A. J. Amoroso, J. C. Jefferey, P. L. Jones, J. A. McCleverty, P. Thornton, M. D. Ward, *Angew. Chem.* **1995**, *107*, 1577–1580; *Angew. Chem. Int. Ed. Engl.* **1995**, *34*, 1443–1446; d) C. Brückner, R. E. Powers, K. N. Raymond, *Angew. Chem.* **1998**, *110*, 1937–1940; *Angew. Chem. Int. Ed. Engl.* **1998**, *37*, 1837–1839; e) D. Caulder, C. Brückner, R. E. Powers, S. König, T. N. Parac, J. A. Leary, K. N. Raymond, *J. Am. Chem. Soc.* **2001**, *123*, 8923–8938; f) R. W. Saalfrank, H. Glaser, B. Demleitner, F. Hampel, M. M. Chowdhry, V. Schünemann, A. X. Trautwein, G. B. M. Vaughan, R. Yeh, A. V. Davis, K. N. Raymond, *Chem. Eur. J.* **2002**, *8*, 493–497.
[5] M. Albrecht, I. Janser, J. Runsink, G. Raabe, P. Weis, R. Fröhlich, *Angew. Chem.* **2004**, *116*, 6832–6836; *Angew. Chem. Int. Ed.* **2004**, *43*, 6662–6666.
[6] a) Y. Pei, K. Brade, E. Brulé, L. Hagberg, F. Lake, C. Moberg, *Eur. J. Org. Chem.* **2005**, 2835–2835; b) C. Moberg, *Angew. Chem.* **1998**, *110*, 260–281; *Angew. Chem. Int. Ed.* **1998**, *37*, 248–268; c) C. Moberg, *Angew. Chem.* **2006**, *118*, 4838–4840; *Angew. Chem. Int. Ed.* **2006**, *45*, 4721–4723; d) see also: S. E. Gibson, M. P. Castaldi, *Angew. Chem.* **2006**, *118*, 4834–4837; *Angew. Chem. Int. Ed.* **2006**, *45*, 4718–4720.
[7] a) T. J. McMurry, M. W. Hosseini, T. M. Garrett, F. E. Hahn, Z. E. Reyes, K. N. Raymond, *J. Am. Chem. Soc.* **1987**, *109*, 7196–7198; b) T. B. Karpishin, T. D. P. Stack, K. N. Raymond, *J. Am. Chem. Soc.* **1993**, *115*, 182–192.
[8] M. Albrecht, I. Janser, S. Kamptmann, P. Weis, B. Wibbeling, R. Fröhlich, *Dalton Trans.* **2004**, 37–43.
[9] For protonation of imine complexes, see: J. R. Nitschke, D. Schultz, G. Bernardinelli, D. Gerard, *J. Am. Chem. Soc.* **2004**, *126*, 16538–16543.
[10] a) A. Aguiari, E. Bullita, U. Casellato, P. Guerriero, S. Tamburini, P. A. Vigato, U. Russo, *Inorg. Chim. Acta* **1994**, *219*, 135; b) A. Aguiari, E. Bullita, U. Casellato, P. Guerriero, S. Tamburini, P. A. Vigato, *Inorg. Chim. Acta* **1992**, *202*, 157–171.
[11] See for comparison: a) S. J. Rodgers, C. W. Lee, C. Y. Ng, K. N. Raymond, *Inorg. Chem.* **1987**, *26*, 1622–1625; b) T. M. Garrett, P. W. Miller, K. N. Raymond, *Inorg. Chem.* **1989**, *28*, 128–133; c) F. E. Hahn, S. Rupprecht, K. H. Moock, *J. Chem. Soc., Chem. Commun.* **1991**, 224–225.
[12] M. Albrecht, I. Janser, R. Fröhlich, *Chem. Commun.* **2005**, 157–165.
[13] H. Pizzala, M. Carles, W. E. E. Stone, A. Thevand, *J. Chem. Soc., Perkin Trans. 2* **2000**, 935–939.
[14] K. Binnemans, K. Lodewyckx, T. N. Para*c*-Vogt, R. Van Deun, B. Goderis, B. Tinant, K. Van Hecke, L. Van Meervelt, *Eur. J. Inorg. Chem.* **2003**, 3028–3033.
[15] E. E. Weinert, R. Dondi, S. Colloredo-Melz, K. N. Frankenfield, C. H. Mitchell, M. Freccero, S. E. Rokita, *J. Am. Chem. Soc.* **2006**, *128*, 11940–11947.
[16] For recent reviews, see: a) C. A. Schalley, *Mass Spectrom. Rev.* **2001**, *20*, 253; b) B. Baytekin, H. T. Baytekin, C. A. Schalley, *Org. Biomol. Chem.* **2006**, *4*, 2825–2841.
[17] M. G. Hutchings, J. Gasteiger, *J. Chem. Soc., Perkin Trans. 2* **1986**, 455–462.
[18] Data have been taken from the NIST Standard Reference Database Number 69, June 2005 release (available online as NIST webbook: http://webbook.nist.gov/).
[19] M. Albrecht, I. Janser, R. Fröhlich, *Synthesis* **2004**, 1977–1982.
[20] A. M. El-Hendawy, A. El-Ghany El-Kourashy, M. M. Shanab, *Polyhedron* **1992**, *11*, 523–530.
[21] Turbomole 5.8, see: R. Ahlrichs, M. Bär, M. Häser, H. Horn, C. Kölmel, *Chem. Phys. Lett.* **1989**, *162*, 165.
[22] M. J. Frisch, G. W. Trucks, H. B. Schlegel, G. E. Scuseria, M. A. Robb, J. R. Cheeseman, J. A. Montgomery Jr, T. Vreven, K. N. Kudin, J. C. Burant, J. M. Millam, S. S. Iyengar, J. Tomasi, V. Barone, B. Mennucci, M. Cossi, G. Scalmani, N. Rega, G. A. Petersson, H. Nakatsuji, M. Hada, M. Ehara, K. Toyota, R. Fukuda, J. Hasegawa, M. Ishida, T. Nakajima, Y. Honda, O. Kitao, H. Nakai, M. Klene, X. Li, J. E. Knox, H. P. Hratchian, J. B. Cross, V. Bakken, C. Adamo, J. Jaramillo, R. Gomperts, R. E. Stratmann, O. Yazyev, A. J. Austin, R. Cammi, C. Pomelli, J. W. Ochterski, P. Y. Ayala, K. Morokuma, G. A. Voth, P. Salvador, J. J. Dannenberg, V. G. Zakrzewski, S. Dapprich, A. D. Daniels, M. C. Strain, O. Farkas, D. K. Malick, A. D. Rabuck, K. Raghavachari, J. B. Foresman, J. V. Ortiz, Q. Cui, A. G. Baboul, S. Clifford, J. Cioslowski, B. B. Stefanov, G. Liu, A. Liashenko, P. Piskorz, I. Komaromi, R. L. Martin, D. J. Fox, T. Keith, M. A. Al-Laham, C. Y. Peng, A. Nanayakkara, M. Challacombe, P. M. W. Gill, B. Johnson, W. Chen, M. W. Wong, C. Gonzalez, J. A. Pople, *Gaussian 03*, Revision C.02, Gaussian, Inc., Wallingford, CT, **2004**.

 © 2007 Wiley-VCH Verlag GmbH & Co. KGaA, Weinheim 

[23] B. Metz, H. Stoll, M. Dolg, *J. Chem. Phys.* **2000**, *113*, 2563.
[24] K. A. Peterson, *J. Chem. Phys.* **2003**, *119*, 11099.
[25] G. Igel-Mann, H. Stoll, H. Preuss, *Mol. Phys* **1988**, *65*, 1321–1328.
[26] C. A. Schalley, T. Müller, P. Linnartz, M. Witt, M. Schäfer, A. Lützen, *Chem. Eur. J.* **2002**, *8*, 3538–3551.
[27] Z. Otwinowski, W. Minor, *Methods Enzymol.* **1997**, *276*, 307–326.
[28] Z. Otwinowski, D. Borek, W. Majewski, W. Minor, *Acta Crystallogr., Sect. A* **2003**, *59*, 228–234.
[29] G. M. Sheldrick, *Acta Crystallogr., Sect. A* **1990**, *46*, 467–473.
Received: December 19, 2006
Published Online: February 26, 2007

 © 2007 Wiley-VCH Verlag GmbH & Co. KGaA, Weinheim 

DOI: 10.1002/ejic.200600758

# Iron(III) Tris(pyridinehydroxamate)s and Related Nickel(II) and Zinc(II) Complexes: Potential Platforms for the Design of Novel Heterodimetallic Supramolecular Assemblies

**Clodagh Mulcahy,[a][‡] Krystyna A. Krot,[a] Darren M. Griffith,[a] Kyrill Yu. Suponitsky,[b] Zoya A. Starikova,[b] and Celine J. Marmion*[a]**

**Keywords:** Iron / Hydroxamic acids / Speciation / Supramolecular chemistry / Crystal packing

The reaction of 3- and 4-pyhaH (pyhaH = pyridinehydroxamic acid) with hydrated metal salts ($Fe^{III}$, $Ni^{II}$, $Zn^{II}$) in aqueous solution affords tris(pyridinehydroxamate)s in the case of $Fe^{III}$ and bis(pyridinehydroxamate)s in the case of $Zn^{II}$ and $Ni^{II}$ in both the solid state and in solution. These metal pyridinehydroxamates that have the hydroxamato moiety coordinated in an O,O′-bidentate fashion all contain free pyridine nitrogen donor atoms that might allow them to be used as building blocks in the construction of pyridinehydroxamato-bridged supramolecular assemblies. The crystal and molecular structures of the two novel $Fe^{III}$ tris(pyridinehydroxamate) building blocks $[Fe^{III}(3\text{-pyha})_3]\cdot 5.125H_2O$ (**1a**) and $[Fe^{III}(4\text{-pyha})_3]\cdot 5.5H_2O$ (**2a**) are found to have different packing systems despite the similar nature of the two complexes. (© Wiley-VCH Verlag GmbH & Co. KGaA, 69451 Weinheim, Germany, 2007)

## Introduction

Hydroxamic acids, which were first discovered by Lossen in the late 19th century,[1] are now firmly established as an important family of biomedical ligands with complex and well-defined chemistry and a wide variety of pharmaceutical properties.[2] While hydroxamic acid containing compounds are most notably associated with Fe transport phenomena, they are ubiquitous in biology, playing vital roles in maintaining the proper function of enzymes in electron and oxygen transport and other life-sustaining processes.[2] The versatile biological activity of hydroxamic acids is due to their strong metal-chelating ability and possibly their nitric oxide releasing properties.[3]

The powerful metal-chelating ability of hydroxamic acids has been utilised to spectacular effect in the construction of a diverse host of fascinating metal complexes. These include hydroxamates,[4] hydroximates[4] and examples in supramolecular chemistry such as metallacrowns,[5] coordination polymers[6] and tetrahedral cluster complexes.[7]

As ligands, hydroxamic acids typically coordinate in an O,O′-bidentate chelating fashion, coordinating through the carbonyl oxygen atom and the deprotonated hydroxy group to form very stable five-membered chelates. Other binding modes are possible, however, such as monodentate binding through the deprotonated nitrogen or oxygen atoms, although these modes require specially designed coordination environments to provide stabilisation.[2,8] Bidentate binding of two metal ions has also been observed in an O,μ-O′-chelating mode.[9] The complexation behaviour of hydroxamic acids can also be dramatically altered by the incorporation of ancillary coordinating groups at adjacent sites in the molecule.[10] Additional deprotonation of the hydroxamato moiety can occur by metal-induced processes, leading to the formation of hydroximato complexes featuring both mono- and bidentate coordination where both the N- and O-atoms of the hydroxamic acid are deprotonated.[11,12]

We recently reported that 2-pyridinehydroxamic acid (2-pyhaH) can coordinate to $Pt^{II}$ to form a novel dinuclear $Pt^{II}$ hydroximate complex, $[\{cis\text{-}Pt(NH_3)_2\}_2(\mu\text{-}2\text{-}pyhaH_{-1})](ClO_4)_2\cdot H_2O$, with the di(ammine)$Pt^{II}$ moieties bridged by the doubly deprotonated pyridinehydroximato ligand, with N,N′-chelation to one *cis*-$Pt(NH_3)_2$ moiety and O,O′-chelation to the other (Figure 1).[4]

We also recently utilised 3- and 4-pyridinehydroxamic acids 3- and 4-pyhaH as bridging scaffolds in the design of $Pt^{II}/M^{II}$ coordination polymers (M = Cu, Ni or Zn) because they can coordinate $Pt^{II}$ in a monodentate fashion through the pyridine nitrogen atom only, thus leaving the hydroxamic acid moiety free to coordinate to a separate metal ion (Figure 2).[6]

[a] Centre for Synthesis & Chemical Biology, Department of Pharmaceutical & Medicinal Chemistry, Royal College of Surgeons in Ireland,
123 St. Stephens Green, Dublin 2, Ireland
Fax: +353-1-402-2168
E-mail: cmarmion@rcsi.ie
[b] X-ray Structural Centre, General and Technical Chemistry Division, Academy of Sciences of Russia,
Vavilov Str. 28, Moscow B-334 117813, Russia
[‡] Present address: School of Chemistry, University of Sydney, Sydney, NSW 2006, Australia
Supporting information for this article is available on the WWW under http://www.eurjic.org or from the author.

 © 2007 Wiley-VCH Verlag GmbH & Co. KGaA, Weinheim 

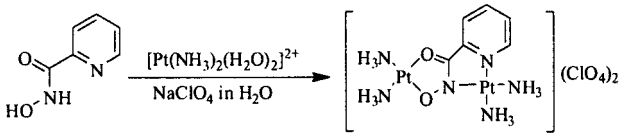


Figure 1. Coordination of 2-pyhaH to $Pt^{II}$ to form the novel dinuclear $Pt^{II}$ hydroximate [{*cis*-$Pt(NH_3)_2$}$_2$(μ-2-pyha$H_{-1}$)]$(ClO_4)_2$·$H_2O$.

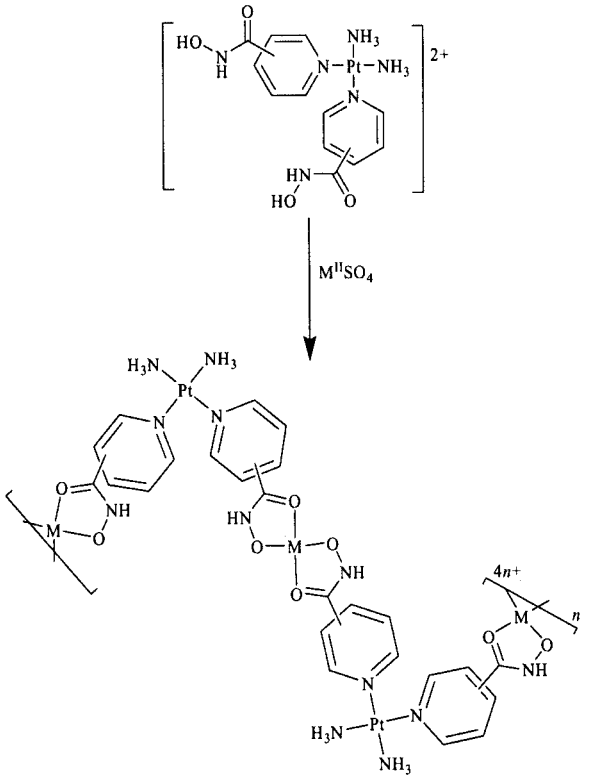


Figure 2. $Pt^{II}/M^{II}$ coordination polymers (M = Cu, Ni or Zn) constructed with 3- and 4-pyhaH as bridging scaffolds.

The present study extends this work to a new family of 3- and 4-pyridinehydroxamato complexes of $Fe^{III}$, $Ni^{II}$ and $Zn^{II}$. We report the synthesis and crystal structures of $[Fe^{III}(3\text{-pyha})_3]\cdot 5.125H_2O$ and $[Fe^{III}(4\text{-pyha})_3]\cdot 5.5H_2O$ and the synthesis and characterisation of related $Ni^{II}$ and $Zn^{II}$ complexes. We hypothesise that such metal pyridinehydroxamates, where the hydroxamato moiety is coordinated to the metal ion in an O,O′-monoanionic way, may act as platforms for the design of novel heterodimetallic supramolecular assemblies because they contain free pyridine nitrogen donor atoms that can coordinate another metal ion. The crystal and molecular structures of the two $Fe^{III}$ tris(pyridinehydroxamate) building blocks are found to have different packing systems despite the similar nature of the two complexes.

## Results and Discussion

### Syntheses of Mono- and Heteronuclear Metal Pyridinehydroxamates

Pyridinehydroxamic acids were synthesised from the corresponding methyl or ethyl esters in high yield and purity. The metal pyridinehydroxamates were generally synthesised by dissolving the hydroxamic acid in water and adding an aqueous solution of the metal salt. This method yielded tris(pyridinehydroxamate)s in the case of $Fe^{III}$ (Figure 3) and bis(pyridinehydroxamate)s in the case of $Ni^{II}$ and $Zn^{II}$ (Figure 4). Upon adjusting the pH to around 5.5, colour changes (to deep red, green and white for the $Fe^{III}$, $Ni^{II}$ and $Zn^{II}$ complexes, respectively) were observed accompanied by precipitation of the metal pyridinehydroxamates. All complexes were formed in reasonably good yields and high purity and were characterised by elemental analysis, IR spectroscopy and, where possible, UV/Vis spectroscopy. Only the $Fe^{III}$ tris(pyridinehydroxamate)s formed crystals of good enough quality for X-ray analysis.

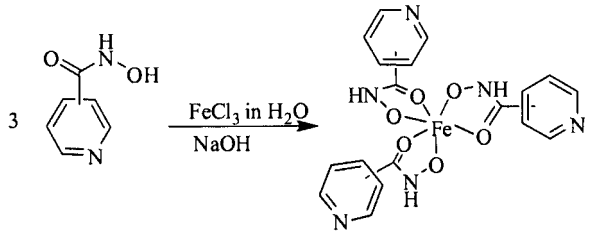


Figure 3. Synthesis of $Fe^{III}$ tris(pyridinehydroxamate)s.

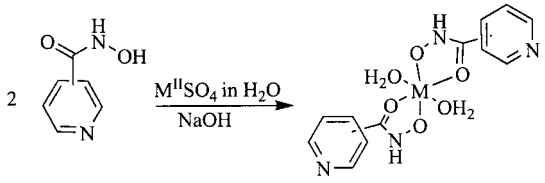


Figure 4. Synthesis of $M^{II}$ bis(pyridinehydroxamate)s (M = Ni or Zn).

IR spectroscopy proved a particularly useful technique for characterisation of the metal pyridinehydroxamates and assigning the coordination modes of the pyridinehydroxamato ligands. The IR spectra of $[Fe^{III}(3\text{-pyha})_3]\cdot 6.5H_2O$ and $[Fe^{III}(4\text{-pyha})_3]\cdot 1.5H_2O$ show a sharp and intense carbonyl stretch at 1600 and 1595 $cm^{-1}$, respectively, which are at lower wavenumbers than in the uncoordinated 3-pyhaH and 4-pyhaH ligands (1660 vs and 1643 s $cm^{-1}$ for 3-pyhaH and 1642 vs and 1608 s $cm^{-1}$ for 4-pyhaH). This indisputably confirms the involvement of the carbonyl oxygen atom in coordination of the $Fe^{III}$ metal ion and is consistent with the X-ray crystallographic results. Similarly, the IR spectra of $[Zn^{II}(3\text{-pyha})_2(H_2O)_2]$ and $[Zn^{II}(4\text{-pyha})_2(H_2O)_2]\cdot H_2O$ each display a carbonyl stretch at 1618 vs and 1613 vs $cm^{-1}$, respectively, each of which has a shoulder at 1599 and 1592 vs $cm^{-1}$, respectively. Analogous shifts in the IR stretching frequencies were observed for the $Ni^{II}$ bis(pyridinehydroxamate)s, indicative of O,O′-hydroxamato coordination. In addition, each metal complex exhibits the

 © 2007 Wiley-VCH Verlag GmbH & Co. KGaA, Weinheim 

characteristic C–N and N–H stretching bands of the hydroxamato moiety in the region 1555–1520 $cm^{-1}$ and 3300–3185 $cm^{-1}$, respectively.

### Crystal Structure of 1a

Crystals of $[Fe^{III}(3\text{-pyha})_3]\cdot 5.125H_2O$ formed from the mother liquor of the reaction between 3-pyhaH and $FeCl_3\cdot 6H_2O$. They were found to be of the monoclinic space group $P2_1/c$ with eight formula units per unit cell. The structure consists of two independent molecules (**A** and **B**) of $Fe^{III}(3\text{-pyha})_3$ (an ORTEP view of **A** and **B** at the 50% probability level is depicted in Figure 5). As expected due to the well-documented high affinity of $Fe^{III}$ for hydroxamic acids,[13] the $Fe^{III}$ core is in a distorted octahedral $O_6$ environment with three 3-pyha chelating ligands coordinating through both oxygen atoms of the hydroxamato moiety to form stable five-membered chelate rings with the pyridine-hydroxamato rings almost planar (Figure 5). The deviations of the $Fe^{III}$ ions from the O–N–C–O planes are rather small (0.01–0.34 Å). The orientations of the pyridine rings with respect to the planes of the corresponding chelating ligands differ significantly for **A** and **B**, as shown by their respective N–C–C–C torsion angles (Table 1).

The range of torsion angles observed can be attributed to the influence of the hydrogen bonds formed between the pyridine nitrogen atoms and water molecules and also the stacking interactions between the pyridine rings. It should be noted that not all of the pyridine nitrogen atoms are involved in hydrogen bonding, whereas all of the pyridine rings are involved in stacking interactions. The degree of rotation of the pyridine ring relative to the hydroxamato functionality does not depend directly on the participation of the corresponding nitrogen atom in hydrogen bonding. For instance, in molecule **A** only two pyridine rings [containing the N(4A), N(6A) atoms], which are nearly coplanar to the connected hydroxamato rings (Table 1), are hydrogen-bonded to water molecules. The opposite situation is observed for molecule **B**, however, in which coplanar pyridine rings are not involved in hydrogen bonding while the other pyridine atom [N(5B)] forms a hydrogen bond with a water molecule. Thus, the conformation of the molecules in **1a** is defined by the effects of the crystal field, which is influenced by the hydrogen-bonding system as well as stacking interactions as a whole.

The $Fe^{III}(3\text{-pyha})_3$ molecules form columns parallel to the screw axis by means of N–H···O hydrogen bonds and stacking interactions. The N(2B)–H(2NB)···O(1A) bond is formed between two independent molecules **A** and **B**, while the N(1B)–H(1NB)···O(3B) hydrogen bond connects molecules of type **B** only (see Figure S1 in the Supporting Information). All other hydrogen bonds involve water molecules. Stacking interactions exist between molecules **A** and **B**, **A** and **B"**, and **B** and **B"**. The formation of columns leaves a space between molecules which is filled with molecules from the neighbouring columns to form an interpenetrated columnar structure with stacking interactions between columns and with channels parallel to the screw axis that are filled with water molecules (see Figure S2 in the Supporting Information).

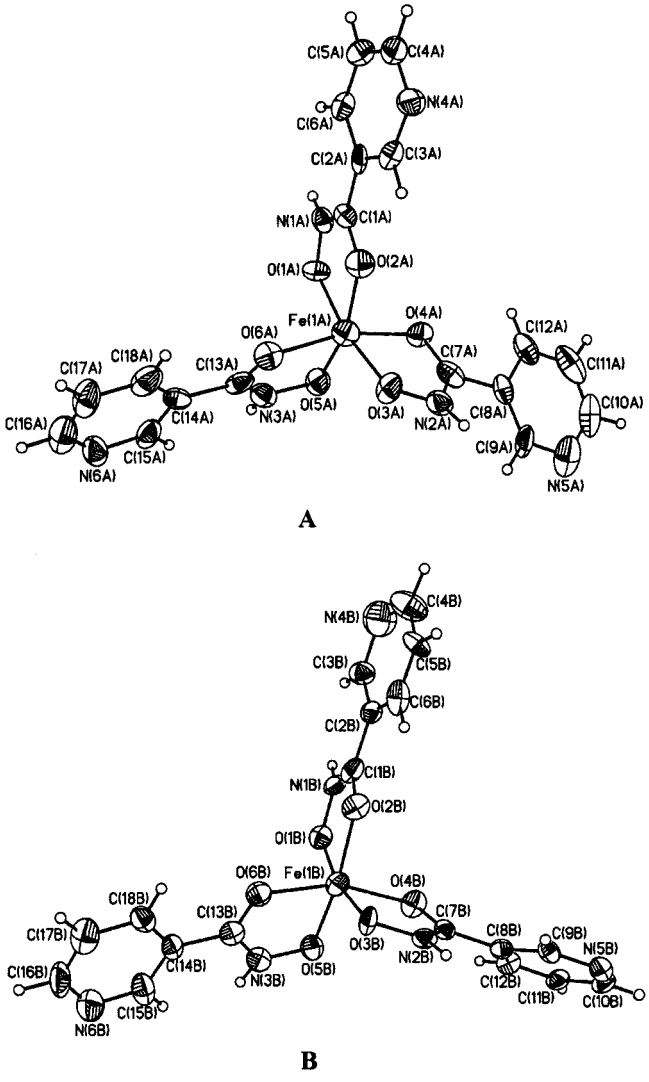


Figure 5. ORTEP drawings (50% probability) of the two independent molecules (**A** and **B**) of **1a** showing the atomic numbering scheme (water molecules of crystallisation have been omitted for clarity).

Table 1. Relative orientation of the pyridine rings and the corresponding hydroxamato rings for **1a** (**A** and **B**).

| Torsion angle [°] | A | B |
|---|---|---|
| N(1)–C(1)–C(2)–C(3) | –174.1(5) | 11.0(8) |
| N(2)–C(7)–C(8)–C(9) | 31.5(8) | –32.7(8) |
| N(3)–C(13)–C(14)–C(15) | 10.1(8) | –1.6(8) |

### Crystal Structure of 2a

$[Fe^{III}(4\text{-pyha})_3]\cdot 5.5H_2O$ crystallises in the tetragonal space group $I4_1a$ with 5.5 water molecules of crystallisation per Fe centre and sixteen formula units in the unit cell. The molecular core consists of an $Fe^{III}$ centre with three almost

 © 2007 Wiley-VCH Verlag GmbH & Co. KGaA, Weinheim 

planar 4-pyha ligands coordinating through both oxygen atoms of the pyridinehydroxamato group to form stable five-membered chelates (Figure 6). The orientations of the pyridine rings with respect to the planes of the corresponding chelating moieties are characterised by their respective N–C–C–C torsion angles (Table 2).

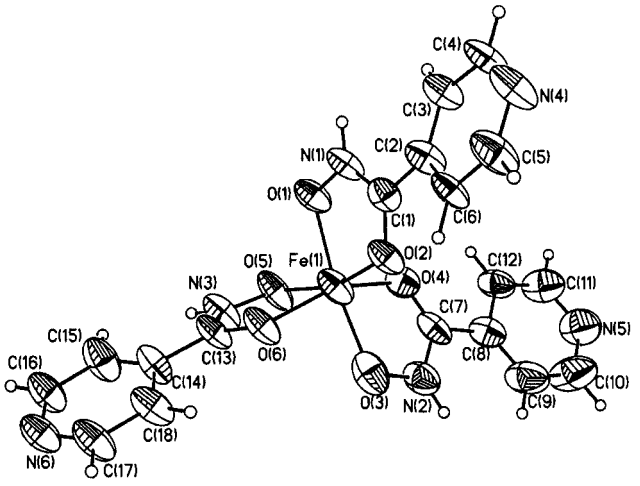


Figure 6. ORTEP view (50% probability) of **2a** showing the atomic numbering scheme (water molecules have been omitted for clarity).

Table 2. Relative orientation of the pyridine rings and corresponding hydroxamato rings in **2a**.

| Atoms | Torsion angle [°] |
|---|---|
| N(1)–C(1)–C(2)–C(3) | –24.7(14) |
| N(2)–C(7)–C(8)–C(9) | –7.5(15) |
| N(3)–C(13)–C(14)–C(15) | –17.6(15) |

The deviations of the $Fe^{III}$ metal ions from the O–N–C–O planes are rather small (0.01–0.34 Å). The crystal packing motif of **2a** is based on two N(1)–H(1N)···O(1) and N(3)–H(3N)···N(6) hydrogen bonds between tris(4-pyha)Fe molecules, which results in a layered structure. Layers parallel to the *ab* crystallographic plane can be described as being built from hydrogen-bonded tetrameric fragments (Figure 7); π-stacking interactions between pyridine rings are also present in the layers (see Figure S3 in the Supporting Information). There are two types of tetrameric fragments in the layer, both of which are formed by molecules related by a fourfold screw axis. The first is formed by N(1)–H(1N)···O(1) interactions and has a butterfly structure, while the other is assembled by means of N(3)–H(3N)···N(6) bonds and is tetrahedral.

The tetrameric fragments are characterised by a chessboard order such that tetramers of the first type are connected to each other by tetramers of the second type, with each molecule participating in both types of tetramers and having four hydrogen-bonded neighbours (Figure 7).

The space between the hydrogen-bonded layers of **2a** is filled with the molecules of neighbouring layers, which results in an interpenetrated layered structure containing channels filled with water molecules. Two types of channels are found in the crystal structure of **2a**: the first is parallel to the *b* axis and the second parallel to the *a* axis (see Figure S3 in the Supporting Information). The crystal structure of **2a** therefore represents a four-layered packing pattern.

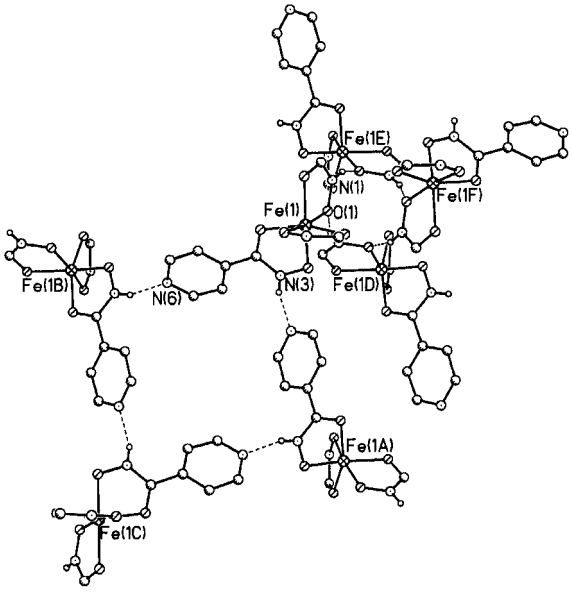


Figure 7. Two tetramers of **2a** formed by N(1)–H(1N)···O(1) and N(3)–H(3N)···N(6) hydrogen bonds (pyridine fragments not involved in hydrogen bonding have been omitted for clarity). Symmetry relations: Fe(1) [*x*, *y*, *z*], Fe(1A) [1.25 – *y*, 0.25 + *x*, 0.25 – *z*], Fe(1B) [–0.25 + *y*, 1.25 – *x*, 0.25 – *z*], Fe(1C) [1 – *x*, 1.5 – *y*, *z*], Fe(1D) [0.75 + *y*, 1.25 – *x*, 0.25 – *z*], Fe(1E) [1.25 – *y*, –0.75 + *x*, 0.25 – *z*], Fe(1F)[2 – *x*, 0.5 – *y*, *z*].

## Formation Constants and Species Distribution Curves

The protonation constants of the pyridinehydroxamic acid ligands 3-pyha ($L^1$) and 4-pyha ($L^2$) and the overall stability constants for the binary ML systems (M = $Fe^{III}$, $Ni^{II}$ or $Zn^{II}$; L = $L^1$ or $L^2$) were calculated from potentiometric data. Two protonation processes were observed for each ligand upon titration with KOH (Figure 8); one proton is released from the pyridine N-atom and a second from the hydroxamate OH group (Table 3). The $pK_{a2}$ value for 3-pyhaH, which corresponds to deprotonation of the hydroxamate OH group, is marginally higher than that for 4-pyhaH.

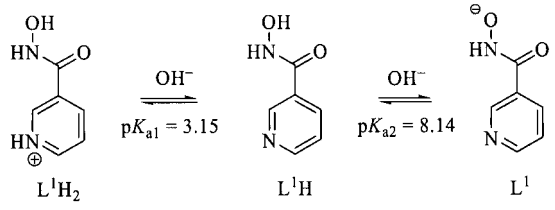


Figure 8. Protonation processes for 3-pyha$H_2$ upon titration with KOH.

 © 2007 Wiley-VCH Verlag GmbH & Co. KGaA, Weinheim 

Table 3. Stability constants ($\log\beta$ values, which refer to the equilibrium $pM + sL + qH \rightleftarrows M_pL_sH_q$) of the proton, $Fe^{III}$, $Ni^{II}$ and $Zn^{II}$ complexes of $L^1$ or $L^2$ ($L^1$ = 3-pyha, $L^2$ = 4-pyha) at 25 °C ($I$ = 0.1 M $KNO_3$).

| Species | *psq* | $\log\beta$ | | |
|---|---|---|---|---|
| $L^1H$ | 011 | 8.14(0.01) | | |
| $L^1H_2$ | 012 | 11.29(0.01) | | |
| $L^2H$ | 011 | 7.74(0.01) | | |
| $L^2H_2$ | 012 | 11.31(0.01) | | |
| | | $Fe^{III}$ | $Ni^{II}$ | $Zn^{II}$ |
| $ML^1$ | 110 | 9.72(0.01) | 4.59(0.02) | 4.60(0.02) |
| $M(L^1)_2$ | 120 | 18.01(0.01) | 8.43(0.02) | 8.47(0.02) |
| $M(L^1)_3$ | 130 | 24.67(0.02) | | |
| $ML^1H_{-1}$ | 11–1 | | –4.14(0.02) | –3.77(0.03) |
| $ML^1H_{-2}$ | 11–2 | | | –12.73(0.01) |
| | | $Fe^{III}$ | $Ni^{II}$ | $Zn^{II}$ |
| $ML^2$ | 110 | 9.77(0.02) | 4.23(0.01) | 4.22(0.02) |
| $M(L^2)_2$ | 120 | 17.38(0.02) | 7.86(0.02) | 7.61(0.02) |
| $M(L^2)_3$ | 130 | 23.13(0.03) | | |
| $ML^2H_{-1}$ | 11–1 | | –4.81(0.03) | –4.41(0.03) |
| $ML^2H_{-2}$ | 11–2 | | | –13.35(0.01) |

For each system studied, the titration curves show significant shifts that are indicative of complex formation. The titration curves for the $FeL^2$ system are shown in Figure 9 as a representative example of the tris(hydroxamato) systems. $Fe^{III}$ forms ML, $ML_2$ and $ML_3$ species with both $L^1$ and $L^2$ (Figure 10) upon increasing pH, as expected, with stability constants slightly lower than those previously reported for the $Fe^{III}$ benzohydroxamate system.[14] We attribute this to the more electron-rich nature of the pyridine ring with respect to benzene.

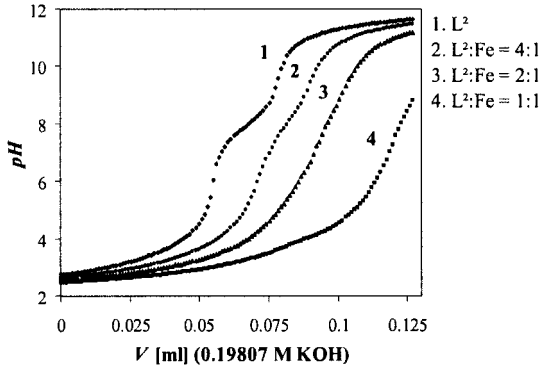


Figure 9. Titration curves for the $Fe^{III}L^2$ binary system.

The speciation studies support the presence of ML and $ML_2$ complexes for the $Ni^{II}$ and $Zn^{II}$ binary systems. The $ML_2$ complexes were also obtained in the solid state (**3**–**6**). The titration curves (Figure 11) and species distribution curves (Figure 12) for the $NiL^2$ system are shown as representative examples of the bis(hydroxamato) systems. The $M(L^1)_2$ complexes ($\log\beta \approx 8.4$) were found to be slightly more stable in solution than their $M(L^2)_2$ analogues ($\log\beta \approx 7.7$).

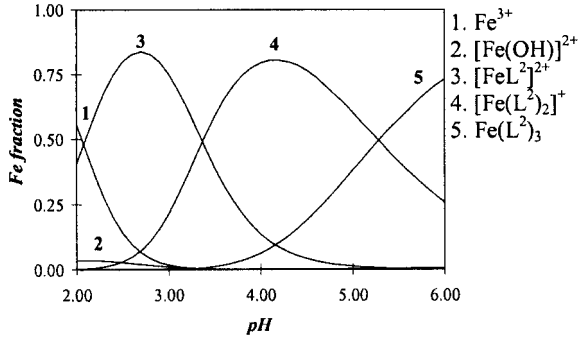


Figure 10. Distribution curves for the $Fe^{III}L^2$ system at pH = 2–6; $[Fe^{III}]$ = 1 mM; $[L^2]$ = 3 mM.

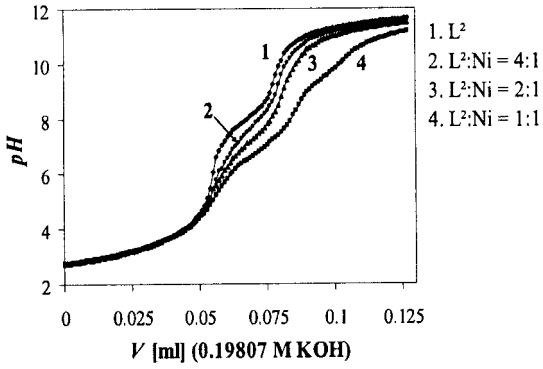


Figure 11. Titration curves for the $Ni^{II}L^2$ binary system.

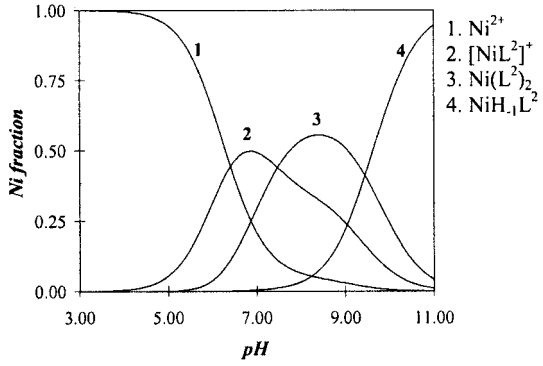


Figure 12. Distribution curves for the $Ni^{II}L^2$ system at pH = 2–6; $[Ni^{II}]$ = 1 mM; $[L^2]$ = 3 mM.

## Spectrophotometric Study

Hydroxamic acids are known to form stable complexes with $Fe^{III}$.[14] The $Fe^{III}$–hydroxamate interaction is characterised in the UV/Vis spectrum by a $\pi(\text{ligand}) \rightarrow d\pi(\text{Fe})$ ligand-to-metal charge-transfer (LMCT) band. We monitored the reaction between $Fe^{III}$ and L [L = 3-pyha ($L^1$) and 4-pyha ($L^2$)] over the pH range of 2.11–5.97 (in line with the speciation studies reported) with an $Fe^{III}$/L ratio of 1:3 by spectrophotometry. Upon increasing the pH, we observed a hypsochromic shift of the LMCT band and an increase in absorption intensity corresponding to the formation of the mono-, bis- and tris(hydroxamato) complexes of $Fe^{III}$ and also consistent with previously reported $Fe^{III}$

 © 2007 Wiley-VCH Verlag GmbH & Co. KGaA, Weinheim 

hydroxamate systems.[14] Precipitation was observed at pH > 5.97. The 1:1 complexes give spectra with $\lambda_{max} \approx 510$ nm, the 1:2 complexes spectra with $\lambda_{max} \approx 480$ nm and the 1:3 complexes spectra with $\lambda_{max} \approx 425$ nm. The UV/Vis spectra of the $Fe^{III}L^2$ system are shown in Figure 13 as a representative example. The spectrophotometric results complement our potentiometry data and further confirm the formation of FeL, $FeL_2$ and $FeL_3$ complexes.

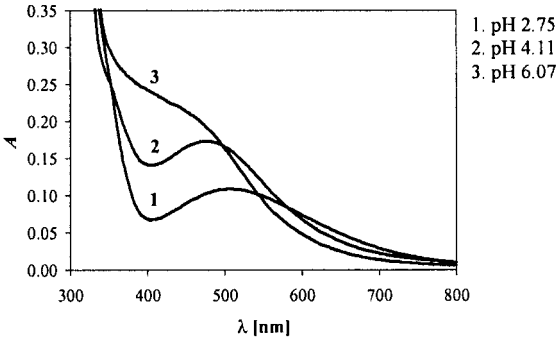


Figure 13. UV/Vis spectra of aqueous solutions of $Fe^{III}$ (0.1 mM) and $L^2$ (0.3 mM) in $KNO_3$ (0.1 mM) at pH = 2.75, 4.11 and 6.07.

## Conclusions

The affinity of hard $Ni^{II}$, $Zn^{II}$ and $Fe^{III}$ centres for hard oxygen donors facilitates the formation of a series of novel metal pyridinehydroxamates where the coordination mode is exclusively hydroxamato-O,O′ with the ligand chelating to the metal centre as a monoanionic species. The crystal and molecular structures of two $Fe^{III}$ tris(pyridinehydroxamate) building blocks have been determined and found to have different packing systems despite the similar nature of the two complexes. A comparative analysis of the crystal packing systems allows us to suggest that the different packing motifs found in **1a** and **2a** might, at least partly, be explained by the participation of the pyridine N-atom in hydrogen bonding to the pyridinehydroxamate ring in **2a**, while in **1a** hydrogen bonds are formed only between the pyridinehydroxamate rings and pyridine N-atoms are involved in hydrogen bonding with water molecules only.

These novel pyridinehydroxamato complexes of $Fe^{III}$, $Ni^{II}$ and $Zn^{II}$ lend themselves to further investigation as potential platforms for the design of novel heterodimetallic supramolecular assemblies.

## Experimental Section

**Materials and Methods:** All reagents, deuteriated solvents and metal salts were purchased from Sigma Aldrich and used without further purification. IR spectra were recorded as KBr discs with a Mattson Genesis II CSI FTIR spectrometer in the 4000–400 $cm^{-1}$ region. UV/Vis spectra were recorded with a Helios Alpha Thermo Spectronic Spectrophotometer in a quartz cell. C, H, N, Fe, Ni and Zn elemental analyses were performed at the Microanalytical Laboratories, University College Dublin, Ireland. $^1$H NMR spectra were recorded with a Bruker Advance DPX 400 FT spectrometer at the Department of Chemistry, Trinity College Dublin, Ireland. The residual undeuterated DMSO signal was used as an internal reference at $\delta = 2.505$ ppm.

**Preparation of the Ligands:** These were prepared as reported previously.[6]

**3-Pyridinehydroxamic Acid (3-pyhaH, $L^1$):** Hydroxylamine hydrochloride (5.07 g, 72 mmol) was added to sodium hydroxide (5.83 g, 146 mmol) in deionised water (37 mL) and the resulting solution was added dropwise to a solution of methyl nicotinate (5.00 g, 36 mmol) in methanol (55 mL). The solution was stirred at room temperature for 72 h, after which it was acidified to pH = 5.5 with 5% HCl. The solvent was removed in vacuo to yield a yellow solid. Methanol (60 mL) was added and sodium chloride was filtered off. The solvent was removed in vacuo to yield a light pink solid, which was recrystallised from water. Yield: 3.00 g (22 mmol, 66%). $C_6H_6N_2O_2$ (138.12): calcd. C 52.17, H 4.38, N 20.28; found C 51.98, H 4.24, N 20.14. $^1$H NMR [400 MHz, $(CD_3)_2SO$, 25 °C]: $\delta$ = 11.41 (s, 1 H, OH), 9.24 (br. s, 1 H, NH), 8.90 (d, $^4J_{H,H}$ = 2.00 Hz, 1 H, H2), 8.70 (dd, $^3J_{H,H}$ = 5.04, $^4J_{H,H}$ = 1.52 Hz, 1 H, H4), 8.10 (dt, $^3J_{H,H}$ = 8.00, $^4J_{H,H}$ = 2.00 Hz, 1 H, H6) 7.51 (dd, $^3J_{H,H}$ = 8.04, $^4J_{H,H}$ = 5.04 Hz, 1 H, H5) ppm. IR (KBr disc): $\tilde{\nu}_{max}$ = 3196 vs (hydroxamate N–H), 2802 s (hydroxamate O–H), 1660 vs and 1643 vs (hydroxamate C=O), 1594 s, 1557 s (hydroxamate C–N) $cm^{-1}$.

**4-Pyridinehydroxamic Acid (4-pyhaH, $L^2$):** This compound was prepared according to the same method as for 3-pyhaH except ethyl isonicotinate was used instead of methyl nicotinate. Yield: 55%. $C_6H_6N_2O_2$ (138.12): calcd. C 52.17, H 4.38, N 20.28; found C 51.94, H 4.29, N 20.12. $^1$H NMR [400 MHz, $(CD_3)_2SO$, 25 °C]: $\delta$ = 11.41 (s, 1 H, OH), 9.37 (br. s, 1 H, NH), 8.70 (d, $^3J_{H,H}$ = 5.6 Hz, 2 H, H2/6), 7.68 (d, $^3J_{H,H}$ = 6.0 Hz, 2 H, H3/5) ppm. IR (KBr disc): $\tilde{\nu}_{max}$ = 3186 vs. (hydroxamate N–H), 2850b (hydroxamate O–H), 1642 vs. and 1608 s (hydroxamate C=O), 1551 s, 1531 s (hydroxamate C–N) $cm^{-1}$.

**Preparation of Metal Pyridinehydroxamates**

**$[Fe^{III}(3\text{-pyha})_3]\cdot 6.5H_2O$ (1):** 3-pyhaH (150 mg, 1.086 mmol) was dissolved in tepid deionised water (5 mL) and, after allowing it to return to room temperature, an aqueous solution (5 mL) of $FeCl_3\cdot 6H_2O$ (97.8 mg, 0.362 mmol) was added. The pH was adjusted to 5.5 with 5% NaOH, which resulted in the precipitation of a red solid. This was filtered, washed with water (3 mL) and dried over $P_2O_5$. Yield: 141 mg (0.253 mmol, 70%). $C_{18}H_{28}FeN_6O_{12.5}$ (584.29): calcd. C 37.00, H 4.83, N 14.38, Fe 9.56; found C 37.00, H 2.87, N 14.00, Fe 9.22. IR (KBr disc): $\tilde{\nu}_{max}$ = 3186 vs (hydroxamato N–H), 1600 vs (hydroxamato C=O), 1549 s, 1518 s (hydroxamato C–N) $cm^{-1}$. UV/Vis ($H_2O$): $\lambda_{max}$ = 430 nm ($\varepsilon$ = 2200 $M^{-1}cm^{-1}$, LMCT). Single crystals of $[Fe^{III}(3\text{-pyha})_3]\cdot 5.125H_2O$ (**1a**) suitable for an X-ray diffraction study, were obtained from the filtrate after standing at room temperature for 2 d.

**$[Fe^{III}(4\text{-pyha})_3]\cdot 1.5H_2O$ (2):** 4-pyhaH (150 mg, 1.086 mmol) was dissolved in tepid deionised water (5 mL) and, after allowing it to return to room temperature, an aqueous solution (5 mL) of $FeCl_3\cdot 6H_2O$ (97.8 mg, 0.362 mmol) was added. The pH was adjusted to 5.5 with 5% NaOH, which resulting in the precipitation of a red solid. This was filtered, washed with water (3 mL) and dried over $P_2O_5$. Yield: 120 mg (0.243 mmol, 67%). $C_{18}H_{18}FeN_6O_{7.5}$ (494.22): calcd. C 43.74, H 3.67, Fe 11.30, N 17.00; found C 43.98, H 3.38, Fe 11.40, N 16.93. IR (KBr disc): $\tilde{\nu}_{max}$ = 3186 vs (hydroxamato N–H), 1595 vs (hydroxamato C=O), 1555 s (hydroxamato C–N) $cm^{-1}$. UV/Vis ($H_2O$): $\lambda_{max}$ = 430 nm ($\varepsilon$

 © 2007 Wiley-VCH Verlag GmbH & Co. KGaA, Weinheim 

= 2800 $M^{-1}cm^{-1}$, LMCT). Single crystals of $Fe^{III}(4\text{-pyha})_3 \cdot 5.5H_2O$ (**2a**) suitable for an X-ray diffraction study were obtained from the filtrate after standing at room temperature for 2 d.

**$[Ni^{II}(3\text{-pyha})_2(H_2O)_2]$ (3):** 3-pyhaH (100 mg, 0.724 mmol) was dissolved in tepid deionised water (5 mL) and an aqueous solution (5 mL) of $NiSO_4 \cdot 6H_2O$ (95 mg, 0.362 mmol) was added. The pH was adjusted to 5.5 with 5% NaOH, which resulted in the precipitation of a green solid. This was filtered, washed with water (3 mL) and dried over $P_2O_5$. Yield: 79 mg (0.213 mmol, 59%). $C_{12}H_{14}N_4NiO_6$ (368.96): calcd. C 39.06, H 3.82, N 15.19, Ni 15.91; found C 38.69, H 3.69, N 14.70, Ni 16.50. IR (KBr disc): $\tilde{\nu}_{max}$ = 3210 vs (hydroxamato N–H), 1611 vs (hydroxamato C=O), 1524 s (hydroxamato C–N) $cm^{-1}$.

**$[Ni^{II}(4\text{-pyha})_2(H_2O)_2]$ (4):** 4-pyhaH (100 mg, 0.724 mmol) was dissolved in tepid deionised water (5 mL) and an aqueous solution (5 mL) of $NiSO_4 \cdot 6H_2O$ (95 mg, 0.362 mmol) was added. The pH was adjusted to 5.5 with 5% NaOH, which resulted in the precipitation of a green solid. This was filtered, washed with water (3 mL) and dried over $P_2O_5$. Yield: 94 mg (0.253 mmol, 70%). $C_{12}H_{14}N_4NiO_6$ (368.96): calcd. C 39.06, H 3.82, N 15.19, Ni 15.91; found C 39.12, H 3.33, N 14.80, Ni 15.83. IR (KBr disc): $\tilde{\nu}_{max}$ = 3185 vs (hydroxamato N–H), 1613 vs, 1586 vs (hydroxamato C=O), 1533 vs (hydroxamato C–N) $cm^{-1}$.

**$[Zn^{II}(3\text{-pyha})_2(H_2O)_2]$ (5):** 3-pyhaH (100 mg, 0.724 mmol) was dissolved in tepid deionised water (10 mL). $ZnSO_4 \cdot 7H_2O$ (104 mg, 0.362 mmol) was added to this solution and the pH was adjusted to 5.5 with 5% NaOH. The resultant white precipitate was filtered, washed with water (3 mL) and dried over $P_2O_5$. Yield: 61 mg (0.163 mmol, 45%). $C_{12}H_{14}N_4O_6Zn$ (375.65): calcd. C 38.37, H 3.76, N 14.91, Zn 17.41; found C 38.16, H 3.58, N 14.70, Zn 16.37. IR (KBr disc): $\tilde{\nu}_{max}$ = 3292 vs (hydroxamato N–H), 1618 vs (hydroxamato C=O), 1547 m (hydroxamato C–N) $cm^{-1}$.

**$[Zn^{II}(4\text{-pyha})_2(H_2O)_2] \cdot H_2O$ (6):** 4-pyhaH (100 mg, 0.724 mmol) was dissolved in tepid deionised water (10 mL). $ZnSO_4 \cdot 7H_2O$ (104 mg, 0.362 mmol) was added to this solution and the pH was adjusted to 6 with 5% NaOH. The resultant white precipitate was filtered, washed with water (3 mL) and dried over $P_2O_5$. Yield: 79 mg (0.199 mmol, 55%). $C_{12}H_{16}N_4O_7Zn$ (393.67): calcd. C 36.61, H 4.10, N 14.23, Zn 16.61; found C 37.06, H 3.04, N 14.28, Zn 16.56. IR (KBr disc): $\tilde{\nu}_{max}$ = 3295 vs (hydroxamato N–H), 1613 vs, 1592 vs (hydroxamato C=O), 1536 s (hydroxamato C–N) $cm^{-1}$.

**Potentiometric Studies:** Potentiometric measurements were carried out using solutions of 0.1 M $KNO_3$ ionic strength at 25 °C. A carbonate-free KOH solution (0.19807 M) standardised with potassium hydrogen phthalate[15] was used as titrant. The pH-metric studies were carried out with a Molspin pH-meter and titration controller with Thermo Russell CMAW711 combined electrode and Hamilton syringe autoburette, in the pH range of 2.5–10.5. The electrode system was calibrated daily by the method of Irving et al.[16] ($pK_w$ = 13.831) and the pH meter readings were converted into hydrogen ion concentrations. The initial volume of the samples was about 2 mL and the ligand concentration was 0.002 M in all systems. Three different metal/ligand ratios (1:1, 1:2 and 1:4) were used. The pH-metric data were used to determine $pK_a$ values and the stoichiometry of the species and to calculate their concentration stability constants. The calculations were performed with the Hyperquad 2000[17] program. Literature data were used for (hydroxido)$Fe^{III}$ complexes: $[FeH_{-1}]^{2+}$: –3.21; $[FeH_{-2}]^{+}$: –6.73; $[Fe_2H_{-2}]^{4+}$: –4.09; $[Fe_3H_{-4}]^{5+}$: –7.58.[18] The standard deviations quoted refer to random errors.

**Spectrophotometric Studies:** UV/Vis spectra for the $Fe^{III}L$ systems ($L^1$ = 3-pyha and $L^2$ = 4-pyha) were obtained with a Helios Alpha Thermo Spectronic Spectrophotometer in the region 300–800 nm. The Fe/L ratios were 1:3 ($[Fe^{III}]$ = 0.1 mM). The pH of the solutions was adjusted with KOH (0.02 M) and $HNO_3$ (0.02 M).

**Crystallographic Measurements for 1a and 2a:** X-ray crystallographic experiments were carried out with a SMART 1000 CCD diffractometer [$\lambda$(Mo-$K_\alpha$) = 0.71073 Å, graphite monochromator, $\omega$-scans] at 120(2) K. The details of the data collection and crystal structure refinements using the SAINT Plus,[19] SADABS and SHELXTL-97[20] program packages are summarised in Table 4. For both structures, hydrogen atoms attached to the nitrogen atoms and to the oxygen atoms of water molecules were located in the difference Fourier maps and were then shifted to the standard X-ray values for N–H and O–H bonds and included in the refinement using the riding approximation. All other hydrogen atoms were placed in geometrically calculated positions and refined with a riding model as well. CCDC-628980 (**1a**) and -628981 (**2a**) contain the supplementary crystallographic data for this paper. These can be obtained free of charge from The Cambridge Crystallographic Data Centre via www.ccdc.ac.uk/data_request/cif.

Table 4. Crystallographic data for **1a** and **2a**.

| Compound | **1a** | **2a** |
|---|---|---|
| Empirical formula | $C_{18}H_{25.25}FeN_6O_{11.13}$ | $C_{18}H_{26}FeN_6O_{11.5}$ |
| Formula mass | 559.54 | 566.30 |
| Crystal colour | red | red |
| Crystal habit | needle | plate |
| Crystal size [mm] | 0.25 × 0.1 × 0.05 | 0.15 × 0.1 × 0.02 |
| Crystal system | monoclinic | tetragonal |
| Space group | $P2_1/c$ | $I4_1/a$ |
| $a$ [Å] | 15.833(4) | 13.872(3) |
| $b$ [Å] | 11.804(3) | 13.872(3) |
| $c$ [Å] | 27.463(6) | 55.462(18) |
| $\beta$ [°] | 105.617(6) | 90 |
| $V$ [Å$^3$] | 4943(2) | 10673(5) |
| $Z$ | 8 | 16 |
| $\rho_{calcd.}$ [g cm$^{-3}$] | 1.504 | 1.410 |
| $F(000)$ | 2322 | 4704 |
| $\mu$ [mm$^{-1}$] | 0.678 | 0.630 |
| $T_{max}$, $T_{min}$ | 0.967, 0.793 | 0.987, 0.796 |
| $\theta$ range [°] | 1.54–26.00 | 1.84–23.03 |
| Reflections collected | 28611 | 21340 |
| Indep reflections, $R_{int}$ | 9637, 0.1500 | 3670, 0.1878 |
| Completeness to $\theta$ [%] | 99.1 | 98.1 |
| Refined parameters | 662 | 333 |
| $GOF$ ($F^2$) | 0.904 | 1.010 |
| Reflections [$I > 2\sigma(I)$] | 3295 | 1544 |
| $R_1(F)$ [$I > 2\sigma(I)$][a] | 0.0675 | 0.0860 |
| $wR_2(F^2)$ (all data)[b] | 0.0905 | 0.2197 |

[a] $R_1 = \Sigma||F_o| - |F_c||/\Sigma(F_o)$. [b] $wR_2 = \Sigma[w(F_o^2 - F_c^2)^2]/\Sigma[w(F_o^2)^2]^{1/2}$.

**Supporting Information** (see footnote on the first page of this article): Crystal packing diagrams of **1a**, crystal packing diagram of **2a** and selected bond lengths for **1a** and **2a**.

## Acknowledgments

We gratefully acknowledge The Research Committee of the Royal College of Surgeons in Ireland, Enterprise Ireland, Dun-Laoghaire Rathdown County Council and the Programme for Research in Third Level Institutions (PRTLI), administered by the HEA, for funding.

 © 2007 Wiley-VCH Verlag GmbH & Co. KGaA, Weinheim 

[1] H. Lossen, *Justus Liebigs Ann. Chem.* **1869**, *150*, 314.
[2] C. J. Marmion, D. Griffith, K. B. Nolan, *Eur. J. Inorg. Chem.* **2004**, 3003 and references therein.
[3] C. J. Marmion, T. Murphy, J. R. Docherty, K. B. Nolan, *Chem. Commun.* **2000**, 1153.
[4] D. Griffith, K. Lyssenko, P. Jensen, P. E. Kruger, C. J. Marmion, *Dalton Trans.* **2005**, 956.
[5] V. L. Pecoraro, A. J. Stemmler, B. R. Gibney, J. J. Bodwin, H. Wang, J. W. Kampt, A. Barinski, "Metallocrowns: A New Class of Molecular Recognition Agents", in *Progress in Inorganic Chemistry*, Wiley, New York, Chichester, **1996**, vol. 45.
[6] C. Mulcahy, F. M. Dolgushin, K. A. Krot, D. Griffith, C. J. Marmion, *Dalton Trans.* **2005**, 1993.
[7] T. Beissel, R. E. Powers, T. N. Parac, K. N. Raymond, *J. Am. Chem. Soc.* **1999**, *121*, 4200.
[8] L. R. Scolnick, A. M. Clements, J. C. Liao, L. M. Hellberg, J. May, T. R. Dean, D. W. Christianson, *J. Am. Chem. Soc.* **1997**, *119*, 850.
[9] A. J. Stemmler, J. L. Kampf, M. L. Kirk, V. L. Pecoraro, *J. Am. Chem. Soc.* **1995**, *117*, 6368.
[10] J. J. Bodwin, A. D. Cutland, R. G. Malkani, V. L. Pecoraro, *Coord. Chem. Rev.* **2001**, *216–217*, 489.
[11] M. D. Hall, T. W. Failes, D. E. Hibbs, T. W. Hambley, *Inorg. Chem.* **2002**, *41*, 1223.
[12] T. W. Failes, M. D. Hall, T. W. Hambley, *Dalton Trans.* **2003**, 1596.
[13] Z. D. Liu, R. C. Hider, *Coord. Chem. Rev.* **2002**, 232,, 151.
[14] E. Farkas, E. Kozma, M. Petho, K. M. Herlihy, G. Micera, *Polyhedron* **1998**, *17*, 3331.
[15] G. Gran, *Acta Chem. Scand.* **1950**, *4*, 599.
[16] H. Irving, M. G. Miles, L. D. Pettit, *Anal. Chim. Acta* **1967**, *38*, 475.
[17] A. Sabatini, A. Vacca, P. Gans, *Coord. Chem. Rev.* **1992**, *120*, 389–405.
[18] C. F. Baes, R. E. Mesmer, *The Hydrolysis of Cations*, Wiley, New York, **1976**.
[19] *SMART and SAINT, Release 5.0, Area Detector Control and Integration Software*, Bruker AXS, Analytical X-ray Instruments, Madison, Wisconsin, USA, **1998**.
[20] G. M. Sheldrick, *SADABS (Version 2.01) and SHELXL (Version 5.01)*, Bruker AXS Inc., Madison, Wisconsin, USA, **1998**.

Received: August 15, 2006
Published Online: February 22, 2007

 © 2007 Wiley-VCH Verlag GmbH & Co. KGaA, Weinheim 

DOI: 10.1002/ejic.200600940

# Gas-Phase Structure and Vibrational Properties of Trifluoromethyl Trifluoromethanesulfonate, $CF_3SO_2OCF_3$

**María E. Tuttolomondo,[a] Pablo E. Argañaraz,[a] Eduardo L. Varetti,[b][‡] Stuart A. Hayes,[c] Derek A. Wann,[c] Heather E. Robertson,[c] David W. H. Rankin,[c] and Aida Ben Altabef*[a][‡]**

**Keywords:** Electron diffraction / IR spectroscopy / Raman spectroscopy / Structure elucidation / Ab initio calculations

Trifluoromethyl trifluoromethanesulfonate, $CF_3SO_2OCF_3$, has been synthesised and its gas-phase structure determined from electron-diffraction data. This structural study was supported by HF, MP2 and DFT (B3LYP and B1B95) calculations, which revealed a strong dependence of the theoretical structure on the polarisation of the basis set. Infrared spectra for the gas and solid and a Raman spectrum for the liquid were obtained, and the observed bands were assigned. The experimental vibrational data, along with theoretical (B3LYP) force constants, were used to define a scaled quantum mechanical force field, which enabled reproduction of the measured frequencies with a final root-mean-square deviation of 6 $cm^{-1}$.
(© Wiley-VCH Verlag GmbH & Co. KGaA, 69451 Weinheim, Germany, 2007)

## Introduction

The synthesis of trifluoromethyl trifluoromethanesulfonate, $CF_3SO_2OCF_3$, was first reported by Noftle and Cady[1] as a product of the thermal decomposition of $(CF_3SO_2)_2O$. Different synthetic routes were later proposed by Olah and Ohyama,[2] Kobayashi et al.[3] and Hassani et al.,[4] but no structural or vibrational studies have been reported.

Our previous studies on derivatives of trifluoromethanesulfonic acid[5–8] have been extended to $CF_3SO_2OCF_3$ in order to investigate further the characteristic conformations and force constants for such molecules. For that purpose, the substance has been synthesised and its gas-phase structure determined by electron diffraction. Additionally, infrared and Raman spectra were recorded for different physical states. These experimental measurements were complemented by quantum chemical calculations to obtain an optimised molecular structure and frequencies corresponding to the normal modes of vibration. Of particular interest is the comparison of the experimental and theoretical molecular geometric parameters and conformational isomers with the experimental results previously obtained for $CF_3SO_2OCH_3$[5] and $ClSO_2OCF_3$,[9] and with those calculated for several $CF_3SO_2X$[6] and $CF_3SO_2OX$[7,8] molecules, which shows that covalent sulfonates prefer a *gauche* conformation (Figure 1).[5]

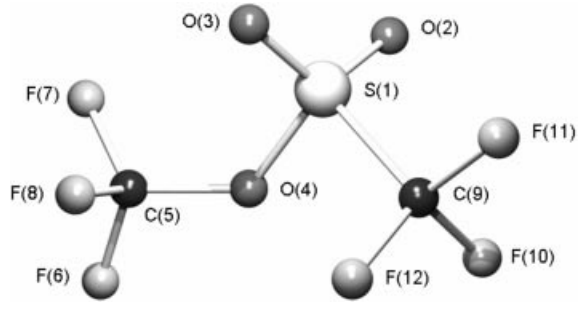


Figure 1. Molecular structure of $CF_3SO_2OCF_3$, showing atom numbering.

## Results and Discussion

### Theoretical Study

A starting geometry for $CF_3SO_2OCF_3$ was obtained by using RHF theory with a 3-21G(d) basis set[10–12] followed by a 6-31G(d) basis set.[13–15] Electron correlation was then accounted for by using the MP2,[16] B3LYP[17] and B1B95[18] methods before increasing the basis set sequentially from 6-31G(d) to 6-311+G(d).[19,20] In addition, the 6-31G(3df) basis set,[21] the Dunning correlation-consistent basis sets, cc-pVDZ and cc-pVTZ[22] and Ahlrichs' TZVP[23] and TZVPP[24] basis sets were used to gauge the

[a] Instituto de Química Física, Facultad de Bioquímica, Química y Farmacia, Universidad Nacional de Tucumán, San Lorenzo 456, 4000 Tucumán, R. Argentina
E-mail: altabef@fbqf.unt.edu.ar
[b] Centro de Química Inorgánica (CEQUINOR, CONICET-UNLP), Departamento de Química, Facultad de Ciencias Exactas, Universidad Nacional de La Plata, C. Correo 962, 1900 La Plata, R. Argentina
[c] School of Chemistry, University of Edinburgh, West Mains Road, Edinburgh, EH9 3JJ, UK
E-mail: d.w.h.rankin@ed.ac.uk
[‡] Members of the Carrera del Investigador Científico, CONICET, R. Argentina
Supporting information for this article is available on the WWW under http://www.eurjic.org or from the author.

 © 2007 Wiley-VCH Verlag GmbH & Co. KGaA, Weinheim 

effect of including further polarisation functions. The results of the geometry optimisations are available in Tables S1 and S2 in the Supporting Information. In all cases, a molecular structure with $C_1$ symmetry was predicted, as shown in Figure 1. The force field obtained at the RHF/6-31G(d) level was then used with the program SHRINK[25] to obtain estimates of the amplitudes of vibration ($u_{h1}$) and perpendicular vibrational correction terms ($k_{h1}$) used in the gas electron diffraction (GED) refinement.

Scans of the potential energy with respect to the C–S–O–C torsion were performed at the RHF/6-31G(d) and MP2/6-31G(d) levels and a third scan at the MP2/6-31G(d) level with the 6-31G(3df) basis set on sulfur (Figure 2). These reveal two symmetrically equivalent minima, corresponding to enantiomers, and O–C(5) eclipses one or other of the S=O bonds when viewed down the S–O(4) bond. As enantiomers are indistinguishable by GED, the subsequent refinement was performed with the eclipsing of the S=O(3) bond by O–C as in the calculated structures. The shallow barrier between the two equivalent conformers is ca. 5–10 kJ mol$^{-1}$, easily surmountable at the experimental temperatures. The quantum chemical calculations predict the existence of two stable, asymmetric (point group $C_1$) and structurally equivalent conformers for $CF_3SO_2OCF_3$, both with a *gauche* conformation with a C–S–O–C dihedral angle of about 110°. As shown in Table 1, this angle is relatively sensitive to changes in method and basis set and has a larger value than that calculated for $CF_3SO_2OCH_3$ (93°).[5] Similar molecules that were previously studied by us were also calculated to have *gauche* conformations, with C–S–O–C dihedral angles of 114.8° in $CF_3SO_2OCH_2CF_3$[7] and 91.5° in $CF_3SO_2OCH_2CH_3$[8] [B3LYP/6-31G(d) values in both cases].

The calculated C–O and C–F bond lengths converged reasonably well with increasing basis set size and showed fairly good agreement between different post-Hartree–Fock methods, as shown in Table 1. Bond lengths to sulfur, however, are extremely sensitive to both method and basis set. Particularly interesting was the result of adding additional polarisation functions to the basis set, which resulted in shortening of the bond lengths, the most significant is a reduction of 5.5 pm for the S–O bond [MP2/6-31G(d) to MP2/6-31G(3df)].

With reference to structural studies on $CF_3SO_2OCH_3$[5] and $ClSO_2OCF_3$,[9] the bond lengths to sulfur were overestimated by B3LYP relative to those obtained by GED and X-ray crystal values (the latter for $ClSO_2OCF_3$ only). With this in mind, the MP2/6-31G(3df) geometry appeared to be the best as both a starting point for the GED refinement and the basis for geometrical restraints.

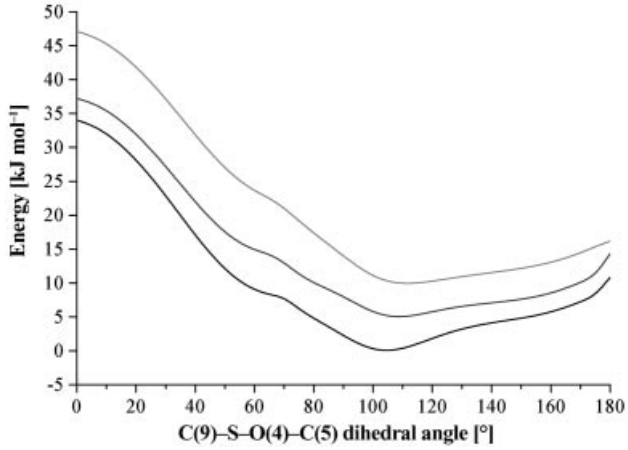


Figure 2. Torsional potential around the S–O(4) bond for $CF_3SO_2OCF_3$, stepped in 5° increments. Calculations were performed at the HF (light grey) and MP2 (dark grey) levels by using a 6-31G(d) basis set and by using MP2/6-31G(d) with 3df polarisation on sulfur (black).

## GED Model

The molecular model for the GED refinement assumed overall $C_1$ symmetry (Figure 1), as predicted by the calculations. The structure of $CF_3SO_2OCF_3$ was defined in terms of 25 independent parameters, comprising 11 bond lengths and differences, 10 bond angles and differences, one tilt angle and three torsional angles, listed in Table 2. The bonded distances S–O(4), O(4)–C(5) and S–C(9) were each defined individually ($p_7$, $p_{10}$ and $p_{11}$, respectively), whilst simple averages were taken of the six C–F bond lengths ($p_1$) and of the two S=O bond lengths ($p_8$). The difference between the average C–F distance in the $CF_3$ group bonded to O(4) (group 1) and the average C–F distance in the $CF_3$ group bonded directly to the sulfur atom (group 2) was defined ($p_2$). For $CF_3$ in group 1, the C–F(6) distance was then found by defining the difference between this distance and the average of the C–F(7) and C–F(8) bond lengths ($p_3$). The difference between the latter two bond lengths was then defined ($p_5$). Similarly, in group 2, the difference between the C–F(11) distance and an average of the other two bond lengths ($p_4$) and the difference between the C–F(12) bond length and the C–F(10) bond length ($p_6$) were defined. The

Table 1. Selected calculated and GED geometrical parameters for $CF_3SO_2OCF_3$ (distances in pm, angles in °).

| | GED | HF/ 6-31G(d) | MP2/ 6-31G(d) | 6-311+G(d) | 6-31G(3df) | cc-pVTZ | TZVPP | B3LYP/ 6-31G(3df) | B1B95/ 6-31G(3df) |
|---|---|---|---|---|---|---|---|---|---|
| *r*C–F average | 133.3(2) | 130.2 | 133.3 | 132.5 | 131.9 | 132.1 | 132.1 | 132.6 | 131.8 |
| *r*S–O | 161.5(4) | 160.3 | 167.7 | 167.1 | 162.2 | 163.9 | 163.8 | 163.6 | 161.8 |
| *r*S=O average | 141.9(3) | 140.9 | 144.7 | 143.4 | 141.9 | 143.1 | 143.1 | 142.0 | 141.4 |
| *r*C–O | 139.3(7) | 137.4 | 139.3 | 138.5 | 139.0 | 139.1 | 139.0 | 139.5 | 138.9 |
| *r*C–S | 181.3(4) | 182.1 | 184.5 | 186.3 | 183.8 | 185.4 | 185.6 | 187.4 | 185.1 |
| ϕC–S–O–C | 119.5(18) | 111.2 | 108.4 | 110.7 | 105.6 | 108.2 | 108.6 | 105.8 | 107.5 |

 © 2007 Wiley-VCH Verlag GmbH & Co. KGaA, Weinheim 

difference between the two S=O double bond lengths ($p_9$) allowed these bond lengths to be defined.

Table 2. GED refined parameters ($r_{h1}$ structure) for $CF_3SO_2OCF_3$ (distances in pm, angles in degrees).

| | Description | Value | MP2/6-31G(3df) | Restraint uncertainty[a] |
|---|---|---|---|---|
| | Independent parameters | | | |
| $p_1$ | *r*C–F average | 133.3(2) | 131.9 | |
| $p_2$ | *r*C–F difference 1 | –0.4(1) | –0.4 | 0.1 |
| $p_3$ | *r*C–F difference 2 | 0.4(1) | 0.4 | 0.1 |
| $p_4$ | *r*C–F difference 3 | 0.2(1) | 0.2 | 0.1 |
| $p_5$ | *r*C–F difference 4 | 0.2(1) | 0.2 | 0.1 |
| $p_6$ | *r*C–F difference 5 | 0.0(1) | 0.0 | 0.1 |
| $p_7$ | *r*S–O | 161.5(4) | 162.2 | |
| $p_8$ | *r*S=O average | 141.9(3) | 141.9 | |
| $p_9$ | *r*S–O difference | 0.4(1) | 0.4 | 0.1 |
| $p_{10}$ | *r*C–O | 139.3(7) | 139.0 | |
| $p_{11}$ | *r*C–S | 181.3(4) | 183.8 | |
| $p_{12}$ | ∠O(4)–S–C | 96.9(10) | 97.0 | 1.0 |
| $p_{13}$ | ∠O–S–O(4) average | 108.0(2) | 108.0 | |
| $p_{14}$ | ∠O–S–O(4) difference | 3.8(4) | 4.4 | 0.5 |
| $p_{15}$ | ∠C–S–O average | 107.9(3) | 107.6 | |
| $p_{16}$ | ∠C–S–O difference | 1.3(2) | 1.3 | 0.2 |
| $p_{17}$ | ∠S–O–C | 121.8(4) | 121.3 | 0.5 |
| $p_{18}$ | ∠O–C–F(6) | 104.6(4) | 105.8 | |
| $p_{19}$ | ∠F–C–F group 1 average | 108.0(2) | 109.3 | |
| $p_{20}$ | ∠F–C–F group 1 difference | 0.3(2) | 0.4 | 0.2 |
| $p_{21}$ | ∠S–C–F tilt | 1.6(5) | 1.6 | 0.5 |
| $p_{22}$ | ∠F–C–F group 2 | 108.6(2) | 109.8 | |
| $p_{23}$ | ϕC–S–O–C | 119.5(18) | 105.6 | |
| $p_{24}$ | ϕS–O–C–F(6) | 195.2(9) | 182.6 | |
| $p_{25}$ | ϕO–S–C–F(11) | 177.2(10) | 178.5 | 2.0 |
| | Dependent parameter | | | |
| $d_1$ | ∠O(2)=S=O(3) | 124.6(8) | 125.1 | 1.0 |

[a] Restraint values are given by the corresponding MP2/6-31G(3df) values.

The geometry around sulfur was described using three angles and two differences: the O(4)–S–C(9) angle ($p_{12}$), the average of the O(2)–S–O(4) and O(3)–S–O(4) angles ($p_{13}$) and their difference ($p_{14}$), and the average of the O(2)–S–C(9) and O(3)–S–C(9) angles ($p_{15}$) and their difference ($p_{16}$).

Fluorine atom positions in $CF_3$ in group 1 were described by using the average of the three internal F–C–F angles ($p_{19}$) and the difference between the F(7)–C–F(8) angle and the angles F(6)–C–F(7) and F(6)–C–F(8) ($p_{20}$), the latter two angles are assumed to be identical. The orientation of this $CF_3$ group with respect to sulfur was defined by using the angles S–O–C ($p_{17}$) and O–C–F(6) ($p_{18}$), and the torsional angles C–S–O–C ($p_{23}$) and S–O–C–F(6) ($p_{24}$).

$CF_3$ in group 2 was described by using a single F–C–F angle ($p_{22}$) and orientated by using a tilt angle ($p_{21}$). A positive tilt was defined as a reduction in the S–C–F(11) angle, with the zero point occurring when the three S–C–F angles are equal. This group was also allowed to rotate around the S–C bond, defined by the torsional angle O(4)–S–C–F(11) ($p_{25}$). In this case, an angle of 180° corresponds to a staggered conformation and a larger angle brings F(11) closer to O(3).

## Electron Diffraction Refinement

The GED refinement (Table 3) was carried out with the SARACEN method,[26] which allows parameters that are poorly defined by GED data alone to be restrained to calculated values with specified uncertainties, on the basis of the degree of convergence of the calculations. Distances were corrected for curvilinear perpendicular motion ($k_{h1}$) and yielded $r_{h1}$ parameters.[25] All 25 independent parameters were refined, along with two individual and eight groups of amplitudes of vibration, to produce an $R_G$ factor of 0.067 ($R_D$ = 0.029). The refined parameters are displayed in Table 2 along with the corresponding values predicted by MP2/6-31G(3df) calculations. The radial-distribution curve is shown in Figure 3, and the molecular-scattering intensity curve is provided as Supporting Information (Figure S1).

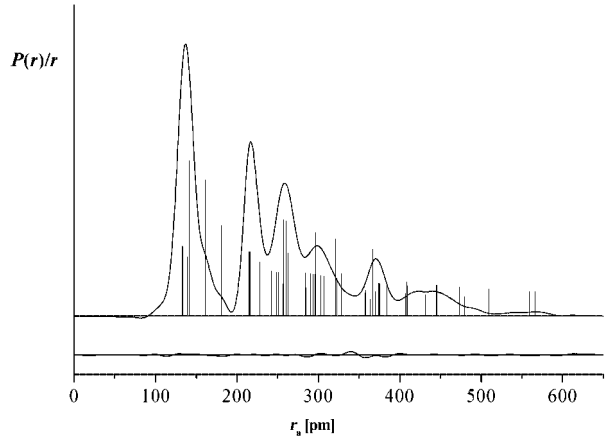


Figure 3. Experimental and difference (experimental – theoretical) radial-distribution curves, $P(r)/r$, for $CF_3SO_2OCF_3$. Before Fourier inversion, the data were multiplied by $s \times \exp[(-0.00002s^2)/(Z_S - f_S)(Z_F - f_F)]$.

Where required, restraints on geometrical parameters were derived from the MP2/6-31G(3df) calculated values. Those applied directly to independent or dependent parameters are given in Table 2, whilst restraints on the differences between independent parameters are provided in Table 3. The only group of amplitudes of vibration allowed to refine

Table 3. Restraints on differences between pairs of independent parameters (distances in pm, angles in degrees).

| Difference | | GED[a] | MP2/6-31G(3df) | Uncertainty[b] |
|---|---|---|---|---|
| $p_{10} - p_1$ | [*r*C–O] – [*r*C–F average] | 6.1(8) | 7.0 | 1.0 |
| $p_{13} - p_{15}$ | [∠O–S–O(4) average] – [∠C–S–O average] | 0.1(2) | 0.3 | 0.2 |
| $p_{22} - p_{19}$ | [∠F–C–F group 2] – [∠F–C–F group 1 average] | 0.5(2) | 0.5 | 0.2 |
| $p_{19} - p_{18}$ | [∠F–C–F group 1 average] – [∠O–C–F(6)] | 3.5(5) | 3.5 | 0.5 |

[a] Refined value. [b] Restraint values are given by the corresponding MP2/6-31G(3df) values.

 © 2007 Wiley-VCH Verlag GmbH & Co. KGaA, Weinheim 

unrestrained was that containing the bonded distances of less than 150 pm. The remaining amplitudes for bonded atom pairs were restrained with uncertainties of 10% of their calculated values, whilst the groups of non-bonded amplitudes were restrained with uncertainties of 20%. A full list of interatomic distances and corresponding calculated and refined amplitudes of vibration are provided in Table S3 (Supporting Information), and the least-squares correlation matrix in Table S4.

### GED and Calculated Structures

Two large discrepancies can be seen between the GED and calculated structures: the S–C bond length and the torsional angles, particularly C–S–O–C. The S–C distance is 2.5 pm shorter than that predicted by MP2/6-31G(3df) calculations. However, the S–O bond length, which for similar compounds is generally poorly defined by theory, is only 0.7 pm shorter experimentally. The MP2/6-31G(3df) calculation is thus significantly more accurate for predicting these bond lengths than other methods or basis sets requiring similar computational resources. For instance, the MP2/6-311+G(d) calculation overestimates the S–O and S–C distances by 5.6 and 3.0 pm, respectively, and B3LYP/6-31G(3df) underestimates the same bond lengths by 2.0 and 6.1 pm, respectively. The B1B95/6-31G(3df) calculation predicts parameter values that are similar to those predicted by MP2, overestimating the respective S–O and S–C distances by 0.3 and 3.8 pm, respectively, relative to the GED values. MP2 and B1B95 are therefore marginally better than B3LYP at describing the geometry of $CF_3SO_2OCF_3$, and for this type of compound, B1B95 is likely be the best compromise between accuracy and computational cost. Comparison of these results with parameters for similar compounds $CF_3SO_2OCH_3$[5] and $FSO_2OSF_5$,[27] studied by GED and B3LYP/6-31G(d) calculations, shows that in these cases, despite the reasonably close agreement between different theoretical methods, the experimental S–O bonds are 5–7 pm shorter. In the case of $CF_3SO_2OCH_3$,[5] the experimentally determined S–C bond is 3.3 pm shorter. The study on $ClSO_2OCF_3$[9] also shows that B3LYP/6-311G(d) underestimates the S–O bond length by 6 to 7 pm, but the B3LYP/6-311+G(3df) calculation reduces this difference to ca. 3 pm. These GED and theoretical results are therefore consistent with the more general observation that distances between sulfur and oxygen are poorly predicted with standard methods [such as MP2/6-31G(d)], and indicate that this may be due primarily to insufficient polarisation functions in the basis set. This conclusion is also consistent with the molecular structures calculated at the MP2 level by using Dunning's cc-pVDZ and cc-pVTZ, and Ahlrichs' TZVP and TZVPP basis sets (Table S2). As was the case for the Pople 6-31G(d) basis set, the cc-pVDZ and TZVP bases contain only a single d-type Gaussian and underestimate the S–O bond length by 8.9 and 6.6 pm, respectively. In contrast, the cc-pVTZ and TZVPP bases, which both incorporate two d-type and one f-type Gaussian, underestimate the S–O bond length by just 2.4 and 2.3 pm, respectively, relative to the GED determined value of 161.5(4) pm. Similar observations can also be made for the S=O and S–C bond lengths, albeit to a lesser extent.

The C–S–O–C torsional angle was found to be 119.5(18)° by GED relative to between 105 and 112° by various theoretical methods. However, the estimated standard deviation of this value does not give a good estimate of its uncertainty, as the refinement can be performed by fixing this angle at any arbitrary value between 100 and 150° without significantly affecting the remaining parameters or the $R_G$ factor. It would, in principle, be possible to replace the rigid model adopted in the refinement by a dynamic model based on the potential function of the C–S–O–C torsion. However, it can be seen from the theoretical potential energy scan (Figure 2) that this potential energy curve is not a simple function, and several parameters would be required to model it. In such cases, the uncertainties of the extra parameters are extremely large, and so the refined values are of little physical significance. We therefore did not use such a dynamic model in this case.

### Vibrational Study

$CF_3SO_2OCF_3$ has $C_1$ symmetry, and therefore its 30 normal modes of vibration are active in the IR and Raman spectra. Representative spectra appear in Figures 4 (IR spectra of the gas and solid) and 5 (Raman spectrum of the liquid), and the frequencies for the observed spectral features are collated in Table 4.

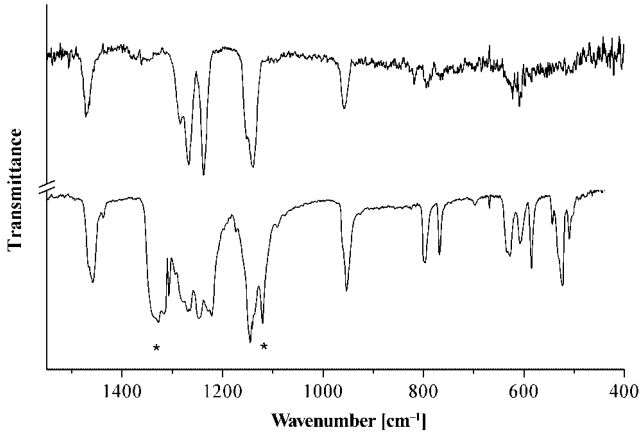


Figure 4. Infrared spectra for $CF_3SO_2OCF_3$ in the gas phase (upper trace; resolution 2 $cm^{-1}$, path length 10 cm, pressure ca. 1.0 Torr) and in the solid phase (lower trace; film on cooled KBr window, resolution 2 $cm^{-1}$). Asterisks indicate solid $SO_2$ bands.

The B3LYP calculations reproduced the normal frequencies of vibration with the following root-mean-square-deviation (RMSD) values for each basis set: 19.8 $cm^{-1}$ for 6-31G(d), 21.6 $cm^{-1}$ for 6-311G(d) and 27.1 $cm^{-1}$ for 6-311+G(d). The first and second basis sets reproduce the experimental frequencies somewhat better, and the results obtained with the 6-31G(d) basis set were used for the vibrational analysis, in order to allow direct comparison with

 © 2007 Wiley-VCH Verlag GmbH & Co. KGaA, Weinheim 

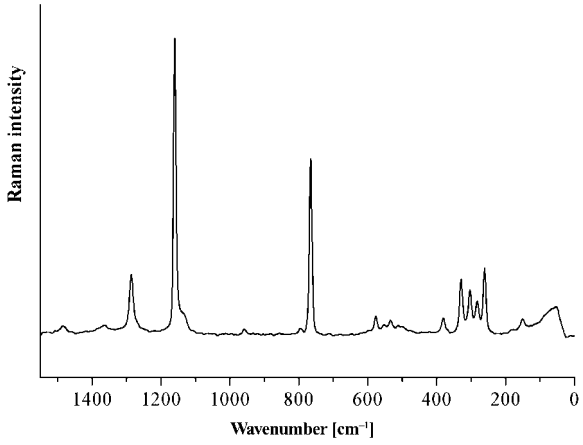


Figure 5. Raman spectrum for liquid $CF_3SO_2OCF_3$ (resolution 4 $cm^{-1}$).

Table 4. Frequencies of observed bands in the infrared and Raman spectra of $CF_3SO_2OCF_3$ (units are $cm^{-1}$).[a]

| Infrared | | Raman[b] | Mode assignment |
|---|---|---|---|
| Gas | Solid | Liquid | |
| 1469 (s) | 1458 (s) | 1458 (3) | $\nu_1$ |
| | | 1342 (3) | ? |
| | 1327 (vs) | | $SO_2$ |
| 1282 (s) | 1277 (s) | | $\nu_2$ |
| 1268 (vs) | 1268 (vs) | 1268 (20) | $\nu_3$ |
| | 1266 (vs) | | $\nu_4$ |
| 1236 (vs) | 1246 (vs) | | $\nu_5$, $\nu_6$ |
| | 1228 (s) | | |
| | 1221 (vs) | | |
| 1150 (sh.) | 1144 (vs) | 1146 (100) | $\nu_7$ |
| 1139 (vs) | 1140 (vs) | | $\nu_8$ |
| | 1119 (s) | | $SO_2$ |
| 956 (s) | 952 (s) | 952 (2) | $\nu_9$ |
| 816 (m) | | | ? |
| 792 (m) | 796 (m) | 794 (2) | $\nu_{10}$ |
| 766 (w) | 767 (m) | 766 (60) | $\nu_{11}$ |
| | 695 (vw) | | $\nu_{12}$ |
| 627 (m) | 628 (m) | | $\nu_{13}$ |
| 606 (m) | 606 (m) | 603 (vvw) | $\nu_{14}$ |
| 586 (w) | 584 (m) | 584 (6) | $\nu_{15}$ |
| | | 560 (3) | $\nu_{16}$ |
| 540 (vw) | 542 (w) | 542 (5) | $\nu_{17}$ |
| | 522 (m) | 520 (3) | ? |
| 508 (w) | 508 (w) | 509 (3) | $\nu_{18}$ |
| | 444 (vvw) | 445 (vvw) | $\nu_{19}$ |
| | | 394 (9) | $\nu_{20}$ |
| | | 345 (19) | $\nu_{21}$ |
| | | 320 (15) | $\nu_{22}$ |
| | | 300 (11) | $\nu_{23}$ |
| | | 280 (23) | $\nu_{24}$ |
| | | 200 (1, br.) | $\nu_{25}$ |
| | | 172 (4) | $\nu_{26}$ |
| | | 150 (sh. | $\nu_{27}$ |

[a] s = strong, m = medium, w = weak, v = very, sh. = shoulder, br. = broad. [b] For the Raman spectrum, relative band heights are given in parentheses.

calculations performed previously for related molecules. The calculated frequencies of vibration appear in Table 5, together with the experimental values.

The proposed assignments of spectral features to the different modes of vibration given in Table 4 are based on the calculated frequencies and on the infrared and Raman intensities and also on comparisons with known data for related molecules.

### *$SO_2$ Group Modes*

The $SO_2$ antisymmetric and symmetric stretching modes appear in the regions 1357–1467 $cm^{-1}$ and 1140–1157 $cm^{-1}$, respectively, in the molecules $CF_3SO_2X$ (X = F, OH, $NH_2$, $CH_3$, $OCH_2CH_3$, $OCH_2CF_3$).[6–8] The intense bands observed at 1469 and 1139 $cm^{-1}$ in the spectrum of the gas can therefore immediately be assigned to these modes. The last mode, however, is a complex mix of several simple vibrations, as discussed below. The medium intensity band at 586 $cm^{-1}$ in the gas infrared spectrum is assigned to the $SO_2$ bend. This frequency is somewhat higher than usual, as this mode appears in the region 488–538 $cm^{-1}$ in the compounds listed above. The bands for the three modes corresponding to the movements of the whole $SO_2$ group appear at relatively low frequencies. The following assignments are proposed, with the corresponding frequency ranges for the molecules mentioned above in parentheses: $SO_2$ wagging, 606 $cm^{-1}$ (611–628 $cm^{-1}$); $SO_2$ rocking, 394 $cm^{-1}$ (382–463 $cm^{-1}$); $SO_2$ twisting, 300 $cm^{-1}$ (310–351 $cm^{-1}$). These assignments are also supported by the calculations.

### *Trifluoromethyl Group Modes*

Inspection of the atomic displacements for the vibrational modes calculated in the 1100–1300 $cm^{-1}$ region shows that the stretching vibrations, especially the symmetric stretches, of the two $CF_3$ groups are strongly coupled. For this reason it is not possible to discuss the assignments of bands for these two groups separately.

The two $CF_3$ symmetric modes are predicted to have large Raman intensities. One mode includes the symmetric stretches of the two $CF_3$ groups, coupled with contributions from the CS and CO stretches and the $SO_2$ symmetric stretch; the latter is out of phase in relation to the other four. The second mode mixes the same five simple vibrations, but with the $SO_2$ symmetric stretch now in phase. These two complex modes are assigned to the strong Raman bands located at 1268 and 1146 $cm^{-1}$. The 1146 $cm^{-1}$ band exhibits a shoulder at ca. 1120 $cm^{-1}$, best defined in the infrared spectrum of the solid, and is assigned to a third mode, which also mixes the two $CF_3$ symmetric stretching vibrations and the CO and CS stretches in an out-of-phase fashion, but with almost no participation of the $SO_2$ symmetric stretch. Four bands should still be assigned to the $CF_3$ antisymmetric stretching vibrations. As not enough arguments are available for precise assignments, those appearing in Table 4 and Table 5 are tentative.

Symmetric deformation modes are observed at 792 $cm^{-1}$ ($CF_3S$ group) and 695 $cm^{-1}$ ($CF_3O$ group) in the gas infrared spectra. The two antisymmetric deformation modes of the $SCF_3$ group appear at 540 and 560 $cm^{-1}$, i.e. about 10 $cm^{-1}$ higher than the calculated values. The antisymmet-

 © 2007 Wiley-VCH Verlag GmbH & Co. KGaA, Weinheim 

Table 5. Observed and calculated frequencies, infrared and Raman intensities and potential-energy distribution for $CF_3SO_2OCF_3$.

| Mode | Observed | Calculated[a] | Calculated SQM[b] | IR intensity[c] | Raman activity[d] | Potential-energy distribution[e] |
|---|---|---|---|---|---|---|
| 1 | 1469 | 1414 | 1461 | 287 | 3.6 | $96S_1$ |
| 2 | 1282 | 1304 | 1283 | 48 | 9.1 | $54S_2 + 20S_8 + 11S_{21}$ |
| 3 | 1268 | 1242 | 1272 | 308 | 0.86 | $31S_2 + 10S_7 + 25S_8$ |
| 4 | 1266 | 1293 | 1263 | 212 | 0.52 | $30S_4 + 10S_5 + 51S_6 + 12S_{13} + 11S_{19}$ |
| 5 | 1236 | 1283 | 1247 | 334 | 0.64 | $51S_4 + 40S_5$ |
| 6 | 1236 | 1264 | 1233 | 515 | 2.1 | $16S_4 + 46S_5 + 31S_6$ |
| 7 | 1150 | 1116 | 1152 | 238 | 6.4 | $21S_3 + 31S_7 + 29S_9 + 22S_{10} + 24S_{12} + 13S_{22}$ |
| 8 | 1139 | 1144 | 1142 | 280 | 2.2 | $15S_3 + 12S_7 + 44S_8 + 36S_9 + 20S_{12}$ |
| 9 | 956 | 933 | 937 | 137 | 1.0 | $28S_3 + 31S_9 + 23S_{11}$ |
| 10 | 792 | 777 | 795 | 26 | 1.5 | $37S_7 + 17S_{10} + 14S_{22}$ |
| 11 | 766 | 737 | 756 | 105 | 16.0 | $21S_3 + 39S_{11} + 12S_{21}$ |
| 12 | 695 | 682 | 696 | 3.87 | 0.53 | $12S_3 + 24S_{12} + 15S_{26}$ |
| 13 | 627 | 613 | 634 | 66 | 0.47 | $12S_6 + 12S_{13} + 19S_{14} + 19S_{19}$ |
| 14 | 606 | 588 | 610 | 114 | 0.60 | $12S_{10} + 12S_{12} + 16S_{13} + 30S_{14}$ |
| 15 | 586 | 567 | 589 | 38 | 3.0 | $38S_{15} + 10S_{17}$ |
| 16 | 560 | 549 | 559 | 0.37 | 2.2 | $54S_{16}$ |
| 17 | 540 | 526 | 536 | 29 | 2.9 | $45S_{17} + 17S_{18}$ |
| 18 | 508 | 487 | 502 | 20 | 1.3 | $19S_{15} + 12S_{17} + 49S_{18}$ |
| 19 | 444 | 430 | 453 | 1.90 | 0.17 | $49S_{13} + 57S_{19}$ |
| 20 | 394 | 380 | 397 | 3.94 | 2.2 | $21S_{16} + 36S_{20} + 21S_{25}$ |
| 21 | 345 | 325 | 341 | 1.05 | 4.8 | $18S_{11} + 28S_{15} + 25S_{21} + 14S_{27}$ |
| 22 | 320 | 304 | 319 | 1.05 | 3.6 | $10S_{11} + 12S_{14} + 14S_{21} + 17S_{22} + 16S_{24}$ |
| 23 | 300 | 275 | 289 | 1.37 | 2.6 | $39S_{23} + 17S_{25}$ |
| 24 | 280 | 263 | 277 | 5.50 | 3.8 | $23S_{22} + 36S_{24}$ |
| 25 | 200 | 185 | 195 | 2.03 | 0.25 | $34S_{20} + 49S_{23} + 56S_{25}$ |
| 26 | 172 | 158 | 170 | 1.07 | 0.44 | $56S_{56} + 23S_{27}$ |
| 27 | 150 | 145 | 154 | 1.31 | 0.26 | $28S_{24} + 19S_{26} + 86S_{27} + 12S_{28} + 15S_{29}$ |
| 28 | – | 66 | 67 | 0.15 | 0.04 | – |
| 29 | – | 51 | 51 | 0.15 | 0.01 | – |
| 30 | – | 36 | 36 | 0.03 | 0.01 | – |
| RMSD | | 19.8 | 6.04 | | | |

[a] B3LYP/6-31G* calculation. Observed and calculated values in $cm^{-1}$. [b] From scaled quantum mechanics force field (see text for further definition). [c] Units are km mol$^{-1}$. [d] Units are Å$^4$(amu)$^{-1}$. [e] See Table 6 for definitions of natural symmetry coordinates.

ric deformation modes of the $CF_3O$ group show a larger splitting, appearing at 508 and 627 $cm^{-1}$.

The $CF_3$ rocking modes were assigned by taking into account the theoretically predicted frequencies and with knowledge of modes in related molecules. In this way, the weak bands located at 200 and 280 $cm^{-1}$ are assigned to the rocking modes of the $CF_3S$ group, which appear at around 200 and 340 $cm^{-1}$ in $CF_3SO_2X$ molecules.[6] Higher frequencies, with values of 340 and 440 $cm^{-1}$, were reported for the $CF_3O$ rocking motions in $CF_3OX$ molecules,[28] and consequently the bands observed at 345 and 444 $cm^{-1}$ for $CF_3SO_2OCF_3$ are assigned to these modes.

### *Skeletal Modes*

The O–S stretching mode appears as a strong Raman band located at 766 $cm^{-1}$. The strong 956 $cm^{-1}$ infrared band in the gas spectrum is well predicted by calculations, in terms of both position and intensity, to be due to the C–O stretch, although the mode is best described as the out-of-phase coupling of the C–O and O–S stretches, as can be observed from the calculated atomic displacements when displayed with the program GaussView.[29]

The 320 $cm^{-1}$ mode shows a strong contribution from the C–S stretch. The CSO bend appears as the main component of the 150 $cm^{-1}$ mode, and is also strongly coupled with the COS bend in the 172 $cm^{-1}$ mode. These last two modes appear as very weak, ill-defined Raman bands.

### *Torsional Modes*

Very weak spectral features were expected for the three torsional modes and, in fact, no bands could be identified to be assigned to these modes.

## Calculation of Force Constants

The Cartesian force field for $CF_3SO_2OCF_3$, as calculated, was transformed into the set of non-redundant, natural coordinates defined in Table 6 through the B-matrix[30] obtained with a standard program. Such coordinates take into account the local symmetry around the C and S atoms and are in accordance with the proposals of Fogarasi et al.[31] The resulting force field was subsequently scaled by using the scheme proposed by Pulay et al.,[32] in which the diagonal force constants are multiplied by scale factors $k_{f,i}$, $k_{f,j}$, etc., and the corresponding interaction constants are multiplied by $(k_{f,i} \times k_{f,j})^{1/2}$. A set of initial scale factors was defined by using values recommended by Kalincsák and Pongor[33] where available and by using unity for the rest. These scale factors were subsequently adjusted by a least-squares procedure in order to obtain the best fit to the experimental frequencies.(initial and final scale factors are available in Table S5, Supporting Information). All vibrational bands were assigned the same weight in the adjustment except for those missing or showing uncertain fre-

 © 2007 Wiley-VCH Verlag GmbH & Co. KGaA, Weinheim 

Table 6. Definitions of natural symmetry coordinates for $CF_3SO_2OCF_3$.[a]

| Label | Definition | Description |
|---|---|---|
| $S_1$ | r(1–2) – r(1–3) | $SO_2$ antisymmetric stretch |
| $S_2$ | 2m(6–5) – m(8–5) – m(7–5) | $OCF_3$ antisymmetric stretch |
| $S_3$ | m(8–5) + m(6–5) + m(7–5) | $OCF_3$ symmetric stretch |
| $S_4$ | d(9–10) – d(9–12) | $SCF_3$ antisymmetric stretch |
| $S_5$ | 2d(9–11) – d(9–10) – d(9–12) | $SCF_3$ antisymmetric stretch |
| $S_6$ | m(8–5) – m(7–5) | $OCF_3$ antisymmetric stretch |
| $S_7$ | d(9–10) + d(9–11) + d(9–12) | $SCF_3$ symmetric stretch |
| $S_8$ | r(1–2) + r(1–3) | $SO_2$ symmetric stretch |
| $S_9$ | p(4–5) | C–O stretch |
| $S_{10}$ | ε(10–9–11) + ε(10–9–12) + ε(11–9–12) – β(10–9–1) – β(11–9–1) – β(12–9–1) | $SCF_3$ symmetric bend |
| $S_{11}$ | l(1–4) | S–O stretch |
| $S_{12}$ | μ(6–5–7) + μ(6–5–8) + μ(7–5–8) – Ω(6–5–4) – Ω(7–5–4) – Ω(8–5–4) | $OCF_3$ symmetric bend |
| $S_{13}$ | μ(8–5–6) – μ(7–5–6) | $OCF_3$ antisymmetric bend |
| $S_{14}$ | ψ(9–1–2) + ψ(9–1–3) – γ(4–1–2) – γ(4–1–3) | $SO_2$ wag |
| $S_{15}$ | 4φ(2–1–3) – ψ(9–1–2) – ψ(9–1–3) – γ(4–1–2) – γ(4–1–3) | $SO_2$ bend |
| $S_{16}$ | ε(10–9–11) – ε(12–9–11) | $SCF_3$ antisymmetric bend |
| $S_{17}$ | 2ε(10–9–12) – ε(10–9–11) – ε(12–9–11) | $SCF_3$ antisymmetric bend |
| $S_{18}$ | 2μ(8–5–7) – μ(8–5–6) – μ(7–5–6) | $OCF_3$ antisymmetric bend |
| $S_{19}$ | Ω(8–5–4) – Ω(7–5–4) | $CF_3$ rock |
| $S_{20}$ | ψ(9–1–2) – ψ(9–1–3) + γ(4–1–2) – γ(4–1–3) | $SO_2$ rock |
| $S_{21}$ | 2Ω(6–5–4) – Ω(8–5–4) – Ω(7–5–4) | $OCF_3$ rock |
| $S_{22}$ | t(1–9) | C–S stretch |
| $S_{23}$ | ψ(9–1–2) – ψ(9–1–3) – γ(4–1–2) + γ(4–1–3) | $SO_2$ twist |
| $S_{24}$ | 2β(11–9–1) – β(10–9–1) – β(12–9–1) | $SCF_3$ rock |
| $S_{25}$ | β(10–9–1) – β(12–9–1) | $SCF_3$ rock |
| $S_{26}$ | α(1–4–5) | SOC bend |
| $S_{27}$ | 4θ(9–1–4) – ψ(9–1–2) – ψ(9–1–3) – γ(4–1–2) – γ(4–1–3) | CSO bend |
| $S_{28}$ | τ(9–1–4–5) + τ(2–1–4–5) + τ(3–1–4–5) | S–O torsion |
| $S_{29}$ | τ(8–5–4–1) + τ(6–5–4–1) + τ(7–5–4–1) | $OCF_3$ torsion |
| $S_{30}$ | τ(10–9–1–2) + τ(11–9–1–2) + τ(12–9–1–2) + τ(10–9–1–3) + τ(11–9–1–3) + τ(12–9–1–3) + τ(10–9–1–4) + τ(11–9–1–4) + τ(12–9–1–4) | $SCF_3$ torsion |

[a] Latin letters denote changes in bonds between the atoms whose numbers appear in parentheses. Greek letters denote changes in angles defined by the atoms that are also indicated with numbers.

quencies, for which zero weights were used. No empirical correction of the theoretical geometry was used. The potential-energy distribution, which shows the relative contribution of the diagonal force constants to each vibrational mode, was subsequently calculated with the resulting scaled quantum mechanics (SQM) force field. The resulting frequencies, final RMSD value and potential-energy distribution are presented in Table 5. It can be seen that only about one half of the modes have a participation of ≥50% of one definite coordinate, whereas the other modes represent complex vibrations where several coordinates are involved.

The force-field transformation, scaling and potential-energy distribution calculations were performed with the program FCARTP.[34] The atomic displacements, given by the calculations for each vibrational mode, served as a tool to help understand qualitatively the nature of the molecular vibrations. The program GaussView was used along with the corresponding data to represent this graphically.[29]

The SQM force field (Table S6, Supporting Information) was used to calculate the internal force constants for $CF_3SO_2OCF_3$ (Table 7), and these are compared to the equivalent values for some related molecules. It can be seen that on moving from $CF_3SO_2OCF_3$ to $CF_3SO_2OCH_3$, the calculated S–O bond becomes shorter (from 168.2 to 162.2 pm), and, consequently, the corresponding force constant increases (from 3.82 to 4.96 mdyn Å$^{-1}$). In contrast, the adjacent O–C bond length increases (from 139.3 to 145.5 pm), and its force constant decreases (from 5.50 to 4.60 mdyn Å$^{-1}$). The highly electronegative $CF_3$ group seems to enhance the participation of the oxygen electronic charge in the O–C bond of $CF_3SO_2OCF_3$, strengthening that bond to the detriment of the S–O bond.

Table 7. Force constants in internal (valence) coordinates for $CF_3SO_2OCF_3$ and related molecules.

| Force constants[a] | $CF_3SO_2OCF_3$ | $CF_3SO_2OCH_3$[b] | $CF_3SO_2OCH_2CF_3$[c] |
|---|---|---|---|
| $k_f$ [C(1)–F] | 6.50 | 5.94 | 5.85 |
| $k_f$ [C(9)–F] | 6.13 | | 6.15 |
| $k_f$ [C–S] | 3.00 | 3.10 | 3.18 |
| $k_f$ [S–O] | 3.82 | 4.96 | 4.62 |
| $k_f$ [S=O] | 11.05 | 10.70 | 10.90 |
| $k_f$ [O–C] | 5.50 | 4.60 | 5.01 |
| $k_f$ [O = S=O] | 1.14 | 1.19 | 1.10 |
| $k_f$ [O–S=O] | 1.26 | 1.26 | 1.25 |
| $k_f$ [C–S–O] | 1.16 | 1.16 | 1.0 |
| $k_f$ [C–S=O] | 1.00 | 1.00 | 1.0 |
| $k_f$ [F–C(1)–F] | 1.24 | 1.29 | 1.29 |
| $k_f$ [F–C(9)–F] | 1.36 | | 1.35 |
| $k_f$ [C–F/C–F] | 0.94 | 0.71 | 0.71 |
| $k_f$ [S=O/S=O] | –0.093 | –0.076 | –0.076 |

[a] Units are mdyn Å$^{-1}$ for stretches and stretch–stretch interactions, and mdyn Å rad$^{-2}$ for angular deformations. [b] Ref.[5] [c] Ref.[7]

 © 2007 Wiley-VCH Verlag GmbH & Co. KGaA, Weinheim 

## Conclusions

$CF_3SO_2OCF_3$ was synthesised in good yields by using a published technique. A complete investigation of its gas-phase molecular structure was carried out by using electron diffraction techniques complemented by theoretical methods. The experimental and theoretical structures both show this molecule as a single *gauche* conformer having a C–S–O–C dihedral angle of 119.5(18)° determined by GED, relative to 105 to 112° calculated by quantum chemistry calculations. A comparison of the bond lengths obtained by GED and those predicted by various ab initio and DFT methods shows that $CF_3SO_2OCF_3$ is a particularly challenging case for theoretical geometry optimisation. The inclusion of multiple polarisation functions in the basis set plays a crucial role, but the choice of method is also significant. These results are consistent with what seem to be common structural characteristics of covalent sulfonates.

Infrared and Raman spectra were obtained for $CF_3SO_2OCF_3$, and bands assignable to 27 out of the expected 30 normal modes of vibration were observed. The vibrational data were used as a basis to define the symmetry (SQM force field) and internal force constants of the molecule.

### Synthesis

$CF_3SO_2OCF_3$ was synthesised by reaction between $CF_3SO_2OH$ and its anhydride, $(CF_3SO_2)_2O$, according to the method reported by Hassani et al.[4] The reactants were heated in a sealed tube for 1 h at approximately 450 K, and after the reaction had occurred, the product was purified by distillation on a vacuum line.

### Gas Electron Diffraction (GED)

Data were collected by using the Edinburgh gas electron diffraction apparatus[35] with an accelerating voltage of ca. 40 kV (ca. 6 pm electron wavelength) on Kodak Electron Image film. Nozzle-to-film distances were determined by using benzene vapour as a standard, immediately after recording the diffraction patterns for $CF_3SO_2OCF_3$. Sample and nozzle temperatures of 195 and 298 K, respectively, were used for both the short and long nozzle-to-camera distances (130.5 and 291.5 mm). The electron scattering pattern was converted into digital form by using an Epson Expression 1680 Pro flatbed scanner with a scanning program that was described elsewhere.[36] Data reduction and least-squares refinements were carried out with the ed@ed program[37] employing the scattering factors of Ross et al.[38] The scale factors, *s* limits, weighting points, correlation parameters and electron wavelengths are given in Table S7 (Supporting Information).

### Infrared and Raman Spectra

Infrared spectra for $CF_3SO_2OCF_3$ in the gas and solid phases were recorded in the 400–4000 $cm^{-1}$ range by using a Perkin–Elmer 1600 FTIR instrument. The spectrum for the solid was obtained after depositing the compound from the vacuum line onto a KBr window, maintained at about 197 K, in a variable temperature RIIC (VLT-2) cell. The Raman spectrum for the liquid at room temperature was obtained with the FRA-106 accessory mounted on a Bruker IFS66 FTIR instrument, by using 1064-nm light from a Nd/YAG laser for excitation.

## Computational Resources

The majority of the calculations described in this paper were performed with a Linux 10-processor Parallel Quantum Solutions (PQS) workstation[39] running the Gaussian 03 suite of programs.[40] The scans of the potential-energy surface and all calculations using the 6-31G(3df), cc-pVTZ, TZVP and TZVPP basis sets were performed with the resources of the EPSRC National Service for Computational Chemistry Software[41] on a cluster of 22 Linux Opteron nodes, where each Opteron server has twin 2.4 GHz Opteron 250 CPUs and 8 GB of memory connected with a high-speed, low-latency Myrinet network.

**Supporting Information** (see footnote on the first page of this article): Details of GED data analysis parameters, interatomic distances, amplitudes of vibrations, distance corrections for perpendicular motion, the least-squares correlation matrix and the molecular-scattering intensity curves used in the GED refinement are presented. Geometric molecular parameters for all ab initio and DFT calculations are also given. GED atomic coordinates and those obtained from MP2/6-31G(3df), MP2/cc-pVTZ, MP2/TZVPP, B3LYP/6-31G(3df) and B1B95/6-31G(3df) calculations are provided, as well as the force field scaling factors.

## Acknowledgments

Research grants from the following Argentine institutions are gratefully acknowledged: CONICET (Consejo Nacional de Investigaciones Científicas y Técnicas), ANPCYT (Agencia Nacional de Promoción Científica y Tecnológica) (PICT 11127), CIUNT (Consejo de Investigaciones de la Universidad Nacional de Tucumán) and UNLP (Universidad Nacional de La Plata). D. A. W. and H. E. R. thank the EPSRC (grant EP/C513649) and S. A. H. thanks the School of Chemistry, University of Edinburgh for funding.

[1] R. E. Noftle, G. Cady, *Inorg. Chem.* **1965**, *4*, 1010.
[2] G. A. Olah, T. Ohyama, *Synthesis* **1976**, 319.
[3] Y. Kobayashi, T. Yoshida, I. Kumadaki, *Tetrahedron Lett.* **1979**, *20*, 3865.
[4] M. O. Hassani, A. Germain, D. Brunel, A. Commeyras, *Tetrahedron Lett.* **1981**, *22*, 65.
[5] F. Trautner, A. Ben Altabef, L. E. Fernández, E. L. Varetti, H. Oberhammer, *Inorg. Chem.* **1999**, *38*, 3051.
[6] L. E. Fernández, A. Ben Altabef, E. L. Varetti, *J. Mol. Struct.* **2002**, *612*, 1.
[7] M. E. Tuttolomondo, L. E. Fernández, A. Navarro, E. L. Varetti, A. Ben Altabef, *Spectrochim. Acta Part A* **2004**, *60*, 611.
[8] M. E. Tuttolomondo, A. Navarro, E. L. Varetti, A. Ben Altabef, *J. Raman Spectrosc.* **2005**, *36*, 427.
[9] M. F. Erben, C. O. Della Vedova, R. Boese, H. Willner, C. Leibold, H. Oberhammer, *Inorg. Chem.* **2003**, *42*, 7297.
[10] J. S. Binkley, J. A. Pople, W. J. Hehre, *J. Am. Chem. Soc.* **1980**, *102*, 939.

 © 2007 Wiley-VCH Verlag GmbH & Co. KGaA, Weinheim 

[11] M. S. Gordon, J. S. Binkley, J. A. Pople, W. J. Pietro, W. J. Hehre, *J. Am. Chem. Soc.* **1982**, *104*, 2797.
[12] W. J. Pietro, M. M. Francl, W. J. Hehre, D. J. DeFrees, J. A. Pople, J. S. Binkley, *J. Am. Chem. Soc.* **1982**, *104*, 5039.
[13] W. J. Hehre, R. Ditchfield, J. A. Pople, *J. Chem. Phys.* **1972**, *56*, 2257.
[14] P. C. Hariharan, J. A. Pople, *Theor. Chim. Acta* **1973**, *28*, 213.
[15] M. S. Gordon, *Chem. Phys. Lett.* **1980**, *76*, 163.
[16] C. Møller, M. S. Plesset, *Phys. Rev.* **1934**, *46*, 618.
[17] C. Lee, W. Yang, R. G. Parr, *Phys. Rev. B* **1988**, *37*, 785; A. D. Becke, *J. Chem. Phys.* **1993**, *98*, 5648.
[18] A. D. Becke, *J. Chem. Phys.* **1996**, *104*, 1040.
[19] A. D. McLean, G. S. Chandler, *J. Chem. Phys.* **1980**, *72*, 5639.
[20] R. Krishnan, J. S. Binkley, R. Seeger, J. A. Pople, *J. Chem. Phys.* **1980**, *72*, 650.
[21] M. J. Frisch, J. A. Pople, J. S. Binkley, *J. Chem. Phys.* **1984**, *80*, 3265.
[22] T. H. Dunning Jr, *J. Chem. Phys.* **1989**, *90*, 1007.
[23] A. Schaefer, H. Huber, R. Ahlrichs, *J. Chem. Phys.* **1994**, *100*, 5829.
[24] F. Weigend, M. Haeser, H. Patzelt, R. Ahlrichs, *Chem. Phys. Lett.* **1998**, *294*, 143.
[25] V. A. Sipachev, *J. Mol. Struct. (THEOCHEM)* **1985**, *121*, 143.
[26] a) N. W. Mitzel, B. A. Smart, A. J. Blake, H. E. Robertson, D. W. H. Rankin, *J. Phys. Chem.* **1996**, *100*, 9339; b) A. J. Blake, P. T. Brain, H. McNab, J. Miller, C. A. Morrison, S. Parsons, D. W. H. Rankin, H. E. Robertson, B. A. Smart, *J. Phys. Chem.* **1996**, *100*, 12280; c) N. W. Mitzel, D. W. H. Rankin, *Dalton Trans.* **2003**, 3650.
[27] C. Leibold, H. Oberhammer, T. D. Thomas, L. J. Saethre, R. Winter, G. L. Gard, *Inorg. Chem.* **2004**, *43*, 3942.
[28] L. E. Fernández, E. L. Varetti, *J. Mol. Struct. (THEOCHEM)* **2003**, *629*, 175.
[29] A. B. Nielsen, A. J. Holder, *GaussView, User's Reference*, Gaussian, Inc., Pittsburgh PA, **1997–1998**.
[30] E. B. Wilson, J. C. Decius, P. C. Cross, *Molecular Vibrations*, McGraw-Hill, New York, **1955**.
[31] G. Fogarasi, X. Zhou, P. W. Taylor, P. Pulay, *J. Am. Chem. Soc.* **1992**, *114*, 8191.
[32] P. Pulay, G. Fogarasi, G. Pongor, J. E. Boggs, A. Vargha, *J. Am. Chem. Soc.* **1983**, *105*, 7037.
[33] F. Kalincsák, G. Pongor, *Spectrochim. Acta Part A* **2002**, *58*, 999.
[34] W. B. Collier, *Program FCARTP (QCPE # 631)*, Department of Chemistry, Oral Roberts University, Tulsa OK, USA, **1992**.
[35] C. M. Huntley, G. S. Laurenson, D. W. H. Rankin, *J. Chem. Soc., Dalton Trans.* **1980**, 954.
[36] H. Fleischer, D. A. Wann, S. L. Hinchley, K. B. Borisenko, J. R. Lewis, R. J. Mawhorter, H. E. Robertson, D. W. H. Rankin, *Dalton Trans.* **2005**, 3221.
[37] S. L. Hinchley, H. E. Robertson, K. B. Borisenko, A. R. Turner, B. F. Johnston, D. W. H. Rankin, M. Ahmadian, J. N. Jones, A. H. Cowley, *Dalton Trans.* **2004**, 2469.
[38] A. W. Ross, M. Fink, R. Hilderbrandt, *International Tables for Crystallography Vol. C* (Ed.: A. J. C. Wilson), Kluwer Academic Publishers, Dordrecht, Boston and London, **1992**, p. 245.
[39] *Parallel Quantum Solutions*, Fayetteville AR, USA.
[40] M. J. Frisch, G. W. Trucks, H. B. Schlegel, G. E. Scuseria, M. A. Robb, J. R. Cheeseman, J. A. Montgomery Jr, T. Vreven, K. N. Kudin, J. C. Burant, J. M. Millam, S. S. Iyengar, J. Tomasi, V. Barone, B. Mennucci, M. Cossi, G. Scalmani, N. Rega, G. A. Petersson, H. Nakatsuji, M. Hada, M. Ehara, K. Toyota, R. Fukuda, J. Hasegawa, M. Ishida, T. Nakajima, Y. Honda, O. Kitao, H. Nakai, M. Klene, X. Li, J. E. Knox, H. P. Hratchian, J. B. Cross, C. Adamo, J. Jaramillo, R. Gomperts, R. E. Stratmann, O. Yazyev, A. J. Austin, R. Cammi, C. Pomelli, J. W. Ochterski, P. Y. Ayala, K. Morokuma, G. A. Voth, P. Salvador, J. J. Dannenberg, V. G. Zakrzewski, S. Dapprich, A. D. Daniels, M. C. Strain, O. Farkas, D. K. Malick, A. D. Rabuck, K. Raghavachari, J. B. Foresman, J. V. Ortiz, Q. Cui, A. G. Baboul, S. Clifford, J. Cioslowski, B. B. Stefanov, G. Liu, A. Liashenko, P. Piskorz, I. Komaromi, R. L. Martin, D. J. Fox, T. Keith, M. A. Al-Laham, C. Y. Peng, A. Nanayakkara, M. Challacombe, P. M. W. Gill, B. Johnson, W. Chen, M. W. Wong, C. Gonzalez, J. A. Pople, *Gaussian 03, Revision B.02*, Gaussian Inc., Pittsburgh PA, **2003**.
[41] EPSRC National Service for Computational Chemistry Software. URL: http://www.nsccs.ac.uk.

Received: October 4, 2006
Published Online: February 21, 2007

 © 2007 Wiley-VCH Verlag GmbH & Co. KGaA, Weinheim 

DOI: 10.1002/ejic.200601028

# Systematic Counterion Tuning of the Solid-State Structure of $[Pt(thiourea)_4]^{2+}$

**Wolfgang Schiessl,[a] Ralph Puchta,[a,b] Živadin D. Bugarčić,[a,c] Frank W. Heinemann,[a] and Rudi van Eldik*[a]**

**Keywords:** Counter ion / Conformers / Crystal engineering

Four different limiting molecular conformations are possible for the homoleptic square-planar complex tetrakis(thiourea)-platinum(II) depending on the up-down orientation of the four thiourea (TU) ligands with respect to the $PtS_4$ plane. The realization of all four possible conformers can be achieved by a systematic variation of the counter anion making use of their individual hydrogen bonding ability. In total, the molecular and crystal structures of seven tetrakis(thiourea)platinum(II) complexes were determined by X-ray diffraction. These are: $[Pt(TU)_4]Cl_2$, $[Pt(TU)_4]I_2$, $[Pt(TU)_4](CF_3SO_3)_2$, $[Pt(TU)_4](BPh_4)_2$, $[Pt(TU)_4](ClO_4)_2$, $[Pt(TU)_4]SiF_6{\cdot}0.25H_2O$ and $[Pt(TU)_4]S_2O_6$. In all cases thiourea is coordinated by the sulfur atom and the two amino groups are not involved in the complex formation. The four independent Pt–S distances do not differ significantly from each other with an average value of 2.324(3) Å. The coordination geometry around the platinum center is distorted square-planar. The orientation of the four TU groups in $[Pt(TU)_4]^{2+}$ depends on the molecular packing forces and hydrogen bonding ability of the counter anion. Hydrogen bonds of the type N–H···X (X = $Cl^-$, $I^-$, $F^-$, O and S) are observed.

(© Wiley-VCH Verlag GmbH & Co. KGaA, 69451 Weinheim, Germany, 2007)

## Introduction

In contrast to its inertness as a metal, platinum and its compounds have become a major field of interest with respect to their possible applications. Besides the common usage of dispersed platinum metal as catalytic material in industrial processes,[1] $Pt^{II}$ complexes are amongst the most commonly used antitumor drugs for certain types of cancer.[2] Intracellular thiols are known to play an important role in the metabolism of Pt antitumor drugs, since they are involved in trapping of the drug,[3] renal toxicity and other side-effects.[4] Thiourea (TU) is one of the best known nucleophiles for $Pt^{II}$ complexes[5,6] and is commonly used in the investigation of ligand-substitution reactions in coordination chemistry. Moreover, thiourea can very easily displace other ligands from $Pt^{II}$ complexes, including S-bonded ligands such as L-cysteine in $[Pt(terpy)(S\text{-}cys)]^+$ with a rate constant of $0.94 \pm 0.02$ $M^{-1}s^{-1}$ at 25 °C, and even much easier guanosine in $[Pt(terpy)(N7\text{-}guo)]^{2+}$ with a rate constant of $4.87 \pm 0.03$ $M^{-1}s^{-1}$.[7] The strong binding ability of S-donor nucleophiles can as well be used to reverse unwanted side-effects in chemotherapy.[8,9] It has been demonstrated that thiourea could restore the biological activity of platinated DNA.[10] Thiourea and other sulfur-containing compounds such as diethyl dithiocarbamate (DEDTC), sodium thiosulfate (STS), glutathione (GSH), *S*-2-(3-(aminopropylamino)ethylphosphorothioic acid (amifostine, WR-2721, Ethiol), methionine, cysteine, penicillamine, biotin, sodium 2-mercaptoethanesulfonate (mesna) and its oxidized S–S bridged dimer (di)mesna (BNP-7787), have been applied as rescue or protective agents, in order to reduce the toxicity of platinum antitumor complexes.[11,12,13] The protective effect of these compounds is either to prevent or to reverse the formation of Pt–S adducts in proteins.

Thiourea coordinates flexibly via the S-donor to the platinum center and the two amino groups are not involved in the complex formation.[14,15] For the proper interaction of drugs with purely organic material, the consideration of different conformations is very important, as the drugs have to fit inside the enzyme pocket.[16] Therefore, the question of conformers should also be addressed in the development of drug mimetics based on metal complexes. The $NH_2$ groups on thiourea can be utilized to form hydrogen-bonded mediated clusters together with suitable anions or other compounds, resulting in interesting structural host-guest motifs.[17] Furthermore, there is current interest in the design of selective receptors for anions,[18,19] which could interact through either electrostatic or hydrogen-bonding interactions.[20,21] The orientation of the four TU groups depends on the molecular packing forces and hydrogen bonding. In the following, these conformers are referred to as OOOO, IOOO, IIOO and IOIO with respect to the flip-flop orientation of the thiourea ligands as shown in Figure 1. Although most of these conformers have been re-

[a] Institute for Inorganic Chemistry, University of Erlangen-Nürnberg,
Egerlandstrasse 1, 91058 Erlangen, Germany
[b] Computer Chemistry Center, University of Erlangen-Nürnberg, Nägelsbachstr. 25, 91052 Erlangen, Germany
[c] Department of Chemistry, Faculty of Science, University of Kragujevac,
P. O. Box 60, 34000 Kragujevac, Serbia
Supporting information for this article is available on the WWW under http://www.eurjic.org or from the author.

 InterScience © 2007 Wiley-VCH Verlag GmbH & Co. KGaA, Weinheim 

ported individually as part of studies focusing on other topics,[22,23,24] we will show in the present study that all four possible conformers of the $[Pt(TU)_4]^{2+}$ unit can be realized by systematic tuning of the molecular structure by the hydrogen-bonding ability of the inorganic counter anion exclusively, without the need of organic substances or additional solvent species as frame works.

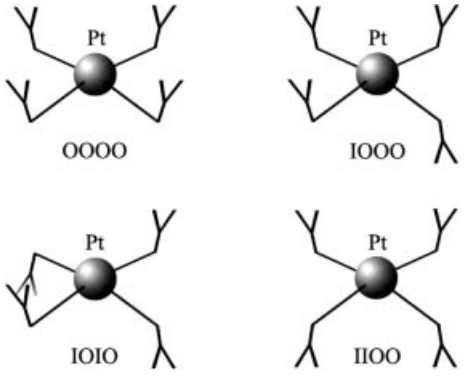


Figure 1. Schematic overview and definition of abbreviations for the four possible $[Pt(TU)_4]^{2+}$ conformers.

As part of our interest in the synthesis, structure and reactivity of coordination complexes of $Pd^{II}$ and $Pt^{II}$, we report here a systematic and detailed study of the crystal structures of $[Pt(TU)_4]X_n$, where X represents the counterions $Cl^-$, $I^-$, $CF_3SO_3^-$, $BPh_4^-$ and $ClO_4^-$ ($n$ = 2), and $S_2O_8^{2-}$ and $SiF_6^{2-}$ ($n$ = 1), in an attempt to gain information on the crystal packing, hydrogen bonding network and orientation of the four TU ligands as a function of the selected counterion.

## Results and Discussion

### Theoretical Calculations

Three of the four possible conformers were calculated applying symmetry constrains. The non-symmetrical IOOO ($C_1$), calculated without symmetry constrains, changed its conformation during the structure optimization and became the energetically most favorable IOIO. On the one hand we attribute this to the low energy barrier for rotation along the Pt–S bond, on the other hand it emphasizes the influence of the counterion. The moderate energy differences between the three conformers (IOIO 0 kcal/mol, IIOO 2 kcal/mol and OOOO 8 kcal/mol) in the gas phase[25] (see Figure 2 and Table 1) are in a range that can be exceeded by extra stabilization via hydrogen bonding. On the basis of 5 to 10 kcal/mol per hydrogen bond in the solid state,[26] already one or two hydrogen bonds should be able to overcome the calculated energy barrier between the different conformers. Since in every $[Pt(TU)_4]^{2+}$ motif 16 $H_{N-H}$ are available for possible hydrogen bond formation, the TU moieties are forced into their respective orientation.

In order to support a distinctive hydrogen network, we selected in addition to halogen anions also oxo and per-

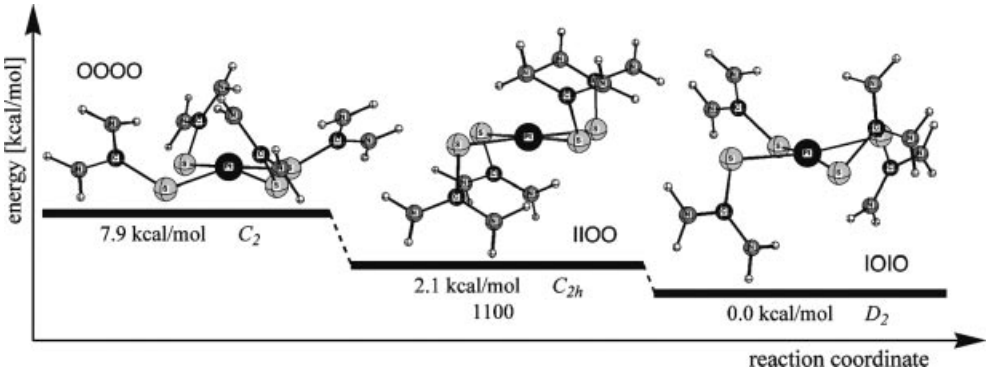


Figure 2. Optimized (RB3LYP/LANL2DZp) structures of the $[Pt(TU)_4]^{2+}$ conformers. (Pt: large black circles, C: small black circles, N: dark grey circles, S: light grey circles, H: white circles).

Table 1. Summary of the calculated (RB3LYP/LANL2DZp) structures of the $[Pt(TU)_4]^{2+}$ conformers.

| | OOOO | IIOO | IOIO |
|---|---|---|---|
| Point group | $C_2$ | $C_{2h}$ | $D_2$ |
| Relative energies (RB3LYP/LANL2DZp) [kcal/mol] | 7.9 | 2.1 | 0.0 |
| Relative energies (RB3LYP/LACV3P+**) [kcal/mol] | 7.6 | 1.7 | 0.0 |
| S–Pt (RB3LYP/LANL2DZp) [Å] | 2.41, 2.42, 2.41, 2.42 | 2.43, 2.43, 2.43, 2.43 | 2.42, 2.42, 2.42, 2.42 |
| Pt deviation of $S_4$ plane (RB3LYP/LANL2DZp) [Å] | 0.30 | 0.00 | 0.00 |
| C–S–Pt angle | 111.3, 116.6, 111.3 | 110.9, 110.9, 110.9 | 111.0, 111.0, 111.0 |
| (RB3LYP/LANL2DZp) [°] | 116.6 | 110.9 | 111.0 |
| S–Pt–S angle (RB3LYP/LANL2DZp) [°] | 91.7, 86.6, 91.7, 86.6 | 83.9, 96.2, 83.9, 96.2 | 97.4, 82.8, 97.4, 82.8 |
| X–S···S–C angle | 149.1, 138.1, 149.1 | –85.8, 127.0, 85.8 | –128.7, 88.1, –128.7 |
| (RB3LYP/LANL2DZp) [°][a] | 138.1 | –127.0 | 88.1 |

[a] X = center of least square plane through the four coordinating sulfur atoms.

 © 2007 Wiley-VCH Verlag GmbH & Co. KGaA, Weinheim 

fluoro anions, viz. $ClO_4^-$, $S_2O_6^{2-}$, $SiF_6^{2-}$ and $CF_3SO_3^-$. Whereas the halogen anions have the rotational symmetric $K_h$ point group, the oxo and perfluoro anions have different symmetry groups with corresponding subgroups. The basic idea was to utilize these symmetry elements to stabilize the suggested $[Pt(TU)_4]^{2+}$ rotamers. In order to obtain the conformational structure of $[Pt(TU)_4]^{2+}$ in the absence of a hydrogen bonding network with the anions, we used $[B(Ph)_4]^-$ as a counterion. As summarized in Table 1, the Pt–S bonds in all conformers are almost identical with 2.42 Å, the $Pt^{II}$ is ideally square-planar coordinated by the four S-donors (except in OOOO) and the C=S–$Pt^{II}$ shows equivalent angles of 111°. The distortion in the OOOO conformer can be explained in terms of only two TU ligands that have a NH-group showing a common orientation toward a neighboring thiourea sulfur (NH···S 2.48 Å), whereas the other two TU exhibit a contact toward their own S atom.

## Crystallographic Results

The molecular structures of the $[Pt(TU)_4]^{2+}$ cations in the complexes $[Pt(TU)_4]SiF_6{\cdot}0.25H_2O$, $[Pt(TU)_4]S_2O_6$, $[Pt(TU)_4](ClO_4)_2$, $[Pt(TU)_4]I_2$, $[Pt(TU)_4](BPh_4)_2$, $[Pt(TU)_4](CF_3SO_3)_2$ and $[Pt(TU)_4]Cl_2$ are shown in Figures 3, 4, 5, and 6 (see also Figures S1 to S3 in the Supporting Information). Selected bond lengths and angles for the various $[Pt(TU)]X_n$ complexes are given in Tables 2, 3, 4, 5, 6, 7, and 8.

In general, TU is coordinated to Pt via its sulfur donor in all the $[Pt(TU)_4]^{2+}$ cations. The coordination geometry around the platinum center is distorted square-planar.

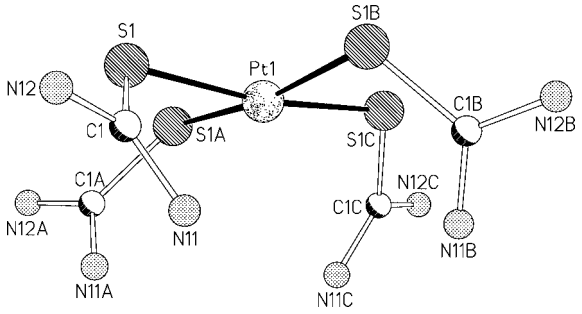


Figure 3. Molecular structure of the $[Pt(TU)_4]^{2+}$ cation of the complex $[Pt(TU)_4]SiF_6{\cdot}0.25H_2O$, (OOOO).

Table 2. Selected bond lengths [Å] and angles [°] for $[Pt(TU)_4]Cl_2$ (IOIO).

| | | | |
|---|---|---|---|
| Pt(1)–S(1) | 2.3168(7) | Pt(1)–S(2) | 2.3222(6) |
| Pt(1)–S(3) | 2.3308(7) | Pt(1)–S(4) | 2.3344(6) |
| S(1)–C(1) | 1.732(3) | C(1)–N(12) | 1.310(3) |
| C(1)–N(11) | 1.324(3) | S(2)–C(2) | 1.730(3) |
| C(2)–N(21) | 1.316(3) | C(2)–N(22) | 1.336(3) |
| S(3)–C(3) | 1.740(2) | C(3)–N(31) | 1.313(3) |
| C(3)–N(32) | 1.321(3) | S(4)–C(4) | 1.739(3) |
| C(4)–N(42) | 1.316(3) | C(4)–N(41) | 1.317(3) |
| | | | |
| S(1)–Pt(1)–S(2) | 83.75(2) | S(1)–Pt(1)–S(3) | 174.46(2) |
| S(2)–Pt(1)–S(3) | 91.84(2) | S(1)–Pt(1)–S(4) | 98.84(2) |
| S(2)–Pt(1)–S(4) | 175.79(2) | S(3)–Pt(1)–S(4) | 85.76(2) |
| C(1)–S(1)–Pt(1) | 110.77(9) | N(12)–C(1)–N(11) | 120.7(2) |
| N(12)–C(1)–S(1) | 123.0(2) | N(11)–C(1)–S(1) | 116.4(2) |
| C(2)–S(2)–Pt(1) | 109.42(9) | N(21)–C(2)–N(22) | 119.4(2) |
| N(21)–C(2)–S(2) | 124.3(2) | N(22)–C(2)–S(2) | 118.3(2) |

Hydrogen bonds for $[Pt(TU)_4]Cl_2$

| D–H···A | *d*(D–H) | *d*(H···A) | *d*(D···A) | <(DHA) |
|---|---|---|---|---|
| N(11)–H(11B)···Cl(2)#1 | 0.88 | 2.48 | 3.329(2) | 161.9 |
| N(11)–H(11A)···S(3)#2 | 0.88 | 2.59 | 3.434(2) | 159.9 |
| N(12)–H(12B)···Cl(1) | 0.88 | 2.67 | 3.347(2) | 134.9 |
| N(12)–H(12B)···S(4) | 0.88 | 2.74 | 3.396(2) | 132.6 |
| N(12)–H(12A)···Cl(1)#3 | 0.88 | 2.44 | 3.236(2) | 151.0 |
| N(21)–H(21B)···S(3) | 0.88 | 2.72 | 3.352(2) | 130.2 |
| N(21)–H(21B)···Cl(2) | 0.88 | 2.74 | 3.505(2) | 146.8 |
| N(21)–H(21A)···Cl(2)#4 | 0.88 | 2.46 | 3.508(2) | 161.7 |
| N(22)–H(22B)···Cl(1)#5 | 0.88 | 2.58 | 3.384(2) | 151.8 |
| N(22)–H(22A)···S(4)#6 | 0.88 | 2.88 | 3.681(2) | 152.5 |
| N(31)–H(31A)···Cl(2)#7 | 0.88 | 2.48 | 3.262(2) | 147.8 |
| N(31)–H(31B)···Cl(1) | 0.88 | 2.63 | 3.293(2) | 133.5 |
| N(32)–H(32B)···Cl(1)#8 | 0.88 | 2.41 | 3.254(2) | 162.1 |
| N(32)–H(32A)···Cl(2)#7 | 0.88 | 2.49 | 3.263(2) | 147.5 |
| N(41)–H(41B)···S(1) | 0.88 | 2.42 | 3.240(2) | 154.7 |
| N(41)–H(41A)···Cl(1)#9 | 0.88 | 2.59 | 3.385(2) | 150.3 |
| N(41)–H(41A)···S(2)#1 | 0.88 | 2.97 | 3.515(2) | 121.9 |
| N(42)–H(42A)···Cl(1)#9 | 0.88 | 2.44 | 3.272(2) | 157.1 |
| N(42)–H(42B)···Cl(2)#10 | 0.88 | 2.28 | 3.144(2) | 166.2 |

Symmetry transformations used to generate equivalent atoms: #1 $-x+1, -y+1, -z$; #2 $x, -y+1/2, z-1/2$; #3 $-x, -y, -z$; #4 $-x+1, y+1/2, -z+1/2$; #5 $-x, -y+1, -z$; #6 $x, y+1, z$; #7 $x-1, y, z$; #8 $-x, y+1/2, -z+1/2$; #9 $x+1, y, z$; #10 $-x+1, y-1/2, -z+1/2$

 © 2007 Wiley-VCH Verlag GmbH & Co. KGaA, Weinheim 

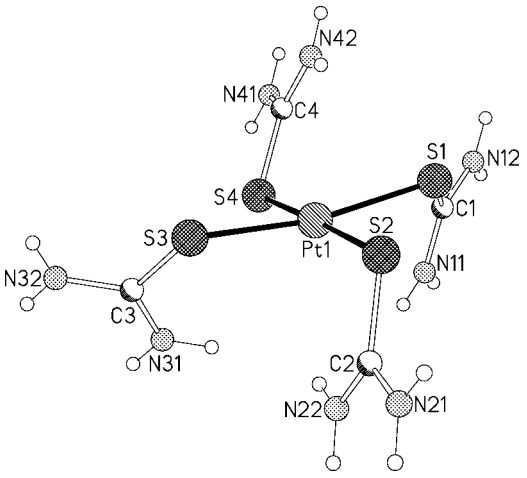


Figure 4. Molecular structure of the $[Pt(TU)_4]^{2+}$ cation of the complex $[Pt(TU)_4]S_2O_6$, (IOOO).

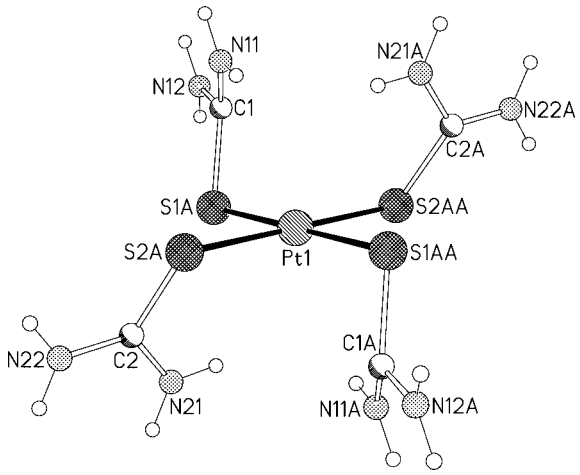


Figure 5. Molecular structure of the $[Pt(TU)_4]^{2+}$ cation of the complex $[Pt(TU)_4](ClO_4)_2$, (IIOO).

Whereas in most of the complexes the largest deviation from the optimum value of 90° for the S–Pt–S angle is less than 4.5°, significantly larger angles of 101.68(2)° in $[Pt(TU)_4](CF_3SO_3)_2$ and 98.84(2)° in $[Pt(TU)_4]Cl_2$ indicate a stronger distortion of the square planar arrangement, which is in good agreement with literature values reported for the chloride complex, viz. 98.3(02)°[14] and 98.9(1)°.[15] The central Pt atom in all investigated complexes is situated well within the $S_4$ plane; the only significant displacement of the Pt center from the square plane is observed for the complex in $[Pt(TU)_4]SiF_6$ [0.180(1) Å] and $[Pt(TU)_4]S_2O_6$ [0.091(1) Å].

The thiourea ligands are arranged in a rotor-like fashion with respect to the $PtS_4$ plane, independent of whether they point upwards or downwards. The dihedral angle between the $PtS_4$ plane and a least-squares plane calculated through the thiourea ligand unit $S=C(N_2)$ varies between 35.3(1)° and 85.2(2)°, with an overall average of 64.9°. The four Pt–S distances in each of the $[Pt(TU)_4]^{2+}$ units do not differ much from each other (see Tables 2, 3, 4, 5, 6, 7, and 8) and cover the narrow range from 2.313(2) Å (shortest distance found in $[Pt(TU)_4](ClO_4)_2$) to 2.345(1) Å (longest distance found in $[Pt(TU)_4](BPh_4)_2$). The overall average value calculated for all Pt–S bond lengths for all investigated $[Pt(TU)_4]X_n$ complexes amounts to 2.324(3) Å. This is in very good

Table 3. Selected bond lengths [Å] and angles [°] for $[Pt(TU)_4]SiF_6 \cdot 0.25H_2O$ (OOOO).

| | | | |
|---|---|---|---|
| Pt(1)–S(1)#1 | 2.3149(7) | Pt(1)–S(1)#2 | 2.3149(7) |
| Pt(1)–S(1)#3 | 2.3149(7) | Pt(1)–S(1) | 2.3149(7) |
| S(1)–C(1) | 1.735(3) | C(1)–N(11) | 1.319(3) |
| C(1)–N(12) | 1.321(3) | Si(1)–F(13)#2 | 1.683(2) |
| Si(1)–F(13)#3 | 1.683(2) | Si(1)–F(13)#1 | 1.683(2) |
| Si(1)–F(13) | 1.683(2) | Si(1)–F(11) | 1.685(3) |
| Si(1)–F(12) | 1.703(3) | N(11)–H(11A) | 0.8800 |
| | | | |
| S(1)#1–Pt(1)–S(1)#2 | 89.654(3) | S(1)#1–Pt(1)–S(1)#3 | 89.654(3) |
| S(1)#2–Pt(1)–S(1)#3 | 171.09(3) | S(1)#1–Pt(1)–S(1) | 171.09(3) |
| S(1)#2–Pt(1)–S(1) | 89.654(3) | S(1)#3–Pt(1)–S(1) | 89.654(3) |
| C(1)–S(1)–Pt(1) | 110.67(9) | N(11)–C(1)–N(12) | 120.0(2) |
| N(11)–C(1)–S(1) | 122.9(2) | N(12)–C(1)–S(1) | 117.1(2) |
| C(1)–N(11)–H(11A) | 120.0 | C(1)–N(11)–H(11B) | 120.0 |
| F(13)#2–Si(1)–F(13)#3 | 179.61(2) | F(13)#2–Si(1)–F(13)#1 | 89.999(1) |
| F(13)#3–Si(1)–F(13) | 89.999(1) | F(13)#1–Si(1)–F(13) | 179.6(2) |

Symmetry transformations used to generate equivalent atoms: #1 $-x+1/2, -y+1/2, z$; #2 $-y+1/2, x, z$; #3 $y, -x+1/2, z$

Hydrogen bonds for $[Pt(TU)_4]SiF_6 \cdot 0.25H_2O$ (OOOO)

| D–H···A | *d*(D–H) | *d*(H···A) | *d*(D···A) | <(DHA) |
|---|---|---|---|---|
| N(11)–H(11A)···F(13)#4 | 0.88 | 2.07 | 2.882(3) | 153.7 |
| N(11)–H(11B)···F(12) | 0.88 | 2.11 | 2.942(3) | 157.9 |
| N(12)–H(12A)···F(11)#5 | 0.88 | 2.25 | 2.975(3) | 139.2 |
| N(12)–H(12A)···F(13)#6 | 0.88 | 2.32 | 3.142(3) | 154.7 |
| N(12)–H(12B)···S(1)#7 | 0.88 | 2.71 | 3.451(3) | 143.2 |
| N(12)–H(21B)···S(1)#8 | 0.88 | 2.97 | 3.563(3) | 126.6 |
| O(1)–H(1A)···F(13)#8 | 0.85 | 2.27 | 3.118(2) | 180.0 |

Symmetry transformations used to generate equivalent atoms: #1 $-x+1/2, -y+1/2, -z$; #2 $-y+1/2, x, z$; #3 $y, -x+1/2, z$; #4 $x+1/2, -y+1, -z+1/$; #5 $-x+1, y+1/2, -x+1/2$; #6 $-y+1, -x+1, -x+1/2$; #7 $-y+1, x+1/2, -z$; #8 $-x+1/2, -y+3/2, z$

 © 2007 Wiley-VCH Verlag GmbH & Co. KGaA, Weinheim 

Table 4. Selected bond lengths [Å] and angles [°] for $[Pt(TU)_4]S_2O_6$ (IOOO).

| | | | |
|---|---|---|---|
| Pt(1)–S(4) | 2.313(2) | Pt(1)–S(3) | 2.321(1) |
| Pt(1)–S(1) | 2.321(2) | Pt(1)–S(2) | 2.344(2) |
| S(1)–C(1) | 1.740(4) | C(1)–N(11) | 1.319(5) |
| C(1)–N(12) | 1.320(5) | S(2)–C(2) | 1.730(5) |
| C(2)–N(21) | 1.315(5) | C(2)–N(22) | 1.325(6) |
| S(3)–C(3) | 1.738(5) | C(3)–N(31) | 1.316(6) |
| C(3)–N(32) | 1.319(6) | S(4)–C(4) | 1.732(4) |
| C(4)–N(41) | 1.312(5) | C(4)–N(42) | 1.319(5) |
| | | | |
| S(4)–Pt(1)–S(3) | 90.58(4) | S(4)–Pt(1)–S(1) | 93.69(4) |
| S(3)–Pt(1)–S(1) | 168.03(4) | S(4)–Pt(1)–S(2) | 177.71(4) |
| S(3)–Pt(1)–S(2) | 89.67(4) | S(1)–Pt(1)–S(2) | 86.51(4) |
| C(1)–S(1)–Pt(1) | 111.0(2) | N(11)–C(1)–N(12) | 120.0(4) |
| N(11)–C(1)–S(1) | 122.5(3) | N(12)–C(1)–S(1) | 117.2(3) |
| C(2)–S(2)–Pt(1) | 107.8(2) | N(21)–C(2)–N(22) | 118.5(4) |
| N(21)–C(2)–S(2) | 118.6(4) | N(22)–C(2)–S(2) | 122.8(3) |

| Hydrogen bonds for $[Pt(TU)_4]S_2O_6$ D–H···A | *d*(D–H) | *d*(H···A) | *d*(D···A) | <(DHA) |
|---|---|---|---|---|
| N(11)–H(11A)···O(63)#1 | 0.88 | 2.12 | 2.988(4) | 169.9 |
| N(11)–H(11B)···O(53)#2 | 0.88 | 2.23 | 3.069(4) | 159.4 |
| N(12)–H(12A)···O(61)#1 | 0.88 | 2.20 | 3.075(5) | 178.2 |
| N(12)–H(12B)···O(51)#3 | 0.88 | 2.47 | 3.173(5) | 137.0 |
| N(21)–H(21A)···O(52)#4 | 0.88 | 2.21 | 2.971(5) | 143.9 |
| N(21)–H(21B)···O(61)#5 | 0.88 | 2.04 | 2.907(5) | 167.3 |
| N(22)–H(22B)···O(53)#2 | 0.88 | 2.26 | 3.030(5) | 146.3 |
| N(22)–H(22A)···S(3)#4 | 0.88 | 2.96 | 3.565(4) | 127.4 |
| N(31)–H(31A)···O(62)#6 | 0.88 | 2.10 | 2.957(5) | 163.3 |
| N(31)–H(31B)···O(53)#2 | 0.88 | 2.13 | 2.979(5) | 161.4 |
| N(31)–H(31B)···S(5)#2 | 0.88 | 2.94 | 3.608(4) | 134.6 |
| N(32)–H(32)···O(63)#6 | 0.88 | 2.13 | 3.005(5) | 169.9 |
| N(32)–H(32)···O(52) | 0.88 | 2.20 | 2.924(5) | 139.4 |
| N(41)–H(41A)···O(62)#7 | 0.88 | 2.29 | 2.996(5) | 137.8 |
| N(41)–H(41B)···S(1)#8 | 0.88 | 2.57 | 3.408(4) | 160.0 |
| N(41)–H(41B)···S(2)#8 | 0.88 | 2.93 | 3.524(4) | 126.4 |
| N(42)–H(42A)···O(51)#3 | 0.88 | 2.40 | 2.931(5) | 119.0 |
| N(42)–H(42B)···S(1) | 0.88 | 2.84 | 3.268(4) | 111.3 |
| N(42)–H(42B)···S(3)#9 | 0.88 | 2.70 | 3.366(4) | 133.6 |

Symmetry transformations used to generate equivalent atoms: #1 $-x+1, -y+1/2, -z+3/2$; #2 $-x+1/2, -y+1, z+1/2$; #3 $-x+3/2, -y+1, z+1/2$; #4 $x-1/2, -y+3/2, -z+1$; #5 $x, y+1, z$; #6 $x-1/2, -y+1/2, -z+1$; #7 $x+1/2, -y+1/2, -z+1$; #8 $-x+1, y-1/2, -z+3/2$; #9 $x+1/2, -y+3/2, -z+1$

agreement with earlier published results (2.324 Å) for $[Pt(TU)]Cl_2$,[15] and is only slightly longer than earlier published data (2.313 Å) for the same complex.[14]

Whereas the parameters for the central $PtS_4$ unit are basically the same for all investigated $[Pt(TU)_4]^{2+}$ cations, remarkable differences are observed for the orientation of the four thiourea ligands with respect to the $PtS_4$ plane that results in one of the conformations OOOO, IOOO, IIOO or IOIO.

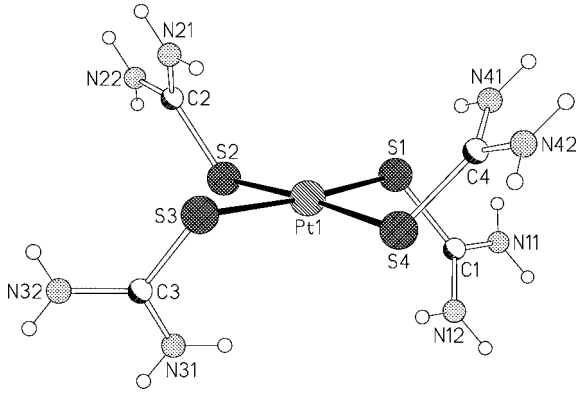


Figure 6. Molecular structure of the $[Pt(TU)_4]^{2+}$ cation of the complex $[Pt(TU)_4]Cl_2$, (IOIO).

### $[Pt(TU)_4]SiF_6 \cdot 0.25H_2O$, Conformation OOOO

Both the $[Pt(TU)_4]^{2+}$ cation and the $SiF_6^{2-}$ anion are situated on a crystallographic fourfold rotation axis ($C_4$ molecule symmetry).[27] Within the crystal the anion is situated exactly above and below the $PtS_4$ plane of the cation (Figure 7), with distances between the axial fluorine atoms (F12 and F11A) and Pt of 3.125(2) and 4.562(2) Å, respectively. The short Pt···F12 distance reflects the fact that F12 is involved in strong hydrogen bonding (Table 3) acting as a fourfold acceptor, thus forcing the OOOO conformation of the cation with the $NH_2$ groups of the thiourea ligands as hydrogen-bond donors. The hydrogen-bond acceptor function of F12 results in a significant longer Si–F bond (1.703(2) Å vs. an average of 1.683(3) Å for the other five Si–F distances). In contrast to these strong intermolecular

 © 2007 Wiley-VCH Verlag GmbH & Co. KGaA, Weinheim 

Table 5. Selected bond lengths [Å] and angles [°] for $[Pt(TU)_4](ClO_4)_2$ (IIOO).

| | | | |
|---|---|---|---|
| Pt(1)–S(1B)#1 | 2.313(2) | Pt(1)–S(1B) | 2.313(2) |
| Pt(1)–S(2A)#1 | 2.313(2) | Pt(1)–S(2A) | 2.313(2) |
| Pt(1)–S(2B) | 2.330(2) | Pt(1)–S(2B)#1 | 2.330(2) |
| Pt(1)–S(1A)#1 | 2.338(2) | Pt(1)–S(1A) | 2.338(2) |
| S(1)–C(1) | 1.819(5) | S(1B)–C(1) | 1.734(5) |
| C(1)–N(11) | 1.253(6) | C(1)–N(12) | 1.330(6) |
| S(2A)–C(2) | 1.802(5) | S(2B)–C(2) | 1.782(5) |
| C(2)–N(21) | 1.274(6) | C(2)–N(22) | 1.309(6) |
| Pt(2)–S(4B)#2 | 2.308(3) | Pt(2)–S(4B) | 2.308(3) |
| Pt(2)–S(4A) | 2.320(3) | Pt(2)–S(4A)#2 | 2.320(3) |
| Pt(2)–S(3B) | 2.328(3) | Pt(2)–S(3B)#2 | 2.328(3) |
| Pt(2)–S(3A) | 2.331(3) | Pt(2)–S(3A)#2 | 2.331(3) |
| S(3A)–C(3) | 1.689(5) | S(3B)–C(3) | 1.806(6) |
| C(3)–N(31) | 1.325(6) | C(3)–N(32) | 1.326(7) |
| S(4A)–C(4) | 1.800(6) | S(4B)–C(4) | 1.715(5) |
| | | | |
| S(1B)#1–Pt(1)–S(1B) | 180.0 | S(1B)#1–Pt(1)–S(2A)#1 | 124.61(8) |
| S(1B)–Pt(1)–S(2A)#1 | 55.39(8) | S(1B)#1–Pt(1)–S(2A) | 55.39(8) |
| S(1B)–Pt(1)–S(2A) | 124.61(8) | S(2A)#1–Pt(1)–S(2A) | 180.0 |
| S(1B)#1–Pt(1)–S(2B) | 87.91(8) | S(1B)–Pt(1)–S(2B) | 92.09(8) |
| S(2A)#1–Pt(1)–S(2B) | 147.33(8) | S(2A)–Pt(1)–S(2B) | 32.67(8) |
| S(1B)#1–Pt(1)–S(2B)#1 | 92.09(8) | S(1B)–Pt(1)–S(2B)#1 | 87.91(8) |
| S(2A)#1–Pt(1)–S(2B)#1 | 32.67(8) | S(2A)–Pt(1)–S(2B)#1 | 147.33(8) |
| S(2B)–Pt(1)–S(2B)#1 | 180.0 | S(1B)#1–Pt(1)–S(1A)#1 | 34.08(8) |
| S(1B)#1–Pt(1)–S(1A)#1 | 145.92(8) | S(2A)#1–Pt(1)–S(1A)#1 | 91.89(8) |
| S(2A)–Pt(1)–S(1A)#1 | 88.11(8) | S(2B)–Pt(1)–S(1A)#1 | 120.69(8) |
| S(2B)#1–Pt(1)–S(1A)#1 | 59.31(8) | S(1B)#1–Pt(1)–S(1A) | 145.92(8) |
| S(1B)–Pt(1)–S(1A) | 34.08(8) | S(2A)#1–Pt(1)–S(1A) | 88.11(8) |
| S(2A)–Pt(1)–S(1A) | 91.89(8) | S(2B)–Pt(1)–S(1A) | 59.31(8) |
| S(2B)#1–Pt(1)–S(1A) | 120.69(8) | S(1A)#1–Pt(1)–S(1A) | 180.0 |

Symmetry transformations used to generate equivalent atoms: #1 $-x+1, -y+1, -z+1$; #2 $-x, -y+1, -z$

Hydrogen bonds for $[Pt(TU)_4](ClO_4)_2$

| D–H···A | *d*(D–H) | *d*(H···A) | *d*(D···A) | <(DHA) |
|---|---|---|---|---|
| N(11)–H(11A)···O(12)#3 | 0.88 | 2.36 | 3.137(5) | 147.2 |
| N(11)–H(11A)···O(21)#4 | 0.88 | 2.50 | 3.126(5) | 128.6 |
| N(12)–H(12B)···O(13) | 0.88 | 2.34 | 3.156(5) | 155.1 |
| N(12)–H(12A)···O(14)#3 | 0.88 | 2.23 | 3.055(5) | 156.8 |
| N(12)–H(12B)···S(4B)#5 | 0.88 | 2.62 | 3.485(9) | 169.1 |
| N(21)–H(21A)···O(22)#6 | 0.88 | 2.55 | 2.997(5) | 112.3 |
| N(21)–H(21A)···O(23)#2 | 0.88 | 2.55 | 3.217(5) | 133.0 |
| N(21)–H(21A)···O(21)#2 | 0.88 | 2.56 | 3.083(5) | 119.1 |
| N(21)–H(21B)···O(13)#1 | 0.88 | 2.20 | 3.004(5) | 151.9 |
| N(21)–H(21B)···S(1A) | 0.88 | 3.01 | 3.477(4) | 115.5 |
| N(22)–H(22A)···O(11)#7 | 0.88 | 2.47 | 3.176(2) | 137.3 |
| N(22)–H(22A)···O(23)#2 | 0.88 | 2.51 | 3.179(5) | 133.4 |
| N(22)–H(22B)···S(2A)#7 | 0.88 | 2.40 | 3.264(5) | 166.4 |
| N(31)–H(31A)···O(23)#8 | 0.88 | 2.55 | 3.254(6) | 137.7 |
| N(31)–H(31B)···S(2B) | 0.88 | 2.49 | 3.175(6) | 135.6 |
| N(31)–H(31B)···S(2A) | 0.88 | 2.96 | 3.805(6) | 161.2 |
| N(32)–H(32A)···O(23)#8 | 0.88 | 2.32 | 3.080(5) | 144.1 |
| N(32)–H(32A)···O(11)#3 | 0.88 | 2.53 | 3.104(5) | 123.6 |
| N(32)–H(32B)···O(24) | 0.88 | 2.22 | 3.032(6) | 154.2 |
| N(41)–H(41A)···O(12)#9 | 0.88 | 2.14 | 3.014(4) | 176.5 |
| N(41)–H(41B)···O(24) | 0.88 | 2.37 | 3.187(5) | 154.7 |
| N(41)–H(41B)···S(3B)#2 | 0.88 | 2.93 | 3.433(5) | 118.3 |
| N(42)–H(42A)···O(21)#10 | 0.88 | 2.22 | 3.005(5) | 148.1 |
| N(42)–H(42B)···S(4B)#5 | 0.88 | 2.64 | 3.511(5) | 169.5 |
| N(42)–H(42B)···S(4A)#5 | 0.88 | 2.80 | 3.644(6) | 160.5 |

Symmetry transformations used to generate equivalent atoms: #1 $-x+1, -y+1, -z+1$; #2 $-x, -y+1, -z$; #3 $x, -y+3/2, -z-1/2$; #4 $x+1, -y+3/2, z+1/2$; #5 $-x+1, -y+1, -z$; #6 $-x, y-1/2, -z+1/2$; #7 $-x, -y+1, -z+1$; #8 $x, -y+3/2, z+1/2$; #9 $-x, y, z-1$; #10 $x+1, y, z$

hydrogen bridges, intramolecular N–H···S hydrogen bonding seems to play only a minor role (H···S distances of 3.12 Å and N–H···S angles of 102.8°).

Within the crystal packing each $SiF_6^{2-}$ anion connects four neighbored $[Pt(TU)_4]^{2+}$ cations via intermolecular N–H···S hydrogen bonds with the equatorial F13 atoms always

 © 2007 Wiley-VCH Verlag GmbH & Co. KGaA, Weinheim 

Table 6. Selected bond lengths [Å] and angles [°] for $[Pt(TU)_4]I_2$ (IOIO).

| | | | |
|---|---|---|---|
| Pt(1)–S(2) | 2.327(2) | Pt(1)–S(2)#1 | 2.327(2) |
| Pt(1)–S(1) | 2.334(2) | Pt(1)–S(2)#1 | 2.334(2) |
| S(1)–C(1) | 1.724(6) | C(1)–N(12) | 1.322(8) |
| C(1)–N(11) | 1.327(8) | S(2)–C(2) | 1.720(6) |
| C(2)–N(22) | 1.321(8) | C(2)–N(21) | 1.330(8) |
| Pt(2)–S(3)#2 | 2.326(2) | Pt(2)–S(3) | 2.326(2) |
| Pt(2)–S(4)#2 | 2.329(2) | Pt(2)–S(4) | 2.329(2) |
| S(3)–C(3) | 1.717(6) | C(3)–N(31) | 1.320(8) |
| C(3)–N(32) | 1.326(8) | S(4)–C(4) | 1.725(6) |
| C(4)–N(41) | 1.323(8) | C(4)–N(42) | 1.315(8) |
| | | | |
| S(2)–Pt(1)–S(2)#1 | 180.000(1) | S(2)–Pt(1)–S(1) | 87.75(6) |
| S(2)#1–Pt(1)–S(1) | 92.25(6) | S(2)–Pt(1)–S(1)#1 | 92.25(6) |
| S(2)#1–Pt(1)–S(1)#1 | 87.75(6) | S(1)–Pt(1)–S(1)#1 | 180.0 |
| S(3)#2–Pt(2)–S(3) | 180.1(2) | S(3)#2–Pt(2)–S(4)#2 | 87.37(6) |
| S(3)–Pt(2)–S(4)#2 | 92.63(6) | S(3)#2–Pt(2)–S(4) | 92.63(6) |
| S(3)–Pt(2)–S(4) | 87.37(6) | S(4)#2–Pt(2)–S(4) | 180.00(7) |
| C(3)–S(3)–Pt(2) | 107.5(2) | N(31)–C(3)–N(32) | 119.2(5) |
| C(1)–S(1)–Pt(1) | 107.0(2) | N(12)–C(1)–N(11) | 119.3(6) |
| N(12)–C(1)–S(1) | 123.0(5) | N(11)–C(1)–S(1) | 117.7(5) |
| C(2)–S(2)–Pt(1) | 109.2(2) | N(22)–C(2)–N(21) | 119.2(6) |
| N(22)–C(2)–S(2) | 122.8(5) | N(21)–C(2)–S(2) | 118.0(5) |

Symmetry transformations used to generate equivalent atoms: #1 $-x+1, -y+1, -z+1$; #2 $-x, -y, -z$

Hydrogen bonds for $[Pt(TU)_4]I_2$

| D–H···A | *d*(D–H) | *d*(H···A) | *d*(D···A) | <(DHA) |
|---|---|---|---|---|
| N(11)–H(11A)···I(2)#3 | 0.88 | 2.76 | 3.603(5) | 159.6 |
| N(11)–H(11B)···I(2)#4 | 0.88 | 2.83 | 3.616(5) | 149.3 |
| N(12)–H(12A)···I(1)#3 | 0.88 | 3.08 | 3.657(5) | 125.0 |
| N(12)–H(12A)···I(2)#3 | 0.88 | 3.17 | 3.925(5) | 145.1 |
| N(12)–H(12B)···I(1) | 0.88 | 2.88 | 3.654(5) | 147.8 |
| N(21)–H(21A)···S(3)#5 | 0.88 | 2.98 | 3.742(6) | 145.5 |
| N(21)–H(21B)···I(1)#5 | 0.88 | 2.79 | 3.670(6) | 173.5 |
| N(22)–H(22A)···S(3)#5 | 0.88 | 2.57 | 3.419(5) | 163.1 |
| N(22)–H(22B)···I(1) | 0.88 | 2.79 | 3.564(5) | 147.5 |
| N(22)–H(22B)···S(1)#1 | 0.88 | 2.88 | 3.288(5) | 110.3 |
| N(31)–H(31A)···I(2)#6 | 0.88 | 2.94 | 3.654(5) | 139.2 |
| N(31)–H(31B)···I(2)#7 | 0.88 | 2.87 | 3.657(5) | 152.3 |
| N(32)–H(32A)···I(1)#6 | 0.88 | 2.68 | 3.535(6) | 164.3 |
| N(32)–H(32B)···I(1)#8 | 0.88 | 2.76 | 3.604(6) | 160.6 |
| N(41)–H(41B)···I(2)#2 | 0.88 | 2.78 | 3.639(5) | 166.3 |
| N(42)–H(42A)···S(1)#9 | 0.88 | 2.62 | 3.462(5) | 160.6 |
| N(42)–H(42B)···I(2)#7 | 0.88 | 2.75 | 3.547(5) | 151.4 |
| N(42)–H(42B)···S(3)#2 | 0.88 | 2.97 | 3.392(5) | 111.4 |

Symmetry transformations used to generate equivalent atoms: #1 $-x+1, -y+1, -z+1$; #2 $-x, -y, -z$; #3 $-x+1, -y, -z+1$; #4 $x, y, z+$; #5 $x+1, y, z$; #6 $x, y-1, z$; #7 $-x+1, -y, -z$; #9 $-x, -y, -z+1$; #9 $x, y-1, z-1$

being the acceptor. Thus, two-dimensional double layers of cations and anions are formed with an up-side (O) face-to-face arrangement of the cations and the anions being located in between. These double layers are linked further by additional intermolecular N–H···S bridges to complete the three-dimensional hydrogen bond network (Figure 8). From the refinement results we concluded the presence of not more than 1/4 water molecule per complex unit. This only partially occupied water molecule is located at a position that allows for the formation of hydrogen bonds to four neighboring $SiF_6^{2-}$ anions depending on the orientation of the $H_2O$ (being situated in the special position *4a* of the space group leading to rotational disorder). This enables the water molecule to further interconnect the anions within layers parallel to the crystallographic *ab* plane (see Figure 8).

### $[Pt(TU)_4]S_2O_6$, Conformation IOOO

The $[Pt(TU)_4]^{2+}$ cation has $C_1$ symmetry and the $S_2O_6^{2-}$ anion is situated above the $PtS_4$ plane with three of the thiourea groups pointing upwards (Figure 9). The dithionate anion is connected to the cation by three hydrogen bonds with the O53 atom acting as acceptor resulting in a Pt–O53 distance of 3.394(3) Å. The fourth down-oriented thiourea ligand is involved in a moderate to strong intramolecular hydrogen bond (N42–H42B···S1) with a donor acceptor distance N42···S1 of 3.268(4) Å (Table 5). Other possible intramolecular hydrogen bonds may be present but are significantly weaker having either longer N···S distances (3.691(4), 4.999(4) Å] or much less favorable N–H···S angles (98.9(1)°]. Each of the eight $NH_2$ groups of the $[Pt(TU)_4]^{2+}$ cation is involved in two or three hydrogen bridges

 © 2007 Wiley-VCH Verlag GmbH & Co. KGaA, Weinheim 

Table 7. Selected bond length [Å] and angles [°] for $[Pt(TU)_4](CF_3SO_3)_2$ (IIOO).

| | | | |
|---|---|---|---|
| Pt(1)–S(2) | 2.3153(7) | Pt(1)–S(3) | 2.3161(7) |
| Pt(1)–S(1) | 2.3175(7) | Pt(1)–S(4) | 2.3229(7) |
| S(1)–C(1) | 1.730(3) | C(1)–N(12) | 1.317(3) |
| C(1)–N(11) | 1.317(3) | S(2)–C(2) | 1.726(3) |
| C(2)–N(22) | 1.317(3) | C(2)–N(21) | 1.322(3) |
| S(3)–C(3) | 1.734(3) | C(3)–N(31) | 1.307(4) |
| C(3)–N(32) | 1.313(4) | S(4)–C(4) | 1.720(3) |
| C(4)–N(42) | 1.314(3) | C(4)–N(41) | 1.331(3) |
| S(5)–O(53) | 1.438(2) | S(5)–O(51) | 1.443(2) |
| S(5)–O(52) | 1.448(2) | S(5)–C(5) | 1.820(3) |
| C(5)–F(51) | 1.323(4) | C(5)–F(53) | 1.330(4) |
| C(5)–F(52) | 1.332(3) | S(6)–O(61) | 1.439(2) |
| S(6)–O(63) | 1.442(2) | S(6)–O(62) | 1.4460(2) |
| S(6)–C(6) | 1.821(3) | C(6)–F(62) | 1.327(3) |
| C(6)–F(63) | 1.329(3) | C(6)–F(61) | 1.330(3) |
| | | | |
| S(2)–Pt(1)–S(3) | 101.68(2) | S(2)–Pt(1)–S(1) | 86.03(2) |
| S(3)–Pt(1)–S(1) | 172.26(2) | S(2)–Pt(1)–S(4) | 174.32(2) |
| S(3)–Pt(1)–S(4) | 83.97(2) | S(1)–Pt(1)–S(4) | 88.31(2) |
| C(1)–S(1)–Pt(1) | 107.20(9) | N(12)–C(1)–N(11) | 119.5(2) |
| N(12)–C(1)–S(1) | 118.0(2) | N(11)–C(1)–S(1) | 122.5(2) |
| C(2)–S(2)–Pt(1) | 109.59(9) | N(22)–C(2)–N(21) | 119.6(2) |
| N(22)–C(2)–S(2) | 123.8(2) | N(21)–C(2)–S(2) | 116.6(2) |
| C(3)–S(3)–Pt(1) | 117.50(9) | N(31)–C(3)–N(32) | 119.8(3) |
| N(31)–C(3)–S(3) | 124.1(2) | N(32)–C(3)–S(3) | 116.0(2) |
| C(4)–S(4)–Pt(1) | 106.79 | N(42)–C(4)–N(41) | 119.0(2) |
| N(42)–C(4)–S(4) | 123.5(2) | N(41)–C(4)–S(4) | 117.5(2) |

Hydrogen bonds for $[Pt(TU)_4](CF_3SO_3)_2$

| D–H···A | *d*(D–H) | *d*(H···A) | *d*(D···A) | <(DHA) |
|---|---|---|---|---|
| N(11)–H(11A)···O(63)#1 | 0.88 | 2.14 | 2.981(3) | 159.6 |
| N(11)–H(11B)···O(61) | 0.88 | 2.23 | 2.855(3) | 128.1 |
| N(12)–H(12A)···O(61)#1 | 0.88 | 2.19 | 3.006(3) | 154.4 |
| N(12)–H(12A)···S(6)#1 | 0.88 | 2.95 | 3.788(2) | 159.6 |
| N(12)–H(12B)···O(63) | 0.88 | 2.08 | 2.850(3) | 145.1 |
| N(21)–H(21A)···O(62)#3 | 0.88 | 2.28 | 3.016(3) | 141.5 |
| N(21)–H(21A)···S(3)#3 | 0.88 | 2.84 | 3.533(2) | 137.0 |
| N(21)–H(21B)···O(51)#4 | 0.88 | 2.20 | 3.032(3) | 156.5 |
| N(22)–H(22A)···S(4)#3 | 0.88 | 2.82 | 3.626(2) | 152.5 |
| N(22)–H(22B)···O(62) | 0.88 | 2.49 | 3.169(3) | 134.9 |
| N(22)–H(22B)···S(3) | 0.88 | 2.72 | 3.428(2) | 138.7 |
| N(31)–H(31A)···O(53)#5 | 0.88 | 2.14 | 3.020(3) | 176.2 |
| N(31)–H(31B)···O(53) | 0.88 | 2.51 | 3.119(3) | 126.9 |
| N(31)–H(31B)···S(2) | 0.88 | 2.69 | 3.324(2) | 129.5 |
| N(32)–H(32A)···O(52)#5 | 0.88 | 2.13 | 2.979(3) | 161.0 |
| N(32)–H(32A)···S(5)#5 | 0.88 | 2.94 | 3.784(3) | 162.6 |
| N(32)–H(32B)···F(53)#6 | 0.88 | 2.52 | 3.065(4) | 120.9 |
| N(41)–H(41A)···O(51)#7 | 0.88 | 2.22 | 3.017(3) | 149.9 |
| N(41)–H(41A)···S(5)#7 | 0.88 | 2.91 | 3.753(2) | 161.4 |
| N(41)–H(41B)···O(62)#8 | 0.88 | 2.08 | 2.927(3) | 160.0 |
| N(42)–H(42A)···O(52)#7 | 0.88 | 2.24 | 3.085(3) | 160.3 |
| N(42)–H(42B)···O(51) | 0.88 | 2.56 | 3.241(3) | 134.4 |

Symmetry transformations used to generate equivalent atoms: #1 $-x+1, y-1/2, -z+3/2$; #2 $x, y-1, z$; #3 $x, -y+5/2, z+1/2$; #4 $x, -y+3/2, z+1/2$; #5 $-x, -y+2, -z+1$; #6 $x, y+1, z$; #7 $x, -y+3/2, z-1/2$; #8 $x, -y+5/2, z-1/2$

(Table 4). The remaining five O atoms of the $S_2O_6^{2-}$ anion act as acceptors for two hydrogen bonds each. Interestingly, one $S_2O_6^{2-}$ anion forms hydrogen bonds to six different cations, thus controlling the packing arrangement.

Within the crystal packing the $[Pt(TU)_4]^{2+}$ cations form zig-zag chains along the crystallographic *b* direction, the cations being connected by intermolecular N–H···S hydrogen bridges with S1, S2 and S3 acting as acceptors, while S4 is only involved in the above mentioned intramolecular H bond. The zig-zag chains form a herringbone arrangement with the $S_2O_6^{2-}$ anions occupying the resulting channels (Figure 10).

### $[Pt(TU)_4](ClO_4)_2$, Conformation IIOO

The $[Pt(TU)_4]^{2+}$ cation is situated on a crystallographic inversion center and, consequently, has $C_i$ symmetry. Similar to the observation made for the OOOO-type complex $[Pt(TU)_4]SiF_6$, the $ClO_4^-$ anions are again arranged above

 © 2007 Wiley-VCH Verlag GmbH & Co. KGaA, Weinheim 

Table 8. Selected bond lengths [Å] and angles [°] for $[Pt(TU)_4](BPh_4)_2$ (IOIO).

| | | | |
|---|---|---|---|
| Pt(1)–S(1)#1 | 2.3226(8) | Pt(1)–S(1) | 2.3226(8) |
| Pt(1)–S(2)#1 | 2.3451(8) | Pt(1)–S(2) | 2.3451(8) |
| S(1)–C(1) | 1.719(3) | C(1)–N(11) | 1.322(4) |
| C(1)–N(12) | 1.322(4) | N(11)–H(11A) | 0.8800 |
| N(11)–H(11B) | 0.8800 | N(12)–H(12A) | 0.8800 |
| N(12)–H(12B) | 0.8800 | S(2)–C(2) | 1.718(3) |
| C(2)–N(22) | 1.314(4) | C(2)–N(21) | 1.327(4) |
| N(21)–H(21A) | 0.8800 | N(21)–H(21B) | 0.8800 |
| N(22)–H(22A) | 0.8800 | N(22)–H(22B) | 0.8800 |
| B(1)–C(41) | 1.637(4) | B(1)–C(21) | 1.642(4) |
| B(1)–C(11) | 1.843(4) | B(1)–C(31) | 1.650(4) |
| C(11)–C(16) | 1.401(4) | C(11)–C(12) | 1.411(4) |
| C(12)–C(13) | 1.380 | C(12)–H(12A) | 0.9500 |
| C(13)–C(14) | 1.398(4) | C(13)–H(13A) | 0.9500 |
| C(14)–C(15) | 1.384(4) | C(14)–H(14A) | 0.9500 |
| C(15)–C(16) | 1.400(4) | C(15)–H(15A) | 0.9500 |
| | | | |
| S(1)#1–Pt(1)–S(1) | 180.00(4) | S(1)#1–Pt(1)–S(2)#1 | 94.46(3) |
| S(1)–Pt(1)–S(2)#1 | 85.54(3) | S(1)#1–Pt(1)–S(2) | 85.54(3) |
| S(1)–Pt(1)–S(2) | 94.46(3) | S(2)#1–Pt(1)–S(2) | 180.0 |
| C(1)–S(1)–Pt(1) | 111.9(2) | N(11)–C(1)–N(12) | 118.8(3) |
| N(11)–C(1)–S(1) | 117.8(2) | N(12)–C(1)–S(1) | 123.3(2) |
| C(1)–N(11)–N(11A) | 120.0 | C(1)–N(11)–H(11B) | 120.0 |
| H(11A)–N(11)–H(11B) | 120.0 | C(1)–N(12)–H(12A) | 120.0 |
| C(1)–N(12)–H(12B) | 120.0 | H(12A)–N(12)–H(12B) | 120.0 |
| C(2)–S(2)–Pt(1) | 110.3(2) | N(22)–C(2)–N(21) | 120.1(3) |
| N(22)–C(2)–S(2) | 122.4(3) | N(21)–C(2)–S(2) | 117.5(3) |
| C(2)–N(21)–H(21A) | 120.0 | C(2)–N(21)–H(21B) | 120.0 |
| H(21A)–N(21)–H(21B) | 120.0 | C(2)–N(22)–H(21A) | 120.0 |
| C(2)–N(22)–H(22B) | 120.0 | H(22A)–N(22)–H(22B) | 120.0 |
| C(41)–B(1)–C(21) | 113.6(2) | C(41)–B(1)–C(11) | 105.6(2) |
| C(21)–B(1)–C(11) | 111.8(2) | C(41)–B(1)–C(31) | 108.5(2) |
| C(21)–B(1)–C(31) | 105.9(2) | C(11)–B(1)–C(31) | 111.5(2) |
| C(16)–C(11)–C(12) | 115.0(3) | C(16)–C(11)–B(1) | 124.9(3) |
| C(12)–C(11)–B(1) | 120.1(3) | C(13)–C(12)–C(11) | 123.1(3) |
| C(12)–C(13)–C(14) | 120.2(3) | C(12)–C(13)–H(13A) | 119.9 |
| C(14)–C(13)–H(13A) | 119.9 | C(15)–C(14)–C(13) | 118.8(3) |
| C(15)–C(14)–H(14A) | 120.6 | C(13)–C(14)–H(14A) | 120.6 |

Symmetry transformations used to generate equivalent atoms: #1 $-x, -y+1, -z+1$

Hydrogen bond for $[Pt(TU)_4](BPh_4)_2$

| D–H···A | *d*(D–H) | *d*(H···A) | *d*(D···A) | <(DHA) |
|---|---|---|---|---|
| N(12)–H(12B)···S(2) | 0.88 | 2.75 | 3.182(3) | 112.0 |
| N(22)–H(22B)···S(1A)#1 | 0.88 | 3.33 | 3.745(3) | 111.4 |

Symmetry transformations used to generate equivalent atoms: #1 $-x, -y+1, -z+1$

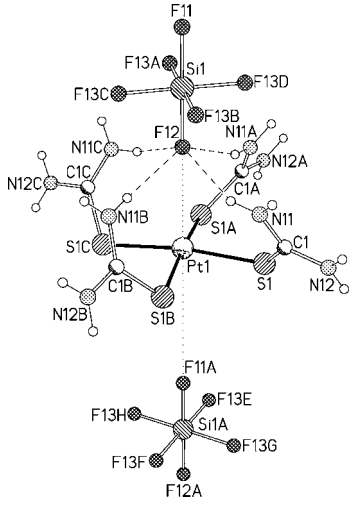


Figure 7. Conformation and H-bonding in $[Pt(TU)_4]SiF_6 \cdot 0.25H_2O$ (OOOO).

and below the $PtS_4$ plane of the $[Pt(TU)_4]^{2+}$ cation, but now form a significantly tilted angle. The angle between the perpendicular axis to the $PtS_4$ plane and the O···Pt···O line amounts to 22.4(1)°, and the corresponding O13···Pt1–S angles are 74.6(1)° (S1A), 73.6(1)° (S2A), 105.4(1)° (S1AA) and 106.4(1)° (S2AA). The oxygen atoms O13 and O13A both act as acceptors for two hydrogen bridges to the up- and down-oriented thiourea ligands (Figure 11), and the distance between Pt and the two symmetry related oxygen atoms O13 and O13A is 3.352(3) Å. Though the asymmetric part of the unit cell contains two independent molecules that are both subjected to disorder with two alternative positions for each of the sulfur atoms, the same arrangement of cations and anions is observed for both. Only one significant intramolecular hydrogen bond is observed in each of the two independent cations, viz. N21–H21B···S1A and N41A–H41B···S3A (see Table 5).

 © 2007 Wiley-VCH Verlag GmbH & Co. KGaA, Weinheim 

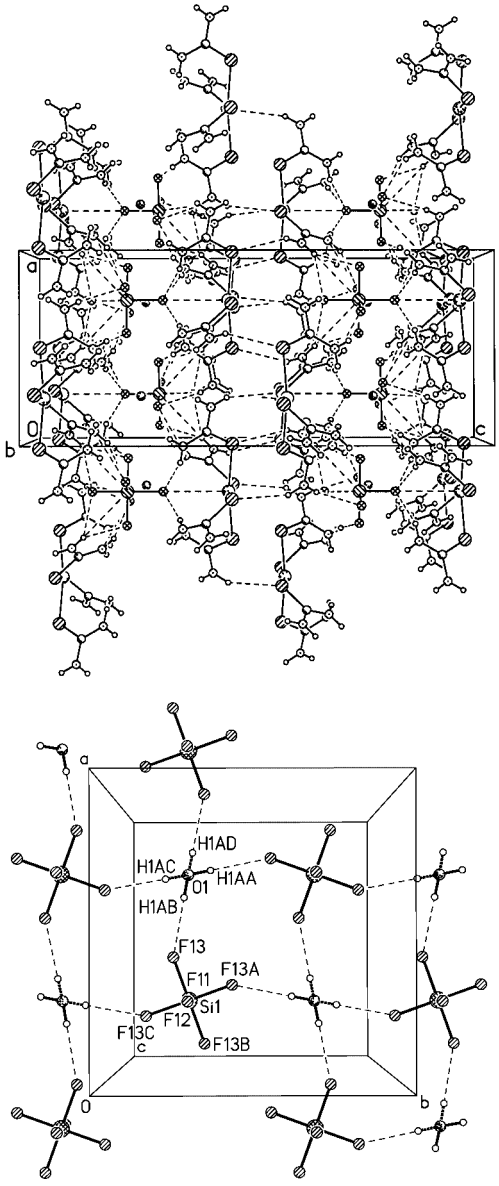


Figure 8. Crystal packing of $[Pt(TU)_4]SiF_6 \cdot 0.25H_2O$ (top) and crystal packing details of $[Pt(TU)_4]SiF_6 \cdot 0.25H_2O$ (bottom) highlighting the intermolecular hydrogen bonds between the partially occupied and disordered water molecules and the $SiF_6^{2-}$ anions parallel to the crystallographic *ab* plane (dashed solid lines between O and H atoms indicate the alternative orientation for the water molecule resulting from symmetry requirements).

The crystal packing is characterized by layers of $[Pt(TU)_4]^{2+}$ cations perpendicular to the *c* direction. Within these layers the cations are connected via intermolecular N–H···S hydrogen bridges. The space between the cation layers is occupied by the $ClO_4^-$ anions connecting the layers via intermolecular N–H···O hydrogen bridges (see Figure 12 and Table 5).

### $[Pt(TU)_4]Cl_2$, Conformation IOIO

We have re-examined the previously reported X-ray structure of $[Pt(TU)_4]Cl_2$.[14,15,22] The $[Pt(TU)_4]^{2+}$ cation in

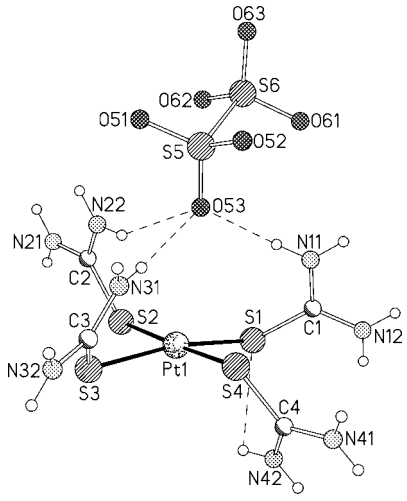


Figure 9. Conformation and H-bonding in $[Pt(TU)_4]S_2O_6$ (IOOO).

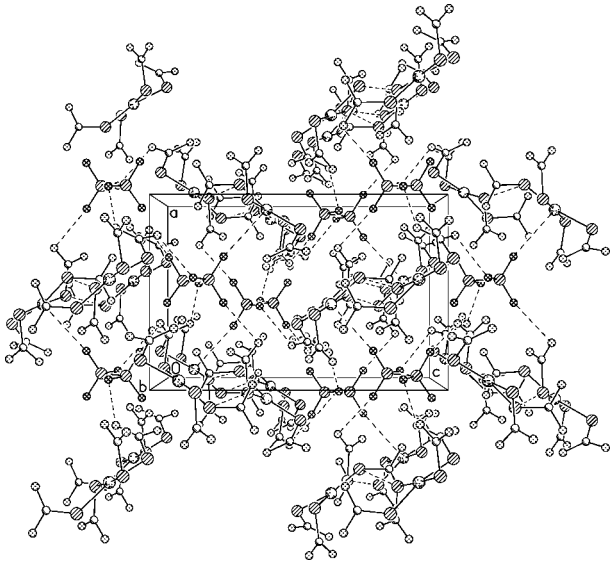


Figure 10. Crystal packing of $[Pt(TU)_4]S_2O_6$.

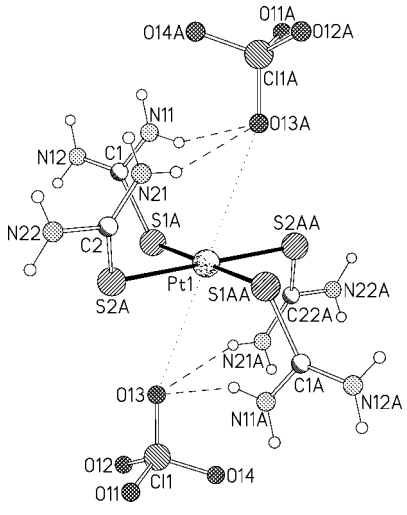


Figure 11. Conformation and H-bonding in $[Pt(TU)_4](ClO_4)_2$.

 © 2007 Wiley-VCH Verlag GmbH & Co. KGaA, Weinheim 

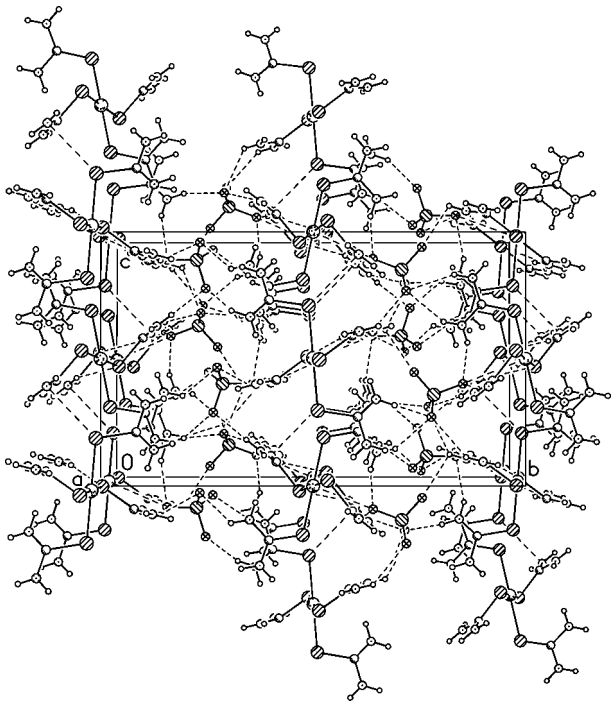


Figure 12. Crystal packing of $[Pt(TU)_4](ClO_4)_2$.

this molecular structure has only $C_1$ symmetry and shows significant deviation from the ideal square planar arrangement as is indicated by the S–Pt–S angles [largest deviation from 90° is observed for S1–Pt1–S4: 98.84(2)°]. The $Cl^-$ anions are situated above and below the $PtS_4$ plane but do not form a straight line with the Pt center any longer, the Cl1···Pt1···Cl2 angle being now 130.16(1)° instead of 180° in the $SiF_6^-$ and $ClO_4^-$ salts. Significant differences are observed for the two Pt···Cl distances [Pt1···Cl1 4.143(1) Å vs. Pt1···Cl2 3.727(1) Å]. Whereas Girling et al.[14] report five and three hydrogen bonds for the two halogen anions, respectively, our data indicate only two hydrogen bonds formed to the above the $PtS_4$ plane positioned chloride anion Cl1 and only one to the below the plane situated single Cl2. Consistent with other findings in the literature,[15] intramolecular N–H···S hydrogen bonding seems to have a stronger effect on the conformation here (see Figure 13 and Table 2). Besides comparably short H···S and N···S distances, the N–H···S angles (> 130°) become more favorable for effective hydrogen bonding.

Within the crystal the $[Pt(TU)_4]^{2+}$ cations are linked by intermolecular N–H···S hydrogen bridges and form stacks running along the crystallographic *a* axis. Each of the $Cl^-$ ions is linked to five neighbored cations by intermolecular N–H···Cl bridges and connects the cation stacks to complete the three-dimensional hydrogen bonding network of the crystal structure (see Figure 14 and Table 2).

### $[Pt(TU)_4](BPh_4)_2$, Conformation IIOO

The molecular and crystal structure of this compound is interesting since the $BPh_4^-$ anion cannot act as a hydrogen-

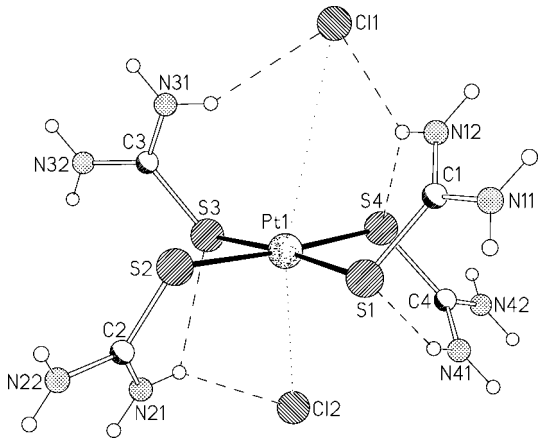


Figure 13. Conformation and H-bonding in $[Pt(TU)_4]Cl_2$.

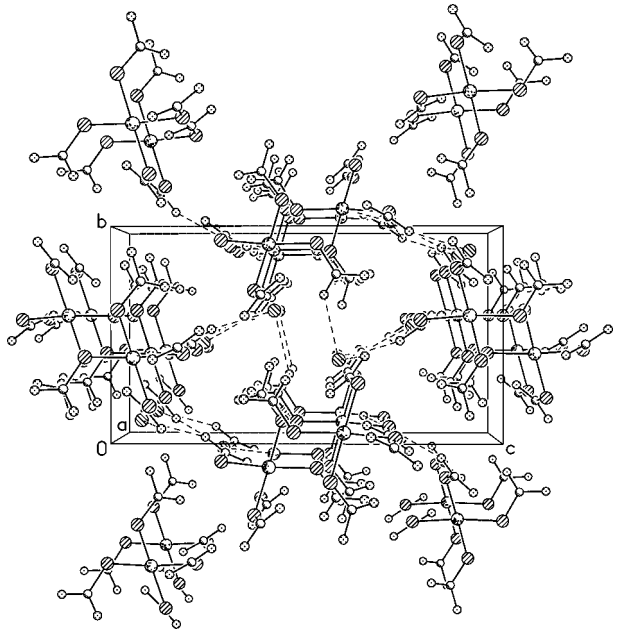


Figure 14. Crystal packing of $[Pt(TU)_4]Cl_2$.

bond acceptor. The $[Pt(TU)_4]^{2+}$ cation has crystallographically imposed $C_i$ symmetry. The rotor-like arrangement of the thiourea ligands with respect to the $PtS_4$ plane features two smaller and two larger dihedral angles of 49.1(1)° and 79.2(1)°, respectively. Surprisingly, intramolecular hydrogen bonds seem to play only a minor role. According to the parameters, only two of them can be mentioned here (Table 8). The crystalline packing can be described as hexagonal close packing of the $BPh_4^-$ anions, whereas the $[Pt(TU)_4]^{2+}$ cations occupy one half of the octahedral interstices.

### $[Pt(TU)_4]I_2$ and $[Pt(TU)_4](CF_3SO_3)_2$, Conformation IIOO

In these two crystal structures the structural motif of the arrangement of the two anions above and below the $[Pt(TU)_4]^{2+}$ moiety is repeated (see $[Pt(TU)_4](ClO_4)_2$). In the iodide compound the corresponding tilt angle between

 © 2007 Wiley-VCH Verlag GmbH & Co. KGaA, Weinheim 

the perpendicular axis to the $PtS_4$ plane and the I···Pt···I line amounts to 22.5(1)°, whereas this angle is 18.4(1)° in the triflate compound (using the sulfur atoms of the two anions for the construction of the line). In both compounds again numerous intermolecular N–H···S bridges force the formation of cation layers. The anions are situated in the space between the layers and connect these by intermolecular hydrogen bonds of the N–H···I or N–H···O and N–H···F type, respectively (see Tables 6 and 7).

## Conclusions

Seven $[Pt(TU)_4]X_n$ (X = $Cl^-$, $I^-$, $CF_3SO_3^-$, $BPh_4^-$ and $ClO_4^-$ ($n$ = 2), and $S_2O_8^{2-}$ and $SiF_6^{2-}$ ($n$ = 1)) complexes were synthesized and their crystal structures were determined by X-ray diffraction. Theoretical calculations show that the possible limiting conformations for the $[Pt(TU)_4]^{2+}$ moiety have only moderate energy differences (OOOO: 7.9 kcal/mol, IIOO: 2.1 kcal/mol (relative energy differences compared to the IOIO conformer)). These energy differences can be overcome by efficient hydrogen bonding, in which each of the $NH_2$ groups of the thiourea ligand can act as hydrogen-bond donor, provided the counterions can serve as acceptors. Consequently, the realization of the four theoretically limiting conformations (OOOO, IOOO, IIOO, IOIO) was achieved by the use of different counterions. Whereas the highly symmetrical $SiF_6^{2-}$ di-anion forced the formation of the all-up conformation (OOOO) using its ability to act as acceptor for four individual equidistant N–H···F hydrogen bridges, the use of other anions resulted in less symmetrical molecular structures. The use of $S_2O_6^{2-}$, the second di-anion in the group of anions in this study leads to the formation of the IOOO conformer of the $[Pt(TU)_4]^{2+}$ cation with three practically equivalent N–H···O hydrogen bridges to one oxygen atom (O53) of the dithionate acting as acceptor, and the remaining five oxygens being involved in an extensive hydrogen bonding network connecting cations and anions. $ClO_4^-$, $CF_3SO_3^-$ and $I^-$ as mono-anions all created an analogous structural motif with one anion above and one below the $PtS_4$ plane, but with a significant tilt angle of roughly 20° between the X···Pt···X line and the perpendicular axis to the $PtS_4$ plane. The resulting arrangement of cation-anion hydrogen interactions leads to the formation of the IIOO conformer in these three crystal structures. The IIOO conformer was also realized in the complex $[Pt(TU)_4](BPh_4)_2$, but without having the possibility of forming intermolecular cation-anion hydrogen bridges. Though intramolecular hydrogen bond formation would be an alternative in the $BPh_4^-$ salt, and is indeed observed to a more or less extent in all investigated $[Pt(TU)_4]^{2+}$ cations, no significantly stronger intramolecular hydrogen bonds have been observed here. From the parameters, a more pronounced influence of intramolecular hydrogen bonding can be attributed to the complex $[Pt(TU)_4]Cl_2$ having the smallest anion and exhibiting the IOIO conformation of the $[Pt(TU)_4]^{2+}$ cation.

Due to the small energy differences between the four limiting conformers, the choice of a suitable anion in terms of size, hydrogen-bond acceptor ability and/or symmetry can force the formation of either of the OOOO, IOOO, IIOO, or IOIO conformers in the solid state.

### Quantum Chemical Methods

We performed RB3LYP[28,29,30]/LANL2DZp[31,32,33,34] hybrid density functional calculations, i.e., with pseudo-potentials on the heavy elements and the valence basis set augmented with polarization functions.[35,36] In addition, we used RB3LYP/LACV3P+**,[32,33,34,37] a basis set originally developed by Schrödinger Inc. Structures were characterized as minima by computation of vibrational frequencies. Relative energies were corrected for zero point vibrational energy. The GAUSSIAN 03 suite of programs was used.[38]

## Experimental Section

Thiourea (Merck, p.a. quality grade) and $K_2[PtCl_4]$ (Johnson Matthey) were of the highest purity commercially available and used as received.

**Tetrakis(thiourea)platinum(II) Chloride, $[Pt(TU)_4]Cl_2$:** Preparation according to a previously published method.[39] $C_4H_{16}Cl_2N_8PtS_4$ (570.46): Calcd. C 8.42, H 2.83, N 19.64, S 22.48; found: C 8.43, H 2.74, N 19.45, S 22.32.

**Tetrakis(thiourea)platinum(II) Dithionate, $[Pt(TU)_4]S_2O_6$:** An acidic aqueous solution (pH 2) of $K_2[PtCl_4]$ (0.2 mM) and thiourea (10 mM) was heated under reflux for 12 h. After formation of the tetrakis(thiourea)platinum(II) complex, the solution was concentrated by a factor of 10 and an equal aliquot of a saturated solution of $Na_2S_2O_6$ was added. Single crystals of $[Pt(TU)_4]S_2O_6$ were obtained by slow evaporation of the solution. Elemental analysis could not be performed due to a very low yield of crystals.

**Tetrakis(thiourea)platinum(II) Hexafluorosilicate, $[Pt(TU)_4]SiF_6 \cdot 0.25H_2O$:** Crystal preparation was done as described above with a saturated solution of $Na_2SiF_6$, and single crystals were obtained within minutes after the saturated counterion solution was added. $C_{16}H_{66}F_{24}N_{32}OPt_4S_{16}Si_4$ (2584.54): Calcd. C 7.44, H 2.57, N 17.34, S 19.85; found: C 7.52, H 2.59, N 17.02, S 20.00.

Crystal preparations for all the other complexes, **$[Pt(TU)_4](ClO_4)_2$**, **$[Pt(TU)_4]I_2$**, **$[Pt(TU)_4](CF_3SO_3)_2$**, and **$[Pt(TU)_4](BPh_4)_2$** were done as described above. The crystals suitable for X-ray measurements were obtained by crystallization from water and after cooling in a refrigerator.

**$[Pt(TU)_4](ClO_4)_2$:** $C_4H_{16}Cl_2N_8O_8PtS_4$ (698.46): Calcd. C 6.88, H 2.31, N 16.04, S 18.36; found: C 7.05, H 2.46, N 15.83, S 18.56.

**$[Pt(TU)_4]I_2$:** No elemental analysis due to a very low yield of crystals.

**$[Pt(TU)_4](CF_3SO_3)_2$:** $C_6H_{16}F_6N_8O_6PtS_6$ (797.68): Calcd. C 9.03, H 2.02, N 14.05, S 24.07; found: C 9.08, H 1.94, N 13.92, S 23.92.

**$[Pt(TU)_4](BPh_4)_2$:** $C_{52}H_{56}B_2N_8PtS_4$ (1138.02): Calcd. C 54.88, H 4.96, N 9.85, S 11.27; found: C 54.84, H 5.20, N 10.27, S 11.57.

**X-ray Crystal Structure Determination of $[Pt(TU)_4]Cl_2$, $[Pt(TU)_4]I_2$, $[Pt(TU)_4](CF_3SO_3)_2$, $[Pt(TU)_4](BPh_4)_2$, $[Pt(TU)_4](ClO_4)_2$, $[Pt(TU)_4]$-**

 © 2007 Wiley-VCH Verlag GmbH & Co. KGaA, Weinheim 

**$SiF_6$·0.25$H_2O$ and [Pt(TU)$_4$]$S_2O_6$:** X-ray intensities were collected at 100 K on a Bruker-Nonius KappaCCD diffractometer using Mo-$K_\alpha$ radiation ($\lambda$ = 0.71073 Å, graphite monochromator). Lorentz and polarization corrections were applied, absorption effects were corrected on the basis of multiple scans using SADABS[40] with the exception of [Pt(TU)$_4$]($BPh_4$)$_2$ where a numerical absorption correction was applied instead. All structures were solved by direct methods and refined using full-matrix least-squares procedures on $F^2$. All non-hydrogen atoms were refined with anisotropic displacement parameters. All hydrogen atoms are placed in positions calculated for optimized geometry, their isotropic displacement parameters were tied to those of their corresponding N

Table 9. Crystallographic data, data collection and crystal structure refinement details.

| | [Pt(TU)$_4$]$Cl_2$ | [Pt(TU)$_4$]($ClO_4$)$_2$ | [Pt(TU)$_4$]$S_2O_6$ | [Pt(TU)$_4$]$SiF_6$·0.25$H_2O$ |
|---|---|---|---|---|
| Molecular formula | $C_4H_{16}Cl_2N_8PtS_4$ | $C_4H_{16}Cl_2N_8O_8PtS_4$ | $C_4H_{16}N_8O_6PtS_6$ | $C_4H_{16.50}F_6N_8O_{0.25}PtS_4Si$ |
| Formula weight | 570.48 | 698.48 | 659.70 | 646.17 |
| Temperature [K] | 100(2) | 100(2) | 100(2) | 100(2) |
| Crystal size (mm) | 0.15 × 0.07 × 0.05 | 0.14 × 0.13 × 0.08 | 0.25 × 0.23 × 0.06 | 0.18 × 0.14 × 0.06 |
| Crystal system | monoclinic | monoclinic | orthorhombic | tetragonal |
| Space group | $P2_1/c$ | $P2_1/c$ | $P2_12_12_1$[#] | $P4/ncc$ |
| $a$ [Å] | 8.9859(4) | 8.3650(5) | 10.022(1) | 9.1575(8) |
| $b$ [Å] | 10.1182(8) | 19.696(2) | 12.355(2) | 9.1575(8) |
| $c$ [Å] | 18.206(2) | 11.7678(7) | 15.298(2) | 22.155(2) |
| $\alpha$ [°] | 90 | 90 | 90 | 90 |
| $\beta$ [°] | 91.206(5) | 90.819(5) | 90 | 90 |
| $\gamma$ [°] | 90 | 90 | 90 | 90 |
| Volume [Å$^3$] | 1654.9(2) | 1938.6(3) | 1894.2(4) | 1857.9(3) |
| $Z$ | 4 | 4 | 4 | 4 |
| Absorption coeff. $\mu$ [mm$^{-1}$] | 9.305 | 7.997 | 8.109 | 8.131 |
| $D_{calcd.}$ [Mg/m$^3$] | 2.290 | 2.393 | 2.313 | 2.310 |
| $F$(000) | 1088 | 1344 | 1272 | 1234 |
| $\theta$ range [°] | 3.74 to 28.70 | 3.20 to 29.00 | 3.56 to 27.88 | 3.64 to 28.69 |
| Reflections collected/unique | 34570/4201 ($R_{int}$ = 0.0422) | 56744/5153 ($R_{int}$ = 0.0651) | 25408/4488 ($R_{int}$ = 0.0588) | 27855/1208 ($R_{int}$ = 0.0444) |
| Reflections observed [$I > 2\sigma(I)$] | 3614 | 3023 | 3913 | 1012 |
| Goodness-of-fit on $F^2$ | 0.926 | 0.978 | 0.910 | 1.091 |
| Final $R$ indices [$I > 2\sigma(I)$] | $R_1$ = 0.0181 $wR_2$ = 0.0344 | $R_1$ = 0.0256 $wR_2$ = 0.0425 | $R_1$ = 0.0227 $wR_2$ = 0.0455 | $R_1$ = 0.0178 $wR_2$ = 0.0347 |
| $R$ indices (all data) | $R_1$ = 0.0277 $wR_2$ = 0.0364 | $R_1$ = 0.0723 $wR_2$ = 0.0513 | $R_1$ = 0.0323 $wR_2$ = 0.0485 | $R_1$ = 0.0273 $wR_2$ = 0.0368 |
| Max. and min. transmission | 0.628 and 0.421 | 0.527 and 0.325 | 0.615 and 0.156 | 0.614 and 0.301 |
| [#] absolute structure (Flack) parameter: 0.025(5) | | | | |

| | [Pt(TU)$_4$]$I_2$ | [Pt(TU)$_4$]($CF_3SO_3$)$_2$ | [Pt(TU)$_4$]($BPh_4$)$_2$ |
|---|---|---|---|
| Molecular formula | $C_4H_{16}I_2N_8PtS_4$ | $C_6H_{16}F_6N_8O_6PtS_6$ | $C_{52}H_{56}B_2N_8PtS_4$ |
| Formula weight | 753.38 | 797.72 | 1138.00 |
| Temperature [K] | 100(2) | 100(2) | 100(2) |
| Crystal size (mm) | 0.07 × 0.05 × 0.05 | 0.20 × 0.15 × 0.07 | 0.39 × 0.14 × 0.04 |
| Crystal system | triclinic | monoclinic | monoclinic |
| Space group | $P\bar{1}$ | $P2_1/c$ | $P2_1/c$ |
| $a$ [Å] | 9.0532(5) | 19.336(2) | 12.371(2) |
| $b$ [Å] | 9.2044(7) | 10.248(1) | 11.841(1) |
| $c$ [Å] | 13.0466(4) | 12.422(2) | 17.307(2) |
| $\alpha$ [°] | 71.304(4) | 90 | 90 |
| $\beta$ [°] | 71.953(4) | 104.80(1) | 109.14(1) |
| $\gamma$ [°] | 63.351(5) | 90 | 90 |
| Volume [Å$^3$] | 902.53(10) | 2379.8(5) | 2395.1(5) |
| $Z$ | 2 | 4 | 2 |
| Absorption coeff. $\mu$ [mm$^{-1}$] | 11.656 | 6.510 | 3.151 |
| $D_{calcd.}$ [Mg/m$^3$] | 2.772 | 2.226 | 1.578 |
| $F$(000) | 688 | 1536 | 1152 |
| $\theta$ range [°] | 3.33 to 27.10 | 3.82 to 27.10 | 3.06 to 27.10 |
| Reflections collected/unique | 20801/3976 ($R_{int}$ = 0.0426) | 56133/5228 ($R_{int}$ = 0.0461) | 53932/5269 ($R_{int}$ = 0.0861) |
| Reflections observed [$I > 2\sigma(I)$] | 3365 | 4561 | 4179 |
| Goodness-of-fit on $F^2$ | 1.163 | 0.987 | 1.073 |
| Final $R$ indices [$I > 2\sigma(I)$] | $R_1$ = 0.0262 $wR_2$ = 0.0517 | $R_1$ = 0.0185 $wR_2$ = 0.0351 | $R_1$ = 0.0261 $wR_2$ = 0.0574 |
| $R$ indices (all data) | $R_1$ = 0.0375 $wR_2$ = 0.0540 | $R_1$ = 0.0272 $wR_2$ = 0.0371 | $R_1$ = 0.0418 $wR_2$ = 0.0636 |
| Max. and min. transmission | 0.558 and 0.458 | 0.634 and 0.353 | 0.881 and 0.449 |
| [#] absolute structure (Flack) parameter: 0.025(5) | | | |

 © 2007 Wiley-VCH Verlag GmbH & Co. KGaA, Weinheim 

or C carrier atoms by a factor of 1.2. The hydrogen atom for the solvent water molecule in the crystal structure of $[Pt(TU)_4]SiF_6 \cdot 0.25H_2O$ (with the oxygen being located in position *4a* of space group *P4/ncc*, no. 130) was taken from a difference fourier syntheses and not refined. The crystal used to determine the structure of **$[Pt(TU)_4](ClO_4)_2$** proved to be a pseudomerohedral twin. The application of an appropriate twin matrix (TWIN 1 0 0 0 –1 0 0 0 –1) resulted in a significant improvement of the refinement though the twinning was present only to a minor extent [BASF = 0.050(2)].

Crystallographic data and a summary of data collection and refinement parameters for all seven complexes are given in Table 9. For structure solution, refinement and graphical representations the SHELXTL NT 6.12 program package was used.[41]

CCDC-631060 (for **$[Pt(TU)_4]Cl_2$**), -631061 (for **$[Pt(TU)_4]I_2$**), -631062 (for **$[Pt(TU)_4](CF_3SO_3)_2$**), and -631063 (for **$[Pt(TU)_4](BPh_4)_2$**), -631064 (for **$[Pt(TU)_4](ClO_4)_2$**), -631065 (for **$[Pt(TU)_4]SiF_6 \cdot 0.25H_2O$**) and -631066 (for **$[Pt(TU)_4]S_2O_6$**) contain the supplementary crystallographic data for this paper. These data can be obtained free of charge from The Cambridge Crystallographic Data Centre via www.ccdc.cam.ac.uk/data_request/cif.

**Supporting Information** (see also the footnote on the first page of this article): Figures S1 to S3 present the molecular structure of the $[Pt(TU)_4]^{2+}$ cation in different complexes of the IIOO type.

## Acknowledgments

The authors gratefully acknowledge financial support from the Deutsche Forschungsgemeinschaft (DFG) and thank Immo Weber, Dr. Nico van Eikema Hommes and Eike Hübner for fruitful discussions, and Christina Wronna for elemental analysis. ZDB thanks Deutscher Akademischer Austauschdienst (DAAD) for a fellowship. We also thank Prof. Tim Clark, Computer Chemistry Center and the Regionales Rechenzentrum Erlangen (RRZE) for computer time.

[1] A. F. Hollemann, N. Wiberg, *Lehrbuch der Anorganischen Chemie*, 101 ed., Walter de Gruyter, Berlin, New York, **1995**.
[2] B. Lippert (Ed.), *Cisplatin: Chemistry and Biochemistry of a Leading Anticancer Drug*, Wiley-VCH, Zurich, **1999**.
[3] P. M. Takahara, C. A. Frederick, S. J. Lippard, *J. Am. Chem. Soc.* **1996**, *118*, 12309–12321.
[4] N. Farrell, in *Transition Metal Complexes as Drugs and Chemotherapeutic Agents* (Eds.: R. Ugo, B. R. James), Kluwer, Dordrecht, The Netherlands, **1989**.
[5] Z. D. Bugarčić, G. Liehr, R. van Eldik, *J. Chem. Soc., Dalton Trans.* **2002**, 2825–2830.
[6] D. Jaganyi, A. Hofmann, R. van Eldik, *Angew. Chem. Int. Ed.* **2001**, *40*, 1680–1683.
[7] Z. D. Bugarčić, F. W. Heinemann, R. van Eldik, *Dalton Trans.* **2004**, 279–286.
[8] J. M. Berry, C. Jacobs, B. Sikic, J. Halsey, R. F. Borch, *J. Clin. Oncol.* **1990**, *8*, 1585–1590.
[9] M. Treskes, U. Holwerda, L. G. J. Nijtmans, H. M. Pinedo, W. J. F. Van der Vijgh, *Cancer Chemother. Pharmacol.* **1992**, *29*, 467–470.
[10] J. Filipski, K. W. Kohn, R. Prather, W. M. Bonner, *Science (Washington, DC, USA)* **1979**, *204*, 181–183.
[11] R. F. Ozols, B. J. Corden, J. Collins, R. C. Young, in *Platinum Coordination Complexes in Cancer Chemotherapy* (Eds.: M. P. Hacker, E. B. Douple, I. H. Krakoff), Martinus Nijhoff, Boston, **1984**, p. 321.
[12] J. H. Burchenal, K. Kalaher, K. Dew, L. Lokys, G. Gale, *Biochimie* **1978**, *60*, 961–965.
[13] J. Reedijk, *Chem. Rev.* **1999**, *99*, 2499–2510.
[14] R. L. Girling, K. K. Chatterjee, E. L. Amma, *Inorg. Chim. Acta* **1973**, *7*, 557–562.
[15] J. Arpalahti, B. Lippert, H. Schoellhorn, U. Thewalt, *Inorg. Chim. Acta* **1988**, *153*, 51–55.
[16] F. Boeckler, H. Lanig, P. Gmeiner, *J. Med. Chem.* **2005**, *48*, 694–709.
[17] T. C. Mak, Q. Li, *Adv. Mol. Struct. Res.* **1998**, *4*, 151–225.
[18] P. D. Beer, P. A. Gale, *Angew. Chem. Int. Ed.* **2001**, *40*, 486–516.
[19] C. R. Bondy, P. A. Gale, S. J. Loeb, *J. Supramol. Chem.* **2003**, *2*, 93–96.
[20] J. Calvo, J. S. Casas, E. Garcia-Martinez, Y. Parajo, A. Sanchez-Gonzalez, J. Sordo, *Z. Anorg. Allg. Chem.* **2004**, *630*, 215–216.
[21] V. Amendola, M. Boiocchi, L. Fabbrizzi, A. Palchetti, *Chem. Eur. J.* **2005**, *11*, 5648–5660.
[22] L. Fuks, N. Sadlej-Sosnowska, K. Samochoka, W. Starosta, *J. Mol. Struct.* **2005**, *740*, 229–235.
[23] P. A. Gale, M. E. Light, R. Quesada, *Chem. Commun.* **2005**, 5864–5866.
[24] P. A. Gale, M. E. Light, R. Quesada, *CrystEngComm* **2006**, *8*, 178–188.
[25] a) We tried to include solvent effects in our calculations by applying the IPCM and PCM solvent model as implemented in Gaussian 03. Due to well documented problems (see, for example ref.[25b,25c]), not all three species could be calculated. The obtained data suggest the same stability trends for the different conformers; b) P. Illner, A. Zahl, R. Puchta, N. J. R. van Eikema Hommes, P. Wasserscheid, R. van Eldik, *J. Organomet. Chem.* **2005**, *690*, 3567–3576; c) R. Puchta, T. Clark, W. Bauer, *J. Mol. Model.* **2006**, *12*, 739–747.
[26] G. R. Desiraju, *Angew. Chem.* **1995**, *107*, 2541–2558.
[27] For the consequences concerning possible enantimerization mechanisms see: R. Puchta, R. Meier, N. J. R. van Eikema Hommes, R. van Eldik, *Eur. J. Inorg. Chem.* **2006**, 4063–4067.
[28] A. D. Becke, *J. Chem. Phys.* **1993**, *98*, 5648–5652.
[29] C. Lee, W. Yang, R. G. Parr, *Phys. Rev. B: Condens. Matter* **1988**, *37*, 785–789.
[30] P. J. Stephens, F. J. Devlin, C. F. Chabalowski, M. J. Frisch, *J. Phys. Chem.* **1994**, *98*, 11623–11627.
[31] T. H. Dunning Jr, P. J. Hay, in *Modern Theoretical Chemistry* (Eds.: H. F. Schaefer III), Plenum, New York, **1976**, vol. 3, p. 1.
[32] W. R. Wadt, P. J. Hay, *J. Chem. Phys.* **1985**, *82*, 284–298.
[33] P. J. Hay, W. R. Wadt, *J. Chem. Phys.* **1985**, *82*, 270–283.
[34] P. J. Hay, W. R. Wadt, *J. Chem. Phys.* **1985**, *82*, 299–310.
[35] S. Huzinaga, *Gaussian Basis Sets for Molecular Calculations*, Elsevier, Amsterdam, **1984**.
[36] The performance of RB3LYP/LANL2DZp is well documented: a) S. Klaus, H. Neumann, H. Jiao, A. Jacobi von Wangelin, D. Goerdes, D. Struebing, S. Huebner, M. Hateley, C. Weckbecker, K. Huthmacher, T. Riermeier, M. Beller, *J. Organomet. Chem.* **2004**, *689*, 3685–3700; b) R. W. Saalfrank, C. Deutscher, H. Maid, A. M. Ako, S. Sperner, T. Nakajima, W. Bauer, F. Hampel, B. A. Hess, N. J. R. van Eikema Hommes, R. Puchta, F. W. Heinemann, *Chem. Eur. J.* **2004**, *10*, 1899–1905; c) A. Scheurer, H. Maid, F. Hampel, R. W. Saalfrank, L. Toupet, P. Mosset, R. Puchta, N. J. R. van Eikema Hommes, *Eur. J. Org. Chem.* **2005**, 2566–2574; d) M. Galle, R. Puchta, N. J. R. van Eikema Hommes, R. van Eldik, *Z. Phys. Chem.* **2006**, *220*, 511–523.
[37] a) The LACV3P basis set is a triple-zeta contraction of the LACVP basis set developed and tested at Schrödinger, Inc. LACV3P is based on the Hay–Wadt-ECPs [33–35] and on the 6-311G basis set; b) T. Clark, J. Chandrasekhar, G. W. Spitznagel, P. von Ragué Schleyer, *J. Comput. Chem.* **1983**, *4*, 294–301;

 © 2007 Wiley-VCH Verlag GmbH & Co. KGaA, Weinheim 

c) M. J. Frisch, J. A. Pople, J. S. Binkley, *J. Chem. Phys.* **1984**, *80*, 3265–3269; d) R. Krishnan, J. S. Binkley, R. Seeger, J. A. Pople, *J. Chem. Phys.* **1980**, *72*, 650–654; e) . A. D. McLean, G. S. Chandler, *J. Chem. Phys.* **1980**, *72*, 5639–5648; f) A. V. Mitin, J. Baker, P. Pulay, *J. Chem. Phys.* **2003**, *118*, 7775–7782.
[38] M. J. Frisch, G. W. Trucks, H. B. Schlegel, G. E. Scuseri, M. A. Robb, J. R. Cheeseman, J. A. Montgomery Jr, T. Vreven, K. N. Kudin, J. C. Burant, J. M. Millam, S. S. Iyengar, J. Tomasi, V. Barone, B. Mennucci, M. Cossi, G. Scalmani, N. Rega, G. A. Petersson, H. Nakatsuji, M. Hada, M. Ehara, K. Toyota, R. Fukuda, J. Hasegawa, M. Ishida, T. Nakajima, Y. Honda, O. Kitao, H. Nakai, M. Klene, X. Li, J. E. Knox, H. P. Hratchian, J. B. Cross, V. Bakken, C. Adamo, J. Jaramillo, R. Gomperts, R. E. Stratmann, O. Yazyev, A. J. Austin, R. Cammi, C. Pomelli, J. W. Ochterski, P. Y. Ayala, K. Morokuma, G. A. Voth, P. Salvador, J. J. Dannenberg, V. G. Zakrzewski, S. Dapprich, A. D. Daniels, M. C. Strain, O. Farkas, D. K. Malick, A. D. Rabuck, K. Raghavachari, J. B. Foresman, J. V. Ortiz, Q. Cui, A. G. Baboul, S. Clifford, J. Cioslowski, B. B. Stefanov, G. Liu, A. Liashenko, P. Piskorz, I. Komaromi, R. L. Martin, D. J. Fox, T. Keith, M. A. Al-Laham, C. Y. Peng, A. Nanayakkara, M. Challacombe, P. M. W. Gill, B. Johnson, W. Chen, M. W. Wong, C. Gonzalez, J. A. Pople, *Gaussian 03 Revision C.02*, Gaussian Inc., Wallingford CT, **2004**.
[39] A. Yamaguchi, R. B. Penland, S. Mizushima, J. T. Lane, C. Curran, J. V. Quagliano, *J. Am. Chem. Soc.* **1958**, *80*, 527–529.
[40] *SADABS 2.06*, Bruker AXS Inc., Madison WI, USA, **2002**.
[41] *SHELXTL NT 6.12*, Bruker AXS Inc., Madison WI, USA, **2002**.

Received: November 1, 2006
Published Online: February 22, 2007

 © 2007 Wiley-VCH Verlag GmbH & Co. KGaA, Weinheim 

DOI: 10.1002/ejic.200601199

# Mononuclear and Heterodinuclear Metal Complexes of Nonsymmetric Ditertiary Phosphanes Derived from $R_2PCH_2OH$

**Gavin M. Brown,[a] Mark R. J. Elsegood,[a] Andrew J. Lake,[a] Noelia M. Sanchez-Ballester,[a] Martin B. Smith,*[a] Thomas S. Varley,[a] and Kevin Blann*[b]**

**Keywords:** Late-transition metals / P ligands / Heterobimetallics / Coordination modes

The new nonsymmetric ditertiary phosphanes, $Ph_2PCH_2N(R)CH_2PAd$ [**3a**: R = $C_6H_5$, **3b**: R = $C_6H_4(4\text{-}CH_3)$] were prepared using a three-step sequence of condensation reactions. Hence treatment of AdP-H (AdP-H = 1,3,5,7-tetramethyl-2,4,8-trioxa-6-phosphaadamantane) with $(CH_2O)_n$ at 110 °C gave the adamantane-derived hydroxymethylphosphane **1**, which upon condensation with $C_6H_5NH_2$ or $C_6H_4(4\text{-}CH_3)NH_2$ gave the secondary aminophosphanes $HN(R)CH_2PAd$ [**2a**: R = $C_6H_5$, **2b**: R = $C_6H_4(4\text{-}CH_3)$]. Further condensation of **2a** or **2b** with $Ph_2PCH_2OH$ gave **3a** or **3b** in high yields (ca. 85 %) containing the sterically encumbered adamantane cage. The coordination capabilities of **2a**, **3a** and **3b** have been explored with various $Pd^{II}$, $Pt^{II}$, $Ru^{II}$, $Ir^{III}$ and $Au^{I}$ metal centres. Bridge cleavage of $\{Pd(\kappa^2\text{-}C,N\text{-}C_{16}H_{16}N)Br\}_2$ with 2 equiv. of **2a** gave the neutral, mononuclear complex $Pd(\kappa^2\text{-}C,N\text{-}C_{16}H_{16}N)Br$(**2a**) (**4**). Reaction of **3a/3b** with $MCl_2$(cod) (M = Pt, Pd) gave the corresponding $\kappa^2$-*P,P′*-chelate complexes *cis*-$MCl_2$(**3**) [**5a**: M = Pt, R = $C_6H_5$, **5b**: Pt, R = $C_6H_4(4\text{-}CH_3)$, **5c**: Pd, R = $C_6H_5$, **5d**: Pd, R = $C_6H_4(4\text{-}CH_3)$]. In contrast, bridge cleavage of the dimers $\{RuCl_2(\eta^6\text{-}p\text{-cym})\}_2$ or $\{IrCl_2(\eta^5\text{-}Cp^*)\}_2$ with **3a** gave the $\kappa^1$-*P*-monodentate complexes $RuCl_2(\eta^6\text{-}p\text{-cym})$(**3a**) (**6**) and $IrCl_2(\eta^5\text{-}Cp^*)$(**3a**) (**7**), respectively, in which the –PAd group is noncoordinating. Reaction of **6** or **7** with AuCl(tht) (tht = tetrahydrothiophene) gave the mixed-metal complexes $\kappa^2$-*P,P′*-μ-$RuCl_2(\eta^6\text{-}p\text{-cym})\{Ph_2PCH_2N(Ph)CH_2PAd(AuCl)\}$ (**8**) and $\kappa^2$-*P,P′*-μ-$IrCl_2(\eta^5\text{-}Cp^*)\{Ph_2PCH_2N(Ph)CH_2PAd(AuCl)\}$ (**9**). All new compounds have been fully characterised by spectroscopic and analytical methods. Furthermore, the structures of **2a**, **4**, **5a**, **5b** and **6**–**9** have been elucidated by single-crystal X-ray crystallography. The X-ray structures of **5a**, **5b** and **6**–**9** represent the first examples of crystallographically characterised nonsymmetric ditertiary phosphane complexes bearing one adamantane moiety.

(© Wiley-VCH Verlag GmbH & Co. KGaA, 69451 Weinheim, Germany, 2007)

## Introduction

As part of ongoing studies[1–5] in our group we have been interested in developing new tertiary and symmetric ditertiary phosphanes using Mannich-based condensation reactions. Compounds of the formula $(R_2PCH_2)_2N(R)$ and $\{(R_2PCH_2)_2N\}_2(R)$ are two such examples[6–10] which have interesting coordination properties, catalytic applications and, more recently, are important ligands for self-assembly reactions using covalent bonds or H-bonding interactions.[1,2,4,11] The tetraphenyl-substituted phosphane $(Ph_2PCH_2)_2N(R)$, closely related to the three-carbon spacer $(Ph_2PCH_2)_2CH_2$ [1,3-bis(diphenylphosphanyl)propane, dppp], has been successfully utilised in several metal-catalysed reactions.[12–14] Furthermore, a related $C_3$ backbone diphosphane structurally comparable to dppp, is the bulky electron-rich diphosphane $(AdPCH_2)_2CH_2$ (bpap) recently reported by Pringle and co-workers.[15,16] Both bpap and related diphospha-adamantane ligands have been shown to form complexes with Ru, Pd and Au metal centres.[15,16] There has also been interest in these adamantane-based phosphane ligands for their important uses in a range of catalytic metal-mediated transformations such as aminations, hydroformylation, hydrogenations, methoxycarbonylation of internal alkenes and Suzuki and Sonogashira couplings.[17–25]

Nonsymmetric ditertiary phosphanes have seldom been studied in relation to their symmetric counterparts possibly reflecting the necessity to perform multistep syntheses.[26–31] When considering possible coordination modes for nonsymmetric diphosphanes of the type $R_2PCH_2XCH_2PR'_2$ various coordination modes are plausible some of which are shown in Figure 1. Hence $\kappa^1$-*P*-monodentate coordination is possible at either $–PR_2$ or $–PR'_2$ centres (structures **I** and **II**) and μ-*PP′* bridging between similar/disparate metal centres (structures **III**–**V**; the presence of a metal–metal interaction is illustrated by a dashed line). Alternatively such mixed ligands may adopt a more classic $\kappa^2$-*PP′*-chelating mode to a single metal centre (structure **VI**). Finally, depending on the nature of the X spacer group [e.g. N-

[a] Department of Chemistry, Loughborough University, Loughborough, Leics,
UK, LE11 3TU, UK
Fax: +44-1509-223925
E-mail: m.b.smith@lboro.ac.uk
[b] Sasol Technology (Pty) Ltd., R&D Division,
1 Klasie Havenga Road, Sasolburg, 1947, South Africa
Fax: +27-11-52-3190
E-mail: kevin.blann@sasol.com

 © 2007 Wiley-VCH Verlag GmbH & Co. KGaA, Weinheim 

$(CH_2)_4$] separating the two phosphorus donor atoms, $\kappa^3$-*PNP′*-tridentate coordination is possible utilising all three group-15 donor atoms (structure **VII**).[8]

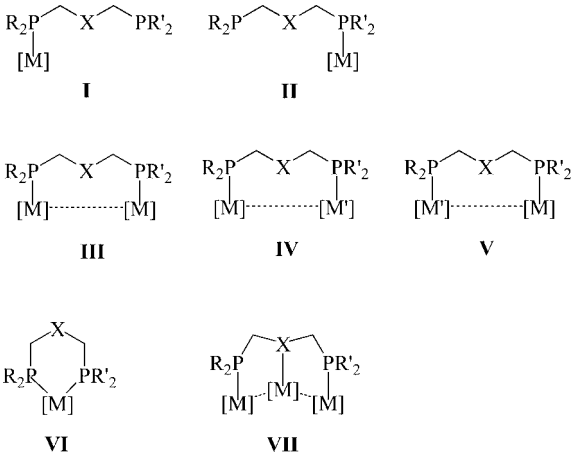


Figure 1. Schematic representation of the possible coordination modes for $R_2PCH_2XCH_2PR'_2$.

Herein we report a simple two-step condensation procedure (Scheme 1, pathway **b/c**) by which ditertiary phosphanes bearing non-equivalent groups (–$PPh_2$ and –PAd) can be obtained. In contrast, while pathway **a** generally affords symmetric diphosphanes, pathway **b** gives initially a secondary aminophosphane that can undergo further reaction with a second different hydroxymethylphosphane precursor (pathway **c**) to yield the desired nonsymmetric diphosphane. We demonstrate that these ligands exhibit diverse coordination behaviour towards a range of late transition metals, and can function in a $\kappa^1$-*P*-monodentate manner in which the –PAd fragment remains non-coordinating (structure **I**). This has allowed us to use these intermediates as "metalloligands" for the construction of heterobimetallic species as exemplified by our syntheses of complexes containing Ru/Au and Ir/Au metal centre combinations. The single-crystal X-ray structures of eight compounds are reported.

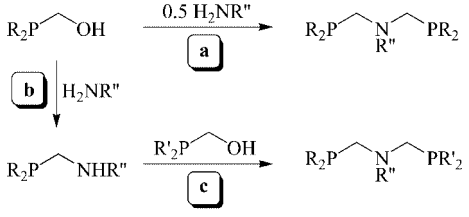


Scheme 1.

## Results and Discussion

### Ligand Syntheses

Previous studies using $Ph_2PCH_2OH$ have shown that condensation with primary amines ($RNH_2$) can be used to access either singly substituted products [of the type $Ph_2PCH_2N(H)R$] or symmetric ditertiary phosphanes [of the type $(Ph_2PCH_2)_2N(R)$] depending on the R group.[1–5] We have found that by using two consecutive Mannich based condensation reactions, nonsymmetric ditertiary phosphanes such as **3a** and **3b** can be realised. Accordingly, insertion of paraformaldehyde into the P–H bond of AdP-H (1:1 ratio) at 110 °C for 90 min affords the hydroxymethyl-functionalised phosphane **1**. Mannich condensation of **1** with $H_2NC_6H_5$ (1:1 ratio) in $CH_3OH$ at room temperature, under anaerobic conditions, gave the secondary aminophosphane **2a** as a racemic mixture of enantiomers. Similarly, **2b** could be prepared from $H_2NC_6H_4(4\text{-}CH_3)$ employing a similar method (Scheme 2). Further treatment of **2a** (or **2b**) with $Ph_2PCH_2OH$ in $CH_3OH$ at room temperature gave the desired nonsymmetric ditertiary phosphanes **3a** (or **3b**) in good yields (ca. 85%). The formulation of these compounds were confirmed by a combination of spectroscopic and analytical methods.

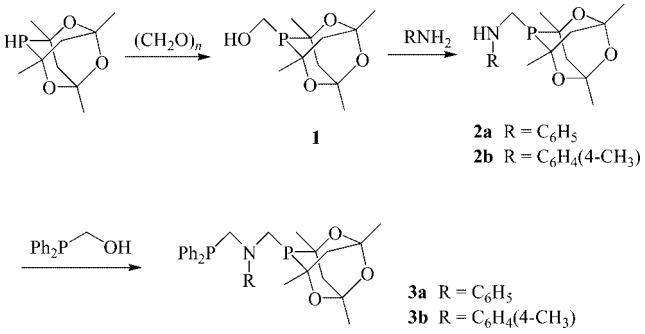


Scheme 2.

The $^{31}P\{^1H\}$ NMR chemical shifts for **1**, **2a** and **2b** are all similar [$\delta$(P) –31.2, –32.2 and –32.4 ppm, respectively], but differ from the starting secondary phosphane AdP-H, by ca. 20 ppm [$\delta$(P) –49.7 ppm, $CDCl_3$].[32] Furthermore, the $^{31}P\{^1H\}$ NMR chemical shifts for **1**, **2a** and **2b** differ by ca. 10 ppm with respect to the phenyl-modified phosphaadamantanes, AdP-Ph, previously reported.[19] Upon second condensation the $^{31}P$ resonance for the –PAd group is shifted upfield by ca. 10 ppm to –41.5 ppm (for **3a**) and –42.0 ppm (for **3b**). The –$PPh_2$ resonance is observed at $\delta$(P) –27.4 ppm (for **3a**) and –27.6 ppm (for **3b**), which differs by ca. 10 ppm with respect to dppp [$\delta$(P) –17.3 ppm, $CDCl_3$]. In the $^1H$ NMR spectra of **2a** and **2b** the $CH_2$ hydrogen atoms are diastereotopic as two separate doublet of doublets are observed at ca. 3.4 and 2.9 ppm. On the basis of FT-IR spectroscopy (KBr pellets), characteristic $\nu_{O-H}$ and $\nu_{N-H}$ stretches were observed at 3470 $cm^{-1}$, 3367 $cm^{-1}$ and 3319 $cm^{-1}$ for **1**, **2a** and **2b**, respectively, yet these frequencies were absent in either **3a** or **3b** as would be expected. Other characterising data are given in Table 1 and the Exp. Sect.

The X-ray structure of **2a** has been determined (Figure 2, Table 2) and confirms the presence of the phospha-adamantane cage. While a few crystallographic examples of sterically hindered phosphanes containing this cage have been reported in the literature[15–19,21,25] this structure represents

 © 2007 Wiley-VCH Verlag GmbH & Co. KGaA, Weinheim 

Table 1. Selected spectroscopic data for compounds **1**–**10**.[a]

| | $\delta$(P) / –$PPh_2$ | $\delta$(P) / –PAd | $^4J$(PP) | $J$(Pt$PPh_2$) | $J$(PtPAd) | $^2J$(PP) | ν(OH)/ ν(NH) | ν(MCl) |
|---|---|---|---|---|---|---|---|---|
| **1** | | –31.2 | | | | | 3470 | |
| **2a** | | –32.2 | | | | | 3367 | |
| **2b** | | –32.4 | | | | | 3319 | |
| **3a** | –27.4 | –41.5 | 5 | | | | | |
| **3b** | –27.6 | –42.0 | 4 | | | | | |
| **4** | | 18.7 | | | | | 3297 | |
| **5a** | –8.0 | –19.0 | | 3233 | 3489 | 19 | | 315, 293 |
| **5b** | –8.0 | –18.9 | | 3230 | 3489 | 19 | | 315, 292 |
| **5c** | 9.6 | –4.0 | | | | 8 | | 304, 291 |
| **5d** | 9.6 | –3.9 | | | | 10 | | 304, 291 |
| **6** | 23.6 | –39.0 | n.r. | | | | | |
| **7** | –5.1 | –38.7 | 5 | | | | | |
| **8** | 28.4 | 24.1 | 11 | | | | | 331 |
| **9** | 17.5 | –3.2 | 9 | | | | | 336 |
| **10**[b] | 14 | 10 | n.r. | | | | | 329 |

[a] Chemical shifts in ppm, coupling constants in Hz. [b] Recorded at –50 °C in $CDCl_3$. n.r. = not resolved.

the first example of such a compound bearing a remote, secondary amine functional group. The P(1)–C(11) [1.8591(19) Å] and C(11)–N(1) [1.456(2) Å] distances are similar to other documented tertiary phosphanes bearing phenyl substituents on phosphorus [P–C 1.8208(19), 1.8515(18) Å; C–N 1.456(2), 1.454(2) Å] illustrating that the adamantane cage has negligible electronic/steric effects on these structural parameters.[1,33]

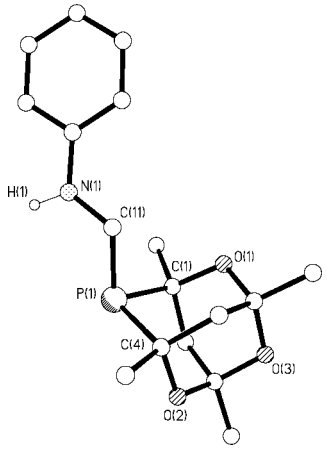


Figure 2. Molecular structure of **2a**; all hydrogen atoms except on N(1) have been removed for clarity.

Table 2. Selected bond lengths [Å] and angles [°] for compounds **2a** and **4**.

| | **2a** | **4** |
|---|---|---|
| Pd(1)–Br(1) | | 2.5676(3) |
| Pd(1)–P(1) | | 2.2522(6) |
| Pd(1)–N(2) | | 2.1291(18) |
| Pd(1)–C(33) | | 2.050(2) |
| N(2)–C(24) | | 1.282(3) |
| P(1)–C(11) | 1.8591(19) | 1.872(2) |
| C(11)–N(1) | 1.456(2) | 1.444(3) |
| Br(1)–Pd(1)–P(1) | | 94.067(16) |
| Br(1)–Pd(1)–C(33) | | 167.48(7) |
| Br(1)–Pd(1)–N(2) | | 89.01(5) |
| P(1)–Pd(1)–C(33) | | 95.42(7) |
| P(1)–Pd(1)–N(2) | | 173.14(5) |
| C(33)–Pd(1)–N(2) | | 82.47(8) |
| Pd(1)–P(1)–C(11) | | 111.02(2) |
| P(1)–C(11)–N(1) | 108.35(13) | 117.08(16) |

## Coordination Studies

Given the paucity of palladium complexes with adamantane-based phosphorus ligands documented in the literature[17,19,25] we prepared the palladium(II) complex **4** by bridge cleavage of the known[34] dimeric compound {Pd($\kappa^2$-*C,N*-$C_{16}H_{16}N$)Br}$_2$ with **2a** in refluxing acetone [Equation (1)]. Compound **4** displayed a singlet at $\delta$(P) 18.7 ppm in the $^{31}P\{^1H\}$ NMR spectrum (Table 1) and furthermore was characterised by single-crystal X-ray crystallography.

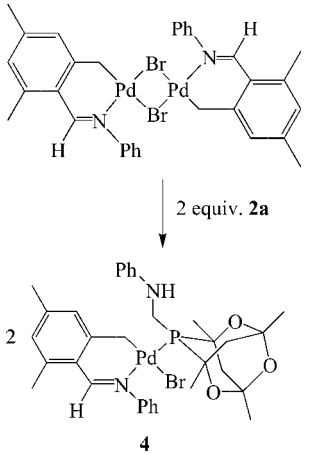


(1)

The X-ray structure (Figure 3, Table 2) confirmed a near square-planar arrangement about palladium with angles in the range 82.47(8)–95.42(7) Å. The Pd(1)–P(1) distance in **4** [2.2522(6) Å] is as expected. As previously observed for

 © 2007 Wiley-VCH Verlag GmbH & Co. KGaA, Weinheim 

other cyclometallated complexes of palladium the phosphane **2a** is *trans* to the imine nitrogen N(2).[35] Within the $\kappa^2$-*C*,*N*-metallated ligand an *E* configuration is adopted by the two arene groups located about the C(24)=N(2) imine double bond. The six-membered $PdC_4N$ metallacycle adopts a nonplanar conformation hinged about C(24)/C(33). The Pd deviates from the P(1)/Br(1)/N(2)/C(33) mean plane by 0.0242 Å. Within the bonded P ligand the intra-cage C–P–C angle is 94.05(10)° which is slightly enlarged with respect to **2a** [92.90(8)°] but similar in magnitude to other coordinated phospha-adamantane ligands.[16,19] The amine group forms an intramolecular hydrogen bond to the coordinated bromide ligand [N(1)···Br(1) 3.265(2) Å, H(1)···Br(1) 2.61(3) Å; N(1)–H(1)···Br(1) 137(2)°].

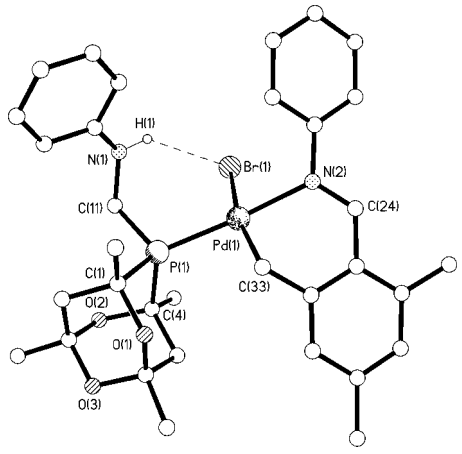


Figure 3. Molecular structure of **4**. All hydrogen atoms except on N(1) have been removed for clarity.

Reaction of **3a** (and **3b**) with $MCl_2$(cod) (M = Pt, Pd) gave the dichloro $\kappa^2$-*P*,*P*′-chelate compounds $MCl_2$(**3a**) [M = Pt **5a**; Pd **5c**] and $MCl_2$(**3b**) [M = Pt **5b**; Pd **5d**] in high yields (Scheme 3). By virtue of the different substituents on each phosphorus the $^{31}P\{^1H\}$ NMR spectra of the chelate complexes **5a**–**5d** are particularly diagnostic showing a classical AX pattern (Table 1). The $^{31}P$ chemical shifts between the two phosphorus nuclei differ by ca. 10 ppm whilst the *J*(PtP) couplings differ by ca. 250 Hz with the *J*(PtP) coupling to the –PAd group being the larger of the two. These variations can presumably be ascribed to the difference in stereoelectronic properties between the two phosphorus centres.

The X-ray structures of the nonsymmetric diphosphane platinum(II) complexes **5a** and **5b** have been determined (Figure 4, Figure 5 and Table 3). Suitable crystals of **5a** and **5b** were obtained by slow diffusion of diethyl ether into a $CDCl_3$ solution. The X-ray structures show that both **5a** and **5b** adopt a chelating coordination mode and furthermore, the coordination environment around platinum is ostensibly square-planar. In **5a** the P(2)–Pt(1)–Cl(2) [83.07(5)°] bond angle is contracted by some 10° with respect to P(1)–Pt(1)–Cl(1) [93.87(6)°] clearly reflecting the different steric effects of phenyl vs. adamantane groups. The P(1)–Pt(1)–P(2) hinge angle is 96.33(5)° which compares favourably with the previously reported angle for the symmetric, bulky diphosphane palladium(II) complex $PdCl_2$(bpap), previously reported by Pringle and coworkers.[15] The Pt–P [2.2362(16), 2.2373(14) Å] and Pt–Cl [2.3545(14), 2.3499(14) Å] bond lengths are similar and illustrate the negligible effect the different substituents on P have on these distances. The Pt is out of the mean plane [defined by the donor atoms P(1), P(2), Cl(1) and Cl(2)] by 0.0139 Å (for **5a**) and 0.0451 Å (for **5b**). The six-membered Pt–P–C–N–C–P′ rings in **5a** and **5b** adopt a conformation in which the Pt(1), P(1), P(2), C(11) and C(18) atoms are essentially flat (to within ±0.07 Å for **5a**; ±0.19 Å for **5b**) and N(1) is out of this plane by 0.74 Å (for **5a**) and 0.66 Å (for **5b**). Furthermore the N–arene torsion angles, defined by the C(11)/N(1)/C(18) and C(12)>C(17) mean planes, are 37° and 76° for **5a** and **5b** respectively. Analysis of the packing in the two crystal structures shows the orientations of the N–arene rings are determined by weak C–H(Me or Ph)···π(N–arene) interactions to neighbouring molecules.

Having established these nonsymmetric ligands successfully *P*,*P*′-chelate to platinum(II) and palladium(II) metal centres we next sought to establish whether the sterically demanding adamantane group could impose a *P*-monodentate mode of binding through the sterically less encumbered $-PPh_2$ group. This sort of *P*-monodentate behaviour, whilst known for flexible small bite angle diphosphanes such as dppm,[36] dppa [bis(phenylphosphanyl)amine][37] and others,[28] is less prevalent with dppp bearing an extended $C_3$ spacer. Gratifyingly when we reacted **3a** with $\{RuCl_2(\eta^6\text{-}p\text{-cym})\}_2$ or $\{IrCl_2(\eta^5\text{-Cp*})\}_2$ in dichloromethane we obtained the $\kappa^1$-*P*-monodentate complexes **6** and **7** in high yields. Presumably under these experimental conditions the –PAd group is too bulky to coordinate to the $RuCl_2(\eta^6\text{-}p\text{-cym})$ or $IrCl_2(\eta^5\text{-Cp*})$ fragments [vide infra for reactions with AuCl(tht)]. The $^{31}P\{^1H\}$ NMR spectra (Table 1) are particularly informative showing new downfield $\delta$(P) resonances for the coordinated $-PPh_2$ group at $\delta$(P) 23.6 ppm (for **6**) and –5.1 ppm (for **7**) whilst the pendant –PAd group is observed at $\delta$(P) ca. –39 ppm (cf. –41.5 ppm for **3a**).

The X-ray structures of the piano-stool complexes **6** and **7** have both been established by X-ray crystallography (see Figures 6 and 7, Table 3). Within the coordination sphere of **6** the Ru–P, Ru–Cl or $Ru-C_{arene}$ bond lengths are comparable to other half-sandwich compounds e. g. $RuCl_2$(*p*-cym)PTA (PTA = 1,3,5-triaza-7-phosphatricyclo[3.3.1.1]-decane), $RuCl_2$(*p*-cym)$Ph_2P(2\text{-}C_5H_4N)$ and $RuCl_2$(*p*-cym)$Ph_2PCH_2Y$ [Y = $-NHC_6H_4(2\text{-}CO_2H)$, $-NHC_6H_4(2\text{-OH})$, $-NHC_6H_4(2\text{-}CH_2OH)$].[1,38] As a consequence of $\kappa^1$-*P*-monodentate coordination the C(11)–N(1)–C(18) bond angle has marginally increased by ca. 3° for **6** (and 4° for **7**) with respect to that observed in the $\kappa^2$-*P*,*P*′-chelate complexes **5a** and **5b**. The P···P separations within **6** and **7** are 4.868 Å and 5.319 Å, respectively.

 © 2007 Wiley-VCH Verlag GmbH & Co. KGaA, Weinheim 

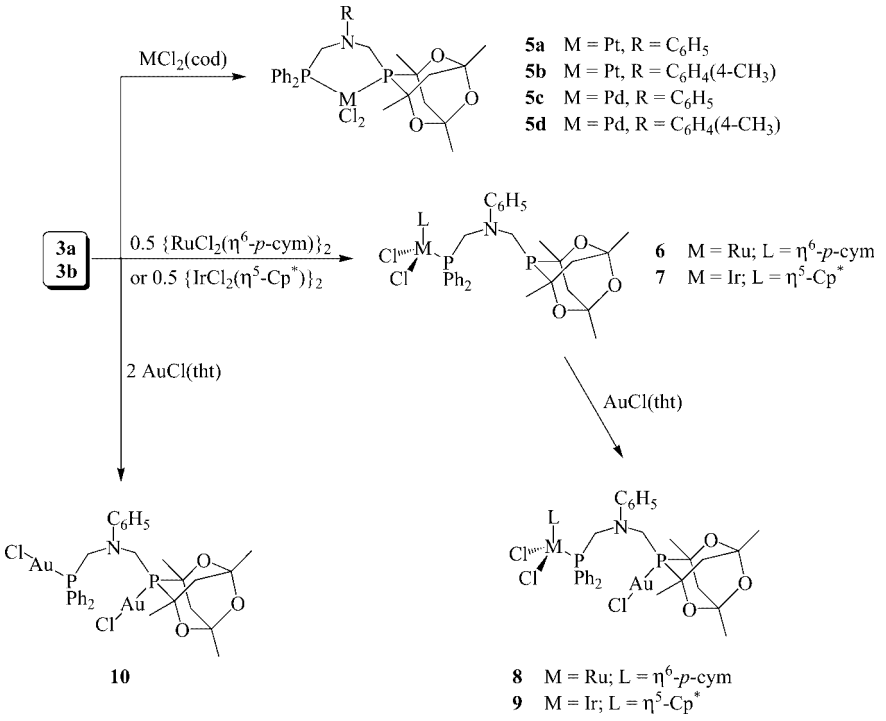


Scheme 3.

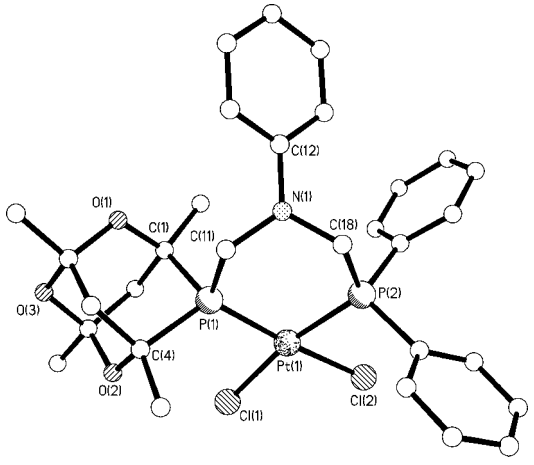


Figure 4. Molecular structure of **5a**. All hydrogen atoms and solvent have been removed for clarity.

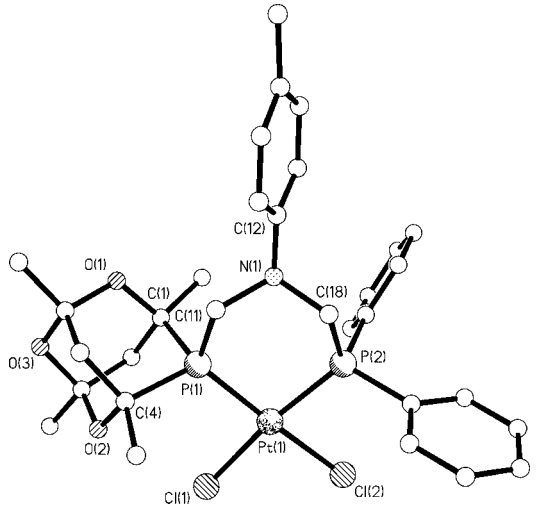


Figure 5. Molecular structure of **5b**. All hydrogen atoms and solvent have been removed for clarity.

In order to pursue the possibility of introducing a second metal centre we elected to react both **6** and **7** with 1 equiv. of AuCl(tht) in dichloromethane at room temperature. After work up the red/orange solids $\kappa^2$-*P*,*P*′-μ-$RuCl_2(\eta^6$-*p*-cym){$Ph_2PCH_2N(Ph)CH_2PAd(AuCl)$} **8** and $\kappa^2$-*P*,*P*′-μ-$IrCl_2(\eta^5$-Cp*){$Ph_2PCH_2N(Ph)CH_2PAd(AuCl)$} **9** were isolated in 93% and 77% yields respectively. The $^{31}P\{^1H\}$ NMR spectra were particularly informative showing a downfield shift for –PAd to $\delta$(P) 24.1 ppm (for **8**) and $\delta$(P) –3.2 ppm (for **9**) with respect to the noncomplexed –PAd group in **6** and **7** (Table 1). Further indication for gold(I) coordination was evident from the IR spectra which clearly showed $\nu_{AuCl}$ vibrations at 331 $cm^{-1}$ and 336 $cm^{-1}$ for **8** and **9**, respectively.

Upon complexation the gold(I) chloride fragment is approximately linear with respect to the coordinated –PAd moiety (see Figures 8 and 9, Table 4). The Au–Cl and Au–P bond lengths are normal and in the region previously observed for phosphane gold(I) complexes.[4,39–41] No significant changes are observed for the M–Cl and M–P (M = Ru or Ir) distances/bond angles upon gold complexation. In addition the Cl(1)–Au(1)–P(1) angles [177.18(4)° for **8**; 174.42(8)° for **9**] suggest very minimal steric congestion between the adamantane cage or neighbouring N–Ph group. Furthermore, the C(11)–N(1)–C(18) angles for **8** and **9** are 115.9(2)° and 115.5(6)°, respectively, whilst the N–arene

 © 2007 Wiley-VCH Verlag GmbH & Co. KGaA, Weinheim 

Table 3. Selected bond lengths [Å] and angles [°] for compounds **5a** and **5b**.

| | 5a | 5b |
|---|---|---|
| Pt(1)–Cl(1) | 2.3545(14) | 2.3544(15) |
| Pt(1)–Cl(2) | 2.3499(14) | 2.3553(14) |
| Pt(1)–P(1) | 2.2362(16) | 2.2436(14) |
| Pt(1)–P(2) | 2.2373(14) | 2.2330(14) |
| P(1)–C(11) | 1.852(6) | 1.833(5) |
| C(11)–N(1) | 1.456(8) | 1.468(7) |
| N(1)–C(18) | 1.462(7) | 1.469(7) |
| C(18)–P(2) | 1.834(6) | 1.830(5) |
| Cl(1)–Pt(1)–P(1) | 93.87(6) | 94.67(5) |
| Cl(1)–Pt(1)–P(2) | 169.29(5) | 171.83(5) |
| Cl(1)–Pt(1)–Cl(2) | 87.05(5) | 85.97(5) |
| Cl(2)–Pt(1)–P(2) | 83.07(5) | 85.91(5) |
| Cl(2)–Pt(1)–P(1) | 174.86(5) | 176.54(5) |
| P(1)–Pt(1)–P(2) | 96.33(5) | 93.38(5) |
| Pt(1)–P(1)–C(11) | 116.9(2) | 118.12(18) |
| P(1)–C(11)–N(1) | 110.7(4) | 113.4(3) |
| C(11)–N(1)–C(18) | 112.4(5) | 112.0(4) |
| N(1)–C(18)–P(2) | 111.6(4) | 110.3(3) |
| C(18)–P(2)–Pt(1) | 117.53(19) | 117.22(19) |

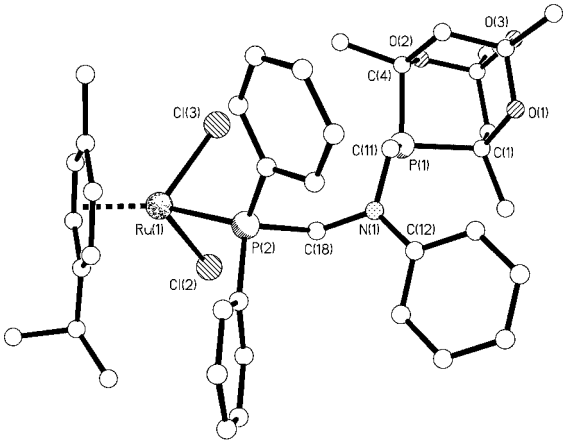


Figure 6. Molecular structure of **6**; all hydrogen atoms and solvent have been removed for clarity.

torsion angles for **6**–**9**, defined by the C(11)/N(1)/C(18) and C(12)>C(17) mean planes, are all in the range 7.6–17.3°. The P···P distances in both heterobimetallic complexes are 5.238 Å and 5.283 Å for **8** and **9**, which also dictate large Ru···Au [8.304 Å] and Ir···Au [8.481 Å] separations. The shortest intermolecular Au···Au separations are 7.628 Å and 5.987 Å, respectively, indicating the absence of any significant aurophilic interactions between neighbouring P–Au–Cl units.[42]

We next sought to demonstrate whether **3a** could bridge two identical metal centres and accordingly prepared the digold(I) compound **10** from 2 AuCl(tht) and 1 equiv. of **3a** in $CH_2Cl_2$. The ambient temperature $^{31}P\{^1H\}$ NMR spectrum of **10** in $CDCl_3$ revealed two broad resonances around $\delta$(P) 15 ppm which sharpened upon cooling to –50 °C (Figure 10). The close similarity of both phosphorus signals makes assignment of these somewhat speculative. The

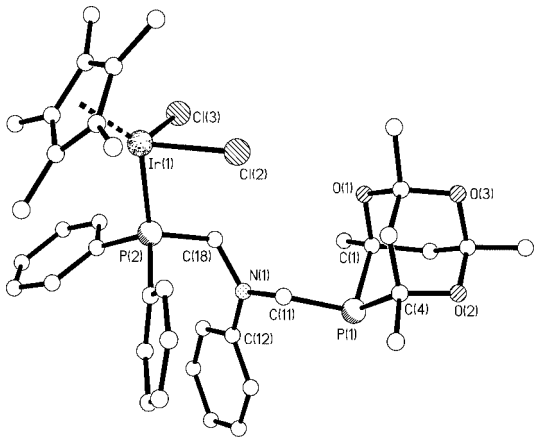


Figure 7. Molecular structure of **7**; all hydrogen atoms and solvent have been removed for clarity.

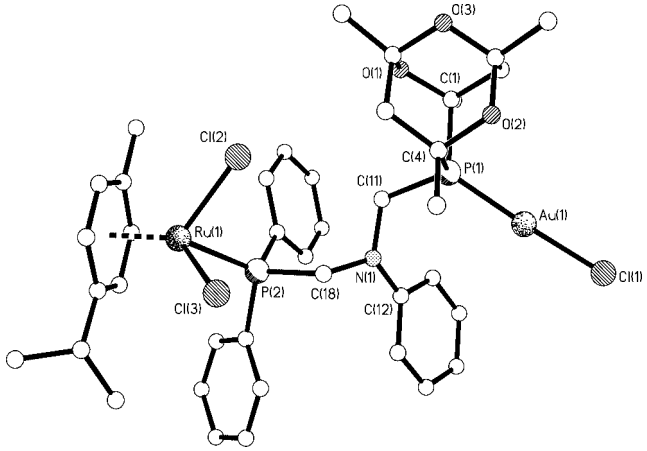


Figure 8. Molecular structure of **8**; all hydrogen atoms and solvent have been removed for clarity.

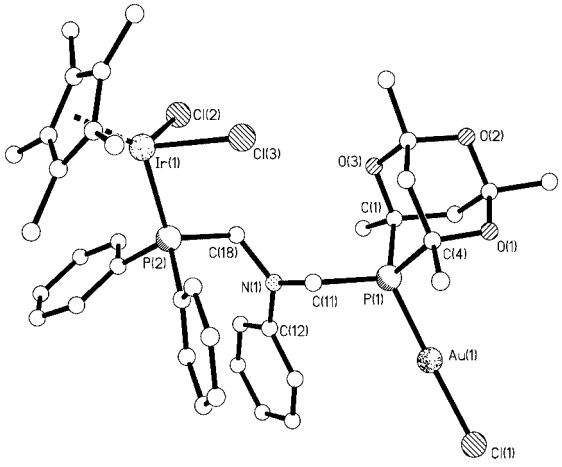


Figure 9. Molecular structure of **9**; all hydrogen atoms have been removed for clarity.

downfield resonance at $\delta$(P) 14 ppm is tentatively assigned to the $-PPh_2(AuCl)$ bonded metal centre by analogy with $PhN(CH_2PPh_2AuCl)_2$ which has recently been reported.[4]

 © 2007 Wiley-VCH Verlag GmbH & Co. KGaA, Weinheim 

Table 4. Selected bond lengths [Å] and angles [°] for compounds **6**–**9**.

| | **6** M = Ru | **7** M = Ir | **8** M = Ru | **9** M = Ir |
|---|---|---|---|---|
| M(1)–Cl(2) | 2.4039(17) | 2.408(2) | 2.4160(8) | 2.4010(19) |
| M(1)–Cl(3) | 2.4063(17) | 2.398(2) | 2.4090(3) | 2.424(2) |
| M(1)–P(2) | 2.3391(18) | 2.3091(19) | 2.3420(8) | 2.3047(19) |
| M(1)–$C_{centroid}$ | 1.698 | 1.814 | 1.709 | 1.805 |
| P(2)–C(18) | 1.894(6) | 1.900(7) | 1.888(3) | 1.881(8) |
| C(18)–N(1) | 1.435(8) | 1.451(9) | 1.454(4) | 1.452(9) |
| N(1)–C(11) | 1.459(8) | 1.474(10) | 1.449(4) | 1.444(9) |
| C(11)–P(1) | 1.885(7) | 1.869(8) | 1.851(3) | 1.869(8) |
| P(1)–Au(1) | | | 2.2227(8) | 2.223(2) |
| Au(1)–Cl(1) | | | 2.2804(9) | 2.280(2) |
| Cl(2)–M(1)–Cl(3) | 88.63(6) | 89.24(8) | 87.45(3) | 89.02(7) |
| Cl(2)–M(1)–P(2) | 83.64(6) | 88.64(7) | 85.55(3) | 85.05(7) |
| Cl(3)–M(1)–P(2) | 84.40(6) | 85.18(7) | 84.49(3) | 88.29(7) |
| M(1)–P(2)–C(18) | 113.3(2) | 112.4(2) | 113.49(10) | 112.0(2) |
| P(2)–C(18)–N(1) | 118.4(4) | 114.4(5) | 116.9(2) | 116.4(5) |
| C(18)–N(1)–C(11) | 115.0(5) | 115.9(6) | 115.9(2) | 115.5(6) |
| N(1)–C(11)–P(1) | 112.5(4) | 113.4(5) | 113.2(2) | 115.1(5) |
| C(11)–P(1)–Au(1) | | | 118.16(10) | 115.6(3) |
| P(1)–Au(1)–Cl(1) | | | 177.18(4) | 174.42(8) |

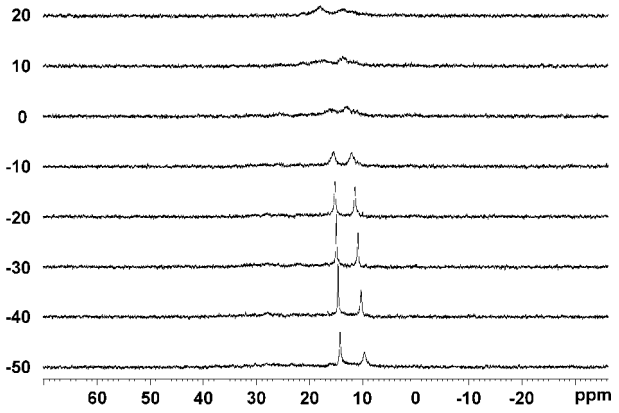


Figure 10. Variable temperature $^{31}P\{^1H\}$ NMR spectra for **10** recorded in the range 20 to –50 °C.

## Conclusions

In summary, we have developed a facile method for the synthesis of two nonsymmetric ditertiary phosphanes bearing one bulky substituent on phosphorus. This procedure is potentially a valuable synthetic route to highly modular nonsymmetric diphosphanes with tuneable stereoelectronic properties. Whilst $\kappa^2$-*P,P′*-chelation is observed upon complexation to square-planar metal centres we have shown the ability of one of these ligands to function as a $\kappa^1$-*P*-monodentate tertiary phosphane. Coordination to a second, different metal, affords new examples of late transition metal heterobimetallic compounds bridged by the phosphane **3a**. This clearly illustrates the importance of steric effects on phosphorus and how this can be implemented in directing variable ligating modes. Our work should be contrasted with that of others who have shown that dppp can readily act as a bridging ligand affording symmetric dinuclear complexes based on e. g. Mo,[43] Ru,[44] Ir,[45] Ni,[46] Pd[47] and Au[48] metal fragments. However, crystallographic examples where dppp bridges two different metal sites are extremely scarce.[45b] Dinuclear Rh/Au complexes[49] have recently been reported using $\kappa^3$-*PN*$_2$-bridged pyridylphosphanes whilst $\{Ph_2PCH_2\}_2PPh$ has been used to generate, amongst others, cationic Ru/Rh and Ru/Ag heteronuclear complexes.[50,51] Further studies are in progress and will be reported in due course.

## Experimental Section

**Materials:** Standard Schlenk techniques were used for the synthesis of **1**, **2a**, **2b**, **3a** and **3b** whilst all other reactions were carried out in air using previously distilled solvents unless otherwise stated. (Diphenylphosphanyl)methanol[52] and the metal complexes AuCl(tht) (tht = tetrahydrothiophene),[53] $\{RuCl_2(\eta^6\text{-}p\text{-cym})\}_2$,[54] $\{IrCl_2(\eta^5\text{-Cp*})\}_2$ (Cp* = 1,2,3,4,5-pentamethylcyclopentadienyl),[55] $MCl_2$(cod) (M = Pd, Pt)[56] and $\{Pd(\kappa^2\text{-}C,N\text{-}C_{16}H_{16}N)Br\}_2$[34] were prepared according to known procedures. All other chemicals were obtained from commercial suppliers and used directly without further purification.

**Instrumentation:** Infrared spectra were recorded as KBr pellets in the range 4000–200 $cm^{-1}$ with a Perkin–Elmer System 2000 Fourier-transform spectrometer, $^1H$ NMR spectra (400 MHz) with a Bruker DPX-400 FT spectrometer with chemical shifts ($\delta$) in ppm to high frequency of $SiMe_4$ and coupling constants ($J$) in Hz, $^{31}P\{^1H\}$ NMR spectra (162 MHz) were recorded with a Bruker DPX-400 FT spectrometer with chemical shifts ($\delta$) in ppm to high frequency of 85% $H_3PO_4$. All NMR spectra were measured in $CDCl_3$ unless otherwise stated. Elemental analyses (Perkin–Elmer 2400 CHN or Exeter Analytical, Inc. CE-440 Elemental Analyzers) were performed by the Loughborough University Analytical Service within the Department of Chemistry.

**Preparation of 1:** 1,3,5,7-Tetramethyl-2,4,8-trioxa-6-phosphaadamantane (0.649 g, 2.91 mmol) and $(CH_2O)_n$ (0.096 g, 3.20 mmol) were heated at 110 °C for 90 min affording a yellow oil which was used directly in subsequent condensation reactions. Compound **1** slowly crystallises upon standing in a freezer. Routinely the purity of **1** was shown, by $^{31}P\{^1H\}$ NMR, to be ca. 85%. $^1H$ NMR ($CDCl_3$): $\delta$ = 4.06 (m, $CH_2$), 2.45 (s, OH), 1.97–1.35 (m, Ad cage) ppm.

**Preparation of 2a:** A solution of $C_6H_5NH_2$ (5.561 g, 59.7 mmol) in methanol (HPLC grade, 35 mL) was added to a methanol (HPLC grade, 35 mL) solution of **1** (2.714 g, 9.37 mmol) by cannula. The resulting mixture was stirred for 17 h and then concentrated under reduced pressure to ca. 10 mL. The solid was collected by suction filtration and dried in vacuo. Yield: 2.455 g, 84%. $^1H$ NMR ($CDCl_3$): $\delta$ = 7.16–6.58 (m, arom. H), 3.85 (NH), 3.43 (dd, $J$ = 12 Hz, 1.6 Hz, $CH_2$), 2.91 (dd, $J$ = 13 Hz, 3.2 Hz, $CH_2$), 1.92–1.30 (m, Ad cage) ppm. $C_{17}H_{24}NO_3P$ (321.37): calcd. C 63.54, H 7.53, N 4.36; found C 63.05, H 7.52, N 4.30. This procedure was also used for the preparation of **2b** albeit in lower yield (53%). For **2b:** $^1H$ NMR ($CDCl_3$): $\delta$ = 7.01 (d, $J$ = 8 Hz, arom. H), 6.60 (d, $J$ = 8.4 Hz, arom. H), 3.90 (NH), 3.48 (dd, $J$ = 13 Hz, 1.4 Hz, $CH_2$), 2.96 (dd, $J$ = 13.2 Hz, 3.2 Hz, $CH_2$), 2.25 ($CH_3$), 1.98–1.33 (m, Ad cage) ppm. $C_{18}H_{26}NO_3P$ (335.4): calcd. C 64.46, H 7.81, N 4.18; found C 64.37, H 7.79, N 4.26.

**Preparation of 3a:** A solution of $Ph_2PCH_2OH$ (0.245 g, 0.906 mmol) in methanol (HPLC grade, 5 mL) was added to a

 © 2007 Wiley-VCH Verlag GmbH & Co. KGaA, Weinheim 

methanol (HPLC grade, 5 mL) suspension of **2** (0.327 g, 0.906 mmol) by cannula. The mixture was stirred for 24 h and the solid **3a** collected by suction filtration and dried in vacuo. Yield: 0.412 g, 87%. For **3a**, $^1$H NMR ($CDCl_3$): $\delta$ = 7.38–6.72 (m, arom. H), 4.33–4.11 (m, $CH_2$), 3.56 (d, $J$ = 14.4 Hz, $CH_2$), 3.10 (dd, $J$ = 14.4 Hz, 5.2 Hz, $CH_2$), 1.88–1.08 (m, Ad cage) ppm. This procedure was also used for the preparation of **3b** (85%). The purity of **3a** (and **3b**) were shown, by $^{31}P\{^1H\}$ NMR, to be ca. 75–80%. For **3b**, $^1$H NMR ($CDCl_3$): $\delta$ = 7.44–7.24 (m, arom. H), 6.97 (d, $J$ = 8.4 Hz, arom. H), 6.76 (d, $J$ = 8.8 Hz, arom. H), 4.26–4.13 (m, $CH_2$), 3.53 (d, $J$ = 14.4 Hz, $CH_2$), 3.10 (dd, $J$ = 14.6 Hz, 5 Hz, $CH_2$), 2.19 ($CH_3$), 1.83–1.02 (m, Ad cage) ppm. All efforts to obtain analytical samples of **3a** (and **3b**) have so far been unsuccessful.

**Preparation of 4:** A mixture of **2a** (0.071 g, 0.221 mmol) and $\{Pd(\kappa^2\text{-}C,N\text{-}C_{16}H_{16}N)Br\}_2$ (0.090 g, 0.110 mmol) in HPLC grade acetone (10 mL) were refluxed for 75 min. After cooling the solution was concentrated under reduced pressure to ca. 2–3 mL and diethyl ether (10 mL)/hexanes (10 mL) added. The solid was collected by suction filtration and dried in vacuo. Yield: 0.113 g, 70%. $^1$H NMR ($CDCl_3$): $\delta$ = 8.22 (d, $J$ = 12.4 Hz, CH=N), 7.67–6.43 (arom. H), 4.70 (NH), 4.23 (d, $J$ = 12.8 Hz, $CH_2$), 3.77–3.63 (m, $CH_2$), 2.43 and 2.24 ($CH_3$), 2.41–1.46 (m, Ad cage) ppm. $C_{33}H_{37}BrN_2O_3PPd$ (726.99): calcd. C 54.52, H 5.13, N 3.85; found C 54.09, H 5.47, N 3.77.

**Preparation of 5a: 3a** (0.119 g, 0.192 mmol) was added as a solid to a $CH_2Cl_2$ (10 mL) solution of $PtCl_2$(cod) (0.072 g, 0.192 mmol). The solution was stirred for 2.5 h and then concentrated to ca. 1–2 mL under reduced pressure. Addition of diethyl ether (20 mL) afforded a solid which was collected by suction filtration and dried in vacuo. Yield: 0.129 g, 85%. $C_{30}H_{35}Cl_2NO_3P_2Pt\cdot 0.5CH_2Cl_2$ (828.04): calcd. C 44.24, H 4.38, N 1.69; found C 43.94, H 3.89, N 2.04. A similar procedure was also used for the preparation of **5b** (92%). $^1$H NMR ($CDCl_3$): $\delta$ = 8.02–7.31 (m, arom. H), 7.04 (d, $J$ = 8.4 Hz, arom. H), 6.80 (d, $J$ = 8.8 Hz, arom. H), 4.27–4.09 (m, $CH_2$), 3.47–3.23 (m, $CH_2$), 2.23 ($CH_3$), 1.76–1.19 (m, Ad cage) ppm. $C_{31}H_{37}Cl_2NO_3P_2Pt\cdot CH_2Cl_2$ (884.53): calcd. C 43.44, H 4.44, N 1.58; found C 42.94, H 4.03, N 1.49. The dichloropalladium(II) complexes **5c** (from **3a**) and **5d** (from **3b**) were prepared in 98% and 92% yields respectively. For **5c:** $C_{30}H_{35}Cl_2NO_3P_2Pd\cdot 0.75CH_2Cl_2$ (760.61): calcd. C 48.56, H 4.84, N 1.84; found C 48.84, H 4.48, N 1.57. For **5d**, $^1$H NMR ($CDCl_3$): $\delta$ = 7.97–7.33 (m, arom. H), 7.04 (d, $J$ = 8 Hz, arom. H), 6.76 (d, $J$ = 8 Hz, arom. H), 4.11–4.03 and 3.52–3.22 (m, $CH_2$), 2.23 ($CH_3$), 1.81–1.27 (m, Ad cage) ppm. $C_{31}H_{37}Cl_2NO_3P_2Pd\cdot 2.5CH_2Cl_2$ (923.27): calcd. C 43.58, H 4.59, N 1.52; found C 43.09, H 4.24, N 1.71.

**Preparation of 6: 3a** (0.098 g, 0.151 mmol) was added as a solid to a $CH_2Cl_2$ (10 mL) solution of $\{RuCl_2(\eta^6\text{-}p\text{-cym})\}_2$ (0.046 g, 0.075 mmol). The solution was stirred for 45 min and then concentrated to ca. 1–2 mL under reduced pressure. Addition of diethyl ether (25 mL) and hexane (25 mL) afforded a red/orange solid which was collected by suction filtration and dried in vacuo. Yield: 0.078 g, 63%. $C_{40}H_{49}Cl_2NO_3P_2Ru\cdot 0.25CH_2Cl_2$ (847.03): calcd. C 57.07, H 5.89, N 1.65; found C 56.97, H 6.27, N 1.66. A similar procedure was also used for the preparation of the iridium(III) complex **7** (96%). For **7**, $^1$H NMR ($CDCl_3$): $\delta$ = 7.86–6.36 (m, arom. H), 5.26 (d, $J$ = 4 Hz, $CH_2$) and 5.08 (d, $J$ = 16 Hz, $CH_2$), 2.98 (dd, $J$ = 15.2 Hz, 4.4 Hz, $CH_2$) and 2.71 (d, $J$ = 15.2 Hz, $CH_2$), 1.79–1.11 (m, Ad cage), 1.28 (d, $J$ = 2 Hz, Cp*) ppm. $C_{40}H_{50}Cl_2IrNO_3P_2\cdot 4.5CH_2Cl_2$ (1300.26): calcd. C 41.11, H 4.57, N 1.08; found C 40.78, H 4.41, N 1.02.

**Preparation of 8:** AuCl(tht) (0.016 g, 0.050 mmol) was added as a solid to a $CH_2Cl_2$ (10 mL) solution of **6** (0.055 g, 0.050 mmol). The solution was stirred for 45 min and then concentrated to ca. 1–2 mL under reduced pressure. Addition of diethyl ether (25 mL) and hexane (25 mL) afforded a red/orange solid which was collected by suction filtration and dried in vacuo. Yield: 0.049 g, 93%. For **8**, $C_{40}H_{49}AuCl_3NO_3P_2Ru$ (1058.22): calcd. C 45.40, H 4.67, N 1.32; found C 46.26, H 4.48, N 1.06. A similar procedure was also used for the preparation of the iridium(III) complex **9** (77%). For **9**, $^1$H NMR ($CDCl_3$): $\delta$ = 7.89–6.45 (m, arom. H), 5.26 (d, $J$ = 16.8 Hz, $CH_2$) and 4.95 (d, $J$ = 16 Hz, $CH_2$), 3.56 (d, $J$ = 16 Hz, $CH_2$) and 3.30 (dd, $J$ = 15.8 Hz, 4.2 Hz, $CH_2$), 2.19–1.10 (m, Ad cage), 1.28 (d, $J$ = 2 Hz, Cp*) ppm. $C_{40}H_{50}AuCl_3IrNO_3P_2$ (1150.36): calcd. C 41.77, H 4.38, N 1.22; found C 41.69, H 4.17, N 1.20.

**Preparation of 10: 3a** (75% purity, 0.117 g, 0.164 mmol) was added as a solid to a $CH_2Cl_2$ (10 mL) solution of AuCl(tht) (0.105 g, 0.328 mmol). The solution was stirred for 45 min in the dark and then concentrated to ca. 1–2 mL under reduced pressure. Addition of diethyl ether (25 mL) and hexane (25 mL) afforded solid **10** which was collected by suction filtration and dried in vacuo. Yield: 0.135 g, 84%. $C_{30}H_{35}Au_2Cl_2NO_3P_2\cdot 0.75C_6H_{14}$ (1049.08): calcd. C 39.50, H 4.37, N 1.34; found C 39.25, H 3.76, N 1.55.

**X-ray Crystallography:** Vapour diffusion of diethyl ether into an acetone solution (for **4**) or $CDCl_3$ solutions (for **5a** or **5b**) over several days afforded suitable X-ray quality crystals. Compound **9** was obtained by slow diffusion of petroleum ether (b.p. 60–80 °C) into a $CDCl_3$ solution whereas slow diffusion of hexane into a $CH_2Cl_2$ solution gave suitable crystals of compound **6**. Compound **2a** was obtained upon allowing a $CH_3OH$ filtrate to stand for several days. Compounds **7** and **8** were obtained by slow evaporation to dryness of a $CH_2Cl_2$/petroleum ether (b.p. 60–80 °C) or $CHCl_3$/hexane solution respectively. Details for the crystal data of **2a** and **4**–**9** and a summary of data collection parameters are given in Table 5 and Table 6.

Measurements were made with either a Bruker AXS SMART 1000 CCD area-detector diffractometer[57] for **2a**, **4**, **5a**, **5b** and **8** using sealed-tube graphite-monochromated Mo-$K_\alpha$ radiation and narrow frame exposures (0.3°) in $\omega$ or a Bruker-Nonius 95 mm CCD kappa diffractometer[58,59] equipped with a rotating anode generator for **6**, **7** and **9**. Cell parameters were refined from the observed $\omega$ angles of all strong reflections in each data set. Intensities were corrected semiempirically for absorption, on the basis of symmetry-equivalent and repeated reflections. The structures were solved by direct methods (Patterson synthesis for **5a**, **5b**, **8** and **9**), and refined on $F^2$ values for all unique data by full-matrix least-squares.[60] Tables 5 and 6 give further details. All non-hydrogen atoms were refined anisotropically. For **5b** a molecule of $Et_2O$ is badly disordered over an inversion centre while in **7** there is a disordered molecule of $CH_2Cl_2$ in a general position; these were modelled by the Platon Squeeze procedure.[61] In **6** a molecule of $CH_2Cl_2$ is disordered over an inversion centre. In **8** a molecule of $CHCl_3$ was disordered with the three Cl atoms split over two sets of positions, the major sites occupied 72.1(3)%. The disorder in **6** and **8** was modelled with restraints applied to assist geometry and anisotropic displacement parameters.

CCDC-629342 to -629349 (for compounds **2a**, **4** and **5a**–**9**) contain the the complete set of X-ray crystallographic structural data. These data can be obtained free of charge from The Cambridge Crystallographic Data Centre via www.ccdc.cam.ac.uk/data_request/cif. at the Cambridge Crystallographic Data Centre, 12 Union Road, Cambridge, CB2 1EZ, UK (Fax: +44-1223-336-033; E-mail: deposit@ccdc.ac.uk) on request, quoting the deposition numbers.

 © 2007 Wiley-VCH Verlag GmbH & Co. KGaA, Weinheim 

Table 5. Crystallographic data for **2a**, **4**, **5a** and **5b**.

| Compound | **2a** | **4** | **5a**·$CHCl_3$ | **5b**·$CHCl_3$·1/2$OEt_2$ |
|---|---|---|---|---|
| Empirical formula | $C_{17}H_{24}NO_3P$ | $C_{33}H_{40}BrN_2O_3PPd$ | $C_{31}H_{36}Cl_5NO_3P_2Pt$ | $C_{34}H_{43}Cl_5NO_{3.5}P_2Pt$ |
| Formula weight | 321.34 | 729.95 | 904.89 | 955.97 |
| Crystal system | monoclinic | triclinic | monoclinic | monoclinic |
| Space group | *C*2/*c* | $P\bar{1}$ | $P2_1/c$ | $P2_1/n$ |
| *a* [Å] | 21.6340(12) | 10.0874(5) | 14.8165(10) | 15.6828(7) |
| *b* [Å] | 8.0270(4) | 12.1965(7) | 16.6937(11) | 12.8162(6) |
| *c* [Å] | 21.0236(12) | 14.4382(8) | 14.3993(10) | 18.2303(8) |
| *α* [°] | | 70.580(2) | | |
| *β* [°] | 116.317(2) | 80.716(2) | 90.655(2) | 93.261(2) |
| *γ* [°] | | 75.021(2) | | |
| Volume [Å$^3$] | 3272.5(3) | 1612.81(15) | 3561.3(4) | 3658.2(3) |
| *Z* | 8 | 2 | 4 | 4 |
| *T* [K] | 150(2) | 200(2) | 150(2) | 150(2) |
| Density (calcd.) [Mg/m$^3$] | 1.304 | 1.503 | 1.688 | 1.736 |
| Absorption coeff. [mm$^{-1}$] | 0.180 | 1.899 | 4.437 | 4.326 |
| Crystal habit | colourless tablet | colourless block | colourless plate | colourless needle |
| Crystal size [mm$^3$] | 0.25 × 0.19 × 0.07 | 0.60 × 0.30 × 0.25 | 0.31 × 0.22 × 0.05 | 0.36 × 0.04 × 0.02 |
| *θ* range [°] | 2.10–29.00 | 1.81–28.88 | 1.84–29.03 | 1.67–29.09 |
| Reflections collected | 14145 | 14148 | 31031 | 31911 |
| Independent reflections | 3988 [$R_{int}$ = 0.030] | 7379 [$R_{int}$ = 0.019] | 8608 [$R_{int}$ = 0.048] | 8854 [$R_{int}$ = 0.039] |
| Final *R*, $R_w$ | 0.041, 0.100 | 0.027, 0.069 | 0.040, 0.101 | 0.040, 0.117 |

Table 6. Crystallographic data for **6**–**9**.

| Compound | **6**·1/2$CH_2Cl_2$ | **7**·$CH_2Cl_2$ | **8**·$CHCl_3$ | **9** |
|---|---|---|---|---|
| Empirical formula | $C_{40.50}H_{50}Cl_3NO_3P_2Ru$ | $C_{41}H_{52}Cl_4IrNO_3P_2$ | $C_{41}H_{50}AuCl_6NO_3P_2Ru$ | $C_{40}H_{50}AuCl_3IrNO_3P_2$ |
| Formula weight | 868.17 | 1002.78 | 1177.50 | 1150.27 |
| Crystal system | triclinic | monoclinic | triclinic | monoclinic |
| Space group | $P\bar{1}$ | *C*2/*c* | $P\bar{1}$ | *C*2/*c* |
| *a* [Å] | 12.7297(12) | 27.2637(13) | 12.5894(6) | 27.5062(17) |
| *b* [Å] | 13.6693(12) | 11.6769(6) | 14.1427(6) | 11.7458(6) |
| *c* [Å] | 13.9918(14) | 27.5628(14) | 15.2006(7) | 27.3935(17) |
| *α* [°] | 65.609(5) | | 64.547(2) | |
| *β* [°] | 68.646(4) | 112.943(2) | 80.820(2) | 111.376(2) |
| *γ* [°] | 66.295(6) | | 68.287(2) | |
| Volume [Å$^3$] | 1972.2(3) | 8080.6(7) | 2270.36(18) | 8241.5(8) |
| *Z* | 2 | 8 | 2 | 8 |
| *T* [K] | 120(2) | 120(2) | 150(2) | 120(2) |
| Density (calcd.) [Mg/m$^3$] | 1.462 | 1.649 | 1.722 | 1.854 |
| Absorption coeff. [mm$^{-1}$] | 0.721 | 3.688 | 4.021 | 7.092 |
| Crystal habit | orange plate | yellow plate | red block | orange lath |
| Crystal size [mm$^3$] | 0.17 × 0.14 × 0.04 | 0.34 × 0.30 × 0.02 | 0.37 × 0.24 × 0.16 | 0.22 × 0.06 × 0.02 |
| *θ* range [°] | 2.97–25.00 | 1.60–27.59 | 1.69–28.99 | 2.91–27.60 |
| Reflections collected | 32530 | 29404 | 20226 | 37377 |
| Independent reflections | 6917 [$R_{int}$ = 0.105] | 8118 [$R_{int}$ = 0.069] | 10522 [$R_{int}$ = 0.020] | 9397 [$R_{int}$ = 0.057] |
| Final *R*, $R_w$ | 0.075, 0.156 | 0.057, 0.177 | 0.028, 0.060 | 0.051, 0.103 |

## Acknowledgments

We thank the EPSRC, Sasol Technology (Pty) Ltd. and Loughborough University for studentships. We are grateful to Cytec Canada Inc. for the kind donation of the secondary cage phosphane used in this work and to Johnson-Matthey for their loan of precious metals. The EPSRC Mass Spectrometry Service centre at Swansea are also acknowledged. The EPSRC X-ray service at Southampton are gratefully acknowledged for the data collection for compounds **6**, **7** and **9**. Finally we thank Dr Mark Edgar for acquiring the variable-temperature NMR spectra for compound **10**.

[1] S. E. Dann, S. E. Durran, M. R. J. Elsegood, M. B. Smith, P. M. Staniland, S. Talib, S. H. Dale, *J. Organomet. Chem.* **2006**, *691*, 4829–4842.

[2] M. R. J. Elsegood, M. B. Smith, P. M. Staniland, *Inorg. Chem.* **2006**, *45*, 6761–6770.

[3] J. H. Downing, M. B. Smith, *Phosphorus Ligands in Comprehensive Coordination Chemistry II*, vol. 1, Elsevier, Oxford, **2004**, 253–296.

[4] M. B. Smith, S. H. Dale, S. J. Coles, T. Gelbrich, M. B. Hursthouse, M. E. Light, *CrystEngComm* **2006**, *8*, 140–149.

[5] S. E. Durran, M. B. Smith, S. H. Dale, S. J. Coles, M. B. Hursthouse, M. E. Light, *Inorg. Chim. Acta* **2006**, *359*, 2980–2988.

[6] L.-C. Song, Z.-Y. Yang, H.-Z. Bian, Y. Liu, H.-T. Wang, X.-F. Liu, Q.-M. Hu, *Organometallics* **2005**, *24*, 6126–6135.

[7] L.-C. Song, F.-H. Su, Q.-M. Hu, E. Grigiotti, P. Zanello, *Eur. J. Inorg. Chem.* **2006**, 422–429.

[8] N. Feeder, J. Geng, P. G. Goh, B. F. G. Johnson, C. M. Martin, D. S. Shepherd, W. Zhou, *Angew. Chem. Int. Ed.* **2000**, *39*, 1661–1664.

 © 2007 Wiley-VCH Verlag GmbH & Co. KGaA, Weinheim 

[9] R. M. Henry, R. K. Shoemaker, D. L. DuBois, M. R. DuBois, *J. Am. Chem. Soc.* **2006**, *128*, 3002–3010.
[10] T. Posset, J. Blümel, *J. Am. Chem. Soc.* **2006**, *128*, 8394–8395.
[11] M. Gonschorowsky, K. Merz, M. Driess, *Eur. J. Inorg. Chem.* **2006**, 455–463.
[12] W. P. Mul, H. Oosterbeek, G. A. Beitel, G.-J. Kramer, E. Drent, *Angew. Chem. Int. Ed.* **2000**, *39*, 1848–1851 and references cited therein.
[13] K. Fuji, T. Morimoto, K. Tsutsumi, K. Kakiuchi, *Chem. Commun.* **2005**, 3295–3297.
[14] P. W. Miller, N. J. Long, A. J. de Mello, R. Vilar, J. Passchier, A. Gee, *Chem. Commun.* **2006**, 546–548.
[15] V. Gee, A. G. Orpen, H. Phetmung, P. G. Pringle, R. I. Pugh, *Chem. Commun.* **1999**, 901–902.
[16] A. Hadzovic, A. J. Lough, R. H. Morris, P. G. Pringle, D. E. Zambrano-Williams, *Inorg. Chim. Acta* **2006**, *359*, 2864–2869.
[17] G. Adjabeng, T. Brenstrum, C. S. Frampton, A. J. Robertson, J. Hillhouse, J. McNulty, A. Capretta, *J. Org. Chem.* **2004**, *69*, 5082–5086.
[18] G. Adjabeng, T. Brenstrum, J. Wilson, C. Frampton, A. Robertson, J. Hillhouse, J. McNulty, A. Capretta, *Org. Lett.* **2003**, *5*, 953–955.
[19] R. A. Baber, M. L. Clarke, K. M. Heslop, A. C. Marr, A. G. Orpen, P. G. Pringle, A. Ward, D. E. Zambrano-Williams, *Dalton Trans.* **2005**, 1079–1085.
[20] R. I. Pugh, E. Drent, P. G. Pringle, *Chem. Commun.* **2001**, 1476–1477.
[21] C.-A. Carraz, D. W. Stephan, *Organometallics* **2000**, *19*, 3791–3796.
[22] D. Gerristma, T. Brenstrum, J. McNulty, A. Capretta, *Tetrahedron Lett.* **2004**, *45*, 8319–8321.
[23] A. Zapf, A. Ehrentraut, M. Beller, *Angew. Chem. Int. Ed.* **2000**, *39*, 4153–4155.
[24] A. Aranyos, D. W. Old, A. Kiyomori, J. P. Wolfe, J. P. Sadighi, S. L. Buchwald, *J. Am. Chem. Soc.* **1999**, *121*, 4369–4378.
[25] J. P. Stambuli, M. Bühl, J. F. Hartwig, *J. Am. Chem. Soc.* **2002**, *124*, 9346–9347.
[26] a) A. Baber, J. G. de Vries, A. G. Orpen, P. G. Pringle, K. von der Luehe, *Dalton Trans.* **2006**, 4821–4828; b) D. L. Dodds, M. F. Haddow, A. G. Orpen, P. G. Pringle, G. Woodward, *Organometallics* **2006**, *25*, 5937–5945.
[27] G. Fries, J. Wolf, K. Ilg, B. Walfort, D. Stalke, H. Werner, *Dalton Trans.* **2004**, 1873–1881.
[28] A. D. Burrows, M. F. Mahon, S. P. Nolan, M. Varrone, *Inorg. Chem.* **2003**, *42*, 7227–7238.
[29] C.-A. Carraz, E. J. Ditzel, A. G. Orpen, D. D. Ellis, P. G. Pringle, G. J. Sunley, *Chem. Commun.* **2000**, 1277–1278.
[30] a) U. W. Meier, F. Hollmann, U. Thewalt, M. Klinga, M. Leskelä, B. Rieger, *Organometallics* **2003**, *22*, 3905–3914; b) C. P. Casey, E. L. Paulsen, E. W. Beuttenmueller, B. R. Proft, B. A. Matter, D. R. Powell, *J. Am. Chem. Soc.* **1999**, *121*, 63–70.
[31] a) A. Hessler, O. Stelzer, H. Dibowski, K. Worm, F. P. Schmidtchen, *J. Org. Chem.* **1997**, *62*, 2362–2369; b) A. Heβler, J. Fischer, S. Kucken, O. Stelzer, *Chem. Ber.* **1994**, *127*, 481–488; c) B. Antelmann, U. Winterhalter, G. Huttner, B. C. Janssen, J. Vogelgesang, *J. Organomet. Chem.* **1997**, *545–546*, 407–420.
[32] M. Epstein, S. A. Buckler, *J. Am. Chem. Soc.* **1961**, *83*, 3279–3282.
[33] M. B. Smith, M. R. J. Elsegood, *Tetrahedron Lett.* **2002**, *43*, 1299–1301.
[34] J. Albert, M. Cadena, J. Granell, *J. Chem. Educ.* **2003**, *80*, 801–802.
[35] J. Albert, J. Granell, A. Luque, M. Font-Bardía, X. Solans, *J. Organomet. Chem.* **1997**, *545–546*, 131–137.
[36] G. K. Anderson, *Adv. Organomet. Chem.* **1993**, *35*, 1–39.
[37] M. Knorr, C. Strohmann, *Organometallics* **1999**, *18*, 248–257.
[38] S. E. Durran, M. B. Smith, A. M. Z. Slawin, T. Gelbrich, M. B. Hursthouse, M. E. Light, *Can. J. Chem.* **2001**, *79*, 780–791.
[39] M. Oswaw, M. Hoshino, M. Akita, T. Wada, *Inorg. Chem.* **2005**, *44*, 1157–1159.
[40] M. R. J. Elsegood, M. B. Smith, S. H. Dale, *Acta Crystallogr., Sect. E* **2006**, *62*, m1850–m1852.
[41] P. Sevillano, A. Habtemariam, S. Parsons, A. Castiñeiras, M. E. García, P. J. Sadler, *J. Chem. Soc., Dalton Trans.* **1999**, 2861–2870.
[42] S. Pathaneni, G. R. Desiraju, *J. Chem. Soc., Dalton Trans.* **1993**, 319–322.
[43] E. C. Alyea, G. Ferguson, K. J. Fisher, R. A. Gossage, M. C. Jennings, *Polyhedron* **1990**, *9*, 2393–2397.
[44] I. del Rio, R. A. Gossage, M. Lutz, A. L. Spek, G. van Koten, *J. Organomet. Chem.* **1999**, *583*, 69–79.
[45] a) W. Keim, P. Kraneburg, G. Dahmen, G. Deckers, U. Englert, K. Linn, T. P. Spaniol, G. Raabe, C. Krüger, *Organometallics* **1994**, *13*, 3085–3094; b) H.-H. Wang, L. H. Pignolet, P. E. Reedy Jr, M. M. Olmstead, A. L. Balch, *Inorg. Chem.* **1987**, *26*, 377–383.
[46] S. E. Duff, S. C. Davies, P. B. Hitchcock, D. J. Evans, *Inorg. Chem. Commun.* **2005**, *8*, 850–852.
[47] J. M. Vila, T. Pereira, J. M. Ortigueira, M. López Torres, A. Castiñeiras, D. Lata, J. J. Fernández, A. Fernández, *J. Organomet. Chem.* **1998**, *556*, 21–30.
[48] W. J. Hunks, M. C. Jennings, R. J. Puddephatt, *Inorg. Chem.* **2002**, *41*, 4590–4598.
[49] J. A. Casares, P. Espinet, J. M. Martin-Álvarez, V. Santos, *Inorg. Chem.* **2006**, *45*, 6628–6636.
[50] Y. Yamamoto, Y. Sinozuka, Y. Tsutsumi, K. Fuse, K. Kuge, Y. Sunada, K. Tatsumi, *Inorg. Chim. Acta* **2004**, *357*, 1270–1282.
[51] Y. Kosaka, Y. Shinozaki, Y. Tsutsumi, Y. Kaburagi, Y. Yamamoto, Y. Sunada, K. Tatsumi, *J. Organomet. Chem.* **2003**, *671*, 8–12.
[52] H. Hellmann, J. Bader, H. Birkner, O. Schumacher, *Justus Liebigs Ann. Chem.* **1962**, *659*, 49–63.
[53] R. Uson, A. Laguna, M. Laguna, *Inorg. Synth.* **1989**, *26*, 85–91.
[54] M. A. Bennett, A. K. Smith, *J. Chem. Soc., Dalton Trans.* **1974**, 233–241.
[55] C. White, A. Yates, P. M. Maitlis, *Inorg. Synth.* **1992**, *29*, 228–234.
[56] a) D. Drew, J. R. Doyle, *Inorg. Synth.* **1972**, *13*, 47–55; b) J. X. McDermott, J. F. White, G. M. Whitesides, *J. Am. Chem. Soc.* **1976**, *98*, 6521–6528.
[57] SMART and SAINT Software for CCD diffractometers, Bruker AXS Inc., Madison, WI, **2001**.
[58] COLLECT: Data Collection Software, R. Hooft, Nonius B. V., **1998**.
[59] DENZO, Z. Otwinowski, W. Minor, in: C. W. Carter Jr, R. M. Sweet (Eds.), Methods in Enzymology, Macromolecular Crystallography, part A, vol. 276, Academic Press, **1997**, 307–326.
[60] G. M. Sheldrick, SHELXTL user manual, version 6.10, Bruker ACS Inc., Madison, WI, **2000**.
[61] A. L. Spek, *Acta Crystallogr., Sect. A* **1990**, *46*, C34.

Received: December 18, 2006
Published Online: February 23, 2007

 © 2007 Wiley-VCH Verlag GmbH & Co. KGaA, Weinheim 

DOI: 10.1002/ejic.200601211

# Tungsten Oxide and Tungsten Oxide-Titania Thin Films Prepared by Aerosol-Assisted Deposition – Use of Preformed Solid Nanoparticles

**Uzma Qureshi,[a] Christopher Blackman,[a] Geoffrey Hyett,[a] and Ivan P. Parkin*[a]**

**Keywords:** Tungsten oxide / Aerosol-assisted CVD / Thin films

Aerosol-assisted deposition (AAD) was used to deposit films of $WO_3$ from a suspension of solid nanoparticulate $WO_3$ in toluene. Titania films were deposited by the aerosol-assisted chemical vapour deposition of $[Ti(OiPr)_4]$ in the presence of $WO_3$ nanoparticles. The $WO_3$ and $TiO_2$ films exhibited photoactivity and photoinduced superhydrophilicity, further the titania films showed very unusual highly crenulated microstructures. These microstructures could not be obtained by sol-gel, atmospheric pressure chemical vapour deposition or evaporation routes. Furthermore, the microstructures could not be obtained from $[Ti(OiPr)_4]$ in the absence of nanoparticulate $WO_3$.
(© Wiley-VCH Verlag GmbH & Co. KGaA, 69451 Weinheim, Germany, 2007)

## Introduction

Nanoparticles are a major research interest worldwide, and a variety of different shapes and compositions can now be produced.[1,2] Many potential applications depend on formation of a nanocomposite, which serves both to immobilise the particles and render them chemically inert. In addition, the incorporation of nanoparticles into a matrix can change the properties of both the particle and the host. One area that has gained rapid attention is the growth of nanoparticles within a host film.[3–10] The presence of nanoparticles can assist in photogenerated charge separation, and this has been exploited in improved titania photocatalysts,[3,11,12] iron oxide photoanodes,[13] and tungsten oxide photochromic and electrochromic films,[14,15] all with incorporated gold nanoparticles.

Several strategies for production of nanoparticles within a host matrix have been devised including; synthesis of the semiconductor matrix followed by addition of pre-formed nanoparticles in a second step.[3,14–16] synthesis of the semiconductor matrix followed by application of metal ions in a second step; high energy ion implantation[6,17,18] and spin coating with a solution of metal ions followed by photocatalytic reduction or heat treatment[8,19] and synthesis of the semiconductor matrix and metal particles in a single step.[13,20,21] In all of these routes the nanoparticle is either used in a charged charge-stabilised or ligand-stabilised form dissolved in solution or generated in situ.[22] Furthermore, the use of a bulk nanoparticulate powder in forming thin films has not been investigated.

The physical state and composition of a precursor are critical in determining the quality of a thin film. In both physical vapour deposition (PVD) and chemical vapour deposition the precursor is transported through a vacuum or gas medium in the form of reactive atoms or molecular entities. These then undergo various surface reactions to form the desired film. The precursors are typically metal or ceramic tablets in the case of PVD, or volatile molecular entities in the case of CVD. On occasions the CVD process has been modified so that molecular precursors that are involatile or that undergo too ready a decomposition are first dissolved in an aerosol, and the aerosol is used as the transport medium to deliver the precursor to the substrate surface. Much work in this area has been pioneered by O'Brien.[23] Preformed bulk solids, suspended in a solution, have not been used in aerosol-assisted chemical vapour deposition. The use of solid particles to form thin films is however well known in a number of processes, in particular cold-spraying, plasma-spraying and thermal-spraying.[24] In these techniques either the solid particles are fired at very high kinetic energies at the surface, normally by a plasma-jet and a coating is formed by "splatting" of the solid on the surface or hybrid thermal-spraying is used in which some movement or reaction of the particles occurs on the surface.[24–26] One very new and emerging area of spraying technology is the use of suspension plasma spraying (SPS), using d.c. or R.F. plasma spray torches, in which powder particles are injected into the plasma flow using a liquid as carrier media, instead of the classical carrier gas.[26] This new approach offers unique possibilities to carry nanosized particles to manufacture finely grained coatings.

This paper details the preparation of $WO_3$ thin films from preformed commercially available solid nanoparticulate $WO_3$ using aerosol-assisted transport. These solid nanoparticles were used in a conventional CVD experiment using an aerosol as a carrier medium. Parallels to spray coating exist except that a high velocity gas stream or reactive plasma was not required. A separate set of experiments

[a] Department of Chemistry, University College London, 20 Gordon Street, London, WC1H OAJ, UK

 © 2007 Wiley-VCH Verlag GmbH & Co. KGaA, Weinheim 

investigated what happened when the $WO_3$ nanoparticles were added to a titanium dioxide AACVD precursor, which was then used to deposit thin films with small tungsten contents but greatly ordered titania microstructures. This work shows that solid nanoparticles can be used and transformed into an adhesive thin film provided that they can be dissolved/suspended in an appropriate carrier solvent and without the use of plasma spraying or high velocity "splatting". Furthermore, these nanoparticulates may act as templates to influence the production of highly unusual microstructures from traditional CVD precursors.

## Results and Discussion

### Preparation of $WO_3$ Thin Films by Aerosol Transport from Solid Nanoparticulate $WO_3$

Tungsten oxide thin films were prepared on glass from the aerosol-assisted deposition (AAD) of commercial nanoparticulate tungsten oxide powder. The films were uniform and pale yellow in colour. They covered the glass substrate. The films passed the Scotch tape test, were adhesive, could not be wiped off but could be scratched with both a brass and steel stylus. Interestingly all of the deposition was on the top substrate plate rather than the heated bottom plate (even with lower substrate temperatures). We have prepared tungsten oxide films by conventional atmospheric pressure chemical vapour deposition, film formation is then on the heated substrate. The films formed previously by conventional APCVD or reported here by aerosol-assisted AAD show similar properties except that by conventional CVD formation of substochiometric $WO_{3-x}$ is an issue.[18]

X-ray powder diffraction of the tungsten oxide films showed that the material was crystalline (Figure 1) with the fully stoichiometric triclinic $WO_3$ structure. This matched exactly by eye the diffraction pattern of the initial powder although perhaps some slight grain growth occurred. The indexed cell constants (from Reitveld analysis[29]) for the starting nanoparticulate powder were $a$ = 7.285(1) Å, $b$ = 7.488(1) Å, $c$ = 7.650(1) Å; $\alpha$ = 89.57(3)°, $\beta$ = 90.18(4)°, $\gamma$ = 90.81(1)° and for the thin film $a$ = 7.321(1) Å, $b$ = 7.525(1) Å, $c$ = 7.683(2) Å; $\alpha$ = 89.58(3)°, $\beta$ = 90.18(1)°, $\gamma$ = 90.78(1)°. These cell constants compare very favourably with those obtained on triclinic $WO_3$ by Woodward et. al.[20] $a$ = 7.312(1) Å, $b$ = 7.525(1) Å, $c$ = 7.689(1) Å; $\alpha$ = 88.847(3)°, $\beta$ = 90.192(4)°, $\gamma$ = 90.94(1)°. The X-ray pattern of the thin film indicates that there is no significant preferred orientation of the crystallites on the surface. This is completely different to conventional atmospheric pressure CVD and aerosol-assisted CVD approaches to tungsten oxide on glass where preferred orientation in the (020) direction predominated.[28] Average crystallite sizes as determined by XRD line broadening using the Scherrer equation (GSAS) were 199(2) Å for the starting powder as and 227(2) Å for the thin film.[29] This indicates some slight grain growth or selective deposition of the slightly larger grains within the weighted average crystallite size.

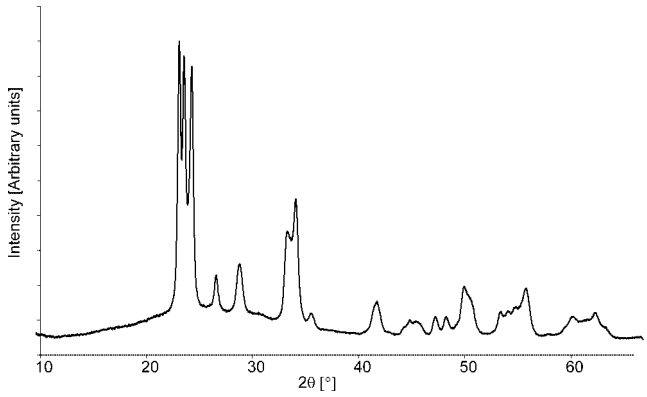


Figure 1. X-ray powder diffraction pattern of the $WO_3$ films formed at 450 °C by the aerosol-assisted deposition of nanoparticulate $WO_3$ suspended in toluene.

Scanning electron microscopy of the tungsten oxide thin films showed a dense continuous film made up of interlocking particles of approximate size 20–50 nm, Figure 2. EDX analysis showed that the films contained only tungsten and oxygen in a 1:3 ratio. The initial tungsten oxide powder was examined by TEM before the aerosol-assisted process. The powder was made up of agglomerates, however a number of small isolated $WO_3$ particles of size 15–20 nm could be seen. The Raman pattern for the as formed $WO_3$ film is identical to the starting material and is a perfect match for triclinic $WO_3$.[21]

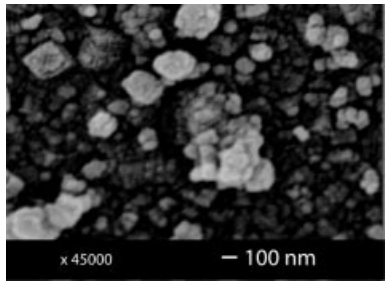


Figure 2. Scanning electron micrograph of the $WO_3$ films formed at 450 °C by the aerosol-assisted deposition of nanoparticulate $WO_3$ suspended in toluene.

The tungsten oxide films displayed two useful functional properties – they were active photocatalysts and they showed photoinduced superhydrophilicity. The contact angle for water droplets on the tungsten oxide thin films was very low – between 3–7°, indicating that the surface is very hydrophilic. This contact angle dropped further to between 0.5–2° on exposure of the surface for 0.5 h to 254-nm radiation. On keeping the samples in the dark for 24 h the contact angle increased to 7–8°, and on further irradiation decreased again to between 0.5–2°. The reversible change in contact angle with light/dark storage has been observed before for $TiO_2$ films.[31] The explanation was that in the light $Ti^{III}$ hydroxide centres are created at the surface which strongly hydrogen bond water and hence reduce the contact angle. A slower oxidative process reverts the $Ti^{III}$ to $Ti^{IV}$ with release of water and loss of the hydroxy groups. In the dark formation of $Ti^{IV}$ predominates as there is no light to

 © 2007 Wiley-VCH Verlag GmbH & Co. KGaA, Weinheim 

promote $Ti^{III}$ formation, and the films become less hydrophilic. The same behaviour could be responsible for what is seen for the tungsten oxide films with formation of a hydroxylated surface in the light and its subsequent loss on oxidation in the dark. A slight colour change was noted between the films kept in the dark which were pale yellow, and those exposed to light which were slightly darker, this could indicate some $W^{V}$ centre formation. The observed water contact angles of the $WO_3$ films are lower – that is the films are more hydrophilic than $WO_3$ made by APCVD and AACVD using traditional soluble molecular precursors.[32] This change in contact angle with time was repeated over many light-dark cycles. The very low initial contact angle puts these films in the class of superhydrophilic films and gives lower measurements to that of titanium dioxide thin films formed from sol-gel or CVD. The contact angle is probably a consequence of the surface being both partially hydroxylated and hence able to hydrogen bond effectively to the water, and having high porosity engendered by having a very fine microstructural form of nanoscaled particles. The $WO_3$ films readily destroyed a stearic acid overlayer and did so with both 254 and 365 nm irradiation, rates of destruction ($1.5 \times 10^{12}$ molecules $cm^{-2}min^{-1}$ for 254 nm) were similar to previously reported CVD prepared $WO_3$ and $TiO_2$ thin films.[30,32,33]

The aerosol transport method provides a ready means of forming thin films from a solid and completely involatile precursor. The fact that the initial tungsten oxide powder was made of nanoparticles probably helped suspension into the toluene solution and facilitated transport of the nanoparticulate solid to the substrate where the aerosol evaporated; and a thin film was laid down on the upper substrate. Notably the initial nanoparticle crystallite sizes (15–20 nm) are considerably smaller than the aerosol droplets (20 μm). The films formed, however, did seem to be composed of nanoparticulates as judged by SEM, although some agglomeration was noted. There seems to have been some sintering and partial crystal growth during the aerosol-assisted transport and deposition. Notably the large agglomerates (micron sized) that were observed in the initial starting powder were not seen in the thin films. Furthermore, these agglomerates did not dissolve in the initial precursor solution and were not found in the reactor flask after the deposition. Some evidence of larger agglomerates was seen in the exhaust of the reactor. Hence in this system we believe that the initial powder gets effectively transferred in the aerosol process. The film that is formed is on the top plate of the reactor and is composed of only relatively small nanoparticulates that are interlocked together – rather than the agglomerated particles seen by TEM in the initial starting powder. The best explanation for this is the thermophoretic effect. Large particles can not diffuse through the stagnant boundary layer effectively due to a buoyancy effect where faster moving gas particles are moving away from the hot surface preventing deposition on the bottom substrate. The cooler top plate is not directly heated making it easier for the smaller particles to penetrate the boundary layer. Hence in the process a degree of nanoscale sieving has occurred. The smaller nanoparticles can be incorporated in a film whilst the larger aggregated ones are repelled and exit to the exhaust.

We have shown that solid nanoparticulate starting materials, provided they can be suspended/dissolved in an appropriate solvent, do make useful precursors for the formation of thin films. This process has not been termed CVD as such as no overriding chemical reaction seems to have occurred, the initial material and final material were very similar by XRD, save some possible grain growth. However some interaction and bonding has occurred between the underlying substrate and the particles as the film is adhesive. The new deposition method developed here is similar to suspension plasma spraying of nanoparticles,[26] but avoids the use of a plasma and a high velocity stream, and hence is much simpler to use and operate.

A comparison was made between the aerosol-assisted process described above and using a spin coating or evaporation technique using the same $WO_3$/toluene nanoparticulate suspension. The films formed by spin coating both before and after firing were nonadhesive and powdery. The SEM of the films are very similar to those formed by AAD with particles matching those seen in the AACVD experiments. However, an important difference is that these films failed the Scotch tape test, and could be wiped off with a tissue, unlike those formed in the AAD process.

### Preparation of Titania Films in the Presence of Tungsten Oxide Nanoparticles

Aerosol-assisted chemical vapour deposition of anatase titania was accomplished from $[Ti(OiPr)_4]$ dissolved in toluene at a deposition temperature of 450 °C in the presence of tungsten oxide nanoparticles. The films of $TiO_2$ formed in the presence of $WO_3$ nanoparticles were generally a very pale yellow-beige – compared to the colourless or white films formed from $[Ti(OiPr)_4]$ alone. Some "rainbow-like" interference fringes could be seen in reflection at the edges of the film due to variations in thickness. The films passed the Scotch tape test and were resistant to wiping but could be scratched with a brass scalpel. They showed minimal specular haze assessed as 2%. The films showed good transmission between 50 and 60% in the visible region. The films formed both on the heated substrate and the top plate – unlike the $WO_3$ nanoparticle experiments where the film was only on the unheated top plate. The same microstructures and analysis were seen for both top and substrate plates.

Wide-area EDAX analysis showed that the films were made up of titanium and oxygen with just a trace of tungsten present (detectable but less than 1 atom% – and so not directly quantifiable). SEM imaging showed a plate-like morphology oriented perpendicular to the substrate of dimension ca 500 nm by 10 nm and underlying plates in a seemingly "wedding cake" structure, Figure 3. This microstructure is to the best of our knowledge unique for a titania film – and was repeatable in over five separate repeat

 © 2007 Wiley-VCH Verlag GmbH & Co. KGaA, Weinheim 

experiments. Indeed each particle seemed to have the self-same highly structured shape and were arranged as if in a mosaic pattern across the surface made up of a similar repeating units. High resolution SEM or spot EDAX analysis did not find any tungsten oxide particles. Previous work on titania by AACVD and APCVD on glass and indeed deposition of $TiO_2$ from $[Ti(OiPr)_4]$ from this work has always formed a smooth continuous film or a random island-like growth.[30] Hence as all other factors were the same the presence of the tungsten nanoparticles is the most likely cause of this unique surface architecture. Side-on SEM images allowed the determination of the film thickness and hence the growth rate of the films. It was found that the film thickness was 7–10 μm depending on the film sample analysed. The growth rate was calculated to be 3.5–10 μm per hour.

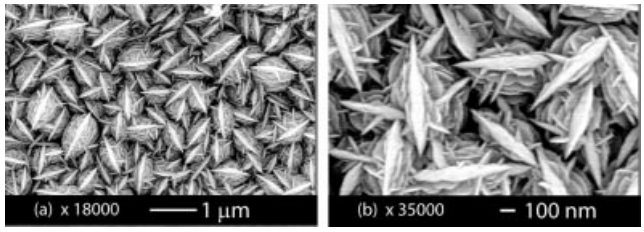


Figure 3. Scanning electron micrograph of the $TiO_2$ films formed at 450 °C by the aerosol-assisted deposition of $[Ti(OiPr)_4]$ in the presence of nanoparticulate $WO_3$: a) at 18000 times magnification; and b) at 35000 times magnification.

The thin film of $TiO_2$ deposited with $WO_3$ nanoparticles was investigated using powder X-ray diffraction, and then modelled using Rietveld refinement.[28] The pattern was found to be well modelled by the anatase phase of $TiO_2$ [$I4_1/amd$, $a$ = 3.7804(3) Å, $c$ = 9.500(2) Å], once the lattice and peak profile parameters were refined and preferred orientation taken into account (See Figure 4 and Figure 5). The preferred orientation was modelled using the March–Dollase model.[34] A good match to the recorded data was found when the 110 plane was used as the preferred plane with a March coefficient of $r$ = 0.542(2), a measure of the sample compression/elongation due to preferred orientation. As the SEM images indicate the crystallites are plate-like (rather than rod-like) then, as the value of $r$ is less than 1, we can conclude that the crystals are preferentially aligned so that the 110 plane is parallel to the deposition surface.[30]

Additional peaks were also found in the pattern for the part of the film that was 5 cm from the reactor inlet (marked with *asterisks* in Figure 5). These could be indexed as belonging to a cubic cell with lattice parameter $a$ = 5.646 Å and systematic absences consistent with face-centred symmetry. These peaks were of much lower intensity than those corresponding to $TiO_2$, suggesting that this phase is present only in small amounts. A search of the inorganic crystal structure database was conducted to identify this phase, but no reasonable match could be found.

The Raman patterns for the titania films (recorded at multiple points across the films surface) showed the expected bands for anatase with bands at 143, 396, 515 and 612 $cm^{-1}$, no evidence was seen for any tungsten oxide phase at any part of the deposited film.

The titania films were very hydrophilic as formed. Typical initial water droplet contact angles were around 5–10°, this is smaller than that found for a typical titania coating formed by CVD which gave initial water contact angles of ca 30°.[32,33] This difference in contact angle can be attributed to the microstructure seen from the SEM measurements. The films exhibited photo-induced superhydrophilicity. The films were also photocatalytically active showing ready destruction of a stearic acid over-layer with both 254 and 365 nm radiation and were comparable in photodegradation ability to previously analysed sol-gel and CVD prepared titania.[35] Using 254-nm light half of the stearic acid coating was removed in 1.2 h ($4 \times 10^{12}$ mole-

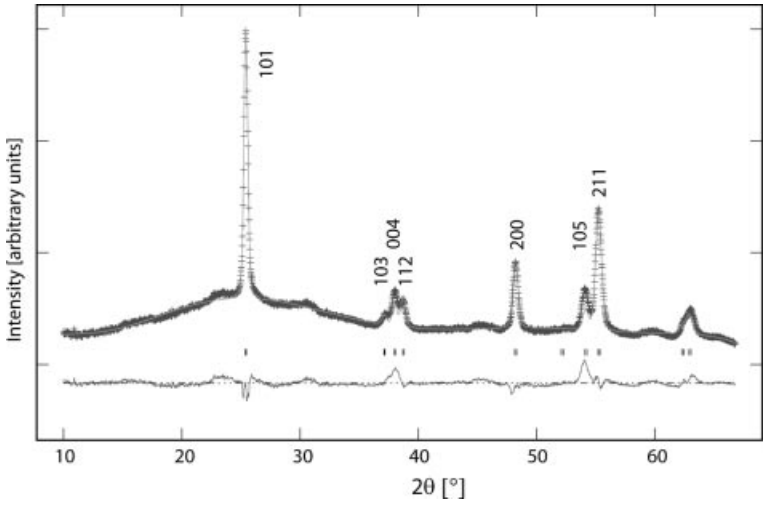


Figure 4. Rietveld refinement of $TiO_2$ films formed at 450 °C by the aerosol-assisted deposition of $[Ti(OiPr)_4]$ in the presence of nanoparticulate $WO_3$. Diffraction data shown by crosses, upper continuous line is the refined model, and lower line is the difference plot. Pattern was obtained from the surface of the glass some 2 cm away from the reactor inlet.

 © 2007 Wiley-VCH Verlag GmbH & Co. KGaA, Weinheim 

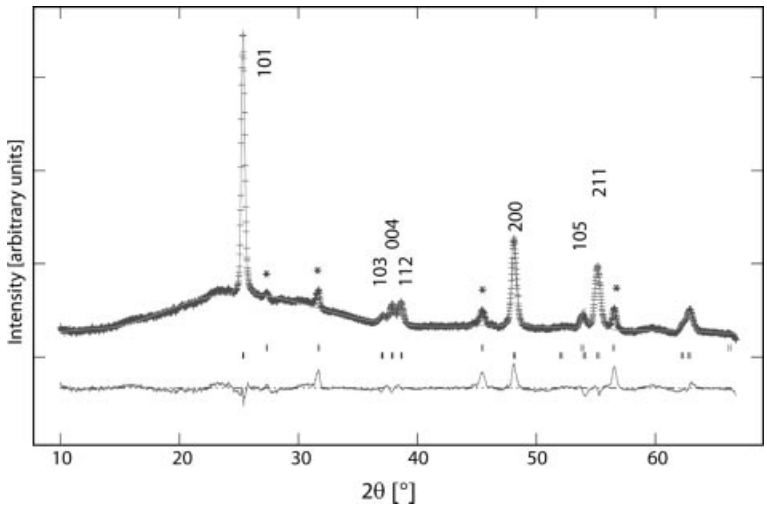


Figure 5. Rietveld refinement of $TiO_2$ films formed at 450 °C by the aerosol-assisted deposition of [Ti(O*i*Pr)$_4$] in the presence of nanoparticulate $WO_3$. Diffraction data shown by crosses, upper continuous line is the refined model, and lower line is the difference plot. The lower set of tick marks correspond to the $TiO_2$ main phase. The higher set of tick marks are the indexed second phase (*F* cubic, $a$ = 5.646 Å), these peaks are also marked by asterisks. Pattern was obtained from the surface 5 cm away from the reactor inlet.

cules cm$^2$ min$^{-1}$ for 254 nm) compared to 2.2 h for a comparable 365-nm source.

As a comparison to the films formed by AACVD the same $WO_3$ nanoparticulate-[Ti(O*i*Pr)$_4$] precursor solution was used to make sol-gel dip-coated films (Figure 6). The reason for this study was to see whether the unusual microstructure would follow in films made from the same precursor solution – but processed in a different way. By using the sol-gel process a nonadhesive, pale yellow, powdery film resulted. This was unlike those formed by AAD that adhered well to the substrate. Furthermore, the SEM of the films showed a particulate microstructure. Hence the fine structure seen in the AAD route was not in evidence and indicates the uniqueness of that approach in controlling – influencing the underlying microstructure. This microstructure gave rise to an important functional property – a very low water contact, much lower than that seen in conventional titania films formed by APCVD, AACVD or sol-gel methods. The unusual microstructure with the crenulated surface texture is most likely responsible for this low value. The ability to have very low contact angles for water is an important criteria for self-cleaning applications for example on windows. Indeed a number of commercial products (Pilkington Activ, Saint Goban Bioclean and PPG sunclean) all make use of this phenomena. The contact angles seen in this work for the structured films are lower than those reported for the commercial products – which typically have values around 10°. One counter point is that the microstructure induces more diffuse specular reflectance (haze) of around 2% compared to commercial windows that have a value of less than 0.2%.

The role of the tungsten oxide nanoparticles in engendering the unusual microstructures has not been fully elucidated in this work. The tungsten oxide obviously plays a major role because in its absence the films of titania formed are continuous and lack the self-similarity across the surface. Tungsten has been detected in the films albeit at ca 1 atom% level. This tungsten has not been seen as individual nanoparticles and spot EDAX analysis can find no evidence of localised high tungsten concentrations. It is possible that some tungsten has been incorporated in the titania lattice in the form of a solid solution- however the Raman and XRD provide no evidence for this in terms of changes in peak position or lattice parameter. The presence of a small amount of secondary phase in the XRD pattern suggests that this could be playing a structurally directing role. The phase is present at only a percent and although few peaks are seen it does match well for a cubic cell.

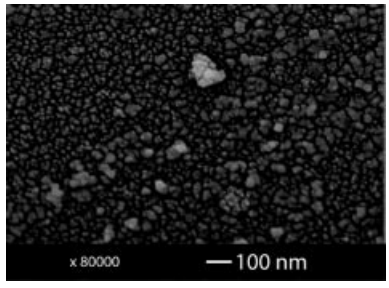


Figure 6. SEM of the $WO_3$–$TiO_2$ film formed by sol-gel dip coating followed by firing at 550 °C.

We have previously reported on the use of preformed – soluble ionic nanoparticles for the formation of composite thin films.[36] In that case gold nanoparticles were generated and then encapsulated in a titania or tungsten oxide matrix. That work is different to that reported here in that the nanoparticles were dissolved in solution rather than acting as a suspension. Further, the films generated did not have any unusual microstructures – the gold was simply embedded in the host matrix. Hence by using a commercial solid nanoparticulate powder we have shown that it is possible to make adherent thin films composed of nanoparticles, and

 © 2007 Wiley-VCH Verlag GmbH & Co. KGaA, Weinheim 

that the presence of these particles can affect the surface morphology of titanium dioxide. The nanoparticles used in these experiments were unlike conventional methods that use nanoparticles – where they are charged or ligand stabilized.

## Conclusions

Aerosol-assisted deposition (AAD) was used to deposit $WO_3$ nanoparticle thin films from a solid nanoscaled precursor. This was a convenient method for applying thin films to glass as it provides reasonable growth rates (3–7 $\mu m\,h^{-1}$) and conformal coverage of the substrate. The films were adhesive and were superhydrophilic. This route shows promise for the formation of thin films of material from involatile nanoscaled solid precursor and is the antithesis of what would normally be required for thin film deposition – i.e. a molecular volatile precursor. Titania films formed in the presence of $WO_3$ nanoparticles form unique microstructures and exhibited two key functional properties, photocatalysis and photoinduced superhydrophilicity. The initial water contact angles of these films are considerably lower than that seen for $TiO_2$ films prepared in the absence of nanoparticles and is attributed to the "fractal-like" microstructure.

## Experimental Section

Solid $WO_3$ nanoparticles and titanium tetraisopropoxide were obtained from Aldrich and used as supplied (99% purity). The pale yellow $WO_3$ nanoparticles (typically 0.2 g, 0.862 mmol) were sonicated by an ultrasonic bath (2 h) to aid dispersion in toluene (40 mL). This produced a pale yellow solution with some undissolved solid. This solution was used as a precursor for aerosol-assisted transport to form $WO_3$ films on glass. A similar concentration solution of $WO_3$ in toluene was used to make $WO_3$–$TiO_2$ thin films – except in that case titanium isopropoxide (0.56 g, 1.972 mmol) was added to the initial precursor solution (W: Ti molar ratio 1:2.28). It should be noted that on leaving the nanoparticulate suspension to stand for 12 h the solution became colourless and by weight seemingly all of the initial particles came out of the solution.

Three series of AACVD experiments were conducted using the following starting solutions/suspensions:

i) A suspension of $WO_3$ nanoparticles (0.2 g, 0.862 mmol) in toluene (40 mL) to form $WO_3$ thin films.

ii) [Ti(O*i*Pr)$_4$] (0.56 g, 1.972 mmol) dissolved in toluene (40 mL) to form $TiO_2$ films.

iii) A mixture of suspended $WO_3$ nanoparticles (0.2 g 0.862 mmol) and [Ti(O*i*Pr)$_4$] (0.56 g, 1.972 mmol) dissolved in toluene (40 mL) to form highly ordered microstructures

All AACVD experiments were performed on a custom built apparatus consisting of a horizontal-bed cold-wall reactor connected to an arrangement of delivery tubing, a bubbler and a humidifier – full details of the reactor have been published previously.[27]

The CVD reactor itself consisted of a silica glass substrate and supported top plate in a cylindrical quartz tube. The cylindrical quartz tube was open at both ends with each end capped by a stainless steel plate. Nitrogen gas entered the system through a brass manifold, which generated an uniform flow of gas across the width of the reactor. The uniform flow then passed between the heated glass bottom plate and the unheated glass top plate that was 5 mm above the heated surface. Thus a channel is present for the gas to flow between. The glass substrates of dimensions $150 \times 45 \times 4$ mm were heated by a graphite block that contained a Whatman cartridge heater. The glass substrates (both top plate and heated bottom plate) were supplied by Pilkington Glass and were pre-coated with a $SiO_2$ barrier layer. This barrier layer prevented atoms within the glass diffusing into the deposited film.

A typical deposition experiment proceeded as follows. The precursor mixture was transferred to the aerosol chamber, a customised PTFE container. A flow of nitrogen (BOC, 99.99%) was passed through the apparatus at all times. The glass substrate was cleaned using a tissue soaked in water, then with a tissue soaked with propan-2-ol. The glass was allowed to dry in air prior to it being mounted in the CVD chamber. The temperature of the glass inside of the reactor was measured by Pt–Rh thermocouples. Depositions were conducted at 400, 450 and 500 °C. Once the temperature was stabilised, an aerosol was then generated using an ultrasonic humidifier, and nitrogen gas passed through the aerosol mist (2 $L\,min^{-1}$), directing the aerosol to the CVD reactor. The aerosol passed through the brass manifold and entered the reactor between the heated substrate and the glass top-plate, placed parallel to the substrate. Any waste products exited through the exhaust. The gas flow was continued until all the precursor mix had passed through the reactor, typically taking 1 to 2 hours depending on the gas flow rate, carbon reactor temperature and solvent. The coated films on glass were cooled to room temperature in situ under a flow of $N_2$, and after cooling were handled and stored in air.

**Spin Coating/ Evaporation Coating:** Films of $WO_3$ and $TiO_2$/$WO_3$ were made by spin and evaporation coating of the precursor solutions mentioned above (0.2 g of $WO_3$ and 0.56 g of [Ti(O*i*Pr)$_4$] in toluene (40 mL). These coatings were fired in a furnace at 550 °C for 1 hour in air. The purpose of these experiments was to explore the differences in microstructure, surface adhesion and durability of the coating compared to those formed by the AACVD route.

**Film Analysis:** X-ray diffraction patterns were measured with a Bruker GADS using Cu-$K_\alpha$ radiation ($K_{\alpha 1}$ = 1.5406 Å). The system had a focussed and movable *x*-*y* stage to analyse various portions of the film. The diffractometer used glancing incident radiation (1.5°). The diffraction patterns were modelled using the Reitveld method with the GSAS suite of programmes and were compared to database standards.[25] EDAX was obtained on a Philips XL30E-SEM instrument and SEM was obtained with a JEOL 6301 instrument. UV/Vis/NIR spectra were recorded in the range 190–1100 nm using a Helios double beam instrument. Reflectance and transmission spectra were recorded between 300 and 1200 nm by a Zeiss miniature spectrometer. Reflectance measurements were standardised relative to a rhodium mirror and transmission relative to air. Raman spectra were acquired with a Renishaw Raman System 1000 using a helium-neon laser of wavelength 632.8 nm. The Raman system was calibrated against the emission lines of neon.

The photocatalytic properties of the samples were assessed by the destruction of an overlayer of a test organic stearic acid on a $3 \times 3$ cm portion of coated glass. This coated glass had been irradiated at 254 nm for 1 h prior to measurement. The stearic acid was applied by dropping 7.5 μL of a 0.4-mmol solution of stearic acid in methanol onto the glass surface which was spun at 1500 revolutions a minute during the dropping procedure. The infrared spectra

 © 2007 Wiley-VCH Verlag GmbH & Co. KGaA, Weinheim 

of the stearic-acid overlayer was measured over the range 2950–2800 $cm^{-1}$. The glass coated with stearic acid was irradiated with 365-nm radiation provided by BDH germicidal lamps (2 × 8 W). The IR spectra of the stearic acid was measured after 30 min intervals for up to 2 h and the areas of the bands that attributed to the C–H stretches were quantified.

The advancing water contact angles were determined by measuring the width of a known volume of water (1 μL) with a travelling microscope and then entering the spread into a simple trigonometric program.

## Acknowledgments

Engineering and Physical Sciences Research Council (EPSRC) and Pilkington Glass are thanked for financial support. The Royal Society and Wolfson Trust are thanked for providing a merit award to IPP.

[1] *Nanoscience and Nanotechnologies*, The Royal Society and The Royal Academy of Engineering, **2004**, London.
[2] G. Schmid (Ed.), *Nanoparticles – From Theory to Applications*, John Wiley & Sons, New York.
[3] V. Subramanian, E. E. Wolf, P. V. Kamat, *J. Am. Chem. Soc.* **2004**, *126*, 4943.
[4] T. Ung, L. M. Liz-Marzan, P. Mulvaney, *Colloids Surfaces A: Physiochem. Eng. Aspects* **2002**, *202*, 119.
[5] X. Xu, M. Stevens, M. B. Cortie, *Chem. Mater.* **2004**, *16*, 2259.
[6] Z. Liu, H. Wang, H. Li, X. Wang, *App. Phys. Lett.* **1998**, *72*, 1823.
[7] T. Mokari, H. Sertchook, A. Aharoni, Y. Ebenstein, D. Avnir, U. Banin, *Chem. Mater.* **2005**, *17*, 258.
[8] K. Naoi, Y. Ohko, T. Tatsuma, *J. Am. Chem. Soc.* **2004**, *126*, 3664.
[9] C. Yang, M. Kalwei, F. Schuth, K. Chao, *App. Catal. A: Gen.* **2003**, *254*, 289.
[10] M. Lee, L. Chae, K. C. Lee, *NanoStructured Mater.* **1999**, *11*, 195.
[11] D. Lahiri, V. Subramanian, T. Shibata, E. E. Wolf, B. A. Bunker, P. V. Kamat, *J. App. Phys.* **2003**, *93*, 2575.
[12] S. Schimpf, M. Lucas, C. Mohr, U. Rodemerck, A. Bruckne, J. Radnik, H. Hofmeister, P. Claus, *Catal. Today* **2002**, *72*, 63.
[13] Y. Hida, H. Kozuka, *Thin Solid Films* **2005**, *476*, 264.
[14] T. He, Y. Ma, Y. Cao, W. Yang, J. Yao, *Phys. Chem. Chem. Phys.* **2002**, *4*, 1637.
[15] T. He, Y. Ma, Y. Cao, W. Yang, J. Yao, *J. Electroanalytical Chem.* **2001**, *514*, 129.
[16] Y. Tian, T. Tatsuma, *Chem. Commun.* **2004**, 1810.
[17] A. L. Stepanov, V. N. Popok, *Technol. Phys. Lett.* **2003**, *29*, 977–979.
[18] K. Fukumi, A. Chayahara, K. Kadono, T. Sakaguchi, Y. Horino, *J. Appl. Phys.* **1994**, *75*, 3075.
[19] E. Stathatos, P. Lianos, P. Falaras, A. Siokou, *Langmuir* **2000**, *16*, 2398.
[20] Y. Yang, J. Shi, W. Huang, S. Dai, L. Wang, *J. Mater. Sci.* **2003**, *38*, 1243.
[21] M. Epifani, C. Giannini, L. Tapfer, L. Vasanelli, *J. Am. Ceram. Soc.* **2000**, *83*, 2385.
[22] C. Bechinger, S. Herminghaus, P. Leiderer, *Thin Solid Films* **1994**, *239*, 156.
[23] C. M. Afzaal, K. Elwood, N. L. Pickett, P. O'Brien, J. Raffety, J. Waters, *J. Mater. Chem.* **2004**, *14*, 1310.
[24] G. Montavon, *High Temp. Mater. Processes* **2004**, *8*, 45.
[25] R. B. Heimann, *Adv. Ceram. Mater. Key Eng. Mater.* **1996**, *122*, 399.
[26] C. Borchers, F. Gartner, T. Stoltenhoff, H. Kreye, *J. Appl. Phys.* **2005**, *96*, 4288.
[27] I. P. Parkin, G. E. Elwin, *Chem. Vap. Dep.* **2000**, *6*, 59.
[28] C. Blackman, I. P. Parkin, *Chem. Mater.* **2005**, *17*, 1583.
[29] A. C. Larson, R. B. Van Dreele, "*General structure analysis system (GSAS)*". Los Alamos national laboratory report LAUR 86–748, **2000**.
[30] P. M. Woodward, A. W. Sleight, J. Voight, *J. Phys. Chem. Solids* **1995**, *56*, 1305.
[31] R. G. Palgrave, I. P. Parkin, *J. Mater. Chem.* **2004**, *14*, 2864; W. B. Cross, I. P. Parkin, S. A. O'Neill, *Chem. Mater.* **2003**, *15*, 2786.
[32] W. B. Cross, I. P. Parkin, *Chem. Commun.* **2003**, 1696.
[33] S. A. O'Neill, I. P. Parkin, R. J. H. Clark, A. Mills, N. Elliott, *J. Mater. Chem.* **2003**, *13*, 56.
[34] W. A. Dollase, *J. Appl. Crystallogr.* **1986**, *19*, 267.
[35] A. Mills, A. Lepre, N. Elliott, S. Bhopal, I. P. Parkin, S. A. O'Neill, *J. Photochem. Photobiol. A: Chem.* **2003**, *160*, 185.
[36] R. Palgrave, I. P. Parkin, *J. Am. Chem. Soc.* **2006**, *128*, 1587.
Received: December 19, 2006
Published Online: February 21, 2007

 © 2007 Wiley-VCH Verlag GmbH & Co. KGaA, Weinheim 

DOI: 10.1002/ejic.200601214

# Luminescent and Electronic Properties of Stilbenoid NCN-Pincer $Pt^{II}$ Compounds

**Guido D. Batema,[a] Koen T. L. van de Westelaken,[a] Javier Guerra,[a] Martin Lutz,[b] Anthony L. Spek,[b] Cornelis A. van Walree,[a] Celso de Mello Donegá,[c] Andries Meijerink,[c] Gerard P. M. van Klink,[a] and Gerard van Koten*[a]**

**Keywords:** Donor–acceptor systems / Luminescence / N-ligands / Platinum

A series of novel 4,4′-disubstituted organic–organometallic stilbenes were synthesized, that is, the 4′-substituted stilbenoid–NCN-pincer platinum(II) complexes [PtCl(NCN–R-4)] (NCN–R-4 = $[C_6H_2(CH_2NMe_2)_2$-2,6-R-4$]^-$ in which R = $C_2H_2C_6H_4$-R′-4′ with R′ = $NMe_2$, OMe, $SiMe_3$, H, I, CN, $NO_2$) (**1**–**7**). In these compounds the PtCl grouping can be considered to be present as a donor substituent. Their synthesis involved a Horner–Wadsworth–Emmons reaction of [PtCl(NCN–CHO-4)] (**9**) with the appropriate phosphonate ester derivatives (**8a**–**g**). Under these reaction conditions, the C–Pt bond in aldehyde **9** was not affected, and the platinated stilbene products were obtained in 53–90 % yield. The solid-state structures of complexes **1**, **2** and **5**–**7** were determined by single-crystal X-ray diffraction, which revealed interesting bent conformations for **2**, **5** and **7**. Linear correlations were found between both the $^{13}C\{^1H\}$ (C *ipso* to Pt) and the $^{195}Pt\{^1H\}$ NMR chemical shift and the Hammett $\sigma_p$ value of the R′ substituent; therefore, these NMR shifts can be used as a qualitative probe for the electronic properties of the delocalized π-system to which it is connected. The platinum–stilbene complexes were investigated for charge-transfer properties in solvents of different polarity. The luminescent properties, shown by donor–acceptor complexes **1**, **6** and **7**, were investigated by fluorescence spectroscopy, and the complexes showed positive solvatochromism, which indicates dipolar character of the excited state. The excited state lifetimes, which were in the picosecond range, and the quantum yields (ranging from 0.002 to 0.2) were also determined for these complexes. It was established that the presence of the transition metal favours nonradiative decay from the excited state to the ground state.

(© Wiley-VCH Verlag GmbH & Co. KGaA, 69451 Weinheim, Germany, 2007)

## Introduction

Conjugated molecules are regarded with high interest for their optoelectronic properties[1] in, for instance, materials with nonlinear optical (NLO)[2] behaviour and for applications in optoelectronic devices such as light-emitting diodes.[3] The properties of these molecules depend on the nature and length of the conjugation path and on the functional groups present in the system. By connecting donor and acceptor groups through a π-electron bridge, intramolecular electron transfer can be achieved. A well-known example of such a push–pull conjugated system is *trans* 4-dimethylamino-4′-nitrostilbene (DANS),[4] a member of the *trans* 4,4′-disubstituted stilbene family (Scheme 1), which has been studied predominantly for its special photophysical and NLO properties.[5–8]

Currently, conjugated systems containing transition metals attract much attention,[9–13] especially because the optoelectronic properties of these systems can be affected by changing the metal ion, the coordinating anions and ligands or by changing the nature of the connecting conjugated system. Interesting examples of metal–organic conjugated molecules studied for their NLO properties are the ferrocene-functionalized donor–acceptor complexes reported by McCleverty and coworkers.[14–17] In our group, bis(pincer–metal)acetylene complexes[18–21] and heterometallic terpyridine–pincer-based complexes[22] were studied in which the communication between two metals by a conjugated ligand bridge was investigated.

We already showed the feasibility of remotely influencing the electron density on the metal centre of the [MX(NCN–R-4)] pincer system (M = Ni, Pd or Pt; X = Cl, Br or I) by altering the *para* substituent R [R = $NO_2$, C(O)Me, COOH,

[a] Organic Chemistry and Catalysis, Faculty of Science, Utrecht University,
Padualaan 8, 3584 CH Utrecht, The Netherlands
Fax: +31-30-2523615
E-mail: g.vankoten@chem.uu.nl
[b] Crystal and Structural Chemistry, Faculty of Science, Utrecht University,
Padualaan 8, 3584 CH Utrecht, The Netherlands
[c] Condensed Matter and Interfaces, Faculty of Science, Utrecht University,
P.O. Box 80.000, Princetonplein 1, 3508 TA Utrecht, The Netherlands

Supporting information for this article is available on the WWW under http://www.eurjic.org or from the author.

 © 2007 Wiley-VCH Verlag GmbH & Co. KGaA, Weinheim 

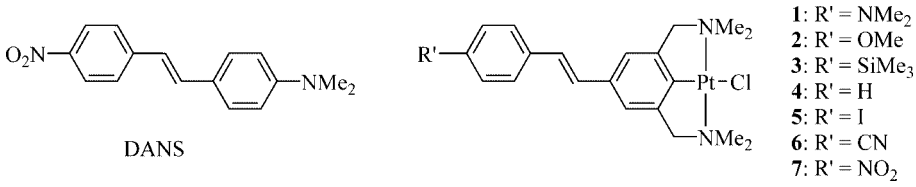


Scheme 1.

CHO, $SO_3H$, $PO(OEt)_2$, PO(OH)(OEt), $PO(OH)_2$, I, Cl, H, $CH_2OH$, OMe, SMe or $NH_2$].[23,24] In this series, a linear correlation was found between the ease of oxidation of the nickel centre and the electron-donating properties of the *para* substituent [redox potential $E_{p,a}$ ($Ni^{II}/Ni^{III}$) versus $\sigma_p$]. Correlations were also found between NMR chemical shifts [$^{13}C\{^1H\}$ and $^{195}Pt\{^1H\}$] of the complexes and the Hammett substituent parameter $\sigma_p$ (for M = Ni: $\delta = {}^{13}C_{ipso}$ versus $\sigma_p$; for M = Pt: $\delta = {}^{195}Pt$ versus $\sigma_p$). Conversely, in the same study, for the carboxylic acid functionalized platinum compound [PtI(NCN–COOH-4)], the Hammett $\sigma_p$ value of the platinum iodide moiety was determined to amount to –1.18 in methanol and –0.72 in water/methanol (1:1). The value and the negative sign of this Hammett substituent constant implied that the *para* platinum iodide group can be considered as an electron-donating substituent comparable in strength to a dimethylamino group [$NMe_2$; $\sigma_p$ = –0.83; the tabulated $\sigma_m$ value of the $CH_2N(Me)_2$ group is 0.00].[25] Consequently, it should be possible to introduce the aryl NCN metal system as the donor group into a donor–acceptor system, like in DANS, that is, to replace the *N*,*N*-dimethylaminobenzene moiety with the NCN–PtCl moiety (Scheme 1). Moreover, recent studies showed that certain $Pt^{II}$–pincer systems have interesting photochemical properties;[26–28] for example, Connick and coworkers studied luminescent NCN–$Pt^{II}$ pincer complexes based on 1,3-bis(piperidylmethyl)benzene.[29–31] Kanbara and coworkers applied a thioamide-based SCS–$Pt^{II}$ pincer complex in a light-emitting diode exhibiting red-coloured electroluminescence.[32]

In the present study we set out to prepare a series of stilbenoid platinum compounds [PtCl{NCN($C_2H_2C_6H_4$-R′-4′)-4}] (**1**–**7**) in which the donor site (the PtCl grouping) is kept constant and the nature of the R′ group is varied (R′ = $NMe_2$, OMe, $SiMe_3$, H, I, CN, $NO_2$). By introducing different substituents at the 4′-position of the stilbenoid–pincer backbone, the donor–acceptor properties of the stilbenoid platinum system could be studied.

An important synthetic objective of the present study was to explore methods for the construction of the stilbene moiety by using a suitable *para*-substituted pincer molecule with the NCN–Pt arrangement already in place. A pronounced influence of the *para* substituent on the (photo)-physical properties of the stilbenoid platinum complexes has been found and will be discussed with the help of the results from solid-state structures, $^{13}C\{^1H\}$ and $^{195}Pt\{^1H\}$ NMR spectroscopic analysis, UV/Vis and emission spectroscopy.

## Results and Discussion

### Synthesis

A series of substituted benzyl phosphonates[33–38] **8b**–**g** was prepared by a Michaelis–Arbuzov reaction between triethyl phosphite and the appropriate *para*-substituted benzylic bromide, which were either commercially available or could be prepared in a single step by a recently improved[39] radical bromination reaction of the available toluene derivative. Phosphonate ester **8a** was synthesized by reduction of 4-dimethylaminobenzaldehyde with sodium borohydride to form 4-dimethylaminobenzyl alcohol,[40] which was then in situ reacted with methanesulfonyl chloride and subsequently converted into the phosphonate ester by an Arbuzov reaction[41] (Scheme 2).

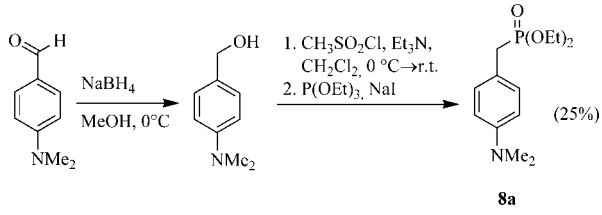


Scheme 2.

Stilbenoid NCN-pincer platinum(II) compounds **1**–**7** were obtained as *trans* compounds in moderate-to-good yield by a Horner–Wadsworth–Emmons condensation reaction of [PtCl(NCN–CHO-4)] (**9**) and the appropriate phosphonate ester **8** in the presence of potassium *tert*-butoxide (Scheme 3).[42–44] Upon hydrolysis of the reaction mixture, the pure *trans* isomers of **1**–**7** precipitated out of the solution and were isolated by filtration as air-stable solids. The solids were fully characterized by $^1H$, $^{13}C\{^1H\}$ and $^{195}Pt\{^1H\}$ NMR spectroscopy, elemental analysis, mass spectrometry, and compounds **1**, **2**, **5**, **6** and **7** were also characterized by single-crystal X-ray structure determination. In this study, only the *trans* isomers of **1**–**7** were obtained in a pure form and further studied. From the filtrate, a *trans*–*cis* mixture (determined by $^1H$ NMR spectroscopy) was obtained of which the *cis* isomer was always present as the minor component. In the solid state, the compounds do not undergo *trans*–*cis* isomerization upon exposure to daylight in contrast to the compounds in solution, which do undergo this *trans*–*cis* isomerization.[5,6] Noteworthy, the Pt–C bond of **9** remains intact throughout the complete reaction under the applied reaction conditions and no visible formation of zero-valent platinum was ob-

 © 2007 Wiley-VCH Verlag GmbH & Co. KGaA, Weinheim 

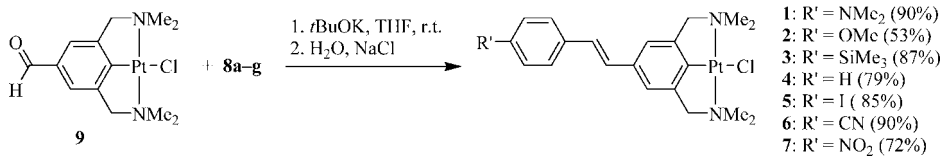


Scheme 3.

served in the olefination reaction induced by the presence of the strong base.

## Crystal Structures

Crystals suitable for single-crystal X-ray structure determination of **1** (Figure 1), **2**, **5**, **6** and **7** (Figure 2) were obtained by slow evaporation of deuterated dichloromethane solutions, which were initially prepared and used for the NMR studies.

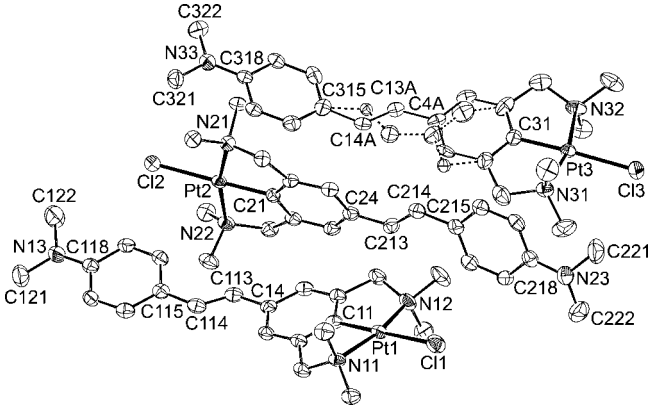

Figure 1. Displacement ellipsoid plot (50% probability level) of the three independent molecules in the crystal structure of **1** (viewed along the crystallographic *b* axis). Hydrogen atoms and partially occupied $CH_2Cl_2$ molecules are omitted for clarity. The minor conformation (19% occupancy) of disordered residue 3 is drawn in dashed lines.

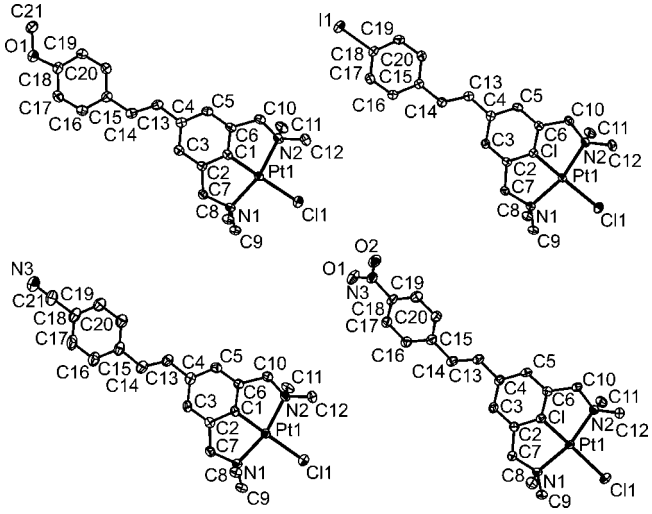

Figure 2. Displacement ellipsoid plot (50% probability level) of complexes **2** (top left), **5** (top right), **6** (bottom left) and **7** (bottom right). Hydrogen atoms have been omitted for clarity.

Compound **1** crystallizes with three independent molecules in the asymmetric unit of which one is disordered about the central double bond (Figure 1). This type of disorder is rather common in *trans*-stilbene and *trans*-azobenzene derivatives.[45] The two ordered molecules have very similar bond lengths and angles (Table 1) but differ in the conformation of the 4-dimethylaminostyryl fragment (Figure S1, Supporting Information). The overall shape of the molecules is bent; the $C_{ipso}$ carbon atoms are 0.448(4) and 0.270(4) Å (for residues 1 and 2, respectively), beneath the least-squares plane of the central double bond (C4–C13–C14–C15). For the corresponding *para* carbon atoms C18, the distances are 0.099(4) and 0.311(4) Å for residues 1 and 2, respectively. In the crystal, the molecules of the metal complex are stacked on top of each other in an antiparallel fashion. These stacks run in the crystallographic [1,0,1] direction (Figure 1). Intermolecular π-stacking interactions could not be observed in this crystal structure.

Despite the different *para* substituents, compounds **2**, **5** and **6** are isostructural in the solid state. They have similar bond lengths and bond angles (Table 2) and also nearly identical conformations and crystal packings. Small differences are observed for intermolecular interactions involving the *para* substituents. Molecular plots of **2**, **5** and **6** are displayed in Figure 2; likewise in the crystal structure of **1**, the molecules have an overall bent shape (Figure 3). Again, the C1 $C_{ipso}$ atom and the C18 aryl carbon atom are beneath the plane of the central double bond with values of 0.382(2), 0.363(3) and 0.343(3) for C1 and 0.307(3), 0.307(4) and 0.101(4) for C18. Also, the crystal structures of **2**, **5** and **6** do not express intermolecular π-stacking interactions. There are only weak intermolecular C–H···π and C–H···Cl interactions, and in some crystals C–H···O (compound **2**) and C–H···N (compound **6**) hydrogen bonds are present. The latter certainly do not determine the packing mode because hydrogen bond interactions in **5** are missing.

All molecules are arranged in the crystallographic *b*-direction in an approximately perpendicular orientation with respect to each other (Figure 4). In the crystallographic *a* direction, layers of polar Pt–Cl units alternate with hydrophobic organic layers.

The molecular geometry of **7** in the crystal is very similar to that of compounds **1**, **2**, **5** and **6** (Table 2). The nitro group in the *para* position is slightly rotated out of the plane with an O2–N3–C18–C17 torsion angle of 165.4(3)°. There is also a slight rotation of the *para* nitrophenyl moiety with respect to the central double bond, expressed in a C13–C14–C15–C16 torsion angle of 167.8(3)°. In contrast to compounds **1**, **2**, **5** and **6**, the shape of **7** is not bent; the C1 $C_{ipso}$ atom and the C18 phenyl carbon are essentially in

 © 2007 Wiley-VCH Verlag GmbH & Co. KGaA, Weinheim 

Table 1. Selected bond lengths [Å], angles [°] and torsion angles [°] of [PtCl{NCN($C_2H_2C_6H_4NMe_2$-4′)-4}] (**1**).

| Residue 1 | | Residue 2 | | Residue 3[a] | |
|---|---|---|---|---|---|
| Pt1–C11 | 1.918(4) | Pt2–C21 | 1.934(4) | Pt3–C31 | 1.915(4) |
| Pt1–N11 | 2.094(3) | Pt2–N21 | 2.084(3) | Pt3–N31 | 2.085(3) |
| Pt1–N12 | 2.088(4) | Pt2–N22 | 2.088(3) | Pt3–N32 | 2.090(4) |
| Pt1–Cl1 | 2.4129(13) | Pt2–Cl2 | 2.4152(11) | Pt3–Cl3 | 2.4134(12) |
| C113–C114 | 1.337(6) | C213–C214 | 1.344(6) | C13A–C14A | 1.339(7) |
| C11–Pt1–N11 | 82.28(16) | C21–Pt2–N21 | 82.15(15) | C31–Pt3–N31 | 82.59(17) |
| C11–Pt1–N12 | 81.89(17) | C21–Pt2–N22 | 82.32(16) | C31–Pt3–N32 | 82.58(18) |
| C11–Pt1–Cl1 | 179.52(12) | C21–Pt2–Cl2 | 178.12(13) | C31–Pt3–Cl3 | 175.11(11) |
| C118–N13–C121 | 119.1(4) | C218–N23–C221 | 120.5(4) | C318–N33–C321 | 121.1(4) |
| C118–N13–C122 | 120.8(4) | C218–N23–C222 | 119.6(4) | C318–N33–C322 | 121.4(4) |
| C14–C113–C114–C115 | 172.1(4) | C24–C213–C214–C215 | 172.9(4) | C4A–C13A–C14A–C315 | 172.0(5) |
| C113–C114–C115–C116 | 169.6(4) | C213–C214–C215–C216 | 177.0(4) | C13A–C14A–C315–C316 | –175.5(5) |
| C117–C118–N13–C121 | 1.4(7) | C217–C218–N23–C221 | –23.5(7) | C317–C318–N33–C321 | –0.6(6) |
| Pt1–N11–C17–C12 | –29.2(4) | Pt2–N21–C27–C22 | 29.2(4) | Pt3–N31–C37–C32 | –25.8(5) |
| Pt1–N12–C110–C16 | –29.4(4) | Pt2–N22–C210–C26 | 25.4(4) | Pt3–N32–C310–C36 | –29.5(5) |
| Angle between planes [°] | | | | | |
| [C11–C12–C13–C14–C15–C16], [C115–C116–C117–C118–C119–C120] | 14.5(2) | [C21–C22–C23–C24–C25–C26], [C215–C216–C217–C218–C219–C220] | 25.5(2) | [C31–C32–C3A–C4A–C5A–C36], [C315–C316–C317–C318–C319–C320] | 13.3(2) |

[a] Only the major conformation (81% occupancy) of disordered residue 3 is given. As a result of the disorder, the geometrical values are less reliable than for residues 1 and 2.

Table 2. Selected bond lengths [Å], angles [°] and torsion angles [°] of **2**, **5**, **6** and **7**.

| | **2** (R′ = OMe) | **5** (R′ = I) | **6** (R′ = CN) | **7** (R′ = $NO_2$) |
|---|---|---|---|---|
| Pt–C1 | 1.920(2) | 1.917(4) | 1.925(3) | 1.915(3) |
| Pt–N1 | 2.0850(18) | 2.087(3) | 2.081(2) | 2.079(2) |
| Pt–N2 | 2.0875(19) | 2.091(3) | 2.091(2) | 2.087(2) |
| Pt–Cl1 | 2.4122(6) | 2.4130(9) | 2.4119(8) | 2.4061(7) |
| C13–C14 | 1.337(4) | 1.345(5) | 1.334(5) | 1.332(4) |
| C1–Pt1–N1 | 81.89(8) | 82.01(12) | 81.99(11) | 82.46(11) |
| C1–Pt1–N2 | 82.01(8) | 81.87(12) | 81.83(11) | 82.30(11) |
| C1–Pt1–Cl1 | 173.69(6) | 173.07(9) | 173.47(9) | 178.33(9) |
| Pt1–N1–C7–C2 | –32.4(2) | –32.4(3) | –32.2(3) | –28.2(3) |
| Pt1–N2–C10–C6 | –28.5(2) | –28.8(3) | –31.2(3) | –29.0(3) |
| C4–C13–C14–C15 | –171.8(2) | –171.8(3) | –175.4(3) | 176.2(3) |
| C13–C14–C15–C16 | 177.4(3) | –177.4(4) | 174.1(4) | 167.8(3) |
| C21–O1–C18–C17 | 177.2(2) | – | – | – |
| C16–C17–C18–I | – | 179.0(3) | – | – |
| C21–C18–C19–C20 | – | – | 178.1(3) | – |
| O2–N3–C18–C17 | – | – | – | 165.4(3) |
| Angle between planes [C1–C2–C3–C4–C5–C6] and [C15–C16–C17–C18–C19–C20] [°] | | | | |
| | 13.64(12) | 21.58(16) | 9.06(17) | 24.65(14) |

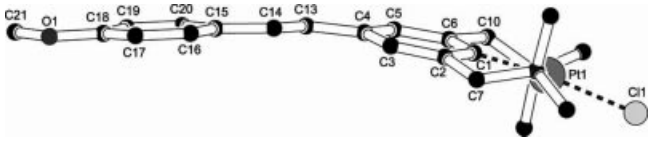


Figure 3. Side view of **2** in the crystal, which shows the overall bent shape. Hydrogen atoms are omitted for clarity. The molecules of **5** and **6** are similarly bent.

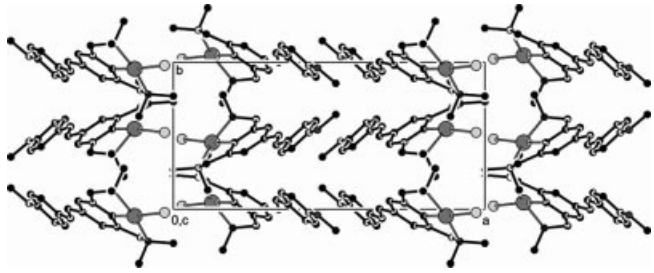


Figure 4. Packing of the molecules in the crystal structure of **2**. Projection along the crystallographic *c* axis. Hydrogen atoms are omitted for clarity. The crystal structures of **5** and **6** are isostructural with **2**.

the plane of the central double bond (Figure 5). The packing of **7** in the crystal is an antiparallel arrangement in the crystallographic [1,1,0] direction (Figure 6). In the crystallographic *c* direction, polar and apolar layers alternate.

Comparison of the molecular structures of **1**, **2** and **5**–**7** with earlier reported [PtCl(NCN)] complexes[21,46–49] shows a similar distorted square-planar geometry around the Pt nucleus in which the carbon atoms of the benzylic substituents (C7 and C10) are positioned above and below the plane

 © 2007 Wiley-VCH Verlag GmbH & Co. KGaA, Weinheim 

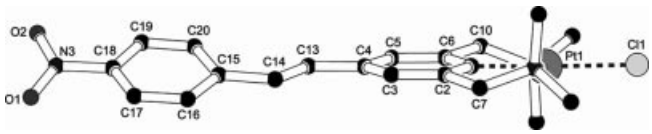


Figure 5. Side view of **7** in the crystal that shows the extended overall shape. Hydrogen atoms are omitted for clarity.

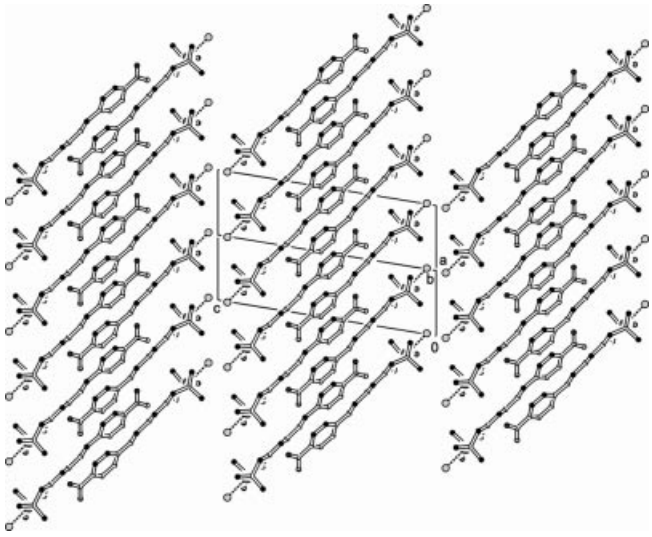

Figure 6. Packing of **7** in the crystal. Hydrogen atoms are omitted for clarity. Projection along the crystallographic [1,–1,0] direction.

defined by C1–N1–Pt1–N2–Cl1. For the two five-membered metallacycles, which are slightly puckered, torsion angles for the Pt1–N1–C7–C2 and Pt1–N2–C10–C6 bonds ranging from 25 to 32° were found. The platinum to $C_{ipso}$ (Pt–C) distances of **1**, **2** and **5**–**7** are in the range of 1.915 to 1.934 Å, as expected.[47]

For the stilbenoid backbone of **1**, **2** and **5**–**7**, similar geometric features were found compared to other reported transition-metal-containing stilbenoid fragments.[9,50,51]

A comparison of the torsion angles between the *trans* bonded 4-styrenyl grouping and the aromatic NCN ring show these fragments to be slightly rotated about the olefinic C–C double bond with torsion angles ranging from 171.8 to 176.2°. For **1** (residues 1 and 3), **2** and **6**, torsion angles between the two aromatic planes (as defined in Tables 1 and 2) of about 9–15° were found. Notable larger torsion angles (ranging from 21° to 26°) were found in **7**, **1** (residue 2) and **5**. As a result of the resonance stabilization energy in conjugated systems, it is expected for stilbenes that the phenyl rings and the ethylene bridge have a nearly coplanar geometry.[52–55] In practice, torsion angles around 0–5° are commonly found in the solid-state structures,[56–58] although a small part of the reported stilbenoid molecules show larger torsion angles ranging from 20 to 27°.[59–61] Such deviations from coplanarity can be explained by a combination of alkenyl-H–*ortho*-H repulsion and by crystal packing forces.

A smaller deviation (1.0–2.7°) from the planar geometry is found for the dihedral angles between the planes formed by the *para* R′ substituent (connected to C18) and its aromatic ring (defined by C15–C16–C17–C18–C19–C20), except for **7** (R′ = $NO_2$), of which the nitro group deviates almost 15° from coplanarity (Table 2, Figure 5). This deviation is commonly found for an aromatic nitro group.[62]

The alternation of bond length $\delta r$ in the phenyl rings provides information about the presence of possible quinoid character in these rings, which reflects ground-state charge-transfer character.[63,64] In benzene, the $\delta r$ value equals 0, whereas values between 0.08 and 0.10 are found in a fully quinoid ring. In the analyses of **2**, **5**, **6** and **7**, for the R′-substituted phenyl ring, $\delta r$ values between 0.003 and 0.016 are found;[65] for the metal-substituted ring, values of $\delta r$ range from 0.015 to 0.019. This indicates that in both substituted rings a slight degree of quinoid character is present. This supports the idea that the metal-containing group acts as an electroactive substituent. The electron donating $NMe_2$ substituent present in **1**, however, seems to induce more quinoid character in the R′ phenyl ring because a value of $\delta r$ = 0.025 in residue 1 and 2 is found. The larger contribution into the quinoid character induced by the $NMe_2$ group was also reported by others.[66] The effect of the $NMe_2$ group seems to oppose that of the metal substituent in **1** because a smaller alternation in the bond length ($\delta r$ = 0.009 and 0.013 for residue 1 and 2, respectively) occurs here relative to that of **2**, **5**, **6** and **7**.

## NMR Spectroscopy

Solutions of **1**–**7** in $CD_2Cl_2$ (0.01 M) were studied by $^1H$, $^{13}C\{^1H\}$ and $^{195}Pt\{^1H\}$ NMR spectroscopy. In the $^1H$ NMR spectra, resonances for the $(CH_3)_2N$ and the $ArCH_2N$ protons of the $CH_2NMe_2$ substituents were observed at $\delta$ = 3.04–3.05 ppm and at $\delta$ = 4.02–4.08 ppm, respectively, and showed characteristic satellites resulting from platinum coupling [$^3J$(H,Pt) ≈ 37 and 46 Hz, respectively]. For compounds **1**, **2** and **4**–**7**, characteristic resonances of the vinylic protons were observed at $\delta$ = 6.8–7.2 ppm with large coupling constants [$^3J$(H,H) = 16 Hz] indicative of a *trans* configuration. For **3**, the chemical shift difference between the vinylic protons was so small that the coupling was not resolved in the higher order pattern.

In the $^{13}C\{^1H\}$ NMR spectra of some of the compounds, a two [$^2J$(C,Pt) = 62–67 Hz] or three bond coupling [$^3J$(C,Pt) = 35–37 Hz] of platinum to carbon was observed. A linear correlation was found ($R^2$ = 0.9842) when the $^{13}C\{^1H\}$ NMR chemical shift of the $C_{ipso}$ (to platinum; Table 3) of **1**–**7** was plotted against the Hammett $\sigma_p$ parameter of the *para* R′ substituents (Figure 7), which suggests that the effect on the electronic character of the conjugated molecule induced by the different *para* substituents can be experienced within the complete system. A previous correlation study on *para*-substituted stilbenoid ferrocene analogues showed a similar substituent effect[67] when the $^{13}C\{^1H\}$ NMR chemical shift of the ferrocenyl carbons was plotted against the Hammett $\sigma_p$ parameter.

 © 2007 Wiley-VCH Verlag GmbH & Co. KGaA, Weinheim 

Table 3. NMR spectroscopic data of [PtCl{NCN($C_2H_2C_6H_4$-R′-4′)-4}] (**1**–**7**).[a]

| Compound | $\sigma_p$ Hammett[b] | $\delta = {}^{13}C\{^1H\}$ [ppm][c] | $\delta = {}^{195}Pt\{^1H\}$ [ppm][d] |
|---|---|---|---|
| **1** (R = $NMe_2$) | –0.83 | 145.6 | –3173 |
| **2** (R = OMe) | –0.27 | 146.7 | –3164 |
| **3** (R = $SiMe_3$) | –0.07 | 147.1 | –3160 |
| **4** (R = H) | 0.00 | 147.0 | –3158 |
| **5** (R = I) | 0.18 | 147.5 | –3149 |
| **6** (R = CN) | 0.66 | 148.6 | –3138 |
| **7** (R = $NO_2$) | 0.78 | 149.1 | –3133 |

[a] 0.01 M solution in $CD_2Cl_2$. [b] Obtained from Ref.[25] [c] Chemical shift of $C_{ipso}$ to Pt. [d] $Na_2PtCl_6$ as external reference.

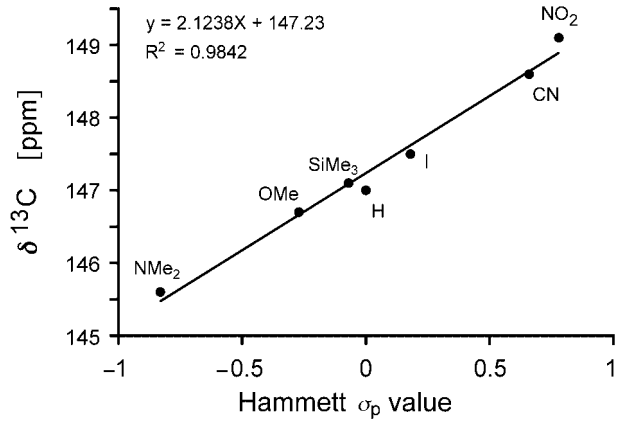


Figure 7. Hammett correlation of the $^{13}C\{^1H\}$ $C_{ipso}$ NMR chemical shift of **1**–**7**.

The electron density at the metal centre of complexes **1**–**7** was probed with $^{195}Pt\{^1H\}$ NMR spectroscopy. The sensitivity of the $^{195}Pt$ nucleus towards changes in, for instance, the geometry and the oxidation state of the metal centre or changes in the electronic nature of the surrounding ligands, is reflected in the $^{195}Pt\{^1H\}$ NMR chemical shift.[68] For **1**–**7**, that is, upon going through the series from an electron-donating ($NMe_2$) to an electron-accepting ($NO_2$) *para* substituent, the $^{195}Pt\{^1H\}$ NMR chemical shift moves to a higher frequency, which points to a less-shielded platinum nucleus (Table 3). A plot of the $^{195}Pt\{^1H\}$ NMR chemical shift against the Hammett $\sigma_p$ parameter resulted in a good linear correlation ($R^2$ = 0.9604, Figure 8). The results show the power of the $^{195}Pt\{^1H\}$ NMR chemical shift as a qualitative probe for the electronic character of the molecule (including $C_{ipso}$) to which the metal is connected. The slope of the line provides information about the efficiency of communication between the substituent and the metal centre, and therefore, it was compared with the slope of a similar graph from an earlier study in which the $^{195}Pt\{^1H\}$ NMR shift of *para*-functionalized phenyl pincers [PtCl(NCN–R-4)] was correlated with the Hammett $\sigma_p$ parameter.[23] Indeed, the slope of 25 in the present study found for the stilbenoid NCN-pincer platinum compounds is less steep relative to the 171 found for the [PtCl(NCN–R-4)] compounds earlier. This smaller number is in agreement with the larger size of the π system in **1**–**7**, over which the effect of the 4-R′ group to the 4-PtCl grouping is spread out.

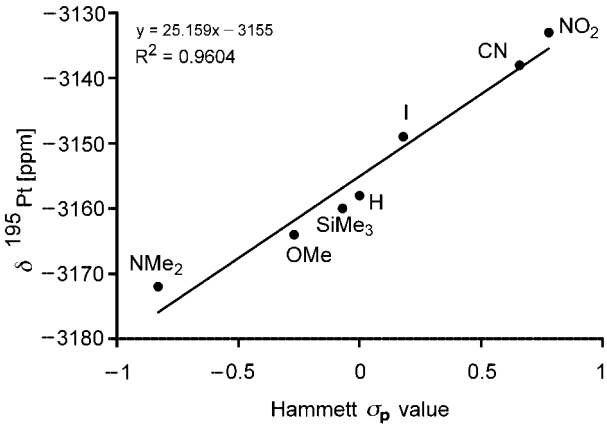


Figure 8. Hammett correlation of the $^{195}Pt\{^1H\}$ NMR chemical shift of **1**–**7**.

As pointed out above, the compounds in solution do undergo *trans–cis* isomerization when exposed to light.[6] Irradiation of a $CD_2Cl_2$ solution of **7** ($9.5\times10^{-3}$ M, $\lambda_{ex}$ = 365 nm) for 2 h resulted in a *trans–cis* mixture. After 1 h, the photostationary state of the isomerization reaction was reached, and a *trans–cis* ratio of exactly 1:1 was observed. In the $^1H$ NMR spectrum, the formation of the *cis* isomer could be observed by the appearance of new peaks for all the protons (Figure 9). The doublets at $\delta$ = 6.65 ppm and $\delta$ = 6.53 ppm are assigned to the *cis* protons of the ethylene bridge which have a characteristic *cis* coupling constant, $^3J$(H,H) = 12 Hz. Recently, this in-solution *trans–cis* isomerization process was also observed by others in a study of cyclometallated $Pt^{II}$ complexes containing substituted 4-styryl-2-phenylpyridine ligands.[69]

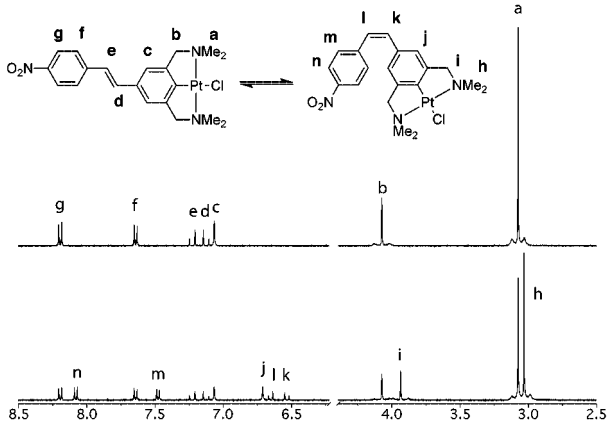


Figure 9. $^1H$ NMR spectra of **7**, before (top; only *trans*) and after (bottom; *trans–cis* mixture) UV irradiation (400 MHz, $CD_2Cl_2$, $9.5\times10^{-3}$ M; $\lambda_{ex}$ = 365 nm, 1 h).

## UV/Vis Spectroscopy

The complexes are well soluble in dichloromethane, but their solubility decreases in solvents like diethyl ether,

 © 2007 Wiley-VCH Verlag GmbH & Co. KGaA, Weinheim 

Table 4. UV/Vis maxima ($\lambda_{max}$) of [PtCl{NCN($C_2H_2C_6H_4$-R′-4′)-4}] (**1**–**7**).[a]

| Solvent | **1** (R = $NMe_2$) | **2** (R = OMe) | **3** (R = $SiMe_3$) | **4** (R = H) | **5** (R = I) | **6** (R = CN) | **7** (R = $NO_2$) |
|---|---|---|---|---|---|---|---|
| Acetonitrile | 366 | 348 | 341 | 347 | 355 | 369 | 402 |
| Dichloromethane | – | 244 (10.9) | 245 (12.4) | 245 (10.8) | 249 (8.2) | 264 (13.1) | 298 (10.7) |
| | 371 (36.9)[b] | 352 (30.6) | 355 (36.0) | 350 (35.6) | 358 (37.3) | 376 (29.4) | 413 (20.6) |
| Tetrahydrofuran | 369 | 353 | 360 | 354 | 363 | 380 | 415 |
| Ethyl acetate | 367 | 352 | 356 | 351 | 361 | 379 | 413 |
| Diethyl ether | 366 | 352 | 357 | 351 | 361 | 376 | 411 |

[a] Absorption wavelength [nm] at room temperature ($c \approx \cdot 10^{-5}$ M), absorption coefficient $\varepsilon$ [$10^3$ $M^{-1}$ $cm^{-1}$] in brackets. [b] Higher energy absorption band not observed.

whereas they are insoluble in cyclohexane. As a result of this restricted solubility, the absorption coefficients of the complexes were only determined in dichloromethane. The absorption spectra for **1**–**7** (Figure 10, Table 4) show a weak band between 244 and 298 nm (not observed for **1**) that originates from the excitation of the singlet ground state ($S_0$) to a higher excited state (e.g. $S_0 \rightarrow S_2$).[1] A more intense lower energy band ($S_0$–$S_1$) is observed in the range of 341 to 415 nm. The position of this band shifts to lower energy with increasing acceptor strength, that is by going from **4** (R′ = H) to **7** (R′ = $NO_2$). Therefore, in the presence of an acceptor functionality, this transition involves intramolecular charge transfer (ICT) in which the NCN–PtCl fragment, as anticipated, behaves as a donor functionality. The observed bathochromic shift is in agreement with calculated charge-transfer properties of 4,4′-substituted donor–acceptor stilbenes,[70] where an increase in the donor–acceptor strength causes the HOMO–LUMO distance of the molecule to decrease, which results in an absorption at lower wavelength. A change in the donor properties of R′ by going through the series from **4** to **1** only slightly affects the absorption maximum ($\lambda_{max}$) of the compounds.

For comparison of **1**–**7** with organic 4,4′-substituted donor–acceptor stilbene analogues, DANS was used as a reference system. In Figure 10 it can be seen that the absorption maxima of **7** and DANS are slightly shifted with respect to each other, which reflects the different nature of the PtCl grouping versus the $NMe_2$ group. Moreover, the absorption measurements of complexes **1**–**7** in different solvents showed no distinct solvent polarity dependence (Table 4), as was reported previously for the organic stilbene analogues,[71,72] which points to a nonpolar ground state of the stilbenoid NCN–Pt compounds.

A qualitative screening of the luminescence of solutions of **1**–**7** in dichloromethane by use of a standard laboratory UV-lamp ($\lambda$ = 365 nm) revealed that, surprisingly, both the 4-donor–4′-donor complex **1** and complexes **6** and **7** with a strong donor–acceptor combination are luminescent. Therefore, these complexes were further studied for their photophysical properties by determination of the fluorescence maxima ($\lambda_{fl}$), quantum yields ($\Phi_{fl}$) and excited state lifetimes ($\tau_{fl}$). From this data, the radiative ($k_r$) and nonradiative ($k_{nr}$) decay constants were calculated. Complexes **2**–**4** showed no luminescence, and complex **5** showed only very weak luminescence, which was too weak to be studied in more detail.

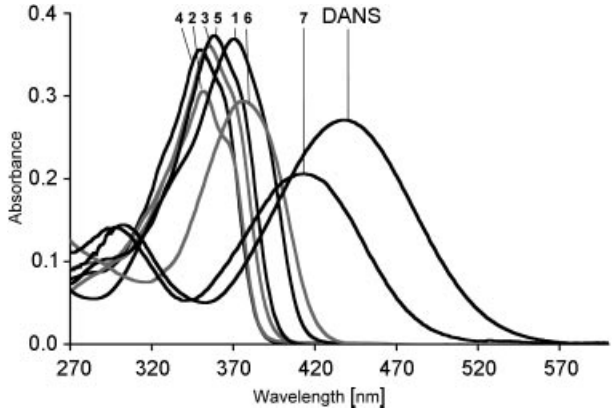


Figure 10. UV/Vis spectra of **1**–**7** in $CH_2Cl_2$. Most intense band, from left to right: R′ = H (**4**), OMe (**2**), $SiMe_3$ (**3**), I (**5**), $NMe_2$ (**1**), CN (**6**), $NO_2$ (**7**) and DANS.

For complexes **1**, **6** and **7**, the emission spectra and excited state lifetimes were recorded in solvents of different polarity (Tables 5 and 6). For all compounds, a bathochromic shift in the emission maximum with an increase in solvent polarity was observed, as is displayed for **6** in Figure 11. The occurrence of this positive solvatochromism, which is the most extensive for **7**, reflects the formation of a charge-separated or dipolar-excited state.

Table 5. Fluorescence data of **1**.

| | [PtCl{NCN($C_2H_2C_6H_4$-$NMe_2$-4′)-4}] (**1**) | | | | |
|---|---|---|---|---|---|
| Solvent | $\lambda_{fl}$ [nm][a] | $\Phi_{fl}$ | $\tau_{fl}$ [ps][b] | $k_r$ [$\cdot 10^7$ $s^{-1}$] | $k_{nr}$ [$\cdot 10^9$ $s^{-1}$] |
| Acetonitrile | 454 | 0.017 | 289 | 5.9 | 3.4 |
| Dichloromethane | 432 | 0.006 | 307 | 2.0 | 3.2 |
| Tetrahydrofuran | 429 | 0.003 | 537 | 0.6 | 1.9 |
| Ethyl acetate | 427 | 0.002 | 463 | 0.4 | 2.2 |
| Diethyl ether | 425 | 0.002 | [c] | | |

[a] Excitation wavelength 370 nm, argon flushed solutions at room temperature, $c \approx \cdot 10^{-6}$ M. [b] Only the values for the slowest component of the biexponential decay curve are reported as the fast component showed values below the detection limit of the setup that was used (<47 ps). [c] Solubility too low to allow measurements.

When the Stokes shift $\nu_{abs}$–$\nu_{fl}$ is plotted versus the solvent polarity parameter $\Delta f$ (defined by the solvent dielectric constant $\varepsilon$ and the refractive index $n$[73]) the difference between the ground and excited state dipole moments $\Delta\mu$ for

 © 2007 Wiley-VCH Verlag GmbH & Co. KGaA, Weinheim 

Table 6. Fluorescence data of **6** and **7**.

| Solvent | [PtCl{NCN($C_2H_2C_6H_4$-CN-4′)-4}] (**6**) | | | | | [PtCl{NCN($C_2H_2C_6H_4$-$NO_2$-4′)-4}] (**7**) | | | | |
|---|---|---|---|---|---|---|---|---|---|---|
| | $\lambda_{fl}$[a] [nm] | $\Phi_{fl}$ | $\tau_{fl}$ [ps] | $k_r$ [$\cdot 10^8$ $s^{-1}$] | $k_{nr}$ [$\cdot 10^9$ $s^{-1}$] | $\lambda_{fl}$[a] [nm] | $\Phi_{fl}$ | $\tau_{fl}$ [ps] | $k_r$ [$\cdot 10^8$ $s^{-1}$] | $k_{nr}$ [$\cdot 10^9$ $s^{-1}$] |
| Acetonitrile | 476 | 0.065 | 271 | 2.4 | 3. 5 | 628 | 0.043 | 343 | 1.3 | 2.8 |
| Dichloromethane | 466 | 0.088 | 206 | 4.3 | 4.4 | 677 | 0.018 | 134 | 1.3 | 7.3 |
| Tetrahydrofuran | 464 | 0.080 | 174 | 4.6 | 5.3 | 592 | 0.042 | 278 | 1.5 | 3.5 |
| Ethyl acetate | 458 | 0.067 | 137 | 4. 9 | 6.8 | 591 | 0.068 | 291 | 2.3 | 3.2 |
| Diethyl ether | 443 | 0.023 | 61 | 3.8 | 16.0 | 546 | 0.197 | 573 | 3.4 | 1.4 |

[a] Excitation wavelength 370 nm, argon flushed solutions at room temperature, $c \approx \cdot 10^{-6}$ M.

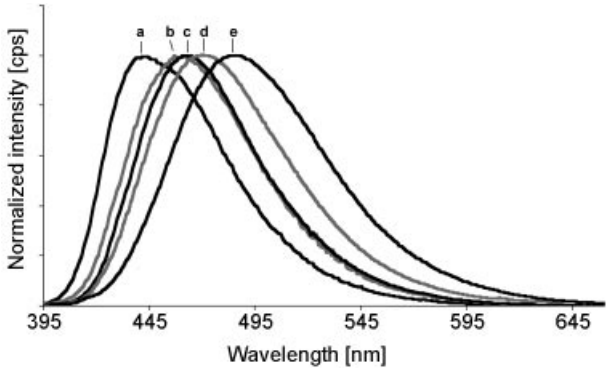


Figure 11. Normalized emission spectra of **6** in different solvents; they show a bathochromic shift with an increase in solvent polarity. Polarity increases from left to right; diethyl ether (a), ethyl acetate (b), tetrahydrofuran (c), dichloromethane (d) and acetonitrile (e).

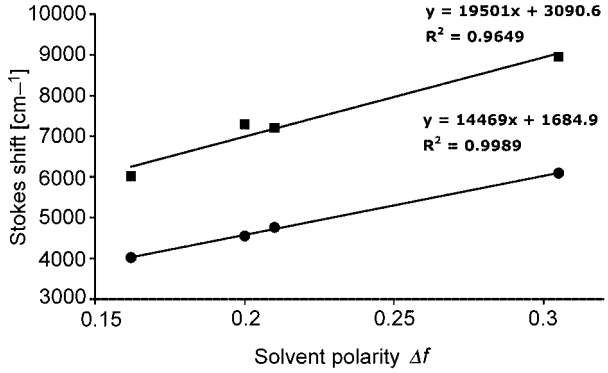


Figure 12. Lippert plot of the Stokes shift versus the solvent polarity parameter $\Delta f$ for **6** (dots) and **7** (squares).

donor–acceptor systems can be approximated by using the Lippert equation [Equation (1)][74]

$$\nu_{abs} - \nu_{fl} = \frac{2\Delta\mu^2}{hc\rho^3}\Delta f + \text{constant}$$

$$\Delta f = \frac{\varepsilon - 1}{2\varepsilon + 1} - \frac{n^2 - 1}{2n^2 + 1} \quad (1)$$

where $h$ is Planck's constant and $c$ is the speed of light. The $\rho$ (Onsager cavity radius) of the molecule can be estimated by numerous methods,[75,76] and in this study the radii of molecules **6** and **7** were estimated from their solid-state structures (estimated to be 4.36 and 4.39 Å, respectively).[77,78]

From the slopes derived from the Lippert plot of **6** and **7** (the values in dichloromethane were excluded from the trend line, Figure 12), $\Delta\mu$ was estimated to be 11 and 13 D, respectively. This implies that in these systems, excited state charge separation is present but to a lesser extent than that found for related 4,4′-substituted stilbenes.[79] The larger dipole moment found for **7** is a result of the stronger electron accepting nitro group.

The excited state behaviour of 4,4′-substituted organic stilbenes has been studied intensively.[8,80–86] For the excited state of the molecule, a three-state kinetic scheme is suggested (Scheme 4).[86] The ground state molecule (E) can be excited into the emissive state E* (planar geometry) in which the molecule is suggested to have biradicaloid character. Emissive relaxation to the ground state from E* is accompanied by two competing relaxation pathways. One proceeds through the nonemissive "phantom-singlet state" (P*), in which the molecule assumes a twisted conformation (double bond twist, including the *trans–cis* isomerization process),[6] also referred to as the photochemical funnel toward the ground state. The alternative follows a pathway which involves rotation about a bond between the aromatic moiety and the central double bond and ends up in a twisted intramolecular charge transfer state A* (TICT state), which is considered to be responsible for the main

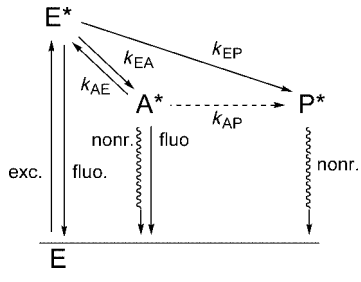


Scheme 4. The three-state kinetic scheme proposed for the relaxation of 4,4′-substituted organic stilbenes after excitation.

 © 2007 Wiley-VCH Verlag GmbH & Co. KGaA, Weinheim 

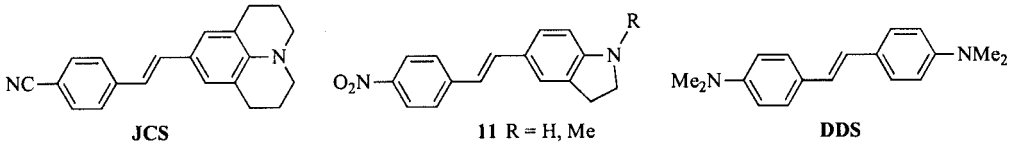


Figure 13. Donor–acceptor stilbenes **JCS** and **11**, donor–donor stilbene **DDS**.

part of the emission. The photophysics of the molecule are dependent on the relative energy of the three different energy states, which are influenced by the solvent polarity and by the donor–acceptor strength of the substituents.

For 4,4′-substituted organic stilbenes in which the donor substituent is an alkylamino group, the TICT state can be reached by a single bond twist about the single bond between the alkylamino group and the aromatic ring or by a twist about the single bond between the anilino group and the double bond. To exclude the alkylamino TICT state, other groups developed and studied the more rigid amino substituted donor–acceptor stilbenes **JCS**[84] and **11**[72] (Figure 13). In our study, the excited state behaviour of **6** and **7** will be compared with that of **JCS** and **11**, respectively, with regard to the NCN–PtCl fragment of **6** and **7** as the rigid donor fragment. So far, we were not able to find a rigid reference system for **1** in the literature; therefore, it was compared with **DDS**[82] (Figure 13), which contains two $NMe_2$ groups.

The fluorescence quantum yields of **1** range from 0.002 to 0.017, and they are remarkably low relative to the values found for **DDS** (ranging from 0.39 to 0.57). Presumably, the presence of the NCN–PtCl fragment favours nonradiative decay by accelerating intersystem crossing. The fluorescence quantum yields of **1** slightly increase with increasing solvent polarity (Table 5), which is probably due to stabilization of the A* state with increasing solvent polarity.[82,87] The fluorescence lifetimes of **1** at room temperature, which were derived from a biexponential decay curve (Table 5; only the slower components of the decay curves are reported here, ranging from 289 to 537 ps), decrease with increasing solvent polarity and are shorter than the value found for **DDS** (900 ps in ethanol at 300 K). It must be noted that the nonradiative decay rates [$k_{nr} = (1 - \Phi_{fl})/\tau_{fl}$] increase with increasing solvent polarity. In more polar solvents, the low-lying A* state is increasingly populated, and the smaller energetic distance to the ground state favours nonradiative decay.

For **6**, an increase in the quantum yield and the lifetime is observed when the polarity of the solvent increases, which can be explained by the dipolar character of the states involved. Both E* and A* are highly polar, with an increased dipole moment for A*; P* has weak or nonpolar properties.[83] Therefore, an increase in the solvent polarity stabilizes E* and A*, and to a much lesser extent P*. As a result, the nonradiative decay, which is governed by the access to P*, becomes less important. For **6**, indeed a decrease in $k_{nr}$ with increasing solvent polarity is found. This is in agreement with what was found for **JCS**,[83,84] for which the yield of the nonradiative decay also decreases with increasing solvent polarity.

For **7**, a reverse dependency of the fluorescence lifetime and quantum yield on the solvent polarity was found. Roughly, an increase in the fluorescence quantum yield and the fluorescence lifetime was observed when the solvent polarity decreases. The remarkable change in the photophysical properties accompanying the change of a cyano group to a nitro group was studied intensively,[72] and the change is also found for **11**. As a consequence of its larger dipole moment, an increase in the solvent polarity results in a decreased energy level of the A* state of **7**. The lower energy minimizes the distance from A* to the ground state and causes radiationless decay from A* to compete with fluorescence. As a result from the energetically low-lying A* state, the P* level plays no significant role, and therefore, relaxation proceeds primarily by way of the A* state.

## Conclusions

A useful and efficient synthetic route towards electronically tunable organometallic stilbenes based on a series of stilbenoid NCN–$Pt^{II}$ pincers is reported. The *trans* configuration of the complexes is maintained in the solid state, but in solution they undergo *trans–cis* isomerization upon exposure to light. The physical data reported for compounds **1**–**7** reflect that a substituent effect can be experienced within the complete delocalized π-system. The linear correlation found between the $^{13}C\{^1H\}$ and $^{195}Pt\{^1H\}$ NMR chemical shifts and the Hammett $\sigma_p$ value indicates that the metal is sensitive to the change in the electronic properties of the delocalized π-system. In this way the metal centre can communicate with a substituent that is situated quite a distance from itself. Therefore, we can regard the platinum centre as a probe by using the $^{195}Pt\{^1H\}$ NMR chemical shift data as a readout for the electronic properties of a conjugated system that is connected to it. The UV/Vis and fluorescence study show that the NCN–PtCl fragment can be qualitatively regarded as an electron-donating group. From the low quantum yields and fast decay rates, it can be concluded that the presence of the platinum centre favours nonradiative decay when compared with the organic stilbene analogues.

## Experimental Section

**General**: All reactions involving air- or moisture-sensitive reagents were performed by using standard Schlenk techniques unless stated otherwise. Light-sensitive compounds and solutions were protected from the light with the use of aluminium foil. Pentane, THF and $Et_2O$ were distilled from Na/benzophenone, $CH_2Cl_2$ was distilled

 © 2007 Wiley-VCH Verlag GmbH & Co. KGaA, Weinheim 

from $CaH_2$ and triethylamine was distilled from KOH prior to use. The platinum precursor $[Pt(p\text{-tol})_2(SEt_2)]_2$,[88,89] [PtBr(NCN–CHO-4)],[90] trimethyl(*p*-tolyl)silane[91] and the respective *para*-substituted diethyl benzylphosphonates **8b**–**g** were prepared according to published procedures of which the benzylic bromination step was performed according to the published procedure of Amijs and coworkers.[39] All other reagents were commercially available and used without further purification. $^1H$ and $^{13}C\{^1H\}$ NMR spectra were recorded at 25 °C with a Bruker AC 300 NMR or Varian Inova 300 or Varian 400 spectrometers, chemical shifts are reported relative to residual solvent resonances. $^{195}Pt\{^1H\}$ NMR spectra were recorded with a Varian Inova 300 MHz NMR spectrometer, referenced to external $Na_2PtCl_6$ (1 M in $D_2O$, $\delta$ = 0 ppm).[92] Elemental analyses were performed by Kolbe, Mikroanalytisches Laboratorium (Mülheim a.d. Ruhr, Germany). ES-MS spectra were obtained from the Biomolecular Mass Spectrometry Group at the Utrecht University. Infrared spectra were recorded with a Perkin–Elmer Spectrum 1 FTIR spectrometer. UV spectra were collected with Cary 1 or Cary 5 spectrophotometers in spectrophotomeric-grade solvents. Fluorescence emission spectra were obtained with a Spex Fluorolog instrument, equipped with a Spex 1680 double excitation monochromator, a Spex 1681 emission monochromator and a Spex 1911F detector. Fluorescence spectra were corrected for the detector spectral response with the aid of a correction file provided by the manufacturer. Fluorescence quantum yields were determined relative to 9,10-diphenylanthracene ($\Phi_{fl}$ = 0.90, excitation wavelength 370 nm).[93] Solvents used for fluorescence measurements were of spectrophotometric grade (Acros). Lifetime measurements were performed with the use of a Pico Quant PDL 800-B laser as the excitation source ($\lambda_{exc}$ = 406 nm, 55 ps pulse width, 2.5–40 MHz repetition rate). The luminescence was collected through a focusing lens, filtered through a crossed polarizer and a combination of suitable optical cut-off filters, dispersed by a 0.1 m monochromator (1350 lines mm$^{-1}$ grating, blazed at 500 nm) and detected by a fast Hamamatsu photomultiplier tube (PMT) (H5738P-01). The PMT signal was amplified by an inverting preamplifier (PAM-102-T – PicoQuant) and used as the start input for a Time Harp 200 multichannel computer card, which was synchronized with the laser pulse by the stop input. The decay curves were obtained by time-correlated single photon counting (TCPCS) by time-to-amplitude conversion (TAC). The ratio of stop to start pulses was kept low (below 0.04) to assure good statistics. The instrument response function (IRF) was measured by using a dilute suspension of silica particles (LUDOX) as the scattering medium and the same experimental conditions used for the fluorescence decay measurements. The raw data was deconvoluted from the IRF and analyzed by fluorescence decay analysis software (Fluofit 3.3). The instrumental resolution was 30 ps (10% of the IRF FWHM).

**Diethyl 4-Dimethylaminobenzylphosphonate (8a):** At 0 °C, methanesulfonyl chloride (0.54 mL, 6.98 mmol) was added dropwise to a solution of 4-dimethylaminobenzyl alcohol (1.0 g, 6.61 mmol) and triethylamine (1.12 mL) in dichloromethane (20 mL). After complete addition, the solution was warmed to room temperature for 1 h. Next, all volatiles were evaporated, and triethylphosphite (4 mL) and NaI (400 mg, 2.67 mmol) were added to the oily residue. The mixture was heated at 110 °C for 2.5 h after which the excess triethylphosphite was distilled off in vacuo. At room temperature, water (10 mL) and ethyl acetate (20 mL) were subsequently added to the residue. The organic layer was separated, washed with saturated $NaHCO_3$ (5 mL) and NaCl solution (5 mL), and dried using $Na_2SO_4$. After evaporation and Kügelrohr distillation, an oily product (0.9 g) was obtained. Further purification of the product could be achieved by column chromatography [neutral $Al_2O_3$, hexane/ethyl acetate (9:1), then gradient elution increasing to pure ethyl acetate] and **8a** (455 mg, 1.68 mmol, 25%) was isolated as an oil. $^1H$ NMR (300 MHz, $C_6D_6$): $\delta$ = 7.29 [dd, $^3J$(H,H) = 8.9 Hz, $^4J$(H,H) = 2.5 Hz, 2 H, ArH], 6.57 [d, $^3J$(H,H) = 8.5 Hz, 2 H, ArH], 3.89 (m, 4 H, $OCH_2$), 3.02 [d, $^2J$(H,P) = 20.9 Hz, 2 H, $CH_2P$], 2.49 [s, 6 H, $N(CH_3)_2$], 0.97 [t, $^3J$(H,H) = 7.1 Hz, 6 H, $CH_3$] ppm. $^{13}C\{^1H\}$ NMR (75 MHz, $C_6D_6$): $\delta$ = 149.8, 130.8 [d, $J$(C,P) = 6.5 Hz], 119.7 [d, $J$(C,P) = 9.3 Hz], 113.0, 61.7 [d, $J$(C,P) = 6.5 Hz], 40.2, 33.1 [d, $J$(C,P) = 139.5 Hz, $CH_2P$], 16.5 [d, $J$(C,P) = 5.4 Hz] ppm. IR (ATR): $\tilde{\nu}$ = 2980, 2906, 2801, 1736, 1615, 1567, 1521, 1479, 1445, 1391, 1348, 1243, 1201, 1191, 1163, 1097, 1052, 1022, 945, 847, 822, 774, 731, 717, 689 cm$^{-1}$. MS (ES+, $CH_2Cl_2$): $m/z$ = 272.15 $[M + H]^+$. $C_{13}H_{22}NO_3P$ (271.30): calcd. C 57.55, H 8.17, N 5.16; found C 57.42, H 8.24, N 5.09.

**[PtCl(NCN–CHO-4)] (9):** [PtBr(NCN–CHO-4)] (1.19 g, 2.40 mmol) in wet acetone (10 mL) was treated with $AgBF_4$ (0.49 g, 2.52 mmol) for 1 h, and the formed precipitate was filtered through Celite. To the filtrate, a solution of NaCl (1.4 g, 23 mmol) in demineralized water (2 mL) was added, and the mixture was stirred for 1.5 h after which all the volatiles were removed in vacuo. After the addition of demineralized water (15 mL) and $CH_2Cl_2$ (15 mL), the mixture was filtered through Celite. The residue was extracted with dichloromethane (3 × 15 mL) after which the organic fraction of the filtrate was separated. The organic fraction was dried with $MgSO_4$, filtered and concentrated in vacuo to yield the crude product as a solid. Purification by column chromatography ($CH_2Cl_2$/MeOH, 9:1, $SiO_2$) yielded **9** (0.86 g, 1.91 mmol, 80%) as a light yellow solid. $^1H$ NMR (300 MHz, $CD_2Cl_2$): $\delta$ = 9.82 (s, 1 H, CHO), 7.32 (s, 2 H, ArH), 4.08 [s, $^3J$(H,Pt) = 46.2 Hz, 4 H, $CH_2$], 3.05 [s, $^3J$(H,Pt) = 38.2 Hz, 12 H, $CH_3$] ppm. $^{13}C\{^1H\}$ NMR (75 MHz, $CD_2Cl_2$): $\delta$ = 192.0 (CHO), 157.5 ($C_{ipso}$ to Pt), 144.7 ($C_{ortho}$ to Pt), 133.4, 121.4 [$^3J$(C,Pt) = 35.6 Hz; $C_{meta}$ to Pt], 77.3 [$^2J$(C,Pt) = 61.0 Hz; $NCH_2$], 54.5 [$N(CH_3)_2$] ppm. $^{195}Pt\{^1H\}$ NMR (64 MHz, $CD_2Cl_2$): $\delta$ = –3068 ppm. IR (ATR): $\tilde{\nu}$ = 3017, 2980, 2929, 1674 (C=O), 1398, 737 cm$^{-1}$. MS (ES+, $CH_3CN$): $m/z$ = 455.14 $[M - Cl + CH_3CN]^+$, 414.10 $[M - Cl]^+$. $C_{13}H_{19}ClN_2OPt$ (449.84): calcd. C 34.71, H 4.26, N 6.23; found C 34.80, H 4.19, N 6.17.

**General Procedure for the Preparation of Stilbenoid Pincer Compounds 1–7:** In a dry Schlenk tube, *para*-aldehyde substituted pincer platinum derivative **9** and the appropriate phosphonate ester **8** were dissolved in dry degassed THF (10–15 mL). While stirring, *t*BuOK (2.5 equiv.) was added to the reaction mixture, under a nitrogen outflow, which directly caused a strong colour change of the reaction mixture. Upon completion of the reaction, monitored by TLC, the mixture was quenched at 0 °C by the addition of ice and an aqueous NaCl solution (to prevent halogen abstraction on the Pt centre). The formed precipitate was isolated by filtration through a glass filter. The residue was dissolved in dichloromethane, dried with $MgSO_4$, filtered and evaporated to leave the crude product. The crude product was purified by precipitation out of a small amount of dichloromethane by the addition of pentane.

**[PtCl{NCN($C_2H_2C_6H_4$-$NMe_2$-4′)-4}] (1):** Diethyl 4-dimethylaminobenzylphosphonate (**8a**; 100 mg, 0.369 mmol), **9** (150 mg, 0.334 mmol). Product isolated as a pale yellow powder (171 mg, 0.302 mmol, 90%). $^1H$ NMR (300 MHz, $CD_2Cl_2$): $\delta$ = 7.37 [d, $^3J$(H,H) = 8.8 Hz, 2 H, ArH], 6.97 [d, $^3J$(H,H) = 16.2 Hz, 1 H, *trans* CH=CH], 6.96 (s, 2 H, ArH), 6.81 [d, $^3J$(H,H) = 16.8 Hz, 1 H, *trans* CH=CH], 6.70 [d, $^3J$(H,H) = 8.8 Hz, 2 H, ArH], 4.02 [s, $^3J$(H,Pt) = 46.2 Hz, 4 H, $CH_2$], 3.04 [s, $^3J$(H,Pt) = 37.9 Hz, 12 H, $CH_3$], 2.96 (s, 6 H, $CH_3$) ppm. $^{13}C\{^1H\}$ NMR (75 MHz, $CD_2Cl_2$): $\delta$ = 150.4 [Ar*C*N$(CH_3)_2$], 145.6 ($C_{ipso}$ to Pt), 144.2, 134.0, 127.4, 126.5, 126.2, 125.8, 117.6 [$^3J$(C,Pt) = 34.9 Hz; $C_{meta}$ to Pt], 112.8,

 © 2007 Wiley-VCH Verlag GmbH & Co. KGaA, Weinheim 

77.9 [$^2J$(C,Pt) = 66.5 Hz; $CH_2N$], 54.6 [$CH_2N(CH_3)_2$], 40.6 [$ArN(CH_3)_2$] ppm. $^{195}Pt\{^1H\}$ NMR (64 MHz, $CD_2Cl_2$): $\delta$ = –3173 ppm. IR (ATR): $\tilde{\nu}$ = 3009, 2978, 2916, 2797, 1604, 1520, 1448, 1351, 1271, 1217, 1187, 1167, 1157, 1127, 1084, 1060, 1041, 944, 880, 835, 808, 706 $cm^{-1}$. MS (ES+, $CH_3CN/CH_2Cl_2$): *m/z* = 566.17 $[M]^+$, 531.19 $[M – Cl]^+$. $C_{22}H_{30}ClN_3Pt$ (566.18): calcd. C 46.60, H 5.33, N 7.41; found C 46.68, H 5.31, N 7.36.

**[PtCl{NCN($C_2H_2C_6H_4$-OMe-4′)-4}] (2):** Diethyl 4-methoxybenzylphosphonate (**8b**; 126 mg, 0.488 mmol), **9** (200 mg, 0.445 mmol). Product isolated as a yellow powder (132 mg, 0.238 mmol, 53%). $^1H$ NMR (300 MHz, $CD_2Cl_2$): $\delta$ = 7.43 [d, $^3J$(H,H) = 8.8 Hz, 2 H, ArH], 7.00 [d, $^3J$(H,H) = 16.2 Hz, 1 H, *trans* CH=CH], 6.97 (s, 2 H, ArH), 6.88 [d, $^3J$(H,H) = 8.8 Hz, 2 H, ArH], 6.87 [d, $^3J$(H,H) = 16.2 Hz, 1 H, *trans* CH=CH], 4.08 [s, $^3J$(H,Pt) = 45.9 Hz, 4 H, $CH_2$], 3.81 (s, 3 H, $OCH_3$), 3.05 [s, $^3J$(H,Pt) = 37.0 Hz, 12 H, $CH_3$] ppm. $^{13}C\{^1H\}$ NMR (75 MHz, $CD_2Cl_2$): $\delta$ = 159.4 (Ar*C*OMe), 146.7 ($C_{ipso}$ to Pt), 144.2, 133.4, 131.0, 128.1, 127.5, 125.4, 117.6 [$^3J$(C,Pt) = 36.0 Hz; $C_{meta}$ to Pt], 114.4, 77.9 [$^2J$(C,Pt) = 62.1 Hz; $CH_2N$], 55.6 ($OCH_3$), 54.5 [$N(CH_3)_2$] ppm. $^{195}Pt\{^1H\}$ NMR (64 MHz, $CD_2Cl_2$): $\delta$ = –3164 ppm. IR (ATR): $\tilde{\nu}$ = 3003, 2973, 2921, 2838, 1625, 1604, 1572, 1509, 1451, 1297, 1252, 1174, 1109, 1083, 1029, 965, 881, 855, 833, 808, 734, 722, 705 $cm^{-1}$. MS (ES+, $CH_3CN$): *m/z* = 559.19 $[M – Cl + CH_3CN]^+$, 518.12 $[M – Cl]^+$. $C_{21}H_{27}ClN_2OPt$ (553.99): calcd. C 45.53, H 4.91, N 5.06; found C 45.46, H 4.87, N 4.88.

**[PtCl{NCN($C_2H_2C_6H_4$-SiMe$_3$-4′)-4}] (3):** Diethyl 4-trimethylsilylbenzylphosphonate (**8c**; 146 mg, 0.486 mmol), **9** (200 mg, 0.445 mmol). Product isolated as a pale white powder (230 mg, 0.386 mmol, 87%). $^1H$ NMR (300 MHz, $CD_2Cl_2$): $\delta$ = 7.50 [d, $^3J$(H,H) = 8.3 Hz, 2 H, ArH], 7.47 [d, $^3J$(H,H) = 8.3 Hz, 2 H, ArH], 7.05 (s, 2 H, ArH), 7.01 (s, 2 H, CH=CH), 4.04 [s, $^3J$(H,Pt) = 45.7 Hz, 4 H, $CH_2$], 3.05 [s, $^3J$(H,Pt) = 37.4 Hz, 12 H, $CH_3$], 0.272 [s, 9 H, $Si(CH_3)_3$] ppm. $^{13}C\{^1H\}$ NMR (75 MHz, $CD_2Cl_2$): $\delta$ = 147.1 ($C_{ipso}$ to Pt), 144.4, 139.8, 138.7, 134.1, 133.1, 130.5, 125.9, 125.7, 118.0 [$^3J$(C,Pt) = 34.9 Hz; $C_{meta}$ to Pt], 77.9 [$^2J$(C,Pt) = 64.3 Hz; $CH_2N$], 54.6 [$N(CH_3)_2$], –1.1 [$Si(CH_3)_3$] ppm. $^{195}Pt\{^1H\}$ NMR (64 MHz, $CD_2Cl_2$): $\delta$ = –3160 ppm. IR (ATR): $\tilde{\nu}$ = 3013, 2953, 1625, 1581, 1451, 1396, 1335, 1298, 1248, 1111, 1084, 1015, 964, 832, 804, 755, 719, 691, 670 $cm^{-1}$. MS (ES+, $CH_2Cl_2$): *m/z* = 596.21 $[M + H]^+$, 560.22 $[M – Cl]^+$. $C_{23}H_{33}ClN_2PtSi$ (596.14): calcd. C 46.34, H 5.58, N 4.70; found C 46.28, H 5.64, N 4.73.

**[PtCl{NCN($C_2H_2C_6H_5$)-4}] (4):** Diethyl benzylphosphonate (**8d**; 61 mg, 0.267 mmol), **9** (100 mg, 0.222 mmol). Product isolated as a pale white powder (92 mg, 0.176 mmol, 79%). $^1H$ NMR (300 MHz, $CD_2Cl_2$): $\delta$ = 7.49 [d, $^3J$(H,H) = 7.1 Hz, 2 H, ArH], 7.33 [t, $^3J$(H,H) = 7.1 Hz, 2 H, ArH], 7.23 [t, $^3J$(H,H) = 7.1 Hz, 1 H, ArH], 7.06 [d, $^3J$(H,H) = 15.9 Hz, 1 H, *trans* CH=CH], 7.01 [d, $^3J$(H,H) = 15.9 Hz, 1 H, *trans* CH=CH], 7.00 (s, 2 H, ArH), 4.04 [s, $^3J$(H,Pt) = 45.9 Hz, 4 H, $CH_2$], 3.05 [s, $^3J$(H,Pt) = 37.9 Hz, 12 H, $CH_3$] ppm. $^{13}C\{^1H\}$ NMR (75 MHz, $CD_2Cl_2$): $\delta$ = 147.0 ($C_{ipso}$ to Pt), 144.4, 138.3, 133.1, 130.3, 129.0, 127.4, 126.4, 125.8, 117.9 ($C_{meta}$ to Pt), 77.9 ($CH_2N$), 54.6 [$N(CH_3)_2$] ppm. $^{195}Pt\{^1H\}$ NMR (64 MHz, $CD_2Cl_2$): $\delta$ = –3158 ppm. IR (ATR): $\tilde{\nu}$ = 3018, 2973, 2920, 1625, 1581, 1496, 1450, 1334, 1300, 1085, 964, 831, 753, 708, 692 $cm^{-1}$. MS (ES+, $CH_3CN/CH_2Cl_2$): *m/z* = 529.18 $[M – Cl + CH_3CN]^+$, 488.12 $[M – Cl]^+$. $C_{20}H_{25}ClN_2Pt$ (523.96): calcd. C 45.85, H 4.81, N 5.35; found C 45.76, H 4.88, N 5.23.

**[PtCl{NCN($C_2H_2C_6H_4$-I-4′)-4}] (5):** Diethyl 4-iodobenzylphosphonate (**8e**; 86 mg, 0.243 mmol), **9** (100 mg, 0.222 mmol). Product isolated as a light yellow powder (123 mg, 0.189 mmol, 85%). $^1H$ NMR (300 MHz, $CD_2Cl_2$): $\delta$ = 7.66 [d, $^3J$(H,H) = 8.2 Hz, 2 H, ArH], 7.25 [d, $^3J$(H,H) = 8.2 Hz, 2 H, ArH], 7.04 [d, $^3J$(H,H) = 16.2 Hz, 1 H, *trans* CH=CH], 6.95 [d, $^3J$(H,H) = 16.2 Hz, 1 H, *trans* CH=CH], 6.99 (s, 2 H, ArH), 4.04 [s, $^3J$(H,Pt) = 45.1 Hz, 4 H, $CH_2$], 3.05 [s, $^3J$(H,Pt) = 37.4 Hz, 12 H, $CH_3$] ppm. $^{13}C\{^1H\}$ NMR (75 MHz, $CD_2Cl_2$): $\delta$ = 147.5 ($C_{ipso}$ to Pt), 144.4, 138.1, 138.0, 132.7, 131.2, 128.2, 124.6, 118.0 ($C_{meta}$ to Pt), 92.1, 77.9 ($CH_2N$), 54.6 [$N(CH_3)_2$] ppm. $^{195}Pt\{^1H\}$ NMR (64 MHz, $CD_2Cl_2$): $\delta$ = –3149 ppm. IR (ATR): $\tilde{\nu}$ = 3002, 2972, 2920, 1622, 1586, 1575, 1483, 1450, 1430, 1398, 1334, 1183, 1085, 1001, 967, 833, 806, 730, 711 $cm^{-1}$. MS (ES+, $CH_3CN/CH_2Cl_2$): *m/z* = 649.06 $[M]^+$, 614.10 $[M – Cl]^+$. $C_{20}H_{24}ClIN_2Pt$ (649.86): calcd. C 36.96, H 3.72, N 4.31; found C 37.04, H 3.78, N 4.28.

**[PtCl{NCN($C_2H_2C_6H_4$-CN-4′)-4}] (6):** Diethyl 4-cyanobenzylphosphonate (**8f**; 155 mg, 0.612 mmol), **9** (250 mg, 0.556 mmol). Product isolated as a yellow powder (275 mg, 0.501 mmol, 90%). $^1H$ NMR (300 MHz, $CD_2Cl_2$): $\delta$ = 7.61 [d, $^3J$(H,H) = 8.5 Hz, 2 H, ArH], 7.39 [d, $^3J$(H,H) = 8.3 Hz, 2 H, ArH], 7.15 [d, $^3J$(H,H) = 16.5 Hz, 1 H, *trans* CH=CH], 7.04 [d, $^3J$(H,H) = 16.5 Hz, 1 H, *trans* CH=CH], 7.02 (s, 2 H, ArH), 4.05 [s, $^3J$(H,Pt) = 45.6 Hz, 4 H, $CH_2$], 3.05 [s, $^3J$(H,Pt) = 37.7 Hz, 12 H, $CH_3$] ppm. $^{13}C\{^1H\}$ NMR (75 MHz, $CD_2Cl_2$): $\delta$ = 148.6 ($C_{ipso}$ to Pt), 144.5, 142.9, 134.0, 132.8, 132.1, 126.7, 123.8, 119.5 (CN), 118.3 [$^3J$(C,Pt) = 37.1 Hz; $C_{meta}$ to Pt], 110.2, 77.8 [$^2J$(C,Pt) = 64.3 Hz, $CH_2N$], 54.5 [$N(CH_3)_2$] ppm. $^{195}Pt\{^1H\}$ NMR (64 MHz, $CD_2Cl_2$): $\delta$ = –3138 ppm. IR (ATR): $\tilde{\nu}$ = 2972, 2919, 2223 (CN), 1664, 1626, 1599, 1579, 1505, 1450, 1333, 1172, 1084, 1016, 955, 882, 864, 833, 818, 725, 707 $cm^{-1}$. MS (ES+, $CH_3CN$): *m/z* = 554.19 $[M – Cl + CH_3CN]^+$, 513.16 $[M – Cl]^+$. $C_{21}H_{24}ClN_3Pt$ (548.97): calcd. C 45.95, H 4.41, N 7.65; found C 46.08, H 4.51, N 7.54.

**[PtCl{NCN($C_2H_2C_6H_4$-NO$_2$-4′)-4}] (7):** Diethyl 4-nitrobenzylphosphonate (**8g**; 122 mg, 0.447 mmol), **9** (182 mg, 0.405 mmol). Product isolated as a brown–red powder (166 mg, 0.292 mmol, 72%). $^1H$ NMR (300 MHz, $CD_2Cl_2$): $\delta$ = 8.18 [d, $^3J$(H,H) = 8.8 Hz, 2 H, ArH], 7.62 [d, $^3J$(H,H) = 8.8 Hz, 2 H, ArH], 7.21 [d, $^3J$(H,H) = 16.4 Hz, 1 H, *trans* CH=CH], 7.10 [d, $^3J$(H,H) = 16.4 Hz, 1 H, *trans* CH=CH], 7.05 (s, 2 H, ArH), 4.06 [s, $^3J$(H,Pt) = 46.7 Hz, 4 H, $CH_2$], 3.06 [s, $^3J$(H,Pt) = 37.4 Hz, 12 H, $CH_3$] ppm. $^{13}C\{^1H\}$ NMR (75 MHz, $CD_2Cl_2$): $\delta$ = 149.1 ($C_{ipso}$ to Pt), 146.6, 145.1, 144.6, 135.1, 132.0, 126.7, 124.5, 123.4, 118.5 [$^3J$(C,Pt) = 34.9 Hz; $C_{meta}$ to Pt], 77.8 [$^2J$(C,Pt) = 63.2 Hz; $CH_2N$], 54.6 [$N(CH_3)_2$] ppm. $^{195}Pt\{^1H\}$ NMR (64 MHz, $CD_2Cl_2$): $\delta$ = –3133 ppm. IR (ATR): $\tilde{\nu}$ = 2978, 2917, 1624, 1592, 1573, 1506, 1450, 1333, 1312, 1180, 1107, 1086, 1020, 955, 910, 859, 839, 749, 711, 691 $cm^{-1}$. MS (ES+, $CH_3CN$): *m/z* = 574.15 $[M – Cl + CH_3CN]^+$, 533.15 $[M – Cl]^+$. $C_{20}H_{24}ClN_3O_2Pt$ (568.96): calcd. C 42.22, H 4.25, N 7.39; found C 42.08, H 4.20, N 7.28.

**X-ray Crystal Structure Determinations:** X-ray intensities were measured with a Nonius KappaCCD diffractometer with rotating anode and graphite monochromator ($\lambda$ = 0.71073 Å) at a temperature of 150 K. The structures were solved with automated Patterson methods[94] and refined with SHELXL-97[95] against $F^2$ of all reflections. The initial atomic coordinates of **2** were taken from isostructural compound **6**. Geometry calculations and checking for higher symmetry were performed with the PLATON[96] program. In structure **1**, the $CH_2Cl_2$ solvent molecule was refined with a partial occupation. One of the metal complexes was disordered about the central double bond. In **1** and **7**, hydrogen atoms were introduced in geometrically optimized positions and refined with a riding model. In **2**, **5** and **6**, all hydrogen atoms were located in the difference Fourier map and refined with a riding model. Further crystallographic details are given in Table 7. CCDC-626890 (compound **1**), -626891 (compound **2**), -626892 (compound **5**), -626893 (compound **6**) and -626894 (compound **7**) contain the supplemen-

 © 2007 Wiley-VCH Verlag GmbH & Co. KGaA, Weinheim 

Table 7. Details of the crystal structure determinations.

| Compound | **1** | **2** | **5** | **6** | **7** |
|---|---|---|---|---|---|
| Formula | $C_{22}H_{30}ClN_3Pt\cdot0.117CH_2Cl_2$ | $C_{21}H_{27}ClN_2OPt$ | $C_{20}H_{24}ClIN_2Pt$ | $C_{21}H_{24}ClN_3Pt$ | $C_{20}H_{24}ClN_3O_2Pt$ |
| Fw | 576.94 | 553.99 | 649.85 | 548.97 | 568.96 |
| Crystal size [$mm^3$] | $0.20\times0.05\times0.01$ | $0.50\times0.38\times0.25$ | $0.27\times0.27\times0.09$ | $0.18\times0.18\times0.06$ | $0.42\times0.21\times0.06$ |
| Crystal colour | colourless | yellow | colourless | yellow | orange |
| Crystal system | monoclinic | monoclinic | monoclinic | monoclinic | triclinic |
| Space group | *C*2/*c* (no. 15) | $P2_1/c$ (no. 14) | $P2_1/c$ (no. 14) | $P2_1/c$ (no. 14) | $P\bar{1}$ (no. 2) |
| *a* [Å] | 46.607(3) | 18.7368(2) | 18.4773(1) | 18.3890(3) | 6.1928(1) |
| *b* [Å] | 8.4291(5) | 8.7213(1) | 8.9170(1) | 8.7258(1) | 8.8369(1) |
| *c* [Å] | 35.055(3) | 12.4729(1) | 12.2858(1) | 12.6978(2) | 18.7268(3) |
| $\alpha$ [°] | 90 | 90 | 90 | 90 | 83.5551(5) |
| $\beta$ [°] | 103.317(3) | 99.8106(4) | 93.1878(5) | 104.9695(7) | 82.0931(5) |
| $\gamma$ [°] | 90 | 90 | 90 | 90 | 78.4925(9) |
| *V* [Å] | 13401.1(15) | 2008.38 | 2021.10(3) | 1968.33(5) | 990.86(3) |
| Z | 24 | 4 | 4 | 4 | 2 |
| $D_{calcd.}$ [$g cm^{-3}$] | 1.716 | 1.832 | 2.136 | 1.853 | 1.907 |
| $\mu$ [$mm^{-1}$] | 6.442 | 7.132 | 8.608 | 7.274 | 7.235 |
| Abs. corr. | multi-scan | multi-scan | multi-scan | multi-scan | analytical |
| Abs. corr. range | 0.50–0.94 | 0.10–0.17 | 0.19–0.46 | 0.41–0.65 | 0.09–0.71 |
| $(\sin\theta/\lambda)_{max}$ [$Å^{-1}$] | 0.61 | 0.65 | 0.65 | 0.65 | 0.65 |
| Refl. (meas./unique) | 137812/12469 | 35146/4599 | 41849/4637 | 29469/4519 | 18904/4499 |
| Param./restraints | 807/66 | 240/0 | 230/0 | 239/0 | 248/0 |
| *R*1/*wR*2 [$I>2\sigma(I)$] | 0.0250/0.0505 | 0.0162/0.0350 | 0.0204/0.0493 | 0.0215/0.0407 | 0.0197/0.0449 |
| *R*1/*wR*2 [all refl.] | 0.0395/0.0550 | 0.0188/0.0357 | 0.0236/0.0589 | 0.0319/0.0433 | 0.0217/0.0460 |
| *S* | 1.022 | 1.086 | 1.129 | 1.052 | 1.086 |

tary crystallographic data for this paper. These data can be obtained free of charge from The Cambridge Crystallographic Data Centre via www.ccdc.cam.ac.uk/data_request/cif.

**Supporting Information** (see footnote on the first page of this article): Results of the BLA calculations (Table S1) and a Quaternion fit of the two ordered molecules in the crystal structure of **1** (Figure S1).

## Acknowledgments

This work was partially supported (G. D. B., M. L. and A. L. S.) by the Council for Chemical Sciences of the Netherlands Organization for Scientific Research (NWO/CW). Duncan M. Tooke is acknowledged for collecting the X-ray data of compound **1**. J. G. thanks the Junta de Comunidades de Castilla-La Mancha for a grant.

[1] H. Meier, *Angew. Chem. Int. Ed.* **2005**, *44*, 2482–2506.
[2] D. R. Kanis, M. A. Ratner, T. J. Marks, *Chem. Rev.* **1994**, *94*, 195–242.
[3] R. H. Friend, R. W. Gymer, A. B. Holmes, J. H. Burroughes, R. N. Marks, C. Taliani, D. D. C. Bradley, D. A. Dos Santos, J. L. Brédas, M. Lögdlund, W. R. Salaneck, *Nature* **1999**, *397*, 121–128.
[4] A. Dulcic, C. Flytzanis, C. L. Tang, D. Pépin, M. Fétizon, Y. Hoppilliard, *J. Chem. Phys.* **1981**, *74*, 1559–1563.
[5] H. Meier, *Angew. Chem. Int. Ed. Engl.* **1992**, *31*, 1399–1420.
[6] D. H. Waldeck, *Chem. Rev.* **1991**, *91*, 415–436.
[7] V. Papper, G. I. Likhtenshtein, *J. Photochem. Photobiol., A* **2001**, *140*, 39–52.
[8] V. Papper, D. Pines, G. Likhtenshtein, E. Pines, *J. Photochem. Photobiol., A* **1997**, *111*, 87–96.
[9] S. K. Hurst, M. G. Humphrey, T. Isoshima, K. Wostyn, I. Asselberghs, K. Clays, A. Persoons, M. Samoc, B. Luther-Davies, *Organometallics* **2002**, *21*, 2024–2026.
[10] H. Lang, R. Packheiser, B. Walfort, *Organometallics* **2006**, *25*, 1836–1850.
[11] A. J. Sandee, C. K. Williams, N. R. Evans, J. E. Davies, C. E. Boothby, A. Köhler, R. H. Friend, A. B. Holmes, *J. Am. Chem. Soc.* **2004**, *126*, 7041–7048.
[12] J. Vicente, M. T. Chicote, M. D. Abrisqueta, M. C. R. de Arellano, P. G. Jones, M. G. Humphrey, M. P. Cifuentes, M. Samoc, B. Luther-Davies, *Organometallics* **2000**, *19*, 2968–2974.
[13] I. R. Whittall, M. G. Humphrey, A. Persoons, S. Houbrechts, *Organometallics* **1996**, *15*, 1935–1941.
[14] I. Asselberghs, K. Clays, A. Persoons, A. M. McDonagh, M. D. Ward, J. A. McCleverty, *Chem. Phys. Lett.* **2003**, *368*, 408–411.
[15] B. J. Coe, C. J. Jones, J. A. McCleverty, D. Bloor, G. Cross, *J. Organomet. Chem.* **1994**, *464*, 225–232.
[16] M. Malaun, R. Kowallick, A. M. McDonagh, M. Marcaccio, R. L. Paul, I. Asselberghs, K. Clays, A. Persoons, B. Bildstein, C. Fiorini, J. M. Nunzi, M. D. Ward, J. A. McCleverty, *J. Chem. Soc., Dalton Trans.* **2001**, 3025–3038.
[17] M. Marcaccio, J. A. McCleverty, W. Akemann, C. Fiorini-Debuisschert, J. M. Nunzi, *J. Photochem. Photobiol., A* **2004**, *163*, 413–417.
[18] S. Back, M. Albrecht, A. L. Spek, G. Rheinwald, H. Lang, G. van Koten, *Organometallics* **2001**, *20*, 1024–1027.
[19] S. Back, R. A. Gossage, H. Lang, G. van Koten, *Eur. J. Inorg. Chem.* **2000**, 1457–1464.
[20] S. Back, M. Lutz, A. L. Spek, H. Lang, G. van Koten, *J. Organomet. Chem.* **2001**, *620*, 227–234.
[21] S. L. James, G. Verspui, A. L. Spek, G. van Koten, *Chem. Commun.* **1996**, 1309–1310.
[22] M. Gagliardo, G. Rodríguez, H. H. Dam, M. Lutz, A. L. Spek, R. W. A. Havenith, P. Coppo, L. De Cola, F. Hartl, G. P. M. van Klink, G. van Koten, *Inorg. Chem.* **2006**, *45*, 2143–2155.
[23] M. Q. Slagt, G. Rodríguez, M. M. P. Grutters, R. J. M. Klein Gebbink, W. Klopper, L. W. Jenneskens, M. Lutz, A. L. Spek, G. van Koten, *Chem. Eur. J.* **2004**, *10*, 1331–1344.
[24] L. A. van de Kuil, H. Luitjes, D. M. Grove, J. W. Zwikker, J. G. M. van der Linden, A. M. Roelofsen, L. W. Jenneskens, W. Drenth, G. van Koten, *Organometallics* **1994**, *13*, 468–477.
[25] C. Hansch, A. Leo, R. W. Taft, *Chem. Rev.* **1991**, *91*, 165–195.
[26] S. J. Farley, D. L. Rochester, A. L. Thompson, J. A. K. Howard, J. A. G. Williams, *Inorg. Chem.* **2005**, *44*, 9690–9703.

 © 2007 Wiley-VCH Verlag GmbH & Co. KGaA, Weinheim 

[27] W. Lu, B. X. Mi, M. C. W. Chan, Z. Hui, N. Y. Zhu, S. T. Lee, C. M. Che, *Chem. Commun.* **2002**, 206–207.
[28] M. Maestri, C. Deuschel-Cornioley, A. von Zelewsky, *Coord. Chem. Rev.* **1991**, *111*, 117–123.
[29] H. Jude, J. A. K. Bauer, W. B. Connick, *Inorg. Chem.* **2002**, *41*, 2275–2281.
[30] H. Jude, J. A. K. Bauer, W. B. Connick, *Inorg. Chem.* **2004**, *43*, 725–733.
[31] H. Jude, J. A. K. Bauer, W. B. Connick, *Inorg. Chem.* **2005**, *44*, 1211–1220.
[32] T. Kanbara, K. Okada, T. Yamamoto, H. Ogawa, T. Inoue, *J. Organomet. Chem.* **2004**, *689*, 1860–1864.
[33] I. O. Donkor, T. L. Huang, B. Tao, D. Rattendi, S. Lane, M. Vargas, B. Goldberg, C. Bacchi, *J. Med. Chem.* **2003**, *46*, 1041–1048.
[34] T. L. Huang, Q. Zhang, A. T. White, S. F. Queener, M. S. Bartlett, J. W. Smith, I. O. Donkor, *Bioorg. Med. Chem. Lett.* **1996**, *6*, 2087–2090.
[35] J. L. H. Jiwan, J. P. Soumillion, *J. Phys. Chem.* **1995**, *99*, 14223–14230.
[36] E. Peeters, P. A. van Hal, S. C. J. Meskers, R. A. J. Janssen, E. W. Meijer, *Chem. Eur. J.* **2002**, *8*, 4470–4474.
[37] S. D. Taylor, C. C. Kotoris, A. N. Dinaut, M. J. Chen, *Tetrahedron* **1998**, *54*, 1691–1714.
[38] R. Wrigglesworth, C. S. J. Walpole, S. Bevan, E. A. Campbell, A. Dray, G. A. Hughes, I. James, K. J. Masdin, J. Winter, *J. Med. Chem.* **1996**, *39*, 4942–4951.
[39] C. H. M. Amijs, G. P. M. van Klink, G. van Koten, *Green Chem.* **2003**, *5*, 470–474.
[40] M. R. Pitts, J. R. Harrison, C. J. Moody, *J. Chem. Soc., Perkin Trans. 1* **2001**, 955–977.
[41] G. Brizius, N. G. Pschirer, W. Steffen, K. Stitzer, H. C. zur Loye, U. H. F. Bunz, *J. Am. Chem. Soc.* **2000**, *122*, 12435–12440.
[42] E. Diez-Barra, J. C. Garcia-Martinez, S. Merino, R. del Rey, J. Rodriguez-Lopez, P. Sanchez-Verdu, J. Tejeda, *J. Org. Chem.* **2001**, *66*, 5664–5670.
[43] H. Meier, J. Gerold, H. Kolshorn, B. Muhling, *Chem. Eur. J.* **2004**, *10*, 360–370.
[44] K. R. J. Thomas, J. T. Lin, K. J. Lin, *Organometallics* **1999**, *18*, 5285–5291.
[45] J. Harada, K. Ogawa, *J. Am. Chem. Soc.* **2004**, *126*, 3539–3544.
[46] M. Albrecht, B. M. Kocks, A. L. Spek, G. van Koten, *J. Organomet. Chem.* **2001**, *624*, 271–286.
[47] M. Albrecht, M. Lutz, A. M. M. Schreurs, E. T. H. Lutz, A. L. Spek, G. van Koten, *J. Chem. Soc., Dalton Trans.* **2000**, 3797–3804.
[48] A. V. Chuchuryukin, P. A. Chase, H. P. Dijkstra, B. M. J. M. Suijkerbuijk, A. M. Mills, A. L. Spek, G. P. M. van Klink, G. van Koten, *Adv. Synth. Catal.* **2005**, *347*, 447–462.
[49] J. G. Donkervoort, J. L. Vicario, J. T. B. H. Jastrzebski, W. J. J. Smeets, A. L. Spek, G. van Koten, *J. Organomet. Chem.* **1998**, *551*, 1–7.
[50] E. A. S. Bustamante, T. Hanemann, W. Haase, I. Svoboda, H. Fuess, *Acta Crystallogr., Sect. C: Cryst. Struct. Commun.* **1995**, *51*, 2192–2196.
[51] D. C. R. Hockless, I. R. Whittall, M. G. Humphrey, *Acta Crystallogr., Sect. C: Cryst. Struct. Commun.* **1996**, *52*, 3222–3224.
[52] J. Catalan, *Chem. Phys. Lett.* **2006**, *421*, 134–137.
[53] S. P. Kwasniewski, L. Claes, J. P. Francois, M. S. Deleuze, *J. Chem. Phys.* **2003**, *118*, 7823–7836.
[54] Z. H. Yu, L. T. Li, W. Fu, L. P. Li, *J. Phys. Chem. A* **1998**, *102*, 2016–2028.
[55] C. H. Choi, M. Kertesz, *J. Phys. Chem. A* **1997**, *101*, 3823–3831.
[56] C. J. Finder, M. G. Newton, N. L. Allinger, *Acta Crystallographica Sect. B: Struct. Sci.* **1974**, *B30*, 411–415.
[57] M. Traetteberg, E. B. Frantsen, F. C. Mijlhoff, A. Hoekstra, *J. Mol. Struct.* **1975**, *26*, 57–68.
[58] J. A. Bouwstra, A. Schouten, J. Kroon, *Acta Crystallographica Sect. C: Crystal Struct. Communications* **1984**, *C40*, 428–431.
[59] Z. Q. Liu, Q. Fang, D. Wang, D. X. Cao, G. Xue, W. T. Yu, H. Lei, *Chem. Eur. J.* **2003**, *9*, 5074–5084.
[60] J. S. Yang, Y. H. Lin, C. S. Yang, *Org. Lett.* **2002**, *4*, 777–780.
[61] S. K. Hurst, M. P. Cifuentes, J. P. L. Morrall, N. T. Lucas, I. R. Whittall, M. G. Humphrey, I. Asselberghs, A. Persoons, M. Samoc, B. Luther-Davies, A. C. Willis, *Organometallics* **2001**, *20*, 4664–4675.
[62] T. M. Gilbert, F. J. Hadley, C. B. Bauer, R. D. Rogers, *Organometallics* **1994**, *13*, 2024–2034.
[63] A. Hilger, J. P. Gisselbrecht, R. R. Tykwinski, C. Boudon, M. Schreiber, R. E. Martin, H. P. Luthi, M. Gross, F. Diederich, *J. Am. Chem. Soc.* **1997**, *119*, 2069–2078.
[64] T. Michinobu, J. C. May, J. H. Lim, C. Boudon, J. P. Gisselbrecht, P. Seiler, M. Gross, I. Biaggio, F. Diederich, *Chem. Commun.* **2005**, 737–739.
[65] See the supporting information for the exact assignment of the bonds and the bond length alternation calculations.
[66] C. A. van Walree, A. W. Maarsman, A. W. Marsman, M. C. Flipse, L. W. Jenneskens, W. J. J. Smeets, A. L. Spek, *J. Chem. Soc., Perkin Trans. 2* **1997**, 809–819.
[67] R. Frantz, J. O. Durand, G. F. Lanneau, *J. Organomet. Chem.* **2004**, *689*, 1867–1871.
[68] J. Mason, *Chem. Rev.* **1987**, *87*, 1299–1313.
[69] B. Yin, F. Niemeyer, J. A. G. Williams, J. Jiang, A. Boucekkine, L. Toupet, H. Le Bozec, V. Guerchais, *Inorg. Chem.* **2006**, *45*, 8584–8596.
[70] C. A. van Walree, O. Franssen, A. W. Marsman, M. C. Flipse, L. W. Jenneskens, *J. Chem. Soc., Perkin Trans. 2* **1997**, 799–807.
[71] L. T. Cheng, W. Tam, S. H. Stevenson, G. R. Meredith, G. Rikken, S. R. Marder, *J. Phys. Chem.* **1991**, *95*, 10631–10643.
[72] H. Gruen, H. Görner, *J. Phys. Chem.* **1989**, *93*, 7144–7152.
[73] Values for $\varepsilon$ and $n$ were taken from: C. Reichardt, *Solvents and Solvent Effects in Organic Chemistry*, 2nd ed., VCH, Weinheim **1988**.
[74] E. Lippert, *Z. Naturforsch., A: Phys. Sci.* **1955**, *10*, 541–546.
[75] Y. V. Il′Ichev, W. Kühnle, K. A. Zachariasse, *Chem. Phys.* **1996**, *211*, 441–453.
[76] A. Kawski, *Z. Naturforsch., A: Phys. Sci.* **2002**, *57*, 255–262.
[77] The Onsager radius was obtained out of the unit cell volume after it was normalized by using the K. P. I. correction; for **6**: $\rho$ = 4.363 Å, for **7**: $\rho$ = 4.391 Å.
[78] I. Majerz, A. Koll, *Acta Crystallogr., Sect. B: Struct. Sci.* **2004**, *60*, 406–415.
[79] R. Lapouyade, A. Kuhn, J. F. Létard, W. Rettig, *Chem. Phys. Lett.* **1993**, *208*, 48–58.
[80] R. Lapouyade, K. Czeschka, W. Majenz, W. Rettig, E. Gilabert, C. Rullière, *J. Phys. Chem.* **1992**, *96*, 9643–9650.
[81] H. LeBreton, B. Bennetau, J. F. Létard, R. Lapouyade, W. Rettig, *J. Photochem. Photobiol., A* **1996**, *95*, 7–20.
[82] J. F. Létard, R. Lapouyade, W. Rettig, *Chem. Phys. Lett.* **1994**, *222*, 209–216.
[83] D. Pines, E. Pines, W. Rettig, *J. Phys. Chem. A* **2003**, *107*, 236–242.
[84] K. Rechthaler, G. Köhler, *Chem. Phys. Lett.* **1996**, *250*, 152–158.
[85] W. Rettig, W. Majenz, *Chem. Phys. Lett.* **1989**, *154*, 335–341.
[86] W. Rettig, W. Majenz, R. Herter, J. F. Létard, R. Lapouyade, *Pure Appl. Chem.* **1993**, *65*, 1699–1704.
[87] J. F. Létard, R. Lapouyade, W. Rettig, *Chem. Phys.* **1994**, *186*, 119–131.
[88] A. J. Canty, J. Patel, B. W. Skelton, A. H. White, *J. Organomet. Chem.* **2000**, *599*, 195–199.
[89] B. R. Steele, K. Vrieze, *Transition Met. Chem.* **1977**, *2*, 140–144.
[90] G. Rodríguez, M. Albrecht, J. Schoenmaker, A. Ford, M. Lutz, A. L. Spek, G. van Koten, *J. Am. Chem. Soc.* **2002**, *124*, 5127–5138.
[91] S. M. Moerlein, *J. Organomet. Chem.* **1987**, *319*, 29–39.

 © 2007 Wiley-VCH Verlag GmbH & Co. KGaA, Weinheim 

[92] P. S. Pregosin, *Coord. Chem. Rev.* **1982**, *44*, 247–291.
[93] D. F. Eaton, *Pure Appl. Chem.* **1988**, *60*, 1107–1114.
[94] P. T. Beurskens, G. Admiraal, G. Beurskens, W. P. Bosman, S. Garcia-Granda, R. O. Gould, J. M. M. Smits, C. Smykalla, *The DIRDIF99 Program System – Technical Report of the Crystallography Laboratory*, University of Nijmegen, The Netherlands, **1999**.
[95] G. M. Sheldrick, *SHELXL-97*: *Program for Crystal Structure Refinement*, University of Göttingen, Germany, **1997**.
[96] A. L. Spek, *J. Appl. Crystallogr.* **2003**, *36*, 7–13.
Received: November 17, 2006
Published Online: February 23, 2007

 © 2007 Wiley-VCH Verlag GmbH & Co. KGaA, Weinheim 

DOI: 10.1002/ejic.200700015

# Preparation and Characterization of Dinuclear $Ni^{II}$ Amine-Thiophenolate Complexes Coligated by $EO_4^-$ (E = Cl, Re) and $EO_4^{2-}$ Oxoanions (E = S, Cr, Mo, W)

**Vasile Lozan[a] and Berthold Kersting*[a]**

**Keywords:** Dinuclear complexes / Macrocyclic ligands / Oxoanions

The ability of dinuclear nickel(II) complexes of the type $[(L^{Me})Ni^{II}_2(L')]$ to coordinate tetrahedral main group and transition metal oxoanions ($L' = EO_4^-$, $EO_4^{2-}$) has been examined ($(L^{Me})^{2-}$ is the deprotonated form of the 24-membered macrocyclic hexaaza-dithiophenolate ligand $H_2L^{Me}$). The following complexes have been synthesized: $[(L^{Me})Ni_2(ClO_4)][ClO_4]$ (**2**$[ClO_4]$), $[(L^{Me})Ni_2(ReO_4)][ReO_4]$ (**3**$[ReO_4]$), $[(L^{Me})Ni_2(SO_4)]$ (**4**), $[(L^{Me})Ni_2(CrO_4)]$ (**5**), $[(L^{Me})Ni_2(MoO_4)]$ (**6**), and $[(L^{Me})Ni_2(WO_4)]$ (**7**). Complexes **2**$[ClO_4]$, **3**$[ReO_4]$, **4**, **5**, and **7** have been characterized by X-ray crystallography. The complexes are isostructural, with the $EO_4^-$ and $EO_4^{2-}$ groups bonded in a $\mu_{1,3}$-bridging mode to generate dioctahedral $N_3Ni(\mu\text{-}S)_2(\mu_{1,3}\text{-}EO_4)NiN_3$ core structures. The doubly charged $EO_4^{2-}$ groups interact more strongly with the $[(L^{Me})Ni_2]^{2+}$ fragment than the $EO_4^-$ groups as reflected by the Ni–O distances which are significantly longer in **2** and **3** than in **4**–**7**. The nickel(II) ions in **4** and **6** are weakly ferromagnetically coupled ($J$ = 24.8 and 3.75 $cm^{-1}$, respectively) and the magnitude of the coupling appears to correlate with the Ni–S–Ni angle.
(© Wiley-VCH Verlag GmbH & Co. KGaA, 69451 Weinheim, Germany, 2007)

## Introduction

The macrocyclic hexaaza-dithiophenolate macrocycle $H_2L^{Me}$ is an effective dinucleating ligand that supports the formation of bioctahedral complexes of the type $[(L^{Me})M_2(L')]^+$ with numerous transition metals such as Mn, Fe, Co, Ni, Zn,[1] and Cd (Scheme 1).[2] These complexes have a rich coordination chemistry since the $[(L^{Me})M_2]^{2+}$ fragments are able to coordinate a large variety of coligands L′. These include $Cl^-$,[3] $OH^-$,[4] $NO_2^-$, $NO_3^-$, $N_3^-$,[5] $BH_4^-$,[6] various carboxylates,[7–9] $N_2H_4$, pyrazolate, and pyridazine,[5] and some biologically relevant molecules such as $HCO_3^-$, $(p\text{-}NO_2C_6H_4O)_2PO_2^-$, and proline.[10]

In earlier work, we have also described the synthesis of a few $[(L^{Me})M_2(L')]^+$ complexes bearing tetrahedral main group and transition metal oxoanions. The X-ray crystal structures of the complexes $[(L^{Me})Co^{II}_2(MoO_4)]$[11] and $[(L^{Me})Ni^{II}_2(O_2P(OH)_2)]^+$ have been reported.[7] In view of the biological, technological and environmental importance of these anions,[12,13] we considered it worthwhile to prepare further complexes of this type to gain more insight into the binding of the oxoanions by the $[(L^{Me})M_2]^{2+}$ fragments. Here we describe the synthesis and characterization of a series of novel dinickel complexes bearing $ClO_4^-$, $ReO_4^-$, $SO_4^{2-}$, $CrO_4^{2-}$, $MoO_4^{2-}$, and $WO_4^{2-}$ ligands and explore their structural features.

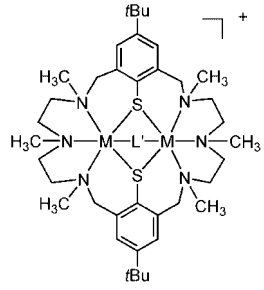


$[(L^{Me})M^{II}_2(L')]^+$
M = Mn, Fe, Co, Ni, Zn
L' = coligand

Scheme 1. Dinuclear $[(L^{Me})M_2(L')]^+$ complexes supported by the $N_6S_2$ macrocycle $(L^{Me})^{2-}$.

## Results and Discussion

### Synthesis of Complexes

The complexes were prepared as indicated in Scheme 2. The perchlorato (**2**) and perrhenato (**3**) complexes were found to be inaccessible by direct reactions of the chloro complex **1** and the respective $EO_4^-$ ligand. In order to achieve their coordination, a $Cl^-$ abstraction was necessary. When **1**$[ClO_4]$ was dissolved in $CH_3CN$ and one equiv. of $Pb(ClO_4)_2$ was added, a dark green solution of **2** formed

[a] Institut für Anorganische Chemie, Universität Leipzig
Johannisallee 29, 04103 Leipzig, Germany
Fax: +49-341-97-36199
E-mail: b.kersting@uni-leipzig.de
Supporting information for this article is available on the WWW under http://www.eurjic.org or from the author.

 © 2007 Wiley-VCH Verlag GmbH & Co. KGaA, Weinheim 

immediately, from which the previously reported perchlorate salt **2**[$ClO_4$] could be isolated as a dark-green, air-stable solid.[6] The $ClO_4^-$ in **2** is extreme labile and proved to be a suitable precursor for the synthesis of other $[(L^{Me})Ni_2(L')]^+$ complexes. Upon treatment of **2** with a large excess of [$n$Bu$_4$N][$ReO_4$] in acetonitrile, both the $ClO_4^-$ ligand and the $ClO_4^-$ counterion can be substituted for $ReO_4^-$ to give **3**[$ReO_4$], as indicated by elemental analyses and IR spectroscopy. Attempts to exchange the $ClO_4^-$ ion by a $MnO_4^-$ ion did not meet with any success. Treatment of **2**[$ClO_4$] with [$n$Bu$_4$N][$MnO_4$] resulted in the formation of an insoluble brown solid, from which no products could be isolated.

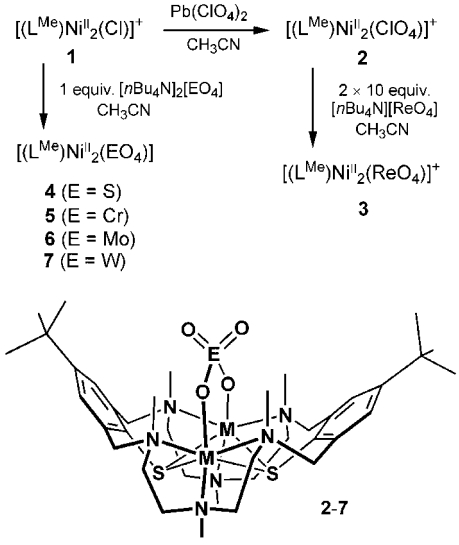


Scheme 2. Synthesis of complexes **2**–**7** from precursor **1**.

Although the $Cl^-$ complex **1** proved to be less labile than the $ClO_4^-$ complex **2**, substitution reactions succeeded with the $EO_4^{2-}$ ions (E = S, Cr, Mo, W); the driving force behind these syntheses presumably being the low solubility of the resulting neutral complexes. Thus, when solutions of $[(L^{Me})Ni^{II}_2(Cl)]^+$ **1** in acetonitrile were treated with equimolar amounts of the respective [$n$Bu$_4$N]$_2$[$EO_4$] salt at room temperature, pale green (**4**, **6**, **7**) or yellow (**5**) $[(L^{Me})Ni_2(EO_4)]$ complexes were formed within 4–12 h in good yields (69–88%). In contrast to **2**[$ClO_4$] and **3**[$ReO_4$], these neutral complexes were found to be sufficiently soluble in $CH_2Cl_2$, acetone, DMF, THF, but virtually insoluble in $CH_3CN$ and MeOH. All complexes were characterized by elemental analysis and standard spectroscopic methods. The crystal structures of **2**[$BPh_4$]·1.5$Me_2CO$·0.5MeOH, **3**[$ReO_4$]·$H_2O$, **4**·2$H_2O$·MeCN, **5**, and **7**·2$H_2O$·MeCN were also determined by X-ray diffraction.

## Spectroscopic Characterization

Infrared data for the complexes and their assignments are listed in Table 1. In addition to the bands arising from the $[(L^{Me})Ni_2]^{2+}$ fragments, all the complexes show strong IR bands for the $[EO_4]^{2-}$ and $[EO_4]^-$ groups. For the sulfato complex **4** two such bands are observed, as in other $SO_4^{2-}$ complexes,[14] at 1120 and 620 $cm^{-1}$; these are assigned to the antisymmetric stretching ($\nu_3$) and bending ($\nu_4$) modes of the sulfate ion. In view of the lowering of the symmetry by coordination to the $[(L^{Me})Ni_2]^{2+}$ fragment, a splitting of the $\nu_3$ mode of the $[EO_4]^{2-}$ ion is expected.[15] For **4** and **5**, this splitting is not resolved. In the case of the molybdato and wolframato complexes **6** and **7**, however, a split $\nu_3$ band is clearly discernible. Each of these compounds reveals two nearly equally intense absorptions in the 800 to 850 $cm^{-1}$ range, typical for coordinated $[MoO_4]^{2-}$,[14] and $[WO_4]^{2-}$ groups.[16] The IR spectra of **2**[$ClO_4$] and **3**[$ReO_4$] both reveal two broad but unsplit bands reflecting the presence of coordinating and non-coordinating $EO_4^-$ species. The observed wavenumbers are not markedly different from those of the free ions.[17–19]

The electronic spectra of the compounds were registered in acetonitrile or dichloromethane solution. Selected data are reported in Table 1. The intense absorptions below 500 nm can be attributed to π-π* transitions within the aromatic rings of the supporting ligand or to $RS^-\rightarrow Ni^{II}$ charge-transfer bands. Above 500 nm, each compound displays two weak absorption bands, typical of six-coordinate nickel(II) complexes.[20,21] Both the $\nu_1$ and the $\nu_2$ transitions are broad and unsymmetrical, indicative of the presence of a significant distortion from octahedral symmetry. The

Table 1. Selected spectroscopic data for complexes **2**–**7**.

| | IR[a] $\tilde{\nu}_3$ [$cm^{-1}$] | $\tilde{\nu}_4$ [$cm^{-1}$] | UV/Vis[b] $\lambda_{max}$ [nm] ($\varepsilon$, $M^{-1}cm^{-1}$) |
|---|---|---|---|
| Free $ClO_4^-$ [17,18] | 1100 | 620 | – |
| Free $ReO_4^-$ [19] | 920 | 322 | – |
| Free $SO_4^{2-}$ [14] | 1105 | 611 | – |
| Free $CrO_4^{2-}$ [19] | 890 | 368 | – |
| Free $MoO_4^{2-}$ [14] | 841 | 338 | – |
| Free $WO_4^{2-}$ [16] | 833 | 324 | – |
| $[(L^{Me})Ni_2(ClO_4)]^+$ **2** | 1097, 1113 | 624 | 578 (129), 1066 (86) |
| $[(L^{Me})Ni_2(ReO_4)]^+$ **3** | 931, 903 | – | 670 (79), 1058 (127) |
| $[(L^{Me})Ni_2(SO_4)]$ **4** | 1120 | 620 | 674 (16), 1122 (34) |
| $[(L^{Me})Ni_2(CrO_4)]$ **5** | 895 | – | 686 (79), 1126 (88) |
| $[(L^{Me})Ni_2(MoO_4)]$ **6** | 854, 817 | – | 690 (104), 1136 (142) |
| $[(L^{Me})Ni_2(WO_4)]$ **7** | 857, 820 | – | 689 (1132), 1132 (130) |

[a] IR spectra were recorded as KBr pellets. [b] The UV/Vis spectra were recorded in MeCN (**2**, **3**) or $CH_2Cl_2$ solution (for **4**–**7**) at ambient temperature.

 © 2007 Wiley-VCH Verlag GmbH & Co. KGaA, Weinheim 

slight differences in the position of the *d-d* transitions show that each complex retains its integrity in solution. The solid state magnetic moments for **4** and **6** are also consistent with an octahedral structure (see below).

### X-ray Crystallography

From a solution of the perchlorate salt of **2** in acetone/methanol to which $NaBPh_4$ had been added, pale green crystals of **2**$[BPh_4]\cdot 1.5Me_2CO\cdot 0.5MeOH$ suitable for X-ray crystallographic analysis were obtained after slow evaporation. The structure consists of dinuclear nickel complexes, tetraphenylborate anions, and acetone and methanol molecules of solvent of crystallization. There are no intermolecular interactions between these components in the solid state. Figure 1 presents an ORTEP view of the cation **2**. Selected bond lengths and angles are given in Table 2 and Table 3. The cation is isostructural with the other nickel complexes, with the perchlorate being coordinated in a bidentate bridging mode and the supporting ligand adopting a bowl-shaped $C_{2v}$ symmetric conformation typical for $[(L^{Me})M^{II}_2(L')]$ complexes coligated by $\mu_{1,3}$-bridging oxyanions.[22] The lability of the perchlorato complex is reflected in the long Ni–O bonds at 2.144(6) Å. In fact, this is the longest Ni–O distance reported for dinuclear $[(L^{Me})Ni_2(L')]^+$ complexes. Note, that the elongation of the Ni–O bonds in **2** is compensated for by an increase of the Ni–N and Ni–S distances. Overall, these structural parameters indicate that the monocharged perchlorate ion binds more weakly to the dinuclear $[(L^{Me})Ni_2]^{2+}$ fragment in **2** than does the doubly charged sulfato ligand in **4**.

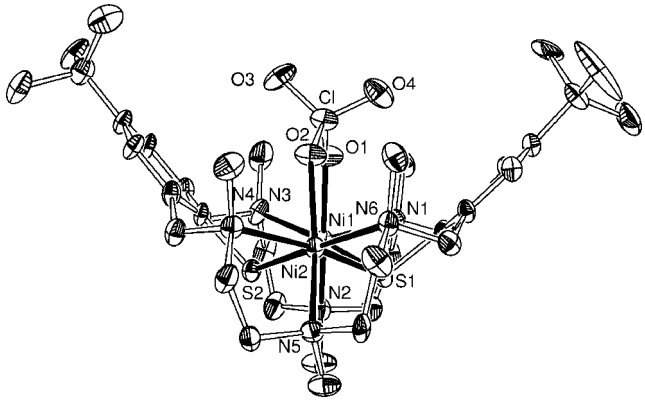


Figure 1. Structure of the cation **2** in crystals of **2**$[BPh_4]\cdot 1.5Me_2CO\cdot 0.5MeOH$. Thermal ellipsoids are drawn at the 30% probability level. Hydrogen atoms are omitted for reasons of clarity.

Pale green crystals of the perrhenato complex **3**$[ReO_4]\cdot H_2O$ suitable for X-ray diffraction analysis were obtained by slow evaporation of an acetonitrile/ethanol solution. The crystal structure consists of the dinuclear perrhenate complex **3**, perrhenate anions and water solvate molecules. As can be seen from Figure 2, complex **3** is isostructural with **2**. Within the $[(L^{Me})Ni_2]^{2+}$ fragments in **2** and **3**, the Ni–S and Ni–N bond lengths are very similar, with the largest difference outside experimental error being ca. 0.1 Å in the Ni–N(6) bonds. The coordination of the larger perrhenate group also results in a slight opening up of the Ni–S–Ni angles to 94.95(7)° thereby causing a larger Ni···Ni separation of 3.630(1) Å. The Ni–O distances are slightly shorter than in **2**, but still larger than those in **4** and **7**. In contrast to **2**, the terminal oxygen atoms of the two $ReO_4^-$ groups are involved in hydrogen bonding interactions with the water molecule of solvent of crystallization. These hydrogen bonds may be classified as moderate based on the bond

Table 2. Selected bond lengths [Å] in complexes **2**–**4** and **7**.

| | **2** (E = Cl) | **3** (E = Re) | **4** (E = S) | **7** (E = W) |
|---|---|---|---|---|
| Ni(1)–O(1) | 2.122(6) | 2.091(5) | 2.001(2) | 2.000(4) |
| Ni(1)–N(1) | 2.245(7) | 2.219(5) | 2.221(3) | 2.220(5) |
| Ni(1)–N(2) | 2.114(7) | 2.114(5) | 2.185(3) | 2.168(5) |
| Ni(1)–N(3) | 2.248(7) | 2.258(6) | 2.339(3) | 2.305(5) |
| Ni(1)–S(1) | 2.433(2) | 2.499(2) | 2.461(1) | 2.498(2) |
| Ni(1)–S(2) | 2.467(2) | 2.434(2) | 2.483(1) | 2.505(2) |
| Ni(2)–O(2) | 2.165(5) | 2.110(5) | 2.017(3) | 2.000(4) |
| Ni(2)–N(4) | 2.277(7) | 2.206(5) | 2.231(3) | 2.229(5) |
| Ni(2)–N(5) | 2.136(6) | 2.132(6) | 2.165(3) | 2.153(5) |
| Ni(2)–N(6) | 2.172(7) | 2.267(5) | 2.298(3) | 2.269(5) |
| Ni(2)–S(1) | 2.434(3) | 2.456(2) | 2.441(1) | 2.454(2) |
| Ni(2)–S(2) | 2.462(2) | 2.462(2) | 2.533(1) | 2.572(2) |
| Ni–N[a] | 2.198(7) | 2.199(6) | 2.240(3) | 2.224(5) |
| Ni–O[a] | 2.144(6) | 2.101(5) | 2.009(2) | 2.000(4) |
| Ni–S[a] | 2.449(3) | 2.463(2) | 2.480(1) | 2.507(2) |
| M(1)···M(2) | 3.547(1) | 3.630(1) | 3.506(1) | 3.655(1) |
| M(1)···E | 3.379(1) | 3.564(1) | 3.263(1) | 3.491(1) |
| M(2)···E | 3.403(1) | 3.563(1) | 3.298(1) | 3.532(1) |
| E–O(1) | 1.446(5) | 1.722(5) [1.703(7)][b] | 1.488(3) | 1.763(4) |
| E–O(2) | 1.451(5) | 1.729(5) [1.716(7)][b] | 1.485(3) | 1.772(4) |
| E–O(3) | 1.444(7) | 1.702(7) [1.705(6)][b] | 1.447(3) | 1.749(4) |
| E–O(4) | 1.407(7) | 1.710(6) [1.698(6)][b] | 1.461(3) | 1.778(5) |
| E–O[a] | 1.437(7) | 1.716(6) [1.706(7)][b] | 1.470(3) | 1.766(4) |

[a] Average values. [b] Values in square brackets refer to the $ReO_4^-$ counteranion.

Table 3. Selected bond angles [°] in complexes **2**, **3**, **4** and **7**.

| | **2** | **3** | **4** | **7** |
|---|---|---|---|---|
| N–M–N[a] | 88.7(3) | 89.6(2) | 87.8(1) | 89.3(2) |
| N–M–S[a] | 95.2(2) | 94.7(2) | 94.16(9) | 94.0(1) |
| O–M–$N_{cis}$ [a] | 86.2(3) | 85.0(2) | 87.3(1) | 85.8(2) |
| O–M–$S_{cis}$ [a] | 93.9(2) | 96.3(2) | 96.10(8) | 97.9(1) |
| S–M–S[a] | 77.96(8) | 76.42(6) | 78.35(4) | 75.74(6) |
| O–M–$N_{trans}$ [a] | 162.6(3) | 161.2(2) | 162.3(1) | 160.4(2) |
| N–M–$S_{trans}$ [a] | 168.6(2) | 166.9(2) | 168.22(9) | 165.9(1) |
| M–S–M[a] | 92.80(9) | 94.95(7) | 90.00(4) | 93.61(6) |
| O(1)–E–O(2) | 108.6(3) | 106.5(2) | 109.59(15) | 106.5(2) |
| O(1)–E–O(3) | 108.6(4) | 110.7(3) | 109.35(17) | 110.9(2) |
| O(1)–E–O(4) | 109.1(4) | 110.1(3) | 108.50(17) | 109.6(2) |
| O(2)–E–O(3) | 109.5(4) | 112.4(3) | 109.71(18) | 109.6(2) |
| O(2)–E–O(4) | 109.8(4) | 109.0(3) | 109.11(18) | 111.9(2) |
| O(3)–E–O(4) | 111.1(5) | 108.1(4) | 110.6(2) | 108.3(2) |

[a] Average values.

 © 2007 Wiley-VCH Verlag GmbH & Co. KGaA, Weinheim 

lengths of ca. 2.8 Å [O(4)···O(9) 2.822 Å, O(6)···O(9) 2.842 Å]. Similar hydrogen-bonding interactions are also observed in **4** and **7**.

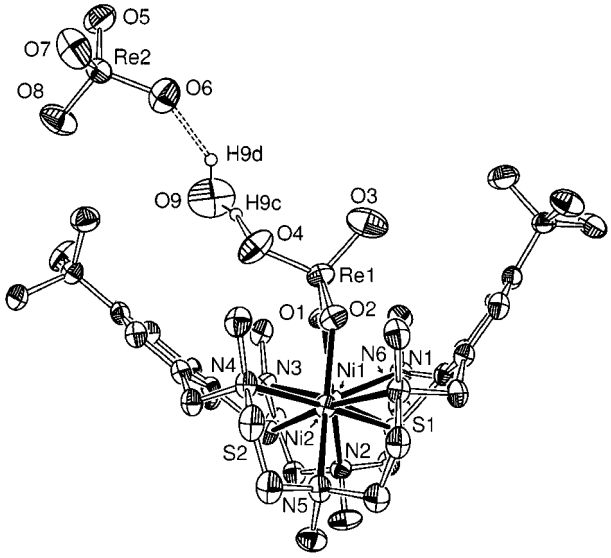


Figure 2. ORTEP plot of the structure of **3**. The hydrogen bonding interactions between the water molecule and the perrhenate groups are shown (dashed lines). Thermal ellipsoids are drawn at the 30% probability level. Hydrogen atoms, except H(9c) and H(9d), are omitted for reasons of clarity.

Pale green crystals of the sulfato complex **4**·2$H_2O$·MeCN were grown by slow evaporation of a mixed (1:1) ethanol/acetonitrile solution of **4**. Figure 3 provides an ORTEP view of the structure of the neutral complex. As in **3**, there is a short O···O distance between the sulfato oxygen atom O(4) and a water molecule [*d*(O(4)···O(5) 2.671 Å] indicative of a hydrogen-bonding interaction. Complex **4** is the first example of a [($L^{Me}$)$Ni_2$(L′)] complex bearing a doubly charged coligand. A comparison of structure **2** with structure **4** allows the effects of $ClO_4^-$ vs. $SO_4^{2-}$ coordination in otherwise identical [($L^{Me}$)$Ni_2$]$^{2+}$ fragments to be evaluated. The only significant differences among these complexes are in the average Ni–O bond lengths, with the sulfato complex having significantly shorter Ni–O bonds than the perchlorato complex, most likely as a consequence of an increased electrostatic interaction. In this regard, it is also interesting to note that the terminal S=O bonds are slightly shorter than the bridging S–O bonds [e.g., 1.454(3) vs. 1.487(3) Å]. A similar behaviour has been noted previously for [($L^{Me}$)-$Co^{II}_2$($MoO_4$)].[11]

Slow evaporation of a $CH_2Cl_2$ solution of the chromato complex **5** gave orange crystals that were analyzed by X-ray crystallography. Although, the structure determination is of low quality and not as good as desired for publication,[23] it can serve to confirm the formulation and the atom connectivity of the neutral $CrO_4^{2-}$ complex. The structure is depicted in Figure 4, but not discussed further.

The wolframato complex **7** is isomorphous with **4**, with very similar unit cell parameters and molecular dimensions. The molecular structure is illustrated in Figure 5, and salient bond lengths and angles are given in Table 2 and

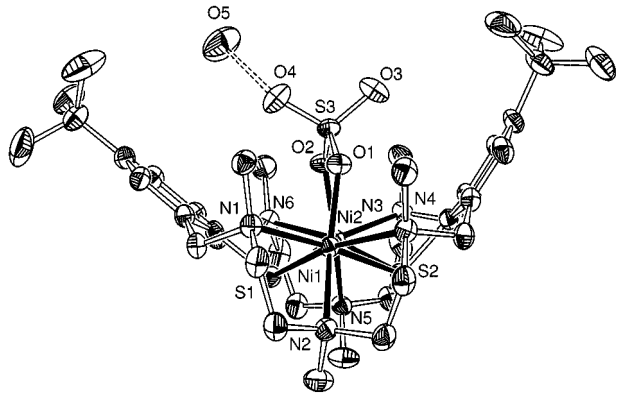


Figure 3. ORTEP plot of the neutral complex **4**. Thermal ellipsoids are drawn at the 30% probability level. Hydrogen atoms are omitted for reasons of clarity. The dashed line indicates the hydrogen bond between the sulfato oxygen atom O(4) and the water molecule O(5).

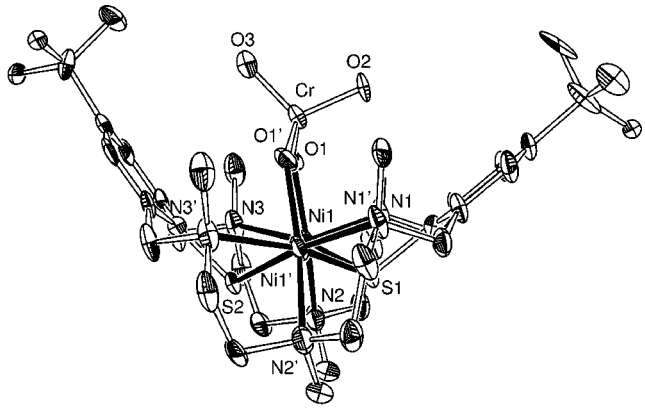


Figure 4. Structure of the neutral complex **5** with thermal ellipsoids drawn at the 50% probability level. Hydrogen atoms are omitted for reasons of clarity. Only one orientation of the disordered *t*Bu groups is displayed. Selected bond lengths [Å] and angles [°]: Ni–O(1) 2.001, Cr–O(1) 1.671, Cr–O(2) 1.639, Cr–O(3) 1.644; Ni(1)–S(1)–Ni(1′) 94.3, Ni(1)–S(2)–Ni(1′) 89.3. Symmetry code used to generate equivalent atoms: *x*, 0.5–*y*, *z* (′).

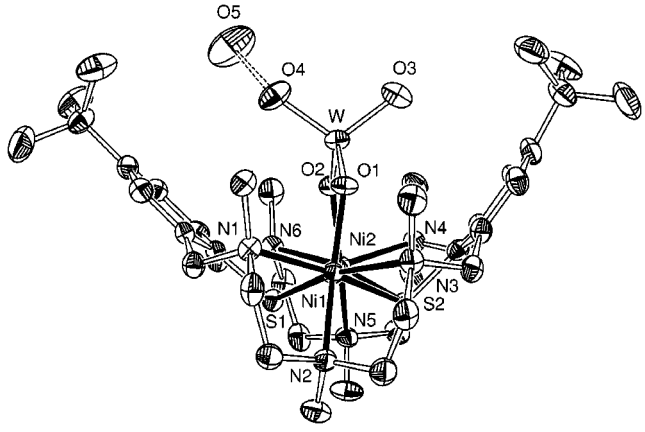


Figure 5. ORTEP plot of complex **7**. Thermal ellipsoids are drawn at 50% probability. Hydrogen atoms have been omitted for reasons of clarity. The dashed line indicates the hydrogen bond between the wolframato oxygen atom O(4) and the water molecule O(5).

 © 2007 Wiley-VCH Verlag GmbH & Co. KGaA, Weinheim 

Table 3. The average Ni–O bond length of 2.000(4) Å resembles that in **4**, again much shorter than in **2** and **3**. In agreement with the splitting of the $v_3$ band in the IR, the coordination about the tungsten atom is not perfectly tetrahedral. The W–O bonds vary between 1.749(4) Å and 1.778(4) Å and the O–W–O bond angles range from 106.5(2) to 111.9(2)°. The Ni···Ni separation is 3.655(1) Å in **7** and is 3.506(1) in **4**. As a consequence, the Ni–S–Ni bond angle in the wolframato complex **7** (93.61(6)°] is wider than in **4** (90.00(4)°].

### Magnetic Properties of Complexes 4 and 6

Temperature-dependent magnetic susceptibility measurements for complexes **4** and **6** were carried out to see whether magnetic exchange interactions are present in these complexes. The temperature dependent susceptibility data for powdered samples of the two complexes have been measured between 4.0 and 289 K by using a Faraday balance in an applied external magnetic field of 1.1 T. Figure 6 displays the temperature dependence of the effective moment ($\mu_{eff}$ per dinuclear complex) for complex **4**. The effective magnetic moment increases from 4.58 $\mu_B$ at 295 K to a maximum value of 5.10 $\mu_B$ at 25 K, and then decreases rapidly to 4.94 $\mu_B$ at 4.4 K. This behaviour indicates an intramolecular ferromagnetic exchange interaction between the two $Ni^{II}$ ions that leads to an S = 2 ground state of complex **4**. The decrease in $\mu_B$ below 22 K is presumably due to zero-field splitting of $Ni^{II}$.

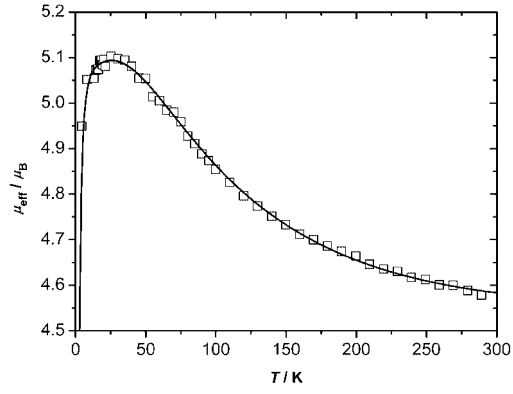


Figure 6. Temperature dependence of $\mu_{eff}$ for **4** (per dinuclear complex). The full line represents the best theoretical fit to eq. (1). Experimental and calculated values are provided as supporting information.

The temperature dependence of the magnetic moment for the wolframato complex **6** is similar to that of the sulfato complex **4** (Figure 7). The effective magnetic moment per dinuclear complex also increases from 4.33 $\mu_B$ at 295 K to a maximum of 5.08 $\mu_B$ at 10 K and then decreases again with decreasing temperature. The fact that the maximum occurs at lower temperatures than in **4** is indicative of a weaker ferromagnetic exchange interaction between the two $Ni^{II}$ ions in **6**.

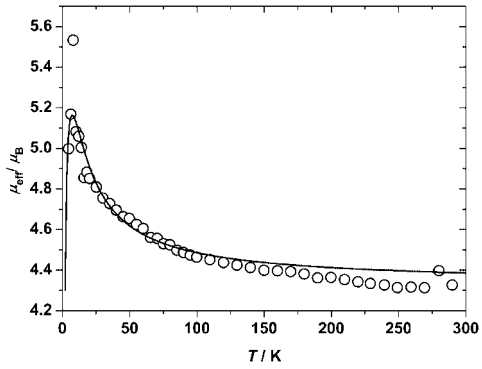


Figure 7. Temperature dependence of $\mu_{eff}$ for the molybdato complex **6** (per dinuclear complex). The full line represents the best theoretical fit to eq. (1). Experimental and calculated values are provided as supporting information.

To determine the magnitude of the exchange interactions, the temperature dependence of the magnetic data were simulated using the appropriate spin-Hamiltonian (1) including the isotropic HDVV exchange, the single-ion zero-field splitting and the single-ion Zeeman interaction by using a full-matrix diagonalization approach.[22,24] For complex **4** an excellent fit was obtained with $J$ = +24.8 $cm^{-1}$, $g$ = 2.08, and $|D|$ = 2.56 $cm^{-1}$. The experimental data for complex **6** were also analyzed in terms of the spin-Hamiltonian in eq. (1) The best fit gave $J$ = +3.75 $cm^{-1}$, $g$ = 2.17, and $|D|$ = 3.27 $cm^{-1}$. Although the experimental data could not be reproduced in every detail in this case, it is clear that the exchange interaction between the two $Ni^{II}$ ions in **6** is also ferromagnetic in nature and that this interaction is significantly weaker than in **4**.

$$H = -2JS_1S_2 + \sum_{i=1}^{2}[D_i(\hat{S}_{zi}^2 - \tfrac{1}{3}S_i(S_i+1)) + g_i\mu_B S_i B] \qquad (1)$$

It has been noted previously, that there exists a relationship between the sign and magnitude of the coupling parameter and the Ni–S–Ni angle in bioctahedral dinickel complexes supported by $(L^{Me})^{2-}$.[5,22] The coupling is antiferromagnetic in nature if the Ni–S–Ni angle deviates by more than about ±10° from 90°. For angles within the 90 ± 10° range a ferromagnetic interaction is observed. Moreover, the closer the Ni–S–Ni angles is at 90° the higher will be the magnitude of the ferromagnetic exchange interaction. Our observations of ferromagnetic exchange interactions in **4** and **6**, for which the Ni–S–Ni angles are in the 90 ± 10° range,[25] are in good agreement with the reported trend.

## Conclusions

The ability of the $[(L^{Me})Ni_2]^{2+}$ fragment to bind tetrahedral oxoanions of various main-group and transition elements has been demonstrated with the synthesis of a series of cationic ($n$ = 1) and neutral complexes ($n$ = 0) of the

 © 2007 Wiley-VCH Verlag GmbH & Co. KGaA, Weinheim 

type $[(L^{Me})Ni_2(EO_4)]^{n+}$, namely $[(L^{Me})Ni_2(ClO_4)]^+$ (**2**), $[(L^{Me})Ni_2(ReO_4)]^+$ (**3**), $[(L^{Me})Ni_2(SO_4)]$ (**4**), $[(L^{Me})Ni_2(CrO_4)]$ (**5**), $[(L^{Me})Ni_2(MoO_4)]$ (**6**), and $[(L^{Me})Ni_2(WO_4)]$ (**7**). All complexes were readily prepared and fully characterized by elemental analysis, IR and UV/Vis spectroscopy. The single-crystal X-ray structure determinations of **2**[$BPh_4$], **3**[$ReO_4$], **4**, **5**, and **7** showed the oxoanions to be coordinated in a $\mu_{1,3}$-bridging mode. Analysis of the structural parameters indicate that the monocharged $EO_4^-$ ions bind more weakly to the dinuclear $[(L^{Me})Ni_2]^{2+}$ fragment in **2** and **3** than the doubly charged $EO_4^{2-}$ groups in **4**–**7**. This was further confirmed by the lability of the $ClO_4^-$ ion in **2**, which renders this complex to be a suitable starting material for other $[(L^{Me})Ni_2(L')]^+$ complexes. The binding and solubility differences of the cationic and neutral $[(L^{Me})Ni_2(EO_4)]$ complexes suggests a possible use of the $[(L^{Me})Ni_2]^{2+}$ fragment in the selective recognition or separation of tetrahedral oxoanions. Studies on these and related topics are in progress in our laboratory.

## Experimental Section

All preparations were carried out under argon. Reagent grade solvents were used throughout. $[(L^{Me})Ni^{II}_2Cl]ClO_4$ (**1**) was prepared as described previously.[3] $[nBu_4N]_2[CrO_4]$ and $[nBu_4N]_2[MoO_4]$ were prepared from $[nBu_4N]OH$ and $CrO_3$ or $MoO_3{\cdot}2H_2O$,[26] respectively, using the procedure reported for $[nBu_4N]_2[WO_4]$.[27] All other reagents were obtained from standard commercial sources and used without further purifications. Melting points were determined in open glass capillaries and are uncorrected. Infrared spectra were recorded on a Bruker VECTOR 22 FT-IR spectrometer. The electronic absorption spectra were measured on a Jasco V-570 UV/Vis/NIR spectrometer. Elemental analyses were carried out with a VARIO EL elemental analyzer. Temperature-dependent (295–2 K) magnetic susceptibility measurements were carried out on Faraday balance (Manics DSM10 magnetometer) over the temperature range 4–295 K in an external magnetic field of 1.1 T. The observed susceptibility data were corrected for the underlying diamagnetism by the use of tabulated Pascal's constants.

***Caution!*** *Perchlorate salts of transition metal complexes are hazardous and may explode. Only small quantities should be prepared and handled with great care.*

**$[(L^{Me})Ni^{II}_2(\mu\text{-}ClO_4)][ClO_4]$ (2[$ClO_4$]):** To a solution of $[(L^{Me})Ni^{II}_2Cl][ClO_4]$ (**1**[$ClO_4$]) (184 mg, 0.200 mmol) in MeCN (50 mL) was added solid $Pb(ClO_4)_2$ (44.7 mg, 0.110 mmol). The reaction mixture was stirred for 2 h before $PbCl_2$ was removed by filtration. To the dark green filtrate was added a solution of $LiClO_4{\cdot}3H_2O$ (321 mg, 2.00 mol) in EtOH (100 mL). The solution was concentrated in vacuo to afford a dark green precipitate which was isolated by filtration and dried in air. Yield: 148 mg (75%). M.p. 308–309 °C (decomp.). IR (KBr): $\tilde{\nu}$ = 3443 (s br), 3045 (w), 3024 (w), 2992 (w), 2958 (s), 2900 (w), 2866 (s), 2815 (w), 1489 (w), 1462 (s), 1426 (w), 1395 (m), 1377 (w), 1363 (m), 1345 (vw), 1326 (w), 1310 (m), 1293 (w), 1262 (m), 1236 (m), 1200 (w), 1170 (m), 1156 (s), 1113 [vs, $\nu_3(ClO_4^-)$], 1097 [vs, $\nu_3(ClO_4^-)$], 1019 (m), 1000 (w), 981 (w), 911 (m), 932 (m), 895 (w), 882 (m), 824 (s), 818 (s), 808 (w), 754 (w), 624 [s, $\nu_4(ClO_4^-)$], 603 (w), 564 (w), 544 (w), 533 (w), 494 (w), 418 (w) $cm^{-1}$. UV/Vis (MeCN): $\lambda$ ($\varepsilon$, $M^{-1}cm^{-1}$) = 578 (129), 1066 (86) nm. $C_{38}H_{64}Cl_2N_6Ni_2O_8S_2{\cdot}EtOH{\cdot}H_2O$ (985.37 + 64.08): calcd. C 45.78, H 6.92, N 8.01, S 6.11; found C 46.06, H 6.82, N 8.06, S. 6.00.

**$[(L^{Me})Ni^{II}_2(ReO_4)][ReO_4]$ (3[$ReO_4$]):** To a solution of $[(L^{Me})Ni_2(ClO_4)][ClO_4]$ (98 mg, 0.100 mmol) in acetonitrile (30 mL) was added an acetonitrile solution (20 mL) of $[nBu_4N][ReO_4]$ (493 mg, 1.00 mmol). The mixture was stirred for 12 h and concentrated in vacuo to give a yellow solid, which was filtered, washed with ethanol and dried in air. To remove traces of perchlorate impurities this material was treated again with a ten-fold molar excess of $[nBu_4N][ReO_4]$ as described above. Recrystallization from a mixed ethanol/acetonitrile solvent system then gave the title compound in analytically pure form. Yield: 107 mg (81%). M.p. > 365 °C (decomp.). IR (KBr): $\tilde{\nu}$ = 3560 (m), 3465 (m), 2961 (s), 2867 (s), 2248 [w, $\nu$(CN)], 1869 (w), 1637 (w), 1597 (w), 1461 (s), 1423 (w), 1394 (m), 1362 (m), 1306 (m), 1262 (m), 1231 (m), 1200 (w), 1168 (w), 1152 (m), 1132 (w), 1102 (w), 1074 (s), 1063 (s), 1041 (s), 998 (w), 977 (w), 963 (w), 931 [s, $\nu_3(ReO_4^-)$], 909 [s, $\nu_3(ReO_4^-)$], 824 (s), 807 (m), 751 (m), 666 (w), 630 (m), 602 (w), 564 (w), 539 (w), 531 (w), 493 (w), 467 (w), 434 (w), 416 (w) $cm^{-1}$. UV/Vis ($CH_3CN$): $\lambda$ ($\varepsilon$, $M^{-1}cm^{-1}$) = 670 (79), 1058 (127) nm. $C_{38}H_{64}N_6Ni_2O_8Re_2S_2{\cdot}CH_3CN$ (1286.88 + 41.05): calcd. C 36.18, H 5.09, N 7.38, S 4.83; found C 36.81, H 5.22, N 7.44, S 5.00.

**$[(L^{Me})Ni^{II}_2(SO_4)]$ (4):** To a solution of $[nBu_4N][HSO_4]$ (0.17 mg, 0.50 mmol) in acetonitrile (50 mL) was added $NEt_3$ (50 mg, 0.50 mmol), followed by $[(L^{Me})Ni_2Cl][ClO_4]$ (184 mg, 0.200 mmol). The reaction mixture was stirred for 12 h to give a pale-green solid which was filtered, washed with methanol and dried in air. Yield: 129 mg (69%). M.p. 340–341 °C (decomp.). IR (KBr): $\tilde{\nu}$ = 3417 (s), 2962 (s), 2867 (s), 2091 (w), 1643 (m), 1461 (s), 1394 (w), 1362 (m), 1309 (w), 1263 (m), 1235 (m), 1202 (w), 1120 [s br, $\nu_3(SO_4^{2-})$], 1056 (s), 1041 (s), 999 (w), 984 (w), 931 (w), 912 (m), 879 (m), 825 (s), 818 (s), 754 (m), 651 (w), 629 (m), 620 [m, $\nu_4(SO_4^{2-})$], 564 (w), 543 (w), 493 (w), 446 (w), 416 (w) $cm^{-1}$. UV/Vis ($CH_2Cl_2$): $\lambda$ ($\varepsilon$, $M^{-1}cm^{-1}$) = 674 (16), 1122 (34) nm. $C_{38}H_{64}N_6Ni_2O_4S_3{\cdot}3H_2O$ (882.53 + 54.05): calcd. C 48.73, H 7.53, N 8.97, S 10.27; found C 48.66, H 7.59, N 8.90, S 10.08.

**$[(L^{Me})Ni^{II}_2(CrO_4)]$ (5):** To a solution of $[nBu_4N]_2[CrO_4]$ (120 mg, 0.200) in acetonitrile (40 mL) was added $[(L^{Me})Ni_2Cl][ClO_4]$ (184 mg, 0.200 mmol). The reaction mixture was stirred for 4 h to give a yellow precipitate which was isolated by filtration, washed with acetonitrile, and dried in air. Yield: 134 mg (73%). M.p. 300–301 °C (decomp.). IR (KBr): $\tilde{\nu}$ = 3409 (s), 3045 (m), 2961 (s), 2866 (s), 1638 (m), 1604 (m), 1480 (s), 1460 (s), 1393 (s), 1362 (s), 1307 (m), 1265 (m), 1232 (m), 1202 (w), 1170 (w), 1153 (m), 1132 (w), 1110 (w), 1080 (s), 1060 (s), 1044 (s), 1000 (w), 981 (w), 895 [s, $\nu_3(CrO_4^{2-})$], 817 (s), 752 (m), 667 (w), 629 (s), 564 (w), 541 (w), 529 (w), 448 (w), 415 (w) $cm^{-1}$. UV/Vis ($CH_2Cl_2$): $\lambda$ ($\varepsilon$, $M^{-1}cm^{-1}$) = 391 (1891), 686 (79), 1126 (88) nm. $C_{38}H_{64}CrN_6Ni_2O_4S_2{\cdot}H_2O$ (902.47 + 18.02): calcd. C 49.58, H 7.23, N 9.13, S 6.97; found C 49.31, H 6.89, N 9.54, S 6.52.

**$[(L^{Me})Ni^{II}_2(MoO_4)]$ (6):** To a solution of $[(L^{Me})Ni_2Cl][ClO_4]$ (92 mg, 0.100 mmol) in acetonitrile (40 mL) was added $[nBu_4N]_2[MoO_4]$ (129 mg, 0.200 mmol). The mixture was stirred for 12 h to give a green solid, which was filtered and dried in air. Yield: 86 mg (88%). M.p. 316–318 °C (decomp.). IR (KBr): $\tilde{\nu}$ = 3416 (s), 2953 (s), 2867 (s), 2248 (w), 2045 (w), 1639 (m), 1460 (s), 1393 (m), 1362 (m), 1306 (m), 1264 (m), 1231 (m), 1203 (w), 1170 (w), 1153 (m), 1131 (w), 1113 (w), 1079 (s), 1065 (s), 1044 (s), 1001 (w), 982 (w), 928 (m), 911 (m), 879 (m), 854 [s, $\tilde{\nu}_3(MoO_4^{2-})$], 817 [s, $\nu_3(MoO_4^{2-})$], 753 (m), 667 (w), 628 (m), 603 (w), 564 (w), 528 (w), 493 (w), 446 (w), 414 (w) $cm^{-1}$. UV/Vis ($CH_2Cl_2$): $\lambda$ ($\varepsilon$, $M^{-1}cm^{-1}$) = 358 (2256), 690 (104), 1136 (142) nm. $C_{38}H_{64}MoN_6Ni_2O_4S_2{\cdot}2H_2O$ (946.41 + 36.03): calcd. C 46.46, H 6.98, N 8.55, S 6.53; found C 46.63, H 6.66, N 9.15, S 6.22.

 © 2007 Wiley-VCH Verlag GmbH & Co. KGaA, Weinheim 

Table 4. Crystallographic data for **2**, **3**, **4**, and **7**.

| Compound | **2**[$BPh_4$]·1.5$Me_2CO$·0.5MeOH | **3**[$ReO_4$]·$H_2O$ | **4**·2$H_2O$·MeCN | **7**·2$H_2O$·MeCN |
|---|---|---|---|---|
| Formula | $C_{67}H_{95}BClN_6Ni_2O_6S_2$ | $C_{38}H_{66}N_6Ni_2O_9Re_2S_2$ | $C_{40}H_{71}N_7Ni_2O_6S_3$ | $C_{40}H_{71}N_7Ni_2O_6S_2W$ |
| $M_r$ [g/mol] | 1308.29 | 1304.91 | 959.64 | 1111.43 |
| Space group | $P\bar{1}$ | $P\bar{1}$ | $P2_1/c$ | $P2_1/c$ |
| $a$ [Å] | 15.820(6) | 11.153(3) | 13.681(2) | 13.759(2) |
| $b$ [Å] | 16.171(5) | 14.408(4) | 19.196(3) | 19.550(2) |
| $c$ [Å] | 16.769(5) | 16.110(4) | 17.814(2) | 17.990(2) |
| $\alpha$ [deg] | 64.85(2) | 68.220(4) | 90.00 | 90 |
| $\beta$ [deg] | 72.37(2) | 69.864(5) | 102.91(3) | 102.01(3) |
| $\gamma$ [deg] | 66.13(2) | 78.117(4) | 90.00 | 90 |
| $V$ [Å$^3$] | 3506(2) | 2248(1) | 4560(1) | 4735(1) |
| $Z$ | 2 | 2 | 4 | 4 |
| $d_{calcd.}$ g/cm$^3$ | 1.239 | 1.928 | 1.398 | 1.559 |
| Crystal size [mm$^3$] | 0.42 × 0.35 × 0.20 | 0.30 × 0.30 × 0.20 | 0.20 × 0.20 × 0.20 | 0.26 × 0.20 × 0.18 |
| $\mu$(Mo-$K_\alpha$) [mm$^{-1}$] | 0.686 | 6.343 | 1.015 | 3.349 |
| $\theta$ limits [deg] | 1.36–28.77 | 1.42–28.87 | 1.58–28.85 | 1.56–28.88 |
| Measured reflections | 10580 | 19924 | 27855 | 17414 |
| Independent reflections | 10536 | 10343 | 10832 | 10583 |
| Observed reflections[a] | 4462 | 7529 | 7503 | 6872 |
| Parameters | 794 | 532 | 512 | 521 |
| $R_1$[b] ($R_1$ all data) | 0.0682 (0.1580) | 0.0400 (0.0626) | 0.0510 (0.0788) | 0.0434 (0.0813) |
| $wR_2$[c] ($wR_2$ all data) | 0.1772 (0.2165) | 0.1158 (0.1272) | 0.1576 (0.1752) | 0.0993 (0.1156) |
| Max./min. peaks [e Å$^3$] | 0.936/–0.818 | 2.085/–2.501 | 2.375/–1.079 | 1.409/–1.855 |
| CCDC number | 631192 | 631193 | 631194 | 631195 |

[a] Observation criterion: $I > 2\sigma(I)$. [b] $R1 = \Sigma||F_o| - |F_c||/\Sigma|F_o|$. [c] $wR2 = \{\Sigma[w(F_o^2 - F_c^2)^2]/\Sigma[w(F_o^2)^2]\}^{1/2}$.

**[($L^{Me}$)$Ni^{II}_2$($WO_4$)] (7):** To a solution of [($L^{Me}$)$Ni_2Cl$][$ClO_4$] (92 mg, 0.100 mmol) in acetonitrile (40 mL) was added [$n$$Bu_4N$]$_2$[$WO_4$] (146 mg, 0.200 mmol). The mixture was stirred for 4 h to give a green solid, which was filtered and dried in air. Yield: 92 mg (86%). M.p. 318–320 °C (decomp.). IR (KBr): $\tilde{\nu}$ = 3399 (s), 2951 (s), 2867 (s), 1685 (m), 1647 (m), 1604 (m), 1459 (s), 1393 (m), 1362 (m), 1306 (w), 1262 (m), 1231 (m), 1203 (w), 1170 (w), 1153 (m), 1131 (w), 1112 (w), 1079 (s), 1065 (s), 1044 (s), 1001 (w), 979 (w), 928 (m), 911 (m), 898 (m), 880 (m), 857 [s, $\nu_3(WO_4^{2-})$], 818 [s, $\nu_3(WO_4^{2-})$], 753 (m), 667 (w), 628 (m), 604 (w), 563 (w), 542 (w), 528 (w), 493 (w), 447 (w), 414 (w) cm$^{-1}$. UV/Vis ($CH_2Cl_2$): $\lambda$ ($\varepsilon$, M$^{-1}$cm$^{-1}$) = 689 (90), 1132 (130) nm. $C_{38}H_{64}N_6Ni_2O_4S_2W$·2$H_2O$ (946.41 + 36.03): calcd. C 42.64, H 6.40, N 7.85, S 5.99; found C 42.82, H 6.27, N 8.71, S 5.50.

**Crystallography:** Crystals of **2**[$BPh_4$]·1.5($Me_2CO$)·0.5$H_2O$ were obtained from an acetone solution of **2**[$ClO_4$] to which a solution of $NaBPh_4$ in methanol had been added. Single-crystals of **5** were grown by recrystallization from $CH_2Cl_2$. All other compounds crystallized upon slow evaporation from 1:1 acetonitrile/ethanol solutions. Crystal data and refinement details are listed in Table 4. The intensity data were collected on a Bruker Smart CCD diffractometer. Graphite-monochromated Mo-$K_\alpha$ radiation ($\lambda$ = 0.71073 Å) was used throughout. The data were processed with SAINT[28] and corrected for absorption using SADABS.[29] The structures were solved by direct methods (SHELXS)[30] and refined by full-matrix least-squares on $F^2$ using SHELXTL (version 5.1).[31] All non-hydrogen atoms were refined with anisotropic displacement parameters, except the C and O atoms of the disordered MeOH molecule in **2**.

Some of the solvate molecules in **2**, **4** and **7** were found to be severely disordered and/or partially occupied. The MeOH molecule in **2** lies near an inversion center such that only half a molecule lies in the asymmetric unit. The occupancy factor of one acetone molecule was also reduced to 0.5, and the C and O atoms were refined with equivalent anisotropic thermal parameters. In addition, one *tert*-butyl group was found to be disordered over two positions. A split atom model with restrained C–C and C···C distances was applied by using appropriate SADI instructions. In the isomorphous complexes **4** and **7**, one water molecule was found to be disordered over two sites with occupation factors of ca. 0.7 and 0.3. The C and N atoms of the acetonitrile molecule in **7** reveal high displacement parameters indicative of disorder. It was not possible to resolve this disorder, and geometric constraints using DFIX instructions were required to keep the structure of the solvate molecule reasonable. The MeCN molecule in **4**·2$H_2O$·MeCN could not be located from Fourier maps. The coordinates of the atoms were taken from the structure of **7** and the acetonitrile molecule was allowed to ride on the oxygen atom O(6b) by using an AFIX 3 instruction. The hydrogen atoms were placed at calculated positions and refined as riding atoms with isotropic displacement parameters, e.g., $U_{iso}$(H) = 1.2 × $U_{iso}$(parent) or $U_{iso}$(H) = 1.5 × $U_{iso}$(C) for methyl groups. The hydrogen atoms of the water molecule in **3** were calculated assuming a O–H distance of 0.96 Å and an ideal tetrahedral geometry. For **4** and **7**, water and acetonitrile hydrogen atoms were not included in the refinement. Graphics were obtained with ORTEP 3 for Windows.[32]

CCDC-631192 to -631195 contain the supplementary crystallographic data for this paper. These data can be obtained free of charge from The Cambridge Crystallographic Data Centre via www.ccdc.cam.ac.uk/data_request/cif.

**Supporting Information** (see also the footnote on the first page of this article): Derivation of the magnetic susceptibility expression for **4** and **6** and magnetic susceptibility data for **4** and **5** as a function of the temperature.

## Acknowledgments

This work was supported by the Deutsche Forschungsgemeinschaft (DFG) (KE 585/3-1,2,3). We are particularly grateful to Prof. Dr. H. Vahrenkamp for providing facilities for IR and X-ray crystallographic measurements.

 © 2007 Wiley-VCH Verlag GmbH & Co. KGaA, Weinheim 

[1] B. Kersting, *Z. Anorg. Allg. Chem.* **2004**, *630*, 765–780.
[2] V. Lozan, B. Kersting, *Eur. J. Inorg. Chem.* **2005**, 504–512.
[3] B. Kersting, G. Steinfeld, *Chem. Commun.* **2001**, 1376–1377.
[4] M. H. Klingele, G. Steinfeld, B. Kersting, *Z. Naturforsch., Teil B* **2001**, *56*, 901–907.
[5] J. Hausmann, V. Lozan, M. H. Klingele, G. Steinfeld, D. Siebert, Y. Journaux, J. J. Girerd, B. Kersting, *Chem. Eur. J.* **2004**, *10*, 1716–1728.
[6] Y. Journaux, J. Hausmann, V. Lozan, B. Kersting, *Chem. Commun.* **2006**, 83–84.
[7] B. Kersting, *Angew. Chem.* **2001**, *113*, 4110–4112; *Angew. Chem. Int. Ed.* **2001**, *40*, 3988–3990.
[8] B. Kersting, G. Steinfeld, *Inorg. Chem.* **2002**, *41*, 1140–1150.
[9] G. Steinfeld, V. Lozan, B. Kersting, *Angew. Chem.* **2003**, *115*, 2363–2365; *Angew. Chem. Int. Ed.* **2003**, *42*, 2261–2263.
[10] B. Kersting, G. Steinfeld, unpublished results.
[11] V. Lozan, B. Kersting, *Inorg. Chem.* **2006**, *45*, 5630–5634.
[12] J. Nelson, V. McKee, R. M. Town in *Macrocyclic Chemistry, Current Trends and Future Perspectives*, K. Gloe (Eds.), Springer, Berlin, **2005**.
[13] *Supramolecular Chemistry of Anions* (Eds.: A. Bianchi, K. Bowman-James, E. Garcia-Espana), Wiley-VCH, New York, **1997**.
[14] R. Coomber, W. P. Griffith, *J. Chem. Soc. A* **1968**, 1128–1131.
[15] K. Nakamoto, *Infrared and Raman Spectra of Inorganic and Coordination Compounds*, 5th ed., part B; VCH-Wiley, New York, **1997**, p. 79ff.
[16] A. Thiele, J. Fuchs, *Z. Naturforsch., Teil B* **1979**, *34*, 145–154.
[17] M. D. Santana, A. Rufete, G. Garcia, G. Lopez, J. Casabo, A. Cabrero, E. Molins, C. Miravitlles, *Polyhedron* **1997**, *16*, 3713–3721.
[18] M. Yonemura, Y. Matsumura, H. Furutachi, M. Ohba, H. Okawa, D. E. Fenton, *Inorg. Chem.* **1997**, *36*, 2711–2717.
[19] N. Weinstock, H. Schulze, A. Müller, *J. Chem. Phys.* **1973**, *59*, 5063–5067.
[20] A. McAuley, S. Subramanian, *Inorg. Chem.* **1990**, *29*, 2830–2837.
[21] K. R. Adam, M. Antolovich, D. S. Baldwin, L. G. Bridgen, P. A. Duckworth, L. F. Lindoy, A. Bashall, M. McPartlin, P. A. Tasker, *J. Chem. Soc., Dalton Trans.* **1992**, 1869–1876.
[22] Y. Journaux, T. Glaser, G. Steinfeld, V. Lozan, B. Kersting, *Dalton Trans.* **2006**, 1738–1748.
[23] Preliminary data of the crystal structure determination of **5**: $C_{38}H_{64}CrN_6Ni_2O_4S_2$, $M_r$ = 902.49, orthorhombic, space group *P*nma, $a$ = 26.91(4), $b$ = 12.30(2), $c$ = 12.84(2) Å, $V$ = 4250(13) Å$^3$, $Z$ = 4, $\mu$(Mo-$K_a$) = 1.27 mm$^{-1}$, $\rho_{calcd.}$ = 1.410 g cm$^{-3}$, $R$ = 0.18 for 5310 reflections with $I > 2\sigma(I)$.
[24] B. Kersting, G. Steinfeld, D. Siebert, *Chem. Eur. J.* **2001**, *7*, 4253–4258.
[25] The average Co–S–Co angle in [($L^{Me}$)$Co_2(MoO_4)$] is at 90.75°, see ref.[10]. We assume that the Ni–S–Ni angles in **4** is also larger in than 90°. We estimate it to be ca. 93° based on the structure of **7**.
[26] G. Brauer, *Handbuch der Präparativen Anorganischen Chemie*, vol. 3, Ferdinand Enke Verlag, Stuttgart, **1981**, p. 1544.
[27] W. Clegg, R. J. Errington, K. A. Fraser, D. G. Richards, *J. Chem. Soc., Chem. Commun.* **1993**, 1105–1107.
[28] *SAINT+*, V6.02, Data Reduction and Frame Integration Program for the CCD Area-Detector System, Bruker AXS, Madison, WI, **1999**.
[29] G. M. Sheldrick, *Program SADABS:* Area-detector absorption correction.
[30] G. M. Sheldrick, *Acta Crystallogr., Sect. A* **1990**, *46*, 467–473.
[31] G. M. Sheldrick, *SHELXTL NT 5*.10, Bruker AXS, Bruker AXS, Madison, WI, **1998**.
[32] a) L. J. Farrugia, ORTEP 3 for Windows, Version 1.05, University of Glasgow, **1997**; L. J. Farrugia, *J. Appl. Crystallogr.* **1997**, *30*, 565.

Received: January 5, 2007
Published Online: February 22, 2007

 © 2007 Wiley-VCH Verlag GmbH & Co. KGaA, Weinheim 

DOI: 10.1002/ejic.200600945

# Synthesis and Structural Characterisation of Diorganotin(IV) and Diphenyllead(IV) Complexes of Pyrimidine-2-thionate Derivatives

**Antonio Rodríguez,[a] Antonio Sousa-Pedrares,[a] J. Arturo García-Vázquez,*[a] Jaime Romero,[a] Antonio Sousa,[a] and Umberto Russo[b]**

**Keywords:** Tin / Lead / N,S ligands / NMR spectroscopy / Moessbauer spectroscopy

The reaction between the ligands 4-(trifluoromethyl)pyrimidine-2-thione (4-$CF_3$pymSH) and 6-methyl-4-(trifluoromethyl)pyrimidine-2-thione (6-Me-4-$CF_3$pymSH) and the corresponding diorganotin(IV) dichloride [$R_2SnCl_2$] (R = Me, *t*Bu or Ph) or diphenyllead(IV) dichloride in the presence of triethylamine yields the diorganotin(IV) complexes [$R_2$Sn(4-$CF_3$pymS)$_2$] and [$R_2$Sn(6-Me-4-$CF_3$pymS)$_2$] or diorganolead-(IV) complexes [$Ph_2$Pb(4-$CF_3$pymS)$_2$] and [$Ph_2$Pb(6-Me-4-$CF_3$pymS)$_2$], respectively. The compounds have been characterised by microanalysis, mass spectrometry and by IR and Mössbauer spectroscopy and, in the case of the compound that was sufficiently soluble, by $^1$H, $^{13}$C, $^{119}$Sn and $^{207}$Pb NMR spectroscopy. The compounds [$Me_2$Sn(4-$CF_3$pymS)$_2$] (**1**), [$Ph_2$Sn(4-$CF_3$pymS)$_2$] (**2**), [$Ph_2$Sn(6-Me-4-$CF_3$pymS)$_2$] (**5**), [*t*$Bu_2$Sn(6-Me-4-$CF_3$pymS)$_2$] (**6**), [$Ph_2$Pb(4-$CF_3$pymS)$_2$] (**7**) and [$Ph_2$Pb(6-Me-4-$CF_3$pymS)$_2$] (**8**) have also been characterised by X-ray diffraction. The X-ray crystal structures show that the metal centre in all these complexes is in a distorted octahedral environment with bonds to two carbon atoms from the aryl or alkyl substituents and to sulfur and heterocyclic nitrogen atoms from the pyrimidine derivative, which acts a ($\kappa^2$-N,S) chelating ligand.
(© Wiley-VCH Verlag GmbH & Co. KGaA, 69451 Weinheim, Germany, 2007)

## Introduction

The chemistry of metal complexes of heterocyclic thione ligands is receiving increasing attention, largely because of the potential relevance of such compounds as models of active sites in metalloenzymes and also their ability to adopt geometries of variable nuclearity and great structural complexity, which is a result of the tendency of thiolate ligands to bridge metal centres to yield oligomeric or polymeric species.[1–8]

However, in comparison with the coordination chemistry of transition metals, the chemistry of main group metals with sulfur ligands remains much less developed.[9–13] In many cases, the interaction of toxic main group metals with biological systems frequently involves bonding of the metal to the sulfhydryl groups present in enzymes. Hence, an insight into the chemistry of main group thiolate compounds is important in terms of understanding the aforementioned interaction and for the design of detoxifying agents.[14,15] This interest has led us to study organotin and organolead compounds that, in a biological medium, react with thiol groups in relevant molecules to yield products that are characterised by metal–thiolate interactions, which are of interest in the design of sequestering agents; indeed, several papers have been dedicated to the design of specific complexing agents.[15,16] In addition, organotin complexes have been studied more recently in terms of their pharmacological and antitumour activity.[17–22]

As a continuation of our studies into the coordination chemistry of sterically hindered heterocyclic thiones,[23] we report here the synthesis and characterisation of diorganotin(IV) and diphenyllead(IV) complexes with 4-(trifluoromethyl)pyrimidine-2-thione and 6-methyl-4-(trifluoromethyl)-pyrimidine-2-thione ligands, the structures of which are shown in Scheme 1. These ligands, besides having solubilising and bulky groups, belong to one of the most versatile types of sulfur ligand in terms of coordination modes. For example, they can act (a) as a neutral monodentate ligand coordinated through the sulfur atom,[24] through one of the nitrogen atoms,[25] and as a bridging ligand through sulfur[26] or as an N,S-chelating ligand,[27,28] or (b) as an anionic ligand, in which case they can be monodentate through the sulfur atom,[29] an N,S-chelating ligand[30–32] or

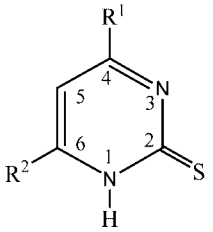


$R^1$ = 4-$CF_3$; $R^2$ = H, $CH_3$

Scheme 1.

[a] Departamento de Química Inorgánica, Universidad de Santiago de Compostela,
15782, Santiago de Compostela, Spain
[b] Dipartartimento di Scienze Chimiche Universiá degli Studi de Padova,
Padova, Italy

 © 2007 Wiley-VCH Verlag GmbH & Co. KGaA, Weinheim 

a binuclear bridging ligand through nitrogen and sulfur,[33] or sulfur only,[34] and as a binuclear triply bridging ligand through sulfur and one of the nitrogen atoms,[31,35] or the two nitrogen and sulfur atoms,[36,37] and as a trinuclear triply bridging system.[38]

Moreover, these ligands were chosen because they are unsymmetrical ambidentate systems and can therefore give rise to linkage isomerism when they are coordinated in some of the aforementioned ways.

## Results and Discussion

A series of diorganotin(IV) and diphenyllead(IV) complexes of general formulae $[R_2Sn(RpymS)_2]$ and $[Ph_2Pb(RpymS)_2]$ were synthesised in reasonable yields (47–74%) from the appropriate diorganotin(IV) dichloride $[R_2SnCl_2]$ (R = Me, Ph, *t*Bu) or diphenyllead(IV) dichloride ($Ph_2PbCl_2$) and the corresponding pyrimidine-2-thione derivative in methanol in the presence of triethylamine, according to Scheme 2.

The complexes reported here are air-stable as solids and do not show a tendency to decompose or oxidise. In addition, they have quite high solubility in the reaction medium, so the resulting solutions were concentrated in order to obtain the corresponding solids. Crystals of $[Ph_2Sn(4\text{-}CF_3pymS)_2]$ (**2**), $[Ph_2Sn(6\text{-Me-}4\text{-}CF_3pymS)_2]$ (**5**), $[Ph_2Pb(4\text{-}CF_3pymS)_2]$ (**7**) and $[Ph_2Pb(6\text{-Me-}4\text{-}CF_3pymS)_2]$ (**8**) suitable for X-ray studies were obtained by slow evaporation of the mother liquor at room temperature; $[Me_2Sn(4\text{-}CF_3pymS)_2]$ (**1**) and $[tBu_2Sn(6\text{-Me-}4\text{-}CF_3pymS)_2]$ (**6**) were obtained by recrystallisation of the initial product from ethanol.

### Molecular Structures of $[Me_2Sn(4\text{-}CF_3pymS)_2]$ (1), $[Ph_2Sn(4\text{-}CF_3pymS)_2]$ (2), $[Ph_2Sn(6\text{-Me-}4\text{-}CF_3pymS)_2]$ (5) and $[tBu_2Sn(6\text{-Me-}4\text{-}CF_3pymS)_2]$ (6)

The molecular structures of **1**, **2**, **5** and **6** are shown in Figures 1, 2, 3 and 4, respectively, together with the atom labelling scheme adopted. Crystallographic data and a se-

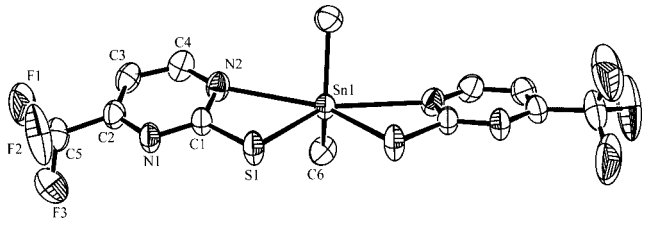


Figure 1. Crystal structure of $[Me_2Sn(4\text{-}CF_3pymS)_2]$ (**1**) (50% probability displacement ellipsoids).

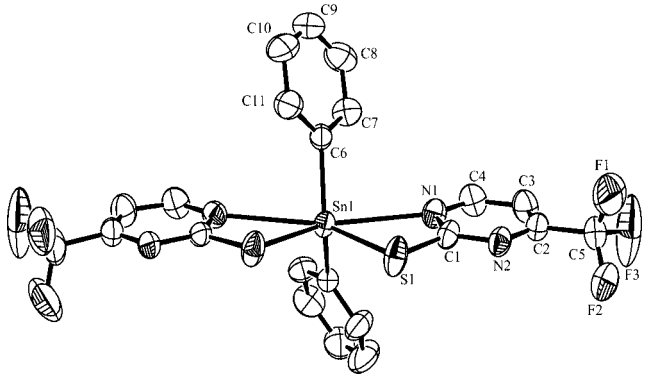


Figure 2. Crystal structure of $[Ph_2Sn(4\text{-}CF_3pymS)_2]$ (**2**) (50% probability displacement ellipsoids).

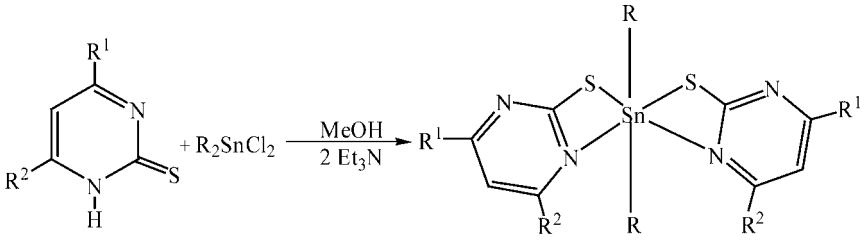


R = Me, *t*Bu, Ph; $R^1 = CF_3$; $R^2$ = H, $CH_3$

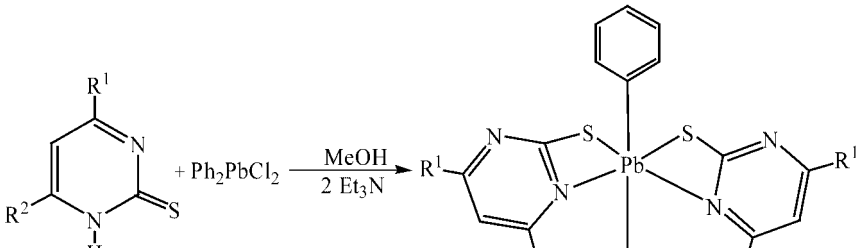


$R^1 = CF_3$; $R^2$ = H, $CH_3$

Scheme 2. General synthesis of the diorganotin(IV) and diphenyllead(IV) complexes.

 © 2007 Wiley-VCH Verlag GmbH & Co. KGaA, Weinheim 

lection of bond lengths and angles (with the estimated standard deviations) are given in the Experimental Section and Tables 1, 2, 3 and 4, respectively.

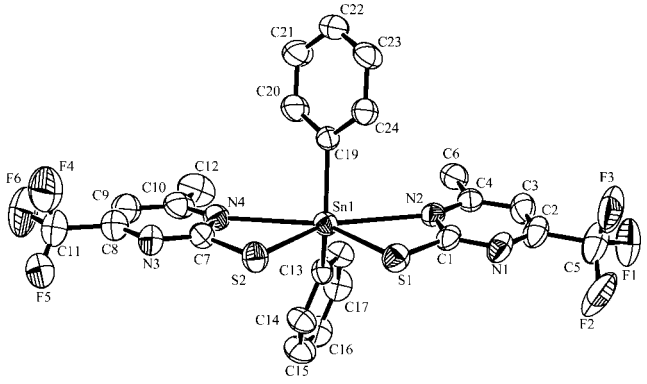


Figure 3. Crystal structure of [$Ph_2Sn$(6-Me-4-$CF_3$pymS)$_2$] (**5**) (50% probability displacement ellipsoids).

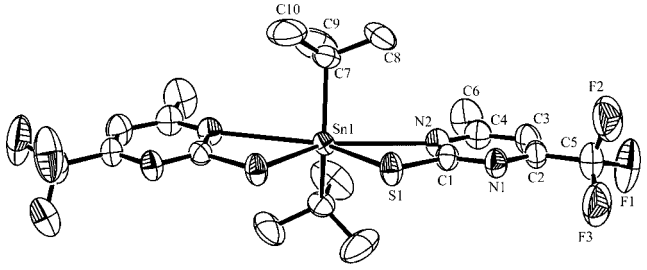


Figure 4. Crystal structure of [$t$Bu$_2$Sn(6-Me-4-$CF_3$pymS)$_2$] (**6**) (50% probability displacement ellipsoids).

Table 1. Selected bond lengths [Å] and angles [°] for [$Me_2$Sn(4-$CF_3$pymS)$_2$] (**1**).[a]

| | | | |
|---|---|---|---|
| Sn(1)–C(6) | 2.108(4) | Sn(1)–S(1) | 2.4836(9) |
| Sn(1)–N(2) | 2.770(3) | S(1)–C(1) | 1.744(3) |
| N(1)–C(2) | 1.327(4) | N(1)–C(1) | 1.335(4) |
| N(2)–C(4) | 1.315(5) | N(2)–C(1) | 1.345(5) |
| C(6)–Sn(1)–C(6)#1 | 123.0(2) | C(6)–Sn(1)–S(1)#1 | 113.87(11) |
| C(6)#1–Sn(1)–S(1)#1 | 107.02(12) | C(6)–Sn(1)–S(1) | 107.02(12) |
| C(6)#1–Sn(1)–S(1) | 113.87(11) | S(1)#1–Sn(1)–S(1) | 86.15(4) |
| C(6)–Sn(1)–N(2) | 85.53(13) | C(6)#1–Sn(1)–N(2) | 82.66(13) |
| S(1)#1–Sn(1)–N(2) | 145.02(7) | S(1)–Sn(1)–N(2) | 59.70(6) |
| C(6)–Sn(1)–N(2)#1 | 82.66(13) | C(6)#1–Sn(1)–N(2)#1 | 85.53(13) |
| S(1)#1–Sn(1)–N(2)#1 | 59.70(6) | S(1)–Sn(1)–N(2)#1 | 145.02(7) |
| N(2)–Sn(1)–N(2)#1 | 155.11(12) | C(4)–N(2)–Sn(1) | 151.8(3) |

| C–H–X interactions[b] | D–H | H···A | D–A | D–H···A |
|---|---|---|---|---|
| C(3)#2–H(3)#2···S(1) | 0.930 | 2.991 | 3.778 | 143.34 |
| C(6)–H(6b)···S(1)#3 | 0.960 | 3.036 | 3.984 | 169.61 |

[a] Symmetry transformations used to generate equivalent atoms: #1: $-x + 1$, $y$, $-z + 3/2$. [b] Symmetry codes: #2: $1.5 - x$, $-0.5 + y$, $1.5 - z$; #3: $x$, $-y$, $0.5 + z$.

The tin atom in **1**, **2** and **6** is located on a twofold rotation axis; accordingly, both methyl, phenyl or *tert*-butyl groups and both pyrimidine-2-thionate derivatives are symmetry equivalent. The molecular structures of **1**, **2**, **5** and **6** consist of neutral monomeric units with the tin atom bonded to two carbon atoms from the alkyl or phenyl groups and two anionic pyrimidinethionate derivatives, which act as chelating ligands through the sulfur atom and

Table 2. Selected bond lengths [Å] and angles [°] for [$Ph_2$Sn(4-$CF_3$pymS)$_2$] (**2**).[a]

| | | | |
|---|---|---|---|
| Sn(1)–C(6) | 2.121(2) | Sn(1)–S(1) | 2.4599(7) |
| Sn(1)–N(1) | 2.859(2) | S(1)–C(1) | 1.734(3) |
| N(1)–C(4) | 1.321(3) | N(1)–C(1) | 1.337(3) |
| N(2)–C(2) | 1.321(4) | N(2)–C(1) | 1.342(3) |
| C(6)–Sn(1)–C(6)#1 | 125.67(13) | C(6)–Sn(1)–S(1) | 112.86(6) |
| C(6)#1–Sn(1)–S(1) | 105.14(6) | C(6)–Sn(1)–S(1)#1 | 105.14(6) |
| C(6)#1–Sn(1)–S(1)#1 | 112.86(6) | S(1)–Sn(1)–S(1)#1 | 89.31(3) |
| C(6)–Sn(1)–N(1)#1 | 81.82(7) | C(6)#1–Sn(1)–N(1)#1 | 86.06(7) |
| S(1)–Sn(1)–N(1)#1 | 147.88(5) | S(1)#1–Sn(1)–N(1)#1 | 58.78(4) |
| C(6)–Sn(1)–N(1) | 86.06(7) | C(6)#1–Sn(1)–N(1) | 81.82(7) |
| S(1)–Sn(1)–N(1) | 58.78(4) | S(1)#1–Sn(1)–N(1) | 147.88(5) |
| N(1)#1–Sn(1)–N(1) | 153.28(8) | C(4)–N(1)–Sn(1) | 154.86(18) |

| C–H–X interactions[b] | D–H | H···A | D–A | D–H···A |
|---|---|---|---|---|
| C(7)#1–H(7)#1···S(1) | 0.930 | 2.772 | 3.573 | 144.79 |
| C(4)#1–H(4)#1···S(1) | 0.930 | 3.007 | 3.838 | 149.52 |
| C(4)#1–H(4)#1···N(2) | 0.930 | 2.929 | 3.807 | 157.94 |

[a] Symmetry transformations used to generate equivalent atoms: #1: $-x + 2$, $y$, $-z + 1/2$. [b] Symmetry code #1: $x$, $-1 + y$, $z$.

Table 3. Selected bond lengths [Å] and angles [°] for [$Ph_2$Sn(6-Me-4-$CF_3$pymS)$_2$] (**5**).

| | | | |
|---|---|---|---|
| Sn(1)–C(13) | 2.126(3) | Sn(1)–C(19) | 2.128(3) |
| Sn(1)–S(2) | 2.4665(10) | Sn(1)–S(1) | 2.4719(10) |
| Sn(1)–N(2) | 2.801(3) | Sn(1)–N(4) | 2.837(3) |
| S(1)–C(1) | 1.753(4) | S(2)–C(7) | 1.750(4) |
| N(1)–C(2) | 1.322(5) | N(1)–C(1) | 1.335(4) |
| N(2)–C(4) | 1.328(4) | N(2)–C(1) | 1.341(4) |
| N(3)–C(8) | 1.309(6) | N(3)–C(7) | 1.338(5) |
| N(4)–C(10) | 1.329(5) | N(4)–C(7) | 1.333(5) |
| C(13)–Sn(1)–C(19) | 126.76(12) | C(13)–Sn(1)–S(2) | 107.90(9) |
| C(19)–Sn(1)–S(2) | 109.24(9) | C(13)–Sn(1)–S(1) | 110.91(9) |
| C(19)–Sn(1)–S(1) | 107.45(9) | S(2)–Sn(1)–S(1) | 87.55(3) |
| C(13)–Sn(1)–N(2) | 84.73(10) | C(19)–Sn(1)–N(2) | 84.11(10) |
| S(2)–Sn(1)–N(2) | 147.22(6) | S(1)–Sn(1)–N(2) | 59.70(6) |
| C(13)–Sn(1)–N(4) | 79.38(10) | C(19)–Sn(1)–N(4) | 88.51(10) |
| S(2)–Sn(1)–N(4) | 59.00(7) | S(1)–Sn(1)–N(4) | 146.38(7) |
| N(2)–Sn(1)–N(4) | 153.45(9) | C(4)–N(2)–Sn(1) | 152.1(2) |

| C–H–X interactions[a] | D–H | H···A | D–A | D–H···A |
|---|---|---|---|---|
| C(15)#1–H(15)#1···S(1) | 0.930 | 3.056 | 3.952 | 162.18 |
| C(6)#2–H(6c)#2···S(2) | 0.960 | 2.767 | 3.677 | 158.48 |

[a] Symmetry codes: #1: $-x + 2$, $-y$, $1 - z$; #2: $x + 0.5$, $-y + 0.5$, $z + 0.5$.

Table 4. Selected bond lengths [Å] and angles [°] for [$t$Bu$_2$Sn(6-Me-4-$CF_3$pymS)$_2$][a] (**6**).

| | | | |
|---|---|---|---|
| Sn(1)–C(7) | 2.216(4) | Sn(1)–S(1) | 2.4886(12) |
| Sn(1)–N(2) | 2.978(4) | S(1)–C(1) | 1.746(5) |
| N(1)–C(2) | 1.336(6) | N(1)–C(1) | 1.342(6) |
| N(2)–C(4) | 1.326(6) | N(2)–C(1) | 1.345(6) |
| C(7)–Sn(1)–C(7)#1 | 131.6(2) | C(7)–Sn(1)–S(1) | 106.37(13) |
| C(7)#1–Sn(1)–S(1) | 109.09(13) | C(7)–Sn(1)–S(1)#1 | 109.09(13) |
| C(7)#1–Sn(1)–S(1)#1 | 106.37(13) | S(1)–Sn(1)–S(1)#1 | 84.12(5) |
| C(7)–Sn(1)–N(2) | 87.31(15) | C(7)#1–Sn(1)–N(2) | 85.26(15) |
| S(1)–Sn(1)–N(2) | 57.10(8) | S(1)#1–Sn(1)–N(2) | 141.05(8) |
| N(2)–Sn(1)–N(2)#1 | 161.82(15) | C(4)–N(2)–Sn(1) | 154.6(3) |

| C–H–X interactions[b] | D–H | H···A | D–A | D–H···A |
|---|---|---|---|---|
| C(6)#1–H(6c)#1···S(1) | 0.960 | 3.165 | 3.733 | 119.54 |
| C(6)#1–H(6b)#1···N(1) | 0.960 | 2.955 Å | 3.401 | 109.70 |

[a] Symmetry transformations used to generate equivalent atoms: #1: $-x + 1$, $y$, $-z + 1/2$. [b] Symmetry code: #1: $x$, $-1 + y$, $z$.

 © 2007 Wiley-VCH Verlag GmbH & Co. KGaA, Weinheim 

one of the nitrogen atoms. Therefore, this pyrimidinethionate derivative is an example of an unsymmetrical ambidentate ligand whose N,S-bidentate coordination to the tin atom could generate linkage isomerism depending on which nitrogen atom is involved. In the case under discussion, the ligand uses the nitrogen atom with less hindrance (i.e., that in position 1), which is the nitrogen atom farthest from the trifluoromethyl substituent in the pyrimidine ring. This suggests that the nitrogen atom involved in the coordination in **1** and **2** is determined by the steric hindrance introduced by the trifluoromethyl group. In the case of the 6-methyl-4-(trifluoromethyl)pyrimidine-2-thionate ligand, the presence of the $CF_3$ group in the 4-position produces greater steric hindrance than the methyl group in the 6-position and, once again, the heterocyclic ligand in $[Ph_2Sn(6\text{-Me-}4\text{-}CF_3pymS)_2]$ (**5**) and $[tBu_2Sn(6\text{-Me-}4\text{-}CF_3pymS)_2]$ (**6**) adopts the same coordination mode as the 4-(trifluoromethyl)pyrimidine-2-thionate ligand in **1** and **2**. Naturally, other factors, such as crystal packing and inter- and/or intramolecular interactions, can also play a role in the coordination mode of the 4-(trifluoromethyl)pyrimidine-2-thionate ligand.

These complexes can be considered to be examples of a hexacoordinate bischelate diorganotin(IV) complex in which the environment around the tin atom is highly distorted octahedral. The C–Sn–C bond angle [123.0(2)° for **1**, 125.67(13)° for **2**, 126.76(12)° for **5** and 131.6(2)° for **6**] is intermediate between the ideal value for the *cis* isomer (90°) and the *trans* isomer (180°), a similar situation to that found in the majority of this type of compounds (122–155°), which suggests that the geometry of **1**, **2**, **5** and **6** can be described as a distorted trapezoidal bipyramid[39] in which the equatorial plane is formed by the sulfur and nitrogen atoms (the longest vertices of the trapezium consist of the two nitrogen atoms and the shortest contain the sulfur atoms) and the axial positions are occupied by the two methyl groups. Another possibility is to consider the compound as a bicapped tetrahedron[40,41] defined by the carbon and sulfur atoms, with four tetrahedral angles close to the ideal value [105.14(6)–113.87(11)°] and two C–Sn–C [123.0(2)–131.6(2)°] and S–Sn–S [84.12(5)–89.31(3)°] angles distorted by the influence of the capping atoms.

The Sn–S bond lengths [2.4599(7)–2.4886(12) Å] are slightly longer than the sum of the covalent radii of these elements (2.42 Å). These values are similar to those found in other hexacoordinate diorganotin(IV) compounds with anionic heterocyclic thionate N,S-chelate ligands, which have values in the range 2.4476(10)–2.503(2) Å.[22,42–46] Examples of such complexes include $[Me_2Sn(pyS)_2]$ [2.487(2) Å],[42] $[Ph_2Sn(4,6\text{-}Me_2\text{-}2\text{-}pymS)_2]$ [2.4476(10)],[44] $[(cyclo\text{-}C_6H_{11})_2Sn(pyS)_2]$ [2.503(2) Å][45] and $[Ph_2Sn(pyS)_2]$ [2.485(1) Å].[46] The Sn–C bond lengths [2.108(4)–2.216(4) Å] are similar to those found in the complexes $[R_2Sn(chelate)_2]$ discussed above, which have values in the range 2.046(14)–2.25(1) Å. The Sn–N bond lengths [2.770(3)–2.978(4) Å] are shorter than the sum of the van der Waals radii of these elements (3.75 Å)[47] but are rather longer than those found in other complexes containing Sn–N bonds {e.g., 2.271(9) and 2.256(9) Å in $[Cl_2Sn(pyS)_2]$}.[48] However, the values obtained for **1**, **2**, **5** and **6** are in the range found in the aforementioned $[R_2Sn(chelate)_2]$ complexes [2.639(6)–3.083(3) Å].

Both heterocyclic ligands in complexes **1**, **2** and **6** are essentially planar, with the sulfur atoms lying practically in the plane of the pyrimidine ring to which they are bonded. On the other hand, the tin atom lies out of these planes by 0.265(6) Å for **1** and 0.171(8) Å for **6** and practically in the plane of the pyrimidine ring in **2** [0.064(4) Å]. Each of the pyrimidine rings in compound **5** is also planar. However, whereas the sulfur and tin atoms are in the plane of the pyrimidine ring to which they are bound [deviation of 0.002 Å for S(1) and 0.028 Å for Sn] for one of these ligands, for the other ligand S(2) (0.094 Å) and Sn (0.228 Å) lie out of the plane of the pyrimidine ring. Moreover, the interplanar angle between the pyrimidine rings in **2** is only 0.23°. Consequently, **2** has an arrangement similar to that found in the complex dimethylbis(pyridine-2-thionato)tin(IV)[42] but is very different to that in the complexes dichloridobis(pyridine-2-thionato)tin(IV),[48] in which the planes of the two ligand molecules are almost perpendicular, and in **1**, **5** and **6**, where the thionate ligands form a dihedral angle [20.2(2)°, 6.89° and 9.09°, respectively] intermediate between those found in the aforementioned complexes.

The S–C [1.734(3)–1.753(4) Å] bond lengths in **1**, **2**, **5** and **6** are intermediate between the values observed in the free ligands 4,6-dimethylpyrimidine-2-thione[28] and 4,6-dimethyl-1-phenylpyrimidine-2-thione[27] [1.692(2) and

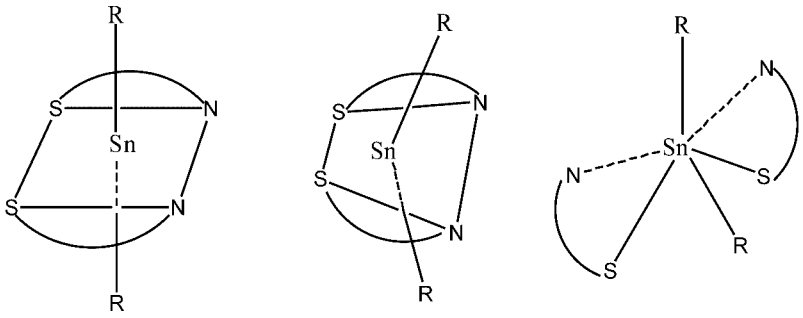


 © 2007 Wiley-VCH Verlag GmbH & Co. KGaA, Weinheim 

1.686(4) Å, respectively], which exist in the thione form in the solid state, and the values of 1.781(2) and 1.782(3) Å found in bis(pyrimidyl)-2,2′-disulfide[49] and bis(4,6-dimethylpyrimidyl)-2,2′-disulfide,[50] which possess a simple C–S bond; this suggests that the ligand is coordinated in a form that is closer to the pyrimidine-2-thionate than to the thione form.

### Molecular Structures of $[Ph_2Pb(4\text{-}CF_3pymS)_2]$ (7) and $[Ph_2Pb(6\text{-}Me\text{-}4\text{-}CF_3pymS)_2]$ (8)

The molecular structures of **7** and **8** are shown in Figure 5 and Figure 6, respectively, together with the atom labelling scheme adopted. Crystallographic data and selected bond lengths and angles are given in the Experimental Section and Tables 5 and 6, respectively.

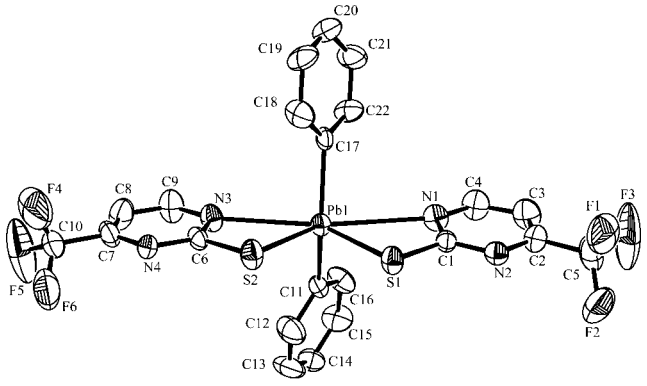


Figure 5. Crystal structure of $[Ph_2Pb(4\text{-}CF_3pymS)_2]$ (**7**) (50% probability displacement ellipsoids).

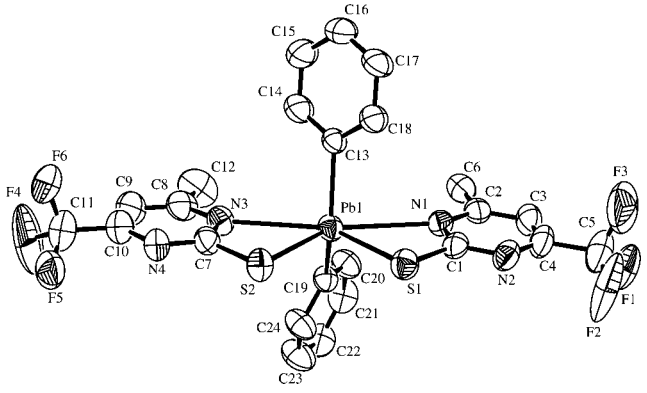


Figure 6. Crystal structure of $[Ph_2Pb(6\text{-}Me\text{-}4\text{-}CF_3pymS)_2]$ (**8**) (50% probability displacement ellipsoids).

The structures determined for these complexes are, as far as we know, the first examples of lead(IV) complexes containing heterocyclic thione ligands, such as pyridine-2-thione or pyrimidine-2-thione. The only previously reported structures containing lead and this type of ligand are the mononuclear complex $[Pb(3\text{-}CF_3pyS)_2]$[9] and trinuclear complex $[Pb_3(3\text{-}Me_3SipyS)_6]$.[51] In both cases the lead atom is in the oxidation state (II). This situation precludes a direct comparison involving the structural parameters of the compounds reported here.

Table 5. Selected bond lengths [Å] and angles [°] for $[Ph_2Pb(4\text{-}CF_3pymS)_2]$ (**7**).

| | | | |
|---|---|---|---|
| Pb(1)–C(17) | 2.189(11) | Pb(1)–C(11) | 2.196(11) |
| Pb(1)–S(2) | 2.577(3) | Pb(1)–S(1) | 2.582(3) |
| Pb(1)–N(3) | 2.824(9) | Pb(1)–N(1) | 2.986(10) |
| S(1)–C(1) | 1.730(11) | S(2)–C(6) | 1.732(11) |
| N(1)–C(4) | 1.309(16) | N(1)–C(1) | 1.346(13) |
| N(2)–C(2) | 1.309(14) | N(2)–C(1) | 1.352(13) |
| N(3)–C(9) | 1.360(16) | N(3)–C(6) | 1.362(13) |
| N(4)–C(6) | 1.332(13) | N(4)–C(7) | 1.336(15) |
| C(17)–Pb(1)–C(11) | 142.8(4) | C(17)–Pb(1)–S(2) | 104.0(3) |
| C(11)–Pb(1)–S(2) | 104.6(3) | C(17)–Pb(1)–S(1) | 104.1(3) |
| C(11)–Pb(1)–S(1) | 102.2(3) | S(2)–Pb(1)–S(1) | 83.96(10) |
| C(17)–Pb(1)–N(3) | 89.7(3) | C(11)–Pb(1)–N(3) | 85.7(3) |
| S(2)–Pb(1)–N(3) | 57.86(19) | S(1)–Pb(1)–N(3) | 141.65(19) |
| C(17)–Pb(1)–N(1) | 85.0(3) | C(11)–Pb(1)–N(1) | 88.2(3) |
| S(2)–Pb(1)–N(1) | 140.23(19) | S(1)–Pb(1)–N(1) | 56.38(19) |
| N(3)–Pb(1)–N(1) | 161.9(2) | C(4)–N(1)–Pb(1) | 154.4(9) |

| C–H–X interactions[a] | D–H | H···A | D–A | D–H···A |
|---|---|---|---|---|
| C(16)#1–H(16)#1···S(1) | 0.930 | 2.778 | 3.694 | 168.38° |
| C(22)#1–H(22)#1···S(1) | 0.930 | 2.785 | 3.704 | 169.80° |
| C(4)#1–H(4)#1···S(1) | 0.930 | 2.964 | 3.753 | 143.65° |
| C(9)#1–H(9)#1···S(2) | 0.930 | 3.081 | 3.847 | 140.79° |
| C(4)#1–H(4)#1···N(2) | 0.930 | 2.711 | 3.598 | 159.66° |
| C(9)#1–H(9)#1···N(4) | 0.930 | 2.639 | 3.543 | 164.16° |

[a] Symmetry code: #1: $x$, $y + 1$, $z$.

Table 6. Selected bond lengths [Å] and angles [°] for $[Ph_2Pb(6\text{-}Me\text{-}4\text{-}CF_3pymS)_2]$ (**8**).

| | | | |
|---|---|---|---|
| Pb(1)–C(13) | 2.187(5) | Pb(1)–C(19) | 2.190(5) |
| Pb(1)–S(2) | 2.5722(1) | Pb(1)–S(1) | 2.5723(1) |
| Pb(1)–N(3) | 2.865(5) | Pb(1)–N(1) | 2.909(4) |
| S(1)–C(1) | 1.748(6) | S(2)–C(7) | 1.747(6) |
| N(1)–C(1) | 1.338(6) | N(1)–C(2) | 1.346(6) |
| N(2)–C(4) | 1.331(7) | N(2)–C(1) | 1.343(6) |
| N(3)–C(8) | 1.337(7) | N(3)–C(7) | 1.341(6) |
| N(4)–C(10) | 1.333(8) | N(4)–C(7) | 1.337(6) |
| C(13)–Pb(1)–C(19) | 134.59(19) | C(13)–Pb(1)–S(2) | 106.99(13) |
| C(19)–Pb(1)–S(2) | 105.48(14) | C(13)–Pb(1)–S(1) | 103.46(13) |
| C(19)–Pb(1)–S(1) | 108.76(14) | S(2)–Pb(1)–S(1) | 87.66(5) |
| C(13)–Pb(1)–N(3) | 90.06(15) | C(19)–Pb(1)–N(3) | 81.31(16) |
| S(2)–Pb(1)–N(3) | 57.72(10) | S(1)–Pb(1)–N(3) | 145.31(10) |
| C(13)–Pb(1)–N(1) | 86.88(14) | C(19)–Pb(1)–N(1) | 84.43(15) |
| S(2)–Pb(1)–N(1) | 144.84(10) | S(1)–Pb(1)–N(1) | 57.41(10) |
| N(3)–Pb(1)–N(1) | 156.65(13) | C(2)–N(1)–Pb(1) | 151.7(4) |

| C–H–X interactions[a] | D–H | H···A | D–A | D–H···A |
|---|---|---|---|---|
| C(23)#1–H(23)#1···S(1) | 0.930 | 2.993 | 3.877 | 159.47 |
| C(6)#2–H(6c)#2···S(2) | 0.960 | 2.914 | 3.755 | 146.89 |

[a] Symmetry codes: #1: $-x + 2$, $-y$, $-z + 2$; #2: $x + 0.5$, $-y + 0.5$, $z + 0.5$.

The complexes $[Ph_2Pb(4\text{-}CF_3pymS)_2]$ (**7**) and $[Ph_2Pb(6\text{-}Me\text{-}4\text{-}CF_3pymS)_2]$ (**8**) consist of neutral monomeric molecules in which the lead atoms are coordinated by two monoanionic thionate ligands and two phenyl groups. The thionate ligands are coordinated to the lead through their sulfur atoms and, more weakly, to one of the nitrogen atoms of each ligand, in such a way that each thionate ligand acts a bidentate chelate system ($\kappa^2$-N,S). In this way, the coordination number for the lead atom is six and the environment around this metal atom can be described as being similar to the analogous tin(IV) complexes **2** and **5**,

 © 2007 Wiley-VCH Verlag GmbH & Co. KGaA, Weinheim 

i.e., a skewed trapezoidal bipyramid or a bicapped tetrahedron. The C–Pd–C bond angles are 142.8(4) Å for **7** and 134.59(19) Å for **8**, which are larger than those found in the diorganotin(IV) complexes previously described. In addition, in **7** and **8** the heterocyclic ligands adopt, for the same reasons, the same coordination mode as in the tin complexes mentioned previously.

The Pb–S bond lengths, 2.577(3) and 2.582(3) Å for **7** and 2.5722(14) and 2.5723(15) Å for **8**, are close to those found in diorganolead(II) tetracoordinate with thiolate ligands; 2.489(6) Å in $[Ph_3PbSMe]$[52] or 2.523(5) and 2.580(4) Å in $[(Ph_3Pb)_2(dmit)]$,[53] where $H_2dmit$ is 4,5-dimercapto-1,3-dithio-2-thione. However, the values found in **7** and **8** are lower than those found in the hexacoordinate thiolate $\{Ph_2Pb[S_2P(OCH_2Ph)_2]_2\}$,[54] 2.679(6) and 2.957(6) Å. The Pb–N bond lengths, 2.824(9) and 2.986(10) Å for **7** and 2.865(5) and 2.909(4) Å for **8**, are much longer than the sum of the corresponding covalent radii for lead (1.600 Å) and nitrogen (0.700 Å) and also longer than those found in other hexacoordinate diorganolead(IV) complexes containing a Pb–N bond; for example, 2.498(7) and 2.461(7) Å in $[Ph_2PbCl_2(imidazole)_2]$.[55] The fact that these distances are shorter than the sum of the van der Waals radii (3.82 Å) suggests that the Pb···N bonds in complexes **7** and **8** are significantly weaker than a normal intermolecular Pb–N bond, a situation similar to that observed in organotin complexes discussed above.

The phenyl and pyrimidine rings are planar [maximum deviation 0.010(3) Å]. The interplanar angle between the pyrimidine rings is only 4.75° in **7** and 3.76(3)° in **8** whereas the rings of the phenyl groups have interplanar angles of 19.63(8)° and 76.04(2)°, respectively. In compound **7**, the sulfur and lead atoms lie approximately in the plane of the pyrimidine ring to which they are bound. However, in **8** the sulfur atoms are approximately in the plane of the pyrimidine rings to which they are bound; 0.038(6) Å for S(1) and 0.067(7) Å for S(2). The lead atom is also practically in the plane of the pyrimidine to which S(1) is bonded [0.055(8) Å] but is out of the plane of the pyrimidine ring to which S(2) is attached [0.296(9) Å].

The average length of the S–C bond, 1.731(11) Å, is similar to that found in other complexes with pyrimidine-2-thionate derivatives, a fact that suggests that this ligand is coordinated in a form that is closer to the thionate than the thione.

## Crystal Packing and Intermolecular Interactions in 1, 2 and 5–8

The crystal packing in compounds **1**, **2** and **5**–**8** is mainly dictated by C–H···X hydrogen-bonding interactions between different C–H groups and the sulfur and nitrogen atoms of the pyrimidine-2-thionate ligands that are not coordinated, as well as interactions involving the $CF_3$ groups (see Tables 1–6).[56,57]

The way in which these C–H···X interactions propagate in space enables the crystal structures of these compounds to be classified into three groups: (1) interactions that propagate in a direction that gives rise to chains that interact weakly with one another; (2) bidimensional interactions that give rise to layers that interact weakly with one another; (3) interactions that are similar in intensity in all three dimensions.

### *Compounds with Crystal Packing in Chains*

The crystal packing arrangements in $[Ph_2Sn(4\text{-}CF_3pymS)_2]$ (**2**), $[tBu_2Sn(6\text{-}Me\text{-}4\text{-}CF_3pymS)_2]$ (**6**) and $[Ph_2Pb(4\text{-}CF_3pymS)_2]$ (**7**) can be described as chains parallel to the crystallographic *b* axis. The pyrimidine rings and the metal atoms are located approximately in the same plane throughout each of the chains. This arrangement is the result of weak C–H···X interactions that propagate along this direction. In **2** and **7**, this arrangement consists of two C–H···S[58,59] interactions between two C–H groups from the phenyl rings and the same sulfur atom of one of the pyrimidine-2-thionate ligands (**7**; see Figure 7) or with a sulfur atom of a different pyrimidine-2-thionate ligand (**2**). This situation is reflected in the angle between the planes of the phenyl rings, which is 19.63(80)° for **7** and 58.96(10)° for **2**. At the same time, and in the same direction, C–H···N[60,61] interactions are established between the uncoordinated nitrogen atom and the symmetry equivalent C–H *para* to this nitrogen (see Figure 7).

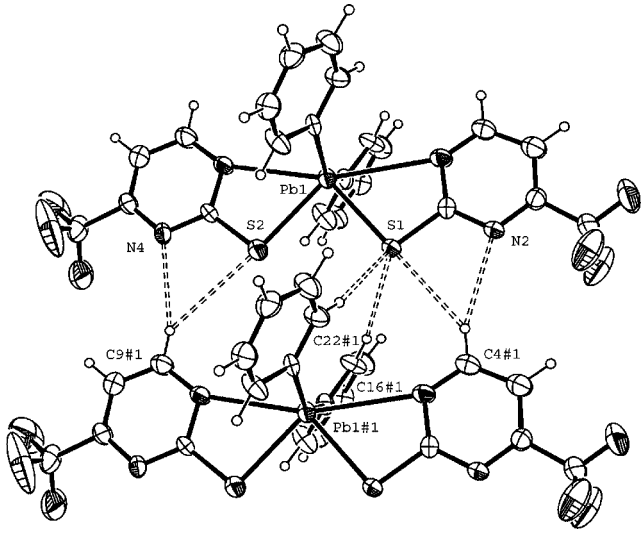


Figure 7. The crystal packing in **7**. Dashed lines show the C–H···S and the C–H···N interactions.

The crystal network of $[tBu_2Sn(6\text{-}Me\text{-}4\text{-}CF_3pymS)_2]$ (**6**) contains the same type of chain along the crystallographic *b* axis, with weak C–H···N and C–H···S interactions similar to those in the two previous cases, although in this case the C–H donor is the methyl group *para* to the uncoordinated nitrogen atom.

In all three cases each of the chains is involved in weak interactions with neighbouring chains in such a way that the planes of the pyrimidine rings along the chain are parallel to one another in the resulting crystal packing. These inter-chain interactions can be classified into two types:

 © 2007 Wiley-VCH Verlag GmbH & Co. KGaA, Weinheim 

those that involve the phenyl (complexes **2** and **7**) or *tert*-butyl (complex **6**), which are established with other chains located above and below the plane of the pyrimidine-2-thionate ligands, and those that involve $CF_3$ groups.[56,57] These $CF_3$ groups are located near to other trifluoromethyl groups in all three cases, a situation that is usual for this type of group.

### *Compounds with Crystal Packing in Layers*

The only compound reported here that shows this type of packing is $[Me_2Sn(4\text{-}CF_3pymS)_2]$ (**1**). Each pyrimidine-2-thionate ligand in this compound establishes two C–H···S interactions between the thionate groups and the C–H groups *para* to the sulfur atoms, as shown in Figure 8. The propagation of these interactions gives rise to layers of molecules parallel to the crystallographic AB plane. Within these layers the $CF_3$ groups are located very close to other $CF_3$ groups in such a way that F···F interactions are also formed within each layer; these interactions are not shown in Figure 8.

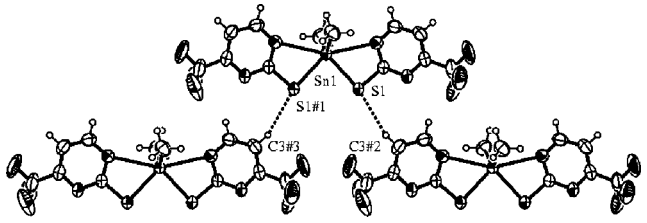


Figure 8. The crystal packing in **1**. Dashed lines show the C–H···S interactions.

The layers that are parallel to the AB planes interact weakly with one another through C–H···S[58,59] interactions between the methyl groups above and below the layers and the sulfur atoms of the pyrimidine-2-thionate ligands in neighbouring layers.

### *Compounds with Three-Dimensional Crystal Packing*

The compounds $[Ph_2Sn(6\text{-Me-}4\text{-}CF_3pymS)_2]$ (**5**) and $[Ph_2Pb(6\text{-Me-}4\text{-}CF_3pymS)_2]$ (**8**) are isomorphous and have identical crystal packing arrangements as a result of interactions of similar strength in three directions in space. The interactions responsible for the packing in these compounds are also C–H···S[58,59] interactions, and each of the thionate groups in the complex is involved in interactions with different C–H groups of other neighbouring complex molecules, as shown in Figure 9.

The S(1) sulfur atom establishes one of these interactions with a C–H group of one of the phenyl rings, while the S(2) sulfur establishes an interaction with a methyl group of a pyrimidine-2-thionate ligand of a neighbouring complex.

There is another type of interaction in addition to the C–H···S interactions, which involves π-π stacking between the phenyl ring not involved in C–H···S interactions and a symmetry equivalent centre of the pyrimidine ring connected to sulfur S(1). This interaction, which is relatively weak, is of the "parallel displaced" type and the centroids of the two rings are separated by 3.920 Å from tin and 3.843 Å from lead. As in the previously discussed complexes, the $CF_3$ groups are located very close to other $CF_3$ groups in such a way that F···F interactions are established.[56,57]

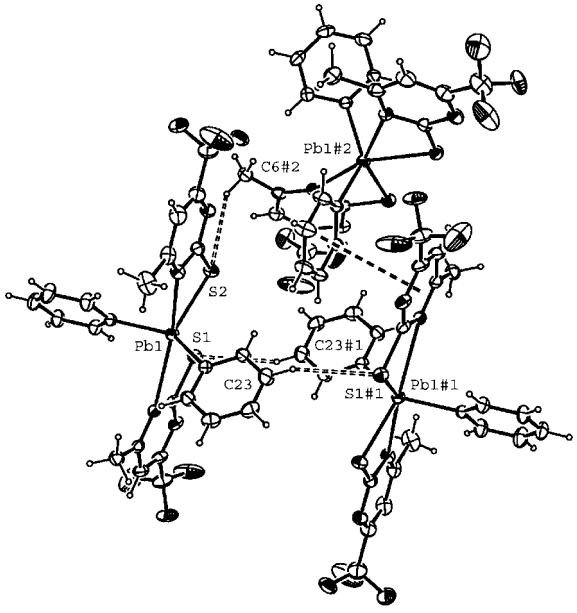


Figure 9. The crystal packing in **8**. Dashed lines show the C–H···S and the π-π stacking interactions.

## Spectroscopic Studies

### *IR Spectroscopy*

The IR spectra of the complexes (see the Experimental Section) show that the ν(N–H) bands of the free pyrimidine-2-thione ligands, which appear between 3200–3050 $cm^{-1}$, are absent from the thionate complexes. This indicates that deprotonation of the thionate group has occurred and therefore that the pyrimidine-2-thione is coordinated in the thionate form. This conclusion is supported by the shift to lower wavenumbers (1580–1550 $cm^{-1}$ in the complexes) of the strong bands due to ν(C=C) and ν(C=N), which appear at 1650–1550 $cm^{-1}$ in the free ligands. The spectra of the complexes also show bands due to the ring breathing vibration in the regions 1110–990 $cm^{-1}$ and 750–620 $cm^{-1}$, which are at higher wavenumbers than the corresponding bands in the free ligands. These shifts provide evidence for coordination of the ligands through the nitrogen atom.[62] The spectra of the methyl and *tert*-butyl derivatives also show additional medium intensity bands at 3100–2900 $cm^{-1}$, which correspond to the vibrations of the methyl groups.

### *NMR Spectra*

The main change in the $^1H$ NMR spectra of the thionate complexes brought about by complexation is the disappearance of the broad signal due to the N–H proton; this confirms that the ligand is in the deprotonated thionate form in the complexes.

 © 2007 Wiley-VCH Verlag GmbH & Co. KGaA, Weinheim 

The $^1$H NMR spectra of the complexes show, in addition to the signals corresponding to the protons on the heterocyclic thionate ligand, signals due to the methyl, *tert*-butyl and phenyl groups of the organometallic fragments. The spectra of the dimethyltin(IV) derivatives also contain a signal at high field ($\delta$ = 1.1 ppm), which is attributed to the protons on the methyl groups of the $Me_2Sn$ fragment. These signals are accompanied by satellite peaks due to coupling of the proton with $^{119}$Sn and $^{117}$Sn nuclei. The $^2J_{^1H,^{119}Sn}$ and $^2J_{^1H,^{117}Sn}$ coupling constants are 74 and 72 Hz, respectively, and these values are similar to those found in other compounds containing the $Me_2Sn$ fragment.[22,63] These $^2J$ coupling constant values can be used to estimate the Me–Sn–Me angle.[64] The values calculated for these angles are 123.9° and 121.8° for **1** and **4**, respectively, and are very similar to one another and also to that found in the solid state for **1** by X-ray diffraction. This suggests that the structures of both compounds in solution are the same as that determined in the solid state for compound **1**.

The $^1$H NMR spectra of the $tBu_2Sn$ derivatives each contain a singlet at around $\delta$ = 1.50 ppm due to the *tert*-butyl protons. Once more, the corresponding satellite peaks can be observed. The $^3J_{^1H,^{119}Sn}$ and $^3J_{^1H,^{117}Sn}$ coupling constants in these cases are 52 and 50 Hz, respectively. The $^1$H NMR spectra of the $Ph_2Sn$ and $Ph_2Pb$ derivatives contain peaks attributable to the aromatic protons. Two groups of signals can be observed. The first is at $\delta$ = 7.8 ppm and is due to the protons *ortho* to the Sn atom. The second group appears at $\delta$ = 7.4 ppm and it is attributable to the other ring protons. The signals in the first group, in the case of the $Ph_2Sn$ derivatives, show satellite signals due to $^1$H-$^{119}$Sn coupling. In these cases, the $^3J_{^1H,^{119}Sn}$ values are close to 75 Hz.

The $^{13}$C NMR spectrum of the free ligand 6-Me-4-$CF_3$pymSH contains twice the expected number of signals for C(2), C(6), $CF_3$ and $CH_3$ as the free ligand exists in two tautomeric forms. This doubling in the number of signals is not observed in the $^{13}$C NMR spectra of the metal complexes. This situation provides evidence that the ligand is coordinated to the metal only in the thionate form in solution. The $^{13}$C NMR spectra of the other complexes that were sufficiently soluble in $CDCl_3$ show, in addition to the expected signals for the thionate ligand, signals attributable to the methyl group ($\delta$ = 6.5–5.5 ppm), phenyl group ($\delta$ = 122–140 ppm) and quaternary and primary carbon atoms from the *t*Bu groups ($\delta$ = 30–40 ppm) in the organometallic fragment.

The $^{119}$Sn NMR spectra of these complexes were recorded at room temperature in $CDCl_3$ using $SnMe_4$ as an external standard. The $^{119}$Sn chemical shifts seem to depend more on the nature of the alkyl or aryl groups bonded to the tin atom than on the pyrimidine ligand. Indeed, it appears that these groups do not have a significant effect on the shielding or deshielding of the tin nucleus. Whereas the $^{119}$Sn chemical shift for the diphenyltin(IV) derivatives appears at $\delta$ = –201.0 ppm for **2** and $\delta$ = –179.3 ppm for **5**, the compounds containing alkyl groups show less negative $^{119}$Sn chemical shifts. For example, the $Me_2Sn$ derivatives exhibit signals at $\delta$ = –70.3 ppm for **1** and $\delta$ = –86.4 ppm for **4**. These values are within the range reported for other complexes of diphenyl- or dimethyltin(IV) with pyrimidine or pyrimidine-2-thionate ligands with the same coordination number.[22,47,65] In the spectra of the $tBu_2Sn$ derivatives, the values of the $^{119}$Sn chemical shift are $\delta$ = –32.1 ppm for **3** and $\delta$ = –4.8 ppm for **6**. These seem to indicate that the complexes have a lower coordination number (tetracoordination) in $CDCl_3$ solution than in the solid state.[66] This change can be explained in terms of the breakdown of Sn–N interactions in solution, with these bonds in **6** (obtained from X-ray crystallography) being longer than the others presented in this work.

The $^{207}$Pb NMR spectra of diphenyllead(IV) complexes were recorded at room temperature in $CDCl_3$ using $PbMe_4$ as an external standard. The $^{207}$Pb chemical shift seems to be particularly sensitive to the electronic environment and is therefore an excellent tool for the study of changes in coordination number.[67] The $^{207}$Pb spectra contain a single peak at around $\delta$ = –199.0 ppm for **7** and $\delta$ = –206.7 ppm for **8**. These values suggest that both complexes of diphenyllead(IV) have the same coordination number in $CDCl_3$ solution (probably hexacoordinate as in the solid state).

### *Mass Spectra*

The tin and lead complexes were also characterised by mass spectrometry using the positive ion FAB technique in 3-nitrobenzyl alcohol (NBA) as matrix. The FAB spectra of dimethyl- and di-*tert*-butyltin with 4-$CF_3$pymS and dimethyltin with 6-Me-4-$CF_3$pymS show the molecular ion peak with the appropriate isotope distribution (*m*/*z* 508, 592 and 536, respectively). In these cases, peaks were also observed due to the fragments produced by the loss of one thionate ligand (*m*/*z* 328, 412 and 342, respectively) or one of these ligands and the two alkyl groups. The spectra of the other tin complexes do not show the molecular ion peaks but do show peaks associated with loss of one phenyl group [*m*/*z* 555 for $PhSn(4\text{-}CF_3pymS)_2$ and 582 for $PhSn(6\text{-}Me\text{-}4\text{-}CF_3pymS)_2$] or one thionate ligand [*m*/*z* 453 for $Ph_2Sn(4\text{-}CF_3pymS)$, 467 for $Ph_2Sn(6\text{-}Me\text{-}4\text{-}CF_3pymS)$ and 427 for $tBu_2Sn(4\text{-}CF_3pymS)_2$].

The FAB mass spectrum of $[Ph_2Pb(4\text{-}CF_3pymS)_2]$ shows the molecular ion peak at *m*/*z* = 720. In this compound, and also in the other lead compound, peaks corresponding to fragments of the parent ions due to loss of different groups from the compounds are observed. For example, peaks are observed at *m*/*z* 540 for **7** and 555 for **8** and these are associated with $Ph_2Pb(RpymS)$ formed by loss of one thionate ligand. Peaks due to the fragments produced by the loss of two phenyl groups and one thionate ligand (*m*/*z* 386 when R = $CF_3$ and 400 when R = 6-Me-4-$CF_3$) are also seen.

### *Mössbauer Spectra*

As expected from their chemical formulae, the Mössbauer spectra of the reported compounds show only a single, slightly asymmetric, quadrupole split doublet (Table 7).

 © 2007 Wiley-VCH Verlag GmbH & Co. KGaA, Weinheim 

The linewidths are narrow enough to rule out any doublet overlap, which implies the existence of just a single tin site in each complex. The isomer shift values are rather surprising as they are grouped around two values, both of which are typical for $SnR_2$ derivatives (1.49 and 1.87 mm s$^{-1}$), in an unexpected way. In fact, the inductive effects of the organic groups would lead to increasing values in the order Ph >> Me > Bu, and so the only explanation must lie in different geometrical distortions or in varying Sn–N bond lengths. A closer analysis of Tables 2, 3, 4, and 5 shows that the average Sn–N bond length for compounds **1**, **2**, and **5**, which have the lowest isomer shift values, is 2.817 ± 0.039 Å, clearly shorter than that of compound **6** [2.978(4) Å]. This value, even though significantly shorter than the sum of the van der Waals radii of these atoms (3.75 Å), indicates that the two Sn–N bonds are rather weak and so the coordination geometry around the tin centre has a considerable fourfold character. This increases the s-electron density at the tin nucleus and so leads to a larger isomer shift. Moreover, the presence of a methyl group in the ligand does not affect the electron density on the tin atom, as expected. The quadrupole splitting values are also very close to each other and quite low, close to values typical for *cis*-$SnR_2$ derivatives (1.7–2.2 mm s$^{-1}$).

Table 7. Mössbauer parameters collected at 80 K. The $\delta$ values are quoted relative to $SnO_2$ at room temperature.

| | $\delta$ [mm s$^{-1}$] | $\Delta E_Q$ [mm s$^{-1}$] | $\Gamma$ [mm s$^{-1}$] | $\Gamma_2/\Gamma_1$ |
|---|---|---|---|---|
| [$Me_2Sn(4\text{-}CF_3pymS)_2$] (**1**) | 1.49 | 2.46 | 0.87 | 0.91 |
| [$Ph_2Sn(4\text{-}CF_3pymS)_2$] (**2**) | 1.49 | 2.68 | 0.87 | 0.97 |
| [$tBu_2Sn(4\text{-}CF_3pymS)_2$] (**3**) | 1.87 | 2.74 | 0.86 | 0.96 |
| [$Ph_2Sn(6\text{-}Me\text{-}4\text{-}CF_3pymS)_2$] (**5**) | 1.49 | 2.54 | 0.85 | 1.03 |
| [$tBu_2Sn(6\text{-}Me\text{-}4\text{-}CF_3pymS)_2$] (**6**) | 1.87 | 2.70 | 0.92 | 0.93 |

Point charge calculations performed by ignoring the influence of the pymS ligand on the electron density around the tin atoms, but taking into account only the experimental C–Sn–C bond angles, afforded values that were too high (2.83–3.14 mm s$^{-1}$) and strongly dependent on the input values. In fact, the C–Sn–C bond angles [123.0–131.6°] are intermediate between the ideal values for the *cis* (90°) and for the *trans* isomer (180°), a situation similar to that found in the majority of this type of compounds (122–155°). The coordination geometry for these compounds can, in fact, be described as a distorted trapezoidal bipyramid[39] in which the equatorial plane is formed by the sulfur and nitrogen atoms, or as a bicapped tetrahedron. These results point to the inability of the point charge method to reproduce the Mössbauer quadrupole splitting in the case of severely distorted structures.

## Conclusions

The work described here involves the synthesis and structural characterisation of a series of compounds obtained by the reaction of the appropriate diorganotin(IV) and diphenyllead(IV) dichlorides with 4-(trifluoromethyl)pyrimidine-2-thione and 6-methyl-4-(trifluoromethyl)pyrimidine-2-thione in methanol in the presence of triethylamine.

The structures of the diorganotin(IV) and diphenyllead(IV) compounds have been investigated and the coordination polyhedron of the metal atom can be described either as a distorted skew-trapezoid or a bicapped tetrahedron, with the heterocyclic thionate acting in a bidentate ($\kappa^2$-N,S) manner. In these arrangements the ligands are unsymmetrical ambidentate and therefore the N,S-bidentate coordination to the metallic atom could generate linkage isomerism through one of the two nitrogen atoms. Only one coordination mode is found in these complexes and this involves the sulfur atom and the less hindered nitrogen atom, which is farthest from the group with the highest level of steric hindrance in the heterocyclic rings; in both cases this is the trifluoromethyl group. Furthermore, it is worth noting that the R groups (methyl, *tert*-butyl or phenyl) of the $R_2M$ moiety do not markedly influence the structure of the complex.

## Experimental Section

**General:** 4-(Trifluoromethyl)pyrimidine-2-thione, 1,1,1-trifluoro-2,4-pentanedione, thiourea, triethylamine, dimethyltin(IV) dichloride, diphenyltin(IV) dichloride, bis(*tert*-butyl)tin dichloride and diphenyllead(IV) dichloride were obtained commercially and used as supplied.

Elemental analysis was performed with a Carlo–Erba EA microanalyser. IR spectra were recorded as KBr mulls with a Bruker IFS-66V spectrophotometer. $^1$H and $^{13}$C NMR spectra were recorded with a Bruker AMX 300 MHz instrument using $CDCl_3$ or [$D_6$]DMSO as solvent. Chemical shifts are quoted relative to TMS as the internal standard. $^{119}$Sn and $^{207}$Pb NMR spectra were recorded with a Bruker AMX500 spectrometer in $CHCl_3$ as solvent using $SnMe_4$ and $PbMe_4$ as an external standard, respectively. The Mössbauer spectra were recorded at $T$ = 80 K in a constant acceleration apparatus and are referenced to $SnO_2$. The mass spectra (FAB) were recorded with a Micromass Autospec spectrometer, with 3-nitrobenzyl alcohol as the matrix material.

**Synthesis of 6-Me-4-$CF_3$pymSH:** This compound was obtained by direct reaction between thiourea (2.428 g, 32 mmol) and 1,1,1-trifluoro-2,4-pentanedione (5 g, 32 mmol) in ethanol in the presence of concentrated hydrochloric acid (1 mL) as a catalyst. The mixture was heated under reflux for 2 h and the resulting dusty yellow solid was filtered off. $C_6H_5F_3N_2S$: calcd. C 37.11, H 2.60, N 14.43, S 16.51; found C 36.39, H 2.60, N 14.26, S 16.38. IR (KBr): $\tilde{\nu}$ = 3100–3200 cm$^{-1}$ m, br, 1615 vs, 1590 vs, 1440 m, 1350 vs, 1320 w, 1200 s, br, 1130 m, 1100 m, 1030 w, 970 s, 920 m, 860 w, 850 m, 705 w, 660 w, 595 w, 570 w, 530 m, 510 w, 470 m, 450 m, 370 w. $^1$H NMR ([$D_6$]DMSO): $\delta$ = 14.40 (s, 1 H, NH), 7.19 (s, 1 H, H-5), 2.39 (s, 3 H, $CH_3$) ppm. $^{13}$C NMR ([$D_6$]DMSO): $\delta$ = 181.00 and 172.13 (s, C-2), 155.86 and 153.72 (q, $^2J_{^{13}C,^{19}F}$ = 35 Hz, C-4), 104.89 (s, C-5), 163.61 (s, C-6), 119.27 and 119.67 (q, $^1J_{^{13}C,^{19}F}$ = 275 Hz, $CF_3$), 23.45 and 18.46 (s, $CH_3$). MS (FAB): *m*/*z* (%) 194 (27) [6-Me-4-$CF_3$pymSH].

**Synthesis of [$Me_2Sn(4\text{-}CF_3pymS)_2$] (1):** Triethylamine (0.128 mL, 0.700 mmol) was added by syringe to a solution of 4-$CF_3$pymSH (0.150 g, 0.832 mmol) in methanol (50 mL) and the resulting solution was stirred for 1 h at room temperature. A solution of dimethyltin dichloride (0.091 g, 0.414 mmol) in methanol (15 mL) was then added and the mixture was heated under reflux for about

 © 2007 Wiley-VCH Verlag GmbH & Co. KGaA, Weinheim 

2.5 h. The solution was filtered and slow evaporation of the solvent gave rise to a cream-coloured solid, which was recrystallised from ethanol to give yellow crystals suitable for X-ray studies. Yield: 0.099 g (47%). $C_{12}H_{10}F_6N_4S_2Sn$ (507.04): calcd. C 28.43, H 1.99, N 11.05, S 12.65; found C 28.44, H 1.65, N 11.03, S 12.71. IR (KBr): $\tilde{\nu}$ = 3050 $cm^{-1}$ w, 1550 s, 1420 m, 1340 vs, 1325 vs, 1200 s, 1160 vs, br, 1110 s, 980 w, 840 sh, 830 s, 780 m, 730 m, 665 m, 555 w, 520 w, 460 w, 355 w, 320 w. $^1$H NMR ($CDCl_3$): $\delta$ = 8.7 (d, $^3J_{H,H}$ = 4.9 Hz, 1 H, H-6), 7.3 (d, $^3J_{H,H}$ = 4.9 Hz, 1 H, H-5), 1.1 (s, 3 H, $CH_3$) ppm. $^{13}$C NMR ($CDCl_3$): $\delta$ = 175 (s, $C^2$), 160 (s, $C^6$), 150 (q, $C^4$), 120 (q, $C^7$), 115 (s, $C^5$), 5.4 ppm (s, Me). $^{119}$Sn NMR ($CDCl_3$): $\delta$ = –70.29 ppm. MS (FAB): *m*/*z* (%) 508 (12) [$Me_2Sn$(4-$CF_3$pymS)$_2$], 328 (100) [$Me_2Sn$(4-$CF_3$pymS)].

**Synthesis of [$Ph_2Sn$(4-$CF_3$pymS)$_2$] (2):** The same procedure as for **1** was used for the synthesis of the diphenyltin derivative. A solution of $Ph_2SnCl_2$ (0.142 g, 0.413 mmol), 4-$CF_3$pymSH (0.150 g, 0.832 mmol) and $NEt_3$ (0.128 mL, 0.700 mmol) in methanol (40 mL) was heated under reflux for 3 h. This solution was concentrated to give single crystals suitable for X-ray studies. Yield: 0.193 g (74%). $C_{22}H_{14}F_6N_4S_2Sn$ (631.18): calcd. C 41.86, H 2.24, N 8.88, S 10.16; found C 42.31, H 2.30, N 8.21, S 10.12. IR (KBr): $\tilde{\nu}$ = 3040 $cm^{-1}$ w, 1550 vs, 1470 m, 1420 s, 1330 vs, br, 1200 s, 1140 m, 1110 m, 1060 w, 1015 w, 990 w, 975 w, 960 vw, 910 w, 830 s, 780 vw, 720 s, 690 m, 665 s, 460 w, 440 m, 355 m, 320 m. $^1$H NMR ($CDCl_3$): $\delta$ = 8.38 (d, $^3J_{H,H}$ = 5.1 Hz, 1 H, H-6), 7.8 (br, phenyl H) and 7.4 (br, phenyl H), 7.08 (d, $^3J_{H,H}$ = 5.1 Hz, 1 H, H-5) ppm. $^{13}$C NMR ($CDCl_3$): $\delta$ = 129–135 ppm (aromatic carbons). NO other signals could be detected due to the poor solubility of this complex. $^{119}$Sn NMR ($CDCl_3$): $\delta$ = –201 ppm. MS (FAB): *m*/*z* (%) 554.8 (12) [PhSn(4-$CF_3$pymS)$_2$], 452.9, (54) [$Ph_2Sn$(4-$CF_3$pymS)], 298.8 (7) [Sn(4-$CF_3$pymS)].

**Synthesis of [*t*$Bu_2$Sn(4-$CF_3$pymS)$_2$] (3):** A solution of *t*$Bu_2SnCl_2$ (0.126 g, 0.414 mmol) in methanol was added to a solution of 4-$CF_3$pymSH (0.150 g, 0.832 mmol) and $NEt_3$ (0.128 mL, 0.421 mmol) in methanol (30 mL) and the reaction mixture was stirred and heated under reflux for 3 h. The resulting solution was slowly evaporated at room temperature to give colourless crystals suitable for X-ray studies. Yield: 0.175 g (74%). $C_{18}H_{22}F_6N_4S_2Sn$ (591.20): calcd. C 36.57, H 3.75, N 9.48, S 10.85; found C 36.74, H 3.14, N 9.50, S 10.96. IR (KBr): $\tilde{\nu}$ = 3050 $cm^{-1}$ w, 2980 w, 2940 w, 2840 m, 1550 s, 1460 m, 1450 m, 1425 m, 1340 w, 1330 vs,br, 1205 s, 1190 m, 1150 m, 1140 m, 1110 m, 1080 vw, 1010 w, 975 w, 935 w, 830 m, 730 m, 665 m, 460 vw, 350 w, 315 w. $^1$H NMR ($CDCl_3$): $\delta$ = 8.8 (d, $^3J_{H,H}$ = 4.9 Hz, 1 H, H-6), 7.4 (d, $^3J_{H,H}$ = 4.9 Hz, 1 H, H-5), 1.50 (s, 9 H, $CH_3$) ppm. $^{13}$C NMR ($CDCl_3$): $\delta$ = 170 (s, $C^2$), 160 (s, $C^6$), 155 (q, $C^4$), 120 (q, $C^7$), 95 (s, $C^5$), 29.7, 30.0 and 31.6 ppm (*t*Bu). $^{119}$Sn NMR ($CDCl_3$): $\delta$ = –32.16 ppm. MS (FAB): *m*/*z* (%) 592 (14) [*t*$Bu_2$Sn(4-$CF_3$pymS)$_2$], 534 (12) [*t*$Bu_2$Sn(4-$CF_3$pymS)$_2$ – 3F], 412 (76) [*t*$Bu_2$Sn(4-$CF_3$pymS)], 298 (100) [Sn(4-$CF_3$pymS)].

**Synthesis of [$Me_2$Sn(6-Me-4-$CF_3$pymS)$_2$] (4):** A solution of $Me_2SnCl_2$ (0.100 g, 0.220 mmol) was added to a solution of (6-Me-4-$CF_3$pymSH) (0.030 g, 0.157 mmol) and $NEt_3$ (0.073 g, 0.233 mmol) in methanol (40 mL) with constant stirring at room temperature. This mixture was heated under reflux for 2.5 h. The solution was the concentrated to give single crystals that were not suitable for X-ray studies. Yield: 0.132 g (54%). $C_{14}H_{14}F_6N_4S_2Sn$ (535.09): calcd. C 31.43, H 2.64, N 10.47, S 11.98; found C 31.52, H 2.52, N 10.51, S 11.72. IR (KBr): $\tilde{\nu}$ = 3080 $cm^{-1}$ w, 3060 w, 1575 m, 1540 s, 1530 vw, 1390 vs, 1365 m, 1310 w, 1265 vs, 1255 m, 1220 w, 1190 w, 1165 w, 1140 m, 1110 m, 1030 w, 990 w, 980 w, 920 m, 875 w, 855 s, 790 m, br, 710 s, 550 m, 515 w, 480 w, 460 w. $^1$H NMR ($CDCl_3$): $\delta$ = 7.14 (s, 1 H, H-5), 2.55 (s, 3 H, H-8), 1.08 (s, 3 H, $CH_3$) ppm. $^{13}$C NMR ($CDCl_3$): $\delta$ = 176.6 (s, $C^2$), 155 (q, $C^4$), 110.6 (s, $C^5$), 171 (s, $C^6$), 120 (q, $C^7$) 24.84 (s, $C^8$), 5.79 ppm (s, Me). $^{119}$Sn NMR ($CDCl_3$): $\delta$ = –86.4 ppm. MS (FAB): *m*/*z* (%) 536 (19) [$Me_2$Sn(6-Me-4-$CF_3$pymS)$_2$], 342 (100) [$Me_2$Sn(6-Me-4-$CF_3$pymS)].

**Synthesis of [$Ph_2$Sn(6-Me-4-$CF_3$pymS)$_2$] (5):** A solution containing diphenyltin dichloride (0.150 g, 0.436 mmol), 6-methyl-4-(trifluoromethyl)pyrimidine-2-thione (0.140 g, 0.721 mmol) and triethylamine (0.110 g, 0.400 mmol) in methanol (30 mL) was heated under reflux for 3 h. It was then evaporated to give white, needle-like crystals that were suitable for X-ray studies. Yield: 0.139 g (52%). $C_{24}H_{18}F_6N_4S_2Sn$ (659.23): calcd. C 43.73, H 2.75, N 8.50, S 9.73; found C 43.12, H 2.49, N 8.38, S 9.62. IR (KBr): $\tilde{\nu}$ = 3080 $cm^{-1}$ w, 1575 s, 1530 s, 1470 w, 1440 w, 1425 m, 1385 s, 1360 m, 1305 vw, 1265 vs, 1250 w, 1220 m, 1190 m, 1170 m, 1135 s, 1110 m, 1070 vw, 995 w, 980 vw, 920 w, 845 s, 730 m, 710 s, 690 m, 545 w, 460 w, 440 m. $^1$H NMR ($CDCl_3$): $\delta$ = 7.85 (m, *ortho*-phenyl), 7.3 (m, phenyl) 7.15 (s, 1 H, H-5), 2.5 (s, 3 H, H-8) ppm. $^{13}$C NMR ($CDCl_3$): $\delta$ = 173.3 (s, $C^2$), 156.0 (q, $C^4$), 141.5–122.4 (phenyl carbons), 112.2 (s, $C^5$), 170.0 (s, $C^6$), 120 (q, $C^7$), 24.13 ppm (s, $C^8$). $^{119}$Sn NMR ($CDCl_3$): $\delta$ = –179.3 ppm. MS (FAB): *m*/*z* (%) 582 (12) [PhSn(6-Me-4-$CF_3$pymS)$_2$], 467 (52) [$Ph_2$Sn(6-Me-4-$CF_3$pymS)], 312 (15) [Sn(4-Me-6-$CF_3$pymS)].

**Synthesis of [*t*$Bu_2$Sn(6-Me-4-$CF_3$pymS)$_2$] (6):** The same procedure as for **4** was used for the synthesis of the di-*tert*-butyltin derivative. A solution of 6-Me-4-$CF_3$pymSH (0.150 g, 0.772 mmol) in methanol (50 mL) was added to a solution containing di-*tert*-butyltin dichloride (0.140 g, 0.461 mmol) and $NEt_3$ (0.110 g, 0.700 mmol) in methanol (15 mL) and the mixture was stirred and heated under reflux for 4 h. It was then filtered and evaporated to give a white crystalline solid (0.136 g, 57%). Crystallisation from ethanol gave single crystals that were suitable for X-ray studies. $C_{20}H_{26}F_6N_4S_2Sn$ (619.26): calcd. C 38.79, H 4.23, N 9.05, S 10.35; found C 38.76, H 4.11, N 8.98, S 10.08. IR (KBr): $\tilde{\nu}$ = 3060 $cm^{-1}$ w, 2980 m, 2940 w, 2840 m, 1570 s, 1530 s, 1450 m, 1430 w, 1390 vs, 1355 w, 1305 m, 1260 vs, br, 1220 m, 1175 m, 1150 vs, br, 1100 w, 1010 w, 970 m, 920 m, 840 s, 800 vw, 780 vw, 655 s, 575 w, 550 m, 480 vw, 450 w. $^1$H NMR ($CDCl_3$): $\delta$ = 7.13 (s, 1 H, H-5), 2.56 (s, 3 H, H-8), 1.49 (s, 9 H, $CH_3$) ppm. $^{13}$C NMR ($CDCl_3$): $\delta$ = 176 (s, $C^2$), 170.2 (s, $C^6$), 112.07 (s, $C^5$), 25.02 (s, $C^8$), 46 [s, $C(CH_3)_3$], 31.82 ppm [s, $C(CH_3)_3$]. $^{119}$Sn NMR ($CDCl_3$): $\delta$ = –4.78 ppm. MS (FAB): *m*/*z* (%) 506.9 (13) [Sn(6-Me-4-$CF_3$pymS)$_2$], 427.0 (72) [*t*$Bu_2$Sn(6-Me-4-$CF_3$pymS)], 312.9 (100) [Sn(6-Me-4-$CF_3$pymS)].

**Synthesis of [$Ph_2$Pb(4-$CF_3$pymS)$_2$] (7):** A solution of 4-$CF_3$pymSH (0.150 g, 0.832 mmol) and $NEt_3$ (0.126 g, 0.700 mmol) in methanol (50 mL) was added to a stirred suspension of diphenyllead dichloride (0.179 g, 0.414 mmol) in methanol (15 mL). The reaction mixture was heated under reflux for 4 h and the yellow solid was filtered off, washed with diethyl ether and dried under vacuum. The mother liquor yielded crystals suitable for X-ray studies (0.112 g, 56%). $C_{22}H_{14}F_6N_4PbS_2$ (719.68): calcd. C 36.72, H 1.96, N 7.78, S 8.91; found C 36.70, H 2.03, N 7.78, S 8.90. IR (KBr): $\tilde{\nu}$ = 3040 $cm^{-1}$ w, 1555 s, 1465 w, 1430 w, 1415 m, 1340 s, 1330 s, 1205 s, 1170 w, 1140 m, 1115 m, 1010 w, 990 m, 975 w, 835 m, 730 m, 720 m, 680 vw, 670 m, 440 m. $^1$H NMR ($CDCl_3$): $\delta$ = 8.54 (d, $^3J_{H,H}$ = 5.0 Hz, 1 H, H-6), 8.14–7.29 (phenyl H), 7.15 ppm (d, $^3J_{H,H}$ = 5.0 Hz, 1 H, H-5). $^{13}$C NMR ($CDCl_3$): $\delta$ = 135–130 ppm (phenyl C). $^{207}$Pb NMR ($CDCl_3$): $\delta$ = –199.0 ppm. MS (FAB): *m*/*z* (%) 720 (6) [$Ph_2$Pb(4-$CF_3$pymS)$_2$], 540 (100) [$Ph_2$Pb(4-$CF_3$pymS)], 386 (40) [Pb(4-$CF_3$pymS)], 284 (28) [PhPb].

**Synthesis of [$Ph_2$Pb(6-Me-4-$CF_3$pymS)$_2$] (8):** A similar procedure to that described above was followed, starting from a suspension

 © 2007 Wiley-VCH Verlag GmbH & Co. KGaA, Weinheim 

of $Ph_2PbCl_2$ (166 mg) in methanol, and a mixture of 6-Me-4-$CF_3$pymSH (150 mg, mmol) and $NEt_3$ (110 mL, mmol) in methanol (50 mL). Concentration of the mother liquor in air at room temperature gave crystals of [$Ph_2Pb$(6-Me-4-$CF_3$pymS)$_2$] suitable for X-ray studies (0.175 g, 61%). $C_{24}H_{18}F_6N_4S_2Pb$ (747.74): calcd. C 38.55, H 2.43, N 7.49, S 8.58; found C 38.84, H 2.64, N 7.28, S 8.51. IR (KBr): $\tilde{\nu}$ = 1570 $cm^{-1}$ m, 1560 m, 1535 w, 1465 w, 1425 w, 1385 vs, 1360 w, 1305 vw, 1260 vs, br, 1220 m, 1190 w, 1170 w, 1130 m, 1110 w, 1010 w, 990 m, 915 w, 840 m, 720 m, 710 m, 680 vw, 540 w, 425 w. $^1$H NMR ($CDCl_3$): $\delta$ = 8.14–7.30 (m, phenyl H), 7.00 (s, 1 H, H-5), 2.32 (s, 3 H, $CH_3$) ppm. $^{13}$C NMR ($CDCl_3$): $\delta$ = 135–130 (phenyl C), 25 ppm (s, C$^8$). $^{207}$Pb NMR ($CDCl_3$): $\delta$ = –206.7 ppm. MS (FAB): *m*/*z* (%) 555.0 (100) [$Ph_2Pb$(6-Me-4-$CF_3$pymS)], 400.4 (45) [Pb(6-Me-4-$CF_3$pymS)], 285 (37) [PhPb], 207 (11) [Pb].

***Caution:*** *Lead is a highly toxic cumulative poison. Compounds should be handled carefully.*

**Crystal Structure Determinations:** X-ray data for compounds **1**, **2** and **5**–**8** were collected on a Bruker Smart CCD 1000 diffractometer with graphite-monochromated Mo-$K_\alpha$ radiation ($\lambda$ = 0.71073 Å). The data were collected at $T$ = 293 K for all structures.

Table 8. Summary of crystal data and structure refinement for ligands and tin and lead compounds.

| Compound | [$Me_2Sn$(4-$CF_3$pymS)$_2$] (**1**) | [$Ph_2Sn$(4-$CF_3$pymS)$_2$] (**2**) | [$Ph_2Sn$(6-Me-4-$CF_3$ pymS)$_2$] (**5**) |
|---|---|---|---|
| Empirical formula | $C_{12}H_{10}F_6N_4S_2Sn$ | $C_{22}H_{14}F_6N_4S_2Sn$ | $C_{24}H_{18}F_6N_4S_2Sn$ |
| Formula weight | 507.05 | 631.18 | 659.23 |
| Crystal size [mm] | 0.35 × 0.25 × 0.20 | 0.40 × 0.34 × 0.15 | 0.55 × 0.20 × 0.05 |
| Temperature [K] | 293(2) | 293(2) | 293(2) |
| Wavelength [Å] | 0.71073 | 0.71073 | 0.71073 |
| Crystal system | monoclinic | monoclinic | monoclinic |
| Space group | *C*2/*c* | *C*2/*c* | $P2_1/n$ |
| *a* [Å] | 17.4481(10) | 16.7891(6) | 13.2553(2) |
| *b* [Å] | 11.8154(7) | 6.4499(3) | 13.4370(3) |
| *c* [Å] | 11.5926(7) | 23.1215(9) | 16.4170(3) |
| *α* [°] | 90 | 90 | 90 |
| *β* [°] | 129.9330(10) | 91.2600(10) | 108.3050(10) |
| *γ* [°] | 90.00 | 90.00 | 90 |
| *V* [Å$^3$] | 1832.55(19) | 2503.18(18) | 2776.09(9) |
| *Z* | 4 | 4 | 4 |
| Calcd. density [Mg m$^{-3}$] | 1.838 | 1.675 | 1.577 |
| $\mu$ [mm$^{-1}$] | 1.682 | 1.250 | 1.131 |
| *F*(000) | 984 | 1240 | 1304 |
| No. reflections collected | 6290 | 8323 | 19798 |
| No. of independent reflections | 2272 [*R*(int) = 0.0382] | 3096 [*R*(int) = 0.0334] | 6832 [*R*(int) = 0.0388] |
| Data/restraints/parameters | 2272/0/141 | 3096/0/187 | 6832/6/390 |
| Goodness-of-fit | 1.024 | 1.018 | 1.003 |
| Final *R* indices [$I > 2\sigma(I)$] | $R_1$ = 0.0394[a] | $R_1$ = 0.0298 | $R_1$ = 0.0399 |
| | $wR_2$ = 0.0905[b] | $wR_2$ = 0.0646 | $wR_2$ = 0.0906 |
| Largest diff. peak and hole [e Å$^{-3}$] | 1.252 and –1.886 | 0.375 and –0.537 | 0.500 and –0.524 |
| | [$t$Bu$_2$Sn(6-Me-4-$CF_3$pymS)$_2$] (**6**) | [$Ph_2Pb$(4-$CF_3$pymS)$_2$] (**7**) | [$Ph_2Pb$(6-Me-4-$CF_3$pymS)$_2$] (**8**) |
| Empirical formula | $C_{20}H_{26}F_6N_4S_2Sn$ | $C_{22}H_{14}F_6N_4PbS_2$ | $C_{24}H_{18}F_6N_4PbS_2$ |
| Formula weight | 619.26 | 719.68 | 747.73 |
| Crystal size, mm | 0.15 × 0.08 × 0.03 | 0.22 × 0.10 × 0.07 | 0.49 × 0.19 × 0.03 |
| Temperature [K] | 293(2) | 293(2) | 293(2) |
| Wavelength [Å] | 0.71073 | 0.71073 | 0.71073 |
| Crystal system | monoclinic | monoclinic | monoclinic |
| Space group | *C*2/*c* | *C*2/*c* | $P2_1/n$ |
| *a* [Å] | 15.1671(11) | 47.497(9) | 12.8826(18) |
| *b* [Å] | 7.5778(5) | 6.2325(12) | 13.707(2) |
| *c* [Å] | 23.3832(17) | 17.665(3) | 16.453(2) |
| *α* [°] | 90 | 90 | 90 |
| *β* [°] | 102.7950(10) | 108.470(3) | 108.732(2) |
| *γ* [°] | 90 | 90 | 90 |
| *V* [Å$^3$] | 2620.8(3) | 4959.8(16) | 2751.4(7) |
| *Z* | 4 | 8 | 4 |
| Calcd. density [Mg m$^{-3}$] | 1.569 | 1.928 | 1.805 |
| $\mu$ [mm$^{-1}$] | 1.192 | 7.035 | 6.344 |
| *F*(000) | 1240 | 2736 | 1432 |
| No. reflections collected | 8267 | 17872 | 17498 |
| No. of independent reflections | 3230 [*R*(int) = 0.0630] | 5039 [*R*(int) = 0.0697] | 5623 [*R*(int) = 0.0396] |
| Data / restraints / parameters | 3230 / 0 / 154 | 5039 / 0 / 316 | 5623 / 6 / 390 |
| Goodness-of-fit | 1.001 | 1.053 | 1.043 |
| Final *R* indices [$I > 2\sigma(I)$] | $R_1$ = 0.0498[a] | $R_1$ = 0.0449 | $R_1$ = 0.0278 |
| | $wR_2$ = 0.0896[b] | $wR_2$ = 0.1013 | $wR_2$ = 0.0506 |
| Largest diff. peak and hole [e Å$^{-3}$] | 0.539 and –1.055 | 1.225 and –1.609 | 0.936 and –0.933 |

[a] $R_1 = \Sigma[|F_o| - |F_c|]/\Sigma[|F_o|]$. [b] $wR_2 = [\Sigma(F_o^2 - F_c^2)^2]/\Sigma(F_o^2)^2]^{1/2}$.

 © 2007 Wiley-VCH Verlag GmbH & Co. KGaA, Weinheim 

The $\omega$-scan technique was employed to measure intensities for all crystals. Decomposition of the crystals did not occur during data collection. The intensities of all data sets were corrected for Lorentz and polarisation effects. Absorption corrections were carried out using SADABS.[68] All the structures were solved by direct methods and refined[69] by full-matrix least-squares based on $F^2$. For all the complexes, hydrogen atoms were also included in idealised positions and refined with isotropic displacement parameters. The $CF_3$ groups of compounds **1**, **2**, **5** and **8** were found to be disordered over two positions with occupancies 73:27 and 52:48 for the groups on C(5) and C(10) in compound **8**, 60:40 for the $CF_3$ group in compound **1**, 50:50 for the $CF_3$ group in **2**, and 55:45 and 62:38 for the groups on C(5) and C(10) in compound **5**.

Atomic scattering factors and anomalous dispersion corrections for all atoms were taken from the International Tables for X-ray Crystallography.[70] The crystal data and summary of data collection and structure refinement for these compounds are given in Table 8. ORTEP 3 drawings,[71] along with the numbering schemes used, are provided in the text.

CCDC-622379 to -622384 (for **1**, **2** and **5**–**8**) contain the supplementary crystallographic data for this paper. These data can be obtained free of charge from The Cambridge Crystallographic Data Centre via www.ccdc.cam.ac.uk/data_request/cif.

## Acknowledgments

This work was supported by the Xunta de Galicia (Spain) (grant PGIDT00PXI20305PR) and by the Ministerio de Ciencia y Tecnología (Spain) (grant BQU2002-01819).

[1] E. S. Raper, *Coord. Chem. Rev.* **1985**, *61*, 115–184.
[2] E. S. Raper, *Coord. Chem. Rev.* **1996**, *153*, 199–225.
[3] E. S. Raper, *Coord. Chem. Rev.* **1997**, *165*, 475–567.
[4] B. Krebs, G. Henkel, *Angew. Chem. Int. Ed. Engl.* **1991**, *30*, 769–788.
[5] I. G. Dance, *Polyhedron* **1986**, *5*, 1037–1104.
[6] P. G. Blower, J. R. Dilworth, *Coord. Chem. Rev.* **1987**, *76*, 121–185.
[7] J. R. Dilworth, J. Hu, *Adv. Inorg. Chem.* **1993**, *40*, 411–459.
[8] P. D. Akrivos, *Coord. Chem. Rev.* **2001**, *213*, 181–210.
[9] A. Sousa-Pedrares, I. Casanova, J. A. García-Vázquez, M. L. Durán, J. Romero, A. Sousa, J. Silver, P. J. Titler, *Eur. J. Inorg. Chem.* **2003**, 678–686.
[10] D. Dakternieks, K. Jurkschat, R. Tozer, J. Hook, E. R. S. Tiekink, *Organometallics* **1997**, *16*, 3696–3706.
[11] J. Fernández, M. B. Hurthouse, M. Laguna, R. Terrota, *J. Organomet. Chem.* **1999**, *574*, 207–212.
[12] S. R. Foley, G. P. A. Yap, D. S. Richeson, *J. Chem. Soc., Dalton Trans.* **2000**, 1663–1668.
[13] R. Jurkschat, V. Pieper, S. Seemeyer, M. Schurmanm, M. Biesmans, I. Verbruggen, R. Willem, *Organometallics* **2001**, *20*, 868–880.
[14] E. Block, G. Ofori-Okai, J. Zubieta, *J. Am. Chem. Soc.* **1989**, *111*, 2327–2329.
[15] M. M. Jones, *Met. Ions Biol. Syst.* **1983**, *16*, 47–83.
[16] K. Abu-Dari, T. B. Karpishim, K. N. Raymond, *Inorg. Chem.* **1993**, *32*, 3052–3055.
[17] M. Gielen, *Coord. Chem. Rev.* **1996**, *151*, 41–51.
[18] M. Gielen, *Appl. Organomet. Chem.* **2002**, *16*, 481–494.
[19] L. Pellerito, L. Nagy, *Coord. Chem. Rev.* **2002**, *224*, 111–150; M. Jain, R. V. Singh, *Appl. Organomet. Chem.* **2003**, *17*, 616–622.
[20] M. N. Xanthopoulou, S. H. Hadjikakou, N. Hadjiliadis, M. Schürmann, K. Jurkschat, A. Michaelides, S. Skoulika, T. Bakas, J. Binolis, S. Karkabounas, K. Charalabopoulos, *J. Inorg. Biochem.* **2003**, *96*, 425–434.
[21] L. S. Zamudio-Rivera, R. George-Tellez, G. López-Mendoza, A. Morales-Pacheco, E. Flores, H. Hupfl, V. Barba, F. J. Férnandez, N. Cabirol, H. Beltrán, *Inorg. Chem.* **2005**, *44*, 5370–5378 and references cited therein.
[22] C. Ma, J. Zhang, G. Tian, R. Zhang, *J. Organomet. Chem.* **2005**, *690*, 519–533 and references cited therein.
[23] J. A. García-Vázquez, J. Romero, A. Sousa, *Coord. Chem. Rev.* **1999**, *193–195*, 691–745.
[24] R. López Garzón, M. D. Gutiérrez Valero, M. L. Godino-Salido, B. K. Kepler, B. Nuber, *J. Coord. Chem.* **1993**, *30*, 111–123.
[25] A. C. Skapski, K. A. Woode, *Acta Crystallogr., Sect. B* **1979**, *35*, 59–62.
[26] P. Karagiannidis, S. K. Hadjikakou, P. Aslanidis, A. Hountas, *Inorg. Chim. Acta* **1990**, *178*, 27–34.
[27] L. R. Battaglia, R. Battistuzzi, A. Bonamartini Corradi, C. Rizzolie, P. Sgarabotto, *J. Crystallogr. Spectrosc. Res.* **1993**, *23*, 937–942.
[28] J. Abbot, D. M. L. Goodgame, Y. Jeeves, *J. Chem. Soc., Dalton Trans.* **1978**, 880–884.
[29] L. Petrilli, F. Caruso, E. Rivarola, *Main Group Met. Chem.* **1994**, *17*, 439–446.
[30] P. K. Baker, P. D. Jackson, M. E. Harman, M. B. Hursthouse, *J. Organomet. Chem.* **1994**, *468*, 171–174.
[31] A. Rodríguez, A. Sousa-Pedrares, J. A. García-Vázquez, J. Romero, A. Sousa, *Eur. J. Inorg. Chem.* **2005**, 2242–2254.
[32] A. Sousa-Pedrares, M. L. Durán, J. Romero, J. A. García-Vázquez, J. C. Monteagudo, A. Sousa, J. R. Dilworth, *Inorg. Chim. Acta* **2006**, *359*, 863–876.
[33] H. Engelking, S. Karentzopoulos, G. Reusmann, B. Krebs, *Chem. Ber.* **1994**, *127*, 2355–2361.
[34] Y. K. Au, K. K. Cheung, W. T. Wong, *J. Chem. Soc., Dalton Trans.* **1995**, 1047–1057.
[35] R. Castro, J. A. García-Vázquez, J. Romero, A. Sousa, R. Pritchard, C. McAuliffe, *J. Chem. Soc., Dalton Trans.* **1994**, 1115–1120.
[36] A. Rodríguez, J. A. García-Vázquez, A. Sousa-Pedrares, J. Romero, A. Sousa, *Inorg. Chem. Commun.* **2003**, *6*, 619–622.
[37] A. Rodríguez, J. A. García-Vázquez, A. Sousa-Pedrares, J. Romero, A. Sousa, *J. Organomet. Chem.* **2004**, *689*, 557–563.
[38] R. Castro, M. L. Durán, J. A. García-Vázquez, J. Romero, A. Sousa, E. E. Castellano, J. Zukerman-Schpector, *J. Chem. Soc., Dalton Trans.* **1992**, 2559–2563.
[39] S. W. Ng, C. Wei, V. G. K. Das, T. C. W. Mak, *J. Organomet. Chem.* **1987**, *334*, 295–305.
[40] T. P. Lockart, J. C. Calabrese, F. Davidson, *Organometallics* **1987**, *6*, 2479–2483.
[41] V. Chandrasekhar, R. O. Day, J. M. Holmes, R. R. Holmes, *Inorg. Chem.* **1988**, *27*, 958–964.
[42] M. V. Castaño, A. Macías, A. Castiñeiras, A. Sánchez-González, E. García-Martínez, J. S. Casas, J. Sordo, W. Hiller, E. E. Castellano, *J. Chem. Soc., Dalton Trans.* **1990**, 1001–1005.
[43] S. K. Hadjikakou, M. A. Demertzis, M. Kubicki, D. Kovala-Demertzi, *Appl. Organomet. Chem.* **2000**, *14*, 727–734.
[44] R. M. Fernandes, E. S. Lang, E. M. V. López, G. F. de Sousa, *Polyhedron* **2002**, *21*, 1149–1153.
[45] M. Boualam, J. Meunier-Piret, M. Biesemans, R. Willem, M. Gielen, *Inorg. Chim. Acta* **1992**, *198*, 249–255.
[46] R. Schmiedgen, F. Huber, H. Preut, *Acta Crystallogr., Sect. C* **1993**, *49*, 1735–1737.
[47] A. Bondi, *J. Phys. Chem.* **1964**, *68*, 441–451.
[48] M. Masaki, S. Matsunami, H. Ueda, *Bull. Chem. Soc. Jpn.* **1978**, *51*, 3298–3301.
[49] S. Furberg, J. Solbakk, *Acta Chem. Scand.* **1973**, *27*, 2536–2542.
[50] J. A. Castro, J. Romero, J. A. García-Vázquez, A. Castiñeiras, A. Sousa, *Polyhedron* **1995**, *14*, 2841–2847.
[51] E. Block, G. Ofori-Okai, H. Kang, J. Wu, J. Zubieta, *Inorg. Chim. Acta* **1991**, *190*, 5–6.

 © 2007 Wiley-VCH Verlag GmbH & Co. KGaA, Weinheim 

[52] G. D. Andreetti, G. Bocelli, G. Calestani, P. Sgarabotto, *J. Organomet. Chem.* **1984**, *273*, 31–45.
[53] S. M. S. V. Doidge-Harrison, J. T. S. Irvine, G. M. Spencer, J. L. Wardell, P. G. Giovanni, V. G. Tapliavini, *Polyhedron* **1996**, *15*, 1807–1815.
[54] M. G. Begley, C. Gaffney, P. G. Harrison, A. Steel, *J. Organomet. Chem.* **1985**, *289*, 281–293.
[55] A. V. Yatsenko, H. Schenk, L. A. Aslanov, *J. Organomet. Chem.* **1994**, *474*, 107–111.
[56] S. R. Halper, S. M. Cohen, *Inorg. Chem.* **2005**, *44*, 4139–4141; S. R. Halper, S. M. Cohen, *Angew. Chem. Int. Ed.* **2004**, *43*, 2385–2388.
[57] A. Nangia, V. M. Lynch, *Chem. Commun.* **2002**, 1304–1305.
[58] Q. B. Song, Y. Z. Li, Y. M. Liang, Y. X. Ma, *Acta Crystallogr., Sect. E* **2003**, *59*, m861–m863.
[59] D. M. Hatch, W. F. Wacholtz, J. T. Mague, *Acta Crystallogr., Sect. C* **2003**, *59*, m452–m453.
[60] F. Tuna, J. Hamblin, G. Clarkson, W. Errington, N. W. Alcock, M. J. Hannon, *Chem. Eur. J.* **2002**, *8*, 4957–4964.
[61] M. Mazik, D. Bläser, R. Boese, *Tetrahedron* **2001**, *57*, 5791–5797.
[62] R. C. Paul, H. S. Makhni, P. Singh, S. L. Chadha, *Z. Anorg. Allg. Chem.* **1970**, *377*, 108–112 and references cited therein; R. D. Kross, V. A. Fassel, M. Hargoshes, *J. Am. Chem. Soc.* **1956**, *78*, 1332–1335.
[63] C. Ma, J. Zhang, R. Zhang, *Can. J. Chem.* **2003**, *81*, 1070–1075; O. Domazetis, B. D. James, M. F. Mackay, R. J. Magee, *J. Inorg. Nucl. Chem.* **1979**, *41*, 1555–1562.
[64] T. P. Lockart, W. F. Manders, *Inorg. Chem.* **1986**, *25*, 892–895.
[65] R. Schmiedgen, F. Huber, A. Silvestri, G. Ruisi, M. Rossi, R. Barbieri, *Appl. Organomet. Chem.* **1998**, *12*, 861–871.
[66] J. Holeček, N. Nádvornik, K. Handlíř, A. Lyčka, *J. Organomet. Chem.* **1986**, *315*, 299–308.
[67] L. A. Margolis, C. D. Schaeffer Jr, C. H. Yoder, *Appl. Organomet. Chem.* **2003**, *17*, 236–238; S. E. Van Bramer, A. Glatfelter, S. Bai, C. Dybowski, G. Neue, D. L. Perry, *Magn. Reson. Chem.* **2006**, *44*, 357–365.
[68] G. M. Sheldrick, *SADABS, An empirical absorption correction program for area detector data*, University of Göttingen, Germany, **1996**.
[69] G. M. Sheldrick, *SHELX-97, Program for the solution a refinement of crystal structures*, University of Göttingen, Germany, **1997**.
[70] *International Tables for X-ray Crystallography*, vol. C, Kluwer, Dordrecht, **1992**.
[71] ORTEP3 for Windows: L. J. Farrugia, *J. Appl. Crystallogr.* **1997**, *30*, 565.

Received: October 5, 2006
Published Online: February 23, 2007

 © 2007 Wiley-VCH Verlag GmbH & Co. KGaA, Weinheim

**The EUChemSoc Societies have taken the significant step into the future by merging their traditional journals, to form two leading chemistry journals, the *European Journal of Inorganic Chemistry* and the *European Journal of Organic Chemistry*. Three further EUChemSoc Societies (Austria, Czech Republic and Sweden) are Associates of the two journals.**

## COVER PICTURE

**The cover picture shows** the synthesis of the mixed-metal Dawson sandwich complexes $[MCo_3(H_2O)_2(P_2W_{15}O_{56})_2]^{16-}$ by the addition of the transition metal cation $M^{2+}$ to the "lacunary" sandwich complex $[NaCo_3(H_2O)_2(P_2W_{15}O_{56})_2]^{17-}$. This "lacunary" species is a good precursor for the preparation mixed-metal sandwich complexes, with promising interesting catalytic, electocatalytic and magnetic properties. Details of the synthesis and the structural characterization in solution are discussed in the article by L. Ruhlmann and R. Touvenot on p. 1493 ff.

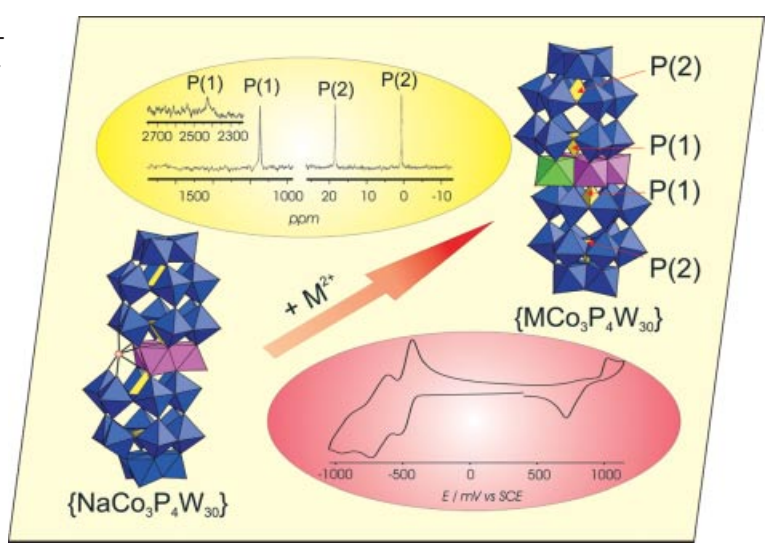


 © 2007 Wiley-VCH Verlag GmbH & Co. KGaA, Weinheim 

# CONTENTS

## MICROREVIEW


### Molecular Electrochemistry

**A. J. L. Pombeiro* ..... 1473–1482**

Characterization of Coordination Compounds by Electrochemical Parameters

**Keywords:** Electrochemistry / Redox potential / Additivity models / Ligand parameters / Ligand effects


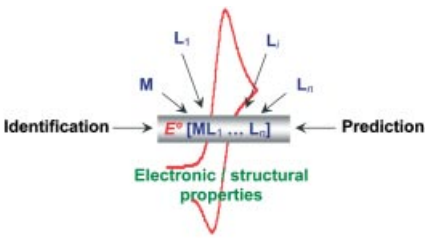



Attention is drawn to the interest shown in the redox potential and derived electrochemical parameters that are used for the caracterization and identification of coordination compounds.


## SHORT COMMUNICATIONS


### Molecular Wires

**C. Femoni, F. Kaswalder, M. C. Iapalucci, G. Longoni,* S. Zacchini ..... 1483–1486**

Infinite Molecular $\{[Pt_{3n}(CO)_{6n}]^{2-}\}_\infty$ Conductor Wires by Self-Assembly of $[Pt_{3n}(CO)_{6n}]^{2-}$ ($n$ = 5–8) Cluster Dianions Formally Resembling CO-Sheathed Three-Platinum Cables

**Keywords:** Carbonyl ligands / Cluster compounds / Platinum / Structure elucidation / Conducting materials


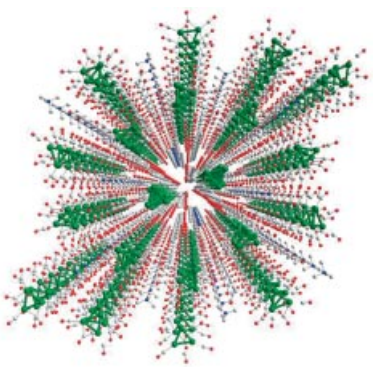


Self-assembly of $[Pt_{3n}(CO)_{6n}]^{2-}$ ($n$ = 5–8) cluster dianions into infinite semicontinuous or continuous $\{[Pt_{3n}(CO)_{3n}(\mu\text{-}CO)_{3n}]^{2-}\}_\infty$ conductor wires is obtained upon crystallization. Pellets of these salts exhibit conductor behavior that roughly depends on the interdianion gap along the wires.

### Inclusion Compounds

**I. Lippold, H. Görls, W. Plass* ..... 1487–1491**

New Aspects for Modeling Supramolecular Interactions in Vanadium Haloperoxidases: β-Cyclodextrin Inclusion Compounds of *cis*-Dioxovanadium(V) Complexes

**Keywords:** Cyclodextrins / Host–guest systems / Inclusion compounds / Vanadium / X-ray diffraction


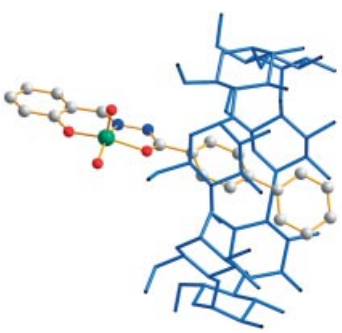


A novel β-cyclodextrin inclusion compound of the *cis*-dioxovanadium(V) complex derived from biphenyl-4-carboxylic acid salicylidene hydrazide has been synthesized. The isolated inclusion compound $K[VO_2(salhybiph)@\beta\text{-CD}]$ has been characterized in solution by NMR spectroscopy and in the solid state by X-ray crystallography. The latter reveals a channel-type packing of head-to-head β-cyclodextrin dimers.

# FULL PAPERS

## Dawson Sandwich Complexes

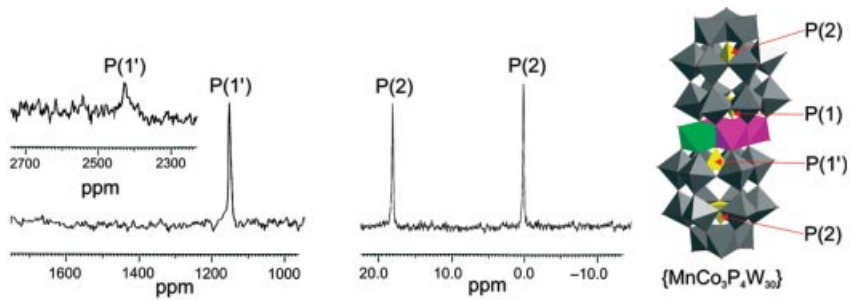


**L. Ruhlmann,* C. Costa-Coquelard, J. Canny, R. Thouvenot* ..... 1493–1500**

Mixed-Metal Dawson Sandwich Complexes: Synthesis, Spectroscopic Characterization and Electrochemical Behaviour of $Na_{16}[M^{II}Co_3(H_2O)_2(P_2W_{15}O_{56})_2]$ (M = Mn, Co, Ni, Zn and Cd)

**Keywords:** Dawson complexes / Paramagnetic $^{31}P$ NMR spectroscopy / Electrochemistry

Mixed-metal Dawson sandwich complexes $[MCo_3(H_2O)_2(P_2W_{15}O_{56})_2]^{16-}$ have been synthesized by the reaction of $M^{2+}$ (where M = Mn, Co, Ni, Zn and Cd) with the "lacunary" sandwich complex $\alpha\beta$-$[NaCo_3(H_2O)_2(P_2W_{15}O_{56})_2]^{17-}$. The $\{MCo_3P_4W_{30}\}$ species were characterized by IR spectroscopy, elemental analysis, $^{31}P$ NMR spectroscopy and electrochemistry.

## Anions of Pentacoordinate P

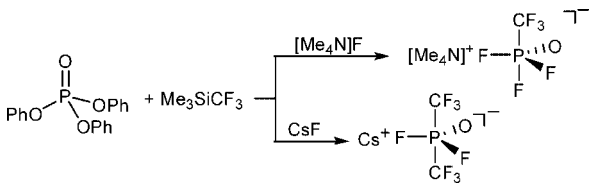


**N. V. Pavlenko, L. A. Babadzhanova, I. I. Gerus, Y. L. Yagupolskii,* W. Tyrra, D. Naumann ..... 1501–1507**

New Anions of Pentacoordinate Phosphorus Containing Fluorine and Trifluoromethyl Groups

**Keywords:** Phosphorus / Fluorides / Silanes / Pentacoordinate anions

The competitive nucleophilic trifluoromethylation/fluorination of $(PhO)_3P(O)$ with $Me_3SiCF_3$ and $[Me_4N]F$ or CsF was investigated.

## Supramolecular Photochemistry

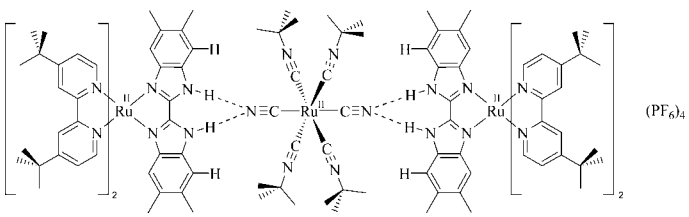


**K. Halbauer, A. Göbel, A. Sterzik, H. Görls, S. Rau, W. Imhof* 1508–1514**

Ruthenium Complex Fragments as Constituents of Trinuclear Photoactive Supramolecular Assemblies Based on Hydrogen Bond Association

**Keywords:** Supramolecular Photochemistry / Bibenzimidazole ligands / Hydrogen bonds / Ruthenium

*cis*- or *trans*-$[Ru(C{\equiv}N\text{-}t\text{Bu})_4(CN)_2]$ and photochemically active [bis(bipyridyl)bibenzimidazole-ruthenium(II)] complexes form supramolecular adducts via hydrogen bond association. Stoichiometry, molecular structure, photophysical properties and association constants of the adducts are reported.

## Olivine – Magnetic Structure

**H. Mikus, H.-J. Deiseroth,* K. Aleksandrov, C. Ritter, R. K. Kremer ..... 1515–1518**

The Magnetic Structure of $Mn_2GeSe_4$

**Keywords:** Olivine / Magnetic structure / Manganese / Germanium / Selenium / Antiferromagnetism

The antiferromagnetic structure on the olivine-type $Mn_2GeSe_4$ is discussed as a potentially canted structure.

 © 2007 Wiley-VCH Verlag GmbH & Co. KGaA, Weinheim 

# CONTENTS

## Organolanthanide Complexes

**S. Zhou, S. Wang,* E. Sheng, L. Zhang, Z. Yu, X. Xi, G. Chen, W. Luo, Y. Li ..... 1519–1528**

Synthesis, Characterization, and Catalytic Activity of Some Neodymium(III), Ytterbium(II), and Europium(II) Complexes with Pyrrolidinyl- and Piperidinyl-Functionalized Indenyl Ligands

**Keywords:** Homolysis / Catalysts / Polymerization / Lanthanoids

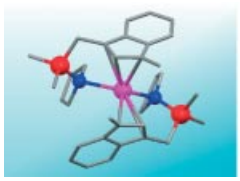

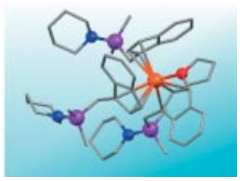

Studies on the reactivity of pyrrolidinyl- and piperidinyl-functionalized indene compounds with the lanthanide(III) amides have led to synthesis and characterization of a series of new organolanthanide(II) complexes and a new neodymium(III) complex. All complexes exhibited moderate to good catalytic activities for the ring-opening polymerization of ε-caprolactone.

## Microclusters

**M. Srnec,* R. Zahradník ..... 1529–1543**

Small Group IIa–VIa Clusters and Related Systems: A Theoretical Study of Physical Properties, Reactivity, and Electronic Spectra

**Keywords:** Ab initio calculations / Cluster compounds / Structural elucidation

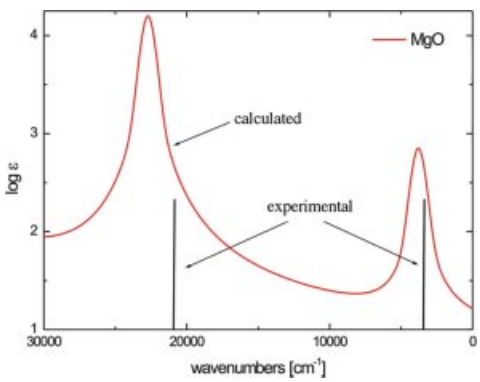


The group IIa–VIa diatomics exhibit electronic transitions in the visible region and the longest wavelength bands are located in the near-infrared region. MgO represents an extreme.

## Semiconducting Oxides

**D. Maestre, J. Ramírez-Castellanos, P. Hidalgo, A. Cremades, J. M. González-Calbet, J. Piqueras* ..... 1544–1548**

Study of the Defects in Sintered $SnO_2$ by High-Resolution Transmission Electron Microscopy and Cathodoluminescence

**Keywords:** Semiconductors / Luminescence / Microstructure / Resistivity

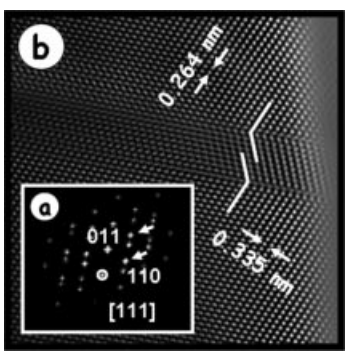


High-resolution images of sintered $SnO_2$ samples annealed under an oxygen atmosphere show structural defects that seem to be related to changes in both the cathodoluminescence spectra and electrical resistivity.

## Nonstoichiometric Compounds

**S. Cobo, R. Fernández, L. Salmon, G. Molnár, A. Bousseksou* ... 1549–1555**

Correlation between the Stoichiometry and the Bistability of Electronic States in Valence-Tautomeric $Rb_xMn[Fe(CN)_6]_y \cdot zH_2O$ Complexes

**Keywords:** Prussian blue analogues / Magnetic properties / Phase transitions / Raman spectroscopy

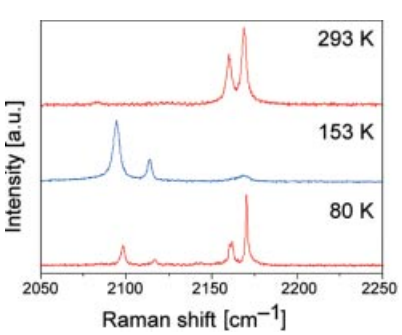


A series of Prussian blue analogues $Rb_xMn[Fe(CN)_6]_y \cdot zH_2O$ with different stoichiometries was synthesized; some of the samples exhibit a first-order phase transition between the $Mn^{II}–Fe^{III}$ and $Mn^{III}–Fe^{II}$ electronic states accompanied by large entropy changes that are mainly of vibrational origin.

 © 2007 Wiley-VCH Verlag GmbH & Co. KGaA, Weinheim 

## Rhenium(I) Complexes

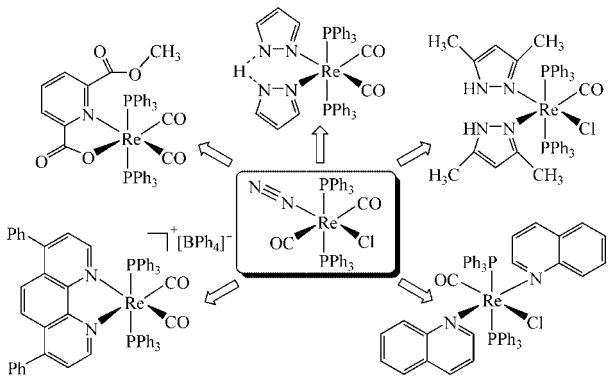

**A. M. Kirillov, M. Haukka, M. F. C. Guedes da Silva, A. J. L. Pombeiro* ..... 1556–1565**

Synthesis, Characterization and Redox Behaviour of Mono- and Dicarbonyl Phosphane Rhenium(I) Complexes Bearing N-, N,N- and N,O-Type Ligands

**Keywords:** Carbonyl ligands / Electrochemistry / N ligands / Rhenium

Pyrazole, quinoline, phenanthroline, picolinate or dipicolinate complexes with $\{Re(CO)_x\}$ ($x$ = 1, 2) sites were prepared from a dinitrogen-complex precursor. The redox behaviour of the complexes was studied and the Lever electrochemical ligand parameter $E_L$ was determined for 4,7-$Ph_2$-phen.

## Metal Sulfide Nanoparticles

Thermolysis of $[M(S_2CPh)_2(tmeda)]$ gave metal sulfide nanoparticles which were characterized by XRD, EDAX and TEM. Both hexagonal and cubic phases of metal sulfide nanoparticles can be prepared by changing experimental conditions.

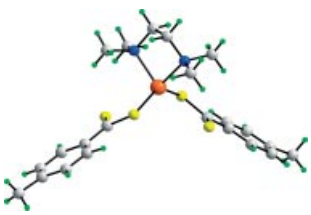

**G. Kedarnath, V. K. Jain,* S. Ghoshal, G. K. Dey, C. A. Ellis, E. R. T. Tiekink* ..... 1566–1575**

Zinc, Cadmium and Mercury Dithiocarboxylates: Synthesis, Characterization, Structure and Their Transformation to Metal Sulfide Nanoparticles

**Keywords:** Zinc / Cadmium / Mercury / Dithiocarboxylates / Nanoparticles

## Nickel(II)-Carbene Intermediates

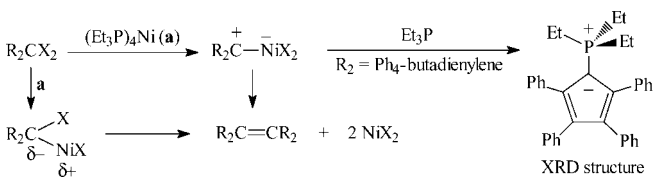


**J. J. Eisch,* Y. Qian, A. L. Rheingold ..... 1576–1584**

Nickel(II)-Carbene Intermediates in Reactions of Geminal Dihaloalkanes with Nickel(0) Reagents and the Corresponding Carbene Capture as the Phosphonium Ylide

**Keywords:** Nickel(0) reagents / Nickel(II)-carbenes / Phosphonium ylides / α-Elimination / Carbon-carbon bond formation

Coupling of geminal dihalides with $(Et_3P)_4Ni$ has been reinvestigated. Failure to trap assumed nickel(0)-carbenes, detection and isolation of Wittig reagents and the failed coupling of 5,5-dibromotetraphenylcyclopentadiene led us to conclude that nickel(II)-carbenes are involved. The X-ray structure of $Ph_4Cp{=}PEt_3$ is best represented as having a zwitterionic C–P bond.

## Stereoselective Alkyne Binding

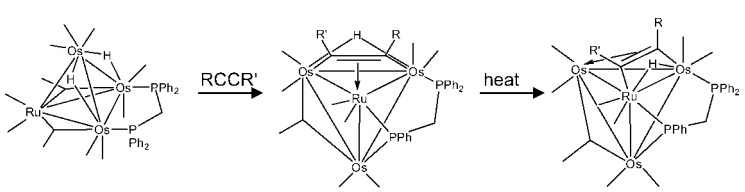

**Y. L. K. Tan, W. K. Leong* ... 1585–1598**

The Ditertiary-Phosphane-Bridged Heteronuclear Cluster $RuOs_3(\mu\text{-}H)_2(CO)_9(\mu\text{-}CO)_2(\mu\text{-}dppm)$: Synthesis and Reactivity with Alkynes

**Keywords:** Heterometallic complexes / Ruthenium / Osmium / Ditertiary phosphanes / Alkynes

The reaction of the dppm-bridged heteronuclear cluster $RuOs_3(\mu\text{-}H)_2(CO)_9(\mu\text{-}CO)_2(\mu\text{-}dppm)$ with alkynes afforded tetrahedral clusters in which the alkyne is aligned parallel to an Os–Os bond (//Os-Os isomer). The clusters incorporating internal alkynes underwent isomerization to the //Ru-Os isomer by alkyne and hydride migration.

 © 2007 Wiley-VCH Verlag GmbH & Co. KGaA, Weinheim 

# CONTENTS

## Cyclopentadienylvanadium CO Structures

**X.-H. Zhang, Q.-S. Li,* Y. Xie, R. B. King,* H. F. Schaefer III ... 1599–1605**

The Binuclear Cyclopentadienylvanadium Carbonyls $(\eta^5\text{-}C_5H_5)_2V_2(CO)_7$ and $(\eta^5\text{-}C_5H_5)_2V_2(CO)_6$: Comparison with Homoleptic Chromium Carbonyls

**Keywords:** Binuclear cyclopentadienylvanadium carbonyls / Density functional theory

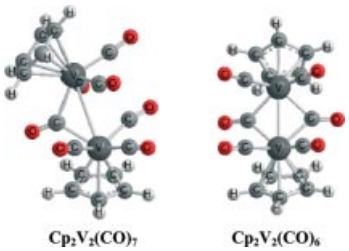


The cyclopentadienylvanadium carbonyls $CpV(CO_n$ ($n$ = 4, 3, 2, 1), $Cp_2V_2(CO)_7$, and $Cp_2V_2(CO)_6$ have been studied by density functional theory using the B3LYP and BP86 functionals. Thermodynamic information from these calculations rationalize why neither $Cp_2V_2(CO)_7$ nor $Cp_2V_2(CO)_6$ have yet been synthesized whereas $Cp_2V_2(CO)_5$ is a known stable compound.

## Thioantimonates

**M. Zhang, T. L. Sheng, X. H. Huang, R. B. Fu, X. Wang, S. M. Hu, S. C. Xiang, X. T. Wu* ..... 1606–1612**

Solvothermal Synthesis, Crystal Structure, and Thermal Stability of Three-Layered Thioantimonate(III) Complexes: $[Ni(C_3H_{10}N_2)_3]Sb_4S_7$, $[C_4H_{14}N_2]Sb_8S_{13}\cdot H_2O$, and $[C_6H_{18}N_2]Sb_{10}S_{16}\cdot H_2O$

**Keywords:** Thioantimonates / Solvothermal synthesis / Cations / Layered compounds

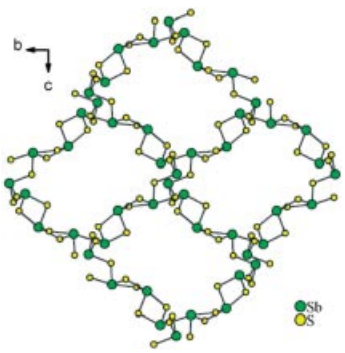


In the compound $[Ni(C_3H_{10}N_2)_3]Sb_4S_7$, a rectangle-like $Sb_{16}S_{16}$ heteroring with dimensions of about 8.1 × 14.7 Å is observed. This is the largest reported pore in layered thioantimonates to date. Further condensation of the $Sb_{16}S_{16}$ heterorings resulted in an unprecedented framework of the five-atom-thick $Sb_xS_y^{n-}$ layer.

**If not otherwise indicated in the article, papers in issue 10 were published online on March 19, 2007**

 © 2007 Wiley-VCH Verlag GmbH & Co. KGaA, Weinheim 

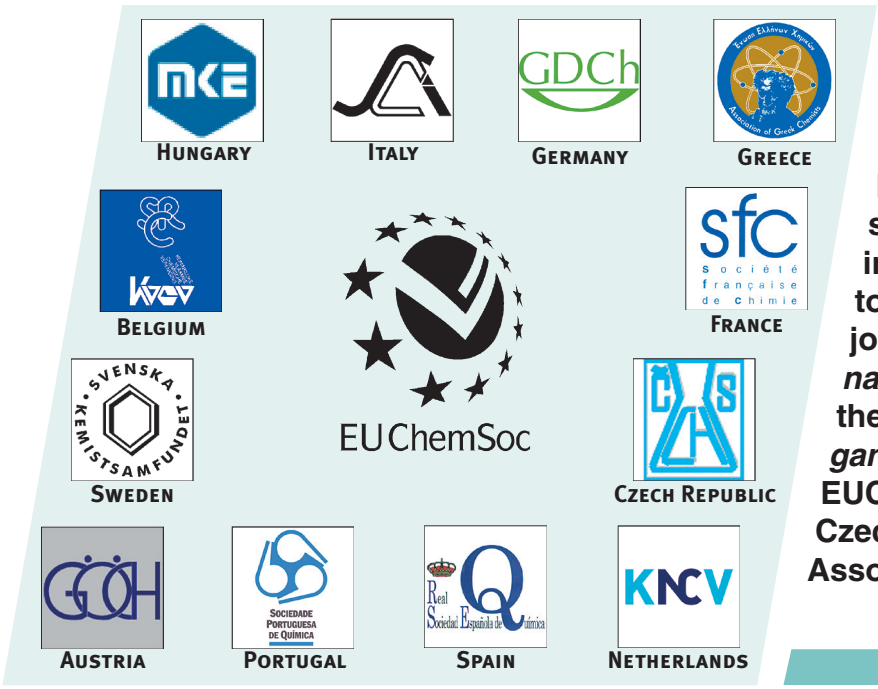


**The EUChemSoc Societies have taken the significant step into the future by merging their traditional journals, to form two leading chemistry journals, the *European Journal of Inorganic Chemistry* and the *European Journal of Organic Chemistry*. Three further EUChemSoc Societies (Austria, Czech Republic and Sweden) are Associates of the two journals.**

## COVER PICTURE

**The cover picture shows** the synthesis of the mixed-metal Dawson sandwich complexes $[MCo_3(H_2O)_2(P_2W_{15}O_{56})_2]^{16-}$ by the addition of the transition metal cation $M^{2+}$ to the "lacunary" sandwich complex $[NaCo_3(H_2O)_2(P_2W_{15}O_{56})_2]^{17-}$. This "lacunary" species is a good precursor for the preparation mixed-metal sandwich complexes, with promising interesting catalytic, electrocatalytic and magnetic properties. Details of the synthesis and the structural characterization in solution are discussed in the article by L. Ruhlmann and R. Thouvenot on p. 1493 ff.

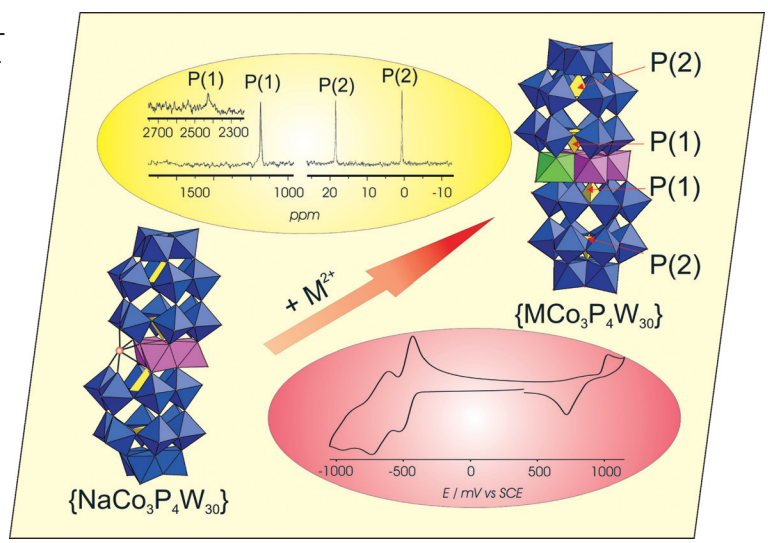


 © 2007 Wiley-VCH Verlag GmbH & Co. KGaA, Weinheim 

DOI: 10.1002/ejic.200601095

# Characterization of Coordination Compounds by Electrochemical Parameters

**Armando J. L. Pombeiro*[a]**

**Keywords:** Electrochemistry / Redox potential / Additivity models / Ligand parameters / Ligand effects

Attention is drawn to the interest in the use of the redox potential for the characterization and identification of coordination compounds on the basis of redox potential-structure relationships that define electrochemical parameters, which are shown for a wide variety of ligands and metal sites.

(© Wiley-VCH Verlag GmbH & Co. KGaA, 69451 Weinheim, Germany, 2007)

1. Introduction
2. Partial Additivity Models – Pickett's and Derived Models
2.1. General
2.2. $P_L$ Ligand Parameter
2.3. $E_s$ and $\beta$ Metal-Site Parameters
3. Full Additivity Lever's Model
3.1. General
3.2. $E_L$ Ligand Parameter and Associated Ones
4. Identification of Coordination Compounds
5. Final Comments

## 1. Introduction

Coordination compounds are usually characterized by common IR and multi-nuclear NMR spectroscopic methods, elemental analysis and, whenever possible, by single-crystal X-ray diffraction. In contrast, electrochemical methods, although being increasingly applied in the last few years (mainly cyclic voltammetry) to measure the redox potential, induce chemical reactions by electron transfer and study the mechanisms of redox processes,[1–4] have not yet found a common application as a characterization or identification tool for such compounds. This is somewhat surprising in view of the useful information associated with the redox potential of a compound.

The main aim of this Microreview is to draw the attention of the coordination and organometallic chemists to the fact that the redox potential of a complex can provide a relevant structural and electronic meaning, allowing for the quantification of the metal and ligand electron acceptor/donor properties, which can then be applied as an important characterization parameter, the use of which has still been neglected. For such a purpose, the review focuses on the seminal works of Pickett and Lever who have proposed useful models for the redox potential/structure relationships in metal complexes, and on the developments thereof, which have been introduced namely by the current author and his research group.

Since the redox potentials of metal complexes have been correlated over the years to a variety of other properties[5–7] that are also dependent on the electronic/structural features of the complexes, one could expect the possibility of using the redox potential to quantify the electron donor/acceptor properties of the ligands and their coordination metal

[a] Centro de Química Estrutural, Complexo I, Instituto Superior Técnico,
Av. Rovisco Pais, 1049-001 Lisboa, Portugal
E-mail: pombeiro@ist.utl.pt

*Armando J. L. Pombeiro, Full Professor (since 1989) at the Instituto Superior Técnico, was born in Porto in 1949 and obtained his D.Phil. degree at the University of Sussex (1976) under the supervision of Professors R. L. Richards and J. Chatt. His main research interests are in the fields of activation, by transition-metal centres, of small molecules (with biological, environmental, pharmacological or industrial significance, such as alkanes, nitriles or oximes), metal-mediated synthesis, catalysis (namely functionalization of alkanes under mild conditions), and molecular electrochemistry of coordination compounds (redox potential-structure relationships, electron-transfer-induced reactions, electrosynthesis, electrocatalysis, mechanisms of redox processes). He has published one book (and edited two more) and ca. 380 original papers, review articles, book contributions and patents. He is a full member of the Academy of Sciences of Lisbon, Vice-President of its Class of Sciences and former Secretary-General. He is the Academy representative at the International Council for Science (ICSU) and the European Academies Science Advisory Council (EASAC). He is a former member of the Higher Council for Science, Technology and Innovation, of international Evaluation Commissions of Portuguese and foreign Universities, and of NATO ASI Advisory Panels. He is a cofounder of the Portuguese Electrochemical Society (former President) and of the Iberoamerican Electrochemical Society.*

 © 2007 Wiley-VCH Verlag GmbH & Co. KGaA, Weinheim 

centres. This would provide an important characterization method for the complexes based on their redox potentials, but would require the establishment of defined relationships between the redox potential and such electronic properties of all the particular ligands and metal sites that constitute the coordination entity under study. To keep matters simple additive effects on the redox potential have been sought.

Following preliminary additivity recognitions,[8,9] within a series of closely related 18-electron first-row transition-metal complexes of the general type $[M(CO)_{6-x}L_x]^{y+}$, which undergo a single-electron reversible oxidation centred at the metal atom, the main systematic approaches have been proposed by Pickett et al.,[10–12] Lever[13–16] and Bursten.[17–19]

The Bursten model is based on a direct linear correlation (with a negative slope) between the HOMO energy and the oxidation potential ($E_{1/2}$) of octahedral $d^6$ metal complexes of the type $[ML_nL'_{6-n}]$ (L = stronger π-acceptor than L′). This potential (viz. HOMO energy) is determined in an additive way by the effects ($B$) of all the $n$L and $(6 - n)$L′ ligands and by the effects ($C$) of the ligands, $x$L and $(4 - x)$L′, that π-interact with the metal dπ orbital comprised in the HOMO of the complex {[Equation (1)] in which $A^0$ depends on the metal atom, in particular its oxidation state, and trivially on the solvent and reference electrode}.

$$E_{1/2} = A^{o} + nB^{L} + (6-n)B^{L'} + xC^{L} + (4-x)C^{L'} \quad (1)$$

In spite of the immediate significance of this model, in terms of the redox potential/redox orbital energy relationship, its basic expression (1) (although it can adopt a simpler form) is considerably complex, requires the differentiation of the ligands in terms of their π-acceptance ability and still remains relatively unexplored. Moreover, it can be correlated to the other models (namely the Pickett one[20]), which are easier to apply and will not be considered further.

It is worth mentioning that, for comparative purposes, the redox potentials have to have a common reference, which often requires a conversion.[21,22] In Pickett's model the potentials have typically been quoted relative to the saturated calomel electrode (SCE), whereas in the Lever one they have been referenced to the normal hydrogen electrode (NHE).

## 2. Partial Additivity Models – Pickett's and Derived Models

In these models, some of the ligands (and therefore their effects) are included in the overall metal centre $\{M_s\}$ to which the other ligand(s) $L_n$ is (are) bonded in the $[M_sL_n]$ complex and therefore the additive effects on the redox potential are assumed only for the $\{M_s\}$ and the $n$L ligand(s). In the extreme case, as in Pickett's model, $n = 1$, i.e. only one ligand is distinct from the binding metal site in the $[M_sL]$ complex, corresponding to a minimum additivity requirement. Extensions of this model to other cases, with a separation of more than one ligand ($n > 1$) from $\{M_s\}$ (a higher additivity assumption), have been proposed by the current author.

### 2.1. General

The linear relationships observed by Pickett et al. between the oxidation potentials ($E^{ox}_{1/2}$) of the members of a series of 18-electron octahedral-type complexes $[M_sL]$ (bearing a variable L ligand at a 16-electron $M_s$ metal centre) and the oxidation potentials of the homologous complexes $[Cr(CO)_5L]$ [with the $\{Cr(CO)_5\}$ site and the common L ligand] can be expressed by the basic Equation (2). Herein, $E_s$ is the oxidation potential of the carbonyl complex $[M_s(CO)]$ [Equation (3)], a measure of the *electron richness* of the metal centre (the higher this property, the lower $E_s$), the slope $\beta$ is the *polarizability* of the metal site (a measure of the sensitivity of the HOMO energy to a variation of the ligand L) and the *ligand $P_L$ parameter* [given by Equation (4)] is the shift in the oxidation potential resulting from the replacement of one CO group in $[Cr(CO)_6]$ by one L ligand.[10]

$$E^{ox}_{1/2}[M_sL] = E_s + \beta P_L \quad (2)$$

$$E_s\{M_s\} = E^{ox}_{1/2}[M_s(CO)] \quad (3)$$

$$P_L(L) = E^{ox}_{1/2}[Cr(CO)_5L] - E^{ox}_{1/2}[Cr(CO)_6] \quad (4)$$

Expression (2) allows (i) the estimate of $E_s$ and $\beta$ of the metal centre from the plot of the oxidation potential of a series of complexes $[M_sL]$ vs. $P_L$, or (ii) the estimate of $P_L$ for the ligand L if $E_s$ and $\beta$ are known for a certain $\{M_s\}$ centre, as well as the oxidation potential of the particular complex $[M_sL]$ with this metal site and the ligand L, or (iii) the estimate of either $E_s$ or $\beta$, when the other parameters and the oxidation potential of an $[M_sL]$ complex is known, or (iv) the prediction of the oxidation potential of any $[M_sL]$ complex provided the corresponding $E_s$, $\beta$ and $P_L$ parameters are known.

The above Pickett's approach has been adapted or extended to complexes of types other than $[M_sL]$ as follows.

Extension of the additivity to 18-electron complexes $[M_sL_n]$ ($n = 2, 3$; $n = 1$ was the original case) leads to Equations (5), (6) and (7),[5,23] with the $P_{nL}$ ligand parameter rep-

$$E^{ox}_{1/2}[M_sL_n] = E_s + \beta P_{nL} \quad (5)$$

$$E_s = E^{ox}_{1/2}[M_s(CO)_n] \quad (6)$$

$$P_{nL} = E^{ox}_{1/2}[Cr(CO)_{6-n}L_n] - E^{ox}_{1/2}[Cr(CO)_6] \quad (7)$$

 © 2007 Wiley-VCH Verlag GmbH & Co. KGaA, Weinheim 

resenting the shift of the oxidation potential upon replacement of *n*CO ligands in $[Cr(CO)_6]$ by *n*L ligands. It is the sum of the *n* individual $P_L$ values [Equation (8)] when the L ligands have independent effects on the oxidation potential.[5,23] The metal centre $\{M_s\}$ is then a 14-electron ($n$ = 2) or a 12-electron ($n$ = 3) site.

$$P_{nL} = n\,P_L \tag{8}$$

For the mixed-ligand complexes $[M_sLL']$, the oxidation potential was shown[24] to be the average of those of the corresponding $[M_sL_2]$ and $[M_sL'_2]$ [Equation (9)] when the metal sites $\{M_sL\}$ and $\{M_sL'\}$ exhibit analogous values of polarizability ($\beta$).

$$E^{ox}_{1/2}[M_sLL'] = 1/2\,\{E^{ox}_{1/2}[M_sL_2] + E^{ox}_{1/2}[M_sL'_2]\} \tag{9}$$

Moreover, the oxidation potential of the complexes $[M_sL_2]$ was demonstrated[25] to be given by Equation (10), showing that the potential of any member of the series can be predicted provided one knows the oxidation potential of the dicarbonyl complex $[M_s(CO)_2]$, the $E_s$ and $\beta$ values of an auxiliary $\{M_sL'\}$ site with the auxiliary L′ ligand and the $P_L$ values of both L and L′. The knowledge of these auxiliary parameters also allows for the estimate of the electron richness and polarizability of the $\{M_sL\}$ centre [Equations (11) and (12)].[25]

These expressions, (9)–(12), with an evident predictive value, have been successfully applied to the series of isocyanido and carbonyl complexes of rhenium(I), *trans*-$[ReLL'(dppe)_2]^+$ (L, L′ = CNR, CO; dppe = $Ph_2PCH_2CH_2PPh_2$) and *trans*-$[ReL_2(dppe)_2]^+$ (L = CNR, CO),[24–25] and of nitrile and carbonyl complexes of iron(II), *trans*-$[FeL_2(depe)_2]^{2+}$ (L = NCR, CO; depe = $Et_2PCH_2CH_2PEt_2$).[26] The $E_s$ and $\beta$ values of the corresponding *trans*-$\{ReL(dppe)_2\}^+$ and *trans*-$\{FeL(depe)_2\}^{2+}$ metal sites have also been estimated (see below).[24–26]

An extension of the model to open-shell 17- and 16-electron complexes has also been carried out.[27,28] The general expressions (2)–(4) can be kept but now the metal site $\{M_s\}$ is a 15- or a 14-electron centre, respectively. The approach has been applied to the 17-electron complexes *cis*-$[ReCl(L)(dppe)_2]^+$ (L = NCR, CO) and *trans*-$[FeBr(L)(depe)_2]^{2+}$, with a 15-electron $Re^{II}$ or $Fe^{III}$ centre,[27] and to the square-planar 16-electron $Rh^I$ complexes $[Rh(O\cap O)(CO)L]$ [O∩O = $MeC(O)CHC(O)Me^-$ (acac), $PhC(O)CHC(O)Me^-$ (bac)].[28]

$$E_s\{M_sL\} = \left[1 - \frac{P_L(L)}{P_L(L')}\right]E^{ox}_{1/2}[M_s(CO)_2] + \frac{P_L(L)}{P_L(L')}E_s\{M_sL'\} \tag{11}$$

$$\beta\{M_sL\} = \frac{\left[1 - \frac{P_L(L)}{P_L(L')}\right]E_s\{M_sL'\} - \left[1 - \frac{P_L(L)}{P_L(L')}\right]E^{ox}_{1/2}[M_s(CO)_2] + \beta\{M_sL'\}P_L(L)}{P_L(L')} \tag{12}$$

### 2.2. $P_L$ Ligand Parameter

The $P_L$ ligand parameter can be obtained from expression (4) if the oxidation potential of the corresponding $[Cr(CO)_5L]$ complex is known, or otherwise by using the general Equation (2) if one knows the oxidation potential of a particular $[M_sL]$ complex with that ligand binding a metal centre $\{M_s\}$ with known $E_s$ and $\beta$ values. It can also be derived from the Lever $E_L$ parameter (see below). $P_L$ values are already known for a wide variety of ligands[5,10,24–56] and lists have been collected[36,56] with particular emphasis on the estimate of the values for carbynes, carbenes, vinylidenes, allenylidenes and alkynyls.[36] Representative examples are given in Table 1, which also includes those reported recently.

The $P_L$ ligand parameter reflects both σ- and π-effects in an overall manner and is considered as a *measure* of the net electron-donor minus the electron-acceptor ability of the ligand L, since the higher this property the less stabilized will be the HOMO for $[Cr(CO)_5L]$ and hence the lower oxidation potential of this complex and the lower the $P_L$ parameter [Equation (4)]. Although the oxidation potential of a compound depends on the energetics of both the compound and its oxidized form, a linear correlation of the oxidation potential with the HOMO energy (see above) is expected for a series of closely related complexes such as $[Cr(CO)_5L]$ with a variable L.

The strongest net π-electron acceptors exhibit the highest $P_L$ values (≥0), namely $NO^+$ (+1.40 V)[10] > carbynes (+0.24 to +0.21 V)[29] > $\eta^2$-vinyl (+0.22 V)[31] > benzoyl isocyanide (+0.20 V)[30] > $PF_3$ (+0.14 V)[32] > aminocarbyne ($=CNH_2^+$) (+0.09 V)[31] > CO (0 V).

Dinitrogen and the phosphaalkyne P≡C*t*Bu, coordinated in the $\eta^1$-mode, have $P_L$ values (–0.07[10] and –0.04[33] V, respectively) close to that of CO (0 V), but this is accounted for by the limited σ-donor and π-acceptor abilities of the former ligands. Similar $P_L$ values can be displayed by both a weak π-acceptor/weak σ-donor ligand and a strong π-acceptor/strong σ-donor one, since $P_L$ is determined by the net π-electron acceptor minus σ-donor character of the ligand.

$$E^{ox}_{1/2}[M_sL_2] = \left[1 - \frac{P_L(L)}{P_L(L')}\right]^2 E^{ox}_{1/2}[M_s(CO)_2] + \left[\frac{2P_L(L)}{P_L(L')} - \frac{P_L^2(L)}{P_L^2(L')}\right]E_s\{M_sL'\} + \frac{P_L^2(L)}{P_L(L')}\beta\{M_sL'\} \tag{10}$$

 © 2007 Wiley-VCH Verlag GmbH & Co. KGaA, Weinheim 

Table 1. $P_L$ and $E_L$ values for selected ligands.[a]

| | $P_L$ [V] | Ref. | $E_L$ [V vs. NHE] | Ref. |
|---|---|---|---|---|
| $NO^+$ | 1.40 | [10] | >1.5 | [13,16] |
| Carbynes (≡CR) | 0.24 to 0.21 | [29] | ca. 1.2 | [29] |
| $\eta^2$-Vinyl ($\eta^2$-$CH_2CCH_2Ph$) | 0.22 | [31] | ca. 1.2 | [36] |
| Benzoyl isocyanide (C≡NCOPh) | 0.20 | [30] | 0.16 | [30] |
| $PF_3$ | 0.14 | [32] | – | – |
| Aminocarbyne (=$CNH_2^+$) | 0.09 | [31] | ca. 1.1 | [36] |
| CO | 0 | [10] | 0.99 | [13] |
| $\eta^1$-Phosphaalkyne ($\eta^1$-P≡C*t*Bu) | –0.04 | [33] | – | – |
| $N_2$ | –0.07 | [10] | – | – |
| Isocyanides (bent) (C≡NR)[b] | –0.07 to –0.18 | [24,25,34,35] | – | – |
| Hydrazinium ($NH_2NH_3^+$) | – | – | 0.80 | [57] |
| Ethylene ($CH_2$=$CH_2$) | – | – | 0.76 | [13] |
| *N*-Pyrrolylphosphanes $PPh_n(NC_4H_4)_{3-n}$ ($n$ = 0–3) | – | – | 0.69 to 0.53 | [28] |
| Vinylidenes (=C=CHR) | 0 to –0.6 | [29,36] | 0.7 to 0.2 | [36] |
| $P(OPh)_3$ | –0.18 | [10] | 0.58 | [13] |
| $\eta^2$-Allene ($\eta^2$-$CH_2$=C=CHPh) | –0.21 | [31] | 0.56 | [36] |
| Metallo-dinitriles (N≡C–X–C≡N–$ML_{n-1}$) | –0.18 to –0.40 | [37] | 0.58 to 0.39 | [36] |
| Ferricinium isocyanides | –0.22 to –0.28 | [38,39] | 0.55 to 0.50 | [36] |
| Nitriles (N≡CR) | –0.23 to –0.58 | [10,27] | 0.49 to 0.33 | [13] |
| C≡N–$BF_3^-$ | –0.24 | [30] | 0.20 | [30] |
| Metallo-cyanides (C≡N–$ML_{n-1}^-$) | –0.25 to –0.61 | [30,40] | 0.50 to 0.21 | [36] |
| Phosphonium isocyanides | –0.28 to –0.36 | [41] | 0.50 to 0.43 | [41] |
| Allenylidenes (=C=C=$CR_2$) | 0 to –0.8 | [36,42] | 0.8 to 0 | [36] |
| $Me_2SO$ (S-coordinated) | –0.19 | [36] | 0.57 | [57] |
| Isocyanides (linear) (C≡NR)[c] | –0.33 to –0.44 | [24,25,34,43] | – | – |
| Organophosphanes | –0.3 to –0.5 | [10,32,45] | 0.5 to 0.3 | [13,36] |
| Bithiophene-carbenes | –0.38 to –0.62 | [44] | 0.41 to 0.21 | [36] |
| Phosphirene | –0.43 | [45] | – | – |
| Protonated indole derivatives | –0.44 to –0.62 | [41] | – | – |
| Indazole | –0.56 | [36] | 0.26 | [71] |
| C≡N–$BPh_3^-$ | –0.51 | [46] | –0.05 | [30] |
| Pyridine | –0.59 | [10] | 0.25 | [13] |
| Oxocarbenes [=C(OR)Y] | –0.51 to –0.64 | [36] | 0.30 to 0.19 | [36] |
| Cyanamides (N≡C–$NR_2$) | –0.57 to –0.85 | [26, 47–49] | 0.25 to 0.0 | [36] |
| Pyrazole | – | – | 0.20 | [13] |
| 4-Methylpyrazole | – | – | 0.18 | [75] |
| Triazole | – | – | 0.18 | [13] |
| 1-Methyltriazole | – | – | 0.17 | [75] |
| Thiocarbenes [=C(SR)Y] | –0.66 to –0.68 | [36] | 0.17 to 0.15 | [36] |
| Aminocarbenes [=C(NRR′)Y] | –0.69 to –0.80 | [5,36] | 0.15 to 0.05 | [36] |
| Hydrotris(pyrazolyl)methane ($HCpz_3$) | – | – | 0.14 | [72] |
| Imidazole | – | – | 0.12 | [13] |
| Benzoyldiazenide ($NNCOPh^-$) | – | – | 0.11 | [72] |
| Benzimidazole | – | – | 0.10 | [75] |
| 1-Alkylimidazole | – | – | 0.08 to 0.06 | [13,75] |
| Ferrocenyl-oxocarbenes | –0.70 to –0.9 | [36] | 0.14 to 0.0 | [36] |
| $NH_3$ | –0.77 | [10] | 0.07 | [13] |
| $CF_3COO^-$ | –0.78 | [10] | –0.15 | [13] |
| Phosphoylide-aminocarbenes | –079 to –0.87 | [41] | 0.06 to 0.0 | [41] |
| Cyanoguanidine [N≡C–$NC(NH_2)_2$] | –0.86 | [50] | – | – |
| Hydrogendicyanamide (N≡CNHCN) | –0.88 | [50] | – | – |
| $NCS^-$ | –0.88 | [10] | – | |
| Tris(pyrazolyl)methanesulfonate ($SO_3Cpz_3^-$) | – | – | –0.09 | [73] |
| Ferrocenyl-aminocarbenes | –0.99 to –1.1 | [36] | –0.11 to –0.21 | [36] |
| Indole derivatives | –0.92 to –1.0 | [41] | – | – |
| C≡$N^-$[d] | –1.00 | [10] | 0.02 | [13] |
| | –0.74 | [30] | –0.26 | [30] |
| Hydrotris(3,5-dimethylpyrazolyl)borate [$HB(Me_2pz)_3^-$] | – | – | –0.23 | [64] |
| Bis(pyrazolyl)borate ($H_2Bpz_2^-$) | – | – | –0.24 | [64] |
| Pyrazolate | –1.14 | [36] | –0.24 | [13] |
| 2-Pyridinecarboxylate (2-$pyCOO^-$)[e] | – | – | –0.24 | [74] |
| Dicyanamide ($NCNCN^-$) | –1.14 | [50] | – | – |
| $I^-$ | –1.15 | [10] | – | – |
| $NCO^-$ | –1.16 | [10] | –0.25 | [13] |
| $Br^-$ | –1.17 | [10] | – | – |

 © 2007 Wiley-VCH Verlag GmbH & Co. KGaA, Weinheim 

Table 1. *(continued)*

| | $P_L$ [V] | Ref. | $E_L$ [V vs. NHE] | Ref. |
|---|---|---|---|---|
| $Cl^-$ | –1.19 | [10] | –0.24 | [13] |
| Acyl- or aroyl-cyanamide $[NCNC(O)R^-]$ | –1.19 | [51] | – | – |
| Monodeprotonated cyanoguanidine $[NCNC(NH)NH_2^-]$ | –1.22 | [50] | – | – |
| Alkynyls ($-C{\equiv}CR^-$) | –0.9 to –1.7 | [5,36,42,52,53] | –0.1 to –0.7 | [36] |
| $H^-$ | –1.22 | [10] | –0.30 | [13] |
| $N_3^-$ | –1.26 | [10] | –0.30 | [13] |
| $Me_2SO$ (O-coordinated) | – | – | –0.37 | [57] |
| $F^-$ | –1.3 | [54] | –0.42 | [13] |
| Hydrogen cyanamide ($NCNH^-$) | –1.34 | [49] | –0.41 | [36] |
| $S_2P(OEt)_2^-$ | –1.34 | [55] | – | – |
| Oxycarbenes (anionic) $[=C(O^-)Y]$ | –1.1 to –1.7 | [36] | –0.16 to –0.73 | [36] |
| $OH^-$ | –1.55 | [10] | –0.59 | [13] |
| Aryls, alkyls, $NO^-$ | –1.7 to –1.9 | [36] | –0.7 to –0.9 | [16] |
| $O^{2-}$ | – | – | –1.8 | [73] |

[a] Ordered generally from higher to lower $P_L$ and/or $E_L$ values; for multidentate ligands the values refer to each ligating arm. [b] At an electron-rich metal centre such as *trans*-$\{MX(dppe)_2\}$ (M = Re, Tc; X = Cl, H). [c] At an electron-poor metal centre such as $\{Cr(CO)_5\}$. [d] The $P_L$ values of –1.0 and –0.74 V have been estimated at the $\{Cr(CO)_5\}$ and *trans*-$\{FeH(dppe)_2\}^+$ centres, respectively. [e] Carboxylate arm.

Isocyanides show $P_L$ values that are spread over a wide range, from +0.2 to –0.4 V (Table 1): benzoyl isocyanide[30] > bent isocyanides[24,25,34,35] > ferricinium isocyanides[38,39] > phosphonium isocyanides[41] ≥ linear isocyanides.[24,25,34,43]

Metallo-cyanide adducts and other cyano adducts are quite sensitive to the Lewis acid but are always stronger net electron acceptors than cyanide: $CNBF_3^-$[30] ≥ $CN–NiCl_2(Pcy_3)^-$[40] > $CN–VCl_3(thf)_2^-$[30] > $CN–BPh_3^-$[46] > $CN–PdCl_2(PPh_3)^-$[40] > $CN^-$.[10,30]

Carbenes and related ligands are spread over an even wider window of $P_L$ values (from 0 to –1.7 V): vinylidenes C=CHR[29,36] ≥ allenylidenes $C{=}C{=}CR_2$[36,42] > bithiophene-carbenes[44] ≥ oxocarbenes C(OR)Y[36] > thiocarbenes C(SR)Y[36] > aminocarbenes C(NRR′) Y,[5,36] ferrocenyl-oxocarbenes[36] ≥ phosphoylide-aminocarbenes[41] > ferrocenyl-aminocarbenes[36] > anionic oxycarbenes $C(O^-)Y$.[36]

Organonitriles ($P_L$ from –0.23 to –0.58 V)[10,27] behave as weaker π-acceptors than analogous isocyanides, whereas cyanamides $N{\equiv}C–NR_2$ (with the electron-donor amino group)[26,47–49] and related species, such as cyanoguanidine $N{\equiv}C–NC(NH_2)_2$,[50] and hydrogen dicyanamide N≡CNHCN,[50] are quite strong net electron-donor neutral ligands, being comparable to $NCS^-$[10] or $CF_3COO^-$.[10]

The strongest net electron-donors are the following, with $P_L$ values below –1.0 V: aryls, alkyls and $NO^-$,[36] $OH^-$,[10] anionic oxycarbenes $[=C(O^-)Y]$,[36] hydrogen cyanamide ($NCNH^-$),[49] $F^-$,[54] $N_3^-$,[10] $H^-$,[10] alkynyls ($C{\equiv}CR^-$),[5,36,42,52,53] monodeprotonated cyanoguanidine $[NCNC(NH)NH_2^-]$,[50] acyl- or aroylcyanamide $[NCNC(O)R^-]$,[51] $Cl^-$,[10] $Br^-$,[10] $NCO^-$,[10] $I^-$,[10] dicyanamide ($NCNCN^-$).[50]

A *modification of a ligand* naturally leads to a change of $P_L$. Hence, protonation is expected to result in an increase of $P_L$ due the promotion of the net electron acceptance (or hampering of the net electron donation), as shown in the following cases (see Table 1): protonation of vinylidenes C=CHR to carbynes $CCH_2R^+$ ($\Delta P_L$ = 0.5 V),[29,36] of a bent isocyanide $C{\equiv}NR$ to an aminocarbyne $C{=}NR_2^+$ (R = H) ($\Delta P_L$ = 0.2 V),[31,36] of phosphoylide-aminocarbenes (protonation at the ylide carbon atom) ($\Delta P_L$ = 0.3 V)[41] and of indole derivatives (protonation at N) ($\Delta P_L$ = 0.5 V).[41]

Oxidation of a metallo-ligand has the same type of effect if there is electronic communication between the two metal atoms, as observed for the ferrocene–isocyanide $C{\equiv}N–Fc$[38,39] and fumaronitrile–iron $N{\equiv}CCH{=}CHC{\equiv}N-\{FeH(dppe)_2\}^+$[37] systems ($\Delta P_L \approx 0.2$ V).

Linkage isomerization with an ambidentate ligand can result in a high $P_L$ variation, as in the case of dimethyl sulfoxide (DMSO) ($\Delta P_L \approx 1.1$ V upon changing from O- to S-binding).[57]

A further important matter concerns the possibility, in some cases, of $P_L$ *dependence on the metal centre*, which was not accounted for by the initial Pickett's model. Although such a behaviour poses difficulties to the application of this model, the recognition of the failure of Equation (2) in particular cases enables us to propose corrections to the $P_L$ values for such cases. This has been recognized for isocyanides,[24,25,34,35] nitriles,[27] cyanamides[26,47–49] and cyanide.[30] A high electron richness of the metal centre and a strong electron release from the *trans* ligand promote the net π-electron acceptance (or hamper the net electron donation) of the ligand under study, resulting in a positive correction (up to 0.34 V) for its usual $P_L$ value.

Hence, in such cases, $P_L$ also conveys information on the electronic properties of the metal centre and, for isocyanides, is also diagnostic of their bent or linear geometry. For *trans*-$\{ReCl(dppe)_2\}$ ($E_s$ = 0.68 V) or for $\{Cr(CO)_5\}$ ($E_s$ = 1.50 V), the former with a much higher electron richness, isocyanides are bent (stronger π-acceptors, higher $P_L$ values

 © 2007 Wiley-VCH Verlag GmbH & Co. KGaA, Weinheim 

by ca. 0.26 V) or linear (weaker π-acceptors), respectively. For *trans*-{TcH(dppe)$_2$}, with a higher electron richness ($E_s$ = 0.34 V), an even greater correction (+0.34 V)[35] is required.

### 2.3. $E_s$ and $\beta$ Metal-Site Parameters

The electron richness ($E_s$) of a metal centre {M$_s$} is given, by definition [Equation (3)], as the oxidation potential of its carbonyl complex [M$_s$(CO)]. It can also be obtained, as well as the polarizability ($\beta$), from the plot of $E^{ox}_{1/2}$[M$_s$L] vs. $P_L$(L) [Equation (2)], comprising as many points as possible. Less direct methods can be applied, namely by considering an auxiliary site {M′$_s$} with known $E_s$ and $\beta$ values, and comparing the oxidation potentials of [M$_s$L] with those of homologues of the related series [M′$_s$L] [from the intercept and the slope of Equation (13), $E_s$ and $\beta$ can be estimated for {M$_s$}]. Other cases have been indicated above [Equations (11) and (12)].

$$E^{ox}[M_sL] - E^{ox}[M'_sL] = (E_s\{M_s\} - E_s\{M'_s\}) + (\beta\{M_s\} - \beta\{M'_s\})\,P_L(L) \quad (13)$$

$E_s$ and $\beta$ values are known[10,24–28,34,35,41,43,56,58–61] for the following {M$_s$} centres, ordered, within each group, according to decreasing $E_s$ values: (a) 16-electron square-pyramidal ones: {FeL(depe)$_2$}$^{2+}$ (L = CO, NCR),[26] {W(≡CR)(CO)$_2$(dppe)}$^+$,[43] {M(CO)$_5$} (M = Cr, Mo, W),[41] {ReL(dppe)$_2$}$^+$ (L = CO, N$_2$, CNR),[5,24,25] {FeX(LL)$_2$}$^+$ (X = Br, H; LL = depe, dppe),[27,10] {Mo(NO)(dppe)$_2$}$^+$,[10] {Mn(CO)(dppm)$_2$}$^+$,[58] {ReX(dppe)$_2$} (X = CN, NCS, Cl, NCO, N$_3$),[34,59,60] *cis*-{ReCl(dppe)$_2$},[27] {TcH(dppe)$_2$},[35] {MoL(dppe)$_2$} (L = CO, N$_2$, NCPh),[10] {Mo(N$_3$)(dppe)$_2$}$^-$;[10] (b) 16-electron half-sandwich ones: {Mo($\eta^7$-C$_7$H$_7$)(LL)}$^+$ (LL = dppe, *t*Bu$_2$-diazabutadiene, bipyridine);[56,61] (c) 15-electron ones: {FeBr(depe)$_2$}$^{2+}$,[27] *cis*-{ReCl(dppe)$_2$}$^+$;[27] (d) 14-electron T-shaped one: {Rh(acac)(CO)}.[28]

The electron richness is unfavoured (increase of $E_s$) by the presence, within {M$_s$}, of ligands (e.g. carbyne or CO) with a strong π-acceptance (high $P_L$), by the increase of charge and by the metal oxidation state. Thus, the least electron-rich sites are the dicationic Fe$^{II}$ centres {FeL(depe)$_2$}$^{2+}$ (L = CO, NCR) ($E_s$ = 2.3–1.7 V vs. SCE),[26] the dicationic Fe$^{III}$ site {FeBr(depe)$_2$}$^{2+}$ ($E_s$ = 1.98 V vs. SCE)[27] and the cationic carbyne-carbonyl centres {W(≡CR)(CO)$_2$(dppe)}$^+$ ($E_s$ = 1.7–1.6 V vs. SCE),[43] followed by the pentacarbonyls {M(CO)$_5$} (M = Cr, Mo, W) ($E_s$ = 1.50 V vs. SCE).[41]

At the other extreme, as the most electron-rich centre, lies the anionic Mo$^0$ site {Mo(N$_3$)(dppe)$_2$}$^-$ ($E_s$ = –1.00 V vs. SCE)[10] with the strong electron-donor azide ligand, followed by the neutral {MoL(dppe)$_2$} (L = NCPh, N$_2$, CO) sites, all with negative $E_s$ values.

Interestingly, the polarizability ($\beta$) of the metal centre also tends to decrease (as does the electron richness) with the increase of the net π-electron acceptor ability of a ligand (increase of $P_L$) comprised in {M$_s$}, as observed for a series of related centres such as *trans*-{M(L)(dppe)$_2$}$^+$ (M = Tc,[35] L = H; M = Re;[5,24,25,34,59,60] L = Cl$^-$, CN$^-$, CNR, CO). In accord, {Mo(NO)(dppe)$_2$}$^+$ and {W(≡CR)(CO)$_2$(dppe)$_2$}, with the very strong π-acceptors NO$^+$ and carbyne/CO ligands, are the centres with the lowest $\beta$ values (0.51[10] and 0.61–0.73,[43] respectively). The delocalization of the HOMO towards the strong π-acceptor ligands in {M$_s$}, as shown by MO calculations in the W–carbyne case,[43] leads to an attenuation effect (energy "buffering", low $\beta$) on the changes of the HOMO energy upon change of another ligand (L) bound to the centre in the complex [M$_s$L].

## 3. Full Additivity Lever's Model

### 3.1. General

In this model, the additivity is extended to all the ligands, and the redox potential of a complex with the M$^{n+1/n}$ redox couple is given by Equation (14) in V vs. NHE, where $S_M$ (slope) and $I_M$ (intercept) depend on the metal and redox couple, the spin state and the stereochemistry, and $E_L$ is an additive ligand parameter that was obtained through a statistical analysis on the known redox potentials of the high number of complexes with the Ru$^{III/II}$ redox couple.[13–16]

$$E_{1/2}[M^{n+1/n}] = S_M(\Sigma E_L) + I_M \quad / \text{V vs. NHE} \quad (14)$$

On account of its wide scope of application, simple use and availability of data, Lever's model became the most popular one and has been reviewed.[13–16] However, its high generality is concomitant with the risk of failure for particular cases, and for strong π-acceptor ligands, e.g. CO, carbynes and isocyanides. Equation (14) requires the use of empirical terms that reflect additional HOMO stabilization effects. Corrections have also been introduced[13] to account for isomeric effects.

The attenuation of the CO ligand additivity effect, also in agreement with electronic spectroscopic and X-ray data, has been recognized[62] for the Os$^{IV/III}$ and Os$^{III/II}$ redox potentials in a series of hexacoordinate mixed halide/carbonyl and halide/carbonyl/nitrile complexes, i.e. the shift of the redox potential upon the first replacement of a halide or a nitrile by a CO ligand is much more pronounced (ca. two to three times) than the shift resulting from the second replacement. Similar nonlinear trends are exhibited by related (isocyanido)Os complexes,[62] although a roughly constant potential shift is observed per each halide replacement by nitrile either in the Os series[62] or in the Ru analogues.[63]

Hence, the mutual influence of the strong π-accepting CO or isocyanido ligands, in such series, leads to an attenuation of the corresponding ligand additivity effects.

The deviation from linearity [Equation (14)] for a wide range of $\Sigma E_L$, as observed for the Re$^{I/II}$ redox system,[14] can be overcome by the consideration of either different

 © 2007 Wiley-VCH Verlag GmbH & Co. KGaA, Weinheim 

expressions along the $\Sigma E_L$ scale or of a curved relationship, the latter is supported by some studies on a series of $Re^{I}$–vinylidene or –nitrile[27] complexes.

Although typically applied only to hexacoordinate complexes, the model has been recently extended by the current author to square-planar tetracoordinate[28,64] and pentacoordinate[28] $Rh^{I/II}$ complexes; the former has also been studied by others[65] although with a smaller number of compounds. Extensions to particular Ru clusters,[66–68] sandwich and half-sandwich complexes,[15,16,69] and to reduction processes centred at ligands[15,16] have also been proposed.

### 3.2. $E_L$ Ligand Parameter and Associated Ones

The ligand $E_L$ parameter depends on the reference electrode (it has been referenced to the NHE), in contrast with the $P_L$ parameter, but both are related by the experimentally observed Equation (15), which, however, fails for strong π-acceptor ligands (see above) when the Lever Equation (14) also requires corrections. Hence, for such ligands, Equation (15) has to be used cautiously for the estimate of the value of one of the parameters from that of the other one. Recognized examples of failure of Equation (15) include, apart from CO, carbynes and bent isocyanides, as well as a number of metallo-cyanide and other cyano adducts e.g. C≡N–A$^-$ [A = $BF_3$,[30] $BPh_3$,[30] $ML_{n-1}$ (M = $V^{III}$, $Re^{V}$, $Ni^{II}$, $Pd^{II}$)[30,40]]. Nevertheless, Equation (15) is valid for allenylidenes and alkynyls.[28,36,42]

$$P_L = 1.17\,E_L - 0.86 \quad (15)$$

$E_L$ values are already known for a wide variety of ligands,[13–16,28–30,36,41,57,64,70–75] including an extensive list of recently estimated values by the current author[36] for many carbyne, carbene, vinylidene, allenylidene and alkynyl ligands. Examples are given in Table 1.

$S_M$ and $I_M$ values (listed in refs.[13–16,36,56]) have already been proposed for the following $M^{n+1/n}$ redox couples: M = Nb ($n$ = 3, 4),[13] Ta ($n$ = 4),[13] Cr ($n$ = 0, 2),[13] Mo ($n$ = 0, 1),[13] Tc ($n$ = 1–3),[14] Re ($n$ = 1–3),[14] Fe ($n$ = 2, 3),[13,26,27] Ru ($n$ = 2, 3),[13,71] Os ($n$ = 2)[13] and Rh ($n$ = 1).[28,64] Normally, the redox centres are six-coordinate, with the exception of the four- and five-coordinate $Rh^{II/I}$,[28,64] and in particular the five-coordinate $Fe^{III/II}$[13] and $Mn^{II/III}$[13] cases. The parameters usually have been obtained in organic media, but different values are observed in water where solvation effects and the complex charge can play a relevant role, as observed for $Cr^{III/II}$,[13] $Fe^{III/II}$,[13] $Ru^{III/II}$ (2+/1+),[13] $Ru^{III/II}$ (1–/2–)[71,75] and $Os^{III/II}$[13] systems. The charge effect has been studied[75] particularly for the $Ru^{III/II}$ system.

Moreover, particular sets of $S_M$ and $I_M$ values, different from the general ones but that better fit an expression of the type (14), have been proposed[26,27] for certain series of complexes.

## 4. Identification of Coordination Compounds

The relationships discussed above [in particular (2) and (14)] between the redox potential of a complex and the electrochemical ligand and metal centre parameters can be used not only to estimate (from the measured redox potential) these parameters that characterize the components of the complex, as discussed above, but also conversely to predict the redox potential of any complex, provided the values of those parameters are known. This latter approach has been much less explored but its significance towards the identification of coordination compounds is rather valuable. It can assist in the identification not only of isolated complexes but also of those generated in situ in a reaction process. This can be conveniently done by cyclic voltammetry, an expedient and rapid method to search for redox waves and measure their potentials, provided these lie within the available solvent/electrolyte potential range and the species have a sufficient lifetime for the wave detection. The redox waves should also be reversible, at least partially, since irreversible processes can lead to considerable shifts in the redox potential.

The identification of the new species generated upon an electron-transfer induced chemical reaction greatly contributes to the understanding of the redox process whose mechanism, in some cases, has been established by digital simulation of the cyclic voltammograms. This is illustrated by the following cases investigated in the author's laboratory.

The trichloro-$Os^{III}$ complex *mer*-$[OsCl_3(NH_3)_2(Me_2S)]$ undergoes, by cyclic voltamemtry in DMSO, a single-electron partially reversible reduction wave ($I^{red}$, Figure 1), which involves heterolytic Os–Cl bond rupture with loss of $Cl^-$ followed by its replacement by DMSO to afford the *S*-coordinated complex $[Os^{II}Cl_2(NH_3)(Me_2S)(DMSO)]$ (Scheme 1).[57] This product as well as an intermediate species that was postulated as the pentacoordinate complex $[OsCl_2(NH_3)_2(Me_2S)]$ were detected by their oxidation waves ($II^{ox}$ and $III^{ox}$, respectively, Figure 1) upon scan reversal following the reduction wave ($I^{red}$) of the starting complex.[57] The identification of the product was based on the very close agreement between the measured value of its oxidation potential ($III^{ox}$) and the predicted one by applying Lever's Equation (14).[57]

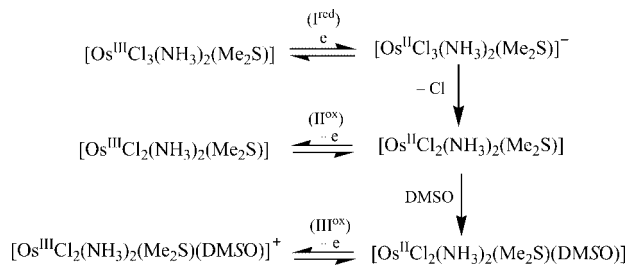


Scheme 1.

 © 2007 Wiley-VCH Verlag GmbH & Co. KGaA, Weinheim 

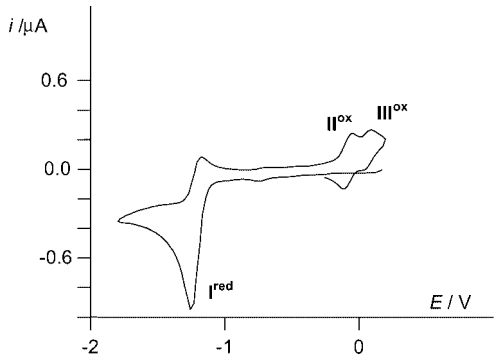


Figure 1. Cyclic voltammogram of *mer*-$[OsCl_3(NH_3)_2(Me_2S)]$ in DMSO with 0.2 M $[Bu_4N][BF_4]$ at a Pt electrode (scan rate: 0.2 $V s^{-1}$).[57]

Other recent examples concern various series of chlorido/azole–ruthenium(III) complexes with antitumor activity, such as $[RuCl_4L_2]^-$[71,75] (L = imidazole, benzimidazole, triazole, pyrazole, indazole or a substituted derivative), $[RuCl_3L_3]$[75] or $[RuCl_2L_4]^+$.[75] They exhibit a single electron reduction (wave $I^{red}$) to the corresponding $Ru^{II}$ complexes, which then readily undergo sequential dechlorination steps upon solvolysis [S = dimethylformamide (DMF) or DMSO] (Scheme 2 for $[RuCl_4L_2]^-$).

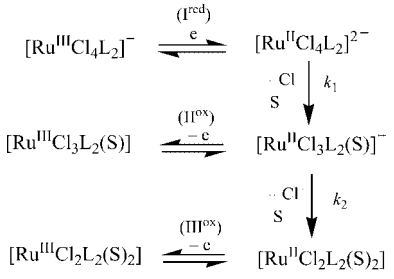


Scheme 2.

The partially dechlorinated/solvated $Ru^{II}$ products, such as $[RuCl_3L_2(S)]^-$ and $[RuCl_2L_2(S)_2]$ derived from $[RuCl_4L_2]^-$, were detected in situ by the appearance of their $Ru^{II}/Ru^{III}$ oxidation waves ($II^{ox}$ and $III^{ox}$, respectively) and identified by the similarity of the corresponding measured oxidation potential values with those predicted by using Lever's Equation (14). A similar behaviour was observed for the other series of azole complexes.

The mechanisms of the processes were investigated in detail by digital simulation of cyclic voltammetry,[71,75] allowing us to estimate the kinetic rate constant of solvolysis upon reduction ($k_1$ and $k_2$), which interestingly were shown to correlate with the redox potential[71,75] (thus, with the azole $E_L$ parameter) and with the anti-tumor activity.[76,77]

## 5. Final Comments

The redox potential of a coordination compound bears rich structural/electronic information, which has started to be explored, in a systematic way, by ligand and metal parameterizations that constitute the bases of simple additive models. The electron donor/acceptor properties of the ligands and binding metal centres can thus be quantified through the values of associated electrochemical parameters, which, conversely, once known, can be used to predict the redox potentials of their complexes.

The latter approach (the estimate of the redox potential) can provide an important contribution towards the identification of unknown complexes by comparing the predicted and the experimentally measured values of the redox potential. The complexes, products or intermediates in reactions, can thus be identified in situ, without the need for their isolation from the solution, lowering the risks of their loss upon further reaction or decomposition.

Another important perspective concerns the possibility of correlating not only the redox potential but also, in a more perceivable way, the above electrochemical ligand (and/or metal site) parameters, with a variety of other properties of the complexes that are also determined by electronic and structural features,[5,6,15,16,69,78] such as ligand IR stretching frequencies,[74] energy of MLCT bands,[16] Hammett's σ-substituent constants and related ones,[69,79,80] Tolman's electronic parameter[81] or metal–metal interaction in ligand-bridged dinuclear complexes. Some of those correlations can allow the estimate of $E_L$ or $P_L$ for further ligands.

Ligand coordination[10,11,34,57] and chemical reactivity[10,37,82–85] criteria have also been proposed in a few cases. A different type of relationship, between the azole $E_L$ ligand parameter and the anticancer activity, has recently been recognized[76,77] for some ruthenium complexes.

However, one should be aware of the model's limitation, associated with the additivity assumption that does not take into account interactions and synergisms. Pickett's model, in its initial form, bears the minimum additivity (only the effect of a single ligand is separated from all the others, taken as a whole) and is expected to be more accurate for particular sets of complexes but has the lowest generality, while Lever's model assumes a full additivity and is more general but has a higher risk of failure in particular cases. These include isomeric effects that require the consideration of corrective terms in Lever's equation,[14] whereas they can be handled by Pickett's model by considering distinct ($E_s$, $\beta$) sets of values for the different isomers.[27,34] The isomeric dependence of the redox potential is particularly relevant in accounting for the type of mechanism of electron-transfer-induced isomerizations in coordination compounds.[86–89]

Another frequent limitation results from the small number of available data (in some cases limited to a single complex) used to estimate the ligand or metal parameters. Many more complexes have to be studied and the values of these parameters averaged.

Although extensions of the initial models have already been proposed, they have still to be further applied to other types of complexes with different metals and ligands, electron counts, geometries, etc. The results so far achieved, as illustrated above, are promising and the field hopefully will attract wider attention.

 © 2007 Wiley-VCH Verlag GmbH & Co. KGaA, Weinheim 

## Acknowledgments

The author gratefully acknowledges all the coauthors cited in the joint publications. This work has been partially supported by the Fundação para a Ciência e a Tecnologia (Portugal) and its POCTI and POCI 2010 programmes (FEDER-funded).

[1] A. J. L. Pombeiro, C. Amatore (Eds.), *Trends in Molecular Electrochemistry*, Marcel Dekker/FontisMedia, New York/Lausanne, **2004**.
[2] A. J. L. Pombeiro, J. McCleverty (Eds.), *Molecular Electrochemistry of Inorganic, Bioinorganic and Organometallic Compounds*, NATO ASI Series, Kluwer, Dordrecht, **1993**.
[3] P. Zanello, *Inorganic Electrochemistry*: *Theory, Practice and Application*, Royal Society of Chemistry, Cambridge, **2003**.
[4] D. Astruc, *Electron Transfer and Radical Processes in Transition-metal Chemistry*, VCH, New York, **1995**.
[5] A. J. L. Pombeiro, *New J. Chem.* **1997**, *21*, 649.
[6] A. J. L. Pombeiro, *Port. Electrochim. Acta* **1983**, *1*, 19.
[7] A. Vlcëk, *Chemtracts – Inorg. Chem.* **1993**, *5*, 1.
[8] A. C. Sarapu, R. F. Fenske, *Inorg. Chem.* **1975**, *14*, 247.
[9] C. J. Pickett, D. Pletcher, *J. Organomet. Chem.* **1975**, *102*, 327.
[10] J. Chatt, C. T. Kan, G. J. Leigh, C. J. Pickett, D. R. Stanley, *J. Chem. Soc., Dalton Trans.* **1980**, 2032.
[11] J. Chatt, *Coord. Chem. Rev.* **1982**, *43*, 337.
[12] C. J. Pickett, in: G. Wilkinson, R. D. Gillard, J. A. McCleverty (Eds.), *Comprehensive Coordination Chemistry*, Pergamon Press, Oxford, **1987**, vol. 1, chapter 8.3, p. 493.
[13] A. B. P. Lever, *Inorg. Chem.* **1990**, *29*, 1271.
[14] A. B. P. Lever, *Inorg. Chem.* **1991**, *30*, 1980.
[15] A. B. P. Lever, E. S. Dodsworth, *Inorganic Electronic Structure and Spectroscopy*, Wiley, New York, **1999**, vol. 2, p. 227.
[16] A. B. P. Lever, in: *Comprehensive Coordination Chemistry II*, vol. 2 (Ed.: A. B. P. Lever), Elsevier, Oxford, **2004**, chapter 2.19, p. 251.
[17] B. E. Bursten, *J. Am. Chem. Soc.* **1982**, *104*, 1299.
[18] B. E. Bursten, M. R. Green, *Prog. Inorg. Chem.* **1988**, *36*, 393.
[19] B. E. Bursten, M. R. Green, V. Katovic, D. Lightner Jr, *Inorg. Chem.* **1986**, *25*, 831.
[20] D. Datta, *J. Chem. Soc., Dalton Trans.* **1986**, 1907.
[21] A. J. Bard, L. R. Faulkner, *Electrochemical Methods*, 2nd ed., Wiley, New York, **2001**.
[22] A. J. L. Pombeiro, M. F. C. Guedes da Silva, M. A. N. D. A. Lemos, *Coord. Chem. Rev.* **2001**, *53*, 219.
[23] A. J. L. Pombeiro, *Port. Electrochim. Acta* **1985**, *3*, 41.
[24] M. F. N. N. Carvalho, A. J. L. Pombeiro, *J. Chem. Soc., Dalton Trans.* **1989**, 1209.
[25] A. J. L. Pombeiro, *Inorg. Chim. Acta* **1985**, *103*, 95.
[26] L. M. D. R. S. Martins, A. J. L. Pombeiro, *Port. Electrochim. Acta* **1996**, *14*, 151.
[27] M. F. C. Guedes da Silva, L. M. D. R. S. Martins, J. J. R. Fraústo da Silva, A. J. L. Pombeiro, *Collect. Czech. Chem. Commun.* **2001**, *66*, 139.
[28] M. F. C. Guedes da Silva, A. M. Trzeciak, J. J. Ziólkowski, A. J. L. Pombeiro, *J. Organomet. Chem.* **2001**, *620*, 174.
[29] S. S. P. R. Almeida, A. J. L. Pombeiro, *Organometallics* **1997**, *16*, 4469.
[30] S. S. P. R. Almeida, M. F. C. Guedes da Silva, J. J. R. Fraústo da Silva, A. J. L. Pombeiro, *Port. Electrochim. Acta* **2001**, *19*, 371.
[31] M. A. N. D. A. Lemos, A. J. L. Pombeiro, *J. Organomet. Chem.* **1988**, *356*, C79.
[32] C. J. Pickett, in *Electrochemistry* (Ed.: D. Pletcher), Royal Society of Chemistry, Cambridge, **1983**, vol. 8, p. 81.
[33] M. F. Meidine, M. A. N. D. A. Lemos, A. J. L. Pombeiro, J. F. Nixon, P. B. Hitchcock, *J. Chem. Soc., Dalton Trans.* **1998**, 3319.
[34] A. J. L. Pombeiro, C. J. Pickett, R. L. Richards, *J. Organomet. Chem.* **1982**, *224*, 285.
[35] Y. Wang, A. J. L. Pombeiro, L. Kaden, M. Wahren in ref.[2], p. 63.
[36] A. J. L. Pombeiro, *J. Organomet. Chem.* **2005**, *690*, 6021.
[37] A. I. F. Venâncio, M. L. Kuznetsov, M. F. C. Guedes da Silva, L. M. D. R. S. Martins, J. J. R. Fraústo da Silva, A. J. L. Pombeiro, *Inorg. Chem.* **2002**, *41*, 6456.
[38] T. El-Shihi, F. Siglmüller, R. Herrman, M. F. N. N. Carvalho, A. J. L. Pombeiro, *J. Organomet. Chem.* **1987**, *335*, 239.
[39] T. El-Shihi, F. Siglmüller, R. Herrman, M. F. N. N. Carvalho, A. J. L. Pombeiro, *Port. Electrochim. Acta* **1987**, *5*, 179.
[40] S. S. P. R. Almeida, M. F. C. Guedes da Silva, A. J. L. Pombeiro, *Collect. Czech. Chem. Commun.* **2003**, *68*, 1663.
[41] G. Facchin, M. Mozzon, R. A. Michelin, M. T. A. Ribeiro, A. J. L. Pombeiro, *J. Chem. Soc., Dalton Trans.* **1992**, 2827.
[42] A. I. F. Venâncio, M. F. C. Guedes da Silva, L. M. D. R. S. Martins, J. J. R. Fraústo da Silva, A. J. L. Pombeiro, *Organometallics* **2005**, *24*, 4654.
[43] L. Zhang, M. F. C. Guedes da Silva, M. L. Kuznetsov, M. P. Gamasa, J. Gimeno, J. J. R. Fraústo da Silva, A. J. L. Pombeiro, *Organometallics* **2001**, *20*, 2782.
[44] A. Limberg, M. A. N. D. A. Lemos, A. J. L. Pombeiro, S. Maiorana, A. Papagni, E. Licandro, *Port. Electrochim. Acta* **1995**, *13*, 319.
[45] A. J. L. Pombeiro, M. T. A. R. S. Costa, Y. Wang, J. F. Nixon, *J. Chem. Soc., Dalton Trans.* **1999**, 3755.
[46] S. S. P. R. Almeida, M. F. C. Guedes da Silva, J. J. R. Fraústo da Silva, A. J. L. Pombeiro, *J. Chem. Soc., Dalton Trans.* **1999**, 467.
[47] S. M. P. R. M. Cunha, M. F. C. Guedes da Silva, A. J. L. Pombeiro, *Port. Electrochim. Acta* **1999**, *17*, 221.
[48] L. M. D. Ribeiro, A. J. L. Pombeiro, *Port. Electrochim. Acta* **1995**, *13*, 329.
[49] M. F. N. N. Carvalho, A. J. L. Pombeiro, *J. Organomet. Chem.* **1991**, *410*, 347.
[50] M. F. N. N. Carvalho, A. J. L. Pombeiro, A. Hills, D. L. Hughes, R. L. Richards, *J. Organomet. Chem* **1993**, *469*, 179.
[51] E. C. B. A. Alegria, S. M. P. R. M. Cunha, L. M. D. R. S. Martins, M. F. C. Guedes da Silva, A. J. L. Pombeiro, *Port. Electrochim. Acta* **2004**, *22*, 19.
[52] A. I. F. Venâncio, L. M. D. R. S. Martins, A. J. L. Pombeiro, *Port. Electrochim. Acta* **2003**, *21*, 85.
[53] A. Hills, D. L. Hughes, N. Kashef, M. A. N. D. A. Lemos, A. J. L. Pombeiro, R. L. Richards, *J. Chem. Soc., Dalton Trans.* **1992**, 1775.
[54] M. F. N. N. Carvalho, M. T. Duarte, A. M. Galvão, A. J. L. Pombeiro, *J. Organomet. Chem.* **1994**, *469*, 79.
[55] L. Zhang, M. P. Gamasa, J. Gimeno, M. F. C. Guedes da Silva, A. J. L. Pombeiro, C. Graiff, M. Lanfranchi, A. Tiripicchio, *Eur. J. Inorg. Chem.* **2000**, 1707.
[56] A. J. L. Pombeiro, in: *Inorganic Electrochemistry* (Eds.: F. Scholz, C. J. Pickett), *Encyclopedia of Electrochemistry*, Wiley-VCH, Weinheim, **2006**, vol. 7A, p.77.
[57] M. F. C. Guedes da Silva, A. J. L. Pombeiro, S. Geremia, E. Zangrando, M. Calligaris, A. V. Zinchenko, V. Yu. Kukushin, *J. Chem. Soc., Dalton Trans.* **2000**, 1363.
[58] G. A. Carriedo, V. Riera, N. G. Connelly, S. J. Raven, *J. Chem. Soc., Dalton Trans.* **1987**, 1769.
[59] M. F. C. Guedes da Silva, J. J. R. Fraústo da Silva, A. J. L. Pombeiro, M. A. Pellinghelli, A. Tiripicchio, *J. Chem. Soc., Dalton Trans.* **1996**, 2763.
[60] Y. Wang, A. J. L. Pombeiro, *Port. Electrochim. Acta* **1993**, *11*, 111.
[61] S. P. M. Disley, R. W. Grime, E. J. L. McInnes, D. M. Spencer, N. Swainston, M. W. Whiteley, *J. Organomet. Chem.* **1998**, *566*, 151.
[62] G. A. Heath, D. G. Humphrey, *J. Chem. Soc., Chem. Commun.* **1991**, 1668.
[63] C. M. Duff, G. A. Health, *J. Chem. Soc., Dalton Trans.* **1991**, 2401.

 © 2007 Wiley-VCH Verlag GmbH & Co. KGaA, Weinheim 

[64] A. M. Trzeciak, B. Borak, Z. Ciunik, J. J. Ziólkowski, M. F. C. Guedes da Silva, A. J. L. Pombeiro, *Eur. J. Inorg. Chem.* **2004**, 1411.
[65] I. Kovacik, O. Gevert, H. Werner, M. Schmittel, R. Söllner, *Inorg. Chim. Acta* **1998**, *275–276*, 435.
[66] H. E. Toma, K. Araki, A. D. P. Alexiou, S. Nikolaou, S. Dovidauskas, *Coord. Chem. Rev.* **2001**, *219*, 187.
[67] D. J. Bierdeman, J. B. Keister, D. A. Jelski, *J. Organomet. Chem.* **2001**, *633*, 51.
[68] W. G. Feighery, H. Yao, A. F. Hollenkamp, R. D. Allendoerfer, J. B. Keister, *Organometallics* **1998**, *17*, 872.
[69] S. Lu, V. V. Strelets, M. F. Ryan, W. J. Pietro, A. B. P. Lever, *Inorg. Chem.* **1996**, *35*, 1013.
[70] For a list of values of Lever's electrochemical parameters see his website: http://www.chem.yorku.ca/profs/lever
[71] E. Reisner, V. B. Arion, M. F. C. Guedes da Silva, R. Lichtenecker, A. Eichinger, B. K. Keppler, V. Yu. Kukushkin, A. J. L. Pombeiro, *Inorg. Chem.* **2004**, *43*, 7083.
[72] E. C. B. Alegria, L. M. D. R. S. Martins, M. F. C. Guedes da Silva, A. J. L. Pombeiro, *J. Organomet. Chem.* **2005**, *690*, 1947.
[73] E. C. B. Alegria, L. M. D. R. S. Martins, M. Haukka, A. J. L. Pombeiro, *Dalton Trans.* **2006**, 4954.
[74] A. M. Kirillov, M. Haukka, M. F. C. Guedes da Silva, J. J. R. Fraústo da Silva, A. J. L. Pombeiro, *J. Organomet. Chem.* **2006**, *691*, 4153.
[75] E. Reisner, V. B. Arion, A. Eichinger, N. Kandler, G. Geister, A. J. L. Pombeiro, B. K. Keppler, *Inorg. Chem.* **2005**, *44*, 6704.
[76] E. Reisner, V. B. Arion, C. G. Hartinger, M. A. Jakupec, A. J. L. Pombeiro, B. K. Keppler in *Education in Advanced Chemistry Vol. 9: Perspectives of Coordination Chemistry* (Ed.: A. Trzeciak), Poznan-Wroclaw, **2005**, p. 215.
[77] E. Reisner, V. B. Arion, B. K. Keppler, A. J. L. Pombeiro, V. Yu. Kukushkin, *J. Russ. Chem. Soc.* **2004**, *48*, 137.
[78] M. Masui, A. B. P. Lever, *Inorg. Chem.* **1993**, *32*, 2199.
[79] M. E. N. P. R. A. Silva, A. J. L. Pombeiro, J. J. R. Fraústo da Silva, R. Herrmann, M. Deus, R. E. Bozak, *J. Organomet. Chem.* **1994**, *480*, 81.
[80] M. E. N. P. R. A. Silva, A. J. L. Pombeiro, J. J. R. Fraústo da Silva, R. Herrmann, N. Deus, T. J. Castilho, M. F. C. Guedes da Silva, *J. Organomet. Chem.* **1991**, *421*, 75.
[81] L. Perrin, E. Clot, O. Eisenstein, J. Loch, R. H. Crabtree, *Inorg. Chem.* **2001**, *40*, 5806.
[82] J. Chatt, G. J. Leigh, H. Neukomm, C. J. Pickett, *J. Chem. Soc., Dalton Trans.* **1980**, 121.
[83] G. J. Leigh, R. H. Morris, C. J. Pickett, D. R. Stanley, *J. Chem. Soc., Dalton Trans.* **1981**, 300.
[84] A. J. L. Pombeiro, *Rev. Port. Quím.* **1981**, *23*, 179.
[85] M. A. N. D. A. Lemos, A. J. L. Pombeiro, *J. Organomet. Chem.* **1992**, *438*, 159.
[86] A. J. L. Pombeiro, M. F. C. Guedes da Silva, M. A. N. D. A. Lemos, *Coord. Chem. Rev.* **2001**, *219–221*, 53.
[87] M. F. C. Guedes da Silva, C. M. P. Ferreira, J. J. R. Fraústo da Silva, A. J. L. Pombeiro, *J. Chem. Soc., Dalton Trans.* **1998**, 4139.
[88] M. F. C. Guedes da Silva, J. J. R. Fraústo da Silva, A. J. L. Pombeiro, C. Amatore, J.-N. Verpeaux, *Inorg. Chem.* **1998**, *37*, 2344.
[89] M. F. C. Guedes da Silva, J. J. R. Fraústo da Silva, A. J. L. Pombeiro, C. Amatore, J.-N. Verpeaux, *Organometallics* **1994**, *13*, 3943.

Received: November 21, 2006
Published Online: March 6, 2007

 © 2007 Wiley-VCH Verlag GmbH & Co. KGaA, Weinheim 

DOI: 10.1002/ejic.200700097

# Infinite Molecular $\{[Pt_{3n}(CO)_{6n}]^{2-}\}_\infty$ Conductor Wires by Self-Assembly of $[Pt_{3n}(CO)_{6n}]^{2-}$ ($n$ = 5–8) Cluster Dianions Formally Resembling CO-Sheathed Three-Platinum Cables

**Cristina Femoni,[a] Francesco Kaswalder,[a] Maria Carmela Iapalucci,[a] Giuliano Longoni,*[a] and Stefano Zacchini[a]**

*Dedicated to Prof. Larry F. Dahl*

**Keywords:** Carbonyl ligands / Cluster compounds / Platinum / Structure elucidation / Conducting materials

Miscellaneous tetrasubstituted ammonium salts of $[Pt_{3n}(CO)_{6n}]^{2-}$ ($n$ = 5–8) clusters, obtained by the stoichiometric oxidation of the corresponding $[Pt_9(CO)_{18}]^{2-}$ salts with tropylium tetrafluoroborate, self-assemble into infinite semicontinuous or continuous $\{[Pt_{3n}(CO)_{3n}(\mu\text{-}CO)_{3n}]^{2-}\}_\infty$ conductor wires upon crystallization. Pellets of these salts exhibit conductor behavior that roughly depends on the interdianion gap along the wires.
(© Wiley-VCH Verlag GmbH & Co. KGaA, 69451 Weinheim, Germany, 2007)

One dimensional molecular metal wires[1,2] and one- and two-dimensional superclusters that are assembled through M–M bonds[3,4] are interesting as low-dimensional molecular materials, and they may find applications in molecular electronics and nanolithography.[5–7] According to EHMO calculations, the LUMO of a $Pt_3(CO)_3(\mu\text{-}CO)_3$ triangular moiety involves the combination of cyclopropenyl-like in-phase Pt $p_z$ atomic orbitals.[8,9] For an infinite stack of neutral $Pt_3(CO)_3(\mu\text{-}CO)_3$ or dianionic $[Pt_3(CO)_3(\mu\text{-}CO)_3]^{2-}$ moieties, the σMO band, which is generated along the $C_3$ axis by the cyclopropenyl-like MOs, should be empty or completely filled, respectively. Therefore, such a stack should not be stable. However, in the case where the stack is generated by the assembly of $[Pt_{3n}(CO)_{6n}]^{2-}$ ($n > 1$) cluster dianions, the above MO band would only be $1/n$ filled; therefore, the stack could be feasible and may behave as a conducting molecular wire.

The first hint of a possible strategy that might favor self-assembly of $[Pt_{3n}(CO)_{6n}]^{2-}$ clusters was suggested by the recent structural characterization of the $[NBu_4]_2[Pt_{12}(CO)_{24}]$ and $[NBu_4]_2[Pt_{24}(CO)_{48}]$ salts.[10,11] In fact, the $[NBu_4]_2[Pt_{12}(CO)_{24}]$ salt is based on zero-dimensional packing of separated $[NBu_4]^+$ and $[Pt_{12}(CO)_{24}]^{2-}$ ions, as it was for the previously characterized $[Pt_{3n}(CO)_{6n}]^{2-}$ ($n$ = 2, 3, 5) dianions in their $[PPh_4]^+$ or $[AsPh_4]^+$ salts.[12] Conversely, the $[NBu_4]_2[Pt_{24}(CO)_{48}]$ salt displays a 2D packing motif based on layers of parallel 1D infinite stacks of $Pt_3(CO)_6$ units intercalated by layers of $[NBu_4]^+$ cations. It was shown by Pauling that the $r^-/r^+$ ratio ($r$ = ionic radius) directs the choice of the ionic lattice of salts of monoatomic ions. In view of the cylindrical shape of the $[Pt_{3n}(CO)_{6n}]^{2-}$ dianions, it appeared more appropriate to substitute $r^-$ with the length of the dianion (L), and consequently, to replace $r^+$ by the diameter of the cation (D), and to use the L/D ratio as a rough guideline to achieve self-assembly of the dianions. In particular, it was speculated that a high L/D ratio would imply a great difference between the sizes of the dianion and the cation and a decreased repulsion between the dianions; the constant 2– charge would be delocalized over an increasing number of $Pt_3(CO)_6$ units. Furthermore, in the case of self-assembly of continuous $[Pt_{3n}(CO)_{6n}]^{2-}$ stacks, L would also determine the amount of filling of the σMO band that develops along the $C_3$ axis.

We have, therefore, reinvestigated the synthesis and structures of miscellaneous $[NR_4]_2[Pt_{3n}(CO)_{6n}]$ salts to assess the effect of the L/D ratio on self-assembly. We report here some significant structural results, as well as preliminary resistivity measurements of the above salts, which point out that stacking of $[Pt_{3n}(CO)_{6n}]^{2-}$ dianions leads to conducting molecular wires.

The investigated salts are collected in Table 1. All $[Pt_{3n}(CO)_{6n}]^{2-}$ ($n$ = 4, 5, 6, and 8) salts have been prepared by the stoichiometric oxidation of the corresponding $[Pt_6(CO)_{12}]^{2-}$ salt[13] with tropylium tetrafluoroborate and crystallized from THF/toluene or acetone/2-propanol mixtures. The formulas of miscellaneous salts were established

[a] Dipartimento di Chimica Fisica ed Inorganica,
Viale Risorgimento 4, 40136 Bologna, Italy
Fax: +051-2093690
E-mail: longoni@ms.fci.unibo.it

 © 2007 Wiley-VCH Verlag GmbH & Co. KGaA, Weinheim 

by single-crystal X-ray diffraction studies, whereas the purities of the crystalline batches were ascertained by elemental analysis, ESI-MS, and IR spectroscopy.[14]

Table 1. Dependence of resistivity from crystal packing and interanionic gap.

| Compound | L/D[a] | Packing | Gap[b] | Resistivity [Ω cm] | Ref. |
|---|---|---|---|---|---|
| $[NBu_4]_2[Pt_{12}(CO)_{24}]$ | 1.0 | 0D | – | $>10^8$ | [10] |
| $[NMe_4]_2[Pt_{12}(CO)_{24}]$ | 2.5 | 0D | – | $>10^8$ | |
| $[NEt_4]_2[Pt_{15}(CO)_{30}]$ | 2.0 | 3D | 3.50 | $2.10^5$ | |
| $[NMe_4]_2[Pt_{18}(CO)_{36}]\cdot 2Me_2CO$ | 3.8 | 1D | 3.09 | $6.10^2$ | |
| $[NEt_4]_2[Pt_{24}(CO)_{48}]$ | 3.3 | 2D | 3.07 | $1.10^2$ | |
| $[NBu_4]_2[Pt_{24}(CO)_{48}]$ | 2.0 | 2D | 3.21 | $2.10^3$ | [11] |

[a] L = (distance between the centroids of the outer $Pt_3$ triangles) + [2 × (van der Waals radius of Pt)]; D = [2 × (average distance between the N and H atoms of the outer $-CH_3$ moiety)] + [2 × (van der Waals radius of H)]. [b] The gap between $[Pt_{3n}(CO)_{6n}]^{2-}$ dianions along the stack is given in Å.

The unit cell of $[NMe_4]_2[Pt_{12}(CO)_{24}]$, in spite of a L/D ratio (2.5) greater than that of $[NBu_4]_2[Pt_{24}(CO)_{48}]$ (see Table 1), contains separated $[Pt_{12}(CO)_{24}]^{2-}$ dianions and $[NMe_4]^+$ cations. As shown in Figure 1, distinct $[Pt_{12}(CO)_{24}]^{2-}$ dianions separated by $[NMe_4]^+$ cations, which hinder the formation of columnar stacks, can be clearly identified. In contrast to the previously characterized $[NBu_4]_2[Pt_{12}(CO)_{24}]$ salt,[10] the cation is also perfectly ordered. The intramolecular parameters of the $[Pt_{12}(CO)_{24}]^{2-}$ dianion are very similar in both salts.

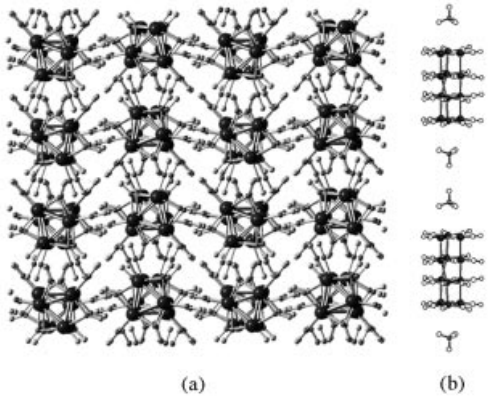


Figure 1. The packing of the $[NMe_4]_2[Pt_{12}(CO)_{24}]$ salt: (a) stacking of $[Pt_{12}(CO)_{24}]^{2-}$ dianions, (b) a portion of one stack that points out the presence of $[NMe_4]^+$ cations separating the $[Pt_{12}(CO)_{24}]^{2-}$ dianions.

The $[NEt_4]_2[Pt_{15}(CO)_{30}]$ salt exhibits incipient columnar self-assembly of $[Pt_{15}(CO)_{30}]^{2-}$ dianions, though it features a smaller L/D ratio (ca. 2) than $[NMe_4]_2[Pt_{12}(CO)_{24}]$. A similar feature was anticipated by the $[EtV^{+\cdot}]_2[EtV^{2+}][Pt_{15}(CO)_{30}]_2$ salt.[17] As shown in Figure 2a, the $[NEt_4]_2[Pt_{15}(CO)_{30}]$ salt displays a 3D packing of quasicontinuous stacks of $Pt_3(CO)_3(\mu\text{-}CO)_3$ units oriented along the four diagonals of the cubic unit cell. The infinite stacks are built from distinct $[Pt_{15}(CO)_{30}]^{2-}$ dianions that are separated by interdianion distances of 3.45–3.54 Å, which are significantly longer than the intraion–intertriangular distances, which are comprised in the 3.06 to 3.15 Å range.

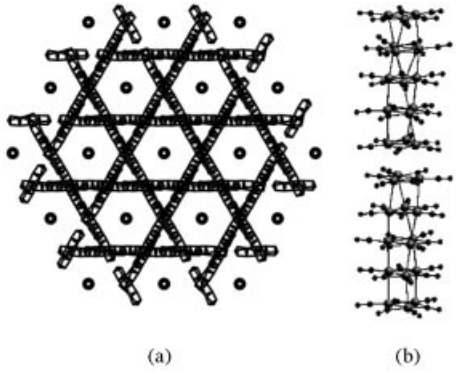


Figure 2. The packing of the $[NEt_4]_2[Pt_{15}(CO)_{30}]$ salt: (a) stacking of $[Pt_{15}(CO)_{30}]^{2-}$ dianions according to the four diagonals of the cubic unit cell (cations and carbonyl groups have been omitted for the sake of clarity), (b) a portion of the $[Pt_{15}(CO)_{30}]^{2-}$ stacks that point out the presence of a gap between the dianions.

Rewardingly, an increase in the L/D ratio beyond 3 enables the formation of continuous stacks of $Pt_3(CO)_3(\mu\text{-}CO)_3$ units, as shown by the structures of $[NMe_4]_2[Pt_{18}(CO)_{36}]\cdot 2Me_2CO$ and $[NEt_4]_2[Pt_{24}(CO)_{48}]$, respectively shown in Figures 3 and 4. They consist of 1D and 2D packing of continuous stacks of $Pt_3(CO)_3(\mu\text{-}CO)_3$ units, in which the individual $[Pt_{18}(CO)_{36}]^{2-}$ and $[Pt_{24}(CO)_{48}]^{2-}$ dianions are no longer distinguishable. Indeed, the $Pt_3(CO)_3(\mu\text{-}CO)_3$ stacks of $[NMe_4]_2[Pt_{18}(CO)_{36}]\cdot 2Me_2CO$ exhibit a constant interlayer periodicity of 3.08 Å, whereas those of $[NEt_4]_2[Pt_{24}(CO)_{48}]$ display alternating interlayer distances of 3.067 and 3.071 Å.

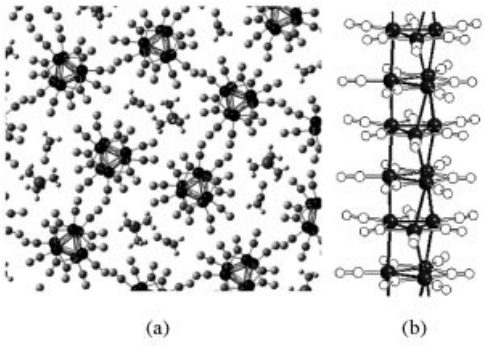


Figure 3. The packing of the $[NMe_4]_2[Pt_{18}(CO)_{36}]\cdot 2Me_2CO$ salt: (a) 1D packing of infinite columnar stacks of $[Pt_{18}(CO)_{36}]^{2-}$ dianions, (b) a portion of the stack that corresponds to a $[Pt_{18}(CO)_{36}]^{2-}$ dianion.

From the above results, it seems reasonable to conclude that L/D ratios > 3 favor self-assembly of $[Pt_{3n}(CO)_{6n}]^{2-}$ ($n \geq 6$) dianions into infinite continuous wires because squeezing these elongated dianions together does not trigger repulsive forces that are too high. Because repulsive forces are expected to increase rapidly for $n \leq 6$, L/D ratios comprised in the 2 to 3 range are less discriminating and may lead to zero-dimensional packing or quasicontinuous wires that are dependent on the length of the dianion. Notably, the formation of infinite $[Pt_{3n}(CO)_{6n}]^{2-}$ continuous wires should be disfavored by Peierls distortions.[18,19] Their effectiveness in

 © 2007 Wiley-VCH Verlag GmbH & Co. KGaA, Weinheim 

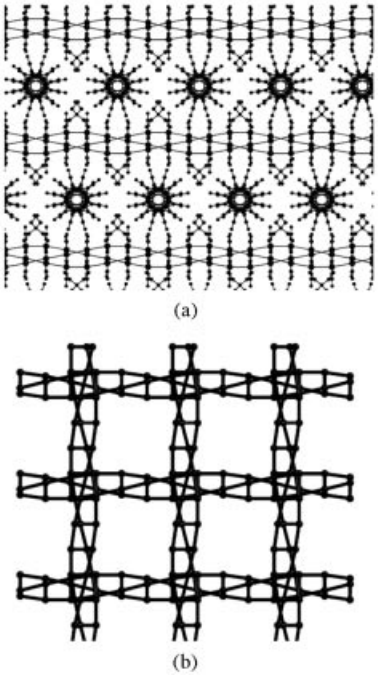


Figure 4. Two different views of the packing of the $[NEt_4]_2[Pt_{24}(CO)_{48}]$ salt: (a) 2D packing of infinite columnar stacks of $[Pt_{24}(CO)_{48}]^{2-}$ dianions according to two directions of the Cartesian axes, which gives rise to two orthogonal layers of parallel stacks, (b) continuity of the stack of $[Pt_{24}(CO)_{48}]^{2-}$ dianions (in this view carbonyl groups and cations are omitted for clarity).

partitioning the stack might be contrasted by the loss of density at the highest L/D ratios.

As shown in Table 1, the resemblance of the infinite $Pt_3(CO)_3(\mu\text{-}CO)_3$ stacks found in $[NMe_4]_2[Pt_{18}(CO)_{36}]\cdot 2Me_2CO$ and $[NEt_4]_2[Pt_{24}(CO)_{48}]$ to CO-insulated platinum cables is not only morphological but also functional. Resistivity measurements were carried out under a nitrogen atmosphere at room temperature with a four-point probe on pressed pellets (ca. $13 \times 1$ mm) of powdered samples. Whereas the zero-dimensional salts expectedly display the resistivity of an insulator material ($>10^8\ \Omega$cm), the salts that are based on quasicontinuous or continuous stacks exhibit resistivity in the $10^5$ to $10^2\ \Omega$cm range. Perhaps, it is significant that the lowest resistivity values are shown by those salts containing continuous columnar stacks of $Pt_3(CO)_3(\mu\text{-}CO)_3$ moieties. Although the resistivity of the above samples was measured on pellets of polycrystalline materials, the lowest observed values are already comparable to those exhibited by single crystals of other mixed-valence molecular chains featuring much shorter M–M bonds, such as $K_2[Pt(CN)_4]Cl_{0.32}\cdot 2.62H_2O$ and $[Rh(MeCN)_4(BF_4)_{1.5}]_x$.[20,21] It seems, therefore, of interest to carry out further physical characterizations (particularly variable temperature resistivity on single-crystals, solid-state $^{195}Pt$ NMR spectroscopic analysis, and magnetic measurements) to better assess the nature of these conductor molecular materials.

A clear effect of the support on self-assembly was observed by STM imaging of HOPG impregnated with water/2-propanol solutions of $[Pt_{3n}(CO)_{6n}]^{2-}$ ($n$ = 4–6) dianions, which pointed out the preferential formation of nanowires over other morphologies.[22] As inferred from TEM images, well-defined Pt morphologies, including Pt nanowires, were also obtained by preparing $[Pt_{3n}(CO)_{6n}]^{2-}$ ($n$ = 2–4) dianions in the micropores of zeolites, followed by thermal decomposition.[23]

The present work demonstrates that self-assembly of $[Pt_{3n}(CO)_{6n}]^{2-}$ ($n$ = 6, 8) into infinite wires readily occurs by crystallization from solution and affords macroscopic crystals that, in favorable cases,[24] enable full elucidation of the wire structure by single-crystal X-ray diffraction studies. In view of the above observations, salts of the $[Pt_{3n}(CO)_{6n}]^{2-}$ ($n$ = 6, 8) dianion with L/D > 3 seem the most promising materials for patterning surfaces with conductor molecular CO-sheathed Pt nano- and microcables, as well as Pt metal nanowires by suitable treatment of the former.

## Acknowledgments

This work was supported by the EU Integrated Project NAIMO (No NMP4-CT-2004–500355)

[1] J. K. Bera, K. R. Dunbar, *Angew. Chem. Int. Ed.* **2002**, *41*, 4453–4457; *Angew. Chem.* **2002**, *114*, 4633–4637.
[2] G. M. Finnis, E. Canadell, C. Campana, K. R. Dunbar, *Angew. Chem. Int. Ed. Engl.* **1996**, *35*, 2772–2774; *Angew. Chem.* **1996**, *108*, 2946–2948.
[3] T. Nakajima, A. Ishiguro, Y. Wakatsuki, *Angew. Chem. Int. Ed.* **2001**, *40*, 1066–1067; *Angew. Chem.* **2001**, *113*, 1096–1099.
[4] C. E. Plechnik, S. Liu, X. Chen, E. A. Meyers, S. G. Shore, *J. Am. Chem. Soc.* **2004**, *126*, 204–213.
[5] R. L. Carroll, C. B. Gorman, *Angew. Chem. Int. Ed.* **2002**, *41*, 4378–4400; *Angew. Chem.* **2002**, *114*, 4556–4579.
[6] G. Schmid, U. Simon, *Chem. Commun.* **2005**, 697–710.
[7] D. Wouters, U. S. Schubert, *Angew. Chem. Int. Ed.* **2004**, *43*, 2480–2495; *Angew. Chem.* **2004**, *116*, 2534–2550.
[8] D. J. Underwood, R. Hoffmann, K. Tatsumi, A. Nakamura, Y. Yamamoto, *J. Am. Chem. Soc.* **1985**, *107*, 5968–5980.
[9] C. Mealli, *J. Am. Chem. Soc.* **1985**, *107*, 2245–2253.
[10] C. Femoni, F. Kaswalder, M. C. Iapalucci, G. Longoni, M. Mehlstäubl, S. Zacchini, *Chem. Commun.* **2005**, 5769–5771.
[11] C. Femoni, F. Kaswalder, M. C. Iapalucci, G. Longoni, M. Mehlstäubl, S. Zacchini, A. Ceriotti, *Angew. Chem. Int. Ed.* **2006**, *45*, 2060–2062; *Angew. Chem.* **2006**, *118*, 2114–2116.
[12] J. C. Calabrese, L. F. Dahl, P. Chini, G. Longoni, S. Martinengo, *J. Am. Chem. Soc.* **1974**, *96*, 2614–2616.
[13] a) G. Longoni, P. Chini, *J. Am. Chem. Soc.* **1976**, *98*, 7225–7231; b) A. Ceriotti, G. Longoni, M. Marchionna, *Inorg. Synth.* **1989**, *26*, 316–319.
[14] *Crystal data for $[NMe_4]_2[Pt_{12}(CO)_{24}]$:* Monoclinic, space group $C2/c$, $a$ = 24.8081(10) Å, $b$ = 13.4980(6) Å, $c$ = 15.1794(6) Å, $\beta$ = 95.797(1)°, $U$ = 5057.0(4) Å$^3$, $Z$ = 4, $D_c$ = 4.153 g/cm$^3$, $T$ = 298 K, graphite-monochromatized Mo-$K_\alpha$ radiation ($\lambda$ = 0.71073 Å), final $R$ value was 0.0252 and $wR$ = 0.0485 for 4443 independent reflections having $I > 2\sigma(I)$. *Crystal data for $[NEt_4]_2[Pt_{15}(CO)_{30}]$:* Cubic, space group $P2_13$, $a$ = 27.5990(3) Å, $U$ = 21022.3(4) Å$^3$, $Z$ = 12, $D_c$ = 3.817 g/cm$^3$, $T$ = 298 K, graphite-monochromatized Mo-$K_\alpha$ radiation ($\lambda$ = 0.71073 Å), final $R$ value was 0.0491 and $wR$ = 0.0860 for 12407 independent reflections having $I > 2\sigma(I)$. *Crystal data for $[NMe_4]_2[Pt_{18}(CO)_{36}]\cdot 2Me_2CO$:* Orthorhombic, space group $Pnnm$, $a$ = 35.191(5) Å, $b$ = 35.570(5) Å, $c$ = 6.1674(9) Å, $U$ = 7720.0(19) Å$^3$, $Z$ = 4, $D_c$ = 4.129 g/cm$^3$, graphite-monochro-

 © 2007 Wiley-VCH Verlag GmbH & Co. KGaA, Weinheim 

matized Mo-$K_\alpha$ radiation ($\lambda$ = 0.71073 Å). Owing to rapid crystal decay at room temperature because of solvent loss, the data had to be collected at 100 K. Furthermore, the structure was recognized to be pseudomerohedrally twinned and a suitable set of BASF/TWIN parameters was used in the refinement, according to the procedure described in SHELX-97: [15] twin law [010 100 00–1]. Final $R$ value was 0.1025 and $wR$ = 0.2521 for 6583 independent reflections having $I > 2\sigma(I)$. *Crystal data for* $[NEt_4]_2[Pt_{24}(CO)_{48}]$*:* Tetragonal, space group $I\bar{4}2d$, $a$ = 12.2675(4) Å, $c$ = 34.251(3) Å, $U$ = 5154.5(5) Å$^3$, $Z$ = 2, $D_c$ = 4.051 g/cm$^3$, $T$ = 298 K, graphite-monochromatized Mo-$K_\alpha$ radiation ($\lambda$ = 0.71073 Å), final $R$ value was 0.0197 and $wR$ = 0.0446 for 2535 independent reflections having $I > 2\sigma(I)$. Data were corrected for Lorentz-polarization and absorption effects (empirical absorption SADABS[16]). The structures were solved by direct methods and refined with full-matrix least-squares (SHELX-97[15]). CCDC-626053 to -626056 contain the supplementary crystallographic data for this paper. These data can be obtained free of charge from The Cambridge Crystallographic Data Centre via www.ccdc.cam.ac.uk/data_request/cif. IR and ESI-MS are unambiguously diagnostic of the purity of the $[Pt_{3n}(CO)_{6n}]^{2-}$ ($n$ = 4, 5, 6) dianions, as a consequence of the varying ratio of number-of-charges/number-of-CO and sufficient stability of those ions in ESI conditions. Given that the $Pt_3(CO)_6$ units are constantly held together by only two electrons, species with $n > 6$ are hardly distinguishable both by IR and ESI-MS because of the leveling of the number-of-charges/number-of-CO ratio and fragmentation under ESI conditions. An almost Gaussian distribution of oligomers with $n \leq 6$ and $n \geq 6$ is observed,[10] even if the presence of oligomers with $n < 6$ in the injected solution is excluded by IR. Therefore, the purity of the $[NEt_4]_2[Pt_{24}(CO)_{48}]$ and $[NBu_4]_2[Pt_{24}(CO)_{48}]$ batches could only be assessed by a combination of IR and elemental analysis.

[15] G. M. Sheldrick, *SHELX-97*, University of Göttingen, Germany, **1997**.
[16] G. M. Sheldrick, *SADABS*, University of Gottingen, Germany, **1996**.
[17] C. Femoni, F. Kaswalder, M. C. Iapalucci, G. Longoni, S. Zacchini, *Coord. Chem. Rev.* **2006**, *250*, 1580–1604.
[18] M.-H. Whangbo, *Acc. Chem. Res.* **1983**, *16*, 95–101.
[19] J. K. Burdett in *Chemical Bonding in Solids*, Oxford University Press, New York, **1995**, pp. 48–65.
[20] K. Krogman, *Angew. Chem. Int. Ed. Engl.* **1969**, *8*, 35–42; *Angew. Chem.* **1969**, *81*, 10.
[21] M. E. Prater, L. E. Pence, R. Clerac, G. M. Finniss, C. Campana, P. Auban-Senzier, D. Jerome, E. Canadell, K. R. Dunbar, *J. Am. Chem. Soc.* **1999**, *121*, 8005–8016.
[22] H. Remita, B. Keita, K. Torigoe, J. Belloni, L. Nadjo, *Surf. Sci.* **2004**, *572*, 301–308.
[23] M. Ichikawa in *Metal Clusters in Chemistry* (Eds.: P. Braunstein, L. A. Oro, P. Raithby), Wiley-VCH, Weinheim, **1999**, vol. 3, pp. 1273–1301.
[24] Notably, $[Pt_{3n}(CO)_{6n}]^{2-}$ ($n$ = 6, 8, and 10) salts have been isolated and formulated by elemental analysis more than 30 years ago.[13a] Attempted structural determination of several salts with miscellaneous tetrasubstituted ammonium or phosphonium cations along the years systematically failed. Their unit cells were often featuring an axis of ca. 3 Å, the cations could not be located, and only unrealistic models of the dianions, on the basis of infinite stacks of perfectly eclipsed $Pt_3(CO)_3$-$(\mu\text{-}CO)_3$ moieties, were obtained by structure solution.

Received: January 24, 2007
Published Online: March 9, 2007

 © 2007 Wiley-VCH Verlag GmbH & Co. KGaA, Weinheim 

DOI: 10.1002/ejic.200601225

# New Aspects for Modeling Supramolecular Interactions in Vanadium Haloperoxidases: β-Cyclodextrin Inclusion Compounds of *cis*-Dioxovanadium(V) Complexes

**Ines Lippold,[a] Helmar Görls,[a] and Winfried Plass*[a]**

**Keywords:** Cyclodextrins / Host–guest systems / Inclusion compounds / Vanadium / X-ray diffraction

The reaction of potassium vanadate and the hydrazone ligand derived from Schiff base condensation of salicylaldehyde and biphenyl-4-carboxylic acid hydrazide ($H_2$salhybiph) in the presence of β-cyclodextrin (β-CD) in water yields the 1:1 inclusion compound K[$VO_2$(salhybiph)@β-CD]. The characterization in solution confirmed the integrity of the inclusion compound in different polar solvents such as DMSO and water. The inclusion compound crystallizes with additional water molecules in the triclinic space group *P*1. The supramolecular aggregation of the inclusion compound in the solid state is established through hydrogen bonding interactions between adjacent β-CD hosts and the π–π stacking ability of the ligand side chain of the guest complexes.
(© Wiley-VCH Verlag GmbH & Co. KGaA, 69451 Weinheim, Germany, 2007)

## Introduction

Vanadium haloperoxidases (V-HPO) are enzymes that catalyze the oxidation of halides to the corresponding hypohalous acids. These oxidized intermediates then readily halogenate organic substrates or convert hydrogen peroxide to singlet oxygen.[1] In addition, these enzymes can also catalyze the oxidation of organic sulfides to sulfoxides.[2] The active site of this class of enzymes consists of a vanadate moiety with a proposed trigonal bipyramidal geometry covalently bound to a histidine residue and held within the protein by strong hydrogen-bonding interactions with several amino acid residues.[3] Furthermore, this active site architecture is also found for certain acid phosphatases,[4] but with subtle distinctions concerning the relative positions of the amino acid residues.[5] The catalytic activity of V-HPO enzymes is proposed to be driven by this hydrogen-bonding network.[6] Therefore, V-HPO model systems need to be designed that provide a polar protic surrounding in order to offer the possibility for such relevant hydrogen-bonding interactions. Examples for such vanadium complexes derived from *N*-salicylidene hydrazides with a hydroxy substituted side chain have recently been reported.[7,8]

An alternative method to provide such an environment for the complex moieties can be through their interaction with appropriate host molecules, which would generate host–guest assemblies. Cyclodextrins (CDs) represent hosts with hydrophobic cavities and hydrophilic outer walls and generate inclusion complexes with various apolar groups that are included partially or completely in the cavity.[9] CDs are well known to form a variety of hydrogen bonds because of their free OH-groups. Parts of the guest protruding out of the CD ring opening could take part in this hydrogen bonding system. CDs and their substituted derivatives could be considered artificial enzymes as a result of their ability to react as catalysts for several asymmetric reactions, such as oxidation reactions, hydrolyses, and racemate separation.[10] Moreover, CDs are known to bind organometallic complexes containing aromatic constituents and such encapsulated complexes often exhibit markedly different physical and chemical properties.[11] Nevertheless, only very few examples of such inclusion complexes reported in the literature have been successfully characterized by single-crystal X-ray diffraction.[12]

We have recently reported the application of the *N*-salicylidene hydrazide ligand system for generating vanadium(V) complexes with a variety of functional groups attached to the ligand core.[7,8,13,14] Extending this approach, we report herein the synthesis and structure of a *cis*-dioxovanadium(V) complex containing an appropriate apolar biphenyl group in the ligand side chain, and its inclusion compound with β-CD.

## Results and Discussion

The *N*-salicylidene hydrazide ligand with apolar side chain used in this study is derived from Schiff base condensation of salicylaldehyde and biphenyl-4-carboxylic acid hydrazide ($H_2$salhybiph; Figure 1). Reaction of potassium

[a] Institut für Anorganische und Analytische Chemie,
Friedrich-Schiller-Universität Jena,
Carl-Zeiss-Promenade 10, 07745 Jena, Germany
Fax: +49-3641-948132
E-mail: Sekr.Plass@uni-jena.de
Supporting information for this article is available on the WWW under http://www.eurjic.org or from the author.

 © 2007 Wiley-VCH Verlag GmbH & Co. KGaA, Weinheim 

vanadate with the $H_2$salhybiph ligand in a methanol/acetone solution leads to the potassium salt of the corresponding *cis*-dioxovanadium(V) complex K[$VO_2$(salhybiph)]. The addition of acetone to the reaction solution is required owing to the very poor solubility of the $H_2$salhybiph ligand system in methanol. After a reaction time of 2 d, K[$VO_2$-(salhybiph)] can be isolated as a yellow crystalline solid material. Notably, the analogous reaction for ammonium vanadate affords the neutral *cis*-dioxovanadium(V) complex [$VO_2$(Hsalhybiph)] as the isolated product in a much lower yield. This is due to the fact that the ligand system under study is prone to variable protonation states at the amide group, which along with the presence of the protolytically active ammonium ions allows the generation of various complex species.[13] Therefore, the potassium vanadate route seems to be more promising for the generation of the relevant inclusion compounds.

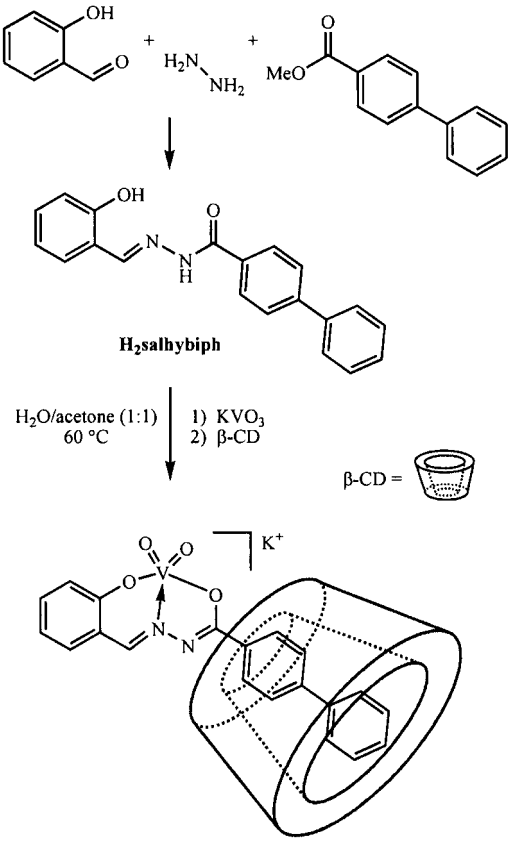


Figure 1. Synthesis of the inclusion compound K[$VO_2$(salhybiph)@β-CD].

The inclusion compound K[$VO_2$(salhybiph)@β-CD] was synthesized by a one-pot reaction of potassium vanadate with the $H_2$salhybiph ligand and β-CD in a water/acetone solution (Figure 1). The presence of β-CD results in a considerably shorter reaction time of about 2 h, and the reaction can be visually followed by the dissolution of the ligand. The 1:1 inclusion compound K[$VO_2$(salhybiph)@β-CD] can be isolated as yellow crystals, which have been fully characterized in solution and in the solid state.

The solution structure of the inclusion compound K[$VO_2$(salhybiph)@β-CD] can be unambiguously established by $^1$H NMR spectroscopy. Proton diffusion-ordered NMR spectroscopy (DOSY) clearly proves the integrity of the inclusion compound in solution, as only one species can be detected. The NOESY NMR spectra exhibit cross-peaks between the proton signals of the biphenyl side chain of the vanadium complex and those of the β-CD host (Figure 2). In particular for the 3-H and 5-H protons of the β-CD that extend into the β-CD host cavity, strong interactions with the aromatic protons of the biphenyl side chain of the guest are observed. The absence of cross-peaks between the 5-H protons of the β-CD and the Hbp7 and Hbp8 protons of the biphenyl group of the guest complex strongly suggests that the guest penetrates into the β-CD cavity from the primary hydroxy side. This is confirmed by the intense cross-peaks that are observed between the 6-H protons of the β-CD host and the Hbp2 and Hbp3 protons of the biphenyl side chain of the guest complex. Moreover, the lack of cross-peaks between the aromatic protons of the salicylidene moiety and the β-CD host proves that this part of the guest complex is distant from the β-CD. This also corroborates the presence of a 1:1 inclusion compound with a clear

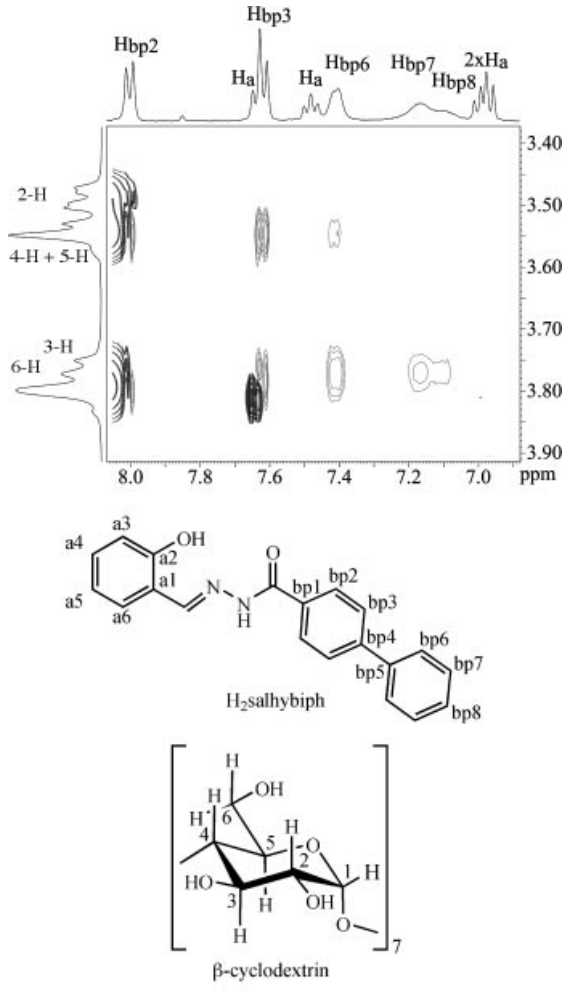


Figure 2. NOESY spectrum of K[$VO_2$(salhybiph)@β-CD] in $D_2O$ and labeling schemes for host and guest.

 © 2007 Wiley-VCH Verlag GmbH & Co. KGaA, Weinheim 

preference for the interaction of the biphenyl side chain with the β-CD host cavity.

For the solid state characterization of the inclusion compound K[$VO_2$(salhybiph)@β-CD], crystals suitable for X-ray analysis were grown by slowly cooling a hot aqueous solution of the inclusion compound. For different batches, a considerable variation in the water content was found. Thermogravimetric analysis (TGA) of these materials reveals a weight loss of about 6.5% (16.6%) in the temperature range form room temperature up to 140 °C, assigned to the removal of water molecules in the interstices between the inclusion compounds. In agreement with the elemental analysis, this indicates anywhere between 6.5 and 18 water molecules of crystallization per host–guest unit in the solid state. Above 200 °C, the inclusion compound starts to decompose. This temperature is somewhat lower than that observed for plain β-CD hydrate which starts to decompose at around 270 °C.[15] This difference can be attributed to the promoting effect of the metal complex host on the decomposition of the β-CD, and this provides further evidence for significant host–guest interaction in the inclusion compound. The final residual masses at 750 °C of 8.8 and 7.1% observed for different batches correspond very well to the values calculated for the formation of potassium orthovanadate, $KVO_3$ (8.1 and 7.3%, respectively; cf. Experimental Section).[16]

Crystallographic investigation shows that this inclusion compound crystallizes in the triclinic space group *P*1. The asymmetric unit contains two inclusion compounds together with the solvent water molecules, with the latter as well as the potassium cations disordered over several crystallographic positions. The molecular structure of the inclusion compound is shown in Figure 3. As expected from the solution NMR spectra, the *cis*-dioxovanadium(V) complex intrudes only partially into the β-CD cavity. Only the biphenyl side chain is located within the hydrophobic cavity of the host, whereas the remaining polar part of the complex is situated outside the primary hydroxy side of the β-CD host.

The vanadium atom of the guest complex exhibits an almost ideal square pyramidal environment with the coordinated $H_2$salhybiph ligand in its dianionic form, which is characterized by $\tau$ values lower than 0.10 ($\tau$ = 0 for ideal tetragonal pyramid; $\tau$ = 1 for ideal trigonal bipyramid). The basal plane of the square pyramid is given by atoms N*i*1, O*i*3, and O*i*4 (*i* = 1, 2) of the ligand and the oxo group O*i*2; the apical position is occupied by the oxo group O*i*1. Relative to the mean plane given by the donor atoms of the chelate ligand system, the vanadium atom is displaced towards the apical oxo group O*i*1 by about 40 pm, whereas the oxo group O*i*2 is slightly tilted towards the opposite side of the ligand plane with a deviation by about 15 pm from that plane. The structural parameters are consistent with those observed for other vanadium(V) complexes containing similar *N*-salicylidene hydrazide ligands, in particular the V=O (O*i*1 and O*i*2) as well as the V–N (N*i*1) and V–O (O*i*3 and O*i*4) bond lengths are within the expected range for such *cis*-dioxovanadium(V) complexes.[8,13]

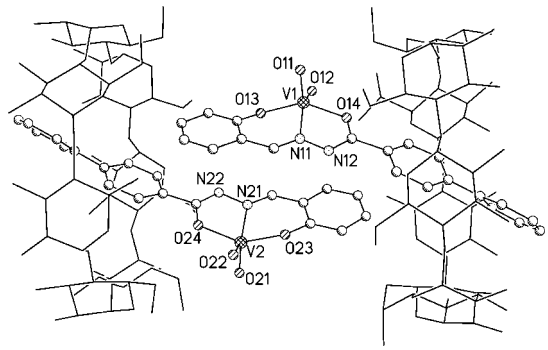


Figure 3. Representation of the molecular structure of the inclusion compound K[$VO_2$(salhybiph)@β-CD] that shows the two independent host–guest assemblies in the asymmetric unit. Selected bond lengths [pm] and angles [°]: V1–O11 159.6(9), V1–O12 159.8(8), V1–O13 189.3(7), V1–O14 196.7(6), V1–N11 215.5(7), N11–N12 139.3(9), O14–C18 127.8(10), N12–C18 129.7(11), O11–V1–O12 106.0(7), O11–V1–O13 102.4(4), O11–V1–O14 104.0(4), O12–V1–O13 98.5(4), O12–V1–O14 94.0(4), O13–V1–O14 146.3(3), O11–V1–N11 99.8(5), O12–V1–N11 153.4(5), O13–V1–N11 82.2(3), O14–V1–N11 73.0(3).

In the solid state, the inclusion compound K[$VO_2$-(salhybiph)@β-CD] forms head-to-head dimers with the secondary hydroxy sides of both β-CD hosts linked by hydrogen bonds as depicted in Figure 4. This arrangement leads to a π–π interaction of the biphenyl side chains of the corresponding guest molecules at a distance of 363 pm. The *cis*-dioxovanadium moieties of the guest molecules protrude from their hosts on the primary hydroxy group side and thereby generate a gap with a distance of about 910 pm between the adjacent head-to-head dimers. The protruding complex fragments of the adjacent dimers possess a staggered arrangement with a nearly coplanar orientation of their ligand planes (defined by N*i*1, O*i*3, and O*i*4 with *i* = 1, 2), which are about 340 pm apart. The overall packing of the head-to-head dimers can be described as a so-called "channel-type" arrangement[17] which is built from host guest dimers that are stringed together. These channels are oriented along the [001] direction and linked through hydrogen bonds between primary hydroxy groups (C-6) of neighboring β-CDs as depicted in Figure 5.

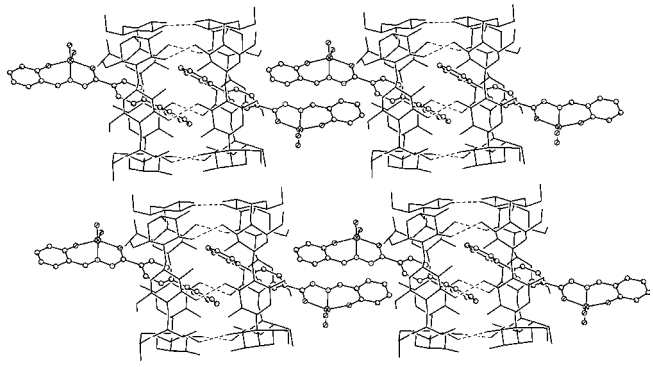

Figure 4. Packing of the inclusion compound K[$VO_2$(salhybiph)@β-CD] viewed approximately perpendicular to the [001] direction of the β-CD channel alignment. Hydrogen bonds between neighboring β-CDs are drawn as broken lines.

 © 2007 Wiley-VCH Verlag GmbH & Co. KGaA, Weinheim 

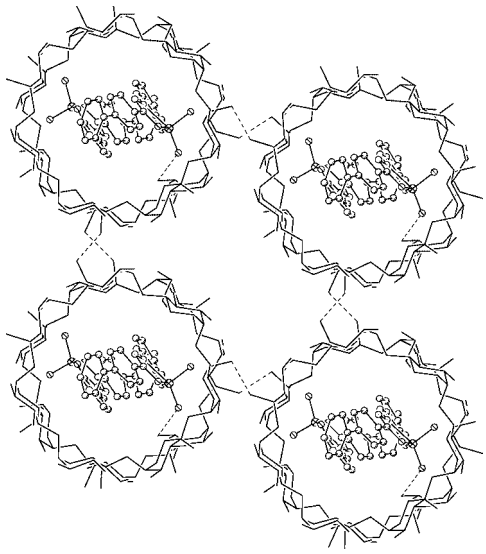

Figure 5. View of the crystal packing along the β-CD channels in the [001] direction. Hydrogen bonds between neighboring β-CDs are drawn as broken lines.

## Conclusions

We present the first supramolecular inclusion compound of a *cis*-dioxovanadium(V) complex with cyclodextrins. To facilitate this, a new vanadium complex derived from *N*-salicylidene hydrazide containing a hydrophobic biphenyl side chain matching the β-CD host cavity was synthesized. The integrity of the isolated inclusion compound K[$VO_2$-(salhybiph)@β-CD] in solution was confirmed by NMR spectroscopy. The solid-state structure reveals a channel-type packing of the head-to-head β-CD dimers which is cross-linked through hydrogen bonds and intercalated potassium cations. Through modification of the CD-host, it should be possible to utilize this concept for the generation of novel systems in oxidation catalysis, including the potential influence of the sugar backbone on chiral induction of vanadium-catalyzed oxidation reactions.

## Experimental Section

**General Remarks:** The synthesis of the ligand biphenyl-4-carboxylic acid salicylidene hydrazide ($H_2$salhybiph) and its neutral *cis*-dioxovanadium(V) complex [$VO_2$(Hsalhybiph)] is described in the Supporting Information. $^1$H, $^{13}$C and $^{51}$V as well as NOESY and DOSY NMR spectra were recorded with a 400 MHz Bruker AVANCE spectrometer. For notation used in the assignment of the atoms, see Figure 2. The chemical shift values for the $^{51}$V NMR spectra are reported relative to $VOCl_3$ as an external standard. Elemental analyses (C, H, N) were carried out with a Leco CHNS-932 elemental analyzer. Mass spectra were measured with a MAT95XL Finnigan instrument utilizing electron spray ionization and observation in the negative mode. IR spectra were recorded with a Bruker IFS55/Equinox spectrometer on samples prepared as KBr pellets. Thermogravimetric analysis (TGA) for powdered samples was performed with a Netzsch STA409PC Luxx apparatus under a constant flow of air ranging from room temperature up to 1000 °C with a heating rate of 5 °C/min. Atomic absorption spectrometry (AAS) was performed with an AA-6800 from Shimadzu.

**K[$VO_2$(salhybiph)]:** A suspension of biphenyl-4-carboxylic acid salicylidene hydrazide (0.200 g, 0.63 mmol) in an acetone/methanol mixture (30:5, 35 mL) was heated to 60 °C. After the addition of $KVO_3$ (0.087 g, 0.63 mmol), the suspension turned yellow–orange, and after 2 d of continuous stirring a clear solution was obtained. Upon removal of the solvent, the crude product was redissolved in hot methanol (30 mL), filtered, and kept for crystallization. Yield: 0.170 g (62%). $^1$H NMR (400 MHz, [$D_6$]DMSO): $\delta$ = 6.78 (t, $J$ = 7.3 Hz, 1 H, $H_{a5}$), 6.80 (d, $J$ = 8.4 Hz, 1 H, $H_{a3}$), 7.35 (t, $J$ = 7.8 Hz, 1 H, $H_{a4}$), 7.39 (tt, $J$ = 7.4 and 2.1 Hz, 1 H, $H_{bp8}$), 7.48 (t, $J$ = 7.5 Hz, 2 H, $H_{bp7}$), 7.57 (d, $J$ = 6.8 Hz, 1 H, $H_{a6}$), 7.52 (d, $J$ = 8.2 Hz, 2 H, $H_{bp3}$), 7.75 (t, $J$ = 8.9 Hz, 2 H, $H_{bp6}$), 8.10 (d, $J$ = 8.3 Hz, 2 H, $H_{bp2}$), 9.00 (s, 1 H, CH=N) ppm. $^{13}$C NMR (100 MHz, [$D_6$]DMSO): $\delta$ = 116.65 ($HC_{a5}$), 119.45, 119.86 ($HC_{a3}$ and $C_{a1}$), 126.34, 126.65 ($HC_{bp3}$ and $HC_{bp6}$), 127.78 ($HC_{bp8}$), 128.29 ($HC_{bp2}$), 128.93 ($HC_{bp7}$), 131.85 ($C_{bp1}$), 132.47 ($HC_{a6}$), 133.03 ($HC_{a4}$), 139.33 ($C_{bp4}$), 141.91 ($C_{bp5}$), 155.51 (C=N), 164.59 ($C_{a2}$), 169.48 (C=O) ppm. $^{51}$V NMR (105 MHz, [$D_6$]DMSO): $\delta$ = –532 ($\nu_{1/2}$ = 1122 Hz) ppm. IR (KBr): $\tilde{\nu}$ = 3447 (s), 3055 (w), 3028 (w), 2929 (w), 1615 (vs), 1550 (m), 1513 (m), 1476 (w), 1446 (m), 1383 (w), 1344 (s), 1278 (m), 1204 (w), 1157 (w), 950 (s), 904 (s), 875 (s), 760 (m), 740 (s), 696 (m) cm$^{-1}$. MS (ESI–, MeOH): $m/z$ (%) = 397 (100) [$VO_2$(salhybiph)]$^-$.$C_{20}H_{14}KN_2O_4V$ (436.38): calcd. C 55.05, H 3.23, N 6.42; found C 55.05, H 3.25, N 6.28.

**K[$VO_2$(salhybiph)@β-Cyclodextrin]·$x$$H_2O$:** Biphenyl-4-carboxylic acid salicylidene hydrazide (0.100 g, 0.32 mmol) was suspended in a solution of β-cyclodextrin (0.359 g, 0.32 mmol) in water (15 mL) at 60 °C. Acetone (15 mL) was added for better solubility of the ligand. Upon addition of $KVO_3$ (0.044 g, 0.32 mmol), the suspension turned yellow and, after stirring for 2 h at 60 °C, became a clear solution. The hot solution was filtered, and acetone was removed under reduced pressure. The solution was heated to 70 °C, allowed to slowly cool to room temperature, and the product precipitated as pale yellow cubic crystals. The water content of the isolated crystalline material varies considerably for different synthetic batches. Yield: 0.29 g (50%). Batch 1: $C_{62}H_{84}KN_2O_{39}V$·6.5$H_2O$ (1697.47): calcd. C 44.10, H 5.79, N 1.67; found C 44.04, H 5.94, N 1.39. TGA: Weight loss up to 140 °C of 6.5% (calcd. 6.9%), residual mass at 750 °C of 8.8% (calcd. 8.1% for $KVO_3$). Batch 2: $C_{62}H_{84}KN_2O_{39}V$·18$H_2O$ (1895.64): calcd. C 39.28, H 6.38, N 1.48, K 2.06; found C 39.79, H 6.39, N 1.21, K 1.2–2.3. TGA: Weight loss up to 140 °C of 16.6% (calcd. 17.1%), residual mass at 750 °C of 7.1% (calcd. 7.3% for $KVO_3$). $^1$H NMR (400 MHz, [$D_6$]DMSO): $\delta$ = 3.25–3.40 (m, 2 H, 2-H and 4-H), 3.50–3.70 (m, 4 H, 3-H, 5-H, and 6-H), 4.44 (t, $J$ = 5.5 Hz, 1 H, C6-OH), 4.82 (d, $J$ = 3.3 Hz, 1 H, 1-H), 5.66 (d, $J$ = 2.2 Hz, 1 H, C3-OH), 5.71 (d, $J$ = 6.9 Hz, 1 H, C2-OH), 6.77 (t, $J$ = 7.2 Hz, 1 H, $H_{a5}$), 6.78 (d, $J$ = 7.4 Hz, 1 H, $H_{a3}$), 7.34 (dt, $J$ = 7.7 and 2.0 Hz, 1 H, $H_{a4}$), 7.38 (tt, $J$ = 7.5 Hz and 1.2 Hz, 1 H, $H_{bp8}$), 7.48 (t, $J$ = 7.6 Hz, 2 H, $H_{bp7}$), 7.56 (dd, $J$ = 8.1 and 1.8 Hz, 1 H, $H_{a6}$), 7.75 (t, $J$ = 8.2 Hz, 4 H, $H_{bp3}$ and $H_{bp6}$), 8.08 (d, $J$ = 8.4 Hz, 2 H, $H_{bp2}$), 8.98 (s, 1 H, CH = N) ppm. $^1$H NMR (400 MHz, $D_2O$): $\delta$ = 3.43 (dd, $J$ = 9.9 Hz and 3.4 Hz, 1 H, 2-H), 3.45–3.50 (m, 2 H, 4-H and 5-H), 3.70–3.80 (m, 3 H, 3-H and 6-H), 4.90 (d, $J$ = 3.5 Hz, 1 H, 1-H), 6.91 (d, $J$ = 8.4 Hz, 1 H, $H_{a3}$), 6.94 (t, $J$ = 7.6 Hz, 1 H, $H_{a5}$), 7.04 (br. s, 1 H, $H_{bp8}$), 7.11 (s, 2 H, $H_{bp7}$), 7.35 (d, $J$ = 6.2 Hz, 2 H, $H_{bp6}$), 7.42 (t, $J$ = 8.0 Hz, 1 H, $H_{a4}$), 7.57 (t, $J$ = 8.0 Hz, 2 H, $H_{bp3}$), 7.57 (t, $J$ = 8.0 Hz, 1 H, $H_{a6}$), 7.95 (d, $J$ = 8.0 Hz, 2 H, $H_{bp2}$), 8.89 (s, 1 H, CH=N) ppm.$^{13}$C NMR (100 MHz, [$D_6$]DMSO): $\delta$ = 59.92 (C-6), 72.04 (C-5), 72.41 (C-2), 73.05 (C-3), 81.54 (C-4), 101.93 (C-1), 116.70 ($HC_{a5}$), 119.51, 119.92 ($HC_{a3}$ and $C_{a1}$),

 © 2007 Wiley-VCH Verlag GmbH & Co. KGaA, Weinheim 

126.43, 126.72 ($HC_{bp3}$ and $HC_{bp6}$), 127.85 ($HC_{bp8}$), 128.33 ($HC_{bp2}$), 129.00 ($HC_{bp7}$), 131.78 ($C_{bp1}$), 132.51 ($HC_{a6}$), 133.11 ($HC_{a4}$), 139.43 ($C_{bp4}$), 141.94 ($C_{bp5}$), 155.60 (C=N), 164.69 ($C_{a2}$), 169.51 (C=O) ppm. $^{51}$V NMR (105 MHz, [D$_6$]DMSO): $\delta$ = –532 ppm ($\nu_{1/2}$ = 1067 Hz). $^{51}$V NMR (105 MHz, $D_2O$): $\delta$ = –533 ppm. IR (KBr): $\tilde{\nu}$ = 3392 (vs), 2929 (m), 1612 (m), 1550 (w), 1509 (w), 1490 (w), 1448 (w), 1388 (w), 1156 (m), 1079 (m), 1028 (s), 945 (m), 906 (m), 759 (w) cm$^{-1}$. MS (ESI–, MeOH): *m*/*z* (%) = 2667 (8) {[$VO_2$(salhybiph)] +2β-CD}$^-$, 1532 (42) {[$VO_2$(salhybiph)] + β-CD}$^-$, 1134 (30) [β-CD – H]$^+$, 397 (100) [$VO_2$(salhybiph)]$^-$.

**X-ray Crystallographic Study of K[$VO_2$(salhybiph)@β-Cyclodextrin]·*x*$H_2O$:** Crystals suitable for X-ray analysis were grown by slow cooling of a hot water solution of the inclusion compound. $C_{62}H_{84}KN_2O_{39}V(\cdot 8H_2O)$, $M_r$ = 1715.48 g mol$^{-1}$, triclinic, space group *P*1, *a* = 1535.37(5), *b* = 1545.54(7), *c* = 2146.64(8) pm, *α* = 94.710(2), β = 98.484(2), *γ* = 102.994(2)°, *V* = 4873.9(3) × 10$^6$ pm$^3$, *Z* = 2, $\mu$(Mo-$K_\alpha$) = 0.229 mm$^{-1}$, 32730 reflections measured with a Nonius KappaCCD diffractometer at 183(2) K in the 2.49 to 27.50° *Θ* range. The structure was solved by direct methods and subsequently refined against $F^2$ with the SHELXL-97 program,[18] which converged at $R_1$ = 0.1126 for 20029 observed reflections with $I > 2\sigma(I)$ and $wR_2$ = 0.3385 for all unique reflections with a goodness-of-fit on $F^2$ of 1.165. All non-hydrogen atoms were refined with anisotropic displacement parameters. All hydrogen atoms bonded to carbon atoms were introduced in theoretical positions but not refined. As known from the analytical data of different batches the content of water molecules is varying. For the measured crystals an overall content of eight water molecules could be assigned. The potassium cations and the water molecules were found to be disordered over several crystallographic positions and refined with partial occupancy factors. The discrimination between potassium and water sites is made on the basis of the potential coordination numbers and hydrogen bonding interactions. For the water molecules, no attached hydrogen atoms were considered. Additional disorder was found for one of the included anionic vanadium complexes (V2) which was refined with a relative ratio of about 1:2. The largest positive and negative residual Fourier peaks after the refinement were equal to 0.82 and –0.51, respectively. CCDC-629924 contains the supplementary crystallographic data for this paper. These data can be obtained free of charge from The Cambridge Crystallographic Data Centre via www.ccdc.cam.ac.uk/data_request/cif.

**Supporting Information** (see footnote on the first page of this article): Experimental details for the synthesis of the $H_2$salhybiph ligand and the [$VO_2$H(salhybiph)] complex.

## Acknowledgments

The authors gratefully acknowledge the financial support of this study by the Deutsche Forschungsgemeinschaft. We wish to thank Brunhilde Dreßler for assistance with the AAS measurements.

[1] a) R. Wever, W. Hemrika in *Handbook of Metalloproteins, Vol. 2* (Eds.: A. Messerschmidt, R. Huber, T. Poulos, K. Wieghardt), John Wiley and Sons Ltd., Chichester, **2001**, pp. 1417–1428; b) A. Butler, *Coord. Chem. Rev.* **1999**, *187*, 17–35; c) D. C. Crans, J. J. Smee, E. Gaidamauskas, L. Yang, *Chem. Rev.* **2004**, *104*, 849–902.

[2] a) M. Andersson, A. Willetts, S. Allenmark, *J. Org. Chem.* **1997**, *62*, 8455; b) H. B. ten Brink, A. Tuynman, H. L. Dekker, W. Hemrika, Y. Izumi, T. Oshiro, H. E. Schoemaker, R. Wever, *Inorg. Chem.* **1998**, *37*, 6780–6784; H. B. ten Brink, H. E. Schoemaker, R. Wever, *Eur. J. Biochem.* **2001**, *268*, 132–138.

[3] a) A. Messerschmidt, R. Wever, *Proc. Natl. Acad. Sci. USA* **1996**, *93*, 392–396; b) A. Messerschmidt, L. Prade, R. Wever, *Biol. Chem.* **1997**, *378*, 309–315; c) M. N. Isupov, A. R. Dalby, A. A. Brindley, Y. Izumi, T. Tanabe, G. N. Murshudov, J. A. Littlechild, *J. Mol. Biol.* **2000**, *299*, 1035–1049; d) M. Weyand, H.-J. Hecht, M. Kiess, M.-F. Liaud, H. Vilter, D. Schomburg, *J. Mol. Biol.* **1999**, *293*, 595–611.

[4] W. Plass, *Angew. Chem.* **1999**, *111*, 960–962; *Angew. Chem. Int. Ed.* **1999**, *38*, 909–912.

[5] K. Ishikawa, Y. Mihara, K. Gondoh, E. Suzuki, Y. Asano, *EMBO J.* **2000**, *19*, 2412–2423.

[6] a) M. Bangesh, W. Plass, *J. Mol Struct. THEOCHEM* **2005**, *725*, 163–175; b) W. Plass, *Abstracts of Papers of the American Chemical Society* **2006**, *232*, 400–Inor (September 10); c) W. Plass, M. Bangesh, S. Nica, A. Buchholz in *Vanadium: The Versatile Metal* (Eds.: K. Kustin, D. C. Crans, J. C. Pessoa), *ACS Symposium Series*, American Chemical Society, Washington, D. C., **2007**, in press.

[7] W. Plass, *Coord. Chem. Rev.* **2003**, *237*, 205–212.

[8] a) S. Nica, A. Pohlmann, W. Plass, *Eur. J. Inorg. Chem.* **2005**, 2032–2036; b) A. Pohlmann, S. Nica, T. K. K. Luong, W. Plass, *Inorg. Chem. Commun.* **2005**, *8*, 289–292.

[9] a) J. Szejtli, *Chem. Rev.* **1998**, *98*, 1743–1753; b) K. Harata, *Chem. Rev.* **1998**, *89*, 1803–1827; c) P. Bortolus, G. Marconi, S. Monti, B. Mayer, G. Köhler, G. Grabner, *Chem. Eur. J.* **2000**, *6*, 1578–1591.

[10] a) R. Breslow, S. D. Dong, *Chem. Rev.* **1998**, *98*, 1997–2011; H. Sakuraba, H. Maekawa, *J. Incl. Phenom. Macrocycl. Chem.* **2006**, *54*, 41–45; b) F. Kramer, W. Dietsche, *Chem. Ber.* **1959**, *92*, 1739–1747.

[11] S. S. Braga, F. A. Almeida Paz, M. Pillinger, J. D. Seixas, C. C. Romão, I. S. Gonçalves, *Eur. J. Inorg. Chem.* **2006**, 1662–1669.

[12] a) Y. Liu, R.-Q. Zhong, H.-Y. Zhang, H.-B. Song, *Chem. Commun.* **2005**, 2211–2213; b) G. Meister, H. Stoeckli-Evans, G. Süss-Fink, *J. Organomet. Chem.* **1993**, *453*, 249–253; c) B. Klingert, G. Rihs, *J. Chem. Soc., Dalton Trans.* **1991**, 2749–2760; d) B. Klingert, G. Rihs, *Organometallics* **1990**, *9*, 1135–1141; e) Y. Odagaki, K. Hirotsu, T. Higuchi, A. Harada, S. Takahashi, *J. Chem. Soc., Perkin Trans. 1* **1990**, 1230–1231; f) D. R. Alston, A. M. Z. Slawin, J. F. Stoddart, D. J. Williams, *Angew. Chem.* **1985**, *97*, 771–772; *Angew. Chem. Int. Ed. Engl.* **1985**, *24*, 786–787.

[13] a) W. Plass, A. Pohlmann, H.-P. Yozgatli, *J. Inorg. Biochem.* **2000**, *80*, 181–183; b) W. Plass, H.-P. Yozgatli, *Z. Anorg. Allg. Chem.* **2003**, *629*, 65–70.

[14] a) J. Becher, I. Seidel, W. Plass, D. Klemm, *Tetrahedron* **2006**, *62*, 5675–5681; b) A. Pohlmann, W. Plass, *J. Inorg. Biochem.* **2001**, *86*, 381; c) S. Nica, M. Rudolph, H. Görls, W. Plass, *Inorg. Chim. Acta* **2007**, DOI:10.1016/j.ica.2006.09.018; d) I. Lippold, S. Nica, M. Mancka, W. Plass, *Abstracts of Papers of the American Chemical Society* **2006**, *232*, 829–Inor (September 10).

[15] A. Harada, K. Saeki, S. Takahashi, *Organometallics* **1989**, *8*, 730–733.

[16] S. Milić, N. Colović, M. Antonijević, F. Gaál, *J. Therm. Anal. Calorim.* **2000**, *61*, 229–238.

[17] W. Saenger, *J. Incl. Phenom. Macrocycl. Chem.* **1984**, *2*, 445–454.

[18] G. Sheldrick, *SHELXS-97* and *SHELXL-97*, University of Göttingen, Germany, **1997**.

Received: December 22, 2006
Published Online: March 6, 2007

 © 2007 Wiley-VCH Verlag GmbH & Co. KGaA, Weinheim 

DOI: 10.1002/ejic.200600942

# Mixed-Metal Dawson Sandwich Complexes: Synthesis, Spectroscopic Characterization and Electrochemical Behaviour of $Na_{16}[M^{II}Co_3(H_2O)_2(P_2W_{15}O_{56})_2]$ (M = Mn, Co, Ni, Zn and Cd)

**Laurent Ruhlmann,*[a] Claire Costa-Coquelard,[a] Jacqueline Canny,[b] and René Thouvenot*[b]**

**Keywords:** Dawson complexes / Paramagnetic $^{31}P$ NMR spectroscopy / Electrochemistry

Mixed-metal Dawson sandwich complexes $[MCo_3(H_2O)_2(P_2W_{15}O_{56})_2]^{16-}$ (represented as $\{MCo_3P_4W_{30}\}$) have been synthesized by the reaction of $M^{2+}$ (where M = Mn, Co, Ni, Zn and Cd) with the "lacunary" sandwich complex αβ-$[NaCo_3(H_2O)_2(P_2W_{15}O_{56})_2]^{17-}$ (represented as $\{NaCo_3P_4W_{30}\}$): $[NaCo_3(H_2O)_2(P_2W_{15}O_{56})_2]^{17-} + M^{2+} \rightarrow [MCo_3(H_2O)_2(P_2W_{15}O_{56})_2]^{16-} + Na^+$. The $\{MCo_3P_4W_{30}\}$ species were characterized by IR spectroscopy, elemental analysis and $^{31}P$ solution NMR spectroscopy. The electrochemical behaviour of these mixed-metal sandwich complexes was investigated in aqueous solution and compared with that of ββ-$[Co_4(H_2O)_2(P_2W_{15}O_{56})_2]^{16-}$ (represented as ββ-$\{Co_4P_4W_{30}\}$) and $\{NaCo_3P_4W_{30}\}$.
(© Wiley-VCH Verlag GmbH & Co. KGaA, 69451 Weinheim, Germany, 2007)

## Introduction

Polyoxometalates (POMs) and their transition-metal-substituted derivatives are metal–oxygen anionic clusters with applications in fields as diverse as magnetochemistry, medicine and catalysis.[1–4]

All investigations centred around this large and growing class of clusters required previous knowledge of their precise composition and structure; therefore, the continuing development of rational methods for the systematic modification of POM systems remains very important.

It is well known that the reaction of the trivacant Dawson anion α-$[P_2W_{15}O_{56}]^{12-}$ with transition-metal cations yields sandwich complexes $[M_4(H_2O)_2(P_2W_{15}O_{56})_2]^{16-}$ ($M^{2+}$ = $Mn^{2+}$, $Co^{2+}$, $Ni^{2+}$, $Zn^{2+}$ and $Cd^{2+}$), in which a sheet of four M atoms (two internal and two external) is sandwiched between two $\{P_2W_{15}\}$ subunits.[5] For all Dawson, tetranuclear, sandwich complexes characterized by X-ray diffraction, the "classical" ββ configuration is observed with β connectivities between both trivacant $\{P_2W_{15}\}$ units and the central $M_4$ tetrad[5c,5e,5f,5h] (Figure 1a). This type of arrangement leads to a molecular anion with $C_{2h}$ symmetry in which the two $\{P_2W_{15}\}$ moieties are equivalent.

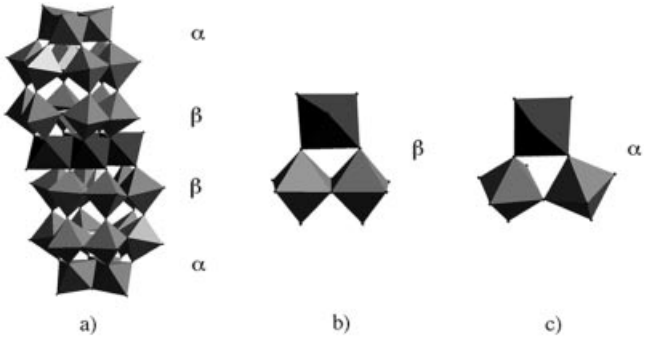


Figure 1. Polyhedral representation of the (a) αββα-$\{M_4P_4W_{30}\}$ sandwich structure, and of the (b) β and (c) α junctions.

The β junction implies a connection between one internal $MO_6$ octahedron and one dimeric $W_2O_{10}$ unit (Figure 1b), whereas for the α junction, this internal $MO_6$ octahedron is connected to two dimeric $W_2O_{10}$ units (Figure 1c).[6]

In the case of cobalt complexes, we previously reported that the synthesis in neutral solution leads to a mixture of symmetrical and unsymmetrical complexes as shown by $^{31}P$ NMR spectroscopy.[7a] One reasonable hypothesis for the structure of the dissymmetrical $\{Co_4P_4W_{30}\}$ species is that it presents both types of junction, α and β, between the two $\{P_2W_{15}\}$ units and the central $Co_4$ sheet.

[a] Laboratoire de Chimie Physique,
UMR CNRS 8000, Université Paris-Sud 11,
Bâtiment 350, 91405 Orsay Cedex, France
Fax: +33-1-69-15-43-28
E-mail: laurent.ruhlmann@lcp.u-psud.fr
[b] Laboratoire de Chimie Inorganique et Matériaux Moléculaires,
UMR CNRS 7071, Université Pierre et Marie Curie – Paris6,
Institut de Chimie Moléculaire FR 2769,
Case Courrier 42, 4, Place Jussieu, 75252 Paris Cedex 05, France
Fax: +33-1-44-27-38-41
E-mail: rth@ccr.jussieu.fr
Supporting information for this article is available on the WWW under http://www.eurjic.org or from the author.

 © 2007 Wiley-VCH Verlag GmbH & Co. KGaA, Weinheim 

Dinuclear and trinuclear sandwich complexes $[Na_2M_2(H_2O)_2(P_2W_{15}O_{56})_2]^{n-}$ and $[NaM_3(H_2O)_2(P_2W_{15}O_{56})_2]^{m-}$ ($M^{2+}$ = $Co^{2+}$, $n$ = 18, $m$ = 17 and $M^{3+}$ = $Fe^{3+}$, $n$ = 16, $m$ = 14) have also been obtained.[7b,7c,8,9]

For the diiron species $[Na_2(H_2O)_2Fe_2(P_2W_{15}O_{56})_2]^{16-}$, the junctions between the trivacant moieties $\{P_2W_{15}\}$ and the metallic sheet are both of the α-type (Figure 2), whereas in the case of the trimetallic complexes ($M^{2+/3+}$ = $Co^{2+}$ or $Fe^{3+}$), the structures may be considered as resulting from the fusion of one α-$\{M_3P_2W_{15}\}$ and one "lacunary" β-$\{M_2P_2W_{15}\}$ unit, and the lacuna is occupied by a $Na^+$ cation.[8–10]

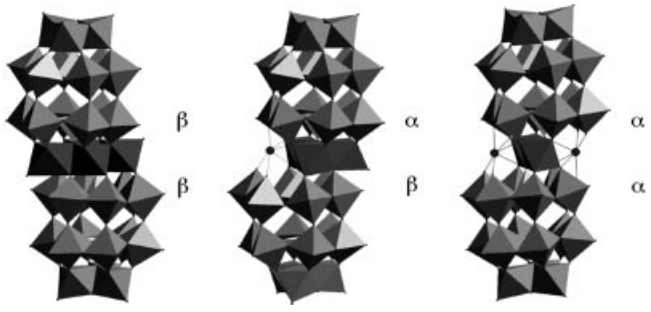


Figure 2. Polyhedral representations of the crystallographically resolved Dawson sandwich structures: ββ-$\{M_4P_4W_{30}\}$ (left), αβ-$\{NaM_3P_4W_{30}\}$ (middle) and αα-$\{Na_2M_2P_4W_{30}\}$ (right). For the "lacunary" structures, the aqua ligands are omitted for clarity.

As the $Na^+$ cations are weakly bonded, the di- and trimetallic complexes may act as divacant and monovacant "lacunary" species, respectively, and mixed-metal sandwich complexes can be obtained by addition of a transition-metal cation $M^{n+}$. Indeed, the reaction of $M^{2+}$ (M = Mn, Co, Ni, Zn) with $\{Na_2Fe_2P_4W_{30}\}$ leads to "saturated" sandwich complexes $[M^{II}_2(H_2O)_2Fe^{III}_2(P_2W_{15}O_{56})_2]^{14-}$ (abbreviated as $\{M_2Fe_2P_4W_{30}\}$).[7b,11,12] In each case, replacement of the two $Na^+$ cations by two $M^{2+}$ metallic cations induces conformational changes that lead to a β connectivity for both $\{P_2W_{15}\}$–$M_2Fe_2$ junctions.

The tricobalt species $[NaCo_3(H_2O)_2(P_2W_{15}O_{56})_2]^{17-}$ (abbreviated as $\{NaCo_3P_4W_{30}\}$)[8] reported recently also appears to be a suitable starting species for the synthesis of mixed-metal sandwich complexes (Figure 3).

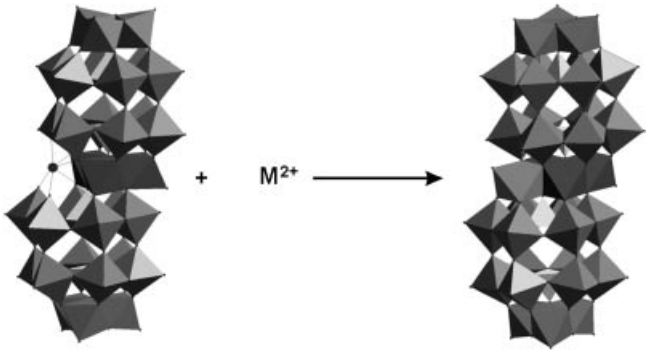


Figure 3. Principle of the synthesis of the mixed-metal Dawson sandwich complexes $\{MCo_3P_4W_{30}\}$.

Such complexes can be used in catalytic reactions as inorganic analogues of metalloporphyrins, and both the redox and the catalytic properties of these complexes can be modulated by the nature of the addendum atom M.[13]

We report here the synthesis and characterization (by IR and $^{31}P$ NMR spectroscopy and elemental analysis) of a new family of these mixed-metal sandwich complexes $[MCo_3(H_2O)_2(P_2W_{15}O_{56})_2]^{16-}$ (abbreviated as $\{MCo_3P_4W_{30}\}$) where $M^{2+}$ = $Mn^{2+}$, $Co^{2+}$, $Ni^{2+}$, $Zn^{2+}$ and $Cd^{2+}$. We also present the electrochemical behaviour of $\{MCo_3P_4W_{30}\}$ and compare it with that of the tetracobalt complex and the trinuclear precursor $\{NaCo_3P_4W_{30}\}$.[8]

## Results and Discussion

### Synthesis

The tricobalt sandwich complex is formally an unsaturated species. As shown by $^{31}P$ NMR spectroscopy, addition of a slight excess of $Co^{2+}$ to the aqueous solution of $\{NaCo_3P_4W_{30}\}$ leads to the immediate and quantitative formation of one dissymmetrical $\{Co_4P_4W_{30}\}$ complex (Figure 4, middle)[8] according to the global reaction [Equation (1)]:

$$[NaCo_3(H_2O)_2(P_2W_{15}O_{56})_2]^{17-} + Co^{2+} \rightarrow \text{dissym-}[Co_4(H_2O)_2(P_2W_{15}O_{56})_2]^{16-} + Na^+ \quad (1)$$

The pH of the solution (initially around 6.5) does not change markedly by addition of $Co^{2+}$. At this pH, the dissymmetrical complex appears very stable, whereas at low pH (ca. 3) it evolves into the symmetrical ββ-$\{Co_4P_4W_{30}\}$ form (Figure 4, bottom).[15] As reported by Coronado and co-workers,[10] the lacunary $\{NaCo_3P_4W_{30}\}$ species presents an αβ connectivity; the rapid addition of $Co^{2+}$ to form the saturated compound likely leads primarily to the αβ-$\{Co_4P_4W_{30}\}$ isomer, which is stable in neutral medium. In acidic medium, however, it isomerizes slowly and irreversibly into ββ-$\{Co_4P_4W_{30}\}$ by formal π/3-rotation of the $\{P_2W_{15}\}$ unit of the α-$\{Co_3P_2W_{15}\}$ moiety leading to β-$\{Co_3P_2W_{15}\}$. The whole process is described as follows [Equation (2)] and [Equation (3)]:

$$\alpha\beta\text{-}[NaCo_3(H_2O)_2(P_2W_{15}O_{56})_2]^{17-} + Co^{2+} \xrightarrow{\text{rapid, pH ca. 6.5}} \alpha\beta\text{-}[Co_4(H_2O)_2(P_2W_{15}O_{56})_2]^{16-} + Na^+ \quad (2)$$

$$\alpha\beta\text{-}[Co_4(H_2O)_2(P_2W_{15}O_{56})_2]^{16-} \xrightarrow{\text{slow, pH ca. 3}} \beta\beta\text{-}[Co_4(H_2O)_2(P_2W_{15}O_{56})_2]^{16-} \quad (3)$$

 © 2007 Wiley-VCH Verlag GmbH & Co. KGaA, Weinheim 

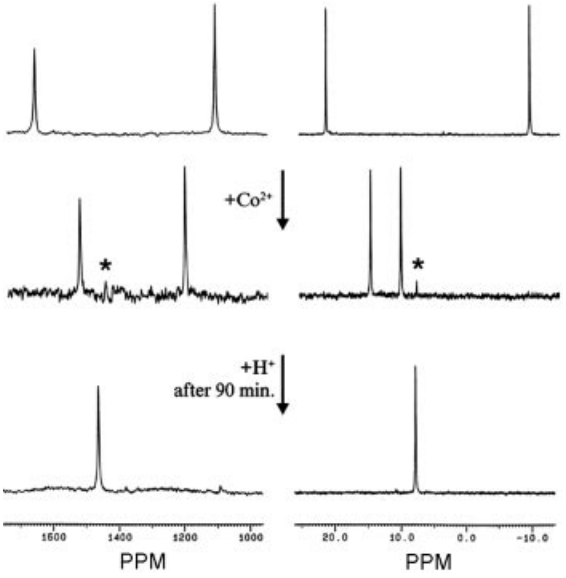


Figure 4. Formation of $\{CoCo_3P_4W_{30}\}$ by addition of $Co^{2+}$ to $\{NaCo_3P_4W_{30}\}$ followed by 121.5 MHz $^{31}P$ NMR spectroscopy. Top: initial spectrum of $\{NaCo_3P_4W_{30}\}$, middle: immediately after addition of 2 equiv. $Co^{2+}$ per $\{NaCo_3P_4W_{30}\}$, bottom: after lowering the pH by addition of 2 equiv. $H_3O^+$. Experimental conditions: $c$ = 0.02 mol L$^{-1}$ in $D_2O/H_2O$ (1:1), $T$ = 300 K.

To obtain analytically pure αβ-$Na_{16}[Co_4(H_2O)_2(P_2W_{15}O_{56})_2]$ it is necessary to use a fourfold excess of $Co^{2+}$ in order to displace the $Na^+$ cation from the central $Na\text{-}Co_3O_{14}(H_2O)_2$ cluster. Actually, by using less than four equivalents of $Co^{2+}$, a mixture of αβ-$\{Co_4P_4W_{30}\}$ and αβ-$\{NaCo_3P_4W_{30}\}$ is always obtained. The crystallisation of $\{MCo_3P_4W_{30}\}$ further requires the addition of NaCl in order to lower the solubility by ionic strength and common cation effects.

The mixed-metal tricobalt sandwich complexes $\{MCo_3P_4W_{30}\}$ (M = $Mn^{2+}$, $Ni^{2+}$, $Zn^{2+}$ and $Cd^{2+}$) are prepared similarly by addition of a fourfold excess of $M^{2+}$ to $\{NaCo_3P_4W_{30}\}$ in 1 mol L$^{-1}$ NaCl. $^{31}P$ NMR spectroscopy shows that the addition reaction is quite selective as no other compound can be detected except for trace amounts of the $\{NaCo_3P_4W_{30}\}$ precursor.

This method, namely simple addition of a transition-metal ion to the "lacunary" tricobalt compound, then leads to a clean reaction without any substitution in the POM subunits. This furnishes a coherent series of new mixed-metal sandwich complexes.

## IR Characterization

The IR spectra of $\{MCo_3P_4W_{30}\}$ ($M^{2+}$ = $Mn^{2+}$, $Co^{2+}$, $Ni^{2+}$, $Zn^{2+}$ and $Cd^{2+}$) are shown in Figure S1 (see Supporting Information) and are compared to that of the precursor compound αβ-$\{NaCo_3P_4W_{30}\}$ and to that of ββ-$\{Co_4P_4W_{30}\}$.

In addition to numerous W–O and W–O–W bands at relatively low wavenumbers (<1000 cm$^{-1}$),[16] the IR spectra of phosphorus-centred polyoxotungstates present well-separated P–O stretching vibrations between 1200 and 1000 cm$^{-1}$.[17]

In our previous papers, we have discussed in detail the pattern of the $PO_4$ stretching region for various ββ-$\{M_4P_4W_{30}\}$ sandwich complexes; it shows two bands at around 1080 (strong) and 1010 cm$^{-1}$ (weak) that are assigned to the unperturbed $PW_9$ moiety and one band at ca. 1055 cm$^{-1}$ (medium) that is attributed to the perturbed $PW_6$ subunit.[7a,8] For the tricobalt precursor αβ-$\{NaCo_3P_4W_{30}\}$, the latter signal is split into two bands, at 1044 cm$^{-1}$ and 1035 cm$^{-1}$, according to the non-equivalence of the two $PW_6$ subunits ($PW_6Co_3$ and $PW_6Co_2Na$).[8,10]

The mixed-tricobalt species $\{MCo_3P_4W_{30}\}$ can be formed from the trimetallic species by replacing the "external" $Na^+$ ion by one transition metal (Figure 3). Unlike those for $\{CdCo_3P_4W_{30}\}$, the two bands for the $PW_6$ subunits in $\{NaCo_3P_4W_{30}\}$ coalesce into one band at ca. 1050 cm$^{-1}$, which shows that the two saturated subunits $PW_6Co_3$ and $PW_6Co_2M$ are nearly equivalent. Such a behaviour was already observed for lacunary and monosubstituted Keggin tungstophosphates, where addition of the transition-metal cation to the lacunary species induces a marked decrease in the splitting of the P–O stretching vibrations.[17a]

Whereas the size of the first row transition-metal cations $Mn^{2+}$ ($r$ = 0.83 Å), $Ni^{2+}$($r$ = 0.69 Å) and $Zn^{2+}$ ($r$ = 0.74 Å) are comparable to that of $Co^{2+}$ ($r$ = 0.74 Å), the cadmium cation is significantly larger ($r$ = 0.95 Å) and it does not fit exactly into the lacuna and therefore does not interact as strongly as the other cations with the oxygen atom of $PO_4$. This accounts for the observation of two bands at around 1045 cm$^{-1}$ ($PW_6Co_3$) and 1035 cm$^{-1}$ (shoulder, $PW_6Co_2Cd$) for $\{CdCo_3P_4W_{30}\}$. Nevertheless, the overall IR spectra of all $\{MCo_3P_4W_{30}\}$ are similar to that of $\{Co_4P_4W_{30}\}$, which indicates a structural similarity throughout the whole series.

## $^{31}P$ NMR Characterization

$^{31}P$ NMR spectroscopy is particularly suitable to check the polyoxometalate purity and to obtain some structural information, i.e. overall symmetry of the species and relative positions of the substituting elements.[12]

The $^{31}P$ NMR spectra of $\{MCo_3P_4W_{30}\}$ ($M^{2+}$ = $Mn^{2+}$, $Co^{2+}$, $Ni^{2+}$, $Zn^{2+}$ and $Cd^{2+}$) are reported in Figure 5 and all data are given in Table 1. Paramagnetic Dawson species always exhibit two markedly different types of $^{31}P$ resonances: the P atoms labelled P(1) in the $PW_6$ subunits close to the paramagnetic centres give rise to broad and strongly shifted (generally towards high frequency) signals, and those labelled P(2) in the $PW_9$ subunits far from the paramagnetic centres give rise to relatively sharp lines at a chemical shift close to that of diamagnetic metallophosphates (between +20 and –20 ppm).[18]

As in the case for $\{NaCo_3P_4W_{30}\}$, the $^{31}P$ NMR spectra of all $\{MCo_3P_4W_{30}\}$ present two relatively narrow lines ($\Delta\nu_{1/2}$: 10–30 Hz) of equal intensity, which are assigned to

 © 2007 Wiley-VCH Verlag GmbH & Co. KGaA, Weinheim 

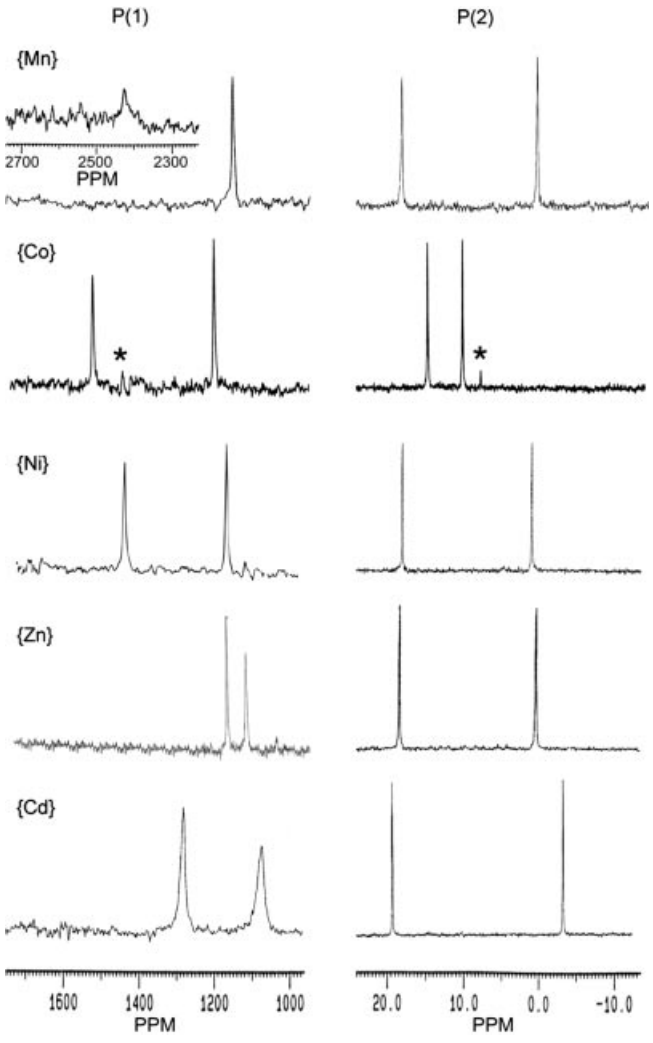


Figure 5. 121.5 MHz $^{31}P$ NMR spectra of various $\{MCo_3P_4W_{30}\}$ [0.02 mol $L^{-1}$ in unbuffered solutions in $D_2O/H_2O$ (1:1)] (from top to bottom: $M^{2+}$ = $Mn^{2+}$, $Co^{2+}$, $Ni^{2+}$, $Zn^{2+}$ and $Cd^{2+}$).

Table 1. $^{31}P$ NMR spectroscopic data for the Dawson sandwich species.[a]

| Compound | P(1)[b] | | P(2)[b] | |
|---|---|---|---|---|
| | $\delta$[c] | $\Delta\nu_{1/2}$[d] | $\delta$[c] | $\Delta\nu_{1/2}$[d] |
| ββ-$\{Co_4P_4W_{30}\}$ | +1483 | 420 | +9.9 | 20 |
| αβ-$\{NaCo_3P_4W_{30}\}$ | +1125 | 450 | –9.3 | 10 |
| | +1673 | 450 | +22.0 | 10 |
| $\{MnCo_3P_4W_{30}\}$ | +1150 | 470 | +0.4 | 17 |
| | +2425 | 2400 | +18.4 | 21 |
| $\{CoCo_3P_4W_{30}\}$ | +1203 | 440 | +10.0 | 14 |
| | +1522 | 540 | +14.5 | 13 |
| $\{NiCo_3P_4W_{30}\}$ | +1164 | 450 | +0.6 | 31 |
| | +1435 | 630 | +17.9 | 31 |
| $\{ZnCo_3P_4W_{30}\}$ | +1163 | 550 | +0.4 | 10 |
| | +1116 | 365 | +18.4 | 10 |
| $\{CdCo_3P_4W_{30}\}$ | +1075 | 250 | –3.2 | 8 |
| | +1283 | 430 | +19.2 | 8 |

[a] Unbuffered 0.02 mol $L^{-1}$ solutions in $D_2O/H_2O$ (1:1) at 300 K. [b] P(1) and P(2) in the $PW_6$ and $PW_9$ subunits, respectively. [c] In ppm with respect to 85% $H_3PO_4$. [d] In Hz.

the two non-equivalent P(2) atoms, and two broad signals attributed to the P(1) atoms (Figure 5). This confirms that the two $\{P_2W_{15}\}$ moieties remain non-equivalent in the $\{MCo_3P_4W_{30}\}$ complexes (Figure 3).

By examination of the data reported in Table 1, we notice that, for all first-row transition-metal species, one P(1) signal is always observed from about +1150 to +1200 ppm. By plotting its $^{31}P$ chemical shift with respect to the atomic number of $M^{2+}$, we observe a moderate and quasilinear variation, whereas the second P(1) signal shifts considerably (Figure 6a). We can tentatively assign the latter signal to the P(1) atom of the $PW_6Co_2M$ subunit that is closer to the addendum $M^{2+}$ cation ($d_{P(1)-M}$: ca. 3.3 Å) rather than to the P(1) atom of the $PW_6Co_3$ subunit ($d_{P(1)-M}$: ca. 4.6 Å). On the contrary, the P(2) chemical shifts are not very sensitive to the nature of $M^{2+}$ with the exception of $Co^{2+}$. Two P(2) signals are observed at around +0.4 to +0.6 ppm and +17.9 to +18.4 ppm, which agrees with phosphorus atoms in the $PW_9$ subunits far from the paramagnetic centres ($d_{P(2)-M} > 7$ Å) and consequently less affected (Figure 6b). It is somewhat puzzling that both the P(2) chemical shifts

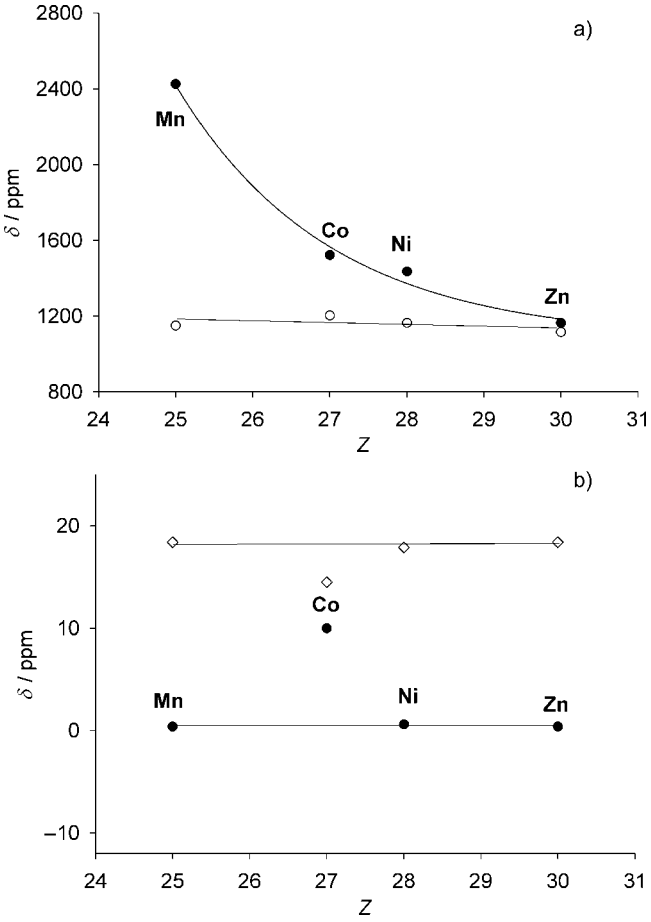


Figure 6. Plot of the variation of a) $\delta_{P(1)}$ and b) $\delta_{P(2)}$ of $\{MCo_3P_4W_{30}\}$ ($M^{2+}$ = $Mn^{2+}$, $Co^{2+}$, $Ni^{2+}$ and $Zn^{2+}$) with respect to the atomic number of M. (For the complete series including $Cd^{2+}$ see Figure S3 of the Supporting Information).

 © 2007 Wiley-VCH Verlag GmbH & Co. KGaA, Weinheim 

for αβ-$\{Co_4P_4W_{30}\}$ do not fall on the line, which may suggest that the $\{MCo_3P_4W_{30}\}$ (M ≠ Co) species present another conformation with ββ connectivities. This question cannot be answered until an X-ray structure determination has been performed.

We notice that the Mn compound presents the largest shift amongst the P(1) signals (+2425 ppm); this $^{31}P$ resonance is also the broadest one (2.4 kHz, Figure 5, top).

## Electrochemistry

### *General Electrochemical Behaviour*

The electrochemical behaviour of complexes $\{NaCo_3P_4W_{30}\}$ and $\{MCo_3P_4W_{30}\}$ was studied in aqueous solution (pH 3.5) by cyclic voltammetry (CV). All electrochemical data are gathered in Table 2, and typical cyclic voltammograms are presented in Figure 7 and Figure 8.

These complexes exhibit three successive reduction processes involving the W centres. For these three couples, the cathodic (and anodic) peak currents are almost proportional to the square root of the scan rate up to 100 mV s$^{-1}$, which indicates that the reduction (and oxidation) processes are both diffusion-controlled.

The voltammograms of $\{ZnCo_3P_4W_{30}\}$, $\{NiCo_3P_4W_{30}\}$ and αβ-$\{Co_4P_4W_{30}\}$ are very similar to that of ββ-$\{Co_4P_4W_{30}\}$ (Figure 7 top and Figure S2), however, with slightly different potentials (Table 2).

In the case of $\{CdCo_3P_4W_{30}\}$, the third reduction process presents a typical pattern that is characteristic of adsorption of metallic Cd at the electrode (Figure 7, bottom). In the forward scan, at –0.859 V, $Cd^{2+}$ is also reduced along with the W centres; this results in the deposition of metallic Cd. In the reverse scan, $Cd^0$ is reoxidized to $Cd^{2+}$, which re-enters the sandwich anion; this gives rise to the intense and symmetrical anodic redissolution peak. The whole reduction and the first reoxidation processes of $\{CdCo_3P_4W_{30}\}$ can be expressed according to Equations (4), (5), (6), (7) and (8).

For all species, controlled-potential coulometry at –0.55 V shows that the solution turns deep blue and consumes between 2.1 and 2.2 electrons per sandwich complex;

$$[CdCo_3(H_2O)_2(P_2W_{15}O_{56})_2]^{16-} + 2e^- \leftrightarrows [CdCo_3(H_2O)_2(P_2W_{15}O_{56})_2]^{18-} \quad (4)$$

$$[CdCo_3(H_2O)_2(P_2W_{15}O_{56})_2]^{18-} + 2e^- \leftrightarrows [CdCo_3(H_2O)_2(P_2W_{15}O_{56})_2]^{20-} \quad (5)$$

$$[CdCo_3(H_2O)_2(P_2W_{15}O_{56})_2]^{20-} + 4e^- + Na^+ \rightarrow [NaCo_3(H_2O)_2(P_2W_{15}O_{56})_2]^{23-} + Cd^0 \quad (6)$$

$$Cd^0 \rightarrow Cd^{2+} + 2e^- \quad (7)$$

$$[NaCo_3(H_2O)_2(P_2W_{15}O_{56})_2]^{23-} + Cd^{2+} \rightarrow [CdCo_3(H_2O)_2(P_2W_{15}O_{56})_2]^{20-} + 2e^- + Na^+ \quad (8)$$

at –0.70 V, the number of exchanged electrons is between 4.1 and 4.3. This shows that both the first and the second processes involve two electrons.

In addition to the cathodic waves as discussed above, the manganese species $\{MnCo_3P_4W_{30}\}$ is also electroactive at a positive potential: an anodic peak at +1.027 V and the associated cathodic peak at +0.719 V correspond to the oxidation and reduction of the Mn centre (Figure 8).[7a,12,19]

Controlled-potential coulometry at +1.10 V results in the passage of 2.2 electrons per complex, whereas subsequent reduction at +0.60 V consumes only 1.1 electron. This suggests that the $Mn^{II}$ is oxidized directly to $Mn^{IV}$, but in the reverse process $Mn^{IV}$ is reduced to $Mn^{III}$; further reduction to recover $Mn^{II}$ in $\{MnCo_3P_4W_{30}\}$ likely leads to a broad peak hardly detectable even after several repetitive scans.

Similar behaviours were previously reported for α$_2$-$[Mn^{II}P_2W_{17}O_{61}]^{8-}$, $[ZnW_{11}MnO_{39}]^{8-}$ and $[Mn_4(H_2O)_2(P_2W_{15}O_{56})_2]^{16-}$ (abbreviated as $\{Mn_4P_4W_{30}\}$); in the last case, the four Mn centres are simultaneously oxidized in a eight-electron process, and the two successive reduction processes $Mn^{IV}$ to $Mn^{III}$ and $Mn^{III}$ to $Mn^{II}$ both consume four electrons.[7a,19]

In that case, the curve-crossing at about 1 V is probably due to the deposition, at the electrode, of the species generated during the oxidation process (Figure 8, dotted line).

Table 2. Electrochemical data of the Dawson sandwich complexes obtained from cyclic voltammetry (scan rate = 20 mV s$^{-1}$) in 0.5 mol L$^{-1}$ $Na_2SO_4$ + $H_2SO_4$ (pH 3.5). All redox potentials $E°'$, approximated by $(E_p^a + E_p^c)/2$ for the reversible steps, are given in V vs. SCE.

| Compound | W(1)[a] | W(2)[a] | W(3)[a] | Mn |
|---|---|---|---|---|
| ββ-$\{Co_4P_4W_{30}\}$ | –0.436 (2e, 71) | –0.641 (2e, 144) | –0.832 (1e, 64)<br>–0.917 (1e, 94) | |
| αβ-$\{NaCo_3P_4W_{30}\}$ | –0.470 (1e, 93)[b]<br>–0.531 (1e, 58)[b] | –0.660 (2e, 83)[c] | –0.835 (2e, 65)[c] | |
| $\{MnCo_3P_4W_{30}\}$ | –0.482 (2e, 106) | –0.673 (2e, 124) | –0.908 (2e, 84) | $E_p^a$ = +1.027<br>$E_p^c$ = +0.719 |
| $\{CoCo_3P_4W_{30}\}$ | –0.467 (2e, 126) | –0.673 (2e, 114) | –0.903 (2e, 110) | |
| $\{NiCo_3P_4W_{30}\}$ | –0.470 (2e, 121) | –0.663 (2e, 116) | –0.896 (2e, 100) | |
| $\{ZnCo_3P_4W_{30}\}$ | –0.465 (2e, 121) | –0.690 (2e, 81) | –0.909 (2e, 101) | |
| $\{CdCo_3P_4W_{30}\}$ | –0.488 (2e, 128) | –0.693 (2e, 151) | –0.859 (4e, 225)[d] | |

[a] In parentheses: number of exchanged electron(s) $n$ and $\Delta E_p = |E_p^a - E_p^c|$. [b] Simultaneous exchange of one electron and one proton (see ref.[7a]). [c] Simultaneous exchange of two electrons and two protons (see ref.[7a]). [d] Irreversible, see text.

 © 2007 Wiley-VCH Verlag GmbH & Co. KGaA, Weinheim 

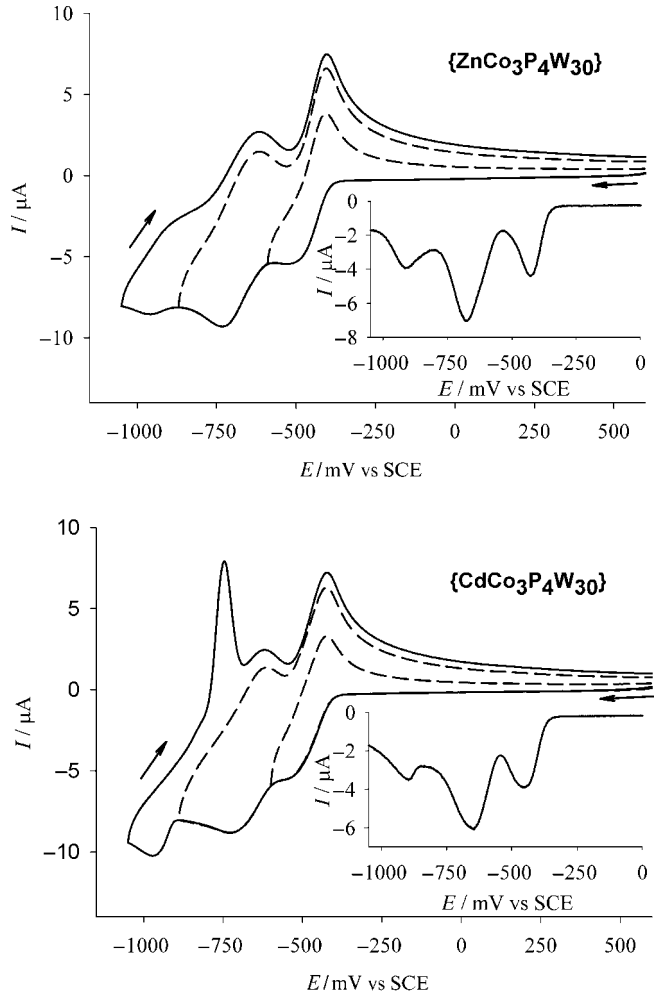


Figure 7. Cyclic voltammograms of $\{ZnCo_3P_4W_{30}\}$ (top) and $\{CdCo_3P_4W_{30}\}$ (bottom) in 0.5 mol L$^{-1}$ $Na_2SO_4$ + $H_2SO_4$ at pH 3.5 with different negative potential limits: –0.60 V, –0.89 V and –1.05 V. Scan rate = 20 mV s$^{-1}$, $c$ = 0.5 mmol L$^{-1}$. Inset: Differential pulse voltammetry at a scan rate of 25 mV s$^{-1}$.

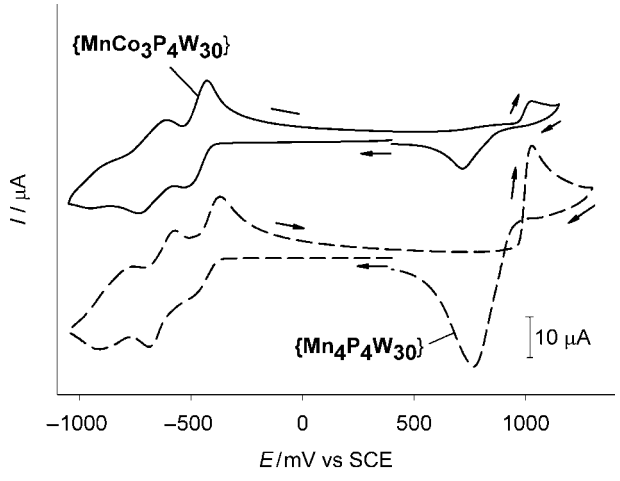


Figure 8. Cyclic voltammograms of $\{MnCo_3P_4W_{30}\}$ (full line) and $\{Mn_4P_4W_{30}\}$ (dotted line) in 0.5 mol L$^{-1}$ $Na_2SO_4$ + $H_2SO_4$ at pH 3.5. Scan rate = 20 mV s$^{-1}$, $c$ = 0.5 mmol L$^{-1}$.

## Summary and Concluding Remarks

In this work, we report for the first time the preparation and characterization of mixed-metal–tricobalt sandwich complexes $[MCo_3(H_2O)_2(P_2W_{15}O_{56})_2]^{16-}$ ($\{MCo_3P_4W_{30}\}$; $M^{2+}$ = $Mn^{2+}$, $Co^{2+}$, $Ni^{2+}$, $Zn^{2+}$ and $Cd^{2+}$).

As in the case for $\{NaCo_3P_4W_{30}\}$, the $^{31}$P NMR spectrum of each $\{MCo_3P_4W_{30}\}$ complex presents two relatively narrow lines of equal intensity assigned to the two non-equivalent P(2) atoms and two broad signals attributed to the P(1) atoms, which indicates that the two $\{P_2W_{15}\}$ moieties remain non-equivalent in the $\{MCo_3P_4W_{30}\}$ complexes. Moreover, by plotting $\delta_{P(1)}$ with respect to the atomic number of M, we notice that one of the two P(1) signals presents a moderate and quasilinear shift with respect to the atomic number, whereas the second P(1) signal changes considerably. This large variation leads us to tentatively assign this signal to the P(1) atom of the $PW_6Co_2M$ subunit that is closer to the addendum $M^{2+}$ cation.

On the contrary, the P(2) signals are not very sensitive to the nature of $M^{2+}$ (with the exception of $Co^{2+}$), which is in agreement with the fact that these phosphorus atoms are in the $PW_9$ subunits far from $M^{2+}$.

The electrochemical behaviours of $\{MCo_3P_4W_{30}\}$ were investigated systematically, with reference to that of αβ-$\{NaCo_3P_4W_{30}\}$ or ββ-$\{Co_4P_4W_{30}\}$. All these compounds exhibit three reversible W-centred reduction processes with slightly different peak potentials, which suggests that the anions have similar structures.

Different electrochemical behaviours can be distinguished: with $Co^{2+}$, $Ni^{2+}$ and $Zn^{2+}$, the metallic centres are not electroactive, whereas with $Mn^{2+}$ and $Cd^{2+}$, redox reactions originating from the metals are observed.

The $Mn^{2+}$ complex presents one oxidation process, corresponding to the $Mn^{II}/Mn^{IV}$ couple, followed, in the reverse scan, by the reduction of $Mn^{IV}$ to $Mn^{III}$. Further reduction to recover $Mn^{II}$ complex is hardly detectable.

The "lacunary" sandwich complex $\{NaCo_3P_4W_{30}\}$ appears to be a good precursor to prepare new classes of mixed-metal polytungstates in which the nature of the metal can be varied considerably. This opens the route to the preparation of mixed-metal sandwich complexes with interesting catalytic and magnetic properties.

## Experimental Section

**General Comment:** Most common laboratory chemicals were of reagent grade purchased from commercial sources, and were used without further purification.

**Preparation of Compounds:** The trinuclear complex αβ-$[NaCo_3(H_2O)_2(P_2W_{15}O_{56})_2]^{17-}$ $\{NaCo_3P_4W_{30}\}$ was prepared as described previously.[8]

For all subsequent compounds, the purity was checked by $^{31}$P NMR spectroscopy: except for $\{CoCo_3P_4W_{30}\}$, no spurious signal could be detected from the noise for all compounds, which shows that the purity is at least 97%.

**αβ-$Na_{16}[Co_4(H_2O)_2(P_2W_{15}O_{56})_2]\cdot 51H_2O$:** $\{NaCo_3P_4W_{30}\}$ (1.00 g, 0.110 mmol) was dissolved in 10 mL of water. By addition of

 © 2007 Wiley-VCH Verlag GmbH & Co. KGaA, Weinheim 

$Co(NO_3)_2{\cdot}6H_2O$ (128.0 mg, 0.440 mmol) while stirring vigorously, the solution immediately turned from dark red to brown. The resulting neutral solution (pH ca. 6.5) was stirred for 2 h, after which NaCl (0.60 g) was added. The solution was concentrated in air in an open vessel, and a greenish brown precipitate appeared after ca. 1 d. The precipitate was collected on a sintered glass frit (porosity 4) after 2 d and dried in air (yield 0.43 g, 43%). $^{31}P$ NMR spectroscopy shows that this sample is contaminated by less than 5% of the symmetrical ββ isomer. $Co_4Na_{16}P_4W_{30}O_{112}{\cdot}53H_2O$ (8989.7): calcd. Co 2.62, P 1.38, W 61.35, $H_2O$ 10.62; found Co 2.60, P 1.38, W 61.21, $H_2O$ 10.62. $^{31}P$ NMR: ($D_2O/H_2O$, 1:1): $\delta$ = +10.0 ($\Delta\nu_{1/2}$ = 14 Hz), +14.5 ($\Delta\nu_{1/2}$ = 13 Hz), +1203 ($\Delta\nu_{1/2}$ = 440 Hz), +1522 ppm ($\Delta\nu_{1/2}$ = 540 Hz).

**$Na_{16}[MnCo_3(H_2O)_2(P_2W_{15}O_{56})_2]{\cdot}51H_2O$.:** This complex was prepared following the same procedure as that for αβ-$\{Co_4P_4W_{30}\}$ by using $MnCl_2{\cdot}6H_2O$ (102.9 mg, 0.440 mmol) instead of $Co(NO_3)_2{\cdot}6H_2O$. The greenish-orange precipitate was collected on a sintered glass frit (porosity 4) after 2 d (yield 0.72 g, 73%). $MnCo_3Na_{16}P_4W_{30}O_{112}{\cdot}53H_2O$ (8985.7): calcd. Co 1.97, Mn 0.61, P 1.38, W 61.38, $H_2O$ 10.63; found Co 1.95, Mn 0.63, P 1.37, W 61.29, $H_2O$ 10.63. $^{31}P$ NMR: ($D_2O/H_2O$, 1:1), $\delta$ = +0.4 ($\Delta\nu_{1/2}$ = 17 Hz), +18.4 ($\Delta\nu_{1/2}$ = 21 Hz), +1150 ($\Delta\nu_{1/2}$ = 470 Hz), +2425 ppm ($\Delta\nu_{1/2}$ = 2.4 kHz).

**$Na_{16}[NiCo_3(H_2O)_2(P_2W_{15}O_{56})_2]{\cdot}49H_2O$:** This complex was prepared following the same procedure as that for αβ-$\{Co_4P_4W_{30}\}$ by using $NiCl_2{\cdot}6H_2O$ (104.4 mg, 0.440 mmol) instead of $Co(NO_3)_2{\cdot}6H_2O$. The yellow-brown precipitate was collected on a sintered glass frit (porosity 4) after 2 d (yield 0.68 g, 69%). $NiCo_3Na_{16}P_4W_{30}O_{112}{\cdot}51H_2O$ (8989.5): calcd. Co 1.97, Ni 0.66, P 1.38, W 61.60, $H_2O$ 10.26; found Co 1.99, Ni 0.63, P 1.39, W 61.70, $H_2O$ 10.26. $^{31}P$ NMR: ($D_2O/H_2O$, 1:1): $\delta$ = +0.6 ($\Delta\nu_{1/2}$ = 31 Hz), +17.9 ($\Delta\nu_{1/2}$ = 31 Hz), +1164 ($\Delta\nu_{1/2}$ = 450 Hz), +1435 ($\Delta\nu_{1/2}$ = 630 Hz).

**$Na_{16}[ZnCo_3(H_2O)_2(P_2W_{15}O_{56})_2]{\cdot}49H_2O$:** This complex was prepared following the same procedure as that for αβ-$\{Co_4P_4W_{30}\}$ by using $ZnCl_2{\cdot}6H_2O$ (107.5 mg, 0.440 mmol) instead of $Co(NO_3)_2{\cdot}6H_2O$. The grey-brown precipitate was collected on a sintered glass frit (porosity 4) after 2 d (yield 0.84 g, 85%). $ZnCo_3Na_{16}P_4W_{30}O_{112}{\cdot}51H_2O$ (8996.1): calcd. Co 1.97, P 1.38, W 61.56, Zn 0.73, $H_2O$ 10.25; found Co 1.96, P 1.35, W 61.91, Zn 0.76, $H_2O$ 10.25. $^{31}P$ NMR: ($D_2O/H_2O$, 1:1): $\delta$ = +0.4 ($\Delta\nu_{1/2}$ = 10 Hz), +18.4 ppm ($\Delta\nu_{1/2}$ = 10 Hz), +1116 ppm ($\Delta\nu_{1/2}$ = 365 Hz), +1163 ($\Delta\nu_{1/2}$ = 550 Hz).

**$Na_{16}[CdCo_3(H_2O)_2(P_2W_{15}O_{56})_2]{\cdot}47H_2O$:** This complex was prepared following the same procedure as that for αβ-$\{Co_4P_4W_{30}\}$ by using $CdCl_2{\cdot}6H_2O$ (128.0 mg, 0.440 mmol) instead of $Co(NO_3)_2{\cdot}6H_2O$. The grey-brown precipitate was collected on a sintered glass frit (porosity 4) after 2 d (yield 0.70 g, 71%). $CdCo_3Na_{16}P_4W_{30}O_{112}{\cdot}49H_2O$ (9043.2): calcd. Cd 1.25, Co 1.97, P 1.38, W 61.48, $H_2O$ 9.84; found Cd 1.22, Co 1.94, P 1.39, W 61.24, $H_2O$ 9.84. $^{31}P$ NMR: ($D_2O/H_2O$, 1:1): $\delta$ = –3.2 ($\Delta\nu_{1/2}$ = 8 Hz), +19.2 ($\Delta\nu_{1/2}$ = 8 Hz), +1075 ($\Delta\nu_{1/2}$ = 250 Hz), +1283 ppm ($\Delta\nu_{1/2}$ = 430 Hz).

**NMR and IR Spectroscopic Measurements:** $^{31}P$ NMR spectra were recorded in 5-mm o.d. tubes on a Bruker AC 300 or a Bruker AvanceII 300 spectrometer operating at 121.5 MHz. The NMR spectra were obtained at 300 K with 0.02 M solutions in $D_2O/H_2O$ (1:1) and were referenced to external 85% $H_3PO_4$ (IUPAC convention) by the substitution method. The $^{31}P$ chemical shifts are pH dependent and some small differences may be observed between the synthetic solution and those obtained after redissolving the solid samples. IR spectra were recorded on a Bio-Rad FTS 165 FTIR spectrophotometer on KBr pellets.

**Electrochemical Experiments:** Water, used for all electrochemical measurements, was obtained by passing through a Milli-$RO_4$ unit and subsequently through a Millipore Q water purification set. $H_2SO_4$ solutions and solid $Na_2SO_4$ were commercial products (Prolabo). The electrolyte was made up from 0.5 M $Na_2SO_4$ aqueous solution, and its pH was precisely adjusted to 3.5 by addition of 0.5 M ($H_2SO_4$ + $Na_2SO_4$) aqueous solution. The solutions were deaerated thoroughly for at least 30 min by bubbling argon (Ar-U from Air Liquide) through the solution and kept under argon atmosphere during the whole experiment.

The source, mounting and polishing of the glassy carbon electrode (GC, Tokai, Japan) have been described previously.[14] The glassy carbon samples had a diameter of 3 mm. The electrochemical apparatus EG&G 273A was driven by a personal computer. Potentials are quoted against a saturated calomel electrode (SCE). The counter electrode was a platinum gauze with a large surface area. All experiments were carried out at room temperature. Controlled potential coulometry experiments were conducted under continuous bubbling and stirring, and a large surface glassy carbon plate ($s$ = 6 $cm^2$) was used.

**Analyses:** Elemental analyses were performed by the Service Central d'Analyse du CNRS, Vernaison (France). The water content was determined by thermogravimetric analysis.

**Supporting Information** (see footnote on the first page of this article): The IR spectra of $\{MCo_3P_4W_{30}\}$ (Figure S1), cyclic voltammograms of ββ-$\{Co_4P_4W_{30}\}$ and αβ-$\{Co_4P_4W_{30}\}$ at pH 3.5 (Figure S2) and plot of the variation of $\delta_{P(1)}$ and $\delta_{P(2)}$ of $\{MCo_3P_4W_{30}\}$, including that of M = $Cd^{2+}$ (Figure S3).

## Acknowledgments

This work was supported by the CNRS and by the Université Paris-Sud 11 and Université Pierre et Marie Curie – Paris6. This work was also supported by the ANR agency, project no. JC05_52436, NCPPOM.

[1] E. Coronado, C. J. Gómez-García, *Chem. Rev.* **1998**, *98*, 273.
[2] M. T. Pope, A. Müller (Eds.), Polyoxometalates: *From Platonic Solids to Anti-Retroviral Activity*, Kluwer, Dordrecht, The Netherlands, **1994**.
[3] J. T. Rhule, C. L. Hill, D. A. Judd, R. F. Schinazi, *Chem. Rev.* **1998**, *98*, 327.
[4] I. V. Kozhevnikov, *Chem. Rev.* **1998**, *98*, 171.
[5] a) R. G. Finke, M. W. Droege, *Inorg. Chem.* **1983**, *22*, 1006; b) R. G. Finke, M. W. Droege, P. J. Domaille, *Inorg. Chem.* **1987**, *26*, 3886; c) T. J. R. Weakley, R. G. Finke, *Inorg. Chem.* **1990**, *29*, 1235; d) J.-P. Ciabrini, R. Contant, *J. Chem. Res.* **1993**, *(S)* 391, *(M)* 2719; e) C. J. Gómez-García, J. J. Borrás-Almenar, E. Coronado, L. Ouahab, *Inorg. Chem.* **1994**, *33*, 4016; f) R. G. Finke, T. J. R. Weakley, *J. Chem. Crystallogr.* **1994**, *24*, 123; g) J. F. Kirby, L. C. W. Baker, *J. Am. Chem. Soc.* **1995**, *117*, 10010; h) X. Zhang, D. C. Duncan, C. F. Campana, C. L. Hill, *Inorg. Chem.* **1997**, *36*, 4208; i) A. Müller, F. Peter, M. Pope, D. Gatteschi, *Chem. Rev.* **1998**, *98*, 239; j) L. Meng, J. F. Liu, *Chem. Res. Chin. Univ.* **1998**, *14*, 1.
[6] R. Thouvenot, M. Fournier, R. Franck, C. Rocchiccioli-Deltcheff, *Inorg. Chem.* **1984**, *23*, 598–605.
[7] a) L. Ruhlmann, L. Nadjo, J. Canny, R. Contant, R. Thouvenot, *Eur. J. Inorg. Chem.* **2002**, 975–986; b) X. Zhang, C. L. Hill, *Chem. Ind.* **1998**, *75*, 519; c) X. Zhang, T. M. Anderson, Q. Chen, C. L. Hill, *Inorg. Chem.* **2001**, *40*, 418–419.

 © 2007 Wiley-VCH Verlag GmbH & Co. KGaA, Weinheim 

[8] L. Ruhlmann, J. Canny, R. Contant, R. Thouvenot, *Inorg. Chem.* **2002**, *41*, 3811–3819.
[9] a) T. M. Anderson, K. I. Hardcastle, N. Okun, C. L. Hill, *Inorg. Chem.* **2001**, *40*, 6418; b) I. M. Mbomekalle, B. Keita, L. Nadjo, W. A. Neiwert, L. Zhang, K. I. Hardcastle, C. L. Hill, T. M. Anderson, *Eur. J. Inorg. Chem.* **2003**, 3924–3928; c) B. Keita, I. M. Mbomekalle, L. Nadjo, T. M. Anderson, C. L. Hill, *Inorg. Chem.* **2004**, *43*, 3257–3263.
[10] J. M. Clemente-Juan, E. Coronado, A. Gaita-Ariño, C. Giménez-Saiz, H.-U. Gu1del, A. Sieber, R. Bircher, H. Mutka, *Inorg. Chem.* **2005**, *44*, 3389–3395.
[11] a) T. M. Anderson, X. Zhang, K. I. Hardcastle, C. L. Hill, *Inorg. Chem.* **2002**, *41*, 2477; b) I. M. Mbomekalle, R. Cao, K. I. Hardcaste, C. L. Hill, M. Amman, B. Keita, L. Nadjo, T. M. Anderson, *C R. Chimie* **2005**, *8*, 1077–1086.
[12] L. Ruhlmann, J. Canny, J. Vaisserman, R. Thouvenot, *Dalton Trans.* **2004**, *5*, 794–800.
[13] a) L. C. W. Baker, Plenary Lecture, Proc. XV International Conference Coordination Chemistry 15th, **1973**; b) D. K. Lyon, W. K. Miller, T. Novet, P. J. Domaille, E. Evitt, D. C. Johnson, R. G. Finke, *J. Am. Chem. Soc.* **1991**, *113*, 7209–7221.
[14] B. Keita, K. Essaadi, L. Nadjo, *J. Electroanal. Chem. Interfacial. Electrochem.* **1989**, *259*, 127–146.
[15] The X-ray structure of ββ-$Na_{16}[Co_4(H_2O)_2(P_2W_{15}O_{56})_2]\cdot 51H_2O$ has been reported in detail recently. The anion $[Co_4(H_2O)_2(P_2W_{15}O_{56})_2]^{16-}$ contains a sheet of four $Co^{II}$ ions forming an oxo–aqua metallic core $Co_4O_{14}(H_2O)_2$, which is sandwiched between two trivacant α-$[P_2W_{15}O_{56}]^{12-}$ ({$P_2W_{15}$}) subunits, with two β connectivities. The crystal structure confirms the $C_{2h}$ symmetry of the whole polyanion, which is in agreement with $^{31}P$ NMR spectroscopy. S. Liu, D. G. Kurth, B. Bredenkőtter, D. Volkmer, *J. Am. Chem. Soc.* **2002**, *124*, 12279–12287.
[16] C. Rocchiccioli-Deltcheff, R. Thouvenot, R. Franck, *Spectrochim. Acta* **1976**, *22A*, 587–597.
[17] a) C. Rocchiccioli-Deltcheff, R. Thouvenot, *J. Chem. Res.* **1977**, *(S)* 46–47, *(M)* 549–571; b) C. Rocchiccioli-Deltcheff, R. Thouvenot, *Spectroscopy Letters* **1979**, *12*, 127–138.
[18] T. L. Jorris, M. Kozik, N. Casañ-Pastor, P. J. Domaille, R. G. Finke, W. K. Miller, L. C. W. Baker, *J. Am. Chem. Soc.* **1987**, *109*, 7402–7408.
[19] L. Cheng, H. Seen, J. Liu, S. Dong, *J. Chem. Soc., Dalton Trans.* **1999**, 2619–2625.

Received: October 5, 2006
Published Online: January 23, 2007

 © 2007 Wiley-VCH Verlag GmbH & Co. KGaA, Weinheim 

DOI: 10.1002/ejic.200600974

# New Anions of Pentacoordinate Phosphorus Containing Fluorine and Trifluoromethyl Groups

**Natalya V. Pavlenko,[a] Lesya A. Babadzhanova,[a] Igor I. Gerus,[b] Yurii L. Yagupolskii,*[a] Wieland Tyrra,[c] and Dieter Naumann[c]**

*Dedicated to Professor Karl Otto Christe on the occasion of his 70th birthday*

**Keywords:** Phosphorus / Fluorides / Silanes / Pentacoordinate anions

The unique pseudo-trigonal-bipyramidal $CF_3PF_3O^-$ and $(CF_3)_2PF_2O^-$ anions were obtained and characterised for the first time. They were formed by the reactions of $(PhO)_3P(O)$, $Me_3SiCF_3$ and the fluoride ion sources $[Me_4N]F$ and CsF, respectively, in glyme. These anions represent the stable transition states postulated for nucleophilic substitution at a tetrahedral phosphorus atom. The salt $Cs[(CF_3)_2PF_2O]$ (**7**) is stable at room temperature for a month, while $[Me_4N][CF_3PF_3O]$ (**1**) dismutates into $[Me_4N][CF_3PF(O)O]$ (**2**) and $[Me_4N][CF_3PF_5]$ (**3**) above 0 °C.
(© Wiley-VCH Verlag GmbH & Co. KGaA, 69451 Weinheim, Germany, 2007)

## Introduction

The importance of fluorinated compounds is rapidly increasing in many fields of modern agrochemistry, pharmaceutical industry and material sciences.[1] During the past several decades numerous methods were developed for the direct introduction of fluorinated substituents, in particular trifluoromethyl groups, into different types of molecules. Among a wide variety of reagents for $CF_3$ group introduction, commercially available trimethyl(trifluoromethyl)-silane had become the reagent of choice.[2] However, only a few phosphorus-containing electrophiles have been used for nucleophilic trifluoromethylation with $Me_3SiCF_3$.[3]

It has been shown that it is possible to convert $P^V$–F compounds into the corresponding $P^V$–$CF_3$ derivatives by reactions of $Me_3SiCF_3$ in the presence of catalytic amounts of $F^-$ sources.[3] In order to avoid the use of toxic phosphorous oxofluorides as starting materials and taking into account two examples of successful trifluoromethylation of aryl esters of $P^{III}$-acids by $Me_3SiCF_3$[3c] and by Ruppert's method,[4] we investigated the reactions of triphenylphosphate and $Me_3SiCF_3$ in the presence of fluoride sources. It should be noted in advance that the results differ from each other depending on the initiator, $[Me_4N]F$ or CsF, and will therefore be described separately.

[a] Institute of Organic Chemistry, National Academy of Sciences of Ukraine,
5 Murmanskaya St., 02094 Kiev 94, Ukraine
[b] Institute of Bioorganic Chemistry and Petrochemistry, National Academy of Sciences of Ukraine,
1 Murmanskaya St., 02094 Kiev 94, Ukraine
[c] Institut für Anorganische Chemie, Universität zu Köln,
Greinstrasse 6, 50939 Köln, Germany

## Results and Discussion

### Reactions of $(PhO)_3P(O)$ with $Me_3SiCF_3$ and $[Me_4N]F$

The reactions of $(PhO)_3P(O)$ with $Me_3SiCF_3$ and $[Me_4N]F$ yielded complex product mixtures. The composition strongly depended on the stoichiometry of the starting materials, the solvent and the temperature. The conditions for obtaining tetramethylammonium trifluoro(trifluoromethyl)phosphoranolate (**1**) as the major phosphorus-containing compound were 4 equiv. $[Me_4N]F$, 1 equiv. $Me_3SiCF_3$ and 1 equiv. $(PhO)_3P(O)$, with dme as the solvent and a temperature of –40 °C (Scheme 1).

Salt **1** contains a unique anion that represents the stable transition state usually postulated in the course of nucleophilic substitution at a tetrahedral phosphorus atom.[5] Compound **1** is stable for a reasonable time, both in solution and in the solid state at temperatures equal to or below 0 °C. It presents one more example of hypervalent compounds whose stability is significantly increased by the introduction of perfluoroalkyl groups.

The formation of the trifluoro(trifluoromethyl)phosphoranolate anion and its structure were established by NMR spectroscopic and mass spectrometric data. NMR spectra recorded at 20 °C are of first order and imply that the anion appears to be rigid at this temperature (Figure 1, Table 1).

The anion exhibits two signals in the $^{19}F$ NMR spectrum for the fluorine atoms attached to the phosphorus centre with an integrative ratio of 1:2. The low-field doublet of triplets ($\delta$ = –46.9 ppm) corresponds to the fluorine atom in the axial position ($^1J_{F_{ax}-P}$ = 812 Hz, $^2J_{F_{ax}-F_{eq}}$ = 82 Hz),

 © 2007 Wiley-VCH Verlag GmbH & Co. KGaA, Weinheim InterScience 

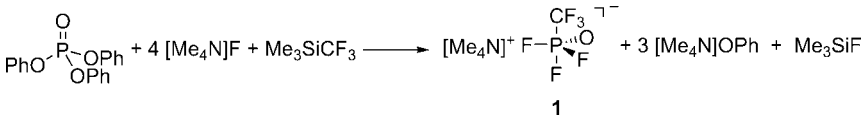


1

Scheme 1.

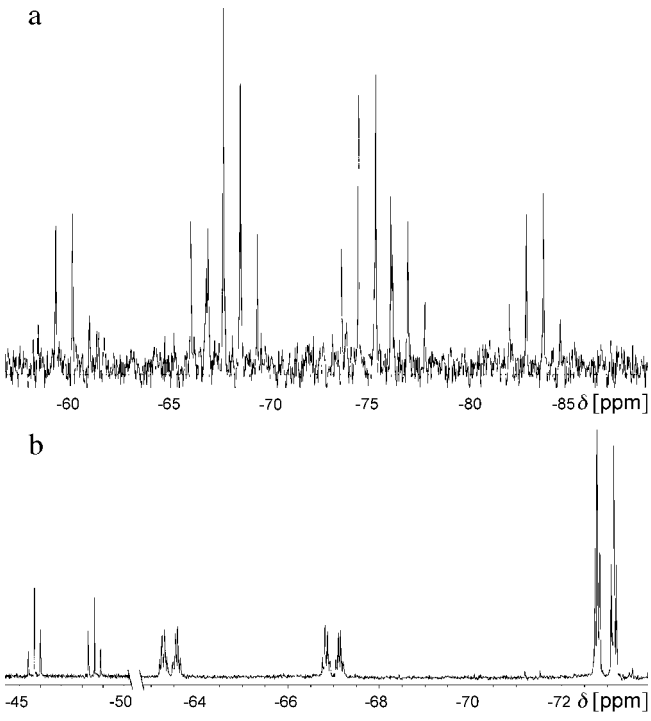


Figure 1. NMR spectra of $[Me_4N][CF_3PF_3O]$ (**1**) recorded in $CD_3CN$: (a) $^{31}P$ spectrum (121.42 MHz) and (b) $^{19}F$ spectrum (282.41 MHz).

and the doublet of doublets of quartets ($\delta$ = –65.2 ppm) is assigned to two equatorial fluorine atoms ($^1J_{F_{eq}-P}$ = 1010 Hz, $^2J_{F_{eq}-F_{ax}}$ = 82 Hz, $^3J_{F_{eq}-CF_3}$ = 15 Hz). The signal of the $CF_3$ group is found at $\delta$ = –73.0 ppm and appears as a doublet of triplets ($^2J_{CF_3-P}$ = 100 Hz, $^3J_{CF_3-F_{eq}}$ = 15 Hz). The chemical shift ($\delta < -70$ ppm) of the $CF_3$ group suggests axial position in comparison with NMR spectroscopic data of related compounds.[7] The triplet of doublets of quartets ($\delta$ = –71.3 ppm) in the $^{31}P$ NMR spectrum falls into the shift range of pentacoordinate phosphorus[7,8] and proves additionally that the anion contains two different types of fluorine atoms and one $CF_3$ group. Thus the anion of salt **1** has the structure of a trigonal bipyramid with one fluorine atom and the trifluoromethyl group in axial positions and two fluorine atoms and the oxygen atom in the equatorial plane. The $^1H$ NMR spectrum shows only the signal of the tetramethylammonium cation at $\delta$ = 2.95 ppm.

Salt **1** undergoes slow dismutation at temperatures above 0 °C, forming stable tetracoordinate and hexacoordinate (compounds **2** and **3**, respectively) phosphorus species (Scheme 2). Therefore, NMR spectra could be run at ambient temperature.

Dismutation of salt **1** presumably proceeds with initial formation of the (trifluoromethyl)phosphonyl difluoride (**A**) by fluoride elimination; **A** reacts with the anion **1** to form the second intermediate, the dimeric anion **B**. The

Table 1. Compilation of $^{19}F$ and $^{31}P$ NMR spectroscopic data of all synthesised compounds.

| | Species (solvent) | $^{31}P$ | $^{19}F$ | | | Coupling constants [Hz] | | | |
|---|---|---|---|---|---|---|---|---|---|
| | | $\delta$ [ppm] | $\delta$ [ppm] | Integral | | $^1J_{P-F}$ | $^2J_{P-CF_3}$ | $^2J_{F-F}$ | $^3J_{F-CF_3}$ |
| **1** | $CF_3PF_3O^-$ ($CD_3CN$) | –71.3 (tdq) | –46.9 (dt) | 1 | $F_{ax}$ | 812 | | 82 | |
| | | | –65.2 (ddq) | 2 | $F_{eq}$ | 1010 | | | 15 |
| | | | –73.0 (dt) | 3 | $CF_3$ | | 100 | | |
| **7** | $(CF_3)_2PF_2O^-$ ($CD_3CN$) | –64.9 (tsept) | –75.0 (dsept) | 1 (2) | $F_{eq}$ | 1080 | | | 16 |
| | | | –74.3 (dt) | 3 (6) | $CF_3$ | | 113 | | |
| **14** | $CF_3PF_2(OPh)O^-$ (dme) | –76.2 (ddq) | –39.0 (dd) | 1 | $F_{ax}$ | 790 | | 74 | |
| | | | –68.9 (ddq) | 1 | $F_{eq}$ | 1004 | | | 14 |
| | | | –72.5 (dd) | 3 | $CF_3$ | | 86 | | |
| **12** | $CF_3P(O)(F)O^-$ ($CD_3CN$) | –8.9 (dq) | –74.3 (dq) | 1 | F | 985 | | | 8 |
| | | | –77.6 (dd) | 3 | $CF_3$ | | 107 | | |
| **2** | $CF_3P(O)(F)O^-$ ($D_2O$) | –6.7 (dq) | –72.4 (dq) | 1 | F | 1020 | | | 12 |
| | | | –73.3 (dd) | 3 | $CF_3$ | | 120 | | |
| **3, 13** | $CF_3PF_5^-$[a,b] ($D_2O$) | –147.5 (quintdq) | –72.9 (dm) | 1 | $F_{ax}$ | 720 | | 42 | 2.5 |
| | | | –73.9 (dm) | 4 | $F_{eq}$ | 819 | | | 13 |
| | | | –69.5 (dquintd) | 3 | $CF_3$ | | 140 | | |
| **8** | $(CF_3)_2P(O)(OH)$[c] ($CD_3CN$) | –5.8 (dsept) | –73.3 (d) | | | | 96 | | |
| **10** | $CF_3P(O)(OH)_2$[c,d] | | | | | | | | |
| | ([D6]dmso) | –6.0 (q) | –71.8 (d) | | | | 92 | | |
| | ($D_2O$) | –3.8 (q) | –74.4 (d) | | | | 107 | | |
| **4** | $F_4PO^-$ ([D6]dmso) | –75.1 (quint) | –54.2 (d) | | | 827 | | | |
| **5** | $F_2P(O)O^-$ ([D6]dmso) | –14.1 (t) | –76.2 (d) | | | 954 | | | |

[a] The spectrum is of higher order ($A_3B_4CX$ spin system). [b] $^{13}C\{^{19}F\}$ NMR ($D_2O$): $\delta$ = 126.2 (d, $^1J_{P-C}$ = 422 Hz) ppm. [c] Cf. ref.[6] [d] $^{13}C\{^{19}F\}$ NMR ($D_2O$): $\delta$ = 122.3 (d, $^1J_{P-C}$ = 248 Hz) ppm.

 © 2007 Wiley-VCH Verlag GmbH & Co. KGaA, Weinheim 

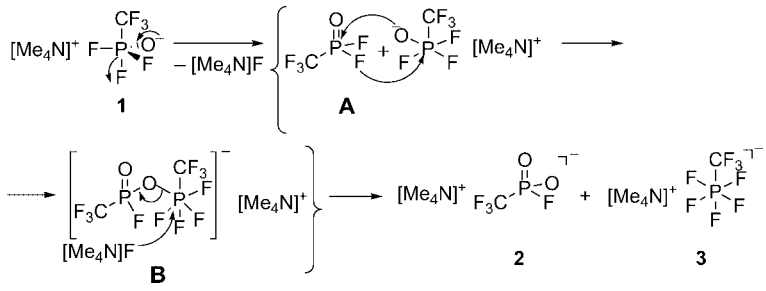

Scheme 2.

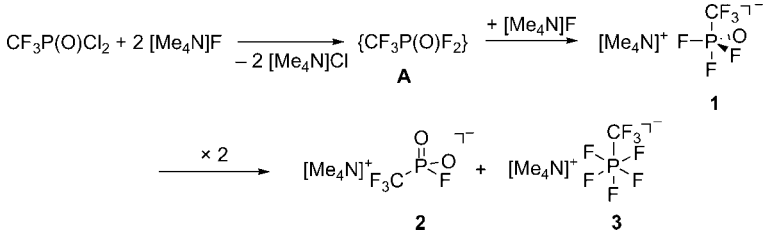

Scheme 3.

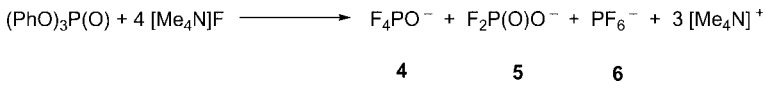

Scheme 4.

fluoride anion liberated in the first reaction step then attacks the hexacoordinate phosphorus atom of intermediate **B** to give salts **2** and **3** as the final reaction products. Both salts were separated by fractional crystallisation and characterised by NMR spectroscopic methods and elemental analyses.

It is explicitly noteworthy that the result of the reaction between $(PhO)_3P(O)$, $Me_3SiCF_3$ and $[Me_4N]F$ provides a new method to obtain two important perfluoroalkyl-containing phosphorus anions, that is, fluoro(trifluoromethyl)-phosphonate (in salt **2**) and hard-to-prepare $\lambda^6$-pentafluoro(trifluoromethyl)phosphate (in salt **3**).[9] The doubtless advantages of this method are the good availability of the starting materials, the mild reaction conditions and the high yields of the target products.

An equimolar mixture of salts **2** and **3** was also obtained by fluorination of (trifluoromethyl)phosphonyl dichloride with $[Me_4N]F$ (Scheme 3).

However, in this case we were unable to isolate salt **1**. It was only detected in the NMR spectra of the mixture together with salts **2** and **3**. This may be explained by the initial formation of (trifluoromethyl)phosphonyl difluoride (**A**) which adds $[Me_4N]F$ to form salt **1**. Similarly the dismutation process starts as outlined earlier, analogous to the elusive tetrafluorophosphate dismutation presented by Christe et al.[8] The latter anion was obtained by $F^-$ addition to $P(O)F_3$, and its composition was elucidated by NMR experiments performed at –140 °C. In one of our experiments, triphenylphosphate was treated with 4 equiv. $[Me_4N]F$ in dme at –40 °C. All phosphorus-containing products were insoluble in dme at this temperature as well as at 20 °C. The $^{19}F$- and $^{31}P$ NMR spectra analysis ([$D_6$]-dmso, room temperature) showed that the reaction mixture contained tetrafluorophosphoranolate (**4**) as the major product and its dismutation products **5** and **6** as minor ones (Scheme 4).

NMR investigations of 1:1 mixtures of $(PhO)_3P(O)$ and $[Me_4N]F$ at –70 °C gave no evidence for the key ion $[(PhO)_3PFO]^-$ but allowed the detection of $(PhO)_2P(O)F$ {$\delta_F$ (dme/[$D_8$]thf, v/v = 50:50, –40 °C) = –78.7 ppm, $^1J_{F–P}$ = 996 Hz; $\delta_P$ (dme/[$D_8$]thf, v/v = 50:50, –40 °C) = –17.0 ppm, $^1J_{F–P}$ = 996 Hz}[10] and its consecutive products **5**, $[(PhO)_2P(O)O]^-$ and $[PhOPF(O)O]^-$.[11,12]

The characteristic NMR spectroscopic data for the compounds **4**, **5** (Table 1) and **6** are in full agreement with the data given by Christe et al.[8] The main advantage of the $[F_4PO]^-$ anion synthesis starting from triphenylphosphate is the relative stability of this anion in the solid state as well as in dmso solution at 20 °C. This result supports the suggestion that the presence of excess $P(O)F_3$ used in the known procedure significantly accelerates the dismutation process.[8]

### Reactions of $(PhO)_3P(O)$ with $Me_3SiCF_3$ and CsF

To our great surprise we were unable to obtain the Cs analogue of salt **1** under the same reaction conditions using CsF instead of $[Me_4N]F$. The product of this reaction was the pentacoordinate phosphorus anion difluorobis(trifluoromethyl)phosphoranolate, $[(CF_3)_2PF_2O]^-$, while reasonable

 © 2007 Wiley-VCH Verlag GmbH & Co. KGaA, Weinheim 

amounts of the starting material triphenylphosphate remained unchanged. Variation of the stoichiometry to 3 equiv. CsF, 2 equiv. $Me_3SiCF_3$ and 1 equiv. $(PhO)_3P(O)$ led to a nearly pure solution of cesium difluorobis(trifluoromethyl)phosphoranolate (**7**) (Scheme 5).

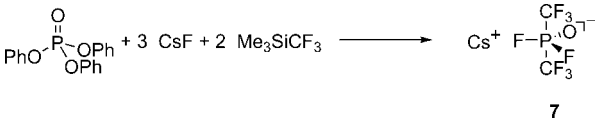


Scheme 5.

By comparison to the known structure[13] and NMR spectroscopic data[7] of the closely related $(CF_3)_2PF_3$ and the easily interpretable $^{19}F$- and $^{31}P$ NMR spectra of salt **7** on a first order basis (Figure 2, Table 1), we propose both $CF_3$ groups reside in axial positions, while the two fluorine atoms and the oxygen atom are located in the equatorial plane of a trigonal bipyramid.

The triplet of septets in the range of pentacoordinate phosphorus ($\delta$ = –64.9 ppm) in the $^{31}P$ NMR spectrum gives evidence that anion **7** contains two magnetically equivalent fluorine atoms and two equivalent $CF_3$ groups. The $^{19}F$ NMR spectrum exhibits the signal of two fluorine atoms bonded to the phosphorus atom as a doublet of septets centred at $\delta$ = –75.0 ppm. Correspondingly, the signals of the trifluoromethyl groups are split into doublets of triplets centred at $\delta$ = –74.3 ppm with $^2J_{CF_3-P}$ = 113 Hz and $^3J_{CF_3-F_{eq}}$ = 16 Hz. The high-field shifts of both signals, compared with values found for compounds with opposite arrangement of the $CF_3$ groups and the fluorine atoms,[7] as well as the value of $^1J_{F-P}$ = 1080 Hz, indicate that the fluorine atoms are located in the equatorial plane of the trigonal bipyramid.

Salt **7** is stable in dme or $CH_3CN$ solutions, as well as in the solid state for months at 20 °C, but it is extremely sensitive to moisture. Also, storing the solid especially in glassware causes decomposition into bis(trifluoromethyl)phosphinic (**8**)[6,14] and (trifluoromethyl)phosphonic (**10**)[6,15] acids (Scheme 6).

The degradation of **7** can be explained on the assumption of the intermediate formation of bis(trifluoromethyl)phosphinyl fluoride (**C**) which is hydrolysed either by replacement of the fluorine atom or the trifluoromethyl group by hydroxy groups. In the latter case, NMR spectroscopic evidence was found for fluoro(trifluoromethyl)phosphonic acid (**9**) [$\delta_F$ ($CD_3CN$) = –71.8 ppm (d, $^1J_{F-P}$ = 980 Hz), –72.7 ppm (d, $^2J_{F-P}$ = 102 Hz); $\delta_P$ ($CD_3CN$) = –8.8 ppm (dq, $^1J_{F-P}$ = 980 Hz, $^2J_{F-P}$ = 102 Hz)] which is rapidly hydrolysed to acid **10**.

In order to obtain the Cs analogue of salt **1**, we performed the reaction of (trifluoromethyl)phosphonyl dichloride with CsF (Scheme 7).

The instability of **11** prevented its detection in NMR spectra of the reaction mixture. Only an equimolar mixture of the dismutation products, fluoro(trifluoromethyl)phosphonate **12** and $\lambda^6$-pentafluoro(trifluoromethyl)phosphate **13** was obtained. The salts were separated by fractional crystallisation, and both compounds were characterised. It is noteworthy that salts with the anion $CF_3PF_5^-$ were reported at the end of the 1960s,[9] but the NMR spectroscopic characterisation had remained insufficient until now. The $^{19}F$- and $^{31}P$ NMR spectroscopic data for salt **13** are shown in Figure 3 (cf. Table 1).

The $^{19}F$ NMR spectrum of the Cs salt **13** is of higher order; the calculated spectrum[16] for an $A_3B_4CX$ spin system matched well with the measured spectrum. While the

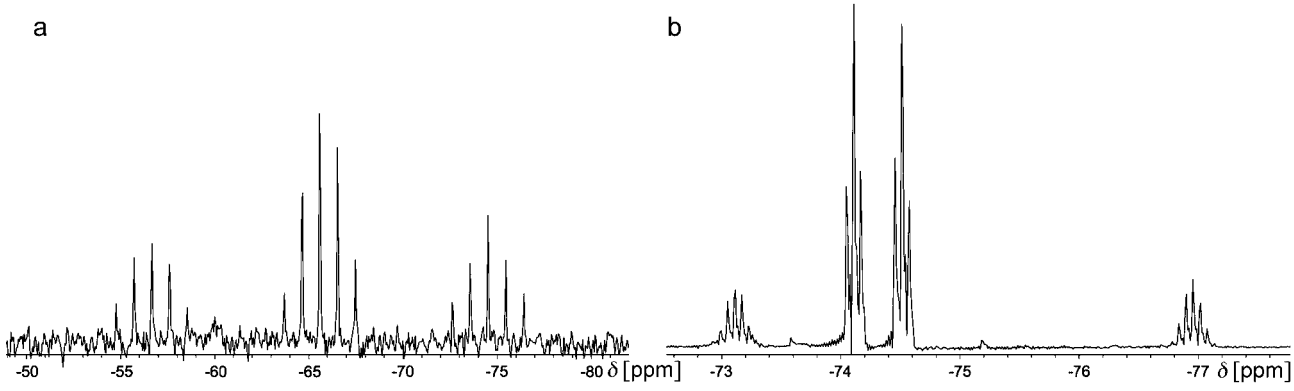


Figure 2. NMR spectra of $Cs[(CF_3)_2PF_2O]$ (**7**) recorded in $CD_3CN$ at 20 °C: (a) $^{31}P$ spectrum (121.42 MHz) and (b) $^{19}F$ spectrum (282.41 MHz).

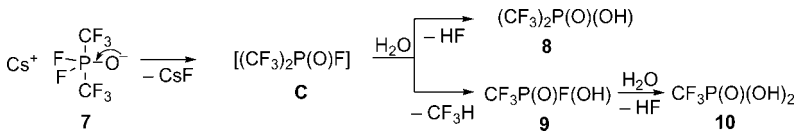


Scheme 6.

 © 2007 Wiley-VCH Verlag GmbH & Co. KGaA, Weinheim 

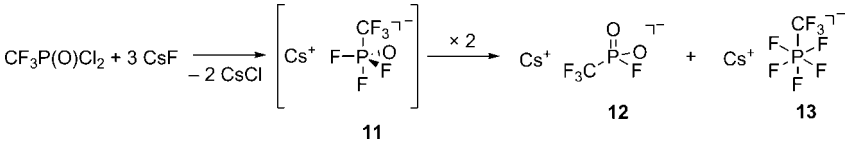


Scheme 7.

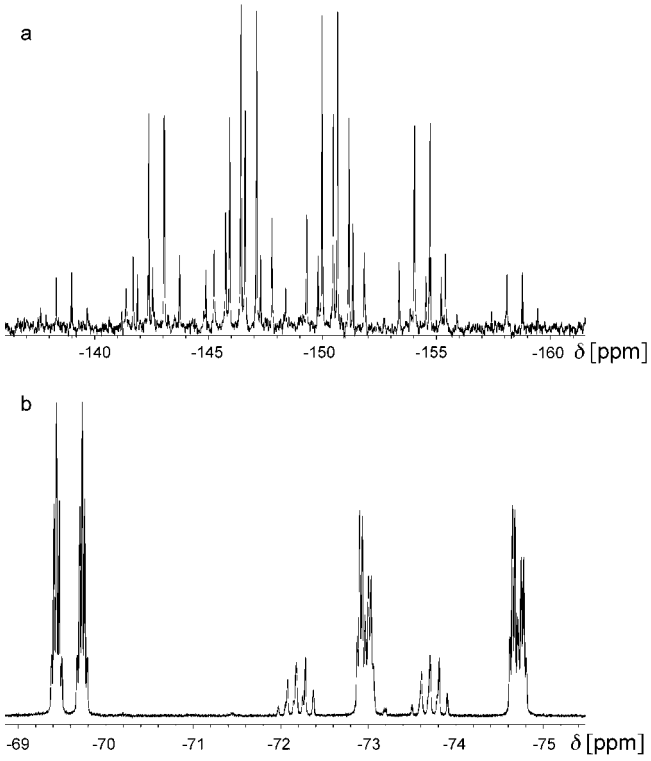


Figure 3. NMR spectra of $Cs[CF_3PF_5]$ (**13**) recorded in $D_2O$ at 20 °C: (a) $^{31}P$ spectrum (202.45 MHz) and (b) $^{19}F$ spectrum (470.54 MHz).

signals for the fluorine atoms directly bonded to phosphorus appear as doublets of complex multiplets ($\delta_{F_{ax}}$ = –72.9 ppm, $\delta_{F_{eq}}$ = –73.9 ppm), the signal of the $CF_3$ group ($\delta$ = –69.5 ppm) can be interpreted as a "first order" doublet ($^2J_{CF_3-P}$ = 140 Hz) of quintets ($^3J_{CF_3-F_{eq}}$ = 13 Hz) of doublets ($^3J_{CF_3-F_{ax}}$ = 2.5 Hz). The doublet of quintets of quartets in the $^{31}P$ NMR spectrum unambiguously confirms the predicted octahedral structure of the anion.

## Conclusions

Some general conclusions can be made thus far. Tetracoordinate triphenylphosphate is converted into the highly fluorinated pentacoordinate phosphorus derivatives **1** or **7** in the reaction with $Me_3SiCF_3$ and sources of fluoride. We assume that the nucleophilic substitution at the tetrahedral phosphorus atom follows the addition-elimination process[5] and, as far as $F^-$ is in excess relative to the second nucleophile "$CF_3^-$", the first step of the reaction is the addition of $F^-$ to the P=O bond of triphenylphosphate to give intermediate **D** (Scheme 8) followed by spontaneous $PhO^-$ elimination to give $(PhO)_2P(O)F$.[10] The ease of adding fluoride to tris(pentafluoroethyl)phosphane oxide[17] and phosphoryl trifluoride[8] further supports this assumption. Upon the substitution of the next PhO group, the highly reactive "$CF_3^-$" nucleophile can compete with the fluoride anion, as is shown in the proposed reaction mechanism (Scheme 8).

One of the facts that supports this scheme is that the intermediate of type **G** (mixed with salt **1**) was observed in the NMR spectra of the reaction mixture with the reagent ratio $(PhO)_3P(O)/Me_3SiCF_3/[Me_4N]F$ = 1:2:1. This intermediate is tetramethylammonium phenyl difluoro(trifluoromethyl)phosphonate (**14**) (Figure 4).

The NMR spectroscopic data (Table 1) allow us to propose the mentioned structure of this unstable anion.

We have characterised three compounds among the possible final structures of type **H**, namely the tetramethylammonium salt of the tetrafluorophosphoranolate ion (**4**), salt **1** with one trifluoromethyl group and salt **7** with two trifluoromethyl groups attached to the phosphorus atom. The stability of anions of type **H** increases significantly in the series $POF_4^- < CF_3POF_3^- < (CF_3)_2POF_2^-$, but their solubility in organic solvents changes in the reverse order. The solvent plays a key role in the investigated reactions; dme is the best choice allowing selective reactions, whereas mix-

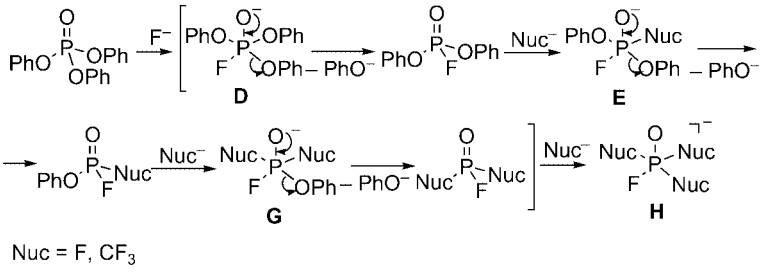


Scheme 8.

 © 2007 Wiley-VCH Verlag GmbH & Co. KGaA, Weinheim 

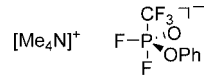

14

Figure 4. Tetramethylammonium phenyl difluoro(trifluoromethyl)-phosphonate (**14**).

tures are formed in thf, and no reaction is observed in ether or propionitrile. The distinct difference in the results depending on whether $[Me_4N]F$ or CsF is used as a fluoride source is probably a result of their different solubility in dme. The less soluble CsF provides a lower concentration of fluoride in solution, and consequently the possibility of the substrate reacting with the competitive nucleophile "$CF_3^-$" is favoured. The result is the formation of salt **7** containing two trifluoromethyl groups. It is noteworthy that we have never observed an anion with three $CF_3$ groups bonded to the phosphorus atom even when using a high excess of trimethyl(trifluoromethyl)silane relative to the fluoride source.

## Experimental Section

**General:** All reactions were carried out under argon, using Schlenk type glassware with rigorous exclusion of traces of moisture and air. The solvents were purified by standard methods and were condensed in vacuo prior to use. $Me_3SiCF_3$ was purchased from ABCR. $[Me_4N]F$[18] and $CF_3P(O)Cl_2$[19] were synthesised according to literature procedures. $[Me_4N]F$ and CsF were carefully dried in vacuo directly before use. Room temp. $^1$H-, $^{19}$F-, $^{31}$P- and $^{13}$C NMR spectra were recorded with either a Varian VXR-300 or a Bruker Avance II 300 spectrometer and in one case (salt **13**) with a Bruker Avance DRX 500 spectrometer. Low-temperature NMR experiments were performed with a Bruker AC 200 spectrometer. Chemical shifts are given in ppm relative to $Me_4Si$ as internal and $CCl_3F$ and 85% $H_3PO_4$ as external standards. The NMR spectroscopic data are compiled in Table 1. Negative ESI mass spectra were recorded with a Finnigan MAT 900 apparatus with a flow rate of 2 μL/min. Intensities are referenced to the most intense peak of a group.

**Tetramethylammonium Trifluoro(trifluoromethyl)phosphoranolate (1):** To a solution of triphenylphosphate (0.60 g, 1.84 mmol) and trimethyl(trifluoromethyl)silane (0.32 g, 2.25 mmol) in dimethoxyethane (dme) (10 mL) at –40 °C was added $[Me_4N]F$ (0.69 g, 7.42 mmol) in small portions over a period of 15 min, and the resulting mixture was stirred for 2 h at this temperature and was then warmed slowly (≈ 4 h) to 0 °C. Stirring was continued at this temperature for 30 min, and the white precipitate was immediately filtered. The solvent was removed in vacuo, and the residue was suspended in diethyl ether (≈ 5 mL) at 0 °C, filtered and dried in vacuo at this temperature to give salt **1**. Yield: 0.38 g (82%). $^1$H NMR ($CD_3CN$): $\delta$ = 2.95 (s, $NCH_3$) ppm. Negative ESI-MS (MeCN): *m*/*z* (%) = 151 (20) $[CF_3(F)P(O)O]^-$, 173 (100) $[CF_3PF_3O]^-$, 223 (68) $[(CF_3)_2PF_2O]^-$, 225 (45) $[CF_3P(O)(OPh)O]^-$. *Note*: Care has to be taken that the operations are performed as quickly as possible to avoid decomposition.

**The Dismutation Reaction of Compound 1:** The solution of **1** (0.38 g, 1.54 mmol) in MeCN (10 mL) was kept at room temp. until $^{31}$P NMR spectra showed complete disappearance of a multiplet at $\delta$ = –71 ppm (≈ 8 h). The solvent was removed in vacuo, and the residue was extracted with hot dme (3 × 10 mL). The solvent was reduced to about 10 mL. After storage of the resultant solution at –17 °C overnight, colourless crystals unsuitable for XRD measurements of **2** were obtained. Yield: 0.13 g (78%). M.p. 110–113 °C (dec.). $^1$H NMR ($D_2O$): $\delta$ = 2.93 (s, $NCH_3$) ppm. $C_5H_{12}F_4NO_2P$ (225.15): calcd. C 26.67, H 5.37, N 6.22; found C 26.35, H 5.72, N 6.13. The residue after extraction was recrystallised from MeCN to give salt **3**. Yield: 0.18 g (86%). M.p. 263–266 °C (dec.). $^1$H NMR ($D_2O$): $\delta$ = 2.89 (s, $NCH_3$) ppm. $C_5H_{12}F_8NP$ (269.15): calcd. C 22.31, H 4.49, N 5.20; found C 22.15, H 4.53, N 5.13.

**Fluorination of (Trifluoromethyl)phosphonyl Dichloride with Tetramethylammonium Fluoride:** To a solution of $CF_3P(O)Cl_2$ (0.50 g, 2.67 mmol) in dme (10 mL) at –40 °C was added $[Me_4N]F$ (0.77 g, 8.27 mmol) in small portions over a period of 15 min. The resulting mixture was stirred for 2 h at this temperature and was then warmed slowly (≈ 4 h) to 0 °C. Stirring was continued at this temperature for 30 min, and the precipitate was filtered off. $^{19}$F- and $^{31}$P NMR spectra of the resultant filtrate showed the presence of compounds **1**, **2** and **3** in a ratio of approximately 2:4:3. The solution was kept at room temp. overnight to complete the dismutation of compound **1**. The solvent was removed in vacuo. The reaction mixture was worked up in the same manner as described earlier. After purification, compounds **2** and **3** were obtained in yields of 72% (0.22 g) and 53% (0.19 g), respectively. Some part of the less soluble salt **3** precipitated together with $[Me_4N]Cl$. Extraction of the primary precipitate with hot MeCN yielded more compound **3** (0.10 g) giving a total yield of compound **3** of 0.29 g (81%).

**Cesium Difluorobis(trifluoromethyl)phosphoranolate (7):** To a solution of triphenylphosphate (0.60 g, 1.84 mmol) and trimethyl(trifluoromethyl)silane (0.55 g, 3.87 mmol) in dme (10 mL) at –40 °C was added CsF (0.84 g, 5.53 mmol) in small portions over a period of 15 min. The resulting mixture was stirred for 2 h at this temperature and was then warmed slowly to room temp. Stirring was continued overnight, the precipitated solid was filtered off, and the solvent was removed in vacuo. The residue was washed with benzene (3 × 5 mL), filtered and dried in vacuo to give salt **7**. Yield: 0.31 g (48%). M.p. 73–75 °C (dec.). Because of the extreme moisture sensitivity of compound **7**, we were unable to obtain satisfactory elemental analytical data. Negative ESI-MS (MeCN): *m*/*z* (%) = 223 (100) $[(CF_3)_2PF_2O]^-$.

**Fluorination of (Trifluoromethyl)phosphonyl Dichloride with Cesium Fluoride:** To a solution of $CF_3P(O)Cl_2$ (0.40 g, 2.14 mmol) in dme (10 mL) at –40 °C was added CsF (0.99 g, 6.52 mmol) in small portions over a period of 15 min. The mixture was stirred for 2 h at this temperature and was then warmed to room temp. Stirring was continued overnight, the solvent was removed in vacuo, and the residue was extracted with hot MeCN (50 mL). After storing the solution at –17 °C, the precipitate was filtered off and recrystallised from a 10:1 (v/v) dioxane/water mixture to yield the pure salt **13** as colourless crystals unsuitable for XRD measurements. Yield: 0.31 g (87%). $CCsF_8P$ (327.89): calcd. C 3.66, P 9.45; found C 3.57, P. 9.52. $^{19}$F- and $^{31}$P NMR spectra of the resultant filtrate showed the presence of salt **12** (Table 1) as the major product (>70%). This compound was not fully characterised because of its high sensitivity to moisture.

## Acknowledgments

Generous financial support of this work by the Deutsche Forschungsgemeinschaft is gratefully acknowledged (436 UKR 113/

 © 2007 Wiley-VCH Verlag GmbH & Co. KGaA, Weinheim 

26). We are indebted to Dr. Mathias Schäfer (Institut für Organische Chemie, Universität zu Köln) for recording the ESI mass spectra.

[1] a) R. Filler, Y. Kobayashi, L. M. Yagupolskii (Eds.), *Organofluorine Compounds in Medicinal Chemistry and Biomedical Applications*, Elsevier, Amsterdam, **1993**; b) R. E. Banks, B. E. Smart, J. C. Tatlow (Eds.), *Organofluorine Chemistry – Principles and Commercial Applications*, Plenum Press, New York, **1994**.

[2] a) G. K. S. Prakash, A. K. Yudin, *Chem. Rev.* **1997**, *97*, 756–786; b) G. G. Furin, *Russ. J. Org. Chem.* **1997**, *33*, 1209–1242; c) R. P. Singh, J. M. Shreeve, *Tetrahedron* **2000**, *56*, 7613–7632; d) E. Abele, E. Lukevics, *Main Group Met. Chem.* **2001**, *24*, 315–350.

[3] a) F. M. Semchenko, O. G. Eremin, B. I. Martynov, *Zh. Obshch. Khim.* **1992**, *62*, 473–474; b) R. P. Singh, A. Vij, R. L. Kirchmeier, J. M. Shreeve, *Inorg. Chem.* **2000**, *39*, 375–377; c) I. Tworowska, W. Dabkowski, J. Michalski, *Angew. Chem. Int. Ed.* **2001**, *40*, 2898–2900.

[4] A. A. Kolomeitsev, M. Görg, U. Dieckbreder, E. Lork, G. V. Röschenthaler, *Phosphorus Sulfur Silicon Relat. Elem.* **1996**, *109–110*, 597–600.

[5] a) K. C. Kumara Swamy, S. S. Krishnamurthy, *Inorg. Chem.* **1986**, *25*, 920–928; b) R. J. P. Corriu, J.-P. Dutheil, G. F. Lanneau, *J. Am. Chem. Soc.* **1984**, *106*, 1060–1065.

[6] T. Mahmood, J. M. Shreeve, *Inorg. Chem.* **1986**, *25*, 3128–3131.

[7] R. Eujen, R. Haiges, *Z. Naturforsch., Teil B* **1998**, *53*, 1455–1460.

[8] K. O. Christe, D. A. Dixon, G. I. Schrobilgen, W. W. Wilson, *J. Am. Chem. Soc.* **1997**, *119*, 3918–3928.

[9] a) S. S. Chan, C. J. Willis, *Can. J. Chem.* **1968**, *46*, 1237–1248; b) J. Jander, D. Börner, U. Engelhardt, *Justus Liebigs Ann. Chem.* **1969**, *726*, 19–24.

[10] W. Dabkowski, J. Michalski, *J. Chem. Soc., Chem. Commun.* **1987**, 755–756.

[11] C. A. Bunton, H. J. Foroudian, N. D. Gilitt, C. R. Whiddon, *Can. J. Chem.* **1998**, *76*, 946–954.

[12] G. S. Reddy, R. Schmutzler, *Z. Naturforsch., Teil B* **1970**, *25*, 1199–1214.

[13] H. Oberhammer, J. Grobe, D. Le Van, *Inorg. Chem.* **1982**, *21*, 275–281.

[14] a) H. J. Emeleus, R. N. Haszeldine, R. C. Paul, *J. Chem. Soc.* **1955**, 563–574; b) A. A. Pinkerton, R. G. Cavell, *Inorg. Chem.* **1971**, *10*, 2720–2723.

[15] F. W. Bennet, H. J. Emeleus, R. N. Haszeldine, *J. Chem. Soc.* **1954**, 3598–3603.

[16] P. H. M Budzelaar, *gNMR Version 4.1*, Cherwell Scientific, Oxford, UK, **1998**.

[17] N. V. Pavlenko, L. M. Yagupolskii, *Zh. Obshch. Khim.* **1989**, *59*, 528–534.

[18] A. A. Kolomeitsev, F. U. Seifert, G. V. Röschenthaler, *J. Fluorine Chem.* **1995**, *71*, 47–49.

[19] J. E. Griffiths, *Spectrochim. Acta* **1968**, *24 A*, 303–305.

Received: October 16, 2006
Published Online: March 1, 2007

 © 2007 Wiley-VCH Verlag GmbH & Co. KGaA, Weinheim 

DOI: 10.1002/ejic.200601233

# Ruthenium Complex Fragments as Constituents of Trinuclear Photoactive Supramolecular Assemblies Based on Hydrogen Bond Association

**Kathi Halbauer,[a] Angela Göbel,[a] Anke Sterzik,[a] Helmar Görls,[a] Sven Rau,[a] and Wolfgang Imhof*[a]**

**Keywords:** Supramolecular Photochemistry / Bibenzimidazole ligands / Hydrogen bonds / Ruthenium

The reaction of the octahedral complexes *cis*- or *trans*-$[Ru(C{\equiv}N\text{-}tBu)_4(CN)_2]$, ($Ru(CN)_2$), with the photochemically active [bis(bipyridyl)bibenzimidazole-ruthenium(II)], ($RubiH_2$), component via hydrogen bond association results in the formation of supramolecular aggregates with modified photophysical properties. The first structural characterization of a supramolecular adduct is reported, in which the N–H functions of the ruthenium bound bibenzimidazole ligand via hydrogen bonds serve as an interface directly toward a cyanide ligand acting as a bridge to another transition metal. In addition, the maximum stoichiometry of the supramolecular associates is estimated by NMR titration experiments and association constants of the hydrogen bonded adducts are determined by the decay of the emission intensity during the titration experiments.

(© Wiley-VCH Verlag GmbH & Co. KGaA, 69451 Weinheim, Germany, 2007)

## Introduction

One of the most challenging goals in chemistry is the conversion of sunlight into electrical, chemical or even mechanical energy. In order to achieve this goal a detailed understanding of suitable chromophore–quencher complexes is a crucial prerequisite for the construction of e.g. photovoltaic cells. Chromophore systems based on transition metals have been widely investigated for polypyridyl complexes[1] or on the basis of porphyrin complexes[2] closely resembling the natural chlorophyll chromophore used in photosynthetic organisms. In general, these efforts may be subdivided into systems in which the chromophore and the quencher are linked via strong interactions like covalent bonds or coordinative bonds on one side and aggregates that are interconnected via weak interactions like hydrogen bonds, hydrophobic interactions or π-stacking effects on the other side.[3]

The construction of multicentred supramolecular assemblies using complementary hydrogen-bond donor and acceptor sites is very appealing due to its synthetic advantages and intrinsic modular approach. In most examples that have been described in the literature up to now metal hybrid assemblies or organic assemblies have been investigated and hydrogen bonds between carboxylic acids (which by definition are self-complementary), nucleobases or protonated cyclam units were used to construct supramolecular assemblies of two different coordination complexes.[3] Campagna as well as Ward and co-workers have shown that $Ru^{II}$ complexes may act as quencher components if they are assembled to suitable chromophore systems via hydrogen bonds realized by cyanide ligands.[3a,3c] Nevertheless, it has to be pointed out that the syntheses of bipy, terpy or porphyrin ligands with pendant nucleobase or cyclam units still are complex multi-step procedures and the distance between the photochemically active metal center and the additional coordination complex subunit is quite large.

We herein report the synthesis and characterisation of supramolecular assemblies between different $Ru^{II}$ complexes where it is possible to control not only the photophysical properties of the chromophore but also the geometry and nuclearity of the aggregates formed. The control over the geometry can be exercised by variation of the H-bond acceptor utilised whereas the nuclearity can be influenced by simple stoichiometry.

## Results and Discussion

Recently, some of us reported the synthesis of complexes of the type $[Ru(bipy^*)_2(biH_2)]^{2+}$ ($biH_2$ = 5,5′,6,6′-tetramethyl-2,2′-bibenzimidazole, bipy* = 4,4′-di-*tert*-butyl-2,2′-bipyridine) which show photophysical properties that are comparable to those of the well-known $[Ru(bipy)_3]^{2+}$ compounds.[4] One of the most important features of the $biH_2$ ligand is the fact that the N–H functions are very efficient hydrogen-bond donor sites leading to the coordination of anions or solvent molecules in almost all structurally

[a] Friedrich-Schiller-Universität, Institute of Inorganic and Analytical Chemistry
August-Bebel-Straße 2, 07743 Jena, Germany
Fax: +49-3641-948102
E-mail: Wolfgang.Imhof@uni-jena.de

Supporting information for this article is available on the WWW under http://www.eurjic.org or from the author.

 © 2007 Wiley-VCH Verlag GmbH & Co. KGaA, Weinheim 

characterized derivatives.[5] It has already been demonstrated that a hydrogen-bonded adduct of this ruthenium complex together with an osmium compound containing a carboxylated bipy ligand exhibits an effective energy transfer from Ru to Os upon irradiation.[3c] So we decided to combine a $[Ru(bipy^*)_2(biH_2)]^{2+}$ complex with compounds of the type $[Ru(C{\equiv}N\text{-}t\text{Bu})_4(CN)_2]$, which are easily accessible as a 1:1 mixture of the *cis*- and *trans*-isomers from the reaction of $Ru_3(CO)_{12}$ with *tert*-butyl isocyanide in the presence of of carbon monoxide ($p$ = 10 atm).[6]

Scheme 1 shows two possible 2:1 adducts of $[Ru(bipy^*)_2(biH_2)]^{2+}$ and $[Ru(C{\equiv}N\text{-}t\text{Bu})_4(CN)_2]$ in *cis*- and *trans*-conformation. The assumption of 2:1 adducts under stoichiometric conditions seems to be reasonable from a thermodynamic point of view because it provides the formation of a maximum number of hydrogen bonds. This assumption is additionally confirmed by NMR titration experiments which show that the signal representing the protons in 4,4′-position of the $biH_2$ ligand is significantly influenced by the stepwise addition of *cis*-$[Ru(C{\equiv}N\text{-}t\text{Bu})_4(CN)_2]$ (Figure 1). Compared to solutions of pure $RubiH_2$ the addition of *cis*-$Ru(CN)_2$ leads to a downfield shift of the corresponding signal. The effect is much less pronounced if the *trans*-isomer of the cyano complex is used presumably due to less steric interaction with the protons in 4,4′-position of the bibenzimidazole ligand in this case. In Figure 2 the product ($m_f \times \Delta\delta$) is plotted against the molar fraction itself. It can be seen that up to a $m_f$ value of app. 0.66 representing a ratio $Ru(CN)_2$:$RubiH_2$ = 2:1 an increase of ($m_f \times \Delta\delta$) is observed whereas for higher $m_f$ values a decrease of ($m_f \times \Delta\delta$) becomes evident. From this behaviour we can conclude that the maximum stoichiometry of hydrogen bonded associates consisting of $Ru(CN)_2$ and $RubiH_2$ in solution is 2:1.[7] Similar NMR titration experiments have also been used to determine the association constants of hydrogen bonded adducts.[3e,8] Nevertheless, this approach is only successful for associates of a 1:1 composition meaning that for the estimation of association constants of the aggregates that are present in our solutions we had to employ another method.

The fact that hydrogen bonds are readily formed in solution and that the so formed associates are quite stable is verified by the IR spectra of the corresponding mixtures which show a shift in the stretching frequencies of the cyanide and isocyanide ligands (cf. Experimental Part). For all molar fractions higher than 0.33 ($Ru(CN)_2$:$RubiH_2$ = 1:2) no bands corresponding to the free cyano complexes are visible in the IR spectra. So e.g. for mixtures of *trans*-$[Ru(C{\equiv}N\text{-}t\text{Bu})_4(CN)_2]$ and $[Ru(bipy^*)_2(biH_2)]^{2+}$ in a 1:2 ratio, the corresponding bands are observed at 2164 and 2101 $cm^{-1}$ compared to 2150 and 2108 $cm^{-1}$ for pure *trans*-$[Ru(C{\equiv}N\text{-}t\text{Bu})_4(CN)_2]$.[6] In the ESI-MS spectra of both compounds, peaks corresponding to the cationic 1:1 supramolecular assemblies $\{[Ru(bipy^*)_2(biH_2)][Ru(C{\equiv}N\text{-}t\text{Bu})_4(CN)_2]\}(PF_6)$ are observed (cf. Experimental Part).

Recrystallization of a mixture of $[Ru(bipy^*)_2(biH_2)](PF_6)_2$ and *trans*-$[Ru(C{\equiv}N\text{-}t\text{Bu})_4(CN)_2]$ in a 2:1 ratio from dichloromethane yielded crystals suitable for X-ray diffraction.[9] The supramolecular structure of the hydrogen-

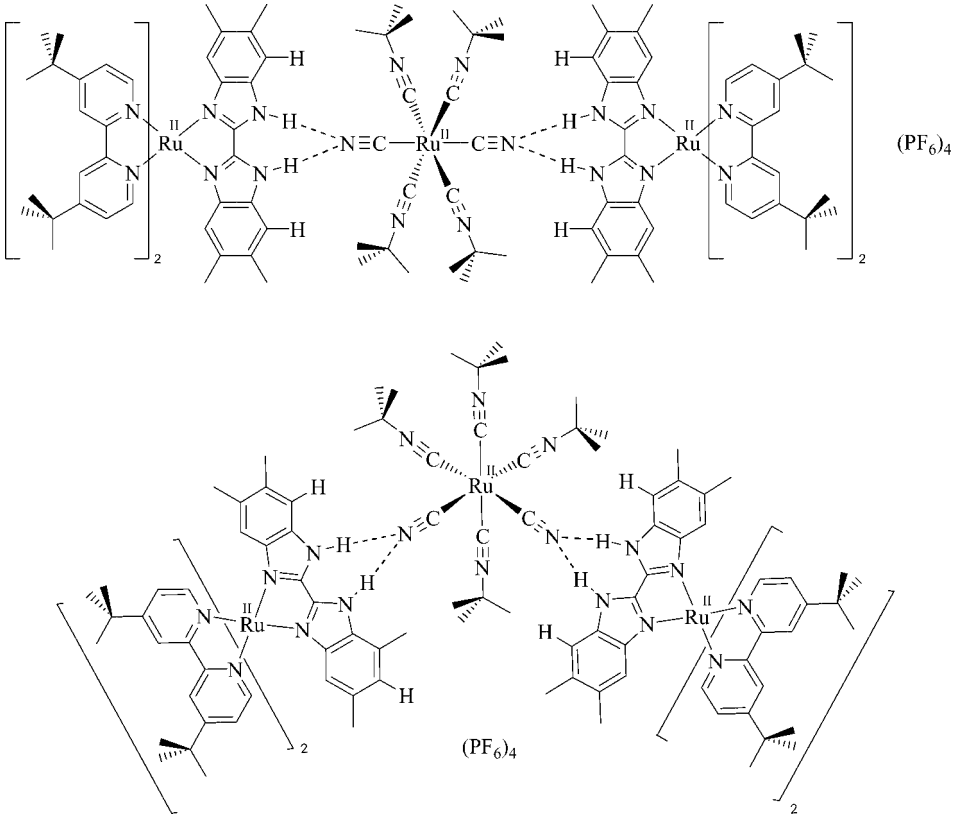


Scheme 1. Hydrogen bonded 2:1 adducts produced by the interaction of N–H functions and cyanide ligands.

 © 2007 Wiley-VCH Verlag GmbH & Co. KGaA, Weinheim 

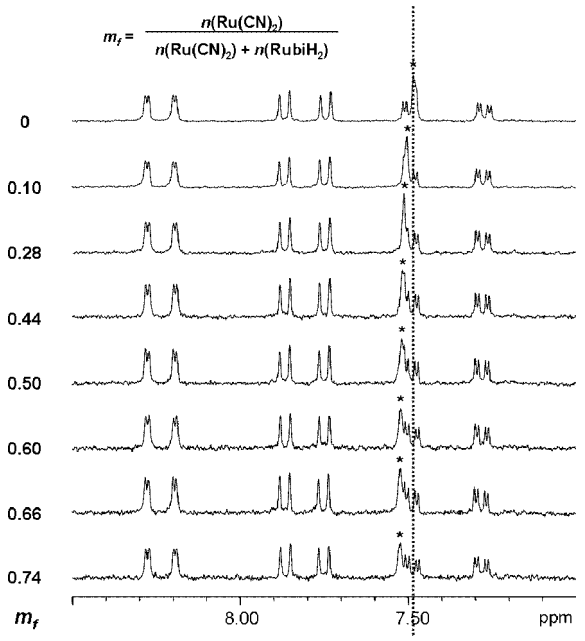


Figure 1. Section of the $^1$H-NMR spectra of [Ru(bipy*)$_2$(biH$_2$)](PF$_6$)$_2$ and [*cis*-Ru(C≡N-*t*Bu)$_4$(CN)$_2$] at various molar fractions ($m_f$ = $n$(Ru(CN)$_2$)/[$n$(Ru(CN)$_2$) + $n$(RubiH$_2$)]; signal of the 4,4′-position marked with an asterisk).

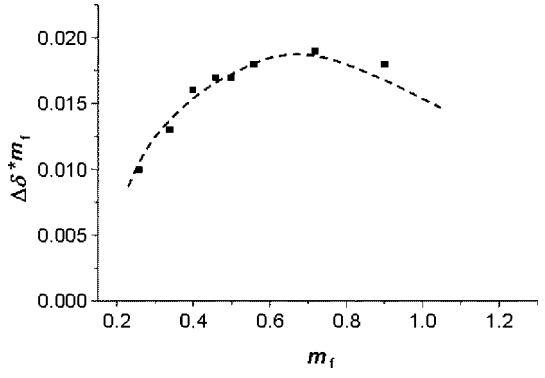


Figure 2. ($\Delta\delta^* \times m_f$) vs. $m_f$ plot showing the maximum stoichiometry of hydrogen bonded adducts in solution to be of the composition Ru(CN)$_2$:RubiH$_2$ = 2:1 ($m_f$ = 0.66).

bonded adduct is depicted in Figure 3. It is obvious that indeed a 2:1 assembly has been formed. All ruthenium atoms show a virtually perfect octahedral coordination sphere and bond lengths and angles of the ligands are as expected (Table 1). The observed monoclinic space group $P2_1/c$ shows Ru2 to be situated at the crystallographic center of inversion. Both N–H functions of the bibenzimidazole ligand are engaged in hydrogen bonds. N2–H2 acts as a hydrogen-bond donor site towards the cyanide nitrogen atom N9 with an N–N distance of 278(2) pm and a N2–H2···N9 bond angle of 166(1) deg. The second N–H group N4–H4 shows a hydrogen bond towards a water molecule (N4–O1w 282(2) pm, N4–H4···O1w 159(1) deg). The distance of 301(2) pm between O1w and N9 is indicative of another weak hydrogen bond between a proton of the water molecule and the cyanide nitrogen atom. The hydrogen bond lengths and angles fit very well to numerous examples of weak hydrogen bonding described in the literature.[10] Figure 3 also shows a view of the hydrogen-bonded adduct down the plane of the bibenzimidazole ligands. All carbon and hydrogen atoms of the bipy*, biH$_2$ (except C1 and C8) and *tert*-butyl groups have been omitted. The angle between the bibenzimidazole plane and the Ru2(CN)$_2$ plane measures to 131(2) deg.

It should be pointed out that from the same recrystallization another crystal has been investigated by means of X-ray crystallography (cf. Supporting Information). Although the quality of this crystal was inferior compared to the structure determination shown in Figure 3, the structural motif in this crystal structure unequivocally reveals a hydrogen bond network with the cyanide ligands being situated symmetrically between the two N–H groups of the bibenzimidazole ligands like it is depicted in Scheme 1. These different supramolecular assemblies clearly demonstrate that polar solvents compete for the hydrogen-bond donor sites with the cyanide ligands.

To the best of our knowledge these compounds are the first structurally characterized adducts of a photochemically active [Ru(bipy*)$_2$(biH$_2$)]$^{2+}$ complex in which the N–H functions are connected via hydrogen bonds directly to a cyanide ligand acting as a bridge to another transition metal. We therefore explored the influence of the binding of the cyano compound to the photochemically active ruthenium bibenzimidazole complex on the photophysical properties of the latter. Solutions of pure [Ru(bipy*)$_2$(biH$_2$)]$^{2+}$ typically exhibit a strong emission at app. 650 nm. Figure 4 illustrates the emission spectra of mixtures of [Ru(bipy*)$_2$(biH$_2$)]$^{2+}$ and *trans*-[Ru(C≡N-*t*Bu)$_4$(CN)$_2$] depending on the molar fraction of the cyano complex. It clearly demonstrates that there is a decay in emission intensity with increasing amount of *trans*-[Ru(C≡N-*t*Bu)$_4$(CN)$_2$] until the emission is almost completely quenched. In addition, the emission is shifted to app. 675 nm. Since the formation of hydrogen bonds may be understood in terms of an acid base reaction this bathochromic shift corresponds to observations reported in the literature, that deprotonation of the N–H functions in [Ru(bipy*)$_2$(biH$_2$)]$^{2+}$ complexes leads to quenching or at least a strong bathochromic shift of the emission band.[11] The emission intensities of solutions of the same concentrations of [Ru(bipy*)$_2$(biH$_2$)]$^{2+}$ are considerably higher than those of mixtures of [Ru(bipy*)$_2$(biH$_2$)]$^{2+}$ and *trans*-[Ru(C≡N-*t*Bu)$_4$(CN)$_2$]. The corresponding plot for *cis*-[Ru(C≡N-*t*Bu)$_4$(CN)$_2$], which may be found in the Supporting Information, is virtually identical. We therefore conclude that in both cases 1:1 and 2:1 adducts are readily formed in the quite diluted solutions that are used for the spectroscopic investigations ($c$(*cis*/*trans*-[Ru(C≡N-*t*Bu)$_4$(CN)$_2$]) + $c$([Ru(bipy*)$_2$(biH$_2$)]$^{2+}$) = $2.573 \times 10^{-6}$ mol L$^{-1}$). In addition, a dilution experiment of a 2:1 mixture of *trans*-[Ru(C≡N-*t*Bu)$_4$(CN)$_2$] and [Ru(bipy*)$_2$(biH$_2$)]$^{2+}$ shows that the emission intensities for the mixtures are significantly lower than the emission intensity of [Ru(bipy*)$_2$(biH$_2$)]$^{2+}$ alone in a blank experiment down

 © 2007 Wiley-VCH Verlag GmbH & Co. KGaA, Weinheim 

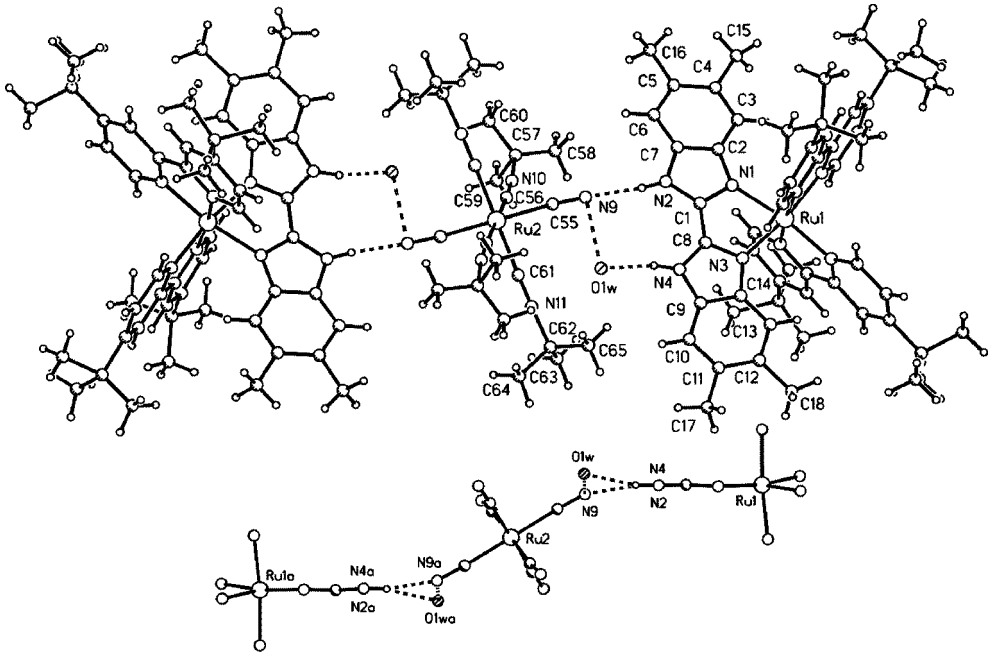


Figure 3. Molecular Structure of $\{[Ru(bipy^*)_2(biH_2)]_2[trans\text{-}Ru(C{\equiv}N\text{-}t\text{Bu})_4(CN)_2]\}^{4+} \times 2H_2O$; anions and additional solvent molecules have been omitted for the sake of clarity.

Table 1. Selected bond lengths [pm] and angles [°] of $\{(trans\text{-}Ru(CN)_2)(RubiH_2)_2\}(PF_6)_4 \times 8\ CH_2Cl_2 \times 6\ H_2O \times 2\ CH_3OH$.

| | | | | | |
|---|---|---|---|---|---|
| Ru1–N1 | 210.0(6) | Ru1–N3 | 210.1(6) | Ru1–N5 | 206.7(7) |
| Ru1–N6 | 204.6(6) | Ru1–N7 | 204.7(6) | Ru1–N8 | 204.4(7) |
| N1–C1 | 133(1) | C1–N2 | 139(1) | N2–C7 | 139(1) |
| C7–C2 | 139(1) | C2–N1 | 141(1) | C1–C8 | 143(1) |
| N3–C8 | 135(1) | C8–N4 | 136(1) | N4–C9 | 136(1) |
| C9–C14 | 142(1) | C14–N3 | 138(1) | Ru2–C55 | 202.6(9) |
| Ru2–C56 | 200(1) | Ru2–C61 | 202.3(9) | C55–N9 | 116(1) |
| C56–N10 | 115(1) | C61–N11 | 115(1) | N2–N9 | 278(2) |
| N4–O1w | 282(2) | N9–O1w | 301(2) | | |
| N1–Ru1–N3 | 77.5(3) | N1–Ru1–N5 | 88.2(3) | N1–Ru1–N6 | 95.4(2) |
| N1–Ru1–N7 | 170.6(3) | N1–Ru1–N8 | 95.7(3) | N3–Ru1–N5 | 93.6(3) |
| N3–Ru1–N6 | 169.5(3) | N3–Ru1–N7 | 95.9(2) | N3–Ru1–N8 | 91.9(3) |
| N5–Ru1–N6 | 78.4(3) | N5–Ru1–N7 | 98.9(3) | N5–Ru1–N8 | 173.9(2) |
| N6–Ru1–N7 | 92.0(2) | N6–Ru1–N8 | 96.5(3) | N7–Ru1–N8 | 77.8(3) |
| N1–C1–N2 | 113.3(7) | C2–N1–C1 | 105.9(6) | N1–C2–C7 | 107.2(7) |
| C2–C7–N2 | 108.2(7) | C7–N2–C1 | 105.3(7) | N1–C1–C8 | 117.0(7) |
| N2–C1–C8 | 129.6(7) | N3–C8–N4 | 111.5(7) | C8–N4–C9 | 107.8(7) |
| N4–C9–C14 | 106.5(7) | C9–C14–N3 | 108.2(7) | C14–N3–C8 | 105.9(6) |
| N3–C8–C1 | 116.4(7) | N4–C8–C1 | 132.1(8) | C55–Ru2–C56 | 89.1(4) |
| C55–Ru2–C61 | 88.0(4) | C56–Ru2–C61 | 95.1(4) | Ru2–C55–N9 | 175.8(9) |
| Ru2–C56–N10 | 173.1(9) | Ru2–C61–N11 | 172.0(9) | | |

to a concentration of app. $5 \times 10^{-7}$ mol $L^{-1}$ demonstrating the stability of the hydrogen bonded adducts.

One major question arising in the investigation of the supramolecular adducts described herein is the question concerning the association constants of these associates. In the literature either NMR titration experiments or Stern–Volmer plots have frequently been employed in similar cases. Nevertheless, these approaches have almost exclusively been applied to 1:1 adducts. From NMR experiments (vide supra) and from the fact that a distinct decrase of the emission intensity is observed up to a $m_f = 0.66$ (and a much less pronounced decrase for higher concentrations of $Ru(CN)_2$) we conclude that in solution adducts of the general formula $\{(RubiH_2)(Ru(CN)_2)_2\}$ are formed. We therefore have to address the question of the equilibrium constant of the following reaction

$$\{(RubiH_2)(Ru(CN)_2)_2\} \rightleftharpoons RubiH_2 + 2\ Ru(CN)_2$$

with the mass-action law

$$K_D = \frac{c(RubiH_2) \cdot c(Ru(CN)_2)^2}{c\{(RubiH_2)(Ru(CN)_2)_2\}}$$

 © 2007 Wiley-VCH Verlag GmbH & Co. KGaA, Weinheim 

providing us with the dissociation constant $K_D$. From the mass-action law we can conclude

$$\log\left(\frac{c(\mathrm{RubiH_2})}{c\{(\mathrm{RubiH_2})(\mathrm{Ru(CN)_2})_2\}}\right) = -2\log(c(\mathrm{Ru(CN)_2})) - \mathrm{p}K_D$$

Applying a methodology that has been used to elucidate the p$K_a$ values of bibenzimidazole ligands in ruthenium complexes from absorption intensities depending on the amount of base present in the solution[12] we are now able to calculate the p$K_D$ value from the emission intensity of pure $RubiH_2$ ($I$($RubiH_2$)), the emission intensities of mixtures with an excess of *cis*/*trans*-$Ru(CN)_2$ ($I$\{($RubiH_2$)($Ru(CN)_2$)$_2$\}) and the emission intensity of the mixtures with different concentrations of *cis*/*trans*-$Ru(CN)_2$ ($I$(M)).

$$\log\left(\frac{I\{(\mathrm{RubiH_2})(\mathrm{Ru(CN)_2})_2\} - I(\mathrm{M})}{I(\mathrm{M}) - I(\mathrm{RubiH_2})}\right) = -2\log(c(\mathrm{Ru(CN)_2})) - \mathrm{p}K_D$$

This means that a plot of the logarithmic term on the left side of the equation vs. –2 log($c$($Ru(CN)_2$)) should give a linear function with the axis intercept representing the p$K_D$ value of the corresponding supramolecular adduct. In Figure 5 a plot of the emission intensity vs. log($c$(*trans*-$Ru(CN)_2$)) showing a sigmoidal shape typical for titration curves and another plot of the logarithmic term of the latter equation vs. –2 log($c$(*trans*-$Ru(CN)_2$)) of linear shape are depicted. The titration of $RubiH_2$ with *cis*-$Ru(CN)_2$ leads to very similar plots although the sigmoidal shape of the titration curve is less pronounced (cf. Supporting Information). From the linear functions we can estimate a p$K_D$ value for \{($Ru(biH_2)$(*cis*-$Ru(CN)_2$)$_2$\} of 7.1 and for

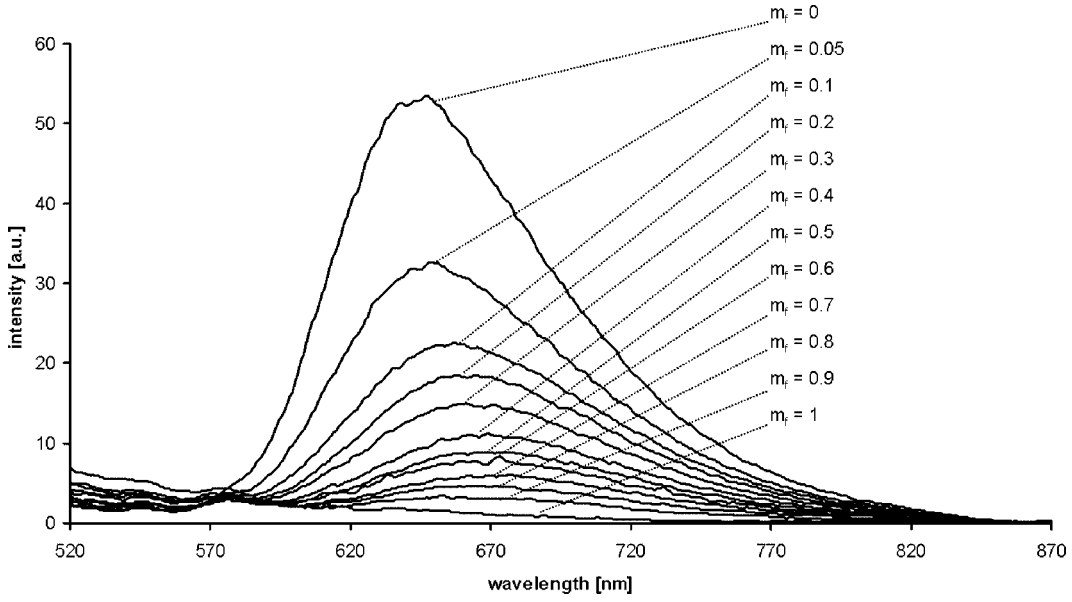


Figure 4. Emission spectra of the mixtures of [$Ru(bipy^*)_2(biH_2)$]($PF_6$)$_2$ and [*trans*-$Ru(C{\equiv}N\text{-}tBu)_4(CN)_2$] at various molar fractions.

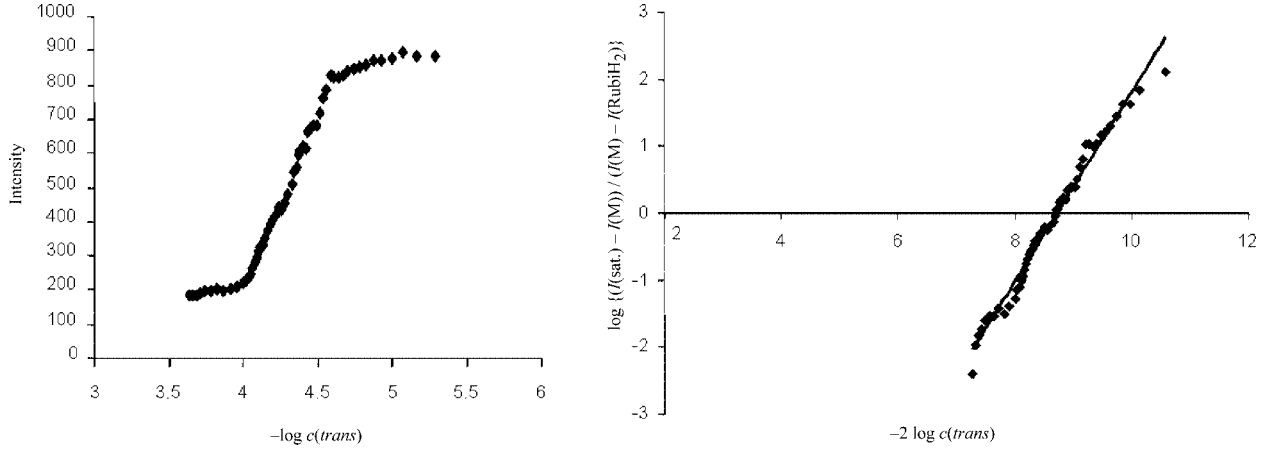


Figure 5. Emission intensity vs. log $c$(*trans*-$Ru(CN)_2$) plot (left) and log \{($I$(sat.) – $I$(M))/($I$(M) – ($I$($RubiH_2$)\} vs. –2 log $c$(*trans*-$Ru(CN)_2$).

 © 2007 Wiley-VCH Verlag GmbH & Co. KGaA, Weinheim 

{(Ru(biH$_2$)(*trans*-Ru(CN)$_2$)$_2$} a p$K_D$ value of 12.3. The adduct of *trans*-Ru(CN)$_2$ thus is much more stable compared to the *cis* analogue which makes sense in terms of less steric interactions with the bibenzimidazole ligand leading to the much better pronounced saturation behaviour and titration curves.

The deactivation of the excited state of the [Ru(bipy*)$_2$(biH$_2$)]$^{2+}$ component may in principle be achieved by either electron or energy transfer from the [Ru(bipy*)$_2$(biH$_2$)]$^{2+}$ fragment to the cyano complex fragment. Taking into account the results described in the literature in connection with related systems[3] as well as cyclovoltammetric investigations of the cyano compounds showing that both isomers may be neither reduced nor oxidised makes the former possibility quite unlikely.

## Experimental Section

All procedures were carried out in anhydrous, freshly distilled solvents. Infrared spectra were recorded on a Perkin–Elmer FT-IR System 2000 using 0.2 mm KBr cuvettes. NMR spectra were recorded on a Bruker DRX400 spectrometer ($^1$H: 400.13 MHz, $^{13}$C: 100.62 MHz, $CDCl_3$ as internal standard). Mass spectra were recorded on a Finnigan MAT SSQ 710 instrument. Elemental analyses were carried out at the laboratory of the Institute of Organic Chemistry and Macromolecular Chemistry, Friedrich-Schiller-Universität, Jena, Germany.

**X-ray Crystallographic Studies:** The structure determinations were carried out on a Enraf Nonius Kappa CCD diffractometer, the crystals being mounted in a stream of cold nitrogen, crystal detector distance 29 mm using graphite-monochromated Mo-$K_\alpha$ radiation. Data were corrected for Lorentz and polarization effects but not for absorption. The structures were dissolved by direct methods and refined by full-matrix least-squares techniques against $F^2$ using the programs SHELXS86 and SHELXL97.[13] All hydrogen atoms were constrained in idealized positions during the final stages of the refinement. The isotropic replacement parameters of all hydrogen atoms were fixed to 1.5 times the value of the corresponding carbon or nitrogen atom. The molecular illustrations were drawn using the program XP.[14]

CCDC-600734 and -600735 contain the supplementary crystallographic data for this paper. These data can be obtained free of charge from The Cambridge Crystallographic Data Centre via www.ccdc.cam.ac.uk/data_request/cif.

***trans*-[Ru(C≡N-*t*Bu)$_4$(CN)$_2$] and [Ru(bipy*)$_2$(biH$_2$)](PF$_6$)$_2$ (1:1):** 20.1 mg (0.0165 mmol) [Ru(bipy*)$_2$(biH$_2$)](PF$_6$)$_2$ dissolved in dichloromethane were added to a solution of 8 mg (0.0165 mmol) *trans*-[Ru(CN)$_2$(C≡N-*t*Bu)$_4$] in dichloromethane at room temperature. After 1 h the solvent was evaporated at room temperature resulting in the formation of a red powder (yield 28 mg). IR ($CH_2Cl_2$): $\tilde{\nu}$ = (CH) 3051 w, 2987 s, ν(-C≡N/-N≡C) 2163 vs, 2126 s, 2103 s, 1606 m, δ(CH) 1479 m, 1423 m, δ(–C(CH$_3$)$_3$) 1372 s, 1246 s, 1096 vs, 1015 vs, 846 vs cm$^{-1}$. MS (Micro-ESI in $CH_2Cl_2$/$CH_3OH$) *m*/*z*(%): 1559(2) [Ru(bipy*)$_2$(biH$_2$)(PF$_6$)Ru(CN)$_2$(C≡N-*t*Bu)$_4$]$^+$, 994(10) [Ru(CN)$_2$(C≡N-*t*Bu)$_4$]$_2$Na$^+$, 927(100) [Ru(bipy*)$_2$(biH$_2$)](-H)$^+$, 509(3) [Ru(CN)$_2$(C≡N-*t*Bu)$_4$]Na$^+$, 487 (3) [Ru(CN)$_2$(C≡N-*t*Bu)$_4$]H$^+$, 464(7) [Ru(bipy*)$_2$(biH$_2$)]$^{++}$. $^1$H NMR (400 MHz, $CD_2Cl_2$): δ = 1.380 (s, 18 H, CH$_3$), 1.497 (s, 18 H, CH$_3$), 1.519 (s, 36 H, CH$_3$), 2.030 (s, 6 H, CH$_3$), 2.321 (s, 6 H, CH$_3$), 5.439 (s, 2 H, CH), 7.539 (dd, $^4J_{HH}$ = 2 Hz, $^3J_{HH}$ = 6 Hz, 2 H, CH), 7.305 (d, $^3J_{HH}$ = 6 Hz, 2 H, CH), 7.399 (s, 2 H, CH), 7.868 (d, $^3J_{HH}$ = 6 Hz, 2 H, CH), 7.729 (d, $^3J_{HH}$ = 6.4 Hz, 2 H, CH), 8.295 (d, $^4J_{HH}$ = 1.6 Hz, 2 H, CH), 8.221 (d, $^4J_{HH}$ = 1.6 Hz, 2 H, CH) ppm. $^{13}$C NMR (400 MHz, $CD_2Cl_2$): δ = 20.649 (CH$_3$), 20.688 (CH$_3$), 30.384 (CH$_3$), 30.612 (CH$_3$), 30.758 (CH$_3$), 35.714 (C), 35.901 (C), 58.114 (C), 113.739 (CH), 115.978 (CH), 120.541 (CH), 124.855 (C), 125.560 (CH), 133.359 (C), 135.163 (C), 136.864 (C), 137.175 (-C≡N), 140.877 (C), 142.313 (-C≡N-*t*Bu), 143.449 (C), 151.859 (C), 152.668 (C), 157.521 (C), 159.180 (C), 161.938 (C), 162.664 (C) ppm.

***trans*-[Ru(CN)$_2$(C≡N-*t*Bu)$_4$] and [Ru(bipy*)$_2$(biH$_2$)](PF$_6$)$_2$ (1:2):** 40.2 mg (0.033 mmol) [Ru(bipy*)$_2$(biH$_2$)](PF$_6$)$_2$ dissolved in dichloromethane were added to a solution of 8 mg (0.0165 mmol) *trans*-[Ru(CN)$_2$(C≡N-*t*Bu)$_4$] in dichloromethane at room temperature. The solvent was evaporated at room temperature (yield 48 mg). Crystallisation from dichloromethane yielded red crystals which were suitable for X-ray diffraction studies. IR ($CH_2Cl_2$) [cm$^{-1}$]: ν(NH) 3379 m, ν(CH) 3072 w, 2968 s, ν(-C≡N/-N≡C) 2164 vs, 2101 s, 1613 m, δ(CH) 1480 m, 1414 m, δ(-C(CH$_3$)$_3$) 1371 s, 1203 s, 1097 vs, 1013 vs, 846 vs, 807 vs, 558 s. MS (Micro-ESI in $CH_2Cl_2$) *m*/*z*(%): 927(100) [Ru(bipy*)$_2$(biH$_2$)](-H)$^+$. $^1$H NMR (400 MHz, $CD_2Cl_2$): δ = 1.384 (s, 36 H, CH$_3$), 1.500 (s, 36 H, CH$_3$), 1.520 (s, 36 H, CH$_3$), 2.041 (s, 12 H, CH$_3$), 2.320 (s, 12 H, CH$_3$), 5.438 (s, 4 H, CH), 7.540 (dd, $^4J_{HH}$ = 2 Hz, $^3J_{HH}$ = 6.2 Hz, 4 H, CH), 7.307 (d, $^3J_{HH}$ = 4.8 Hz, 4 H, CH), 7.410 (s, 4 H, CH), 7.870 (d, $^3J_{HH}$ = 6 Hz, 4 H, CH), 7.729 (d, $^3J_{HH}$ = 6 Hz, 4 H, CH), 8.299 (d, $^4J_{HH}$ = 1.6 Hz, 4 H, CH), 8.225 (d, $^4J_{HH}$ = 1.6 Hz, 4 H, CH) ppm. $^{13}$C NMR (400 MHz, $CD_2Cl_2$): δ = 20.632 (CH$_3$), 20.706 (CH$_3$), 30.429 (CH$_3$), 30.659 (CH$_3$), 30.802 (CH$_3$), 35.764 (C), 35.939 (C), 58.297 (C), 113.846 (CH), 115.997 (CH), 120.581 (CH), 124.895 (C), 125.609 (CH), 133.418 (C), 134.248 (C), 137.028 (C), 138.005 (-C≡N), 140.901 (C), 142.313 (-C≡N-*t*Bu), 143.305 (C), 151.891 (C), 152.687 (C), 157.574 (C), 159.245 (C), 162.040 (C), 162.757 (C) ppm.

***cis*-[Ru(CN)$_2$(C≡N-*t*Bu)$_4$] and [Ru(bipy*)$_2$(biH$_2$)](PF$_6$)$_2$ (1:1):** 20.1 mg (0.0165 mmol) [Ru(bipy*)$_2$(biH$_2$)](PF$_6$)$_2$ dissolved in dichloromethane were added to a solution of 8 mg (0.0165 mmol) *cis*-[Ru(CN)$_2$(C≡N-*t*Bu)$_4$] in dichloromethane at room temperature. The solvent was evaporated at room temperature after stirring the solution for 1 h (yield: 28 mg). IR ($CH_2Cl_2$) [cm$^{-1}$]: ν(CH) 3071 w, 2971 s, ν(-C≡N/-N≡C) 2220 m, 2169 vs, 2117 s, 1613 m, δ(CH) 1480 m, 1414 m, δ(-C(CH$_3$)$_3$) 1371 s, 1236 m, 1204 s, 1097 s, 1013 d, 846 vs, 807 s, 558 s. MS (Micro-ESI in $CH_2Cl_2$) *m*/*z*(%): 1559([Ru(bipy*)$_2$Ru(biH$_2$)(PF$_6$)Ru(CN)$_2$(C≡N-*t*Bu)$_4$]$^+$, 1413(1) [Ru(bipy*)$_2$(biH$_2$)Ru(CN)$_2$(C≡N-*t*Bu)$_4$]$^{++}$, 927(100) [Ru(bipy*)$_2$(biH$_2$)](-H)$^{++}$. $^1$H NMR (400 MHz, $CD_2Cl_2$): δ = 1.380 (s, 18 H, CH$_3$), 1.499 (s, 18 H, CH$_3$), 1.441 (s, 18 H, CH$_3$), 1.519 (s, 36 H, CH$_3$), 2.028 (s, 6 H, CH$_3$), 2.312 (s, 6 H, CH$_3$), 5.415 (s, 2 H, CH), 7.532 (dd, $^4J_{HH}$ = 2 Hz, $^3J_{HH}$ = 6 Hz, 2 H, CH), 7.290 (d, $^3J_{HH}$ = 6 Hz, 2 H, CH), 7.604 (s, 2 H, CH), 7.867 (d, $^3J_{HH}$ = 6 Hz, 2 H, CH), 7.721 (d, $^3J_{HH}$ = 6 Hz, 2 H, CH), 8.296 (d, $^4J_{HH}$ = 2 Hz, 2 H, CH), 8.219 (d, $^4J_{HH}$ = 1.2 Hz, 2 H, CH) ppm. $^{13}$C NMR (400 MHz, $CD_2Cl_2$): δ = 20.587 (CH$_3$), 20.698 (CH$_3$), 30.433 (CH$_3$), 30.664 (CH$_3$), 30.664 (CH$_3$), 30.918 (CH$_3$), 35.753 (C), 35.934 (C), 58.384 (C), 114.518 (CH), 115.734 (CH), 120.563 (CH), 124.872 (C), 125.529 (CH), 133.691 (C), 135.053 (C), 136.764 (C), 139.460 (-C≡N), 140.906 (C), 141.437 (-C≡N-*t*Bu), 141.637 (-C≡N-*t*Bu), 143.504 (C), 151.854 (C), 152.661 (C), 157.610 (C), 159.244 (C), 161.961 (C), 162.701 (C) ppm.

***cis*-[Ru(CN)$_2$(C≡N-*t*Bu)$_4$] and [Ru(bipy*)$_2$(biH$_2$)](PF$_6$)$_2$ (1:2):** 49.7 mg (0.0408 mmol) [Ru(bipy*)$_2$(biH$_2$)](PF$_6$)$_2$ dissolved in dichloromethane were added to a solution of 9.9 mg (0.0204 mmol)

 © 2007 Wiley-VCH Verlag GmbH & Co. KGaA, Weinheim 

*cis*-[Ru(CN)$_2$(C≡N-*t*Bu)$_4$] in dichloromethane at room temperature. After 1 h the solvent was evaporated at room temperature (yield 59 mg). IR ($CH_2Cl_2$) [cm$^{-1}$]: ν(CH) 3051 w, 2987 s, ν(-C≡N/–N≡C) 2163 m, 2123 m, 1675 m, δ(CH) 1440 s, 1423 s, δ(-C-(CH$_3$)$_3$) 1363 s, 1223 s, 1090 m, 1048 m, 1031 m, 846 vs. MS (Micro-ESI in $CH_2Cl_2$/$CH_3OH$) *m*/*z*(%): 1559(9) [Ru(bipy*)$_2$(biH$_2$)(PF$_6$)-Ru(CN)$_2$(C≡N-*t*Bu)$_4$]$^+$, 994(2) [Ru(CN)$_2$(C≡N-*t*Bu)$_4$]$_2$Na$^+$, 927(100) [Ru(bipy*)$_2$(biH$_2$)](-H)$^+$, 509(3) [Ru(CN)$_2$(C≡N-*t*Bu)$_4$]-Na$^+$, 464(33) [Ru(bipy*)$_2$(biH$_2$)]$^{++}$. $^1$H NMR (400 MHz, $CD_2Cl_2$): $\delta$ = 1.379 (s, 36 H, $CH_3$), 1.500 (s, 36 H, $CH_3$), 1.442 (s, 18 H, $CH_3$), 1.562 (s, 18 H, $CH_3$), 2.028 (s, 12 H, $CH_3$), 2.301 (s, 12 H, $CH_3$), 5.417 (s, 4 H, CH), 7.533 (dd, $^4J_{HH}$ = 2 Hz, $^3J_{HH}$ = 6 Hz, 4 H, CH), 7.282 (d, $^3J_{HH}$ = 5.2 Hz, 4 H, CH), 7.540 (s, 4 H, CH), 7.870 (d, $^3J_{HH}$ = 6.4 Hz, 4 H, CH), 7.730 (d, $^3J_{HH}$ = 6 Hz, 4 H, CH), 8.296 (d, $^4J_{HH}$ = 2 Hz, 4 H, CH), 8.219 (d, $^4J_{HH}$ = 2 Hz, 4 H, CH) ppm. $^{13}$C NMR (400 MHz, $CD_2Cl_2$): $\delta$ = 20.546 ($CH_3$), 20.685 ($CH_3$), 30.377 ($CH_3$), 30.602 ($CH_3$), 30.602 ($CH_3$), 30.846 ($CH_3$), 35.684 (C), 35.871 (C), 58.289 (C), 114.435 (CH), 115.636 (CH), 120.494 (CH), 124.762 (C), 125.467 (CH), 133.864 (C), 134.847 (C), 137.525 (C), 139.768 (-C≡N), 140.904 (C), 141.126 (-C≡N-*t*Bu), 141.362 (-C≡N-*t*Bu), 143.706 (C), 151.812 (C), 152.576 (C), 157.493 (C), 159.180 (C), 161.779 (C), 162.546 (C) ppm.

**Supporting Information** (see also the footnote on the first page of this article): Molecular structure of {[Ru(bipy*)$_2$(biH$_2$)]$_2$[*trans*-Ru(C≡N-*t*Bu)$_4$(CN)$_2$]}(PF$_6$)$_4$, emission spectra of the mixtures of [Ru(bipy*)$_2$(biH$_2$)](PF$_6$)$_2$ and [*cis*-Ru(C≡N-*t*Bu)$_4$(CN)$_2$], emission intensity vs. log *c*(*cis*-Ru(CN)$_2$) plot and log {(*I*(sat.) – *I*(M))/(*I*(M) – (*I*(RubiH$_2$)} vs. –2 log *c*(*cis*-Ru(CN)$_2$).

## Acknowledgments

Financial support from the Deutsche Forschungsgemeinschaft (DFG) (IM 22/6-1), the Fonds der Chemischen Industrie and the Free State of Thuringia (Ph.D. grant for K. H.) is gratefully acknowledged.

[1] Selected recent examples: a) J. Lombard, S. Romain, S. Dumas, J. Chauvin, M.-N. Collomb, D. Daveloose, A. Deronzier, J.-C. Lepretre, *Eur. J. Inorg. Chem.* **2005**, 3320; b) B. Wenger, M. Grätzel, J.-E. Moser, *J. Am. Chem. Soc.* **2005**, *127*, 12150; c) S. Y. Reece, D. G. Nocera, *J. Am. Chem. Soc.* **2005**, *127*, 9448; d) M. H. V. Huynh, D. M. Dattelbaum, T. J. Meyer, *Coord. Chem. Rev.* **2005**, *249*, 457; e) P. V. Kamat, M. Haria, S. Hotchandani, *J. Phys. Chem. B* **2004**, *108*, 5166; f) J. Andersson, F. Puntoriero, S. Serroni, A. Yartsev, T. Pascher, T. Polivka, S. Campagna, V. Sundstroem, *J. Chem. Soc., Faraday Trans.* **2004**, *127*, 295; g) S. Serroni, S. Campagna, F. Puntoriero, F. Loiseau, V. Ricevuto, R. Passalacqua, M. Galetta, *Compt. Rend. Chim.* **2003**, *6*, 883; h) D. M. Kaschak, S. A. Johnson, C. C. Waraksa, J. Pogue, T. E. Mallouk, *Coord. Chem. Rev.* **1999**, *185–186*, 403; i) A. Vlček Jr., *Coord. Chem. Rev.* **2000**, *200–202*, 933; j) M. D. Ward, F. Barigeletti, *Coord. Chem. Rev.* **2001**, *216*, 127; k) A. Prodi, M. T. Indelli, C. J. Kleverlaan, E. Alessio, F. Scandola, *Coord. Chem. Rev.* **2002**, *229*, 51; l) N. R. M. Simpson, M. D. Ward, A. Farran Morales, B. Ventura, F. Barigeletti, *J. Chem. Soc., Dalton Trans.* **2002**, 2455; m) M. A. Rampi, M. T. Indelli, F. Scandola, F. Pina, A. J. Parola, *Inorg. Chem.* **1996**, *35*, 3355.

[2] Selected recent examples: a) J. Rosenthal, J. Bachmann, J. L. Dempsey, A. J. Esswein, T. G. Gray, J. M. Hodgkiss, D. R. Manke, T. D. Luckett, B. J. Pistorio, A. S. Veige, D. G. Nocera, *Coord. Chem. Rev.* **2005**, *249*, 1316; b) G. Knör, A. Strasser, *Inorg. Chem. Commun.* **2005**, *8*, 471; c) F. D'Souza, M. E. El-Khouly, S. Gadde, A. L. McCarty, P. A. Karr, M. E. Zandler, Y. Araki, O. Ito, *J. Phys. Chem. B* **2005**, *109*, 10107; d) A.-H. Bae, T. Hatano, K. Sugiyasu, T. Kishida, M. Takeuchi, S. Shinkai, *Tetrahedron Lett.* **2005**, *46*, 3169; e) F. D'Souza, R. Chitta, S. Gadde, M. E. Zandler, A. S. D. Sandanayaka, Y. Araki, O. Ito, *Chem. Commun.* **2005**, 1279; f) M. Itou, M. Otake, Y. Araki, O. Ito, H. Kido, *Inorg. Chem.* **2005**, *44*, 1580; g) A. Harriman, M. Mehrabi, B. G. Maiya, *Photochem. Photobiol. Sci.* **2005**, *4*, 47; h) T. Yamamura, A. Momotake, T. Arai, *Tetrahedron Lett.* **2005**, *45*, 9219; i) A. Dreuw, G. A. Worth, L. S. Cederbaum, M. Head-Gordon, *J. Phys. Chem. B* **2004**, *108*, 19049; j) B. J. Coe, N. R. M. Curati, *Comments Inorg. Chem.* **2004**, *25*, 147; k) L. Flamigni, F. Barigeletti, N. Armaroli, J.-P. Collin, M. Dixon, J.-P. Sauvage, J. A. G. Williams, *Coord. Chem. Rev.* **1999**, *190–192*, 671.

[3] a) M. D. Ward, *Chem. Soc. Rev.* **1997**, *26*, 365; b) M. D. Ward, *Int. J. Photoenerg.* **1999**, *1*, 121; c) F. Loiseau, G. Marzanni, S. Quici, M. T. Indelli, S. Campagna, *Chem. Commun.* **2003**, 286; d) S. Rau, B. Schäfer, S. Schebesta, A. Grüßing, W. Poppitz, D. Walther, M. Duati, W. R. Browne, J. G. Vos, *Eur. J. Inorg. Chem.* **2003**, 1503; e) C. M. White, M. F. Gonzalez, D. A. Bardwell, L. H. Rees, J. C. Jeffery, M. D. Ward, N. Armaroli, G. Calogero, F. Barigelletti, *J. Chem. Soc., Dalton Trans.* **1997**, 727.

[4] a) S. Rau, L. Böttcher, S. Schebesta, M. Stollenz, H. Görls, *Eur. J. Inorg. Chem.* **2002**, 2800; b) S. Rau, T. Büttner, C. Temme, M. Ruben, H. Görls, D. Walther, M. Duati, F. Fanni, J. G. Vos, *Inorg. Chem.* **2000**, *39*, 1621; c) S. Rau, B. Schäfer, A. Grüßing, S. Schebesta, K. Lamm, J. Vieth, H. Görls, D. Walther, M. Rudolph, U. W. Grummt, E. Birkner, *Inorg. Chim. Acta* **2004**, *357*, 4496.

[5] a) S. Rau, H. Görls, *J. Coord. Chem.* **2004**, *57*, 1587; b) F. Baril-Robert, A. L. Beauchamp, *Polyhedron* **2004**, *23*, 1139; c) L. De Souza, K. E. Bessler, E. Schulz-Lang, *Zeitschr. Anorg. Allg. Chem.* **1998**, *624*, 701; d) L. De Souza, K. E. Bessler, E. Schulz-Lang, *Zeitschr. Anorg. Allg. Chem.* **1998**, *624*, 30; e) N. G. Larsen, P. D. W. Boyd, S. J. Rodgers, G. E. Wünschell, C. A. Koch, S. Rasmussen, J. R. Tate, B. S. Erler, C. A. Reed, *J. Am. Chem. Soc.* **1986**, *108*, 6950.

[6] D. Dönnecke, W. Imhof, *Dalton Trans.* **2003**, 2737.

[7] C.-S. Wilcox, in *Frontiers in Supramolecular Organic Chemistry and Photochemistry* (Eds.: H.-J. Schneider, H. Dürr), VCH, Weinheim, **1991**, 123.

[8] a) I. Horman, B. Dreux, *Anal. Chem.* **1983**, *55*, 1219; b) C. J. Creswell, A. L. Allred, *J. Phys. Chem.* **1962**, *66*, 1469.

[9] Crystal data. {[Ru(bipy*)$_2$(biH$_2$)]$_2$[*trans*-Ru(C≡N-*t*Bu)$_4$-(CN)$_2$]}(PF$_6$)$_4$ × 8 $CH_2Cl_2$ × 6 $H_2O$ × 2 $CH_3OH$, *FW* = 3773.54 g mol$^{-1}$, monoclinic, space group $P2_1/c$, $a$ = 12.838(1), $b$ = 33.376(3), $c$ = 23.594(2) Å, $\beta$ = 103.923(4)°, $V$ = 9813(1) Å$^3$, $D_{calc}$ = 1.277 g cm$^{-3}$, $Z$ = 2, $T$ = 183 K, 29611 reflections collected, 18343 unique, $R_{int}$ = 0.0645, 13608 observed reflections [$I > 2\sigma(I)$], $R_1$ = 0.1108, $wR_2$ = 0.3223.

[10] G. R. Desiraju, T. Steiner, *The Weak Hydrogen Bond*, Oxford Science Publications, **1999**.

[11] S. Rau, T. Büttner, C. Temme, M. Ruben, H. Görls, D. Walther, M. Duati, S. Fanni, J. G. Vos, *Inorg. Chem.* **2000**, *39*, 1621 and literature cited therein.

[12] a) A. M. Bond, M. Haga, *Inorg. Chem.* **1986**, *25*, 4507; b) M. Haga, A. Tsunemitsu, *Inorg. Chim. Acta* **1989**, *164*, 137; c) M. Haga, T. Ano, K. Kano, S. Yamabe, *Inorg. Chem.* **1991**, *30*, 3843; d) M. Haga, T. Ano, T. Ishizaki, K. Kano, K. Nozaki, T. Ohno, *J. Chem. Soc., Dalton Trans.* **1994**, 263.

[13] G. Sheldrick, University of Göttingen, Germany, **1986**; G. Sheldrick, University of Göttingen, Germany, **1997**.

[14] Siemens Analytical Xray Inst. Inc., XP – Interactive Molecular Graphics, Vers. 4.2, **1990**.

Received: December 22, 2006
Published Online: February 26, 2007

 © 2007 Wiley-VCH Verlag GmbH & Co. KGaA, Weinheim 

DOI: 10.1002/ejic.200600770

# The Magnetic Structure of $Mn_2GeSe_4$

**Holger Mikus,[a] Hans-Jörg Deiseroth,*[a] Krassimir Aleksandrov,[a] Clemens Ritter,[b] and Reinhard K. Kremer[c]**

**Keywords:** Olivine / Magnetic structure / Manganese / Germanium / Selenium / Antiferromagnetism

The magnetic structure of the olivine type $Mn_2GeSe_4$ is investigated by powder neutron diffraction between 2 K and ambient temperature. Based on a number of "magnetic reflections" occurring below $T_c$ = 66 K a model for the magnetic structure of the $Mn^{2+}$ ions ($d^5$) is derived by structure refinements based on the FULLPROF program system. Most important result is an antiferromagnetic arrangement of the $Mn^{2+}$ moments in successive layers along [001] ("easy direction"). This ordering evolves gradually with decreasing temperature as can be seen from the temperature dependence of the resultant magnetization of the two magnetic sublattices. The magnetization direction of one of the magnetic sublattices shows a weak tendency at low temperatures to deviate from the easy direction [001] towards [100]. The magnetic structure proposed for the title compound is comparable with the ones found for other magnetic thio- and seleno-olivines although a comprehensive picture for the magnetic properties of this group of solids is still lacking. The explanation for the "weak ferromagnetism" below $T_c$ = 66 K with a saturation magnetization of about 0.5 $\mu_B$ per $Mn^{2+}$ ion in a field of 7 T (2 K) as derived from earlier susceptibility measurements remains still speculative. It may result from local non-zero components that do not show up in the overall magnetic structure.
(© Wiley-VCH Verlag GmbH & Co. KGaA, 69451 Weinheim, Germany, 2007)

## Introduction

$Mn_2GeSe_4$ is one of the rare ternary selenides that crystallizes in the olivine structure type with Se atoms forming a hexagonal close packing. The $Mn^{2+}$ ions ($3d^5$) occupy half of the octahedral and the $Ge^{4+}$ one eighth of the tetrahedral holes. Crystal structure and temperature dependence of the magnetic susceptibility for $Mn_2GeSe_4$ were recently determined[1]. Above 150 K the susceptibility shows a clear paramagnetic field independent Curie–Weiss behaviour with an extrapolated Curie temperature $\Theta$ = –240(5) K indicating predominant antiferromagnetic exchange interactions between the $Mn^{2+}$ ions. Below 150 down to 66 K significant deviations from an ideal Curie–Weiss behaviour are observed until below $T_c$ = 66 K the susceptibility increases and becomes clearly field dependent. Consequently $1/\chi$ drops sharply for the low field data which we ascribe to a weak ferromagnetic component that is saturated in the high field measurement.

In this paper we present the results of elastic neutron scattering measurements on powder samples obtained at the ILL Grenoble using the instruments D2B and D20. The model for the magnetic structure of $Mn_2GeSe_4$ at different temperatures is based on Rietveld refinements and discussed on the background of earlier susceptibility and magnetisation measurements. A particular problem of a detailed comparison between the susceptibility measurement and the magnetic structure as obtained by neutron diffraction is that the latter one is measured under *zero* field conditions whereas the magnetization measurements require a *non-zero* field. So a *weak* magnetization detected by a susceptibility measurement may not necessarily be reflected by the magnetic structure.

[a] Anorganische Chemie, Universität Siegen,
Adolf Reichwein Strasse 2, 57076 Siegen, Germany
Fax: +49-271-7402555
E-mail: deiseroth@chemie.uni-siegen.de
[b] Institute Laue Langevin,
B. P. 156, 38042 Grenoble Cedex 9, France
[c] Max Planck Institut für Festkörperforschung,
Heisenbergstrasse 1, 70569 Stuttgart, Germany
Fax: +49-711-6891091
E-mail: rkre@fkf.mpg.de

## Results and Discussion

### General

A few investigations concerning magnetic properties (susceptibility, magnetic structure) of sulfur and selenium containing olivines which are closely related to the title compound, have been carried out in the past. They were initiated by the surprising observation of a *sharp* local $1/\chi$ minimum between 83 and 85 K for $Mn_2SiS_4$[2,3,4] accompanied by the occurrence of "weak ferromagnetism". This effect might be related to "metamagnetism" occurring in certain antiferromagnetic compounds under special conditions as a function of an external field (see, for example, ref.[5]). Indeed below 85 K $Mn_2SiS_4$ is antiferromagnetic with a change of the easy direction from [010] to [100] between 83 and 85 K. Above 85 K the compound is paramag-

 © 2007 Wiley-VCH Verlag GmbH & Co. KGaA, Weinheim 

netic. In particular the *sharp* local $1/\chi$ minimum is unique among the chalcogen containing olivines investigated so far. A further example is $Mn_2SiSe_4$ which is comparable to $Mn_2SiS_4$ in its *general* susceptibility behaviour, but is characterized by a *broad* local $1/\chi$ minimum between 66 and 30 K[6,7]. The $Mn^{2+}$ ions in $Mn_2SiSe_4$ show an antiferromagnetic ordering (easy direction: [001]). A complex behaviour with respect to the temperature dependence of susceptibility and magnetization was discussed on the basis of several measurements in two independent publications for the olivine type $Fe_2GeS_4$ ($T_N$ = 144 K)[3,8]. This compound shows an antiferromagnetic ordering below 144 K (easy direction [010]) followed by a change of the easy direction to [001] at lower temperatures. The susceptibility behaviour of $Mn_2GeS_4$ is unknown but its antiferromagnetic structure was determined at 4.2 K[9] (easy direction [010]).

## The Olivine Structure

Some important aspects of the well known olivine structure[10] with respect to an understanding of the magnetic structure of $Mn_2GeSe_4$ are summarized subsequently. Olivine and spinel are frequent competitors for solids with the general chemical composition $A_2BX_4$. The olivine structure is preferred if relatively large cations (A = $Mn^{2+}$) occupy the octahedral and relatively small cations (B = $Ge^{4+}$) the tetrahedral holes. The opposite is true for spinel (further details see, for example, ref.[11,12]).

Concerning the magnetic structure it is important to mention that the $MnSe_6$ octahedra are arranged in layers perpendicular to [001] at $z \approx 0$ and $z \approx 0.5$. *Inside* the layers the octahedra share *common edges* and form zig-zag chains which are separated by $GeSe_4$ tetrahedra. Between successive layers along [001] the $AX_6$ octahedra share *corners* only (Figure 1). A section of the resulting three dimensional arrangement of the $Mn^{2+}$ ions in layers perpendicular to [001] referring to the just mentioned zig-zag arrangement of $MnSe_6$ octahedra is shown in Figure 2. It can be seen that the $Mn^{2+}$ ions form isolated triangular strands along [010]. In the (110) plane the strands are separated by $GeSe_4$ tetrahedra (not shown in Figures 1 and 2). Interatomic distances between $Mn^{2+}$ ions inside the strands are around 400 pm between adjacent strands they are greater than 479 pm in all directions.

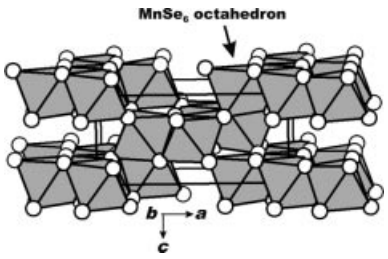


Figure 1. Section of the $Mn_2GeSe_4$ structure emphasizing the arrangement of the $MnSe_6$ octahedra. The $GeSe_4$ tetrahedra are omitted for clarity.

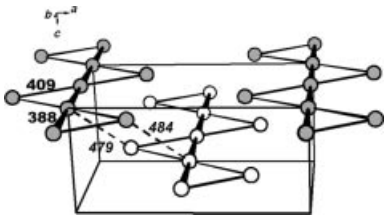


Figure 2. Perspective drawing of the arrangement of $Mn^{2+}$ ions (approximately along [010]) in $Mn_2GeSe_4$ with shortest interatomic distances *d*(Mn–Mn) inside and between the strands.

## Magnetic Structure and Magnetization

Figure 3 shows a Rietveld plot (3 K) and Figure 4 neutron scattering diagrams (D2B, low 2Theta section) for three different temperatures (3, 63 and 196 K). Upon cooling below 66 K five significant magnetic reflections with increasing intensity can be indexed as 100, 110, 300, 310 and 120. The Miller indices of these magnetic reflections can be assigned on the basis of the chemical unit cell, but apparently violate the a-glide plane in *Pnma*. They are similar to those ones found in the 1.4 K measurement for $Mn_2SiSe_4$[6,7] but are different from the ones found for $Fe_2GeS_4$[8] at 85 and 4.2 K.

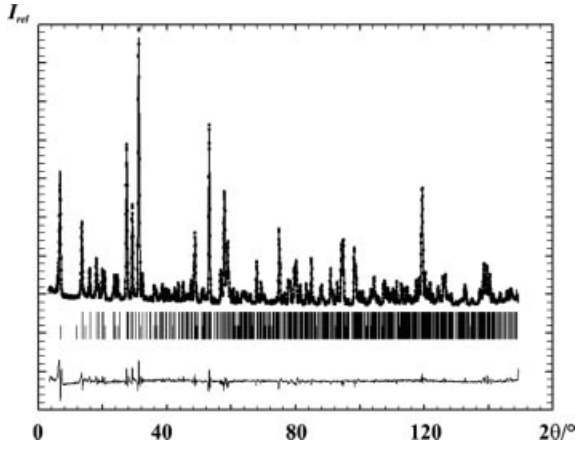


Figure 3. A Rietveld plot of a neutron scattering measurement of $Mn_2GeSe_4$ at 3 K.

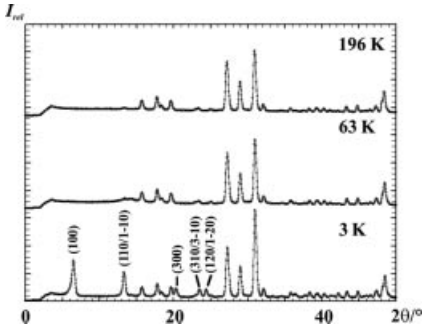


Figure 4. Neutron scattering diagrams for $Mn_2GeSe_4$ at 196, 63 and 3 K. The magnetic reflections are marked by their Miller indices.

 © 2007 Wiley-VCH Verlag GmbH & Co. KGaA, Weinheim 

As in the case of $Mn_2SiSe_4$, [001] reflections are basically absent (see however discussion below). This indicates an antiferromagnetic arrangement of $Mn^{2+}$ ions in the layers at $z \approx 0$ and $z \approx 0.5$ with the magnetic vector aligned along [001] ("easy direction") similar to the magnetic structure of $Mn_2SiSe_4$ (see above). In accordance with $Mn_2SiSe_4$ we assumed for our initial Rietveld refinements (3 K data obtained with the D2B instrument) a model based on an ordered magnetic phase characterized by a $C_z(4a) - C_z(4b)$ coupling. 4a and 4b are the Wyckoff positions for the two crystallographically different $Mn^{2+}$ ions and $C_z$ refers to Bertauts notation[13] for this type of coupling in space group *Pnma*. Relevant refinement data for different temperatures based on the magnetic reflections are given in Table 1. Further details are discussed in ref.[14]

Table 1. Reliability factors for the chemical ($R_B$) and the magnetic structure (magnetic $R$) of $Mn_2GeSe_4$ between 10 and 65 K as obtained by Rietveld refinements with neutron powder data at different temperatures.

| $T$/K | $M_{4a}/\mu_B$ | $M_{4c}/\mu_B$ | $R_B$/%[a] | Magnetic $R$/%[b] |
|---|---|---|---|---|
| 10 | 4.11(4) | 4.26(5) | 2.76 | 9.99 |
| 12 | 4.05(4) | 4.23(5) | 3.36 | 10.1 |
| 15 | 3.97(4) | 4.22(5) | 2.87 | 10.7 |
| 17 | 3.90(4) | 4.20(5) | 2.80 | 11.0 |
| 20 | 3.84(4) | 4.17(5) | 2.77 | 11.3 |
| 24 | 3.74(4) | 4.14(5) | 3.09 | 12.0 |
| 28 | 3.61(4) | 4.13(5) | 3.08 | 12.7 |
| 32 | 3.48(4) | 4.05(5) | 3.30 | 13.8 |
| 36 | 3.30(4) | 3.99(5) | 3.34 | 15.2 |
| 43 | 3.06(4) | 3.84(5) | 3.64 | 17.4 |
| 46 | 2.82(4) | 3.70(5) | 3.92 | 19.6 |
| 49 | 2.64(4) | 3.53(6) | 4.21 | 21.9 |
| 52 | 2.46(4) | 3.39(6) | 4.38 | 24.9 |
| 55 | 2.29(5) | 3.21(6) | 4.26 | 28.3 |
| 57 | 2.04(5) | 2.97(7) | 4.95 | 33.2 |
| 59 | 1.94(5) | 2.85(7) | 4.96 | 34.7 |
| 61 | 1.72(6) | 2.61(7) | 5.17 | 40.9 |

[a] $R_B = [\sum_h |I_{obs,h} - I_{calc,h}|]/[\sum_h |I_{obs,h}|]$. [b] The magnetic $R$ is defined as $R_B$ but it is applied to magnetic intensities.

As a result of these initial calculations it can be stated that the magnetic structures of $Mn_2SiSe_4$ and the title compound (Figure 5, a) are similar, except a possible transverse component of one of the magnetic sublattices (see below). In most of the other chalcogeno-olivines investigated up to now such a transverse component of at least one magnetic sublattice is superimposed to the general antiferromagnetic order. Such transverse components evolve either continuously with decreasing temperature or they occur in an intermediate temperature range. A good example is the just mentioned $Mn_2SiSe_4$ where a transverse component was discussed but could not be verified significantly by the magnetic structure.[6,7] Indeed a closer inspection of details of the magnetic scattering diagrams of the title compound in combination with Rietveld refinements based on the D2B data showed a weak indication for a transverse component of *one* of the two magnetic sublattices (Figure 5, b). In particular the very weak and somewhat diffuse scattering intensity at the 2Theta position where the magnetic 001 reflection occurs (marked by an arrow in Figure 4) is a (weak) indicator for a possible deviation from the [001] direction. There is low significance but an apparent tendency from our refinement calculations that this deviation is associated to those $Mn^{2+}$ ions which belong to the Wyckoff position 4(a). A final proof based on the existing data is, however, not possible presently.

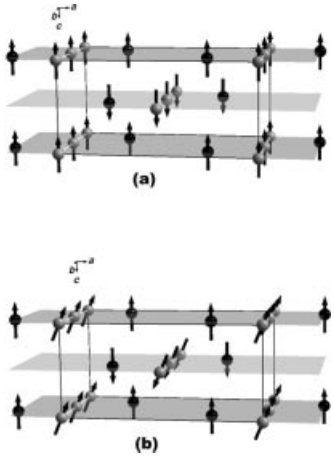


Figure 5. (a) The magnetic structure of $Mn_2GeSe_4$ as obtained by *initial* Rietveld refinements based on 3 K neutron scattering data. Mn atoms belonging to Wyckoff position 4(a): light gray balls, Wyckoff position 4(b): black balls. (b) Possible magnetic structure below 66 K including a deviation of the $Mn^{2+}$ in Wyckoff position 4(a) from the easy direction [001] towards [100] (qualitative representation of the unknown inclination angle).

It is further interesting to look at the magnetization per $Mn^{2+}$ ion for the two magnetic sublattices (Figure 6), derived from the evaluation of the D20 neutron data. One can see clearly that the successive ordering with decreasing temperature evolves with different velocities for the two sublattices, although both end up with a resultant magnetization per $Mn^{2+}$ ion of 4.25 $\mu_B$. This value corresponds to the one found for $Mn_2SiSe_4$ (4.5 $\mu_B$ see ref.[6,7]) and is in good agreement with the assumed $d^5$ configuration for $Mn^{2+}$.

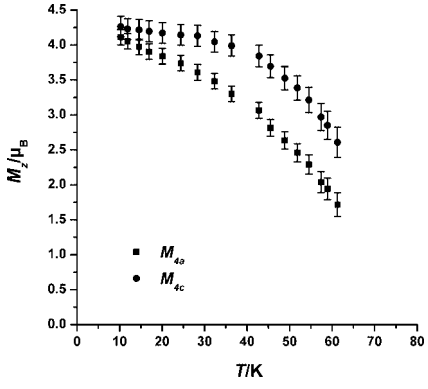


Figure 6. The resultant magnetization for the two magnetic sublattices as derived from the refinements of powder neutron diffraction diagrams between 10 and 60 K.

 © 2007 Wiley-VCH Verlag GmbH & Co. KGaA, Weinheim 

Neither the deviation alone nor the antiferromagnetic basis structure, however, account for the very weak resultant ferromagnetic magnetization ($< 0.05\ \mu_B$ per $Mn^{2+}$ ion) of the title compound even in low fields at low temperatures. As Figure 7 shows this weak magnetization, which may result from non-compensating local components in the overall antiferromagnetic sample, saturates even in an external field of 7 T to about 0.5 $\mu_B$ per $Mn^{2+}$ ion only.

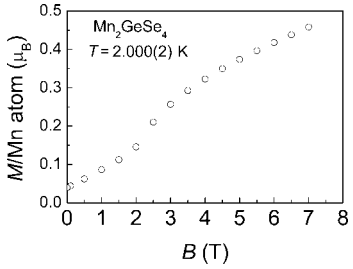


Figure 7. The resultant overall magnetization per $Mn^{2+}$ at 2 K in an external field between 0 and 7 T.

One cannot expect from neutron powder diffraction data to reflect the origin of such a weak resultant magnetization in the magnetic structure. Speculations about magnetically non compensated grain boundaries and domain size effects as possible origins can be found in the literature (e.g., ref.[6,7]). Moreover we note the slight anomaly in the *M* vs. *B* curve (Figure 7) between 2 and 4 T which is not discussed in this paper but seems to be an indication for more subtle magnetic properties of the title compound.

## Experimental Section

Powder samples of $Mn_2GeSe_4$ were obtained by the experimental procedure described in ref.[1] The neutron diffraction measurements were carried out with the D2B and D20 powder diffractometer at the ILL in Grenoble with samples contained in cylindrical vanadium containers and loaded into a standard helium flow cryostat. Data were collected at the temperatures 3 K, 63 K, 196 K (D2B) and with the instrument D20 in the temperature range 10 K $< T <$ 75 K using different $\Delta T$ steps. The wavelength was 1.594 Å. Data sets cover a range in $2\Theta$ up to 160° and have an angular resolution of 0.05°. The Rietveld method (Fullprof package[15,16]) was used to refine at first the chemical structure at room temperature. In subsequent refinement cycles based on low temperature data various refinement strategies were used. In these calculations the magnetic moment vectors of all eight $Mn^{2+}$ ions in the Wyckoff positions 4(a) and 4(c) were refined either independently or partly fixed by constraints. The room-temperature data served as basis for the positional parameters of the chemical structure. In addition to the magnetic moment vectors only thermal parameters and lattice constants were refined with low-temperature data.

## Acknowledgments

The authors are grateful to the Deutsche Forschungsgemeinschaft (DFG) and Fonds der Chemischen Industrie for their continuous financial support. Helpful discussions with Prof. Dr. H. Lueken and Dr. P. Mueller (RWTH Aachen) are acknowledged.

[1] H. J. Deiseroth, K. Aleksandrov, R. K. Kremer, *Z. Anorg. Allg. Chem.* **2005**, *631*, 448–450.
[2] A. M. Lamarche, G. Lamarche, C. Church, J. C. Woolley, I. P. Swainson, *J. Magnetism Magnet. Mater.* **1994**, *137*, 305–312.
[3] A. Junod, K. Q. Wang, G. Triscone, G. Lamarche, *J. Magnetism Magnet. Mater.* **1995**, *146*, 21–29.
[4] G. Lamarche, F. Lamarche, A. M. Lamarche, *Physica B* **1994**, *B194–196*, 219–220.
[5] E. A. Nagelschmitz, W. Jung, R. Feiten, P. Müller, H. Lueken, *Z. Anorg. Allg. Chem.* **2001**, *627*, 523–532.
[6] F. Bodénan, V. B. Cajipe, G. Ouvrard, G. André, *J. Magnetism. Magnet. Mater.* **1996**, *164*, 233–240.
[7] S. Jobic, F. Bodénan, P. Le Boterf, G. Ouvrard, *J. Alloys Compd.* **1995**, *230*, 16–22.
[8] H. Vincent, E. F. Bertaut, *J. Phys. Chem. Solids* **1973**, *34*, 151–158.
[9] T. Duc, H. Vincent, E. F. Bertaut, V. van Qui, *Sol. State Commun.* **1969**, *7*, 641–645.
[10] R. W. G. Wyckoff, *Crystal Structures*, 2nd ed., vol. 3, Interscience Publisher Inc., New York, **1965**.
[11] K. Kugimiya, H. Steinfink, *Inorg. Chem.* **1968**, *7*, 1762–1770.
[12] H. Vincent, E. F. Bertaut, W. H. Baur, R. D. Shannon, *Acta Crystallogr., Sect. B* **1976**, *32*, 1749–1755.
[13] E. F. Bertaut, *Acta Crystallogr., Sect. A* **1968**, *24*, 217–231.
[14] H. Mikus, PhD Thesis, in progress, University of Siegen (Germany).
[15] J. Rodriguez-Carvajal, *FULLPROF*, Version 3.20 (**2005**), Laboratoire Léon Brillouin (CEA-CNRS), France.
[16] T. Roisnel, J. Rodriguez-Carvajal, *WINPLOTR* (**2005**), Laboratoire Léon Brillouin (CEA-CNRS), France.

Received: August 18, 2006
Published Online: February 26, 2007

 © 2007 Wiley-VCH Verlag GmbH & Co. KGaA, Weinheim 

DOI: 10.1002/ejic.200601102

# Synthesis, Characterization, and Catalytic Activity of Some Neodymium(III), Ytterbium(II), and Europium(II) Complexes with Pyrrolidinyl- and Piperidinyl-Functionalized Indenyl Ligands

**Shuangliu Zhou,[a] Shaowu Wang,*[a,b] Enhong Sheng,[a] Lijun Zhang,[a] Zeyan Yu,[a] Xiaobing Xi,[a] Guodong Chen,[a] Wei Luo,[a] and Yan Li[a]**

**Keywords:** Homolysis / Catalysts / Polymerization / Lanthanoids

A series of organolanthanide complexes with pyrrolidinyl- and piperidinyl- functionalized indenyl ligands were synthesized by reaction of $[(Me_3Si)_2N]_3Ln^{III}(\mu\text{-}Cl)Li(THF)_3$ (Ln = Yb, Eu, Nd) with the corresponding indene compounds. Treatment of $[(Me_3Si)_2N]_3Yb^{III}(\mu\text{-}Cl)Li(THF)_3$ with 2 equiv. of $C_9H_6$-1-R-3-$CH_2SiMe_2NC_4H_8$ (R = H, $CH_3$) in refluxing toluene produced the corresponding organoytterbium(II) complexes with formula $[\eta^m{:}\eta^1\text{-}C_9H_5\text{-}1\text{-}R\text{-}3\text{-}CH_2SiMe_2NC_4H_8]_2Yb^{II}$ [$m$ = 5, R = H (**2**); $m$ = 3, R = $CH_3$ (**3**)] in 49 and 58 % yield, respectively. Treatment of $[(Me_3Si)_2N]_3Ln^{III}(\mu\text{-}Cl)Li(THF)_3$ (Ln = Yb, Eu, Nd) with 2 equiv. of $C_9H_7CH_2SiMe_2NC_5H_{10}$ (**1**) in toluene at moderately high temperatures afforded, after workup, the corresponding organolanthanide complexes with formula $[\eta^5{:}\eta^1\text{-}C_9H_6CH_2SiMe_2NC_5H_{10}]_2Yb^{II}$ (**4**), $[\eta^5{:}\eta^1\text{-}C_9H_6CH_2SiMe_2NC_5H_{10}]_2Eu^{II}$ (**5**), and $[C_9H_6CH_2SiMe_2NC_5H_{10}]_3Nd^{III}\cdot THF$ (**6**) in 37, 71, and 29 % yield, respectively. All the compounds were fully characterized by spectroscopic methods and elemental analyses. The structures of complexes **2**, **3**, **5**, and **6** were additionally determined by single-crystal X-ray analyses. The catalytic properties of all the organolanthanide complexes on the ring-opening polymerization of ε-caprolactone have been studied. The effects of temperature, solvent, and coordination on the catalytic activities of the complexes were examined.
(© Wiley-VCH Verlag GmbH & Co. KGaA, 69451 Weinheim, Germany, 2007)

## Introduction

Over the past few decades, great progress has been made in the chemistry of divalent organolanthanide complexes. Divalent organolanthanide complexes exhibited a particularly rich reaction chemistry based on their strong reductive properties.[1] A variety of complexes have been synthesized and used in organic synthesis and polymer chemistry.[2] Generally, divalent organolanthanide complexes were synthesized by metathesis reaction of alkaline metal salts of a ligand with $LnI_2$ or by reductive reaction of lanthanide(III) halides with metallic atoms.[3]

Lanthanide complexes have received much interest for their potential application as homogeneous catalysts or catalyst precursors for various useful transformations such as olefin polymerization,[4] hydroamination of olefins and alkynes,[5] hydrophosphination of olefins and alkynes,[6] Tishchenko reactions,[7] ring-opening polymerization of ε-caprolactone and δ-valerolactone,[8] and insertion reactions.[9] Recently, our group has reported that the tetracoordinate lanthanide amides $[(Me_3Si)_2N]_3Ln^{III}(\mu\text{-}Cl)Li(THF)_3$ can work as efficient catalysts for the aldol-condensation reaction,[10] or initiators for the Cannizzaro-type disproportionation of aromatic aldehydes to amides and alcohols.[11]

At the same time, we have also demonstrated that the interactions of indene compounds having nitrogen-containing substituents or oxygen-containing substituents with the lanthanide(III) amides $[(Me_3Si)_2N]_3Ln(\mu\text{-}Cl)Li(THF)_3$ (Ln = Yb, Eu) produced organolanthanide(II) complexes.[12] The formation pathway of the organolanthanide(II) complexes is proposed to proceed through a tandem silylamine elimination[13]/homolysis of the Ln–N bonds, thus it provides a new methodology for the preparation of the lanthanide(II) complexes. Especially, the reaction of heterocyclic-functionalized indene compound $C_9H_7CH_2SiMe_2NC_4H_8$ with the europium(III) amide $[(Me_3Si)_2N]_3Eu(\mu\text{-}Cl)Li(THF)_3$ has led to the isolation and characterization of the unexpected novel triple-decker tetranuclear europium(II) complex with the linked indenyl ligands,[12e] and a novel ytterbium(II) complex having the indenyl ligand bonded to the metal through a benzo ring with an $\eta^4$ hapticity has been isolated and characterized by treatment of the *N*-piperidinylethyl functionalized indene compound with the ytterbium(III) amide $[(Me_3Si)_2N]_3Yb(\mu\text{-}Cl)Li(THF)_3$,[12d] indicating the ligands' effects on the reactivity patterns and coordination modes. In order to further study the reduction potentials of the lanthanides and the ligands' effect on reactivity patterns and the bonding modes between the ligands

[a] Anhui Key Laboratory of Functional Molecular Solids, Institute of Organic Chemistry, School of Chemistry and Materials Science, Anhui Normal University,
Wuhu, Anhui 241000, China
[b] State Key Laboratory of Organometallic Chemistry, Shanghai Institute of Organic Chemistry, Chinese Academy of Sciences, Shanghai 200032, China

 © 2007 Wiley-VCH Verlag GmbH & Co. KGaA, Weinheim 

and the lanthanide metals, we have studied the reactions of $C_9H_6$-1-R-3-$CH_2SiMe_2NC_4H_8$ (R = H, Me), and $C_9H_7CH_2SiMe_2NC_5H_{10}$ with the lanthanide(III) amides $[(Me_3Si)_2N]_3Ln(\mu\text{-}Cl)Li(THF)_3$ (Ln = Yb, Eu, Nd).

In this paper, we will report the interactions of $C_9H_6$-1-R-3-$CH_2SiMe_2NC_4H_8$ (R = H, Me), and $C_9H_7CH_2SiMe_2NC_5H_{10}$ with the lanthanide(III) amides $[(Me_3Si)_2N]_3Ln(\mu\text{-}Cl)Li(THF)_3$ (Ln = Yb, Eu, Nd) leading to preparation and characterization of a series of new organolanthanide(II) complexes and an organoneodymium(III) complex. The catalytic activities of these complexes as single-component ε-caprolactone polymerization catalysts were also examined.

## Results and Discussion

### Synthesis and Characterization of $C_9H_7CH_2SiMe_2NC_5H_{10}$ (1)

Interaction of $C_9H_7Li$ with 1 equiv. of $ClSiMe_2CH_2Cl$, followed by treatment with 1 equiv. of lithium piperidinide $C_5H_{10}NLi$, gave piperidinyl-functionalized indene compound $C_9H_7CH_2SiMe_2NC_5H_{10}$ (**1**) in good yield (Scheme 1). The compound was fully characterized by spectroscopic methods and elemental analysis. The nucleophilic substitution reaction of $C_9H_7Li$ with $ClSiMe_2CH_2Cl$ occurs at the C–Cl bond, not at the Si–Cl bond on the basis of the NMR analyses of the reaction products. Similar results were observed in the reaction of $C_5Me_4HLi$ or $Ph_2PLi$ with $ClSiMe_2CH_2Cl$, giving the corresponding product $C_5HMe_4CH_2SiMe_2Cl$[14] or $Ph_2PCH_2SiMe_2Cl$,[15] indicating the electronic and steric effects on the reactivity of the C–Cl and Si–Cl bonds.

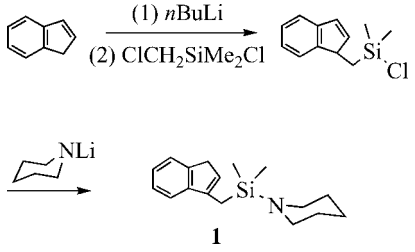


Scheme 1.

### Synthesis and Characterization of Organolanthanide Complexes with Pyrrolidinyl- and Piperidinyl-Functionalized Indenyl Ligands

Treatment of the lanthanide(III) amides $[(Me_3Si)_2N]_3Ln^{III}(\mu\text{-}Cl)Li(THF)_3$ (Ln = Yb, Eu) with 2 equiv. of $C_9H_6$-1-R-3-$CH_2SiMe_2NC_4H_8$ (R = H, $CH_3$) and $C_9H_7CH_2SiMe_2NC_5H_{10}$ in toluene produced the lanthanide(II) complexes with formula $[\eta^m\text{:}\eta^1\text{-}C_9H_5\text{-}1\text{-}R\text{-}3\text{-}CH_2SiMe_2NC_4H_8]_2Yb^{II}$ [*m* = 5, R = H (**2**); *m* = 3, R = $CH_3$(**3**)] and $[\eta^5\text{:}\eta^1\text{-}C_9H_6CH_2SiMe_2NC_5H_{10}]_2Ln^{II}$ [Ln = Yb(**4**); Ln = Eu(**5**)] (Scheme 2). The complexes **2**, **3**, **4**, and **5** are sensitive to air and moisture, they are soluble in polar solvents such as THF, DME, and pyridine, and slightly soluble in toluene, but insoluble in *n*-hexane. All the complexes were fully characterized by spectroscopic methods and elemental analyses. The structures of the complexes **2**, **3**, and **5** were determined by single-crystal X-ray analyses. X-ray analyses showed that the complexes **2**, **3**, and **5** were a monomeric structure, not a triple-decker sandwich tetranuclear structure analogous to the complex[12e] from the reaction of $[(Me_3Si)_2N]_3Eu^{III}(\mu\text{-}Cl)Li(THF)_3$ with $C_9H_7CH_2SiMe_2NC_4H_8$, probably due to different reduction potentials of lanthanide ions, and the ligands' steric and electronic effects.

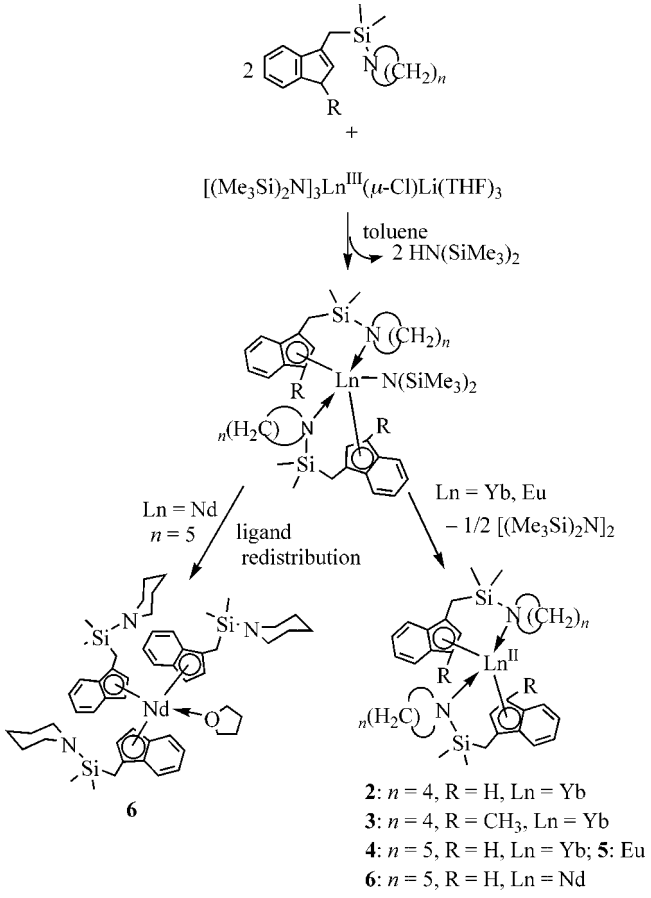


Scheme 2.

Estimated $Ln^{3+}/Ln^{2+}$ reduction potentials are as follows:[16] $E°(Eu^{3+}/Eu^{2+})$ = –0.35 V, $E°(Yb^{3+}/Yb^{2+})$ = –1.15 V, $E°(Nd^{3+}/Nd^{2+})$ = –2.62 V. This suggested that europium(III) and ytterbium(III) could be more easily reduced to europium(II) and ytterbium(II) than other lanthanide(III) metal ions. To probe reduction potential effects on the reactivity, the reaction of $[(Me_3Si)_2N]_3Nd^{III}(\mu\text{-}Cl)Li(THF)_3$ with $C_9H_7CH_2SiMe_2NC_5H_{10}$ (**1**) was studied.

The reaction of $[(Me_3Si)_2N]_3Nd^{III}(\mu\text{-}Cl)Li(THF)_3$ with 2 equiv. of $C_9H_7CH_2SiMe_2NC_5H_{10}$ (**1**) in refluxing toluene produced, after recrystallization from *n*-hexane, a neodymium(III) complex $[C_9H_6CH_2SiMe_2NC_5H_{10}]_3Nd^{III}\cdot THF$ (**6**) (Scheme 2). The complex is sensitive to air and moisture. It is soluble in THF, DME, toluene, and pyridine, and slightly

 © 2007 Wiley-VCH Verlag GmbH & Co. KGaA, Weinheim 

soluble in *n*-hexane. The complex was fully characterized by spectroscopic methods and elemental analysis. Its structure was determined by single-crystal X-ray analysis. X-ray analysis showed that complex **6** is a trivalent neodymium(III) complex composed of three indenyl ligands π-bonded with the central metal and one coordinated tetrahydrofuran. Homolysis of the Nd–N bond was not observed probably due to the reduction potential of the $Nd^{3+}/Nd^{2+}$ and steric effects.

We have proved that the interactions of indene compounds without donor-substituted groups on the indene ring with lanthanide(III) amides $[(Me_3Si)_2N]_3Ln(\mu\text{-}Cl)Li(THF)_3$ (Ln = Yb, Eu) produced lanthanide(III) amides $(Ind')_2LnN(SiMe_3)_2$ (Ind′ = indenyl- or ethylene-bridged indenyl ligands), while the interactions of the heteroatom side-arm functionalized indene compounds with $[(Me_3Si)_2N]_3Ln(\mu\text{-}Cl)Li(THF)_3$ (Ln = Yb, Eu) produced lanthanide(II) complexes; the formation pathway of the lanthanide(II) complexes has been proposed via a tandem silylamine elimination/homolysis of the Ln–N bond (Ln = Yb, Eu) based on the experimental results.[12] Thus, the formation of the above europium(II) and ytterbium(II) complexes is proposed to go through a tandem silylamine elimination/homolysis of the Ln–N (Ln = Yb, Eu) bonds, but the formation of neodymium(III) complex **6** may go through a silylamine elimination, followed by a ligand redistribution reaction (Scheme 2).

### Molecular Structures of Complexes 2, 3, 5, and 6

X-ray analyses revealed that the central metal ions of the complexes **2** (Figure 1), **3** (Figure 2), and **5** (Figure 3) exist in a +2 oxidation state. The results further confirmed that the formation of these organolanthanide(II) complexes involves a one-electron reductive elimination process. The selected bond lengths and angles are listed in Table 1. It can be seen that the lanthanide contraction is clearly reflected by the average Ln–C and Ln–N distances.

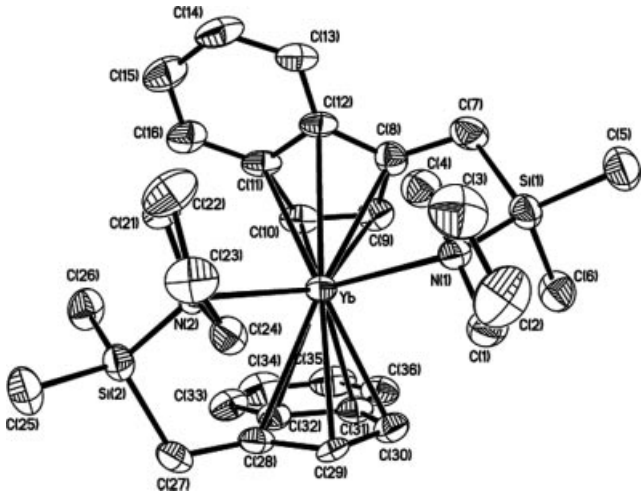


Figure 1. Molecular structure of $[\eta^5:\eta^1\text{-}(C_9H_6CH_2SiMe_2NC_4H_8)]_2Yb^{II}$ (**2**). Hydrogen atoms are omitted for clarity.

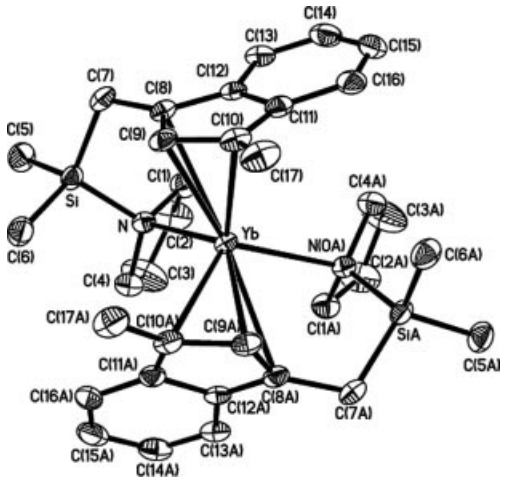


Figure 2. Molecular structure of $[\eta^3:\eta^1\text{-}C_9H_5\text{-}1\text{-}CH_3\text{-}3\text{-}CH_2SiMe_2NC_4H_8]_2Yb^{II}$ (**3**). Hydrogen atoms are omitted for clarity.

Table 1. Selected bond lengths [Å] and bond angles [°].

| **2** | | **3** | | **5** | | **6** | |
|---|---|---|---|---|---|---|---|
| Yb–N(1) | 2.671(8) | Yb–N | 2.634(4) | Eu(1)–N(1) | 2.794(2) | Nd(1)–O(1) | 2.547(4) |
| Yb–N(2) | 2.619(7) | | | | | Nd(1)–C(1) | 2.718(5) |
| Yb–C(8) | 2.792(9) | Yb–C(8) | 2.811(4) | Eu(1)–C(1) | 2.802(3) | Nd(1)–C(2) | 2.719(5) |
| Yb–C(9) | 2.649(9) | Yb–C(9) | 2.714(4) | Eu(1)–C(2) | 2.813(3) | Nd(1)–C(3) | 2.921(5) |
| Yb–C(10) | 2.672(9) | Yb–C(10) | 2.794(4) | Eu(1)–C(3) | 2.941(3) | Nd(1)–C(8) | 2.980(5) |
| Yb–C(11) | 2.889(8) | Yb–C(11) | 2.944(4) | Eu(1)–C(8) | 2.968(3) | Nd(1)–C(9) | 2.844(5) |
| Yb–C(12) | 2.930(8) | Yb–C(12) | 2.929(4) | Eu(1)–C(9) | 2.900(2) | Nd(1)–C(18) | 2.720(5) |
| Yb–C(28) | 2.798(9) | | | | | Nd(1)–C(19) | 2.714(5) |
| Yb–C(29) | 2.713(8) | | | | | Nd(1)–C(20) | 2.896(5) |
| Yb–C(30) | 2.708(9) | | | | | Nd(1)–C(25) | 2.966(5) |
| Yb–C(31) | 2.840(9) | | | | | Nd(1)–C(26) | 2.859(5) |
| Yb–C(32) | 2.868(9) | | | | | Nd(1)–C(35) | 2.724(5) |
| | | | | | | Nd(1)–C(36) | 2.708(5) |
| | | | | | | Nd(1)–C(37) | 2.954(5) |
| | | | | | | Nd(1)–C(42) | 3.043(5) |
| N(2)–Yb–N(1) | 106.6(2) | N–Yb–N#1 | 106.50(16) | N(1)#1–Eu(1)–N(1) | 109.99(8) | Nd(1)–C(43) | 2.908(5) |
| Yb–C(av) | 2.786(9) | Yb–C(av) | 2.838(4) | Eu–C(av) | 2.885(3) | Nd–C(av) | 2.845(5) |

 © 2007 Wiley-VCH Verlag GmbH & Co. KGaA, Weinheim 

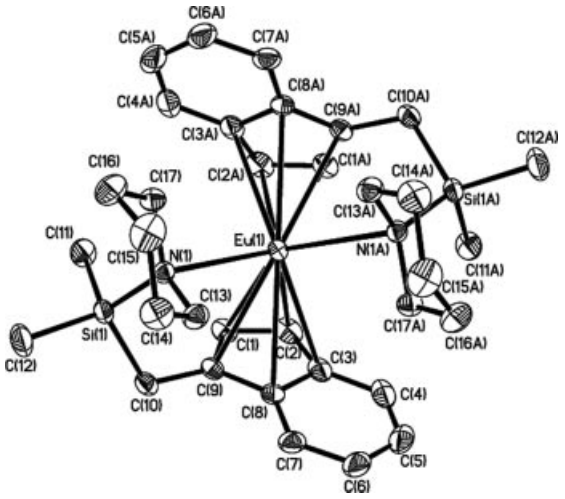


Figure 3. Molecular structure of $[\eta^5{:}\eta^1\text{-}C_9H_6CH_2SiMe_2NC_5H_{10}]_2\text{-}Eu^{II}$ (**5**). Hydrogen atoms are omitted for clarity.

From Table 1, we can see that the Yb–C bond lengths in complex **2** range from 2.649(9) to 2.930(8) Å, with an average of 2.786(9) Å, which is comparable to the average Yb–C distances of 2.806(12) and 2.778(14) Å found in the corresponding indenyl ytterbium(II) complexes $[\eta^5{:}\eta^1\text{-}Me_2Si(Me_2NCH_2CH_2C_9H_5)(NHtBu)]_2Yb^{II}$,[12a] $[\eta^5{:}\eta^1\text{-}(Me_2NCH_2CH_2C_9H_5SiMe_3)]_2Yb^{II}$.[12a] This average Yb–C distance of 2.786(9) Å found in **2** is longer than the corresponding values of 2.722(10) Å found in $[\eta^5{:}\eta^1\text{-}(Me_2NCH_2CH_2C_9H_6)]_2Yb^{II}$,[12a] 2.723(14) Å found in $[\eta^5{:}\eta^1\text{-}(2\text{-}C_5H_4NCH_2)C_9H_6]_2Yb^{II}$,[12f] 2.737(4) Å found in $[\eta^5{:}\eta^1\text{-}(MeOCH_2CH_2C_5H_4)]_2Yb^{II}(THF)$,[17] and 2.75 Å found in $[Me_3Si(C_5H_4)]_2Yb(THF)_2$.[18] The above differences in the average Yb–C distances of different ytterbium(II) complexes may be due to steric effects and ionic radii differences.

The Yb to C(11) and C(12), which are shared by both C5 and C6 rings, distances of 2.944(4) and 2.929(4) Å in complex **3** are significantly longer than those of others [ranging from 2.714(4) to 2.811(4) Å], suggesting that the Yb atom tends to bond with indenyl ligands in an $\eta^3$-mode. The average Yb–C distance of 2.838(4) Å found in **3** is obviously longer than the corresponding value of 2.786(9) Å found in **2**. This distance is also longer than those of 2.818(3) Å in $[\eta^5\text{-}Me_2Si(C_9H_6)(C_2B_{10}H_{11})]Yb(THF)[(\mu\text{-}\eta^5){:}\sigma\text{-}Me_2Si(C_9H_6)(C_2B_{10}H_{10})]Na(THF)_3$,[19] 2.814(7) Å in $[\eta^5{:}\eta^1{:}\sigma\text{-}Me_2Si(C_9H_5CH_2CH_2OMe)(C_2B_{10}H_{10})]Yb(DME)\text{-}(THF)$,[20] 2.806(12) Å in $[\eta^5{:}\eta^1\text{-}Me_2Si(Me_2NCH_2CH_2\text{-}C_9H_5)(NHtBu)]_2Yb^{II}$,[12a] 2.778(14) Å found in $[\eta^5{:}\eta^1\text{-}(Me_2NCH_2CH_2C_9H_5SiMe_3)]_2Yb^{II}$,[12a] and 2.732(18) Å in $[\eta^5{:}\eta^1\text{-}(C_4H_7OCH_2C_9H_5SiMe_3)]_2Ln^{II}$,[12g] indicating steric and electronic effects.

The average Yb–N bond length of 2.645(8) Å in **2** is compared with the average Yb–N distances of 2.634(4) Å in **3**, 2.673(11) Å in $[\eta^5{:}\eta^1\text{-}Me_2Si(Me_2NCH_2CH_2C_9H_5)(NHtBu)]_2\text{-}Yb^{II}$,[12a] and 2.650(12) Å in $[\eta^5{:}\eta^1\text{-}(Me_2NCH_2CH_2C_9H_5Si\text{-}Me_3)]_2Yb^{II}$,[12a] but longer than those of 2.561(7) Å in $[\eta^5{:}\eta^1\text{-}(2\text{-}C_5H_4NCH_2)C_9H_6]_2Yb^{II}$,[12f] and 2.588(7) Å in $[\eta^5{:}\eta^1\text{-}(Me_2NCH_2CH_2C_9H_6)]_2Yb^{II}$,[12a] respectively. The above difference in the average Yb–N distances in different ytterbium(II) complexes may be due to steric effects and

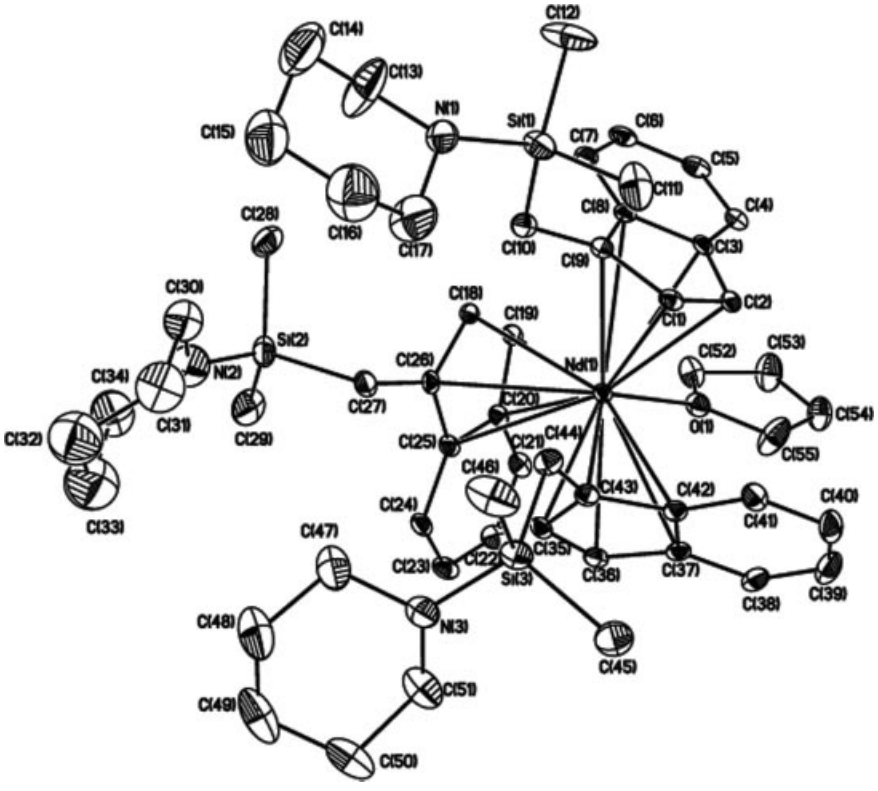


Figure 4. Molecular structure of $[C_9H_6CH_2SiMe_2NC_5H_{10}]_3Nd^{III}\cdot THF$ (**6**). Hydrogen atoms are omitted for clarity.

 © 2007 Wiley-VCH Verlag GmbH & Co. KGaA, Weinheim 

the hybridization state of nitrogen atoms. The N–Yb–N angle of 106.6(2)° in **2** is comparable to the corresponding angle of 106.50(16)° in **3**, but larger than the corresponding angles of 95.1(4), 92.8(5), and 103.7(2)° found in $[\eta^5{:}\eta^1$-$Me_2Si(Me_2NCH_2CH_2C_9H_5)(NHtBu)]_2Yb^{II}$,[12a] $[\eta^5{:}\eta^1$-$(Me_2NCH_2CH_2C_9H_5SiMe_3)]_2Yb^{II}$,[12a] and $[\eta^5{:}\eta^1$-$(Me_2NCH_2CH_2C_9H_6)]_2Yb^{II}$,[12a] respectively, suggesting steric and electronic effects.

The average Eu–C bond length of 2.885(3) Å in complex **5** is comparable to the average Eu–C bond lengths of 2.883(11), 2.873(10), and 2.841(7) Å found in the corresponding indenyl europium(II) complexes $[\eta^5{:}\eta^1$-$Me_2Si(Me_2NCH_2CH_2C_9H_5)(NHtBu)]_2Eu^{II}$,[12c] $[\eta^5{:}\eta^1$-$(Me_2NCH_2CH_2C_9H_5SiMe_3)]_2Eu^{II}$,[12c] and $[\eta^5{:}\eta^1$-$(Me_2NCH_2CH_2C_9H_6)]_2Eu^{II}$,[12c] but shorter than that of 2.911(18) Å in $[\eta^5{:}\eta^1$-$C_9H_5$-1-Me-3-$CH_2SiMe_2NC_4H_8]_2Eu^{II}$.[12e] The above differences in the average Eu–C bond lengths of different europium(II) complexes may be due to steric effects.

The average Eu–N bond length of 2.794(2) Å in **5** is longer than those of 2.753(16), 2.748(9), 2.744(8), and 2.711(6) Å found in $[\eta^5{:}\eta^1$-$C_9H_5$-1-Me-3-$CH_2SiMe_2NC_4H_8]_2Eu^{II}$,[12e] $[\eta^5{:}\eta^1$-$Me_2Si(Me_2NCH_2CH_2C_9H_5)(NHtBu)]_2Eu^{II}$,[12c] $[\eta^5{:}\eta^1$-$(Me_2NCH_2CH_2C_9H_5SiMe_3)]_2Eu^{II}$,[12c] and $[\eta^5{:}\eta^1$-$(Me_2NCH_2CH_2C_9H_6)]_2Eu^{II}$,[12c] respectively, suggesting steric effects. The N–Eu–N angle of 109.99(8)° in **2** is close to the corresponding angle of 110.19(15)° in $[\eta^5{:}\eta^1$-$C_9H_5$-1-Me-3-$CH_2SiMe_2NC_4H_8]_2Eu^{II}$,[12e] but larger than those of 96.1(3), 92.9(3), and 104.7(2)° found in $[\eta^5{:}\eta^1$-$Me_2Si(Me_2NCH_2CH_2C_9H_5)(NHtBu)]_2Eu^{II}$,[12c] $[\eta^5{:}\eta^1$-$(Me_2NCH_2CH_2C_9H_5SiMe_3)]_2Eu^{II}$,[12c] and $[\eta^5{:}\eta^1$-$(Me_2NCH_2CH_2C_9H_6)]_2Eu^{II}$,[12c] respectively, indicating steric and electronic effects.

X-ray analysis reveals that the central metal ion of complex **6** (Figure 4) exists in a +3 oxidation state, and the central metal in complex **6** is coordinated by three indenyl ligands tending to $\eta^3$ bonding modes based on the determined Nd–C distances, and by an oxygen atom of the tetrahydrofuran in $\eta^1$-mode.

The average value of the Nd–C distances of 2.845(5) Å found in **6** is longer than the average Nd–C distances of 2.83(3) Å found in $(C_9H_7)_3Nd{\cdot}THF$,[21] 2.836(9) Å found in $[Na(C_4H_8O)_6][Nd(\eta^5$-$C_9H_7)_3(\mu$-C1)$Nd(\eta^5$-$C_9H_7)_3]$,[22] but shorter than the average Nd–C distance of 2.91(5) Å found in $(C_5Me_5)_3Nd$,[23] indicating steric effects on the coordination and bonding.

### Ring-Opening Polymerization of ε-Caprolactone

The complexes as single-component catalysts in ε-caprolactone polymerization were examined. It was found that all of the complexes exhibited good catalytic activities for ring-opening polymerization of ε-caprolactone in toluene, THF, and DME (Table 2). From Table 2, we can see that the complexes with piperidinyl-functionalized indenyl ligands exhibited higher catalytic activities in temperature ranges of 60 to –30 °C than those of the complexes with pyrrolidinyl-functionalized indenyl ligands, indicating the ligands' effects on catalytic activities of the complexes. From Table 2, we can also see that the catalyst **3** showed a higher catalytic activity than that of the catalyst **2** especially at relatively high temperatures, probably due to different bonding modes between the ligands and the central metals.

Examination of the solvents effects on the catalytic activities of the catalysts **2**–**6** indicated that the catalytic activities of the catalysts have good activity in toluene, THF, or DME. Simultaneously, we found that the molecular weights of the polymers obtained in toluene were higher than those obtained in THF and DME, indicating the solvents' effects on the chain propagation process. It was also found that the molecular weight distributions of the polymers obtained in toluene were slightly broader than those obtained in THF and DME.

The results of the temperature effects on the catalytic activities of the complexes **2**–**6** are listed in Table 2. In the table, we can see that the complexes **4**–**6** showed high catalytic activities in temperature ranges of 60 to –30 °C, but the complexes **2**, and **3** showed the highest catalytic activities at 0 °C. It was also found that the molecular weights of the polymers generally increase as the polymerization temperatures decrease, indicating that a chain propagation process is favored at relatively low temperatures.

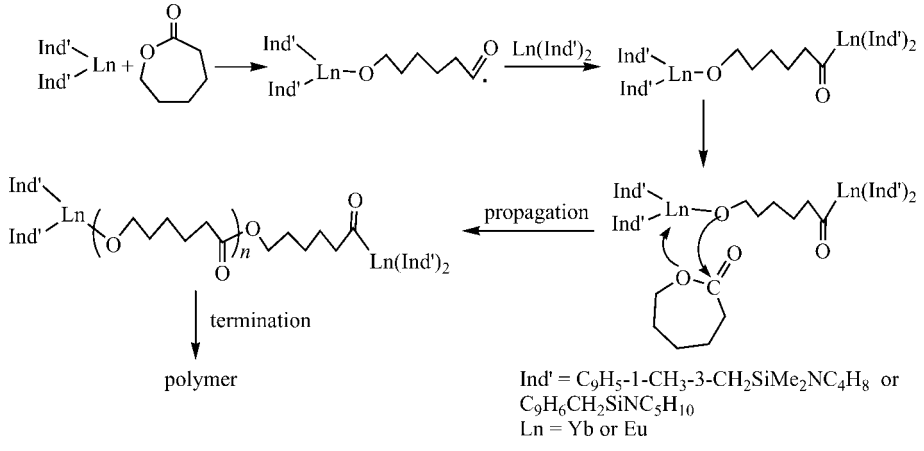


Scheme 3.

 © 2007 Wiley-VCH Verlag GmbH & Co. KGaA, Weinheim 

Table 2. Data for the polymerization of ε-caprolactone (ε-CL).[a]

| Catalyst | Solvent | *T*p /°C | Time /min | $M_n \times 10^{-4}$ | $M_w \times 10^{-4}$ | $M_w/M_n$ | Conv. % | Activity ($\times 10^{-6}$) |
|---|---|---|---|---|---|---|---|---|
| **2** | THF | 30 | 8 | 1.58 | 2.36 | 1.49 | 58 | 0.30 |
| | | 0 | 1 | 3.77 | 6.48 | 1.58 | 69 | 2.35 |
| | | –15 | 10 | 8.67 | 13.70 | 1.72 | 52 | 0.26 |
| | | –30 | 20 | – | – | – | 0 | 0 |
| | toluene | 30 | 20 | 5.67 | 9.93 | 1.75 | 57 | 0.10 |
| | | 0 | 1 | 1.11 | 3.13 | 2.82 | 67 | 2.78 |
| | | –15 | 1 | 6.24 | 16.9 | 2.71 | 47 | 1.96 |
| | | –30 | 1 | 8.31 | 15.8 | 1.90 | 63 | 2.59 |
| | DME | 30 | 20 | 0.99 | 1.45 | 1.46 | 42 | 1.43 |
| | | 0 | 12 | 2.17 | 3.31 | 1.53 | 51 | 1.76 |
| | | –15 | 20 | 1.18 | 1.81 | 1.53 | 9 | 0.065 |
| | | –30 | 20 | – | – | – | 0 | 0 |
| **3** | THF | 60 | 30 | 1.94 | 3.23 | 1.66 | 48 | 0.055 |
| | | 30 | 5 | 1.41 | 2.44 | 1.73 | 71 | 0.43 |
| | | 0 | 1 | 2.39 | 4.58 | 1.92 | 65 | 1.93 |
| | | –30 | 30 | 3.98 | 6.97 | 1.75 | 37 | 0.036 |
| | toluene | 60 | 30 | 2.38 | 4.86 | 2.04 | 51 | 0.051 |
| | | 30 | 5 | 2.64 | 4.67 | 1.77 | 78 | 0.47 |
| | | 0 | 1 | 3.18 | 4.41 | 1.39 | 57 | 1.71 |
| | | –30 | 30 | 4.84 | 8.66 | 1.79 | 46 | 0.046 |
| | DME | 60 | 30 | 1.63 | 2.11 | 1.30 | 40 | 0.039 |
| | | 30 | 5 | 3.27 | 5.94 | 1.82 | 67 | 0.40 |
| | | 0 | 1 | 3.93 | 6.90 | 1.76 | 52 | 1.55 |
| | | –30 | 30 | – | – | – | 0 | 0 |
| **4** | THF | 60 | 2 | 1.47 | 1.59 | 1.09 | 89 | 1.55 |
| | | 30 | 2 | 1.58 | 1.69 | 1.07 | 92 | 1.57 |
| | | 0 | 2 | 2.19 | 3.79 | 1.73 | 83 | 1.41 |
| | | –30 | 10 | 3.01 | 5.71 | 1.90 | 68 | 0.239 |
| | | –60 | 60 | 5.94 | 10.32 | 1.74 | 52 | 0.0291 |
| | toluene | 60 | 2 | 5.34 | 14.70 | 2.75 | 94 | 1.60 |
| | | 30 | 2 | 6.24 | 18.38 | 2.95 | 79 | 1.36 |
| | | 0 | 10 | 9.86 | 18.21 | 1.87 | 57 | 0.191 |
| | | –30 | 10 | 9.40 | 21.82 | 2.32 | 45 | 0.153 |
| | | –60 | 60 | 13.50 | 37.23 | 2.76 | 19 | 0.0109 |
| | DME | 60 | 2 | 2.87 | 6.48 | 2.12 | 96 | 1.61 |
| | | 30 | 2 | 1.49 | 1.59 | 1.06 | 86 | 1.45 |
| | | 0 | 2 | 2.75 | 4.91 | 1.78 | 80 | 1.36 |
| | | –30 | 10 | 4.53 | 7.48 | 1.65 | 82 | 0.276 |
| | | –60 | 60 | 6.86 | 10.07 | 1.47 | 57 | 0.0327 |
| **5** | THF | 60 | 1 | 3.15 | 6.68 | 2.12 | 100 | 3.43 |
| | | 30 | 1 | 3.26 | 5.73 | 1.76 | 97 | 3.39 |
| | | 0 | 1 | 5.13 | 9.42 | 1.83 | 100 | 3.42 |
| | | –30 | 1 | 7.37 | 10.59 | 1.44 | 86 | 2.91 |
| | | –60 | 10 | 7.74 | 14.93 | 1.93 | 73 | 0.247 |
| | toluene | 60 | 1 | 10.27 | 26.66 | 2.60 | 92 | 3.12 |
| | | 30 | 1 | 10.05 | 22.76 | 2.26 | 97 | 3.33 |
| | | 0 | 1 | 12.91 | 27.03 | 2.09 | 98 | 3.39 |
| | | –30 | 1 | 27.11 | 72.11 | 2.66 | 95 | 3.24 |
| | | –60 | 10 | 50.66 | 90.27 | 1.78 | 78 | 0.265 |
| | DME | 60 | 1 | 1.60 | 2.74 | 1.71 | 96 | 3.29 |
| | | 30 | 1 | 1.50 | 1.93 | 1.29 | 91 | 3.11 |
| | | 0 | 1 | 2.22 | 2.61 | 1.17 | 89 | 3.05 |
| | | –30 | 1 | 4.85 | 7.37 | 1.52 | 90 | 3.04 |
| | | –60 | 10 | 5.32 | 6.32 | 1.18 | 58 | 0.196 |
| **6** | THF | 60 | 1 | 2.08 | 3.81 | 1.84 | 94 | 3.23 |
| | | 30 | 1 | 2.74 | 5.03 | 1.84 | 88 | 3.07 |
| | | 0 | 1 | 2.85 | 5.11 | 1.79 | 85 | 2.90 |
| | | –30 | 1 | 4.88 | 8.76 | 1.79 | 76 | 2.68 |
| | | –60 | 10 | 77.15 | 10.37 | 1.34 | 37 | 0.129 |
| | toluene | 60 | 1 | – | – | – | 93 | 3.20 |
| | | 30 | 1 | 2.61 | 6.88 | 2.63 | 82 | 2.83 |
| | | 0 | 1 | 4.85 | 18.83 | 3.88 | 87 | 2.86 |
| | | –30 | 1 | 7.68 | 15.21 | 1.98 | 79 | 2.73 |
| | | –60 | 10 | 10.29 | 23.55 | 2.29 | 28 | 0.0963 |
| | DME | 60 | 1 | 1.68 | 2.28 | 1.36 | 89 | 2.99 |
| | | 30 | 1 | 1.50 | 2.08 | 1.38 | 86 | 2.97 |
| | | 0 | 1 | 1.92 | 2.56 | 1.34 | 80 | 2.67 |
| | | –30 | 10 | 5.19 | 9.47 | 1.82 | 71 | 0.248 |
| | | –60 | 30 | – | – | – | 19 | 0.0221 |

[a] Condition: solvent/ε-CL (v/v) = 3:1; Cat./ε-CL (mol/mol) = 1:500; Activity: g polymer·mol$^{-1}$(cat)·h$^{-1}$; *T*p: polymerization temperature.

 © 2007 Wiley-VCH Verlag GmbH & Co. KGaA, Weinheim 

The proposed mechanism of the ε-CL polymerization catalyzed by the lanthanide(II) complexes is that the lanthanide(II) complexes are oxidized by the lactone at the first stage, which forms an alkoxyl lanthanide(III) species.[24] Then, the chain propagation process was performed through a coordination-insertion process (Scheme 3).[25] However, the possible mechanism of the polymerization catalyzed by the neodymium(III) complex is through a coordination–insertion process.[25]

## Conclusions

In summary, a series of organolanthanide(II) complexes and an organolanthanide(III) complex with pyrrolidinyl- and piperidinyl-functionalized indenyl ligands were synthesized by the reactions of $C_9H_6$-1-R-3-$CH_2SiMe_2NC_4H_8$ (R = H, Me) or $C_9H_7CH_2SiMe_2NC_5H_{10}$ with the lanthanide(III) amides $[(Me_3Si)_2N]_3Ln(\mu\text{-}Cl)Li(THF)_3$ (Ln = Yb, Eu, Nd). This work demonstrated that the reduction potentials of $Ln^{3+}/Ln^{2+}$ and the ligands have an influence on the reactivity patterns. The formation pathway of the lanthanide(II) complexes and the neodymium(III) complex was proposed on the basis of our previous experimental results. Structural analyses of the complexes indicated that substituents on the ligands have an influence on the bonding modes between the ligands and the central metals. The results of the catalytic activities of the newly prepared complexes indicated that the temperatures, solvents, ligands, and the bonding modes between the ligands and the central metals have an influence on the catalytic activities of the catalysts, the molecular weights, and the molecular weight distributions of the polymers.

## Experimental Section

**General Remarks:** All syntheses and manipulations of air- and moisture-sensitive materials were performed under dry argon and an oxygen-free atmosphere using standard Schlenk techniques or in a glovebox. All solvents were refluxed and distilled from either finely divided $LiAlH_4$ or sodium benzophenone ketyl under argon prior to use unless otherwise noted. $CDCl_3$ was dried with activated 4-Å molecular sieves. ε-Caprolactone (ε-CL) was dried with finely divided $CaH_2$ and distilled before use. $ClCH_2SiMe_2Cl$ was bought from Aldrich Chemicals and distilled before use. $C_9H_6$-1-R-3-$CH_2SiMe_2NC_4H_8$ (R = H, $CH_3$)[12e] and $[(Me_3Si)_2N]_3Ln^{III}(\mu\text{-}Cl)Li(THF)_3$ (Ln = Yb,[12a] Eu,[26] Nd[26]) were prepared according to literature methods. Elemental analyses data were obtained with a Perkin–Elmer 2400 Series II elemental analyzer. IR spectra were recorded with a Perkin–Elmer 983(G) spectrometer (CsI crystal plate, Nujol mulls). $^1H$ NMR and $^{13}C$ NMR spectra for analyses of compounds were recorded with a Bruker AV-300 NMR spectrometer in $C_5D_5N$ ([$D_5$]pyridine) for lanthanide complexes and in $CDCl_3$ for organic compounds. Gel permeation chromatography (GPC) analyses of polymer samples were carried out at 30 °C using THF as an eluent with a Waters-2414 instrument and calibrated using monodispersed polystyrene standards at a flow rate of 1.0 mL min$^{-1}$.

**Preparation of $C_9H_7CH_2SiMe_2NC_5H_{10}$ (1):** To a solution of indene (10.0 mL, 85.2 mmol) in THF (80.0 mL) was slowly added a 1.57-M *n*BuLi solution (54.0 mL, 85.2 mmol) at 0 °C. The reaction mixture was stirred for 12 h at room temperature, and was then cooled to 0 °C. To the reaction mixture was added fresh $ClSiMe_2CH_2Cl$ (11.3 mL, 85.2 mmol) in one portion. The reaction mixture was stirred for 12 h at room temperature. The solvents were pumped off under reduced pressure. The residue was extract with diethyl ether (2 × 20.0 mL), the extractions were combined, and solvent was pumped off under vacuum. Distillation of the resulting liquid gives the product $C_9H_7CH_2SiMe_2Cl$ as a colorless oil (14.9 g, 79% yield). B.p. 88–90 °C/0.02 Torr. $^1H$ NMR (300 MHz, $CDCl_3$, 25 °C): $\delta$ = 7.52 (m, 2 H), 7.27 (m, 2 H), 7.01 (d, $J$ = 4.52 Hz, 1 H), 6.68 (dd, $J$ = 4.52, 6.99 Hz, 1 H), 3.78 (d, $J$ = 6.99 Hz, 1 H), 2.80 (s, 2 H), 0.06 (s, 6 H) ppm. $^{13}C$ NMR (300 MHz, $CDCl_3$, 25 °C): $\delta$ = 144.2, 144.1, 134.4, 129.8, 125.2, 123.9, 122.6, 121.2, 43.7, 24.9, –5.8 ppm. $C_{12}H_{15}ClSi$ (222.79): calcd. C 64.69, H 6.79; found C 64.51, H 7.02. To a freshly prepared THF (50 mL) solution of lithium piperidinide $C_5H_{10}NLi$ (3.37 g, 36.6 mmol) was added slowly the above prepared indene compound $C_9H_7CH_2SiMe_2Cl$ (8.14 g, 36.6 mmol) at 0 °C. The reaction mixture was then stirred for 12 h at 50 °C. The solvent was pumped off under reduced pressure. The residue was extracted with diethyl ether (2 × 20.0 mL), the extractions were combined, and the solvents were pumped off under vacuum. Distillation of the residue gave **1** as a colorless oil (8.03 g, 81% yield). B.p. 118–121 °C/0.02 Torr. $^1H$ NMR (300 MHz, $CDCl_3$, 25 °C): $\delta$ = 7.49–7.20 (m, 4 H), 6.09 (s, 1 H), 3.39 (d, $J$ = 7.53, 2 H), 2.87 (m, 4 H), 2.09 (s, 2 H), 1.58 (m, 4 H), 1.42 (m, 4 H), 0.09 (s, 6 H) ppm. $^{13}C$ NMR (300 MHz, $CDCl_3$, 25 °C): $\delta$ = 146.4, 144.4, 141.6, 126.1, 125.8, 124.3, 123.5, 119.4, 47.3, 46.6, 37.8, 27.9, 27.0, 25.6, 17.4, –2.1 ppm. IR (Nujol mulls): $\tilde{\nu}$ = 2953 (s), 2923 (s), 2853 (s), 1601 (w), 1573 (w), 1460 (m), 1376 (m), 1252 (m), 1170 (w), 1060 (m), 962 (m), 838 (m), 765 (s), 718 (m), 413 (w) cm$^{-1}$. $C_{17}H_{25}NSi$ (271.47): calcd. C 75.21, H 9.28, N 5.16; found C 75.06, H 9.24, N 4.80.

**Preparation of $[\eta^5{:}\eta^1\text{-}(C_9H_6CH_2SiMe_2NC_4H_8)]_2Yb^{II}$ (2):** To a toluene (10.0 mL) solution of $C_9H_7CH_2SiMe_2NC_4H_8$ (0.617 g, 2.40 mmol) was added a toluene (50.0 mL) solution of $[(Me_3Si)_2N]_3Yb^{III}(\mu\text{-}Cl)Li(THF)_3$ (1.096 g, 1.20 mmol) at room temperature. After the reaction mixture was stirred at room temperature for 6 h, the mixture was then refluxed for 12 h, the solution gradually changed from yellow to green to red. The solvent was evaporated under reduced pressure. The residue was washed with *n*-hexane (10.0 mL). The resulting solid was extracted with toluene (2 × 15.0 mL). The extractions were combined and concentrated to about 15.0 mL. The red crystals were obtained by cooling the concentrated solution at 0 °C for several days (0.403 g, 49% yield). M.p. 169–170 °C. $^1H$ NMR (300 MHz, $C_5D_5N$, 25 °C): $\delta$ = 7.55 (m, 4 H), 7.18 (m, 4 H), 6.96 (m, 2 H), 6.03 (m, 2 H) ($C_9H_6$), 2.11 (s, 4 H) ($CH_2$), 2.85 (m, 8 H), 1.52 (m, 8 H) ($C_4H_8N$), 0.10 (s, 12 H) [$Si(CH_3)_2$] ppm. IR (Nujol mulls): $\tilde{\nu}$ = 2925 (s), 2855 (s), 2333 (w), 1714 (m), 1604 (m), 1546 (m), 1461 (m), 1377 (s), 1249 (m), 1194 (w), 1006 (m), 829 (m), 755 (m), 721 (m), 467 (w) cm$^{-1}$. $C_{32}H_{44}N_2Si_2Yb$ (685.02): calcd. C 56.03, H 6.47, N 4.08; found C 55.79, H 6.45, N 3.92.

**Preparation of $[\eta^3{:}\eta^1\text{-}C_9H_5\text{-}1\text{-}CH_3\text{-}3\text{-}CH_2SiMe_2NC_4H_8]_2Yb^{II}$(3):** This compound was prepared as red crystals in 58% yield from the reaction of $[(Me_3Si)_2N]_3Yb^{III}(\mu\text{-}Cl)Li(THF)_3$ (1.096 g, 1.20 mmol) with $C_9H_6$-1-$CH_3$-3-$CH_2SiMe_2NC_4H_8$ (0.650 g, 2.40 mmol) by using procedures similar to those used for the preparation of **2**. M.p. 178–181 °C. $^1H$ NMR (300 MHz, $C_5D_5N$, 25 °C): $\delta$ = 7.36 (m, 8 H), 5.93 (s, 2 H) ($C_9H_6$), 2.82 (m, 8 H) ($C_4H_8N$), 2.03 (s, 4 H) ($CH_2$), 1.49 (m, 8 H) ($C_4H_8N$), 1.18 (m, 6 H) ($CH_3$), 0.06 (s, 12 H) [$Si(CH_3)_2$] ppm. IR (Nujol mulls): $\tilde{\nu}$ = 2961 (s), 2869 (m), 1603 (m), 1559 (m), 1540 (s), 1457 (m), 1354 (w), 1256 (m), 1153 (w),

 © 2007 Wiley-VCH Verlag GmbH & Co. KGaA, Weinheim 

1019 (m), 877 (m), 751 (m), 668 (m), 419 (w) $cm^{-1}$. $C_{34}H_{48}N_2Si_2Yb$ (713.97): calcd. C 57.20, H 6.78, N 3.92; found C 57.42, H 6.67, N 4.44.

**Preparation of $[\eta^5:\eta^1\text{-}C_9H_6CH_2SiMe_2NC_5H_{10}]_2Yb^{II}$ (4):** This compound was prepared as a red powder in 37% yield from the reaction of $[(Me_3Si)_2N]_3Yb^{III}(\mu\text{-Cl})Li(THF)_3$ (1.278 g, 1.40 mmol) with $C_9H_7CH_2SiMe_2NC_5H_{10}$ (**1**) (0.759 g, 2.80 mmol) in refluxing toluene by using procedures similar to those used for the preparation of **2**. M.p. 153–155 °C. $^1H$ NMR (300 MHz, $C_5D_5N$, 25 °C): $\delta$ = 7.38 (m, 8 H), 6.08 (d, 4 H) ($C_9H_6$), 2.69 (m, 8 H) ($C_5H_{10}N$), 2.03 (s, 4 H) ($CH_2$), 1.38 (m, 8 H) ($C_5H_{10}N$), 1.24 (m, 4 H) ($C_5H_{10}N$), 0.03 (m, 12 H) [$Si(CH_3)_2$] ppm. $C_{34}H_{48}N_2Si_2Yb$ (713.97): calcd. C 57.20, H 6.78, N; 3.92; found C 57.13, H 6.54, N 4.55.

**Preparation of $[\eta^5:\eta^1\text{-}C_9H_6CH_2SiMe_2NC_5H_{10}]_2Eu^{II}$ (5):** This compound was prepared as yellow crystals in 71% yield from the reaction of $[(Me_3Si)_2N]_3Eu^{III}(\mu\text{-Cl})Li(THF)_3$ (1.247 g, 1.40 mmol) with $C_9H_7CH_2SiMe_2NC_5H_{10}$ (**1**) (0.759 g, 2.80 mmol) in toluene at 60 °C by using procedures similar to those used for the preparation of **2**. NMR ($C_5D_5N$) spectra of the compound were not informative due to lack of locking signals for the paramagnetic property of the europium(II) complex. M.p. 132–133 °C. IR (Nujol mulls): $\tilde{\nu}$ = 3064 (w), 2931 (s), 2852 (m), 1540 (m), 1507 (m), 1490 (m), 1459 (m), 1448 (m), 1249 (s), 1059 (m), 962 (m), 833 (s), 766 (s), 719 (m), 668 (m) $cm^{-1}$. $C_{34}H_{48}EuN_2Si_2$ (692.89): calcd. 58.94, H 6.98, N 4.04; found C 58.77, H 7.32, N 3.83.

**Preparation of $[C_9H_6CH_2SiMe_2NC_5H_{10}]_3Nd^{III}\cdot THF$ (6):** To a toluene (10.0 mL) solution of $C_9H_7CH_2SiMe_2NC_5H_{10}$ (**1**) (0.759 g, 2.80 mmol) was added a toluene (50.0 mL) solution of $[(Me_3Si)_2N]_3Nd^{III}(\mu\text{-Cl})Li(THF)_3$ (1.238 g, 1.40 mmol) at room temperature. After the reaction mixture was stirred at room temperature for 6 h, the mixture was then refluxed for 12 h. The solvent was evaporated under reduced pressure. The residue was extracted with *n*-hexane (2 × 15.0 mL). The extractions were combined and concentrated to about 20.0 mL. The green crystals were obtained by cooling the concentrated solution at 0 °C for several days [0.417 g, 29% yield based on $[(Me_3Si)_2N]_3Nd^{III}(\mu\text{-Cl})Li(THF)_3$]. NMR ($C_5D_5N$) spectra of the compound were not informative due to lack of locking signals for the paramagnetic property of the neodymium(III) complex. M.p. 146–148 °C. IR (Nujol mulls): $\tilde{\nu}$ = 2933 (m), 1601 (m), 1520 (m), 1445 (m), 1398 (m), 1292 (m), 1251 (s), 1203 (w), 1030 (m), 962 (m), 870 (s), 853 (s), 766 (s), 720 (m), 668 (w) $cm^{-1}$. $C_{51}H_{72}N_3NdSi_3$ (955.63): calcd. C 64.10, H 7.59, N 4.40; found C 64.25, H 7.16, N 5.07.

**X-ray Crystallography:** Suitable crystals of complexes **2**, **3**, **5**, and **6** were each mounted in a sealed capillary. Diffraction was performed with a Siemens SMART CCD-area detector diffractometer using graphite-monochromated Mo-$K_\alpha$ radiation ($\lambda$ = 0.71073 Å); temperature 293(2) K; $\phi$ and $\omega$ scan technique; SADABS effects and empirical absorption were applied in the data corrections. All structures were solved by direct methods (SHELXTL-97),[27] completed by subsequent difference Fourier syntheses, and refined by full-matrix least-squares calculations based on $F^2$ (SHELXTL-97).[27] See Table 3 for crystallographic data.

CCDC-627924 (for **2**), -627925 (for **3**), -627923 (for **5**), and -627922 (for **6**) contain the supplementary crystallographic data for this paper. These data can be obtained free of charge from The Cambridge Crystallographic Data Centre via www.ccdc.cam.ac.uk/data_request/cif.

**ε-Caprolactone Polymerization:** ε-CL polymerization reactions were performed in a 50-mL Schlenk flask, placed in an external temperature-controlled bath, on a Schlenk line or in a glovebox. In a typical procedure, the catalyst (20–50 mg) was loaded into the Schlenk flask and the solvent was added. The ε-CL was added through a gastight syringe after the external bath temperature was stabilized. The polymer product was precipitated into hydrochloric acid (0.1 M, 50.0 mL), washed with hydrochloric acid (0.1 M), and then dried to a constant weight in a vacuum oven at 50 °C. The molecular weights of the polymers were analyzed by GPC techniques.

## Acknowledgments

This work was co-supported by the National Natural Science Foundation of China (20472001, 20672002), the program for

Table 3. X-ray experimental data of complexes **2**, **3**, **5** and **6**.

| | **2** | **3** | **5** | **6** |
|---|---|---|---|---|
| Empirical formula | $C_{32}H_{44}N_2Si_2Yb$ | $C_{34}H_{48}N_2Si_2Yb$ | $C_{34}H_{48}EuN_2Si_2$ | $C_{55}H_{80}N_3NdOSi_3$ |
| Formula weight | 685.91 | 713.96 | 692.88 | 1027.73 |
| Crystal system | monoclinic | monoclinic | monoclinic | monoclinic |
| Space group | *P*2(1)/*n* | *C*2/*c* | *Cc* | *P*21/*c* |
| *a* [Å] | 13.7350(10) | 15.7405(14) | 16.518(3) | 22.192(2) |
| *b* [Å] | 11.9791(2) | 10.2816(9) | 9.6420(16) | 11.5905(12) |
| *c* [Å] | 19.1269(2) | 19.7404(17) | 20.069(3) | 21.538(2) |
| $\beta$ [°] | 101.96 | 91.6130(10) | 92.922(3) | 90 |
| *V* [$Å^3$] | 3078.75(6) | 3193.5(5) | 3192.2(9) | 5540.0(10) |
| *T* [K] | 293(2) | 293(2) | 293(2) | 293(2) |
| $D_{calcd.}$ [$g\,cm^{-3}$] | 1.480 | 1.485 | 1.433 | 1.232 |
| *Z* | 4 | 4 | 4 | 4 |
| *F*(000) | 1392 | 1456 | 1412 | 2164 |
| Number of reflections collected | 9220 | 4734 | 7905 | 27380 |
| Number of unique reflections | 5296 ($R_{int}$ = 0.0406) | 2790 ($R_{int}$ = 0.0198) | 2821 ($R_{int}$ = 0.0284) | 9764 ($R_{int}$ = 0.0474) |
| Number of parameters | 334 | 177 | 179 | 622 |
| $\lambda$ [Å] (Mo-$K_\alpha$) | 0.71073 | 0.71073 | 0.71073 | 0.71073 |
| $\mu$ [$mm^{-1}$] | 3.138 | 3.029 | 2.065 | 1.040 |
| $\theta$ range [deg] | 2.02 to 25.01 | 2.37 to 25.09 | 2.03 to 25.02 | 1.89 to 25.01 |
| Goodness of fit | 1.093 | 1.148 | 1.083 | 1.050 |
| $R$ [$I > 2\sigma(I)$] | 0.0566 | 0.0292 | 0.0218 | 0.0378 |
| $wR_2$ | 0.1268 | 0.0662 | 0.0621 | 0.0890 |
| Largest diff. peak and hole [e·$Å^{-3}$] | 2.124 and –1.534 | 0.520 and –1.337 | 0.590 and –0.909 | 0.710 and –0.356 |

 © 2007 Wiley-VCH Verlag GmbH & Co. KGaA, Weinheim 

theNew Century Excellent Talents (NCET) (NCET-04-0590), the Excellent Young Scholars Foundation of Anhui Province (04046079) and a grant from Anhui Education Department (2005hbz06). Prof. Baohui Du and Jiping Hu's assistance in running IR and NMR spectra are also gratefully acknowledged.

[1] a) W. J. Evans, *Coord. Chem. Rev.* **2000**, *206–207*, 263–283; b) W. J. Evans, *Polyhedron* **1987**, *6*, 803–835; c) W. J. Evans, *J. Organomet. Chem.* **2002**, *647*, 2–11; d) P. M. Zeimentz, S. Amdt, B. R. Elvidge, J. Okuda, *Chem. Rev.* **2006**, *106*, 2404–2433; e) Z. Hou, Y. Wakatsuki, *Coord. Chem. Rev.* **2002**, *231*, 1–22; f) W. J. Evans, B. L. Davis, *Chem. Rev.* **2002**, *102*, 2119–2136; g) A. A. Trifonov, E. A. Fedorova, G. K. Fukin, E. V. Baranov, N. O. Druzhkov, M. N. Bochkarev, *Chem. Eur. J.* **2006**, *12*, 2752–2757; h) A. A. Trifonov, E. A. Fedorova, G. K. Fukin, N. O. Druzhkov, M. N. Bochkarev, *Angew. Chem. Int. Ed.* **2004**, *43*, 5045–5048; *Angew. Chem. Int. Ed.* **2004**, *116*, 5155–5158; i) A. A. Trifonov, M. N. Bochkarev, H. Schumann, J. Loebel, *Angew. Chem. Int. Ed. Engl.* **1991**, *30*, 1149–1151.

[2] a) J. Moore, A. Cowley, J. Gordon, *Organometallics* **2006**, *25*, 5207–5209; b) A. M. Kawaoka, T. J. Marks, *J. Am. Chem. Soc.* **2005**, *127*, 6311–6324; c) I. L. Fedushkin, S. Dechert, H. Schumann, *Organometallics* **2000**, *19*, 4066–4076; d) Y. Nakayama, H. Yasuda, *J. Organomet. Chem.* **2004**, *689*, 4489–4498; e) S. Arndt, T. P. Spaniol, J. Okuda, *Organometallics* **2003**, *22*, 775–781; f) M. Schultz, J. M. Boncella, D. J. Berg, T. D. Tilley, R. A. Andersen, *Organometallics* **2002**, *21*, 460–472; g) C. Qian, H. Li, J. Sun, W. Nie, *J. Organomet. Chem.* **1999**, *585*, 59–62; h) A. A. Trifonov, E. N. Kirillov, A. Fischer, F. T. Edelmann, M. N. Bochkarev, *Chem. Commun.* **1999**, 2203–2204; i) C. J. Burns, R. A. Andersen, *J. Am. Chem. Soc.* **1987**, *109*, 915–917; j) M. Deng, Y. Yao, Q. Shen, Y. Zhang, J. Sun, *Dalton Trans.* **2004**, 944–950; k) Z. Hou, Y. Zhang, O. Tardif, Y. Wakatsuki, *J. Am. Chem. Soc.* **2001**, *123*, 9216–9217; l) W. J. Evans, G. Zucchi, J. W. Ziller, *J. Am. Chem. Soc.* **2003**, *125*, 10–11; m) H. M. Dietrich, H. Grove, K. W. Törnroos, R. Anwander, *J. Am. Chem. Soc.* **2006**, *128*, 1458–1459; n) W. Hieringer, J. Eppinger, R. Anwander, W. A. Herrmann, *J. Am. Chem. Soc.* **2000**, *122*, 11983–11994; and references cited therein.

[3] M. N. Bochkarev, *Coord. Chem. Rev.* **2004**, *248*, 835–851.

[4] a) A. A. Trifonov, G. G. Skvortsov, D. M. Lyubov, N. A. Skorodumova, G. K. Fukin, E. V. Baranov, V. N. Glushakova, *Chem. Eur. J.* **2006**, *12*, 5320–5327; b) Y. Yao, Z. Zhang, H. Peng, Y. Zhang, Q. Shen, J. Lin, *Inorg. Chem.* **2006**, *45*, 2175–2183; c) R. Gauvin, A. Mortreux, *Chem. Commun.* **2005**, 1146–1148; d) F. Bonnet, A. Hillier, A. Collins, S. Dubberley, P. Mountford, *Dalton Trans.* **2005**, 421–423; e) M. T. Gamer, M. Rastätter, P. W. Roesky, A. Steffens, M. Glanz, *Eur. J. Chem.* **2005**, *11*, 3165–3172; f) Y. Nakayama, H. Yasuda, *J. Organomet. Chem.* **2004**, *689*, 4489–4498; g) H. Ma, T. P. Spaniol, J. Okuda, *Angew. Chem. Int. Ed.* **2006**, *45*, 7818–7821; h) S. Arndt, K. Beckerle, P. M. Zeimentz, T. P. Spaniol, J. Okuda, *Angew. Chem. Int. Ed.* **2005**, *44*, 7473–7477; i) S. Arndt, J. Okuda, *Adv. Synth. Catal.* **2005**, *347*, 339–354; j) H. Ma, J. Okuda, *Macromolecules* **2005**, *38*, 2665–2673; k) A. Fischbach, M. G. Klimpel, M. Widenmeyer, E. Herdtweck, W. Scherer, R. Anwander, *Angew. Chem. Int. Ed.* **2004**, *43*, 2234–2239; *Angew. Chem.* **2004**, *116*, 2284–2289; l) A. Fischbach, C. Meermann, G. Eickerling, W. Scherer, R. Anwander, *Macromolecules* **2006**, *39*, 6811–6816; m) H. M. Dietrich, K. W. Törnroos, R. Anwander, *J. Am. Chem. Soc.* **2006**, *128*, 9298–9299.

[5] a) J. Zhao, T. J. Marks, *Organometallics* **2006**, *25*, 4763–4772; b) P. W. Roesky, T. E. Müller, *Angew. Chem. Int. Ed.* **2003**, *42*, 2708–2710; c) Y. K. Kim, T. Livinghouse, Y. Horino, *J. Am. Chem. Soc.* **2003**, *125*, 9560–9561; d) K. C. Hultzsch, F. Hampel, T. Wagner, *Organometallics* **2004**, *23*, 2601–2612; e) S. Hong, S. Tian, M. Metz, T. Marks, *J. Am. Chem. Soc.* **2003**, *125*, 14768–14783; f) J. S. Ryu, T. J. Marks, F. E. McDonald, *Org. Lett.* **2001**, *3*, 3091–3094; g) J. S. Ryu, T. J. Marks, F. E. McDonald, *J. Org. Chem.* **2004**, *69*, 1038–1052; h) V. M. Arredondo, S. Tian, F. E. McDonald, T. J. Marks, *J. Am. Chem. Soc.* **1999**, *121*, 3633–3639; i) D. V. Gribkov, K. C. Hultzsch, F. Hampel, *Eur. J. Chem.* **2003**, *9*, 4796–4810; j) T. K. Panda, A. Zulys, M. T. Gamer, P. W. Roesky, *Organometallics* **2005**, *24*, 2197–2202; k) P. N. O'Shaughnessy, P. Scott, *Tetrahedron: Asymmetry* **2003**, *14*, 1979–1983; l) J. Collin, J. Daran, E. Schulza, A. Trifonov, *Chem. Commun.* **2003**, 3048–3049; m) J. Collin, J. Daran, O. Jacquet, E. Schulz, A. Trifonov, *Chem. Eur. J.* **2005**, *11*, 3455–3462.

[6] a) M. R. Douglass, T. J. Marks, *J. Am. Chem. Soc.* **2000**, *122*, 1824–1825; b) M. R. Douglass, M. Ogasawara, S. Hong, M. V. Metz, T. J. Marks, *Organometallics* **2002**, *21*, 283–292; c) A. M. Kawaoka, M. R. Douglass, T. J. Marks, *Organometallics* **2003**, *22*, 4630–4632.

[7] a) H. Berberich, P. W. Roesky, *Angew. Chem. Int. Ed.* **1998**, *37*, 1569–1571; b) M. R. Bürgstein, H. Berberich, P. W. Roesky, *Chem. Eur. J.* **2001**, *7*, 3078–3085; c) G. B. Deacon, A. Gitlits, P. W. Roesky, M. R. Bürgstein, K. C. Lim, B. W. Skelton, A. H. White, *Chem. Eur. J.* **2001**, *7*, 127–138.

[8] a) P. W. Roesky, M. T. Gamer, M. Puchner, A. Greiner, *Chem. Eur. J.* **2005**, *8*, 5265–5271; b) F. Kerton, A. Whitwood, C. Willans, *Dalton Trans.* **2004**, 2237–2244; c) Y. Yao, M. Ma, X. Xu, Y. Zhang, Q. Shen, W. Wong, *Organometallics* **2005**, *24*, 4014–4020; d) K. C. Hultsch, T. P. Spaniol, J. Okuda, *Organometallics* **1997**, *16*, 4845–4846; e) E. Martin, P. Dubois, R. Jerome, *Macromolecules* **2000**, *33*, 1530–1535; f) H. Noss, M. Oberthür, C. Fischer, W. P. Kretschmer, R. Kempe, *Eur. J. Inorg. Chem.* **1999**, 2283–2288; and references cited therein.

[9] a) J. Zhang, R. Cai, L. Weng, X. Zhou, *Organometallics* **2004**, *23*, 3303–3308; b) J. Zhang, X. Zhou, R. Cai, L. Weng, *Inorg. Chem.* **2005**, *44*, 716–722; c) H. Li, Y. Yao, Q. Shen, L. Weng, *Organometallics* **2002**, *21*, 2529–2532; d) G. R. Giesbrecht, G. D. Whitener, J. Arnold, *J. Chem. Soc., Dalton Trans.* **2001**, 923–927.

[10] L. Zhang, S. Wang, E. Sheng, S. Zhou, *Green Chem.* **2005**, *7*, 683–686.

[11] L. Zhang, S. Wang, S. Zhou, S. Yang, E. Sheng, *J. Org. Chem.* **2006**, *71*, 3149–3153.

[12] a) E. Sheng, S. Wang, G. Yang, S. Zhou, L. Cheng, K. Zhang, Z. Huang, *Organometallics* **2003**, *22*, 684–692; b) K. Zhang, W. Zhang, S. Wang, E. Sheng, G. Yang, M. Xie, S. Zhou, Y. Feng, L. Mao, Z. Huang, *Dalton Trans.* **2004**, 1029–1037; c) E. Sheng, S. Zhou, S. Wang, G. Yang, Y. Wu, Y. Feng, L. Mao, Z. Huang, *Eur. J. Inorg. Chem.* **2004**, 2923–2932; d) S. Wang, X. Tang, A. Vega, J. Saillard, E. Sheng, G. Yang, S. Zhou, Z. Huang, *Organometallics* **2006**, *25*, 2399–2401; e) S. Wang, S. Zhou, E. Sheng, G. Yang, M. Xie, K. Zhang, L. Cheng, Y. Feng, L. Mao, Z. Huang, *Organometallics* **2003**, *22*, 3546–3552; f) S. Wang, Y. Feng, L. Mao, E. Sheng, G. Yang, M. Xie, S. Wang, Y. Wei, Z. Huang, *J. Organomet. Chem.* **2006**, *691*, 1265–1274; g) Y. Wu, S. Wang, C. Qian, E. Sheng, M. Xie, G. Yang, Q. Feng, L. Zhang, X. Tang, *J. Organomet. Chem.* **2005**, *690*, 4139–4149.

[13] a) A. Dash, A. Razavi, A. Mortreux, C. Lehmann, J. Carpentier, *Organometallics* **2002**, *21*, 3238–3249; b) W. A. Herrmann, J. Eppinger, M. Spiegler, O. Runte, R. Anwander, *Organometallics* **1997**, *16*, 1813–1815; c) R. Anwander, O. Runte, J. Eppinger, G. Gerstberger, M. Spiegler, E. Herdtweck, *J. Chem. Soc., Dalton Trans.* **1998**, 847–858; d) J. Eppinger, M. Spiegler, W. Hieringer, W. A. Herrmann, R. Anwander, *J. Am. Chem. Soc.* **2000**, *122*, 3080–3096.

[14] A. A. Trifonov, T. P. Spaniol, J. Okuda, *Organometallics* **2001**, *20*, 4869–4874.

[15] L. Lefort, T. W. Crane, M. D. Farwell, D. M. Baruch, J. A. Kaeuper, R. J. Lachicotte, W. D. Jones, *Organometallics* **1998**, *17*, 3889–3899.

[16] L. Morss, *Chem. Rev.* **1976**, *76*, 827–841.

[17] D. Deng, C. Qian, *J. Organomet. Chem.* **1993**, *443*, 79–83.

 © 2007 Wiley-VCH Verlag GmbH & Co. KGaA, Weinheim 

[18] M. F. Lappert, I. W. Yarrow, J. L. Atwood, R. Shakir, *J. Chem. Soc.; Chem. Commun.* **1980**, 987–988.
[19] Z. Xie, S. Wang, Q. Yang, T. Mak, *Organometallics* **1999**, *18*, 2420–2427.
[20] S. Wang, H. Li, Z. Xie, *Organometallics* **2004**, *23*, 2469–2478.
[21] J. W. Guan, Q. Shen, R. D. Fischer, *J. Organomet. Chem.* **1997**, *549*, 203–212.
[22] M. Chen, G. Wu, W. Wu, S. Zhuang, Z. Huang, *Organometallics* **1988**, *7*, 802–806.
[23] W. J. Evans, C. A. Seibel, J. W. Ziller, *J. Am. Chem. Soc.* **1998**, *120*, 6745–6752.
[24] a) M. Nishiura, Z. Hou, T. Koizumi, T. Imamoto, Y. Wakatsuki, *Macromolecules* **1999**, *32*, 8245–8251; b) W. J. Evans, H. Katsumata, *Macromolecules* **1994**, *27*, 2330–2332.
[25] X. Deng, M. Yuan, C. Xiong, X. Li, *J. Appl. Polym. Sci.* **1999**, *73*, 1401–1408.
[26] S. Zhou, S. Wang, G. Yang, X. Liu, E. Sheng, K. Zhang, L. Cheng, Z. Huang, *Polyhedron* **2003**, *22*, 1019–1024.
[27] G. M. Sheldrick, *SHELXTL*, version 5.10, Bruker Analytical X-ray Systems Inc., Madison, WI, **1997**.

Received: November 22, 2006
Published Online: March 1, 2007

 © 2007 Wiley-VCH Verlag GmbH & Co. KGaA, Weinheim 

DOI: 10.1002/ejic.200600816

# Small Group IIa–VIa Clusters and Related Systems: A Theoretical Study of Physical Properties, Reactivity, and Electronic Spectra

**Martin Srnec*[a] and Rudolf Zahradník[b]**

**Keywords:** Ab initio calculations / Cluster compounds / Structural elucidation

In the monomeric form, the title systems assume unexpected optical properties, and as oligomers they can serve as candidates for molecular devices. In bulk they are attractive in the area of material science. A broad set of quantum chemical methods ranging from density functional theory by the Hartree–Fock method and the Møller–Plesset perturbation theory to the coupled-cluster method, in connection with nonrelativistic Dunning's basis sets as well as with relativistic SDD basis sets were used. Electronic spectra were analyzed by means of time-dependent DFT, with the symmetry-adapted cluster configuration interaction and with the internally contracted multireference configuration interaction. The Douglas–Kroll–Hess quasirelativistic Hamiltonian served as a basis for the estimation of the role of relativistic effects. All the diatomics representing 25 elements of a matrix formed by the combination of group IIa (Be, ..., Ba) with group VIa (O, ..., Po) atoms were characterized by calculated bond length, valence vibration, dipole moment, and the Hartree–Fock frontier orbital energies. Calculated characteristics were confronted with experimental data. The geometry of the oligomers (from dimers through hexamers) was investigated systematically, and the nature of the located stationary points on the respective potential energy surfaces was established. Special attention was paid to the four lightest elements of the group IIa–VIa matrix, i.e. BeO, BeS, MgO, and MgS. As for electronic spectra, the systems of the first column (BeO, ..., BaO), the first row (BeO, ..., BePo), and the systems of the main diagonal (BeO, ..., BaPo) were calculated in the form of monomers and dimers. Analogous calculations were performed for a few group Ia–VIIa, IIIa–Va, IVa–IVa, and IIb–VIa systems. The group IIa–VIa and IIb–VIa diatomics exhibit electronic transitions in the visible region of the spectrum, and the longest wavelength bands are located in the near-infrared region. MgO represents an extreme with the first band appearing at about 3500 $cm^{-1}$, which strictly speaking makes the use of the Born–Oppenheimer approximation questionable. Whenever experimental transitions are available, the agreement between the calculated and observed band positions is good. Passing from monomers to oligomers is always associated with a significant hypsochromic shift in the first transition.

(© Wiley-VCH Verlag GmbH & Co. KGaA, 69451 Weinheim, Germany, 2007)

## Introduction

Contemporary electronics, material science, molecular engines, an urgent desire to build computers on the basis of appropriate molecules and macromolecules, and a general tendency to miniaturize prompted us to search for species and materials with the desired properties. These compounds require special physical, chemical, and mechanical characteristics.

For years conjugated organic systems have attracted attention on the basis of the above-mentioned aims and also in connection with the investigation of structure–color relationships. Special interest has been paid to intensively colored species[1a,2] and to systems possessing the longest wavelength transition in the near-infrared region.[1b] Such systems exhibit a very narrow gap between the highest occupied and the lowest unoccupied molecular orbitals (HOMO and LUMO, respectively).

Inorganic systems were, except for various transition-metal complexes, on the periphery of interest. This changed after the discovery of interesting facets (including semiconductivity) of some solids derived, for example, from group IIb–VIa binary compounds, such as, ZnO, ZnS, CdO, and CdS.[3a–3c] Species that are derived from group IIa–VIa elements have received much less attention than the group IIb–VIa compounds. It was shown recently that monomeric forms of group IIa–VIa binary species and small oligomers thereof absorb in the visible and near-infrared regions.[4] Passing from monomers to oligomers of increasing size manifests itself by a hypsochromic shift, which is opposite to that which is known for conjugated organic species.

The group IIa–VIa combination of atoms can be extended to other isoelectronic pairs: groups Ia–VIIa, IIIa–Va, and IVa–IVa. When considering the five elements com-

[a] Department of Molecular Modeling, Institute of Organic Chemistry and Biochemistry, Academy of Sciences of the Czech Republic,
Flemingovo nam.,16610 Prague 6. Czech Republic
E-mail: srnec@uochb.cas.cz
[b] J. Heyrovský of Physical Chemistry, Academy of Sciences of the Czech Republic,
Dolejškova St. 3, 18223 Prague 8. Czech Republic

Supporting information for this article is available on the WWW under http://www.eurjic.org or from the author.

 © 2007 Wiley-VCH Verlag GmbH & Co. KGaA, Weinheim 

prising the individual groups of the periodic table, 25 species are derived for each of these combinations. The lightest species consists of LiF, BeO, BN, and $C_2$. These prototypes are followed by 24 molecules; the total number of nonidentical group IVa–IVa combinations amounts to $n(n-1)/2$ (where $n$ is the number of elements in the group), five of them being homonuclear, the remaining, heteronuclear.

In all these instances, 1–10 nm clusters of these parent species represent systems in which the properties are tunable by their size and/or by passing from one element to another element belonging to the same group.

With the group IIa–VIa systems, mostly species containing beryllium and magnesium were investigated. The majority of studies on beryllium compounds, probably because of their toxicity,[5–23] is more theoretical than experimental. Magnesium compounds, mainly MgO, were studied in the context of group IIa–VIa compounds most frequently.[24–50] The number of studies of binary systems containing heavier group IIa metals (Ca, Sr, Ba) is smaller.[24,51–56] Widely investigated were group IIb–VIa systems because of their practical importance. However, only papers having some relevance to systems dealt with in this work are cited.[3a–3c,57–74]

Species of these classes attract attention as nanoparticle[56,62,63,66,68,71,75] materials for quantum dots,[56,58,59] as clusters[24,25,31,43,52,57,59,64a,64b,69] and semiconductors,[3c,57,60,74] and as materials used in the preparation of nanotubes and nanowires.[50,52] The transition between clusters and bulk was investigated.[76] The band structure[7] of BeO and MgO surfaces[26,44a,44b] (and their infrared spectra[37]), as well as doped MgO,[26] were also subjects of scrutiny. Trends in the series BeO through BaO[10] and BeS through BeTe[15,19,23] were described. BeS[6,9,12,17] and MgS[25,33,40] represent materials worth mentioning. Not only closed-shell parent systems, but also radical–ions[13,14,27a,29,35,36] derived from them were subjects of studies, sometimes by means of photoelectron spectroscopy.[27a,38] The electron affinity of BeO is so high that complexes with rare gases were described.[8]

In addition to the currently widely used Hartree–Fock, Møller–Plesset, and coupled-cluster methods (vide infra), density functional theory[10,11,22,34,49,53,73] and empirical potentials[24,46,51] served to describe large systems, clusters in particular. A full configuration interaction (CI) was used to study[5] the electronic structure of BeO.

Electronic spectra investigations[16,27b,27c,34,48,56] involved mainly MgO (size-dependency of the MgO clusters[42]). In ref.[54] spectra of CaO, SrO, and BaO were analyzed. A correlation was found to exist between the energy of the Khon–Sham orbitals and the excitation energies.[77] Infrared spectra of MgO[37] and BeO complexes with noble gases[21,22] are available.

Calculations of dissociation energies (e.g. for MgO,[28] $MgO^+$, and $SrO^+$ in ref.[28]), as well as heats of formation (BeO, MgO, CaO),[20] still represent a rather demanding task.

In this paper, we utilize various quantum chemical methods to determine the structural and electronic characteristics of monomeric through hexameric group IIa–VIa species (group IIa: Be through Ba; group VIa: O through Po) and to determine how these characteristics vary with different elements, cluster size, and geometrical structure. We focus on the following features: (1) Screening structural and physical properties of all 25 group IIa–VIa monomers. (2) Detailing the study of the properties of the four lightest MX monomers (M = Be, Mg; X = O, S). (3) Testing relativistic effects on the properties of a representative molecule, CaSe. (4) Characterizing geometries of oligomeric isomers. (5) Characterizing electronic spectra for the most stable isomers. (6) Evaluating trends of physical characteristics in a series of oligomers.

## Computational Details

Quantum chemical methods were used for the computation of the structural and physical properties of selected group IIa–VIa diatomics MX, their oligomers $M_iX_i$ (from dimers to hexamers, $i$ = 2,.., 6), and for some related systems by using the Gaussian 03 program package.[78]

In the first part concerning diatomics, attention was focused on screening the bond lengths, the harmonic valence vibrations, the electric dipole moments, and frontier orbital energies. The following computational schemes were used: density functional theory (DFT) with the B3LYP exchange-correlation functional, the Hartree–Fock method (HF), and the second-order Møller–Plesset perturbation theory (MP2). Calculations were performed for all the matrix elements (diatomics) of the group IIa–VIa matrix. Relativistic pseudopotentials were used throughout the calculations so as to describe relativistic effects, which increase with $Z^4$ and $Z^2$ ($Z$ – proton number) for inner and outer electrons, respectively. The SDD basis sets[79a] are appropriate for this purpose and are available in the Gaussian 03 standard library. Analysis of the wavefunctions was carried out by means of the CASSCF method[79b] by using the MOLPRO 02 program.[79c]

The second part relates to the four lightest members of the group IIa–VIa matrix. These diatomics were extensively characterized by means of the DFT method using nonrelativistic Dunning's basis sets[80a–80c] (cc-pVXZ from double-zeta to quintuple-zeta) and the calculated characteristics were almost always extrapolated to the complete basis set (CBS) limit according to the (quasi)linear dependency between the physical characteristics and the reciprocals of the total number of basis set functions.[81] Unless otherwise stated, the geometry optimization of the oligomers was always performed at the B3LYP/cc-pVTZ level. The positions of the first electronic valence (the longest wavelength) bands of these species were estimated by means of the time-dependent density functional method (TD–B3LYP). These results were then compared with the experimental data (if available) and with the results of two more robust methods, namely, the symmetry-adapted cluster configuration interaction (SAC–CI),[82] including single and double excitations, and the internally contracted multireference config-

 © 2007 Wiley-VCH Verlag GmbH & Co. KGaA, Weinheim 

uration interaction (icMRCI),[83a,83b] also with single and double excitations. Specification of the reference configuration space related to icMRCI calculations will be mentioned with concrete instances. The electronic transitions were fitted with equal-weighted Gauss/Lorentz curves with half-maximum widths of 1000 $cm^{-1}$; the Frank–Condon factors were not considered.

In the third part, we were interested in the trends of some structural and spectral features along the horizontal (the first row), the vertical (the first column), and the main diagonal directions of the group IIa–VIa matrix (Figure 1). The second-order Douglas–Kroll–Hess (DKH)[84a–84c] scalar quasirelativistic Hamiltonian was explored in the local spin density basis set DZVP[85] and the large-core SDD pseudopotential technique (vide supra), both within the B3LYP procedure. The DKH method neglects the two-electron relativistic corrections and also spin-orbit coupling. This method is based on the free-particle Foldy–Wouthuysen (FW)[84d] transformation, which separates the electronic and positronic solutions of the Dirac equation by the unitary transformation of the Dirac–Coulomb–Breit Hamiltonian. The approximate scheme of the DKH method applies the free-particle FW transformation to the molecular bare-nucleus Hamiltonian and, moreover, also applies additional transformations to remove off-diagonal Hamiltonian elements, which results in variational stability.

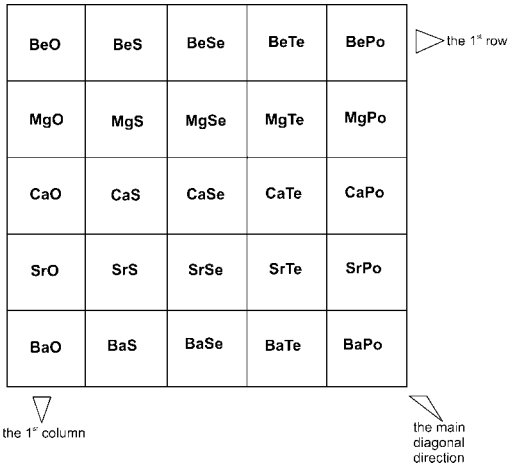


Figure 1. Diatomics formed by a combination of atoms of groups IIa and VIa. Three main directions are indicated.

The adiabatic and vertical ionization potentials ($I_a$ and $I_v$, respectively) and the adiabatic and vertical electron affinities ($A_a$ and $A_v$, respectively) are defined as follows [Equations (1), (2), (3), and (4)]:

$$I_a = E_{M_iX_i^{+-}}\left(M_iX_i^{+-}\right) - E_{M_iX_i}\left(M_iX_i\right) + \frac{1}{2}h\sum_j^{3N-6}\left[\nu_j\left(M_iX_i^{++}\right) - \nu_j\left(M_iX_i\right)\right] \quad (1)$$

$$I_v = E_{M_iX_i^{+-}}\left(M_iX_i\right) - E_{M_iX_i}\left(M_iX_i\right) \quad (2)$$

$$A_a = E_{M_iX_i^{--}}\left(M_iX_i^{--}\right) - E_{M_iX_i}\left(M_iX_i\right) + \frac{1}{2}h\sum_j^{3N-6}\left[\nu_j\left(M_iX_i^{--}\right) - \nu_j\left(M_iX_i\right)\right] \quad (3)$$

$$A_v = E_{M_iX_i^{--}}\left(M_iX_i\right) - E_{M_iX_i}\left(M_iX_i\right) \quad (4)$$

where the lower index and the index in parentheses specify chemical species and the structure, which was optimized, respectively. The adiabatic forms include the zero-point energy (ZPE) corrections; $\nu_j$ stands for the $j$th vibrational mode. The energy of the open-shell species was calculated by unrestricted methods.

The energy of formation of the oligomers was calculated by means of the following expression [Equation (5)]:

$$\Delta E = (iE_M + iE_x - E_{M_iX_i})/i \quad (5)$$

Equation (5) permits the estimation of the relative stability of the isomers. The basis set superposition error (BSSE) was calculated by using the function counterpoise method[86] and included throughout. It necessarily tends to zero when approaching complete basis sets.

The Mulliken population analysis was used for semiquantitative estimates of partial charges at the atoms.

## Results and Discussion

### Monomers: Screening of Structural and Selected Physical Properties

The ground state of all the studied species is a singlet state. The only uncertainty is related to BaPo. Again, a singlet represents the ground state with the SDD basis set (S–T split amounts to 3.6 kcal $mol^{-1}$ with B3LYP). With the ECP-CRENBL[87] basis set, however, the opposite is true (T–S split is equal to 13.5 kcal $mol^{-1}$ with B3LYP). The semiquantitative estimates of the S–T splittings for all group IIa–VIa species are available on request from the authors.

Bond lengths, valence vibrations, dipole moments, and frontier orbital energies for 25 group IIa–VIa diatomics are summarized in Figure 2. The bond length dependencies (A, B) are monotonic and reflect the empirical statement that passing from the first-row element to its nearest neighbor manifests itself roughly with the same degree of change relative to that found by passing between the second and the fifth period. The B3LYP, HF, and MP2 bond length courses overlap significantly. Average deviations between calculated and observed[88] bond lengths for the species of the first matrix column amount to 29 (B3LYP/SDD), 24 (HF/SDD), and 70 pm (MP2/SDD).

Dependences C and D in Figure 2 have to do with harmonic wavenumbers ($\tilde{\nu}$), which decrease monotonically in the columns and rows of the matrix. By contrast, force constants of magnesium chalcogenides exert minima. This agrees well with the remarkable reactivity of MgO.[31] Again, the features of the species that include first-row ele-

 © 2007 Wiley-VCH Verlag GmbH & Co. KGaA, Weinheim 

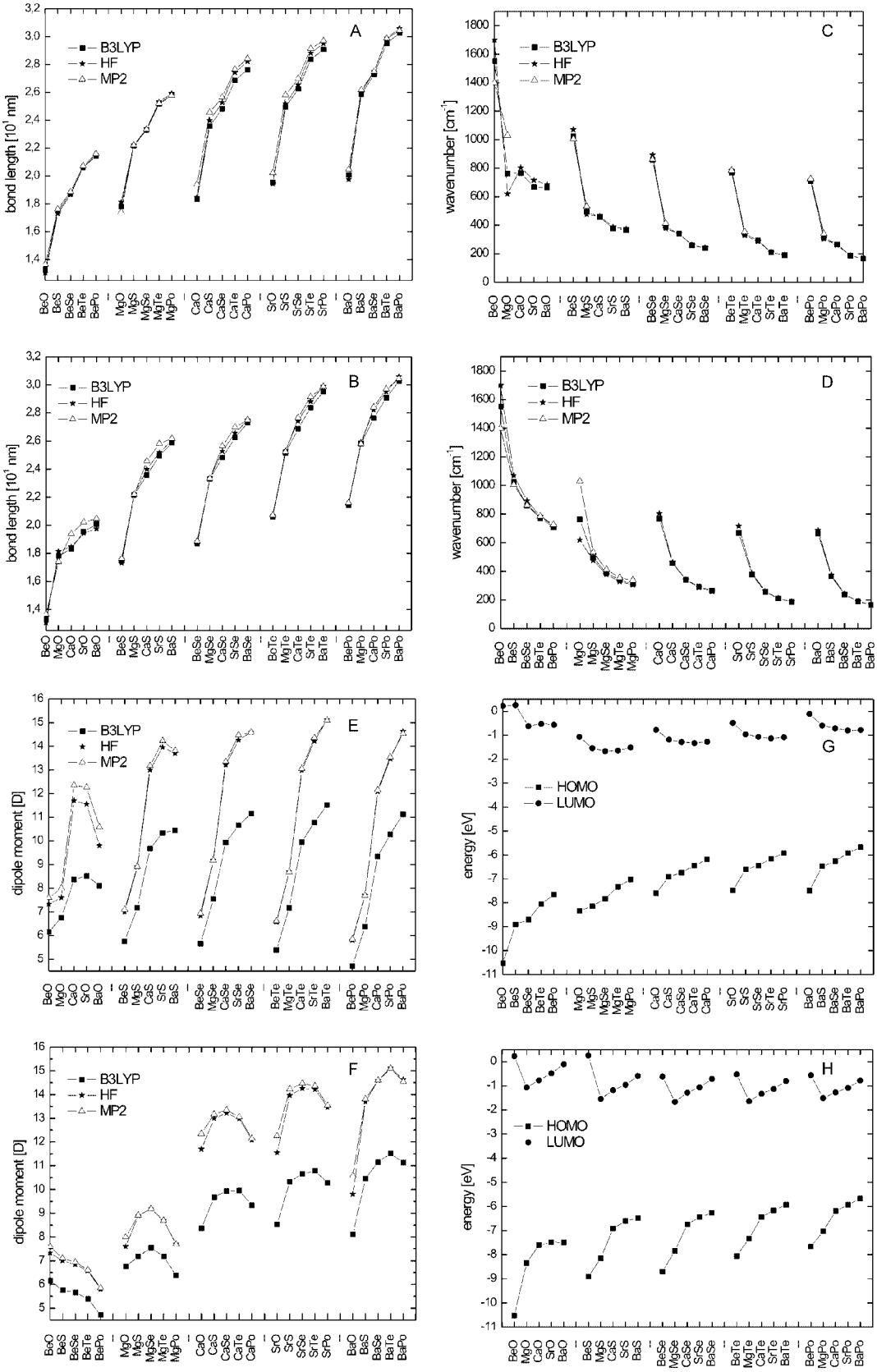


Figure 2. Trends of bond lengths, $\ell$(A, B), wavenumbers of valence vibrations, $\tilde{\nu}$(C, D), electric dipole moments, $\mu$(E, F), and energies of frontier orbitals, $E$(G, H) for 25 group IIa–VIa diatomics: oxides, sulfides, selenides, tellurides, polonides of beryllium, magnesium, calcium, strontium, and barium, respectively. Computational methods and units used are indicated in the graphs. The DFT (B3LYP), HF, and MP2 methods were used with pseudopotential SDD basis sets. HF frontier orbital energies correspond, except for signs, to Koopmans' ionization potential and electron affinity.

 © 2007 Wiley-VCH Verlag GmbH & Co. KGaA, Weinheim 

ments are shifted from the data for the rest of the systems. This is particularly obvious for BeO. There is a fair agreement between B3LYP/SDD and experimental wavenumbers for species of the first matrix column. The largest deviation was observed for MgO (16%), whereas for BaO it amounted to only 0.6%.

The dipole moments (Figure 2, E and F) indicate significantly the ionic nature of all the systems. There is a rather dramatic difference between the B3LYP and the HF and MP2 values (always with the SDD basis sets). Reasonable agreement between B3LYP and highly accurate theoretical values for BeO (6.16 and 6.15–6.25 D,[18] respectively) and BeS (5.76 and 5.19 D,[17] respectively) suggest the superiority of the B3LYP estimates with respect to the two other procedures. This confirms our previous experience.[81] In contrast to dependencies for species in columns, the dependencies in the rows exerts (except for beryllium chalcogenides) well-developed maxima for selenides or tellurides. On the whole, the B3LYP dipole moments assume values between 5 and 11 D.

The HF frontier orbital energies (Figure 2, G and H) represent, within the framework of the Koopmans' theorem, the first vertical ionization potential (HOMO) and the first vertical electron affinity (LUMO). The ionization potentials decrease and the electron affinities increase in the rows of the matrix. Dependencies for electron affinities

Table 1. Calculated bond lengths ($R_e$), dipole moments ($\mu$), wavenumber of valence vibrations ($\tilde{\nu}$), vertical ionization potential ($I_v$), vertical electron affinity ($A_v$), and formation enthalpy corresponding to the process $MX(^1\Sigma^+) = M(^1S) + X(^1D)$ for BeO, BeS, MgO, and MgS. The B3LYP and MP2 methods were obtained for Dunnig's basis sets (n; cc-pVXZ with X = D, T, Q, 5). Only in a few cases were very sophisticated calculated values used as a benchmark instead of experimental values.

| | | B3LYP | | | | | |
|---|---|---|---|---|---|---|---|
| Species | *n* | $R_e$ [$10^{-10}$ m] | $\mu$ [D] | $\tilde{\nu}$ [$cm^{-1}$] | $I_v$ [eV] | $A_v$ [eV] | $\Delta E$[a] [kJ/mol] |
| BeO | D | 1.3381 | 5.71 | 1510 | 9.85 | 2.00 | –686 |
| | T | 1.3233 | 6.11 | 1551 | 9.90 | 2.13 | –721 |
| | Q | 1.3193 | 6.27 | 1554 | 10.13 | 2.14 | –729 |
| | 5 | 1.3195 | 6.39 | 1551 | 10.15 | 2.17 | –731 |
| | liter. | 1.331[c] | 6.15–6.25[b] | 1487[c] | 10.1 ± 0.4[c] | – | –544 ± 50[d] |
| BeS | D | 1.7540 | 4.90 | 1000 | 9.08 | 2.13 | –478 |
| | T | 1.7414 | 5.24 | 1009 | 9.24 | 2.24 | –490 |
| | Q | 1.7375 | 5.32 | 1012 | 9.25 | 2.28 | –493 |
| | 5 | 1.7374 | 5.34 | 1012 | 9.25 | 2.31 | –493 |
| | liter. | 1.742[c] | 5.19[e] | 998[c] | – | – | – |
| MgO | D | 1.7493 | 6.28 | 814 | 7.61 | 1.72 | –448 |
| | T | 1.7430 | 6.86 | 822 | 7.76 | 1.77 | –471 |
| | Q | 1.7388 | 7.19 | 826 | 7.81 | 1.83 | –483 |
| | 5 | 1.7343 | 7.35 | 826 | 7.83 | 1.84 | –489 |
| | liter. | 1.749[c] | – | 785[c] | 8.76 ± 0.22[c] | – | –594 ± 42[c] |
| MgS | D | 2.1620 | 6.88 | 523 | 7.68 | 1.94 | –342 |
| | T | 2.1514 | 7.30 | 527 | 7.80 | 2.00 | –353 |
| | Q | 2.1490 | 7.46 | 527 | 7.81 | 2.05 | –356 |
| | 5 | 2.1414 | 7.52 | 530 | 7.82 | 2.05 | –358 |
| | liter. | 2.143[c] | – | 529[c] | – | – | – |
| | | MP2 | | | | | |
| BeO | D | 1.3746 | 7.17 | 1337 | 9.88 | 1.65 | –696 |
| | T | 1.3535 | 7.36 | 1406 | 10.11 | 1.87 | –760 |
| | Q | 1.3480 | 7.48 | 1414 | 10.29 | 1.94 | –780 |
| | 5 | 1.3479 | 7.56 | 1414 | 10.40 | 1.99 | –788 |
| | liter. | 1.331[c] | 6.15–6.25[b] | 1487[c] | 10.1 ± 0.4[c] | – | –544 ± 50[d] |
| BeS | D | 1.7710 | 6.24 | 991 | 9.09 | | –470 |
| | T | 1.7592 | 6.42 | 994 | 9.20 | | –504 |
| | Q | 1.7522 | 6.48 | 1002 | 9.30 | | –519 |
| | 5 | 1.7500 | 6.49 | 1004 | 9.34 | | –526 |
| | liter. | 1.742[c] | 5.19[e] | 998[c] | – | | – |
| MgO | D | 1.7341 | 7.74 | 1068 | 8.73 | | –502 |
| | T | 1.7377 | 8.43 | 1033 | 8.98 | | –564 |
| | Q | 1.7398 | 8.81 | 1022 | 9.08 | | –587 |
| | 5 | 1.7413 | 9.04 | 1012 | 9.14 | | –598 |
| | liter. | 1.749[c] | – | 785[c] | 8.76 ± 0.22[c] | | –594 ± 42[c] |
| MgS | D | 2.1662 | 8.75 | 559 | 7.39 | 1.63 | –351 |
| | T | 2.1556 | 9.08 | 561 | 7.69 | 1.82 | –388 |
| | Q | 2.1514 | 9.25 | 562 | 7.78 | 1.89 | –403 |
| | 5 | 2.1474 | 9.32 | 564 | 7.82 | 1.91 | –410 |
| | liter. | 2.143[c] | – | 529[c] | – | – | – |

[a] Formation enthalpy $MX(^1\Sigma^+) = M(^1S) + X(^1D)$. [b] Value recommended on the basis of theoretical results.[18] [c] Taken from Huber–Herzberg collection.[88] [d] Taken from experimental work.[96] [e] Theoretical value from ref.[17]

 © 2007 Wiley-VCH Verlag GmbH & Co. KGaA, Weinheim 

along the columns exert clear minima for the Mg-containing species.

The differences between the calculated (HF, Koopmans' theorem) and observed[89] ionization potentials for the species in the first column ($\Delta I = I_{calcd.} - I_{exp.}$) amount to 0.42, –0.43, –0.80, –0.88, and –0.89 eV. Notably, CI vectors in the CASSCF approach suggest an admixture of 7 to 10% of excited configurations in the ground states.

### The BeO, BeS, MgO, and MgS Systems

The results of DFT and MP2 calculations for bond length, dipole moment, valence vibration, vertical ionization potential and electron affinity, and heat of formation for the title diatomics are presented in Table 1. The bond lengths and valence vibrations can be obtained for the set of diatomics under study with satisfactory precision.

The MP2 CBS bond lengths, when compared to experimental values, exhibit an average deviation of 0.7 pm. The B3LYP CBS values underestimate the experiment by 1.1 pm. The average deviation of wavenumbers is smallest for the B3LYP procedure and amounts in the CBS limit to 36 $cm^{-1}$.

Vertical ionization potentials and electron affinities were obtained from Equations (2) and (4). The overall agreement is satisfactory, which also applies to HF data (not included in Table 1) with the use of Koopmans' theorem.

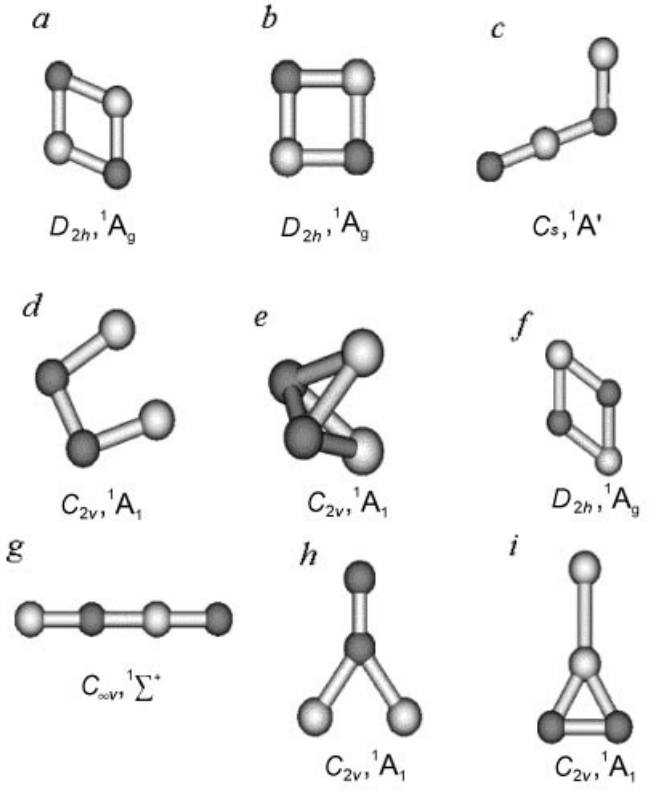


| | | a | b | c | d | e | f | g | h | i |
|---|---|---|---|---|---|---|---|---|---|---|
| $Be_2O_2$ | A | GM | LM | LM | LM | LM | LM | - | S1 | S1 |
| | B | No | No | No | 94;5 | 74;25 | 58;40 | - | - | - |
| | C | 0.0 | 157 | 268 | 546 | 552 | 270 | - | - | - |
| $Be_2S_2$ | A | GM | LM | LM | LM | S1 | S1 | S1 | LM | S1 |
| | B | No | No | No | 95;2 | - | - | - | 97;1 | - |
| | C | 0.0 | 277 | 312 | 350 | - | - | - | 564 | - |
| $Mg_2O_2$ | A | GM | LM | - | LM | - | LM | S1 | LM | LM |
| | B | 97;1 | 97;1 | - | 58;41 | - | 58:42 | - | 87;6 | 96;2 |
| | C | 0.0 | 36 | - | 214 | - | 214 | - | 397 | 410 |
| $Mg_2S_2$ | A | GM | LM | LM | LM | LM | S1 | S1 | LM | LM |
| | B | No | No | No | 89;5 | 82;16 | - | - | 88;6 | 96:4 |
| | C | 0.0 | 125 | 23 | 224 | 222 | - | - | 339 | 303 |

Figure 3. Localized stationary points on the B3LYP/cc-pVDZ energy hypersurfaces of $Be_2O_2$, $Be_2S_2$, $Mg_2O_2$, and $Mg_2S_2$. Each of them is described by symmetry point group and electronic ground state. White and grey balls correspond to metal (Be, Mg) and chalcogen (O, S) atoms, respectively. In the presented table, basic information about the isomers found is collected in the following way: A – nature of stationary point (GM – global minimum, LM – local minimum, S*n* – saddle point of *n*th order); B – multireference wavefunction character of isomer [percentage ratio of the two most dominant wavefunctions; analysis with CASSCF(4,6)]; C – relative energies of dimer isomers (in $kJ\,mol^{-1}$).

 © 2007 Wiley-VCH Verlag GmbH & Co. KGaA, Weinheim 

### Calcium Selenide: Testing System for Relativistic Contribution Estimate

This system consisting of the fourth row elements was used for estimating the role of relativistic effects. The comparison was made with nonrelativistic B3LYP/cc-pVTZ and quasirelativistic DKH-B3LYP/cc-pVTZ methods. The latter method includes those components of relativistic corrections which can be considered essential. The calculations were performed for the monomer ($^1A_{1g}$) and the dimer ($^1B_{3u}$) and concerned molecular geometry, heat of formation, the first adiabatic ionization potential and electron affinity, wavenumbers of vibrational modes, and excitation energies for the longest wavelength electronic transition. The results are transparent: except for the heats of formation, the changes are not significant. In the case of the (negative) heats of formation, the relativistic values are about 20% bigger than the nonrelativistic ones.

### Structure of Oligomers $M_iX_i$ (M = Be, Mg; X = O, S; *i* = 2–6)

*Dimers:* Stationary points on the respective potential energy surfaces have been obtained by the energy minimization of numerous initial structures selected on the basis of chemical intuition and fantasy. The nature of the located stationary points was ascertained by means of the eigenvalue signs of the respective Hessians. This made it possible to distinguish global and local minima and the first- and higher-order saddle points. Except for minima, only the first-order saddle points are of chemical relevance, and they represent activated complexes of the Eyring absolute rate theory. The structures investigated with the dimers and detailed information on the nature of the located stationary points is presented in Figure 3. For the sake of simplicity, we concluded that the rhombic structure with acute angles at chalcogens represented a global minimum not only with $Be_2O_2$, $Be_2S_2$, $Mg_2O_2$, and $Mg_2S_2$ but in general also with analogue dimers. We observe that the opposite is true with group IIIa–Va dimers: acute angles are associated with the metal atoms.[90] Moreover, all these species represent single-reference systems. Figure 3 shows that a local minimum is only a little higher in energy than the global minimum. However, in the case of $Mg_2O_2$, structure *b* is about 36 kJ mol$^{-1}$ above the global minimum, and with $Mg_2S_2$, structre *c* is 23 kJ mol$^{-1}$ above the global minimum.

Passing from monomers to dimers is accompanied by a lengthening of the M–X bond by 16, 18, 12, and 17 pm for $Be_2O_2$, $Be_2S_2$, $Mg_2O_2$, and $Mg_2S_2$, respectively (B3LYP/cc-pVDZ). The softer nature of these bonds is indicated by the $b_{1u}$ harmonic normal vibrational modes of the dimers.

*Trimers:* Despite great effort, it seems that the only significant minimum on the PES of these systems are hexagons possessing the $D_{3h}$ structure. They are products of strong electrostatic (head–tail) interactions of three building units. It is tempting to try to ascribe the stability of the $D_{3h}$ structures to a kind of aromaticity. Although there is a significant formal similarity between the systems under study and moieties such as benzene and cyclic $C_6$ ($D_{3h}$), the great difference in the electronegativity of the atoms that form building units (e.g. Be and O) reduces delocalization considerably. Again, the angles at the chalcogen atoms of the trimers are smaller than those at metal atoms. The structure of the group IIIa–Va and group IIb–VIa species is analogous.[69,90] Chemical intuition has strong support in molecular dynamics. We have been able to show by a simulated annealing procedure[91] the superiority of the $D_{3h}$ structure for the four dimers which were thoroughly studied. Heavier trimers from the group IIIa–Va matrix prefer[90] a three-dimensional structure, which was ascribed to the low-lying d orbitals and energy diminution due to higher coordination numbers. We might add that linear trimers represent saddle points of the higher order. The bond lengths in trimers are equal 146.7, 190.9, 184.0, and 229.9 pm for the BeO, BeS, MgO, and MgS bonds, respectively. This means that all the bonds are about 3 pm shorter than the analogous bonds in the dimers.

*Tetramers:* We have been able to localize three stationary points with all four building units under study (Figure 4). The BeO tetramer is the most stable in a planar octagonal form ($D_{4h}$). $Mg_4O_4$ and $Mg_4S_4$ assume a heterocubic structure ($T_d$); with $Be_4S_4$ the situation is somewhat more involved. A minimum of $D_{2d}$ symmetry passes through an extremely low-lying transition state of $D_{4h}$ symmetry into an equivalent $D_{2d}$ system. The B3LYP/cc-pVTZ barrier

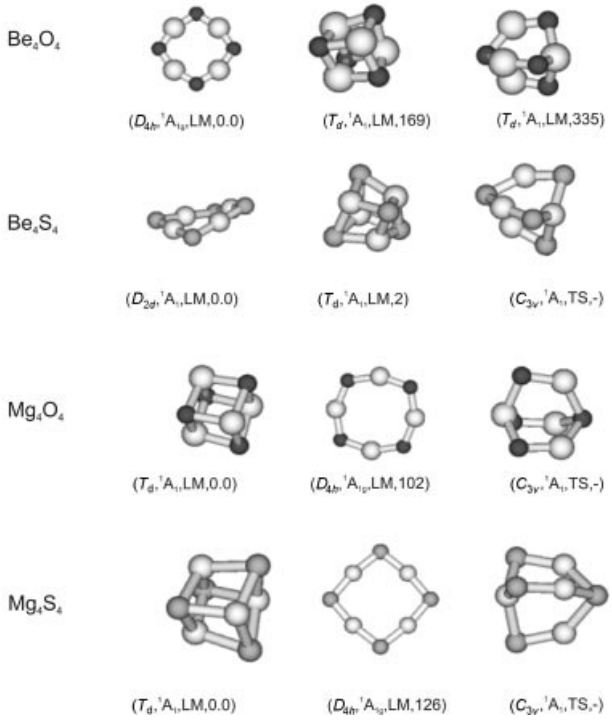


Figure 4. Localized stationary points on the B3LYP/cc-pVDZ energy hypersurfaces of $Be_4O_4$, $Be_4S_4$, $Mg_4O_4$, and $Mg_4S_4$. Symmetry group, electronic state, nature of the stationary point, and relative energy (kJ mol$^{-1}$) with respect to the most stable isomer are in parentheses. Dark spheres stand for chalcogen. Local minima (LM) and transition states (TS).

 © 2007 Wiley-VCH Verlag GmbH & Co. KGaA, Weinheim 

amounts to 0.5 kJ mol$^{-1}$ and can be neglected at room temperature. The $A_1$ ground state is not degenerate and therefore the deviation from coplanarity cannot be attributed to the Jahn–Teller effect. However, pseudo Jahn–Teller distortion is applicable, which is supported by arguments in ref.[60] The HOMO ($b_{1u}$) and LUMO ($a_{1g}$) orbitals in the $D_{2d}$ geometry are transformed into $a_1$ orbitals, which are capable of mixing. The mixing is probably not very pronounced because of the large energy gap between these orbitals estimated on the basis of the first electronic transition (3.9 eV; TD-B3LYP/cc-pVDZ). At this level, the energy difference between the $D_{2d}$ and $T_d$ structures is so small that the order of isomers can be changed when passing to a higher level of theory.

The $Be_4O_4$, $Mg_4O_4$, and $Mg_4S_4$ clusters with $D_{4h}$ symmetry and $Be_4S_4$ with $D_{2d}$ symmetry have bond lengths equal to 145.3, 182.6, 228.6 and 190.1 pm, respectively (B3LYP/cc-pVDZ), which correspond roughly to the values of the bond lengths in the trimers. The contraction of bond lengths with respect to those of dimers could indicate heteroaromatic behavior of the rings. The bond lengths in the most stable isomers of $Mg_4O_4$ and $Mg_4S_4$ (both with $T_d$ symmetry) are 195.7 and 243.0 pm, which is in agreement with the expected increase in bond lengths when passing to bulk: $(MgO)_\infty$, 210.6 and $(MgS)_\infty$, 260.0 pm.

*Pentamers:* Localized stationary points are summarized in Figure 5. Only $Be_5O_5$ assumes a planar monocyclic structure (decagon) with $D_{5h}$ symmetry. Another isomer has a naphthalene-like structure with $C_{2v}$ symmetry. The other three pentamers are most stable in a nonplanar structure ($C_s$). Monocyclic structures with $Be_5S_5$ are nonplanar ($C_s$), whereas with $Mg_5O_5$ they are planar ($D_{5h}$). The $D_{5h}$ structure of $Mg_5S_5$ is a second-order saddle point. The addition of one electron to the monocyclic nonplanar $C_s$ structure of $Be_5S_5$ causes planarization of the ring ($D_{5h}$) accompanied by reduction of the Be–Be distance. Ladder structures have been localized with pentamers except $Be_5O_5$, but they have little chemical relevance.

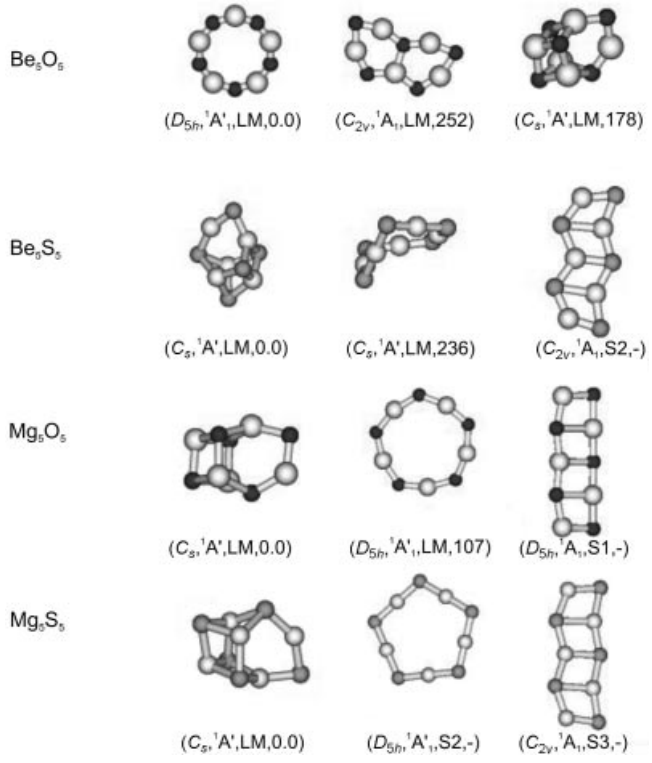


Figure 5. Localized stationary points on the B3LYP/cc-pVDZ energy hypersurfaces of $Be_5O_5$, $Be_5S_5$, $Mg_5O_5$, and $Mg_5S_5$. Symmetry group, electronic state, nature of the stationary point, and relative energy (kJ mol$^{-1}$) with respect to the most stable isomer are in parentheses. Dark spheres stand for chalcogen. Local minima (LM) and saddle points of the *n*th order (S*n*).

*Hexamers:* Ten local minima are among 16-localized stationary points for the four systems under study (Figure 6). With all hexamers, the most stable forms have $D_{3d}$ structure, which consists of six-membered cycles in a stacking arrangement. This form represents a building unit of wurzite crystals, which concerns beryllium oxide and sulfide. Magnesium compounds crystallize frequently into a cubic structure, which, at the level of hexamers, is represented by the $D_{2h}$ structure. It can be considered a kind of "sandwich" consisting of three stable rhombic units. Only $Mg_6O_6$ and $Mg_6S_6$ represent local minima; the beryllium containing systems of the $D_{2h}$ structure are saddle points.

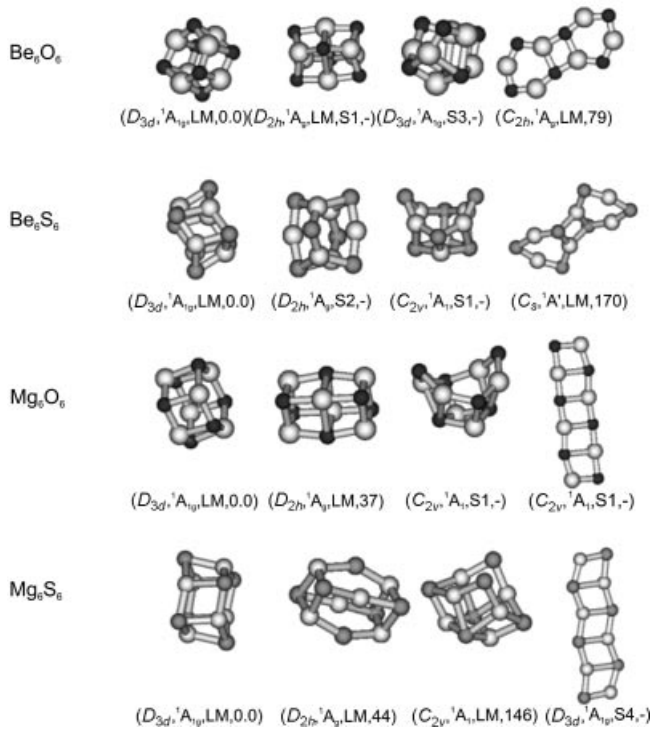


Figure 6. Localized stationary points on the B3LYP/cc-pVDZ energy hypersurfaces of $Be_6O_6$, $Be_6S_6$, $Mg_6O_6$, and $Mg_6S_6$. Symmetry group, electronic state, nature of the stationary point, and relative energy (kJ mol$^{-1}$) with respect to the most stable isomer are in parentheses. Dark spheres stand for chalcogen. Local minima (LM) and saddle points of the *n*th order (S*n*).

Bowl-like $C_{2v}$ structures consisting of tetragons, in contrast to $Zn_6S_6$ and $Zn_6Se_6$ clusters,[60] are not stable species; they are just saddle points. $Mg_6S_6$ assumes a special posi-

 © 2007 Wiley-VCH Verlag GmbH & Co. KGaA, Weinheim 

tion by being a local minimum. This might be tentatively ascribed to the d orbitals of S and Mg, which stabilize systems with atoms having high coordination numbers.

The $Be_6O_6$ system exists with a local minimum ($C_{2h}$) consisting of two hexagons and one (connecting) rhombic motif. Therefore, there is a formal resemblance between this system and diphenylene in the benzenoid hydrocarbon series. With reference to $Be_6S_6$, this $C_{2h}$ structure converges to a nonplanar system with $C_s$ structure, whereas $Mg_6O_6$ and $Mg_6S_6$ pass into a ladder structure of a saddle-point nature.

Time consumption connected with the B3LYP/cc-pVDZ geometry optimization of hexamers can be reduced considerably by using the PM3 preoptimization.[92]

## Electronic Spectra

We believe we have shown convincingly[4] that for BeO, BeS, MgO, and MgS the longest wavelength transitions calculated by TD-B3LYP/cc-pVDZ and SAC-CI(SD)/cc-pVDZ mutually agree satisfactorily. The same is true when

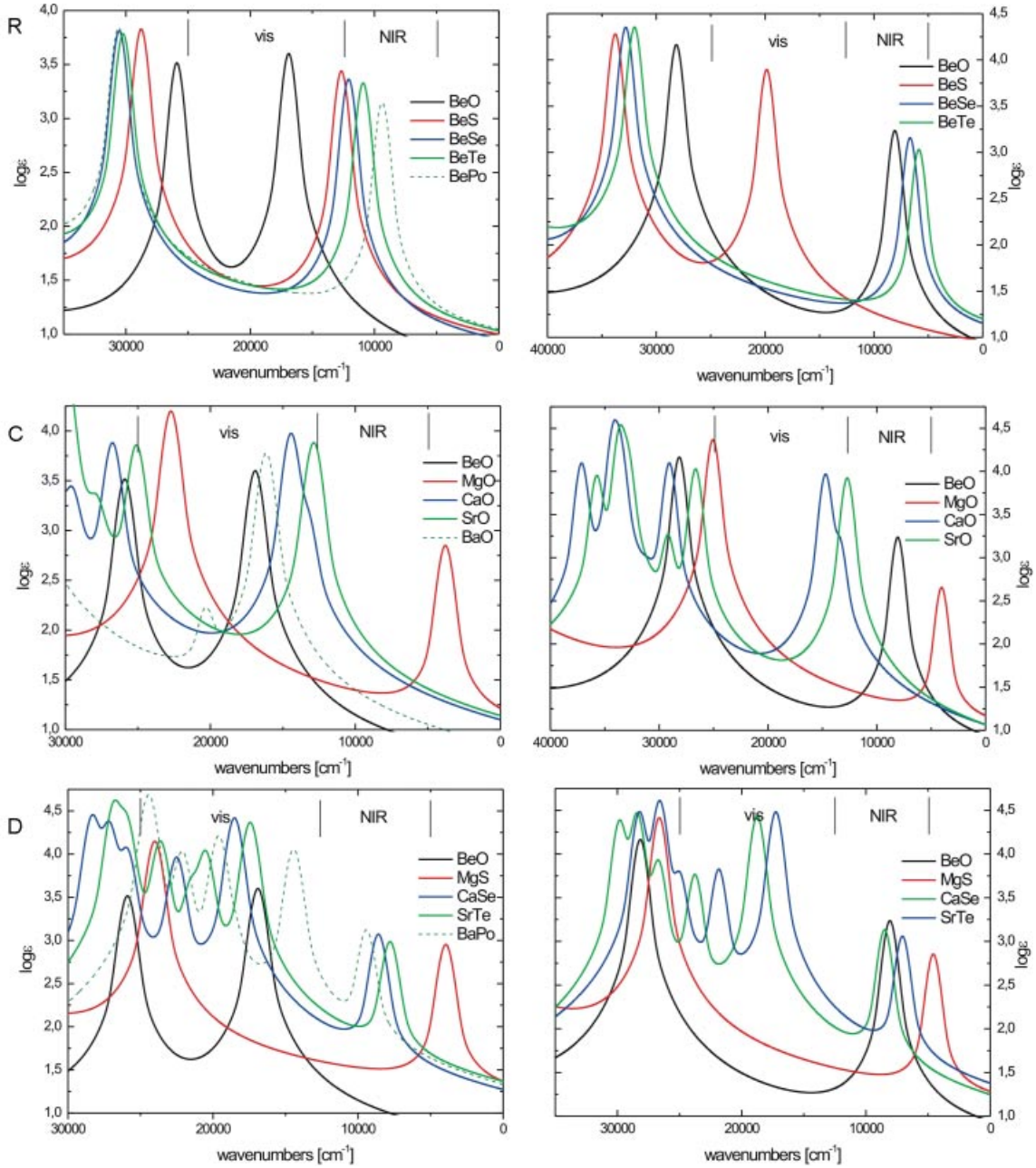


Figure 7. Computed electronic spectra of the group IIa–VIa diatomics at the TD-B3LYP/SDD (the left column) and DKH-B3LYP/VDZP (the right column) level. Three directions in the group IIa–VIa matrix are considered (the first column, C; the first row, R; the main diagonal, D). The regions of visible (vis) and near-infrared regions (NIR) are indicated.

 © 2007 Wiley-VCH Verlag GmbH & Co. KGaA, Weinheim 

comparing calculated and observed[4] band positions in the near-infrared and visible regions of the spectrum. An analogous statement is valid for dimers of the above-mentioned diatomics, except that there are no experimental data available. In all instances, passing from monomer to dimer is accompanied by a very large hypsochromic shift. Moreover, it has been shown with the monomers that the use of the icMRCI procedure produces similar results. Although passing from DZ to TZ brings about an improvement in all three methods relative to the experimental values, the TD-B3LYP/cc-pVDZ method is well-suited and a relatively economic procedure for good semiquantitative predictions.

The order of transitions with oxides forming the first column (BeO, ..., BaO) remains unchanged ($X^1\Sigma^+ \rightarrow A^1\Pi$, $X^1\Sigma^+ \rightarrow B^1\Sigma^+$, $X^1\Sigma^+ \rightarrow B^1\Pi$, and $X^1\Sigma^+ \rightarrow C^1\Sigma^+$) between BeO and CaO. For SrO, the two first transitions are approximately equal in energy, and with BaO, the first band connected with the $\Sigma^+ \rightarrow \Sigma^+$ transition is observed.

Instead of calculating the electronic spectroscopic data for all matrix elements and the dimers thereof, we dealt with systems of the first column (BeO, ..., BaO), of the first row (BeO, ..., BePo), and with systems formed from the main diagonal (BeO, ..., BaPo) (cf. Figure 1). The respective theoretical absorption curves are depicted in Figure 7 for di-

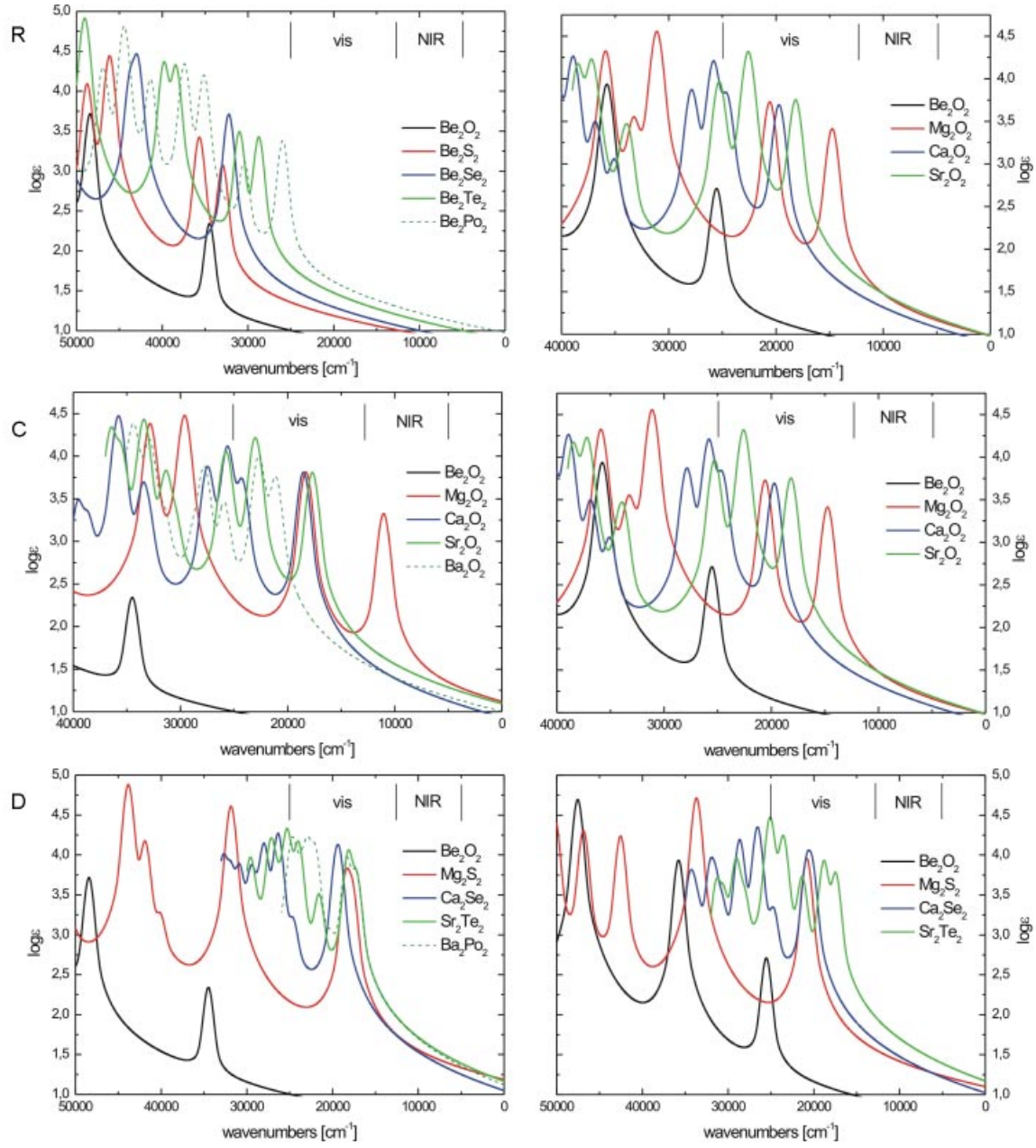


Figure 8. Computed electronic spectra of dimers of the group IIa–VIa diatomics at the TD-B3LYP/SDD (the left column) and DKH-B3LYP/VDZP (the right column) level. Three directions in the group IIa–VIa matrix are considered (the first column, C; the first row, R; the main diagonal, D). The regions of visible (vis) and near-infrared regions (NIR) are indicated.

 © 2007 Wiley-VCH Verlag GmbH & Co. KGaA, Weinheim 

atomics and in Figure 8 for their dimers. On the basis of comparison between calculated and observed band positions for all group IIa oxides and BeS and MgS, it is possible to say that the curves in Figures 7 and 8 offer a realistic picture of the electronic spectra. The first absorption band is either in the near-infrared region (in the majority of cases) or in the visible region. The overall picture is quite similar for both theoretical levels used, but the DKH procedure seems to be more reliable. However, the only real failure of the pseudopotential basis set (SDD) is for BeO and its dimer.

Calculated electronic spectra for the most stable pairs of isomers of the dimers, tetramers, and hexamers of MgO suggest the possibility to use this type of spectroscopy for structure elucidation (Supporting Information, see Figure S1).

### Trends in Physical Characteristics in Series of Oligomers

A summarizing note on the geometry of clusters will be augmented by remarks on ionization potentials and elec-

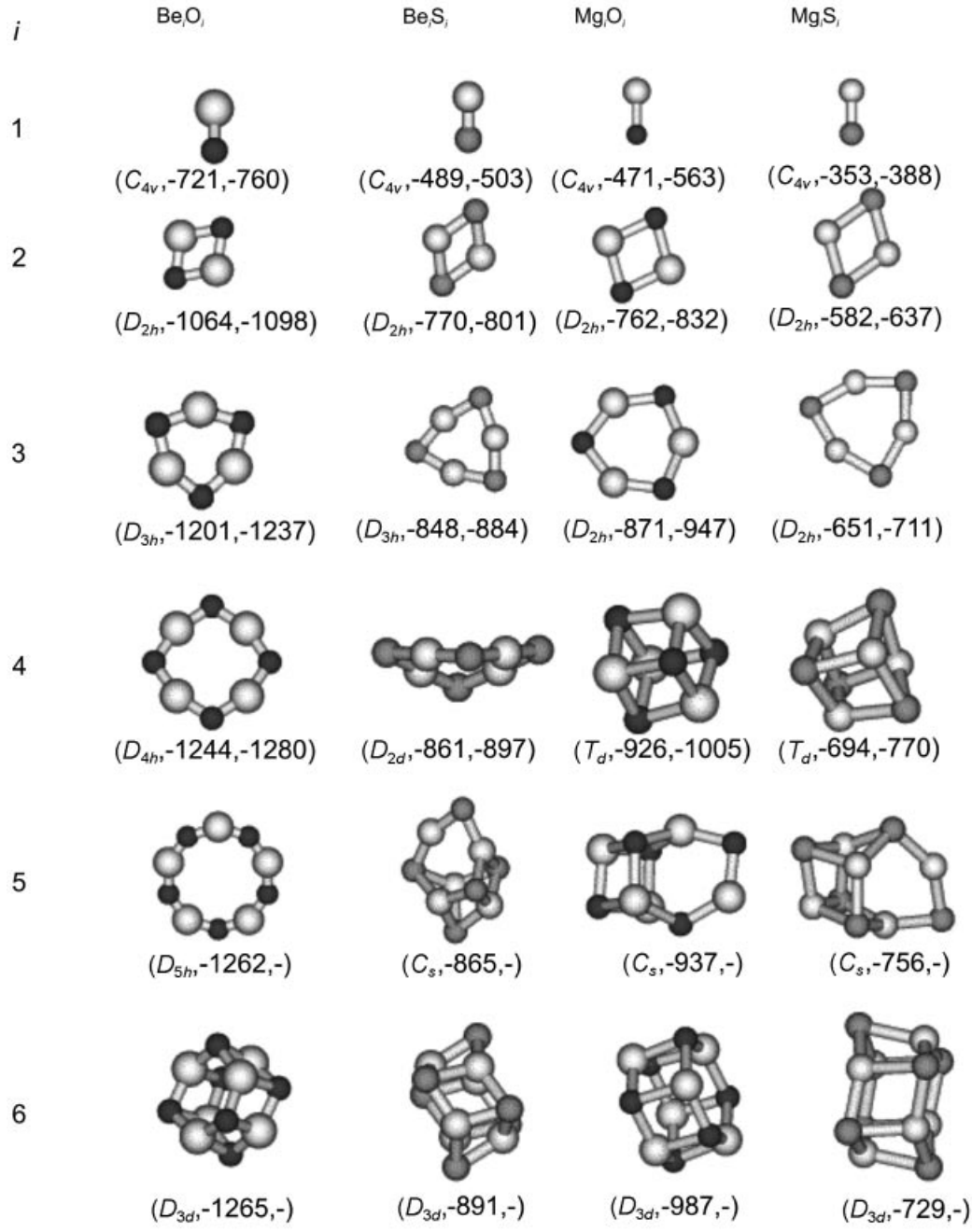


Figure 9. Structure of global minima of $(MX)_i$ on the respective energy hypersurface. Symmetry group and calculated energy of formation, $\Delta E$ (B3LYP/cc-pVTZ and MP2/cc-pVTZ) per MX unit (kJ mol$^{-1}$). Basis set superposition error is included. Dark spheres mean chalcogen.

 © 2007 Wiley-VCH Verlag GmbH & Co. KGaA, Weinheim 

tron affinities. Assumed global minima are summed up in Figure 9. Notably, higher oligomers consist of rhombic and hexagonal motifs. Specific energies of formation of oligomers, that is energies per monomer unit, are defined by Equation (5). The two sets of formation energies (DFT and MP2) are available up to tetramer and differ by about 5%. It is hardly possible to say which of the methods should be preferred. Obviously, however, it is desirable to have for small oligomers such a comparison available and, for more extensive systems, the DFT procedure represents the only, remarkably reliable, chance. Increasing specific formation energy suggests the increasing stability of larger oligomers and also their decreasing reactivity. It is known from the literature[3c,69] that attempts to obtain cohesion energy of a crystal by extrapolating the formation energy of small clusters are not successful. Internal energy of BeO and MgO crystals are 1180 and 995 kJ mol$^{-1}$.[93]

Ionization potentials, $I$, and electron affinities, $A$, are valuable characteristics in several respects. The BeO clusters are used as representatives. Adiabatic and vertical values are defined by Equations (1)–(4). In opposition to the formation energies, the plots of $I$ and $A$ against the cluster size are not smooth (Figure 10). Relative maxima with ionization potentials correspond to $i$ = 3 and 5, whereas minima are at $i$ = 2, 4, and 6. This suggests that there is stabilization of cycles with 6 and 10 atoms; minima on the plot are connected with 4, 8, and 12 atoms in the ring. It is at least formally an analogy to the aromatic and nonaromatic cyclic, conjugated hydrocarbons. The same was observed in the BN series, that is aromaticity with $(BN)_3$ and $(BN)_5$.[94] the adiabatic and vertical values differ very little, which indicates an absence of dramatic geometry changes after removal or addition of an electron. The trends are the same for both methods used.

In Table S1 (Supporting Information), we summarize the values of the partial charges at the metal atoms for the oligomers depicted in Figure 9. We wish to underline two points: (1) The ionic character increases with cluster size, which correlates to a hypsochromic shift in the electronic spectra (vide infra). The partial charges are also significantly influenced by the coordination environment and that is apparent in the series of $Be_iO_i$, $i$ = 1–6. Only the $Be_6O_6$ system has a different coordination number of atoms and is not consistent with the smooth trend for $i$ = 1–5. (2) The MgO molecule exerts significant covalency; the growth of ionic character for the MgO clusters with increasing $i$ is most dramatic among species included in Figure 9.

The dependence of the positions on the longest wavelength bands for oxides and sulfides of beryllium and magnesium is shown in Figure 11. The only structurally homogeneous series for $i$ = 1–5 is BeO: the first band of the cyclic structures exhibits a dramatic hypsochromic shift from about 10 000 ($i$ = 1) to 60 000 cm$^{-1}$ ($i$ = 5). The bathochromic shift when passing from pentamer to hexamer is, no doubt, due to structural changes, namely to the transition to a three-dimensional structure ($D_{3d}$). The courses for the remaining three systems support the plausibility of this assumption because a change from hypsochromicity to bathochromicity manifests itself by passing from trimer to tetramer, which coincides with passing from planarity to three-dimensional structures.

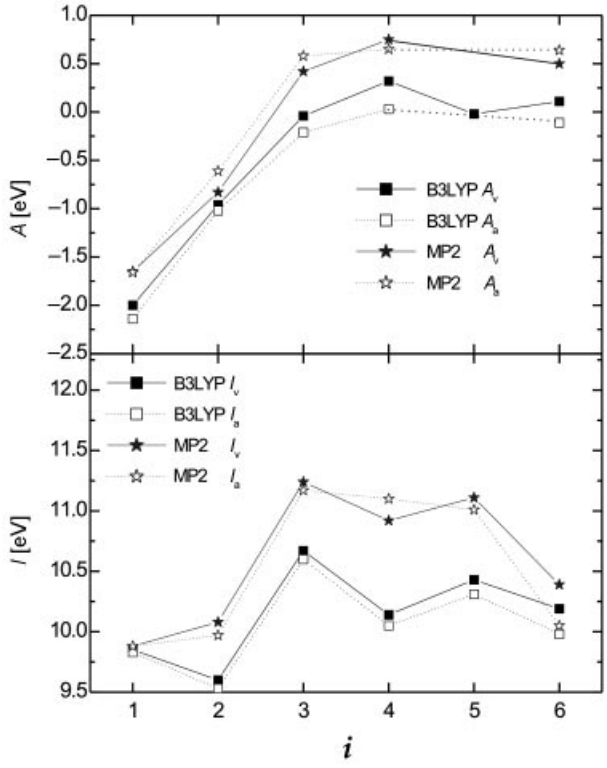


Figure 10. Vertical and adiabatic ionization potentials and electron affinities plotted against the size of the most stable $(BeO)_i$ oligomers (eV). In adiabatic values zero-point energy is included [cf. Equations (1)–(4)]. B3LYP/cc-pVDZ (squares: full-vertical, empty-adiabatic), MP2/cc-pVDZ (stars: full-vertical, empty-adiabatic) calculations.

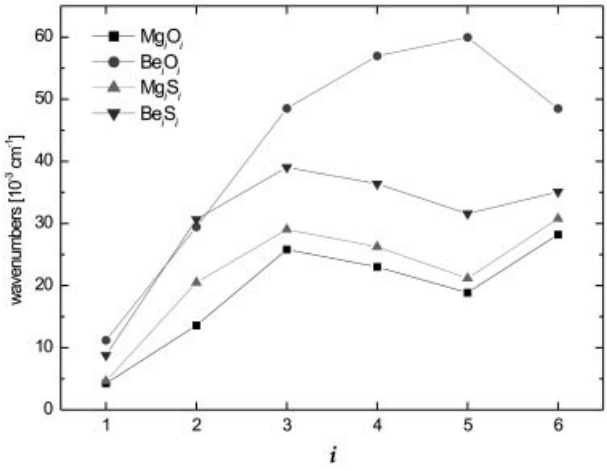


Figure 11. The shift in the position of the longest wavelength absorption band in the electronic spectra in four series of systems ranging from monomer up to hexamer. The calculations have been performed at the TD-B3LYP/cc-pVTZ level.

A remarkably close correlation exists between TD DFT excitation energies (for transitions which dominate the HOMO–LUMO excitation) and differences of Khon–Sham

 © 2007 Wiley-VCH Verlag GmbH & Co. KGaA, Weinheim 

eigenvalues, which result from the solution of Kohn–Sham equations with the B3LYP functional. Recently, such correlations were observed and analyzed.[70,77] This finding is valuable because it makes estimates of the first-band position on the basis of a calculation possible, which, for extensive systems, are significantly more economic than complete TD DFT calculations.

Finally, let us briefly comment on the first and second excitation energies in the isoelectronic series of diatomics related to the second row of the periodic table. The wavenumbers [$cm^{-1}$] are as follows: LiF: 40530, 45600; BeO: 9410, 21250; BN: 27880, –; and $C_2$: 720, –. These values were obtained at the TD-B3LYP/cc-pVTZ level (LiF, BeO) or taken from ref.[95] (BN, $C_2$). Except for group IIa–VIa species, in all instances the passing from monomers (diatomics) to dimers is associated with a bathochromic shift.

The related group IIb–VIa diatomics MX (M = Zn, Cd, Hg; X = O, S) exert the first two bands in similar regions as the group IIa–VIa species. Whereas the first peak (TD-B3LYP/cc-pVTZ [$cm^{-1}$]) is located in the near-infrared or infrared region (ZnO: 5570; ZnS: 5040; CdO: 2810; CdS: 2810; HgO: 3350; HgS: 1960) with very low intensity, the second one, which is more intensive by about two orders of magnitude, is shifted to the near-UV region (ZnO: 31470; ZnS: 32290; CdO: 28400; CdS: 28730; HgO: 32560; HgS: 32635).

## Conclusions

Although the group IIa–VIa system in bulk does not attract the attention of many chemists, which is (partly) due to a big gap between valence and conduction bands and their chemical inertness, the opposite is true for group IIa–VIa diatomics and clusters thereof. We found that the diatomics unexpectedly exert the first absorption band in the near-infrared or visible regions and this band is progressively shifted toward shorter wavelengths with growing cluster size.

The structural variety of group IIa–VIa species is significantly limited by strong ionic interaction of metal–chalcogen poles. Therefore, the most stable structures of larger clusters could be considered as a combination of a few, rhombic and hexagonal, patterns.

We feel strongly that catalytic properties of bulk surfaces could be enhanced by deposing cluster-like structures. In this work, we tried to demonstrate how electronic characteristics are tunable by varying the metal and chalcogen, cluster size, and isomerization. We hope that the group IIa–VIa species can be valuable for new molecular devices similar to the group IIb–VIa species.

**Supporting Information** (see footnote on the first page of this article): Electronic spectra and partial charges at metal atoms.

## Acknowledgments

Our sincere thanks are due to Mr. J. Novotney and Mrs. R. Žohová for significant help with the preparation of the final version of the manuscript.

[1] a) J. Fabian, R. Zahradník, *Angew. Chem. Int. Ed. Engl.* **1989**, *28*, 677; b) D. F. Perepichka, M. R. Bryce, *Angew. Chem. Int. Ed.* **2005**, *44*, 5370.
[2] a) J. Koutecký, R. Zahradník, *Collect. Czech. Chem. Commun.* **1960**, *25*, 811.
[3] a) Ch. W. Bauschlicher Jr, S. R. Langhoff, *Chem. Phys. Lett.* **1986**, *126*, 163; b) T. Hiratani, K. Konishi, *Angew. Chem. Int. Ed.* **2004**, *43*, 5943; c) J. M. Matxain, J. M. Mercero, J. E. Fowler, J. M. Ugalde, *J. Phys. Chem. A* **2003**, *107*, 9918.
[4] M. Srnec, R. Zahradník, *Chem. Phys. Lett.* **2005**, *407*, 283.
[5] Ch. W. Bauschlicher Jr, S. R. Langhoff, *Theor. Chim. Acta* **1988**, *73*, 43.
[6] N. Benosman, N. Amrane, S. Méçabih, H. Aourag, *Physica B* **2001**, *304*, 214.
[7] K. J. Chang, S. Froyen, M. L. Cohen, *J. Phys. C: Solid State Phys.* **1983**, *16*, 3475.
[8] G. Frenking, W. Koch, J. Gauss, D. Cremer, *J. Am. Chem. Soc.* **1988**, *110*, 8007.
[9] O. Fuchs, L. Weinhardt, C. Heske, E. Umbach, A. Fleszar, C. Bostedt, L. J. Terminello, R. C. C. Perera, *Advanced Light Source Comp.* **2001**.
[10] P. Fuentealba, A. Savin, *J. Phys. Chem. A* **2000**, *104*, 10882.
[11] Y. H. Hu, *J. Am. Chem. Soc.* **2003**, *125*, 4388.
[12] D.-Y. Hwang, A. M. Mebel, *J. Am. Chem. Soc.* **2000**, *122*, 11406.
[13] K. D. Jordan, *Chem. Phys. Lett.* **1978**, *54*, 320.
[14] K. D. Jordan, *Chem. Phys. Lett.* **1979**, *62*, 143.
[15] G. Landwehr, A. Waag, F. Fischer, H.-J. Lugauer, K. Schüll, *Physica E* **1998**, *3*, 158.
[16] S. R. Langhoff, Ch. W. Bauschlicher Jr, H. Partridge, *J. Chem. Phys.* **1986**, *84*, 4474.
[17] J. Noga, T. Pluta, *Chem. Phys. Lett.* **1997**, *264*, 101.
[18] V. Parasuk, P. Neogrády, H. Lischka, M. Urban, *J. Phys. Chem.* **1996**, *100*, 6325.
[19] R. L. Sarkar, S. Chatterjee, *J. Phys. C: Solid State Phys.* **1977**, *10*, 57.
[20] M. B. Sullivan, M. A. Iron, P. C. Redfern, J. M. L. Martin, L. A. Curtiss, L. Radom, *J. Phys. Chem. A* **2003**, *107*, 5617.
[21] C. A. Thompson, L. Andrews, *J. Am. Chem. Soc.* **1994**, *116*, 423.
[22] A. A. Thompson, L. Andrews, *J. Phys. Chem.* **1996**, *100*, 12214.
[23] A. Waag, Th. Litz, F. Fischer, H.-J. Lugauer, T. Baron, K. Shüll, U. Zehnder, T. Gerhard, U. Lunz, M. Keim, G. Reuscher, G. Landwehr, *J. Crystal Growth* **1998**, *184/185*, 1.
[24] A. Aguado, J. M. López, *J. Phys. Chem. B* **2000**, *104*, 8398.
[25] M. A. Al-Laham, G. W. Trucks, K. Raghavachari, *J. Chem. Phys.* **1992**, *96*, 1137.
[26] A. L. Almeida, J. B. L. Martins, E. Longo, N. C. Furtado, C. A. Taft, J. R. Sambrano, W. A. Lester Jr, *Int. J. Quantum Chem.* **2001**, *84*, 705.
[27] a) Ch. W. Bauschlicher Jr, H. Partridge, *Chem. Phys. Lett.* **2001**, *342*, 441; b) Ch. W. Bauschlicher Jr, B. H. Lengsfield III, D. M. Silver, D. R. Yarkony, *J. Chem. Phys.* **1981**, *74*, 2379; c) Ch. W. Bauschlicher Jr, D. M. Silver, D. R. Yarkony, *J. Chem. Phys.* **1980**, *73*, 2867.
[28] Ch. W. Bauschlicher Jr, B. H. Lengsfield III, B. Liu, *J. Chem. Phys.* **1982**, *77*, 4084.
[29] D. K. Böhme, H. Schwarz, *Angew. Chem. Int. Ed.* **2005**, *44*, 2.
[30] A. I. Boldyrev, J. Simons, P. R. von Schleyer, *Chem. Phys. Lett.* **1995**, *233*, 266.
[31] A. I. Boldyrev, J. Simons, *J. Phys. Chem.* **1996**, *100*, 8023.
[32] A. I. Boldyrev, I. L. Shamovsky, P. R. von Schleyer, *J. Am. Chem. Soc.* **1992**, *114*, 6469.
[33] C. Bradford, C. B. O'Donnell, B. Urbaszek, A. Balocchi, C. Morhain, K. A. Prior, B. C. Cavenett, *Appl. Phys. Lett.* **2000**, *76*, 3929.
[34] G. Cappellini, F. Finocchi, S. Bouette-Russo, C. Noguera, *Comput. Mater. Sci.* **2001**, *20*, 401.

 © 2007 Wiley-VCH Verlag GmbH & Co. KGaA, Weinheim 

[35] N. F. Dalleska, P. B. Armentrout, *Int. J. Mass Spectrosc. Ion Processes.* **1994**, *134*, 203.
[36] M. Gutowski, P. Skurski, X. Li, L.-S. Wang, *Phys. Rev. Lett.* **2000**, *85*, 3145.
[37] E. Kagi, T. Hirano, S. Takano, K. Kawaguchi, *J. Mol. Spectrosc.* **1994**, *168*, 109.
[38] J. H. Kim, L.-S. Wang, H. L. de Clerq, C. A. Fancher, O. C. Thomas, K. H. Bowen, *J. Chem. Phys. A* **2001**, *105*, 5709.
[39] S. Kohiki, M. Arai, H. Yoshikawa, S. Fukushima, *J. Phys. Chem. B* **1999**, *103*, 5296.
[40] A. Lichanot, A. Dargelos, C. Larrieu, *Solid State Commun.* **1994**, *90*, 189.
[41] E. Lucas, S. Decker, A. Khaleel, A. Seitz, S. Fultz, A. Ponce, W. Li, C. Carnes, K. J. Klabunde, *Chem. Eur. J.* **2001**, *7*, 2505.
[42] I. Onal, S. Senkan, *Industrial & Engineering Chem. Res.* **1997**, *36*, 4028.
[43] J. M. Recio, R. Pandey, A. Ayuela, A. B. Kunz, *J. Chem. Phys.* **1993**, *98*, 4783.
[44] a) D. Ricci, C. Di Valentin, G. Pacchioni, P. V. Sushko, A. L. Shluger, E. Giamello, *J. Am. Chem. Soc.* **2003**, *125*, 738; b) D. Ricci, G. Pacchioni, P. V. Sushko, A. Shluger, *J. Chem. Phys.* **2002**, *117*, 2844.
[45] C. Roberts, R. L. Johnston, *Phys. Chem. Chem. Phys.* **2001**, *3*, 5024.
[46] A. J. Rowley, P. Jemmer, M. Wilson, P. A. Madden, *J. Chem. Phys.* **1998**, *108*, 10209.
[47] M. Stener, G. Fronzoni, R. De Francesco, *Chem. Phys.* **2004**, *298*, 141.
[48] S. Stankic, M. Müller, O. Diwald, M. Sterrer, E. Knözinger, J. Bernardi, *Angew. Chem. Int. Ed.* **2005**, *44*, 4917.
[49] S. Veliah, R. Pandey, Y. S. Li, J. M. Newsam, B. Vessal, *Chem. Phys. Lett.* **1995**, *53*, 235.
[50] Y. Wu, H. Yan, M. Huang, B. Messer, J. H. Song, P. Yang, *Chem. Eur. J.* **2002**, *8*, 1261.
[51] A. Aguado, L. Bernasconi, P. A. Madden, *J. Chem. Phys.* **2003**, *118*, 5704.
[52] A. R. Armstrong, J. Canales, P. G. Bruce, *Angew. Chem. Int. Ed.* **2004**, *43*, 4899.
[53] P. Cortona, *Int. J. Quantum Chem.* **2004**, *99*, 828.
[54] R. W. Field, *J. Chem. Phys.* **1974**, *60*, 2400.
[55] C. N. Jarman, R. A. Hailey, P. F. Bernath, *J. Chem. Phys.* **1992**, *96*, 5571.
[56] C. Wang, K. Tang, Q. Yang, C. An, B. Hai, G. Shen, Y. Qian, *Chem. Phys. Lett.* **2002**, *351*, 385.
[57] A. P. Alivisatos, *J. Phys. Chem.* **1996**, *100*, 13226.
[58] R. E. Bailey, S. Nie, *J. Am. Chem. Soc.* **2003**, *125*, 7100.
[59] D. Battaglia, J. J. Li, Y. Wang, X. Peng, *Angew. Chem. Int. Ed.* **2003**, *42*, 5035.
[60] P. Deglmann, R. Ahlrichs, K. Tsereteli, *J. Chem. Phys.* **2002**, *116*, 1585.
[61] K. Gokhberg, A. Glozman, E. Lifshitz, T. Maniv, M. C. Schlamp, P. Alivisatos, *J. Chem. Phys.* **2002**, *117*, 2909.
[62] J. Hu, Y. Bando, J. Zhan, D. Golberg, *Angew. Chem. Int. Ed.* **2004**, *43*, 4606.
[63] J. Hu, Y. Bando, D. Golberg, *Small* **2005**, *1*, 95.
[64] a) J.-O. Joswig, G. Seifert, T. A. Niehaus, M. Springborg, *J. Phys. Chem. B* **2003**, *107*, 2897; b) J.-O. Joswig, M. Springborg, G. Seifert, *J. Phys. Chem. B* **2000**, *104*, 2617.
[65] M. Kurtz, J. Strunk, O. Hinrichsen, M. Muhler, K. Fink, B. Meyer, C. Wöll, *Angew. Chem. Int. Ed.* **2005**, *44*, 2790.
[66] Q. Li, C. Wang, *J. Am. Chem. Soc.* **2003**, *125*, 9892.
[67] J. J. Li, Y. A. Wang, W. Guo, J. C. Keay, T. D. Mishima, M. B. Johnson, X. Peng, *J. Am. Chem. Soc.* **2003**, *125*, 12567.
[68] Z. Li, Y. Ding, Y. Xiong, Q. Yang, Y. Xie, *Chem. Eur. J.* **2004**, *10*, 5823.
[69] J. Matxain, J. M. Mercero, J. E. Fowler, J. M. Ugalde, *J. Phys. Chem. A* **2004**, *108*, 10502.
[70] J. M. Matxain, J. M. Mercero, J. E. Fowler, J. M. Ugalde, *J. Am. Chem. Soc.* **2003**, *125*, 9494.
[71] T. Nann, J. Riegler, *Chem. Eur. J.* **2002**, *8*, 4791.
[72] C. Pacholski, A. Kornowski, H. Weller, *Angew. Chem. Int. Ed.* **2002**, *41*, 1188.
[73] E. Spanó, S. Hamad, C. R. A. Catlow, *J. Phys. Chem. B* **2003**, *107*, 10337.
[74] H. Weller, *Angew. Chem. Int. Ed. Engl.* **1993**, *32*, 41.
[75] U. Drechsler, B. Erdogan, V. M. Rotello, *Chem. Eur. J.* **2004**, *10*, 5570.
[76] A. Pramann, K. Rademann, *Chem. Phys. Lett.* **2001**, *347*, 46.
[77] A. Savin, C. J. Umrigar, X. Gonze, *Chem. Phys. Lett.* **1998**, *288*, 391.
[78] M. J. Frisch, G. W. Trucks, H. B. Schlegel, G. E. Scuseria, M. A. Robb, J. R. Cheeseman, J. A. Montgomery Jr, T. Vreven, K. N. Kudin, J. C. Burant, J. M. Millam, S. S. Iyengar, J. Tomasi, V. Barone, B. Mennucci, M. Cossi, G. Scalmani, N. Rega, G. Petersson, H. Nakatsuji, M. Hada, M. Ehara, K. Toyota, R. Fukuda, J. Hasegama, M. Ishida, T. Nakajima, Y. Honda, O. Kitao, H. Nakai, M. Klene, X. Li, J. E. Knox, P. Hratchian, J. B. Cross, C. Adamo, J. Jaramillo, R. Gomperts, R. E. Stratmann, O. Yazyev, A. J. Austin, R. Cammi, C. Pomelli, J. W. Ochterski, P. Y. Ayala, K. Morokuma, G. A. Voth, P. Salvador, J. J. Dannenberg, V. G. Zakrzewski, S. Dapprich, A. D. Daniels, M. C. Strain, O. Farkas, D. K. Malick, A. D. Rabuck, K. Raghavachari, J. B. Foresman, J. V. Ortiz, Q. Cui, A. G. Baboul, S. Clifford, J. Ciolowski, B. B. Stefanov, G. Liu, A. Liashenko, P. Piskorz, I. Komaromi, R. L. Martin, D. J. Fox, T. Keith, M. A. Al-Laham, C. Y. Peng, A. Nanayakkara, M. Challacombe, P. M. W. Gill, B. Johnson, W. Chen, M. W.Wong, C. Gonzales, J. A. Pople, *Gaussian 03*, *Revision B.02*, Gaussian, Inc., Pittsburgh, **2003**.
[79] a) T. Leininger, A. Nicklass, H. Stoll, M. Dolg, P. Schwerdtfeger, *J. Chem. Phys.* **1996**, *105*, 1052; b) H.-J. Werner, P. J. Knowles, *J. Chem. Phys.* **1985**, *82*, 5053; c) H.-J. Werner, P. J. Knowles, M. Schütz, R. Lindh, P. Celani, T. Korona, G. Rauhut, F. R. Manby, R. D. Amos, A. Bernhardsson, A. Berning, D. L. Cooper, M. J. O. Deegan, A. J. Dobbyn, F. Eckert, C. Hampel, G. Hetzer, A. W. Lloyd, S. J. McNicholas, W. Meyer, M. E. Mura, A. Nicklass, P. Palmieri, R. Pitzer, U. Schumann, H. Stoll, A. J. Stone, R. Tarroni, T. Thorsteinsson, *MOLPRO 2002.3: A Package of Ab Initio Programs.*
[80] a) T. H. Dunning Jr, *J. Chem. Phys.* **1989**, *90*, 1007; b) R. A. Kendall, T. H. Dunning Jr, R. J. Harrison, *J. Chem. Phys.* **1992**, *96*, 6796; c) D. E. Woon, T. H. Dunning Jr, *J. Chem. Phys.* **1993**, *98*, 1358.
[81] R. Zahradník, L. Šroubková, *Isr. J. Chem.* **2003**, *43*, 243.
[82] H. Nakatsuji, *Chem. Phys. Lett.* **1978**, *59*, 362.
[83] a) H.-J. Werner, P. J. Knowles, *J. Chem. Phys.* **1988**, *89*, 5803; b) P. J. Knowles, H.-J. Werner, *Chem. Phys. Lett.* **1988**, *145*, 514.
[84] a) M. Douglas, N. M. Kroll, *Ann. Phys. (N. Y)* **1974**, *82*, 89; b) B. A. Hess, *Phys. Rev. A* **1986**, *33*, 3742; c) G. Jansen, B. A. Hess, *Phys. Rev. A* **1989**, *39*, 6016; d) L. L. Foldy, S. A. Wonthuysen, *Phys. Rev.* **1950**, *78*, 29.
[85] N. Godbout, D. R. Salahub, J. Andzelm, E. Wimmer, *Can. J. Chem.* **1992**, *70*, 560.
[86] S. F. Boys, F. Bernardi, *Mol. Phys.* **1970**, *19*, 553.
[87] a) R. B. Ross, J. M. Powers, T. Atashroo, W. C. Ermler, L. A. LaJohn, P. A. Christiansen, *J. Chem. Phys.* **1990**, *93*, 6654; b) R. B. Ross, J. M. Powers, T. Atashroo, W. C. Ermler, L. A. LaJohn, P. A. Christiansen, *J. Chem. Phys.* **1994**, *101*, 1098.
[88] K. P. Huber, G. Herzberg, *Molecules Spectra and Molecular Structure IV: Constants of Diatomic Molecules*, Van Nostrand Reinold, New York, **1979**.
[89] A. A. Radzig, B. M. Smirnov, *Reference Data on Atoms, Molecules and Ions*, Springer, Berlin, **1985**.
[90] A. Costales, A. K. Kandalam, R. Franco, R. Pandey, *J. Phys. Chem. B* **2002**, *106*, 1940.
[91] R. A. Elber, C. Rotberg, C. Simmerling, R. Goldstein, H. Y. Li, G. Verkhivker, C. Keasar, J. Zhang, A. Ulitsky, *Comput. Phys. Commun.* **1995**, *91*, 159.
[92] J. J. P. Stewart, *J. Comput. Chem.* **1989**, *10*, 209.

 © 2007 Wiley-VCH Verlag GmbH & Co. KGaA, Weinheim 

[93] D. R. Lide, *Handbook of Chemistry and Physics*, 85th ed., CRC Press, New York, **2004**.
[94] J. M. Matxain, J. M. Ugalde, M. D. Towler, R. J. Needs, *J. Phys. Chem. A* **2003**, *107*, 10004.
[95] K. A. Peterson, *J. Chem. Phys.* **1995**, *102*, 262.
[96] T. E. Sorensen, W. B. England, *Int. J. Quantum Chem.* **2000**, *76*, 259.

Received: September 4, 2006
Published Online: February 28, 2007

 © 2007 Wiley-VCH Verlag GmbH & Co. KGaA, Weinheim 

DOI: 10.1002/ejic.200600990

# Study of the Defects in Sintered $SnO_2$ by High-Resolution Transmission Electron Microscopy and Cathodoluminescence

David Maestre,[a] Julio Ramírez-Castellanos,[b] Pedro Hidalgo,[a] Ana Cremades,[a] José M. González-Calbet,[b] and Javier Piqueras*[a]

**Keywords:** Semiconductors / Luminescence / Microstructure / Resistivity

The defect structure of sintered $SnO_2$ was investigated by high-resolution transmission electron microscopy (HRTEM), cathodoluminescence (CL), and electrical measurements. HRTEM shows the presence of the SnO phase in the sintered samples as well as twinning, stacking faults, and disordered intergrowths. The sintered samples annealed under an oxygen atmosphere show changes in the defect structure and in the CL spectra. In particular, the intensity of a CL band at 1.94 eV, related to oxygen vacancies, decreased as the electrical resistivity increased. The results are discussed by considering the presence of stoichiometric defects such as oxygen vacancies and Sn interstitials in the final structure and their evolution during the annealing process under an oxygen atmosphere.
(© Wiley-VCH Verlag GmbH & Co. KGaA, 69451 Weinheim, Germany, 2007)

## Introduction

$SnO_2$ is a semiconducting oxide of interest for technological applications such as gas sensors, transparent electrical contacts, or optoelectronics.[1–3] It is commonly accepted that its electrical conductivity is related to its nonstoichiometry, which is due to a large concentration of oxygen vacancies that act as shallow donors close to the conduction band.[4] However, this vacancy model seems to raise a few fundamental questions with regard to the general understanding of the phenomenon of transparent conductivity. Some theoretical results[5] point to an important role of the interstitial Sn atoms, which present unusual stability owing to the multivalence of tin, under different chemical potential conditions in $SnO_2$.

In this work, the defect structure of sintered $SnO_2$ ceramic samples and its correlation with optical and electrical properties were investigated. In particular, the role of oxygen vacancies and of tin interstitials in the luminescence and electrical resistivity of the sintered samples was analyzed. Samples prepared under different thermal treatments were characterized by the cathodoluminescence (CL) mode in a scanning electron microscope (SEM), x-ray diffraction (XRD), high-resolution transmission electron microscopy (HRTEM), and electrical resistivity measurements.

[a] Departamento de Física de Materiales, Facultad de Ciencias Físicas, Universidad Complutense de Madrid,
28040 Madrid, Spain
Fax: +34-91-394-4547
E-mail: piqueras@fis.ucm.es
[b] Departamento de Química Inorgánica, Facultad de Ciencias Químicas, Universidad Complutense de Madrid,
28040 Madrid, Spain

## Results

The sintered samples have irregular-shaped grains with different sizes and porosities as a function of the annealing temperature. We have previously reported[6] that the cathodoluminescence spectra of $SnO_2$-sintered samples show three main contributions centered around 1.94, 2.25, and 2.58 eV, whose relative intensities depend on the sintering treatment. The 1.94 eV emission has been related to the presence of oxygen vacancies[6,7] which act as shallow donors in $SnO_2$.

Figure 1 shows CL spectra recorded at 80 K on samples sintered in air for 10 h at 1200 °C, and subsequently treated under an oxygen atmosphere at 600 and 900 °C. As a reference, the spectrum of the sample sintered in air for 10 h at 1200 °C, is also represented. No significant changes in the spectrum can be appreciated after the treatment under an oxygen atmosphere at 600 °C. However, thermal treatments at higher temperatures (900 °C) produce a decrease in the total CL signal, but mainly of the 1.94 eV emission intensity. Figure 2 shows CL spectra of samples sintered in air for 10 h at 1500 °C, with and without subsequent treatment in an oxygen atmosphere. The 2.25 eV emission is dominant in the three spectra, whereas the 1.94 eV emission has almost disappeared. A decrease in the CL intensity is also observed as the temperature of the oxygen annealing is increased.

In order to investigate the changes that these treatments produce in the oxide microstructure and composition of $SnO_2$, analysis by means of XRD and HRTEM were carried out. XRD of the samples sintered at 1200 °C and 1500 °C show a crystalline structure of rutile type, with a tetragonal unit cell and parameters $a$ = 0.4738 nm and $c$ =

 © 2007 Wiley-VCH Verlag GmbH & Co. KGaA, Weinheim 

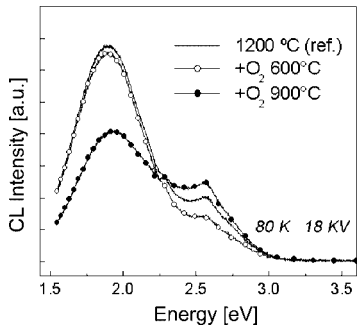


Figure 1. CL spectra of samples sintered in air at 1200 °C, some of which were subsequently treated under an oxygen atmosphere at 600 or 900 °C.

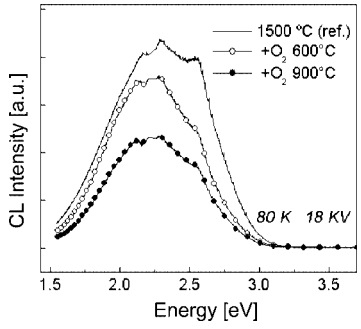


Figure 2. CL spectra of samples sintered in air at 1500 °C for 10 h, and samples further annealed under an atmosphere of oxygen at 600 and 900 °C.

0.3187 nm, and $P4_2/mnm$ space group. SAED and HRTEM studies show the presence of different defects, including twinning, stacking faults, disordered intergrowths, domains, and amorphization.

Figure 3a shows the fast Fourier transform (FFT) pattern along the [001] zone axis of the sample sintered at 1200 °C, which can be indexed on the basis of the rutile crystal structure. The corresponding HRTEM image (Figure 3b) shows a very well-ordered material with interplanar distances of 0.47 nm.

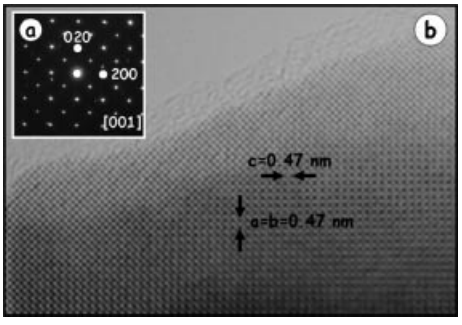


Figure 3. FFT pattern along the [001] axis (a), and HRTEM image (b) of a sample sintered in air at 1200 °C for 10 h.

In contrast, Figure 4a shows the FFT pattern along the [111] zone axis of the same sample, which can also be indexed on the basis of the rutile crystal structure. However, the splitting of the main diffraction spots (marked by arrows) suggests the existence of twining. In the corresponding HRTEM image (Figure 4b), twin planes along (011) are observed. These straight twin boundaries are coherent and consist of Sn atoms shared by the two neighboring components of the twin.[8] Huang et al.[9] reported that the Sn sublattice is mirror symmetric to the coherent twin boundary (CTB), whereas the oxygen atoms forming octahedral cages around the Sn atoms are not mirror symmetric to the CTB.

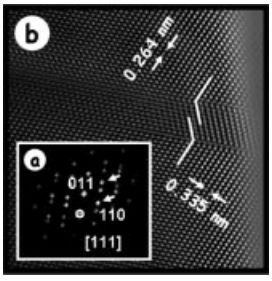


Figure 4. FFT pattern along the [111] zone axis (a) of a sample sintered in air at 1200 °C for 10 h and the corresponding HRTEM image (b), showing twin planes along (011).

Figure 5 corresponds to a different area of the same sample. The inset (Figure 5a) shows the corresponding FFT pattern along the [111] zone axis, which shows both splitting and streaking of the diffraction spots; this is indicative of high structural disorder, as it can be seen in the corresponding HRTEM micrograph (Figure 5b) where recurrent twinning and disorder intergrowths are observed. HRTEM characterization also shows that after annealing under an oxygen atmosphere at 900 °C, the density of defects decreases.

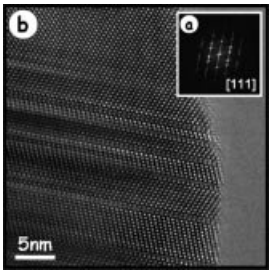


Figure 5. FFT pattern along the [111] axis (a) and HRTEM image showing structural disorder and recurrent twinnings (b) corresponding to a different area of the sample observed in Figures 3 and 4.

Alternatively, Figure 6a shows the SAED pattern of the sample treated at 1500 °C in air for 10 h. The diffuse rings indicate the presence of an amorphous phase. Moreover, the intensity and discrete spots in this FFT pattern (Figure 6b) suggest the presence of randomly oriented grains of very small dimensions. Figure 6c reveals a complex microstructure, where crystallized domains (dashed circle) in an amorphous matrix are observed. Therefore, in some crystals of this sample, interplanar distances of 0.48 nm were measured (Figure 7a), which corresponds to the *c* axis of the SnO phase. The inset (Figure 7b) shows the corresponding

 © 2007 Wiley-VCH Verlag GmbH & Co. KGaA, Weinheim 

FFT pattern. Notably, further thermal treatment at 900 °C under an oxygen atmosphere led to better recrystallization of the sample.

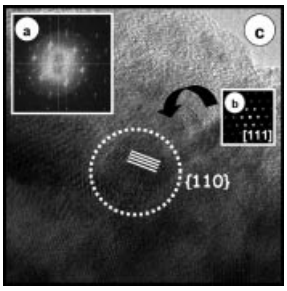


Figure 6. SAED (a) and FFT pattern (b) of a sample sintered in air at 1500 °C for 10 h. HRTEM image (c) reveals the presence of crystallized domains in an amorphous matrix.

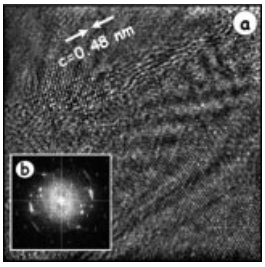


Figure 7. HRTEM image (a) of a sample sintered in air at 1500 °C for 10 h. The inset shows the corresponding FFT pattern.

As the presence of oxygen vacancies acting as donors determines the electrical properties of $SnO_2$, resistivity measurements were carried out. Results are presented in Table 1 and Figure 8.

Table 1. Evolution of the samples resistivity as a function of the sintering temperature and post annealing under an oxygen atmosphere at 900 °C.

| Temperature [°C] | Resistivity [Ω cm] | + $O_2$ (900 °C) |
|---|---|---|
| 1000 | $(0.9 \pm 0.2)\ 10^3$ | $(3.1 \pm 0.5)\ 10^4$ |
| 1100 | $(3.5 \pm 0.7)\ 10^3$ | |
| 1200 | $(2.3 \pm 0.4)\ 10^4$ | $(1.2 \pm 0.2)\ 10^4$ |
| 1300 | $(9.0 \pm 1.5)\ 10^5$ | |

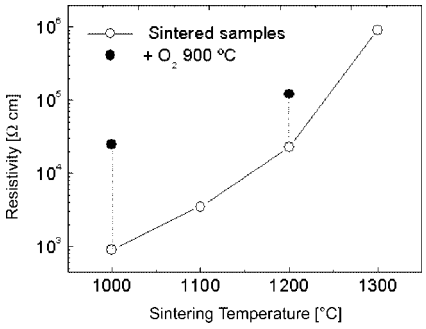


Figure 8. Resistivity of samples as a function of the sintering temperature and further annealing under an oxygen atmosphere at 900 °C.

The results show a rise in the resistivity as the temperature used during the sintering treatments was increased. Note that the *y* axis in Figure 8 is logarithmic-scaled, which denotes a faster increase in the resistivity at higher sintering temperatures. Moreover, the annealing process, which is performed under an oxygen atmosphere heated at 900 °C, also causes an increase in the resistivity, as shown in Figure 8. The samples sintered at temperatures above 1300 °C present a resistivity higher than $10^8\ \Omega$cm, but exact values could not be obtained with the experimental setup used.

## Discussion

The influence of oxygen vacancies ($V_O$) on the electrical conduction, structure, or luminescence properties of $SnO_2$ has been often considered, whereas the influence of Sn interstitials ($Sn_i$) is usually ignored. Different authors[4,10] have pointed out that oxygen vacancies are mainly responsible for several optical and electrical properties of $SnO_2$, and they act as shallow donor levels below the conduction band. Both donor defects, $V_O$ and $Sn_i$, can donate electrons to the conduction band without increasing the optical interband absorption, which explains the coexistence of conductivity and transparency in this material. Themlin et al.,[11] from their synchrotron results on the $SnO_2$ (110) surface, concluded the existence of states sensitive to oxygen chemisorption, situated 1.4 eV above the valence band top. These levels, related to the $Sn^{2+}$ cation and associated with the presence of oxygen vacancies, are compatible with the transitions leading to the 1.94 eV emission observed in the present work. Also, our previous studies[6] showed the connection between this emission and the oxygen vacancies. The fact that treatment of the sample under an oxygen atmosphere heated at 900 °C causes the intensity of the 1.94 eV band to decrease, also indicates an annealing-induced decrease in the vacancy concentration as a result of thermally activated oxygen diffusion. In the samples sintered at 1500 °C without additional treatments, the 1.94 eV CL emission hardly appears; therefore, subsequent oxygen treatments cannot affect this emission intensity as much as in the samples sintered at 1200 °C. The kinetics of the oxygen–$SnO_2$ reaction, as well as the oxygen diffusion mechanism, were previously investigated. Kamp et al.[12] concluded that at temperatures below 800 °C, only surface reactions like adsorption occurs, which is the diffusion process that is activated at higher temperatures. These processes would be related to a change in the oxidation state of the adsorbed oxygen at 450 °C,[13] which turns $O_2^-$ into $O^-$ (the latter being more reactive). Themlin et al.[11] observed that an increase in the temperature to 630 °C initiates the bulk-oxygen diffusion process. Our CL results (Figure 1) show a decrease in the 1.94 eV emission, related to the oxygen vacancies, that occurs during the treatment of the sample under an oxygen atmosphere heated at 900 °C, which agrees with these observations. Sintering at high temperatures, up to 1500 °C, results in the progressive disappearance of the oxygen vacancies' concentration, as suggested not only by

 © 2007 Wiley-VCH Verlag GmbH & Co. KGaA, Weinheim 

the decrease in the 1.94 eV emission, but also for the charge effects appearing during the observations in SEM. The resistivity increase that is produced at higher sintering temperatures and during oxygen treatments, shown in Figure 8, agrees with a decrease in the vacancy concentration detected by the evolution of the 1.94 eV band. Indeed, perfectly stoichiometric samples are highly resistive.[14] Paria et al.[15] obtained similar resistivity results on sintered $SnO_2$ to those presented here. The crystallinity improvement produced by the oxygen treatments agrees with the well-ordered appearance observed in the HRTEM images. Conversely, sintering treatments can also increase the presence of defects (as shown in Figures 5 and 7), which reduces the carriers mobility, and the conductivity as well. Previous work confirms the decrease in the conductivity as the pressure and the oxygen content in the reactive atmosphere is increased.[16]

SAED and HRTEM analyses show that planar defects, such as recurrent twinning, stacking faults, and vacancies, are present in these samples. In addition, at high temperatures, the material seems to consist of both a polycrystalline $SnO_2$ phase and an amorphous SnO phase.[17] Moreover, the decomposition of $SnO_2$ into SnO, according to the reaction $SnO_2 \rightarrow SnO + V_O^-$, at high temperatures, has to be considered. These processes begin with the formation of intermediate phases, such as $Sn_3O_4$, SnO, and even metallic Sn, by internal oxygen disproportionate allocation, depending on the temperature and atmosphere conditions, as described by Cahen et al.[18] Many crystal defects, including twinning, crystallographic shear planes (CSP), stacking faults, and oxygen vacancies, are formed during these processes. In our case, the partial SnO formation was observed when the $SnO_2$ material was treated at high temperatures in air. Because both compounds are structurally related, it is reasonable to think that they can easily exist in the same crystal, as observed in samples treated at 1500 °C in air (Figure 7). In the $SnO_2$ rutile structure, each Sn atom has six oxygen neighbors, which form a distorted octahedral. The distance between the Sn and O atoms within one octahedron is 0.21 nm. In SnO, each Sn atom has four oxygen neighbors, but all of them are located on the same side of the Sn atoms, as shown by the pyramid consisting of one Sn atom and four O atoms in the SnO unit cell. The Sn–O bonds have a length of 0.222 nm. Accordingly, the $SnO_2$ phase can be easily transformed into the SnO phase by removing the O atoms from $SnO_2$ and by slightly adjusting the position of the Sn atoms. The formation of $Sn_i$ requires the rearrangement of its atomic environment by ionic relaxations resembling the local structure of SnO, which can also explain the observed SnO phase.

The sintered samples that were treated under an oxygen atmosphere were found mainly to consist of the $SnO_2$ phase. This shows that the SnO phase formed by the reduction of $SnO_2$ at high temperature is unstable under oxidation conditions and will be transformed into the $SnO_2$ rutile phase through an oxidation process. During this process, a decrease in the $V_O$ and $Sn_i$ concentration takes place along with an increase in resistivity.

## Conclusions

Sintering $SnO_2$ in air at high temperatures results in a high density of defects, as observed by SAED and HRTEM, as well as in the presence of the SnO phase which can be explained by $Sn_i$ formation. The sintering treatments modify the CL signal, mainly the 1.94 eV emission, which disappears at temperatures greater than 1500 °C. This emission, which has been associated with the presence of oxygen vacancies, is decreased during post sintering treatments under an oxygen atmosphere. This process governed by oxygen diffusion, was detected after treatments at 900 °C. The decrease in the $V_O$ concentration is associated with a large increase in resistivity. Annealing under an oxygen atmosphere at high temperatures improves the crystallinity of the samples and leads to the formation of a pure $SnO_2$ rutile phase.

## Experimental Section

The starting material used was commercial $SnO_2$ powder (Aldrich Chemical Company Inc., 99.9% purity). The powder, consisting of particles and aggregates of rounded particles with sizes of about 200 nm, was compacted under a compressive load of 2 tons to form disc-shaped samples that were about 7 mm in diameter and 2 mm thick. The samples were sintered in air for 10 h at temperatures between 1000 °C and 1500 °C and some of them were subsequently annealed for 2 h under an oxygen atmosphere at 600 °C and 900 °C.

The samples were observed in the secondary electron (SE) and cathodoluminescence (CL) modes with a Hitachi S-2500 or a Leica 440 SEM, at accelerating voltages ranging from 10 to 30 kV at a temperature of 80 K. The CL spectra were recorded either with the photomultiplier tube attached to an Oriel 78215 computer-controlled monochromator or with a CCD camera with a built-in spectrograph (Hamamatsu PMA-11). Resistivity measurements were performed by means of the Van der Pauw technique, in air and at room temperature. Structural information of the samples was obtained by X-ray diffraction (XRD) performed with a Philips diffractometer and high resolution transmission energy microscopy (HRTEM) with a JEOL 300 FEG electron microscope.

## Acknowledgments

This work was supported by MEC (project MAT 2003-00455) and by UCM-CM (Group 910146).

[1] B. Drevillon, S. Kumer, P. R. Carbarrocas, J. M. Siefert, *J. Appl. Phys. Lett.* **1989**, *54*, 2088.
[2] G. Martinelli, M. C. Carotta, E. Traversa, G. Ghiotti, *MRS Bull.* **1999**, *24*, 30.
[3] A. Lousa, S. Gimeno, J. Marti, Vacuum **1994**, *45*, 1143.
[4] D. F. Cox, T. B. Fryberger, S. Semacik, *Phys. Rev. B* **1988**, *38*, 2072.
[5] C. Kiliç, A. Zunger, *Phys. Rev. Lett.* **2002**, *88*, 095501.
[6] D. Maestre, A. Cremades, J. Piqueras, *J. Appl. Phys.* **2003**, *95*, 3027.
[7] D. Maestre, A. Cremades, J. Piqueras, *Semicond. Sci. Technol.* **2004**, *19*, 1236.
[8] J. G. Zheng, X. Pen, M. Scheweizer, F. Zhou, U. Weimar, W. Gopel, M. Ruhle, *J. Appl. Phys.* **1996**, *79*, 7688.

 © 2007 Wiley-VCH Verlag GmbH & Co. KGaA, Weinheim 

[9] J. Y. Huang, B. H. Park, D. Jan, X. Q. Pan, Y. T. Zhu, Q. X. Jia, *Philos. Magn. A* **2002**, *82*, 735.
[10] S. Samson, C. G. Fonstad, *J. Appl. Phys.* **1973**, *44*, 4618.
[11] J. M. Themlin, R. Sporken, J. Darville, R. Caudano, J. M. Gilles, R. L. Johnson, *Phys. Rev. B* **1990**, *42*, 11914.
[12] B. Kamp, R. Merkle, J. Maier, *Sens. Actuators, B* **2001**, *77*, 534.
[13] U. Pulkkinen, T. T. Rantala, T. S. Rantala, V. Lantto, *J. Mol. Catal. A* **2001**, *166*, 15.
[14] C. Terrier, J. P. Chatelon, R. Berjoan, J. A. Roger, *Thin Solid Films* **1995**, *263*, 37.
[15] M. K. Paria, H. S. Maiti, *J. Mater. Sci.* **1983**, *18*, 2101.
[16] B. Sterjna, C. G. Granqviest, A. Seidel, L. Häggström, *J. Appl. Phys.* **1990**, *68*, 6241.
[17] Z. W. Chen, J. K. L. Lai, C. H. Shek, *J. Solid State Chem.* **2005**, *178*, 892.
[18] S. Cahen, N. David, J. M. Fiorani, A. Maitre, M. Vilasi, *Thermochim. Acta* **2003**, *403*, 275.

Received: October 20, 2006
Published Online: March 2, 2007

 © 2007 Wiley-VCH Verlag GmbH & Co. KGaA, Weinheim 

DOI: 10.1002/ejic.200601023

# Correlation between the Stoichiometry and the Bistability of Electronic States in Valence-Tautomeric $Rb_xMn[Fe(CN)_6]_y \cdot zH_2O$ Complexes

**Saioa Cobo,[a] Raquel Fernández,[a] Lionel Salmon,[a] Gábor Molnár,[a] and Azzedine Bousseksou*[a]**

**Keywords:** Prussian blue analogues / Magnetic properties / Phase transitions / Raman spectroscopy

A series of Prussian blue analogues, $Rb_xMn[Fe(CN)_6]_y \cdot zH_2O$ with different stoichiometries have been synthesized. Elemental analyses reveal a quasilinear decrease in *x* and *y* when *z* increases. Some of these samples present a first-order phase transition between the $Mn^{II}$–$Fe^{III}$ and $Mn^{III}$–$Fe^{II}$ electronic states with large thermal hysteresis loops observed in the magnetic susceptibility. The phase-transition temperatures correlate with the stoichiometry, but quantitative predictions cannot be made because of the disordered nature of the compounds. Contrary to previous literature reports, calorimetric and Raman spectroscopic measurements reveal that the charge-transfer phase transition is accompanied by a significant entropy change, $\Delta S = 48–59\ J\,K^{-1}\,mol^{-1}$, of mainly vibrational origin. In addition to the thermal phase transition, Raman spectra also show that below ca. 120 K a photoinduced $Mn^{III}$–$Fe^{II}$ to $Mn^{II}$–$Fe^{III}$ conversion occurs in certain stoichiometries.

(© Wiley-VCH Verlag GmbH & Co. KGaA, 69451 Weinheim, Germany, 2007)

## Introduction

The bistability of electronic states in transition-metal complexes represents an important field of research in coordination chemistry. The bistability in these compounds generally arises from strong electron-lattice couplings. Typical examples are spin crossover phenomena,[1,2] and valence-tautomerism.[3] In this latter class, valence-tautomeric Prussian blue analogues of transition metals with general formula $A_xM^{II}[M'^{III}(CN)_6]_y \cdot nH_2O$ (where A is an alkali metal cation, and M and M′ are divalent or trivalent transition-metal cations) have attracted considerable interest because of their remarkable magnetic properties, such as high Curie temperatures[4,5] or photomagnetic phenomena.[6–8] In some of these complexes, a first-order thermal phase transition was observed and associated with metal-to-metal electron transfer.[9,10] The compound $Rb_xMn[Fe(CN)_6]_y \cdot zH_2O$ shown in Figure 1 (noncoordinated water molecules and rubidium atoms are not represented) is one of the most studied members of this family.[10,11] It exhibits switching phenomena between the high-temperature (HT) $Fe^{III}$($S$ = 1/2)–CN–$Mn^{II}$($S$ = 5/2) and the low-temperature (LT) $Fe^{II}$($S$ = 0)–CN–$Mn^{III}$($S$ = 2) states that can be induced by changing the sample temperature or pressure as well as by light irradiation.[10–18] The two phases display markedly different magnetic, optical, and electric properties.

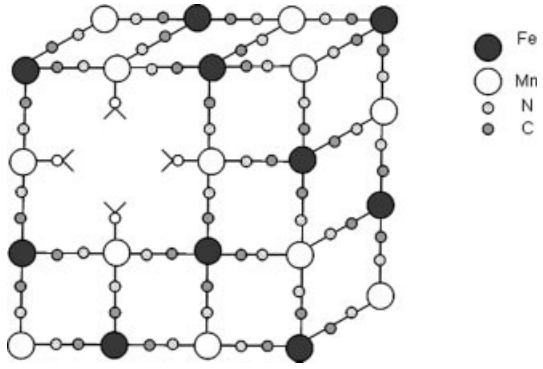


Figure 1. Schematic structure of $Rb_xMn[Fe(CN)_6]_y \cdot zH_2O$ with a $Fe(CN)_6^{3-}$ vacancy. (Noncoordinated water molecules and rubidium atoms are not represented.)

Even if $Rb_xMn[Fe(CN)_6]_y \cdot zH_2O$ has been the object of many investigations, several questions remain to be clarified. Notably, the control of the phase-transition temperature is an important issue because these compounds present very large thermal hysteresis loops (up to 138 K).[18] Such a large bistability domain is an appealing property for the application of these materials in various devices (e.g. memories). In preliminary results, Ohkoshi et al.[17] found a correlation between the hysteresis width and the stoichiometry of these compounds, but further measurements performed by the same group[18] and others[11] appear to escape this correlation. Another important question concerns the origin of the thermal phase transition. This question has been investigated extensively in the case of spin-crossover complexes and it is now generally accepted that thermal spin

[a] Laboratoire de Chimie de Coordination, CNRS UPR-8241, 205 Route de Narbonne, 31077 Toulouse, France
Fax: +33-561-553-003
E-mail: boussek@lcc-toulouse.fr

 © 2007 Wiley-VCH Verlag GmbH & Co. KGaA, Weinheim 

crossover is an entropy-driven phenomenon and coupling between the electronic states and the phonon system plays a fundamental role.[19] Data on Prussian blue analogues are considerably less extensive.[20] However, it seems a reasonable assumption to attribute a similar importance to the vibrations because the most prominent structural changes in both cases are the metal–ligand bond length. Therefore, it is very surprising that the transition entropy for the title compound was found hardly of the order of the electronic entropy change.[10,21] This paper has been written in order to discuss these questions. In this aim, we have synthesized nine samples of different stoichiometry and characterized them by using Raman spectroscopy, elemental analysis, and magnetic and calorimetric measurements.

## Results and Discussion

### Stoichiometry and Magnetic Properties

Elemental analysis reveals significant differences between the different $Rb_xMn[Fe(CN)_6]_y{\cdot}zH_2O$ samples. For each compound, a chemical formula, taking into account the chemical arrangement of the system, the weight percentage of each element, and the electroneutrality, is proposed (Table 1). Figure 2 shows the $Rb^+$ ($x$) and $H_2O$ ($z$) content of each sample and those reported in refs.[11,17] as a function of the iron proportion. Clearly, independent of the synthetic method, a quasilinear correlation exists between these quantities, which can be understood as follows. In each case, the system contains a certain amount of $[Fe(CN)_6]^{3-}$ vacancies (Figure 1). The formation of these vacancies leads to a lower $Rb^+$ proportion ($x$) in order to maintain the charge neutrality. Indeed, the regression analysis shows that for each missing $[Fe(CN)_6]^{3-}$ unit, ca. three $Rb^+$ ions are removed from the crystal lattice. Moreover, the $H_2O$ content ($z$) increases because the water molecules complete the coordination around the $Mn^{II}$ ions at the place of the missing $[Fe(CN)_6]^{3-}$ entities and we can safely state that the non-stoichiometric crystal lattice contains a relatively large amount of noncoordinated water molecules as well. However, according to Figure 2b, the formation of one $[Fe(CN)_6]^{3-}$ vacancy leads to the uptake of ca. 22 water molecules; 6 of which would complete the coordination sphere of the $Mn^{II}$ ions at the place of the missing N atoms, and the remaining water molecules become encapsulated in the remaining cavities. Let us also note that the reproducibility of the synthesis (samples **7**–**9**) is relatively poor owing mainly to the extreme insolubility and the disordered nature of the sample.

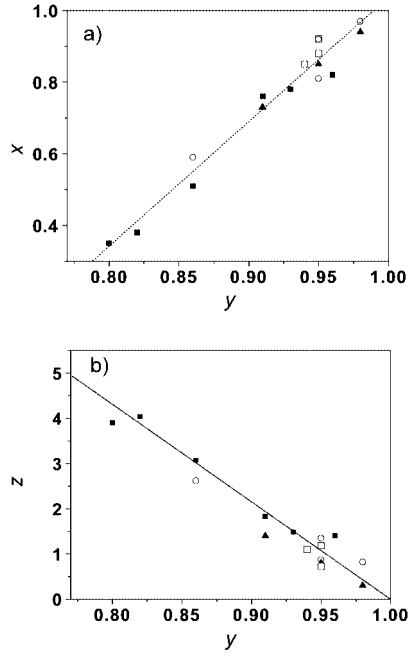


Figure 2. $Rb^+$ content (a) and $H_2O$ content (b) as a function of Fe content in $Rb_xMn[Fe(CN)_6]_y{\cdot}zH_2O$. (Full squares: samples **1**–**6**, open squares: samples **7**–**9**, open circles: data from ref.,[11] full triangles: data from ref.[17]) Straight lines represent linear fits on the data.

Table 1. Elemental analysis data and proposed formula for the different samples.

| Sample | | C | N | Mn | Fe | Rb | Proposed formula |
|---|---|---|---|---|---|---|---|
| **1** | Observed | 18.19 | 20.80 | 16.78 | 13.71 | 9.12 | $Rb_{0.35}Mn[Fe(CN)_6]_{0.80}{\cdot}3.90H_2O$ |
| | Calculated | 17.57 | 20.5 | 16.78 | 13.63 | 9.12 | |
| **2** | Observed | 18.19 | 20.82 | 16.24 | 13.51 | 9.80 | $Rb_{0.38}Mn[Fe(CN)_6]_{0.82}{\cdot}4.04H_2O$ |
| | Calculated | 17.49 | 20.4 | 16.24 | 13.55 | 9.61 | |
| **3** | Observed | 18.62 | 21.34 | 16.37 | 14.33 | 12.88 | $Rb_{0.51}Mn[Fe(CN)_6]_{0.86}{\cdot}3.07H_2O$ |
| | Calculated | 18.46 | 21.53 | 16.37 | 14.31 | 12.99 | |
| **4** | Observed | 19.26 | 22.06 | 15.83 | 14.66 | 18.70 | $Rb_{0.76}Mn[Fe(CN)_6]_{0.91}{\cdot}1.83H_2O$ |
| | Calculated | 18.87 | 22.02 | 15.83 | 14.63 | 18.71 | |
| **5** | Observed | 19.62 | 22.55 | 15.80 | 15.04 | 19.30 | $Rb_{0.78}Mn[Fe(CN)_6]_{0.93}{\cdot}1.48H_2O$ |
| | Calculated | 19.29 | 22.5 | 15.8 | 14.96 | 19.2 | |
| **6** | Observed | 19.60 | 22.49 | 15.63 | 15.18 | 19.90 | $Rb_{0.82}Mn[Fe(CN)_6]_{0.96}{\cdot}1.40H_2O$ |
| | Calculated | 19.64 | 22.91 | 15.63 | 15.22 | 19.9 | |
| **7** | Observed | 19.6 | 22.6 | 15.2 | 16.0 | 21.1 | $Rb_{0.85}Mn[Fe(CN)_6]_{0.94}{\cdot}1.10H_2O$ |
| | Calculated | 19.7 | 22.9 | 15.2 | 15.3 | 21.1 | |
| **8** | Observed | 19.9 | 22.5 | 15.5 | 15.0 | 21.1 | $Rb_{0.88}Mn[Fe(CN)_6]_{0.95}{\cdot}1.18H_2O$ |
| | Calculated | 19.3 | 22.5 | 15.5 | 15.0 | 21.2 | |
| **9** | Observed | 19.8 | 22.8 | 15.8 | 15.4 | 22.5 | $Rb_{0.92}Mn[Fe(CN)_6]_{0.95}{\cdot}0.72H_2O$ |
| | Calculated | 19.6 | 22.9 | 15.8 | 15.2 | 22.6 | |

 © 2007 Wiley-VCH Verlag GmbH & Co. KGaA, Weinheim 

Figure 3 shows the product of molar magnetic susceptibility and the temperature for samples **1**–**9** as a function of temperature. One of the interesting points of the $\chi_M T$–$T$ plots is that the values for compounds **1**–**3** are around 5.0 $cm^3 mol^{-1}$ K for the whole range of temperatures, which indicates that the ground state consists mainly of the $Fe^{III}{}_{LS}$–CN–$Mn^{II}{}_{HS}$ configuration (HT phase). In contrast, the $\chi_M T$ value for compounds **4**–**6** and **7**–**9** varies significantly with the temperature and reveals a HT→LT phase transition with a large hysteresis loop. We can explain these results by using the arguments proposed for the first time in ref.[11] In the idealized formula Rb:Mn:Fe = 1:1:1 for $Rb_xMn[Fe(CN)_6]_y \cdot zH_2O$, the ground state is the $Fe^{II}{}_{LS}$–CN–$Mn^{III}{}_{HS}$ configuration, which remains stable up to ca. 300 K. Above this temperature, the $Fe^{III}{}_{LS}$–CN–$Mn^{II}{}_{HS}$ configuration becomes the thermodynamically stable phase because of its higher entropy (vide infra). On the contrary, in a nonidealized formula with vacant $Fe(CN)_6$ sites, oxygen atoms of the water molecule coordinate to the Mn ions instead of the nitrogen atoms of the cyanide, and the average environment of the manganese ions changes to $Mn^{III}(O_2H)_x(NC)_{6-x}$. As a result, the ligand field strength of the $Mn^{III}$ ions becomes weaker and consequently the redox potential of the $Mn^{III}/Mn^{II}$ couple increases leading finally to the oxidation of the $Fe^{II}$ ion. If the water content is sufficiently high, the redox potential increases to such an extent that the $Fe^{III}{}_{LS}$–CN–$Mn^{II}{}_{HS}$ form becomes stable at very low temperatures.

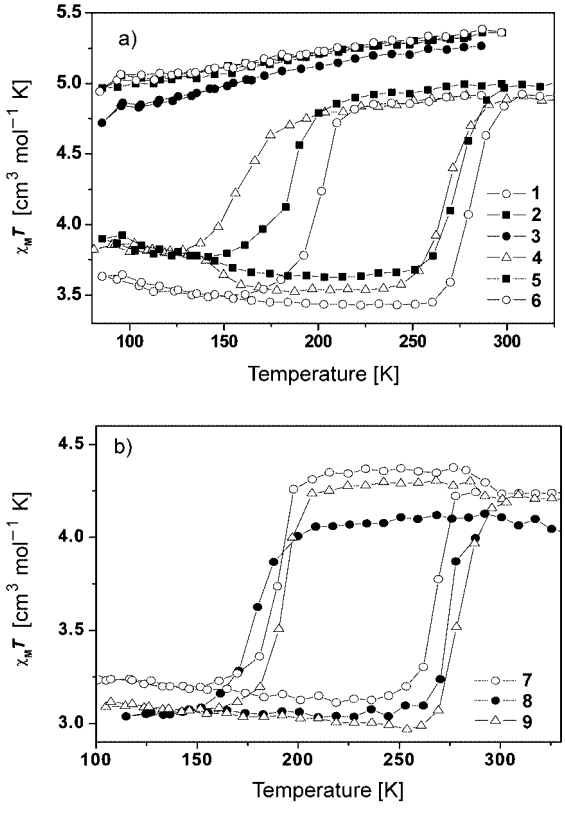


Figure 3. $\chi_M T$ versus $T$ curves for samples **1**–**6** (a) and **7**–**9** (b). (Data points are connected to guide the eye.)

The $\chi_M T$–$T$ curve for compound **4** decreases abruptly from 4.7 $cm^3 mol^{-1}$ K to 3.6 $cm^3 mol^{-1}$ K below 184 K upon cooling and, conversely, as the sample was warmed in the LT phase, the $\chi_M T$ value increased around 272 K and reached the HT value. The width of the thermal hysteresis loop (112 K) is defined by $T_{1/2}\downarrow$ = 160 K and $T_{1/2}\uparrow$ = 272 K. The $\chi_M T$–$T$ plots for sample **6** showed $\Delta T$ = 81 K, $T_{1/2}\downarrow$ = 201 K, $T_{1/2}\uparrow$ = 282 K, and for sample **5** $\Delta T$ = 87 K, $T_{1/2}\downarrow$ = 184 K, $T_{1/2}\uparrow$ = 271 K. This series of compounds agrees with Ohkoshi's proposition,[17] that is, the $\Delta T$ value increases as the Fe/Mn ratio decreases. To prove the reproducibility of the synthesis, and Ohkoshi's findings, we have synthesized three more compounds, **7**–**9**. Figure 4 shows the $\Delta T$, $T_{1/2}\downarrow$, and $T_{1/2}\uparrow$ values for each sample and for those reported in refs.[11,17] as a function of the $Rb^+$ proportion (although the relevant parameter is the Fe content, we have chosen to plot them as a function of the Rb content because [Fe] and [Rb] are proportional and the sample-to-sample changes in [Rb] are higher). This figure appears to indeed reveal some general trends. When decreasing the value of $x$ (i.e. the Rb content) from 0.97 to 0.73, the phase transition shifts from 301 K (240 K) to

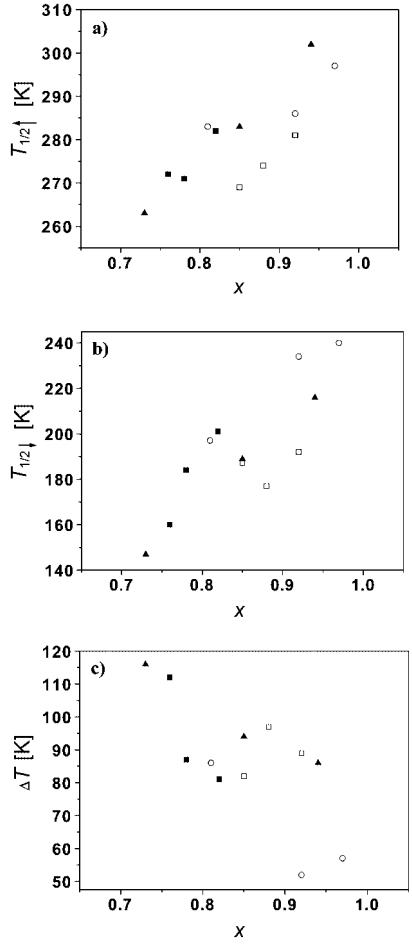


Figure 4. Phase transition temperatures in the heating (a) and cooling (b) modes and hysteresis width (c) as a function of the Rb content in $Rb_xMn[Fe(CN)_6]_y \cdot zH_2O$. (Full squares: samples **1**–**6**, open squares: samples **7**–**9**, open circles: data from ref.,[11] full triangles: data from ref.[17])

 © 2007 Wiley-VCH Verlag GmbH & Co. KGaA, Weinheim 

263 K (147 K) in the heating (cooling) cycles, and accordingly the hysteresis width increases. It is interesting to note that the increase in the hysteresis width is due to the fact that $T_{1/2}\downarrow$ changes more than $T_{1/2}\uparrow$. In fact, according to the Ising-like model developed in ref.,[22] the hysteresis loop width is proportional to $J/T_c$, where $J$ is a phenomenological parameter for the cooperativity and $T_c$ is the transition temperature. Because $T_c \cong (T_{1/2}\downarrow + T_{1/2}\uparrow)/2$, this inverse proportional relationship explains the increase in the hysteresis width when $T_{1/2}\downarrow$ decreases.

Nonetheless, the data are rather scattered and one can observe differences as much as 20–30 K for samples having the same composition. Let us also note that the sample reported in ref.,[18] which contains also an important amount of the reduced form, $Fe^{II}$–CN–$Mn^{II}$ escapes even the loose correlation seen in Figure 4. In summary, however, we find that the general tendency is the shift in the phase transition to lower temperatures with increasing deviations from the idealized (Rb:Mn:Fe = 1:1:1) stoichiometry. As explained above, this observation can be understood as a result of the weakening ligand field on the manganese ions and associated change of the redox properties. We believe that the fact that the correlation is rather vague is a result of the disordered nature of these compounds containing various types of defects in arbitrary distribution.

### Entropy Change on Phase Transition

As already mentioned, the valence-tautomeric thermal phase transition is entropy driven. The entropy change can be represented as the sum of electronic, vibrational, configurational, rotational, and translational terms. The two latter are excluded from consideration in the solid state. Moreover, in the absence of orientational disorder the configurational term can also be neglected. The electronic term may contain spin and orbital contributions. Assuming the idealized cubic symmetry of the Prussian blue structure, the LT phase [$Mn^{III}(^5E_g$)–$Fe^{II}(^1A_{1g})$] has a 2(orbital) × 5(spin) = 10-fold degeneracy, whereas the degeneracy of the HT phase [$Mn^{II}(^6A_{1g}$)–$Fe^{III}(^2T_{2g})$] is 3(orbital) × 12(spin) = 36-fold. This would lead to an electronic entropy change of $\Delta S_{el} = R\ln(36/10) = 10.6\ J\,K^{-1}\,mol^{-1}$. However, the orbital degeneracy of the $Mn^{III}$ ion is removed by the Jahn–Teller effect[10] and it is reasonable to assume also that in the non-stoichiometric disordered structures, the local symmetry around the iron atoms are not perfectly octahedral either, and therefore, the orbital moment of the $Fe^{III}$ ion is quenched, which leads to the $^5B_{1g}$ and $^2B_{2g}$ terms for $Mn^{III}$ and $Fe^{III}$, respectively. Then, one obtains the spin-only value of $\Delta S_{el} = R\ln(12/5) = 7.3\ J\,K^{-1}\,mol^{-1}$. This value is indeed quite close to the experimentally observed value of $6\ J\,K^{-1}\,mol^{-1}$.[10] However, it is well-known that the weakening of the metal–ligand bonds results in a strong increase in the vibrational partition functions.[23] In the case of $Rb_xMn[Fe(CN)_6]_y{\cdot}zH_2O$, the formation of the LT phase is accompanied by a discontinuous lattice contraction of ca. 10% and a reduction in the average Fe–Mn distance from 5.27 Å to 5.10 Å! Such a huge change in the bond lengths must lead to observable differences in the vibrational entropy. For this reason, we have carried out DSC measurements. Figure 5 shows the DSC curves of sample **7**, which exhibits singularities around 170 K and 280 K in the cooling and heating modes, respectively. These peaks clearly correspond to the charge-transfer phase transition. The enthalpy variation associated with the phase transition is $\Delta H = 11\ kJ\,mol^{-1}$. Then, assuming that $T_c \cong (T_{1/2}\downarrow + T_{1/2}\uparrow)/2 = 230$ K (calculated from the more accurate magnetic data), one obtains $\Delta S = \Delta H/T_c = 48\ J\,K^{-1}\,mol^{-1}$. Fairly similar results ($\Delta H = 13.6\ kJ\,mol^{-1}$, $\Delta S = 59\ J\,K^{-1}\,mol^{-1}$) were obtained for sample **6** as well, whereas sample **2**, which remains in the HT phase in the whole temperature range, showed no singularity in the calorimetric data. These results are therefore in significant disagreement with the results of other groups,[10,11] but seem to be more realistic for us taking into account the electronic and structural changes discussed above.

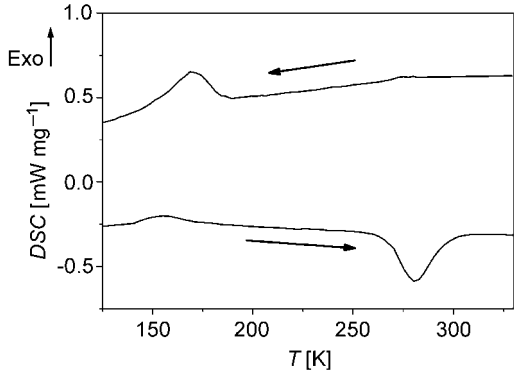


Figure 5. DSC curves of sample **7** in the heating and cooling cycles.

The calorimetric data strongly suggest that the phase transition is associated with a significant change in the vibrational entropy (ca. 40–50 $J\,K^{-1}\,mol^{-1}$), which should be obviously reflected by the vibrational spectra of the compound. Representative Raman spectra of **7** are shown in Figure 6. In agreement with previous IR spectroscopic data on this complex,[12] the CN stretching modes can be chosen to follow the electron transfer. In the HT phase, two intense Raman modes were observed around 2159 and 2170 $cm^{-1}$ and assigned to the stretching modes of the CN moiety bridged between $Fe^{III}$ and $Mn^{II}$. It should be also noted that the completely reduced form $Fe^{II}$–CN–$Mn^{II}$ of the compound was not observed in the Raman spectra. When decreasing the temperature, the spectra change drastically and at 120 K, two Raman modes are observed at ca. 2096 and 2114 $cm^{-1}$, which can be assigned to the stretching modes of the CN ligand linked to the $Fe^{II}$ and $Mn^{III}$ in the LT phase. The phase transition appears to be incomplete at low temperatures. CN stretching modes thus provide very useful diagnostic features concerning the electronic configuration of the system, but their contribution to the vibrational entropy is negligible as only the frequencies below ca. 600 $cm^{-1}$ can give significant contributions.[23] Low frequency Raman spectra in the two phases are shown in Fig-

 © 2007 Wiley-VCH Verlag GmbH & Co. KGaA, Weinheim 

ure 6b. Without isotope-substitution data, the assignment of these modes is not feasible, but we note that, according to literature data,[24] frequencies around 550, 450, and 200 $cm^{-1}$ in Prussian blue analogues can be attributed to $\nu$(FeC), $\delta$(FeCN), and $\delta$(CFeC) modes, respectively. Indeed, a number of modes appear around these frequencies. Although the former do not seem to be very sensitive to the actual electronic configuration, huge changes are observed at lower frequencies (180–320 $cm^{-1}$), which thus tend to support the large vibrational entropy changes revealed by the calorimetry data.

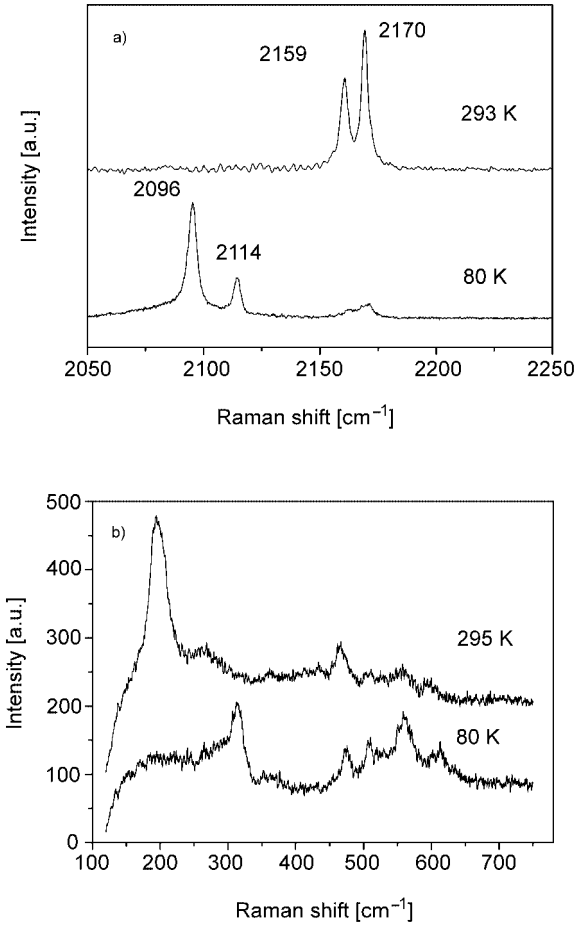


Figure 6. Raman spectra of sample **7** in the $\nu_{CN}$ (a) and low-frequency (b) regions at selected temperatures (cooling mode).

### Additional Raman Spectroscopic Data

During the Raman spectroscopic study, other interesting phenomena were uncovered as well. As the temperature is decreased below ca. 120 K in certain samples, the LT phase starts to transform back to the HT phase and at 80 K the Raman spectrum becomes fairly similar to the 293 K spectrum (Figure 7). In agreement with the observations made by Moritomo et al.,[16] this LT→HT transformation at low temperatures is clearly a photoinduced effect due to the laser light used to excite Raman scattering. However, this photoinduced effect was only observed in samples **4**–**6** and **8**, but no effect was detected at all in samples **7** and **9** (Figure 6). Note also that samples **1**–**3** cannot display such phenomenon as they remain in the HT phase down to 80 K. It was established by Escax et al.[7,8] that defects play an important role in the photoconversion efficiency in Co–Fe Prussian blue analogues. In fact, vacancies provide certain flexibility to the lattice and thus allow an easier relaxation of the lattice strain induced by the volume expansion during light irradiation. However, in our case it seems difficult to find a clear link between the occurrence of the photoinduced transformation and the sample stoichiometries (see Table 1). A detailed investigation of the temperature dependence of the photoconversion efficiency and the stability of the metastable phases down to liquid helium temperatures will be necessary to determine the pertinent parameters governing this phenomenon.

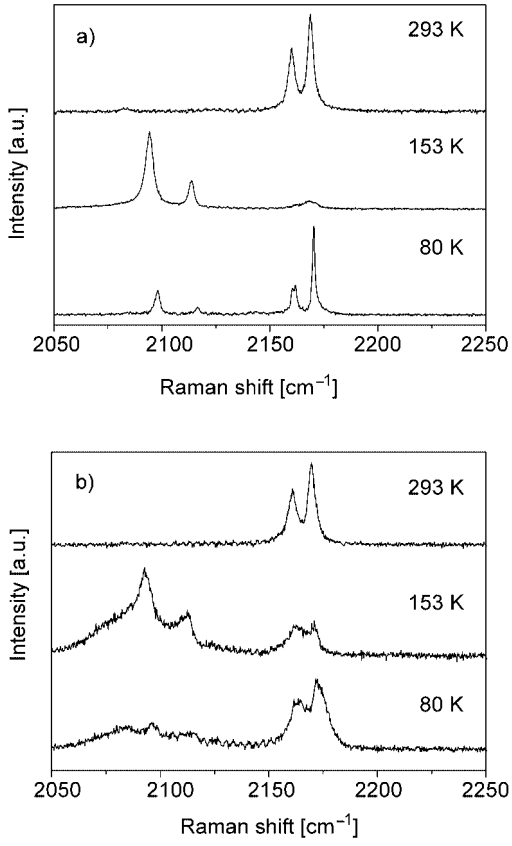


Figure 7. Raman spectra of sample **8** (a) and sample **5** (b) in the $\nu_{CN}$ frequency region at selected temperatures (cooling mode).

Figure 7 also shows that in sample **5** the Raman frequencies at low temperatures become extremely broad and unresolved. Such broadening of Raman modes can be expected as the degree of disorder increases as a result of the broader distribution in the bond lengths and the bond angles. Furthermore, as the disordered phase loses symmetry the associated selection rules may also change and one can also expect mode splittings and the appearance of modes, which are otherwise forbidden by the selection rules in the higher symmetry (i.e. more stoichiometric) forms. While in the LT phase the frequencies become badly re-

 © 2007 Wiley-VCH Verlag GmbH & Co. KGaA, Weinheim 

solved, the broadening of the modes in the HT phase can be used for diagnostic purposes as suggested by Vertelman et al.[11] In agreement with these authors, we observed that complexes exhibiting a conversion between the two valence-tautomeric forms show considerably narrower Raman linewidths in the CN-stretching region than complexes which do not present this phase transition (Figure 8).

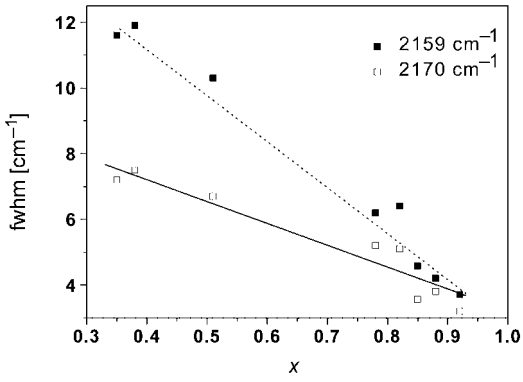


Figure 8. Full width at half maximum of selected Raman modes in $Rb_xMn[Fe(CN)_6]_y{\cdot}zH_2O$ at 298 K as a function of the Rb content. (Straight lines represent linear fits on the data.)

## Conclusions

We have synthesized a series of nonstoichiometric $Rb_xMn[Fe(CN)_6]_y{\cdot}zH_2O$ compounds, some of which display charge-transfer phase-transition phenomena as a function of their composition. We have found, independently of the reaction conditions, a fairly good quantitative correlation between the Rb, Fe, and $H_2O$ proportions, which can be explained by simple arguments based on the chemical arrangement of the system. The general tendency between the phase transition temperature and the sample stoichiometry, initially proposed by Ohkoshi et al.,[17] was confirmed. However, the quantitative correlation they propose was not observed probably because of the inherent disorder in these systems. Contrary to two independent reports,[10,21] we found that the phase transition is accompanied by an important change in the entropy of mainly vibrational origin, which is reflected in the huge changes observed in low frequency Raman spectra. Further work should address the question of the properties of the light-induced metastable phase, which was observed in the Raman spectra.

## Experimental Section

**Syntheses:** A solution of $MnCl_2{\cdot}4H_2O$ (Aldrich) in Millipore $H_2O$ (3 $cm^3$) was slowly mixed with a solution of $K_3Fe(CN)_6$ (Aldrich) and RbCl (Aldrich) in Millipore $H_2O$ (3 $cm^3$). All solutions were stirred mechanically and kept at a temperature of 50 °C during the addition procedure. A brown powder precipitate was filtered, washed with Millipore $H_2O$ and dried in air at room temperature. Nine different syntheses were realized (Table 2), six to observe the effect of concentrations (samples **1**–**6**) and three more to observe the reproducibility of the synthesis (samples **7**–**9**).

Table 2. Concentration of reactants used for the synthesis of different samples.

| Sample | $MnCl_2{\cdot}4H_2O$ [mol $dm^{-3}$] | RbCl [mol $dm^{-3}$] | $K_3Fe(CN)_6$ [mol $dm^{-3}$] |
|---|---|---|---|
| **1** | 0.11 | 0.48 | 0.1 |
| **2** | 0.14 | 1.01 | 0.1 |
| **3** | 0.1 | 2.03 | 0.1 |
| **4** | 0.06 | 1 | 0.1 |
| **5** | 0.11 | 1 | 0.1 |
| **6** | 0.07 | 1.02 | 0.1 |
| **7** | 0.11 | 1 | 0.1 |
| **8** | 0.11 | 1 | 0.1 |
| **9** | 0.06 | 1 | 0.1 |

**Microanalyses:** Analysis for C, H, and N were performed after combustion at 850 °C by using IR detection and gravimetry by means of a Perkin–Elmer 2400 series II device. Fe, Mn, Rb, and K concentration were determined with ICP–AES (Inductively Coupled Plasma Atomic Emission Spectroscopy) after acid digestion in $H_2SO_4/HNO_3$. Standard deviations of the measured metal concentrations were typically around 2 rel.%. The O and H atoms were assumed to be the only other elements present in the samples and the $H_2O$ content was obtained by difference to 100%. (The K concentration was found to be negligible.)

**Spectroscopy:** Raman spectra were collected between 300 K and 80 K with a LabRAM-HR (Jobin Yvon) Raman microspectrometer and a Linkam THMS-600 cryostage. The 632.8 nm line of a He–Ne laser was used as the excitation source and a spectral resolution of ca. 1 $cm^{-1}$ was obtained.

**Magnetic Studies:** Magnetic susceptibility measurements were carried out between 350–80 K by using a homemade Faraday-type magnetometer equipped with a continuous-flow Oxford Instruments cryostat. Measurements were done isothermally by steps of 10 K in 5 different magnetic fields between 4500 and 15000 Oe. Calibration of magnetic susceptibility was performed by using the reference compound $HgCo(SCN)_4$. Data were corrected for diamagnetic contributions.

**Differential Scanning Calorimetry (DSC):** DSC analysis was carried out with a Netsch DSC 204 instrument under helium purging gas (20 $cm^3\,min^{-1}$) at a scan rate of 10 $K\,min^{-1}$ both in heating and cooling modes. Temperature and enthalpy ($\Delta H$) were calibrated by using the melting transition of standard materials (Hg, In, Sn). The uncertainty in the transition enthalpy ($\Delta H_{HL}$) and entropy ($\Delta S_{HL}$) is estimated at ca. 10% because of the subtraction of the unknown baseline and uncertainties in the residual (i.e. nontransformed) fractions.

## Acknowledgments

S. Seyrac and J.-F. Meunier (LCC-CNRS) are acknowledged for CHN, DSC, and magnetic measurements. The ICP-AES analysis was made by the Service Central d'Analyse du CNRS (Vernaison).

[1] P. Gütlich, A. Hauser, H. Spiering, *Angew. Chem. Int. Ed. Engl.* **1994**, *33*, 2024.
[2] A. Bousseksou, G. Molnár, G. Matouzenko, *Eur. J. Inorg. Chem.* **2004**, 4353.
[3] D. N. Hendrickson, C. G. Pierpont, *Top. Curr. Chem.* **2004**, *234*, 63.
[4] T. Mallah, S. Thiébaut, M. Verdaguer, P. Veillet, *Science* **1993**, *262*, 1554.

 © 2007 Wiley-VCH Verlag GmbH & Co. KGaA, Weinheim 

[5] M. Verdaguer, A. Bleuzen, V. Marvaud, J. Vaissermann, M. Seuleiman, C. Desplanches, A. Scuiller, C. Train, R. Garde, G. Gelly, C. Lomenech, I. Roseman, P. Veillet, C. Cartier, F. Villain, *Coord. Chem. Rev.* **1999**, *190–192*, 1023.
[6] O. Sato, T. Iyoda, A. Fujishima, K. Hashimoto, *Science* **1996**, *272*, 704.
[7] V. Escax, A. Bleuzen, C. Cartier, F. Villain, A. Goujon, F. Varret, M. Verdaguer, *J. Am. Chem. Soc.* **2001**, *123*, 12536.
[8] V. Escax, A. Bleuzen, J. P. Itié, P. Munsch, F. Varret, M. Verdaguer, *J. Phys. Chem. B* **2003**, *107*, 4763.
[9] N. Shimamoto, S. Ohkoshi, O. Sato, K. Hashimoto, *Inorg. Chem.* **2002**, *41*, 678.
[10] S. Ohkoshi, H. Tokoro, K. Hashimoto, *Coord. Chem. Rev.* **2005**, *249*, 1830.
[11] E. J. M. Vertelman, E. Maccallini, D. Gournis, P. Rudolf, T. Bakas, J. Luzon, R. Broer, A. Pugzlys, T. T. A. Lummen, P. H. M. van Loosdrecht, P. J. van Koningsbruggen, *Chem. Mater.* **2006**, *18*, 1951.
[12] S. Ohkoshi, H. Tokoro, M. Utsunomiya, M. Mizuno, M. Abe, K. Hashimoto, *J. Phys. Chem. B* **2002**, *106*, 2423.
[13] H. Tokoro, S. Ohkoshi, K. Hashimoto, *Appl. Phys. Lett.* **2003**, *82*, 1245.
[14] H. Tokoro, T. Matsuda, K. Hashimoto, K. S. Ohkoshi, *J. Appl. Phys.* **2005**, *97*, 10M508.
[15] T. Yokoyama, H. Tokoro, S. Ohkoshi, K. Hashimoto, K. Okamoto, T. Ohta, *Phys. Rev. B* **2002**, *66*, 184111.
[16] Y. Moritomo, M. Hanawa, Y. Ohishi, K. Kato, M. Takata, A. Kuriki, E. Nishibori, M. Sakata, S. Ohkoshi, H. Tokoro, K. Hashimoto, *Phys. Rev. B* **2003**, *68*, 144106.
[17] S. Ohkoshi, T. Matsuda, H. Tokoro, K. Hashimoto, *Chem. Mater.* **2005**, *17*, 81.
[18] H. Tokoro, S. Miyashita, K. Hashimoto, S. Ohkoshi, *Phys. Rev. B* **2006**, *73*, 172415.
[19] M. Sorai, S. Seki, *J. Phys. Chem. Solids* **1974**, *35*, 555.
[20] S. Gawali-Salunke, F. Varret, I. Maurin, C. Enachescu, M. Malarova, K. Boukheddaden, E. Codjovi, H. Tokoro, S. Ohkoshi, K. Hashimoto, *J. Phys. Chem. B* **2005**, *109*, 8251.
[21] E. J. M. Vertelman, P. J. van Koningsbruggen at the *International Symposium on Molecular Materials based on Coordination and Organometallic Chemistry*, June 7–10th **2006**, Lyon, France.
[22] A. Bousseksou, J. Nasser, J. Linares, K. Boukheddaden, F. Varret, *J. Phys. I* **1992**, *2*, 1381.
[23] A. Bousseksou, J. J. McGarvey, F. Varret, J. A. Real, J. P. Tuchagues, A. C. Dennis, M. L. Boillot, *Chem. Phys. Lett.* **2000**, *318*, 409.
[24] S. N. Ghosh, *J. Inorg. Nucl. Chem.* **1974**, *36*, 2465.

Received: October 31, 2006
Published Online: March 6, 2007

 © 2007 Wiley-VCH Verlag GmbH & Co. KGaA, Weinheim 

DOI: 10.1002/ejic.200601026

# Synthesis, Characterization and Redox Behaviour of Mono- and Dicarbonyl Phosphane Rhenium(I) Complexes Bearing N-, N,N- and N,O-Type Ligands

**Alexander M. Kirillov,[a] Matti Haukka,[b] M. Fátima C. Guedes da Silva,[a] and Armando J. L. Pombeiro*[a]**

**Keywords:** Carbonyl ligands / Electrochemistry / N ligands / Rhenium

New mono- and dicarbonyl phosphane $Re^{I}$ complexes $[ReCl(L)_2(CO)(PPh_3)_2]$ {L = 3,5-$Me_2$-Hpz (**3**), quin (**4**)} and $[Re(L)_n(CO)_2(PPh_3)_2][BPh_4]_m$ {L = pz/Hpz, $n$ = 2, $m$ = 0 (**2**); L = 4,7-$Ph_2$-phen, $n$ = 1, $m$ = 1 (**5**); L = 2-Me-dipic, $n$ = 1, $m$ = 0 (**6**)} were prepared by reaction of the dinitrogen $Re^{I}$ precursor $[ReCl(N_2)(CO)_2(PPh_3)_2]$ (**1**), in refluxing methanol or methanol/benzene mixture, with 3,5-dimethylpyrazole (3,5-$Me_2$-Hpz), quinoline (quin), pyrazole (Hpz), 4,7-diphenyl-1,10-phenanthroline (4,7-$Ph_2$-phen) and dipicolinic acid ($H_2$dipic), respectively, with esterification of the latter in **6** to afford the 2-methoxycarbonyl-6-pyridinecarboxylate (2-Me-dipic) moiety. Complexes **2**–**6** were characterized by IR spectroscopy, $^{1}$H-, $^{31}$P{$^{1}$H}- and $^{13}$C{$^{1}$H} NMR spectroscopy, FAB-MS, cyclic voltammetry, elemental analyses and single-crystal X-ray diffraction (for **2**, **5** and **6**) analyses which indicate mutually *trans* triphenylphosphane ligands. The redox behaviour of the obtained complexes in solution was studied, and the Lever electrochemical ligand parameter $E_L$ was determined, for the first time, for 4,7-$Ph_2$-phen. Compounds **2**–**6** represent the first examples of *mono*- and *dicarbonyl* Re complexes bearing these types of ligands.

(© Wiley-VCH Verlag GmbH & Co. KGaA, 69451 Weinheim, Germany, 2007)

## Introduction

Dinitrogen complexes of rhenium are an important class of compounds within the low-oxidation-state coordination chemistry of this metal, particularly because of their significance in the field of nitrogen fixation and as versatile synthons for a variety of new rhenium derivatives.[1,2] The lability of the coordinated $N_2$ in Re complexes allows its displacement by a variety of small molecules (e.g., CO, $H_2$, $CS_2$, NO, nitriles, oximes, alkynes, azides, cyanates, etc.) and various P-, N-, O-, S- or mixed-donor ligands.[1,3] In this respect, the bis(diphosphane) complex *trans*-$[ReCl(N_2)(dppe)_2]$ {dppe = 1,2-bis(diphenylphosphanyl)-ethane} is the most studied member within the whole family of Re dinitrogen complexes.[1b,1e,1g,3a,3e,4] A few studies have been performed on the monophosphane analogues $[ReCl(N_2)(L)_4]$ (L = $PMe_2Ph$ or $PMePh_2$),[1b,5a,5b] whereas the reactivity of the related mixed $N_2$/CO complex $[ReCl(N_2)(CO)_2(PPh_3)_2]$ (**1**) appears to have been investigated only in a couple of cases; one instance involved its reactions with some amino acids conjugated with 2-aminothiazole (L) to afford monocarbonyl $Re^{II}$ complexes of the general formula $[ReCl(L)(CO)(PPh_3)_2]$.[5c] The other case led to the $Re^{I}$ dinitrogen compound $[Re(pic)(N_2)(CO)(PPh_3)_2]$ (pic = picolinate) by reaction of **1** with picolinic acid (Hpic),[6a] thus initially extending to the low $Re^{I}$ oxidation state (and to picolinate) our interest in higher-oxidation-state rhenium complexes with N- or O-ligands, namely some benzoyldiazenido-$Re^{III}$[6b] and oxo-$Re^{V}$[6c] compounds which were shown to act as catalysts for the peroxidative oxidation[6b] or carboxylation[6c] of alkanes. To further explore the use of **1** as a convenient precursor for the synthesis of new $Re^{I}$ compounds with N-, N,N- or N,O-ligands, we studied its reactions with various N-heterocycle species, that is, pyrazole, 3,5-dimethylpyrazole, quinoline, 4,7-diphenyl-1,10-phenanthroline and dipicolinic acid (Scheme 1), and we prepared and characterized a series of derived mono- and dicarbonyl complexes. Although heterocycle ligands of such types are rather simple and commonly used in coordination chemistry, their complexes with the monocarbonyl {Re(CO)} or dicarbonyl {$Re(CO)_2$} core are still very rare.[7] This contrasts with the tricarbonyl {$Re(CO)_3$} core, whose coordination chemistry was extensively developed over the last two decades,[8] with application in nuclear-medical research, in the preparation of photoluminescent materials, in catalysis and in supramolecular chemistry.[7a,9]

[a] Centro de Química Estrutural, Complexo I, Instituto Superior Técnico,
Av. Rovisco Pais, 1049–001 Lisbon, Portugal
Fax: +351-21-846-4455
E-mail: pombeiro@ist.utl.pt
[b] Department of Chemistry, University of Joensuu,
P.O. Box 111, 80101, Joensuu, Finland

Supporting information for this article is available on the WWW under http://www.eurjic.org or from the author.

 InterScience © 2007 Wiley-VCH Verlag GmbH & Co. KGaA, Weinheim 

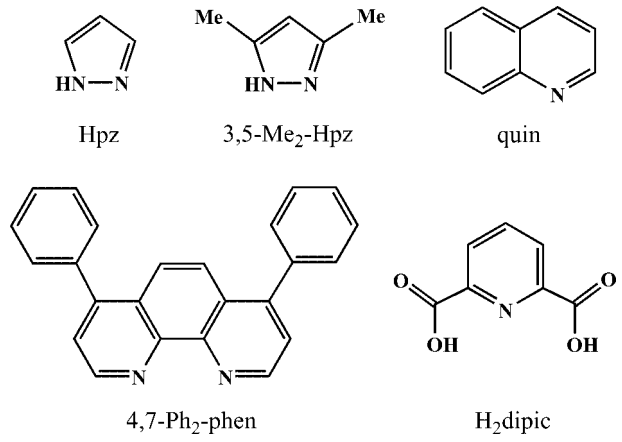


Scheme 1.

In particular, despite the fact that a number of *tricarbonyl* Re complexes with these ligands were already known,[10] to the best of our knowledge, there were no examples of *mono*- and *dicarbonyl* Re complexes comprising pyrazole, 3,5-dimethylpyrazole or quinoline ligands, as well as any phenanthroline or dipicolinate derivatives. The redox properties of the synthesized complexes were also investigated by cyclic voltammetry, and the value of the electrochemical Lever ligand parameter $E_L$[11] was estimated, for the first time, for the 4,7-$Ph_2$-phen ligand.

## Results and Discussion

### Synthesis and Spectroscopic Characterization

The reactions of the dinitrogen rhenium(I) complex $[ReCl(N_2)(CO)_2(PPh_3)_2]$ (**1**) with the N-heterocycle ligands of Scheme 1 in refluxing methanol or a methanol/benzene mixture led to the displacement of the $N_2/Cl^-$ ligands, or of the $N_2$ and one CO ligand in **1** (Scheme 2), thus allowing the formation of the new mono- and dicarbonyl rhenium(I) complexes $[ReCl(L)_2(CO)(PPh_3)_2]$ {L = 3,5-$Me_2$-Hpz (**3**), quin (**4**)} and $[Re(L)_n(CO)_2(PPh_3)_2][BPh_4]_m$ {L = pz/Hpz, $n$ = 2, $m$ = 0 (**2**); L = 4,7-$Ph_2$-phen, $n$ = 1, $m$ = 1 (**5**); L = 2-Me-dipic (2-methoxycarbonyl-6-pyridinecarboxylate), $n$ = 1, $m$ = 0 (**6**)}, which were isolated as air-stable crystalline solids in 78–44% yields. Hence, the reaction of **1** with pyrazole (Hpz, Scheme 2, reaction 1) gave the pale-yellow dicarbonyl complex $[Re(pz)(Hpz)(CO)_2(PPh_3)_2]$ (**2**) with one pyrazolate ($pz^-$) ligand and one pyrazole (Hpz) ligand, formed upon $N_2$ and HCl elimination, while the use of 3,5-dimethylpyrazole (3,5-$Me_2$-Hpz, reaction 2) led to the displacement of $N_2$ and one CO ligand, yielding the yellow monocarbonyl dipyrazole compound $[ReCl(3,5\text{-}Me_2\text{-}Hpz)_2(CO)(PPh_3)_2]$ (**3**). The related deep-purple monocarbonyl complex $[ReCl(quin)_2(CO)(PPh_3)_2]$ (**4**) was obtained by treatment of the starting material **1** with an excess of quinoline (quin, Scheme 2, reaction 3). The reactions of 4,7-diphenyl-1,10-phenanthroline (4,7-$Ph_2$-phen) and dipicolinic (2,6-pyridinedicarboxylic) acid ($H_2$dipic) with **1** (reactions 4, 5) led to the deep-red ionic Re compound $[Re(4,7\text{-}Ph_2\text{-}phen)(CO)_2(PPh_3)_2][BPh_4]$ (**5**) (upon addition of $Na[BPh_4]$) and the orange neutral complex $[Re(2\text{-}Me\text{-}dipic)(CO)_2(PPh_3)_2]$ (**6**), respectively. The complexes **2**–**6** were characterized by IR spectroscopy, FAB-MS, $^1$H-, $^{31}P\{^1H\}$- and $^{13}C\{^1H\}$ NMR spectroscopy, cyclic voltammetry, elemental analyses and single-crystal X-ray diffraction (for **2**, **5** and **6**) structural analyses.

Complex **2** bears both one Hpz ligand and its anionic conjugate base ($pz^-$). However, the $^1$H- and $^{13}C\{^1H\}$ NMR spectra show their magnetic equivalence as accounting for a single set of resonances attributable to proton or carbon atoms of both ligands. In the $^1$H NMR spectrum of **2**, the broad 1 H intensity N*H* signal at $\delta$ = 11.26 ppm is assigned to N–*H*···N, although the upfield shift relative to uncoordinated pyrazole [$\delta$(N*H*) = 13.60 ppm, $CCl_4$ (0.5 M)][12] cannot be directly related to the effects of the hydrogen bond and/or of a dynamic proton exchange since in other cases[10a] they led to lowfield shifts. The solid-state IR spectrum of **2** exhibits an intense ν(NH) band with a maximum at 3317 $cm^{-1}$, whose broad character is indicative of hydrogen bonding.

In contrast, both 3,5-$Me_2$-Hpz ligands are neutral in complex **3**. Its $^1$H NMR spectrum shows a 2 H intensity N*H* signal at $\delta$ = 11.06 ppm, which is also shifted upfield relative to free 3,5-dimethylpyrazole [$\delta$(N*H*) = 12.29 ppm, $CDCl_3$ (1.0 M)],[12] while the IR spectrum of this compound exhibits a ν(NH) band at 3222 $cm^{-1}$.

In complex **6** the dipicolinate ligand (2-Me-dipic) is bidentate, exhibiting N,O-coordination and one free arm whose esterification to give a methyl acetate moiety occurred during the synthesis in methanol solution, conceivably being promoted by the $Re^I$ centre since the methyl ester was not detected in a blank experiment upon refluxing dipicolinic acid in methanol for several hours in the absence of a metal complex. The same type of esterification was previously observed[6c] by us in the course of the synthesis of $Re^V$ complexes such as $[ReOCl_2(2\text{-}Me\text{-}dipic)(PPh_3)]$ and $[ReOCl\{(OCH_2CH_2)N(CH_2COO)(CH_2COOCH_3)\}(PPh_3)]$ derived from dipicolinic and *N*-(2-hydroxyethyl)iminodiacetic acids, respectively. The presence of the methyl ester group in **6** is corroborated by the detection of the corresponding $CH_3$ resonances in the $^1$H- ($\delta$ = 4.19 ppm) and $^{13}C\{^1H\}$ ($\delta$ = 53.91 ppm) NMR spectra. Moreover, the IR spectrum of **6** shows strong bands at 1740 and 1435 $cm^{-1}$ associated with $\nu_{as}$ and $\nu_s$ vibrations, respectively, of the COOMe fragment.

The $^{13}C\{^1H\}$ NMR spectra of the dicarbonyl complexes exhibit two *C*O signals, lying in the $\delta$ range of ca. 203–189 ppm for complexes **2** and **6**, whereas in **5** they are significantly shifted upfield to $\delta$ = 166.74 and 166.04 ppm. In the monocarbonyl complex **3** the corresponding *C*O resonance is observed at $\delta$ = 197.80 ppm. The $^{31}P\{^1H\}$ NMR spectra of all complexes **2**–**6** indicate the stereochemically favoured *trans* phosphane coordination in view of the single resonance detected in the $\delta$ range of ca. 32–20 ppm (relative to external $H_3PO_4$), which is shifted downfield from that ($\delta$ = –5.47 ppm) of free triphenylphosphane. These signals and all other NMR resonances of complexes **2**–**6** are unexcep-

 © 2007 Wiley-VCH Verlag GmbH & Co. KGaA, Weinheim 

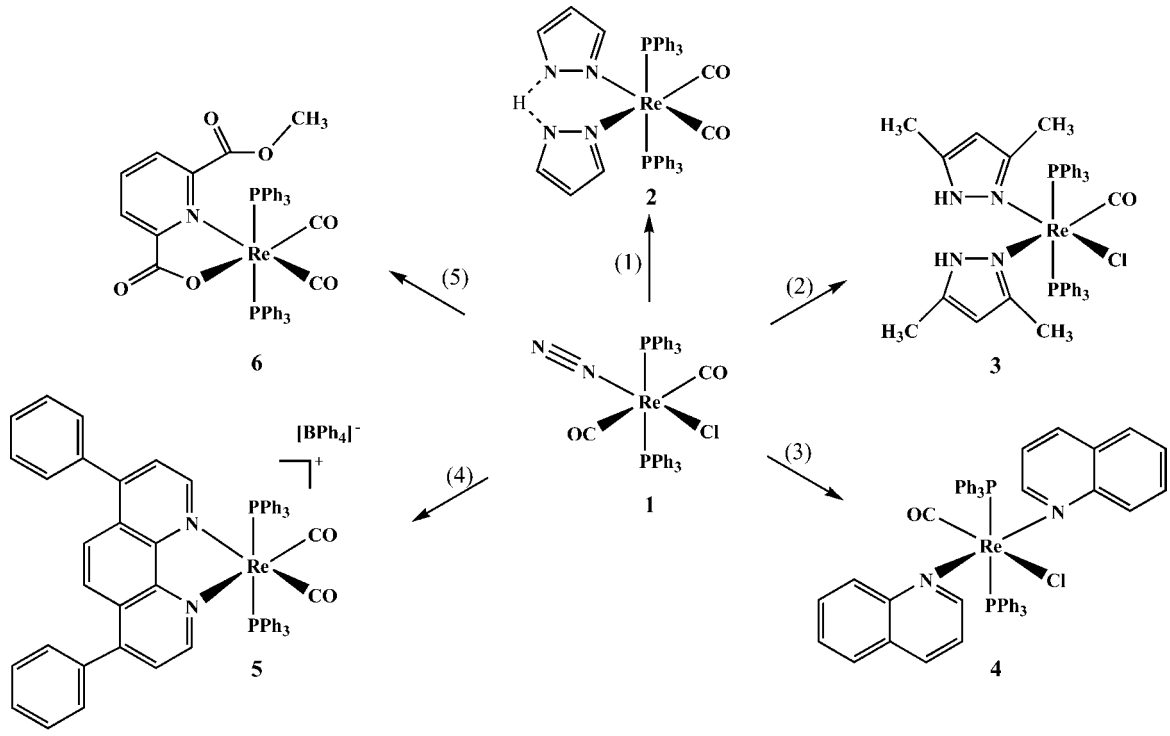


Scheme 2. (1): + Hpz – $N_2$ – HCl; (2): + 3,5-$Me_2$-Hpz – $N_2$ – CO; (3): + quin – $N_2$ – CO; (4): + 4,7-$Ph_2$-phen + Na[$BPh_4$] – $N_2$ – NaCl; (5): + $H_2$dipic – $N_2$ – HCl.

tional and comparable to those found in related rhenium complexes.[6,10a,10e–g,13]

The IR spectra of the dicarbonyl complexes **2**, **5** and **6** exhibit two strong ν(CO) bands in the 1929–1924 and 1853–1841 $cm^{-1}$ ranges, similar to those of the starting material **1** (1921 and 1844 $cm^{-1}$) and other dicarbonyl $Re^{I}$ complexes containing the *cis*-{$Re(CO)_2$} moiety, for example, [$Re(L)(CO)_2(PPh_3)_2$] {L = MeCOO or EtCOO;[14a] $OC(NH_2)S$, OC(NHPh)S or $OC(NHC_6H_4Me\text{-}4)S$}[14b] and [$Re(L)(CO)_2$(bipy)] {bipy = 2,2′-bipyridine, L = diethyl-2-(*N*-*p*-tolylimino)-3-(hydroxymethylene)butane-1,2-dicarboxylate}.[14c] An additional ν(CO) band is detected at 2032 $cm^{-1}$ in the spectrum of **2**, as observed with other rhenium carbonyl complexes comprising pyrazole moieties.[14d] Two strong ν(CO) bands at 1922 and 1839 $cm^{-1}$ are also shown by **3**, whereas in complex **4** the ν(CO) band is detected at 1778 $cm^{-1}$, being considerably shifted to a lower-energy region more typical for a bridging carbonyl group.[14e] Nevertheless, we believe that compound **4** is mononuclear and bears a terminal carbonyl ligand *trans* to the ligated $Cl^-$, as formulated in Scheme 2. This is in agreement with (i) an X-ray single-crystal diffraction analysis of **4** which indicates its basic and mononuclear structure, with the *trans*-CO/Cl arrangement, although with a too-high error to be reported, as well as with (ii) a FAB-MS(+) analysis which clearly detects the molecular ion [$ReCl(quin)_2(CO)(PPh_3)_2$]$^+$ as the heaviest observed fragment (see later). A low IR ν(CO) value (ca. 1800 $cm^{-1}$)[4e] was also found for the $Re^{I}$ monocarbonyl complex *trans*-[$ReCl(CO)(dppe)_2$] with the strong electron-donor chloro ligand which promotes the electron release from $d_\pi$ orbitals of the metal to the π*(CO) orbitals, as it also conceivably occurs in complex **4**. This is also assisted by the limited π-electron acceptance of the two quinoline ligands in comparison with the CO and $N_2$ ligands in compound **1**. The IR spectra of complexes **3**–**6** also show a set of bands due to the $\nu_{as}$ and $\nu_s$ vibrations of CH groups in the typical 3060–3050 and 3000–2925 $cm^{-1}$ ranges, respectively. The characteristic ν(PPh) bands due to the $PPh_3$ ligands are observed at 747–743 and 697–695 $cm^{-1}$.

The positive FAB-MS spectra of compounds **3**–**6** exhibit the molecular ions $[M]^+$ with the expected isotopic patterns at *m*/*z* values of 966, 1032, 1099 and 947, respectively, while the protonated molecular ion $[M + H]^+$ is detected at *m*/*z* = 903 in the spectrum of **2**. Fragmentation pathways involve the stepwise loss of CO, Cl and $PPh_3$ ligands as well as of N-, N,N- or N,O-moieties. A comparative analysis of peak intensities concerned with typical fragmentations suggests that in complexes **3**–**6** the elimination of one $PPh_3$ ligand is a favourable process, in agreement with the detection of very intense signals assigned to the [M – $PPh_3$] (in **3**, **4**), [M – $PPh_3$ – 2CO] (in **5**) and [M – $PPh_3$ – CO] (in **6**) fragments. In contrast, the release of one or two pyrazole ligands is more favourable in **2** since a set of intense peaks attributed to the [M – pz], [M – pz – CO], [M – pz – Hpz] and [M – pz – Hpz – CO] fragments is observed. The presence of the $[BPh_4]^-$ counterion in **5** is clearly confirmed by the negative FAB-MS spectrum (the intense signal of the $[M]^-$ molecular ion at *m*/*z* = 319 with the expected isotopic pattern) and by the IR spectrum. Also, elemental analyses

 © 2007 Wiley-VCH Verlag GmbH & Co. KGaA, Weinheim 

of all compounds are consistent with the proposed formulations (Scheme 2) which are further confirmed by single-crystal X-ray diffraction studies (for **2**, **5** and **6**).

### X-ray Crystal Structures

The molecular structures of complexes **2**, **5** and **6** are shown in Figures 1, 2 and 3, respectively, and selected bond lengths and angles are given in Table 1. All compounds crystallize in the monoclinic crystal system (space group $P2_1/n$) and exhibit a distorted octahedral coordination environment about rhenium filled by the N-, N,N- or N,O-ligand(s), two triphenylphosphane groups and two carbonyl groups.

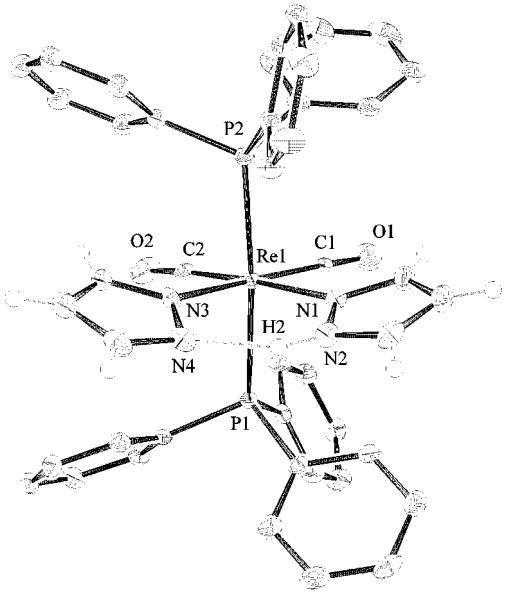


Figure 1. An ORTEP representation of **2** with ellipsoids shown at the 50% probability level. Phenyl hydrogen atoms are omitted for clarity.

The molecular structure of **2** (Figure 1) shows the $pz^-$ and Hpz ligands *trans* to the carbonyl groups. The Re1–C1 and Re1–C2 bond lengths of 1.920(4) and 1.893(4) Å, respectively, are common for rhenium carbonyl complexes,[10a,10d–g,15] while the carbonyl C1–O1 and C2–O2 distances of 1.141(5) and 1.162(5) Å, respectively, are comparable to the C≡O bond of ca. 1.128 Å[16] in molecular carbon monoxide. The binding of the Hpz/$pz^-$ ligands to rhenium is characterized by a slight difference between the Re1–N1 [2.219(3) Å] and Re1–N3 [2.176(3) Å] bond lengths which agree with those reported for other rhenium carbonyl complexes comprising pyrazole or hydrotris(pyrazolyl)-borate $[HB(pz)_3]^-$ derivatives, for example, $[Re(pz)(Hpz)_2(CO)_3]$,[10a] $[Re\{HB(pz)_3\}(CO)_2L]$ (L = THF or $PPh_3$)[15b] and $[\{Re(B(Hpz)_3)(CO)_2\}_2(N_2)]$.[17] Although only one NH proton is crystallographically localized at one of the pyrazole moieties of **2**, its assignment to the N2 atom is rather formal and in reality it may be split between N2 and N4. This agrees with the observation of a rather short N2–H2···N4 intramolecular hydrogen bond with N2···N4 distance of 2.627(5) Å [N2–H2 0.94(4) Å and H2···N4 1.74(5) Å; N2–H2···N4 156(4)°], which connects two pyrazole groups forming the Re1–N1–N2···N4–N3 ring with the N1–Re1–N3 angle of 89.22(12)°. Related features of the NH protons assignment and splitting, and the hydrogen-bonding interactions within the Hpz and $pz^-$ fragments were observed in some Re, Ru, Co, Pd, Pt and Zn complexes.[10a] The triphenylphosphane groups are bound almost linearly, and the Re–P distances range from 2.4251(10) to 2.4453(10) Å being comparable to those of compounds **5** and **6** and in accordance with those reported for other carbonyl rhenium complexes with *trans* $PPh_3$ ligands.[14a,18]

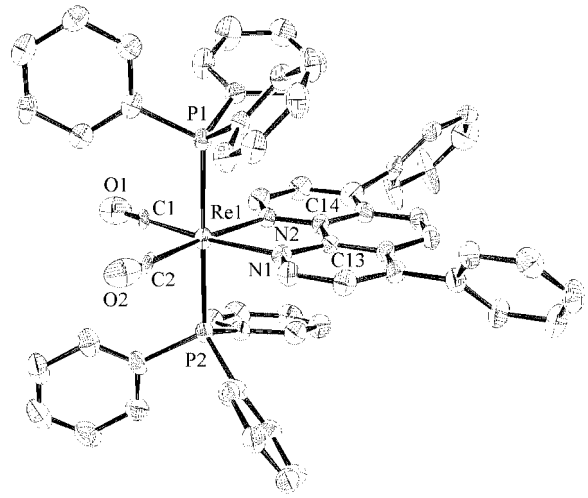


Figure 2. An ORTEP representation of the cationic part of **5** with ellipsoids shown at the 50% probability level. All hydrogen atoms and the solvent molecule are omitted for clarity.

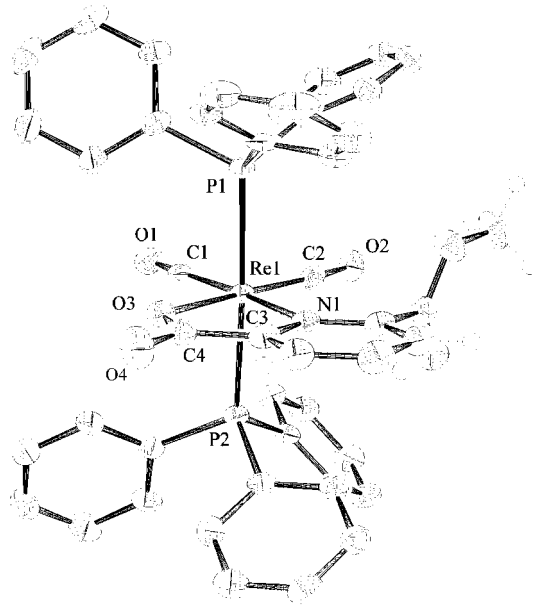


Figure 3. An ORTEP representation of **6** with ellipsoids shown at the 50% probability level. Phenyl hydrogen atoms and the solvent molecule are omitted for clarity.

 © 2007 Wiley-VCH Verlag GmbH & Co. KGaA, Weinheim 

Table 1. Selected bond lengths [Å] and angles [°] for compounds **2**, **5** and **6**.

| | **2** | **5**·0.5$CH_2Cl_2$ | **6**·EtOH |
|---|---|---|---|
| Re1–C1 | 1.920(4) | 2.004(6) | 1.918(6) |
| Re1–C2 | 1.893(4) | 2.042(7) | 1.887(7) |
| Re1–N1 | 2.219(3) | 2.162(4) | 2.216(4) |
| Re1–N2 | – | 2.147(4) | – |
| Re1–N3 | 2.176(3) | – | – |
| Re1–O3 | – | – | 2.176(4) |
| Re1–P1 | 2.4251(10) | 2.4434(12) | 2.4273(13) |
| Re1–P2 | 2.4453(10) | 2.4439(13) | 2.4246(13) |
| C1–O1 | 1.141(5) | 0.977(6) | 1.126(6) |
| C2–O2 | 1.162(5) | 0.860(6) | 1.167(7) |
| C1–Re1–C2 | 93.81(16) | 95.5(2) | 85.0(2) |
| C1–Re1–N1 | 85.54(13) | 168.77(17) | 172.8(2) |
| C1–Re1–N2 | – | 93.05(17) | – |
| C2–Re1–N1 | 176.20(14) | 95.7(2) | 102.1(2) |
| C2–Re1–N2 | – | 171.45(19) | – |
| C2–Re1–O3 | – | – | 176.63(18) |
| N1–Re1–N2 | – | 75.73(14) | – |
| N1–Re1–N3 | 89.22(12) | – | – |
| N1–Re1–O3 | – | – | 74.51(16) |
| C1–Re1–P1 | 90.65(11) | 89.78(14) | 89.19(14) |
| C2–Re1–P1 | 84.02(12) | 90.66(17) | 90.87(16) |
| C1–Re1–P2 | 91.66(11) | 88.90(14) | 89.18(14) |
| C2–Re1–P2 | 91.69(12) | 91.74(17) | 91.35(16) |
| N1–Re1–P1 | 92.24(9) | 89.94(10) | 90.37(11) |
| N1–Re1–P2 | 92.07(9) | 90.90(10) | 90.95(11) |
| P1–Re1–P2 | 175.26(3) | 177.36(4) | 177.13(5) |
| Re1–C1–O1 | 176.6(3) | 179.2(6) | 176.9(5) |
| Re1–C2–O2 | 175.8(4) | 178.2(8) | 176.1(5) |

The major deviation from the octahedral geometry in **2** concerns the C2–Re1–P1 angle of 84.02(12)°; the other bond angles are relatively close to the idealized 90° and 180°.

Compound **5** is the first structurally characterized example with the 4,7-diphenyl-1,10-phenanthroline ligand within the large family of phenanthroline Re complexes. Its molecular structure comprises the $[Re(4,7\text{-}Ph_2\text{-}phen)(CO)_2(PPh_3)_2]^+$ cation and the $[BPh_4]^-$ anion, with the separation between rhenium and boron centres being ca. 8.91 Å. The cationic part also contains two phosphane ligands in *trans* position, whereas the equatorial sites are occupied by the bidentate phenanthroline ligand and the two carbonyl groups (Figure 2). The octahedral environment around rhenium is more distorted than that of complex **2**, exhibiting a major deviation from an idealized geometry with a minimal N1–Re1–N2 angle of 75.73(14)°. The Re1–C1 and Re1–C2 bonds of 2.004(6) and 2.042(7) Å, respectively, are lengthened by ca. 0.10–0.15 Å relative to the corresponding distances in **2** and other complexes with a phenanthroline moiety.[10d–g,15a] Such an elongation of the Re–C distances is concomitant with the shortening of the C1–O1 and C2–O2 bonds to 0.977(6) and 0.860(6) Å, respectively; the latter distance is unusually short and this is not reflected in ν(CO) which is comparable to the other complexes. The phenanthroline molecule is bound to the metal forming a N1–C13–C14–N2–Re1 chelate ring, and the Re1–N1 and Re1–N2 bonds of 2.162(4) and 2.147(4) Å, respectively, lie in the range of ca. 2.14–2.22 Å reported for other phenanthroline Re complexes.[10d–g,15a]

The structure of **6** (Figure 3), with a chelating methyldipicolinate ligand, is similar to that of **2** comprising the pyrazolate/pyrazole ligands in the equatorial sites. In the monoesterificated dipicolinate ligand, the nitrogen N1 is *trans* to the C1–O1 carbonyl group and the carboxylate oxygen O3 is *trans* to the C2–O2 ligand, forming a Re1–N1–C3–C4–O3 chelate ring with a N1–Re1–O3 bite angle of 74.51(16)° which is the most deviated angle from the idealized 90° around the distorted octahedral geometry of the Re1 centre. The bond lengths within the dipicolinate moiety in **6** are analogous to those of $[ReBr\{C_5H_3N(COOEt)(COOMe)\}(CO)_3]$[10i] and $[ReOCl_2(2\text{-Me-dipic})]$,[6c] although the latter contains a rather short Re–$O_{dipic}$ bond [2.037(2) Å] relative to the corresponding Re1–O3 distance of 2.176(4) Å in **6**. The Re1–C1 [1.918(6) Å] and Re1–C2 [1.887(7) Å] bonds as well as the C1–O1 [1.126(6) Å] and C2–O2 [1.167(7) Å] distances in **6** are standard and very close to those of **2** (Table 1) and other carbonyl rhenium complexes.[10a,10d–g,15] In the structure of **6**·EtOH, O–H···O hydrogen-bonding interactions are observed between the dipicolinate oxygen O4 and the hydroxy group of the ethanol crystallization molecule [O99···O4 2.671(8) Å], as well as between two ethanol molecules from adjacent units [O99···O99 2.869(2) Å].

## Electrochemical Studies

Complexes **2**, **3**, **5** and **6** exhibit, by cyclic voltammetry at a Pt electrode in 0.2 M $[nBu_4N][BF_4]/CH_2Cl_2$ solution, a first single-electron reversible (or quasireversible) (for **2** and **5**) or irreversible (for **3** and **6**) oxidation at ${}^{I}E_{1/2}{}^{ox}$ = 0.67 (**2**) and 1.22 (**5**) V or ${}^{I}E_{p}{}^{ox}$ = 0.75 (**3**) and 0.87 (**6**) V vs. SCE (Table 2, Figure 4 for **5**), assigned to the $Re^{I} \rightarrow Re^{II}$ oxidation, followed by a second reversible (for **2** and **3**) or irreversible (for **6**) oxidation at close potentials (1.00 to 1.15 V vs. SCE), most likely caused by the $Re^{II} \rightarrow Re^{III}$ oxidation. A third irreversible oxidation wave is also observed for compounds **2**, **3** and **6** at a higher potential (ca. 1.34–1.43 V vs. SCE). Complex **4** could not be studied by cyclic voltammetry because of its instability in the solvent/electrolyte medium.

For the quasireversible waves, increasing the scan rate from 0.2 to 0.5 or 1.0 $V s^{-1}$ usually led to an enhancement of the degree of reversibility. The oxidation potentials of the neutral complexes **2**, **3** and **6** are lower than the corresponding potentials for the starting compound **1** (${}^{I}E_{1/2}{}^{ox}$ = 0.94, ${}^{II}E_{p}{}^{ox}$ = 1.79 V vs. SCE, measured[6a] under identical experimental conditions). This confirms the stronger electron-donor character of the N- and N,O-ligands in **2**, **3** and **6** relative to ligated $Cl^-$ + $N_2$ or $N_2$ + CO in **1**, in agreement with the π-electron-acceptor character of $N_2$ and CO. The highest oxidation potential is observed for $[Re(4,7\text{-}Ph_2\text{-}phen)(CO)_2(PPh_3)_2]^+$ in **5** (${}^{I}E_{1/2}{}^{ox}$ = 1.22 V vs. SCE) on account of its positive charge.

In addition, compounds **5** and **6** show (Table 2, Figure 4 for **5**) one reversible reduction wave at an unusually high potential (${}^{I}E_{1/2}{}^{red}$ = –0.01 and –0.18 V vs. SCE, respec-

 © 2007 Wiley-VCH Verlag GmbH & Co. KGaA, Weinheim 

Table 2. Cyclic voltammetric data for the $Re^{I}$ complexes.[a]

| | ${}^{I}E_{1/2}^{ox}$ (${}^{I}E_{p}^{ox}$) | ${}^{II}E_{1/2}^{ox}$ (${}^{II}E_{p}^{ox}$) | (${}^{III}E_{p}^{ox}$) | ${}^{I}E_{1/2}^{red}$ | ${}^{II}E_{1/2}^{red}$ |
|---|---|---|---|---|---|
| **1**[b] | 0.94 | (1.79) | – | – | – |
| **2**[c] | 0.67 | 1.00 | (1.41) | – | – |
| **3**[d] | (0.75)[e] | 1.00 | (1.34) | – | – |
| **5**[f] | 1.22 | – | – | –0.01 | –1.21 |
| **6** | (0.87) | (1.15)[e] | (1.43) | –0.18 | –0.57 |

[a] Values given in V ± 0.02 vs. SCE ($CH_2Cl_2$/[$n$Bu$_4$N][$BF_4$], $v$ = 0.2 V s$^{-1}$, for further details see Exp. Sect.); $E_{1/2}$ corresponds to half-wave potential of reversible or quasireversible wave; peak potentials ($E_p$) for irreversible waves are given in brackets. [b] Included for comparison from ref.[6a] [c] Two new reduction waves at $E_p^{red}$ = –0.30 V and $E_{1/2}^{red}$ = –0.79 V (not observed in initial oxidation and reduction scans) appeared over time, conceivably caused by decomposition products. [d] Two new reduction waves at $E_{1/2}^{red}$ = –0.21 V and $E_{1/2}^{red}$ = –0.70 V (not observed in initial oxidation and reduction scans) appeared over time, conceivably caused by decomposition products. [e] This wave becomes quasireversible at higher scan rates ($v$ = 0.5 or 1.0 V s$^{-1}$). [f] An additional wave was observed at $E_p^{ox}$ = 0.97 V as a result of the oxidation of the counterion [$BPh_4$]$^-$.

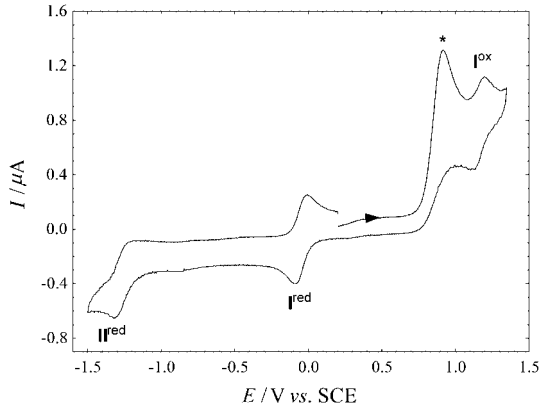


Figure 4. Cyclic voltammogram of [Re(4,7-$Ph_2$-phen)(CO)$_2$($PPh_3$)$_2$]-[$BPh_4$] (**5**) ($8.5 \times 10^{-4}$ mol L$^{-1}$), in 0.2 M [$n$Bu$_4$N][$BF_4$]/$CH_2Cl_2$, at a Pt working electrode and at a scan rate of 0.2 V s$^{-1}$; * wave due to the oxidation of the counterion [$BPh_4$]$^-$.

tively), followed by a second quasireversible reduction wave at ${}^{II}E_{1/2}^{red}$ = –1.21 (**5**) and –0.57 (**6**) V vs. SCE. The evidence for considering the wave at $E_{1/2}$ = –0.01 V vs. SCE in compound **5** as a reduction wave is apparent from its position in the $I$ (current) scale in the cyclic voltammogram (Figure S1 in the Supporting Information). Further proof is provided by controlled potential electrolysis (CPE) at a potential slightly lower than that of $I^{red}$ (i.e., at –0.30 V), which led to a colour change of solution (i.e., from deep brown to clear green), while neither alteration in colour was detected nor charge was measured upon attempted CPE at a potential above that of the same wave.

According to literature data for other $Re^{I}$ compounds with aromatic N-heterocycle ligands[7b,19–22] (e.g., [{ReCl(CO)$_3$}$_2$(ddpq)] {ddpq = 6,7-dimethyl-2,3-bis(2-pyridyl)quinoxaline}, [Re(bpa)(bqu)(CO)$_3$]$^+$ {bpa = 1,2-bis(4-pyridyl)ethane, bqu = 2,2′-biquinoline}, [Re(bpy)(4,4′-bpy)(CO)$_3$]$^+$ {bpy = 2,2′-bipyridine, 4,4′-bpy = 4,4′-bipyridine}, etc.),[19,20] the waves (one or two) observed at less negative potentials (i.e., from –0.2 to –1.1 V vs. SCE) are expected to correspond to N,N(N,O)-ligand-centred reductions, whereas the waves at more negative potentials can be assigned to the $Re^{I} \rightarrow Re^{0}$ reduction. Although our measured less-negative potentials are considerably higher than most of those in the literature, they are comparable to, for example, $E_{1/2}^{red}$ = –0.24 V vs. SCE reported for a ligand-centred process in [{Re(CO)$_3$(CH$_3$CN)}$_2$(ppz)]$^{2+}$ (ppz = 4′,7′-phenanthrolino-5′,6′:5,6-pyrazine).[20] However, one should mention that the free 4,7-$Ph_2$-phen species does not show any waves in the window from –2.0 to +2.0 V vs. SCE.

The possible ligand-centred character of the $I^{red}$ wave (Figure 4) is also supported by the UV/Vis spectrum of **5** recorded in $CH_2Cl_2$ solution, which reveals the presence of a rather broad and intense ($\varepsilon \approx 9200$ L mol$^{-1}$ cm$^{-1}$) band with a maximum at ca. 400 nm, most likely related to a metal-to-ligand charge-transfer (MLCT) process and in agreement with reported data for $Re^{I}$ systems with polypyridyl ligands.[7b,20–22] For example, MLCT bands with a rather close absorption maximum and intensity have been observed for [Re(bpy)(py)(CO)$_2${P(OEt)$_3$}][$PF_6$][7b] (bpy = 2,2′-bipyridine, py = pyridine) ($\lambda_{max}$ = 397 nm), [Re(bpy)(CO)$_2$($PPh_3$)$_2$][$PF_6$][7b] ($\lambda_{max}$ = 401 nm), [Re{(CF$_3$)$_2$-bpy}(CO)$_2${P(OEt)$_3$}$_2$][$PF_6$][7b] {(CF$_3$)$_2$bpy = 4,4′-bis(trifluoromethyl)bipyridine} ($\lambda_{max}$ = 404 nm) and [ReCl(bppz)-(CO)$_3$][20] {bppz = 2,3-bis(2-pyridyl)pyrazine} ($\lambda_{max}$ = 417 nm).

The measured first oxidation potential (upon conversion to the NHE scale) for the rhenium(I) complex [Re(4,7-$Ph_2$-phen)(CO)$_2$($PPh_3$)$_2$]$^+$ in **5** (${}^{I}E_{1/2}^{ox}$ = 1.22 V vs. SCE, i.e., 1.22 + 0.245[11] = 1.47 V vs. NHE) was applied to calculate the electrochemical Lever $E_L$ parameter[11,23] for the 4,7-$Ph_2$-phen ligand according to the Lever's equation (1), valid for octahedral complexes, where $\sum E_L$ is the sum of the $E_L$ values for all the ligands, and $S_M$ and $I_M$ are standard parameters dependent on the metal redox couple, spin state and stereochemistry.[11]

$$E = S_M(\sum E_L) + I_M, \text{ V vs. NHE} \quad (1)$$

Thus, applying the corresponding $S_M$ = 0.76 and $I_M$ = –0.95 V vs. NHE values for the $Re^{II/I}$ couple[11b] and the $E_L$ values for the CO and $PPh_3$ ligands ($E_L$ = 0.99 and 0.39 V vs. NHE, respectively),[11a,23] we have estimated, for the first time, the value of the electrochemical Lever ligand parameter, $E_L$ = 0.21 V vs. NHE, for each binding arm of the 4,7-$Ph_2$-phen ligand. This value is comparable to those previously established[11a,23] for monodentate 1,10-phenanthroline ($E_L$ = 0.26 V vs. NHE) and 4,7-dimethyl-1,10-phenanthroline ($E_L$ = 0.23 V vs. NHE) ligands.

## Conclusions

This study shows that the mixed dinitrogen-dicarbonyl complex [ReCl(N$_2$)(CO)$_2$($PPh_3$)$_2$] (**1**) constitutes a convenient starting material for the synthesis of new low-oxidation-state Re complexes bearing N-, N,N- or N,O-ligands with unsaturated N-heterocycle groups coordinated to {Re(CO)} or {Re(CO)$_2$} centres. It is thus possible to open

 © 2007 Wiley-VCH Verlag GmbH & Co. KGaA, Weinheim 

a suitable entry to mono- and dicarbonyl Re complexes with such types of ligands, allowing the extension to the $\{Re(CO)_n\}$ ($n$ = 1 or 2) centres of the rich coordination chemistry that is being developed for complexes with the tricarbonyl $\{Re(CO)_3\}$ site[8] which has found applications in various fields such as nuclear medicine, pharmacology, photoluminescent materials, supramolecular chemistry and catalysis.[7a,9]

It is also necessary to mention that the axial bisphosphane *trans*-$\{Re(PPh_3)_2\}^+$ core in complex **1** remains during the substitution reactions which involve only the equatorial $N_2$/CO/$Cl^-$ ligands. The observed behaviour can be accounted for by a combination of various factors, namely the usual lability of the dinitrogen ligand (a rather weak σ-electron donor),[24] the labilization of the chloro ligand upon loss of $N_2$ (a π-electron acceptor that, when *trans* to $Cl^-$, enhances the electron release from the latter to the metal), the strong *trans* influence of the effective π-acceptor CO ligands in *trans* position (with their resulting mutual labilization), the protic-acid character of the new ligand precursor and the chelating effect of a possible bidentate new ligand.

Hence, on reactions of **1** with acidic N-heterocycle ligands (pyrazole or dipicolinic acid, reactions 1 and 5, respectively), $N_2$ and $Cl^-$ are the replaced ligands (the substitution of the latter being assisted by protonation), whereas the reactions of **1** with nonacidic and nonchelating N-heterocycle ligands (3,5-dimethylpyrazole and quinoline, reactions 2 and 3, respectively) occur by displacement of $N_2$ and one CO ligand. Chelation of the new ligand(s) leads to CO *trans*-to-*cis* isomerization with the formation of *cis*-dicarbonyl products (reactions 1, 4 and 5) from the *trans*-dicarbonyl starting complex **1**. However, *cis*- to *trans*-Cl/CO isomerization can occur (reaction 3) with a nonchelating bulky ligand, resulting in a particularly favourable π-donor/π-acceptor interaction between the former ligands (compound **4**).

The synthetic significance of those observations, namely in terms of selectivity, deserves further exploration, by taking advantage of the versatile structural/electronic features of the mixed $N_2$/CO complex **1** as demonstrated in this study.

## Experimental Section

### General Materials and Procedures

All synthetic work was performed under dinitrogen using standard Schlenk techniques. The solvents were dried and degassed by standard methods. Potassium perrhenate (Merck), triphenylphosphane (Aldrich), benzoylhydrazine (Aldrich), carbon monoxide (Air Products), pyrazole (Aldrich), 3,5-dimethylpyrazole (Aldrich), quinoline (Merck), 4,7-diphenyl-1,10-phenanthroline (Aldrich), sodium tetraphenylborate (Aldrich) and 2,6-pyridinedicarboxylic acid (Aldrich) were obtained from commercial sources and used as received. $[ReCl(N_2)(CO)_2(PPh_3)_2]$ (**1**) was prepared by a published method.[1g]

C, H and N elemental analyses were carried out by the Microanalytical Service of the Instituto Superior Técnico. The FAB mass spectra were obtained with a Trio 2000 instrument by bombarding 3-nitrobenzyl alcohol (*m*-NBA) matrices of the samples with 8 keV (ca. 1.18 $10^{15}$ J) Xe atoms. Mass calibration for data system acquisition was achieved using CsI. Infrared spectra (4000–400 $cm^{-1}$) were recorded with a Jasco FT/IR-430 instrument in KBr pellets. $^1H$-, $^{31}P\{^1H\}$- and $^{13}C\{^1H\}$ NMR spectra were measured with a Varian UNITY 300 spectrometer at ambient temp. The $^{31}P$ chemical shifts are relative to external 85% $H_3PO_4$ aqueous solution. UV/Vis spectra were recorded with a Jasco model 7800 UV/Vis spectrophotometer.

The electrochemical experiments were carried out with an EG&G PAR 273A potentiostat/galvanostat connected to a personal computer through a GPIB interface. Cyclic voltammetry (CV) studies were undertaken in a two-compartment three-electrode cell, at platinum-wire working electrode (d = 0.5 mm) and counter electrodes, in 0.2 M $[nBu_4N][BF_4]/CH_2Cl_2$ solution. A Luggin capillary connected to a silver-wire pseudoreference electrode was used to control the working electrode potential. Controlled potential electrolysis (CPE) experiments were carried out in electrolyte solutions with the mentioned composition, in a two-compartment three-electrode cell with platinum-gauze working electrode and counter electrodes in compartments separated by a glass frit; a Luggin capillary, probing the working electrode, was connected to a silver-wire pseudoreference electrode. The CPE experiments were monitored regularly by cyclic voltammetry, thus assuring that no significant potential drift occurred along the electrolyses. The oxidation potentials of the complexes were measured by CV in the presence of ferrocene as the internal standard, and the redox potential values are quoted relative to the SCE by using the $[Fe(\eta^5\text{-}C_5H_5)_2]^{0/+}$ ($E_{1/2}^{ox}$ = 0.525 V vs. SCE) redox couple in 0.2 M $CH_2Cl_2$/$[Bu_4N][BF_4]$ solution.[25] The obtained potentials vs. SCE can be converted into the NHE scale by addition of 0.245 V.[11]

**$[Re(pz)(Hpz)(CO)_2(PPh_3)_2]$ (2):** A mixture of **1** (50 mg, 0.060 mmol) and pyrazole (41 mg, 0.60 mmol) was refluxed in MeOH (20 mL) for 2 d to produce a brown suspension. It was filtered off, washed with MeOH (3 × 10 mL), $C_6H_6$ (3 × 5 mL) and $Et_2O$ (3 × 10 mL) and dried in vacuo to yield complex **2** as a pale-yellow microcrystalline solid. Yield: 78% (42 mg), based on **1**. Further purification of **2** can be achieved by recrystallization from a $CH_2Cl_2/C_6H_6$/EtOH mixture. $C_{44}H_{36}N_4O_2P_2Re$ (901.9): calcd. C 58.59, H 4.13, N 6.21; found C 58.27, H 4.21, N 5.89. FAB-MS(+): $m/z$ = 903 $[M + H]^+$, 835 $[M – pz]^+$, 807 $[M – pz – CO]^+$, 778 $[M – Hpz – 2CO]^+$, 767 $[M – pz – Hpz]^+$, 739 $[M – pz – Hpz – CO]^+$, 709 $[Re(PPh_3)_2 – 2H]^+$, 613 $[M – PPh_3 – CO + H]^+$, 449 $[RePPh_3]^+$. IR (KBr): $\tilde{\nu}$ = 3317 (s br) ν(NH), 3148 (w) $\nu_{as}$(CH) and 3055 (w) $\nu_s$(CH), 2032 (m), 1924 (s) and 1841 (s) ν(CO), 743 (s) and 697 (s) ν(PPh) $cm^{-1}$. $^1H$ NMR ($CDCl_3$): $\delta$ = 11.26 (s br, 1 H, N*H*), 7.81 [m, 2 H, pz*H*(3/5)], 7.68–7.50 (m, 12 H, $PPh_3$), 7.45–7.30 (m, 18 H, $PPh_3$), 6.81 [d, $J$ = 2.0 Hz, 2 H, pz*H*(3/5)], 5.88 [t, $J$ = 2.1 Hz, 2 H, pz*H*(4)] ppm. $^{13}C\{^1H\}$ NMR ($CDCl_3$): $\delta$ = 202.86 and 202.04 (*C*O), 142.15 (pz*C*), 134.75–134.30 (m, $PPh_3$), 133.91 (pz*C*), 129.77 (d, $J_{CP}$ = 9.4 Hz, $PPh_3$), 128.70–128.35 (m, $PPh_3$), 107.61 (pz*C*) ppm. $^{31}P\{^1H\}$ NMR ($CDCl_3$): $\delta$ = 20.75 (s) ppm. X-ray-quality crystals of **2** were grown by slow evaporation at 5 °C of a $CH_2Cl_2/C_6H_6$/EtOH solution of **2**.

**$[ReCl(3,5\text{-}Me_2\text{-}Hpz)_2(CO)(PPh_3)_2]$ (3):** A mixture of **1** (50 mg, 0.060 mmol) and 3,5-dimethylpyrazole (58 mg, 0.60 mmol) was refluxed in MeOH (20 mL) for 2.5 d to produce a brown-yellow cloudy solution. The solid was filtered off, washed with MeOH (3 × 10 mL) and $Et_2O$ (3 × 10 mL) and dried in vacuo to yield complex **3** as a yellow microcrystalline solid. Further purification of **3** can be achieved by recrystallization from a $C_6H_6$/EtOH(MeOH)

 © 2007 Wiley-VCH Verlag GmbH & Co. KGaA, Weinheim 

solution. Yield: 67% (39 mg), based on **1**. $C_{47}H_{46}ClN_4OP_2Re$ (966.5): calcd. C 58.41, H 4.80, N 5.80; found C 58.08, H 4.56, N 5.50. FAB-MS(+): *m*/*z* = 966 $[M]^+$, 834 $[M - \{3,5\text{-}Me_2\text{-}Hpz\} - Cl - H]^+$, 802 $[M - 2\{3,5\text{-}Me_2\text{-}Hpz\} + CO]^+$, 774 $[M - 2\{3,5\text{-}Me_2\text{-}Hpz\}]^+$, 746 $[M - 2\{3,5\text{-}Me_2\text{-}Hpz\} - CO]^+$, 739 $[M - 2\{3,5\text{-}Me_2\text{-}Hpz\} - Cl]^+$, 704 $[M - PPh_3]^+$, 668 $[M - PPh_3 - Cl - H]^+$, 640 $[M - PPh_3 - Cl - CO - H]^+$, 608 $[M - PPh_3 - \{3,5\text{-}Me_2\text{-}Hpz\}]^+$, 580 $[M - PPh_3 - \{3,5\text{-}Me_2\text{-}Hpz\} - CO]^+$, 531 $[M - PPh_3 - \{3,5\text{-}Me_2\text{-}Hpz\} - Ph]^+$, 512 $[M - PPh_3 - 2\{3,5\text{-}Me_2\text{-}Hpz\}]^+$, 503 $[M - PPh_3 - \{3,5\text{-}Me_2\text{-}Hpz\} - CO - Ph]^+$, 484 $[M - PPh_3 - 2\{3,5\text{-}Me_2\text{-}Hpz\} - CO]^+$, 407 $[M - 2PPh_3 - Cl - 2H]^+$, 329 $[M - PPh_3 - 2\{3,5\text{-}Me_2\text{-}Hpz\} - CO - 2Ph - H]^+$. IR (KBr): $\tilde{\nu}$ = 3222 (s) ν(NH), 3059 (w) $\nu_{as}$(CH), 3002 (w) and 2925 (w) $\nu_s$(CH), 1922 (s) and 1839 (s) ν(CO), 1571 (m) ν(C=N), 746 (m) and 695 (s) ν(PPh) $cm^{-1}$. $^1H$ NMR ($CDCl_3$): $\delta$ = 11.06 (s, 2 H, N*H*), 7.65–7.10 (m, 30 H, $PPh_3$), 5.34 (s, 2 H, pz*H*), 1.76–1.56 (m, 12 H, pz$CH_3$) ppm. $^{13}C\{^1H\}$ NMR ($CDCl_3$): $\delta$ = 197.80 (*C*O), 152.44 and 139.74 (pz*C*), 134.90–134.20 (m, $PPh_3$), 129.82 (s, $PPh_3$), 128.60–128.30 (m, $PPh_3$), 107.76 (pz*C*), 15.95 and 11.44 (pz$CH_3$) ppm. $^{31}P\{^1H\}$ NMR ($CDCl_3$): $\delta$ = 21.04 (s) ppm.

**$[ReCl(quin)_2(CO)(PPh_3)_2]$ (4):** Complex **1** (50 mg, 0.060 mmol) was refluxed in a quinoline (0.50 mL) and methanol (20 mL) mixture for 15 h to produce a deep-brown cloudy solution. The solid was filtered off, washed with MeOH (5 × 10 mL) and $Et_2O$ (3 × 10 mL) and dried in vacuo to yield complex **4** as a deep-purple microcrystalline solid. Yield: 70% (43 mg), based on **1**. $C_{55}H_{44}ClN_2OP_2Re$ (1032.6): calcd. C 63.98, H 4.30, N 2.71; found C 63.66, H 4.63, N 2.72. FAB-MS(+): *m*/*z* = 1032 $[M]^+$, 770 $[M - PPh_3]^+$, 641 $[M - PPh_3 - quin]^+$, 613 $[M - PPh_3 - quin - CO]^+$, 484 $[M - PPh_3 - 2quin - CO]^+$. IR (KBr): $\tilde{\nu}$ = 3051 (m) $\nu_{as}$(CH), 3000 (w) $\nu_s$(CH), 1778 (s) ν(CO), 745 (s) and 695 (s) (PPh) $cm^{-1}$. $^1H$ NMR ($CDCl_3$): $\delta$ = 7.71–7.40, 7.33–7.12 and 7.06–6.92 (m, 10 H + 18 H + 16 H, $PPh_3$ + quin*H*) ppm. $^{31}P\{^1H\}$ NMR ($CDCl_3$): $\delta$ = 30.79 (s) ppm. No reliable $^{13}C\{^1H\}$ NMR spectrum could be accumulated because of the gradual decomposition of **4** in $CDCl_3$ or [$D_6$]acetone. Single crystals were grown by slow evaporation at 5 °C of a $CH_2Cl_2$/$Me_2CO$(EtOH) solution of **4**. The proposed formulation of **4** with the *trans*-CO/Cl arrangement was also confirmed by a single-crystal X-ray diffraction analysis, but with a rather high error due to a heavy disorder.

**$[Re(4,7\text{-}Ph_2\text{-}phen)(CO)_2(PPh_3)_2][BPh_4]$ (5):** A mixture of **1** (50 mg, 0.060 mmol) and 4,7-diphenyl-1,10-phenanthroline (60 mg, 0.18 mmol) was refluxed in a MeOH (10 mL) and $C_6H_6$ (20 mL) mixture overnight. The resulting deep-green clear solution was concentrated under reduced pressure to give a green oil which was dissolved in EtOH (15 mL) and treated with an ethanol solution (30 mL) of $Na[BPh_4]$ (205 mg, 0.60 mmol). The obtained deep-green suspension was almost completely dissolved upon addition of acetone (30 mL). The resulting green clear solution was filtered and left to evaporate in air in a beaker at ambient temp. Deep-red crystals formed in a few days from that green solution. They were isolated by filtration, washed gently with $Et_2O$, collected and dried in vacuo to yield compound **5**. Yield: 64% (54 mg), based on **1**. $C_{86}H_{66}BN_2O_2P_2Re$ (1418.4): calcd. C 72.82, H 4.69, N 1.97; found C 72.47, H 4.86, N 2.25. FAB-MS(+): *m*/*z* = 1099 $[M]^+$, 1071 $[M - CO]^+$, 837 $[M - PPh_3]^+$, 808 $[M - PPh_3 - CO - H]^+$, 781 $[M - PPh_3 - 2CO]^+$, 767 $[M - \{4,7\text{-}Ph_2\text{-}phen\}]^+$, 739 $[M - \{4,7\text{-}Ph_2\text{-}phen\} - CO]^+$, 703 $[M - PPh_3 - 2CO - Ph - H]^+$, 625 $[M - PPh_3 - 2CO - 2Ph - 2H]^+$. FAB-MS(–): *m*/*z* = 319 $[BPh_4]^-$. IR (KBr): $\tilde{\nu}$ = 3054 (m br) $\nu_{as}$(CH), 2999 (w) and 2983 (w) $\nu_s$(CH), 1927 (s) and 1852 (s) ν(CO), 744 (s) and 697 (s) (PPh) $cm^{-1}$. $^1H$ NMR ($CDCl_3$): $\delta$ = 7.90–6.40 (m, 66 H, $PPh_3$ + $BPh_4$ + phen*H*) ppm. $^{13}C\{^1H\}$ NMR ($CDCl_3$): $\delta$ = 166.04 and 164.74 (*C*=O), 140.15 (m), 137.08, 133.24 (m), 130.97, 130.18 (d, $J_{CP}$ = 6.0 Hz), 129.32 (m), 126.62 (m), 126.09 (m) and 122.17 ($PPh_3$ + $BPh_4$ + phen*C*) ppm. $^{31}P\{^1H\}$ NMR ($CDCl_3$): $\delta$ = 22.51 (s) ppm. X-ray-quality crystals of **5**·0.5$CH_2Cl_2$ were grown by slow evaporation of an EtOH/$Me_2CO$/$CH_2Cl_2$ solution of **5**.

**$[Re(2\text{-}Me\text{-}dipic)(CO)_2(PPh_3)_2]$ (6):** To a solution of **1** (50 mg, 0.060 mmol) in MeOH (20 mL) and $C_6H_6$ (10 mL) was added an excess of 2,6-pyridinedicarboxylic acid (108 mg, 0.60 mmol), and the reaction mixture was refluxed for 1 d. The resulting deep-orange clear solution was concentrated under reduced pressure to give an orange oil which was treated with MeOH (15 mL). The solid that separated out from the resulting solution was filtered off and discarded. The filtrate was evaporated under reduced pressure giving an orange oily solid to which $Et_2O$ (30 mL) was added to form an orange precipitate. It was filtered off, washed with $Et_2O$ (3 × 10 mL) and dissolved on a filter in $Me_2CO$ (5 mL) to form a deep-orange solution which was taken to dryness under reduced pressure yielding an orange oil. Further addition of $Et_2O$ (30 mL) led to the formation of a solid which was filtered off, washed with $Et_2O$ (3 × 10 mL) and dried in vacuo to give complex **6** as an orange microcrystalline material. Yield: 44% (25 mg), based on **1**. $C_{46}H_{36}NO_6P_2Re$ (946.9): calcd. C 58.35, H 3.83, N 1.48; found C 58.03, H 3.49, N 1.84. FAB-MS(+): *m*/*z* = 947 $[M]^+$, 919 $[M - CO]^+$, 767 $[M - \{2\text{-}Me\text{-}dipic\}]^+$, 739 $[M - \{2\text{-}Me\text{-}dipic\} - CO]^+$, 657 $[M - PPh_3 - CO]^+$, 642 $[M - PPh_3 - CO - Me]^+$, 629 $[M - PPh_3 - 2CO]^+$, 614 $[M - PPh_3 - 2CO - Me]^+$, 505 $[M - PPh_3 - \{2\text{-}Me\text{-}dipic\}]^+$, 447 $[RePPh_3 - 2H]^+$. IR (KBr): $\tilde{\nu}$ = 3058 (m) $\nu_{as}$(CH), 2954 (w) $\nu_s$(CH), 1929 (s) and 1853 (s) ν(CO), 1740 (s) $\nu_{as}$(COOMe), 1692 (s) $\nu_{as}$(COO), 1482 (m) $\nu_s$(COO), 1435 (s) $\nu_s$(COOMe), 747 (s) and 696 (s) ν(PPh) $cm^{-1}$. $^1H$ NMR ($CDCl_3$): $\delta$ = 8.59 (t, *J* = 7.9 Hz, 1 H, py*H*), 8.49 (t, *J* = 7.8 Hz, 1 H, py*H*), 8.30 (m, 1 H, py*H*), 7.91–7.32 (m, 30 H, $PPh_3$), 4.19 (s, 3 H, $CH_3$) ppm. $^{13}C\{^1H\}$ NMR ($CDCl_3$): $\delta$ = 208.54 and 189.24 (*C*O), 166.31 (*C*OO), 153.53 (*C*OOMe), 140.27, 139.08, 132.37, 131.62 and 127.65 (py*C*), 134.83 (d, $J_{CP}$ = 9.3 Hz), 134.42–134.26 (m), 130.25 and 129.63–128.30 (m, $PPh_3$), 53.91 ($CH_3$) ppm. $^{31}P\{^1H\}$ NMR ($CDCl_3$): $\delta$ = 31.96 (s) ppm. X-ray-quality crystals of **6**·EtOH were grown by slow evaporation at 5 °C of an EtOH/$Me_2CO$ or EtOH/$C_6H_6$ solution of **6**.

**X-ray Crystal Structure Determinations:** The X-ray diffraction data of **2**, **5** and **6** were collected with a Nonius Kappa CCD diffractometer using Mo-$K_\alpha$ radiation. The Denzo-Scalepack[26] program package was used for cell refinements and data reductions. All structures were solved by direct methods using the SHELXS-97,[27] SIR97[28] or SIR2002[29] programs with the WinGX[30] graphical user interface. An empirical absorption correction was applied to all data ($T_{max}/T_{min}$: 0.6242/0.5545, 0.8965/0.5149, 0.5172/0.7256 for **2**, **5** and **6**, respectively) using SORTAV[31] or XPREP in SHELXTL v.6.14–1[32] program. Structural refinements were carried out with SHELXL-97.[33] In **2** the NH hydrogen atom was located from the difference Fourier map and refined isotropically. In **5** one of the phenyl groups in 4,7-$Ph_2$-phen is disordered over two sites with occupancies 0.72 and 0.28. In these groups the aromatic rings were refined with fixed C–C distances of 1.39 Å. Moreover, the disordered $CH_2Cl_2$ solvent molecule was modelled by placing the two chlorines over three sites with equal occupancies. The solvent was partially lost from the structure, and all in all only half a molecule of $CH_2Cl_2$ was introduced into the structure. Because of the disorder, $CH_2Cl_2$ was refined only isotropically and the hydrogen atoms were omitted. In **6** the carbon atoms of the EtOH molecule are disordered over two sites with occupancies 0.55 and 0.45. The OH hydrogen atom of EtOH was located from the difference Fourier map but not refined ($U_{iso}$ = 0.12). Other hydro-

 © 2007 Wiley-VCH Verlag GmbH & Co. KGaA, Weinheim 

Table 3. Crystal data and structure refinement details for complexes **2**, **5** and **6**.

| | **2** | **5**·0.5$CH_2Cl_2$ | **6**·EtOH |
|---|---|---|---|
| Empirical formula | $C_{44}H_{37}N_4O_2P_2Re$ | $C_{86.5}H_{67}BClN_2O_2P_2Re$ | $C_{48}H_{42}NO_7P_2Re$ |
| Formula weight | 901.92 | 1460.82 | 992.97 |
| Temperature [K] | 120(2) | 120(2) | 120(2) |
| $\lambda$ [Å] | 0.71073 | 0.71073 | 0.71073 |
| Crystal system | monoclinic | monoclinic | monoclinic |
| Space group | $P2_1/n$ | $P2_1/n$ | $P2_1/n$ |
| $a$ [Å] | 11.5079(2) | 14.7466(3) | 10.0823(2) |
| $b$ [Å] | 16.6886(3) | 14.7938(2) | 11.9229(2) |
| $c$ [Å] | 19.7901(3) | 32.5113(6) | 35.7524(7) |
| $\alpha$ [°] | 90 | 90 | 90 |
| $\beta$ [°] | 99.4790(10) | 97.335(8) | 91.1040(10) |
| $\gamma$ [°] | 90 | 90 | 90 |
| $V$ [Å$^3$] | 3748.81(11) | 7034.6(2) | 4297.01(14) |
| $Z$ | 4 | 4 | 4 |
| $\rho_{calcd.}$ [Mg m$^{-3}$] | 1.598 | 1.379 | 1.535 |
| $\mu$(Mo-$K_\alpha$) [mm$^{-1}$] | 3.371 | 1.862 | 2.955 |
| Number of collected reflections | 40567 | 72404 | 24191 |
| Number of unique reflections | 8585 | 12266 | 7372 |
| $R_{int}$ | 0.0584 | 0.0836 | 0.0586 |
| Final $R_1$,[a] $wR_2$[b] ($I \geq 2\sigma$) | 0.0289, 0.0617 | 0.0430, 0.0926 | 0.0368, 0.0868 |
| $R_1$, $wR_2$ (all data) | 0.0490, 0.0864 | 0.0696, 0.1034 | 0.0525, 0.0947 |
| GOF on $F^2$ | 1.127 | 1.048 | 1.063 |
| Largest diff. peak and hole [e Å$^{-3}$] | 0.844, –2.736 | 1.467, –0.965 | 1.560, –1.088 |

[a] $R_1 = \Sigma||F_o| - |F_c||/\Sigma|F_o|$. [b] $wR_2 = \{\Sigma[w(F_o^2 - F_c^2)^2]/\Sigma[w(F_o^2)^2]\}^{1/2}$.

gen atoms were placed in idealized positions and constrained to ride on their parent atom. The crystallographic data are summarized in Table 3.

CCDC-623918 to -623920 (for **2**, **5**·0.5$CH_2Cl_2$ and **6**·EtOH, respectively) contain the supplementary crystallographic data for this paper. These data can be obtained free of charge from The Cambridge Crystallographic Data Centre via www.ccdc.cam.ac.uk/data_request/cif.

**Supporting Information** (see also the footnote on the first page of this article): Supplementary figure (Figure S1) showing the cyclic voltammogram of **5** initiated by the anodic and cathodic sweep.

## Acknowledgments

This work has been partially supported by the Fundação para a Ciência e a Tecnologia (FCT), Portugal and its POCI 2010 programme (FEDER funded). A. M. K. is grateful to the FCT and the POCTI and POCI programme for a fellowship (BD/6287/01).

[1] a) B. A. MacKay, M. D. Fryzuk, *Chem. Rev.* **2004**, *104*, 385; b) U. Abram, in *Comprehensive Coordination Chemistry* (Eds.-in-Chief: J. A. McCleverty, T. J. Meyer), 2nd ed., Elsevier, Amsterdam, **2003**, vol. 5 (Eds.: E. C. Constable, J. R. Dilworth), ch. 5.3, pp. 271–402; c) A. J. L. Pombeiro, M. F. C. Guedes da Silva, R. H. Crabtree, in *Encyclopedia of Inorganic Chemistry* (Ed.: R. B. King), 2nd ed., Wiley, New York, **2005**, vol. IX, pp. 5499–5516; d) M. D. Fryzuk, S. A. Johnson, *Coord. Chem. Rev.* **2000**, *200–202*, 379; e) M. Hidai, Y. Mizobe, *Chem. Rev.* **1995**, *95*, 1115; f) J. Chatt, J. R. Dilworth, R. L. Richards, *Chem. Rev.* **1978**, *78*, 589; g) J. Chatt, J. R. Dilworth, G. J. Leigh, *J. Chem. Soc., Dalton Trans.* **1973**, 612.

[2] a) N. C. Mosch-Zanetti, S. Kopke, R. Herbst-Irmer, M. Hewitt, *Inorg. Chem.* **2002**, *41*, 3513; b) G. Albertin, S. Antoniutti, E. Bordignon, E. Visentin, *Inorg. Chem.* **2001**, *40*, 5465; c) G. Albertin, S. Antoniutti, A. Bacchi, E. Bordignon, F. Miani, G. Pelizzi, *Inorg. Chem.* **2000**, *39*, 3283; d) R. M. Chin, J. Barrera, R. H. Dubois, L. E. Helberg, M. Sabat, T. Y. Bartucz, A. J. Lough, R. H. Morris, W. D. Harman, *Inorg. Chem.* **1997**, *36*, 3553.

[3] a) A. J. L. Pombeiro, *Inorg. Chem. Commun.* **2001**, *4*, 585; b) A. J. L. Pombeiro, M. F. C. Guedes da Silva, R. A. Michelin, *Coord. Chem. Rev.* **2001**, *218*, 43; c) R. A. Michelin, A. J. L. Pombeiro, M. F. C. Guedes da Silva, *Coord. Chem. Rev.* **2001**, *218*, 75; d) A. J. L. Pombeiro, M. F. C. Guedes da Silva, *J. Organomet. Chem.* **2001**, *617*, 65; e) A. J. L. Pombeiro, R. L. Richards, *Coord. Chem. Rev.* **1990**, *104*, 13; f) R. L. Richards, *Coord. Chem. Rev.* **1996**, *154*, 83; g) A. J. L. Pombeiro, *New J. Chem.* **1994**, *18*, 163; h) J. Chatt, W. Hussain, G. J. Leigh, H. M. Ali, C. J. Pickett, D. A. Rankin, *J. Chem. Soc., Dalton Trans.* **1985**, 1131.

[4] a) M. F. C. Guedes da Silva, J. J. R. Fraústo da Silva, A. J. L. Pombeiro, *Inorg. Chem.* **2002**, *41*, 219; b) M. F. C. Guedes da Silva, M. A. N. D. A. Lemos, J. J. R. Fraústo da Silva, A. J. L. Pombeiro, M. A. Pellinghelli, A. Tiripicchio, *J. Chem. Soc., Dalton Trans.* **2000**, 373; c) M. F. N. N. Carvalho, A. M. Galvao, A. J. L. Pombeiro, *J. Chem. Soc., Dalton Trans.* **2000**, 3393; d) M. F. N. N. Carvalho, M. T. Duarte, A. M. Galvao, A. J. L. Pombeiro, R. Henderson, H. Fuess, I. Svoboda, *J. Organomet. Chem.* **1999**, *583*, 56; e) M. F. C. Guedes da Silva, C. M. P. Ferreira, J. J. R. Fraústo da Silva, A. J. L. Pombeiro, *J. Chem. Soc., Dalton Trans.* **1998**, 4139; f) C. M. P. Ferreira, M. F. C. Guedes da Silva, V. Yu. Kukushkin, J. J. R. Fraústo da Silva, A. J. L. Pombeiro, *J. Chem. Soc., Dalton Trans.* **1998**, 325.

[5] a) A. J. L. Pombeiro, P. B. Hitchcock, R. L. Richards, *J. Chem. Soc., Dalton Trans.* **1987**, 319; b) A. J. L. Pombeiro, M. T. A. R. S. Costa, Y. Wang, J. F. Nixon, *J. Chem. Soc., Dalton Trans.* **1999**, 3755; c) A. Lazzaro, G. Vertuani, P. Bergamini, N. Mantovani, A. Marchi, L. Marvelli, R. Rossi, V. Bertolasi, V. Ferretti, *J. Chem. Soc., Dalton Trans.* **2002**, 2843.

[6] a) A. M. Kirillov, M. Haukka, M. F. C. Guedes da Silva, J. J. R. Fraústo da Silva, A. J. L. Pombeiro, *J. Organomet. Chem.* **2006**, *691*, 4153; b) A. M. Kirillov, M. Haukka, M. F. C. Guedes da Silva, A. J. L. Pombeiro, *Eur. J. Inorg. Chem.* **2005**, 2071; c) A. M. Kirillov, M. Haukka, M. V. Kirillova, A. J. L. Pombeiro, *Adv. Synth. Catal.* **2005**, *347*, 1435.

[7] a) D. Rattat, P. A. Schubiger, H. G. Berke, H. Schmalle, R. Alberto, *Cancer Biother. Radio.* **2001**, *16*, 339; b) K. Koike, J.

 © 2007 Wiley-VCH Verlag GmbH & Co. KGaA, Weinheim 

Tanabe, S. Toyama, H. Tsubaki, K. Sakamoto, J. R. Westwell, F. P. A. Johnson, H. Hori, H. Saitoh, O. Ishitani, *Inorg. Chem.* **2000**, *39*, 2777; c) D. Veghini, S. E. Nefedov, H. Schmalle, H. Berke, *J. Organomet. Chem.* **1996**, *526*, 117; d) J. E. Joachim, C. Apostolidis, B. Kanellakopulos, D. Meyer, B. Nuber, K. Raptis, J. Rebizant, M. L. Ziegler, *J. Organomet. Chem.* **1995**, *492*, 199.

[8] For recent reviews, see: a) I. Santos, A. Paulo, J. D. G. Correia, *Top. Curr. Chem.* **2005**, *252*, 45; b) R. Schibli, P. A. Schubiger, *Eur. J. Nucl. Med. Mol. Imaging* **2002**, *29*, 1529; c) S. S. Sun, A. J. Lees, *Coord. Chem. Rev.* **2002**, *230*, 171; d) D. R. Striplin, G. A. Crosby, *Coord. Chem. Rev.* **2001**, *211*, 163; e) S. S. Sun, A. J. Lees, *J. Am. Chem. Soc.* **2000**, *122*, 8956; f) R. V. Slone, K. D. Benkstein, S. Belanger, J. T. Hupp, I. A. Guzei, A. L. Rheingold, *Coord. Chem. Rev.* **1998**, *171*, 221.

[9] a) D. Rattat, A. Verbruggen, H. Schmalle, H. Berke, R. Alberto, *Tetrahedron Lett.* **2004**, *45*, 4089; b) G. Tamagnan, R. M. Baldwin, N. S. Kula, R. J. Baldessarini, R. B. Innis, *Bioorg. Med. Chem. Lett.* **2000**, *10*, 1113; c) E. Schutte, J. B. Helms, S. M. Woessner, J. Bowen, B. P. Sullivan, *Inorg. Chem.* **1998**, *37*, 2618; d) D. Nietlispach, D. Veghini, H. Berke, *Helv. Chim. Acta* **1994**, *77*, 2197.

[10] a) G. A. Ardizzoia, G. La Monica, A. Maspero, M. Moret, N. Masciocchi, *Eur. J. Inorg. Chem.* **1998**, 1503; b) G. A. Ardizzoia, G. La Monica, A. Maspero, N. Masciocchi, M. Moret, *Eur. J. Inorg. Chem.* **1999**, 1301; c) N. M. Iha, G. Ferraudi, *J. Chem. Soc., Dalton Trans.* **1994**, 2565; d) K. K.-W. Lo, K. H.-K. Tsang, W.-K. Hui, N. Zhu, *Chem. Commun.* **2003**, 2704; e) E. Hevia, J. Perez, V. Riera, D. Miguel, *Organometallics* **2002**, *21*, 1966; f) A. A. Marti, G. Mezei, L. Maldonado, G. Paralitici, R. G. Raptis, J. L. Colon, *Eur. J. Inorg. Chem.* **2005**, 118; g) K. K.-W. Lo, W.-K. Hui, D. C.-M. Ng, K.-K. Cheung, *Inorg. Chem.* **2002**, *41*, 40; h) O. S. Wenger, L. M. Henling, M. W. Day, J. R. Winkler, H. B. Gray, *Inorg. Chem.* **2004**, *43*, 2043; i) M. L. Creber, K. G. Orrell, A. G. Osborne, V. Sik, M. B. Hursthouse, M. E. Light, *Polyhedron* **2001**, *20*, 1973.

[11] a) A. B. P. Lever, *Inorg. Chem.* **1990**, *29*, 1271; b) A. B. P. Lever, *Inorg. Chem.* **1991**, *30*, 1980.

[12] *SDBSWeb:* http://www.aist.go.jp/RIODB/SDBS/ (National Institute of Advanced Industrial Science and Technology).

[13] a) E. C. B. Alegria, L. M. D. R. S. Martins, M. F. C. Guedes da Silva, A. J. L. Pombeiro, *J. Organomet. Chem.* **2005**, *690*, 1947; b) E. Hevia, J. Perez, V. Riera, *Inorg. Chem.* **2002**, *41*, 4673.

[14] a) C. J. Cameron, P. E. Fanwick, M. Leeaphon, R. A. Walton, *Inorg. Chem.* **1989**, *28*, 1101; b) R. Rossi, A. Marchi, A. Duatti, L. Magon, A. Cassellato, R. Graziani, *J. Chem. Soc., Dalton Trans.* **1987**, 2299; c) E. Hevia, J. Perez, V. Riera, D. Miguel, *Organometallics* **2003**, *22*, 257; d) N. Burzlaff, I. Hegelmann, B. Weibert, *J. Organomet. Chem.* **2001**, *626*, 16; e) N. Colthup, L. Daly, S. Wiberley, *Introduction to Infrared and Raman Spectroscopy*, 3rd ed., Academic Press, San Diego, **1990**.

[15] a) L. Wallace, C. Woods, D. P. Rillema, *Inorg. Chem.* **1995**, *34*, 2875; b) M. Angaroni, G. A. Ardizzoia, G. D'Alfonso, G. La Monica, N. Masciocchi, M. Moret, *J. Chem. Soc., Dalton Trans.* **1990**, 1895.

[16] J. E. Huheey, E. A. Keiter, R. L. Keiter, *Inorganic Chemistry: Principles of Structure and Reactivity*, 4th ed., Harper Collins, New York, **1993**.

[17] T. B. Gunnoe, M. Sabat, W. D. Harman, *J. Am. Chem. Soc.* **1998**, *120*, 8747.

[18] a) R. Melenkivitz, J. S. Southern, G. L. Hillhouse, T. E. Concolino, L. M. Liable-Sands, A. L. Rheingold, *J. Am. Chem. Soc.* **2002**, *124*, 12068; b) J. S. Southern, G. L. Hillhouse, A. L. Rheingold, *J. Am. Chem. Soc.* **1997**, *119*, 12406; c) N. W. Hoffman, N. Prokopuk, M. J. Robbins, C. M. Jones, N. M. Doherty, *Inorg. Chem.* **1991**, *30*, 4177; d) R. Rossi, A. Marchi, A. Duatti, L. Magon, U. Casellato, R. Graziani, *J. Chem. Soc., Dalton Trans.* **1988**, 899.

[19] R. Lin, Y. Fu, C. P. Brock, T. F. Guarr, *Inorg. Chem.* **1992**, *31*, 4346, and references therein.

[20] B. J. Yoblinski, M. Stathis, T. F. Guarr, *Inorg. Chem.* **1992**, *31*, 5.

[21] D. J. Stufkens, A. Vlcek Jr, *Coord. Chem. Rev.* **1998**, *177*, 127.

[22] V. W.-W. Yam, K. M.-C. Wong, K.-K. Cheung, *Organometallics* **1997**, *16*, 1729, and references therein.

[23] A list of values of the electrochemical $E_L$ Lever parameter can be found at http://www.chem.yorku.ca/profs/lever/research.html.

[24] A. J. L. Pombeiro, V. Yu. Kukushkin, in *Comprehensive Coordination Chemistry* (Eds.-in-Chief: J. A. McCleverty, T. J. Meyer), 2nd ed., Elsevier, Amsterdam, **2003**, vol. 1 (Ed.: A. B. P. Lever), chapter 1.29, pp. 585–594.

[25] A. J. L. Pombeiro, M. F. C. Guedes da Silva, M. A. N. D. A. Lemos, *Coord. Chem. Rev.* **2001**, *219–221*, 53.

[26] Z. Otwinowski, W. Minor, in *Methods in Enzymology, Volume 276, Macromolecular Crystallography, Part A* (Eds.: C. W. Carter, J. Sweet), Academic Press, New York, USA, **1997**, pp. 307–326.

[27] G. M. Sheldrick, *SHELXS-97, Program for Crystal Structure Determination*, University of Göttingen, Göttingen, Germany, **1997**.

[28] A. Altomare, M. C. Burla, M. C. Camalli, C. Giacovazzo, A. Guagliardi, A. G. G. Moliterni, G. Polidori, R. Spagna, *J. Appl. Crystallogr.* **1999**, *32*, 115.

[29] M. C. Burla, M. Camalli, B. Carrozzini, G. L. Cascarano, C. Giacovazzo, G. Polidori, R. Spagna, *J. Appl. Crystallogr.* **2003**, *36*, 1103.

[30] L. J. Farrugia, *J. Appl. Crystallogr.* **1999**, *32*, 837.

[31] R. H. Blessing, *Acta Crystallogr., Sect. A* **1995**, *51*, 33.

[32] G. M. Sheldrick, *SHELXTL v. 6.14–1*, Bruker Analytical X-ray Systems, Bruker AXS, Inc., Madison, Wisconsin, USA, **2005**.

[33] G. M. Sheldrick, *SHELXL-97, Program for Crystal Structure Refinement*, University of Göttingen, Göttingen, Germany, **1997**.

Received: October 31, 2006
Published Online: March 2, 2007

 © 2007 Wiley-VCH Verlag GmbH & Co. KGaA, Weinheim 

DOI: 10.1002/ejic.200601059

# Zinc, Cadmium and Mercury Dithiocarboxylates: Synthesis, Characterization, Structure and Their Transformation to Metal Sulfide Nanoparticles

**Gotluru Kedarnath,[a] Vimal K. Jain,*[a] Shamik Ghoshal,[a] Gautam K. Dey,[b] Carol A. Ellis,[c] and Edward R. T. Tiekink*[c]**

**Keywords:** Zinc / Cadmium / Mercury / Dithiocarboxylates / Nanoparticles

Reactions of $M(OAc)_2{\cdot}nH_2O$ and $M(OAc)_2$(tmeda) with dithiocarboxylic acids gave $[M(S_2CTol)_2]_n$ (**1**) (M = Zn or Cd; Tol = $C_6H_4Me$-4) and $[M(S_2CAr)_2(tmeda)]$ (**3**) (M = Zn, Cd, Hg; Ar = Ph or Tol), respectively, in high yields as deep-colored crystalline solids. The former are soluble in pyridine to give pyridine adducts $[M(S_2CTol)_2(py)]$ (**2**). These complexes were characterized by elemental analysis, UV/Vis and NMR ($^1H$, $^{13}C$) spectroscopy. The absorptions in the electronic spectra have been assigned to ligand-to-ligand charge-transfer transitions. The crystal and molecular structures of the monomeric species $[Zn(S_2CTol)_2(py)]$ (**2**), $[Zn(S_2CPh)_2(tmeda)]$ (**3a**), $[Zn(S_2CTol)_2(tmeda)]$ (**3b**) and $[Cd(S_2CTol)_2(tmeda)]$ (**3d**) have been established by X-ray crystallography. In $[Zn(S_2CTol)_2(py)]$, chelating dithiocarboxylate ligands and pyridine define a coordination geometry intermediate between square pyramidal and trigonal bipyramidal. In each of **3a** and **3b**, tetrahedral $N_2S_2$ coordination geometries are found as the dithiocarboxylate ligands are effectively monodentate; evidence for the greater coordination potential is found for $^-S_2CTol$ over $^-S_2CPh$. Chelating dithiocarboxylate ligands in $[Cd(S_2CTol)_2(tmeda)]$ (**3d**) lead to an octahedral geometry. Thermal behavior has been studied by thermogravimetric analysis. The $[M(S_2CAr)_2(tmeda)]$ complexes underwent a three-step decomposition. Pyrolysis in the temperature range 300–500 °C and solvothermal decomposition in ethylenediamine and hexadecylamine (HDA) gave metal sulfide nanoparticles. The MS (M = Zn, Cd, Hg) nanoparticles were characterized by XRD, EDAX, absorption/emission spectroscopy and electron microscopy (TEM). Solvothermal decomposition gave hexagonal phases of nanoparticles whereas heating in a furnace gave cubic ZnS and HgS, and hexagonal CdS.

(© Wiley-VCH Verlag GmbH & Co. KGaA, 69451 Weinheim, Germany, 2007)

## Introduction

During the past two decades considerable effort has been made to prepare high-quality monodispersed surface-passivated nanoparticles of II–VI semiconductors.[1] Owing to their quantum-confinement effect, semiconductor nanoparticles exhibit remarkable size- and shape-dependent optical properties which have led to their use in opto-electronic devices[2–6] and biological imaging.[7,8] Although a wide range of synthetic routes have been developed to prepare II–VI semiconductor nanoparticles,[8–11] decomposition of single-source molecular precursors in a suitable solvent has proved quite successful for isolation of high-quality nanoparticles within a narrow size distribution. The area has been dominated by ZnE and CdE (E = S, Se, Te) nanoparticles with limited investigations on HgE. Metal organochalcogenolates, $[M(EPh)_2(tmeda)]$ (M = Zn or Cd; E = S, Se or Te),[12] thiocarboxylates $[M(SCOR)_2L_2]$ (M = Zn or Cd; L = tmeda, 2-lutidene; R = Me, *t*Bu)[13] and $[Cd(SCOPh)_2(2,2'\text{-bipyridine})]$,[14] selenocarboxylates, $[M(SeCOAr)_2(tmeda)]$ (M = Zn or Cd),[15] xanthates $[M(S_2COR)_2]$ (M = Zn or Cd; R = Et, *i*Pr),[16,17] dithiocarbamates $[M(S_2NRR')_2]$ (M = Zn or Cd)[18,19] and dithiophosphinates $[M(S_2P\textit{i}Bu_2)_2]$ (M = Zn, Cd)[20] have been employed for the preparation of ME (M = Zn, Cd; E = S, Se, Te) nanoparticles/thin films.

Chemistry of the zinc-triad 1,1-dithiolates has been of considerable interest due to their numerous applications (e.g., lubricating oil in combustion engine, vulcanization of rubber, floating agents in metallurgy) and diverse structural features.[21–24] Subtle changes in organic substituents on the dithiolate group or in an auxiliary ligand often result in different structural motifs. Thus, molecules with zero- (discrete mono- and bi-nuclear complexes), one-, two- and three-dimensional structural motifs have been isolated and structurally characterized.[24] The 1,1-dithiolate chemistry of the zinc-triad has been dominated by ligands of the type **A**–**D** with relatively little attention to dithiocarboxylates (**E**), Scheme 1.[25–27] With the above in mind, it was consid-

[a] Chemistry Division, Bhabha Atomic Research Centre, Mumbai 400085, India
E-mail: jainvk@apsara.barc.ernet.in
[b] Materials Science Division, Bhabha Atomic Research Centre, Mumbai 400085, India
[c] Department of Chemistry, The University of Texas at San Antonio, One UTSA Circle, Texas 78249–0698, USA
E-mail:Edward.Tiekink@utsa.edu

Supporting information for this article is available on the WWW under http://www.eurjic.org or from the author.

 © 2007 Wiley-VCH Verlag GmbH & Co. KGaA, Weinheim 

ered worthwhile to explore the dithiocarboxylate chemistry of zinc, cadmium and mercury with the aim of isolating new structural motifs and also to develop a new family of promising single-source molecular precursors for the synthesis of MS nanoparticles. Results of this work are described herein.

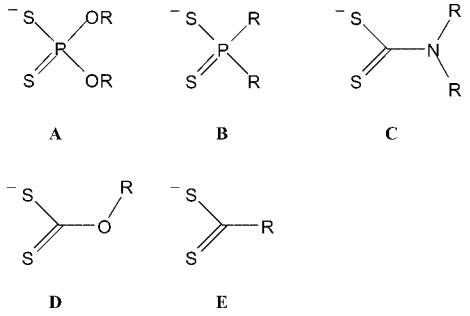


Scheme 1.

## Results and Discussion

Treatment of $M(OAc)_2 \cdot 2H_2O$ with *p*-tolyldithiocarboxylic acid in methanol gave sparingly soluble orange complexes of composition $[M(S_2Ctol)_2]$ (**1**) [M = Zn (**1a**) or Cd (**1b**)]. The complexes dissolved readily in pyridine solution, with concomitant formation of the corresponding pyridine adducts $[Zn(S_2CTol)_2(py)]$ (**2**). The reaction of $[M(OAc)_2$-(tmeda)] with dithiocarboxylic acid in benzene afforded deep-colored complexes of the general formula, $[M(S_2COAr)_2(tmeda)]$ (**3**) [Equation (1)].

$$[M(OAc)_2(tmeda)] + 2\ ArCS_2H \rightarrow [M(S_2CAr)_2(tmeda)] + 2\ AcOH\ldots \quad (1)$$

**3**

| M | Ar | |
|---|---|---|
| Zn | Ph | **3a** |
| Zn | Tol | **3b** |
| Cd | Ph | **3c** |
| Cd | Tol | **3d** |
| Hg | Ph | **3e** |
| Hg | Tol | **3f** |

The electronic spectra of these complexes in dichloromethane solution displayed two (Ar = Ph) and three (Ar = Tol) absorption bands and are assigned for transitions in thiocarbonyl group. The electronic spectra of metal dithiocarboxylates have been reported to display characteristic absorption maxima in the region 250–550 nm attributable to π–π* and n–π* transitions.[28] The $^1H$ NMR spectra exhibited characteristic peaks due to tmeda and dithiolate ligand protons. The absence of singlets ascribed to the SH proton in the spectra indicate deprotonation of the acid. The $NMe_2$ and $NCH_2$ protons resonances appeared as singlets in the ranges 2.39–2.65 and 2.57–2.73 ppm, respectively. The resonance due to 2,6-protons of the aryl ring are deshielded with reference to the free ligand. The $^{13}C\{^1H\}$ NMR spectra showed singlets for $NMe_2$ and $NCH_2$ carbon atoms of tmeda at ca. 46.0 ppm and ca. 56.5 ppm, respectively. The resonance due to thiocarbonyl carbon (C=S) is deshielded (<20 ppm) on complexation, deshielding being greater in cadmium complexes than the corresponding zinc derivatives.

### Structural Characteristics

The molecular structure of $[Zn(S_2CTol)_2(py)]$ (**2**) is represented in Figure 1 (a). The molecule is disposed about a crystallographic twofold axis which bisects the pyridine molecule and contains the zinc atom. The zinc atom is five-coordinate within a $NS_4$ donor set defined by two asymmetrically chelating dithiocarboxylate ligands and the pyridine-N atom. The Zn–S1 and Zn–S2 bond lengths are 2.3499(9) and 2.6046(11) Å, respectively and this asymmetry is reflected in the associated C–S distances so that S1–C1 is significantly longer than S2–C2, i.e., 1.716(3) and 1.679(3) Å,

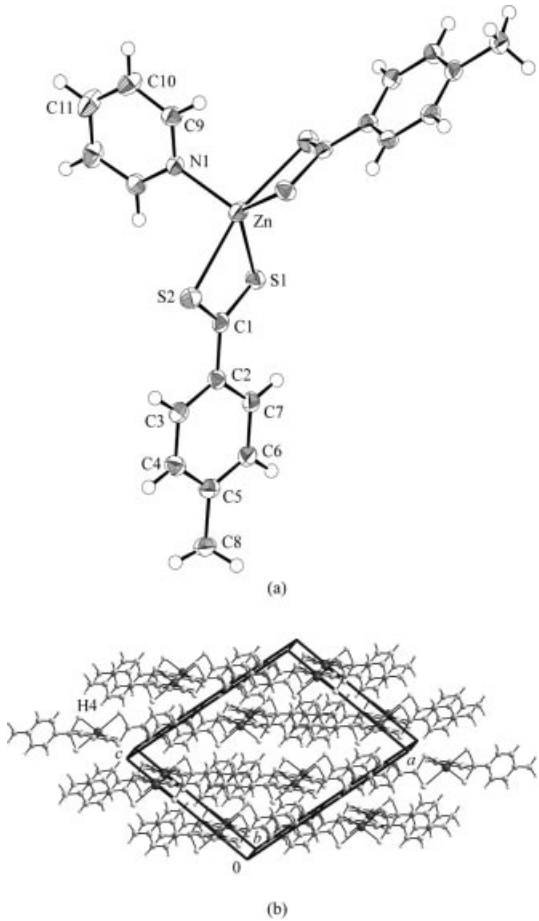


Figure 1. (a) Molecular structure and (b) unit cell contents for $[Zn(S_2CTol)_2(py)]$ (**2**).

 © 2007 Wiley-VCH Verlag GmbH & Co. KGaA, Weinheim 

respectively; the Zn–N1 distance is 2.046(3) Å. The dihedral angle between the two $ZnS_2C$ chelate rings is 53.96(7)° and each of these is effectively orthogonal to the pyridine ring, dihedral angle = 79.87(10)°. The range of angles subtended at the zinc atom extends from 72.04(2)°, for the S1–Zn–S2 chelate angle to 164.55(4)°, for S2–Zn–S2$^{i}$; symmetry operation *i*: *–x*, *y*, 1/2 – *z*. The coordination geometry is intermediate between square pyramidal ($\tau$ = 0) and trigonal bipyramidal ($\tau$ = 1) as exemplified in the value of $\tau$ of 0.61.[29] The closely related structure of [Zn($S_2CC_6H_2$-4-OH-3,5-$t$Bu$_2$)$_2$(py)][26] also features an intermediate geometry but one more inclined towards a square-pyramidal geometry as judged by the $\tau$ value of 0.43. The 1,1-dithiolate ligand is not strictly planar, there being a twist about the C1–C2 bond in **2** as seen in the value of –162.7(2)° for the S1/C1/C2/C3 torsion angle. In the crystal structure, Figure 1 (b), molecules pack in layers along (101). The primary contacts within layers are π···π interactions of 3.7202(19) Å between interdigitated C2–C7 rings (symmetry operation: 1/2 – *x*, 1/2 – *y*, *–z*). The interactions between successive layers are of the type C–H···π. Thus, the C4–H···ring centroid (pyridine) distance is 2.88 Å with an angle of 153° subtended at the H4 atom (symmetry operation: 1/2 + *x*, 1/2 + *y*, *z*).

A formal decrease in the coordination number of zinc is found in the structure of [Zn($S_2$CTol)$_2$(tmeda)] (**3b**). The molecule, Figure 2 (a), has twofold symmetry, with the axis bisecting the tmeda ligand and containing zinc atom. The zinc atom is four-coordinate with the $N_2S_2$ coordination geometry defined by chelating tmeda and monodentate dithiocarboxylate ligands. The respective Zn–S1 and Zn–S2 distances are 2.3238(7) and 3.0860(9) Å, and these distances are significantly shorter and longer than the equivalent distances in the pyridine analog, respectively. The asymmetric mode of coordination is reflected in the respective S1–C1 and S2–C1 bond lengths of 1.705(3) and 1.667(3) Å; the Zn–N1 distance is 2.170(2) Å. The range of angles subtended at the tetrahedrally coordinated zinc atom is 84.11(11)°, for the N1–Zn–N1$^{i}$ chelate angle, to 132.46(5)° for S1–Zn–S1$^{i}$; symmetry operation *i*: *–1 – x*, *–y*, *z*. The wider angle is certainly due to the close approach of the S2 atoms. A small twist is apparent between the $S_2C$ and aromatic ring as seen in the S1/C1/C2/C3 torsion angle of 174.88(18)°. In the crystal structure, Figure 2 (b), the molecules form chains along the *c* axis stabilized by $C_{methyl}$–H···π interactions so that the C8–H···ring centroid of C2–C7 distance is 2.88 Å and angle at H of 130° for symmetry operation: –1/2 – *x*, *y*, –1/2 + *z*.

The influence of substituting the $^{-}S_2$CTol ligand by $^{-}S_2$CPh was investigated by examining the crystal and molecular structure of [Zn($S_2$CPh)$_2$(tmeda)] (**3a**). The molecule, Figure 3 (a), has twofold symmetry as described for **3b** but the structures are not isomorphous. To a first approximation, the coordination geometry for both structures is the same. Thus, the zinc atom exists is a distorted tetrahedral geometry defined by a $N_2S_2$ donor set. The Zn–S1 and Zn–S2 distances of 2.3079(12) and 3.2736(14) Å are respectively, shorter and longer than the comparable distances in **3b**. This is reflected in the S1–C1 and S2–C1 distances of

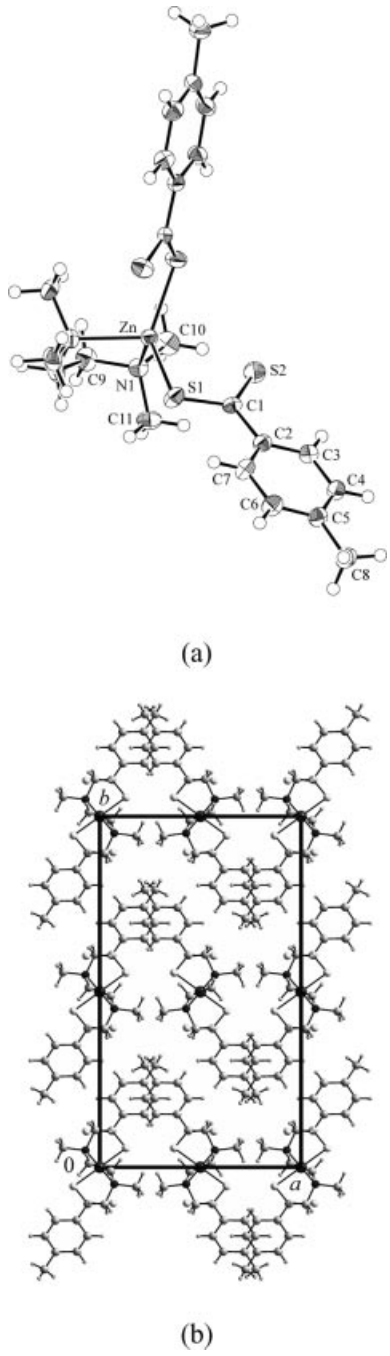


Figure 2. (a) Molecular structure and (b) unit cell contents for [Zn($S_2$CTol)$_2$(tmeda)] (**3b**).

1.725(5) and 1.653(5) Å. The difference in mode of coordination of the two 1,1-dithiolate ligands can be conveniently realized by considering the Δ(Zn–S) and the associated Δ(C–S) values, with greater values been correlated with greater asymmetry. Thus, in **3b** these compute to 0.76 and 0.04 Å, respectively, which are smaller than the values found for **4a** of 0.97 and 0.07 Å, respectively. Further, the Zn–N1 distance of 2.127(4) Å is shorter in the present structure. These results correlate in the expected fashion with the electron-donating ability of the methyl group in the $^{-}S_2$CTol ligand that makes this a comparatively better

 © 2007 Wiley-VCH Verlag GmbH & Co. KGaA, Weinheim 

chelating agent. However, it is noted that there is a significant twist about the C1–C2 bond of the $^{-}S_2CTol$ ligand as seen in the value of 142.8(4)° for the S1/C1/C2/C3 torsion angle, and so the negative inductive effect exerted by the methyl group is not the reason for the different coordinating abilities. By contrast to the previously described crystal structures, in the absence of π···π and C–H···π interactions, C–H···S interactions dominate the crystal packing in **3a**. Thus, in addition to a variety of intramolecular C–H···S interactions, three intermolecular C–H···S interactions may be discerned in the stabilization of the crystal structure. A view of the unit-cell contents is shown in Figure 3 (b). Here, two C–H···S interactions are highlighted and show adjacent C–H atoms of an aromatic ring bridging S1 and S2 atoms of different ligands but of the same molecule. The parameters associated with interaction "(a)" are C6–H···S1$^{i}$ of 3.10 Å with an angle of 164° subtended at the H6 atom, and "(b)" C5–H···S2$^{ii}$ of 3.06 Å and angle 125°; symmetry operations *i*: *–x*, 1 – *y*, 1 – *z* and *ii*: *x*, 1 – *y*, –1/2 + *z*. Orthogonal C8–H···S2$^{iii}$ interactions, i.e., involving methylene-H atoms, of 3.02 Å and angle 173°, link translationally related molecules along the *b*-direction into chains; symmetry operation *iii*: *x*, 1 + *y*, *z*.

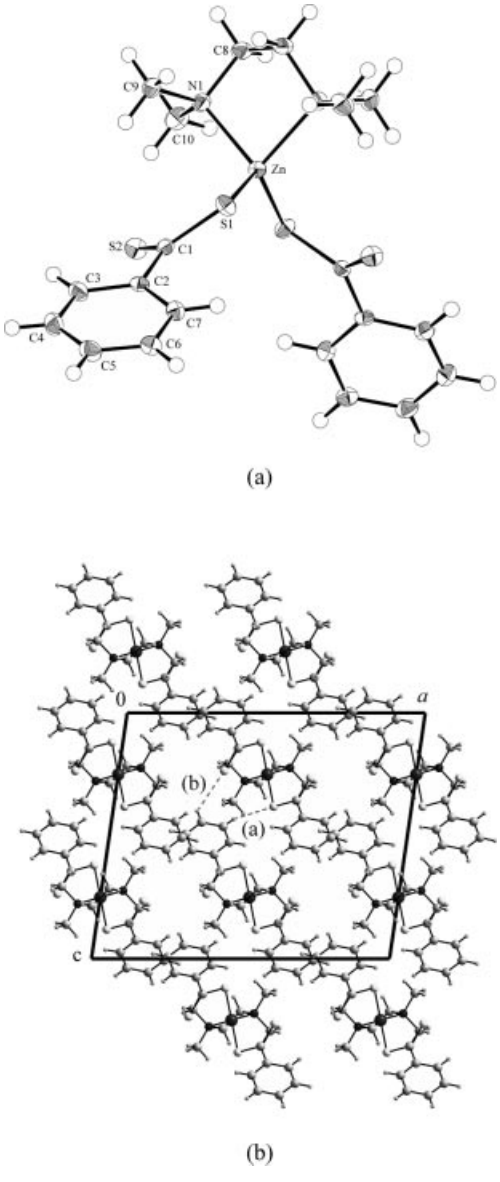


Figure 3. (a) Molecular structure and (b) unit cell contents for [Zn($S_2CPh$)$_2$(tmeda)] (**3a**).

The remaining structure to be described is that of [Cd($S_2CTol$)$_2$(tmeda)] (**3d**), shown in Figure 4. This structure is isomorphous with the zinc analog described above, but the coordination geometry is different. Here, owing to the greater propensity of the larger cadmium atom to increase its coordination number, the coordination geometry is based on a distorted octahedron within a $N_2S_4$ donor set. The dithiocarboxylate ligand forms nearly symmetric Cd–S bonds of 2.6508(8) and 2.7336(9) Å, Δ(Cd–S) is only 0.08 Å; the Cd–N1 bond length is 2.416(2) Å. Distortions from the ideal octahedral geometry may be traced to the acute chelate angles of 66.18(2)°, for S1–Cd–S2, and 76.15(12)°, for N1–Cd–N1$^{i}$; symmetry operation *i*: *–x*, *–y*, *z*. The $CS_2$ and aromatic portions of the 1,1-dithiolate ligand are effectively co-planar as evidenced by the S1/C1/C2/C3 torsion angle of –174.3(2)°. The crystal packing is as described above for **3d** with a C8–H···ring centroid of C2–C7 distance is 2.94 Å and angle at H of 131° for symmetry operation: –1/2 – *x*, *y*, 1/2 + *z*.

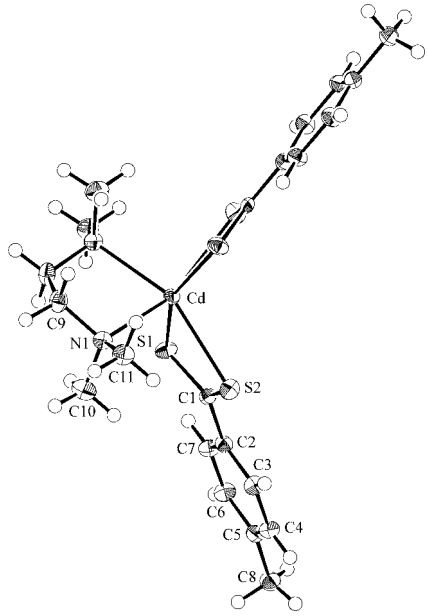


Figure 4. Molecular structure of [Cd($S_2CTol$)$_2$(tmeda)] (**3d**).

## Thermal Studies

TG analyses were carried out to study the thermal behavior and suitability of these complexes for the preparation of metal sulfides. These complexes underwent a three-step decomposition, exemplified for [Zn($S_2CPh$)$_2$(tmeda)] (**3a**) in Figure S1 (see Supporting Information), with the formation of metal sulfides as inferred from the weight loss (e.g. **3a**, calculated weight loss: 80.0% and observed weight loss:

 © 2007 Wiley-VCH Verlag GmbH & Co. KGaA, Weinheim 

76.5%) and confirmed from the XRD patterns of the residues. The onset temperatures are **3a**, 194 °C; **3b**, 178 °C; **3c**, 175 °C; **3d**, 180 °C. The TG curves of the zinc complexes showed slightly separated steps while for the cadmium and mercury derivatives they were poorly resolved indicating instability of the intermediate species. The first step, based on percentage of weight loss (e.g. **3a**, calcd. weight loss for tmeda: 23.8% and obsd. weight loss for first step: 23.8%) has been attributed to the elimination of tmeda. The second and third steps can be characterized for decomposition of dithiocarboxylate groups.

Pyrolysis of $[M(S_2CAr)_2(tmeda)]$ (Ar = Ph, Tol) was carried out at 350 °C under flowing nitrogen for 2 h. In each case metal sulfides (MS; M = Zn, Cd, Hg) were formed as confirmed by their XRD patterns (see Figure 5 and Figures S2–S3 in the Supporting Information) and EDAX analysis (Ar = Ph) (ZnS: calcd 67.1, S 32.9; found Zn 60.2, S 39.8. CdS: calcd Cd 77.8, S 22.2; found Cd 74.3, S 25.7. HgS: calcd. Hg 86.2, S 13.8; found Hg 84.2, S 15.8). The XRD patterns of ZnS and HgS were consistent with the formation of cubic phase of the material,[30,31] whereas CdS was isolated in the hexagonal phase.[32] The pyrolysis of $[Cd(S_2CPh)_2(tmeda)]$ (**3c**), carried out at 300, 400 and 500 °C, also gave hexagonal CdS with the average particle sizes of 18, 36 and 43 nm, respectively, from the Scherrer equation.[33] This indicates that particle size increases with increasing decomposition temperature at a given time. The absorption spectrum of CdS nanoparticles (obtained at 300 °C) showed a broad peak at 505 nm. The emission profile displayed a band at 521 nm, which may be due to surface traps (Figure 6). The particles are of 15 nm in size as estimated from the Brus expression.[34]

Solvothermal decomposition of $[M(S_2CPh)_2(tmeda)]$ (M = Zn, Cd, Hg) was examined in different coordinating solvents, such as ethylenediamine and HDA, to assess their suitability as precursors for the preparation of MS nanoparticles. Pyrolysis of $[M(S_2CPh)_2(tmeda)]$ in refluxing ethylenediamine gave hexagonal phases of MS (from XRD) nanoparticles which were isolated as cream (ZnS), yellow-orange (CdS) and orange (HgS) powders by centrifugation (Figure S4 in the Supporting Information). The particle sizes, estimated from the Scherrer formula,[33] are 34 (ZnS), 29 (CdS) and 103 (HgS) nm. The mercury complex can be pyrolyzed in ethylenediamine at a temperature as low as 57 °C with the formation of hexagonal HgS, having an average particle size (diameter) of 21 nm. The absorption spectra of CdS and HgS nanoparticles (obtained at 122 °C in ethylenediamine) displayed peaks at 480 and 401 nm, respectively. Emission profile (Figure 7) of these CdS nanoparticles exhibited a band at 518 nm (bulk CdS bandgap is 515 nm), which may be due to surface traps.

Nanoparticles prepared under different conditions are known to give different phases and sizes due to different nucleation mechanisms.[35] It is likely that in the present circumstances different nanoparticles are obtained owing to different mechanisms of formation and temperatures. Thus, when the precursor is heated without solvent, initially tmeda is released (as inferred from TG curve) followed by decomposition of the complex, whereas in a coordinating solvent, the coordinating ligand helps in passivating the surface of the particles resulting in different phases.

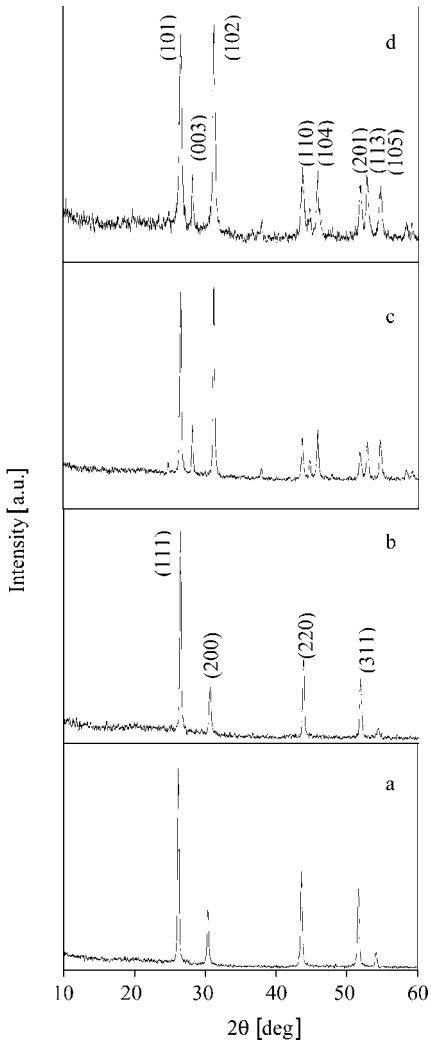


Figure 5. XRD patterns of the HgS nanoparticles prepared under different conditions from $[Hg(SC_2Ph)_2(tmeda)]$; a) heated in a furnace at 250 °C, b) heated in a furnace at 350 °C, c) thermolysis in ethylenediamine at 125 °C and d) thermolysis in HDA at 125 °C.

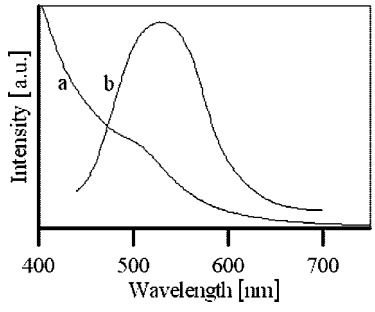


Figure 6. a) Absorption and b) emission spectra of CdS nanoparticles obtained by the pyrolysis of $[Cd(S_2CPh)_2(tmeda)]$ in a furnace at 300 °C under flowing nitrogen.

Pyrolysis of $[Cd(S_2CPh)_2(tmeda)]$ (**3c**) and $[Hg(S_2CPh)_2(tmeda)]$ (**3e**) was also carried out in HDA either at different

 © 2007 Wiley-VCH Verlag GmbH & Co. KGaA, Weinheim 

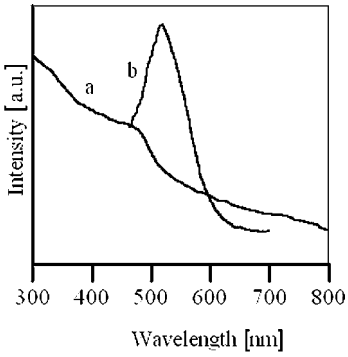


Figure 7. a) Absorption and b) emission spectra of CdS nanoparticles obtained by pyrolysis of $[Cd(S_2CPh)_2(tmeda)]$ in ethylenediamine at 122 °C.

temperatures and/or different concentrations of the precursor. Thermolysis of **3c** in HDA at 188, 188, and 225 °C having precursor/solvent mol ratio of 1:34, 1:55, and 1:55, respectively gave yellow-orange nanoparticles of hexagonal CdS with particle sizes 17, 26, and 34 nm, respectively. Their absorption spectra (Figure 8) in toluene showed exciton peaks at 466, 473 and 503 nm, respectively, which are blue shifted from bulk CdS (515 nm). The emission spectra of the samples prepared at 188 °C of precursor: solvent mol ratio of 1:34 and 1:55 exhibited a broad emission at 523 and 546 nm, respectively. Both absorption and emission maxima are red-shifted with increasing size of the CdS nanoparticles. Pyrolysis of **3e** in HDA (precursor/HDA mol ratio = 1:70) at 125 °C afforded the hexagonal phase of HgS,[36] whereas at 160 °C it gave cubic HgS with particle size of 26 nm and 34 nm (from the Scherrer formula[33]), respectively.

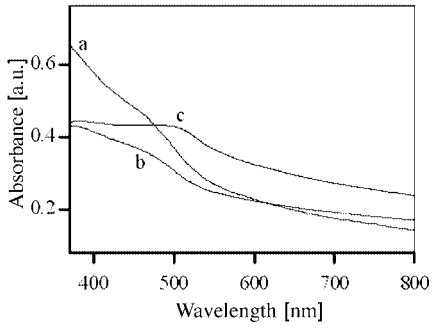


Figure 8. Absorption spectra of CdS nanoparticles obtained by the pyrolysis of $[Cd(S_2CPh)_2(tmeda)]$ with precursor: coordinating solvent mole ratio a) 1:34 (188 °C), b) 1:55 (188 °C) and c) 1:55 (225 °C).

Thermolysis of **3c** in HDA at 188, 188 and 225 °C having precursor/solvent mol ratio of 1:34, 1:55 and 1:55, respectively, gave nanoparticles of hexagonal CdS with different particle sizes. At fixed precursor/solvent mol ratio and duration, particle size increases with increase of temperature. This may be due to the growth of particles that accelerates with increasing temperature.[37] Thermolysis at a fixed duration and temperature with different precursor/solvent mol ratio 1:34 (particle size is 17 nm) and 1:55 (particle size is 26 nm) also gave different particle sizes which may be due to Ostwald ripenening.[38]

### Electron Microscopy

The Selected Area Electron Diffraction (SAED) patterns of MS nanoparticles (Figure 9; Figures S5–S6 in the Supporting Information) obtained by pyrolysis of $[M(S_2CPh)_2(tmeda)]$ in a furnace at 350 °C for M = Zn, and in ethylenediamine for M = Cd (122 °C) and Hg (57 °C) revealed the formation of crystalline material. The diffraction rings in the SAED pattern of ZnS corresponds to the lattice planes (111), (220) and (311) which are assigned for the cubic phase. Concentric rings in the SAED patterns of MS (M = Cd or Hg) have been attributed to the lattice planes (100), (002), (101), (102), (110), (103) and (112) (CdS); (101), (102), (110), (104) and (105) (HgS), respectively, of the hexagonal phases of MS. The phases determined from the SAED and XRD patterns are in agreement. The TEM image of MS showed that ZnS nanoparticles [Figure S5 (Supporting Information)] are spherical in shape with an average diameter of 10 nm, while those of CdS (Figure 9) and HgS (Figure S6, Supporting Information) are nearly spherical with the average size of 20 and 25 nm, respectively. However, in the case of CdS, the presence of a small amount of nanorods of 20–60 nm in length and diameter of 12–20 nm

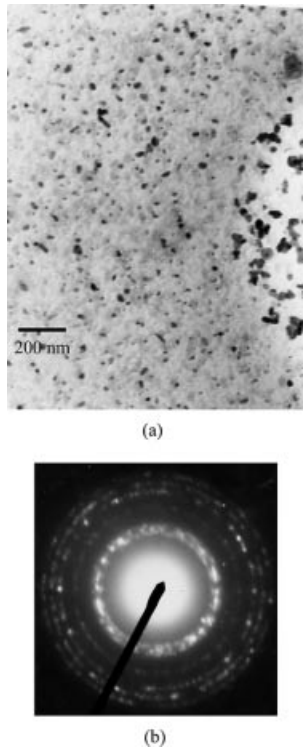


Figure 9. a) TEM image and b) SAED pattern of CdS nanoparticles obtained by pyrolysis of $[Cd(S_2CPh)_2(tmeda)]$ in ethylenediamine at 122 °C. In b) the inner ring is assigned to planes (100), (002) and (101), with the remaining rings from inner to outer corresponding to planes (102), (110), (103) and (112), respectively.

 © 2007 Wiley-VCH Verlag GmbH & Co. KGaA, Weinheim 

was also observed. Co-formation of nanoparticles of different morphology is known and optimization of reaction conditions can lead to the preferential deposition of one form over another.[39] The particle sizes of ZnS and HgS nanoparticles obtained from TEM images are in agreement with the sizes estimated from XRD pattern using the Scherrer formula,[33] whereas the sizes evaluated by these techniques differs for CdS nanoparticles. This inconsistency could be due to the deviation from spherical morphology of the CdS particles.[40]

## Conclusions

Zinc, cadmium and mercury dithiocarboxylate complexes are conveniently prepared in high yields and are stable at room temperature for several months. The homoleptic derivatives are associated in the solid state and are sparingly soluble in non-coordinating solvents. The complexes with neutral donor ligands (e.g., py or tmeda) are discrete monomers. These complexes undergo facile decomposition both in the solid state (furnace heating) and in solution (solvothermal) to yield metal sulfide nanoparticles. The solvothermal decomposition affords nanoparticles at moderately low temperatures which can be as low as 57 °C for the preparation of HgS. Different phases (cubic/hexagonal) can be obtained under different experimental conditions. Thus, owing to the synthetic ease and facile conversion into phase pure metal sulfide nanoparticles, these complexes prove to be reliable precursors for the generation of MS, M = Zn, Cd and Hg.

## Experimental Section

**General:** Elemental analyses were carried out by Radio Chemistry Division of B.A.R.C. $^1$H and $^{13}$C{$^1$H} NMR spectra were recorded with a Bruker DPX-300 NMR spectrometer operating at 300 and 75.47 MHz, respectively. Chemical shifts are relative to internal chloroform resonances at $\delta$ = 7.26 ppm for $^1$H and $\delta$ = 77.0 ppm for $^{13}$C{$^1$H}. UV/Vis absorption spectra were recorded with a Chemito Spectrascan UV 2600 double beam UV/Vis spectrophotometer. Fluorescence spectra were recorded using a Hitachi F-4500 FL spectrofluorometer.

Thermogravimetric analyses (TGA) were carried out with a Nitzsch STA PC-Luxx TG-DTA instrument, which was calibrated with $CaC_2O_4{\cdot}H_2O$. TG curves were recorded at a heating rate of 5 °C min$^{-1}$ under a flow of nitrogen. Solvents were dried and distilled before use under nitrogen. HPLC-grade toluene was used in all experiments involving HDA as a capping agent while methanol was used in case of ethylenediamine as the capping agent. Dimethylformamide was used in pyrolysis experiments for optical studies. X-ray powder diffraction patterns were measured using Cu-$K_\alpha$ radiation with a Philips PW1820 powder diffractometer. EDAX were carried out with a Tescan Vega 2300T/40 instrument. A JEOL-2000FX transmission electron microscope operating at accelerating voltages up to 200 kV was used for TEM studies. The samples for TEM and SAED were prepared by placing a drop of sample dispersed in acetone on a carbon-coated copper grid.

**Materials:** Zinc, cadmium and mercury acetates, *N*,*N*,*N*′,*N*′-tetramethylethylenediamine (tmeda), hexadecylamine (HDA) and ethylenediamine (en), solvents were obtained from commercial sources. [M(OAc)$_2$(tmeda)] (M = Zn, Cd and Hg) were prepared by refluxing metal acetates with an excess of tmeda in dichloromethane under an inert atmosphere for 2 h. Dithiocarboxylic acids, $RCS_2H$ (R = Ph, *p*-Tol) [NMR in $CDCl_3$ for R = Ph, $^1$H NMR: $\delta$ = 6.40 (br. s, SH), 7.39 (br., 2 H, 3,5-H), 7.57 (br., 1 H, 4-H), 8.07 (br., *J* = 8.2 Hz, 2 H, 2,6-H) ppm. $^{13}$C{$^1$H} NMR: $\delta$ = 126.7 (C-3,5), 128.2 (C-4), 133.0 (C-2,6), 143.5 (C-1), 225.2 ($CS_2$) ppm. $^1$H NMR for R = *p*-Tol: $\delta$ = 2.38 (s, *Me*-tol), 4.71 (s, SH), 7.19 (d, *J* = 8.3 Hz, 2 H, 3,5-H), 7.98 (d, *J* = 8.2 Hz, 2 H, 2,6-H) ($C_6H_4$) ppm. $^{13}$C{$^1$H} NMR: $\delta$ = 21.5 (Me), 126.9 (C-2,6), 129.0 (C-3,5), 141.1 (C-4), 144.2 (C-1), 224.6 ($CS_2$) ppm] were prepared by the reaction of RMgBr with $CS_2$ in diethyl ether as described in the literature method.[41]

**Preparation of [Zn(S$_2$CTol)$_2$] (1a):** A methanolic solution of $Zn(OAc)_2{\cdot}2H_2O$ (390 mg, 1.78 mmol) was added to a benzene solution (20 mL) of $HS_2CTol$ (600 mg, 3.56 mmol), with vigorous stirring which continued for 2 h under nitrogen. The solvents were evaporated under vacuum to afford an orange residue (660 mg, 93%), m.p. 175 °C. $C_{16}H_{14}S_4Zn$ (399.94): calcd. C 48.0, H 3.5, S 32.1; found C 47.5, H 3.4, S 32.6. UV/Vis ($CH_2Cl_2$): $\lambda$ = 334, 350 and 392 nm. $^1$H NMR ($CDCl_3$): $\delta$ = 2.43 (s, C*H*$_3$C$_6$H$_4$CS$_2$), 7.22 (d, 7.5 Hz, $C_6H_4$), 8.28 (d, 7.5 Hz, $C_6H_4$) ppm. A portion of the residue was recrystallized as red crystals from dichloromethane containing few drops of pyridine. The $^1$H NMR spectrum of these crystals, [Zn(S$_2$CTol)$_2$(py)] (**2**), showed resonances due to coordinated pyridine: $^1$H NMR: $\delta$ = 2.73 (s, C*H*$_3$C$_6$H$_4$CS$_2$), 7.15 (d, *J* = 7.7 Hz, $C_6H_4$), 7.70 (d, *J* = 7 Hz, $C_6H_4$), 7.31 (br.), 8.38 (br.), 8.64 (br., py); this formulation was confirmed by an X-ray crystallographic study for red crystals grown by the slow evaporation of a dichloromethane solution of the compound.

**Preparation of [Cd(S$_2$CTol)$_2$] (1b):** This was prepared in a manner similar to the zinc complex in 92% yield as a red-orange crystalline solid; m.p. 160 °C. $C_{16}H_{14}CdS_4$ (446.96): calcd. C 43.0, H 3.2, S 28.7; found C 43.0, H 3.1, S 29.4. UV/Vis ($CH_2Cl_2$): $\lambda$ = 321, 345, 360 nm. $^1$H NMR ($CDCl_3$): $\delta$ = 2.37 (s, C*H*$_3$C$_6$H$_4$CS$_2$), 7.12 (br., *C*$_6$*H*$_4$), 8.30 (br., $C_6H_4$) ppm.

**Preparation of [Zn(S$_2$CTol)$_2$(tmeda)] (3b):** Solid [Zn(OAc)$_2$(tmeda)] (590 mg, 1.97 mmol) was added to a benzene solution (20 mL) of $HS_2CTol$ (660 mg, 3.92 mmol), with vigorous stirring, which continued for 2 h under nitrogen. The solvent was removed under vacuum to yield an orange residue which was recrystallzed from dichloromethane/toluene (1:3) mixture to give red crystals (930 mg, 91% yield), m.p. 173 °C. $C_{22}H_{30}N_2S_4Zn$ (516.14): calcd. C 51.2, H 5.9, N 5.4, S 24.9; found C 51.3, H 5.9, N 5.4, S 25.0. UV/Vis ($CH_2Cl_2$): $\lambda$ = 307, 326, 366 nm. $^1$H NMR ($CDCl_3$): $\delta$ = 2.35 (s, C*H*$_3$C$_6$H$_4$CS$_2$), 2.62 (s, $NMe_2$), 2.70 (s, $NCH_2$), 7.10 (d, *J* = 7.4 Hz, $C_6H_4$), 8.36 (d, *J* = 7.3 Hz, $C_6H_4$) ppm. $^{13}$C{$^1$H} NMR ($CDCl_3$): $\delta$ = 21.4 (*C*H$_3$-C$_6$H$_4$CS$_2$), 46.2 ($NMe_2$), 56.9 ($NCH_2$), 127.2, 128.1, 128.7, 142.7 ($C_6H_4$), 245.0 (C=S) ppm. Red crystals for X-ray diffraction were grown by the slow evaporation of a dichloromethane/toluene (3:1) solution of the compound.

**Preparation of [Zn(S$_2$CPh)$_2$(tmeda)] (3a):** This was prepared in a manner similar to [Zn(S$_2$CTol)$_2$(tmeda)] and recrystallized from dichloromethane/toluene as dark-red crystals in 92% yield, m.p. 152 °C (dec). $C_{20}H_{26}N_2S_4Zn$ (488.08): calcd. C 49.2, H 5.4, N 5.7, S 26.3; found C 49.5, H 5.4, N 5.9, S 25.7. UV/Vis ($CH_2Cl_2$): $\lambda$ = 302, 366 nm. $^1$H NMR ($CDCl_3$): $\delta$ = 2.65 (s, $NMe_2$), 2.73 (s, $NCH_2$), 7.30 (t, *J* = 7.7 Hz), 7.47 (t, *J* = 7.2 Hz), 8.44 (d, *J* = 7.4 Hz, Ph) ppm. $^{13}$C{$^1$H} NMR ($CDCl_3$): $\delta$ = 46.1 ($NMe_2$), 56.7 ($NCH_2$), 126.9, 127.3, 131.7, 145.4 (Ph), 245.9 (C=S) ppm. Red crystals for X-ray crystallography were grown by the slow evapora-

 © 2007 Wiley-VCH Verlag GmbH & Co. KGaA, Weinheim 

tion of a dichloromethane/toluene (3:1) solution of the compound.

**Preparation of [Cd($S_2$CPh)$_2$(tmeda)] (3c):** This complex was prepared in a similar fashion to its zinc analog and recrystallized from dichloromethane/hexane or dichloromethane/toluene mixture as orange crystals in 90% yield; m.p. 164 °C (dec). $C_{20}H_{26}CdN_2S_4$ (535.11): calcd. C 44.9, H 4.9, N 5.2, S 24.0; found C 45.4, H 4.8, N 4.8, S 24.5. UV/Vis ($CH_2Cl_2$): $\lambda$ = 304, 368 nm. $^1$H NMR ($CDCl_3$): $\delta$ = 2.60 (s, $NMe_2$), 2.69 (s, $NCH_2$), 7.32 (t, $J$ = 7.8 Hz), 7.48 (t, $J$ = 7.3 Hz), 8.47 (d, $J$ = 7.7 Hz) (Ph) ppm. $^{13}$C{$^1$H} NMR ($CDCl_3$): $\delta$ = 46.0 ($NMe_2$), 56.7 ($NCH_2$), 127.3, 128.2, 131.9, 145.4 (Ph), 249.0 (s, C=S) ppm. Red crystals for X-ray diffraction were grown by the slow evaporation of a chloroform/toluene (3:1) solution of the compound.

**Preparation of [Cd($S_2$CTol)$_2$(tmeda)] (3d):** This was prepared similarly to [Zn($S_2$CTol)$_2$(tmeda)] and recrystallized from dichloromethane/toluene in 90% yield as orange crystals; m.p. 176 °C. $C_{22}H_{30}CdN_2S_4$ (563.16): calcd. C 46.9, H 5.4, N 5.0, S 22.8; found C 47.3, H 5.4, N 5.1, S 23.0. UV/Vis ($CH_2Cl_2$): $\lambda$ = 316, 328, 376 nm. $^1$H NMR ($CDCl_3$): $\delta$ = 2.37 (s, C$H_3$C$_6$H$_4$CS$_2$), 2.57 (s, $NMe_2$), 2.66 (s, $NCH_2$), 7.10 (d, $J$ = 7.8 Hz, $C_6H_4$), 8.39 (d, $J$ = 7.8 Hz, $C_6H_4$) ppm. $^{13}$C{$^1$H} NMR ($CDCl_3$): $\delta$ = 21.4 (*C*H$_3$-C$_6$H$_4$CS$_2$), 46.0 ($NMe_2$), 57.0 ($NCH_2$), 127.7, 128.1, 142.9, 143.4 (Ph), 248.4 (C=S) ppm.

**Preparation of [Hg($S_2$CPh)$_2$(tmeda)] (3e):** The complex was obtained as a brown solid similarly to the previous mercury complex in 90% yield; m.p. 78 °C (dec). $C_{20}H_{26}HgN_2S_4$ (623.29): calcd. C 38.5, H 4.2, N 4.5, S 20.6; found C 37.9, H 3.7, N 4.3, S 21.2. UV/Vis ($CH_2Cl_2$): $\lambda$ = 298 (sh), 310 nm. $^1$H NMR ($CDCl_3$): $\delta$ = 2.43 (s, $NMe_2$), 2.66 (s, $NCH_2$), 7.38 (t, $J$ = 7 Hz), 7.56 (t, $J$ = 7.2 Hz), 8.19 (br., Ph) ppm. $^{13}$C{$^1$H} NMR ($CDCl_3$): $\delta$ = 45.2 ($NMe_2$), 56.2 ($NCH_2$), 126.9, 127.9, 132.7, 144.3 (Ph) ppm; the resonance due to C=S was not resolved.

**Preparation of [Hg($S_2$CTol)$_2$(tmeda)] (3f):** This was prepared similarly to its zinc, cadmium analogs as a brown solid in 91%; m.p. 112 °C. $C_{22}H_{30}HgN_2S_4$ (651.34): calcd. C 40.6, H 4.6, N 4.3, S 19.7; found C 40.1, H 4.1, N 4.0, S 20.3. UV/Vis ($CH_2Cl_2$): $\lambda$ = 315, 335, 361 nm. $^1$H NMR ($CDCl_3$): $\delta$ = 2.39 (s, $NMe_2$), 2.38 (s, C$H_3$C$_6$H$_4$CS$_2$), 2.57 (s, $NCH_2$), 7.16 (d, $J$ = 7.7 Hz, $C_6H_4$), 8.15 (br., $C_6H_4$) ppm.

**X-ray Crystallography:** Intensity data for [Zn($S_2$CTol)$_2$(py)], [Zn($S_2$CTol)$_2$(tmeda)], [Zn($S_2$CPh)$_2$(tmeda)] and [Cd($S_2$CTol)$_2$-(tmeda)] were measured with a Rigaku AFC12/Saturn724 CCD fitted with Mo-$K_\alpha$ radiation so that $\theta$ = 27.5°. The structures were solved by heavy-atom methods[42] and refinement was on $F^2$ [43] using data that had been corrected for absorption effects with an empirical procedure,[44] with non-hydrogen atoms modeled with anisotropic displacement parameters, with hydrogen atoms in their calculated positions, and using a weighting scheme of the form $w = 1/[\sigma^2(F_o^2) + (aP)^2 + bP]$ where $P = (F_o^2 + 2F_c^2)/3$. The absolute configuration of [M($S_2$CTol)$_2$(tmeda)], M = Zn and Cd, was determined on the basis of differences in Friedel pairs included in the data sets and confirmed by the near-zero value of the Flack parameter in each case, i.e. 0.006(12) and –0.01(3), respectively.[45] A residual electron density peak of 2.02 e Å$^{-3}$ was noted in the final difference map for [Zn($S_2$CPh)$_2$(tmeda)], this was located between the Zn and S1 atoms. A residual of 1.05 e Å$^{-3}$ was located 0.02 Å from the Cd atom in [Cd($S_2$CTol)$_2$(tmeda)]. Molecular structures shown in Figures 1, 2, 3, and 4 were drawn at the 50% probability level using ORTEP.[46] The DIAMOND program[47] was used for the remaining crystallographic figures. Data manipulation and analyses were performed with teXsan[48] and PLATON.[49] Crystallographic data and refinement details are given in Table 1.

**Preparation of Metal Sulfide Nanoparticles**

**(a) Pyrolysis in a Furnace:** A weighed quantity of a sample (ca. 200 mg) in a quartz boat, was pyrolyzed at 350 °C (unless otherwise stated) in a furnace under flowing nitrogen for 2 h. After cooling, the residue in the quartz boat was again weighed and characterized by XRD and in some cases by UV/Vis spectroscopy. The pyrolysis of **3c** was carried out at three different temperatures, 300, 400 and 500 °C and the dark-red residual powder was characterized by XRD.

Table 1. Crystallographic parameters and refinement details for [Zn($S_2$CTol)$_2$(py)], [Zn($S_2$CTol)$_2$(tmeda)], [Zn($S_2$CPh)$_2$(tmeda)] and [Cd($S_2$CTol)$_2$(tmeda)].

| Parameter | [Zn($S_2$CTol)$_2$·py] | [Zn($S_2$CTol)$_2$(tmeda)] | [Zn($S_2$CPh)$_2$(tmeda)] | [Cd($S_2$CTol)$_2$(tmeda)] |
|---|---|---|---|---|
| Formula | $C_{21}H_{19}NS_4Zn$ | $C_{22}H_{30}N_2S_4Zn$ | $C_{20}H_{26}N_2S_4Zn$ | $C_{22}H_{30}CdN_2S_4$ |
| *Fw* | 478.98 | 516.09 | 488.04 | 563.12 |
| Crystal system | monoclinic | orthorhombic | monoclinic | orthorhombic |
| Space group | *C*2/*c* | *Aba*2 | *C*2/*c* | *Aba*2 |
| *a* [Å] | 17.451(6) | 13.140(3) | 18.419(4) | 12.644(3) |
| *b* [Å] | 9.023(2) | 23.098(5) | 8.0230(16) | 23.859(5) |
| *c* [Å] | 13.979(4) | 7.8304(15) | 15.404(3) | 7.9794(16) |
| $\beta$ [°] | 107.038(6) | 90 | 98.251(4) | 90 |
| *V* [Å$^3$] | 2104.6(11) | 2376.6(8) | 2252.9(8) | 2407.1(9) |
| *Z* | 4 | 4 | 4 | 4 |
| $\mu$ [cm$^{-1}$] | 1.570 | 1.397 | 1.469 | 1.266 |
| $D_{calcd.}$ [g cm$^{-3}$] | 1.512 | 1.442 | 1.439 | 1.554 |
| Independent reflections | 2412 | 2720 | 2582 | 2741 |
| Observed reflections with $I > 2\sigma(I)$ | 2340 | 2677 | 2506 | 2717 |
| *R* (obsd. data) | 0.049 | 0.034 | 0.054 | 0.026 |
| *a*, *b* in weighting scheme | 0.065, 5.371 | 0.052, 1.787 | 0.042, 42.646 | 0.031, 4.477 |
| $R_w$ (all data) | 0.127 | 0.084 | 0.160 | 0.062 |
| CCDC numbers[a] | 616718 | 616716 | 616717 | 616715 |

[a] The supplementary crystallographic data for this paper can be obtained free of charge from The Cambridge Crystallographic Data Centre (CCDC) via www.ccdc.cam.ac.uk/data_request/cif.

 © 2007 Wiley-VCH Verlag GmbH & Co. KGaA, Weinheim 

**(b) Preparation of MS (M = Zn, Cd, Hg) Nanoparticles in Coordinating Solvents:** All experiments were performed similarly. A typical experiment is described below:

In a three-necked flask fitted with a thermometer, HDA (hexadecylamine) (5 g) was degassed at 120 °C under argon for 1 h with continuous stirring. The temperature was slowly raised to 225 °C and stabilized at this temperature. To this, a solution of **3c** (200 mg, 0.37 mmol) in dichloromethane (3 mL) was injected rapidly. The temperature dropped to 195 °C and was slowly raised to 225 °C and maintained at this temperature for 10 min. This hot solution was maintained at 225 °C for 20 min and was cooled to 70 °C and methanol was added to precipitate yellow CdS nanoparticles. The yellow flocculate was given a thorough washing with methanol followed by centrifuging and drying under vacuum.

Similarly, experiments were carried out at different temperatures and at different concentrations of precursor and coordinating solvent. Metal sulfide nanoparticles prepared in ethylenediamine were isolated by centrifuging rather than precipitating with methanol. The particles thus separated were thoroughly washed with methanol and dried. In case of experiments performed in ethylenediamine, a sudden surge in temperature to 135–140 °C was observed when the precursor (zinc, cadmium and mercury) was injected at 115 °C into ethylenediamine.

**Supporting Information** (see also the footnote on the first page of this article): XRD slides of nanoparticles of different colors, SAED patterns and TEM images of ZnS, HgS nanoparticles.

## Acknowledgments

We thank Drs. T. Mukherjee and S. K. Kulshreshtha for encouragement of this work. The authors are grateful to Dr. S. K. Gupta and his group for EDAX measurements and Dr. V. K. Manchanda and his group for providing microanalysis of these complexes.

[1] a) H. S. Nalwa, Encyclopedia of Nanoscience and Nanotechnology (Eds.: P. Reiss, A. Pron), American Scientific Publishers, USA, vol. 6, **2004**, 587–604; b) A. P. Alivisatos, *Science* **1996**, *271*, 933–937.
[2] V. L. Colvin, M. C. Schlamp, A. P. Alivisatos, *Nature* **1994**, *370*, 354–357.
[3] V. I. Klimov, A. A. Mikhailovsky, S. Xu, A. Malko, J. A. Hollingsworth, C. A. Leatherdale, H.-J. Eisler, M. G. Bawendi, *Science* **2000**, *290*, 314–317.
[4] S. Coe, W. K. Woo, M. G. Bawendi, V. Bulovic, *Nature* **2002**, *420*, 800–803.
[5] W. U. Huynh, J. J. Dittmer, A. P. Alivisatos, *Science* **2002**, *295*, 2425–2427.
[6] http://www.nrel.gov/ncpv/ncpv.html.
[7] M. Green, *Angew. Chem. Int. Ed.* **2004**, *43*, 4129–4131.
[8] W. C. W. Chan, S. M. Nie, *Science* **1998**, *281*, 2016–2018.
[9] P. V. Braun, P. Osenar, S. I. Stupp, *Nature* **1996**, *380*, 325–328.
[10] T. Trindade, P. O'Brien, N. L. Pickett, *Chem. Mater.* **2001**, *13*, 3843–3858.
[11] O. Masala, R. Seshadri, *Annu. Rev. Mater. Res.* **2004**, *34*, 41–81.
[12] a) M. Yosef, A. K. Schaper, M. Froba, S. Schlecht, *Inorg. Chem.* **2005**, *44*, 5890–5896; b) Y. W. Jun, J. E. Koo, J. Cheon, *Chem. Commun.* **2000**, 1243–1244.
[13] a) M. D. Nyman, M. J. Hampden-Smith, E. N. Duesler, *Adv. Mater. CVD* **1996**, *5*, 171–174; b) M. D. Nyman, M. J. Hampden-Smith, E. N. Duesler, *Inorg. Chem.* **1997**, *36*, 2218–2224.
[14] Z. H. Zhang, W. S. Chin, J. J. Vittal, *J. Phys. Chem. B* **2004**, *108*, 18569–18574.
[15] G. Kedarnath, L. B. Kumbhare, V. K. Jain, P. P. Phadnis, M. Nethaji, *Dalton Trans.* **2006**, 2714–2718.
[16] J. Cheon, D. S. Talaga, J. I. Zink, *J. Am. Chem. Soc.* **1997**, *119*, 163–168.
[17] D. Barreca, A. Gasparotto, C. Maragno, R. Seraglia, E. Tondello, A. Venzo, V. Krishnan, H. Bertagnolli, *Appl. Organomet. Chem.* **2005**, *19*, 59–67.
[18] a) M. Motevalli, P. O'Brien, J. R. Walsh, *Polyhedron* **1996**, *15*, 2801–2808; b) M. Lazell, P. O'Brien, *Chem. Commun.* **1999**, 2041–2042; c) M. Chunggaze, M. A. Malik, P. O'Brien, *J. Mater. Chem.* **1999**, *9*, 2433–2438.
[19] Y. W. Jun, S. Min Lee, N.-J. Kang, J. Cheon, *J. Am. Chem. Soc.* **2001**, *123*, 5150–5151.
[20] C. Byron, M. A. Malik, P. O'Brien, A. P. J. White, D. J. Williams, *Polyhedron* **2000**, *19*, 211–215.
[21] I. Haiduc, D. B. Sowerby, S. F. Lu, *Polyhedron* **1995**, *14*, 3389–3472.
[22] G. Hogarth, *Prog. Inorg. Chem.* **2005**, *53*, 71–561.
[23] E. R. T. Tiekink, I. Haiduc, *Prog. Inorg. Chem.* **2005**, *54*, 127–319.
[24] E. R. T. Tiekink, *CrystEngComm* **2003**, *5*, 101–113.
[25] M. Bonamico, G. Dessy, V. Fares, L. Scaramuzza, *J. Chem. Soc., Dalton Trans.* **1972**, 2515–2517.
[26] D. J. Darensbourg, M. J. Adams, J. C. Yarbrough, *Inorg. Chem. Commun.* **2002**, *5*, 38–41.
[27] H. Adams, A. C. Albeniz, N. A. Bailey, D. W. Bruce, A. S. Cherodian, R. Dhillon, D. A. Dunmer, P. Espinet, J. L. Feijoo, E. Lalinde, P. M. Maitlis, R. M. Richardson, G. Ungar, *J. Mater. Chem.* **1991**, *1*, 843–856.
[28] a) N. Kano, T. Kawashima, *Top. Curr. Chem.* **2005**, *251*, 141–180; b) C. Furlani, M. L. Luciani, *Inorg. Chem.* **1968**, *7*, 1586–1592.
[29] A. W. Addison, T. N. Rao, J. Reedijk, J. van Rijn, G. C. Verschoor, *J. Chem. Soc., Dalton Trans.* **1984**, 1349–1356.
[30] *International Center for Diffraction data*, JCPDS File No. 80–0020, **1997**.
[31] *International Center for Diffraction data*, JCPDS File No. 75–1538, **1997**.
[32] *International Center for Diffraction data*, JCPDS File No. 77–2306, **1997**.
[33] a) B. D. Cullity, *Elements of X-ray diffraction*, Addison-Wesley Inc., London, **1978**; b) N. Bhatt, R. Vaidya, S. G. Patel, A. R. Jani, *Bull. Mater. Sci.* **2004**, *27*, 23–25.
[34] J. Z. Zhang, *J. Phys. Chem. B* **2000**, *104*, 7239–7253.
[35] Y. Jun, J. Lee, J. Choi, J. Cheon, *J. Phys. Chem. B* **2005**, *109*, 14795–14806.
[36] *International Center for Diffraction data*, JCPDS File No. 06–0256, **1997**.
[37] C. B. Murray, D. J. Norris, M. G. Bawendi, *J. Am. Chem. Soc.* **1993**, *115*, 8706–8715.
[38] X. Peng, J. Wieckham, A. P. Alivisatos, *J. Am. Chem. Soc.* **1998**, *120*, 5343–5344.
[39] P. S. Nair, G. D. Scholes, *J. Mater. Chem.* **2006**, *16*, 467–473.
[40] P. S. Nair, T. Radhakrishnan, N. Revaprasadu, G. A. Kolawole, P. O'Brien, *Chem. Commun.* **2002**, 564–565.
[41] a) P. Beslin, A. Dlubala, G. Levesue, *Synthesis* **1987**, 835–837; b) R. W. Bost, W. J. Mattox, *J. Am. Chem. Soc.* **1930**, *52*, 332–335.
[42] P. T. Beurskens, G. Admiraal, G. Beurskens, W. P. Bosman, S. García-Granda, J. M. M. Smits, C. Smykalla, *The DIRDIF program system*, Technical Report of the Crystallography, Laboratory, University of Nijmegen, Nijmegen, The Netherlands, **1992**.
[43] G. M. Sheldrick, *SHELXL97*. Program for crystal structure refinement. University of Göttingen, Germany, **1997**.
[44] T. Higashi, *ABSCOR*, Empirical Absorption Correction based on Fourier Series Approximation, Rigaku Corporation, 3-9-12 Matsubara, Akishima, Japan, **1995**.

 © 2007 Wiley-VCH Verlag GmbH & Co. KGaA, Weinheim 

[45] H. D. Flack, *Acta Crystallogr., Sect. A* **1983**, *39*, 876–881.
[46] C. K. Johnson, *ORTEP II*, Report ORNL-5136, Oak Ridge National Laboratory, Oak Ridge, TN, **1976**.
[47] *Crystal Impact*, *DIAMOND*, *Version 3.1*. Crystal Impact GbR, Postfach 1251, 53002 Bonn, Germany, **2006**.
[48] *teXsan*, Structure Analysis Package, Molecular Structure Corporation, Houston, TX, **1992**.
[49] A. L. Spek, *PLATON*, A Multipurpose Crystallographic Tool, Utrecht University, Utrecht, The Netherlands, **2006**.
Received: November 12, 2006
Published Online: March 6, 2007

 © 2007 Wiley-VCH Verlag GmbH & Co. KGaA, Weinheim 

DOI: 10.1002/ejic.200601106

# Nickel(II)-Carbene Intermediates in Reactions of Geminal Dihaloalkanes with Nickel(0) Reagents and the Corresponding Carbene Capture as the Phosphonium Ylide[‡]

**John J. Eisch,*[a] Yun Qian,[a] and Arnold L. Rheingold[b]**

**Keywords:** Nickel(0) reagents / Nickel(II)-carbenes / Phosphonium ylides / α-Elimination / Carbon-carbon bond formation

In a previous study of geminal bond cleavages of substrates of the type $R_2CE_2$ [$E_2 = X_2$, O, S, Li($SO_2$Ph)] by nickel(0) reagents [$L_nNi$, $L_n$ = $(Cod)_2$, $(Et_4P)_4$], leading to $R_2C{=}CR_2$ as products, the tentative hypothesis had been proposed that such reactions likely proceed via nickel(0)-carbene intermediates (J. J. Eisch, Y. Qian, M. Singh, *J. Organomet. Chem.* **1996**, *512*, 207). Because such proposed nickel(0)-carbenes do not satisfactorily account for reactions encountered with such α-eliminations, a detailed reexamination of the reaction of these nickel(0) reagents with geminal dihalides has been undertaken. For example, two reactions of such presumed nickel(0)-carbenes remained anomalous: (1) the failure of 5,5-dibromotetraphenylcyclopentadiene to form its expected dimer, octaphenylphenylfulvalene and instead the formation of triethylphosphonium tetraphenylcyclopentadienide in its reaction with $(Et_3P)_4Ni$; and (2) the presumed capture of intermediate $R_2C{=}Ni^0$ in presence of the trapping agent (benzaldehyde or benzophenone). As to the first anomaly, a detailed study has shown that no trace of octaphenylfulvalene was formed. As to the second anomaly, the $R_2C$ fragment could be trapped by the carbonyl reagents only in reactions involving $(Et_3P)_4Ni$, but not in reactions with $(Cod)_2Ni$. This finding compels one to conclude that the carbonyl reagent is capturing the Wittig reagent, $R_2C{=}PEt_3$, and not $R_2C{=}Ni^0$. Based upon all present data, the mechanism of such C=C bond dimerizations is best explicable in terms of nickel(II)-carbenes. The triethylphosphonium tetraphenylcyclopentadienide formed here has by single-crystal X-ray structure determination, complemented by $^{13}C$ NMR spectroscopic data, been found to have the zwitterionic structure $Ph_4Cp^-$–$^+PEt_3$ as its paramount resonance contributor.

(© Wiley-VCH Verlag GmbH & Co. KGaA, 69451 Weinheim, Germany, 2007)

## Introduction

The oxidative addition of nickel(0) complexes ($L_nNi$, **1**) into σ-covalent bonds between carbon and a wide variety of heteroatoms or even another carbon [**2**; E = X, O (of epoxide ring or allylic ether), N, C, S, P, Al][2,3] produces organonickel intermediates (**3**) pivotal in olefin isomerization,[3] olefin and diolefin oligomerization,[3] desulfurization of aromatic sulfur heterocycles,[4] epoxide deoxygenation[5] and the Kumada carbon–carbon cross coupling[6] [Equation (1)].

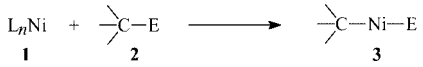


**1** **2** **3** (1)

A recent study of nickel(0)-induced α-eliminations from geminal disubstituted alkanes **4** leading directly to carbon–carbon π-bond coupling also appears to involve such oxidative addition by nickel(0) to produce **5**[7] (Scheme 1). However, in this situation adduct **5** could lead to C=C bond coupling via two distinctly different routes: (1) **5** could itself undergo an α-elimination yielding a nickel(II)-carbene complex (**6**); or (2) alternatively, **5** could undergo a second oxidative addition with **1** to produce dinickelaalkane **7**, which upon elimination of NiAB (**8**) would yield nickel(0)-carbene complex **9**. Then via a dimerization-elimination of nickel(II)-carbene **6** (path 1) or by a coupling process through nickel(0)-carbene **9** and **4** (path 2) the olefin dimer **10** would result. This previous global investigation of α-eliminations of geminally disubstituted hydrocarbons by nickel(0) rea-

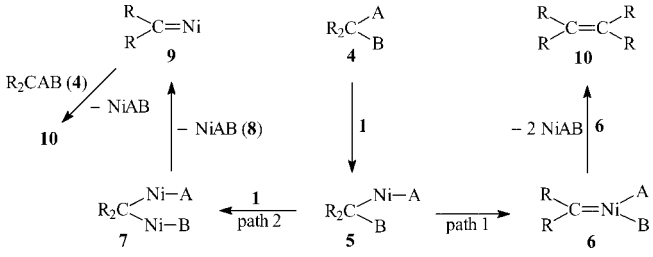


Scheme 1.

[‡] Organic Chemistry of Subvalent Transition Metal Complexes, 40; Part 39: Ref.[1]

[a] State University of New York at Binghamton, Department of Chemistry,
P. O. Box 6000, Binghamton, NY 13902-6000, USA
Fax: +1-607-777-4865
E-mail: jjeisch@binghamton.edu
[b] University of California, San Diego, Department of Chemistry and Biochemistry,
9500 Gilman Drive, m/c 0358, LaJolla, CA 92093-0332, USA

 © 2007 Wiley-VCH Verlag GmbH & Co. KGaA, Weinheim 

gents has embraced in its survey dihalo, sulfonyl lithio, ketonic, thioketonic and even cyclopropene reagents.[7]

Since the ring-opening and alkyne-insertion reactions of 1,2,3-triphenylcyclopropene (**11**) with nickel(0) complexes to produce intermediate **12** seemed to be explicable only in terms of path 2 (Scheme 2; Diels–Alder capture of **12** by diphenylacetylene and subsequent $Ni^0$-elimination to yield **13**), we made the preliminary hypothesis that all such geminal disubstituted derivatives would similarly involve nickel(0)-carbene intermediates.

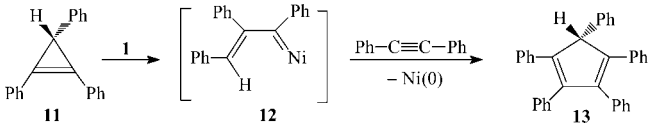


Scheme 2.

But in extending path 2 to the reactions of $L_nNi$ (**1**) with geminal dichlorides, for example, one would have to invoke the unlikely polarization **14** to explain the coupling with $R_2CCl_2$ (**15**) to form olefin dimer **10** or the purported capture of **9** as **17** with an aldehyde or ketone $R_2C{=}O$ (**16**), benzaldehyde or benzophenone for **9** in ref.[7] (Scheme 3). On the contrary, with late transition metal or Fischer carbenes, the carbene center is known to exhibit *electrophilic* (**18**), rather than nucleophilic (**14**) character. Accordingly, resonance structure **14** would be only a minor contributor to the actual π-electron distribution in **9**.

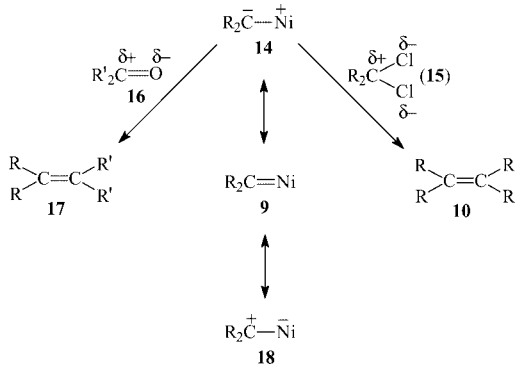


Scheme 3.

Because of these incongruities between the experimental observations made in the reactions of geminal dihalides (e.g. **15**) with nickel(0) reagents **1** and the postulated role of nickel(0)-carbenes (Scheme 1; path 2: **4** → **5** → **7** → **9** → **10**), we have reinvestigated these reactions in a more searching manner. We have tried to detect and identify all possible by-products and side products. Most of all, we have striven to explain the anomalous course of the attempted carbon–carbon π-bond coupling of 5,5-dibromotetraphenylcyclopentadiene (**19**) by tetrakis(triethylphosphane)nickel(0), $(Et_3P)_4Ni$ (**20**). Instead of dimerizing to octaphenylfulvalene (**21**), the corresponding phosphonium ylide or Wittig reagent **22c** was formed in high yield[7] (Scheme 4). Any acceptable reaction mechanism, in our opinion, would have to explain how such Wittig reagents could readily arise in the course of such couplings. We will show that only the intermediacy of nickel(II)-carbene complexes (Scheme 1; path 1: **4** → **5** → **6** → **10**) can readily lead to Wittig reagents in situ.

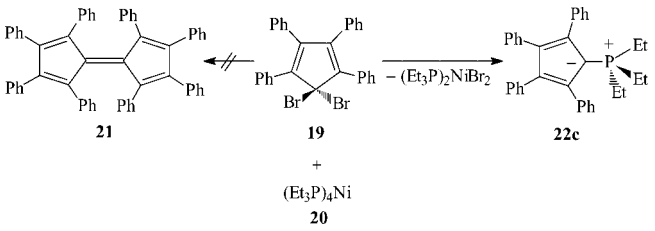


Scheme 4.

## Results and Discussion

### Anomalous Reaction of 5,5-Dibromotetraphenylcyclopentadiene (19) with $(Et_3P)_4Ni$ (20)

The reaction mixture of a 1:3 molar ratio of **19** and **20** in THF at room temp. was freed of volatiles and the resulting residue was extracted with warm cyclohexane. The extract deposited 70% of triethylphosphonium tetraphenylcyclopentadienide (**22c**).[8a] From the concentrated and cooled cyclohexane filtrate were obtained 80% of the expected $(Et_3P)_2NiBr_2$. Finally, treating the last filtrate with deoxygenated 6 N aqueous HCl led upon hydrolytic workup to the isolation of 1,2,3,4-tetraphenylcyclopentadiene (**23**, 24%) as the only detectable organic product with no sign of fulvalene **21**. The hydrocarbon **23** can be considered as the expected reductive cleavage product of phosphonium ylide **22c** by **20** and acid, shown in Scheme 5, a reaction having ample precedent.[8b] From this detailed analysis of the reaction products, we therefore conclude that the formation of phosphonium ylide in Scheme 3 has proceeded essentially to completion without the generation of any **21**. The failure of any fulvalene like **21** to form in such a reaction cannot be ascribed to any inherent instability of these substituted fulvalenes. Both 1,2,3,4-tetraphenylfulvalene (m.p. 202 °C)[9a] and octaphenylfulvalene [**21**, m.p. 170 °C (dec.)][9b] have been prepared as brilliant orange-red solids and have been found to be indefinitely stable below 100 °C.

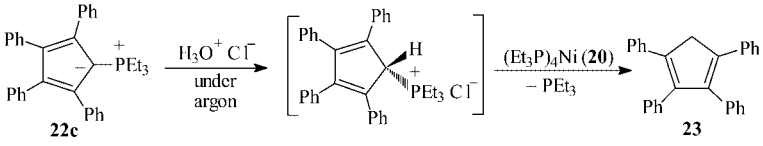


Scheme 5.

 © 2007 Wiley-VCH Verlag GmbH & Co. KGaA, Weinheim 

### The Stability and Structure of Triethylphosphonium Tetraphenylcyclopentadienide (22c)

Although the phosphonium ylide **22c** has all the structural features of a typical Wittig reagent, it is stable to air and moisture when stored at room temperature and does not react with either benzaldehyde or benzophenone in warm cyclohexane to give a fulvene, the expected Wittig methylenation reaction product. But the corresponding triphenylphosphonium cyclopentadienide has also been shown by Ramirez and Levy not to react with cyclohexanone even at elevated temperatures.[10] In both instances, the delocalization of the anionic charge and Hückel aromaticity of such a cyclopentadienyl ring could be viewed as the cause for the inertness of such Wittig reagents.

The single-crystal X-ray structure determination of phosphonium ylide **22c** (Figure 1 and Tables 1 and 2) sheds light on the extent of delocalization of the negative charge in the cyclopentadienyl moiety of **22c**, namely the relative importance of resonance structures **22a**, **22b** and **22c**, as well as the relative importance of the neutral phosphorane resonance structure **22d**, often invoked with Wittig reagents. It should be noted that this XRD structure of **22c** is not the first trisubstituted phosphonium cyclopentadienide whose structure has been determined in the crystalline state. The crystal structure of triphenylphosphonium cyclopentadienide (**24**) has been determined by X-ray crystallography and the question of the degree of ylide-ylene character in the cyclopentadienyl carbon–phosphorus bond carefully addressed.[11a] This prior work has been most valuable in our present attempt to evaluate the relative contributions of resonance structures **22a**–**22d**.

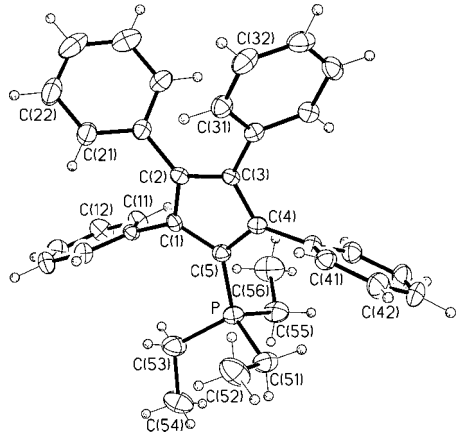


Figure 1. ORTEP projection of triethylphosphonium tetraphenylcyclopentadienide (**22c**) with ellipsoids at the 30% probability level.

In Table 1 are listed the experimentally determined C(5)–P and C–C bond lengths of greatest relevance in evaluating the relative contributions of resonance structures **22a**–**22d**. The observed C–C bond lengths within the cyclopentadienyl ring, as shown in **22d**, can be profitably compared with those of the cyclopentadienyl anion.[12] Of analogous use is a comparison of C(5)–P bond length in **22a**–**d** with that of the similar phosphonium ylide **24** and that of naphthalene derivative **25**.[13a]

Table 1. Selected bond lengths and angles of triethylphosphonium tetraphenylcyclopentadienide (**22c**).

| Bond lengths [Å] | | | |
|---|---|---|---|
| P–C(5) | 1.756(5) | C(1)–C(16) | 1.492(6) |
| P–C(51) | 1.807(5) | C(2)–C(3) | 1.420(7) |
| P–C(53) | 1.812(6) | C(2)–C(26) | 1.483(7) |
| P–C(55) | 1.825(5) | C(3)–C(4) | 1.400(6) |
| C(1)–C(2) | 1.399(6) | C(3)–C(36) | 1.476(6) |
| C(1)–C(5) | 1.425(6) | C(4)–C(5) | 1.428(6) |
| **Bond angles [°]** | | | |
| C(5)–P–C(51) | 112.3(3) | C(4)–C(3)–C(2) | 108.5(4) |
| C(5)–P–C(53) | 112.0(3) | C(3)–C(4)–C(5) | 107.4(5) |
| C(5)–P–C(55) | 113.6(2) | C(1)–C(5)–C(4) | 108.1(4) |
| C(2)–C(1)–C(5) | 107.4(4) | C(1)–C(5)–P | 126.6(4) |
| C(1)–C(2)–C(3) | 108.6(4) | C(4)–C(5)–P | 125.0(4) |

Table 2. Crystal data and structure refinement for triethylphosphonium tetraphenylcyclopentadienide (**22c**).

| | |
|---|---|
| Empirical formula | $C_{35}H_{35}P$ |
| Formula weight | 486.60 |
| Diffractometer | Siemens P4 (scintillation counter) |
| Temperature | 296(2) K |
| Wavelength | 0.71073 Å |
| Crystal system | monoclinic |
| Space group | *P*2(1) |
| Unit cell dimensions | $a$ = 10.757(2) Å; $\alpha$ = 90°<br>$b$ = 11.076(2) Å; $\beta$ = 94.57(2)°<br>$c$ = 11.988(3) Å; $\gamma$ = 90° |
| Volume | 1423.8(5) Å$^3$ |
| $Z$ | 2 |
| Density (calculated) | 1.135 mg/m$^3$ |
| Absorption coefficient | 0.117 mm$^{-1}$ |
| $F$(000) | 520 |
| Crystal size | 0.32 × 0.28 × 0.24 mm |
| $\theta$ range for data collection | 2.45–22.50° |
| Index ranges | $-11 \leq h \leq 11$, $0 \leq k \leq 11$, $0 \leq l \leq 12$ |
| Reflections collected | 2076 |
| Independent reflections | 1970 [$R$(int) = 0.0205] |
| Completeness to $\theta$ = 22.50° | 99.6% |
| Absorption correction | none |
| Max. and min. transmission | 0.9724 and 0.9635 |
| Refinement method | full-matrix least squares on $F^2$ |
| Data/restraints/parameters | 1970/1/325 |
| Goodness-of-fit on $F^2$ | 0.795 |
| Final $R$ indices [$I > 2\sigma(I)$] | $R1$ = 0.0371, $wR2$ = 0.0645 |
| $R$ indices (all data) | $R1$ = 0.0715, $wR2$ = 0.0722 |
| Absolute structure parameter | 0.04(17) |
| Largest diff. peak and hole | 0.118 and –0.168 e Å$^{-3}$ |

In the first place, the clearly alternating C–C bond lengths of the cyclopentadienyl ring (1.40 ± 0.02 Å) of **22a**–**d** indicate that resonance structures **22a** and **22b** make relatively lesser contributions to the π-electron distribution. In the cyclopentadienyl anion of KCp(18-crown-6), however, the ring C–C bond lengths range from 1.37 to 1.41 Å with a mean of 1.40 Å. The distances in **22a**–**d** might be considered the same within experimental error, if their bond length alternation did not so nicely parallel the C–C bonding in resonance structures **22c** or **22d**.

 © 2007 Wiley-VCH Verlag GmbH & Co. KGaA, Weinheim 

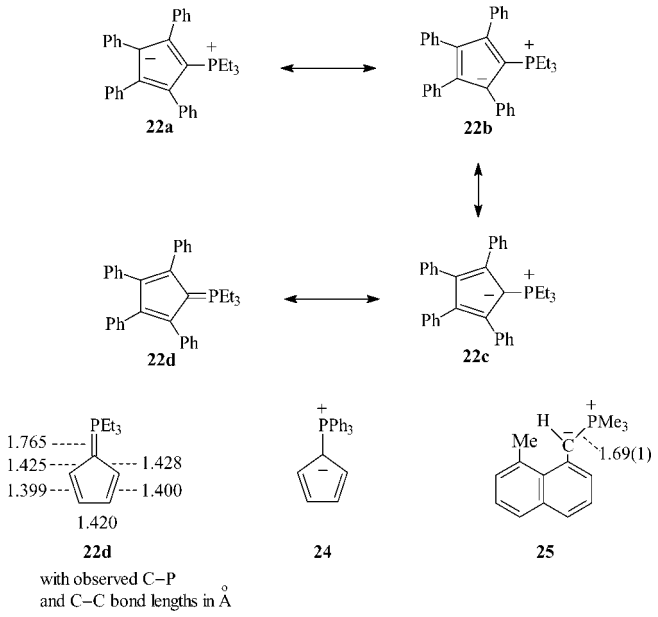


The question of ionic or double character of the carbene–carbon bonding with phosphorus can reasonably be judged on the basis of the carbene C–P bond in **25**, one of the few open-chain phosphoranes with alkyl substituents, whose XRD structures have been measured. At 1.69 Å the C–P bond in **25** should have more C=P bond character than that in **22a**–**d**, 0.08 Å longer. Another indication of lessened C=P bonding in **22a**–**d** results from comparing the bond lengths of the C–P bonds of the three ethyl groups attached to phosphorus, 1.81 Å, with the carbene C(5)–P bond, 1.77 Å. A change in the C($sp^3$) hybridization of the ethyl in **22** to the C($sp^2$) hybridization of the phenyl in $Ph_4P^+$ (1.81 → 1.79 Å) suggests that the $sp^2$-hybridized carbene-carbon–phosphorus bond length would be 1.79 Å for an ordinary single C–P bond. This length is so close to the observed 1.77 Å as to indicate that there is markedly less phosphorane character in **22**, as suggested by **22c** than there is in **25** (C–P bond of 1.69 Å) or even in **24** (C–P bond of 1.72 Å). Therefore, the carbon–phosphorus linkage is best represented by the single resonance structure **22c**. The greater zwitterionic character in the carbene-carbon–phosphorus bond of **22c**, compared with that of **24**, can be attributed to the following electronic stabilization: (1) the presence of electron-donating ethyl groups on P, instead of phenyl groups, stabilizing the cationic P-center; and (2) the presence of π-electron-withdrawing phenyl groups on the cyclopentadienyl ring, instead of hydrogens, stabilizing the anionic C-center. Assigning a reliable percentage of ylene-ylide character to the C–P bond, however, seems to be beset with great uncertainty.[11b]

The $^{13}C$ NMR spectrum of **22c** provides confirmation of the higher charge density of carbon C(5) over that of centers C(1) or C(4).[13b] The doublet centered at $\delta$ = 124.85 ppm displays the largest $^{13}C$-$^{31}P$ coupling (60 Hz) whereas the doublets at $\delta$ = 127.10 ppm and 127.80 ppm are split by 25 Hz and 18 Hz, respectively. As expected, the doublet with the largest splitting must be assigned to C(5), which is closest to the phosphorus. Since C(5) is the closest to phosphorus and its signal is the most shielded, it would thus have a higher electron density than those of C(1) and C(4).

### Possible Mechanistic Routes to Triethylphosphonium Tetraphenylcyclopentadienide (22c)

Two quite divergent pathways leading from 5,5-dibromotetraphenylcyclopentadiene (**19**) and $(Et_3P)_4Ni$ (**20**) to **22c** can be envisioned, the one an integral part of the nickel(II)-carbene pathway proposed here for the coupling of geminal dihalides to yield dimeric olefins via intermediates analogous to **26** and **27** (cf. infra) (path a; Scheme 6) and the other involving an initially formed quarternary phosphonium salt (**28**), followed by oxidative addition of $Ni^0$ from **20** to produce **29** and concluded by elimination of $NiBr_2$ (path b).[14] Clearly, the latter route would involve no nickel-carbene complex as such.

As will be discussed below, there is ample precedent for the coupling of geminal dihalides by $Ni^0$ reagents, either $(Et_3P)_4Ni$ (**20**) or $(Cod)_2Ni$ (**34**), via intermediates like **26** and **27**, when steric factors do not prevent their coupling. Thus, the feasibility of path a is evident. On the other hand, path b requires as its first step the slow quaternization of $Et_3P$ (**20a**) by **19** to form **28**, a process known to require a combination of higher temperatures, peroxides and/or ultraviolet radiation to be initiated and widely considered to involve free-radical chain reactions.[15a,15b] By contrast, it

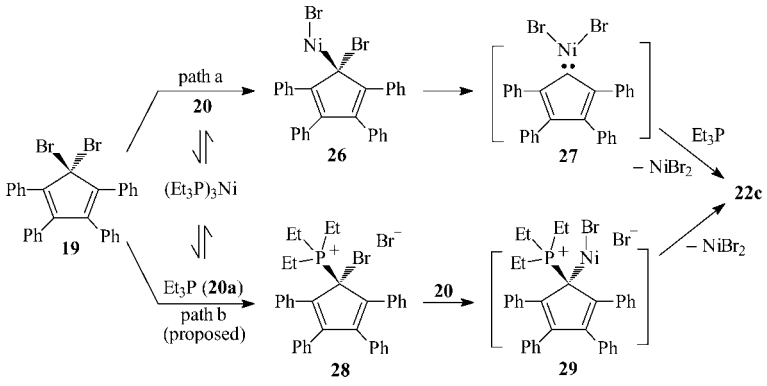


Scheme 6.

 © 2007 Wiley-VCH Verlag GmbH & Co. KGaA, Weinheim 

should be noted that the reaction of **19** with **20** proceeds readily at room temperature in oxygen- and peroxide-free THF with no special illumination. Furthermore, the reaction of putative intermediate **28** with **20** to yield the necessary **29** is obviously fraught with steric hindrance. Finally and decisively, the attempted interaction of **19** with **20a** in THF, with the conditions under which **19** and **20** react completely (18 h at 25 °C), failed altogether. Since this proposed first step of path b has been attempted in this study without success, path b can be dismissed as a viable alternative to path a.

### Reactions of α,α-Dichlorotoluene (30) with Nickel(0) Reagents

In our previous report we observed that a 1:2 mixture of α,α-dichlorotoluene (**30**) and $(Et_3P)_4Ni$ (**20**) reacted in THF at 25 °C to give 98% of *trans*-stilbene (**31**) [Equation (2)].[16]

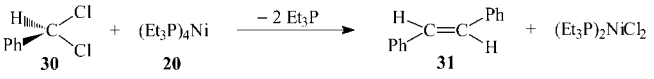


(2)

In a parallel reaction conducted at 0 °C, the 1:2 mixture of **30** and **20** was allowed to react in the presence of 1 equiv. of benzophenone (**32**). Hydrolytic workup led to the isolation of 40% of **31** and 47% of triphenylethylene (**33**). The formation of **33** was at first thought to have originated from a Wittig-like reaction of the nickel(0)-carbene, PhCH=Ni, with **32** through the elimination of NiO [Equation (3)].

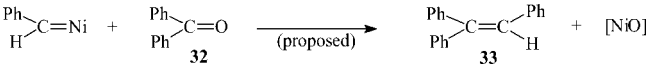


(3)

But the present findings, employing $(Cod)_2Ni$ (**34**) with **30**, tend to rule out this interpretation. Certainly, a 1:2 mixture of **30** and **34** reacted equally smoothly in THF at 25 °C to produce a high yield of *trans*-stilbene (96%). But the corresponding attempted trapping experiment involving a 1:2:1 mixture of **30**, **34** and **32** again led only to a high conversion to *trans*-stilbene (94%) with no detectable amount of the trapping product **33**. If the nickel(0)-carbene, PhCH=Ni, were the source of **33**, it should also have been present in this mixture and therefore have been trapped. Since no such trapping product was detected, we suggest an alternative and mechanically more reasonable source of **33**. We now propose, instead, that a nickel(II)-carbene (**36**) is generated in these coupling reactions and that coupling occurs through the reaction between **36** and oxidative-addition product **35**. The matched polarities of carbon–nickel bond of **35** and the Fischer-carbene-carbon–nickel(II) bond of **36** should foster rapid C–C bond formation to yield **31**. Only in the C–C couplings employing reagent **20** would the triethylphosphane be present to undergo a competitive reaction with the electrophilic carbon of nickel(II)-carbene **36**, leading to the displacement of nickel(II) chloride as its $Et_3P$ complex and the generation of phosphane ylide **37** (Scheme 7). The reaction of benzophenone (**32**) with this Wittig reagent, rather than the dubious reaction with the previously suggested nickel(0)-carbene, is therefore concluded to be the actual source of the triphenylethylene (**33**) [Equation (4)].

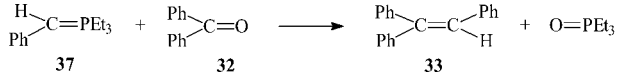


(4)

The observation of phosphonium ylide **22c** as the ultimate Wittig-like reagent from dibromo compound **19** and nickel reagent **20**, as well as the aforementioned detection of **37** in the reaction of geminal dichloro compound **30** with **20**, show that phosphonium ylides can occur as intermediates in such C–C bond-coupling reactions. That they are necessary intermediates, however, seems most unlikely.[17]

### Generalized Mechanism for the Nickel(0)-Promoted Coupling of Geminal Disubstituted Hydrocarbons

The foregoing coupling mechanism, having nickel(II)-carbenes as key intermediates, can be rationally applied to the other geminal dihalohydrocarbons already studied, namely dibromomethane, dichlorodiphenylmethane and 5,5-dibromo-1,2,3,4-tetraphenylcyclopentadiene (**19**) (Scheme 8).

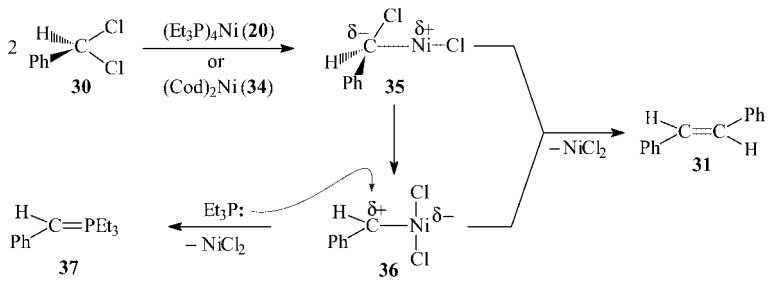


Scheme 7.

 © 2007 Wiley-VCH Verlag GmbH & Co. KGaA, Weinheim 

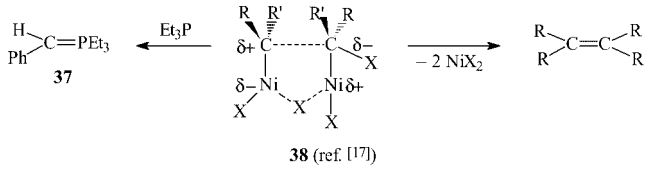


Scheme 8.

Considering **38** as an appropriate activated complex,[18] it is clear that when R and R′ are space-filling groups as in the reaction of 5,5-dibromotetraphenylcyclopentadiene (**19**) (R and R′ combined as a 1,4-tetraphenylbutadienylene group), then C–C bond formation will be relatively slow and the $Et_3P$ attack will form the Wittig reagent selectively. With R and R′ as phenyl groups, C–C bonding is still possible but backside attack at the pseudo-tertiary carbene-carbon by $Et_3P$ should be slow. This view is in agreement with our previous finding that the reaction of $(Et_3P)_4Ni$ with dichlorodiphenylmethane in the presence of benzaldehyde leads to 95% of tetraphenylethylene with no sign of triphenylethylene, the expected Wittig reaction product expected to arise from benzaldehyde and $Ph_2C{=}PEt_3$.[19]

Finally, with R = Ph and R′ = H, as was presented in Scheme 5, C–C bond formation would occur along the internuclear line in **38** with the phenyl groups *trans* to each other for steric reasons. In this case, the carbene-carbon is pseudo-secondary and hence more accessible to backside attack by $Et_3P$ and thus the formation of the corresponding Wittig reagent. With R and R′ as H in dihalomethanes, the frontside C–C coupling in **38** and the backside attack by $Et_3P$ should be of comparable facility and therefore C–C coupling and Wittig-reagent formation both are possible and in fact observed.

The coupling mechanism operative with other geminal disubstituted hydrocarbon derivatives, such as thioketones and α-lithioorganic sulfones, is also most likely one involving analogous nickel(II)-carbene intermediates.[20] Even the behavior of benzylic sulfones toward nickel(0) reagents indicates the possible intermediacy of nickel(II)-carbene complexes. Benzyl phenyl sulfone (**39**), for example, reacted with $(Cod)_2Ni$ in toluene at 25 °C over an extended period to give the deposition of nickel metal. Hydrolytic workup gave a 40% yield of *trans*-stilbene (**31**) with no trace of bibenzyl (Scheme 9). The absence of bibenzyl is consistent with the absence of reductive cleavage of the C–S bond. The formation of *trans*-stilbene can be readily explained through the oxidative addition process depicted in Scheme 9, which would lead to a nickel(II)-carbene (**40**) and thus to C–C bond coupling analogous to that in Scheme 7.

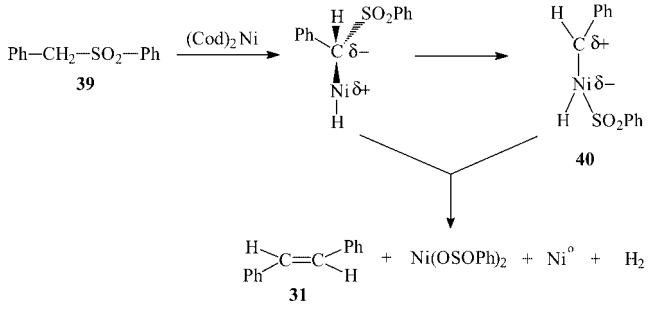


Scheme 9.

## Conclusions

The bond cleavages of geminal dihalides of the type $R_2CX_2$ by nickel(0) reagents is best depicted as leading to dimers $R_2C{=}CR_2$ via nickel(II)-carbenes by the following sequence of reactions: (1) oxidative addition of $Ni^0$ to produce $XR_2C–Ni–X$;to provide the nickel(II)-carbene, $R_2C^+–{}^-NiX_2$; (3) C=C bond formation between $XR_2C^{\delta-}–{}^{\delta+}NiX_2$ and $R_2C^+–{}^-NiX_2$ because of opposite polarities. If step 3 is too slow in the reactions involving $(Et_3P)_4Ni$, then any free $Et_3P$ can displace the $NiX_2$ from $R_2C^+–{}^-NiX_2$ and capture the $R_2C$ ligand as the Wittig reagent, $R_2C{=}PEt_3$. Such a Wittig reagent, rather than the previously assumed nickel(0)-carbene, $R_2C{=}Ni^0$, is responsible for the formation of $R_2C{=}CR'R''$ when $R'R''C{=}O$ is added to such reaction mixtures.

Triethylphosphonium tetraphenylcyclopentadienide (**22c**), the Wittig reagent obtained in high yield from the unsuccessful attempt to couple 5,5-dibromotetraphenylcyclopentadiene to produce octaphenylfulvalene (cf. supra: slow step 3), was subjected to X-ray crystallographic structure determination. Such structural data, together with its $^{13}C$ NMR chemical shifts and $^{13}C$-$^{31}P$ coupling constants, are clearly consistent with the electronic structure **22c**, where the ring C(5)–P bond is essentially a zwitterionic single C–P bond and the negative charge of the *pseudo*-cyclopentadiene anion greatest on C(5).

## Experimental Section

**General Procedures and Techniques:** All reactions were carried out under a positive pressure of anhydrous, oxygen-free argon. All solvents employed with organometallic compounds were dried and distilled from a sodium metal/benzophenone ketyl mixture prior to use. The preparation and purification of oxygen- and moisture-sensitive reagents were carried out under argon with the use of Schlenk techniques.[21] The IR spectra were recorded with a Perkin–Elmer instrument, model 457 and samples were measured either as mineral oil mulls or as KBr films. The NMR spectra ($^1H$ and $^{13}C$) were recorded with a Bruker spectrometer, model AM-360 and tetramethylsilane (TMS) was used as the internal standard. The chemical shifts reported are expressed on the $\delta$-scale and in parts per million (ppm) from the reference TMS signal. The gas-chromatographic analyses were carried out with a Hewlett–Packard instrument, model 5880, provided with a 6 ft OV-101 packed column or with a Hewlett–Packard instrument, model 5890, having a 30 m SE-30 capillary column, respectively. Melting points were determined with a Thomas-Hoover Unimelt capillary melting point apparatus and are uncorrected. The $(Cod)_2Ni$ was prepared according to a procedure adapted from those of Semmelhack[22] and of Schunn.[23] The yield of product has been improved to 95% by purifying the starting materials with extreme care.

The $(Et_3P)_4Ni$ was prepared according to the method of Cundy[24] and the (Cod)(Bpy)Ni by the procedure of Dinjus et al.[25] The α,α-dichlorotoluene, dichlorodiphenylmethane and dibromomethane

 © 2007 Wiley-VCH Verlag GmbH & Co. KGaA, Weinheim 

were purchased at 98+% of purity and their purity further checked by gas chromatography.

The 5,5-dibromotetraphenylcyclopentadiende (**19**) was prepared for the first time by the following procedure developed in this laboratory. A solution of 3.76 g (10.0 mmol) of 1,2,3,4-tetraphenylcyclopentadiene (**23**) in 80 mL of $CCl_4$ was treated with 3.65 g (20.5 mmol) of *N*-bromosuccinimide (99%) and the suspension heated at reflux until all suspended solid had risen to the surface (90 min). During the heating, a small illuminated UV lamp was focused on the reaction flask. The hot solution was then filtered from the succinimide and the filtrate freed of solvent in a rotary evaporator. The pale yellow solid residue of 5.1 g was essentially pure **19** because the peak at $\delta = 4.0$ ppm in the $^1$H NMR spectrum of the starting diene was absent. Recrystallization from 95% ethanol yielded 4.4 g (83%) of pure **19**, m.p. 154–155 °C. $C_{29}H_{20}Br_2$ (528.30): C 65.31, H 3.78; found C 65.69, H 3.82.

The sample of octaphenylfulvalene (**21**) was prepared by the following route. A suspension of 1.50 g (2.80 mmol) of **19**, prepared in the foregoing method, and 5.0 g (76 mmol) of zinc dust in 50 mL of benzene was treated with a crystal of iodine as an activator and was then stirred under reflux for 6 h. The resulting deep red suspension was filtered hot. The filtrate was freed of solvent in a rotary evaporator to leave a deep red gummy residue. Stirring this residue with hot portions of a 1:1 (v/v) mixture of benzene/95% ethanol gave a deep red extract. Concentration and cooling of the extract gave 710 mg (69%) of brilliant orange-red solid (**21**), which had multiplets of proton signals between $\delta = 7.0$ ppm and 7.4 ppm in the $^1$H NMR spectrum and whose mass spectrum at 70eV had a parent peak at $m/z = 736$, characteristic of fulvalene **21**. No peaks were present indicative of any **19** or any other bromine-containing component (with isotopic $^{79}$Br and $^{81}$Br components). This sample melted at 170 °C with decomposition, despite several recrystallizations from 95% ethanol/toluene. $C_{58}H_{40}$ (736.77): calcd. C 94.54, H 5.46; found C 94.10, H 5.16.

**X-ray Crystallographic Study of Triethylphosphonium Tetraphenylcyclopentadienide (22). Crystal Mounting and Data Collection:** Data were collected at room temperature with a Siemens P4 diffractometer equipped with a scintillation counter. An orange crystal was mounted on a glass fiber with epoxy cement and a unit cell determined from the angular settings of 25 centered reflections. Systematic absences in the diffraction data indicated either the monoclinic space groups $P2_1$ or $P2_1/m$. *E* statistics initially indicated the noncentrosymmetric alternative, and the structure that was developed in this setting proved to be incompatible with mirror-plane symmetry. All non-hydrogen atoms were refined with anisotropic thermal parameters and hydrogen atoms were treated as idealized contributions. The correctness of the reported hand was affirmed by the value of the refined Flack parameter: 0.04(17). All software used was contained in the SHELXTL and data collection libraries of programs provided by the Siemens Corporation (Madison, WI). The pertinent crystal data and structure refinement are presented in Table 2. CCDC-628202 contains the supplementary crystallographic data for this paper. These data can be obtained free of charge from The Cambridge Crystallographic Data Centre via www.ccdc.cam.ac.uk/data_request/cif.

**Preparation of Triethylphosphonium Tetraphenylcyclopentadienide (22c) from 5,5-Dibromotetraphenylcyclopentadiene (19) and $(Et_3P)_4$-Ni (20):** A solution of 1.94 g (3.66 mmol) of **19** in 60 mL of THF was treated with 640 mg (1.20 mmol) of **20** at 25 °C. The dark red solution was stirred for 18 h and then the THF was removed under reduced pressure. The dark residue was extracted with warm cyclohexane (6 10-mL portions of deoxygenated solvent). The hot extracts were filtered, concentrated to 2/3 of volume and chilled to deposit 1.24 g of amber-colored **22c** (70%). Recrystallization from cyclohexane yielded pale orange **22c**, m.p. 200–202 °C, which was submitted to X-ray single-crystal determination (Table 2). $^1$H NMR ($C_6D_6$): $\delta = 0.41$–0.50 (m, 9 H), 1.02–1.21 (m, 6 H), 6.82–7.59 (m, 304) ppm. $^{13}$C NMR ($C_6D_6$): $\delta = 15.98$ (d), 20.17 (3), 124.85 (d), 127.10 (d), 127.80 (m, high intensity), 132.45 (d) ppm. The $J_{C,P}$ values of the doublets at $\delta = 124.85$, 127.10 and 127.80 ppm are 60, 25 and 18 Hz, respectively.

The original cyclohexane filtrate from which **22c** had crystallized was concentrated to dryness under reduced pressure and the residue dissolved in dry, deoxygenated $C_6H_6$. The $^1$H NMR spectrum of this solution displayed only very broad absorptions, characteristic of the presence of paramagnetic components. Hence, the entire $C_6D_6$ solution was treated with deoxygenated 6 N aqueous HCl. Hydrolytic workup yielded 107 mg of a reddish solid, whose $^1$H NMR spectrum showed it to be largely **23** (m.p. 180–181 °C, 24%, $^1$H NMR peak at $\delta = 4.0$ ppm).

The deep red reaction residue remaining after the cyclohexane extraction of the reaction mixture was redissolved in THF and cooled to –78 °C. Long dark red needles of $(Et_3P)_2NiBr_2$ were formed (440 mg, 80%).[26] The $^1$H NMR spectrum showed no aromatic proton absorptions.

**Attempted Reaction of 5,5-Dibromotetraphenylcyclopentadiene (19) with Triethylphosphane (20a). Test of the First Proposed Step, 19 + 20 → 28, of Path b in Scheme 6:** A solution of 3.88 g (7.32 mmol) of **19** and 0.87 g (7.4 mmol) of **20a** dissolved in 120 mL of anhydrous, deoxygenated THF was allowed to stand under an argon atmosphere for 18 h at 25 ± 5 °C in a Schlenk flask sheathed in aluminum foil, so as to exclude light. During this time, the initially pale yellow solution did not change color nor did any solid precipitate. All volatiles were then removed under reduced pressure at 25 °C and the resulting residue was shown to be essentially pure **19** by $^1$H and $^{13}$C NMR spectroscopic analysis.

**Reaction of $(Cod)_2Ni$ (34) with α,α-Dichlorotoluene (30):** In our previous report on the reactions of geminal dihaloalkanes with nickel(0) reagents[7] the experimental details for the individual reactions of α,α-dichlorotoluene, dichlorodiphenylmethane and dibromomethane with $(Et_3P)_4Ni$ or for the reaction of dichlorodiphenylmethane with $(Cod)_2Ni$ have already been published. The following experiment is described here for the first time.

A solution of $(Cod)_2Ni$ (**34**, 1.35 g, 4.90 mmol) and α,α-dichlorotoluene (**30**, 0.40 g, 2.40 mmol) in 20 mL of THF was stirred for 2 h at 25 °C. Quenching with deoxygenated 6 N HCl under argon. Usual workup (diethyl ether extraction, neutralization with solid $NaHCO_3$, solvent removal and flash chromatography) permitted the isolation of only *trans*-stilbene (**31**) (225 mg, 96%).

**Reactions of $(Cod)_2Ni$ (34) with α,α-Dichlorotoluene (30) in the Presence of Benzophenone (28):** A reaction run almost identical to the foregoing was conducted, except that 1 equiv. of benzophenone (**32**) was present. The analogous workup of the reaction mixture and flash chromatography led only to *trans*-stilbene (94%), with 90% of the benzophenone recovered.

**Reaction of $(Cod)_2Ni$ (34) with Benzyl Phenyl Sulfone (39):** A solution of **34** (1.24 g, 4.50 mmol) and **39** (1.05 g, 4.50 mmol) in 60 mL of dry, deoxygenated toluene became black upon mixing the components. The black mixture was stirred at 25 °C for 4 h and then at reflux for 3 h, during which latter period a nickel mirror appeared on the flask wall. Hydrolysis of the mixture with deoxygenated, aqueous 6 N HCl led to gas evolution. Separation and drying of the toluene layer, removal of solvent and flash

 © 2007 Wiley-VCH Verlag GmbH & Co. KGaA, Weinheim 

chromatography led to the isolation of *trans*-stilbene (0.81 g, 39%) and recovered **39**. No sign of bibenzyl was seen in the $^1$H NMR spectrum of the crude reaction product.

## Acknowledgments

This research has received the financial support of Akzo Corporate Research America Inc. and the Boulder Scientific Company, Mead, Colorado. Furthermore, through an Alexander von Humboldt Senior Scientist Award, the corresponding author was able to spend his sabbatical leave during the academic year of 2005–2006 in the Institute of Inorganic Chemistry of the Munich Technical University, Germany. There, in the research group of Wolfgang A. Herrmann, he received much insight into the chemistry of nitrogenr heterocyclic carbene complexes of transition metal salts. Finally, the authors are grateful for valuable orienting experiments with nickel(0) and zirconium(II) carbenoid reactions to former coworkers, Drs. Adetenu Adeosun, Tomasz Dluzniewski, Somnath Dutta and Xin Ma.

[1] J. J. Eisch, A. A. Adeosun, J. M. Birmingham, *Eur. J. Inorg. Chem.* **2007**, 39–43.
[2] a) P. W. Jolly, G. Wilke, *The Organic Chemistry of Nickel*, Academic Press, New York, **1974**, vol. 1, pp. 110ff., 139ff., 329ff.; b) P. W. Jolly, G. Wilke, *The Organic Chemistry of Nickel*, Academic Press, New York, **1975**, vol. 2, p. 400.
[3] J. J. Eisch, S. R. Sexsmith, *Res. Chem. Intermed.* **1990**, *13*, 149–152.
[4] J. J. Eisch, L. E. Hallenbeck, K. I. Han, *J. Am. Chem. Soc.* **1986**, *108*, 7763–7767.
[5] J. J. Eisch, K. R. Im, *J. Organomet. Chem.* **1977**, *139*, C45–C50.
[6] T. Hayashi, M. Kumada, *Acc. Chem. Res.* **1982**, *15*, 395–401.
[7] J. J. Eisch, Y. Qian, M. Singh, *J. Organomet. Chem.* **1996**, *512*, 207–217.
[8] a) Cf. infra for the XRD and $^{13}$C NMR evidence justifying the ylide resonance structure **22c** as the paramount contributor to the π-electron distribution of this molecule: b) M. P. Cooke Jr, R. M. Parlman, *J. Org. Chem.* **1975**, *40*, 531–532.
[9] a) E. C. Schreiber, E. I. Becker, *J. Am. Chem. Soc.* **1954**, *76*, 6125–6127; b) the preparative procedure for **21** has been developed in this laboratory and is published here for the first time.
[10] F. Ramirez, S. Levy, *J. Org. Chem.* **1956**, *21*, 488–489.
[11] a) H. L. Ammon, G. L. Wheeler, P. H. Waats Jr, *J. Am. Chem. Soc.* **1973**, *95*, 6158–6163; b) in ref.[11a], such percentages for **24** ranged from 20% to 80%, depending upon the method of calculation.
[12] S. Neander, F. E. Tio, R. Buschman, U. Behrens, F. Olbrich, *J. Organomet. Chem.* **1999**, *582*, 58–65. For the potassium (18-crown-6) salt the C–C bonds range from 1.371–1.411 Å.
[13] a) L. M. Engelhardt, R. I. Papasergio, C. L. Raston, G. Salem, C. R. Whitaker, *J. Chem. Soc. Dalton Trans.* **1987**, 1647–1653; b) R. M. Silverstein, G. C. Bassler, T. C. Morill, *Spectroscopic Identification of Organic Compounds*, 5th ed., John Wiley, New York, **1991**, p. 239: "Shifts (in the $^{13}$C NMR signals) of the aromatic carbon atom directly attached to the substituent have been correlated with substituent electronegativity after correcting for magnetic anisotropy effects". On the Allred-Rochow scale phosphorus at 2.06 is electron-releasing relative to carbon at 2.50 and thus magnetically shielding towards carbon.
[14] A referee has been helpful in suggesting the possibility of path b as an alternative possibility for producing **22c** from **19** and **20** without the intermediacy of a nickel(II)-carbene. In addition, the same referee suggested the key experiment for deciding on the viability of path b as a competing mechanism, namely whether or not **19** and **20a** would react with each other at 25 °C.
[15] a) F. Ramirez, N. McKelvie, *J. Am. Chem. Soc.* **1957**, *79*, 5829–5830. b) Although this report appeared 50 years ago, it has not been repudiated since and in fact is treated as reliable in a classic monograph on organophosphorus reactions: R. F. Hudson, *Structure and Mechanism in Organo-Phosphorus Chemistry*, Academic Press, New York, **1965**, pp. 297–299.
[16] When the THF solution of the final reaction mixture was concentrated to half its volume and then cooled to 0 °C, dark red crystals of bis(triethylphosphane)nickel(II) chloride were deposited, mp. 113–115 °C (68%); D. T. Doughty, G. Gordon, R. P. Stewart Jr, *J. Am. Chem. Soc.* **1979**, *101*, 2645–2648.
[17] A referee has proposed that in such coupling reactions of geminal dihalides with $(Et_3P)_4Ni$ (**20**) perhaps metal carbenes are not involved at all, that maybe they are just phosphonium ylide adducts, $R_3P^+–CR_2–^-NiCl_2$ and, as Milstein and co-workers have shown, that ylides could be converted to metal-carbenes by late transition metal compounds (M. Gandelman, K. M. Naing, B. Rybtchinski, E. Poverenov, Y. Ben-David, N. Ashkenazi, R. M. Gauvin, D. Milstein, *J. Am. Chem. Soc.* **2005**, *127*, 15265–15272). Admittedly, our work has shown that phosphonium ylide **22c** is readily formed from dibromo compound **19** and $(Et_3P)_4Ni$ (**20**) and that **30** and **20** produce Wittig reagent **37** in solution, which is capable of being captured in a Wittig reaction with benzophenone. Despite the presence of **37** in such reactions, such phosphonium ylides or their complexes with $NiCl_2$ cannot be essential intermediates in these coupling reactions, because **30** can be converted into olefin dimer **31** in over 90% yield either by $(Et_3P)_4Ni$ or by $(Cod)_2Ni$. Obviously, the latter nickel(0) complex could not involve any phosphonium ylide. In fact, any phosphonium ylide generated with **30** may be in ready equilibrium with the crucial carbene intermediate **36a** (**36** with coordinated $Et_3P$):

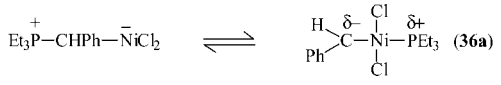

**(36a)**

[18] The likelihood of a bridging halide between the nickel centers in the proposed activated complex **38** is supported by the known dimeric structure of η$^4$-tetraphenylcyclobutadiene–nickel(II) bromide where the two units of the monomer are held together by two Ni···Br···Ni bridges.
[19] The failure to detect triphenylethylene in this trapping experiment with benzaldehyde can stem from either of two causes: (1) the supposed ylide, $Ph_2C{=}PEt_2$, is too slow to react with PhCHO, before it reacts thus: $Ph_2C{=}PEt_3 + Ph_2C(Cl)NiCl \rightarrow Ph_2C{=}CPh_2 + (Et_3P)_2NiCl_2$; or (2) in analogy with Scheme 7, $Et_3P$ is unable, for steric reasons, to react with $Ph_2C–NiCl_2$ (**36**) before coupling occurs via **38**.
[20] The α-elimination of lithium benzenesulfinate from Ph–CHLi–$SO_2$Ph cannot be effected by heating this dry salt under argon at 90–120 °C for 5 h. No trace of either *cis*- or *trans*-stilbene could be detected upon hydrolytic workup and 90% of the starting sulfone was recovered. By contrast, irradiation of Ph–CHLi–$SO_2$Ph in THF under argon in a quartz tube in a Rayonet rotating reactor (model 100), equipped with lamptubes of 254 nm wavelength for 24 h and subsequent hydrolysis yielded upon liquid chromatography on silica gel with a hexane eluent: (a) a 1:1.3 mixture of *cis*- and *trans*-stilbenes (33%); and (b) *cis*- and *trans*-1,2,3-triphenylcyclopropanes (25%), besides recovered Ph–$CH_2$–$SO_2$–Ph. The cyclopropanes were identified by their C-H proton singlets at $\delta$ = 2.82 (*cis*) and 2.73 (*trans*) ppm ($CDCl_3$) and the mass spectrum of the mixture: MS (70eV): *m/z* = 270 [M], 179, 178, 152, 89, 77 (Y. Qian, Masters Thesis, SUNY-Binghamton, **1992**, p. 57; Y. Qian, Research Notebook No. 1, May 22, **1991**, p. 36). More to the point of this study, however, is the finding that 1–10 mol-% of Ni(acac)$_2$ can cause the catalytic elimination of LiOSOPh from Ph–CHLi–$SO_2$Ph in THF from 0 °C to reflux, leading to variable proportions of solely *trans*-stilbene and *trans*-1,2,3-triphenylcyclopropane, as attested to by their IR, $^1$H NMR and

 © 2007 Wiley-VCH Verlag GmbH & Co. KGaA, Weinheim 

mass spectra on pure samples separated by column chromatography (silica gel/hexane). In two separate further experiments, one with 1,1-diphenylethylene and the other with diphenylacetylene, the benzylidene fragment from Ph–CHLi–$SO_2$Ph was trapped as 1,1,2-triphenylcyclopropane and 1,2,3-triphenylcyclopropene, respectively (ref.[7]; Y. Qian, Doctoral Dissertation, SUNY-Binghamton, **1996**, pp. 117–118; Y. Qian, Research Notebook No. 1, October 19, **1991**, p. 66). The detailed mechanisms of these carbenoid oligomerizations are under further investigation.

[21] J. J. Eisch, *Organometallic Syntheses*, Academic Press, New York, **1981**, vol. 2, pp. 1–84.

[22] M. F. Semmelhack, *Org. React.* **1972**, *19*, 178–179.

[23] R. A. Schunn, *Inorg. Synth.* **1974**, *15*, 5–9.

[24] C. S. Cundy, *J. Organomet. Chem.* **1974**, *69*, 305–310.

[25] E. Dinjus, I. Gorski, E. Uhlig, H. Walther, *Z. Anorg. Allg. Chem.* **1976**, *75*, 422–428.

[26] T. Yamamoto, T. Kohara, K. Osakada, A. Yamamota, *Bull. Chem. Soc. Jpn.* **1983**, *56*, 2147–2153.

Received: November 22, 2006
Published Online: February 26, 2007

 © 2007 Wiley-VCH Verlag GmbH & Co. KGaA, Weinheim 

DOI: 10.1002/ejic.200601118

# The Ditertiary-Phosphane-Bridged Heteronuclear Cluster $RuOs_3(\mu\text{-}H)_2(CO)_9(\mu\text{-}CO)_2(\mu\text{-}dppm)$: Synthesis and Reactivity with Alkynes

**Yong Leng Kelvin Tan[a] and Weng Kee Leong*[a]**

**Keywords:** Heterometallic complexes / Ruthenium / Osmium / Ditertiary phosphanes / Alkynes

A high-yielding alternative synthesis of the dppm-bridged heteronuclear cluster $RuOs_3(\mu\text{-}H)_2(CO)_9(\mu\text{-}CO)_2(\mu\text{-}dppm)$ (**1**) [dppm = bis(diphenylphosphanyl)methane] has been developed. Thermolysis of **1** resulted in dephenylation of both phosphane groups to afford the butterfly cluster $RuOs_3(CO)_{12}(\mu_4,\kappa^2\text{:}\kappa^2\text{-}PhPCH_2PPh)$ (**2**). The reaction of **1** with selected alkynes afforded the products $RuOs_3(\mu\text{-}H)(CO)_8(\mu\text{-}CO)(\mu_3,\kappa^2\text{:}\kappa^1\text{-}PhPCH_2PPh_2)(\mu_3,\eta^1\text{:}\eta^2\text{:}\eta^1\text{-}L)$ (**3**) (L = alkyne) in which the alkyne is aligned parallel to an Os–Os bond (// Os-Os isomer). The clusters incorporating internal alkynes underwent isomerization to the //Ru-Os isomer by alkyne and hydride migration. Several other cluster products of these reactions were also identified, including $RuOs_3(\mu\text{-}H)(CO)_8(\mu\text{-}CO)(\mu_3,\kappa^2\text{:}\kappa^1\text{-}PhPCH_2PPh_2)(\mu_3,\eta^1\text{:}\eta^2\text{:}\eta^1\text{-}t\text{Bu}C_2CHO)$ (**6**) in which the methyl group of the alkyne has been oxidized to an aldehyde.
(© Wiley-VCH Verlag GmbH & Co. KGaA, 69451 Weinheim, Germany, 2007)

## 1. Introduction

Ditertiary phosphane ligands continue to play an important role in the chemistry of transition-metal clusters because they have the ability to maintain the integrity of the metal framework during chemical reactions, preventing cluster fragmentation and enhancing the catalytic activity of the ditertiary-phosphane-stabilized cluster. Several tri- and tetranuclear ruthenium clusters containing ditertiary phosphane ligands have been studied for their catalytic potential in alkene hydrogenation and isomerization reactions.[1] For these studies, the presence of the phosphane ligand ensured that cluster nuclearity was maintained even under severe reaction conditions. These clusters were found to exhibit greater thermal stability and lower tendency towards decomposition at higher pressure, clearly pointing to the cluster-stabilizing properties of the ditertiary phosphane ligand. In contrast, the catalytic potential of heteronuclear clusters incorporating ditertiary phosphane ligands remains relatively unexplored. The combination of different transition metals within the same framework in heteronuclear clusters may induce novel forms of substrate activation, thus giving rise to interesting chemistry. We have been investigating the chemistry of the hetero group 8 tetranuclear cluster $RuOs_3(\mu\text{-}H)_2(CO)_{13}$ and its derivatives.[2] In the course of our investigations, we have found that the cluster fragments at elevated temperatures. Our efforts to incorporate the dppm ligand onto the cluster by TMNO (trimethylamine-*N*-oxide) activation have led to the isolation of $RuOs_3(\mu\text{-}H)_2(CO)_9(\mu\text{-}CO)_2(\mu\text{-}dppm)$ (**1**) in moderate yield (57%), together with other products.[3] We were interested in further exploring the reactivity and catalytic potential of **1**. In this paper, we would like to report an alternative, high-yield, synthetic route to **1** and our investigations into its reactions with a number of representative alkynes.

## 2. Results and Discussion

### 2.1. Synthesis and Thermal Stability of $RuOs_3(\mu\text{-}H)_2(CO)_9(\mu\text{-}CO)_2(\mu\text{-}dppm)$ (1)

The mononuclear ruthenium complex $Ru(CO)_4(\kappa^1\text{-}dppm)$, which can be prepared in situ by treating dppm with $Ru(CO)_4(C_2H_4)$,[4] has been shown to be a versatile building block for increasing cluster nuclearity. The pendant arm of the ditertiary phosphane can aid the joining of the mononuclear complex to the target cluster; subsequently, metal–metal interactions can be facilitated between the two units held in close proximity to each other.[5] Thus the addition of $Os_3(\mu\text{-}H)_2(CO)_{10}$ to a hexane solution of $Ru(CO)_4(\kappa^1\text{-}dppm)$ resulted in an instantaneous color change to light yellow. Subsequent workup afforded **1** in 82% yield; the minor side products obtained were $Ru_3(CO)_{12}$ and $RuOs_3(\mu\text{-}H)_2(CO)_{13}$ (Scheme 1).

Thermolysis of **1** in refluxing hexane afforded the novel butterfly cluster $RuOs_3(CO)_{12}(\mu_4,\kappa^2\text{:}\kappa^2\text{-}PhPCH_2PPh)$ (**2**) and the trinuclear cluster $Os_3(\mu\text{-}H)_2(CO)_8(\mu\text{-}dppm)$ in 69% and 15% yields, respectively. The unsaturated, 46-electron hydrido osmium cluster $Os_3(\mu\text{-}H)_2(CO)_8(\mu\text{-}dppm)$ has previously been obtained by the treatment of either $Os_3(\mu\text{-}H)(CO)_8[Ph_2PCH_2PPh(C_6H_4)]$ or $Os_3(\mu\text{-}H)_2(CO)_7(\mu\text{-}dppm)(\mu_3\text{-}CN_2)$ with hydrogen gas at elevated tempera-

[a] Department of Chemistry, National University of Singapore, Kent Ridge, Singapore 119260
Supporting information for this article is available on the WWW under http://www.eurjic.org or from the author.

 © 2007 Wiley-VCH Verlag GmbH & Co. KGaA, Weinheim 

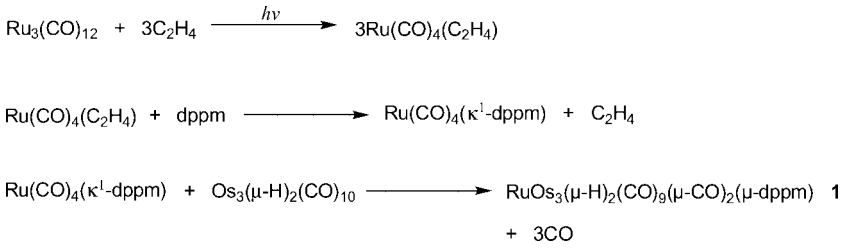


Scheme 1.

tures.[6] The novel cluster **2** has been completely characterized by spectroscopic, elemental and single-crystal X-ray crystallographic analyses; an ORTEP plot showing the atomic numbering scheme and selected bond parameters are given in Figure 1.

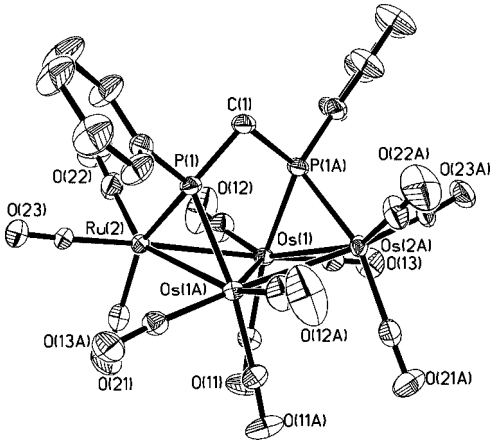


Figure 1. ORTEP diagram (50% probability thermal ellipsoids, organic hydrogen atoms omitted). Selected bond lengths [Å] and angles [°] for **2**: Os(1)–Os(1A) = 2.9067(6), Os(1)–Ru(2) = 2.9289(6), Os(1A)–Ru(2) = 2.8236(6), P(1)–Os(1A) = 2.3591(14), P(1)–Ru(2) = 2.3228(15); Ru(2)–Os(1)–Os(1A) = 61.456(16), Os(1)–Os(1A)–Ru(2) = 57.875(12), Os(1A)–Ru(2)–Os(1) = 60.669(13), Ru(2)–P(1)–Os(1A) = 74.18(4). There is Ru/Os disorder (1:1) over Ru(2) and Os(2A).

The cluster valence electron count for cluster **2** is 62, which is in accord with that predicted by the effective atomic number (EAN) rule for a tetranuclear cluster with five metal–metal bonds.[7] The dihedral angle between the two wings of the butterfly core of **2** is 150.9°. Dephenylation at each phosphane of the ligand has led to phosphanido bridges across two metal–metal bonds. The phenyl groups were probably lost as benzenes with the cluster-bound hydrides.[1c,8] There is a total of twelve carbonyl groups on the cluster, compared to eleven in cluster **1**, the additional carbonyl ligand presumably coming from other decomposition products of the reaction.

The spectroscopic data obtained confirms that the solid-state structure of **2** is retained in solution. The $^{31}P\{^1H\}$ NMR spectrum comprised two sets of doublets at $\delta$ = 77.40 and –22.34 ppm. A downfield shift of the phosphorus signals relative to those observed for **1**, in addition to the large $^2J_{PP}$ of 116.4 Hz, supported the presence of two bridging phosphanido moieties.[9] On the basis of previous observations that a phosphanido bridge across an Os–Os bond resonates at a higher field than one across a Ru–Os edge,[2b,10] the higher-field phosphorus resonance has been assigned to the phosphanido bridging the Os–Os bond.

### 2.2. Reaction of 1 with Alkynes

The reaction of **1** with the alkynes diphenylacetylene, 2-pentyne, 4,4-dimethyl-2-pentyne, phenylacetylene, or *tert*-butylacetylene, at elevated temperatures, afforded up to two products, **3** and **4**, each with the general formula $RuOs_3(\mu\text{-}H)(CO)_8(\mu\text{-}CO)(\mu_3,\kappa^2\text{:}\kappa^1\text{-}PhPCH_2PPh_2)(\mu_3,\eta^1\text{:}\eta^2\text{:}\eta^1\text{-}L)$ [L = PhCCPh (**a**), $C_2H_5CCCH_3$ (**b**), *t*BuCCCH$_3$ (**c**) for **3** and **4**; PhCCH (**d**), *t*BuCCH (**e**) for **3** (products **4d** and **4c** were not obtained)], as well as some other minor products in some cases (Scheme 2).

Clusters **3** and **4** are isomers differing in whether the $\mu_3,\eta^1\text{:}\eta^2\text{:}\eta^1$-bonded alkyne is parallel to an Os–Os edge (// Os-Os isomer, **3**), or to an Ru–Os edge (// Ru-Os isomer, **4**). Clusters **3** and **4** are also of interest because, in general, tetranuclear clusters tend to form butterfly clusters on reaction with alkynes, i.e., cleavage of a metal–metal bond is common.[11] Thus there are rarely examples in which the tetrahedral core is retained.[2g,12] In the formation of these clusters, dephenylation of one of the phosphane groups of the dppm ligand has occurred. Clusters **3** and **4** have been characterized spectroscopically and analytically, and for **3a**–**e** and **4a**–**b**, by single-crystal X-ray crystallographic studies as well; the ORTEP plots for **3b** and **4b** are shown in Figure 2 and Figure 3, respectively.

### 2.3. Structural Discussion on 3 and 4

Selected bond parameters and a common atomic numbering scheme for clusters **3a**–**e** are given in Table 1.

The metal core in clusters **3** adopts a closed tetrahedral geometry, with a valence electron count of 60, as predicted by the EAN rule.[7] The five-electron donor $PhPCH_2PPh_2$ phosphanido-phosphane ligand caps the Os(1)–Os(2)–Ru(4) triangular metal face of the tetrahedron, the phosphanido group adopting an asymmetrical bridging mode in which the Os(2)–P(2) bond is significantly shorter than the Ru(4)–P(2) bond. C–C bond elongation of the coordinated alkynes is observed, with lengths ranging from 1.366(14) to 1.426(12) Å, which are in the ranges of carbon–carbon $sp^2$–$sp^2$ double and single bonds (1.32 and 1.48 Å, respectively).[13] In principle, for such unsymmetrical alkynes, there is the possibility of alkyne isomerism, i.e., the forma-

 © 2007 Wiley-VCH Verlag GmbH & Co. KGaA, Weinheim 

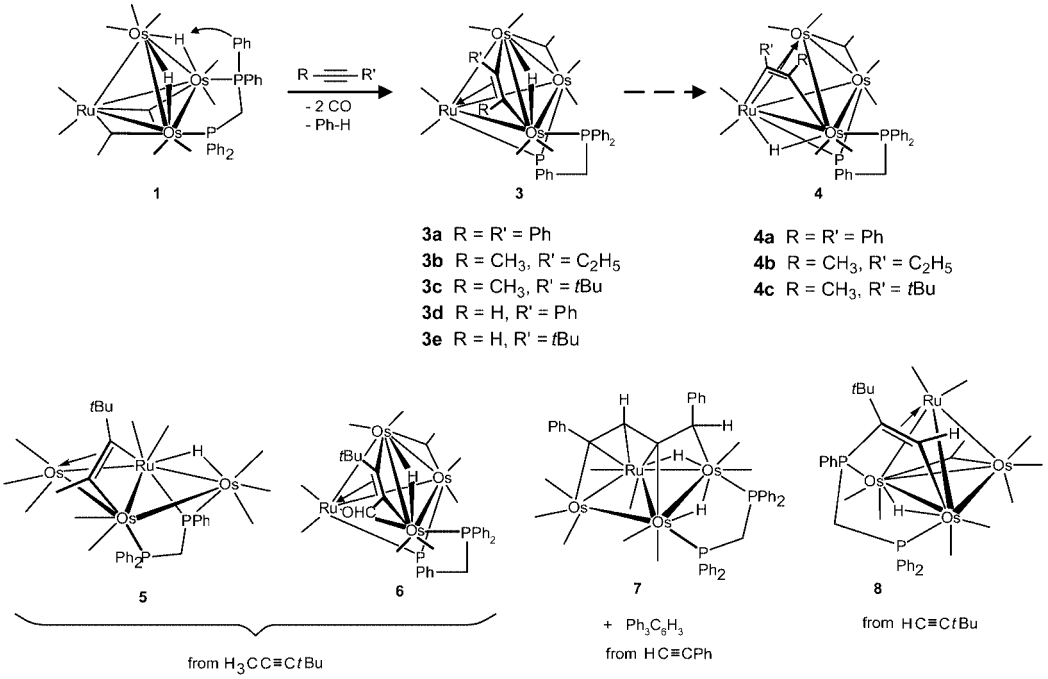


Scheme 2.

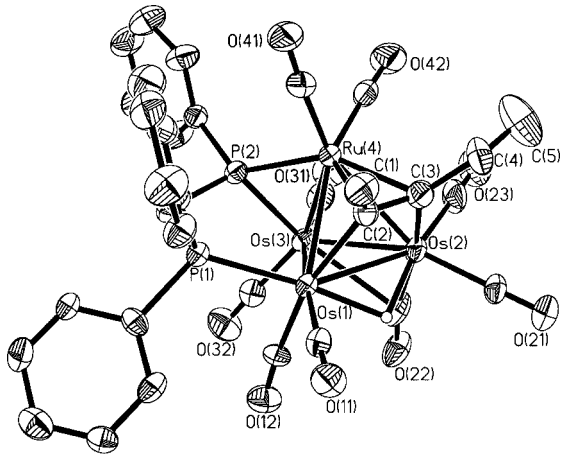


Figure 2. ORTEP diagram (50% probability thermal ellipsoids, organic hydrogen atoms omitted) for **3b**.

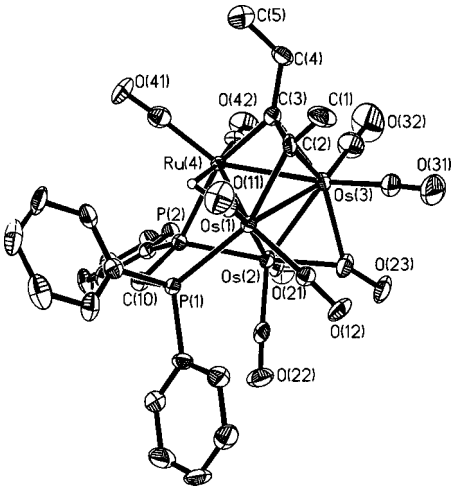


Figure 3. ORTEP diagram (50% probability thermal ellipsoids, organic hydrogen atoms omitted) for **4b**.

tion of isomers which differ in the orientation of the substituents on the alkyne with respect to the phosphanido bridge.[14] The stereoselectivity in **3** may be rationalized by the steric interaction between the phosphane ligand and the bulkier substituent on the alkyne moiety.

The metal–metal bond lengths for **3** show some fairly clear trends. The longest metal–metal contact in the tetrahedral core is in the triangular metal face capped by the phosphanido-phosphane moiety; the lengthening of the Os(1)–Os(2) vector is likely to have resulted from the need to accommodate the steric demands imposed by the phosphanido-phosphane ligand. In comparison to the corresponding distances in $RuOs_3(\mu\text{-}PPh_2)(\mu\text{-}H)_3(CO)_{11}$, $RuOs_3(\mu\text{-}PPh_2)_2(\mu\text{-}H)_2(CO)_{10}$, $RuOs_3(\mu\text{-}PPh_2)_2(\mu\text{-}H)_4(CO)_9$, and $RuOs_3(\mu\text{-}PPh_2)(\mu\text{-}H)_3(CO)_{10}(PPh_3)$,[2b] the phosphanido-bridged Os(2)–Ru(4) bond in **3** (average 2.788 Å) is shorter. One interesting feature is that the Os(1)–Os(3) bond does not display the usual lengthening associated with a hydride-bridged metal–metal vector. This may be ascribed to the presence of the alkyne ligand, which also spans the same edge, therefore countering the normal lengthening effect. The shortest metal–metal separation in the cluster [Os(2)–Os(3)] is associated with the bridging carbonyl group.

A similar tabulation for **4a** and **4b** is given in Table 2; attempts to grow suitable crystals of **4c** proved unsuccessful. There are two crystallographically independent molecules

 © 2007 Wiley-VCH Verlag GmbH & Co. KGaA, Weinheim 

Table 1. Common atomic numbering scheme and selected bond parameters for clusters **3**.

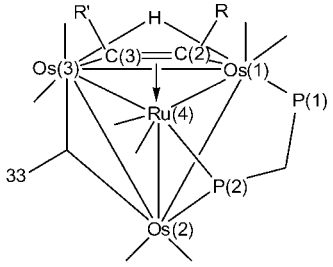


**3a** R = R' = Ph
**3b** R = $CH_3$, R' = $C_2H_5$
**3c** R = $CH_3$, R' = *t*Bu
**3d** R = H, R' = Ph
**3e** R = H, R' = $^t$Bu

| | **3a** | **3b** | **3c** | **3d** | **3e**[a] |
|---|---|---|---|---|---|
| Bond lengths [Å] | | | | | |
| Os(1)–Os(2) | 2.9138(4) | 2.9090(5) | 2.8837(4) | 2.9005(3) | 2.8856(11) |
| Os(1)–Os(3) | 2.8564(4) | 2.8607(5) | 2.8394(4) | 2.8607(3) | 2.8667(7) |
| Os(1)–Ru(4) | 2.7691(6) | 2.7756(8) | 2.7760(5) | 2.7594(4) | 2.7743(7) |
| Os(2)–Os(3) | 2.6662(4) | 2.7171(5) | 2.7174(4) | 2.7028(3) | 2.7307(11) |
| Os(2)–Ru(4) | 2.7950(6) | 2.7799(8) | 2.7713(5) | 2.7983(4) | 2.7977(11) |
| Os(3)–Ru(4) | 2.8631(6) | 2.8060(8) | 2.8045(5) | 2.8268(4) | 2.8237(7) |
| Os(1)–P(1) | 2.3584(18) | 2.336(2) | 2.3405(17) | 2.3406(14) | 2.337(3) |
| Os(2)–P(2) | 2.2472(19) | 2.242(2) | 2.2514(17) | 2.2362(14) | 2.231(3) |
| Ru(4)–P(2) | 2.3503(18) | 2.340(3) | 2.3436(17) | 2.3210(14) | 2.326(3) |
| Os(2)–C(33) | 2.525(8) | 2.582(10) | 2.575(7) | 2.578(6) | 2.565(16) |
| Os(3)–C(33) | 2.004(9) | 1.960(13) | 1.981(7) | 1.955(7) | 1.948(16) |
| Os(1)–C(2) | 2.191(7) | 2.138(10) | 2.168(6) | 2.141(5) | 2.117(13) |
| Os(3)–C(3) | 2.080(8) | 2.133(10) | 2.159(6) | 2.102(5) | 2.12(13) |
| C(2)–C(3) | 1.423(10) | 1.386(14) | 1.409(9) | 1.401(7) | 1.397(18) |
| Bond angles [°] | | | | | |
| Os(2)–P(2)–Ru(4) | 74.84(6) | 74.68(7) | 74.15(5) | 75.74(4) | 75.71(10) |
| Os(2)–C(33)–Os(3) | 71.1(3) | 72.0(3) | 71.9(2) | 71.7(2) | 73.0(5) |

[a] Disorder of ruthenium over Os(2) and Ru(4).

in the asymmetric unit of **4a**; their bond parameters are fairly similar. The crystals of both **4a** and **4b** exhibited disorder of the ruthenium atom about two alternative sites in the metal framework. This disorder was solved with ruthenium occupancies of about 0.08 and 0.92 at M(3) and M(4), respectively, for **4a**, and 0.07 and 0.93 at M(3) and M(4), respectively, for **4b**. As in **3**, the phosphanido-phosphane bridged Os(1)–Os(2) edge is the longest metal–metal bond in the tetrahedral core, while the carbonyl-bridged Os(2)–Os(3) bond is the shortest.

The NMR spectra of both **4a** and **4b** indicated the presence of two isomers in an approximately 11:1 ratio in solution. The hydride resonances for each of these isomers appear as doublets of doublets of doublets; the coupling constants have been confirmed by selective decoupling experiments. The splitting pattern and values of the coupling constants provided further evidence that the hydride bridges the same metal–metal edge as the phosphanido-phosphane ligand and is found in a *cisoid* position relative to the two phosphorus atoms. Both the $^{31}P\{^1H\}$ and the $^1H$ NMR spectra of **4c** indicated that three isomers are present in an approximately 8:1:1 ratio in solution. $^{31}P\{^1H\}$-$^{31}P\{^1H\}$ COSY and $^{31}P\{^1H\}$-$^1H$ HMBC experiments were carried out to aid the elucidation of the P-P and P-H correlations, while the coupling constants were confirmed by $^1H\{^{31}P\}$ selective decoupling experiments. A 2D $^1H$ EXSY experiment performed at ambient temperature indicated no chemical exchange between the three isomers of **4c**. The proposed solution-state structures and tentative NMR assignments for **4a**–**c** are shown in Figure 4, and at least for **4a** and **4b**, are consistent with the disorder observed in the solid state.[2c–2f]

The hydride resonances for **4** were shifted upfield relative to those for the corresponding isomer **3**. This may be ascribed to an increase in electron density at the hydride for **4**, since the hydride spans the Os(1)–Ru(4) edge, which contains the bridging phosphanido-phosphane ligand and is thus expected to be the most electron-rich metal–metal bond.[15] The two phosphorus resonances for **4a**–**c** are also shifted downfield relative to **3a**–**c**. More notably, the values of the $^2J_{PP}$ coupling constants for **4a**–**c** are almost twice those found for **3a**–**c**, although the P–C–P bond angle in the two isomers do not differ significantly.

### 2.4. Isomerism of 3a–c to 4a–c

Thermolysis of **3a**–**c** afforded the isomeric products **4a**–**c**, respectively; clusters **3d** and **3e** (which incorporated terminal alkynes) did not exhibit isomerization under similar

 © 2007 Wiley-VCH Verlag GmbH & Co. KGaA, Weinheim 

Table 2. Common atomic numbering scheme and selected bond parameters for **4a** and **4b**.

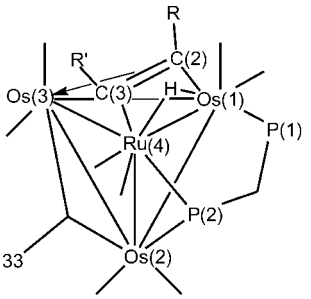


**4a** R = R' = Ph
**4b** R = $CH_3$, R' = $C_2H_5$

| | **4a** (Molecule A)[a] | **4a** (Molecule B)[a] | **4b**[b] |
|---|---|---|---|
| Bond lengths [Å] | | | |
| Os(1)–Os(2) | 2.9210(14) | 2.9184(14) | 2.9272(5) |
| Os(1)–Os(3) | 2.7774(15) | 2.7730(15) | 2.7744(5) |
| Os(1)–Ru(4) | 2.837(2) | 2.843(2) | 2.8360(7) |
| Os(2)–Os(3) | 2.6114(15) | 2.6290(16) | 2.6281(5) |
| Os(2)–Ru(4) | 2.821(2) | 2.807(2) | 2.7955(7) |
| Os(3)–Ru(4) | 2.786(2) | 2.777(2) | 2.7682(7) |
| Os(1)–P(1) | 2.384(7) | 2.377(7) | 2.376(2) |
| Os(2)–P(2) | 2.338(7) | 2.331(7) | 2.335(2) |
| Ru(4)–P(2) | 2.327(7) | 2.325(7) | 2.341(9) |
| Os(2)–C(33) | 1.96(3) | 2.00(3) | 2.039(9) |
| Os(3)–C(33) | 2.39(3) | 2.36(3) | 2.287(9) |
| Os(1)–C(2) | 2.18(2) | 2.21(2) | 2.134(9) |
| Ru(4)–C(3) | 2.13(3) | 2.15(3) | 2.111(8) |
| C(2)–C(3) | 1.42(3) | 1.42(3) | 1.411(12) |
| Bond angles [°] | | | |
| Os(2)–P(2)–Ru(4) | 74.4(2) | 74.2(2) | 73.42(6) |
| Os(2)–C(33)–Os(3) | 73.1(10) | 73.6(9) | 74.6(3) |

[a] Disorder of Ru over Os(3) and Ru(4), with Ru occupancies of 8 and 92%, respectively. [b] Disorder of Ru over Os(3) and Ru(4), with Ru occupancies of 7 and 93%, respectively.

conditions. Clusters **3** and **4** are the kinetic and thermodynamic products, respectively. It has been noticed that, in several heterometallic clusters, the coordinated alkynes are apparently oriented such that the π-bond is directed towards the less electron-rich metal.[16] Likewise, in ditertiary-phosphane-substituted triosmium clusters incorporating hydride ligands, the hydride is observed to occupy the most electron-rich metal–metal bond in the cluster.[15] In **4**, the Os(1) and Ru(4) metal atoms are electron-rich as a result of σ-donation from the ligating phosphanidophosphane moiety, which probably is the driving force for the reorientation of the alkyne and hydride over the Os(1)–Os(3)–Ru(4) edge.

The isomerization of **3a**–**c** to **4a**–**c** involves a flipping of the alkyne ligand about the Os(1)–Os(3)–Ru(4) face, coupled with hydride migration from the Os(1)–Os(3) to the Os(1)–Ru(4) edge. It is envisaged that this dynamic process occurs via an intermediate in which the alkyne is coordinated in a $\mu_3,\eta^2{:}\eta^2$ perpendicular fashion (Scheme 3). Such a process has been previously proposed to account for the observed rotation of parallel-coordinated alkynes on a triosmium cluster.[17] More recently, a reversed scheme termed *switchback motion* has been suggested to explain the fluxional behavior of the triruthenium cluster $[\{Cp^*Ru(\mu\text{-}H)\}_3(\mu_3,\eta^2{:}\eta^2\text{-}C_5H_6)]$.[18] We have monitored the isomerization of **3c** to **4c** by $^1H$ NMR spectroscopy and found that it is a very slow process at ambient temperature. After five months at ambient temperature, the mixture was heated in refluxing hexane for 4 h in order to obtain the equilibrium concentrations. The final spectrum recorded after thermolysis of the mixture gave $K_{eqm} = [\mathbf{4c}]_{eqm}/[\mathbf{3c}]_{eqm} = 10.9$ and $\Delta G = -RT \ln K_{eqm} = -5.92\ kJ\,mol^{-1}$. The half-life for the isomerization was estimated to be ca. 77 d.

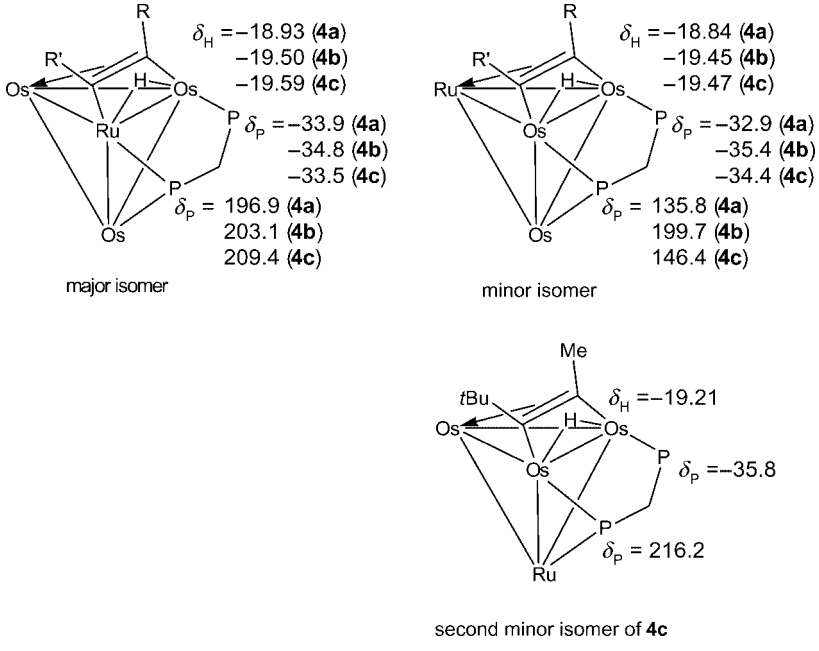


Figure 4. Proposed solution-state structures and tentative NMR assignments for **4** (carbonyl and phenyl groups omitted).

 © 2007 Wiley-VCH Verlag GmbH & Co. KGaA, Weinheim 

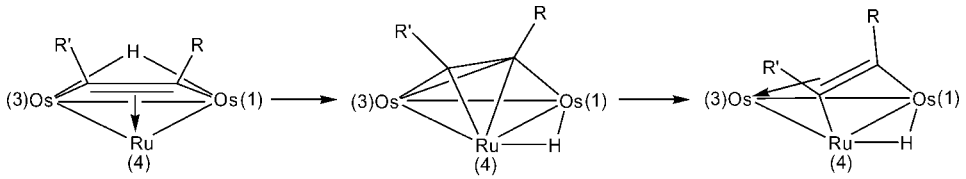


**3a** R = R' = Ph
**3b** R = $CH_3$, R' = $C_2H_5$
**3c** R = $CH_3$, R' = *t*Bu

**4a** R = R' = Ph
**4b** R = $CH_3$, R' = $C_2H_5$
**4c** R = $CH_3$, R' = *t*Bu

Scheme 3.

### 2.5. Other Products

A number of other novel clusters were also isolated from these reactions with alkynes, viz. $RuOs_3(\mu\text{-H})(CO)_{10}(\mu_3,\kappa^2{:}\kappa^1\text{-}PhPCH_2PPh_2)(\mu_3,\eta^1{:}\eta^2{:}\eta^1\text{-}t\text{BuC}_2CH_3)$ (**5**) and $RuOs_3(\mu\text{-H})(CO)_8(\mu\text{-CO})(\mu_3,\kappa^2{:}\kappa^1\text{-}PhPCH_2PPh_2)(\mu_3,\eta^1{:}\eta^2{:}\eta^1\text{-}t\text{BuC}_2CHO)$ (**6**) from 4,4-dimethyl-2-pentyne, $RuOs_3(\mu\text{-H})_2(CO)_9(\mu\text{-}Ph_2PCH_2PPh_2)(\mu_4,\eta^1{:}\eta^2{:}\eta^2{:}\eta^1\text{-}PhCCHCCHPh)$ (**7**) from phenylacetylene, and $RuOs_3(\mu\text{-H})(CO)_9(\mu\text{-CO})[\mu_3,\eta^1{:}\eta^2{:}\kappa^1{:}\kappa^1\text{-}(HC{=}Ct\text{Bu})PhPCH_2PPh_2]$ (**8**) from *tert*-butylacetylene. The characterization of all these clusters is complete, including single-crystal X-ray diffraction studies. The ORTEP plots and selected bond parameters for **5**–**8** are given in Figure 5, Figure 6, Figure 7, and Figure 8.

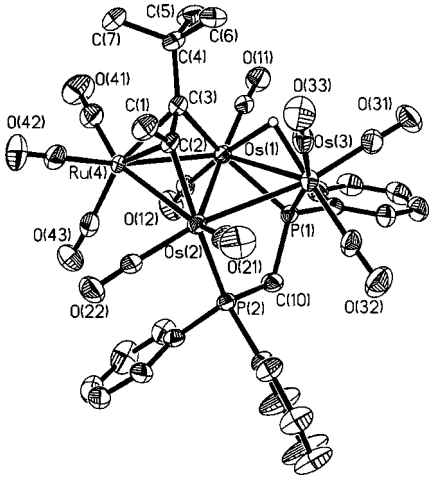


Figure 5. ORTEP diagram (50% probability thermal ellipsoids, organic hydrogen atoms omitted). Selected bond lengths [Å] and angles [°] for **5**: Os(1)–Os(2) = 2.7947(4), Os(1)–Os(3) = 2.8787(4), Os(1)–Ru(4) = 2.7535(5), Os(2)–Os(3) = 2.9403(4), Os(2)–Ru(4) = 2.7854(4), Os(1)–P(1) = 2.3010(16), Os(3)–P(1) = 2.3364(17), Os(2)–P(2) = 2.3965(17), Os(1)–C(3) = 2.204(7), Os(2)–C(2) = 2.089(6), Ru(4)–C(2) = 2.262(7), Ru(4)–C(3) = 2.181(7); Os(1)–P(1)–Os(3) = 76.74(4).

The molecular structure of **5** shows disorder of the heavy atoms, which was solved with ruthenium occupancies of 0.33 and 0.67 at M(1) and M(4), respectively. Cluster **5** comprises an open butterfly-shaped tetranuclear metal core, the two wings of the butterfly cluster having a dihedral angle of 157.6° between them. A metal-bound hydride bridges the Os(1)–Os(3) vector. The position of this hydride was located by a low-angle difference map and verified by XHYDEX calculations.[19] One triangular wing of the but-

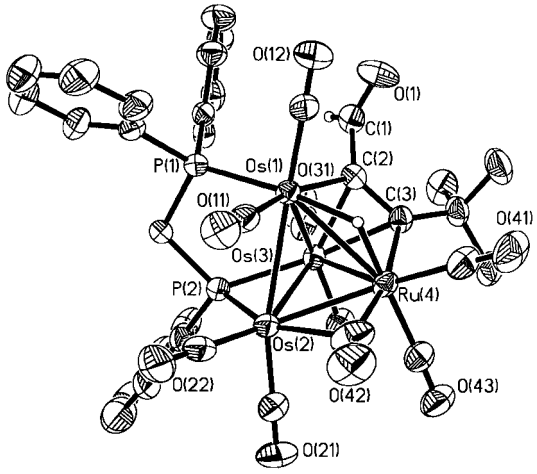


Figure 6. ORTEP diagram (50% probability thermal ellipsoids, organic hydrogen atoms omitted). Selected bond lengths [Å] and angles [°] for **6**: Os(1)–Os(2) = 2.9020(4), Os(1)–Os(3) = 2.7885(5), Os(1)–Ru(4) = 2.8649(5), Os(2)–Os(3) = 2.7861(5), Os(2)–Ru(4) = 2.7061(5), Os(3)–Ru(4) = 2.8001(5), Os(1)–P(1) = 2.3516(18), Os(2)–P(2) = 2.252(2), Os(3)–P(2) = 2.321(2), Os(1)–C(2) = 2.164(7), Os(3)–C(2) = 2.156(7), Os(3)–C(3) = 2.235(7), Ru(4)–C(3) = 2.135(7); Os(2)–P(2)–Os(3) = 75.05(6), Ru(4)–C(42)–Os(2) = 74.1(3).

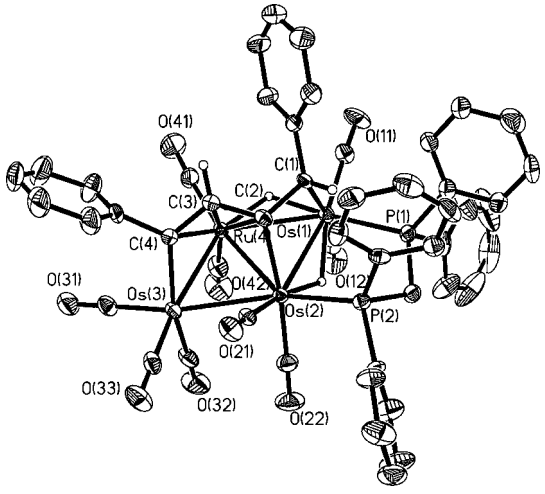


Figure 7. ORTEP diagram (50% probability thermal ellipsoids, organic hydrogen atoms omitted). Sselected bond lengths [Å] and angles [°] for **7**: Os(1)–Os(2) = 3.0121(4), Os(1)–Ru(4) = 2.9363(6), Os(2)–Os(3) = 2.9305(4), Os(2)–Ru(4) = 2.8499(6), Os(3)–Ru(4) = 2.6858(6), Os(1)–P(1) = 2.3303(18), Os(2)–P(2) = 2.3546(18), Os(1)–C(1) = 2.240(7), Os(2)–C(2) = 2.098(7), Os(3)–C(4) = 2.081(7), Ru(4)–C(2) = 2.301(7), Ru(4)–C(3) = 2.239(7), Ru(4)–C(4) = 2.249(7), C(1)–C(2) = 1.464(9), C(2)–C(3) = 1.425(10), C(3)–C(4) = 1.434(9); P(1)–Os(1)–Os(2) = 93.90(4), P(2)–Os(2)–Os(1) = 86.17(4).

 © 2007 Wiley-VCH Verlag GmbH & Co. KGaA, Weinheim 

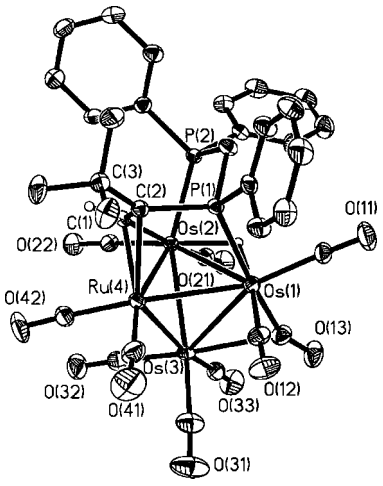


Figure 8. ORTEP diagram (50% probability thermal ellipsoids, organic hydrogen atoms omitted). Selected bond lengths [Å] and angles [°] for **8**: Os(1)–Os(2) = 2.9290(2), Os(1)–Os(3) = 2.8684(2), Os(1)–Ru(4) = 2.8484(3), Os(2)–Os(3) = 2.8319(2), Os(2)–Ru(4) = 2.7656(3), Os(3)–Ru(4) = 2.6588(3), Os(1)–P(1) = 2.3726(10), Os(2)–P(2) = 2.3382(10), Os(2)–C(1) = 2.149(4), P(1)–C(2) = 1.805(4), C(1)–C(2) = 1.407(5), Os(1)–C(13) = 1.984(5), Os(3)–C(13) = 2.478(5); Os(1)–C(13)–Os(3) = 79.16(16).

terfly cluster is capped by the dephenylated dppm ligand, while the other wing is capped by the alkyne moiety, and these ligands are orientated on opposite sides of the plane defined by the four metal atoms.

The $^{31}P\{^1H\}$ and $^1H$ NMR spectra of **5** showed that there were two isomers in solution. The NMR resonances have been assigned with the aid of $^1H\{^{31}P\}$ selective decoupling and $^{31}P\{^1H\}$-$^1H$ HMBC experimental data, and also on the basis of earlier observations that $^{31}P$ chemical shifts for a phosphanido bridges across Ru–Os edges are found downfield relative to those across Os–Os bonds.[2b,10] The proposed solution-state structures and their tentative NMR assignments are displayed in Figure 9, and are in agreement with the disorder in the solid-state structure. Thermolysis of **5** afforded **3c** and **4c** in 49% and 46% yields (with respect to the amount of **5** that reacted), respectively, indicating that **5** may be a precursor to **3c**. The formation of **3c** from **5** should be a multistep process, involving the elimination of one CO ligand, migration of hydride and CO ligands, metal–carbon bond cleavage and formation, and metal–metal bond formation, but the sequence of these processes remains unknown.

The crystal of **6** also exhibited disorder of the metal framework, which was solved with ruthenium occupancies of about 0.42 and 0.58 at M(3) and M(4), respectively. Cluster **6** is structurally very similar to **3c**, and it contains almost the same ligand set. The main structural difference is the replacement of the methyl substituent on the coordinated alkyne moiety by an aldehyde functional group. Both the $^1H$ and $^{31}P\{^1H\}$ NMR spectra of **6** displayed two sets of signals integrating to give a 7:1 ratio, indicating the presence of two isomers in solution. The proposed solution-state structures for the two isomers of **6**, which are in agreement with the disorder observed in the solid-state crystal

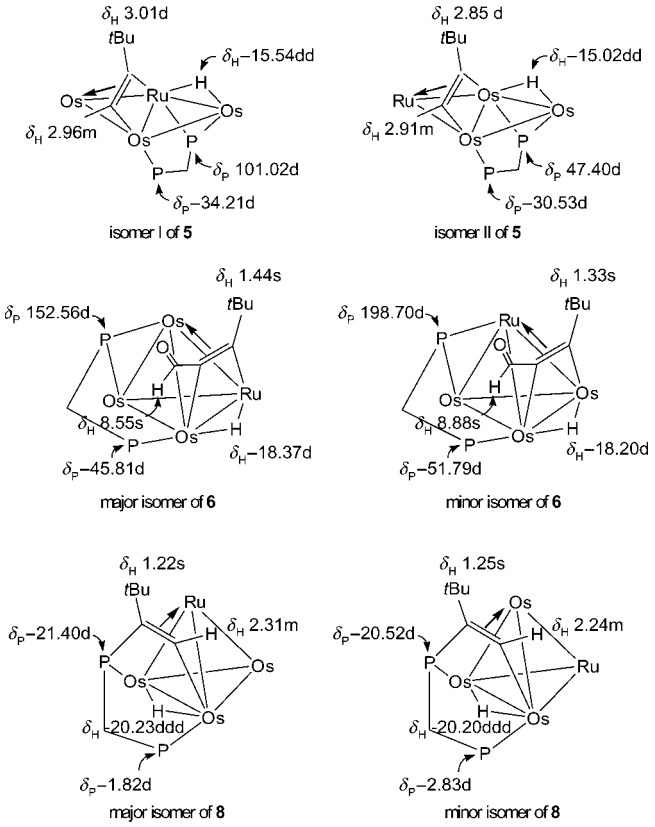


Figure 9. Proposed solution-state structures and tentative NMR assignments for **5**, **6**, and **8** (carbonyl and phenyl groups omitted).

structure, are shown in Figure 9 together with the tentative NMR assignments.

We have carried out a number of experiments to understand how the aldehyde group in **6** could have been formed. Monitoring the reaction of **1** with 4,4-dimethyl-2-pentyne in degassed $[D_{12}]$cyclohexane by $^1H$ NMR spectroscopy indicated that formation of the aldehyde occurred during the reaction. Carrying out the reaction in the presence of air resulted in a slightly higher yield of **6** (15% vs. 12% in the degassed sample). Cluster **6** was formed even when the reaction was carried out under anhydrous conditions; similarly, the yield of **6** did not increase upon addition of water to the system. Thermolysis of **3c**, **4c**, or **5** in air did not result in the formation of **6**. Oxidation of the methyl group to form the aldehyde prior to alkyne coordination to the metal cluster is unlikely, as previously reported reactions between clusters and unsaturated aldehydes or ketones gave products in which the oxygen atom of the organic carbonyl ligand is coordinated to the metal core.[20] Presumably the alkyne is oxidized in the presence of **1** to afford **6**, while **3c**, **4c**, and **5** appear not to be involved in this process, although the oxidant remains unknown.

Cluster **7** is another butterfly-shaped tetranuclear cluster, with a dihedral angle of 166.4° between the wing planes. The Os(1)–Os(2) edge is bridged by the dppm ligand, and the metal–phosphorus bond lengths do not differ significantly from those found for the parent cluster **1**. The XHYDEX program indicated that hydride ligands bridged

 © 2007 Wiley-VCH Verlag GmbH & Co. KGaA, Weinheim 

both Os(1)–Os(2) and Os(1)–Ru(4); this is supported by the observation that these vectors are long [3.0121(4) and 2.9363(6) Å, respectively]. In **7**, two phenylacetylenes have coupled head-to-head, and the resulting four-carbon ligand is coordinated to all four metal atoms, with an $\eta^3$-allylic interaction to Ru(4);[21] there is no evidence of another isomer displaying head-to-tail coupling, although both types of products have been reported for ruthenium and osmium clusters.[22] The organic moiety formally donates six electrons, resulting in a cluster electron count of 62 for **7**, in accordance with the effective atomic number (EAN) rule.[7] Carbon–carbon bond lengths within the organic ligand range from 1.425(10) to 1.464(9) Å, which are in the ranges of carbon–carbon $sp^2$–$sp^2$ double and single bonds (1.32 and 1.48 Å, respectively),[13] suggesting some electron delocalization over the entire carbon chain. Dimerization of the two alkyne units also resulted in a hydrogen atom shift, which has been postulated to precede the C–C coupling step.[23] The spectroscopic data for **7** clearly points to the retention of the solid-state structure in solution.

Cluster **8** retains the tetrahedral metal framework of the parent cluster **1**; the long Os(1)–Os(2) edge [2.9290(2) Å] is bridged by both a hydride and a dephenylated dppm moiety. A salient structural feature in **8** is the formation of a phosphorus–carbon bond between the dephenylated phosphane P(1) and the C(2) carbon of the vinyl organic fragment [P(1)–C(2) = 1.805(4) Å], resulting in the capping of the Os(1)–Os(2)–Ru(4) triangular face of the metal tetrahedron by the novel ligand (HC=C*t*Bu)$PhPCH_2PPh_2$ in a $\mu_3,\eta^1{:}\eta^2{:}\kappa^1{:}\kappa^1$ manner. Reports of P–C coupling between two separate ligands are rare in cluster chemistry, few examples are known.[24] This ligand donates a total of seven electrons to the cluster, and **8** is formally a 60-electron species in accordance with the observed tetrahedral metal core. The crystal of **8** also exhibited disorder of the metal framework, which was solved with ruthenium occupancies of about 0.11 and 0.89 at M(3) and M(4), respectively.

The NMR spectra of **8** showed that there are two isomers present in an approximate 9:1 ratio in solution. $^1H\{^{31}P\}$ as well as $^1H\{^1H\}$ selective decoupling experiments have been utilized to aid the assignment of the signals. The proposed solution-state structures for the isomers of **8** and their tentative NMR assignments are given in Figure 9; the structures, as well as their relative proportions, are in agreement with those expected from the disorder found in the solid state. On prolonged standing in solution, **8** was found to slowly convert to **3e**; this process could be speeded up by thermolysis. Thus, **8** is a precursor to **3e**, but this conversion has to be a multistep process.

In addition to **3d** and **7**, the reaction with phenylacetylene afforded, as characterized by mass spectrometry and $^1H$ NMR spectroscopy, a mixture of 1,3,5- and 1,2,4-triphenylbenzene.[25] Gas chromatography-mass spectrometry (GC-MS) analysis indicated that these cyclotrimerized products were present in a 1:2 ratio. We have found that **3d** catalyzed the cyclotrimerization of phenylacetylene; the cluster was recoverable quantitatively and no intermediates could be isolated. A number of organometallic compounds are known to catalyze the [2+2+2]-cyclotrimerization of alkynes,[26] but few cluster catalysts are known.[27] Thus far, attempts at optimization showed that **3d** is at best a modest catalyst, with TON $< 2$ for a catalyst loading of 1 mol-%. In contrast, **7** failed to react with phenylacetylene under similar conditions, suggesting that it is not directly involved in the catalytic step. Furthermore, **7** was not obtained in the reaction of **3d** with phenylacetylene, indicating that it is not a side product of the catalytic reaction. No cyclotrimerization product was obtained from the reaction of **2** with the other alkynes reported here, and **3d** also failed to catalyze the cyclotrimerization of diphenylacetylene (an internal alkyne) or *tert*-butylacetylene (a terminal alkyne).

## 3. Concluding Remarks

In this study, we have found that **1** reacts with both terminal and internal alkynes to afford initially cluster **3** in which the alkyne is bonded in a $\mu_3,\eta^1{:}\eta^2{:}\eta^1$ fashion and the alkyne C≡C bond is parallel to an Os–Os edge; the tetrahedral core of the cluster is retained. The binding of the alkyne appears to be highly stereoselective, since for unsymmetrical alkynes, the bulkier substituent is oriented away from the dephenylated dppm moiety. In the case of internal alkynes, **3** isomerized slowly to form **4**. This isomerization process involved migration of both the alkyne and hydride across a triangular metal face to bridge the most electron-rich metal–metal bond of the cluster, which is that bridged by the dephenylated dppm; the stereoselectivity appears to be similar to that in **3**. Cluster **3d** was also found to be a modest catalyst for the cyclotrimerization of phenylacetylene.

These results point to stereoselective binding of alkynes in such heterometallic clusters, and indicate that the ditertiary phosphane ligand can play an important role in the high stereoselectivity exhibited as well as in keeping the cluster framework intact. Hence, such clusters may play a useful role in the stereocontrol of reactions with alkynes and provide a possible direction for future work.

## 4. Experimental Section

**4.1. General Procedures:** All reactions and manipulations were carried out under nitrogen by using standard Schlenk techniques. Solvents were purified, dried, distilled, and stored under nitrogen prior to use. The products were separated by thin layer chromatography (TLC), by using plates coated with silica gel 60 F254 of 0.25 or 0.5 mm thickness and extracted with dichloromethane. Routine NMR spectra were acquired with a Bruker ACF300 NMR spectrometer, while decoupling and 2D NMR spectra were obtained with a Bruker Avance DRX500 or Bruker AMX500 machine. The solvent used was deuterated chloroform unless otherwise stated. Chemical shifts reported are referenced to that for the residual proton of the solvent for $^1H$, and to 85% aqueous $H_3PO_4$ (external standard) for $^{31}P\{^1H\}$. Mass spectra were obtained with a Finnigan MAT95XL-T spectrometer in an *m*-nitrobenzyl alcohol matrix. Microanalyses were carried out by the microanalytical laboratory at the National University of Singapore. GC-MS analysis was car-

 © 2007 Wiley-VCH Verlag GmbH & Co. KGaA, Weinheim 

ried out with an Agilent GC 6890 with Mass Selective Detector MS 5973, using a 300 mm × 0.25 mm × 0.25 μm HP-1 MS column. The cluster $Os_3(\mu\text{-}H)_2(CO)_{10}$ was prepared according to the literature method.[28] $Ru_3(CO)_{12}$ was purchased from Oxkem Ltd; all other reagents were from commercial sources and were used as supplied.

**4.2. Synthesis of $RuOs_3(\mu\text{-}H)_2(CO)_9(\mu\text{-}CO)_2(\mu\text{-}dppm)$ (1):** $Ru_3(CO)_{12}$ (8.0 mg, 0.013 mmol) was placed with hexane (20 mL) into a 100-mL round-bottomed flask fitted with a Teflon valve. After three freeze-pump-thaw cycles, ethene gas at ca. 20 psi was introduced at ambient temperature. The mixture was then irradiated with a 60W Phillips reflector lamp, while being cooled in an ice-water bath, until the solution became colorless (ca. 2 h). $Ru(CO)_4(C_2H_4)$ was formed in quantitative yield, as characterized by infrared spectroscopy. A stoichiometric equivalent of dppm was added to the solution which was still kept in the ice-water bath. Formation of $Ru(CO)_4(\kappa^1\text{-dppm})$ was established by its infrared spectroscopic data. Addition of $Os_3(\mu\text{-}H)_2(CO)_{10}$ (30.1 mg, 0.036 mmol) resulted in an immediate color change to light yellow. The mixture was stirred under a nitrogen atmosphere for 1.5 h. Removal of the solvent and volatiles in vacuo and column chromatographic separation of the residue, with hexane and dichloromethane as eluants, yielded three bands. [Yields are calculated with respect to $Os_3(\mu\text{-}H)_2(CO)_{10}$ used.] The first two bands were identified from their infrared spectra as $Ru_3(CO)_{12}$ (1.2 mg, 0.002 mmol) and $RuOs_3(\mu\text{-}H)_2(CO)_{13}$ (5.6 mg, 15%), respectively. The third band was identified from its infrared spectrum as $RuOs_3(\mu\text{-}H)_2(CO)_9(\mu\text{-}CO)_2(\mu\text{-}dppm)$ (**1**) (40.3 mg, 82%).

**4.3. Thermolysis of 1:** To a Schlenk tube containing **1** (16.9 mg, 0.012 mmol) was added hexane (30 mL), and the reaction mixture was stirred and heated under reflux for 4 h. The solvent was removed under reduced pressure, and the residue obtained was redissolved in a minimum of dichloromethane and chromatographed on TLC plates. Elution with hexane/dichloromethane (4:1, v/v) yielded two bands. Band 1 ($R_f$ = 0.49) gave dark red crystals of $RuOs_3(CO)_{12}(\mu_4,\kappa^2\text{:}\kappa^2\text{-}PhPCH_2PPh)$ (**2**). Yield: 10.4 mg, 69%. Band 2 ($R_f$ = 0.19) gave dark red crystals of $Os_3(\mu\text{-}H)_2(CO)_8(\mu\text{-dppm})$. Yield: 2.1 mg, 15%. IR ($CH_2Cl_2$) $\nu$(CO) : $\tilde{\nu}$ = 2068 (s), 2005 (vs), 1983 (vs, br), 1955 (w), 1943 (w) $cm^{-1}$. $^{31}P\{^1H\}$ NMR: $\delta$ = –0.02 (s) ppm. $^1H$ NMR: $\delta$ = 7.35 (m, 20 H, Ph), 4.19 (t, $^2J_{PH}$ = 10.5 Hz, 2 H, $CH_2$), –10.26 (t, $^2J_{PH}$ = 9.9 Hz, 2 H, Os*H*Os) ppm. MS (FAB): *m*/*z* calcd. for $[M]^+$ 1181; found 1181. X-ray data: Orthorhombic, *Pbca*, *a* = 16.2438(4) Å, *b* = 16.8441(5) Å, *c* = 25.3499(7) Å, *V* = 6936.0(3) $Å^3$. Data are in agreement with literature values.[6a]

**4.4. Reactions of 1 with Alkynes:** In a typical reaction, to a Schlenk tube containing **1** and hexane (30 mL) was added the alkyne, and the reaction mixture was stirred and heated under reflux for 6 h. The solvent was removed under reduced pressure, and the residue obtained was redissolved in a minimum of dichloromethane and chromatographed on TLC plates with hexane/dichloromethane (3:2, v/v) as the mobile phase. The reaction conditions and yields are summarized in Table 3, and spectroscopic and analytical data for all new products are given in Table 4 and Table 5.

**4.5. Thermolysis of 3:** In a typical reaction, to a Schlenk tube containing **3a** (20.2 mg, 14 μmol) was added hexane (30 mL), and the

Table 3. Reaction of **1** with alkynes.

| Amount of **1** | Alkyne (amount) | Product | Color | $R_f$ | Yield |
|---|---|---|---|---|---|
| 20.1 mg, 0.014 mmol | PhCCPh (8.0 mg, 0.045 mmol) | **3a** | dark brown | 0.27 | 19.2 mg, 95% |
| 22.4 mg, 0.016 mmol | $C_2H_5CCCH_3$ (0.1 mL) | **4b** | red-orange | 0.57 | 8.1 mg, 39% |
| | | **3b** | red-orange | 0.51 | 7.9 mg, 38% |
| 20.2 mg, 0.014 mmol | *t*BuCCCH$_3$ (0.1 mL) | **5** | dark brown | 0.43 | 3.1 mg, 17% |
| | | **4c** | dark brown | 0.31 | 4.7 mg, 25% |
| | | **3c** | dark brown | 0.26 | 5.7 mg, 30% |
| | | **6** | dark brown | 0.19 | 2.1 mg, 12% |
| 20.6 mg, 0.014 mmol | PhCCH (0.1 mL) | triphenylbenzene | yellow | 0.69 | 2.1 mg |
| | | **3d** | dark brown | 0.54 | 8.2 mg, 44% |
| | | **7** | dark brown | 0.40 | 8.2 mg, 39% |
| 25.8 mg, 0.018 mmol | *t*BuCCH (0.1 mL) | **3e** | dark brown | 0.57 | 12.8 mg, 55% |
| | | **8** | dark brown | 0.37 | 10.2 mg, 40% |

Table 4. Infrared and analytical data for all new products.

| Cluster | IR ($CH_2Cl_2$) $\nu$(CO) [$cm^{-1}$] | Elemental analysis: found (calculated) [%] |
|---|---|---|
| **2** | 2090 m, 2061 vs, 2030 s, 1997 w (br), 1985 mw | $C_{25}H_{12}O_{12}Os_3P_2Ru\cdot 1/4C_6H_{14}$: C, 25.35 (25.27); H, 1.00 (1.24)[a] |
| **3a** | 2065 s, 2018 s, 2005 vs, 1998 vs, 1984 s, 1960 m, 1921 w | $C_{42}H_{28}O_9Os_3P_2Ru\cdot 1/2CH_2Cl_2$: C, 34.99 (35.13); H, 1.95 (2.01)[b] |
| **3b** | 2062 s, 2016 s, 2000 vs, 1995 vs, 1979 s, 1956 m, 1931 w, 1915 w | – |
| **3c** | 2059 s, 2014 s, 2000 vs, 1994 vs, 1979 s, 1959 m, 1915 w | $C_{35}H_{30}O_9Os_3P_2Ru$: C, 31.85 (31.61); H, 2.39 (2.25) |
| **3d** | 2065 s, 2042 w, 2022 s, 2005 vs (br), 1984 s, 1918 w | $C_{36}H_{24}O_9Os_3P_2Ru$: C, 33.27 (33.28); H, 2.08 (1.79) |
| **3e** | 2060 s, 2018 s, 2004 vs, 1996 vs, 1984 s, 1966 m, 1935 w (br) | $C_{34}H_{28}O_9Os_3P_2Ru$: C, 31.35 (31.07); H, 1.90 (2.15) |
| **4a** | 2052 w, 2022 s, 2004 m, 1983 w, 1968 w, 1950 vw (sh) | – |
| **4b** | 2061 w, 2050 m, 2016 s, 2001 s, 1979 m, 1964 m | $C_{33}H_{26}O_9Os_3P_2Ru\cdot 1/2C_6H_{14}$: C, 32.41 (32.19); H, 2.41 (2.48)[a] |
| **4c** | 2058 w, 2049 w, 2015 vs, 2000 s, 1979 m, 1963 m | $C_{35}H_{30}O_9Os_3P_2Ru$: C, 31.39 (31.61); H, 2.00 (2.25) |
| **5** | 2078 w (sh), 2064 vs, 2052 w (sh), 2017 m (sh), 1997 s, 1954 w, 1919 vw | $C_{36}H_{30}O_{10}Os_3P_2Ru$: C, 32.28 (31.88); H, 2.02 (2.23) |
| **6** | 2064 w, 2012 s, 2002 ms, 1989 m, 1966 w | $C_{35}H_{28}O_{10}Os_3P_2Ru$: C, 31.29 (31.29); H, 2.34 (2.09) |
| **7** | 2067 s, 2030 s, 2011 ms, 2000 s, 1988 vs, 1951 w (sh) | $C_{50}H_{36}O_9Os_3P_2Ru\cdot 1/2C_6H_{14}$: C, 40.68 (40.84); H, 2.58 (2.76)[a] |
| **8** | 2073 w, 2061 m, 2031 m, 2008 s, 1987 m, 1960 w, 1918 vw (br) | $C_{34}H_{28}O_9Os_3P_2Ru\cdot 1/2CH_2Cl_2$: C, 30.82 (30.79); H, 1.85 (2.11)[b] |

[a] $^1H$ NMR spectroscopy confirmed the presence of hexane in the sample. [b] $^1H$ NMR spectroscopy confirmed the presence of dichloromethane in the sample.

 © 2007 Wiley-VCH Verlag GmbH & Co. KGaA, Weinheim 

reaction mixture was stirred and heated under reflux for 4 h. The solvent was removed under reduced pressure, and the residue obtained was redissolved in a minimum of dichloromethane and chromatographed on TLC plates with hexane/dichloromethane (3:2, v/v) as the mobile phase to afford unreacted **3a** ($R_f$ = 0.27, yield = 10.1 mg) and **4a** ($R_f$ = 0.22, yield = 10.0 mg, 50%). Similar thermolysis of **3b** (12.5 mg, 10 μmol) afforded **4b** ($R_f$ = 0.57, yield = 7.0 mg, 54%) and unreacted **3b** ($R_f$ = 0.51, yield = 5.1 mg); and of **3c** (14.7 mg, 11 μmol) afforded **4c** ($R_f$ = 0.31, yield = 12.2 mg, 81%) and unreacted **3c** ($R_f$ = 0.26, yield = 2.0 mg). For **3d** and **3e**, the infrared spectra and TLC analyses revealed only the presence of the starting clusters.

Table 5. NMR spectroscopic and MS data for all products.

| Cluster | $^{31}P\{^1H\}$ NMR, $\delta$ | $^1H$ NMR, $\delta$ | FAB-MS, *m*/*z* found (calculated for $M^+$) |
|---|---|---|---|
| **2** | 77.40 (d, Ru*P*Os, $^2J_{PP}$ = 116.4 Hz)<br>–22.34 (d, Os*P*Os) | 7.64 (m, 5 H, Ph), 7.42 (s, 5 H, Ph), 5.97 (m, 1 H, $CH_2$), 5.59 (m, 1 H, $CH_2$) | 1239 (1238) |
| **3a** | 194.46 (d, PPh, $^2J_{PP}$ = 53.4 Hz),<br>–49.64 (d, $PPh_2$) | 7.93–6.85 (m, 25 H, Ph), 5.25 (m, 2 H, $CH_2$),<br>–17.43 (d, 1 H, Os*H*Os, $^2J_{PH}$ = 25.6 Hz) | 1411 (1410) |
| **3b** | 190.86 (d, PPh, $^2J_{PP}$ = 53.5 Hz),<br>–46.88 (d, $PPh_2$) | 7.90–7.10 (m, 10 H, Ph), 5.79 (m, 1 H, $CH_2$), 4.53 (m, 1 H, $CH_2$),<br>2.55 (m, 2 H, $CH_2$), 1.86 (s, 3 H, $CH_3$), 1.06 (t, 3 H, $CH_3$),<br>–18.09 (d, 1 H, Os*H*Os, $^2J_{PH}$ = 26.2 Hz) | 1300 (1300) |
| **3c** | 190.55 (d, PPh, $^2J_{PP}$ = 53.4 Hz),<br>–48.57 (d, $PPh_2$) | 7.92–7.49 (m, 15 H, Ph), 5.83 (m, 1 H, $CH_2$), 5.95 (m, 1 H, $CH_2$),<br>2.27 (s, 3 H, $CH_3$), 2.07 (s, 9 H, *t*Bu), –18.03 (d, 1 H, Os*H*Os, $^2J_{PH}$ = 27.2 Hz) | 1329 (1328) |
| **3d** | 196.28 (d, PPh, $^2J_{PP}$ = 49.6 Hz),<br>–45.82 (d, $PPh_2$) | 7.82–7.39 (m, 20 H, Ph), 5.44 (m, 1 H, $CH_2$), 4.88 (m, 1 H, $CH_2$),<br>1.27 (s, 1 H, CH), –17.74 (d, 1 H, Os*H*Os, $^2J_{PH}$ = 26.4 Hz) | 1335 (1334) |
| **3e** | 203.52 (d, PPh, $^2J_{PP}$ = 53.4 Hz),<br>–47.32 (d, $PPh_2$) | 7.82–7.30 (m, 15 H, Ph), 5.51 (m, 1 H, $CH_2$), 4.86 (m, 1 H, $CH_2$),<br>1.73 (s, 1 H, CH), 1.26 (s, 9 H, *t*Bu), –18.02 (d, 1 H, Os*H*Os, $^2J_{PH}$ = 26.4 Hz) | 1314 (1314) |
| **4a** [major isomer] | 196.92 (d, PPh, $^2J_{PP}$ = 93.5 Hz),<br>–33.94 (d, $PPh_2$) | 7.75–6.99 (m, 25 H, Ph), 4.02 (m, 2 H, $CH_2$),<br>–18.93 (ddd, 1 H, Ru*H*Os, $^2J_{PH}$ = 9.9 Hz, $^2J_{PH}$ = 8.9 Hz, $^4J_{HH}$ = 3.3 Hz) | 1410 (1410) |
| [minor isomer] | 135.84 (d, PPh, $^2J_{PP}$ = 87.7 Hz),<br>–32.92 (d, $PPh_2$) | 7.75–6.99 (m, 25 H, Ph), 4.02 (m, 2 H, $CH_2$),<br>–18.84 (ddd, 1 H, Os*H*Os, unresolved) | |
| **4b** [major isomer] | 203.11 (d, PPh, $^2J_{PP}$ = 97.3 Hz),<br>–34.84 (d, $PPh_2$) | 7.75–6.91 (m, 15 H, Ph), 3.98 (m, 1 H, $CH_2$), 3.85 (m, 1 H, $CH_2$),<br>3.11 (d, 2 H, $CH_2$), 2.96 (s, 3 H, $CH_3$), 1.40 (t, 3 H, $CH_3$),<br>–19.50 (ddd, 1 H, Ru*H*Os, $^2J_{PH}$ = 16.5 Hz, $^2J_{PH}$ = 10.7 Hz, $^4J_{HH}$ = 3.3 Hz) | 1300 (1300) |
| [minor isomer] | 199.66 (d, PPh, $^2J_{PP}$ = 99.2 Hz),<br>–35.38 (d, $PPh_2$) | 7.75–6.91 (m, 15 H, Ph), 3.98–3.11 (m, 4 H, $CH_2$), 2.96 (s, 3 H, $CH_3$),<br>1.36 (t, 3 H, $CH_3$), –19.45 (ddd, 1 H, Os*H*Os, unresolved) | |
| **4c** [major isomer] | 209.36 (d, PPh, $^2J_{PP}$ = 99.2 Hz),<br>–35.54 (d, $PPh_2$) | 7.73–6.87 (m, 15 H, Ph), 3.82 (m, 2 H, $CH_2$), 3.29 (s, 12 H, *t*Bu, $CH_3$),<br>–19.59 (ddd, 1 H, Ru*H*Os, $^2J_{PH}$ = 15.3 Hz, $^2J_{PH}$ = 10.3 Hz, $^4J_{HH}$ = 3.3 Hz) | 1328 (1328) |
| [minor isomer I] | 146.38 (d, PPh, $^2J_{PP}$ = 91.6 Hz),<br>–34.35 (d, $PPh_2$) | 7.60–6.87 (m, 15 H, Ph), 4.20 (m, 1 H, $CH_2$), 3.85 (m, 1 H, $CH_2$),<br>2.95 (s, 12 H, *t*Bu, $CH_3$), –19.47 (ddd, 1 H, Os*H*Os, $^2J_{PH}$ = 14.0 Hz,<br>$^2J_{PH}$ = 8.3 Hz, $^4J_{HH}$ = 2.5 Hz) | |
| [minor isomer II] | 216.21 (d, PPh, $^2J_{PP}$ = 91.6 Hz),<br>–35.80 (d, $PPh_2$) | 7.60–6.87 (m, 15 H, Ph), 4.37 (m, 1 H, $CH_2$), 3.85 (m, 1 H, $CH_2$),<br>3.32 (s, 12 H, *t*Bu, $CH_3$), –19.21 (ddd, 1 H, Os*H*Os, $^2J_{PH}$ = 13.8 Hz,<br>$^2J_{PH}$ = 8.0 Hz, $^4J_{HH}$ = 2.7 Hz) | |
| **5** [isomer I] | 101.02 (d, PPh, $^2J_{PP}$ = 125.9 Hz),<br>–34.21 (d, $PPh_2$) | 7.70–7.32 (m, 15 H, Ph), 5.12 (m, 1 H, $CH_2$), 4.71 (m, 1 H, $CH_2$),<br>3.01 (d, 9 H, *t*Bu, $^5J_{PH}$ = 3.3 Hz), 2.96 (m, 3 H, $CH_3$),<br>–15.54 (dd, 1 H, Ru*H*Os, $^2J_{PH}$ = 17.3 Hz, $^3J_{PH}$ = 8.3 Hz) | 1356 (1356) |
| [isomer II] | 47.40 (d, PPh, $^2J_{PP}$ = 125.9 Hz),<br>–30.53 (d, $PPh_2$) | 7.70–7.32 (m, 15 H), 5.00 (m, 1 H, $CH_2$), 4.36 (m, 1 H, $CH_2$),<br>2.91 (m, 3 H, $CH_3$), 2.85 (d, 9 H, *t*Bu, $^5J_{PH}$ = 3.3 Hz),<br>–15.02 (dd, 1 H, Os*H*Os, $^2J_{PH}$ = 12.4 Hz, $^3J_{PH}$ = 9.1 Hz) | |
| **6** [major isomer] | 152.56 (d, PPh, $^2J_{PP}$ = 53.4 Hz),<br>–45.81 (d, $PPh_2$) | 8.55 (s, 1 H, C*H*O), 7.67–7.59 (m, 15 H, Ph), 5.79 (m, 1 H, $CH_2$),<br>4.92 (m, 1 H, $CH_2$), 1.44 (s, 9 H, *t*Bu), –18.37 (d, 1 H, Ru*H*Os, $^2J_{PH}$ =<br>23.6 Hz) | 1343 (1343) |
| [minor isomer] | 198.70 (d, PPh, $^2J_{PP}$ = 49.6 Hz),<br>–51.79 (d, $PPh_2$) | 8.88 (s, 1 H, C*H*O), 7.90–7.83 (m, 15 H, Ph), 4.66 (m, 1 H, $CH_2$),<br>4.21 (m, 1 H, $CH_2$), 1.33 (s, 9 H, *t*Bu), –18.20 (d, 1 H, Os*H*Os, $^2J_{PH}$ = 27.2 Hz) | |
| **7** | 3.86 (d, $PPh_2$, $^2J_{PP}$ = 45.8 Hz),<br>–6.34 (d, $PPh_2$) | 7.55–6.89 (m, 30 H, Ph), 6.58 (s, 1 H, PhC=C*H*CCHPh),<br>5.78 (m, 1 H, PhC=CHCC*H*Ph), 4.66 (m, 1 H, $CH_2$), 3.79 (m, 1 H, $CH_2$),<br>–13.12 (dt, 1 H, Ru*H*Os, $^2J_{PH}$ = 16.5, $^3J_{PH}$ = 5.0, $^2J_{HH}$ = 5.0 Hz),<br>–17.62 (dt, 1 H, Os*H*Os, $^2J_{PH}$ = 11.5, $^2J_{PH}$ = 11.5, $^2J_{HH}$ = 5.0 Hz) | 1514 (1514) |
| **8** [major isomer] | –21.40 (d, PPh, $^2J_{PP}$ = 36.3 Hz),<br>–1.82 (d, $PPh_2$) | 7.62–7.49 (m, 10 H, Ph), 7.22–7.11 (m, 5 H, Ph), 5.40 (m, 2 H, $CH_2$),<br>2.24 (m, 1 H, CH), 1.22 (s, 9 H, *t*Bu), –20.23 (ddd, 1 H, Os*H*Os,<br>$^2J_{PH}$ = 19.0 Hz, $^2J_{PH}$ = 12.8 Hz, $^4J_{HH}$ = 5.8 Hz) | 1344 (1342) |
| [minor isomer] | –20.52 (d, PPh, $^2J_{PP}$ = 40.0 Hz),<br>2.83 (d, $PPh_2$) | 7.75–7.65 (m, 10 H, Ph), 7.19–7.12 (m, 5 H, Ph), 5.51 (m, 2 H, $CH_2$),<br>2.31 (m, 1 H, CH), 1.25 (s, 9 H, *t*Bu), –20.20 (ddd, 1 H, Os*H*Os,<br>$^2J_{PH}$ = 18.3 Hz, $^2J_{PH}$ = 14.0 Hz, $^4J_{HH}$ = 5.0 Hz) | |

 © 2007 Wiley-VCH Verlag GmbH & Co. KGaA, Weinheim 

**4.6. Thermolysis of 5:** To a Schlenk tube containing **5** (10.3 mg, 0.008 mmol) was added hexane (30 mL), and the reaction mixture was stirred and heated under reflux for 4 h. Subsequent treatment as above afforded unreacted **5** (3.5 mg), **4c** (2.5 mg, 23%), and **3c** (3.7 mg, 34%).

**4.7. Reaction of 1 with 4,4-Dimethyl-2-pentyne in Air:** To a 100-mL two-necked, round-bottomed flask containing **1** (12.1 mg, 0.009 mmol) and hexane (30 mL) was added $t$BuCCCH$_3$ (0.1 mL). Air was bubbled into the mixture by means of a compressor pump and the reaction mixture was stirred and heated under reflux for 6 h. Subsequent treatment as above afforded **5** (1.8 mg, 15%), **4c** (2.9 mg, 24%), **3c** (3.5 mg, 29%) and **6** (1.8 mg, 15%).

**4.8. Thermolysis of 3c, 4c, or 5 in Air:** To a 100-mL two-necked, round-bottomed flask containing **3c** (7.1 mg, 0.005 mmol), **4c** (5.2 mg, 0.004 mmol), or **5** (8.4 mg, 0.006 mmol) was added hexane (30 mL). Air was bubbled into the mixture by means of a compressor pump and the reaction mixture was stirred and heated under reflux for 6 h. Subsequent treatment as above revealed the presence of all three clusters for the thermolysis of **5**. Clusters **3c** and **4c** were obtained from the reaction of **3c**, while only the unreacted starting cluster was observed when **4c** was heated.

**4.9. Reaction of 1 with Phenylacetylene:** To a Schlenk tube containing **1** (9.9 mg, 0.007 mmol) and hexane (30 mL) was added phenylacetylene (0.1 mL), and the reaction mixture was stirred and heated under reflux for 12 h. Subsequent treatment as above afforded triphenylbenzene (1.0 mg), **3d** (3.3 mg, 36%) and **7** (4.9 mg, 46%).

**4.10. Thermolysis of 8:** To a Schlenk tube containing **8** (8.4 mg, 0.006 mmol) was added hexane (30 mL), and the reaction mixture was stirred and heated under reflux for 4 h. Subsequent treatment as above afforded unreacted **8** (3.8 mg) and **3e** (4.3 mg, 54%).

**4.11. Cyclotrimerization Reactions of Phenylacetylene:** In a typical reaction, the cluster **3d** and PhCCH were placed in a Carius tube containing hexane (10 mL), degassed by three freeze-pump-thaw cycles, and heated.

**4.12. Reaction of 3d with Diphenylacetylene and *tert*-Butylacetylene:** To a Schlenk tube containing **3d** (5.2 mg, 0.004 mmol) and hexane (30 mL) was added PhCCPh (6.1 mg, 0.030 mmol) or $t$BuCCH (0.1 mL), and the reaction mixture was stirred and heated under reflux for 12 h. Subsequent treatment as above revealed the presence of unreacted **3d** only.

**4.13 X-ray Crystal Structure Determinations**

Crystals were mounted on quartz fibers. X-ray data were collected with a Bruker AXS APEX system, by using Mo-$K_\alpha$ radiation, with the SMART suite of programs.[29] Data were processed and corrected for Lorentz and polarization effects with SAINT,[30] and for absorption effects with SADABS.[31] Structural solution and refinement were carried out with the SHELXTL suite of programs.[32] Crystal and refinement data are summarized in Table 6, Table 7, and Table 8.

The structures were solved by direct methods to locate the heavy atoms, followed by difference maps for the light, non-hydrogen atoms. The hydrides were generally placed by potential energy calculations with the program XHYDEX,[19] given fixed isotropic thermal parameters, and refined riding on an osmium atom to which they are attached. Organic hydrogen atoms were generally placed in calculated positions and refined with a riding model. All non-hydrogen atoms were generally given anisotropic displacement parameters in the final model.

Cluster **2** sits across a $C_2$ symmetry axis, which passes through the methylene carbon of the dppm ligand and the midpoint of the

Table 6. Crystal data for **2**, **3a**–**c**.

| Compound | **2** | **3a** | **3b** | **3c** |
|---|---|---|---|---|
| Formula | $C_{25}H_{12}O_{12}Os_3P_2Ru$ | $C_{42}H_{28}O_9Os_3P_2Ru{\cdot}1/2CH_2Cl_2$ | $C_{33}H_{26}O_9Os_3P_2Ru$ | $C_{35}H_{30}O_9Os_3P_2Ru{\cdot}1/2C_6H_{14}$ |
| Formula weight | 1237.96 | 1452.72 | 1300.15 | 1371.29 |
| Temperature [K] | 193(2) K | 223(2) | 223(2) | 223(2) |
| Crystal system | Monoclinic | Triclinic | Tetragonal | Triclinic |
| Space group | $C2/c$ | $P\bar{1}$ | $I\bar{4}2d$ | $P\bar{1}$ |
| Unit cell dimensions | | | | |
| $a$ [Å] | 16.119(3) | 9.1091(2) | 31.5814(6) | 9.0388(4) |
| $b$ [Å] | 9.2446(17) | 13.6379(3) | 31.5814(6) | 12.2045(5) |
| $c$ [Å] | 21.004(4) | 17.8813(5) | 15.6854(6) | 18.9635(8) |
| $\alpha$ [°] | 90 | 96.0940(10) | 90 | 74.2140(10) |
| $\beta$ [°] | 98.507(9) | 99.4940(10) | 90 | 81.7690(10) |
| $\gamma$ [°] | 90 | 97.656(2) | 90 | 78.3480(10) |
| Volume [Å$^3$] | 3095.3(10) | 2152.68(9) | 15644.4(7) | 1962.90(14) |
| $Z$ | 4 | 2 | 16 | 2 |
| $\rho_c$ [g cm$^{-3}$] | 2.656 | 2.241 | 2.208 | 2.320 |
| $\mu$(Mo-$K_\alpha$) [mm$^{-1}$] | 12.916 | 9.359 | 10.222 | 10.190 |
| $F$(000) | 2240 | 1350 | 9568 | 1278 |
| Crystal size [mm$^3$] | $0.34\times0.28\times0.18$ | $0.10\times0.20\times0.26$ | $0.30\times0.26\times0.20$ | $0.34\times0.16\times0.10$ |
| $\theta$ range [°] | 2.55 to 29.98 | 2.03 to 28.28 | 2.04 to 26.37 | 2.24 to 28.28 |
| Reflections collected | 12731 | 19531 | 58395 | 27491 |
| Independent reflections ($R_{int}$) | 4308 [$R$(int) = 0.0402] | 10590 (0.0395) | 8009 (0.0432) | 9695 (0.0441) |
| Completeness%, (to $\theta$, deg) | 95.7 (29.98) | 99.2 (28.28) | 99.9 (26.37) | 99.5 (28.28) |
| Transmission range | 0.2046 and 0.0965 | 0.298003–0.170804 | 0.2343–0.1494 | 0.4289–0.1292 |
| Data/restraints/parameters | 4308/0/195 | 10590/0/544 | 8009/0/436 | 9695/1/468 |
| Goodness-of-fit on $F^2$ | 1.066 | 1.011 | 1.162 | 1.051 |
| Final $R$ indices [$I>2\sigma(I)$] | $R_1$ = 0.0313, $wR_2$ = 0.0734 | $R_1$ = 0.0410, $wR_2$ = 0.1037 | $R_1$ = 0.0298, $wR_2$ = 0.0857 | $R_1$ = 0.0392, $wR_2$ = 0.0930 |
| $R$ indices (all data) | $R_1$ = 0.0362, $wR_2$ = 0.0769 | $R_1$ = 0.0508, $wR_2$ = 0.1073 | $R_1$ = 0.0323, $wR_2$ = 0.0868 | $R_1$ = 0.0485, $wR_2$ = 0.0970 |
| Largest diff. peak and hole [e Å$^{-3}$] | 1.271 and –2.538 | 2.405 and –1.342 | 1.754 and –0.747 | 2.953 and –1.566 |

 © 2007 Wiley-VCH Verlag GmbH & Co. KGaA, Weinheim 

Table 7. Crystal data for **3d**–**e** and **4a**–**b**.

| Compound | **3d** | **3e** | **4a** | **4b** |
|---|---|---|---|---|
| Formula | $C_{36}H_{24}O_9Os_3P_2Ru$ | $C_{34}H_{28}O_9Os_3P_2Ru$ | $C_{42}H_{28}O_9Os_3P_2Ru$ | $C_{33}H_{26}O_9Os_3P_2Ru$ |
| Formula weight | 1334.16 | 1314.17 | 1410.25 | 1300.15 |
| Temperature [K] | 223(2) | 193(2) | 223(2) | 223(2) |
| Crystal system | Triclinic | Triclinic | Monoclinic | Monoclinic |
| Space group | $P\bar{1}$ | $P\bar{1}$ | $Cc$ | $P2_1/c$ |
| Unit cell dimensions | | | | |
| $a$ [Å] | 8.7605(2) | 8.8328(4) | 11.5027(11) | 9.0451(8) |
| $b$ [Å] | 12.5261(3) | 12.3241(5) | 21.5495(19) | 26.643(2) |
| $c$ [Å] | 17.1932(3) | 16.9444(7) | 33.708(3) | 14.7236(12) |
| $\alpha$ [°] | 103.2880(10) | 96.4610(10) | 90 | 90 |
| $\beta$ [°] | 96.6360(10) | 92.4220(10) | 92.971(4) | 102.134(2) |
| $\gamma$ [°] | 98.3850(10) | 100.2260(10) | 90 | 90 |
| Volume [Å$^3$] | 1794.65(7) | 1800.02(13) | 8344.3(14) | 3468.9(5) |
| $Z$ | 2 | 2 | 8 | 4 |
| $\rho_c$ [g cm$^{-3}$] | 2.469 | 2.425 | 2.245 | 2.489 |
| $\mu$(Mo-$K_\alpha$) [mm$^{-1}$] | 11.142 | 11.107 | 9.592 | 11.525 |
| $F$(000) | 1228 | 1212 | 5232 | 2392 |
| Crystal size [mm$^3$] | 0.36 × 0.28 × 0.22 | 0.14 × 0.08 × 0.02 | 0.12 × 0.08 × 0.04 | 0.22 × 0.20 × 0.02 |
| $\theta$ range [°] | 2.33 to 28.28 | 2.57 to 29.49 | 2.01 to 24.71 | 2.08 to 26.37 |
| Reflections collected | 16218 | 21674 | 28930 | 50407 |
| Independent reflections ($R_{int}$) | 8827 (0.0283) | 8932 (0.0651) | 10896 (0.0797) | 7096 (0.0825) |
| Completeness%, (to $\theta$, deg) | 99.0 (28.28) | 99.3 (26.37) | 99.8 (24.71) | 99.9 (26.37) |
| Transmission range | 0.1930–0.1080 | 0.6659–0.4714 | 0.7002–0.3923 | 0.8022–0.1859 |
| Data/restraints/parameters | 8827/0/468 | 8932/0/449 | 10896/8/608 | 7096/0/439 |
| Goodness-of-fit on $F^2$ | 1.066 | 1.074 | 0.964 | 1.020 |
| Final $R$ indices [$I > 2\sigma(I)$] | $R_1$ = 0.0311, $wR_2$ = 0.0737 | $R_1$ = 0.0472, $wR_2$ = 0.0925 | $R_1$ = 0.0531, $wR_2$ = 0.1006 | $R_1$ = 0.0404, $wR_2$ = 0.0996 |
| $R$ indices (all data) | $R_1$ = 0.0366, $wR_2$ = 0.0757 | $R_1$ = 0.0652, $wR_2$ = 0.1035 | $R_1$ = 0.0950, $wR_2$ = 0.1211 | $R_1$ = 0.0514, $wR_2$ = 0.1054 |
| Largest diff. peak and hole [e Å$^{-3}$] | 2.201 and –1.347 | 1.947 and –1.660 | 1.921 and –2.259 | 3.143 and –1.816 |

Table 8. Crystal data for **5**–**8**.

| Compound | **5** | **6** | **7** | **8** |
|---|---|---|---|---|
| Formula | $C_{36}H_{30}O_{10}Os_3P_2Ru$ | $C_{35}H_{28}O_{10}Os_3P_2Ru{\cdot}1/2CH_2Cl_2$ | $C_{50}H_{36}O_9Os_3P_2Ru$ | $C_{35}H_{28}O_{10}Os_3P_2Ru{\cdot}CH_2Cl_2$ |
| Formula weight | 1356.21 | 1384.65 | 1514.40 | 1427.11 |
| Temperature [K] | 223(2) | 223(2) | 223(2) | 193(2) |
| Crystal system | Triclinic | Monoclinic | Monoclinic | Triclinic |
| Space group | $P\bar{1}$ | $C2/c$ | $P2_1/c$ | $P\bar{1}$ |
| Unit cell dimensions | | | | |
| $a$ [Å] | 10.2517(6) | 34.9452(14) | 18.7787(6) | 10.8185(4) |
| $b$ [Å] | 10.7899(6) | 12.7259(5) | 12.0922(4) | 12.4511(5) |
| $c$ [Å] | 19.2191(10) | 24.3102(9) | 22.0276(7) | 15.3985(6) |
| $\alpha$ [°] | 93.9060(10) | 90 | 90 | 88.2510(10) |
| $\beta$ [°] | 96.1960(10) | 129.3270(10) | 111.0870(10) | 75.3930(10) |
| $\gamma$ [°] | 113.9100(10) | 90 | 90 | 86.3140(10) |
| Volume [Å$^3$] | 1917.43(18) | 8362.7(6) | 4667.0(3) | 2002.80(13) |
| $Z$ | 2 | 8 | 4 | 2 |
| $\rho_c$ [g cm$^{-3}$] | 2.349 | 2.200 | 2.155 | 2.366 |
| $\mu$(Mo-$K_\alpha$) [mm$^{-1}$] | 10.432 | 9.632 | 8.584 | 10.123 |
| $F$(000) | 1256 | 5128 | 2840 | 1324 |
| Crystal size [mm$^3$] | 0.10 × 0.12 × 0.24 | 0.38 × 0.27 × 0.10 | 0.32 × 0.18 × 0.05 | 0.38 × 0.26 × 0.08 |
| $\theta$ range [°] | 2.15 to 26.37 | 2.17 to 24.71 | 2.05 to 29.48 | 2.08 to 30.03 |
| Reflections collected | 28297 | 62952 | 65040 | 29989 |
| Independent reflections ($R_{int}$) | 7791 (0.0350) | 7119 (0.0432) | 12163 (0.0542) | 11306 (0.0324) |
| Completeness%, (to $\theta$, deg) | 99.4 (26.37) | 99.9 (24.71) | 93.7 (29.48) | 96.4 (30.03) |
| Transmission range | 0.4218–0.1886 | 0.4459–0.1208 | 0.6735–0.1698 | 0.4981–0.1137 |
| Data/restraints/parameters | 7791/2/476 | 7119/18/490 | 12163/0/586 | 11306/0/497 |
| Goodness-of-fit on $F^2$ | 1.037 | 1.097 | 1.308 | 1.043 |
| Final $R$ indices [$I > 2\sigma(I)$] | $R_1$ = 0.0319, $wR_2$ = 0.0796 | $R_1$ = 0.0528, $wR_2$ = 0.1070 | $R_1$ = 0.0533, $wR_2$ = 0.0991 | $R_1$ = 0.0274, $wR_2$ = 0.0716 |
| $R$ indices (all data) | $R_1$ = 0.0369, $wR_2$ = 0.0822 | $R_1$ = 0.0364, $wR_2$ = 0.0847 | $R_1$ = 0.0590, $wR_2$ = 0.1011 | $R_1$ = 0.0310, $wR_2$ = 0.0731 |
| Largest diff. peak and hole [e Å$^{-3}$] | 2.728 and –1.418 | 1.851 and –1.000 | 2.368 and –1.375 | 2.552 and –1.897 |

 © 2007 Wiley-VCH Verlag GmbH & Co. KGaA, Weinheim 

hinge metal–metal bond. Cluster **3b** was refined as a racemic twin. There were two molecules in the asymmetric unit for **4a**. Disorder of the heavy atom positions were found for **2**, **3e**, **4a**, **4b**, **5**, **6**, and **8**. Solvent molecules were found in the crystals of **3a** (half molecule of $CH_2Cl_2$), **3c** (half molecule of hexane), and **6** (half molecule of $CH_2Cl_2$).

CCDC-628206–CCDC-628217 contain the supplementary crystallographic data for this paper. These data can be obtained free of charge from The Cambridge Crystallographic Data Centre via www.ccdc.cam.ac.uk/data_request/cif.

**Supporting Information** (see footnote on the first page of this article): Details on the treatment of disorder, metal hydride placement and refinement, and of solvent molecules in the X-ray crystallographic studies; $^{31}P\{^1H\}$-$^1H$ HMBC spectra for **4c**, **5**, and **7**; $^{31}P\{^1H\}$-$^{31}P\{^1H\}$ COSY spectrum for **4c**; the isomerization of **3c** and **4c** (percentages against time, as obtained from $^1H$ NMR spectra); cyclotrimerization reactions of **3d** with phenylacetylene.

## Acknowledgments

This work was supported by the National University of Singapore (Research Grant No. *R*143–000–267–112) and one of us (Y. L. K. T.) thanks the University for a Research Scholarship.

[1] a) B. Fontal, M. Reyes, T. Suàrez, F. Bellandi, J. C. Diaz, *J. Mol. Catal. A* **1999**, *149*, 75; b) B. Fontal, M. Reyes, T. Suàrez, F. Bellandi, J. C. Diaz, *J. Mol. Catal. A* **1999**, *149*, 87; c) C. Bergounhou, J. J. Bonnet, P. Fompeyrine, G. Lavigne, N. Logun, F. Mansilla, *Organometallics* **1986**, *5*, 60; d) C. Bergounhou, J. J. Bonnet, P. Fompeyrine, G. Commenges, *J. Mol. Catal.* **1988**, *48*, 285; e) U. Matteoli, V. Baghetto, A. Scrivanti, *J. Mol. Catal. A* **1996**, *109*, 45; f) V. Moberg, P. Homanen, S. Selva, R. Persson, M. Haukka, T. A. Pakkanen, M. Monari, E. Nordlander, *Dalton Trans.* **2006**, 279.

[2] a) L. Pereira, W. K. Leong, S. Y. Wong, *J. Organomet. Chem.* **2000**, *609*, 104; b) L. J. Pereira, K. S. Chan, W. K. Leong, *J. Organomet. Chem.* **2005**, *690*, 1033; c) L. J. Pereira, W. K. Leong, *J. Organomet. Chem.* **2006**, *691*, 1941; d) L. J. Pereira, W. K. Leong, *J. Organomet. Chem.* **2006**, *691*, 2448; e) L. J. Pereira, W. K. Leong, *Polyhedron* **2006**, *25*, 2392; f) Y. L. K. Tan, W. K. Leong, *J. Organomet. Chem.* **2006**, *691*, 2048; g) Y. L. K. Tan, C. W. A. Koh, T. B. Lim, W. K. Leong, *J. Cluster Sci.* **2006**, *17*, 509; h) Y. L. K. Tan, W. K. Leong, *J. Organomet. Chem*. **2007**, *692*, 768.

[3] Y. L. K. Tan, W. K. Leong, *J. Organomet. Chem*. in press.

[4] a) G.-Y. Kiel, J. Takats, *Organometallics* **1989**, *8*, 839; b) K. A. Buntem, D. H. Farrar, A. J. Poë, A. J. Lough, *Organometallics* **2000**, *19*, 3674.

[5] N. E. Leadbeater, J. Lewis, P. R. Raithby, A. J. Edwards, *J. Organomet. Chem.* **1997**, *545–546*, 567.

[6] a) J. A. Clucas, M. M. Harding, A. K. Smith, *J. Chem. Soc., Chem. Commun.* **1985**, 1280; b) S. M. T. Abedin, K. I. Hardcastle, S. E. Kabir, K. M. A. Malik, M. A. Mottalib, E. Rosenberg, M. J. Abedin, *Organometallics* **2000**, *19*, 5623.

[7] R. K. Pomeroy in *Comprehensive Organometallic Chemistry II* (Eds.: G. Wilkinson, F. G. A. Stone, E. W. Abel), Pergamon, Oxford, New York, **1995**, vol. 7, ch. 15.

[8] M. I. Bruce, E. Horn, O. bin Shawkataly, M. R. Snow, E. R. T. Tiekink, M. L. Williams, *J. Organomet. Chem.* **1986**, *316*, 187.

[9] A. J. Carty, S. A. MacLauglin, D. Nuciurone in *Phosphorus-31 NMR Spectroscopy in Stereochemical Analysis: Organic Compounds and Metal Complexes* (Eds.: J. G. Verkade; L. D. Quinn), VCH, New York, **1987**.

[10] a) G. Hogarth, J. A. Phillips, F. Van Gastel, N. J. Taylor, T. B. Marder, A. J. Carty, *J. Chem. Soc., Chem. Commun.* **1988**, 1570; b) G. Hogarth, N. Hadj-Bagheri, N. J. Taylor, A. J. Carty, *J. Chem. Soc., Chem. Commun.* **1990**, 1352; c) L. M. Bullock, J. S. Field, R. J. Haines, E. Minshall, M. H. Moore, F. Mulla, D. N. Smit, L. M. Steer, *J. Organomet. Chem.* **1990**, *381*, 429; d) A. M. Arif, T. Bright, D. E. Heaton, R. A. Jones, C. M. Nunn, *Polyhedron* **1990**, *9*, 1573; e) V. Patel, A. Cherkas, D. Nucciarone, N. J. Taylor, A. J. Carty, *Organometallics* **1985**, *4*, 1793.

[11] a) A. A. Koridze, *Russ. Chem. Bull.* **2000**, *49*, 1135; b) S. Deabate, R. Giordano, E. Sappa, *J. Cluster Sci.* **1997**, *8*, 407; c) E. Sappa, A. Tiripicchio, A. J. Carty, G. E. Toogood, *Prog. Inorg. Chem.* **1987**, *35*, 437; d) P. R. Raithby, M. J. Rosales, *Adv. Inorg. Chem. Radiochem.* **1985**, *29*, 169; e) E. Sappa, A. Tiripicchio, P. Braunstein, *Chem. Rev.* **1983**, *83*, 203.

[12] a) V. Ferrand, G. Süss-Fink, A. Neels, H. Stoeckli-Evans, *J. Chem. Soc., Dalton Trans.* **1998**, 3825; b) V. Ferrand, G. Süss-Fink, A. Neels, H. Stoeckli-Evans, *Eur. J. Inorg. Chem.* **1999**, 853.

[13] M. B. Smith, J. March, *March's Advanced Organic Chemistry*, 5th ed., Wiley, New York, **2001**, p. 20.

[14] a) P. Srinivasan, W. K. Leong, *Eur. J. Inorg. Chem.* **2006**, 464; b) G. Wilkinson, F. G. A. Stone, E. W. Abel (Eds.), *Comprehensive Organometallic Chemistry II*, Pergamon, Oxford-New York, **1995**; c) L. F. Dahl, D. L. Smith, *J. Am. Chem. Soc.* **1962**, *84*, 2450; d) R. J. Haines, N. D. C. T. Steen, M. Laing, P. Sommerville, *J. Organomet. Chem.* **1980**, *198*, C72 and references cited therein.

[15] a) M. R. Churchill, R. A. Lashewycz, *Inorg. Chem.* **1978**, *17*, 1950; b) R. D. Adams, N. M. Golembeski, J. P. Selegue, *J. Am. Chem. Soc.* **1981**, *103*, 546.

[16] E. Sappa, A. Tiripicchio, P. Braunstein, *Coord. Chem. Rev.* **1985**, *65*, 219.

[17] a) A. J. Deeming, M. Underhill, *J. Chem. Soc., Dalton Trans.* **1974**, 1415; b) A. J. Deeming, *J. Organomet. Chem.* **1978**, *150*, 123; c) A. J. Deeming, I. P. Rothewell, M. B. Hursthouse, J. D. Backer-Dirks, *J. Chem. Soc., Dalton Trans.* **1981**, 1879.

[18] T. Takao, S. Kakuta, R. Tenjimbayashi, T. Takemori, E. Murotani, H. Suzuki, *Organometallics* **2004**, *23*, 6090.

[19] A. G. Orpen, *XHYDEX*, School of Chemistry, University of Bristol, UK, **1997**.

[20] a) A. J. Deeming, *J. Mol. Catal.* **1983**, *21*, 25; b) A. J. Deeming, P. J. Manning, I. P. Rothwell, M. B. Hursthouse, N. P. C. Walker, *J. Chem. Soc., Dalton Trans.* **1984**, 2039; c) E. Boyar, A. J. Deeming, A. J. Arce, Y. De Sanctis, *J. Organomet. Chem.* **1984**, *276*, C45; d) A. J. Arce, Y. De Sanctis, A. J. Deeming, *J. Organomet. Chem.* **1985**, *295*, 365; e) A. J. Arce, Y. De Sanctis, A. J. Deeming, *Polyhedron* **1988**, *7*, 979.

[21] a) S. Aime, L. Milone, D. Osella, M. Valle, *J. Chem. Res. (S)* **1978**, 77; b) S. Aime, D. Osella, *Organomet. Synth.* **1988**, *4*, 253; c) M. I. Bruce, A. C. Meier, B. W. Skelton, A. H. White, N. N. Zaitseva, *Aust. J. Chem.* **2001**, *54*, 319.

[22] a) G. Gervasio, E. Sappa, A. M. M. Lanfredi, A. Tiripicchio, *Inorg. Chim. Acta* **1983**, *68*, 171; b) V. Ferrand, C. Gambs, N. Derrien, C. Bolm, H. Stoeckli-Evans, G. Süss-Fink, *J. Organomet. Chem.* **1997**, *549*, 275; c) L. J. Farrugia, N. Macdonald, R. D. Peacock, *Polyhedron* **1998**, *17*, 2877.

[23] a) O. Gambino, E. Sappa, A. M. M. Lanfredi, A. Tiripicchio, *Inorg. Chim. Acta* **1979**, *36*, 189; b) R. D. Adams, J. E. Babin, M. Tasi, J.-G. Wang, *Organometallics* **1988**, *7*, 755.

[24] a) J. F. Corrigan, S. Doherty, N. J. Tylor, A. J. Carty, *Organometallics* **1993**, *12*, 1365; b) M. I. Bruce, J. R. Hinchcliff, P. A. Humphrey, R. J. Surynt, B. W. Skelton, A. H. White, *J. Organomet. Chem.* **1998**, *552*, 109; c) M. I. Bruce, S. I. Pyke, N. N. Zaitseva, B. W. Skelton, A. H. White, *Helv. Chim. Acta* **2001**, *84*, 3197.

[25] a) K. Lonsdale, *Nature* **1934**, *133*, 67; b) K. S. Krishnan, S. Banerjee, *Nature* **1934**, *133*, 497; c) G. Booth, J. M. Rowe, *Chem. Ind.* **1960**, 661.

[26] See for example: a) M. S. Sigman, A. W. Fatland, B. E. Eaton, *J. Am. Chem. Soc.* **1998**, *120*, 5130; b) Y. Sato, K. Ohashi, M. Mori, *Tetrahedron Lett.* **1999**, *40*, 5231; c) N. Mori, S. Ikeda, K. Odashima, *Chem. Commun.* **2001**, 181.

 © 2007 Wiley-VCH Verlag GmbH & Co. KGaA, Weinheim 

[27] a) W. Hübel, C. Hoogzand, *Chem. Ber.* **1960**, *93*, 103; b) M. Valle, G. Cetini, O. Gambino, E. Sappa, *Atti Accad. Sci. Torino* **1969**, *105*, 913; c) G. A. Vaglio, O. Gambino, R. P. Ferrari, G. Cetini, *Inorg. Chim. Acta* **1973**, *7*, 193; d) C. C. Yin, A. J. Deeming, *J. Organomet. Chem.* **1978**, *144*, 351; e) C. Y. Ren, W. C. Cheng, W. C. Chan, C. H. Yeung, C. P. Lau, *J. Mol. Catal.* **1990**, *59*, L1; f) W. Baidossi, N. Goren, J. Blum, H. Schumann, H. Hemling, *J. Mol. Catal.* **1993**, *85*, 153; g) A. J. Edwards, N. E. Leadbeater, J. Lewis, P. R. Raithby, *J. Chem. Soc., Dalton Trans.* **1995**, 3985; h) T. Sugihara, A. Wakabayashi, Y. Nagai, H. Takao, H. Imagawa, M. Nishizawa, *Chem. Commun.* **2002**, 576; i) M. Deng, W. K. Leong, *Organometallics* **2002**, *21*, 1221.
[28] H. D. Kaesz, *Inorg. Synth.* **1990**, *28*, 238.
[29] *SMART* version 5.628, Bruker AXS Inc. Madison, Wisconsin, USA, **2001**.
[30] *SAINT*+ version 6.22a, Bruker AXS Inc. Madison, Wisconsin, USA, **2001**.
[31] G. M. Sheldrick, *SADABS*, **1996**.
[32] *SHELXTL* version 5.1, Bruker AXS Inc., Madison, Wisconsin, USA, **1997**.

Received: November 27, 2006
Published Online: March 6, 2007

 © 2007 Wiley-VCH Verlag GmbH & Co. KGaA, Weinheim 

DOI: 10.1002/ejic.200601172

# The Binuclear Cyclopentadienylvanadium Carbonyls $(\eta^5\text{-}C_5H_5)_2V_2(CO)_7$ and $(\eta^5\text{-}C_5H_5)_2V_2(CO)_6$: Comparison with Homoleptic Chromium Carbonyls

**Xiuhui Zhang,[a] Qian-shu Li,*[a] Yaoming Xie,[b] R. Bruce King,*[b] and Henry F. Schaefer III[b]**

**Keywords:** Binuclear cyclopentadienylvanadium carbonyls / Density functional theory

The cyclopentadienylvanadium carbonyls $CpV(CO)_n$ ($n$ = 4, 3, 2, 1), $Cp_2V_2(CO)_7$, and $Cp_2V_2(CO)_6$ have been studied by density functional theory using the B3LYP and BP86 functionals. The optimized structure of $CpV(CO)_4$ is close to that found experimentally by X-ray and electron diffraction methods. For the coordinately unsaturated $CpV(CO)_n$ ($n$ = 3, 2, 1) the computed ν(CO) frequencies by BP86 are related to those found in low-temperature matrix isolation experiments but show some significant differences for $n$ = 3 and 2 in band spacings suggesting some matrix effects on the geometries. An optimized structure for $Cp_2V_2(CO)_7$ is found with one symmetrical bridging carbonyl group and a V–V distance of 3.306 Å (BP86) suggesting a single bond. Energetically competitive structures for $Cp_2V_2(CO)_6$ include a doubly symmetrically bridged singlet structure with only two-electron donor carbonyl groups, a triplet doubly semibridged structure, and a singlet structure with one four-electron donor bridging carbonyl group. Thermodynamic considerations rationalize why neither $Cp_2V_2(CO)_7$ nor $Cp_2V_2(CO)_6$ have yet been synthesized. Thus $Cp_2V_2(CO)_7$ is predicted to be unstable with respect to dissociation into $CpV(CO)_4$ + $CpV(CO)_3$. Furthermore, the dissociation energy of the lowest lying singlet isomer from $Cp_2V_2(CO)_6$ to $Cp_2V_2(CO)_5$ is only 10.8 kcal/mol (BP86) consistent with the formation of $Cp_2V_2(CO)_5$ rather than $Cp_2V_2(CO)_6$ upon decomposition of the presumed $CpV(CO)_3H_2$ dihydride generated by acidification of the dianion $CpV(CO)_3^{2-}$.

(© Wiley-VCH Verlag GmbH & Co. KGaA, 69451 Weinheim, Germany, 2007)

## 1. Introduction

Cyclopentadienylvanadium tetracarbonyl, $CpV(CO)_4$ ($Cp = \eta^5\text{-}C_5H_5$), which was originally synthesized in 1958 by E. O. Fischer,[1] can be regarded as an analogue of the long known $Fe(CO)_5$ or $Cr(CO)_6$ or the unknown $Ti(CO)_7$ depending on whether the $\eta^5\text{-}C_5H_5$ ring replaces one, two, or three carbonyl groups, respectively, in the corresponding homoleptic metal carbonyl. Photolysis of $Fe(CO)_5$ has been known[2] since 1927 to give $Fe_2(CO)_9$ (Figure 1), with the formal Fe–Fe single bond required to give each iron atom the favored 18-electron configuration.[3] However, no evidence has been found for any binuclear $Cr_2(CO)_n$ derivatives from the photolysis or thermolysis of $Cr(CO)_6$ including $Cr_2(CO)_{11}$ with a Cr–Cr single bond required to give each chromium atom the favored 18-electron configuration. This latter observation has been rationalized by our theoretical studies indicating even the lowest energy isomer of $Cr_2(CO)_{11}$ to be thermodynamically unstable with respect to mononuclear $Cr(CO)_6$ and $Cr(CO)_5$ fragments.[4] By comparison, laboratory photolysis of $CpV(CO)_4$ goes directly to $Cp_2V_2(CO)_5$ with the formal V≡V triple bond required to give both vanadium atoms the favored 18-electron configuration[5–8] (Figure 1) without any evidence for $Cp_2V_2(CO)_7$ and $Cp_2V_2(CO)_6$ intermediates expected to have formal V–V single and V = V double bonds, respectively, by the 18-electron rule.[3] We now present computational studies on these intermediate $Cp_2V_2(CO)_7$ and $Cp_2V_2(CO)_6$ molcules in order to predict structures and to understand why they have not been found in the photolysis of $CpV(CO)_4$ or other reactions of cyclopentadienylvanadium carbonyl derivatives.

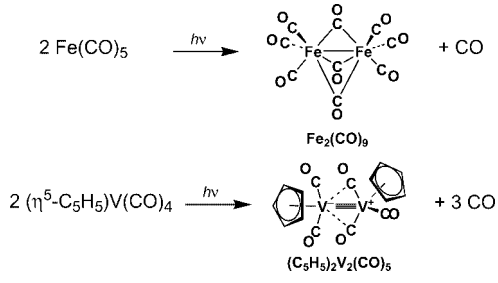


Figure 1. A comparison of the photolyses of $Fe(CO)_5$ and $CpV(CO)_4$.

[a] Institute of Chemical Physics, Beijing Institute of Technology, Beijing 100081, P. R. China
[b] Department of Chemistry and Center for Computational Chemistry, University of Georgia, Athens, Georgia 30602, USA

Supporting information for this article is available on the WWW under http://www.eurjic.org or from the author.

 © 2007 Wiley-VCH Verlag GmbH & Co. KGaA, Weinheim 

## 2. Theoretical Methods

Electron correlation effects were considered by employing density functional theory (DFT) methods, which have evolved as a practical and effective computational tool, especially for organometallic compounds.[9–17] Two DFT methods were used in this study. The first functional is the hybrid B3LYP method, which is the hybrid HF/DFT method using the combination of the three-parameter Becke functional (B3) with the Lee–Yang–Parr (LYP) generalized gradient correlation functional.[18,19] The other DFT method used in this paper is BP86, which combines Becke's 1988 exchange functional (B) with Perdew's 1986 gradient corrected correlation functional method (P86).[20,21] It has been noted elsewhere that the BP86 method may be somewhat more reliable than B3LYP for the type of organometallic systems considered in this paper.[22–24]

All calculations were performed using the double-ζ plus polarization (DZP) basis sets. The DZP basis sets used for carbon and oxygen add one set of pure spherical harmonic d functions with orbital exponents $\alpha_d(C) = 0.75$ and $\alpha_d(O) = 0.85$ to the standard Huzinaga-Dunning contracted DZ sets[25,26] and are designated (9s5p1d/4s2p1d). For hydrogen, a set of p polarization functions $\alpha_p(H) = 0.75$ was added to the Huzinaga-Dunning DZ set. The loosely contracted DZP basis set for vanadium is the Wachters primitive set[27] augmented by two sets of p functions and a set of d functions, contracted following Hood, Pitzer and Schaefer,[28] designated (14s11p6d/10s8p3d).

The geometries of all structures were fully optimized using the DZP B3LYP and DZP BP86 methods, and the vibrational frequencies were determined by evaluating analytically the second derivatives of the energy with respect to the nuclear coordinates. The corresponding infrared intensities were also evaluated analytically. All of the computations were carried out with the Gaussian 03 program,[29] exercising the fine grid option (75 radial shells, 302 angular points) for evaluating integrals numerically, while the tight ($10^{-8}$ hartree) designation is the default for the self-consistent field (SCF) convergence.

The low-magnitude imaginary vibrational frequencies are suspect because of significant limitations in the numerical integration procedures used in the DFT computations. Ziegler et al.[30] have suggested that all imaginary vibrational frequencies with magnitudes less than 100 $cm^{-1}$ may be suspect, owing to the possibility of numerical errors arising from the use of standard integration grids. Therefore, we do not always follow such low imaginary vibrational frequencies unless they appear to be chemically meaningful.

## 3. Results

### 3.1 Mononuclear Cyclopentadienylvanadium Carbonyl Derivatives

Figure 2 and Table 1 depict and describe the optimized structures for $CpV(CO)_n$ ($n$ = 4, 3, 2, 1). Among these compounds $CpV(CO)_4$ is a stable 18-electron metal complex[1] whereas the coordinately unsaturated derivatives $CpV(CO)_n$ ($n$ = 3, 2, 1) have been generated by the photolysis of $CpV(CO)_4$ in frozen gas matrices (argon, methane) at 12 K.[31]

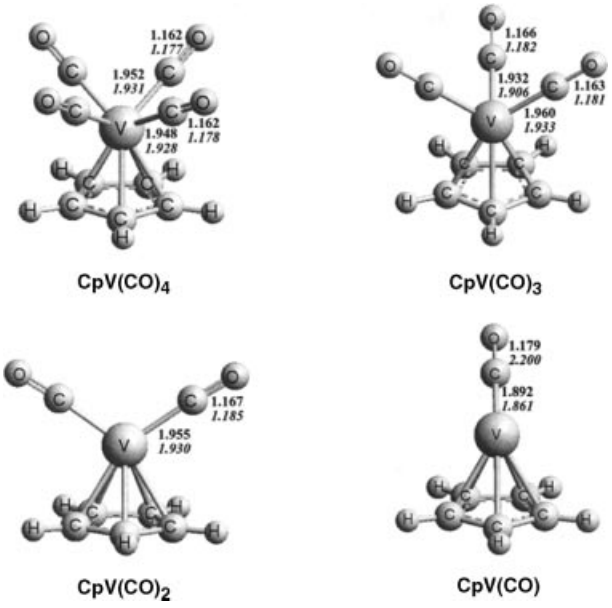


Figure 2. The optimized structures of $CpV(CO)_n$ ($n$ = 4, 3, 2, 1).

The optimized structure for $CpV(CO)_4$ is close to those found experimentally by X-ray[32] and electron diffraction[33] for crystalline and gas-phase $CpV(CO)_4$, respectively, with the latter perhaps being more accurate since the X-ray diffraction study is a rather old one predating automatic diffractometers. Thus the theoretical V–CO and C–O distances from our DFT studies are 1.948/1.952 Å (B3LYP) or 1.928/1.931 Å (BP86) and 1.162 Å (B3LYP) or 1.178 Å (BP86), respectively. This compares with 1.88/1.94 Å and 1.18/1.12 Å found by X-ray diffraction and 1.963 Å and 1.135 Å found by electron diffraction.

Table 1. The total energies ($E$, Hartree) for $CpV(CO)_n$ ($n$ = 4, 3, 2, 1). The number of imaginary vibrational frequencies (Nimg) for each structure is also listed.

| Singlet | | $CpV(CO)_4$ ($C_s$) | $CpV(CO)_3$ ($C_s$) | $CpV(CO)_2$ ($C_s$) | CpV(CO) ($C_s$) |
|---|---|---|---|---|---|
| B3LYP | $E$ | –1591.065026 | –1477.674671 | –1364.278723 | –1250.877952 |
| | Nimg | 1 (15$i$)[a] | 0 | 0 | 0 |
| BP86 | $E$ | –1591.244927 | –1477.841138 | –1364.430801 | –1251.019000 |
| | Nimg | 1 (17$i$)[a] | 0 | 0 | 0 |

[a] These imaginary frequencies were reduced to 0$i$ (B3LYP) or 2$i$ (BP86) by using the larger (120, 974) integration grid.

 © 2007 Wiley-VCH Verlag GmbH & Co. KGaA, Weinheim 

Table 2. Infrared-active ν(CO) vibrational frequencies ($cm^{-1}$) predicted for the mono-nuclear molecules: $CpV(CO)_n$ ($n$ = 4, 3, 2, 1) (infrared intensities in parentheses are given in km/mol).

| | B3LYP | BP86 | Experimental[a] |
|---|---|---|---|
| $CpV(CO)_4$ | 2008 (1539), 2008 (1544), 2019 (7), 2085 (624) | 1928 (1290), 1928 (1293), 1934 (4),[b] 2004 (497) | 1931, 1952,[b] 2030 |
| $CpV(CO)_3$ | 1983 (714), 1985 (1701), 2062 (718) | 1892 (1406), 1896 (536), 1967 (581) | 1857, 1887, 1953 |
| $CpV(CO)_2$ | 1954 (1964), 2028 (741) | 1854 (1634), 1924 (561) | 1894, 1992 |
| CpV(CO) | 1929 (1370) | 1823 (1039) | 1830 |

[a] Data taken from the literature (R. B. Hitam, A. J. Rest, *Organometallics* **1989**, *8*, 1598) for the ν(CO) frequencies in methane matrices at 12 K averaging out reported matrix splitting. [b] The infrared "inactive" $b_1$ ν(CO) frequency for $CpV(CO)_4$.

The infrared ν(CO) frequencies computed for $CpV(CO)_n$ ($n$ = 4, 3, 2, 1) are listed in Table 2 along with the experimental ν(CO) frequencies reported in methane matrices.[31]

The BP86 calculated frequencies for $CpV(CO)_4$ and CpV(CO) agree very well with the experimental frequencies. However, there are significant differences between the ν(CO) frequencies calculated by the usually more reliable BP86 method and those found in matrices for $CpV(CO)_3$ and $CpV(CO)_2$. In particular, although the positions of the calculated ν(CO) frequencies are reasonably close to those found experimentally, the calculated frequency separations are significantly different from those found experimentally. Thus for $CpV(CO)_2$ the two theoretical ν(CO) frequencies (Table 2) are separated by 74 $cm^{-1}$ (B3LYP) or 70 $cm^{-1}$ (BP86), whereas the experimental ν(CO) frequencies assigned to the matrix studies are separated by 98 $cm^{-1}$. The nature of the matrix experiments may be responsible for this discrepancy since the initial geometries generated by loss of a CO ligand may not fully relax to the optimized geometries at the low temperatures involved.

### 3.2 The Binuclear Derivatives $Cp_2V_2(CO)_n$ ($n$ = 7, 6)

#### *3.2.1 $Cp_2V_2(CO)_7$*

Only one optimized structure was found for $Cp_2V_2(CO)_7$ with a V–V distance short enough to imply any significant interaction between the $CpV(CO)_4$ and $CpV(CO)_3$ fragments. This structure (**7S-1** in Figure 3 and Table 3) has $C_2$ symmetry with one symmetrical bridging CO group and six terminal CO groups. The bridging CO group has V–C distances of 2.214 Å (B3LYP) or 2.185 Å (BP86) and leads to a predicted ν(CO) frequency (Table 4) of 1759 $cm^{-1}$ (BP86). The V–C distances to the terminal CO groups are in the range 1.933–1.988 Å (B3LYP) or 1.918–1.972 Å (BP86). The V–V distance of 3.382 Å (B3LYP) or 3.306 Å (BP86) is in agreement with the single bond required to give both vanadium atoms the favored 18-electron configuration.

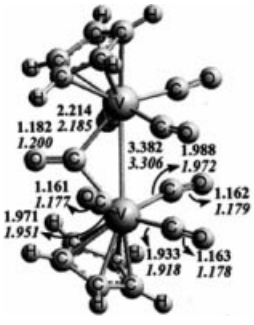


Figure 3. Optimized structure of $Cp_2V_2(CO)_7$ (**7S-1**).

Table 3. The total energy ($E$, Hartree), number of imaginary vibrational frequencies, (Nimg), and V–V distances for $Cp_2V_2(CO)_7$ (**7S-1**) by B3LYP and BP86.

| Singlet | | $Cp_2V_2(CO)_7$ ($C_2$) (**7S-1**) |
|---|---|---|
| B3LYP | $E$ | –3068.725630 |
| | V–V | 3.382 Å |
| | Nimg | 1 (19$i$) |
| BP86 | $E$ | –3069.086435 |
| | V–V | 3.306 Å |
| | Nimg | 1 (18$i$) |

This structure for $Cp_2V_2(CO)_7$ exhibits a very small imaginary vibrational frequency at 19$i$ $cm^{-1}$ (B3LYP) or 18$i$ $cm^{-1}$ (BP86). Following the corresponding normal mode causes $Cp_2V_2(CO)_7$ to dissociate into $CpV(CO)_4$ + $CpV(CO)_3$ fragments with an energy minimum at a clearly non-bonding vanadium-vanadium distance of 5.307 Å (B3LYP) or 5.283 Å (BP86). In addition, energy calculations indicate that the dissociation [Equation (1)]

$$Cp_2V_2(CO)_7 \rightarrow CpV(CO)_4 + CpV(CO)_3 \quad (1)$$

is either exothermic by 8.8 kcal/mol (B3LYP) or only very slightly endothermic by 0.2 kcal/mol (BP86). All of these observations indicate that $Cp_2V_2(CO)_7$ is unstable with respect to dissociation into $CpV(CO)_4$ + $CpV(CO)_3$ [Equation (1)] and thus unlikely to be prepared as an isolable molecule.

#### *3.2.2 $Cp_2V_2(CO)_6$*

Five low-lying stationary points are found for $Cp_2V_2(CO)_6$ (Figure 4 and Table 4 and Table 5). The B3LYP and BP86 methods disagree with respect to the relative energies of these isomers as well as key features of the optimized lowest energy triplet structure **6T-1**.

The global minimum for $Cp_2V_2(CO)_6$ using the BP86 method is a $C_{2v}$ singlet **6S-1** (Figure 4) with two symmetrical bridging carbonyl groups having equal V–C distances of

 © 2007 Wiley-VCH Verlag GmbH & Co. KGaA, Weinheim 

Table 4. Infrared active ν(CO) vibrational frequencies ($cm^{-1}$) predicted for $Cp_2V_2(CO)_7$ (**7S-1**) and the $Cp_2V_2(CO)_6$ isomers [infrared intensities in parentheses are in km/mol; bridging ν(CO) frequencies are printed in **bold**].

| | B3LYP | BP86 |
|---|---|---|
| **7S-1** | **1847** (**495**), 1982 (68), 1992 (439), | **1759** (**405**), 1896 (97), 1907 (431), |
| ($C_2$) | 2006 (48), 2006 (987), 2027 (2172), 2074 (664) | 1922 (121), 1923 (733), 1945 (1726), 1988 (577) |
| **6S-1** | **1780** (**755**), **1833** (**283**), 2008 (0), | **1733** (**587**), **1767** (**221**), 1922 (0), |
| ($C_{2v}$) | 2013 (758), 2025 (1531), 2076 (1206) | 1934 (555), 1939 (1249), 1987 (995) |
| **6T-1** | 1929 (802), 1944 (671), 1988 (627), | **1799** (**609**), **1810** (**311**), 1915 (1), |
| ($C_2$) | 2001 (8), 2025 (1556), 2072 (1087) | 1915 (885), 1934 (1127), 1982 (1091) |
| **6T-2** | **1791** (**756**), **1836** (**284**), 2000 (1604), | **1778** (**629**), **1798** (**226**), 1907 (0), |
| ($C_{2v}$) | 2019 (0), 2021 (1486), 2071 (1346) | 1920 (654), 1935 (1095), 1978 (1142) |
| **6S-2** | **1731** (**446**), 1970 (166), 1989 (1297), | **1678** (**353**), 1880 (97), 1902 (1081), |
| ($C_1$) | 2015 (827), 2031 (879), 2086 (489) | 1925 (307), 1931 (1205), 1985 (434) |
| **6S-3** | 1958 (123), 1976 (200), 2002 (580), | 1871 (7),1893 (28), 1909 (404), |
| ($C_s$) | 2011 (888), 2015 (2108), 2070 (853) | 1918 (1814), 1923 (926), 1978 (806) |

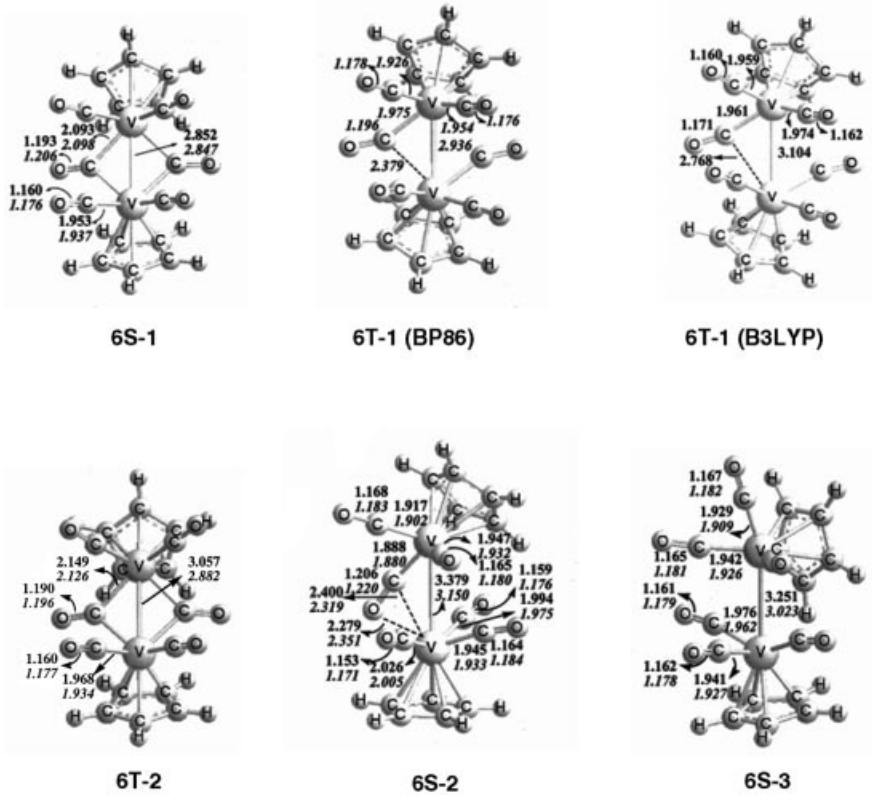


Figure 4. The stationary points of $Cp_2V_2(CO)_6$ showing the different structures for **6T-1** by BP86 and B3LYP.

Table 5. The total energies (*E*, hartree), relative energies (Δ*E*, kcal/mol), number of imaginary vibrational frequencies (Nimg), and V–V distances for the $Cp_2V_2(CO)_6$ stationary states.

| Singlet | | **6S-1** ($C_{2v}$) | **6T-1** ($C_2$) | **6T-2** ($C_{2v}$) | **6S-2** ($C_1$) | **6S-3** ($C_s$) |
|---|---|---|---|---|---|---|
| B3LYP | *E* | –2955.369144 | –2955.380720 | –2955.361110 | –2955.374370 | –2955.359829 |
| | Δ*E* | 7.3 | 0.0 | 12.3 | 4.0 | 13.1 |
| | Nimg | 0 | 0 | 3 (304*i*, 8*i*, 6*i*) | 0 | 0 |
| | V–V | 2.852 | 3.104 | 3.057 | 3.379 | 3.251 |
| BP86 | *E* | –2955.732464 | –2955.728933 | –2955.724138 | –2955.722935 | –2955.709504 |
| | Δ*E* | 0.0 | 2.2 | 5.2 | 6.0 | 14.4 |
| | Nimg | 0 | 0 | 1 (371*i*) | 0 | 0 |
| | V–V | 2.847 | 2.936 | 2.882 | 3.150 | 3.023 |

 © 2007 Wiley-VCH Verlag GmbH & Co. KGaA, Weinheim 

2.093 Å (B3LYP) or 2.098 Å (BP86) and exhibiting ν(CO) frequencies in the normal range for such bridging carbonyl groups, namely 1767 and 1733 $cm^{-1}$ (BP86, Table 4). For the four terminal carbonyls in **6S-1**, the V–C distances are 1.953 Å (B3LYP) or 1.937 Å (BP86). The V–V distance in **6S-1** is 2.852 Å (B3LYP) or 2.847 Å (BP86), which is the shortest vanadium-vanadium distance found in any of the $Cp_2V_2(CO)_6$ isomers and consistent with the V=V double bond required to give each vanadium atom in $Cp_2V_2(CO)_6$ the favored 18-electron configuration[3] when all of the CO groups are the usual two-electron donors. The dissociation energy of $Cp_2V_2(CO)_6$ (**6S-1**) to 2 $CpV(CO)_3$ is 31.5 kcal/mol (BP86) indicating that $Cp_2V_2(CO)_6$, unlike $Cp_2V_2(CO)_7$, is stable with respect to dissociation.

The two methods disagree on the structure of the lowest lying triplet **6T-1** of $Cp_2V_2(CO)_6$ (Figure 4). The BP86 method predicts **6T-1** to be a structure with two semibridging CO groups having V–C distances of 1.975 Å and 2.379 Å and exhibiting ν(CO) frequencies in the usual bridging range at 1799 and 1810 cm.$^{-1}$ (Table 4). The V–V bond length of 2.936 Å in **6T-1** can be interpreted as a single bond somewhat shortened by the presence of the two semibridging CO groups thereby giving both metal atoms the 17-electron configurations expected for a binuclear triplet. Using the B3LYP method gives a significantly different structure for **6T-1** with two much more unsymmetrical semibridging CO groups having V–C distances of 1.961 Å and 2.768 Å. The latter V–C distance indicates very weak interactions so that these highly unsymmetrical bridging CO groups are essentially undistinguishable from terminal CO groups consistent with their V–C–O angles close to 180°. Thus these two semibridging CO groups give ν(CO) frequencies in the terminal CO range. The V–V distance of 3.104 Å in **6T-1** found by B3LYP is nearly 0.2 Å longer than that found by BP86. This can be rationalized by the fact that the semibridging CO groups in **6T-1** found by B3LYP are so highly unsymmetrical that they function effectively as terminal CO groups and thus do not shorten the V–V distance. By either method isomer **6T-1** for $Cp_2V_2(CO)_6$ is found to have relatively little spin contamination ($<S^2>$ = 2.05 and 2.01 for B3LYP and BP86, respectively).

A triplet stationary point for $Cp_2V_2(CO)_6$ similar to **6S-1** is **6T-2**, which lies 12.3 kcal/mol above **6T-1** (B3LYP) or 5.2 kcal/mol above **6S-1** (BP86). The apparent spin contamination in **6T-2** is quite small ($<S^2>$ = 2.07 and 2.02 for B3LYP and BP86, respectively). Structure **6T-2** has one substantial imaginary vibrational frequency, namely, 304*i* $cm^{-1}$ (B3LYP) or 371*i* $cm^{-1}$ (BP86). Following the corresponding normal mode leads to structure **6T-1**. For the bridging carbonyls, the V–C distances in **6T-2** are 2.149 Å (B3LYP) or 2.126 Å (BP86) and their ν(CO) frequencies are the normal values of 1798 and 1778 $cm^{-1}$. The V–C distances to the terminal carbonyls are 1.968 Å (B3LYP) or 1.934 Å (BP86). The V–V distance in **6T-2** is 3.057 Å (B3LYP) or 2.882 Å (BP86) consistent with the single bond required to give each vanadium the 17-electron configuration for a binuclear triplet with only two-electron donor CO groups.

The next singlet structure **6S-2** for $Cp_2V_2(CO)_6$ lies 6.0 kcal/mol above **6S-1** (BP86) or 4.0 kcal/mol above **6T-1** (B3LYP). This structure has one semibridging CO group with V–C distances of 1.888 Å (B3LYP) or 1.880 Å (BP86) and 2.400 Å (B3LYP) or 2.319 Å (BP86). The V–C–O bond angle is almost linear. One of these semibridging CO group has a relatively short V–O distance of 2.279 Å (B3LYP) or 2.351 Å (BP86) indicating that it is a $\eta^2$-μ-CO group donating four electrons using both a σ-bond and a π-bond. This four-electron donor CO group is responsible for the very low bridging ν(CO) frequency of 1678 $cm^{-1}$ (Table 4). The V–V distance in **6S-2** is 3.379 Å (B3LYP) or 3.150 Å (BP86). This is longer than that in **6T-1** by ca. 0.3 Å (B3LYP) or ca. 0.2 Å (BP86) but consistent with the single bond needed to give both vanadium atoms in **6S-2** the favored 18-electron configuration in a structure with one four-electron donor bridging CO group.

The last isomer **6S-3** of $Cp_2V_2(CO)_6$ is a $C_s$ unbridged structure lying above **6T-1** by 13.1 kcal/mol (B3LYP) or above **6S-1** by 14.4 kcal/mol (BP86). Structure **6S-3** has all real vibrational frequencies. For the six carbonyls, the V–C distances are in the range of 1.929–1.976 Å (B3LYP) or 1.909–1.962 Å (BP86). The V–C–O bond angles are almost linear. The V–V distance in **6S-3** is 3.251 Å (B3LYP) or 3.023 Å (BP86), which is longer than that of **6T-1** by ca. 0.1 Å.

### 3.3 Dissociation Energies

Table 6 summarizes the calculated dissociation energies for the successive removal of carbonyl groups from the lowest lying singlet isomers of $Cp_2V_2(CO)_7$ and $Cp_2V_2(CO)_6$, namely isomers **7S-1** (Figure 2) and **6S-1** (Figure 3) for $Cp_2V_2(CO)_7$ and $Cp_2V_2(CO)_6$, respectively, as well as the calculated lowest energy singlet isomers of $Cp_2V_2(CO)_5$ and $Cp_2V_2(CO)_4$. Note that the dissociation energy for decarbonylation of $Cp_2V_2(CO)_5$ to $Cp_2V_2(CO)_4$ is considerably larger than that for decarbonylation of $Cp_2V_2(CO)_7$ to $Cp_2V_2(CO)_6$ or for $Cp_2V_2(CO)_6$ to $Cp_2V_2(CO)_5$. This thermodynamic factor may be one reason why the photochemical decarbonylation[6] of $CpV(CO)_4$ goes all the way to $Cp_2V_2(CO)_5$ without stopping at $Cp_2V_2(CO)_7$ or $Cp_2V_2(CO)_6$. In addition, $Cp_2V_2(CO)_5$ was first synthesized[5] by acidification of the anion $CpV(CO)_3^{2-}$, with the expected carbonyl dihydride $CpV(CO)_3H_2$ decomposing according to the following Equation (2).

$$2\ CpV(CO)_3H_2 \rightarrow Cp_2V_2(CO)_5 + 2\ H_2 + CO \quad (2)$$

Table 6. Dissociation energies (kcal/mol) for the successive removal of carbonyl groups from the lowest lying singlet isomers of $Cp_2V_2(CO)_n$ ($n$ = 7, 6, 5, 4).

| | B3LYP | BP86 |
|---|---|---|
| $Cp_2V_2(CO)_7 \rightarrow Cp_2V_2(CO)_6 + CO$ | 17.5 | 16.8 |
| $Cp_2V_2(CO)_6 \rightarrow Cp_2V_2(CO)_5 + CO$ | 1.2 | 10.8 |
| $Cp_2V_2(CO)_5 \rightarrow Cp_2V_2(CO)_4 + CO$ | 29.5 | 34.7 |

 © 2007 Wiley-VCH Verlag GmbH & Co. KGaA, Weinheim 

The fact that $Cp_2V_2(CO)_5$, rather than the expected dimer $Cp_2V_2(CO)_6$, is produced in this reaction relates to our calculation of a low dissociation energy of one CO group from $Cp_2V_2(CO)_6$ to give $Cp_2V_2(CO)_5$ (Table 6).

## 4. Discussion

A cyclopentadienyl ring is electronically equivalent to three carbonyl groups[34] but, because of its compact nature, sterically equivalent to only two carbonyl groups. Using the latter relationship the binuclear cyclopentadienylvanadium carbonyls studied in this work can be compared with the corresponding homoleptic chromium carbonyls studied previously[4,35] by replacing two carbonyl groups in the chromium derivatives with a single cyclopentadienyl ring in the vanadium derivatives. In this way $Cp_2V_2(CO)_7$ is an analogue of $Cr_2(CO)_{11}$ and thus was found to be unstable with respect to dissociation into $CpV(CO)_4$ + $CpV(CO)_3$ just as $Cr_2(CO)_{11}$ was found earlier[4] to be unstable with respect to dissociation into $Cr(CO)_6$ + $Cr(CO)_5$. The monobridged structure for $Cp_2V_2(CO)_7$, namely $Cp_2V_2(CO)_6(\mu\text{-CO})$, found in this work (Figure 2) is analogous to a monobridged structure $Cr_2(CO)_{10}(\mu\text{-CO})$ found for $Cr_2(CO)_{11}$ in the previous work.[4]

The other binuclear cyclopentadienylvanadium carbonyl derivative discussed in this paper, namely $Cp_2V_2(CO)_6$, is an analogue of $Cr_2(CO)_{10}$.[35] Both $Cp_2V_2(CO)_6$ and $Cr_2(CO)_{10}$ are predicted to be thermodynamically stable with respect to dissociation into the corresponding mononuclear fragments, namely $CpV(CO)_3$ and $Cr(CO)_5$, respectively. For $Cp_2V_2(CO)_6$ the global minimum using the BP86 functional, namely **6S-1**, is a doubly bridged structure with a V=V distance of 2.85 Å suggesting the double bond required to give both vanadium atoms the favored 18-electron configuration. Similar Cr=Cr distances are found in the lowest lying $Cr_2(CO)_{10}$ isomers, which are also doubly bridged singlets.[35] Using the B3LYP functional for $Cp_2V_2(CO)_6$ leads to a different global minimum, namely an essentially unbridged triplet **6T-1** with a predicted V–V single-bond length of 3.10 Å. This triplet structure, with 17-electron configurations for the vanadium atoms, is closely related to the structure of the experimentally known singlet $Cp_2Cr_2(CO)_6$ determined by X-ray crystallography[36] to have no bridging CO groups and a Cr–Cr single bond length of 3.28 Å consistent with 18-electron configurations for the chromium atoms. The triplet structure for $Cr_2(CO)_{10}$ corresponding to this triplet structure for $Cp_2V_2(CO)_6$ lies 12.7 kcal/mol (B3LYP) or 13.2 kcal/mol (BP86) above its singlet global minimum.[35] The singlet structure **6S-2** for $Cp_2V_2(CO)_6$, with one four-electron donor bridging carbonyl group and a V–V distance of 3.150 Å (BP86) suggesting a single bond, has no counterpart in the singlet structures[35] predicted for $Cr_2(CO)_{10}$ in previous research.

**Supporting Information** (see also the footnote on the first page of this article): Tables S1–S6: The theoretical harmonic vibrational frequencies for the $Cp_2V_2(CO)_7$ and $Cp_2V_2(CO)_6$ structures using the BP86 method; Tables S7–S12: The theoretical Cartesian coordinates for the $Cp_2V_2(CO)_7$ and $Cp_2V_2(CO)_6$ structures using the BP86 method.

## Acknowledgments

We are indebted to the National Science Foundations of the U. S. (grant CHE-0209857) and the 111 Project (B07012) in China for support of this work.

[1] E. O. Fischer, S. Vigoureux, *Chem. Ber.* **1958**, *91*, 2205.
[2] E. Speyer, H. Wolf, *Ber. Dtsch. Chem. Ges.* **1927**, *60*, 1424.
[3] P. Pyykkö, *J. Organomet. Chem.* **2006**, *691*, 4336.
[4] N. A. Richardson, Y. Xie, R. B. King, H. F. Schaefer, *J. Phys. Chem. A* **2001**, *105*, 11134.
[5] E. O. Fischer, R. J. J. Schneider, *Angew. Chem.* **1967**, *79*, 537.
[6] W. A. Herrmann, J. Plank, *Chem. Ber.* **1979**, *112*, 392.
[7] F. A. Cotton, L. Kruczynski, *J. Organomet. Chem.* **1978**, *160*, 93.
[8] J. C. Huffman, L. N. Lewis, K. G. Caulton, *Inorg. Chem.* **1980**, *19*, 2755.
[9] A. W. Ehlers, G. Frenking, *J. Am. Chem. Soc.* **1994**, *116*, 1514.
[10] B. Delly, M. Wrinn, H. P. Lüthi, *J. Chem. Phys.* **1994**, *100*, 5785.
[11] J. Li, G. Schreckenbach, T. Ziegler, *J. Am. Chem. Soc.* **1995**, *117*, 486.
[12] V. Jonas, W. Thiel, *J. Chem. Phys.* **1995**, *102*, 8474.
[13] T. A. Barckholtz, B. E. Bursten, *J. Am. Chem. Soc.* **1998**, *120*, 1926.
[14] S. Niu, M. B. Hall, *Chem. Rev.* **2000**, *100*, 353.
[15] P. Macchi, A. Sironi, *Coord. Chem. Rev.* **2003**, *238*, 383.
[16] J.-L. Carreon, J. N. Harvey, *Phys. Chem. Chem. Phys.* **2006**, *8*, 93.
[17] M. Bühl, H. Kabrede, *J. Chem. Theor. Comput.* **2006**, *2*, 1282.
[18] A. D. Becke, *J. Chem. Phys.* **1993**, *98*, 5648.
[19] C. Lee, W. Yang, R. G. Parr, *Phys. Rev. B* **1988**, *37*, 785.
[20] A. D. Becke, *Phys. Rev. A* **1988**, *38*, 3098.
[21] J. P. Perdew, *Phys. Rev. B* **1986**, *33*, 8822.
[22] See especially F. Furche, J. P. Perdew, *J. Chem. Phys.* **2006**, *124*, 044103.
[23] H. Y. Wang, Y. Xie, R. B. King, H. F. Schaefer, *J. Am. Chem. Soc.* **2005**, *127*, 11646.
[24] H. Y. Wang, Y. Xie, R. B. King, H. F. Schaefer, *J. Am. Chem. Soc.* **2006**, *128*, 11376.
[25] T. H. Dunning, *J. Chem. Phys.* **1970**, *53*, 2823.
[26] S. Huzinaga, *J. Chem. Phys.* **1965**, *42*, 1293.
[27] A. J. H. Wachters, *J. Chem. Phys.* **1970**, *52*, 1033.
[28] D. M. Hood, R. M. Pitzer, H. F. Schaefer, *J. Chem. Phys.* **1979**, *71*, 705.
[29] M. J. Frisch, G. W. Trucks, H. B. Schlegel, G. E. Scuseria, M. A. Robb, J. R.Cheeseman, J. A. Montgomery Jr, T. Vreven, K. N. Kudin, J. C. Burant, J. M. Millam, S. S. Iyengar, J. Tomasi, V. Barone, B. Mennucci, M. Cossi, G. Scalmani, N. Rega, G. A. Petersson, H. Nakatsuji, M. Hada, M. Ehara, K. Toyota, R. Fukuda, J. Hasegawa, M. Ishida, T. Nakajima, Y. Honda, O. Kitao, H. Nakai, M. Klene, X. Li, J. E. Knox, H. P. Hratchian, J. B. Cross, V. Bakken, C. Adamo, J. Jaramillo, R. Gomperts, R. E. Stratmann, O. Yazyev, A. J. Austin, R. Cammi, C. Pomelli, J. W. Ochterski, P. Y. Ayala, K. Morokuma, G. A. Voth, P. Salvador, J. J. Dannenberg, V. G. Zakrzewski, S. Dapprich, A. D. Daniels, M. C. Strain, O. Farkas, D. K. Malick, A. D. Rabuck, K. Raghavachari, J. B. Foresman, J. V. Ortiz, Q. Cui, A. G. Baboul, S. Clifford, J. Cioslowski, B. B. Stefanov, G. Liu, A. Liashenko, P. Piskorz, I. Komaromi, R. L. Martin, D. J. Fox, T. Keith, M. A. Al-Laham, C. Y. Peng, A. Nanayakkara, M. Challacombe, P. M. W. Gill, B. Johnson, W. Chen, M. W. Wong, C. Gonzalez, J. A. Pople, *Gaussian 03*, Revision C.02, Gaussian, Inc., Wallingford CT, **2004**.

 © 2007 Wiley-VCH Verlag GmbH & Co. KGaA, Weinheim 

[30] H. Jacobsen, T. Ziegler, *J. Am. Chem. Soc.* **1996**, *118*, 4631.
[31] R. B. Hitam, A. J. Rest, *Organometallics* **1989**, *8*, 1598.
[32] J. B. Wilford, A. Whitla, H. M. Powell, *J. Organomet. Chem.* **1967**, *8*, 495.
[33] M. J. Almond, E. M. Page, D. A. Rice, K. Hagen, *J. Organomet. Chem.* **1996**, *511*, 303.
[34] R. Hoffmann, *Angew. Chem. Int. Ed. Engl.* **1982**, *21*, 711.
[35] S. Li, N. A. Richardson, Y. Xie, R. B. King, H. F. Schaefer, *J. Chem. Soc., Faraday Trans.* **2003**, *124*, 315.
[36] M. D. Curtis, W. M. Butler, *J. Organomet. Chem.* **1978**, *155*, 131.

Received: November 20, 2006
Published Online: March 6, 2007

 © 2007 Wiley-VCH Verlag GmbH & Co. KGaA, Weinheim 

DOI: 10.1002/ejic.200601030

# Solvothermal Synthesis, Crystal Structure, and Thermal Stability of Three-Layered Thioantimonate(III) Complexes: $[Ni(C_3H_{10}N_2)_3]Sb_4S_7$, $[C_4H_{14}N_2]Sb_8S_{13}\cdot H_2O$, and $[C_6H_{18}N_2]Sb_{10}S_{16}\cdot H_2O$

**Meng Zhang,[a,b] Tian Lu Sheng,[a] Xi He Huang,[a] Rui Biao Fu,[a] Xin Wang,[a] Sheng Min Hu,[a] Sheng Chang Xiang,[a] and Xin Tao Wu*[a]**

**Keywords:** Thioantimonates / Solvothermal synthesis / Cations / Layered compounds

Three new thioantimonate(III) complexes $[Ni(1,2\text{-PDA})_3]Sb_4S_7$ (**1**) (1,2-PDA = 1,2-propanediamine), $[dmenH_2^{2+}]Sb_8S_{13}\cdot H_2O$ (**2**) (dmen = *N*,*N*-dimethylethylenediamine), and $[deenH_2^{2+}]Sb_{10}S_{16}\cdot H_2O$ (**3**) (deen = *N*,*N*-diethylethylenediamine), prepared under solvothermal conditions, have been characterized by single-crystal X-ray diffraction, elemental analysis, and DTA-TG measurements. In compound **1**, a rectangle-like $Sb_{16}S_{16}$ heterоring whose dimensions are about $8.1 \times 14.7$ Å is observed, this is the largest reported pore in layered thioantimonates to date. Further condensation of the $Sb_{16}S_{16}$ heterorings resulted in an unprecedented framework of the five-atom thick $Sb_xS_y^{n-}$ layer. In **2**, a new member of $Sb_nS_n$ ($n$ = 2, 3, 4, 8, 16, 30, 31, 32) heterocycles $Sb_{15}S_{15}$ heterоring has been obtained as the first example. In compound **3**, the most particular feature is that when the secondary Sb–S bonds are considered the Sb2 atom becomes sevenfold coordinated.

(© Wiley-VCH Verlag GmbH & Co. KGaA, 69451 Weinheim, Germany, 2007)

## Introduction

The design and synthesis of chalcogenidometalates have received considerable attention[1–3] during the past decades. To design and synthesize more compounds with various configurations, it is very important to understand which factors affect the structures of chalcogenidometalates. We have in some extent studied how the structures of the sulfur-containing transition-metal polymers are influenced by the size and charge of the cations.[1,2] By using different cations such as $[Nd(DMF)_8]^{3+}$ and $[La(DMF)_8]^{3+}$, we have successfully synthesized and characterized a large number of complexes with different structure.[4] Now we further spread our interest to the study of thioantimonates.

Dozens of open-framework thioantimonates, in which transition-metal complex cations[5–18,25] and organic amine cations[19–24] serve as charge balancing ions, have been prepared in recent years, and the synthesis of these compounds is generally completed in the presence of organic amines as structure-directing agents.[10,20,26,27,34] The organic species used are often aliphatic amines, polyamines, and alicyclic amines.[21–32] The solvothermal method was proven to be very successful in the synthesis of these compounds. Although the size and charge of cations obviously have important effects on the final structure of the anions,[17,19,23,27,32] a clear relationship between them has not been observed.[12,13] Therefore, more examples of such compounds need to be prepared for further understanding.

In this work, $[Ni(1,2\text{-PDA})_3]Sb_4S_7$ (**1**) is the first example of a thioantimonate(III) in which a 1,2-propanediamine complex of a transition metal serves as the counterion. As a result of the use of two N-substituted polyamines, *N*,*N*-dimethylethylenediamine and *N*,*N*-diethylethylenediamine, we successfully prepared two additional thioantimonate(III) complexes: $[C_4H_{14}N_2]Sb_8S_{13}\cdot H_2O$ (**2**) and $[C_6H_{18}N_2]Sb_{10}S_{16}\cdot H_2O$ (**3**).

## Results and Discussion

The structure of compound **1** is composed of isolated $[Ni(1,2\text{-PDA})_3]^{2+}$ cations and $^2_\infty[Sb_4S_7]^{2-}$ anions. The $Ni^{2+}$ ion is sixfold coordinated by six nitrogen atoms of bichelate 1,2-PDA ligands, which forms a distorted octahedron (Figure 1), as is suggested by the octahedral axial $N\text{–}Ni\text{–}N_{trans}$ angles between 171.6(4)° and 172.4(4)°. The Ni–N distances between 2.091(9) and 2.135(9) Å (Table 1) are comparable with those reported in the literature.[33,34] The $^2_\infty[Sb_4S_7]^{2-}$ anion consists of two $SbS_3$ trigonal pyramids and two $SbS_4$ units. The Sb–S distances in $SbS_3$ pyramids vary from 2.373(3) to 2.561(2) Å with S–Sb–S angles between 90.89(7)° and 98.19(9)° (Table 1). For $SbS_4$ units, both Sb

[a] State Key Laboratory of Structural Chemistry, Fujian Institute of Research on the Structure of Matter, The Chinese Academy of Sciences,
Fuzhou, Fujian 350002, China
Fax: +86-591-83714947
E-mail: wxt@fjirsm.ac.cn
[b] Graduate University of the Chinese Academy of Sciences, Beijing 100039, China

Supporting information for this article is available on the WWW under http://www.eurjic.org or from the author.

 InterScience® © 2007 Wiley-VCH Verlag GmbH & Co. KGaA, Weinheim 

atoms have two short and two longer distances to neighboring S atoms with longer Sb–S separations in the *trans* position, the Sb–S bond lengths and S–Sb–S angles range, respectively, from 2.429(2) to 2.744(3) Å and from 81.29(8)° to 169.84(8)° (Table 1). These values are normal and comparable to other thioantimonate(III) complexes.[13,35,36] The interconnection of primary building units (PBUs) $Sb1S_4$, $Sb2S_3$, $Sb3S_3$, and $Sb4S_4$ results in an $Sb_4S_{10}$ chain (Figure 2). Through sharing S1 and S2 atoms, four chains of this condense to an $Sb_{16}S_{16}$ ring whose dimensions are about $8.1 \times 14.7$ Å (measured from coordinate to coordinate); this is the largest pore in layered thioantiomonates by far.[10,12,13,20] Further condensation of $Sb_{16}S_{16}$ rings through common S7 and S7b atoms leads to the two-dimensional layered $[Sb_4S_7]^{2-}$ anion, which is the first "five-atom"-thick layer; an overwhelming number of thioantimonate(III) complexes that have two-atom-thick layers are often found.[12] The layers lie in the (100) plane, and they are stacked onto each other along the *a* axis to form tunnels also in this direction (Figure 3). The cations are located between the layers.

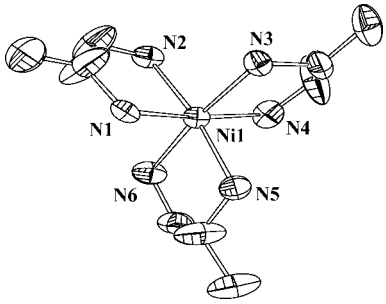


Figure 1. Structure of $[Ni(1,2\text{-}PDA)_3]^{2+}$ cation in **1** with labeling. Hydrogen atoms are omitted for clarity, displacement ellipsoids are drawn at the 50% probability level.

Table 1. Selected distances [Å] and angles [°] for $[Ni(C_3H_{10}N_2)_3]Sb_4S_7$ (**1**).[a]

| | | | |
|---|---|---|---|
| Sb1–S1 | 2.368(2) | Sb4–S2a | 2.429(2) |
| Sb1–S4 | 2.459(3) | Sb4–S7 | 2.469(2) |
| Sb1–S2 | 2.680(3) | Sb4–S6 | 2.700(2) |
| Sb1–S3 | 2.842(3) | Sb4–S1a | 2.744(3) |
| Sb2–S3 | 2.373(3) | Ni1–N2 | 2.091(9) |
| Sb2–S5 | 2.447(3) | Ni1–N1 | 2.112(8) |
| Sb2–S4 | 2.489(3) | Ni1–N5 | 2.125(8) |
| Sb3–S6 | 2.422(2) | Ni1–N6 | 2.130(9) |
| Sb3–S7b | 2.470(2) | Ni1–N4 | 2.130(9) |
| Sb3–S5 | 2.561(2) | Ni1–N3 | 2.135(9) |
| S1–Sb1–S4 | 103.25(9) | S6–Sb3–S7b | 97.64(8) |
| S1–Sb1–S2 | 86.32(8) | S6–Sb3–S5 | 92.72(8) |
| S4–Sb1–S2 | 90.27(9) | S7b–Sb3–S5 | 87.82(8) |
| S1–Sb1–S3 | 90.11(8) | S2a–Sb4–S7 | 104.05(9) |
| S4–Sb1–S3 | 81.29(8) | S2a–Sb4–S6 | 89.14(8) |
| S2–Sb1–S3 | 169.84(8) | S7–Sb4–S6 | 89.97(8) |
| S3–Sb2–S5 | 98.19(9) | S2a–Sb4–S1a | 83.73(8) |
| S3–Sb2–S4 | 90.87(9) | S7–Sb4–S1a | 83.73(8) |
| S5–Sb2–S4 | 98.08(9) | S6–Sb4–S1a | 169.04(8) |

[a] Symmetry codes: a: $-x+5/2$, $y+1/2$, $-z+1/2$, b: $-x+3$, $-y+2$, $-z+1$.

The structure of compound **2** consists of double-protonated dmen cations and $^2_\infty[Sb_8S_{13}]^{2-}$ anions, seven $SbS_3$ trigonal pyramids, and one $SbS_4$ unit as the PBUs condense to form the $[Sb_8S_{13}]^{2-}$ anion through sharing common corners and edges (Figure 4). The Sb–S separations of the $SbS_3$ pyramids vary from 2.396(2) to 2.567(2) Å with the S–Sb–S angles between 85.69(4)° and 98.23(4)°. In the $Sb6S_4$ unit, the Sb6 atom has two short [2.447(2) and 2.532(2) Å] and two relatively longer distances [2.747(2) and 2.728(2) Å], the longer distances being in the *trans* position [170.00(4)°]

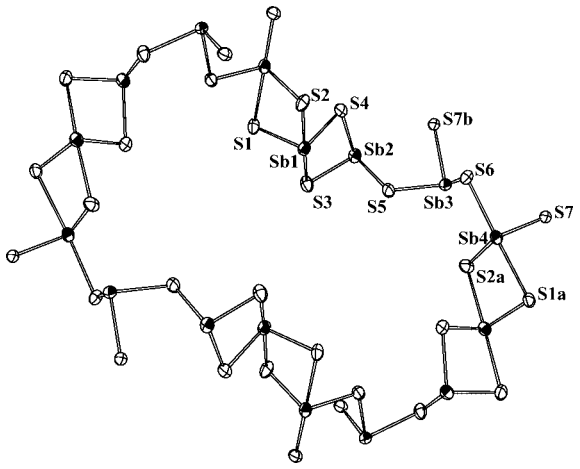


Figure 2. $Sb_4S_{10}$ chain with labeling and further condensation to form $Sb_{16}S_{16}$ ring in $[Ni(C_3H_{10}N_2)_3]Sb_4S_7$ (**1**). Symmetry codes: a: $-x+5/2$, $y+1/2$, $-z+1/2$, b: $-x+3$, $-y+2$, $-z+1$. Displacement ellipsoids are drawn at the 50% probability level.

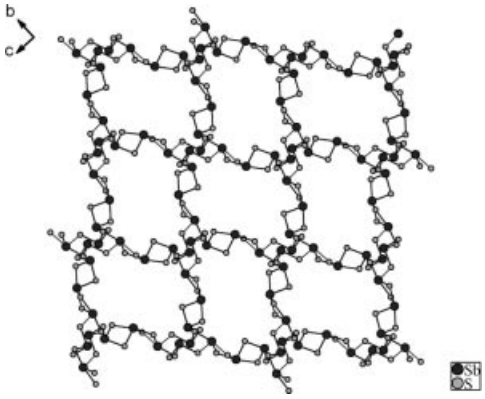


Figure 3. The layer composed of $Sb_{16}S_{16}$ rings in $[Ni(C_3H_{10}N_2)_3]Sb_4S_7$ (**1**).

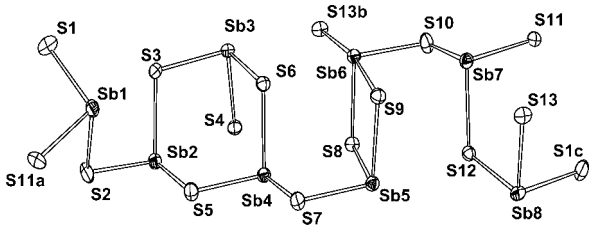


Figure 4. Condensation of seven $SbS_3$ trigonal pyramids and one $SbS_4$ unit to form the $[Sb_8S_{13}]^{2-}$ anion with numbering scheme in $[C_4H_{14}N_2]Sb_8S_{13}\cdot H_2O$ (**2**). Symmetry codes: a: –x, $-1/2+y$, $1/2-z$, b: $-1+x$, $y$, $z$, c: $-x$, $1/2+y$, $1/2-z$. Displacement ellipsoids are drawn at the 50% probability level.

 © 2007 Wiley-VCH Verlag GmbH & Co. KGaA, Weinheim 

(Table 2). All these values are normal in thioantimonate(III) complexes.[19,22,23] Further interconnection of the $[Sb_8S_{13}]^{2-}$ anions yields undulated layers extending in the (001) plane, in which the $Sb_{15}S_{15}$ heterorings are for the first time observed (shadowed area in Figure 5). There exist nearly circular pores with dimensions of about $7.9 \times 8.4$ Å (measured from coordinate to coordinate) in these heterorings. The layers are stacked onto each other to build channels along the *c* axis, in which the organic cations and the water molecules are accommodated (Figure 5). Compound **3** is composed of double-protonated deen cations and $^2_\infty[Sb_{10}S_{16}]^{2-}$ anions. The $[Sb_{10}S_{16}]^{2-}$ anions are formed by the interconnection of nine $SbS_3$ trigonal pyramids and one $SbS_4$ unit by common corners and edges (Figure 6). In the $SbS_3$ pyramids, Sb–S distances vary from 2.404(3) to 2.595(3) Å and S–Sb–S angles are between 87.58(10)° and 98.70(10)°; in the $Sb6S_4$ moieties there are three short [2.460(3), 2.506(3), Sb6–S9: 2.585(3) Å] and one extraordinarily long Sb–S bonds [Sb6–S15a: 2.929(3) Å] with the S9–Sb6–S15a angle being 169.61(10)° (Table 3). All of these values are in the typical range.[21,22,27] Further condensation of the $[Sb_{10}S_{16}]^{2-}$ anions resulted in the two-dimensional layers extending in the (001) plane, which could be thought

Table 2. Selected distances [Å] and angles [°] for $[C_4H_{14}N_2]$-$Sb_8S_{13}\cdot H_2O$ (**2**).[a]

| | | | |
|---|---|---|---|
| Sb1–S11a | 2.437(2) | S11a–Sb1–S1 | 100.59(5) |
| Sb1–S2 | 2.440(2) | S2–Sb1–S1 | 93.48(5) |
| Sb1–S1 | 2.452(2) | S3–Sb2–S5 | 97.22(4) |
| Sb2–S3 | 2.445(2) | S3–Sb2–S2 | 90.89(4) |
| Sb2–S5 | 2.451 (2) | S5–Sb2–S2 | 88.88(5) |
| Sb2–S2 | 2.496(2) | S4–Sb3–S6 | 92.99(4) |
| Sb3–S4 | 2.396 (2) | S4–Sb3–S3 | 92.43(4) |
| Sb3–S6 | 2.507(2) | S6–Sb3–S3 | 96.60(4) |
| Sb3–S3 | 2.513 (2) | S6–Sb4–S5 | 93.30(4) |
| Sb4–S6 | 2.465(2) | S6–Sb4–S7 | 90.12(4) |
| Sb4–S5 | 2.498(2) | S5–Sb4–S7 | 92.93(4) |
| Sb4–S7 | 2.533(2) | S9–Sb5–S7 | 94.62(4) |
| Sb5–S9 | 2.417(2) | S9–Sb5–S8 | 89.98(4) |
| Sb5–S7 | 2.535(2) | S7–Sb5–S8 | 98.23(4) |
| Sb5–S8 | 2.567(2) | S8–Sb6–S10 | 93.34(5) |
| Sb6–S8 | 2.447(2) | S8–Sb6–S9 | 85.69(4) |
| Sb6–S10 | 2.532(2) | S10–Sb6–S9 | 93.96(4) |
| Sb6–S9 | 2.728(2) | S8–Sb6–S13b | 88.99(4) |
| Sb6–S13b | 2.747(2) | S10–Sb6–S13b | 94.80(4) |
| Sb7–S10 | 2.461(2) | S9–Sb6–S13b | 170.00(4) |
| Sb7–S12 | 2.475(2) | S10–Sb7–S12 | 89.89(4) |
| Sb7–S11 | 2.497(2) | S10–Sb7–S11 | 93.07(5) |
| Sb8–S13 | 2.413(2) | S12–Sb7–S11 | 94.81(4) |
| Sb8–S12 | 2.477(2) | S13–Sb8–S12 | 96.50(4) |
| Sb8–S1c | 2.524(2) | S13–Sb8–S1c | 96.17(5) |
| S11a–Sb1–S2 | 86.82(5) | S12–Sb8–S1c | 91.96(4) |

[a] Symmetry codes: a: -x, y–1/2, –*z*+1/2, b: x–1, *y*, *z*, c: –x, *y*+1/2, –*z*+1/2.

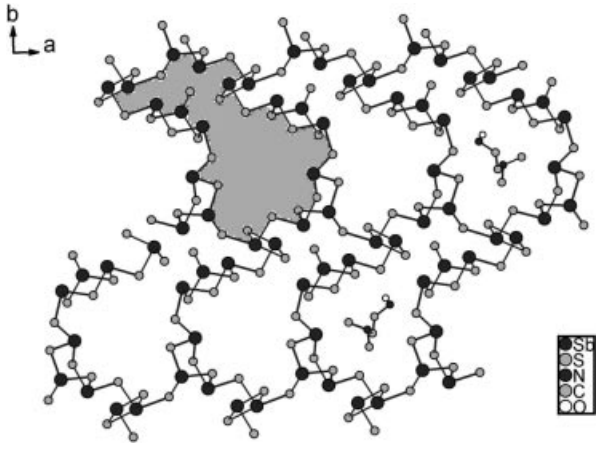


Figure 5. $Sb_{15}S_{15}$ heteroring (shadowed area) in layer of $[C_4H_{14}N_2]$-$Sb_8S_{13}\cdot H_2O$ (**2**). The organic cations and water molecules are accommodated in the channels. Hydrogen atoms, some organic cations, and $H_2O$ molecules are omitted for clarity.

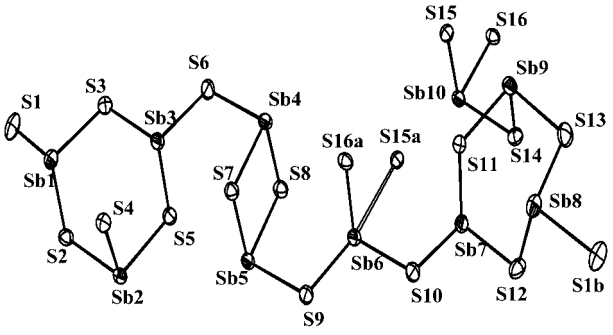


Figure 6. Interconnection of nine $SbS_3$ and one $SbS_4$ units, which results in the $[Sb_{10}S_{16}]^{2-}$ anion with labeling in $[C_6H_{18}N_2]$-$Sb_{10}S_{16}\cdot H_2O$ (**3**). Symmetry codes: a: 2 –*x*, -y, 2 –*z*, b: 1 –*x*, –1/2 + *y*, 3/2 –*z*.

Table 3. Selected distances [Å] and angles [°] for $[C_6H_{18}N_2]$-$Sb_{10}S_{16}\cdot H_2O$ (**3**).[a]

| | | | |
|---|---|---|---|
| Sb1–S2 | 2.443(3) | S2–Sb1–S1 | 89.70(11) |
| Sb1–S3 | 2.469(3) | S3–Sb1–S1 | 89.75(12) |
| Sb1–S1 | 2.498(3) | S4–Sb2–S5 | 96.04(10) |
| Sb2–S4 | 2.404(3) | S4–Sb2–S2 | 91.50(11) |
| Sb2–S5 | 2.468(3) | S5–Sb2–S2 | 96.88(10) |
| Sb2–S2 | 2.521(3) | S5–Sb3–S3 | 94.97(11) |
| Sb3–S5 | 2.453(3) | S5–Sb3–S6 | 90.46(11) |
| Sb3–S3 | 2.492(3) | S3–Sb3–S6 | 93.73(11) |
| Sb3–S6 | 2.515(3) | S8–Sb4–S7 | 89.30(10) |
| Sb4–S8 | 2.449(3) | S8–Sb4–S6 | 94.84(11) |
| Sb4–S7 | 2.519(3) | S7–Sb4–S6 | 97.61(10) |
| Sb4–S6 | 2.521(3) | S7–Sb5–S9 | 93.36(10) |
| Sb5–S7 | 2.480(3) | S7–Sb5–S8 | 87.58(10) |
| Sb5–S9 | 2.521(3) | S9–Sb5–S8 | 98.70(10) |
| Sb5–S8 | 2.564(3) | S16a–Sb6–S10 | 93.16(11) |
| Sb6–S16a | 2.460(3) | S16a–Sb6–S9 | 90.40(10) |
| Sb6–S10 | 2.506(3) | S10–Sb6–S9 | 93.66(10) |
| Sb6–S9 | 2.585(3) | S16a–Sb6–S15a | 81.83(9) |
| Sb6–S15a | 2.929(3) | S10–Sb6–S15a | 93.65(9) |
| Sb7–S10 | 2.461(3) | S9–Sb6–S15a | 169.61(10) |
| Sb7–S11 | 2.495(3) | S10–Sb7–S11 | 91.73(10) |
| Sb7–S12 | 2.498(3) | S10–Sb7–S12 | 92.73(12) |
| Sb8–S12 | 2.438(3) | S11–Sb7–S12 | 95.03(10) |
| Sb8–S1b | 2.444(4) | S12–Sb8–S1b | 88.40(12) |
| Sb8–S13 | 2.459(4) | S12–Sb8–S13 | 98.68(13) |
| Sb9–S14 | 2.457(3) | S1b–Sb8–S13 | 92.68(13) |
| Sb9–S11 | 2.478(3) | S14–Sb9–S11 | 96.13(10) |
| Sb9–S13 | 2.509(3) | S14–Sb9–S13 | 93.58(12) |
| Sb10–S15 | 2.422(3) | S11–Sb9–S13 | 92.78(11) |
| Sb10–S16 | 2.519(3) | S15-Sb10–S16 | 91.75(10) |
| Sb10–S14 | 2.595(3) | S15-Sb10–S14 | 92.37(10) |
| S2–Sb1–S3 | 97.59(11) | S16-Sb10–S14 | 98.31(10) |

[a] Symmetry codes: a: 2–*x*, –y, 2–*z*, b: 1–*x*, –1/2+*y*, 3/2–*z*.

 © 2007 Wiley-VCH Verlag GmbH & Co. KGaA, Weinheim 

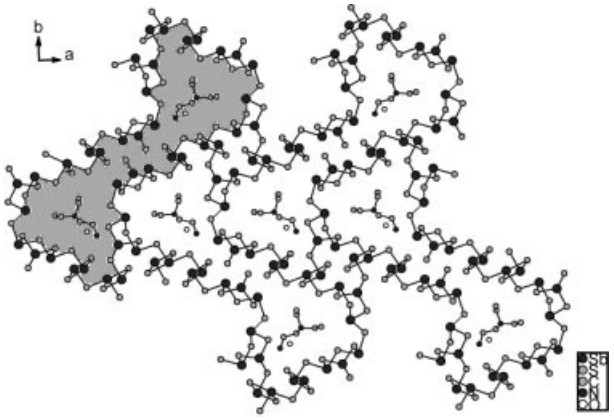


Figure 7. $[Sb_{10}S_{16}]^{2-}$ layer consists of $Sb_{30}S_{30}$ rings (shaded area) in $[C_6H_{18}N_2]Sb_{10}S_{16}\cdot H_2O$ (**3**). Organic cations and water molecules are held in tunnels. Hydrogen atoms are omitted for clarity.

to be composed of the "double-ellipsoidal"[20] $Sb_{30}S_{30}$ rings in two perpendicular directions (Figure 7). The dimensions of the ellipsoidal pores in the $Sb_{30}S_{30}$ rings are about $8.8 \times 10.1$ Å (measured from coordinate to coordinate). The layers are stacked onto each other in the [001] direction, which forms channels where the cations and water molecules are located (Figure 7).

In all three title compounds, relatively short H···S distances are observed. The short H···S separations in compound $[Ni(C_3H_{10}N_2)_3]Sb_4S_7$ scatter from 2.51 to 2.69 Å with N–H···S angles ranging from 157.5° to 177.9° (Table 4). In $[C_4H_{14}N_2]Sb_8S_{13}\cdot H_2O$, four short H···S contacts from 2.53 to 2.82 Å are found with N–H···S (or O–H···S) angles between 136.1° and 163.8° (Table 4). Several short H···S separations (2.46 to 2.60 Å) in $[C_6H_{18}N_2]$-$Sb_{10}S_{16}\cdot H_2O$ are also observed, and the N–H···S (or O–H···S) angles are in the range of 140.6 to 164.2° (Table 4). All the values indicate that weak hydrogen bonding interconnections exist between the cations and the $Sb_xS_y^{n-}$ anions.

When the secondary Sb–S bonds (sum of van der Waals' radii: $Sb_{vdw} + S_{vdw} \approx 3.85$ Å[37]) are taken into account, most Sb atoms in the three title compounds enhance their coordination numbers. In compound **1**, the Sb3 and Sb4 atoms are fivefold coordinated to form ψ-$SbS_5$ octahedra, and the Sb2 atom is surrounded by four S atoms to yield ψ-SbS4 trigonal bipyramids (Table 5). In compound **2**, the Sb1 and Sb7 atoms enhance their coordination numbers to five and the Sb2, Sb3, Sb4, Sb5, Sb6, and Sb8 atoms become sixfold coordinated (Table 5). In compound **3**, the Sb1 atom, the Sb7 and Sb8 atoms, and the Sb3, Sb4, Sb5, Sb6, Sb9, and Sb10 atoms are surrounded by four, five, and six S atoms, respectively. The most distinct character is that the Sb2 atom becomes seven-coordinate (Figure 8) with the Sb–S bond lengths varying from 3.1909(31) to 3.7607(34) Å and the S–Sb–S angles being in the range of 59.91(8)° to111.29(8)° [67.98(7) to113.14(6)° for other Sb atoms] (Table 5). To the best of our knowledge, compound **3** is the first thioantimonate in which there exists seven-coordinate Sb atoms with Sb–S distances under 3.8 Å.

In the three title compounds, the sequence of the cationic size is $[Ni(C_3H_{10}N_2)_3]^{2+}$ (in **1**) > $[C_6H_{18}N_2]^{2+}\cdot H_2O$ (in **3**) > $[C_4H_{14}N_2]^{2+}\cdot H_2O$ (in **2**), correspondingly the dimensions of pores in compounds are **1** ($8.1 \times 14.7$ Å) > **3** ($8.8 \times 10.1$ Å) > **2** ($7.9 \times 8.4$ Å), the cations and the water molecules are

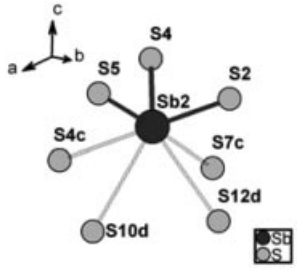


Figure 8. Seven-coordinated Sb2 atom in $[C_6H_{18}N_2]Sb_{10}S_{16}\cdot H_2O$ (**3**). Symmetry code: c: –x, -y, 1 –*z*, d: 1 –*x*, -y, 1 –*z*.

Table 4. Proposed hydrogen bonding geometry for $[Ni(C_3H_{10}N_2)_3]Sb_4S_7$ (**1**), $[C_4H_{14}N_2]Sb_8S_{13}\cdot H_2O$ (**2**), and $[C_6H_{18}N_2]Sb_{10}S_{16}\cdot H_2O$ (**3**).

| D–H | A | *d*(H···A) | *d*(D···A) | <DHA | Symmetry code |
|---|---|---|---|---|---|
| $[Ni(C_3H_{10}N_2)_3]Sb_4S_7$ | | | | | |
| N1–H1A | S1 | 2.55 | 3.396(8) | 157.5 | |
| N1–H1B | S5 | 2.69 | 3.570(9) | 164.6 | x-1, *y*, *z* |
| N2–H3A | S4 | 2.63 | 3.526(9) | 177.9 | –*x* + 3/2, y-1/2, –*z* + 1/2 |
| N2–H3B | S6 | 2.57 | 3.451(9) | 165.4 | –*x* + 3/2, y-1/2, –*z* + 1/2 |
| N3–H2B | S5 | 2.51 | 3.365(9) | 159.3 | x-1, *y*, *z* |
| $[C_4H_{14}N_2]Sb_8S_{13}\cdot H_2O$ | | | | | |
| N2–H2A | S7 | 2.54 | 3.404(6) | 163.8 | –x-1, –*y* + 1, –*z* + 1 |
| N2–H2C | S1 | 2.82 | 3.516(6) | 136.1 | |
| O1–H1D | S10 | 2.58 | 3.265(5) | 138.3 | |
| O1–H1E | S1 | 2.53 | 3.302(5) | 152.0 | x-1, *y*, *z* |
| $[C_6H_{18}N_2]Sb_{10}S_{16}\cdot H_2O$ | | | | | |
| N1–H1C | S2 | 2.60 | 3.338(11) | 140.6 | x + 1, *y*, *z* |
| N1–H1D | S9 | 2.59 | 3.367(13) | 146.9 | –x, *y* + 1/2, –*z* + 3/2 |
| O1–H1F | S6 | 2.46 | 3.284(11) | 164.2 | x + 1, *y*, *z* |

 © 2007 Wiley-VCH Verlag GmbH & Co. KGaA, Weinheim 

Table 5. The long Sb–S bonds [Å] and some S–Sb–S angles [°] in compounds **1**–**3**.[a]

| | | | |
|---|---|---|---|
| $[Ni(C_3H_{10}N_2)_3]Sb_4S_7$ (**1**) | | | |
| Sb2–S7b | 3.6197(24) | Sb3–S2a | 3.4969(25) |
| Sb3–S6b | 3.0593(25) | Sb4–S3c | 3.5010(26) |
| $[C_4H_{14}N_2]Sb_8S_{13}{\cdot}H_2O$ (**2**) | | | |
| Sb1–S12a | 3.2707(13) | Sb5–S4f | 3.0826(13) |
| Sb1–S3 | 3.3016(13) | Sb5–S12 | 3.2860(13) |
| Sb2–S4 | 3.1035(13) | Sb5–S7h | 3.5613(14) |
| Sb2–S7b | 3.7021(13) | Sb6–S6 | 3.1086(13) |
| Sb2–S4g | 3.7351(13) | Sb6–S13j | 3.6998(14) |
| Sb3–S9b | 3.2233(13) | Sb7–S9 | 3.1479(14) |
| Sb3–S13b | 3.3178(15) | Sb7–S13 | 3.2971(13) |
| Sb3–S11i | 3.4816(13) | Sb8–S4f | 3.2472(13) |
| Sb4–S4 | 3.0214(13) | Sb8–S8f | 3.3889(12) |
| Sb4–S8 | 3.1146(13) | Sb8–S2h | 3.7584(15) |
| Sb4–S4g | 3.6241(13) | | |
| $[C_6H_{18}N_2]Sb_{10}S_{16}{\cdot}H_2O$ (**3**) | | | |
| Sb1–S4 | 3.0925(31) | Sb7–S15a | 3.1317(31) |
| Sb3–S4 | 3.0495(31) | Sb7–S14 | 3.3374(31) |
| Sb3–S7 | 3.1997(31) | Sb8–S2b | 3.2598(31) |
| Sb4–S16a | 3.1594(33) | Sb8–S11 | 3.2789(30) |
| Sb4–S14a | 3.1863(31) | Sb9–S15 | 3.0792(31) |
| Sb4–S14j | 3.5548(33) | Sb9–S8a | 3.5946(30) |
| Sb5–S4c | 3.0754(31) | Sb9–S3i | 3.6282(34) |
| Sb5–S5 | 3.2465(32) | Sb10-S15a | 3.1056(30) |
| Sb5–S9d | 3.3800(34) | Sb10-S11a | 3.1312(30) |
| Sb6–S8 | 3.1415(33) | Sb10-S6h | 3.4291(37) |
| Sb6–S4h | 3.5750(32) | | |
| Sb2–S4c | 3.1909(31) | Sb2–S12d | 3.4002(33) |
| Sb2–S7c | 3.3842(30) | Sb2–S10d | 3.7607(34) |
| S7c–Sb2–S4c | 85.05(8) | S10d–Sb2–S4c | 67.30(7) |
| S12d–Sb2–S4c | 111.29(8) | S10d–Sb2–S7c | 107.10(7) |
| S12d–Sb2–S7c | 72.57(8) | S10d–Sb2–S12d | 59.91(8) |

[a] Symmetry codes: for $[Ni(C_3H_{10}N_2)_3]Sb_4S_7$: a: $-x+5/2$, $y+1/2$, $-z+1/2$, b: $-x+3$, $-y+2$, $-z+1$, c: $x+1$, $y$, $z$; for $[C_4H_{14}N_2]Sb_8S_{13}{\cdot}H_2O$: a: –x, y–1/2, $-z+1/2$, b: x–1, $y$, $z$, f: $x+1$, $y$, $z$, g: –x–1, $-y+1$, –z, h: -x, $-y+1$, –z, i: -x, $-y+1$, $-z+1$, j: $-x+1$, $-y+1$, $-z+1$; for $[C_6H_{18}N_2]Sb_{10}S_{16}{\cdot}H_2O$: a: $-x+2$, $-y$, $-z+2$, b: $-x+1$, y–1/2, $-z+3/2$, c: –x, $-y$, $-z+1$, d: $-x+1$, $-y$, $-z+1$, h: $x+1$, $y$, $z$, i: $-x+1$, $-y$, $-z+2$, j: x–1, $y$, $z$.

located above or under the pores. So it is obvious that the cations play an important role in the formation of $Sb_xS_y^{n-}$ structures.

### Thermal Investigations

Compound **1** decomposes in a two-step manner which is accompanied by two signals in the DTA curve ($T_p$ = 192 and 286 °C; Figure S1) and the extrapolated onset temperature $T_e$ was 175 °C. The experimental total mass loss was 24.4%, which corresponds to the emission of organic amine ($-\Delta m_{theo}$ = 22.4%). For **2**, the mechanism of decomposition is more complicated and two obvious steps can be identified. In the first step, the extrapolated onset temperature $T_e$ was 140 °C and $T_p$ was 150 °C (Figure S2). The weight loss was 1.2%, which is in good agreement with the expected value for the removal of water molecules ($-\Delta m_{theo}$ = 1.0%). On further heating, another endothermic event occurred with the DTA signal at $T_p$ = 274 °C, the mass loss was 8.4% which can be attributed to the complete emission of organic ligands ($-\Delta m_{theo}$ = 6.0%). In the TG curve of **3** a smooth decrease from 63 °C to 223 °C is observed with a weight change of 1.1% (Figure S3), as corresponds to the removal of water molecules ($-\Delta m_{theo}$ = 1.0%). On further heating, a sharp weight loss of 7.6% occurred, which was accompanied by the endothermic event at $T_e$ = 247 °C and $T_p$ = 260 °C in the DTA curve. The experimental value is in good agreement with that determined for the emission of the organic component ($-\Delta m_{theo}$ = 6.3%). During the heating process, besides the removal of organic amine and water molecules, some $H_2S$ molecules were formed and emitted.[13,27] This may explain the discrepancy between the experimental and theoretic values.

## Experimental Section

**1**: Yellow crystals of $[Ni(1,2\text{-PDA})_3]Sb_4S_7$ (**1**) were obtained from Ni (0.0586 g, 1 mmol) or $NiCl_2{\cdot}6H_2O$ (0.273 g, 1 mmol), Sb (0.1217 g, 1 mmol), and S (0.1280 g, 4 mmol) in a water solution of 1,2-PDA (60%, 5 mL) under solvothermal conditions. The mixture was heated at 140 °C for 6 d in Teflon-lined steel autoclaves with an inner volume of 25 mL and then cooled to room temperature over 5 h. After the reaction mixture was filtered, the residual solid product was washed with alcohol. The yellow crystals were obtained in 30% yield (according to Sb), and they are stable in air and alcohol, but have good dissolvability in water. $C_9H_{30}N_6NiSb_4S_7$ (992.52): calcd. C 10.8, H 3.02, N 8.46; found C 10.54, H 3.23, N 8.95.

**2**: Red crystals of $[dmenH_2^{2+}]Sb_8S_{13}{\cdot}H_2O$ (**2**) were prepared from the reaction of Zn (0.0915 g, 1.4 mmol), Sb (0.1217 g, 1 mmol), and S (0.1280 g, 4 mmol) in an aqueous solution of dmen (50%, 5 mL). The mixture was heated at 140 °C for 6 d in Teflon-lined steel autoclaves and then cooled to room temperature. The reacted mixture was filtered and washed with water and alcohol to give 30% yield of crystalline **2** (based on Sb). The product is stable in air, water, and ethanol. In the absence of Zn in the reaction mixture, a decreased yield was observed. $C_4H_{16}N_2Sb_8S_{13}O$ (1498.97): calcd. C 3.20, H 1.06, N 1.87; found C 3.55, H 1.36, N 1.67.

**3**: The procedure for the synthesis of $[deenH_2^{2+}]Sb_{10}S_{16}{\cdot}H_2O$ (**3**) is the same as that of **2**. Zn (0.0729 g, 1.1 mmol), Sb (0.1217 g, 1 mmol), S (0.0712 g, 2.2 mmol), aqueous solution of deen (50%, 5 mL). Yield: 35%. In the absence of Zn in the reaction mixture, a decreased yield was observed. $C_6H_{20}N_2Sb_{10}S_{16}O$ (1866.70): calcd. C 3.86, H 1.07, N 1.50; found C 3.82, H 1.35, N 1.23.

**Structure Determination:** Intensities were collected at 293(2) K with a Simens SMART-CCD diffractometer (for **1**), at 294(2) K with a Rigaku SATURN70 CCD diffractometer (for **2**), and at 293(2) K with a Rigaku Mercury CCD diffractometer (for **3**) by using graphite-monochromated Mo-$K_a$ radiation [$\lambda$ = 0.71073 Å]. Data for all three compounds were corrected for Lorentz, polarization, and absorption effects. The structures were solved and refined by full-matrix least-squares techniques on $F^2$ by using SHELXL-97,[38] all non-hydrogen atoms were refined anisotropically. Hydrogen atoms were generated geometrically and allowed to ride on their parent atoms with fixed isotropic displacement parameters. The crystallographic data are summarized in Table 6.

CCDC-626004 (for **1**), -626005 (for **2**), and -626006 (for **3**) contain the supplementary crystallographic data for this paper. These data

 © 2007 Wiley-VCH Verlag GmbH & Co. KGaA, Weinheim 

Table 6. Crystallographic data for $[Ni(C_3H_{10}N_2)_3]Sb_4S_7$ (**1**), $[C_4H_{14}N_2]Sb_8S_{13}\cdot H_2O$ (**2**), and $[C_6H_{18}N_2]Sb_{10}S_{16}\cdot H_2O$ (**3**).

| | **1** | **2** | **3** |
|---|---|---|---|
| Color, habit | yellow block | red sheet | red block |
| Crystal size [mm] | $0.25\times0.25\times0.20$ | $0.18\times0.12\times0.01$ | $0.24\times0.22\times0.20$ |
| Crystal system | monoclinic | monoclinic | monoclinic |
| Space group | *P*21/*n* | *P*21/*c* | *P*21/*c* |
| *a* [Å] | 10.809(1) | 9.143(2) | 11.537(3) |
| *b* [Å] | 15.795(1) | 23.515(4) | 25.110(7) |
| *c* [Å] | 16.1152(2) | 13.871(2) | 13.748(4) |
| $\beta$ [°] | 90.75(1) | 105.00(1) | 111.29(1) |
| *V* [Å$^3$] | 2751.11(5) | 2880.6(8) | 3711.0(18) |
| *Z* | 4 | 4 | 4 |
| Formula weight [g mol$^{-1}$] | 992.52 | 1498.97 | 1866.70 |
| Calculated density [g cm$^{-3}$] | 2.396 | 3.456 | 3.341 |
| $\mu$ [mm$^{-1}$] | 5.091 | 8.332 | 8.070 |
| *F*(000) | 1880 | 2712 | 3376 |
| Temperature [K] | 293(2) | 293(2) | 293(2) |
| $\theta$ range for data collection [°] | 1.81 to 25.66 | 2.30 to 27.47 | 2.27 to 27.48 |
| *h*, *k*, *l*, range | –13 to 8 | –11 to 11 | –14 to 11 |
| | –19 to19 | –30 to 23 | –30 to 32 |
| | –19 to 16 | –18 to 18 | –15 to 17 |
| Reflections measured | 14489 | 22025 | 28691 |
| Independent reflections | 5201 | 6496 | 8491 |
| Observed reflection [$I>2\sigma(I)$] | 4488 | 5725 | 7281 |
| $R_{int.}$ | 0.0363 | 0.0322 | 0.0639 |
| Min./max. trans. | 0.8146/1.0000 | 0.6135/1.0000 | 0.2476/0.2952 |
| $R$[a] | 0.0446 | 0.0213 | 0.0622 |
| $Rw$[b] | 0.0890 | 0.0552 | 0.1516 |
| Goodness of fit | 1.096 | 1.199 | 1.177 |
| Max./min. $\Delta\rho$ [e Å$^{-3}$] | 1.286/–0.954 | 1.242/–1.187 | 1.861/–1.954 |

[a] $R = \Sigma(||F_o| - |F_c||)/\Sigma|F_o|$. [b] $Rw = \{\Sigma w[(F_o^2 - F_c^2)^2]/\Sigma w[(F_o^2)^2]\}^{1/2}$, $w = 1/[\sigma^2(F_o^2)+(aP)^2+bP]$, $P = (F_o^2+2F_c^2)/3$, $a = 0.1110$, $b = 14.4871$.

can be obtained free of charge from The Cambridge Crystallographic Data Centre via www.ccdc.cam.ac.uk/data_request/cif.

**Thermoanalytical Measurements:** Thermoanalytical measurements were performed with a DTA-TG device STA 449C from Netzsch. All measurements were performed under a nitrogen atmosphere (flow-rate: 20 mL min$^{-1}$) with $Al_2O_3$ crucibles. The heating rates are 10 K min$^{-1}$.

**X-ray Powder Diffractometry:** The X-ray powder diffraction patterns were acquired with a DMAX-2500 diffractometer by using Cu $K_a$ radiation at ambient environment.

**Supporting Information** (see footnote on the first page of this article): DTA-TG figures of the title compounds and X-ray powder patterns of crystals **2** and **3**.

## Acknowledgments

This work was supported by grants from the State Key Laboratory of Structure Chemistry, Fujian Institute of Research on the Structure of Matter, Chinese Academy of Sciences (CAS), the 973 Program (2006CB932900), the National Science Foundation of China (20333070, 90206040, 90406024, and 20673118), the Science Foundation of CAS, and Fujian Province (2006J0014, 2005HZ01–1, and 2004HZ01–1).

[1] L. Chen, X. T. Wu in *Inorganic Chemistry in Focus II* (Eds.: G. Meyer, D. Naumann, L. Weseman), Wiley; New York, **2005**, p. 207.

[2] X. T. Wu, Q. Huang, Q. M. Wang, T. L. Sheng, J. X. Lu in *Transition Metal Sulfur Chemistry: Biological and Industrial Significance* (Eds.: E. I. Stiefel, K. Matsumoto), ACS Symposium Series 653, American Chemical Society, Washington DC, **1996**, p. 282.

[3] M. Schaefer, D. Kurowski, A. Pfitzner, C. Na1ther, Z. Rejai, K. Mo1ller, N. Ziegler, W. Bensch, *Inorg. Chem.* **2006**, *45*, 3726.

[4] For examples, see: a) H. Yu, W. J. Zhang, X. T. Wu, T. L. Sheng, Q. M. Wang, P. Lin, *Angew. Chem. Int. Ed.* **1998**, *37*, 2520; b) Q. Huang, X. T. Wu, Q. M. Wang, T. L. Sheng, J. X. Lu, *Angew. Chem. Int. Ed. Engl.* **1996**, *35*, 868–869; c) Q. Huang, X. T. Wu, T. L. Sheng, Q. M. Wang, *Inorg. Chem.* **1995**, *34*, 4931–4932; d) Q. Huang, X. T. Wu, J. X. Lu, *Inorg. Chem.* **1996**, *35*, 7445–7447; e) Q. Huang, X. T. Wu, J. X. Lu, *Chem. Commun.* **1997**, 703; f) L. Chen, X. T. Wu, X. C. Gao, W. J. Zhang, P. Lin, *J. Chem. Soc., Dalton Trans.* **1999**, 4303–4307.

[5] R. Stähler, B.-D. Mosel, H. Eckert, W. Bensch, *Angew. Chem. Int. Ed.* **2002**, *41*, 4487.

[6] H.-O. Stephan, M. G. Kanatzidis, *J. Am. Chem. Soc.* **1996**, *118*, 12226.

[7] R. Stähler, W. Bensch, *Eur. J. Inorg. Chem.* **2001**, 3073.

[8] R. Stähler, W. Bensch, *J. Chem. Soc., Dalton Trans.* **2001**, 2518.

[9] H.-O. Stephan, M. G. Kanatzidis, *Inorg. Chem.* **1997**, *36*, 6050.

[10] R. Stähler, W. Bensch, *Z. Anorg. Allg. Chem.* **2002**, *628*, 1657.

[11] W. Bensch, C. Näther, R. Stähler, *Chem. Commun.* **2001**, 477.

[12] R. Stähler, C. Näther, W. Bensch, *Eur. J. Inorg. Chem.* **2001**, 1835.

[13] R. Stähler, C. Näther, W. Bensch, *J. Solid State Chem.* **2003**, *174*, 264.

[14] M. Schaefer, C. Näther, W. Bensch, *Solid State Sci.* **2003**, *5*, 1135.

[15] R. Kiebach, W. Bensch, R.-D. Hoffmann, R. Pöttgen, *Z. Anorg. Allg. Chem.* **2003**, *629*, 532.

[16] M. Schur, W. Bensch, *Z. Naturforsch., Teil B* **2002**, *57*, 1.

[17] W. Bensch, M. Schur, *Z. Naturforsch., Teil B* **1997**, *52*, 405.

[18] M. Schur, C. Näther, W. Bensch, *Z. Naturforsch., Teil B* **2001**, *56*, 79.

 © 2007 Wiley-VCH Verlag GmbH & Co. KGaA, Weinheim 

[19] L. Engelke, C. Näther, W. Bensch, *Eur. J. Inorg. Chem.* **2002**, 2936–2941.
[20] R. Kiebach, C. Näther, W. Bensch, *Z. Naturforsch., Teil B* **2004**, *59*, 1314–1319.
[21] X. Q. Wang, L. M. Liu, A. J. Jacobson, *J. Solid State Chem.* **2000**, *155*, 409–416.
[22] X. Q. Wang, F. Liebau, *J. Solid State Chem.* **1994**, *111*, 385–389.
[23] V. Spetzler, R. Kiebach, C. Näther, W. Bensch, *Z. Anorg. Allg. Chem.* **2004**, *630*, 2398–2404.
[24] P. Vaqueiro, D. P. Darlow, A. V. Powell, A. M. Chippindale, *Solid State Ionics* **2004**, *172*, 601–605.
[25] M. Schaefer, D. Kurowski, A. Pfitzner, C. Näther, W. Bensch, *Acta Crystallogr., Sect. E* **2004**, *60*, m183–m185.
[26] A. V. Powell, R. J. E. Lees, A. M. Chippindale, *Inorg. Chem.* **2006**, *45*, 4261–4267.
[27] A. Puls, M. Schaefer, C. Näther, W. Bensch, A. V. Powell, S. Boissière, A. M. Chippindale, *J. Solid State Chem.* **2005**, *178*, 1171–1181.
[28] R. Stähler, C. Näther, W. Bensch, *Acta Crystallogr., Sect. C* **2001**, *57*, 26–27.
[29] P. Vaqueiro, A. M. Chippindale, A. V. Powell, *Inorg. Chem.* **2004**, *43*, 7963–7965.
[30] D. X. Jia, Q. Y. Zhu, J. Dai, W. Lu, W. J. Guo, *Inorg. Chem.* **2005**, *44*, 819–821.
[31] D. X. Jia, Q. X. Zhao, Y. Zhang, J. Dai, J. L. Zuo, *Inorg. Chem.* **2005**, *44*, 8861–8867.
[32] R. Kiebach, F. Studt, C. Näther, W. Bensch, *Eur. J. Inorg. Chem.* **2004**, 2553–2556.
[33] D. X. Jia, Y. Zhang, J. Dai, Q. Y. Zhu, X. M. Gua, *J. Solid State Chem.* **2004**, *177*, 2477–2483.
[34] M. Schur, W. Bensch, *Acta Crystallogr., Sect. C* **2000**, *56*, 1107–1108.
[35] A. Puls, C. Näther, W. Bensch, *Acta Crystallogr., Sect. E* **2006**, *62*, m674–m676.
[36] L. Engelke, R. Stähler, M. Schur, C. Näther, W. Bensch, R. Pöttgen, M. H. Möller, *Z. Naturforsch., Teil B* **2004**, *59*, 869–876.
[37] A. Bondi, *J. Phys. Chem.* **1964**, *68*, 441.
[38] G. M. Sheldrick, *SHELXS-97*, University of Göttingen, Germany, **1997**.

Received: November 2, 2006
Published Online: February 28, 2007

 © 2007 Wiley-VCH Verlag GmbH & Co. KGaA, Weinheim 

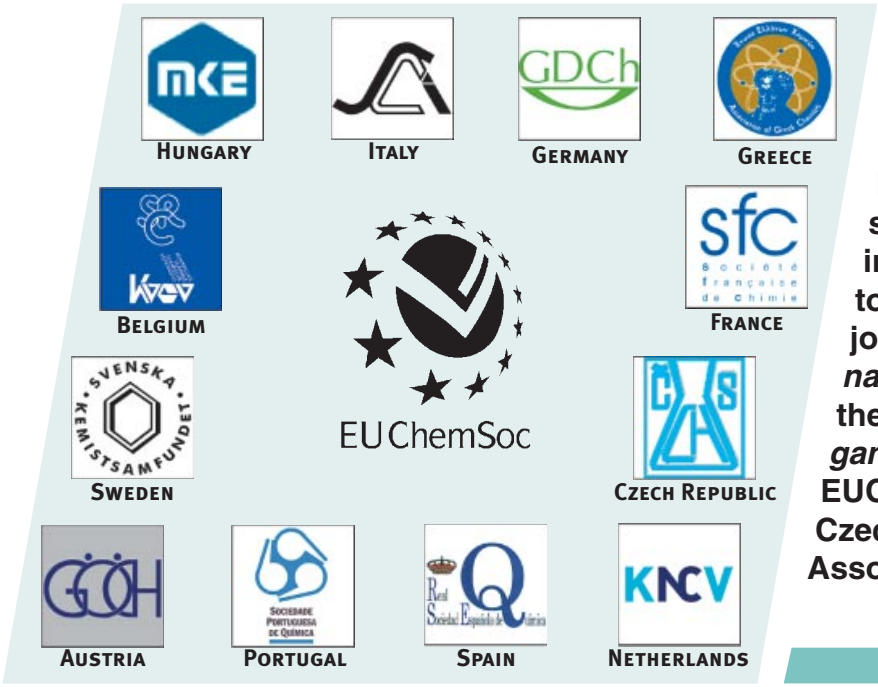


**The EUChemSoc Societies have taken the significant step into the future by merging their traditional journals, to form two leading chemistry journals, the *European Journal of Inorganic Chemistry* and the *European Journal of Organic Chemistry.* Three further EUChemSoc Societies (Austria, Czech Republic and Sweden) are Associates of the two journals.**

## COVER PICTURE

**The cover picture shows** a crown-based lateral macrobicycle designed by our research group as a potential ligand for $Pb^{II}$ complexation. Lead is recognized worldwide as a serious environmental pollutant, and although it is a natural component of soil, water and vegetation, anthropogenic emissions have contributed to the dramatic increase in its level in the environment. The removal of lead from the environment and biological systems is the aim of many research groups. In particular, we are interested in the design of $Pb^{II}$-complexing agents based on crown frameworks. In this picture, the complexed $Pb^{II}$ ion has been replaced by our beautiful but polluted blue planet. The cover picture symbolizes the need for innovative ideas to solve the problem of environmental lead pollution – one solution includes the design of selective complexing agents. Details are discussed in the article by A. de Blas, T. Rodríguez-Blas et al. on p. 1635 ff.

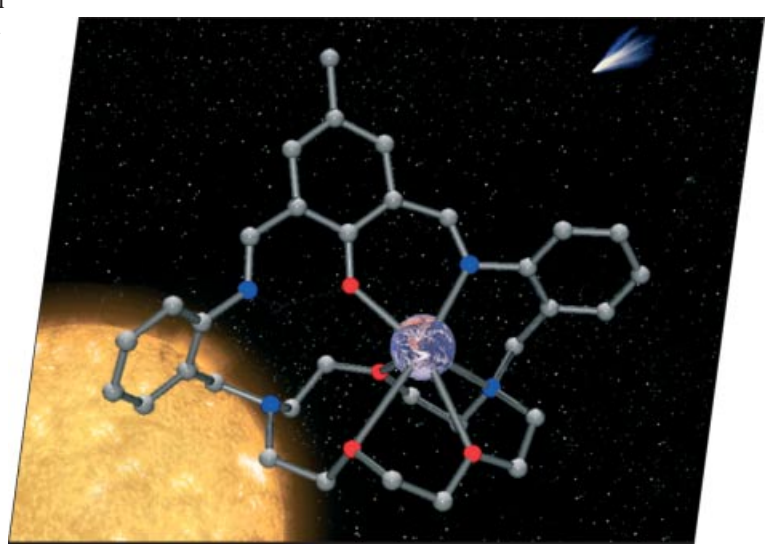

 © 2007 Wiley-VCH Verlag GmbH & Co. KGaA, Weinheim 

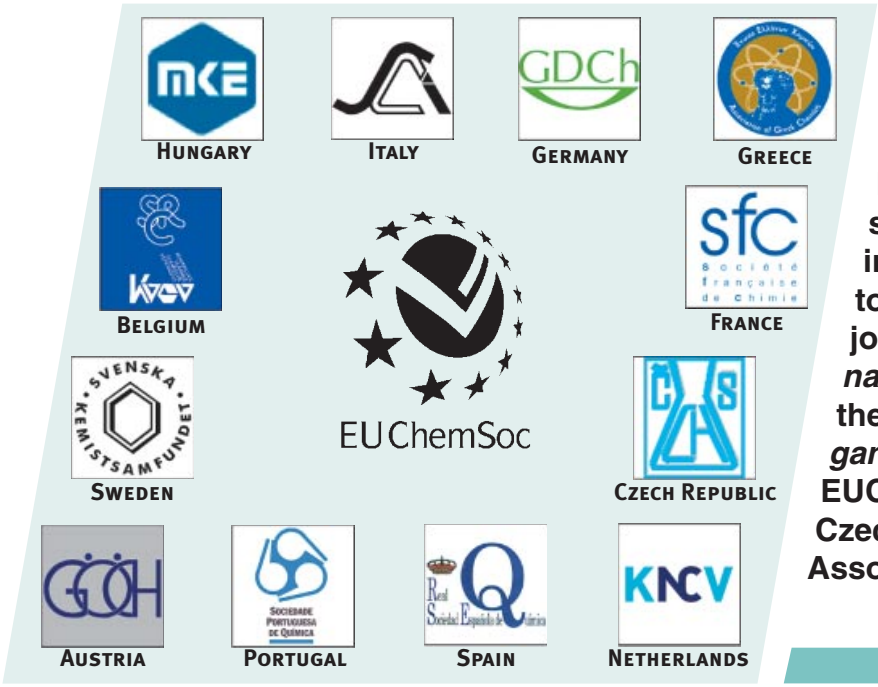


**The EUChemSoc Societies have taken the significant step into the future by merging their traditional journals, to form two leading chemistry journals, the *European Journal of Inorganic Chemistry* and the *European Journal of Organic Chemistry.* Three further EUChemSoc Societies (Austria, Czech Republic and Sweden) are Associates of the two journals.**

## COVER PICTURE

**The cover picture shows** a crown-based lateral macrobicycle designed by our research group as a potential ligand for $Pb^{II}$ complexation. Lead is recognized worldwide as a serious environmental pollutant, and although it is a natural component of soil, water and vegetation, anthropogenic emissions have contributed to the dramatic increase in its level in the environment. The removal of lead from the environment and biological systems is the aim of many research groups. In particular, we are interested in the design of $Pb^{II}$-complexing agents based on crown frameworks. In this picture, the complexed $Pb^{II}$ ion has been replaced by our beautiful but polluted blue planet. The cover picture symbolizes the need for innovative ideas to solve the problem of environmental lead pollution – one solution includes the design of selective complexing agents. Details are discussed in the article by A. de Blas, T. Rodríguez-Blas et al. on p. 1635 ff.

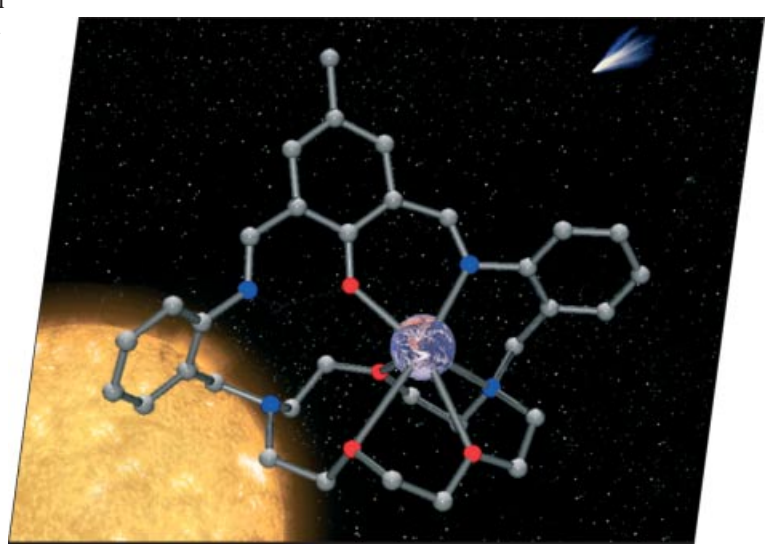

 © 2007 Wiley-VCH Verlag GmbH & Co. KGaA, Weinheim 

# CONTENTS

## SHORT COMMUNICATIONS

### Ligand Indexing

**M. Minakawa, K. Takenaka, Y. Uozumi* ..... 1629–1631**

Pd Pincer Complex as a Probe To Index the Coordination Ability of Various Ligands

**Keywords:** Pincer complexes / Coordination / Palladium / Phosphane ligands / Mondentate ligands

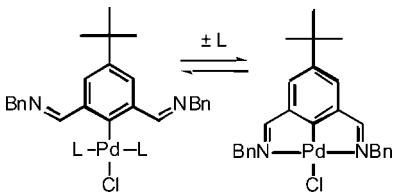


The coordination constants of 27 monodentate ligands (L) with a pincer palladium complex to form complexes of the type $ArPd(L)_2Cl$ were determined by *1*H NMR spectroscopy. This allowed the coordination ability of a wide variety of ligands, including P-, N-, and As-coordinating ligands, to be indexed.

### Bioorganometallic Re Complexes

**R. S. Herrick,* C. J. Ziegler,* A. Çetin, B. R. Franklin ..... 1632–1634**

Structure of the Triaquatricarbonylrhenium(I) Cation and Its Conjugate Base

**Keywords:** Aqua ligands / Carbonyl ligands / Hydrolysis / Rhenium

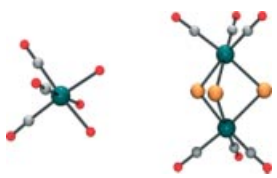

The crystal structure of the $Re(CO)_3(H_2O)_3^+$ cation has been determined, once with the $Re_2(CO)_9(\mu_3\text{-}Br)_3^-$ anion and once co-crystallized with the conjugate base, $Re(CO)_3(OH)(H_2O)_2$, with a $PF_6^-$ anion. The unexpected stability of the hydroxo compound may be due to disordering of the hydroxo and aqua ligands.

## FULL PAPERS

### Lead(II) Coordination

**D. Esteban-Gómez, C. Platas-Iglesias, F. Avecilla, A. de Blas,* T. Rodríguez-Blas* ..... 1635–1643**

Effect of Protonation and Interaction with Anions on a Lead(II) Complex with a Lateral Macrobicycle Containing a Phenol Schiff-Base Spacer

**Keywords:** Lead / Macrocycles / N,O ligands / Density functional calculations

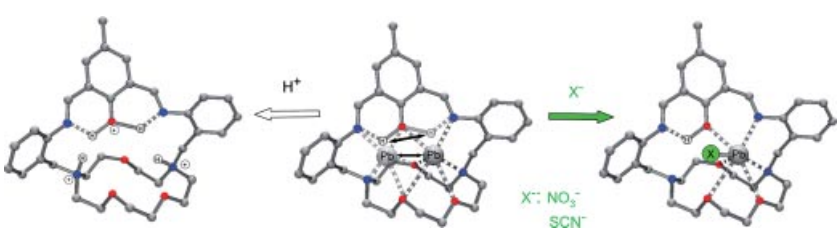


The macrobicyclic receptor derived from 1,10-diaza-15-crown-5 incorporating a phenol Schiff-base spacer forms stable complexes with lead(II). In $[Pb(L^4)(ClO_4)](ClO_4)\cdot CH_3CN$ the $Pb^{II}$ ion is asymmetrically placed at the one end of the macrobicyclic cavity inducing chirality in the corresponding complex. The effect of the protonation on the complex at room temperature has been studied, finding that protonation causes demetallation of the complex without receptor destruction i.e. the receptor is recovered in its protonated form. Likewise, since in solution the $Pb^{II}$ ion is coordinatively unsaturated in the complex, the interaction of the $Pb^{II}$ complex with anions such as $NO_3^-$ and $SCN^-$ has been evaluated by using spectrophotometric titrations in acetonitrile.

 © 2007 Wiley-VCH Verlag GmbH & Co. KGaA, Weinheim 

## Tetracopper Clusters

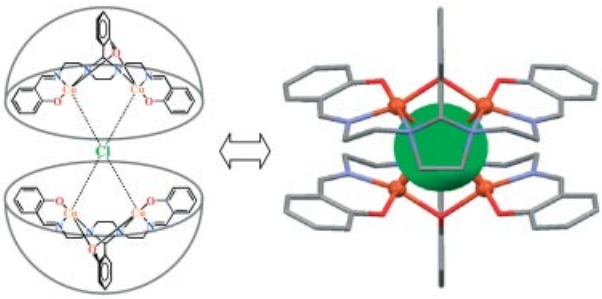

**A. R. Paital, C. S. Hong, H. C. Kim, D. Ray* ..... 1644–1653**

[$Cu^{II}_4$] Clusters From the Self-Assembly of Two Imidazolidinyl 2-Phenolate-Bridged [$Cu^{II}_2$] Units: The Role of the Chloride Bridge

**Keywords:** Template synthesis / Self-assembly / Cluster compounds / Copper / Magnetic properties

The new cluster $[Cu_4(\mu_4\text{-}Cl)L_2]ClO_4{\cdot}12H_2O$ is obtained by self-assembly of two $[Cu_2L]^+$ cations around the spherical $Cl^-$ anion and shows an unprecedented single atom nucleating exogenous symmetric bridging mode. This anion-centred cluster formation is responsible for $Cl^-$ entrapment during metal coordination in a $\mu_4$ fashion.

## Helical Coordination Polymers

**P. S. Subramanian,* E. Suresh, L. Casella* ..... 1654–1660**

Supramolecular Helical Architectures Dictated by Folded and Extended Conformations of the Amino Acid in Ternary $Cu^{II}$/Diamine/Racemic Amino Acid Complexes

**Keywords:** Helicates / Self-assembly / Copper / Chiroptical properties / Amino acids

Self-assembled ternary $Cu^{II}$ complexes containing a diamine and a racemic amino acid are shown to form optically pure homochiral and racemic helicates. The folded and extended conformations of the amino acid moieties in $[Cu(DA)(D,L\text{-phe})]^+$ (DA = 1,10-phenanthroline; D,L-phe = racemic phenylalanine) are found to form novel chiral helical structures

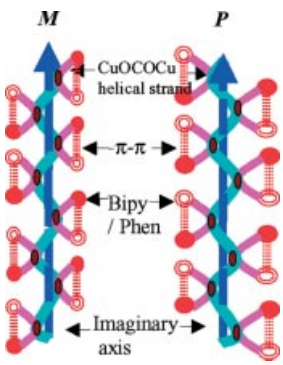


## Helicates

**M. Bröring,* S. Link, C. D. Brandt, E. C. Tejero ..... 1661–1670**

Helical Transition-Metal Complexes of Constrained 2,2′-Bidipyrrins

**Keywords:** 2,2′-Bidipyrrins / Helicates / Constrained ligands / Porphyrinoids / Coordination modes

Helical mono- and dinuclear transition-metal chelates form upon treatment of simple $Ni^{II}$, $Pd^{II}$, $Cu^{II}$ and $Zn^{II}$ salts with new constrained 2,2′-bidipyrrin ligands. X-ray crystallographic work revealed that dinuclear helicates of $Cu^{II}$ and $Zn^{II}$ form interesting packing patterns in the solid.

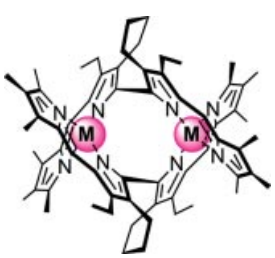


## Cationic Organogallanes

**J. D. Young, M. A. Khan, D. R. Powell, R. J. Wehmschulte* ..... 1671–1681**

*m*-Terphenylaluminum and -gallium Compounds: Synthesis and Conversion into Low-Coordinate Organogallium Cations

**Keywords:** Aluminum / Cations / Gallium / Lewis acids / Low coordination

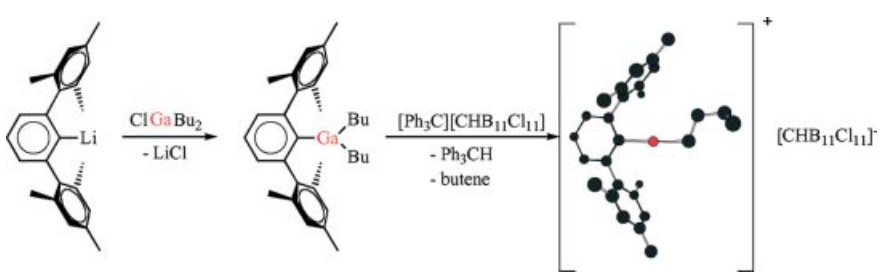


*m*-Terphenylalanes and -gallanes are obtained from the reaction of *m*-terphenyllithium with $MCl_3$, $AlH_3{\cdot}NMe_3$, or $ClGaBu_2$. Butanide abstraction from the dibutyl(*m*-terphenyl)gallanes [(terph)-$GaBu_2$] with trityl salts of weakly coordinating anions ($[A]^-$) affords the ionic species $[(terph)GaBu]^+[A]^-$.

 © 2007 Wiley-VCH Verlag GmbH & Co. KGaA, Weinheim 

# CONTENTS

## Host–Guest Chemistry

**N. Nunes, R. Amaro, F. Costa, E. Rombi, M. A. Carvalho, I. C. Neves,* A. M. Fonseca ..... 1682–1689**

Copper(II)–Purine Complexes Encapsulated in NaY Zeolite

**Keywords:** N ligands / Copper / NaY / Encapsulation / Host–guest chemistry / Oxidation

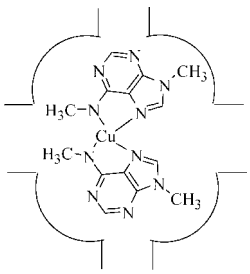

**A**

Copper–purine complexes were encapsulated in Y zeolite. A combination of different characterization techniques (XPS, SEM, XRD, ICP-AES, EPR, FTIR, UV/Vis and TGA) was used to identify the different copper–purine species. Complex **A** was formed at pH ≥ 7.

## Supramolecular Chemistry

**N. L. S. Yue, M. C. Jennings, R. J. Puddephatt* ..... 1690–1697**

Supramolecular Chemistry and Anion Binding in Palladium(II) and Silver(I) Complexes Containing *N*,*N*′-Dipyridylxanthene-4,5-dicarboxamide Ligands

**Keywords:** Supramolecular / Polymers / Silver / Palladium

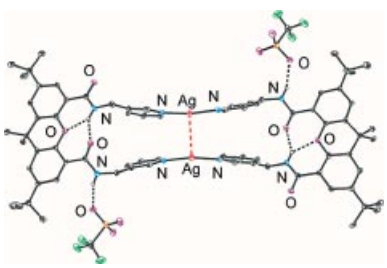

Hydrogen bonding in ligands containing *N*,*N*′-dipyridylxanthene-4,5-dicarboxamide units can orient the pyridine donor groups to favor macrocycle formation, in complexes of silver(I) or palladium(II), and can either enhance anion binding or control self-assembly of supramolecular polymers.

## Ferrimagnets

**X.-P. Shen, Y.-Z. Li, Y. Song, Z. Xu,* G.-C. Guo ..... 1698–1702**

Single-Crystal Structure and Magnetic Behavior of a Molecule-Based Ferrimagnet $Mn[Mn_{0.2}Cr_{0.8}(CN)_6]\cdot 4H_2O$

**Keywords:** Prussian blue analogue / Crystal structure / Magnetic properties / Chromium / Manganese

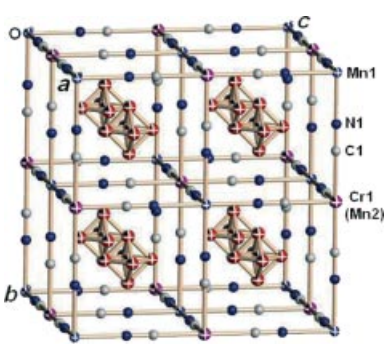


A novel Prussian-blue-type ferrimagnet $Mn[Mn_{0.2}Cr_{0.8}(CN)_6]\cdot 4H_2O$ has been characterized by single-crystal X-ray structure analysis and magnetic measurements. The complex has a face-centered cubic lattice and indicates ferrimagnetic ordering below $T_c$ = 63 K.

## Organosoluble Phthalocyanines

**A. Bilgin,* B. Ertem, Y. Gök ..... 1703–1712**

Highly Organosoluble Metal-Free Phthalocyanines and Metallophthalocyanines: Synthesis and Characterization

**Keywords:** Soluble phthalocyanine / Phthalonitrile / Macrocycles / Nickel / Zinc

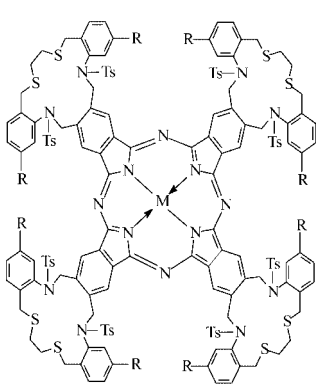

M: 2H, Zn, Cu, Ni
R: *tert*-butyl, X: CN or Br

Cation-binding abilities, electrical conductivities and thermal properties of metal-free phthalocyanines and metallophthalocyanines containing macrocyclic units were evaluated.

 © 2007 Wiley-VCH Verlag GmbH & Co. KGaA, Weinheim 

## Classical Polyhydrido Complexes

Protonation of heptacoordinate mixed-ligand mono- and dihydridorhenium(III) complexes with $HBF_4 \cdot Et_2O$ leads to $Re^V$ polyhydrido derivatives, whereas treatment with terminal alkynes affords vinylrhenium complexes.

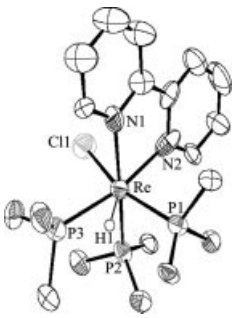


**G. Albertin,* S. Antoniutti, J. Castro, S. García-Fontán, G. Schipilliti ..... 1713–1722**

Preparation and Reactivity of Hydridorhenium Complexes with Polypyridine and Phosphonite Ligands

**Keywords:** Hydrido ligands / P ligands / Protonation / Rhenium / Vinyl complexes

## Heterogeneous Catalysis

By a combination of sol-gel synthesis and subsequent photochemical oxidation, nanoparticles of CuO and ZnO are imbedded into a matrix of amorphous silica. The composites show a high specific surface area and a considerable activity in methanol synthesis.

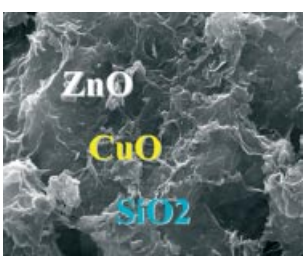


**B. Rohe, R. Weiss, S. Vukojević, C. Baltes, M. Muhler, M. Tausch, M. Epple* ..... 1723–1727**

CuO/ZnO Nanoparticles in a Matrix of Amorphous Silica as High-Surface Precursors for Methanol Synthesis

**Keywords:** Heterogeneous catalysis / Copper / Zinc oxide / Silica / Nanoparticles / Surface coating

## Molybdenum(VI) Chelates

The molybdenum(VI) binding properties of bis(3-hydroxy-2-methyl-4-pyridinone)IDA and -EDTA derivatives were studied. Both of the ligands form quite stable 1:1 $Mo^{VI}$ complexes. However, the extra functional groups of the EDTA derivative can improve the bioavailability of the complexes and also potentiate extra interactions with biological sites.

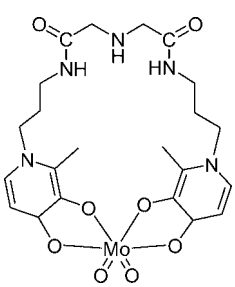


**M. A. Santos,* S. Gama, J. C. Pessoa, M. C. Oliveira, I. Tóth, E. Farkas* ..... 1728–1737**

Complexation of Molybdenum(VI) with Bis(3-hydroxy-4-pyridinone)amino Acid Derivatives

**Keywords:** Molybdenum / Hydroxypyridinones / Hydroxypyridinonate complexes / Chelates

## Low-Valent Rh Complexes

New rhodium complexes with κ*N*-monodentate and κ*N*,κ*O*-bidentate β-amino alcohols, as well as chelating 1,2-diamine ligands, were prepared. Coordination chemistry and catalytic C=O hydrogenation reactions were investigated.

**L. Dahlenburg,* H. Treffert, C. Farr, F. W. Heinemann, A. Zahl .... 1738–1751**

Rhodium(I) Complexes Containing β-Amino Alcohol and 1,2-Diamine Ligands: Syntheses, Structures, and Catalytic Applications

**Keywords:** Rhodium / N,O ligands / N,N ligands / X-ray diffraction / Catalysis

 © 2007 Wiley-VCH Verlag GmbH & Co. KGaA, Weinheim 

# CONTENTS

## Ru-Labelled Purines

**M. Vrábel, M. Hocek,* L. Havran, M. Fojta,* I. Votruba, B. Klepetářová, R. Pohl, L. Rulíšek, L. Zendlová, P. Hobza, I-h. Shih, E. Mabery, R. Mackman ..... 1752–1769**

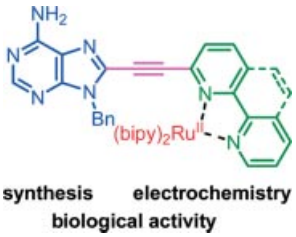


Purines Bearing Phenanthroline or Bipyridine Ligands and Their $Ru^{II}$ Complexes in Position 8 as Model Compounds for Electrochemical DNA Labeling – Synthesis, Crystal Structure, Electrochemistry, Quantum Chemical Calculations, Cytostatic and Antiviral Activity

**Keywords:** Purines / Nucleobases / Bipyridines / Phenanthrolines / Ru complexes / Electrochemistry

Model compounds for DNA labeling: a series of diverse adenine- and oligopyridine-type ligand conjugates and their Ru and Os complexes were prepared by cross-coupling and/or complexation reactions. Interesting electrochemical properties and strong antiviral activity were found and are discussed.

## Ytterbium Complexes

**L. Cheng, Y. Feng, S. Wang,* W. Luo, W. Yao, Z. Yu, X. Xi, Z. Huang ..... 1770–1777**

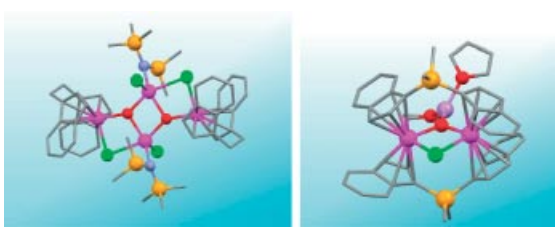

Synthesis and Structural Characterization of Novel Ytterbium(III) Complexes with both a μ-Oxo Group and Bridged Indenyl Ligands, and Ytterbium(II) Complexes with Bridged Indenyl Ligands

**Keywords:** Organometallic compounds / Lanthanoids / Synthesis / Ytterbium / X-ray diffraction

The reaction of the ytterbium(III) amide $[(Me_3Si)_2N]_3Yb(\mu\text{-}Cl)Li(thf)_3$ with different bridged indene compounds in the presence of external donor ligands led to the isolation and characterization of ytterbium(II) and ytterbium(III) complexes containing μ-oxo group(s), depending on the reaction conditions.

**If not otherwise indicated in the article, papers in issue 11 were published online on March 27, 2007**

 © 2007 Wiley-VCH Verlag GmbH & Co. KGaA, Weinheim 

DOI: 10.1002/ejic.200700037

# Pd Pincer Complex as a Probe To Index the Coordination Ability of Various Ligands

**Maki Minakawa,[a] Kazuhiro Takenaka,[a] and Yasuhiro Uozumi*[a]**

**Keywords:** Pincer complexes / Coordination / Palladium / Phosphane ligands / Mondentate ligands

An NCN pincer palladium complex was developed as a probe molecule to index the coordination ability of various monodentate ligands. Coordination constants of 27 monodentate ligands (L) with a pincer palladium complex to form complexes of the type $ArPd(L)_2Cl$ were determined by $^1H$ NMR spectroscopy. This allowed the coordination ability of a wide variety of ligands, including P-coordinating ligands (phosphane, phosphite), as well as As-coordinating $AsPh_3$, and N-coordinating pyridine, to be indexed. The differential between the highest/lowest coordination constants was $10^{12}$. The relative coordination ability is described in a logarithmic manner, $\log(K_{eq(L)}/K_{eq(PPh_3)})$, with respect to the value of $PPh_3$ to exhibit high linearity in the Hammett plot.

(© Wiley-VCH Verlag GmbH & Co. KGaA, 69451 Weinheim, Germany, 2007)

## Introduction

Transition-metal–ligand complexes have emerged as versatile and functional molecules in the domain of chemistry. Vast arrays of functional metal complexes have been developed in which ligands undergo drastic change and/or fine-tuning of their chemical and physical properties. Transition-metal-catalyzed organic transformations are the most commonly employed reactions where the choice of ligands is essential in controlling the catalytic reaction pathway. Coordination ability is one of the most fundamental and important properties of ligands and, therefore, quite a few studies have appeared that index the ligand coordination ability. However, to the best of our knowledge, no direct or precise method has appeared that allows the determination of the relative strength/weakness of the coordination ability of $PPh_3$ to palladium, for example, versus $AsPh_3$, pyridine, $PCy_3$, etc. Clearly, although pioneering strides have been made, additional studies on the ordering of the coordination abilities of ligands are warranted.

Because the coordination ability is controlled by both the electronic and steric properties of the ligand, this renders quantitative description difficult. Indeed, although the two controlling factors (electronic and steric) have been defined,[1,2] all of the well-developed research on the determination of the coordination ability of various ligands has been limited to isolated reports.[3] If a practical probe for the direct and exact observation of the coordination–dissociation equilibria of a wide range of ligands were developed, a scale of the coordination ability of various ligands would be achieved. This would provide fundamental and useful information for catalytic as well as organic, inorganic, organometallic, and materials research fields. We would like to propose pincer palladium complex **1** as a novel probe to titrate the coordination ability of various nonchelating igands to palladium to form palladium complexes $ArPd(L)_2X$. Many of these complexes are recognized as key intermediates in various palladium-catalyzed processes (e.g. cross-couplings, the Heck reaction, carbonylation, etc.).

## Results and Discussion

We have previously prepared various NCN pincer palladium complexes[4] by the ligand introduction route [Scheme 1, Equation (1)].[5] From our detailed studies on the pincer complexation process, we found that intermediate complex **2** was in equilibrium with pincer complex **1**. The coordination–dissociation behavior of the $PPh_3$ ligand of intermediate complex **2** was observed by $^1H$ and $^{31}P\{^1H\}$ NMR spectroscopy, and the coordination constant $K_{eq(PPh_3)}$ was unambiguously determined by the $^1H$ NMR spectroscopic measurement of the intramolecular $CH$=N$CH_2$Ph ligand groups [*Ha* and/or *Hb* indicated in Scheme 1, Equation (2)]. These observations led us to the conclusion that complex **1** would be a good probe to index the coordination abilities of various ligands. By using probe complex **1**, a wide range of coordination constants (the difference between the highest and lowest constants is $10^{12}$) were determined with high accuracy by $^1H$ NMR spectroscopic measurements, which allowed the relative coordination ability of 27 different ligands to be indexed.

[a] Institute for Molecular Science (IMS)
Myodaiji, Okazaki, Aichi 444-8787, Japan
Fax: +81-564-59-5574
E-mail: uo@ims.ac.jp

Supporting information for this article is available on the WWW under http://www.eurjic.org or from the author.

 © 2007 Wiley-VCH Verlag GmbH & Co. KGaA, Weinheim 

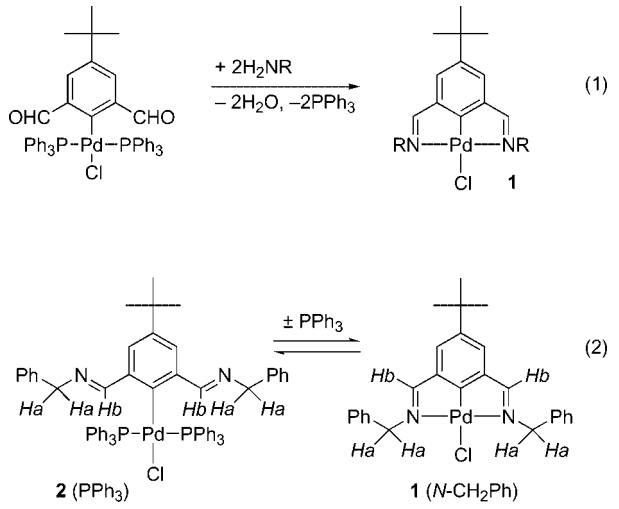


Scheme 1. Preparation and substitution equilibrium of the pincer complex: (1) ligand introduction route to pincer complexation; (2) ligand substitution equilibrium.

A typical procedure for the equilibria study by NMR spectroscopy for $PPh_3$ is as follows: Complex **1** was dissolved in $CD_2Cl_2$ (12.7 mM) at 298 K and $PPh_3$ (2 mol equiv. to **1**) was added under a nitrogen atmosphere. The resulting mixture was analyzed by $^1H$ NMR spectroscopy, where the resonances of *Ha* for complexes **2** (phosphane complex) and **1** (pincer complex) were observed at $\delta$ = 4.50 and 5.01 ppm, respectively, to provide $K_{eq(PPh_3)} = 2.06 \times 10^5$ M$^{-2}$ in $CD_2Cl_2$ (298 K). The coordination constants of 27 ligands obtained by similar NMR spectroscopic experiments are shown in Table 1. Ligands, whose coordination constants could not be determined by the present method because their coordination ability was either too strong or too weak, are also listed in Table 1 to demonstrate the scope and limitation of this system. The coordination constants of $Ph_2P(C_6H_4$-2-Me), $Ph_2P(C_6F_5)$, $P[C_6H_3$-3,5-$(CF_3)_2]_3$, $P$(2-furyl)$_3$, $P(OPh)_3$, pyridine, and $AsPh_3$ were so small that the VT-NMR spectroscopic studies were performed at lower temperatures to observe both peaks of **1** and **2** (Table 1, Entries 22–28), and their $K_{eq(L)}$ values at 298 K were estimated by a van't Hoff plot (see Supporting Information). The relative coordination ability (RCA) is described in a logarithmic manner, $\log(K_{eq(L)}/K_{eq(PPh_3)})$, with respect to the value of $PPh_3$.

Several representative and/or typical features obtained by this indexation include: (1) The coordination ability of ligands having the same cone angle was strictly determined by their electronic character (vide infra). (2) The coordination constant of $AsPh_3$ is $10^{10}$ smaller than that of $PPh_3$. (3) $P(OPh)_3$ exhibits a $10^7$ smaller value than that of its carbon analogue $P(CH_2Ph)_3$. (4) The order of the coordination ability of phosphane ligands bearing six-membered ring substituents is $PCy_3 > PPh_3 > PPh_2Cy > PPhCy_2$.[6] (5) The coordination ability is significantly affected by the steric bulkiness of the ligand [e.g. $PPh_3$ versus $PPh_2$Tol-*o* (Table 1, Entries 9 and 22)]. These features would be difficult to predict without direct observation of the $K_{eq}$ values.

Table 1. Coordination constants of various ligands.[a]

**1** + 2L ⇌ **2** (L)

| Entry | Ligand | $K_{eq(L)}$ [M$^{-2}$][b] | RCA[c] |
|---|---|---|---|
| 1 | $P(n$Bu$)_3$ | N/A | >3 |
| 2 | $Ph_2P(C_6H_4$-4-$NMe_2)$ | $2.38 \times 10^7$ | 2.06 |
| 3 | $P(C_6H_4$-4-$OMe)_3$ | $1.61 \times 10^7$ | 1.89 |
| 4 | $PCy_3$ | $9.45 \times 10^6$ | 1.64 |
| 5 | $PhP(C_6H_4$-4-$OMe)_2$ | $4.58 \times 10^6$ | 1.35 |
| 6 | $P(C_6H_4$-4-$Me)_3$ | $2.20 \times 10^6$ | 1.03 |
| 7 | $Ph_2P(C_6H_4$-4-Me) | $1.04 \times 10^6$ | 0.703 |
| 8 | $P(C_6H_4$-3-$Me)_3$ | $8.15 \times 10^5$ | 0.597 |
| 9 | $PPh_3$ | $2.06 \times 10^5$ | 0.00 |
| 10 | $P(CH_2CH_2CN)_3$ | $1.52 \times 10^5$ | –0.132 |
| 11 | $PBn_3$ | $1.27 \times 10^5$ | –0.210 |
| 12 | $P(C_6H_3$-3,5-$Me_2)_3$ | $1.16 \times 10^5$ | –0.249 |
| 13 | $P(C_6H_4$-4-$F)_3$ | $1.10 \times 10^5$ | –0.272 |
| 14 | $Ph_2PCy$ | $9.35 \times 10^4$ | –0.343 |
| 15 | $P(C_6H_4$-3-$OMe)_3$ | $3.59 \times 10^4$ | –0.759 |
| 16 | $PhPCy_2$ | $1.63 \times 10^4$ | –1.10 |
| 17 | $P(C_6H_4$-4-$Cl)_3$ | $1.39 \times 10^4$ | –1.17 |
| 18 | $P(C_6H_4$-3-$Cl)_3$ | $2.07 \times 10^3$ | –2.00 |
| 19 | $P(C_6H_4$-3-$F)_3$ | $1.30 \times 10^3$ | –2.20 |
| 20 | $Ph_2P(C_6H_4$-2-OMe) | $1.73 \times 10^2$ | –3.08 |
| 21 | $P(C_6H_4$-4-$CF_3)_3$ | $1.28 \times 10^2$ | –3.21 |
| 22[d] | $Ph_2P(C_6H_4$-2-Me) | 5.93 | –4.54 |
| 23[d] | $Ph_2P(C_6F_5)$ | 0.267 | –5.89 |
| 24[d] | $P[C_6H_3$-3,5-$(CF_3)_2]_3$ | 0.120 | –6.23 |
| 25[d] | P(2-furyl)$_3$ | $8.80 \times 10^{-2}$ | –6.37 |
| 26[d] | $P(OPh)_3$ | $2.09 \times 10^{-2}$ | –7.00 |
| 27[d] | Pyridine | $1.06 \times 10^{-4}$ | –9.29 |
| 28[d] | $AsPh_3$ | $2.49 \times 10^{-5}$ | –9.92 |
| 29 | $P(C_6H_4$-2-$Me)_3$ | N/A | <–10 |
| 30 | $P(t$Bu$)_3$ | N/A | <–10 |
| 31 | $CyP(t$Bu$)_2$ | N/A | <–10 |
| 32 | $Cy_2P(t$Bu) | N/A | <–10 |
| 33 | $PhP(C_6H_4$-2-$OMe)_2$ | N/A | <–10 |
| 34 | $P(C_6F_5)_3$ | N/A | <–10 |
| 35 | $PhP(C_6F_5)_2$ | N/A | <–10 |
| 36 | $Cy_2P$(2-biphenyl) | N/A | <–10 |

[a] All titrations were performed by $^1H$ NMR spectroscopic measurements at 298 K. [b] Average of two or three measurements. [c] RCA = $\log(K_{eq(L)}/K_{eq(PPh_3)})$. [d] $K_{eq}$ value was estimated by the van't Hoff plot obtained by VT-NMR spectroscopic experiments (see Supporting Information).

Figure 1 is the Hammett plot for the RCA values of various triarylphosphanes to quantify the electronic effect of the P substituents. Triarylphosphanes with *para* and *meta* monosubstituted aromatic groups having cone angles of 145 ° show excellent proportionality for the σ values[7] of the aromatic groups. Thus, the RCA value decreased proportionally as the σ value of the aromatics increased and the RCA–σ relationship exhibits high linearity (Figure 1, black solid line: $R^2$ = 0.9925), which demonstrates the high accuracy of the RCA values measured by the present method. This observation should make the prediction of the RCA value of various triarylphosphane ligands having *para* or *meta* monosubstitution possible by inter-/extrapolation (dotted line), even if the RCA value is out of the measurement range with highly electron-rich or -deficient substituents. The RCA values of triarylphosphane ligands of the 147 ° cone angle were slightly smaller than those of the plot for the ligands of the 145 ° cone angle. Thus, $P(C_6H_3$-

 © 2007 Wiley-VCH Verlag GmbH & Co. KGaA, Weinheim 

3,5-$Me_2$)$_3$ and P[$C_6H_3$-3,5-($CF_3$)$_2$]$_3$ exhibited RCA values of –0.249 and –6.23, respectively (Table 1, Entries 12 and 24). More sterically demanding ligands gave lower RCA values (Table 1, Entries 20, 22, and 23).

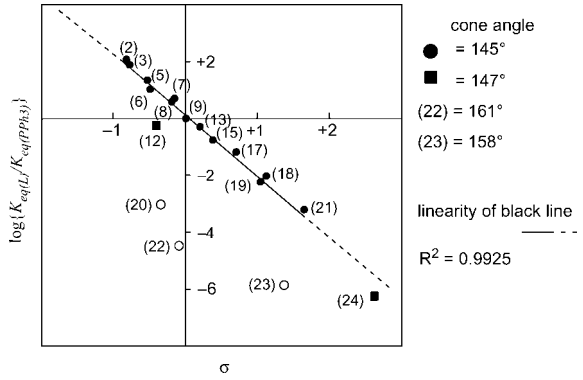


Figure 1. Hammett plot for the RCA values: $\log(K_{eq(L)}/K_{eq(PPh_3)})$ versus Taft's σ value of aromatic substituents of the triarylphosphane ligands. The numbers in parentheses correspond to the entry numbers in Table 1.

## Conclusions

We have developed pincer palladium complex **1** as a novel probe for the determination of the coordination ability of various ligands to form $ArPd(L)_2Cl$, with the relative coordination abilities of 27 ligands being determined easily by $^1$H NMR spectroscopic experiments. A two-dimensional analysis using probe complexes of different steric demands (with the use of various NR groups), as well as the application of the indexation protocol to ligands bearing other coordination sites, e.g. carbene, S, Sb, etc., are currently underway and will be reported in due course.

## Experimental Section

**General Equilibria Studies by NMR Spectroscopy:** Complex **1** and a ligand (2 equiv.) were dissolved in [$D_2$]dichloroethane. The equilibrium constant, $K_{eq}$, was determined by the integration of the resonances: the resonance integration ratio **1/2** = $x$:$y$; $K_{eq}$ = $(1/4)[\{y(x + y)^2\}/x^3][\mathbf{1}]_0^2$ ($M^{-2}$). All NMR spectroscopic data (charts, chemical shifts, integration data, etc) are provided in the Supporting Information.

**Supporting Information** (see footnote on the first page of this article): $^1$H NMR spectroscopic data with their measurement conditions for Table 1, Entries 2–28.

## Acknowledgments

This work was supported by the CREST program, sponsored by the JST. We also thank the JSPS and the MEXT for partial financial support of this work.

[1] For some recent experimental and theoretical work on the electronic effects of phosphane ligands, see: a) J. Huang, C. M. Haar, S. P. Nolan, W. J. Marshall, K. G. Moloy, *J. Am. Chem. Soc.* **1998**, *120*, 7806–7815; b) S. Serron, S. P. Nolan, Y. A. Abramov, L. Brammer, *Organometallics* **1998**, *17*, 104–110; c) C. M. Haar, S. P. Nolan, *Inorg. Chim. Acta* **1999**, *291*, 32–38; d) C. Li, S. Serron, S. P. Nolan, *Organometallics* **1996**, *15*, 4020–4029; e) J. Huang, S. Serron, S. P. Nolan, *Organometallics* **1998**, *17*, 4004–4008; f) S. T. N. Freeman, F. R. Lemke, C. M. Haar, S. P. Nolan, J. L. Petersen, *Organometallics* **2000**, *19*, 4828–4833; g) E. J. M. Meier, W. Kozminski, A. Linden, P. Lustenberger, W. Philipsborn, *Organometallics* **1996**, *15*, 2469–2477; h) N. Mathew, B. R. Jagirdar, R. S. Gopalan, G. U. Kulkarni, *Organometallics* **2000**, *19*, 4506–4517; i) C. R. Landis, S. Feldgus, J. Uddin, C. E. Wozniak, K. G. Moloy, *Organometallics* **2000**, *19*, 4878–4886; j) C. H. Suresh, N. Koga, *Inorg. Chem.* **2002**, *41*, 1573–1578; k) A. Streitwieser, A. E. McKeown, F. Hasanayn, N. R. Davis, *Org. Lett.* **2005**, *7*, 1259–1262.

[2] a) C. A. Tolman, *Chem. Rev.* **1977**, *77*, 313–348; b) T. L. Brown, K. J. Lee, *Coord. Chem. Rev.* **1993**, *128*, 89–116; c) T. L. Brown, *Inorg. Chem.* **1992**, *31*, 1286–1294.

[3] a) R. J. Angelici, C. M. Ingemanson, *Inorg. Chem.* **1969**, *8*, 83–86; ligand exchange process with [$W(CO)_5(PhNH_2)$]: b) W. Partenheimer, *Inorg. Chem.* **1972**, *11*, 743–746; measurement of $\Delta H$ value of the Pd-ligand complexation: c) L. E. Manzer, C. A. Tolman, *J. Am. Chem. Soc.* **1975**, *97*, 1955–1956; $\Delta H$ value of the Pt-ligand complexation: d) R. P. Pinnell, C. A. Megerle, S. L. Manett, P. A. Kroon, *J. Am. Chem. Soc.* **1973**, *95*, 977–978; based on the $^{31}$P NMR spectroscopic coupling constants of P–Se; five examples: e) W.-Y. Jeong, R. A. Holwerda, *Inorg. Chem.* **1989**, *28*, 2674–2679; based on the $^{31}$P NMR spectroscopic $\Delta\delta$ values between a complex and the free phosphane, seven examples: f) L. Perrin, E. Clot, O. Eisenstein, J. Loch, R. H. Crabtree, *Inorg. Chem.* **2001**, *40*, 5806–5811.

[4] a) K. Takenaka, M. Minakawa, Y. Uozumi, *J. Am. Chem. Soc.* **2005**, *127*, 12273–12281; b) K. Takenaka, Y. Uozumi, *Org. Lett.* **2004**, *6*, 1833–1835.

[5] For other applications of the ligand introduction route, see: a) K. Takenaka, Y. Uozumi, *Adv. Synth. Catal.* **2004**, *346*, 1693–1696; b) T. Kimura, Y. Uozumi, *Organometallics* **2006**, *25*, 4883–4887.

[6] The orders of steric and electronic factors of these phosphane ligands are reverse to each other [steric (small to large): $PPh_3$ > $PPh_2Cy$ > $PPhCy_2$ > $PCy_3$; electronic (basicity): $PCy_3$ > $PPhCy_2$ > $PPh_2Cy$ > $PPh_3$] and, therefore, the order of their coordination ability is difficult to predict. The spectroscopic direct observation of the coordination ability should be required to determine the order of their coordination ability.

[7] a) C. Hansch, A. Leo, R. W. Taft, *Chem. Rev.* **1991**, *91*, 165–195; b) M. T. Tribble, J. G. Traynham, *J. Am. Chem. Soc.* **1969**, *91*, 379–388, and references cited therein.

Received: December 11, 2006
Published Online: March 14, 2007

 © 2007 Wiley-VCH Verlag GmbH & Co. KGaA, Weinheim 

DOI: 10.1002/ejic.200700118

# Structure of the Triaquatricarbonylrhenium(I) Cation and Its Conjugate Base

**Richard S. Herrick,*[a] Christopher J. Ziegler,*[b] Anıl Çetin,[b] and Brenton R. Franklin[a]**

**Keywords:** Aqua ligands / Carbonyl ligands / Hydrolysis / Rhenium

The crystal structure of the $Re(CO)_3(H_2O)_3^+$ cation has been determined from crystals obtained by evaporation of an aqueous solution of $[Re(CO)_3(H_2O)_3]Br$. The bromide ion is incorporated in the $Re_2(CO)_9(\mu_3\text{-}Br)_3^-$ anion. A second structure was obtained by removal of bromide as AgBr and precipitation of the $Re(CO)_3(H_2O)_3^+$ cation with $PF_6^-$. In the latter structure the conjugate base, $Re(CO)_3(OH)(H_2O)_2$ is co-crystallized in the structure. Each structure along with the previously known cubane $[Re(CO)_3(\mu_3\text{-}OH)]_4\cdot 4H_2O$ was obtained multiple times during crystallization studies. The use of other anions to generate crystalline products was unsuccessful.
(© Wiley-VCH Verlag GmbH & Co. KGaA, 69451 Weinheim, Germany, 2007)

## Introduction

The discoveries of the $Re(CO)_3(H_2O)_3^+$ cation **1**$^+$ and its technetium congener[1,2] sparked intense interest in recent years for their potential as reagents in aqueous organometallic chemistry. One focal point is the search for viable $d^6$ $M(CO)_3L^+$ (M = $^{186/188}$Re, $^{99m}$Tc) compounds for use as therapeutic and imaging agents, respectively, in nuclear medicine.[3,4] Kinetic and thermodynamic details of water exchange and ligand substitution for these aquacarbonyl ions have been reported[5,6] and many syntheses utilizing these important synthons have been published.[7–11] Several crystal structures have been solved that formally result from the deprotonation of **1**$^+$ in aqueous solution and subsequent aggregation.[12] Although the preparation and isolation of [**1**]Br have been described[13] and attempts to grow crystals of this cation have been reported,[12] its structure has not appeared. There are, in fact, only a limited number of elucidated structures of aquacarbonyl complexes in the chemical literature, and only four structures with exclusively water and carbon monoxide as ligands.[14–17] We have discovered that crystals containing **1**$^+$ are surprisingly easy to prepare. We now report the first crystal structures of salts of **1**$^+$ and the formal appearance of its conjugate base, $Re(CO)_3(OH)(H_2O)_2$ **2** in a crystal structure.[18]

## Results and Discussion

Our initial attempt at growing crystals containing **1**$^+$ consisted of dissolving [**1**]Br in distilled water in air and allowing the water to evaporate. Crystals in two separate morphologies were obtained along with some non-crystalline material. The majority of the product was in the form of small colorless rods, with a smaller fraction of large colorless, crystalline blocks. X-ray crystallographic analysis of the blocks showed the presence of the known cubane structure $[Re(CO)_3(\mu_3\text{-}OH)]_4\cdot 4H_2O$ (**3**)[13] which had not previously been crystallized from aqueous solution. Crystallographic characterization of the rods showed the presence of the desired cation in the salt [**1**][$Re_2(CO)_6(\mu_2\text{-}Br)_3$]·$6H_2O$.[19]

Figure 1 shows the structure of [**1**][$Re_2(CO)_6(\mu_2\text{-}Br)_3$]·$6H_2O$. The cation has the expected octahedral geometry with a facial disposition of both carbon monoxide and water ligands. The identity of the anion was unexpected, but it is supposed that the bromide ion competes as a ligand with water molecules when the solvent evaporates as shown in Equation (1). The dimeric anion $Re_2(CO)_6(\mu_2\text{-}Br)_3^-$ has

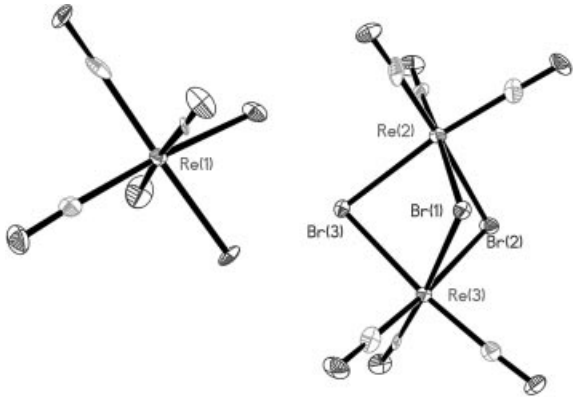


Figure 1. Structure of [**1**][$Re_2(CO)_6(\mu_2\text{-}Br)_3$]·$6H_2O$ with 50% thermal ellipsoids. Solvent water and hydrogen atoms have been omitted.

[a] Department of Chemistry, College of the Holy Cross, Worcester, MA 01610, USA
Fax: +1-508-793-3530
E-mail: rherrick@holycross.edu
[b] Department of Chemistry, University of Akron, Akron, OH 44325, USA
Fax: +1-330-972-7370
E-mail: ziegler@uakron.edu

 © 2007 Wiley-VCH Verlag GmbH & Co. KGaA, Weinheim 

been seen before and has the expected $D_{3h}$ geometry.[20,21] The IR spectrum of [**1**][$Re_2(CO)_6(\mu_2\text{-}Br)_3$]·$6H_2O$ shows two sets of tricarbonyl bands as predicted.

$$3\ \mathbf{1}^+ + 3\ Br^- \rightarrow [\mathbf{1}][Re_2(CO)_6(\mu_2\text{-}Br)_3]\cdot 6H_2O \quad (1)$$

We were interested in seeing if $\mathbf{1}^+$ could be crystallized with other anions in the hope of increasing the yield of the cation by preventing formation of the $Re_2(CO)_6(\mu_2\text{-}Br)_3^-$ anion and minimizing formation of **3**. A variety of bromide-free crystallization experiments were set up with different non-coordinating anions, $PF_6^-$, $CF_3SO_2^-$ or $NO_3^-$, at various pH values adjusted by the appropriate acid. Only the $PF_6^-$ trials produced crystals. Crystals grown with $PF_6^-$ as the counterion at acidic pH (ca. 1.5–4) produced primarily a single crystalline form of product. These needles were analyzed and can be formally represented as **2**·[**1**][$PF_6$]·$H_2O$,[22] corresponding to the co-crystallization of **2** with [**1**][$PF_6$]. In distilled water, pH = 5.6, with the $PF_6^-$ anion, crystals of **3** formed along with **2**·[**1**][$PF_6$]·$H_2O$. Figure 2 shows the structure of **2**·[**1**][$PF_6$]·$H_2O$.

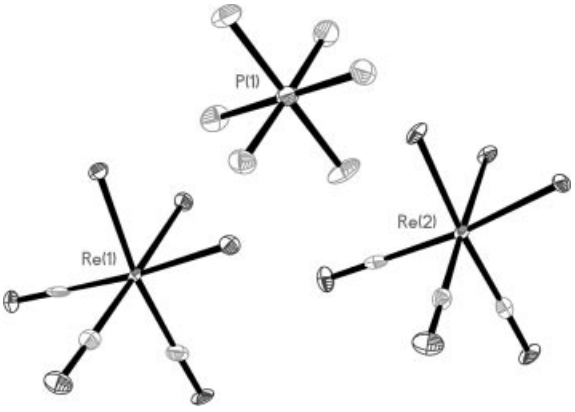


Figure 2. Structure of **2**·[**1**][$PF_6$]·$H_2O$ with 50% thermal ellipsoids. See text for explanation of the assignments of $\mathbf{1}^+$ and **2**. Solvent water and hydrogen atoms have been omitted.

Because the hydrogen atoms were not observed directly by the difference map, the assignments of $\mathbf{1}^+$ and **2** are problematic. Table 1 lists the average distances for the structures. Each monomeric rhenium species in the two structures shows a slight elongation of the octahedral geometry along the $C_3$ axis as observed for $Ru(CO)_3(H_2O)_3^{2+}$.[15] The average Re–C distance of $\mathbf{1}^+$ in [**1**][$Re_2(CO)_6(\mu_2\text{-}Br)_3$]·$6H_2O$ is 0.03 Å longer than it is in either rhenium unit in **2**·[**1**][$PF_6$]·$H_2O$. This difference may be due in part to a decrease in hydrogen bonding in **2**·[**1**][$PF_6$]·$H_2O$ vs. [**1**][$Re_2(CO)_6(\mu_2\text{-}Br)_3$]·$6H_2O$. The average Re–O distance in $\mathbf{1}^+$ in the first structure and in Re(1) in **2**·[**1**][$PF_6$]·$H_2O$ are nearly identical. The corresponding value for Re(2) in **2**·[**1**][$PF_6$]·$H_2O$ is about 0.02 Å shorter. At issue is whether the differences in these two average Re–O bond lengths are meaningful with regard to protonation state.

Table 1. Comparison of selected average bond lengths and angles[a] for compounds reported.

| | $\mathbf{1}^+$[b] | Re(1)[c] | Re(2)[d] | **4**[e] |
|---|---|---|---|---|
| Re–C [Å] | 1.912(12) | 1.887(8) | 1.887(14) | 1.908(4) |
| Re–O [Å] | 2.201(14) | 2.195(10) | 2.178(10) | 2.132(3) |
| C–Re–O [°] | 96.1(8) | 96.2(21) | 96.8(14) | – |

[a] Errors cover the range of observed values. [b] Average values for the cation from [**1**][$Re_2(CO)_6(\mu_2\text{-}Br)_3$]·$6H_2O$. [c] Average values associated with Re(1) in **2**·[**1**][$PF_6$]·$H_2O$. [d] Average values associated with Re(2) in **2**·[**1**][$PF_6$]·$H_2O$. [e] From ref.[23].

The sixteen structurally characterized $Re^I$ compounds that have a CO *trans* to a water ligand, including $Re(CO)_5(H_2O)^+$,[17] were analyzed to compare bond lengths. In these compounds the Re–C bond lengths span the range 1.80–1.92 Å, while the Re–O distances vary from 2.17–2.26 Å. There is only one characterized rhenium compound, Re(dmbpy)$(CO)_3$(OH) **4** (dmbpy = 4,4′-dimethyl-2,2′-bipyridine), with a terminal hydroxide *trans* to a carbon monoxide ligand.[23] In this compound, the Re–C(*trans*) bond length measures 1.908(4) Å and the Re–O bond length is 2.132(3) Å.[24] From the structural data for **2**·[**1**][$PF_6$]·$H_2O$ the evidence is not conclusive as to whether the hydroxide is disordered over the three possible positions [making Re(1) the center of $\mathbf{1}^+$ and Re(2) the center of **2**] or over the six possible positions of the two rhenium species (meaning that the identity of $\mathbf{1}^+$ and **2** is ambiguous). However, the IR spectrum of crystals of **2**·[**1**][$PF_6$]·$H_2O$ shows a single tricarbonyl pattern suggesting that rapid proton exchange involving water ligands on both tricarbonyl species is likely.

Previous compounds crystallized from aqueous solutions of $\mathbf{1}^+$ include [$NEt_4$][$Re_2(CO)_6(\mu_2\text{-}OH)_3$] (**5**) and [$NEt_4$]-[$Re_3(CO)_9(\mu_2\text{-}OH)_3(\mu_3\text{-}OH)$] (**6**).[1] Both of these were separately prepared by addition of a stoichiometric amount of NaOH and allowing the solutions to stand. The structure of the tetranuclear cluster associated with **3** has been reported previously with other solvates but typically it was prepared from wet organic solvents and not from water directly.[12,13] Compound **2** has also been observed in solution previously, but was proposed to be an intermediate which promptly produced dimers, trimers and tetramers.[12] In all of our crystallization trials the only rhenium-containing crystalline products we observed were [**1**][$Re_2(CO)_6(\mu_2\text{-}Br)_3$]·$6H_2O$, **2**·[**1**][$PF_6$]·$H_2O$ and **3**. Each was observed multiple times indicating that despite expectations $\mathbf{1}^+$ is a stable crystallizable species.

## Conclusions

This work has shown that it is possible to crystallize the rhenium(I)triaquatricarbonyl cation under specific conditions and with specific anions. Work is in progress to crystallize other Group 7 aqua carbonyl complexes.

## Experimental Section

**[1][$Re_2(CO)_6(\mu_2\text{-}Br)_3$]·$6H_2O$:** [**1**]Br[13] (50 mg) was dissolved in distilled water (3 mL). Slow evaporation gave a solid that consisted of

 © 2007 Wiley-VCH Verlag GmbH & Co. KGaA, Weinheim 

large colorless blocks of **3**, small colorless rods of [**1**][$Re_2(CO)_6(\mu_2$-$Br)_3$]·$6H_2O$ and a non-crystalline solid. The rods were the major component of the solid. IR of separated crystals: $\tilde{\nu}$ = 2021, 2028, 1920, 1888 $cm^{-1}$.

**2·[1][$PF_6$]·$H_2O$:** 100 mg (0.22 mmol) of [**1**]Br was dissolved in 3 mL of distilled water. Addition of 55 mg (0.22 mmol) of $AgPF_6$, produced copious precipitation which was removed by centrifugation. The solution was allowed to evaporate. Large colorless blocks of **3**, rods consisting of **2**·[**1**][$PF_6$]·$H_2O$ and non-crystalline material were found. IR of separated crystals: $\tilde{\nu}$ = 2036, 1905 $cm^{-1}$.

Other attempts to grow crystals: Aqueous solutions of [**1**][$PF_6$] were created with pH values between 1.5 and 4. The solutions were allowed to slowly evaporate. In each case crystals of **2**·[**1**][$PF_6$]·$H_2O$ were obtained along with non-crystalline material. **3** was also observed in one trial due to incomplete precipitation of bromide.

## Acknowledgments

Financial support from the Research Corporation, Pfizer/CBIA, and the National Science Foundation (CHE-0116041) for support of this research is gratefully acknowledged.

[1] R. Alberto, A. Egli, U. Abram, K. Hegetschweiler, V. Gramlich, P. A. Schubiger, *J. Chem. Soc. Dalton Trans.* **1994**, 2815–2820.
[2] R. Alberto, R. Schibli, A. Egli, P. A. Schubiger, W. A. Herrmann, G. Artus, U. Abram, T. A. Kaden, *J. Organomet. Chem.* **1995**, *493*, 119–127.
[3] R. Schibli, P. A. Schubiger, *Eur. J. Nuclear Medicine Mol. Imaging* **2002**, *29*, 1529–1542.
[4] R. S. Herrick, T. J. Brunker, C. Maus, K. Crandall, A. Cetin, C. J. Ziegler, *Chem. Commun.* **2006**, 4330–4331.
[5] P. V. Grundler, B. Salignac, S. Cayemittes, R. Alberto, A. E. Merbach, *Inorg. Chem.* **2004**, *43*, 865–873.
[6] B. Salignac, P. V. Grundler, S. Cayemittes, U. Frey, R. Scopelliti, A. E. Merbach, R. Hedinger, K. Hegetschweiler, R. Alberto, U. Prinz, G. Raabe, U. Koelle, S. Hall, *Inorg. Chem.* **2003**, *42*, 3516–3526.
[7] R. Alberto, R. Schibli, R. Waibel, U. Abram, A. P. Schubiger, *Coord. Chem. Rev.* **1999**, *190–192*, 901–919.
[8] R. S. Herrick in *New Developments in Organometallic Research* (Ed.: M. A. Cato), Nova Science Publishers, Inc., New York, **2006**, pp. 117–149.
[9] H. He, M. Lipowska, X. Xu, A. T. Taylor, M. Carlone, L. G. Marzilli, *Inorg. Chem.* **2005**, *44*, 5437–5446.
[10] R. Alberto, *Top. Curr. Chem.* **2005**, *252*, 1–44.
[11] L. Maria, A. Paulo, I. C. Santos, I. Santos, P. Kurz, B. Spingler, R. Alberto, *J. Am. Chem. Soc.* **2006**, *128*, 14590–14598.
[12] A. Egli, K. Hegetschweiler, R. Alberto, U. Abram, R. Schibli, R. Hedinger, V. Gramlich, R. Kissner, P. A. Schubiger, *Organometallics* **1997**, *16*, 1833–1840.
[13] N. Lazarova, S. James, J. Babich, J. Zubieta, *Inorg. Chem. Commun.* **2004**, *7*, 1023–1026.
[14] U. C. Meier, R. Scopelliti, E. Solari, A. E. Merbach, *Inorg. Chem.* **2000**, *39*, 3816–3822.
[15] T. Funaioli, C. Cavazza, F. Marchetti, G. Fachinetti, *Inorg. Chem.* **1999**, *38*, 3361–3368.
[16] R. E. Marsh, *Acta Crystallogr. Sect. B: Struct. Sci. Sect. B* **2002**, *58*, 893–899.
[17] E. Horn, M. R. Snow, *Aust. J. Chem.* **1984**, *37*, 1375–1393.
[18] CCDC-631412 and -631413 contain the supplementary crystallographic data for this paper. These data can be obtained free of charge from The Cambridge Crystallographic Data Centre via www.ccdc.cam.ac.uk/data_request/cif.
[19] Crystallographic data was collected at 100 K (Bruker KRYOFLEX) with a Bruker SMART APEX CCD-based X-ray diffractometer (Mo-$K_\alpha$ radiation, $\lambda$ = 0.71073 Å). The structures were refined using the Bruker SHELXTL Software Package (Version 6.10) and were solved until the final anisotropic full-matrix, least-squares refinement of $F^2$ converged. Crystal data for [**1**][$Re_2(CO)_6(\mu_2$-$Br)_3$]·$6H_2O$: $C_9Br_3O_{17}Re_3H_{16}$, $M_r$ = 1193.66, crystal size 0.10 mm × 0.10 mm × 0.05 mm, monoclinic, $P2_1/c$, $a$ = 9.264(2), $b$ = 10.075(2), $c$ = 27.121(6) Å, $\beta$ = 94.870(4)°, $V$ = 2522.1(10) $Å^3$, $Z$ = 4, $\rho$ = 3.103 $mg\,m^{-3}$. A total of 18827 reflections was collected (4954 independent reflections). $F(000)$ = 2080, $R_1$ = 0.0472, $wR_2$ = 0.1024 [for 4954 $I_o$, $I_o > 2\sigma(I_o)$].
[20] A. C. da Silva, H. Piotrowski, P. Mayer, K. Polborn, K. Severin, *J. Chem. Soc. Dalton Trans.* **2000**, 2960–2963.
[21] R. Alberto, R. Schibli, A. Egli, U. Abram, S. Abram, T. A. Kaden, P. A. Schubiger, *Polyhedron* **1998**, *17*, 1133–1140.
[22] Crystal data for **2**·[**1**][$PF_6$]·$H_2O$: $C_6F_6O_{13}PRe_2$, $M_r$ = 811.91, crystal size 0.30 mm × 0.08 mm × 0.06 mm, monoclinic, $P2_1/c$, $a$ = 12.778(3), $b$ = 6.1002(12), $c$ = 23.576(5) Å, $\beta$ = 101.065(3)°, $V$ = 1803.5(6) $Å^3$, $Z$ = 4, $\rho$ = 2.937 $mg\,m^{-3}$, a total of 14901 reflections were obtained (4216 were independent). $R_1$ = 0.0392, $wR_2$ = 0.0840 [for 4216 $I_o$, $I_o > 2\sigma(I_o)$].
[23] F. H. Allen, *Acta Crystallogr. Sect. B* **2002**, *58*, 380–388. Search performed on Dec. 21, **2006**.
[24] D. H. Gibson, Y. Xiaolong, H. Haiyang, M. S. Mashuta, *Organometallics* **2003**, *22*, 337–346.

Received: January 9, 2007
Published Online: March 14, 2007

 © 2007 Wiley-VCH Verlag GmbH & Co. KGaA, Weinheim 

DOI: 10.1002/ejic.200601003

# Effect of Protonation and Interaction with Anions on a Lead(II) Complex with a Lateral Macrobicycle Containing a Phenol Schiff-Base Spacer

**David Esteban-Gómez,[a] Carlos Platas-Iglesias,[a] Fernando Avecilla,[a] Andrés de Blas,*[a] and Teresa Rodríguez-Blas*[a]**

**Keywords:** Lead / Macrocycles / N,O ligands / Density functional calculations

The macrobicycle receptor **L⁴**, derived from 1,10-diaza-15-crown-5 incorporating a phenol Schiff-base spacer, forms stable complexes with lead(II). In $[Pb(L^4)(ClO_4)](ClO_4)\cdot CH_3CN$ (**1**), the lead(II) ion is asymmetrically placed at the one end of the macrobicyclic cavity, because of the intramolecular hydrogen bonding interaction that occurs between an imine nitrogen atom and the phenol group. This asymmetric position of the metal ion inside the macrobicyclic cavity induces chirality in this system. Variable temperature $^1H$ NMR spectroscopic experiments indicate that the asymmetric coordination of the metal ion inside the macrocyclic cavity is maintained in acetonitrile solution, but a translocation of the $Pb^{II}$ ion from one end of the macrobicyclic cavity to the second one occurs. This dynamic behaviour, which corresponds to the interconversion between the two possible enantiomeric forms of the complex, is fast on the NMR timescale at 320 K but slow at low temperatures, and we have estimated an activation barrier of $\Delta G^{\ddagger} = 68 \pm 2$ kJ mol$^{-1}$. We have also studied the effect of the protonation on **1** by NMR and UV/Vis spectroscopy in $CH_3CN$ solutions at room temperature, finding that diprotonation causes demetallation of the complex without receptor destruction, recovering **L⁴** in its protonated form. On the other hand, the interaction of compound **1** with anions such as $NO_3^-$ and $SCN^-$ has been evaluated by using spectrophotometric titrations in acetonitrile solution, finding log *K* values of 5.83(1) for $NO_3^-$ and 6.27(2) for $SCN^-$. The $[Pb(L^4)]^{2+}$, $[Pb(L^4)(NO_3)]^+$, $[Pb(L^4)(NCS)]^+$ and $[Pb(L^4)(SCN)]^+$ systems were characterized by means of density functional theory calculations (DFT) performed by using the B3LYP model, and the coordination geometry as well as the role of the $Pb^{II}$ lone pair has been investigated and discussed.
(© Wiley-VCH Verlag GmbH & Co. KGaA, 69451 Weinheim, Germany, 2007)

## Introduction

Lead is regarded as a serious environmental pollutant.[1] Considered as a cheap and convenient material to convey water to the consumers' tap, lead has been widely used for municipal service pipes, household plumbing, joints and solders. Other major uses also include electric storage batteries, paint pigments, gasoline additives or ammunition.[2] The awareness of its environmental and health effects has led the authorities to ban some of these uses in most of the developed countries, which has contributed to a decrease in the lead level in the environment. Even so, this level is still a high risk for health, and lead continues to be one of the ten most common pollutants. In fact, the concentration in drinking water, diets and ambient air is significant in some areas.[2–5]

The removal of toxic heavy metal contaminants from aqueous waste streams is currently one of the most important environmental issues under investigation. Precipitation, activated carbon absorption, bioremediation, reverse osmosis, electrolysis, cementation, irradiation, zeolite absorption, evaporation, membrane processes or ion flotation are some of the treatment methods used for heavy metal-containing waste remediation.[6] Solvent extraction and treatment with cation exchange resins are also important, especially when selective extractions are required and/or low concentrations of the target metal ion are present. Solvent extraction occurs when a metal ion associates with an organic complexant to form a species that is transferred from the aqueous to the organic phase in a two-phase system, whereas cation exchange resins are formed by a polymeric skeleton functionalized with a complexant agent capable of binding to the desired metal ion; therefore, these two methods require the presence of a selective complexant agent. The efficient use of $Pb^{II}$ complexant agents capable of acting as extracting agents requires that the following conditions are met: (i) fast binding of the metal ion by the complexant agent; (ii) selective ion complexation; (iii) sufficiently high binding strength for the metal ion to be extracted; (iv) high stability against hydrolysis, and (v) reversible complexation allowing for the total recovery of the metal without significant extracting agent destruction.[7] The search for novel

[a] Dpto. Química Fundamental, Facultade de Ciencias, Campus da Zapateira s/n, Universidade da Coruña,
15071 A Coruña, Spain
Fax: +34-981-167065
E-mail: mayter@udc.es
Supporting information for this article is available on the WWW under http://www.eurjic.org or from the author.

 © 2007 Wiley-VCH Verlag GmbH & Co. KGaA, Weinheim 

highly selective complexant agents for $Pb^{II}$ requires a great knowledge of the chemical behaviour of this cation, which has caused a resurgence of interest in its chemistry.[8–12] In recent years many reports concerning coordination chemistry of $Pb^{II}$ with a great variety of receptors have been published. The $Pb^{II}$ cation exhibits a rich and interesting coordination chemistry: it binds to a broad range of donor groups, assumes a wide range of coordination numbers and geometries and can exhibit the so-called "inert-pair effect".

Because of the highly favoured complexation, thanks to the chelate and macrocyclic effects, chelate and macrocyclic ligands have been widely used for metal extractions. Particularly, crown ethers have been recognized as a very effective class of compounds to achieve selective separation of heavy metal ions from aqueous solutions. Separation processes based on crown ether complexes of $Pb^{II}$ have been reported and are often quite selective.[13] In particular, we are interested in the design of selective complexant agents for $Pb^{II}$ based on crown frameworks. In a recent work[14] we have found that the macrobicyclic receptor **L⁵** (see Scheme 1), derived from 4,13-diaza-18-crown-6, incorporating a pyridinyl Schiff-base spacer, allows reversible and fast complexation of $Pb^{II}$. This, together with the inertia of the receptor towards hydrolysis, opens very interesting perspectives for the use of this receptor as a new lead(II) extracting agent.[15] As a continuation of this work we discuss the potential of the related receptor **L⁴** as a complexant agent for this metal ion. Likewise, the effect that the presence of different counterions and the protonation of the receptor has on the $Pb^{II}$ coordination environment have also been investigated. Receptors **L⁴** and **L⁵** derive structurally from the bibracchial lariat ethers **L¹** and **L²**, respectively, and belong to the group defined as (Schiff base) lateral macrobicycles.[16] Although both Schiff-base macrocycles and cryptands have been proposed as excellent platforms for the complexation of a wide variety of metal ions,[17,18] no example of a Schiff-base lateral macrobicycle was reported until 1999[19] when we prepared the macrobicycles **L³**–**L⁶** (see Scheme 1). Subsequent studies have demonstrated that these systems possess very promising coordinating properties.[20–22]

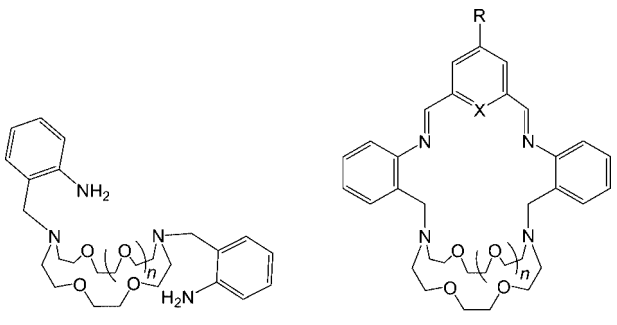


$Pb(L^4)(ClO_4)_2 \cdot 0.5\,H_2O$ (**1**) $[H_3L^4](ClO_4)_3 \cdot 3\,CH_3CN$ (**2**)

Scheme 1.

## Results and Discussion

Reaction between the barium complex $[Ba(L^4)](ClO_4)_2$ and $Pb(ClO_4)_2 \cdot 6H_2O$ yields the $Pb^{II}$ compound of formula $Pb(L^4)(ClO_4)_2 \cdot 0.5H_2O$ (**1**). The absence of peaks corresponding to species containing the $[Ba(L^4)]^+$ fragment in the FAB-mass spectrum coupled with the presence of an intense peak from $[Pb(L^4)(ClO_4)]^+$ confirmed that the macrobicycle **L⁴** remains intact and that transmetallation has occurred.

Slow diffusion of diethyl ether into a solution of **1** in acetonitrile gave X-ray quality crystals of this compound. Crystals comprise the cation $[Pb(L^4)(ClO_4)]^+$, a well-separated perchlorate group and an acetonitrile molecule. Figure 1 illustrates the structure of the complex cation, while selected bond lengths and angles of the coordination sphere are compiled in Table 1. The $Pb^{II}$ ion is set into the macrobicyclic cavity, bound to six of the eight heteroatoms of the receptor **L⁴** and two oxygen atoms of a perchlorate group. The interaction between the $Pb^{II}$ ion and this perchlorate group is very weak, as indicated by the $Pb–O_{perchlorate}$ distances, Pb–O(11) 2.838(5) and Pb–O(9) 3.000(7). Very often these weak interactions have been described as "semicoordination",[23] and it is usually attributed to crystal packing forces in the solid state.

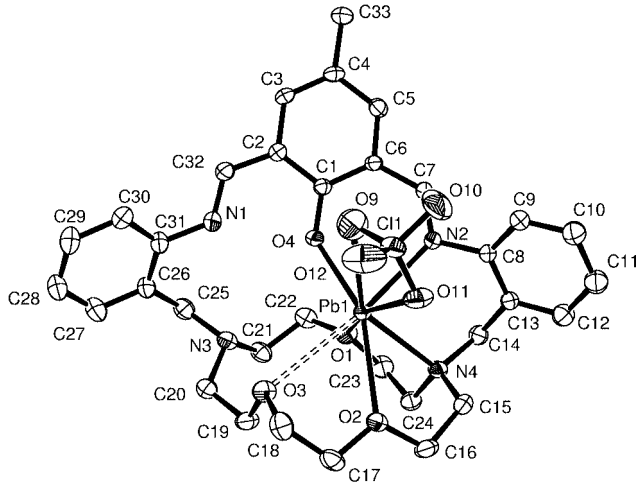


Figure 1. X-ray crystal structure of the cation in compound **1** with atom labelling; hydrogen atoms are omitted for simplicity; the ORTEP plot is drawn at the 30% probability level.

As shown in Figure 1, in $[Pb(L^4)(ClO_4)]^+$ the $Pb^{II}$ ion is asymmetrically placed at one end of the macrobicyclic cavity, coordinated to one imine nitrogen atom, N(2), one pivotal nitrogen atom, N(4), the phenol oxygen atom, O(4), and the three oxygen atoms of the crown moiety, O(1), O(2) and O(3). The $Pb^{II}$ ion is clearly closer to O(1) than to O(2) and O(3), and the considerably long Pb–O(3) and Pb–O(2) distances [3.117(5) and 2.844(4) Å, respectively] suggest that the interaction of $Pb^{II}$ with these oxygen donor atoms is

 © 2007 Wiley-VCH Verlag GmbH & Co. KGaA, Weinheim 

Table 1. Selected bond lengths [Å] and angles [°] for **1**.

| | | | |
|---|---|---|---|
| Pb–O(1) | 2.556(4) | Pb–O(9) | 3.000(7) |
| Pb–O(2) | 2.844(4) | Pb–O(11) | 2.838(5) |
| Pb–O(3) | 3.117(5) | Pb–N(2) | 2.537(5) |
| Pb–O(4) | 2.379(4) | Pb–N(4) | 2.588(5) |
| O(4)–Pb(1)–N(2) | 74.51(15) | O(4)–Pb(1)–O(1) | 74.82(14) |
| N(2)–Pb(1)–O(1) | 95.29(15) | O(4)–Pb(1)–N(4) | 131.15(16) |
| N(2)–Pb(1)–N(4) | 79.29(15) | O(1)–Pb(1)–N(4) | 67.35(15) |
| O(4)–Pb(1)–O(11) | 117.73(14) | N(2)–Pb(1)–O(11) | 76.25(16) |
| O(1)–Pb(1)–O(11) | 161.21(15) | N(4)–Pb(1)–O(11) | 94.38(16) |
| O(4)–Pb(1)–O(2) | 156.31(14) | N(2)–Pb(1)–O(2) | 129.14(14) |
| O(1)–Pb(1)–O(2) | 98.75(14) | N(4)–Pb(1)–O(2) | 62.23(15) |
| O(11)–Pb(1)–O(2) | 75.03(14) | O(4)–Pb(1)–O(9) | 72.11(16) |
| N(2)–Pb(1)–O(9) | 72.64(17) | O(1)–Pb(1)–O(9) | 146.73(17) |
| N(4)–Pb(1)–O(9) | 136.21(17) | O(11)–Pb(1)–O(9) | 46.96(16) |
| O(2)–Pb(1)–O(9) | 113.02(16) | O(4)–Pb(1)–O(3) | 99.15(13) |
| N(2)–Pb(1)–O(3) | 173.36(13) | O(1)–Pb(1)–O(3) | 84.78(13) |
| N(4)–Pb(1)–O(3) | 106.76(14) | O(11)–Pb(1)–O(3) | 105.58(14) |
| O(2)–Pb(1)–O(3) | 57.26(12) | O(9)–Pb(1)–O(3) | 103.76(16) |

weak. The other two heteroatoms of the macrobicyclic receptor, the imine and pivotal nitrogen atoms N(1) and N(3), do not belong to the metal ion coordination environment, as evidenced by the observed Pb–N(1) and Pb–N(3) distances of 4.4515(4) and 4.0474(3) Å, respectively. Moreover, the X-ray data suggest that the imine nitrogen atom N(1) and the phenol donor O(4) are involved in an intramolecular hydrogen bonding interaction [N(1)···H(1N), 0.84(7) Å; N(1)···O(4) 2.598(7) Å, O(4)···H(1N) 1.95(8) Å, N(1)–H(1N)–O(4) 133(7)°]. These distances also indicate that proton transfer from the phenol group to the imine atom N(1) has occurred. This proton transfer has also been observed in the related complexes $[Ba(L^4)(ClO_4)(CH_3CN)]^+$[24] and $[Pb(L^6)]^{2+}$,[21] where the guest metal ion is also asymmetrically located in the macrobicyclic cavity. A remarkable characteristic of the complex is the presence of chirality induced by the asymmetric position of the metal ion inside the macrobicyclic cavity. Inspection of the crystal data reveals that in **1** both enantiomers cocrystallize in equal amounts (racemate).

The fold of $\mathbf{L^4}$ around the $Pb^{II}$ ion allows the five donors of the crown moiety, [O(1), O(2), O(3), N(3) and N(4)], to be essentially coplanar (mean deviation from plane 0.0762 Å), with the metal ion located 1.6955 Å above this plane. The coordination polyhedron may be described as a distorted monocapped pentagonal bipyramid (Figure 2). The torsion angles C(1)–C(6)–C(7)–N(2) [–6.8(10)°] and C(1)–C(2)–C(32)–N(1) [–5.1(10)°] indicate that both imine groups are slightly rotated from coplanarity with the phenol ring. This planarity loss is related to the structure of the receptor and the coordinative requirements of the metal ion guest that force the receptor to fold increasing the stress of its structure. The lateral aromatic rings of $\mathbf{L^4}$ in **1** are in different planes and intersect at 47.08°, a value substantially different from that found in the analogous barium complex $[Ba(L^4)(ClO_4)(CH_3CN)]^+$ (57.62°).[24] Likewise, the phenol ring forms a dihedral angle of 43.48° with the plane containing the benzyl ring attached to the pivotal nitrogen atom N(4), and an angle of 48.65° with the plane containing the other aromatic ring. The former is 23.9° larger than that found in $[Ba(L^4)(ClO_4)(CH_3CN)]^+$, whereas the latter is 16.3° smaller.[24] These results highlight the ability of $\mathbf{L^4}$ to adapt its conformation to the steric and electronic requirements of the metal ion.

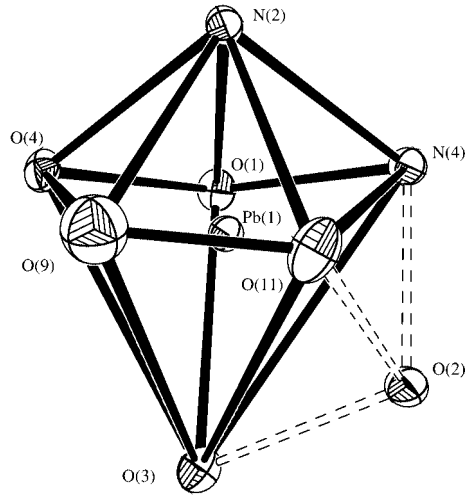


Figure 2. Coordination polyhedron around the metal ion in $[Pb(L^4)(ClO_4)]^+$.

The conductivity measurement for an ca. $10^{-3}$ M solution of **1** in acetonitrile at 20 °C ($\Lambda_M$ = 255 $cm^2\,\Omega^{-1}\,mol^{-1}$) reveals that this compound behaves as a 2:1 electrolyte in this solvent,[25] indicating that the perchlorate anions are not coordinated to the metal ion in the acetonitrile solution. This is expected when taking into account the weak interaction of a perchlorate anion with the metal ion observed in the solid state. The $^1H$ NMR spectrum of **1** recorded in $CD_3CN$ solution at 320 K is consistent with the presence of a single complex species in solution with an effective $C_s$ symmetry (Figure 3). Upon decreasing the temperature the signals corresponding to the imine and aromatic protons gradually broaden and finally split into two different signals, reflecting intramolecular conformational exchange processes (Figure 3). The spectrum recorded at 248 K shows two resonances at $\delta$ = 8.79 and 8.75 ppm attributable to the protons of the imine units, and two signals at $\delta$ = 7.90 and 7.78 ppm with a $^4J$ = 2.4 Hz from the aromatic protons of the phenol group. This is consistent with the presence of a single species in solution with $C_1$ symmetry, in agreement with the X-ray crystal structure described above. Indeed, in the solid state the $Pb^{II}$ ion is placed at one end of the macrobicyclic cavity, which results in a complex with $C_1$ symmetry. Thus, the dynamic bevaviour of compound **1** in acetonitrile solution can be attributed to a translocation of the $Pb^{II}$ ion from one end of the macrobicyclic cavity to the other. This dynamic process is fast on the NMR timescale at high temperature, thus resulting in a spectrum corresponding to a species with an effective $C_s$ symmetry in solution. From the coalescence temperature of signals corresponding to the aromatic protons of the phenol unit, which occurs at 309 K, we can estimate an activation barrier of $\Delta G^{\ddagger} = 68 \pm 2$ kJ $mol^{-1}$ for this intramolecular dy-

 © 2007 Wiley-VCH Verlag GmbH & Co. KGaA, Weinheim 

namic process. As discussed above, the presence of the $Pb^{II}$ ion at one end of the macrocyclic cavity in **1** induces chirality in the complex. Thus, the dynamic process observed for this compound in solution corresponds to the interconversion between the two possible enantiomeric forms of the complex.

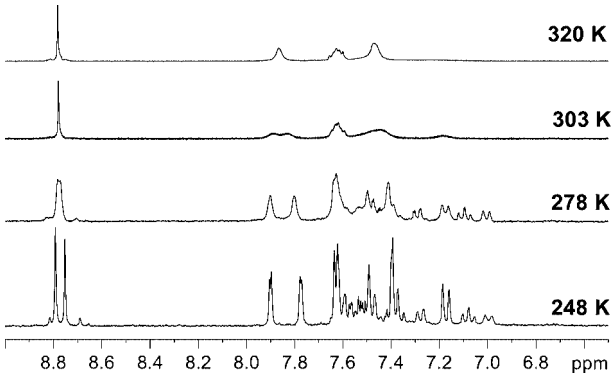


Figure 3. Part of the 300-MHz $^1$H-NMR spectra of compound **1** recorded in $CD_3CN$ at different temperatures.

The $[Pb(L^4)]^{2+}$ system was characterized by means of DFT calculations at the B3LYP level. On the basis of our previous experience for these calculations we used the standard 6-31G(d) basis set for the ligand atoms, while the LanL2DZ valence and effective core-potential functions were used for Pb.[26] The calculated structure for this complex (Figure 4) resembles the X-ray crystal structure of **1**, with the calculated bond lengths of the metal coordination environment in reasonable agreement with those obtained experimentally (Table 2). The experimental and calculated bond lengths differ by less than 0.08 Å, except the Pb–O(3) distance, which differs by ca. 0.18 Å from the experimental value. However, this is not surprising since the experimental value of the Pb–O(3) distance [3.117(5) Å] indicates a weak interaction between the metal ion and O(3). Shimoni-Livny et al.[27] have investigated a close relation between the role of a lone pair of $Pb^{II}$ and the coordination geometry for a large number of $Pb^{II}$ complexes. They have found two general structural categories of $Pb^{II}$ compounds: holodirected and hemidirected, which are distinguished by the disposition of ligands around the metal ion. In the hemidirected form there is a void in the liganding attributable to the stereochemical activity of the $Pb^{II}$ lone pair that is not found in holodirected geometry. The calculated Pb–O(1) bond length [2.479 Å] is clearly shorter than distances between the metal ion and the remaining oxygen atoms of the crown moiety. This, together with the presence of an identifiable void in the disposition of the donor atoms of the ligand around the metal ion, suggests that the $Pb^{II}$ lone pair is stereochemically active in $[Pb(L^4)]^{2+}$. The analysis of the natural bond orbitals (NBO) in $[Pb(L^4)]^{2+}$ shows that the $Pb^{II}$ lone pair orbital is predominantly 6s, but polarized by some 6p contribution: s[98.02%]p[1.98%]. Similar p contributions (>1%) have been calculated for hemidirected $Pb^{II}$ complexes with related ligands, which clearly confirm that the $Pb^{II}$ lone pair is stereochemically active in $[Pb(L^4)]^{2+}$.[26] However, we notice that in the X-ray crystal structure the Pb–O(1) bond length is slightly longer than the calculated one, which suggests that the presence of a weakly coordinating perchlorate anion around the $Pb^{II}$ ion decreases the stereochemical activity of the $Pb^{II}$ lone pair.

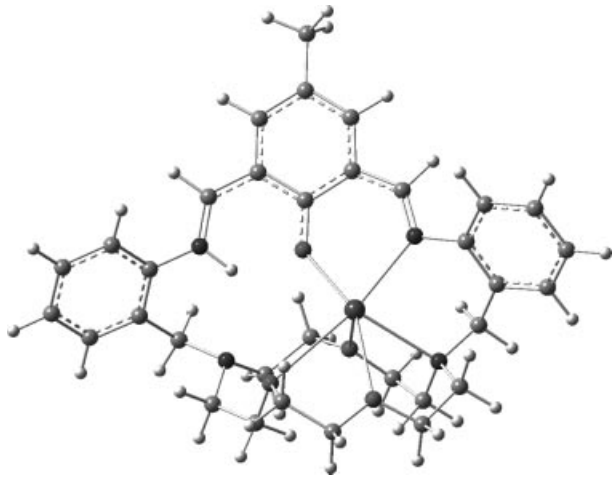

Figure 4. Structure of $[Pb(L^4)]^{2+}$ as optimized in vacuo at the B3LYP/6-31G(d) level.

Table 2. Calculated (B3LYP/6-31G(d)) bond lengths [Å] of the $Pb^{II}$ coordination environment obtained for the $[Pb(L^4)]^{2+}$, $[Pb(L^4)(NO_3)]^+$ and $[Pb(L^4)(NCS)]^+$ systems (see Figure 1 for numbering scheme).

| | $[Pb(L^4)]^{2+}$ | $[Pb(L^4)(NO_3)]^+$ | $[Pb(L^4)(NCS)]^+$ | $[Pb(L^4)(SCN)]^+$ |
|---|---|---|---|---|
| Pb–O(1) | 2.479 | 2.843 | 2.965 | 2.916 |
| Pb–O(2) | 2.772 | 2.835 | 2.757 | 2.831 |
| Pb–O(3) | 2.935 | 3.191 | 2.862 | 2.916 |
| Pb–O(4) | 2.316 | 2.439 | 2.396 | 2.329 |
| Pb–N(2) | 2.485 | 2.550 | 2.565 | 2.535 |
| Pb–N(4) | 2.610 | 2.725 | 2.874 | 2.881 |
| Pb–$ONO_2$ | | 2.429/2.479 | | |
| Pb–NCS | | | 2.308 | |
| Pb–SCN | | | | 2.870 |

## Interaction with Anions

Since in solution the $Pb^{II}$ ion is coordinatively unsaturated in **1**, we have studied the interaction of this compound with anions such as $NO_3^-$ and $SCN^-$ by using spectrophotometric titrations in acetonitrile solution. The UV/Vis spectrum of **1** (Figure 5) displays a band centred at 456 nm typical of the C=N chromophores.[28,29] Upon addition of $NO_3^-$ or $SCN^-$ anions this band undergoes a blue shift to ca. 423 nm as its intensity decreases. Nonlinear least-squares analyses of the titration profiles (absorbance versus equivalents of anion added, see insets of Figure 5) clearly indicated the formation of 1:1 complexes in every case, and allowed us to estimate the association constants defined as [Equation (1)].

$$[Pb(L^4)]^{2+} + X^- \rightleftarrows [Pb(L^4)(X)]^+, \text{ where } X^- = NO_3^- \text{ or } SCN^- \quad (1)$$

 © 2007 Wiley-VCH Verlag GmbH & Co. KGaA, Weinheim 

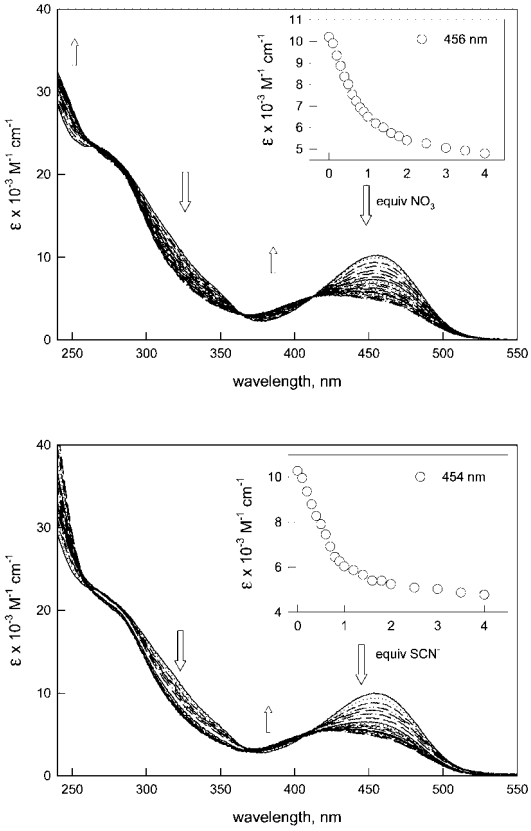


Figure 5. UV/Vis spectra taken over the course of the titration of a $10^{-5}$ M solution of compound **1** with a standard solution of tetrabutylammonium nitrate (top) or thiocyanate (bottom). The insets show titration profiles at selected wavelengths.

The analysis of the experimental data provides log *K* values of 5.83(1) ($X^- = NO_3^-$) and 6.27(2) ($X^- = SCN^-$). These results clearly confirm that the metal ion is coordinatively unsaturated in the $Pb^{II}$ complex of $\mathbf{L^4}$, and indicate that the $SCN^-$ ligand binds more strongly to $[Pb(L^4)]^{2+}$ than $NO_3^-$.

DFT calculations performed on the $[Pb(L^4)(NO_3)]^+$ system (see Supporting Information) indicate that the coordination of the nitrate anion has an important effect on the bond lengths of the metal coordination environment, which increase by ca. 0.06–0.36 Å with respect to those calculated for $[Pb(L^4)]^{2+}$ (Table 2). The $NO_3^-$ ligand coordinates in a nearly symmetrical bidentate fashion [Pb–O 2.429 and 2.479 Å]. In order to understand if the coordination of the thiocyanate ligand occurs through the nitrogen atom or through the sulfur one we have also carried out DFT calculations on the $[Pb(L^4)(NCS)]^+$ and $[Pb(L^4)(SCN)]^+$ systems. $Pb^{II}$ is classified as "intermediate" in the Pearson HSAB classification,[30] and thus it is not particularly surprising that both *N*-bonded and *S*-bonded $Pb^{II}$ complexes of thiocyanate exist.[31] The optimized geometries for both compounds are given in the Supporting Information. Our calculations predict that the *N*-bonded thiocyanate ligand results in a more stable structure, where the in vacuo relative energy of the $[Pb(L^4)(SCN)]^+$ system with respect to the $[Pb(L^4)(NCS)]^+$ is 5.47 kcal mol$^{-1}$. This is in agreement with the X-ray structure of the $Pb^{II}$ thiocyanate complex with the related macrobicycle $\mathbf{L^3}$, which shows that the thiocyanate ligand is *N*-bonded.[22] This is probably because the steric hindrance around the metal ion, caused by the coordination of the macrobicyclic receptor, favours the coordination of the $SCN^-$ ligands through the N donor atom.[32] On the other hand, the analysis of the NBOs in $[Pb(L^4)(NO_3)]^+$ indicates that the 6p contribution decreases upon coordination of the nitrate anion: s[98.57%]p[1.43%]. As a consequence the coordination geometry in $[Pb(L^4)(NO_3)]^+$ is less hemidirected than in $[Pb(L^4)]^{2+}$, and the Pb–O(1) bond length increases (Table 3). Replacing the nitrate anion by a *N*-bonded thiocyanate ligand results in a somewhat lower polarization of the Pb 6s lone pair, as follows from the NBOs analysis: s[98.72%]p[1.28%]. Furthermore, the presence of a *S*-bonded thiocyanate ligand causes a further decrease of the polarization of the Pb 6s lone pair: s[99.28%]p[0.72%]. Thus, the polarization of the Pb lone pair decreases when hard donor atoms such as O atoms of the nitrate group are replaced by softer donor atoms such as the N or S donor atoms of a thiocyanate ligand. These results are in agreement with previous observations that indicated that the coordination of soft-donor atoms favours holodirected ligand geometries in $Pb^{II}$ complexes.[26,27]

Table 3. $^1$H- and $^{13}$C-NMR spectroscopic data [ppm] for compound $[H_2L^4]^{2+}$ in $CD_3CN$ solution at 298 K.[a]

| H atom[b] | δ values | C atom | δ values |
|---|---|---|---|
| H1 | 2.41 (s, 3 H) | C1 | 20.1 |
| H3 | 7.70 (s, 2 H) | C2 | 130.8 |
| H6 | 8.66 (s, 2 H) | C3 | 140.8 |
| H8 | 7.31 (d, 2 H) | C4 | 122.4 |
| H9 | 7.60 (td, 2 H) | C5 | 158.4 |
| H10 | 7.40 (t, 2 H) | C6 | 166.6 |
| H11 | 7.49 (d, 2 H) | C7 | 151.0 |
| H13 | 4.31 (d, 2 H) | C8 | 120.8 |
| H13′ | 4.72 (d, 2 H) | C9 | 132.9 |
| H14 | 3.43 (m, 2 H) | C10 | 128.6 |
| H14′ | 3.43 (m, 2 H) | C11 | 132.7 |
| H15 | 3.40 (m, 2 H) | C12 | 124.3 |
| H15′ | 3.64 (m, 2 H) | C13 | 58.9 |
| H16 | 2.99 (m, 2 H) | C14 | 55.6 |
| H16′ | 3.41 (m, 2 H) | C15 | 64.8 |
| H17 | 3.42 (m, 2 H) | C16 | 69.8 |
| H17′ | 3.88 (m, 2 H) | C17 | 56.9 |
| H18 | 3.78 (m, 2 H) | C18 | 65.1 |
| H18′ | 4.01 (m, 2 H) | | |

[a] See Figure 6 for labelling. [b] $^3J_{8,9}$ = 7.9 Hz; $^3J_{11,10}$ = 7.4 Hz; $^4J_{9,11}$ = 1.3 Hz; $^2J_{13,13'}$ = 13.8 Hz.

## Protonation Studies

The protonation of $Pb(L^4)(ClO_4)_2 \cdot 0.5H_2O$ (**1**) has been followed by NMR and UV/Vis spectroscopy in $CH_3CN$ solutions at room temperature. Upon addition of trifluoroacetic acid to a solution of **1** in $CD_3CN$ a new set of signals is observed in the $^1$H NMR spectra whose chemical shifts do not vary with the amount of trifluoroacetic acid added,

 © 2007 Wiley-VCH Verlag GmbH & Co. KGaA, Weinheim 

thereby confirming the formation of a single protonated species in acetonitrile solution. Upon addition of two equivalents of acid the signals of compound **1** nearly disappear, in agreement with the formation of the diprotonated species $[H_2L^4]^{2+}$ (see Figure 6). The two protonations probably occur on the pivotal nitrogen atoms, as previously observed for $[H_2L^5]^{2+}$.[33] The $^1H$ and $^{13}C$ NMR spectra of $[H_2L^4]^{2+}$ could be fully assigned on the basis of two-dimensional COSY, HSQC and HMBC experiments at 298 K (Table 3, see Figure 6 for labelling). The $^{13}C$ NMR spectrum shows 18 signals for the 33 carbon nuclei of the ligand, indicating an effective $C_s$ symmetry of $[H_2L^4]^{2+}$ in acetonitrile solution. The methylene protons H13/H13′ yield an AB spin pattern ($^2J_{13,13'}$ = 13.8 Hz) in the $^1H$ NMR spectrum, while the protons of the crown moiety give AA′BB′ spin patterns (Figure 6). This is indicative of a relatively rigid structure of $[H_2L^4]^{2+}$ in solution, probably because of the presence of intramolecular hydrogen bonding interactions between the protonated pivotal nitrogen atoms and oxygen atoms of the crown moiety.

Figure 7 shows a family of UV/Vis spectra recorded during the course of a titration of a $10^{-4}$ M solution of **1** with trifluoroacetic acid in $CH_3CN$ solution. Upon addition of trifluoroacetic acid the band at 456 nm experiences a blue shift to 364 nm. The presence of two sharp isosbestic points at 394 and 335 nm indicates that only two species co-exist at the equilibrium, while the profile shown in the inset of Figure 7 indicates the formation of a diprotonated species in solution upon addition of trifluoroacetic acid. Data can be interpreted on the basis of equilibrium (2).

$$[Pb(L^4)]^{2+} + 2\ H^{+} \rightleftarrows [(H_2L^4)]^{2+} + Pb^{2+},\ \beta_{12} \qquad (2)$$

A nonlinear least-squares treatment of the titration profile provides $\log\beta_{12}$ = 9.14(1). These results confirm that addition of acid to a solution of **1** causes the demetallation of the complex together with the formation of the diprotonated form of the ligand, as previously observed for $[Pb(L^5)]^{2+}$.[14] However, in the latter case the demetallation process has been shown to occur in two steps, with the formation of an intermediate monoprotonated complex species $[Pb(HL^5)]^{3+}$. By contrast, the demetallation of $[Pb(L^4)]^{2+}$ appears to occur in a single step, as described by Equation (2).

Addition of a large excess of $CF_3COOH$ to a solution of $[H_2L^4]^{2+}$ provokes further changes in the UV/Vis spectrum (Figure 7); the band from the imine group at 364 nm shows a red shift towards 495 nm. This result suggests that a third protonation process occurs in the presence of a large excess of acid. Slow evaporation of a solution of **1** in the presence of 10 equiv. of $CF_3COOH$ allowed us to obtain single crystals of $[H_3L^4](ClO_4)_3{\cdot}3CH_3CN$ (**2**) suitable for single-crystal X-ray diffraction studies, which confirms the formation of the triprotonated form of the macrobicycle under these conditions. Crystals of **2** contain the cation $[H_3L^4]^{3+}$, three perchlorate anions and acetonitrile molecules. Figure 8 shows the structure of the cation in **2**. Bond lengths and angles do not show significant deviations from the expected values. The conformation of the macrobicycle in **2** is conditioned by the presence of intramolecular hydrogen bonding interactions (Table 4) involving each pivotal nitrogen atom with two oxygen atoms of the crown moiety and both imine nitrogen atoms with the oxygen atom of the phenol group. This type of interaction seems to be responsible for the relatively rigid structure found in solution for the related diprotonated receptor $[H_2L^4]^{2+}$ described above.

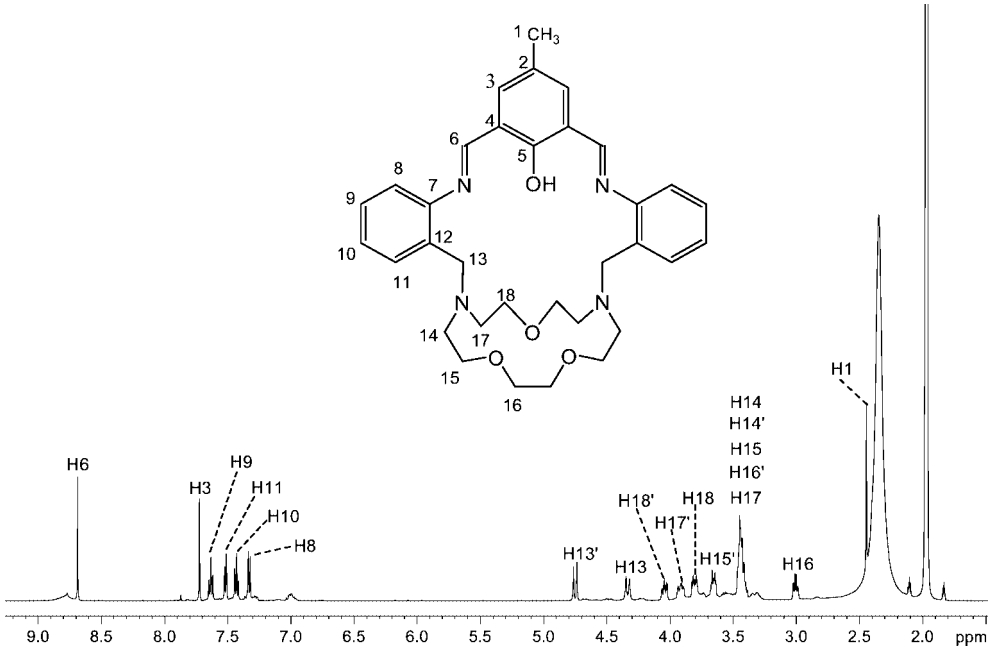


Figure 6. $^1H$-NMR spectrum of $[H_2L^4]^{2+}$ recorded in $CD_3CN$ solution at 298 K.

 © 2007 Wiley-VCH Verlag GmbH & Co. KGaA, Weinheim 

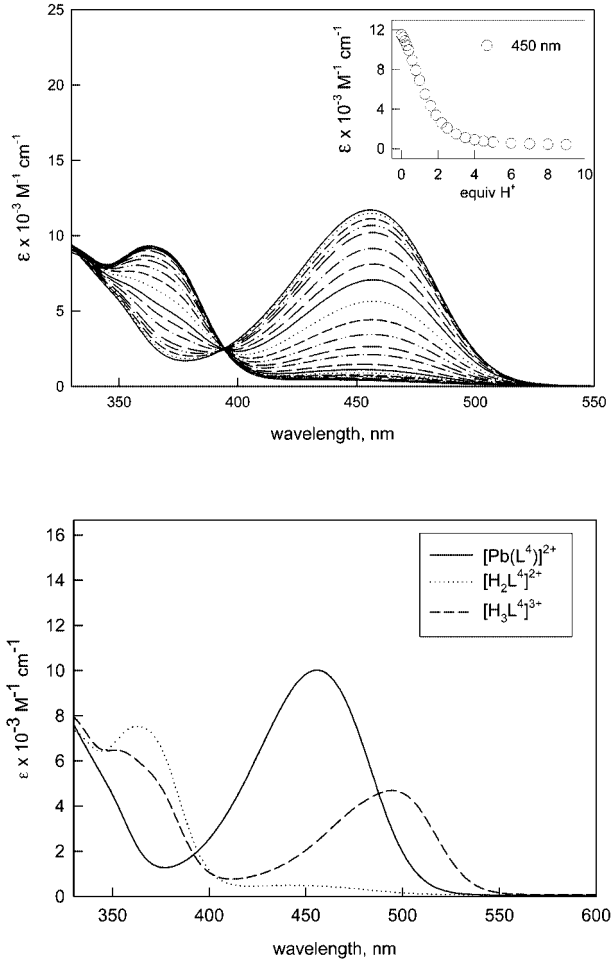


Figure 7. Top: family of spectra taken over the course of the titration of an acetonitrile solution $10^{-5}$ M in **1** with a standard solution of $CF_3COOH$ at 298 K. The titration profile is reported in the inset. Bottom: comparison of the UV/Vis spectra of $[Pb(L^4)]^{2+}$, $[H_2L^4]^{2+}$ and $[H_3L^4]^{3+}$ as recorded in acetonitrile solution.

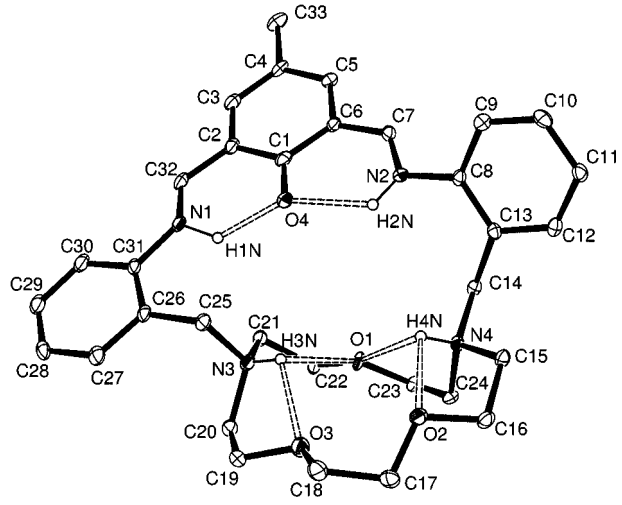


Figure 8. ORTEP diagram (30% probability) of $[H_3L^4]^{3+}$ in **2**, showing the atomic numbering scheme. For the sake of clarity hydrogen atoms are omitted, except those involved in intramolecular hydrogen bonds.

Table 4. Distances [Å] and angles [°] of intramolecular hydrogen bonds in compound **2**.[a]

| D–H···A | H···A | D···A | D–H···A |
|---|---|---|---|
| N(3)–H(3N)···O(1) | 2.33(6) | 2.679(4) | 102(4) |
| N(3)–H(3N)···O(3) | 2.21(5) | 2.714(5) | 113(3) |
| N(4)–H(3N)···O(1) | 2.49(5) | 2.778(4) | 100(3) |
| N(4)–H(3N)···O(2) | 2.43(5) | 2.726(6) | 100(3) |
| N(1)–H(3N)···O(4) | 1.73(5) | 2.533(4) | 128(4) |
| N(2)–H(3N)···O(4) | 2.05(4) | 2.656(4) | 121(3) |

[a] For atom labels see Figure 7.

## Conclusions

The Schiff-base lateral macrobicycle **L$^4$**, derived from 1,10-diaza-15-crown-5 incorporating a phenol Schiff-base spacer, forms stable complexes with $Pb^{II}$. The X-ray crystal structure of $[Pb(L^4)(ClO_4)](ClO_4)\cdot CH_3CN$ (**1**) shows that the lead(II) ion is asymmetrically placed at the one end of the macrobicyclic cavity, because of the intramolecular hydrogen bonding interaction that occurs between an imine nitrogen atom and the phenol group. This asymmetric position of the metal ion inside the macrobicyclic cavity induces chirality in this system. The asymmetric coordination of the metal ion inside the macrocyclic cavity found in the solid state is also maintained in acetonitrile solution, but a translocation of the $Pb^{II}$ ion from one end of the macrobicyclic cavity to the other occurs. This dynamic behaviour, which actually corresponds to the interconversion between the two possible enantiomeric forms of the complex, is fast on the NMR timescale at 320 K but slow at low temperatures, and we have estimated an activation barrier of $\Delta G^{\ddagger} = 68 \pm 2$ kJ mol$^{-1}$.

Both the solid state and solution structure of $[Pb(L^4)]^{2+}$ indicate that the complex is coordinatively unsaturated so that interactions with anions such as $NO_3^-$ and $SCN^-$ are possible. Spectrophotometric titrations in acetonitrile solution indicate that the $SCN^-$ ligand binds more strongly to $[Pb(L^4)]^{2+}$ than $NO_3^-$, which follows from the values of the binding constants obtained: [$\log K = 5.83(1)$ and 6.27(2) for $NO_3^-$ and $SCN^-$, respectively]. The coordination geometry as well as the role of a lone pair of $Pb^{II}$ of the systems $[Pb(L^4)]^{2+}$, $[Pb(L^4)(NO_3)]^+$, $[Pb(L^4)(NCS)]^+$ and $[Pb(L^4)(SCN)]^+$ have been investigated by means of DFT calculations. The analysis of the natural bond orbitals (NBO) in $[Pb(L^4)]^{2+}$ shows that the $Pb^{II}$ lone pair is stereochemically active in $[Pb(L^4)]^{2+}$. The 6p contribution decreases upon coordination of the nitrate anion, and so the coordination geometry in $[Pb(L^4)(NO_3)]^+$ is less hemidirected than in $[Pb(L^4)]^{2+}$. Replacing the nitrate anion by a *N*-bonded thiocyanate ligand results in a lower polarization of the Pb 6s lone pair, which further decreases when the $SCN^-$ ligand is *S*-bonded. Finally, we have found that protonation of **1** with trifluoroacetic acid in acetonitrile solution causes demetallation of the complex without receptor destruction, with receptor **L$^4$** recovered in its protonated form. This opens interesting perspectives for the use of this receptor as a potential lead(II) extracting agent.

 © 2007 Wiley-VCH Verlag GmbH & Co. KGaA, Weinheim 

## Experimental Section

**Materials and Synthesis:** $[Ba(L^4)](ClO_4)_2$ was prepared as described previously by us.[19] All other chemicals were purchased from commercial sources and used without further purification. Solvents were of reagent grade purified by the usual methods. Caution! Although we have experienced no difficulties with the perchlorate salts, these should be regarded as potentially explosive and handled with care.[34]

**$Pb(L^4)(ClO_4)_2·0.5H_2O$ (1):** A solution of $Pb(ClO_4)_2·6H_2O$ (0.0131 g, 0.025 mmol) in absolute ethanol (5 mL) was added while stirring to a solution of $[Ba(L^4)](ClO_4)_2$ (0.0224 g, 0.025 mmol) in the same solvent (20 mL). The reaction mixture was stirred and refluxed for 48 h. After the reaction was complete the resultant yellow solution was allowed to stand for a few days and an orange precipitate was formed, which was collected by filtration and air dried (0.016 g, 66%). $C_{33}H_{40}Cl_2N_4O_{12}Pb·0.5H_2O$ (971.2): calcd. C 40.7, H 4.2, N 5.7; found C 40.3, H 4.2, N 5.5. MS (FAB): $m/z$ = 863 $[Pb(L^4)(ClO_4)]^+$. IR (KBr): $\tilde{\nu}$ = $(C{=}N)_{imine}$ 1633, $\nu(OH)_{phenol}$ 3470, $\nu_{as}$(Cl–O) 1092, $\delta_{as}$(O–Cl–O) 623 $cm^{-1}$. X-ray quality crystals of formula $[Pb(L^4)(ClO_4)](ClO_4)·CH_3CN$ were grown by slow diffusion of diethyl ether into a solution of **1** in acetonitrile.

**Physical Methods:** Elemental analyses were carried out with a Carlo–Erba 1108 elemental analyzer. FAB mass spectra were recorded using a FISONS QUATRO mass spectrometer with a Cs ion-gun and 3-nitrobenzyl alcohol as the matrix. IR spectra were recorded, as KBr discs or nujol mulls, using a Bruker Vector 22 spectrophotometer. Conductivity measurements were carried out with a Crison Micro CM 2201 conductivimeter using ca. $10^{-3}$ M solutions of the complex in acetonitrile. $^1H$ and $^{13}C$ NMR spectra were run at 25 °C with Bruker Avance 300-MHz or Bruker WM-500 spectrometers. Chemical shifts are reported in $\delta$ values. Spectral assignments were based in part on two-dimensional COSY, HMQC and HMBC experiments. Electronic spectra in the UV/Vis range were recorded at 20 °C with a Perkin–Elmer Lambda 900 UV/Vis spectrophotometer using 1.0 cm quartz cells. Spectrophotometric titrations were performed at 25 °C on $10^{-5}$ or $10^{-4}$ M solutions of compound **1** in acetonitrile (polarographic grade). Typically, aliquots of a fresh standard solution of the titrant salt ($10^{-3}$ or $10^{-2}$ M) were added and the UV/Vis spectra of the samples were recorded. All spectrophotometric titration curves were fitted with the HYPERQUAD program.[35]

**X-ray Crystallography:** Crystal data and details on data collection and refinement are summarized in Table 5. Three dimensional X-ray data for $[Pb(L^4)(ClO_4)](ClO_4)·CH_3CN$ (**1**) and $[H_3L^4](ClO_4)_3·3CH_3CN$ (**2**) were collected with a Bruker Smart 1000 CCD diffractometer. Data were corrected for Lorentz and polarization effects and for absorption by semi-empirical methods. Complex scattering factors were taken from the program package SHELXTL[36] for **1**, and SHELX97[37] for **2**. Both structures were solved by direct methods and refined by full-matrix least-squares on $F^2$. Refinement converged with anisotropic displacement parameters for all non-hydrogen atoms. The hydrogen atoms were included in calculated positions and refined by using a riding model, except for the hydrogen atom H(1N) in **1**, and H(1N), H(2N), H(3N) and H(4N) in **2**, which were first located in a difference electron-density map and then left to freely refine. The crystal of **1** presents a disorder on the ionic perchlorate and 162 restraints had to be imposed. This disorder has been solved and two atomic sites for each oxygen atom have been observed. The site occupancy factor was 0.491 for the four oxygen atoms, O(5A), O(6A), O(7A) and O(8A). The crystal of **2** also presents disorder on one of the acetonitrile solvent molecules [site occupancy factor: 0.526 for N(7A), C(38A) and C(31A)]. CCDC-624582 and -624583 contain the supplementary crystallographic data for the structures included in this paper. These data can be obtained free of charge from The Cambridge Crystallographic Data Centre via http://www.ccdc.cam.ac.uk/datarequest/cif.

Table 5. Crystal data and refinement details for compounds **1** and **2**.

| | **1** | **2** |
|---|---|---|
| Formula | $C_{35}H_{43}Cl_2N_5O_{12}Pb$ | $C_{39}H_{52}Cl_3N_7O_{16}$ |
| Mol. mass [g mol$^{-1}$] | 1003.83 | 981.23 |
| Crystal system | triclinic | monoclinic |
| Space group | $P\bar{1}$ | $C2/c$ |
| Temperature [K] | 293(2) | 100(2) |
| $a$ [Å] | 9.5083(9) | 36.377(5) |
| $b$ [Å] | 13.1472(12) | 13.3500(19) |
| $c$ [Å] | 16.2475(15) | 23.350(3) |
| $\alpha$ [°] | 96.506(2) | 90 |
| $\beta$ [°] | 101.7200 | 125.674(2) |
| $\gamma$ [°] | 97.083(2) | 90 |
| $V$ [Å$^3$] | 1953.4(3) | 9212(2) |
| $F(000)$ | 1000.0 | 4112 |
| $Z$ | 2 | 8 |
| $\rho_{calcd.}$ [g cm$^{-3}$] | 1.707 | 1.415 |
| $\mu$ [mm$^{-1}$] | 4.523 | 0.275 |
| $2\theta$ range [°] | 1.29–28.29 | 1.76–29.29 |
| $R_{int}$ | 0.0432 | 0.1473 |
| Measured reflections | 13860 | 53909 |
| Unique reflections | 9472 | 11624 |
| Observed reflections [$I > 2\sigma(I)$] | 6929 | 4919 |
| Goodness-of-fit on $F^2$ | 0.981 | 0.935 |
| $R_1$ [$I > 2\sigma(I)$][a] | 0.0440 | 0.0683 |
| $wR_2$ (all data)[b] | 0.1078 | 0.2023 |

[a] $R_1 = \Sigma||F_o| - |F_c||/\Sigma|F_o|$. [b] $wR_2 = \{\Sigma[w(|F_o|^2 - |F_c|^2)^2]/\Sigma[w(F_o^4)]\}^{1/2}$.

**Computational Methods:** The $[Pb(L^4)]^{2+}$, $[Pb(L^4)(NO_3)]^+$, $[Pb(L^4)(NCS)]^+$ and $[Pb(L^4)(SCN)]^+$ systems were fully optimized by using the B3LYP density functional model.[38,39] In these calculations we have used the standard 6-31G(d) basis set for the ligand atoms, while the LanL2DZ valence and effective core potential functions were used for Pb.[40] The stationary points found on the potential energy surfaces as a result of the geometry optimizations have been tested to represent energy minima rather than saddle points via frequency analysis. The relative free energy of the $[Pb(L^4)(NCS)]^+$ and $[Pb(L^4)(SCN)]^+$ complexes was calculated in vacuo at the same computational level, and it includes nonpotential energy (NPE) contributions (that is, zero point energy and thermal terms) obtained by frequency analysis. The wave functions of some of the lead complexes were analyzed by natural bond orbital analyses, involving natural atomic orbital (NAO) populations and natural bond orbitals (NBO).[41,42] All DFT calculations were performed by using the Gaussian 03 program package (Revision C.01).[43]

**Supporting Information** (see also the footnote on the first page of this article): Figure S1 showing B3LYP-optimized structures of the $[Pb(L^4)(NO_3)]^+$, $[Pb(L^4)(NCS)]^+$ and $[Pb(L^4)(SCN)]^+$ systems, and in-vacuo-optimized Cartesian coordinates [Å] for the $[Pb(L^4)]^{2+}$, $[Pb(L^4)(NO_3)]^+$, $[Pb(L^4)(NCS)]^+$ and $[Pb(L^4)(SCN)]^+$ systems.

## Acknowledgments

The authors thank Xunta de Galicia (PGIDIT03TAM10301PR and PGIDIT06TAM10301PR) for generous financial support. The

 © 2007 Wiley-VCH Verlag GmbH & Co. KGaA, Weinheim 

authors are indebted to Centro de Supercomputación of Galicia (CESGA) for providing the computer facilities.

[1] R. M. Harrison, D. R. H. Laxen, *Lead Pollution*, Chapman & Hall, London, **1981**.
[2] J. M. Christensen, J. Kristiansen, in: *Handbook of Metals in Clinical and Analytical Chemistry* (Eds.: H. G. Seiler, A. Sigel, H. Sigel), Marcel Dekker, New York, **1994**, pp. 425–440.
[3] B. P. Lanphear, D. A. Burgoon, S. W. Rust, S. Eberly, W. Galke, *Environmental Res.* **1998**, *76*, 120–130.
[4] T. G. Spiro, W. M. Stigliani, *Chemistry of the Environment*, Prentice Hall, Upper Saddle River, NJ, **1996**.
[5] F. Cuenot, M. Meyer, A. Bucaille, R. Guilard, *J. Mol. Liquids* **2005**, *118*, 89–99.
[6] A. T. Yordanov, D. M. Roundhill, *Coord. Chem. Rev.* **1998**, *170*, 93–124.
[7] A. Deratani, B. Sebille, *Anal. Chem.* **1981**, *53*, 1742–1746.
[8] J. Parr, *Polyhedron* **1997**, *16*, 551–566.
[9] C. E. Holloway, M. Melnik, *Main Group Met. Chem.* **1997**, *20*, 107–132.
[10] C. E. Holloway, M. Melnik, *Main Group Met. Chem.* **1997**, *20*, 399–495.
[11] C. E. Holloway, M. Melnik, *Main Group Met. Chem.* **1997**, *20*, 583–625.
[12] E. Claudio, E. S. Godwin, H. A. Magyar, *Prog. Inorg. Chem.* **2003**, *51*, 1–144.
[13] See for instance: a) M. P. Biehl, R. M. Izatt, J. D. Lamb, J. J. Christensen, *Sep. Sci. Technol.* **1982**, *17*, 289–294; b) R. M. Izatt, G. A. Clark, J. J. Christensen, *Sep. Sci. Technol.* **1986**, *21*, 865–872; c) R. M. Izatt, R. L. Bruening, G. A. Clark, J. D. Lamb, J. J. Christensen, *Sep. Sci. Technol.* **1987**, *22*, 661–675.
[14] D. Esteban-Gómez, R. Ferreirós, S. Fernández-Martínez, F. Avecilla, C. Platas-Iglesias, A. de Blas, T. Rodríguez-Blas, *Inorg. Chem.* **2005**, *44*, 5428–5436.
[15] *Spanish patent* 2233187 B1, A. de Blas, T. Rodríguez-Blas, F. Avecilla, C. Platas-Iglesias, D. Esteban-Gómez.
[16] J.-M. Lehn, *Pure Appl. Chem.* **1980**, *52*, 2441–2459.
[17] a) C. Platas, F. Avecilla, A. de Blas, T. Rodriguez-Blas, J.-C.-G. Bünzli, *J. Chem. Soc., Dalton Trans.* **1999**, 1763–1772; b) R. Rodriguez-Cortiñas, F. Avecilla, C. Platas-Iglesias, D. Imbert, J.-C. G. Bünzli, A. de Blas, T. Rodriguez-Blas, *Inorg. Chem.* **2002**, *41*, 5336–5349.
[18] W. Radecka-Paryzek, V. Patroniak, J. Lisowski, *Coord. Chem. Rev.* **2005**, *249*, 2156–2175.
[19] D. Esteban, D. Bañobre, R. Bastida, A. de Blas, A. Macías, A. Rodríguez, T. Rodríguez-Blas, D. E. Fenton, H. Adams, J. Mahía, *Inorg. Chem.* **1999**, *38*, 1937–1944.
[20] D. Esteban, D. Bañobre, A. de Blas, T. Rodríguez-Blas, R. Bastida, A. Macías, A. Rodríguez, D. E. Fenton, H. Adams, J. Mahía, *Eur. J. Inorg. Chem.* **2000**, 1445–1456.
[21] D. Esteban, F. Avecilla, C. Platas-Iglesias, J. Mahía, A. de Blas, T. Rodríguez-Blas, *Inorg. Chem.* **2002**, *41*, 4337–4347.
[22] D. Esteban, F. Avecilla, C. Platas-Iglesias, A. de Blas, T. Rodríguez-Blas, *Polyhedron* **2003**, *22*, 2709–2717.
[23] M. N. Gowda, S. B. Naikar, G. K. Reddy, *Adv. Inorg. Radiochem.* **1984**, *28*, 255–299.
[24] F. Avecilla, D. Esteban, C. Platas-Iglesias, A. de Blas, T. Rodríguez-Blas, *Acta Crystallogr., Sect. C* **2003**, *59*, m93–m94.
[25] W. J. Geary, *Coord. Chem. Rev.* **1971**, *7*, 81–122.
[26] D. Esteban, C. Platas-Iglesias, T. Enríquez-Pérez, F. Avecilla, A. de Blas, T. Rodríguez-Blas, *Inorg. Chem.* **2006**, *45*, 5407–5416.
[27] L. Shimoni-Livny, J. P. Glusker, C. W. Bock, *Inorg. Chem.* **1998**, *37*, 1853–1867.
[28] C. Platas, F. Avecilla, A. de Blas, T. Rodríguez-Blas, C. F. G. C. Geraldes, É. Tóth, A. E. Merbach, J.-C. G. Bünzli, *J. Chem. Soc., Dalton Trans.* **2000**, 611–618.
[29] M. González-Lorenzo, C. Platas-Iglesias, F. Avecilla, S. Faulkner, S. J. A. Pope, A. de Blas, T. Rodríguez-Blas, *Inorg. Chem.* **2005**, *44*, 4254–4262.
[30] R. G. Pearson, R. Mawby, *J. Halogen Chem.* **1967**, *3*, 55–84.
[31] C. Platas-Iglesias, D. Esteban-Gómez, T. Enríquez-Pérez, F. Avecilla, A. de Blas, T. Rodríguez-Blas, *Inorg. Chem.* **2005**, *44*, 2224–2233.
[32] B. Metz, R. Weiss, *Inorg. Chem.* **1974**, *13*, 2094–2098.
[33] F. Avecilla, D. Esteban, C. Platas-Iglesias, S. Fernández-Martínez, A. de Blas, T. Rodríguez-Blas, *Acta Crystallogr., Sect. C* **2005**, *61*, o92–o94.
[34] W. C. Wolsey, *J. Chem. Educ.* **1973**, *50*, A335–A337.
[35] P. Gans, A. Sabatini, A. Vacca, *Talanta* **1996**, *43*, 1739–1753.
[36] G. M. Sheldrick, *SHELXTL Bruker Analytical X-ray System*, release 5.1, Madison, WI, **1997**.
[37] *SHELX97* [Includes *SHELXS97*, *SHELXL97*, *CIFTAB*] - Programs for Crystal Structure Analysis (Release 97-2). G. M. Sheldrick, Institut für Anorganische Chemie der Universität, Tammanstrasse 4, 37077 Göttingen, Germany, **1998**.
[38] A. D. Becke, *J. Chem. Phys.* **1993**, *98*, 5648–5652.
[39] C. Lee, W. Yang, R. G. Parr, *Phys. Rev. B* **1988**, *37*, 785–789.
[40] P. J. Hay, W. R. Wadt, *J. Chem. Phys.* **1985**, *82*, 284–298.
[41] E. D. Glendening, A. E. Reed, J. E. Carpenter, F. Weinhold, *NBO version 3.1*.
[42] A. E. Reed, L. A. Curtiss, F. Weinhold, *Chem. Rev.* **1988**, *88*, 899–926.
[43] M. J. Frisch, G. W. Trucks, H. B. Schlegel, G. E. Scuseria, M. A. Robb, J. R. Cheeseman, J. A. Montgomery Jr, T. Vreven, K. N. Kudin, J. C. Burant, J. M. Millam, S. S. Iyengar, J. Tomasi, V. Barone, B. Mennucci, M. Cossi, G. Scalmani, N. Rega, G. A. Petersson, H. Nakatsuji, M. Hada, M. Ehara, K. Toyota, R. Fukuda, J. Hasegawa, M. Ishida, T. Nakajima, Y. Honda, O. Kitao, H. Nakai, M. Klene, X. Li, J. E. Knox, H. P. Hratchian, J. B. Cross, C. Adamo, J. Jaramillo, R. Gomperts, R. E. Stratmann, O. Yazyev, A. J. Austin, R. Cammi, C. Pomelli, J. W. Ochterski, P. Y. Ayala, K. Morokuma, G. A. Voth, P. Salvador, J. J. Dannenberg, V. G. Zakrzewski, S. Dapprich, A. D. Daniels, M. C. Strain, O. Farkas, D. K. Malick, A. D. Rabuck, K. Raghavachari, J. B. Foresman, J. V. Ortiz, Q. Cui, A. G. Baboul, S. Clifford, J. Cioslowski, B. B. Stefanov, G. Liu, A. Liashenko, P. Piskorz, I. Komaromi, R. L. Martin, D. J. Fox, T. Keith, M. A. Al-Laham, C. Y. Peng, A. Nanayakkara, M. Challacombe, P. M. W. Gill, B. Johnson, W. Chen, M. W. Wong, C. Gonzalez, J. A. Pople, *Gaussian*, Inc., Wallingford CT, **2004**.

Received: October 24, 2006
Published Online: January 19, 2007

 © 2007 Wiley-VCH Verlag GmbH & Co. KGaA, Weinheim 

DOI: 10.1002/ejic.200600917

# [$Cu^{II}_4$] Clusters From the Self-Assembly of Two Imidazolidinyl 2-Phenolate-Bridged [$Cu^{II}_2$] Units: The Role of the Chloride Bridge

**Alok Ranjan Paital,[a] Chang Seop Hong,[b] Hyoung Chan Kim,[c] and Debashis Ray*[a]**

**Keywords:** Template synthesis / Self-assembly / Cluster compounds / Copper / Magnetic properties

A new family of tetracopper clusters [$Cu_4(\mu_4$-X)$L_2$]$ClO_4$·$nH_2O$ (**1a**–**c**) [X = Cl, Br, I; $n$ = 12, 2, 2; $H_3L$ = 2-(2′-hydroxyphenyl)-1,3-bis[4-(2-hydroxyphenyl)-3-azabut-3-enyl]-1,3-imidazolidine] have been synthesised and characterised. The X-ray crystal structure of **1a** reveals that the template action of the spherical $Cl^-$ anion ($\mu_4$-$Cl^-$), which features a unique rectangular planar bridging mode, is responsible for the self-assembly of two $[Cu_2L]^+$ units in complex **1a**. In this family of complexes the spherical halides serve as templates to assemble the dimeric unit into tetrameric complexes, which gives an insight into the role of the halide bridge in tetranuclear complex formation. The capacity of this bridge to mediate magnetic coupling has been examined by bulk magnetic measurements for complex **1a**.
(© Wiley-VCH Verlag GmbH & Co. KGaA, 69451 Weinheim, Germany, 2007)

## Introduction

Cluster-like metal-organic assemblies can be obtained from cation-[1] and anion-templated[2] syntheses, and several recent reports have demonstrated that anions can be successfully employed as a template for the formation of a wide range of organic[3] and metal-organic[4] assemblies. The anionic species in these syntheses plays a templating role by using its directing properties and determines the geometry and connectivity of the final structure. The spherically symmetrical $Cl^-$ ion has recently been shown to direct the self-assembly of four trimethylphosphane-stabilised diphenylstibenium ions.[5] Anion-templated synthesis is expected to yield novel structures with properties of chemical significance. Single-atom-nucleated paramagnetic $M_4$ assemblies can generate interesting structures depending upon the number and nature of the coordination bonds they form in space.[6] The size, charge and nature of the nucleating atom also control the geometry and stability of the cluster. The $\mu_4$-$Cl^-$ coordination mode is rare for $Cu_4$ clusters of polydentate ligands and can have either tetrahedral (A)[7] or square-pyramidal (B)[2b,2c,8] geometries (Scheme 1). In these two coordination modes, the {$Cu^{II}_4(\mu_4$-Cl)} core is further supported by either phosphate or halide auxiliary bridges. The presence of auxiliary bridging ligands helps the nucleation around the chloride anion in a particular mode of binding.

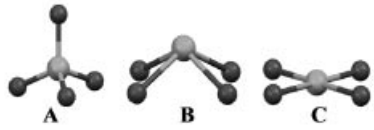


Scheme 1. Left: tetrahedral $\mu_4$-Cl (ref.[7]); middle: pyramidal $\mu_4$-Cl (ref.[2b]); right: part of complex **1a**; grey: Cl; black: Cu. Structures generated with the Mercury X-ray crystallography software package (version 1.4).

On the other hand the rectangular planar structure (C), which has $C_{2h}$ symmetry and long M–Cl bonds, is not known in the literature for complexes of polydentate ligands. Recently, we have shown that the spherical $O^{2-}$ anion can function as a nucleating group that allows isolation of the tetrahedral {$Cu^{II}_4(\mu_4$-O)} core of two different non-bridging hexadentate ligands.[9] No analogous $\mu_4$-Cl-templated tetranuclear complex of a 3d element is known with similar Schiff-base ligand systems. Currently, efforts are be-

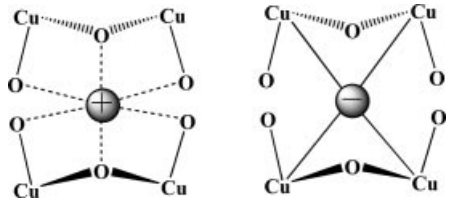


Figure 1. Schematic presentation of a cation-centred assembly around octahedral $Na^+$ (left, ref.[11]) and the anion-centred assembly around spherical $Cl^-$ in complex **1a** (right).

[a] Department of Chemistry, Indian Institute of Technology, Kharagpur 721 302, India
Fax: +91-3222-82252
E-mail: dray@chem.iitkgp.ernet.in
[b] Department of Chemistry and Center for Electro- and Photo-Responsive Molecules, Korea University, Seoul 136-701, Korea
[c] Systems Research Team, Research & Development Division, Nuclear Fusion Research Center, Daejeon 305-333, Korea


InterScience
© 2007 Wiley-VCH Verlag GmbH & Co. KGaA, Weinheim

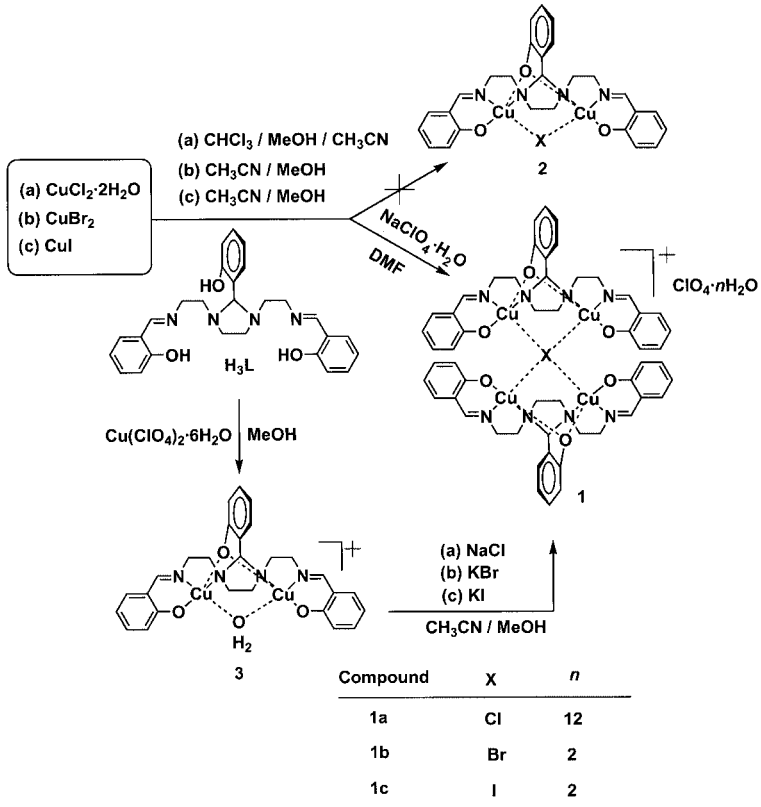


Scheme 2.

ing made to rationalize the role of the $Cu_4$ cluster based catalytic site, which has never before been found in biology, for the reduction of $N_2O$ to $N_2$.[10] The ligand $H_3L$ [2-(2′-hydroxyphenyl)-1,3-bis[4-(2-hydroxyphenyl)-3-azabut-3-enyl]-1,3-imidazolidine] has recently been shown to undergo the cation (sodium)-centred assembly of two $[Cu_2L]^+$ units upon octahedral coordination of $Na^+$ to the terminal phenolate oxygen atoms of two ligands[11] (Figure 1, left).

Here, we report the preferential formation of a rectangular {$Cu^{II}_4(\mu_4\text{-Cl})$} core in **1a**, where two $Cu_2$ units assemble around the meridian of the spherical chloride anion (Figure 1, right). The centrosymmetric geometry reduces the ligand's steric crowding. The anion (chloride)-centred assembly of two $[Cu_2L]^+$ units is responsible for its entrapment in the final complex and coordination in a $\mu_4$ mode (**1**) instead of bridging (**2**) or terminal monodentate (**6** in Scheme 3) coordination in dinuclear complex formation (Scheme 2).

## Results and Discussion

### Syntheses and Spectroscopic Characterisation

The μ-bis(tetradentate) ligand $H_3L$ [2-(2′-hydroxyphenyl)-1,3-bis[4-(2-hydroxyphenyl)-3-azabut-3-enyl]-1,3-imidazolidine] was prepared according to a literature procedure,[12] and a general procedure was followed for the synthesis of complexes **1a**–**c**. The reaction of $H_3L$ in a $CH_2Cl_2$/MeOH (1:1) solvent mixture with an $CH_3CN$/MeOH (1:1) solution of $CuCl_2·2H_2O$ in air followed by addition of $N(C_2H_5)_3$ (1:2:3 molar ratio) at room temperature afforded a green precipitate of $[Cu_4(\mu_4\text{-Cl})L_2]Cl·2H_2O$. Addition of a saturated solution of $NaClO_4·H_2O$ in MeOH to the above precipitate in dmf produced a green solution, which yielded green crystalline **1a** upon slow evaporation in air for six days. The elemental analysis and solution electrical conductivity data in dmf are consistent with the formula $[Cu_4(\mu_4\text{-Cl})L_2]ClO_4·12H_2O$ (**1a**); the yield was found to be 80%. Complexes $[Cu_4(\mu_4\text{-Br})L_2]ClO_4·2H_2O$ (**1b**) and $[Cu_4(\mu_4\text{-I})L_2]ClO_4·2H_2O$ (**1c**) were synthesised in a similar manner but with $CuBr_2$ and CuI, respectively, in $CH_3CN$/MeOH (1:1). During the synthesis of **1c** the light-yellow colour of the reaction mixture changed to green after 10 min.

All the compounds are insoluble in water and separate immediately from the reaction mixture. Elemental analysis, metal estimation, solution electrical conductivity and FT-IR and UV/Vis studies confirmed the formation of **1a**–**c**. Based on tetranuclear formulations, the molar conductivity values ($\Lambda_M$) in dmf are 90, 95 and 92 $\Omega^{-1}cm^2mol^{-1}$ (28 °C) for **1a**, **1b** and **1c**, respectively. These values correspond to the 1:1 electrolyte behaviours of **1a**–**c** in dmf and indicate the stability of the $Cu_4$ clusters in solution.[13] In the strong donor solvent dmf solvolysis of the clusters to $[Cu_2(dmf)_2L]X$ (X = Cl, Br and I) is not observed. The sharp peaks in the IR spectra of complexes **1a**–**c** at 1633, 1636 and 1632 $cm^{-1}$, respectively, are characteristic of the C=N functionality of the ligand and the broad/medium bands at

 © 2007 Wiley-VCH Verlag GmbH & Co. KGaA, Weinheim 

3388, 3427 and 3392 $cm^{-1}$, respectively, are observed for $\nu(OH)_{H_2O}$ of the lattice water molecules. Compounds **1a–c** show broad electronic absorption bands at 660 ($\varepsilon$ = 440), 620 ($\varepsilon$ = 510) and 635 nm ($\varepsilon$ = 745 $M^{-1}cm^{-1}$), respectively, for the d–d transitions. In dmf solution the $L \rightarrow Cu^{II}$ charge-transfer (CT) transitions are observed around 377 ($\varepsilon$ = 7810, 15425 and 16305 $M^{-1}cm^{-1}$). The intra-ligand CT transitions are seen around 280 nm ($\varepsilon$ = 20150, 21800 and 22425 $M^{-1}cm^{-1}$). Similarly, peaks at 1627 and 3388 $cm^{-1}$ in the IR spectrum of complex **3** are characteristic of the C=N functionality of the ligand and the $\nu(OH)_{H_2O}$ stretch of the water molecules. Compound **3** shows a broad electronic absorption band at 640 nm ($\varepsilon$ = 440 $M^{-1}cm^{-1}$) for the d–d transition and bands at 402 ($\varepsilon$ = 2770 $M^{-1}cm^{-1}$) and 273 nm ($\varepsilon$ = 22041 $M^{-1}cm^{-1}$) are observed for the charge-transfer transitions.

The nature of the final reaction product is greatly influenced by the ligand, solvent system and sequence of addition of the reactants. For example, under similar reaction conditions $H_3L$ and a substituted analogue of $H_3L$ ($H_3$mhbai in ref.[14])[15] react differently with $NaN_3$ to give the cation- and anion-centred tetranuclear copper complexes $[NaCu_4L_2(N_3)_2]ClO_4 \cdot H_2O$[11] and $[Cu_4L_2(N_3)]Cl \cdot 16H_2O$,[15] respectively. Following several synthetic trials with $NaN_3$, we failed to obtain same products ($\mu_2$-$N_3^-$ or $\mu_4$-$N_3^-$) for either of these two ligands in varying solvent systems and reaction conditions. Thus, the ligands play the deciding role for final product formation and act independently of the nature of the solvent and sequence of addition of reagents. It is an inherent property of the ligand systems that they show different self-assembly behaviours for cluster formation. Likewise, for ligand $H_3L$ reported in this paper, the dinuclear complex **2** was not obtained (Scheme 3) when a methanolic solution of the ligand was added to $CuCl_2 \cdot 2H_2O$ in MeOH/$H_2O$ (2:1) in a 1:2 molar ratio.

Complexes **1a–c** can also be obtained by an indirect route via the exogenous aqua-bridged dinuclear complex $[Cu_2L(H_2O)]ClO_4 \cdot 2H_2O$ (**3**). Complex **3** is obtained from the reaction of $Cu(ClO_4)_2 \cdot 6H_2O$ with $H_3L$ in the presence of $Et_3N$ in MeOH in a 2:1:3 molar ratio (Scheme 3). Complex **3** reacts further with NaCl, KBr or KI in a 2:1 molar ratio to give complexes **1a–c** (Scheme 2). In a two-step reaction, complex **3** initially reacts with $N_3^-$ to form the dicopper species **4** in solution. The basal-apical mode of azide coordination and face-to-face orientation of two such species provides a cavity to accommodate a $Na^+$ ion and give tetrameric complex **5**.[11] In this work, we have shown that the larger halide anions prefer metal coordination in an apical-apical mode to produce **1a–c**. The $\mu_4$-X centred $Cu_4$ complexes **1a–c**, which have four Cu–X apical bonds, also react with $NaN_3$ in MeOH/$CH_3CN$ (1:1) to produce **5**, which contains two apical and two basal Cu–N(azide) bonds. These reactions also demonstrate the successful replacement of halide groups with weaker apical-apical coordination by strong azide coordination in a basal-apical mode. So far, we have been unable to synthesise complexes **6** and **7** by varying the solvents and reaction conditions (Scheme 3).

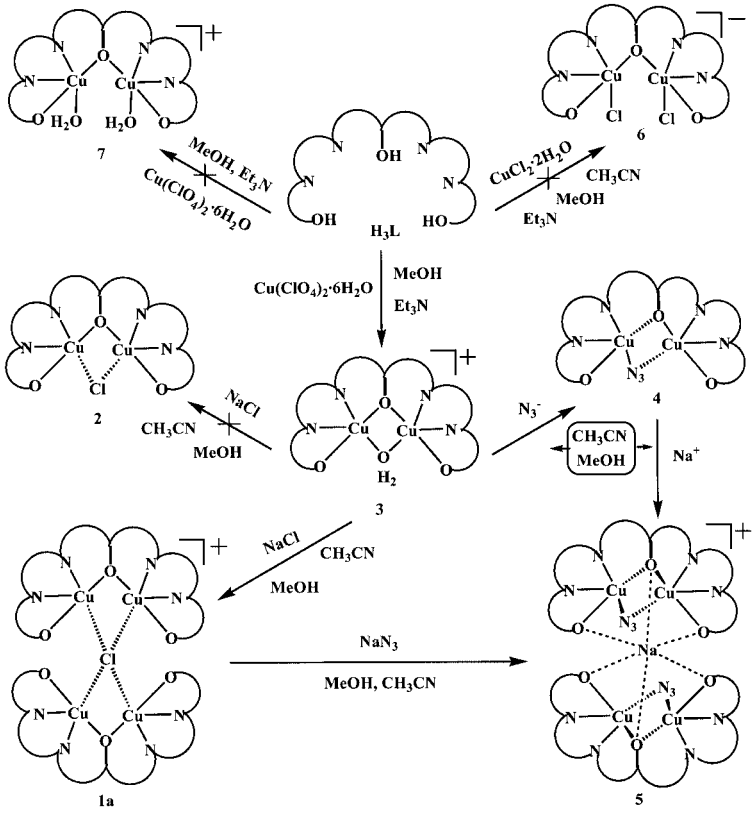


Scheme 3.

 © 2007 Wiley-VCH Verlag GmbH & Co. KGaA, Weinheim 

### X-ray Structure of $[Cu_4(\mu_4\text{-}Cl)L_2]ClO_4\cdot 12H_2O$ (1a)

Single crystals of **1a** suitable for X-ray diffraction were obtained by slow evaporation of a dmf solution of the compound. It consists of a tetracopper cluster cation $[Cu_4(\mu_4\text{-}Cl)L_2]^+$ along with a disordered $ClO_4^-$ anion and twelve water molecules. An ORTEP view of $[Cu_4(\mu_4\text{-}Cl)L_2]^+$ is shown in Figure 2, and selected bond lengths and bond angles are listed in Table 1.

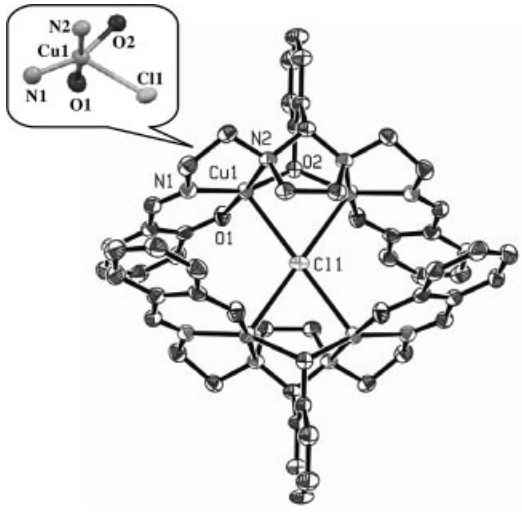


Figure 2. ORTEP representation of $[Cu_4(\mu_4\text{-}Cl)L_2]^+$ (**1a**) with ellipsoids at the 40% probability level. Hydrogen atoms have been omitted for clarity. Only independent non-carbon atoms are labelled.

Table 1. Selected bond lengths [Å] and bond angles [°] in complex **1a**.

| Bond lengths [Å] | |
|---|---|
| Cu1–O1 | 1.906(3) |
| Cu1–N1 | 1.935(3) |
| Cu1–N2 | 2.070(3) |
| Cu1–O2 | 1.971(2) |
| Cu1–Cl1 | 2.776(5) |
| **Bond angles [°]** | |
| O1–Cu1–N1 | 93.50(14) |
| N1–Cu1–N2 | 83.94(14) |
| N2–Cu1–O2 | 91.16(13) |
| O1–Cu1–O2 | 89.92(13) |
| N1–Cu1–O2 | 157.70(14) |
| O1–Cu1–N2 | 175.66(12) |
| Cu1–O2–Cu1 | 110.63(17) |
| Cu1–Cl1–Cu1 | 71.44(13) |

A rectangular arrangement of four crystallographically equivalent $Cu^{II}$ ions as two pairs of metal ions is seen in $[Cu_4(\mu_4\text{-}Cl)L_2]^+$. The cationic tetramer has crystallographic 2/*m* symmetry, with the central Cl atom at the 2/*m* centre. The metal ions within each $[Cu_2]$ pair are bridged and chelated by one $\mu\text{-}L^{3-}$ ligand. These dinuclear units are in turn linked exclusively by one unsupported $Cl^-$ ligand in a $\mu_4$-bridging mode. The polydentate ligand $L^{3-}$ within each dinuclear unit bridges the metal ions through one imidazolidine and one phenoxide moiety while further coordinating the copper ions through two terminal phenoxide and imine groups. The four copper atoms are placed at the vertices of a regular rectangle, with the chloride ligand lying at the centre of the rectangle. Each $[Cu_2]$ pair, spanning the short axis of the $[Cu_4Cl]$ rectangle is also bridged by one end of the $\mu_4\text{-}Cl^-$ ligand. The $Cl^-$ ligand fills the fifth apical coordination site of each copper. Within the $[Cu_2L]^+$ units, the bridging $Cl^-$ ions show an apical-apical coordination mode, which is different from the apical-basal binding mode of the azide ions in $[NaCu_4L_2(N_3)_2]ClO_4$.[11] At the same time, this mode of bridging also forces the imidazolidinyl phenolate oxygens to exhibit a complementary basal-apical coordination. This apical-basal and basal-apical combination is responsible for the formation of an interdimer cavity that nicely accommodates $Na^+$ ion in **5**. Contrary to this, the apical-apical halide bridging within $[Cu_2L]^+$ in **1a**–**c** retains the basal-basal coordination mode of the imidazolidinyl phenolate oxygens (Scheme 4). The four $Cu^{II}$ ions in **1a** are pentacoordinate and feature a distorted square-pyramidal $N_2O_2Cl$ environment ($\tau$ = 0.30).[16] The polyhedra around copper share the chlorine atom Cl(1) as a common apical vertex and the ligand phenolate oxygen atoms O(2) and O(2)$^{\#}$ as the shared basal donors. The sum of the angles around the oxygen atom of the central phenolate bridge is 330.61° in all basal coordinations and shows a pyramidal distortion arising from a folding of the ligand around the imidazolidine backbone, while the chlorine

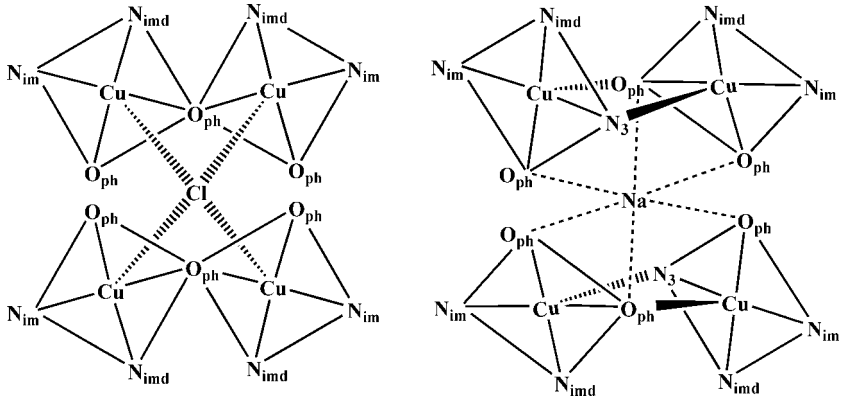


Scheme 4.

 © 2007 Wiley-VCH Verlag GmbH & Co. KGaA, Weinheim 

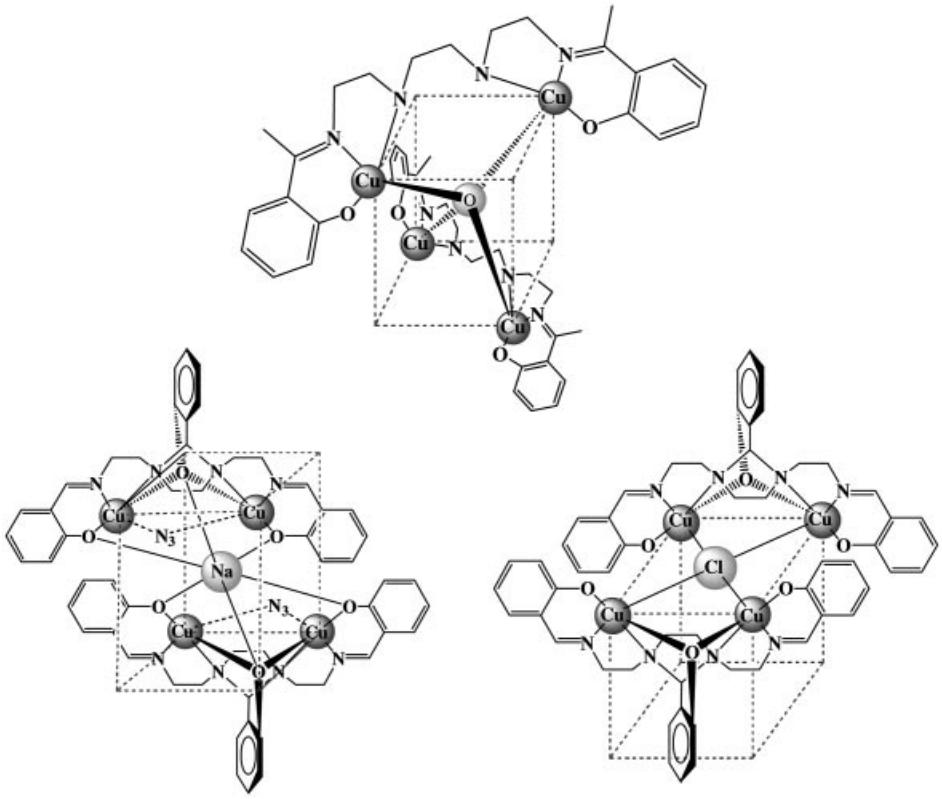


Figure 3. Three single atom nucleating self-assemblies with different polyhedral geometries: a tetrahedral $\mu_4$-$O^{2-}$-directed self-assembly (top, ref.[9]), an octahedral $Na^+$-templated self-assembly (bottom left, ref.[11]) and a planar $\mu_4$-$Cl^-$-templated self-assembly (bottom right, **1a**).

atom for apical coordination to $Cu^{II}$ presents a perfect planar geometry (sum of angles is 360°). The angle between the basal planes of the pyramids is 139.78°, thereby highlighting the non-coplanarity induced by the folded ligand system.

Each copper centre lies 0.220 Å above the mean $N_2O_2$ basal plane and is shifted towards $Cl^-$. To the best of our knowledge, this is the first $\mu_4$-chloride copper cluster of any multidentate ligand. The conformation of the $\mu_4$-$Cl^-$ moiety in **1a** is different from the two previously reported cases with respect to its symmetry (Scheme 1).[2b,7] The Cu···Cu distances within the [$Cu_4$] rectangle of **1a** are 3.241(8) Å within each [$Cu_2$] pair and 4.507(6) Å when spanned by only the $\mu_4$-$Cl^-$ ligand. The first distance is longer and the second distance is shorter than the values (3.040 and 6.009 Å, respectively) for a $Na^+$-templated tetramer of the same ligand with a rectangular disposition of the $Cu^{II}$ ions.[11] These differences are due to basal-apical coordination of the imidazolidinyl phenolic oxygen in the case of [$NaCu_4$] compared to basal-basal coordination in the present case. In the case of the [$NaCu_4$][11] cluster, the azide apical-basal coordinations provide space for $Na^+$, which controls the positions of the phenolate donors, whereas in the [$Cu_4Cl$] cluster the chloride ion with four apical bonds controls the $Cu^{II}$ positions in the cluster (Figure 3).

The Cu(1)–Cl(1) bond is inclined towards O(2), as indicated by the O(2)–Cu(1)–Cl(1) angle of 84.01° (inset of Figure 2). The C=N and C–O distances of the salicylaldimine fragments are 1.280(5) and 1.316(5) Å, respectively, consistent with the coordination of the deprotonated form of the salicylaldimine functionalities.[11] The single chloride anion binds all four Cu ions sitting at the corners of the rectangle with an average Cu···Cl distance of 2.775(5) Å, which is slightly longer than complexes containing tetrahedral and pyramidal $\mu_4$-Cl.[2b,2f,7] The C–C distance within the imid-

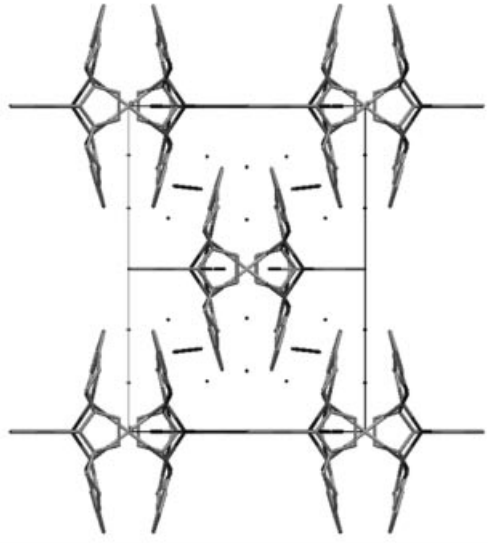

Figure 4. Packing diagram of **1a** along the crystallographic *c* axis.

 © 2007 Wiley-VCH Verlag GmbH & Co. KGaA, Weinheim 

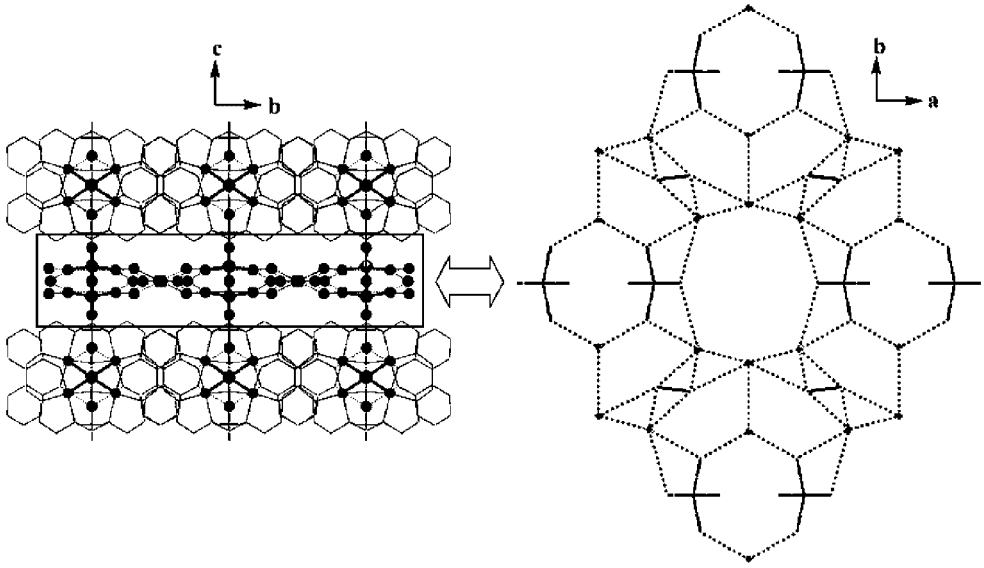


Figure 5. Packing diagram of **1a** along the crystallographic *a* axis (left) and the water–anion net inside the channel viewed along the crystallographic *c* axis (right).

azolidine ring is longer [1.527(8) Å] than the distance in the ethylenediamine backbone [1.46(2) Å].[9] The Cu–$N_{imine}$ [1.935(3) Å] and Cu–$N_{amine}$ [2.070(3) Å] distances are clearly different. The terminal Cu–$O_{phenolate}$ distance [1.906(3) Å] is shorter than the distance involving the central bridging phenolate arm [1.971(2) Å], and the intradimer Cu–Cl–Cu angle [71.44(2)°] is much smaller than the Cu–O–Cu angle [88.2(3)°] in a previously reported $Cu_2$ complex of the same ligand.[17] The $Cl^-$ ligand serves as a template and assembles two $Cu_2$ units in an inverted configuration, which reduces the steric crowding of the central imidazolidinyl phenolate parts of the ligands. Convex molecules of **1a** pack nicely along the crystallographic *c* axis (Figure 4).

The crystal packing diagram along the *a* axis clearly shows the formation of a novel water-anion net within the intercluster space (Figure 5). This net forms hydrogen bonds with the terminal phenolate oxygens (O1) that are held tight in the intercluster space. The presence of these water molecules is crucial for cluster stability and crystal growth.

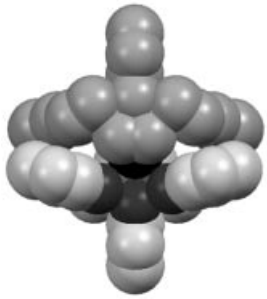

Figure 6. Two inverted crown $[Cu_2L]^+$ motifs sandwiching the chloride anion in a space filling model (ligand carbon atoms are shown in light grey and grey; black: oxygen; deep black: chlorine).

A space filling view of **1a** shows that two $Cu_2$ units sit over each other in an inverted fashion and the spherical chloride anion is trapped inside the complex (Figure 6).

### Magnetochemistry of $[Cu^{II}_4(\mu_4\text{-}Cl)L_2]ClO_4\cdot 12H_2O$ (1a)

To determine the effect of a planar $\mu_4$-Cl-bridging mode on the magnetic exchange within the cluster, bulk magnetisation measurements were carried out under a constant magnetic field of 5000 G between 1.8 and 300 K. The magnetic susceptibility data, corrected for the diamagnetic contribution of the complex and the sample holder, and TIP (temperature-independent paramagnetism) of 0.0016 $cm^3$ $mol^{-1}$, are shown in Figure 7.

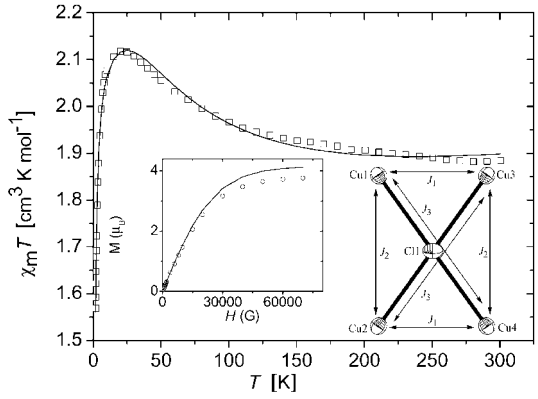


Figure 7. Plot of $\chi_m T$ vs. $T$ in a magnetic field of 5000 G. The solid lines represent the best fit. The left inset shows the field-dependence of the magnetisation at $T$ = 1.8 K. The solid line denotes the Brillouin curve calculated from two independent $S$ = 1 spin system. The right inset shows the $Cu_4Cl$ topology of the complex.

 © 2007 Wiley-VCH Verlag GmbH & Co. KGaA, Weinheim 

At 300 K, the $\chi_m T$ value of 1.88 $cm^3 K mol^{-1}$ is slightly higher than the expected value for four uncoupled copper(II) ions. $\chi_m T$ increases on lowering the temperature, reaching a maximum of 2.12 $cm^3 K mol^{-1}$ at 20 K and then decreasing rapidly. The initial rise in $\chi_m T$ on cooling implies the existence of dominant ferromagnetic interactions within the cluster. Based on the structural parameters, there are three possible magnetic exchange pathways, as illustrated in the inset of Figure 7. One is through the phenoxide bridge and the Cu–*N*–C–*N*–Cu route ($J_1$), in which the main magnetic contribution would arise from the former because of the longer pathway of the latter; the other two occur via the central Cl atom ($J_2$ and $J_3$). The magnetic data were properly fitted using the isotropic exchange Hamiltonian $H = -2J_1(S_1 \cdot S_3 + S_2 \cdot S_4) - 2J_2(S_1 \cdot S_2 + S_3 \cdot S_4) - 2J_3(S_1 \cdot S_4 + S_2 \cdot S_3)$.[18] A best fit gives magnetic parameters of $g = 2.08$, $J_1 = 33.4$, $J_2 = -0.25$ and $J_3 = -0.25$ $cm^{-1}$. These magnetic results are reliable as the bond length between Cu and the apical Cl atom is significantly longer (2.775 Å) than the $Cu–O_{phenoxide}$ distance (1.980 Å). It is reasonable to suppose that the magnetic exchange coupling for $J_1$ is strong whereas $J_2$ and $J_3$ are very weak. The ferromagnetic nature through the $J_1$ pathway can arise from the counter complementary effect between the phenoxide ligand and an NCN link from the Schiff base.[19] Accurate values of $J_2$ and $J_3$ could not be determined, although overall weak antiferromagnetic interactions through pathways $J_2$ and $J_3$ are still evident. The $\mu_4$-Cl bridge mediates the magnetic coupling ineffectively because of the longer metal–chloride distance. This can be compared with the $\mu_4$-O unit, which can transmit a stronger antiferromagnetic interaction.[9] The magnetic strength through the $J_1$ pathway is stronger than in the [$NaCu_4$] cluster ($J = 5.43$ $cm^{-1}$)[11] and the tetranuclear carbonate complex ($2J = 39.44$ $cm^{-1}$).[20] From a magnetostructural point of view the magnetic orbital $d_{x^2-y^2}$ lies in the basal plane.[21] The pronounced exchange coupling ($J_1$) through the phenoxide route, compared with the [$NaCu_4$], can be understood by taking into account that the phenoxide ligand bridges two adjacent Cu centres in basal positions. This leads to effective overlap of the magnetic orbitals residing on the two Cu ions. In contrast, the apical-basal bridging mode of the phenoxide that operates in the [$NaCu_4$] cluster gives rise to a weaker overlap.[11] The field dependence of the magnetisation is plotted in the inset of Figure 7. The experimental data lie below the theoretical values derived from two uncoupled $S = 1$ spin systems. This result indicates that there are weak antiferromagnetic interactions between two pairs with an $S = 1$ ground state created by the intradimer ferromagnetic couplings at 1.8 K, which is consistent with the $\chi_m T$ vs. $T$ plot.

### Electrochemistry of $[Cu^{II}_4(\mu_4\text{-}Cl)L_2]ClO_4 \cdot 12H_2O$ (1a)

The electron-transfer behaviour of $[Cu^{II}_4(\mu_4\text{-}Cl)L_2]ClO_4 \cdot 12H_2O$ (**1a**) in dmf was studied by cyclic voltammetry at room temperature. A glassy-carbon working electrode with tetrabutylammonium perchlorate (TBAP) as supporting electrolyte at 298 K was used. The cyclic voltammogram was recorded in the potential range between –1.0 and +1.0 V vs. an Ag/AgCl reference electrode at a scan rate of 100 mV $s^{-1}$. Complexes **1b** and **1c** do not display any characteristic cyclic voltammetric response within the above-mentioned potential window, and only the $\mu_4$-chlorido-bridged complex **1a** exhibits a quasi-reversible ($i_{pc}/i_{pa} = 0.8$) response at $E_{1/2} = 0.515$ V ($\Delta Ep = 156$ mV; Figure 8). The formal potential value for the copper(II) to copper(III) oxidation is similar to other complexes containing phenoxido donor ligands.[22] No characteristic voltammetric wave was observed on the negative side (vs. Ag/AgCl) of the potential window. The observed quasi-reversible peak is assigned to a one-electron transfer process [Equation (1)] for a metal-centred oxidation. The present electrochemical redox reaction in dmf is consistent with a quasi-reversible one-electron transfer process.[23]

$$[Cu^{III}Cu^{II}_3(\mu_4\text{-}Cl)L_2]^{2+}\ (\mathbf{1a^{2+}}) + e^- \leftrightarrow [Cu^{II}_4(\mu_4\text{-}Cl)L_2]^{+}\ (\mathbf{1a^{+}}) \quad (1)$$

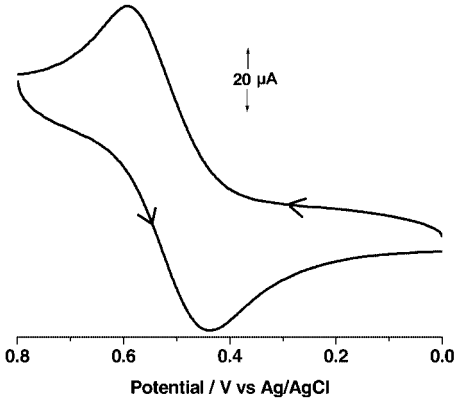


Figure 8. Cyclic voltammogram (scan rate 100 mV $s^{-1}$) of $10^{-3}$ M solutions of **1a** in dimethylformamide at a glassy-carbon electrode ($T = 298$ K).

The quasi-reversible nature of the voltammogram indicates the formation of a copper(III) centre within the cluster that is still coordinated to the $\mu_4$-$Cl^-$. The absence of any voltammetric response in the analogous bromido- and iodido-bridged complexes **1b** and **1c** indicates that the trivalent state is only stable in solution when coordinated to chloride. At 298 K the oxidized species is only stable on the voltammetric timescale.

## Concluding Remarks

We have shown that entrapment of a chloride ion by four copper ions is possible by isolating a {$Cu_4(\mu_4$-Cl)} core within a tetranuclear cluster. Two [$Cu_2$] units can be assembled around the spherical chloride ion, which serves as an anion template to give a rectangular planar geometry. The new supramolecular chlorido complex is formed in a discrete centrosymmetrical structure. The in-plane single atom nucleating coordination mode of $Cl^-$ is the first example of its kind and exclusively binds four copper(II) centres without any auxiliary bridging units. The templating role of

 © 2007 Wiley-VCH Verlag GmbH & Co. KGaA, Weinheim 

$Cl^-$ has been demonstrated with the help of the reaction of $[Cu_2L(H_2O)]ClO_4{\cdot}2H_2O$ (**3**) with NaCl. In **1a**, a weak antiferromagnetic interaction is observed between two [$Cu^{II}_2$] units with an $S = 1$ ground state that is created by an intradimer ferromagnetic coupling mediated by the basal-basal bridging mode of the phenoxido groups.

## Experimental Section

**Materials and Physical Measurements:** Triethylenetetramine was obtained from S.D. Fine Chem. (India) and 2-hydroxybenzaldehyde from SRL (India). Cupric perchlorate hexahydrate was prepared by treating copper(II) carbonate with $HClO_4$ in a 1:1 ratio and crystallised after concentration in a water bath. All other chemicals and solvents were reagent-grade materials and were used as received without further purification. The elemental analyses (C, H, N) were performed with a Perkin–Elmer model 240 C elemental analyzer. IR spectra were recorded with a Perkin–Elmer 883 spectrophotometer. The solution electrical conductivity and electronic spectra were obtained with a Unitech type U131C digital conductivity meter with a solute concentration of about $10^{-3}$ M and a Shimadzu UV 3100 UV/Vis/NIR spectrophotometer, respectively. The room-temperature magnetic susceptibilities in the solid state were measured using a home built Gouy balance fitted with a Polytronic d.c. power supply. The experimental magnetic susceptibilities were corrected for the diamagnetic response using Pascal's constants. Magnetic measurements were carried out on polycrystalline samples (ca. 30 mg) using a Quantum Design MPMS-7 SQUID magnetometer operating at a constant magnetic field of 5000 G between 1.8 and 300 K. The experimental magnetic moment was corrected for the diamagnetic contribution from the sample holder and the diamagnetic response from the sample, which was evaluated from Pascal's constants. Electrochemical measurements were made using a PAR model 173 potentiostat/galvanostat, 175 universal programmer, 178 electrometer, and 377-cell system. A glassy carbon working electrode, a platinum-wire auxiliary electrode, and an Ag/AgCl reference electrode were used in a three-electrode configuration. A digital series 2000 Omni Graphic recorder was used to trace the voltammograms. Electrochemical measurements were performed under nitrogen in dry dmf.

All experimental procedures were performed in air at room temperature. The ligand $H_3L$ [2-(2′-hydroxyphenyl)-1,3-bis[4-(2-hydroxyphenyl)-3-azabut-3-enyl]-1,3-imidazolidine) was prepared according to a literature procedure.[12]

**Synthesis of Complexes:** Two methods were followed for the synthesis and isolation of tetranuclear complexes **1a**–**c**. Method **1** is a direct method where the complexes were synthesised from the ligand and the corresponding copper salts. Method **2** is an indirect synthetic pathway from complex **3**. Details are given below for the representative cases.

**$[Cu^{II}_2(\mu\text{-}H_2O)L]{\cdot}ClO_4{\cdot}2H_2O$ (3):** A methanolic solution of triethylamine (0.55 mL, 4 mmol) was added to a solution of the ligand (0.50 g, 1.09 mmol) in 15 mL of dichloromethane followed by a methanolic solution of $Cu(ClO_4)_2{\cdot}6H_2O$ (0.80 g, 2.18 mmol) and the mixture was stirred at ambient temperature for one hour. The solvent was then evaporated in air, and the deep green precipitate obtained was filtered and washed with water, ethanol and finally dried in vacuo over $P_4O_{10}$. Yield: 0.60 g (75%). $C_{27}H_{33}ClCu_2N_4O_{10}$ (736.12): calcd. C 44.05, H 4.51, Cu 17.26, N 7.61; found C 43.82, H 4.94, Cu 16.90, N 7.37. IR (KBr disk): $\tilde{\nu}$ = 3388 $cm^{-1}$ br, 2936 m, 1627 s, 1595 s, 1537 s, 1447 s, 1312 s, 1094 s, 914 s, 722 s. Molar conductance (MeCN solution): $\Lambda_M$ = 130 $\Omega^{-1}cm^2mol^{-1}$. UV/Vis (dmf): $\lambda_{max}$ ($\varepsilon$) = 640 nm (290 $M^{-1}cm^{-1}$), 402 (2770), 273 (22041).

**$[Cu_4(\mu_4\text{-}Cl)L_2]ClO_4{\cdot}12H_2O$ (1a)**

**Method 1:** A solution of $H_3L$ (0.5 g, 1.09 mmol) in $CH_2Cl_2$/MeOH (1:1) (15 mL) was added to a solution of $CuCl_2{\cdot}2H_2O$ (0.371 g, 2.18 mmol) in $CH_3CN$/MeOH (1:1; 20 mL) then $Et_3N$ (0.5 mL, 3.58 mmol) was added dropwise. The mixture was stirred for 1 h and $[Cu_4(\mu_4\text{-}Cl)L_2]Cl$ precipitated as a green solid in about 80% yield. This solid was isolated, washed with cold methanol, and dried under vacuum over $P_4O_{10}$. It was then dissolved in dmf and a stoichiometric amount of $NaClO_4$ was added. Single crystals suitable for X-ray analysis were obtained from the above mixture after 6 d. $C_{54}H_{78}Cl_2Cu_4N_8O_{22}$ (1516.3): calcd. C 42.77, H 5.18, Cu 16.76, N 7.39; found C 42.48, H 5.46, Cu 16.42, N 6.98. Molar conductance (dmf): $\Lambda_M$ = 90 $\Omega^{-1}cm^2mol^{-1}$. UV/Vis spectrum (dmf): $\lambda_{max}$ ($\varepsilon$) = 660 nm (440 $M^{-1}cm^{-1}$), 377 (7810), 280 (20150). Selected IR bands (KBr) $\tilde{\nu}$ = 3388 $cm^{-1}$ vs, 1633 vs, 1445 m, 1304 m, 1120 w, 1091 m, 770 w, 667 m.

***Caution!*** *Perchlorates are potentially explosive and should be handled only in very small quantities.*

**Method 2:** A methanolic solution of NaCl (0.016 g, 0.27 mmol) was added dropwise to an acetonitrile solution (50 mL) of complex **3** (0.4 g, 0.54 mmol) and stirring was continued for 1 h to give a greenish crystalline product. This solid was isolated, washed with cold methanol/water and dried under vacuum over $P_4O_{10}$. Analytical and spectroscopic data indicated the formation of complex **1a**.

**$[Cu_4(\mu_4\text{-}Br)L_2]ClO_4{\cdot}2H_2O$ (1b)**

**Method 1:** A solution of $H_3L$ (0.5 g, 1.09 mmol) in methanol (15 mL) was added to an acetonitrile solution (30 mL) of $CuBr_2$ (0.486 g, 2.18 mmol) and then $Et_3N$ (0.5 mL, 3.58 mmol) was added dropwise. The mixture was stirred for 1 h, whereupon the complex precipitated as a green solid (ca. 74% yield). This solid was isolated, washed with cold methanol, and dried under vacuum over $P_4O_{10}$. It was then dissolved in dmf and a stoichiometric amount of $NaClO_4$ was added. After one week the resulting crystals of **1b** were isolated and dried under vacuum over $P_4O_{10}$. $C_{54}H_{58}BrClCu_4N_8O_{12}$ (1380.6): calcd. C 46.97, H 4.23, Cu 16.76, N 8.11; found C 46.88, H 4.44, Cu 16.62, N 7.86. Molar conductance (dmf): $\Lambda_M$ = 95 $\Omega^{-1}cm^2mol^{-1}$. UV/Vis ($CH_3CN$): $\lambda_{max}$ ($\varepsilon$) = 620 nm (510 $M^{-1}cm^{-1}$), 377 (15426), 280 (21800). Selected IR data (KBr): $\tilde{\nu}$ = 3427 $cm^{-1}$ vs, 1636 vs, 1458 s, 1307 m, 1130 m, 1088 s, 762 s.

**Method 2:** A methanolic solution of KBr (0.032 g, 0.27 mmol), was added dropwise to an acetonitrile solution (30 mL) of complex **3** (0.4 g, 0.54 mmol) and stirring was continued for 1 h to give a greenish crystalline product. This solid was isolated, washed with cold methanol/water and dried under vacuum over $P_4O_{10}$. All analytical and spectroscopic data indicated formation of complex **1b**. All attempts to obtain crystals of **1b** suitable for an X-ray structure determination were unsuccessful.

**$[Cu_4(\mu_4\text{-}I)L_2]ClO_4{\cdot}2H_2O$ (1c)**

**Method 1:** A solution of $H_3L$ (0.5 g, 1.09 mmol) in methanol (15 mL) was added to an acetonitrile solution (50 mL) of CuI (0.415 g, 2.18 mmol) and then $Et_3N$ (0.5 mL, 3.58 mmol) was added dropwise. The mixture was stirred for 1 h, and the complex precipitated as a green solid (ca. 69% yield). This solid was isolated, washed with cold methanol, and dried under vacuum over $P_4O_{10}$. It was then dissolved in dmf and a stoichiometric amount of $NaClO_4$ was added. After one week crystals of **1c** were isolated and dried under vacuum over $P_4O_{10}$. $C_{54}H_{58}ClCu_4IN_8O_{12}$ (1427.6):

 © 2007 Wiley-VCH Verlag GmbH & Co. KGaA, Weinheim 

calcd. C 45.43, H 4.09, Cu 17.80, N 7.84; found C 45.28, H 4.34, Cu 17.70, N 7.52. Molar conductance (dmf): $\Lambda_M$ = 92 $\Omega^{-1}cm^2mol^{-1}$. UV/Vis ($CH_3CN$): $\lambda_{max}$ ($\varepsilon$) 635 nm (747 $M^{-1}cm^{-1}$), 377 (16305), 280 (22426). Selected IR bands (KBr): $\tilde{\nu}$ = 3392 $cm^{-1}$ vs, 1632 vs, 1536 m, 1448 s, 1311 m, 1196 m, 1090 s, 766 s.

**Method 2:** A methanolic solution of KI (0.044 g, 0.27 mmol) was added dropwise to an acetonitrile solution (50 mL) of complex **3** (0.4 g, 0.54 mmol) and stirring was continued for 2 h to give a greenish crystalline solid. This solid was isolated, washed with cold methanol/water and dried under vacuum over $P_4O_{10}$. All analytical and spectroscopic data indicated formation of complex **1c**. All attempts to obtain crystals of **1c** suitable for X-ray structure determination were unsuccessful.

**$[NaCu_4L_2(N_3)_2]ClO_4\cdot H_2O$ (5)**

**Method 1:** A methanolic solution of $Cu(ClO_4)_2\cdot 6H_2O$ (0.80 g, 2.18 mmol) was added to a dichloromethane solution (10 mL) of the ligand (0.50 g, 1.09 mmol) and then a methanolic solution of $NaN_3$ (0.07 g, 1.09 mmol) was added dropwise whilst stirring at ambient temperature in air. After 15 min, a dilute methanolic solution of $Et_3N$ (0.45 mL ,3.27 mmol) was added and the reaction mixture was stirred for 1 h more. The complex precipitated as a green solid (ca. 85% yield), which was isolated, washed with water, and dried under vacuum over $P_4O_{10}$. Single crystals suitable for X-ray analysis were obtained from MeOH/MeCN (1:1) after five days. $C_{54}H_{56}ClCu_4N_{14}NaO_{11}$ (1389.8): calcd. C 46.66, H 4.06, Cu 18.28, N 14.10; found C 46.64, H 4.25, Cu 18.50, N 13.88. Molar conductance (dmf): $\Lambda_M$ = 73 $\Omega^{-1}cm^2mol^{-1}$. UV/Vis (dmf): $\lambda_{max}$ ($\varepsilon$) = 650 nm (150 $M^{-1}cm^{-1}$), 398 (2660), 271 (16062). IR (KBr disk): $\tilde{\nu}$ = 3425 $cm^{-1}$ br, 2926 m, 2076 s, 1633 s, 1595 s, 1537 s, 1447 s, 1312 s, 1274 s, 1081 s, 747 s, 625 s.

***Caution!*** *Azide derivatives are potentially explosive and should be handled only in very small quantities.*

**Method 2:** A methanolic solution of $NaN_3$ (0.035 g, 0.54 mmol) was added dropwise to an acetonitrile solution (50 mL) of complex **3** (0.4 g, 0.54 mmol) and stirring was continued for 2 h to give a greenish crystalline product, which was isolated, washed with cold methanol/water and dried under vacuum over $P_4O_{10}$. All analytical and spectroscopic data indicated the formation of complex **5**.

**Method 3:** A methanolic solution of $NaN_3$ (0.025 g, 0.395 mmol) was added dropwise to an acetonitrile solution (50 mL) of complex **1a** (0.3 g, 0.197 mmol) and stirring was continued for 1 h to give a greenish crystalline product, which was isolated, washed with cold methanol/water and dried under vacuum over $P_4O_{10}$. All analytical and spectroscopic data indicated the formation of complex **5**.

**X-ray Crystallographic Study of $[Cu_4(\mu_4\text{-}Cl)L_2]ClO_4\cdot 12H_2O$ (1a):** Green block-shaped single crystals of $[Cu_4(\mu_4\text{-}Cl)L_2]ClO_4\cdot 12H_2O$ suitable for X-ray analysis were grown by the slow evaporation of a dmf solution of the complex. The intensity data for the complex were collected on a CAD-4 single-crystal X-ray diffractometer equipped with a graphite-monochromated Mo-$K_\alpha$ radiation source ($\lambda$ = 0.71073 Å) by the ω-scan method for a single crystal with dimensions 0.14 × 0.12 × 0.11 $mm^3$. Precise unit cell dimensions were determined by least-squares refinement of 25 strong reflections having $2\theta$ values between 1.57 and 24.97 °. Data were collected at 298 K. A total of 3127 reflections were recorded with Miller indices $h_{min}$ = 0, $h_{max}$ = 16, $k_{min}$ = 0, $k_{max}$ = 22 and $l_{min}$ = –15, $l_{max}$ = 15. In the final cycles of full-matrix least-squares refinement on $F^2$ all non-hydrogen atoms were assigned anisotropic thermal parameters and refinement converged at $R$ = 0.0473. The residual electron density was in the range +0.491 to –0.541 e $Å^{-3}$. The structure was solved with the SHELX-97 programme system[24] and refined using full-matrix least-squares with all non-hydrogen atoms treated anisotropically and hydrogens included at calculated positions as riding on their carrier atoms. H-atoms on water molecules could not be located. The $ClO_4^-$ anion and some solvent water molecules were found to be disordered. Further information concerning X-ray data collection and structure refinement of the compound is summarised in Table 2.

Table 2. Crystallographic data for compound $[Cu_4(\mu_4\text{-}Cl)L_2]ClO_4\cdot 12H_2O$ (**1a**).

| | |
|---|---|
| Molecular formula | $C_{54}H_{78}N_8O_{22}Cl_2Cu_4$ |
| Molecular weight | 1516.33 |
| Crystal system | monoclinic |
| Space group | *C*2/*m* |
| *a* [Å] | 13.643(3) |
| *b* [Å] | 18.619(8) |
| *c* [Å] | 13.139(2) |
| $\beta$ [°] | 100.25(2) |
| *V* [$Å^3$] | 3284.3(17) |
| $D_c$ [$g\,cm^{-3}$] | 1.541 |
| *Z* | 2 |
| *F*(000) | 1552 |
| $\lambda$ [Å] | 0.71073 |
| *T* [K] | 298(1) |
| Crystal size [mm] | 0.14 × 0.12 × 0.11 |
| $\mu$ [$mm^{-1}$] | 1.441 |
| *R*,[a] $R_w$[b] [$I > 2\sigma(I)$] | 0.0473, 0.1190 |
| GOF | 1.047 |
| Max., min. residual electron density [e $Å^{-3}$] | 0.491, –0.541 |

[a] $R = \Sigma(||F_o| - |F_c||)/\Sigma|F_o|$. [b] $R_w = [\Sigma w(|F_o| - |F_c|)^2/\Sigma w(F_o)^2]^{1/2}$; $w = 0.75/[\sigma^2(F_o) + 0.001F_o^2]$.

CCDC-611922 contains the supplementary crystallographic data for this paper. These data can be obtained free of charge from The Cambridge Crystallographic Data Centre via www.ccdc.cam.ac.uk/data_request/cif.

## Acknowledgments

We are grateful to the Council of Scientific and Industrial Research, New Delhi, for financial support. C. S. H. acknowledges financial support from the Korean Government (MOEHRD, Basic Research Promotion Fund) (KRF-2005-070-C00068) and H. C. K. acknowledges financial support from the Korean Government.

[1] a) A. V. Davis, K. N. Raymond, *J. Am. Chem. Soc.* **2005**, *127*, 7912; b) J. L. Atwood, L. J. Barbour, S. J. Dalgarno, M. J. Hardie, C. L. Raston, H. R. Webb, *J. Am. Chem. Soc.* **2004**, *126*, 13170; c) C. J. Pedersen, *J. Am. Chem. Soc.* **1967**, *89*, 7017.

[2] a) C. S. Campos-Fernandez, B. L. Schottel, H. T. Chifotides, J. K. Bera, J. Bacsa, J. M. Koomen, D. H. Russell, K. R. Dunbar, *J. Am. Chem. Soc.* **2005**, *127*, 12909; b) Q.-F. Zhang, R. D. Adams, D. Fenske, *J. Mol. Struct.* **2005**, *741*, 129; c) B.-J. Liaw, T. S. Lobana, Y.-W. Lin, J.-C. Wang, C. W. Liu, *Inorg. Chem.* **2005**, *44*, 9921; d) R. Vilar, *Angew. Chem. Int. Ed.* **2003**, *42*, 1460; e) P. A. Gale, *Coord. Chem. Rev.* **2003**, *240*, 191; f) W. Xu, J. J. Vittal, R. J. Puddephatt, *J. Am. Chem. Soc.* **1995**, *117*, 8362.

[3] a) B. Tomapatanaget, T. Tuntulani, J. A. Wisner, P. D. Beer, *Tetrahedron Lett.* **2004**, *45*, 663; b) J. A. Wisner, P. D. Beer, M. G. B. Drew, *Angew. Chem. Int. Ed.* **2001**, *40*, 3606; c) G. M. Hubner, J. Glaser, C. Seel, F. Vögtle, *Angew. Chem. Int. Ed.* **1999**, *38*, 383.

 © 2007 Wiley-VCH Verlag GmbH & Co. KGaA, Weinheim 

[4] a) J. W. Anthis, R. J. Staples, *Inorg. Chem.* **2002**, *41*, 278; b) C. S. Campos-Fernandez, R. Clerac, J. M. Koomen, D. H. Russell, K. R. Dunbar, *J. Am. Chem. Soc.* **2001**, *123*, 773; c) S.-T. Cheng, E. Doxiadi, R. Vilar, A. J. P. White, D. J. Williams, *J. Chem. Soc., Dalton Trans.* **2001**, 2239; d) C. S. Campos-Fernandez, R. Clerac, K. R. Dunbar, *Angew. Chem. Int. Ed.* **1999**, *38*, 3477; e) D. A. McMorran, P. J. Steel, *Angew. Chem. Int. Ed.* **1998**, *37*, 3295.
[5] J. W. Wielandt, N. L. Kilah, A. C. Willis, S. B. Wild, *Chem. Commun.* **2006**, 3679.
[6] a) Y. Lee, A. A. N. Sarjeant, K. D. Karlin, *Chem. Commun.* **2006**, 621; b) K. Tokuda, K. Okamoto, T. Konno, *Inorg. Chem.* **2000**, *39*, 333; c) A. M. Atria, A. Vega, M. Contreras, J. Valenzuela, E. Spodine, *Inorg. Chem.* **1999**, *38*, 5681; d) F. Jiang, X. Lei, Z. Huang, M. Hong, B. Kang, D. Wu, H. Liu, *J. Chem. Soc., Chem. Commun.* **1990**, 1655.
[7] V. Chandrasekhar, S. Kingsley, *Angew. Chem. Int. Ed.* **2000**, *39*, 2320.
[8] W. Xu, J. J. Vittal, R. J. Puddephatt, *J. Am. Chem. Soc.* **1993**, *115*, 6456.
[9] M. Bera, W. T. Wong, G. Aromí, J. Ribas, D. Ray, *Inorg. Chem.* **2004**, *43*, 4787.
[10] M. Prudêncio, A. S. Pereira, P. Tavares, S. Besson, I. Cabrito, K. Brown, B. Samyn, B. Devreese, J. V. Beeumen, F. Rusnak, G. Fauque, J. J. G. Moura, M. Tegoni, C. Cambillau, I. Moura, *Biochemistry* **2000**, *39*, 3899.
[11] P. K. Nanda, G. Aromí, D. Ray, *Inorg. Chem.* **2006**, *45*, 3143.
[12] E. Wong, S. Liu, T. Luegger, F. E. Hahn, C. Orvig, *Inorg. Chem.* **1995**, *34*, 93.
[13] W. J. Geary, *Coord. Chem. Rev.* **1971**, *7*, 81.
[14] M. Bera, W. T. Wong, G. Aromí, D. Ray, *Eur. J. Inorg. Chem.* **2005**, 2526.
[15] P. K. Nanda, G. Aromí, D. Ray, *Chem. Commun.* **2006**, 3181.
[16] A. W. Addison, T. N. Rao, J. Reedijk, J. van Rijn, G. C. Verschoor, *J. Chem. Soc., Dalton Trans.* **1984**, 1349.
[17] P. K. Nanda, M. Bera, G. Aromí, D. Ray, *Polyhedron* **2006**, *25*, 2791.
[18] Y. Song, C. Massera, O. Roubeau, P. Gamez, A. M. M. Lanfredi, J. Reedijk, *Inorg. Chem.* **2004**, *43*, 6842.
[19] M. Fondo, N. Ocampo, A. M. García-Deibe, M. Corbella, M. R. Bermejo, J. Sanmartín, *Dalton Trans.* **2005**, 3785.
[20] M. Fondo, A. M. García-Deibe, M. Corbella, E. Ruiz, J. Tercero, J. Sanmartín, M. R. Bermejo, *Inorg. Chem.* **2005**, *44*, 5011.
[21] M. Julve, M. Verdaguer, A. Gleizes, M. Philoche-Levisalles, O. Kahn, *Inorg. Chem.* **1984**, *23*, 3808.
[22] a) F. C. Anson, T. J. Collins, T. G. Richmond, B. D. Santarsiero, J. E. Toth, B. G. R. T. Treco, *J. Am. Chem. Soc.* **1987**, *109*, 2974; b) R. Ruiz, C. Surville-Barland, A. Aukauloo, E. Anxolabehere-Mallart, Y. Journaux, J. Cano, M. C. Muñoz, *J. Chem. Soc., Dalton Trans.* **1997**, 745.
[23] H. Shimakoshi, W. Ninomiya, Y. Hisaeda, *J. Chem. Soc., Dalton Trans.* **2001**, 1971.
[24] G. M. Sheldrick, SHELXS-97, *Program for the Refinement of Crystal Structures*, University of Göttingen, Germany, **1997**.

Received: September 28, 2006
Published Online: March 13, 2007

 © 2007 Wiley-VCH Verlag GmbH & Co. KGaA, Weinheim 

DOI: 10.1002/ejic.200600967

# Supramolecular Helical Architectures Dictated by Folded and Extended Conformations of the Amino Acid in Ternary $Cu^{II}$/Diamine/Racemic Amino Acid Complexes

**Palani Sivagnana Subramanian,*[a] Eringathodi Suresh,[a] and Luigi Casella*[b]**

**Keywords:** Helicates / Self-assembly / Copper / Chiroptical properties / Amino acids

The ternary $Cu^{II}$ complexes [Cu(D,L-phe)(bpy)]·($ClO_4$) (**1**), [Cu(D,L-phe)(phen)($H_2O$)]·$ClO_4$·$H_2O$ (**2**), and [Cu(L-phe)(bpy)($H_2O$)]·$ClO_4$·$H_2O$ (**3**) (bpy = 2,2′-bipyridine, phen = 1,10-phenanthroline) adopt helical structures in the crystal state, as determined by an X-ray structural analysis. The supramolecular helical assembly of these complexes was also investigated by single-crystal X-ray crystallography. The complexes derived from racemic amino acids (**1** and **2**) undergo spontaneous resolution in the solid state to form separate helical chains of the ternary complex that carry a single enantiomer of the amino acid. In the case of complex **1**, the two helical chains resulting from the L- and D-phe complexes bear opposite chirality, which means that the bulk crystalline sample is racemic. In contrast, the two helical chains generated by L- and D-phe complexes in **2** have the same twist and pack together in a right-handed assembly. The (*P*)/(*M*) handedness of the helical chains is dictated by the conformational chirality (λ/δ) of the chelate rings of the D/L-amino acids.

(© Wiley-VCH Verlag GmbH & Co. KGaA, 69451 Weinheim, Germany, 2007)

## Introduction

Compounds that are achiral in nature but gain chiroptical properties upon formation of supramolecular helical architectures have received a great deal of interest in recent years.[1] A number of ternary $Cu^{II}$/diamine (DA) complexes with optically active D- and L-amino acids (AA), where the latter residues can be present in folded and extended conformations, are known, and their optical properties in solution have been studied extensively.[2–4] Many of the investigations on such [$Cu^{II}$(DA)(AA)][5–9] complexes reported so far have focused mainly on structure/reactivity correlations and conformational studies; no correlation between their structural architecture and solid-state optical properties has been reported. Inorganic metallohelicates[10] are known to have interesting chiroptical properties. Intensive efforts to amplify the chiroptical properties obtained by supramolecular helicity by introducing various chiral residues or molecules such as chiral spacers,[11,12] amino acids,[13,14] and chiragens[14] into the helical skeleton have been made by a number of researchers, including Raymond et al.[15] and Albrecht et al.[16] Recent articles by Kuroda et al.,[1a,17] however, have explored the chiroptical properties exhibited by achiral complexes. The self-assembled, single-stranded supramolecular architecture of ternary [$Cu^{II}$(DA)(AA)] complexes obtained from a simple one-pot reaction that contain the amino acid in their helical skeleton inspired us to investigate their optical behavior. In the structure of the complexes [Cu(D,L-phe)(bpy)]·$ClO_4$ (**1**), [Cu(D,L-phe)(phen)($H_2O$)]·$ClO_4$·$H_2O$ (**2**), and [Cu(L-phe)(bpy)($H_2O$)]·$ClO_4$·$H_2O$ (**3**) that we describe here (bpy = 2,2′-bipyridyl; phen = 1,10-phenanthroline), the difference in the orientation of the phenylalanine side chain results in folded and extended conformations of the amino acid chelate ring that lead to noncovalently propagated supramolecular helical architectures. Folded and extended forms of ternary aromatic amino acid complexes have been reported by many researchers,[2,5,7–9] and here we show how these conformations can influence the helicity of the polymeric structure of the ternary complexes. Complexes **1** and **2**, which contain racemic phenylalanine, undergo spontaneous resolution in the crystalline state and their different supramolecular helical structures result in interesting differences in chiroptical properties in the solid state. The potential sources of optical activity in the ternary complexes **1**–**3** are discussed in terms of the Δ/Λ configuration of the $Cu^{II}$ chromophoric units, the supramolecular helicity (*P*)/(*M*), and the λ/δ conformational chirality of the nonplanar D/L-amino acid chelate rings.

[a] Analytical Science Division, Central Salt and Marine Chemicals Research Institute,
Gijubhai Badhegha Marg, Bhavnagar, 364002, Gujarat, India
Fax: +91-278-256-6970
E-mail: siva@csmcri.org
[b] Dipartimento di Chimica Generale, Università di Pavia,
Via Taramelli 12, 27100 Pavia, Italy
Fax: +39-0382-528-544
E-mail: bioinorg@unipv.it

Supporting information for this article is available on the WWW under http://www.eurjic.org or from the author.

 © 2007 Wiley-VCH Verlag GmbH & Co. KGaA, Weinheim 

## Results and Discussion

### Crystal Structures and Molecular Association

ORTEP diagrams of complexes **1**–**3** with the atom numbering schemes are given in Figure 1. A summary of the crystallographic data is given in the Experimental Section and selected bond lengths and angles for **1**–**3** are given in Table 1. The $Cu^{II}$ ions in complexes **1**–**3** possess a distorted square-pyramidal geometry where the base of the square pyramid is constituted by the pyridyl nitrogen atoms of the heterocyclic diamines and the $NH_2$ and $CO_2$ groups of the amino acids (L-, D-phe). The fifth axial ligand is different and consists of a carboxylate oxygen atom in **1** and a water molecule in **2** and **3**. The long $Cu^{II}$–carboxylate oxygen bonds [Cu1–O4 2.274(2), Cu2–O2 2.261(2) Å] formed by O2 and O4 of phenylalanine in **1** define a folded single-stranded helical, cationic polymeric chain along the *a* axis. The carboxylate oxygen atom O2 coordinated to Cu(2) possesses an additional weak short contact with one of the two bipyridyl nitrogen atoms (O2–N4 2.910 Å) that may have some significance for the helical arrangement. The helical chain is constructed from –Cu1–OCO–Cu2– bonds with $Cu^{II}$ centers sitting alternatively at distances of 5.883 and 5.864 Å. The aromatic rings of the amino acids C13 to C18 and C32 to C37 adopt only a folded conformation in complex **1** and are oriented almost parallel to the bpy rings, with a slight deviation of 2.74 and 6.99°, respectively, from the mean plane, which facilitates strong intra- and intermolecular stacking interactions (Figure 2A).

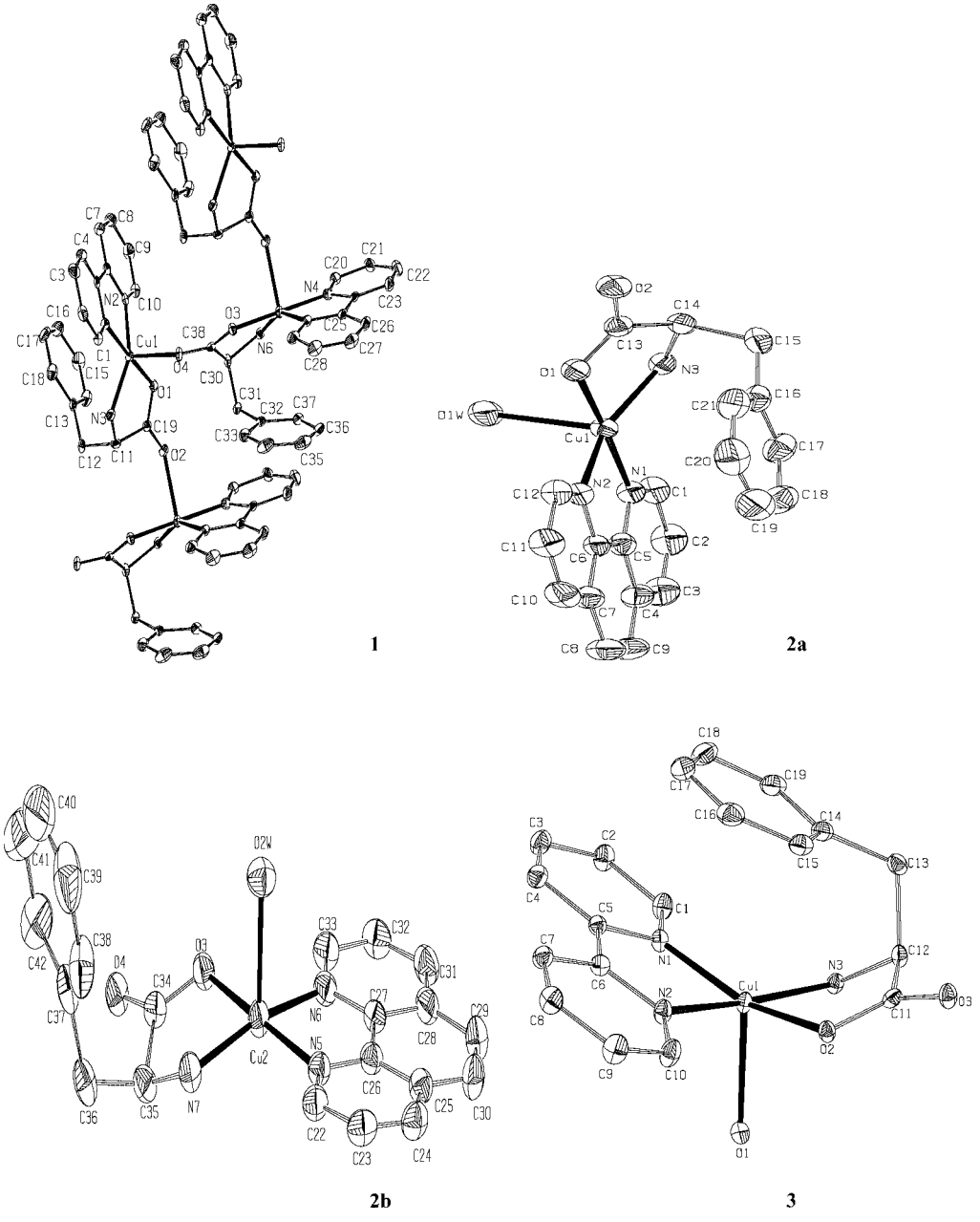


Figure 1. ORTEP diagrams of the structures of complexes **1**–**3**.

 © 2007 Wiley-VCH Verlag GmbH & Co. KGaA, Weinheim 

Table 1. Selected bond lengths [Å]and bond angles [°] for complexes **1**–**3**.[a]

| | | | |
|---|---|---|---|
| | **1** | | |
| Cu1–O1 | 1.9432 | Cu2–O3 | 1.9462 |
| Cu1–N2 | 1.9883 | Cu2–N6 | 1.9902 |
| Cu1–N3 | 1.9932 | Cu2–N4 | 1.9923 |
| Cu1–N1 | 1.9953 | Cu2–N5 | 1.9953 |
| Cu1–O4 | 2.2742 | Cu2–O2#1 | 2.2612 |
| O1–Cu1–N2 | 96.0810 | O3–Cu2–N6 | 84.479 |
| O1–Cu1–N3 | 84.419 | O3–Cu2–N4 | 177.7310 |
| N2–Cu1–N3 | 151.8610 | N6–Cu2–N4 | 97.6710 |
| O1–Cu1–N1 | 177.549 | O3–Cu2–N5 | 96.3010 |
| N2–Cu1–N1 | 81.5610 | N6–Cu2–N5 | 150.9910 |
| N3–Cu1–N1 | 97.9910 | N4–Cu2–N5 | 81.4611 |
| O1–Cu1–O4 | 94.588 | O3–Cu2–O2#1 | 94.198 |
| N2–Cu1–O4 | 107.939 | N6–Cu2–O2#1 | 103.079 |
| N3–Cu1–O4 | 100.059 | N4–Cu2–O2#1 | 86.099 |
| N1–Cu1–O4 | 85.529 | N5–Cu2–O2#1 | 105.789 |
| | **2** | | |
| Cu1–O1 | 1.952617 | Cu2–O3 | 1.936417 |
| Cu1–N3 | 2.0042 | Cu2–N5 | 1.9972 |
| Cu1–N2 | 2.0072 | Cu2–N6 | 2.0052 |
| Cu1–N1 | 2.0102 | Cu2–N4 | 2.0122 |
| Cu1–O1w | 2.2852 | Cu2–O2w | 2.3512 |
| O1–Cu1–N3 | 83.748 | O3–Cu2–N5 | 94.488 |
| O1–Cu1–N2 | 93.728 | O3–Cu2–N6 | 83.088 |
| N3–Cu1–N2 | 159.669 | N5–Cu2–N6 | 167.9510 |
| O1–Cu1–N1 | 176.058 | O3–Cu2–N4 | 176.538 |
| N3–Cu1–N1 | 100.099 | N5–Cu2–N4 | 82.439 |
| N2–Cu1–N1 | 82.358 | N6–Cu2–N4 | 99.629 |
| O1–Cu1–O1w | 86.0810 | O3–Cu2–O2w | 95.438 |
| N3–Cu1–O1w | 100.1310 | N5–Cu2–O2w | 97.0910 |
| N2–Cu1–O1w | 99.819 | N6–Cu2–O2w | 94.8911 |
| N1–Cu1–O1w | 94.1410 | N4–Cu2–O2w | 86.538 |
| | **3** | | |
| Cu1–O2 | 1.972916 | Cu1–N2 | 1.980919 |
| Cu1–N3 | 1.9992 | Cu1–N1 | 2.001919 |
| Cu1–O1 | 2.301414 | | |
| O2–Cu1–N2 | 92.068 | O2–Cu1–N3 | 82.396 |
| N2–Cu1–N3 | 171.508 | O2–Cu1–N1 | 160.797 |
| N2–Cu1–N1 | 81.087 | N3–Cu1–N1 | 102.148 |
| O2–Cu1–O1 | 90.736 | N2–Cu1–O1 | 98.247 |
| N3–Cu1–O1 | 88.307 | N1–Cu1–O1 | 107.957 |

[a] Symmetry operation for atom #1 = $x-1$, $y$, $z$.

Complex **2** differs from **1** and **3** by crystallizing with two independent molecules in the asymmetric unit; one contains the D isomer of the amino acid in the folded form only (henceforth referred to as **2a**), while the other contains only the L-amino acid in an extended form (henceforth referred to as **2b**). Similar folded and extended conformations have already been reported in analogous ternary copper(II) complexes such as [Cu(L-trypO)(phen)]$^+$,[18] [Cu(L-phe)(phen)Cl]·3$H_2O$,[8] [Cu(L-*o*-Me-phe)(phen)($H_2O$)]$ClO_4$,[5c] [Cu(L-$NH_2$Phe)(bpy)]·$NO_3$·$H_2O$,[8] and [Cu(L-tyr)(phen)($H_2O$)]·$ClO_4$·1.5$H_2O$,[8] etc. We have also recently reported a folded conformation of L-phe in the ternary complex [Cu(L-phe)(bpy)($H_2O$)]·$ClO_4$.[9] The coordination around $Cu^{II}$ remains almost the same for both **2a** and **2b**, although the phenylalanine side chain varies somewhat in its orientation. The apical coordination of the $Cu^{II}$ square pyramid is fulfilled by long bonds with water molecules [Cu1–O1w 2.285 (**2a**), Cu2–O2w 2.351 Å (**2b**)] in both cases, while the square base resembles that present in complexes **1** and **3**.

Similar to complex **1**, the phenyl ring of D-phe in **2a** is almost parallel to the phenanthroline ring (tilt angle of 5.29°) and forms a folded isomer. However, the phenyl moiety of L-phe in **2b** is inclined towards the perpendicular of the phenanthroline ring (tilt angle of 71.96°) to yield an extended isomer. The folded and extended isomers **2a** and **2b**, respectively, in Figure 2 are packed with the phenyl ring of the amino acid pair pointing in opposite directions and give effective π···π stacking interactions, as shown in Figure 2D. The offset inter- and intramolecular π···π stacking interactions between the phenyl rings of the bpy/phen ligands and the aromatic rings of the amino acids in complexes **1** and **2** are depicted in Figure 2; the stacking distances are given in the figure caption. The weak π···π interactions clearly play a significant role: the aromatic ring of the folded phenylalanine causes the intramolecular π···π stacking interaction and that of the extended form facilitates the intermolecular π···π stacking interaction, as indicated by the double-headed arrows in Figure 2. Further, the phenanthroline units of the folded and extended forms generate interhelical π···π stacking through the centroids [$Cg_3$(ext)···$Cg_2$(fold) 3.539 Å] of their aromatic rings.

### Supramolecular Helical Association and Chirality

The stereochemical descriptors (*P*) or (*M*) can be assigned to the helical assemblies in **1**–**3** depending on the clockwise or anticlockwise bias of the helical strand, respectively. It is noteworthy that the supramolecular packing in complexes **1**–**3** generates a one-dimensional inner-sphere helical arrangement running through the metal centers by a combination of weak inter- and intramolecular π···π stacking and hydrogen-bonding interactions, as shown in Figure 2. An imaginary helical axis drawn between the metal centers along the *a* axis is shown in Figure 3. In all cases the bipyridyl ligand and the phenyl ring of the amino acid that projects outwards revolve around the helical axis with good intra- and intermolecular π···π stacking interactions. The intramolecular helical structure running through the Cu1–OCO–Cu2 strands in complex **1** contains only folded phenylalanine isomers. As expected, therefore, the arrangement of the two polymeric helical chains containing the D- and L-amino acids in this complex occurs through the formation of alternately packed (*P*) and (*M*) helices, as shown in Figure 3A.

The coordinated O1w and O2w molecules of the folded and extended conformers in complex **2** propagate the hydrogen-bonded helical architecture through Cu1–O1w···O2CO1–Cu1 and Cu2–O2w···O4CO3–Cu2 bonds, respectively, diagonal to the *ac* plane. The O1w and O2 (carboxylate oxygen) atoms of the adjacent molecular units of the folded form are interconnected by hydrogen bonds (O1w···O2 2.747 Å) to form a single-stranded helical chain. Similarly, the O2w and O4 (carboxylate oxygen) atoms (O2w···O4 2.857 Å) of the extended form are interlinked

 © 2007 Wiley-VCH Verlag GmbH & Co. KGaA, Weinheim 

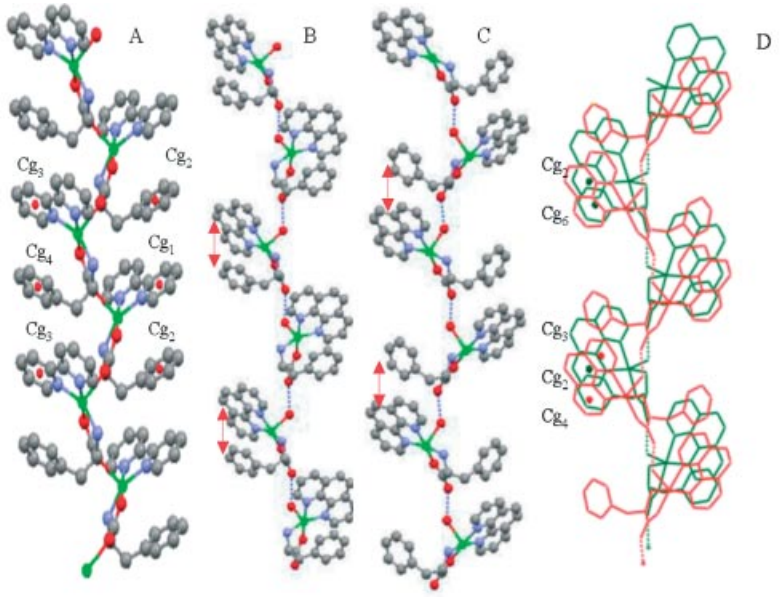


Figure 2. Stacking interactions of the phenyl rings in complexes **1** and **2** along the *a* axis. The double-headed arrows indicate the inter- and intramolecular stacking interactions. A: complex **1** [inter: Cg(1)···Cg(2) 4.158 Å; intra: Cg(1)···Cg(2) 4.154 Å; inter: Cg(3)···Cg(4) 4.264 Å; intra: Cg(3)···Cg(4) 4.044 Å]; B: complex **2** (only folded form); C: complex **2** (only extended form); D: merged packing of **2a** and **2b** [intra: Cg(2)···Cg(6) 3.882 Å; inter: Cg(3)···Cg(2) 3.539 Å]. Color scheme: red = carboxylate oxygen; green = Cu(II).

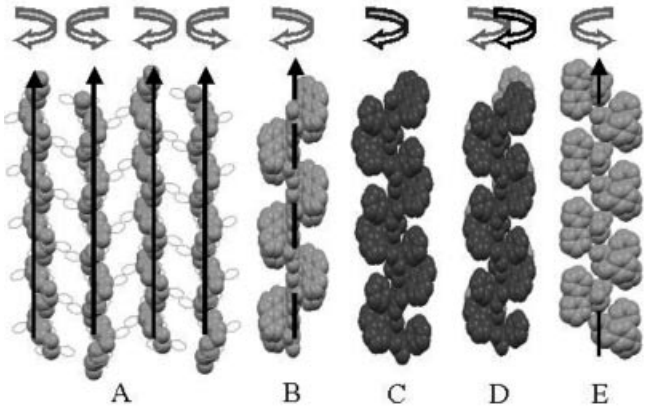


Figure 3. Space-filling model of the single-stranded supramolecular helical arrangements formed by Cu–OCO–Cu connectivity (light gray = folded; dark gray = extended). A: **1**; B: **2a**, C:**2b**; D: addition of both **2a** and **2b**; E: **3**.

through hydrogen bonding to create another helical chain. An alternate arrangement of O–H···O interactions with the lattice water molecule O3w and N–H···O bonds brings the adjacent folded and extended helical chains into close proximity to create a sheet-like architecture that restores the helical superstructure of the complex. The combined effect of various O–H···O and N–H···O interactions involving O3w–O2 (2.742 Å), O3w···O2w (2.745 Å), and N(3)H···O4 (3.024 Å) and π···π stacking interactions brings the $Cu^{II}$ centers into closer contact (5.928 Å). The hydrogen-bonded helical superstructure formed by both the folded and extended isomers can be designated as (*P*) because of the clockwise sense of its molecular rotation, as shown in Figure 3D. The folded and extended forms are shown separately in Figures 3B and C to better visualize their similar helical chirality.

Supramolecular helices usually pack in a racemic fashion,[19] and reports on homochiral helicates are rare. Supramolecular packing of **1**, for instance, occurs with the usual racemic pattern comprising both the (*P*) and (*M*) alternate helical chains, while in the crystal structure of complex **2** packing of two (*P*) helices occurs stereospecifically to give a homochiral superstructure, as shown in Figures 3B–D. In complex **3**, the free carboxylate oxygen atom (O2) involved in N···H···O interactions [N(3)–H···O2 3.027 Å] forms a single-stranded inner-sphere helical chain through the Cu1–N3···O2CO1–Cu1 bonds along the *bc* plane, as shown in Figure 3E.

## Chiroptical Properties

In order to understand the correlation between the supramolecular helical architecture and the chiroptical properties, CD spectra for complexes **1**–**3** were recorded both in solution and on ground crystals. In general, the optical activity could be derived from the (*P*)/(*M*) helical chain chiral descriptors, the geometrical Δ/Λ descriptors of the chiral metal centers (Scheme 1), and the λ/δ conformational chirality[20] of the nonplanar L/D-amino acid chelate rings. For systems **1**–**3**, therefore, an attempt to correlate their chiroptical properties can be made. Chirality at the metal centers can be derived by taking into account the non-coplanar arrangement of the donor atoms at the base of the square pyramid in the structures of the $Cu^{II}$ centers; the descriptors[21] Δ and Λ are thus assigned depending upon the clockwise (Δ isomer) and anticlockwise (Λ isomer) operation of the chromophore $O_{(aa)} \rightarrow N_{(aa)} \rightarrow N_{(py)}$

 © 2007 Wiley-VCH Verlag GmbH & Co. KGaA, Weinheim 

→ $N_{(py)}$ around the $Cu^{II}$ center, as shown in Scheme 1. In complex **1**, the (*P*) sense of the helix is associated with ΔΔΔΔ... configurations at the metal centers, while the (*M*) sense involves ΛΛΛΛ... configurations at the Cu atoms. The amino acids in complex **2** exist in folded (**2a**) and extended (**2b**) forms, both of which selectively assemble into (*P*) helical chains, although the configuration at the metal centers is ΛΔΛΔ... in the skeleton of the two helices. Furthermore, as complexes **1** and **2** possess very similar chemical compositions, the difference in their spatial arrangement caused by the folded and extended isomer and the extra space provided by the phenanthroline ligand may be the reason for its homochiral nature.

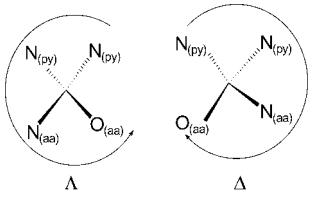


Scheme 1. Geometrical descriptors.

As regards the conformation of the amino acid chelate rings, it should be noted that the folded isomer has λ chirality for the L-phe and δ chirality for the D-phe residues, and that the opposite chirality occurs for the corresponding extended isomers (Scheme 2). The amino acids in the helical chains of complexes **1** and **3** adopt the folded conformation (λ for L-phe and δ for D-phe), although both the folded D-phe residue in **2a** and the extended L-phe residue in **2b** bear the same δ chirality.

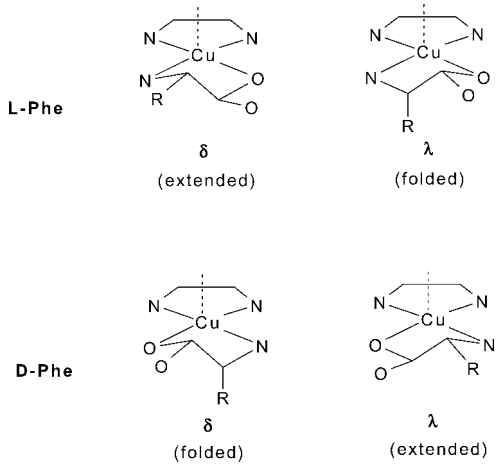


Scheme 2. Conformations of the amino acid chelate rings.

Complex **1** assembles in alternating (*P*) and (*M*) helices through Cu1–OCO–Cu2 chains, therefore both the contributions to the overall chirality by the conformation of the amino acid chelate rings and the configuration at the $Cu^{II}$ centers perfectly cancel each other out in the enantiomeric (*P*) and (*M*) helices. In contrast, the two supramolecular helical chains built up by the D- and L-phe complexes in complex **2** bear the same (*P*) chirality. This shows that the chirality of the helical chain is dictated by the conformational chirality of the amino acid chelate ring rather than the absolute (L/D) configuration of the amino acid, with a λ conformation inducing an (*M*) helix and a δ conformation a (*P*) helix. The self-assembly process generating the helical chains is thus enantioselectively dictated by the folded or extended disposition assumed by the side-chain of the phe residues.

As expected, the CD spectra of complexes **1** and **2** in solution are flat as the polymeric structure is destroyed; the solid-state CD spectrum of complex **1** is also essentially flat, taking into account the low resolution of the experiment, whereas crystals of complex **2** appear to exhibit optical activity in the solid state, with weak but clearly detectable CD activity with a positive sign between 500 and 600 nm. The dominant CD activity for complex **3** has a negative sign and remains unchanged both in the solid state ($\lambda_{max} \approx$ 620 nm) and in solution [CD data in methanol: $\lambda_{max} \approx 565$ ($\Delta\varepsilon = -0.44\ M^{-1}\,cm^{-1}$) and 725 nm (+0.10)], thus clearly indicating that no significant change occurs in the chiral arrangement of the complex. The CD activity observed for complexes **2** and **3** in the $Cu^{II}$ d-d bands therefore reflects the opposite chirality of the amino acid chelate rings and of the corresponding helical chains associated with the two complexes in the crystalline state.

## Conclusion

We have described the formation of a series of single-stranded helical coordination polymers that contain both covalent and hydrogen bonds as a construction element. The two separate helical chains of the ternary complex carrying L- and D-phe residues in complex **1** bear opposite chirality, which means that the crystalline sample as a whole is racemic. In contrast, the two helical chains generated by the L- and D-phe complexes in **2** have the same (*P*) chirality and together form two right-handed helical assemblies. In principle, a supramolecular arrangement involving two helical chains with (*M*) chirality, built from the folded (L) and extended (D) forms of the racemic amino acid, is possible for this complex, but is probably not observed in the crystalline state due to the less favorable packing. Further studies on chiral amplification to monitor the crystallization process of metal complexes containing optically pure and racemic amino acids are currently under way in our laboratory.

## Experimental Section

**Materials:** L-Phenylalanine, D,L-phenylalanine, 2,2′-bipyridyl, and 1,10-phenanthroline were purchased from Sigma–Aldrich and used as received. All the other reagents and solvents were commercially available and used without further purification. Microanalysis of the complexes was performed with a Perkin–Elmer PE 2400 series II CHNS/O elemental analyzer. FT-IR spectra for KBr pellets (1% w/w) were recorded with a Schimadzu FT-COM 1 spectrophotometer. The CD spectra were measured for KBr pellets or methanol solutions of the complexes with a JASCO J710 dichrograph; a smoothing program from JASCO (version 1.53.00) was used to reduce the noise of the solid-state spectra.

 © 2007 Wiley-VCH Verlag GmbH & Co. KGaA, Weinheim 

Table 2. Summary of the crystallographic parameters for complexes **1**–**3**.

| | **1** | **2** | **3** |
|---|---|---|---|
| Empirical formula | $C_{38}H_{36}Cl_2Cu_2N_6O_{12}$ | $C_{42}H_{42}Cl_2Cu_2N_6O_{15}$ | $C_{19}H_{20}ClCuN_3O_7$ |
| Formula mass | 966.71 | 1068.80 | 501.37 |
| Crystal size [mm] | $0.45\times0.20\times0.08$ | $0.35\times0.20\times0.10$ | $0.36\times0.26\times0.24$ |
| Crystal description | plates | plates | blocks |
| Crystal system | triclinic | monoclinic | monoclinic |
| Space group | $P\bar{1}$ | $P2_1/n$ | $P2_1$ |
| $a$ [Å] | 8.3033(8) | 13.3582(10) | 7.2743(7) |
| $b$ [Å] | 13.7280(13) | 25.3803(18) | 11.3581(10) |
| $c$ [Å] | 18.2520(18) | 14.1334(10) | 12.5857(11) |
| $\alpha$ [°] | 68.282(2) | 90.00 | 90.00 |
| $\beta$ [°] | 84.708(2) | 113.775(10) | 102.845(2) |
| $\gamma$ [°] | 82.050(2) | 90 | 90 |
| Volume [Å$^3$] | 1912.3(3) | 4385.1(5) | 1013.84(16) |
| $Z$ | 2 | 4 | 2 |
| $D_{calcd.}$ [g cm$^{-3}$] | 1.679 | 1.619 | 1.642 |
| $F(000)$ | 988 | 2192 | 514 |
| $\mu$ (Mo-$K_\alpha$) [mm$^{-1}$] | 1.326 | 1.170 | 1.258 |
| Temperature [K] | 293(2) | 293(2) | 293(2) |
| $2\theta$ max | 22.50 | 28.24 | 28.27 |
| Observed reflections [$I > 2\sigma(I)$] | 4930 | 10159 | 3636 |
| Parameters refined | 541 | 756 | 352 |
| Goodness of fit | 1.054 | 1.050 | 1.054 |
| Final $R_1$ (observed data) | 0.0435 | 0.0441 | 0.0222 |
| Final $wR_2$ (observed data) | 0.1263 | 0.1270 | 0.0581 |

### Preparation of the Complexes

**[Cu(D,L-phe)(bpy)]·ClO$_4$ (1):** A mixture of D,L-phenylalanine (0.82 g, 10 mmol) and NaOH (0.20 g, 10 mmol) in distilled water (50 mL) was added to an aqueous solution (25 mL) of $CuSO_4{\cdot}5H_2O$ (1.25 g, 10 mmol) and stirred for 30 min. The solution was stirred at 50 °C for another 2 h until a pale-blue precipitate had formed. An ethanolic solution (20 mL) of bipyridyl (0.78 g) was then added dropwise and the pale-blue precipitate was observed to dissolve to form a clear blue solution. At the end of the reaction, $NaClO_4{\cdot}H_2O$ (0.7 g, 10 mmol), dissolved in distilled water (20 mL), was added. $C_{19}H_{18}ClCuN_3O_6$ (483.36): calcd. C 47.30, H 3.73, N 8.71; found C 47.35, H 3.76, N 8.63. IR: $\tilde{\nu}$ = 3450–2910, 1631, 1593 (s), 1444, 1386 (m), 1320 (m), 1131, 1103, 1057 (br., s), 763, 618 (m) cm$^{-1}$.

**[Cu(D,L-phe)(phen)(H$_2$O)]·ClO$_4$·H$_2$O (2):** This complex was synthesized according to the above procedure but with phenanthroline (0.94 g, 10 mmol) in place of bipyridyl. $C_{21}H_{21}ClCuN_3O_{7.5}$ (530.40): calcd. C 47.19, H 3.96, N 7.86; found C 47.42, H 4.54, N 7.27. IR: $\tilde{\nu}$ = 3519–2940 (br., s), 1609, 1589 ($\nu_{COO}$, s), 1520 (m), 1429, 1399 (m), 1149, 1100, 1085 ($\nu_{ClO_4}$, br, s), 851 (m), 622 (m) cm$^{-1}$.

**[Cu(L-phe)(bpy)(H$_2$O)]·ClO$_4$·H$_2$O (3):** Synthesized and characterized according to the reported procedure.[9]

**Crystal Structure Determination:** Data collection for **1**–**3** was performed with a Bruker Apex CCD diffractometer using Mo-$K_\alpha$ radiation ($\lambda$ = 0.71073 Å) at 100(2) K. Absorption corrections were applied with the multi-scan program SADABS.[22a] Further details are given in Table 2. The structures were solved by direct methods and all non-hydrogen atoms were refined anisotropically by least-squares on $F^2$ using the program SHELXTL.[22b] Hydrogen atoms were generated with a riding model. CCDC-281899 (**1**), -281900 (**2**), and -281901 (**3**) contain the supplementary crystallographic data for this paper. These data can be obtained free of charge from The Cambridge Crystallographic Data Centre via www.ccdc.cam.ac.uk/data_request/cif.

**Supporting Information** (see footnote on the first page of this article): Table summarizing hydrogen-bonding network for complexes **1** and **2**.

## Acknowledgments

P. S. and E. S. are grateful to Dr. P. K. Ghosh, Director of the Central Salt and Marine Chemicals Research Institute, for his keen interest and encouragement, and Dr. A. Granata for recording the CD spectra.

[1] a) S. G. Telfer, T. Sato, R. Kuroda, *Angew. Chem.* **2004**, *116*, 591; *Angew. Chem. Int. Ed.* **2004**, *43*, 581; b) M. Ziegler, A. V. Davis, D. W. Johnson, K. N. Raymond, *Angew. Chem.* **2003**, *115*, 689; *Angew. Chem. Int. Ed.* **2003**, *42*, 665; c) G. Tian, G. Zhu, X. Yang, Q. Fang, M. Xue, J. Sun, Y. Wei, S. Qin, *Chem. Commun.* **2005**, 1396; d) X.-M. Chen, G.-F. Liu, *Chem. Eur. J.* **2002**, *8*, 4811; e) M. Suareez, N. Branda, J.-M. Lehn, A. Decian, J. Fischer, *Helv. Chim. Acta* **1998**, *81*, 1; f) E. Yashima, K. Maeda, T. Nishimura, *Chem. Eur. J.* **2004**, *10*, 42.

[2] a) O. Yamauchi, A. Odani, M. Takani, *J. Chem. Soc., Dalton Trans.* **2002**, 3411; b) O. Yamauchi, A. Odani, *J. Am. Chem. Soc.* **1981**, *103*, 391; c) O. Yamauchi, A. Odani, T. Kohzuma, H. Masuda, K. Toriumi, K. Saito, *Inorg. Chem.* **1989**, *28*, 4066; d) F. Zhang, A. Odani, H. Masuda, O. Yamauchi, *Inorg. Chem.* **1996**, *35*, 7148; e) O. Yamauchi, A. Odani, *J. Am. Chem. Soc.* **1985**, *107*, 5938.

[3] a) J. Pasan, J. Sanchiz, C. Ruiz-Perez, F. Lloret, M. Julve, *Eur. J. Inorg. Chem.* **2004**, 4081; b) T. Kahzuma, H. Masuda, O. Yamauchi, *J. Am. Chem. Soc.* **1989**, *111*, 3431.

[4] a) H. Sigel, R. Malini-Balakrishnan, U. K. Haring, *J. Am. Chem. Soc.* **1985**, *107*, 5137; b) E. Dubler, U. K. Haring, K. H. Scheller, P. Sigel, *Inorg. Chem.* **1984**, *23*, 3785; c) A. Castineiras, A. G. Sicilia-Zafra, J. M. Gonzalez-Perez, D. Choquesillo-Lazarte, J. Niclos-Gutierrez, *Inorg. Chem.* **2002**, *41*, 6956.

[5] a) S. Suzuki, K. Yamaguchi, N. Nakamura, Y. Tagawa, H. Kuma, T. Kawamoto, *Inorg. Chim. Acta* **1998**, *283*, 260; b) U. Mukhopadhyay, D. Choquesillo-Lazarte, J. Niclos-Gutierrez,

 © 2007 Wiley-VCH Verlag GmbH & Co. KGaA, Weinheim 

I. Bernal, *Cryst. Eng. Commun.* **2004**, *6*, 627; c) F. Zhang, T. Yajima, H. Masuda, A. Odani, O. Yamauchi, *Inorg. Chem.* **1997**, *36*, 5777; d) L. H. Abdel-Rahman, L. P. Battaglia, M. R. Mahmoud, *Polyhedron* **1996**, *15*, 327.

[6] a) N. Nakamura, T. Kohzuma, H. Kuma, S. Suzuki, *J. Am. Chem. Soc.* **1992**, *114*, 6550; b) . J. L. Seymour, F. Turecek, A. V. Malkov, P. Kocovsky, *J. Mass. Spectrom.* **2004**, *39*, 1044.

[7] M. Mizutani, S. Tomosue, H. Kinoshita, K. Jitsukawa, H. Masuda, H. Einaga, *Bull. Chem. Soc. Jpn.* **1999**, *72*, 981.

[8] T. Sugimori, H. Masuda, N. Ohata, K. Koiwai, A. Odani, O. Yamauchi, *Inorg. Chem.* **1997**, *36*, 576.

[9] P. S. Subramanian, E. Suresh, P. Dastidar, S. Waghmode, D. Srinivas, *Inorg. Chem.* **2001**, *40*, 4291.

[10] a) V. G. Machado, P. N. W. Baxter, J.-M. Lehn, *J. Braz. Chem. Soc.* **2001**, *12*, 431; b) J.-M. Lehn, A. Rigault, J. Siegel, J. Harrowfield, B. Chevrier, D. Moras, *Proc. Natl. Acad. Sci. USA* **1987**, *84*, 2565; c) C. Piguet, G. Bernardinelli, G. Hopfgartner, *Chem. Rev.* **1997**, *97*, 2005.

[11] a) R. Prabaharan, N. C. Fletcher, M. Nieuwenhuyzen, *J. Chem. Soc., Dalton Trans.* **2002**, 602; b) Y.-T. Way, M.-L. Tong, H.-H. Fan, H.-Z. Wang, X.-M. Chen, *Dalton Trans.* **2005**, 424.

[12] L. J. Prins, P. Timmerman, D. N. Reinhoudt, *J. Am. Chem. Soc.* **2001**, *123*, 10153.

[13] a) C. J. Carrano, K. N. Raymond, *J. Am. Chem. Soc.* **1978**, *100*, 5371; b) A.-K. Duhme, Z. Dauter, R. C. Hider, S. Pohl, *Inorg. Chem.* **1996**, *35*, 3059.

[14] a) M. Duggeli, C. Goujon-Ginglinger, S. R. Ducotterd, D. Mauron, C. Bonte, A. V. Zelewsky, H. Stoeckli-Evans, A. Neels, *Org. Biomol. Chem.* **2003**, *1*, 1894; b) O. Mamula, A. V. Zelewsky, T. Bark, G. Bernardinelli, *Angew. Chem.* **1999**, *111*, 3129; *Angew. Chem. Int. Ed.* **1999**, *38*, 2945; c) O. Mamula, F. J. Monlien, A. Porquet, G. Hopfgartner, A. E. Merbach, A. V. Zelewsky, *Chem. Eur. J.* **2001**, *7*, 533; d) A. V. Zelewsky, *Coord. Chem. Rev.* **1999**, *190–192*, 811.

[15] a) M. Meyer, B. Kersting, R. E. Powers, K. N. Raymond, *Inorg. Chem.* **1997**, *36*, 5179; b) B. Kresting, M. Meyer, R. E. Powers, K. N. Raymond, *J. Am. Chem. Soc.* **1996**, *118*, 7221; c) D. Caulder, K. N. Raymond, *J. Chem. Soc., Dalton Trans.* **1999**, 1185; d) J. Xu, T. N. Parac, K. N. Raymond, *Angew. Chem.* **1999**, *111*, 3055; *Angew. Chem. Int. Ed.* **1999**, *38*, 2878.

[16] a) M. Albrecht, O. Spieß, M. Schneider, P. Weis, *Chem. Commun.* **2002**, 786; b) M. Albrecht, M. Napp, M. Schneider, P. Weis, R. Frohlich, *Chem. Eur. J.* **2001**, *7*, 3966; c) M. Albrecht, M. Napp, M. Schneider, P. Weis, R. Fröhlich, *Chem. Commun.* **2001**, 409.

[17] a) S. J. Telfer, R. Kuroda, *Chem. Eur. J.* **2005**, *11*, 57.

[18] K. Akoi, H. Yamazaki, *J. Chem. Soc., Dalton Trans.* **1987**, 2017.

[19] J. Breu, H. Domel, A. Stoll, *Eur. J. Inorg. Chem.* **2000**, 2401.

[20] L. Casella, M. Gullotti, *J. Am. Chem. Soc.* **1981**, *103*, 6338.

[21] a) L.-S. Long, J.-W. Cai, Y.-P. Ren, Y.-X. Tong, X.-M. Chen, L.-N. Ji, R.-B. Huang, L.-S. Zheng, *J. Chem. Soc., Dalton Trans.* **2001**, 845; b) H. Miyasaka, S. Okamura, T. Nakashima, N. Matsumoto, *Inorg. Chem.* **1997**, *36*, 4329.

[22] a) G. M. Sheldrick, *SADABS 2.05*, University of Göttingen, Germany; b) *SHELXTL 6.10*, Bruker Analytical Instrumentation, Madison, WI, **2000**.

Received: October 13, 2006
Published Online: March 6, 2007

 © 2007 Wiley-VCH Verlag GmbH & Co. KGaA, Weinheim 

DOI: 10.1002/ejic.200600986

# Helical Transition-Metal Complexes of Constrained 2,2′-Bidipyrrins

**Martin Bröring,*[a] Stephan Link,[a] Carsten D. Brandt,[a] and Esther Cónsul Tejero[a]**

**Keywords:** 2,2′-Bidipyrrins / Helicates / Constrained ligands / Porphyrinoids / Coordination modes

Nickel(II), palladium(II), zinc(II) and copper(II) complexes of new constrained 2,2′-bidipyrrin ligands ($H_2$BDP) with a peripheral eight-membered ring were prepared and examined with respect to coordination modes and conformation. $Ni^{II}$ and $Pd^{II}$ ions form mononuclear complexes with a distorted square-planar $N_4$ coordination, which was determined for the palladium derivative by single-crystal X-ray diffraction. $Zn^{II}$ ions lead to the formation of dinuclear $M_2L_2$ helicates, and for $Cu^{II}$ ions both coordination modes are realized. X-ray crystallographic analyses reveal short M···M distances for the dinuclear helicates of $Cu^{II}$ and $Zn^{II}$ bidipyrrins and individually distinct packing patterns for both in the solid state.
(© Wiley-VCH Verlag GmbH & Co. KGaA, 69451 Weinheim, Germany, 2007)

## Introduction

For a long time the coordination chemistry of open-chain tetrapyrroles was limited to bioinspired studies on the metal-binding capabilities of biliverdin-IXα (BV) and closely related model ligands.[1] Naturally occurring heme degradation processes[2] and the unexpected lability of Fe–BV complexes[3] have been the major driving forces for this research, and many questions have remained unanswered until today. Open-chain tetrapyrroles with a non-natural backbone, on the other hand, have been prepared mainly as precursors for different template-directed macrocyclizations to porphyrinoids.[4] Signs of a stand-alone coordination chemistry of such ligands hardly appeared in the literature prior to 1990.[5]

The interest in open-chain tetrapyrroles as multifunctional chelate ligands started in 1996 with Mizutani's work on the chiral recognition of amino acids by helical Zn–BV derivatives.[6] In 1998 two groups reported, independently, that open-chain oligopyrroles are useful templates for the construction of supramolecular coordination assemblies,[7] including earlier findings on similar dinuclear species.[8] A very elegant approach along this line was reported by Thompson et al., who introduced chiral carboxylic ester side chains in order to investigate stereoselective helix formation triggered by metal insertion.[9] The first bioinorganic use of linear tetrapyrroles besides heme degradation studies was reported in 2001.[10] It could be demonstrated that a dimeric manganese(III) complex of BV-IXα-dimethyl ester catalyzes the decomposition of hyperoxide, and that therefore this complex should be addressed as a functional SOD model. However, reports on investigations of possible medical applications have not yet appeared.

A tetrapyrrolic system with a particularly simple architecture is found in the non-natural 2,2′-bidipyrrin,[7b,11] which is constituted of two directly linked dipyrrin units, and which can in principle rotate around this central pyrrole–pyrrole link. 2,2′-Bidipyrrins have been shown in recent years to support a multitude of different coordination modes (Figure 1).[12] Because of the robustness of methyl-terminated 2,2′-bidipyrrins and their straightforward preparation in large amounts, these ligands would be an ideal candidate for a reference system of the natural BV-IXa and especially of the hitherto almost elusive iron complexes thereof.[13] Unfortunately, however, and similar to other natural and non-natural open-chain tetrapyrroles, 2,2′-bidipyrrins do not form sufficiently stable iron chelates.

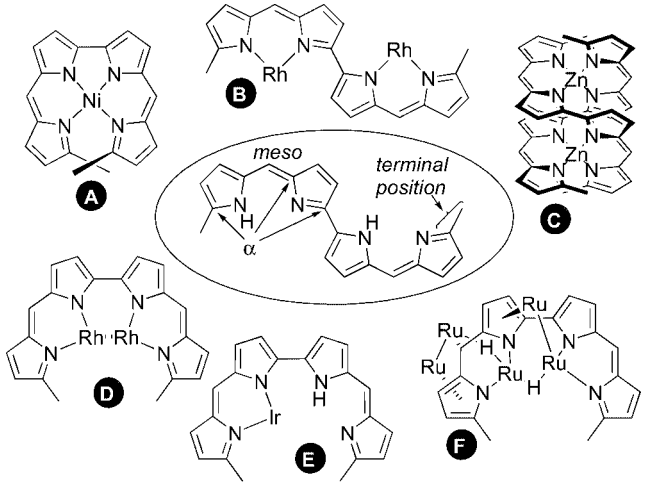


Figure 1. Nomenclature and selected coordination compounds with different binding modes (A–F) of 2,2′-bidipyrrins (alkyl substituents and CO coligands on Rh, Ir and Ru omitted).

[a] Fachbereich Chemie, Philipps-Universität Marburg, Hans-Meerwein-Straße, 35032 Marburg, Germany
Fax: +49-6421-282-5653
E-mail: Martin.Broering@chemie.uni-marburg.de

 © 2007 Wiley-VCH Verlag GmbH & Co. KGaA, Weinheim 

2,2′-Bidipyrrins typically reside in an *anti* conformation in the solid state and in solution,[11b,11c,14] and we expected that, enforcing a *syn*- (or *syn-gauche*-) conformation as shown on the right in Figure 2, the formation of 1:1 chelate complexes of type **A** with kinetically labile ions should be favoured. We report here on the synthesis of such conformationally restricted 2,2′-bidipyrrins **1** and **2** and their coordination behaviour to 3d transition metals.

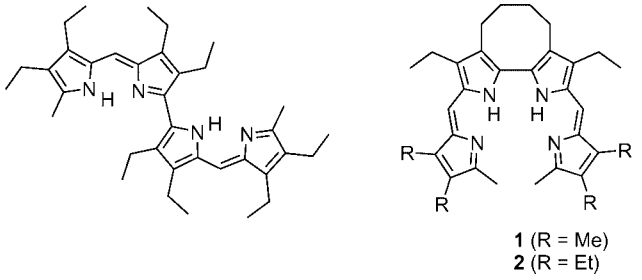


Figure 2. Conformational preferences of unrestrained and restrained 2,2′-bidipyrrins.

## Results and Discussion

The synthesis of the new 2,2′-bidipyrrin ligands **1** and **2** is illustrated in Scheme 1. We have chosen an eight-membered ring as an intermediately severe constraint for our purpose. A bis(indole)-based $N_4$ ligand with an identical restraint was prepared and studied before in the field of anion sensing,[15] and a maximum bis(indole) torsion angle of 65° was estimated for this compound. This estimate fits well for our intention to produce a 2,2′-bidipyrrin with a restriction to the *syn*- and/or *syn-gauche* conformation.

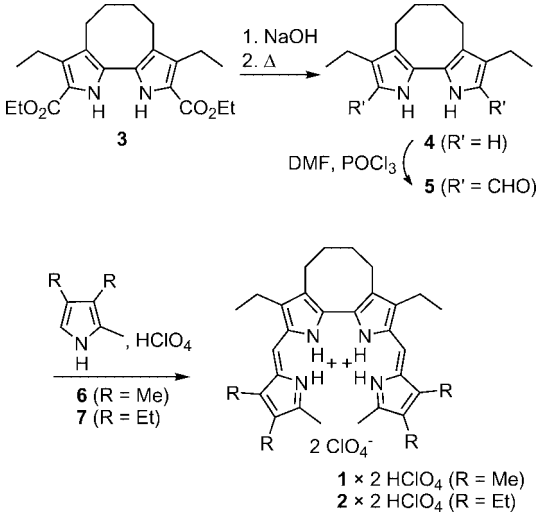


Scheme 1. Preparation of restrained 2,2′-bidipyrrins **1** and **2** as bis(hydroperchlorate) salts.

The new ligands **1** and **2** were obtained analogously to simpler 2,2′-bidipyrrins recently described.[11c,11d] Dialdehyde **5** was prepared from the recently communicated diester **3**[16] by a saponification-decarboxylation-formylation sequence. The electron-rich bipyrrole **4** proved to be extremely sensitive to light and air, and was therefore used directly in the Vilsmeyer formylation to yield **5** as a yellow powder in an overall yield of 72%. The acid-promoted double condensation of **5** with 2 equiv. of a 5-unsubstituted pyrrole (either **6** or **7**) was carried out at 60 °C in methanol solution. Perchloric acid was found to be the agent of choice, as the protonated products **1**·2 $HClO_4$ and **2**·2 $HClO_4$ directly crystallize from the hot reaction mixture. The yields of 50 and 48%, however, are significantly lower compared to the almost quantitative formation of nonhindered 2,2′-bidipyrrins.

The formation of the desired tetrapyrroles **1** and **2** is indicated mass spectrometrically by the signals for the $[M + 1]^+$ ions at *m*/*z* 481 and 537, respectively. Combustion analyses in combination with thermogravimetric investigations point to the presence of hydrates, that is [**1**·2$HClO_4$·$H_2O$] and [**2**·2$HClO_4$·3$H_2O$]. Further characterization was performed by $^1H$ and $^{13}C$ NMR spectroscopy. Proton NMR spectra of [**1**·2$HClO_4$·$H_2O$] and [**2**·2$HClO_4$·3$H_2O$] show broad singlets for two types of NH protons at 12.23 and 11.47 (**1**) or 11.17 and 10.55 ppm (**2**) in addition to a sharp resonance line for the *meso* H atoms at 7.06 (**1**) or 7.25 ppm (**2**). The singlet for the terminal methyl groups is found at 2.76 (**1**) and 2.73 ppm (**2**), and the $C_4$-bridge leads to broadened multiplets for the benzylic and homobenzylic methylene protons at $\delta$ = 2.7 and 1.8 ppm, respectively (Figure 3).

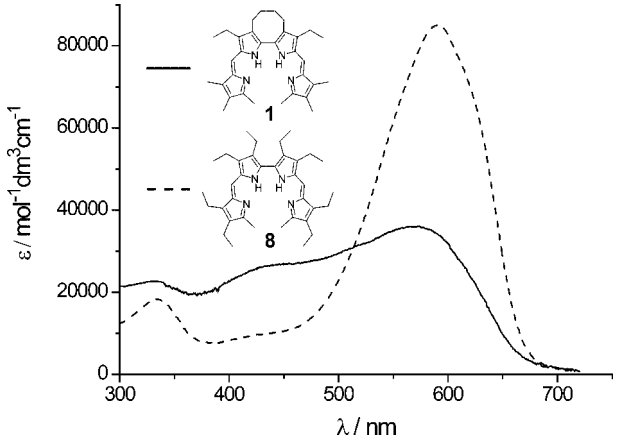


Figure 3. UV/Vis spectra ($CH_2Cl_2$) of free base **1** and octaethyldimethyl-2,2′-bidipyrrin **8**.[11d]

While the data discussed above give no direct hint to a special conformation of the new tetrapyrroles, the restricted rotation of **1** and **2** is well documented in the optical spectra. Figure 3 shows the UV/Vis absorption spectra of restrained **1** and of the unrestrained 2,2′-bidipyrrin **8**.[11d] Compared to octaethyldimethyl-2,2′-bidipyrrin **8** the optical transitions of **1** are significantly broader and largely equal in intensity, but very similar with respect to the absorption maxima. A possible interpretation of this spectral pattern is that the presence of the eight-membered ring in **1** prevents a single minimum conformation for the tetrapyrrole in solution. Instead, a number of energetically similar *syn-gauche* conformations exist and slowly interconvert into

 © 2007 Wiley-VCH Verlag GmbH & Co. KGaA, Weinheim 

each other. The observed line-broadening for the $C_4$-bridge methylene proton signals in the $^1H$ NMR spectra of **1** and **2** as well as the relatively high solubility of the new tetrapyrroles provide additional support for this thesis. An attempt to investigate this issue further by variable temperature NMR spectroscopy on **1** failed, however, because of severely overlapping resonances in the aliphatic region.

Metal coordination was studied using divalent metal acetates and excess base (sodium acetate, ammonia or sodium methoxide) in methanolic solution. Only zinc(II), copper(II), nickel(II) and palladium(II) yielded isolable complexes with **1** or **2** while no binding was observed for iron(II), manganese(II) and vanadyl(IV), and only decomposition products were detected after treatment with cobalt(II) acetate. The successful attempts are summarized in Scheme 2.

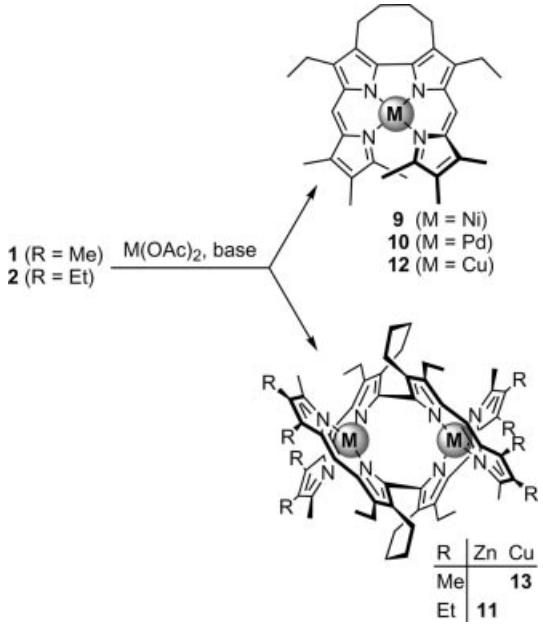


Scheme 2. Formation of nickel(II), palladium(II), zinc(II) and copper(II) chelates **9**–**13** from rotationally restricted 2,2′-bidipyrrins **1** and **2**.

The formation of nickel and palladium chelates **9** and **10** is easily monitored by an immediate colour change from dark green to brownish green and red, respectively, upon addition of metal acetate and sodium acetate to a solution of **1**. Isolation can be effected in good yields after chromatographic workup and recrystallization. As expected, the new complexes are of type **A** with a distorted square-planar arrangement of the *N* donors and therefore analogous to known nonbridged nickel- and palladium-2,2′-bidipyrrins of, for example, **8**.[12c,12d] Results from high-resolution mass spectrometry, NMR spectroscopy and UV/Vis measurements further support the assignments. In particular, the small high-field shift for the terminal methyl proton resonances at 2.44 (**9**) and 2.57 ppm (**10**) is a good indication for the strain, which is typically present at this position in helical dimethyl-2,2′-bidipyrrins of type **A**. In addition, the resonances of the *meso* protons are also detected high-field shifted at 6.24 (**9**) and 6.40 ppm (**10**). Unlike for the protonated **1** and **2**, the signals for the methylene protons of the $C_4$ bridge show sharp absorptions and indicate a rigid conformation of the eight-membered ring. The optical spectra of the nickel and palladium chelates **9** and **10** show two major absorptions at 430/530 or 430/520 nm, respectively, and are almost indistinguishable from those of their unrestrained analogues with ligand **8** (Figure 4).[12c,12d]

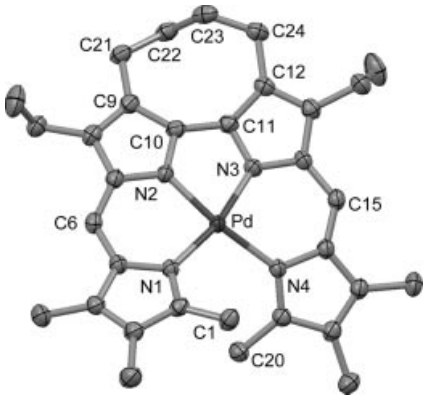


Figure 4. Molecular structure of **10**. Ellipsoids are set at 50% probability (hydrogen atoms omitted for clarity).

A detailed picture of the coordination and the degree of molecular distortion was derived from X-ray crystallographic work performed on the palladium derivative **10**. Suitable crystals were obtained by slow evaporation of a solution of **10** in dichloromethane/*n*-hexane. The compound crystallizes monoclinically in the space group $P2_1/n$ and forms green metallic plates. The molecular structure of **10** is given in Figure 4. Table 1 summarizes selected angles and distances.

The palladium(II) ion is coordinated to the four nitrogen donors of the 2,2′-bidipyrrin in a distorted square-planar fashion with Pd–N distances of 1.963(2)–2.071(2) Å. The *in-plane* distortion is mainly due to the presence of the bipyrrolic subunit, which allows an N2–Pd–N3 angle of only 78.32(9)°. More interestingly, the *out-of-plane* distortion caused by the close proximity of the terminal methyl groups C1 and C20 can be analyzed using different torsion angles. Values relevant for comparison are the torsion angles N2–C9–C10–N3, C8–C9–C10–C11 and C2–C10–C11–C19, which are found to be 11.8(3), 27.3(6) and 21.4(1)°, respectively, in **10**. These angles are reduced by 4.7, 7.3 and 6.3° with respect to the unconstrained $Pd^{II}$ chelate from ligand **8** and, in combination with the shorter C1–C20 distance of 3.217(4) Å (3.473 Å for Pd-**8**), a slight planarization of **10** becomes visible. The differences between the solid-state structures of **10** and the literature precedent, however, are quite small. In both cases the distances between the terminal methyl groups clearly undercut the sum of the *van der Waals* distances and prove the strained situation at these positions. The annelated eight-membered ring of **10** itself resides in a twist conformation, and no disorder is found in the crystal at this position (Figure 5).

The preparation of the zinc chelate **11** is straightforward. The action of sodium methoxide and excess zinc acetate on

 © 2007 Wiley-VCH Verlag GmbH & Co. KGaA, Weinheim 

Table 1. Selected structural data for **10**, **11** and **13**.[a]

| Compound | **10** | **11** | | | | **13** | | |
|---|---|---|---|---|---|---|---|---|
| | Pd | Zn-Ia[b] | Zn-Ib[b] | Zn-IIa[b] | Zn-IIb[b] | Cu-Ia[b] | Cu-Ib[b] | Cu-II[b] |
| N1–M | 2.060(2) | 2.004(3) | 2.002(3) | 2.009(3) | 2.017(3) | 2.005(6) | 1.971(5) | 1.983(6) |
| N2–M | 1.963(2) | 1.995(3) | 2.001(3) | 1.987(3) | 1.992(3) | 1.947(5) | 1.942(6) | 1.939(6) |
| N3–M | 1.964(2) | 1.974(3) | 1.986(3) | 1.992(3) | 1.992(3) | 1.951(6) | 1.938(5) | 1.969(5) |
| N4–M | 2.071(2) | 2.030(4) | 2.024(3) | 2.001(3) | 1.988(3) | 1.996(6) | 2.001(6) | 1.999(6) |
| C5–C6 | 1.382(4) | 1.373(5) | 1.365(5) | 1.374(8) | 1.372(4) | 1.394(13) | 1.366(13) | 1.374(13) |
| C6–C7 | 1.397(4) | 1.389(6) | 1.395(5) | 1.394(9) | 1.386(4) | 1.394(11) | 1.400(12) | 1.400(12) |
| C10–C11 | 1.458(4) | 1.443(6) | 1.446(6) | 1.439(6) | 1.441(6) | 1.457(11) | 1.433(11) | 1.436(11) |
| C14–C15 | 1.400(4) | 1.435(8) | 1.398(6) | 1.401(6) | 1.388(7) | 1.401(11) | 1.383(11) | 1.385(11) |
| C15–C16 | 1.382(4) | 1.356(8) | 1.378(6) | 1.361(6) | 1.357(8) | 1.375(11) | 1.362(11) | 1.378(11) |
| C9–C21 | 1.500(4) | 1.508(7) | 1.512(6) | 1.485(19) | 1.511(6) | 1.503(13) | 1.50(5) | 1.489(13) |
| C21–C22 | 1.517(4) | 1.517(9) | 1.488(10) | 1.496(12) | 1.523(8) | 1.50(2) | 1.50(5) | 1.528(13) |
| C22–C23 | 1.533(4) | 1.498(12) | 1.541(16) | 1.500(13) | 1.508(10) | 1.44(3) | 1.51(4) | 1.516(14) |
| C23–C24 | 1.512(4) | 1.497(13) | 1.363(14) | 1.467(11) | 1.481(11) | 1.499(19) | 1.378(18) | 1.504(14) |
| C24–C12 | 1.508(4) | 1.483(11) | 1.498(7) | 1.561(8) | 1.519(8) | 1.512(11) | 1.508(13) | 1.512(10) |
| M···M′ | – | 3.4427(7) | | 3.3579(7) | | 3.0629(13) | | 3.0123(13) |
| Δ(1,2,6)[c] | 0.5386(2) | 0.1942(4) | 0.2450(4) | 0.1306(4) | 0.1119(4) | 0.0929(9) | 0.0622(9) | 0.0363(9) |
| Δ(3,4,15)[c] | 0.4796(2) | 0.1519(4) | 0.1385(4) | 0.1055(4) | 0.1253(4) | 0.0167(9) | 0.0460(9) | 0.0252(9) |
| N1–M–N2 | 88.78(9) | 93.50(12) | 94.11(12) | 95.19(13) | 93.50(12) | 94.1(2) | 93.8(2) | 92.3(2) |
| N1–M–N3 | 164.93(9) | 118.83(12) | 117.14(13) | 106.76(12) | 114.25(12) | 104.5(3) | 101.1(2) | 104.5(2) |
| N1–M–N4 | 104.52(8) | 122.13(12) | 119.97(14) | 119.18(13) | 121.63(13) | 122.7(2) | 127.5(3) | 125.9(2) |
| N2–M–N3 | 78.32(9) | 127.47(12) | 129.75(13) | 130.24(13) | 131.78(14) | 144.4(3) | 141.2(3) | 143.7(3) |
| N2–M–N4 | 164.54(9) | 102.72(13) | 103.31(13) | 113.39(12) | 104.87(15) | 102.6(2) | 105.6(3) | 102.5(3) |
| N3–M–N4 | 89.41(8) | 93.80(13) | 94.10(15) | 94.11(11) | 93.39(15) | 92.7(2) | 93.4(2) | 93.3(2) |
| C5–C6–C7 | 127.5(2) | 129.5(4) | 129.5(4) | 130.4(4) | 129.2(3) | 128.6(7) | 130.5(7) | 127.4(7) |
| C14–C15–C16 | 127.8(2) | 129.2(4) | 131.0(5) | 128.8(4) | 129.6(4) | 127.8(7) | 129.1(7) | 128.8(7) |
| C9–C21–C22 | 114.3(2) | 113.7(4) | 115.3(5) | 118.9(6) | 111.9(4) | 113.1(10) | 129(4) | 116.4(8) |
| C21–C22–C23 | 112.8(2) | 116.9(6) | 118.7(7) | 118.8(7) | 114.5(5) | 117.7(15) | 132(4) | 117.2(8) |
| C22–C23–C24 | 112.9(2) | 123.9(8) | 113.2(9) | 117.6(6) | 118.2(7) | 120.6(14) | 124(2) | 118.9(9) |
| C23–C24–C12 | 114.1(2) | 119.9(6) | 124.9(7) | 114.3(5) | 117.2(5) | 121.1(10) | 117.2(11) | 117.4(8) |
| N2–C10–C11–N3 | 11.8(3) | 41.3(6) | 39.9(5) | 38.4(6) | 37.9(6) | 38.4(12) | 40.0(12) | 41.1(10) |
| C9–C10–C11–C12 | 27.3(6) | 52.4(8) | 51.0(7) | 47.1(8) | 48.0(8) | 51.5(14) | 54.9(16) | 53.4(13) |
| C21–C22–C23–C24 | 131.1(2) | 63.3(10) | 75.6(11) | 64.4(11) | 57.6(7) | 72(2) | 51(5) | 74.5(13) |

[a] Unified numbering scheme used for all compounds, see Figure 5. [b] I and II correspond to crystallographically distinct helicates, a and b determine the respective BDP in each dimer. [c] Out-of-plane distance of the metal ion from the N1–N2–C6 or N3–N4–C15 plane.

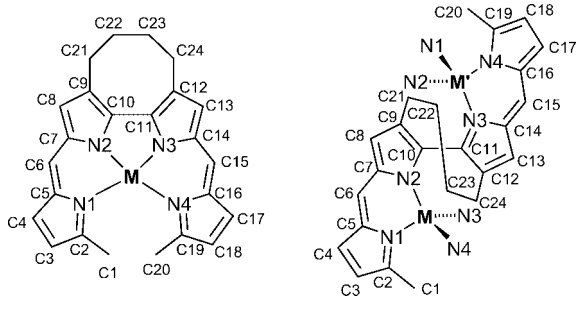


Figure 5. Unified numbering scheme used for the complexes and/or single-strand fragments of **10**, **11** and **13** in Figures 4, 6, 7, 9 and 10, and in Table 1.

ligand **2** in methanolic solution results in an immediate colour change from dark to light green. Because of the high solubility of the product **11** in most organic solvents the new complex can conveniently be isolated from this mixture by repeated pentane extraction, and forms green plates after crystallization. The results from mass spectrometry clearly point to the formation of a dinuclear zinc complex of type **C** with a complicated isotope pattern around *m*/*z* 1200. Proton NMR shows the formation of a symmetric compound, in which the terminal methyl proton signal is strongly shifted to high field with respect to **2** and can be observed as a singlet at $\delta$ = 1.66 ppm. The signal for the *meso* protons, however, appears at $\delta$ = 6.95 ppm without any significant shift (Figure 6).

For further characterization an X-ray crystallographic analysis was performed on **11**. Suitable green plates were obtained by slow evaporation of a solution of **11** in dichloromethane/*n*-hexane (1:3). Complex **11** crystallizes in the triclinic space group $P\bar{1}$. Two independent molecules I and II and their respective enantiomers are found in the unit cell. Multiple disorder was found for the orientation of nine ethyl substituents, which had to be refined with restraints. In addition, three of the four $C_4$ bridges are found to be strongly disordered and were refined assuming two conformations with occupancy factors for the atoms of concern of 0.5. Only data of molecule I will be discussed. Data for molecule II, however, are presented in Table 1 for comparison. The molecular structure of **11-I** is depicted in Figure 6. For the numbering scheme, see Figure 5.

The molecular structure of **11** shows a dinuclear double-stranded helicate with the zinc ions embedded in four N donor centres with a distorted tetrahedral geometry. Each zinc ion is coordinated to two N donor atoms of each 2,2′-

 © 2007 Wiley-VCH Verlag GmbH & Co. KGaA, Weinheim 

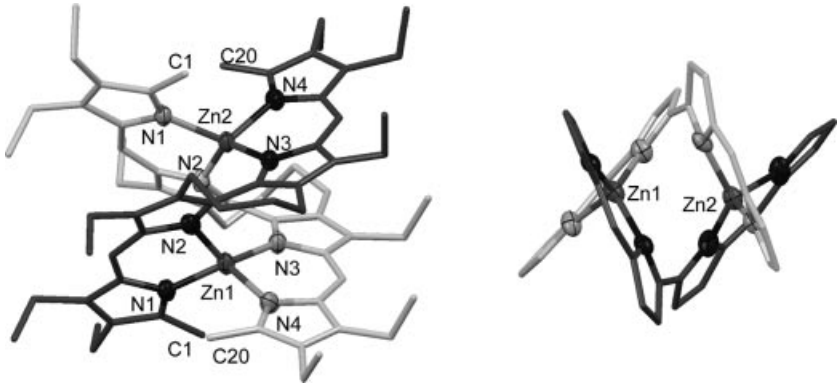


Figure 6. Molecular structure of **11**. Left side: *P* enantiomer of molecule I (carbon atoms as capped sticks and hydrogen atoms omitted for clarity); right side: view of the coordination environments of the zinc ions (alkyl substituents and hydrogen atoms removed). Ellipsoids are set at 40% probability.

bidipyrrin ligand. To allow the binding of two zinc centres to the same ligand the tetrapyrrole has to rotate around the central pyrrole–pyrrole bond C10–C11. The torsion at this position is, however, restricted to 41.3(6)/39.9(5) and 52.4(8)/51.0(7)° [N2–C10–C11–N3 and C9–C10–C11–C12 for the two strands of molecule I, respectively] by the annelated-eight membered ring, so that the ligand resides in the *syn-gauche* conformation with compressed $ZnN_4$ units. In the literature precedent of a nonrestrained dinuclear bidipyrrinato-helicate of zinc[7b] respective torsion angles are as large as 112.3 and 108.8° and indicate an *anti-gauche* conformation of the tetrapyrrole. The compression of the tetrahedral binding environment of the zinc ions in **11** can best be viewed by the dihedral angles between N1–Zn–N2 and N3–Zn–N4 planes, which should be 90° for a tetrahedron but range from 75.8 to 80.9° for **11**. The unrestrained analogue, on the other hand, shows an enlarged dihedral angle of 102.0°. The Zn–N distances of **11** [1.974(3)–2.030(4) Å] and the literature precedent (1.982–1.996 Å) do not differ much, but the zinc···zinc distance of **11** shrinks dramatically from 4.891 Å to 3.443 Å as a result of the backbone constraint. It should be noticed that the eight-membered rings do not form a single low-energy conformer but are found to reside either in a twist or boat conformation.[17]

The helicates of **11** arrange in pillars, which propagate along the crystallographic *b* axis (Figure 7). Next neighbours within these pillars are always of a different structure (i.e., molecule I next to molecule II and vice versa), and are alternately 10.116 and 10.149 Å apart from each other. With respect to the stereochemistry of the helicates, it is remarkable that only one enantiomeric form is contained in each chain, thus forming chiral *M*- or *P*-helical pillars. Heli-

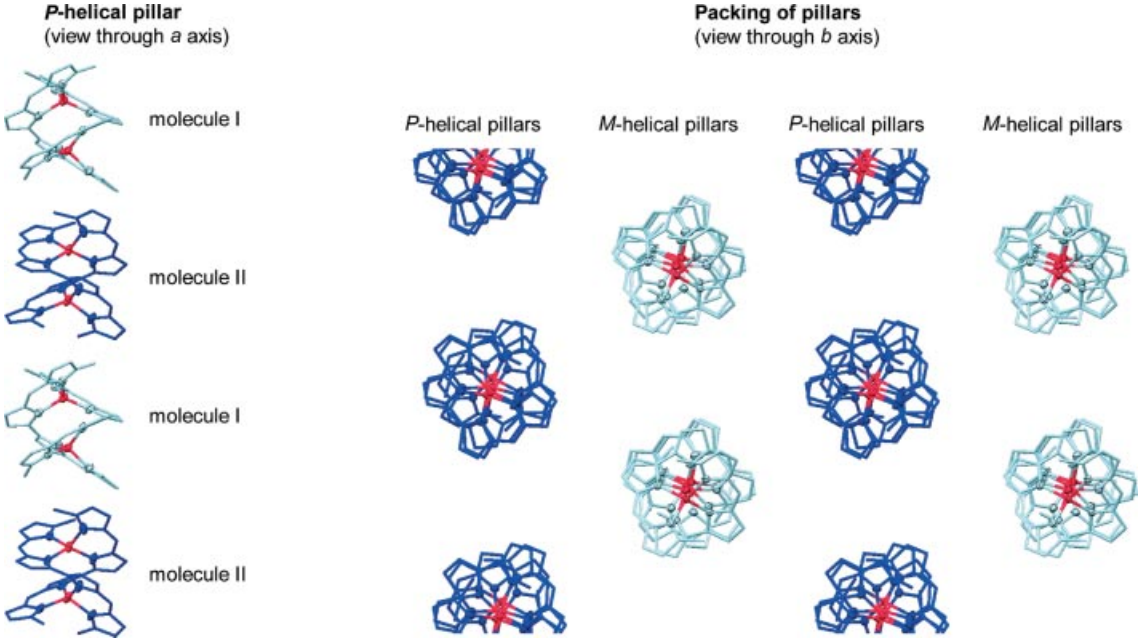


Figure 7. Packing of **11** in the crystal. Left side: *P*-helical pillar formed by the alternating arrangement of *P*-helical isomers of molecules I (bright) and II (dark). Right side: view along the pillars propagating in the crystallographic *b* axis (*P*-helices dark, *M*-helices bright). The ellipsoids are set at 40% probability. Alkyl side chains and hydrogen atoms removed for clarity.

 © 2007 Wiley-VCH Verlag GmbH & Co. KGaA, Weinheim 

cal pillars with both senses are then densely packed in the crystal as shown on the right in Figure 7.

Copper complexes of 2,2′-bidipyrrins usually form either in the type **A** or the type **C** structure, depending on the reaction conditions.[11f,12c] In this case, the outcome of the reaction of **1** and copper acetate depends critically on the choice of the added base. If concentrated ammonia is added to a mixture of **1** and excess copper(II) acetate in methanol, only the immediate formation of a brownish-red monomeric species **12** of type **A** is observed. Using sodium methoxide results in a mixture of **12** and some green dimeric species **13** of type **C**, which becomes the major component if only sodium acetate is added to absorb the released protons. In either case, however, the separation and isolation of **12** and **13** is quite simple because of their large differences in solubility. Monomeric **12** tends to crystallize almost quantitatively from methanolic solutions (up to 65% yield), while **13** is soluble even in cold pentane and can thus be conveniently extracted from the reaction mixtures and isolated in up to 54% yield. The compositions of both compounds were confirmed by combustion analysis and mass spectrometry.

EPR spectroscopy shows the expected signal for **12** in dichloromethane solution at ambient temperature with $g_{iso}$ = 2.096 and a quartet with $A_{Cu}$ = 82.1 G. This spectrum is identical to the one described before for the copper chelate of the unrestrained ligand **8**.[12c] Complex **13**, on the other hand, is EPR-silent under these conditions. As no well-resolved $^1$H NMR spectrum was observed, we conclude that the $Cu^{II}$ atoms of **13** are weakly antiferromagnetically coupled. The UV/Vis spectra of **12** and **13** are shown in Figure 8. Both are clearly governed by the π–π* transitions of their 2,2′-bidipyrrin ligands, which obviously change with different conformations.

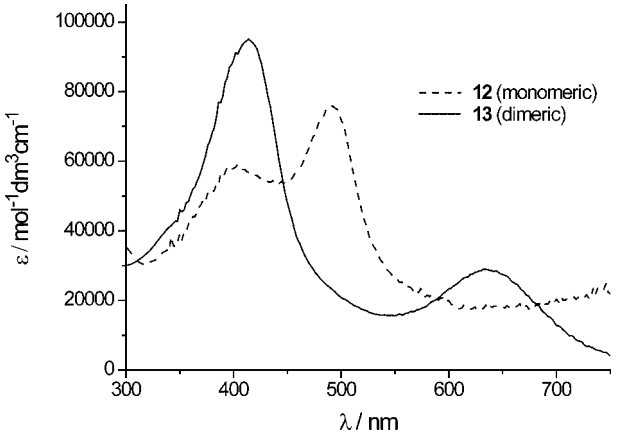


Figure 8. UV/Vis spectra ($CH_2Cl_2$, 293 K) of monomeric and dimeric copper(II) chelates **12** and **13**.

An X-ray crystallographic analysis shows that **13** resides in the assumed bishelical structure. The complex crystallized by slow evaporation of a solution of **13** in dichloromethane/pentane as a solvate **13**·$^1/_3C_5H_{12}$ in the orthorhombic system, space group *Pbcn*. Two independent molecules I and II and their respective enantiomers are found in the unit cell. Crystallographically molecule II as well as the solvent are situated on inversion centres, which explains the formula of the solvate. The eight-membered rings of molecule I and the solvent are disordered. Because of the severity of the disorder the solvent molecule was treated with the SQUEEZE command in Platon. The disorder of the eight-membered rings of molecule I is very severe, and the most disordered methylene groups had to be refined in two positions with occupancy factors of 0.5 (C22, C23) and 0.8422/0.1578 (C53, C54) and with additional restraints. Only the molecular parameters of molecule II (Figure 9) will be discussed further. Data for both molecules are presented in Table 1.

As for the zinc complex **11** shown above, the copper atoms of **13** are coordinated to both tetrapyrrole strands, which reside in a *syn-gauche* conformation with N2–C10–C11–N3 and C9–C10–C11–C12 torsion angles of 41.1(10) and 53.4(13)°, respectively, in order to accommodate two transition-metal ions. The copper $N_4$ coordination is again that of a compressed tetrahedron, which shows Cu–N bond lengths of 1.939(6)–1.999(6) Å and angles between the N1–Cu–N2 and N3–Cu–N4 planes of 65.18°, even smaller than those seen in **11**. The two copper(II) ions are located only 3.0123(13) Å apart from each other, so that a noticeable antiferromagnetic exchange interaction can be expected. This finding is in agreement with the EPR-silent character of **13**.

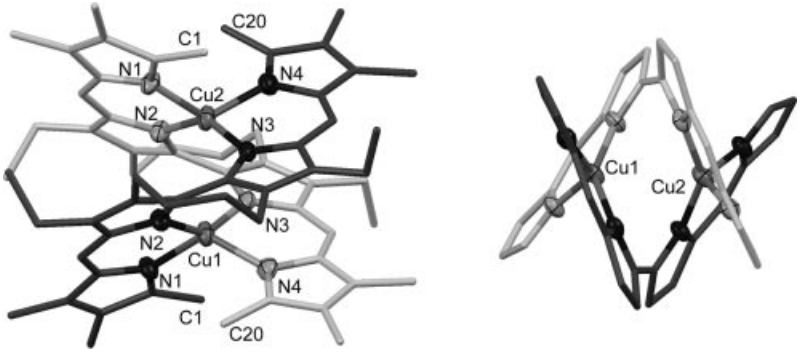


Figure 9. Molecular structure of **13**. Left side: *P* enantiomer of molecule II (carbon atoms as capped sticks and hydrogen atoms omitted for clarity); right side: view of the coordination environments of the copper ions (alkyl substituents and hydrogen atoms removed). Ellipsoids are set at 40% probability.

 © 2007 Wiley-VCH Verlag GmbH & Co. KGaA, Weinheim 

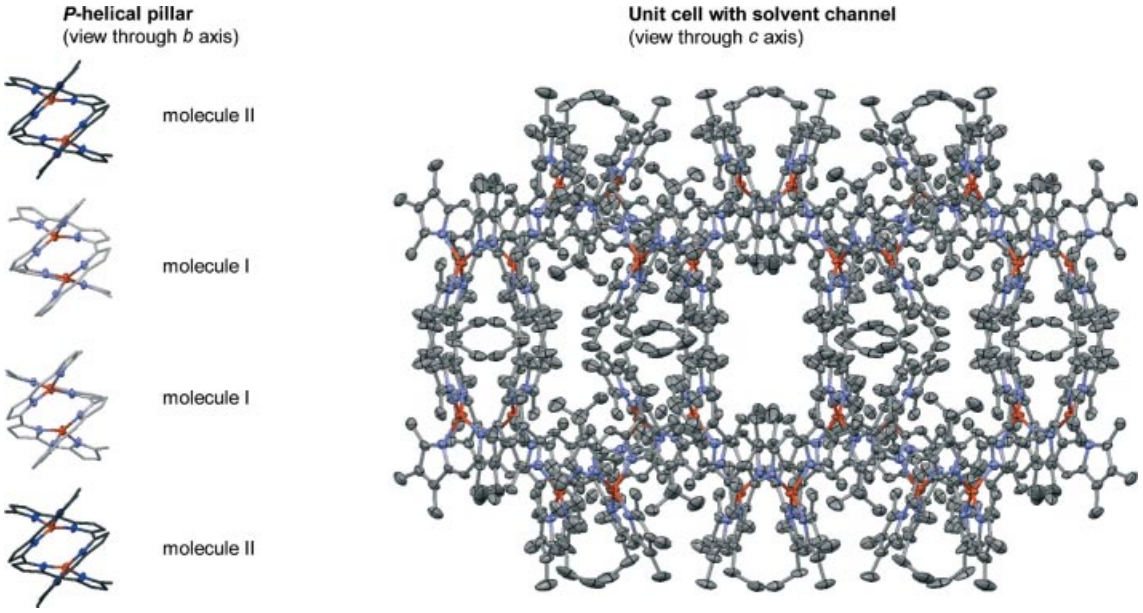


Figure 10. Packing of **13** in the crystal. Left side: *P*-helical pillar formed by *P*-helical isomers of molecule I (bright) and II (dark). Alkyl side chains and hydrogen atoms are removed for clarity. Right side: View down the solvent channel along the crystallographic *c* axis of the unit cell of **13** (solvent removed). The ellipsoids are set at 40% probability. Hydrogen atoms were removed for clarity.

The similarity between the solid-state structures of **11** and **13** comprises even the formation of enantiopure helical pillars from 1D strands of individual molecules, which are found along the crystallographic *a* axis in the crystal of **13**. The molecules are arranged in alternating distances of 9.628 and 11.124 Å (Figure 10). The obvious deviations of the packing pattern, however, originate from the differing sequences of molecules I and II within these strands, which are I – II – I – II for **11** but I – I – II – I – I – II for **13**. This nonalternating mode of the latter opens inner channels along the *c* axis (right in Figure 10), which are filled with disordered solvent molecules in order to stabilize the crystal lattice.

## Conclusions

In summary, we have prepared the first examples of conformationally restricted 2,2′-bidipyrrins **1** and **2** and described syntheses, spectroscopic properties and structural investigations for several transition-metal complexes of type **A** and type **C**. Concerning the coordination modes and binding abilities for different transition-metal ions, the constrained 2,2′-bidipyrrins **1** and **2** are amazingly similar to the unconstrained ones like **8**, although conformative differences in the molecular fine-tune have been shown by the crystallographic analyses. The aim of stabilizing labile ions in the 2,2′-bidipyrrin environment could not be achieved by this approach. However, structural information on dinuclear copper chelates of tetrapyrrolic ligands was obtained for the first time, and the unexpected finding of enantiopure 1D helical pillars for dinuclear complexes with short M···M distances points to further investigations into the use of such restricted ligands for anisotropic materials, metal-organic frameworks (MOFs) and the like.

## Experimental Section

**General:** All reagents and solvents were purchased from commercial sources and used as received. Bipyrrole diester **3**,[16] trimethylpyrrole **6**[18] and diethylmethylpyrrole **7**[19] were prepared as previously reported. NMR spectra were obtained with a Bruker AMX 400 spectrometer in the solvents indicated below. EPR spectra were measured with a Bruker ESP 300 instrument at X-band. Mass spectra were recorded with a Finnigan 90 MAT or a Micromass AutoSpec instrument. *m*/*z* values are given for the most abundant isotopes only. UV/Vis spectra were measured with a Hitachi U-3200 in the range 300–800 nm. Melting points were determined by DTA with a Thermoanalyzer DuPont 9000. For X-ray crystallographic measurements a Bruker Smart Apex with D8 goniometer was used.

CCDC-271753 to -271755 contain the supplementary crystallographic data for this paper. These data can be obtained free of charge from The Cambridge Crystallographic Data Centre via www.ccdc.cam.ac.uk/data_request/cif.request/cif.

**Synthesis of 3,3′-(1,4-Butanediyl)-4,4′-diethyl-2,2′-bipyrrole-5,5′-dicarbaldehyde (5):** The bipyrrole diester **3** (6.95 g, 18.0 mmol) and sodium hydroxide (1.45 g, 36.0 mmol) were mixed with ethylene glycol (120 mL) and heated to reflux with good stirring and under strict exclusion of dioxygen and light for 2 h. Upon cooling in ice, a yellow, light-sensitive solid started to form. Degassed ice water (90 mL) was added dropwise at this temperature, and the solid was filtered, washed with additional water, and dried in the dark in high vacuo. The material was then dissolved in DMF (100 mL) with exclusion of air and moisture and cooled to 0 °C. At this temperature phosphoryl chloride (3.80 mL, 41.0 mmol) was added dropwise. Ten minutes after the addition, cooling was stopped and the mixture stirred at ambient temperature for another 2 h. The mixture was poured into water (400 mL) in an open flask, and a solution of sodium hydroxide in water (30%) was added, until a solid formed. This solid was filtered, washed carefully with water and dried in high vacuo to yield the title compound as a yellow powder. Yield 3.86 g (82%). M.p. 130 °C. $^1$H NMR (400 MHz, $CDCl_3$, 25 °C): $\delta$ = 1.22 (t, 6 H, $J$ = 7.3 Hz, $CH_3CH_2$pyr), 1.81 (br. s, 4 H,

 © 2007 Wiley-VCH Verlag GmbH & Co. KGaA, Weinheim 

C$H_2$CH$_2$pyr), 2.75–2.70 (m, 8 H, CH$_2$C$H_2$pyr and CH$_3$C$H_2$pyr), 9.65 (br. s, 2 H, CHO), 11.56 (br. s, 2 H, NH) ppm. $^{13}$C{$^1$H} NMR (100 MHz, $CDCl_3$, 25 °C): $\delta$ = 17.0, 17.1, 21.9, 26.5, 124.4, 129.3, 130.0, 138.9, 177.4 ppm. HRMS (ESI) calcd. for $C_{18}H_{22}N_2O_2$: 298.1681; obsd. 298.1672, $\Delta$ = 0.9 mmu. $C_{18}H_{22}N_2O_2$ (298.38): calcd. C 72.46, H 7.43, N 9.39; found C 72.39, H 7.26, N 9.45.

**Synthesis of 3,3′-(1,4-Butanediyl)-4,4′-diethyl-8,8′,9,9′,10,10′-hexamethyl-2,2′-bidipyrrin (1) as Bis(hydroperchlorate):** A suspension of **5** (100 mg, 0.33 mmol) and 2,3,4-trimethylpyrrole (**6**) (80 mg, 0.74 mmol) in methanol (5 mL) was heated to 60 °C. At this temperature perchloric acid (1 mL of a 70% solution in water) was added at once and heating was discontinued. The colour of the mixture changed immediately to dark green. The product crystallized upon cooling in ice as a dark solid, which was filtered, washed with small portions of ice-cold methanol, and dried in vacuo to yield a green solid. Yield 123 mg (50%). M.p. 151 °C (dec.). $^1$H NMR (400 MHz, $CDCl_3$, 25 °C): $\delta$ = 1.19 (t, 6 H, $J$ = 7.3 Hz, C$H_3$CH$_2$pyr), 1.80 (m, 4 H, C$H_2$CH$_2$pyr), 2.00, 2.25 (2×s, 12 H, 2×C$H_3$pyr), 2.58–2.73 (m, 8 H, CH$_2$C$H_2$pyr and CH$_3$C$H_2$pyr), 2.76 (s, 6 H, *term*-CH$_3$), 7.06 (s, 2 H, *meso*-H), 11.47 (br. s, 2 H, NH), 12.23 (br. s, 2 H, NH) ppm. $^{13}$C{$^1$H} NMR (100 MHz, $CDCl_3$, 25 °C): $\delta$ = 9.2, 10.4, 14.0, 16.2, 18.2, 22.6, 26.1, 118.9, 127.7, 128.9, 129.6, 131.7, 137.1, 143.5, 144.9, 161.7 ppm. MS (FAB): 481 [M – ($HCl_2O_8$)]$^+$. UV/Vis ($CH_2Cl_2$): $\lambda_{max}$ ($\varepsilon$, L mol$^{-1}$ cm$^{-1}$) = 330 (23000), 435 (27000), 565 (36000) nm. $C_{32}H_{42}Cl_2N_4O_8 \cdot 3H_2O$ (735.649): calcd. C 52.25, H 6.58, N 7.62; found C 52.39, H 6.56, N 7.85.

**Synthesis of 3,3′-(1,4-Butanediyl)-4,4′,8,8′,9,9′-hexaethyl-10,10′-dimethyl-2,2′-bidipyrrin (2) as Bis(hydroperchlorate):** Complex **2** was prepared from **3** (100 mg, 0.33 mmol) and 3,4-diethyl-2-methylpyrrole (**7**) (100 mg, 0.74 mmol) as described above for **1** and yielded a brown-violet powder. Yield 128 mg (48%). M.p. 236 °C (dec.). $^1$H NMR (400 MHz, $CD_2Cl_2$, 25 °C): $\delta$ = 1.17, 1.25, 1.27 (6×t, 18 H, $J$ = 7.3 Hz, C$H_3$CH$_2$pyr), 1.86 (m, 4 H, C$H_2$CH$_2$pyr), 2.54 (q, 4 H, $J$ = 7.3 Hz, CH$_3$C$H_2$pyr), 2.68–2.82 (m, 12 H, CH$_2$C$H_2$pyr and CH$_3$C$H_2$pyr), 2.73 (s, 6 H, *term*-CH$_3$), 7.25 (s, 2 H, *meso*-H), 10.55 (br. s, 2 H, NH), 11.17 (br. s, 2 H, NH) ppm. $^{13}$C{$^1$H} NMR (100 MHz, $CD_2Cl_2$, 25 °C): $\delta$ = 13.7, 14.4, 15.9, 16.6, 17.0, 17.4, 18.4, 22.6, 26.2, 119.2, 129.3, 130.4, 131.3, 133.8, 137.2, 145.8, 150.4, 162.5 ppm. MS (FAB): 537 [M – ($HCl_2O_8$)]$^+$. UV/Vis ($CH_2Cl_2$): $\lambda_{max}$ ($\varepsilon$, L mol$^{-1}$ cm$^{-1}$) = 330 (24000), 430 (27000), 565 (37000) nm. $C_{36}H_{50}Cl_2N_4O_8 \cdot H_2O$ (755.725): calcd. C 57.22, H 6.94, N 7.41; found C 57.35, H 6.66, N 7.42.

**Synthesis of 3,3′-(1,4-Butanediyl)-4,4′-diethyl-8,8′,9,9′,10,10′-hexamethyl-2,2′-bidipyrrinatonickel(II) (9):** A solution of nickel acetate tetrahydrate (50 mg, 0.20 mmol) in methanol (3 mL) was added to a suspension of **1** (100 mg, 0.15 mmol) and sodium acetate (100 mg, 1.21 mmol) in methanol (10 mL) and the resulting mixture was stirred for 30 min at ambient temperature. The solvent was removed in vacuo, and the residue was purified by silica chromatography with dichloromethane/*n*-hexane (1:1). The greenish-brown fraction was collected and the solvent was removed to yield **9** as a violet solid. Yield 44 mg (54%). M.p. 239 °C. $^1$H NMR (400 MHz, $C_6D_6$, 25 °C): $\delta$ = 1.10 (t, 6 H, $J$ = 7.3 Hz, C$H_3$CH$_2$pyr), 1.39 (s, 6 H, CH$_3$pyr), 1.58–1.54 (m, 2 H, C$H_2$CH$_2$pyr), 1.66 (s, 6 H, CH$_3$pyr), 1.85–1.75 (m, 2 H, C$H_2$CH$_2$pyr), 2.20–2.52 (m, 8 H, CH$_2$C$H_2$pyr and CH$_3$C$H_2$pyr), 2.44 (s, 6 H, *term*-CH$_3$), 6.24 (s, 2 H, *meso*-H) ppm. $^{13}$C{$^1$H} NMR (100 MHz, $C_6D_6$, 25 °C): $\delta$ = 9.3, 9.7, 16.3, 17.9, 18.4, 25.2, 26.6, 120.2, 125.1, 126.2, 133.8, 138.8, 140.8, 141.9, 152.1, 168.4 ppm. HRMS (ESI) calcd. for $C_{32}H_{38}N_4Ni$: 536.24498; obsd. 536.24629, $\Delta$ = 1.31 mmu. UV/Vis ($CH_2Cl_2$): $\lambda_{max}$ ($\varepsilon$, L mol$^{-1}$ cm$^{-1}$) = 350 (20000), 430 (81000), 530 (18000), 610sh (12000) nm. $C_{32}H_{38}N_4Ni$ (537.364): calcd. C 71.52, H 7.13, N 10.43; found C 71.13, H 6.96, N 10.09.

**Synthesis of 3,3′-(1,4-Butanediyl)-4,4′-diethyl-8,8′,9,9′,10,10′-hexamethyl-2,2′-bidipyrrinatopalladium(II) (10):** A solution of palladium acetate (59 mg, 0.26 mmol) in methanol (5 mL) was added to a suspension of **1** (180 mg, 0.26 mmol) and sodium acetate (100 mg, 1.21 mmol) in methanol (10 mL) and the resulting mixture was stirred for 30 min at ambient temperature. The solvent was removed in vacuo, and the residue was purified by radial chromatography on silica with dichloromethane/*n*-hexane (1:1). The deep red fraction was collected, the solvent was removed and the residue was recrystallized from dichloromethane/*n*-hexane (1:2) to yield **10** as brownish-red crystals. Yield 94.0 mg (62%). M.p. 202 °C. $^1$H NMR (400 MHz, $C_6D_6$, 25 °C): $\delta$ = 1.12 (t, 6 H, $J$ = 7.3 Hz, C$H_3$CH$_2$pyr), 1.52 (s, 6 H, C$H_3$pyr), 1.71–1.75 (m, 2 H, C$H_2$CH$_2$pyr), 1.77 (s, 6 H, C$H_3$pyr), 1.81–1.86 (m, 2 H, C$H_2$CH$_2$pyr), 2.35–2.41 (m, 6 H, CH$_2$C$H_2$pyr and CH$_3$C$H_2$pyr), 2.54–2.61 (m, 2 H, CH$_2$C$H_2$pyr), 2.57 (s, 6 H, *term*-CH$_3$), 6.40 (s, 2 H, *meso*-H) ppm. $^{13}$C{$^1$H} NMR (100 MHz, $C_6D_6$, 25 °C): $\delta$ = 9.6, 9.9, 16.8, 17.0, 18.1, 22.7, 27.6, 120.6, 124.8, 126.8, 132.4, 138.1, 138.2, 142.0, 151.6, 165.4 ppm. HRMS (ESI) calcd. for $C_{32}H_{38}N_4Pd$: 584.21311; obsd. 584.21205, $\Delta$ = 1.06 mmu. UV/Vis ($CH_2Cl_2$): $\lambda_{max}$ ($\varepsilon$, L mol$^{-1}$ cm$^{-1}$) = 430 (82000), 520 (32000), 770 (11000) nm. $C_{32}H_{38}N_4Pd$ (585.09): calcd. C 65.69, H 6.55, N 9.58; found C 65.42, H 6.41, N 9.37.

**Crystallographic Data for 10:** $C_{32}H_{38}N_4Pd$, green plates obtained by slow concentration of a $CH_2Cl_2$/*n*-hexane solution, crystal size: 0.40 × 0.40 × 0.30 mm, monoclinic, space group $P2_1/n$, $a$ = 8.8497(10), $b$ = 24.160(3), $c$ = 12.8685(14) Å, $\beta$ = 98.421(2)°, $V$ = 2721.7(5) Å$^3$, $\rho_{calcd.}$ = 1.428 g cm$^{-3}$, $Z$ = 4, $2\theta_{max}$ = 50°, Mo-$K_\alpha$ radiation, $\lambda$ = 0.71073 Å, scan mode: $\omega$-scans, $T$ = 193(2) K, 31431 measured, 4798 independent reflections, 4620 reflections observed for $I > 2\sigma(I)$, $\mu$ = 0.710 mm$^{-1}$, solved by Patterson method, refined with full-matrix least-squares on $F^2$ [20], 342 parameters, H atoms refined with isotropic temperature factors. $R$ = 0.0340, $wR$ = 0.0821, residual electron density $\rho$ = 0.730/–0.313 e Å$^{-3}$.

**Bis[3,3′-(1,4-butanediyl)-4,4′,8,8′,9,9′-hexaethyl-10,10′-dimethyl-2,2′-bidipyrrinatozinc(II)] (11):** A suspension of **2**·2HClO$_4$ (85.0 mg, 0.11 mmol) and sodium methoxide (54 mg, 1.0 mmol) in methanol (5 mL) is stirred for 5 min. Zinc acetate hydrate (39 mg, 0.18 mmol) is then added at once, and the solution turns to dark green. After 30 min at ambient temperature the solvent is removed in vacuo, and the dark residue is extracted into pentane. The product is purified by alumina chromatography (basic alumina I) with dichloromethane/*n*-hexane (1:1), and the intense green main fraction is collected. Crystallization from dichloromethane/*n*-hexane (1:3) yields **11** as bronze-coloured plates. Yield 55.0 mg (84%). $^1$H NMR (400 MHz, $C_6D_6$, 25 °C): $\delta$ = 0.96 (t, 12 H, $J$ = 7.4 Hz, C$H_3$CH$_2$pyr), 1.22 (t, 12 H, $J$ = 7.4 Hz, C$H_3$CH$_2$pyr), 1.24 (t, 12 H, $J$ = 7.3 Hz, C$H_3$CH$_2$pyr), 1.32–1.40 (m, 16 H, C$H_2$CH$_2$pyr and CH$_2$C$H_2$pyr), 1.66 (s, 12 H, *term*-CH$_3$), 2.10–2.31 (m, 8 H, CH$_3$C$H_2$pyr), 2.51–2.61 (m, 16 H, CH$_3$C$H_2$pyr), 6.95 (s, 4 H, *meso*-H) ppm. $^{13}$C{$^1$H} NMR (100 MHz, $C_6D_6$, 25 °C): $\delta$ = 14.3, 14.4, 15.7, 17.9, 18.5, 23.0 29.8, 30.1, 32.3, 120.3, 130.0, 137.8, 141.2, 143.5, 150.9, 159.7 ppm; the signals four two C(sp$^2$) atoms are probably hidden underneath the solvent signal. HRMS (ESI) calcd. for $C_{72}H_{92}N_8Zn_2$: 1196.60275; obsd. 1196.60215, $\Delta$ = 0.60 mmu. UV/Vis ($CH_2Cl_2$): $\lambda_{max}$ ($\varepsilon$, L mol$^{-1}$ cm$^{-1}$) = 360 (52000), 475 (138000), 620 (48000) nm. $C_{72}H_{92}N_8Zn_2$ (1200.33): calcd. C 72.04, H 7.73, N 9.34; found C 71.72, H 7.39, N 9.05.

**Crystallographic Data for 11:** $C_{72}H_{92}N_8Zn_2$, green plates obtained by slow concentration of a $CH_2Cl_2$/*n*-hexane solution, crystal size:

 © 2007 Wiley-VCH Verlag GmbH & Co. KGaA, Weinheim 

$0.20 \times 0.18 \times 0.17$ mm, triclinic, space group $P\bar{1}$, $a$ = 14.0038(16), $b$ = 20.206(2), $c$ = 24.556(3) Å, $\alpha$ = 72.719(2), $\beta$ = 84.446(2), $\gamma$ = 78.961(2)°, $V$ = 6505.9(13) Å$^3$, $\rho_{calcd.}$ = 1.225 g cm$^{-3}$, $Z$ = 4, $2\theta_{max}$ = 56.532°, Mo-$K_\alpha$ radiation, $\lambda$ = 0.71073 Å, scan mode: $\omega$-scans, $T$ = 153(2) K, 45469 measured, 22898 independent reflections, 17802 reflections observed for $I > 2\sigma(I)$, $\mu$ = 0.785 mm$^{-1}$, solved by Patterson method, refined with full-matrix least-squares on $F^2$ [20], 1638 parameters and 107 restraints, H atoms refined with isotropic temperature factors. $R$ = 0.0607, $wR$ = 0.1783, residual electron density $\rho$ = 0.969/–0.641 e Å$^{-3}$.

**3,3′-(1,4-Butanediyl)-4,4′-diethyl-8,8′,9,9′,10,10′-hexamethyl-2,2′-bidipyrrinatocopper(II) (12):** A suspension of **1**·2HClO$_4$ (50 mg, 0.07 mmol) in methanol (4 mL) was treated with a solution of copper acetate hydrate (20.0 mg, 0.10 mmol) in ammonia (1 mL of a conc. solution in water) at once. The colour immediately changed from dark green to brown. After 5 min the precipitated product was filtered off and washed with methanol. The solid was extracted with dichloromethane, again filtered, and the solution evaporated in vacuo to leave the title compound as a brown solid. Yield 25.0 mg (65%). M.p. 150 °C. EPR (293 K, $CH_2Cl_2$): $g_{iso}$ = 2.096, $A_{Cu}$ = 82.1 G. MS (FAB): 541 ($M^+$). UV/Vis ($CH_2Cl_2$): $\lambda_{max}$ ($\varepsilon$, L mol$^{-1}$ cm$^{-1}$) = 405 (57000), 495 (76000) nm. $C_{32}H_{38}CuN_4$ (542.217): calcd. C 70.88, H 7.06, N 10.33; found C 70.88, H 7.20, N 10.51.

**Bis[3,3′-(1,4-butanediyl)-4,4′-diethyl-8,8′,9,9′,10,10′-hexamethyl-2,2′-bidipyrrinatocopper(II)] (13):** A suspension of **1**·2HClO$_4$ (50 mg, 0.07 mmol) and sodium acetate (40.0 mg, 0.48 mmol) in methanol (4 mL) was treated with a solution of copper acetate hydrate (20.0 mg, 0.10 mmol). The mixture turned brown, then dark green after 1 min of stirring. After 1 h at ambient temperature the solvent was removed in vacuo and the residue was extracted with pentane. Evaporation of the solvent yielded the title compound as a dark green powder. Yield 20.0 mg (54%). M.p. 108 °C (dec.). HRMS (ESI) calcd. for $C_{64}H_{76}Cu_2N_8$: 1082.47846; obsd. 1082.47874, $\Delta$ = 0.28 mmu. UV/Vis ($CH_2Cl_2$): $\lambda_{max}$ ($\varepsilon$, L mol$^{-1}$ cm$^{-1}$) = 410 (94000), 630 (29000) nm. $C_{64}H_{76}Cu_2N_8$ (1084.434): calcd. C 70.88, H 7.06, N 10.33; found C 70.55, H 6.87, N 10.01.

**Crystallographic Data for 13:** $C_{64}H_{76}N_8Cu_2$, red cubes obtained by slow concentration of a $CH_2Cl_2$/pentane solution, crystal size: $0.27 \times 0.17 \times 0.15$ mm, orthorhombic, space group *Pbcn*, $a$ = 30.3691(19), $b$ = 25.1323(16), $c$ = 22.6084(14) Å, $V$ = 17255.8(19) Å$^3$, $\rho_{calcd.}$ = 1.251 g cm$^{-3}$, $Z$ = 8, $2\theta_{max}$ = 56.488°, Mo-$K_\alpha$ radiation, $\lambda$ = 0.71073 Å, scan mode: $\omega$-scans, $T$ = 173(2) K, 243067 measured, 15182 independent reflections, 12807 reflections observed for $I > 2\sigma(I)$, $\mu$ = 0.786 mm$^{-1}$, solved by direct methods, refined with full-matrix least-squares on $F^2$ [20], 1061 parameters and 74 restraints, H atoms refined with isotropic temperature factors. $R$ = 0.1130, $wR$ = 0.2517, residual electron density $\rho$ = 1.111/–0.642 e Å$^{-3}$.

## Acknowledgments

This work was funded by the Deutsche Forschungsgemeinschaft (DFG). The assistance of Dr. Dirk Leusser with the X-ray analysis of **11** is gratefully acknowledged.

[1] See, e.g.: a) J. Subramanian, J.-H. Fuhrhop in *The Porphyrins* (Ed.: D. Dolphin), Academic Press, New York, **1978**, vol. 2, p. 255; b) R. Bonnett, D. G. Buckley, D. Hamzetash, *J. Chem. Soc., Perkin Trans. 1* **1981**, 322; c) A. L. Balch, M. Mazzanti, B. C. Noll, M. M. Olmstead, *J. Am. Chem. Soc.* **1994**, *116*, 9114; d) R. Koerner, M. M. Olmstead, A. Ozarowski, S. L. Phillips, P. M. Van Calcar, K. Winkler, A. L. Balch, *J. Am. Chem. Soc.* **1998**, *120*, 1274; e) P. A. Lord, B. C. Noll, M. M. Olmstead, A. L. Balch, *J. Am. Chem. Soc.* **2001**, *123*, 10554; f) L. Latos-Grażyński, J. Wojaczyński, R. Koerner, J. J. Johnson, A. L. Balch, *Inorg. Chem.* **2001**, *40*, 4971; g) P. A. Lord, L. Latos-Grażyński, A. L. Balch, *Inorg. Chem.* **2002**, *41*, 1011.

[2] A. Wilks, *Antioxidants Redox Signaling* **2002**, *4*, 603.

[3] a) J.-H. Fuhrhop, A. Salek, J. Subramanian, C. Mengersen, S. Besecke, *Justus Liebigs Ann. Chem.* **1975**, 1131; b) P. K. W. Wasser, J.-H. Fuhrhop, *Ann. N.Y. Acad. Sci.* **1973**, *206*, 533.

[4] See e.g.: a) A. W. Johnson, I. T. Kay, R. Rodrigo, *J. Chem. Soc.* **1963**, 2336; A. W. Johnson, I. T. Kay, *J. Chem. Soc.* **1965**, 1620; P. Bamfield, R. Grigg, A. W. Johnson, R. W. Kenyon, *J. Chem. Soc., C* **1968**, 1259; A. Eschenmoser, *Pure Appl. Chem.* **1969**, *20*, 1; J. Engel, H. H. Inhoffen, *Justus Liebigs Ann. Chem.* **1977**, 767; K. M. Barkigia, M. W. Renner, H. Xie, K. M. Smith, J. Fajer, *J. Am. Chem. Soc.* **1993**, *115*, 7894; S. Neya, K. Nishinaga, K. Ohyama, N. Funasaki, *Tetrahedron Lett.* **1998**, *39*, 5217; E. Vogel, B. Binsack, Y. Hellwig, C. Erben, A. Heger, J. Lex, Y.-D. Wu, *Angew. Chem.* **1997**, *109*, 2725; *Angew. Chem. Int. Ed. Engl.* **1997**, *36*, 2612; R. Paolesse in *The Porphyrin Handbook* (Eds.: K. M. Kadish, K. M. Smith, R. Guilard), Academic Press, San Diego/London, **2000**, vol. 2, p. 201; K. M. Smith in *The Porphyrin Handbook* (Eds.: K. M. Kadish, K. M. Smith, R. Guilard), Academic Press, San Diego/London, **2000**, vol. 1, p. 119.

[5] a) H. Falk, *The Chemistry of Linear Oligopyrroles and Bile Pigments*, Springer, Vienna, **1989**; b) R. G. Khoury, M. O. Senge, J. E. Colchester, K. M. Smith, *J. Chem. Soc., Dalton Trans.* **1996**, 3937.

[6] a) S. Yagi, T. Morinaga, T. Nomura, T. Takagishi, T. Mizutani, S. Kitagawa, H. Ogoshi, *J. Org. Chem.* **2001**, *66*, 3848; b) S. Yagi, H. Sadachi, Y. Kashiwagi, T. Takagishi, T. Mizutani, S. Kitagawa, H. Ogoshi, *Chem. Lett.* **2000**, 1054; c) T. Mizutani, K. Wada, S. Kitagawa, *J. Org. Chem.* **2000**, *65*, 6097; d) T. Mizutani, N. Sakai, S. Yagi, T. Takagishi, S. Kitagawa, H. Ogoshi, *J. Am. Chem. Soc.* **2000**, *122*, 748; e) T. Mizutani, S. Yagi, A. Honmaru, T. Goldacker, S. Kitagawa, M. Furusyo, T. Takagishi, H. Ogoshi, *Supramol. Chem.* **1999**, *10*, 297; f) S. Yagi, R. Yamada, T. Takagishi, N. Sakai, H. Takahashi, T. Mizutani, S. Kitagawa, H. Ogoshi, *Chem. Commun.* **1999**, 911; g) T. Mizutani, S. Yagi, T. Moninaga, T. Nomura, T. Takagishi, S. Kitagawa, H. Ogoshi, *J. Am. Chem. Soc.* **1999**, *121*, 754; h) T. Mizutani, S. Yagi, A. Honmaru, S. Murakami, M. Furusyo, T. Takagishi, H. Ogoshi, *J. Org. Chem.* **1998**, *63*, 8769; i) T. Mizutani, S. Yagi, A. Honmaru, H. Ogoshi, *J. Am. Chem. Soc.* **1996**, *118*, 5318.

[7] a) R. G. Khoury, L. Jaquinod, K. M. Smith, *Tetrahedron* **1998**, *54*, 2339; b) Y. Zhang, A. Thompson, S. J. Rettig, D. Dolphin, *J. Am. Chem. Soc.* **1998**, *120*, 13537; c) A. Thompson, S. J. Rettig, D. Dolphin, *Chem. Commun.* **1999**, 631; d) A. Thompson, D. Dolphin, *Org. Lett.* **2000**, *2*, 1315; e) A. Thompson, D. Dolphin, *J. Org. Chem.* **2000**, *65*, 7870.

[8] a) G. Struckmeier, U. Thewalt, J.-H. Fuhrhop, *J. Am. Chem. Soc.* **1976**, *98*, 278; b) W. S. Sheldrick, J. Engel, *J. Chem. Soc., Chem. Commun.* **1980**, 5.

[9] a) T. E. Wood, A. C. Ross, N. D. Dalgleish, E. D. Power, A. Thompson, X. Chen, Y. Okamoto, *J. Org. Chem.* **2005**, *70*, 9967; b) T. E. Wood, N. D. Dalgleish, E. D. Power, A. Thompson, X. Chen, Y. Okamoto, *J. Am. Chem. Soc.* **2005**, *127*, 5740.

[10] a) I. Spasojević, I. Batinić-Haberle, *Inorg. Chim. Acta* **2001**, *317*, 230; b) I. Spasojević, I. Batinić-Haberle, R. D. Stevens, P. Hambright, A. N. Thorpe, J. Grodkowski, P. Neta, I. Fridovich, *Inorg. Chem.* **2001**, *40*, 726.

[11] a) H. S. Gill, I. Finger, I. Bozidarevic, F. Szydlo, M. J. Scott, *New J. Chem.* **2005**, *29*, 68; b) L. Simkhovich, I. Goldberg, Z. Gross, *Org. Lett.* **2003**, *5*, 1241; c) M. Bröring, D. Griebel, C. Hell, A. Pfister, *J. Porphyrins Phthalocyanines* **2001**, *5*, 708; d) M. Bröring, *Synthesis* **2000**, 1291; e) H. Falk, H. Flödl, U. G.

 © 2007 Wiley-VCH Verlag GmbH & Co. KGaA, Weinheim 

Wagner, *Monatsh. Chem.* **1988**, *119*, 739; f) D. Dolphin, R. L. N. Harris, J. L. Huppatz, A. W. Johnson, I. T. Kay, J. Leng, *J. Chem. Soc., C* **1966**, 98.
[12] a) M. Bröring, E. Cónsul-Tejero, *J. Organomet. Chem.* **2005**, *690*, 5290; b) M. Bröring, C. D. Brandt, E. Cónsul-Tejero, *Z. Anorg. Allg. Chem.* **2005**, *631*, 1793; c) M. Bröring, C. D. Brandt, J. Bley-Escrich, J.-P. Gisselbrecht, *Eur. J. Inorg. Chem.* **2002**, 910; d) M. Bröring, C. D. Brandt, J. Lex, H.-U. Humpf, J. Bley-Escrich, J.-P. Gisselbrecht, *Eur. J. Inorg. Chem.* **2001**, 2549; e) M. Bröring, A. Pfister, K. Ilg, *Chem. Commun.* **2000**, 1407.
[13] For the only exceptions see: a) K. T. Nguyen, S. P. Rath, L. Latos-Grażyński, M. M. Olmstead, A. L. Balch, *J. Am. Chem. Soc.* **2004**, *126*, 6210; b) A. L. Balch, L. Latos-Grażyński, B. C. Noll, M. M. Olmstead, L. Szterenberg, N. Safari, *J. Am. Chem. Soc.* **1993**, *115*, 1422; c) A. L. Balch, L. Latos-Grażyński, B. C. Noll, M. M. Olmstead, N. Safari, *J. Am. Chem. Soc.* **1993**, *115*, 9056.
[14] M. Bröring, C. Hell, C. D. Brandt, E. Cónsul Tejero, *J. Porphyrins Phthalocyanines* **2003**, *7*, 214.
[15] V. Hegde, P. Madhukar, J. D. Madura, R. P. Thummel, *J. Am. Chem. Soc.* **1990**, *112*, 4549.
[16] M. Bröring, S. Link, *Synthesis* **2002**, 67.
[17] R. W. Saalfrank, *Angew. Chem.* **1977**, *89*, 184; *Angew. Chem. Int. Ed. Engl.* **1977**, *16*, 185.
[18] A. Treibs, D. Dinelli, *Justus Liebigs Ann. Chem.* **1935**, *517*, 152.
[19] J. Tang, J. G. Verkade, *J. Org. Chem.* **1994**, *59*, 7793.
[20] G. Sheldrick, *SHELXL-97, Program for Crystal Structure Refinement*, University of Göttingen, Germany, **1997**.

Received: October 19, 2006
Published Online: February 13, 2007

 © 2007 Wiley-VCH Verlag GmbH & Co. KGaA, Weinheim 

DOI: 10.1002/ejic.200601049

# *m*-Terphenylaluminum and -gallium Compounds: Synthesis and Conversion into Low-Coordinate Organogallium Cations

**Jackie D. Young,[a] Masood A. Khan,[a] Douglas R. Powell,[a] and Rudolf J. Wehmschulte*[b]**

**Keywords:** Aluminum / Cations / Gallium / Lewis acids / Low coordination

The reaction of two or 3 equiv. of *m*-terphenyllithium with $MCl_3$ or $AlH_3{\cdot}NMe_3$ (M = Al, Ga) affords the bis(terphenyl)-aluminum and -gallium chloride compounds [{2,6-(4-*t*$BuC_6H_4)_2C_6H_3$}$_2$GaCl] (**1**), [{2,6-(3,5-$Me_2C_6H_3)_2C_6H_3$}$_2$GaCl] (**2**), [{2,6-(4-*t*$BuC_6H_4)_2C_6H_3$}$_3$Ga] (**3**), [(2,6-$Mes_2C_6H_3)_2$AlCl] (**5**), and [(2,6-$Mes_2C_6H_3)_2$AlH] (**7**; Mes = 2,4,6-$Me_3C_6H_2$). While the gallium compounds can be obtained at room temperature, heating is required for the aluminum derivatives. The dibutyl compounds [(2,6-$Mes_2C_6H_3$)$GaBu_2$] (**8**) and [(2,6-$Dipp_2C_6H_3$)$GaBu_2$] (**9**; Dipp = 2,6-*i*$Pr_2C_6H_3$) have also been synthesized by the reaction of *m*-terphenyllithium with $ClGaBu_2$. A metathesis reaction of **2** with Li[Al{$OCH(CF_3)_2$}$_4$] gives the ionic species [(2,6-$Mes_2C_6H_3)_2$Ga]$^+$[Li{Al-[$OCH(CF_3)_2$]$_4$}$_2$]$^-$ (**11**). The cationic butyl(terphenyl)gallium compounds [(2,6-$Mes_2C_6H_3$)GaBu]$^+$ ([**13**]$^+$) and [(2,6-$Dipp_2C_6H_3$)GaBu]$^+$ ([**14**]$^+$) have been prepared by butanide abstraction with the trityl salts of the weakly coordinating anions $[B(C_6F_5)_4]^-$, $[CHB_{11}Br_6Me_5]^-$, and $[CHB_{11}Cl_{11}]^-$. These ionic species are stable at room temperature for days or weeks, although their combinations with the borate anion $[B(C_6F_5)_4]^-$ suffer from $C_6F_5$ migration, which is slow at room temperature and faster at elevated temperatures. The compound [**14**]$^+[CHB_{11}Cl_{11}]^-$ is stable at 70 °C for at least 23 h. Addition of 1-octene to a solution of [**14**]$^+[CHB_{11}Cl_{11}]^-$ in $C_6D_6$ results in olefin exchange and formation of the octyl species [(2,6-$Dipp_2C_6H_3$)Ga(octyl)]$^+$ ([**17**]$^+$), and a slow alkylation of the solvent to afford various octylbenzenes. Hydrolysis of **8** and [**13**]$^+[CHB_{11}Br_6Me_5]^-$ gives the compounds [{(2,6-$Mes_2C_6H_3$)GaBu(μ-OH)}$_2$] (**10**) and [$(BuGa)_4$(μ-$OH)_6$]$^{2+}[CHB_{11}Br_6Me_5]^-_2$ (**16**). All compounds have been characterized by $^1H$ and $^{13}C\{^1H\}$ NMR spectroscopy and mass spectrometry, and compounds **3**, **5**, **7**, **10**, and **16**·4.5$C_6H_6$ have also been characterized by single-crystal X-ray crystallography.
(© Wiley-VCH Verlag GmbH & Co. KGaA, 69451 Weinheim, Germany, 2007)

## Introduction

The enormous progress in the development of weakly coordinating anions during the past 10–15 years has invigorated the research of previously inaccessible, often highly reactive, cationic species.[1–4] Some recent examples in main group chemistry include a three-coordinate stannylium cation [$(Trip)_3Sn$]$^+$ (Trip = 2,4,6-*i*$Pr_3C_6H_2$),[5] two-coordinate gallium and aluminum cations [(2,6-$Mes_2C_6H_3)_2M$]$^+$ (M = Ga,[6] Al;[7] Mes = 2,4,6-$Me_3C_6H_2$), monosubstituted group 14 cations [Cp*Si]$^+$[8] and [(2,6-$Trip_2C_6H_3$)Pb]$^+$,[9] or the interesting phosphorus-based cations $[P_2X_5]^+$ and $[P_5X_2]^+$.[10] On the more applied side, there have been several studies of the potential of low-coordinate cationic organoaluminum compounds as catalysts for olefin oligomerization and polymerization.[11–14] Three-coordinate species have been obtained using monoanionic bidentate ligands,[15,16] and quasi-two-coordination has been achieved by employing two large *m*-terphenyl substituents at a single cationic aluminum center.[7] In an effort to increase the reactivity of the cationic species, we have begun to investigate methods to achieve two-coordination that do not rely on excessive steric protection, which tends to decrease and change reactivity patterns. Based on the observed close secondary Al···C contacts in [(2,6-$Mes_2C_6H_3)_2$Al]$^+$ involving the *ipso*- and *ortho*-carbon atoms of the flanking mesityl groups,[7] we speculate that a single *m*-terphenyl substituent in conjunction with the least-coordinating anions should be sufficient for the stabilization of a low-coordinate cationic center. The bulky substituents are expected to prevent close anion···cation contacts such as those observed in [$Et_2Al$]-[$CB_{11}H_6X_6$] (X = Cl, Br)[13] and to stabilize the electron-poor center through secondary M···C contacts. Ideally, the internal stabilization would be sufficiently labile to allow facile cation···substrate interactions (Scheme 1).

Here, we report the synthesis of a series of terphenylaluminum and -gallium precursor molecules and the conversion of a selection of these into cationic species.

[a] Department of Chemistry and Biochemistry,
University of Oklahoma,
620 Parrington Oval, Room 208, Norman, OK 73019, USA
[b] Department of Chemistry, Florida Institute of Technology,
150 West University Blvd., Melbourne, FL 32901, USA
Fax: +1-321-674-8951
E-mail: rwehmsch@fit.edu

## Results and Discussion

A series of mono- and diterphenylgallium halides and alkyl derivatives has been prepared from standard organo-

 © 2007 Wiley-VCH Verlag GmbH & Co. KGaA, Weinheim 

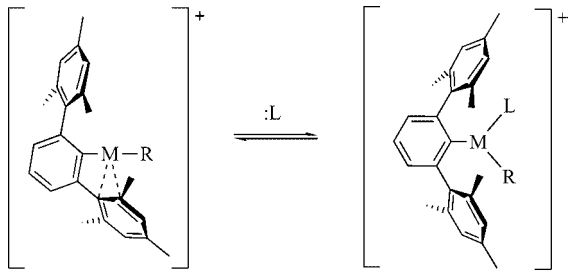


M = Al, Ga; R = alkyl; L = Lewis base, olefin

Scheme 1.

metallic procedures.[17] Selected examples have been converted into cationic species either by salt elimination or alkanide abstraction. Most of the latter reactions were performed on a small (ca. 50 μmol) scale, and the products were characterized by multinuclear NMR spectroscopy and mass spectrometry.

### Diterphenylgallium Compounds

The diterphenylgallium chloride species [{2,6-(4-$t$BuC$_6$H$_4$)$_2$C$_6$H$_3$}$_2$GaCl] (**1**) and [{2,6-(3,5-Me$_2$C$_6$H$_3$)$_2$-C$_6$H$_3$}$_2$GaCl] (**2**) were obtained in moderate yields by the metathesis reaction of 2 equiv. of the coresponding terphenyllithium compound with $GaCl_3$ at room temperature in hexane solution according to Equation (1). Compounds **1** and **2** were isolated as colorless microcrystalline solids that are readily soluble in aromatic solvents or $CH_2Cl_2$ but practically insoluble in hexanes. The synthesis of **1** under slightly different conditions and its X-ray crystal structure have been reported independently.[18] Crystals of **1** obtained from toluene solution are essentially identical to those crystallized from $Et_2O$ solution described by Robinson et al. after taking low-temperature effects in the present data set into consideration.[18]

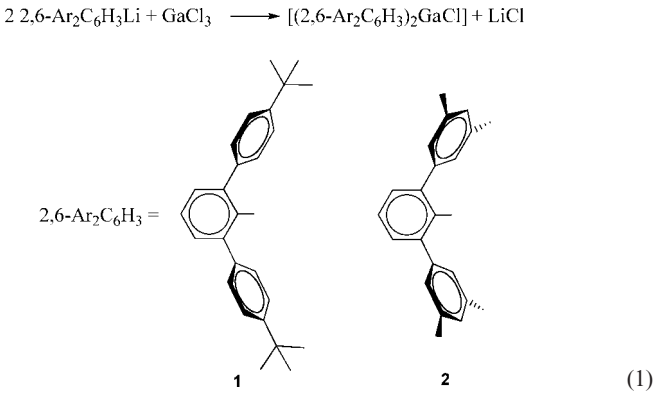


(1)

### Triterphenylgallium

The very crowded compound [{2,6-(4-$t$BuC$_6$H$_4$)$_2$-C$_6$H$_3$}$_3$Ga] (**3**) was initially obtained in small amounts during an attempt to prepare the methyl derivative [{2,6-(4-$t$BuC$_6$H$_4$)$_2$C$_6$H$_3$}$_2$GaMe] by methylation of **1** with methyllithium. Ligand migration in arylgallium compounds is not uncommon and has been described previously.[17] The systematic reaction involving 3 equiv. of 2,6-(4-$t$BuC$_6$H$_4$)$_2$-C$_6$H$_3$Li gave **3** in 34% yield as a colorless, high-melting (m.p. 281 °C), crystalline solid. Its structure (Figure 1) features a slightly distorted trigonal-planar gallium center [Σ(C–Ga–C) = 359.3°] that is efficiently protected by three *m*-terphenyl substituents. The Ga–C bond lengths [1.989(2)–2.010(2) Å] fall within the upper range observed previously for diterphenylgallanes.[18–21] The slightly elongated Ga(1)–C(16) bond [2.010(2) Å] and the corresponding widening of the C(38)–Ga(1)–C(68) angle to 122.57(10)° may be attributed to the steric demands of the *m*-terphenyl substituents. The substituents are arranged in the typical propeller fashion,[18,22,23] and the planes of the central arene rings are rotated out of the $GaC_3$ plane by 39° [C(38) ring], 47° [C(16) ring], and 64° [C(68) ring]. Some minor distortions are found for the C(38) substituent. The central C(38) ring is bent away from the normal linear arrangement by 18.6°, as judged from the angle between the Ga(1)–C(38) and C(38)–C(41) vectors. Similarly, there is a 6.6° angle between the C(39)–C(43) and C(43)–C(46) vectors of the flanking C(43) ring. The shortest C···C contacts between neighboring arene rings are 3.22 Å for C(38)···C(18) and 3.24 Å for C(16)···C(70). Overall, the structure of **3** bears close resemblance to that of the indium analogue [{2,6-(4-$t$BuC$_6$H$_4$)$_2$C$_6$H$_3$}$_3$In].[18]

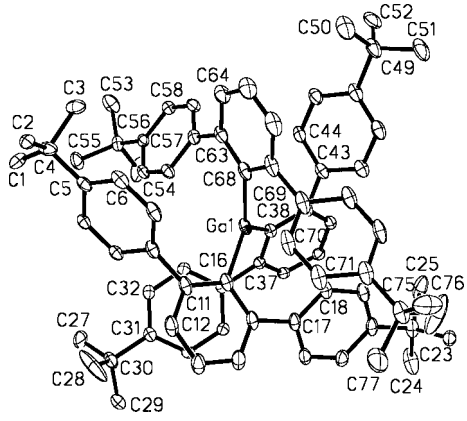


Figure 1. Thermal ellipsoid plot (50% probability ellipsoids) showing the molecular structure of **3**. Hydrogen atoms have been omitted for clarity.

### Diterphenylaluminum Compounds

Whereas the synthesis of the di- and triterphenylgallium compounds **1**–**3** as well as the more crowded species [(2,6-Mes$_2$C$_6$H$_3$)$_2$GaCl][24] (**4**) proceeds at room temperature, the preparation of the aluminum analogue [(2,6-Mes$_2$C$_6$H$_3$)$_2$-AlCl] (**5**) was complicated by the formation of a stable intermediate tentatively characterized as the alanate [(2,6-Mes$_2$C$_6$H$_3$)AlCl$_3$]Li. A closely related compound has been previously observed in the reaction of 2,6-Mes$_2$C$_6$H$_3$Li with $AlBr_3$.[25] The reaction of 2 equiv. of 2,6-Mes$_2$C$_6$H$_3$-

 © 2007 Wiley-VCH Verlag GmbH & Co. KGaA, Weinheim 

Li with $AlCl_3$ at room temperature for 20 h resulted in the formation of a new *m*-terphenyl compound (the alanate) and unreacted 2,6-$Mes_2C_6H_3Li$ in an approximately 1:1 ratio according to $^1H$ NMR spectroscopy. The introduction of the second terphenyl substituent requires refluxing in benzene solution. Inadvertent Al–C bond hydrolysis during reflux reduced the yield significantly, and it was difficult to isolate pure **5**. Its crystal structure (Figure 2) is isostructural with that of the gallium congener,[24] but features a significantly shorter Al–Cl bond with a value of 2.1098(12) Å [2.177(5) Å for **4**], which indicates the higher Lewis acidity of aluminum. The Al–C bond lengths, with average values of 1.978 Å, are identical with the Ga–C distances observed for **4**. The shorter Al–Cl distance results in a slight decrease of the C–M–C angle from 153.5(5)° in **4** to 147.52(13)°. Evidence for the steric crowding brought about by two large *m*-terphenyl substituents is apparent in some distortions. For example, as in **3**, the central rings of the substituents are bent away from the ideal linear alignment by 16.2° [C(15) ring] and 12.9° [C(39) ring]. Furthermore, the flanking mesityl groups are pushed out of the plane of the C(15) ring by 12.8° [C(9) mesityl] and 10.4° [C(16) mesityl].

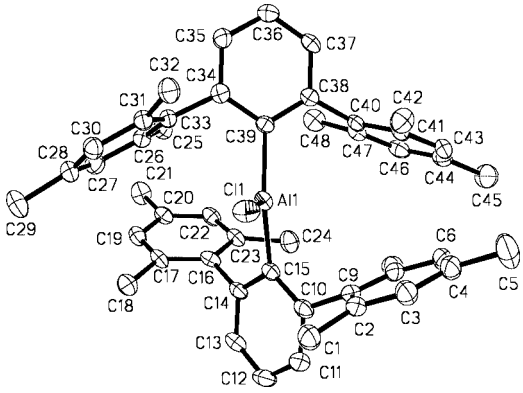


Figure 2. Thermal ellipsoid plot (50% probability ellipsoids) showing the molecular structure of **5**. Hydrogen atoms have been omitted for clarity.

The hydride derivative [(2,6-$Mes_2C_6H_3)_2GaH$] (**6**) has been prepared by the reaction of the chloride **4** with LiHBEt$_3$.[21] Because **5** could only be isolated in moderate yields, a different route was selected for the preparation of the aluminum hydride [(2,6-$Mes_2C_6H_3)_2AlH$] (**7**). Thus, reaction of 2,6-$Mes_2C_6H_3Li$ with [(2,6-$Mes_2C_6H_3)AlH_2$]·$OEt_2$[26] [Equation (2)] at 70 °C for 30 min afforded **7** in moderate to good yields in the form of well-shaped colorless crystals.[7]

$$2,6\text{-}Mes_2C_6H_3Li + [(2,6\text{-}Mes_2C_6H_3)AlH_2]\cdot OEt_2 \longrightarrow [(2,6\text{-}Mes_2C_6H_3)_2AlH] + LiH \quad (2)$$

**7**

Compound **7** is only the second example of an aluminum hydride that is three-coordinate in the solid state.[27] Similar to [Mes*$_2$AlH][27] (Mes* = 2,4,6-$tBu_3C_6H_2$), the monomeric character of **7** is also due to steric protection, as can clearly be seen in the crystal structure (Figure 3). The overall structural features are similar to those of **5** and **6**, although the distortions are less pronounced than in the structure of **5**. The Al–H distance is 1.436(18) Å and the Al–C distances average 1.990 Å. As was found for the corresponding gallium compounds **4** and **6**, the C–Al–C angle in **7**, with a value of 137.62(5)°, is also significantly smaller than in the chloride **5** [147.52(13)°, see above]. The terphenyl substituents display a staggered arrangement with respect to each other to minimize steric repulsion. The angles between the Al(1)–C(15) and C(15)–C(12) vectors and the Al(1)–C(39) and C(39)–C(36) vectors are 11.7° and 12.8°, respectively, and there are only minor distortions within the terphenyl substituents, thus indicating less steric crowding than for **5**.

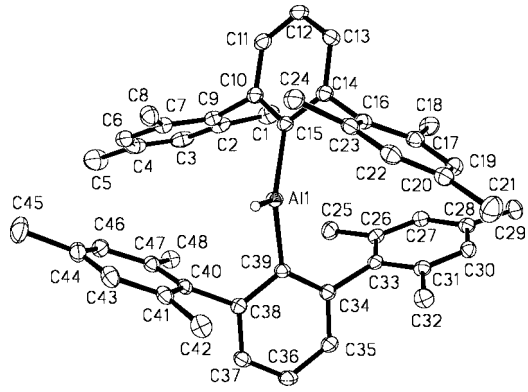


Figure 3. Thermal ellipsoid plot (50% probability ellipsoids) showing the molecular structure of **7**. Hydrogen atoms, with the exception of the hydrogen atom bound to the aluminum atom, have been omitted for clarity.

### Dibutylgallium Compounds

The dibutyl(terphenyl)gallanes [(2,6-$Mes_2C_6H_3)GaBu_2$] (**8**) and [(2,6-$Dipp_2C_6H_3)GaBu_2$] (**9**) (Dipp = 2,6-*i*$Pr_2C_6H_3$) were synthesized by the reaction of terphLi with $ClGaBu_2$ [Equation (3)].

$$2,6\text{-}Ar_2C_6H_3Li + ClGaBu_2 \longrightarrow [(2,6\text{-}Ar_2C_6H_3)GaBu_2] + LiCl \quad (3)$$

2,6-$Ar_2C_6H_3$ =

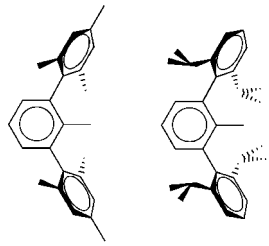

**8** **9**

The presence of the flexible *n*-butyl groups apparently prevents the formation of crystals of sufficient quality for X-ray diffraction. In fact, **8** could only be obtained as fine colorless needles, and **9** was initially isolated as a colorless oil, which eventually solidified after a month at room temperature. Despite several attempts, compounds **8** and **9**

 © 2007 Wiley-VCH Verlag GmbH & Co. KGaA, Weinheim 

could not be obtained analytically pure. Both compounds are readily soluble in aliphatic and aromatic solvents. Their composition was confirmed by $^1H$ and $^{13}C\{^1H\}$ NMR spectroscopy as well as the isolation of a hydrolysis product of **8**, namely $[\{(2,6\text{-}Mes_2C_6H_3)GaBu(\mu\text{-}OH)\}_2]$ (**10**). The latter compound was isolated during an attempt to grow X-ray quality crystals by slow concentration of a 1-octene solution of **8** inside a dry box. Its structure (Figure 4) closely resembles those of the related dimeric hydroxy-bridged compounds $[\{(2,6\text{-}Mes_2C_6H_3)GaMe(\mu\text{-}OH)\}_2]$ and $[\{(2,6\text{-}Mes_2C_6H_3)GaCl(\mu\text{-}OH)\}_2]$.[21] The terphenyl substituents in the centrosymmetric molecule are positioned in a mutual *trans* orientation. The Ga–O bond lengths are essentially identical [1.947(5) and 1.952(5) Å] and are close to those found in the above-mentioned methyl derivatives and chlorides.[21]

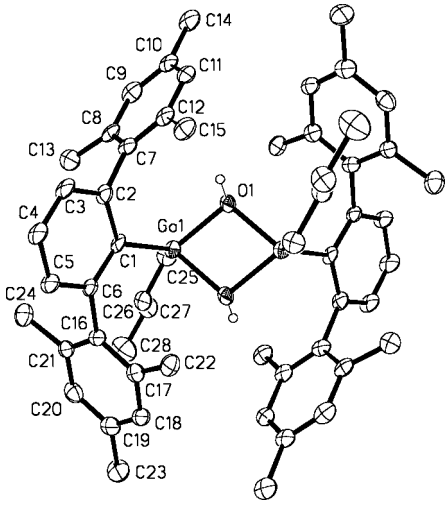


Figure 4. Thermal ellipsoid plot (50% probability ellipsoids) showing the molecular structure of **10**. Hydrogen atoms, with the exception of those bound to oxygen atoms, have been omitted for clarity.

## Cation Formation

We have shown previously that the two-coordinate cationic species $[(2,6\text{-}Mes_2C_6H_3)_2Ga]^+$ and $[(2,6\text{-}Mes_2C_6H_3)_2Al]^+$ can be prepared by chloride abstraction[6] with the lithium alanate $Li[Al\{OCH(CF_3)_2\}_4]$ or by alkanide or hydride abstraction with the trityl salt $[Ph_3C]^+[B(C_6F_5)_4]^-$.[7,21] Chloride abstraction with 2 equiv. of $Li[Al\{OCH(CF_3)_2\}_4]$ also converted the sterically less encumbered diterphenylgallium chloride **2** cleanly into the cationic species $[(2,6\text{-}Ar_2C_6H_3)_2Ga]^+[Li(Al\{OCH(CF_3)_2\}_4)_2]^-$ (**11**; Ar = 3,5-$Me_2C_6H_3$). Interestingly, the analogous reaction with compound **1** to afford **12** (Ar = 4-*t*Bu$C_6H_4$) did not proceed. Monitoring of the reaction in $C_6D_5Cl$ by $^1H$ NMR spectroscopy showed broadening of some of the aromatic signals ($\delta$ = 7.4–7.0 ppm), but no further reaction was observed even after prolonged heating at 70 °C. Although attempts to isolate crystals of **11** have not yet been successful, the stoichiometry of the products is supported by the presence of the methine hydrogen signal of the anion in a relative intensity corresponding to eight hydrogen atoms in the $^1H$ NMR spectra. In addition, mass spectrometric analysis of the solution showed the presence of the cation $[\{2,6\text{-}(3,5\text{-}Me_2C_6H_3)_2C_6H_3\}_2Ga]^+$. Chlorobenzene solutions of **11** remain unchanged at room temperature for days, which suggests a surprising stability of this cationic species considering that the related electron-deficient diterphenylboranes $(2,6\text{-}Ar_2C_6H_3)_2BH$ undergo C–H activation below room temperature to give 9-borafluorenes and $H_2$.[28]

Conversion of the dibutyl(terphenyl)gallanes **8** and **9** into the cationic species $[(2,6\text{-}Mes_2C_6H_3)GaBu]^+$ ([**13**]$^+$) and $[(2,6\text{-}Dipp_2C_6H_3)GaBu]^+$ ([**14**]$^+$), was accomplished by treatment with the trityl salts $[CPh_3]^+[A]^-$ [A = $B(C_6F_5)_4$,[29] $CHB_{11}Br_6Me_5$,[30] $CHB_{11}Cl_{11}$[31]] according to Equation (4).

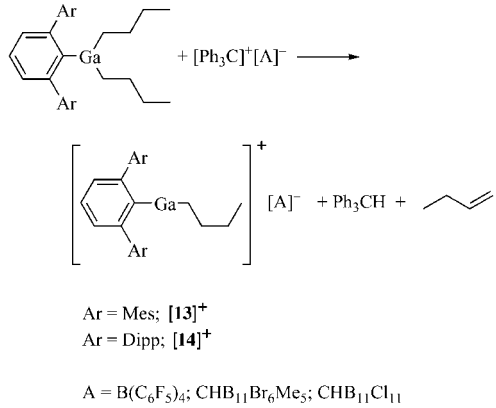


(4)

These reactions were performed in NMR tubes sealed with J. Young valves or in small Schlenk flasks. The progress of the reactions was monitored by recording the signals due to C*H*$Ph_3$ and C*H*$_2$C*H*$CH_2CH_3$ in the $^1H$ NMR spectrum. The reactions are relatively fast: they are complete within a few hours when both reactants are soluble in the chosen solvent. Otherwise, the reaction rate is dependent on the solubility of the trityl salt, with $[CPh_3]^+[CHB_{11}Cl_{11}]^-$ being the least soluble. Despite the small scale, all reactions are readily reproducible. It has not been possible to isolate any of the products in pure or crystalline form so far due to their tendency to form oils. Nevertheless, the identities of the products have been established by multinuclear NMR spectroscopy and ESI mass spectrometry. The best general strategy for obtaining the highest-purity samples involves performing the reaction in benzene solution followed by phase separation and washing of the dense phase containing the product with benzene. All ionic products are soluble in chlorobenzene, bromobenzene, or their mixtures with benzene. Only [**13**]$^+[CHB_{11}Br_6Me_5]^-$ is readily soluble in benzene. The other combinations of [**13**]$^+$[A]$^-$ and [**14**]$^+$[A]$^-$ form dense liquid phases, so-called liquid clathrates.[32] The solubility of [**13**]$^+[CHB_{11}Cl_{11}]^-$ lies between these extremes: a liquid clathrate separates at high concentrations (ca. 0.08 M) which can be redissolved upon dilution with $C_6D_6$. Clathrate formation has been observed previously in our laboratory for the compounds $[(2,6\text{-}Mes_2C_6H_3)_2M]^+$-

 © 2007 Wiley-VCH Verlag GmbH & Co. KGaA, Weinheim 

$[B(C_6F_5)_4]^-$ (M = Al, Ga), which exist as separate ions.[7,21] Hence, we propose clathrate formation as supporting evidence for anion/cation separation in $[\mathbf{13}]^+[A]^-$ and $[\mathbf{14}]^+[A]^-$. Additional evidence is found in the $^{19}F$ NMR chemical shifts of $[\mathbf{13}]^+[B(C_6F_5)_4]^-$ and $[\mathbf{14}]^+[B(C_6F_5)_4]^-$, which are close to the values reported for the "free" anion.[16] However, a weak cation···$XC_6H_5$ (solvent) contact (X = Cl, Br) cannot be ruled out. Such interactions have been described for [(*i*Pr$_2$-ATI)MR][$B(C_6F_5)_4$](ClPh) (M = Al, Ga, In; *i*Pr$_2$-ATI = *N*,*N*′-diisopropylaminotroponiminate).[33]

The $^1H$ NMR spectrum of a $C_6D_6$ solution of $[\mathbf{13}]^+[CHB_{11}Br_6Me_5]^-$ shows two sets of signals for the *o*- and *o*′′-methyl groups and the *m*- and *m*′′-hydrogen atoms of the flanking mesityl groups of the *m*-terphenyl ligand due to a loss of symmetry. This, together with the fact that $[\mathbf{13}]^+[CHB_{11}Br_6Me_5]^-$ is soluble in benzene, may be viewed as good evidence for its existence as a tight ion-pair with close Ga···Br contacts similar to those observed for $[Et_2Al]^+[CB_{11}H_6X_6]^-$ (X = Cl, Br).[13] In keeping with an intermediate behavior, the $^1H$ NMR spectrum of $[\mathbf{13}]^+[CHB_{11}Cl_{11}]^-$ in $C_6D_6$ solution does not display an analogous broadening.

All ionic compounds described here are stable in solution at room temperature for days if not weeks. The $[B(C_6F_5)_4]^-$ salts are susceptible to $C_6F_5$ migration at elevated temperatures, a common occurrence for this anion in combination with strong Lewis acids.[34] For example, heating of a solution of $[\mathbf{14}]^+[B(C_6F_5)_4]^-$ at 60 °C for 16 h results in the clean formation of a 1:1 mixture of [(2,6-Dipp$_2$C$_6$H$_3$)GaBu($C_6F_5$)] (**15**) and $B(C_6F_5)_3$. These compounds were identified by $^1H$ and $^{19}F$ NMR spectroscopy, the latter by comparison with an authentic sample and published data[35] and the former by the similarity of its $^{19}F$ NMR signals with those of the related (pentafluorophenyl)aluminum species [$Me_nAl(C_6F_5)_{3-n}$].[34] On the other hand, no change of the NMR spectra of the carborane salt $[\mathbf{14}]^+[CHB_{11}Cl_{11}]^-$ was observed after heating at 68–70 °C for 23 h, thereby indicating a surprisingly high stability of this compound.

The difficulty of obtaining pure samples of any of the new ionic compounds may be illustrated by the fact that repeated attempts to crystallize $[\mathbf{13}]^+[CHB_{11}Br_6Me_5]^-$ only afforded a few crystals of the hydrolysis product $[(BuGa)_4(\mu\text{-}OH)_6]^{2+}[CHB_{11}Br_6Me_5]^-_2$ (**16**), whose structure consists of layers of $[(BuGa)_4(\mu\text{-}OH)_6]^{2+}$ dications and $[CHB_{11}Br_6Me_5]^-$ anions separated by benzene molecules. The cations and anions are well separated, but are kept in contact through hydrogen bonding between the hydroxy hydrogen atoms of the cations and bromine atoms of the anions. These contacts can be as close as 2.44 Å for H(3)···Br(3A). The dications are cage molecules with a distorted adamantane $Ga_4O_6$ framework (Figure 5). The neutral analogue $[\{(Me_3Si)_3Ga\}_4(\mu\text{-}OH)_4(\mu\text{-}O)_2]$ has been reported previously.[36] The metric parameters of both compounds are comparable, with average Ga–O and Ga–C bond lengths of 1.897(6) and 1.933(1) Å and O–Ga–O and Ga–O–Ga angles of 96.9(1.8)° and 130.8(1.0)° in **16** (Table 3) vs. 1.895 and 1.998 Å and 100.46 and 125.42°, respectively, in $[\{(Me_3Si)_3Ga\}_4(\mu\text{-}OH)_4(\mu\text{-}O)_2]$.

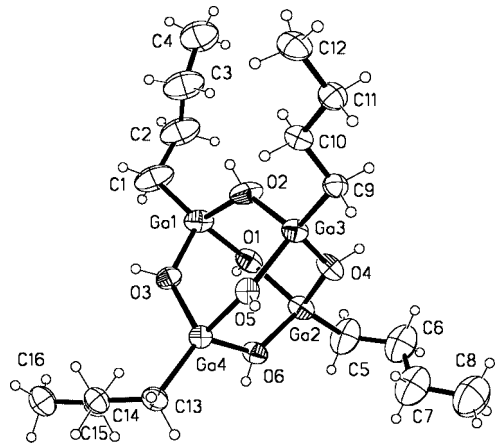


Figure 5. Thermal ellipsoid plot (30% probability ellipsoids) showing the molecular structure of the dication in **16**.

### Reaction of $[\mathbf{14}]^+$ with 1-Octene

One of the goals of the preparation of low-coordinate aluminum and gallium cations was the investigation of their interactions with olefins. The NMR spectra obtained during the monitoring of the syntheses of the various cation/anion combinations $[\mathbf{13}]^+[A]^-$ and $[\mathbf{14}]^+[A]^-$ indicated a rather slow reaction with 1-butene. Since $[\mathbf{14}]^+[CHB_{11}Cl_{11}]^-$ is thermally stable, its interaction with 1-octene was investigated more closely. Approximately 1.2 equiv. of 1-octene was added to a solution of $[\mathbf{14}]^+[CHB_{11}Cl_{11}]^-$ in a 6:1 mixture of $C_6D_6$ and $C_6D_5Cl$, and the progress of the reaction was monitored by $^1H$ NMR spectroscopy. About 15 min after the 1-octene addition, the $^1H$ NMR spectrum showed a broadening of the α-C$H_2$ signal, and signals of free 1-octene and 1-butene in an approximately 2:1 ratio were discernible. After 48 h at room temperature, the olefinic signals had almost completely disappeared, and an additional 2.4 equiv. of 1-octene was added after a reaction time of 54 h. This time, only a small amount of free 1-butene was generated, and most of the signals due to the butyl compound $[\mathbf{14}]^+$ were replaced by similar signals that were slightly shifted from their previous positions. Two more additions of 1-octene were undertaken after the olefin had been almost completely consumed. After a total reaction time of 21 d at room temperature, no more olefin signals were present, and the spectrum was dominated by octyl signals, although a slightly broadened multiplet at $\delta$ = 0.21 ppm indicated the presence of a Ga-C$H_2$ group. Analysis of the mixture by ESI mass spectrometry and GC-MS showed the presence of the octyl species [(2,6-Dipp$_2$C$_6$H$_3$)Ga(octyl)]$^+$ ($[\mathbf{17}]^+$) and various octylbenzenes. These preliminary results suggest a facile olefin/alkyl exchange followed by octene isomerization and benzene alkylation. Scheme 2 shows a proposed reaction mechanism. Further work in this area is in progress.

 © 2007 Wiley-VCH Verlag GmbH & Co. KGaA, Weinheim 

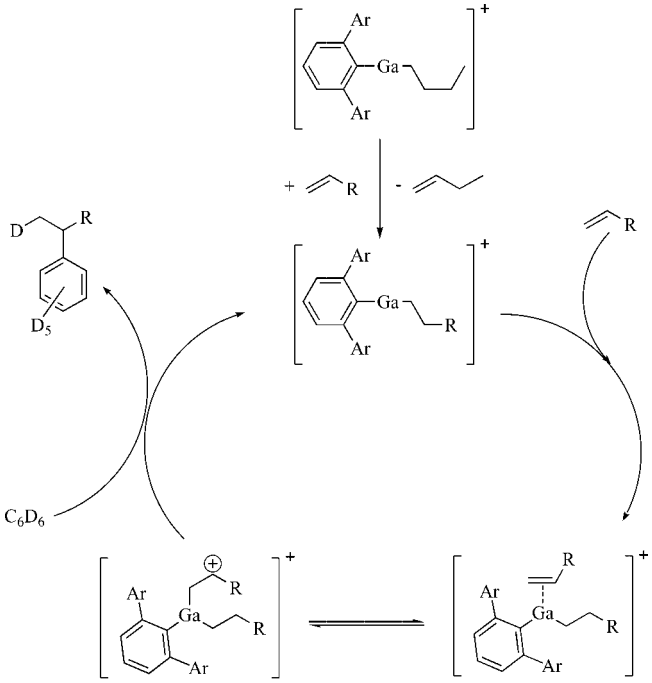


Scheme 2.

## Conclusion

Diterphenylaluminum and -gallium compounds have been prepared by the treatment of 2 equiv. of terphenyllithium with $MCl_3$ or $H_3Al{\cdot}NMe_3$; the synthesis of the aluminum species requires more forcing conditions. Dibutyl(terphenyl)gallanes have also been obtained by treating terphenyllithium with $ClGaBu_2$. The best method for the preparation of cationic gallium species $[(terph)GaR]^+$ is treatment with trityl salts of weakly coordinating anions, although chloride abstraction with a fluorinated lithium tetraalkoxidoalanate can also be used for selected gallium chloride precursors. The ionic compounds are at least moderately stable in aromatic solvents at room temperature, with the compound $[\mathbf{14}]^+[CHB_{11}Cl_{11}]^-$ being thermally stable up to 70 °C. All ionic compounds, with the exception of $[\mathbf{13}]^+[CHB_{11}Br_6Me_5]^-$, form clathrates in benzene solution, which suggests the presence of only weak ion-pairing or even "free" ions. A preliminary study on the interaction of $[\mathbf{14}]^+[CHB_{11}Cl_{11}]^-$ with 1-octene has found facile alkyl/olefin exchange at the cationic gallium center and slow octene isomerization and benzene alkylation.

## Experimental Section

**General Procedures:** All work was performed under anaerobic and anhydrous conditions by using either modified Schlenk techniques or an Innovative Technologies or Vacuum Atmospheres drybox. Solvents were freshly distilled under $N_2$ from sodium, potassium, sodium/potassium alloy, or calcium hydride and degassed twice prior to use, or they were dispensed from an MBraun Solvent Purification System. $AlCl_3$, $GaCl_3$, *n*-butyllithium (1.6 M in hexanes), and MeLi (1.6 M in $Et_2O$) were obtained from commercial suppliers. Compounds 2,6-(4-*t*Bu$C_6H_4$)$_2C_6H_3$Br,[37] 2,6-(4-*t*Bu$C_6H_4$)$_2$-$C_6H_3$Li,[38] 2,6-(3,5-$Me_2C_6H_3$)$_2C_6H_3$Li,[28] [(2,6-$Mes_2C_6H_3$)$_2$AlH] (**7**),[7] $ClGaBu_2$,[39] 2,6-$Mes_2C_6H_3$Li,[40] 2,6-$Dipp_2C_6H_3$Li,[41] and $[Ph_3C][B(C_6F_5)_4]$[29] were synthesized according to literature methods. The carborane compounds $[Ph_3C][CHB_{11}Br_6Me_5]$ and $[Ph_3C][CHB_{11}Cl_{11}]$ were supplied by Prof. Christopher A. Reed and Dr. Kee-Chan Kim from the University of California, Riverside. NMR spectra were recorded with a Varian Mercury 300 MHz, a Varian Unity Plus 400 MHz, a Bruker AMX 360, or a Bruker Avance 400 MHz spectrometer. $^1$H NMR chemical shift values were determined relative to the residual protons in $C_6D_6$ or $CDCl_3$ as internal reference ($\delta$ = 7.15 or 7.26 ppm). $^{13}$C NMR spectra were referenced to the solvent signal ($\delta$ = 128.0 or 77.0 ppm). $^{19}$F NMR spectra were referenced to an external solution of $C_6H_5CF_3$ in $C_6D_6$ ($\delta$ = –63.72 ppm). IR spectra were recorded in the range 4000–400 $cm^{-1}$ with a Nicolet Nexus 470 FTIR spectrometer. Electron impact mass spectra were recorded with a Finnigan MAT Polaris spectrometer and electrospray mass spectra with a Micromass Q-ToF or a JEOL AccuTOF DART spectrometer. Melting points were determined in Pyrex capillary tubes sealed under nitrogen with a Mel-Temp apparatus and are uncorrected. Elemental analyses were performed by Desert Analytics in Tucson, AZ.

**[{(4-*t*Bu$C_6H_4$)$_2C_6H_3$}$_2$GaCl] (1):** A solution of (4-*t*Bu$C_6H_4$)$_2$-$C_6H_3$Br (1.00 g, 2.4 mmol) in hexanes (60 mL) was treated with a hexane solution of *n*-butyllithium (0.97 mL, 2.78 M) at –78 °C. The reaction mixture was warmed to room temperature and stirred overnight. The volatile material was removed from the cloudy suspension under reduced pressure. $GaCl_3$ (0.21 g, 1.2 mmol) was added to a suspension of the resulting colorless to beige solid in hexanes (50 mL) at –78 °C. Warming to room temperature and stirring overnight afforded a suspension of **1** and LiCl. Decanting of the mother liquor, washing with hexanes and extraction with benzene gave **1** as a fine colorless solid after removal of the solvent in vacuo. Yield: 0.54 g (57%). Crystals suitable for X-ray diffraction were grown from a concentrated toluene solution at –24 °C. M.p. 202–208 °C. $^1$H NMR (300 MHz, $C_6D_6$, 25 °C): $\delta$ = 7.32 (d, $J$ = 7.5 Hz, *m*-H, 4 H), 7.28 (s, 4-*t*Bu$C_6H_4$, 16 H), 7.19 (t, $J$ = 7.5 Hz, *p*-H, 2 H), 1.16 (s, C$H_3$, 36 H) ppm. $^{13}$C{$^1$H} NMR (90.567 MHz, $C_6D_6$, 25 °C): $\delta$ = 150.89, 149.51, 147.05 (*i*-C), 142.96; 129.75 (*p*-C), 128.65 [*o*-C(4-*t*Bu$C_6H_4$)], 127.93 (*m*-C), 126.30 [*p*-C(4-*t*Bu$C_6H_4$)], 34.45 [$C(CH_3)_3$], 31.29 [C($CH_3$)$_3$] ppm. MS (DART, $C_6D_6$ solution): calcd. for [$M^+$ – Cl] 751.3794, found 751.3595.

**[{(3,5-$Me_2C_6H_3$)$_2C_6H_3$}$_2$GaCl] (2):** $GaCl_3$ (0.39 g, 2.2 mmol) was added through an addition funnel for solids to a suspension of 2,6-(3,5-$Me_2C_6H_3$)$_2C_6H_3$Li (1.37 g, 4.7 mmol) in hexanes at –78 °C. After 15 min, the reaction mixture was allowed to slowly warm to room temperature to give a cream-colored suspension and a dark grey solid on the bottom of the flask. After 3 d at room temperature, the dark solid was consumed. The insoluble material (1.09 g), which is a mixture of **2** and LiCl, was collected on a glass frit. Redissolution in $CH_2Cl_2$ (20 mL), followed by separation of LiCl by decantation, concentration of the clear yellow solution to ca. 2 mL and cooling at 4 °C for 2 d afforded a fine crystalline solid (0.2 g). A second batch (0.05 g) was obtained from the concentrated mother liquor at 4 °C after 3 d. Yield: 0.25 g (17%). M.p. softens at 178 °C, melts at 188–192 °C. $^1$H NMR (400 MHz $C_6D_6$, 25 °C): $\delta$ = 7.43 (d, $J$ = 7.6 Hz, *m*-H, 4 H), 7.31(s, $J$ = 7.6 Hz, *p*-H, 2 H), 7.00 [s, *o*-H(3,5-$Me_2C_6H_3$), 8 H], 6.66 [s, *p*-H(3,5-$Me_2C_6H_3$), 4 H], 1.93 (s, C$H_3$, 24 H) ppm. $^{13}$C{$^1$H} NMR (100.13 MHz, $C_6D_6$, 25 °C): $\delta$ = 149.00, 148.22, 145.82, 139.26, 129.82, 129.80, 128.31, 126.85, 21.14 ($CH_3$) ppm.

 © 2007 Wiley-VCH Verlag GmbH & Co. KGaA, Weinheim 

**[{(4-*t*BuC$_6$H$_4$)$_2$C$_6$H$_3$}$_3$Ga] (3):** $GaCl_3$ (0.18 g, 1.0 mmol) was added to a suspension of 4-(*t*BuC$_6$H$_4$)$_2$C$_6$H$_3$Li (1.07 g, 3.1 mmol) in hexanes (50 mL) at –78 °C through an addition funnel for solids. The mixture was warmed to room temperature and stirred for 20 h. The resulting fine, colorless precipitate was separated by filtration, and the product was obtained by crystallization of the colorless supernatant liquid at –24 °C for several days. Yield: 0.64 g (58%). Crystals suitable for X-ray diffraction were grown from a concentrated toluene solution at –24 °C. M.p. 281–283 °C. $^1$H NMR (300 MHz, $C_6D_6$, 25 °C): $\delta$ = 7.19 [d, $J$ = 8.4 Hz, 12 H, *o*- or *p*-(4-*t*BuC$_6$H$_4$)], 6.97 [d, $J$ = 8.1 Hz, 12 H, *o*- or *p*-(4-*t*BuC$_6$H$_4$)], 6.97 (s, 9 H, *m*- and *p*-H), 1.22 (s, 54 H, C*H*$_3$) ppm. $^{13}$C{$^1$H} NMR (75.45 MHz, $C_6D_6$, 25 °C): $\delta$ = 151.06 (*i*-C), 148.86, 148.60, 142.71, 129.80 [*o*-(4-*t*BuC$_6$H$_4$)], 127.93 (*m*- or *p*-C), 124.85 [*p*-(4-*t*BuC$_6$H$_4$)], 34.49 [*C*(CH$_3$)$_3$], 31.53 [C(*C*H$_3$)$_3$] ppm. $C_{78}H_{87}Ga$ (1094.3): calcd. C 85.61, H 8.01; found C 84.35, H 8.21.

**[(2,6-Mes$_2$C$_6$H$_3$)$_2$AlCl] (5):** $AlCl_3$ (0.25 g, 1.9 mmol) was added to a solution of 2,6-Mes$_2$C$_6$H$_3$Li (1.28 g, 4.0 mmol) in benzene (10 mL) through an addition funnel for solids with cooling in an ice bath. After warming to room temperature, the mixture was stirred for 14 h and heated to reflux for another 2 h. After cooling to room temperature, the clear yellow solution was decanted off the fine colorless precipitate, and the volatile material was distilled off under reduced pressure to give a pale-yellow foamy solid. Addition of hexanes (5–6 mL) afforded the precipitation of **5** as a fine pale-yellow powder (0.32 g) which was found to be contaminated with 22% 2,6-Mes$_2$C$_6$H$_4$. Crystals of a quality suitable for X-ray diffraction were obtained by crystallization from a saturated toluene solution at –20 °C for 7 d, although an analytically pure bulk sample could not be isolated. $^1$H NMR (400 MHz, $C_6D_6$, 25 °C): $\delta$ = 7.05 (t, $J$ = 7.6 Hz, 2 H, *p*-H), 6.85 [s, 8 H, *m*-H(Mes)], 6.63 (d, $J$ = 7.6 Hz, 4 H, *m*-H), 2.25 (s, 12 H, *p*-C*H*$_3$), 1.83 (s, 24 H, *o*-C*H*$_3$) ppm. $^{13}$C{$^1$H} NMR (100.61 MHz, $C_6D_6$, 25 °C): $\delta$ = 150.68, 143.73 (*i*-C), 141.78, 137.58 [*o*-C(Mes)], 136.99, 130.21 (*p*-C), 129.13 [*m*-C(Mes)], 128.43 (*m*-C), 21.91 (*o*-*C*H$_3$), 21.29 (*p*-*C*H$_3$) ppm. MS (DART, solid): calcd. for [M + H$^+$] 689.3495, found 689.3583.

**[(2,6-Mes$_2$C$_6$H$_3$)GaBu$_2$] (8):** A suspension of a 9:1 mixture of 2,6-Mes$_2$C$_6$H$_3$Li/2,6-Mes$_2$C$_6$H$_4$ (2.27 g, 6.4 mmol 2,6-Mes$_2$C$_6$H$_3$Li) in hexanes (30 mL) was added slowly to a solution of $ClGaBu_2$ (1.40 g, 6.4 mmol) in hexanes (20 mL) at –78 °C. The mixture was kept at –78 °C for 30 min, then warmed to room temperature and stirred overnight. The pale-yellow solution was decanted off the fine colorless precipitate, concentrated to 5 mL, and cooled to –40 °C for 2 d. As no crystals had formed, the solution was further concentrated to about 1 mL and cooled to –40 °C for 5 d to afford fine, colorless needles (1.21 g). A second batch was obtained from the concentrated mother liquor after cooling at –40 °C for 4 d (0.81 g). Yield: 2.02 g (58%). The needles were contaminated with approximately 13% 2,6-Mes$_2$C$_6$H$_4$. $^1$H NMR (300 MHz, $C_6D_6$, 25 °C): $\delta$ = 7.31 (t, $J$ = 7.5 Hz, 1 H, *p*-H), 7.02 (d, $J$ = 7.5 Hz, 2 H, *m*-H), 6.81 [s, 4 H, *m*-H(Mes)], 2.16 (s, 12 H, *o*-Me), 2.13 (s, 6 H, *p*-Me), 1.23 (m, 4 H, β-C*H*$_2$), 1.04 (m, 4 H, γ-C*H*$_2$), 0.83 (t, $J$ = 6.9 Hz, 6 H, δ-C*H*$_3$), 0.54 ("t", $J$ = 7.8 Hz, 4 H, α-C*H*$_2$) ppm. $^{13}$C{$^1$H} NMR (75.45 MHz, $C_6D_6$, 25 °C): $\delta$ = 155.61, 147.00, 140.98, 137.01, 136.17, 128.88 [*m*-C(Mes)], 128.45 (*p*-C), 126.04 (*m*-C), 28.32 (β- or γ-*C*H$_2$), 28.13 (β- or γ-*C*H$_2$), 21.11 (*o*-*C*H$_3$), 21.05 (*p*-*C*H$_3$), 19.33 (α-*C*H$_2$), 14.24 (δ-*C*H$_3$) ppm.

**[(2,6-Dipp$_2$C$_6$H$_3$)GaBu$_2$] (9):** A suspension of 2,6-Dipp$_2$C$_6$H$_3$Li (2.51 g, 6.2 mmol) in hexanes (30 mL) was added slowly to a solution of $ClGaBu_2$ (1.30 g, 5.9 mmol) in hexanes (20 mL) at –78 °C. The mixture was kept at –78 °C for 30 min, warmed to room temperature and stirred overnight. The cloudy, pale-yellow solution was filtered through a sintered glass frit, and the pale-yellow filtrate was concentrated to 5 mL and cooled to –40 °C for 4 d. As no crystals had formed, the volatile material was removed under reduced pressure to give crude **9** as a pale-yellow oil, which solidified after a month at room temperature. The main impurity was identified as the arene 2,6-Dipp$_2$C$_6$H$_3$I in amounts of approximately 5%. $^1$H NMR (300 MHz, $C_6D_6$, 25 °C): $\delta$ = 7.25 (m, 5 H), 7.16 (m, 4 H), 3.09 [sept, $J$ = 6.9 Hz, 4 H, C*H*(CH$_3$)$_2$], 1.27 [d, $J$ = 6.9 Hz, 12 H, CH(C*H*$_3$)$_2$], 1.14 (m, 8 H, β-, γ-CH$_2$), 1.07 [d, $J$ = 6.9 Hz, 12 H, CH(C*H*$_3$)$_2$], 0.84 (t, $J$ = 7.2 Hz, 6 H, δ-CH$_3$), 0.45 (m, 4 H, α-CH$_2$) ppm. $^{13}$C{$^1$H} NMR (75.45 MHz, $C_6D_6$, 25 °C): $\delta$ = 156.31, 147.10, 145.64, 141.89, 128.72, 127.80, 126.98, 123.36, 30.54 [*C*H(CH$_3$)$_2$], 28.24 (β- or γ-*C*H$_2$), 27.46 (β- or γ-*C*H$_2$), 26.22 [CH(*C*H$_3$)$_2$], 22.66 [CH(*C*H$_3$)$_2$], 19.93 (α-*C*H$_2$), 14.00 (δ-*C*H$_3$) ppm.

**[{(2,6-Mes$_2$C$_6$H$_3$)GaBu(μ-OH)}$_2$] (10):** A solution of crude **8** (30 mg) in $C_6D_6$ (1 mL) was placed in a small vial inside a glovebox, and the solvent was allowed to slowly evaporate through the partially tightened lid over a period of two weeks to afford a pale-yellow glass. Redissolution in 1-octene (1 mL) and subsequent slow concentration over a period of six weeks gave fine colorless needles of **10** of sufficient quality for X-ray diffraction. $^1$H NMR (400 MHz, $C_6D_6$, 25 °C): $\delta$ = 7.21 (t, $J$ = 7.2 Hz, 2 H, *p*-H), 6.91 (d, $J$ = 7.2 Hz, 4 H, *m*-H), 6.87 [s, 8 H, *m*-H(Mes)], 2.35 (s, 12 H, *p*-Me), 2.08 (s, 24 H, *o*-Me), 1.21 (m, 4 H, β-, γ-C*H*$_2$), 0.88 (t, $J$ = 6.8 Hz, 6 H, δ-C*H*$_3$), 0.13 ("t", $J$ = 8.1 Hz, 4 H, α-C*H*$_2$), 0.09 (s, 2 H, O*H*) ppm. $^{13}$C{$^1$H} NMR (100.75 MHz, $C_6D_6$, 25 °C): $\delta$ = 148.30, 141.76, 136.38, 136.14, 128.59, 128.42, 126.95, 28.38 (β-or γ-*C*H$_2$), 28.24 (β-or γ-*C*H$_2$), 21.51 (*p*-*C*H$_3$), 21.32 (*o*-*C*H$_3$), 15.82 (α-*C*H$_2$), 14.00 (δ-*C*H$_3$) ppm. FTIR (thin film between CsI plates): $\tilde{\nu}$ = 3642 [m, ν(OH)] cm$^{-1}$.

**[{2,6-(3,5-Me$_2$C$_6$H$_3$)$_2$C$_6$H$_3$}$_2$Ga]$^+$[Li(Al{OCH(CF$_3$)$_2$}$_4$)$_2$]$^-$ (11):** A solution of **2** (32 mg, 47 μmol) in $C_6D_5Cl$ (1.0 mL) was added to finely powdered LiAl[OCH(CF$_3$)$_2$]$_4$ (70 mg, 0.1 mmol) in an NMR tube fitted with a J. Young valve. The NMR tube was shaken for 1 min and then rotated for 16 h around its long axis using a standard overhead stirrer lying on its side. The fine colorless precipitate was allowed to settle, and the clear colorless supernatant liquid containing essentially pure **11** was pipetted off. $^1$H NMR (400 MHz, $C_6D_5Cl$, 25 °C): $\delta$ = 7.58 (t, $J$ = 8.0 Hz, 2 H, *p*-H), 7.53 (d, $J$ = 8.0 Hz, 4 H, *m*-H), 6.72 [s, 4 H, *p*-H of xylyl], 6.40 [s, 8 H, *o*-H of xylyl], 4.84 [sept, $J_{H,F}$ = 5.4 Hz, 8 H, C*H*(CF$_3$)$_2$], 1.95 (s, 24 H, C*H*$_3$) ppm. $^{13}$C{$^1$H} NMR (100.61 MHz, $C_6D_5Cl$, 25 °C): $\delta$ = 148.23, 146.74, 144.42, 131.51, 125.68, 122.34 (q, $^1J_{C,F}$ = 285 Hz, *C*F$_3$), 121.14, 70.86 [sept, $^2J_{C,F}$ = 33 Hz, *C*H(CF$_3$)$_2$], 20.67 (*C*H$_3$) ppm. MS (DART, $C_6D_5Cl$ solution): calcd. 639.2542, found 639.2497; (neg. ion): calcd. for [Al{OCH(CF$_3$)$_2$}$_4$]$^-$ 694.9542, found 694.9511.

**[(2,6-Mes$_2$C$_6$H$_3$)GaBu]$^+$[B(C$_6$F$_5$)$_4$]$^-$ {[13]$^+$[B(C$_6$F$_5$)$_4$]$^-$}:** An NMR tube equipped with a J. Young valve was charged with **8** (27 mg, 50 μmol), [Ph$_3$C][B(C$_6$F$_5$)$_4$] (43 mg, 47 μmol), and $C_6D_6$ (0.7 mL), and the resulting mixture was shaken for 1 min to give a pale-yellow solution above a dense red layer (ca. 0.1 mL). The mixture was rotated at room temperature for 5 h to afford a dense, dark orange-yellow layer (0.1 mL) and a pale-yellow top layer. The top layer was pipetted off, and the bottom layer was washed with $C_6D_6$ (2 × 0.25 mL) and then dissolved in $C_6D_5Br$ (0.35 mL) to give a yellow solution. The solution contained mainly [**13**]$^+$[B(C$_6$F$_5$)$_4$]$^-$, which was contaminated with 15% of an unknown 2,6-Mes$_2$C$_6$H$_3$-containing species. $^1$H NMR [400.13 MHz, $C_6D_6$/$C_6D_5Br$ (1:3), 25 °C]: $\delta$ = 7.48 (t, $J$ = 7.6 Hz, 1 H, *p*-H), 7.10 (d, $J$ = 7.6 Hz, 2 H, *m*-H), 6.88 [s, 4 H, *m*-H(Mes)], 2.22 (s, 6 H, *p*-C*H*$_3$), 1.96 (s, 12

 © 2007 Wiley-VCH Verlag GmbH & Co. KGaA, Weinheim 

H, *o*-C$H_3$), 0.65 (m, 2 H, β-C$H_2$), 0.56 (s, 5 H, γ-C$H_2$, δ-C$H_3$), 0.25 (t, $J$ = 7.5 Hz, 2 H, α-C$H_2$) ppm. $^{13}C\{^1H\}$ NMR [100.61 MHz, $C_6D_6/C_6D_5Br$ (1:3); signals referenced to $\delta$ = 122.45 ppm for *i*-C($C_6D_5Br$), 25 °C]: $\delta$ = 148.83 (br. d, $^1J_{C,F}$ = 243 Hz), 146.57, 140.47, 138.71 [br. d, $^1J_{C,F}$ = 243 Hz, *p*-C($C_6F_5$)], 138.24, 136.82 (br. d, $^1J_{C,F}$ = 246 Hz), 135.81 [*o*-C(Mes)], 133.77 (*p*-C), 130.71 [*m*-C(Mes)], 27.28 (γ-*C*$H_2$), 25.66 (β-*C*$H_2$), 21.97 (br., α-*C*$H_2$), 20.94 (*p*-*C*$H_3$), 20.82 (*o*-*C*$H_3$), 13.32 (δ-*C*$H_3$) ppm. $^{19}F$ NMR (284.34 MHz, $C_6D_6/C_6D_5Cl$ (1:1), 25 °C): $\delta$ = –132.15 (br. d, $J$ = 9.9 Hz, 8 F, *o*-F), –162.28 (t, $J$ = 20.9 Hz, 4 F, *p*-F), –166.24 (br. s, 8 F, *m*-F) ppm. MS (DART, $C_6D_6/C_6D_5Br$ (1:3) solution): calcd. 439.1916, found 439.1919.

**[(2,6-$Mes_2C_6H_3$)GaBu]$^+$[$CHB_{11}Cl_{11}$]$^-$ {[13]$^+$[$CHB_{11}Cl_{11}$]$^-$}:** An NMR tube equipped with a J. Young valve was charged with **8** (24 mg, 45 μmol), [$Ph_3C$][$CHB_{11}Cl_{11}$]·0.8$C_7H_8$ (33 mg, 39 μmol) and $C_6D_6$ (0.6 mL), and the resulting mixture was shaken for 1 min to give a pale-yellow solution above a fine yellow solid. The mixture was rotated at room temperature for 26 h to afford a dense orange-yellow layer (0.06 mL) and a yellow top layer. In order to ensure complete consumption of the trityl salt, an additional 5 mg of **8** was added, and the tube was rotated for another 4 h. This resulted in a significant fading of the color of both layers. The top layer was pipetted off, and the bottom layer (ca. 0.03 mL) was dissolved in $C_6D_6$ (0.6 mL). The NMR spectra are in agreement with the formation of [**13**]$^+$[$CHB_{11}Cl_{11}$]$^-$, which still contained around 22% $Ph_3CH$. No further purification was attempted. The NMR spectroscopic data are given for [**13**]$^+$[$CHB_{11}Cl_{11}$]$^-$. $^1H$ NMR (400.13 MHz, $C_6D_6$, 25 °C): $\delta$ = 7.15 (obscured by $C_6D_5H$, *p*-H), 6.85 (d, $J$ = 7.6 Hz, 2 H, *m*-H), 6.79 [s, 4 H, *m*-H(Mes)], 2.08 (s, 12 H, *o*-C$H_3$), 2.05 (s, 6 H, *p*-C$H_3$), 1.24 (m, 2 H, β-C$H_2$), 1.12 (br. s, 2 H, α-C$H_2$), 0.97 (sext, $J$ = 7.2 Hz, 2 H, γ-C$H_2$), 0.71 (t, $J$ = 7.2 H, 3 Hz, δ-C$H_3$) ppm. $^{13}C\{^1H\}$ NMR (100.61 MHz, $C_6D_6$, 25 °C): $\delta$ = 147.48, 139.39, 138.53, 136.50 [*o*-C(Mes)], 131.98, 130.16 [*m*-C(Mes)], 48.03 (br., *C*H$B_{11}Cl_{11}$), 26.76 (γ-*C*$H_2$), 26.47 (β-*C*$H_2$), 21.55 (*o*-*C*$H_3$), 20.92 (*p*-*C*$H_3$), 13.51 (δ-*C*$H_3$) ppm.

**[(2,6-$Mes_2C_6H_3$)GaBu]$^+$[$CHB_{11}Br_6Me_5$]$^-$ {[13]$^+$[$CHB_{11}Br_6Me_5$]$^-$}:** A small tube equipped with a Teflon valve was charged with **8** (28 mg, 52 μmol), [$Ph_3C$][$CHB_{11}Br_6Me_5$]·2.3$C_7H_8$ (60 mg, 52 μmol), and $C_6D_6$ (1.5 mL), and the resulting mixture was rotated at room temperature for 16 h to afford a clear, orange solution. The volatile material was distilled off in vacuo, and the resulting orange-red oil was dissolved in hexanes (1 mL). The slightly cloudy solution was cooled to –20 °C for 2 h to precipitate $Ph_3CH$. The yellow-orange supernatant liquid was pipetted off, and the solvent was allowed to evaporate slowly inside a drybox. The resulting yellow glass was investigated by $^1H$ NMR spectroscopy, and the spectra were found to be in agreement with the formulation [**13**]$^+$[$CHB_{11}Br_6Me_5$]$^-$. Small amounts of 2,6-$Mes_2C_6H_4$, $Ph_3CH$ and *n*-hexane were also present. $^1H$ NMR (400 MHz, $C_6D_6$, 25 °C): $\delta$ = 6.95 (br. s, $w_{1/2}$ = 6.9 Hz, 2 H, *m*-H of Mes), 6.73 (br. s, $w_{1/2}$ = 7.6 Hz, 2 H, *m*-H of Mes), 2.49 (br. s, $w_{1/2}$ = 6.4 Hz, 6 H, *o*-C$H_3$), 2.06 (s, 6 H, *p*-C$H_3$), 1.94 (br. s, $w_{1/2}$ = 6.4 Hz, 6 H, *o*-C$H_3$), 1.50 (m, 4 H, α-, β-C$H_2$), 1.21 [m, 2 H, γ-C*H* (obscured by hexane C$H_2$)], 0.80 (t, $J$ = 7.5 Hz, 3 H, δ-C$H_3$), 0.25 (s, 15 H, B-C$H_3$) ppm. Further attempts at purification were unsuccessful and eventually led to the formation of **16** (vide infra).

**[(2,6-$Dipp_2C_6H_3$)GaBu)]$^+$[$B(C_6F_5)_4$]$^-$ {[14]$^+$[$B(C_6F_5)_4$]$^-$}:** A solution of **9** (39 mg, 67 μmol) in $C_6D_6$ (0.8 mL) was added to [$Ph_3C$][$B(C_6F_5)_4$] (62 mg, 67 μmol) in an NMR tube equipped with a J. Young valve at room temperature. The mixture was shaken, and a dense red liquid phase separated after standing for a few minutes. After 2 h at room temperature, only a small amount of $Ph_3CH$ could be detected by $^1H$ NMR spectroscopy. The sample was rotated slightly off axis for 18 h, after which time the $^1H$ NMR spectrum showed the consumption of **9**. The yellow upper phase was pipetted off, and the dense red oily phase was washed with $C_6D_6$ (0.6 mL and 1.2 mL). The remaining red oily liquid was dissolved in a mixture of $C_6D_6/C_6D_5Cl$ (4.5:1.5). $^1H$ NMR (300 MHz, $C_6D_6/C_6D_5Cl$ (4.5:1.5), 25 °C): $\delta$ = 7.26 (t, $J$ = 6.9 Hz, 1 H, *p*-H), 7.24 (t, $J$ = 7.8 Hz, 2 H, *p*-H of Dipp), 7.14 (d, $J$ = 6.9 Hz, 2 H, *m*-H), 7.07 (d, $J$ = 7.8 Hz, 4 H, *m*-H of Dipp), 2.52 [sept, $J$ = 6.8 Hz, 4 H, C*H*$(CH_3)_2$], 0.95, [d, $J$ = 6.8 Hz, 12 H, CH(C$H_3$)$_2$], 0.92, [d, $J$ = 6.8 Hz, 12 H, CH(C$H_3$)$_2$], 0.41 (br. s, 7 H, β-, γ-C$H_2$, δ-C$H_3$), 0.04 ("t", $J$ = 6.8 Hz, 2 H, α-C$H_2$) ppm. $^{13}C\{^1H\}$ NMR (75.45 MHz, $C_6D_6/C_6D_5Cl$ (4.5:1.5), 25 °C): $\delta$ = 149.1 (br. d, $^1J_{C,F}$ = 238 Hz), 147.83, 145.81, 133.54 (*p*-C), 138.8 (br. d, $^1J_{C,F}$ = 249 Hz, *p*-*C*F), 138.05, 137.0 (br. d, $^1J_{C,F}$ = 249 Hz), 131.77 [*m*-C(Dipp)], 129.22 (*m*-C), 125.63 [*m*-C(Dipp)], 30.95 [*C*H$(CH_3)_2$], 27.44 (β- or γ-*C*$H_2$), 25.38 (β- or γ-*C*$H_2$), 24.95 [CH(*C*$H_3$)$_2$], 23.43 [CH(*C*$H_3$)$_2$], 21.58 (α-*C*$H_2$), 13.28 (δ-*C*$H_3$) ppm. $^{19}F$ NMR (284.34 MHz, $C_6D_6/C_6D_5Cl$ (4.5:1.5), 25 °C): $\delta$ = –133.12 (br. d, $J$ = 7.7 Hz, 8 F, *o*-F), –163.93 (t, $J$ = 20.8 Hz, 4 F, *p*-F), –167.72 ppm (br. t, $J$ = 18.9 Hz, 8 F, *m*-F).

**[(2,6-$Dipp_2C_6H_3$)GaBu]$^+$[$CHB_{11}Cl_{11}$]$^-$ {[14]$^+$[$CHB_{11}Cl_{11}$]$^-$}:** An NMR tube equipped with a J. Young valve was charged with **9** (36 mg, 62 μmol, 30% excess) and [$Ph_3C$][$CHB_{11}Cl_{11}$]·0.8$C_7H_8$ (40 mg, 47 μmol), and $C_6D_6$ (0.75 mL) was added. The sample was rotated horizontally slightly off axis at room temperaturefor 5 d during which time a dense orange liquid layer formed (ca. 0.1 mL). The pale-yellow upper layer was pipetted off, and the lower layer was washed twice with $C_6D_6$ (0.5 and 0.3 mL). $C_6D_5Cl$ (0.45 mL) was added to the remaining liquid to give a clear yellow orange solution of [**14**]$^+$[$CHB_{11}Cl_{11}$]$^-$. $^1H$ NMR (400.13 MHz, $C_6D_5Cl/C_6D_6$ (3:1), 25 °C): $\delta$ = 7.55 (t, $J$ = 7.6 Hz, 1 H, *p*-H), 7.48 (t, $J$ = 7.8 Hz, 2 H, *p*-H of Dipp), 7.39 (d, $J$ = 7.6 Hz, 2 H, *m*-H), 7.27 (d, $J$ = 7.8 Hz, 4 H, *m*-H of Dipp), 2.86 (br. s, 1 H, C*H*$B_{11}Cl_{11}$), 2.66 [sept, $J$ = 6.8 Hz, 4 H, C*H*$(CH_3)_2$], 1.11 [d, $J$ = 6.8 Hz, 12 H, CH(C$H_3$)$_2$], 1.07 [d, $J$ = 6.8 Hz, 12 H, CH(C$H_3$)$_2$], 0.69 (quint, $J$ = 6.8 Hz, 2 H, β-C$H_2$), 0.55 (t, $J$ = 7.6 Hz, 2 H, α-C$H_2$), 0.49 (br. s, 5 H, γ-C$H_2$, δ-C$H_3$) ppm. $^{13}C\{^1H\}$ NMR [100.61 MHz, $C_6D_5Cl/C_6D_6$ (3:1); signals referenced to $\delta$ = 133.69 ppm for *i*-C($C_6D_5Cl$), 25 °C]: $\delta$ = 149.14 (*i*-C), 147.27 [*o*-C(Dipp)], 145.40, 137.79, 133.46 (*p*-C), 131.58, 128.51, 125.49 [*m*-C(Dipp)], 46.76 (br., *C*H$B_{11}Cl_{11}$), 30.52 [*C*H$(CH_3)_2$], 24.60 [CH(*C*$H_3$)$_2$], 23.46 [CH(*C*$H_3$)$_2$], 13.20 (δ-*C*$H_3$) ppm. MS (ESI, acetonitrile solution): calcd. for [$C_{34}H_{46}Ga^+$] 523.286, found 523.3; calcd. for [$M^+$ + $CH_3CN$] 564.312, found 564.4.

**Thermal Stability of [14]$^+$[$B(C_6F_5)_4$]$^-$:** A solution of [**14**]$^+$[$B(C_6F_5)_4$]$^-$ (ca. 5 μmol) in $C_6D_6/C_6D_5Cl$ (ca. 12:1 ratio, 0.6 mL) in an NMR tube equipped with a J. Young valve was heated at 60 °C for 16 h. During that time, the phase separation disappeared and a pale-yellow solution was obtained. The NMR spectroscopic data are in accordance with the presence of two compounds, namely [(2,6-$Dipp_2C_6H_3$)GaBu($C_6F_5$)] (**15**)[34] and $B(C_6F_5)_3$.[35] $^1H$ NMR (300 MHz, $C_6D_6/C_6D_5Cl$ (12:1), 25 °C): $\delta$ = 7.26 (br. s, 3 H, *m*-, *p*-H), 7.00 [d, $J$ = 7.5 Hz, 4 H, *m*-H of Dipp], 2.99 [sept, $J$ = 6.8 Hz, 4 H, C*H*$(CH_3)_2$], 1.15, [d, $J$ = 6.8 Hz, 12 H, CH(C$H_3$)$_2$], 0.99, [d, $J$ = 6.8 Hz, 12 H, CH(C$H_3$)$_2$], 0.68 ("t", $J$ = 6.0 Hz, 3 H, δ-C$H_3$), 0.45 ("t", $J$ = 8.0 Hz, 2 H, α-C$H_2$) ppm. $^{19}F$ NMR [284.34 MHz, $C_6D_6/C_6D_5Cl$ (12:1), 25 °C]: **15**: $\delta$ = –121.90 (m, *o*-F), –155.18 (t, $J$ = 19.9 Hz, *p*-F), –162.18 (m, *m*-F) ppm; $B(C_6F_5)_3$: $\delta$ = –129.89 (m, *o*-F), –142.86 (m, *p*-F), –161.18 (m, *m*-F) ppm.

**[$(BuGa)_4(\mu\text{-}OH)_6$]$^{2+}$[$CHB_{11}Br_6Me_5$]$^-_2$ (16):** The solution of [**13**]$^+$[$CHB_{11}Br_6Me_5$]$^-$ that was used to measure the $^1H$ NMR spectrum

 © 2007 Wiley-VCH Verlag GmbH & Co. KGaA, Weinheim 

was transferred to a small vial inside the glove box, and the solvent was allowed to slowly evaporate. The resulting colorless crystals were analyzed by X-ray diffraction as $Ph_3CH{\cdot}C_6H_6$[42] and **16**·4.5$C_6D_6$.

**Reaction of [14]$^+$[$CHB_{11}Cl_{11}$]$^-$ with 1-Octene:** A solution of [**14**]$^+$[$CHB_{11}Cl_{11}$]$^-$ (11 mg, 12 μmol) in a 6:1 mixture of $C_6D_6$/$C_6D_5Cl$ (0.6 mL) was treated with 1-octene (14 μmol, 2.4 μL) at room temperature. The reaction was monitored by $^1$H NMR spectroscopy. After most of the free olefin had been consumed, additional olefin was added at various intervals starting after 54 h (5 μL), then after an additional 8 d (5 μL), and finally after further 4 d (10 μL). The last olefin added had been consumed at room temperature after 7 d. Two drops of the reaction mixture were used for ESI mass spectrometry. The rest was poured into a vial in air, the solvent was allowed to evaporate, and the remaining oil was investigated by GC/MS. MS (ESI, acetonitrile solution): calcd. for $C_{38}H_{54}Ga$ [M$^+$] 579.35; found 579.6; calcd. for $C_{40}H_{57}GaN$ [M$^+$ + MeCN] 620.37; found 620.6. GC/MS: $t_R$ = 11.62 min (16%), calcd. for $C_{14}H_{16}D_6$ (4-octylbenzene) 196.21, found 196.1; 11.73 min (25%), calcd. for $C_{14}H_{16}D_6$ (3-octylbenzene) 196.21, found 196.1; 11.97 min (59%), calcd. for $C_{14}H_{16}D_6$ (2-octylbenzene) 196.21, found 196.1. Assignments were made based on the fragmentation patterns.

**X-ray Crystallography:** Crystals of **1**, **3**, and **5** were obtained by crystallization from concentrated toluene solutions at –24 °C, crystals of **7** were obtained from a concentrated benzene solution at 3–4 °C, and crystals of **10** and **16** at room temperature from a 1-octene or benzene solution of **8** or [**13**]$^+$[$CHB_{11}Br_6Me_5$]$^-$, respectively, by slow evaporation of the solvents inside a drybox. Crystals of **1**, **3**, **5**, and **7** were removed from the Schlenk tube under a stream of $N_2$ and immediately covered with a layer of hydrocarbon oil, and crystals of **10** and **16** were covered with a layer of hydrocarbon oil inside a drybox. A suitable crystal was selected, attached to a glass fiber, and immediately placed in the low-temperature nitrogen stream. Crystals of **16** experienced a phase transition around 170 K, and the data were collected at 178 K. The data were collected with a Bruker Apex diffractometer using Mo-$K_\alpha$ ($\lambda$ = 0.71073 Å) radiation. Absorption corrections using a multi-scan method from equivalent reflections were applied for **1**, **3**, **5**, **7**, and **10**; a semi-empirical method was used for **16**.[43] The structures were solved by direct methods using the SHELXTL program suite (version 6.1[44]) and refined by full-matrix least squares on $F^2$ including all reflections. All non-hydrogen atoms were refined anisotropically, and all hydrogen atoms were included in the refinement with idealized parameters. The OH hydrogen atoms in compounds **10** and **16** were not observed, but were placed into calculated positions using riding and distance restraints, respectively. The X-ray crystal structure of **1** at room temperature was reported recently.[18] Its parameters are very similar to the ones given here with the exception of a slightly larger unit cell. The structure of **16** displayed some serious disorder problems. The structure includes one dication, two monoanions, and four and one half benzene molecules. One of the solvent molecules was severely disordered and was best modeled using the Squeeze program.[45] Three of the *n*-butyl groups on the cation were disordered and each was modeled in two orientations. The occupancies of atoms C(1)–C(4), C(5)–C(8), and C(13)–C(16) refined to 0.689(12) and 0.311(12), 0.627(11) and 0.373(11), and 0.797(9) and 0.203(9) for the unprimed and primed atoms, respectively. Restraints were placed on the positional and displacement parameters of the disordered atoms and the solvent atoms as well as the positional parameters of the hydrogen atoms bonded to the oxygen atoms and the hydrogen atoms on C(1A) and C(1B). Some details of the crystal data and refinement are given in Table 1, and selected bond lengths and angles are listed in

Table 1. Crystal data and structural refinement details for **1**, **3**, **5**, **7**, **10**, and **16**·4.5$C_6H_6$.

| | **1** | **3** | **5** | **7** | **10** | **16**·4.5$C_6H_6$ |
|---|---|---|---|---|---|---|
| Empirical formula | $C_{52}H_{58}ClGa$ | $C_{78}H_{87}Ga$ | $C_{48}H_{50}AlCl$ | $C_{48}H_{51}Al$ | $C_{56}H_{70}Ga_2O_2$ | $C_{55}H_{101}B_{22}Br_{12}Ga_4O_6$ |
| Formula mass | 788.15 | 1094.2 | 689.31 | 654.87 | 914.56 | 2333.98 |
| $T$ [K] | 100(2) | 100(2) | 130(2) | 120(2) | 110(2) | 178(2) |
| Wavelength [Å] | 0.71073 | 0.71073 | 0.71073 | 0.71073 | 0.71073 | 0.71073 |
| Crystal system | monoclinic | monoclinic | monoclinic | orthorhombic | triclinic | monoclinic |
| Space group | $P2_1/n$ | $P2_1/c$ | $P2_1/n$ | $P2_12_12_1$ | $P\bar{1}$ | $C2/c$ |
| $a$ [Å] | 17.1401(9) | 9.9494(8) | 11.9518(16) | 11.9283(5) | 9.010(6) | 33.122(5) |
| $b$ [Å] | 13.7377(7) | 33.470(3) | 20.391(3) | 15.8012(7) | 12.163(7) | 18.094(2) |
| $c$ [Å] | 19.7484(10) | 18.6120(15) | 16.157(2) | 20.3941(9) | 12.211(7) | 31.434(4) |
| $\alpha$ [°] | 90 | 90 | 90 | 90 | 67.407(7) | 90 |
| $\beta$ [°] | 110.2180(10) | 94.3920(10) | 100.167(2) | 90 | 78.940(8) | 112.014(5) |
| $\gamma$ [°] | 90 | 90 | 90 | 90 | 82.428(7) | 90 |
| $V$ [Å$^3$] | 4363.6(4) | 6179.6(9) | 3875.9(9) | 3843.9(3) | 1210.1(13) | 17465(4) |
| $Z$ | 4 | 4 | 4 | 4 | 1 | 8 |
| $D_{calcd.}$ [Mg m$^{-3}$] | 1.200 | 1.176 | 1.181 | 1.132 | 1.255 | 1.775 |
| $\mu$(Mo-$K_\alpha$) [mm$^{-1}$] | 0.725 | 0.489 | 0.154 | 0.085 | 1.153 | 0.71073 |
| $F$(000) | 1672 | 2344 | 1472 | 1408 | 484 | 9064 |
| Crystal size [mm] | 0.16 × 0.12 × 0.06 | 0.38 × 0.22 × 0.20 | 0.26 × 0.18 × 0.04 | 0.28 × 0.22 × 0.18 | 0.48 × 0.08 × 0.02 | 0.24 × 0.22 × 0.14 |
| Crystal color and habit | colorless prism | colorless plate | colorless prism | colorless prism | colorless needle | colorless prism |
| $2\Theta_{max}$ [°] | 54.3 | 52.8 | 52.2 | 54.0 | 52.0 | 52.0 |
| No. of obsd. recflections | 9643 | 12644 | 7663 | 8384 | 4581 | 17168 |
| No. of variables | 499 | 760 | 463 | 458 | 271 | 983 |
| $R_1$[a] [$I > 2\sigma(I)$] | 0.0347 | 0.0509 | 0.0625 | 0.0332 | 0.0859 | 0.0671 |
| $wR_2$[b] [$I > 2\sigma(I)$] | 0.0803 | 0.1155 | 0.1081 | 0.0906 | 0.2364 | 0.1772 |
| Goodness-of-fit on $F^2$ | 1.005 | 1.006 | 1.011 | 1.026 | 1.068 | 1.027 |
| Largest diff. peak [e Å$^{-3}$] | 0.418 | 0.648 | 0.301 | 0.280 | 1.842 | 1.804 |

[a] $R_1 = \Sigma||F_o| - |F_c||/\Sigma|F_o|$. [b] $wR_2 = (\Sigma w||F_o| - |F_c||^2/\Sigma w|F_o|^2)^{1/2}$.

 © 2007 Wiley-VCH Verlag GmbH & Co. KGaA, Weinheim 

Tables 2 and 3. CCDC-626538 to -626542 and 626654 contain the supplementary crystallographic data for this paper. These data can be obtained free of charge from The Cambridge Crystallographic Data Centre via www.ccdc.cam.ac.uk/datarequest/cif.

Table 2. Selected bond lengths [Å] and angles [°] for **1**, **3**, **5**, and **7**.

| | **1** (M = Ga) | **3** (M = Ga) | **5** (M = Al; X = Cl) | **7** (M = Al; X = H) |
|---|---|---|---|---|
| M–C | 1.9701(16) | 2.010(2) | 1.976(3) | 1.9936(13) |
| | 1.9816(17) | 1.989(2) | 1.979(3) | 1.9864(13) |
| | | 1.996(3) | | |
| M–X | 2.1786(5) | | 2.1098(12) | 1.436(18) |
| C–M–C | 138.26(7) | 117.64(10) | 147.52(13) | 137.62(5) |
| | | 119.05(10) | | |
| | | 122.57(10) | | |
| C–M–X | 107.04(5) | | 105.22(10) | 113.8(7) |
| | 114.52(5) | | 107.26(9) | 108.6(7) |

Table 3. Selected bond lengths [Å] and angles [°] for **10** and **16**.

| Compound **10** | | | |
|---|---|---|---|
| Ga(1)–O(1) | 1.947(5) | O(1)–Ga(1)–O(1A) | 78.4(2) |
| Ga(1)–O(1A) | 1.952(5) | O(1)–Ga(1)–C(1) | 111.0(2) |
| Ga(1)–C(1) | 1.992(6) | O(1A)–Ga(1)–C(1) | 110.8(3) |
| Ga(1)–C(25) | 1.967(7) | O(1)–Ga(1)–C(25) | 108.1(3) |
| | | O(1A)–Ga(1)–C(25) | 107.0(3) |
| | | C(25)–Ga(1)–C(1) | 129.7(3) |
| Compound **16** | | | |
| Ga(1)–O(1) | 1.889(6) | Ga(3)–O(5) | 1.890(5) |
| Ga(1)–O(2) | 1.903(5) | Ga(4)–O(3) | 1.887(5) |
| Ga(1)–O(3) | 1.898(5) | Ga(4)–O(5) | 1.901(5) |
| Ga(2)–O(1) | 1.901(6) | Ga(4)–O(6) | 1.898(5) |
| Ga(2)–O(4) | 1.893(5) | Ga(1)–C(1) | 1.932(5) |
| Ga(2)–O(6) | 1.907(5) | Ga(2)–C(5) | 1.933(5) |
| Ga(3)–O(2) | 1.903(5) | Ga(3)–C(9) | 1.932(4) |
| Ga(3)–O(4) | 1.896(5) | Ga(4)–C(13) | 1.934(5) |
| O(1)–Ga(1)–O(2) | 97.0(3) | O(3)–Ga(4)–O(5) | 95.1(2) |
| O(1)–Ga(1)–O(3) | 97.2(2) | O(3)–Ga(4)–O(6) | 97.5(2) |
| O(2)–Ga(1)–O(3) | 96.8(3) | O(5)–Ga(4)–O(6) | 96.4(2) |
| O(1)–Ga(2)–O(4) | 98.3(2) | Ga(1)–O(1)–Ga(2) | 129.5(3) |
| O(1)–Ga(2)–O(6) | 96.0(2) | Ga(1)–O(2)–Ga(3) | 130.1(3) |
| O(4)–Ga(2)–O(6) | 97.3(2) | Ga(1)–O(3)–Ga(4) | 132.5(3) |
| O(2)–Ga(3)–O(4) | 93.1(3) | Ga(2)–O(4)–Ga(3) | 130.9(3) |
| O(2)–Ga(3)–O(5) | 100.4(3) | Ga(3)–O(5)–Ga(4) | 130.6(3) |
| O(4)–Ga(3)–O(5) | 98.1(2) | Ga(2)–O(6)–Ga(4) | 131.1(3) |

## Acknowledgments

Financial support for this work from the University of Oklahoma, the Florida Institute of Technology, and the donors of the Petroleum Research Fund, administered by the American Chemical Society, is gratefully acknowledged. We also thank Prof. Christopher A. Reed and Dr. Kee-Chan Kim from the University of California, Riverside, for valuable discussions and the donation of the carborane trityl salts used in this study. We are also grateful to Dr. Li Zhang for the ESI mass spectra collected at the University of Oklahoma and to Prof. Nasri Nesnas for the DART mass spectra collected at the Florida Institute of Technology. We are furthermore grateful to the National Science Foundation for the purchase of the Bruker Avance 400 NMR spectrometer (CHE 03422510).

[1] S. H. Strauss, *Chem. Rev.* **1993**, *93*, 927.
[2] C. A. Reed, *Acc. Chem. Res.* **1998**, *31*, 133.
[3] E. Y.-X. Chen, T. J. Marks, *Chem. Rev.* **2000**, *100*, 1391.
[4] I. Krossing, I. Raabe, *Angew. Chem. Int. Ed.* **2004**, *43*, 2066.
[5] J. B. Lambert, L. Lin, S. Keinan, T. Mueller, *J. Am. Chem. Soc.* **2003**, *125*, 6022.
[6] R. J. Wehmschulte, J. M. Steele, J. D. Young, M. A. Khan, *J. Am. Chem. Soc.* **2003**, *125*, 1470.
[7] J. D. Young, M. A. Khan, R. J. Wehmschulte, *Organometallics* **2004**, *23*, 1965.
[8] P. Jutzi, A. Mix, B. Rummel, W. W. Schöller, B. Neumann, H.-G. Stammler, *Science* **2004**, *305*, 849.
[9] S. Hino, M. Brynda, A. D. Phillips, P. P. Power, *Angew. Chem. Int. Ed.* **2004**, *43*, 2655.
[10] M. Gonsior, I. Krossing, L. Müller, I. Raabe, M. Jansen, L. van Wüllen, *Chem. Eur. J.* **2002**, *8*, 4475.
[11] M. P. Coles, D. C. Swenson, R. F. Jordan, V. G. Young Jr, *Organometallics* **1997**, *16*, 5183.
[12] A. V. Korolev, E. Ihara, I. A. Guzei, V. G. Young Jr, R. F. Jordan, *J. Am. Chem. Soc.* **2001**, *123*, 8291.
[13] K.-C. Kim, C. A. Reed, G. S. Long, A. Sen, *J. Am. Chem. Soc.* **2002**, *124*, 7662.
[14] P. H. M. Budzelaar, G. Talarico, *Struct. Bonding (Berlin)* **2003**, *105*, 141.
[15] C. E. Radzewich, I. A. Guzei, R. F. Jordan, *J. Am. Chem. Soc.* **1999**, *121*, 8673.
[16] S. Dagorne, I. A. Guzei, M. P. Coles, R. F. Jordan, *J. Am. Chem. Soc.* **2000**, *122*, 274.
[17] C. Elschenbroich, *Organometallics*, 3rd ed., Wiley-VCH, Weinheim, Germany, **2006**.
[18] B. Quillian, Y. Wang, P. Wei, A. Handy, G. H. Robinson, *J. Organomet. Chem.* **2006**, *691*, 3765.
[19] R. C. Crittendon, X.-W. Li, J. Su, G. H. Robinson, *Organometallics* **1997**, *16*, 2443.
[20] R. C. Crittendon, B. C. Beck, J. Su, X.-W. Li, G. H. Robinson, *Organometallics* **1999**, *18*, 156.
[21] R. J. Wehmschulte, J. M. Steele, M. A. Khan, *Organometallics* **2003**, *22*, 4678.
[22] O. T. Beachley Jr, M. R. Churchill, J. C. Pazik, J. W. Ziller, *Organometallics* **1986**, *5*, 1814.
[23] M. A. Petrie, P. P. Power, H. V. R. Dias, K. Ruhlandt-Senge, K. M. Waggoner, R. J. Wehmschulte, *Organometallics* **1993**, *12*, 1086.
[24] X.-W. Li, W. T. Pennington, G. H. Robinson, *Organometallics* **1995**, *14*, 2109.
[25] X.-W. Li, J. Su, G. H. Robinson, *Chem. Commun.* **1998**, 1281.
[26] R. J. Wehmschulte, W. J. Grigsby, B. Schiemenz, R. A. Bartlett, P. P. Power, *Inorg. Chem.* **1996**, *35*, 6694.
[27] A. H. Cowley, H. S. Isom, A. Decken, *Organometallics* **1995**, *14*, 2589.
[28] R. J. Wehmschulte, A. A. Diaz, M. A. Khan, *Organometallics* **2003**, *22*, 83.
[29] E. Ihara, V. G. Young Jr, R. F. Jordan, *J. Am. Chem. Soc.* **1998**, *120*, 8277.
[30] D. Stasko, C. A. Reed, *J. Am. Chem. Soc.* **2002**, *124*, 1148.
[31] Z. Xie, C.-W. Tsang, E. T.-P. Sze, Q. Yang, D. T. W. Chan, T. C. W. Mak, *Inorg. Chem.* **1998**, *37*, 6444.
[32] J. L. Atwood, in *Coordination Chemistry of Aluminum* (Ed.: G. H. Robinson), VCH, New York, **1993**, pp. 197.
[33] A. V. Korolev, F. Delpech, S. Dagorne, I. A. Guzei, R. F. Jordan, *Organometallics* **2001**, *20*, 3367.
[34] M. Bochmann, M. J. Sarsfield, *Organometallics* **1998**, *17*, 5908.
[35] T. Beringhelli, D. Maggioni, G. D'Alfonso, *Organometallics* **2001**, *20*, 4927.
[36] C. Schnitter, H. W. Roesky, T. Albers, H.-G. Schmidt, C. Riipken, E. Parisini, G. M. Sheldrick, *Chem. Eur. J.* **1997**, *3*, 1783.
[37] R. J. Wehmschulte, M. A. Khan, B. Twamley, B. Schiemenz, *Organometallics* **2001**, *20*, 844.

 © 2007 Wiley-VCH Verlag GmbH & Co. KGaA, Weinheim 

[38] R. J. Wehmschulte, M. A. Khan, S. I. Hossain, *Inorg. Chem.* **2001**, *40*, 2756.
[39] R. A. Kovar, G. Loaris, H. Derr, J. O. Callaway, *Inorg. Chem.* **1974**, *13*, 1476.
[40] K. Ruhlandt-Senge, J. J. Ellison, R. J. Wehmschulte, F. Pauer, P. P. Power, *J. Am. Chem. Soc.* **1993**, *115*, 11353.
[41] B. Schiemenz, P. P. Power, *Angew. Chem. Int. Ed. Engl.* **1996**, *35*, 2150.
[42] A. Allemand, R. Gerdil, *Acta Crystallogr., Sect. A* **1975**, *31*, S130.
[43] G. M. Sheldrick, University of Göttingen, Germany, **2002**.
[44] G. M. Sheldrick, Bruker AXS, Madison, WI, **2000**.
[45] P. van der Sluis, A. L. Spek, *Acta Crystallogr., Sect. A* **1990**, *46*, 194.

Received: November 8, 2006
Published Online: March 6, 2007

 © 2007 Wiley-VCH Verlag GmbH & Co. KGaA, Weinheim 

DOI: 10.1002/ejic.200601036

# Copper(II)–Purine Complexes Encapsulated in NaY Zeolite

Natércia Nunes,[a] Raquel Amaro,[a] Filomena Costa,[a] Elisabetta Rombi,[b] M. Alice Carvalho,[a] Isabel C. Neves,*[a] and António M. Fonseca[a]

**Keywords:** N ligands / Copper / NaY / Encapsulation / Host–guest chemistry / Oxidation

Y-encapsulated $Cu^{II}$–purine complexes were synthesized, characterized and studied in the catalytic oxidation of cyclohexene. Encapsulation was achieved by ion-exchanging the complex from aqueous solutions containing both the purine ligand, 9-methyl-6-(methylamino)purine, and copper, in different pH, with a purine/$Cu^{II}$ molar ratio of 5:1. The resulting materials were characterized by surface analysis (XPS, SEM and XRD), chemical analysis, spectroscopic methods (EPR, FTIR and UV/Vis) and thermal analysis (TGA), which indicated that the $Cu^{II}$–purine complexes were effectively encapsulated in NaY, most probably inside the supercages, without any modification of the morphology and structure of the zeolite. Different $Cu^{II}$–purine complexes were formed, depending on the pH during synthesis. The coordination geometry of Y-encapsulated $Cu^{II}$–purine complexes was obtained with preferentially 1:2 and 1:3 Cu/L stoichiometry: complexes **A** and **B** (1:2) and complex **C** (1:3). Complex **A** was formed at pH ≥ 7, and complexes **B** and **C** (Scheme 2) were formed at pH = 5.4. Oxidation of cyclohexene with *t*BuOOH (TBHP) as the oxygen source, gave 2-cyclohexene-1-one, 2-cyclohexene-1-ol, cyclohexene oxide and 3-*tert*-butylcyclohexenyl peroxide.
(© Wiley-VCH Verlag GmbH & Co. KGaA, 69451 Weinheim, Germany, 2007)

## Introduction

During the last two decades the preparation and catalytic activity of transition-metal complexes encapsulated in zeolite structures have been extensively investigated because of their industrial significance. The use of metal complexes immobilized into solid supports as heterogeneous catalysts has become very important for ecofriendly industrial processes. These new catalysts can be easily separated from the reaction mixture and which also improves the recycling of the expensive catalyst.[1,2]

Encapsulation of transition-metal complexes with redox properties, in zeolites or other molecular sieves, is a theme of current research because of their potential use as heterogeneous redox catalysts. The peculiar adsorptive properties of Y zeolites originate from the positively charged exchangeable ions, which are located inside the 3D pore structure of the solid to balance the negative charge on the framework Al atoms and which can be coordinated by different functionalized ligands.[3]

The oxyfunctionalization of inexpensive hydrocarbons to produce more valuable organic compounds, such as alcohols, aldehydes and ketones, requires the selective oxidation of strong C–H bonds.[4,5] In this field, homogeneous catalysis is not suitable for applications on a large scale, because of low conversions, catalyst deactivation, the cost of the complexes and lack of recycling methods.

Y-encapsulated $Cu^{II}$–histidine complexes showed good catalytic activity in the oxidation of alcohols and alkenes in the presence of hydrogen peroxide at ambient temperatures.[6–10] Alkene oxidation led to different products, depending on the structure of both the substrate and the oxidant.[11] Heterogenized copper(II)–amino-acid complexes $[Cu(AA)_n]^{m+}$ were obtained by Weckhuysen et al.[6] by encapsulation in Y zeolites through ion exchange from aqueous solutions containing both the amino acid (AA) and copper(II), with an AA/$Cu^{II}$ ratio of 5:1. Copper(II) was chosen as the transition-metal ion because it forms the most stable coordination complexes, which typically consist of four nearby donor atoms approximately arranged in a plane around the transition-metal ion.[6–8]

The present work deals with the multistep preparation, characterization and catalytic studies of new heterogeneous materials, namely $Cu^{II}$–purine complexes encapsulated in Y zeolites. The preparation procedure includes (i) the synthesis of purine ligands and (ii) the ion-exchange procedure for encapsulating the metal complex in the NaY zeolite. The obtained samples were fully characterized by chemical analysis, spectroscopic methods (EPR, FTIR and UV/Vis), powder X-ray diffraction (XRD), X-ray photoelectron spectroscopy (XPS), scanning electron microscopy (SEM) and thermal analysis (TGA). The cyclohexene oxidation reaction was performed in liquid phase, at 30 °C, by using *tert*-butyl hydroperoxide (*t*BuOOH) as the oxygen source.

[a] Departamento de Química, Centro de Química, Universidade do Minho,
Campus de Gualtar, 4710-057 Braga, Portugal
Fax: +351-253-678983
E-mail: ineves@quimica.uminho.pt
[b] Dipartimento di Scienze Chimiche, Università di Cagliari, Monserrato, Italy

 InterScience © 2007 Wiley-VCH Verlag GmbH & Co. KGaA, Weinheim 

## Results and Discussion

### The 9-Methyl-6-(methylamino)purine Ligand

The biomonomer under investigation, 9-methyl-6-(methylamino)purine, a potentially polydentate ligand, can offer only nitrogen atoms as donor atoms. It was suggested that the most basic centre in purine resides in the pyrimidine ring, especially at $N^1$. However, protonation can also occur at $N^7$ and $N^9$.[12]

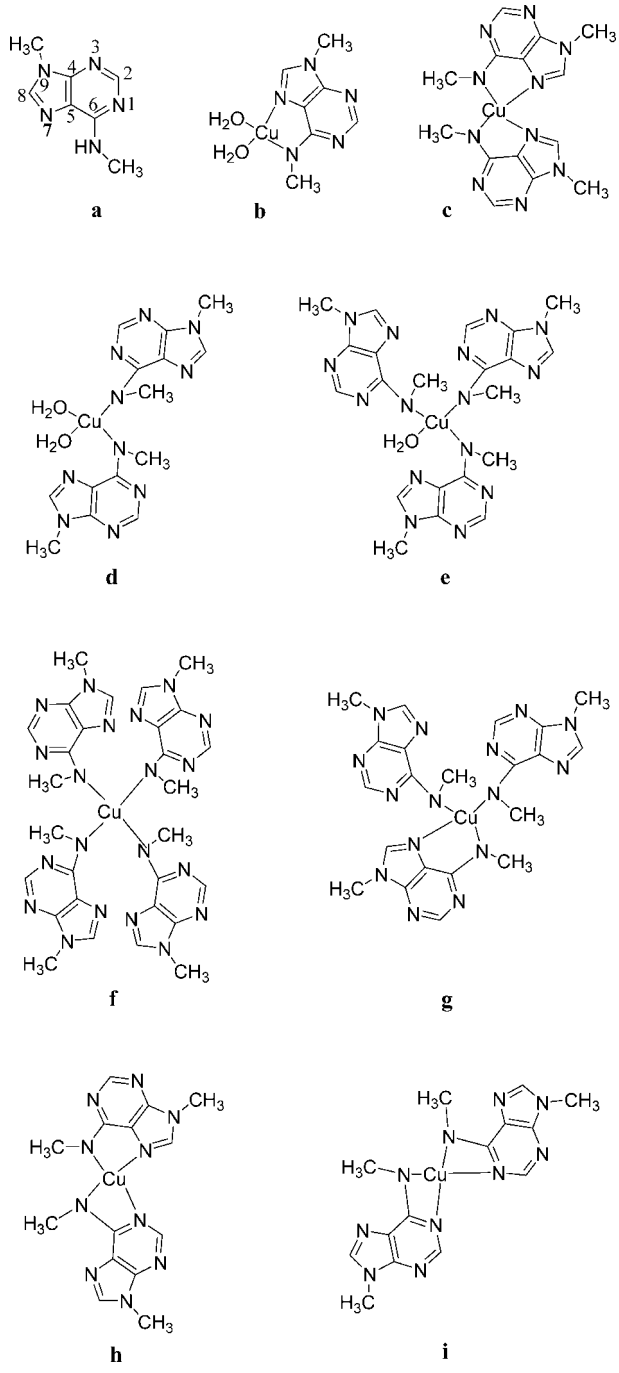


Scheme 1. Molecular structures of the used ligand and possible models of purine coordination in copper complexes: **a**: 9-methyl-6-(methylamino)purine; **b**: $N_{am}N^7O_wO_w$; **c**: $N_{am}(1)N^7(1)N_{am}(2)N^7(2)$; **d**: $N_{am}(1)N_{am}(2)O_wO_w$; **e**: $N_{am}(1)N_{am}(2)N_{am}(3)O_w$; **f**: $N_{am}(1)$-$N_{am}(2)N_{am}(3)N_{am}(4)$; **g**: $N_{am}(1)N_{am}(2)N_{am}(3)N^7(3)$; **h**: $N_{am}(1)$-$N^7(1)N_{am}(2)N^1(2)$; and **i**: $N_{am}(1)N^1(1)N_{am}(2)N^1(2)$ coordination. The axial ligands are omitted in these representations.

Since $N^9$ is substituted in the 9-methyl-6-(methylamino)-purine ligand, the coordination of the ligand with the copper ion can occur at $N^1$ and $N^7$ on the purine ring and at the *N*-amino nitrogen ($N_{am}$), which is bonded to $C^6$ carbon of the six-membered ring. Accordingly, different models of purine coordination in copper complexes can be derived (Scheme 1).

As shown in Scheme 1, the purine ligand can coordinate with the copper ion to generate complexes with four- and five-membered chelating rings; however, the latter ones lead to minor ring tension and to less steric hindrance, being thus preferred.

The purine ligand was characterized by spectroscopic methods. The electronic absorption spectrum of the purine ligand for pH = 7.0 and 10.0 exhibits three slight bands at $\lambda_{max}$(EtOH) = 305, 320 and 335 nm, which can be assigned to ligand n-π* transitions, and a high intense broad band at $\lambda_{max}$(EtOH) = 269 nm due to π-π* transitions.[13,14] A similar spectrum was obtained for pH = 5.4, however, a small shift to higher transition energies due to $N^1$ nitrogen protonation was observed.

The FTIR spectrum of the ligand in KBr is dominated by the characteristic bands of the purine ring ($\tilde{\nu}_{max}$ = 1617–1300 $cm^{-1}$) and by bands of the methylamino group on the 6-position of the ring ($\tilde{\nu}_{max}$ = 3273 and 1679 $cm^{-1}$). The strong and medium bands appearing between $\tilde{\nu}_{max}$ = 1617 and 1300 $cm^{-1}$ can be attributed to skeletal vibrations of the purine ring, while the methylamino group is indicated by the typical free N–H stretching vibrations at $\tilde{\nu}_{max}$ = 3273 $cm^{-1}$ and by the N–H bending vibration at $\tilde{\nu}_{max}$ = 1679 $cm^{-1}$.[13]

### Ion-Exchange Encapsulation Process of $Cu^{II}$–Purine Complexes

As it is commonly known, NaY zeolite is a microporous aluminosilicate based on sodalite cages joined by O bridges between the hexagonal faces. Eight such sodalite cages are linked together, forming a large central cavity or supercage, with a diameter of 12.5 Å. The supercages share a 12-membered ring with an open diameter of 7.4 Å. Thus, $Cu^{II}$–purine complexes can be ion-exchanged and encapsulated into the zeolite cavities.[15] In earlier studies, we showed that the methodologies used for the encapsulation/immobilization of the metal complexes in zeolites[16] and clays[17] are largely determined by the supports.

In this work, the modified zeolites with the entrapped metal complex were prepared by ion exchange in aqueous solutions, using an excess of the purine ligand (purine/$Cu^{II}$ molar ratio = 5:1). Chemical analysis (ICP-AES), and FTIR and UV/Vis spectroscopic analyses were performed at different stages of the preparation procedure in order to better characterize the prepared materials. In particular, the residual solutions obtained from the encapsulation process

 © 2007 Wiley-VCH Verlag GmbH & Co. KGaA, Weinheim 

were analyzed before and after Soxhlet extraction. The results are summarized in Table 1.

Table 1. Chemical analysis of the residual solutions after the ion-exchange procedure for the preparation of the $[Cu^{II}L]_nY$ samples.

| Sample | $Cu^{II}$ [a] [mmol] | $Cu^{II}$ [b] [mmol] | $Cu^{II}$ [c] [mmol] | $Cu^{II}$ [d] [mmol] |
|---|---|---|---|---|
| $[Cu^{II}L]_{5.4}Y$ | $3.52\times10^{-2}$ | $1.65\times10^{-5}$ | $3.518\times10^{-2}$ | – |
| $[Cu^{II}L]_7Y$ | $3.52\times10^{-2}$ | $3.15\times10^{-5}$ | $3.517\times10^{-2}$ | $3.38\times10^{-2}$ |
| $[Cu^{II}L]_{10}Y$ | $3.52\times10^{-2}$ | $1.57\times10^{-5}$ | $3.518\times10^{-2}$ | – |

[a] Initial copper amount in the ion-exchange solution. [b] Residual copper amount. [c] Copper loading on NaY. [d] Copper loading on NaY after the treatment with $NaNO_3$.

It appears that the residual $Cu^{II}$ content was very low, indicating that about 99% of the copper initially present was retained inside the zeolite. This finding was also confirmed by the disappearance of the brown-green colour of the starting solution after six hours under ion exchange with the zeolite.

For the sample of $[Cu^{II}L]_7Y$ submitted to the treatment with $NaNO_3$, the amount of uncomplexed copper ions in solution was equal to $1.40\times10^{-3}$ mmol, implying a copper loading on NaY of $3.38\times10^{-2}$ mmol. The small decrease observed in the loaded amount of $Cu^{II}$, on the $[Cu^{II}L]_7Y$ sample after the $NaNO_3$ treatment, seems to indicate that almost all the adsorbed metal (96%) reacted with the purine ligand and the resulting complex became entrapped inside the zeolite.

### *$[Cu^{II}L]_nY$ before Soxhlet Extraction*

To obtain information about the adsorption of the purine ligand on zeolite, the residual solutions of the ion-exchange procedure were further analyzed by UV/Vis and FTIR spectroscopy. The presence of the purine ligand in the residual solutions is shown by the appearance of the band at $\lambda_{max}$(EtOH) = 269 nm in the UV/Vis spectra, thus indicating that the excess ligand in the initial solutions, not adsorbed by zeolite, was removed by filtration. The IR measurements also reveal the presence of bands due to the ligand, thus confirming the UV/Vis spectra results.

### *$[Cu^{II}L]_nY$ after Soxhlet Extraction*

Zeolites with the hosted metal complex, which were a brown-green colour, were extracted with ethanol to remove both the residual metal complex physically adsorbed on the external surface and the uncomplexed ligand. The resulting samples retained their initial colour after extraction. FTIR and UV/Vis spectroscopic analyses were performed on the extracting solvent; typical absorption bands of the purine ligand and complexes were present in the obtained spectra. These results confirmed that Soxhlet extraction was able to remove the entire adsorbed complex on the external surface and the uncomplexed ligand. This finding might indicate that the adsorbed ligand is fully coordinated with copper ions and that the encapsulated complex can not exit the zeolite.

### Characterization of the Modified Zeolite

The final $[Cu^{II}L]_nY$ samples obtained after the ion-exchange encapsulation process were characterized by surface analysis (XRD, SEM and XPS), spectroscopic methods (FTIR and EPR), chemical analysis (CA) and thermal analysis (TGA).

Powder X-ray diffraction patterns of the $[Cu^{II}L]_nY$ samples and the parent NaY are very similar. The unit-cell parameters were calculated from the (5 3 3), (6 4 2) and (5 5 5) reflection peak positions which were determined using the (1 1 1) reflection of the quartz ($2\theta$ = 26.64187) as an internal standard by ASTM D 3942–80. No variation was observed in the zeolite lattice parameters after the encapsulation process. This result shows that no significant structural changes in the zeolite framework occur (i.e., crystallinity of NaY is preserved) during the encapsulation process and that the zeolite structure is retained upon metal-complex encapsulation. Peaks due to the neat complex were not detected, probably because of its very low percentage loading.

$[Cu^{II}L]_nY$ samples obtained after the ion-exchange encapsulation process were analyzed by SEM. Analysis of the SEM micrographs of the parent and modified samples indicates that there were no changes in the NaY morphology and structure upon complex encapsulation (Figure 1). Furthermore, the SEM results confirm that Soxhlet extraction is a suitable method for removing all the uncomplexed ligand and the residual metal complex physically adsorbed on the external surface of zeolite.

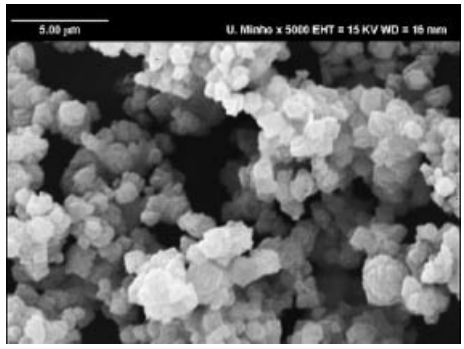


Figure 1. Scanning electron micrograph of $[Cu^{II}L]_{10}Y$ after Soxhlet extraction.

The infrared spectra of the parent NaY (**A**), $[Cu^{II}L]_7Y$ (**B**) and purine ligand (**C**) are presented in Figure 2. As the FTIR spectroscopic patterns of the $[Cu^{II}L]_nY$ samples prepared at different pH values were very similar, the sample $[Cu^{II}L]_7Y$ was chosen as a representative example.

The spectra of the parent zeolite and $[Cu^{II}L]_7Y$ are dominated by the strong bands attributable to the zeolite structure. No shift or broadening of the zeolite vibration bands are observed upon inclusion of the complex, which provides further evidence that the zeolite structure remains unchanged after the encapsulation procedure. In the $[Cu^{II}L]_7Y$ spectrum, the presence of the encapsulated organic complexes can be detected by small bands at $\tilde{\nu}_{max}$ = 1503, 1465 and 1395 $cm^{-1}$, typical of the purine ring, which appear shifted relative to those of the free ligand. The absence of N–H stretching vibration at $\tilde{\nu}_{max}$ = 3273 $cm^{-1}$ is evidence of the copper-ion coordination with the purine

 © 2007 Wiley-VCH Verlag GmbH & Co. KGaA, Weinheim 

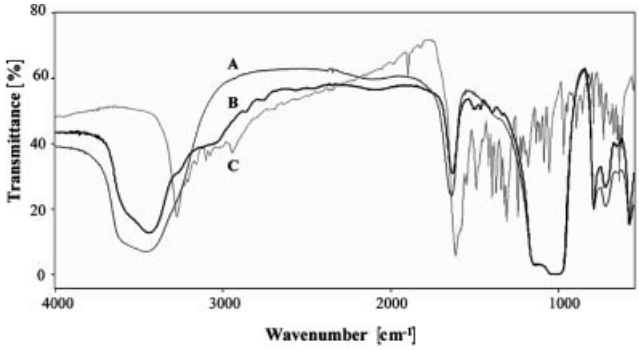


Figure 2. FTIR spectra of (A) NaY, (B) $[Cu^{II}L]_7Y$ and (C) purine ligand.

ligand and of the absence of free ligand within the zeolitic matrix. The obtained FTIR spectroscopic data indicate that the metal complex has been encapsulated in the Y zeolite and also suggest the presence of host–guest interactions with the zeolite structure.

Chemical analyses were also carried out on the solid $[Cu^{II}L]_nY$ samples. The obtained results, together with the molar Si/Al ratio and the estimated number of copper ions per unit cell, are presented in Table 2.

Table 2. Chemical analysis of the solid $[Cu^{II}L]_nY$ samples.

| | Elemental analysis [wt.-%] | | | | | | Cu/C | Cu/N |
|---|---|---|---|---|---|---|---|---|
| | Si/Al | $Cu^{II}$ [a] | $Cu^{II}$/UC | C | H | N | (w/w) | (w/w) |
| NaY | 2.88 | – | – | – | – | – | – | – |
| $[Cu^{II}L]_{5.4}Y$ | 2.95 | 0.43 | 1.10 | 1.70 | 3.20 | 1.50 | 0.25 | 0.28 |
| $[Cu^{II}L]_7Y$ | 2.98 | 0.32[b] | 0.76[b] | 1.00 | 3.00 | 0.90 | 0.32 | 0.35 |
| $[Cu^{II}L]_{10}Y$ | 2.93 | 0.41 | 0.96 | 1.30 | 2.90 | 1.10 | 0.32 | 0.37 |

[a] Copper loading on NaY. [b] Copper loading after the $NaNO_3$ treatment on NaY.

Table 2 shows that the maximum of one metal ion per unit cell is obtained on the $[Cu^{II}L]_{5.4}Y$ sample. It can also be calculated that the $(AlO_4)^-$ charges in the modified samples are not fully compensated by $Cu^{2+}$ and $Na^+$ ions. Most likely, protons balance the remaining charges through the following reaction taking place in aqueous solution:

$$\text{purine(aq)} + Cu^{2+}(aq) + H^+(aq) + Na^+(Z) \rightarrow Cu[\text{purine}]_n(Z) + Na^+(aq) + H^+(Z)$$

Charge compensation by co-exchange of protons led to some residual acidity in the zeolite, even in the samples for which NaOH was used to adjust the pH value during the preparation procedure. This residual acidity could have an effect on the catalytic behaviour of the samples in the cyclohexene oxidation reaction.[8]

The molar Si/Al ratio in $[Cu^{II}L]_nY$ samples did not change substantially upon $Cu^{II}$ complex exchange, indicating that dealumination does not occur during the encapsulation procedure. The comparisons of the molar Si/Al ratios for NaY and the modified samples confirm that the preparation method used in this work does not modify the zeolite structure, in agreement with XRD and FTIR results.

The success of the encapsulation of $Cu^{II}$–purine complexes in NaY was confirmed by the analytical data of carbon and nitrogen obtained by elemental analysis and by the copper loading obtained by ICP-AES (Table 2). The results suggest the presence of different structures of $Cu^{II}$–purine complexes with preferential Cu/ligand stoichiometry of 1:2 and 1:3.

For the 9-methyl-6-(methylamino)purine ligand, with a cation $pK_a$ value equal to 4.2,[18] the ratio of ligand·$H^+$/ligand observed at different pH syntheses is $5 \times 10^{-2}$ for pH = 5.4, $1.3 \times 10^{-3}$ for pH = 7.0 and $1.3 \times 10^{-7}$ for pH = 10.0. In acidic media, the purine ring can be protonated at $N^1$ (the more basic centre in the purine ring). This protonation hinders the coordination of the purine-ring nitrogen atoms ($N^1$ and $N^7$) with the copper ion; the formation of complexes such as **g** and **h** (Scheme 1) may be then favoured. In neutral medium, complex **h** is mainly present with two purine ligands that coordinate through the nitrogen atoms (NNNN) around the copper ion.[19,20] In more basic solutions, the nitrogen atoms of the purine ring are activated to coordinate with the copper ion, and complex **c** may be formed.

The XPS technique, which allows an analysis of the inner structure and cavity contents up to a depth of about 50 Å,[21] can provide information about the presence and distribution of $Cu^{II}$–purine complexes through the surface layer of NaY as well as on the oxidation state of the metal. All samples revealed the presence of oxygen, silicon and aluminium in their XPS resolution spectra. In the $[Cu^{II}L]_nY$ samples, the presence of the copper and nitrogen from the metal complexes was detected. In the Cu $2p_{3/2}$ and N 1s region, bands typical of the $Cu^{II}$ complexes, scarcely intense because of their low loading (as confirmed by XRD analyses), were identified. Table 3 presents the surface atomic content of sodium, silicon, aluminium and copper, obtained from the area of the relevant bands in the XPS spectrum for $[Cu^{II}L]_nY$ samples.

Table 3. Areas under the XPS Al 2p, Si 2p, Na 1s, C 1s, N 1s and Cu 2p bands for the samples.

| | XPS [atom-%] | | | | |
|---|---|---|---|---|---|
| | Si | Al | Na | $Cu^{II}$ | Si/Al |
| NaY | 23.8 | 7.4 | 11.4 | – | 3.10 |
| $[Cu^{II}]Y$ | 23.5 | 7.6 | 8.5 | 0.30 | 2.98 |
| $[Cu^{II}L]_{5.4}Y$ | 25.1 | 5.6 | 3.3 | 0.10 | 4.32 |
| $[Cu^{II}L]_7Y$ | 22.4 | 7.1 | 7.0 | 0.50 | 3.03 |
| $[Cu^{II}L]_{10}Y$ | 22.1 | 7.3 | 8.6 | 0.40 | 2.92 |

The increase in the Si/Al ratio in the modified $[Cu^{II}L]_{5.4}Y$ sample suggests that a certain dealumination takes place at the surface of the material during the encapsulation process in this case.

For $[Cu^{II}L]_7Y$ and $[Cu^{II}L]_{10}Y$ samples, the amount of Cu from XPS is very similar to the bulk copper content (Table 2). Probably, the $Cu^{II}$–purine complexes are homogeneously distributed throughout the NaY structure. However, for $[Cu^{II}L]_{5.4}Y$ the metal complexes diffuse through NaY and are preferentially located within the inner cavities.

 © 2007 Wiley-VCH Verlag GmbH & Co. KGaA, Weinheim 

A medium binding-energy value of 932.2 eV for Cu $2p_{3/2}$ is obtained from the XPS spectra of $[Cu^{II}L]_nY$ samples, which confirms that the metal is in a +2 oxidation state, in agreement with the copper coordination sphere of the free complex. The same oxidation state is observed for the $[Cu^{II}]Y$ sample. All samples exhibit N 1s as a band centred at 400 eV, due to the contribution of the amine nitrogen atom of the 9-methyl-6-(methylamino)purine ligand. This result shows that the host matrix environment does not affect the valence state of the metal atom of the complexes.

Powder EPR spectra of all $[Cu^{II}L]_nY$ samples obtained at room temperature are typical of magnetically diluted samples, implying that the $Cu^{II}$–purine complexes are dispersed within the supercages of NaY, which acts as a diamagnetic matrix. The corresponding $g_{\|}$ and $A_{\|}$ values, summarized in Table 4, are axial type and exhibit well-resolved hyperfine couplings with copper ($^{63}Cu/^{65}Cu$, $I = 3/2$) in the region of low magnetic fields.[9,10]

Table 4. EPR data of the solid $[Cu^{II}L]_nY$ samples.

| Sample | $g_{\|}$ | $g_{\perp}$ | $A_{\|}$ / $10^{-4}$ cm$^{-1}$ |
|---|---|---|---|
| $[Cu^{II}L]_{5.4}Y$ | 2.490 | 2.045 | 150 |
| $[Cu^{II}L]_{7}Y$ | 2.309 | 2.049 | 180 |
| $[Cu^{II}L]_{10}Y$ | 2.302 | 2.047 | 175 |

EPR spectra of the samples prepared at pH = 7.0 and pH = 10.0 (Figure 3) show $g$ and $A$ values typical of planar coordination of nitrogen and/or oxygen in the first coordination sphere around $Cu^{II}$.[8,9,16,19] In contrast, the EPR spectrum of the $[Cu^{II}L]_{5.4}Y$ sample is complex, probably because of the presence of more than one complex species. The increase in $A_{\|}$ and the decrease in $g_{\|}$ values (see Table 4) suggest an NNNN coordination around the $Cu^{2+}$ ion.[20,22–24]

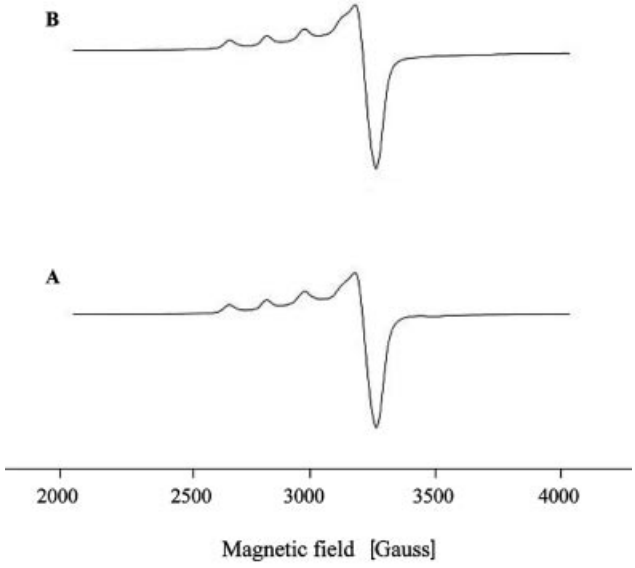


Figure 3. EPR spectra of (A) $[Cu^{II}L]_7Y$ and (B) $[Cu^{II}L]_{10}Y$.

In agreement with Weckhuysen et al. who reported two different coordination modes of the $Cu^{II}$–histidine complexes encapsulated in NaY zeolite,[6–10,20] three different $Cu^{II}$–purine complexes are proposed for inside the zeolitic supercage: (i) complexes **A** and **B** with a 1:2 Cu/L stoichiometry and (ii) complex **C** with a 1:3 Cu/L stoichiometry. As shown in Scheme 2, $Cu^{II}$ is coordinated with the 9-methyl-6-(methylamino)purine ligands in complex **A** by means of two $N_{am}N^7$ chelating groups [with an $N_{am}(1)N^7(1)$-$N_{am}(2)N^7(2)$ coordination, where the numbers in brackets refer to the 9-methyl-6-(methylamino)purine molecule], while complex **B** is characterized by an $N_{am}(1)N_{am}(2)O_wO_z$ coordination, in which $O_w$ and $O_z$ symbolize a water and a zeolite framework oxygen, respectively. An $N_{am}(1)N_{am}(2)$-$N_{am}(3)O_z$ coordination is finally observed for complex **C**.

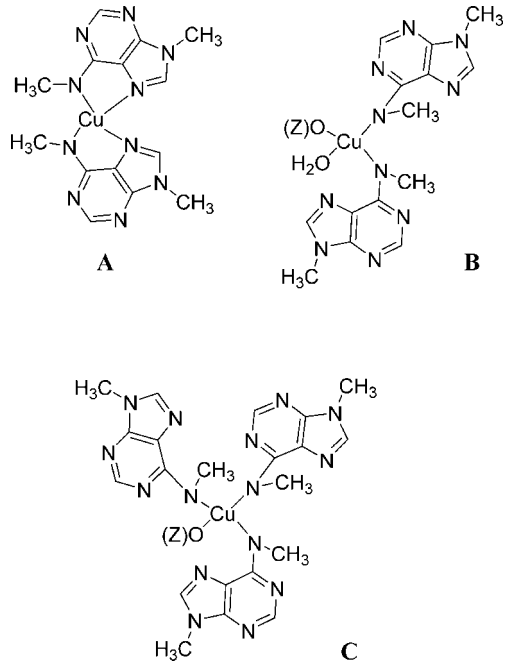


Scheme 2. Structures of copper(II)–purine complexes in Y zeolite: complex **A** with $N_{am}(1)N^7(1)N_{am}(2)N^7(2)$ coordination; complex **B** with $N_{am}(1)N_{am}(2)O_zO_w$ coordination; complex **C** with $N_{am}(1)$-$N_{am}(2)N_{am}(3)O_z$ coordination.

Although complex **A** is the dominant configuration for all samples, the relative amount of the different structures depends on the preparation conditions of the samples. It seems that the pH value during the synthesis determines the mode of coordination of the $Cu^{II}$ ion with the purine ligand; higher values (pH = 7.0 and 10.0) foster the formation of complex **A**, which accounts for 80% in both cases, while at lower pH (5.4) an increase in the amount of complexes **B** and **C** was observed.

Complementary studies performed by using thermal analysis (TGA) contributed to a better understanding of the different configurations of the encapsulated metal (depending on the pH value during the synthesis) on the thermal properties of the samples. The TGA curve of NaY shows a weight loss at 120 °C which can be attributed to the removal of intrazeolite water. After encapsulation of $Cu^{II}$–purine complexes, two major stages of weight loss can be found in a broad temperature range (i.e., 110–490 °C). The first stage occurs above 110 °C with comparable weight

 © 2007 Wiley-VCH Verlag GmbH & Co. KGaA, Weinheim 

losses for the three $[Cu^{II}L]_nY$ samples, and it is most likely caused by intrazeolite water desorption and by desorption of water associated with the encapsulated complexes. However, differences were observed at higher temperatures in the second stage of the TGA curves, which corresponds to the decomposition of the encapsulated complexes, both in the onset temperature of the decomposition process and in the weight-loss extent. Results are summarized in Table 5.

Table 5. Thermogravimetric analysis results of the solid $[Cu^{II}L]_nY$ samples.

| Sample | $T_1$[a] [°C] | $T_2$[b] [°C] | Weight loss[c] [%] |
|---|---|---|---|
| NaY | 120 | – | – |
| $[Cu^{II}L]_{5.4}Y$ | 110 | 350 | 5.4 |
| $[Cu^{II}L]_7Y$ | 110 | 420 | 3.2 |
| $[Cu^{II}L]_{10}Y$ | 110 | 480 | 3.7 |

[a] Temperature of water desorption obtained from DTG curve. [b] Temperature of complex decomposition obtained from DTG curve. [c] Weight loss due to complex decomposition obtained from DTG curve.

Differences in weight losses and onset temperatures of the complex decomposition are most probably related to (i) different coordination configurations of the $Cu^{II}$ ion with the 9-methyl-6-(methylamino)purine ligand which leads to three $Cu^{II}$–purine complexes, in agreement with chemical analysis and EPR results, and (ii) predominance of one of these $Cu^{II}$–purine complexes for high pH syntheses.

### Catalytic Behaviour of the Modified Zeolite

The effect of $Cu^{II}$–purine complexes encapsulated in NaY zeolite on the oxidation of cyclohexene with *t*BuOOH (TBHP) in decane was studied, and the results are shown in Table 6.

Table 6. Catalytic performance of the $[Cu^{II}L]_nY$ samples in cyclohexene oxidation.[a]

| Catalyst | Conversion[a] | Selectivity [%] | | |
|---|---|---|---|---|
| | [%] | Ketone[b] | Alcohol[c] | Oxide[d] |
| – | 40.3 | 62.7 | 37.3 | 0.0 |
| NaY | 40.8 | 59.0 | 41.0 | 0.0 |
| $[Cu^{II}]Y$ | 46.4 | 65.9 | 34.1 | 0.0 |
| $[Cu^{II}L]_{5.4}Y$ | 47.6 | 49.3 | 42.4 | 8.3 |
| $[Cu^{II}L]_7Y$ | 55.8 | 48.4 | 37.0 | 14.6 |
| $[Cu^{II}L]_{10}Y$ | 65.9 | 48.9 | 41.3 | 9.8 |

[a] In decane, 30 °C, TBHP/cyclohexene molar ratio = 5:3. [b] 2-Cyclohexene-1-one. [c] 2-Cyclohexene-1-ol. [d] Cyclohexene oxide.

Cyclohexene conversion and product selectivity were compared at 24 hours on-stream. Blank runs were performed to check the contribution of the radical mechanism; it was found that it accounted for about 40% of cyclohexene conversion. Only allylic oxidation occurred with the formation of 2-cyclohexene-1-one, 2-cyclohexene-1-ol and 3-*tert*-butylcyclohexenyl peroxide, as also reported in ref.,[25] while the formation of cyclohexene oxide was not observed. The NaY sample showed a quite similar behaviour.

When sodium was ion-exchanged with copper in NaY ($[Cu^{II}]Y$), a slight increase was observed both in conversion and in 2-cyclohexene-1-one selectivity. The increase in conversion from 46.4% to 65.9%, which is found by comparing the $[Cu^{II}]Y$ and $[Cu^{II}L]_{10}Y$ samples, indicates that in the presence of the purine ligand the catalytic activity is increased by a factor of 1.42. From the results in Table 6, it is evident that 2-cyclohexene-1-one is selectively formed in the presence of all catalysts. However, cyclohexene oxide is formed only on the $[Cu^{II}L]_nY$ catalysts, when $Cu^{II}$ is coordinated to the purine ligands. The selectivity value towards the epoxide seems to have a slight maximum for the $[Cu^{II}L]_7Y$ sample, while conversion increases continuously with the pH value used during the catalyst preparation. The 2-cyclohexene-1-ol selectivity also shows an increase for all the $[Cu^{II}L]_nY$ catalysts with respect to the $[Cu^{II}]Y$ sample. Further, in agreement with the findings of other authors,[7,25] the presence of 1,2-cyclohexanediol was not observed.

The formation of the allylic oxidation products, 2-cyclohexene-1-one and 2-cyclohexene-1-ol, suggests the preferential attack of the activated C–H bond over the C=C bond. Furthermore, the formation of 3-*tert*-butylcyclohexenyl peroxide is an indication of the occurrence of radical reactions.[25–28] TBHP as the oxidant promotes the allylic oxidation pathway and the extent of epoxidation is reduced. The effect of molecular oxygen in the cyclohexene epoxidation reaction with *t*BuOOH has also been reported.[29,30] It was found that when molecular oxygen acts as an oxidant in the reaction, 2-cyclohexene-1-one and 2-cyclohexene-1-ol are mainly formed.

## Conclusions

In light of the obtained results, it can be concluded that $Cu^{II}$–purine complexes coordinated with a 9-methyl-6-(methylamino)purine ligand can be encapsulated in NaY zeolite by an ion-exchange adsorption process, without structural modification or loss of crystallinity of the zeolite framework. Depending on the pH of the exchange solution, three different structures for the $Cu^{II}$–purine complexes have been proposed in the Y zeolite supercage: (i) complex **A** is located in the centre of the supercage, for which all equatorial coordination sites are provided by the purine molecules; (ii) complex **B** is coordinated to two purine molecules, for which the other two ligands are supplied by the zeolite and a water molecule; and (iii) complex **C** is coordinated to three purine ligands and to one framework oxygen atom from the zeolite.

$[Cu^{II}L]_nY$ catalysts are active in the cyclohexene oxidation reaction with TBHP. The product distribution is mainly consistent with the allylic oxidation to 2-cyclohexene-1-one and 2-cyclohexene-1-ol.

## Experimental Section

**Materials:** NaY zeolite (Si/Al = 2.88) was supplied by Grace GmbH. Chemicals for the purine ligand synthesis, the encapsulation procedure [EtOH, NaOH, HCl, $Cu(NO_3)_2{\cdot}3H_2O$ and

 © 2007 Wiley-VCH Verlag GmbH & Co. KGaA, Weinheim 

$NaNO_3$] and the oxidation reaction (cyclohexene, decane, *t*BuOOH [70% solution in water]) were purchased from Aldrich. All used materials were reagent grade.

**Sample Preparation:** The 9-methyl-6-(methylamino)purine ligand was synthesized as described in detail elsewhere.[31] Zeolite-encapsulated $Cu^{II}$–purine complexes were prepared according to the following experimental procedure: aqueous solutions of $Cu(NO_3)_2 \cdot 3H_2O$ (8.5 mg, $3.52 \times 10^{-2}$ mmol) and the 9-methyl-6-(methylamino)purine ligand (29.0 mg, $1.76 \times 10^{-1}$ mmol) in distilled water (100 $cm^3$) (purine/$Cu^{II}$ = 5:1; this molar ratio ensures that the purine ligand is not the limiting reactant during the encapsulation process) were added to NaY (0.5 g; previously calcined at 500 °C during 8 h under a dry air stream) at different pH (5.4, 7.0 and 10.0). Aqueous solutions of NaOH and/or HCl (0.1 mol $dm^{-3}$) were used to adjust the pH value, which was continuously monitored. The resulting mixtures were stirred at room temp. for 24 h, until the brown-green aqueous solutions became colourless, indicating that the complex was adsorbed by the zeolite. Then the suspension was filtered off, and the solid was washed with distilled water and dried at 60 °C for 8 h. The excess or uncoordinated ligand, as well as the residual metal complex physically adsorbed on the external surface, was removed by Soxhlet extraction with ethanol for 6 h. Finally, the samples were dried in an oven at 100 °C, under vacuum, for 12 h. The obtained samples are denoted as $[Cu^{II}L]_nY$, where L represents the 9-methyl-6-(methylamino)purine ligand and *n* is the pH value. A $[Cu^{II}]Y$ sample, with the same amount of copper as $[Cu^{II}L]_nY$, was also prepared for comparison. A portion of the $[Cu^{II}L]_7Y$ sample was further treated, for 6 h at room temp., with an aqueous solution of $NaNO_3$ (0.1 mol $dm^{-3}$) in order to remove the remaining uncomplexed copper ions from the zeolite; it was subsequently filtered off, washed with hot distilled water and finally dried at 60 °C for 12 h.

**Characterization:** Elemental chemical analyses (Si, Al, Na and Cu) were performed by inductively coupled plasma atomic emission spectrometry (ICP-AES) using a Philips ICP PU 7000 Spectrometer. The decomposition of solid samples was carried out by alkaline fusion; the method involves the use of lithium metaborate as the fluxing agent, which grants thermal stabilization of elements during the fusion stage at 1050 °C.[15] Chemical analysis of C, H and N were carried out with a Leco CHNS-932 analyzer. X-ray photoelectron spectroscopy analyses were obtained at the C. A. C. T. I. (Vigo University, Spain) with a VG Scientific ESCALAB 250iXL spectrometer using monochromatic Al-$K_\alpha$ radiation (1486.92 eV). Powder EPR spectra were obtained with a Bruker EMX spectrometer working at the X-band microwave frequencies (ca. 9.5 GHz) at room temp. Phase analysis was performed by XRD using a Philips PW1710 diffractometer. Scans were taken at room temp. in a $2\theta$ range between 4 and 80°, using Cu-$K_\alpha$ radiation. The SEM micrographs were collected with a LEICA Cambridge S360 Scanning Microscope equipped with an EDS system. To avoid the surface charging, samples were coated with gold in vacuo, by using a Fisons Instruments SC502 sputter coater, before being observed. Room temp. FTIR spectra of ligand and sample materials were obtained from powdered samples on KBr pellets, using a Bomem MB104 spectrometer in the range 4000–500 $cm^{-1}$ by averaging 20 scans at a maximum resolution of 4 $cm^{-1}$. The electronic UV/Vis absorption spectra of the purine ligand and residual solutions were collected in the range 600–200 nm with a Shimadzu UV/2501PC spectrophotometer using quartz cells at room temp. Thermogravimetric analyses (TGA) of the samples were carried out using a TGA 50 Shimadzu instrument under a high-purity helium flow (50 $cm^3 min^{-1}$). All samples were characterized between 25 and 600 °C with a heating rate of 6 °C $min^{-1}$.

**Catalytic Runs**

Experimental runs lasting 24 h were performed in a magnetically agitated batch reactor, equipped with an external water jacket and with a refrigerant, each connected with a cryothermostat in order to control the reaction and condensation temperatures, respectively. Prior to the catalytic tests, samples were activated in an oven at 250 °C for 2 h. The reaction conditions were $T$ = 30 °C, catalyst: 30 mg, cyclohexene: 100 μL, *t*BuOOH (5.5 mol $dm^{-3}$ in decane): 945 μL, oxidant/substrate molar ratio = 5:3 and solvent: decane.

Chromatographic analyses of the reaction mixture, sampled at 1-h intervals, were carried out using a GC HP 6890 (equipped with a capillary column SUPELCO Petrocol DH and a FID) and allowed qualitative and quantitative determination of (by the internal standard method) the reactant, cyclohexene and the following reaction products: cyclohexene oxide, 2-cyclohexene-1-one, 2-cyclohexene-1-ol and 1,2-cyclohexanediol. Other products were also observed (but not quantified) and identified by GC-MS: 3-*tert*-butylcyclohexenyl peroxide and very small amounts of 2,3-epoxycyclohexanone and 2,3-epoxycyclohexanol, together with those derived from the thermal decomposition of the *t*BuOOH.

## Acknowledgments

Dr. C. S. Rodriguez (C. A. C. T. I., Vigo University, Spain) is gratefully acknowledged for performing and interpreting the XPS analyses. Acknowledgments are also due to Dr. C. L. Remesar (GIQIMO, Santiago de Compostela University, Spain) for the EPR measurements. We thank Dr. A. S. Azevedo for collecting the powder diffraction data and Dr. C. Ribeiro for performing chemical analyses (Departamento de Ciências da Terra of Universidade do Minho). This work was supported by the Centro de Química (University of Minho, Portugal) and by Fundação para a Ciência e Tecnologia (FCT Portugal), under programme POCTI-SFA-3-686.

[1] P. P. Knops-Gerrits, D. E. De Vos, F. Thibault-Starzyk, P. A. Jacobs, *Nature* **1994**, *369*, 543–546.
[2] D. E. De Vos, P. P. Knops-Gerrits, R. F. Parton, B. M. Weckhuysen, P. A. Jacobs, R. A. Schoonheydt, *J. Inclusion Phenom. Mol. Recognit. Chem.* **1995**, *21*, 185–213.
[3] A. Corma, H. Garcia, *Eur. J. Inorg. Chem.* **2004**, 1143–1164.
[4] H. Arakawa, M. Aresta, J. N. Armor, M. A. Barteau, E. J. Beckman, A. T. Bell, J. E. Bercaw, C. Creutz, E. Dinjus, D. A. Dixon, K. Domen, D. L. DuBois, J. Eckert, E. Fujita, D. H. Gibson, W. A. Goddard, D. W. Goodman, J. Keller, G. J. Kubas, H. H. Kung, J. E. Lyons, L. E. Manzer, T. J. Marks, K. Morokuma, K. M. Nicholas, R. Periana, L. Que, J. Rostrup-Nielson, W. M. H. Sachtler, L. D. Schmidt, A. Sen, G. A. Somorjai, P. C. Stair, B. R. Stults, W. Tumas, *Chem. Rev.* **2001**, *101*, 953–996.
[5] T. Katsuki, *Coord. Chem. Rev.* **1995**, *140*, 189–214.
[6] B. M. Weckhuysen, A. A. Verberckmoes, I. P. Vannijvel, J. A. Pelgrins, P. L. Buskens, P. A. Jacobs, R. A. Schoonheydt, *Angew. Chem. Int. Ed. Engl.* **1996**, *34*, 2652–2654.
[7] B. M. Weckhuysen, A. A. Verberckmoes, L. Fu, R. A. Schoonheydt, *J. Phys. Chem.* **1996**, *100*, 9456–9461.
[8] B. M. Weckhuysen, H. Leeman, R. A. Schoonheydt, *Phys. Chem. Chem. Phys.* **1999**, *1*, 2875–2880.
[9] R. Grommen, P. Manikandan, Y. Gao, T. Shane, J. J. Shane, R. A. Schoonheydt, B. M. Weckhuysen, D. Goldfarb, *J. Am. Chem. Soc.* **2000**, *122*, 11488–11496 and references therein.
[10] D. Baute, D. Arieli, F. Neese, H. Zimmermann, B. M. Weckhuysen, D. Goldfarb, *J. Am. Chem. Soc.* **2004**, *126*, 11733–11745.
[11] G. Sienel, R. Rieth, K. T. Rowbottom, *Ulmann's Encyclopedia of Industrial Chemistry*, 7th ed., Wiley-VCH, **2004**, vol. A9, p. 531–545.

 © 2007 Wiley-VCH Verlag GmbH & Co. KGaA, Weinheim 

[12] J. H. Lister, *Chemistry of Heterocyclic Compounds*, Wiley-Interscience, New York, **1971**, vol. 24 (II).
[13] G. Shaw, *Comprehensive Heterocyclic Chemistry I* (Eds.: K. T. Potts), Pergamon Press, Oxford, **1984**, vol. 5.
[14] J. B. Lambert, H. F. Shurvell, D. A. Lightner, R. G. Cooks, *Organic Structural Spectroscopy*, Prentice-Hall, New Jersey, **1998**.
[15] N. Nunes, F. Costa, A. M. Fonseca, I. C. Neves, M. A. Carvalho, C. Ribeiro, *Mater. Sci. Forum* **2006**, *514–516*, 1246–1249.
[16] I. Neves, C. Freire, A. N. Zakharov, B. Castro, J. L. Figueiredo, *Colloids Surf., A* **1996**, *115*, 249–256.
[17] F. Costa, C. J. R. Silva, M. M. M. Raposo, A. M. Fonseca, I. C. Neves, A. P. Carvalho, J. Pires, *Microporous Mesoporous Mater.* **2004**, *72*, 111–118.
[18] D. J. Brown, N. W. Jacobsen, *J. Chem. Soc.* **1965**, 3770–3778.
[19] J. G. Mesu, T. Visser, F. Soulimani, E. E. van Faassen, P. de Peinder, A. M. Beale, B. M. Weckhuysen, *Inorg. Chem.* **2006**, *45*, 1960–1971.
[20] J. G. Mesu, T. Visser, A. M. Beale, F. Soulimani, B. M. Weckhuysen, *Chem. Eur. J.* **2006**, *12*, 7167–7177.
[21] J. C. Vendrine, *Catalyst Characterization. Physical Techniques for Solid Materials* (Eds.: B. Imelik, J. C. Vendrine), Plenum Press, New York, **1994**, p. 467.
[22] H. J. Scholl, J. Hutermann, *J. Phys. Chem.* **1992**, *96*, 9684–9691.
[23] R. Lontie, *Copper Proteins and Copper Enzymes*, CRC Press, Boca Raton, FL, **1984**, vols. 1–3.
[24] A. Neves, C. N. Verani, M. A. Brito, I. Vencato, A. Mangrich, G. Oliva, D. D. H. F. Souza, A. A. Batista, *Inorg. Chim. Acta* **1999**, *290*, 207–212.
[25] M. Salavati-Niasari, M. Hassani-Kabutarkhani, F. Davar, *Catal. Commun.* **2006**, *7*, 955–962.
[26] J. D. Koola, J. K. Kochi, *J. Org. Chem.* **1987**, *52*, 4545–4553.
[27] R. A. Sheldon, J. K. Kochi, *Adv. Catal.* **1976**, *25*, 272–413.
[28] S. V. Kotov, S. Boneva, T. Kolev, *J. Mol. Catal. A* **2000**, *154*, 121–129.
[29] T. G. Carrell, S. Cohen, G. C. Dismukes, *J. Mol. Catal. A* **2002**, *187*, 3–15.
[30] P. Forzatti, F. Trifirò, *React. Kinet. Catal. Lett.* **1974**, *1*, 367–372.
[31] R. K. Robins, H. H. Lin, *J. Am. Chem. Soc.* **1957**, *79*, 490–494.
Received: November 3, 2006
Published Online: March 13, 2007

 © 2007 Wiley-VCH Verlag GmbH & Co. KGaA, Weinheim 

DOI: 10.1002/ejic.200700033

# Supramolecular Chemistry and Anion Binding in Palladium(II) and Silver(I) Complexes Containing *N*,*N*′-Dipyridylxanthene-4,5-dicarboxamide Ligands

**Nancy L. S. Yue,[a] Michael C. Jennings,[a] and Richard J. Puddephatt*[a]**

**Keywords:** Supramolecular / Polymers / Silver / Palladium

Two new ligands, 2,7-di-*tert*-butyl-9,9-dimethyl-*N*,*N*′-di(3-pyridyl)- (**1**) and -*N*,*N*′-bis[(3-pyridyl)methyl]xanthene-4,5-dicarboxamide (**2**), and their complexes with palladium(II) and silver(I) are reported. Intramolecular hydrogen bonding orients the ligands so as to favour formation of macrocyclic complexes, and the structures of $[Pd_2X_4(\mu\text{-}\mathbf{1})_2]$ (**3a**), X = Cl; (**3b**) X = Br, and $[Ag_2(\mu\text{-}\mathbf{2})_2](CF_3SO_3)_2$ (**5a**) are reported. Intermolecular hydrogen bonding can also occur and can lead to supramolecular self-assembly to give sheet **3a** or ribbon **5a** structures, or serve to bind anions or solvent molecules.
(© Wiley-VCH Verlag GmbH & Co. KGaA, 69451 Weinheim, Germany, 2007)

## Introduction

In the field of host–guest chemistry, there is increasing interest in the use of hybrid organic–inorganic receptors, which can be synthesized easily by the techniques of self-assembly, and in which both the organic and inorganic components can have useful functions in binding different types of guest molecules or ions.[1–5] If the organic component contains hydrogen-bonding functionality, such as an amide group, this can be used to control the ligand conformation through intraligand hydrogen bonding, and hence to determine the primary structure of the complex (for example, chelate complex, macrocycle or polymer).[6,7] In addition, the hydrogen-bonding component may control secondary or tertiary structure through further interligand hydrogen bonding, and it may be used to enhance host–guest interactions.[1–15] Thus, the combination of dynamic coordination chemistry and hydrogen bonding has proved to be particularly useful for the self-assembly of functional molecular materials.

Ligands based on the xanthene or dibenzofuran skeletons have been widely used in catalysis, because the wide bite angles that are typical with ligands of type **A** or **B** (Scheme 1) can lead to unusual reactivity.[16–23] However, they have been used less frequently in studies of self-assembly or host–guest chemistry,[24–26] though interesting ligands such as **C** (Scheme 1) have been designed.[25] In addition, xanthene skeletons with additional amide functions incorporated, such as **D** (Scheme 1), have been used as mimics for β turns in protein analogs, using intramolecular hydrogen bonds to control the β-turn orientation.[27,28] Following our interest in the self-assembly of host molecules,[29–38] this article reports silver(I) and palladium(II) complexes derived from the *N*,*N*′-di(3-pyridyl)- or *N*,*N*′-bis[(3-pyridyl)methyl]xanthene-4,5-dicarboxamide ligands **1** and **2** (Scheme 1). The ligand is designed to give easy self-

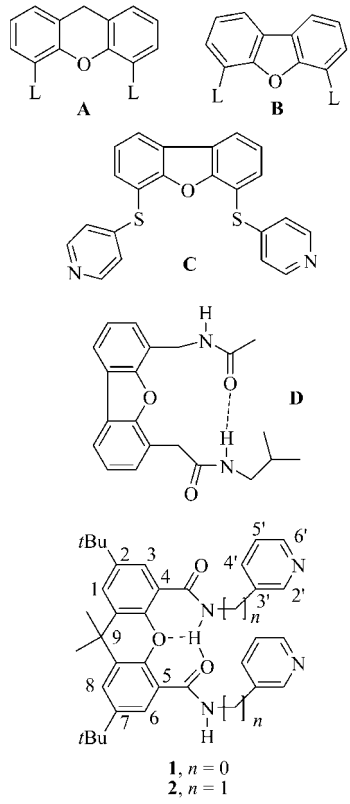


Scheme 1. The *N*,*N*′-dipyridyl-substituted xanthenedicarboxamide ligands **1** and **2**, and some related compounds containing the xanthene or dibenzofuran scaffold unit. The labelling system is defined for ligands **1** and **2**.

[a] Department of Chemistry, University of Western Ontario, London, Ontario N6A 5B7, Canada
E-mail: pudd@uwo.ca


© 2007 Wiley-VCH Verlag GmbH & Co. KGaA, Weinheim

assembly of metallacyclic complexes by dynamic coordination using the pyridine groups as donors. In addition, the amide groups can be used both to orient the donor groups through intramolecular NH···O=C hydrogen bonding and to control either intermolecular assembly or host-guest chemistry through the second NH, C=O group functionality.[27–38]

## Results and Discussion

### Properties of the Ligands 1 and 2

The ligands were prepared according to Equation (1).

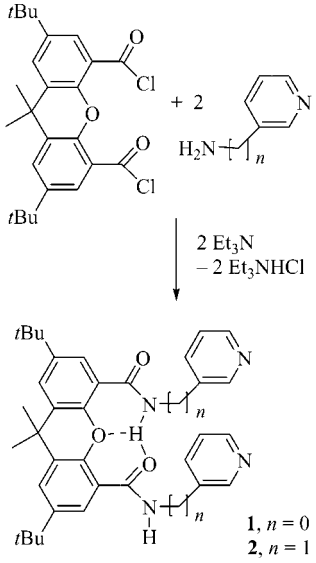


(1)

The ligand **2** was sufficiently soluble in $CD_2Cl_2$ to allow a study by variable-temperature NMR (Figure 1). It has previously been shown that in xanthenecarboxamide derivatives hydrogen-bonded NH proton signals appear in the region $\delta$ = 7–9 ppm and exhibit a large temperature dependence [$\Delta\delta/\Delta T < -10$ ppb/K], while free N–*H* signals appear at $\delta \approx 6$ ppm and exhibit a small temperature dependence [$\Delta\delta/\Delta T \approx -1$ ppb/K].[27,28] The resonance for the NH protons of ligand **2** occurs at $\delta$ = 8.18 ppm at 299 K and gives a value of $\Delta\delta/\Delta T = -12$ ppb/K. Only a single set of aromatic resonances was observed, indicating effective twofold symmetry (Figure 1). These data indicate that there is an easy equilibrium between the conformers **2a**, **2b** and **2c** in solution, with the equilibrium favoring the hydrogen-bonded forms (Scheme 2). The ligand **1** was insufficiently soluble in $CD_2Cl_2$ to allow a similar NMR study, but it is likely that a similar equilibrium is present. In the $^1$H NMR spectrum of **1** in $CD_2Cl_2/CD_3OD$, the NH proton exchanged rapidly with the methanol proton and so was not observed.

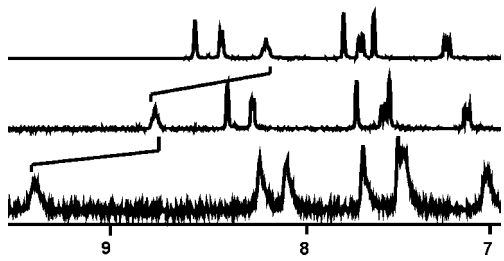


Figure 1. Variable-temperature $^1$H NMR spectra (400 MHz, top, 299 K; center, 233 K; bottom, 193 K) of ligand **2** in $CD_2Cl_2$. The bars indicate the movement of the resonance for the NH protons.

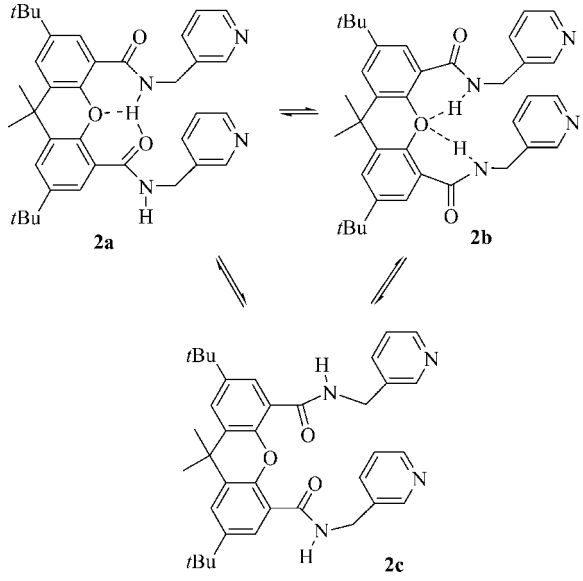


Scheme 2. Probable conformers of ligand **2** arising from rotation of the amide groups.

### Palladium(II) Complexes

Reaction of equimolar amounts of ligand **1** and $[PdX_2(NCPh)_2]$ gave the corresponding macrocyclic complexes $[Pd_2X_4(\mu\text{-}\mathbf{1})_2]$ (**3a**), X = Cl; (**3b**), X = Br (Scheme 3). Complex **3a** was essentially insoluble in common organic solvents, but **3b** was sufficiently soluble in [$D_7$]DMF to give a $^1$H NMR spectrum. The spectrum indicated effective twofold symmetry, because only a single set of resonances for the ligand **1** was observed. The amide NH resonance for **3b** was observed at $\delta$ = 10.75 ppm.

Single crystals of **3a** and **3b** were grown by slow diffusion of a solution of ligand **1** in acetonitrile/methanol into a solution of $[PdX_2(NCPh)_2]$, X = Cl or Br, in dichloromethane, under which conditions each complex crystallized as the acetonitrile solvate $[Pd_2X_4(\mu\text{-}\mathbf{1})_2]\cdot 4MeCN$. The molecular structures are shown in Figure 2. The complexes exist as macrocycles, with each palladium(II) center having the *trans*-$PdCl_2N_2$ square-planar coordination. There is a crystallographically imposed inversion center in both **3a** and **3b** (Figure 2). All amide groups are in the usual *trans* conformation. Each ligand has one NH and one C=O group directed inwards, with a transannular NH···O=C hydrogen bond between them, and one NH and C=O group directed

 © 2007 Wiley-VCH Verlag GmbH & Co. KGaA, Weinheim 

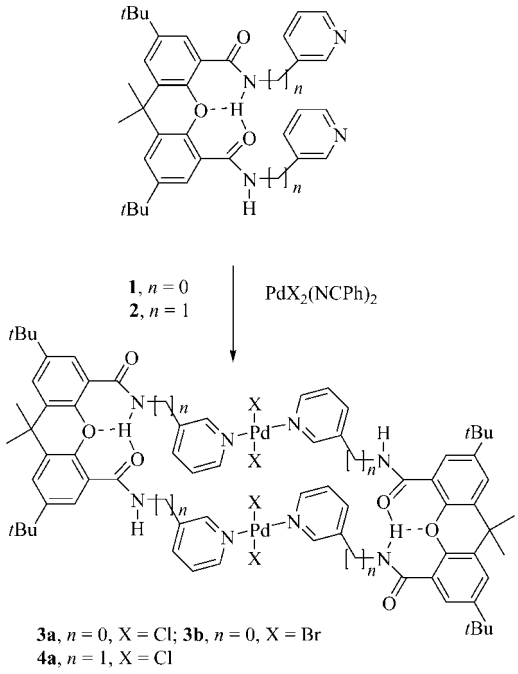


Scheme 3. Synthesis of macrocyclic palladium(II) complexes.

outwards. The inward NH group is also hydrogen-bonded to the xanthene oxygen atom (Figure 2). In complex **3b**, the outward NH group is hydrogen-bonded to an acetonitrile solvate molecule (Figure 2), but in **3a** the hydrogen bonding of the outward NH group is more complex, as described below. The other main difference in molecular structures of **3a** and **3b** is related to the conformations of the 3-pyridyl groups. In complex **3a** both pyridyl donors are roughly *syn* to the amide carbonyl group [dihedral angles C(8)N(7)C(3)C(2) –19.7°, C(34)N(36)C(37)C(38) –19.8°], but in complex **3b** one of the pyridyl groups is roughly *syn* and the other roughly *anti* to the amide carbonyl group [dihedral angles C(8)N(7)C(3)C(2) –34.7°, C(34)N(36)C(37)C(38) –136.9°]. The above torsion angles and the illustrations in Figure 2 also illustrate how the 3-pyridyl groups are distorted out of the plane of the amide units to a greater extent in **3b** compared to **3a**. As a result of the conformational difference, the palladium atoms are closer and the macrocycle more rectangular in shape in **3b** compared to **3a** [Pd···PdA 5.67 Å in **3a**; Pd···PdA 4.26 Å in **3b**].

In complex **3a** the acetonitrile molecules of solvation are not involved in hydrogen bonding with the outward NH group. Instead this NH group forms an intermolecular hydrogen bond to a chloride ligand of a neighboring molecule (Figure 3a). Each macrocycle **3a** is involved in four such hydrogen-bonding interactions through the two outward-directed NH groups and two of the four chloride ligands (Figure 3b). The overall result is that the macrocycles are assembled into sheets as shown in part b of Figure 3. This intermolecular hydrogen bonding is evidently strong enough to make complex **3a** much less soluble than **3b**. The outward-directed carbonyl group is not involved in hydrogen bonding in either complex **3a** or **3b**, and so it appears that the strength of intermolecular hydrogen bonding of the

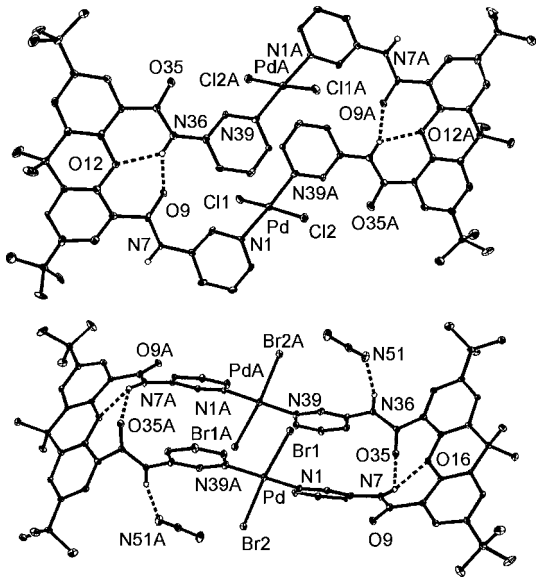


Figure 2. Molecular structures of complexes **3a** and **3b**. Selected distances: **3a**; Pd–Cl(1) 2.320(2); Pd–Cl(2) 2.293(2); Pd–N(1) 2.040(6); Pd–N(39A) 1.997(6) Å. **3b**; Pd–N(1) 1.999(7); Pd–N(39A) 2.016(7); Pd–Br(2) 2.419(1); Pd–Br(1) 2.442(1) Å. Hydrogen bond lengths: **3a**; N(36)···O(12) 2.706(8); N(36)···O(9) 2.843(7) Å. **3b**; N(7)···O(16) 2.641; N(7)···O(35) 3.081; N(36)···N(51) 3.02(1) Å.

outward NH group follows the series NH···ClPd (observed in **3a**) > NH···NCMe (observed in **3b**) > NH···BrPd, NH···O=C (not observed).

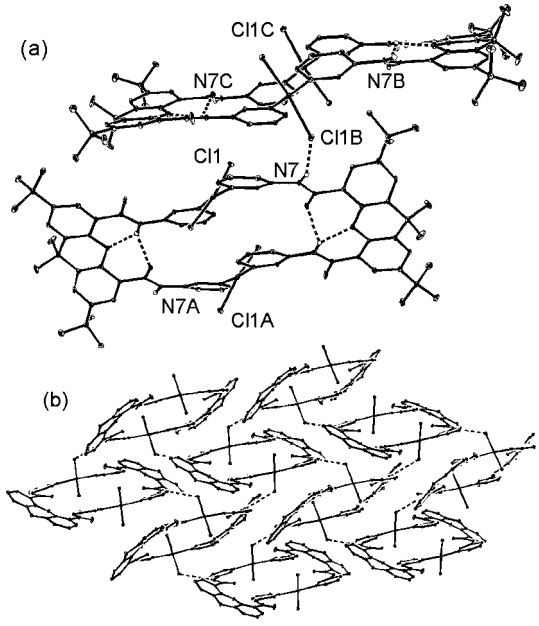


Figure 3. The self-assembly of the macrocyclic complexes **3a**: (a) an intermolecular NH···Cl interaction with distance N(7)···Cl(1B) 3.585(7) Å; (b) the sheet structure arising from the self-assembly process.

The apparent twofold symmetry of complex **3b** in solution, as determined by its $^1$H NMR spectrum, requires easy rotation of the pyridylamido units and it is likely that the

 © 2007 Wiley-VCH Verlag GmbH & Co. KGaA, Weinheim 

conformers **3-A** (as seen in the solid-state structure of **3a**) and **3-B** (as seen in **3b**) are two of several that may be involved in the fluxionality (Scheme 4).

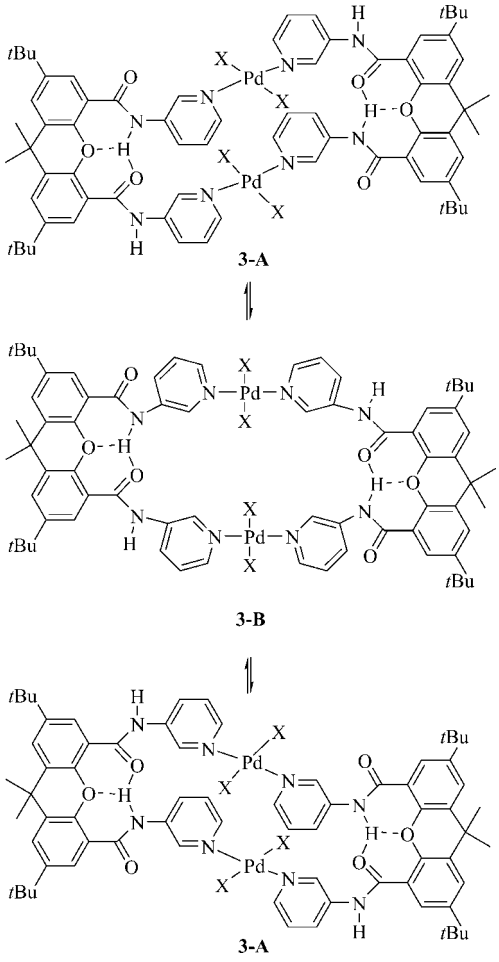


Scheme 4. Proposed mechanism of fluxionality of complex **3b** (X = Br).

The reaction of ligand **2** with $[PdCl_2(NCPh)_2]$ was more complex. The product analysed as "$PdCl_2$(**2**)", but the $^1$H NMR spectrum indicated the presence of two isomers in a roughly 3:2 ratio, each having twofold symmetry (see Exp. Sect.). Single crystals for X-ray structure determination could not be obtained. The ESI-MS gave the highest mass peak envelope centered at *m*/*z* = 1499, corresponding to $[Pd_2Cl_3(\mu\text{-}\mathbf{2})_2]^+$, as expected for loss of one chloride ligand from **4a**. Hence, it is likely that one of the isomers present is **4a** but the nature of the other isomer is not known.

### Silver(I) Complexes

The reactions of ligand **1** with silver(I) salts gave insoluble complexes which could not be characterized, but the similar reaction with the more flexible ligand **2** gave the more soluble complexes $[Ag_2(\mu\text{-}\mathbf{2})]_2(X)_2$, **5a**, X = $CF_3SO_3$; **5b**, X = $CF_3CO_2$; **5c**, X = $NO_3$; **5d**, X = $BF_4$; **5e**, X = $PF_6$. Complex **5a** was not easily soluble in dichloromethane but it was sufficiently soluble in a $CD_2Cl_2$/$CD_3OD$ mixture to give a $^1$H NMR spectrum. The $^1$H NMR spectrum in the temperature range 299–193 K indicated effective twofold symmetry of the ligand units **2**, presumably due to easy rotation of the pyridylamido units. In contrast to the case of complex **4a**, only one isomer was present (Figure 4). The resonance for the NH protons of complex **5a** occurs at $\delta$ = 9.17 ppm at 299 K and gives a value of $\Delta\delta/\Delta T$ = –3 ppb/K.

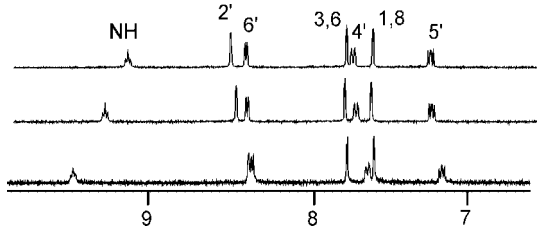


Figure 4. $^1$H NMR spectrum (400 MHz) of complex **5a** in $CD_2Cl_2$/$CD_3OD$ at (top) 299 K; (center) 273 K; (bottom) 243 K.

The structure of complex **5a** is shown in Figure 5. The complex exists in the form of a macrocycle with distorted linear silver(I) coordination [N(1)–Ag–N(41A) 168.9(3)°]. The distortion from linearity allows the silver(I) centers to form a transannular argentophilic interaction [Ag–Ag(A) 3.134(1) Å]. The conformation of the amido groups is similar to those observed in **3a** and **3b**, in which the inward NH group hydrogen bonds to both the xanthene oxygen atom and the inward directed carbonyl oxygen atom (Figure 5). The outward directed NH groups hydrogen bond to triflate anions.

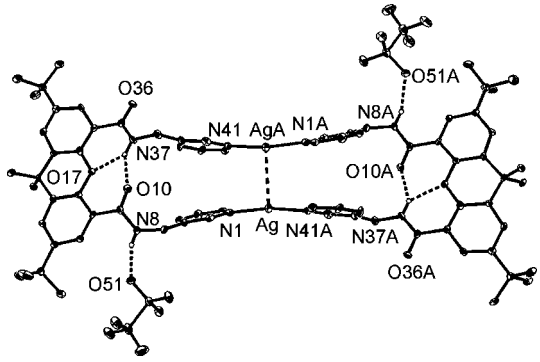


Figure 5. Structure of the silver(I) complex **5a**. Selected parameters: Ag–N(1) 2.130(7), Ag–N(41A) 2.148(7), Ag–Ag(A) 3.134(1) Å; N(1)–Ag–N(41A) 168.9(3)°. Hydrogen bonding distances: N(8)···O(51) 2.92(1), N(37)···O(10) 2.83(1), N(37)···O(17) 2.71(1) Å.

The complex **5a** undergoes further self-assembly in the solid state to give a ribbon structure, as shown in Figure 6. Each triflate ion is hydrogen-bonded to an outward-directed NH group through one of its oxygen atoms (O51), as shown in Figure 5, but each triflate also bridges between the two silver(I) centers of a neighboring macrocycle through a second oxygen atom (O52), as shown in Figure 6. Each macrocycle then interacts with four bridging triflate ions through secondary Ag···O or NH···O interactions, as shown in Figure 6, and a ribbon structure is formed.

 © 2007 Wiley-VCH Verlag GmbH & Co. KGaA, Weinheim 

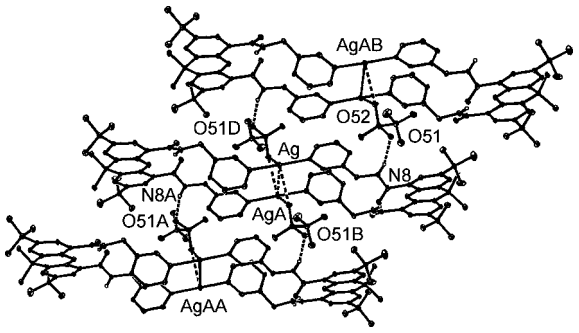


Figure 6. The ribbon structure formed by self-assembly of **5a**, showing how each macrocycle binds to two neighboring macrocycles through four bridging triflate ions. Selected distances: Ag···O(52B) and AgA···O(52D) 2.77(1), Ag···O(52D) and AgA···O(52B) 2.83(1) Å.

The interactions of complexes **5a**–**5e** with anions in dilute acetonitrile solution were studied by ESI-MS. The highest mass peaks for complexes **5a**–**5e** were observed in envelopes centered at *m*/*z* = 1546, 1511, 1458, 1483, and 1541, corresponding to $[^{107}Ag_2(\mathbf{2})_2X]^+$, with X = $O_3SCF_3$, $O_2CCF_3$, $NO_3$, $BF_4$, and $PF_6$, respectively. A dilute solution of complex **5a** ($0.5 \times 10^{-3}$ M) in acetonitrile was treated with increasing amounts of $Bu_4N^+X^-$ (X = $NO_3$, $HSO_4$, $ClO_4$, $BF_4$ and $PF_6$) to give 1:0.6, 1:0.8, 1:1.0, 1:1.2 and 1:1.4 molar ratios. By monitoring the decrease in intensity of the envelope of peaks for $[Ag_2(\mathbf{2})_2(O_3SCF_3)]^+$ at *m*/*z* = 1545, accompanied by the increase in intensity of the peaks for $[Ag_2(\mathbf{2})_2X]^+$, it is possible to estimate the relative binding abilities of the anions $X^-$. Typical spectra are shown in Figure 7. The anion binding follows the sequence $NO_3^- > HSO_4^- > CF_3SO_3^- > ClO_4^- > BF_4^-, PF_6^-$. This is consistent either with the series of p$K_a$ values of the corresponding acids [approximate p$K_a$ for $HNO_3$ –1; $H_2SO_4$ –3; $HClO_4$ –10; $CF_3SO_3H$ –13] or with the coordinating ability of the anions.[39] Hence it is not obvious if the anions mainly associate with the cation $[Ag_2(\mu\text{-}\mathbf{2})_2]^{2+}$ primarily by coordination to silver(I) or by hydrogen bonding to one of the outward-directed NH groups.

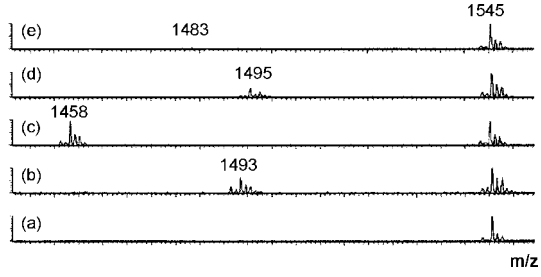


Figure 7. ESI-MS for complex **5a** in acetonitrile either alone (a) or in the presence of 1.4 equiv. of $Bu_4NX$: (b) X = $HSO_4$; (c) X = $NO_3$; (d) X = $ClO_4$; (e) X = $BF_4$.

## Conclusions

The intramolecular hydrogen bonding observed for ligands **1** and **2** serves to favor a U-shaped molecule [Scheme 1, Equation (1)] and this in turn favors formation of macrocyclic complexes with palladium(II) and silver(I). In the case of the ligand **1** only macrocyclic complexes **3a** and **3b** are formed with palladium(II) halides (Scheme 3, Figure 2) but, in the case of the more flexible ligand **2** a second isomer is formed. Examination by molecular mechanics indicates that either a monomer with chelating ligand **2** or a *cis*,*cis* dimer with bridging ligands **2** are possible for this second isomer. With silver(I), the ligand **2** forms a macrocyclic complex $[Ag_2(\mu\text{-}\mathbf{2})_2]^{2+}$ and, in the triflate salt, the anions form secondary bonds to both silver(I) and to an NH group of the ligand.

An interesting feature of the macrocyclic complexes is that there are two outward-directed NH groups available to take part in hydrogen bonding (Scheme 2). In the palladium(II) complexes **3a** and **3b**, these NH groups form hydrogen bonds to either solvent molecules (**3b**) or to chloride ligands of neighboring macrocycles (**3a**) (Figure 2 and Figure 3). In complex **3a**, this intermolecular hydrogen bonding leads to supramolecular self-assembly of a sheet structure (Figure 3). In the silver(I) complex **5a**, the outward-directed NH groups form hydrogen bonds to triflate anions (Figure 5). The triflate anions then use a second oxygen atom to form a weak coordinate bond to the two silver(I) centers of a neighboring macrocycle. The overall result is then the formation of a supramolecular "ribbon of macrocycles" structure (Figure 6). The ESI-MS of **5a** in acetonitrile solution indicates that at least partial association between the cations $[Ag_2(\mu\text{-}\mathbf{2})_2]^{2+}$ and triflate anions occurs giving the major ion $[Ag_2(\mu\text{-}\mathbf{2})_2(CF_3SO_3)]^+$. As expected, anion exchange occurs easily with other anions $X^-$ such as $HSO_4^-$, $NO_3^-$, $ClO_4^-$, $BF_4^-$ and $PF_6^-$ to give the corresponding ions $[Ag_2(\mu\text{-}\mathbf{2})_2(X)]^+$ (Figure 7). In all of the complexes, there is easy exchange in solution between the inward and outward directed NH groups, and this occurs by easy rotation of the 3-pyridylamide units (Scheme 4).

Overall, this first study of coordination complexes of ligands with amide group substituents on the xanthene scaffold indicates the promise that exists for both supramolecular self-assembly and host-guest chemistry through various forms of hydrogen bonding with the outward-directed NH groups.

## Experimental Section

NMR spectra were recorded with a Varian Inova 400 MHz spectrometer. For atom labeling see Scheme 1.

**2,7-Di-*tert*-butyl-9,9-dimethyl-*N*,*N*′-di(3-pyridyl)xanthene-4,5-dicarboxamide (1):** A solution of 3-aminopyridine (0.21 g, 2.23 mmol) in dichloromethane (20 mL) was added to a solution of 2,7-di-*tert*-butyl-9,9-dimethylxanthene-4,5-dicarbonyl dichloride (0.50 g, 1.12 mmol) and triethylamine (0.34 g, 3.35 mmol) in dry dichloromethane (50 mL). The reaction mixture was stirred overnight under nitrogen, then the solvent was evaporated under vacuum, and the residue was washed with water and acetone to give the product as a white solid. Yield: 0.33 g (52%). $^1$H NMR ($CD_2Cl_2$/$CD_3OD$): $\delta$ = 8.59 (s, 2 H, 2′-H), 8.19 (d, $J_{HH}$ = 5 Hz, 2 H, 6′-H), 7.98 (d, $J_{HH}$ = 7 Hz, 2 H, 4′-H), 7.78 (s, 2 H, 3-H, 6-H), 7.66 (s, 2 H, 1-H, 8-

 © 2007 Wiley-VCH Verlag GmbH & Co. KGaA, Weinheim 

H), 7.11 (dd, $J_{HH}$ = 5 Hz, 7 Hz, 2 H, 5′-H), 1.70 (s, 6 H, $CH_3$), 1.36 (s, 18 H, *t*Bu) ppm. $C_{35}H_{38}N_4O_3$ (562.71): calcd. C 74.71, H 6.81, N 9.96; found C 74.41, H 6.42, N 10.44.

**2,7-Di-*tert*-butyl-9,9-dimethyl-*N*,*N*′-bis[(3-pyridyl)methyl]xanthene-4,5-dicarboxamide (2):** This compound was prepared according to the procedure described above for **1**. 3-(Aminomethyl)pyridine was used instead of 3-aminopyridine. Yield: 35%. $^1$H NMR ($CD_2Cl_2$): $\delta$ = 8.57 (s, 2 H, 2′-H), 8.44 (d, $J_{HH}$ = 5 Hz, 2 H, 6′-H), 8.19 (t, $J_{HH}$ = 5 Hz, 2 H, CONH), 7.77 (s, 2 H, 3-H, 6-H), 7.69 (d, $J_{HH}$ = 8 Hz, 2 H, 4′-H), 7.60 (s, 2 H, 1-H, 8-H), 7.21 (dd, $J_{HH}$ = 5 Hz, 8 Hz, 2 H, 5′-H), 4.51 (d, $J_{HH}$ = 5 Hz, 4 H, $CH_2$), 1.68 (s, 6 H, $CH_3$), 1.33 (s, 18 H, *t*Bu) ppm. $^{13}$C NMR: $\delta$ = 167.6 (C=O), 148.9, 148.3, 146.8, 146.2, 136.5, 135.9, 130.6, 127.0, 126.1, 124.4, 121.7, 41.52 ($CH_2$), 35.1 ($CH_3$), 33.0 ($CH_3$), 51.5 (*t*Bu) ppm. $C_{37}H_{42}N_4O_3$ (590.76): calcd. C 75.23, H 7.17, N 9.48; found C 75.28, H 7.20, N 9.09.

**[Pd$_2$Cl$_4$(μ-1)$_2$] (3a):** A solution of the ligand **1** (0.0154 g, 0.026 mmol) in $CH_2Cl_2$ (10 mL) was added to a solution of [$PdCl_2$(NCPh)$_2$] (0.010 g, 0.026 mmol) in $CH_2Cl_2$ (10 mL) was added. The solution was stirred overnight, then pentane (40 mL) was added, and the yellow solid product which precipitated was collected by filtration and dried under vacuum. Yield: 0.013 g. The product was insufficiently soluble to give an NMR spectrum. $C_{70}H_{76}Cl_4N_8O_6Pd_2$ (1480.03): calcd. C 56.81, H 5.18, N 7.57; found C 56.64, H 5.00, N 7.47.

**[Pd$_2$Br$_4$(μ-1)$_2$] (3b):** A solution of the ligand **1** (0.036 g; 0.064 mmol) in dichloromethane (10 mL) was added to a solution [$PdBr_2$(NCPh)$_2$] (0.030 g, 0.064 mmol) in a mixture of acetonitrile (5 mL) and dichloromethane (5 mL). The solution was stirred overnight, then pentane (40 mL) was added, and the yellow solid product was collected by filtration and dried under vacuum. Yield: 0.043 g. $^1$H NMR ([D$_7$]DMF): $\delta$ = 10.75 (s, 4 H, CONH), 9.30 (s, 4 H, -2′-H), 8.82 (d, $J_{HH}$ = 6 Hz, 4 H, 6′-H), 8.04 (d, $J_{HH}$ = 8 Hz, 4′-H), 7.84 (d, $J_{HH}$ = 2 Hz, 4 H, 3-H, 6-H), 7.69 (d, $J_{HH}$ = 2 Hz, 4 H, 1-H, 8-H), 7.18 (dd, $J_{HH}$ = 6 Hz, 8 Hz, 4 H, 5′-H), 1.77 (br. s, 12 H, $CH_3$), 1.38 (br. s, 36 H, *t*Bu) ppm. $C_{70}H_{76}Br_4N_8O_6Pd_2 \cdot H_2O$ (1657.84): calcd. C 50.17, H 4.69, N 6.69; found C 50.40, H 4.54, N 6.45.

**[Pd$_2$Cl$_4$(μ-2)$_2$] (4):** A solution of the ligand **2** (0.0154 g; 0.026 mmol) in $CH_2Cl_2$ (10 mL) was added to a solution of [$PdCl_2$(NCPh)$_2$] (0.010 g; 0.026 mmol) in $CH_2Cl_2$ (10 mL). The solution was stirred overnight and the product was isolated as above. Yield: 0.013 g. $^1$H NMR ($CD_2Cl_2$/$CD_3OD$), isomer (**a**): $\delta$ = 9.15 (s, 2 H, 2′-H), 8.80 (d, $J_{HH}$ = 6 Hz, 2 H, 6′-H), 8.20 (br. t, 2 H, CONH), 7.68 (d, $J_{HH}$ = 8 Hz, 2 H, 4′-H), 7.65 (s, 2 H, 3-H, 6-H), 7.56 (s, 2 H, 1-H, 8-H), 7.16 (dd, $J_{HH}$ = 8 Hz, 6 Hz, 2 H, 5′-H), 4.36 (s, 4 H, $CH_2$), 1.66 (s, 6 H, $CH_3$), 1.33 (s, 18 H, *t*Bu) ppm. Isomer (**b**): $\delta$ = 9.20 (s, 2 H, 2′-H), 8.70 (d, $J_{HH}$ = 6 Hz, 2 H, 6′-H), 8.45 (br. t, 2 H, CONH), 7.88 (d, $J_{HH}$ = 8 Hz, 2 H, 4′-H), 7.67 (s, 2 H, 3-H, 6-H), 7.59 (s, 2 H, 1-H, 8-H), 7.48 (dd, $J_{HH}$ = 8 Hz, 6 Hz, 2 H, 5′-H), 4.23 (s, 4 H, $CH_2$), 1.64 (s, 6 H, $CH_3$), 1.30 (s, 18 H, *t*Bu) ppm. $C_{74}H_{87}Cl_4N_8O_6Pd_2$ (1539.16): calcd. C 57.86, H 5.51, N 7.29; found C 57.84, H 5.85, N 7.32.

**[Ag$_2$(μ-2)$_2$][CF$_3$SO$_3$]$_2$ (5a):** A solution of the ligand **2** (0.046 g, 0.078 mmol) in THF (10 mL) was added to a solution of $AgO_3SCF_3$ (0.020 g, 0.078 mmol) in acetone (10 mL). The solution was stirred overnight. The solvent was evaporated to give a white solid, which was washed with hexane and dried under vacuum. Yield: 0.055 g. $^1$H NMR ($CD_2Cl_2$/$CD_3OD$): $\delta$ = 9.17 (t, $J_{HH}$ = 6 Hz, 4 H, CONH), 8.53 (s, 4 H, 2′-H), 8.44 (d, $J_{HH}$ = 5 Hz, 4 H, 6′-H), 7.81 (d, $J_{HH}$ = 2 Hz, 4 H, 3-H, 6-H), 7.76 (d, $J_{HH}$ = 8 Hz, 4 H, 4′-H), 7.63 (d, $J_{HH}$ = 2 Hz, 4 H, 1-H, 8-H), 7.37 (dd, $J_{HH}$ = 5 Hz, 8 Hz, 4 H, 5′-H), 4.53 (d, $J_{HH}$ = 6 Hz, 8 H, $CH_2$), 1.66 (s, 12 H, $CH_3$), 1.33 (s, 36 H, *t*Bu) ppm. $C_{76}H_{84}Ag_2F_6N_8O_{12}S_2 \cdot H_2O \cdot$THF: calcd. C 53.81, H 5.31, N 6.28; found C 53.85, H 5.17, N 6.08. Colourless plate crystals of **5a**·4$CHCl_3$ were obtained by slow diffusion of a concentrated solution of ligand **2** in chloroform into a concentrated solution of [$AgO_3SCF_3$] in acetone.

Similarly were prepared: **[Ag$_2$(μ-2)$_2$][CF$_3$CO$_2$]$_2$ (5b):** Yield: 34%. $^1$H NMR ($CD_2Cl_2$/$CD_3OD$): $\delta$ = 9.02 (br. t, 4 H, CONH), 8.47 (br. s, 4 H, 2′-H), 8.38 (d, $J_{HH}$ = 6 Hz, 4 H, 6′-H), 7.80 (d, $J_{HH}$ = 2 Hz, 4 H, 3-H, 6-H), 7.78 (br. m, 4 H, 4′-H), 7.62 (d, $J_{HH}$ = 3 Hz, 4 H, 1-H, 8-H), 7.27 (br. dd, $J_{HH}$ = 6 Hz, 8 Hz, 4 H, 5′-H), 4.53 (br. d, $J_{HH}$ = 4 Hz, 8 H, $CH_2$), 1.66 (s, 12 H, $CH_3$), 1.33 (s, 36 H, *t*Bu) ppm. $C_{78}H_{84}Ag_2F_6N_8O_{10} \cdot 2CH_2Cl_2 \cdot 2H_2O \cdot 2(CH_3)_2CO \cdot C_5H_{12}$ (1623.29): calcd. C 54.18, H 5.80, N 5.55; found C 54.39, H 4.95, N 5.64. **[Ag$_2$(μ-2)$_2$][NO$_3$]$_2$ (5c):** Yield: 84%. $^1$H NMR ($CD_2Cl_2$/$CD_3OD$): $\delta$ = 9.23 (br. t, $J_{HH}$ = 6 Hz, 4 H, CONH), 8.52 (br. s, 4 H, 2′-H), 8.42 (d, $J_{HH}$ = 5 Hz, 4 H, 6′-H), 7.82 (br. d, $J_{HH}$ = 8 Hz, 4 H, 4′-H), 7.81 (d, $J_{HH}$ = 2 Hz, 4 H, 3-H, 6-H), 7.64 (d, $J_{HH}$ = 3 Hz, 4 H, 1-H, 8-H), 7.34 (dd, $J_{HH}$ = 5 Hz, 8 Hz, 4 H, 5′-H), 4.48 (br. d, $J_{HH}$ = 4 Hz, 8 H, $CH_2$), 1.67 (s, 12 H, $CH_3$), 1.33 (s, 36 H, *t*Bu) ppm. $C_{76}H_{90}Ag_2N_{10}O_{12} \cdot 6H_2O$: calcd. C 55.01, H 6.20, N 8.44; found C 54.98, H 5.57, N 8.46. **[Ag$_2$(μ-2)$_2$][BF$_4$]$_2$ (5d):** Yield: 62%. $^1$H NMR ($CD_2Cl_2$/$CD_3OD$): $\delta$ = 9.06 (br. t, $J_{HH}$ = 6 Hz, 4 H, CONH), 8.52 (br. s, 4 H, 2′-H), 8.41 (d, $J_{HH}$ = 5 Hz, 4 H, 6′-H), 7.82 (br. d, $J_{HH}$ = 8 Hz, 4 H, 4′-H), 7.80 (d, $J_{HH}$ = 2 Hz, 4 H, 3-H, 6-H), 7.64 (d, $J_{HH}$ = 2 Hz, 4 H, 1-H, 8-H), 7.33 (br. dd, $J_{HH}$ = 6 Hz, 8 Hz, 4 H, 5′-H), 4.55 (br. d, $J_{HH}$ = 5 Hz, 8 H, $CH_2$), 1.67 (s, 12 H, $CH_3$), 1.33 (s, 36 H, *t*Bu) ppm. $C_{94}H_{132}Ag_2B_2Cl_6F_8N_8O_{12} \cdot 4H_2O \cdot (CH_3)_2CO$ (2168.18): calcd. C 54.37, H 5.81, N 6.59; found C 54.33, H 5.59, N 6.49. **[Ag$_2$(μ-2)$_2$][PF$_6$]$_2$ (5e):** Yield: 72%. $^1$H NMR ($CD_2Cl_2$/$CD_3OD$): $\delta$ = 9.16 (br. t, $J_{HH}$ = 6 Hz, 4 H, CONH), 8.47 (br. d, $J_{HH}$ = 2 Hz, 4 H, 2′-H), 8.41 (br. d, $J_{HH}$ = 5 Hz, 4 H, 6′-H), 7.86 (br. d, $J_{HH}$ = 8 Hz, 4 H, 4′-H), 7.76 (d, $J_{HH}$ = 2 Hz, 4 H, 3-H, 6-H), 7.63 (d, $J_{HH}$ = 2 Hz, 4 H, 1-H, 8-H), 7.41 (dd, $J_{HH}$ = 5 Hz, 8 Hz, 4 H, 5′-H), 4.54 (br. d, $J_{HH}$ = 6 Hz, 8 H, $CH_2$), 1.65 (s, 12 H, $CH_3$), 1.31 (s, 36 H, *t*Bu) ppm. $C_{76}H_{90}Ag_2F_{12}N_8O_6P_2 \cdot H_2O$: calcd. C 52.60, H 5.34, N 6.46; found C 52.74, H 5.51, N 6.12.

**ESI-MS:** All ESI mass spectra were recorded with a Micromass LCT spectrometer and were calibrated with NaI at a concentration of 2 μg/μL in propan-2-ol/water (50:50). The injection flow rate at 20.0 μL/min was used throughout all experiments. The procedure for anion exchange between **5a** and $Bu_4N^+NO_3^-$ was as follows. A stock solution of $Bu_4N^+NO_3^-$ in acetonitrile ($5 \times 10^{-3}$ M) was used to prepare standard solutions of $Bu_4N^+NO_3^-$ at varying concentrations. To a solution of **5a** in acetonitrile (1 mL, $5 \times 10^{-4}$ M) was added a solution of $Bu_4N^+NO_3^-$ in acetonitrile (1 mL, $7 \times 10^{-4}$ M). After 30 min, the ESI-MS was recorded and the ratio of [Ag$_2$(μ-**2**)$_2$($O_3SCF_3$)]$^+$ to [Ag$_2$(μ-**2**)$_2$($NO_3$)]$^+$ was estimated. The procedure was repeated at several concentrations of $Bu_4N^+NO_3^-$. The same procedure was used to study anion exchange between complex **5a** and $Bu_4N^+X^-$ (X = $HSO_4^-$, $ClO_4^-$, $BF_4^-$, and $PF_6^-$).

**X-ray Structure Determinations:** Crystals were mounted on glass fibers, and data were collected at 150 K with a Nonius Kappa-CCD diffractometer with COLLECT (Nonius, 1998) software. The unit cell parameters were calculated and refined from the full data set. Crystal cell refinement and data reduction were carried out using the Nonius DENZO package. The data were scaled using SCALEPACK (Nonius, 1998). The SHELXTL-NT V6.1 (G. M. Sheldrick, Madison, WI) program package was used to solve and refine the structures by direct methods. The hydrogen atom posi-

 © 2007 Wiley-VCH Verlag GmbH & Co. KGaA, Weinheim 

Table 1. Crystal data and structure refinement for the complexes.

| Complex | **3a**·4MeCN | **3b**·4MeCN | **5a**·2$CHCl_3$ |
|---|---|---|---|
| Formula | $C_{78}H_{88}Cl_4N_{12}O_6Pd_2$ | $C_{78}H_{88}Br_4N_{12}O_6Pd_2$ | $C_{40}H_{44}AgCl_6F_3N_4O_6S$ |
| *Fw* | 1644.20 | 1822.04 | 1086.42 |
| *T* [K] | 150(2) | 150(2) | 150(2) |
| $\lambda$ [Å] | 0.71073 | 0.71073 | 0.71073 |
| Crystal system | monoclinic | monoclinic | monoclinic |
| Space group | $P2_1/c$ | $P2_1/c$ | $P2_1/c$ |
| Cell dimensions | | | |
| *a* [Å] | 20.643(2) | 25.421(2) | 13.2529(5) |
| *b* [Å] | 12.3582(8) | 16.839(1) | 37.775(1) |
| *c* [Å] | 16.020(1) | 9.3664(6) | 9.1803(4) |
| $\beta$ [°] | 112.822(3) | 99.653(3) | 94.697(2) |
| *V* [Å$^3$] | 3767.0(5) | 3952.6(4) | 4580.5(3) |
| *Z* | 2 | 2 | 4 |
| $d_{calcd.}$ [Mgm$^{-3}$] | 1.450 | 1.531 | 1.575 |
| Absorption coefficient [mm$^{-1}$] | 0.680 | 2.535 | 0.897 |
| *F*(000) | 1696 | 1840 | 2208 |
| Reflections | 22349 | 29296 | 36296 |
| Independent reflections | 11397 | 6886 | 7595 |
| Absorption correction | semi-empirical | semi-empirical | semi-empirical |
| Data/restraints/parameters | 11397/4/471 | 6886/2/460 | 7595/0/550 |
| Goof | 1.051 | 0.856 | 0.882 |
| $R_1$ [$I > 2\sigma(I)$] | 0.077 | 0.061 | 0.059 |
| $wR_2$[$I > 2\sigma(I)$] | 0.140 | 0.092 | 0.103 |

tions were calculated geometrically and were included as riding on their respective carbon atoms. Details of the data collection and refinement are given in Table 1. In all three structures, the molecule had a crystallographically imposed center of symmetry.

Orange plate-like crystals of [$Pd_2Cl_4$(μ-**1**)$_2$]·4MeCN were grown from $CH_2Cl_2$/MeCN/MeOH. The crystal was twinned and the twin law was determined by using ROTAX, and confirmed by successful refinement. All heavy atoms were refined anisotropically but there were some anomalous thermal parameters and a large $R_{int}$, associated with imperfect treatment of the crystal twinning and with unresolved disorder of the solvent molecules.

Yellow crystals of [$Pd_2Br_4$(μ-**1**)$_2$]·4MeCN were grown from $CH_2Cl_2$/MeCN/MeOH, a concentrated dichloromethane/acetonitrile/methanol solution. One MeCN molecule was well ordered, but the other was not and its geometry was constrained to be the same as the well-ordered one.

Colorless crystals of [$Ag_2$(μ-**2**)$_2$][$CF_3SO_3$]$_2$·4$CHCl_3$, were grown from $CHCl_3$/$Me_2CO$. The refinement was straightforward in this case.

CCDC-632844 to -632846 contain the supplementary crystallographic data for this paper. These data can be obtained free of charge from The Cambridge Crystallographic Data Centre via www.ccdc.cam.ac.uk/data_request/cif.

## Acknowledgments

We thank the Natural Sciences and Engineering Research Council of Canada (NSERC) for financial support and R. J. P. thanks the Government of Canada for a Canada Research Chair.

[1] S. R. Seidel, P. J. Stang, *Acc. Chem. Res.* **2002**, *35*, 972–983.
[2] M. Fujita, M. Tominaga, A. Hori, B. Therrien, *Acc. Chem. Res.* **2005**, *38*, 371–380.
[3] P. D. Beer, P. A. Gale, *Angew. Chem. Int. Ed.* **2001**, *40*, 486–516.
[4] C. R. Bondy, S. J. Loeb, *Coord. Chem. Rev.* **2003**, *240*, 77–99.
[5] S.-L. Zheng, M.-L. Tong, X.-M. Chen, *Coord. Chem. Rev.* **2003**, *246*, 185–202.
[6] C. L. Chen, B. S. Kang, C. Y. Su, *Austral. J. Chem.* **2006**, *59*, 3–18.
[7] A. N. Khlobystov, A. J. Blake, N. R. Champness, D. A. Lemenovskii, A. G. Majouga, N. V. Zyk, M. Schroder, *Coord. Chem. Rev.* **2001**, *222*, 155–192.
[8] D. Braga, F. Grepioni, *Acc. Chem. Res.* **2000**, *33*, 601–608.
[9] M. W. Hosseini, *Acc. Chem. Res.* **2005**, *38*, 313–323.
[10] D. S. Lawrence, T. Jiang, M. Levett, *Chem. Rev.* **1995**, *95*, 2229–2260.
[11] J. Sola, A. Lopez, R. A. Coxall, W. Clegg, *Eur. J. Inorg. Chem.* **2004**, 4871–4881.
[12] L. Applegarth, A. E. Goeta, J. W. Steed, *Chem. Commun.* **2005**, 2405–2406.
[13] A. M. L. Fuller, D. A. Leigh, P. J. Lusby, A. M. Z. Slawin, D. B. Walker, *J. Am. Chem. Soc.* **2005**, *127*, 12612–12619.
[14] B.-C. Tzeng, B.-S. Cho, H.-T. Yeh, G.-H. Lee, S.-M. Peng, *New J. Chem.* **2006**, *30*, 1087–1092.
[15] C.-L. Chen, H.-Y. Tan, J.-H. Yao, Y.-Q. Wan, C.-Y. Su, *Inorg. Chem.* **2005**, *44*, 8510–8520.
[16] P. C. J. Kamer, P. W. M. van Leeuwen, J. N. H. Reek, *Acc. Chem. Res.* **2001**, *34*, 895–904.
[17] A. Miedamer, J. W. Raebiger, C. J. Curtis, S. M. Miller, D. L. Dubois, *Organometallics* **2004**, *23*, 2670–2679.
[18] T. Wada, K. Tanaka, *Eur. J. Inorg. Chem.* **2005**, 3832–3839.
[19] R. Begum, T. Komura, H. Tobita, *Chem. Commun.* **2006**, 432–433.
[20] P. J. Cox, A. Kaltzoglou, P. Aslanidis, *Inorg. Chim. Acta* **2006**, *359*, 3183–3190.
[21] M. J. McNevin, J. R. Hagadorn, *Inorg. Chem.* **2004**, *43*, 8547–8554.
[22] E. Deschamps, B. Deschamps, J. L. Dormieux, L. Ricard, N. Mezailles, P. Le Floch, *Dalton Trans.* **2006**, 594–602.
[23] F. Li, R. Delgado, A. Coelho, M. G. B. Drew, V. Felix, *Tetrahedron* **2006**, *62*, 8550–8558.
[24] L. R. Hanton, A. G. Young, *Cryst. Growth Des.* **2006**, *6*, 833–835.
[25] P. L. Caradoc-Davies, L. R. Hanton, *Dalton Trans.* **2003**, 1754–1758.
[26] K. Aikawa, T. Nagata, *Inorg. Chim. Acta* **2000**, *306*, 223–226.

 © 2007 Wiley-VCH Verlag GmbH & Co. KGaA, Weinheim 

[27] K. T. Tsang, H. Diaz, N. Graciani, J. W. Kelly, *J. Am. Chem. Soc.* **1994**, *116*, 3988–4005.
[28] K. McWilliams, J. W. Kelly, *J. Org. Chem.* **1996**, *61*, 7408–7414.
[29] N. L. S. Yue, Z. Qin, M. C. Jennings, D. J. Eisler, R. J. Puddephatt, *Inorg. Chem. Commun.* **2003**, *6*, 1269–1271.
[30] N. L. S. Yue, D. J. Eisler, M. C. Jennings, R. J. Puddephatt, *Inorg. Chem.* **2004**, *43*, 7671–7681.
[31] N. L. S. Yue, D. J. Eisler, M. C. Jennings, R. J. Puddephatt, *Inorg. Chem. Commun.* **2005**, *8*, 31–33.
[32] N. L. S. Yue, M. C. Jennings, R. J. Puddephatt, *Inorg. Chem.* **2005**, *44*, 1125–1131.
[33] Z. Qin, M. C. Jennings, R. J. Puddephatt, *Inorg. Chem.* **2002**, *41*, 3967–3974.
[34] Z. Qin, M. C. Jennings, R. J. Puddephatt, *Inorg. Chem.* **2003**, *42*, 1956–1965.
[35] N. L. S. Yue, M. C. Jennings, R. J. Puddephatt, *Dalton Trans.* **2006**, 3886–3893.
[36] T. J. Burchell, D. J. Eisler, R. J. Puddephatt, *Dalton Trans.* **2005**, 268–272.
[37] T. J. Burchell, D. J. Eisler, R. J. Puddephatt, *Cryst. Growth Des.* **2006**, *6*, 974–982.
[38] T. J. Burchell, D. J. Eisler, R. J. Puddephatt, *Chem. Commun.* **2004**, 944–945.
[39] J. P. Guthrie, *Can. J. Chem.* **1978**, *56*, 2342.

Received: January 10, 2007
Published Online: March 9, 2007

 © 2007 Wiley-VCH Verlag GmbH & Co. KGaA, Weinheim 

DOI: 10.1002/ejic.200600062

# Single-Crystal Structure and Magnetic Behavior of a Molecule-Based Ferrimagnet $Mn[Mn_{0.2}Cr_{0.8}(CN)_6]\cdot 4H_2O$

Xiao-Ping Shen,[a,b] Yi-Zhi Li,[a] You Song,[a] Zheng Xu,*[a] and Guo-Cong Guo[c]

**Keywords:** Prussian blue analogue / Crystal structure / Magnetic properties / Chromium / Manganese

The compound with the stoichiometry $Mn^{III}[Mn^{III}_{0.2}Cr^{III}_{0.8}(CN)_6]\cdot 4H_2O$ (**1**), which was prepared by slow diffusion of an aqueous solution of $K_3[Cr(CN)_6]$ and a methanol solution of [Mn(saltn)]$ClO_4$ [saltn = *N*,*N*′-1,3-propylenebis(salicylideneiminato) dianion] through a U-shaped tube containing silica gel, has been characterized by elemental analysis, ICP analysis, XPS, single-crystal X-ray structure analysis, and magnetic measurements. The complex has a face-centered cubic lattice analogous to Prussian blue and indicates ferrimagnetic ordering below $T_c$ = 63 K.
(© Wiley-VCH Verlag GmbH & Co. KGaA, 69451 Weinheim, Germany, 2007)

## Introduction

There has been continuous interest in the molecule-based magnetic materials of cyano-bridged dimetallic assemblies because of their interesting magnetic, magneto-optical and optoelectronic properties.[1,2] It is known that Prussian blue (PB) analogues, derived from hexacyanometalate ions $[M(CN)_6]^{n-}$ and simple transition metal ions, exhibit magnetic ordering at critical temperatures as high as 376 K and form a family of magnetic materials.[2] On the basis of powder XRD results, PB analogues are generally thought to have a face-centered cubic structure, but detailed structural studies are still limited because of the difficulty in obtaining single crystals.[3] On the other hand, in order to clarify the magnetostructural correlation of cyano-bridged dimetallic systems, a wide variety of hybrid Prussian blue complexes derived from $[M(CN)_6]^{n-}$ (M = Fe, Cr, Mn, Co) and coordinatively unsaturated transition metal complexes have been studied structurally and magnetically.[4] These complexes assume oligonuclear, 1D, 2D, and 3D structures and exhibit ferro-, ferri-, and metamagnetic behavior. For instance, the reaction between [Mn(salen)]$ClO_4$ [salen = *N*,*N*′-ethylenebis(salicylideneiminato) dianion] and $[M(CN)_6]^{3-}$ (M = Fe, Cr) has already led to two dimetallic heptanuclear $Mn_6M$ clusters.[5] Recently, we had expected to obtain another cyano-bridged $Mn^{III}$–$Cr^{III}$ cluster by using [Mn(saltn)]$ClO_4$ [saltn = *N*,*N*′-1,3-propylenebis(salicylideneiminato) dianion] instead of [Mn(salen)]$ClO_4$ as a building block. Surprisingly, we found a novel PB analogue $Mn[Mn_{0.2}Cr_{0.8}(CN)_6]\cdot 4H_2O$ (**1**), which has a face-centered cubic lattice and shows ferrimagnetic ordering below 63 K. Here we report on its synthesis, crystal structure, and magnetic properties.

[a] State Key Laboratory of Coordination Chemistry, Nanjing University,
Nanjing 210093, P. R. China
Fax: +86-25-83314502
E-mail: zhengxu@netra.nju.edu.cn
[b] School of Chemistry and Chemical Engineering, Jiangsu University,
Zhenjiang 212003, P. R. China
[c] State Key Laboratory of Structural Chemistry, Fujian Institute of Research on the Structure of Matter, Chinese Academy of Sciences,
Fuzhou 350002, P. R. China

## Results and Discussion

### Synthesis and Characterization

Complex **1** was obtained as brown-yellow, quasi-ball-shaped single crystals by slow diffusion of a methanol solution of [Mn(saltn)]$ClO_4$ and an aqueous solution of $K_3[Cr(CN)_6]$ through a U-tube containing silica gel. It is insoluble in usual inorganic and organic solvents and stable in air. The elemental and inductively coupled plasma (ICP) analyses confirm the composition of **1** (see Experimental Section). The IR spectrum of **1** shows a sharp $\nu$(C≡N) peak at 2161 $cm^{-1}$. The blue shift of the band $\nu$(C≡N) relative to that of $K_3[Cr(CN)_6]$ (2130 $cm^{-1}$)[6] suggests the formation of cyano bridges. A strong broad band around 3400 $cm^{-1}$ indicates the presence of $H_2O$. The characteristic peaks from the ligand saltn are not found in the IR spectrum. The X-ray photoelectron spectroscopy (XPS) of **1** shows the peaks for Cr($2p_{3/2}$) at 576.95 eV and for Mn($2p_{3/2}$) at 641.9 eV, with a molar ratio Cr/Mn = 1:1.6. As shown in Table 1, the Mn $2p_{3/2}$ binding energy of **1** is close to those found for $K_3[Mn^{III}(CN)_6]$ and $Mn_2O_3$, and obviously different from those of $Mn^{II}_3[Cr(CN)_6]_2\cdot 16H_2O$, MnO, and $MnO_2$, which supports the oxidation state of +3 for Mn. The composition of $Mn[Mn_{0.2}Cr_{0.8}(CN)_6]\cdot 4H_2O$ for complex **1** is in agreement with the results of the crystal structural analysis and magnetic studies as discussed below.

 © 2007 Wiley-VCH Verlag GmbH & Co. KGaA, Weinheim 

Table 1. Manganese $2p_{3/2}$ binding energies [eV] of some manganese compounds.

| Complex **1** | $Mn_3[Cr(CN)_6]_2\cdot 16H_2O$[3e] | $K_3[Mn(CN)_6]_3$ | MnO | $Mn_2O_3$ | $MnO_2$ | Ref. |
|---|---|---|---|---|---|---|
| 641.9 | 641.35 | 641.65<br>641.6 | | | | This work<br>[2g] |
| | | | 641.0 | 641.9 | 642.5 | [7] |
| | | | 640.9 | 641.8 | 642.5 | [8] |
| | | | 641.0 | 641.7 | 642.2 | [9] |

It can be inferred that the six-membered ring $MnN_2C_3$ in $[Mn(saltn)]^+$ has a lower stability with respect to the five-membered ring $MnN_2C_2$ in $[Mn(salen)]^+$ because of the less favorable entropy change required for the formation of six-membered rings.[10] Therefore, the $[Mn(saltn)]^+$ can dissociate more easily into $Mn^{3+}$, which reacts with $[Cr(CN)_6]^{3-}$ to produce the more stable complex **1**. The formation reactions for complex **1** can be shown as follows:

$[Mn(saltn)]^+ \rightarrow Mn^{3+} + saltn^{2-}$

$1.2Mn^{3+} + [Cr(CN)_6]^{3-} + 4H_2O \rightarrow Mn[Mn_{0.2}Cr_{0.8}(CN)_6]\cdot 4H_2O + 0.2Cr^{3+}$

It should be pointed out that complex **1** can only be obtained in low yields by the above slow diffusion method and cannot be synthesized as a bulk powder by directly mixing the same ingredients in solution (i.e. without the method with the U-tube); direct mixing immediately results in a black precipitate. The IR spectrum of the black product shows a $\nu(C\equiv N)$ peak at 2126 $cm^{-1}$ and a series of characteristic peaks for saltn, which suggests the formation of the $[Cr(CN)_6]^{3-}/[Mn(saltn)]^+$ adduct. Although the reason of the formation of the two different products is not clear at present, according to the reaction conditions, we infer that the synthesis of complex **1** would be dominated by thermodynamic factors, while that of the black product would be controlled by kinetic factors.

## Crystal Structure

X-ray crystallography shows that **1** belongs to the cubic space group $Fm\bar{3}m$, $a = b = c = 10.7632(7)$ Å, $V = 1246.9(1)$ Å$^3$. These data are comparable to those for $NaMn[Cr(CN)_6]$,[3a] $Mn_3[Mn(CN)_6]_2\cdot xH_2O$,[3b] $Mn_3[Cr(CN)_6]_2\cdot xH_2O$,[3e] and $K_{0.2}Mn_{1.4}[Cr(CN)_6]\cdot 6H_2O$.[3g] The crystal structure of **1** is shown in Figure 1. Each unit cell contains four $Mn[Mn_{0.2}Cr_{0.8}(CN)_6]\cdot 4H_2O$ units. The Mn1 atom occupies the position (0, 1/2, 1/2) and Cr1(Mn2) atom is in the position (1/2, 1/2, 1/2). Because of the Cr/Mn molar ratio of 2:3 on the basis of ICP analysis, the Cr atoms are partially replaced by Mn atoms and the occupancy of Cr1/Mn2 is 0.8:0.2, which is similar to that of $NMe_4Mn[(Mn, Cr)(CN)_6]\cdot 3H_2O$[3c] reported by Babel et al. In complex **1**, both the Mn and Cr atoms are six-coordinate and have an octahedral geometry, and are linked through cyano-bridges to form a face-centered cubic framework. The Cr atom is bonded to the carbon atoms of the $CN^-$ ligands as in $K_3[Cr(CN)_6]$. The Mn1 atom is coordinated to the nitrogen atoms of the $CN^-$ groups and the Mn2 atom to the carbon atoms, which would result in Mn1 and Mn2 with high-spin and low-spin ground states, respectively. The Mn1–N–C–Cr1(Mn2) linkage is linear, and the bond lengths are 2.155(9) Å [Mn1–N], 1.120(10) Å [C–N], and 2.106(14) Å [Cr1(Mn2)–C]. The Mn1···Cr1(Mn2) distance is 5.3816 Å. Because of the Jahn–Teller effect, the high-spin (HS) $Mn^{III}$ ions should usually occupy the distorted octahedral sites. For example, the structure of the $Mn^{III}$ (HS)-$Fe^{II}$ Prussian blue analogues in a low-temperature state is not face-centered cubic but tetragonal because of the Jahn–Teller effect.[11] In complex **1**, it is likely that Jahn–Teller distortion occurs, but the macroscopic X-ray diffraction technique only presents a statistical distribution of distorted $Mn^{III}$ polyhedron. Water molecules occupy the vacancies in the unit cell, and O2 is structurally disordered. It must be pointed out that the structure of complex **1** could not be solved properly according to the $Mn_3[Cr(CN)_6]_2\cdot xH_2O$ model.[3b,3e] This fact further supports the oxidation state of +3 for Mn. Generally, the structure and composition of a generic PB-like compound $A_p[B(CN)_6]_q\cdot x$H2O depend on the oxidation states of the cations A and B: for A(III) and B(III), a A/B molar ratio of 1:1 is found, while for A(II) and B(III), a ratio of 3:2 is found. For the former, the coordination spheres of A and B are $\{A(NC)_6\}$ and $\{B(CN)_6\}$, while for the latter, one third of the $[B(III)(CN)_6]$ vacancies are filled by water molecules, therefore, the coordination sphere of B is the same but the mean coordination sphere of A becomes $\{A(NC)_4(H_2O)_2\}$.[1a] Complex **1** is a unique example in which the valence of both the cations A and B is +3, but the A/B molar ratio is 3:2 instead of 1:1. The reason for the special stoichiometry that **1** presents is unclear at present.

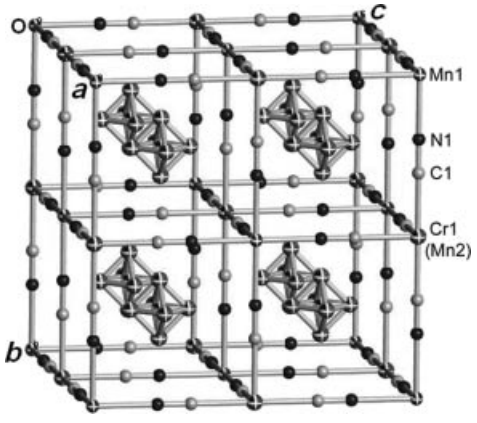


Figure 1. Unit cell diagram of complex **1**.

 © 2007 Wiley-VCH Verlag GmbH & Co. KGaA, Weinheim 

## Magnetic Properties

The magnetic susceptibilities of complex **1** were measured with an applied field of $H$ = 100 Oe in the temperature range 2–300 K. The plot of $\chi_M T$ vs. $T$ is given in Figure 2. At room temperature, the value of $\chi_M T$ per $Mn_{1.2}Cr_{0.8}$ unit is 5.02 $cm^3\,K\,mol^{-1}$ (6.34 $\mu_B$), which is slightly higher than the spin-only value of 4.7 $cm^3\,K\,mol^{-1}$ (6.13 $\mu_B$) expected for an uncoupled spin system ($1{\cdot}S_{Mn}$ = 2, $0.2{\cdot}S_{Mn}$ = 1, $0.8{\cdot}S_{Cr}$ = 3/2) with $g$ = 2.0. On lowering the temperature, the $\chi_M T$ value gradually decreases and reaches a minimum of 4.43 $cm^3\,K\,mol^{-1}$ (5.95 $\mu_B$) at 140 K (inset in Figure 2). Upon further cooling, $\chi_M T$ increases to a maximum of 3005 $cm^3\,K\,mol^{-1}$ (155 $\mu_B$) at 52 K and then decreases below this temperature. The dependence of $1/\chi_M$ on $T$ obeys the Curie–Weiss law [$\chi = C/(T-\theta)$] in the temperature range 300–140 K with a Weiss constant of $\theta$ = –44 K. The negative Weiss constant and the shallow minimum in the $\chi_M T$ vs. $T$ curve both indicate the presence of an antiferromagnetic coupling between adjacent $Mn^{III}$ ($S$ = 2) and $Cr^{III}$ ($S$ = 3/2) [or $Mn^{III}$ ($S$ = 1)] ions through the cyanide bridges. The abrupt increase in the $\chi_M T$ value at about 65 K suggests the onset of the three-dimensional magnetic ordering. The decrease in the $\chi_M T$ value below 52 K may be due to the zero-field splitting effect and/or the field saturation of the magnetization. This is characteristic of ferrimagnetic behavior. The temperature dependence of the zero-field alternating current (ac) magnetic susceptibility taken at 10 Hz (Figure 3) shows that the real part ($\chi'$) and the imaginary part ($\chi''$) of the ac magnetic susceptibility both have a maximum at 63 K and 64 K, respectively, which indicates that $T_c$ of **1** is 63 K.

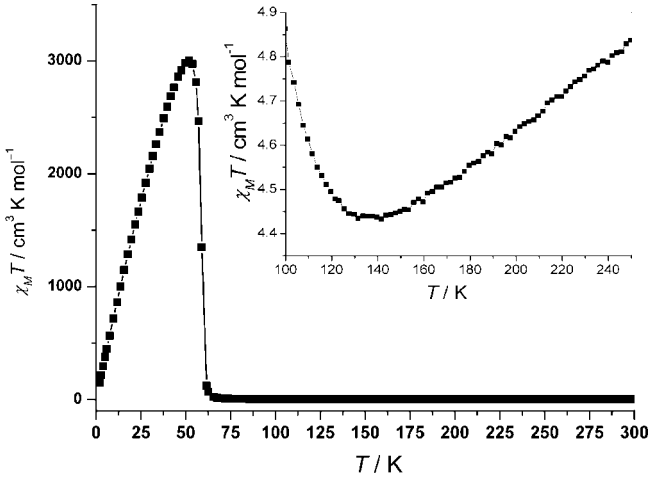


Figure 2. Temperature dependence of $\chi_M T$ for complex **1** measured at 100 Oe. Inset displays the minimum of $\chi_M T$ at 142 K, the signature of ferrimagnetism.

The field dependence of the magnetization with an applied field of 0–70 kOe, measured at 1.8, 55 and 80 K, respectively, is shown in Figure 4. At 80 K, the magnetization increases linearly and shows typical paramagnetic behavior. At 55 K, the magnetization first increases sharply and then slowly, thus displaying a property of a magnet. At

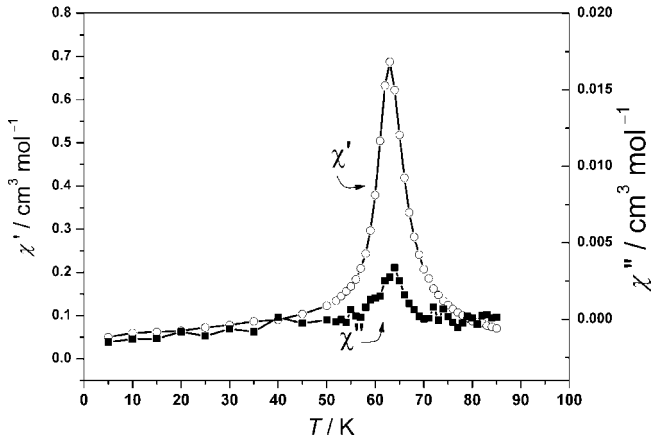


Figure 3. Real ($\chi'$) and imaginary ($\chi''$) ac magnetic susceptibilities as a function of temperature at 10 Hz for complex **1**.

1.8 K, the magnetization increases sharply in the low-field region and reaches saturation above ca. 1.0 kOe. The saturation magnetization $M_s$ = 3.1 N$\beta$ is much higher than the expected value of 1.2 N$\beta$ for the antiferromagnetic $Mn_{1.2}Cr_{0.8}$ system. The inconsistency in $M_s$ values was also observed in some other PB analogues.[2a,2f,3a] The higher $M_s$ value of **1** is perhaps due to the disorder of the paramagnetic ions.[2f] The magnetic hysteresis loop at 1.8 K (Figure 5) reveals no significant hysteretic behavior typical of a soft magnet, which is consistent with the symmetrical cubic three-dimensional structure.[2a–2c,3a] The antiferromagnetic interaction between the $Mn^{III}$ ($S$ = 2) and $Cr^{III}$ ($S$ = 3/2) [or $Mn^{III}$ ($S$ = 1)] ions can be rationalized in terms of the overlap of the magnetic orbitals of these ions.[1a]

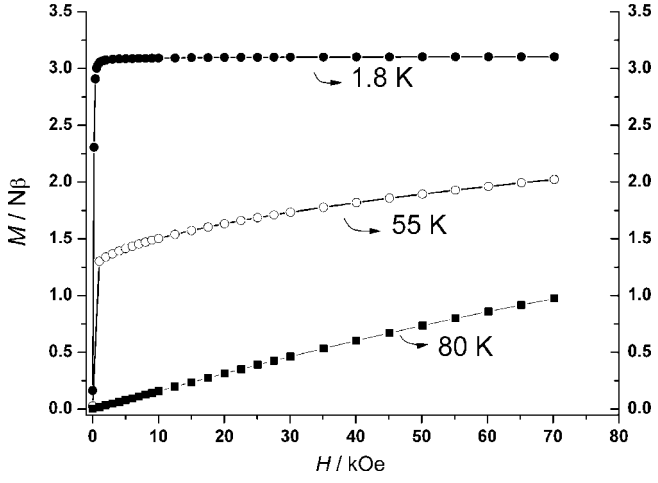


Figure 4. Field dependence of the magnetization at 1.8, 55, and 80 K for complex **1**.

It should be mentioned that the magnetic properties of complex **1** are similar to those of the $Mn^{II}/Cr^{III}$ complexes, such as $[Mn(en)]_3[Cr(CN)_6]_2{\cdot}4H_2O$ ($T_c$ = 69 K),[4d,4m] $Mn_3[Cr(CN)_6]_2{\cdot}12H_2O$ ($T_c$ = 63 K),[4m] $NaMn[Cr(CN)_6]$ ($T_c$ = 60 K),[3a] and $K_{0.2}Mn_{1.4}[Cr(CN)_6]{\cdot}6H_2O$ ($T_c$ = 66 K).[3g] Especially, it is somewhat surprising that the $Mn^{III}$-based

 © 2007 Wiley-VCH Verlag GmbH & Co. KGaA, Weinheim 

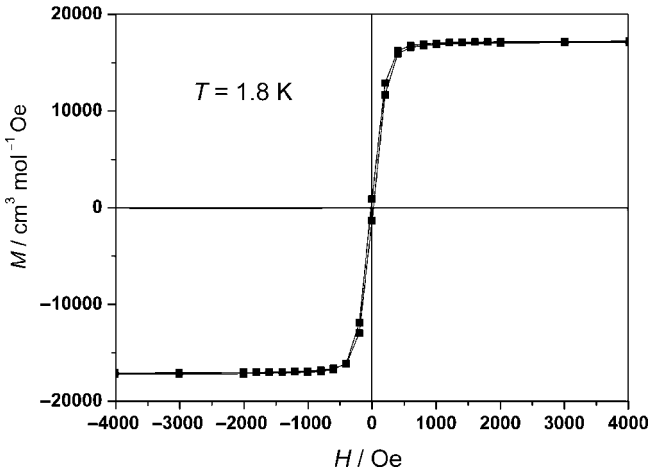


Figure 5. Magnetic hysteresis loop at 1.8 K for complex **1**.

system of **1** has such a low coercive field as found for $Mn^{II}$-based systems since both high- and low-spin (LS) $Mn^{III}$ are much more anisotropic than high-spin (HS) $Mn^{II}$. This may be related to the extremely complex magnetic properties of the $Mn^{III}$ (LS) species because of strong spin-orbit coupling. In addition, it is interesting to note that $[Mn(en)]_3[Cr(CN)_6]_2\cdot 4H_2O$ has a higher magnetic phase-transition temperature ($T_c$) than the ligand-free $Mn^{II}/Cr^{III}$ and $Mn^{III}/Cr^{III}$ systems. Lu et al.[3g] recently demonstrated that the $T_c$ value of $K_{0.2}Mn_{1.4}[Cr(CN)_6]\cdot 6H_2O$ can be substantially modulated through a dehydration/rehydration treatment and increases to 99 K after dehydration in which a weight loss of 23.4% is reached. This indicates that the $T_c$ value is sensitive to subtle changes in structure and composition. By considering the fact that the $Mn^{II}/Mn^{III}$ Prussian blue analogues, such as $Mn^{II}_3[Mn^{III}(CN)_6]_2\cdot xH_2O$ ($T_c$ = 35.5 K) [3b] and $CsMn^{II}[Mn^{III}(CN)_6]\cdot 1/2H_2O$ ($T_c$ = 31 K),[12] have lower magnetic phase-transition temperatures than the $Mn^{II}/Cr^{III}$ analogues, it would be expected that the partial substitution of low-spin $Mn^{III}$ for $Cr^{III}$ in complex **1** would reduce its $T_c$ value. On the other hand, unlike complex $Mn_3[Cr(CN)_6]_2\cdot 12H_2O$,[4m] complex **1** does not have $[Cr(CN)_6]^{3-}$ vacancies in the crystal structure, which would increase the $T_c$ value. The above two factors counteract each other, which results in a value of $T_c$ = 63 K in complex **1**. From the magnetic point of view, complex **1** is essentially a ternary metal Prussian blue system [high-spin $Mn^{III}$/low-spin $Mn^{III}/Cr^{III}$]. Hashimoto et al.[13] have systematically investigated the magnetic behavior of a series of ternary-metal Prussian blue analogues $(Ni^{II}_xMn^{II}_{1-x})_{1.5}[Cr^{III}(CN)_6]\cdot zH_2O$, which incorporate both ferromagnetic $Ni^{II}$–$Cr^{III}$ ($J_{NiCr}$) and antiferromagnetic $Mn^{II}$–$Cr^{III}$ ($J_{MnCr}$) exchange interactions. The magnetic properties such as the saturation magnetization, the Weiss constant, and the coercive field could be tuned by changing the molar ratios $x$. However, the $T_c$ values of these complexes almost remained the same (≈ 70 K). In complex **1**, both $Mn^{III}$(HS)–$Cr^{III}$ and $Mn^{III}$(HS)–$Mn^{III}$(LS) exchange interactions are antiferromagnetic. Therefore, unlike the situation in the $(Ni^{II}_xMn^{II}_{1-x})_{1.5}[Cr^{III}(CN)_6]\cdot zH_2O$ system, the magnetic properties of **1** could not change from antiferromagnetic to ferromagnetic by changing the molar ratios of the metal ions.

## Conclusions

A novel Prussian blue type ferrimagnet $Mn[Mn_{0.2}Cr_{0.8}(CN)_6]\cdot 4H_2O$ has been structurally and magnetically characterized. The complex has a cubic lattice and shows ferrimagnetic ordering below 63 K. This temperature is relatively high in all cyano-bridged complexes characterized by single-crystal structure analysis.[3,4] To the best of our knowledge, complex **1** is the first A(III)-B(III) type PB analogue characterized by single-crystal structure analysis and provides a unique example for the study of structure and magnetic properties of the PB analogues.

## Experimental Section

**Measurements:** Elemental analyses for C, H and N were performed with a Perkin–Elmer 240C analyzer. Mn and Cr analyses were carried out with a Jarrell–Ash 1100+2000 inductively coupled plasma quantometer. IR spectra were recorded on a Nicolet FT-170SX spectrometer with KBr pellets in the 4000–400 $cm^{-1}$ region. X-ray photoelectron spectra (XPS) were obtained by using an ESCALAB MK-II spectrometer. The magnetic measurements were performed on microcrystalline powder obtained from crushed single crystals by using a Quantum Design MPMS-XL SQUID magnetometer. Diamagnetic corrections were made by using Pascal's constants. Effective magnetic moments were calculated with the equation $\mu_{eff} = 2.828(\chi_M \times T)^{1/2}$, where $\chi_M$ is the magnetic susceptibility per formula unit.

**Preparations:** All chemicals and solvents were reagent grade and were used without further purification. $[Mn(saltn)]ClO_4$ was synthesized by mixing $Mn(OAc)_3\cdot 2H_2O$, saltn$H_2$, and $NaClO_4$ in a molar ratio of 1:1:1.5 in methanol according to a method reported previously.[14] $K_3[Cr(CN)_6]$ was prepared by the literature method.[15]

**Caution:** Perchlorate salts of metal complexes with organic ligands are potentially explosive and should be handled in small quantities with care.

**$Mn[Mn_{0.2}Cr_{0.8}(CN)_6]\cdot 4H_2O$ (1):** Complex **1** was obtained as brown-yellow, quasi-ball-shaped single crystals by slow diffusion of a methanol solution (15 $cm^3$) of $[Mn(saltn)]ClO_4$ (0.15 mmol) and an aqueous solution (15 $cm^3$) of $K_3[Cr(CN)_6]$ (0.15 mmol) through a U-tube containing silica gel at room temperature. The resulting crystals were collected, washed with $H_2O$ and EtOH, and dried in air. This complex is insoluble in usual inorganic and organic solvents and stable in air. Yield: 4.8 mg. $C_6H_8Cr_{0.8}Mn_{1.2}N_6O_4$ (335.71): calcd. C 21.46, H 2.4, Cr 12.39, Mn 19.64, N 25.04; found C 21.21, H 2.61, Cr 12.3, Mn 20.0, N 24.95. IR: $\tilde{\nu}_{max}$ = 3400 (vs), 2161 (s), 1613 (s), 990 (m), 478 (s) $cm^{-1}$.

**X-ray Crystallography:** Diffraction data were collected at 293(2) K on a Bruker SMART APEX CCD area detector diffractometer by using graphite-monochromated Mo-$K_\alpha$ radiation ($\lambda$ = 0.71073 Å) with the $\phi$ and $\omega$ scan mode. Empirical absorption correction was made with SADABS. The structures were solved by direct methods and refined by full-matrix least-squares techniques based on $F^2$ with the SHELXTL-97 program package. Crystal data for **1**: $C_6H_8Cr_{0.8}Mn_{1.2}N_6O_4$, $M$ = 335.71, cubic, space group $Fm\bar{3}m$, $a$ =

 © 2007 Wiley-VCH Verlag GmbH & Co. KGaA, Weinheim 

10.7632(7) Å, $\alpha = 90°$, $V = 1246.9(1)$ Å$^3$, $Z = 4$, $D_c = 1.788$ g/cm$^3$, $F(000) = 167$, $\mu = 1.928$ mm$^{-1}$, $S = 0.91$. 1887 reflections measured, 106 unique. Final $R_1 = 0.029$ and $wR_2 = 0.074$ for 62 observed reflections [$I > 2\sigma(I)$]. CCDC-284959 contains the supplementary crystallographic data for complex **1**. These data can be obtained free of charge from the Cambridge Crystallographic Data Centre via www.ccdc.cam.ac.uk/data_request/cif.

## Acknowledgments

This work was supported by NNSF under major project (No. 20490210) and the Natural Science Foundation of Jiangsu Province (No. BK2005056). The authors also thank the anonymous reviewers for their critical comments and suggestions, which enabled us to improve the manuscript significantly.

[1] a) M. Verdaguer, A. Bleuzen, V. Marvaud, J. Vaissermann, M. Seuleiman, C. Desplanches, A. Scuiller, C. Train, R. Garde, G. Gelly, C. Lomenech, I. Rosenman, P. Veillet, C. Cartier, F. Villain, *Coord. Chem. Rev.* **1999**, *190–192*, 1023–1047; b) M. Ohba, H. Okawa, *Coord. Chem. Rev.* **2000**, *198*, 313–328; c) J. Cernak, M. Orendac, I. Potocnak, J. Chomic, A. Orendacova, J. Skorsepa, A. Feher, *Coord. Chem. Rev.* **2002**, *224*, 51–66; d) J. J. Sokol, A. G. Hee, J. R. Long, *J. Am. Chem. Soc.* **2002**, *124*, 7656–7657.

[2] a) S. M. Holmes, G. S. Girolami, *J. Am. Chem. Soc.* **1999**, *121*, 5593–5594; b) S. Mallah, S. Thiebaut, M. Verdaguer, P. Veillet, *Science* **1993**, *262*, 1554–1557; c) S. Ferlay, T. Mallah, R. Ouahes, P. Veillet, M. Verdaguer, *Inorg. Chem.* **1999**, *38*, 229–234; d) O. Sato, T. Iyoda, A. Fujishima, K. Hashimoto, *Science* **1996**, *272*, 704–705; e) W. R. Ently, G. S. Girolami, *Science* **1995**, *268*, 397–400; f) Q. Hatlevik, W. E. Buschmann, J. Zhang, J. L. Manson, J. S. Miller, *Adv. Mater.* **1999**, *11*, 914–918; g) W. E. Buschmann, J. S. Miller, *Inorg. Chem.* **2000**, *39*, 2411–2421.

[3] a) W. Dong, L. N. Zhu, H. B. Song, D. Z. Liao, Z. H. Jiang, S. P. Yan, P. Cheng, S. Gao, *Inorg. Chem.* **2004**, *43*, 2465–2467; b) P. Franz, C. Ambrus, A. Hauser, D. Chernyshov, M. Hostettler, J. Houser, L. Keller, K. Kramer, H. Stoeckli-Evans, P. Pattison, H. B. Burgi, S. Decurtins, *J. Am. Chem. Soc.* **2004**, *126*, 16472–16477; c) M. Witzel, B. Ziegler, D. Babel, *Z. Anorg. Allg. Chem.* **2000**, *626*, 471–477; d) M. Schwarten, D. Babel, *Z. Anorg. Allg. Chem.* **2000**, *626*, 1921–1928; e) H. U. Güdel, H. Stucki, A. Ludi, *Inorg. Chim. Acta* **1973**, *7*, 121–124; f) B. Zeigler, M. Witzel, M. Schwrter, D. Babel, *Z. Naturforsch., Teil B* **1999**, *54*, 870–874; g) Z. L. Lu, X. Y. Wang, Z. L. Liu, F. Liao, S. Gao, R. G. Xiong, H. W. Ma, D. Q. Zhang, D. B. Zhu, *Inorg. Chem.* **2006**, *45*, 999–1004.

[4] a) M. Ohba, N. Maruono, H. Okawa, T. Enoki, J. M. Latour, *J. Am. Chem. Soc.* **1994**, *116*, 11566–11567; b) H. J. Choi, J. J. Sokol, J. R. Long, *Inorg. Chem.* **2004**, *43*, 1606–1608; c) C. P. Berlinguette, D. Vaughn, C. Canada-Vilalta, J. R. Galan-Mascaros, K. R. Dunbar, *Angew. Chem. Int. Ed.* **2003**, *42*, 1523–1526; d) M. Ohba, N. Usuki, N. Fukita, H. Okawa, *Angew. Chem. Int. Ed.* **1999**, *38*, 1795–1798; e) H. Z. Kou, S. Gao, J. Zhang, G. H. Wen, G. Su, R. K. Zheng, X. X. Zhang, *J. Am. Chem. Soc.* **2001**, *123*, 11809–11810; f) H. Z. Kou, Y. B. Jiang, B. C. Zhou, R. J. Wang, *Inorg. Chem.* **2004**, *43*, 3271–3276; g) J. Koo, D. Kim, Y. S. Kim, Y. Do, *Inorg. Chem.* **2003**, *42*, 2983–2987; h) A. H. Yuan, J. Z. Zou, B. L. Li, Z. G. Zha, C. Y. Duan, Y. J. Liu, Z. Xu, S. Keizer, *Chem. Commun.* **2000**, 1297–1298; i) H. Miyasaka, N. Matsumoto, H. Okawa, N. Re, E. Gallo, C. Floriani, *J. Am. Chem. Soc.* **1996**, *118*, 981–994; j) M. S. El Fallah, E. Rentschler, A. Caneschi, R. Sessoli, D. Gatteschi, *Angew. Chem. Int. Ed. Engl.* **1996**, *35*, 1947–1949; k) J. Larionova, M. Gross, M. Pilkington, H. Andres, H. Stoeckli-Evans, H. U. Gudel, S. Decurtins, *Angew. Chem. Int. Ed.* **2000**, *39*, 1605–1609; l) C. P. Berlinguette, J. R. Galan-Mascaros, K. R. Dunbar, *Inorg. Chem.* **2003**, *42*, 3416–3422; m) N. Usuki, M. Yamada, M. Ohba, H. Okawa, *J. Solid State Chem.* **2001**, *159*, 328–335.

[5] a) X. P. Shen, B. L. Li, J. Z. Zou, H. M. Hu, Z. Xu, *J. Mol. Struct.* **2003**, *657*, 325–331; b) X. P. Shen, B. L. Li, J. Z. Zou, Z. Xu, Y. P. Yu, S. X. Liu, *Transitiion Met. Chem.* **2002**, *27*, 372–376.

[6] K. Nakamoto, *Infrared and Raman Spectra of Inorganic and Coordination Compounds*, 3rd ed., Wiley, New York, **1978**.

[7] V. Di Castro, G. Polzonetti, *J. Electron Spectrosc. Relat. Phenom.* **1989**, *48*, 117–123.

[8] M. Borges-Soares, F. Menes, R. Fontaine, R. Caillat, *J. Microsc. Spectrosc. Electron.* **1983**, *8*, 93–97.

[9] M. Benson, Thesis, *X-ray Photoelectron Spectroscopy of Lithium Manganese Spinels*, University of Auckland, **1996**.

[10] a) C. R. Bertsch, W. C. Fernelius, B. P. Block, *J. Phys. Chem.* **1958**, *62*, 444–450; b) M. S. Newman, D. H. Busch, G. E. Cheney, C. R. Gustafson, *Inorg. Chem.* **1972**, *11*, 2890–2893.

[11] S. Ohkoshi, H. Tokoro, K. Hashimoto, *Coord. Chem. Rev.* **2005**, *249*, 1830–1840.

[12] W. R. Entley, G. S. Girolami, *Inorg. Chem.* **1994**, *33*, 5165–5166.

[13] a) S. Ohkoshi, O. Sato, T. Iyoda, A. Fujishima, K. Hashimoto, *Inorg. Chem.* **1997**, *36*, 268–269; b) S. Ohkoshi, K. Hashimoto, *Phys. Rev. B* **1999**, *60*, 12820–12825.

[14] N. Matsumoto, N. Takemoto, A. Ohyoshi, H. Okawa, *Bull. Chem. Soc. Jpn.* **1988**, *61*, 2984–2988.

[15] J. H. Bigelow, J. C. Bailar, *Inorg. Synth.* **1946**, *2*, 203–206.

Received: January 21, 2006
Revised Version Received: January 18, 2007
Published Online: March 9, 2007

 © 2007 Wiley-VCH Verlag GmbH & Co. KGaA, Weinheim 

DOI: 10.1002/ejic.200600943

# Highly Organosoluble Metal-Free Phthalocyanines and Metallophthalocyanines: Synthesis and Characterization

**Ahmet Bilgin,*[a] Beytullah Ertem,[b] and Yaşar Gök[c]**

**Keywords:** Soluble phthalocyanine / Phthalonitrile / Macrocycles / Nickel / Zinc

The syntheses and characterization of metal-free and metal-containing (Zn and Ni) derivatives of a symmetrically octa-substituted phthalocyanine derived from 4,5:12,13-bis(4′-*tert*-butylbenzo)-8,9-(4′′,5′′-dicyanobenzo)-6,11-ditosyl-6,11-diaza-2,15-dithiacyclohexadeca-4,8,12-triene and CuPc from 4,5:12,13-bis(4′-*tert*-butylbenzo)-8,9-(4′′,5′′-dibromobenzo)-6,11-ditosyl-6,11-diaza-2,15-dithiacyclohexadeca-4,8,12-triene were carried out. Pentanuclear silver(I) and palladium(II) complexes have also been prepared from nickel(II) phthalocyaninate derivatives. The prepared phthalocyanines were semiconducting materials in the range of $10^{-5}$ to $10^{-10}$ S cm$^{-1}$ in vacuo and under atmospheric pressure. The extraction abilities of NiPc and detosylated phthalocyanines were evaluated in chloroform/water by using several heavy-metal picrates such as $Ag^{+}$, $Cd^{2+}$, $Cu^{2+}$, $Hg^{2+}$, $Pb^{2+}$, $Pd^{2+}$, and $Zn^{2+}$. The extraction affinities of NiPc and detosylated phthalocyanines for $Ag^{+}$ were found to be the highest in solvent extraction experiments. The new compounds were characterized by using elemental analysis, UV/Vis, FTIR, NMR, MS spectroscopic data and DTA/TG.
(© Wiley-VCH Verlag GmbH & Co. KGaA, 69451 Weinheim, Germany, 2007)

## Introduction

Phthalocyanines have been shown to have very interesting properties coupled with excellent stability to heat, light, and harsh chemical environments. Their optical and electronic properties have been exploited in various applications such as pigments in paints and printing inks, infrared security devices, information storage, and computer disk writing, conducting polymers and photoconductors, catalysts for oxidation of thiols, disulfides, chemical sensors, and in photodynamic therapy of cancer.[1,2] Transition-metal-based phthalocyanines have attracted attention in the areas of fuel cells, gas sensors, and biosensors.[1,2] Most of these applications require the use of phthalocyanines in the form of thin films. Further, it is desirable to have ordered, well-packed, and oriented molecular layers of phthalocyanines on various substrates.

Applications of peripherally unsubstituted phthalocyanines are restricted because of their insolubility in common solvents and water.[3,4] Phthalocyanines own an extended π-conjugated electron system which allows π stacking (aggregation) between planar macrocycles, provided the distance between the macrocycles is small.[5] By the peripheral attachment of bulky (e.g. *tert*-butyl),[6] long-chain groups (e.g. alkyl or alkoxy),[7] N-tosyl derivatives,[8] crown ether analogs[9–12] or macrobicyclic[13,14] and macrotricyclic[15] moieties to the macrocycles, transition-metal phthalocyanine complexes and their bridged systems can be made soluble in common organic solvents, for example chloroform or toluene,[4–6] because these substituents increase the distance between the stacked phthalocyanines and enable their solvation.[5,16] The *tert*-butyl group is especially suitable to increase the solubility of phthalocyanines in organic solvents.[5] Heteroatom-functionalized substituents were introduced onto the periphery of the phthalocyanine nucleus.[8–17] These peripheral groups are capable of binding alkali metal ions and provide donor sites for binding transition-metal ions, which leads to homo- and heteronuclear complexes.

Unfortunately, for many applications it is preferable to have both soluble and symmetric phthalocyanines. With this idea in mind, we set out to synthesize symmetrical di-*tert*-butylphtholonitrile and di-*tert*-butyl-*o*-dibromobenzene derivatives for condensation to very soluble symmetrical octa-*tert*-butyl-substituted phthalocyanines in this study. The electrical conductivities of the phthalocyanines as Au/MPc/Au sandwiches in vacuo and air atmosphere were examined. Additionally, the heavy metal extraction properties of **11** and **14** were investigated.

[a] Department of Science Education, Kocaeli University, 41380-Kocaeli, Turkey
Fax: +90-262303-2403
E-mail: abilgin@kou.edu.tr
[b] Department of Chemistry, Karadeniz Technical University, 61080 Trabzon, Turkey
[c] Department of Chemistry, Pamukkale University, Kınıklı Campus, 20070 Kınıklı, Denizli, Turkey

## Results and Discussion

### Synthetic Procedure and Characterization

The synthetic routes to **3**–**10** are summarized in Scheme 1 and **11**–**14** are summarized in Scheme 2. 1,2-Bis(4-*tert*-bu-

 © 2007 Wiley-VCH Verlag GmbH & Co. KGaA, Weinheim 

tyl-2-nitrobenzylthio)ethane (**3**) was prepared by a modified literature[18] procedure by the reaction of 1,2-ethandithiol (**1**) with 4-*tert*-butyl-2-nitrobenzyl chloride (**2**) in methanol in 62% yield. In this work, we were able to easily obtain nitro derivative **3** as a pure solid by simple crystallization, whereas Sakata and coworkers[18] obtained an oily product

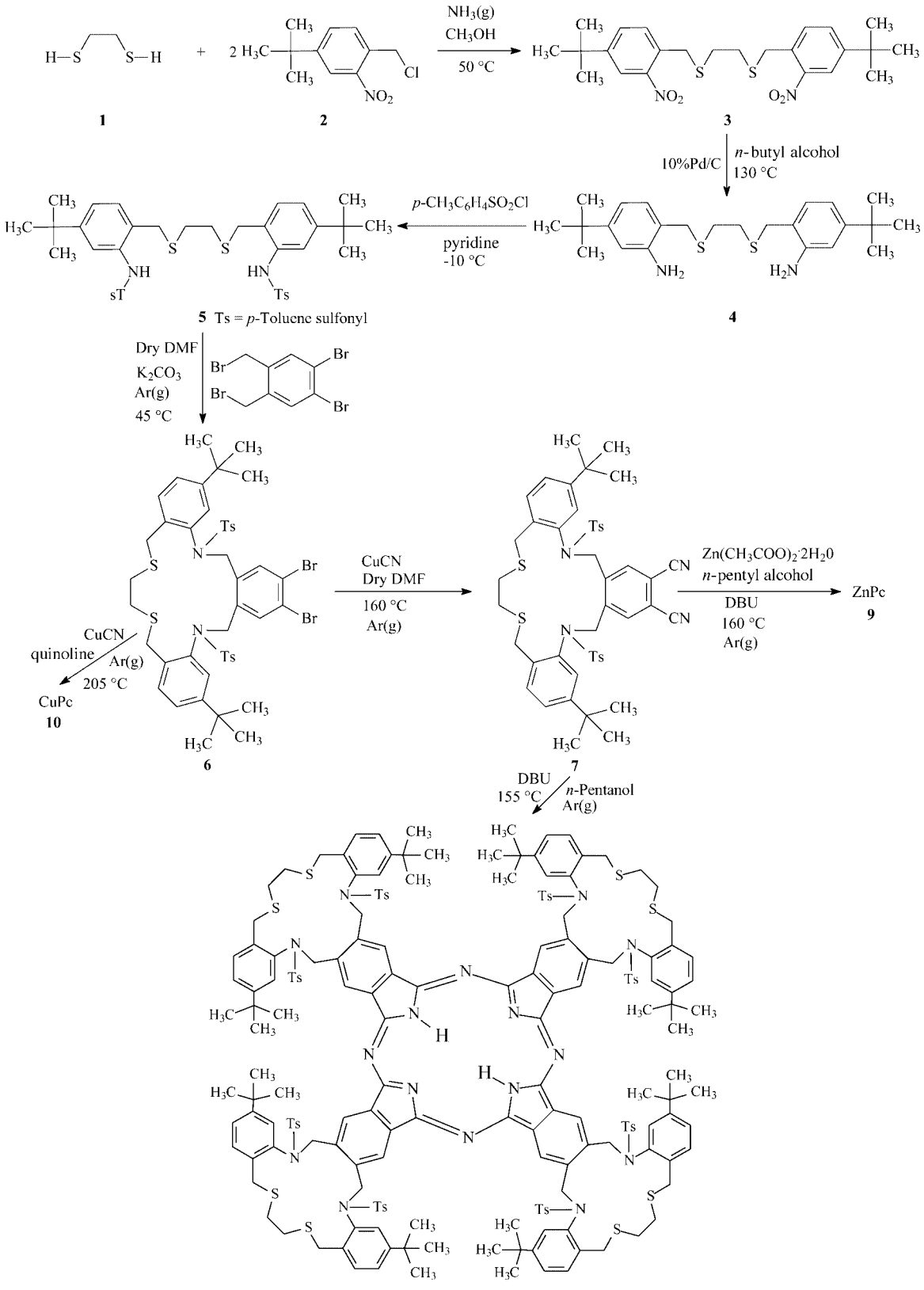


Scheme 1. Synthesis of metal-free phthalocyanines and metallo(Zn, Cu)phthalocyanines.

 © 2007 Wiley-VCH Verlag GmbH & Co. KGaA, Weinheim 

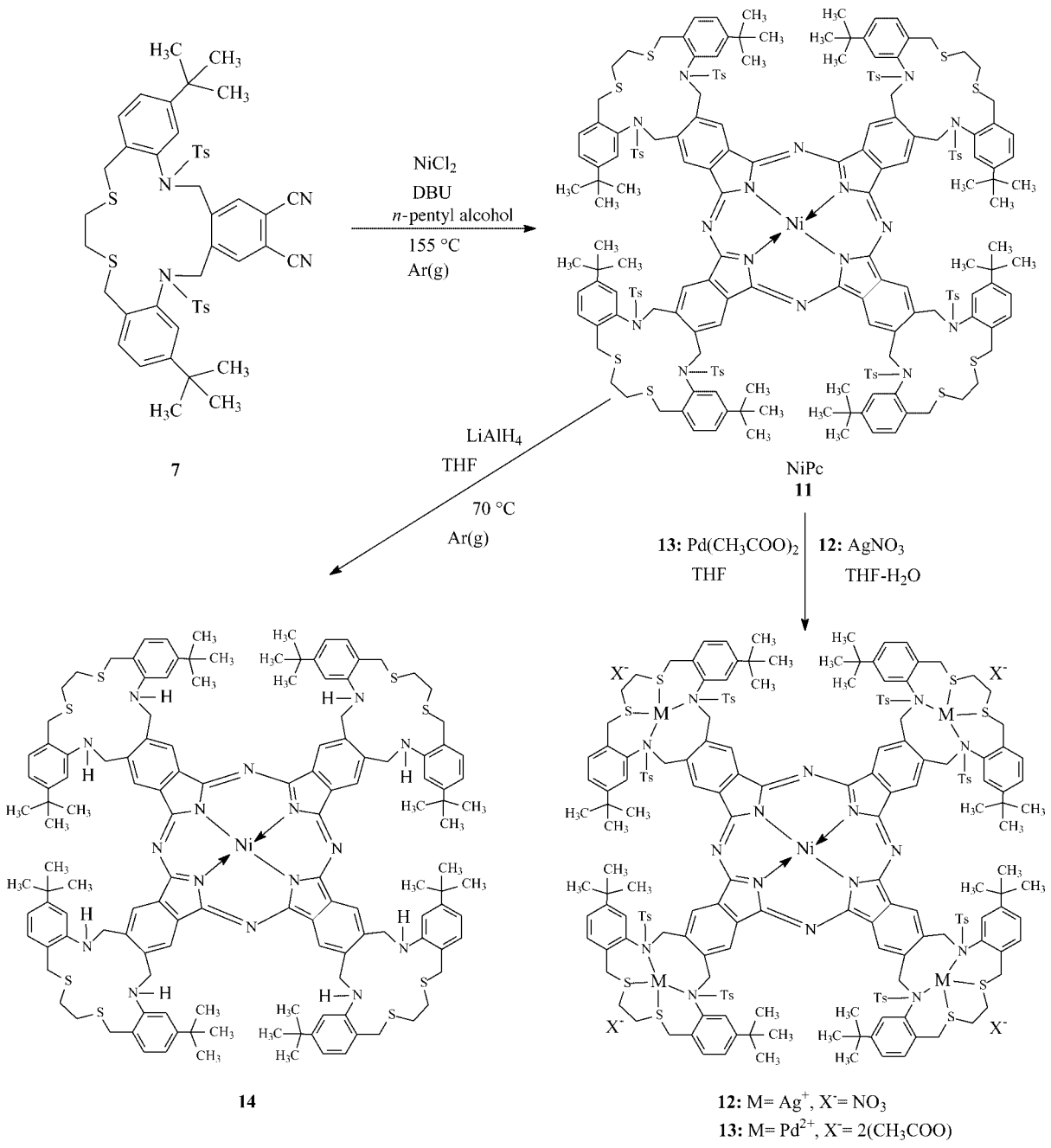


Scheme 2. Synthesis of nickel phthalocyanine and its derivatives.

after a more exhausting and time consuming column chromatography method. This compound was characterized spectroscopically and analytically. The $^1$H NMR spectrum of **3** showed characteristic signals for Ar–$CH_2$–S and S$CH_2$–$CH_2$S protons at $\delta$ = 4.20 and 2.70 ppm, respectively. The $^{13}$C NMR spectrum of this compound also clearly indicates the presence of expected signals related to the above-mentioned groups at $\delta$ = 31.90 and 32.45 ppm, respectively. The IR spectrum featured a band at 684 cm$^{-1}$, which is attributable to the C–S bonds. The EI mass spectrum of this compound exhibited a molecular ion peak at $m/z$ = 476.23 $[M]^+$, that also supports the structure.

Diamino derivative **4** was obtained by the reduction of **3** with 10%Pd/C (palladium activated charcoal), hydrazinium hydrate, and *n*-butyl alcohol in 78% overall yield. Because this method is more advantageous than the others, we preferred this one.[19] The disappearance of the signals for the $NO_2$ groups at 1543 and 1340 cm$^{-1}$ and the appearance of the signals of the $NH_2$ groups at 3430–3320 cm$^{-1}$ and bending signals at 1610 cm$^{-1}$ in the IR spectrum confirmed the formation of amino derivative **4**. The $^1$H and $^{13}$C NMR spectra of **4** were very similar to those of precursor compound **3** except for the signals of the $NH_2$ groups at $\delta$ = 3.82 and 145.56 ppm, respectively. The EI mass spectrum

 © 2007 Wiley-VCH Verlag GmbH & Co. KGaA, Weinheim 

displayed the $[M]^+$ parent ion peak at $m/z$ = 416.09, which confirms the same structure.

Reaction of *p*-toluenesulfonyl chloride with compound **4** in dry pyridine[20] afforded compound **5** in 97.5% yield. The IR spectrum of compound **5** shows the signals related to the tosyl groups at 1343–1140 $cm^{-1}$ and the N–H groups at 3270–1592 $cm^{-1}$, which indicates that the tosylation reaction was clearly achieved. A molecular ion peak at $m/z$ = 724.19 $[M]^+$ in its mass spectrum together with elemental analysis data clearly supports the structure of compound **5**. The $^1H$ NMR spectrum of compound **5** exhibits signals for both the N–H and tosyl groups at $\delta$ = 8.29 ppm and $\delta$ = 7.85–7.35 (Tosyl–Ar–H) and 2.32 ppm (Tosyl–$CH_3$), respectively. The $^{13}C$ NMR spectrum shows the signals at $\delta$ = 148.56 ppm (Ar–C–NH) and 144.62, 135.32, 130.23, 127.44 ppm (Ts–Ar), and 21.34 (Tosyl–$CH_3$), respectively. All these spectroscopic data confirm the proposed structure.

Dibromobenzene derivative **6** was obtained from the reaction of compound **5** and α,α′-dibromomethyl-4,5-dibromobenzene in 36% yield as a pale brown solid. From the IR spectrum, the formation of the C–Br bond was confirmed by the presence of the peak at 632 $cm^{-1}$, and the signals for the N–H group of compound **5** at 3270–1592 $cm^{-1}$ disappeared. Other IR peaks are similar to those of compound **5**. The N–H signals observed for compound **5** at $\delta$ = 8.29 ppm in the $^1H$ NMR spectrum disappeared and a new peak arose at $\delta$ = 7.75 ppm, which results from α,α′-dibromomethyl-4,5-dibromobenzene. The $^{13}C$ NMR spectra of **6** was very similar to that of the precursor compound **5** except for the carbon signal at $\delta$ = 149.41 ppm for the Ar–C–N– group. MS (FAB positive): $m/z$ = 983.3 $[M]^+$ also confirmed the structure.

Substitution of the bromo groups in **6** with cyanide moieties by a Rosenmund–von Braun reaction with cuprous cyanide[21] afforded corresponding phthalonitrile **7** in 58% yield. In the IR spectrum of **7**, the signal at 632 $cm^{-1}$ for the C–Br bond vanished and a new peak at 2224 $cm^{-1}$ appeared which was attributed to the dicyano groups. In the $^{13}C$ NMR spectrum of this compound, the presence of the signal at $\delta$ = 115.62 ppm, attributable to the nitrile carbon atom, indicated that the conversion had taken place; the $^1H$ NMR spectrum displayed similarities with that of precursor compound **6**. The mass spectrum of compound **7** should a peak at $m/z$ = 876.29 $[M]^+$ and this is in a good accord with the suggested structure.

Because of the eight *tert*-butyl and eight tosyl peripheral groups, all phthalocyanines except for **12** and **13** possess good solubility in common organic solvents and they can be purified by column chromatography by using appropriate solvent systems as coeluents that break up the molecular aggregation and increase the mobility of these compounds on silica gel or neutral alumina columns.

Metal-free phthalocyanine **8** was synthesized from the reaction of phthalonitrile derivative **7**, dry *n*-pentyl alcohol, and a catalytic amount of DBU. According to the IR spectrum of **8**, the signals for the C≡N groups at 2224 $cm^{-1}$ for compound **7** disappeared and new peaks appeared at 3320–1040 $cm^{-1}$ and 1630 $cm^{-1}$ that are dedicated to the N–H and C=N bonds in the phthalocyanine core of **8**, respectively. In the $^1H$ NMR spectrum, a peak at $\delta$ = –5.24 ppm, which is very characteristic for metal-free phthalocyanines, was detected and confirmed the suggested structure. The peak related to the C≡N groups in the $^{13}C$ NMR spectrum of **7** vanished in the case of metal-free phthalocyanine **8**. Other $^1H$- and $^{13}C$ NMR spectra peaks resembled those of precursor compound **7**. The mass spectrum of **8** was measured as $m/z$ = 3507.45 $[M]^+$ and is in good accord with the suggested structure.

Cyclization of **7** with zinc(II) acetate or nickel(II) chloride in the presence of DBU in *n*-pentyl alcohol then furnished the corresponding (phthalocyaninato)metal complexes **9** or **11**. The elemental analysis and mass spectroscopic data of **9** ($m/z$ = 3570.31 $[M]^+$) and **11** ($m/z$ = 3563.15 $[M]^+$) are consistent with their calculated values. The $^1H$ NMR spectra of these compounds were almost identical to those of metal-free phthalocyanine **8**. The differences in the $^1H$ NMR spectra of $H_2Pc$, ZnPc, and NiPc were the broad signals encountered in the case of compound **9** and **11** as a result of the aggregation of phthalocyanine cores at the considerable high concentration used for the NMR measurements.[22] The other characteristics of these compounds were quite similar to those of **7** and **8**. Cyclotetramerization of **7** was confirmed by the disappearance of the sharp C≡N stretching vibration at 2224 $cm^{-1}$ in the IR spectrum. The IR spectra of NiPc and ZnPc are also very similar to that of the precursor $H_2Pc$ except for the disappearance of the N–H vibration of the phthalocyanine core.

Copper(II) phthalocyanine (**10**) was synthesized directly from dibromo derivative **6**, CuCN, and quinoline in 42% yield. The comparison of the IR spectra obtained from **6** and **10** confirmed the conversion of the bromo groups into the characteristic skeleton moiety of phthalocyanine. In this case, the C–Br band at 632 $cm^{-1}$ disappeared and a C=N stretching vibration at 1642 $cm^{-1}$ appeared. The mass spectrum of **10** showed a peak corresponding to $[M + 1]^+$ at $m/z$ = 3568.15.

Metal-free phthalocyanine **8** and metallophthalocyanines **9**–**11** and **14** displayed typical UV/Vis electronic spectra with two significant absorption bands, one of them in the visible region at about 710–600 nm corresponding to the Q band, and the other in the UV, approximately at 300 nm. The Q band absorptions of **8** in chloroform at $\lambda_{max}$ = 710, 672, and 656 nm and the other absorption at 376 and 310 nm are consistent with the results obtained previously for similar phthalocyanines (Figure 1A).[23] The Q band absorption present in **8** can be attributed to the fact that the symmetry of the metal-free phthalocyanine is nondegenerate ($D_{2h}$) and is split in a $Q_x$ and a $Q_y$ peak as shown in the spectrum.[24] The bands between 300–500 nm show superimposed bands of phthalocyanine due to the existence of the Soret band of phthalocyanine (Pc).

The UV/Vis absorption spectra of metallophthalocyanines **9** and **10** are given in Figure 1A and **11** and **14** are given in Figure 2 in chloroform at room temperature. These compounds showed the expected absorptions at the main

 © 2007 Wiley-VCH Verlag GmbH & Co. KGaA, Weinheim 

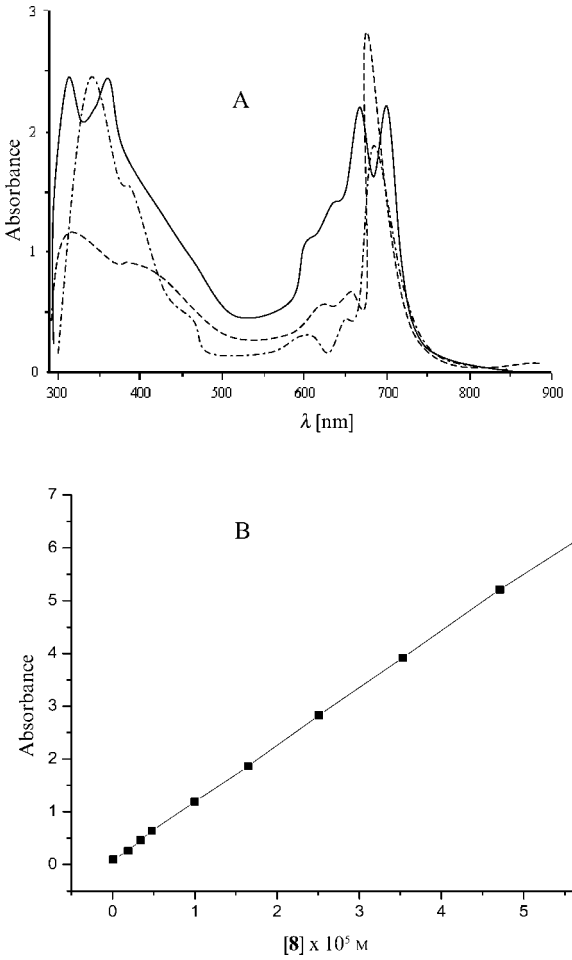


Figure 1. A) UV/Vis spectra of **8** (——), **9** (----) and **10** (-·-·-·) in chloroform ($1 \times 10^{-5}$ M). B) Plot of the Q-band (624 nm) absorbance versus concentration (from $2.5 \times 10^{-7}$ to $5.80 \times 10^{-5}$ M) in chloroform.

peaks of the Q- and B bands appearing at $\lambda_{max}$ = 690, 692, 694, 683 nm and 330, 355, 341, 332 nm, respectively. This result is typical of metal complexes of substituted and unsubstituted Pc with $D_{4h}$ symmetry.[2,25] Although ZnPc (**9**), CuPc (**10**), and NiPc (**11**) have a typical spectral pattern in the UV/Vis region for metallophthalocyanines, CuPc, NiPc, and detosylated **14** showed the new absorption bands at around 400 nm (466, 419, and 460 nm, respectively) in addition to the B band.[26] These new bands are sometimes observed, which can be ascribed to metal-to-ligand charge-transfer or ligand-to-metal charge-transfer transitions because metal ions have partially filled d orbitals. Alternatively, when the UV/Vis spectra data of **11** and **14** are compared, the Q bands in the UV/Vis spectra of **14** are shifted to shorter wavelengths with a decrease in the molar absorption coefficient as a result of the tendency to undergo aggregation.

Because of the eight bulky *tert*-butyl and eight tosyl substituents, these phthalocyanines are expected to be relatively nonaggregated in solution. This was confirmed by variable-concentration UV/Vis studies of compounds **8**–**11** in

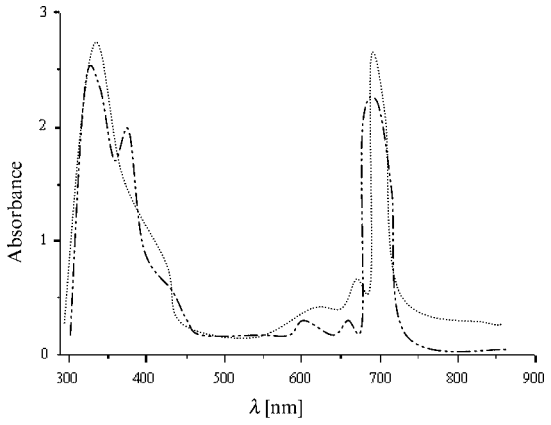


Figure 2. UV/Vis spectra of **11** (···) ($1 \times 10^{-5}$ M) and **14** (–··–··) in chloroform ($1 \times 10^{-5}$ M).

$CHCl_3$. For these four compounds, plots of the Q-band absorbance versus concentration (from $2.50 \times 10^{-7}$ to $5.80 \times 10^{-5}$ mol $L^{-1}$) gave nearly straight lines, which shows that the compounds follow the Beer–Lambert law. This observation indicates that the compounds mainly exist in the monomeric form under the conditions employed. Complex **14**, however, is slightly aggregated at higher concentrations (ca. $10^{-4}$ mol $L^{-1}$). This situation can be attributed to an increase in the intermolecular interaction between the phthalocyanine units after removing the bulky tosyl groups in **11**.

Nickel(II) phthalocyaninate derivatives of pentanuclear silver(I) complex **12** and palladium(II) complex **13** were prepared by treatment of **11** with $AgNO_3$ or $Pd(CH_3COO)_2$, respectively. From the IR spectra of products **12** and **13**, the vibrations belonging to the $NO_3^-$ groups are observed at 1382 $cm^{-1}$ and also symmetrical and asymmetrical vibrations of the $CH_3COO^-$ groups are observed at 1580 and 1420 $cm^{-1}$, respectively, which confirmed the complexation of silver(I) or palladium(II) cations. The $^1H$ NMR spectra of **12** and **13** show downfield changes in all the chemical shifts of the protons in the macrocyclic rings upon complex formation. This can be attributed to the fact that the silver(I) and palladium(II) cations are strongly coordinated to the N and S atoms in the macrocyclic rings. The chemical shifts assigned to the acetate groups, which were observed at $\delta$ = 2.39 ppm, also confirmed the formation of target pentanuclear complex **13**. The FAB mass spectra of products **12** and **13**, which were recorded in a triflouroacetic acid/*m*-nitrobenzyl alcohol matrix, show peaks at *m*/*z* 4244.92 $[M + 2]^+$ and 4242.56 $[M]^+$, and 4461.50 $[M + 1]^+$, 4460.02 $[M]^+$, respectively. Elemental analyses of **12** and **13** also confirmed the formation of complexes with silver(I) or palladium(II) ions.

The tosyl groups in **11** were removed by treatment with excess $LiAlH_4$ in THF to give complex **14** containing free amino groups. Comparison of the IR data gives sufficient support for the proposed structure. The difference between the spectra of tosylated and free amino groups is clear from the presence of $SO_2$ vibrations in **11** at 1140 and 1343 $cm^{-1}$ and the free N–H stretching vibrations for **14** at 3290 $cm^{-1}$.

 © 2007 Wiley-VCH Verlag GmbH & Co. KGaA, Weinheim 

The tosyl groups' signals observed for compound **11** in the $^1$H NMR spectrum disappeared and a new peak appeared at $\delta$ = 3.21 ppm belonging to the N–H signals in **14**. After detosylation, the tosyl groups' signals in the $^{13}$C NMR spectrum of **14** disappeared. The mass spectrum of compound **14** was 2338.08 $[M + Li]^+$and 2332.14 $[M + 1]^+$. All these spectroscopic data confirm the proposed structure.

The structures of the obtained phthalocyanines were an Au/MPc/Au sandwich in the configuration commonly used for the electrical conductivity measurements.[27] To prepare the samples, powdered materials were pressed at a load of 4 tons for 5 min into disk-shaped compacts with a thickness of 0.55–0.62 mm. The a.c. conductivity and parallel capacitance were measured with an Autolab 30 Voltammetry-FRA 2 impedance analyzer. The frequency range was 100 Hz to 1 MHz and the applied amplitude (rms) was 10 mV. The electrical conductivities of the obtained phthalocyanines were measured in a vacuum and under atmospheric pressure. Table 1 shows the a.c. electrical conductivities of phthalocyanines **8**–**14**. The conductivity values obtained under atmospheric pressure were higher than those under vacuum for all phthalocyanines probably because of absorbed oxygen.[27] These values correspond with those for semiconductive materials as encountered in a number of substituted phthalocyanine derivatives.[28] Relative to the conductivities of **11** and **14**, detosylated **14** shows a partial increase in the conductivity that is due to the removal of the bulky tosyl groups, which prevent the interaction of delocalized π-electrons on the phthalocyanine planes. Sixteen-membered diazadithiamacrocyclic substituents are expected to provide new chances to enhance the stacking of phthalocyanine units whereas their size and donor atoms are extremely harmonius to bond with transition metal cations in a 1:1 (metal/macrocycle ring) ratio.[29] Similar to the alkali metal complexes of analogous crown ether substituted phthalocyanines, planarity of the phthalocyanine nucleus will be extended. As a result, interaction of π-electrons will be achieved to realize charge transport. A.c. conductivities of nickel(II) phthalocyanine with four silver(I) or palladium(II) cations in the diazadithiamacrocyclic rings indicate a clear increase in the case of nitrate or acetate counterions.

The thermal properties of the synthesized macrocyclic compounds were investigated by DTA/TG.[30] Phthalocyanines are resistant to thermal oxidation. The DTA curves exhibited exothermic changes for all phthalocyanines **8**–**14** in the region investigated.[31] The initial decomposition temperature decreased in the order **9** > **7** > **11** > **8** > **13** > **14** > **6** > **10** > **12** (Table 2). Cu-containing phthalocyanine **10** was the most rapidly degrading metallophthalocyanine whereas Zn- and Ni-containing metallophthalocyanine showed good thermal stability under the working conditions. These results are in good agreement with the literature.[32] The DTA thermogram of **12** showed an endothermic peak at 230 °C, which is due to the dissociation of the nitrate groups. The thermal stabilities of **12** and **13** were lower than that of compound **11**. The thermal stabilities of **12** and **13** indicate that the dopants are rather weakly bound in the macrocyclic cavities because the bulky tosyl and *tert*-butyl groups in the macrocyclic ring have a steric effect.

The heavy metal binding ability of N–S-macrocyclic units is a well-known property. The binding abilities of the heavy metal ions in the N–S-macrocyclic units were esti-

Table 2. Thermal properties of the polymeric phthalocyanines.

| Compound | Dissociation of $NO_3$ $T_{max}$ [°C] | Initial decomposition temp. [°C] | Main decomposition temp. [°C] |
|---|---|---|---|
| **6** | – | 331 | 387 |
| **7** | | 348 | 415 |
| **8** | – | 337 | 425 |
| **9** | – | 376 | 494 |
| **10** | | 324 | 428 |
| **11** | | 345 | 454 |
| **12** | 230 | 320 | 430 |
| **13** | | 350 | 443 |
| **14** | – | 335 | 438 |

Table 3. Heavy metal picrate extractions for **11**[a] and **14**[a] under liquid–liquid phase conditions.

| Metal ion | Extractabilities of **11** and **14** [%][b] | | $\lambda_{max}$ of metal picrate |
|---|---|---|---|
| | **11** | **14** | [nm] |
| $Ag^+$ | 55.62 ± 0.01 | 86.23 ± 0.01 | 350 |
| $Cd^{2+}$ | 35.41 ± 0.01 | 54.36 ± 0.01 | 362 |
| $Cu^{2+}$ | 23.48 ± 0.01 | 48.54 ± 0.01 | 355 |
| $Hg^{2+}$ | 16.33 ± 0.01 | 42.27 ± 0.01 | 360 |
| $Pb^{2+}$ | 12.46 ± 0.01 | 35.67 ± 0.01 | 354 |
| $Pd^{2+}$ | 39.80 ± 0.01 | 68.98 ± 0.01 | 360 |
| $Zn^{2+}$ | 9.54 ± 0.01 | 31.73 ± 0.01 | 349 |

[a] Temperature 25 ± 1 °C; aqueous phase (10 mL), [picrate] = $3.0 \times 10^{-3}$ M; organic phase (chloroform, 10 mL), [host molecule] = $3.0 \times 10^{-3}$ M. [b] Average and standard deviation for three independent measurements.

Table 1. Electrical conductivity of the phthalocyanines at room temperature.

| Compound | M | Conductivity [$S cm^{-1}$] in air | in vacuo | Pellet thickness [mm] |
|---|---|---|---|---|
| **8** | 2H | $7.75 \times 10^{-9}$ | $6.23 \times 10^{-10}$ | 0.60 |
| **9** | Zn | $3.53 \times 10^{-8}$ | $1.64 \times 10^{-9}$ | 0.55 |
| **10** | Cu | $2.74 \times 10^{-7}$ | $2.36 \times 10^{-8}$ | 0.65 |
| **11** | Ni | $1.58 \times 10^{-7}$ | $3.47 \times 10^{-8}$ | 0.60 |
| **12** | Ni·4$AgNO_3$ | $2.42 \times 10^{-5}$ | $3.15 \times 10^{-6}$ | 0.62 |
| **13** | Ni·4Pd$(CH_3COO)_2$ | $3.50 \times 10^{-6}$ | $3.97 \times 10^{-7}$ | 0.56 |
| **14** | Ni-8Ts | $6.72 \times 10^{-7}$ | $4.95 \times 10^{-8}$ | 0.60 |

 © 2007 Wiley-VCH Verlag GmbH & Co. KGaA, Weinheim 

mated by solvent extraction of heavy metal picrates from the aqueous phase to an organic phase (Table 3). Picrate was used as the counter anion for all compounds. As depicted in Table 3, the highest extraction affinities of **11** and **14** were determined as 55.62 and 86.23% for $Ag^+$, respectively. The extraction affinity of **14** was more than that of **11** for all working cations. This indicates that cations are able to bind to **14** easier than they can to **11** after the bulky tosyl groups were removed.

## Conclusions

In this paper, we have described the synthesis and characterization of new very soluble octa-substituted metal-free phthalocyanines and metallophthalocyanines (M = 2 H, Zn, Cu, and Ni) by using proper materials. Zn- and Ni-containing phthalocyanines showed good thermal stability whereas Cu-containing phthalocyanine degraded the most rapidly. The DTA thermogram of **12** showed an endothermic peak at 230 °C, which is due to the dissociation of the nitrate groups. Also, the thermal stabilities of **12** and **13** were lower than that of compound **11**. The electrical conductivities of the obtained phthalocyanines were found to be $10^{-10}$–$10^{-5}$ $Scm^{-1}$ in vacuo and air. The extraction abilities of **11** and **14** were evaluated by using a solvent extraction technique and the highest extraction affinities were observed for $Ag^+$ for all working conditions. The extraction affinity of **14** was more than that of **11** for all working cations.

## Experimental Section

**Materials:** Reactions were performed under an atmosphere of argon. 4-*tert*-Butyl-2-nitrobenzyl chloride (**2**) was prepared according to the literature.[18] All other reagents and solvents were of reagent grade quality, purchased from commercial suppliers, and they were dried before use as described in the literature.[33] Silica gel (70–230 mesh) and Merck 90 active neutral alumina were used for chromatographic separations.

**Measurements:** Melting points were determined with an electrothermal apparatus and are uncorrected. $^1H$ and $^{13}C$ NMR spectroscopic data were recorded with a Varian XL-200 spectrometer and IR spectra were obtained with a Perkin–Elmer Spectrum One spectrometer. Optical spectra in the UV/Vis region were recorded with a model Shimadzu 1601 UV/Vis spectrometer with the use of 1-cm pathlength cuvettes at room temperature. The a.c. conductivity was measured with an Autolab 30 Voltammetry-FRA 2 frequency analyzer. The frequency range was 100 Hz to1 MHz and the applied amplitude (rms) was 10 mV. Mass spectra were measured with a Varian MAT 711 or a Micromass Quatro LC/ULTIMA LC-MS/MS spectrometer by using triflouroacetic acid/*m*-nitrobenzyl alcohol as the matrix. Elemental analyses were determined with a CHNS-932 LECO instrument. The metal content of the metallophthalocyanines was determined with a Unicam 929 AA spectrophotometer.

**1,2-Bis(4-*tert*-butyl-2-nitrobenzylthio)ethane (3):** 1,2-ethandithiol (2 mL, 60 mmol), 4-*tert*-butyl-2-nitrobenzyl chloride (11.35 g, 50 mmol), and methanol (10 mL) were stirred inside a washing bottle at 50 °C while ammonia gas was bubbled through the solution for 2 h. The mixture was then cooled down to room temperature, benzene (100 mL) was added, and the salt was removed by filtration. The solvent was evaporated and methanol (15 mL) was added to the residue, which was then kept inside the refrigerator overnight. The yellow crystals were separated by filtration, dried in vacuo, and then recrystallized from *n*-butyl alcohol. Yield: 7.3 g (62%). M.p. 139–142 °C. $^1H$ NMR (200 MHz, $CDCl_3$): $\delta$ = 8.01–7.48 (m, 6 H, Ar-H), 4.20 (s, 4 H, Ar-$CH_2$-S), 2.70 (t, 4 H, -$SCH_2$-$CH_2$S-), 1.32 [s, 18 H, $(CH_3)_3$C-] ppm. $^{13}C$ NMR (50 MHz, $CDCl_3$): $\delta$ = 149.5 (Ar-C-$NO_2$), 147.2, 128.2, 124.3, 119.3, 117.2, 34.1 [Ar-C-$(CH_3)_3$], 32.5 (S-$CH_2$-$CH_2$-S), 31.9 (Ar-$CH_2$-S), 30.6 [(-$CH_3)_3$] ppm. IR (KBr): $\tilde{\nu}$ = 3043 (CH aromatic), 2954–2849($CH_2$ aliphatic), 1543, 1340 ($NO_2$), 684 (C–S) $cm^{-1}$. MS (EI): *m*/*z* = 477.01 $[M + 1]^+$, 476.23 $[M]^+$, 475.30, 285.12, 284.07, 193.24, 192.15 $[M - C_{13}H_{18}NO_2S_2]^+$. $C_{24}H_{32}N_2O_4S_2$ (476.12): calcd. C 60.49, H 6.72, N 5.88, S 13.47; found C 60.32, H 6.92, N 5.69, S 13.62.

**1,2-Bis(4-*tert*-butyl-2-aminobenzylthio)ethane (4):** 1,2-Bis(4-*tert*-butyl-2-nitrobenzylthio)ethane (7.3 g, 153 mmol) was dissolved in *n*-butyl alcohol (200 mL) and heated at 80 °C. The temperature was then adjusted to 60 °C and 10%Pd/C (0.91 g) was added, and the reaction mixture was heated at reflux. Hydrazinium hydrate (30.6 mL) was added dropwise to the reaction mixture over a period of 30 min. After the addition, the mixture was heated at reflux for 10 h, and then the reaction was filtered over celite while it was hot. *n*-Butyl alcohol was removed under reduced pressure, and methanol (25 mL) was added to the residue, which was then kept in the refrigerator overnight. The precipitated white crystals were filtered off and washed several times with petroleum ether and dried in vacuo. Yield 3.5 g (78%). M.p. 106–108 °C. $^1H$ NMR (200 MHz, $CDCl_3$): $\delta$ = 7.29–6.56 (m, 6 H, Ar-H), 3.82 (br. s, 4 H, -$NH_2$), 3.62 (s, 4 H, Ar-$CH_2$-S), 2.91 (t, 4 H, -$SCH_2$-$CH_2$S-), 1.29 [s, 18 H, $(CH_3)_3$C-] ppm. $^{13}C$ NMR (50 MHz, $CDCl_3$): $\delta$ = 145.6 (Ar-C-$NH_2$), 143.2, 127.1, 123.3, 118.8, 116.5, 34.0 [Ar-C-$(CH_3)_3$], 31.6 (S-$CH_2$-$CH_2$-S), 30.8 (Ar-$CH_2$-S), 30.2 [(-$CH_3)_3$] ppm. IR (KBr): $\tilde{\nu}$ = 3430–3320 ($NH_2$), 3025 (C–H aromatic), 2965–2864 ($CH_2$ aliphatic), 1610 ($NH_2$, bending), 1512, 1450, 1234 and 670 (C–S) $cm^{-1}$. MS (EI): *m*/*z* = 417.23 $[M + 1]^+$, 416.09 $[M]^+$, 254.15, 163.17 $[M + 1 - C_{13}H_{20}NS_2]^+$, 162.08 $[M - C_{13}H_{20}NS_2]^+$. $C_{24}H_{36}N_2S_2$ (416.12): calcd. C 69.21, H 8.65, N 6.73, S 15.40; found C 68.97, H 8.54, N 6.86, S 15.65.

**1,2-Bis(4-*tert*-butyl-2-tosylaminobenzylthio)ethane (5):** *p*-Toluenesulfonyl chloride (1.233 g, 6.47 mmol) in pyridine (2.5 mL) was added dropwise over a period of 2 h to a –10 °C solution of 1,2-bis(4-*tert*-butyl-2-aminobenzylthio)ethane (**3**; 1.344 g, 3.23 mmol) in pyridine (2.5 mL). The reaction was stirred overnight at –10 °C and then stirred at room temperature for 15 h under a nitrogen atmosphere. The reaction mixture was gently poured into ice (50–100 g), conc. HCl (6 mL) was added, and the mixture stirred for 24 h. The precipitated solid was filtered off and washed several times with deionized water until the washing solvent was neutral. The pale yellow solid product was then dried in vacuo and recrystallized from acetone. Yield 2.28 g (97.5%). M.p. 220–222 °C. $^1H$ NMR (200 MHz, $CDCl_3$): $\delta$ = 8.29 (s, 2 H, N-H), 7.85 (d, 4 H, Tosyl-Ar-H), 7.35 (d, 4 H, Tosyl-Ar-H), 6.40–6.98 (m, 6 H, Ar-H), 3.67 (s, 4 H, Ar-$CH_2$-S), 2.73 (t, 4 H, -$SCH_2$-$CH_2$S-), 2.32 (s, 6 H, Tosyl-$CH_3$), 1.27 [s, 18 H, $(CH_3)_3$C-] ppm. $^{13}C$ NMR (50 MHz, $CDCl_3$): $\delta$ = 148.6 (Ar-C-NH), 144.6 (Ts-Ar), 143.4, 135.3 (Ts-Ar), 130.2 (Ts-Ar), 127.4 (Ts-Ar), 127.2, 123.4, 118.9, 116.2, 34.1 [Ar-C-$(CH_3)_3$], 31.3 (S-$CH_2$-$CH_2$-S), 30.6 (Ar-$CH_2$-S), 30.2 [(-$CH_3)_3$], 21.5 (Ar-$CH_3$) ppm. IR (KBr): $\tilde{\nu}$ = 3270 (N–H), 3050 (CH aromatic), 2990–2835($CH_2$ aliphatic), 1592 (N–H bending), 1343 and 1140 ($SO_2$), 674 (C–S) $cm^{-1}$. MS (FAB+): *m*/*z*: = 725.30 $[M + 1]^+$,

 © 2007 Wiley-VCH Verlag GmbH & Co. KGaA, Weinheim 

724.19 $[M]^+$, 570.42 $[M + 1 - Ts]^+$, 471.41, 470.12, 415.08 $[M + 1 - 2Ts]^+$, 414.14$[M - 2Ts]^+$. $C_{38}H_{48}N_2O_4S_4$ (724.24): calcd. C 62.96, H 6.62, N 3.87, S 17.71; found C 62.74, H 6.40, N 3.73, S 17.85.

**4,5:12,13-Bis(4′-*tert*-butylbenzo)-8,9-(4′′,5′′-dibromobenzo)-6,11-ditosyl-6,11-diaza-2,15-dithiacyclohexadeca-4,8,12-triene (6):** A 500-mL three-necked round-bottomed flask containing anhydrous DMF (100 mL) and fitted with a condenser was evacuated, refilled three times with argon gas and connected to a vacuum line. Under an argon atmosphere, the flask was charged with **5** (2.28 g, 3.15 mmol) and finely ground anhydrous $K_2CO_3$ (2.174 g, 15.75 mmol). The reaction mixture was stirred for 1 h at 45 °C. α,α′-Dibromomethyl-4,5-dibromobenzene (1.349 g, 3.15 mmol) in anhydrous DMF (50 mL) was added dropwise to the reaction mixture over a period of 6 h, and the reaction mixture was heated at reflux under an argon atmosphere for 6 d. The reaction was monitored by thin layer chromatography [chloroform/petroleum ether (7:3)]. At the end of this period, the mixture was cooled to room temperature, filtered, and washed with dry DMF and dichloromethane. The filtrate and the washing solvents were combined and the solvents evaporated to dryness under reduced pressure. The residue was added to ice (100 g) and stirred for 1 d. Thus, a pale brown solid was obtained and washed with deionized water (50 mL) and then dried in vacuo. The final purification of the product was carried out by column chromatography on silica gel (chloroform) to give a pale brown solid. Yield 1.12 g (36%). M.p. 264–265 °C. $^1$H NMR (200 MHz, $CDCl_3$): $\delta$ = 7.75 (s, 2 H, Ar-H), 7.57 (d, 4 H, Tosyl-Ar-H), 7.30 (d, 4 H, Tosyl-Ar-H), 6.51–6.78 (m, 6 H, Ar-H), 4.92 (s, 4 H Ar-$CH_2$-N), 3.71 (s, 4 H, Ar-$CH_2$-S), 2.70 (t, 4 H, -$SCH_2$-$CH_2$S-), 2.40 (s, 6 H, Tosyl-$CH_3$), 1.22 [s, 18 H, $(CH_3)_3$C-] ppm. $^{13}$C NMR (50 MHz, $CDCl_3$): $\delta$ = 149.4 (Ar-C-N-), 144.9 (Ts-Ar), 142.7, 139.4, 134.7, 130.5, 127.5, 127.0, 125.5, 124.4, 119.7, 117.5, 49.7 (Ar-$CH_2$-N-Ar), 34.3 [Ar-C-$(CH_3)_3$], 31.7 (S-$CH_2$-$CH_2$-S), 31.7 (Ar-$CH_2$-S), 29.3 [(-$CH_3)_3$], 21.8 (Ar-$CH_3$) ppm. IR (KBr): $\tilde{\nu}$ = 3048 (CH aromatic), 2995–2865($CH_2$ aliphatic), 1340 and 1145 ($SO_2$), 676 (C–S), 632 (C–Br) cm$^{-1}$. MS (FAB+): *m*/*z* = 982.23 $[M]^+$. $C_{46}H_{52}Br_2N_2O_4S_4$ (984.05): calcd. C 56.09, H 5.28, N 2.85, S 13.03; found C 56.39, H 5.47, N 2.63, S 13.41.

**4,5:12,13-Bis(4′-tert-butylbenzo)-8,9-(4′′,5′′-dicyanobenzo)-6,11-ditosyl-6,11-diaza-2,15-dithiacyclohexadeca-4,8,12-triene (7):** Compound **6** (3.05 g, 3.1 mmol) in anhydrous DMF (30 mL) and CuCN (0.95 g, 10.66 mmol) were added to a 250-mL round-bottomed flask. Under an argon atmosphere, the reaction mixture was gently heated to 160 °C and stirred for 24 h. The reaction mixture was then cooled to room temperature, a 25% $NH_3$ solution (150 mL) was added, and oxygen gas was bubbled through the reaction mixture for 24 h. The precipitated solid was then filtered off and washed several times with deionized water until the filtrate was neutral. The pale brown product was dried in vacuo over $P_2O_5$. The crude product was purified by column chromatography on silica gel [chloroform/petroleum ether/methanol (6:3:1)] to give a pale brown solid. Yield: 1.58 g (58%). M.p. 208–210 °C. $^1$H NMR (200 MHz, $CDCl_3$): $\delta$ = 7.90 (s, 2 H, Ar-H), 7.60 (d, 4 H, Tosyl-Ar-H), 7.35 (d, 4 H, Tosyl-Ar-H), 6.56–6.79 (m, 6 H, Ar-H), 4.98 (s, 4 H Ar-$CH_2$-N), 3.75 (s, 4 H, Ar-$CH_2$-S), 2.74 (t, 4 H, -$SCH_2$-$CH_2$S-), 2.42 (s, 6 H, Tosyl-$CH_3$), 1.24 [s, 18 H, $(CH_3)_3$C-] ppm. $^{13}$C NMR (50 MHz, $CDCl_3$): $\delta$ = 147.2 (Ar-C-N-), 144.4, 142.2, 140.7, 133.7, 130.3, 127.5, 127.0, 124.0, 118.7, 116.3, 115.6 (C≡N), 114.1, 51.1 (Ar-$CH_2$-N-Ar), 35.0 [Ar-C-$(CH_3)_3$], 32.9 (S-$CH_2$-$CH_2$-S), 32.5 (Ar-$CH_2$-S), 30.1 [(-$CH_3)_3$], 20.9 (Ar-$CH_3$) ppm. IR (KBr): $\tilde{\nu}$ = 3045 (CH aromatic), 2980–2854($CH_2$ aliphatic), 2224 (C≡N), 1500, 1460, 1343 and 1148 ($SO_2$), 675 (C–S) cm$^{-1}$. MS (FAB+): *m*/*z* = 876.32 $[M]^+$. $C_{48}H_{52}N_4O_4S_4$ (876.24): calcd. C 65.74, H 5.93, N 6.39, S 14.64; found C 65.44, H 5.68, N 6.64, S 14.02.

**Metal-Free Phthalocyanine 8:** Under a dry argon atmosphere, a standard Schlenk tube was charged with phthalonitrile derivative **7** (150 mg, 0.171 mmol), dry *n*-pentyl alcohol (1.5 mL), and 3–4 drops of DBU, and the mixture was degassed several times. The reaction mixture was heated at reflux (155 °C) for 16 h, cooled to room temperature, and diethyl ether (2–3 mL) was added. The precipitated light green solid product was filtered off and dried. This product was purified by column chromatography on silica gel [dichloromethane/methanol (100:1)]. The combined solvents were evaporated and light green metal-free phthalocyanine **8** was obtained and then dried in vacuo. Yield: 42 mg (28%). M.p. >300 °C. $^1$H NMR (200 MHz, $CDCl_3$): $\delta$ = 8.06 (s, 8 H, Ar-H), 7.72–6.72 (m, 56 H, Ar-H), 4.78 (s, 16 H, Ar-$CH_2$-N), 3.69 (s, 16 H, Ar-$CH_2$-S), 2.80 (t, 16 H, -$SCH_2$-$CH_2$S-), 2.48 (s, 24 H, Tosyl-$CH_3$), 1.27 [s, 72 H, $(CH_3)_3$C-], –5.24 (br. s, 2 H, N-H) ppm. $^{13}$C NMR (50 MHz, $CDCl_3$): $\delta$ = 156.3, 146.4, 143.9, 141.6, 141.0, 137.1, 131.5, 129.4, 128.1, 126.8, 122.2, 119.8, 112.7, 53.1, 34.1, 31.8, 30.3, 29.5, 22.2 ppm. IR (KBr): $\tilde{\nu}$ = 3320 (N–H), 3054 (CH aromatic), 2963–2874 ($CH_2$ aliphatic), 1630 (C=N), 1510, 1480, 1340 and 1150 ($SO_2$), 1040 (N–H), 750, 680 (C–S) cm$^{-1}$. UV/Vis ($CHCl_3$): $\lambda_{max}$ (log$\varepsilon$) = 710 (5.34), 672 (5.35), 656 (5.19), 624 (5.08), 376 (5.38), 310 (5.39) nm. MS (FAB+): *m*/*z* = 3507.45 $[M]^+$. $C_{192}H_{210}N_{16}O_{16}S_{16}$ (3506.96): calcd. C 65.70, H 5.99, N 6.39, S 14.63; found C 65.96, H 5.90, N 6.57, S 14.97.

**Phthalocyaninato Zinc(II) (9):** Under a dry argon atmosphere, a standard Schlenk tube was charged with phthalonitrile derivative **7** (100 mg, 0.114 mmol), dry *n*-pentyl alcohol (1.5 mL), $Zn(CH_3COO)_2 \cdot 2H_2O$ (6.4 mg, 0.029 mmol), and 3–4 drops of DBU, and the mixture was degassed several times. The reaction mixture was heated at reflux (160 °C) for 15 h, cooled to room temperature, and diethyl ether (2–3 mL) was added. The precipitated green solid product was filtered off, washed with ethanol, water, and diethyl ether, respectively, and then dried. The obtained light green product was purified by column chromatography on silica gel [dichloromethane/methanol (100:1)]. The collected solvents were evaporated and light green $Zn^{II}$ phthalocyaninate **9** obtained and then dried in vacuo. Yield 38.7 mg (38%). M.p. > 300 °C. $^1$H NMR (200 MHz, $CDCl_3$): $\delta$ = 7.90 (br. s, 8 H, Ar-H), 7.67–6.50 (m, 56 H, Ar-H), 4.70 (s, 16H Ar-$CH_2$-N), 3.63 (s, 16 H, Ar-$CH_2$-S), 2.73 (t, 16 H, -$SCH_2$-$CH_2$S-), 2.39 (s, 24 H, Tosyl-$CH_3$), 1.22 [s, 72 H, $(CH_3)_3$C-] ppm. $^{13}$C NMR (50 MHz, $CDCl_3$): $\delta$ = 153.1, 145.9, 142.4, 141.1, 139.6, 137.3, 130.5, 129.4, 128.3, 127.0, 122.1, 119.7, 110.6, 52.2, 34.9, 32.5, 31.3, 29.5, 22.0 ppm. IR (KBr): $\tilde{\nu}$ = 3050 (CH aromatic), 2990–2848 ($CH_2$ aliphatic), 1632 (C=N), 1512, 1485, 1341 and 1134 ($SO_2$), 756, 672 (C–S) cm$^{-1}$. UV/Vis ($CHCl_3$): $\lambda_{max}$ (log$\varepsilon$) = 690 (5.45), 665 (4.90), 627 (4.83), 390 (4.96), 330 (5.07) nm. MS (FAB+): *m*/*z* = 3571.54 $[M + 1]^+$, 3570.31 $[M]^+$, 3506.12 $[M + 1 - Zn]^+$. $C_{192}H_{208}N_{16}O_{16}S_{16}Zn$ (3570.34): calcd. C 64.53, H 5.83, N 6.27, S 14.37, Zn 1.83; found C 64.28, H 5.69, N 6.43, S 14.61, Zn 1.71.

**Phthalocyaninato Copper(II) (10):** A mixture of dibromo derivative **6** (250 mg, 0.254 mmol), CuCN (68.2 mg, 0.762 mmol), and quinoline (1 mL) was placed in a stoppered Schlenk tube under an argon atmosphere, gently heated to 205 °C and refluxed for 22 h. The reaction mixture was then cooled to room temperature, ethanol (10 mL) added, stirred for 15 min, and filtered. The solid product was heated with a 3 N NaCN solution (3 × 25 mL) in order to remove excess CuCN over a period of 5 h. The dark green residue was filtered off and dried. This product was charged into a Soxhlet extraction column and extracted with chloroform for 18 h. The solvent was removed and solid product obtained. This green $Cu^{II}$ phthalocyanine derivative was purified by column chromatography on neutral alumina (chloroform) to give a dark green solid product.

 © 2007 Wiley-VCH Verlag GmbH & Co. KGaA, Weinheim 

Yield 95 mg (42%). M.p. > 300 °C. IR (KBr): $\tilde{\nu}$ = 3060 (CH aromatic), 2985–2862 ($CH_2$ aliphatic), 1642 (C=N), 1515, 1495, 1350 and 1138 ($SO_2$), 755, 673 (C–S) $cm^{-1}$. UV/Vis ($CHCl_3$): $\lambda_{max}$ (log$\varepsilon$) = 692 (5.26), 655 (4.73), 611 (4.66), 466 (4.75), 394 (5.20), 355 (5.38) nm. MS (FAB+): *m/z* = 3568.15 $[M + 1]^+$, 3504.72 $[M + 1 – Cu]^+$. $C_{192}H_{208}CuN_{16}O_{16}S_{16}$ (3568.42): calcd. C 64.57, H 5.83, N 6.28, S 14.37, Cu 1.78; found C 64.74, H 6.03, N 6.49, S 14.85, Cu 1.94.

**Phthalocyaninato Nickel(II) (11):** Dicyano derivative **7** (80 mg, 0.091 mmol), dry *n*-pentyl alcohol (1.5 mL), $NiCl_2$ (12 mg, 0.092 mmol), and 3–4 drops of DBU were placed into a standard Schlenk tube under a dry argon atmosphere, and reaction mixture was evacuated several times and refilled with dry argon. Under an argon atmosphere, the reaction mixture was heated at reflux (155 °C) for 18 h. The reaction mixture was then cooled to room temperature, filtered, and dried. The obtained product was purified by column chromatography on silica gel [chloroform/methanol (100:1)]. The combined solvents were evaporated and dark green $Ni^{II}$ phthalocyaninate **9** was obtained and dried in vacuo. Yield 26.5 mg (32.6%). M.p. > 300 °C. $^1$H NMR (200 MHz, $CDCl_3$): $\delta$ = 7.93 (br. s, 8 H, Ar-H), 7.68–6.54 (m, 56 H, Ar-H), 4.73 (s, 16H Ar-$CH_2$-N), 3.61 (s, 16 H, Ar-$CH_2$-S), 2.77 (t, 16 H, -$SCH_2$-$CH_2$S-), 2.42 (s, 24 H, Tosyl-$CH_3$), 1.20 [s, 72 H, $(CH_3)_3$C-] ppm. $^{13}$C NMR (50 MHz, $CDCl_3$): $\delta$ = 153.5, 145.6, 142.3, 140.2, 139.9, 137.2, 130.4, 129.3, 128.1, 127.9, 121.6, 119.5, 109.8, 51.2, 35.0, 32.5, 31.1, 29.0, 22.1 ppm. IR (KBr): $\tilde{\nu}$ = 3057 (CH aromatic), 2981–2856 ($CH_2$ aliphatic), 1645 (C=N), 1505, 1489, 1346 and 1130 ($SO_2$), 762, 678 (C–S) $cm^{-1}$. UV/Vis ($CHCl_3$): $\lambda_{max}$ (log$\varepsilon$) = 694 (5.38), 668 (4.85), 622 (4.59), 419 (4.90), 341 (5.41) nm. MS (FAB+): *m/z* = 3563.15 $[M]^+$, 3505.62 $[M – Ni]^+$. $C_{192}H_{208}N_{16}NiO_{16}S_{16}$ (3563.66): calcd. C 64.65, H 5.84, N 6.29, S 14.39, Ni 1.65; found C 64.49, H 6.14, N 6.11, S 14.56, Ni 1.79.

**Silver(I) Complex of 11 (12):** Nickel(II) phthalocyanine derivative **11** (0.10 g, 0.028 mmol) was dissolved in tetrahydrofuran/water (5.1:0.1) in a 100-mL three-necked round-bottomed flask. Silver nitrate (0.038 g, 0.225 mmol) in the same solvent mixture (5.1:0.1) was added. The mixture was heated at reflux for 4 h, and a bluish–green product formed. The product was filtered off and washed with hot water, hot ethanol, and then diethyl ether. The deep blue product was then dried with $P_2O_5$ in vacuo. Yield: 0.069 g (58%). $^1$H NMR (200 MHz, $CF_3COOD$): $\delta$ = 7.95 (br. s, 8 H, Ar-H), 7.70–6.52 (m, 56 H, Ar-H), 4.80 (s, 16 H, Ar-$CH_2$-N), 3.69 (s, 16 H, Ar-$CH_2$-S), 2.84 (t, 16 H, -$SCH_2$-$CH_2$S-), 2.41 (s, 24 H, Tosyl-$CH_3$), 1.21 [s, 72 H, $(CH_3)_3$C-] ppm. IR (KBr): $\tilde{\nu}$ = 3045, 2942, 1615, 1480, 1382 ($NO_3$), 1340, 1235, 1120, 1100, 1048, 1015, 840, 760, 681 $cm^{-1}$. MS (FAB+): *m/z* = 4244.92 $[M + 2]^+$, 4242.56 $[M]^+$, 4180.26 $[M – NO_3]^+$, 4118.17 $[M – 2NO_3]^{2+}$, 4056.08 $[M – 3NO_3]^{3+}$. $C_{192}H_{208}Ag_4N_{20}NiO_{28}S_{16}$ (4243.14): calcd. C 54.30, H 4.90, N 6.60, S 12.09, Ni 1.38, Ag 10.17; found C 54.16, H 4.67, N 6.86, S 12.31, Ni 1.54, Ag 10.42.

**Palladium(II) Complex of 11 (13):** Metallophthalocyanine **11** (0.10 g, 0.028 mmol) was dissolved in tetrahydrofuran (5 mL) and a solution of $Pd(CH_3COO)_2$ (0.0503 g, 0.2236 mmol) in THF (5 mL) was added. The color became bluish–green while heated at reflux for 5 h and then precipitation occurred. The product was separated by centrifugation and washed several times successively with hot water, hot ethanol, and then diethyl ether. The bluish–green product was filtered off and dried with $P_2O_5$ in vacuo. Yield: 0.081 g (65%). $^1$H NMR (200 MHz, $CF_3COOD$): $\delta$ = 8.12 (br. s, 8 H, Ar-H), 7.75–6.50 (m, 56 H, Ar-H), 4.79 (s, 16H Ar-$CH_2$-N), 3.70 (s, 16 H, Ar-$CH_2$-S), 2.85 (t, 16 H, -$SCH_2$-$CH_2$S-), 2.43 (s, 24 H, Tosyl-$CH_3$), 2.39 (s, 24 H, $CH_3COO$), 1.21 [s, 72 H, $(CH_3)_3$C-] ppm. IR (KBr): $\tilde{\nu}$ = 3055, 2980, 1630, 1580 (asym.$CH_3COO$), 1503, 1470, 1420 (sym. $CH_3COO$), 1343, 1220, 1110, 1090, 1040, 1010, 740, 674 $cm^{-1}$. MS (FAB+): *m/z* = 4461.50 $[M + 1]^+$, 4460.02 $[M]^+$, 4400.13 $[M – CH_3COOH]^+$. $C_{208}H_{232}N_{16}NiO_{32}Pd_4S_{16}$ (4461.26): calcd. C 55.95, H 5.20, N 5.02, S 11.50, Ni 1.32, Pd 9.54; found C 56.14, H 5.32, N 4.87, S 11.65, Ni 1.49, Pd 9.75.

**Detosylation of 11 with $LiAlH_4$ – Compound 14:** A solution of **11** (0.100 g, 0.028 mmol) in dry THF (100 mL) was slowly added to a stirred suspension of $LiAlH_4$ (0.11 g, 2.8 mmol) in dry THF (100 mL) at room temperature under an argon atmosphere. The resulting mixture was stirred and heated at reflux for 5 d. A mixture of ethyl acetate and water was carefully added with stirring at 0 °C to decompose the excess $LiAlH_4$. The resulting precipitate was filtered and washed thoroughly with ethyl acetate and $CH_2Cl_2$. The combined filtrates were dried ($MgSO_4$) and the solvents evaporated. The residue was purified by chromatography on silica gel [$CH_2Cl_2$/$CH_3OH$/$NH_4OH$ (98:1:1)]. Evaporation of the solvent gave **14** as a green solid. Yield: 0.016 g (25%). $^1$H NMR (200 MHz, $CDCl_3$): $\delta$ = 7.94 (br., 8 H, Ar-H), 7.17–6.59 (m, 24 H, Ar-H), 4.69 (s, 16H Ar-$CH_2$-N), 3.65 (s, 16 H, Ar-$CH_2$-S), 3.21 (br. s, 8 H, N-H, $D_2O$ exchange), 2.78 (t, 16 H, -$SCH_2$-$CH_2$S-), 1.24 [s, 72 H, $(CH_3)_3$C-] ppm. $^{13}$C NMR (50 MHz, $CDCl_3$): $\delta$ = 152.6, 150.1, 147.8, 139.4, 136.3, 127.8, 123.8, 122.6, 118.5, 112.3, 45.6, 34.0, 32.5, 31.1, 28.9 ppm. IR (KBr): $\tilde{\nu}$ = 3290 (N–H), 3040 (CH aromatic), 2960–2859 ($CH_2$ aliphatic), 1632 (C=N), 1500, 1490, 1240, 1120 (N–H), 760, 672 (C–S) $cm^{-1}$. UV/Vis ($CHCl_3$): $\lambda_{max}$ (log$\varepsilon$) = 683 (5.33), 658 (4.38), 606 (4.51), 460 (4.80), 379 (5.30), 332 (5.39) nm. MS (FAB+): *m/z* = 2338.08 $[M + Li]^+$, 2332.14 $[M + 1]^+$, 2331.16 $[M – Li]^+$. $C_{136}H_{160}N_{16}NiS_8$ (2331.18): calcd. C 70.01, H 6.86, N 9.61, S 11.00, Ni 2.52; found C 70.21, H 6.68, N 9.54, S 11.27, Ni 2.69.

**Measurements of Heavy Metal-Binding Properties of 11 and 14:** The extraction properties of **11** and **14** were investigated under liquid–liquid phase and neutral conditions by using heavy metal picrates ($Ag^+$, $Cd^{2+}$, $Cu^{2+}$, $Hg^{2+}$, $Pb^{2+}$, $Pd^{2+}$, and $Zn^{2+}$) as substrates and by measuring with UV/Vis the amounts of metal picrate in the aqueous phase before and after treatment with the related compounds. Heavy metal picrates were prepared by the mixture of metal nitrates ($4 \times 10^{-2}$ M) and picric acid ($1.5 \times 10^{-2}$ M) in deionized water. We also prepared solutions ($3 \times 10^{-3}$ M) of related compounds **11** and **14** in dichloromethane. Equal volumes of both metal picrate solutions and compound solutions were then added into plastic bottles, kept closed, and shaken for 10 h by a shaker at 25 ± 1 °C. After shaking, the aqueous phases were separated and the percent of picrate salt extracted ($E$%) was determined by UV spectrophotometry. For each combination of host and metal picrate, the picrate extraction was conducted on three different samples and the average value of percent picrate extracted, with standard deviation, was calculated. The picrate extraction results are presented in Table 3. In the absence of host, blank experiment, no metal ion picrate extraction was detected. The extractability was determined on the basis of the absorbance of picrate ions in the aqueous solutions. The extractability was calculated by using the equation below:

$$E(\%) = [(A_{before} - A_{after})/A_{before}] \times 100$$

where $A_{before}$ is the absorbance in the absence of ligand. $A_{after}$ denotes the absorbance in the aqueous solution phase after extraction.

## Acknowledgments

This study was supported by The Scientific & Technical Research Council of Turkey (TUBITAK), Project Number: TBAG-

 © 2007 Wiley-VCH Verlag GmbH & Co. KGaA, Weinheim 

2453(104T065) (Ankara, Turkey) and the Research Fund of Karadeniz Technical University, Project Number: 2002.111.2.8 (Trabzon/Turkey). We are also indebted to Dr. Ayhan Çelik (University of Edinburgh/England) for assistance with some spectroscopic data.

[1] a) E. Ben-Hur, W. S. Chan in *The Porphyrin Handbook* (Eds.: K. M. Kadish, K. M. Smith, R. Guilard), Academic Press, New York, **2003**, vol. 19, pp. 1–36; b) M. Bouvet in *The Porphyrin Handbook* (Eds.: K. M. Kadish, K. M. Smith, R. Guilard), Academic Press, New York, **2003**, vol. 19, pp. 37–98; c) P. Erk, H. Hengelsberg in *The Porphyrin Handbook* (Eds.: K. M. Kadish, K. M. Smith, R. Guilard), Academic Press, New York, **2003**, vol. 19, pp. 105–149; d) M. Kimura, H. Shirai in *The Porphyrin Handbook* (Eds.: K. M. Kadish, K. M. Smith, R. Guilard), Academic Press, New York, **2003**, vol.19, pp.151–189; e) M. L'Her, A. Pondaven in *The Porphyrin Handbook* (Eds.: K. M. Kadish, K. M. Smith, R. Guilard), Academic Press, New York, **2003**, vol. 16, pp. 117–169.

[2] a) C. C. Leznoff, A. B. P. Lever (Eds.), *Phthalocyanines: Properties and Applications*, VCH, Weinheim, **1989**–**1996**, vols.1–4; b) N. B. McKeown, *Phthalocyanine Materials*: *Synthesis Structure and Function*, Cambridge University Press, Cambridge, **1998**.

[3] W. Eberhardt, M. Hanack, *Synthesis* **1997**, 95–100.

[4] N. Bhardwaj, J. Andraos, C. C. Leznoff, *Can. J. Chem.* **2002**, *80*, 141–147.

[5] M. Hanack, M. Lang, *Adv. Mater.* **1994**, *6*, 819–833.

[6] M. Hanack, S. Knecht, R. Polley, *Chem. Ber.* **1995**, *128*, 929–933.

[7] S. Foley, G. Jones, R. Liuzzi, D. J. McGarvey, M. H. Perry, T. G. Truscott, *J. Chem. Soc., Perkin Trans. 2* **1997**, 1725–1730.

[8] S. Z. Yıldız, H. Kantekin, Y. Gök, *J. Porphyrins Phthalocyanines* **2001**, *5*, 367–375.

[9] J. Sly, P. Kasák, E. G. Nadal, C. Rovira, L. Górriz, P. Thordarson, D. B. Amabilino, A. E. Rowan, R. J. M. Nolte, *Chem. Commun.* **2005**, 1255–1257.

[10] S. Dabak, A. G. Gürek, E. Musluoğlu, V. Ahsen, *New J. Chem.* **2001**, *25*, 1583–1587.

[11] M. Koçak, A. Cihan, A. İ. Okur, A. Gül, Ö. Bekâroğlu, *Dyes Pigments* **2000**, *45*, 9–14.

[12] N. Sheng, R. Li, C. F. Choi, W. Su, D. K. P. Ng, X. Cui, K. Yoshida, N. Kobayashi, J. Jiang, *Inorg. Chem.* **2006**, *45*, 3794–3802.

[13] Y. Gök, H. Kantekin, A. Bilgin, D. Mendil, İ. Değirmencioğlu, *Chem. Commun.* **2001**, 285–286.

[14] A. Bilgin, Y. Gök, *Supramol. Chem.* **2006**, *18*, 491–499.

[15] A. Bilgin, B. Ertem, Y. Gök, *Polyhedron* **2005**, *24*, 1117–1124.

[16] M. Hanack, P. Haisch, *Synthesis* **1995**, 1251–1256.

[17] a) A. Bilgin, Ç. Yağcı, U. Yıldız, *Macromol. Chem. Phys.* **2005**, *206*, 2257–2268; b) A. Bilgin, B. Ertem, Y. Gök, *Supramol. Chem.* **2005**, *17*, 277–281; c) A. Bilgin, B. Ertem, Y. Gök, *Tetrahedron Lett.* **2003**, *44*, 3829–3833; d) A. G. Gürek, V. Ahsen, A. Gül, Ö. Bekâroğlu, *J. Chem. Soc., Dalton Trans.* **1991**, 3367–3371; e) L. S. Beall, N. S. Mani, A. J. P. White, D. J. Williams, A. G. M. Barrett, B. M. Hoffman, *J. Org. Chem.* **1998**, *63*, 5806–5817; f) B. Cabezon, E. Quesada, S. Esperanza, T. Torres, *Eur. J. Org. Chem.* **2000**, 2767–2775; g) P. Thordarson, R. J. M. Nolte, A. E. Rowanin in *The Porphyrin Handbook* (Eds.: K. M. Kadish, K. M. Smith, R. Guilard), Academic Press, New York, **2003**, vol. 18, pp. 281–300.

[18] K. Sakata, K. Matsumoto, M. Hashimoto, *Inorg. Chim. Acta* **1994**, *227*, 113–118.

[19] D. Mendil, A. Bilgin, Y. Gök, H. B. Şentürk, *J. Incl. Phenom.* **2002**, *43*, 265–270.

[20] J. E. Richman, T. J. Atkins, *J. Am. Chem. Soc.* **1974**, *96*, 2268–2270.

[21] G. Ellis, T. Romney-Alexander, *Chem. Rev.* **1987**, *87*, 779–794.

[22] a) A. W. Snow in *The Porphyrin Handbook* (Eds.: K. M. Kadish, K. M. Smith, R. Guilard), Academic Press, New York, **2003**, vol. 17, pp. 129–167; b) M. Brewis, G. J. Clarkson, M. Helliwell, A. M. Holder, N. B. McKeown, *Chem. Eur. J.* **2000**, *6*, 4630–4636.

[23] a) T. Ceylan, Ö. Bekâroğlu, *Monatsh. Chem.* **2002**, *133*, 71–78; b) M. Q. Tian, T. Wada, H. Sasabe, *Dyes Pigments* **2002**, *52*, 1–8.

[24] G. Gümüş, Z. Z. Öztürk, V. Ahsen, A. Gül, Ö. Bekâroğlu, *J. Chem. Soc., Dalton Trans.* **1992**, 2485–2489.

[25] K. Takahashi, M. Kawashima, Y. Tomita, M. Itoh, *Inorg. Chim. Acta* **1995**, *232*, 69–73.

[26] a) D. Attila, V. Ahsen, *J. Porphyrins Phthalocyanines* **2002**, *6*, 593–601; b) F. Yılmaz, D. Attila, V. Ahsen, *Polyhedron* **2004**, *23*, 1931–1937.

[27] a) J. Simon, J. J. Andre, *Molecular Semiconductors* (Eds.: J. M. Lehn, C. W. Rees), Springer, Berlin, **1985**, p. 136; b) D. Schlettwein, N. I. Jaeger, T Oekermann in *The Porphyrin Handbook* (Eds.: K. M. Kadish, K. M. Smith, R.), Academic Press, New York, **2003**, vol. 16, pp. 247–285.

[28] a) H. Pagnia, N. Sotnik, *Phys. Status Solidi (a)* **1988**, *108*, 11–65; b) A. Ahmad, R. A. Collins, *Phys. Status Solidi (a)* **1991**, *123*, 201–211; c) D. Dini, M. Hanack in *The Porphyrin Handbook* (Eds.: K. M. Kadish, K. M. Smith, R. Guilard), Academic Press, New York, **2003**, vol. 17, pp. 1–31.

[29] Z. Z. Öztürk, A. Altındal, A. G. Gürek, Ö. Bekâroğlu, *Synth. Met.* **1992**, *52*, 291–297.

[30] A. D. Delman, J. J. Kelly, A. A. Stein, F. B. Simms, *Thermal Analysis: Proceedings of the 2nd International Conference*, Academic Press, New York, **1969**, vol. 1, p. 539.

[31] H. Shirai, K. Kobayashi, Y. Takemae, A. Suzuki, O. Hirabaru, N. Hojo, *Makromol. Chem.* **1979**, *180*, 2073–2084.

[32] T. R. Walton, J. R. Griffith, *J. Appl. Polm. Sci., Appl. Polm. Symp.* **1975**, *26*, 429–429.

[33] D. D. Perin, W. L. F. Armarego, *Purification of Laboratory Chemicals*, 2nd ed., Pergamon Press, Oxford, **1989**.

Received: October 5, 2006
Published Online: March 6, 2007

 © 2007 Wiley-VCH Verlag GmbH & Co. KGaA, Weinheim 

DOI: 10.1002/ejic.200601056

# Preparation and Reactivity of Hydridorhenium Complexes with Polypyridine and Phosphonite Ligands

**Gabriele Albertin,*[a] Stefano Antoniutti,[a] Jesús Castro,[b] Soledad García-Fontán,[b] and Giorgio Schipilliti[a]**

**Keywords:** Hydrido ligands / P ligands / Protonation / Rhenium / Vinyl complexes

The hydrido complexes $[ReH(Cl)(N–N)P_3]BPh_4$ [P = $PPh(OEt)_2$; N–N = 2,2′-bipyridine (bpy), 5,5′-dimethylbipyridine (5,5′-$Me_2$bpy), 1,10-phenanthroline (phen)] have been prepared by allowing $ReCl_3P_3$ to react with the polypyridine in refluxing ethanol. The dihydrido $[ReH_2(bpy)P_3]BPh_4$ complex has also been prepared by treating $[ReHCl(bpy)P_3]^+$ cation with $NaBH_4$ in ethanol. Similarly, the hydrido tricarbonyl derivative $[ReH_2(bpy)(CO)_3]BPh_4$ has been synthesized by allowing $[ReH(bpy)(CO)_3]$ to react with $HBF_4·Et_2O$. All complexes have been characterized spectroscopically (IR and NMR spectroscopic data) and the $[ReHCl(bpy)\{PPh(OEt)_2\}_3]BPh_4$ derivative by X-ray crystallography. Protonation of both $[ReHCl(bpy)P_3]BPh_4$ and $[ReH_2(bpy)P_3]BPh_4$ with $HBF_4·Et_2O$ leads to the classical cations $[ReH_2Cl(bpy)P_3]^{2+}$ and $[ReH_3(bpy)P_3]^{2+}$, respectively. The vinyl complexes $[Re\{CH=C(H)R\}_2(bpy)P_3]BPh_4$ (R = Ph, *p*-tolyl, *tert*-butyl) have also been prepared by allowing the dihydrido derivative $[ReH_2(bpy)P_3]BPh_4$ to react with an excess of terminal alkyne in 1,2-dichloroethane.

(© Wiley-VCH Verlag GmbH & Co. KGaA, 69451 Weinheim, Germany, 2007)

## Introduction

The chemistry of rhenium polyhydrido complexes has received considerable attention in recent years due to their various reactivity modes and unusual structural properties, including the presence of $\eta^2$-$H_2$ ligands.[1–4] The ancillary ligands used in this chemistry mainly involve π-acceptors such as carbonyls and mono- or polydentate tertiary phosphane groups.[1–4] In contrast, much less attention has been devoted to the use of nitrogen-donor ligands, and only one paper[5] has reported the use of polypyridines as supporting ligands[6,7] in rhenium polyhydrido complexes. This is somewhat surprising because rhenium complexes with polypyridine ligands are used in photo- and electrocatalytic reduction of $CO_2$.[6,7c,8] Changes in the nature of the ancillary ligands may also greatly change both the properties of complexes and the reactivity of the M–H bond, and recent results from our laboratory have confirmed the important influence of polypyridine ligands in the chemistry of classical and non-classical hydrido complexes of the iron triad.[9]

We have developed the chemistry of hydrido complexes of transition metals over several years using monodentate phosphites as supporting ligands.[9,10] Recently, in the case of rhenium, we reported the synthesis and reactivity of mono- and polyhydrido complexes of the type $[ReH(CO)_nP_{5-n}]$, $[Re(\eta^2\text{-}H_2)(CO)_nP_{5-n}]^+$, $ReH_5P_3$, $ReH_3P_4$, $Re_2H_8P_4$, and $[ReH_4(\eta^2\text{-}H_2)P_3]^+$ (P = phosphite; $n$ = 1–4).[11] We have now extended these studies, with the aim of introducing nitrogen-donor ligands such as 2,2′-bipyridine and 1,10-phenanthroline into rhenium polyhydrido chemistry. Our results on the synthesis and reactivity of mixed-ligand cationic hydridorhenium complexes with phosphonite and polypyridine are reported here.

[a] Dipartimento di Chimica, Università Ca' Foscari Venezia, Dorsoduro 2137, 30123 Venezia, Italy
[b] Departamento de Química Inorgánica, Universidade de Vigo, Facultade de Química, Edificio de Ciencias Experimentais, 36310 Vigo, Galicia, Spain

## Results and Discussion

### Synthesis of Hydrido Complexes

The trichlorido complex $[ReCl_3\{PPh(OEt)_2\}_3]$ was treated with an excess of polypyridine (N–N) in refluxing ethanol to give the cation $[ReHCl(N–N)\{PPh(OEt)_2\}_3]^+$, which was isolated as its $BPh_4$ salt and characterized (Scheme 1).

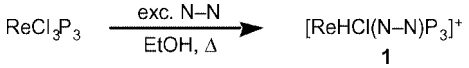


Scheme 1. P = $PPh(OEt)_2$; N–N = 2,2′-bipyridine (bpy) **a**, 5,5′-dimethyl-2,2′-bipyridine (5,5′-$Me_2$bpy) **b**, 1,10-phenanthroline (phen) **c**.

The reaction proceeds with substitution of the chlorido ligand by the polypyridine and formation of a heptacoordinate hydrido cation. The hydrido ligand presumably arises from abstraction of hydrogen from the ethanol solvent. Although this could not be proved conclusively, numerous precedents[1a] support this hypothesis.

 © 2007 Wiley-VCH Verlag GmbH & Co. KGaA, Weinheim 

The nature of the phosphane ligand is crucial for the synthesis of heptacoordinate hydrido complex **1**, which was obtained in pure form only with the phosphonite $PPh(OEt)_2$. The reaction of the related precursors $[ReCl_3(PPh_2OEt)_3]$ with polypyridines gave a mixture of products containing only small amounts of the $[ReHCl(N–N)(PPh_2OEt)_3]^+$ derivatives.

The hydrido complexes $[ReHCl(N–N)P_3]BPh_4$ (**1**) were treated with $NaBH_4$ in ethanol to give the dihydrido cations $[ReH_2(N–N)P_3]^+$ which, in the case of the bpy ligand, was isolated in good yield and characterized (Scheme 2). The reaction of **1** with $NaBH_4$ also proceeded with 5,5′-dimethylpyridine and 1,10-phenanthroline as a ligand but, in these cases, complexes **2** were rather unstable and decomposed during crystallization.

$$[ReHCl(N–N)P_3]^+ \xrightarrow[EtOH,\ \Delta]{NaBH_4} [ReH_2(N–N)P_3]^+$$
**1** **2a**

Scheme 2. P = $PPh(OEt)_2$; N–N = 2,2′-bipyridine (bpy) **a**.

Hydridorhenium complexes containing polypyridine as a supporting ligand are rare[5,6] and the only known examples were obtained from polyhydrido $[ReH_7(PPh_3)_2]$ or $[ReCl(bpy)(CO)_3]$ precursors. The reaction of $[ReCl_3P_3]$ with polypyridine in ethanol is therefore a new method for preparing mixed-ligand hydridorhenium complexes.

Hydrido complexes **1** and **2a** are dark-green (**1**) or red-brown (**2a**) solids that are stable in air and in solution in polar organic solvents, where they behave as 1:1 electrolytes.[12] The analytical and spectroscopic (IR, NMR; Table 1) data confirm the proposed formulation for the complexes. Further support comes from the X-ray crystal structure of $[ReHCl(bpy)\{PPh(OEt)_2\}_3]BPh_4$ (**1a**), the cation of which is shown in Figure 1. The geometrical parameters of the anion were as expected and do not require further comment.

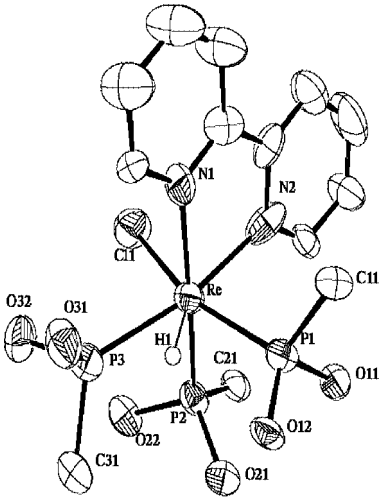


Figure 1. Perspective view of the crystal structure of the cation $[ReHCl(bpy)\{PPh(OEt)_2\}_3]^+$ **1a**, with thermal ellipsoids drawn at the 50% probability level. The ethyl and phenyl groups of the phosphites are omitted for clarity.

The rhenium atom in the cation is coordinated by three phosphorus atoms from three phosphonite ligands, two nitrogen atoms from the bipyridine ligand, and a chlorine atom. There is also significant residual electronic density close to the rhenium atom (at 1.23 Å; see Experimental Section), probably due to the presence of the hydrogen atom in this region, but unfortunately its position could not be refined due to the well-known inability of X-ray diffractometry to detect hydrido ligands coordinated to third-row transition metals. The presence of this ligand was also confirmed by the values of the angles around the metal, which are far from the theoretical values for an octahedron as a consequence of the heptacoordinate environment of the metal. Without knowing the position of the hydrido ligand it is difficult to propose a geometry around the metal. The N(1)–Re–P(2) axis [171.7(2)°], for example, could indicate a monocapped octahedron or a pentagonal bipyramid. The chelate angle N(1)–Re–N(2) has a value of only 75.7(4)° – virtually the same as that found in other 2,2′-bipyridine complexes of $Re^{III}$[13] – and is an important source of distortion since one of the nitrogen atoms is in the axis and the other in the equatorial plane. The angles in the plane for a pentagonal bipyramidal geometry should be close to 72°, although the different steric requirements of the hydrido and the rest of the ligands may enlarge these angles. The angles in the cation complex range from 79.2(2)° to 90.6(1)°. This, and the distortion of the axis, allows us to propose a monocapped octahedral geometry around the metal, with the hydrido ligand situated in the trigonal face occupied by the three phosphorus atoms.

The Re–N [2.172(10) and 2.180(9) Å] and Re–Cl [2.450(3) Å] bond lengths are slightly longer than those found for other octahedrally coordinated complexes,[13] as expected due to the increase in coordination number. The Re–P bond lengths range from 2.286(3) to 2.365(3) Å and are slightly shorter than those found in the cationic complex $[ReCl(PhN_2)\{PPh(OEt)_2\}_4]BPh_4$,[14] the only example of a complex containing both $Re^{III}$ and a phosphonite $PPh(OEt)_2$ ligand found in the CCDC (version 5.27, update August 2006).[15] This shortening is due to the pseudo *trans* effect exerted by the nitrogen or chlorine atoms in the heptacoordinate complex when compared with the cited octahedral cation, which has the phosphonite ligands mutually *trans*.

The IR spectra of monohydrido complexes $[ReHCl(N–N)P_3]BPh_4$ (**1**) show the bands characteristic of polypyridine and phosphonite ligands ($\nu_{PO}$ = 1098–1020 $cm^{-1}$), but none attributable to the $\nu_{ReH}$ of the hydrido ligand. However, its presence was confirmed by the $^1H$ NMR spectra, which show signals for the $PPh(OEt)_2$ and polypyridine ligands and a multiplet between $\delta$ = –7.98 and –8.30 ppm that is characteristic of a hydrido ligand. As the $^{31}P\{^1H\}$ NMR spectrum is an $A_2M$ multiplet for all complexes **1** in the temperature range between +20 and –80 °C, the hydrido pattern can be simulated by an $A_2MX$ model (X = $^1H$), with the parameters listed in Table 1. In addition, the values of the two $J_{P,H}$ coupling constants are similar, which suggests that the hydrido is in a mutually *cis* position with re-

 © 2007 Wiley-VCH Verlag GmbH & Co. KGaA, Weinheim 

Table 1. IR, $^1H$ and $^{31}P\{^1H\}$ NMR spectroscopic data for rhenium complexes.

| Compound | $^1H$ NMR[a] $\delta$ | Assignment | $^{31}P\{^1H\}$ NMR[a,b] Spin system | $\delta$ |
|---|---|---|---|---|
| $[ReHCl(bpy)\{PPh(OEt)_2\}_3]BPh_4$ (**1a**) | 9.28–6.51 (m) | Ph + bpy | $A_2M$ | $\delta_A$ = 126.8 |
| | 3.64 (m) | $CH_2$ | | $\delta_M$ = 119.9 |
| | 1.19 (t) | $CH_3$ | | $J_{A,M}$ = 37.7 |
| | 1.16 (t) | | | |
| | 1.08 (t) | | | |
| | $A_2MX$ | ReH | | |
| | $\delta_X$ = –8.28 | | | |
| | $J_{A,X}$ = 44 | | | |
| | $J_{M,X}$ = 58 | | | |
| $[ReHCl(5,5'\text{-}Me_2bpy)\{PPh(OEt)_2\}_3]BPh_4$ (**1b**) | 9.57–6.15 (m) | Ph + bpy | $A_2M$ | $\delta_A$ = 126.9 |
| | 3.68 (m) | $CH_2$ | | $\delta_M$ = 121.2 |
| | 2.34 (s) | $CH_3$ bpy | | $J_{A,M}$ = 36.2 |
| | 2.22 (s) | | | |
| | 1.21 (t) | $CH_3$ phos | | |
| | 1.19 (t) | | | |
| | 1.08 (t) | | | |
| | $A_2MX$ | ReH | | |
| | $\delta_X$ = –8.30 | | | |
| | $J_{AX}$ = 44 | | | |
| | $J_{MX}$ = 58 | | | |
| $[ReHCl(phen)\{PPh(OEt)_2\}_3]BPh_4$ (**1c**) | 9.64–6.13 (m) | Ph + phen | $A_2M$ | $\delta_A$ = 127.0 |
| | 3.70 (m) | $CH_2$ | | $\delta_M$ = 119.8 |
| | 1.28 (t) | $CH_3$ | | $J_{A,M}$ = 37.4 |
| | 1.03 (t) | | | |
| | $A_2MX$ | ReH | | |
| | $\delta_X$ = –7.98 | | | |
| | $J_{A,X}$ = 42 | | | |
| | $J_{M,X}$ = 58 | | | |
| $[ReH_2(bpy)\{PPh(OEt)_2\}_3]BPh_4$ (**2a**) | 9.27–6.86 (m) | Ph + bpy | | 141 m, b |
| | 3.60 (m) | $CH_2$ | | |
| | 3.31 (m) | | | |
| | 0.96 (br. m) | $CH_3$ | | |
| | –5.20 (br. m) | ReH | | |
| | 9.20–6.80 (m)[c] | Ph + bpy | $AM_2$[c] | $\delta_A$ 145.7 |
| | 3.57 (m) | $CH_2$ | | $\delta_M$ 134.3 |
| | 3.23 (m) | | | $J_{A,M}$ = 27.0 |
| | 1.25 (t) | $CH_3$ | | |
| | 0.98 (t) | | | |
| | $AM_2X_2$ | ReH | | |
| | $\delta_X$ –5.31 | | | |
| | $J_{A,X}$ = 12 | | | |
| | $J_{M,X}$ = 66 | | | |
| $[ReH_2(bpy)(CO)_3]BPh_4$ (**3a**)[d] | 9.03–7.68 (m) | Ph + bpy | | |
| | –13.07 d | $ReH_2$ | | |
| | –17.47 d | | | |
| | $J_{H,H}$ = 3.4 | | | |
| $[ReH_2Cl(bpy)\{PPh(OEt)_2\}_3]^{2+}$ (**4a**) | 9.55–6.50 (m)[e] | Ph + bpy | $AM_2$[e] | $\delta_A$ = 163.4 |
| | 3.75 (m) | $CH_2$ | | $\delta_M$ = 124.1 |
| | 1.26 (m) | $CH_3$ | | $J_{A,M}$ = 52.3 |
| | –5.50 (br. dt) | $ReH_2$ | $AM_2$[e] | $\delta_A$ = 155.0 |
| | –7.84 (br. m) | | | $\delta_M$ = 125.5 |
| | | | | $J_{A,M}$ = 49.4 |
| $[ReH_3(bpy)\{PPh(OEt)_2\}_3]^{2+}$ (**5a**) | 9.25–6.85 (m)[f] | Ph + bpy | $A_2B$[f] | $\delta_A$ = 127.8 |
| | 4.20–3.35 (m) | $CH_2$ | | $\delta_B$ = 126.5 |
| | 1.20 (m) | $CH_3$ | | $J_{A,B}$ = 31.0 |
| | –2.2 (br. m) | $ReH_3$ | | |
| | –3.1 (br. m) | | | |
| $[Re\{CH{=}C(H)Ph\}_2(bpy)\{PPh(OEt)_2\}_3]BPh_4$ (**6a**) | 7.30–6.82 (m) | Ph + bpy | $AB_2$ | $\delta_A$ = 139.3 |
| | 7.08 (m) | $=CH_\alpha$ | | $\delta_B$ = 138.2 |
| | 6.47 (m) | $=CH_\beta$ | | $J_{A,B}$ = 32.6 |
| | 4.35–3.60 (m) | $CH_2$ | | |
| | 1.52 (t) | $CH_3$ | | |
| | 1.15 (t) | | | |
| | 1.07 (t) | | | |

 © 2007 Wiley-VCH Verlag GmbH & Co. KGaA, Weinheim 

Table 1. *(continued)*

| Compound | $^1$H NMR[a] | | $^{31}$P{$^1$H} NMR[a,b] | |
|---|---|---|---|---|
| | $\delta$ | Assignment | Spin system | $\delta$ |
| [Re{CH=C(H)-*p*-tolyl}$_2$(bpy){PPh(OEt)$_2$}$_3$]BPh$_4$ (**7a**) | 9.32–6.86 (m) | Ph + bpy | $AB_2$ | $\delta_A$ = 136.4 |
| | $AB_2XY$ | =CH | | $\delta_B$ = 135.2 |
| | (X = $H_\alpha$, Y = $H_\beta$) | | | $J_{A,B}$ = 31.8 |
| | $\delta_X$ = 7.04 | | | |
| | $\delta_Y$ = 6.45 | | | |
| | $J_{A,X}$ = 4.0 | | | |
| | $J_{A,Y}$ = 4.35 | | | |
| | $J_{B,X}$ = 7.10 | | | |
| | $J_{B,Y}$ = 5.20 | | | |
| | $J_{X,Y}$ = 7.7 | | | |
| | 4.30–3.30 (m) | $CH_2$ | | |
| | 2.44 (s) | $CH_3$ *p*-tolyl | | |
| | 1.51 (t) | $CH_3$ phos | | |
| | 1.15 (t) | | | |
| | 0.99 (t) | | | |
| [Re{CH=C(H)-*tert*-butyl}$_2$(bpy){PPh(OEt)$_2$}$_3$]BPh$_4$ (**8a**) | 9.28–6.87 (m) | Ph + bpy | $AB_2$ | $\delta_A$ = 137.0 |
| | $AB_2XY$ | =CH | | $\delta_B$ = 135.5 |
| | (X = $H_\alpha$, Y = $H_\beta$) | | | $J_{A,B}$ = 31.6 |
| | $\delta_X$ = 7.09 | | | |
| | $\delta_Y$ = 6.51 | | | |
| | $J_{A,X}$ = 6.85 | | | |
| | $J_{A,Y}$ = 3.60 | | | |
| | $J_{B,X}$ = 8.10 | | | |
| | $J_{B,Y}$ = 4.30 | | | |
| | $J_{X,Y}$ = 8.40 | | | |
| | 4.32–3.32 (m) | $CH_2$ | | |
| | 1.50 (t) | $CH_3$ phos | | |
| | 1.14 (t) | | | |
| | 1.10 (t) | | | |
| | 1.07 (s) | $CH_3$ *t*Bu | | |

[a] In $CD_2Cl_2$ at 25 °C, unless otherwise noted. Chemical shifts are given in ppm and coupling constants in Hz. [b] Positive shifts downfield from 85% $H_3PO_4$. [c] At –30 °C. [d] IR data for the complex in a KBr pellet: $\nu_{CO}$ = 2049 (s), 1989 (s), 1924 cm$^{-1}$ (s). [e] At –50 °C. [f] At –70 °C.

spect to all the phosphonite ligands. Lastly, the two methyl substituents of the 5,5′-dimethyl-2,2′-bipyridine ligand are magnetically inequivalent in **1b** (two methyl singlets at $\delta$ = 2.34 and 2.22 ppm in the $^1$H NMR spectrum of the complex).

The geometry of the heptacoordinate hydrido complexes **1** may be discussed in terms of three limiting structures, namely pentagonal bipyramidal, monocapped octahedral, or monocapped trigonal prismatic. The spectroscopic data do not allow us to distinguish between these possible structures, although it is plausible that the same geometry observed in the solid state for **1a** is also maintained in solution. A monocapped octahedral geometry of type **I**, which contains two magnetically equivalent phosphites that are different from the third and the hydrido ligand in a *cis* position with respect to each of the three phosphite groups, is in full accordance with the observed NMR spectroscopic data.

The $^1$H and $^{31}$P NMR spectra of the [ReH$_2$(bpy)P$_3$]$^+$ cation **2a** indicate that the complex is fluxional. The broad signals present at room temperature in the $^{31}$P NMR spectrum resolve into an $AM_2$ multiplet at –30 °C, thereby suggesting the presence of two phosphonites that are magnetically equivalent and different from the third. At the same temperature, the $^1$H NMR spectrum shows sharp signals

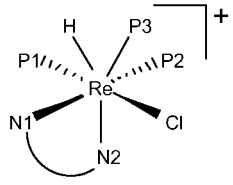


**I**

attributable to phosphonite and bpy ligands and a multiplet at $\delta$ = –5.31 ppm for the hydrido ligands. Variable-temperature $T_1$ measurements (200 MHz) on this signal gave a $T_{1min}$ value of 104 ms (Table 2), in agreement[16] with the classical nature of the dihydrido derivative **2a**. The hydrido multiplet at $\delta$ = –5.31 ppm can also be simulated with an $AM_2X_2$ (X = $^1$H) model, with the parameters listed in

Table 2. $^1$H NMR spectroscopic data (200 MHz; $\delta$ values, ppm) in the hydrido region for some rhenium complexes.

| Compound | $T$ [K] | $\delta$ (M–H) | $T_{1min}$ [ms] |
|---|---|---|---|
| [ReH$_2$(bpy){PPh(OEt)$_2$}$_3$]BPh$_4$ (**2a**) | 205 | –5.45 | 104 |
| [ReH$_2$(bpy)(CO)$_3$]BPh$_4$ (**3a**) | 198 | –13.1 | 112 |
| [ReH$_2$Cl(bpy){PPh(OEt)$_2$}$_3$]$^{2+}$ (**4a**) | 200 | –7.84 | 76 |
| [ReH$_3$(bpy){PPh(OEt)$_2$}$_3$]$^{2+}$ (**5a**) | 208 | –2.15 | 65 |
| | 203 | –3.10 | 83 |

 © 2007 Wiley-VCH Verlag GmbH & Co. KGaA, Weinheim 

Table 1, and the good fit between experimental and calculated spectra indicates the magnetic equivalence of the two hydrido ligands.

The spectroscopic data strongly support the proposed formulation for complex **2a** but do not allow us to unambiguously assign its geometry in solution. However, by analogy with the related monohydrido **1**, a monocapped octahedral geometry of type **II** may also be proposed for dihydrido complex **2a**; this ligand arrangement fits the reported NMR spectroscopic data.

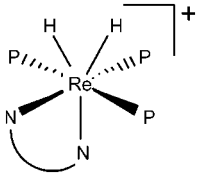


**II**

The easy synthesis of mono- and dihydridorhenium(III) complexes **1** and **2a** prompted us to extend our studies to related complexes containing carbonyl ligands. The method used was the protonation of $Re^{I}$ compounds of the type $[ReH(bpy)(CO)_3]$[17] and $[ReBr(bpy)(CO)_3]$ (Scheme 3).

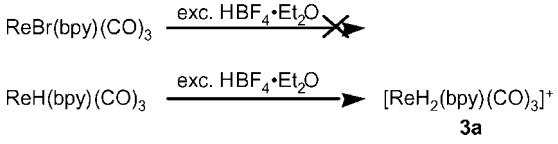


Scheme 3.

Although $[ReBr(bpy)(CO)_3]$ was found to be unreactive toward an excess of $HBF_4$, $[ReH(bpy)(CO)_3]$ reacts quickly with $HBF_4$ to give the dihydrido cation $[ReH_2(bpy)(CO)_3]^+$, which was isolated as its $BPh_4$ salt and characterized. Good analytical data were obtained for complex **3**, which is a yellow solid that is stable in air and in solution in polar organic solvents, where it behaves as a 1:1 electrolyte.[12] The IR spectrum of **3a** shows three strong absorptions in the $\nu_{CO}$ region attributable to three carbonyl ligands in a mutually *fac* position. Besides the signals of the bpy ligand and the $BPh_4$ anion, the $^1H$ NMR spectrum shows two doublets at $\delta$ = –13.07 and –17.47 ppm ($J_{H,H}$ = 3.4 Hz) for the two hydrido ligands, which means they are magnetically inequivalent. $T_1$ measurements on these hydrido signals were also performed and gave $T_{1min}$ values near 112 ms, in good agreement[16] with the classical nature of these hydrido ligands. On this basis, we hypothesize that the reaction of $[ReH(bpy)(CO)_3]$ with $HBF_4$ does not proceed by protonation of the Re–H bond to give an $\eta^2$-$H_2$ ligand but involves the oxidative addition of $H^+$ to yield the formal cationic $Re^{III}$ derivative $[ReH_2(bpy)(CO)_3]^+$. Oxidative addition of $H^+$ to a $Re^{I}$ complex is rather rare[3e] as formation of the dihydrogen [Re]-$\eta^2$-$H_2$ complex is the more usual result of protonation.[3i,4a,11b] The presence of the bpy ligand probably strongly influences the course of the protonation reaction that leads to the $Re^{III}$ species **3**.

Although the IR and NMR spectroscopic data do not allow us to assign geometries to the complex, a monocapped octahedral geometry of type **III**, like those proposed for complexes **1** and **2a**, fits the spectroscopic data and may be tentatively proposed for the $[ReH_2(bpy)(CO)_3]^+$ derivative **3a**.

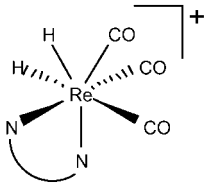


**III**

## Reactivity

Protonation of the new hydrido complexes **1**, **2a**, and **3a** with a Brønsted acid was studied with the aim of testing whether $\eta^2$-$H_2$ complexes could be formed. The results show that, although $[ReH_2(bpy)(CO)_3]^+$ (**3a**) is unreactive towards an excess of $HBF_4$·$Et_2O$, phosphonite complexes **1a** and **2a** give the new $Re^{V}$ hydrido complexes **4** and **5**, respectively, as shown in Scheme 4.

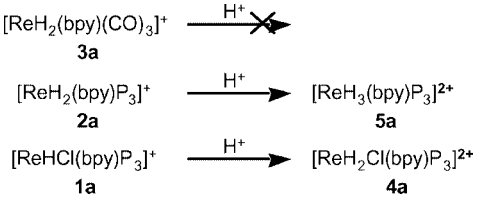


Scheme 4. P = $PPh(OEt)_2$.

The protonation was carried out at variable temperature and was monitored by $^1H$ and $^{31}P$ NMR spectroscopy. The addition of $HBF_4$·$Et_2O$ to a $CD_2Cl_2$ solution of the dihydrido cation $[ReH_2(bpy)P_3]^+$ (**2a**) at –80 °C caused the disappearance of the hydrido signal at $\delta$ = –5.4 ppm in the $^1H$ NMR spectrum and the appearance of two new multiplets with an intensity ratio of 2:1 at $\delta$ = –2.2 and at –3.1 ppm, respectively. Variable-temperature $T_1$ measurements (Table 2) on these signals gave $T_{1min}$ values (200 MHz) of 65 and 83 ms, respectively, which suggests a classical structure for the protonated $[ReH_3(bpy)P_3]^+$ derivatives. Protonation of the dihydrido cation $[ReH_2(bpy)P_3]^+$ therefore proceeds by oxidative addition of $H^+$ to the metal center to give the octacoordinate $Re^{V}$ trihydrido derivative **5a**. It should be noted that a twofold excess of $HBF_4$·$Et_2O$ must be used to complete the formation of **5a**, the $^{31}P$ NMR spectrum of which shows an $A_2B$ multiplet at –80 °C that can be simulated with the parameters listed in Table 1.

Addition of an excess of $NEt_3$ to a solution of **5a** regenerates the starting dihydrido complex $[ReH_2(bpy)P_3]^+$ and, although complex **5a** was not isolated, its spectroscopic data strongly support its formulation as the mixed-ligand rhenium(V) trihydrido complex $[ReH_3(bpy)P_3]^{2+}$, which contains three phosphonites and a bipyridine.

 © 2007 Wiley-VCH Verlag GmbH & Co. KGaA, Weinheim 

Protonation of cationic hydrido complexes has been reported previously[9,19] and often proceeds, in the presence of a large excess of Brønsted acid, to give $\eta^2$-$H_2$ derivatives. The relatively easy oxidative addition of $H^+$ to a cationic $Re^{III}$ hydrido complex to yield a $Re^V$ polyhydrido complex similar to **5a** may be due to the presence of the polypyridine ligand, which is able to stabilize classical dicationic hydrido complexes in a high oxidation state.

Reaction of the hydrido-chlorido $[ReH(Cl)(bpy)P_3]^+$ cation **1a** also proceeds with $HBF_4{\cdot}Et_2O$ at –80 °C to give the new hydrido cation $[ReH_2Cl(bpy)P_3]^{2+}$ (**4a**) (Scheme 4), although in this case a large excess of acid is required to complete the reaction. The $^1H$ and $^{31}P\{^1H\}$ NMR spectroscopic data also suggest the presence of two isomers for **4a**, which shows two multiplets at $\delta$ = –5.50 and –7.84 ppm in the $^1H$ NMR spectrum and two $A_2M$ multiplets in the $^{31}P$ NMR spectrum. $T_1$ measurements on the hydrido proton multiplets (Table 2) confirmed the classical nature of the protonated complex, which suggests that oxidative addition of $H^+$ also takes place in the hydrido-chlorido complexes to yield the rhenium(V) polypyridine derivative **4a**. The two $Re^{III}$ hydrido complexes **1a** and **2a**, which contain a polypyridine and phosphonites as supporting ligands, therefore show parallel behavior during the oxidative addition of $H^+$ and afford a dicationic octacoordinate polyhydrido $Re^V$ complex.

Reactivity studies on hydrido cations **1** and **2a** were extended to substitution and insertion reactions, and the results revealed the relatively high stability of both complexes. Substitution reactions with carbonyl, phosphane, nitrile, or isocyanide ligands and insertion reactions with unsaturated molecules such as $ArN_2^+$, $RCH{=}CH_2$, $CO_2$, $CS_2$, etc. proved impossible for both complexes. However, one reaction was observed for **2a**, which reacts with terminal alkynes to give the bis(vinyl) derivatives $[Re\{CH{=}C(H)R\}_2(bpy)P_3]^+$ (**6a**, **7a**, and **8a**), as shown in Scheme 5.

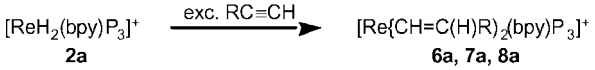


Scheme 5. P = $PPh(OEt)_2$; R = Ph **6a**, *p*-tolyl **7a**, *tert*-butyl **8a**.

The reaction is quite slow at room temperature, and the synthesis of pure vinyl complexes **6a**–**8a** can be achieved only at reflux conditions. In every case, the reaction proceeds with the insertion of two alkynes into the Re–H bond to give only bis(vinyl) derivatives **6a**, **7a**, and **8a**. The absence of any mono-insertion product such as $[ReH\{CH{=}C(H)R\}_2(bpy)P_3]^+$ is probably due to a faster insertion rate of the second alkyne with respect to the first into the Re–H bond of **2a**. The need for reflux conditions to obtain the vinyl complexes may be explained by the fact that the mechanism proposed[20] for the insertion of an alkyne into an M–H bond usually requires a vacant site, and only at higher temperatures can the substitution of one ligand by an alkyne take place.

Vinyl complexes of rhenium are rare[21] and in some cases have been proposed only as intermediates.[22] Our reaction of dihydrido compound **2a** with a terminal alkyne provides new examples of this class of derivatives. Vinyl complexes **6a**–**8a** are green solids that are stable in air and in solution in polar organic solvents, where they behave as 1:1 electrolytes.[12] The analytical and spectroscopic data (Tables 1 and 3) support their proposed formulation. Thus, besides the signals of the polypyridine, phosphites, and the $BPh_4$ anion, the $^1H$ NMR spectrum shows a slightly broad multiplet at around $\delta$ = 6.45–6.51 ppm due to $H_\beta$ of the vinyl ligand. This multiplet was correlated in a COSY experiment with a signal overlapping the phenyl resonances at $\delta$ = 7.04–7.09 ppm, which was attributed to the $H_\alpha$ proton of the vinyl ligand. As the $^{31}P$ NMR spectrum in the temperature range between +20 and –80 °C is an $AB_2$ multiplet, the $H_\alpha$ and $H_\beta$ vinyl signals can be simulated with an $AB_2XY$ (X = $H_\alpha$, Y = $H_\beta$) model with the parameters listed in Table 1. The values of the proton-proton coupling constants $J_{X,Y}$ of 7.7 (**7a**) and 8.4 Hz (**8b**) also suggest a *cis* arrangement[23] of the two vinyl protons.

Table 3. $^{13}C\{^1H\}$ NMR spectroscopic data for vinyl complexes **7a** and **8a**.

| Compound | $^{13}C\{^1H\}$ NMR[a] | |
|---|---|---|
| | $\delta$ | Assignment |
| **7a** | 165–122 (m) | Ph + bpy |
| | 131.2 (s) | $=CH_\beta$ |
| | 128.6 (m) | $=CH_\alpha$ |
| | 67.4 (d) | $CH_2$ |
| | 66.4 (d) | |
| | 16.6 (m) | $CH_3$ phos |
| | 11.3 (s) | $CH_3$ *p*-tolyl |
| **8a** | 163–122 (m) | Ph + bpy |
| | 129.1 (m) | $=CH_\alpha$ |
| | 123.8 (s) | $=CH_\beta$ |
| | 67.4 (m) | $CH_2$ |
| | 65.4 (s) | $C(CH_3)_3$ |
| | 30.5 (s) | $C(CH_3)_3$ |
| | 16.9 (m) | $CH_3$ phos |

[a] In $CD_2Cl_2$ at 25 °C. Chemical shifts are given in ppm and coupling constants in Hz.

The $^{13}C$ NMR spectra (Table 3) confirm the presence of the vinyl group in compounds **6**–**8** by the presence of a multiplet at $\delta$ = 128–129 ppm attributed to $C_\alpha$ and another at $\delta$ = 123–131 ppm attributed to $C_\beta$ of the vinyl ligand. HMQC and HMBC experiments confirmed this assignment as the multiplets at $\delta$ = 123–131 ppm in the $^{13}C$ spectra are correlated to the proton signals near $\delta$ = 6.5 ppm due to the $H_\beta$ vinyl resonance, whereas the $^{13}C$ signal at $\delta$ = 128–129 ppm is correlated with the signal at $\delta$ = 7.04–7.09 ppm due the $H_\alpha$ vinyl proton, in agreement with the proposed assignment of these signals.

These spectroscopic data strongly support the proposed formulation for the complexes but do not allow us to unambiguously assign geometries to the complexes. Assuming a monocapped octahedral geometry for these vinyl complexes as well, a structure of type **IV**, with two magnetically equiv-

 © 2007 Wiley-VCH Verlag GmbH & Co. KGaA, Weinheim 

alent vinyl groups and two magnetically equivalent phosphonites that are different from the third, fits the spectroscopic data. However, the absence of any X-ray crystal structure due to the poor quality of the obtained crystals means that geometry **IV** is only a tentative proposal.

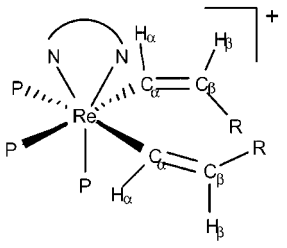

**IV**

## Conclusions

We have described the synthesis of the mixed-ligand hydridorhenium(III) complexes $[ReHCl(N–N)P_3]BPh_4$ (**1**) and $[ReH_2(N–N)P_3]BPh_4$ (**2a**), both of which contain phosphonite and polypyridine ligands. The hydrido carbonyl cations $[ReH_2(bpy)(CO)_3]^+$ have also been obtained by the oxidative addition of $H^+$ to $Re^I$ derivatives. The structural parameters for the heptacoordinate $[ReHCl(bpy)P_3]^+$ cation have been obtained by X-ray crystallography. Among the properties shown by the new $Re^{III}$ hydrido complexes we can highlight the easy protonation of cationic complexes **1** and **2a** to give classical $Re^V$ hydrido derivatives, and the reaction of **2a** with terminal alkynes to afford new examples of vinyl complexes of rhenium.

## Experimental Section

**General:** All synthetic work was carried out under an inert atmosphere (Ar, $N_2$) using standard Schlenk techniques or a dry box (Vacuum Atmospheres, Mecaplex, CH). All solvents were dried with appropriate drying agents, degassed on a vacuum line, and distilled into vacuum-tight storage flasks. $Re_2(CO)_{10}$ was a Pressure Chemical Co. (USA) product, while Re powder was purchased from Chempur (Germany); both were used as received. The phosphonite $PPh(OEt)_2$ and phosphinite $PPh_2OEt$ were prepared according to Rabinowitz and Pellon.[24] Other reagents were purchased from commercial sources with the highest available purity and used as received. IR spectra were recorded with a Nicolet Magna 750 or Perkin–Elmer Spectrum One FT-IR spectrophotometer. NMR spectra ($^1H$, $^{31}P$, $^{13}C$) were obtained with an AC200 or Avance 300 Bruker spectrometer at temperatures between –80 and +30 °C, unless otherwise noted. $^1H$ and $^{13}C$ NMR spectra are referenced to internal tetramethylsilane; $^{31}P\{^1H\}$ chemical shifts are reported with respect to 85% $H_3PO_4$, with downfield shifts considered positive. The COSY, HMQC, and HMBC NMR experiments were performed using the standard programs. Values of $T_{1min}$ (±10%) were determined by the inversion recovery method between –90 and +30 °C in $CD_2Cl_2$ with a standard 180°–τ–90° pulse sequence. The SwaN-MR software package[25] was used to treat NMR spectroscopic data. The conductivity of $10^{-3}$ M solutions of the complexes in $CH_3NO_2$ at 25 °C was measured with a Radiometer CDM 83. Elemental analyses were determined by the Microanalytical Laboratory of the Dipartimento di Scienze Farmaceutiche of the University of Padua, Italy.

**Synthesis of Complexes:** $[ReCl_3P_3]$, $[ReBr(CO)_5]$, and $[ReH(CO)_5]$ [P = $PPh(OEt)_2$, $PPh_2OEt$] were prepared following the previously reported methods.[11a,26]

**$[ReHCl(N–N)\{PPh(OEt)_2\}_3]BPh_4$ (1) [N–N = 2,2′-bipyridine (bpy) (a), 5,5′-dimethylbipyridine (5,5′-$Me_2$bpy) (b), 1,10-phenanthroline (phen) (c)]:** $[ReCl_3\{PPh(OEt)_2\}_3]$ (0.50 g, 0.56 mmol) and the appropriate polypyridine N–N (1.7 mmol) were placed in a 50-mL, three-necked, round-bottomed flask and dissolved in 30 mL of ethanol. The resulting mixture was refluxed for 5 h and then the solvent was removed under reduced pressure to give a brown solid from which the hydrido complex was extracted with five 10-mL portions of $CH_2Cl_2$. The combined extracts were evaporated to dryness to give an oil, which was treated with ethanol (5 mL) containing an excess of $NaBPh_4$ (1.7 mmol, 0.58 g). A dark-green solid separated out. This solid was filtered and crystallized from $CH_2Cl_2$ and ethanol. Yields: 0.45 g for **1a** (62%), 0.48 g for **1b** (65%), 0.33 g for **1c** (45%).

**1a:** $C_{64}H_{74}BClN_2O_6P_3Re$ (1292.7): calcd. C 59.47, H 5.77, Cl 2.74, N 2.17; found C 59.39, H 5.63, Cl 2.58, N 2.24. $\Lambda_M$ = 54.9 $S\,cm^2\,mol^{-1}$.

**1b:** $C_{66}H_{78}BClN_2O_6P_3Re$ (1320.7): calcd. C 60.02, H 5.95, Cl 2.68, N 2.12; found C 59.87, H 6.02, Cl 2.80, N 2.21. $\Lambda_M$ = 51.3 $S\,cm^2\,mol^{-1}$.

**1c:** $C_{66}H_{74}BClN_2O_6P_3Re$ (1316.7): calcd. C 65.38, H 5.66, Cl 2.69, N 2.13; found C 65.16, H 5.75, Cl 2.86, N 2.05. $\Lambda_M$ = 52.8 $S\,cm^2\,mol^{-1}$.

**$[ReH_2(bpy)\{PPh(OEt)_2\}_3]BPh_4$ (2a):** $[ReCl_3\{PPh(OEt)_2\}_3]$ (0.50 g, 0.56 mmol) and 2,2′-bipyridine (0.266 g, 1.7 mmol) were placed in a 50-mL, three-necked, round-bottomed flask and 20 mL of ethanol was added. The mixture was stirred and refluxed for 5 h and then allowed to reach room temperature. An excess of $NaBH_4$ (0.211 g, 5.6 mmol) in ethanol (10 mL) was then added and the mixture refluxed for 1 h. The solvent was removed under reduced pressure to give an oil, from which the hydrido complex was extracted with five 10-mL portions of $CH_2Cl_2$. The extracts were evaporated to dryness to give an oil, which was triturated with ethanol (5 mL) containing an excess of $NaBPh_4$ (1.7 mmol, 0.58 g). A red-brown solid slowly separated out. This solid was filtered and crystallized from $CH_2Cl_2$ and ethanol. Yield: 0.40 g (57%). $C_{64}H_{75}BN_2O_6P_3Re$ (1258.2): calcd. C 61.09, H 6.01, N 2.23; found C 61.25, H 5.84, N 2.12. $\Lambda_M$ = 54.7 $S\,cm^2\,mol^{-1}$.

**$[ReH(bpy)(CO)_3]$:** This compound was prepared by a new method rather than that reported in the literature.[6] Thus, $[ReH(CO)_5]$ (0.35 mL, 2.05 mmol) and one equivalent of 2,2′-bipyridine (0.32 g, 2.05 mmol) were placed in a 250-mL, three-necked, round-bottomed flask and 100 mL of toluene was added. The reaction mixture was refluxed for 4 h and then the solvent was removed under reduced pressure to give an oil, which was triturated with ethanol (5 mL). An orange solid slowly separated out from the resulting stirring solution. This solid was filtered and dried under vacuum. Yield: 0.307 g (35%). $C_{13}H_9N_2O_3Re$ (427.43): calcd. C 36.53, H 2.12, N 6.55; found C 36.71, H 2.05, N 6.42. IR (KBr): $\tilde{\nu}$ = 2032 (m), 1976 (s), 1912 $cm^{-1}$ [s ($\nu_{CO}$)]. $^1H$ NMR ($CD_2Cl_2$, 25 °C): $\delta$ = 9.13–7.56 (m, bpy), –13.02 (s, ReH) ppm.

**$[ReBr(bpy)(CO)_3]$:** This compound was prepared by a slight modification of the reported method.[27] Thus, $[ReBr(CO)_5]$ (1 g,

 © 2007 Wiley-VCH Verlag GmbH & Co. KGaA, Weinheim 

2.46 mmol) and 2,2′-bipyridine (1.15 g, 7.38 mmol) were placed in a 100-mL, three-necked, round-bottomed flask and 30 mL of toluene was added. The mixture was stirred, refluxed for 5 h, and then allowed to reach room temperature. A yellow solid separated out which, after 1 h of stirring, was filtered and dried under vacuum. Yield: 1.01 g (81%). $C_{13}H_8BrN_2O_3Re$ (506.32): calcd. C 30.84, H 1.59, N 5.53; found C 30.66, H 1.68, N 5.40. IR (KBr): $\tilde{\nu}$ = 2012 (m), 1905 (s), 1882 $cm^{-1}$ [s ($\nu_{CO}$)]. $^1H$ NMR ($CD_2Cl_2$, 25 °C): $\delta$ = 9.06–7.53 (m, bpy) ppm.

**[$ReH_2$(bpy)$(CO)_3$]$BPh_4$ (3a):** An excess of $HBF_4{\cdot}Et_2O$ (2.3 mmol, 0.33 mL of a 54% solution in diethyl ether) was added to a solution of [ReH(bpy)$(CO)_3$] (0.100 g, 0.23 mmol) in $CH_2Cl_2$ (7 mL) at –196 °C. The reaction mixture was then brought to room temperature and stirred for 2 h. The solvent was removed under reduced pressure to give an oil, which was triturated with ethanol (2 mL) containing an excess of $NaBPh_4$ (0.46 mmol, 0.157 g). A yellow solid slowly separated out from the resulting solution. This solid was filtered and crystallized from $CH_2Cl_2$ and ethanol; yield 0.134 g (78%). $C_{37}H_{30}BN_2O_3Re$ (747.67): calcd. C 59.44, H 4.04, N 3.75; found C 59.27, H 4.01, N 3.68. $\Lambda_M$ = 53.5 $S cm^2 mol^{-1}$.

**[$ReH_2$(Cl)(bpy){PPh$(OEt)_2$}$_3$]$^{2+}$ (4a) and [$ReH_3$(bpy){PPh$(OEt)_2$}$_3$]$^{2+}$ (5a):** These cationic complexes were prepared in $CD_2Cl_2$ solution by protonation of the precursors [ReH(Cl)(bpy)$P_3$]$BPh_4$ (**1a**) and [$ReH_2$(bpy)$P_3$]$BPh_4$ (**2a**) with $HBF_4{\cdot}Et_2O$. In a typical experiment, a $CD_2Cl_2$ solution (0.5 mL) of **1a** or **2a** (30–40 mg, 0.02–0.03 mmol) was placed in a screw-cap 5-mm NMR tube placed in a dry box. The tube was sealed, cooled to –80 °C, and then increasing amounts (from one to four equivalents) of $HBF_4{\cdot}Et_2O$ were added with a microsyringe. The tube was then transferred into the instrument's probe, which had been pre-cooled to –80 °C, and the spectra collected.

**[Re{CH=C(H)R}$_2$(bpy){PPh$(OEt)_2$}$_3$]$BPh_4$ (6–8) [R = Ph (6a), *p*-tolyl (7a), *tert*-butyl (8a)]:** An excess of the appropriate alkyne RC≡CH (0.8 mmol) was added to a solution of [$ReH_2$(bpy){PPh$(OEt)_2$}$_3$]$BPh_4$ (0.100 g, 0.079 mmol) in 12 mL of 1,2-dichloroethane and the reaction mixture refluxed for 1 h. The solvent was removed under reduced pressure to give an oil, which was triturated with ethanol (2 mL) containing an excess of $NaBPh_4$ (0.2 mmol, 68 mg). A green solid slowly separated out from the resulting solution. This solid was filtered and crystallized from $CH_2Cl_2$ and ethanol. Yield 0.079 g for **6a** (68%), 0.081 g for **7a** (69%), 0.082 g for **8a** (73%).

**6a:** $C_{80}H_{87}BN_2O_6P_3Re$ (1462.5): calcd. C 65.70, H 6.00, N 1.92; found C 65.49, H 5.93, N 1.88. $\Lambda_M$ = 53.1 $S cm^2 mol^{-1}$.

**7a:** $C_{82}H_{91}BN_2O_6P_3Re$ (1490.6): calcd. C 66.08, H 6.15, N 1.88; found C 65.91, H 6.24, N 1.80. $\Lambda_M$ = 54.6 $S cm^2 mol^{-1}$.

**8a:** $C_{76}H_{95}BN_2O_6P_3Re$ (1422.5): calcd. C 64.17, H 6.73, N 1.97; found C 64.38, H 6.86, N 2.08. $\Lambda_M$ = 52.8 $S cm^2 mol^{-1}$.

**Crystallographic Analysis of [ReHCl(bpy){PPh$(OEt)_2$}$_3$]$BPh_4$ (1a):** Data collection was performed on a SIEMENS Smart CCD area-detector diffractometer with graphite-monochromated Mo-$K_\alpha$ radiation. Absorption correction was carried out using SADABS.[28] The structure was solved and refined with the Oscail program[29] by Patterson methods and refined by a full-matrix least-squares procedure on $F^2$.[30] Non-hydrogen atoms were refined with anisotropic displacement parameters. Hydrogen atoms were included in idealized positions and refined with isotropic displacement parameters except that bonded to the rhenium atom, which was neither located nor included in the model. Atomic scattering factors and anomalous dispersion corrections for all atoms were taken from International Tables for X-ray Crystallography.[31] Details of crystal data and structural refinement are given in Table 4 and selected bond lengths and angles are listed in Table 5.

Table 4. Crystal data and structure refinement for [ReHCl(bpy){PPh$(OEt)_2$}$_3$]$BPh_4$ (**1a**).

| | |
|---|---|
| Empirical formula | $C_{64}H_{74}BClN_2O_6P_3Re$ |
| Formula weight | 1292.68 |
| Temperature | 173(2) K |
| Wavelength | 0.71073 Å |
| Crystal system | monoclinic |
| Space group | $P2_1/c$ |
| Unit cell dimensions | $a$ = 14.7335(18) Å<br>$b$ = 14.7029(19) Å<br>$c$ = 27.823(4) Å<br>$\beta$ = 90.929(4)° |
| Volume | 6026.4(13) $Å^3$ |
| $Z$ | 4 |
| Density (calculated) | 1.421 $Mg m^{-3}$ |
| Absorption coefficient | 2.192 $mm^{-1}$ |
| $F$(000) | 2636 |
| Crystal size | 0.25 × 0.16 × 0.10 $mm^3$ |
| Theta range for data collection | 1.38–28.02° |
| Index ranges | $-19 \le h \le 19$<br>$-13 \le k \le 19$<br>$-36 \le l \le 32$ |
| Reflections collected | 31483 |
| Independent reflections | 13368 [$R$(int) = 0.1562] |
| Reflections observed (>2σ) | 3916 |
| Data completeness | 0.915 |
| Absorption correction | Semi-empirical from equivalents |
| Max. and min. transmission | 1.000 and 0.791 |
| Refinement method | Full-matrix least-squares on $F^2$ |
| Data/restraints/parameters | 13368/0/709 |
| Goodness-of-fit on $F^2$ | 0.692 |
| Final $R$ indices [$I > 2\sigma(I)$] | $R_1$ = 0.0659, $wR_2$ = 0.0835 |
| $R$ indices (all data) | $R_1$ = 0.2677, $wR_2$ = 0.1154 |
| Largest diff. peak and hole | 1.128 and –1.397 e $Å^{-3}$ |

Table 5. Selected bond lengths [Å] and angles [°] for [ReH(Cl)(bpy){PPh$(OEt)_2$}$_3$]$BPh_4$ (**1a**).

| | | | |
|---|---|---|---|
| Re–N(2) | 2.172(10) | Re–N(1) | 2.180(9) |
| Re–P(1) | 2.286(3) | Re–P(2) | 2.316(3) |
| Re–P(3) | 2.365(3) | Re–Cl(1) | 2.450(3) |
| N(2)–Re–N(1) | 75.7(4) | N(2)–Re–P(1) | 80.2(2) |
| N(1)–Re–P(1) | 99.9(2) | N(2)–Re–P(2) | 101.3(3) |
| N(1)–Re–P(2) | 171.7(2) | P(1)–Re–P(2) | 87.06(10) |
| N(2)–Re–P(3) | 168.7(3) | N(1)–Re–P(3) | 98.7(3) |
| P(1)–Re–P(3) | 110.68(11) | P(2)–Re–P(3) | 82.84(10) |
| N(2)–Re–Cl(1) | 79.2(2) | N(1)–Re–Cl(1) | 84.7(2) |
| P(1)–Re–Cl(1) | 157.02(10) | P(2)–Re–Cl(1) | 87.09(10) |
| P(3)–Re–Cl(1) | 90.58(10) | | |

CCDC-626730 contains the supplementary crystallographic data for this paper. These data can be obtained free of charge from The Cambridge Crystallographic Data Center via www.ccdc.cam.ac.uk/data_request/cif.

## Acknowledgments

Financial support from Ministero dell'Università e della Ricerca (MIUR) (grant no. PRIN 2004) is gratefully acknowledged. We also thank Daniela Baldan for technical assistance.

 © 2007 Wiley-VCH Verlag GmbH & Co. KGaA, Weinheim 

[1] a) E. L. Muetterties, *Transition Metal Hydrides*, Marcel Dekker, Inc., New York, **1971**; b) A. Dedieu, *Transition Metal Hydrides*, Wiley-VCH, New York, **1992**; c) M. Peruzzini, R. Poli, *Recent Advances in Hydride Chemistry*, Elsevier, Amsterdam, **2001**; d) G. J. Kubas, *Metal Dihydrogen and σ-Bond Complexes*, Kluwer Academic, Plenum Publishers, New York, **2001**.

[2] a) P. Jessop, R. H. Morris, *Coord. Chem. Rev.* **1992**, *121*, 155–284; b) D. M. Heinekey, W. J. Oldham Jr, *Chem. Rev.* **1993**, *93*, 913–926; c) R. H. Crabtree, *Angew. Chem. Int. Ed. Engl.* **1993**, *32*, 789–805.

[3] a) D. R. Root, K. E. Meyer, R. A. Walton, *Inorg. Chem.* **1989**, *28*, 2503–2506; b) F. A. Cotton, R. L. Luck, D. R. Root, R. A. Walton, *Inorg. Chem.* **1990**, *29*, 43–47; c) M. T. Costello, P. E. Fanwick, M. A. Green, R. A. Walton, *Inorg. Chem.* **1992**, *31*, 2359–2365; d) X. L. R. Fontaine, E. H. Fowles, T. P. Leyzell, B. L. Shaw, M. Thornton-Pett, *J. Chem. Soc., Dalton Trans.* **1991**, 1519–1524; e) X.-L. Luo, D. Michos, R. H. Crabtree, *Inorg. Chem.* **1991**, *30*, 4286–4288; f) D. Michos, X.-L. Luo, J. A. K. Howard, R. H. Crabtree, *Inorg. Chem.* **1992**, *31*, 3914–3916; g) X. L. R. Fontaine, T. P. Layzell, B. L. Shaw, *J. Chem. Soc., Dalton Trans.* **1994**, 917–924; h) M. Leeaphon, K. Rohl, R. J. Thomas, P. E. Fanwick, R. A. Walton, *Inorg. Chem.* **1993**, *32*, 5562–5568; i) D. G. Gusev, D. Nietlispach, I. L. Eremenko, H. Berke, *Inorg. Chem.* **1993**, *32*, 3628–3636; j) Y. Kim, H. Deng, J. C. Gallucci, A. Wojcicki, *Inorg. Chem.* **1996**, *35*, 7166–7173; k) Z. Lin, M. B. Hall, *J. Am. Chem. Soc.* **1994**, *116*, 4446–4448.

[4] a) D. M. Heinekey, C. E. Radzewich, M. H. Voges, B. M. Schomber, *J. Am. Chem. Soc.* **1997**, *119*, 4172–4181; b) T. M. McKinney, P. E. Fanwick, R. A. Walton, *Inorg. Chem.* **1999**, *38*, 1548–1554; c) N. V. Belkova, E. S. Shubina, A. V. Ionidis, L. M. Epstein, H. Jacobsen, A. Messmer, H. Berke, *Inorg. Chem.* **1997**, *36*, 1522–1525; d) J. Huhmann-Vincent, B. L. Scott, G. J. Kubas, *J. Am. Chem. Soc.* **1998**, *120*, 6808–6809; e) S. Bolaño, L. Gonsalvi, P. Barbaro, A. Albinati, S. Rizzato, E. Gutsul, N. Belkova, L. Epstein, E. Shubina, M. Peruzzini, *J. Organomet. Chem.* **2006**, *691*, 629–637.

[5] G. A. Moehring, R. A. Walton, *Inorg. Chem.* **1987**, *26*, 2910–2912.

[6] B. P. Sullivan, T. J. Meyer, *J. Chem. Soc., Chem. Commun.* **1984**, 1244–1245.

[7] The organometallic chemistry of rhenium polypyridine complexes is also relatively undeveloped, see: a) J. Guilhem, C. Pascard, J.-M. Lehn, R. Ziessel, *J. Chem. Soc., Dalton Trans.* **1989**, 1449–1454; b) J. V. Caspar, B. P. Sullivan, T. J. Meyer, *Inorg. Chem.* **1984**, *23*, 2104–2109; c) D. H. Gibson, X. Yin, H. He, M. S. Mashuta, *Organometallics* **2003**, *22*, 337–346.

[8] a) J. Hawecker, J.-M. Lehn, R. Ziessel, *J. Chem. Soc., Chem. Commun.* **1983**, 536; b) B. P. Sullivan, C. M. Bolinger, D. Conrad, T. J. Vining, T. J. Meyer, *J. Chem. Soc., Chem. Commun.* **1985**, 1414; c) P. Christensen, A. Hamnett, A. V. G. Muit, G. A. Timney, *J. Chem. Soc., Dalton Trans.* **1992**, 1455; d) G. J. Stor, F. Hartl, J. W. M. van Outersterp, D. J. Stufkens, *Organometallics* **1995**, *14*, 115; e) F. P. A. Johnson, M. W. George, F. Hartl, J. J. Turner, *Organometallics* **1996**, *15*, 3374; f) A. Klein, C. Vogler, W. Kaim, *Organometallics* **1996**, *15*, 236.

[9] a) G. Albertin, S. Antoniutti, M. Bortoluzzi, *Inorg. Chem.* **2004**, *43*, 1328–1335; b) G. Albertin, S. Antoniutti, A. Bacchi, C. D′Este, G. Pelizzi, *Inorg. Chem.* **2004**, *43*, 1336–1349; c) G. Albertin, S. Antoniutti, S. Pizzol, *J. Organomet. Chem.* **2004**, *689*, 1639–1647.

[10] a) S. Antoniutti, G. Albertin, P. Amendola, E. Bordignon, *J. Chem. Soc., Chem. Commun.* **1989**, 229–230; b) P. Amendola, S. Antoniutti, G. Albertin, E. Bordignon, *Inorg. Chem.* **1990**, *29*, 318–324; c) G. Albertin, P. Amendola, S. Antoniutti, E. Bordignon, *J. Chem. Soc., Dalton Trans.* **1990**, 2979–2984; d) G. Albertin, S. Antoniutti, D. Baldan, E. Bordignon, *Inorg. Chem.* **1995**, *34*, 6205–6210; e) G. Albertin, S. Antoniutti, M. Bettiol, E. Bordignon, F. Busatto, *Organometallics* **1997**, *16*, 4959–4969; f) G. Albertin, S. Antoniutti, E. Bordignon, M. Pegoraro, *J. Chem. Soc., Dalton Trans.* **2000**, 3575–3584; g) Albertin, S. Antoniutti, A. Bacchi, B. Fregolent, G. Pelizzi, *Eur. J. Inorg. Chem.* **2004**, 1922–1938; h) G. Albertin, S. Antoniutti, M. Bortoluzzi, G. Zanardo, *J. Organomet. Chem.* **2005**, *690*, 1726–1738; i) G. Albertin, S. Antoniutti, C. Busato, J. Castro, S. Garcia-Fontán, *Dalton Trans.* **2005**, 2641–2649.

[11] a) S. Garcia-Fontán, A. Marchi, L. Marvelli, R. Rossi, S. Antoniutti, G. Albertin, *J. Chem. Soc., Dalton Trans.* **1996**, 2779–2785; b) G. Albertin, S. Antoniutti, S. Garcia-Fontán, R. Carballo, F. Padoan, *J. Chem. Soc., Dalton Trans.* **1998**, 2071–2081.

[12] W. J. Geary, *Coord. Chem. Rev.* **1971**, *7*, 81–122.

[13] B. Machura, R. Kruszynski, M. Jaworska, P. Lodowski, *Polyhedron* **2005**, *24*, 701–709.

[14] G. Albertin, S. Antoniutti, A. Bacchi, E. Bordignon, F. Miani, G. Pelizzi, *Inorg. Chem.* **2000**, *39*, 3283–3293.

[15] F. H. Allen, *Acta Crystallogr., Sect. B* **2002**, *58*, 380–388.

[16] a) D. G. Hamilton, R. H. Crabtree, *J. Am. Chem. Soc.* **1988**, *110*, 4126–4136; b) M. T. Bautista, K. A. Earl, P. A. Maltby, R. H. Morris, C. T. Schweitzer, A. Sella, *J. Am. Chem. Soc.* **1988**, *110*, 7031–7036; c) P. J. Desrosiers, L. Cai, Z. Lin, R. Richards, J. Halpern, *J. Am. Chem. Soc.* **1991**, *113*, 4173–4184.

[17] We have prepared the $[ReH(bpy)(CO)_3]$ complex by substituting carbonyl ligands with bpy in the pentacarbonyl derivative $[ReH(CO)_5]$. A *mer* arrangement of the three CO ligands is suggested by the presence of one band of medium intensity (2032 $cm^{-1}$) and two strong ones (1976 and 1912 $cm^{-1}$) in the $\nu_{CO}$ region,[18] while the presence of the hydrido ligand is confirmed by the sharp singlet at $\delta = -13.02$ ppm observed in the $^1H$ NMR spectrum. The previously reported species $[ReH(bpy)(CO)_3]$[6] was prepared from the $[Re(bpy)(CO)_3(H_2O)]^+$ cation and showed a *fac* geometry with the hydrido signal surprisingly being found at $\delta = +1.54$ ppm in the $^1H$ NMR spectrum. Such a high frequency assignment for the hydrido is questionable.

[18] D. A. Adams, *Metal-ligand and Related Vibrations*, St. Martin's Press, New York, **1968**.

[19] a) M. Schlaf, A. J. Lough, P. A. Maltby, R. H. Morris, *Organometallics* **1996**, *15*, 2270–2278; b) E. Rocchini, A. Mezzetti, H. Rügger, U. Burckhardt, V. Gramlich, A. Dal Zotto, P. Martinuzzi, P. Rigo, *Inorg. Chem.* **1997**, *36*, 711–720; c) T. A. Luther, D. M. Heinekey, *Inorg. Chem.* **1998**, *37*, 127–132; d) S. E. Landau, R. H. Morris, A. J. Lough, *Inorg. Chem.* **1999**, *38*, 6060–6068; e) K. T. Smith, M. Tilset, R. Kuhlman, K. G. Caulton, *J. Am. Chem. Soc.* **1995**, *117*, 9473–9480.

[20] X. Li, T. Vogel, C. D. Incarvito, R. H. Crabtree, *Organometallics* **2005**, *24*, 62–76 and references cited therein.

[21] W. G. Hatton, J. A. Gladysz, *J. Am. Chem. Soc.* **1983**, *105*, 6157–6158.

[22] M. Leeaphon, A. L. Ondracek, R. J. Thomas, P. E. Fanwick, R. A. Walton, *J. Am. Chem. Soc.* **1995**, *117*, 9715–9724.

[23] a) J. Navarro, E. Sola, M. Martin, I. T. Dobrinovitch, F. J. Lahoz, L. A. Oro, *Organometallics* **2004**, *23*, 1908–1917; b) M. Bassetti, S. Marini, J. Diaz, M. P. Gamasa, J. Gimeno, Y. Rodriguez-Alvarez, S. Garcia-Granda, *Organometallics* **2002**, *21*, 4815–4822; c) Y. Gao, M. C. Jennings, R. L. Puddephatt, *Dalton Trans.* **2003**, 261–265; d) D. S. Frohnapfel, P. S. White, J. L. Templeton, *Organometallics* **2000**, *19*, 1497–1506; e) M. L. Buil, M. A. Esteruelas, *Organometallics* **1999**, *18*, 1798–1800; f) X. Li, L. N. Appelhans, J. W. Faller, R. H. Crabtree, *Organometallics* **2004**, *23*, 3378–3387; g) I. de los Rios, M. Jimenez-Tenorio, M. C. Puerta, P. Valerga, *J. Am. Chem. Soc.* **1997**, *119*, 6529–6538; h) Y. Wakatsuki, N. Koga, H. Werner, K. Morokuma, *J. Am. Chem. Soc.* **1997**, *119*, 360–366.

[24] R. Rabinowitz, J. Pellon, *J. Org. Chem.* **1961**, *26*, 4623–4626.

[25] G. Balacco, *J. Chem. Inf. Comput. Sci.* **1994**, *34*, 1235–1241.

[26] M. A. Urbancic, J. R. Shapley, *Inorg. Synth.* **1990**, *28*, 165–168.

[27] E. W. Abel, G. Wilkinson, *J. Chem. Soc.* **1959**, 1501–1505.


 © 2007 Wiley-VCH Verlag GmbH & Co. KGaA, Weinheim 

[28] G. M. Sheldrick, *SADABS, An empirical absorption correction program for area detector data*, University of Göttingen, Germany, **1996**.
[29] P. McArdle, *J. Appl. Crystallogr.* **1995**, *28*, 65.
[30] G. M. Sheldrick, *Shelxl97. Program for the solution and refinement of crystal structures*, University of Göttingen, Germany, **1997**.
[31] *International Tables for X-ray Crystallography*, vol. C, Kluwer, Dordrecht, The Netherlands, **1992**.

Received: November 10, 2006
Published Online: March 9, 2007

 © 2007 Wiley-VCH Verlag GmbH & Co. KGaA, Weinheim 

DOI: 10.1002/ejic.200601084

# CuO/ZnO Nanoparticles in a Matrix of Amorphous Silica as High-Surface Precursors for Methanol Synthesis

**Bernd Rohe,[a] Rainer Weiss,[b] Sascha Vukojević,[c] Christian Baltes,[c] Martin Muhler,[d] Michael Tausch,[e] and Matthias Epple*[b]**

**Keywords:** Heterogeneous catalysis / Copper / Zinc oxide / Silica / Nanoparticles / Surface coating

An intimate mixture of CuO/ZnO nanocrystals was prepared by an easy sol-gel synthesis (precipitation in methanol by hydroxide in the presence of a silane). The organic substituents of the silane were almost completely removed by a subsequent photochemical oxidation. The resulting amorphous $SiO_2$ prevented the growth of the catalytically active particles to larger crystals. The coating layer of silica can easily be penetrated by gaseous reactants, as shown by the high specific surface area of about 110–130 $m^2 g^{-1}$ (probably due to both silica and nanocrystalline CuO/ZnO) and the good catalytic activity in methanol synthesis from $CO/CO_2/H_2$ synthesis gas (7 to 37 %, compared to an industrial standard methanol catalyst). The ratio of CuO to ZnO can be easily varied by the used preparation method.
(© Wiley-VCH Verlag GmbH & Co. KGaA, 69451 Weinheim, Germany, 2007)

## Introduction

Cu/ZnO is a widely used model catalyst system for investigations in heterogeneous catalysis.[1] In most cases, the methanol synthesis and the steam reforming reaction are studied. The industrial catalyst is based on Cu/ZnO/$Al_2O_3$,[1,2] but often Cu/ZnO is examined as simplified binary model system.[3–15] Although copper is the more important catalytically active component,[16,17] pure ZnO is itself active in methanol synthesis[18–20] The most common preparation methods for the catalyst precursor CuO/ZnO are based on the co-precipitation of carbonates or oxalates, followed by thermolysis to the corresponding oxides.[6,8,11,14,21–23] We have recently shown that active catalysts can also be prepared by thermolysis of bimetallic coordination compounds,[24] xerogels and aerogels,[25] and tartrate mixed crystals.[26] Copper nanoparticles in liquid dispersion were recently shown to be active as methanol catalysts,[27] as well as metal-loaded mesoporous silicates[28] and metal-oxide frameworks (MOFs).[29]

Here we report on the preparation, characterization and catalytic activity of ZnO and CuO/ZnO nanocomposites which were obtained by a combination of sol-gel synthesis and photochemical oxidation which was applied earlier to prepare nanoscale ZnO.[30] By precipitating the oxides in the presence of a silane in alcohol, a highly dispersed mixture of the oxides with a high specific surface area[31] is obtained because the silane prevents the growth and agglomeration of the oxide crystals.[32] Subsequently, the organic substituents of the silane are photochemically oxidized and almost completely removed.[30] The ratio of copper to zinc can be easily varied by this method, opening a way to nanocrystalline systems of CuO/ZnO in amorphous silica with a high overall specific surface area. Copper oxide can then be reduced to Cu, resulting in Cu/ZnO/$SiO_2$, i.e. the active methanol catalyst, preserving a high specific surface area which is advantageous for a high catalytic activity. This approach to co-precipitate the nanoparticles with a porous inorganic matrix is different from the often applied approach to fill an already existing porous template.

[a] Sachtleben Chemie GmbH,
Dr.-Rudolf-Sachtleben-Str. 4, 47198 Duisburg, Germany
[b] Inorganic Chemistry, University of Duisburg-Essen,
Universitätsstrasse 5–7, 45117 Essen, Germany
Fax: +49-201-183-2621
[c] Max-Planck-Institute for Coal Research,
Kaiser-Wilhelm-Platz 1, 45470 Mülheim an der Ruhr, Germany
[d] Industrial Chemistry, Ruhr University of Bochum,
Universitaetsstrasse 150, 44801 Bochum, Germany
[e] University of Wuppertal,
Gaussstr. 20, 42119 Wuppertal, Germany

## Result and Discussion

Four samples with different ratios of CuO/ZnO (**A**: 0.76 wt.-% Cu; **B**: 4.37 wt.-% Cu; **C**: 15.6 wt.-% Cu; **D**: 34.4 wt.-% Cu) were prepared by a combination of sol-gel synthesis and photochemical oxidation and compared to a sample of pure ZnO (**Z**), prepared by the same method.[30] The coating with silane prevented crystal growth and agglomeration of the primary oxides. The subsequent photochemical treatment almost completely destroyed the organic fragments of the silane and led to the formation of X-ray amorphous silica ("$SiO_2$").

Scanning electron microscopy (SEM) showed an agglomerated material with particle sizes of a few hundred nano-

 © 2007 Wiley-VCH Verlag GmbH & Co. KGaA, Weinheim 

metres (Figure 1). The "coating layer" probably results from amorphous silica which remains after the photochemical oxidation. The high specific surface area from BET experiments (Table 1) indicates a high internal porosity that we tentatively attribute to the silica. X-ray powder diffraction shows broad diffraction peaks for ZnO and CuO, confirming the nanocrystallinity of the primary particles (Figure 2). A semi-quantitative determination of the crystallite size for ZnO by the Scherrer equation[33] results in 6–7 nm. It was not possible to determine the size of the CuO particles due to peak overlap, but a visual examination of the peak in Figure 2 suggests a crystallite size of the same order. Temperature-programmed reduction (TPR) gave the amount of CuO (Figure 3), followed by the quantitative determination of the specific copper surface area with reactive frontal chromatography (RFC). All analytical results are comprised in Table 1. It should be noted that the content of zinc is in all cases lower than expected from the synthesis (Table 1). This means that copper preferentially precipitates during the synthesis.

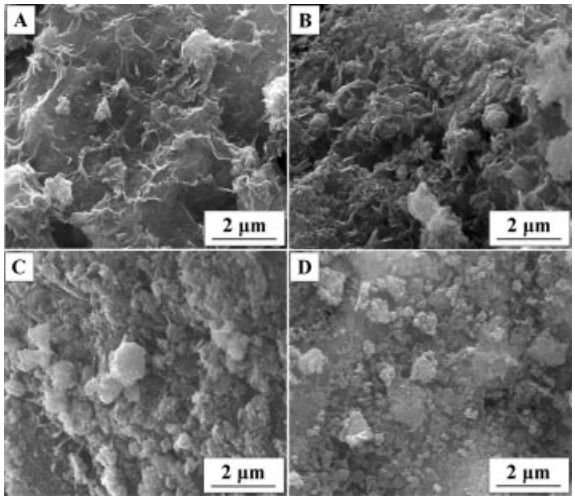


Figure 1. Scanning electron micrographs of the CuO/ZnO samples **A** to **D** (see Table 1). The samples consist of agglomerated particles with sizes of a few hundred nanometers (**A**: 0.76 wt.-% Cu; **B**: 4.37 wt.-% Cu; **C**: 15.6 wt.-% Cu; **D**: 34.4 wt.-% Cu). CuO and ZnO cannot be distinguished, i.e. they form an intimate mixture, together with X-ray amorphous $SiO_2$.

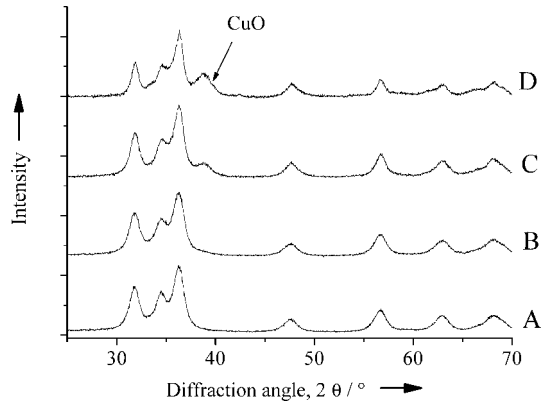


Figure 2. X-ray powder diffraction patterns of samples **A**, **B**, **C** and **D**. All reflections of the samples **A** and **B** belong to ZnO (zincite), except for the reflection at 38.9 °2$\Theta$ which belongs to CuO (tenorite). All patterns show strong peak broadening due to the small size of the primary nanoparticles (**A**: 0.76 wt.-% Cu; **B**: 4.37 wt.-% Cu; **C**: 15.6 wt.-% Cu; **D**: 34.4 wt.-% Cu).

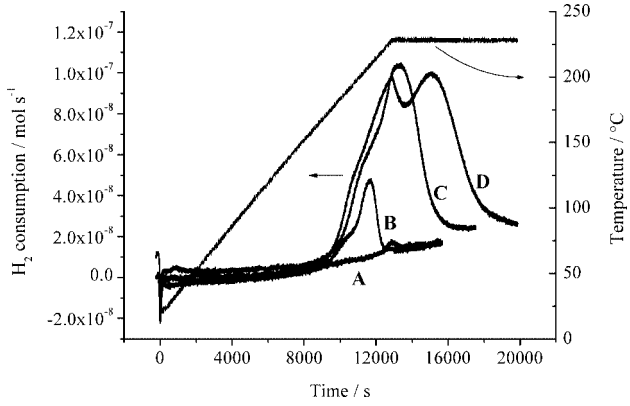


Figure 3. Reduction profiles of CuO to Cu obtained by heating under diluted hydrogen (TPR: temperature-programmed reduction; **A**: 0.76 wt.-% Cu; **B**: 4.37 wt.-% Cu; **C**: 15.6 wt.-% Cu; **D**: 34.4 wt.-% Cu).

The total specific surface area was determined by BET after drying for 2 h at 110 °C under air (Table 1). The BET surface areas were very high (higher than those of CuO/ZnO from co-precipitated carbonate precursors which are typically 40 $m^2 g^{-1}$ or less[31]). In addition, they are almost

Table 1. Chemical and morphological parameters and catalytic activity of all samples.

| Sample | wt.-%[a] Zn | wt.-%[a] Cu | wt.-% Cu (by TPR) | wt.-%[b] C | wt.-%[b] H | wt.-%[b] $SiO_2$ | ZnO crystallite size[d] / nm | Specific surface area[a,e] / $m^2 g^{-1}$ | Specific Cu surface[a–f] area / $m^2 g^{-1}$ | Catalytic activity (%)[g] |
|---|---|---|---|---|---|---|---|---|---|---|
| **Z** (pure ZnO) | 67.0 | 0.0 | – | 2.6 | 0.8 | 16.6 | 6 | 127.8 | 0.0 | – |
| **A** (CuO/ZnO) | 66.4 | 0.76 | 0.3 | 2.2 | 0.7 | 13.5 | 6 | 110.0 | 0.1 | 7 |
| **B** (CuO/ZnO) | 61.2 | 4.37 | 3.7 | 2.6 | 0.5 | 15.3 | 6 | 134.8 | 0.3 | 16 |
| **C** (CuO/ZnO) | 53.3 | 15.6 | 13.6 | 2.9 | 0.6 | 10.6 | 7 | 132.0 | 0.3 | 35 |
| **D** (CuO/ZnO) | 35.7 | 34.4 | 26.8 | 3.2 | 0.6 | 8.7 | 7 | 113.3 | 5.5 | 37 |

[a] By ICP. [b] By combustion elemental analysis. [c] The contents of zinc and copper were used to compute the amount of ZnO and CuO in the sample (stoichiometric factors 1.245 and 1.252, respectively). The sum of ZnO, ZnO, C and H was computed, and the difference to 100% was tentatively ascribed to $SiO_2$. [d] By application of the Scherrer equation;[33] the full-width at half maximum (FWHM) was typically 1.2–1.6° 2$\Theta$ for the (102), (110), and (103) peaks of ZnO with no differences among these peaks. [e] By BET. [f] By reactive frontal chromatography (RFC). [g] Compared to the activity of an ICI reference methanol catalyst, consisting of 64 wt.-% CuO, 24 wt.-% ZnO and 10 wt.-% $Al_2O_3$ (data from the manufacturer).

 © 2007 Wiley-VCH Verlag GmbH & Co. KGaA, Weinheim 

independent from the composition of the samples, suggesting that silica is mostly responsible for this high surface area. We conclude that the nature of the metal cation does not play a significant role for the micromorphology of the precatalyst, and we also conclude that most of the surface must be ascribed to internal pores, given the fact that the samples appear agglomerated and not nanoparticulate in SEM. The amorphous silicon dioxide which is left after photooxidation[30,32] is probably responsible for this effect, preventing the fusion of the oxide nanoparticles by formation of a porous coating layer. Note that the UV-photooxidation is not complete, as indicated by the residual content of carbon and hydrogen (Table 1) and also by weak characteristic C–H vibrations in IR spectroscopy (data not shown). In total, about 10–15 wt.-% of silica and carbon-containing residues together are present in the samples (see Table 1), both being X-ray amorphous (Figure 2).

This coating effect may explain the comparatively small specific copper surface area obtained by reactive frontal chromatography (RFC). Except for a very high content of copper, the copper surface area is small compared to the BET surface areas, unlike oxide mixtures from carbonate precursors.[31] We assume sintering of the copper particles due to the high reduction temperature (>200 °C) which caused a small specific surface area. Nevertheless, the catalytic activity of the samples is much higher than it would have been predicted from this small specific copper surface area.[12] The catalytic activity was compared to a ternary $CuO/ZnO/Al_2O_3$ benchmark catalyst (ICI Katalco 51-8) whose activity was set to 100%. This proves that the silica-embedded copper and zinc oxide particles are still well accessible by the synthesis gas. We speculate that the silica layer itself has a high internal pore surface which can be penetrated by the gaseous molecules, so it also serves as a kind of membrane on the catalytically active particles (ZnO and Cu).

We explain the mismatch between the low specific copper surface area and the good catalytic activity as follows: the specific copper surface area after TPR does not correspond to the copper surface area which is present in the active catalyst because of different reduction conditions. In TPR which is followed by RFC, CuO is reduced with diluted hydrogen (4.1% $H_2$ in Ar) at atmospheric pressure at 223 °C. Figure 3 shows that the reduction temperature is comparatively high, i.e. the copper oxide is not easily reduced (possibly not even fully, but mostly; see Table 1). In the catalytic test, the catalyst is reduced by a prescribed procedure for the commercial catalyst involving several steps, e.g. heating to 170 °C in 5% $H_2/N_2$, keeping it at that temperature for a certain period of time, then increasing the temperature and the concentration of $H_2$ and finally reaching 245 °C in pure $H_2$ under 25 bar pressure. Subsequently and prior to the measurement of the catalytic activity, the catalysts are equilibrated at the final operating pressure and gas composition mixture ($H_2/CO/CO_2$). Therefore, it is likely that there is a difference between the copper surface area measured by RFC and the copper surface area of the materials during catalytic testing (it is well known that dynamic effects are controlling the size and shape of the Cu crystals during reduction[4,7]). The fact that the content of copper found by TPR is about 20% smaller than the content of copper by elemental analysis may indicate an incomplete reduction due to a surface layer of impenetrable silica. However, this also indicates that most of the copper (about 80%) was reduced. The small specific copper surface area may be due to sintering of the crystals under the TPR conditions which does not occur upon reduction under higher pressure in the parallel reactor.

## Conclusions

$CuO/ZnO/SiO_2$ composites with high specific surface area and good catalytic activity in heterogeneous methanol synthesis can be prepared by a combination of sol-gel chemistry and photochemistry. The ratio of copper to zinc can be easily varied in the precipitation process. The primary nanoparticles of ZnO and CuO are covered by silica, but still accessible for gases as demonstrated by the high BET surface area (indicating pores in the silica) and the good catalytic activity. The catalytic activity increases with the content of copper oxide in the precatalyst. The X-ray amorphous silica prevents the fusion of the catalytically active CuO/ZnO nanoparticles and also serves as a membrane which can be penetrated by the gaseous reactants (CO, $CO_2$, $H_2$, $CH_3OH$).

## Experimental Section

**Sol-Gel Synthesis and Photochemical Oxidation:** In the first step, silane-coated CuO/ZnO was synthesized according to refs.[30,32]. 11.12 g (45 mmol) (3-methacryloxypropyl)trimethoxysilane was added to 333 g methanol at 55 °C in a 1-L round-bottomed flask. At 60 °C, zinc acetate dihydrate and copper acetate monohydrate were added (Table 2) and a solution of 50.3 g (0.89 mol) potassium hydroxide in 167 g methanol was added dropwise. The precipitate was filtered off and washed four times with methanol. After centrifugation of the gelatineous precipitate, the product was dried at 130 °C. In the second step, 1.5 g of the synthesized silane-coated CuO/ZnO were dispersed in 450 mL water and transferred into a water-cooled UV-lamp reactor. The suspension was irradiated with a 125-W mercury high-pressure lamp (HPK 125 W, Philips) for 60 min whilst stirring to destroy the organic parts of the silane while bubbling air through the dispersion. The material was then centrifuged (10 min, 2000 rpm) and dried at 150 °C for 24 h.

Table 2. Preparation conditions of all samples.

| Sample | *n*(zinc acetate dihydrate) /(mmol) | *n*(copper(II) acetate monohydrate) /(mmol) |
|---|---|---|
| **Z** | 448 | – |
| **A** | 448 | 5 |
| **B** | 448 | 23 |
| **C** | 405 | 45 |
| **D** | 336 | 123 |

**Solid-State Characterization Methods:** BET measurements were conducted with a Micromeritics instrument Flow Sorb II 2300. Ele-

 © 2007 Wiley-VCH Verlag GmbH & Co. KGaA, Weinheim 

mental analysis of copper and zinc were carried out with an inductively coupled plasma-optical emission spectrometer (ICP-OES) Varian VISTA MPX with a radial plasma. X-ray powder diffraction (XRD) was performed on a Siemens D 500 instrument with Cu-$K_\alpha$ radiation. Scanning electron microscopy was performed with a FEI ESEM Quanta 400 FEG instrument on gold-sputtered samples.

**Catalytic Performance:** Measurements were performed in a high-throughput 49-parallel channel reactor.[11] The samples (100 mg diluted with 200 mg quartz per well) were placed in a sample holder consisting of a stainless steel cartridge closed at the bottom by a stainless-steel sinter metal frit. Prior to the catalytic measurements the catalysts were reduced with a $H_2/N_2$ mixture at 518 K following the prescribed procedure for the commercial benchmark catalyst ICI Katalco 51-8 (see above). Before measuring the catalytic activity, all samples were equilibrated for 3 h (reaction pressure 4.5 MPa, reaction temperature 518 K, analytic flow 20 mL min$^{-1}$). The reaction gas consisted of 70% $H_2$, 24% CO, and 6% $CO_2$. A double GC system (HP GC 6890) equipped with a methanizer FID was used for online gas analysis. Oxo-product separation ($H_3COH$, $HCOOCH_3$, $H_3CCOOCH_3$, $H_3CCH_2OH$) was carried out on a SuppelcoWAX 0.53 mm column and CO, $CO_2$ and $CH_4$ were separated on a Carboxen 1006 column. Methanol productivities for all measured samples were compared to the productivity of the industrial benchmark catalyst ICI Katalco 51-8 ($P_{ICI}$ = 40 mol MeOH/($kg_{cat}$ h) at 518 K and 4.5 MPa).

**Temperature-Programmed Reduction (TPR) and Reactive Frontal Chromatography (RFC):** The set-up used for TPR and $N_2O$ RFC consisted of a gas supply unit, a specially designed reactor and furnace, and a gas analysis section. The gas supply unit was equipped with mass flow controllers and included gas lines for pure Ar, a 4.2% $H_2$/Ar gas mixture, and a 1.0% $N_2O$/Ar gas mixture. The reactor was made of two concentric quartz tubes of an optimized geometry with respect to back-mixing of gas and the axial temperature profile. The design of the reactor and the furnace followed the work of Monti and Baiker.[34] The temperature of the furnace was controlled by a programmable PID controller (Eurotherm 2416). The gas analysis section included a cooling trap (filled with isopropyl alcohol and dry ice) for water removal, a thermal conductivity detector (Hydros) to monitor the uptake of $H_2$, and an dispersive IR detector (Uras) to monitor the uptake of $N_2O$. The set-up was operated by a personal computer via a program based on the software package LabView.

The TPR experiments were carried out to determine the specific Cu content of samples and to reduce samples prior to $N_2O$ RFC. A 100 mg sample was heated from 303 K to 513 K (furnace temperature; sample temperature 500 K) with a heating rate of 2 K min$^{-1}$ and the final temperature was held for 1 h. The inlet concentration of $H_2$ was fixed to 4.2% and the total flow rate of the $H_2$/Ar gas mixture was set to 84 mL min$^{-1}$. The low values of the heating rate, the final temperature, and the inlet concentration of $H_2$ were chosen to minimize sintering of the copper particles due to heat released by the reduction process or too high temperature.

The determination of the specific Cu surface area by $N_2O$ RFC was carried out consecutively to the TPR experiment. After cooling to room temperature in the flowing $H_2$/Ar gas mixture, the reactor was flushed for 15 min with pure Ar (50 mL min$^{-1}$). After bypassing the reactor and the cooling trap the Uras IR detector was calibrated, first in pure Ar and then in a 1.0% $N_2O$/Ar gas mixture (10 mL min$^{-1}$). When the calibration was finished the reactor was set on-line and the uptake of $N_2O$ from the $N_2O$/Ar gas mixture (10 mL min$^{-1}$) was measured. The measurement was finished when no further uptake of $N_2O$ was detectable. This method is based on the decomposition of $N_2O$ on exposed Cu atoms accompanied by the formation of adsorbed atomic oxygen $O_{ads}$ and gas-phase $N_2$. For calculation of the exposed Cu surface area an average surface atom density of $1.47 \times 10^{19}$ Cu atoms m$^{-2}$ was used. The specific Cu surface area was obtained by dividing the exposed Cu surface area by the initial sample mass [35].

All gas volumes correspond to standard conditions at 0 °C and 1013 mbar.

## Acknowledgments

This work was supported by the Deutsche Forschungsgemeinschaft (DFG) within the scope of the Collaborative Research Center SFB 558: Metal-substrate interactions in heterogeneous catalysis. We also acknowledge the support of the experimental section of Grillo-Werke AG, Duisburg. We are grateful to Prof. F. Schüth, Mülheim/Ruhr, for helpful discussions.

[1] J. M. Thomas, W. J. Thomas, *Principles and practice of heterogeneous catalysis*, VCH, Weinheim, **1996**.
[2] J. R. Jensen, T. Johannessen, S. Wedel, H. Livbjerg, *J. Catal.* **2003**, *218*, 67–77.
[3] C. V. Ovesen, B. S. Clausen, J. Schiotz, P. Stoltze, H. Topsøe, J. K. Nørskov, *J. Catal.* **1997**, *168*, 133–142.
[4] J. D. Grunwaldt, A. M. Molenbroek, N. Y. Topsoe, H. Topsoe, B. S. Clausen, *J. Catal.* **2000**, *194*, 452–460.
[5] S. A. French, A. A. Sokol, S. T. Bromley, C. R. A. Catlow, S. C. Rogers, F. King, P. Sherwood, *Angew. Chem.* **2001**, *113*, 4569–4572; *Angew. Chem. Int. Ed.* **2001**, *40*, 4437–4440.
[6] M. M. Günter, T. Ressler, B. Bems, C. Büscher, T. Genger, O. Hinrichsen, M. Muhler, R. Schlögl, *Catal. Lett.* **2001**, *71*, 37–44.
[7] P. L. Hansen, J. B. Wagner, S. Helveg, J. R. Rostrup-Nielsen, B. S. Clausen, H. Topsoe, *Science* **2002**, *295*, 2053–2055.
[8] B. Bems, M. Schur, A. Dassenoy, H. Junkes, D. Herein, R. Schlögl, *Chem. Eur. J.* **2003**, *9*, 2039–2052.
[9] M. C. Carroll, B. Skrotzki, M. Kurtz, M. Muhler, G. Eggeler, *Scripta Mater.* **2003**, *49*, 527–532.
[10] S. A. French, A. A. Sokol, S. T. Bromley, C. R. A. Catlow, P. Sherwood, *Top. Catal.* **2003**, *24*, 161–172.
[11] C. Kiener, M. Kurtz, H. Wilmer, C. Hoffmann, H. W. Schmidt, J. D. Grunwaldt, M. Muhler, F. Schüth, *J. Catal.* **2003**, *216*, 110–119.
[12] M. Kurtz, H. Wilmer, T. Genger, O. Hinrichsen, M. Muhler, *Catal. Lett.* **2003**, *86*, 77–80.
[13] M. Schur, B. Bems, A. Dassenoy, I. Kassatkine, J. Urban, H. Wilmes, O. Hinrichsen, M. Muhler, R. Schlögl, *Angew. Chem.* **2003**, *115*, 3945–3947; *Angew. Chem. Int. Ed.* **2003**, *42*, 3815–3817.
[14] B. L. Kniep, T. Ressler, A. Rabis, F. Girgsdies, M. Baenitz, F. Steglich, R. Schlögl, *Angew. Chem.* **2004**, *116*, 114–117; *Angew. Chem. Int. Ed.* **2004**, *43*, 112–115.
[15] T. Ressler, B. L. Kniep, I. Kasatkin, R. Schlögl, *Angew. Chem.* **2005**, *117*, 4782–4785; *Angew. Chem. Int. Ed.* **2005**, *44*, 4704–4707.
[16] R. B. Rasmussen, P. M. Holmblad, T. Askgaard, C. V. Ovesen, P. Stoltze, J. K. Nørskov, I. Chorkendorff, *Catal. Lett.* **1994**, *26*, 373–381.
[17] J. Yoshihara, C. T. Campbell, *J. Catal.* **1996**, *161*, 776–782.
[18] H. Wilmer, M. Kurtz, K. Klementiev, O. Tkachenko, W. Grünert, O. Hinrichsen, A. Birkner, S. Rabe, K. Merz, M. Driess, C. Wöll, M. Muhler, *Phys. Chem. Chem. Phys.* **2003**, *5*, 4736–4742.
[19] M. Kurtz, J. Strunk, O. Hinrichsen, M. Muhler, K. Fink, B. Meyer, C. Wöll, *Angew. Chem.* **2005**, *117*, 2850–2854; *Angew. Chem. Int. Ed.* **2005**, *44*, 2790–2794.

 © 2007 Wiley-VCH Verlag GmbH & Co. KGaA, Weinheim 

[20] S. Polarz, J. Strunk, V. Ischenko, M. W. E. van den Berg, O. Hinrichsen, M. Muhler, M. Driess, *Angew. Chem.* **2006**, *118*, 3031–3035; *Angew. Chem. Int. Ed.* **2006**, *45*, 2965–2969.
[21] C. Chauvin, J. Jaussey, J. C. Lavalley, H. Idriss, J. P. Hidermann, A. Kiennemann, P. Chaumette, P. Coutry, *J. Catal.* **1990**, *121*, 56–69.
[22] G. J. Hutchings, J. C. Vedrine, in *Basic principles in applied catalysis, vol. 75* (Ed.: M. Baerns), Springer, New York, **2004**, pp. 217–258.
[23] M. Saito, K. Murata, *Catal. Surveys from Asia* **2004**, *8*, 285–294.
[24] R. Weiss, Y. Guo, S. Vukojevic, L. Khodeir, R. Boese, F. Schüth, M. Muhler, M. Epple, *Eur. J. Inorg. Chem.* **2006**, 1796–1802.
[25] Y. Guo, W. Meyer-Zaika, M. Muhler, S. Vukojevic, M. Epple, *Eur. J. Inorg. Chem.* **2006**, 4774–4781.
[26] R. Weiss, S. Vukojevic, C. Baltes, R. Naumann d'Alnoncourt, M. Muhler, M. Epple, *Eur. J. Inorg. Chem.* **2006**, 4782–4786.
[27] S. Vukojevic, O. Trapp, J. D. Grunwaldt, C. Kiener, F. Schüth, *Angew. Chem.* **2005**, *117*, 8192–8195; *Angew. Chem. Int. Ed.* **2005**, *44*, 7978–7981.
[28] R. Becker, H. Parala, F. Hipler, O. P. Tkachenko, K. V. Klementiev, W. Grünert, H. Wilmer, O. Hinrichsen, M. Muhler, A. Birkner, C. Wöll, S. Schäfer, R. A. Fischer, *Angew. Chem.* **2004**, *116*, 2899–2901; *Angew. Chem. Int. Ed.* **2004** *43*, 2839–2842.
[29] S. Hermes, M. K. Schröter, R. Schmid, L. Khodeir, M. Muhler, A. Tissler, R. W. Fischer, R. A. Fischer, *Angew. Chem.* **2005**, *117*, 6394–6397; *Angew. Chem. Int. Ed.* **2005**, *44*, 6237–6241.
[30] B. Rohe, W. S. Veeman, M. Tausch, *Nanotechnology* **2006**, *17*, 277–282.
[31] G. E. Parris, K. Klier, *J. Catal.* **1986**, *97*, 374–384.
[32] M. Kotecha, B. Rohe, W. S. Veeman, M. Tausch, *Microporous Mesoporous Materials* **2006**, *95*, 66–75.
[33] H. P. Klug, L. E. Alexander, *X-ray diffraction procedures for polycrystalline and amorphous materials*, Wiley-Interscience, New York, **1974**.
[34] D. A. M. Monti, A. Baiker, *J. Catal.* **1983**, *83*, 323–335.
[35] O. Hinrichsen, T. Genger, M. Muhler, *Chem. Eng. Technol.* **2000**, *11*, 956–959.

Received: November 19, 2006
Published Online: March 13, 2007

 © 2007 Wiley-VCH Verlag GmbH & Co. KGaA, Weinheim 

DOI: 10.1002/ejic.200601088

# Complexation of Molybdenum(VI) with Bis(3-hydroxy-4-pyridinone)amino Acid Derivatives

M. Amélia Santos,*[a] Sofia Gama,[a] João Costa Pessoa,[a] M. Conceição Oliveira,[a] Imre Tóth,[b] and Etelka Farkas*[b]

**Keywords:** Molybdenum / Hydroxypyridinones / Hydroxypyridinonate complexes / Chelates

The molybdenum(VI) binding properties of a series of 3-hydroxy-2-methyl-4-pyridinones (3,4-HP), namely bis(3,4-HP) chelators, were investigated in solution and as solids; in particular, the complexation of $Mo^{VI}$ with iminobis{acetyl[1-(3′-aminopropyl)-3-hydroxy-2-methyl-4-pyridinone]}, IDAPr-(3,4-HP)$_2$, and ethylenediamino-*N*,*N*′-bis(methylcarboxyl)-*N*,*N*′-bis{acetyl[1-(3′-aminopropyl)-3-hydroxy-2-methyl-4-pyridinone]}, EDTAPr(3,4-HP)$_2$, as well as three model compounds: 1,2-dimethyl-3-hydroxy-4-pyridinone (DFP), iminodiacetic acid (IDA), and ethylenediaminodiacetic acid (EDDA). Solution studies show that the complexation occurs at low pH values by the coordination modes of the hydroxypyridinone moiety, and with the formation of bischelated $MoO_2^{2+}$ species. As the pH is increased, hydrolytic processes start with the formation of monochelated $MoO_3$ complexes and is followed by the total recovery of the free ligand, at pH > 8 for most of the systems, but at pH 10 for EDTAPr-(3,4-HP)$_2$. The obtained solid molybdenum complexes showed evidence for the presence of mononuclear species in solution, whereas the dinuclear species, $(MoO_2)_2$EDTAPr(3,4-HP)$_2$, were only detected for the EDTA derivative. Aqueous solution studies were performed by pH–potentiometry, spectrophotometry, $^1$H NMR and $^{17}$O NMR spectroscopy, and solid complex species were characterized by elemental analysis, IR spectroscopy, and ESI-MS.

(© Wiley-VCH Verlag GmbH & Co. KGaA, 69451 Weinheim, Germany, 2007)

## Introduction

3-Hydroxy-4-pyridinones (3,4-HP) are compounds of considerable biological interest because of their ability to form very stable complexes with several metal ions, in particular iron(III) and group 13 metal ions. They have been identified as the main candidates for medical application, either for the control of metal toxicity situations in the body (e.g. Fe[1–3] and Al[4–6]), or for clinical diagnosis (e.g. $^{67,68}$Ga, $^{111}$In).[7,8] In particular, the commercially available deferiprone (2-methyl-3-hydroxy-4-pyridinone) has been used as an orally active chelating agent for the decorporation of iron from iron-overload disease situations.[2,3] As part of an ongoing project aimed at the development of new polydentate 3-hydroxy-4-pyridinone-based derivatives,[9,10] two tetradentate bis(3,4-HP)amino acid derivatives were recently obtained. They present well-balanced lipo–hydrophilic character and improvement on metal-chelating efficacy in solution and in vivo relative to the bidentate monoderivatives; thus, good perspectives of their potential clinical use in much lower doses, to minimize drug-induced toxicity, are envisaged.[11,12]

Molybdenum complexation with 3,4-HP-based ligands has emerged as an important research target. In fact, molybdenum is of great biological relevance because of its role as the cofactor component in various redox enzymes,[13] as a determinant factor for siderophore production (e.g. secretion of azotochelin by *Azotobacter vinelandii*),[14] and also as an insulin mimetic for the prevention or amelioration of cardiac dysfunction in diabetic hearts.[15] However, research on molybdenum(VI) complexation with 3,4-HP-based ligands is quite scarce and is limited to solid-state studies with monochelators,[14–16] which is in contrast to Mo complexation with other O,O-donor ligands (e.g. hydroxamate and cathecholate siderophore analogues, for which solution studies are known[14,17,18]). Furthermore, the bis(3,4-HP) ligands are expected to form stable 1:1 complexes, and so they are better suited for optimal complexation with the $MoO_2^{2+}$ unit (with four available coordination sites) than the corresponding monoderivatives.[15,16,19] Thus, we present herein a molybdenum(VI) complexation study with two bis(3,4-HP)amino acid derivatives recently reported.[11,12] These polydentate compounds have two 3,4-HP binding groups attached to linear hydrophilic amino–carboxylic backbones (see Scheme 1), namely iminodiacetic acid (IDA) and ethylenodiaminotetraacetic acid (EDTA),

[a] Centro de Química Estrutural, Complexo I, Instituto Superior Técnico, UT Lisboa
Av. Rovisco Pais, 1049-001 Lisboa, Portugal
E-mail: masantos@ist.utl.pt
[b] Department of Inorganic and Analytical Chemistry, University of Debrecen,
4010 Debrecen, Hungary
E-mail: efarkas@delfin.klte.hu

Supporting information for this article is available on the WWW under http://www.eurjic.org or from the author.

 © 2007 Wiley-VCH Verlag GmbH & Co. KGaA, Weinheim 

to give iminobis{acetyl[1-(3′-aminopropyl)-3-hydroxy-2-methyl-4-pyridinone]}, IDAPr(3,4-HP)$_2$, and ethylenediamino-*N*,*N*′-bis(methylcarboxyl)-*N*,*N*′-bis{acetyl[1-(3′-aminopropyl)-3-hydroxy-2-methyl-4-pyridinone]}, EDTAPr(3,4-HP)$_2$, respectively. To aid in the rationalization of the results, analogous studies are also carried out for some model compounds, namely 1,2-dimethyl-3-hydroxy-4-pyridinone (3,4-DMHP or DFP), iminodiacetic acid (IDA), and ethylenediaminodiacetic acid (EDDA). The aqueous solution study involves potentiometric and spectroscopic techniques (UV/Vis, $^1$H and $^{17}$O NMR) to evaluate the chelating affinity and the coordination modes. Several solid complexes are also characterized by elemental analysis, IR spectroscopy, and ESI-MS.

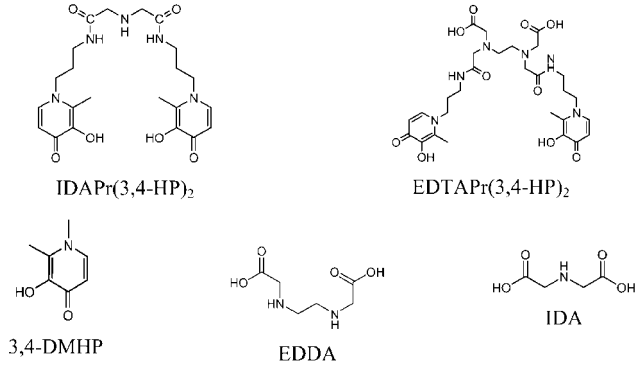


Scheme 1.

## Results and Discussion

Before starting the analysis and discussion of the results, some peculiar properties of the hydrolytic species associated with the $Mo^{VI}$-containing systems should be noted. In aqueous solution, numerous molybdenum species are present, whereas the free metal ion does not exist. As usual, $MoO_4^{2-}$ is chosen as the metal component (M) in the calculations. In aqueous solution above pH 7, $MoO_4^{2-}$ predominates, whereas below pH 7 some mononuclear species can exist but polyoxomolybdates are the main species. The equilibrium model determined previously under the conditions used in the present investigation, and the calculated overall stability constants ($\log\beta$) are summarized in Table S1. All these hydrolytic species were included in the equilibrium models to assess the complex species associated to the molybdenum(VI) ligand systems because there is always competition between the hydrolytic processes and the complex formation reactions with molybdenum(VI).[20]

One of the main objectives of this work is to study the molybdenum-binding capabilities of a set of bis(hydroxypyridinone) chelators with the IDA and EDTA backbones, namely in comparison with mono(hydroxypyridinone) derivatives. Therefore, for the rationalization of the complexation results, the interaction of $MoO_4^{2-}$ with mono(3-hydroxy-4-pyridinone), 3,4-DMHP, as well as with some parent compounds (EDDA and IDA) was also studied. The results are also compared with those previously obtained for mono- and bis(hydroxamate) ligands which proved to form very stable complexes with $Mo^{VI}$.[21]

### Mono(3-hydroxy-4-pyridinone): 3,4-DMHP

The protonation constants of 1,2-dimethyl-3-hydroxy-4-pyridinone (3,4-DMHP, Table 1) were calculated by best-fit analysis of the pH–potentiometric curve. As expected, two protons can react with the anionic form of a 3,4-DMHP molecule, and the corresponding $\log K_i$ constants are assigned to the protonation of the enolate group (9.74) and the pyridine N atom (3.66). These are in close agreement with the values previously reported (9.77 and 3.68, respectively).[22]

Table 1. Stepwise protonation constants ($\log K_i$) of the ligands 3,4-DMHP, IDAPr(3,4-HP)$_2$, EDTAPr(3,4-HP)$_2$, EDDA, and IDA, and global stability constants ($\log\beta$) for the corresponding molybdenum(VI) complex species ($I$ = 0.2 M KCl, $T$ = 25 °C).

| Ligand | $\log K_i$ | Species | $\log\beta$ |
|---|---|---|---|
| 3,4-DMHP | 9.749(4), 9.77[a] | $MoO_2(L)_2$ | 40.22(4) |
| (HL) | 3.655(7), 3.68[a] | $MoO_3(L)$ | 20.0(1) |
| IDAPr(3,4-HP)$_2$ | 9.91(3), 9.94[b] | | |
| ($H_2L$) | 9.37(3), 9.44[b] | $MoO_2(LH)$ | 40.33(4) |
| | 5.34(4), 5.42[b] | $MoO_2(L)$ | 36.41(7) |
| | 3.46(5), 3.54[b] | $[MoO_3(LH_2)]$ | |
| | 3.06(6), 3.11[b] | | |
| EDTAPr(3,4-HP)$_2$ | 10.12(1), 10.12[c] | | |
| ($H_4L$) | 9.54(8), 9.53[c] | $MoO_2(LH)$ | 45.02(2) |
| | 7.05(1), 7.04[c] | $MoO_3(LH_2)$ | 38.31(2) |
| | 4.02(2), 4.03[c] | $MoO_3(LH)$ | 30.53(3) |
| | 3.39(1), 3.38[c] | $MoO_3(L)$ | 22.12(4) |
| | 2.85(2), 2.84[c] | | |
| EDDA | 9.524(4), 9.60[d] | $MoO_2(L)$ | 26.74(4) |
| ($H_2L$) | 6.489(6), 6.51[d] | $MoO_3(LH)$ | 23.38(5) |
| | 2.169(9), 2.12[d] | $MoO_3(L)$ | 19.18(3) |
| IDA | 9.17(2), 9.34[e] | $MoO_2(L)$ | 22.73(5) |
| ($H_2L$) | 2.53(3), 2.62[e] | $MoO_3(L)$ | 18.15(4), 18.3[f] |

[a] Ref.[22] $I$ = 0.10 M KCl, $T$ = 25.0 °C. [b] Ref.[11] $I$ = 0.10 M $KNO_3$, $T$ = 25.0 °C. [c] Ref.[12] $I$ = 0.20 M KCl, $T$ = 25.0 °C. [d] Ref.[24] $I$ = 0.10 M $KNO_3$, $T$ = 25.0 °C. [e] Ref.[25] $I$ = 0.20 M KCl, $T$ = 25.0 °C. [f] Ref.[26] $I$ = 0.15 M $KNO_3$, $T$ = 25.0 °C.

Under the analytical concentration conditions usually used in the pH–potentiometric measurements for the complexation studies, there was some precipitation of the $Mo^{VI}$–3,4-DMHP complexes and this is indicated by the dashed lines in the pH–metric titration curves (Figure 1). Therefore, pH–metric experimental data was not used to calculate the equilibrium constants for any of the $Mo^{VI}$–3,4-DMHP complexes formed in solution. However, as complexes containing the dioxomolybdenum core usually have intense UV bands with $\lambda_{max}$ at ca. 290 nm (molar absorptivity ca. 2500 $M^{-1}cm^{-1}$),[16,20] this system could be studied by spectrophotometry. In this UV region, there are no measurable bands for the polyoxomolybdates and molybdate itself,[20] but for the ligand. Therefore, the spectral parameters (molar absorptivities, $\lambda_{max}$ values) of the pro-

 © 2007 Wiley-VCH Verlag GmbH & Co. KGaA, Weinheim 

tonated and nonprotonated forms of 3,4-DMHP need to be independently determined. Figure 2a shows spectra recorded at several pH values for 3,4-DMHP. The individually calculated spectra (molar absorptivity versus $\lambda_{max}$) for $H_2L^+$, HL, and $L^-$ are presented in the inset of this figure. The high molar absorptivities allowed the use of quite low analytical concentrations (ca. $10^{-5}$ M) during the UV spectroscopic measurements and so, under these conditions, precipitation did not occur in the solutions containing $Mo^{VI}$ and 3,4-DMHP. Representative spectra recorded for this system at various pH values are shown in Figure 2b. Comparison of Figure 2a and Figure 2b shows significant differences between the spectra obtained, namely in the acidic solutions.

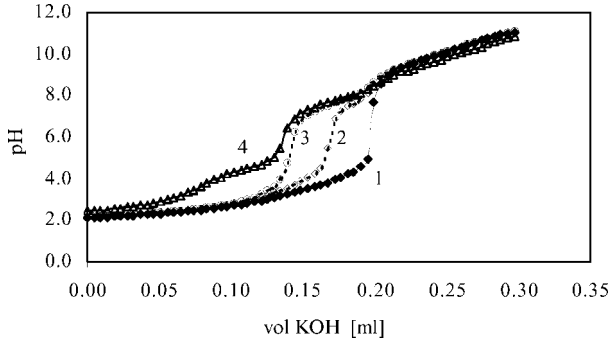


Figure 1. Potentiometric titration curves of aqueous solutions containing $Mo^{VI}$ and 3,4-DMHP. Symbols ♦ and △ represent titration points where no precipitation occurred. 1: $C_L = 4.647 \times 10^{-3}$ M; 2: $C_L = 4.650 \times 10^{-3}$ M, $C_M = 4.633 \times 10^{-3}$ M; 3: $C_L = 4.647 \times 10^{-3}$ M, $C_M = 2.315 \times 10^{-3}$ M; 4: $C_L = 1.164 \times 10^{-3}$ M, $C_M = 4.658 \times 10^{-3}$ M.

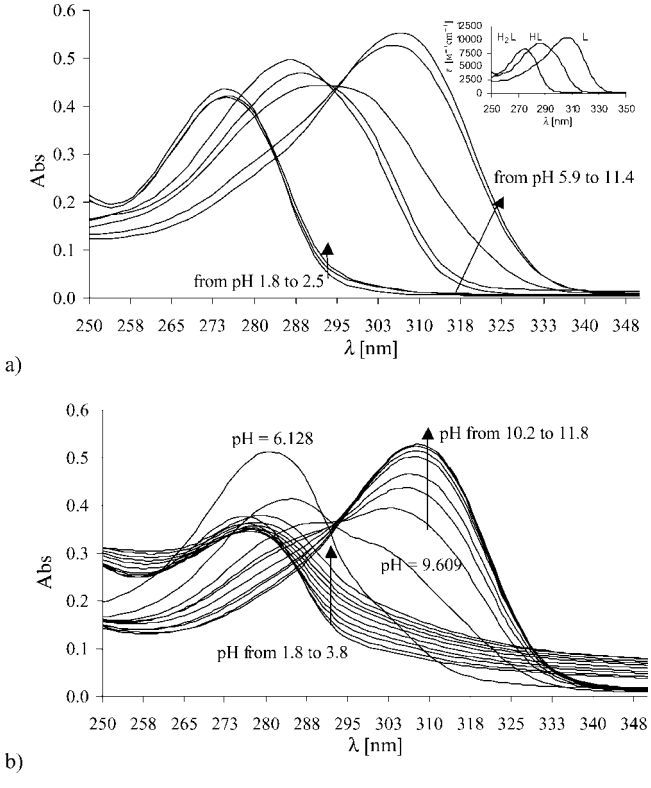


Figure 2. UV spectra for aqueous solutions containing: a) 3,4-DMHP, $C_L = 5.297 \times 10^{-5}$ M; b) $Mo^{VI}$ and 3,4-DMHP, at indicated pH values, $C_L = 4.946 \times 10^{-5}$ M, $C_M = 2.468 \times 10^{-5}$ M. ($I = 0.2$ M (KCl), $T = 25.0$ °C). The inset in a) represents individually calculated spectra for the $H_2L^+$, HL, and $L^-$ forms of the ligand.

The calculated ligand absorptivity was included in the input files of the PSEQUAD program,[23] together with the set of spectrophotometric data for the ligand in the presence of molybdenum, to fit the spectra obtained for the $Mo^{VI}$–3,4-DMHP system. The best fit was obtained with the equilibrium model and the stability constants shown in Table 1.

According to the results, within the experimental concentration range, the complexation of $Mo^{VI}$ with 3,4-DMHP involves the formation of the mono- and bischelated complexes. The stability constants obtained are presented in Table 1, and they correspond to the equilibrium processes in Equations (1) and (2).

$$MoO_4^{2-} + 2\,L^- + 4H^+ \rightleftarrows [MoO_2(L)_2] + 2\,H_2O \quad (1)$$

$$MoO_4^{2-} + 2\,L^- + 2H^+ \rightleftarrows [MoO_3(L)]^- + H_2O \quad (2)$$

Analysis of the concentration distribution curves (Figure 3a) show that if the ligand-to-metal ion concentration ratio is at least 2:1, even at very low analytical concentrations ($C_{Mo} = 2.468 \times 10^{-5}$ M), the bischelated species $[MoO_2(L)_2]$ predominates below ca. pH 4. This complex starts do decompose above ca. pH 4 by formation of the monochelated species $[MoO_3(L)]^-$. Above ca. pH 8, there is no $Mo^{VI}$–3,4-DMHP complex in solution.

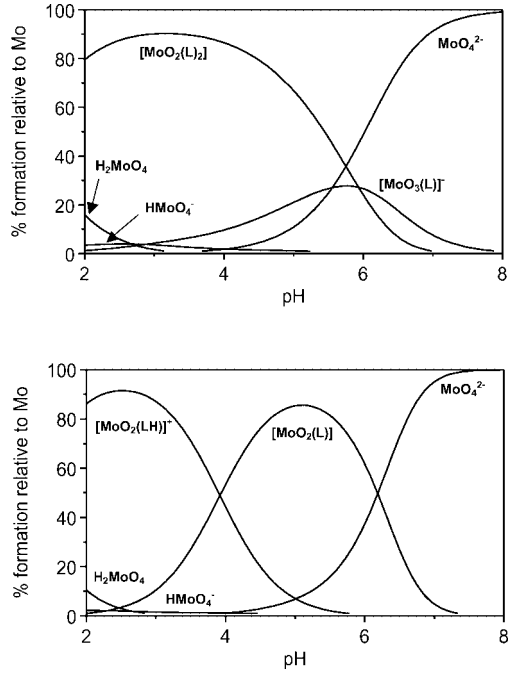


Figure 3. Concentration distribution curves of aqueous solutions containing $Mo^{VI}$ and a) 3,4-DMHP at 2:1 ligand-to-metal molar ratio and $C_M = 2.47 \times 10^{-5}$ M; b) IDAPr(3,4-HP) at 1:1 ligand-to-metal molar ratio and $C_M = 3.52 \times 10^{-3}$ M.

Similar results were previously obtained for the complexation of $Mo^{VI}$ with hydroxamate-based ligands in aqueous solution, where the bischelated complexes, $MoO_2$–(hydrox-

 © 2007 Wiley-VCH Verlag GmbH & Co. KGaA, Weinheim 

amate)$_2$, predominate in acidic solution (generally below pH 3), but decompose through the formation of a trioxomolybdenum-containing monohydroxamate species, $MoO_3$–hydroxamate, at ca. pH 8.[21]

### Bis(3-hydroxy-4-pyridinone)s: IDAPr(3,4-HP)$_2$ and EDTAPr(3,4-HP)$_2$

There are three main objectives directed at the design of these bis(hydroxypyridinone)s:[11,12] (1) the improvement of the metal-binding capability, which is higher for the multichelators than the corresponding monochelators, at least in the dilute conditions that prevail under physiological conditions, (2) the reinforcement of the hydrophilic character of the ligand–metal complexes, (3) the capacity for further backbone extra-functionalization for biological interactions or pharmacokinetic modifications. Therefore, two chelating moieties are appended to hydrophilic polyaminocarboxylic acid scaffolds, IDA and EDTA. The chain size of the propylene linker was considered to be long enough to allow the wrapping of the metal moiety by the hydroxypyridinone chelating units without interference of the amino acid backbone, which could be used for further biological interactions.

### $Mo^{VI}$–IDAPr(3,4-HP)$_2$ System

The fully protonated form of this ligand involves five dissociable protons. Although only the protonation macroconstants were determined, chemical evidence and $^1$H NMR spectra recorded at different pH values indicate that the two pyridine N atoms are the less basic amino groups, whereas the hydroxy groups present the highest basicity. The imino N atom is much less basic in this molecule ($\log K$ = 5.34) than it is in the parent molecule, IDA ($\log K$ = 9.34[25]), which may be attributed to the amidation of the neighbor carboxylic groups. In spite of the quite hydrophilic nature of the IDA-based backbone of the molecule, the $Mo^{VI}$ complexes with IDAPr(3,4-HP)$_2$ are not water-soluble under the usual concentrations used for pH–metric measurements. Therefore, as spectrophotometry allows the use of much lower analytical concentrations, as in the case of the $Mo^{VI}$–(3,4-DMHP) system, this method was used to determine the stoichiometry and stability constants of the $Mo^{VI}$–IDAPr(3,4-HP)$_2$ complexes. Comparison between the spectra obtained for the free ligand (Figure S1a) and the molybdenum-containing systems (Figure S1b) in the acidic pH range shows significant differences, which can be used to establish the equilibrium model and to determine the corresponding stability constants, as well as the concentration distribution curves (Figure 3b).

For the solution containing $Mo^{VI}$ and IDAPr(3,4-HP)$_2$, the spectrum obtained at pH 9.10 corresponds to the spectrum of the free ligand (cf. Figure S1a and S1b). In the pH range 6 to 9, the spectra could not be recorded because of the absence of any buffer capacity of the solutions. By fitting all the spectra recorded in the pH range 1.7 to 5.5, the equilibrium model and overall stability constants shown in Table 1 were determined. According to this equilibrium model, two $Mo^{VI}$ complexes are formed in the acidic pH range, which corresponds to the equilibrium processes represented by Equations (3) and (4):

$$MoO_4^{2-} + L^{2-} + 5H^+ \rightleftarrows [MoO_2(LH)]^+ + 2\ H_2O \quad (3)$$

$$MoO_4^{2-} + L^{2-} + 4H^+ \rightleftarrows [MoO_2(L)] + 2H_2O \quad (4)$$

For the species $[MoO_2(LH)]^+$, both hydroxypyridinonate moieties of a single molecule are most probably coordinated to the same dioxomolybdenum core, and the imino N atom is protonated. In $[MoO_2(L)]$, this proton is released. Comparison of the $\log\beta$ values obtained for this ligand with those of the monohydroxypyridinone, and the observed decrease in the imino N basicity upon coordination with the metal ion, agree with the proposed equilibrium model and binding mode. However, it should be emphasized that it is not possible to differentiate between processes depicted in Equations (4) and (5) as both have the same pH effect.

$$MoO_4^{2-} + L^{2-} + 4H^+ \rightleftarrows [MoO_3(LH_2)] + 2H_2O \quad (5)$$

To obtain further support for this equilibrium model, $^1$H NMR titrations were carried out for ligand solutions in the absence, and in the presence of $Mo^{VI}$, to support the identification of the different species in solution as well as their pH dependence. Because the metal coordination involves the hydroxypyridinone oxygen atoms, the peaks associated with the pyridinic protons (5-H and 6-H of the hydroxypyridinone ring) are the most informative ones. Therefore, for the $^1$H NMR titration curves those chemical shifts were registered as a function of pD* (Figure S2). Analysis of these $^1$H NMR titration curves shows that in the range ca. pH 2 to 4 only one complex species is formed, which corresponds to the bischelated species. Above pH 4 a new species is detected, with a deshielding effect on those protons, whereas the free ligand also starts to be formed. The observation of this second complex species agrees with the hypothetical formation of the monochelated trioxo species. The decomposition of the complex is completed between pH 6 and 8. Thus, the profiles of these $^1$H NMR titration curves support the model involving the three species suggested by the spectrophotometric results.

### $Mo^{VI}$–EDTAPr(3,4-HP)$_2$ System

In its fully protonated form, EDTAPr(3,4-HP)$_2$ has eight dissociable protons. According to our results, two of them are released below the measurable pH region. Because the protonation microconstants were not evaluated, we cannot discuss much about the acid–base properties of the individual groups. However, on the basis of chemical evidence,[12,14] it is possible to conclude that the two hydroxy groups are the most basic groups, and that the value $\log K$ = 7.04 should be mostly attributed to the deprotonation of one of the ethylenediamine N atoms.

 © 2007 Wiley-VCH Verlag GmbH & Co. KGaA, Weinheim 

The EDTA derivative has two hydroxypyridinonate arms, as with IDAPr(3,4-HP)$_2$, but it also contains an EDDA moiety that may offer an alternative coordination mode (at least theoretically) for several metal ions. To compare the molybdenum(VI) binding ability of the two "multichelating parts" of the EDTAPr(3,4-HP)$_2$ molecule, studies of the Mo$^{VI}$–ethylenediaminodiacetic acid (EDDA) system were also carried out, and calculations were made for the hypothetical ternary system Mo$^{VI}$ –EDDA–(3,4-DMHP).

The potentiometric titrations of the Mo$^{VI}$–EDDA system were carried out without precipitation problems (some titration curves are included in the Supporting Information, Figure S3). These titration curves could be fitted well with an equilibrium model including the species $[MoO_2(L)]$, $[MoO_3(LH)]^-$, and $[MoO_3(L)]^{2-}$, whose stability constants are shown in Table 1. The concentration distribution curves calculated for the Mo$^{VI}$–EDDA complex species (Figure S4), under the concentration conditions used herein, indicate that an ethylenediaminodiacetate ligand cannot effectively compete with the Mo$^{VI}$ hydrolytic processes. At 1:1 metal-to-ligand molar ratio and at an analytical concentration of ca. $4\times10^{-5}$ M of the components, the maximum relative amount of the metal complex found is 20% at pH ca. 2. By increasing the pH, the Mo$^{VI}$ hydrolytic species becomes more and more dominant.

Therefore, the results obtained for the Mo$^{VI}$–EDDA system indicate that, for EDTAPr(3,4-HP)$_2$, only the hydroxypyridinonate arms are the effective binding sites for Mo$^{VI}$. The preference of the hydroxypyridinone over the EDDA coordination mode can also be clearly illustrated by the concentration distribution curves calculated for the hypothetical ternary system Mo$^{VI}$–EDDA–(3,4-DMHP) at 1:1:2 molar ratio (Figure S5). According to this speciation curves, the percentage of Mo$^{VI}$–EDDA complexes formed do not exceed 5–6% of total Mo$^{VI}$. Consequently, if there is no excess of the metal in solution, we expect simple hydroxypyridinonate-type coordination of EDTAPr(3,4-HP)$_2$ towards Mo$^{VI}$. Because the formation of dinuclear species can be expected under conditions where excess metal is present, some studies were also performed at a ligand-to-metal ion molar ratio of 1:2.

As the solubility of the complexes formed in the Mo$^{VI}$–EDTAPr(3,4-HP)$_2$ system are slightly higher than those with the former hydroxypyridinonate derivatives, it was possible to titrate some samples without precipitation (see titration curves in Figure 4).

Besides the pH–potentiometric titrations, spectrophotometric measurements were also performed, and the spectra of the free ligand and the Mo$^{VI}$–ligand system were recorded at several pH values. (Figure S6).

The best-fit for both the pH–potentiometric and spectrophotometric data was obtained with the equilibrium model and the stability constants shown in Table 1. The corresponding concentration distribution curves are shown in Figure 5.

By taking also into account the results obtained for the model ligands, EDDA and 3,4-DMHP, the following assumptions can be made regarding the equilibrium processes

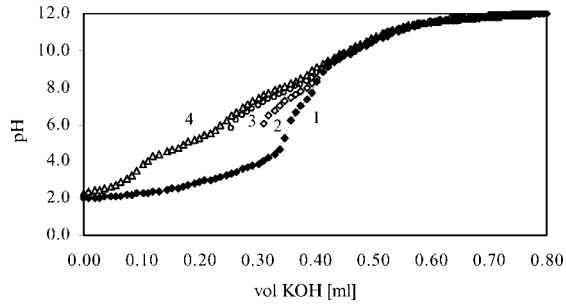


Figure 4. Potentiometric titration curves of aqueous solutions containing Mo$^{VI}$ and EDTAPr(3,4-HP)$_2$: 1: $C_L = 3.523\times10^{-3}$ M; 2: $C_L = 3.451\times10^{-3}$ M, $C_M = 1.654\times10^{-3}$ M; 3: $C_L = 3.523\times10^{-3}$ M, $C_M = 3.355\times10^{-3}$ M; 4: $C_L = 2.864\times10^{-3}$ M, $C_M = 5.732\times10^{-3}$ M.

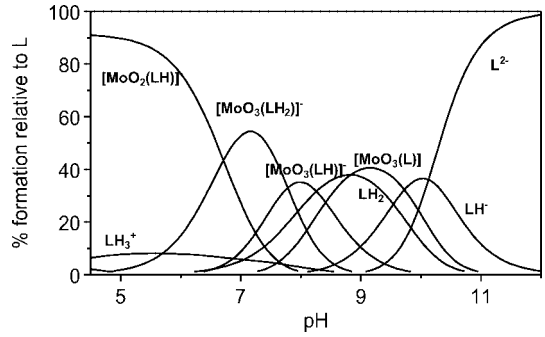


Figure 5. Concentration distribution curves for the complexes formed in Mo$^{VI}$–EDTAPr(3,4-HP)$_2$ system for solutions containing $C_L = 9.175\times10^{-3}$ M and $C_M = 8.39\times10^{-3}$ M.

and the possible bonding modes of EDTAPr(3,4-HP)$_2$: in the acidic pH range, the complex species $[MoO_2(LH)]^-$ predominates, in which the coordination of the two hydroxypyridinone moieties to the dioxomolybdenum core is the most plausible, while one of the ethylenediamine N atoms remains protonated. The corresponding equilibrium constant in Table 1 corresponds to the process shown in Equation (6):

$$MoO_4^{2-} + L^{2-} + 5H^+ \rightleftarrows [MoO_2(LH)]^- + 2H_2O \quad (6)$$

As the pH is increased, two types of processes can occur: (1) $[MoO_2(L)]^{2-}$ can be formed by the deprotonation of the noncoordinating ethylenediamine N atom,

$$[MoO_2(LH)]^- \rightleftarrows [MoO_2(L)]^{2-} + H^+ \quad (7a)$$

the calculated stability constant corresponding to Equation (7):

$$(MoO_4^{2-} + L^{2-} + 4H^+ \rightleftarrows [MoO_2(L)]^{2-} + 2H_2O) \quad (7)$$

(2) Partial hydrolysis of the complex may occur through formation of a monochelated complex with a trioxomolybdenum core, which has the noncoordinating amino and hydroxy groups in the protonated form.

$$[MoO_2(LH)]^- + H_2O \rightleftarrows [MoO_3(LH_2)]^- + H^+ \quad (8a)$$

In such a hypothesis, the stability constant in Table 1 would correspond to Equation (8):

$$(MoO_4^{2-} + L^{2-} + 4H^+ \rightleftarrows [MoO_3(LH_2)]^- + H_2O) \quad (8)$$

 © 2007 Wiley-VCH Verlag GmbH & Co. KGaA, Weinheim 

As the formation of $[MoO_2(L)]^{2-}$ and $[MoO_3(LH_2)]^-$ via **8a** and **7a**, respectively, have the same pH effect, they cannot be distinguished by pH-potentiometry. However, analyzing the UV/Vis spectra, we concluded that the best fit of the spectra could be obtained if the latter species was involved in the model. At ca. pH 5.5, there is a change in the UV/Vis spectra, which indicates that free hydroxypyridinone groups start to be present in the system, thus supporting the formation of $MoO_3$-type complexes in which one of the hydroxypyridinone groups is not coordinated. Further increase in the pH leads to the stepwise deprotonation of the noncoordinated groups in $[MoO_3(LH_2)]^-$ (Equations 9a and 10a), with the final formation of the molybdate anion by the complete decomposition of the metal complexes [Equation (11)].

$$[MoO_3(LH_2)]^- \rightleftarrows [MoO_3(LH)]^{2-} + H^+ \quad (9a)$$

$$(MoO_4^{2-} + L^{2-} + 3H^+ \rightleftarrows [MoO_3(LH)]^- + H_2O) \quad (9)$$

$$[MoO_3(LH)]^{2-} \rightleftarrows [MoO_3(L)]^{3-} + H^+ \quad (10a)$$

$$(MoO_4^{2-} + L^{2-} + 2H^+ \rightleftarrows [MoO_3(L)]^{2-} + H_2O) \quad (10)$$

$$[MoO_3(LH)]^{2-} + H_2O \rightleftarrows MoO_4^{2-} + LH_2 + H^+ \quad (11)$$

Because these solution equilibriums are quite complex and different isomers may correspond to the same stoichiometry, $^1H$ NMR titrations were also carried out to obtain additional information. These studies were performed for solutions containing free ligand, $EDTAPr(3,4\text{-}HP)_2$, and the $Mo^{VI}$–$EDTAPr(3,4\text{-}HP)_2$ system, under experimental conditions as close as possible to those used in the potentiometric measurements. The set of results is depicted in Figure 6.

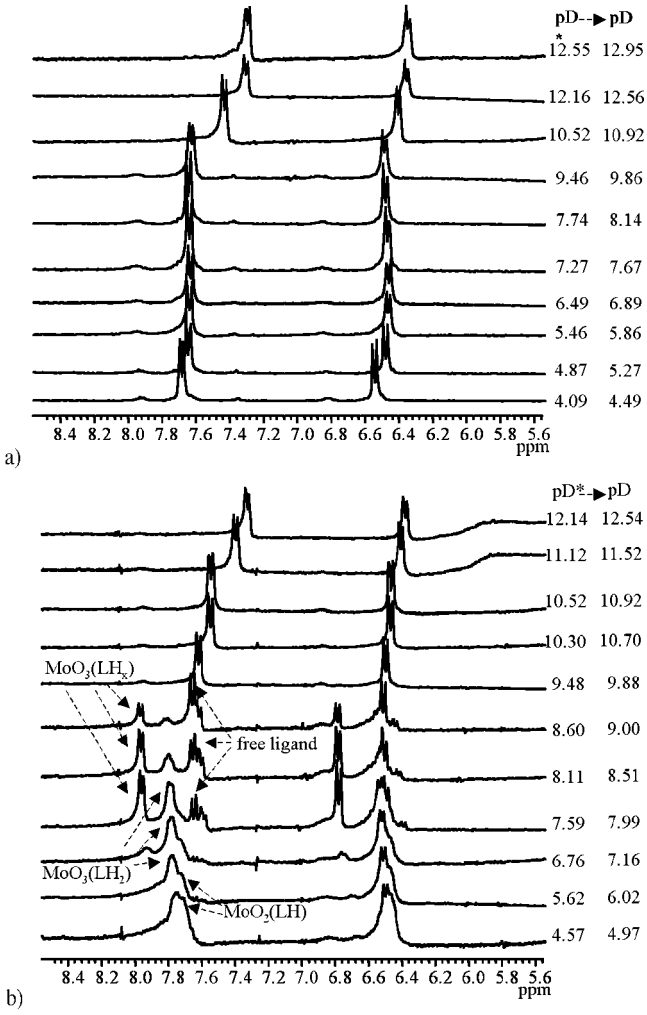


Figure 6. $^1H$ NMR spectra, at indicated pD* and pD, corresponding to the 5-H and 6-H peaks of the hydroxypyridinone ring of: a) solution containing the free ligand $EDTAPr(3,4\text{-}HP)_2$ $C_L = 8.73 \times 10^{-3}$ M; b) solution containing $Mo^{VI}$ and $EDTAPr(3,4\text{-}HP)_2$ with $C_L = 9.175 \times 10^{-3}$ M and $C_M = 8.39 \times 10^{-3}$ M.

Analysis of the $^1H$ NMR spectra obtained for the $Mo^{VI}$–$EDTAPr(3,4\text{-}HP)_2$ system and their comparison with the corresponding free ligand spectra led to the following conclusions: (1) at pH 4, there is only one complex species, (2) at pH ca. 5, another one starts to form, (3) at pH ca. 7, a third distinct complex species appears. These three species are completely hydrolyzed at pH > 9, with the formation of the free ligand. The ligand band is split between pH 6 and 9, thus indicating the existence of two types of "free ligand" hydroxypyridinone moieties in this pH range. One of them should correspond to a noncoordinated hydroxypyridinone and the other one to a species with only one of the noncoordinated arms.

With the use of the Mestre C program,[27] deconvolution of some spectra and a comparative analysis of the relative intensities of the individual peaks and their pH dependence with the species distribution curves enabled the peak attribution to the species present in solution. Table 2 includes the calculated relative percentages for each peak, and the assignment of the corresponding species. We can conclude that there is a good fit between the values obtained for the concentration distribution species on the basis of the deconvolution of the $^1H$ NMR spectroscopic signals and on the potentiometric results.

To aid in the rationalization of the present results, $^{17}O$ NMR spectroscopic studies were also performed because the chemical shifts present high-dependence on the number and type of oxo ligands bonded to the molybdenum cores. The chemical shift of $MoO_4^{2-}$ is ca. 532 ppm; *cis* $MoO_3$ appears at lower field (ca. 700 ppm) followed by the *cis* $MoO_2^{2+}$ core at ca. 900 ppm.[17,19] Therefore, to obtain further evidence for the proposed equilibrium model of the $Mo^{VI}$–$EDTAPr(3,4\text{-}HP)_2$ system in aqueous solution, two $^{17}O$ NMR titrations were carried out at 1:1 and 1:2 ligand-to-metal molar ratios. This is shown in Figure S7.

A distinct peak appears at $\delta$ = 532 ppm, which corresponds to $MoO_4^{2-}$; at ca. 680 ppm, the $MoO_3^-$ moiety can be identified between pH 7 and 9. However, it was not possible to observe any peak corresponding to the $MoO_2^{2+}$ core. This is probably due to precipitation and/or some fast chemical exchange between the oxygen atoms involved in the coordination, as a result of the intramolecular exchange between the different bonding isomers formed, which suppresses the $^{17}O$ NMR spectroscopic signal.

 © 2007 Wiley-VCH Verlag GmbH & Co. KGaA, Weinheim 

Table 2. Calculated speciation for the hydroxypyridinone-containing species, at indicated pD*, on the basis of the integration of the $^1$H NMR spectroscopic peaks corresponding to the 5-H and 6-H protons of the hydroxypyridinone ring. The values in parentheses represent the corresponding data obtained from the potentiometric results under the same conditions ($C_L = 9.175 \times 10^{-3}$ M, $C_{Mo}^{VI} = 8.39 \times 10^{-3}$ M).

| Peaks 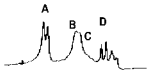 | pD*=8.60 | pD*=8.11 | pD*=7.59 | pD*=6.76 | pD*=4.57 | Attributions |
|---|---|---|---|---|---|---|
| A | 45 (40) | 58 (55) | 57 (51) | 16 (13) | -- | $MoO_3LH_x$, $x$=0,1 |
| B | 5 (10) | 10 (4) | 18 (21) | 54 (55) | 0 (2) | $MoO_3LH_2$ |
| C | -- | -- | -- | 30 (20) | 100 (90) | $MoO_2LH$ |
| D | 50 (47) | 32 (37) | 25 (28) | 0 (12) | 0 (8) | Free ligand |

By taking into account the molecular structure of EDTAPr(3,4-HP)$_2$, formation of dinuclear species could be expected for solutions containing this ligand and excess of $Mo^{VI}$, with the metal centers coordinated either by the hydroxypyridinone groups or the "EDDA skeleton". However, from the experimental data obtained in aqueous solution, calculations with the PSEQUAD program[23] were not successful for all the equilibrium models in which those species were included. This means that, mathematically, it was not possible to obtain any log$\beta$ for the dimeric species, thus suggesting a low probability for the existence of dinuclear species in our solution conditions. Then again, if we consider the results obtained in the $^1$H NMR titration, and if the aliphatic part of the spectra is carefully compared (see Figure S8), there is evidence that, at high pH, the spectrum recorded for the ligand–$Mo^{VI}$ system is the same as that of the free ligand. At pH < 6, only the bands for the protons which feel the coordination of the hydroxypyridinonate chelate (1,6) show significant broadening. However, when the bischelated dioxomolybdenum species starts to decompose, and some monochelated trioxomolybdenum species starts to be formed, the hydroxypyridinonate arms become noncoordinated and different species are suggested by the spectra with the broadening and splitting of the aliphatic peaks. This means that, probably, there is a dynamic intramolecular exchange between the different binding isomers formed, and not a real exchange between the coordination of the hydroxypyridinone and the "EDDA skeleton".

## Solid State Studies

As mentioned above, for most of the systems precipitation occurred along the pH–metric titrations. Several of those solids were isolated by performing similar batch experiments, but with the use of higher concentrations of metal ion and ligand. The molybdenum solid complexes obtained were characterized by IR, elemental analysis, and ESI-MS experiments. Some relevant data of the IR results are included in Table 3. The selected IR data are representative of the differences between the free ligand and the complexes. Complex formation is confirmed by the emergence of two strong new bands characteristic of the Mo–O stretching vibrations ($\nu_{Mo=O}$, as strong peaks in the range 800–950 cm$^{-1}$).[28] Concerning the $MoO_2^{2+}$ core, its characteristic stretching bands, $\nu_{MoO_2}$ (symmetric) and $\nu_{MoO_2}$ (asymmetric), appear around 920 and 890 cm$^{-1}$, respectively.[29] For the $MoO_3$ unit, the characteristic bands normally appear around 890 and 840 cm$^{-1}$.[30] For the hydroxypyridinone derivatives there is also a characteristic infrared four-band spectral pattern between 1610 and 1400 cm$^{-1}$.[16,31,32] Those bands can be assigned to $\nu_{C=O}$ and $\nu_{ring}$ that are very difficult to differentiate. Upon coordination, this pattern is usually preserved, but a bathochromic shift and a reordering of the peaks can be observed. For the solid complexes obtained, comparison with the free ligand spectra shows that the four-band pattern remains with some change in the intensity of some of the peaks, and some small shifts to lower wavenumbers.

Table 3. Infrared spectroscopic data for the hydroxypyridinone derivatives and the corresponding $Mo^{VI}$ complexes.

| Compound | Selected IR data [cm$^{-1}$] | | | | | | | | |
|---|---|---|---|---|---|---|---|---|---|
| | $\nu_{O-H}$ | $\nu_{C=C} + \nu_{C=O}$ | | | | $\nu_{C-O}$ | $\nu_{Mo-O}$ | | $\nu_{Mo-O-Mo}$ |
| 3,4-DMHP | 3146(br. s)[a] | 1631 | 1568 | 1530 | 1515 | 1234(s) | – | | – |
| [$MoO_2$(3,4-DMHP)$_2$·$H_2O$] | – | 1616 | 1556 | 1514 | 1495 | – | 919(s) | 892(s) | – |
| IDAPr(3,4-HP)$_2$ | 3227(br. s)[a] | 1682 | 1628 | 1560 | 1507 | 1251(s) | – | | – |
| {$Mo_3O_8$[IDAPr(3,4-HP)$_2$]·3$H_2O$} | 3412(br. s)[a] | 1652 | 1614 | 1556 | 1496 | 1267(s) | 918(m) | 891(m) | 828, 753(m) |
| EDTAPr(3,4-HP)$_2$ | 3328(br. s)[a] | 1684 | 1634 | 1560 | 1508 | 1252(s) | –- | | – |
| {($MoO_2$)$_2$[EDTAPr(3,4-HP)$_2$]·7$H_2O$} | 3410(br. s)[a] | 1635 | | 1558 | 1496 | – | 940(br. m) | | 899(br. s) |

[a] Only one $\nu_{O-H}$ vibration band is found in the spectra thus disabling independent attributions to the hydroxypyridinone–OH or other OH groups.

 © 2007 Wiley-VCH Verlag GmbH & Co. KGaA, Weinheim 

For the $Mo^{VI}$–(3,4-DMHP)$_2$ complex, elemental analysis fits the formulation as a monohydrated complex in which two 3,4-DMHP molecules are coordinated to one $MoO_2^{2+}$ unit [$MoO_2$(3,4-DMHP)$_2$·$H_2O$]. The IR spectrum shows a redshift of the four-band pattern corresponding to the hydroxypyridinone spectra, and two strong peaks are obtained at 919 and 892 $cm^{-1}$, which can be attributed to the two characteristic IR bands of the $MoO_2^{2+}$ unit.

Concerning the $Mo^{VI}$–IDAPr(3,4-HP)$_2$ solid complex isolated, an entirely different structure was obtained. From the elemental analysis of the yellow solid we can conclude that a complex with one ligand and three molybdenum atoms was formed: [$Mo_3O_8$(IDAPr(3,4-HP)$_2$)·3$H_2O$]. In the IR spectra of the complex, besides the bathochromic shifts of the $\nu_{C=O}$ and $\nu_{ring}$ bands, which indicate coordination through the hydroxypyridinone groups, and the two characteristic Mo–O bands at ca. 918 and 891 $cm^{-1}$, two new bands appear at 828 and 753 $cm^{-1}$ (see Table 3). By taking into account that the IR bands in the 735 to 850 $cm^{-1}$ range have been attributed to Mo–O–Mo stretching modes,[28,33–35] identical assignment can be assumed for [$Mo_3O_8$(IDAPr(3,4-HP)$_2$)·3$H_2O$]. Furthermore, on the basis of molecular structures reported in the literature for other molybdenum complexes, such as $Na_4$[$Mo_6O_8$(EDTA)$_3$·14$H_2O$],[36] [$Mo_3Cu_2O_{10}$(pz)]$_n$[28] with pz = pyrazine, and [{$MoO_2$(MCM(3,4-HP))O}$_2$]$^{2-}$[34] with MCM(3,2-HP) = 1-[(methoxycarbonyl)methyl]-3-hydroxy-2-pyridinone, we suggest that for [$Mo_3O_8$(IDAPr(3,4-HP)$_2$)·3$H_2O$], a structure with three $Mo^{VI}$ atoms bonded by oxygen bridges, that is a $\mu_3$-oxo-trismolybdenum(VI) complex exists. However, because no suitable crystals were obtained for X-ray diffraction studies, such an assumption cannot be confirmed.

From solutions containing $Mo^{VI}$ and EDTAPr(3,4-HP)$_2$, a yellow solid complex was obtained at acidic pH. Its elemental analysis indicates a dinuclear structure in which two $MoO_2^{2+}$ units are coordinated by one ligand molecule: [$(MoO_2)_2$(EDTAPr(3,4-HP)$_2$)·7$H_2O$]. The IR spectra of the solid compound showed bands at 940 and 899 $cm^{-1}$ (Table 3), which are characteristic of the $\nu_{Mo-O}$ in the $MoO_2^{2+}$ core.

Some of the solids obtained (dissolved in water) and their mother solutions were also analyzed by ESI-MS. Some ESI mass spectra were obtained from the solutions of "batch" samples of the $Mo^{VI}$–IDAPr(3,4-HP)$_2$ system, at different pH conditions. One of the spectra (see Figure S9a) contains an intense peak at *m*/*z* = 590, ascribed to the monoprotonated neutral complex {[$(MoO_2)$(L–2 H)] + H}$^+$, in which L is IDAPr(3,4-HP)$_2$, having the hydroxy groups deprotonated and coordinated to one $MoO_2^{2+}$ unit. The other spectrum (Figure S9b) shows two peaks at *m*/*z* = 484 and 612, which correspond to the ions [L + Na]$^+$ and {[$(MoO_2)$(L–2 H)] + Na}$^+$, respectively.

The mass spectrum obtained for the solutions containing $Mo^{VI}$ and EDTAPr(3,4-HP)$_2$ (Figure S10a) presents three intense peaks at *m*/*z* = 787, 825, and 863, attributed to the ions {[$(MoO_2)$(L–2 H)] + K}$^+$, {[$(MoO_2)$(L–2 H) – H] + 2 K}$^+$, and {[$(MoO_2)$(L–2 H) – 2H] + 3 K}$^+$, respectively. Also in this case, [$(MoO_2)$(L–2 H)], in which L is EDTAPr(3,4-HP)$_2$, represents the neutral complex with the two hydroxypyridinone moieties deprotonated and coordinated to the $MoO_2^{2+}$ core, but with the two carboxylic groups protonated. Therefore, the first species is just the neutral complex charged by a potassium cation. As the relative amount of $K^+$ increases with the addition of KOH to the solutions, the carboxylic groups deprotonate and the proton is substituted by K cations.

Although in the solution-phase molybdenum complexation studies with EDTAPr(3,4-HP)$_2$, dinuclear species were not found, ESI-MS data obtained for the solid material and the corresponding mother solution are in agreement with the elemental analysis results obtained for the solids. The peak at *m*/*z* = 873 presented in the spectrum of this solid (Figure S10b) is assigned to the complex ion {[$(MoO_2)_2$(L–4 H)] + H}$^+$, a dinuclear species $C_{28}H_{37}Mo_2N_6O_{14}^+$. The more intense peak at *m*/*z* = 947 corresponds to the water adduct of the cationic dinuclear complex, {[$(MoO_2)_2$(L–4 H)] + K, 2·$H_2O$}$^+$. The relative intensities of the isotopic peaks of the molybdenum-containing species agree, within experimental error, with the characteristic patterns resulting from two molybdenum atoms, which provide further support for the above assignments. [$(MoO_2)_2$(L–4 H)] represents the neutral complex with one $MoO_2^{2+}$ core coordinated by the two deprotonated hydroxypyridinone groups, and another one coordinated by the "EDDA part", which involves both the deprotonated carboxylic groups of the ligand. The spectrum also shows a much less intense peak at *m*/*z* = 749 which corresponds to the protonated mononuclear species, {[$(MoO_2)$(L–2 H)] + H}$^+$, with the relative intensities of the isotopic peaks characteristic for one molybdenum unit. The additional peak at *m*/*z* = 805 is attributed to the water adduct of the mononuclear cationic species {[$(MoO_2)$(L–2 H)] + K, $H_2O$}$^+$.

This set of results demonstrates that structure and/or stoichiometry of predominant species in diluted solutions may differ from those of precipitated solids or corresponding mother solutions. The difference observed between solution and solid-state studies can be attributed to the low water solubility of the complexes, thus rendering difficult their detection in solution, at least under dilute experimental conditions.

## Conclusions

Two bis(3-hydroxy-4-pyridinone) chelators, having IDA and EDTA backbones with two bearing 3-hydroxy-4-pyridinone chelating moieties, were shown to be able to form quite stable bischelated 1:1 $MoO_2$ complexes under acidic conditions. An increase in the pH of the solution to basic values leads to the stepwise hydrolysis of the complexes and subsequent formation of monochelate species and the free ligand. Although under dilute conditions only soluble mononuclear species with hydroxypyridinone coordination modes were found, increasing concentration conditions and excess amounts of metal lead to water-insoluble polynuclear

 © 2007 Wiley-VCH Verlag GmbH & Co. KGaA, Weinheim 

species. Moreover, it was shown that the ligand scaffold determines the tuning of some molybdenum complex properties, namely water solubility and stability to hydrolysis. As compared to the remaining mono- or bischelated systems, the $Mo^{VI}$–EDTAPr(3,4-HP)$_2$ system presents the most interesting behavior as a result of the EDTA scaffold. In fact, there are fewer water-insolubility problems associated with the complex, and under conditions where there is not an excess of metal, the coordination only involves the hydroxypyridinone moieties, which leaves the EDDA moiety free for further metal-ion coordination or extra-interaction with biological sites.

## Experimental Section

**General:** Unless otherwise indicated, analytical grade reagents were used as supplied. The IDAPr(3,4-HP)$_2$ and the EDTAPr(3,4-HP)$_2$ ligands were synthesized, purified and fully characterized as described previously.[11,12]

The aqueous molybdenum(VI) stock solution was prepared from the required amount of $Na_2MoO_4$ (Reanal product) dissolved in bidistilled water, and the exact metal-ion concentration was checked gravimetrically by precipitation of its quinolin-8-olate complex. The concentration of each ligand and HCl stock solutions were determined by pH–potentiometry using the Gran's method.[37] For the aqueous solution studies, a MOLSPIN pH-meter, a Methrom 6.0234.100 combined electrode, and a computer-controlled Mol-AcS microburette were used to carry out the potentiometric and also some of the spectrophotometric titrations, at 25.0 ± 0.1 °C and ionic strength of 0.2 M (KCl). The electrode calibrations were made according to the Irving method,[38] and the pH readings could therefore be converted into hydrogen ion concentration. The titrant used was a carbonate-free KOH solution (0.2 M) and its concentration was also determined by potentiometry using the Gran's method.[37] For all samples, the total volume was 3 mL, the ligand concentration was around $4 \times 10^{-3}$ M and the ligand-to-metal ion molar ratios between 1 and 4. Under the experimental conditions used, the value determined for the ionization constant ($pK_w$) was 13.76.

Spectral determinations were carried out with a HP 8453 spectrophotometer equipped with 1.0-cm-matched quartz cells at 25.0 ± 0.2 °C and $I$ = 0.2 M KCl. For solutions containing $Mo^{VI}$, the spectra were recorded in the range 200 to 350 nm by using 3.00 mL samples, ligand concentrations of ca. $5 \times 10^{-5}$ M and metal concentrations of $2.5–5.0 \times 10^{-5}$ M. The equilibrium models were established and the complex formation constants were calculated with the PSEQUAD computer program[23] by using the previously reported ($\log\beta$) values of the $Mo^{VI}$ hydrolytic species.[20]

A Varian Unity 300 instrument was used to perform the $^1$H NMR measurements. The titrations were performed at room temperature with ligand concentrations of $5–9 \times 10^{-5}$ M in $D_2O$ with DSS, sodium 3-(trimethylsilyl)-[2,2,3,3–$^2D_4$]propionate, as the internal reference. The direct reading of the $H_2O$ calibrated pH meter, here called pD*, was converted to pD values by using the expression pD = pD* + 0.4.[39]

For the $Mo^{VI}$–EDTAPr(3,4-HP)$_2$ system, $^{17}$O NMR spectroscopic measurements were carried out at 1:1 and 1:2 ligand-to-metal ion ratio with $C_M = 5.0 \times 10^{-2}$ M. The samples were prepared in 82% $H_2O$, 10% $D_2O$, and 8% $D_2O$ enriched for $^{17}$O (37.8% $^{17}$O and 48.8% $^{18}$O). The enrichment occurs in the Mo = O oxygen atoms and usually the ligand oxygen atoms are inert towards oxygen exchange. A Bruker AM 360 was used to record the spectra, and the chemical shifts are reported from the signal of the water which is considered as the internal reference, $\delta$ = 0 ppm.

The ESI mass spectra were obtained with a LCQ Duo (Finnigan, San Jose, CA, USA) ion trap mass spectrometer equipped with an electrospray ion source, operated in the positive mode. The spray voltage was kept at ±4.5 kV. The temperature of the heated capillary was set at 220 °C. The flow rate of the electrospray solution was 5 μL min$^{-1}$. Other parameters, including capillary voltage, lens and octapole voltages, and sheath gas flow rate were optimized for maximum abundance of the ions of interest.

The complex [$MoO_2$(3,4-DMHP)$_2$] was synthesized by a method similar to that described by Griffith,[29] by mixing an ammonium molybdate (5 mL, 230 mg, 1 mmol) aqueous solution with an equivalent amount of 3,4-DMHP (140 mg) previously dissolved in water (10 mL). The yellow solution was stirred for ca. 1 h at room temperature, and the precipitate was obtained, filtered, then washed with water, methanol, and ether, and dried in vacuo. A similar procedure was used for the ligands IDAPr(3,4-HP)$_2$ and EDTAPr(3,4-HP)$_2$, and the corresponding $Mo^{VI}$ complexes were obtained as yellow solids. [$MoO_2$(3,4-DMHP)$_2$.$H_2O$]: $C_{14}H_{18}MoN_2O_7$ (422.24): calcd. C 39.82, H 4.30, N 6.63; found C 39.8, H 4.1, N 6.8. [$Mo_3O_8$(IDAPr(3,4-HP)$_2$)·3$H_2O$]: $C_{22}H_{35}Mo_3N_5O_{17}$ (929.37): calcd. C 28.43, H 3.80, N 7.56, Mo 30.97; found C 28.2, H 3.9, N 7.7, Mo 31. [($MoO_2$)$_2$(EDTAPr(3,4-HP)$_2$)·7$H_2O$]: $C_{28}H_{50}Mo_2N_6O_{21}$ (998.60): calcd. C 33.68, H 5.05, N 8.42; found C 33.9, H 4.6, N 8.3.

For the $Mo^{VI}$ complexation with ligands IDAPr(3,4-HP)$_2$ and EDTAPr(3,4-HP)$_2$, "batch synthesis" procedures were also carried out. $Na_2MoO_4$ (0.0414 M; 8.46 mL, 0.350 mmol) was added to an aqueous solution (100 mL) of IDAPr(3,4-HP)$_2$ (0.170 mmol), and the initial pH was 9.98. This solution was divided into 10 mL samples at different pH values, set with 2 N and 0.2 N HCl solutions. When precipitation of the product occurred at pH < 7, the samples were filtered and the solids isolated. For the EDTAPr(3,4-HP)$_2$ system, a similar procedure was used, namely mixing a 0.0014 M ligand stock solution (50 mL, 0.070 mmol) with a 0.016 M ($NH_4$)$_6$-$Mo_7O_{24}$·4$H_2O$ solution (1.260 mL, 0.138 mmol of $Mo^{VI}$) and pH adjustment up to 9.16 with 2 M KOH solution. Several sample solutions were prepared at different pH values by using a 0.1 M HCl solution. Precipitation started at pH < 3, and the yellow solids were filtered and the corresponding mother solutions were preserved. The solutions were analyzed by ESI-MS whereas some of the solids were characterized by IR spectroscopy and elemental analysis.

**Supporting Information** (see footnote on the first page of this article): Overall stability constants for the species formed in measurable concentrations in the $H^+$–$MoO_4^{2-}$ equilibrium system; UV spectra for solutions containing free IDAPr(3,4-HP)$_2$ and IDAPr(3,4-HP)$_2$, and $Mo^{VI}$; graphical representation of the chemical shifts of the 5-H and 6-H of the hydroxypyridinone ring for the free ligand and for the $Mo^{VI}$–IDAPr(3,4-HP)$_2$ system; potentiometric titration curves of aqueous solutions containing $Mo^{VI}$ and EDDA at different molar ratios; concentration distribution curves for the complexes formed in the $Mo^{VI}$–EDDA system; concentration distribution curves but for the complexes formed in a hypothetical ternary system; UV spectra for solutions containing EDTAPr(3,4-HP)$_2$ free ligand, and in the presence of $Mo^{VI}$ and EDTAPr(3,4-HP)$_2$. $^{17}$O NMR spectra of solutions containing $Mo^{VI}$ and EDTAPr(3,4-HP)$_2$ at the indicated pH values and at ligand-to-metal ratio of 1:1; $^1$H NMR spectra of the aliphatic region for the same

 © 2007 Wiley-VCH Verlag GmbH & Co. KGaA, Weinheim 

systems; ESI-MS of $Mo^{VI}$–IDAPr(3,4-HP)$_2$ and $Mo^{VI}$–EDTAPr(3,4-HP)$_2$.

## Acknowledgments

The authors thank the Portuguese Foundation for Science and Technology (FCT) (PhD grant SFRH/BD/8743/02; Proj. PCDT/QUI/56985/04), the Hungarian Scientific Research Fund (OTKA T034674), and the COST D21/001 program for financial support. The authors are also grateful to the Group of Environmental and Biological Mass Spectrometry for providing the facilities to obtain the mass spectra.

[1] Z. D. Liu, R. C. Hider, *Med. Res. Rev.* **2002**, *22*, 26–64.
[2] G. J. Kontoghiorghes, *Br. Med. J. (Clin. Res. Ed.)*. **1988**, *296*, 1672–1673.
[3] G. J. Kontoghiorghes, *Hemoglobin* **2006**, *30*, 183–200; G. J. Kontoghiorghes, E. Eracleous, C. Economides, A. Kolganou, *Curr. Med. Chem.* **2005**, *12*, 2663–2681.
[4] M. Gomez, J. L. Esparza, J. L. Domingo, J. Corbella, P. K. Singh, M. M. Jones, *Pharmacol Toxicol (Copenhagen)* **1998**, *82*, 295–300.
[5] R. W. Shin, T. P. A. Kruck, H. Murayama, T. Kitamoto, *Brain Res.* **2003**, *961*, 139–146.
[6] M. A. Santos, *Coord. Chem. Rev.* **2002**, *228*, 187–203.
[7] Z. Zhang, D. M. Lyster, G. A. Webb, C. Orvig, *Int. J. Appl. Instrum. B* **1992**, *19*, 327–331.
[8] B. L. Ellis, C. B. Sampson, R. D. Abeysinghe, J. B. Porter, R. C. Hider, *Eur. J. Nucl. Med.* **1999**, *26*, 1400–1406.
[9] S. Chaves, M. Gil, S. Marques, L. Gano, M. A. Santos, *J. Inorg. Biochem.* **2003**, *97*, 161–172.
[10] M. A. Santos, M. Gil, L. Gano, S. Chaves, *J. Biol. Inorg. Chem.* **2005**, *10*, 564–580.
[11] M. A. Santos, S. Gama, L. Gano, G. Cantinho, E. Farkas, *Dalton Trans.* **2004**, 3772–3781.
[12] M. A. Santos, S. Gama, L. Gano, E. Farkas, *J. Inorg. Biochem.* **2005**, *99*, 1845–1852.
[13] A. Sigel, H. Sigel, *Molybdenum and Tungsten: Their Roles in Biological Processes*, Marcel Dekker, New York, **2002**, p. 810.
[14] A.-K. Duhme-Klair, G. Vollmer, C. Mars, R. Frohlich, *Angew. Chem. Int. Ed.* **2000**, *39*, 1626–1628.
[15] S. J. Lord, N. A. Epstein, R. L. Paddock, C. M. Vogels, T. L. Hennigar, M. J. Zaworotko, N. J. Taylor, W. R. Driedzic, T. L. Broderick, S. A. Westcott, *Can. J. Chem.* **1999**, *77*, 1249–1261.
[16] N. A. Epstein, J. L. Horton, C. M. Vogels, N. J. Taylor, S. A. Westcott, *Austr. J. Chem.* **2000**, *53*, 687–691.
[17] E. Farkas, P. Buglyo, E. A. Enyedy, V. A. Gerlei, M. A. Santos, *Inorg. Chim. Acta* **2002**, *339*, 215–223.
[18] E. Farkas, H. Csóka, I. Tóth, *Dalton Trans.* **2003**, 1645–1652.
[19] M. K. J. Gagnon, T. R. St. Germain, R. A. McNamara, C. M. Vogels, S. A. Westcott, *Austr. J. Chem.* **2000**, *53*, 693–697.
[20] E. Farkas, H. Csóka, G. Micera, A. Dessi, *J. Inorg. Biochem.* **1997**, *65*, 281–286.
[21] E. Farkas, K. Megyeri, L. Somsák, L. Kovács, *J. Inorg. Biochem.* **1998**, *70*, 41–47.
[22] E. T. Clarke, A. E. Martell, *Inorg. Chim. Acta* **1992**, *191*, 57–63.
[23] L. Zékány, I. Nagypál, *Computational Methods for the Determination of Stability Constants*, Plenum Press, New York, **1985**, pp. 291–353.
[24] R. J. Gualtieri, W. A. E. McBryde, H. K. J. Powell, *Can. J. Chem.* **1979**, *57*, 113–118.
[25] D. Sanna, I. Bodi, S. Bouhsina, G. Micera, T. Kiss, *J. Chem. Soc., Dalton Trans.* **1999**, 3275–3282.
[26] R. J. Kula, D. L. Rabenstein, *Anal. Chem.* **1966**, *38*, 1934–1936.
[27] J. C. Cobas, F. J. Sardina, *Concepts Magn. Reson. Part A* **2003**, *19A*, 80–96.
[28] Y. Liang, M. Hong, W. Su, R. Cao, J. Chen, *Helv. Chim. Acta* **2001**, *84*, 3393–3402.
[29] W. P. Griffith, S. I. Mostafa, *Polyhedron* **1992**, *11*, 2997–3005.
[30] E. I. Stiefel, *Comprehensive Coordination Chemistry*, Pergamon Press, **1987**, pp. 1375–1420.
[31] Z. Zhang, S. J. Rettig, C. Orvig, *Inorg. Chem.* **1991**, *30*, 509–515.
[32] A. R. Katritzky, R. A. Jones, *J. Chem. Soc.* **1960**, 2942–2947.
[33] B. Korpar-Colig, M. Cindric, D. Matkovic-Calogovic, V. Vrdoljak, B. Kamenar, *Polyhedron* **2002**, *21*, 147–153.
[34] E. J. Brown, A. C. Whitwood, P. H. Walton, A.-K. Duhme-Klair, *Dalton Trans.* **2004**, 2458–2462.
[35] E. Kahrovica, K. Molcanov, L. Tusek-Bozic, B. Kojic-Prodic, *Polyhedron* **2006**, *25*, 2459–2464.
[36] A. Bino, F. A. Cotton, Z. Dori, *J. Am. Chem. Soc.* **1979**, *101*, 3842–3847.
[37] G. Gran, *Acta Chem. Scand.* **1950**, *4*, 559–577.
[38] H. M. Irving, M. G. Miles, L. D. Pettit, *Anal. Chim. Acta* **1967**, *38*, 475–488.
[39] A. Krezel, W. Bal, *J. Inorg. Biochem.* **2004**, *98*, 161–166.

Received: November 20, 2006
Published Online: March 16, 2007

 © 2007 Wiley-VCH Verlag GmbH & Co. KGaA, Weinheim 

DOI: 10.1002/ejic.200601215

# Rhodium(I) Complexes Containing β-Amino Alcohol and 1,2-Diamine Ligands: Syntheses, Structures, and Catalytic Applications

**Lutz Dahlenburg,*[a] Harald Treffert,[a] Christian Farr,[a] Frank W. Heinemann,[a] and Achim Zahl[a]**

**Keywords:** Rhodium / N,O ligands / N,N ligands / X-ray diffraction / Catalysis

The bridge-opening reaction of $[(\eta^4\text{-}C_8H_{12})_2Rh_2(\mu\text{-}Cl)_2]$ with chiral and achiral β-amino alcohol nucleophiles gave mononuclear complexes $[(\eta^4\text{-}C_8H_{12})RhCl\{HN(R)\cap OH\text{-}\kappa N\}]$ containing the amino alcohol ligands in N-monodentate coordination; HN(R)∩OH = ethanolamine (**4**), 2-amino-2-methyl-1-propanol (**5**), and either enantiomer of (*R*)-, (*S*)-2-amino-3-methyl-1-butanol (D-, L-valinol) [(*R*)-**6**, (*S*)-**6**], (*R*)-, (*S*)-2-pyrrolidinemethanol (D-, L-prolinol) [(*R*)-**7**, (*S*)-**7**], (1*S*,2*R*)-, (1*R*,2*S*)-2-amino-1-phenyl-1-propanol (D-, L-norephedrine) [(1*S*,2*R*)-**8**, (1*R*,2*S*)-**8**], and (1*S*,2*R*)-, (1*R*,2*S*)-*cis*-1-amino-2-indanol [(1*S*,2*R*)-**9**, (1*R*,2*S*)-**9**]. Coordination of the free hydroxy function of the N,O ligands was brought about by both dehydrochlorination, which furnished the neutral valinolato chelate complex $[(\eta^4\text{-}C_8H_{12})Rh\{(S)\text{-}H_2NCH(CHMe_2)CH_2O\text{-}\kappa N,\kappa O\}]$, (*S*)-**10**, and by precipitation of the metal-bound chloride with $TlO_3SCF_3$ to produce ionic chelate complexes $[(\eta^4\text{-}C_8H_{12})Rh\{HN(R)\cap OH\text{-}\kappa N,\kappa O\}]O_3SCF_3$; HN(R)∩OH = 2-amino-2-methyl-1-propanol (**11**), (*S*)-2-amino-3-methyl-1-butanol [(*S*)-**12**], (*S*)-2-pyrrolidinemethanol [(*S*)-**13**], (1*R*,2*S*)-2-amino-1-phenyl-1-propanol [(1*R*,2*S*)-**14**], and (1*R*,2*S*)-*cis*-1-amino-2-indanol [(1*R*,2*S*)-**15**]. Except for only two in situ characterized $[\{(R)\text{-binap}\}Rh(H_2N\cap OH\text{-}\kappa N,\kappa O)]^+$ cations, where H₂N∩OH = L-valinol or L-norephedrine, no compound containing the various N,O ligands in addition to mono- or bidentate phosphanes could be prepared. In contrast, the $P_2/N_2$-coordinated chelate complexes $[\{(R)\text{-binap}\}Rh(H_2N\cap NH_2)]BF_4$ with $H_2N\cap NH_2 = H_2NCMe_2CMe_2NH_2$ [(*R*)-(**16**)], (*R*,*R*)-$H_2NCH(Ph)CH(Ph)NH_2$ [(*R*),(*R*,*R*)-**17**], and (*R*,*R*)-1,2-$(H_2N)_2C_6H_{10}$ [(*R*),(*R*,*R*)-**18**] were easily obtained from $[(\eta^4\text{-}C_8H_{12})Rh\{(R)\text{-binap}\}]BF_4$ and 1,2-diamines. Oxidative addition of HCl to (*R*),(*R*,*R*)-**17** produced *trans*-$[\{(R)\text{-binap}\}Rh(H)(Cl)\{(R,R)\text{-}H_2NCH(Ph)CH(Ph)NH_2\}]BF_4$ [(*R*),(*R*,*R*)-**19**]. If activated by strong base (KOH), (*R*),(*R*,*R*)-**17** and (*R*),(*R*,*R*)-**19** acted as moderately active and enantioselective catalysts for the reduction of acetophenone by both direct and transfer hydrogenation: $ee_{max}$: 71% (*S*). The crystal structures of **4**, (*S*)-**6**, (*R*)-**7**, (1*R*,2*S*)-**8**, (*S*)-**10**, (1*R*,2*S*)-**14**, (1*R*,2*S*)-**15**, (*R*)-**16**, (*R*),(*R*,*R*)-**17**, and two alcohol/alcoholato addition compounds, $[(\eta^4\text{-}C_8H_{12})Rh(H_2NCMe_2CH_2O\text{-}\kappa N,\kappa O)][(\eta^4\text{-}C_8H_{12})Rh(H_2NCMe_2CH_2OH\text{-}\kappa N,\kappa O)][(\eta^4\text{-}C_8H_{12})RhCl_2]$ [**1·2**], and $[(\eta^4\text{-}C_8H_{12})Rh(H_2NCMe_2CH_2O\text{-}\kappa N,\kappa O)][(\eta^4\text{-}C_8H_{12})Rh(H_2NCMe_2CH_2OH\text{-}\kappa N,\kappa O)]Cl$ [**1·3**], were determined.

(© Wiley-VCH Verlag GmbH & Co. KGaA, 69451 Weinheim, Germany, 2007)

## Introduction

Our recent activities have focused on the catalytic potential of iridium (and rhodium) complexes bearing various β-aminophosphanes derived from optically active amino alcohols in asymmetric C=O hydrogenation reactions.[1] Following these studies, we have turned our attention to coordination compounds of the two platinum metals containing the very same β-amino alcohols and some akin 1,2-diamines as ligands.

Whereas ruthenium(II) complexes with N,O- and N,N donors − in particular, *N*-methyl-1,2-diphenylethanolamine and 1,2-diphenylethylenediamine − are well known to serve as efficient catalysts for the asymmetric hydrogenation and transfer hydrogenation of ketones and imines,[2] virtually no systematic studies on amino alcohol compounds of rhodium or iridium in their +1 or +3 oxidation states have so far been reported. Noteworthy exceptions are (1) the (amino alcoholato)rhodium(III) chelate $[\{\eta^5\text{-}C_5Me_4\text{-}(1R,2S)\text{-}C_6H_4CH_2NHCH(Me)CH(Ph)O\text{-}\kappa N,\kappa O\}RhCl]$, which contains an *N*-benzyl-(L)-norephedrine component tethered to a tetramethylcyclopentadienyl ligand and has been used as a highly active catalyst for the asymmetric reduction of ketones,[3] and (2) the acetate salt of the $[(\eta^4\text{-}C_8H_{12})Rh\{(S)\text{-}H_2NCH(Ph)CH_2OH\text{-}\kappa N,\kappa O\}]^+$ cation published only recently in this journal.[4]

Furthermore, notwithstanding that cationic $[(\eta^4\text{-}C_8H_{12})M(diamine)]^+$ complexes, where M = Rh or Ir and diamine = ethylenediamine, *o*-phenylenediamine, 1,8-diaminonaphthalene, and the like, are well-documented,[5] we are not aware of any previously described diphosphane(diamine)-coordinated cations $[M(R_2P\cap PR_2)(H_2N\cap NH_2)]^+$ or $[M(X)(Y)(R_2P\cap PR_2)(H_2N\cap NH_2)]^+$ (X, Y = halide, hy-

[a] Institut für Anorganische Chemie der Universität Erlangen-Nürnberg
Egerlandstrasse 1, 91058 Erlangen, Germany
Fax: +49-9131-85-27387
E-mail: Lutz.Dahlenburg@chemie.uni-erlangen.de

 InterScience © 2007 Wiley-VCH Verlag GmbH & Co. KGaA, Weinheim 

dride) which, at least from a structural point of view, bear a direct resemblance to the famous $[Ru(X)(Y)(R_2P\cap PR_2)(H_2N\cap NH_2)]$ hydrogenation catalysts. A limited number of examples coming closest to the so far unknown diphosphane(diamine) chelate compounds of the two metals include the dihydrides $[MH_2(PPh_3)_2(H_2NC_2H_4NH_2)]^+$ (M = Rh,[6] Ir[7]) along with only two in situ characterized $Rh^{I}$ species, $[Rh\{(S)\text{-binap}\}(NEt_3)_2]^+$[8] and $[Rh(dppe)(NH_3)_2]^+$,[9] respectively.

Using the chlorido-bridged dimer $[(\eta^4\text{-}C_8H_{12})_2Rh_2(\mu\text{-}Cl)_2]$ as a common starting material, we have obtained a family of (cyclooctadiene)rhodium(I) complexes containing both chiral and achiral amino alcohols in κ*N*-monodentate and κ*N*,κ*O*-bidentate coordination. It is envisaged that such compounds and some related (diphosphane)diamine chelate complexes $[Rh\{(R)\text{-binap}\}(H_2N\cap NH_2)]^+$, both of which are the subject of this communication, can be useful for the construction of stereoselective catalysts,[10] and a first account of their application to homogeneous C=O hydrogenation is given in the following.

## Results and Discussion

### β-Amino Alcohol Complexes

Initial attempts were directed towards the synthesis of amino alcoholato derivatives of $Rh^{I}$ by treating $[(\eta^4\text{-}C_8H_{12})_2Rh_2(\mu\text{-}Cl)_2]$ with solutions of the respective sodium alkoxides $H_2N\cap ONa$ in $H_2N\cap OH$/toluene. Although such experiments did produce amino alcoholato complexes as desired, their results remained inconclusive in that mixtures of the neutral and ionic chelates, $[(\eta^4\text{-}C_8H_{12})Rh(H_2N\cap O\text{-}\kappa N,\kappa O)]$ and $[(\eta^4\text{-}C_8H_{12})Rh(H_2N\cap OH\text{-}\kappa N,\kappa O)]^+$, were formed. Thus, the sodium salt of 2-amino-2-methyl-1-propanol reacted in $H_2NCMe_2CH_2OH$/toluene to give $[(\eta^4\text{-}C_8H_{12})Rh(H_2NCMe_2CH_2O\text{-}\kappa N,\kappa O)]$ (**1**) as the wanted target complex but also furnished the amino alcohol chelated salts $[(\eta^4\text{-}C_8H_{12})Rh(H_2NCMe_2CH_2OH\text{-}\kappa N,\kappa O)][(\eta^4\text{-}C_8H_{12})RhCl_2]$ (**2**) and $[(\eta^4\text{-}C_8H_{12})Rh(H_2NCMe_2CH_2OH\text{-}\kappa N,\kappa O)]Cl$ (**3**) as unwanted byproducts. Repeated crystallizations of such mixtures and subsequent single-crystal X-ray diffraction studies revealed that **1** and **2** cocrystallized from thf/*n*-pentane as the addition compound **1·2**·thf stabilized by multiple O–H···O, N–H···O, and N–H···Cl hydrogen bonding interactions, whereas **1** and **3** were separated from solution as the likewise hydrogen-bonded adduct **1·3**, if crystallized from toluene/*n*-hexane mixtures.

In the structure of **1·2**·thf, the two rhodium-alcohol(ato) constituents were located on crystallographically independent positions of a triclinic unit cell (space group $P\bar{1}$) and, hence, could be distinguished without difficulty (Figure 1). In contrast, the tetragonal unit cell of **1·3** (crystallizing in the space group $P\bar{4}2c$) was found to contain neutral $[(\eta^4\text{-}C_8H_{12})Rh(H_2NCMe_2CH_2O\text{-}\kappa N,\kappa O)]$ and cationic $[(\eta^4\text{-}C_8H_{12})Rh(H_2NCMe_2CH_2OH\text{-}\kappa N,\kappa O)]^+$ on symmetry-related sites such that the mixed composition of the compound was only evident from the presence of one chloride anion spread with quarter occupancies over special positions *a* and *b* of the cell (Figure 2). For the two structures, the rhodium–oxygen and rhodium–nitrogen bond lengths fall in the usual range.[11] The molecular parameters of the $[(\eta^4\text{-}C_8H_{12})RhCl_2]^-$ anion also deserve no further comment as they are very similar to those previously measured for the same ion in a number of related $[(\eta^4\text{-}C_8H_{12})RhL_2][(\eta^4\text{-}C_8H_{12})RhCl_2]$ complexes.[11]

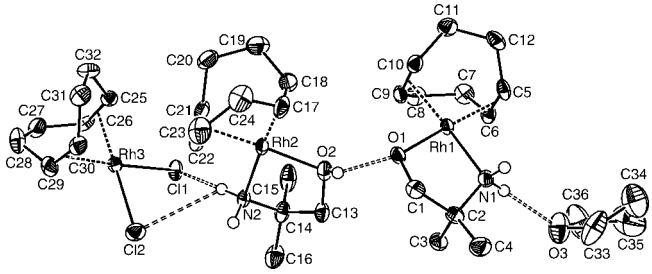


Figure 1. Molecular structure of the addition compound $[(\eta^4\text{-}C_8H_{12})Rh(H_2NCMe_2CH_2O\text{-}\kappa N,\kappa O)]\cdot[(\eta^4\text{-}C_8H_{12})Rh(H_2NCMe_2CH_2OH\text{-}\kappa N,\kappa O)][(\eta^4\text{-}C_8H_{12})RhCl_2]\cdot$thf (**1·2**·thf), which shows the multiple O–H···O, N–H···O, and N–H···Cl hydrogen bonding interactions (H atoms of the diolefin ligand are omitted for clarity). Selected bond lengths [Å] and angles [°]: Rh1–O1, 2.053(3); Rh1–N1, 2.093(4); Rh2–O2, 2.065(4); Rh2–N2, 2.098(4); Rh3–Cl1, 2.387(1); Rh3–Cl2, 2.372(2). O1–Rh1–N1, 81.2(1); O2–Rh2–N2, 80.4(1); Cl1–Rh3–Cl2, 89.47(5). Hydrogen-bonding interactions as D–H, H···A, D···A, D–H···A [Å °]: O2–H···O1, 0.82, 1.79, 2.417(5), 132.5; N1–H···O3, 0.92, 2.15, 3.015(6), 155.4; N2–H···Cl1, 0.92, 2.55, 3.447(4), 165.5; N2–H···Cl2, 0.92, 2.95, 3.422(5), 113.6; N1–H···Cl1_#1, 0.92, 2.40, 3.289(5), 163.3; N2–H···Cl2_#2, 0.92, 2.65, 3.353(4), 133.6. Symmetry transformations used to generate equivalent atoms: #1 = $x$, $y+1$, $z$; #2 = $-x+1$, $-y-1$, $-z$.

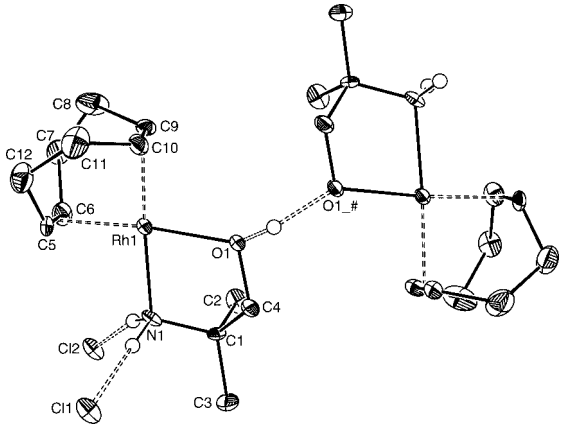


Figure 2. Molecular structure of the hydrogen-bonded amino alcohol/amino alcoholato adduct $[(\eta^4\text{-}C_8H_{12})Rh(H_2NCMe_2CH_2O\text{-}\kappa N,\kappa O)]\cdot[(\eta^4\text{-}C_8H_{12})Rh(H_2NCMe_2CH_2OH\text{-}\kappa N,\kappa O)]Cl$ (**1·3**), where the two complex moieties reside on symmetry-related positions and the chloride counterion is distributed with 1/4 occupancies over special sites *a* (0, 0, 3/4) and *b* (0, 1/2, 3/4) of space group $P\bar{4}2c$ (H atoms of the diolefin ligand are omitted for clarity). Selected bond lengths [Å] and angles [°]: Rh1–O1, 2.074(5); Rh1–N1, 2.112(5). O1–Rh1–N1, 81.0(2). Hydrogen-bonding interactions as D–H, H···A, D···A, D–H···A [Å °]: O1–H···O1_#, 0.85, 1.55, 2.396(9), 171.3; N1–H···Cl1, 0.92, 2.43, 3.339(5), 168.9; N1–H···Cl2, 0.92, 2.51, 3.418(5), 167.9. Symmetry transformation used to generate equivalent atoms: #1 = $-x+1$, $y$, $-z+1$.

The transformation of $[(\eta^4\text{-}C_8H_{12})_2Rh_2(\mu\text{-}Cl)_2]$ by the $H_2NCMe_2CH_2ONa/H_2NCMe_2CH_2OH$ mixture to give, in

 © 2007 Wiley-VCH Verlag GmbH & Co. KGaA, Weinheim 

addition to neutral alcoholato complex **1**, the ionic products $[(\eta^4\text{-}C_8H_{12})Rh(H_2NCMe_2CH_2OH\text{-}\kappa N,\kappa O)][(\eta^4\text{-}C_8H_{12})RhCl_2]$ (**2**) and $[(\eta^4\text{-}C_8H_{12})Rh(H_2NCMe_2CH_2OH\text{-}\kappa N,\kappa O)]Cl$ (**3**) is reminiscent of some bridge-cleaving reactions of the dimer with a number of aliphatic diamines described in earlier work, where either ion-pair complexes $[(\eta^4\text{-}C_8H_{12})Rh(diamine)][(\eta^4\text{-}C_8H_{12})RhCl_2]$ or chloride-containing products $[(\eta^4\text{-}C_8H_{12})Rh(diamine)Cl]$ were obtained. Different from **3**, however, the latter were formulated as neutral pentacoordinate rather than ionic tetracoordinate species.[5e]

From the above results it was inferred that better-defined products could arise from preparations that avoid the presence of alkoxide base in the initial reaction solutions. Hence, further experiments used the $[(\eta^4\text{-}C_8H_{12})_2Rh_2(\mu\text{-}Cl)_2]$ starting compound together with toluene dilutions of the pure amino alcohols. Under these conditions, smooth opening of the chloride bridges by the amine nucleophiles was observed to give high yields of mononuclear products $[(\eta^4\text{-}C_8H_{12})RhCl\{HN(R)\cap OH\text{-}\kappa N\}]$ (R = H, alkyl), **4**–**9**, containing the amino alcohol ligands in monodentate coordination: HN(R)∩OH = ethanolamine (**4**), 2-amino-2-methyl-1-propanol (**5**), as well as either enantiomer of (*R*)-, (*S*)-2-amino-3-methyl-1-butanol (D-, L-valinol) [(*R*)-**6**, (*S*)-**6**], (*R*)-, (*S*)-2-pyrrolidinemethanol (D,- L-prolinol) [(*R*)-**7**, (*S*)-**7**], (1*S*,2*R*)-, (1*R*,2*S*)-2-amino-1-phenyl-1-propanol (D-, L-norephedrine) [(1*S*,2*R*)-**8**, (1*R*,2*S*)-**8**], and (1*S*,2*R*)-, (1*R*,2*S*)-*cis*-1-amino-2-indanol [(1*S*,2*R*)-**9**, (1*R*,2*S*)-**9**], respectively (Scheme 1).

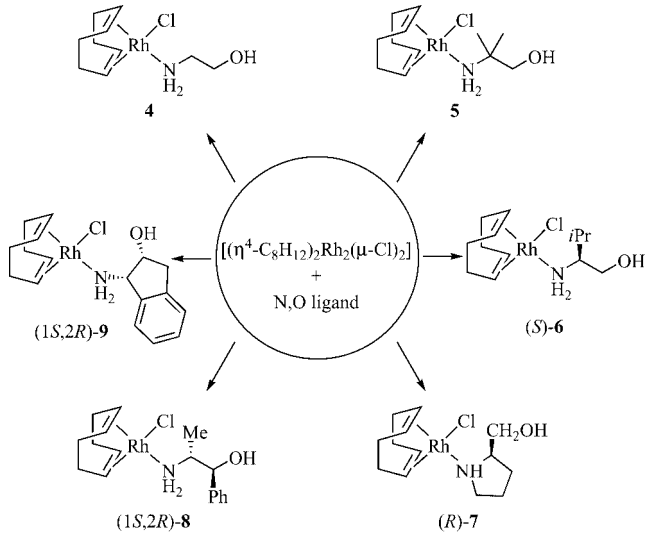


Scheme 1. Synthesis of κ*N*-monodentate amino alcohol complexes **4**–**9**; only one enantiomer of chiral molecules **6**–**9** is drawn.

Complexes **4**–**9** form relatively air-stable yellow crystals which are readily soluble in the more polar solvents, for example methanol, thf, $CHCl_3$, $CH_2Cl_2$, and the like. From such solutions, compounds **4**, (*S*)-**6**, (*R*)-**7**, and (1*R*,2*S*)-**8** (crystallizing as a solvate with the idealized composition $[(\eta^4\text{-}C_8H_{12})RhCl\{(1R,2S)\text{-}H_2NCH(Me)CH(Ph)CH_2OH\}]\cdot 1/4CH_2Cl_2\cdot 1/4thf$) were isolated as single-crystals and subjected to X-ray structure analyses (Figures 3, 4, 5, and 6. Whereas the asymmetric units of **4** and (*S*)-**6** comprised one complex molecule each, two crystallographically independent molecules with partially disordered pyrrolidine and cyclooctadiene rings were found in structures (*R*)-**7** and (1*R*,2*S*)-**8**. In the solid-state packing of the four compounds, the individual complexes are assembled through O–H···Cl and N–H···Cl hydrogen bonds from the dangling hydroxy group and the ligated amino groups to the chlorido ligands of neighboring molecules. Not unexpectedly, neither the Rh–Cl distances (2.381–2.398 Å) nor the Rh–$NH_2$ bond lengths (2.127–2.137 Å) displayed any significant differences.

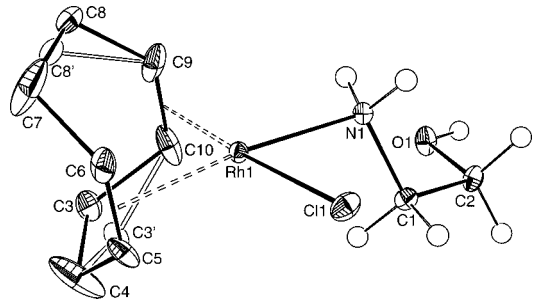


Figure 3. Molecular structure of $[(\eta^4\text{-}C_8H_{12})RhCl\text{-}(H_2NCH_2CH_2OH\text{-}\kappa N)]$ (**4**), which shows the twofold disorder of two methylene C atoms in the $C_8H_{12}$ ring (H atoms of the diolefin ligand are omitted for clarity). Selected bond lengths [Å] and angles [°]: Rh1–Cl1, 2.3930(4); Rh1–N1, 2.128(2). Cl1–Rh1–N1, 88.38(4). Hydrogen-bonding interactions as D–H, H···A, D···A, D–H···A [Å [°]]: O1–H···Cl1_#1, 0.84, 2.39, 3.128(2), 147.5; N1–H···Cl1_#2, 0.92, 2.73, 3.623(2), 164.5; N1–H···O1_#3, 0.92, 2.19, 3.002(2), 147.3. Symmetry transformations used to generate equivalent atoms: #1 = $-x+2$, $y+1/2$, $-z+1/2$; #2 = $x$, $-y+11/2$, $z-1/2$; #3 = $x$, $-y+11/2$, $z+1/2$.

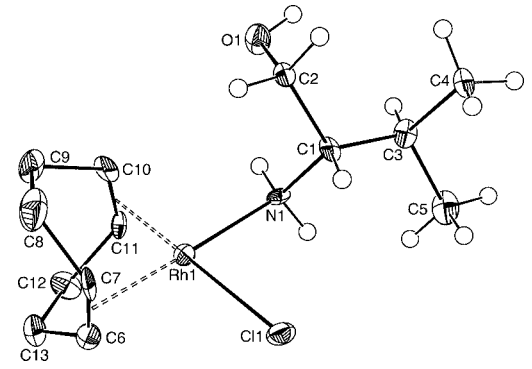


Figure 4. Molecular structure of $[(\eta^4\text{-}C_8H_{12})RhCl\{(S)\text{-}H_2NCH(CHMe_2)CH_2OH\text{-}\kappa N\}]$, (*S*)-**6** (H atoms of the diolefin ligand are omitted for clarity). Selected bond lengths [Å] and angles [°]: Rh1–Cl1, 2.395(3); Rh1–N1, 2.127(8). Cl1–Rh1–N1, 86.5(2). Hydrogen-bonding interactions as D–H, H···A, D···A, D–H···A [Å [°]]: O1–H···Cl1_#1, 0.84, 2.42, 3.250(8), 171.5; N1–H···Cl1_#2, 0.92, 2.57, 3.301(9), 137.2. Symmetry transformations used to generate equivalent atoms: #1 = $-x+1$, $y+1/2$, $-z$; #2 = $-x$, $y+1/2$, $-z$.

For converting the $[(\eta^4\text{-}C_8H_{12})RhCl\{HN(R)\cap OH\text{-}\kappa N\}]$ complexes into N,O-chelated derivatives, two obvious approaches can be taken into account: (1) removal of both the chlorido ligand and the OH proton by base to give neutral amino alcoholato products $[(\eta^4\text{-}C_8H_{12})Rh\{HN(R)\cap O\text{-}$

 © 2007 Wiley-VCH Verlag GmbH & Co. KGaA, Weinheim 

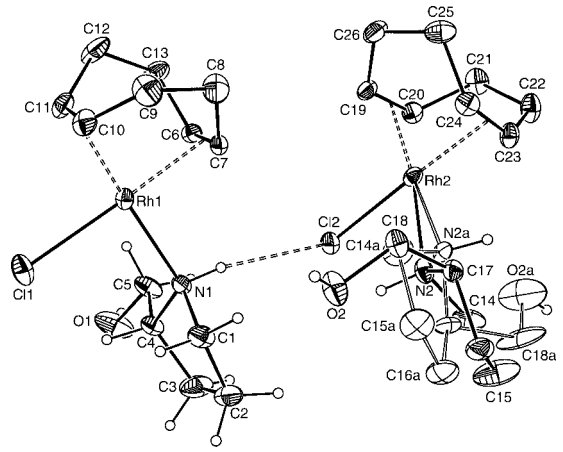


Figure 5. Structure of the two crystallographically independent hydrogen-bonded molecules of $[(\eta^4\text{-}C_8H_{12})RhCl\{(R)\text{-}HN(CH_2CH_2CH_2CH)CH_2OH\text{-}\kappa N\}]$, (*R*)-**7** (H atoms of the diolefins and the disordered D-prolinol ligand are omitted for clarity). Selected bond lengths [Å] and angles [°]: Rh1–Cl1, 2.381(2); Rh1–N1, 2.134(4); Rh2–Cl2, 2.397(2); Rh2–N2, 2.13(1); Rh2–N2A, 2.18(1). Cl1–Rh1–N1, 90.3(1); Cl2–Rh2–N2, 77.4(3); Cl2–Rh2–N2A, 95.4(3). Hydrogen-bonding interactions as D–H, H···A, D···A, D–H···A [Å [°]]: N1–H···Cl2, 0.92, 2.52, 3.432(4), 170.0; O1–H···Cl1_#1, 0.83, 2.24, 3.057(7), 167.8; O2–H···Cl2_#2, 0.83, 2.32, 3.13(1), 164.6; O2A–H···O1_#3, 0.83, 2.10, 2.51(2), 110.3; N2A–H···Cl1_#3, 0.92, 2.84, 3.72(1), 161.2. Symmetry transformations used to generate equivalent atoms: #1 = *x*, *y*+1, *z*; #2 = *x*, *y*–1, *z*; #3 = *x*–1, *y*, *z*.

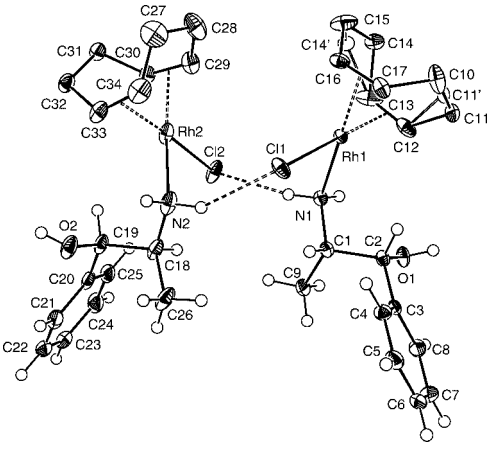


Figure 6. Structure of the two crystallographically independent hydrogen-bonded complex molecules (1*R*,2*S*)-**8** of $[(\eta^4\text{-}C_8H_{12})RhCl\{(1R,2S)\text{-}H_2NCH(Me)CH(Ph)OH\text{-}\kappa N\}]\cdot 1/4CH_2Cl_2\cdot 1/4thf$, which shows the twofold disorder of two methylene C atoms in one of the $C_8H_{12}$ ligands (cyclooctadiene H atoms and solvate molecules are omitted for clarity). Selected bond lengths [Å] and angles [°]: Rh1–Cl1, 2.3912(4); Rh1–N1, 2.134(2); Rh2–Cl2, 2.3982(5); Rh2–N2, 2.137(2). Cl1–Rh1–N1, 88.16(5); Cl2–Rh2–N2, 88.54(5). Hydrogen-bonding interactions as D–H, H···A, D···A, D–H···A [Å [°]]: N1–H···Cl2, 0.92, 2.38, 3.281(2), 167.7; N2–H···Cl1, 0.92, 2.52, 3.338(2), 148.8; O1–H···Cl2_#1, 0.84, 2.28, 3.109(2), 171.8; O2–H···Cl1_#3, 0.84, 2.28, 3.111(2), 172.6; N1–H···ClCH$_2$Cl_#2, 0.92, 2.88, 3.703(3), 149.5; N2–H···ClH$_2$Cl_#3, 0.92, 2.83, 3.646(5), 148.8; N2–H···OC$_4$H$_8$_#3, 0.92, 2.34, 3.137(4), 144.5. Symmetry transformations used to generate equivalent atoms: #1 = -*x*+1, *y*–1/2, –*z*+1; #2 = –*x*+1, *y*+1/2, –*z*+1; #3 = –*x*+1, *y*+1/2, –*z*+2.

κ*N*,κ*O*}]; (2) precipitation of the metal-bound chloride as, for example, AgCl or TlCl to afford cationic amino alcohol chelates $[(\eta^4\text{-}C_8H_{12})Rh\{HN(R)\cap OH\text{-}\kappa N,\kappa O\}]^+$.

Method (1) was probed by using $[(\eta^4\text{-}C_8H_{12})RhCl\{(S)\text{-}H_2NCH(CHMe_2)CH_2OH\text{-}\kappa N\}]$ [(*S*)-**6**] together with powdered KOH in $CH_2Cl_2$ (Scheme 2). This dehydrochlorination reaction furnished the "valinolato" chelate complex $[(\eta^4\text{-}C_8H_{12})Rh\{(S)\text{-}H_2NCH(CHMe_2)CH_2O\text{-}\kappa N,\kappa O\}]$ [(*S*)-**10**] which crystallized from the reaction solution in the (rare) triclinic space group *P*1 with one molecule of lattice water per formula unit. The water of crystallization served to assemble two molecules of (*S*)-**10**·$H_2O$ in the unit cell by multiple N–H···$OH_2$ and O–H···O hydrogen bonds, as shown in Figure 7. The metal-to-nitrogen und metal-to-oxygen bond lengths as well as the O–Rh–N angles closely resemble those measured for $[(\eta^4\text{-}C_8H_{12})Rh(H_2NCMe_2\text{-}CH_2O\text{-}\kappa N,\kappa O)]$ (**1**) in its thf-solvated addition compound with $[(\eta^4\text{-}C_8H_{12})Rh(H_2NCMe_2CH_2OH\text{-}\kappa N,\kappa O)][(\eta^4\text{-}C_8H_{12})RhCl_2]$ (**2**).

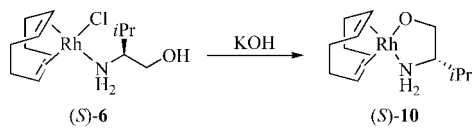


Scheme 2. Formation of L-valinolato chelate complex (*S*)-**10** by dehydrochlorination of (*S*)-**6**.

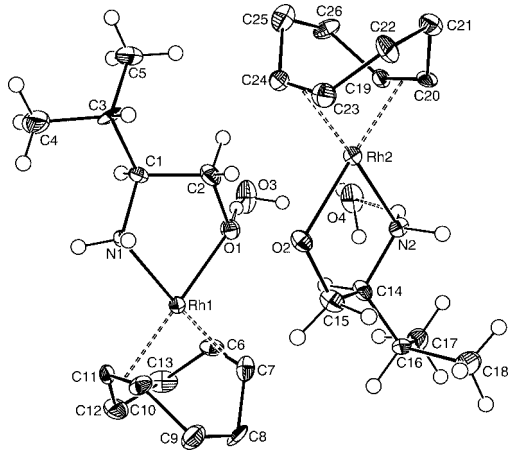


Figure 7. Structure of the two lattice water-containing molecules $[(\eta^4\text{-}C_8H_{12})Rh\{(S)\text{-}H_2NCH(CHMe_2)CH_2O\text{-}\kappa N,\kappa O\}]\cdot H_2O$ [(*S*)-**10**·$H_2O$] which fill the triclinic unit cell of space group *P*1 (cyclooctadiene H atoms are omitted for clarity). Selected bond lengths [Å] and angles [°]: Rh1–O1, 2.037(7); Rh1–N1, 2.102(7); Rh2–O2, 2.041(6); Rh2–N2, 2.126(8). O1–Rh1–N1, 82.9(3); O2–Rh2–N2, 81.4(3). Hydrogen-bonding interactions as D–H, H···A, D···A, D–H···A [Å [°]]: O3–H···O1, 0.85, 2.00, 2.83(1), 167.0; N2–H···O4, 0.92, 1.94, 2.77(1), 148.9; O3–H···O2_#1, 0.85, 1.95, 2.77(1), 162.2; O4–H···O2_#1, 0.85, 1.94, 2.69(1), 146.5; N1–H···O3_#2, 0.92, 2.00, 2.92(1), 171.6. Symmetry transformations used to generate equivalent atoms: #1 = *x*–1, *y*, *z*; #2 = *x*+1, *y*, *z*.

Attempts to induce chelation of the unligated hydroxy groups of complexes **4**–**9** by reaction with soluble silver salts such as $AgBF_4$ or $AgO_3SCF_3$ according to method (2) resulted in the deposition of elemental silver rather than silver chloride with concomitant decomposition of the com-

 © 2007 Wiley-VCH Verlag GmbH & Co. KGaA, Weinheim 

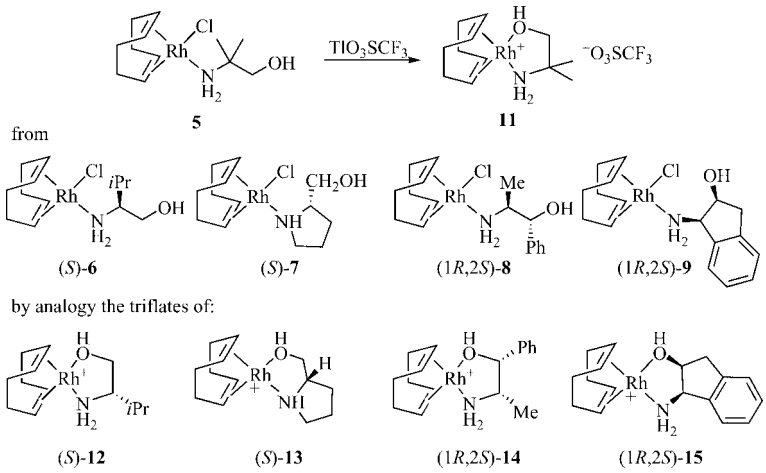


Scheme 3. Synthesis of triflate salts **11**–**15** containing chelated β-amino alcohol ligands.

pounds. Reduction of the $Ag^+$ ion is most likely caused by the free OH functions of the amino alcohols as may be judged from the standard electrode potentials for the equilibria "$Ag^+ + e^- = Ag$" ($E^0 = +0.799$ V) and, as a rough estimate, "$CH_3CHO + 2\ H^+ + 2\ e^- = C_2H_5OH$" ($E^0 = +0.192$ V).[12] Because of the low standard potential of the redox couple $Tl^+/Tl$ ($E^0 = -0.336$ V), thallium(I) trifluoromethanesulfonate proved to be a more suitable chloride-precipitating reagent, which smoothly converted the [($\eta^4$-$C_8H_{12}$)RhCl{HN(R)∩OH-κ*N*}] complexes into the triflate salts [($\eta^4$-$C_8H_{12}$)Rh{HN(R)∩OH-κ*N*,κ*O*}]$O_3SCF_3$, where HN(R)∩OH-κ*N*,κ*O* stands for chelated 2-amino-2-methyl-1-propanol (**11**), (*S*)-2-amino-3-methyl-1-butanol (L-valinol) [(*S*)-**12**], (*S*)-2-pyrrolidinemethanol (L-prolinol), [(*S*)-**13**], (1*R*,2*S*)-2-amino-1-phenyl-1-propanol (L-norephedrine) [(1*R*,2*S*)-**14**], and (1*R*,2*S*)-*cis*-1-amino-2-indanol [(1*R*,2*S*)-**15**] (Scheme 3). As mentioned in the introductory section, the closely related (*S*)-2-amino-2-phenylethanol containing compound [($\eta^4$-$C_8H_{12}$)Rh{(*S*)-$H_2$NCH(Ph)-$CH_2$OH-κ*N*,κ*O*}]$O_2$CMe was only recently isolated from the bridge-cleaving reaction of the amino alcohol with the [($\eta^4$-$C_8H_{12}$)$_2$Rh$_2$(μ-$O_2$CMe)$_2$] dimer.[4]

Complexes (1*R*,2*S*)-**14** and (1*R*,2*S*)-**15** were fully characterized by single-crystal X-ray diffraction (Figures 8 and 9). In both structures, the complex cations and their counterions are linked by hydrogen-bonding interactions from the coordinated amino and hydroxy donors to the triflate anion acceptors. Relative to the metal-to-oxygen bond lengths measured for the two crystallographically independent molecules of alcoholato complex (*S*)-**10**, 2.037(7) and 2.041(6) Å, the Rh–O separations observed for (1*R*,2*S*)-**14**, 2.125(3) Å, and the two cations filling the asymmetric unit of (1*R*,2*S*)-**15**, 2.086(4) and 2.089(4) Å, tend to be slightly elongated, which thereby reflects the weaker bonding capabilities of neutral alcohol than those of anionic alkoxo donor groups.

In the $^1$H NMR spectra of both the monodentate and the chelated amino alcohol complexes [($\eta^4$-$C_8H_{12}$)-RhCl{HN(R)∩OH-κ*N*}] (**4**–**9**) and [($\eta^4$-$C_8H_{12}$)Rh{HN(R)-∩OH-κ*N*,κ*O*}]$O_3SCF_3$ (**11**–**15**) measured at ambient temperature, largely unresolved broad multiplets, each accounting for four protons, are observed for the allylic $CH_2$ ($\delta \approx$ 1.6–1.8 and 2.3–2.5 ppm) and the olefinic CH groups ($\delta \approx$ 4.0–4.2 ppm) of the diene ligand. In the $^{13}$C NMR spectra, the olefinic carbon atoms similarly give rise to very broad signals centered at $\delta \approx$ 77–83 ppm; the resonances of the methylene carbon atoms appear as either one or two singlets ($\delta \approx$ 29–32 ppm), which likewise show line broadening. From these NMR spectroscopic data it is apparent that a dynamic process occurs in solution, which averages the chemical nonequivalency of the CH=CH groups that are bound *trans* to N and Cl in **4**–**9** and *trans* to N and O in **11**–**15**, respectively.

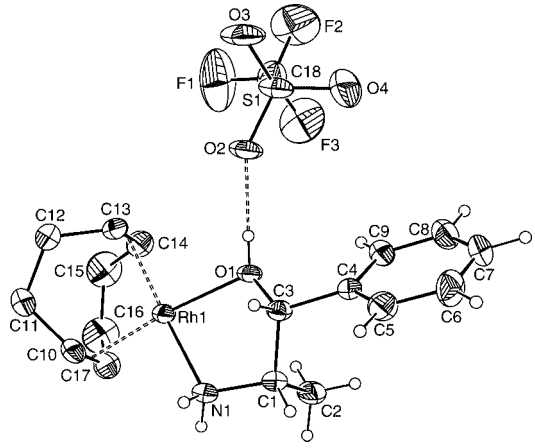


Figure 8. Structure of the ion pair [($\eta^4$-$C_8H_{12}$)Rh{(1*R*,2*S*)-$H_2$NCH(Me)CH(Ph)OH-κ*N*,κ*O*}]$O_3SCF_3$ [(1*R*,2*S*)-**14**] (cyclooctadiene H atoms are omitted for clarity). Selected bond lengths [Å] and angles [°]: Rh1–O1, 2.125(3); Rh1–N1, 2.112(4). O1–Rh1–N1, 78.8(1). Hydrogen-bonding interactions as D–H, H···A, D···A, D–H···A [Å [°]]: O1–H···O2, 0.82, 1.86, 2.672(5), 174.2; N1–H···O2_#1, 0.90, 2.20, 3.074(7), 164.2; N1–H···O3_#2, 0.90, 2.09, 2.968(6), 164.5. Symmetry transformations used to generate equivalent atoms: #1 = $x-1/2, -y+1/2, -z$; #2 = $x-1, y, z$.

This interconversion of the double bonds could not be frozen by lowering the temperature in the case of the monodentate amino alcohol complexes. Thus, the $^{13}$C NMR

 © 2007 Wiley-VCH Verlag GmbH & Co. KGaA, Weinheim 

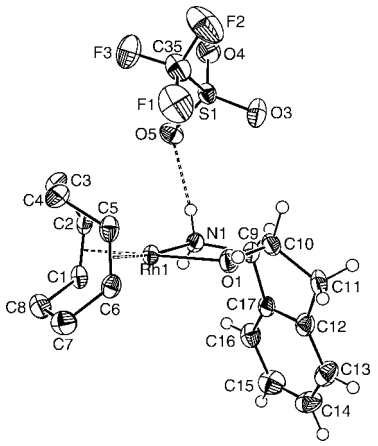


Figure 9. Structure of one of the two crystallographically independent ion pairs of $[(\eta^4\text{-}C_8H_{12})Rh\{(1R,2S)\text{-}H_2NCH[CH(OH)CH_2]\text{-}C_6H_4\text{-}\kappa N,\kappa O\}]O_3SCF_3$ [(1*R*,2*S*)-**15**] (cyclooctadiene H atoms are omitted for clarity). Selected bond lengths [Å] and angles [°]: Rh1–O1, 2.089(4); Rh1–N1, 2.109(4). O1–Rh1–N1, 79.6(2). Analogous parameters for ion pair 2: Rh2–O2, 2.086(4); Rh2–N2, 2.124(5). O2–Rh2–N2, 78.6(2). Hydrogen-bonding interactions as D–H, H···A, D···A, D–H···A [Å [°]]: N1–H···O5, 0.91, 2.09, 2.981(6), 165.7; N1–H···O6_#1, 0.91, 2.26, 3.001(6), 137.9; O1–H···O7_#2, 0.84, 1.82, 2.665(6), 175.4 (both from complex 1 to triflate 2); N2–H···O3_#3, 0.91, 2.27, 3.139(6), 159.0; N2–H···O4_#3, 0.91, 2.65, 3.158(6), 116.3; O2–H···O5_#4, 0.85, 1.81, 2.651(6), 171.6 (all from complex 2 to triflate 1). Symmetry transformations used to generate equivalent atoms: #1 = *x*, *y*, *z* + 1; #2 = –*x*, *y* + 1/2, –*z*; #3 = –*x*, *y* – 1/2, –*z* + 1; #4 = *x*, *y*, *z* – 1.

spectrum of $[(\eta^4\text{-}C_8H_{12})RhCl(H_2NCMe_2CH_2OH\text{-}\kappa N)]$, **5**, which displays two broad signals for the $CH_2$ and CH carbon atoms ($\delta$ = 30.6 and 77.1 ppm) in $[D_6]$DMSO at 30 °C, still showed considerable line-broadening for the cyclooctadiene resonances when recorded in $[D_4]$methanol at –25 °C: $\delta$ = 29.6, 30.7 (both $CH_2$), and 81.7 (CH) ppm. Conversely, it could be demonstrated for the chelated L-norephedrine compound $[(\eta^4\text{-}C_8H_{12})Rh\{(1R,2S)\text{-}H_2NCH(Me)CH(Ph)OH\text{-}\kappa N,\kappa O\}]O_3SCF_3$ [(1*R*,2*S*)-**14**] that a $^{13}C$ NMR spectrum consistent with a rigid $C_1$-symmetric structure of the cation can in fact be observed if a $[D_4]$methanol solution cooled to –35 °C is used. Both the methylene and the olefinic carbon atoms then resolve into four distinct signals, the former protons appear as singlets ($\delta$ = 30.31, 30.90, 32.11, and 32.45 ppm), and the latter protons resonate as $^{103}Rh$-coupled doublets ($\delta$ = 73.41, 73.85, 84.32, and 84.51 ppm; $J_{Rh,C}$ = 11.7–16.9 Hz).

We do not know the mechanism of the olefin site interchange of the coordinated diene in compounds **4**–**9** and **11**–**15** but note that analogous scrambling of two chemically nonequivalent CH=CH bonds was previously described for a number of related four-coordinate rhodium(I) compounds $[(\eta^4\text{-}C_8H_{12})RhCl(R_2P\cap E\text{-}\kappa P)]$ and $[(\eta^4\text{-}C_8H_{12})Rh\{R_2P\cap E\text{-}\kappa P,\kappa E)]^+$ containing different P,N and P,S chelate ligands bonded in a mono- or bidentate fashion.[13] For the chlorido complexes containing "dangling" donor groups similar to the free hydroxy functions of **4**–**9**, the exchange dynamics were accounted for in terms of a fast equilibrium between the square planar form of the molecule and small amounts of a pentacoordinate chelated isomer undergoing rapid pseudorotation.[13a] For the cationic chelate complexes that bear some structural resemblance to **11**–**15**, a mechanism involving breaking of the Rh–N or Rh–S linkage, followed by rotation around the Rh–P bond and rebuilding of the four-coordinate chelate structure was proposed as an alternative.[13b–13d] As a further alternative, the diene dynamics were ascribed to diolefin rotation proceeding by cleavage of one Rh–diene bond, rotation through 180° around the remaining metal–olefin bond, and recoordination of the free CH=CH group either *cis* or *trans* to one of the two different donors of the chelate ligand.[13e]

### 1,2-Diamine Complexes

For catalytic applications, it seemed desirable to substitute P donors, in particular chiral diphosphanes, for the cyclooctadiene ligand of the newly prepared complexes bearing the diverse amino alcohols in κ*N*-monodentate or κ*N*,κ*O*-bidentate coordination. Accordingly, numerous attempts were made to obtain phosphane-coordinated products by reaction of the amino alcohol compounds with both chiral and achiral mono- and ditertiary phosphanes or, vice versa, by combining phosphane-containing precursors such as $[(i\text{Pr}_3P)_2Rh_2(\mu\text{-}Cl)_2]$[14] and $[(\eta^4\text{-}C_8H_{12})Rh\{(R)\text{-binap}\}]BF_4$[15] with amino alcohol ligands. So far, all of these experiments failed in that reaction mixtures were produced from which only ill-defined or unwanted compounds could be isolated, some of which were already known. Thus, reactions of the dinuclear bis(triisopropylphosphane) complex with L-valinol or L-norephedrine in thf under a nitrogen atmosphere repeatedly furnished the well-known dinitrogen compound *trans*-$[(i\text{Pr}_3P)_2RhCl(N_2)]$[16] rather than any amino alcohol containing material, whereas both $[(i\text{Pr}_3P)_2Rh_2(\mu\text{-}Cl)_2]$ and $[(\eta^4\text{-}C_8H_{12})Rh\{(R)\text{-binap}\}]BF_4$ afforded mixtures of multifarious unidentified derivatives, if combined with a number of different amino alcohols in $CH_2Cl_2$ or thf under an atmosphere of argon or hydrogen. Largely unidentified products were also formed upon treatment of several $[(\eta^4\text{-}C_8H_{12})RhCl\{HN(R)\cap OH\text{-}\kappa N\}]$ or $[(\eta^4\text{-}C_8H_{12})Rh\{HN(R)\cap OH\text{-}\kappa N,\kappa O\}]O_3SCF_3$ precursors with a number of different mono- or bidentate phosphanes.

For the time being, only L-valinol and L-norephedrine chelate complexes (*S*)-**12** and (1*R*,2*S*)-**14** and the (*R*)-binap ligand reacted to give defined mixtures of products. $^{31}P$ and $^1H$ NMR spectroscopy disclosed the predominant presence (>90%; see Experimental Section) of each an (*R*)-binap-coordinated $C_1$-symmetric species assumed to be $[\{(R)\text{-binap}\}Rh\{(S)\text{-}H_2NCH(CHMe_2)CH_2OH\text{-}\kappa N,\kappa O\}]^+$ and $[\{(R)\text{-binap}\}Rh\{(1R,2S)\text{-}H_2NCH(Me)CH(Ph)OH\text{-}\kappa N,\kappa O\}]^+$, respectively, but all attempts to isolate these cations as pure compounds resulted in their degradation to unidentified materials.

In contrast to the largely unsuccessful reactions of β-amino alcohols with, for example, $[(\eta^4\text{-}C_8H_{12})Rh\{(R)\text{-binap}\}]BF_4$, 1,2-diamines such as 1,1′,2,2′-tetramethylethyl-

 © 2007 Wiley-VCH Verlag GmbH & Co. KGaA, Weinheim 

enediamine and (*R*,*R*)-1,2-diphenylethylenediamine, and (*R*,*R*)-1,2-diaminocyclohexane smoothly displaced the $C_8H_{12}$ ligand from the metal giving the chelate complexes [{(*R*)-binap}Rh($H_2N\cap NH_2$)]$BF_4$, if allowed to interact with the diene(diphosphane) complex in thf under a hydrogen atmosphere; $H_2N\cap NH_2$ = $H_2NCMe_2CMe_2NH_2$ [(*R*)-(**16**)], (*R*,*R*)-$H_2NCH(Ph)CH(Ph)NH_2$ [(*R*),(*R*,*R*)-**17**], (*R*,*R*)-1,2-$(H_2N)_2C_6H_{10}$ [(*R*),(*R*,*R*)-**18**]. Further reaction of (*R*),(*R*,*R*)-**17** with hydrogen chloride afforded *trans*-[{(*R*)-binap}Rh(H)(Cl){(*R*,*R*)-$H_2NCH(Ph)CH(Ph)NH_2$}]$BF_4$ [(*R*),(*R*,*R*)-**19**], by oxidative addition (Scheme 4). From a structural point of view, the cation of the latter can be regarded as a blueprint of the neutral $Ru^{II}$ complex *trans*-[{(*R*)-binap}Ru(H)(Cl){(*R*,*R*)-$H_2NCH(Ph)CH(Ph)NH_2$}], known to be an excellent catalyst precursor for the stereoselective hydrogenation of ketones and imines.[17a]

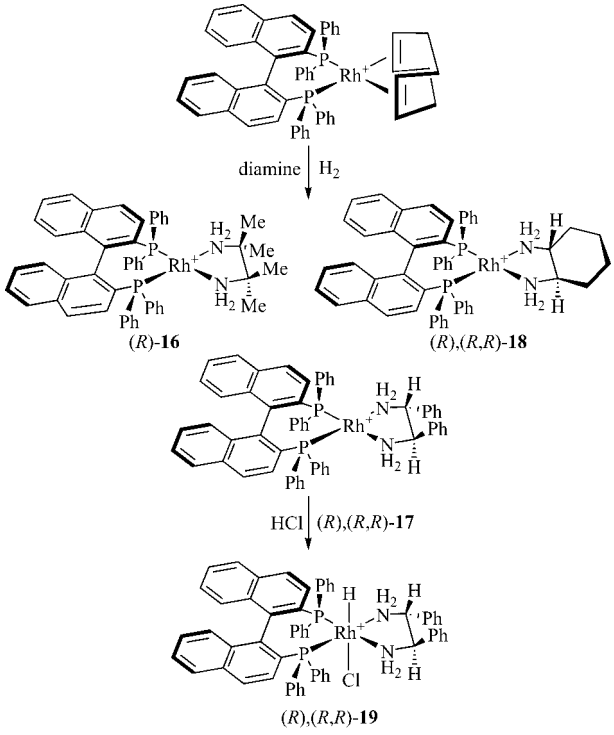


Scheme 4. Preparation of (*R*)-binap/1,2-diamine complexes (all as $BF_4^-$ salts).

Single-crystals of (*R*)-**16** and (*R*),(*R*,*R*)-**17** containing solvent molecules of crystallization [i.e. (*R*)-**16**·1/2$Me_2CO$·1/4thf and (*R*),(*R*,*R*)-**17**·$CH_2Cl_2$] were obtained upon slow diffusion of diethyl ether into concentrated solutions of the two complexes in acetone/thf and dichloromethane, respectively. As anticipated, the X-ray structure analyses of the two compounds revealed the presence of N–H···F hydrogen-bonded [{(*R*)-binap}Rh($H_2N\cap NH_2$)]$BF_4$ ion pairs with the rhodium atoms in a close to planar coordination geometry (Figures 10 and 11). The metal-to-phosphane and metal-to-amine linkages measure 2.213(2)–2.223(2) Å and 2.147(7)–2.156(7) Å, respectively, which is slightly shorter than, but still comparable to, the Ru–P and Ru–N bond lengths previously reported for the octahedral molecules *trans*-[{(*R*)-binap}Ru(X)(Cl){(*R*,*R*)-$H_2NCH(Ph)CH(Ph)NH_2$}] (X = H[17a] or Cl[18]), where *d*(Ru–P) = 2.238–2.282 Å and *d*(Ru–N) = 2.164–2.198 Å.

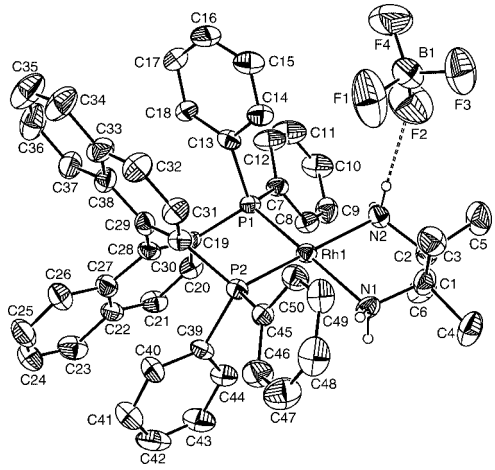

Figure 10. Structure of the ion pair [{(*R*)-binap}Rh($H_2NCMe_2CMe_2NH_2$)]$BF_4$ [(*R*)-**16**] as observed for the solid state of (*R*)-**16**·1/2$Me_2CO$·1/4thf (phenyl and methyl H atoms are omitted for clarity). Selected bond lengths [Å] and angles [°]: Rh1–P1, 2.223(2); Rh1–P2, 2.219(2); Rh1–N1, 2.155(6); Rh1–N2, 2.147(7). P1–Rh1–P2, 90.86(8); P1–Rh1–N1, 170.8(2); P1–Rh1–N2, 98.1(2); P2–Rh1–N1, 94.3(2); P2–Rh1–N2, 166.2(2); N1–Rh1–N2, 78.3(3). Hydrogen-bonding interactions as D–H, H···A, D···A, D–H···A [Å [°]]: N2–H···F2, 0.90, 2.26, 3.15(1), 171.1; N2–H···F3_#, 0.90, 2.23, 3.13(1), 176.7. Symmetry transformation used to generate equivalent atom: # = $-x$, $y-1/2$, $-z+1/2$.

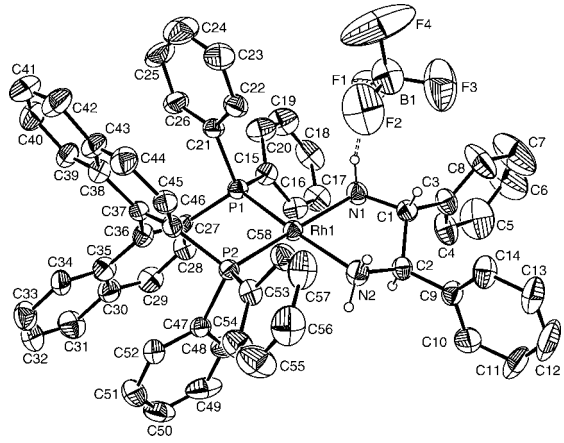

Figure 11. Structure of the ion pair [{(*R*)-binap}Rh{(*R*,*R*)-$H_2NCH(Ph)CH(Ph)NH_2$}]$BF_4$ [(*R*),(*R*,*R*)-**17**] as observed for the solid state of (*R*),(*R*,*R*)-**17**·$CH_2Cl_2$ (phenyl H atoms are omitted for clarity). Selected bond lengths [Å] and angles [°]: Rh1–P1, 2.219(2); Rh1–P2, 2.213(2); Rh1–N1, 2.147(7); Rh1–N2, 2.156(7). P1–Rh1–P2, 91.00(8); P1–Rh1–N1, 94.3(2); P1–Rh1–N2, 170.0(2); P2–Rh1–N1, 173.0(3); P2–Rh1–N2, 97.3(2); N1–Rh1–N2, 78.0(3). Hydrogen-bonding interaction as D–H, H···A, D···A, D–H···A [Å [°]]: N1–H···F1, 0.90, 2.05, 2.92(1), 163.2.

## Catalytic C=O Hydrogenation

The close structural relationship of the ionic $Rh^I$ and $Rh^{III}$ complexes (*R*),(*R*,*R*)-**17** and (*R*),(*R*,*R*)-**19** to the neutral $Ru^{II}$ ketone hydrogenation (pre)catalysts *trans*-[{(*R*)-

 © 2007 Wiley-VCH Verlag GmbH & Co. KGaA, Weinheim 

binap}Ru(X)(Cl){(*R*,*R*)-$H_2NCH(Ph)CH(Ph)NH_2$}] (X = H,[17a] Cl[18]) prompted us to also inspect the two rhodium compounds for their ability to form C=O hydrogenation catalysts. In these probing experiments, which were run in 2-propanol with acetophenone at a substrate-to-catalyst (*s*:*c*) ratio of 200:1 under the conditions summarized in Table 1, virtually no conversion to 1-phenylethanol was observed on attempted catalysis in the absence of an activating basic additive (Table 1, Entries 1 and 4). Only when combined with strong base (typically, 5 equiv. of KOH) did both complexes behave as relatively sluggish catalysts for the hydrogenation of the ketone functionality − irrespective of whether the reactions were carried out in the absence of hydrogen gas (Table 1, Entries 2 and 5) or under $H_2$ pressure (Table 1, Entries 3 and 6). These observations clearly demonstrate that neither the $d^8$ species [{(*R*)-binap}Rh{(*R*,*R*)-$H_2NCH(Ph)CH(Ph)NH_2$)]$BF_4$ nor its HCl adduct *trans*-[{(*R*)-binap}Rh(H)(Cl){(*R*,*R*)-$H_2NCH(Ph)CH(Ph)NH_2$)]$BF_4$ as such can act as catalysts for C=O hydrogenation, whereas the two base-modified systems are able to catalyze the transfer of $H^+$ and $H^-$ equivalents both from the solvent and the gas molecule to the carbonyl dipole. Reduction of the substrate is slower in the absence than in the presence of hydrogen gas, which indicates that the two catalytic systems favor the direct hydrogenation by $H_2$ gas over the transfer of hydrogen from solvent molecules. The product alcohol was obtained in higher (albeit still modest) enantiomeric excess for the (*S*) enantiomer by transfer hydrogenation (64 and 71% *ee*) than by direct hydrogenation (30 and 33% *ee*).

Table 1. Hydrogenation of acetophenone in the presence of (*R*),(*R*,*R*)-**17** and (*R*),(*R*,*R*)-**19** as precatalysts.[a]

| No. | Complex/base (equiv. rel. to $C_{Rh}$) | $p(H_2)$ [bar] | *t* [h] | % PhCH(OH)Me | % *ee* (config.) |
|---|---|---|---|---|---|
| 1 | (*R*),(*R*,*R*)-**17**/none | 10 | 20 | | |
| 2 | (*R*),(*R*,*R*)-**17**/KOH (5) | | 5 | 57 | 71 (*S*) |
| 3 | (*R*),(*R*,*R*)-**17**/KOH (5) | 10 | 2.5 | 100 | 33 (*S*) |
| 4 | (*R*),(*R*,*R*)-**19**/none | 10 | 20 | | |
| 5 | (*R*),(*R*,*R*)-**19**/KOH (5) | | 5 | 30 | 64 (*S*) |
| 6 | (*R*),(*R*,*R*)-**19**/KOH (5) | 10 | 2.5 | 75 | 30 (*S*) |

[a] Acetophenone (2.0 mmol) together with (*R*),(*R*,*R*)-**17** or (*R*),(*R*,*R*)-**19** (0.01 mmol), plus added base, in 2-propanol (3 mL) at 50 °C.

Recent results of Rautenstrauch, Morris et al. have shown that the established $Ru^{II}$-based ketone hydrogenation precatalyst *trans*-[{(*S*)-tolbinap}$RuCl_2${(*S*,*S*)-$H_2NCH(Ph)CH(Ph)NH_2$}] (tolbinap = the di-*p*-tolyl analogue of binap) and its (*R*),(*R*,*R*) enantiomer also display catalytic activity for ketone transfer hydrogenation, if modified by strong alkaline base (usually KO*t*Bu) in 2-propanol.[17b] Relative to rhodium precatalysts (*R*),(*R*,*R*)-**17** and (*R*),(*R*,*R*)-**19**, the ruthenium complexes form much more active systems and work very fast at *s*:*c* = $10^5$–$10^6$ under the conditions of direct hydrogenation and with a reduced rate, but still much faster than both (*R*),(*R*,*R*)-**17** and (*R*),(*R*,*R*)-**19**, at *s*:*c* = $10^4$–$10^5$ under transfer hydrogenation conditions. With acetophenone as the substrate ketone, the (*R*),(*R*,*R*) forms of both the ruthenium and the rhodium catalysts favor the formation of the product alcohol as the (*S*) enantiomer. In direct hydrogenation, distinctly higher *ee*'s are achieved with the Ru systems than the Rh systems (≈80% versus ≈30%), although the latter give somewhat better optical yields than the former if allowed to operate on the pathway of transfer hydrogenation (64–71% versus 42–62%).

## Conclusions

This work shows that β-amino alcohols behave as N-monodentate ligands towards the dirhodium complex [($\eta^4$-$C_8H_{12}$)$_2$$Rh_2$(μ-Cl)$_2$] to form [($\eta^4$-$C_8H_{12}$)RhCl{HN(R)∩OH-κ*N*}] by nucleophilic cleavage of the chlorido bridges. Coordination of the free hydroxy function of the N,O ligands can be brought about either by dehydrochlorination to furnish alcoholato chelates [($\eta^4$-$C_8H_{12}$)Rh($H_2$N∩O-κ*N*,κ*O*)] or by precipitation of the metal-bound chloride as TlCl, which converts the neutral [($\eta^4$-$C_8H_{12}$)RhCl{HN(R)∩OH-κ*N*}] compounds into cationic [($\eta^4$-$C_8H_{12}$)Rh{HN(R)∩OH-κ*N*,κ*O*}]$^+$ amino alcohol chelate complexes. Whereas the exploratory studies aimed at the coordination of the amino alcohols to phosphane-containing rhodium compounds remain largely inconclusive, similar complexes could easily be made from [($\eta^4$-$C_8H_{12}$)Rh{(*R*)-binap}]$BF_4$ and 1,2-diamine ligands. If activated by strong base, the resulting products [{(*R*)-binap}Rh($H_2$N∩$NH_2$)]$BF_4$ can act as moderately active and selective catalysts for the reduction of acetophenone by both direct and transfer hydrogenation, as was demonstrated for [{(*R*)-binap}Rh{(*R*,*R*)-$H_2NCH(Ph)CH(Ph)NH_2$)]$BF_4$ and its HCl adduct *trans*-[{(*R*)-binap}Rh(H)(Cl){(*R*,*R*)-$H_2NCH(Ph)CH(Ph)NH_2$)]$BF_4$.

## Experimental Section

**General:** All manipulations were performed under a nitrogen or argon atmosphere, except for the preparation of the 1,2-diamine complexes [{(*R*)-binap}Rh($H_2$N∩$NH_2$)]$BF_4$ (**16**–**18**) from [($\eta^4$-$C_8H_{12}$)Rh{(*R*)-binap}]$BF_4$, which were carried out under a hydrogen atmosphere. Solvents were distilled from the appropriate drying agents prior to use. IR spectra were obtained with a Mattson Polaris spectrometer. $^1$H, $^{13}$C, and $^{31}$P NMR were obtained with Bruker DPX 300 or Bruker DRX 400 spectrometers with $SiMe_4$ as the internal standard or with $H_3PO_4$ as the external standard (downfield positive) at ambient temperature, unless stated otherwise ("m" = deceptively simple multiplet). HPLC were obtained with a Thermoquest P 4000 (UV detector) apparatus. The amino alcohols, as well as the diphosphane and diamine ligands (*R*)-2,2′-bis(diphenylphosphanyl)-1,1′-binaphthyl, (*R*,*R*)-1,2-diphenylethylenediamine, and (*R*,*R*)-1,2-diaminocyclohexane, were used as obtained commercially. 1,1′,2,2′-Tetramethylethylenediamine,[19] [($\eta^4$-$C_8H_{12}$)$_2$$Rh_2$(μ-Cl)$_2$],[20] [($\eta^2$-$C_8H_{14}$)$_4$$Rh_2$(μ-Cl)$_2$],[21] and [($\eta^4$-$C_8H_{12}$)Rh{(*R*)-binap}]$BF_4$[15] were prepared according to published procedures or slight modifications thereof.

 © 2007 Wiley-VCH Verlag GmbH & Co. KGaA, Weinheim 

**Monodentate Amino Alcohol Complexes [(η⁴-$C_8H_{12}$)RhCl{HN-(R)∩OH-κ*N*}] (4–9):** Toluene solutions (5–10 mL) of [(η⁴-$C_8H_{12}$)$_2$-$Rh_2$(μ-Cl)$_2$] (0.20–0.70 mmol) were treated with the respective amino alcohol (2.1–2.5 equiv.) for 1 h at ambient conditions. Slow addition of *n*-pentane (50 mL) caused the products to separate from the mixtures as yellow microcrystals, which were separated by filtration, washed with *n*-pentane (3 × 10 mL), and dried under vacuum.

**[(η⁴-$C_8H_{12}$)RhCl($H_2NCH_2CH_2OH$-κ*N*)] (4):** From [(η⁴-$C_8H_{12}$)$_2$-$Rh_2$(μ-Cl)$_2$] (250 mg, 0.51 mmol) and ethanolamine (66 mg, 1.08 mmol) in toluene (10 mL). Yield: 260 mg (85%). $^1$H NMR (300.1 MHz, $CDCl_3$): δ = 1.64, 2.30 (both m, 4 H each, both diene $CH_2$), 2.5 (br., 2 H, $NH_2$), 2.67, 3.80 (both t, *J* = 4.95 Hz, 2 H each, $NCH_2CH_2O$), 4.0 (br., 4 H, diene CH) ppm. $^{13}$C NMR (75.5 MHz, $CDCl_3$): δ = 31.60 (s, diene $CH_2$), 46.80 (s, $NCH_2$), 62.90 (s, $CH_2O$), 79.7 (br., diene CH) ppm. $C_{10}H_{19}ClNORh$ (307.62): calcd. C 39.04, H 6.23, N 4.55; found C 39.25, H 6.26, N 4.56.

**[(η⁴-$C_8H_{12}$)RhCl($H_2NCMe_2CH_2OH$-κ*N*)] (5):** From [(η⁴-$C_8H_{12}$)$_2$-$Rh_2$(μ-Cl)$_2$] (152 mg, 0.31 mmol) and 2-amino-2-methyl-1-propanol (57 mg, 0.64 mmol) in toluene (5 mL). Yield: 190 mg (91%). $^1$H NMR (300.1 MHz, [$D_6$]DMSO): δ = 1.11 (s, 6 H, $CH_3$), 1.69, 2.29 (both m, 4 H each, both diene $CH_2$), 3.18 (s, $CH_2O$), 4.0 (br., 4 H, diene CH), 5.2 (br., 2 H, $NH_2$) ppm. $^1$H NMR (400.1 MHz, $CD_3OD$, –25 °C): δ = 1.30 (s, 6 H, $CH_3$), 1.81, 2.40 (both m, 4 H each, both diene $CH_2$), 3.41 (br., $CH_2O$), 3.8, 4.2 (both br., 2 H each, both diene CH) ppm. $^{13}$C NMR (75.5 MHz, [$D_6$]DMSO): δ = 25.13 (s, $CH_3$), 30.6 (br., diene $CH_2$), 55.04 (s, N*C*$Me_2$), 71.62 (s, $CH_2O$), 77.1 (br., diene CH) ppm. $^{13}$C NMR (100.6 MHz, $CD_3OD$, –25 °C): δ = 24.13 (s, $CH_3$), 29.6, 30.7 (both br, both diene $CH_2$), 56.92 (s, N*C*$Me_2$), 70.3 (br., diene CH), 76.12 (s, $CH_2O$), 81.7 (br., diene CH) ppm. $C_{12}H_{23}ClNORh$ (335.68): calcd. C 42.94, H 6.91, N 4.17; found C 43.89, H 6.85, N 4.76.

**[(η⁴-$C_8H_{12}$)RhCl{(*R*)-$H_2NCH(CHMe_2)CH_2OH$-κ*N*}] [(*R*)-6 and Enantiomer (*S*)-6]:** From [(η⁴-$C_8H_{12}$)$_2$$Rh_2$(μ-Cl)$_2$] (200 mg, 0.41 mmol) and (*R*)- or (*S*)-2-amino-3-methyl-1-butanol (D-, L-valinol) (104 mg, 1.03 mmol) in toluene (10 mL). Yield: 275 mg (96%). $^1$H NMR (300.1 MHz, $CD_2Cl_2$): δ = 0.86 (d, *J* = 6.78 Hz, 6 H, $CH_3$), 1.68–1.80 (m, 5 H, C*H*$Me_2$ partially superimposed by 4 diene $CH_2$), 2.3–2.5 (br. m, 7 H, NCH and $NH_2$, partially superimposed by 4 diene $CH_2$), 3.61 (dd, $^2J$ = 12.06 Hz, $^3J$ = 4.50 Hz, 1 H, 1 $CH_2O$), 4.00 (br., 4 H, diene CH), 4.21 (dd, $^2J$ = 12.06 Hz, $^3J$ = 2.64 Hz, 1 H, 1 $CH_2O$) ppm. $^1$H NMR (400.1 MHz, [$D_8$]thf): δ = 0.83, 0.88 (both d, *J* = 6.60, 6.84 Hz, 3 H each, both $CH_3$), 1.63 (m, 4 H, diene $CH_2$, partially superimposed by solvent), 1.82 ("dq", *J* = 6.60, 6.84 Hz, 1 H, C*H*$Me_2$), 2.26 (m, 4 H, diene $CH_2$), 2.49 (m, 1 H, NCH), 2.9 (br., 2 H, $NH_2$), 3.51 (dd, $^2J$ = 11.24 Hz, $^3J$ = 4.88 Hz, 1 H, 1 $CH_2O$), 3.94 (m, 3 H, 2 diene CH superimposing 1 $CH_2O$), 3.97 (m, 2 H, diene CH) ppm. $^1$H NMR (400.1 MHz, [$D_8$]thf, –25 °C): δ = 0.80, 0.85 (both d, *J* = 6.60, 6.84 Hz, 3 H each, both $CH_3$), 1.62 (m, 4 H, diene $CH_2$, partially superimposed by solvent), 1.81 ("dq", *J* = 6.60, 6.84 Hz, 1 H, C*H*$Me_2$, 2.21 (m, 4 H, diene $CH_2$), 2.56 (br., 1 H, NCH), 2.78, 2.93 (both br, 1 H each, $NH_2$), 3.59 (m, 1 H, 1 $CH_2O$), 3.8–4.1(br. m, 5 H, 4 diene CH superimposing 1 $CH_2O$) ppm. $^{13}$C NMR (75.5 MHz, $CDCl_3$): δ = 18.71, 18.89 (both s, both $CH_3$), 30.44, 30.56 (both s, diene $CH_2$ and *C*H$Me_2$), 61.14 (s, NCH), 62.61 (s, $CH_2O$), 78.7 (br., diene CH) ppm. $C_{13}H_{25}ClNORh$ (349.70): calcd. C 44.65, H 7.21, N 4.01; found C 45.22, H 7.24, N 4.35.

**[(η⁴-$C_8H_{12}$)RhCl{(*R*)-HN($CH_2CH_2CH_2CH$)$CH_2OH$-κ*N*}] [(*R*)-7 and Enantiomer (*S*)-7]:** From [(η⁴-$C_8H_{12}$)$_2$$Rh_2$(μ-Cl)$_2$] (220 mg, 0.45 mmol) and (*R*)- or (*S*)-2-pyrrolidinemethanol (D-, L-prolinol) (99 mg, 0.98 mmol) in toluene (10 mL). Yield: 280 mg (89%). $^{13}$C NMR (75.5 MHz, $CDCl_3$): δ = 25.25, 26.81 (both s, prolinol C*C*$H_2$*C*$H_2$C), 30.80, 31.45 (both s, both diene $CH_2$), 49.84 (s, $NCH_2$), 61.65 (s, NCH), 68.38 (s, $CH_2O$), 83.0 (br., diene CH) ppm. $C_{13}H_{23}ClNORh$ (347.68): calcd. C 44.91, H 6.67, N 4.03; found C 45.28, H 6.66, N 4.33.

**[(η⁴-$C_8H_{12}$)RhCl{(1*S*,2*R*)-$H_2NCH(Me)CH(Ph)OH$-κ*N*}] [(1*S*,2*R*)-8 and Enantiomer (1*R*,2*S*)-8]:** From [(η⁴-$C_8H_{12}$)$_2$$Rh_2$(μ-Cl)$_2$] (346 mg, 0.70 mmol) and (1*S*,2*R*)- or (1*R*,2*S*)-2-amino-1-phenyl-1-propanol (D-, L-norephedrine) (230 mg, 1.52 mmol) in toluene (10 mL). Yield: 510 mg (92%). $^1$H NMR (300.1 MHz, $CD_2Cl_2$): δ = 0.97 (d, *J* = 6.39 Hz, 3 H, $CH_3$), 1.83 (m, 4 H, diene $CH_2$), 2.47 (m, 5 H, NCH, partially superimposed by 4 diene $CH_2$), 3.19 (m, 1 H, CHO), 4.1 (br., 4 H, diene CH), 5.7 (br., 2 H, $NH_2$), 7.31–7.42 (m, 5 H, $C_6H_5$) ppm. $^{13}$C NMR (75.5 MHz, $CD_2Cl_2$): δ = 16.87 (s, $CH_3$), 31.50 (s, diene $CH_2$), 56.21 (s, NCH), 76.30 (s, CHO), 80.0 (br., diene CH), 126.68, 128.14, 129.05, 141.79 (all s, all $C_6H_5$) ppm. $C_{17}H_{25}ClNORh$ (397.74): calcd. C 51.34, H 6.34, N 3.52; found C 51.49, H 6.35, N 3.80.

**[(η⁴-$C_8H_{12}$)RhCl{(1*S*,2*R*)-$H_2NCH[CH(OH)CH_2]C_6H_4$-κ*N*}] [(1*S*,2*R*)-9 and Enantiomer (1*R*,2*S*)-9]:** From [(η⁴-$C_8H_{12}$)$_2$$Rh_2$(μ-Cl)$_2$] (148 mg, 0.30 mmol) and (1*S*,2*R*)- or (1*R*,2*S*)-*cis*-1-amino-2-indanol (94 mg, 0.63 mmol) in toluene (5 mL). Yield: 225 mg (94%). $^1$H NMR (300.1 MHz, $CD_2Cl_2$): δ = 1.82, 2.57 (both m, 4 H each, both diene $CH_2$), 2.97 (dd, $^2J$ = 16.40 Hz, $^3J$ = 3.21 Hz, 1 H, 1 C*H*$_2$CH), 3.17 (dd, $^2J$ = 16.40 Hz, $^3J$ = 5.67 Hz, 1 H, 1 C*H*$_2$CH), 4.1 (br., 4 H, diene CH), 4.40 (d, *J* = 3.21 Hz, 1 H, CHN), 4.79 (m, 1 H, CHO), 7.31 (m, 3 H, phenylene H), 7.70 (m, 1 H, phenylene H) ppm. $^{13}$C NMR (75.5 MHz, $CD_2Cl_2$): δ = 31.51, 31.58 (both s, both diene $CH_2$), 39.41 (s, *C*$H_2$CH), 61.88 (s, NCH), 73.85 (CHO), 80.3 (br., diene CH), 126.29, 126.13, 127.64, 129.25, 141.69, 141.89 (all s, all $C_6H_4$) ppm. $C_{17}H_{23}ClNORh$ (395.73): calcd. C 51.60, H 5.86, N 3.54; found C 51.54, H 6.13, N 3.91.

**[(η⁴-$C_8H_{12}$)Rh{(*S*)-$H_2NCH(CHMe_2)CH_2O$-κ*N*,κ*O*}]·$H_2O$, (*S*)-10·$H_2O$:** Powdered potassium hydroxide (300 mg, 5.35 mmol) was added to a solution of [(η⁴-$C_8H_{12}$)RhCl{(*S*)-$H_2NCH(CHMe_2)$-$CH_2OH$-κ*N*}], [(*S*)-**6**; (105 mg, 0.30 mmol] in dichloromethane (5 mL). The mixture was stirred for 16 h at room temperature and excess KOH was removed by filtration. Orange crystals identified as (*S*)-**9**·$H_2O$ by X-ray structure determination (see below) were deposited from the filtrate upon standing for several days at ambient conditions.

**Chelated Amino Alcohol Complexes [(η⁴-$C_8H_{12}$)Rh{HN(R)∩OH-κ*N*,κ*O*}]$O_3SCF_3$ (11–15):** Solid thallium trifluoromethanesulfonate was added in 10–20% excess to stirred solutions of the required monodentate amino alcohol complex [(η⁴-$C_8H_{12}$)RhCl(HN-(R)∩OH-κ*N*)] (0.25–0.40 mmol) in dichloromethane (5–10 mL). After stirring for 30 min at room temperature, the precipitated thallium chloride was filtered off and the products were isolated as yellow powders by removing all volatile material from the filtrates.

**[(η⁴-$C_8H_{12}$)Rh($H_2NCMe_2CH_2OH$-κ*N*,κ*O*)]$O_3SCF_3$ (11):** From **5** (99 mg, 0.29 mmol) and $TlO_3SCF_3$ (125 mg, 0.35 mmol) in $CH_2Cl_2$ (5 mL). Yield: 115 mg (88%). $^1$H NMR (300.1 MHz, $CD_3OD$): δ = 1.33 (s, 6 H, $CH_3$), 1.84, 1.86 (both m, 4 H each, both diene $CH_2$), 3.47 (s, 2 H, $CH_2O$), 4.1 (br., 4 H, diene CH) ppm. $^{13}$C NMR (75.5 MHz, $CD_3OD$): δ = 25.57 (s, $CH_3$), 31.7 (br., diene $CH_2$), 57.13 (s, N*C*$Me_2$), 76.15 (s, $CH_2O$), 82.0 (br., diene CH), 122.21 (q, $^1J_{F,C}$ = 318.6 Hz, $CF_3$) ppm. $C_{13}H_{23}F_3NO_4RhS$ (449.29): calcd. C 34.75, H 5.16, N 3.12, S 7.12; found C 34.14, H 5.34, N 3.12, S 6.87.

**[(η⁴-$C_8H_{12}$)Rh{(*S*)-$H_2NCH(CHMe_2)CH_2OH$-κ*N*,κ*O*}]$O_3SCF_3$ [(*S*)-12]:** From (*S*)-**6** (108 mg, 0.31 mmol) and $TlO_3SCF_3$ (105 mg,

 © 2007 Wiley-VCH Verlag GmbH & Co. KGaA, Weinheim 

0.30 mmol) in $CH_2Cl_2$ (5 mL). Yield: 130 mg (90%). $^1$H NMR (300.1 MHz, $CDCl_3$): $\delta$ = 0.89, 0.93 (both d, $J$ = 6.78 Hz each, 3 H each, both $CH_3$), 1.68–1.84 (m, 5 H, 4 diene $CH_2$ superimposing 1 C*H*Me$_2$), 2.36 (m, 4 H, diene $CH_2$), 2.5 (br., 1 H, NCH), 2.9, 3.0 (both br, 1 H each, $NH_2$), 3.55 ("t", $^2J$ + $^3J$ = 10.35 Hz, 1 H, 1 $CH_2O$), 3.79 (dd, $^2J$ = 10.56 Hz, $^3J$ = 3.76 Hz, 1 H, 1 $CH_2O$), 4.1 (br., 4 H, diene CH) ppm. $^1$H NMR (400.1 MHz, [D$_8$]thf): $\delta$ = 0.83, 0.87 (both d, $J$ = 6.60, 6.84 Hz, 3 H each, both $CH_3$), 1.73 (m, 5 H, 4 diene $CH_2$ superimposing 1 C*H*Me$_2$), 2.31 (m, 4 H, diene $CH_2$), 2.5 (br., 1 H, NCH), 3.3, 3.6 (both br., 1 H each, $NH_2$), 3.50 (m, 1 H, 1 $CH_2O$, partially superimposed by solvent), 3.74 (dd, $^2J$ = 10.40, $^3J$ = 4.16 Hz, 1 H, 1 $CH_2O$), 4.06, 4.13 (both m, 2 H each, both diene CH) ppm. $^{13}$C NMR (75.5 MHz, $CDCl_3$): $\delta$ = 19.48, 19.74 (both s, both $CH_3$), 30.04, 30.44, 30.82 (all s, diene $CH_2$ and *C*HMe$_2$), 61.50 (s, NCH), 68.35 (s, $CH_2O$), 79.0 (br., diene CH), 120.54 (q, $^1J_{F,C}$ = 319.2 Hz, $CF_3$) ppm. $C_{14}H_{25}F_3NO_4RhS$ (463.32): calcd. C 36.29, H 5.44, N 3.02, S 6.92; found C 36.98, H 5.72, N 3.09, S 6.67.

**[(η$^4$-C$_8$H$_{12}$)Rh{(*S*)-HN(CH$_2$CH$_2$CH$_2$CH)CH$_2$OH-κ*N*,κ*O*}]-O$_3$SCF$_3$ [(*S*)-13]:** From (*S*)-**7** (86 mg, 0.25 mmol) and $TlO_3SCF_3$ (131 mg, 0.37 mmol) in $CH_2Cl_2$ (5 mL). Yield: 98 mg (85%). $^1$H NMR (400.1 MHz, $CD_3OD$): $\delta$ = 1.59, 1.79 (both m, 1 and 3 H, prolinol $CCH_2CH_2C$), 1.95 (m, 4 H, diene $CH_2$), 2.40, 2.52 (both m, 2 H each, both diene $CH_2$), 2.89 (br. m, 2 H, $NCH_2$), 3.68 (br. m, 1 H, NCH), 3.51, 3.71 (both m, 1 H each, $CH_2O$), 4.08, 4.21 (both m, 2 H each, both diene CH) ppm. $^{13}$C NMR (100.6 MHz, $CD_3OD$): $\delta$ = 23.37, 24.70 (both s, prolinol C*C*H$_2$*C*H$_2$C), 29.40, 30.32 (both s, both diene $CH_2$), 46.66 (s, $NCH_2$), 61.98 (s, NCH), 67.81 (s, $CH_2O$), 78.4 (br., diene CH), 120.48 (q, $^1J_{F,C}$ = 318.9 Hz, $CF_3$) ppm. $C_{14}H_{23}F_3NO_4RhS$ (461.30): calcd. C 36.45, H 5.03, N 3.04, S 6.95; found C 35.69, H 4.91, N 2.89, S 6.10.

**[(η$^4$-C$_8$H$_{12}$)Rh{(1*R*,2*S*)-H$_2$NCH(Me)CH(Ph)OH-κ*N*,κ*O*}]O$_3$SCF$_3$ [(1*R*,2*S*)-14]:** From (1*R*,1*S*)-**8** (150 mg, 0.38 mmol) and $TlO_3SCF_3$ (160 mg, 0.45 mmol) in $CH_2Cl_2$ (5 mL). Yield: 182 mg (94%). $^1$H NMR (400.1 MHz, $CD_3OD$): $\delta$ = 1.08 (d, $J$ = 6.80 Hz, 3 H, $CH_3$), 1.93, 2.53 (both m, 4 H each, both diene $CH_2$), 3.25 (m, 1 H, NCH), 4.2 (br., 4 H, diene CH), 4.99 (d, $J$ = 3.92 Hz, 1 H, CHO), 7.40–7.66 (m, 5 H, $C_6H_5$) ppm. $^1$H NMR (400.1 MHz, $CD_3OD$, –35 °C): $\delta$ = 1.03 (d, $J$ = 6.36 Hz, 3 H, $CH_3$), 1.94, 2.54 (both m, 4 H each, both diene $CH_2$), 3.18 (m, 1 H, NCH), 4.0, 4.1 (both br, 1 H each, 2 diene CH), 4.4 (br., 2 H, 2 diene CH), 5.00 (d, $J$ = 3.68 Hz, 1 H, CHO), 7.44–7.74 (m, 5 H, $C_6H_5$) ppm. $^{13}$C NMR (100.6 MHz, $CD_3OD$): $\delta$ = 15.62 (s, $CH_3$), 31.18, 31.48 (both s, both diene $CH_2$), 55.07 (s, NCH), 68.84 (s, CHO), 79.2 (br., diene CH), 121.89 (q, $^1J_{F,C}$ = 320.0 Hz, $CF_3$), 127.78, 129.60, 138.06 (all s, $C_6H_5$) ppm. $^{13}$C NMR (100.6 MHz, $CD_3OD$, –35 °C): $\delta$ = 15.94 (s, $CH_3$), 30.31, 30.90, 32.11, 32.45 (all s, all diene $CH_2$), 54.94 (s, NCH), 68.94 (s, CHO), 73.41, 73.85, 84.32, 84.51 (all d, $J_{Rh,C}$ = 13.20, 16.87, 11.73, 14.67 Hz, all diene CH), 121.69 (q, $^1J_{F,C}$ = 317.0 Hz, $CF_3$), 127.08, 127.94, 129.68, 138.06 (all s, $C_6H_5$) ppm. $C_{18}H_{25}F_3NO_4RhS$ (511.36): calcd. C 42.28, H 4.93, N 2.74, S 6.27; found C 42.23, H 5.13, N 2.93, S 5.96.

**[(η$^4$-C$_8$H$_{12}$)Rh{(1*R*,2*S*)-H$_2$NCH[CH(OH)CH$_2$]C$_6$H$_4$-κ*N*,κ*O*}]-O$_3$SCF$_3$ [(1*R*,2*S*)-15]:** From (1*R*,1*S*)-**9** (94 mg, 0.24 mmol) and $TlO_3SCF_3$ (100 mg, 0.28 mmol) in of $CH_2Cl_2$(10 mL). Yield: 120 mg (98%). $^1$H NMR (300.1 MHz, $CD_3OD$): $\delta$ = 1.78, 2.31 (both m, 4 H each, both diene $CH_2$), 3.03 (dd, $^2J$ = 16.74, $^3J$ = 3.00 Hz, 1 H, 1 C*H*$_2$CH), 3.18 (dd, $^2J$ = 16.74, $^3J$ = 4.89 Hz, 1 H, 1 C*H*$_2$CH), 4.00, 4.14 (both br. m, 2 H each, both diene CH), 4.33 (d, $J$ = 4.50 Hz, 1 H, CHN), 4.76 (m, 1 H, CHO), 7.32–7.45 (m, 4 H, phenylene H) ppm. $^{13}$C NMR (75.5 MHz, $CD_3OD$): $\delta$ = 30.40 (s, diene $CH_2$), 40.36 (s, *C*H$_2$CH), 63.36 (s, NCH), 79.0 (br., diene CH), 83.66 (CHO), 122.22 (q, $^1J_{F,C}$ = 318.5 Hz, $CF_3$), 125.64, 126.93, 128.56, 128.94, 130.47, 141.30 (all s, all $C_6H_4$) ppm. $C_{18}H_{23}F_3NO_4RhS$ (509.34): calcd. C 42.45, H 4.55, N 2.75, S 6.29; found C 41.66, H 4.44, N 2.71, S 6.27.

**1,2-Diamine Complexes [{(*R*)-binap}Rh(H$_2$N∩NH$_2$)]BF$_4$ (16–18):** A thf solution (8 mL) of [(η$^4$-$C_8H_{12}$)Rh{(*R*)-binap}]$BF_4$ (0.10–0.15 mmol) was combined with the required 1,2-diamine ligand in a 1:1 stoichiometry and allowed to react for 24 h at room temperature under an atmosphere of hydrogen. Evaporation of the solvent to a residual volume of ca. 2 mL followed by the slow addition of diethyl ether (15 mL) induced the precipitation of the product as a crystalline solid which was washed with diethyl ether (5 mL) and dried under vacuum.

**[{(*R*)-binap}Rh(H$_2$NCMe$_2$CMe$_2$NH$_2$)]BF$_4$ [(*R*)-16]:** From [(η$^4$-$C_8H_{12}$)Rh{(*R*)-binap}]$BF_4$ (110 mg, 0.12 mmol) and 1,1′,2,2′-tetramethylethylenediamine (14 mg, 0.12 mmol). Yield: 82 mg (74%), red needles. $^1$H NMR (300.1 MHz, [D$_6$]acetone): $\delta$ = 1.04, 1.15 (both s, 6 H each, both $CH_3$), 1.34, 4.17 (both br. d, $^2J$ = 12.9 Hz, 2 H each, both $NH_2$), 6.27–7.74 (m, 32 H, aryl H) ppm. $^{13}$C NMR (75.5 MHz, $CD_2Cl_2$): $\delta$ = 25.86, 26.18 (both s, both $CH_3$), 60.81 (s, *C*Me$_2$), 125.65–138.79 (m, aryl C) ppm. $^{31}$P NMR (121.5 MHz, [D$_6$]acetone): $\delta$ = 61.43 (d, $^1J_{Rh,P}$ = 173.9 Hz) ppm. $C_{50}H_{48}BF_4N_2P_2Rh$ (928.59): calcd. C 64.67, H 5.22, N 3.02; found C 64.75, H 5.69, N 2.75.

**[{(*R*)-binap}Rh{(*R*,*R*)-H$_2$NCH(Ph)CH(Ph)NH$_2$}]BF$_4$ [(*R*),(*R*,*R*)-17]:** From [(η$^4$-$C_8H_{12}$)Rh{(*R*)-binap}]$BF_4$ (120 mg, 0.13 mmol) and (*R*,*R*)-1,2-diphenylethylenediamine (28 mg, 0.13 mmol). Yield: 100 mg (75%), dark red needles. $^1$H NMR (300.1 MHz, $CD_3CN$): $\delta$ = 2.40, 3.27, 4.24 (all m, 2 H each, CHN and $NH_2$), 6.48–7.95 (m, 42 H, aryl H) ppm. $^{13}$C NMR (75.5 MHz, $CD_2Cl_2$): $\delta$ = 63.35 (s, CHN), 124.52–138.14 (m, aryl C) ppm. $^{31}$P NMR (121.5 MHz, $CD_2Cl_2$): $\delta$ = 62.36 (d, $^1J_{Rh,P}$ = 175.7 Hz) ppm. $C_{58}H_{48}BF_4N_2P_2Rh$ (1024.69): calcd. C 67.99, H 4.73, N 2.74; found C 67.39, H 4.92, N 2.79.

**[{(*R*)-binap}Rh{(*R*,*R*)-1,2-(H$_2$N)$_2$C$_6$H$_{10}$}]BF$_4$ [(*R*),(*R*,*R*)-18]:** From [(η$^4$-$C_8H_{12}$)Rh{(*R*)-binap}]$BF_4$ (120 mg, 0.13 mmol) and (*R*,*R*)-1,2-diaminocyclohexane (15 mg, 0.13 mmol). Yield: 71 mg (59%), orange crystals. $^1$H NMR (300.1 MHz, $CD_3CN$): $\delta$ = 0.92, 1.04, 1.46, 1.53 (all m, 2 H each, all $CH_2$), 1.66, 2.22, 3.20 (all m, 2 H each, CHN and $NH_2$), 6.41–7.96 (m, 32 H, aryl H) ppm. $^{13}$C NMR (75.5 MHz, $CD_3CN$): $\delta$ = 23.88, 34.10 (both s, both $CH_2$), 58.72 (s, CHN), 125.41–133.87 (m, aryl C) ppm. $^{31}$P NMR (121.5 MHz, $CD_3CN$): $\delta$ = 61.84 (d, $^1J_{Rh,P}$ = 173.9 Hz) ppm. $C_{50}H_{46}BF_4N_2P_2Rh$ (926.22): calcd. C 64.78, H 5.01, N 3.02; found C 63.95, H 5.40, N 2.98.

**[{(*R*)-binap}Rh(H)(Cl){(*R*,*R*)-H$_2$NCH(Ph)CH(Ph)NH$_2$}]BF$_4$ [(*R*),(*R*,*R*)-19]:** Dropwise addition of a saturated solution of hydrogen chloride in diethyl ether (2.5 mL) to (*R*),(*R*,*R*)-**17** (85 mg, 0.08 mmol) in thf (10 mL) caused an immediate change in color from dark red to bright yellow. The resulting mixture was stirred for 30 min at ambient conditions and then reduced in volume to 2 mL. Dilution with *n*-pentane (10 mL) gave the product as an off-white precipitate which was collected by filtration, washed with *n*-pentane (2 × 4 mL), and dried under vacuum. Yield: 61 mg (72%). $^1$H NMR (300.1 MHz, $CD_2Cl_2$): $\delta$ = –14.06 ("dt", $^1J_{Rh,H}$ = 20.86 Hz, $\Sigma^2J_{P,H}$ = 39.01 Hz, 1 H, RhH), 2.54, 2.76, 3.34, 4.43 (all m, 6 H, CHN and $NH_2$), 6.20–8.16 (m, 42 H, aryl H) ppm. $^{31}$P NMR (121.5 MHz, $CD_2Cl_2$): $\delta$ = 44.23 (dd, $^1J_{Rh,P}$ = 122.1 Hz, $^2J_{P,P}$ = 35.1 Hz), 57.32 (dd, $^1J_{Rh,P}$ = 120.2 Hz) ppm. $C_{58}H_{49}BClF_4N_2P_2Rh$ (1060.21): calcd. C 65.65, H 4.67, N 2.64; found C 65.27, H 4.53, N 2.58.

 © 2007 Wiley-VCH Verlag GmbH & Co. KGaA, Weinheim 

**Reaction of $[(\eta^4\text{-}C_8H_{12})_2Rh_2(\mu\text{-}Cl)_2]$ with $H_2NCMe_2CH_2ONa$/$H_2NCMe_2CH_2OH$:** A solution of $[(\eta^4\text{-}C_8H_{12})_2Rh_2(\mu\text{-}Cl)_2]$ (50 mg, 0.10 mmol) in toluene (3 mL) was treated with a solution of $H_2NCMe_2CH_2ONa$ in 2-amino-2-methyl-1-propanol (1.1 M, 0.2 mL), prepared by dissolving the required amount of sodium metal in that amino alcohol. Stirring at room temperature for several minutes produced a yellow precipitate which was collected by filtration. Slow diffusion of *n*-pentane into a saturated thf solution of the solid afforded the addition compound $[(\eta^4\text{-}C_8H_{12})Rh(H_2NCMe_2CH_2O\text{-}\kappa N,\kappa O)]\cdot[(\eta^4\text{-}C_8H_{12})Rh(H_2NCMe_2CH_2OH\text{-}\kappa N,\kappa O)][(\eta^4\text{-}C_8H_{12})RhCl_2]\cdot$thf (**1·2·**thf), while recrystallization of the crude product from a toluene/*n*-hexane mixture resulted in the isolation of the adduct $[(\eta^4\text{-}C_8H_{12})Rh(H_2NCMe_2CH_2O\text{-}\kappa N,\kappa O)]\cdot[(\eta^4\text{-}C_8H_{12})Rh(H_2NCMe_2CH_2OH\text{-}\kappa N,\kappa O)]Cl$ (**1·3**), as shown by X-ray structure analyses (see below).

**Formation of *trans*-$[(i\text{Pr}_3\text{P})_2RhCl(N_2)]$:** L-Valinol was added in slight excess to the solution formed by mixing $[(\eta^2\text{-}C_8H_{14})_4Rh_2(\mu\text{-}Cl)_2]$ (103 mg, 0.14 mmol) in thf (5 mL)with $Pi\text{Pr}_3$ (0.11 mL, ca. 4 equiv.) under a nitrogen atmosphere at room temperature. Gentle warming of the solution resulted in an immediate change in color from dark red to orange. All volatile materials were then removed, and the remaining orange solid was redissolved in $CH_2Cl_2$. Slow evaporation of the solvent induced the deposition of orange crystals which X-ray crystallography showed to be *trans*-$[(i\text{Pr}_3\text{P})_2RhCl(N_2)]$ (see below). $^{31}$P NMR (121.5 MHz, $CDCl_3$): $\delta$ = 49.52 (d, $^1J_{Rh,P}$ = 120.3 Hz); ref.[15b]: $\delta$ = 41.8 (d, $^1J_{Rh,P}$ = 122.5 Hz) in [D$_8$]toluene. No identifiable products were formed when the reaction was carried out under an atmosphere of argon or hydrogen.

**Reaction of $[(\eta^4\text{-}C_8H_{12})Rh(H_2N\cap OH\text{-}\kappa N,\kappa O\})]O_3SCF_3$ Chelate Complexes (*S*)-12 and (1*R*,2*S*)-14 with (*R*)-binap:** (*a*) A solution of L-valinol complex (*S*)-**12** (55 mg, 0.12 mmol) in thf (5 mL) was treated with an equimolar quantity of (*R*)-binap (74 mg). The color of the mixture changed immediately from yellow to red–orange. After stirring for 3 h at ambient temperature, the solvent was removed to leave an orange powder (109 mg), the $^{31}$P NMR spectrum of which revealed the presence of an (*R*)-binap-coordinated $C_1$-symmetric species, assumed to originate from the $[\{(R)\text{-binap}\}Rh\{(S)\text{-}H_2NCH(CHMe_2)CH_2OH\text{-}\kappa N,\kappa O\}]^+$ cation. $^{31}$P NMR (121.5 MHz, [D$_8$]thf): $\delta$ = 47.58 (dd, $^1J_{Rh,P}$ = 172.7 Hz, $^2J_{P,P}$ = 62.4 Hz), 55.71 (dd, $^1J_{Rh,P}$ = 207.2 Hz); comparative $^{31}$P NMR spectroscopic data ($CD_2Cl_2$) for an in situ generated cationic complex formulated as $[\{(R)\text{-binap}\}Rh\{(S)\text{-nobin}\}]^+$ ($SbF_6^-$ salt; nobin = 2′-amino-1,1′-binaphth-2-ol): $\delta$ = 39.4 (dd, $^1J_{Rh,P}$ = 203.6 Hz, $^2J_{P,P}$ = 89.3 Hz), 40.1 (dd, $^1J_{Rh,P}$ = 201.5 Hz) ppm.[10] The product also contained traces of uncoordinated (*R*)-binap ($\delta$ = –14.19 ppm) in addition to minor quantities (ca. 6%) of oxidized forms of the ligand, that is, (*R*)-binap(O) ($\delta$ = –13.76, 26.84 ppm) and (*R*)-binap(O)$_2$ ($\delta$ = 29.39 ppm); ref.[22] $\delta$ = –14.3, 28.1 ppm for binap(O) and $\delta$ = 29.3 ppm for binap(O)$_2$. Only inferior amounts (ca. 4%) of the $[(\eta^4\text{-}C_8H_{12})Rh\{(R)\text{-binap}\}]^+$ cation resulting from substitution of the amino alcohol rather than the diolefin were detected by $^{31}$P NMR spectroscopic analysis: $\delta$ = 26.71 (d, $^1J_{Rh,P}$ = 147.1 Hz) ppm; comparative data for authentic $[(\eta^4\text{-}C_8H_{12})Rh\{(R)\text{-binap}\}]BF_4$ (121.5 MHz, $CDCl_3$): $\delta$ = 26.65 (d, $^1J_{Rh,P}$ = 144.8 Hz) ppm. The predominant replacement of the diene ligand by the diphosphane was also evident from the $^1$H NMR spectrum (300.1 MHz,

Table 2. Crystal data and structure refinement for compounds **1·2·**thf, **1·3**, **4**, (*S*)-**6**, and (*R*)-**7**.

| Compound | **1·2·**thf | **1·3** | **4** | (*S*)-**6** | (*R*)-**7** |
|---|---|---|---|---|---|
| Empirical formula | $C_{36}H_{65}Cl_2N_2O_3Rh_3$ | $C_{24}H_{45}ClN_2O_2Rh_2$ | $C_{10}H_{19}ClNORh$ | $C_{13}H_{25}ClNORh$ | $C_{13}H_{23}ClNORh$ |
| $M$ [g mol$^{-1}$] | 953.53 | 634.89 | 307.62 | 349.70 | 347.68 |
| Crystal size [mm] | 0.50 × 0.28 × 0.08 | 0.48 × 0.27 × 0.23 | 0.23 × 0.18 × 0.17 | 0.41 × 0.35 × 0.20 | 0.32 × 0.17 × 0.13 |
| $T$ [°C] | –150 ± 2 | –150 ± 2 | –173 ± 2 | –150 ± 2 | –60 ± 2 |
| Crystal system | triclinic | tetragonal | monoclinic | monoclinic | monoclinic |
| Space group | $P\bar{1}$ | $P\bar{4}2c$ | $P2_1/c$ | $P2_1$ | $P2_1$ |
| $a$ [Å] | 11.643(5) | 11.220(2) | 14.1313(3) | 7.202(2) | 11.220(2) |
| $b$ [Å] | 12.877(8) | 11.220(2) | 9.0605(5) | 9.354(3) | 7.267(1) |
| $c$ [Å] | 15.343(2) | 21.023(8) | 8.9213(4) | 11.046(3) | 17.461(3) |
| $\alpha$ [°] | 102.85(2) | 90 | 90 | 90 | 90 |
| $\beta$ [°] | 101.60(2) | 90 | 92.405(3) | 100.53(2) | 90.99(2) |
| $\gamma$ [°] | 111.12(4) | 90 | 90 | 90 | 90 |
| $V$ [Å$^3$] | 1989.6(17) | 2646.6(12) | 1141.25(8) | 731.6(4) | 1423.5(4) |
| $Z$ | 2 | 4 | 4 | 2 | 4 |
| $D_{calcd.}$ [g cm$^{-3}$] | 1.592 | 1.593 | 1.790 | 1.587 | 1.622 |
| $F$(000) | 976 | 1304 | 624 | 360 | 712 |
| $\mu$ [mm$^{-1}$] | 1.399 | 1.370 | 1.699 | 1.335 | 1.372 |
| $\theta$ range [°] | 1.97 to 25.17 | 1.94 to 26.27 | 3.66 to 28.70 | 1.88 to 25.15 | 1.17 to 26.97 |
| $h$; $k$; $l$ range | –13, 12; 0, 15; –18, 17 | –13, 13; 0, 10; 0, 25 | –19, 19; –12, 12; –12, 12 | –8, 8; –11, 11; –13, 13 | 0, 14; –9, 9; –22, 22 |
| Reflections collected | 7491 | 5115 | 25405 | 3030 | 6500 |
| Unique reflections | 7148 ($R_{int.}$ = 0.0272) | 2685 ($R_{int.}$ = 0.0630) | 2929 ($R_{int.}$ = 0.0206) | 2625 ($R_{int.}$ = 0.0521) | 6183 ($R_{int.}$ = 0.0423) |
| Complete to $\theta_{max}$ [%] | 100.0 | 99.7 | 99.8 | 100.0 | 99.7 |
| Intensities $I > 2\sigma(I)$ | 5747 | 2018 | 2779 | 2147 | 5630 |
| $T_{min}/T_{max}$ | 0.668/0.894 | 0.578/0.731 | 0.670/0.749 | 0.652/0.763 | 0.739/0.835 |
| Parameters refined | 435 | 146 | 146 | 157 | 374 |
| $wR_2$ (all data) | 0.1032 | 0.1290 | 0.0394 | 0.1353 | 0.0980 |
| $R_1$ [$I > 2\sigma(I)$] | 0.0410 | 0.0466 | 0.0170 | 0.0547 | 0.0371 |
| $GoF$ on $F^2$ | 1.043 | 1.081 | 1.102 | 1.096 | 1.039 |
| $\rho_{max}/\rho_{min}$ [$e$ Å$^{-3}$] | 1.17/–0.87 | 1.27/–0.68 | 0.59/- 0.57 | 1.16/–1.30 | 0.76/–0.62 |
| Flack parameter $x$[29] | | 0.41(9)[a] | | 0.01(10) | 0.01(5) |

[a] Racemic twin.

 © 2007 Wiley-VCH Verlag GmbH & Co. KGaA, Weinheim 

[$D_8$]thf) showing free cyclooctadiene ($\delta$ = 2.22 and 5.39 ppm) together with coordinated L-valinol: $\delta$ = 0.54, 0.75 (both d, $J$ = 6.60, 6.78 Hz, 3 H each, both $CH_3$), 1.98 ("dq", $J$ = 6.60, 6.78 Hz, 1 H, C*H*Me$_2$), 2.48 (br. m, 3 H, NCH and $NH_2$ superimposed), 3.38 (m, 1 H, 1 $CH_2O$), 3.76 (dd, $^2J$ = 9.98 Hz, $^3J$ = 3.48 Hz, 1 H, $CH_2O$); comparative data for free L-valinol: $\delta$ = 0.71, 0.72 (both d, $J$ = 6.78 Hz each, 3 H each, both $CH_3$), 1.41 ("dq", $J$ = 6.78 Hz, 1 H C*H*Me$_2$), 2.36 (m, 1 H, NCH), 2.4 (br., 2 H, $NH_2$), 3.11 (m, 1 H, 1 $CH_2O$), 3.42 (dd, $^2J$ = 10.53, $^3J$ = 3.75 Hz, 1 H, $CH_2O$). (*b*) The unwanted formation of the binap(O), binap(O)$_2$, and [($\eta^4$-$C_8H_{12}$)-Rh{(*R*)-binap}]$^+$ byproducts could be suppressed by using a slight deficiency of the diphosphane as shown by the reaction of the L-norephedrine chelate complex (1*R*,2*S*)-**14** (129 mg, 0.25$_2$ mmol) with the (*R*)-binap ligand (156 mg, 0.25$_0$ mmol) in dichloromethane (4 mL). $^{31}$P NMR spectroscopic data (121.5 MHz, $CD_2Cl_2$) attributed to the [{(*R*)-binap}Rh{(1*R*,2*S*)-$H_2$NCH(Me)CH(Ph)OH-κ*N*,κ*O*}]$^+$ cation: $\delta$ = 47.39 (dd, $^1J_{Rh,P}$ = 173.8 Hz, $^2J_{P,P}$ = 60.1 Hz, 55.70 (dd, $^1J_{Rh,P}$ = 204.2 Hz) ppm. So far, all attempts to isolate the suspected (*R*)-binap/amino alcohol complexes as pure compounds resulted in their decomposition to unidentified products.

**General Procedure for Catalytic C=O Hydrogenation:** A 10-mL Schlenk tube equipped with a small magnetic stirring bar was charged with the catalyst complex dissolved in 2-propanol (typically 0.01 mmol in 3.0 mL). The required equivalent of potassium hydroxide (if any; see Table 1) and acetophenone (2.0 mmol) were added, the mixture was stirred for 10 min at ambient conditions, and the tube was inserted into an argon-filled stainless steel autoclave. The autoclave was sealed and, in direct hydrogenation experiments, vented several times with $H_2$ (Messer-Griesheim; 99.999%), subsequently pressurized to 10 bar and kept at 50 °C with stirring. Transfer hydrogenation experiments were carried out under an atmosphere of argon. At the end of the reaction, the pressure was vented, the solvent removed under vacuum, and the residue was diluted with *n*-pentane to precipitate the catalyst as a red oil. The pentane solution was decanted and chromatographed on silica gel (diethyl ether/*n*-pentane, 1:1). Volatile material was distilled off, and the mixture of products was analyzed by $^1$H NMR spectroscopy. Conversions and product compositions were determined on the basis of the integrations of the PhC(O)C*H*$_3$ and PhCH(OH)C*H*$_3$ signals. Enantiomeric excesses were measured by HPLC by using a Daicel Chiralcel OD column.

**X-ray Structure Determinations:** Single-crystals of the addition compounds **1·2**·thf and **1·3** were obtained by crystallizing the precipitates formed upon treatment of [($\eta^4$-$C_8H_{12}$)$_2$Rh$_2$(μ-Cl)$_2$] with $H_2$NCMe$_2$CH$_2$ONa/$H_2$NCMe$_2$CH$_2$OH from thf/*n*-pentane and toluene/*n*-hexane, respectively. Crystals suitable for X-ray work of **4**, (*S*)-**6**, (*R*)-**7**, (1*R*,2*S*)-**14**, and (1*R*,2*S*)-**15** were grown from dichloromethane. Crystal growth of (1*R*,2*S*)-**8** from thf/$CH_2Cl_2$ and (*R*)-**16** from diethyl ether/acetone/thf afforded solvent-containing specimens having the idealized compositions (1*R*,2*S*)-**8**·1/4$CH_2Cl_2$·1/4thf and (*R*)-**16**·1/2Me$_2$CO·1/4thf (see below). Crystals of (*S*)-**10**·$H_2O$ grew from the mother liquor of the reaction between (*S*)-**6** and powdered KOH in $CH_2Cl_2$; those of (*R*),(*R*,*R*)-**17**·$CH_2Cl_2$ were deposited upon slow diffusion of diethyl ether into a concentrated dichloromethane solution of the complex. Diffraction measurements were made with an Enraf–Nonius CAD-4 MACH 3 diffractometer (compounds **1·2**·thf, **1·3**, (*S*)-**6**, (*S*)-**10**·$H_2O$, (1*R*,2*S*)-**15**, (*R*)-**7**, (1*R*,2*S*)-**14**, (*R*)-**16**·1/2Me$_2$CO·1/4thf, and (*R*),(*R*,*R*)-

Table 3. Crystal data and structure refinement for compounds (1*R*,2*S*)-**8**·1/4$CH_2Cl_2$·1/4thf,[a] (*S*)-**10**·$H_2O$, (1*R*,2*S*)-**14**, (1*R*,2*S*)-**15**, and (*R*)-**16**·1/2Me$_2$CO·1/4thf.

| Compound | (1*R*,2*S*)-**8**·1/4$CH_2Cl_2$·1/4thf | (*S*)-**10**·$H_2O$ | (1*R*,2*S*)-**14** | (1*R*,2*S*)-**15** | (*R*)-**16**·1/2Me$_2$CO·1/4thf |
|---|---|---|---|---|---|
| Empirical formula | $C_{36.611}H_{55.222}Cl_{2.926}N_2O_{2.537}Rh_2$[b] | $C_{13}H_{26}NO_2Rh$ | $C_{18}H_{25}F_3NO_4RhS$ | $C_{18}H_{23}F_3NO_4RhS$ | $C_{52.50}H_{53}BF_4N_2O_{0.75}P_2Rh$ |
| $M$ [g mol$^{-1}$] | 873.62 | 331.26 | 511.36 | 509.34 | 957.63 |
| Crystal size [mm] | 0.23 × 0.18 × 0.16 | 0.38 × 0.25 × 0.19 | 0.50 × 0.33 × 0.28 | 0.45 × 0.40 × 0.35 | 0.43 × 0.35 × 0.10 |
| $T$ [°C] | –173 ± 2 | –150 ± 2 | +20 ± 2 | –70 ± 2 | +20 ± 2 |
| Crystal system | monoclinic | triclinic | orthorhombic | monoclinic | orthorhombic |
| Space group | $P2_1$ | $P\bar{1}$ | $P2_12_12_1$ | $P2_1$ | $P2_12_12_1$ |
| $a$ [Å] | 10.9864(3) | 7.288(2) | 10.3321(9) | 10.7614(7) | 11.448(2) |
| $b$ [Å] | 14.2188(13) | 10.139(1) | 10.3563(9) | 16.7785(13) | 15.002(2) |
| $c$ [Å] | 12.3624(4) | 10.521(1) | 21.9557(18) | 11.5551(13) | 30.887(4) |
| $\alpha$ [°] | 90 | 91.59(1) | 90 | 90 | 90 |
| $\beta$ [°] | 105.747(2) | 107.27(2) | 90 | 108.621(8) | 90 |
| $\gamma$ [°] | 90 | 103.52(3) | 90 | 90 | 90 |
| $V$ [Å$^3$] | 1858.7(2) | 717.8(2) | 2135.3(3) | 1977.2(3) | 5305.1(14) |
| $Z$ | 2 | 2 | 4 | 4 | 4 |
| $D_{calcd.}$ [g cm$^{-3}$] | 1.561 | 1.533 | 1.591 | 1.711 | 1.222 |
| $F$(000) | 898 | 344 | 1040 | 1032 | 2016 |
| $\mu$ [mm$^{-1}$] | 1.135 | 1.181 | 0.946 | 1.021 | 0.432 |
| $\theta$ range [°] | 3.44 to 28.70 | 2.04 to 26.17 | 2.04 to 25.48 | 1.86 to 24.06 | 2.33 to 25.16 |
| $h$; $k$; $l$ range | –14, 13; –19, 19; –16, 16 | 0, 9; –12, 12; –13, 12 | –12, 9; 0, 12; –24, 0 | –12, 11; –19, 0; 0, 13 | –13, 13; –17, 17; –36, 36 |
| Reflections collected | 40881 | 3114 | 4037 | 3422 | 10486 |
| Unique reflections | 9540 ($R_{int.}$ = 0.0213) | 3114 | 3769 ($R_{int.}$ = 0.0248) | 3249 ($R_{int.}$ = 0.0155) | 9451 ($R_{int.}$ = 0.0378) |
| Complete to $\theta_{max}$ [%] | 99.3 | 100.0 | 100.0 | 99.9 | 99.1 |
| Intensities $I > 2\sigma(I)$ | 9232 | 3082 | 3161 | 3114 | 6569 |
| $T_{min}/T_{max}$ | 0.727/0.830 | 0.655/0.798 | 0.668/0.763 | 0.665/0.699 | 0.794/0.958 |
| Parameters refined | 473 | 314 | 257 | 511 | 601 |
| $wR_2$ (all data) | 0.0421 | 0.0648 | 0.0861 | 0.0593 | 0.1951 |
| $R_1$ [$I > 2\sigma(I)$] | 0.0187 | 0.0223 | 0.0371 | 0.0232 | 0.0731 |
| $GoF$ on $F^2$ | 1.137 | 1.143 | 1.097 | 1.044 | 1.034 |
| $\rho_{max}/\rho_{min}$ [$e$ Å$^{-3}$] | 0.52/–0.67 | 0.99/–0.60 | 0.57/–0.48 | 0.53/- 0.52 | 1.05/–0.69 |
| Flack parameter $x$[29] | –0.010(14) | 0.01(5) | 0.03(5) | 0.01(3) | –0.05(5) |

[a] Formula idealized for integer number of atoms in unit cell (see text). [b] Empirical formula given for the hydrogen-bonded dimeric unit (see Figure 6) including the solvent of crystallization.

 © 2007 Wiley-VCH Verlag GmbH & Co. KGaA, Weinheim 

**17**·$CH_2Cl_2$) and a Bruker-Nonius Kappa CCD instrument (compounds **4** and (1*R*,2*S*)-**8**·1/4$CH_2Cl_2$·1/4thf), by using Mo-$K_\alpha$ radiation ($\lambda$ = 0.71073 Å); data corrected for absorption either semiempirically from equivalents[23] (**4** and (1*R*,2*S*)-**8**·1/4$CH_2Cl_2$·1/4thf) or by $\psi$-scans.[24]

The structures were solved by direct methods and subsequently refined by full-matrix least-squares procedures on $F^2$ with allowance for anisotropic thermal motion of all non-hydrogen atoms employing both the SHELXTL NT 6.12[25] and the WinGX[26a] packages with some of the relevant programs (SIR-97,[27] SHELXL-97,[28] ORTEP-3[26b]) implemented therein. Crystals of **1·3** showed racemic twinning which was refined to give a twin component ratio close to 1:1. The split occupancies for the disordered cyclooctadiene carbon atoms in structure **4** (Figure 3) refined to 0.55 and 0.45, those of (1*R*,2*S*)-**8**·1/4$CH_2Cl_2$·1/4thf (Figure 6) to 0.74 and 0.26, and those of the atoms belonging to the disordered D-prolinol ligand in structure (*R*)-**7** (Figure 5) to 0.73 and 0.27. The residual electron density remaining after refinement of the structural model resulting for complex (*R*)-**16** was modeled by assuming the presence of solvent of crystallization (acetone and thf) with site occupancies fixed to 0.5 for the acetone and 0.25 for the thf molecule: (*R*)-**16**·1/2$Me_2CO$·1/4thf. Similarly, the final $\Delta F$ maps of the structure analysis of (1*R*,2*S*)-**8** indicated that in the crystal under study two different solvent molecules ($CH_2Cl_2$ and thf) shared a single crystallographic site with occupancies refining to 0.23 for the $CH_2Cl_2$ and 0.27 for the thf of crystallization, that is, close to (1*R*,2*S*)-**8**·1/4$CH_2Cl_2$·1/4thf. Further details of the X-ray structure determinations and results of the structure refinements are provided in Tables 2 3, and 4. For comparison with previously published data,[16b] the results of the structure determination carried out for the already known dinitrogen complex *trans*-[($i$Pr$_3$P)$_2$RhCl($N_2$)] have also been included in Table 4.

Table 4. Crystal data and structure refinement for compounds (*R*),(*R*,*R*)-**17**·$CH_2Cl_2$ and *trans*-[($i$Pr$_3$P)$_2$RhCl($N_2$)].

| Compound | (*R*),(*R*,*R*)-**17**·$CH_2Cl_2$ | *trans*-[($i$Pr$_3$P)$_2$RhCl($N_2$)] |
|---|---|---|
| Empirical formula | $C_{59}H_{50}BCl_2F_4N_2P_2RhS$ | $C_{18}H_{42}ClN_2P_2Rh$ |
| $M$ [g mol$^{-1}$] | 511.36 | 486.84 |
| Crystal size [mm] | 0.40 × 0.31 × 0.30 | 0.22 × 0.12 × 0.09 |
| $T$ [°C] | +20 ± 2 | –70 ± 2 |
| Crystal system | orthorhombic | monoclinic |
| Space group | $P2_12_12_1$ | $P2_1/c$ [$P2_1/c$][a] |
| $a$ [Å] | 11.355(1) | 8.105(2) [8.062(2)][a] |
| $b$ [Å] | 15.545(1) | 8.887(3) [8.883(2)][a] |
| $c$ [Å] | 31.979(3) | 16.551(8) [16.431(4)][a] |
| $\alpha$ [°] | 90 | 90 |
| $\beta$ [°] | 90 | 93.07(5) [92.45(1)][a] |
| $\gamma$ [°] | 90 | 90 |
| $V$ [Å$^3$] | 5644.7(8) | 1189.1(8) |
| $Z$ | 4 | 2[b] |
| $D_{calcd.}$ [g cm$^{-3}$] | 1.306 | 1.360 [1.375][a] |
| $F$(000) | 2272 | 512 |
| $\mu$ [mm$^{-1}$] | 0.505 | 0.969 |
| $\theta$ range [°] | 1.90 to 25.16 | 2.46 to 27.04 |
| $h$; $k$; $l$ range | 0, 13; 0, 18; 0, 38 | –10, 10; 0, 11; –21, 21 |
| Reflections collected | 5595 | 2779 |
| Unique reflections | 5595 | 2599 ($R_{int.}$ = 0.0226) |
| Complete to $\theta_{max}$ [%] | 99.4 | 99.7 |
| Intensities $I > 2\sigma(I)$ | 4286 | 2089 |
| $T_{min}/T_{max}$ | 0.756/0.856 | 0.892/0.915 |
| Parameters refined | 667 | 124 |
| $wR_2$ (all data) | 0.1661 | 0.0720 |
| $R_1$ [$I > 2\sigma(I)$] | 0.0609 | 0.0294 [0.024][a] |
| $GoF$ on $F^2$ | 1.055 | 1.014 |
| $\rho_{max}/\rho_{min}$ [$e$ Å$^{-3}$] | 0.77/–0.56 | 0.51/–0.30 |
| Flack parameter $x$[29] | 0.15(6) | |

[a] Crystal and refinement data obtained at –160 °C[16b] given in brackets. [b] Cl and $N_2$ ligands disordered about center of symmetry.

CCDC-631170 (for **1·2**·thf), -631171 (for **1·3**), -631172 (for **4**), -631173 [for (*S*)-**6**], -631174 [for (*R*)-**7**], -631175 [for (1*R*,2*S*)-**8**·1/4$CH_2Cl_2$·1/4thf], -631176 [for (*S*)-**10**·$H_2O$], -631177 [for (1*R*,2*S*)-**14**], -631178 [for (1*R*,2*S*)-**15**], -631179 [for (*R*)-**16**·1/2$Me_2CO$·1/4thf], -631180 [for (*R*),(*R*,*R*)-**17**·$CH_2Cl_2$], and -631181 [for *trans*-[($i$Pr$_3$P)$_2$RhCl($N_2$)] contain the supplementary crystallographic data for this paper. These data can be obtained free of charge from The Cambridge Crystallographic Data Centre via www.ccdc.cam.ac.uk/data_request/cif.

## Acknowledgments

Support of this work by the Deutsche Forschungsgemeinschaft (Bonn, SFB 583) is gratefully acknowledged. We are also indebted to Mrs. S. Hoffmann and Mr. P. Bakatselos for their skilful assistance.

[1] a) L. Dahlenburg, *J. Organomet. Chem.* **2001**, *619*, 88–98; b) L. Dahlenburg, R. Götz, *Inorg. Chem. Commun.* **2003**, *6*, 443–446; c) L. Dahlenburg, R. Götz, *Eur. J. Inorg. Chem.* **2004**, 888–905; d) L. Dahlenburg, R. Götz, *Inorg. Chim. Acta* **2004**, *357*, 2875–2880.

[2] For leading overviews, see: a) R. Noyori, S. Hashiguchi, *Acc. Chem. Res.* **1997**, *30*, 97–102; b) M. J. Palmer, M. Wills, *Tetrahedron: Asymmetry* **1999**, *10*, 2045–2061; c) M. Wills, M. Gamble, M. Palmer, A. Smith, J. Studley, J. Kenny, *J. Mol. Catal. A* **1999**, *146*, 139–148; d) R. Noyori, T. Ohkuma, *Angew. Chem.* **2001**, *113*, 40–75; *Angew. Chem. Int. Ed.* **2001**, *40*, 40–74; e) R. Noyori, *Angew. Chem.* **2002**, *114*, 2108–2123; *Angew. Chem. Int. Ed.* **2002**, *41*, 2008–2022 (2001 Nobel Lecture in Chemistry); f) S. E. Clapham, A. Hadzovic, R. H. Morris, *Coord. Chem. Rev.* **2004**, *248*, 2201–2237; g) T. Ohkuma, R. Noyori, in M. Beller, C. Bolm (Eds.), *Transition Metals for Organic Synthesis*, 2nd ed., Wiley-VCH, Weinheim, **2004**, vol. 2, pp. 29–113; h) M. Kitamura, R. Noyori in *Ruthenium in Organic Synthesis* (Ed.: S.-I. Murahashi) Wiley-VCH, Weinheim, **2004**, pp. 3–52; i) T. Ikariya, K. Murat, R. Noyori, *Org. Biomol. Chem.* **2006**, *4*, 393–406; j) S. Gladiali, E. Alberico, *Chem. Soc. Rev.* **2006**, *35*, 226–236.

[3] D. J. Cross, I. Houson, A. M. Kawamoto, M. Wills, *Tetrahedron Lett.* **2004**, *45*, 843–846.

[4] M. Enamullah, A. Sharmin, M. Hasegawa, T. Hoshi, A.-C. Chamayou, C. Janiak, *Eur. J. Inorg. Chem.* **2006**, 2146–2154.

[5] a) J. Chatt, L. M. Venanzi, *J. Chem. Soc.* **1957**, 4735–4741; b) G. Zassinovich, G. Mestroni, A. Camus, *J. Organomet. Chem.* **1975**, *91*, 379–388; c) R. Uson, L. A. Oro, C. Claver, M. A. Garralda, *J. Organomet. Chem.* **1976**, *105*, 365–370; d) L. A. Oro, M. J. Fernandez, J. Modrego, J. M. Lopez, *J. Organomet. Chem.* **1985**, *287*, 409–417; e) M. A. Garralda, L. Ibarlucea, *J. Organomet. Chem.* **1986**, *311*, 225–231; f) J. G. Donkervoort, M. Bühl, J. M. Ernsting, C. J. Elsevier, *Eur. J. Inorg. Chem.* **1999**, 27–33.

[6] D. B. MacQueen, F. D. Petersen, *Inorg. Chem.* **1990**, *29*, 2313–2320.

[7] P. A. Harding, S. D. Robinson, *J. Chem. Soc., Dalton Trans.* **1987**, 947–954.

[8] S.-I. Inoue, H. Takaya, K. Tani, S. Otsuka, T. Sato, R. Noyori, *J. Am. Chem. Soc.* **1990**, *112*, 4897–4905.

[9] W. Leitner, J. M. Brown, H. Brunner, *J. Am. Chem. Soc.* **1993**, *115*, 152–159.

[10] During the preparation of this manuscript, a Japanese group described a Rh$^I$-based catalytic system used for enantioselective cyclizations of 1,6-enynes, which was made by mixing the

 © 2007 Wiley-VCH Verlag GmbH & Co. KGaA, Weinheim 

biphep [2,2′-bis(diphenylphosphanyl)- 1,1′-biphenyl] and binap norbornadiene complexes $[(\eta^4\text{-}C_7H_8)Rh(P\cap P)]SbF_6$ with the β-amino alcohol nobin (2′-amino-1,1′-binaphth-2-ol) in $CH_2Cl_2$ under hydrogen. $^{31}P$ NMR spectroscopy indicated the presence in solution of diphosphane-coordinated cations formulated as $[(biphep)Rh(nobin)]^+$ and $[(binap)Rh(nobin)]^+$, respectively: K. Mikami, S. Kataoka, K. Wakabayshi, K. Aikawa, *Tetrahedron Lett.* **2006**, *47*, 6361–6364.

[11] F. H. Allen, O. Kennard, *Chem. Des. Autom. News* **1993**, *8*, 1.

[12] a) W. M. Latimer, *The Oxidation States of the Elements and Their Potentials in Aqueous Solutions*, 2nd ed., Prentice-Hall, Englewood Cliffs, N. J., **1952**; b) A. J. Bard, R. Parsons, J. Jordan, *Standard Potentials in Aqueous Solutions*, Dekker, New York, **1985**.

[13] a) E. Rotondo, G. Battaglia, S. G. Arena, F. Faraone, *J. Organomet. Chem.* **1991**, *419*, 399–402; b) H. Berger, R. Nesper, P. S. Pregosin, H. Rüegger, M. Wörle, *Helv. Chim. Acta* **1993**, *76*, 1520–1538; c) A. Albinati, J. Eckert, P. Pregosin, H. Rüegger, R. Salzmann, C. Stössel, *Organometallics* **1997**, *16*, 579–590; d) M. Valentini, K. Selvakumar, M. Wörle, P. S. Pregosin, *J. Organomet. Chem.* **1999**, *587*, 244–251; e) S. Gladiali, F. Grepioni, S. Medici, A. Zucca, Z. Berente, L. Kollár, *Eur. J. Inorg. Chem.* **2003**, 556–561; f) D. J. Brauer, K. W. Kottsieper, S. Roßenbach, O. Stelzer, *Eur. J. Inorg. Chem.* **2003**, 1748–1755.

[14] P. Binger, J. Haas, G. Glasser, R. Goddard, C. Krüger, *Chem. Ber.* **1994**, *127*, 1927–1929.

[15] a) K. Tani, T. Yamagata, S. Akutagawa, H. Kumobayashi, T. Taketomi, H. Takaya, A. Miyashita, R. Noyori, S. Otsuka, *J. Am. Chem. Soc.* **1984**, *106*, 5208–5217; b) K. Mashima, T. Akutagawa, X. Zhang, H. Takaya, T. Taketomi, H. Kumobayashi, S. Akutagawa, *J. Organomet. Chem.* **1992**, *428*, 213–222.

[16] a) C. Busetto, A. D'Alfonso, F. Maspero, G. Perego, A. Zazetta, *J. Chem. Soc., Dalton Trans.* **1977**, 1828–1834; b) D. L. Thorn, T. H. Tulip, J. A. Ibers, *J. Chem. Soc., Dalton Trans.* **1979**, 2022–2025; c) R. L. Harlow, D. L. Thorn, R. T. Baker, N. L. Jones, *Inorg. Chem.* **1992**, *31*, 993–997.

[17] a) K. Abdur-Rashid, A. J. Lough, R. H. Morris, *Organometallics* **2001**, *20*, 1047–1049; b) V. Rautenstrauch, X. Hoang-Cong, R. Churlaud, K. Abdur-Rashid, R. H. Morris, *Chem. Eur. J.* **2003**, *9*, 4954–4967.

[18] H. Doucet, T. Ohkuma, K. Murata, T. Yokozawa, M. Kozawa, E. Katayama, A. F. England, T. Ikariya, R. Noyori, *Angew. Chem.* **1998**, *110*, 1792–1796; *Angew. Chem. Int. Ed.* **1998**, *37*, 1703–1707.

[19] C. Hirel, K. E. Vostrikova, J. Pécaut, V. I. Ovcharenko, O. Rey, *Chem. Eur. J.* **2001**, *7*, 2007–2014.

[20] G. Giordano, R. H. Crabtree, *Inorg. Synth.* **1979**, *19*, 218–220; G. Giordano, R. H. Crabtree, *Inorg. Synth.* **1990**, *28*, 88–90.

[21] A. van der Ent, A. L. Onderdelinden, *Inorg. Synth.* **1973**, *14*, 92–95; A. van der Ent, A. L. Onderdelinden, *Inorg. Synth.* **1990**, *28*, 90–92.

[22] K. A. Bunten, D. H. Farrar, A. J. Poë, A. Lough, *Organometallics* **2002**, *21*, 3344–3350.

[23] *SADABS*, Program for Absorption Correction for Area Detectors, v. 2.06, Bruker-AXS, Inc., Madison, WI, **2002**.

[24] A. C. T. North, D. C. Phillips, F. S. Mathews, *Acta Crystallogr., Sect. A* **1968**, *24*, 351–359.

[25] *SHELXTL NT*, Program Library for Structure Solution and Molecular Graphics, v. 6.12, Bruker AXS, Inc., Madison, WI, **2002**.

[26] a) L. J. Farrugia, *J. Appl. Crystallogr.* **1999**, *32*, 837–838; b) L. J. Farrugia, *J. Appl. Crystallogr.* **1997**, *30*, 565.

[27] A. Altomare, M. C. Burla, M. Camalli, G. L. Cascarano, C. Giacovazzo, A. Guagliardi, A. G. G. Moliterni, G. Polidori, R. Spagna, *J. Appl. Crystallogr.* **1999**, *32*, 115–119.

[28] G. M. Sheldrick, *SHELXL-97*, Program for the Refinement of Crystal Structures (release 97–2), University of Göttingen, Germany, **1998**.

[29] H. D. Flack, *Acta Crystallogr., Sect. A* **1983**, *39*, 876–881.

Received: December 20, 2006
Published Online: March 6, 2007

 © 2007 Wiley-VCH Verlag GmbH & Co. KGaA, Weinheim 

DOI: 10.1002/ejic.200700030

# Purines Bearing Phenanthroline or Bipyridine Ligands and Their $Ru^{II}$ Complexes in Position 8 as Model Compounds for Electrochemical DNA Labeling – Synthesis, Crystal Structure, Electrochemistry, Quantum Chemical Calculations, Cytostatic and Antiviral Activity

**Milan Vrábel,[a] Michal Hocek,*[a] Luděk Havran,[b] Miroslav Fojta,*[b] Ivan Votruba,[a] Blanka Klepetářová,[a] Radek Pohl,[a] Lubomír Rulíšek,[c] Lucie Zendlová,[c] Pavel Hobza,[c] I-hung Shih,[d] Eric Mabery,[d] and Richard Mackman[d]**

**Keywords:** Purines / Nucleobases / Bipyridines / Phenanthrolines / Ru complexes / Electrochemistry

A series of ethynyl- or (4-boronophenyl)bipyridines and -phenanthrolines were prepared as versatile building blocks for attachment of bidentate N-ligands to other molecules via cross-coupling reactions. Their complexation with $Ru(bpy)_2Cl_2$ gave the corresponding $Ru^{II}$ complexes. 9-Benzyladenine derivatives bearing the bipyridine or phenanthroline complexes in position 8, attached via a conjugate acetylene or phenylene linker were prepared by cross-coupling reactions of the ethynyl- or 4-boronophenylbipyridines and -phenanthrolines with 9-benzyl-8-bromoadenine. Their complexation with $Ru(bpy)_2Cl_2$ afforded the corresponding Ru complexes as model compounds for electrochemical DNA labeling. The same compounds were also prepared directly by cross-coupling of 9-benzyl-8-bromoadenine with Ru complexes of the alkynes and boronic acids. Both approaches are compared in terms of potential applications for labeling of nucleic acids. The crystal structures of two Ru complexes were determined by X-ray diffraction. The electrochemistry of the model purines bearing the phenanthroline or bipyridine ligands and the Ru complexes was studied by means of cyclic or square-wave voltammetry with carbon paste and mercury electrodes. The experimental redox potentials of the title compounds were compared with quantum chemical calculations. A very good agreement between experiment and theory was obtained, with a standard deviation of 0.13 V. It was shown that theoretical calculations can be of a limited predictive power for new $Ru^{II}$ complexes, though it was difficult to reproduce differences smaller than 0.05 V. Several compounds of this series exhibited a considerable cytostatic effect and activity against the hepatitis C virus (HCV).
(© Wiley-VCH Verlag GmbH & Co. KGaA, 69451 Weinheim, Germany, 2007)

## Introduction

DNA biosensors and chips[1] are increasingly utilized in current molecular biology, biochemistry, biomedicine and related disciplines. On the basis of DNA hybridization, these devices are used to analyze nucleotide sequences of DNAs or RNAs, searching for mutations, monitoring of gene expression, etc. DNA damage and interaction of DNA with different toxic or biologically active species can also be detected by DNA sensors. In addition to optical methods involved in most of the commercially available systems, electrochemical detection has attracted attention as a less expensive alternative offering comparable sensitivity.

Nucleic acids are electroactive species producing analytically useful oxidation and reduction signals at mercury or solid electrodes.[2,3] In addition to label-free DNA detection, different electroactive (or enzyme) tags tethered to target DNAs or hybridization probes are used to improve sensitivity and/or specificity of the analysis.[3] For example, ferrocene-labeled oligonucleotides (ON) were used as reporter (signaling) probes[4] or as an electrochemical variant of a "molecular beacon."[5] Osmium tetroxide complexes reacting selectively with thymine residues were applied in recently proposed double-surface (biomagnetic) electrochemical DNA hybridization techniques.[3,6] In analogy with the multicolor optical coding, combination of electrochemical tags yielding different signals makes it possible to detect several target DNA sequences in parallel.[7]

[a] Gilead & IOCB Research Center, Institute of Organic Chemistry and Biochemistry, v. v. i., Academy of Sciences of the Czech Republic,
Flemingovo nám. 2, 16610 Prague 6, Czech Republic
Fax: +420-220183559
E-Mail: hocek@uochb.cas.cz
[b] Institute of Biophysics, v. v. i., Academy of Sciences of the Czech Republic,
Královopolská 135, 61265 Brno, Czech Republic
E-Mail: fojta@ibp.cz
[c] Center for Complex Molecular Systems and Biomolecules, Institute of Organic Chemistry and Biochemistry, Academy of Sciences of the Czech Republic,
Flemingovo nám. 2, 16610 Prague 6, Czech Republic
[d] Gilead Sciences, Inc.,
333 Lakeside Drive, Foster City, CA 94404, USA
Supporting information for this article is available on the WWW under http://www.eurjic.org or from the author.

 © 2007 Wiley-VCH Verlag GmbH & Co. KGaA, Weinheim 

Complexes of transition metals, for instance ferrocene,[8] or complexes of bidentate N-ligands[9] (in particular phenanthrolines and bipyridines) with transition metals (Ru, Rh, Ni, Cu, Co, Pt, Pd, Os etc.) possess unique electrochemical and photophysical properties. Some of the phenanthroline complexes, which are also efficient DNA intercallators, have been extensively used as luminescent and electroactive DNA labels.[10] Attachment of probes based on metal complexes directly to a nucleobase via conjugate linkers should increase the efficiency of the charge transfer and thus enhance sensitivity. There are many examples of such probes connected to pyrimidine nucleobases. 5-(Ferrocenylethynyl)pyrimidine nucleosides were synthesized by Sonogashira coupling of 5-iodopyrimidines with ethynylferrocene and incorporated into DNA as electroactive redox markers.[11] Covalently bound conjugates of pyrimidine nucleotides and phenanthroline complexes of Ru and Os have been studied[12] as fluorescence probes for DNA hybridization and charge transfer through DNA. However, there are very few reports of probes conjugated to purines, presumably due to the greater difficulty in preparation and incorporation. Recently, we have reported[13] on the synthesis of model 9-benzyl-8-(ferrocenylethynyl)adenine by cross-coupling of ethynylferrocene with 8-bromoadenine. Preliminary electrochemical and quantum chemical studies showed that even small electronic changes are effectively transferred through the conjugated system and are electrochemically detectable. Moreover, these effects could be reliably calculated and predicted using ab initio calculations. However, the corresponding protected phosphoramidite of 8-(ferrocenylethynyl)-2′-deoxyadenosine was not efficiently incorporated to oligonucleotides[14] presumably due to oxidation of ferrocene followed by nucleophilic displacement. Therefore, our next probes of choice for labeling purines are complexes (Ru and Os) of bipyridine and phenanthroline. Here we describe the synthesis of model adenine derivatives by two different approaches and the study of their electrochemical properties in order to verify applicability of such complexes as probes for labeling nucleic acids. We were also interested in the biological activity of these novel types of adenine derivatives and metal complex conjugates.

## Results and Discussion

### Synthesis

Two different approaches to the synthesis of target 9-benzyladenines bearing phenanthroline complexes $Ru^{II}$ and $Os^{II}$ in position 8 have been designed and verified in terms of their efficiency, practicability, and compatibility with rather labile nucleic acids. The first one consisted of cross-coupling of 8-bromoadenine with ethynyl- or (4-boronophenyl)-2,2′-bipyridines or -phenanthrolines followed by complexation of the resulting purine-ligand conjugates with a metal. The second approach was based on direct cross-coupling of 8-bromoadenine with preformed Ru complexes of the ligand building blocks. For both approaches we needed the acetylene and boronic acid derivatives of the bidentate N-ligands.

#### *Synthesis of Ligand Building Blocks*

1,10-Phenanthroline (phen), 2,2′-bipyridine (bpy), and 2,2′:6′,2"-terpyridine (tpy) are the most commonly used polypyridine ligands in the chemistry of coordinating compounds[15] and are often used as building blocks for the construction of molecular and supramolecular devices.[16] Cross-coupling reactions are the most versatile tools for construction of molecules containing these ligands connected via conjugate (and thus charge conducting) acetylene or phenylene linkers. However, the chemistry of the corresponding synthetic equivalents for cross-coupling reactions, i.e. boronic acids and acetylene derivatives of oligopyridine ligands, is still underdeveloped and rather difficult. Therefore our first task was to prepare a series of such reagents (some of them were hitherto unknown compounds) not only by application but also by modification and optimization of known methods.

Common starting compounds in the synthesis of the building blocks were halogenated phenanthrolines and bipyridines **1**. 2-Chloro-1,10-phenanthroline (**1a**) was prepared[17] in four steps from the commercially available phenanthroline monohydrate. The Sonogashira cross-coupling reaction of **1a** with (trimethylsilyl)acetylene and subsequent deprotection of the TMS group by treatment with KF in MeOH/THF mixture, led to the desired new 2-ethynyl-1,10-phenanthroline (**2a**) (Scheme 1). Known 6-(ethynyl)-2,2′-bipyridine (**2b**) and 5-(ethynyl)-2,2′-bipyridine (**2c**) were prepared by analogous literature procedures[18] from 6-bromo-2,2′-bipyridine (**1b**) and 5-bromo-2,2′-bipyridine (**1c**), respectively (Scheme 1, Table 1).

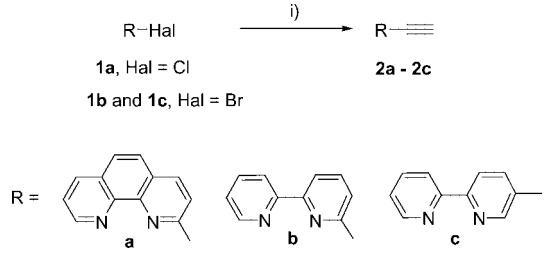


Scheme 1. Synthesis of the ligands: i) 1. $[Pd(PPh_3)_2Cl_2]$ (5–10 mol-%), CuI (10 mol-%), TMSA (2.2 equiv.), $Et_3N$ (3.2 equiv.), DMF or THF, 60–70 °C; 2. MeOH/THF KF (2 equiv.).

Table 1. Synthesis of the ethynyl ligands **2**.

| Entry | R-hal | Product | Yield [%] |
|---|---|---|---|
| 1 | **1a** | **2a** | 60 |
| 2 | **1b** | **2b** | 82 |
| 3 | **1c** | **2c** | 83 |

(4-Bromophenyl)bipyridines, -phenanthroline and -terpyridine **3a**–**3d** were the key intermediates for the synthesis of the corresponding boronates **4a**–**4d**. 2-(4-Bromophenyl)-phenanthroline (**3a**) was prepared in 69% yield by a known[19] procedure involving addition of 4-bromophenyllithium to phenanthroline monohydrate followed by oxi-

 © 2007 Wiley-VCH Verlag GmbH & Co. KGaA, Weinheim 

dation with $MnO_2$. The Suzuki cross-coupling reactions of 6-bromo-2,2′-bipyridine or 5-bromo-2,2′-bipyridine with 4-bromophenylboronic acid afforded the *p*-bromophenylene-substituted bipyridines **3b** and **3c** (compound **3c** was reported earlier via heterocyclizations[20]). 4′-(*p*-Bromophenyl)-2,2′:6′,2"-terpyridine **3d** was prepared by a known multistep procedure[21] from 2-acetylpyridine and 4-bromobenzaldehyde. All these bromo derivatives **3a**–**3d** were subjected to cross-coupling reactions with bis(pinacolato)-diboron[22] in the presence of $Pd(dppf)Cl_2$ and KOAc in dioxane at 80 °C to give the series of pinacol boronates **4a**–**4d** in good yields of 60–91% (Scheme 2, Table 2). Compounds **4a** and **4b** were new, while known compounds **4c**[23] and **4d**[21a] were prepared by this method in much higher yields (91 and 81%, respectively) than alternative methods reported in the literature (30 and 42%, respectively).

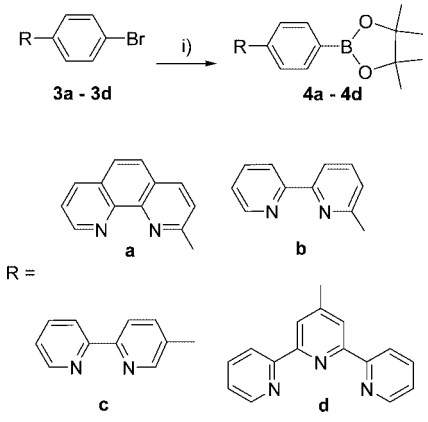


Scheme 2. Synthesis of the ligands: i) bis(pinacolatodiboron) (1.2 equiv.), [$Pd(dppf)Cl_2$] (5 mol-%), KOAc (1.5 equiv.), dioxane, 80 °C.

Table 2. Synthesis of the phenylene-bridged ligands.

| Entry | Bromo derivative | Product | Yield [%] |
|---|---|---|---|
| 1 | **3a** | **4a** | 60 |
| 2 | **3b** | **4b** | 86 |
| 3 | **3c** | **4c** | 91 |
| 4 | **3d** | **4d** | 81 |

### *Synthesis of Ru Complex-Containing Building Blocks*

Among many transition metals used in coordination chemistry of bipyridine-type ligands, $Ru^{II}$ complexes are one of the most popular due to their chemical stability and favorable redox and photophysical properties.[24] Surprisingly, acetylene or boronic acid building blocks containing the $Ru^{II}$ complexes, ready for a single-step attachment to any aromatic skeleton by cross-coupling reactions, are virtually unknown with the exception of (3- and 4-ethynyl-1,10-phenanthroline)$Ru^{2+}(bipy)_2 \cdot 2PF_6^-$.[25] We have prepared the whole series of $Ru^{II}$ complexes of the ligands **2b**–**2c** and **4a**–**4d**.

Commercially available $Ru(bpy)_2Cl_2 \cdot 2H_2O$ was the compound of choice for the complexation reactions. Its complexation with ligands **2** and **4a**–**4c** under standard conditions,[26] e.g. mixing of the reagents in MeOH or EtOH and refluxing the mixture for several hours under an inert atmosphere, afforded the desired products **5** and **6** in poor yields (12–30%) accompanied by some byproducts. When ethylene glycol was used as the solvent,[27] the yields were improved up to 66% (Scheme 3, Table 3) and the amounts of byproducts significantly decreased. A typical procedure involved a suspension of the starting compounds in ethylene glycol heating the mixture at 150 °C for 2 h, distillation of the solvent and anion exchange precipitation from aqueous solution by treatment with $NH_4PF_6$. The solid was further purified on a silica gel column using a mixture of acetonitrile, water, and saturated $KNO_3$ as the eluent. However, during this separation, partial anion exchange occurred and therefore it was crucial to re-precipitate the final product once again from its aqueous solution by treatment with $NH_4PF_6$. Only after this procedure and final re-crystallization were pure samples of hexafluorophosphate salts **5b**–**5c** and **6a**–**6c** isolated. In the case of terpyridine derivative **4d**, $Ru(tpy)Cl_3$ complex[28] was used as the complexation agent under the same conditions as described above to yield the complex **6d**. It should be mentioned that all the pinacol esters of boronate ligands **4a**–**4d** were cleaved simultaneously during the complexation to afford free boronic acids **6a**–**6d**.

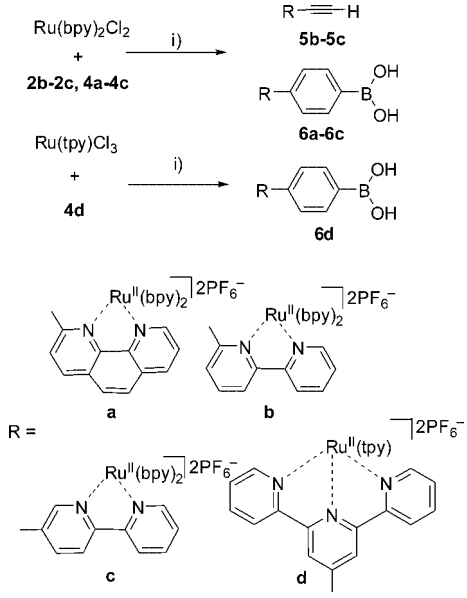


Scheme 3. Complexation reactions: i) 1. ethylene glycol, 150 °C, 2 h; 2. saturated aqueous solution of $NH_4PF_6$.

Table 3. Complexations of the ligands **2** and **4**.

| Entry | Ligand | Complex | Yield [%][a] |
|---|---|---|---|
| 1 | **2b** | **5b** | 49 |
| 2 | **2c** | **5c** | 32 |
| 3 | **4a** | **6a** | 66 |
| 4 | **4b** | **6b** | 47 |
| 5 | **4c** | **6c** | 42 |
| 6 | **4d** | **6d** | 69 |

[a] Yields after crystallization.

 © 2007 Wiley-VCH Verlag GmbH & Co. KGaA, Weinheim 

### *Synthesis of Adenine–Ligand Conjugates*

Cross-coupling reactions are often used for introduction of C-substituents to position 8 of purines.[29] The Suzuki–Miyaura reactions with arylboronic acids are usually used[30] for attachment of an aryl group while the Sonogashira reactions with terminal acetylenes are used[13,31] for alkynyl groups. Therefore, these reactions were our methods of choice for the synthesis of the conjugates of adenine with oligopyridine-type ligands connected via acetylene or phenylene bridges.

The Sonogashira cross coupling reactions of 9-benzyl-8-bromoadenine (**7**) with the terminal alkynes **2a**–**2c** in the presence of $[Pd(dppf)Cl_2]$, CuI, and $Et_3N$ in DMF at 90 °C afforded the corresponding acetylene-bridged conjugates **8a**–**8c** in the yields of ca. 55% after crystallization (Scheme 4, Table 4). The Suzuki–Miyaura cross coupling reaction of bromoadenine **7** with pinacol boronates **4a**–**4d** gave the phenylene-linked conjugates **9a**–**9d** (Scheme 4) in ca. 50% yield. All the cross-coupling reactions proceeded very well and quite cleanly. Their moderate isolated yields may have been caused by partial complexation of the Pd-catalysts by the oligopyridine moiety and by some loss during the silica gel chromatography of the quite polar substrates.

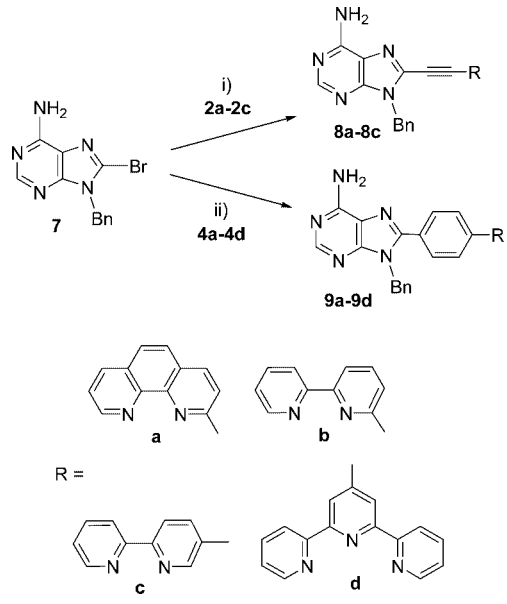


Scheme 4. Synthesis of the conjugates: i) $[Pd(dppf)Cl_2]$ (5 mol-%), CuI (5 mol%), $Et_3N$ (8 equiv.), DMF, 90 °C; ii) $[Pd(dppf)Cl_2]$ (5 mol-%), $K_2CO_3$ (4 equiv.), DMF, 90 °C.

Table 4. Synthesis of the conjugates.

| Entry | Ligand | Conjugate | Yield [%][a] |
|---|---|---|---|
| 1 | **2a** | **8a** | 55 |
| 2 | **2b** | **8b** | 58 |
| 3 | **2c** | **8c** | 56 |
| 4 | **4a** | **9a** | 47 |
| 5 | **4b** | **9b** | 53 |
| 6 | **4c** | **9c** | 52 |
| 7 | **4d** | **9d** | 46 |

[a] Yields after crystallization.

### *Synthesis of Adenine–Complex Conjugates by Complexation*

One of the approaches to the desired title model conjugates of adenine and $Ru^{II}$ complexes is the complexation of the adenine-ligand conjugates **8** and **9** (Scheme 5, Table 5). The complexation reactions with either $Ru(bpy)_2Cl_2 \cdot 2H_2O$ or the $Ru(tpy)Cl_3$ complex were performed in ethylene glycol in analogy to the synthesis of the building blocks **5** and **6**. Once again problems were encountered with anion exchange during chromatography and the desired $Ru^{II}$ complexes **10a**–**10c** and **11a**–**11d** could only be isolated in good yields of 65–81% after re-precipitation and recrystallization (Table 5). There was no significant difference in the rate and yield of complexation between the less sterically hindered 5-substituted bipyridines **8c**,**9c** and the more hindered 6-substituted bipyridines **8b**,**9b**.

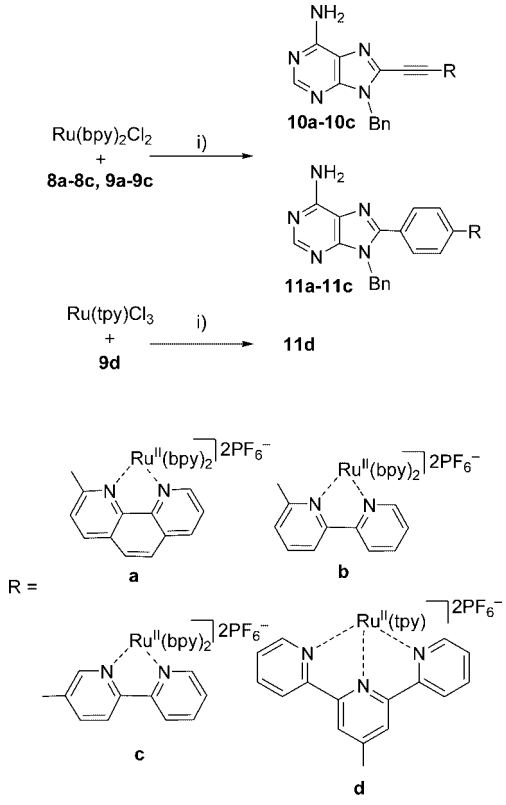


Scheme 5. Complexations of the conjugates: i) 1. ethylene glycol, 150 °C, 2 h; 2. saturated aqueous solution of $NH_4PF_6$.

In order to compare the chemical and electrochemical properties of the $Ru^{II}$ complexes with the corresponding $Os^{II}$ we have prepared the Os complex **12b** (Scheme 6), using the complexation of **8b** with $Os(bipy)_2Cl_2$[32] under the same conditions as for Ru complexes. In this case the Os complex **12b** was obtained in good yield of 74%.

 © 2007 Wiley-VCH Verlag GmbH & Co. KGaA, Weinheim 

Table 5. Complexation of conjugates.

| Entry | Conjugate | Complex | Yield [%] |
|---|---|---|---|
| 1 | **8a** | **10a** | 69 |
| 2 | **8b** | **10b** | 80 |
| 3 | **8c** | **10c** | 75 |
| 4 | **9a** | **11a** | 72 |
| 5 | **9b** | **11b** | 74 |
| 6 | **9c** | **11c** | 81 |
| 7 | **9d** | **11d** | 65 |

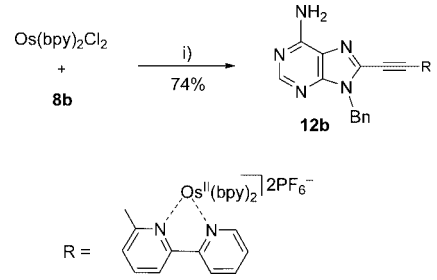


Scheme 6. Synthesis of the $Os^{II}$ complex: i) 1. ethylene glycol, 150 °C, 2 h; 2. saturated aqueous solution of $NH_4PF_6$.

### *Synthesis of Adenine–Complex Conjugates by Direct Cross-Coupling*

The second approach to the title conjugates **10** and **11** was based on direct cross-coupling reactions of **7** with Ru complex containing building blocks **5** and **6**. At first we tried to apply the same cross-coupling conditions utilized in the synthesis of ligand conjugates **8** and **9** (reactions in DMF, $Pd(dppf)Cl_2$ as catalyst and CuI, $Et_3N$ for the terminal alkynes and $K_2CO_3$ for the boronic acids). Unfortunately, none of these reactions proceeded and partial decomposition of the starting materials was observed under prolonged reaction times. Therefore, we tried to apply the aqueous-phase cross-coupling reactions that have been recently successfully used in the attachment of aryl groups[33] including hydrophilic amino acid residues[34] to the 8-position of purine nucleosides. The cross-coupling reactions of **7** with boronic acids **6a**–**6d** using $Pd(OAc)_2$ as the catalyst, water soluble $P(Ph–SO_3Na)_3$ ligand and $Cs_2CO_3$ as a base in a mixture of acetonitrile/water (1:1) proceeded relatively well to give the desired products **11a**–**11d** in moderate yields 24–63% (Scheme 7, Table 6). Application of the aqueous conditions for the Sonogashira cross coupling reactions of **7** with acetylenes **5** was not successful. In conclusion, direct cross-coupling of 8-bromoadenine with Ru complex-containing organometallics is possible with the application of aqueous-phase conditions for attachment of aryl groups by the Suzuki–Miyaura reaction. Presumably, due to the relatively mild conditions and tolerance to unprotected functional groups,[34] this could be the method of choice for direct labeling of nucleotides and oligonucleotides with complexes containing phenylene linkers but not for the attachment of acetylenes.

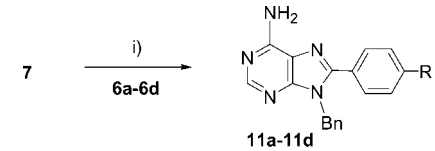


Scheme 7. Cross coupling reactions with complexes. i) $[Pd(OAc)_2]$ (10 mol-%), $P(Ph-SO_3Na)_3$ (50 mol-%), $Cs_2CO_3$ (3 equiv.), $CH_3CN/H_2O$ (1:1).

Table 6. Cross coupling reactions with Ru complexes.

| Entry | Ru complex | Product | Yield [%] |
|---|---|---|---|
| 1 | **6a** | **11a** | 40 |
| 2 | **6b** | **11b** | 24 |
| 3 | **6c** | **11c** | 53 |
| 4 | **6d** | **11d** | 63 |

### Crystal Structures

Complexes **5b** and **10b** gave monocrystals suitable for X-ray diffraction. However, the crystals of **10b** diffracted rather poorly, which resulted in weak reflections. Consequently, the precision of the structure determination is not excellent, but it still describes reasonably well all the main structural features of this Ru complex. The structures of complexes **5b** and **10b** are depicted in Figure 1.

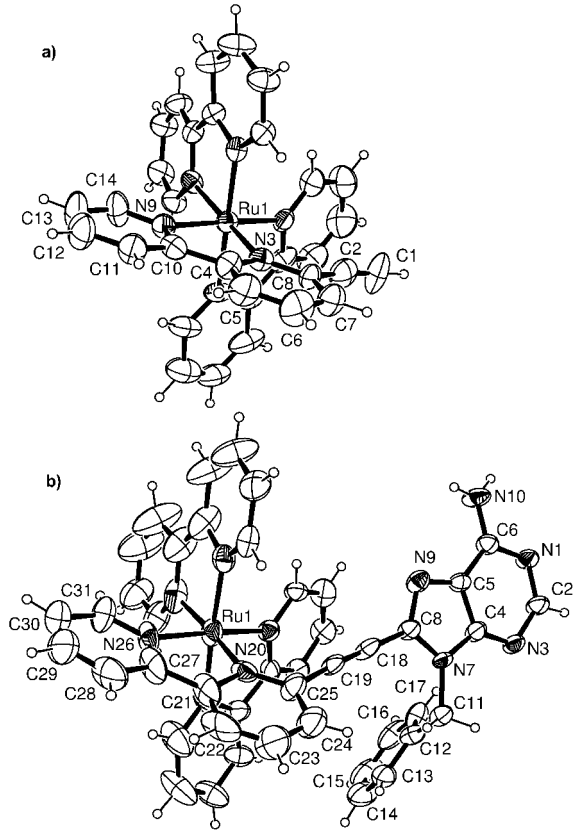


Figure 1. ORTEP diagram of **5b** (a) and **10b** (b) (thermal ellipsoids drawn at the 30% probability level).

The Ru–N bond lengths of **10b** and **5b** are generally comparable to those of the parent ion $[Ru(bpy)_3]^{2+}$ (2.055 Å),[35] with the exception of the shorter bond Ru1–N50 [**10b**,

 © 2007 Wiley-VCH Verlag GmbH & Co. KGaA, Weinheim 

2.013(9) Å], Ru1–N33 [**5b**, 2.097(10) Å] and especially the significantly elongated bonds Ru1–N20 [**10b**, 2.109(9) Å] and the corresponding bond Ru1–N3 [**5b**, 2.110(6) Å]. This elongation is caused by the steric hindrance of the adjacent 9-benzyl-8-ethynyladenine (**10b**) or acetylene (**5b**) groups and seems to be typical for all structures containing any group attached to the C25 carbon that were found in the Cambridge Structural Database.[36] The structure of the central octahedron in both complexes is more or less the same, but the bipyridine units are slightly shifted due to the presence of substituents (see Figure S1 in the Supporting Information).

## Electrochemistry

The conjugates **10a**–**10c**, **11a**–**11d**, and **12b** involve several electrochemically active centers, including the adenine moiety (potentially reducible at mercury and oxidizable at carbon electrodes[37]), triple bond of the ethynyl bridge (reducible at mercury electrodes[38]) as well as the ruthenium or osmium chelates (expected to undergo reversible one-electron $Ru^{II}/Ru^{III}$ or $Os^{II}/Os^{III}$ oxidation[39]). Using the hanging mercury drop electrode (HMDE), we observed cathodic signals attributable to the adenine (with all conjugates) as well to the triple bond (with **10a**–**10c** and **12b**, see Table 7). Potentials of 9-benzyladenine reduction were influenced by the substituents to some extent. In general, the adenine moiety was reduced more easily in bipyridine conjugates with the phenylene linker than in analogues with the ethynyl linker (**10b** vs. **11b** and **10c** vs. **11c**), in the phenanthroline conjugates (**10a** vs. **11a**), the opposite was true. The potential of the adenine signal in the bipyridine conjugates was also influenced by the position of the bipyridine substitution, being markedly more negative for the 5-substituted (**b**) than for 6-substituted (**c**) bipyridines. The ethynyl linker produced a single reduction peak in conjugates of phenanthroline (**a**) and 6-substituted bipyridine (**b**). In the 5-substituted bipyridine compounds (**a**) involving the acetylene moiety, two cathodic peaks were observed. As expected,[38] reduction of the triple bond was easier in the conjugate **10c** (involving disubstituted acetylene) than in the building block **5c** (monosubstituted acetylene).

With respect to the prospective utilization of the conjugates as DNA labels, our attention was focused mainly on processes related to the metal complexes. Cyclic voltammetry (CV) at a carbon paste electrode (CPE) revealed couples of reversible redox signals for all ruthenium complexes at potentials around +1.2 V (not shown). The CV peaks were, however, relatively poorly developed due to their occurrence at rather positive potentials close to background discharge. We therefore chose square-wave voltammetry (SWV), a technique offering better separation of signals from the background,[40] in further experiments. Peak potentials due to the ruthenium complexes resulting from these measurements are summarized in Table 7. All compounds involving the bipyridine ligand covalently linked to the adenine moiety, regardless of the bridge type or position of the bipyridine substitution, produced net SWV peaks at +1.21 V (compounds **10b**, **10c**, **11b**, and **11c**; in Figure 2 shown for

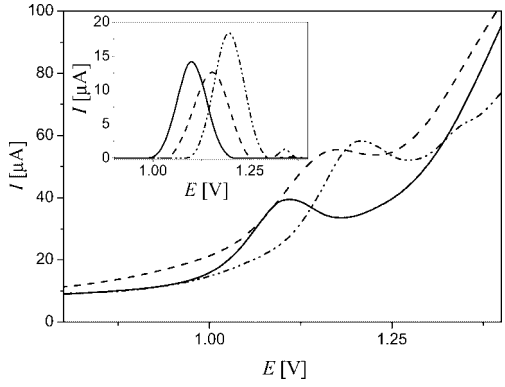


Figure 2. Sections of square-wave voltammograms of unsubstituted complex $[Ru(bipy)_3]^{2+}$ (solid), compound **5b** (dash) and compound **10b** (dash-dot-dot) measured at the CPE. Inset shows the same voltammograms after baseline subtraction.

Table 7. Potentials of electrochemical signals of the synthesized compounds.

| | Oxidation at PGE | | Reduction at HMDE | | |
|---|---|---|---|---|---|
| | $E^{net}$ [a] [V] | $\Delta E^{net}$ [b] [mV] | $E^{ade}$ [c] [V] | $\Delta E^{ade}$ [d] [mV] | $E^{eth}$ [e] [V] |
| $[Ru(bipy)_3]^{2+}$ | 1.095 | 0 | – | – | – |
| 9-benzyladenine | – | – | –1.362 | 0 | – |
| **5c** | 1.175 | 80 | – | – | –1.263; –1.362 |
| **10c** | 1.210 | 115 | –1.355 | 7 | –0.810; –0.886 |
| **10b** | 1.210 | 115 | –1.414 | –52 | –1.062 |
| **6c** | 1.165 | 70 | – | – | – |
| **11c** | 1.210 | 115 | –1.316 | 46 | – |
| **11b** | 1.210 | 115 | –1.378 | –16 | – |
| **10a** | 1.220 | – | –1.372 | –10 | –0.950 |
| **11a** | 1.215 | – | –1.326 | 36 | – |
| **11d** | 1.265 | – | – | – | – |
| **12b** | 0.790 | – | –1.390 | –28 | –1.024 |

[a] $E^{net}$ is the apparent redox potential of the $Ru^{II}/Ru^{III}$ or $Os^{II}/Os^{III}$ couple measured on the net square-wave voltammogram (CPE). [b] $\Delta E^{net}$ is the potential shift relative to unsubstituted $[Ru(bipy)_3]^{2+}$ complex. [c] $E^{ade}$ is the potential of reduction of the 9-benzyladenine moiety in the conjugate measured by linear scan voltammetry (HMDE). [d] $\Delta E^{ade}$ is the potential shift relative to unsubstituted 9-benzyladenine. [e] $E^{eth}$ are potentials of peaks related to reduction of the ethynyl linker triple bond (HMDE). All potentials are measured against a Ag/AgCl/3 M KCl reference electrode.

 © 2007 Wiley-VCH Verlag GmbH & Co. KGaA, Weinheim 

**10b**). Apparent redox potentials of complexes with covalently coupled phenanthroline ligands **10a**,**11a** were slightly more positive (+1.220 or +1.215 V, respectively) than those of the bipyridine analogues, while the complex **11d** (with ruthenium coordinated by two terpyridines) yielded a peak at +1.265 V. The osmium complex **12b** underwent reversible oxidation at +0.79 V, in agreement with a less positive redox potential of the $Os^{II}/Os^{III}$ couple, compared to $Ru^{II}/Ru^{III}$[39] (not shown).

Compared to unsubstituted $[Ru(bipy)_3]^{2+}$, the apparent redox potentials of compounds **10b–c** and **11b–c** were significantly more positive (see Table 7). This phenomenon can be explained by electron-withdrawing effects of the adenine residue linked via the unsaturated bridges. Reducing electron density at ruthenium results in its more difficult oxidation. Similar effects were recently observed[13] with ferrocenylethyne–adenine conjugates in which the iron oxidation was found to be more difficult, compared to unsubstituted ferrocene or to ferrocene linked to the adenine moiety via a saturated bridge, due to electronic coupling between ferrocene and adenine via the alkyne bridge. Influence of conjugated unsaturated substituents on electrochemical properties of the ruthenium complex is evident from the series $[Ru(bipy)_3]^{2+}$–**5b**–**10b** (Table 7, Figure 2) and series $[Ru(bipy)_3]^{2+}$–**6b**–**11b** (Table 7). The ethynyl (**5b**) or phenylene (**6b**) groups themselves cause shifts in the redox potential of the ruthenium complex by 80 or 70 mV, respectively, towards more positive values. Attachment of the purine moiety offering further electronic conjugation resulted in higher positive potential shifts (about 115 mV relative to the $[Ru(bipy)_3]^{2+}$ for both **10b** and **11b** as well as **10c** and **11c** which involve 5-substituted bipyridine instead of 6-substituted bipyridine present in the series **b**). Similar shifts of the $Ru^{II}/Ru^{III}$ redox potential were observed also with compounds in which the adenine moiety was replaced by another aromatic system (*p*-tolyl, not shown). More details about the electrochemistry of the conjugates and/or the building blocks at carbon or mercury electrodes will be published elsewhere.

### Quantum Chemical Calculations of the Redox Potentials of the Studied Complexes

DFT calculations have been performed in order to verify the potential utilization of these methods for theoretical prediction of redox potentials of the title complexes. Listed in Table 8 are the calculated values of redox potentials for the synthesized compounds, using Equations (1) and (2) (see Experimental Section). It can be seen that the calculated and experimental results are in good agreement (with a standard deviation of 130 mV). The systematic (mean) error of –60 mV can be attributed to several factors: (i) neglect of spin-orbit coupling (SOC) in the nonrelativistic treatment which has been estimated to account for approximately +30 mV on the model $Ru^{2+/3+}$ complex[41] (this effect is by one order of magnitude greater for $Os^{II}$ complexes, viz. Table 8, and has been calculated to account for 200 mV on a small model complex),[41] (ii) the single reference treatment of the triple (quasi)degenerate ground state in $[Ru(bipy)_3]^{3+}$ complexes, (iii) the uncertainty in the absolute potential of SHE, (iv) the difference between the theoretical calculations and the experimental setup (presence of counterions and the adsorption of complexes on the electrode).

Table 8. The calculated redox potentials of the synthesized compounds (vs. Ag/AgCl/3 M KCl reference electrode).

| | Oxidation $Ru^{2+/3+}$ ($Os^{2+/3+}$) | | | Reduction |
|---|---|---|---|---|
| | $E^0_{calc}$ [V][a] | $\Delta E^0_{calc}$ [mV][b] | $\Delta E^0_{exp}$ [mV][c] | $E^0_{calc}$ [V] |
| $[Ru(bipy)_3]^{2+}$ | 1.082a | 0 | 0 | –1.450 |
| **5c** | 1.074 | –8 | 80 | –1.557 |
| **10c** | 1.183 | 101 | 115 | –1.144 |
| **10b** | 1.238 | 156 | 115 | –1.357 |
| **6c** | 1.368 | 286 | 70 | –1.429 |
| **11c** | 0.987 | –95 | 115 | –1.292 |
| **11b** | 1.130 | 48 | 115 | –1.411 |
| **10a** | 1.165 | 83 | (125) | –1.234 |
| **11a** | 1.189 | 107 | (120) | –1.484 |
| **11d** | 0.960 | –122 | (170) | –1.389 |
| **12b** | 1.127 | 45 | (–305) | –1.498 |

[a] $E^0_{calc}$ were calculated using the B3LYP/def2-TZVP//PBE/def2-SVP energies, PBE/def2-SV(P) frequencies, ideal gas approximation for thermodynamic functions, the COSMO solvation model, 4.34 V as the absolute potential of the SHE, and 0.207 V as the potential of the reference electrode used in the electrochemical measurements (Table 7). [b] $\Delta E^0_{calc/exp}(X) = E^0_{calc/exp}(X) - E^0_{calc/exp}([Ru(bipy)_3]^{2+})$. [c] Experimental data taken from Table 7; values in parentheses have not been presented in Table 7 (showing effects of conjugated unsaturated substituents on the $[Ru(bipy)_3]^{2+/3+}$ redox potential) because compounds **10a**, **11a**, **11d** and **12b** involve complexes of different types.

To account for these systematic errors, we further discuss the values of $\Delta E^0$ [$\Delta E^0(X) = E^0(X) - E^0([Ru(bipy)_3]^{2+})$], though it can be noted that an excellent agreement between the calculated and experimental values of $E^0([Ru(bipy)_3]^{2+})$ has been obtained ($E^0_{calc}$ = 1.082 V vs. $E^0_{exp}$ = 1.095 V).

Considering that 100 mV corresponds to ca. 10 kJ mol$^{-1}$, we can see that most of the calculated values are within an error bar of the quantum chemical methods. Specifically, the values of $\Delta E^0$ for four studied complexes (**10c**, **11b**, **10a**, **11a**) are within 42 mV of the experimental values, which can be considered an excellent agreement between theory and experiment. Another two complexes, **5c** and **11b**, deviate by 88 and 67 mV, respectively, which is still a very good agreement. The largest errors are found for **6c** (+216 mV), **11c** (–210 mV), and **11d** (–292 mV). However, an analysis of the spin densities have shown that for the latter two complexes, the unpaired electron is not localized on the Ru atom (Figure 3), but rather resides on the adenine moiety. This finding explains the observed discrepancy between the calculations and experimental data. Whether this is an artifact of the DFT method or an observable phenomenon is a subject of subsequent study.[41] As mentioned above, the discrepancy of +350 mV for **12b** ($Os^{2+/3+}$ complexes) can be mostly attributed to spin-orbit coupling effects, which are not included in the DFT calculations. This is a general effect exercised in octahedral $Os^{2+/3+}$ complexes and may ex-

 © 2007 Wiley-VCH Verlag GmbH & Co. KGaA, Weinheim 

plain the lower redox potential of the $Os^{2+/3+}$ pair (compared to $Ru^{2+/3+}$).

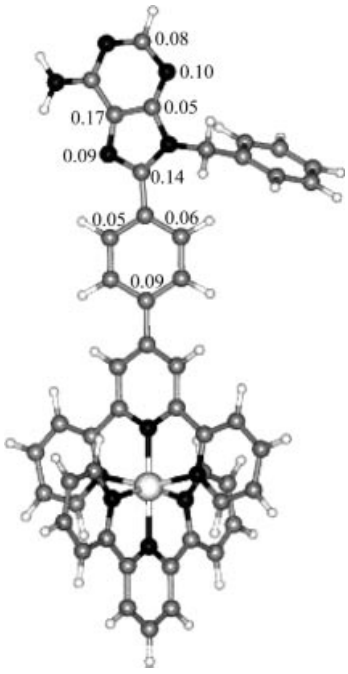


Figure 3. The equilibrium geometry of **11d**. Denoted are the calculated spin densities for the oxidized $Ru^{III}$ complex demonstrating that the unpaired electron is localized on the adenine moiety rather than on the Ru atom.

Structurally, we can observe only very small geometry changes associated with the $Ru^{2+/3+}$ oxidation and $Ru^{2+/1+}$ reduction. The most important parameters, the Ru–N distances, are shortened by ca. 0.004 Å upon the reduction and lengthened by ca. 0.006 Å upon oxidation. All the values of the Ru–N distances are summarized in Table S1 (see supporting information).

Also listed in Table 8 are the values of redox potentials for the reduction of the studied compounds. The interpretation of these values, i.e., the assignment of the formal redox states to subsystems in the studied complexes, is more complicated. In general, the calculated data are in the range of the experimental values: (–1.144, –1.557 V) vs. (–0.810, –1.414 V). The spin densities are strongly delocalized on the ligands, which suggests that these redox potential values do not refer to the reduction of the metal center, in agreement with the experimental data (Table 7).

In summary, it has been demonstrated that the theoretical calculations can satisfactorily reproduce the experimental data and can serve for prediction of redox potentials of new molecules with a reasonable level of fidelity. However, the anticipated differences in redox potential should be higher than ca. 100 mV (which has been shown as an error bar of the method), and care must be taken when interpreting the calculated data, i.e., to formally assign oxidation states and check whether they correspond to the experimentally observed process.

## Biological Activity

HCV chronically infects about 170 million people and the only approved therapy (a combination of interferon-α and ribavirin) is expensive and effective in only 50–60% of patients infected with HCV genotype 1. Development of effective antivirals for combating this pathogen is of great interest within pharmaceutical research. Common nucleoside *anti*-HCV agents are intracellularly phosphorylated to their triphosphates and then inhibit viral RNA synthesis mediated by the HCV RNA-dependent RNA polymerase.[42] Apart from that, there are numerous non-nucleoside inhibitors of this enzyme under current study.[43] Ru complexes of oligopyridine ligands are known to bind to DNA and thus exert antitumor and antiparasitic activity.[44] Some other types of Ru complexes are inhibitors of protein kinases.[45] To the best of our knowledge, neither oligopyridine ligands nor their transition metal complexes have been reported to possess *anti*-HCV activity. Therefore, we have also studied the biological activity (cytostatic effect and *anti*-HCV activity) of the model adenine-ligand and adenine complex conjugates.

Selected compounds and their respective Ru or Os complexes were evaluated in the HCV subgenomic replicon assay and their activity is presented in Table 9.[46] In general, the Ru and Os complex-based inhibitors displayed similar or weaker antiviral activity than their corresponding precursors with the exception of **10c**. However, analog **10c** despite improved antiviral activity compared to its precursor **8c** also showed less than 5-fold selectivity thereby confounding further interpretation of the data. Two of the most potent compounds were the structurally related analogs **9a** and **8a** in which the main structural difference is the bridging group between the purine and metal chelating motif

Table 9. Replicon activity and NS5B 1b enzymatic potency of selected compounds.

| | Replicon $EC_{50}$/μM | Huh-7 $CC_{50}$/μM | NS5B 1b $IC_{50}$/μM | Ru/Os salt complex | Replicon $EC_{50}$/μM | Huh-7 $CC_{50}$/μM |
|---|---|---|---|---|---|---|
| **8a**[a] | 0.73 | 2 | n.d. | **10a** | 17 | 100 |
| **8b** | 5 | >50 | >2 | **10b** | 28 | cytostatic |
| **8c** | >50 | >50 | n.d. | **10c** | 10 | 50 |
| **9a** | 0.49 | 0.89 | >2 | **11a** | 27 | >100 |
| **9b** | 3.0 | 14 | >2 | **11b** | 1.0 | 28 |
| | | | | **12b** | 2.0 | 32 |
| **9c** | 4.0 | 50 | n.d. | **11c** | 11 | cytostatic |
| **9d** | 0.23 | >50 | >2 | **11d** | 28 | 23 |

[a] Compound required low pH for dissolution in DMSO; n.d. = not determined.

 © 2007 Wiley-VCH Verlag GmbH & Co. KGaA, Weinheim 

(alkynyl or phenyl). Unfortunately, both of these analogs also displayed poor selectivity (less than 3-fold). Analog **9d** was the most potent and selective (at least 200-fold) inhibitor in the series.

Several compounds, including **9d**, were tested for inhibition toward HCV NS5B polymerase 1b (Table 9).[47] None of the noncomplexed analogs demonstrated activity up to 2 μM. Because of poor solubility in the assay buffer, inhibitory activity beyond 2 μM could not be measured. Therefore, determination of whether **9d** inhibits HCV NS5B weakly through an allosteric mechanism, or whether it has other cellular or viral targets will require further study.

The in vitro evaluation of the cell growth inhibition was estimated in mouse lymphocytic leukemia L1210 cells (ATCC CCL 219), CCRF-CEM T lymphoblastoid cells (human acute lymphoblastic leukemia, ATCC CCL 119), human promyelocytic leukemia HL-60 cells (ATCC CCL 240), and human cervix carcinoma HeLa S3 cells (ATCC CCL 2.2). Significant cytostatic activity was found only in compounds **8a** and **9d**. Surprisingly, compound **9a** in contrast to Huh-7 hepatocytes does not exert any cytotoxicity at 10 μmol $L^{-1}$. This discrepancy was rechecked by the analysis of the cell cycle course using flow cytometry. The data revealed that 0.7 μM compound **8a** considerably influences the cell cycle profile, which is characterized by apoptosis inducing activity and reduced proportion of G1 (from 49.4 to 17.5%) and G2/M phases (from 19.7 to 4.9%) compensated by an increase of the S phase (from 30.8 to 77.6%). On the other hand, compound **9a** does not affect the cell cycle pattern even at 2 μM, which represents more than twice the Huh7 $CC_{50}$ value. These results indicate different susceptibilities of various cell lines towards the model adenine ligands (Table 10).

Table 10. Cytostatic activity of selected compounds.

| | $IC_{50}$, μmol $L^{-1}$ | | | |
|---|---|---|---|---|
| | L1210 | HL60 | HeLa S3 | CCRF-CEM |
| **8a** | 0.88 ± 0.06 | 0.57 ± 0.05 | 1.10 ± 0.08 | 1.40 ± 0.10 |
| **9d** | 0.97 ± 0.08 | 1.40 ± 0.08 | > 20 | 1.65 ± 0.11 |

## Conclusions

9-Benzyladenine derivatives bearing Ru complexes in position 8 were prepared as model compounds for electrochemical DNA labeling. Two strategies of synthesis have been explored: (i) synthesis of adenine derivatives of bipyridine ligands followed by complexation with Ru or (ii) cross-coupling of 8-bromoadenine derivatives with boronic acids derived from Ru complexed ligands. None of the two approaches is truly efficient but, due to the relatively harsh conditions, difficult separation, and moderate yields of the complexation in the first approach, the second approach seems to be more suitable for applications in labile nucleosides or oligonucleotides despite its moderate yields. The new Ru-containing acetylene or boronate building blocks **5** and **6** will certainly be useful in labeling of other types of molecules by a direct cross-coupling.

The model compounds have been systematically studied by several methods. Electrochemistry revealed both oxidation and reduction patterns with relatively minor substituent effects. Quantum-chemical calculations were able to predict the values of redox potentials with the precision of ca. 100 mV, which might not always be sufficient for the prediction of differences in redox potentials in DNA. Despite these problems, we will continue our efforts in the synthesis of oligonucleotide probes bearing such transition metal complexes. The most interesting (and rather unexpected) finding was the significant antiviral activity against HCV of the adenine–oligopyridine conjugates, which is unfortunately accompanied by considerable cytotoxicity. Nevertheless, these compounds represent a completely new structural lead in the search for novel antiviral agents.

## Experimental Section

**General Remarks:** All cross-coupling reactions were performed under argon. $Et_3N$ was degassed in vacuo and stored over molecular sieves under argon. Compounds **1a** [ref.[17]], **1b**, **1c**, **2b**, **2c** [ref.[18]], **3a** [ref.[19]], and **3d** [ref.[20]] were prepared according to literature procedures. Other chemicals were purchased from commercial suppliers and used as received. NMR spectra were recorded with Bruker Avance 500 (500 MHz for $^1H$ and 125.8 MHz for $^{13}C$) and Bruker Avance 400 ($^1H$ at 400, $^{13}C$ at 100.6 MHz) spectrometers in $CDCl_3$, [$D_6$]DMSO, or [$D_6$]acetone. Chemical shifts (in ppm, $\delta$ scale) were referenced to TMS (for $^1H$ NMR spectra in $CDCl_3$) and/or to the solvent signal ($CDCl_3$ δ = 7.26 ppm for $^1H$ NMR and δ = 77.0 ppm for $^{13}C$ NMR; [$D_6$]DMSO for $^1H$ NMR ($\delta$ = 2.5 ppm) and for $^{13}C$ NMR ($\delta$ = 39.7 ppm), [$D_6$]acetone for $^1H$ NMR ($\delta$ = 2.05 ppm) and for $^{13}C$ NMR ($\delta$ = 29.8 ppm, $CD_3$ group), coupling constants $J$ are given in Hz. The assignment of proton and carbon signals was based on H,H-COSY, H,C-HSQC, and H,C-HMBC experiments. Melting points were determined on a Kofler block and are uncorrected. Mass spectra were measured on a ZAB-EQ (VG Analytical) spectrometer using FAB (ionization by Xe, accelerating voltage 8 kV, glycerol matrix) or on a LCQ classic spectrometer using electrospray ionization (ESI). X-ray crystallographic analysis of single crystals of **10b** (red, 0.03 × 0.14 × 0.27 mm) and **5b** (red, 0.08 × 0.31 × 0.40 mm) was performed with Xcalibur X-ray diffractometer with Cu-$K_\alpha$ ($\lambda$ = 1.54180 Å), data collected at 150 K (**10b**) and 295 K (**5b**).

**2-Ethynyl-1,10-phenanthroline (2a):** A solution of 2-chloro-1,10-phenanthroline (0.5 g, 2.3 mmol), bis(triphenylphosphane)palladium dichloride (160 mg, 0.23 mmol), CuI (44 mg, 0.23 mmol), $Et_3N$ (1 mL, 7.2 mmol), and (trimethylsilyl)acetylene (0.7 mL, 5.16 mmol) in DMF (5 mL) was stirred at 60 °C under argon for 12 h. The solvent was removed under reduced pressure, the residue was dissolved in $CHCl_3$, and washed with a saturated solution of EDTA. The organic layers were collected and the solvents evaporated to dryness. The crude intermediate was diluted in methanol (5 mL) and $K_2CO_3$ (2.17 mmol, 300 mg) was added. The mixture was stirred for 6 h at room temperature. After evaporation of the solvent under reduced pressure, the crude product was purified by column chromatography (ethyl acetate/hexanes, 1:1) to give 285 mg of **1a** (60%) as brownish crystals with m.p. 52–58 °C. $^1H$ NMR (400 MHz, $CDCl_3$): $\delta$ = 3.27 (s, 1 H, HC≡C–), 7.65 (dd, $J_{8,7}$ = 8.1, $J_{8,9}$ = 4.4, 1 H, 8-H), 7.77 (d, $J_{5,6}$ = 8.8, 1 H, 5-H), 7.79 (d, $J_{3,4}$ =

 © 2007 Wiley-VCH Verlag GmbH & Co. KGaA, Weinheim 

8.2, 1 H, 3-H), 7.81 (d, $J_{6,5}$ = 8.8, 1 H, 6-H), 8.22 (d, $J_{4,3}$ = 8.2, 1 H, 4-H), 8.25 (dd, $J_{7,8}$ = 8.1, $J_{7,9}$ = 1.8, 1 H, 7-H), 9.23 (dd, $J_{9,8}$ = 4.4, $J_{9,7}$ = 1.8, 1 H, 9-H) ppm. $^{13}$C NMR (100.6 MHz, $CDCl_3$): $\delta$ = 78.43 (H*C*≡C–), 83.56 (–*C*≡CH), 123.31 (C-8), 126.04 (C-5), 126.54 (C-3), 127.43 (C-6), 127.91 (C-4a), 128.89 (C-6a), 135.95 (C-7), 136.12 (C-4), 142.56 (C-2), 145.66 (C-10a), 146.28 (C-10b), 150.70 (C-9) ppm. FAB MS: *m*/*z* (%) = 205 (100) [M$^+$ + H]. HRMS (FAB): for $C_{14}H_9N_2$ calcd. 205.0766; found 205.0769. IR ($CHCl_3$): $\tilde{\nu}$ = 3304, 3049, 2968, 2835, 1505, 853 cm$^{-1}$. $C_{14}H_8N_2{\cdot}H_2O$ (222.24): calcd. C 75.66, H 4.54, N 12.6; found C 75.71, H 4.88, N 12.3.

**6-(4-Bromophenyl)-2,2′-bipyridine (3b):** A mixture of 6-bromo-2,2′-bipyridine (1 g, 4.25 mmol), (4-bromophenyl)boronic acid (1.28 g, 5.3 mmol, 1.5 equiv.), $K_2CO_3$ (1.18 g, 8.5 mmol, 2 equiv.), and $Pd(PPh_3)_4$ (245 mg, 0.21 mmol, 5 mol-%) in toluene (5 mL) was stirred under argon for 8 h at 100 °C. After evaporation of the solvent the residue was dissolved in chloroform, washed with saturated solution of EDTA and dried with $MgSO_4$. The product was purified by silica gel column chromatography (ethyl acetate/hexanes, 1:10). The product was obtained as a colorless solid (1.14 g, 86%). $^1$H NMR (500 MHz, $CDCl_3$): $\delta$ = 7.33 (ddd, $J_{5',4'}$ = 7.5, $J_{5',6'}$ = 4.8, $J_{5',3'}$ = 1.2, 1 H, 5′-H), 7.63 (m, 2 H, H$^m$ phenylene), 7.74 (dd, $J_{5,4}$ = 7.8, $J_{5,3}$ = 1.0, 1 H, 5-H), 7.85 (ddd, $J_{4',3'}$ = 8.0, $J_{4',5'}$ = 7.5, $J_{4',6'}$ = 1.8, 1 H, 4′-H), 7.89 (t, $J_{4,5}$ = 7.8, $J_{4,3}$ = 7.8, 1 H, 4-H), 8.03 (m, 2 H, H$^o$ phenylene), 8.39 (dd, $J_{3,4}$ = 7.8, $J_{3,5}$ = 1.0, 1 H, 3-H), 8.60 (dt, $J_{3',4'}$ = 8.0, $J_{3',5'}$ = 1.2, $J_{3',6'}$ = 0.9, 1 H, 3′-H), 8.70 (ddd, $J_{6',5'}$ = 4.8, $J_{6',4'}$ = 1.8, $J_{6',3'}$ = 0.9, 1 H, 6′-H) ppm. $^{13}$C NMR (125.8 MHz, $CDCl_3$): $\delta$ = 119.64 (C-3), 120.01 (C-5), 121.25 (C-3′), 123.45 (C$^p$ phenylene), 123.84 (C-5′), 128.49 (C$^o$ phenylene), 131.85 (C$^m$ phenylene), 136.88 (C-4′), 137.84 (C-4), 138.21 (C$^i$ phenylene), 149.11 (C-6′), 155.23 (C-6), 155.88 (C-2), 156.12 (C-2′) ppm. IR ($CHCl_3$): $\tilde{\nu}$ = 3011, 2985, 1582, 1562, 1454, 1431, 1009, 817, 637 cm$^{-1}$. FAB MS: *m*/*z* (%) = 311 (100). HRMS (FAB): for $C_{16}H_{12}BrN_2$ calcd. 311.0184; found 311.0179. $C_{16}H_{11}BrN_2$ (311.18): calcd. C 61.76, H 3.56, N 9.00; found C 61.82, H 3.61, N 9.05.

**5-(4-Bromophenyl)-2,2′-bipyridine (3c):** A mixture of 5-bromo-2,2′-bipyridine (1 g, 4.25 mmol), (4-bromophenyl)boronic acid (1.03 g, 5.1 mmol, 1.2 equiv.), $K_2CO_3$ (1.18 g, 8.5 mmol, 2 equiv.), and $Pd(PPh_3)_4$ (245 mg, 0.21 mmol, 5 mol-%) in DMF (5 mL) was stirred under argon for 8 h at 100 °C. After evaporation of the solvent the residue was dissolved in chloroform, washed with saturated solution of EDTA, and dried with $MgSO_4$. The product was purified by silica gel column chromatography (ethyl acetate/hexanes, 1:10). The product was obtained as a colorless solid (780 mg, 59%), which gave analytical data identical to those previously reported.[20]

**General Procedure for Preparation of the Pinacolboronates. Method A:** A bromo derivative (**3a/3d**) (3.5 mmol), bis(pinacolato)diboron (4.2 mmol, 1.2 equiv.), $PdCl_2$ (0.175 mmol, 5 mol-%), dppf (0.175 mmol, 5 mol-%), and KOAc (5.25 mmol, 1.5 equiv.) were combined and stirred under argon in dry dioxane at 80 °C until the TLC showed complete consumption of the starting material. After evaporation of the solvent the residue was dissolved in chloroform, washed with a saturated solution of EDTA and purified by silica gel column chromatography (ethyl acetate/hexanes).

**Pinacol [4-(1,10-Phenanthroline-3-yl)phenyl]boronate (4a):** The product was obtained as brownish crystals in 60% yield (Method A). M.p. 192–193 °C. $^1$H NMR (400 MHz, $CDCl_3$): $\delta$ = 1.39 (s, 12 H, $CH_3$ dioxaborolane), 7.65 (dd, $J_{8,7}$ = 8.0, $J_{8,9}$ = 4.4, 1 H, 8-H), 7.79 (d, $J_{6,5}$ = 8.8, 1 H, 6-H), 7.83 (d, $J_{5,6}$ = 8.8, 1 H, 5-H), 7.99 (m, 2 H, H$^m$ phenylene), 8.15 (d, $J_{3,4}$ = 8.4, 1 H, 3-H), 8.27 (dd, $J_{7,8}$ = 8.0, $J_{7,9}$ = 1.7, 1 H, 7-H), 8.32 (d, $J_{4,3}$ = 8.4, 1 H, 4-H), 8.36 (m, 2 H, H$^o$ phenylene), 9.26 (dd, $J_{9,8}$ = 4.4, $J_{9,7}$ = 1.7, 1 H, 9-H) ppm. $^{13}$C NMR (100.6 MHz, $CDCl_3$): $\delta$ = 24.92 ($CH_3$ dioxaborolane), 83.88 (C dioxaborolane), 120.86 (C-3), 122.89 (C-8), 126.38 and 126.40 (C-5 and C-6), 127.14 (C$^o$ phenylene), 127.73 (C-4a), 129.08 (C-6a), 135.22 (C$^m$ phenylene), 136.14 (C-7), 136.83 (C-4), 141.94 (C$^i$ phenylene), 146.13 (C-10b), 146.42 (C-10a), 150.45 (C-9), 157.36 (C-2) ppm; C$^p$ phenylene signal not observed. FAB MS: *m*/*z* (%) = 282.1 (70), 382.2 (100) [M$^+$]. HRMS (FAB): for $C_{24}H_{24}BN_2O_2$ calcd. 383.1931; found 383.1924. IR ($CHCl_3$): $\tilde{\nu}$ = 3010, 2981, 1610, 1522, 1360, 1144, 1089, 1017, 858, 842, 662, 650 cm$^{-1}$. $C_{24}H_{23}BN_2O_2{\cdot}1/3H_2O$ (400.28): calcd. C 74.53, H 6.12, N 7.24; found C 74.74, H 6.07, N 6.99.

**Pinacol [4-(2,2′-Bipyridin-6-yl)phenyl]boronate (4b):** The product was obtained as white crystals in 86% yield (Method A). M.p. 121–123 °C. $^1$H NMR (500 MHz, $CDCl_3$): $\delta$ = 1.38 (s, 12 H, $CH_3$ dioxaborolane), 7.33 (ddd, $J_{5',4'}$ = 7.5, $J_{5',6'}$ = 4.8, $J_{5',3'}$ = 1.2, 1 H, 5′-H), 7.81 (dd, $J_{5,4}$ = 7.8, $J_{5,3}$ = 1.1, 1 H, 5-H), 7.86 (td, $J_{4',3'}$ = 8.0, $J_{4',5'}$ = 7.5, $J_{4',6'}$ = 1.8, 1 H, 4′-H), 7.89 (t, $J_{4,5}$ = 7.8, $J_{4,3}$ = 7.8, 1 H, 4-H), 7.95 (m, 2 H, H$^m$ phenylene), 8.16 (m, 2 H, H$^o$ phenylene), 8.39 (dd, $J_{3,4}$ = 7.8, $J_{3,5}$ = 1.1, 1 H, 3-H), 8.64 (dt, $J_{3',4'}$ = 8.0, $J_{3',5'}$ = 1.2, $J_{3',6'}$ = 1.0, 1 H, 3′-H), 8.70 (ddd, $J_{6',5'}$ = 4.8, $J_{6',4'}$ = 1.8, $J_{6',3'}$ = 1.0, 1 H, 6′-H) ppm. $^{13}$C NMR (125.8 MHz, $CDCl_3$): $\delta$ = 24.89 ($CH_3$ dioxaborolane), 83.88 (C dioxaborolane), 119.57 (C-3), 120.58 (C-5), 121.34 (C-3′), 123.75 (C-5′), 126.13 (C$^o$ phenylene), 135.17 (C$^m$ phenylene), 136.89 (C-4′), 137.67 (C-4), 141.81 (C$^i$ phenylene), 149.04 (C-6′), 155.80 (C-2), 156.23 (C-6), 156.31 (C-2′) ppm; C$^p$ phenylene signal not observed. FAB MS: *m*/*z* (%) = 258.1 (65), 358.2 (100) [M$^+$]. HRMS (FAB): for $C_{22}H_{24}BN_2O_2$ calcd. 359.1931; found 359.1938. IR ($CHCl_3$): $\tilde{\nu}$ = 3010.2998, 2983, 1611, 1566, 1430, 1391, 1361, 1321, 1144, 1088, 1018, 859, 662 cm$^{-1}$. $C_{22}H_{23}BN_2O_2$ (358.24): calcd. C 73.76, H 6.47, N 7.82; found C 73.58, H 6.47, N 7.60.

**Pinacol [4-(2,2′-Bipyridin-5-yl)phenyl]boronate (4c):** The product was obtained as white crystals in 91% yield (Method A) which gave analytical data identical to those previously reported.[23] $^1$H NMR (400 MHz, $CDCl_3$): $\delta$ = 1.38 (s, 12 H, $CH_3$ dioxaborolane), 7.33 (ddd, $J_{5',4'}$ = 8.0, $J_{5',6'}$ = 4.8, $J_{5',3'}$ = 1.2, 1 H, 5′-H), 7.67 (m, 2 H, H$^o$ phenylene), 7.84 (td, $J_{4',3'}$ = $J_{4',5'}$ = 8.0, $J_{4',6'}$ = 1.9, 1 H, 4′-H), 7.94 (m, 2 H, H$^m$ phenylene), 8.05 (dd, $J_{4,3}$ = 8.3, $J_{4,6}$ = 2.4, 1 H, 4-H), 8.45 (dt, $J_{3',4'}$ = 8.0, $J_{3',5'}$ = 1.2, $J_{3',6'}$ = 1.0, 1 H, 3′-H), 8.48 (dd, $J_{3,4}$ = 8.3, $J_{3,6}$ = 0.9, 1 H, 3′-H), 8.71 (ddd, $J_{6',5'}$ = 4.8, $J_{6',4'}$ = 1.9, $J_{6',3'}$ = 1.0, 1 H, 6′-H), 8.94 (dd, $J_{6,4}$ = 2.4, $J_{6,3}$ = 0.9, 1 H, 6-H) ppm. $^{13}$C NMR (100.6 MHz, $CDCl_3$): $\delta$ = 24.87 ($CH_3$ dioxaborolane), 83.95 (C dioxaborolane), 120.96 and 121.10 (C-3 and C-3′), 123.72 (C-5′), 126.32 (C$^o$ phenylene), 135.29 (C-4), 135.52 (C$^m$ phenylene), 136.30 (C-5), 136.95 (C-4′), 140.20 (C$^i$ phenylene), 147.72 (C-6), 149.23 (C-6′), 155.14 (C-2), 155.84 (C-2′) ppm; C$^p$ phenylene signal not observed.

**Pinacol [4-(2,2′:6′,2"-Terpyridine-4′-yl)phenyl]boronate (4d):** The product was isolated as white crystals in 81% yield (Method A). M.p. 187–196 °C. $^1$H NMR (400 MHz, $CDCl_3$): $\delta$ = 1.39 (s, 12 H, $CH_3$ dioxaborolane), 7.36 (ddd, $J_{5',4'}$ = 7.5, $J_{5',6'}$ = 4.8, $J_{5',3'}$ = 1.2, 2 H, 5′-H), 7.88 (td, $J_{4',3'}$ = 8.0, $J_{4',5'}$ = 7.5, $J_{4',6'}$ = 1.8, 2 H, 4′-H), 7.92 (m, 2 H, H$^o$ phenylene), 7.96 (m, 2 H, H$^m$ phenylene), 8.68 (dt, $J_{3',4'}$ = 8.0, $J_{3',5'}$ = 1.2, $J_{3',6'}$ = 0.9, 2 H, 3′-H), 8.74 (ddd, $J_{6',5'}$ = 4.8, $J_{6',4'}$ = 1.8, $J_{6',3'}$ = 0.9, 2 H, 6′-H), 8.76 (s, 2 H, 3-H) ppm. $^{13}$C NMR (100.6 MHz, $CDCl_3$): $\delta$ = 24.93 ($CH_3$ dioxaborolane), 83.98 (C dioxaborolane), 118.94 (C-3), 121.42 (C-3′), 123.85 (C-5′), 126.59 (C$^o$ phenylene), 135.37 (C$^m$ phenylene), 136.90 (C-4′), 140.98 (C$^i$ phenylene), 149.15 (C-6′), 150.15 (C-4), 155.98 (C-2), 156.26 (C-2′) ppm; C$^p$ phenylene signal not observed. FAB MS: *m*/*z* (%) = 336 (25), 436 (100) [M$^+$ + H]. HRMS (FAB): for

 © 2007 Wiley-VCH Verlag GmbH & Co. KGaA, Weinheim 

$C_{27}H_{27}BN_3O_2$: calcd. 436.2196; found 436.2187. IR ($CHCl_3$): $\tilde{\nu}$ = 3010, 2983, 1603, 1586, 1469, 1388, 1364, 1144, 1092, 1019, 859, 787, 662 $cm^{-1}$.

**9-Benzyl-8-[(1,10-Phenanthroline-2-yl)ethynyl]adenine (8a):** 9-Benzyl-8-bromoadenine (0.5 g, 1.64 mmol), 2-ethynylphenanthroline (402 mg, 1.97 mmol, 1.2 equiv.), $PdCl_2$ (14.5 mg, 0.082 mmol, 5 mol-%), dppf (45.5 mg, 0.082 mmol, 5 mol-%), CuI (16 mg, 0.082 mmol, 5 mol-%), and $Et_3N$ (2 mL, 14.3 mmol) were combined in dry DMF (5 mL) and stirred under argon at 90 °C for 12 h. The solvent was removed under reduced pressure, the residue was dissolved in chloroform, washed with a saturated solution of EDTA, evaporated, and purified by silica gel column chromatography ($CHCl_3$ + 1–10% MeOH). Crystallization from $CHCl_3$ (plus a few drops of MeOH) and heptane gave the product as a yellowish solid (385 mg, 55%). M.p. 288–291 °C. $^1$H NMR (500 MHz, [$D_6$]-DMSO): $\delta$ = 5.60 (s, 2 H, $CH_2$), 7.29 (m, 1 H, H$^p$ phenylene), 7.37 (m, 2 H, H$^m$ phenylene), 7.49 (m, 2 H, H$^o$ phenylene), 7.62 (br. s, 2 H, $NH_2$), 7.83 (dd, $J_{8',7'}$ = 8.1, $J_{8',9'}$ = 4.3, 1 H, 8′-H), 8.05 (d, $J_{5',6'}$ = 8.8, 1 H, 5′-H), 8.06 (d, $J_{3',4'}$ = 8.3, 1 H, 3′-H), 8.09 (d, $J_{6',5'}$ = 8.8, 1 H, 6′-H), 8.27 (s, 1 H, H-2), 8.54 (dd, $J_{7',8'}$ = 8.1, $J_{7',9'}$ = 1.8, 1 H, 7′-H), 8.63 (d, $J_{4',3'}$ = 8.3, 1 H, 4′-H), 9.15 (dd, $J_{9',8'}$ = 4.3, $J_{9',7'}$ = 1.8, 1 H, 9′-H) ppm. $^{13}$C NMR (125.8 MHz, [$D_6$]DMSO): $\delta$ = 46.61 ($CH_2$), 78.45 (pur-*C*≡C), 94.32 (phen-*C*≡C), 119.45 (C-5), 124.08 (C-8′), 126.44 and 126.63 (C-3′, C-5′), 127.98 (C$^o$ phenylene), 128.08 (C$^p$ phenylene), 128.46 (C-4a′), 128.52 (C-6′), 128.99 (C$^m$ phenylene), 129.12 (C-6a′), 132.41 (C-8), 136.57 (C-7′), 136.68 (C$^i$ phenylene), 137.37 (C-4′), 140.44 (C-2′), 145.02 (C-10a′), 146.03 (C-10b′), 149.65 (C-4), 150.61 (C-9′), 154.57 (C-2), 156.27 (C-6) ppm. FAB MS: *m*/*z* (%) = 428 (25) [M$^+$ + H], 231 (80). HRMS (FAB): for $C_{26}H_{18}N_7$ calcd. 428.1623; found 428.1630. IR (KBr): $\tilde{\nu}$ = 3481, 3413, 3034, 1631, 1572, 1486, 1287, 850, 732 $cm^{-1}$. UV/Vis (MeOH): $\lambda_{max}$ ($\varepsilon$) = 364 (24345), 333 (25380), 279 (21220) nm. $C_{26}H_{17}N_7 \cdot 1/2CHCl_3$ (487.15): calcd. C 65.34, H 3.62, N 20.13; found C 65.95, H 3.62, N 20.15.

**9-Benzyl-8-[(2,2′-bipyridine-6-yl)ethynyl]adenine (8b):** 9-Benzyl-8-bromoadenine (0.5 g, 1.64 mmol), 6-ethynylbipyridine (355 mg, 1.97 mmol, 1.2 equiv.), $PdCl_2$ (14.5 mg, 0.082 mmol, 5 mol-%), dppf (45.5 mg, 0.082 mmol, 5 mol-%), CuI (16 mg, 0.082 mmol, 5 mol-%), and $Et_3N$ (2 mL, 14.3 mmol) were combined in DMF (3 mL) and stirred under argon at 90 °C for 8 h. The workup was performed in the same way as for **8a**. Crystallization of the crude product from $CHCl_3$ (plus a few drops of MeOH)/heptane gave **8b** as a colorless solid (384 mg, 58%). M.p. 242–244 °C. $^1$H NMR (500 MHz, [$D_6$]DMSO): $\delta$ = 5.44 (s, 2 H, $CH_2$), 7.29 (m, 1 H, H$^p$ phenylene), 7.35 (m, 2 H, H$^m$ phenylene), 7.47 (m, 2 H, H$^o$ phenylene), 7.52 (ddd, $J_{5'',4''}$ = 7.5, $J_{5'',6''}$ = 4.7, $J_{5'',3''}$ = 1.2, 1 H, 5″-H), 7.62 (br. s, 2 H, $NH_2$), 7.83 (dd, $J_{5',4'}$ = 7.7, $J_{5',3'}$ = 1.1, 1 H, 5′-H), 8.01 (td, $J_{4'',3''}$ = 8.0, $J_{4'',5''}$ = 7.5, $J_{4'',6''}$ = 1.8, 1 H, 4″-H), 8.09 (t, $J_{4',3'}$ = 8.0, $J_{4',5'}$ = 7.7, 1 H, 4′-H), 8.27 (s, 1 H, H-2), 8.42 (dt, $J_{3'',4''}$ = 8.0, $J_{3'',5''}$ = 1.2, $J_{3'',6''}$ = 1.0, 1 H, 3″-H), 8.49 (dd, $J_{3',4'}$ = 8.0, $J_{3',5'}$ = 1.1, 1 H, 3′-H), 8.73 (ddd, $J_{6'',5''}$ = 4.7, $J_{6'',4''}$ = 1.8, $J_{6'',3''}$ = 1.0, 1 H, 6″-H) ppm. $^{13}$C NMR (125.8 MHz, [$D_6$]DMSO): $\delta$ = 46.54 ($CH_2$), 77.94 (pur-*C*≡C-), 93.58 (bipy-*C*≡C-), 119.31 (C-5), 120.86 (C-3″), 121.55 (C-3′), 125.00 (C-5″), 128.03 (C$^o$ phenylene), 128.16 (C$^p$ phenylene), 128.27 (C-5′), 128.95 (C$^m$ phenylene), 132.40 (C-8), 136.74 (C$^i$ phenylene), 137.78 (C-4″), 138.63 (C-4′), 140.32 (C-6′), 149.62 (C-4), 149.66 (C-6″), 154.33 (C-2″), 154.56 (C-2), 156.27 (C-6), 156.34 (C-2′) ppm. FAB MS: *m*/*z* (%) = 79.1 (100), 187.0 (20), 279.1 (20), 404.2 (10) [M$^+$ + H]. HRMS (FAB): for $C_{24}H_{18}N_7$ calcd. 404.1624; found 404.1628. IR (KBr): $\tilde{\nu}$ = 3430, 3316, 1649, 1559, 1425, 775 $cm^{-1}$. UV/Vis (MeOH): $\lambda_{max}$ ($\varepsilon$) = 327 (23755), 282 (15335) nm. $C_{24}H_{17}N_7 \cdot 1/2H_2O$ (421.45): calcd. C 69.89, H 4.40, N 23.77; found C 70.08, H 4.06, N 23.79.

**9-Benzyl-8-[(2,2′-bipyridine-5-yl)ethynyl]adenine (8c):** 8-Bromo-9-benzyladenine (0.5 g, 1.64 mmol), 5-ethynylbipyridine (355 mg, 1.97 mmol, 1.2 equiv.), $PdCl_2$ (14.5 mg, 0.082 mmol, 5 mol-%), dppf (45.5 mg, 0.082 mmol, 5 mol-%), CuI (16 mg, 0.082 mmol, 5 mol-%), and $Et_3N$ (2 mL, 14.3 mmol) were combined in DMF (5 mL) and stirred under argon at 85 °C for 12 h. The workup was performed in the same way as for **8a**. Crystallization of crude product from $CHCl_3$ (plus a few drops of MeOH)/heptane gave **8c** as a white solid (373 mg, 56%). M.p. 273–278 °C. $^1$H NMR (400 MHz, [$D_6$]DMSO): $\delta$ = 5.55 (s, 2 H, $CH_2$), 7.29 (m, 1 H, H$^p$ phenylene), 7.33–7.41 (m, 4 H, H$^{m,o}$ phenylene), 7.51 (ddd, $J_{5'',4''}$ = 7.5, $J_{5'',6''}$ = 4.7, $J_{5'',3''}$ = 1.2, 1 H, 5″-H), 7.60 (br. s, 2 H, $NH_2$), 8.00 (td, $J_{4'',3''}$ = 7.9, $J_{4'',5''}$ = 7.5, $J_{4'',6''}$ = 1.8, 1 H, 4″-H), 8.22 (dd, $J_{4',3'}$ = 8.3, $J_{4',6'}$ = 2.2, 1 H, 4′-H), 8.25 (s, 1 H, H-2), 8.43 (dt, $J_{3'',4''}$ = 7.9, $J_{3'',5''}$ = 1.2, $J_{3'',6''}$ = 0.9, 1 H, 3″-H), 8.49 (dd, $J_{3',4'}$ = 8.3, $J_{3',6'}$ = 0.9, 1 H, 3′-H), 8.74 (ddd, $J_{6'',5''}$ = 4.7, $J_{6'',4''}$ = 1.8, $J_{6'',3''}$ = 0.9, 1 H, 6″-H), 8.94 (dd, $J_{6',4'}$ = 2.2, $J_{6',3'}$ = 0.9, 1 H, 6′-H) ppm. $^{13}$C NMR (125.8 MHz, [$D_6$]DMSO): $\delta$ = 46.39 ($CH_2$), 83.01 (pur-*C*≡C-), 91.58 (bipy-*C*≡C-), 117.69 (C-5′), 119.28 (C-5), 120.34 (C-3′), 121.25 (C-3″), 125.04 (C-5″), 127.82 (C$^o$ phenylene), 128.06 (C$^p$ phenylene), 128.96 (C$^m$ phenylene), 132.66 (C-8), 136.83 (C$^i$ phenylene), 137.75 (C-4″), 140.36 (C-4′), 149.66 (C-4), 149.78 (C-6″), 152.01 (C-6′), 154.28 (C-2″), 154.44 (C-2), 155.58 (C-2′), 156.21 (C-6) ppm. FAB MS: *m*/*z* (%) = 93 (100), 259 (5), 404.2 (10) [M$^+$ + H]. HRMS (FAB): for $C_{24}H_{18}N_7$ calcd. 404.1624 found 404.1614. IR (KBr): $\tilde{\nu}$ = 3421, 3321, 3032, 1660, 1586, 1325, 1021, 195, 745 $cm^{-1}$. UV/Vis (MeOH): $\lambda_{max}$ ($\varepsilon$) = 336 (21515), 257 (5228) nm. $C_{24}H_{17}N_7 \cdot 1H_2O$ (421.45): calcd. C 69.89, H 4.40, N 23.77; found C 70.20, H 4.15, N 23.63.

**9-Benzyl-8-[4-(1,10-phenanthroline-2-yl)phenyl]adenine (9a):** 9-Benzyl-8-bromoadenine (0.215 g, 0.7 mmol), 4-(1,10-phenanthroline-3-yl)pinacolboronate (270 mg, 0.7 mmol, 1 equiv.), $PdCl_2$ (6 mg, 0.035 mmol, 5 mol-%), dppf (19 mg, 0.035 mmol, 5 mol-%), $K_2CO_3$ (390 mg, 2.8 mmol, 4 equiv.) were combined in DMF (4 mL) and three drops of water and stirred under argon at 90 °C for 10 h. The workup was performed in the same way as for **8a**. Crystallization of crude product from $CHCl_3$ (plus a few drops of MeOH)/heptane gave **9a** as a yellowish solid (160 mg, 47%). M.p. 286–293 °C. $^1$H NMR (400 MHz, [$D_6$]DMSO): $\delta$ = 5.62 (s, 2 H, $CH_2$), 7.07 (m, 2 H, H$^o$ phenylene), 7.24 (m, 1 H, H$^p$ phenylene), 7.30 (m, 2 H, H$^m$ phenylene), 7.46 (br. s, 2 H, $NH_2$), 7.81 (dd, $J_{8',7'}$ = 8.1, $J_{8',9'}$ = 4.3, 1 H, 8′-H), 7.94 (m, 2 H, H$^o$ phenylene), 8.01 (d, $J_{6',5'}$ = 8.8, 1 H, 6′-H), 8.05 (d, $J_{5',6'}$ = 8.8, 1 H, 5′-H), 8.22 (s, 1 H, H-2), 8.48 (d, $J_{3',4'}$ = 8.5, 1 H, 3′-H), 8.52 (dd, $J_{7',8'}$ = 8.1, $J_{7',9'}$ = 1.8, 1 H, 7′-H), 8.58 (m, 2 H, H$^m$ phenylene), 8.61 (d, $J_{4',3'}$ = 8.5, 1 H, 4′-H), 9.18 (dd, $J_{9',8'}$ = 4.3, $J_{9',7'}$ = 1.8, 1 H, 9′-H) ppm. $^{13}$C NMR (100.6 MHz, [$D_6$]DMSO): $\delta$ = 46.46 ($CH_2$), 118.89 (C-5), 120.42 (C-3′), 123.66 (C-8′), 126.53 (C$^o$ phenylene), 126.59 (C-5′), 127.06 (C-6′), 127.71 (C$^p$ phenylene, C$^m$ phenylene), 127.95 (C-4a′), 128.96 (C$^m$ Ph), 129.10 (C-6a′), 129.38 (C$^o$ phenylene), 130.90 (C$^i$ phenylene), 136.54 (C-7′), 137.24 (C$^i$ Ph), 137.74 (C-4′), 139.98 (C$^p$ phenylene), 145.51 (C-10b′), 145.76 (C-10a′), 149.51 (C-8), 150.24 (C-9′), 151.76 (C-4), 153.15 (C-2), 154.67 (C-2′), 156.13 (C-6) ppm. FAB MS: *m*/*z* (%) = 282 (5%), 390 (8%) 480 (35) [M$^+$]. HRMS (FAB): for $C_{30}H_{22}N_7$ calcd.480.1937 found 480.1945. IR (KBr): $\tilde{\nu}$ = 3438, 3133, 1666, 1292, 1113 $cm^{-1}$. UV/Vis (MeOH): $\lambda_{max}$ ($\varepsilon$) = 355 sh (9720), 321 (21792), 303 sh (21792), 233 (26572) nm. $C_{30}H_{21}N_7 \cdot 1H_2O$ (497.55): calcd. C 72.42, H 4.66, N 19.71; found C 72.40, H 4.19, N 19.53.

**9-Benzyl-8-[4-(2,2′-bipyridine-6-yl)phenyl]adenine (9b):** 9-Benzyl-8-bromoadenine (0.5 g, 1.64 mmol), 4-(2,2′-bipyridin-6-yl)pinacolboronate (600 mg, 1.8 mmol, 1.1 equiv.), $PdCl_2$ (14.5 mg, 0.082 mmol, 5 mol-%), dppf (45.5 mg, 0.082 mmol, 5 mol-%), and

 © 2007 Wiley-VCH Verlag GmbH & Co. KGaA, Weinheim 

$K_2CO_3$ (905 mg, 6.56 mmol, 4 equiv.) were combined in DMF (5 mL) and three drops of water and stirred under argon at 90 °C for 8 h. The workup was performed in the same way as for **8a**. Crystallization of crude product from $CHCl_3$ (plus a few drops of MeOH)/heptane gave **9b** as a white solid (401 mg, 53%). M.p. 252–255 °C. $^1$H NMR (500 MHz, [D$_6$]DMSO): $\delta$ = 5.58 (s, 2 H, $CH_2$), 7.05 (m, 2 H, H$^o$ Ph), 7.24 (m, 1 H, H$^p$ Ph), 7.29 (m, 2 H, H$^m$ Ph), 7.40 (br. s, 2 H, $NH_2$), 7.49 (ddd, $J_{5'',4''}$ = 7.5, $J_{5'',6''}$ = 4.7, $J_{5'',3''}$ = 1.2, 1 H, 5″-H), 7.88 (m, 2 H, H$^o$ phenylene), 8.00 (td, $J_{4'',3''}$ = 7.9, $J_{4'',5''}$ = 7.5, $J_{4'',6''}$ = 1.8, 1 H, 4″-H), 8.07 (t, $J_{4',5'}$ = 7.9, $J_{4',3'}$ = 7.7, 1 H, 4′-H), 8.13 (br. d, $J_{5',4'}$ = 7.9, 1 H, 5′-H), 8.21 (s, 1 H, H-2), 8.38 (m, 2 H, H$^m$ phenylene), 8.39 (dd, $J_{3',4'}$ = 7.7, $J_{3',5'}$ = 1.1, 1 H, 3′-H), 8.60 (dt, $J_{3'',4''}$ = 7.9, $J_{3'',5''}$ = 1.2, $J_{3'',6''}$ = 0.9, 1 H, 3″-H), 8.72 (ddd, $J_{6'',5''}$ = 4.7, $J_{6'',4''}$ = 1.8, $J_{6'',3''}$ = 0.9, 1 H, 6″-H) ppm. $^{13}$C NMR (125.8 MHz, [D$_6$]DMSO): $\delta$ = 46.43 ($CH_2$), 118.88 (C-5), 119.82 (C-3′), 120.97 (C-3″, C-5′), 124.59 (C-5″), 126.45 (C$^o$ Ph), 127.04 (C$^m$ phenylene), 127.66 (C$^p$ Ph), 128.95 (C$^m$ Ph), 129.36 (C$^o$ phenylene), 130.65 (C$^i$ phenylene), 137.20 (C$^i$ Ph), 137.61 (C-4″), 138.80 (C-4′), 139.61 (C$^p$ phenylene), 149.51 (C-6″, C-8), 151.69 (C-4), 153.11 (C-2), 154.56 (C-6′), 155.32 (C-2′, C-2″), 156.10 (C-6) ppm. FAB MS: *m*/*z* (%) = 91 (100), 258 (10), 366 (15), 456 (75%) [M$^+$ + H]. HRMS (FAB): for $C_{28}H_{22}N_7$ calcd.456.1937 found 456.1927. IR (KBr): $\tilde{\nu}$ = 3444, 3062, 1649, 1582, 1429, 755 cm$^{-1}$. UV/Vis (MeOH): $\lambda_{max}$ ($\varepsilon$) = 310 (26420), 238 (21188) nm. $C_{28}H_{21}N_7 \cdot H_2O$ (473.53): calcd. C 71.02, H 4.90, N 20.71; found C 71.24, H 4.55, N 20.59.

**9-Benzyl-8-[4 -(2,2′-bipyridine-5-yl)phenyl]adenine (9c):** 9-Benzyl-8-bromoadenine (0.5 g, 1.64 mmol), 4-(2,2′-bipyridin-5-yl)pinacolboronate (600 mg, 1.8 mmol, 1.1 equiv.), $PdCl_2$ (28 mg, 0.165 mmol, 10 mol-%), dppf (90 mg, 0.165 mmol, 5 mol-%), and $K_2CO_3$ (905 mg, 6.56 mmol, 4 equiv.) were combined in DMF (9 mL) and three drops of water and stirred under argon at 90 °C for 8 h. The workup was performed in the same way as for **8a**. Crystallization of crude product from $CHCl_3$ (plus a few drops of MeOH)/heptane gave **9c** as a white solid (400 mg, 52%). M.p. 267–272 °C. $^1$H NMR (400 MHz, [D$_6$]DMSO): $\delta$ = 5.58 (s, 2 H, $CH_2$), 7.04 (m, 2 H, H$^o$ Ph), 7.22–7.33 (m, 4 H, H$^{m,p}$ Ph), 7.43 (br. s, 2 H, $NH_2$), 7.48 (ddd, $J_{5'',4''}$ = 7.5, $J_{5'',6''}$ = 4.8, $J_{5'',3''}$ = 1.2, 1 H, 5″-H), 7.86 (m, 2 H, H$^o$ phenylene), 7.95–8.01 (m, 3 H, 4″-H and H$^m$ phenylene), 8.20 (s, 1 H, H-2), 8.34 (dd, $J_{4',3'}$ = 8.3, $J_{4',6'}$ = 2.4, 1 H, 4′-H), 8.44 (dt, $J_{3'',4''}$ = 7.9, $J_{3'',5''}$ = 1.2, $J_{3'',6''}$ = 1.0, 1 H, 3″-H), 8.49 (dd, $J_{3',4'}$ = 8.3, $J_{3',6'}$ = 0.9, 1 H, 3′-H), 8.79 (ddd, $J_{6'',5''}$ = 4.8, $J_{6'',4''}$ = 1.8, $J_{6'',3''}$ = 1.0, 1 H, 6″-H), 9.10 (dd, $J_{6',4'}$ = 2.4, $J_{6',3'}$ = 0.9, 1 H, 6′-H) ppm. $^{13}$C NMR (125.8 MHz, [D$_6$]DMSO): $\delta$ = 46.42 ($CH_2$), 118.88 (C-5), 120.67 and 120.70 (C-3′ and C-3″), 124.51 (C-5″), 126.39 (C$^o$ Ph), 127.22 (C$^m$ phenylene), 127.65 (C$^p$ Ph), 128.95 (C$^m$ Ph), 129.60 (C$^o$ phenylene), 129.80 (C$^i$ phenylene), 134.69 (C-5′), 135.43 (C-4′), 137.19 (C$^i$ Ph), 137.57 (C-4″), 137.96 (C$^p$ phenylene), 147.59 (C-6′), 149.41 (C-8), 149.60 (C-6″), 151.69 (C-4), 153.09 (C-2), 154.76 (C-2′), 154.97 (C-2″), 156.08 (C-6) ppm. FAB MS: *m*/*z* (%) = 456.2 (45%) [M$^+$]. HRMS (FAB): for $C_{28}H_{22}N_7$ calcd.456.1937 found 456.1921. IR (KBr): $\tilde{\nu}$ = 3446, 1643, 1589, 1330, 1001, 753 cm$^{-1}$. UV/Vis (MeOH): $\lambda_{max}$ ($\varepsilon$) = 315 (20980), 259 (6656) nm. $C_{28}H_{21}N_7 \cdot CHCl_3$ (574.89): calcd. C 60.59, H 3.86, N 17.05; found C 60.43, H 3.36, N 16.73.

**9-Benzyl-8-[4′-(2′,2": 6′,2"-terpyridine-1′-yl)phenyl]adenine (9d):** 9-Benzyl-8-bromoadenine (0.35 g, 1.15 mmol), 4′-phenylene-2,2′:6′,2′′-terpyridine (500 mg, 1.15 mmol, 1 equiv.), $PdCl_2$ (10 mg, 0.058 mmol, 5 mol-%), dppf (32 mg, 0.058 mmol, 5 mol-%), and $K_2CO_3$ (475 mg, 3.45 mmol, 3 equiv.) were combined in DMF (5 mL)and three drops of water and stirred under argon at 85 °C for 10 h. The workup was performed in the same way as for **8a**. Crystallization of crude product from $CHCl_3$ (plus a few drops of MeOH)/heptane gave **9d** as a white solid (283 mg, 46%). M.p. 269–271 °C. $^1$H NMR (400 MHz, [D$_6$]DMSO): $\delta$ = 5.60 (s, 2 H, $CH_2$), 7.06 (m, 2 H, H$^o$ Ph), 7.42 (m, 1 H, H$^p$ Ph), 7.30 (m, 2 H, H$^m$ Ph), 7.46 (br. s, 2 H, $NH_2$), 7.54 (ddd, 2 H, $J_{5'',4''}$ = 7.5, $J_{5'',6''}$ = 4.8, $J_{5'',3''}$ = 1.2, 2 H, 5″-H), 7.92 (m, 2 H, H$^o$ phenylene), 8.04 (ddd, $J_{4'',3''}$ = 8.0, $J_{4'',5''}$ = 7.5, $J_{4'',6''}$ = 1.8, 2 H, 4″-H), 8.07 (m, 2 H, H$^m$ phenylene), 8.21 (s, 1 H, H-2), 8.68 (dt, $J_{3'',4''}$ = 8.0, $J_{3'',5''}$ = 1.2, $J_{3'',6''}$ = 0.9, 2 H, 3″-H), 8.76 (s, 2 H, H-3′), 8.76 (ddd, $J_{6'',5''}$ = 4.8, $J_{6'',4''}$ = 1.8, $J_{6'',3''}$ = 0.9, 2 H, 6″-H) ppm. $^{13}$C NMR (100.6 MHz, [D$_6$]-DMSO): $\delta$ = 46.51 ($CH_2$), 118.14 (C-3′), 118.93 (C-5), 121.22 (C-3″), 124.88 (C-5″), 126.58 (C$^o$ Ph), 127.49 (C$^m$ phenylene), 127.73 (C$^p$ Ph), 128.99 (C$^m$ Ph), 129.86 (C$^o$ phenylene), 130.91 (C$^i$ phenylene), 137.19 (C$^i$ Ph), 137.77 (C-4″), 138.72 (C$^p$ phenylene), 148.65 (C-4′), 149.29 (C-8), 149.59 (C-6″), 151.78 (C-4), 153.22 (C-2), 155.05 (C-2″), 156.06 (C-2′), 156.16 (C-6) ppm. FAB MS: *m*/*z* (%) = 91 (90), 336 (35), 436 (100), 533 (15) [M$^+$]. HRMS (FAB): for $C_{33}H_{25}N_8$ calcd. 533.2202 found 533.2231. IR (KBr): $\tilde{\nu}$ = 3401, 3299, 3060, 1637, 1584, 1390, 1330, 842, 792 cm$^{-1}$. UV/Vis (MeOH): $\lambda_{max}$ ($\varepsilon$) = 318 sh (30620), 285 (34170), 248 (32715) nm. $C_{33}H_{24}N_8 \cdot H_2O$ (550.6): calcd. C 71.98, H 4.74, N 20.35; found C 71.24, H 4.47, N 20.31.

**General Procedure for the Complexation Reactions. Method B:** Compounds **2b**–**2c**, **4a**–**4c**, **8a**–**8c** or **9a**–**9c** (1.5 mmol) were combined with commercially available $Ru(bipy)_2Cl_2 \cdot 2H_2O$ (1.65 mmol, 1.1 equiv.) or **4d** or **9d** with $Ru(terpy)Cl_3$ (1.65 mmol, 1.1 equiv.) in ethylene glycol and were then heated for 2 h at 150 °C. The solvent was distilled off under reduced pressure. The residue was dissolved in water and saturated solution of $NH_4PF_6$ was added to the mixture. The precipitate thus formed was collected by filtration. The crude product was purified by silica gel column chromatography using a mixture of $CH_3CN/H_2O$/saturated $KNO_3$ (10:1:0.1) as eluent. The corresponding fractions were combined and the solvent removed in vacuo. The residue was dissolved in a small amount of EtOH and the $KNO_3$ was filtered off. The product was dissolved in water and a saturated solution of $NH_4PF_6$ was added. The product precipitated as hexafluorophosphate salts from the solution. The solid was filtered off. Crystallization from acetone or acetonitrile/*i*PrOH gave pure desired products **5**, **6**, **10** or **11**.

**Complex 5b:** The product was isolated as a red solid in 49% yield (Method B). M.p. 265–274 °C (decomposition). $^1$H NMR (400 MHz, [D$_6$]acetone): $\delta$ = 3.60 (s, 1 H, HC≡C), 7.43 (ddd, $J_{5,4}$ = 7.6, $J_{5,6}$ = 5.7, $J_{5,3}$ = 1.4, 1 H, 5-H bipy), 7.51–7.59 (m, 3 H, 5′-H and 2 × 5-H bipy), 7.63 (ddd, $J_{5,4}$ = 7.6, $J_{5,6}$ = 5.7, $J_{5,3}$ = 1.4, 1 H, 5-H bipy), 7.82 (dd, $J_{5,4}$ = 7.8, $J_{5,3}$ = 1.3, 1 H, 5-H), 7.91–7.97 (m, 4 H, 6′-H and 3 ×6-H bipy), 8.08 (ddd, $J_{4,3}$ = 8.1, $J_{4,5}$ = 7.6, $J_{4,6}$ = 1.5, 1 H, 4-H bipy), 8.18–8.27 (m, 5 H, 4-H, 4′-H and 3 ×4-H bipy), 8.33 (ddd, $J_{6,5}$ = 5.7, $J_{6,4}$ = 1.5, $J_{6,3}$ = 0.8, 1 H, 6-H bipy), 8.71 (ddd, $J_{3,4}$ = 8.1, $J_{3,5}$ = 1.4, $J_{3,6}$ = 0.8, 1 H, 3-H bipy), 8.78–8.84 (m, 4 H, 3′-H and 3 ×3-H bipy), 8.84 (dd, $J_{3,4}$ = 8.2, $J_{3,5}$ = 1.3, 1 H, 3-H) ppm. $^{13}$C NMR (100.6 MHz, [D$_6$]acetone): $\delta$ = 79.31 (*C*≡CH), 88.56 (H*C*≡C), 124.92, 124.98, 125.02, 125.50 and 125.53 (C-3′ and C-3 bipy), 126.04 (C-3), 128.45, 128.50, 128.70, 128.79 and 129.08 (C-5′ and C-5 bipy), 135.16 (C-5), 138.88, 138.97, 139.04, 139.10, 139.14 and 139.33 (C-4, C-4′ and C-4 bipy), 148.19 (C-6), 152.39, 152.44, 152.52, 152.91 and 153.75 (C-6′ and C-6 bipy), 158.03, 158.17, 158.25 and 158.32 (C-2 bipy), 158.79 (C-2′), 159.22 (C-2) ppm. ESI MS: *m*/*z* (%) = 739 (65) [M$^+$ + PF$_6^-$], 297 (100) [M$^{2+}$ – 2PF$_6^-$]. IR (KBr): $\tilde{\nu}$ = 3435, 3280, 2118 1568, 1466, 1426, 839, 558 cm$^{-1}$. $C_{32}H_{24}F_{12}N_6P_2Ru \cdot H_2O$ (901.6): calcd. C 42.63, H 2.91, N 9.32; found C 43.18, H 3.07, N 9.01.

**Complex 5c:** The product was isolated as a red solid in 32% yield (Method B). M.p. 185–193 °C. $^1$H NMR (500 MHz, [D$_6$]acetone):

 © 2007 Wiley-VCH Verlag GmbH & Co. KGaA, Weinheim 

$\delta$ = 4.12 (s, 1 H, HC≡C), 7.55–7.62 (m, 5 H, 5″-H and 4×5-H bipy), 7.99–8.10 (m, 6 H, 6′-H, 6″-H and 4×6-H bipy), 8.17–8.27 (m, 6 H, 4′-H, 4″-H and 4×4-H bipy), 8.78–8.85 (m, 6 H, 3′-H, 3″-H, 4×3-H bipy) ppm. $^{13}$C NMR (125.8 MHz, [D$_6$]acetone): $\delta$ = 78.97 (*C*≡CH), 86.89 (H*C*≡C), 123.71 (C-5′), 124.89, 125.29, 125.33, 125.36, 125.46 and 125.93 (C-3′, C-3″ and C-3 bipy), 128.71, 128.74, 128.80 and 129.04 (C-5″ and C-5 bipy), 138.97, 139.04 and 139.06 (C-4″ and C-4 bipy), 141.42 (C-4′), 152.58, 152.73, 152.82, 152.84 and 153.09 (C-6″ and C-6 bipy), 154.81 (C-6′), 157.50 (C-2′), 157.79, 158.00, 158.09, 158.12 and 158.17 (C-2″ and C-2 bipy) ppm. ESI MS: *m*/*z* (%) = 738.9 (35) [M$^+$ + PF$_6^-$], 297 (100) [M$^{2+}$ – 2PF$_6^-$]. IR (KBr): $\tilde{\nu}$ = 3435, 3270, 2117 1559, 1466, 1465, 839, 558 cm$^{-1}$. $C_{32}H_{24}F_{12}N_6P_2Ru\cdot H_2O$ (901.6): calcd. C 42.63, H 2.91, N 9.32; found C 42.80, H 3.06, N 9.10.

**Complex 6a:** The product was isolated as a red solid in 66% yield (Method B). M.p. 182–188 °C. $^1$H NMR (400 MHz, [D$_6$]acetone): $\delta$ = 6.24 (br. m, 1 H, H$^m$ phenylene), 6.94 (ddd, $J_{5,4}$ = 7.6, $J_{5,6}$ = 5.6, $J_{5,3}$ = 1.3, 1 H, 5-H bipy), 7.22 (s, 2 H, B(OH)$_2$), 7.28 (br. m, 1 H, H$^o$ phenylene), 7.31 (ddd, $J_{6,5}$ = 5.6, $J_{6,4}$ = 1.5, $J_{6,3}$ = 0.7, 1 H, 6-H bipy), 7.40, 7.47 and 7.50 (3×ddd, $J_{5,4}$ = 7.6, $J_{5,6}$ = 5.6, $J_{5,3}$ = 1.3, 3×1 H, 3×5-H bipy), 7.55 (br. m, 1 H, H$^m$ phenylene), 7.60 (br. m, 1 H, H$^o$ phenylene), 7.68 (td, $J_{4,3}$ = 8.2, $J_{4,5}$ = 7.6, $J_{4,6}$ = 1.5, 1 H, 4-H bipy), 7.79 and 7.83 (2×ddd, $J_{6,5}$ = 5.6, $J_{6,4}$ = 1.5, $J_{6,3}$ = 0.7, 2×1 H, 2×6-H bipy), 7.84 (d, $J_{3,4}$ = 8.3, 1 H, 3-H), 7.85 (dd, $J_{8,9}$ = 8.3, $J_{8,7}$ = 5.3, 1 H, 8-H), 8.12, 8.14 and 8.23 (3×ddd, $J_{4,3}$ = 8.2, $J_{4,5}$ = 7.6, $J_{4,6}$ = 1.5, 3×1 H, 3×4-H bipy), 8.26 (dd, $J_{9,8}$ = 5.3, $J_{9,7}$ = 1.3, 1 H, 9-H), 8.28 (ddd, $J_{6,5}$ = 5.6, $J_{6,4}$ = 1.5, $J_{6,3}$ = 0.7, 1 H, 6-H bipy), 8.32 (ddd, $J_{3,4}$ = 8.2, $J_{3,5}$ = 1.3, $J_{3,6}$ = 0.7, 1 H, 3-H bipy), 8.45 (d, $J_{6,5}$ = 8.9, 1 H, 6-H), 8.50 (d, $J_{5,6}$ = 8.9, 1 H, 5-H), 8.67, 8.70 and 8.73 (3×dt, $J_{3,4}$ = 8.2, $J_{3,5}$ = 1.3, $J_{3,6}$ = 0.7, 3×1 H, 3×3-H bipy), 8.81 (dd, $J_{7,8}$ = 8.3, $J_{7,9}$ = 1.3, 1 H, 7-H), 8.92 (d, $J_{4,3}$ = 8.3, 1 H, 4-H) ppm. $^{13}$C NMR (100.6 MHz, [D$_6$]acetone): $\delta$ = 124.18, 125.16, 125.19 and 125.28 (C-3 bipy), 126.77 (C-8′), 126.96 (C$^m$ phenylene), 127.54 (C-5 bipy), 127.81 (C$^m$ phenylene), 127.97, 128.67, 128.95 and 128.97 (C-6 and C-5 bipy), 129.34 and 129.36 (C-3 and C-5), 131.27 (C-4a), 132.60 (C-6a), 134.86 (C$^o$ phenylene), 135.28 (C$^i$ phenylene), 136.90 (C-4 bipy), 137.89 (C-7), 138.53 (C-4), 138.91 and 139.11 (C-4 bipy), 141.28 (C$^p$ phenylene), 148.55 (C-10b), 149.03 (C-10a), 152.13, 152.89 and 152.94 (C-6 bipy), 153.46 (C-9′), 153.81 (C-6 bipy), 157.56, 158.11, 158.43 and 159.03 (C-2 bipy), 168.67 (C-2′) ppm. ESI MS: *m*/*z* (%) = 859 (65) [M$^+$ + PF$_6^-$], 357 (70) [M$^{2+}$ – 2PF$_6^-$]. IR (KBr): $\tilde{\nu}$ = 3435, 3082, 2924, 1242, 1202, 840, 558 cm$^{-1}$. $C_{38}H_{29}BF_{12}N_6O_2P_2Ru\cdot H_2O$ (1021.5): calcd. C 44.68, H 3.06, N 8.23; found C 44.65, H 2.90, N 8.32.

**Complex 6b:** The product was isolated as a red solid in 47% yield (Method B). M.p. 180–200 °C. $^1$H NMR (400 MHz, [D$_6$]acetone): $\delta$ = 6.15 (br. m, 1 H, H$^m$ phenylene), 6.78 (br. m, 1 H, H$^o$ phenylene), 6.97 (ddd, $J_{5,4}$ = 7.6, $J_{5,6}$ = 5.6, $J_{5,3}$ = 1.3, 1 H, 5-H bipy), 7.06 (br. m, 1 H, H$^o$ phenylene), 7.27 (ddd, $J_{6,5}$ = 5.6, $J_{6,4}$ = 1.5, $J_{6,3}$ = 0.7, 1 H, 6-H bipy), 7.41 (ddd, $J_{5,4}$ = 7.6, $J_{5,6}$ = 5.6, $J_{5,3}$ = 1.3, 1 H, 5-H bipy), 7.45 (br. m, 1 H, H$^m$ phenylene), 7.48 (dd, $J_{5,4}$ = 7.7, $J_{5,3}$ = 1.4, 1 H, 5-H), 7.50 (ddd, $J_{5',4'}$ = 7.6, $J_{5',6'}$ = 5.6, $J_{5',3'}$ = 1.3, 1 H, 5′-H), 7.61 (ddd, $J_{5,4}$ = 7.6, $J_{5,6}$ = 5.6, $J_{5,3}$ = 1.3, 1 H, 5-H bipy), 7.67 (ddd, $J_{6,5}$ = 5.6, $J_{6,4}$ = 1.5, $J_{6,3}$ = 0.7, 1 H, 6-H bipy), 7.70 (ddd, $J_{5,4}$ = 7.6, $J_{5,6}$ = 5.6, $J_{5,3}$ = 1.3, 1 H, 5-H bipy), 7.73 (ddd, $J_{4,3}$ = 8.2, $J_{4,5}$ = 7.6, $J_{4,6}$ = 1.5, 1 H, 4-H bipy), 7.89 (ddd, $J_{6',5'}$ = 5.6, $J_{6',4'}$ = 1.5, $J_{6',3'}$ = 0.7, 1 H, 6′-H), 8.07 (ddd, $J_{4,3}$ = 8.2, $J_{4,5}$ = 7.6, $J_{4,6}$ = 1.5, 1 H, 4-H bipy), 8.13 (ddd, $J_{6,5}$ = 5.6, $J_{6,4}$ = 1.5, $J_{6,3}$ = 0.7, 1 H, 6-H bipy), 8.21 (ddd, $J_{4,3}$ = 8.2, $J_{4,5}$ = 7.6, $J_{4,6}$ = 1.5, 1 H, 4-H bipy), 8.22 (ddd, $J_{4',3'}$ = 8.2, $J_{4',5'}$ = 7.6, $J_{4',6'}$ = 1.5, 1 H, 4′-H), 8.28 (ddd, $J_{4,3}$ = 8.2, $J_{4,5}$ = 7.6, $J_{4,6}$ = 1.5, 1 H, 4-H bipy), 8.31 (t, 1 H, $J_{4,3}$ = 8.2, $J_{4,5}$ = 7.7, 1 H, 4-H), 8.32 (ddd, $J_{3,4}$ = 8.2, $J_{3,5}$ = 1.3, $J_{3,6}$ = 0.7, 1 H, 3-H bipy), 8.37 (ddd, $J_{6,5}$ = 5.6, $J_{6,4}$ = 1.5, $J_{6,3}$ = 0.7, 1 H, 6-H bipy), 8.64, 8.71 and 8.73 (3×ddd, $J_{3,4}$ = 8.2, $J_{3,5}$ = 1.3, $J_{3,6}$ = 0.7, 3×1 H, 3×3-H bipy), 8.89 (ddd, $J_{3',4'}$ = 8.2, $J_{3',5'}$ = 1.3, $J_{3',6'}$ = 0.7, 1 H, 3′-H), 8.93 (dd, $J_{3,4}$ = 8.2, $J_{3,5}$ = 1.4, 1 H, 3-H) ppm. $^{13}$C NMR (100.6 MHz, [D$_6$]-acetone): $\delta$ = 124.27 (C-3 bipy), 124.48 (C-3), 125.18, 125.36 and 125.39 (C-3 bipy), 125.97 (C-3′), 127.57 and 128.08 (C-5 bipy), 128.18 (C$^m$ phenylene), 128.27 (C-5′), 128.80 (C$^m$ phenylene), 128.86 and 128.93 (C-5 bipy), 129.31 (C$^o$ phenylene), 130.59 (C-5′), 137.07 (C-4 bipy), 138.94, 138.97, 139.05 and 139.07 (C-4′ and C-4 bipy), 139.18 (C-4), 139.82 (C$^p$ phenylene), 151.90 (C-6 bipy), 152.58 (C-6′), 152.70 and 153.78 (C-6 bipy), 157.30, 158.16 and 158.26 (C-2 bipy), 158.61, 159.06 and 159.10 (C-2, C-2′ and C-2 bipy), 167.75 (C-6) ppm; C$^i$ phenylene signal not observed. ESI MS: *m*/*z* (%) = 834 (5) [M$^+$ + PF$_6^-$], 345 (15) [M$^{2+}$ – 2PF$_6^-$]. IR (KBr): $\tilde{\nu}$ = 3437, 3083, 2342, 1242, 1225, 842, 558 cm$^{-1}$. $C_{36}H_{29}BF_{12}N_6O_2P_2Ru$ (979.5): calcd. C 44.15, H 2.98, N 8.58; found C 44.11, H 3.16, N 8.29.

**Complex 6c:** The product was isolated as a red solid in 42% yield (Method B). M.p. 151–172 °C. $^1$H NMR (500 MHz, [D$_6$]acetone): $\delta$ = 7.35 (s, 1 H, B–OH), 7.44 (m, 2 H, H$^m$ phenylene), 7.55–7.65 (m, 5 H, 5″-H and 4×5-H bipy), 7.89 (m, 2 H, H$^o$ phenylene), 8.07, 8.08 and 8.10 (3×ddd, $J_{6,5}$ = 5.6, $J_{6,4}$ = 1.5, $J_{6,3}$ = 0.7, 3×1 H, 3×6-H bipy), 8.11 (dd, $J_{6,4}$ = 2.1, $J_{6,3}$ = 0.6, 1 H, 6′-H), 8.17 (ddd, $J_{6,5}$ = 5.6, $J_{6,4}$ = 1.5, $J_{6,3}$ = 0.7, 1 H, 6-H bipy), 8.18–8.28 (m, 6 H, 6″-H, 4″-H and 4×4-H bipy), 8.50 (dd, $J_{4',3'}$ = 8.6, $J_{4',6'}$ = 2.1, 1 H, 4′-H), 8.70, 8.83, 8.835 and 8.84 (4×dt, $J_{3,4}$ = 8.3, $J_{3,5}$ = 1.3, $J_{3,6}$ = 0.7, 4H 4×3-H bipy), 8.86 (dt, $J_{3,4}$ = 8.3, $J_{3,5}$ = 1.3, $J_{3,6}$ = 0.7, 4 H, 3″-H), 8.89 (dd, $J_{3',4'}$ = 8.6, $J_{3',6'}$ = 0.6, 1 H, 3′-H) ppm. $^{13}$C NMR (125.8 MHz, [D$_6$]acetone): $\delta$ = 125.24, 125.31, 125.36 and 125.45 (C-3′, C-3″ and C-3 bipy), 126.88 (C$^m$ phenylene), 128.64, 128.68, 128.72 and 128.81 (C-5″ and C-5 bipy), 135.91 (C$^o$ phenylene), 136.65 (C-4′), 137.14 (C$^p$ phenylene), 138.88 and 138.92 (C-4″ and C-4 bipy), 140.77 (C-5′), 149.90 (C-6′), 152.64, 152.68, 153.02 and 153.07 (C-6″ and C-6 bipy), 156.79 (C-2′), 157.91, 158.03, 158.09, 158.15 and 158.27 (C-2″ and C-2 bipy) ppm; C$^i$ phenylene signal not observed. ESI MS: *m*/*z* (%) = 835 (100) [M$^+$ + PF$_6^-$], 345 (30) [M$^{2+}$ – 2PF$_6^-$]. IR (KBr): $\tilde{\nu}$ = 3435, 3083, 2981, 1244, 1222, 840, 558 cm$^{-1}$. $C_{36}H_{29}BF_{12}N_6O_2P_2Ru$ (979.5): calcd. C 44.15, H 2.98, N 8.58; found C 44.58, H 3.51, N 8.13.

**Complex 6d:** The product was isolated as a red solid in 69% yield (Method B). M.p. >310 °C. $^1$H NMR (500 MHz, [D$_6$]acetone): $\delta$ = 7.33 and 7.34 (2×ddd, $J_{5',4'}$ = 7.5, $J_{5',6'}$ = 5.5, $J_{5',3'}$ = 1.3, 2×2 H, 5′-H terpy and 5′-H Ph-terpy), 7.52 (br. s, 1 H, B–OH), 7.72 (ddd, $J_{6',5'}$ = 5.5, $J_{6',4'}$ = 1.5, $J_{6',3'}$ = 0.7, 2 H, 6′-H Ph-terpy), 7.81 (ddd, $J_{6',5'}$ = 5.5, $J_{6',4'}$ = 1.5, $J_{6',3'}$ = 0.7, 2 H, 6′-H terpy), 8.08 and 8.09 (2×ddd, $J_{4',3'}$ = 8.2, $J_{4',5'}$ = 7.5, $J_{4',6'}$ = 1.5, 2×2 H, 4′-H terpy and 4′-H Ph-terpy), 8.22 (m, 2 H, H$^o$ phenylene), 8.33 (m, 2 H, H$^m$ phenylene), 8.58 (t, $J_{4,3\&5}$ = 8.2, 1 H, 4-H terpy), 8.82 (ddd, $J_{3',4'}$ = 8.2, $J_{3',5'}$ = 1.3, $J_{3',6'}$ = 0.7, 2 H, 6′-H terpy), 9.07 (ddd, $J_{3',4'}$ = 8.2, $J_{3',5'}$ = 1.3, $J_{3',6'}$ = 0.7, 2 H, 6′-H Ph-terpy), 9.08 (d, $J_{3\&5,4}$ = 8.2, 2 H, 3,5-H terpy), 9.45 (s, 2 H, 3,5-H Ph-terpy) ppm. $^{13}$C NMR (125.8 MHz, [D$_6$]acetone): $\delta$ = 122.30 (C-3,5 Ph-terpy), 124.78 (C-3,5 terpy), 125.41 (C-3′ terpy), 125.65 (C-3′ Ph-terpy), 127.57 (C$^m$ phenylene), 128.60 (C-5′ Ph-terpy and C-5′ terpy), 136.08 (C$^o$ phenylene), 138.97 (C$^p$ phenylene), 139.05 and 139.12 (C-4′ Ph-terpy and C-4′ terpy), 149.13 (C-4 Ph-terpy), 153.41 and 153.48 (C-6′ Ph-terpy and C-6′ terpy), 156.41 (C-2,6 terpy), 156.65 (C-2,6 Ph-terpy), 159.20 (C-2′ terpy), 159.36 (C-2′ Ph-terpy) ppm; C$^i$ phenylene signal not observed. ESI MS: *m*/*z* (%) = 833 (50) [M$^+$ + PF$_6^-$], 344 (40) [M$^{2+}$ – 2PF$_6^-$], 687 (75) [M$^+$ – 2PF$_6^-$]. IR (KBr): $\tilde{\nu}$ = 3435, 3083, 2981, 1244, 1222, 840, 558 cm$^{-1}$.

 © 2007 Wiley-VCH Verlag GmbH & Co. KGaA, Weinheim 

$C_{36}H_{27}BF_{12}N_6O_2P_2Ru·H_2O$ (995.5): calcd. C 43.44, H 2.94, N 8.60; found C 43.63, H 2.95, N 8.23.

**Complex 10a:** The product was isolated as an orange solid in 69% yield (Method B). M.p. 261–264 °C. $^1$H NMR (500 MHz, [D$_6$]acetone): $\delta$ = 5.28 and 5.42 (2 × d, $J_{gem}$ = 15.5, 2 H, $CH_2$Ph), 6.91 (br. s, 1 H, NH), 6.99 (ddd, $J_{5,4}$ = 7.6, $J_{5,6}$ = 5.6, $J_{5,3}$ = 1.4, 1 H, 5-H bipy), 7.23 (m, 2 H, H$^o$ Ph), 7.25–7.32 (m, 3 H, H$^{m,p}$ Ph), 7.37 and 7.51 (2 × ddd, $J_{5,4}$ = 7.6, $J_{5,6}$ = 5.6, $J_{5,3}$ = 1.4, 2 × 1 H, 2 × 5-H bipy), 7.52 (ddd, $J_{4,3}$ = 8.3, $J_{4,5}$ = 7.6, $J_{4,6}$ = 1.5, 1 H, 4-H bipy), 7.56 (ddd, $J_{5,4}$ = 7.6, $J_{5,6}$ = 5.6, $J_{5,3}$ = 1.4, 1 H, 5-H bipy), 7.71 and 7.86 (2 × ddd, $J_{6,5}$ = 5.6, $J_{6,4}$ = 1.5, $J_{6,3}$ = 0.7, 2 × 1 H, 2 × 6-H bipy), 7.91 (dd, $J_{8',9'}$ = 8.2, $J_{8',7'}$ = 5.3, 1 H, 8′-H), 7.97 (ddd, $J_{6,5}$ = 5.6, $J_{6,4}$ = 1.5, $J_{6,3}$ = 0.7, 1 H, 6-H bipy), 8.17 (d, $J_{3',4'}$ = 8.4, 1 H, 3′-H), 8.18–8.24 (m, 4 H, 6-H bipy and 3 × 4-H bipy), 8.29 (s, 1 H, H-2), 8.33 (dd, $J_{9',8'}$ = 5.3, $J_{9',7'}$ = 1.3, 1 H, 9′-H), 8.44 (d, $J_{5',6'}$ = 8.9, 1 H, 5′-H), 8.47 (d, $J_{6',5'}$ = 8.9, 1 H, 6′-H), 8.56 (ddd, $J_{3,4}$ = 8.3, $J_{3,5}$ = 1.4, $J_{3,6}$ = 0.7, 1 H, 3-H bipy), 8.78–8.84 (m, 4 H, 7′-H and 3 × 3-H bipy), 8.91 (d, $J_{4',3'}$ = 8.4, 1 H, 4′-H) ppm. $^{13}$C NMR (125.8 MHz, [D$_6$]acetone): $\delta$ = 47.33 ($CH_2$Ph), 89.14 (C≡*C* pur), 90.68 (*C*≡C pur), 120.07 (C-5), 125.23, 125.44, 125.49 and 125.51 (C-3 bipy), 127.33 (C-8′), 128.26 and 128.57 (C-5 bipy), 128.61 (C$^o$ Ph), 128.81 (C-5 bipy), 128.97 (C$^p$ Ph), 129.10 and 129.13 (C-5′ and C-5 bipy), 129.65 (C$^m$ Ph), 130.02 (C-6′), 131.60 (C-4a′), 132.12 (C-8), 132.77 (C-6a′), 133.60 (C-3′), 137.29 (C$^i$ Ph), 137.67 (C-4 bipy), 138.07 (C-7′), 138.39 (C-4′), 139.07, 139.15 and 139.41 (C-4 bipy), 147.60 (C-2′), 148.65 (C-10a′), 149.59 (C-10b′), 150.77 (C-4), 152.30, 152.45 and 152.73 (C-6 bipy), 153.67 (C-3′), 153.77 (C-9′), 155.79 (C-2), 157.29 (C-6), 157.82, 158.01, 158.19 and 158.76 (C-2 bipy) ppm. ESI MS: *m*/*z* (%) = 840 (50) [M$^+$ – 2PF$_6^-$], 420 (100) [M$^{2+}$ – 2PF$_6^-$]. IR (KBr): $\tilde{\nu}$ = 2220, 1637, 840, 558 cm$^{-1}$. UV/Vis (MeOH): $\lambda_{max}$ ($\varepsilon$) = 439 (14454), 373 (19412), 285 (81332) nm. $C_{46}H_{33}F_{12}N_{11}P_2Ru·H_2O$ (1148.9): calcd. C 48.09, H 3.07, N 13.41; found C 48.40, H 3.29, N 13.09.

**Complex 10b:** The product was isolated as an orange solid in 80% yield (Method B). M.p. 295–301 °C. $^1$H NMR (500 MHz, [D$_6$]acetone): $\delta$ = 5.22 and 5.34 (2 × d, $J_{gem}$ = 15.5, $CH_2$Ph), 6.87 (br. s, 1 H, NH), 6.91 (ddd, $J_{5,4}$ = 7.6, $J_{5,6}$ = 5.6, $J_{5,3}$ = 1.3, 1 H, 5-H bipy), 7.20 (m, 2 H, H$^o$ Ph), 7.27–7.31 (m, 3 H, H$^{m,p}$ Ph), 7.47 (ddd, $J_{4,3}$ = 8.5, $J_{4,5}$ = 7.6, $J_{4,6}$ = 1.5, 1 H, 4-H bipy), 7.50 (ddd, $J_{5,4}$ = 7.6, $J_{5,6}$ = 5.6, $J_{5,3}$ = 1.3, 1 H, 5-H bipy), 7.56 (ddd, $J_{5'',4''}$ = 7.6, $J_{5'',6''}$ = 5.6, $J_{5'',3''}$ = 1.3, 1 H, 5″-H), 7.58 and 7.69 (2 × ddd, $J_{5,4}$ = 7.6, $J_{5,6}$ = 5.6, $J_{5,3}$ = 1.3, 2 × 1 H, 5-H bipy), 7.78 and 7.88 (2 × ddd, $J_{6,5}$ = 5.6, $J_{6,4}$ = 1.5, $J_{6,3}$ = 0.7, 2 × 1 H, 6-H bipy), 7.92 (dd, $J_{5',4'}$ = 7.8, $J_{5',3'}$ = 1.4, 1 H, 5′-H), 7.94 (ddd, $J_{6'',5''}$ = 5.6, $J_{6'',4''}$ = 1.5, $J_{6'',3''}$ = 0.7, 1 H, 6″-H), 7.97 (ddd, $J_{6,5}$ = 5.6, $J_{6,4}$ = 1.5, $J_{6,3}$ = 0.7, 1 H, 6-H bipy), 8.17 (ddd, $J_{4,3}$ = 8.5, $J_{4,5}$ = 7.6, $J_{4,6}$ = 1.5, 1 H, 4-H bipy), 8.23 (ddd, $J_{4'',3''}$ = 8.5, $J_{4'',5''}$ = 7.6, $J_{4'',6''}$ = 1.5, 1 H, 4″-H), 8.26 (ddd, $J_{4,3}$ = 8.5, $J_{4,5}$ = 7.6, $J_{4,6}$ = 1.5, 1 H, 4-H bipy), 8.27 (s, 1 H, H-2), 8.28 (ddd, $J_{4,3}$ = 8.5, $J_{4,5}$ = 7.6, $J_{4,6}$ = 1.5, 1 H, 4-H bipy), 8.32 (t, $J_{4',3'}$ = 8.3, $J_{4',5'}$ = 7.8, 1 H, 4′-H), 8.40 (ddd, $J_{6,5}$ = 5.6, $J_{6,4}$ = 1.5, $J_{6,3}$ = 0.7, 1 H, 6-H bipy), 8.49, 8.77 and 8.83 (3 × ddd, $J_{3,4}$ = 8.5, $J_{3,5}$ = 1.3, $J_{3,6}$ = 0.7, 3 × 1 H, 3 × 3-H bipy), 8.87 (ddd, $J_{3'',4''}$ = 8.5, $J_{3'',5''}$ = 1.3, $J_{3'',6''}$ = 0.7, 1 H, 3″-H), 8.92 (dd, $J_{3',4'}$ = 8.3, $J_{3',5'}$ = 1.4, 1 H, 3′-H) ppm. $^{13}$C NMR (125.8 MHz, [D$_6$]acetone): $\delta$ = 47.27 ($CH_2$Ph), 87.58 (C≡*C* pur), 90.40 (*C*≡C pur), 118.92 (C-5), 125.31, 125.37, 125.44, 125.57 and 126.19 (C-3′, C-3″ and C-3 bipy), 128.42 and 128.44 (C-5 bipy), 128.59 (C$^o$ Ph), 128.75 (C-5 bipy), 128.94 (C$^p$ Ph and C-5 bipy), 129.06 (C-5″), 129.63 (C$^m$ Ph), 132.23 (C-8), 135.78 (C-5′), 137.26 (C$^i$ Ph), 137.39, 139.03, 139.14, 139.22, 139.25 and 139.37 (C-4′, C-4″ and C-4 bipy), 147.41 (C-6′), 150.72 (C-4), 152.21, 152.23, 152.44, 152.67 and 153.76 (C-6″ and C-6 bipy), 155.70 (C-2), 157.27 (C-6), 157.97, 158.01 and 158.79 (C-2″ and C-2 bipy), 159.72 (C-2′) ppm. ESI MS: *m*/*z* (%) = 816 (15) [M$^+$ – 2PF$_6^-$], 408 (100) [M$^{2+}$ – 2PF$_6^-$]. IR (KBr): $\tilde{\nu}$ = 2218, 1639, 841, 558 cm$^{-1}$. UV/Vis (MeOH): $\lambda_{max}$ ($\varepsilon$) = 442 (17095), 355 sh (26410), 287 (88079) nm. $C_{44}H_{33}F_{12}N_{11}P_2Ru·H_2O$ (1124.8): calcd. C 46.98, H 3.14, N 13.7; found C 46.83, H 3.03, N 13.56.

**Complex 10c:** The product was isolated as an orange solid in 75% yield (Method B). M.p. 284–291 °C. $^1$H NMR (500 MHz, [D$_6$]acetone): $\delta$ = 5.45 (s, 2 H, $CH_2$Ph), 6.88 (br. s, 2 H, $NH_2$), 7.26–7.34 (m, 5 H, H-*o,m,p*-Ph), 7.54–7.63 (m, H-5″, 5 H, 4 × 5-H bipy), 8.00, 8.04 and 8.07 (3 × ddd, $J_{6,5}$ = 5.6, $J_{6,4}$ = 1.4, $J_{6,3}$ = 0.6, 1 H, 3 × 6-H bipy), 8.09 (ddd, $J_{6'',5''}$ = 5.6, $J_{6'',4''}$ = 1.4, $J_{6'',3''}$ = 0.6, 1 H, 6″-H), 8.14–8.25 (m, 6 H, 4″-H, 4 × 4-H bipy and 6-H bipy), 8.25 (s, 1 H, H-2), 8.29 (dd, $J_{6',4'}$ = 1.9, $J_{6',3'}$ = 0.7, 1 H, 6′-H), 8.39 (dd, $J_{4',3'}$ = 8.5, $J_{4',6'}$ = 1.9, 1 H, 4′-H), 8.78, 8.81, 8.82 and 8.86 (4 × dt, $J_{3,4}$ = 8.3, $J_{3,5}$ = 1.5, $J_{3,6}$ = 0.6, 5 H, 3″-H and 4 × 3-H bipy), 8.90 (dd, $J_{3',4'}$ = 8.5, $J_{3',6'}$ = 0.7, 1 H, 3′-H) ppm. $^{13}$C NMR (100.6 MHz, [D$_6$]acetone): $\delta$ = 47.21 ($CH_2$Ph), 86.09 (C≡*C* pur), 89.84 (*C*≡C pur), 120.62 (C-5), 122.55 (C-5′), 125.00 (C-3′), 125.33, 125.46 and 126.18 (C-3″ and C-3 bipy), 128.50 (C$^o$ Ph), 128.2, 128.75, 128.82, 128.84 and 129.18 (C$^p$ Ph, C-5″ and C-5 bipy), 129.63 (C$^m$ Ph), 133.26 (C-8), 137.50 (C$^i$ Ph), 138.98, 139.03 and 139.10 (C-4″ and C-4 bipy), 141.03 (C-4′), 150.89 (C-4), 152.54, 152.77, 152.84, 152.88 and 153.09 (C-6″ and C-6 bipy), 154.66 (C-6′), 155.50 (C-2), 157.10 (C-6), 157.37 (C-2′), 157.99, 158.04, 158.12, 158.04 and 158.30 (C-2″ and C-2 bipy) ppm. ESI MS: *m*/*z* (%) = 816 (5) [M$^+$ – 2PF$_6^-$], 408 (100) [M$^{2+}$ – 2PF$_6^-$]. IR (KBr): $\tilde{\nu}$ = 2221, 1635, 840, 558 cm$^{-1}$. UV/Vis (MeOH): $\lambda_{max}$ ($\varepsilon$) = 442 sh (18007), 365 (34598), 286 (85546) nm. $C_{44}H_{33}F_{12}N_{11}P_2Ru·H_2O$ (1124.8): calcd. C 46.98, H 3.14, N 13.7; found C 46.26, H 3.08, N 13.35.

**General Procedure for Cross-Coupling of Complexes 6a–6d with 7 - Method C**

9-Benzyl-8-bromoadenine (20 mg, 0.065 mmol), the corresponding complex (**6a**–**6d**) (0.072 mmol, 1.1 equiv.), and $Cs_2CO_3$ (64 mg, 0.195 mmol, 3 equiv.) were combined and a mixture of degassed $CH_3CN/H_2O$ (1:1, 1 mL) was added. To this mixture was added a solution of Pd(OAc)$_2$ (0.0065 mmol, 10 mol-%) and water soluble P(Ph-*m*$SO_3Na$)$_3$ (0.0325 mmol, 5 equiv. to Pd, 50 mol-%) in $CH_3CN/H_2O$ (1:1, 0.5 mL). The whole mixture was degassed and the flask filled with argon. The mixture was stirred under argon at 95 °C for 7 h. The solvent was than evaporated and the products were purified by silica gel column chromatography using a mixture of $CH_3CN/H_2O$/saturated $KNO_3$ (10:1:0.1) as eluent. The crystallization from acetonitrile or acetone/*i*PrOH, diethylether gave the desired products **11a**–**11d**.

**Complex 11a:** The product was isolated as an orange solid in 72% yield (Method B) and in 40% yield (Method C). M.p. 210–215 °C. $^1$H NMR (500 MHz, [D$_6$]acetone): $\delta$ = 5.57 and 5.62 (2 × d, $J_{gem}$ = 16.7, 2 H, $CH_2$Ph), 6.38 (br. m, 1 H, H$^m$ phenylene), 6.98 (ddd, $J_{5,4}$ = 7.7, $J_{5,6}$ = 5.6, $J_{5,3}$ = 1.3, 1 H, 5-H bipy), 7.10 (m, 2 H, H$^o$ Ph), 7.22 (br. m, 1 H, H$^o$ phenylene), 7.29–7.37 (m, 3 H, H$^{m,p}$ Ph), 7.37 (ddd, $J_{6,5}$ = 5.6, $J_{6,4}$ = 1.4, $J_{6,3}$ = 0.7, 1 H, 6-H bipy), 7.41, 7.46 and 7.47 (3 × ddd, $J_{5,4}$ = 7.7, $J_{5,6}$ = 5.6, $J_{5,3}$ = 1.3, 3 × 1 H, 3 × 5-H bipy), 7.51 (br. m, 1 H, H$^o$ phenylene), 7.72 (br. m, 1 H, H$^m$ phenylene), 7.75 (td, $J_{4,3}$ = 8.1, $J_{4,5}$ = 7.7, $J_{4,6}$ = 1.5, 1 H, 4-H bipy), 7.77 (ddd, $J_{6,5}$ = 5.6, $J_{6,4}$ = 1.4, $J_{6,3}$ = 0.7, 1 H, 6-H bipy), 7.85 (dd, $J_{8',9'}$ = 8.2, $J_{8',7'}$ = 5.3, 1 H, 8′-H), 7.88 (d, $J_{3',4'}$ = 8.3, 1 H, 3′-H), 7.89 (ddd, $J_{6,5}$ = 5.6, $J_{6,4}$ = 1.4, $J_{6,3}$ = 0.7, 1 H, 6-H bipy), 8.11, 8.13 and 8.20 (3 × ddd, $J_{4,3}$ = 8.1, $J_{4,5}$ = 7.7, $J_{4,6}$ = 1.5, 3 × 1 H, 3 × 4-H bipy), 8.20 (ddd, $J_{6,5}$ = 5.6, $J_{6,4}$ = 1.4, $J_{6,3}$ = 0.7, 1 H, 6-H bipy), 8.25 (dt, $J_{3,4}$ = 8.1, $J_{3,5}$ = 1.3, $J_{3,6}$ = 0.7, 1 H, 3-H bipy), 8.27 (dd, $J_{9',8'}$ = 5.3, $J_{9',7'}$ = 1.3, 1 H, 9′-H), 8.37 (s, 1 H, H-2), 8.46 (d, $J_{6',5'}$ = 8.9, 1 H, 6′-H), 8.51 (d, $J_{5',6'}$ = 8.9, 1 H, 5′-H),

 © 2007 Wiley-VCH Verlag GmbH & Co. KGaA, Weinheim 

8.59, 8.66 and 8.69 (3×dt, $J_{3,4}$ = 8.1, $J_{3,5}$ = 1.3, $J_{3,6}$ = 0.7, 3×1 H, 3×3-H bipy), 8.82 (dd, $J_{7',8'}$ = 8.2, $J_{7',9'}$ = 1.3, 1 H, 7′-H), 8.95 (d, $J_{4',3'}$ = 8.3, 1 H, 4′-H) ppm. $^{13}$C NMR (125.8 MHz, [D$_6$]acetone): δ = 47.61 ($CH_2$Ph), 117.89 (C-5), 124.45, 125.16, 125.18 and 125.25 (C-3 bipy), 126.85 (C-8′), 127.29 (C$^o$ Ph), 127.86, 128.04, 128.52, 128.62, 128.74, 128.99, 129.11, 129.30, 129.39, 129.47 and 129.56 (C-3′, C-5′, C-6′, C-5-bipy, C$^{o,m}$ phenylene and C$^p$ Ph), 129.74 (C$^m$ Ph), 131.10 (C$^i$ phenylene), 131.36 (C-4a′), 132.60 (C-6a′), 137.64 (C$^i$ Ph), 137.80 (C-7′), 137.93 (C-4 bipy), 138.69 (C-4′), 138.92 and 139.15 (C-4 bipy), 141.15 (C$^p$ phenylene), 148.75 (C-10b′), 148.95 (C-10a′), 151.04 (C-8), 151.34 (C-2), 152.10 (C-6 bipy), 152.62 (C-4), 152.64 and 153.15 (C-6 bipy), 153.46 (C-9′), 153.67 (C-6 bipy), 155.17 (C-6), 157.40, 158.01, 158.38 and 158.79 (C-2 bipy), 167.55 (C-2′) ppm. ESI MS: *m*/*z* (%) = 892 (25) [M$^+$ – 2PF$_6^-$], 447 (100) [M$^{2+}$ – 2PF$_6^-$]. IR (KBr): ṽ = 1636, 840, 558 cm$^{-1}$. UV/Vis (MeOH): $\lambda_{max}$ (ε) = 446 (15810), 287 (72639), 268 sh (63625) nm. $C_{50}H_{37}F_{12}N_{11}P_2Ru{\cdot}2H_2O$ (1218.9): calcd. C 49.27, H 3.39, N 12.64; found C 49.34, H 3.06, N 12.52.

**Complex 11b:** The product was isolated as an orange solid in 74% yield (Method B) and in 24% yield (Method C). M.p. 208–210 °C. $^1$H NMR (500 MHz, [D$_6$]acetone): δ = 5.52 and 5.54 (2×d, $J_{gem}$ = 16.8, 2 H, $CH_2$Ph), 6.25 (br. m, 1 H, H$^m$ phenylene), 6.95 (ddd, $J_{5,4}$ = 7.7, $J_{5,6}$ = 5.6, $J_{5,3}$ = 1.3, 1 H, 5-H bipy), 7.07 (m, 2 H, H$^o$ Ph), 7.13 (br. m, 2 H, H$^o$ phenylene), 7.27–7.36 (m, 4 H, 6-H bipy and H$^{m,p}$ Ph), 7.41 (ddd, $J_{5,4}$ = 7.7, $J_{5,6}$ = 5.6, $J_{5,3}$ = 1.3, 1 H, 5-H bipy), 7.42 (br. m, 1 H, H$^m$ phenylene), 7.51 (ddd, $J_{5'',4''}$ = 7.7, $J_{5'',6''}$ = 5.6, $J_{5'',3''}$ = 1.3, 1 H, 5″-H), 7.92 (dd, $J_{5',4'}$ = 7.7, $J_{5',3'}$ = 1.3, 1 H, 5′-H), 7.61 (ddd, $J_{5,4}$ = 7.7, $J_{5,6}$ = 5.6, $J_{5,3}$ = 1.3, 1 H, 5-H bipy), 7.65 (ddd, $J_{6,5}$ = 5.6, $J_{6,4}$ = 1.5, $J_{6,3}$ = 0.7, 1 H, 6-H bipy), 7.68 (ddd, $J_{5,4}$ = 7.7, $J_{5,6}$ = 5.6, $J_{5,3}$ = 1.3, 1 H, 5-H bipy), 7.73 (ddd, $J_{4,3}$ = 8.2, $J_{4,5}$ = 7.7, $J_{4,6}$ = 1.5, 1 H, 4-H bipy), 7.91 (ddd, $J_{6'',5''}$ = 5.6, $J_{6'',4''}$ = 1.5, $J_{6'',3''}$ = 0.7, 1 H, 6″-H), 8.07 (ddd, $J_{4,3}$ = 8.2, $J_{4,5}$ = 7.7, $J_{4,6}$ = 1.5, 1 H, 4-H bipy), 8.17 (ddd, $J_{6,5}$ = 5.6, $J_{6,4}$ = 1.5, $J_{6,3}$ = 0.7, 1 H, 6-H bipy), 8.19–8.28 (m, 4 H, 4″-H, 3-H bipy, 2×4-H bipy and 6-H bipy), 8.31 (s, 1 H, H-2), 8.34 (t, $J_{4',3'}$ = 8.2, $J_{4',5'}$ = 7.7, 1 H, 4′-H), 8.58, 8.62 and 8.70 (3×ddd, $J_{3,4}$ = 8.2, $J_{3,5}$ = 1.3, $J_{3,6}$ = 0.7, 3×1 H, 3×3-H bipy), 8.88 (ddd, $J_{3'',4''}$ = 8.2, $J_{3'',5''}$ = 1.3, $J_{3'',6''}$ = 0.7, 1 H, 3″-H), 8.93 (dd, $J_{3',4'}$ = 8.2, $J_{3',5'}$ = 1.3, 1 H, 3′-H) ppm. $^{13}$C NMR (100.6 MHz, [D$_6$]acetone): δ = 47.45 ($CH_2$Ph), 120.18 (C-5), 124.49 (C-3 bipy), 124.61 (C-3′), 125.13, 125.29 and 125.36 (C-3 bipy), 125.94 (C-3″), 127.24 (C$^o$ Ph), 127.73 and 128.12 (C-5 bipy), 128.34 (C-5″), 128.44 (C$^m$ phenylene), 128.54 (C$^p$ Ph), 128.93 and 128.97 (C-5 bipy), 129.37 (C$^m$ phenylene), 129.49 (C$^o$ phenylene), 129.70 (C$^m$ Ph), 130.41 (C-5′), 131.12 (C$^i$ phenylene), 137.67 (C-4 bipy), 137.85 (C$^i$ Ph), 138.95, 138.98, 139.06 and 139.08 (C-4″ and C-4 bipy), 139.35 (C-4′), 140.96 (C$^p$ phenylene), 150.52 (C-8), 151.83 (C-6 bipy), 152.41 (C-2), 152.57 (C-6″), 152.76 (C-4), 152.90 and 153.62 (C-6 bipy), 155.98 (C-6), 157.11, 158.07 and 158.21 (C-2 bipy), 158.88 and 158.92 (C-2′, C-2″ and C-2 bipy), 166.81 (C-6′) ppm. ESI MS: *m*/*z* (%) = 868 (5) [M$^+$ – 2PF$_6^-$], 434 (65) [M$^{2+}$ – 2PF$_6^-$]. IR (KBr): ṽ = 1634, 841, 558 cm$^{-1}$. UV/Vis (MeOH): $\lambda_{max}$ (ε) = 448 (10816), 289 (63986) nm. $C_{48}H_{37}F_{12}N_{11}P_2Ru{\cdot}3H_2O$ (1212.9): calcd. C 47.53, H 3.57, N 12.7; found C 47.62, H 3.09, N 12.58.

**Complex 11c:** The product was isolated as an orange solid in 81% yield (Method B) and in 53% yield (Method C). M.p. 280–283 °C. $^1$H NMR (500 MHz, [D$_6$]acetone): δ = 5.58 (s, 2 H, $CH_2$Ph), 6.76 (br. s, 2 H, $NH_2$), 7.06 (m, 2 H, H$^o$ Ph), 7.23–7.30 (m, 3 H, H$^{m,p}$ Ph), 7.54–7.65 (m, 7 H, 5″-H, 4×5-H bipy and H$^m$ phenylene), 7.79 (m, 2 H, H$^o$ phenylene), 8.05 (ddd, $J_{6,5}$ = 5.6, $J_{6,4}$ = 1.5, $J_{6,3}$ = 0.7, 1 H, 6-H bipy), 8.08 (ddd, $J_{6'',5''}$ = 5.6, $J_{6'',4''}$ = 1.5, $J_{6'',3''}$ = 0.7, 1 H, 6″-H), 8.10 (ddd, $J_{6,5}$ = 5.6, $J_{6,4}$ = 1.5, $J_{6,3}$ = 0.7, 1 H, 6-H bipy), 8.16–8.24 (m, 7 H, 6′-H, 4″-H, 3×4-H bipy and 2×6-H bipy), 8.24 (s, 1 H, H-2), 8.26 (td, $J_{4,3}$ = 8.3, $J_{4,5}$ = 7.6, $J_{4,6}$ = 1.5, 1 H, 4-H bipy), 8.54 (dd, $J_{4',3'}$ = 8.6, $J_{4',6'}$ = 2.1, 1 H, 4′-H), 8.79, 8.82, 8.83 and 8.88 (4×dt, $J_{3,4}$ = 8.3, $J_{3,5}$ = 1.5, $J_{3,6}$ = 0.7, 5 H, 3″-H and 4×3-H bipy), 8.91 (dd, $J_{3',4'}$ = 8.6, $J_{3',6'}$ = 0.6, 1 H, 3′-H) ppm. $^{13}$C NMR (100.6 MHz, [D$_6$]acetone): δ = 47.35 ($CH_2$Ph), 120.09 (C-5), 125.24, 125.31, 125.34, 125.45 and 125.48 (C-3′, C-3″ and C-3 bipy), 127.32 (C$^o$ Ph), 128.16 (C$^m$ phenylene), 128.42 (C$^p$ Ph), 128.69, 128.72 and 128.81 (C-5″ and C-5 bipy), 129.58 (C$^m$ Ph), 130.55 (C$^o$ phenylene), 132.21 (C$^i$ phenylene), 136.75 (C-4′), 136.88 (C$^p$ phenylene), 137.99 (C$^i$ Ph), 138.94 (C-4″ and C-4 bipy), 139.81 (C-5′), 150.02 (C-6′), 150.37 (C-8), 152.62 and 152.66 (C-6 bipy), 153.00 (C-4), 153.03 and 153.08 (C-6″ and C-6 bipy), 153.80 (C-2), 156.73 (C-6), 157.12 (C-2′), 157.82, 158.00, 158.10, 158.14 and 158.26 (C-2″ and C-2 bipy) ppm. ESI MS: *m*/*z* (%) = 1014 (70) [M$^+$ – PF$_6^-$], 434 (100) [M$^{2+}$ – 2PF$_6^-$]. IR (KBr): ṽ = 1635, 840, 558 cm$^{-1}$. UV/Vis (MeOH): $\lambda_{max}$ (ε) = 451 (13145), 320 sh (34814), 286 (77563) nm. $C_{48}H_{37}F_{12}N_{11}P_2Ru{\cdot}2H_2O$ (1194.9): calcd. C 48.25, H 3.46, N 12.89; found C 48.10, H 3.24, N 12.84.

**Complex 11d:** The product was isolated as an orange solid in 65% yield (Method B) and in 63% yield (Method C). M.p. >320 °C. $^1$H NMR (500 MHz, [D$_6$]acetone): δ = 5.74 (s, 2 H, $CH_2$Ph), 6.82 (br. s, 2 H, $NH_2$), 7.19 (m, 2 H, H$^o$ Ph), 7.29–7.39 (m, 7 H, 5′-H terpy, 5′-H Ph-terpy, H$^{m,p}$ Ph), 7.73 (ddd, $J_{6',5'}$ = 5.6, $J_{6',4'}$ = 1.5, $J_{6',3'}$ = 0.6, 2 H, 6′-H Ph-terpy), 7.81 (ddd, $J_{6',5'}$ = 5.6, $J_{6',4'}$ = 1.5, $J_{6',3'}$ = 0.6, 2 H, 6′-H terpy), 8.08 (ddd, $J_{4',3'}$ = 8.2, $J_{4',5'}$ = 7.5, $J_{4',6'}$ = 1.5, 2 H, 4′-H Ph-terpy), 8.09 (ddd, $J_{4',3'}$ = 8.2, $J_{4',5'}$ = 7.5, $J_{4',6'}$ = 1.5, 2 H, 4′-H terpy), 8.10 (m, 2 H, H$^o$ phenylene), 8.48 (m, 2 H, H$^m$ phenylene), 8.59 (t, $J_{4,3\&5}$ = 8.2, 1 H, 4-H terpy), 8.82 (ddd, $J_{3',4'}$ = 8.2, $J_{3',5'}$ = 1.3, $J_{3',6'}$ = 0.6, 2 H, 6′-H terpy), 9.06 (ddd, $J_{3',4'}$ = 8.2, $J_{3',5'}$ = 1.3, $J_{3',6'}$ = 0.6, 2 H, 6′-H Ph-terpy), 9.09 (d, $J_{3\&5,4}$ = 8.2, 2 H, 3,5-H terpy), 9.49 (s, 2 H, 3,5-H Ph-terpy) ppm. $^{13}$C NMR (125.8 MHz, [D$_6$]acetone): δ = 47.48 ($CH_2$Ph), 120.24 (C-5), 122.26 (C-3,5 Ph-terpy), 124.81 (C-3,5 terpy), 125.43 (C-3′ terpy), 125.71 (C-3′-Ph_terpy), 127.41 (C$^o$ Ph), 128.50 (C$^p$ Ph), 128.62 and 128.67 (C-5′ Ph-terpy and C-5′ terpy), 128.80 (C$^m$ phenylene), 129.69 (C$^m$ Ph), 133.02 (C$^i$ Ph), 137.08 (C$^o$ phenylene), 138.16 (C$^i$ Ph), 138.60 (C$^p$ phenylene), 139.07 and 139.16 (C-4′ Ph-terpy and C-4′ terpy), 147.88 (C-4 Ph-terpy), 150.44 (C-8), 153.15 (C-4), 153.45 and 153.48 (C-6′ Ph-terpy and C-6′ terpy), 154.14 (C-2), 156.38 (C-2,6 terpy), 156.77 (C-2,6 Ph-terpy), 157.02 (C-6), 159.18 and 159.29 (C-2′ terpy and C-2′ Ph-terpy) ppm. ESI MS: *m*/*z* (%) = 866 (15) [M$^+$ – PF$_6^-$], 433 (100) [M$^{2+}$ – 2PF$_6^-$]. IR (KBr): ṽ = 1633, 842, 558 cm$^{-1}$. UV/Vis (MeOH): $\lambda_{max}$ (ε) = 490 (32975), 333 sh (60225), 311 (71050), 283 (60350), 275 sh (59375) nm. $C_{48}H_{35}F_{12}N_{11}P_2Ru{\cdot}3H_2O$ (1210.9): calcd. C 47.61, H 3.41, N 12.72; found C 47.70, H 3.21, N 12.70.

**Complex 12b:** The complex was prepared according to general procedures for complexation (Method B) using Os(bipy)$_2$Cl$_2$ as the complexation agent. The product was isolated as a dark green solid in 74% yield. M.p. >320 °C. $^1$H NMR (500 MHz, [D$_6$]acetone): δ = 5.21 and 5.34 (2×d, $J_{gem}$ = 15.4, $CH_2$Ph), 6.86 (ddd, $J_{5,4}$ = 7.4, $J_{5,6}$ = 5.7, $J_{5,3}$ = 1.4, 1 H, 5-H bipy), 6.87 (br. s, 1 H, NH), 7.19 (m, 2 H, H$^o$ Ph), 7.26–7.31 (m, 4 H, 4-H bipy and H$^{m,p}$ Ph), 7.44 (ddd, $J_{5,4}$ = 7.4, $J_{5,6}$ = 5.7, $J_{5,3}$ = 1.4, 1 H, 5-H bipy), 7.46 (ddd, $J_{5'',4''}$ = 7.4, $J_{5'',6''}$ = 5.7, $J_{5'',3''}$ = 1.4, 1 H, 5″-H), 7.50 and 7.59 (2×ddd, $J_{5,4}$ = 7.4, $J_{5,6}$ = 5.7, $J_{5,3}$ = 1.4, 2×1 H, 2×5-H bipy), 7.65, 7.73 and 7.81 (3×ddd, $J_{6,5}$ = 5.7, $J_{6,4}$ = 1.5, $J_{6,3}$ = 0.7, 3×1 H, 3×6-H bipy), 7.84 (dd, $J_{5',4'}$ = 7.8, $J_{5',3'}$ = 1.4, 1 H, 5′-H), 7.87 (ddd, $J_{6'',5''}$ = 5.7, $J_{6'',4''}$ = 1.5, $J_{6'',3''}$ = 0.7, 1 H, 6″-H), 7.99 (ddd, $J_{4,3}$ = 8.4, $J_{4,5}$ = 7.4, $J_{4,6}$ = 1.5, 1 H, 4-H bipy), 8.02 (ddd, $J_{4'',3''}$ = 8.4, $J_{4'',5''}$ = 7.4, $J_{4'',6''}$ = 1.5, 1 H, 4″-H), 8.08 and 8.09 (2×ddd, $J_{4,3}$ = 8.4, $J_{4,5}$ = 7.4, $J_{4,6}$ = 1.5, 2×1 H, 2×4-H bipy), 8.13 (t, $J_{4',3'}$ = 8.3, $J_{4',5'}$ = 7.8, 1 H, 4′-H), 8.27 (s, 1 H, H-2), 8.31 (ddd, $J_{6,5}$ =

 © 2007 Wiley-VCH Verlag GmbH & Co. KGaA, Weinheim 

5.6, $J_{6,4}$ = 1.5, $J_{6,3}$ = 0.7, 1 H, 6-H bipy), 8.49, 8.77, 8.79 and 8.81 (4 × ddd, $J_{3,4}$ = 8.4, $J_{3,5}$ = 1.4, $J_{3,6}$ = 0.7, 4 × 1 H, 4 × 3-H bipy), 8.86 (ddd, $J_{3'',4''}$ = 8.4, $J_{3'',5''}$ = 1.4, $J_{3'',6''}$ = 0.7, 1 H, 3″-H), 8.90 (dd, $J_{3',4'}$ = 8.3, $J_{3',5'}$ = 1.4, 1 H, 3′-H) ppm. $^{13}$C NMR (125.8 MHz, [D$_6$]acetone): $\delta$ = 47.29 ($CH_2$Ph), 88.05 (C≡*C* pur), 90.45 (*C*≡C pur), 120.12 (C-5), 125.34, 125.41, 125.48, 125.57 and 125.76 (C-3′ and C-3 bipy), 126.35 (C-3″), 128.59 (C$^o$ Ph), 128.74, 128.92, 128.94, 129.12, 129.40 and 129.46 (C-5″ C-5-bipy and C$^p$ Ph), 129.63 (C$^m$ Ph), 132.25 (C-8), 135.97 (C-5′), 136.83 (C-4 bipy), 137.26 (C$^i$ Ph), 138.36, 138.47, 138.64 and 139.09 (C-4′, C-4″ and C-4 bipy), 146.91 (C-6′), 150.72 (C-4), 151.15, 151.19 and 151.40 (C-6 bipy), 151.99 (C-6″), 153.33 C-6 bipy), 155.68 (C-2), 157.24 (C-6), 159.02, 159.79, 159.92 and 160.64 (C-2″ and C-2 bipy), 162.53 (C-2′) ppm. ESI MS: *m*/*z* (%) = 1052 (100) [M$^+$ – $PF_6^-$], 453 (15) [M$^{2+}$ – 2$PF_6^-$]. IR (KBr): $\tilde{\nu}$ = 1635, 842, 558 cm$^{-1}$. $C_{44}H_{33}F_{12}N_{11}OsP_2$ (1197.2): calcd. C 44.19, H 2.78, N 12.88; found C 44.15, H 2.74, N 12.83.

**Electrochemistry:** All voltammetric measurements were performed with an Autolab analyzer (Eco Chemie, The Netherlands) in connection with VA-Stand 663 (Metrohm, Switzerland). The three-electrode system was always used. Carbon paste electrodes (CPE) or hanging mercury drop electrodes (HMDE) were used as working electrodes, a Ag/AgCl/3 M KCl electrode as reference and platinum wire as the auxiliary electrode. The CPE was prepared by hand mixing of graphite powder CR-5 (Tesla, Czech Republic) with mineral oil (Sigma) in a weight ratio of 70/30 and filled in a Teflon electrode body. The surface of the CPE was renewed by wiping with wet filtration paper. Square-wave voltammetric measurements at the CPEs were performed with the following settings: frequency 200 Hz, amplitude 25 mV, potential step 5 mV, scan rate: 1 V s$^{-1}$, initial potential: –1.0 V, end potential: +1.6 V. For measurements at the HMDE, linear sweep or cyclic voltammetry was used: scan rate: 1 V s$^{-1}$, potential step 5 mV, initial potential: 0.0 V, end (switching) potential: –1.6 V. All measurements were performed in 0.2 acetate buffer (pH 5.0) at room temperature (22 to 25 °C). Before each measurement at the HMDE, the solution of the background electrolyte was deaerated with argon.

**Computational Details:** All density functional theory (DFT) calculations reported in the study were carried out using the Turbomole 5.8 program.[48] The Perdew–Burke–Ernzerhof (PBE)[49] and hybrid three-parameter Becke's[50] (B3LYP) functionals were used throughout. The calculations were expedited by expanding the Coulomb integrals in an auxiliary basis set, the resolution-of-identity (RI-J) approximation.[51,52] All the geometry optimizations were carried out using the def2-SVP basis set,[53] whereas the single point energies were recomputed in a larger basis set, def2-TZVP (triple-zeta valence with two polarization functions on each atom).[53]

To account for solvation effects, the conductor-like screening model (COSMO) method[54,55] was used with the dielectric constant corresponding to an equimolar mixture of water and acetonitrile ($\varepsilon_r$ = 57). The Gibbs free energy was then calculated as the sum of these contributions [Equation (1)]

$$G = E_{el} + G_{solv} + (E_{ZPE} + nRT - TS) \quad (1)$$

where $E_{el}$ is the in vacuo energy of the system (at the B3LYP/def2-TZVP level and the geometry optimized at the RI-PBE/def2-SVP level), $G_{solv}$ is the solvation free energy (at the RI-PBE/def2-SVP level) and the ($E_{ZPE}$ + $nRT$ – $TS$) term is the zero-point energy, thermal correction to the Gibbs free energy, and entropic term (obtained from a frequency calculation with the same method and software as for the geometry optimizations at the RI-PBE/def2-SV(P) level, 298 K and 1 atm pressure, using an ideal-gas approximation.[56])

The redox potentials were then calculated according to the equation (2)

$$E^0\,[\mathrm{V}] = 27.21(G_{ox}\,[\mathrm{a.u.}] - G_{red}\,[\mathrm{a.u.}]) - 4.34\,\mathrm{V} \quad (2),$$

where $G_{ox/red}$ are free energy values calculated according to Equation (1), and 4.34 V is an absolute redox potential of the standard hydrogen electrode (SHE).[57]

**X-ray Diffraction:** X-ray crystallographic analysis of single crystals of **10b** (red, 0.03 × 0.14 × 0.27 mm) and **5b** (red, 0.08 × 0.31 × 0.40 mm) was performed with the Xcalibur X-ray diffractometer with Cu-$K_\alpha$ ($\lambda$ = 1.54180 Å), data collected at 150 K (**10b**) and 295 K (**5b**). Both structures were solved by direct methods with SIR92[58] and refined by full-matrix least-squares methods based on F with CRYSTALS.[59] Friedel pairs were not merged. Hydrogen atoms were located in a difference map, but those attached to carbon atoms were repositioned geometrically and then refined with riding constraints, all other atoms were refined anisotropically in both cases.

**Crystal Data for 10b:** $C_{44}H_{33}F_{12}N_{11}P_2Ru_1$, monoclinic, space group $P2_1/n$, $a$ = 9.041(4), $b$ = 11.983(4), $c$ = 45.72(2) Å, $\beta$ = 94.34(4)°, $V$ = 4939(3) Å$^3$, $Z$ = 4, $M$ = 1106.81, 73413 reflections measured, 18674 independent reflections. Final $R$ = 0.0866, $wR$ = 0.0701 for 5598 reflections with $I > 1.96\sigma(I)$ and 694 parameters. Several thermal similarity restraints were used in the refinement of the bipyridine units and the hexafluorophosphate anions. The two hexafluorophosphate anions were found to be disordered in three positions with their site occupation factors being 0.75, 0.75, and 0.50.

**Crystal Data for 5b:** $C_{34}H_{24}F_{12}N_6P_2Ru_1$, orthorhombic, space group $Pna2_1$, $a$ = 13.5397(2), $b$ = 25.6956(3), $c$ = 10.0094(2) Å, $V$ = 3482.38(10) Å$^3$, $Z$ = 4, $M$ = 883.58, 56076 reflections measured, 7377 independent reflections. Final $R$ = 0.0331, $wR$ = 0.0380 for 2940 reflections with $I > 1.96\sigma(I)$ and 478 parameters.

CCDC-628693 (for **10b**) and -629224 (for **5b**) contain the supplementary crystallographic data for this paper. These data can be obtained free of charge from The Cambridge Crystallographic Data Centre via www.ccdc.cam.ac.uk/data_request/cif.

**Biological Activity Screening:** The HCV subgenomic replicon assay was performed according to the published procedure.[46] Inhibition of HCV NS5B polymerase 1b assay was performed according to ref.[47] Cytostatic activity screening was done according to ref.[60] The cell cycle analysis was carried out by the propidium iodide method[61] and evaluated by means of ModFit LT software (Verity Software House, Topsham, ME, USA).

## Acknowledgments

This work is a part of the research project Z4 055 0506. It was supported by EC Specific Targeted Research Project, Control of Assembly and Charge Transport Dynamics of Immobilized DNA (CIDNA) (to M. V. and M. H.), by the Grant Agency of the Czech Republic (a grant No. 203/05/0043 to M. V., M. H., L. H., and M. F. and 203/05/H001 to L. Z.), by the Czech Ministry of Education LC512 and LC06035 (to L. R., L. Z., P. H. and L. H., M. F., respectively) and by Gilead Sciences, Inc. (Foster City, CA, USA).

[1] M. J. Heller, *Annu. Rev. Biomed. Eng.* **2002**, *4*, 129–153.
[2] a) M. Fojta, *Electroanalysis* **2002**, *14*, 1449–1463; b) M. Fojta, *Collect Czech. Chem. Commun.* **2004**, *69*, 715–747; c) M. Fojta

 © 2007 Wiley-VCH Verlag GmbH & Co. KGaA, Weinheim 

in *Electrochemistry of Nucleic Acids and Proteins. Towards Electrochemical Sensors for Genomics and Proteomics* (Eds.: E. Paleček, F. Scheller, J. Wang), Elsevier, Amsterdam, **2005**, pp. 386–430.

[3] a) E. Paleček, M. Fojta, *Anal. Chem.* **2001**, *73*, 74A–83A; b) E. Paleček, M. Fojta in *Bioelectronics* (Eds.: I. Wilner, E. Katz), Wiley VCH, Weinheim, **2005**, pp. 127–192; c) N. Popovich, H. Thorp, *Interface* **2002**, *11*, 30–34; d) J. Wang in *Electrochemistry of Nucleic Acids and Proteins. Towards Electrochemical Sensors for Genomics and Proteomics* (Eds.: E. Paleček, F. Scheller, J. Wang), Elsevier, Amsterdam, **2005**, pp. 175–190.

[4] T. Ihara, M. Nakayama, M. Murata, K. Nakano, M. Maeda, *Chem. Commun.* **1997**, *17*, 1609–1610.

[5] a) C. Fan, K. W. Plaxco, A. J. Heeger, *Proc. Natl. Acad. Sci. USA* **2003**, *100*, 9134–9137; b) E. Paleček, *Trends Biotechnol.* **2004**, *22*, 55–58; c) A. E. Radi, J. L. A. Sanchez, E. Baldrich, C. K. O′Sullivan, *J. Am. Chem. Soc.* **2006**, *128*, 117.

[6] a) M. Fojta, L. Havran, S. Billová, P. Kostecka, M. Masarik, R. Kizek, *Electroanalysis* **2003**, *15*, 431–440; b) M. Fojta, L. Havran, R. Kizek, S. Billová, E. Paleček, *Biosens. Bioelectron.* **2004**, *20*, 985–994; c) E. Paleček, M. Fojta, F. Jelen, *Bioelectrochemistry* **2002**, *56*, 85–90.

[7] J. Wang, G. Liu, A. Merkoci, *J. Am. Chem. Soc.* **2003**, *125*, 3214–3215.

[8] D. R. Van Staveren, N. Metzler-Nolte, *Chem. Rev.* **2004**, *104*, 5931–5985.

[9] V. Balzani, A. Juris, M. Venturi, *Chem. Rev.* **1996**, *96*, 759–833.

[10] a) P. K. Bhattacharya, H. J. Lawson, J. K. Barton, *Inorg. Chem.* **2003**, *42*, 8811–8818; b) C. Stinner, M. D. Wightman, S. O. Kelley, M. G. Hill, J. K. Barton, *Inorg. Chem.* **2001**, *40*, 5245–5250; c) J. L. Kisko, J. K. Barton, *Inorg. Chem.* **2000**, *39*, 4942–4949; d) R. E. Holmlin, J. A. Yao, J. K. Barton, *Inorg. Chem.* **1999**, *38*, 174–189; e) S. J. Franklin, C. R. Treadway, J. K. Barton, *Inorg. Chem.* **1998**, *37*, 5198–5210.

[11] a) P. Meunier, I. Ouattara, B. Gautheron, J. Tirouflet, D. Camboli, J. Besancon, *Eur. J. Med. Chem.* **1991**, *26*, 351–362; b) E. Bucci, L. De Napoli, G. Di Fabio, A. Messere, D. Montesarchio, A. Romanelli, G. Piccialli, M. Varra, *Tetrahedron* **1999**, *55*, 14435–14450; c) C. J. Yu, H. Yowanto, Y. J. Wan, T. J. Meade, Y. Chong, M. Strong, L. H. Donilon, J. F. Kayyem, M. Gozin, G. F. Blackburn, *J. Am. Chem. Soc.* **2000**, *122*, 6767–6768; d) A. R. Pike, L. C. Ryder, B. R. Horrocks, W. Clegg, M. R. J. Elsegood, B. A. Connolly, A. Houlton, *Chem. Eur. J.* **2002**, *8*, 2891–2899; e) W. A. Wlassoff, G. C. King, *Nucleic Acids Res.* **2002**, *30*, e58.

[12] a) D. J. Hurley, Y. Tor, *J. Am. Chem. Soc.* **2002**, *124*, 3749–3762; b) D. J. Hurley, Y. Tor, *J. Am. Chem. Soc.* **2002**, *124*, 13231–13241; c) H. Weizman, Y. Tor, *J. Am. Chem. Soc.* **2002**, *124*, 1568–1569; d) D. J. Hurley, Y. Tor, *J. Am. Chem. Soc.* **1998**, *120*, 2194–2195; e) D. J. Hurley, S. E. Seaman, J. C. Mazura, Y. Tor, *Org. Lett.* **2002**, *4*, 2305–2308.

[13] M. Hocek, P. Štěpnička, J. Ludvík, I. Císařová, I. Votruba, D. Řeha, P. Hobza, *Chem. Eur. J.* **2004**, *10*, 2058–2066.

[14] a) M. Hocek, I. Rosenberg, unpublished results. Independently, it was confirmed by another laboratory; b) A. R. Pike, L. C. Ryder, B. R. Horrocks, W. Clegg, B. A. Connoly, A. Houlton, *Chem. Eur. J.* **2005**, *11*, 344–353.

[15] a) Y. Tor, *Synlett* **2002**, 1043–1054; b) U. S. Schubert, C. Eschenbauer, *Angew. Chem. Int. Ed.* **2002**, *41*, 2892–2926; c) J. P. Sauvage, J. P. Collin, J. C. Chamdron, S. Guillerez, Ch. Coudret, *Chem. Rev.* **1994**, *94*, 993–1019.

[16] Selected references for metal-containing materials: a) C.-T. Chen, K. S. Suslick, *Coord. Chem. Rev.* **1993**, *128*, 293–322; b) I. Manners, *Angew. Chem. Int. Ed. Engl.* **1996**, *35*, 1602–1621; c) V. Balzani, A. Credi, M. Venturi, *Coord. Chem. Rev.* **1998**, *171*, 3–16; d) R. Ziessel, M. Hissler, A. El-ghayoury, A. Harriman, *Coord. Chem. Rev.* **1998**, *180*, 1251–1298; e) For multiphoton, multielectron transfer processes in metal-containing polymers, see: L. A. Worl, W. E. Jones, G. F. Strouse, J. N. Younathan, E. Danielson, K. A. Maxwell, M. Sykora, T. J. Meyer, *Inorg. Chem.* **1999**, *38*, 2705–2708.

[17] B. E. Halcrow, W. O. Kermack, *J. Chem. Soc.* **1946**, 155–157.

[18] V. Grosshenny, F. M. Romero, R. Ziessel, *J. Org. Chem.* **1997**, *62*, 1491–1500.

[19] C. D. Buchecker, B. Colasson, M. Fujita, A. Hori, N. Geum, S. Sakamoto, K. Yamaguchi, J. P. Sauvage, *J. Am. Chem. Soc.* **2003**, *125*, 5717–5725.

[20] a) B. M. Kelly-Basetti, D. J. Cundy, S. M. Pereira, W. H. F. Sasse, G. P. Savage, G. W. Simpson, *Bioorg. Med. Chem. Lett.* **1995**, *24*, 2989–2992; b) V. N. Kozhevnikov, D. N. Kozhevnikov, O. V. Shabunina, V. L. Rusinov, O. N. Chupakhin, *Tetrahedron Lett.* **2005**, *46*, 1791–1793.

[21] a) C. J. Aspley, J. A. G. Williams, *New J. Chem.* **2001**, *25*, 1136–1147; b) G. W. V. Cave, C. L. Raston, *J. Chem. Soc., Perkin Trans. 1* **2001**, 3258–3264.

[22] T. Isiyama, M. Murate, N. Miyaura, *J. Org. Chem.* **1995**, *60*, 7508–7510.

[23] T. Haino, H. Araki, Y. Fujiwara, Y. Tanimoto, Y. Fukazawa, *Chem. Commun.* **2002**, 2148–2149.

[24] a) V. Balzani, A. Juris, M. Venturi, *Chem. Rev.* **1996**, *96*, 759–833; b) C. M. Elliott, E. J. Hershenhart, *J. Am. Chem. Soc.* **1982**, *104*, 7519–7526; c) A. Juris, V. Balzani, F. Barigelletti, S. Campagna, P. Belser, A. Von Zelewsky, *Coord. Chem. Rev.* **1988**, *84*, 85–277.

[25] a) D. Tzalis, Y. Tor, *Chem. Commun.* **1996**, 1043–1044; b) E. C. Glazer, D. Magde, Y. Tor, *J. Am. Chem. Soc.* **2005**, *127*, 4190–4192.

[26] P. J. Connors, D. Tzalis, A. L. Dunnick, Y. Tor, *Inorg. Chem.* **1998**, *37*, 1121–1123.

[27] a) F. Hartl, S. Vernier, P. Belser, *Collect. Czech. Chem. Commun.* **2005**, *70*, 1891–1908; b) D. Martineau, P. Gros, M. Beley, Y. Fort, *Eur. J. Inorg. Chem.* **2004**, 3984–3986.

[28] B. P. Sullivan, J. M. Calvert, T. J. Meyer, *Inorg. Chem.* **1980**, *19*, 1404–1407.

[29] a) Reviews: M. Hocek, *Eur. J. Org. Chem.* **2003**, 245–254; b) L. A. Agrofoglio, I. Gillaizeau, Y. Saito, *Chem. Rev.* **2003**, *103*, 1875–1916; c) M. K. Lakshman, *J. Organomet. Chem.* **2002**, *653*, 234–251.

[30] a) Examples: M. Havelková, D. Dvořák, M. Hocek, *Synthesis* **2001**, 1704–1710; b) M. Hocek, D. Hocková, J. Štambaský, *Collect. Czech. Chem. Commun.* **2003**, *68*, 837–848; c) M. Hocek, D. Hocková, H. Dvořáková, *Synthesis* **2004**, 889–894; d) N. Amann, H.-A. Wagenknecht, *Synlett* **2002**, 687–691; e) E. Mayer, L. Valis, R. Huber, N. Amann, H.-A. Wagenknecht, *Synthesis* **2003**, 2335–2340; f) N. Kohyama, T. Katashima, Y. Yamamoto, *Synthesis* **2004**, 2799–2804.

[31] a) Examples: R. Volpini, S. Constanzi, C. Lambertucci, S. Vittori, K.-N. Klotz, A. Lorenzen, G. Cristalli, *Bioorg. Med. Chem. Lett.* **2001**, *11*, 1931–1934; b) S. Manfredini, P. G. Baraldi, R. Bazzanini, M. Marangoni, D. Simoni, J. Balzarini, E. De Clercq, *J. Med. Chem.* **1995**, *38*, 199–203; c) H. Gunji, A. Vasella, *Helv. Chim. Acta* **2000**, *83*, 2975–2992; d) P. Lang, G. Magnin, G. Mathis, A. Burger, J.-F. Biellmann, *J. Org. Chem.* **2000**, *65*, 7825–7832; e) J. L. Sessler, R. Wang, *J. Am. Chem. Soc.* **1996**, *118*, 9808–9809; f) J. L. Sessler, R. Wang, *J. Org. Chem.* **1998**, *63*, 4079–4091; g) J. L. Sessler, R. Wang, *Angew. Chem. Int. Ed.* **1998**, *37*, 1726–1729; h) J. L. Sessler, M. Sathiosatham, C. T. Brown, T. A. Rhodes, G. Wiederrecht, *J. Am. Chem. Soc.* **2001**, *123*, 3655–3660.

[32] E. M. Kober, J. V. Caspar, B. P. Sullivan, T. J. Meyer, *Inorg. Chem.* **1988**, *27*, 4587–4598.

[33] a) E. C. Western, J. R. Daft, E. M. Johnson, P. M. Gannett, K. H. Shaughnessy, *J. Org. Chem.* **2003**, *68*, 6767–6774; b) E. C. Western, K. H. Shaughnessy, *J. Org. Chem.* **2005**, *70*, 6378–6388; c) P. Čapek, M. Vrábel, Z. Hasník, R. Pohl, M. Hocek, *Synthesis* **2006**, 3515–3526.

[34] a) P. Čapek, M. Hocek, *Synlett* **2005**, 3005–3007; b) P. Čapek, R. Pohl, M. Hocek, *Org. Biomol. Chem.* **2006**, *4*, 2278–2284.

 © 2007 Wiley-VCH Verlag GmbH & Co. KGaA, Weinheim 

[35] D. P. Rillema, D. S. Jones, H. A. Levy, *J. Chem. Soc., Chem. Commun.* **1979**, 849–851.
[36] a) D. Onggo, M. L. Scudder, D. C. Craig, H. A. Goodwin, *J. Mol. Struct.* **2005**, *738*, 129–136; b) R. Chotalia, E. C. Constable, M. J. Hannon, D. A. Tocher, *J. Chem. Soc., Dalton Trans.* **1995**, *22*, 3571–3580; c) S. Encias, A. F. Morales, F. Barigelletti, A. M. Barthram, C. M. White, S. M. Couchman, J. C. Jeffery, M. D. Ward, D. C. Grills, M. W. George, *J. Chem. Soc., Dalton Trans.* **2001**, *22*, 3312–3319.
[37] E. Paleček, F. Jelen in *Electrochemistry of Nucleic Acids and Proteins. Towards Electrochemical Sensors for Genomics and Proteomics* (Eds.: E. Palecek, F. Scheller, J. Wang), Elsevier, Amsterdam, **2005**, pp. 74–174.
[38] H. Kiesele, J. Heinze in *Organic Electrochemistry* (Eds.: H. Lund, M. M. Baizer), Dekker, New York, **1991**, p. 331.
[39] P. A. Ropp, H. H. Thorp, *Chem. Biol.* **1999**, *6*, 599–605.
[40] A. J. Bard, L. R. Faulkner, Electrochemical Methods, 2nd ed., John Wiley, New York, **2001**.
[41] M. Srnec, J. Chalupský, M. Hocek, L. Zendlová, P. Hobza, L. Rulíšek, to be published.
[42] a) Examples: A. B. Eldrup, C. R. Allerson, C. F. Bennett, S. Bera, B. Bhat, N. Bhat, M. R. Bosserman, J. Brooks, C. Burlein, S. S. Carroll, P. D. Cook, K. L. Getty, M. MacCoss, D. R. McMasters, D. B. Olsen, T. P. Prakash, M. Prhavc, Q. L. Song, J. E. Tomassini, J. Xia, *J. Med. Chem.* **2004**, *47*, 2283–2295; b) D. B. Olsen, A. B. Eldrup, L. Bartholomew, B. Bhat, M. R. Bosserman, A. Ceccacci, L. F. Colwell, J. F. Fay, O. A. Flores, K. L. Getty, J. A. Grobler, R. L. LaFemina, E. J. Markel, G. Migliaccio, M. Prhavc, M. W. Stahlhut, J. E. Tomassini, M. MacCoss, D. J. Hazuda, S. S. Carroll, *Antimicrob. Agents Chemother.* **2004**, *48*, 3944–3953; c) A. B. Eldrup, M. Prhavc, J. Brooks, B. Bhat, T. P. Prakash, Q. L. Song, S. Bera, N. Bhat, P. Dande, P. D. Cook, C. F. Bennett, S. S. Carroll, R. G. Ball, M. Bosserman, C. Burlein, L. F. Colwell, J. F. Fay, O. A. Flores, K. Getty, R. L. LaFemina, J. Leone, M. MacCoss, D. R. McMasters, J. E. Tomassini, D. Von Langen, B. Wolanski, D. B. Olsen, *J. Med. Chem.* **2004**, *47*, 5284–5297.
[43] Recent examples: a) P. L. Beaulieu, J. Gillard, D. Bykowski, C. Brochu, N. Dansereau, J. S. Duceppe, B. Hache, A. Jakalian, L. Lagace, S. LaPlante, G. McKercher, E. Moreau, S. Perreault, T. Stammers, L. Thauvette, J. Warrington, G. Kukolj, *Bioorg. Med. Chem. Lett.* **2006**, *16*, 4987–4993; b) H. Li, J. Tatlock, A. Linton, J. Gonzalez, A. Borchardt, P. Dragovich, T. Jewell, T. Prins, R. Zhou, J. Blazel, H. Parge, R. Love, M. Hickey, C. Doan, S. Shi, R. Duggal, C. Lewis, S. Fuhrman, *Bioorg. Med. Chem. Lett.* **2006**, *16*, 4834–4838; c) B. K. Biswal, M. T. Wang, M. M. Cherney, L. Chan, C. G. Yannopoulos, D. Bilimoria, J. Bedard, M. N. G. James, *J. Mol. Biol.* **2006**, *361*, 33–45.
[44] Recent reviews: a) I. Kostova, *Curr. Med. Chem.* **2006**, *13*, 1085–1107; b) M. J. Clarke, *Coord. Chem. Rev.* **2002**, *232*, 69–93.
[45] a) G. E. Atilla-Gokcumen, D. S. Williams, H. Bregman, N. Pagano, E. Meggers, *ChemBioChem* **2006**, *7*, 1443–1450; b) J. E. Debreczeni, A. N. Bullock, G. E. Atilla, D. S. Williams, H. Bregman, S. Knapp, E. Meggers, *Angew. Chem. Int. Ed.* **2006**, *45*, 1580–1585; c) H. Bregman, P. J. Carroll, E. Meggers, *J. Am. Chem. Soc.* **2006**, *128*, 877–884; d) D. S. Williams, G. E. Atilla, H. Bregman, A. Arzoumanian, P. S. Klein, E. Meggers, *Angew. Chem. Int. Ed.* **2005**, *44*, 1984–1987.
[46] V. Lohmann, F. Korner, J. O. Koch, U. Herian, L. Theilmann, R. Bartenschlager, *Science* **1999**, *285*, 110–113.
[47] a) M. Hung, C. S. Gibbs, M. Tsiang, *Antiviral Res.* **2002**, *56*, 99–114; b) M. Hocek, P. Šilhár, I. H. Shih, E. Mabery, R. Mackman, *Bioorg. Med. Chem. Lett.* **2006**, *16*, 5290–5293.
[48] R. Ahlrichs, M. Bär, M. Häser, H. Horn, C. Kölmel, *Chem. Phys. Lett.* **1989**, *162*, 165.
[49] J. P. Perdew, K. Burke, M. Ernzerhof, *Phys. Rev. Lett.* **1996**, *77*, 3865–3868.
[50] a) A. D. Becke, *Phys. Rev. A* **1988**, *38*, 3098–3100; b) C. T. Lee, W. T. Yang, R. G. Parr, *Phys. Rev. B* **1988**, *37*, 785–789; c) A. D. Becke, *J. Chem. Phys.* **1993**, *98*, 5648–5652; d) P. J. Stephens, F. J. Devlin, C. F. Chabalowski, M. J. Frisch, *J. Phys. Chem.* **1994**, *98*, 11623–11627.
[51] K. Eichkorn, O. Treutler, H. Öhm, M. Häser, R. Ahlrichs, *Chem. Phys. Lett.* **1995**, *240*, 283–290.
[52] K. Eichkorn, F. Weigen, O. Treutler, R. Ahlrichs, *Theor. Chim. Acta* **1997**, *97*, 119–124.
[53] a) A. Schäfer, H. Horn, R. Ahlrichs, *J. Chem. Phys.* **1992**, *97*, 2571–2577; b) F. Weigend, R. Ahlrichs, *Phys. Chem. Chem. Phys.* **2006**, *7*, 3297–3305.
[54] A. Klamt, G. Schuurmann, *J. Chem. Soc., Perkin Trans. 2* **1993**, 799–805.
[55] A. Schäfer, A. Klamt, D. Sattel, J. C. W. Lohrenz, F. Eckert, *Phys. Chem. Chem. Phys.* **2000**, *2*, 2187–2193.
[56] F. Jensen, *Introduction to Computational Chemistry*, John Wiley & Sons, New York, **1999**.
[57] J. Llano, L. A. Ericsson, *Phys. Chem. Chem. Phys.* **2004**, *6*, 4707–4713.
[58] A. Altomare, G. Cascarano, G. Giacovazzo, A. Guagliardi, M. C. Burla, G. Polidori, M. Camalli, *J. Appl. Crystallogr.* **1994**, *27*, 435–435.
[59] P. W. Betteridge, J. R. Carruthers, R. I. Cooper, K. Prout, D. J. Watkin, *J. Appl. Crystallogr.* **2003**, *36*, 1487–1487.
[60] M. Hocek, A. Holý, I. Votruba, H. Dvořáková, *J. Med. Chem.* **2000**, *43*, 1817–1825.
[61] J. You, R. C. Bird, *J. Cell Physiol.* **1995**, *164*, 424–433.

Received: November 30, 2006
Published Online: March 6, 2007

 © 2007 Wiley-VCH Verlag GmbH & Co. KGaA, Weinheim 

DOI: 10.1002/ejic.200601141

# Synthesis and Structural Characterization of Novel Ytterbium(III) Complexes with both a μ-Oxo Group and Bridged Indenyl Ligands, and Ytterbium(II) Complexes with Bridged Indenyl Ligands

**Lin Cheng,[a] Yan Feng,[a] Shaowu Wang,*[a,b] Wei Luo,[a] Wei Yao,[a] Zeyan Yu,[a] Xiaobing Xi,[a] and Zixiang Huang[c]**

**Keywords:** Organometallic compounds / Lanthanoids / Synthesis / Ytterbium / X-ray diffraction

The reactivity of the ytterbium(III) amide $[(Me_3Si)_2N]_3Yb(\mu\text{-}Cl)Li(thf)_3$ with different bridged indene compounds in the presence of external donor ligands was studied. Reaction of $[(Me_3Si)_2N]_3Yb(\mu\text{-}Cl)Li(thf)_3$ with the corresponding 1,2-bis-(indenyl)ethane $[(CH_2)_2(C_9H_7)_2]$ or $Me_2Si(C_9H_7)_2$, followed by the addition of excess thf, produced a novel tetranuclear ytterbium complex $[\{\eta^5\text{:}\eta^5\text{-}(CH_2)_2(C_9H_6)_2\}Yb(\mu\text{-}Cl)(\mu_3\text{-}O)Yb\text{-}(Cl)N(SiMe_3)_2Li(thf)_4]_2$ (**1**) or a novel dinuclear ytterbium complex $[\eta^5\text{:}\eta^5\text{-}(CH_3)_2Si(C_9H_6)_2Yb]_2(\mu\text{-}Cl)(\mu\text{-}O)Li(thf)_2$ (**2**), respectively. Treatment of $[(Me_3Si)_2N]_3Yb(\mu\text{-}Cl)Li(thf)_3$ with $(CH_2)_2(C_9H_6SiMe_3)_2$ (**3**) or $Me_2Si(C_9H_7)_2$ under different conditions produced ytterbium(II) complexes $[\eta^5\text{:}\eta^5\text{-}(CH_2)_2\text{-}(C_9H_5SiMe_3)_2]Yb(thf)_2\cdot(C_6H_{14})_{0.5}$ (**4**) and $[\eta^5\text{:}\eta^5\text{-}(CH_2)_2\text{-}(C_9H_5SiMe_3)_2]Yb\cdot dme$ (**5**) or $[\eta^5\text{:}\eta^5\text{-}(CH_3)_2Si(C_9H_6)_2]Yb\cdot$tmeda (**6**), respectively. Interaction of the ytterbium(III) amide $[\eta^5\text{:}\eta^5\text{-}(CH_2)_2(C_9H_6)_2]YbN(SiMe_3)_2$ with excess tmeda afforded the ytterbium(II) complex $[\eta^5\text{:}\eta^5\text{-}(CH_2)_2(C_9H_6)_2]Yb\cdot$tmeda (**7**). All the compounds were fully characterized by spectroscopic methods and elemental analyses. Complexes **1**, **2**, and **4** were additionally characterized by single-crystal X-ray diffraction analyses. The solvents and temperature effects on the reaction are discussed.

(© Wiley-VCH Verlag GmbH & Co. KGaA, 69451 Weinheim, Germany, 2007)

## Introduction

Lanthanide complexes have received continuous interest because of their potential applications as catalysts in a wide range of olefin transformations such as olefin polymerization,[1] hydroamination/cyclization,[2] hydrophosphanation,[3] and hydrosilylation of a variety of unsaturated compounds, for example, functionalized alkenes, -alkynes, -allenes, and -dienes.[4] The lanthanide complexes with a Ln–N bond are among the lanthanide complexes that show diverse reactivity toward the Tishchenko reaction,[5] ring-opening polymerization of ε-caprolactone and δ-valerolactone,[6] olefin polymerization,[1,7] hydroamination/cyclization,[2] hydrosilylation,[4a,4b] dimerization of terminal alkyne,[8a] as well as toward the Cannizzaro-type disproportionation of aromatic aldehydes to amides and alcohols.[8b]

It has been documented that lanthanide complexes with pentamethylcyclopentadienyl,[9] Schiff base,[10] dipyrrolide,[11] triamidoamine,[12] carborane,[13] and porphyrinogen[14] ligands can react with thf or oxygen-containing compounds such as epoxides to give the μ-oxo-containing or enolate complexes. It was also reported that the alkyl lanthanide complexes can thermally decompose to give the enolate complexes in the presence of thf/LiCl.[15] However, the synthesis and characterization of lanthanide complexes with either indenyl ligands or the μ-oxo-containing group has been far less studied.

We have reported that the treatment of functionalized indene compounds having internal donor-substituted groups such as the *N*,*N*-dimethylaminoethyl group[16] and the methoxyethyl[17] group with $[(Me_3Si)_2N]_3Ln^{III}(\mu\text{-}Cl)\text{-}Li(thf)_3$ (Ln = Yb, Eu) affords organolanthanide(II) complexes. The treatment of the indenes $C_9H_6$-1-R-3-$CH_2SiMe_2NC_4H_8$ (R = H, $CH_3$) with $[(Me_3Si)_2N]_3Eu^{III}(\mu\text{-}Cl)\text{-}Li(thf)_3$ were also studied, and novel tetranuclear triple-decker and monomeric europium(II) complexes were isolated and characterized.[18a] A novel ytterbium(II) complex in which the indenyl ligand is bonded to the metal through the benzo ring with an $\eta^4$-hapticity was isolated and characterized by treatment of the *N*-piperidinylethyl-functionalized indene compound with the ytterbium(III) amide $[(Me_3Si)_2N]_3Yb(\mu\text{-}Cl)Li(THF)_3$.[18b] The above study indicated that the electronic and steric effects of the ligands have an influence on the homolytic reaction of the Ln–N (Ln = Yb, Eu) bond. In this paper, we report on the reactivity of the ytterbium(III) amide with bridged indene com-

[a] Anhui Key Laboratory of Functional Molecular Solids, Institute of Organic Chemistry, College of Chemistry and Materials Science, Anhui Normal University,
Wuhu, Anhui 241000, China
Fax: +86-553-3883517
E-mail: swwang@mail.ahnu.edu.cn
[b] State Key Laboratory of Organometallic Chemistry, Shanghai Institute of Organic Chemistry,
Shanghai 200032, China
[c] Fujian Institute of Research on the Structure of Matters, Chinese Academy of Sciences,
Fuzhou 350002, China

 © 2007 Wiley-VCH Verlag GmbH & Co. KGaA, Weinheim 

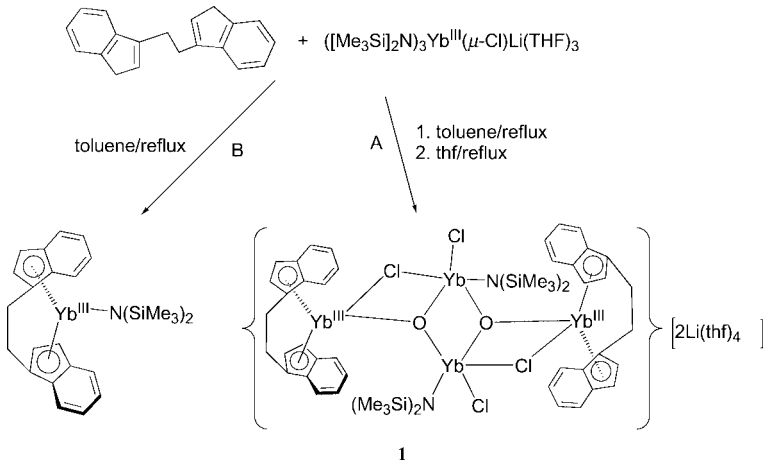


**1**

Scheme 1.

pounds in the presence of external donor ligands such as thf, dme, and tmeda, with the isolation and characterization of a series of novel ytterbium(III) and ytterbium(II) complexes. The effect of the donor ligands and the temperature on the reactivity of the Yb–N bond is also discussed.

## Results and Discussion

### Synthesis and Characterization of Ytterbium(III) and Ytterbium(II) Complexes

Treatment of 1,2-bis(indenyl)ethane with 1 equiv. $[(Me_3Si)_2N]_3Yb^{III}(\mu\text{-}Cl)Li(thf)_3$ in refluxing toluene overnight, followed by the addition of excess thf afforded, after workup, a novel tetranuclear ytterbium(III) complex $[\{\eta^5\text{:}\eta^5\text{-}(CH_2)_2(C_9H_6)_2\}Yb(\mu\text{-}Cl)(\mu_3\text{-}O)Yb(Cl)N(SiMe_3)_2\text{-}Li(thf)_4]_2$ (**1**) as red crystals (Scheme 1, path A). This result is different from that of our previous studies, which showed that the treatment of indene compounds having internal donor substituents with lanthanide(III) amides $[(Me_3Si)_2N]_3\text{-}Ln^{III}(\mu\text{-}Cl)Li(THF)_3$ (Ln = Yb, Eu) produce the lanthanide(II) complexes through a tandem silylamine elimination and homolysis of the Ln–N bond.[16–18] This result is also different from that obtained from the direct treatment of 1,2-bis(indenyl)ethane with 1 equiv. $[(Me_3Si)_2N]_3Yb^{III}(\mu\text{-}Cl)Li(thf)_3$ in refluxing toluene, the indenyl ytterbium(III) amide complex $[\eta^5\text{:}\eta^5\text{-}(CH_2)_2(C_9H_6)_2]YbN(SiMe_3)_2$ (Scheme 1, path B).[16a] The color change from yellow to dark blue and the isolation of indenyl ytterbium(III) amide $[\eta^5\text{:}\eta^5\text{-}(CH_2)_2(C_9H_6)_2]YbN(SiMe_3)_2$ from the dark blue solution suggests that the formation of complex **1** may occur via the indenyl ytterbium(III) amide as intermediate.

X-ray analysis reveals that complex **1** is a centrosymmetric structure and contains a discrete dianion $[\{\eta^5\text{:}\eta^5\text{-}(CH_2)_2\text{-}(C_9H_6)_2\}Yb(\mu\text{-}Cl)(\mu_3\text{-}O)Yb(Cl)N(SiMe_3)_2]_2^{2-}$, with two $\mu_3$-O atoms, and the cations $Li(thf)_4^+$. The presence of the oxygen atoms in **1** likely arises from cleavage of thf, a process that is well documented in lanthanide chemistry.[9–15] In order to extend the scope of the reaction, the reaction of $Me_2Si(C_9H_7)_2$ with $[(Me_3Si)_2N]_3Yb^{III}(\mu\text{-}Cl)Li(thf)_3$ was studied.

Treatment of $Me_2Si(C_9H_7)_2$ with $[(Me_3Si)_2N]_3Yb^{III}(\mu\text{-}Cl)Li(thf)_3$ in toluene, followed by the addition of excess thf and by heating the mixture at reflux for 6 h produced an ytterbium(III) complex $[\eta^5\text{:}\eta^5\text{-}(CH_3)_2Si(C_9H_6)_2Yb]_2(\mu\text{-}Cl)(\mu\text{-}O)Li(thf)_2$ (**2**) (Scheme 2).

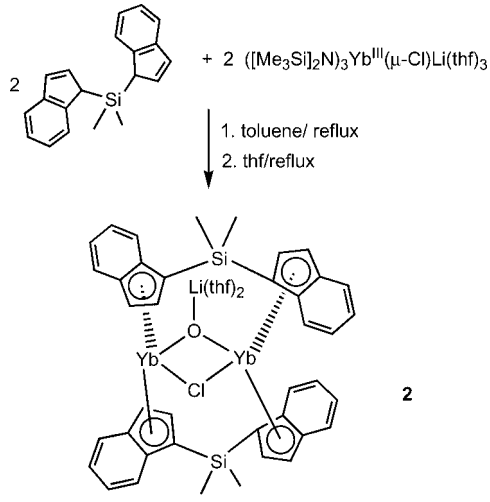


**2**

Scheme 2.

Complexes **1** and **2** are soluble in thf and pyridine, but they are insoluble in toluene and hexane. They were fully characterized by spectroscopic methods and elemental analyses, and their structures were determined by single-crystal X-ray analyses. $^1H$ NMR analyses of the complexes gave no information because of the lack of locking signals, which probably results from the strong paramagnetic property of the complexes. This suggests that the oxidation state of the central ytterbium metal atom may be +3, which was confirmed by X-ray structural analyses. The formation of complexes **1** and **2** is somewhat different from the thermal decomposition of alkyl lanthanide complexes to form the enolate complexes in the presence of thf/LiCl.[15]

When $(CH_2)_2(C_9H_6SiMe_3)_2$ (**3**) and 1 equiv. ytterbium(III) amide $[(Me_3Si)_2N]_3Yb^{III}(\mu\text{-}Cl)Li(thf)_3$ were treated in refluxing thf and not in toluene, with the addition

 © 2007 Wiley-VCH Verlag GmbH & Co. KGaA, Weinheim 

of excess thf, an ytterbium(II) complex $[\eta^5{:}\eta^5\text{-}(CH_2)_2(C_9H_5SiMe_3)_2]Yb(thf)_2{\cdot}(C_6H_{14})_{0.5}$ (**4**) (Scheme 3) was isolated and characterized on the basis of elemental, spectroscopic, and single-crystal X-ray analyses. The solvated *n*-$C_6H_{14}$ and coordinated thf can be evaporated under vacuum, as suggested by the elemental analyses data. The formation of the ytterbium(II) complex **4** suggests that the reaction involves a one-electron reductive elimination process, which is different from process for the formation of complexes **1** and **2** and indicates the temperature or solvent effects on the reaction that result from the difference in the boiling points of the refluxing toluene and thf. The experiments to prove the hypothesis that the formation of complexes **1** and **2** occurs via an ytterbium(II) intermediate, which then reacts with thf to give the μ-oxo complexes that results from the abstraction of the oxygen atom of the thf ring, by heating complex **4** in toluene at reflux were unsuccessful. This is because of the formation of an insoluble solid, which is difficult to purify by recrystallization or other techniques. Formation of complex **4** indicates that interaction of the Yb–N bond with an external donor ligand may provide a new method for the preparation of organolanthanide(II) complexes. Thus, the interactions of the Yb–N bond with other external donor ligands such as dme and tmeda were studied.

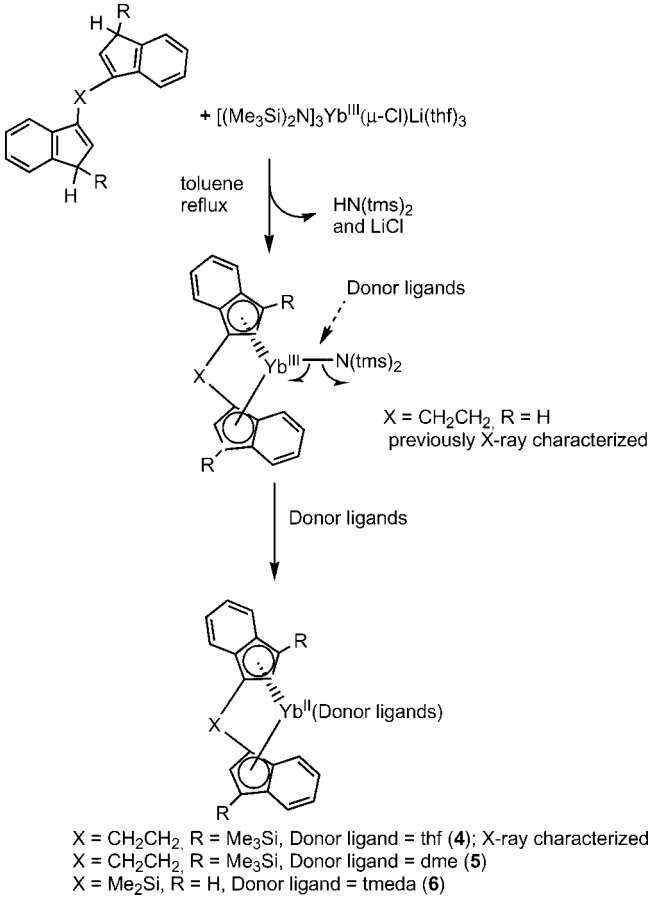


Scheme 3.

Reaction of $[(Me_3Si)_2N]_3Yb^{III}(\mu\text{-}Cl)Li(thf)_3$ with $(CH_2)_2(C_9H_6SiMe_3)_2$ (**3**) in refluxing dme for 24 h produced, after workup, an ytterbium(II) complex $[\eta^5{:}\eta^5\text{-}(CH_2)_2(C_9H_5SiMe_3)_2]Yb{\cdot}dme$ (**5**) (Scheme 3). The reaction of $[(Me_3Si)_2N]_3Yb^{III}(\mu\text{-}Cl)Li(thf)_3$ and $(CH_2)_2(C_9H_6SiMe_3)_2$ (**3**) in toluene at first, followed by the addition of excess dme also produced complex **5**, on the basis of elemental and spectroscopic analyses. Treatment of $Me_2Si(C_9H_7)_2$ with $[(Me_3Si)_2N]_3Yb^{III}(\mu\text{-}Cl)Li(thf)_3$ in refluxing toluene for 6 h, followed by the addition of excess tmeda, produced, after workup, an ytterbium(II) complex $[\eta^5{:}\eta^5\text{-}(CH_3)_2Si(C_9H_6)_2]Yb{\cdot}tmeda$ (**6**) (Scheme 3). The μ-oxo-containing complex has not been isolated in the above reactions. $^1H$ NMR analyses showed that the ratio of the indenyl ligand and the dme or tmeda ligands is 1:1. The diamagnetic property of the complexes suggests that the oxidation state of the central metal is +2. These complexes are extremely air- and moisture sensitive and they are soluble in thf and dme.

The fact that reaction of the ytterbium(III) amide $[\eta^5{:}\eta^5\text{-}(CH_2)_2(C_9H_6)_2]YbN(SiMe_3)_2$ with tmeda produced the ytterbium(II) complex $[\eta^5{:}\eta^5\text{-}(CH_2)_2(C_9H_6)_2]Yb{\cdot}tmeda$ (**7**) (Scheme 4) suggests that the formation of **4**–**6** may involve indenyl ytterbium(III) amide as an intermediate. Moreover, homolysis of the Yb–N bond has not been observed either by heating the indenyl ytterbium(III) amide $[\eta^5{:}\eta^5\text{-}(CH_2)_2(C_9H_6)_2]YbN(SiMe_3)_2$ at reflux in toluene for 3 d, by heating the ytterbium(III) amide $[(Me_3Si)_2N]_3Yb^{III}(\mu\text{-}Cl)Li(thf)_3$ at reflux in toluene, or by sublimation of the amide $[(Me_3Si)_2N]_3Yb^{III}(\mu\text{-}Cl)Li(thf)_3$ in vacuo.

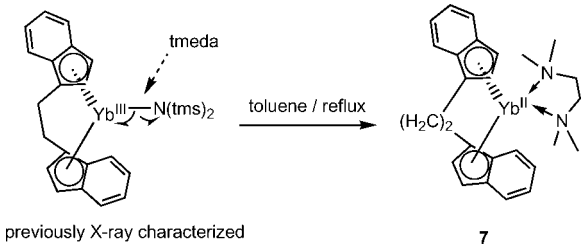


Scheme 4.

The above results suggest that a one-electron reductive elimination process occurs after the formation of the indenyl ytterbium(III) amides $[\eta^5{:}\eta^5\text{-}(X)(C_9H_5R)_2]Yb^{III}N(SiMe_3)_2$ (X = bridging group $CH_2CH_2$ or $Me_2Si$; R = H or $Me_3Si$) resulting from the reactions of the indene compounds with the ytterbium(III) amide $[(Me_3Si)_2N]_3Yb^{III}(\mu\text{-}Cl)Li(thf)_3$. Reactions of external donor ligands such as thf, dme, or tmeda with the resulting indenyl ytterbium(III) amides $[\eta^5{:}\eta^5\text{-}(X)(C_9H_5R)_2]Yb^{III}N(SiMe_3)_2$ produce the ytterbium(II) complexes. The above results also indicate that this method for the preparation of organoytterbium(II) complexes by interaction of the Yb–N bond with external donor ligands at moderately high temperatures can be suitable for different cases.

On the basis of these results, the pathway for the formation of ytterbium(II) complexes **4**–**6** is proposed as follows: the reactions of the bridged indene compounds $(X)(C_9H_6R)_2$ (X = bridging group $CH_2CH_2$ or $Me_2Si$; R = H

 © 2007 Wiley-VCH Verlag GmbH & Co. KGaA, Weinheim 

or $Me_3Si$) with the ytterbium(III) amide $[(Me_3Si)_2N]_3Yb^{III}(\mu\text{-}Cl)Li(thf)_3$ produces the indenyl ytterbium(III) amide $[\eta^5{:}\eta^5\text{-}(X)(C_9H_5R)_2]Yb^{III}N(SiMe_3)_2$, which then reacts with external donor ligands to give the ytterbium(II) complex $[\eta^5{:}\eta^5\text{-}(X)(C_9H_5R)_2]Yb^{II}(D)$ (D = thf, dme, or tmeda) by coordination of the donor ligands to the central metal, leading to the homolysis of the Yb–N bond that resulted in the reduction of ytterbium(III) to ytterbium(II) (Scheme 3). Thus, the method for the preparation of the ytterbium(II) complexes through homolysis of the Yb–N bond by treatment of internally substituted indene compounds with $[(Me_3Si)_2N]_3Yb^{III}(\mu\text{-}Cl)Li(thf)_3$ may be extended to the reaction of ytterbium complexes having the Yb–N bond with suitable external donor ligands at moderately high temperatures such that the reduction of ytterbium(III) to ytterbium(II) may proceed relatively easily.[16–18] However, the formation pathway of complexes **1** and **2** remains to be further examined.

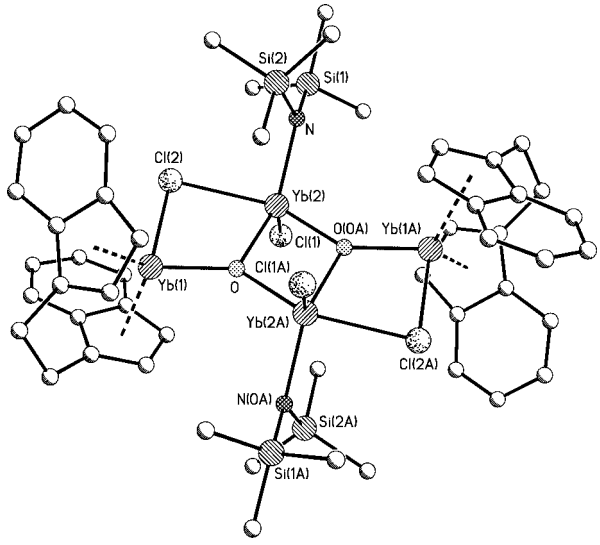


Figure 1. Molecular structure of the dianion $[\{\eta^5{:}\eta^5\text{-}(CH_2)_2(C_9H_6)_2\}Yb(\mu\text{-}Cl)(\mu_3\text{-}O)Yb(Cl)N(SiMe_3)_2]_2^{2-}$ in **1**.

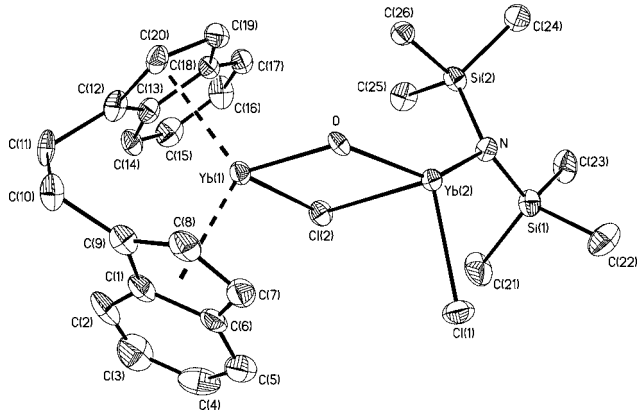


Figure 2. Structure of one symmetrical unit of the dianion in **1**. The atoms are labelled.

## Molecular structure

The structures of complexes **1** (Figures 1 and 2), **2** (Figure 3), and **4** (Figure 4) were determined by single-crystal X-ray analyses, which reveals that both **1** and **2** are oxygen-containing complexes and that the central ytterbium atoms are in the +3 oxidation state.

The key structural feature of complex **1** (Figures 1 and 2) is that the four ytterbium atoms Yb(1), Yb(1A), Yb(2), Yb(2A), the two oxygen atoms O and O(OA), and two chlorine atoms Cl(2), Cl(2A) are coplanar with a mean deviation of 0.0588 Å on the basis of a least-squares calculation. It represents the first example of a tetranuclear ytterbium complex containing both μ-oxo groups and bridged indenyl ligands in the molecular structure.[19] The Yb–O distances of 2.126(8), 2.107(9), and 2.200(9) Å (Table 1) in **1** are also notable – these distances are longer than the Sm–O distance in $[(C_5Me_5)_2Sm]_2(\mu\text{-}O)$[9] {2.094(1) Å} but are comparable to that in $\{[Cy(C_4H_3N)_2]Sm\}_4(\mu\text{-}O)$[11] {2.1844(4) Å}. The Yb–O distances in **1** are shorter than the average Sm–O($\mu_4$-O) distance of 2.346(1) Å in $[\{[\eta^5\text{-}Me_2Si(C_5Me_4)(C_2B_{10}H_{11})]Sm\}_2(\mu_2\text{-}Cl)_3(\mu_3\text{-}Cl)_4Li(OEt_2)_2Li(thf)_2Sm(\mu_4\text{-}O)]_2$[13b] and the average Sm–O distance of 2.211(8) Å found in $[\{\eta^5\text{-}(Me_3Si)_2C_2B_4H_4\}Sm]_3[\{\eta^5\text{-}(Me_3Si)_2C_2B_4H_4\}Li]_3(\mu_3\text{-}OMe)][\mu_3\text{-}Li(thf)]_3(\mu_3\text{-}O)$.[13a] The differences in the bond lengths may arise because of the different ionic radii of the lanthanide metals and the O atom and because of the steric effects in the complex.

The structural feature of the oxygen-containing dinuclear complex **2** (Figure 3) is that the silylene-bridged indenyl ligand adopts a bridging coordination, instead of the normal chelating coordination found in organometallic compounds with ligands that contain a silylene-bridge and two cyclopentadienyl or two tetramethylcyclopentadienyl groups.[20] The bridging coordination phenomenon is similar to those found in lanthanide complexes with silylene-bridged fluorenyl cyclopentadienyl ligands.[21]

The Yb(2)–O–Yb(1) angle of 109.7(2)° (Table 1) in **2** is smaller than the Yb(1)–O–Yb(2) angle of 113.4(4)° and the Yb(2A)–O–Yb(1) angle of 144.6(5)° in **1**, but larger than the Yb(2A)–O–Yb(2) angle of 101.9(3)° in **1**. The Yb(1)–Cl–Yb(2) angle of 80.40(7)° in **2** is also smaller than the Yb(1)–Cl(2)–Yb(2) angle of 84.98(11)° in **1**. Both the Yb(1)–Cl(2)–Yb(2) angle of 84.98(11)° in **1** and the Yb(1)–Cl–Yb(2) angle of 80.40(7)° in **2** is smaller than the Yb(1)–Cl(3)–Yb(1a) angle of 104.54(8)° in the dimeric ytterbium(III) chloride $[\{\eta^5{:}\eta^1{:}\sigma\text{-}Me_2Si(C_9H_5CH_2CH_2NMe_2)(C_2B_{10}H_{10})\}Yb(\mu\text{-}Cl)]_2$.[22] The Yb–O distances of 2.070(5) Å and 2.063(5) Å in **2** are comparable to the Sm–O distance of 2.094(1) Å in $[(C_5Me_5)_2Sm]_2(\mu\text{-}O)$ if the difference in ionic radii is taken into account.[23] The Yb–Cl distances of 2.603(3) Å and 2.632(2) Å in **2** are longer than the Yb(1)–Cl(2) distance of 2.572(4) Å and the Yb(2)–Cl(1) bond length of 2.532(4) Å in **1**, but shorter than the Yb(2)–Cl(2) bond length of 2.778(4) Å in **1**. The average Yb–C distance ($C_5$ ring) of 2.657(10) Å in **2** is shorter than that in **1** [2.691(17) Å]. These differences are probably due to the differences in the ionic radii and due to steric effects.

 © 2007 Wiley-VCH Verlag GmbH & Co. KGaA, Weinheim 

Table 1. Selected bond lengths [Å] and bond angles [°] in **1**, **2**, and **4**.

| **1** | | **2** | | **4** | |
|---|---|---|---|---|---|
| Yb(1)–O | 2.126(8) | Yb(1)–O | 2.070(5) | Yb–O(1) | 2.381(6) |
| Yb(2)–O | 2.200(9) | Yb(2)–O | 2.063(5) | Yb–O(2) | 2.381(5) |
| Yb(1)–Cl(2) | 2.572(4) | Yb(1)–Cl | 2.603(3) | Yb–C(4) | 2.811(7) |
| Yb(2)–Cl(2) | 2.778(4) | Yb(2)–Cl | 2.632(2) | Yb–C(5) | 2.849(6) |
| Yb(2)–Cl(1) | 2.532(4) | Yb(1)–C(11) | 2.649(8) | Yb–C(10) | 2.812(7) |
| Yb(2)–O(OA) | 2.107(9) | Yb(1)–C(12) | 2.602(8) | Yb–C(11) | 2.749(7) |
| Yb(2)–N | 2.226(11) | Yb(1)–C(13) | 2.650(9) | Yb–C(12) | 2.735(8) |
| Yb(1)–C(1) | 2.804(15) | Yb(1)–C(14) | 2.727(10) | Yb–C(15) | 2.719(7) |
| Yb(1)–C(6) | 2.769(16) | Yb(1)–C(15) | 2.697(8) | Yb–C(16) | 2.800(7) |
| Yb(1)–C(7) | 2.602(17) | Yb(1)–C(31) | 2.651(8) | Yb–C(21) | 2.852(7) |
| Yb(1)–C(8) | 2.570(15) | Yb(1)–C(32) | 2.618(8) | Yb–C(22) | 2.799(9) |
| Yb(1)–C(9) | 2.677(15) | Yb(1)–C(33) | 2.655(10) | Yb–C(23) | 2.714(7) |
| Yb(1)–C(12) | 2.694(14) | Yb(1)–C(34) | 2.665(10) | Yb–C(av.) | 2.784(9) |
| Yb(1)–C(13) | 2.766(14) | Yb(1)–C(35) | 2.685(9) | O(2)–Yb–O(1) | 91.1(2) |
| Yb(1)–C(18) | 2.777(13) | Yb(2)–C(22) | 2.643(8) | | |
| Yb(1)–C(19) | 2.651(16) | Yb(2)–C(23) | 2.648(9) | | |
| Yb(1)–C(20) | 2.598(16) | Yb(2)–C(24) | 2.647(9) | | |
| Yb–C(av.) | 2.691(17) | Yb(2)–C(25) | 2.667(9) | | |
| O(OA)–Yb(2)-O | 78.1(3) | Yb(2)–C(26) | 2.671(8) | | |
| O–Yb(2)–Cl(2) | 77.5(2) | Yb(2)–C(42) | 2.610(9) | | |
| O–Yb(1)–Cl(2) | 83.6(3) | Yb(2)–C(43) | 2.619(9) | | |
| Yb(1)–O–Yb(2) | 113.4(4) | Yb(2)–C(44) | 2.649(10) | | |
| Yb(2A)–O–Yb(1) | 144.6(5) | Yb(2)–C(45) | 2.727(9) | | |
| Yb(2A)–O–Yb(2) | 101.9(3) | Yb(2)–C(46) | 2.667(9) | | |
| N–Yb(2)–Cl(2) | 89.9(3) | Yb–C(av.) | 2.657(10) | | |
| N–Yb(2)–Cl(1) | 108.0(3) | Li–O | 1.830(18) | | |
| O–Yb(2)–N | 140.5(4) | Li–O(1) | 1.97(2) | | |
| N–Yb(2)–Cl(1) | 108.0(3) | Li–O(2) | 1.98(2) | | |
| O(OA)–Yb(2)–N | 106.7(4) | O–Yb(1)–Cl | 85.27(15) | | |
| Yb(1)–Cl(2)–Yb(2) | 84.98(11) | O–Yb(2)–Cl | 84.65(15) | | |
| | | Yb(1)–Cl–Yb(2) | 80.40(7) | | |
| | | Yb(2)–O–Yb(1) | 109.7(2) | | |

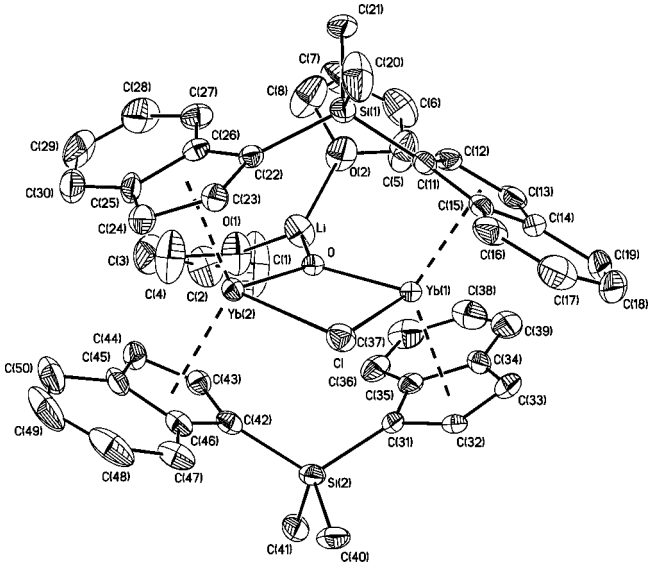


Figure 3. Molecular structure of $[\eta^5{:}\eta^5\text{-}(CH_3)_2Si(C_9H_6)_2Yb]_2(\mu\text{-}Cl)(\mu\text{-}O)Li(thf)_2$ (**2**).

X-ray analyses confirmed that the central ytterbium atom of complex **4** (Figure 4) is in the +2 oxidation state. The central ytterbium atom is coordinated by two indenyl ligands in an $\eta^5$ mode and by two oxygen atoms of the thf molecules in distorted tetrahedral geometry. The Yb–C distances range from 2.714(7) to 2.852(7) Å (Table 1), with an average length of 2.784(9) Å, which is slightly longer than those in $(\eta^5{:}\eta^1\text{-}MeOCH_2CH_2C_9H_5SiMe_3)_2Yb$[17] {2.741(14) Å} and in $(\eta^5{:}\eta^1\text{-}Me_2NCH_2CH_2C_9H_5SiMe_3)_2$-Yb {2.778(14) Å}.[16a] The average Yb–O distance of 2.381(6) Å in **4** is slightly shorter than that in $(\eta^5{:}\eta^1\text{-}MeOCH_2CH_2C_9H_5SiMe_3)_2Yb$[17] {of 2.462(9) Å}, but the O(2)–Yb–O(1) angle of 91.1(2)° in **4** is larger than those in $(\eta^5{:}\eta^1\text{-}MeOCH_2CH_2C_9H_5SiMe_3)_2Yb$[17] {84.5(3)° and 86.3(3)°}, which indicates the influence of steric effects on the coordination geometry of the complex.

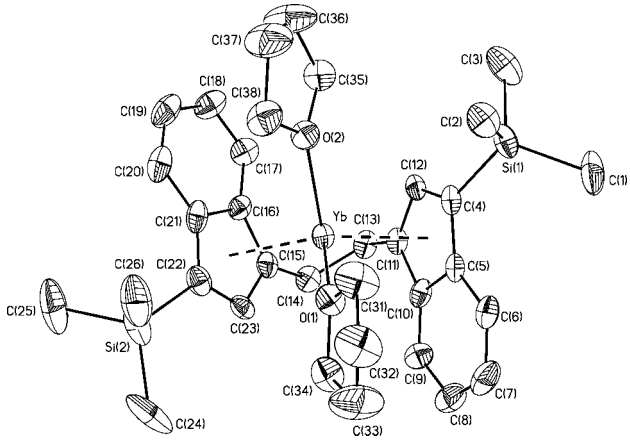


Figure 4. Molecular structure of $[\eta^5{:}\eta^5\text{-}(CH_2)_2(C_9H_5SiMe_3)_2]$ $Yb(thf)_2$ (**4**), solvated *n*-$C_6H_{14}$ is omitted for clarity.

 © 2007 Wiley-VCH Verlag GmbH & Co. KGaA, Weinheim 

## Conclusions

In summary, the reaction of the ytterbium(III) amide $[(Me_3Si)_2N]_3Yb(\mu\text{-}Cl)Li(thf)_3$ with various bridged indene compounds in the presence of external donor ligands was studied for the first time. In contrast to the result that the indenyl ytterbium(III) amide $[\eta^5\text{:}\eta^5\text{-}(CH_2)_2(C_9H_6)_2]YbN(SiMe_3)_2$ was isolated by direct treatment of the bridged indene compound $(CH_2)_2(C_9H_7)_2$ with the ytterbium(III) amide $[(Me_3Si)_2N]_3Yb(\mu\text{-}Cl)Li(thf)_3$ in refluxing toluene, the ytterbium(II) complexes were isolated and characterized by direct treatment of indenyl ytterbium(III) amide with external donor ligands such as tmeda or treatment of the bridged indene compounds with the ytterbium(III) amide $[(Me_3Si)_2N]_3Yb(\mu\text{-}Cl)Li(thf)_3$ at moderately high temperatures in the presence of excess external donor ligands such as dme or tmeda. This work also demonstrates that when thf was used as the external donor ligand, the reaction products were complicated depending on the reaction temperatures and the indenyl ligands; when the reaction was carried out in the refluxing toluene in the presence of excess thf, a novel tetranuclear or dinuclear ytterbium(III) complex containing μ-oxo group(s) was isolated, and when the reaction was performed in refluxing thf, and not in toluene with the addition of excess thf, an ytterbium(II) complex was isolated. Thus, this work indicates that reactions of lanthanide(III) complexes having the Ln–N bond with suitable external donor ligands at moderately high temperatures may provide a new method for the preparation of organolanthanide(II) complexes.

## Experimental Section

**General Remarks:** All syntheses and manipulations of air- and moisture-sensitive materials were carried out in flamed Schlenk-type glassware on a Schlenk line. All solvents were refluxed and distilled from either finely divided $LiAlH_4$ or sodium benzophenone ketyl under argon prior to use unless otherwise noted. $CDCl_3$ was dried with activated by 4-Å molecular sieves. $[(Me_3Si)_2N]_3Yb^{III}(\mu\text{-}Cl)Li(thf)_3$,[16a] $(CH_2)_2(C_9H_7)_2$,[24] and $[\eta^5\text{:}\eta^5\text{-}(CH_2)_2(C_9H_6)_2]YbN(SiMe_3)_2$[16a] were prepared according to the reported procedures. Elemental analyses data were obtained with a Perkin–Elmer 2400 Series II elemental analyzer. IR spectra were recorded with a Perkin–Elmer 983(G) spectrometer (CsI crystal plate, Nujol and Fluorolube mulls. Melting points were determined in sealed capillaries without correction. $^1H$ NMR and $^{13}C$ NMR spectra for analyses of compounds were recorded with a Bruker Avance-300 NMR spectrometer in $[D_5]$pyridine for lanthanide complexes and in $CDCl_3$ for organic compounds, and chemical shifts for $^1H$ and $^{13}C$ NMR spectra were reported with reference to internal solvent resonances.

**$[\{\eta^5\text{:}\eta^5\text{-}(CH_2)_2(C_9H_6)_2\}Yb(\mu\text{-}Cl)(\mu_3\text{-}O)Yb(Cl)N(SiMe_3)_2Li(thf)_4]_2$ (1)**: To a toluene solution (50.0 mL) of $[(Me_3Si)_2N]_3Yb^{III}(\mu\text{-}Cl)Li(thf)_3$ (2.208 g, 2.42 mmol) was added $(CH_2)_2(C_9H_7)$ (0.624 g, 2.42 mmol). The reaction mixture was heated at reflux overnight, and the color of the solution changed to dark blue. An ytterbium(III) amide complex with the formula $[\eta^5\text{:}\eta^5\text{-}(CH_2)_2(C_9H_6)_2]YbN(SiMe_3)_2$ (determined by X-ray data) was isolated from this solution. To the reaction mixture was added thf (2.0 mL, 24.66 mmol, excess). The reaction mixture was then heated at reflux for 2 d. The color of the mixture gradually changed from dark blue to dark purple. The solvents were pumped off under vacuum. The residue was washed with *n*-hexane (10.0 mL) and was then extracted with thf (2 × 10.0 mL). The extract was combined and concentrated to about 10.0 mL. Dark red crystals were obtained by cooling the concentrated solution at –10 °C for several days (1.49 g, 44%). M.p. 243–245 °C (dec.). NMR analyses were not informative because of the lack of locking signals, which results from the paramagnetic property of the complex. IR (Nujol and Fluorolube mulls): $\tilde{\nu}$ = 2952 (s), 2851 (s), 2725 (s), 1693 (w), 1606 (w), 1461 (s), 1377 (s), 1305 (w), 1260 (m), 1094 (m), 1019 (m), 933 (w), 805 (m), 768 (m), 720 (m), 393 (w) $cm^{-1}$. $C_{84}H_{132}Cl_4Li_2N_2O_{10}Si_4Yb_4$ (2290.12): calcd. C 44.06, H 5.81, N 1.22; found C 44.32, H 5.74, N 1.10.

**$[\eta^5\text{:}\eta^5\text{-}(CH_3)_2Si(C_9H_6)_2Yb]_2(\mu\text{-}Cl)(\mu\text{-}O)Li(thf)_2$ (2):** To a toluene solution (30.0 mL) of $[(Me_3Si)_2N]_3Yb^{III}(\mu\text{-}Cl)Li(thf)_3$ (1.10 g, 1.20 mmol) was slowly added a toluene solution (10.0 mL) of $(CH_3)_2Si(C_9H_7)_2$ (0.35 g, 1.20 mmol). The reaction mixture was stirred and heated at reflux for 6 h. To the reaction mixture was added thf (1.0 mL, 12.33 mmol, excess). The reaction mixture was heated at reflux for another 24 h. The color of the mixture gradually changed to dark red. The solvent was pumped off under vacuum, leaving a dark red solid. The solid was washed with *n*-hexane (10.0 mL), and the residue was extracted with toluene (2 × 10.0 mL). The extract was combined and concentrated to about 15.0 mL. Dark red crystals were obtained by cooling the solution at 0 °C for several days (0.75 g, 56%). M.p. 180–182 °C. NMR analyses were not informative because of the lack of locking signals, which probably results from the paramagnetic property of the complex. IR (Nujol and Fluorolube mulls): $\tilde{\nu}$ = 2930 (s), 2958 (s), 1461 (m), 1383 (m), 1251 (w), 1143 (w), 1025 (w), 959 (w), 810 (w), 715 (w) $cm^{-1}$. $C_{48}H_{52}ClLiO_3Si_2Yb_2{\cdot}C_7H_8$ (1213.70): calcd. C 54.42, H 4.98; found C 53.91, H 5.25.

**$(CH_2)_2(C_9H_6SiMe_3)_2$ (3):** To a diethyl ether solution of $(CH_2)_2(C_9H_7)_2$ (6.0 g, 23.3 mmol) was slowly added a 1.59 M *n*-hexane solution of *n*BuLi (29.3 mL, 46.6 mmol) at 0 °C. The reaction temperature was gradually raised to room temperature, and the reaction mixture was stirred at room temperature overnight. The reaction mixture was cooled to 0 °C. To the reaction mixture was added $Me_3SiCl$ (15.0 mL, 119.0 mmol, excess) in one portion. The mixture was then stirred at room temperature overnight. The precipitate was filtered off, and the solvent and excess $Me_3SiCl$ was evaporated under reduced pressure to leave a yellow solid, which was then washed with *n*-hexane to give a pale yellow solid (7.4 g, 65%). M.p. 143–145 °C. $^1H$ NMR ($CDCl_3$): $\delta$ = 7.10–7.50 (m, 8 H), 6.36 (m, 2 H), 3.36 (m, 2 H, $C_9H_6$), 2.96 (m, 4 H, $CH_2CH_2$), –0.09 [s, 18 H, $Si(CH_3)_3$] ppm. $^{13}C$ NMR ($CDCl_3$): $\delta$ = 146.0, 144.4, 141.6, 130.1, 124.6, 123.7, 122.9, 119.0, 44.6 ($C_9H_6$), 27.2 ($CH_2CH_2$), –2.3 $[Si(CH_3)_3]$ ppm. IR (Nujol and Fluorolube mulls): $\tilde{\nu}$ = 2923 (s), 2854 (s), 1714 (m), 1604 (m), 1461 (s), 1377 (m), 1345 (m), 1259 (m), 1248 (m), 1034 (m), 937 (w), 877 (m), 763 (m), 737 (w), 699 (w), 615 (w), 368 (w) $cm^{-1}$. $C_{26}H_{34}Si_2$ (402.66): calcd. C 77.54, H 8.51; found C 77.32, H 8.81.

**$[\eta^5\text{:}\eta^5\text{-}(CH_2)_2(C_9H_5SiMe_3)_2]Yb(thf)_2{\cdot}(C_6H_{14})_{0.5}$ (4):** To a thf solution (30.0 mL) of $[(Me_3Si)_2N]_3Yb^{III}(\mu\text{-}Cl)Li(thf)_3$ (1.290 g, 1.41 mmol) was added a thf solution (10.0 mL) of $(CH_2)_2(C_9H_6SiMe_3)_2$ (0.570 g, 1.41 mmol). After the reaction mixture was heated at reflux for 24 h, the solvent was evaporated under vacuum, leaving a red solid. The residue was extracted with *n*-hexane (2 × 10.0 mL), and the extract was combined and concentrated to about 10.0 mL. Red crystals were obtained by cooling the concentrated solution at –10 °C for several days (0.46 g, 46%). M.p. 154–

 © 2007 Wiley-VCH Verlag GmbH & Co. KGaA, Weinheim 

157 °C. $^1$H NMR ([D$_5$]pyridine): $\delta$ = 8.63–8.46 (m, 8 H), 7.16 (s, 2 H, C$_9H_5$), 4.78 (m, 8 H, OC$_4H_8$), 2.73 (m, 8 H, OC$_4H_8$), 2.22 (m, 2 H), 1.88 (m, 2 H, C$H_2$C$H_2$), 1.10 [s, 18 H, Si(C$H_3$)$_3$] ppm. $^{13}$C NMR ([D$_5$]py): $\delta$ = 147.7, 145.8, 142.8, 137.1, 136.5, 125.1, 124.4, 121.1, 68.94, 26.9, 4.2, 3.7, 3.3, –1.2, –1.8 ppm. IR (Nujol and Fluorolube mulls): $\tilde{\nu}$ = 2949 (m), 2600 (m), 1249 (m), 1160 (w), 1031 (m), 931 (w), 878 (m), 839 (s), 763 (m), 722 (m), 617 (w), 239 (w) cm$^{-1}$. $C_{26}H_{32}Si_2Yb$ (**4** – 2thf – 1/2$C_6H_{14}$) (573.69): calcd. C 54.45, H 5.62; found C 54.54, H 6.07.

Heating **4** in toluene at reflux led to an insoluble solid, which could not be purified by recrystallization and other methods.

**[$\eta^5$:$\eta^5$-(CH$_2$)$_2$(C$_9$H$_5$SiMe$_3$)$_2$]Yb·dme (5):** To a dme solution (30.0 mL) of [(Me$_3$Si)$_2$N]$_3$Yb$^{III}$($\mu$-Cl)Li(thf)$_3$ (1.414 g, 1.55 mmol) was added a dme solution (10.0 mL) of (CH$_2$)$_2$(C$_9$H$_6$SiMe$_3$)$_2$ (0.624 g, 1.55 mmol). After the reaction mixture was heated at reflux for 24 h, the solvent was pumped off, leaving a red solid. The solid was washed with *n*-hexane (8.0 mL). The solid was extracted with toluene (2 × 10.0 mL), and the extract was combined and concentrated to about 10.0 mL. The red crystalline solid was obtained by cooling the concentrated solution at –10 °C for several days (0.57 g, 55%). M.p. 165–168 °C. $^1$H NMR ([D$_5$]pyridine): $\delta$ = 7.30–6.43 (m, 10 H, C$_9H_5$), 3.46 (m, 4 H), 3.23 (m, 4 H, CH$_3$OC$H_2$C$H_2$-OCH$_3$), 2.71 (s, 6 H, C$H_3$OCH$_2$CH$_2$OC$H_3$), –0.10 [s, 18 H, Si-(C$H_3$)$_3$] ppm. IR (Nujol and Fluorolube mulls): $\tilde{\nu}$ = 2925 (s), 2855 (s), 1602 (m), 1460 (s), 1377 (m), 1260 (m), 1249 (m), 1104 (m), 1029 (m), 931 (m), 878 (m), 839 (s), 763 (m), 722 (m), 696 (m), 617 (m), 393 (w) cm$^{-1}$. $C_{30}H_{42}O_2Si_2Yb$ (663.83): calcd. C 54.28, H 6.38; found C 54.10, H 6.38.

Heating the reaction mixture of [(Me$_3$Si)$_2$N]$_3$Yb$^{III}$($\mu$-Cl)Li(thf)$_3$ and (CH$_2$)$_2$(C$_9$H$_6$SiMe$_3$)$_2$ in toluene at reflux for 6 h followed by the addition of excess dme also produced complex **5**. The complex was characterized by elemental and spectroscopic analyses.

**[$\eta^5$:$\eta^5$-(CH$_3$)$_2$Si(C$_9$H$_6$)$_2$]Yb·tmeda (6):** To a toluene solution (30.0 mL) of [(Me$_3$Si)$_2$N]$_3$Yb$^{III}$($\mu$-Cl)Li(thf)$_3$ (1.10 g, 1.20 mmol) was slowly added a toluene solution (10.0 mL) of (CH$_3$)$_2$Si-(C$_9$H$_7$)$_2$ (0.35 g, 1.20 mmol). The reaction mixture was stirred at room temperature for 6 h. To the reaction mixture was added tmeda [(CH$_3$)$_2$NCH$_2$CH$_2$N(CH$_3$)$_2$] (1.0 mL, 6.62 mmol, excess). The reaction mixture was then heated at reflux for 24 h. The color of the solution changed to purple. The solvent was pumped off under vacuum, and the solid residue was washed with *n*-hexane (10.0 mL). The solid was extracted with toluene (2 × 10.0 mL), and the extract was combined and concentrated to about 15.0 mL. The purple crystalline solid was obtained by cooling the solution at 0 °C for several days (0.47 g, 68%). M.p. 98–100 °C. $^1$H NMR ([D$_5$]pyridine): $\delta$ = 7.63–7.56 (m, 8 H), 7.26–7.19 (m, 4 H, C$_9H_6$), 2.19 (m, 4 H), 2.13 [s, 12 H, (C$H_3$)$_2$NC$H_2$C$H_2$N(C$H_3$)$_2$], 0.71–1.04 [m, 6 H, Si(C$H_3$)$_2$] ppm. $C_{26}H_{34}N_2SiYb$ (547.66): calcd. C 54.25, H 5.95, N 4.86; found C 54.23, H 6.20, N 4.83.

**[$\eta^5$:$\eta^5$-(CH$_2$)$_2$(C$_9$H$_6$)$_2$]Yb·tmeda (7):** To a toluene solution (15 mL) of [$\eta^5$:$\eta^5$-(CH$_2$)$_2$(C$_9$H$_6$)$_2$]YbN(SiMe$_3$)$_2$ (0.347 g, 0.059 mmol) was added a tmeda (1.20 mL, 7.95 mmol, excess). The mixture was heated at reflux for 24 h. The color of the mixture completely changed from dark blue to red. The solvent was evaporated under vacuum, and the resulting solid was washed with *n*-hexane and extracted with diethyl ether (2 × 10.0 mL). The extract was combined and was then evaporated to dryness to afford **7** as a red solid (0.13 g, 43%). M.p. 183–185 °C. $^1$H NMR ([D$_5$]pyridine): $\delta$ = 7.36–7.21 (m, 8 H), 7.16–7.07 (m, 4 H, C$_9H_6$), 2.24 (m, 2 H), 1.89 (m, 2 H, C$H_2$C$H_2$), 2.20 (m, 4 H), 2.15 [s, 12 H, (C$H_3$)$_2$NC$H_2$-C$H_2$N(C$H_3$)$_2$] ppm. $C_{28}H_{32}N_2Yb$ (569.61): calcd. C 57.27, H 5.87, N 5.13; found C 56.92, H 6.02, N 5.04.

**Crystal Structure Analyses of 1, 2 and 4:** Suitable crystals of complexes **1**, **2** and **4** were mounted in sealed capillaries. Diffraction was performed on a Siemens SMART CCD-area detector diffractometer with graphite-monochromated Mo-$K_\alpha$ radiation ($\lambda$ = 0.71073 Å), temperature 293(2) K, the $\phi$ and $\omega$ scan technique; SADABS effects and empirical absorption were applied to the data for correction. All structures were solved by direct methods (SHELXTL-97),[24] completed by subsequent difference Fourier syntheses, and refined by full-matrix least-square calculations based on $F^2$ (SHELXTL-97). The hydrogen atom coordinates were calculated with SHELXTL by using an appropriate riding model

Table 2. Crystal Data for **1**, **2** and **4**.

| | **1** | **2** | **4** |
|---|---|---|---|
| Empirical formula | $C_{84}H_{132}N_2Cl_4Li_2O_{10}Si_4Yb_4$ | $C_{48}H_{52}ClLiO_3Si_2Yb_2$ | $C_{37}H_{54}O_2Si_2Yb$ |
| Formula weight | 2290.12 | 1121.55 | 760.02 |
| Crystal system | triclinic | monoclinic | orthorhombic |
| Space group | $P\bar{1}$ | $P2_1/n$ | $Fdd2$ |
| $a$ [Å] | 14.3978(4) | 11.3899(2) | 33.0471(6) |
| $b$ [Å] | 14.4560(3) | 19.5632(3) | 35.7088(2) |
| $c$ [Å] | 14.7510(3) | 20.0532(3) | 14.9298(3) |
| $\alpha$ [°] | 110.2180(10) | 90 | 90 |
| $\beta$ [°] | 107.8010(10) | 94.1760(10) | 90 |
| $\gamma$ [°] | 96.8200(10) | 90 | 90 |
| $V$ [Å$^3$] | 2655.16(11) | 4456.45(12) | 17618.2(5) |
| $T$ [K] | 293(2) | 293(2) | 293(2) |
| $D_{calcd.}$ [g cm$^{-3}$] | 1.432 | 1.672 | 1.146 |
| $Z$ | 1 | 4 | 16 |
| $F$(000) | 1140 | 2208 | 6240 |
| No. Reflections collected | 13686 | 14956 | 22293 |
| No. Unique Reflections | 9193 ($R_{int}$ = 0.054) | 7766 ($R_{int}$ = 0.035) | 5786 ($R_{int}$ = 0.040) |
| No. of Parameters | 541 | 514 | 376 |
| $\lambda$ [Å] Mo-$K_\alpha$ | 0.71073 | 0.71073 | 0.71073 |
| $\mu$ [mm$^{-1}$] | 3.682 | 4.325 | 2.202 |
| $\theta$ range [°] | 1.89 to 25.06 | 1.46 to 25.04 | 2.37 to 25.06 |
| Goodness of fit | 1.154 | 1.162 | 1.080 |
| $R$ [$I > 2\sigma(I)$] | 0.078 | 0.048 | 0.034 |
| $wR_2$ | 0.155 | 0.081 | 0.078 |

 © 2007 Wiley-VCH Verlag GmbH & Co. KGaA, Weinheim 

with varied thermal parameters. All the non-hydrogen atoms were refined anisotropically. The residual electron densities were of no chemical significance. Crystal data and details of the data collection and structure refinements are given in Table 1, and selected bond lengths and angles are compiled in Table 2.

CCDC-262319 for **1**, CCDC-262320 for **2**, CCDC-262321 for **4** contain the supplementary crystallographic data for this paper. These data can be obtained free of charge from The Cambridge Crystallographic Data Centre via www.ccdc.cam.ac.uk/data_request/cif.

## Acknowledgments

This work is co-supported by the National Natural Science Foundation of China (20472001, 20672002), the Program for NCET (NCET-04–0590), the Excellent Young Scholars Foundation of Anhui Province (04046079), and the Anhui Education Department (for a grant). We are grateful to Prof. Baohui Du and Jiping Hu for running the IR and NMR spectra.

[1] a) Z. Hou, Y. Luo, X. Li, *J. Organomet. Chem.* **2006**, *691*, 3114–3121; b) H. Yasuda, *J. Organomet. Chem.* **2002**, *647*, 128; c) Z. Hou, Y. Wakatsuki, *Coord. Chem. Rev.* **2002**, *231*, 1; d) Y. Nakayama, H. Yasuda, *J. Organomet. Chem.* **2004**, *689*, 4489; and references cited therein.

[2] a) H. Kim, T. Livinghouse, J. H. Shim, S. G. Lee, P. H. Lee, *Adv. Synth. Catal.* **2006**, *348*, 701–704; b) D. V. Gribkov, K. C. Hultzsch, F. Hampel, *J. Am. Chem. Soc.* **2006**, *128*, 3748–3759; c) S. Hong, T. J. Marks, *Acc. Chem. Res.* **2004**, *37*, 673–686; d) K. C. Hultzsch, F. Hampel, T. Wagner, *Organometallics* **2004**, *23*, 2601–2612; e) F. Lauterwasser, P. G. Hayes, S. Brase, W. E. Piers, L. L. Schafer, *Organometallics* **2004**, *23*, 2234–2237; f) J.-S. Ryu, T. J. Marks, F. E. McDonald, *J. Org. Chem.* **2004**, *69*, 1038–1052; g) S. Hong, A. M. Kawaoka, T. J. Marks, *J. Am. Chem. Soc.* **2003**, *125*, 15878–15892; h) S. Hong, S. Tian, M. V. Metz, T. J. Marks, *J. Am. Chem. Soc.* **2003**, *125*, 14768–14783; i) Y. K. Kim, T. Livinghouse, Y. Horino, *J. Am. Chem. Soc.* **2003**, *125*, 9560–9561; j) S. Hong, T. J. Marks, *J. Am. Chem. Soc.* **2002**, *124*, 7886–7887; k) G. A. Molander, E. D. Dowdy, S. K. Pack, *J. Org. Chem.* **2001**, *66*, 4344–4347; l) J. Collin, J.-C. Daran, E. Schulz, A. Trifonov, *Chem. Commun.* **2003**, 3048–3049; m) Y. K. Kim, T. Livinghouse, *Angew. Chem. Int. Ed.* **2002**, *41*, 3645–3647; n) Y. K. Kim, T. Livinghouse, J. E. Bercaw, *Tetrahedron Lett.* **2001**, *42*, 2933; o) D. V. Gribkov, K. C. Hultzsch, F. Hampel, *Eur. J. Chem.* **2003**, *9*, 4796–4810; p) D. Riegert, J. Collin, A. Meddour, E. Schulz, A. Trifonov, *J. Org. Chem.* **2006**, *71*, 2514–2517; q) K. C. Hultzsch, *Adv. Synth. Catal.* **2005**, *347*, 367–391.

[3] a) A. M. Kawaoka, M. R. Douglass, T. J. Marks, *Organometallics* **2003**, *22*, 4630–4632; b) K. Takaki, G. Koshoji, K. Komeyama, M. Takeda, T. Shishido, A. Kitani, K. Takehira, *J. Org. Chem.* **2003**, *68*, 6554–6565; c) M. R. Douglass, C. L. Stern, T. J. Marks, *J. Am. Chem. Soc.* **2001**, *123*, 10221–10238; d) M. R. Douglass, T. J. Marks, *J. Am. Chem. Soc.* **2000**, *122*, 1824–1825; e) K. Komeyama, T. Kawabata, K. Takehira, K. Takaki, *J. Org. Chem.* **2005**, *70*, 7260–7266.

[4] a) Y. Horino, T. Livinghouse, *Organometallics* **2004**, *23*, 12–14; b) D. V. Gribkov, F. Hampel, K. C. Hultzsch, *Eur. J. Inorg. Chem.* **2004**, 4091–4101; c) A. A. Trifonov, T. P. Spaniol, J. Okuda, *Organometallics* **2001**, *20*, 4869–4874; d) Z. Hou, Y. Zhang, O. Tardif, Y. Wakatsuki, *J. Am. Chem. Soc.* **2001**, *123*, 9216–9217; e) A. Z. Voskoboynikov, A. K. Shestakova, I. P. Beletskaya, *Organometallics* **2001**, *20*, 2794–2801.

[5] a) H. Berberich, P. W. Roesky, *Angew. Chem. Int. Ed.* **1998**, *37*, 1569; b) M. R. Bürgstein, H. Berberich, P. W. Roesky, *Chem. Eur. J.* **2001**, *7*, 3078.

[6] a) K. C. Hultsch, T. P. Spaniol, J. Okuda, *Organometallics* **1997**, *16*, 4845; b) E. Martin, P. Dubois, R. Jerome, *Macromolecules* **2000**, *33*, 1530.

[7] a) M. A. Giardello, Y. Yamamoto, L. Brard, T. J. Marks, *J. Am. Chem. Soc.* **1995**, *117*, 3276; b) C. Qian, G. Zuo, Y. F. Chen, J. Sun, *Organometallics* **2001**, *20*, 3106; c) C. Boisson, F. Barbotin, R. Spitz, *Macromol. Chem. Phys.* **1999**, *200*, 1163; d) C. Qian, W. L. Nie, J. Sun, *Organometallics* **2000**, *19*, 4134; e) S. Zhou, S. Wang, G. Yang, X. Liu, E. Sheng, K. Zhang, L. Cheng, Z. Huang, *Polyhedron* **2003**, *22*, 1019–1024.

[8] a) K. Komeyama, T. Kawabata, K. Takehira, K. Takaki, *J. Org. Chem.* **2005**, *70*, 7260–7266; b) L. Zhang, S. Wang, S. Zhou, G. Yang, E. Sheng, *J. Org. Chem.* **2006**, *71*, 3149–3153.

[9] W. J. Evans, J. W. Grate, I. Bloom, W. E. Hunter, J. L. Atwood, *J. Am. Chem. Soc.* **1985**, *107*, 405–409.

[10] T. Dubé, S. Gambarotta, G. P. A. Yap, *Organometallics* **1998**, *17*, 3967–3973.

[11] a) T. Dubé, S. Gambarotta, G. P. A. Yap, *Angew. Chem. Int. Ed.* **1999**, *38*, 1432–1435; b) T. Dubé, S. Conoci, S. Gambarotta, G. P. A. Yap, *Organometallics* **2000**, *19*, 1182–1185.

[12] H. C. Aspinall, M. R. Tillotson, *Inorg. Chem.* **1996**, *35*, 2163–2164.

[13] a) N. S. Hosmane, Y. Wang, A. R. Oki, H. Zhang, J. A. Maguire, *Organometallics* **1996**, *15*, 626; b) G. Zi, Q. Yang, T. C. W. Mak, Z. Xie, *Organometallics* **2001**, *20*, 2359–2366.

[14] J. Jubb, S. Gambarotta, R. Duchateau, J. H. Teuben, *J. Chem. Soc., Chem. Commun.* **1994**, 2461–2462.

[15] W. J. Evans, R. Dominguez, T. P. Hanusa, *Organometallics* **1986**, *5*, 1291–1296.

[16] a) E. Sheng, S. Wang, G. Yang, S. Zhou, L. Cheng, K. Zhang, Z. Huang, *Organometallics* **2003**, *22*, 684–692; b) E. Sheng, S. Zhou, S. Wang, G. Yang, Y. Wu, Y. Feng, L. Mao, Z. Huang, *Eur. J. Inorg. Chem.* **2004**, 2923–2932.

[17] K. Zhang, W. Zhang, S. Wang, E. Sheng, G. Yang, M. Xie, S. Zhou, Y. Feng, L. Mao, Z. Huang, *Dalton Trans.* **2004**, 1029–1037.

[18] a) S. Wang, S. Zhou, E. Sheng, M. Xie, K. Zhang, L. Cheng, Y. Feng, L. Mao, Z. Huang, *Organometallics* **2003**, *22*, 3546–3552; b) S. Wang, X. Tang, A. Vega, J. Saillard, E. Sheng, G. Yang, S. Zhou, Z. Huang, *Organometallics* **2006**, *25*, 2399–2401.

[19] For recent reviews, see: a) H. Schumann, J. A. Messe-Markscheffel, L. Esser, *Chem. Rev.* **1995**, *95*, 865; b) F. T. Edelmann, in *Comprehensive Organometallic Chemistry II* (Eds.: E. W. Abel, F. G. A. Stone, G. Wilkinson), Pergamon, New York, **1995**, vol. 4, p. 11; c) H. C. Aspinall, *Chem. Rev.* **2002**, *102*, 1807–1850; d) F. T. Edelmann, D. M. M. Freckmann, H. Schumann, *Chem. Rev.* **2002**, *102*, 1851–1896; e) S. Arndt, J. Okuda, *Chem. Rev.* **2002**, *102*, 1953–1976; f) M. N. Bochkarev, *Chem. Rev.* **2002**, *102*, 2089–2118; g) W. J. Evans, B. L. Davis, *Chem. Rev.* **2002**, *102*, 2119–2136.

[20] a) W. Abriel, J. Heck, *J. Organomet. Chem.* **1986**, *302*, 363; b) G. Jeske, L. E. Schock, P. N. Swepston, H. Schumann, T. J. Mark, *J. Am. Chem. Soc.* **1985**, *107*, 8103; c) C. M. Fendrick, E. A. Mintz, L. D. Schertz, T. J. Marks, V. W. Day, *Organometallics* **1984**, *3*, 819.

[21] C. Qian, W. Nie, J. Sun, *Organometallics* **2000**, *19*, 4134–4140.

[22] S. Wang, H.-W. Li, Z. Xie, *Organometallics* **2004**, *23*, 3780–3787.

[23] R. D. Shannon, *Acta Crystallogr., Sect. A* **1976**, *32*, 751.

[24] G. M. Sheldrick, *SHELXTL*, version 5.10, Bruker Analytical X-ray Systems, Inc., Madison, WI, **1997**.

Received: December 2, 2006
Published Online: March 6, 2007

 © 2007 Wiley-VCH Verlag GmbH & Co. KGaA, Weinheim

**The EUChemSoc Societies have taken the significant step into the future by merging their traditional journals, to form two leading chemistry journals, the *European Journal of Inorganic Chemistry* and the *European Journal of Organic Chemistry.* Three further EUChemSoc Societies (Austria, Czech Republic and Sweden) are Associates of the two journals.**

## COVER PICTURE

**The cover picture shows** the crystal structures of three diiron complexes with bridging hydrocarbyl ligands of increasing size and complexity: from the bridging aminocarbyne (at the back) through to the bridging vinyliminium (in the middle) to the allylidene complex (in the front). The complexes are the result of subsequent additions of alkynes and acetylides that take place at the bridging unit. For each step, the bridging coordination provides activation and also regio- and stereocontrol of the addition reactions. Thus, the nature and conformation of the growing bridging organic frame can be largely predicted and properly designed. Details are discussed in the article by V. Zanotti et al. on p. 1799 ff.

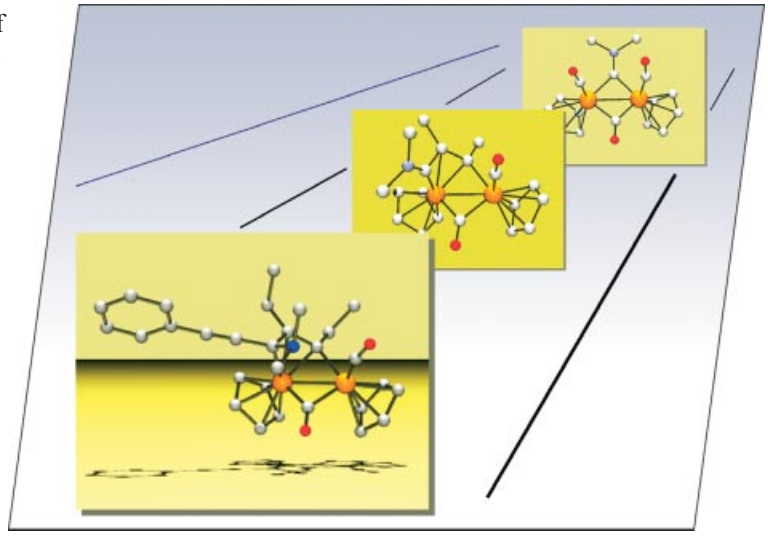

 © 2007 Wiley-VCH Verlag GmbH & Co. KGaA, Weinheim

**The EUChemSoc Societies have taken the significant step into the future by merging their traditional journals, to form two leading chemistry journals, the *European Journal of Inorganic Chemistry* and the *European Journal of Organic Chemistry.* Three further EUChemSoc Societies (Austria, Czech Republic and Sweden) are Associates of the two journals.**

## COVER PICTURE

**The cover picture shows** the crystal structures of three diiron complexes with bridging hydrocarbyl ligands of increasing size and complexity: from the bridging aminocarbyne (at the back) through to the bridging vinyliminium (in the middle) to the allylidene complex (in the front). The complexes are the result of subsequent additions of alkynes and acetylides that take place at the bridging unit. For each step, the bridging coordination provides activation and also regio- and stereocontrol of the addition reactions. Thus, the nature and conformation of the growing bridging organic frame can be largely predicted and properly designed. Details are discussed in the article by V. Zanotti et al. on p. 1799 ff.

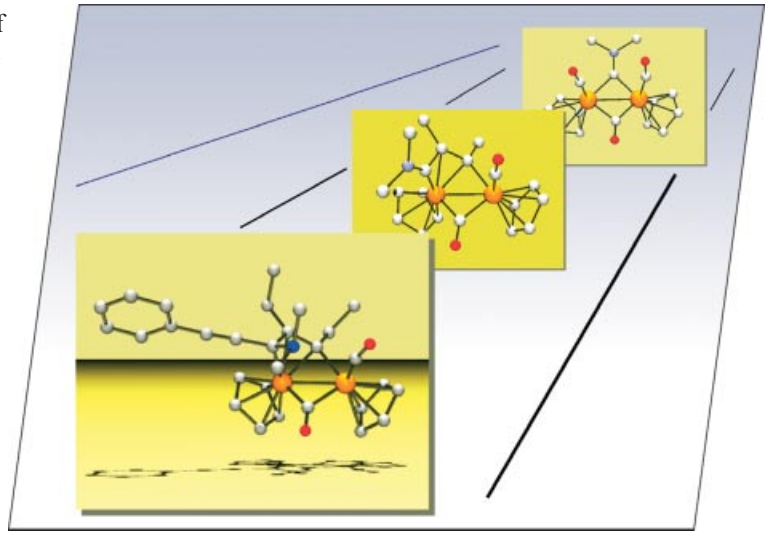

 © 2007 Wiley-VCH Verlag GmbH & Co. KGaA, Weinheim 

# CONTENTS

## SHORT COMMUNICATION


### Dihydrogen Activation

**H. Kameo, Y. Nakajima, H. Suzuki* ..... 1793–1798**

Hydrogenation of a Trinuclear $\mu_3$-Imido Complex of Ruthenium: Homolytic or Heterolytic H–H Bond Cleavage?

**Keywords:** Hydrido complexes / Ruthenium / Cleavage reactions / Imido complexes / Trinuclear complexes


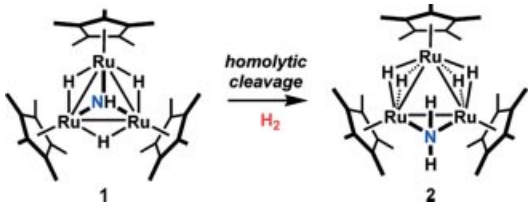



To elucidate the mode of hydrogen–hydrogen bond cleavage at transition metal sites, the hydrogenation of $(Cp^*Ru)_3(\mu_3\text{-}NH)(\mu\text{-}H)_3$ ($Cp^* = \eta5\text{-}C_5Me_5$) with deuterium was carried out. The percentage of deuterium content in the amido ligand of $(Cp^*Ru)_3(\mu\text{-}NH_2)(\mu\text{-}H)_4$ proved the mode of cleavage of dihydrogen in the reaction.


## FULL PAPERS


### Growing Bridging Organic Frames

**L. Busetto, F. Marchetti, S. Zacchini, V. Zanotti* ..... 1799–1807**

Acetylide Addition to Bridging Vinyliminium Ligands in Dinuclear Complexes

**Keywords:** Acetylides / Dinuclear complexes / Bridging ligands / C–C bond formation


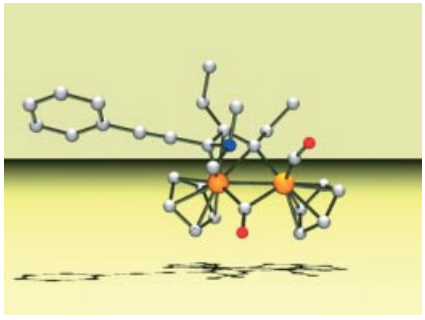


Functionalized organic frameworks are built on diiron complexes by the addition of acetylides to bridging vinyliminium ligands under regio- and stereocontrolled conditions.

### Organoboron Complexes

**Y. Ren, X. Liu, W. Gao, H. Xia, L. Ye, Y. Mu* ..... 1808–1814**

Boron Complexes with Chelating Anilido-Imine Ligands: Synthesis, Structures and Luminescent Properties

**Keywords:** Organoboron compounds / Schiff-base ligands / Luminescence


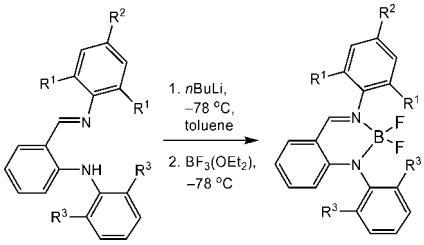



Three new organoboron complexes with anilido-imine ligands were synthesized. All complexes were characterized by $^1H$, $^{11}B$, $^{13}C$ and $^{19}F$ NMR spectroscopy, X-ray crystallography, elemental analyses and mass spectrometry. These complexes show excellent luminescent properties.

### Ligand-Exchange Mechanisms

**E. Pasgreta, R. Puchta, A. Zahl, R. van Eldik* ..... 1815–1822**

Ligand-Exchange Processes on Solvated Lithium Cations: Acetonitrile and Hydrogen Cyanide

**Keywords:** Lithium / Acetonitrile / Hydrogen cyanide / Solvation / Exchange mechanism


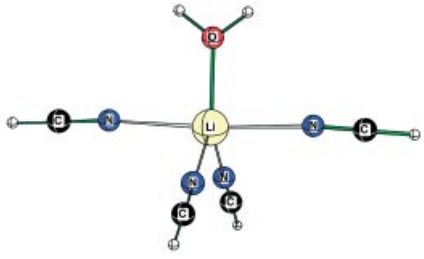



Experimental and theoretical studies indicate that $Li^+$ is four coordinate in $CH_3CN$ and in $CH_3CN$/water mixtures. Water coordinates strongly to $Li^+$ such that addition of water immediately leads to the formation of $[Li(H_2O)_4]^+$. Ligand-exchange reactions on $Li^+$ most probably follow an associative mechanism.

## Luminescent Coordination Polymers

**H. N. Peindy, F. Guyon,* A. Khatyr, M. Knorr,* C. Strohmann ..... 1823–1828**

Construction of 1D and 2D Copper(I) Coordination Polymers Assembled by $PhS(CH_2)_nSPh$ ($n$ = 1, 2) Dithioether Ligands: Surprising Effect of the Spacer Length on the Dimensionality, Cluster Nuclearity and the Fluorescence Properties of the Metal–Organic Framework

**Keywords:** Dithioethers / Copper / Fluorescence / Coordination polymers / Metal–metal interactions

Treatment of CuI with $PhS(CH_2)_nSPh$ ($n$ = 1, 2) affords the strongly luminescent 1D metal–organic coordination polymer, $[Cu_4I_4\{\mu\text{-}PhS_2CH_2SPh\}_2]_n$, and the 2D coordination polymer, $[(CuI)_2\{\mu\text{-}PhS(CH_2)_2SPh\}_2]_n$, respectively, by a self-assembly reaction.

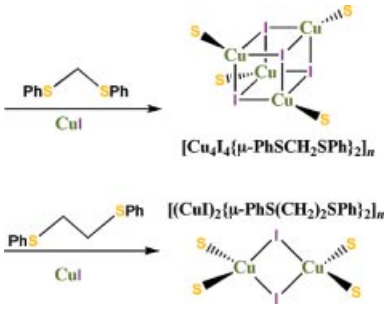


## Nanostructures

**Q.-R. Zhao, X. Zhu, X. Bai, H.-H. Fan, Y. Xie* ..... 1829–1834**

Synthesis and Optical Properties of β-$BaB_2O_4$ Network-Like Nanostructures

**Keywords:** Nonlinear optics / Materials science / Sol–gel processes / Borates

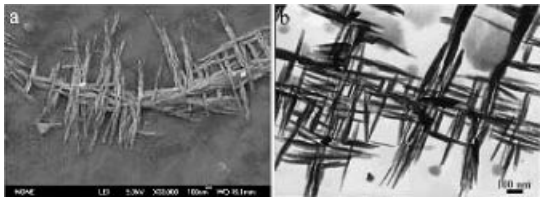


Network-like nanostructures made from the nonlinear optical material beta barium metaborate (β-$BaB_2O_4$, β-BBO) have been successfully synthesized from a BBO gel precursor using a sol–gel method. The morphology of the synthesized β-$BaB_2O_4$ materials exerts a significant influence on the second harmonic generation (SHG) efficiency.

## Biomimetic Dihydrogen Evolution

**C. Greco, M. Bruschi, P. Fantucci, L. De Gioia* ..... 1835–1843**

Influence of a Large σ-Donor Ligand on Structural and Catalytic Properties of Di-Iron Compounds Related to the Active Site of Fe-Hydrogenase – A DFT Investigation

**Keywords:** Hydrogenases / Biomimetic chemistry / Catalytic $H_2$ evolution / Density functional calculations / Iron

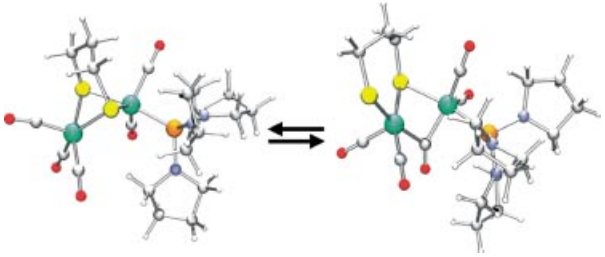

The structural and electronic properties of $(\mu\text{-pdt})[Fe_2(CO)_5P(NC_4H_8)_3]$, a recently synthesized model of the active site of Fe-hydrogenase, have been studied by means of density functional theory. The unprotonated, mono-, and di-protonated forms of this compound were taken into account, in order to disclose the geometric features of the various intermediates involved in the electrocatalytic process of $H_2$ evolution.

## Porphyrinoids

**S.-N. Song, D.-M. Li,* J.-F. Wu, C.-F. Zhuang, H. Ding, W.-B. Song, L.-F. Cui, G.-Z. Cao, G.-F. Liu .... 1844–1853**

Syntheses and Characterization of Molybdenum/Zinc Porphyrin Dimers Bridged by Aromatic Linkers

**Keywords:** Porphyrinoids / Heteronuclear complexes / Bridging ligands / Molybdenum / Zinc / Electrochemistry

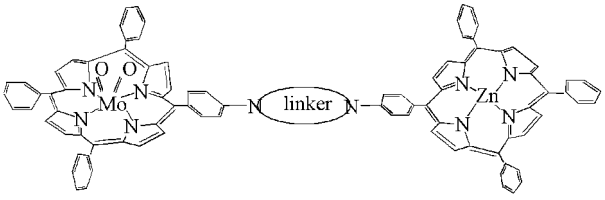


Heterobinuclear porphyrin dimers are obtained by two different methods. They are characterized by UV/Vis, IR, XPS, $^1H$ NMR, and luminescence spectroscopy and their TG-DTA and electrochemical properties determined.

 © 2007 Wiley-VCH Verlag GmbH & Co. KGaA, Weinheim 

# CONTENTS

## Coordination Polymers

**H.-P. Zhou,* P. Wang, Z.-J. Hu, L. Li, J.-J. Chen, Y. Cui, Y.-P. Tian,* J.-Y. Wu, J.-X. Yang, X.-T. Tao, M.-H. Jiang ..... 1854–1866**

Synthesis, Crystal Structures, and Photoluminescence of a Series of Coordination Polymers with Two Homologous Functional Flexible Ligands

**Keywords:** Coordination polymers / Flexible ligands / Supramolecular chemistry / Luminescence

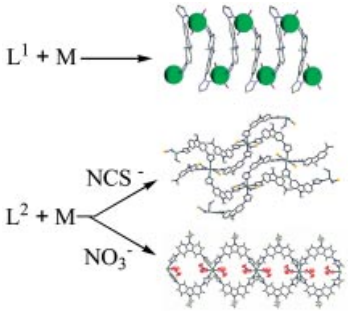


The functional flexible ligands 3,6-dipyrazolyl-9-ethylcarbazole and 3,6-diimidazolyl-9-ethylcarbazole are shown to be capable of coordinating to metal centers through their imidazolyl or pyrazolyl nitrogen atoms to form novel 2D or 3D polymers through different nonbonding and π–π interactions.

## Polynuclear Copper(II) Complexes

**A. Fernández-Botello, A. Escuer, X. Solans, M. Font-Bardía, A. Holý, H. Sigel, V. Moreno* ..... 1867–1873**

New Ternary Complexes of Copper(II) with 2,2′-Bipyridine (Bpy) and Phosphocholine ($PCh^-$) or the Quaternary 1-(2-Phosphonomethoxy)ethyl Derivative of 2,4-Diaminopyrimidine ($PMEDAPy^-$)

**Keywords:** Ternary complexes / Oxido bridges / Phosphonate bridges / Copper(II) / Magnetic properties

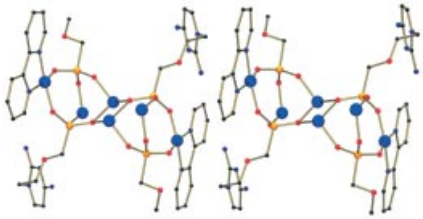

Ternary tetra- and hexanuclear copper(II) models of multicopper proteins were synthesised from the reaction of copper salts with bpy and phosphonate ligands which act as tri- or tetradentate bridges. Structural and magnetic properties were also studied.

## Crown Ether Complexation

**L. Vaiana, C. Platas-Iglesias, D. Esteban-Gómez, F. Avecilla, A. de Blas,* T. Rodríguez-Blas* ..... 1874–1883**

Receptor versus Counterion: Capability of *N*,*N*′-Bis(2-aminobenzyl)-diazacrowns for Giving Endo- and/or Exocyclic Coordination of $Zn^{II}$

**Keywords:** Zinc / Macrocyclic ligands / Crown compounds / Coordination modes / Density functional calculations

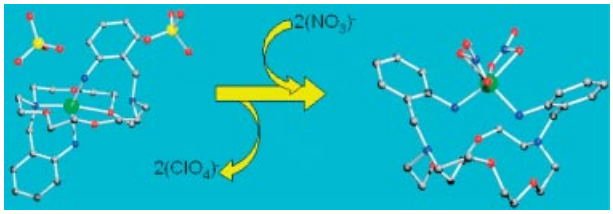


$Zn^{II}$ binding by the lariat crown ethers $L^1$ and $L^2$ [$L^1$ = *N*,*N*′-bis(2-aminobenzyl)-1,10-diaza-15-crown-5 and $L^2$ = *N*,*N*′-bis(2-aminobenzyl)-4,13-diaza-18-crown-6] in the presence of different counterions has been studied. The cavity of $L^2$ is rather large for $Zn^{II}$, so that endo- or exocyclic coordinations are observed for the metal cation depending on the coordinative properties of the counterion.

## Alkaline Niobates

**C. Sun, X. R. Xing,* J. Chen, J. X. Deng, L. Li, R. B. Yu, L. J. Qiao, G. R. Liu ..... 1884–1888**

Hydrothermal Synthesis of Single Crystalline (K,Na)$NbO_3$ Powders

**Keywords:** Hydrothermal synthesis / Crystal growth / Crystal morphology / Niobates

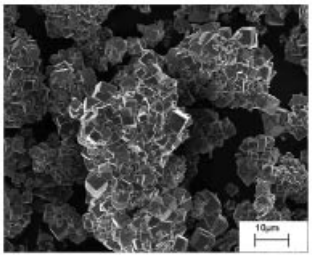


$(K_{1-x}Na_x)NbO_3$ single crystalline powders with perovskite structure were synthesized by a hydrothermal method under moderate conditions. The mechanism of formation of $(K_{1-x}Na_x)NbO_3$ was concluded. FE-SEM images showed that the morphological structures of niobates were cubes and nanofingers.

 © 2007 Wiley-VCH Verlag GmbH & Co. KGaA, Weinheim 

## Amido-thiolato Ln Complexes

Protonolysis reactions of $[(Me_3Si)_2N]_3Ln(\mu\text{-}Cl)Li(thf)_3$ (Ln = Pr, Sm) with an equimolar amount of *t*BuSH or EtSH afforded four amidolanthanide alkylthiolate complexes $[\{(Me_3Si)_2N\}_2Ln(\mu\text{-}StBu)]_2$ and $[Li(thf)_4][\{(Me_3Si)_2N\}_4Ln_4(\mu_4\text{-}SEt)(\mu\text{-}SEt)_8]$ (Ln = Pr, Sm). These compounds show catalytic activity in ring-opening polymerization reactions.

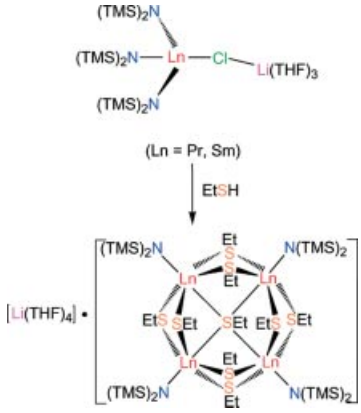


**M.-L. Cheng, H.-X. Li, W.-H. Zhang, Z.-G. Ren, Y. Zhang, J.-P. Lang* ..... 1889–1896**

Protonolysis Reactions of $[(Me_3Si)_2N]_3Ln(\mu\text{-}Cl)Li(thf)_3$ with *t*BuSH or EtSH: Isolation, Structures and Catalytic Properties of Dinuclear Complexes $[\{(Me_3Si)_2N\}_2Ln(\mu\text{-}StBu)]_2$ and Tetranuclear Complexes $[Li(thf)_4][\{(Me_3Si)_2N\}_4Ln_4(\mu_4\text{-}SEt)(\mu\text{-}SEt)_8]$ (Ln = Pr, Sm)

**Keywords:** Amidolanthanides / Alkylthiolates / Synthesis / Crystal structure / Ring-opening polymerization

## Real Structure Analysis

The real structure of a new partially ordered cluster phase of the ternary system La–Al–I was determined by a combined methodical approach of electron microscopy techniques and X-ray diffraction. The arrangement of neighboring clusters is comparable to chemically related, but strongly disordered cluster phases.

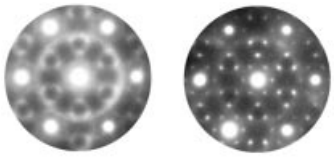

**L. Kienle,* O. Oeckler, T. Weber, V. Duppel, H. Mattausch, A. Simon ..... 1897–1902**

Order and Disorder in Cluster Phases – The Case of $La_{\approx 0.7}(Al_{\approx 0.1}I_{\approx 0.9})$

**Keywords:** Electron microscopy / X-ray diffraction / Rare earth metal compounds / Clusters / Halides / Disorder

## Thioether Coordination Chemistry

The first series of $W^{VI}$ dioxidodihalide complexes with soft thioether co-ligands are described, together with a range of new $Mo^{VI}$ thioether complexes; crystal structures of representative examples are described.

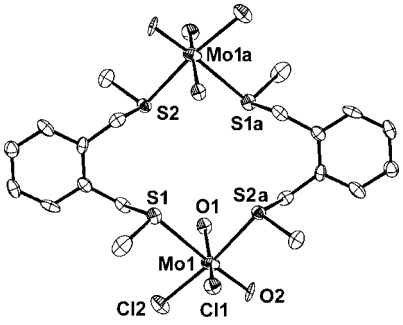


**M. F. Davis, W. Levason, M. E. Light, R. Ratnani, G. Reid,* K. Saraswat, M. Webster ..... 1903–1910**

Tungsten(VI) and Molybdenum(VI) Complexes with Soft Thioether Ligand Coordination – Synthesis, Spectroscopic and Structural Studies

**Keywords:** Tungsten / Thioether / Molybdenum

## Iridium(III) Polypyridine Complexes

Three new polypyridine iridium(III) complexes $[Ir^{III}Cl(L)(tterpy)](PF_6)_2$ {L = phen (**1**), dpphen (**2**), and dmbpy (**3**)} were prepared. The calculated energies of the lowest singlet and triplet states in the $[Ir^{III}(L)_2](PF_6)_3$ {L = tterpy (**5**) and terpy (**6**)} complexes are in good agreement with the experimental absorption and phosphorescence spectra.

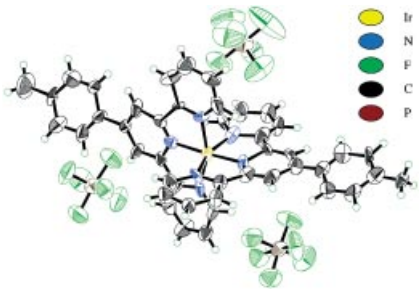


**N. Yoshikawa,* S. Yamabe, N. Kanehisa, Y. Kai, H. Takashima, K. Tsukahara ..... 1911–1919**

Synthesis, Characterization, and DFT Investigation of $Ir^{III}$ Tolylterpyridine Complexes

**Keywords:** Iridium / Terpyridine / Absorption / Emission / Density functional calculations

 © 2007 Wiley-VCH Verlag GmbH & Co. KGaA, Weinheim 

# CONTENTS

## Polynuclear Complexes

**V. Vertlib, J. Figueira, J. Mesquita, J. Rodrigues,* K. Nättinen, K. Rissanen* ..... 1920–1924**

A Trinuclear Aqua Cyano-Bridged Ruthenium Complex $[\{(\eta^5\text{-}C_5H_5)(PPh_3)_2Ru(\mu\text{-}CN)\}_2RuCl_2(PPh_3)(H_2O)]PF_6$: Synthesis, Characterization and Crystal Structure

**Keywords:** Ruthenium / Trinuclear complexes / Bridging ligands / X-ray structure / Metal–metal interactions / Chain structures

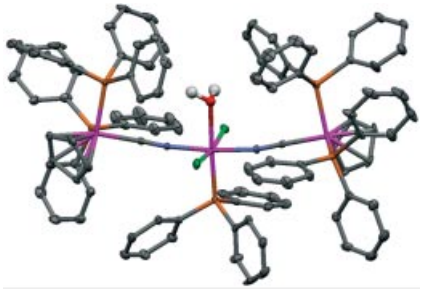

An unusual organometallic trinuclear aqua cyano-bridged complex $[\{(\eta^5\text{-}C_5H_5)(PPh_3)_2Ru(\mu\text{-}CN)\}_2RuCl_2(PPh_3)(H_2O)]PF_6$ was isolated and structurally characterized by FTIR, $^1H$, $^{13}C$, and $^{31}P$ NMR spectroscopy, mass spectrometry, elemental analysis, single-crystal X-ray diffraction, and cyclic voltammetry. The complex represents a rare example of a Ru–C≡N–Ru′–N≡C–Ru array with Ru-coordinated water.

## Water Chains

**Y. Jin, Y. Che, S. R. Batten, P. Chen, J. Zheng* ..... 1925–1929**

Unusual T4(1) Water Chain Stabilized in the One-Dimensional Chains of a Copper(II) Coordination Polymer

**Keywords:** Water chain / Self assembly / One dimensional / Coordination polymers

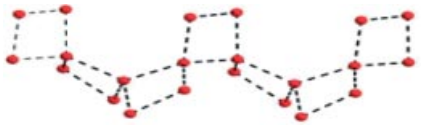

The water chain within the $Cu^{II}$ coordination polymer lies about the $3_2$ screw axes. The water tetramers are connected through the shared O(4) corners to form a chain with T4(1) symmetry.

## Suzuki Cross-Coupling

**R. Venkateswaran, M. S. Balakrishna,* S. M. Mobin ..... 1930–1938**

The Iminophosphorane-Phosphane $Ph_2P\text{-}C_6H_4OC_6H_4PPh_2{=}NP(O)(OPh)_2$: Synthesis, Reactivity, and Catalytic Activity in Suzuki Cross-Coupling and the Homogeneous Hydrogenation of Olefins

**Keywords:** Monoimination / Monophosphane / Iminophosphorane-phosphane / Staudinger reaction / Suzuki cross-coupling

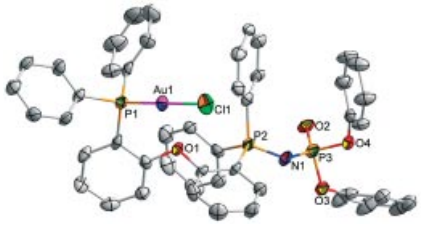


The synthesis of the iminophosphorane-phosphane ligand $Ph_2PC_6H_4OC_6H_4PPh_2{=}NP(O)(OPh)_2$ (**1**) and its Pt, Pd, Au and Rh complexes is reported. Its catalytic utility in Suzuki cross-coupling reactions and the hydrogenation of olefins is also described.

**If not otherwise indicated in the article, papers in issue 12 were published online on April 4, 2007**

 © 2007 Wiley-VCH Verlag GmbH & Co. KGaA, Weinheim 

DOI: 10.1002/ejic.200700173

# Hydrogenation of a Trinuclear $\mu_3$-Imido Complex of Ruthenium: Homolytic or Heterolytic H–H Bond Cleavage?

**Hajime Kameo,[a] Yumiko Nakajima,[a] and Hiroharu Suzuki*[a]**

**Keywords:** Hydrido complexes / Ruthenium / Cleavage reactions / Imido complexes / Trinuclear complexes

To elucidate the mode of hydrogen–hydrogen bond cleavage at transition metal sites that cooperate with a heteroatom, the hydrogenation of trinuclear $\mu_3$-imido complex $(Cp^*Ru)_3(\mu_3\text{-}NH)(\mu\text{-}H)_3$ ($Cp^* = \eta^5\text{-}C_5Me_5$) (**1**) with deuterium was carried out. The percentage of deuterium content in the amido ligand of $(Cp^*Ru)_3(\mu\text{-}NH_2)(\mu\text{-}H)_4$ (**2**), which was generated as an intermediate in the reaction of **1** with dihydrogen, proved that hydrogenation of **1** to **2** proceeded through homolytic cleavage of dihydrogen.

(© Wiley-VCH Verlag GmbH & Co. KGaA, 69451 Weinheim, Germany, 2007)

## Introduction

Activation of dihydrogen at transition metal sites is a critical issue in a wide field ranging from inorganic and organometallic chemistry to enzymology.[1] One focus of interest is the mode of hydrogen–hydrogen bond cleavage. Two possible pathways, namely homolysis and heterolysis, are proposed for the activation of dihydrogen. H–H bond cleavage by oxidative addition of dihydrogen to the metal center to form a dihydridometal species is a typical example of homolysis. In contrast, [FeFe]- and [FeNi]hydrogenase, of which the active site consists of iron and nickel ions bridged by two sulfur atoms and another heteroatom, is recognized to activate dihydrogen in a heterolytic manner to generate hydride and a proton.[2] In connection with the enzymatic reaction, the reaction of dihydrogen with a complex whose metal center cooperates with a heteroatom has engaged the attention of inorganic chemists.[3]

We have reported, thus far, that the reaction of triruthenium pentahydrido complex, $(Cp^*Ru)_3(\mu\text{-}H)_3(\mu_3\text{-}H)_2$ (**3**), with ammonia or hydrazine leads to the formation of the corresponding mono($\mu_3$-imido) complex, $(Cp^*Ru)_3(\mu\text{-}H)_3(\mu_3\text{-}NH)$ (**1**).[4,5] The resulting $\mu_3$-imido complex **1** readily undergoes hydrogenation with 5 atm of dihydrogen to afford **3** and ammonia, quantitatively (Scheme 1).

Complex **1** has a Lewis basic nitrogen atom directly bound to the ruthenium center and it would be of interest to determine whether the hydrogenation reaction proceeds by way of homolytic cleavage of dihydrogen at one of the ruthenium atoms or by heterolytic cleavage with participation of the adjacent nitrogen atom (Figure 1). In the homolysis step with the use of deuterium instead of hydrogen (Figure 1a), the deuterium molecule can access the ruthenium atom from the opposite face of the $\mu_3$-NH ligand with respect to the $Ru_3$ plane as a result of the decreased steric hindrance; therefore, the deuterium molecule can undergo oxidative addition to form a dideuterido species. Alternatively, a deuterium molecule approaching the reaction site from the NH-bridged face might be expected to undergo heterolytic cleavage by interaction with both the nitrogen and ruthenium atoms (Figure 1b). We report herein a mech-

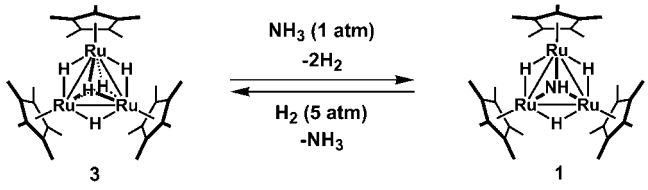


Scheme 1. Activation of N–H bonds of ammonia by trinuclear polyhydrido cluster **3** and hydrogenolysis of $\mu_3$-imido complex **1**.

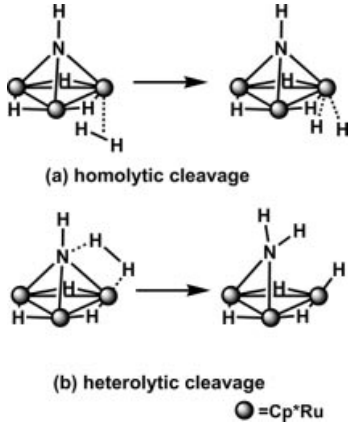


Figure 1. Activation of dihydrogen on the metal imido cluster.

[a] Department of Applied Chemistry
Graduate School of Science and Engineering Tokyo Institute of Technology
O-okayama, Meguro-ku, Tokyo 152-8552, Japan
Fax: +81-3-5734-3913
E-mail: hiroharu@n.cc.titech.ac.jp

 © 2007 Wiley-VCH Verlag GmbH & Co. KGaA, Weinheim 

anistic study of the hydrogenation of $\mu_3$-imido complex **1** where deuterium-labeling experiments showed conclusively that the reaction proceeds through oxidative addition of deuterium to the ruthenium atom.

## Results and Discussion

Hydrogenation of $\mu_3$-imido complex **1** proceeds via intermediary μ-amido complex **2**.[5] The reaction of **1** with 1 atm of hydrogen at room temperature was monitored by $^1$H NMR spectroscopy, and the formation of μ-amido complex **2** was revealed; the yields of **2** and pentahydride **3** reached 91 and 6%, respectively, after 170 h. Intermediary μ-amido complex **2** underwent subsequent hydrogenation at 60 °C for 90 h to lead to the quantitative formation of **3** and ammonia (Scheme 2).

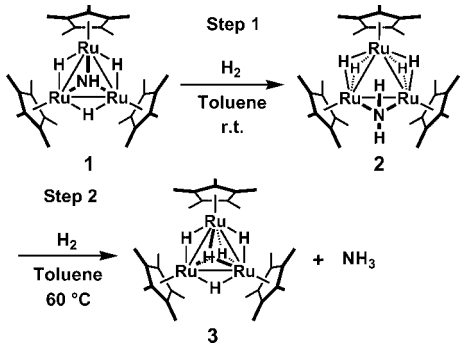


Scheme 2. Stepwise hydrogenolysis of $\mu_3$-imido cluster **1** to generate **3** and $NH_3$ via μ-amido cluster **2**.

Compound **2** was isolated by crystallization from a cold (–30 °C) toluene solution of a mixture of **1**, **2**, and **3**. The structure of compound **2** was determined by an X-ray diffraction study with the use of a single crystal that was obtained from the NMR sample solution (Figure 2). The nitrogen atom of the amido ligand is located above the plane defined by the three ruthenium atoms. Notably, one of the hydrogen atoms attached to the nitrogen atom, $H_A$, is located inside the $Ru_3N$ core and the other hydrogen atom, $H_B$, is located outside the $Ru_3N$ core. The broad resonance signals which appeared at $\delta$ = 2.86 and 5.05 ppm in the $^1$H NMR spectrum of **2** recorded at –60 °C were assigned to $H_A$ and $H_B$, respectively, on the basis of shielding/deshielding effects of the aromatic ring current. The resonance signal of the proton located inside the $Ru_3N$ core is shielded by the ring current, and as a result it is shifted upfield. Variable temperature $^1$H NMR spectra exhibited broadening of signals for both $H_A$ and $H_B$ and a reduction in the difference of the chemical shifts between these two μ-amido protons along with the rise in temperature. This showed the site-exchange between $H_A$ and $H_B$, possibly by a pivot motion (Scheme 3), and was confirmed by an SST experiment.[6] This type of dynamic process, namely, in-to-out site-exchange of protons, was reported for several trinuclear transition-metal clusters.[7]

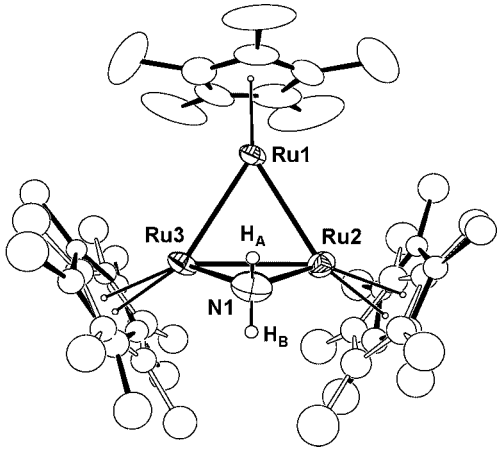


Figure 2. Molecular structure of μ-amido complex **2** with thermal ellipsoids at the 30% probability level.

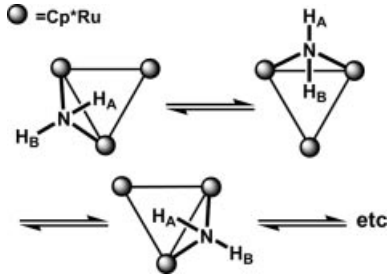


Scheme 3. Exchange of the sites between $H_A$ and $H_B$.

Two sets of hydrido ligands of **2** exchange the coordination site with each other, and their resonance signals coalesce around room temperature. The enthalpy and entropy of activation for this exchange process were estimated at $\Delta H^{\ddagger} = 12.6 \pm 0.6$ kcal mol$^{-1}$ and $\Delta S^{\ddagger} = 3.6 \pm 0.1$ cal mol$^{-1}$ K$^{-1}$, respectively, on the basis of line-shape analysis with the use of a *g*-NMR program package (vide infra). Interestingly, the hydrido ligands and the amido hydrogen of **2** do not undergo coordination site-exchange whereas the hydrido ligands mutually exchange the coordination sites. It should be noted that there is also no site-exchange process between the imido hydrogen and the hydrido ligands in **1**.

As mentioned above, amido complex **2** reacted with 1 atm of hydrogen to afford **3** with an equimolar amount of ammonia. In contrast, complex **2** underwent disproportionation to yield **1** and **3** in the absence of hydrogen, but the conversion of **2** is at most 4% after 120 h at room temperature.

On the basis of the above observations, the reaction of **1** with deuterium was examined to elucidate the mode of hydrogen activation in the hydrogenolysis of the ruthenium–nitrogen bond. The reaction was monitored by $^1$H NMR spectroscopy, and the product and isotopomer ratios were estimated on the basis of the integral intensity of the resonance signals.[8]

The reaction of $\mu_3$-imido complex **1** with 1 atm of deuterium in [$D_8$]toluene was monitored at ambient temperature by $^1$H NMR spectroscopy by using cyclooctane ($\delta$ =

 © 2007 Wiley-VCH Verlag GmbH & Co. KGaA, Weinheim 

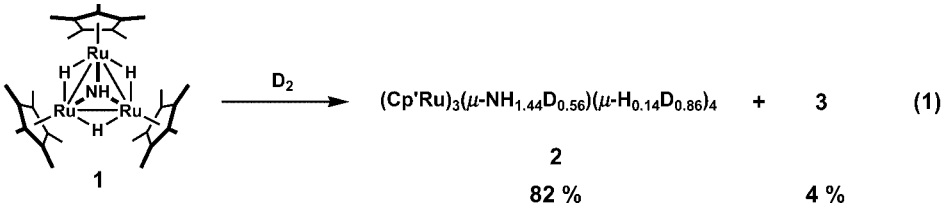


1.49 ppm, [$D_8$]toluene, 23 °C) as an internal standard. Conversion of **1** reached 86% after 125 h, and the molar ratio among **1**, μ-amido complex **2**, and pentahydrido complex **3** was 14:82:4 [Equation (1)].

In the hydrido region of the $^1$H NMR spectrum, two singlet peaks assignable to the signal of the hydrido ligands of isotopomers $(Cp^*Ru)_3(\mu\text{-}H)_2(\mu\text{-}D)(\mu_3\text{-}NH)$ (**1**-$d_1$) and $(Cp^*Ru)_3(\mu\text{-}H)(\mu\text{-}D)_2(\mu_3\text{-}NH)$ (**1**-$d_2$) appeared at $\delta$ = –14.51 and –14.73 ppm, respectively. Notably, the hydrido signal of isotopomer **1**-$d_0$ ($\delta$ = –14.30 ppm) disappeared. Although the hydrido signal of isotopomer $(Cp^*Ru)_3(\mu\text{-}D)_3(\mu_3\text{-}NH)$ (**1**-$d_3$) was, of course, not observable, the amount of **1**-$d_3$ formed in the reaction was unambiguously estimated on the basis of the integral intensity ratio between the Cp* proton signal and the hydrido signals. As a result, the isotopomer ratio **1**-$d_0$/**1**-$d_1$/**1**-$d_2$/**1**-$d_3$ was estimated at 0:1:4:9, and the percentage of deuterium content in the hydrido ligand of unconverted **1** was 86%. Here, it should be stressed that the hydrogen of the imido ligand was not replaced by deuterium at all, and this clearly shows the absence of a direct exchange process between the hydrogen at the imido nitrogen and atmospheric deuterium.

Conversely, the integral intensity of the signal for the amido proton of **2** formed in the reaction was 1.44 H, and the percentage of deuteration for the amido proton was estimated to be 28%, whereas that for the hydrido ligand was estimated at 86% (0.56 H). Interestingly, the percentage of deuteration was practically equal for both amido signals at $\delta$ = 2.86 and 5.05 ppm. This strongly supports the presence of a dynamic process, such as a pivot-motion mentioned above, which exchanges the site of the two amido protons, $H_A$ and $H_B$.

We then examined the reaction of **2**, which was isolated in the reaction of **1** with dihydrogen, with deuterium. The reaction of **2** with deuterium (1 atm) was monitored by $^1$H NMR spectroscopy with the use of cyclooctane as an internal standard. The reaction proceeded slowly at ambient temperature, and the conversion yield from **2** to **3** is at most 4% after 280 h. The hydrido ligand of unconverted amido complex **2** was partially deuterated, and the percentage of deuteration of the hydrido ligand was estimated at 74%. In contrast to the hydrido ligand, the integral intensity of the amido proton signal remained almost unchanged despite a long reaction time, and the percentage of deuteration was estimated at less than 5%.

These results show that there is not any direct exchange process between the hydrogen atom of the amido ligand and atmospheric deuterium. According to these observations, we concluded that the deuterium was incorporated into the amido ligand of **2** through hydrogenolysis of the Ru–N bond of **1**, which involves the heterolytic activation of $D_2$ (path **a**) or through reductive coupling between the imido group and the deuterido ligand formed as a result of the homolytic activation, namely, oxidative addition of $D_2$ (path **b**). The two possible reaction paths are shown in Scheme 4.

If hydrogenation of **1** proceeded by path **a**, the percentage of deuteration of the amido ligand should be 50%. This value is far from the observed one, and path **a** should, therefore, be disregarded.

Path **b** involves the formation of $\mu_3$-imido-pentahydrido species **B**. The formation of 48e species **B** is rationalized because the H/D exchange reaction between the hydrido ligand of **1** and $D_2$ likely proceeds through an associative pathway rather than a dissociative path by way of an intermediary $\mu_3$-imido-monohydrido species (44e). In the first stage, deuterium would oxidatively add to $\mu_3$-imido complex **1** via an intermediary $\sigma$-$D_2$ complex to generate isotopomer **B**-$d_2$ (48e), in which the coordination sites were exchanged between the deuterides and the hydrides. As a result, the deuterium atom would scramble around the coordination sites for the hydrido ligand. Rapid scrambling of the deuterido ligand is proved by the fact that the $^1$H NMR spectroscopic signals for the three $C_5Me_5$ groups are observed to be equivalent at any percentage of deuterium content in **1**-$d_n$. Isotopomer **B**-$d_2$ would then undergo reductive coupling between the imido nitrogen and the hydrido ligand to yield μ-amido complex **2**-$d_2$. The percentage of deuterium content in the amido ligand should, therefore, be 20% (0.4 D/2 H). In contrast, the liberation of hydrogen ($H_{1.2}D_{0.8}$) from **B**-$d_2$ affords $\mu_3$-imido complex **1**-$d_{1.2}$. Isotopomer **1**-$d_{1.2}$ would react again with deuterium to generate **2**-$d_{3.2}$, which should contain 0.64 D (32% deuterium content) at the amido nitrogen atom. The observed value of 28% for the percentage of deuterium content in the amido ligand in **2** is approximately consistent with that anticipated for the reaction paths involving homolytic activation, namely, oxidative addition of deuterium. This is strongly supported by the time-course of the yield of **2** and the percentage of deuterium content in the amido ligand (Figure 3). The percentage of deuterium content is about 20% in the early stage of the reaction, and grows gradually along with the progress of the reaction. The deuterium content finally reached 28% after 125 h. Path **b** rationally accounts for these results.

 © 2007 Wiley-VCH Verlag GmbH & Co. KGaA, Weinheim 

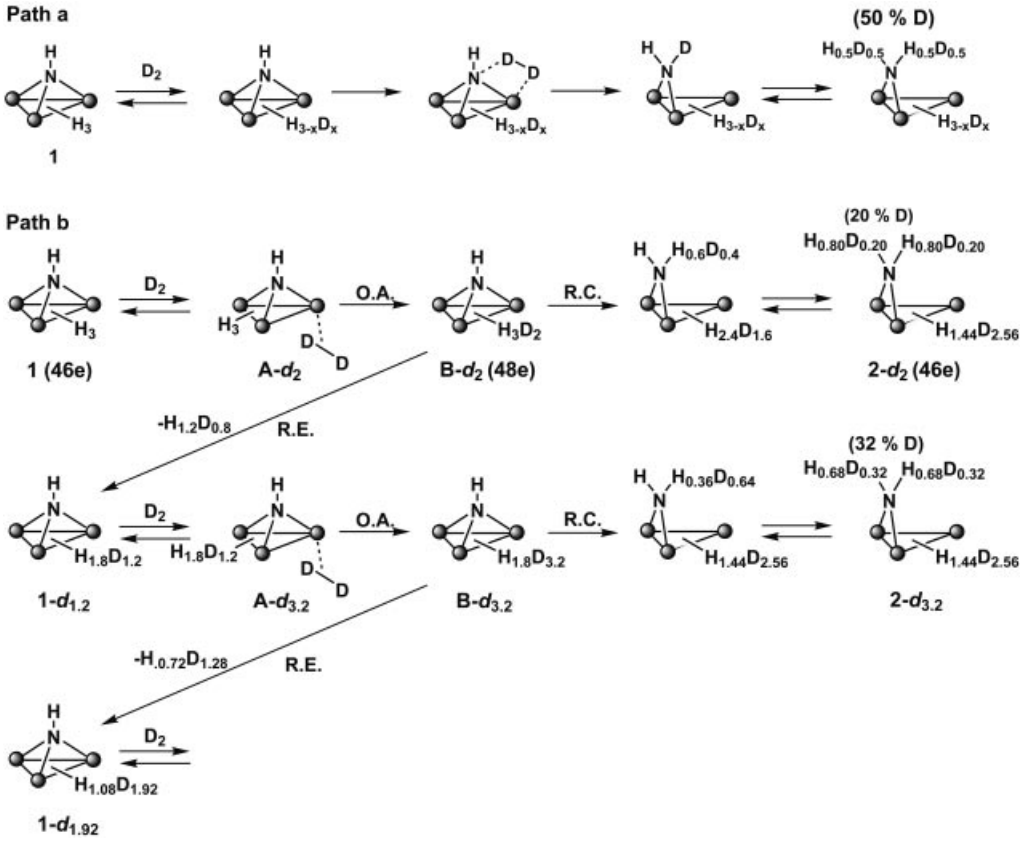


Scheme 4. Plausible mechanism for the reaction of **1** with $D_2$.

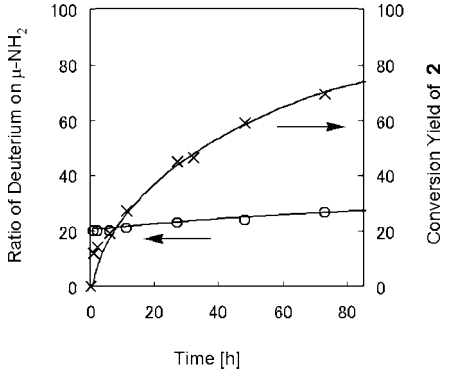


Figure 3. Time conversion regarding the reaction of **1** with $D_2$ (×: conversion yield of **2**, ○: the percentage of deuteration for the amido proton).

## Conclusion

We have experimentally elucidated that hydrogenation of triruthenium $\mu_3$-imido complex **1** to yield μ-amido complex **2** (Step 1, Scheme 2) proceeds through homolytic cleavage of dihydrogen. However, the reaction path for the hydrogenation of **2** to form **3** and ammonia (Step 2, Scheme 2) still remains unclear. Theoretical study is now in progress by using $[(C_5H_5)Ru]_3(\mu\text{-}H)_3(\mu_3\text{-}NH)$ as a model compound.

## Experimental Section

**General Procedure:** The compounds described below were handled under an argon atmosphere with rigorous exclusion of air and water by using Schlenk techniques. Dihydrogen and deuterium were obtained from Fujii Co. Ltd., and no further purification was performed. $(Cp^*Ru)_3(\mu\text{-}H)_3(\mu_3\text{-}NH)$ (**1**), $(Cp^*Ru)_3(\mu\text{-}H)_4(\mu\text{-}NH)$ (**2**), and $(Cp^*Ru)_3(\mu\text{-}H)_3(\mu_3\text{-}H)_2$ (**3**) were prepared as described previously.[4,5] $[D_8]$toluene was dried with sodium benzophenone ketyl and distilled under an argon atmosphere. $^1H$ and $^{13}C$ NMR spectra were recorded with a Varian INOVA 400 Fourier transform spectrometer with tetramethylsilane as an internal standard.

**Reaction of $(Cp^*Ru)_3(\mu_3\text{-}NH)(\mu\text{-}H)_3$ (1) with $H_2$. Formation of μ-Amido Complex 2:** An NMR sample tube equipped with a Teflon stopcock was charged with **1** (6.1 mg, 0.0084 mmol), $[D_8]$toluene (0.4 mL), and cyclooctane (1 μL) as an internal standard. The sample tube was evacuated at –196 °C, and atmospheric pressure of dihydrogen (2.6 mL, 0.12 mmol) was introduced. The reaction was performed at room temperature and monitored by $^1H$ NMR spectroscopy. After 170 h, $(Cp^*Ru)_3(\mu\text{-}NH_2)(\mu\text{-}H)_4$ (**2**) and $(Cp^*Ru)_3(\mu_3\text{-}H)_2(\mu\text{-}H)_3$ (**3**) were formed in 91 and 6% yield, respectively. The reaction was further carried out at 60 °C for 90 h to generate **3** quantitatively. Data for **2**: $^1H$ NMR (400 MHz, $[D_8]$toluene, –80 °C, TMS): $\delta$ = –17.71 (s, 2 H, Ru-*H*), –5.48 (s, 2 H, Ru-*H*), 1.81 (s, 30 H, Cp*-*Me*), 2.06 (s, 15 H, Cp*-*Me*), 2.88 (br. s, 1 H, $w_{1/2}$ = 10.5 Hz, N-*H*), 5.09 (br. s, 1 H, $w_{1/2}$ = 10.4 Hz, N-*H*) ppm. $^1H$ NMR (400 MHz, $[D_8]$toluene, 80 °C, TMS): $\delta$ = –11.83 (br. s, 4 H, $w_{1/2}$ = 45.2 Hz, Ru-*H*), 1.76 (s, 30 H, $C_5Me_5$), 1.96 (s, 15 H, $C_5Me_5$), 2.78 (br. s, 1 H, $w_{1/2}$ = 20.5 Hz, N-*H*), 4.85 (br. s, 1 H,

 © 2007 Wiley-VCH Verlag GmbH & Co. KGaA, Weinheim 

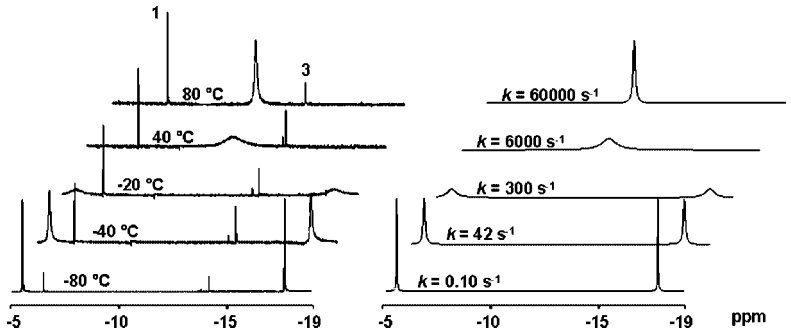


Figure 4. Experimental (left) and simulated (right) variable-temperature $^1$H NMR spectra of **2**, which shows the region of the hydride protons.

$w_{1/2}$ = 20.3 Hz, N-*H*) ppm. $^{13}$C NMR (100 MHz, [D$_8$]toluene, 23 °C, TMS): $\delta$ = 12.4 (q, $J_{CH}$ = 125.6 Hz, Cp*-*Me*), 13.2 (q, $J_{CH}$ = 125.4 Hz, Cp*-*Me*), 84.1 (s, Cp*-ring), 85.1 (s, Cp*-ring) ppm. $C_{30}H_{51}N_1Ru_3$ (728.9): calcd. C 49.57, H 6.79, N 1.92; found C 49.22, H 6.81, N 2.03.

**X-ray Diffraction Studies:** A single crystal of **2** for X-ray analysis was obtained directly from the preparations described above and mounted on glass fibers. The diffraction experiment was performed with a Rigaku R-AXIS RAPID imaging plate diffractometer with graphite-monochromated Mo-$K_\alpha$ radiation ($\lambda$ = 0.71069 Å) at 173 K within 3.28° < $\theta$ < 27.48°. Cell refinement and data reduction were performed with the PROCESS-AUTO program.[9] Intensity data were corrected for Lorentz-polarization effects and for empirical absorption. The structure of **2** was solved by the Patterson method by using the SHELX-97 program package.[10] All non-hydrogen atoms were found by the difference Fourier synthesis and were refined anisotropically except for the disordered atoms described below. The refinement was carried out by least-squares methods based on $F^2$ with all measured reflections. For **2**, disorder at Cp* ligands bonded at Ru(2) and Ru(3) were refined in the ratio of 40:60. Crystal data for **2**: monoclinic, space group $P2_1/n$ (No. 14), $a$ = 11.9713(10), $b$ = 11.7390(10), $c$ = 22.540(2) Å, $\beta$ = 102.602(8)°, $V$ = 3091.3(5) Å$^3$, $Z$ = 4, $\rho_{calcd.}$ = 1.566 Mg m$^{-3}$, $\mu$(Mo$_{Ka}$) = 1.464 mm$^{-1}$, of the 24614 reflections that were collected, 7410 were unique ($R_{int}$ = 0.0981), $R_1$ = 0.1089 [$I > 2\sigma(I)$], $wR_2$ = 0.3149 [$I > 2\sigma(I)$], GOF = 1.250, $\Delta\rho_{min/max}$ = +4.030/–1.855 e Å$^{-3}$. CCDC-630784 contains the supplementary crystallographic data for this paper. These data can be obtained free of charge from The Cambridge Crystallographic Data Centre via www.ccdc.cam.ac.uk/data_request/cif.

**Measurement of 2 by Variable-Temperature $^1$H NMR Spectroscopy:** An NMR sample tube equipped with a Teflon stopcock was charged with **2** (10.2 mg, 0.0014 mmol), [D$_8$]toluene (0.5 mL), and cyclooctane (1 μL) as an internal standard. Figure 4 shows the $^1$H NMR spectra (hydride region) of **2** at variable temperatures. The signals on the left-hand side are the experimental set, and the right-hand side shows the signals simulated. The activation parameters were estimated by line-shape analysis using the g-NMR program. Temperature dependence of the rate constants gave activation parameters $\Delta H^\ddagger$ = 12.6 ± 0.6 kcal mol$^{-1}$, $\Delta S^\ddagger$ = 3.6 ± 0.1 cal mol$^{-1}$ K$^{-1}$, and $\Delta G^\ddagger$ = 13.2 ± 0.6 kcal mol$^{-1}$. This exchange process is shown in Scheme 5.

**Thermolysis of 2:** An NMR sample tube equipped with a Teflon stopcock was charged with **2** (8.1 mg, 0.011 mmol), [D$_8$]toluene (0.4 mL), and cyclooctane (1 μL) as an internal standard. The reaction was performed at room temperature and monitored by $^1$H NMR spectroscopy. After 120 h, the $^1$H NMR spectrum showed

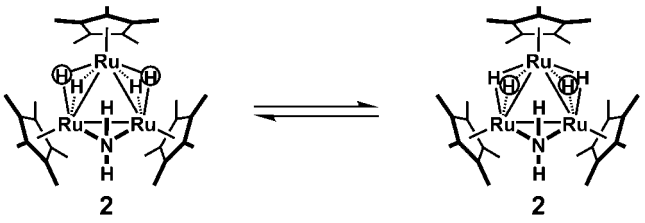


Scheme 5. Coordination site exchange between the two sets of hydrido ligands of **2**.

that **2** underwent disproportionation to afford **1** and **3**, both in 2% yield.

**Reaction of Complex 1 with Molecular Deuterium:** An NMR sample tube equipped with a Teflon stopcock was charged with **1** (8.3 mg, 0.011 mmol), [D$_8$]toluene (0.4 mL), and cyclooctane (1 μL) as an internal standard. The sample tube was evacuated at –196 °C, and atmospheric pressure of molecular deuterium (2.6 mL, 0.12 mmol) was introduced. The reaction was performed at room temperature and monitored by $^1$H NMR spectroscopy. After 125 h, the $^1$H NMR spectrum showed the formation of **1**, **2**, and **3** in 14, 82, and 4% yield, respectively. The percentages of deuteration of unconverted **1** for the imido proton and the hydrido ligand were estimated at 0 and 86%, respectively. The percentages of deuteration of **2** for the amido proton and the hydrido ligand were estimated at 28 and 86%, respectively.

**Reaction of Complex 2 with Molecular Deuterium:** An NMR sample tube equipped with a Teflon stopcock was charged with **2** (7.5 mg, 0.010 mmol), [D$_8$]toluene (0.4 mL), and cyclooctane (1 μL) as an internal standard. The sample tube was evacuated at –196 °C, and atmospheric pressure of molecular deuterium (2.6 mL, 0.12 mmol) was introduced. The reaction was performed at room temperature and monitored by $^1$H NMR spectroscopy. After 280 h, the $^1$H NMR spectrum showed the formation of **2** and **3** in 96 and 4% yield, respectively. The percentage of deuteration of **2** for the hydrido ligand was estimated at 74%, and that for the amido proton was estimated at less than 5%.

## Acknowledgments

The present research is supported by the Ministry of Education, Culture, Sports, Science, and Technology, Japan by grant No. 18064007 (Priority Area "Synergy of Elements") and from Japan Society of the Promotion of Science by grant No.18105002 [Scientific Research (S)]. The authors are also grateful to Kanto Chemical Co., Inc., for a generous supply of pentamethylcyclopentadiene.

 © 2007 Wiley-VCH Verlag GmbH & Co. KGaA, Weinheim 

[1] a) G. J. Kubas, *Metal Dihydrogen and σ-Bond Complexes*, Kluwer Academic, New York, **2001**; b) R. H. Crabtree, *The Organometallic Chemistry of Transition Metals*, Wiley, New York, **1988**; c) S. Sabo-Etienne, B. Chaudret, *Chem. Rev.* **1998**, *98*, 2077–2091; d) D. M. Heinekey, W. J. Oldham, *J. Chem. Rev.* **1993**, 913–926; e) S. E. Clapham, A. Hadzovic, R. H. Morris, *Coord. Chem. Rev.* **2004**, *248*, 2201–2237; f) R. K. Thauer, A. R. Klein, G. C. Hartmann, *Chem. Rev.* **1996**, *96*, 3031–3042; g) P. Maire, T. Büttner, F. Breher, P. L. Floch, H. Grützmacher, *Angew. Chem. Int. Ed.* **2005**, *44*, 6318–6323.

[2] a) X. Liu, S. K. Ibrahim, C. Tard, C. J. Pickett, *Coord. Chem. Rev.* **2005**, *249*, 1641–1652; b) T. B. Rauchfuss, *Inorg. Chem.* **2004**, *43*, 14–26; c) M. Y. Darensbourg, E. J. Lyon, J. J. Smee, *Coord. Chem. Rev.* **2000**, *206*, 533–561; d) Y. Higuchi, H. Ogata, K. Miki, N. Yasuoka, T. Yaghi, *Structure* **1999**, *7*, 549–556; e) S. Niu, N. B. Hall, *Inorg. Chem.* **2001**, *40*, 6201–6203; f) F. A. Armstrong, *Curr. Opin. Chem. Biol.* **2004**, *8*, 133–140.

[3] a) G. Zampella, M. Bruschi, P. Fantucci, L. D. Gioia, *J. Am. Chem. Soc.* **2005**, *127*, 13180–13189; b) A. Ienco, M. J. Calhorda, J. Reinhold, F. Reinen, C. Bianchini, M. Peruzzini, F. Vizza, C. Mealli, *J. Am. Chem. Soc.* **2004**, *126*, 11954–11965; c) R. C. Linck, R. J. Pafford, T. B. Rauchfuss, *J. Am. Chem. Soc.* **2001**, *123*, 8856–8857; d) Y. Ohki, N. Matsuura, T. Marumoto, H. Kawaguchi, K. Tatsumi, *J. Am. Chem. Soc.* **2003**, *125*, 7978–7988; e) D. Sellmann, F. Geipel, M. Moll, *Angew. Chem. Int. Ed.* **2000**, *39*, 561–563; f) D. Sellmann, R. Prakash, F. W. Heinemann, M. Moll, M. Klimowicz, *Angew. Chem. Int. Ed.* **2004**, *43*, 1877–1880.

[4] a) Y. Nakajima, H. Suzuki, *Organometallics* **2003**, *22*, 959–969; b) H. Suzuki, T. Kakigano, K. Tada, M. Igarashi, K. Matsubara, A. Inagaki, M. Oshima, T. Takao, *Bull. Chem. Soc. Jpn.* **2005**, *78*, 67.

[5] Y. Nakajima, H. Kameo, H. Suzuki, *Angew. Chem. Int. Ed.* **2006**, *45*, 950–952.

[6] The spin saturation transfer experiment was carried out at 80 °C with complex **2**. It was observed that irradiation of the amido peak at $\delta$ = 2.78 ppm led to an approximately 80% decrease in intensity of another N–H signal at $\delta$ = 4.85 ppm in the $^1$H NMR spectrum. This observation can be interpreted to result from an in-to-out exchange process of the protons.

[7] a) F. H. Försterling, C. E. Barnes, *J. Am. Chem. Soc.* **1997**, *119*, 7585–7586; b) S. E. Kabir, M. Day, M. Irving, T. McPhillips, H. Minassian, E. Rossenberg, K. I. Hardcastle, *Organometallics* **1991**, *10*, 3997–4004; c) Y. Sanctis, A. J. Arce, F. Canãvera, R. Machado, A. J. Deeming, T. González, E. Galarza, *J. Organomet. Chem.* **2004**, *689*, 2025–2028; d) $(Cp^*Ru)_2(Cp^*Ir)(\mu\text{-}PMe_2)(\mu\text{-}H)_4$ demonstrated that the site exchange between methyl group $Me_A$, located inside the $Ru_2Ir$ core, and $Me_B$, located outside the $Ru_2Ir$ core, occurs by a pivot motion.

[8] The longitudinal relaxation time $T_1$ of the amido proton signals at $\delta$ = 2.88 and 5.09 ppm are 313 and 323 ms, respectively, at room temperature. The signals are sharpened at low temperature. We, therefore, recorded the $^1$H NMR spectra at –80 °C with a relaxation delay (D1) of 10 s.

[9] *PROCESS-AUTO*, Automatic Data Acquisition and Processing Package for Imaging Plate Diffractometer, Rigaku Corporation, Tokyo, Japan, **1998**.

[10] G. M. Sheldrick, *SHELX-97*, Program for Crystal Structure Determination, University of Göttingen, Göttingen, Germany, **1997**.

Received: December 28, 2006
Published Online: March 23, 2007

 © 2007 Wiley-VCH Verlag GmbH & Co. KGaA, Weinheim 

DOI: 10.1002/ejic.200601047

# Acetylide Addition to Bridging Vinyliminium Ligands in Dinuclear Complexes

**Luigi Busetto,[a] Fabio Marchetti,[b][‡] Stefano Zacchini,[a] and Valerio Zanotti*[a]**

**Keywords:** Acetylides / Dinuclear complexes / Bridging ligands / C–C bond formation

The (vinyliminium)diiron complexes $[Fe_2\{\mu\text{-}\eta^1{:}\eta^3\text{-}C_\gamma(R')=C_\beta(R')C_\alpha{=}N(Me)(R)\}(\mu\text{-}CO)(CO)(Cp)_2][SO_3CF_3]$ [R = Xyl, R′ = Me (**1a**); R = Xyl, R′ = Et (**1b**); R = R′ = Me (**1c**); R = Me, R′ = Et (**1d**); R = $CH_2Ph$, R′ = Me (**1e**); Xyl = 2,6-$Me_2C_6H_3$] undergo regio- and stereoselective addition by lithium acetylides. Addition of LiC≡CR′′ (R′′ = Tol, Ph, $SiMe_3$; Tol = 4-$MeC_6H_4$) to *trans*-**1a** occurs at the $C_\beta$ atom of the vinyliminium ligand and results in the formation of the bis(alkylidene) complexes *cis*-$[Fe_2\{\mu\text{-}\eta^1{:}\eta^2\text{-}C(Me)C(Me)(C{\equiv}CR'')CN(Me)(Xyl)\}(\mu\text{-}CO)(CO)(Cp)_2]$ [R′′ = Tol (**2a**), Ph (**2b**), $SiMe_3$ (**2c**)]. The molecular structure of **2a** has been determined by X-ray diffraction. Similarly, the diruthenium complex $[Ru_2\{\mu\text{-}\eta^1{:}\eta^3\text{-}C(Me)=C(Me)C=N(Me)(Xyl)\}(\mu\text{-}CO)(CO)(Cp)_2][SO_3CF_3]$ (**3**) reacts with LiC≡CTol to give the bis(alkylidene) compound $[Ru_2\{\mu\text{-}\eta^1{:}\eta^2\text{-}C(Me)C(Me)(C{\equiv}CTol)CN(Me)(Xyl)\}(\mu\text{-}CO)(CO)(Cp)_2]$ (**4**). Conversely, **1c** and **1d** undergo acetylide attack at the $C_\alpha$ atom of the vinyliminium ligand to yield the allylidene complexes $[Fe_2\{\mu\text{-}\eta^1{:}\eta^3\text{-}C(R')C(R')C(C{\equiv}CR'')N(Me)_2\}(\mu\text{-}CO)(CO)(Cp)_2]$ [R′ = Me, R′′ = Tol (**5a**); R′ = Me, R′′ = Ph (**5b**); R′ = Me, R′′ = $SiMe_3$ (**5c**); R′ = Me, R′′ = *n*Bu (**5d**); R′ = Me, R′′ = $C(Me)=CH_2$ (**5e**); R′ = Me, R′′ = H (**5f**); R′ = Et, R′′ = Tol (**5g**); R′ = Et, R′′ = Ph (**5h**); R′ = Et, R′′ = $SiMe_3$ (**5i**); R′ = Et, R′′ = $C(Me)=CH_2$ (**5j**)]. Analogously, the reaction of **1e** with LiC≡CPh affords $[Fe_2\{\mu\text{-}\eta^1{:}\eta^3\text{-}C(Me)C(Me)C(C{\equiv}CPh)N(Me)(CH_2Ph)\}(\mu\text{-}CO)(CO)(Cp)_2]$ (**6**). The molecular structure of **5h** has been determined by X-ray diffraction. Finally, **1b**, in both its *cis* and *trans* forms, undergoes acetylide attack at the $C_\alpha$ atom of the vinyliminium ligand to give the complexes $[Fe_2\{\mu\text{-}\eta^1{:}\eta^3\text{-}C(Et)C(Et)C(C{\equiv}CR'')N(Me)(Xyl)\}(\mu\text{-}CO)(CO)(Cp)_2]$ [R′′ = $SiMe_3$ (**7a**), H (**7b**)].
(© Wiley-VCH Verlag GmbH & Co. KGaA, 69451 Weinheim, Germany, 2007)

## Introduction

Dinuclear complexes are expected to provide new reactivity patterns that are distinct from those of similar monometallic complexes and open novel perspectives in the field of homogeneous catalysis and metal-assisted organic synthesis.[1] Our interest in this area has been focused on the chemistry of the vinyliminium-bridged diiron complexes **I** and **II** (Figure 1), which are obtained by the insertion of primary and secondary alkynes, respectively, into the metal–carbyne bond of $[Fe_2\{CN(Me)(R)\}(\mu\text{-}CO)(CO)(NCMe)(Cp)_2][SO_3CF_3]$.[2]

The carbon skeleton of the bridging framework in **I** and **II** should be able to be expanded by addition of appropriate carbon nucleophiles by taking advantage of the electrophilic character of the vinyliminium ligand. Thus, it has been found that the addition of $CN^-$ can be selectively directed to the iminium carbon atom ($C_\alpha$) or to the adjacent $C_\beta$ atom to afford $\mu\text{-}\eta^1{:}\eta^3$-vinylalkylidene and $\mu\text{-}\eta^1{:}\eta^2$-bis(alkylidene) ligands, respectively,[3] in a similar way to that reported for hydride addition.[4] However, the acidity of the

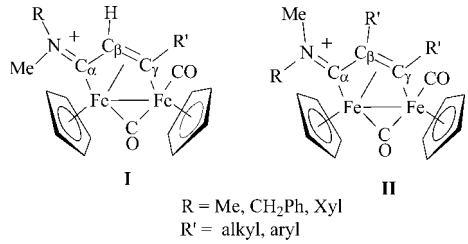


Figure 1. μ-Vinyliminium complexes.

$C_\beta$-H proton in complexes of type **I** represents a serious limitation to the addition of carbon nucleophiles. Indeed, reactions with organolithium reagents result in $C_\beta$-H proton removal rather than nucleophilic addition.[5] To overcome this limitation, further studies have been restricted to vinyliminium complexes of type **II**, which do not contain $C_\beta$-H protons. Nevertheless, organolithium reagents (LiMe, LiPh) have been found to attack the $C_5H_5$ ring instead of the bridging ligand. This initial attack is followed by hydride migration from the $C_5H_5R$ ring to the iminium carbon atom ($C_\alpha$).[6]

Moreover, we have recently communicated that the reaction of *cis*-$[Fe_2\{\mu\text{-}\eta^1{:}\eta^3\text{-}C(Me)=C(Me)C=N(Me)(Xyl)\}(\mu\text{-}CO)(CO)(Cp)_2][SO_3CF_3]$ with acetylides occurs at the carbonyl group with cleavage of the carbon–oxygen bond.[7] The three-carbon-atom chain of the bridging frame grows

[a] Dipartimento di Chimica Fisica e Inorganica, Università di Bologna,
Viale Risorgimento 4, 40136 Bologna, Italy
E-mail: valerio.zanotti@unibo.it
[b] Dipartimento di Chimica e Chimica Industriale, Università di Pisa,
Via Risorgimento 35, 56126 Pisa, Italy
[‡] Born in Bologna in 1974

 © 2007 Wiley-VCH Verlag GmbH & Co. KGaA, Weinheim 

by several units due to the inclusion of both the alkynyl (C≡CR′′) and the $C_\delta$ atom, which originates from the CO ligand (Scheme 1).

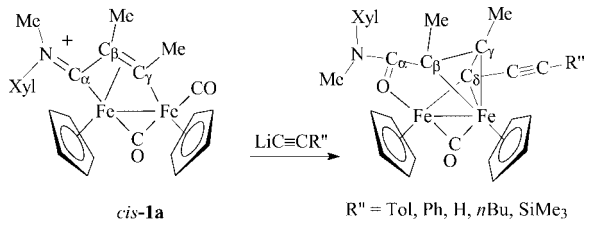


Scheme 1.

Herein we report on an extension of these studies, the aim of which was to establish whether the reaction reported above has a general character or if other reaction paths are available. A number of μ-vinyliminium complexes containing different substituents on the bridging ligand and displaying *cis* or *trans* geometry were examined in order to determine possible steric and electronic effects.

## Results and Discussion

The vinyliminium complexes investigated in this work are shown in Figure 2. They were obtained by insertion of the appropriate disubstituted alkyne into the Fe–aminocarbyne bond of the complexes $[Fe_2\{\mu\text{-}CN(Me)(R)\}(\mu\text{-}CO)(CO)(NCMe)(Cp)_2][SO_3CF_3]$ and $[Fe_2\{\mu\text{-}CN(Me)(R)\}(\mu\text{-}CO)(CO)(Cl)(Cp)_2]$ according to published methods.[2] It should be remembered that compounds **1a** and **1b** assume a *trans* geometry when they are obtained from the aminocarbyne complexes $[Fe_2\{\mu\text{-}CN(Me)(R)\}(\mu\text{-}CO)(CO)(Cl)(Cp)_2]$ by chloride abstraction in the presence of the appropriate alkyne, and that they can be converted into the corresponding *cis* isomers by heating in refluxing thf. Conversely, complexes **1c**–**e** are only isolated as their *cis* isomers.[2b]

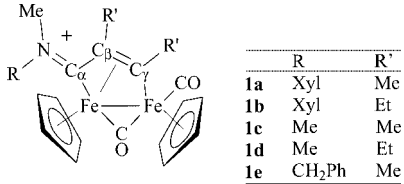

| | R | R′ |
|---|---|---|
| **1a** | Xyl | Me |
| **1b** | Xyl | Et |
| **1c** | Me | Me |
| **1d** | Me | Et |
| **1e** | $CH_2Ph$ | Me |

Figure 2. Vinyliminium complexes examined in this work.

Complex *trans*-**1a** reacts with LiC≡CR′′ (R′′ = Tol, Ph, $SiMe_3$; Tol = 4-$MeC_6H_4$) in thf solution to afford the corresponding acetylene-functionalised bis(alkylidene) complexes $[Fe_2\{\mu\text{-}\eta^1\text{:}\eta^2\text{-}C(Me)C(Me)(C{\equiv}CR'')CN(Me)(Xyl)\}(\mu\text{-}CO)(CO)(Cp)_2]$ (**2a**–**c**) as a consequence of nucleophilic addition at the $C_\beta$ atom of the vinyliminium ligand (Scheme 2).

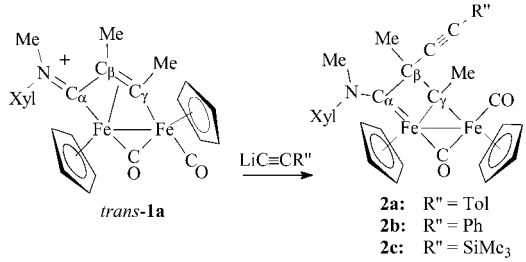


Scheme 2.

Thus, the reaction of *trans*-**1a** has a completely different outcome to that of the corresponding *cis* isomer (Scheme 1). Compounds **2a**–**c** were obtained in good yields (ca. 70%) after purification by column chromatography on alumina and were characterised by IR and NMR spectroscopy.

The structure of **2a** was determined by X-ray diffraction: the ORTEP molecular diagram is shown in Figure 3 and relevant bond lengths and angles are listed in Table 1.

The bridging ligand is coordinated to the Fe atoms through a bridging alkylidene carbon atom ($C_\gamma$) and an aminocarbene moiety. The main bond lengths and angles are similar to those of the analogous bis(alkylidene) complex $[Fe_2\{\mu\text{-}\eta^1\text{:}\eta^2\text{-}C(CO_2Me)CH_2CN(Me)(Xyl)\}(\mu\text{-}CO)(CO)(Cp)_2]$, which was obtained by hydride addition to $C_\beta$ of the vinyliminium ligand in *cis*-$[Fe_2\{\mu\text{-}\eta^1\text{:}\eta^3\text{-}C(CO_2Me){=}C(H)C{=}N(Me)(Xyl)\}(\mu\text{-}CO)(CO)(Cp)_2][SO_3CF_3]$.[4a] In particular, both the N(1)–C(15) [1.321(7) Å] and the Fe(1)–C(15) [1.899(6) Å] interactions show some double-bond character, which is typical for a terminal aminocarbene ligand.[8] In agreement with this, both C(15) and N(1) adopt a nearly perfect $sp^2$ hybridisation [sum of angles: 360.1(8)° and 360.0(8)°, respectively]. Moreover, the iron atoms are bound through nearly pure σ-interactions to the $C_\gamma$ atom [Fe(1)–C(13) 1.970(6), Fe(2)–C(13) 1.992(5) Å], as expected for a bridging alkylidene. Finally, the C(13)–C(14) [1.562(8) Å] and C(14)–C(15) [1.510(7) Å] interactions are typical for pure C–C single bonds, in agreement with the $sp^3$ hybridisation assumed by C(14); conversely, the C(17)–C(18) interaction [1.189(8) Å] exhibits a triple-bond character and the C(14)–C(17)–C(18)–C(19) unit is almost perfectly linear, as expected for an alkynyl group [C(14)–C(17)–C(18) 172.6(6), C(17)–C(18)–C(19) 179.6(7)°].

The spectroscopic data for **2a**–**c** are consistent with the structure of **2a**. The IR spectra (in $CH_2Cl_2$ solution) exhibit absorptions for a terminal and a bridging carbonyl group (1919 and 1749 $cm^{-1}$ for **2a**), and a band attributable to the $C_\alpha$–N interaction at about 1510 $cm^{-1}$. The $^{13}C$ NMR spectra contain a low-field resonance due to the aminocarbene carbon atom $C_\alpha$ ($\delta$ = 268.8 ppm for **2a**) and the $C_\gamma$ resonance ($\delta$ = 181.5 ppm for **2a**), in the range typical for alkylidene carbon atoms. Moreover, NOE experiments indicate that **2a**–**c** adopt the same geometry in solution as in the solid, with the Cp ligands mutually *cis* and a (*Z*) configuration for the Me and Xyl groups. Therefore, the acetylide addition is accompanied by *trans*/*cis* isomerisation.[9] The

 © 2007 Wiley-VCH Verlag GmbH & Co. KGaA, Weinheim 

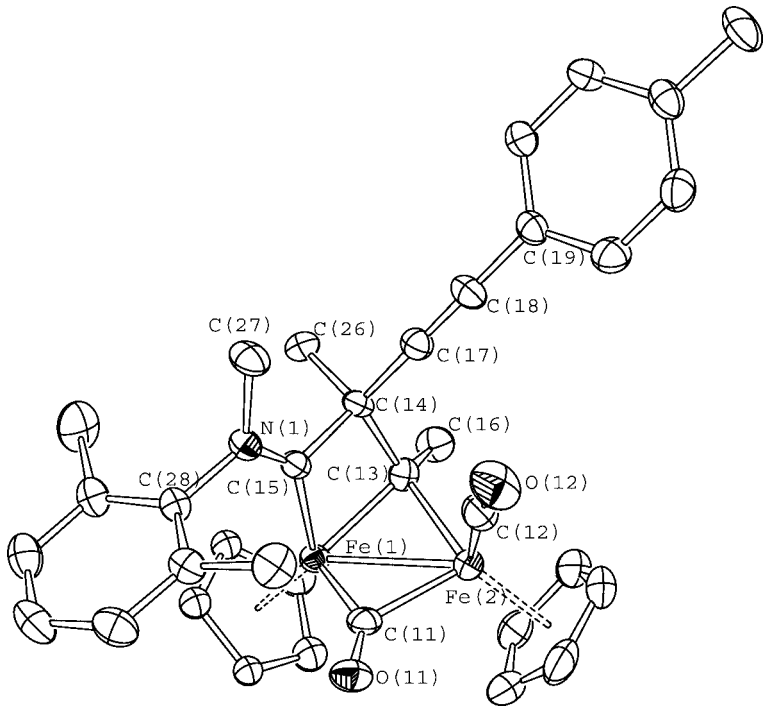


Figure 3. ORTEP drawing of $[Fe_2\{\mu\text{-}\eta^1\text{:}\eta^2\text{-}C(Me)C(Me)(C{\equiv}CTol)CN(Me)(Xyl)\}(\mu\text{-}CO)(CO)(Cp)_2]$ (**2a**). All H atoms have been omitted for clarity. Thermal ellipsoids are at the 30% probability level.

Table 1. Selected bond lengths [Å] and angles [°] for $[Fe_2\{\mu\text{-}\eta^1\text{:}\eta^2\text{-}C(Me)C(Me)(C{\equiv}CTol)CN(Me)(Xyl)\}(\mu\text{-}CO)(CO)(Cp)_2]$ (**2a**).

| | | | |
|---|---|---|---|
| Fe(1)–Fe(2) | 2.5085(12) | C(13)–C(14) | 1.562(8) |
| Fe(2)–C(12) | 1.747(8) | C(14)–C(15) | 1.510(7) |
| Fe(1)–C(11) | 1.832(6) | C(13)–C(16) | 1.512(8) |
| Fe(2)–C(11) | 1.965(6) | C(14)–C(17) | 1.479(8) |
| Fe(1)–C(13) | 1.970(6) | C(17)–C(18) | 1.189(8) |
| Fe(2)–C(13) | 1.992(5) | C(18)–C(19) | 1.430(8) |
| Fe(1)–C(15) | 1.899(6) | C(14)–C(26) | 1.551(8) |
| C(11)–O(11) | 1.198(7) | C(15)–N(1) | 1.321(7) |
| C(12)–O(12) | 1.155(8) | C(27)–N(1) | 1.471(7) |
| Fe(2)–C(13)–Fe(1) | 78.6(2) | C(14)–C(15)–Fe(1) | 97.8(4) |
| Fe(2)–C(13)–C(14) | 118.2(4) | C(14)–C(17)–C(18) | 172.6(6) |
| C(13)–C(14)–C(15) | 94.5(4) | C(17)–C(18)–C(19) | 179.6(7) |
| C(15)–N(1)–C(27) | 124.2(5) | C(27)–N(1)–C(28) | 114.8(5) |
| C(15)–N(1)–C(28) | 121.0(4) | Fe(1)–C(11)–Fe(2) | 82.6(3) |
| C(14)–C(15)–N(1) | 124.2(5) | N(1)–C(15)–Fe(1) | 138.1(4) |

NMR spectra of **2a**–**c** also show that only one isomer is present in solution, thereby indicating that the acetylide addition, which generates a stereogenic centre at $C_\beta$, is stereospecific. Thus, we assume that the acetylene fragment is exclusively placed on the opposite side to the sterically demanding Cp ligands, as shown by the structure of **2a** in the solid.

Interestingly, the observed nucleophilic addition at the $C_\beta$ position of the bridging ligand does not correspond to the reactivity expected for a non-coordinated vinyliminium functionality, which should react at the iminium carbon atom ($C_\alpha$) or at the conjugated $C_\gamma$ position. This unusual reactivity shown by the bridging $C_3$ frame presumably originates from the stability of the bis(alkylidene) coordination mode, which is assumed to be a consequence of the nucleophilic addition and C–C bond formation at $C_\beta$.

The most relevant feature of the reactions described above is the completely different outcome of the acetylide addition for *cis*-**1a** and *trans*-**1a**. The mutual arrangement of ancillary ligands in dinuclear complexes rarely exerts any relevant influence on the reactivity of adjacent ligands,[10] although the results reported above are not entirely unexpected. In a very similar and previously reported reaction, the *cis* and *trans* isomers of **1b** were found to react with $NaBH_4$ in different ways: the *cis* isomer was found to undergo hydride addition at $C_\alpha$, whereas the *trans* isomer reacts at $C_\beta$.[4b] This seems to indicate that the *trans* arrangement of the Cp ligands is more favourable than the *cis* one for addition at the $C_\beta$ position.

A second point to be noted is that neither *cis*-**1a** nor *trans*-**1a** undergo acetylide attack at the iminium carbon atom ($C_\alpha$), in spite of its strongly electrophilic character. This can be explained in terms of restricted access to the $C_\alpha$ position due to the presence of the sterically demanding Xyl group.

Since (μ-vinyliminium)diruthenium complexes analogous to **1a**–**e** are known, and their chemistry generally parallels that of their diiron counterparts,[11] we extended the investigation to the diruthenium species in order to detect possible effects due to the nature of the metal atom. Thus, we studied the reactions of the *trans* and *cis* isomers of the diruthenium complex $[Ru_2\{\mu\text{-}\eta^1\text{:}\eta^3\text{-}C(Me){=}C(Me)C{=}N(Me)(Xyl)\}(\mu\text{-}CO)(CO)(Cp)_2][SO_3CF_3]$ (**3**), which is an ana-

 © 2007 Wiley-VCH Verlag GmbH & Co. KGaA, Weinheim 

logue of **1a**, with lithium acetylides. Surprisingly, both *trans* and *cis* isomers react in the same way to give the acetylene-functionalised bis(alkylidene) compound $[Ru_2\{\mu\text{-}\eta^1{:}\eta^2\text{-}C(Me)C(Me)(C{\equiv}CTol)CN(Me)(Xyl)\}(\mu\text{-}CO)(CO)(Cp)_2]$ (**4**; Scheme 3).

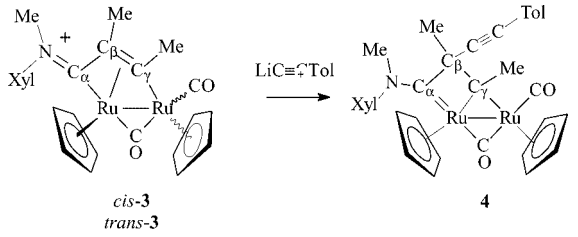


Scheme 3.

Complex **4**, which is an analogue of the diiron compound **2a**, was characterised by spectroscopy and elemental analysis. In particular, its NMR spectroscopic data well parallel those of **2a** (see Experimental Section), thereby suggesting that the two compounds adopt identical geometries.

Further investigations concerned the complexes $[Fe_2\{\mu\text{-}\eta^1{:}\eta^3\text{-}C(R')=C(R')C=N(Me)_2\}(\mu\text{-}CO)(CO)(Cp)_2][SO_3CF_3]$ [R′ = Me (**1c**), Et (**1d**)], which exist only as *cis* isomers. Compounds **1c** and **1d** differ from **1a** in that they contain a methyl group instead of a Xyl group in the iminium moiety. Therefore, in the absence of steric protection due to the Xyl group, the iminium carbon atom is expected to be the preferential site of addition. Accordingly, the reactions of **1c** and **1d** with a series of lithium acetylides LiC≡CR′′ [R′′ = H, Ph, Tol, $SiMe_3$, $C(Me)=CH_2$] resulted in the formation of the novel bridging acetylene-functionalised allylidene complexes **5a**–**j**, as reported in Scheme 4.

Compounds **5a**–**j** were obtained in good yields after purification by column chromatography on alumina and were characterised by IR and NMR spectroscopy. The structure of **5h** was determined by X-ray diffraction; the ORTEP molecular diagram is shown in Figure 4 and selected bond lengths and angles are listed in Table 2.

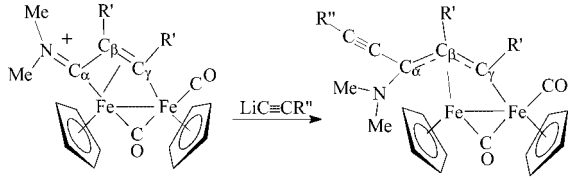


| | R′ | R″ | |
|---|---|---|---|
| **1c** | Me | Tol | **5a** |
| **1c** | Me | Ph | **5b** |
| **1c** | Me | $SiMe_3$ | **5c** |
| **1c** | Me | *n*Bu | **5d** |
| **1c** | Me | $C(Me)=CH_2$ | **5e** |
| **1c** | Me | H | **5f** |
| **1d** | Et | Tol | **5g** |
| **1d** | Et | Ph | **5h** |
| **1d** | Et | $SiMe_3$ | **5i** |
| **1d** | Et | $C(Me)=CH_2$ | **5j** |

Scheme 4.

Table 2. Selected bond lengths [Å] and angles [°] for $[Fe_2\{\mu\text{-}\eta^1{:}\eta^3\text{-}C(Et)C(Et)C(C{\equiv}CPh)N(Me)_2\}(\mu\text{-}CO)(CO)(Cp)_2]$ (**5h**).

| | | | |
|---|---|---|---|
| Fe(1)–Fe(2) | 2.5362(8) | C(13)–C(14) | 1.425(4) |
| Fe(2)–C(12) | 1.750(4) | C(14)–C(15) | 1.463(4) |
| Fe(1)–C(11) | 1.903(3) | C(13)–C(16) | 1.520(4) |
| Fe(2)–C(11) | 1.946(3) | C(14)–C(18) | 1.528(4) |
| Fe(1)–C(13) | 2.010(3) | C(15)–C(22) | 1.452(4) |
| Fe(2)–C(13) | 1.987(3) | C(22)–C(23) | 1.199(4) |
| C(11)–O(11) | 1.168(4) | C(23)–C(24) | 1.438(4) |
| C(12)–O(12) | 1.137(4) | C(15)–N(1) | 1.455(4) |
| Fe(1)–C(14) | 2.040(3) | Fe(1)–C(15) | 2.098(3) |
| Fe(2)–C(13)–Fe(1) | 78.77(11) | C(14)–C(15)–N(1) | 119.8(2) |
| Fe(1)–C(11)–Fe(2) | 82.43(13) | C(14)–C(15)–C(22) | 117.8(2) |
| Fe(2)–C(13)–C(14) | 126.1(2) | C(15)–C(22)–C(23) | 169.0(3) |
| C(13)–C(14)–C(15) | 120.1(2) | C(22)–C(23)–C(24) | 176.1(4) |

The $C_3$-bridged coordination framework exhibits some changes as a consequence of acetylide addition, although it remains σ-bound to Fe(2) [Fe(2)–C(13) 1.987(3) Å] and $\eta^3$-coordinated to Fe(1) [Fe(1)–C(13) 2.010(3), Fe(1)–C(14) 2.040(3), Fe(1)–C(15) 2.098(3) Å]. The usual description for this bonding mode is a mix of vinylalkylidene and allylidene

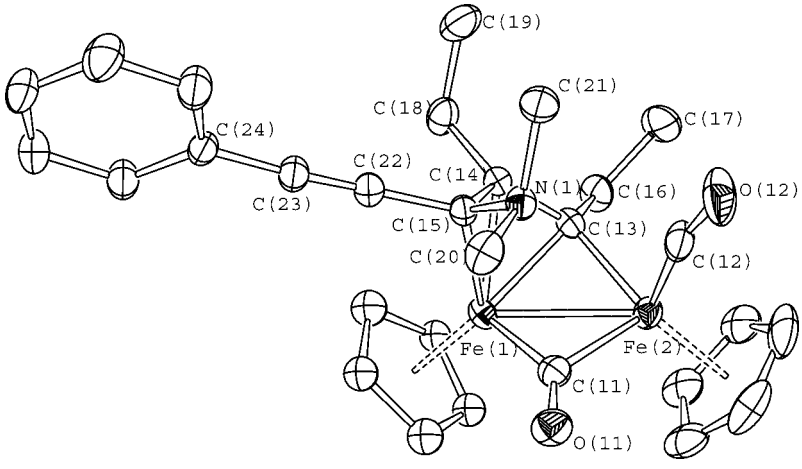


Figure 4. ORTEP drawing of $[Fe_2\{\mu\text{-}\eta^1{:}\eta^3\text{-}C(Et)C(Et)C(C{\equiv}CPh)N(Me)_2\}(\mu\text{-}CO)(CO)(Cp)_2]$ (**5h**). All H atoms have been omitted for clarity. Thermal ellipsoids are at the 30% probability level.

 © 2007 Wiley-VCH Verlag GmbH & Co. KGaA, Weinheim 

contributions (Figure 5, **A** and **B**, respectively).[12] The structure of **5h** can be compared to that of the related complexes $[Fe_2\{\mu\text{-}\eta^1\text{:}\eta^3\text{-}C_\gamma(Tol)C_\beta(H)C_\alpha(H)N(Me)_2\}(\mu\text{-}CO)(CO)(Cp)_2]$ (**III**),[4a] $[Fe_2\{\mu\text{-}\eta^1\text{:}\eta^3\text{-}C_\gamma(SiMe_3)C_\beta(H)C_\alpha(CN)N(Me)_2\}(\mu\text{-}CO)(CO)(Cp)_2]$ (**IV**),[3] and $[Fe_2\{\mu\text{-}\eta^1\text{:}\eta^3\text{-}C_\gamma(Me)C_\beta(Me)C_\alpha(CN)N(Me)_2\}(\mu\text{-}CO)(CO)(Cp)_2]$ (**V**),[3] which were obtained by hydride or cyanide addition.[3] Compound **III** has a $C_\alpha$–$C_\beta$ bond length [1.408(9) Å] shorter than that of $C_\beta$–$C_\gamma$ [1.441(8) Å], and has been described as containing a bridging vinylalkylidene. Conversely, **5h** shows the opposite trend, namely the $C_\beta$-$C_\gamma$ bond length [1.435(4) Å] is shorter than that of $C_\alpha$–$C_\beta$ [1.463(4) Å], and because of this closely resembles **IV** and **V** [$C_\beta$–$C_\gamma$ 1.414(3) and 1.419(3), $C_\alpha$–$C_\beta$ 1.447(3) and 1.449(3) Å, respectively], which were more appropriately described as allylidene complexes (Figure 5, **B**). This observation, together with the fact that the C(15)–N(1) ($C_\alpha$–N) [1.455(4) Å] and Fe(1)–C(15) interactions [2.098(3) Å] are almost a single bond and both C(15) and N(1) deviate appreciably from $sp^2$ hybridisation [sum of angles: 348.5(3) and 334.6(4)°, respectively], suggests that the ligand can also be described in terms of a $\eta^1$:$\eta^2$-vinyl contribution (Figure 5, **C**), although the most representative description is as an allylidene (**B**).

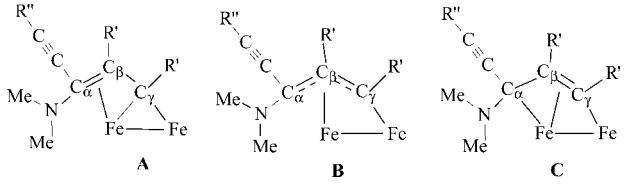


Figure 5. Description of the bridging ligand in complexes of type **5**.

A further difference between **5h** and the complexes derived by hydride addition to $C_\alpha$ (**III**) consists in the orientation of the $NMe_2$ group. Thus, in the acetylene-functionalised compound **5h** it lies *trans* to the R substituent of $C_\beta$ whereas it is *cis* in complex **III**.[4a] In this respect **5h** more closely resembles the products obtained by cyanide addition (**IV** and **V**), which display an analogous *trans* orientation.[3]

The spectroscopic data of **5a**–**j** are fully consistent with the proposed formulation. The IR spectra (in $CH_2Cl_2$ solution) exhibit the usual ν(CO) band pattern and a weak absorption at 2120–2180 $cm^{-1}$ for the C≡C bond. The $^1H$ NMR spectra suggest a single isomer in solution, which indicates that the reaction is regio- and stereoselective. In particular, NOE investigations carried out on **5b** show that irradiation of the $C_\beta$-*Me* resonance ($\delta$ = 2.18 ppm) results in a significant enhancement of the *N*-methyl resonance at $\delta$ = 1.64 ppm, whereas no NOE is detected between $C_\beta$-*Me* and the other N–*Me* ($\delta$ = 2.31 ppm) or between the *N*-bound methyl groups and the Cp ligands. Indeed, looking at the structure of **5h**, the $NMe_2$ group is placed on the side opposite to the Cp ligand and one *N*-methyl group lies much closer to the $C_\beta$ substituent than the other.

The major features of the $^{13}C$ NMR spectra concern the $C_\alpha$ and $C_\gamma$ resonances: the latter is found downfield ($\delta$ = 203.4 ppm for **5h**), whereas the former is shifted upfield ($\delta$ = 72.8 ppm for **5h**), with respect to the vinyliminium precursors. These data are consistent with the alkyl nature of $C_\alpha$ and the vinyl character of $C_\gamma$. Finally, two signals in the range $\delta$ = 89–107 ppm can be assigned to the sp carbon atoms ($\delta$ = 92.4 and 91.1 ppm for **5h**).

The reaction of $[Fe_2\{\mu\text{-}\eta^1\text{:}\eta^3\text{-}C(Me)=C(Me)C=N(Me)(CH_2Ph)\}(\mu\text{-}CO)(CO)(Cp)_2][SO_3CF_3]$ (**1e**) with LiC≡CPh was also investigated. Compared to **1a** and **1c**, compound **1e** has one benzyl group as an *N*-substituent. The aim of this study was to determine to what extent substituents with a steric hindrance intermediate between Me and Xyl can exert steric protection on the iminium carbon atom ($C_\alpha$). The addition occurs selectively at $C_\alpha$ and results in the formation of complex **6** (Scheme 5).

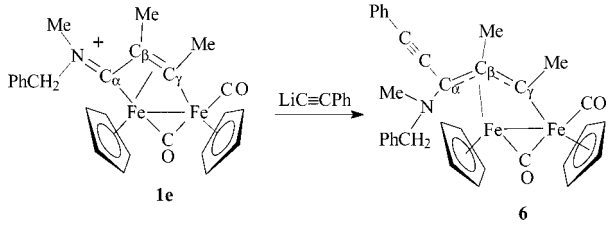


Scheme 5.

The spectroscopic data of **6** are similar to those of **5a**–**j**. However, by contrast with **5a**–**j**, complex **6** contains minor amounts of a second isomeric form in solution (isomer ratio about 12:1). These isomers are presumably due to the different orientations that the methyl and benzyl substituents can adopt as a consequence of hindered rotation around the $C_\alpha$–N bond. NOE experiments on the major isomer suggest that the most favourable geometry is that with the bulkier benzyl group pointing toward the bridging and terminal CO.

Finally, the reactions of compound **1b** with LiC≡CR′ (R′ = $SiMe_3$, H) resulted in the formation of complexes $[Fe_2\{\mu\text{-}\eta^1\text{:}\eta^3\text{-}C(Et)C(Et)C(C{\equiv}CR')N(Me)(Xyl)\}(\mu\text{-}CO)(CO)(Cp)_2]$ (R′ = $SiMe_3$ **7a**, H **7b**) in low yields (20–30%; Scheme 6).

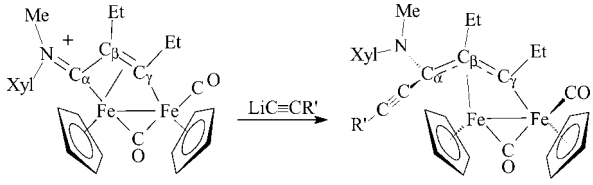


| | R′ | |
|---|---|---|
| **1b** | $SiMe_3$ | **7a** |
| **1b** | H | **7b** |

Scheme 6.

It is noteworthy that both *cis*- and *trans*-**1b** react in the same way. Unexpectedly, the addition occurs selectively at the iminium carbon atom rather than producing CO cleavage, in spite of the presence of the Xyl group and a *cis* arrangement of the Cp ligands.

 © 2007 Wiley-VCH Verlag GmbH & Co. KGaA, Weinheim 

Compounds **7a** and **7b** are unstable and decompose in $CH_2Cl_2$ solution at room temperature after 12 h. Nonetheless, they could be purified by chromatography on alumina and characterised by IR and NMR spectroscopy. Their NMR spectroscopic data, and in particular the $C_\alpha$, $C_\beta$ and $C_\gamma$ resonances (see Experimental Section), are consistent with their acetylene-functionalised allylidene nature. NOE studies were carried out on complex **7b**. Thus, irradiation of the Cp resonance at $\delta$ = 3.68 ppm resulted in significant enhancement of the resonances at $\delta$ = 4.67 (Cp), 2.62 (N-*Me*) and 1.29 ppm (Xyl-*Me*). This indicates that the Cp ligands adopt a *cis* geometry and the N(Me)(Xyl) is close to one Cp ring. Thus, the geometry of the substituents at the $C_\alpha$ atom seems to be different from that found in **5h**, since the alkynyl moiety in **7b** points toward the CO ligands.

## Conclusions

Complexes containing bridging vinyliminium ligands are very reactive toward acetylides: they undergo nucleophilic addition with C–C bond formation at the $C_3$ bridging ligand. Several reaction paths have been evidenced, in addition to the nucleophilic attack to CO and its cleavage, previously communicated. The results evidence that, although several sites of addition are available, the reactions are selective and do not produce mixtures of isomers. The site of addition is largely determined by steric arguments, related to the nature of the substituents on the vinyliminium ligand. Thus, the iminium carbon atom ($C_\alpha$) appears as the most reactive site, but it is made hardly accessible by the presence of the sterically demanding Xyl substituent. Likewise, nucleophilic addition at the $C_\beta$ position is hampered when the Cp ligands are mutually *cis*, or in the presence of $C_\beta$ substituents more sterically demanding than a methyl group. When all these factors operate, the acetylide attack is directed to the CO and is soon followed by an intramolecular rearrangement involving the vinyliminium ligand. Thus, the reactions lack a general character and, in some cases, are difficult to predict. On the other hand, the bridging $C_3$ moiety displays a variety of possible ways in which it can add an alkynyl group to generate new bridging hydrocarbyl ligands with more complex architectures.

## Experimental Section

**General:** All reactions were routinely carried out under nitrogen using standard Schlenk techniques. Solvents were distilled immediately before use under nitrogen from appropriate drying agents. Chromatographic separations were performed on columns of deactivated alumina (4% w/w water). Glassware was oven-dried before use. IR spectra were recorded with a Perkin–Elmer Spectrum 2000 FT-IR spectrophotometer and elemental analyses were performed with a ThermoQuest Flash 1112 Series EA Instrument. All NMR measurements were performed with Varian Gemini 300 and Mercury Plus 400 instruments. The chemical shifts for $^1H$ and $^{13}C$ were referenced to internal TMS. The spectra were fully assigned by DEPT experiments and $^1H$,$^{13}C$ correlation through gs-HSQC and gs-HMBC experiments.[13] All NMR spectra were recorded at 298 K; NMR signals due to a second isomeric form (where it was possible to detect and/or resolve them) are *italicized*. NOE measurements were recorded using the DPFGSE-NOE sequence.[14] All reagents were commercial products (Aldrich) of the highest purity available and were used as received. $[Fe_2(CO)_4(Cp)_2]$ was purchased from Strem and used as received. Complexes $[Fe_2\{\mu\text{-}\eta^1\text{:}\eta^3\text{-}C(R')=C(R')C=N(Me)(R)\}(\mu\text{-}CO)(CO)(Cp)_2][SO_3CF_3]$ (**1a**–**e**)[2] and $[Ru_2\{\mu\text{-}C(Me)=C(Me)C=N(Me)(Xyl)\}(\mu\text{-}CO)(CO)(Cp)_2][CF_3SO_3]$ (**3**)[11] were prepared as described in the literature.

**Synthesis of $[Fe_2\{\mu\text{-}\eta^1\text{:}\eta^2\text{-}C(Me)C(Me)(C{\equiv}CR'')CN(Me)(Xyl)\}(\mu\text{-}CO)(CO)(Cp)_2]$ [R'' = Tol (2a), Ph (2b), $SiMe_3$ (2c)]:** A solution of *trans*-**1a** (201 mg, 0.311 mmol), in thf (8 mL), was treated at room temperature with a thf solution of LiC≡CTol (1.2 mL, 0.620 mmol) freshly prepared from *n*BuLi and HC≡CTol. The mixture was stirred for 30 min, then it was concentrated under reduced pressure. Chromatography of the residue on alumina, using diethyl ether as eluent, afforded a red band corresponding to **2a**. Yield: 137 mg (72%). Crystals suitable for X-ray diffraction were obtained by layering a diethyl ether solution of **2a** with petroleum ether (b.p. 40–60 °C) at –20 °C. $C_{35}H_{35}Fe_2NO_2$ (613.35): calcd. C 68.54, H, 5.75; found C 68.36, H 5.70. IR ($CH_2Cl_2$): ν(CO) 1919 (vs), 1749 (s); ν($C_\alpha$N) 1511 (w) $cm^{-1}$. $^1H$ NMR ($CDCl_3$): $\delta$ = 7.64–6.98 (m, 7 H, $Me_2C_6H_3$ and $C_6H_4Me$), 4.58, 3.95 (s, 10 H, Cp), 3.43 (s, 3 H, $C_\gamma$Me), 3.40 (s, 3 H, NMe), 2.32 (s, 3 H, $C_6H_4Me$), 2.25, 2.20 (s, 6 H, $Me_2C_6H_3$), 2.01 (s, 3 H, $C_\beta$Me) ppm. $^{13}C$ NMR ($CDCl_3$): $\delta$ = 283.2 (μ-CO), 268.8 ($C_\alpha$), 216.5 (CO), 181.5 ($C_\gamma$), 146.1 (*ipso*-$Me_2C_6H_3$), 137.3–127.3 ($Me_2C_6H_3$ and $C_6H_4Me$), 94.1, 85.9 (C≡C), 87.9, 85.2 (Cp), 75.0 ($C_\beta$), 43.0 (NMe), 39.3 ($C_\gamma Me$), 27.5 ($C_\beta Me$), 21.4 ($C_6H_4Me$), 18.4, 17.7 ($Me_2C_6H_3$) ppm. Complexes **2b** and **2c** were obtained according to the same procedure described for the synthesis of **2a** by treating *trans*-**1a** (190 mg) with LiC≡CPh and LiC≡C$SiMe_3$, respectively. **2b:** Yield: 124 mg (74%). Colour: red. $C_{34}H_{33}Fe_2NO_2$ (599.32): calcd. C 68.14, H, 5.55; found C 68.21, H 5.62. IR ($CH_2Cl_2$): ν(CO) 1918 (vs), 1749 (s); ν($C_\alpha$N) 1511 (w) $cm^{-1}$. $^1H$ NMR ($CDCl_3$): $\delta$ = 7.71–6.39 (m, 8 H, $Me_2C_6H_3$ and Ph), 4.58, 3.95 (s, 10 H, Cp), 3.44 (s, 3 H, $C_\gamma$Me), 3.40 (s, 3 H, NMe), 2.25, 2.20 (s, 6 H, $Me_2C_6H_3$), 2.03 (s, 3 H, $C_\beta$Me) ppm. $^{13}C$ NMR ($CDCl_3$): $\delta$ = 282.3 (μ-CO), 268.4 ($C_\alpha$), 216.6 (CO), 181.2 ($C_\gamma$), 146.7 (*ipso*-$Me_2C_6H_3$), 135.1–125.9 ($Me_2C_6H_3$ and $C_6H_5$), 94.1, 85.9 (C≡C), 87.9, 85.2 (Cp), 75.0 ($C_\beta$), 43.0 (NMe), 39.3 ($C_\gamma Me$), 27.5 ($C_\beta Me$), 18.4, 17.7 ($Me_2C_6H_3$) ppm. **2c:** Yield: 119 mg (68%). Colour: red. $C_{31}H_{37}Fe_2NO_2Si$ (595.41): calcd. C 62.53, H, 6.26; found C 62.55, H 6.20. IR ($CH_2Cl_2$): ν(CO) 1918 (vs), 1750 (s); ν($C_\alpha$N) 1511 (w) $cm^{-1}$. $^1H$ NMR ($CDCl_3$): $\delta$ = 7.10–6.80 (m, 3 H, $Me_2C_6H_3$), 4.54, 3.91 (s, 10 H, Cp), 3.37 (s, 3 H, $C_\gamma$Me), 3.36 (s, 3 H, NMe), 2.23, 2.17 (s, 6 H, $Me_2C_6H_3$), 1.92 (s, 3 H, $C_\beta$Me), 0.45 (s, 9 H, $SiMe_3$) ppm. $^{13}C$ NMR ($CDCl_3$): $\delta$ = 282.3 (μ-CO), 266.2 ($C_\alpha$), 216.5 (CO), 181.1 ($C_\gamma$), 147.4 (*ipso*-$Me_2C_6H_3$), 137.2–126.4 ($Me_2C_6H_3$), 113.7, 90.1 (C≡C), 87.8, 85.2 (Cp), 78.8 ($C_\beta$), 42.9 (NMe), 39.1 ($C_\gamma Me$), 29.7 ($C_\beta Me$), 18.3, 17.7 ($Me_2C_6H_3$) ppm.

**Synthesis of $[Ru_2\{\mu\text{-}\eta^1\text{:}\eta^2\text{-}C(Me)C(Me)(C{\equiv}CTol)CN(Me)(Xyl)\}(\mu\text{-}CO)(CO)(Cp)_2]$ (4):** A solution of **3** (300 mg, 0.407 mmol) in thf (15 mL), was treated at room temperature with a thf solution of LiC≡CTol (1.6 mL, 0.827 mmol) freshly prepared from *n*BuLi and HC≡CTol. The mixture was stirred for 30 min, then the solvent was removed under reduced pressure. Chromatography of the residue on alumina, using diethyl ether as eluent, afforded a red band corresponding to **4**. Yield: 203 mg (71%). $C_{35}H_{35}NO_2Ru_2$ (703.8): calcd. C 59.73, H, 5.01; found C 59.92, H 4.89. IR ($CH_2Cl_2$): ν(C≡C) 2159 (w); ν(CO) 1918 (vs), 1744 (s) $cm^{-1}$. $^1H$ NMR ($CDCl_3$): $\delta$ = 7.67–7.09 (m, 7 H, $Me_2C_6H_3$ and $C_6H_4Me$), 5.12, 4.51 (s, 10 H, Cp), 3.57 (s, 3 H, NMe), 3.08 (s, 3 H, $C_\gamma$Me), 2.34 (s, 3 H, $C_6H_4Me$), 2.24, 2.23 (s, 6 H, $Me_2C_6H_3$), 1.87 (s, 3 H, $C_\beta$Me)

 © 2007 Wiley-VCH Verlag GmbH & Co. KGaA, Weinheim 

ppm. $^{13}C$ NMR ($CDCl_3$): $\delta$ = 252.1 ($C_\alpha$), 249.29 (μ-CO), 204.5 (CO), 156.2 ($C_\gamma$), 147.0 (*ipso*-$Me_2C_6H_3$), 137.7 (*ipso*-$C_6H_4Me$), 133.4, 132.6, 132.4, 131.4–128.0 ($Me_2C_6H_3$ and $C_6H_4Me$), 94.1, 89.0 (C≡C), 90.0, 86.9 (Cp), 76.3 ($C_\beta$), 42.2 (NMe), 40.0 ($C_\gamma Me$), 28.1 ($C_\beta Me$), 21.8 ($C_6H_4Me$), 18.7, 17.9 ($Me_2C_6H_3$) ppm.

**Synthesis of [Fe$_2${μ-η$^1$:η$^3$-C(Me)C(Me)C(C≡CR′′)N(Me)$_2$}(μ-CO)-(CO)(Cp)$_2$] [R′′ = Tol (5a), Ph (5b), SiMe$_3$ (5c), *n*Bu (5d), C(Me)=CH$_2$ (5e), H (5f)]:** A solution of complex **1c** (99 mg, 0.178 mmol), in thf (10 mL) was treated with LiC≡CTol (0.552 mmol) according to the same procedure described for the synthesis of **2a**–**c**. The reaction afforded **5a** as red crystals in 69% yield (64 mg). $C_{28}H_{29}Fe_2NO_2$ (523.22): calcd. C 64.27, H 5.59; found C 64.29, H 5.54. IR ($CH_2Cl_2$): ν(C≡C) 2181 (w); ν(CO) 1939 (vs), 1769 (s) cm$^{-1}$. $^1H$ NMR ($CDCl_3$): $\delta$ = 7.43–7.09 (m, 4 H, $C_6H_4Me$), 4.81, 4.33 (s, 10 H, Cp), 3.86 (s, 3 H, $C_\gamma Me$), 2.34 (s, 3 H, $C_6H_4Me$), 2.29, 1.61 (s, 6 H, NMe), 2.15 (s, 3 H, $C_\beta Me$) ppm. $^{13}C$ NMR ($CDCl_3$): $\delta$ = 275.8 (μ-CO), 214.5 (CO), 193.7 ($C_\gamma$), 136.9, 132.3, 130.6, 129.0, 121.8 ($C_6H_4Me$), 93.1, 91.8 (C≡C), 89.7 ($C_\beta$), 88.4, 87.1 (Cp), 72.9 ($C_\alpha$), 48.4, 41.1 (NMe), 39.4 ($C_\gamma Me$), 22.8 ($C_\beta Me$), 21.5 ($C_6H_4Me$) ppm. Complexes **5b**–**f** were obtained analogously by treating **1c** (150 mg) with the appropriate lithium acetylide. **5b:** Yield: 113 mg (82%). Colour: red. $C_{27}H_{27}Fe_2NO_2$ (509.20): calcd. C 63.68, H, 5.34; found C 63.72, H 5.44. IR ($CH_2Cl_2$): ν(C≡C) 2181 (w); ν(CO) 1940 (vs), 1768 (s) cm$^{-1}$. $^1H$ NMR ($CDCl_3$): $\delta$ = 7.56–7.26 (m, 5 H, Ph), 4.82, 4.35 (s, 10 H, Cp), 3.87 (s, 3 H, $C_\gamma Me$), 2.31, 1.64 (s, 6 H, NMe), 2.18 (s, 3 H, $C_\beta Me$) ppm. $^{13}C$ NMR ($CDCl_3$): $\delta$ = 272.4 (μ-CO), 214.7 (CO), 194.0 ($C_\gamma$), 132.4–124.9 (Ph), 93.0, 92.6 (C≡C), 89.8 ($C_\beta$), 88.4, 87.1 (Cp), 72.5 ($C_\alpha$), 48.4, 41.1 (NMe), 39.4 ($C_\gamma Me$), 22.6 ($C_\beta Me$) ppm. **5c:** Yield: 119 mg (87%). Colour: red. $C_{24}H_{31}Fe_2NO_2Si$ (505.28): calcd. C 57.05, H, 6.18; found C 57.08, H 6.16. IR ($CH_2Cl_2$): ν(C≡C) 2118 (m); ν(CO) 1940 (vs), 1769 (s) cm$^{-1}$. $^1H$ NMR ($CDCl_3$): $\delta$ = 4.79, 4.25 (s, 10 H, Cp), 3.82 (s, 3 H, $C_\gamma Me$), 2.19 (s, 3 H, $C_\beta Me$), 2.04, 1.54 (s, 6 H, NMe), 0.21 (s, 9 H, $SiMe_3$) ppm. $^{13}C$ NMR ($CDCl_3$): $\delta$ = 272.4 (μ-CO), 214.6 (CO), 193.9 ($C_\gamma$), 107.1, 96.1 (C≡C), 89.6 ($C_\beta$), 88.4, 87.5 (Cp), 72.8 ($C_\alpha$), 48.1, 40.9 (NMe), 39.3 ($C_\gamma Me$), 22.3 ($C_\beta Me$), 0.78 ($SiMe_3$) ppm. **5d:** Yield: 105 mg (80%). Colour: ochre yellow. $C_{25}H_{31}Fe_2NO_2$ (489.21): calcd. C 61.38, H 6.39; found C 61.44, H 6.35. IR ($CH_2Cl_2$): ν(CO) 1934 (vs), 1762 (s) cm$^{-1}$. $^1H$ NMR ($CDCl_3$): $\delta$ = 4.77, 4.26 (s, 10 H, Cp), 3.83 (s, 3 H, $C_\gamma Me$), 2.32 (m, 2 H, C≡C$CH_2$), 2.18 (s, 3 H, $C_\beta Me$), 2.04, 1.52 (s, 6 H, NMe), 1.58–1.32 (m, 4 H, C≡CC$H_2$C$H_2$C$H_2$), 0.93 (m, 3 H, C≡CC$H_2$C$H_2$C$H_2$C$H_3$) ppm. $^{13}C$ NMR ($CDCl_3$): $\delta$ = 272.8 (μ-CO), 214.8 (CO), 193.6 ($C_\gamma$), 92.7, 89.2 (C≡C), 89.2 ($C_\beta$), 88.3, 87.2 (Cp), 71.3 ($C_\alpha$), 48.3, 41.0 (NMe), 39.5 ($C_\gamma Me$), 32.0, 22.2, 19.3 ($CH_2$), 22.5 ($C_\beta Me$), 13.8 ($CH_2CH_2CH_2CH_3$) ppm. **5e:** Yield: 63 mg (74%). Colour: ochre yellow. $C_{24}H_{27}Fe_2NO_2$ (473.17): calcd. C 60.92, H 5.75; found C 60.99, H 5.67. IR ($CH_2Cl_2$): ν(C≡C) 2159 (w); ν(CO) 1938 (vs), 1764 (s) cm$^{-1}$. $^1H$ NMR ($CDCl_3$): $\delta$ = 5.15, 5.08 (m, 2 H, $CH_2$), 4.73, 4.22 (s, 10 H, Cp), 3.77 (s, 3 H, $C_\gamma Me$), 2.15 (s, 3 H, $C_\beta Me$), 2.01, 1.49 (s, 6 H, NMe), 1.91 (s, 3 H, C≡CC$Me$) ppm. $^{13}C$ NMR ($CDCl_3$): $\delta$ = 272.3 (μ-CO), 214.6 (CO), 193.8 ($C_\gamma$), 127.9 (C≡C$C$Me), 118.3 ($CH_2$), 94.4, 91.7 (C≡C), 89.7 ($C_\beta$), 88.4, 87.1 (Cp), 72.7 ($C_\alpha$), 48.3, 41.0 (NMe), 39.4 ($C_\gamma Me$), 24.3 (C≡CC$Me$), 22.6 ($C_\beta Me$) ppm. **5f:** Yield: 24 mg (21%). Colour: ochre yellow. $C_{21}H_{23}Fe_2NO_2$ (433.10): calcd. C 58.24, H 5.35; found C 58.30, H 5.34. IR ($CH_2Cl_2$): ν(CO) 1942 (vs), 1771 (s) cm$^{-1}$. $^1H$ NMR ($CDCl_3$): $\delta$ = 4.79, 4.27 (s, 10 H, Cp), 3.83 (s, 3 H, $C_\gamma Me$), 2.64 (s, 1 H, C≡CH), 2.20 (s, 3 H, $C_\beta Me$), 2.05, 1.54 (s, 6 H, NMe) ppm. $^{13}C$ NMR ($CDCl_3$): $\delta$ = 272.0 (μ-CO), 214.5 (CO), 194.0 ($C_\gamma$), 89.7 ($C_\beta$), 88.4, 87.3 (Cp), 85.3, 82.1 (C≡C), 69.9 ($C_\alpha$), 47.9, 40.9 (NMe), 39.4 ($C_\gamma Me$), 22.1 ($C_\beta Me$) ppm.

**Synthesis of [Fe$_2${μ-η$^1$:η$^3$-C(Et)C(Et)C(C≡CR′′)N(Me)$_2$}(μ-CO)-(CO)(Cp)$_2$] [R′′ = Tol (5g), Ph (5h), SiMe$_3$ (5i), C(Me)=CH$_2$ (5j)]:** Complexes **5g**–**j** were obtained by the same procedure described for the synthesis of **5a** by treating **1d** (180 mg) with the appropriate lithium acetylide. Crystals of **5h** suitable for X-ray analysis were collected by layering a diethyl ether solution with *n*-pentane at –20 °C. **5g:** Yield: 115 mg (65%). Colour: red. $C_{30}H_{33}Fe_2NO_2$ (551.28): calcd. C 65.36, H, 6.03; found C 65.42, H 6.11. IR ($CH_2Cl_2$): ν(C≡C) 2180 (w); ν(CO) 1940 (vs), 1769 (s) cm$^{-1}$. $^1H$ NMR ($CDCl_3$): $\delta$ = 7.35–6.95 (m, 4 H, $C_6H_4Me$), 4.79, 4.35 (s, 10 H, Cp), 4.46, 4.09 (m, 2 H, $C_\gamma CH_2$), 3.19, 2.18 (m, 2 H, $C_\beta CH_2$), 2.33 (s, 3 H, $C_6H_4Me$), 2.18, 1.59 (s, 6 H, NMe), 1.67 (t, $^3J_{H,H}$ = 7 Hz, 3 H, $C_\gamma CH_2CH_3$), 1.26 (t, $^3J_{H,H}$ = 7 Hz, 3 H, $C_\beta CH_2CH_3$) ppm. $^{13}C$ NMR ($CDCl_3$): $\delta$ = 272.5 (μ-CO), 214.7 (CO), 203.3 ($C_\gamma$), 136.8–121.9 ($C_6H_4Me$), 93.7 ($C_\beta$), 91.5, 91.1 (C≡C), 88.4, 86.5 (Cp), 73.1 ($C_\alpha$), 49.0, 41.6 (NMe), 44.8 ($C_\gamma CH_2$), 29.5 ($C_\beta CH_2$), 21.5 ($C_6H_4Me$), 20.5 ($C_\gamma CH_2CH_3$), 16.4 ($C_\beta CH_2CH_3$) ppm. **5h:** Yield: 104 mg (60%). Colour: red. $C_{29}H_{31}Fe_2NO_2$ (537.25): calcd. C 64.83, H, 5.82; found C 64.86%; H 5.82. IR ($CH_2Cl_2$): ν(C≡C) 2180 (w); ν(CO) 1941 (vs), 1768 (s) cm$^{-1}$. $^1H$ NMR ($CDCl_3$): $\delta$ = 7.45–7.24 (m, 5 H, Ph), 4.81, 4.38 (s, 10 H, Cp), 4.50, 4.10 (m, 2 H, $C_\gamma CH_2$), 3.22, 2.19 (m, 2 H, $C_\beta CH_2$), 2.21, 1.62 (s, 6 H, NMe), 1.70 (t, $^3J_{H,H}$ = 7 Hz, 3 H, $C_\gamma CH_2CH_3$), 1.28 (t, $^3J_{H,H}$ = 7 Hz, 3 H, $C_\beta CH_2CH_3$) ppm. $^{13}C$ NMR ($CDCl_3$): $\delta$ = 272.3 (μ-CO), 214.6 (CO), 203.4 ($C_\gamma$), 130.7, 128.2, 126.8, 125.0 (Ph), 93.8 ($C_\beta$), 92.4, 91.1 (C≡C), 88.4, 86.5 (Cp), 72.8 ($C_\alpha$), 49.1, 41.6 (NMe), 44.8 ($C_\gamma CH_2$), 29.5 ($C_\beta CH_2$), 20.5 ($C_\gamma CH_2CH_3$), 16.5 ($C_\beta CH_2CH_3$) ppm. **5i:** Yield: 119 mg (69%). Colour: ochre yellow. $C_{26}H_{35}Fe_2NO_2Si$ (533.34): calcd. C 58.55, H 6.61; found C 58.50, H 6.69. IR ($CH_2Cl_2$): ν(C≡C) 2118 (m), ν(CO) 1940 (vs), 1766 (s) cm$^{-1}$. $^1H$ NMR ($CDCl_3$): $\delta$ = 4.78, 4.28 (s, 10 H, Cp), 4.43, 4.06 (m, 2 H, $C_\gamma CH_2$), 3.10, 2.19 (m, 2 H, $C_\beta CH_2$), 2.06, 1.52 (s, 6 H, NMe), 1.65 (t, $^3J_{H,H}$ = 7 Hz, 3 H, $C_\gamma CH_2CH_3$), 1.21 (t, $^3J_{H,H}$ = 8 Hz, 3 H, $C_\beta CH_2CH_3$), 0.19 (s, 9 H, $SiMe_3$) ppm. $^{13}C$ NMR ($CDCl_3$): $\delta$ = 272.6 (μ-CO), 214.8 (CO), 203.5 ($C_\gamma$), 106.9, 94.0 (C≡C), 93.7 ($C_\beta$), 88.4, 86.9 (Cp), 72.9 ($C_\alpha$), 48.8, 41.4 (NMe), 44.7 ($C_\gamma CH_2$), 28.9 ($C_\beta CH_2$), 20.3 ($C_\gamma CH_2CH_3$), 16.1 ($C_\beta CH_2CH_3$), 0.67 ($SiMe_3$) ppm. **5j:** Yield: 134 mg (83%). Colour: ochre yellow. $C_{26}H_{31}Fe_2NO_2$ (501.22): calcd. C 62.30, H, 6.23; found C 62.20, H 6.18. IR ($CH_2Cl_2$): ν(C≡C) 2160 (w); ν(CO) 1938 (vs), 1764 (s) cm$^{-1}$. $^1H$ NMR ($CDCl_3$): $\delta$ = 5.20, 5.14 (m, 2 H, $CH_2$), 4.78, 4.32 (s, 10 H, Cp), 4.46, 4.06 (s, 2 H, $C_\gamma CH_2$), 3.15, 2.05 (s, 2 H, $C_\beta CH_2$), 2.09, 1.54 (s, 6 H, NMe), 1.96 (s, 3 H, C≡CC$Me$), 1.66 (dd, $^3J_{H,H}$ = 7.14 Hz, $^3J_{H,H}$ = 7.69 Hz, 3 H, $C_\gamma CH_2CH_3$), 1.23 (dd, $^3J_{H,H}$ = 7.14 Hz, $^3J_{H,H}$ = 7.69 Hz, 3 H, $C_\gamma CH_2CH_3$) ppm. $^{13}C$ NMR ($CDCl_3$): $\delta$ = 272.5 (μ-CO), 214.7 (CO), 203.3 ($C_\gamma$), 127.9 (C≡C$C$Me), 118.2 ($CH_2$), 93.7 ($C_\beta$), 92.4, 91.4 (C≡C), 88.4, 86.5 (Cp), 72.9 ($C_\alpha$), 49.0, 41.5 (NMe), 44.8 ($C_\gamma CH_2$), 29.4 ($C_\beta CH_2$), 24.3 (C≡CC$Me$), 20.5 ($C_\gamma CH_2CH_3$), 16.4 ($C_\beta CH_2CH_3$) ppm.

**Synthesis of [Fe$_2${μ-η$^1$:η$^3$-C(Me)C(Me)C(C≡CPh)N(Me)(CH$_2$-Ph)}(μ-CO)(CO)(Cp)$_2$] (6):** This complex was obtained according to the same procedure described for the synthesis of **5a** by treating **1e** (120 mg, 0.190 mmol) with LiC≡CPh. Yield: 80 mg (72%). Colour: ochre yellow. $C_{33}H_{31}Fe_2NO_2$ (585.29): calcd. C 67.72, H 5.34; found C 67.78, H 5.40. IR ($CH_2Cl_2$): ν(C≡C) 2181 (w); ν(CO) 1953 (vs), 1767 (s) cm$^{-1}$. $^1H$ NMR ($CDCl_3$): $\delta$ = 7.54–7.13 (m, 10 H, Ph), 4.86, *4.83*, 4.39, *4.31* (s, 10 H, Cp), 4.53, 3.30 (d, $^2J_{H,H}$ = 12.64 Hz, 2 H, C$H_2$Ph), 3.92, *3.84* (s, 3 H, $C_\gamma Me$), 2.31, *2.27* (s, 3 H, $C_\beta Me$), *2.22*, 1.54 (s, 3 H, NMe) ppm. Isomer ratio 12: 1. $^{13}C$ NMR ($CDCl_3$): $\delta$ = 270.7 (μ-CO), 213.8 (CO), 194.3 ($C_\gamma$), 138.8–124.8 (Ph), 93.6, 93.4 (C≡C), 89.1 ($C_\beta$), *88.7*, 88.5, *87.6*, 87.4 (Cp), 73.7 ($C_\alpha$), *65.4*, 59.7 (*C*$H_2$Ph), 45.5, *42.1* (NMe), 39.6, *37.7* ($C_\gamma Me$), *23.8*, 23.0 ($C_\beta Me$) ppm.

 © 2007 Wiley-VCH Verlag GmbH & Co. KGaA, Weinheim 

**Syntheses of [$Fe_2${μ-η$^1$:η$^3$-C(Et)C(Et)C(C≡CR′′)N(Me)(Xyl)}(μ-CO)(CO)$(Cp)_2$] [R′′ = $SiMe_3$ (7a), H (7b)]:** A solution of *cis*-**1b** (180 mg, 0.267 mmol) in thf (10 mL) was treated with a thf solution of LiC≡C$SiMe_3$ (0.40 mL, 0.40 mmol) freshly prepared from *n*BuLi and HC≡C$SiMe_3$. Solvent removal and chromatography of the residue on alumina, using $CH_2Cl_2$ as eluent, afforded a brown band corresponding to **7a** (45 mg, 27%). $C_{33}H_{41}Fe_2NO_2Si$ (623.46): calcd. C 63.57, H 6.63; found C 63.65, H 6.57. IR ($CH_2Cl_2$): ν(CO) 1943 (vs), 1762 (s) cm$^{-1}$. $^1$H NMR ($CDCl_3$): δ = 7.17–6.78 (m, 3 H, $Me_2C_6H_3$), 4.59, 4.35 (s, 10 H, Cp), 4.26, 3.97 (m, 2 H, $C_\gamma CH_2$), 2.89 (s, 3 H, NMe), 2.57, 1.14 (m, 2 H, $C_\beta CH_2$), 1.48, 1.35 (s, 6 H, $Me_2C_6H_3$), 1.31 (m, 3 H, $C_\gamma CH_2CH_3$), 0.85 (m, 3 H, $C_\beta CH_2CH_3$), 0.07 (s, 9 H, $SiMe_3$) ppm. $^{13}$C NMR ($CDCl_3$): δ = 273.8 (μ-CO), 212.6 (CO), 202.8 ($C_\gamma$), 155.5 (*ipso*-$Me_2C_6H_3$), 134.8–122.7 ($Me_2C_6H_3$), 106.5, 88.6 (C≡C), 97.3 ($C_\alpha$), 89.4 ($C_\beta$), 88.1, 85.8 (Cp), 43.4 ($C_\gamma CH_2$), 39.9 (NMe), 25.4 ($C_\beta CH_2$), 19.5, 19.2 ($Me_2C_6H_3$), 17.3 ($C_\gamma CH_2CH_3$), 14.9 ($C_\beta CH_2CH_3$), 1.34 ($SiMe_3$) ppm. Complex **7b** was obtained according to the same procedure described for the synthesis of **7a** by treating *cis*-**1b** (180 mg) with LiC≡CH. **7b:** Yield: 37 mg (25%). Colour: brownish green. $C_{30}H_{33}Fe_2NO_2$ (551.28): calcd. C 65.36, H 6.03; found C 65.42, H 6.00. IR ($CH_2Cl_2$): ν(CO) 1945 (vs), 1762 (s) cm$^{-1}$. $^1$H NMR ($CDCl_3$): δ = 7.19–6.96 (m, 3 H, $Me_2C_6H_3$), 4.67, 3.68 (s, 10 H, Cp), 3.76 (m, 2 H, $C_\gamma CH_2$), 2.62 (s, 3 H, NMe), 2.18 (s, 1 H, C≡CH), 2.02, 1.68 (m, 2 H, $C_\beta CH_2$), 1.29, 1.26 (s, 6 H, $Me_2C_6H_3$), 1.22 (t, $^3J_{H,H}$ = 7 Hz, 3 H, $C_\gamma CH_2CH_3$), 0.43 (t, $^3J_{H,H}$ = 7 Hz, 3 H, $C_\beta CH_2CH_3$) ppm.

**X-ray Crystallography**: The X-ray intensity data for **2a** and **5h** were collected at room temperature with a Bruker AXS SMART 2000 CCD diffractometer using Mo-$K_\alpha$ radiation. Intensity data were measured over full diffraction spheres using 0.3°-wide ω-scans and a crystal-to-detector distance of 5.2 cm. Cell dimensions and orientation matrixes were initially determined from least-squares refinements on reflections measured in three sets of 20 exposures collected in three different ω-regions and eventually refined against all reflections. The software SMART[15] was used for collecting frames of data, indexing reflections and determining the lattice parameters. The collected frames were then processed for integration by the software SAINT and empirical absorption corrections were applied with SADABS.[16] The structure was solved by direct methods and refined by full-matrix least squares based on all data using $F^2$.[17] Crystal data are listed in Table 3. Non-H atoms were refined anisotropically, unless otherwise stated; H atoms were placed in calculated positions and treated isotropically using the 1.2-fold $U_{iso}$ value of the parent atoms, except methyl protons, which were assigned the 1.5-fold $U_{iso}$ value of the parent C atoms. One Cp ligand in both **2a** and **5h** is disordered. Disordered atomic positions were split and refined isotropically using similar distance and similar *U* restraints and one occupancy parameter per disordered group. CCDC-626314 (**2a**) and -626315 (**5h**) contain the supplementary crystallographic data for this paper. These data can be obtained free of charge from The Cambridge Crystallographic Data Centre via www.ccdc.cam.ac.uk/data_request/cif.

Table 3. Crystal data and experimental details for **2a** and **5h**.

| Complex | **2a** | **5h** |
|---|---|---|
| Empirical formula | $C_{35}H_{35}Fe_2NO_2$ | $C_{29}H_{31}Fe_2NO_2$ |
| Formula mass | 613.34 | 537.25 |
| λ [Å] | 0.71073 | 0.71073 |
| Crystal system | monoclinic | triclinic |
| Space group | $P2_1/c$ | $P\bar{1}$ |
| *a* [Å] | 14.2068(6) | 9.2783(19) |
| *b* [Å] | 9.1543(4) | 11.275(2) |
| *c* [Å] | 22.3490(10) | 12.226(2) |
| α [°] | 90 | 95.73(3) |
| β [°] | 94.0690(10) | 100.61(3) |
| γ [°] | 90 | 92.50(3) |
| *V* [Å$^3$] | 2899.2(2) | 1248.3(4) |
| *Z* | 4 | 2 |
| $D_c$ [g cm$^{-3}$] | 1.405 | 1.429 |
| μ [mm$^{-1}$] | 1.033 | 1.188 |
| *F*(000) | 1280 | 560 |
| Crystal size [mm] | 0.21 × 0.18 × 0.12 | 0.24 × 0.21 × 0.13 |
| θ limits [°] | 1.44–24.11 | 1.70–26.37 |
| Reflections collected | 22967 | 12447 |
| Independent reflections | 4629 ($R_{int}$ = 0.1321) | 5099 ($R_{int}$ = 0.0319) |
| Data/restraints/parameters | 4629/26/363 | 5099/27/309 |
| Goodness on fit on $F^2$ | 1.061 | 1.013 |
| $R_1$ [$I > 2\sigma(I)$] | 0.0696 | 0.0435 |
| $wR_2$ (all data) | 0.1865 | 0.1232 |
| Largest diff. peak/hole [e Å$^{-3}$] | 0.550/–1.053 | 0.526/–0.334 |

## Acknowledgments

We thank the Ministero dell'Università e della Ricerca Scientifica e Tecnologica (M.U.R. project: "New strategies for the control of reactions: interactions of molecular fragments with metallic sites in unconventional species") and the University of Bologna for financial support.

[1] Selected examples: a) P. Braunstein, J. Rosè, in *Metal Clusters in Chemistry* (Eds.: P. Braunstein, L. A. Oro, P. R. Raithby), Wiley-VCH, Weinheim, **1999**; b) R. D. Adams, B. Captain, *J. Organomet. Chem.* **2004**, *689*, 4521–4529; c) J. C. Qin, A. Gavrilova, B. Bosnich, *Pure Appl. Chem.* **2001**, *73*, 221–226; d) E. K. Van Den Beuken, B. L. Feringa, *Tetrahedron* **1998**, *54*, 12985–13011; e) K. Severin, *Chem. Eur. J.* **2002**, *8*, 1514–1518; f) M. Cowie, *Can. J. Chem.* **2005**, *83*, 1043–1055; g) G. Onodera, H. Matsumoto, Y. Nishibayashi, S. Uemura, *Organometallics* **2005**, *24*, 5799–5801.

[2] a) V. G. Albano, L. Busetto, F. Marchetti, M. Monari, S. Zacchini, V. Zanotti, *Organometallics* **2003**, *22*, 1326–1331; b) V. G. Albano, L. Busetto, F. Marchetti, M. Monari, S. Zacchini, V. Zanotti, *J. Organomet. Chem.* **2004**, *689*, 528–538.

[3] V. G. Albano, L. Busetto, F. Marchetti, M. Monari, S. Zacchini, V. Zanotti, *J. Organomet. Chem.* **2006**, *691*, 4234–4243.

[4] a) V. G. Albano, L. Busetto, F. Marchetti, M. Monari, S. Zacchini, V. Zanotti, *Organometallics* **2004**, *23*, 3348–3354; b) V. G. Albano, L. Busetto, F. Marchetti, M. Monari, S. Zacchini, V. Zanotti, *J. Organomet. Chem.* **2005**, *690*, 837–846.

[5] L. Busetto, F. Marchetti, S. Zacchini, V. Zanotti, *Organometallics* **2005**, *24*, 2297–2306.

[6] V. G. Albano, L. Busetto, F. Marchetti, M. Monari, S. Zacchini, V. Zanotti, *J. Organomet. Chem.* **2005**, *690*, 4666–4667.

[7] L. Busetto, F. Marchetti, S. Zacchini, V. Zanotti, *Eur. J. Inorg. Chem.* **2006**, 285–289.

[8] a) V. Zanotti, S. Bordoni, L. Busetto, L. Carlucci, A. Palazzi, R. Serra, V. G. Albano, M. Monari, F. Prestopino, F. Laschi, P. Zanello, *Organometallics* **1995**, *14*, 5232–5241; b) V. G. Albano, S. Bordoni, L. Busetto, F. Marchetti, M. Monari, V. Zanotti, *J. Organomet. Chem.* **2003**, *684*, 37–43.

[9] a) R. D. Adams, F. A. Cotton, *J. Am. Chem. Soc.* **1973**, *95*, 6589–6594; b) C. P. Casey, K. P. Gable, D. M. Roddick, *Organometallics* **1990**, *9*, 221–226; c) N. C. Schroeder, R. Funchess, R. A. Jacobson, R. J. Angelici, *Organometallics* **1989**, *8*, 521–529; d) A. F. Dyke, S. A. R. Knox, M. Morris, P. J. Naish, *J. Chem. Soc., Dalton Trans.* **1983**, 1417–1426; e) R. E. Colborn, A. F. Dyke, S. A. R. Knox, K. A. Mead, P. Woodward, *J. Chem. Soc., Dalton Trans.* **1983**, 2099–2108; f) R. E. Colborn, D. L. Davies, A. F. Dyke, S. A. R. Knox, K. A. Mead, A. G. Orpen, *J. Chem. Soc., Dalton Trans.* **1989**, 1799–1805; g) M. A.

 © 2007 Wiley-VCH Verlag GmbH & Co. KGaA, Weinheim 

Guillevic, E. L. Hancox, B. E. Mann, *J. Chem. Soc., Dalton Trans.* **1992**, 1729–1733.
[10] G. Hogarth, M. H. Lavander, K. Shukri, *J. Organomet. Chem.* **1997**, *527*, 247–258.
[11] L. Busetto, F. Marchetti, S. Zacchini, V. Zanotti, *J. Organomet. Chem.* **2006**, *691*, 2424–2439.
[12] a) R. E. Colborn, A. F. Dyke, B. P. Gracey, S. A. R. Knox, K. A. Macpherson, K. A. Mead, A. G. Orpen, *J. Chem. Soc., Dalton Trans.* **1990**, 761–771; b) D. L. Davies, S. A. R. Knox, K. A. Mead, M. J. Morris, P. Woodward, *J. Chem. Soc., Dalton Trans.* **1984**, 2293–2299; c) A. F. Dyke, S. A. R. Knox, P. J. Naish, G. E. Taylor, *J. Chem. Soc., Dalton Trans.* **1982**, 1297–1307.
[13] W. Wilker, D. Leibfritz, R. Kerssebaum, W. Beimel, *Magn. Reson. Chem.* **1993**, *31*, 287–292.
[14] K. Stott, J. Stonehouse, J. Keeler, T. L. Hwang, A. J. Shaka, *J. Am. Chem. Soc.* **1995**, *117*, 4199–4200.
[15] *SMART & SAINT Software Reference Manuals*, version 5.051, Bruker Analytical X-ray Instruments Inc., Madison, WI, **1998**.
[16] G. M. Sheldrick, *SADABS, Program for empirical absorption correction*, University of Göttingen, Germany, **1996**.
[17] G. M. Sheldrick, *SHELX97, Program for crystal structure determination*, University of Göttingen, Germany, **1997**.

Received: November 7, 2006
Published Online: February 2, 2007

 © 2007 Wiley-VCH Verlag GmbH & Co. KGaA, Weinheim 

DOI: 10.1002/ejic.200600841

# Boron Complexes with Chelating Anilido-Imine Ligands: Synthesis, Structures and Luminescent Properties

Yi Ren,[a] Xiaoming Liu,[a] Wei Gao,[a] Hong Xia,[a] Ling Ye,[a] and Ying Mu*[a]

**Keywords:** Organoboron compounds / Schiff-base ligands / Luminescence

Three new boron complexes with anilido-imine ligands, *ortho*-$C_6H_4(NAr^1)(CH{=}NAr^2)BF_2$ [$Ar^1$ = 2,6-$Et_2C_6H_3$, $Ar^2$ = *p*-$MeC_6H_4$ (**3a**); $Ar^1$ = 2,6-*i*$Pr_2C_6H_3$, $Ar^2$ = *p*-$MeC_6H_4$ (**3b**); $Ar^1$ = 2,6-*i*$Pr_2C_6H_3$, $Ar^2$ = 2,6-$Me_2C_6H_3$ (**3c**)] were synthesized by the reaction of $BF_3(OEt_2)$ with the lithium salt of the corresponding ligands. All complexes were characterized by $^1H$, $^{11}B$, $^{13}C$ and $^{19}F$ NMR spectroscopy, elemental analyses and mass spectrometry. The molecular structures of complexes **3a**–**3c** were determined by X-ray crystallography. DSC analysis of **3a**–**3c** demonstrates their good thermal stability. Luminescent properties of the ligands and the complexes **3a**–**3c** in solution and the solid state were studied.
(© Wiley-VCH Verlag GmbH & Co. KGaA, 69451 Weinheim, Germany, 2007)

## Introduction

Luminescent tricoordinate and tetracoordinate boron complexes, due to their high thermal stability, adequate electron transport and excellent luminescent properties, have recently attracted a great deal of attention in the field of organic light-emitting devices (OLEDs) application.[1] Marder et al.[2] and Cornu et al.[3] focus their works on the three-coordinate organoboron compounds and π-conjugated systems incorporating closo-dodecaborate clusters, respectively, and study their optical properties. Wang and co-workers have explored some devices made from $BR_2q$ [R = Et, Ph, 2-naphthyl, q = 8-hydroxyquinolato][4] and boron complexes with modified 8-hydroxyquinoline ligands,[5] which not only are promising emitters, but also were found to possess excellent electron transport properties. Y. Wang's group has reported some boron complexes with phenol-pyridyl ligands and investigated their applications in OLEDs.[6] Meanwhile, many boron complexes with N,N-chelate ligands were reported.[7] Some of these complexes provide excellent luminescent properties, and cover almost the entire visible region when changing substituents on the ligands.[7a–7f] Recently, some luminescent complexes with Schiff-base ligands were synthesized and showed potential applications in organic optoelectronics.[8] However, luminescent boron complexes with Schiff-base ligands are rather rare. We recently reported a new class of aluminum complexes with Schiff base type chelating anilido-imine ligands showing good luminescent properties.[9] However, the aluminum complexes are usually vulnerable, to some extent, to air and moisture.[10] In contrast, the boron complexes are generally chemically and thermally stable, and thus more promising for practical applications.[7b,11] We have therefore synthesized a number of new boron complexes with anilido-imine ligands: *ortho*-$C_6H_4(NAr^1)(CH{=}NAr^2)BF_2$ [$Ar^1$ = 2,6-$Et_2C_6H_3$, $Ar^2$ = *p*-$MeC_6H_4$ (**3a**); $Ar^1$ = 2,6-*i*$Pr_2C_6H_3$, $Ar^2$ = *p*-$MeC_6H_4$ (**3b**); $Ar^1$ = 2,6-*i*$Pr_2C_6H_3$, $Ar^2$ = 2,6-$Me_2C_6H_3$ (**3c**)]. Herein, we report the syntheses, characterizations, and fluorescent properties of these complexes.

[a] Key Laboratory for Supramolecular Structure and Materials of Ministry of Education, School of Chemistry, Jilin University, 2699 Qianjin Street, Changchun 130012, People's Republic of China
Fax: +86-431-85193421
E-mail: ymu@mail.jlu.edu.cn

## Results and Discussion

### Synthesis of Ligands

Anilido-imine ligands *ortho*-$C_6H_4(NHAr^1)(CH{=}NAr^2)$ [$Ar^1$ = 2,6-$Et_2C_6H_3$, $Ar^2$ = *p*-$MeC_6H_4$ (**2a**); $Ar^1$ = 2,6-*i*$Pr_2C_6H_3$, $Ar^2$ = *p*-$MeC_6H_4$ (**2b**); $Ar^1$ = 2,6-*i*$Pr_2C_6H_3$, $Ar^2$ = 2,6-$Me_2C_6H_3$ (**2c**)] were synthesized in good yields by the reaction of *ortho*-$C_6H_4F(CH{=}NAr^2)$ (**1**) with corresponding $LiN(H)Ar^1$ (Scheme 1) according to the literature procedure.[9,12] Among the ligands, **2a** and **2b** are new compounds while **2c** has been reported previously.[9] The reaction was carried out in THF and the crude products were purified by crystallization from methanol. Compounds **2a** and **2b** were characterized by $^1H$ and $^{13}C$ NMR spectroscopy along with elemental analyses. The $^1H$ NMR spectra of both compounds exhibit resonances around $\delta$ 8.59 ppm for the CH protons in –CH=N– group, with the corresponding $^{13}C$ NMR resonances occurring about $\delta$ = 162.4 ppm. The NH resonances appear at characteristically low field ($\delta$ = 10.65, 10.60 ppm). The infrared absorption bands of the imine C=N stretching occur at 1615 and 1624 $cm^{-1}$. These data are similar to the corresponding values of **2c**.[9]


© 2007 Wiley-VCH Verlag GmbH & Co. KGaA, Weinheim

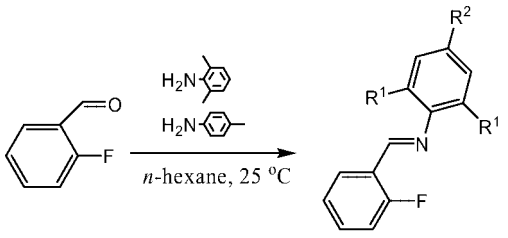


**1a** $R^1$ = H, $R^2$ = Me
**1b** $R^1$ = Me, $R^2$ = H

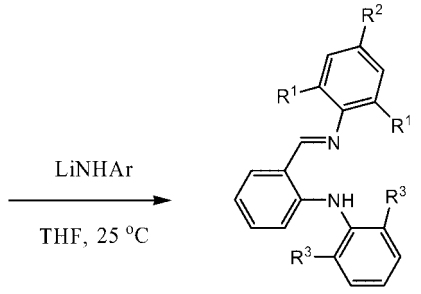


**2a** $R^1$ = H, $R^2$ = Me, $R^3$ = Et
**2b** $R^1$ = H, $R^2$ = Me, $R^3$ = *i*Pr
**2c** $R^1$ = Me, $R^2$ = H, $R^3$ = *i*Pr

Scheme 1. Synthetic procedure of ligand **2a**–**2c**.

## Synthesis of Complexes

The boron difluoride complexes **3a**–**3c** were synthesized in reasonable yields (71–78%) by the reaction of $BF_3(OEt_2)$ with the lithium salt of corresponding ligand that was generated in situ by treating the free ligand with *n*BuLi in toluene at –78 °C (Scheme 2). These complexes are well soluble in dichloromethane, diethyl ether, toluene and THF, but less soluble in saturated hydrocarbons. All complexes **3a**–**3c** were characterized by elemental analyses, $^1$H, $^{13}$C, $^{19}$F and $^{11}$B NMR spectroscopy, and satisfactory analytic results were obtained. In the $^1$H NMR spectra of **3a**–**3c**, the resonances for the imino CH protons are at $\delta$ = 8.37, 8.37 and 8.12 ppm, respectively. While the resonances ($\delta$ = 159.9–163.9 ppm) for the imino C-atoms in the $^{13}$C NMR spectra shift to high field in comparison with the corresponding signals of the free ligands and the dichloride aluminum complexes.[13] The N–H signals of the free ligands disappear in the $^1$H NMR spectra of the complexes **3a**–**3c**, which is indicative of the formation of B–N bond in these complexes. The two methyl groups of the isopropyl units in complexes **3b** and **3c** are inequivalent, since the coordination of the anilido-imine ligands to the boron center causes rotation about the N–aryl bond to become slow on the NMR time scale.[14] In addition, in the $^1$H and $^{13}$C NMR spectra of these complexes **3a**–**3c**, the resonances for 2,6-substituents of the aromatic ring at the amido nitrogen are equal, which indicates these complexes all have Cs-symmetric structures in solution. In $^{11}$B NMR spectra, complexes **3a**–**3c** exhibit triplet at $\delta$ 4.534, 4.527 and 4.335 ppm respectively, due to coupling with two equivalent fluorine atoms. These resonances of complexes **3a**–**3c** are in lower field compared to those of 2,4-diethyl-4,4-difluoro-1,3,5,7,8-pentamethyl-4-bora-3a,4a-diaza-*s*-indacene ($\delta_B$ = 3.8)[15a] and *p*-Tol$_2$nacnacBF$_2$ ($\delta_B$ 2.0),[15b] while in substantially higher field in comparison with that of tricoordinate boron complex [(Tolylnacnac)BMe]$^+$[MeB(C$_6$F$_5$)$_3$]$^-$ ($\delta_B$ = 37.1).[15b] The narrow linewidth of $^{11}$B NMR spectra for all complexes is consistent with tetrahedral boron. Complexes **3a**–**3c** are air- and moisture-stable in solution and solid state. Differential scanning calorimetry (DSC) analysis of complexes **3a**–**3c** shows that complexes **3a**–**3c** melt at 159.8, 176.8 and 221.5 °C, respectively. These data are close to the melting points of similar tetra-coordinated boron complexes, 2-(4′-methylquinolinyl)-2-phenolato)BPh$_2$ (210 °C),[16a] and 1,6-bis(2-hydroxyphenyl)pyridylboron–2-methoxybenzene (227 °C).[16b] DSC analysis of **3a**–**3c** also exhibits their high thermal stability since they can be heated to 250 °C without decomposition. They also have good thermal stability in solution and can be heated in boiling toluene or ethanol for several hours without obvious decomposition.

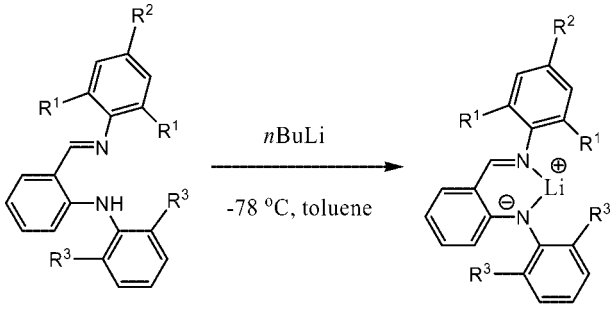


**2a** $R^1$ = H, $R^2$ = Me, $R^3$ = Et
**2b** $R^1$ = H, $R^2$ = Me, $R^3$ = *i*Pr
**2c** $R^1$ = Me, $R^2$ = H, $R^3$ = *i*Pr

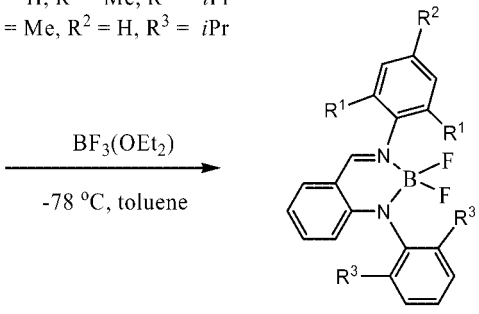


**3a** $R^1$ = H, $R^2$ = Me, $R^3$ = Et
**3b** $R^1$ = H, $R^2$ = Me, $R^3$ = *i*Pr
**3c** $R^1$ = Me, $R^2$ = H, $R^3$ = *i*Pr

Scheme 2. Synthetic procedure of complexes **3a**–**3c**.

## Crystal Structures

Molecular structures of the complexes **3a**–**3c** were determined by X-ray crystallographic analysis. The crystals of complexes **3a**–**3c** suitable for crystal structure analysis were obtained from *n*-hexane at 5 °C. The ORTEP drawings of molecular structures of **3a**, **3b** and **3c** are shown in Fig-

 © 2007 Wiley-VCH Verlag GmbH & Co. KGaA, Weinheim 

ures 1, 2, and 3, respectively. Selected bond lengths and angles for these complexes are given in Table 1. The X-ray analysis reveals that complexes **3a**–**3c** are four-coordinate and adopt a distorted tetrahedral geometry at the boron center. Complex **3a** belongs to the monoclinic space group $P2_1/n$, **3b**,**3c** to the triclinic space group $P\bar{1}$. In these complexes, the anilido-imine ligands chelate to the boron center to form the six-membered chelating rings that are nearly planar with the boron atom lying 0.0594 Å, 0.3127 Å, and 0.3020 Å out of the plane, respectively. The imino C=N bonds in these complexes retain their double bond character, being 1.307(2) Å, 1.302(2) Å, and 1.306(3) Å for **3a**, **3b**, and **3c**, respectively. The B–N (amido) distances (1.510(3) Å for **3a**, 1.521(3) Å for **3b**, 1.531(3) Å for **3c**) are shorter than the B–N (imine) distances (1.564(3) Å for **3a**, 1.580(2) Å for **3b**, 1.581(3) Å for **3c**) which is consistent with the fact that the B–N (amido) bond is a covalent bond while the B–N (imine) bond is a coordination bond. The B–N (imine) distances are larger than those values (1.550(3) Å and 1.553(3) Å] previously reported for *p*-Tol$_2$nacnacBF$_2$,[15b] while the B–N (amido) distances are shorter than the values (1.740(4) Å] of 2,6-(NMe$_2$)$_2$C$_6$H$_3$BCl(Ph).[15c] The average B–F bond lengths of 1.382(9) Å in those boron complexes are close to those values of 2,2-difluoro-1,3,4,6-tetramethyl-3-aza-1-azonia-2-bora-4,6-cyclohexadiene (1.403(2) Å][17a] and 4,4-difluoro-1,3,5,7,9-pentamethyl-3a,4a-diaza-4-bora-*s*-indacene (1.394(3) Å].[17b,17c] The F–B–F bond angles (107.5(2)° for **3a**, 108.86(18)° for **3b**, 108.5(2)° for **3c**) of those complexes are similar, which are slightly larger than 107.1(2)° for 2,2-difluoro-1,3,4,6-tetramethyl-3-aza-1-azonia-2-bora-4,6-cyclohexadiene,[17a] but smaller than the ideal tetrahedral angles (109.49°). The dihedral angles between the six-membered chelating ring and the aromatic ring at the amido nitrogen are 87.00° for **3a**, 83.65° for **3b**, and 82.00° for **3c**, while the dihedral angles between the six-membered chelating ring and the aromatic ring at the imine nitrogen are 51.40°, 55.17° and 80.60° for **3a**, **3b** and **3c**, respectively.

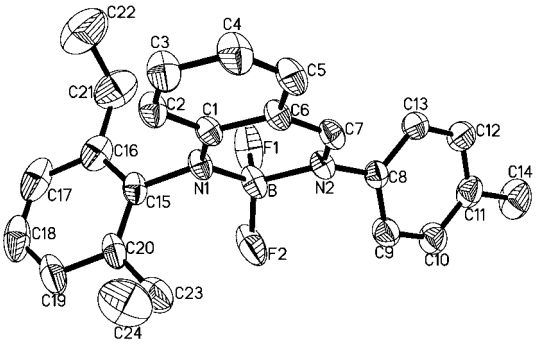


Figure 1. Molecular structure of complex **3a** (thermal ellipsoids are drawn at the 30% probability level).

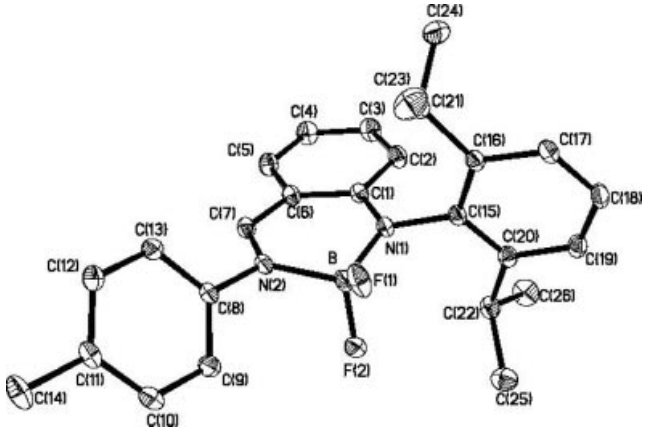


Figure 2. Molecular structure of complex **3b** (thermal ellipsoids are drawn at the 30% probability level).

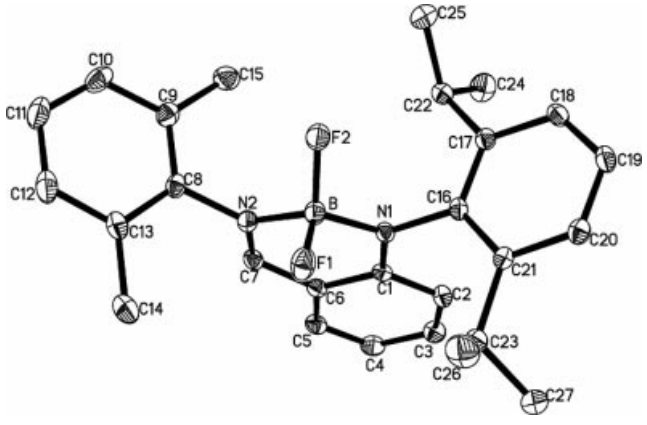


Figure 3. Molecular structure of complex **3c** (thermal ellipsoids are drawn at the 30% probability level).

Table 1. Selected bond lengths [Å] and angles [°].

| | | | |
|---|---|---|---|
| Complex **3a** | | | |
| N(1)–B | 1.510(3) | C(1)–N(1)–B | 124.97(16) |
| N(2)–B | 1.564(3) | F(2)–B–N(2) | 110.3(2) |
| F(1)–B | 1.387(3) | C(15)–N(1)–B | 116.93(15) |
| F(2)–B | 1.368(3) | C(7)–N(2)–B | 121.67(18) |
| N(1)–C(1) | 1.364(2) | C(8)–N(2)–B | 118.67(16) |
| N(2)–C(7) | 1.307(2) | F(1)–B–F(2) | 107.5(2) |
| N(1)–B–N(2) | 110.15(17) | F(1)–B–N(1) | 112.0(2) |
| F(1)–B–N(2) | 105.88(18) | F(2)–B–N(1) | 110.95(19) |
| Complex **3b** | | | |
| N(1)–B | 1.521(3) | C(1)–N(1)–B | 123.68(15) |
| N(2)–B | 1.580(2) | F(2)–B–N(2) | 106.75(17) |
| F(1)–B | 1.367(3) | C(15)–N(1)–B | 117.34(14) |
| F(2)–B | 1.395(3) | C(7)–N(2)–B | 120.86(16) |
| N(1)–C(1) | 1.358(2) | C(8)–N(2)–B | 119.83(14) |
| N(2)–C(7) | 1.302(2) | F(1)–B–F(2) | 108.86(18) |
| N(1)–B–N(2) | 108.00(15) | F(1)–B–N(1) | 112.08(17) |
| F(1)–B–N(2) | 108.81(17) | F(2)–B–N(1) | 112.15(17) |
| Complex **3c** | | | |
| B–F(2) | 1.384(3) | F(1)–B–N(1) | 111.85(19) |
| B–F(1) | 1.389(3) | F(2)–B–N(2) | 109.70(18) |
| B–N(1) | 1.531(3) | F(1)–B–N(2) | 107.93(18) |
| B–N(2) | 1.581(3) | N(1)–B–N(2) | 107.28(18) |
| C(1)–N(1) | 1.365(3) | C(1)–N(1)–B | 123.69(18) |
| C(7)–N(2) | 1.306(3) | C(16)–N(1)–B | 117.35(16) |
| F(2)–B–F(1) | 108.5(2) | C(7)–N(2)–B | 122.19(18) |
| F(2)–B–N(1) | 111.53(19) | C(8)–N(2)–B | 119.59(17) |

 © 2007 Wiley-VCH Verlag GmbH & Co. KGaA, Weinheim 

### UV/Vis and Fluorescent Properties

Table 2 summarizes the UV/Vis and fluorescent properties of compounds **2a**–**2c** and **3a**–**3c** determined in both solution and the solid state. The free ligands **2a**–**2c** all display weak blue fluorescence with emission maxima of 448, 446 and 420 nm, respectively. UV/Vis absorptions of complexes **3a**–**3c** are displayed in Figure 4. The maximal absorptions of **3a**–**3c** ($\lambda_{abs}$ = 440, 440 and 429 nm) are close to those of their aluminum analogues ($\lambda_{abs}$ = 437, 436, 436, 447 nm).[13] The fluorescent spectra of complexes **3a**–**3c** are shown in Figure 5. Complexes **3a**–**3c** in solution all give a broad emission band (bandwidth at half-height: 64, 61, 69 nm) with $\lambda_{max}$ = 511, 512 and 491 nm, respectively. The quantum yields of these complexes are relatively high in solution. The emission energies of these complexes are significantly red-shifted in comparison with their free ligands. As previous reported,[9,13] the observed luminescence of these complexes could be attributed to π*–π transition of their conjugated chelating anilido-imine ligands. The role of the coordination of the ligand to the boron atom in the luminescence of **3a**–**3c** should be twofold as pointed out in literatures for coordination complexes.[18] The formation of the B–N bond via the donation of lone-pair of the N atom to the B atom lowers the energy gap between π* and π of the ligand, and the chelating ring makes the ligand more rigid, which can reduce the loss of energy via vibrational motions and increase the emission efficiency. The emission maxima of complexes **3a** and **3b** are close to each other, while the emission maximum of **3c** is blue-shifted for about 20 nm compared to the ones of **3a** and **3b**. Such a result might be attributed to the differences in the number and size of the *ortho*-substituents on the rotatable aryl rings of their ligands that could affect the dihedral angles between the six-membered chelating ring and the aromatic ring at the imine nitrogen and thus the conjugated extent of these complexes.[5,19a,19b] In addition, the lower basicity and electron density of the anilido may also be responsible for the emission red shift in **3a** and **3b**.[19c] Compared to its aluminum analogue, [*ortho*-$C_6H_4N(C_6H_3i Pr_2$-2,6)-(CH=$NC_6H_3Me_2$-2,6)$AlCl_2$] ($\lambda_{max}$ = 510),[13] the emission maximum of complex **3c** is blue-shifted by 19 nm in hexane. The emission energies of complexes **3a**–**3c** in solution are close to or slightly higher than those of related boron compounds, 4,4-difluoro-8-(4-hydroxyphenyl)-4-bora-3a,4a-diaza-*s*-indacene ($\lambda_{abs}$ = 518 nm)[20a] and 2,4-diethyl-4-fluoro-1,3,5,7,8-pentamethyl-4-phenyl-4-bora-3a,4a-diaza-*s*-indacene ($\lambda_{abs}$ = 536 nm).[20b] All complexes **3a**–**3c** exhibit bright

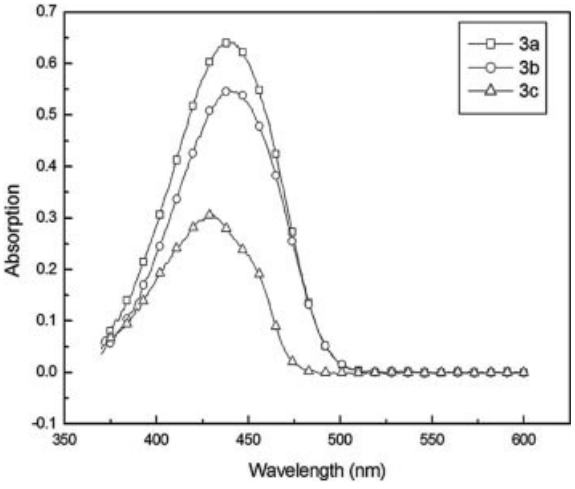


Figure 4. UV/Vis absorption of complexes **3a**–**3c** in hexane.

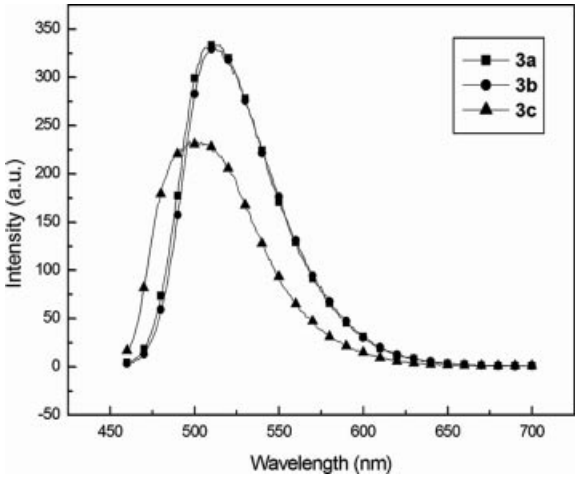


Figure 5. Emission spectra of complexes **3a**–**3c** in *n*-hexane.

Table 2. Photoluminescent data for ligands **2a**–**2c** and complexes **3a**–**3c**.

| Compound | Conditions | $\lambda_{abs}$ [nm] | $\lambda_{em}$ [nm] | ε [M·cm$^{-1}$] | Quantum yields [$\Phi$][a] |
|---|---|---|---|---|---|
| **2a** | hexane, 298 K | 386 | 448 | 12587 | 0.027 |
| | solid, 298 K | | 468 | | |
| **2b** | hexane, 298 K | 386 | 446 | 10358 | 0.032 |
| | solid, 298 K | | 461 | | |
| **2c** | hexane, 298 K | 371 | 420 | 11265 | 0.029 |
| | solid, 298 K | | 432 | | |
| **3a** | hexane, 298 K | 440 | 511 | 9521 | 0.549 |
| | solid, 298 K | | 527 | | |
| **3b** | hexane, 298 K | 440 | 512 | 9785 | 0.574 |
| | solid, 298 K | | 518 | | |
| **3c** | hexane, 298 K | 429 | 491 | 9840 | 0.582 |
| | solid, 298 K | | 519 | | |

[a] Determined using quinine sulfate in 0.1 M sulfuric acid as a standard.

 © 2007 Wiley-VCH Verlag GmbH & Co. KGaA, Weinheim 

fluorescence in the solid state when irradiated with an adequate excitation wavelength. The emission spectra of these complexes in the solid state are shown in Figure 6. Complexes **3a**, **3b**, and **3c** each has a relatively narrow emission band (bandwidth at half-height: 55, 75, 74 nm) with $\lambda_{max}$ = 527, 518 and 519 nm, respectively. The emission maxima of these complexes in the solid state are red-shifted compared to their corresponding emission maxima in solution. Red shifting of emission maximum can be normally observed for most fluorescent compounds in the solid state due probably to π-π staking of aromatic rings in the molecules.

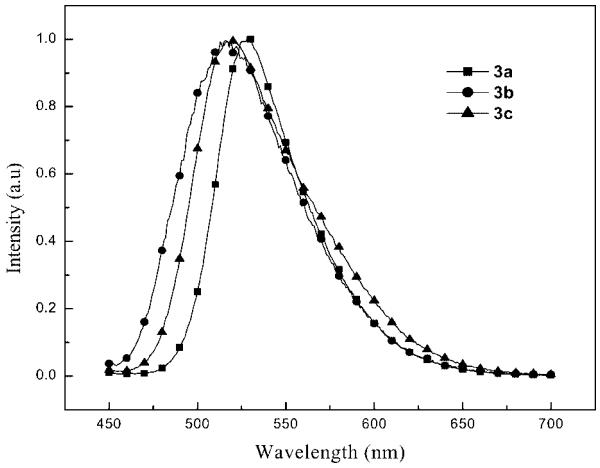


Figure 6. Emission spectra of complexes **3a**–**3c** in the solid state.

## Experimental Section

**General:** All reactions were performed using standard Schlenk techniques in an atmosphere of high-purity nitrogen or glove-box techniques. Toluene, hexane, THF, and diethyl ether were dried by reflux over sodium and benzophenone and distilled under nitrogen prior to use. $C_6D_6$ was dried with activated 4-Å molecular sieves and vacuum-transferred to a sodium-mirrored air-free flask. $CDCl_3$ was dried with $CaH_2$ for 48 h and vacuum-transferred to an air-free flask. $BF_3(OEt_2)$ and *n*BuLi were purchased from Aldrich and used as received. The pre-ligands and the ligands were synthesized according to literature procedures.[9,12] $^1H$ and $^{13}C$ NMR spectra were measured using a Bruker AVANCE-500 NMR spectrometer. $^{11}B$ NMR spectra were measured using a Bruker AVANCE-500 NMR spectrometer at 160 MHz with $BF_3(OEt_2)$ as external reference (positive values downfield).$^{19}F$ NMR spectra were measured using a Bruker AVANCE-500 NMR spectrometer at 376.27 MHz with $CFCl_3$ as external reference (positive values downfield). The elemental analysis was performed with a Perkin–Elmer 2400 microanalyzer. UV/Vis absorption spectra were recorded on a PE UV-lambdazo spectrophotometer. Fluorescence measurements were carried out on a Shimadzu RF-5301PC. The melting points were determined on a Fisher–Johns melting point apparatus. Differential scanning calorimetric measurements were performed on a NETZSCH DSC204 instrument.

***ortho*-$C_6H_4NH(C_6H_3Et_2$-2,6)(CH=$NC_6H_4$Me-*p*) (2a):** A solution of *n*BuLi (25.29 mL, 30.35 mmol) in hexanes was added to a solution of 2,6-diethylaniline (5.0 mL, 30.35 mmol) in THF (20 mL) at –78 °C. The reaction mixture was warmed to room temperature and stirred overnight. The resulting solution of LiNHAr was transferred into a solution of *ortho*-$C_6H_4F(CH{=}NC_6H_4Me$-*p*) (6.47 g, 30.35 mmol) in THF (20 mL) at 25 °C. After stirring for 24 h, the reaction was quenched with $H_2O$ (20 mL), the mixture was extracted with *n*-hexane, and the organic phase evaporated to dryness in vacuo to give the crude product as yellow solid. Pure product (7.79 g, 75%) was obtained as yellow crystals by recrystallization from ethanol at –20 °C. $C_{24}H_{26}N_2$ (342.48): calcd. C 84.17, H 7.65, N 8.18; found C 84.12, H 7.67, N 8.21%. $^1H$ NMR (500 MHz, $CDCl_3$, 293 K): $\delta$ = 1.09 (t, 6 H, $CH_2CH_3$), 2.30 (s, 3 H, $CH_3$), 2.47 (q, 2 H, $CH_2CH_3$), 2.57 (q, 2 H, $CH_2CH_3$), 6.18 (d, 1 H, Ph-*H*), 6.62 (t, 1 H, Ph-*H*), 7.03–7.34 (m, 9 H, Ph-*H*), 8.59 (s, 1 H, C*H*=NAr) 10.65 (s, 1 H, N*H*) ppm. $^{13}C\{^1H\}$ NMR (125 MHz, $CDCl_3$, 293 K): $\delta$ = 15.1 ($CH_3$), 21.0 ($CH_2CH_3$), 25.1 ($CH_2CH_3$), 76.8, 77.1, 77.3, 111.9, 115.5, 117.1, 120.9, 126.8, 127.0, 127.6, 129.9, 132.0, 134.6, 142.9, 149.0, 149.1, 162.4 (*C*H=NAr) ppm.

***ortho*-$C_6H_4NH(C_6H_3iPr_2$-2,6)(CH=$NC_6H_3C_6H_4$Me-*p*) (2b):** A solution of *n*BuLi (22.1 mL, 26.5 mmol) in hexanes was added to a solution of 2,6-diisopropylaniline (5.0 mL, 26.5 mmol) in THF (20 mL) at –78 °C. The reaction mixture was warmed to room temperature and stirred overnight. The resulting solution of LiNHAr was transferred into a solution of *ortho*-$C_6H_4F(CH{=}NC_6H_4Me$-*p*) (5.7 g, 26.5 mmol) in THF (20 mL) at 25 °C. After stirred for 24 h, the reaction was quenched with $H_2O$ (20 mL), the mixture was extracted with *n*-hexane and the organic phase evaporated to dryness in vacuo to give the crude product as yellow solid. Pure product (7.7 g, 78%) was obtained as yellow crystals by recrystallization from ethanol at –20 °C. $C_{26}H_{30}N_2$ (370.53): calcd.C 84.28, H 8.16, N 7.56; found C 84.31, H 8.11, N 7.58%. $^1H$ NMR (500 MHz, $CDCl_3$, 293 K): $\delta$ = 1.07 (d, 6 H, $CH(CH_3)_2$), 1.10 (d, 6 H, $CH(CH_3)_2$), 2.29 (s, 3 H, $CH_3$), 3.09 (sept, 2 H, $CH(CH_3)_2$), 6.18 (d, 1 H, Ph-*H*), 6.61 (t, 1 H, Ph-*H*), 7.02–7.33 (m, 9 H, Ph-*H*), 8.59 (s, 1 H, C*H*=NAr), 10.60 (s, 1 H, N*H*). $^{13}C\{^1H\}$ NMR (125 MHz, $CDCl_3$, 293 K): $\delta$ = 21.1 ($CH_3$), 22.9 ($CH(CH_3)_2$), 25.0 ($CH(CH_3)_2$), 28.6 ($CH(CH_3)_2$), 76.8, 77.1, 77.3, 112.1, 115.4, 116.9, 120.9, 123.8, 127.4, 129.8, 132.0, 134.5, 135.0, 135.5, 147.6, 149.0, 149.8, 162.4 (*C*H=NAr).

***ortho*-$C_6H_4N(C_6H_3Et_2$-2,6)(CH=$NC_6H_4$Me-*p*)$BF_2$ (3a):** 0.49 mL of an *n*BuLi solution (0.58 mmol) was added to the solution of the ligand **2a** *ortho*-$C_6H_4NH(C_6H_3Et_2$-2,6)(CH=$NC_6H_4$Me-*p*) (0.2 g, 0.58 mmol) in toluene with stirring at –78 °C. The mixture was warmed to room temperature and stirred overnight. The resulting mixture was added dropwise to a toluene suspension of $BF_3(OEt_2)$ (0.71 mL, 0.58 mmol) at –78 °C with stirring. The mixture was warmed to room temperature, then stirred overnight at 80 °C. The solvent was removed in vacuo. The 9 mL of hexane was added to the yellow solid residue. Insoluble material was removed by filtration through Celite. Yellow crystals (0.18 g, 78%) were obtained from *n*-hexane solution at 5 °C. $C_{24}H_{25}BF_2N_2$ (390.28): calcd. C 73.86, H 6.46, N 7.18; found C 73.89, H 6.41, N 7.14%. $^1H$ NMR (500 MHz, $CDCl_3$, 293 K): $\delta$ = 1.11 (t, 6 H, $CH_2CH_3$), 2.40 (s, 3 H, $CH_3$), 2.45 (q, 2 H, $CH_2CH_3$), 2.64 (q, 2 H, $CH_2CH_3$), 6.25 (d, 1 H, Ph-*H*), 6.70 (t, 1 H, Ph-*H*), 7.24–7.49 (m, 9 H, Ph-*H*), 8.37 (s, 1 H, C*H*=NAr) ppm. $^{13}C\{^1H\}$ NMR (125 MHz, $CDCl_3$, 293 K): $\delta$ = 14.7 ($CH_3$), 21.3 ($CH_2CH_3$), 23.9 ($CH_2CH_3$), 76.8, 77.2, 77.4, 77.7, 112.9, 115.6, 116.5, 124.1, 126.6, 127.6, 130.2, 133.3, 137.6, 137.7, 138.7, 141.2, 142.9, 151.9, 159.9 (*C*H=NAr) ppm. $^{11}B$ NMR ($CDCl_3$, 160 MHz, 293 K): $\delta$ = 4.534 (t, 1:2:1, $J$ = 28.32 Hz) ppm. $^{19}F$ NMR ($CDCl_3$, 470 MHz, 293 K): $\delta$ = 49.7 (q, 1:1:1:1) pm. MS, *m*/*z*: 371 [(M – F)$^+$].

***ortho*-$C_6H_4N(C_6H_3iPr_2$-2,6)(CH=$NC_6H_3C_6H_4$Me-*p*)$BF_2$ (3b):** An *n*BuLi solution (0.45 mL, 0.54 mmol) was added to a toluene solution (6 mL) of the ligand **2b** *ortho*-$C_6H_4NH(C_6H_3iPr_2$-

 © 2007 Wiley-VCH Verlag GmbH & Co. KGaA, Weinheim 

2,6)(CH=NC$_6$H$_3$C$_6$H$_4$Me-*p*) (0.2 g, 0.54 mmol) at –78 °C. The mixture was warmed to room temperature, then stirred overnight. The resulting mixture was added dropwise to a toluene suspension of $BF_3(OEt_2)$ (0.66 mL, 0.54 mmol) at –78 °C with stirring. The mixture was warmed to room temperature, then stirred overnight at 80 °C. The solvent was removed in vacuo. Then 9 mL of hexane was added to the yellow solid residue. Insoluble material was removed by filtration through Celite. Yellow crystals (0.16 g, 73%) were obtained from the *n*-hexane solution at 5 °C. $C_{26}H_{29}BF_2N_2$ (418.33): calcd. C 74.65, H 6.99, N 6.70; found C 74.66, H 6.96, N 6.67%. $^1$H NMR (500 MHz, $CDCl_3$, 293 K): $\delta$ = 0.99 (d, 6 H, CH(C$H_3$)$_2$), 1.22 (d, 6 H, CH(C$H_3$)$_2$), 2.40 (s, 3 H, C$H_3$), 3.02 (sept, 2 H, C*H*(CH$_3$)$_2$), 6.28 (d, 1 H, Ph-*H*), 6.68 (t, 1 H, Ph-*H*), 7.22–7.50 (m, 9 H, Ph-*H*), 8.37 (s, 1 H, C*H*=NAr) ppm. $^{13}$C{$^1$H} NMR (125 MHz, $CDCl_3$, 293 K): $\delta$ = 21.3 (*C*H$_3$), 24.4 (CH(*C*H$_3$)$_2$), 25.1 (CH(*C*H$_3$)$_2$), 28.5 (*C*H(CH$_3$)$_2$), 76.8, 77.2, 77.4, 77.7, 112.8, 116.3, 116.4, 124.2, 124.5, 128.0, 130.2, 133.3, 135.7, 137.4, 138.6 147.9, 152.3, 160.0 (*C*H=NAr) ppm. $^{11}$B NMR ($CDCl_3$, 160 MHz, 293 K): $\delta$ = 4.527 (t, 1:2:1, $J$ = 27.84 Hz) ppm. $^{19}$F NMR ($CDCl_3$, 470 MHz, 293 K): $\delta$ = 51.0 (q, 1:1:1:1) ppm. MS, *m*/*z*: 399.1 [(M – F)$^+$].

***ortho*-C$_6$H$_4$N(C$_6$H$_3$*i*Pr$_2$-2,6)(CH=NC$_6$H$_3$Me$_2$-2,6)BF$_2$ (3c):** 0.43 mL of an *n*BuLi solution (0.52 mmol) was added to the toluene of the ligand **2c** *ortho*-C$_6$H$_4${NH(C$_6$H$_3$*i*Pr$_2$-2,6)}(CH=NC$_6$H$_3$Me$_2$-2,6) (0.2 g, 0.52 mmol) at –78 °C. The mixture was warmed to the room temperature, then stirred until room temperature was reached. The resulting mixture was added dropwise to a toluene suspension of $BF_3(OEt_2)$ (0.64 mL, 0.52 mmol) at –78 °C with stirring. The mixture was stirred until room temperature was reached, stirring was continued overnight at 80 °C. The solvent was removed in vacuo. Then 9 mL of hexane was added to the yellow solid residue. Insoluble material was removed by filtration through Celite. Yellow crystals (0.16 g, 71%) were obtained from *n*-hexane solution at 5 °C. $C_{27}H_{31}BF_2N_2$ (432.36): calcd. C 75.01, H 7.23, N 6.48; found C 75.04, H 7.19, N 6.51%. $^1$H NMR (500 MHz, $CDCl_3$, 293 K): $\delta$ = 1.01 (d, 6 H, CH(C$H_3$)$_2$), 1.21 (d, 6 H, CH(C$H_3$)$_2$), 2.34 (s, 6 H, C$H_3$), 3.13 (sept, 2 H, C*H*(CH$_3$)$_2$), 6.30 (d, 1 H, Ph-*H*), 6.68 (t, 1 H, Ph-*H*), 7.14–7.39 (m, 9 H, Ph-*H*), 8.12 (s, 1 H, C*H*=NAr) ppm. $^{13}$C{$^1$H} NMR (125 MHz, $CDCl_3$, 293 K): $\delta$ = 18.6 (*C*H$_3$), 24.5 (CH(*C*H$_3$)$_2$), 25.3 (CH(*C*H$_3$)$_2$), 28.5 (*C*H(CH$_3$)$_2$), 76.8, 77.3, 77.7, 116.2, 116.4, 124.6, 128.0, 128.3, 128.8, 133.3, 134.5, 135.6, 137.5, 147.8, 152.6, 163.9 (*C*H=NAr) ppm. $^{11}$B NMR ($CDCl_3$, 160 MHz, 293 K): $\delta$ = 4.335 (t, 1:2:1, $J$ = 28.48 Hz) ppm. $^{19}$F NMR ($CDCl_3$, 470 MHz, 293 K): $\delta$ = 49.7 (s) ppm. MS, *m*/*z*: 413.1 [(M – F)$^+$].

**PL Quantum Yield Measurements:** Room-temperature luminescence quantum yields were measured at a single excitation wavelength (360 nm) referenced to quinine sulfate in sulfuric acid aqueous solution ($\Phi$ = 0.546). The quantum yields were calculated using known procedures.[21] The excitation wavelength was 440, 440, and 429 nm for complexes **3a**, **3b** and **3c**, respectively.

**X-ray Structure Determinations of 3a, 3b and 3c:** Single crystals of **3a**, **3b** and **3c** suitable for X-ray structural analysis were obtained from *n*-hexane. Diffraction data were collected at 293 K with a Rigaku R-AXIS RAPID IP diffractometer equipped with graphite-monochromated Mo-$K_\alpha$ radiation ($\lambda$ = 0.71073 Å) for **3a**, **3b** and **3c**. Details of the crystal data, data collections, and structure refinements are summarized in Table 2 and Table 3. The structures were solved by direct methods[22] and refined by full-matrix least-squares on $F^2$. All non-hydrogen atoms were refined anisotropically and the hydrogen atoms were included in idealized position. All calculations were performed using the SHELXTL[23] crystallographic software packages.

CCCD-619766 (for **3a**), -619767 (for **3b**), and -619768 (for **3c**) contain the supplementary crystallographic data for this paper. These data can be obtained free of charge from The Cambridge Crystallographic Data Centre via www.ccdc.cam.ac.uk/data_request/cif.

Table 3. Crystal data and structural refinements details for **3a**, **3b** and **3c**.

| | **3a** | **3b** | **3c** |
|---|---|---|---|
| Empirical formula | $C_{24}H_{25}BF_2N_2$ | $C_{28}H_{29}BF_2N_2$ | $C_{27}H_{31}BF_2N_2$ |
| Formula mass | 390.27 | 442.34 | 432.35 |
| Temp. [K] | 293(2) | 293(2) | 293(2) |
| Crystal system | monoclinic | triclinic | triclinic |
| Space group | $P2_1/n$ | $P\bar{1}$ | $P\bar{1}$ |
| $a$ [Å] | 11.225(2) | 9.2815(19) | 8.8684(9) |
| $b$ [Å] | 14.649(3) | 11.852(2) | 11.5381(13) |
| $c$ [Å] | 12.857(3) | 12.451(3) | 12.3418(12) |
| $\alpha$ [°] | 90 | 111.57(3) | 73.654(5) |
| $\beta$ [°] | 90.61(3) | 91.95(3) | 73.645(4) |
| $\gamma$ [°] | 90 | 110.71(3) | 81.066(2) |
| Volume [Å$^3$] | 2114.0(7) | 1170.0(4) | 1158.8(2) |
| $Z$ | 4 | 2 | 2 |
| $D_{calcd.}$ [Mg cm$^{-3}$] | 1.226 | 1.256 | 1.239 |
| $F(000)$ | 824 | 468 | 460 |
| $\theta$ range for data collection [°] | $2.11 \le 2\theta \le 27.48$ | $3.19 \le 2\theta \le 27.47$ | $1.78 \le 2\theta \le 27.48$ |
| Limiting indices | $-14 \le h \le 0$ | $-12 \le h \le 11$ | $0 \le h \le 11$ |
| | $-19 \le k \le 0$ | $-14 \le k \le 15$ | $-14 \le k \le 14$ |
| | $-16 \le l \le 16$ | $-16 \le l \le 16$ | $-14 \le l \le 16$ |
| Data/restraints/parameters | 4840/0/263 | 5233/0/285 | 5177/0/380 |
| Goodness-of-fit on $F^2$ | 0.773 | 1.041 | 0.951 |
| Final $R$ indices [$I > 2\sigma(I)$] | $R_1$ [a] = 0.0485 | $R_1$ [a] = 0.0512 | $R_1$ [a] = 0.0498 |
| | $wR_2$ [b] = 0.1132 | $wR_2$ [b] = 0.1369 | $wR_2$ [b] = 0.1073 |
| $R$ indices (all data) | $R_1$ [a] = 0.1402 | $R_1$ [a] = 0.0970, | $R_1$ [a] = 0.1165, |
| | $wR_2$ [b] = 0.1330 | $wR_2$ [b] = 0.1599 | $wR_2$ [b] = 0.1310 |
| Largest diff. peak/hole [e·Å$^{-3}$] | 0.210, –0.191 | 0.174, –0.186 | 0.218, –0.249 |

[a] $R_1 = \Sigma||F_o| - |F_c||/\Sigma|F_o|$. [b] $wR_2 = \{\Sigma[w(F_o^2 - F_c^2)^2]/\Sigma[w(F_o^2)^2]\}^{1/2}$.

 © 2007 Wiley-VCH Verlag GmbH & Co. KGaA, Weinheim 

## Acknowledgments

This work was supported by the National Natural Science Foundation of China (20674024 and 20374023) and the Ministry of Science and Technology of China (2002CB6134003).

[1] a) T. Noda, Y. Shirota, *J. Am. Chem. Soc.* **1998**, *120*, 9714–9715; b) T. Noda, H. Ogawa, Y. Shirota, *Adv. Mater.* **1999**, *11*, 283–285; c) Y. Shirota, M. Kinoshita, T. Noda, K. Okumoto, T. Ohara, *J. Am. Chem. Soc.* **2000**, *122*, 11021–11022; d) M. Kinoshita, H. Kita, Y. Shirota, *Adv. Funct. Mater.* **2002**, *12*, 780–786; e) H. Doi, M. Kiinoshita, K. Okumoto, Y. Shirota, *Chem. Mater.* **2003**, *15*, 1080–1089; f) C. Goze, G. Ulrich, L. J. Mallon, B. D. Allen, A. Harriman, R. Zieseel, *J. Am. Chem. Soc.* **2006**, *128*, 10231–10239; g) T. Sano, Y. Nishio, Y. Hamada, H. Takahashi, T. Usuki, K. Shibata, *J. Mater. Chem.* **2000**, *10*, 157–161.

[2] a) M. Halik, W. Wenseleers, C. Grasso, F. Stellacci, E. Zojer, S. Barlow, J. L. Bredas, J. W. Perry, S. R. Marder, *Chem. Commun.* **2003**, 1490–1491; b) C. D. Entwistle, T. B. Marder, *Chem. Mater.* **2004**, *16*, 4574–4585; c) C. D. Entwistle, T. B. Marder, *Angew. Chem. Int. Ed.* **2002**, *41*, 2927–2931.

[3] a) R. Bernard, D. Cornu, J. P. Scharff, R. Chiriac, P. Miele, *Inorg. Chem.* **2006**, *45*, 8743–8748; b) R. Bernard, D. Cornu, P. L. Baldeck, J. Caslavsky, J. M. Letoffe, J. P. Scharff, P. Miele, *Dalton Trans.* **2005**, 3065–3071.

[4] Q. Wu, M. Esteghamatian, N. X. Hu, Z. Popovic, G. Enright, Y. Tao, M. D′Iorio, S. Wang, *Chem. Mater.* **2000**, *12*, 79–83.

[5] Y. Cui, Q. D. Liu, D. R. Bai, W. L. Jia, Y. Tao, S. Wang, *Inorg. Chem.* **2005**, *44*, 601–609.

[6] a) Q. D. Liu, Y. Liu, W. M. Bu, D. Lu, Y. Wu, Y. Wang, *Chem. Mater.* **2000**, *12*, 2672–2675; b) J. S. Chen, D. G. Ma, Y. Liu, Y. Wang, *J. Phys. D: Appl. Phys.* **2005**, *38*, 3366–3370; c) Y. Q. Li, Y. Liu, W. M. Bu, J. H. Guo, Y. Wang, *Chem. Commun.* **2000**, 1551–1552; d) H. Y. Zhang, C. Huo, K. Q. Ye, P. Zhang, W. J. Tian, Y. Wang, *Inorg. Chem.* **2006**, *45*, 2788–2794.

[7] a) Q. D. Liu, M. S. Mudadu, H. Schmider, R. Thummel, Y. Tao, S. Wang, *Organometallics* **2002**, *21*, 4743–4749; b) Q. Wu, M. Esteghamatian, N. X. Hu, Z. Popovic, G. Enright, S. R. Breeze, S. Wang, *Angew. Chem. Int. Ed.* **1999**, *38*, 985–998; c) Q. G. Wu, G. Wu, L. Brancaleon, S. Wang, *Organometallics* **1999**, *18*, 2553–2556; d) S. F. Liu, Q. Wu, H. L. Schmider, H. Aziz, N. X. Hu, Z. Popovic, S. Wang, *J. Am. Chem. Soc.* **2000**, *122*, 3671–3678; e) C. C. Cheng, W. S. Yu, P. T. Chou, S. M. Peng, G. H. Lee, P. C. Wu, Y. H. Song, Y. Chi, *Chem. Commun.* **2003**, 2628–2629; f) Q. D. Liu, M. S. Mudadu, R. Thummel, Y. Tao, S. Wang, *Adv. Funct. Mater.* **2005**, *15*, 143–154; g) W. Baruah, W. W. Qin, A. Renaud, L. Vallee, D. Beljonne, T. Rohand, W. Dehaen, N. Boens, *Org. Lett.* **2005**, *7*, 4377–4380; h) M. Baruah, W. W. Qin, C. Flors, J. Hofkens, R. A. L. Vallee, D. Beljonne, M. V. D. Auweraer, W. M. D. Borggraeve, N. Boens, *J. Phys. Chem. A* **2006**, *110*, 5998–6009; i) L. Bi, D. H. Kim, J. Y. Ju, *J. Am. Chem. Soc.* **2006**, *128*, 2542–2543; j) L. Zeng, E. W. Miller, A. Pralle, E. Y. Isacoff, C. J. Chang, *J. Am. Chem. Soc.* **2006**, *128*, 10–11.

[8] a) H. F. Xiang, S. C. Chan, K. Y. Wu, C. M. Che, P. T. Lai, *Chem. Commun.* **2005**, 1408–1410; b) C. M. Che, S. C. Chan, H. F. Xiang, M. C. W. Chan, Y. Liu, Y. Wang, *Chem. Commun.* **2004**, 1484–1485; c) J. Qiao, L. D. Wang, L. Duan, Y. Li, D. Q. Zhang, Y. Qiu, *Inorg. Chem.* **2004**, *43*, 5096–5102; d) F. Galbrecht, X. H. Yang, B. S. Nehls, D. Neher, T. Farrel, U. Scherf, *Chem. Commun.* **2005**, 2378–2380; e) J. Qiao, Y. Qiu, L. D. Wang, L. Duan, Y. Yi, D. Q. Zhang, *Appl. Phys. Lett.* **2002**, *81*, 4913–4915; f) T. Sano, Y. Nishio, Y. Hamada, H. Takahashi, T. Usuki, K. Shibata, *J. Mater. Chem.* **2000**, *10*, 157–161.

[9] X. M. Liu, W. Gao, Y. Mu, G. Li, L. Ye, H. Xia, Y. Ren, S. H. Feng, *Organometallics* **2005**, *24*, 1614–1619.

[10] a) L. M. Leung, W. Y. Lo, S. K. So, K. M. Lee, W. K. Choi, *J. Am. Chem. Soc.* **2000**, *122*, 5640–5641; b) Y. Peng, H. Fan, H. Zhu, H. W. Roesky, J. Magull, C. E. Hughes, *Angew. Chem. Chem. Int. Ed.* **2004**, *43*, 3443–3445; c) V. Jancik, Y. Peng, H. W. Roesky, J. Li, D. Neculai, A. M. Neculai, R. Herbst-Irmer, *J. Am. Chem. Soc.* **2003**, *125*, 1452–1453; d) V. Jancik, L. W. Pineda, J. Pinas, H. W. Roesky, D. Neculai, A. M. Neculai, R. Herbst-Irmer, *Angew. Chem. Int. Ed.* **2004**, *43*, 2142–2145; e) G. Bai, Y. Peng, H. W. Roesky, J. Li, H.-G. Schmidt, M. Noltemeyer, *Angew. Chem. Int. Ed.* **2003**, *42*, 1132–1135.

[11] a) A. Hassan, S. Wang, *Chem. Commun.* **1998**, 211–212; b) W. Liu, A. Hassan, S. Wang, *Organometallics* **1997**, *16*, 4257–4259; c) J. Ashenhurst, L. Brancaleon, A. Hassan, W. Liu, H. Schmider, S. Wang, Q. Wu, *Organometallics* **1998**, *17*, 3186–3195.

[12] P. G. Hayes, G. C. Welch, D. J. H. Emslie, C. L. Noack, W. E. Piers, M. Parvez, *Organometallics* **2003**, *22*, 1577–1579.

[13] X. M. Liu, H. Xia, W. Gao, L. Ye, Y. Mu, Q. Su, Y. Ren, *Eur. J. Inorg. Chem.* **2006**, 1216–1222.

[14] a) J. C. Jenkins, M. Brookhart, *Organometallics* **2003**, *22*, 250–256; b) B. Y. Lee, X. H. Bu, G. C. Bazan, *Organometallics* **2001**, *20*, 5425–5431; c) V. C. Gibson, J. A. Segal, A. J. P. White, D. J. Williams, *J. Am. Chem. Soc.* **2000**, *122*, 7120–7121; d) C. E. Radezewich, I. A. Guzei, R. F. Jordan, *J. Am. Chem. Soc.* **1999**, *121*, 8673–8674.

[15] a) R. Ziessel, L. Bonardi, P. Retailleau, G. Ulrich, *J. Org. Chem.* **2006**, *71*, 3093–3102; b) B. X. Qian, S. W. Baek, M. R. Smith III, *Polyhedron* **1999**, *18*, 2405–2414.

[16] a) S. F. Liu, C. Seward, H. Aziz, N. X. Hu, Z. Popovic, S. N. Wang, *Organometallics* **2000**, *19*, 5709–5714; b) H. Zhang, C. Huo, K. Ye, P. Zhang, W. Tian, Y. Wang, *Inorg. Chem.* **2006**, *45*, 2788–2794.

[17] a) N. Kuhn, A. Kuhn, M. Speis, D. Blaser, R. Boese, *Chem. Ber.* **1990**, *123*, 1301–1306; b) A. Treibs, F. H. Kreuzer, *Justus Liebigs Ann. Chem.* **1968**, *718*, 208–223; c) C. L. Picou, E. D. Stevens, M. Shah, J. H. Boyer, *Acta Crystallogr., Sect. C* **1990**, *46*, 1148–1150.

[18] a) S. F. Lim, R. H. Friend, I. D. Rees, J. Li, Y. G. Ma, K. Robinson, A. B. Holmes, E. Hennebicq, D. Beljonne, F. Cacialli, *Adv. Funct. Mater.* **2005**, *15*, 981–988; b) F. Cacialli, B. S. Chuah, R. H. Friend, S. C. Moratti, A. B. Holmes, *Synth. Met.* **2000**, *111*, 155–158; c) M. Klessinger, J. Michl, *Excited State and Photochemistry of Organic Molecules*, VCH Publishers, New York, **199**5.

[19] a) D. Rendell (Ed.), *Fluorescence and Phosphorescence*, Wiley, New York, **1987**; b) H. Yersin, A. Vogler (Eds.), *Photochemistry and Photophysics of Coordination Compounds*, Springer-Verlag, Berlin, **1987**; c) A. W. Adamson, P. D. Fleischauer (Eds.), *Concepts of Inorganic Photochemistry*, Wiley, New York, **1975**.

[20] a) M. Baruah, W. W. Qin, N. Basaric, W. M. D. Borggraeve, N. Boebs, *J. Org. Chem.* **2005**, *70*, 4152–4157; b) C. Goze, G. Ulrich, L. J. Mallon, B. D. Allen, A. Harriman, R. Ziessel, *J. Am. Chem. Soc.* **2006**, *128*, 10231–10239.

[21] K. Ye, J. Wang, H. Sun, Y. Liu, Z. Mu, F. Li, S. Jiang, J. Zhang, Y. Wang, C. M. Che, *J. Phys. Chem. B* **2004**, *109*, 8008–8016.

[22] G. M. Sheldrick, *SHELXTL*, PC Siemens Analytical X-ray Instruments, Madison, WI, **1993**.

[23] G. M. Sheldrick, *SHELXTL Structure Determination Programs*, Version 5.0, PC Siemens Analytical Systems, Madison, WI (USA), **1994**.

Received: September 9, 2006
Published Online: March 14, 2007

 © 2007 Wiley-VCH Verlag GmbH & Co. KGaA, Weinheim 

DOI: 10.1002/ejic.200600930

# Ligand-Exchange Processes on Solvated Lithium Cations: Acetonitrile and Hydrogen Cyanide[‡]

Ewa Pasgreta,[a] Ralph Puchta,[a,b] Achim Zahl,[a] and Rudi van Eldik*[a]

**Keywords:** Lithium / Acetonitrile / Hydrogen cyanide / Solvation / Exchange mechanism

Solutions of $LiClO_4$ in solvent mixtures of acetonitrile and water, or acetonitrile and nitromethane, were studied by $^7Li$ NMR spectroscopy. Measured chemical shifts indicate that the $Li^+$ cation is coordinated by four acetonitrile molecules. In the binary water/acetonitrile mixture, water coordinates more strongly to $Li^+$ than acetonitrile such that addition of water immediately leads to the formation of $[Li(H_2O)_4]^+$. The solvent-exchange mechanism for $[Li(L)_4]^+$ (L = $CH_3CN$ and HCN) was studied by using DFT calculations (RB3LYP/6-311+G**). This process was found to follow a limiting associative mechanism involving the formation of relatively stable five-coordinate intermediates. The suggested mechanisms are discussed with reference to available experimental and theoretical data.
(© Wiley-VCH Verlag GmbH & Co. KGaA, 69451 Weinheim, Germany, 2007)

## Introduction

The ongoing discussion on sustainability in chemistry[1] is partly focused on the role of solvents and especially on alternatives for common organic solvents. Such alternatives could be, for example, ionic liquids[2–5] or supercritical carbon dioxide.[6–10] A detailed knowledge of the properties and structural motifs, as well as of elementary reactions such as solvent-exchange processes in different solvents, is an important prerequisite for selecting, optimizing and tailoring the ideal solvent.

Acetonitrile is a common solvent in chemical laboratories, for example it is used in reactions[11,12] or in the investigation of complexation phenomena and complex-formation constants.[13–18] Use of its hydrogen derivative HCN is mostly prevented by its high toxicity and its boiling point of 25 °C. Experimental studies dating back to the middle of the 20th century show that HCN is a water-like solvent that is well suited for dissolving organic and inorganic compounds. Salts such as LiCl, LiBr or $LiClO_4$ are highly soluble in Hydrogen cyanide, most likely because of its high dielectric constant of 123 (at 15.6 °C).[19–23] However, HCN serves as an excellent simplified model of $CH_3CN$ and thus can be used instead in quantum chemical studies of $CH_3CN$.

The behaviour of pure acetonitrile and acetonitrile mixtures was studied experimentally[24,25] and computationally.[24,26] Since an ion in solution strongly disturbs the local solvent structure,[27] a detailed knowledge of the environment is an essential prerequisite for understanding reactions in the neighbourhood of the ion. Several studies investigated solvated $Li^+$ ions in acetonitrile both experimentally with various spectroscopic techniques[28–31] and computationally with different classical molecular dynamics (MD) methods[32–35] and Monte Carlo simulations of solvated alkali and halide ions in $CH_3CN$.[36] Over the past decade, DFT and ab initio calculations on $[Li(CH_3CN)_n]^+$ and related clusters were also performed by different groups.[30,37–40]

There has been a special interest in the properties of Li salts, such as conductivity,[41–44] transport abililty,[45–47] viscosity,[48] and osmotic behaviour[49], in solvents and solvent mixtures because of the use of $Li^+$ ions in batteries of high energy density.[50] Such studies are not restricted to liquid systems. $Li^+$ mobility in potential solid electrolytes was also investigated intensively both experimentally and theoretically.[51–53]

To the best of our knowledge, however, investigations of solvent-exchange reactions in acetonitrile and acetonitrile/water mixtures or in HCN and HCN/water mixtures have not been performed. Whereas experimental investigations study reactions under real conditions in a whole ensemble of molecules,[54,55] quantum chemical calculations focus on one molecule and a small number of solvent molecules, for example, the first solvent shell.[56–60] This approach enables a more detailed mechanistic insight.

In this contribution, we extend our combined quantum chemical and experimental investigations on ligand coordination and ligand exchange on $Li^+$ in acetonitrile and

[‡] Part IV; for part III see: E. Pasgreta, R. Puchta, M. Galle, N. J. R. van Eikema Hommes, A. Zahl, R. van Eldik; Ligand-Exchange Processes on Solvated Lithium Cations: DMSO and Water/DMSO Mixtures; *ChemPhysChem*, in press.

[a] Institute for Inorganic Chemistry, University of Erlangen-Nürnberg,
Egerlandstraße 1, 91058 Erlangen, Germany
E-mail: vaneldik@chemie.uni-erlangen.de
[b] Computer Chemistry Center, University of Erlangen-Nürnberg, Nägelsbachstraße 25, 91052 Erlangen, Germany

 © 2007 Wiley-VCH Verlag GmbH & Co. KGaA, Weinheim 

HCN, as well as in $CH_3CN/H_2O$ and $HCN/H_2O$ mixtures. The calculations mainly focus on HCN for two reasons: (1) to gain a deeper insight into this solvent, which is not used often, and (2) HCN is a good working model for $CH_3$–CN as its use prevents well known problems associated with rotating $CH_3$ groups and to facilitate studies with solvent models.

## Results and Discussion

### Coordination Number of $Li^+$

The structures of $Li^+$–acetonitrile solvates are in general less well known than the structures of $Li^+$–water solvates. The $Li^+$ ion was found to be four coordinate by NMR spectroscopic studies in which acetonitrile was gradually replaced by water when water was added to an acetonitrile solution of $LiClO_4$ (1.6 M),[61] and on the basis of IR spectroscopic intensities measured for the acetonitrile CN stretching vibrations.[62,63] Even compounds with mixed coordination of a counterion and acetonitrile were reported to be four coordinate, namely $[Li(CH_3CN)_3Br]$ formed from 0.58 M LiBr in $CH_3CN$.[64] Extensive concentration-dependent ion-pairing was also found for weak coordinating counterions, such as in $LiBF_4$[30] and $LiClO_4$,[62] by studying the CN vibration.[65] These findings for the coordination number are in good agreement with published X-ray structures.[66–68]

However, Sajeevkumar and Singh found the average coordination number to be 4.7,[69] whereas Megyes et al. found up to six acetonitrile molecules surrounding the $Li^+$ ion in the gas phase by means of mass spectrometry.[70] Therefore, we reinvestigated the maximum coordination number of $[Li(CH_3CN)_n]^+$ both experimentally and computationally, and purely quantum chemically for $[Li(NCH)_n]^+$.

In order to determine the coordination number of $Li^+$ by using NMR techniques, the concentration of $LiClO_4$ was kept constant and the $CH_3CN$ concentration was varied over a wide range. To use this method, the cation must be dissolved in solvent mixtures consisting of one coordinating and one non-coordinating component. The measured chemical shifts are then plotted against the mol ratio of cation to coordinating solvent. When such a plot shows a marked discontinuity, the appropriate solvent/cation ratio can be taken as the coordination number of the cation. There are, however, a few conditions that must be obeyed. An inert non-coordinating solvent must be available that will dissolve all solution components, a measurable parameter must exist that is a function of the solvent composition, and the formation constant of the solvate must be sufficiently large so that a limiting value of the parameter can be reached. In this case, the selected parameter was the $Li^+$ NMR signal; its position in the NMR spectrum depends on the composition of the coordination sphere of the studied ion. Typical alkali metal salts are not appreciably soluble in truly inert solvents. Therefore, it is necessary to select a solvent that minimally interacts with $CH_3CN$ and the alkali metal ion.[71]

Nitromethane (Gutmann donor number $DN$ = 2.7)[72] represents a good compromise for the various requirements. It appreciably dissolves alkali metal salts and its interaction with $Li^+$ is much weaker than that between $CH_3CN$ (Gutmann donor number $DN$ = 14.1) and a metal cation. The mol ratio data obtained confirms the "inertness" of this solvent and indicates that it is in fact sufficiently unreactive for the purpose of this study.

Figure 1 and Figure 2 illustrate the results obtained from the $^7Li$ NMR spectroscopic study. Figure 2 shows a plot of the chemical shift as a function of the mol ratio of the $CH_3CN/LiClO_4$ system; the $LiClO_4$ concentration was kept at 0.05 M in nitromethane. A clear break can be observed at a $[CH_3CN]/[Li^+]$ ratio of 4:1, which indicates that $Li^+$ is coordinated by 4 acetonitrile molecules under these conditions. It appears, therefore, that NMR studies of alkali metal ion coordination can be carried out even in solvents that are not totally inert toward the reacting metal ion provided that the interaction between the metal ion and the stronger donor solvent dominates.

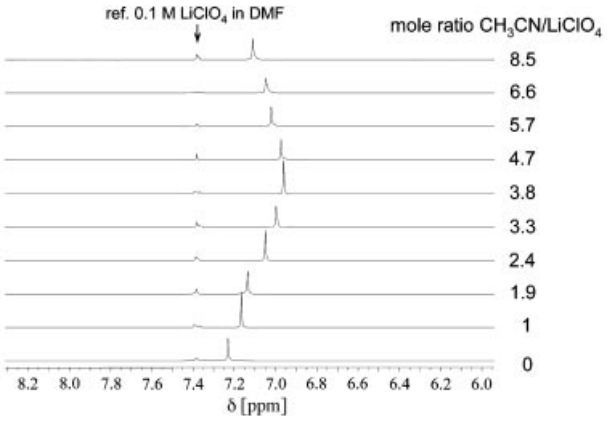


Figure 1. $^7Li$ NMR spectra recorded as a function of $CH_3CN/LiClO_4$ mol ratio (0.05 M $LiClO_4$ in the $CH_3CN$/nitromethane mixture) at 25 °C.

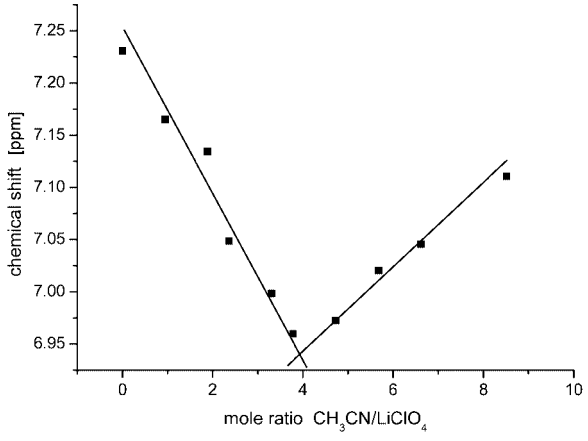


Figure 2. $^7Li$ NMR shift measured for 0.05 M $LiClO_4$ in $CH_3CN$/nitromethane solvent mixtures.

 © 2007 Wiley-VCH Verlag GmbH & Co. KGaA, Weinheim 

### Selective Coordination of $Li^+$

Selective coordination occurs when the solvate prefers one of the solvent components over the other. The exchange of ions between different environments is usually rapid with respect to the NMR time scale, and this results in only one resonance signal at an average frequency determined by the magnetic shielding and lifetime of the nucleus in each of the sites. Variation of parameters such as concentration, counterions and solvent produces changes in the relative proportion and type of environment, which may be reflected by the NMR spectra in terms of chemical shift, line shape and/or line width of the observed resonance.[73]

We performed the measurements by keeping the concentration of $LiClO_4$ constant (0.1 M) and by changing the composition of the $H_2O/CH_3CN$ mixtures. The concentration of $H_2O$ (molar ratio) was increased from 0 to 100%. For each sample, the $^7Li$ NMR spectrum was recorded. The chemical shift changed as the amount of water in the sample was varied.

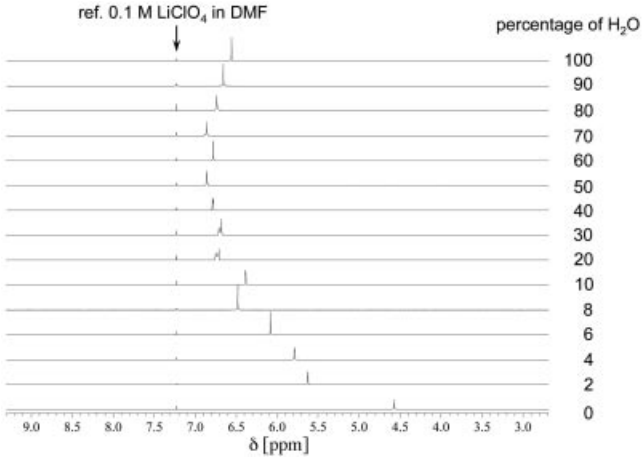


Figure 3. $^7Li$ NMR spectra of 0.1 M $LiClO_4$ in $H_2O/CH_3CN$ mixtures.

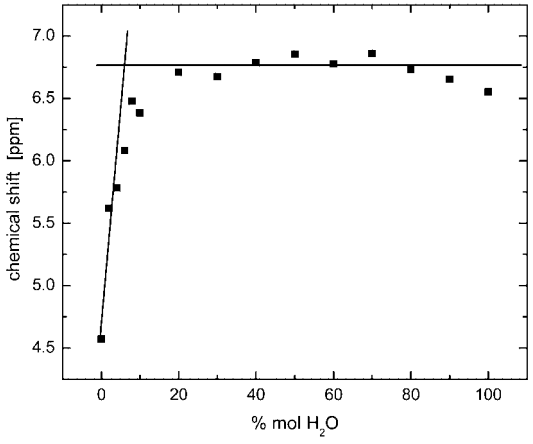


Figure 4. $^7Li$ NMR shift for 0.1 M $LiClO_4$ as a function of the $H_2O/CH_3CN$ composition.

It was observed that the position of the NMR signal moved significantly (from 4.5 to 6.4 ppm) even when the amount of added water was very small (only 10% $H_2O$). The chemical shift value then increased slightly and remained almost constant when the amount of water was changed from 10 to 100% (see Figure 3 and Figure 4). This observation confirms that water coordinates much more strongly to the $Li^+$ ion than acetonitrile. Thus, addition of water immediately leads to the formation of the aquated cation.

### Ligand Exchange on Solvated $Li^+$

It was not possible to follow the exchange process for $CH_3CN$ on $Li^+$ experimentally. As reported before, the rate constant of water exchange on $Li^+$ is extremely fast (approximately $10^9$ $s^{-1}$ at 25 °C) although water is a relatively strong donor (*DN* = 33.0). As $CH_3CN$ coordinates much more weakly (*DN* = 14.1), its exchange on $Li^+$ is even faster, which makes it impossible to study experimentally. Therefore, theoretical calculations are essential and may be very useful in such investigations.

### Quantum Chemical Calculations

We studied the ligand exchange process in more detail and provide computational evidence for a limiting associative exchange mechanism on the HCN- and $CH_3CN$-solvated lithium cation. As mentioned before, HCN was employed as a simplified working model to perform quantum chemical calculations on $CH_3CN$. Our calculations corroborated the results of the experimental study in solution (vide supra)[29] and in the solid state,[68] which showed that the first coordination sphere around $Li^+$ consists of four tightly bound $CH_3CN$ and HCN molecules. The five-coordinate intermediates are 3.7 kcal/mol and 4.6 kcal/mol [3.2 kcal/mol B3LYP(IPCM: acetonitrile)/6-311+G**//B3LYP/6-311+G**] higher in energy for acetonitrile and HCN, respectively. The computed Li–N distance for $Li(NCH)_4$ and $Li(NCCH_3)_4$ are 2.06 and 2.05 Å, respectively. Additional solvent molecules do not coordinate to $Li^+$, but instead form a second coordination sphere, mainly through electrostatic interactions. The gas-phase binding energy for the fifth acetonitrile molecule in $[Li(NCCH_3)_4(NCCH_3)]^+$ is 6.1 kcal/mol, with a Li–N distance of 6.65 Å. The fifth molecule is stabilized only by a weak $H_{CH_3}$–NC–$CH_3$ interaction of 2.32 Å. The fifth HCN molecule is bound through a weak hydrogen bond (2.04 Å) in the second coordination sphere. This bond stabilizes the system by 8.9 kcal/mol (see Figure 5).

The HCN exchange itself proceeds through a trigonal-bipyramidal intermediate $[Li(NCH)_5]^+$ that is reached via a late transition state. The entering HCN molecule approaches the lithium cation directly and pushes three coordinated solvent molecules away toward the equatorial positions. In line with the experimental observation of a very fast exchange process (vide supra), the computed activation

 © 2007 Wiley-VCH Verlag GmbH & Co. KGaA, Weinheim 

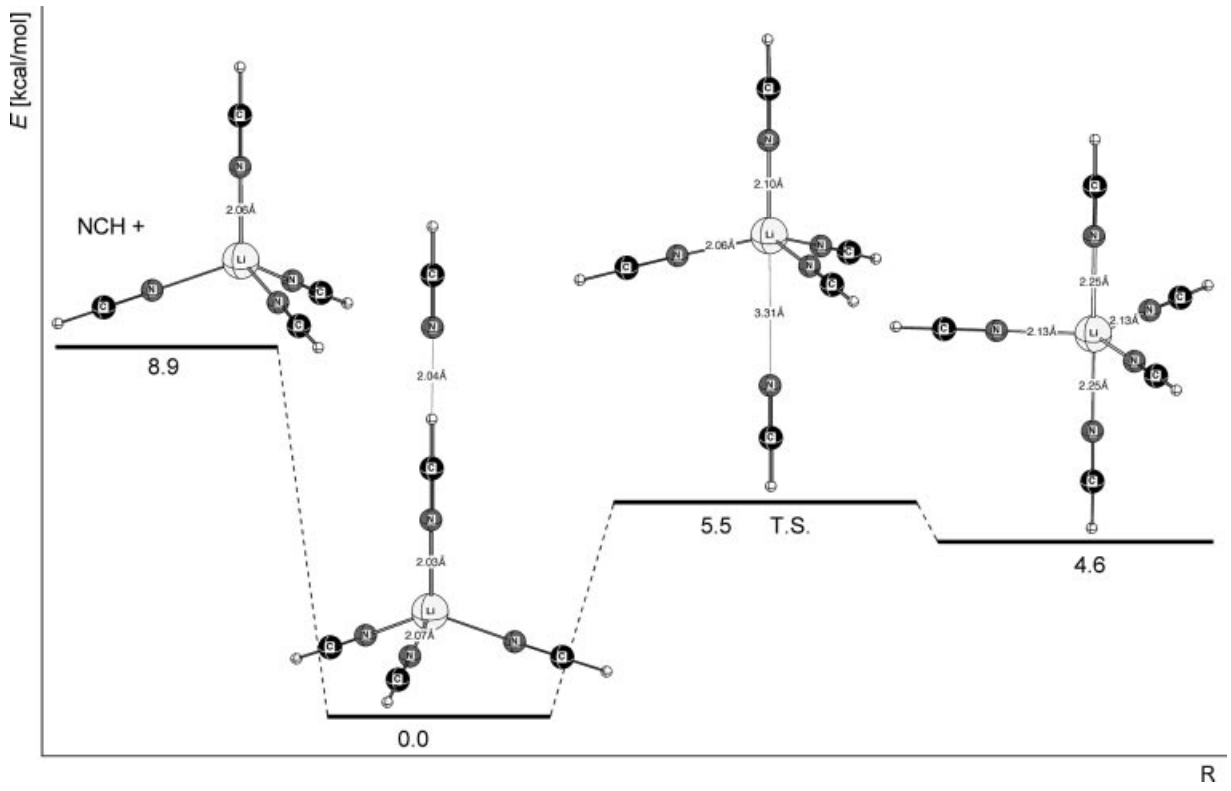


Figure 5. Energy profile (RB3LYP/6-311+G**) for the exchange of HCN on $[Li(NCH)_4]^+$.

barrier is only 5.5 kcal/mol, while the five-coordinate intermediate is 4.6 kcal/mol less stable than the precursor complex. The very low barrier toward dissociation of only 0.9 kcal/mol means that the five-coordinate intermediate is very short-lived. The evaluation of the energy at the MP2(full)/6-311+G**//B3LYP/6-311+G** and B3LYP/6-311+G**//B3LYP/6-311+G** levels shows only minor differences in the computed energies, except in those for the intermediate ($[Li(L)_4(L)]^+$) (see Table 1). We attribute this to an incorrectly balanced description of the metal–ligand and hydrogen-bond strengths by DFT methods as observed earlier by Rotzinger and others in studies on water exchange reactions.[74,75] Inclusion of solvent effects at the B3LYP(CPCM)/6-311+G**//B3LYP/6-311+G** and B3LYP(IPCM)/6-311+G**//B3LYP/6-311+G** level clearly favours a four-coordinate structure with NCH in the second coordination sphere or uncoordinated. Therefore, the transition state is also stabilized since the entering NCH molecule can best be addressed as uncoordinated (see Table 1 and Figure 5). Unfortunately, the transition state is modelled as being too stable in the B3LYP(IPCM)/6-311+G**//B3LYP/6-311+G** approximation, irrespective of whether acetonitrile or water is used in the modelling by the IPCM formalism.

In trigonal-bipyramidal $[Li(NCH)_5]^+$, the axial Li–N distances are 0.11 Å longer than the equatorial distances, which may be taken as a clear indication that one of the axial ligands will be expelled. The energy profile for the exchange of acetonitrile on $[Li(NCCH_3)_4]^+$ shows the same topology, only the energy differences are somewhat smaller.

Table 1. Calculated relative energies (in kcal/mol) for the exchange of L at $[Li(L)_4]^+$ (L = HCN, $CH_3CN$).[a]

| L = HCN | $[Li(L)_4]^+ + L$ | $[Li(L)_4\cdots(L)]^+$ | TS | $[Li(L)_4(L)]^+$ |
|---|---|---|---|---|
| B3LYP | 8.9 | 0.0 | 5.5 | 4.6 |
| MP2(full) | 9.5 | 0.0 | 3.2 | 0.5 |
| IPCM | –2.8 | 0.0 | –2.6 | 3.2 |
| CPCM | –0.4 | 0.0 | 1.8 | 1.4 |
| L = $H_3CCN$ | | | | |
| B3LYP | 6.1 | 0.0 | 4.1 | 3.7 |

[a] B3LYP: B3LYP/6-311+G**//B3LYP/6-311+G**; MP2(full): MP2(full)/6-311+G**//B3LYP/6-311+G**; IPCM: B3LYP/(IPCM: acetonitrile)/6-311+G**//B3LYP/6-311+G**; CPCM: B3LYP/(CPCM: water)/6-311+G**//B3LYP/6-311+G**.

We attribute this difference to stabilization effects caused by the methyl group and to the absence of hydrogen bonding. A detailed investigation was prevented since a local minimum was not reached with $[Li(NCCH_3)_4(NCCH_3)]^+$ because of the rotation of the methyl groups, and the IPCM calculations show the well-documented problems in reaching an energy convergence.[4,76]

These findings fully corroborate the results expected for small ions coordinated by small ligands. The dissociation of a molecule of HCN from $[Li(NCH)_4]^+$ results in the intermediate $[Li(NCH)_3]^+$ with a $D_{3h}$ symmetry, which is 14.3 kcal/mol higher in energy and less favourable. In addition, there is no visible steric crowding, which is necessary for a dissociative mechanism. Interchange mechanisms are known for $Li^+$, e.g. in the case of ammonia exchange on

 © 2007 Wiley-VCH Verlag GmbH & Co. KGaA, Weinheim 

Table 2. Calculated energies for the subsequent reactions of $[Li(NCH)_4]^+$ with water.

| B3LYP(IPCM)/6-311+G**//B3LYP/6-311+G** [kcal/mol] | Gas phase | IPCM: acetonitrile | IPCM: water |
|---|---|---|---|
| $[Li(NCH)_4]^+ + H_2O \rightarrow [Li(H_2O)(NCH)_3]^+ + NCH$ | –0.5 | +1.7 | +1.6 |
| $[Li(H_2O)(NCH)_3]^+ + H_2O \rightarrow [Li(H_2O)_2(NCH)_2]^+ + NCH$ | –0.5 | –1.4 | –1.6 |
| $[Li(H_2O)_2(NCH)_2]^+ + H_2O \rightarrow [Li(H_2O)_3(NCH)]^+ + NCH$ | –0.3 | –3.6 | –3.9 |
| $[Li(H_2O)_3(NCH)]^+ + H_2O \rightarrow [Li(H_2O)_4]^+ + NCH$ | +0.1 | –0.9 | –1.2 |
| $\Sigma$ | –1.3 | –4.2 | –5.1 |

$Li^+$,[77] but requires a five-coordinate transition state that would contradict the five-coordinate intermediate in our mechanism. Analogous arguments can also be applied for the second reaction under investigation.

Under actual experimental conditions water can never be excluded. Therefore, and because of the importance of solvent mixtures in technical and laboratory applications, we modelled the HCN/$H_2O$ exchange process exemplarily for $[Li(NCH)_4]^+$ to $[Li(NCH)_3(H_2O)]^+$ (Table 2). In this case, NCH can again be considered as a model for acetonitrile.

From experiments (vide supra) and from the Gutmann donor number for acetonitrile, which is only 50% of that for water, it is known that addition of water to solutions of lithium ions in acetonitrile leads to the formation of a water-coordinated $Li^+$ complex. This can be reproduced for HCN as a model by quantum chemical calculations (RB3LYP/6-311+G**).

By including solvent effects at the B3LYP(IPCM)/6-311+G**//B3LYP/6-311+G** level, the reaction energies are significantly increased, regardless of whether water or acetonitrile is selected as solvent.

We investigated the mechanism of the first reaction step in detail (see Figure 6). As shown before,[29,68] the first coordination sphere around $Li^+$ consists of four tightly bound acetonitrile molecules, here NCH molecules. An additional solvent molecule does not coordinate to the $Li^+$ ion; a second coordination sphere is formed in which water is bound by one linear hydrogen bond (1.88 Å). The gas-phase hydrogen-bond energy for the $H_2O$ molecule in $[Li(NCH)_4\cdots(OH_2)]^+$ is 9.5 kcal/mol. Again, the entering solvent, here water, approaches the $Li^+$ ion directly through a face of the $[Li(NCH)_4]^+$ tetrahedron and pushes three coordinated HCN molecules away. According to the movement of the water molecule in the transition state (7.1 kcal/mol higher in energy), one would expect an intermediate with three HCN molecules in equatorial positions and the fourth together with the $H_2O$ molecule in the axial positions. During the optimization steps, the structure rearranges to form an intermediate 3.7 kcal/mol lower in energy, with two HCN molecules in the axial positions and the $H_2O$ molecule together with the two remaining HCN molecules in the equatorial positions. The bonds for the axial molecules are

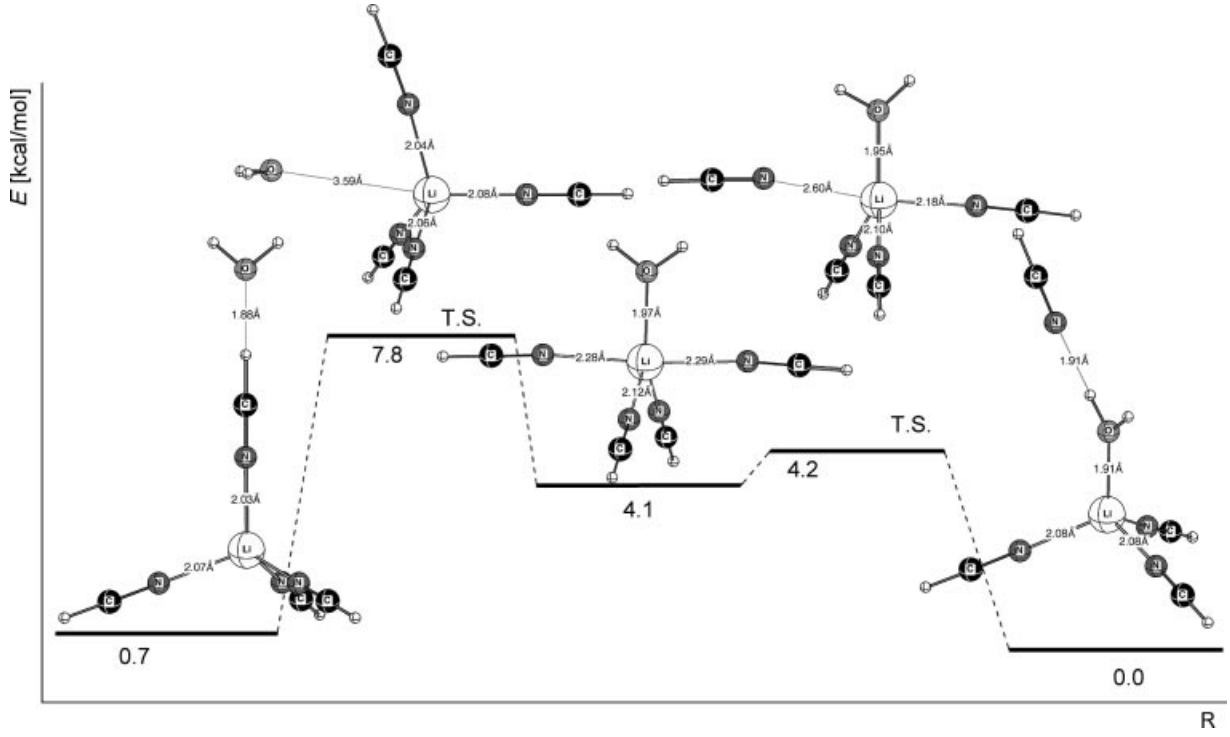


Figure 6. Energy profile (RB3LYP/6-311+G**) for the HCN/water exchange on $[Li(NCH)_4]^+$.

 © 2007 Wiley-VCH Verlag GmbH & Co. KGaA, Weinheim 

0.16 Å longer than those for the equatorial HCN ligands – it can be concluded that one axial ligand will be expelled to reach a four-coordinate product. The activation barrier for the release of an axial HCN molecule is rather low (0.1 kcal/mol), which means that the five-coordinate intermediate will be very short-lived. On the assumption that the expelled HCN molecule will form a hydrogen bond with the nearest hydrogen atom, one would expect the product $[Li(NCH)_3(H_2O)\cdots(NCH)]^+$ to form at an energy that is 4.2 kcal/mol lower than that of the second transition state. The energy required to destroy this hydrogen bond is 9.7 kcal/mol (Table 3).

Table 3. Calculated relative energies for the exchange of $H_2O$/NCH at $[Li(NCH)_4]^+$ (L = HCN; W = $H_2O$).[a]

| | $[Li(L)_4\cdots W]^+$ | TS | $[Li(L)_2\{W(L)_2\}]^+$ | TS | $[Li(L)_3(W)\cdots L]^+$ |
|---|---|---|---|---|---|
| B3LYP | 0.7 | 7.8 | 4.1 | 4.2 | 0.0 |
| MP2(full) | 0.9 | 6.1 | 0.6 | 1.2 | 0.0 |
| IPCM | 0.1 | 2.8 | 1.3 | 1.8 | 0.0 |
| CPCM | 0.1 | 5.6 | 1.0 | 1.5 | 0.0 |

[a] B3LYP: B3LYP/6-311+G**//B3LYP/6-311+G**; MP2(full): MP2(full)/6-311+G**//B3LYP/6-311+G**; IPCM: B3LYP/(IPCM: acetonitrile)/6-311+G**//B3LYP/6-311+G**; CPCM: B3LYP/(CPCM: water)/6-311+G**//B3LYP/6-311+G**.

Whereas MP2(full)/6-311+G**//B3LYP/6-311+G** calculations show typical discrepancies, the application of the IPCM- and CPCM-solvent models dramatically lowers the energy for the intermediate and the transition states. The barriers of 2.8 and 1.8 kcal/mol corroborate the experimental findings for an efficient formation of a water-coordinated $Li^+$ complex.

## Conclusions

It was confirmed both experimentally and theoretically that $Li^+$ is coordinated by four acetonitrile molecules. In the binary mixture of water and acetonitrile, water is coordinated more strongly to the $Li^+$ ion than acetonitrile. Thus, addition of water immediately leads to the formation of the aquated cation. Ligand exchange reactions on $Li^+$ most probably follow an associative mechanism as indicated by the formation of stable five-coordinate intermediates.

## Experimental Section

**General Procedures:** All transformations were carried out under a Ar or $N_2$ atmosphere by using standard Schlenk techniques, under Ar atmosphere in a glove box, or under vacuum. $LiClO_4$ (Aldrich, battery grade) was vacuum dried at 120 °C for 48 h and was then stored under dry nitrogen. Acetonitrile (Acros, extra dry, water < 10 ppm) was used as received. Nitromethane (Roth) was purified and dried by a previously reported method.[78] Solutions of $LiClO_4$ were prepared under dry nitrogen. For $^7$Li NMR spectroscopic studies, these solutions were sealed under a Ar atmosphere in 5-mm NMR tubes.

**$^7$Li NMR Spectroscopy:** Fourier transform $^7$Li NMR spectra were recorded at a frequency of 155 MHz on a Bruker Avance DRX 400WB spectrometer equipped with a superconducting BC-94/89 magnet system. Spinning 5-mm tubes were used with a 1-mm o.d. melting point capillary inserted coaxially in the spinning tube and filled with an external reference solution (usually 1 M $LiClO_4$ in DMF). The experiments were conducted at room temperature and at ambient pressure. For a typical kinetic run, 0.8 mL of solution was transferred under Ar to a Wilmad screw cap NMR tube equipped with a poly(tetrafluoroethylene) septum. All samples were prepared in the same way.

**Quantum Chemical Calculations:** All structures were fully optimized at the B3LYP/6-311+G**[79–82] level of theory and characterized as minima or transition-state structures by computation of vibrational frequencies (for minima, all frequencies are positive, NIMAG = 0; for transition-state structures, exactly one imaginary frequency is present, NIMAG = 1). Single-point energy calculations were performed at the MP2(full)/6-311+G**//B3LYP/6-311+G** level;[83] the influence of the bulk solvent was probed by using the IPCM[84] and CPCM[85,86] formalism and water or acetonitrile as solvent, i.e. B3LYP(IPCM)/6-311+G**//B3LYP/6-311+G** and B3LYP(CPCM)/6-311+G**//B3LYP/6-311+G**.[87] The Gaussian 03 suite of programs was used throughout.[88]

## Acknowledgments

This work was supported by the EC TMR network HPRN-CT-2000-19 ("Solvation Dynamics and Ionic Mobility in Conventional and Polymer Solvents") and the Deutsche Forschungsgemeinschaft (SFB 583 on Redox-active Metal Complexes). We would like to thank Michael Galle for preliminary calculations, Dr. Nico van Eikema Hommes for fruitful discussions, Prof. Tim Clark for hosting this work in the CCC, and the Regionales Rechenzentrum Erlangen (RRZE) for a generous allotment of computer time.

[1] P. T. Anastas, T. C. Williamson (Eds.), *Green Chemistry: Designing Chemistry for the Environment* (Symposium at the 208th National Meeting of the American Chemical Society, Washington, DC, August 21–25, 1994.) [In: ACS Symp. Ser. 1996, 626], **1996**, p. 251.
[2] P. Wasserscheid, T. Welton, *Ionic Liquids in Synthesis*, Wiley-VCH Verlag GmbH & Co. KGaA, Weinheim, Germany, **2003**, p. 364.
[3] P. Wasserscheid, *Chem. Unserer Zeit* **2003**, *37*, 52–63.
[4] P. Illner, A. Zahl, R. Puchta, N. van Eikema Hommes, P. Wasserscheid, R. van Eldik, *J. Organomet. Chem.* **2005**, *690*, 3567–3576.
[5] C. F. Weber, R. Puchta, N. J. R. van Eikema Hommes, P. Wasserscheid, R. van Eldik, *Angew. Chem. Int. Ed.* **2005**, *44*, 6033–6038.
[6] A. Clifford, T. Clifford, *Fundamentals of Supercritical Fluids*, Oxford University Press, Oxford, **1999**, p. 228.
[7] C. Erkey, *J. Supercrit. Fluids* **2000**, *17*, 259–287.
[8] R. S. Oakes, A. A. Clifford, C. M. Rayner, *J. Chem. Soc., Perkin Trans. 1* **2001**, *9*, 917–941.
[9] D. A. Morgenstern, R. M. LeLacheur, D. K. Morita, S. L. Borkowsky, S. Feng, G. H. Brown, L. Luan, M. F. Gross, M. J. Burk, W. Tumas, *ACS Symp. Ser.* **1996**, *626*, 132–151.
[10] P. G. Jessop, T. Ikariya, R. Noyori, *Science* **1995**, *269*, 1065–1069.
[11] W. J. Kinart, E. Sniec, I. Tylak, C. M. Kinart, *Phys. Chem. Liq.* **2000**, *38*, 193–201.
[12] B. S. Babu, K. K. Balasubramanian, *Synlett* **1999**, *8*, 1261–1262.
[13] A. D'Aprano, M. Salomon, V. Mauro, *J. Solution Chem.* **1995**, *24*, 685–702.
[14] M. Shamsipur, T. Madrakian, *J. Coord. Chem.* **2000**, *52*, 139–149.

 © 2007 Wiley-VCH Verlag GmbH & Co. KGaA, Weinheim 

[15] M. Shamsipur, E. Karkhaneei, A. Afkhami, *J. Coord. Chem.* **1998**, *44*, 23–32.
[16] E. Karkhaneei, J. Zolgharnein, A. Afkhami, M. Shamsipur, *J. Coord. Chem.* **1998**, *46*, 1–11.
[17] A. F. D. de Namor, J. C. Y. Ng, M. A. L. Tanco, M. Salomon, *J. Phys. Chem.* **1996**, *100*, 14485–14491.
[18] A. R. Fakhari, M. Shamsipur, *J. Inclusion Phenom.* **1996**, *26*, 243–251.
[19] G. Jander, W. Klemm, *Die Chemie in Wasserähnlichen Lösungsmitteln*, Springer-Verlag, Berlin, **1949**, p. 367.
[20] J. Jander, C. Lafrenz, *Wasserähnliche Lösungsmittel*, Springer-Verlag, Berlin, **1968**, Vol. 3, p. 212.
[21] J. Jander, G. Tuerk, *Chem. Ber.* **1962**, *95*, 881–888.
[22] J. Jander, G. Tuerk, *Chem. Ber.* **1962**, *95*, 2314–2320.
[23] J. Jander, G. Tuerk, *Chem. Ber.* **1965**, *98*, 894–903.
[24] I. Bako, T. Megyes, G. Palinkas, *Chem. Phys.* **2005**, *316*, 235–244.
[25] H. Lu, J. Wang, Y. Zhao, X. Xuan, K. Zhuo, *J. Chem. Eng. Data* **2001**, *46*, 631–634.
[26] R. Rivelino, B. J. C. Cabral, K. Coutinho, S. Canuto, *Chem. Phys. Lett.* **2005**, *407*, 13–17.
[27] M. Hojo, *Bunseki Kagaku* **2004**, *53*, 1279–1293.
[28] A. K. Mollner, P. A. Brooksby, J. S. Loring, I. Bako, G. Palinkas, W. R. Fawcett, *J. Phys. Chem. A* **2004**, *108*, 3344–3349.
[29] J. Barthel, R. Buchner, E. Wismeth, *J. Solution Chem.* **2000**, *29*, 937–954.
[30] X. Xuan, H. Zhang, J. Wang, H. Wang, *J. Phys. Chem. A* **2004**, *108*, 7513–7521.
[31] J. S. Loring, W. R. Fawcett, *J. Phys. Chem. A* **1999**, *103*, 3608–3617.
[32] M. Maroncelli, *J. Chem. Phys.* **1991**, *94*, 2084–2103.
[33] J. Richardi, P. H. Fries, H. Krienke, *J. Chem. Phys.* **1998**, *108*, 4079–4089.
[34] E. Guardia, R. Pinzon, *J. Mol. Liq.* **2000**, *85*, 33–44.
[35] D. Spångberg, K. Hermansson, *Chem. Phys.* **2004**, *300*, 165–176.
[36] R. Fischer, J. Richardi, P. H. Fries, H. Krienke, *J. Chem. Phys.* **2002**, *117*, 8467–8478.
[37] Y. Dimitrova, *THEOCHEM* **1995**, *334*, 215–222.
[38] E. M. Cabaleiro-Lago, M. A. Rios, *Chem. Phys.* **2000**, *254*, 11–23.
[39] L. Pejov, *Int. J. Quantum Chem.* **2002**, *86*, 356–367.
[40] I. Bako, T. Megyes, T. Radnai, G. Palinkas, M. Probst, W. R. Fawcett, *Z. Phys. Chem.* **2004**, *218*, 643–658.
[41] A. D′Aprano, M. Iammarino, V. Mauro, B. Sesta, *J. Electroanal. Chem.* **1995**, *392*, 27–33.
[42] M. Hojo, T. Ueda, M. Nishimura, H. Hamada, M. Matsui, S. Umetani, *J. Phys. Chem. B* **1999**, *103*, 8965–8972.
[43] J. Barthel, M. Kleebauer, R. Buchner, *J. Solution Chem.* **1995**, *24*, 1–17.
[44] F. Croce, A. D′Aprano, C. Nanjundiah, V. R. Koch, C. W. Walker, M. Salomon, *J. Electrochem. Soc.* **1996**, *143*, 154–159.
[45] A. D′Aprano, B. Sesta, A. Capalbi, M. Iammarino, V. Mauro, *J. Electroanal. Chem.* **1996**, *403*, 257–260.
[46] V. Mauro, A. D'Aprano, F. Croce, M. Salomon, *J. Power Sources* **2005**, *141*, 167–170.
[47] C. L. Faverio, P. R. Mussini, T. Mussini, *Anal. Chem.* **1998**, *70*, 2589–2595.
[48] D. Brouillette, G. Perron, J. E. Desnoyers, *Electrochim. Acta* **1999**, *44*, 4721–4742.
[49] J. Barthel, R. Neueder, H. Poepke, H. Wittmann, *J. Solution Chem.* **1999**, *28*, 489–503.
[50] B. Mandal, T. Sooksimuang, B. Griffin, A. Padhi, R. Filler, *Solid State Ionics* **2004**, *175*, 267–272.
[51] S. Murugavel, B. Roling, *J. Phys. Chem. B* **2004**, *108*, 2564–2567.
[52] C. R. Mariappan, G. Govindaraj, B. Roling, *Solid State Ionics* **2005**, *176*, 723–729.
[53] A. Heuer, S. Murugavel, B. Roling, *Phys. Rev. B: Condens. Matter Mater. Phys.* **2005**, *72*, 174304/174301–174304/174307.
[54] L. Helm, A. E. Merbach, *Chem. Rev.* **2005**, *105*, 1923–1959.
[55] L. Helm, A. E. Merbach, *Coord. Chem. Rev.* **1999**, *187*, 151–181.
[56] H. Erras-Hanauer, T. Clark, R. van Eldik, *Coord. Chem. Rev.* **2003**, *238–239*, 233–253.
[57] M. Hartmann, T. Clark, R. van Eldik, *J. Am. Chem. Soc.* **1997**, *119*, 7843–7850.
[58] M. Hartmann, T. Clark, R. Van Eldik, *J. Phys. Chem. A* **1999**, *103*, 9899–9905.
[59] F. P. Rotzinger, *Chem. Rev.* **2005**, *105*, 2003–2037.
[60] R. Puchta, N. van Eikema Hommes, R. van Eldik, *Helv. Chim. Acta* **2005**, *88*, 911–922.
[61] R. G. Keil, D. W. Johnson, M. A. Fryling, J. F. O'Brien, *Inorg. Chem.* **1989**, *28*, 2764–2766.
[62] W. R. Fawcett, G. Liu, P. W. Faguy, C. A. Foss Jr, A. J. Motheo, *J. Chem. Soc., Faraday Trans.* **1993**, *89*, 811–816.
[63] J. Barthel, R. Deser, *J. Solution Chem.* **1994**, *23*, 1133–1146.
[64] T. Cartailler, W. Kunz, P. Turq, M. C. Bellisent-Funel, *J. Phys.: Condens. Matter* **1991**, *3*, 9511–9520.
[65] L. A. Solovieva, S. K. Akopyan, E. Vilaseca, *Spectrochim. Acta Part A* **1994**, *50*, 683–688.
[66] N. R. Brooks, W. A. Henderson, W. H. Smyrl, *Acta Crystallogr., Sect. E: Struct. Rep. Online* **2002**, *58*, m176–m177.
[67] S. Chitsaz, J. Pauls, B. Neumuller, *Z. Naturforsch. B: Chem. Sci.* **2001**, *56*, 245–248.
[68] Y. Yokota, V. G. Young Jr, J. G. Verkade, *Acta Crystallogr., Sect. C: Cryst. Struct. Commun.* **1999**, *55*, 196–198.
[69] V. A. Sajeevkumar, S. Singh, *J. Mol. Struct.* **1996**, *382*, 101–110.
[70] T. Megyes, T. Radnai, A. Wakisaka, *J. Mol. Liq.* **2003**, *103–104*, 319–329.
[71] B. W. Maxey, A. I. Popov, *J. Am. Chem. Soc.* **1968**, *90*, 4470–4472.
[72] V. Gutmann, *Electrochim. Acta* **1976**, *21*, 661–670.
[73] Y. M. Cahen, P. R. Handy, E. T. Roach, A. I. Popov, *J. Phys. Chem.* **1975**, *79*, 80–85.
[74] F. P. Rotzinger, *J. Phys. Chem. B* **2005**, *109*, 1510–1527.
[75] H. Hanauer, R. Puchta, T. Clark, R. van Eldik, *Inorg. Chem.* **2007**, *46*, 1112–1122.
[76] R. Puchta, T. Clark, W. Bauer, *J. Mol. Model.* **2006**, *12*, 739–747.
[77] R. Puchta, M. Galle, N. Van Eikema Hommes, E. Pasgreta, R. Van Eldik, *Inorg. Chem.* **2004**, *43*, 8227–8229.
[78] J. F. Coetzee, T. H. Chang, *Pure Appl. Chem.* **1986**, *58*, 1541–1545.
[79] P. J. Stephens, F. J. Devlin, C. F. Chabalowski, M. J. Frisch, *J. Phys. Chem.* **1994**, *98*, 11623–11627.
[80] A. D. Becke, *J. Chem. Phys.* **1993**, *98*, 5648–5652.
[81] C. Lee, W. Yang, R. G. Parr, *Phys. Rev. B: Condens. Matter Mater. Phys.* **1988**, *37*, 785–789.
[82] W. Koch, M. C. Holthausen, *A Chemist's Guide to Density Functional Theory, 2nd Edition*, John Wiley & Sons, Inc., Chichester, UK, **2001**, p. 528.
[83] W. J. Hehre, L. Radom, P. v. R. Schleyer, J. A. Pople, *Ab initio Molecular Orbital Theory*, John Wiley & Sons, New York, **1986**, p. 548.
[84] J. B. Foresman, T. A. Keith, K. B. Wiberg, J. Snoonian, M. J. Frisch, *J. Phys. Chem.* **1996**, *100*, 16098–16104.
[85] V. Barone, M. Cossi, *J. Phys. Chem. A* **1998**, *102*, 1995–2001.
[86] M. Cossi, N. Rega, G. Scalmani, V. Barone, *J. Comput. Chem.* **2003**, *24*, 669–681.
[87] In the CPCM formalism, some molecules failed while using symmetry in the molecular cavity generation. This problem was solved successfully by the keyword "nosymm".
[88] M. J. Frisch, G. W. Trucks, H. B. Schlegel, G. E. Scuseria, M. A. Robb, J. R. Cheeseman, J. A. Montgomery Jr, T. Vreven, K. N. Kudin, J. C. Burant, J. M. Millam, S. S. Iyengar, J. Tomasi, V. Barone, B. Mennucci, M. Cossi, G. Scalmani, N. Rega, G. A. Petersson, H. Nakatsuji, M. Hada, M. Ehara, K. Toyota, R. Fukuda, J. Hasegawa, M. Ishida, T. Nakajima, Y. Honda,


 © 2007 Wiley-VCH Verlag GmbH & Co. KGaA, Weinheim 

O. Kitao, H. Nakai, M. Klene, X. Li, J. E. Knox, H. P. Hratchian, J. B. Cross, V. Bakken, C. Adamo, J. Jaramillo, R. Gomperts, R. E. Stratmann, O. Yazyev, A. J. Austin, R. Cammi, C. Pomelli, J. W. Ochterski, P. Y. Ayala, K. Morokuma, G. A. Voth, P. Salvador, J. J. Dannenberg, V. G. Zakrzewski, S. Dapprich, A. D. Daniels, M. C. Strain, O. Farkas, D. K. Malick, A. D. Rabuck, K. Raghavachari, J. B. Foresman, J. V. Ortiz, Q. Cui, A. G. Baboul, S. Clifford, J. Cioslowski, B. B. Stefanov, G. Liu, A. Liashenko, P. Piskorz, I. Komaromi, R. L. Martin, D. J. Fox, T. Keith, M. A. Al-Laham, C. Y. Peng, A. Nanayakkara, M. Challacombe, P. M. W. Gill, B. Johnson, W. Chen, M. W. Wong, C. Gonzalez, J. A. Pople, *Gaussian 03, Revision B.03*, Gaussian Inc., Wallingford, CT, **2004**.

Received: October 2, 2006
Published Online: March 23, 2007

 © 2007 Wiley-VCH Verlag GmbH & Co. KGaA, Weinheim 

DOI: 10.1002/ejic.200600954

# Construction of 1D and 2D Copper(I) Coordination Polymers Assembled by $PhS(CH_2)_nSPh$ ($n$ = 1, 2) Dithioether Ligands: Surprising Effect of the Spacer Length on the Dimensionality, Cluster Nuclearity and the Fluorescence Properties of the Metal–Organic Framework

**Harmel N. Peindy,[a] Fabrice Guyon,*[a] Abderrahim Khatyr,[a] Michael Knorr,*[a] and Carsten Strohmann[b]**

*Dedicated to the memory of Prof. Liliane G. Hubert-Pfalzgraf*

**Keywords:** Dithioethers / Copper / Fluorescence / Coordination polymers / Metal–metal interactions

Treatment of CuI with $PhSCH_2SPh$ in MeCN solution affords, by a self-assembly reaction, the monodimensional metal–organic coordination polymer $[Cu_4I_4\{\mu\text{-}PhS_2CH_2SPh\}_2]_n$ (**1**), in which $Cu_4(\mu^3\text{-}I)_4$ cluster units are linked by the dithioether ligand in a 1D necklace structure. In contrast, the reaction of $PhSCH_2CH_2SPh$ with CuI results in the formation of the metallopolymer $[(CuI)_2\{\mu\text{-}PhS(CH_2)_2SPh\}_2]_n$ (**2**). The 2D network of **2** is built from dimeric $Cu_2I_2$ units which are connected by 1,2-bis(phenylthio)ethane bridging ligands. The solid-state luminescence spectrum of **1** exhibits a strong emission around 532 nm, whereas a weak emission centred at 413 nm is observed in the case of **2**.
(© Wiley-VCH Verlag GmbH & Co. KGaA, 69451 Weinheim, Germany, 2007)

## Introduction

It is well established that interaction of various nucleophiles (L) such as phosphanes, aniline and pyridyl type ligands with copper(I) halides often affords tetranuclear cubane-like $Cu_4X_4L_4$ clusters by a self-assembly process.[1] The interest in these polymetallic systems, in particular those incorporating the $Cu_4I_4$ unit, stems from their remarkable photophysical properties,.[2] Therefore these compounds have also been the object of theoretical studies.[3] Less common is the incorporation of the tetranuclear $Cu_4I_4$ core in a metal–organic network. The known examples of 1D to 3D coordination polymers including $Cu_4I_4$ cores were assembled by using an alkanedinitrile ligand,[4] difunctional pyridyl ligands,[5] dimethylsufide and diethylsulfide,[6a,6b] a functionalized dithioether ligand,[6c] polydentate thioether macrocycles,[7] and a triselenoether macrocycle.[8] The topology of extended networks based on flexible bidentate thioether ligands has been shown in the case of silver(I) to be very dependent on the spacer between the coordinated functions.[9] Our interest in the coordination chemistry of bi- and polydentate thioether ligands[10] has led us to investigate the reactivity of the flexible dithioether ligands $PhS–(CH_2)_n–SPh$ ($n$ = 1–2) towards CuI in order to evaluate the influence of the spacer on the resulting framework.

## Results and Discussion

The reaction of CuI with an equimolar amount of bis(phenylthio)methane in acetonitrile gave colourless crystals of the general formula $[Cu_4I_4\{\mu\text{-}PhSCH_2SPh\}_2]_n$ (**1**) (Scheme 1). Modification of the molar ratio, for example from 1:1 to 1:2, had no influence on the composition of the resulting material, and only compound **1** was formed. This observation is in contrast to the results reported by Sheldrick et al., who used an alkanedinitrile ligand (L) to obtain the 1:1 and 2:1 coordination polymers, $[(CuI)_2L_2]$ and $[(CuI)_4L_2]$, respectively, from the appropriate molar ratio of reactants.[4]

The crystal structure of **1**, viewed along the $c$ axis in Figure 1, consists of cubane-like $Cu_4I_4$ clusters linked by bridging dithioether ligands to form an infinite chain with Cu–S distances of 2.292(2) and 2.301(2) Å. The Cu–I bond lengths range from 2.6077(11) to 2.7704(11) Å. The Cu···Cu distances [2.6173(18)–2.7864(14) Å], comparable to the sum of the van der Waals radii (2.8 Å), lie in the range of distances reported for this interaction in other structurally

[a] Institut UTINAM, UMR CNRS 6213, Université de Franche-Comté, Faculté des Sciences et des Techniques, 16, Route de Gray, 25030 Besançon, France
E-mail: michael.knorr@univ-fcomte.fr
fabrice.guyon@univ-fcomte.fr
[b] Institut für Anorganische Chemie der Universität Würzburg, Am Hubland, 97074 Würzburg, Germany
Supporting information for this article is available on the WWW under http://www.eurjic.org or from the author.

 © 2007 Wiley-VCH Verlag GmbH & Co. KGaA, Weinheim 

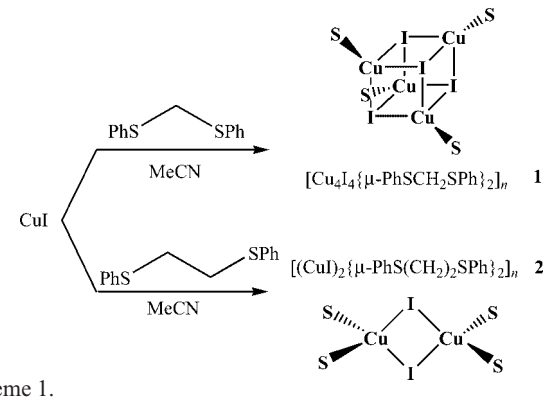


Scheme 1.

characterized $Cu_4I_4$ units. Two adjacent $Cu_4I_4$ cores are linked by two flexible dithioether ligands leading thus to the formation of a 1D necklace structure. Note also that the phenyl substituents adopt a parallel orientation with a short $C_{ipso}$–$C_{ipso}$ distance of 3.502 Å.

Despite the fact that the phenyl groups of neighbouring ribbons are somewhat interpenetrated, there are no close inter-ribbon interactions between the 1D chains of coordination polymer **1**, the separation between the midpoints of two adjacent $Cu_4I_4$ units being 11.64 Å (Figure 2).

The colourless crystals obtained from the reaction between equimolar amounts of CuI and 1,2 bis(phenylthio)-ethane in acetonitrile were identified by an X-ray study as the coordination polymer $[(CuI)_2\{\mu\text{-}PhS(CH_2)_2SPh\}_2]_n$ (**2**). This framework consists of centrosymmetric $Cu_2(\mu^2\text{-}I)_2$ rhomboid dimers, each connected to an adjacent unit via one $\mu^2$-bridging dithioether ligand (Figure 3). Each Cu atom is in a distorted tetrahedral environment, coordinated to the bridging iodido ligand and thioether group of two different ligands.

The 2D network resulting from this coordination mode includes centrosymmetric 24-membered metallomacrocycles constituted from four dithioether ligands, six Cu atoms and two iodido ligands (Figure 4). The average length of the two Cu–S bonds [2.3000(11) and 2.3855(10) Å] is somewhat greater than that in **1**. The Cu···Cu separation of 2.8058(11) Å is much greater than those observed in the above-mentioned $Cu_4I_4$ unit of **1**. A survey of the literature indicates that Cu···Cu separations vary in $[Cu(\mu^2\text{-}I)_2Cu]$ compounds. A dithioether-functionalized tetrathiafulvalene Cu complex was reported to have a relatively small Cu···Cu separation of 2.65 Å.[11a] Distances close to the value in **2** have been reported for $[Cu_2I_2[16]aneS_4]_n$ ([16]aneS$_4$ = 1,5,9,13-tetrathiacyclohexadecane) [2.8079(12) Å][7] and $[\{MeSi(CH_2SMe)_3\}CuI]_2$ [2.862(2) Å].[11b] A far longer

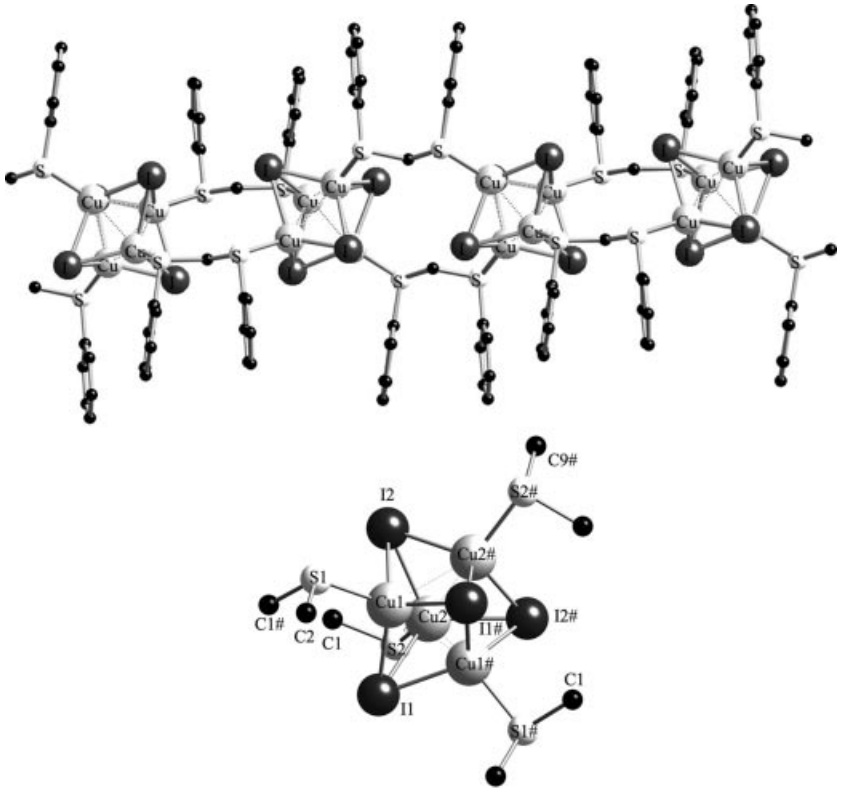


Figure 1. (top) View on the 1D chain of **1** along the *c* axis. H atoms are omitted for clarity. Selected bond lengths [Å]: Cu(1)–S(1) 2.292(2), Cu(2)–S(2) 2.301(2), Cu(1)–Cu(2) 2.7864(14), Cu(1)–Cu(1)#2 2.6173(18), Cu(1)–Cu(2)#2 2.6464(13), Cu(2)–Cu(2)#2 2.663(2), Cu(1)–I(1) 2.6486(15), Cu(1)–I(2) 2.7621(11), Cu(2)–I(2)#2 2.6077(10), Cu(2)–I(2) 2.6825(12), Cu(2)–I(1) 2.7704(11), I(1)–Cu(1)#2 2.6228(12), I(2)–Cu(2)#2 2.6077(11), C(1)–S(2) 1.804(7), C(1)–S(1)#1 1.818(7). (bottom) View of the tetranuclear $Cu_4(\mu^3\text{-}I)_4$ core of **1**. Only the *ipso* carbon atoms C2 and C9 of the phenyl groups are shown for clarity. Symmetry operations used to generate equivalent atoms: #1: $-x + 2, -y + 1, -z$; #2: $-x + 2, y, -z + 1/2$.

 © 2007 Wiley-VCH Verlag GmbH & Co. KGaA, Weinheim 

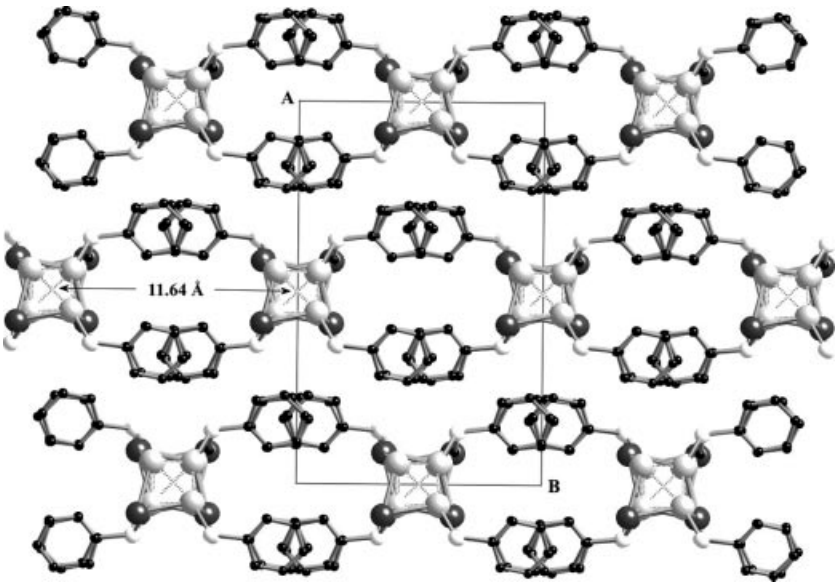


Figure 2. View of packing of **1** on the *ab* plane.

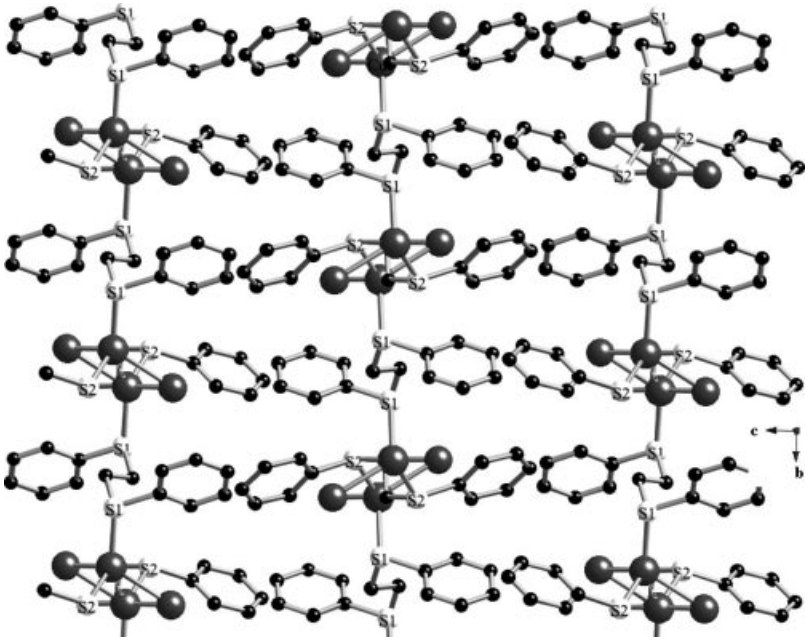


Figure 3. View of the packing of **2** on the *bc* plane.

Cu···Cu interaction of 3.18 Å has been found in the two-dimensional sheet structure of polymeric $[Cu_2I_2(dtpcp)_2]$·thf (dtpcp = 2,11-dithia[3.3]paracyclophane).[11c–11d] Our discovery that a subtle steric modification of the dithioether has a major impact on the cluster nuclearity suggests that a small energetic difference exists between the centrosymmetric rhomboid $Cu_2I_2$ motif and the cubane-like $Cu_4I_4$ cluster. Note that treatment of $[Cu(MeCN)_4][BF_4]$ with 1,2-bis(phenylthio)ethane affords the mononuclear chelate complex $[Cu\{PhS(CH_2)_2SPh\}_2][BF_4]$, which has been reported to undergo facile ligand dissociation in solution.[12]

The solid-state emission spectra of **1** and **2** are shown in Figure 5. Upon excitation at 360 nm, a strong emission band was observed for the tetranuclear adduct, **1**, with a maximum at 532 nm. Emissions in a similar spectral range have been observed for nitrogen-substituted $Cu_4I_4L_4$ clusters and were attributed to an emission from a triplet cluster centred excited state ($^3$CC).[3b,13] In fact, this broad CC excited state emission is mixed in character with equal contributions of iodine to copper charge transfer (XMCT) and copper orbital centred (d→s) transitions.[3b] In contrast, the emission spectrum recorded for polymeric **2** containing the

 © 2007 Wiley-VCH Verlag GmbH & Co. KGaA, Weinheim 

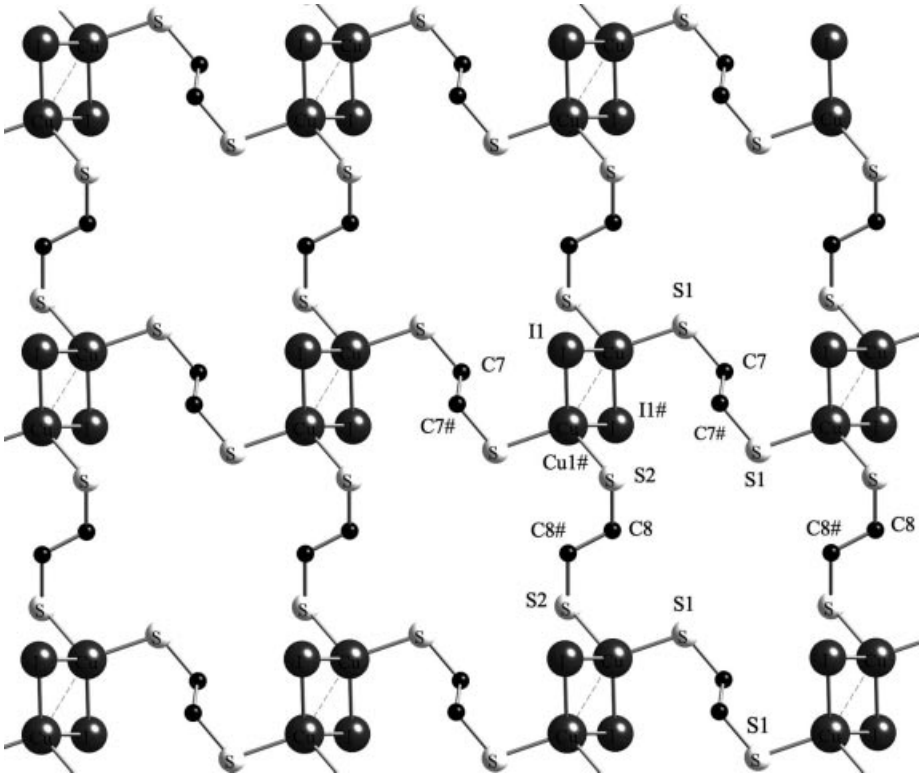


Figure 4. View of the core structure of **2** on the *ab* plane. H atoms and phenyl groups are omitted for clarity. Selected bond lengths [Å] and angles [°]: Cu(1)–S(1) 2.3000(11), Cu(1)–S(2) 2.3855(10), Cu(1)–I(1) 2.6108(7), Cu(1)–I(1)#3 2.6169(8), Cu(1)–Cu(1)#3 2.8058(10), C(7)–S(1) 1.820(3), C(8)–S(2) 1.816(4); S(1)–Cu(1)–S(2) 109.24(4), S(1)–Cu(1)–I(1) 120.26(3), S(1)–Cu(1)–I(1)#3 105.57(3), S(2)–Cu(1)–I(1)#3 110.00(3), S(2)–Cu(1)–I(1) 96.12(3), I(1)#3–Cu(1)–I(1) 115.08(2), Cu(1)#3–I(1)–Cu(1) 64.92(2), C(7)–S(1)–Cu(1) 110.61(11). Symmetry operations used to generate equivalent atoms: #1: $-x + 2, -y + 2, -z$; #2: $-x + 1, -y + 1, -z$; #3: $-x + 2, -y + 1, -z$.

dinuclear $Cu_2I_2$ unit exhibits, under similar experimental conditions, only a very weak emission centred at 413 nm with a shoulder at 438 nm. Although less studied than the tetranuclear systems, photophysical properties of some dinuclear $Cu_2X_2$ compounds have been reported in the literature, but are currently limited to those of *N*-heterocyclic ligands.[3c,14] The observation of a shoulder suggests a mixed emission with different contributions from the XMCT and Cu (d→s) transitions. To confirm this hypothesis, advanced photophysical studies and ab initio calculations are in progress. Solution measurements carried out in acetonitrile at room temperature show no luminescence for either **1** or **2**. This is probably due to a disassembly of the cluster units by this strongly coordinating solvent.

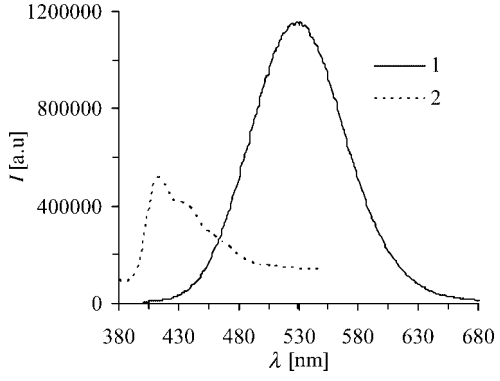


Figure 5. Corrected solid-state luminescence spectra recorded at room temperature for compounds **1** (solid) and **2** (dotted).[15]

## Conclusions

In summary, this work has shown that the dithioether ligand spacer length has a significant impact on the dimensionality of the resulting coordination polymer and the cluster nuclearity. It therefore determines, indirectly, the luminescence properties of the resulting metal–organic framework. We are currently varying the spacer length and nature of the copper salt systematically in order to establish a correlation between $PhS(CH_2)_nSPh$ and the motif of the framework. In addition, detailed photophysical studies and theoretical computations on these coordination polymers are underway.

## Experimental Section

$PhSCH_2SPh$ and $PhS(CH_2)_2SPh$ were prepared according to ref.[16] and ref.,[17] respectively. The solid-state emission spectra were recorded at room temperature with a Jobin–Yvon Fluorolog-3 spectrometer using a cylindrical 0.5 cm diameter quartz capillary with a scan speed of 1 nm/s. Intensity scales are presented in arbitrary units.

 © 2007 Wiley-VCH Verlag GmbH & Co. KGaA, Weinheim 

**Preparation of 1 and 2**: To a suspension of CuI (191 mg, 1.0 mmol) in acetonitrile (10 mL) was added $PhSCH_2SPh$ (232 mg, 1.0 mmol). The mixture was heated at reflux for 15 min, then the solution was allowed to reach room temperature. After one day, colourless crystals of **1** formed. Yield 0.22 g, 72%. $C_{13}H_{12}Cu_2I_2S_2$ (613.23): calcd. C 25.46, H 1.97; found C 25.89, H 2.05. The reaction of CuI with $PhS(CH_2)_2SPh$ under similar conditions afforded compound **2**. Yield 0.33 g, 75%. $C_{14}H_{14}CuIS_2$ (436.81): calcd. C 38.49, H 3.23; found C 38.77, H 3.30.

**X-ray Crystallography:** Crystal data and experimental details are given in Table 1. Data were collected with a Stoe IPDS diffractometer at 173(2) K. The intensities were determined and corrected with the program INTEGRATE in IPDS.[18] An empirical absorption correction was employed using the FACEIT program in IPDS.[19] All structures were solved by applying direct and Fourier methods. For each structure, the non-hydrogen atoms were refined anisotropically. All hydrogen atoms were placed in geometrically calculated positions, and each was assigned a fixed isotropic displacement parameter based on a riding model. Refinement of the structures was carried out by full-matrix least-squares methods based on $F_o^2$. All calculations were performed with the WinGX crystallographic software package, using the programs SHELXS-90[20] and SHELXL-97.[21] CCDC-623106 and -623107 contain the supplementary data for **1** and **2**, respectively. These data can be obtained free of charge from The Cambridge Crystallographic Data Centre via www.ccdc.cam.ac.uk/data_request/cif.

Table 1. Crystal data and structure refinement details for **1** and **2**.

| Compound | **1** | **2** |
|---|---|---|
| Empirical formula | $C_{13}H_{12}Cu_2I_2S_2$ | $C_{14}H_{14}CuIS_2$ |
| Formula weight | 613.13 | 436.81 |
| $T$ [K] | 173(2) | 173(2) |
| Crystal system | monoclinic | monoclinic |
| Space group | $C2/c$ | $P2_1/n$ |
| $a$ [Å] | 20.857(4) | 9.4711(18) |
| $b$ [Å] | 11.656(2) | 7.928(2) |
| $c$ [Å] | 15.530(3) | 19.632(4) |
| $\beta$ [°] | 119.42(3) | 97.78(2) |
| $V$ [Å$^3$] | 3288.5(11) | 1460.5(6) |
| $Z$ | 8 | 4 |
| $\rho_{calcd.}$ [g/cm$^3$] | 2.477 | 1.987 |
| $\mu$ [mm$^{-1}$] | 6.578 | 3.874 |
| $F$(000) | 2288 | 848 |
| Crystal size [mm] | 0.40 × 0.20 × 0.20 | 0.30 × 0.30 × 0.10 |
| $\theta$ range [°] | 2.22 to 25.00 | 2.28 to 26 |
| Index ranges | $-24 \le h \le 24$ | $-11 \le h \le 11$ |
| | $-12 \le k \le 13$ | $-9 \le k \le 9$ |
| | $-18 \le l \le 18$ | $-24 \le l \le 24$ |
| Reflections collected | 9932 | 13463 |
| Independent reflections | 2871 | 2782 |
| Refinement method | | full-matrix least squares on $F^2$ |
| Data/restraints/parameters | 2871/0/172 | 2782/0/164 |
| Goodness-of-fit on $F^2$ | 1.033 | 1.066 |
| $R_1$, $wR_2$ [$I > 2\sigma(I)$] | 0.0463, 0.1404 | 0.0353, 0.0874 |
| $R_1$, $wR_2$ [all data] | 0.0480, 0.1421 | 0.0395, 0.0898 |
| $\Delta\rho$(min), $\Delta\rho$(max) [e·Å$^3$] | 1.119, –1.104 | 1.060, –0.759 |

**Supporting Information** (see footnote on the first page of this article): View of the structure and packing of **2** along the *b* axis and of **1** on the *bc* plane.

## Acknowledgments

Financial support from the Région Franche-Comté for the fluorescence spectrometer is gratefully acknowledged.

[1] See for example a) N. P. Rath, E. M. Holt, K. Tanimura, *Inorg. Chem.* **1985**, *24*, 3934–3938; b) L. M. Engelhardt, P. C. Healy, J. D. Kildea, A. H. White, *Austr. J. Chem.* **1989**, *42*, 107–113; c) M. R. Churchill, B. G. DeBoer, S. J. Mendak, *Inorg. Chem.* **1975**, *14*, 2041–2047; d) G. Hu, G. J. Mains, E. M. Holt, *Inorg. Chim. Acta* **1995**, *240*, 559–565; e) R.-H. Wang, M.-C. Hong, J.-H. Luo, R. Cao, J.-B. Weng, *Eur. J. Inorg. Chem.* **2002**, 3097–3100.

[2] a) P. C. Ford, E. Cariati, J. Bourassa, *Chem. Rev.* **1999**, *99*, 3625–3647; b) M. Vitale, P. C. Ford, *Coord. Chem. Rev.* **2001**, *219–221*, 3–16; c) H. D. Hardt, A. Pierre, *Inorg. Chim. Acta* **1977**, *25*, L59–60.

[3] a) A. Vega, J.-Y. Saillard, *Inorg. Chem.* **2004**, *43*, 4012–4018; b) M. Vitale, W. E. Palke, P. C. Ford, *J. Phys. Chem.* **1992**, *96*, 8329–8336; c) M. Vitale, C. K. Ryu, W. E. Palke, P. C. Ford, *Inorg. Chem.* **1994**, *33*, 561–566; d) for a general review on the photochemical properties of $d^{10}$ metal complexes see: C. Kutal, *Coord. Chem. Rev.* **1990**, *99*, 213–252.

[4] M. Heller, W. S. Sheldrick, *Z. Anorg. Allg. Chem.* **2004**, *630*, 1869–1874.

[5] a) A. J. Blake, N. R. Brooks, N. R. Champness, M. Crew, A. Deveson, D. Fenske, D. H. Gregory, L. R. Hanton, P. Hubberstey, M. Schröder, *Chem. Commun.* **2001**, 1432–1433; b) S. Hu, M.-L. Tong, *Dalton Trans.* **2005**, 1165–1167.

[6] a) J. S. Filippo Jr, L. E. Zyontz, J. Potenza, *Inorg. Chem.* **1975**, *14*, 1667–1671; b) J. Zhou, G.-Q. Bian, J. Dai, Y. Zhang, Q.-Y. Zhu, W. Lu, *Inorg. Chem.* **2006**, *45*, 8486–8488; c) T. H. Kim, K. Y. Lee, Y. W. Shin, S.-T. Moon, K.-M. Park, J. S. Kim, Y. Kang, S. S. Lee, J. Kim, *Inorg. Chem. Commun.* **2005**, *8*, 27–30.

[7] a) P. R. Ashton, A. L. Burns, C. G. Claessens, G. K. H. Shimizu, K. Small, J. F. Stoddart, A. J. P. White, D. J. Williams, *J. Chem. Soc., Dalton Trans.* **1997**, 1493–1496; b) N. R. Brooks, A. J. Blake, N. R. Champness, P. A. Cooke, P. Hubberstey, D. M. Proserpio, C. Wilson, M. Schröder, *J. Chem. Soc., Dalton Trans.* **2001**, 456–465.

[8] R. D. Adams, K. T. McBride, R. D. Rogers, *Organometallics* **1997**, *16*, 3895–3901.

[9] J.-R. Li, R.-H. Zhang, X.-H. Bu, *Cryst. Growth Des.* **2003**, *3*, 829–835.

[10] a) H. N. Peindy, F. Guyon, I. Jourdain, M. Knorr, D. Schildbach, C. Strohmann, *Organometallics* **2006**, *25*, 1472–1479; b) H. N. Peindy, F. Guyon, M. Knorr, C. Strohmann, *Z. Anorg. Allg. Chem.* **2005**, *631*, 2397–2400; c) H. N. Peindy, F. Guyon, M. Knorr, A. B. Smith, J. A. Farouq, S. A. Islas, D. Rabinovich, J. A. Golen, C. Strohmann, *Inorg. Chem. Commun.* **2005**, *8*, 479–482; d) M. Knorr, H. N. Peindy, F. Guyon, H. Sachdev, C. Strohmann, *Z. Anorg. Allg. Chem.* **2004**, *630*, 1955–1961; e) C. Strohmann, S. Lüdtke, O. Ulbrich, *Organometallics* **2000**, *19*, 4223–4227; f) C. Strohmann, *Chem. Ber.* **1995**, *128*, 167–172; g) C. Strohmann, S. Lüdtke, E. Wack, *Chem. Ber.* **1996**, *129*, 799–805; h) C. Strohmann, E. Wack, *Z. Naturforsch.* **2004**, *59b*, 1570–1578; i) I. Pavel, K. Strohfeldt, C. Strohmann, W. Kiefer, *Inorg. Chim. Acta* **2004**, *357*, 1920–1930.

[11] a) W. Lu, Z.-M. Yan, J. Dai, Y. Zhang, Q.-Y. Zhu, D.-X. Jia, W.-J. Guo, *Eur. J. Inorg. Chem.* **2005**, 2339–2345; b) H. W. Yim, D. Rabinovich, K.-C. Lam, J. A. Golen, A. L. Rheingold, *Acta Crystallogr., Sect. E* **2003**, *59*, 556–558; c) M. Munakata, L. P. Wu, T. Kuroda-Sowa, M. Maekawa, Y. Suenaga, S. Nakagawa, *J. Chem. Soc., Dalton Trans.* **1996**, 1525–1530; d) the mean value found in a variety of $[Cu(\mu\text{-}I)_2Cu]$ derivatives is ca. 2.76 Å: F. H. Allen, *Acta Crystallogr., Sect. B* **2002**, *58*, 380–388.

 © 2007 Wiley-VCH Verlag GmbH & Co. KGaA, Weinheim 

[12] J. R. Black, W. Levason, *J. Chem. Soc., Dalton Trans.* **1994**, 3225–3230.
[13] E. Lindsay, P.-C. Ford, *Inorg. Chim. Acta* **1996**, *242*, 51–56.
[14] a) N. P. Rath, J. L. Maxwell, E. M. Holt, *J. Chem. Soc., Dalton Trans.* **1986**, 2449–2453; b) M. Henary, J. L. Wotton, S. I. Khan, J. I. Zink, *Inorg. Chem.* **1997**, *36*, 796–801; c) H. Araki, K. Tsuge, Y. Sasaki, S. Ishizaka, N. Kitamura, *Inorg. Chem.* **2005**, *44*, 9667–9675 and the references cited therein.
[15] As pointed out by a referee, the direct comparisons between two different solid samples on an absolute intensity scale are qualitative at best, since (unlike solutions) both the absorption of the excitation light and the collection of the emission depend on the physical characteristics of the solid powder sample, including particle size and homogeneity.
[16] S. G. Murray, W. Levason, H. E. Tuttlebee, *Inorg. Chim. Acta* **1981**, *51*, 185–189.
[17] a) F. R. Hartley, S. G. Murray, W. Levason, H. E. Soutter, C. A. McAuliffe, *Inorg. Chim. Acta* **1979**, *35*, 265–277; b) B.-H. Hou, L.-N. Zhou, Q.-X. Yin, J.-K. Wang, W. Chen, *Acta Crystallogr., Sect. E* **2005**, *61*, 2482–2483.
[18] *INTEGRATE-IPDS*, Stoe & Cie GmbH, Darmstadt, **1999**.
[19] *FACEIT-IPDS*, Stoe & Cie GmbH, Darmstadt, **1999**.
[20] G. M. Sheldrick, *SHELXS-90*, Universität Göttingen, **1990**.
[21] G. M. Sheldrick, *SHELXL-97*, Universität Göttingen, **1997**.

Received: October 10, 2006
Published Online: March 16, 2007

 © 2007 Wiley-VCH Verlag GmbH & Co. KGaA, Weinheim 

DOI: 10.1002/ejic.200600969

# Synthesis and Optical Properties of β-$BaB_2O_4$ Network-Like Nanostructures

Qingrui Zhao,[a] Xi Zhu,[a] Xue Bai,[a] Haihua Fan,[b] and Yi Xie*[a]

**Keywords:** Nonlinear optics / Materials science / Sol–gel processes / Borates

Network-like nanostructures made from the nonlinear optical material beta barium metaborate (β-$BaB_2O_4$, β-BBO) have been successfully synthesized from a BBO gel precursor by a sol–gel method. The homogeneous BBO gel precursor is prepared by the hydrolysis and condensation of barium acetate, sorbitol, and boric acid in a mixture of polyethylene glycol (PEG200) and water. We have also demonstrated that the morphology of the synthesized β-$BaB_2O_4$ materials exerts a significant influence on the second harmonic generation (SHG) efficiency. Importantly, the preparation and second-order nonlinear optical studies with different shapes will offer great opportunities to explore the dependence of a material's second-order nonlinear optical properties on its morphology and is essential for the manufacture of potential nanoscale optoelectronic and nonlinear optical devices.

(© Wiley-VCH Verlag GmbH & Co. KGaA, 69451 Weinheim, Germany, 2007)

## Introduction

Much attention has been focused on nonlinear optical (NLO) materials during the past decades owing to their promising future applications in a number of fields such as laser medicine, optical communication, and signal processing.[1–5] Among the nonlinear optical bulk crystals, beta barium metaborate (β-$BaB_2O_4$, β-BBO) has shown good promise due to its large second harmonic generation (SHG) coefficients. SHG is a well-documented nonlinear optical effect that occurs when laser radiation strikes the surface of a material and a fraction of the incident light is frequency-doubled.[6,7] Generally, β-$BaB_2O_4$ single crystals are prepared by high temperature solution growth, such as the Czochralski technique[8] and Flux method.[9] Recent developments in the fast evolving field of nanoscience and nanotechnology, where size and shape are crucial for the optoelectronic properties of materials, especially the preparation of various β-BBO nanostructures such as nanowires, nanorods, and nanotubes and studies on their SHG performance on the nanoscale, are worthy of note.[10,11] Most recently, Hong et al. have reported that β-BBO nanoparticles with a diameter of 40 nm,[12] which show promising applications in the photoelectronic industry, can be prepared by coprecipitation followed by annealing at 700 °C. Despite this excellent progress in our ability to prepare β-BBO nanoparticles, no reports concerning the synthesis of one-dimensional (1D) nanostructures are available as yet, which therefore limits the shape-and-size dependent nonlinear optical responses of this functional material.

1D Nanostructures are an ideal system not only for understanding the functional phenomena in low-dimensional systems but also for developing new generation nanodevices with high performance. Furthermore, it is generally accepted that 1D nanostructures provide a good system to investigate the relationship between size and properties.[11] However, as far as NLO materials are concerned, including $KNbO_3$, $KH_2PO_4$ (KDP), α-$LiIO_3$, and β-BBO etc., there are few reports on the synthesis of 1D nanostructures. Only recently, for example, have Magrez et al. reported the growth of $KNbO_3$ nanowires by a hydrothermal route.[13] Similarly, Pribošič et al. have recently prepared $KNbO_3$ perovskite in the form of nanoneedles and nanoplatelets by crystallization of the amorphous gel.[14] Further research efforts are therefore needed to develop the fabrication of 1D NLO nanostructures from only $KNbO_3$ to other NLO materials such as β-BBO.

Inspired by these ideas, in this paper we report a simple, inexpensive, and efficient sol–gel approach as the first example of a morphology-controlled synthesis of β-$BaB_2O_4$ nanostructures with novel and interesting 1D morphologies. Interestingly, we show that the prepared β-$BaB_2O_4$ nanorods self-organize to form network-like structures. β-BBO nanoparticles can also be fabricated by varying the experimental parameters. In addition, the second-harmonic generation (SHG) efficiency of β-BBO network-like nanostructures and nanoparticles are described. The experimental results indicate that the β-BBO network-like nanostructures and nanoparticles have obvious differences in their SHG efficiency, which suggests that SHG is sensitive to the electronic properties of nanostructures of varying shape, size,

[a] Nanomaterials and Nanochemistry, Hefei National Laboratory for Physical Sciences at Microscale, University of Science & Technology of China,
Hefei, Anhui 230026, P. R. China
[b] State Key Laboratory of Optoelectronic Materials and Technologies, Sun Yat-Sen University,
Guangzhou, 510275, China
Fax: +86-551-3603987
E-mail: yxie@ustc.edu.cn

 © 2007 Wiley-VCH Verlag GmbH & Co. KGaA, Weinheim 

composition, and spatial organization.[15–18] Thus, the preparation and properties of β-BBO nanostructures provide a fine example of the dependence of a material's second-order nonlinear optical properties on its morphology and will find many interesting applications in the field of NLO devices.

## Results and Discussion

The crystal structure and phase composition of the as-prepared product were characterized by X-ray powder diffraction (XRD). Figure 1 (a) shows a typical XRD pattern of the as-prepared product. All the peaks can be readily indexed to the hexagonal phase of β-BBO (JCPDS file, no. 80-1489), with lattice constants of $a$ = 12.53 and $c$ = 12.72 Å (Figure 1, b). No characteristic peaks were observed for any impurities.

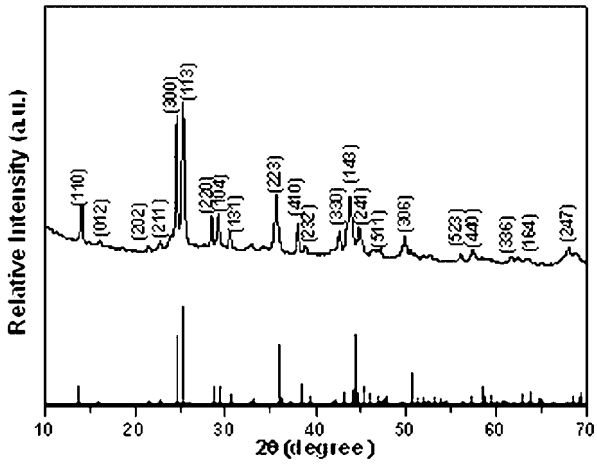


Figure 1. XRD pattern of network-like β-$BaB_2O_4$ nanostructures.

X-ray photoelectron spectra were also recorded to further characterize the product; the results are shown in Figure 2. High resolution spectra were recorded in the Ba 3d (Figure 2, a), B 1s (Figure 2, b), and O 1s (Figure 2, c) regions. The peak at 781.7 eV can be attributed to Ba $3d_{5/2}$, and the peak at 193.5 eV corresponds to B 1s of β-$BaB_2O_4$. The O 1s binding energy of 532.8 eV (Figure 2, c) indicates that the oxygen atoms are present as $O^{2-}$ species in the compounds. These results are in good agreement with the values for crystalline β-$BaB_2O_4$ found in the literature.[19]

Further evidence for the composition of the sample was obtained from the Raman and IR spectra. The β-BBO crystal belongs to the $C_{3v}^6$ space group and group theory analysis predicts the zone–center optical modes $A_1$ and E, both of which are Raman and IR active. Figure 3 (a) shows the Raman spectra of a typical sample. The peaks centered at 1539, 784, 632, and 597 $cm^{-1}$ can be assigned to $A_1$ [transversal-optical (TO) photon mode], and the peaks at 971, 661, 480, 384, and 703 $cm^{-1}$ can be assigned to E [longitudinal-optical (LO) photon mode].[20] We also measured the IR spectra of the sample (Figure 3b). The full-range IR spectra between 800 and 3000 $cm^{-1}$ shows broad absorptions in the range 900–1500 $cm^{-1}$ for the characteristic absorption of β-BBO. The absorption peaks at 1078 and 1243 $cm^{-1}$ are due to the B–O stretching modes in the $BO_3^{3-}$

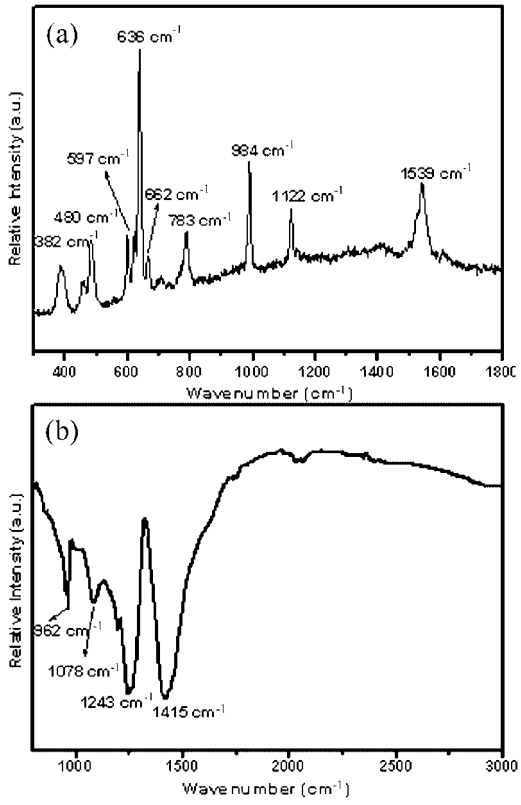


Figure 3. a) Raman and b) full-range IR spectra of the as-obtained β-$BaB_2O_4$ nanostructures.

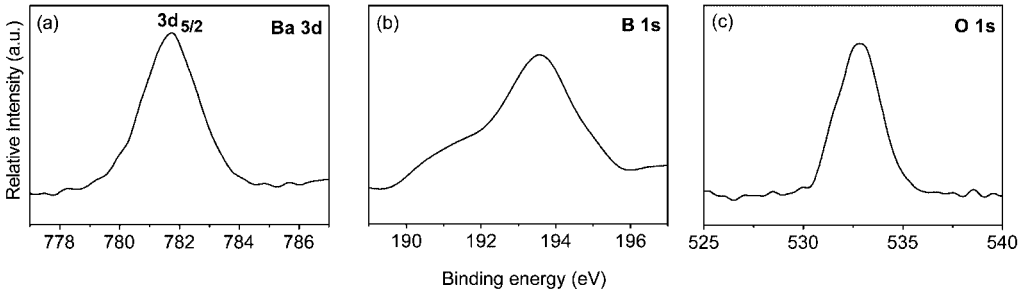


Figure 2. XPS spectra of network-like β-$BaB_2O_4$ nanostructures: a) high-resolution Ba region; b) high-resolution B region; c) high-resolution O region.

 © 2007 Wiley-VCH Verlag GmbH & Co. KGaA, Weinheim 

unit, which is a component of the $(B_3O_6)^{3-}$ ring.[21] The bands observed at 962 and 1415 $cm^{-1}$ are B–O extra-ring stretching modes,[22] which is further evidence that high quality β-BBO nanocrystals have been obtained.

Figure 4 presents typical FESEM, TEM, and HRTEM images of the β-BBO network-like nanostructures obtained at different magnifications. The low magnification FESEM image in Figure 4 (a) shows the panoramic morphology of the products and the three-dimensional features and regularity of the network. Part b of Figure 4 is a TEM image, which reveals that the building blocks of the network-like nanostructures are uniform nanorods. These nanorods interlink in an orderly fashion that resembles a nanoweb. The average diameter of the nanorods is about 30 nm and their lengths range from 300 to 400 nm. Some building blocks of the network-like nanostructures are bundles of nanorods. For HRTEM imaging the samples were dispersed in ethanol and deposited on carbon-coated copper grids. The HRTEM image shown in parts c and d of Figure 4 show the high crystallinity of the product; defects such as twin structures, stacking faults, or dislocations are not seen in this image. This typical HRTEM image indicates that β-BBO nanostructures are single crystals that grow preferentially along the *a* [113] direction.

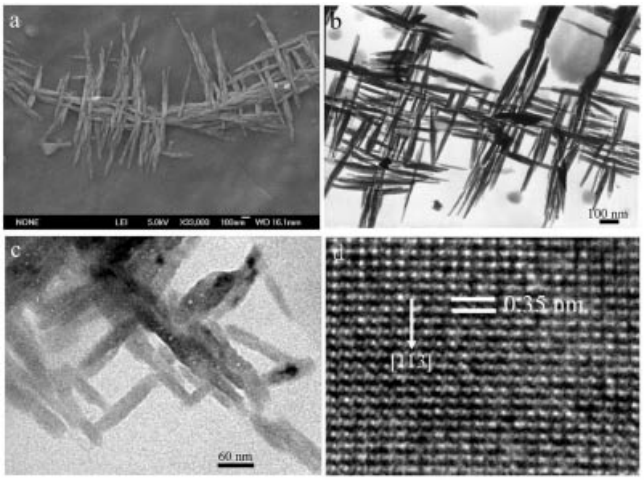


Figure 4. Electron microscopy images of the β-$BaB_2O_4$ network-like nanostructures: a) FESEM image; b) TEM image; c) high-magnification TEM image; d) HRTEM image along the [113] axis.

The sol–gel technique has been widely adopted to fabricate various nanostructures.[23] In our process, sorbitol coordinates to boric acid to form complexes by dehydration, which could prevent boric acid from volatilizing.[24] This complex solution then reacts with barium acetate, which loses its acetate to form the precursor.[25] When this mixture is heated continually it forms a homogeneous sol that then undergoes polycondensation and crosslinking to produce a gel. When calcined, this gel decomposes to form β-BBO nanostructures. The whole process is summarized in Scheme 1.

These β-BBO nanostructures are synthesized from a BBO gel precursor in a mixture of polyethylene glycol (PEG200) and water. The representative IR absorption

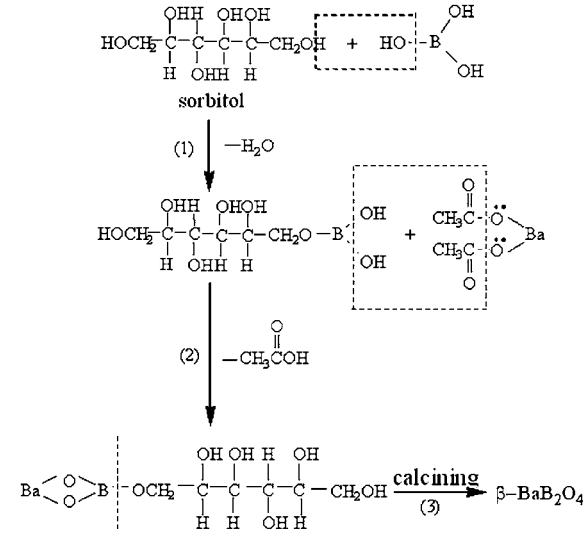


Scheme 1. The formation of β-$BaB_2O_4$.

spectra of the sol and gel shown in parts a and b of Figure 5 provide a direct way of investigating the sol–gel process. The bands at 2875, 1455, and 1351 $cm^{-1}$ in part a of Figure 5 are assigned to the vibration of the C–H bond of PEG,[21] whereas the absorption peaks at 831, 888, and 944 $cm^{-1}$ are due to the B–O stretching modes, which is a component of the $(B_3O_6)^{3-}$ ring.[21] The bands at 1100 and 1249 $cm^{-1}$ are due to the vibration of the C–O bond,[26] and the intense bands at 1657 $cm^{-1}$ are due to the presence of a carbonyl group.[27] Bands at around 1574, 1408, and 1069 $cm^{-1}$ are clearly observed in Figure 5 (b). The strong absorption band from the carbonyl group at 1657 $cm^{-1}$ has disappeared, which implies that acetic acid is released during the sol–gel process. The characteristic bands of PEG at 2875, 1455, and 1351 $cm^{-1}$ have also disappeared, which indicates that the PEG has been removed completely. The appearance of a band at 1574 $cm^{-1}$ indicates the presence of Ba–O. The absorption peak at 1069 $cm^{-1}$ is due to the B–O stretching modes in the $BO_3^{3-}$ unit and the band observed at 1408 $cm^{-1}$ can be attributed to B–O extra-ring stretching modes.[21] The characteristic peaks of B–O at 1408 and 1069 $cm^{-1}$ gradually shift to lower frequency and decrease in intensity, which suggests that polycondensation reactions of the $H_3BO_3$ precursor have occurred.

The cross-linking reagent PEG200 plays an important role in the formation of a gel precursor with high homogeneity, and hence a low degree of aggregation of the resulting nanostructures,[28] in this system, as can be seen from the IR spectra in Figure 5. The hydrolysis and polycondensation velocity of the precursor is lowered in the presence of PEG200, which minimizes the aggregation of the nanostructures during calcination. In addition, the short chain polymer PEG200 also acts as a structure-directing agent in the formation of 1D β-BBO nanostructures. PEG200 is easily adsorbed on the surface of the colloid due to its uniform and ordered chain structure, as reported previously.[29] From a kinetic point of view, if the polymer adsorbs on the surface of the growing colloid, thereby

 © 2007 Wiley-VCH Verlag GmbH & Co. KGaA, Weinheim 

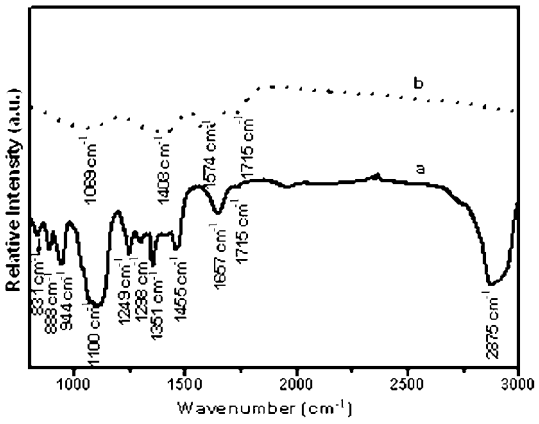


Figure 5. IR spectra of the samples in the sol–gel process: a) the precursor sol [$Ba(OAc)_2$ + $H_3BO_3$ + sorbitol + PEG); b) the precursor gel.

blocking this region, the growth of the colloid in one direction will be restricted. Therefore, the addition of PEG200 to the solution will modify the growth kinetics of the colloid, which finally leads to anisotropic growth of the samples. Previous research has provided many excellent samples where a polymer helps the growth of 1D nanostructures.[30] In the present work, PEG200 can efficiently adsorb to the surfaces of the precursor colloids, which leads to the growth of β-BBO along a certain direction.

We also performed a series of experiments to investigate the effect of the reaction conditions on the formation of β-BBO network-like nanostructures. We found that the use of PEG200 and the appropriate proportion of PEG200 and $H_2O$ had a decisive effect on the formation of network-like β-BBO nanostructures. Our experiment showed that only β-BBO nanoparticles with an average diameter of 80 nm, as shown in Figure 6 (a), are formed in water with no PEG200, which confirms its important role as a structure-directing agent. When the experiment was carried out in the absence of water the reaction did not initiate and therefore no β-BBO was obtained. This result suggests that the addition of water increases the solubility of barium acetate, sorbitol, and boric acid and facilitates the formation of the homogeneous sol and the gel. The appropriate proportion of PEG200 is also critical for the formation of 1D β-BBO nanostructures. When the experiment was done with a PEG200 and $H_2O$ ration 2:1 under otherwise identical conditions β-BBO shuttle-like nanostructures (Figure 6, b) were obtained. When the volume ratio of PEG200 and $H_2O$ was changed to 1:1, however, β-BBO network-like nanostructures were obtained. This phenomenon might occur because the different amount of PEG200 results in a different rate of hydrolysis and condensation of the precursors.[31] The addition of an appropriate amount of PEG200 could control the rate of hydrolysis and condensation of the precursors and prevent the early precipitation of the metal ions from solution, thus allowing the formation of a homogeneous gel.

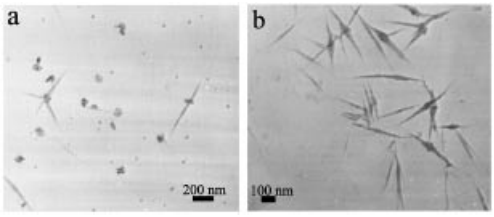


Figure 6. TEM images of as-prepared β-$BaB_2O_4$ samples formed in the presence of different amounts of PEG and $H_2O$: a) nanoparticles (without PEG); b) nanoshuttles (volume ratio of PEG and $H_2O$ of 2:1).

It is known that β-BBO crystals have a high transmissivity from 190 to 3500 nm. Figure 7 (a) shows the UV/Vis/NIR absorption data of the as-obtained products. It can be seen that β-BBO is transparent up to 200 nm (6.22 eV). The absorption spectra are relatively featureless, and the broad and overall constant low absorbance from 200 to 1600 nm is consistent with the reported values for single crystals,[31] thus demonstrating that it is transparent from ultraviolet to the mid-infrared regions. The room temperature PL spectrum of the β-BBO network-like nanostructures (Figure 7, b) was recorded at an excitation wavelength of 245 nm. It can be seen that the spectrum features a strong emission band at 377 nm (approx. 3.3 eV). Earlier reports have indicated that β-BBO exhibits a dominant peak near 355 nm (3.5 eV).[32] The luminescence of these β-BBO network-like nanostructures at 3.3 eV is an intrinsic property of β-BBO due to radiative annihilation of the self-trapped exciton.[32]

Generally, NLO materials lacking an inversion symmetry and containing a π-electron conjugated system should exhibit an efficient SHG. Furthermore, SHG is sensitive to the electronic properties of nanostructures of varying shape, size, composition, and spatial organization. The structure of β-BBO (Scheme 2) is made up of slightly distorted $(B_3O_6)^{3-}$ anionic hexagonal groupings with a threefold axis. These plane-like $(B_3O_6)^{3-}$ units are stacked along the *c* axis.[33] The boroxyl ring $(B_3O_6)^{3-}$ is the unit that contributes most to the material's non-linearity.

Powder SHG measurements of the β-BBO network-like nanostructures (Figure 8) were performed to determine its second-order nonlinear optical behavior and hopefully allow us to determine the relationship between their properties and morphologies. The β-BBO nanostructures were irradiated with the fundamental laser wavelength of 1064 nm and light transmitted through the β-BBO nanostructures was found to have a wavelength of 531–533 nm, thus proving the generation of frequency doubling. The results in Figure 8 reveal that the SHG efficiency of the β-BBO network-like nanostructures is 78% relative to that of the reference sample (urea). At the same time, the contrast experiment found that the SHG efficiency of β-BBO nanostructures is nearly 10 times that of the β-BBO nanoparticles with a diameter of about 80 nm prepared without PEG200. These results indicate that the morphology of the materials has an important effect on their nonlinear optical properties and that the SHG is sensitive to the electronic properties of nanostructures of varying shape, size, composition,

 © 2007 Wiley-VCH Verlag GmbH & Co. KGaA, Weinheim 

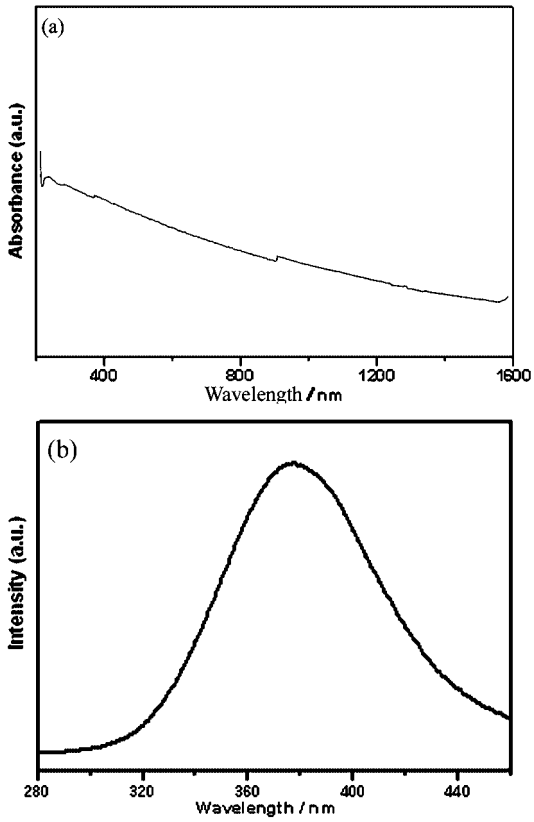


Figure 7. a) Absorption and b) PL spectra of β-$BaB_2O_4$ network-like nanostructures.

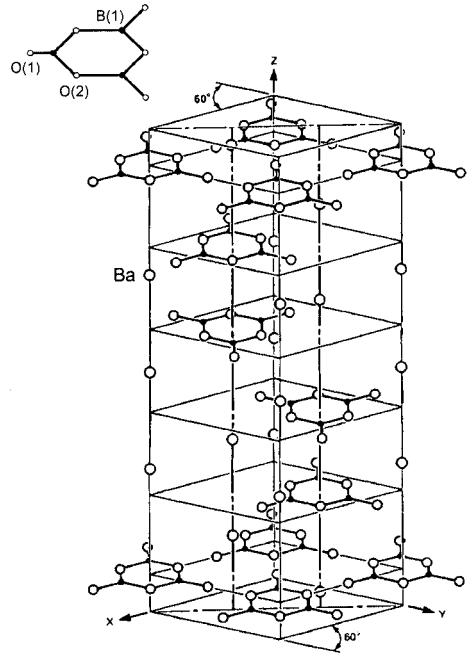


Scheme 2. Crystal structure of β-$BaB_2O_4$, which consists of nearly planar $(B_3O_6)^{3-}$ rings perpendicular to the polar axis that are bonded together through the barium atoms.

and spatial organization. For example, the measured second-order susceptibilities of ZnO nanowires are different from those of ZnO nanoribbons, which may be due to subtle changes in their structural or electronic properties.[34] This suggests that an in-depth investigation of the relationship between the structures and their second-order nonlinear optical susceptibilities is needed. Meanwhile, it is reasonable to suggest that some more complicated or special morphologies of β-BBO nanostructures with higher SHG intensity and wider transmissions might exist. This lays the groundwork for possible practical applications of nonlinear optical nanomaterials by replacing their single crystalline counterparts, and this kind of work on nonlinear optical nanomaterials provides new physical insights, which will be helpful to researchers in applied physics. Thus, there is still a long way to go in synthesizing nonlinear optical nanomaterials and studying their optical properties in the future.

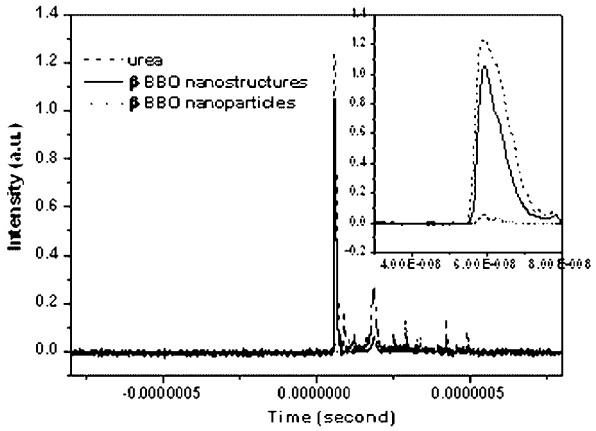


Figure 8. Powder SHG measurements of β-$BaB_2O_4$ network-like nanostructures, β-$BaB_2O_4$ nanoparticles, and reference sample urea. The inset is a high-magnification image.

## Conclusions

In summary, a sol–gel method using the polymer PEG200 as structure-directing agent has been successfully used to synthesize β-BBO network-like nanostructures on a large scale. PEG200 plays an important role in the formation of β-BBO network-like nanostructures. This method has a lot of merits, such as not requiring complicated procedures and a short processing time. Investigations into the optical properties of β-BBO network-like nanostructures reveal that they have a wide transparency range from 200 to 1600 nm and a strong PL emission. The SHG efficiency of β-BBO nanostructures is close to that of urea and larger than that of β-BBO nanoparticles. Consequently, the fabrication and study of different β-$BaB_2O_4$ nanostructures has revealed the existence of a profound shape/property relationship and the potential promise for their application in the photoelectronics industry and as nonlinear optical devices.

## Experimental Section

In a typical experiment, 6 mL of an aqueous solution containing barium acetate (0.25 g, 1 mmol), sorbitol (0.18 g, 1 mmol), and bo-

 © 2007 Wiley-VCH Verlag GmbH & Co. KGaA, Weinheim 

ric acid (0.13 g, 2 mmol) was put in a conical flask and stirred with a magnetic stirrer until a transparent solution had formed. This solution was then mixed with 6 mL of polyethylene glycol (PEG200, $M_w$ = 200), in which the volume ratio of PEG200 and water was 1:1, and transferred into a 15-mL Teflon-lined stainless-steel autoclave. The mixed solution was kept at 180 °C for 12 h to homogenize the precursor sol. After the reaction was complete, the solution was heated to 330 °C for 5 h to form a homogeneous gel and then to 800 °C for 2 h under oxygen. The resultant white products were collected and rinsed several times with distilled water and absolute ethanol, and then dried under vacuum at 40 °C for 4 h.

The samples were characterized by X-ray powder diffraction (XRD) with a Japan Rigaku D/max rA X-ray diffractometer equipped with graphite-monochromated high-intensity Cu-$K_\alpha$ radiation ($\lambda$ = 1.54178 Å) in the $2\theta$ range from 10° to 70°. The transmission electron microscopy (TEM) images were recorded with a Hitachi Model H-800 instruments with a tungsten filament, using an accelerating voltage of 200 kV. The high-resolution transmission electron microscopy (HRTEM) images were recorded with a JEOL-2010 TEM at an acceleration voltage of 200 kV. The field emission scanning electron microscopy (FE-SEM) images were recorded with a JEOL JSM-6700F SEM. X-ray photoelectron spectroscopy (XPS) was performed with an ESCALAB MKII with Mg-$K_\alpha$ radiation ($hv$ = 1253.6 eV) as the excitation source. The binding energies obtained in the XPS spectral analysis were corrected for specimen charging by referencing the C 1s peak to 284.6 eV. FT-IR absorption spectra were recorded with a Nicolet FT-IR-170SX spectrometer in the range 800–3000 $cm^{-1}$ at room temperature, in transmission mode in a KBr pellet. Absorption spectra were recorded with a Shimadzu UV-365 UV/Vis-NIR Recording Spectrophotometer. The room-temperature photoluminescence (PL) spectra were recorded with a Jobin Yvon–Labram Steady-State/Lifetime Spectrofluorometer with an HeCd laser. The second-order nonlinear optical intensities were estimated for powder samples with a diameter of 76–154 μm in the form of a pellet. The thickness of each pellet was about 0.8 mm. The experimental arrangement for the nonlinear optical properties utilizes an OPG pumped by a PC2143 series laser at a repetition rate of 10 Hz. The selected wavelength is 1064 nm. After the selection of the wavelength, the laser beam is split into two parts, one of which is used to generate the second harmonic signal in the reference (urea pellet).

## Acknowledgments

This work was financially supported by the National Nature Science Foundation of China (No. 20621061) and the State Key Project of Fundamental Research of Nanomaterials and Nanostructures (2005CB623601).

[1] L. F. Weaver, C. S. Petty, D. Eimerl, *J. Appl. Phys.* **1990**, *68*, 2589–2598.
[2] M. H. Dunn, M. Ebrahimzadeh, *Science* **1999**, *286*, 1513–1517.
[3] C. C. Chen, B. Wu, A. Jiang, G. You, *Science Sin. B* **1985**, *28*, 235–243.
[4] E. Delahaye, N. Tancrez, T. Yi, I. Ledoux, J. Zyss, S. Brasselet, R. Clément, *Chem. Phys. Lett.* **2006**, *429*, 533–537.
[5] T. Yi, R. Clément, C. Haut, L. Catala, T. Gacoin, N. Tancrez, I. Ledoux, J. Zyss, *Adv. Mater.* **2005**, *17*, 335–338.
[6] H. Nakatani, W. R. Bosenberg, L. K. Cheng, C. L. Tang, *Appl. Phys. Lett.* **1988**, *53*, 2587–2589.
[7] M. I. Stockman, D. J. Bergman, C. Anceau, S. Brasselet, J. Zyss, *Phys. Rev. Lett.* **2004**, *92*, 057402.
[8] H. Kouta, S. Imoto, Y. Kuwano, *J. Cryst. Growth* **1993**, *128*, 938–944.
[9] R. S. Feigelson, R. J. Raymeker, R. K. Route, *J. Cryst. Growth* **1989**, *97*, 352–366.
[10] J. Hu, T. W. Odom, C. M. Lieber, *Acc. Chem. Res.* **1999**, *32*, 435–445.
[11] Y. N. Xia, P. D. Yang, Y. G. Sun, Y. Y. Wu, B. Mayer, B. Gates, Y. D. Yin, F. Kim, H. Q. Yan, *Adv. Mater.* **2003**, *15*, 353–389.
[12] Y. F. Zhou, M. C. Hong, Y. Q. Xu, B. Q. Chen, C. Z. Chen, Y. S. Wang, *J. Cryst. Growth* **2005**, *276*, 478–484.
[13] A. Magrez, E. Vasco, J. W. Seo, C. Dieker, N. Setter, L. Forró, *J. Phys. Chem. B* **2006**, *110*, 58–61.
[14] I. Pribošič, D. Makovec, M. Drofenik, *Chem. Mater.* **2005**, *17*, 2953–2958.
[15] M. D. McMahon, R. Lopez, R. F. Haglund, *Phys. Rev. B* **2006**, *73*, 041401.
[16] R. C. Johnosn, J. T. Li, J. T. Hupp, G. C. Scatz, *Chem. Phys. Lett.* **2002**, *356*, 534–540.
[17] A. Podlipensky, J. Lange, G. Seifert, H. Graener, I. Cravetchi, *Opt. Lett.* **2003**, *28*, 716–718.
[18] E. C. Hao, G. C. Schatz, R. C. Johnson, J. T. Hupp, *J. Chem. Phys.* **2002**, *117*, 5963–5966.
[19] S. C. Sabharwal, S. K. Kulkarni, B. D. Padalia, *J. Mater. Sci.: Mater. Electronics* **2000**, *11*, 325–329.
[20] P. Ney, M. D. Fontana, K. Polgar, *J. Phys.: Condens. Networks* **1998**, *10*, 673–681.
[21] S. Hirano, T. Yogo, K. Kikuta, K. Yamagiwa, *J. Am. Ceram. Soc.* **1992**, *75*, 1697–1700.
[22] U. Moryc, W. S. Ptark, *J. Mol. Struct.* **1999**, *512*, 241–249.
[23] H. G. Yang, H. C. Zeng, *J. Phys. Chem. B* **2003**, *107*, 12244–12255.
[24] L. J. Q. Maria, M. I. B. Bernardi, A. R. Zanatta, A. C. Hernandes, V. R. Martelaro, *Mater. Sci. Eng. B* **2004**, *107*, 33–38.
[25] B. Guo, Z. L. Liu, L. Hong, H. X. Jiang, *Surf. Coat. Technol.* **2005**, *198*, 24–29.
[26] Y. Djaoued, P. V. Ashrit, S. Badilescu, R. Bruning, *J. Sol-Gel Sci. Technol.* **2003**, *28*, 235–244.
[27] G. Montanari, A. L. Costa, S. Albonetti, *J. Sol-Gel Sci. Technol.* **2005**, *36*, 203–211.
[28] H. L. Su, Y. Xie, P. Gao, Y. J. Xiong, Y. T. Qian, *J. Mater. Chem.* **2001**, *11*, 684–686.
[29] Z. Q. Li, Y. J. Xiong, Y. Xie, *Inorg. Chem.* **2003**, *42*, 8105–8109.
[30] Y. J. Xiong, Y. Xie, C. Z. Wu, J. Yang, Z. Q. Li, F. Xu, *Adv. Mater.* **2003**, *15*, 405–408.
[31] T. Yogo, K. Kikuta, K. Niwa, M. Ichida, A. Nakamura, S. Hirano, *J. Sol-Gel Sci. Technol.* **1997**, *9*, 201–209.
[32] I. N. Ogorodnikov, V. A. Pustovarov, A. V. Kruzhalov, L. I. Isaenko, M. Kirm, G. Zimmerer, *Phys. Solid State* **2000**, *42*, 1846–1853.
[33] D. Eimerl, L. Davis, S. Velsko, *J. Appl. Phys.* **1987**, *62*, 1968–1983.
[34] J. C. Johnson, K. P. Knutsen, H. Yan, M. Law, Y. F. Zhang, P. D. Yang, R. J. Saykally, *Nano. Lett.* **2004**, *4*, 197–204.

Received: October 15, 2006
Published Online: March 16, 2007

 © 2007 Wiley-VCH Verlag GmbH & Co. KGaA, Weinheim 

DOI: 10.1002/ejic.200601097

# Influence of a Large σ-Donor Ligand on Structural and Catalytic Properties of Di-Iron Compounds Related to the Active Site of Fe-Hydrogenase – A DFT Investigation

**Claudio Greco,[a] Maurizio Bruschi,[b] Piercarlo Fantucci,[a] and Luca De Gioia*[a]**

**Keywords:** Hydrogenases / Biomimetic chemistry / Catalytic $H_2$ evolution / Density functional calculations / Iron

The complex $(S_2C_3H_6)[Fe_2(CO)_5P(NC_4H_8)_3]$ (**A**), a recently synthesized functional model of the active site of Fe-hydrogenases, is able to electrocatalyze proton reduction, leading to molecular hydrogen evolution. Experimental results suggested that the presence of the electron donor $P(NC_4H_8)_3$ ligand in **A** could favor the formation of a μ-CO species similar to that observed in the enzymatic cluster. However, insight into the structural features of key catalytic intermediates deriving from reduction and protonation of **A** was still lacking. Here we present results obtained using density functional theory to evaluate structures, relative stabilities, and spectroscopic properties of several species relevant for the electrocatalytic $H_2$ evolving process. The results enabled us to unravel the structure of the μ-CO complex experimentally detected after monoelectronic reduction of **A**. Moreover, we show that the introduction of the large electron-donor ligand $P(NC_4H_8)_3$ in the biomimetic complex does not favour the stabilization of terminal-hydrido adducts, which are expected to be very reactive in terms of $H_2$ production. The comparison of our findings with previous theoretical and experimental results obtained on similar model complexes suggests that the introduction of an electron donor ligand as good as $P(NC_4H_8)_3$, but less sterically demanding, could represent a better choice to facilitate the formation of μ-CO complexes more closely resembling the structure of the enzymatic cluster.

(© Wiley-VCH Verlag GmbH & Co. KGaA, 69451 Weinheim, Germany, 2007)

## Introduction

The possibility of producing molecular hydrogen through eco-compatible, hydrocarbon-independent processes has been stimulating chemists towards the synthesis of inexpensive catalytic materials that could replace the currently used platinum-containing electrocatalysts.[1] The search for cheaper, but still efficient catalysts could take advantage from the study of hydrogenases,[2] which are metallo-enzymes that are able to catalyze the evolution of molecular hydrogen at high rates starting from protons and electrons.

Three classes of hydrogenases have been characterized so far: Ni–Fe hydrogenases, which include both iron and nickel atoms as metal centers of functional importance, and two classes of iron-dependent enzymes, i.e. the "iron-sulfur-cluster-free" hydrogenases,[3] and another group of proteins containing $Fe_xS_x$ clusters, commonly referred to as "Iron-only" or Fe-hydrogenases. X-ray crystallographic studies on Fe-hydrogenases from *C. pasteurianum*[4] and *D. desulfuricans*[5] have shown that the active site of these enzymes includes an $Fe_2S_2$ sub-site bearing CO and $CN^-$ ligands. The iron atoms of the sub-site are bridged by two sulfur atoms of a 1,3-propanedithiolato (pdt) or a related bis(thiomethyl)amino unit. One of the iron atoms shares a cysteinyl sulfur ligand with a classical $Fe_4S_4$ cluster; the resulting iron–sulfur complex is usually referred to as the H-cluster. Experimental results[6] indicate that the unprotonated, $Fe^{I}$-$Fe^{II}$ form of the H-cluster di-iron subsite should correspond to a catalytically active state characterized by the presence of a carbonyl ligand bridging the two iron centers. As shown in Scheme 1, the coordination site *trans* to the bridging CO remains vacant, and this observation suggests that protons and dihydrogen could occupy such a position during the catalytic process. Upon monoelectronic reduction of the H-cluster, the bridging CO moves to a terminal position, but it still remains localized in the region of space between the iron ions (see Scheme 1).[6]

The above-mentioned studies have stimulated experimental chemists towards the synthesis of organometallic models that could reproduce the main structural and functional features of the H-cluster.[7] Unfortunately, the biomimetic clusters obtained so far fail to reproduce the precise orientation of ligands found in the H-cluster, a fact that is expected to be at the basis of the reduced catalytic efficiency of synthetic assemblies. For example, in the complex (μ-

[a] Department of Biotechnology and Biosciences, University of Milano-Bicocca,
Piazza della Scienza 2, 20126 Milano, Italy
Fax: +39-02-64483478
E-mail: luca.degioia@unimib.it
[b] Department of Environmental Sciences, University of Milano-Bicocca,
Piazza della Scienza 1, 20126 Milano, Italy

 © 2007 Wiley-VCH Verlag GmbH & Co. KGaA, Weinheim 

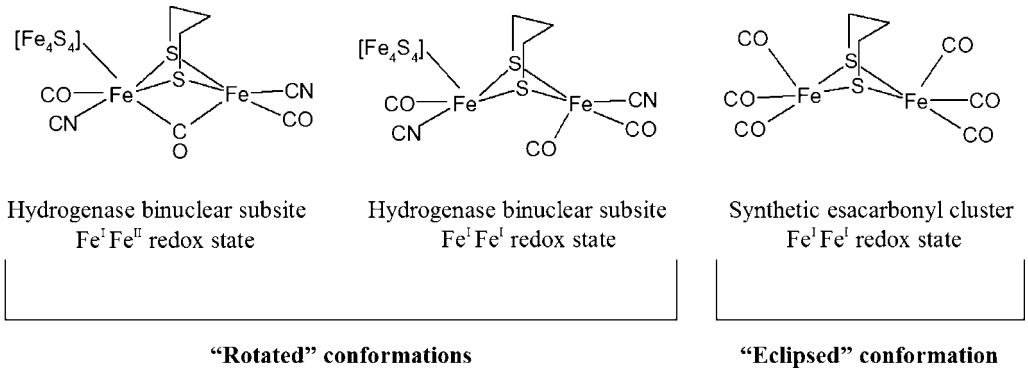


Scheme 1. Structures of the Fe-hydrogenase binuclear subsite in two different redox states, and geometry of the synthetic complex (μ-pdt)[Fe(CO)$_3$]$_2$.

pdt)[Fe(CO)$_3$]$_2$, the simplest functional model of the active site of Fe-hydrogenases, all the carbonyl groups are in the terminal position.[7h] Such an arrangement of ligands will be referred to as the "eclipsed conformation," as opposed to the "rotated conformation" that can be observed in Fe-hydrogenases (Scheme 1).

Theoretical studies have been carried out to understand the causes of the structural difference between synthetic models and the enzyme active site.[8,9] It turned out that the presence of good electron donor ligands bound to the metal centers can help in stabilizing the rotated conformation of di-iron clusters. Such observations have been recently taken into account by Hou and collaborators, who probed the effects of the introduction of tris(*N*-pyrrolidinyl)phosphane, a very good donor ligand, on the structural and functional properties of the synthetic species (μ-pdt)[Fe$_2$(CO)$_5$P(NC$_4$H$_8$)$_3$] (**A**).[10] It turned out that **A** (Scheme 2) is characterized by eclipsed conformation, while monoelectronic reduction leads to the formation of a μ-CO species that was tentatively assigned, on the basis of IR data, to a rotated conformer closely resembling the unprotonated form of the H-cluster (species **A2**$^-$, Scheme 2). Nothing is known about the regiochemistry of protonation of this synthetic cluster, an issue that is expected to be relevant to rationalize the electrocatalytic properties shown by (μ-pdt)[Fe$_2$(CO)$_5$P(NC$_4$H$_8$)$_3$] (for details on the mechanism proposed by Hou and collaborators for hydrogen evolution mediated by the di-iron assembly, see Scheme 2). In order to shed light on the structure-function relationships in **A**, we carried out a DFT investigation of structures, spectroscopic properties, and relative stabilities of several plausible isomers of this biomimetic compound, both in its protonated and unprotonated forms. Results allowed us to obtain a detailed structural characterization of key intermediate species, and a better understanding of the electrocatalytic cycle. DFT results are expected to be helpful also for the design of better bioinspired electrocatalytic compounds.

## Methods

DFT calculations have been carried out using the pure functional BP86[11] in conjunction with a valence triple-ζ basis set with polarization on all atoms (TZVP).[12]

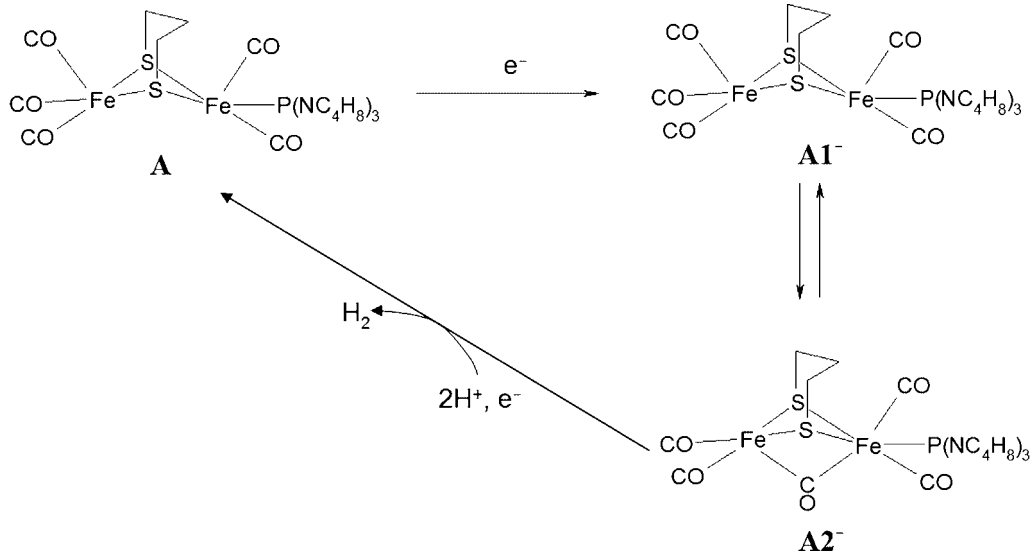


Scheme 2. The electrocatalytic mechanism of $H_2$ evolution mediated by (μ-pdt)[Fe$_2$(CO)$_5$P(NC$_4$H$_8$)$_3$], as proposed in ref.[10]

 © 2007 Wiley-VCH Verlag GmbH & Co. KGaA, Weinheim 

Calculations have been carried out with the TURBOMOLE 5.7 suite[13] applying the resolution-of-the-identity technique.[14]

Stationary points of the energy hypersurface have been located by means of energy gradient techniques and full vibrational analysis has been carried out to further characterize each stationary point. In order to characterize isomeric forms, DFT optimizations were repeated several times, starting from different initial geometries.

Free energy ($G$) values have been obtained from the electronic SCF energy considering three contributions to the total partition function ($Q$), namely $q_{translational}$, $q_{rotational}$, $q_{vibrational}$, under the assumption that $Q$ may be written as the product of such terms.[15] In order to evaluate enthalpy and entropy contributions, the value for the temperature, pressure, and scaling factor for the SCF wavenumbers have been set to 298.15 K, 1 bar, and 0.9914, respectively. Rotations have been treated classically and vibrational modes described according to the harmonic approximation.

The optimized structures of the complexes reported in the present study always correspond to low spin states; high spin states are characterized by higher energies (not shown), as expected considering the characteristics of the ligands forming the coordination environment of the metal atoms.

The relative energies discussed in the present work are Gibbs free energies where the contributions described above are taken into account. The effect of the solvent (acetonitrile, $\varepsilon$ = 36.64) has been evaluated according to the COSMO approach.[16]

## Results and Discussion

For the sake of clarity, hereafter experimental complexes will be designated with capital bold letters, while computational models will be referred to using lower case bold letters. As for the nomenclature of the iron atoms, the metal center bound to the phosphane ligand will be referred to as the "proximal iron" ($Fe_p$), while the other iron ion will be named "distal" ($Fe_d$).

In order to validate the computational approach adopted in this paper (BP86/TZVP, see Methods), we initially opti-

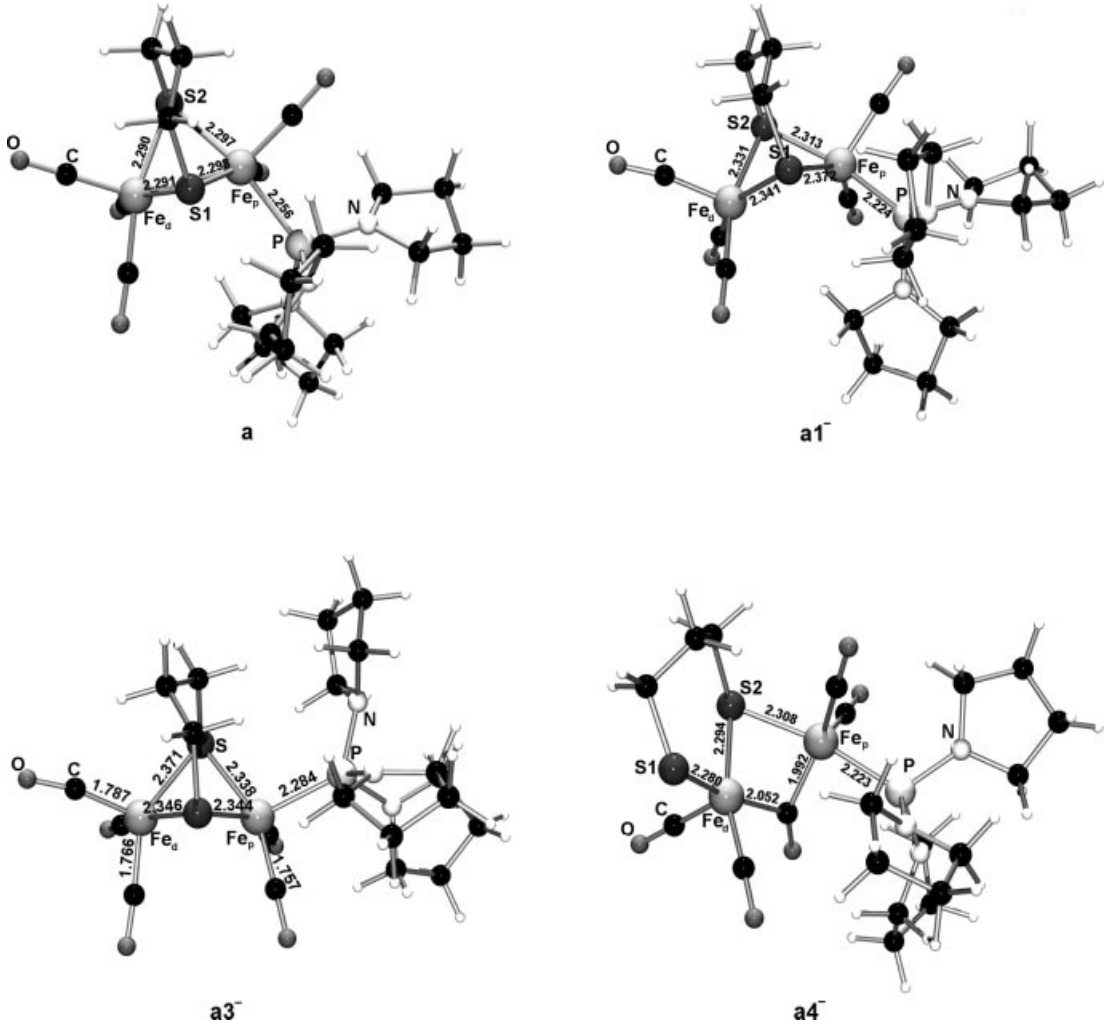


Figure 1. Optimized geometries of complexes **a**, **a1**$^-$, **a3**$^-$ and **a4**$^-$; $S$ = 0 and 1/2 for neutral and monoanionic complexes, respectively. Selected distances are given in Å.

 © 2007 Wiley-VCH Verlag GmbH & Co. KGaA, Weinheim 

mized the geometry of complex **a**, and compared the resulting structure (see Figure 1) with its experimental counterpart. As shown in Table 1, the differences in bond lengths between **a** and **A** never exceed 0.059 Å. Similarly good results are obtained when bond angles are considered: in fact, the maximum difference between calculated and experimental values is very low (4.7 deg; for the $Fe_p$–$Fe_d$–C angle, the latter atom belonging to the carbonyl group *trans* to the S2 atom of pdt. See Figure 1).

Table 1. Comparison between experimental and computed bond lengths for complex **A**. Distances in Å.

| Bond | Experimental bond lengths (**A**) | Calculated bond lengths (**a**) | Difference |
|---|---|---|---|
| $Fe_d$–$Fe_p$ | 2.5527 | 2.611 | 0.0583 |
| $Fe_p$–S | 2.2418; 2.2675 | 2.279; 2.300 | 0.0372; 0.0325 |
| $Fe_d$–S | 2.2542; 2.2615 | 2.286; 2.297 | 0.0318; 0.0355 |
| $Fe_p$–P | 2.2563 | 2.286 | 0.0297 |
| P–N | 1.662; 1.670; 1.682 | 1.711; 1.721; 1.731 | 0.049; 0.051; 0.049 |

An excellent correlation between computed and experimental CO stretching frequencies was also found, confirming that the BP86/TZVP level of theory is well suited to describe this class of compounds.[17] In fact, linear regression analysis gives rise to a $R^2$ value as large as 0.997 (Figure 2).

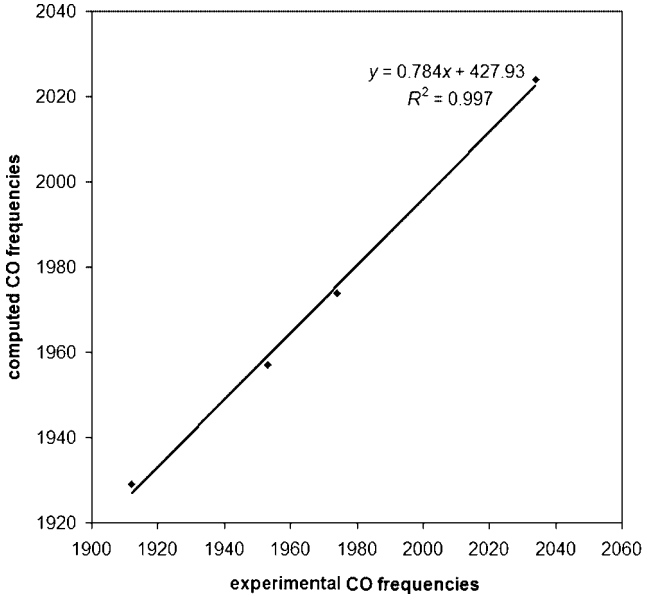


Figure 2. Linear fitting of calculated and experimental CO stretching frequencies for species **A**.

## Structural Characterization of the Experimentally Observed Monoanionic Derivatives

The first optimized monoanionic isomer considered as a plausible product of the monoelectron reduction of **a** is **a1**$^-$, which shares a high degree of structural similarity with the parent complex **a**, the main differences being restricted to a limited decrease of the $Fe_p$–P bond length, while all the other bonds are slightly elongated in **a1**$^-$ (see Figure 1).

Hou et al.[10] proposed that **A1**$^-$ could undergo a conformational rearrangement leading to a μ-CO species structurally related to the enzymatic $Fe_2S_2$ subsite (complex **A2**$^-$, see Scheme 2). Prompted by these considerations, we carried out the geometry optimization of $(CO)_2Fe_d(\mu\text{-pdt})(\mu\text{-CO})Fe_p(CO)_2[P(NC_4H_8)_3]$ (**a2**$^-$), a species in which one of the terminal carbonyls bound to $Fe_d$ in **a1**$^-$ has moved to a bridging position. However, it turned out that **a2**$^-$ (structure not shown) corresponds to a third-order saddle point on the potential energy surface (imaginary frequencies: 47.95i, 29.72i, 14.91i $cm^{-1}$). Moreover, **a2**$^-$ is 12.5 kcal $mol^{-1}$ less stable than **a1**$^-$. DFT optimizations started from slightly different initial geometries converged on **a1**$^-$ or **a2**$^-$. Taken as a whole, these results indicate that **a2**$^-$ cannot correspond to the μ-CO species experimentally observed (**A2**$^-$).

In principle, another isomer closely resembling the structure of the unprotonated enzymatic cofactor could be present in solution: in fact, a terminal CO bound to $Fe_p$ could move to a bridging position, thus giving place to $(CO)_3Fe_d(\mu\text{-pdt})(\mu\text{-CO})Fe_p(CO)[P(NC_4H_8)_3]$, see Scheme 3. However, all the attempts to obtain such a geometry as a result of DFT optimization failed: several calculations were carried out starting from slightly different guess structures, but all of them fell back towards the **a1**$^-$ conformation. This indicates that a minimum corresponding to such a μ-CO geometry does not exist on the PES of $(\mu\text{-pdt})[Fe_2(CO)_5P(NC_4H_8)_3]$. The instability of this structure can be ascribed to the presence of a μ-CO group *trans* to another π-acid carbonyl ligand, and to a vacant coordination site.

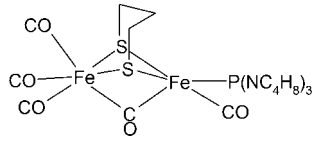


Scheme 3. Schematic structure of a hypothetical adduct showing rotated conformation.

Previous computational studies[18,19] have shown that the stabilization of rotated conformations in di-iron biomimetic complexes can be achieved positioning a good σ-donating group *trans* to the incipient μ-CO. In view of this observation, we have evaluated (i) if the sterically impeded ligand $P(NC_4H_8)_3$ can move to assume an apical position on $Fe_p$ in an eclipsed conformer, and (ii) if such a disposition of ligands on $Fe_p$ can favor the rotation of ligands around $Fe_d$. In fact, an eclipsed geometry showing an apical $P(NC_4H_8)_3$ ligand corresponds to an energy minimum structure (adduct **a3**$^-$, Figure 1). **a3**$^-$ is 4.1 kcal $mol^{-1}$ less stable than **a1**$^-$ due to the unfavorable interactions between the pyrrolidine rings of the phosphane ligand and the alkyl chain of pdt. These repulsive interactions played a relevant role in the optimization of the corresponding rotated species **a3-rotated**$^-$, see Scheme 4. In fact, the distortion of pdt geometry led one of its sulfur atoms to detach from the proximal

 © 2007 Wiley-VCH Verlag GmbH & Co. KGaA, Weinheim 

iron ion, a rearrangement accompanied by bridging-to-terminal movement of the μ-CO group, resulting in a four-coordinate $Fe_p$ atom (structure not shown).

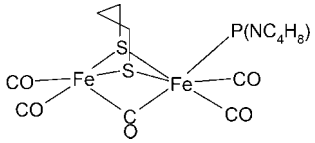


Scheme 4. Starting structure used for geometry optimization of **a3-rotated**$^-$.

The instability of μ-CO anionic complexes leaves unanswered the question of the nature of the spectroscopically characterized μ-CO species. Indeed, it was recently shown that hexacarbonyl di-iron complexes including a pdt ligand can assume a structure in which a sulfur atom of pdt has moved from a bridging to a terminal position;[20] such a rearrangement may allow one of the terminal CO ligands to become a μ-CO. Analysis of **a1**$^-$ suggests that this species might undergo a similar rearrangement: in fact, one of the Fe–S bonds ($Fe_p$–S1, 2.372 Å, see Figure 1) is significantly elongated with respect to the other three Fe–S bonds (2.313, 2.331, 2.341 Å). The weakening of the bonding interaction between $Fe_p$ and S1 could favor isomerization, giving place to the DFT-optimized species **a4**$^-$ (see Figure 1). Notably, this isomer is only slightly less stable (2.9 and 5.0 kcal mol$^{-1}$ when considering SCF energy differences and $\Delta G$ values, respectively) than **a1**$^-$; thus, these two adducts could be present simultaneously in solution, with **a1**$^-$ representing the main product of the monoelectronic reduction of **a**.

The co-existence of **a4**$^-$ and **a1**$^-$ is also supported by the comparison between the computed CO stretching frequencies of these two species and the experimental IR bands: in fact, the IR spectrum collected after electrochemical reduction of **a** is characterized by six distinct bands – five intense bands in the region between 1845 and 2015 cm$^{-1}$, and a weak absorption at lower wavenumbers (1778 cm$^{-1}$). In light of our computational results, we propose that the spectrum region above 1850 cm$^{-1}$ is dominated by the stretching modes of the five terminal carbonyls included in the main reduction product **a1**$^-$; the less stable **a4**$^-$ species is detectable thanks to its bridging CO group, whose predicted IR stretching frequency (1742 cm$^{-1}$) is located largely below 1845 cm$^{-1}$. All the other computed CO peaks from **a4**$^-$ fall in a narrow region between 1872 and 1953 cm$^{-1}$, where the most populated **a1**$^-$ isomer gives place to intense absorption bands. As a further support to this hypothesis, a very good correlation between the selected six computed IR frequencies and the corresponding experimental bands could be evidenced after linear regression fitting analysis ($R^2$ = 0.990, see Figure 3).

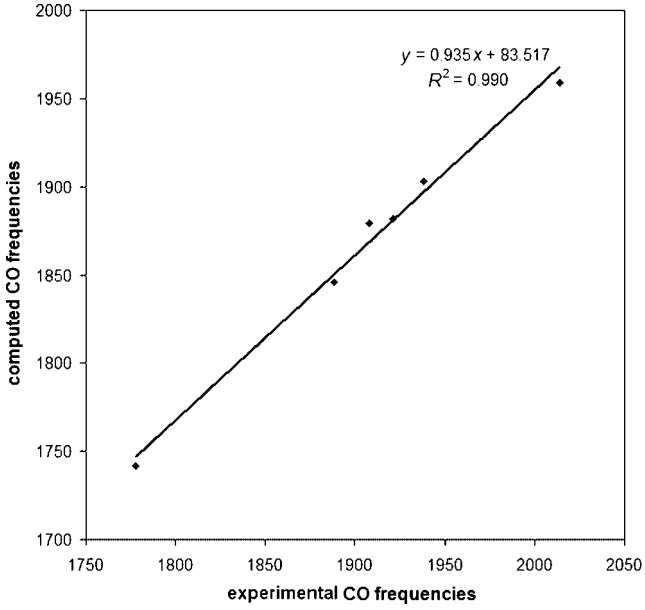


Figure 3. Linear fitting of the calculated and experimental CO frequencies for the anionic adducts coming from monoelectronic reduction of **A**.

## Protonation of Monoanionic Derivatives

In the electrocatalytic cycle, monoelectronic reduction of **A** should be followed by protonation of the resulting monoanionic complex. The regiochemistry of protonation can influence the efficiency of hydrogen evolution, as shown recently for the biomimetic di-iron compound $[Fe_2(S_2C_2H_4)(\mu\text{-CO})(H)(CO)(PMe_3)_4]^+$, which revealed that a hydrido ligand terminally bound to one of the iron ions is much more reactive than a μ-H group.[21] This result supports the hypothesis that the formation of a terminal hydrido *trans* to a μ-CO or a semi-bridging carbonyl is crucial to explain the very high efficiency of Fe-hydrogenases (Scheme 5). However, in the case of simple Fe-hydrogenase functional models such as (μ-pdt)$[Fe(CO)_3]_2$, formation of μ-H derivatives (as opposed to terminal-hydrido adducts) is highly favored.[20a,22]

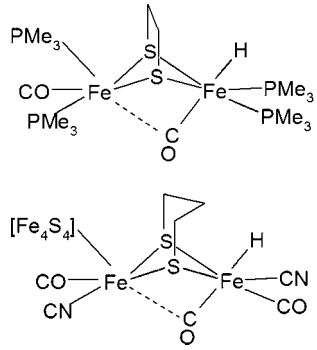


Scheme 5. Schematic structure of the synthetic complex obtained by Rauchfuss et al.,[21] and hypothetical structural features of the corresponding state of the active site of Fe-hydrogenase.

In view of these observations, we have studied the effects of the introduction of the donor ligand $P(NC_4H_8)_3$ on the relative stabilities of monoprotonated pentacarbonyl diiron complexes. To this end, we carried out geometry optimization of several different isomers, whose optimized structures are collected in Figure 4.

 © 2007 Wiley-VCH Verlag GmbH & Co. KGaA, Weinheim 

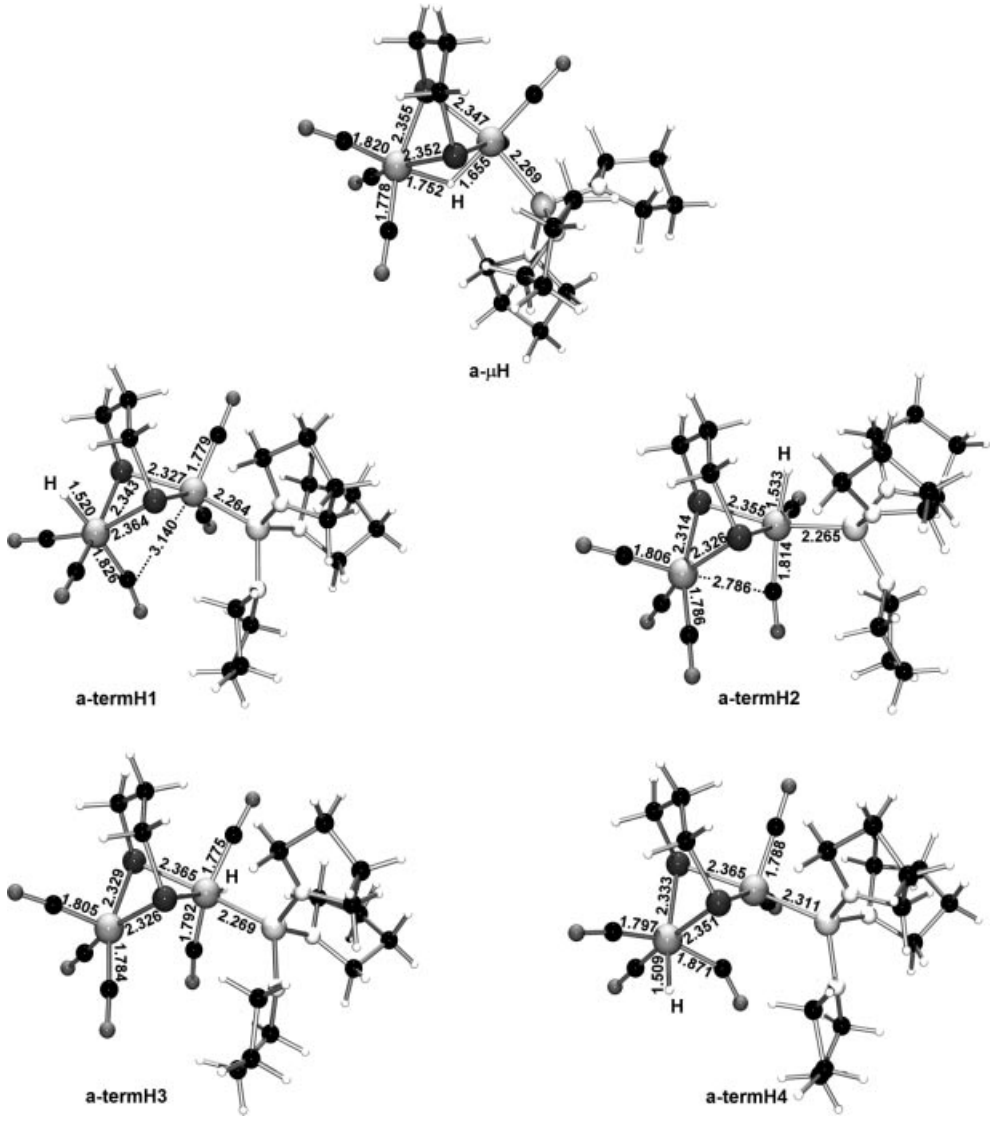


Figure 4. Optimized geometries of complexes **a-μH**, **a-termH1**, **a-termH2**, **a-termH3**, and **a-termH4**; for all these species $S = 1/2$. Selected distances are given in Å. The hydrido group has been labelled for the sake of clarity.

In line with previous observations regarding the protonated form of (μ-pdt)[Fe(CO)$_3$]$_2$,[20] the μ-H species **a-μH** is more stable than all the terminal-hydrido adducts considered in the present study (see Table 2 for a summary of the calculated $\Delta G$ values). Particularly relevant in the context of relative stabilities analysis are the cases of **a-termH1** and **a-termH2**: these complexes feature a terminal hydrido ligand *trans* to a carbonyl ligand, and can thus be considered the isomers with greater similarity to the most plausible protonated form of the enzymatic di-iron subsite (Figure 4). However, the free energy difference between **a-termH1** and **a-μH** is large ($\Delta G_{\mathbf{a\text{-}termH1-a\text{-}\mu H}}$ = 11.3 kcal mol$^{-1}$) and, more importantly, it is even larger than the energy difference between the corresponding monoprotonated hexacarbonyl complexes (**b-μH** and **b-termH**, see Figure 5; $\Delta G_{\mathbf{b\text{-}termH1-b\text{-}\mu H}}$ = 8.2 kcal mol$^{-1}$). The increase in the energy gap observed going from the hexacarbonyl to the pentacarbonyl species is due to steric repulsion between the carbonyl *trans* to the terminal hydrido in **a-termH1** and the phosphane ligand bound to Fe$_p$. In fact, this CO group can be considered a terminal carbonyl in the pentacarbonyl complex, since the Fe$_p$–C distance is as long as 3.140 Å, while the corresponding interatomic distance in (μ-pdt)[Fe(H)(CO)$_3$]$_2$ is significantly shorter (2.856 Å).

Table 2. Free energy difference between the μ-H adduct **a-μH** and the various terminal-hydrido isomers considered in this paper.

| Adduct | Free energy difference relative to **a-μH** [kcal mol$^{-1}$] |
|---|---|
| **a-termH1** | 11.3 |
| **a-termH2** | 10.3 |
| **a-termH3** | 11.2 |
| **a-termH4** | 18.0 |

When **a-termH2** is considered, a large energy difference relative to **a-μH** is also observed ($\Delta G_{\mathbf{a\text{-}termH1-a\text{-}\mu H}}$ = 10.3 kcal mol$^{-1}$). In this case, however, the CO *trans* to the

 © 2007 Wiley-VCH Verlag GmbH & Co. KGaA, Weinheim 

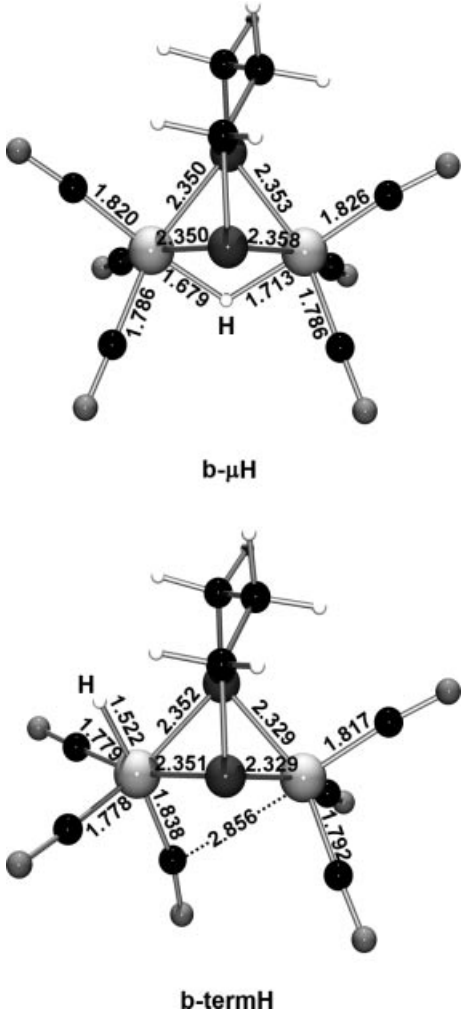


Figure 5. Optimized geometries of complexes **b-μH** and **b-termH**; for these two species $S = 1/2$. Selected distances are given in Å. The hydrido group has been labelled for the sake of clarity.

terminal hydrido on $Fe_p$ remains closer to the second iron center ($Fe_d$–C bond length: 2.786 Å, see Figure 4), a behavior that is again correlated with the repulsive interactions between the carbonyl ligand and the pyrrolidine rings included in $P(NC_4H_8)_3$.

To complete the characterization of the monoprotonated species, we optimized also the structures of two adducts bearing a hydrido *trans* to the sulfur atoms of pdt (**a-termH3** and **a-termH4**, see Figure 4); both of them show free energy gaps larger than 11 kcal mol$^{-1}$, when compared to **a-μH**.

In summary, our computational results demonstrate that the formation of terminal-hydrido ligands should have small, if any, importance in the electrocatalytic cycle mediated by (μ-pdt)[$Fe_2(CO)_5P(NC_4H_8)_3$]. Moreover, the comparison between theoretical data obtained for (μ-pdt)[$Fe(CO)_3]_2$ and (μ-pdt)[$Fe_2(CO)_5P(NC_4H_8)_3$] indicates that the introduction of the electron donor ligand $P(NC_4H_8)_3$ does not lead to stabilization of terminal-hydrido complexes.

### Diprotonated Neutral Complexes

Experimental data show that (μ-pdt)[$Fe_2(CO)_5P(NC_4H_8)_3$] undergoes two reduction and two protonation steps to allow $H_2$ evolution and closure of the catalytic cycle. Formation of diprotonated neutral species could thus have a role in electrocatalysis. In view of this, we studied neutral species derived from reduction and protonation of neutral, monoprotonated model complexes. In particular, we investigated the possible outcome of monoelectronic reduction and protonation of both a μ-H adduct (**a-μH**), and a terminal-hydrido compound (**a-termH1**).

It is important to note that the catalytic cycle of Fe-hydrogenases has been proposed to involve diprotonated intermediates in which a $H_2$ molecule is terminally bound to one of the iron centers in the binuclear subsite[23] (see Scheme 6). However, reduction and protonation of both **a-μH** and **a-termH1** does not lead to $H_2$-bound complexes: the addition of one electron and one proton to **a-μH** led to **a-$H_2$** (Figure 6), in which both hydrogen atoms, which are separated by 1.78 Å, occupy terminal positions on the two iron centers.

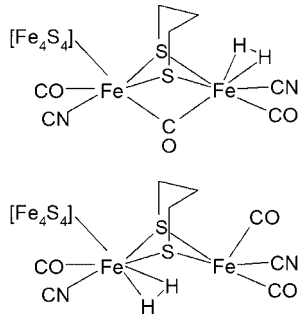


Scheme 6. The two possible versions of the $H_2$ bound H-cluster, as reported in ref.[23]

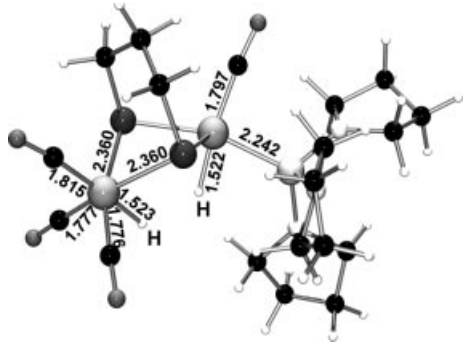


Figure 6. Optimized geometry of complex **a-$H_2$**, a diprotonated neutral complex in the singlet state ($S = 0$). Selected distances are given in Å. Labels are added only to metal-bound hydrogen atoms.

Interestingly, during the optimization of a species obtained by mono-electron reduction and protonation of **a-termH1**, the release of $H_2$ from the complex was observed. This result corroborates the hypothesis that the formation of **a-termH1** during electrocatalysis would give rise to a very efficient $H_2$ evolving route. Therefore, efforts aiming at the stabilization of pentacarbonyl diiron adducts bearing a ter-

 © 2007 Wiley-VCH Verlag GmbH & Co. KGaA, Weinheim 

minal hydrido ligand could assume great relevance for the development of better electrocatalytic materials.

## Conclusions

In the first part of this work, we investigated the structural properties of several plausible isomers obtained by monoelectron reduction of the biomimetic complex (μ-pdt)[$Fe_2(CO)_5P(NC_4H_8)_3$]. Our computational study allowed us to show that complexes **a1**$^-$ and **a4**$^-$ should coexist in solution. The former adduct corresponds to a "classical" eclipsed conformation, while the second one is a μ-CO species structurally not related to the Fe-hydrogenases binuclear subsite. Therefore, the possibility that a rotated conformer closely resembling the H-cluster geometry can be formed during electrocatalysis is excluded. The ineffectiveness of $P(NC_4H_8)_3$ in stabilizing the rotated form of the synthetic assembly can be rationalized in light of recent theoretical results regarding monosubstituted derivatives of (μ-pdt)[$Fe(CO)_3$]$_2$ (i.e., adducts in which only one carbonyl has been replaced by a good σ-donor).[18,19] In fact, it has been shown that a good electron-donating ligand (L) is able to stabilize the rotated conformation of (μ-pdt)[$Fe(CO)_3$-$Fe(CO)_2(L)$]$^-$ complexes, when L is *trans* to the incipient bridging CO group.[18,19] Nevertheless, if L corresponds to $P(NC_4H_8)_3$, it is not possible to place the σ-donor *trans* to the incipient μ-CO, since in such a configuration the alkyl chain of pdt would cause steric clashes with the pyrrolidine rings included in $P(NC_4H_8)_3$. These observations suggest that the introduction of an electron donor ligand as good as $P(NC_4H_8)_3$, but less sterically demanding, could represent a better choice to facilitate the formation of more stable rotated adducts.

In the second part of the study, we have shown that the most stable protonated, uncharged form of (μ-pdt)-[$Fe_2(CO)_5P(NC_4H_8)_3$] corresponds to a μ-H adduct (**a-μH**), and that terminal-hydrido complexes – which turned out to be highly reactive according to DFT results – are not involved in the electrocatalytic cycle. In fact, all the terminal-hydrido species here investigated are less stable than the hydrido-bridged isomer **a-μH** by at least 10 kcal mol$^{-1}$. The steric repulsion between the $P(NC_4H_8)_3$ ligand and the carbonyl ligands plays a relevant role in determining such large energy gaps.

In conclusion, DFT results allowed us to rationalize why the synthetic complex (μ-pdt)[$Fe_2(CO)_5P(NC_4H_8)_3$] is significantly less efficient then the enzyme in $H_2$ production,[10,24] and might contribute to the design and synthesis of novel functional models of the active site of Fe-hydrogenase.


[1] M. Y. Darensboug, *Nature* **2005**, *433*, 589.

[2] S. P. Albracht, *Biochim. Biophys. Acta* **1994**, *167*, 1188; E. G. Graf, R. K. Thauer, *FEBS Lett.* **1981**, *136*, 165; M. W. W. Adams, *Biochim. Biophys. Acta* **1990**, *115*, 1020; R. Cammack, *Nature* **1999**, *397*, 214; Y. Nicolet, B. J. Lemon, J. C. Fontecilla-Camps, J. W. Peters, *Trends Biochem. Sci.* **2000**, *25*, 138; J. W. Peters, *Curr. Opin. Struct. Biol.* **1999**, *9*, 670; D. S. Horner, B. Heil, T. Happe, T. M. Embley, *Trends Biochem. Sci.* **2002**, *27*, 148; Y. Nicolet, C. Cavazza, J. C. Fontecilla-Camps, *Inorg. Biochem.* **2002**, *91*, 1; R. Cammack, M. Frey, R. Robson, *Hydrogen as Fuel – Learning from Nature*, Taylor and Francis, London, **2001**; F. A. Armstrong, *Curr. Opin. Chem. Biol.* **2004**, *8*, 133.

[3] E. J. Lyon, S. Shima, G. Buurman, S. Chowdhuri, A. Batschauer, K. Steinbach, R. K. Thauer, *Eur. J. Biochem.* **2004**, *271*, 195; O. Pilak, B. Mamat, S. Vogt, C. H. Hagemeier, R. K. Thauer, S. Shima, C. Vonrhein, E. Warkentin, U. Ermler, *J. Mol. Biol.* **2006**, *358*, 798.

[4] J. W. Peters, W. N. Lanzilotta, B. J. Lemon, L. C. Seefeldt, *Science* **1998**, *282*, 1853.

[5] Y. Nicolet, C. Piras, P. Legrand, C. E. Hatchikian, J. C. Fontecilla-Camps, *Structure* **1999**, *7*, 13.

[6] Y. Nicolet, A. L. de Lacey, X. Vernede, V. M. Fernandez, E. C. Hatchikian, J. C. Fontecilla-Camps, *J. Am. Chem. Soc.* **2001**, *123*, 1596.

[7] a) W. Gao, J. Liu, C. Ma, L. Weng, K. Jin, C. Chen, B. Akermark, L. Sun, *Inorg. Chim. Acta* **2006**, *359*, 1071; b) L.-C. Song, C. Jea, J. Yan, H.-T. Wang, X.-F. Liu, X. Q.-M. Hu, *Organometallics* **2006**, *25*, 1544; c) S. Jiang, J. Liu, L. Sun, *Inorg. Chem. Commun.* **2006**, *9*, 290; d) J.-F. Capon, F. Gloaguen, P. Schollhammer, J. Talarmin, *Coord. Chem. Rev.* **2005**, *249*, 1664; e) C. Tard, X. Liu, S. K. Ibrahim, M. Bruschi, L. De Gioia, S. C. Daview, X. Yang, L.-S. Wang, G. Sawers, C. J. Pickett, *Nature* **2005**, *433*, 610; f) L.-C. Song, Z.-Y. Yang, H.-Z. Bian, Y. Liu, H.-T. Wang, X.-F. Liu, Q.-M. Hu, *Organometallics* **2005**, *24*, 6126; g) J. W. Tye, J. Lee, H.-W. Wang, R. Mejia-Rodriguez, J. H. Reibenspies, M. B. Hall, M. Y. Darensbourg, *Inorg. Chem.* **2005**, *44*, 5550; h) S. J. Borg, T. Behrsing, S. P. Best, M. Razavet, X. Liu, C. J. Pickett, *J. Am. Chem. Soc.* **2004**, *126*, 16988; i) S. Ott, M. Kritikos, B. Akermark, L. Sun, R. Lomoth, *Angew. Chem. Int. Ed.* **2004**, *43*, 1006; j) T. Liu, M. Wang, Z. Shi, H. Cui, W. Dong, J. Chen, B. Akermark, L. Sun, *Chem. Eur. J.* **2004**, *10*, 4474; k) R. Mejia-Rodriguez, D. Chong, J. H. Reibenspies, M. P. Soriaga, M. Y. Darensborg, *J. Am. Chem. Soc.* **2004**, *126*, 12004; l) J.-F. Capon, F. Gloaguen, P. Schollhammer, J. Talarmin, *J. Electroanal. Chem.* **2003**, *566*, 241; m) D. Chong, I. P. Georgakaki, R. Mejia-Rodriguez, J. Sanabria-Chinchilla, M. P. Soriaga, M. Y. Darensbourg, *Dalton Trans.* **2003**, 4158; n) F. Gloaguen, J. D. Lawrence, T. B. Rauchfuss, M. Bénard, M.-M. Rohmer, *Inorg. Chem.* **2002**, *41*, 6573; o) F. Gloaguen, J. D. Lawrence, T. B. Rauchfuss, *J. Am. Chem. Soc.* **2001**, *123*, 9476.

[8] M. Bruschi, P. Fantucci, L. De Gioia, *Inorg. Chem.* **2004**, *43*, 3733.

[9] J. W. Tye, M. Y. Darensbourg, M. B. Hall, *Inorg. Chem.* **2006**, *45*, 1552.

[10] J. Hou, X. Peng, Z. Zhou, S. Sun, X. Zhao, S. Gao, *J. Org. Chem.* **2006**, *71*, *691*, 4633.

[11] A. D. Becke, *Phys. Rev. A* **1988**, *38*, 3098; J. P. Perdew, *Phys. Rev. B* **1986**, *33*, 8822.

[12] A. Schafer, C. Huber, R. Ahlrichs, *J. Chem. Phys.* **1994**, *100*, 5829.

[13] R. Ahlrichs, M. Bar, M. Haser, H. Horn, C. Kolmel, *Chem. Phys. Lett.* **1989**, *162*, 165.

[14] K. Eichkorn, F. Weigend, O. Treutler, R. Ahlrichs, *Theor. Chem. Acc.* **1997**, *97*, 119.

[15] F. Jensen, *Introduction to Computational Chemistry*, John Wiley & Sons, Chichester, England.

[16] A. Klamt, *J. Phys. Chem.* **1995**, *99*, 2224; A. Klamt, *J. Phys. Chem.* **1996**, *100*, 3349.

[17] G. Zampella, M. Bruschi, P. Fantucci, M. Razavet, C. J. Pickett, L. De Gioia, *Chemistry* **2005**, *11*, 509.

[18] M. Y. Darensbourg, E. J. Lyon, X. Zhao, I. P. Georgakaki, *Proc. Natl. Acad. Sci. USA* **2003**, *100*, 3683; I. P. Georgakaki, L. M. Thomson, E. J. Lyon, M. B. Hall, M. Y. Darensbourg, *Coord. Chem. Rev.* **2003**, *238–239*, 255.


 © 2007 Wiley-VCH Verlag GmbH & Co. KGaA, Weinheim 

[19] It is interesting to note that a similar stabilizing effect exerted by the ligand *trans* to the μ-CO could be operative also in the enzyme active site. In fact, the $Fe_4S_4$ subcluster included in the H-cluster proved to be a good electron-donating group (see ref.[7e]) and it has been demonstrated that good donors localized at the position occupied by the Fe–S cubane can favor the rotation of ligands bound to the distal iron center (see ref.[8]).
[20] S. J. Borg, J. W. Tye, M. B. Hall, S. P. Best, *Inorg. Chem.* **2007**, *46*, 384; C. Greco, G. Zampella, L. Bertini, M. Bruschi, P. Fantucci, L. De Gioia, *Inorg. Chem.* **2007**, *46*, 108.
[21] J. I. van der Vlugt, T. B. Rauchfuss, C. M. Whaley, S. R. Wilson, *J. Am. Chem. Soc.* **2005**, *127*, 16012.
[22] T. Zhou, Y. Mo, A. Liu, Z. Zhou, K. R. Tsai, *Inorg. Chem.* **2004**, *43*, 923.
[23] M. Bruschi, G. Zampella, P. Fantucci, L. De Gioia, *Coord. Chem. Rev.* **2005**, *249*, 1620.
[24] J. N. Butt, M. Filipiak, W. R. Hagen, *Eur. J. Biochem.* **1997**, *245*, 116.

Received: November 21, 2006
Published Online: March 14, 2007

 © 2007 Wiley-VCH Verlag GmbH & Co. KGaA, Weinheim 

DOI: 10.1002/ejic.200600853

# Syntheses and Characterization of Molybdenum/Zinc Porphyrin Dimers Bridged by Aromatic Linkers

Sai-Nan Song,[a] Dong-Mei Li,*[a,b] Jun-Feng Wu,[a] Chang-Fu Zhuang,[a] Hong Ding,[a] Wen-Bo Song,[a] Li-Feng Cui,[a] Geng-Zhen Cao,[a] and Guo-Fa Liu[a]

**Keywords:** Porphyrinoids / Heteronuclear complexes / Bridging ligands / Molybdenum / Zinc / Electrochemistry

Two new heterobinuclear porphyrin dimers, namely [{$Mo^{VI}O_2$}-DBPA-Zn] (**1**; $H_4$DBPA = *N*,*N*′-dibenzylidenebis-[4-(10,15,20-triphenyl-21*H*,23*H*-porphin-5-yl)phenylamine]) and [{$Mo^{VI}O_2$}-PBDA-Zn] (**2**; $H_4$PBDA = *N*,*N*′-bis[4-(10,15,20-triphenyl-21*H*,23*H*-porphin-5-yl)phenyl]-1,3-benzenedicarboxamide), have been synthesized. These bis-(porphyrin)s were obtained by treating 5-(*p*-aminophenyl)-10,15,20-triphenylporphyrinatomolybdenum and -zinc with benzene-1,4-dicarboxaldehyde or benzene-1,3-dicarboxylic acid. They have been characterized by UV/Vis, IR, X-ray photoelectron, luminescence, and $^1$H NMR spectroscopy, and their TG-DTA behavior and molar conductances have also been determined. Th *cis*-dioxomolybdenum(VI) unit in these complexes is contained in one of the porphyrin moieties and zinc(II) ion is tetracoordinated in the other. Their electrochemical properties have also been investigated in detail.
(© Wiley-VCH Verlag GmbH & Co. KGaA, 69451 Weinheim, Germany, 2007)

## Introduction

Large π-conjugated macrocyclic systems like porphyrins are fascinating functional materials with high chemical and thermal stability whose photophysical and photochemical properties can be finely tuned by structural modifications involving the substitution of functional groups or different metal coordination.[1–3] Among the many porphyrins and metalloporphyrin complexes, dimeric and oligomeric porphyrins with extensive electronic delocalization have attracted increasing interest due to their potential applications in molecular electronics and photonics, which range from light-emitting diodes,[4] nonlinear optical (NLO) materials,[5] information storage materials,[6] photovoltaic cells,[7–9] chemical sensors,[10] biomimetic systems,[11,12] photosensitizers in photodynamic therapy,[13,14] and so forth. Optional linkages connecting monomeric porphyrin rings would allow the spatial configuration of porphyrins to be adjusted, thereby altering the sizes and shapes of the porphyrinato cavities. Generally speaking, three kinds of linkages are observed in porphyrin dimers and oligomers: (1) a flexible spacer such as a variable-length hydrocarbon or one containing mixed atoms;[15] (2) a rigid spacer such as diphenylanthracene, diphenylene, or *o*-phenylene;[16] (3) a direct *meso*-linked dimer or oligomer.[17,18]

Bis(porphyrin) complexes containing different metal ions, for example Mo/Os, W/Ru, Sn/Mo, and Gd/Co,[19–22] afford heterometallic dimers with extremely interesting magnetic or bifunctional catalytic properties compared with homometallic bis(porphyrin)s (Co/Co, Pd/Pd).[23,24] Molybdenum exhibits oxidation states from +2 to +6 in its porphyrin complexes[25–27] and several studies have demonstrated that high-valent molybdenum porphyrin complexes with *trans*-diperoxo, *cis*-dioxo, and *cis*-oxo-peroxo groups exhibit good oxygen transport activity in vivo and high catalytic activity toward oxygenation reactions.[28–31] We are currently focussing on heterometallic bis(porphyrin)s containing molybdenum in a high oxidation state (+6), and in this paper we report the syntheses, spectral characterization, and electrochemical properties of two new molybdenum–zinc porphyrin dimers, namely [{$Mo^{VI}O_2$}-DBPA-Zn] (**1**; $H_4$DBPA = *N*,*N*′-dibenzylidene-bis[4-(10,15,20-triphenyl-21*H*,23*H*-porphin-5-yl)phenylamine]) and [{$Mo^{VI}O_2$}-PBDA-Zn] (**2**; $H_4$PBDA = *N*,*N*′-bis[4-(10,15,20-triphenyl-21*H*,23*H*-porphin-5-yl)phenyl]-1,3-benzenedicarboxamide) that contain a *p*-bis(Schiff base)phenyl or a *meta*-diimidophenyl as a linking spacer.

## Results and Discussions

### Synthesis of the Complexes

Bis(porphyrin)s can be obtained by self-assembly of monomeric porphyrins through van der Waals or π–π interactions.[32–34] Herein, two kinds of linkers have been chosen, one of which is formed by simple acylation of a diacid and 5-(*p*-aminophenyl)-10,15,20-triphenylporphyrin [5-(*p*-$NH_2$)-TPP] whilst the other is obtained by direct reaction of a dialdehyde and 5-(*p*-$NH_2$)TPP. Two strategies to insert dif-

[a] College of Chemistry, Jilin University,
Jiefang Road 2519, Changchun 130023, P. R. China
[b] Nanoscale Physics & Devices Laboratory, Institute of Physics, Chinese Academy of Sciences,
Beijing 100080, P. R. China
E-mail: dmli@aphy.iphy.ac.cn

 © 2007 Wiley-VCH Verlag GmbH & Co. KGaA, Weinheim 

ferent metal ions into the bis(porphyrin) cavities have also been followed, both of which gave satisfactory results. One approach involves the reaction of one molar equivalent of the mononuclear porphyrin complexes [{5-(*p*-$NH_2$)TPP}-Zn] (**3**) and [{5-(*p*-$NH_2$)TPP}$Mo^{VI}O_2$] (**4**) with the bridge-linking reagents (see Scheme 1).

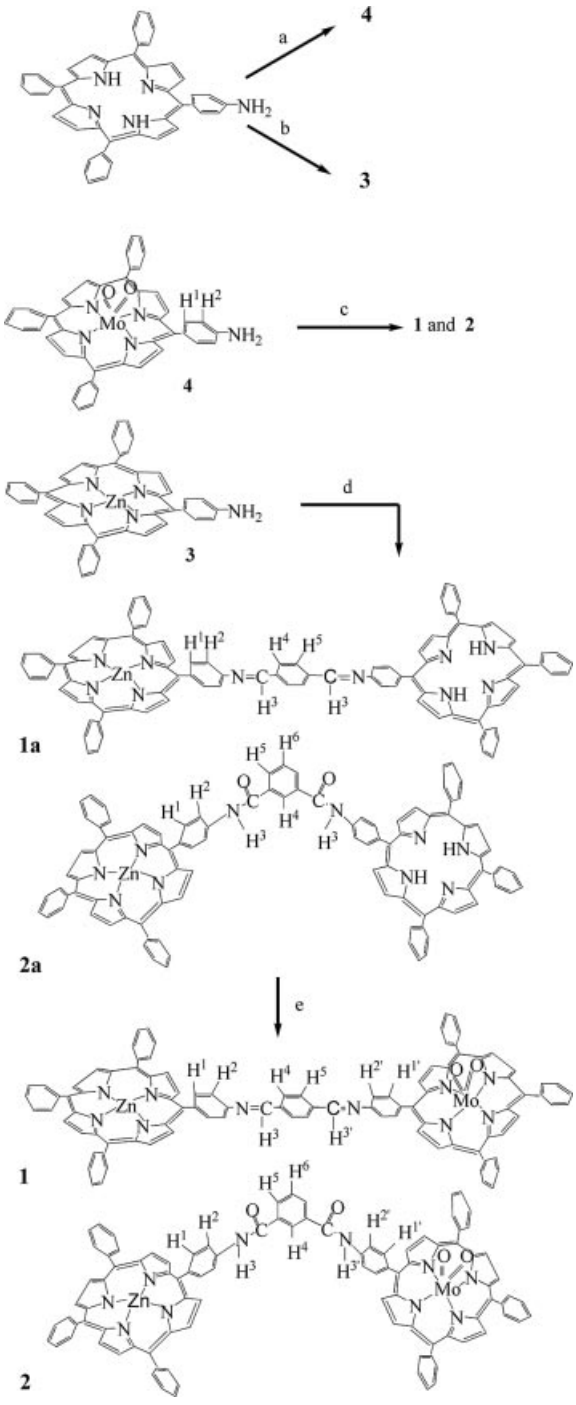


Scheme 1. a: $Mo(CO)_6$, 1,2,4-trichlorobenzene; b: $Zn(OAc)_2{\cdot}2H_2O$, dmf; c: **3** and benzene-1,4-dicarbaldehyde in dmf (to yield **1**) or benzene-1,3-dicarboxylic acid in dmf (to yield **2**); d: 5-(*p*-$NH_2$)TPP and benzene-1,4-dicarbaldehyde (to yield **1a**) or benzene-1,3-dicarboxylic acid in dmf (to yield **2a**); e: $Mo(CO)_6$, 1,2,4-trichlorobenzene.

The progress of the reaction was monitored by recording the UV/Vis absorption spectra. Completion of the reaction was indicated by a change in the relative intensities of the bands centered at about 555 and 595 nm and the appearance of a new band at around 450 nm. However, this reaction also produces several by-products and therefore requires further purification steps. Follow-up experiments revealed that adjusting the molar ratio (1:1) and the charging sequence of the starting materials improves the yield.

The second synthetic strategy consists of two steps: preparation of the mono-zinc bis(porphyrin) complexes **1a** and **2a**, and subsequent treatment of **1a**, **2a** with $Mo(CO)_6$ to give the Mo/Zn compounds.[35] This method produces fewer by-products, although the yield of compound **2** is low, presumably due to the cleavage of the imido linkage at higher temperatures.

### Composition of the Complexes

The heterobimetallic porphyrin complexes **1** and **2** were isolated as stable, purple, microcrystalline solids, although recrystallization from different organic solvents failed to give crystals suitable for an X-ray diffraction study. This lack of crystals led us to seek alternative ways to deduce the possible coordination modes of the central metals. The formulations [{$Mo^{VI}O_2$}-DBPA-Zn] (**1**) and [{$Mo^{VI}O_2$}-PBDA-Zn] (**2**) are proposed based on the elemental analyses, mass spectra, molar conductance, and XPS (as well as spectral and electrochemical characteristics, see below). First, the elemental analyses of **1**, **2**, and **4** are consistent with their respective compositions, thus implying that the *cis*-dioxomolybdenum unit has been successfully inserted into the porphyrinato rings. Second, the mass spectrum of [{5-(*p*-$NH_2$)TPP}$Mo^{VI}O_2$] (**4**) shows the molecular ion peak at *m*/*z* 757 $[M + 2]^+$ and the base peak at *m*/*z* 741 $[M + 2 - O]^+$. The MALDI-TOF spectrum of **1** matches the calculated abundance, thereby confirming its elemental composition and the dimeric structure (peaks at *m*/*z* 736.0 and 692.1 attributable to [{5-(*p*-$NH_2$)TPP}$Mo^{VI}O$] and [{5-(*p*-$NH_2$)TPP}Zn], respectively). This evidence suggests that four nitrogen atoms from the porphyrin β-pyrroles are chelated to the molybdenum atom with the two oxo ligands adopting a *cis* configuration on the same side of the porphyrin ring. Third, the molar conductance values in $1.0 \times 10^{-3}$ M chloroform solution at 25 °C are 0.028, 0.039, 0.022, 0.030, 0.030, and 0.033 $\Omega^{-1}\,cm^2\,mol^{-1}$ for dimers **1**, **2**, **1a**, and **2a** and monomers **3** and **4**, respectively, thus indicating that all these porphyrin complexes exhibit nonelectrolytic behavior.[36] Finally, X-ray photoelectron spectroscopy (XPS) was employed to determine the oxidation state of the molybdenum atoms in the Mo/Zn dimers. Mo $3d_{5/2}$ binding energies of 232.3 eV for compound **1** and 232.6 eV for compound **2** were observed, which suggests that the valence state of molybdenum atom in the two compounds is +6.[37,38] Thus, on the basis of the data available, it is assumed that the zinc(II) ion in these Mo/Zn dimers is tetracoordinate to the four pyrrole nitrogens from one

 © 2007 Wiley-VCH Verlag GmbH & Co. KGaA, Weinheim 

porphyrin ring while the molybdenum(VI) atom is hexacoordinate to the other porphyrin ring with the two oxygen atoms located in a *cis* position, as illustrated in Scheme 1.

No axial ligand is present in the porphyrinatozinc subunits of **1** and **2** as two important effects of axial ligands are not observed.[39–41] Thus, the absorption spectrum of [{5-(*p*-$NH_2$)TPP}Zn] (**3**) was obtained in chloroform, a poorly coordinating solvent, which means that no solvent molecule is ligated to the zinc ion. The other complexes **1a**, **2a**, **1**, and **2** did not show a red shift of their Soret bands relative to **3**. Similarly, no change in the relative intensities of the bands at around 550 and 590 nm is observed (see UV/vis section below).[39] This kind of coordination mode for two metal centers is different from the known anthracene-bridged Mo/Zn porphyrin dimer with an oxomolybdenum(V) unit[42] and other zinc porphyrin complexes with different axial ligands.[43] In fact, some mixed-metal Zn/M bis(porphyrin) complexes (M = Pd, Zn, $H_2$) possess a similar coordination mode, mainly due to the different synthetic methodologies.[15,44,45]

### Infrared Spectra

The mono-zinc and heterometallic Mo/Zn bis(porphyrin) complexes give complicated IR spectra. However, they display characteristic IR absorptions that are helpful for identifying the functional groups. For example, the mono-zinc bis(porphyrin) **1a** shows strong stretching bands at 1659 and 1628 $cm^{-1}$ for the C=N bond of the Schiff base, while the mono-zinc bis(porphyrin) **2a** exhibits intense bands at 1652 and 1635 $cm^{-1}$ due to the symmetric C=O stretching vibrations of the imido groups. Upon coordination of the mono-zinc bis(porphyrin)s to the molybdenum atom these bands shift to higher wavenumbers (1697 and 1651 $cm^{-1}$ for **1** and 1652 $cm^{-1}$ for **2**). This shift is primarily associated with the increasing asymmetry of the molecule as a whole. Furthermore, additional bands at 910 and 951 $cm^{-1}$ are observed in **1** and **2**, respectively, due to the Mo=O stretching vibrations. Similar bands have also been found in other molybdenum porphyrin complexes such as [O=Mo(TPP)OH] and [O=Mo(TPP)X] [X = OMe, OEt, O*i*Pr, O*t*Bu].[43]

### UV/Vis Spectra

The bis(porphyrin)s with different bridges exhibit typical UV/Vis spectra in chloroform in the visible and near-ultraviolet regions. Their maximum absorption wavelengths are listed in Table 1 along with the corresponding monoporphyrin compounds.

As can be seen in Figure 1 (a) and Table 1, Mo/Zn bis(porphyrin) complexes **1** and **2** show very similar absorptions and the mono-zinc bis(porphyrin) complexes **1a** and **2a** also give quite similar absorptions. Apparently, the two different linkers do not significantly influence the UV/Vis absorptions of the bis(porphyrin)s. The Mo/Zn dimers give two Soret absorptions at around 340 and 424 nm, which suggest that both $Mo^{VI}$ and Zn ions can be introduced into the porphyrin rings since the absorptions in the ranges 330–340 nm and 420–425 nm are much closer to those found in the monomeric complexes **4** and **3**, respectively. Figure 1 (b) shows the UV/Vis spectra of **3** and **4** as well as their superposition. It is to be expected, and is indeed observed, that the overlapping peaks of **3** and **4** should be similar to those of **1** and **2** (there is no obvious shift in the Soret bands). This result strongly suggests that no axial ligand (e.g., ethanol) is coordinated to the $Zn^{2+}$ ion.

### $^1$H NMR Spectra

Further confirmation of the identity of **1** and **2** was provided by their $^1$H NMR spectra. We collected the $^1$H NMR spectroscopic data of mono-zinc bis(porphyrin)s **1a** and **2a** and Mo/Zn porphyrin dimers **1** and **2** in $CDCl_3$. A weak signal at $\delta$ = –2.75 ppm was observed for **1a** and **2a** due to the pyrrolic nitrogen protons. This signal disappears after the four pyrrolic nitrogens become coordinated to the molybdenum atom. On the other hand, the broad singlet at $\delta$ = 4.11 ppm due to the amino protons in **4** disappears after

Table 1. UV/Vis spectra of the ligands and complexes.

| Compounds | $\lambda_{max}$ [nm] ($\varepsilon$ [$10^3$ $M^{-1}$ $cm^{-1}$]) Soret band | Q bands | | | | Ref. |
|---|---|---|---|---|---|---|
| 5-(*p*-$NH_2$)TPP | 426 (263.4) | 518 (28.7) | 554 (15.8) | 592 (9.1) | 648 (7.6) | this work |
| **3** | 428 (277.6) | | 554 (19.8) | 596 (7.7) | | this work |
| **4** | 341 (50.7) | 459 (66.5) | | | 647 (14.9) | this work |
| **1a** | 429 (269.3) | 517 (18.3) | 554 (27.3) | 595 (12.5) | 648 (4.9) | this work |
| **2a** | 428 (277.1) | 519 (17.2) | 554 (26.0) | 594 (11.8) | 650 (4.9) | this work |
| **1** | 337 (62.4) 425 (285.6) | 454 (68.1) | 552 (29.0) | 593 (13.4) | 625 (7.6) | this work |
| **2** | 340 (59.8) 424 (293.8) | 458 (89.5) | 553 (24.1) | 590 (14.5) | 626 (9.7) | this work |
| **5**[a] | 341 (81.1) 414 (249) | 458 (41.4) | 545 (16.8) | 575 (16.9) | 598 (4.7) | [42] |
| **6**[b] | 425 (214) | 487 (4.6) | 535 (15.2) | 562 (11) | | [44] |
| **7**[c] | 453 (182) | 540 (3.5) | 581 (15.9) | 620 (10.9) | 540 (3.5) | [43] |

[a] **5** = (DPA)[$Mo^{V}O$(OMe)][Zn(MeOH)] (DPA = 1,8-bis[5-(2,8,13,17-tetraethyl-3,7,12,18-tetramethylporphyrinyl)]anthracene). [b] **6** = [$MoO_2$(TTP)] (TTP = 5,10,15,20-tetra-*p*-tolylporphyrin). [c] **7** = [MO(TPP)OEt] (TPP = 5,10,15,20-tetraphenylporphyrin).

 © 2007 Wiley-VCH Verlag GmbH & Co. KGaA, Weinheim 

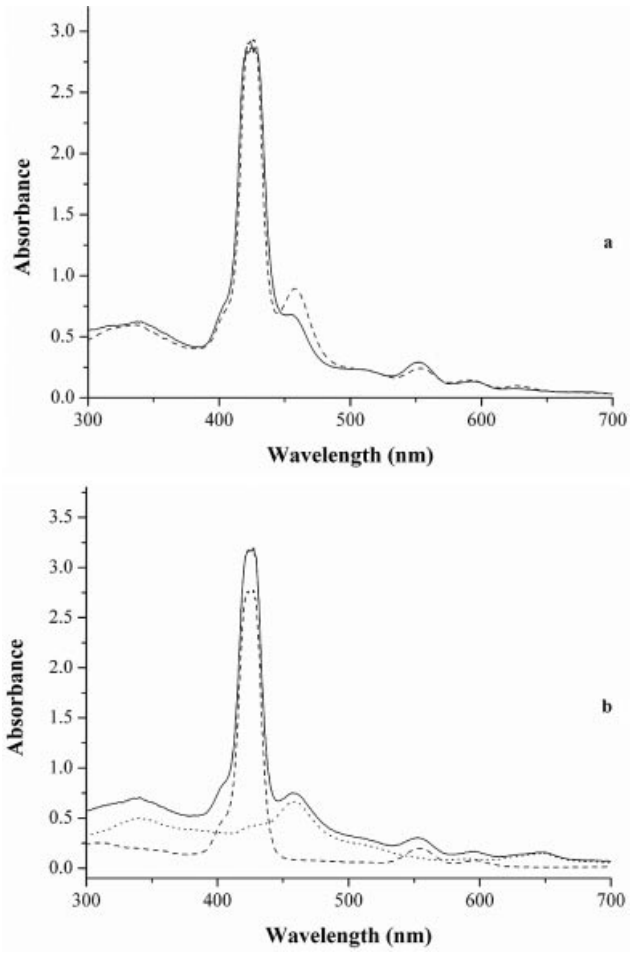


Figure 1. UV/Vis spectra of a series of porphyrin complexes in chloroform at room temperature: (a) Mo/Zn bis(porphyrin) complexes **1** (solid line) and **2** (dashed line); (b) [{5-(*p*-$NH_2$)TPP}Zn] (dashed line), [{5-(*p*-$NH_2$)TPP}$Mo^{VI}O_2$] (dotted line), and their difference spectrum (solid line).

reaction with the linkers. New broad singlets at around $\delta$ = 10.15 ppm due to the protons of the Schiff base [C(*H*)=N] are observed in **1a** and **1**, whereas a new resonance at around $\delta$ = 10.30 ppm is found for the amide proton [C(O)-N*H*] in **2a** and **2**. Mono-substitution on the phenyl rings impose an effective $C_s$ symmetry on the metalloporphyrin moiety, which leads to a splitting of the pyrrole resonances. This tendency is also observed here, where the pyrroles adjacent to the 5-*meso* position bear non-equivalent pairs of protons (see Experimental Section). Besides, **1a** shows a singlet at $\delta$ = 8.23 ppm due to the *ortho* protons, two doublets at $\delta$ = 7.89 and 7.77 ppm due to the *para* and *meta* protons of the *meso*-substituted phenyls, respectively, and two doublets at $\delta$ = 8.08 and 7.63 ppm due to the 5-*meso*-substituted phenyl. For the corresponding Mo/Zn complex **1**, these signals are observed at $\delta$ = 8.24, 7.86, 7.76, 8.07, and 7.69 ppm, respectively. Obviously, these values are too similar to allow any distinctive differences between the two compounds to be determined. Similar phenomena are observed for **2a** and **2**. As regards the Schiff base linker, **1a** shows two doublets at $\delta$ = 7.57 and 7.53 ppm attributable to the phenyl protons, and these resonances are observed at $\delta$ = 7.53 and 7.50 ppm for **1**. For the imido linkage, **2a** shows signals at $\delta$ = 8.01 and 7.95 ppm due to the phenyl protons while signals at $\delta$ = 7.99, 7.88, and 7.46 ppm are observed for **2**. Therefore, the ring current originating from the neighboring porphyrin macrocycle does not cause a significant upfield shift of the phenyl protons *para* or *meta* to the bis(porphyrin)s.[45]

## Thermal Studies

Thermogravimetric analyses of monoporphyrins **3** and **4** and bis(porphyrin)s **1a**, **1**, **2a**, and **2** were carried out. These six compounds were found to be thermally stable up to 150 °C, as indicated by a horizontal plateau in their TG curves. However, the mono- and bis(porphyrin)s show slightly different thermal processes. Monomers **3** and **4**, for example, exhibit similar TG curves with three obvious weight-loss processes. For **4**, the first stage, which involves the loss of a small amount of adsorbent water, four *meso*-phenyl groups, and one terminal oxygen atom, starts at 150 °C and is complete at 301.5 °C. The observed weight loss is 54.56%, in good agreement with the calculated weight loss of 54.90%. This is a continuous exothermic process. The second stage, which corresponds to the collapse of the porphyrinato skeleton, involves a strong exotherm at 373.5 °C; the process is complete at 457.8 °C. This stage leads to the stable product $MoO_3$ with a total weight loss of 26.16%, in agreement with the theoretical value of 26.03%. Following the second step, a medium exothermic process occurs with a further weight loss of 4.85%, thus indicating that $MoO_3$ is not the final product in compound **4**. According to the literature, a possible explanation for this may be the occurrence of self-heating or autocatalysis to yield a nonstoichiometric molybdenum oxide with the formula $MoO_{2.56}$.[46] In contrast to the monomers, the bis(porphyrin)s exhibit continuous decomposition processes. Figure 2 shows the TG and DTA curves for compound **2**. The decomposition of **2** starts at 150 °C and the process ends at

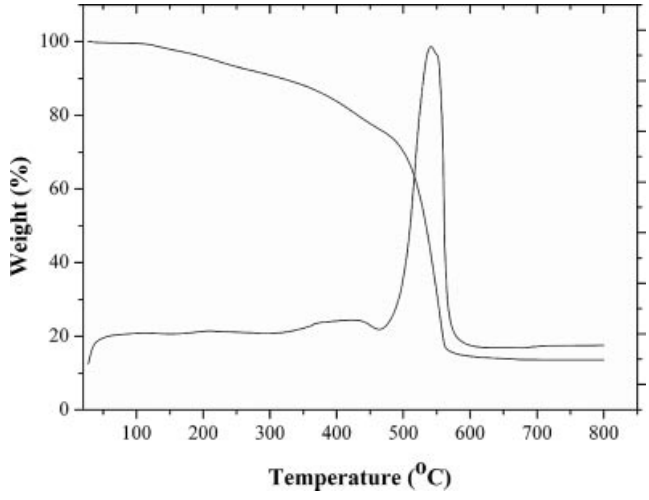


Figure 2. TG and DTA curves of compound **2**.

 © 2007 Wiley-VCH Verlag GmbH & Co. KGaA, Weinheim 

600 °C, as revealed by the weight loss curve. The experimental weight loss for the process is 85.57%, in good agreement with the expected value of 85.72%. This step involves the loss of a small amount of adsorbed water and the collapse of the whole porphyrin framework; the final products are expected to be $MoO_3$ and ZnO. Therefore, one possible reason why the yield of **2** is so low could be that Mo/Zn bis(porphyrin)s with an imidophenyl linkage are not very stable at high temperature.

### Luminescence Studies

Excited-state processes in porphyrins are extremely important for their applications in molecular devices. Two fluorescence bands [S2 (B band) and S1 (Q band)] are observed in the porphyrin complexes. These are attributable to the transitions from the second excited singlet state (S2) to the ground state (S0; S2→S0) and from the lowest excited singlet state (S1) to S0 (S1→S0), respectively. The room-temperature fluorescence spectra of monomers **3** and **4** and bis(porphyrin)s **1a**, **1**, **2a**, and **2** in chloroform ($1 \times 10^{-5}$ M) were recorded. The excitation spectra are approximately mirror images of the absorption spectra in the Q-band region. The emission spectra obtained at an excitation wavelength of 420 nm are shown in Figure 3.[47]

The Q(0–0) fluorescence bands of these metalloporphyrin complexes are observed in the region 601–608 nm, with the Q(0–1) fluorescence bands in the region 651–655 nm, although they differ with respect to their relative intensities and fluorescent yields. It should be noted that the Q(1–0) absorption bands around 560 nm observed in the zinc tetraarylporphyrin complexes do not appear in the emission spectra of our monomer or dimers. This is probably because this band is too weak to be observed.[47] Several interesting results can be extracted from Table 3: first, the monozinc bis(porphyrin) complex **1a** has weaker Q(0–0) and more intense Q(0–1) bands than **2a**, probably due to a radiationless deactivation process. Second, the Mo/Zn porphyrin dimers **1** and **2** give almost identical fluorescence spectra, thus suggesting that the two *meso* linkages have no significant influence on the fluorescence spectra of these dimers. Third, the emission spectra of monomers **3** and **4** are obviously different, for example an intense Q(0–0) band is observed in **3** while an intense Q(0–1) band is found in **4**. The different coordination modes of the central metals are likely to be responsible for this difference − the molybdenum unit is six-coordinate while the zinc ion is only four-coordinate. Thus, the extent of spin-orbit coupling is strongly dependent on the axial ligands of the porphyrins, such as O, Cl, Br, and I. Fourth, the fluorescent yields of all six porphyrin compounds are less than 0.2, which is in accordance with those reported previously, thereby implying that the excited state S1 is primarily deactivated by radiation-less decay in porphyrins.[47] Monomers **3** and **4** give three- to five-times higher fluorescent yields than ZnTPP due to the effect of the *para*-$NH_2$ group on the rate of nonradiative quenching of S1 (as shown in Table 2). Furthermore, the fluorescence

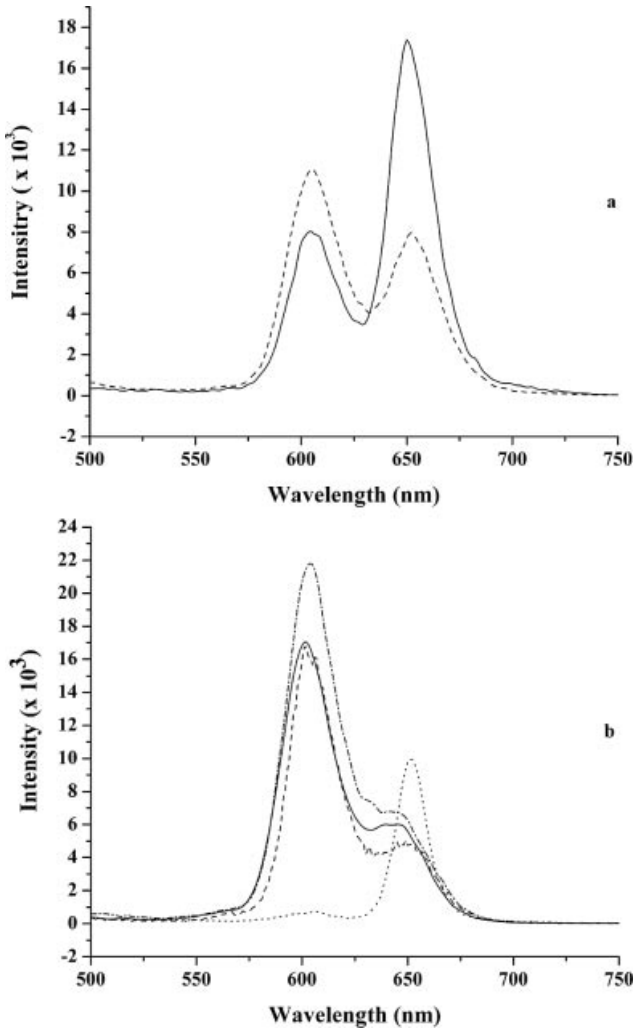


Figure 3. Emission spectra of (a) monozinc bis(porphyrin) **1a** (solid line) and **2a** (dashed line); (b) Mo-Zn porphyrin dimers **1** (solid line) and **2** (dashed line) and monomeric porphyrin complexes **3** (dash dotted line) and **4** (dotted line).

is also dependent on the coplanarity of the compounds. The coplanarity of **3** is better than that of **4**, which leads to its relatively high fluorescence yield. The fluorescent yields of bis(porphyrin)s **1a**, **2a**, **1**, and **2** are quite close to that of ZnTPP, which is due to the lack of interaction between two porphine π systems or a larger dihedral angle between the

Table 2. Emission spectra data and quantum yields ($\Phi_f$) of the monomers and dimers.

| Compounds | Q(0–0) | Q(0–1) | $\Phi_f$ |
|---|---|---|---|
| 5-(*p*-$NH_2$)TPP | | 651 | 0.032 |
| **3** | 605 | 647 | 0.167 |
| **4** | 605 | 651 | 0.105 |
| **1a** | 605 | 650 | 0.043 |
| **2b** | 605 | 650 | 0.040 |
| **1** | 604 | 649 | 0.042 |
| **2** | 602 | 649 | 0.041 |
| [ZnTPP][a] | 598 | 647 | 0.033 |

[a] ZnTPP = 5,10,15,20-tetraphenylporphyrinatozinc(II).

 © 2007 Wiley-VCH Verlag GmbH & Co. KGaA, Weinheim 

two planes, which means that the two porphine π systems in the dimers exhibit independent fluorescence properties.

### Electrochemistry

The electrochemical behavior of **1a**, **1**, **2a**, and **2** was investigated by cyclic voltammetry in dmf containing 0.1 M TEAP. The redox properties of three precursor monoporphyrinates, namely 5-(*p*-$NH_2$)TPP, **3**, and **4** were also studied under the same experimental conditions for comparison. The potentials were scanned positively at either +1.0 $V s^{-1}$ for 5-(*p*-$NH_2$)TPP, **1a**, **2**, **3**, and **4**, or at +1.25 $V s^{-1}$ for **1** and **2a**. All potentials are quoted relative to an $Ag^+/Ag$ electrode.

As shown in Figure 4 (c), complex **4** gives a complicated cyclic voltammogram. It undergoes four reduction steps at $E_{1/2}$ = –1.86, –1.46, –1.16, and –0.43 V (vs. $Ag^+/Ag$; labeled as peaks I–IV). An irreversible oxidation process is also ob-

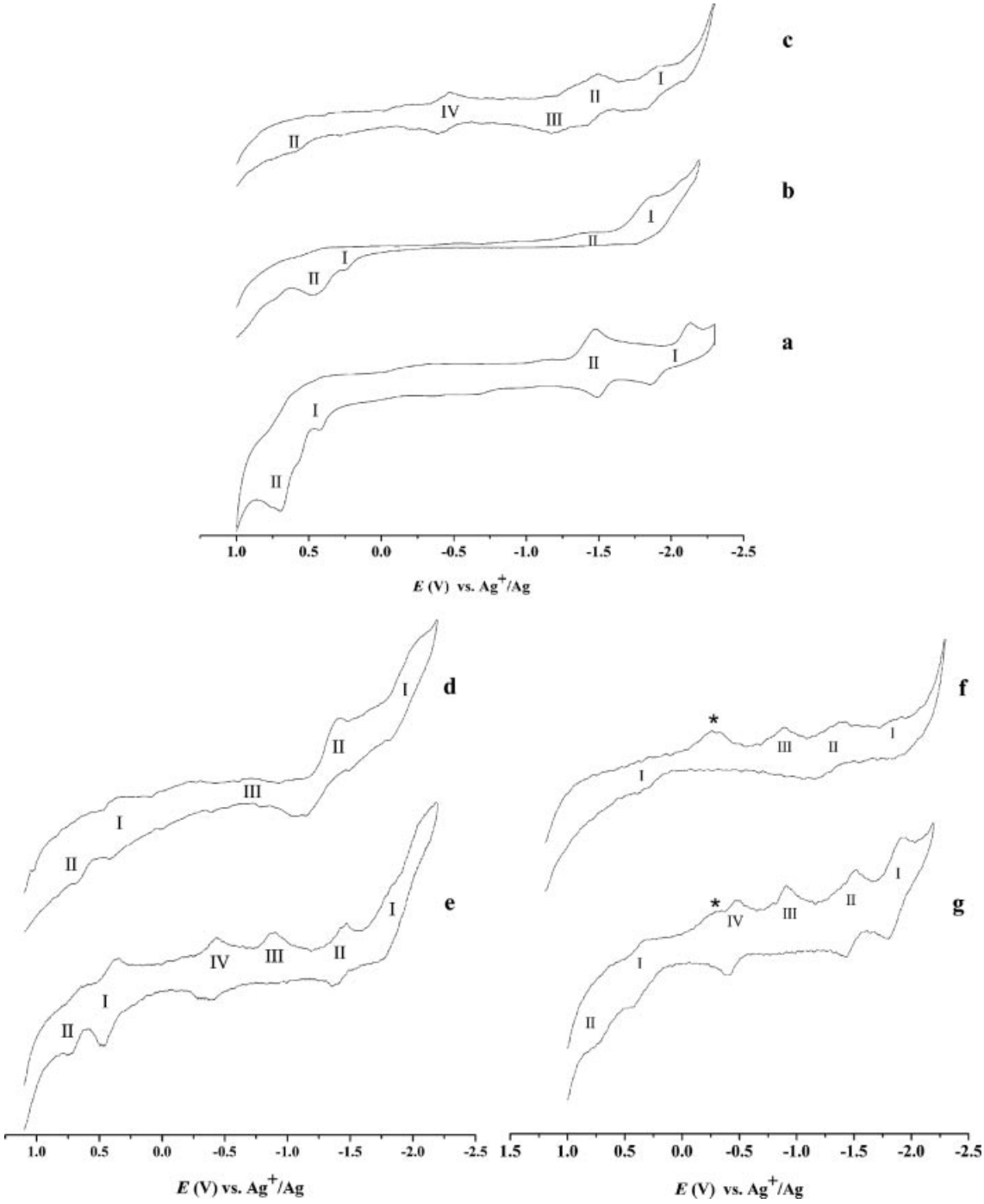


Figure 4. Cyclic voltammograms of 5-(*p*-$NH_2$)TPP (a), [{5-(*p*-$NH_2$)TPP}Zn] (**3**; b), [{5-(*p*-$NH_2$)TPP}$Mo^{VI}O_2$] (**4**; c), [($H_2$DBPA)Zn] (**1a**; d), [{$Mo^{VI}O_2$}-DBPA-Zn] (**1**; e), [{$H_2$PBDA}Zn] (**2a**; f), and [{$Mo^{VI}O_2$}-PBDA-Zn] (**2**; g) in dmf + 0.1 M TEAP. The cathodic peaks marked with asterisks (*) at around –0.3 V in **2a** and **2** are due to impurities.

 © 2007 Wiley-VCH Verlag GmbH & Co. KGaA, Weinheim 

served at $E_p$ = 0.51 V (vs. $Ag^+/Ag$). Each of these processes is a one-electron reduction or oxidation. The first two quasi-reversible reduction steps were assigned to the reductions of the central Mo (waves IV and III), namely $Mo^{VI}$ to $Mo^{V}$ and $Mo^{V}$ to $Mo^{IV}$, while the reduction reactions occurring at the porphyrin ring (waves I and II) yield the dianion and anion radical. These reactions are shown in Scheme 2.[48] Kadish et al. have systematically investigated the electrochemistry of monomeric molybdenum porphyrins such as $[Mo^{VI}O_2(TPP)]$, $[Mo^{VI}O(TMP)(O_2)]$ (TMP = 5,10,15,20-tetramesitylporphyrinato dianion), $[Mo^{V}O(TPP)(X)]$ (X = $MeO^-$, $OAc^-$, $Cl^-$), $[Mo^{IV}O(TPP)]$ in dichloromethane.[30,49–54] A comparison with these molybdenum porphyrin compounds indicates that the two oxidation potentials at around 1.22 and 1.49 V (vs. SCE) in $[Mo^{VI}O_2(TPP)]$ are not observed in compound **4**, although a weak oxidation peak at 0.51 V, which is assumed to be due to the formation of the porphyrin cation radical $[Mo^{VI}O_2(por)]^{\cdot+}$, is found.[49] Furthermore, the electroreductions on the porphyrin rings of **4** in dmf are more negative than those for $[Mo^{VI}O_2(TPP)]$ in dichloromethane or 1,2-dichloroethane (–1.13 and –1.48 V vs. SCE).[54] The use of a different solvent (dmf or dichloromethane) may be the cause of this. This was further confirmed by the electrochemical behavior of the free porphyrin 5-(*p*-$NH_2$)TPP and the corresponding zinc complex (see parts a and b in Figure 4). [{5-(*p*-$NH_2$)TPP}Zn] (**3**) gives two reduction potentials at –1.81 and –1.45 V for $por^-/por^{2-}$ and $por/por^-$ and two oxidation potentials at 0.26 and 0.48 V for $por^{\cdot+}/por$ and $por^{\cdot2+}/por^+$, respectively. It should be noted that all three potentials related to the reductions of the porphyrin ring of **3** and **4** are shifted slightly to more positive potentials upon metalation relative the free-base porphyrin ($E_{1/2}$ = –2.00, –1.49 V). The presence of amine groups has been reported to bring about a multi-electron oxidation, particularly the potentials at 0.5–0.6 V vs. SCE that occur in $H_2T$(*p*-$NH_2$)PP in dichloromethane, although this kind of oxidation could not be distinguished in these three compounds.[54]

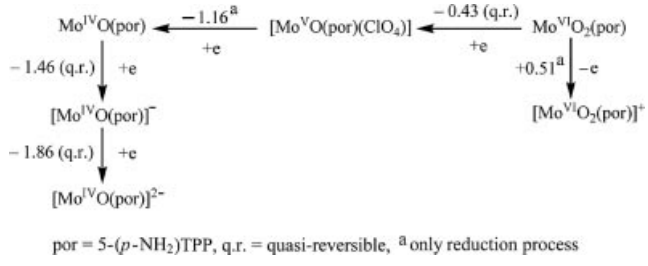


Scheme 2. The electrochemical oxidation and reduction of **4**. Values are quoted in volts.

The four bis(porphyrin) complexes **1a**, **1**, **2a**, and **2** (d–g, respectively, in Figure 4) exhibit systematic redox processes. The Mo/Zn dimers **1** and **2** exhibit similar cyclic voltammograms while the monozinc bis(porphyrin)s **1a** and **2a** also have similar properties, thus indicating that the introduction of Schiff-base or imido linkers at the periphery of porphyrins has a similar influence on their redox potential values. As seen in Table 3, the two oxidation waves at around 0.40 and 0.70 V and the two reduction waves in the ranges –1.30 to –1.45 V and –1.86 to –1.91 V correspond to the reduction of the porphyrin units in these four cases. The new totally irreversible cathodic potential at around –0.90 V that appears in the bis(porphyrin)s was assigned to the reduction of the porphyrin ligands. It is thus supposed that the increased asymmetry of bis(porphyrin)s **1a**, **2a**, **1**, and **2** may result in multiple redox processes at the porphyrin rings. Only one quasi-reversible reduction at the central metal ($Mo^{VI}/Mo^{V}$) is observed in **1** and **2** ($E_{1/2}$ = –0.44 V), thus indicating that further reduction from $Mo^{V}$ to $Mo^{IV}$ is difficult when **4** is connected to another zinc porphyrin subunit by the bridging linker.

Table 3. Half-wave potentials (V vs. $Ag^+/Ag$) for some porphyrin complexes in dmf containing 0.1 M TEAP as supporting electrolyte.

| Ligand/complex | Reduction waves | | | | Oxidation waves | |
|---|---|---|---|---|---|---|
| | I | II | III | IV | I | II |
| 5-(*p*-$NH_2$)TPP | –2.00 | –1.49 | | | 0.43[a] | 0.70[a] |
| **3** | –1.81 | –1.45[b] | | | 0.26[a] | 0.48[a] |
| **4** | –1.86 | –1.46 | –1.16[a] | –0.43 | | 0.51[a] |
| **1a** | –1.91 | –1.30 | –0.71[b] | | 0.38 | 0.68[a] |
| **1** | –1.86 | –1.45 | –0.89[b] | –0.44 | 0.43 | 0.70 |
| **2a** | –1.88 | –1.30 | –0.90[b] | | 0.37[a] | |
| **2** | –1.86 | –1.48 | –0.91[b] | –0.45 | 0.39 | 0.74[a] |
| $[MoO_2(TPP)]$[48] | | –1.48 | –1.13 | | 1.22 | 1.49 |

[a] Only reduction process. [b] Only oxidation process.

The abstraction of an electron from $Mo^{VI}$, $Zn^{II}$, or the oxo ligand of the four bis(porphyrin) complexes is impossible, therefore the only reasonable site for oxidation is the porphyrin system; this yields the radical cations. Figure 4 (parts d–g) shows the almost identical oxidation reactions that occur at around 0.40 and 0.70 V at the porphyrin moiety, similar to those of monomeric **3** and **4**. However, these peaks are weak in comparison with those found in dichloromethane. It is noteworthy that a large decrease of the HOMO–LUMO gap, as expressed by the half-wave potential difference $E_{1/2}$(1st ox) – $E_{1/2}$(1st red), is observed for **1** and **2** (approx. 0.85 V), in comparison with the corresponding monoporphyrin complexes (approx. 1.80 V), monozinc bis(porphyrin) complexes (approx. 1.10 V), and anthracene-bridged Mo/Zn porphyrin dimer (1.27 V).[42,55] Detailed investigations of this phenomenon are currently underway.

## Conclusions

We have reported the synthesis of two kinds of Mo/Zn bis(porphyrin) complexes by treating 5-(4-aminophenyl)-10,15,20-triphenylporphyrinatomolybdenum/zinc complexes with benzene-1,4-dicarbaldehyde or benzene-1,3-dicarboxylic acid. Unfortunately, we have not been able to obtain good quality single crystals for an X-ray diffraction analysis. However, we have thoroughly investigated them by

 © 2007 Wiley-VCH Verlag GmbH & Co. KGaA, Weinheim 

recording their electronic absorption spectra, thermal stability, luminescent spectra, and electrochemical properties. Taking into consideration previously reported Mo and Mo/Zn porphyrin complexes, we suggest that the dioxomolybdenum(VI) unit is inserted into the porphyrin ring with the two oxo groups in a *cis* configuration.

## Experimental Section

**Materials:** Unless otherwise stated, all reagents, such as $Zn(OAc)_2 \cdot 2H_2O$, $Mo(CO)_6$, benzene-1,4-dicarbaldehyde and benzene-1,3-dicarboxylic acid, were obtained commercially and used without further purification. *N*,*N*-Dimethylformamide (dmf) for electrochemical measurement was distilled from 4 Å molecular sieves under reduced pressure before use. 5-(*p*-Aminophenyl)-10,15,20-triphenylporphyrin [5-(*p*-$NH_2$)TPP] and its zinc complex [{5-(*p*-$NH_2$)TPP}Zn] (**3**) were prepared following a literature procedure.[56–58] TEAP (tetraethylammonium perchlorate) was also obtained by the literature method.[59]

**Physical and Chemical Measurements:** UV/Vis spectra were recorded with a Shimadzu UV2155 spectrometer. IR spectra were measured with a Tensor 27 Fourier Transform spectrometer in the region 4000–400 $cm^{-1}$ using KBr pellets. Elemental analyses (C,H,N) were determined with a Perkin–Elmer 2400 LSII elemental analyzer. Excitation and emission spectra were recorded with a Shimadzu PTI-600 fluorescence spectrometer at room temperature in the range from 300 to 800 nm; the quantum yields were calculated using [Zn(TPP)] as standard ($\Phi_f$ = 0.033). Molar conductances of a $1 \times 10^{-3}$ M solution in chloroform at 25 °C were measured with a DDX-111A conductometer. $^1$H NMR spectra were recorded with a Varian-Unity 500 NMR spectrometer for solutions in $CDCl_3$ with tetramethylsilane (TMS) as an internal standard. The MALDI-TOF mass spectrum for **1** was recorded with a Bruker BIFLEX III spectrometer. The ESI MS spectrum for **4** was measured with a Finnigan MATLCQ electrospray ionization-ion trap mass spectrometer. Thermogravimetric analyses (TGA) and differential thermal analyses (DTA) were performed with a thermoanalyzer (TA SDT 2960) in air at a heating rate of 10 °C $min^{-1}$. The redox behaviors of the complexes (ca. $1 \times 10^{-3}$ M) were determined at a scan rate of 100 mV $s^{-1}$ with an EG&G Princeton Applied Research Model 263A potentiostat/galvanostat at room temperature. An ohmic drop compensation was applied during the CV acquisition. A conventional three-electrode system was used in all electrochemical measurements, consisting of a platinum plate electrode as working electrode, a platinum-wire electrode as counter electrode, and a standard $Ag^+/Ag$ (0.1 M $AgNO_3$ in dmf containing 0.1 M TEAP) reference electrode. The solutions were thoroughly degassed with nitrogen for at least 15 min prior to measurements.

**Method 1. Preparation of [{5-(*p*-$NH_2$)TPP}$Mo^{VI}O_2$] (4):** 5-(*p*-$NH_2$)TPP (200 mg, 0.32 mmol) and $Mo(CO)_6$ (200 mg, 0.76 mmol) were added to 15 mL of 1,2,4-trichlorobenzene under $N_2$ and the mixture was heated at 190 °C for 2 h while stirring. The progress of the reaction was monitored by UV/Vis spectroscopy. After cooling to room temperature, the solution was passed through a silica gel column (2 × 20 cm). The first band eluted with $CHCl_3$ was the free-base porphyrin. The second green band eluted with 2% $C_2H_5OH/CHCl_3$ (v:v) was collected, and the solvents evaporated to dryness to give the desired product as a brown-green powder (80.44 mg, 35%). $C_{44}H_{29}N_5MoO_2$ (755.67): calcd. C 69.93, H 3.87, N 9.27; found C 68.87, H 4.04, N 8.89. ESI-MS: *m*/*z* 757 [M + 2H]$^{2+}$. UV/Vis ($CHCl_3$): $\lambda_{max}$ ($\varepsilon$) = 341 nm [50.7 ($\times 10^3$ $M^{-1}cm^{-1}$)], 459 (66.5), 647 (14.9). IR (KBr): $\tilde{\nu}$ = 3418 br s, ($\nu_{N-H}$), 2953 w, 2923 m, 2853 m ($\nu_{C-H}$), 1625 s ($\nu_{C-N}$), 1125 w ($\nu_{C-O}$), 946 m, 910 w ($\nu_{Mo-O}$) $cm^{-1}$. $^1$H NMR (500 MHz, $CDCl_3$): $\delta$ = 8.95 (br. s, 2 H, β-pyrrole), 8.23 (br. s, 6 H, β-pyrrole), 7.97 (br. s, 6 H, *ortho* ArH), 7.81 (br. s, 2 H$^1$, ArH *meta* to amido), 7.71 (dd, *J* = 4, 7 Hz, 3 H, *para* ArH), 7.54 (d, *J* = 2 Hz, 3 H, *meta* ArH), 7.05 (s, 2 H$^2$, ArH *meta* to amido), 4.11 (br. s, 2 H, NH) ppm.

**Preparation of [{$Mo^{VI}O_2$}-DBPA-Zn] (1):** [{5-(*p*-$NH_2$)TPP}Zn] (**3**; 37 mg, 0.053 mmol) and benzene-1,4-dicarbaldehyde (10 mg, 0.075 mmol) were dissolved in 20 mL of dmf. The solution was refluxed for 30 min while being stirred under $N_2$. [{5-(*p*-$NH_2$)-TPP}$Mo^{VI}O_2$] (50 mg, 0.053 mmol) was added to the above mixture and refluxing was continued for another 3 h. After the mixture had cooled to room temperature, the suspension was mixed with $CHC1_3$ and extracted several times with distilled water. The chloroform layer was collected and dried with anhydrous $Na_2SO_4$. After removal of the solvent, the residue was purified by chromatography on a neutral alumina column (2 × 10 cm) using 2% $C_2H_5OH/CHCl_3$ (v:v) as eluent to give the desired product. Recrystallization from $CHCl_3$ gave [{$Mo^{VI}O_2$}-DBPA-Zn], which was dried under vacuum to give a purple powder (46 mg, 57%). $C_{96}H_{60}MoN_{10}O_2Zn$ (1546.9): calcd. C 74.55, H 3.91, N 9.06; found C 73.18, H 3.60, N 8.68. MALDI-TOF MS: *m*/*z* 1526.0, 736.0, 692.1. UV/Vis ($CHCl_3$): $\lambda_{max}$ ($\varepsilon$) = 337 nm [62.4 ($\times 10^3$ $M^{-1}cm^{-1}$)], 425 (285.6), 454 (68.1), 552 (29.0), 593 (13.4), 625 (7.6). IR (KBr): $\tilde{\nu}$ = 3434 m, 1697 s, 1651 s, 1523 m, 910 m, 844 w $cm^{-1}$. $^1$H NMR (500 MHz, $CDCl_3$): $\delta$ = 10.14 (s, 1 H, C*H*$^3$=N), 10.00 (s, 1 H, C*H*$^{3'}$=N), 9.05 (d, *J* = 4 Hz, 2H$_\beta$, β-pyrrole), 8.96 (d, *J* = 5 Hz, 12 H$_\beta$, β-pyrrole), 8.90 (br. s, 2 H, β-pyrrole), 8.24 (br. s, 12 H, *ortho* ArH), 8.07 (d, *J* = 8 Hz, 2 H$^1$ and 2 H$^{1'}$, ArH *meta* to Schiff base), 7.86 (d, *J* = 8 Hz, 6 H, *para* ArH), 7.76 (s, 12 H, *meta* ArH), 7.69 (br. s, 2 H$^2$ and 2 H$^{2'}$, ArH *para* to Schiff base), 7.53 (br., 2 H$^4$, bridge-phenyl), 7.50 (d, *J* = 8 Hz, 2 H$^5$, bridge-phenyl) ppm.

**Preparation of [{$Mo^{VI}O_2$}-PBDA-Zn] (2):** [{5-(*p*-$NH_2$)TPP}Zn] (30 mg, 0.043 mmol) and benzene-1,3-dicarboxylic acid (12 mg, 0.072 mmol) were dissolved in 20 mL of dmf and the solution was refluxed for 30 min under $N_2$. [{5-(*p*-$NH_2$)TPP}$MoO_2$] (**4**; 28 mg, 0.039 mmol) was then added to the reaction solution and reflux was continued for another 3 h. After the mixture had cooled to room temperature the suspension was poured into 70 mL of $CHC1_3$ and extracted three times with distilled water. The chloroform layer was collected and dried with anhydrous $Na_2SO_4$. After the removal of the solvent, the residue was purified by chromatography on a neutral alumina column (2 × 10 cm) using 2% $C_2H_5OH/CHCl_3$ (v:v) as eluent to afford the desired product, which was dried under vacuum to give a purple powder (44 mg, 59%). $C_{96}H_{60}MoN_{10}O_4Zn$ (1578.9): calcd. C 73.04, H 3.80, N 8.88; found C 72.38, H 4.15, N 8.11. UV/Vis ($CHCl_3$): $\lambda_{max}$ ($\varepsilon$) = 340 nm [59.8 ($\times 10^3$ $M^{-1}cm^{-1}$)], 424 (293.8), 458 (89.5), 553 (24.1), 590 (14.5), 626 (9.7). IR (KBr): $\tilde{\nu}$ = 3434 s, 1652 m, 1620 br. s, 1520 s, 951 br m, 875 br w, $cm^{-1}$. $^1$H NMR (500 MHz, $CDCl_3$): $\delta$ = 10.30 (br. s, 2 H, O=C–N*H*$^3$–), 8.95 (m, 12 H$_\beta$, β-pyrrole), 8.84 (br. s, 4 H$_\beta$, β-pyrrole), 8.231 (d, *J* = 6 Hz, 12 H, *ortho* ArH), 7.99 (s, 1 H$^4$, bridge-phenyl), 7.94 (br., 2 H$^1$, ArH *meta* to imido), 7.88 (d, *J* = 5 Hz, 2 H$^5$, bridge-phenyl), 7.75 (br. s, 8 H, *meta* ArH), 7.62 (m, 4 H, *meta* ArH), 7.53 (t, *J* = 6 Hz, 6 H, *para* ArH), 7.46 (t, *J* = 8 Hz, 1 H$^6$, bridge-phenyl), 7.18 (m, 2 H$^{1'}$, ArH *meta* to imido), 6.91 (d, *J* = 3 Hz, 2 H$^2$, ArH *ortho* to imido), 6.64 (br., 2 H$^{2'}$, ArH *ortho* to imido) ppm.

**Method 2. Preparation of [($H_2$DBPA)Zn] (1a):** 5-(*p*-$NH_2$)TPP (200 mg, 0.32 mmol) and benzene-1,4-dicarbaldehyde (50 mg, 0.37 mmol) were added to 30 mL of dmf and the mixture was re-

 © 2007 Wiley-VCH Verlag GmbH & Co. KGaA, Weinheim 

fluxed for 30 min under $N_2$. [{5-(*p*-$NH_2$)TPP}Zn] (220 mg, 0.32 mmol) was then added and the reflux was maintained for another 3 h, during which time the process was monitored by UV/Vis spectroscopy every 10 min. After cooling to room temperature, 70 mL of $CHC1_3$ was poured into the solution and this mixture extracted several times with distilled water. The $CHCl_3$ layer was collected, dried with anhydrous $Na_2SO_4$, filtered to remove the drying agent, and finally evaporated to a small volume. The crude product was purified by chromatography on a neutral alumina column (3.0 × 10 cm). The first band, which eluted with $CHCl_3$, was unreacted [{5-(*p*-$NH_2$)TPP}Zn]. The main purple band, which eluted with 2% $C_2H_5OH/CHCl_3$ (v:v), was collected and condensed to dryness on a rotary evaporator to afford the desired product (108 mg, 24%). $C_{96}H_{62}N_{10}Zn$ (1421.0): calcd. C 81.14, H 4.40, N 9.86; found C 79.98, H 4.55, N 8.97. UV/Vis ($CHCl_3$), $\lambda_{max}$ ($\varepsilon$): 429 nm [269.3 ($10^3$ м$^{-1}$ cm$^{-1}$)], 517 (18.3), 554 (27.3), 595 (12.5), 648 (4.9). IR (KBr): $\tilde{\nu}$ = 3430 s, 1659 m, 1628 s, 1550 m, 963 m cm$^{-1}$. $^1$H NMR (500 MHz, $CDCl_3$): $\delta$ = 10.16 (s, 2 H, C*H*$^3$=N–), 9.02 (br., 2 $H_\beta$, β-pyrrole), 8.95 (d, *J* = 9 Hz, 4 $H_\beta$, β-pyrrole), 8.85 (d, J = 5 Hz, 4 $H_\beta$, β-pyrrole), 8.64–8.58 (br., 6 $H_\beta$, β-pyrrole), 8.23 (br. s, 12 H, o*rtho* ArH), 8.08 (d, *J* = 9 Hz, 4 H$^1$, ArH, *meta* to Schiff base), 7.89 (d, *J* = 8 Hz, 6 H, *para* ArH), 7.77 (d, *J* = 7 Hz, 12 H, *meta* ArH), 7.63 (d, *J* = 6 Hz, 4 H$^2$, ArH, *para* to Schiff base), 7.57 (d, *J* = 7 Hz, 2 H$^4$, bridge-phenyl), 7.53 (d, *J* = 9 Hz, 2 H$^5$, bridge-phenyl), –2.75 (s, 2 H, N–H) ppm.

**Preparation of [($H_2$PBDA)Zn] (2a):** 5-(*p*-$NH_2$)TPP (200 mg, 0.32 mmol) and benzene-1,3-dicarboxylic acid (60 mg, 0.36 mmol) were added to 30 mL of dmf and the mixture was refluxed for 30 min under $N_2$. [{5-(*p*-$NH_2$)TPP}Zn] (**3**; 220 mg, 0.32 mmol) was then added and the mixture was refluxed for another 3 h, during which the process was monitored by UV/Vis spectroscopy every 10 min. After cooling to room temperature, 70 mL of $CHC1_3$ was poured into the solution and the mixture extracted several times with distilled water. The $CHCl_3$ layer was collected, dried with anhydrous $Na_2SO_4$, filtered to remove the drying agent, and finally evaporated to a small volume. The crude product was purified by chromatography on a neutral alumina column (2× 10 cm). The first band, which eluted with $CHCl_3$, was unreacted [{5-(*p*-$NH_2$)-TPP}Zn]. The main purple band, which eluted with 2% $C_2H_5OH/CHCl_3$ (v:v), was collected and the solvents evaporated to dryness to obtain the desired product (164 mg, 35%). $C_{96}H_{62}N_{10}O_2Zn$ (1453.0): calcd. C 79.35, H 4.30, N 9.64; found C 77.97, H 3.98, N 9.17. UV/Vis ($CHCl_3$): $\lambda_{max}$ ($\varepsilon$) = 428 nm [277.1 ($10^3$ м$^{-1}$ cm$^{-1}$)], 519 (17.2), 554 (26.0), 594 (11.8), 650 (4.9). IR (KBr): $\tilde{\nu}$ = 3380 m, 1652 s, 1635 s, 1532 m, 966 w cm$^{-1}$. $^1$H NMR (500 MHz, $CDCl_3$): $\delta$ = 10.27 (br. s, 2 H, O=C–N*H*$^3$–), 8.87–8.83 (br., 12 H, β-pyrrole), 8.81–8.80 (br., 4 $H_\beta$, β-pyrrole), 8.21 (d, *J* = 6 Hz, 12 H, *ortho* ArH), 8.01 (s, 2 H$^4$, bridge-phenyl), 7.95 (d, *J* = 7 Hz, 2 H$^5$, bridge-phenyl), 7.93 (br. s, 4 H$^1$, *meta* ArH), 7.74 (t, *J* = 6 Hz, 12 H, *meta* ArH), 7.53 (t, *J* = 6 Hz, 6 H, *para* ArH), 6.91 (br., 4 H$^2$, ArH *ortho* to imido), –2.75 (s, 2 H, N–H) ppm.

**Preparation of [{$Mo^{VI}O_2$}-DBPA-Zn] (1):** [($H_2$DBPA)Zn] (**1a**; 50 mg, 0.035 mmol) and $Mo(CO)_6$ (50 mg, 0.190 mmol) were added to 10 mL of 1,2,4-trichlorobenzene and the mixture was refluxed while stirring for 4 h under $N_2$. The progress of the reaction was monitored by UV/Vis spectroscopy. After cooling to room temperature, the solution was transferred directly onto a neutral alumina column (2 × 10 cm). The first red band, which eluted with $CHCl_3$, was unreacted [($H_2$DBPA)Zn]. The second purple-red band, which eluted with 2% $C_2H_5OH/CHCl_3$ (v:v), was collected and the solvents evaporated to dryness to give the desired product (23 mg, 42%).

**Preparation of [{$Mo^{VI}O_2$}-PBDA-Zn] (2):** [($H_2$PBDA)Zn] (50 mg, 0.035 mmol) and $Mo(CO)_6$ (50 mg, 0.190 mmol) were added to 10 mL of 1,2,4-trichlorobenzene and the mixture was refluxed while stirring for 4 h under $N_2$. The progress of the reaction was monitored by UV/Vis spectroscopy. After cooling to room temperature, the solution was transferred directly onto a neutral alumina column (2 × 10 cm). The first red band, which eluted with $CHCl_3$, was unreacted [($H_2$PBDA)Zn]. The second purple-red band, which eluted with 2% $C_2H_5OH/CHCl_3$ (v:v), was collected and the solvents evaporated to dryness to give the desired product (10 mg, 5.5%).

## Acknowledgments

We would like to thank the Jilin University Youth Foundation for financial support. The permanent, generous support of Prof. Guo-Fa Liu and Prof. Qing-Bo Meng is gratefully acknowledged.

[1] O. Siri, L. Jaquinod, K. M. Smith, *Tetrahedron Lett.* **2000**, *41*, 3583–3587.
[2] T.-G. Zhang, Y. Zhao, I. Asselberghs, A. Persoons, K. Clays, M. J. Therien, *J. Am. Chem. Soc.* **2005**, *127*, 9710–9720.
[3] J. P. Collman, J. M. Garner, *J. Am. Chem. Soc.* **1990**, *112*, 166–173.
[4] H. Mizuseki, R. V. Belosludov, A. A. Farajian, N. Igarashi, Y. Kawazoe, *Mater. Sci. Eng., C* **2005**, *25*, 718–721.
[5] T. Morotti, M. Pizzotti, R. Ugo, S. Quici, M. Bruschi, P. Mussini, S. Righetto, *Eur. J. Inorg. Chem.* **2006**, 1743–1757.
[6] J. Jiao, F. Anariba, H. Tiznado, I. Schmidt, J. S. Lindsey, F. Zaera, D. F. Bocian, *J. Am. Chem. Soc.* **2006**, *128*, 6965–6974.
[7] Q. Wang, W. M. Campbell, E. E. Bonfantani, K. W. Jolley, D. L. Officer, P. J. Walsh, K. Gordon, R. Humphry-Baker, M. K. Nazeeruddin, M. Gratzel, *J. Phys. Chem. B* **2005**, *109*, 15397–15409.
[8] L. Schmidt-Mende, W. M. Campbell, Q. Wang, K. W. Jolley, D. L. Officer, M. K. Nazeeruddin, M. Gratzel, *ChemPhysChem.* **2005**, *6*, 1253–1258.
[9] S. Cherian, C. C. Wamser, *J. Phys. Chem. B* **2000**, *104*, 3624–3629.
[10] C. A. Hunter, S. Tomas, *J. Am. Chem. Soc.* **2006**, *128*, 8975–8979.
[11] M. O. Senge, *Chem. Commun.* **2006**, 243–256.
[12] R. S. Loewe, R. K. Lammi, J. R. Diers, C. Kirmaier, D. F. Bocian, D. Holten, J. S. Lindsey, *J. Mater. Chem.* **2002**, *12*, 1530–1552.
[13] C. J. Byrne, M. A. Cooper, P. A. Cowled, R. Johnstone, L. Mackenzie, L. V. Marshallsay, I. K. Morris, C. A. Muldoon, M. J. Raftery, S. S. Yin, A. D. Ward, *Austr. J. Chem.* **2004**, *57*, 1091–1102.
[14] M. Schaffer, P. M. Schaffer, L. Corti, M. Gardiman, G. Sotti, A. Hofstetter, G. Jori, E. Duhmke, *J. Photochem. Photobiol., B* **2002**, *66*, 157–164.
[15] J. Borowiec, I. Trojnar, S. Wolowiec, *Polyhedron* **2004**, *23*, 33–39.
[16] S. Faure, C. Stern, R. Guilard, P. D. Harvey, *Inorg. Chem.* **2005**, *44*, 9232–9241.
[17] H. Shinmori, T. K. Ahn, H. S. Cho, D. Kim, N. Yoshida, A. Osuka, *Angew. Chem. Int. Ed.* **2003**, *42*, 2754–2758.
[18] K. Susumu, T. Shimidzu, K. Tanaka, H. Segawa, *Tetrahedron Lett.* **1996**, *37*, 8399–8402.
[19] J. P. Collman, S. T. Harford, S. Franzen, J.-C. Marchon, P. Maldivi, A. P. Shreve, W. H. Woodruff, *Inorg. Chem.* **1999**, *38*, 2085–2092.
[20] J. P. Collman, S. T. Harford, S. Franzen, A. P. Shreve, W. H. Woodruff, *Inorg. Chem.* **1999**, *38*, 2093–2097.
[21] E. Malinowska, J. Niedziolka, E. Rozniecka, M. E. Meyerhoff, *J. Electroanal. Chem.* **2001**, *514*, 109–117.

 © 2007 Wiley-VCH Verlag GmbH & Co. KGaA, Weinheim 

[22] P. D. Harvey, N. Proulx, G. Martin, M. Drouin, D. J. Nurco, K. M. Smith, F. Bolze, C. P. Gros, R. Guilard, *Inorg. Chem.* **2001**, *40*, 4134–4142.
[23] S. Faure, C. Stern, R. Guilard, P. D. Harvey, *Inorg. Chem.* **2005**, *44*, 9232–9241.
[24] J. P. Collman, P. Denisevich, Y. Konai, M. Marrocco, C. Koval, F. C. Anson, *J. Am. Chem. Soc.* **1980**, *102*, 6027–6036.
[25] Y. Matsuda, Y. Murakami, *Coord. Chem. Rev.* **1988**, *92*, 157–192.
[26] H. Brand, J. Arnold, *Coord. Chem. Rev.* **1995**, *140*, 137–168.
[27] T. S. Srivastava, E. B. Fleischer, *J. Am. Chem. Soc.* **1970**, *92*, 5518–5519.
[28] T. Fujihara, Y. Sasaki, T. Imamura, *Chem. Lett.* **1999**, 403–404.
[29] T. Fujihara, N. H. Rees, K. Umakoshi, J. Tachibana, U. Sasaki, W. McFarlane, T. Imamura, *Chem. Lett.* **2000**, 102–103.
[30] T. Fujihara, K. Myougan, A. Ichimura, Y. Sasaki, T. Imamura, *Chem. Lett.* **2001**, 178–179.
[31] J. P. Collman, P. S. Wagenknecht, J. E. Hutchison, *Angew. Chem. Int. Ed. Engl.* **1994**, *33*, 1537–1554.
[32] T. Haino, T. Fujii, Y. Fukazawa, *J. Org. Chem.* **2006**, *71*, 2572–2580.
[33] M. Takeuchi, S. Tanaka, S. Shinkai, *Chem. Commun.* **2005**, 5539–5541.
[34] K. Ogawa, A. Ohashi, Y. Kobuke, K. Kamada, K. Ohta, *J. Am. Chem. Soc.* **2003**, *125*, 13356–13357.
[35] J. Borowiec, I. Trojnar, S. Wolowiec, *Polyhedron* **2004**, *23*, 33–39.
[36] W. J. Geary, *Coord. Chem. Rev.* **1971**, *7*, 81–122.
[37] S. O. Grim, L. J. Matienzo, *Inorg. Chem.* **1975**, *14*, 1014–1018.
[38] J.-Q. Xu, X.-H. Zhou, L.-M. Zhou, T.-G. Wang, B. A. Averill, *Inorg. Chim. Acta* **1999**, *285*, 152–154.
[39] M. Nappa, J. S. Valentine, *J. Am. Chem. Soc.* **1978**, *100*, 5075–5080.
[40] E. Deiters, V. Bulach, M. W. Hosseini, *New J. Chem.* **2006**, *30*, 1289–1294.
[41] T. Morotti, M. Pizzotti, R. Ugo, S. Quici, M. Bruschi, P. Mussini, S. Righetto, *Eur. J. Inorg. Chem.* **2006**, 1743–1757.
[42] T. Fujihara, K. Tsuge, Y. Sasaki, Y. Kaminaga, T. Imamura, *Inorg. Chem.* **2002**, *41*, 1170–1176.
[43] H. J. Ledon, M. C. Bonnet, Y. Brigandat, F. Varescon, *Inorg. Chem.* **1980**, *19*, 3488–3491.
[44] H. J. Ledon, M. C. Bonnet, J.-Y. Lallemand, *J. Chem. Soc., Chem. Commun.* **1979**, 702–704.
[45] S. Wolowiec, *Polyhedron* **1998**, *17*, 1295–1301.
[46] M. I. Diaz-Guemes, *Thermochim. Acta* **1986**, *106*, 125–132.
[47] D. J. Quimby, F. R. Longo, *J. Am. Chem. Soc.* **1975**, *97*, 5111–5117.
[48] T. Malinski, P. M. Hanley, K. M. Kadish, *Inorg. Chem.* **1986**, *25*, 3229–3235.
[49] J.-H. Fuhrhop, K. M. Kadish, D. G. Davis, *J. Am. Chem. Soc.* **1973**, *95*, 5140–5147.
[50] T. Malinski, H. Ledon, K. M. Kadish, *J. Chem. Soc., Chem. Commun.* **1983**, 1077–1079.
[51] H. Ledon, F. Varescon, F. Varescon, T. Malinski, K. M. Kadish, *Inorg. Chem.* **1984**, *23*, 261–263.
[52] Y. Matsuda, S. Yamada, Y. Murakami, *Inorg. Chem.* **1981**, *20*, 2239–2246.
[53] K. M. Danish, T. Malinski, H. Ledon, *Inorg. Chem.* **1982**, *21*, 2982–2987.
[54] A. Bettelheim, B. A. White, S. A. Raybuck, R. W. Murray, *Inorg. Chem.* **1987**, *26*, 1009–1017.
[55] P. Bhyrappa, M. Sankar, B. Varghese, *Inorg. Chem.* **2006**, *45*, 4136–4149.
[56] D.-M. Li, Z.-X. Zhao, S.-Q. Liu, G.-F. Liu, T.-S. Shi, X.-X. Liu, *Synth. Commun.* **2000**, *30*, 4017–4026.
[57] W. J. Kruper Jr, T. A. Chamberlin, M. Kochanny, *J. Org. Chem.* **1989**, *54*, 2753–2756.
[58] A. D. Alder, F. R. Longo, V. Varadi, *Inorg. Synth.* **1976**, *16*, 213–220.
[59] H. O. House, E. Feng, N. P. Peet, *J. Org. Chem.* **1971**, *36*, 2371–2375.

Received: September 13, 2006
Published Online: March 13, 2007

 © 2007 Wiley-VCH Verlag GmbH & Co. KGaA, Weinheim 

DOI: 10.1002/ejic.200600887

# Synthesis, Crystal Structures, and Photoluminescence of a Series of Coordination Polymers with Two Homologous Functional Flexible Ligands

Hong-Ping Zhou,*[a] Peng Wang,[a] Zhang-Jun Hu,[a] Lin Li,[a] Jing-Jin Chen,[a] Yang Cui,[a] Yu-Peng Tian,*[a–c] Jie-Ying Wu,[a] Jia-Xiang Yang,[a] Xu-Tang Tao,[b] and Min-Hua Jiang[b]

**Keywords:** Coordination polymers / Flexible ligands / Supramolecular chemistry / Luminescence

Two functional, flexible ligands, namely 3,6-dipyrazolyl-9-ethylcarbazole (**L¹**) and 3,6-diimidazolyl-9-ethylcarbazole (**L²**) have been synthesized and characterized and their coordination to various $Ag^{I}$, $Cd^{II}$, and $Co^{II}$ salts investigated. Six new complexes, **1**–**6**, have been obtained and fully characterized by IR spectroscopy, elemental analysis, and single-crystal X-ray diffraction. The 2D double helix framework of the complex $[CdL^{1}I_2]_n$ (**1**) is formed by C–H···I hydrogen bonds, whereas the same 2D double helix framework of compound $[\{AgL^{1}SO_3PhCH_3\}_2(CH_3OH)(H_2O)]_n$ (**2**) is formed by S–O···H and C–H···O hydrogen bonds and weak π–π interactions. The coordination modes of $Cd^{II}$ and $Co^{II}$ in $[CdL^{2}_2(NCS)_2]_n$(**3**),$[CoL^{2}_2(NCS)_2(CHCl_3)_2]_n$(**4**),$[CdL^{2}_2(NO_3)_2(CH_3OH)_2]_n$ (**5**), and $[CoL^{2}_2(NO_3)_2(CH_3OH)_2]_n$ (**6**) are the same, but in the packing diagram interlayers form a 3D network through C–H···S interactions and π–π interactions in **3**, interlayers form a 3D network through S···S interactions and π–π interactions in **4**, novel 3D structures are formed by interchain O···H–C hydrogen bonding and interlayer O···H–C hydrogen-bonding and π–π interactions in **5** and **6**. The structural differences between these complexes show the influence of the orientation of the coordinating group of the ligand. These results also show that the metal ion, anion, and nonbonding and π–π interactions are significant factors in controlling the structural topology of these metal-organic supramolecular architectures. In addition, the luminescence properties of **L¹**, **1**, **L²**, and **3** are investigated in the solid state at room temperature.
(© Wiley-VCH Verlag GmbH & Co. KGaA, 69451 Weinheim, Germany, 2007)

## Introduction

Much recent work has been devoted to the design, synthesis, and structural characterization of novel multidimensional metal-organic frameworks (MOFs),[1–3] with the increasing volume of research being reflected in the exponential growth of the number of structures reported over the past few years. These structures are assembled by very strong and highly directional coordinative interactions, nonbonding weak interactions, and π–π interactions and display properties related to both the pure organic and inorganic compounds. The motivation behind such research lies in the large variety of peculiar architectures, together with the various potential applications of these compounds as functional materials (e.g., porosity allied with guest exchange, catalysis, gas storage, photoluminescence, nonlinear optical properties, chirality, clathration abilities, and magnetic properties).[4,5]

Biimidazole and bipyrazole have been widely used as biomimetic ligands in bioinorganic chemistry,[6] bridging ligands in organometallic chemistry for catalysis,[7] antitumor drugs,[8] and as building blocks of multidimensional MOFs due to their ability to coordinate to several metal centers in various modes.[9] However, it is difficult to model the structural and functional aspects of these complexes. It is well known that organic ligands with special functionality for use in supramolecular architectures have rarely been reported to date due to the synthetic difficulties involved. We expected to be able to combine such functionality by coordination using the ligands 9-ethyl-3,6-dipyrazolylcarbazole (**L¹**) and 9-ethyl-3,6-diimidazolylcarbazole (**L²**; Scheme 1). As imidazole[10] and pyrazole are electron-rich aromatic compounds, we introduced imidazolyl or pyrazolyl groups at the carbazole ring, in high yield, by a two-step Ullmann reaction. This functionalization of the organic molecule (addition of donor atoms such as N or O) allows its incorporation into inorganic coordination complexes, which have the advantage of higher thermal stability and solvent resistance than organic materials. Compared with our previous reports concerning 9-ethyl-3,6-bis[2-(2-pyridyl)ethenyl]carbazole and 9-ethyl-3,6-bis[2-(4-pyridyl)ethenyl]carbazole,[11]

[a] Department of Chemistry, Anhui University,
Hefei 230039, P. R. China
E-mail: zhpzhp@263.net
yptian@ahu.edu.cn
[b] State Key Laboratory of Crystal Materials, Shandong University,
Jinan, 250100, P. R. China
[c] State Key Laboratory of Coordination Chemistry, Nanjing University,
Nanjing 210093, P. R. China

 InterScience © 2007 Wiley-VCH Verlag GmbH & Co. KGaA, Weinheim 

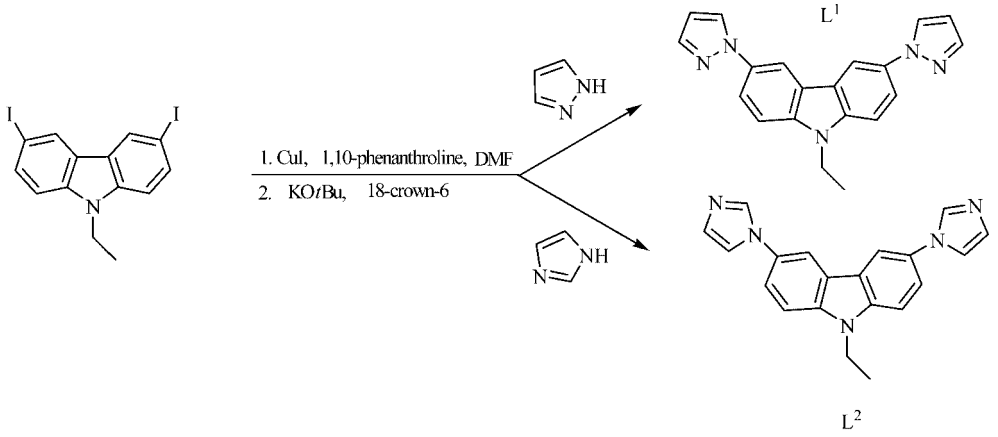


Scheme 1. Synthesis of ligands **L¹**, and **L²**.

replacement of the two pyridylethene groups with two imidazolyl or pyrazolyl groups enhances the flexibility of the ligand greatly. These ligands have a greater number of possible coordination modes than their more rigid analogs due to their flexibility and low symmetry since they can adopt different orientations according to the geometric needs of different metal ions. As a result of a systematic study of these ligands, this paper will describe a series of novel 2D and 3D coordination polymers with intermolecular weak non-bonding and π–π interactions and their photoluminescence properties. All the compounds have been characterized by IR spectroscopy, elemental analysis, and X-ray crystallography. In addition, the luminescence properties of the ligands and complexes **1** and **3** in the solid state are investigated.

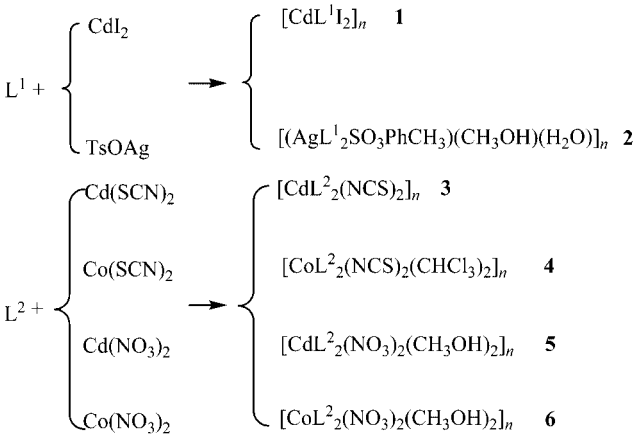


Scheme 2. Summary of the reactions between ligands and transition-metal salts.

## Results and Discussion

We synthesized the ligands 9-ethyl-3,6-dipyrazolylcarbazole and 9-ethyl-3,6-diimidazolylcarbazole in good yield by a ligand-accelerated catalytic Ullmann reaction. The Ullmann reaction of aryl halides with amines or heterocycles is traditionally carried out by heating the reagent with copper powder in the presence of a base such as sodium carbonate or hydroxide.[12] However, we found that the Ullmann reaction of 9-ethyl-3,6-diiodocarbazole and imidazole or pyrazole could not be carried out under these conditions. Fortunately, addition of 1,10-phenanthroline and 18-crown-6 allowed **L¹** and **L²** to be synthesized in 84% and 79% yield, respectively.

### Crystal Structures

The ligands react readily with a variety of $Cd^{II}$, $Co^{II}$, and $Ag^{I}$ salts to form complexes **1**–**6**, which were fully characterized by IR spectroscopy, elemental analysis, and single-crystal X-ray diffraction. The general reaction is shown in Scheme 2. The coordination of $Cd^{II}$ and $Ag^{I}$ salts to **L¹** produced 2D polymer chains **1** and **2**, while the coordination of $Cd^{II}$ and $Co^{II}$ salts to **L²** produced the 3D polymers **3**–**6**.

#### *Crystal Structure of $[CdL^1I_2]_n$ (1)*

Single-crystal X-ray diffraction analysis revealed that the structure of the complex presents unusual double helices, as depicted in Figure 2 below. Further crystallographic details are given in the Experimental Section, and selected bond lengths and angles are listed in Table 1. It can clearly be seen from Figure 1 that the cadmium(II) ion displays a distorted tetrahedral geometry with two nitrogens from two $L^1$ ligands and two iodines in the coordination sphere. The bond angles around Cd(1) are in the range 99.73(16)–119.22(3)°, and the bond lengths between the $Cd^{II}$ center and nitrogen range from 2.288(6) to 2.309(6) Å. The two pyrazolyl rings of each $L^1$ ligand have opposite orientations in complex **1**, and the pyrazolyl rings of the two independent $L^1$ ligands are twisted to meet the requirements of steric hindrance, with the dihedral angles between the pyrazolyl rings and the corresponding carbazolyl rings linked to them being 44.5° and 53.3°. Furthermore, the dihedral angle between the pyrazolyl rings in $L^1$ is 64.1°.

The helical polymer is composed of $[CdL^1I_2]$ monomers. A loose, single-stranded helical chain is formed by self-assembly of $[CdL^1I_2]$ by coordination of the metal-bound peripheral pyrazole-N of this unit to the neighboring $Cd^{II}$

 © 2007 Wiley-VCH Verlag GmbH & Co. KGaA, Weinheim 

Table 1. Selected intra- and intermolecular bond lengths [Å] and angles [°] for **1**–**6**. Symmetry operation used to generate equivalent atoms: **1**: A: $x + 1/2, -y + 1/2, -z$. **2**: A: $-x, y + 1/2, -z + 1/2$. **3**: A: $-x, -y, -z$. **4**: A: $-x, -y, -z$; B: $-x + 1/2, y + 1/2, -z + 1/2$; C: $x - 1/2, -y - 1/2, z - 1/2$. **5**: A: $-x, -y, -z$; B: $x + 1/2, y + 1/2, z$; C: $-x + 1/2, -y + 1/2, -z$. **6**: A: $-x, -y, -z$; B: $x + 1/2, y + 1/2, z$; C: $-x + 1/2, -y + 1/2, -z$.

| | | | |
|---|---|---|---|
| | | **1** | |
| Cd(1)–I(1) | 2.7151(8) | N(3)–Cd(1)–I(1) | 111.11(18) |
| Cd(1)–I(2) | 2.7189(8) | N(5A)–Cd(1)–I(2) | 105.67(14) |
| Cd(1)–N(3) | 2.309(6) | N(3)–Cd(1)–I(2) | 99.73(16) |
| Cd(1)–N(5A) | 2.288(6) | N(5A)–Cd(1)–N(3) | 100.7(2) |
| N(5A)–Cd(1)–I(1) | 117.49(13) | I(1)–Cd(1)–I(2) | 119.22(3) |
| | | **2** | |
| Ag(1)–O(1) | 2.467(14) | N(5A)–Ag(1)–N(3) | 152.3(6) |
| Ag(1)–N(3) | 2.19(2) | N(5A)–Ag(1)–O(1) | 102.7(6) |
| Ag(1)–N(5A) | 2.056(16) | N(3)–Ag(1)–O(1) | 97.6(5) |
| Ag(2)–O(4) | 2.539(15) | N(8)–Ag(2)–N(10A) | 151.3(6) |
| Ag(2)–N(8) | 2.17(2) | N(8)–Ag(2)–O(4) | 112.4(5) |
| Ag(2)–N(10A) | 2.274(14) | N(10A)–Ag(2)–O(4) | 93.6(5) |
| | | **3** | |
| Cd(1)–N(1) | 2.345(2) | N(5)–C(11) | 1.363(4) |
| Cd(1)–N(5) | 2.322(3) | C(11)–C(13) | 1.342(5) |
| Cd(1)–N(6) | 2.347(3) | N(5A)–Cd(1)–N(5) | 180.00(3) |
| N(1)–C(8) | 1.313(4) | N(5)–Cd(1)–N(1) | 90.25(9) |
| N(1)–C(19) | 1.362(4) | N(5A)–Cd(1)–N(1) | 89.75(9) |
| N(2)–C(8) | 1.349(4) | N(1)–Cd(1)–N(1A) | 180.0 |
| N(2)–C(14) | 1.366(4) | N(5A)–Cd(1)–N(6) | 91.41(12) |
| C(14)–C(19) | 1.359(5) | N(5)–Cd(1)–N(6) | 88.59(12) |
| N(4)–C(17) | 1.340(4) | N(1)–Cd(1)–N(6) | 91.04(11) |
| N(4)–C(13) | 1.365(4) | N(1)–Cd(1)–N(6A) | 88.96(11) |
| N(5)–C(17) | 1.313(4) | N(6)–Cd(1)–N(6A) | 180.0 |
| | | **4** | |
| Co(1)–N(1) | 2.128(3) | N(5)–C(6) | 1.376(5) |
| Co(1)–N(4C) | 2.144(3) | C(6)–C(7) | 1.351(6) |
| Co(1)–N(2A) | 2.161(3) | N(1)–Co(1)–N(1A) | 180.0 |
| N(2)–C(2) | 1.318(5) | N(1)–Co(1)–N(4B) | 90.97(12) |
| N(2)–C(4) | 1.368(5) | N(1A)–Co(1)–N(4B) | 89.03(12) |
| N(3)–C(2) | 1.350(5) | N(4B)–Co(1)–N(4C) | 180.0 |
| N(3)–C(3) | 1.372(5) | N(1)–Co(1)–N(2A) | 89.66(12) |
| C(3)–C(4) | 1.344(5) | N(1)–Co(1)–N(2) | 90.34(12) |
| N(4)–C(5) | 1.311(5) | N(4C)–Co(1)–N(2A) | 87.92(11) |
| N(4)–C(7) | 1.364(5) | N(4B)–Co(1)–N(2A) | 92.08(11) |
| N(5)–C(5) | 1.352(5) | N(2A)–Co(1)–N(2) | 180.00(5) |
| | | **5** | |
| Cd(1)–O(1) | 2.258(10) | N(5)–C(4) | 1.361(9) |
| Cd(1)–N(2) | 2.307(7) | C(5)–C(6) | 1.337(12) |
| Cd(1)–N(4B) | 2.328(6) | O(1A)–Cd(1)–O(1) | 180.000(2) |
| N(2)–C(1) | 1.280(10) | O(1A)–Cd(1)–N(2) | 94.1(4) |
| N(2)–C(3) | 1.360(12) | O(1)–Cd(1)–N(2) | 85.9(4) |
| N(3)–C(2) | 1.335(10) | N(2)–Cd(1)–N(2A) | 180.000(1) |
| N(3)–C(1) | 1.356(10) | O(1A)–Cd(1)–N(4B) | 94.3(4) |
| C(2)–C(3) | 1.406(12) | O(1)–Cd(1)–N(4B) | 85.7(4) |
| N(4)–C(4) | 1.293(9) | N(2)–Cd(1)–N(4B) | 85.8(2) |
| N(4)–C(6) | 1.389(11) | N(2A)–Cd(1)–N(4B) | 94.2(2) |
| N(5)–C(5) | 1.345(10) | N(4B)–Cd(1)–N(4C) | 180.000(1) |
| | | **6** | |
| Co(1)–N(2) | 2.117(5) | N(5)–C(5) | 1.353(8) |
| Co(1)–O(1) | 2.182(5) | C(5)–C(6) | 1.318(9) |
| Co(1)–N(4B) | 2.121(5) | N(2A)–Co(1)–N(2) | 180.0(3) |
| N(2)–C(1) | 1.318(7) | N(2)–Co(1)–N(4B) | 93.27(18) |
| N(2)–C(3) | 1.364(8) | N(2)–Co(1)–N(4C) | 86.73(18) |
| N(3)–C(1) | 1.350(7) | N(4B)–Co(1)–N(4C) | 180.0(3) |
| N(3)–C(2) | 1.375(7) | N(2A)–Co(1)–O(1) | 89.9(2) |
| C(2)–C(3) | 1.350(9) | N(2)–Co(1)–O(1) | 90.1(2) |
| N(4)–C(4) | 1.317(7) | N(4B)–Co(1)–O(1) | 92.8(2) |
| N(4)–C(6) | 1.374(8) | N(4C)–Co(1)–O(1) | 87.2(2) |
| N(5)–C(4) | 1.347(7) | O(1)–Co(1)–O(1A) | 180.0(4) |

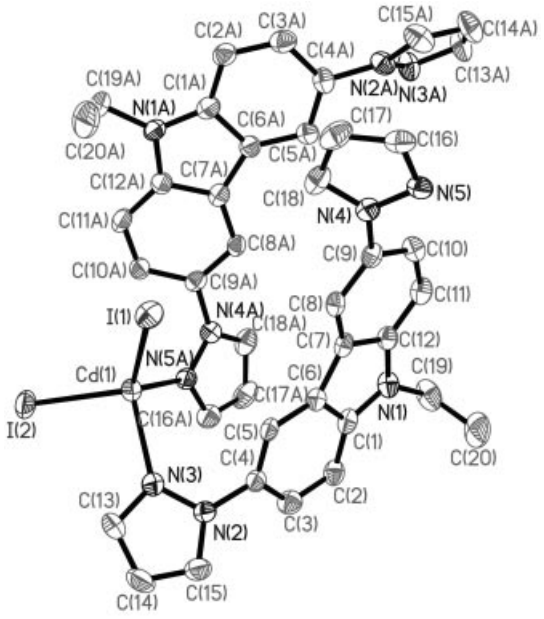


Figure 1. ORTEP diagram showing the structure of compound **1** with thermal ellipsoids at the 50% probability level and the atom-labeling scheme. Hydrogen atoms have been omitted for clarity.

center running along the *a* direction with a long pitch of about 3.819 Å (distance between two Cd centers with the same phase). At the widest point the diameter of the helix is 8.990 Å. The adjacent helical chains in $[CdL^1I_2]_n$, one of which is left-handed and the other right-handed, are not entangled but interact through C–H···I interactions (H···I 3.207 Å, ∠C–H···I 156.2°) between two helical chains to generate a very loose double-stranded helical chain [Figure 2(b)]. To illustrate this more clearly, the left- and right-handed helical chains are represented in Figures 2(a) and (c), respectively. These double-stranded helical chains are further extended into a two-dimensional architecture by C–H···I (H···I 3.207 Å, ∠C–H···I 156.2°; H···I 3.135 Å, ∠C–H···I 175.2°) interactions along the *b* axis (Figure 3). Taking the van der Waals radii of H and I to be 1.20 and 2.15 Å, respectively, any H···I contact of less than 3.35 Å and C–H···I angle greater than 130° can therefore be considered as being significant.[13–15] Because left- and right-handed helical chains coexist in the crystal structure, the whole crystal is mesomeric and does not exhibit chirality.

### *Crystal Structure of $[\{AgL^1SO_3PhCH_3\}_2(CH_3OH)(H_2O)]_n$ (2)*

The structure of complex **2** consists of a novel two-dimensional double helical chain. As depicted in Figure 4, the structure of **2** reveals that the asymmetric unit contains two crystallographically and conformationally inequivalent molecules (a) and (b). Each silver(I) center is three-coordinate to two nitrogen donors of two independent $L^1$ ligands [Ag(1)–N(3) 2.19(2) Å, Ag(1)–N(5A) 2.056(16), Ag(2)–N(8)

 © 2007 Wiley-VCH Verlag GmbH & Co. KGaA, Weinheim 

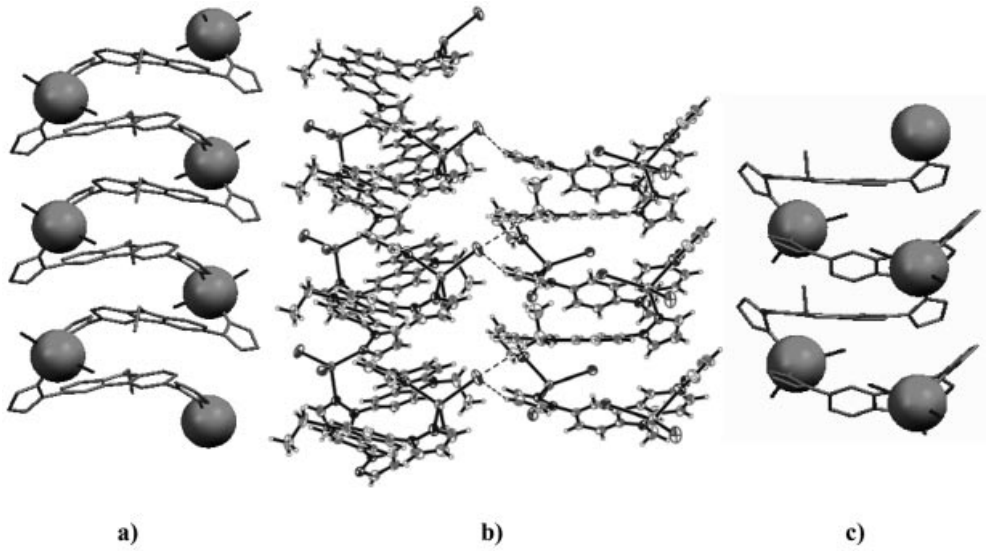


Figure 2. Ball-and-stick model of **1**. Cd atoms are given as balls and H atoms have been omitted for clarity. (a) Left-handed chain and (b) ball-and-stick plot of the double helix bridged by C–H···I interactions (dotted lines) in complex **1**; (c) right-handed chain.

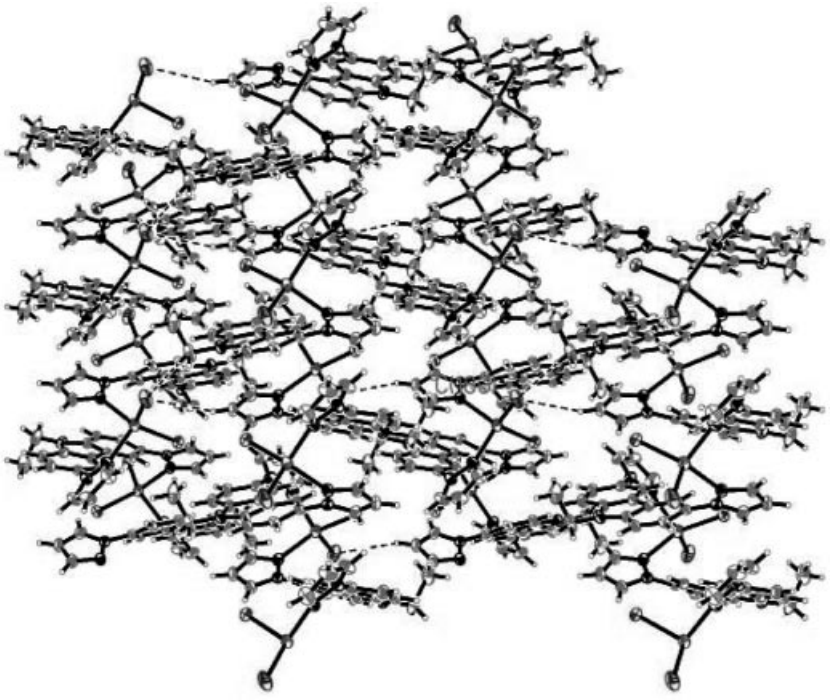

Figure 3. 2D network viewed along the *ab* plane in complex **1** showing C–H···I interactions as dotted lines.

2.17(2), Ag(1)–N(10A) 2.274(16) Å] and one oxygen atom of one *p*-toluenesulfonate anion [Ag(1)–O(1) 2.467(14), Ag(1)–O(4) 2.539(15) Å] to form a distorted trigonal geometry. The two pyrazolyl rings of $L^1$ also exhibit opposite orientations in complex **2**. These components connect to form an infinite polymeric chain structure similar to complex **1**. The dihedral angle between the two pyrazolyl rings of $L^1$ is about 71.4° or 108.6° and the dihedral angles between pyrazolyl rings and the corresponding carbazolyl rings linked to them are 57.6° and 43.0° in the Ag(1) chain. The dihedral angle between the two pyrazolyl rings of $L^1$ is about 73.9° or 106.1° and the dihedral angles between the pyrazolyl rings and the corresponding carbazolyl rings linked to them are 42.3° and 63.0° in the Ag(2) chain. Two loose single-stranded helical chains are formed by self-assembly of $[AgL^1{}_2SO_3PhCH_3]$ through coordination of the *meta*-bound peripheral pyrazole-N of this unit to the neighboring $Ag^I$ center running along the crystallographic $2_1$ axis in the *b* direction with a long pitch of about 5.3385 Å; at the widest point the diameter of the helix is 8.7711 Å.

 © 2007 Wiley-VCH Verlag GmbH & Co. KGaA, Weinheim 

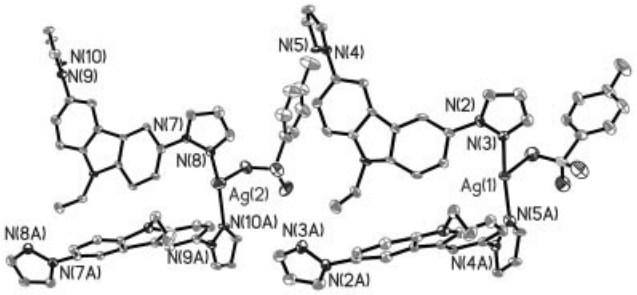


Figure 4. ORTEP diagram showing the structure of compound **2** with thermal ellipsoids at the 50% probability level. H atoms and water and methanol molecules have been omitted for clarity.

In addition, like complex **1**, the adjacent helical chains in compound **2**, one of which is left-handed and the other right-handed, are not entangled together but interact through an S–O···H interaction (H···O 2.469 Å, ∠ S–O···H 136.5°), which alternates between the two helical chains to generate a loose, double-stranded helical chain. Taking the van der Waals radii of H and O to be 1.20 and 1.40 Å, respectively, any H···O contact less than 2.60 Å and S–O···H angle above 130° can be considered to be significant. To illustrate this clearly, the left- and right-handed helical chains are represented in Figure 5. Like complex **1**, these double-stranded helical chains are further extended into a two-dimensional architecture by O···H–C hydrogen-bond interactions between the ligands and oxygen atoms of adjacent chains (O···H 2.455 Å, ∠ O···H–C 152.1°) and a very weak π–π stacking interaction (the shortest distance between carbazolyl rings is 4.3477 Å) along the *a* axis in compound **2** (Figure 6). The whole crystal is mesomeric and does not exhibit chirality, just like compound **1**.

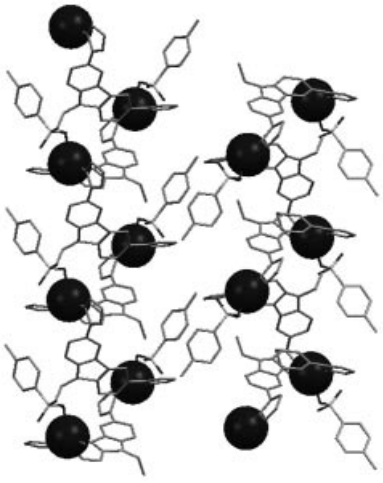

Figure 5. A ball-and-stick model of complex **2** showing the helicity. Ag atoms are given as balls and H atoms and water and methanol molecules have been omitted for clarity.

### *Crystal Structure of $[CdL^2_2(NCS)_2]_n$ (3)*

The coordination environment of the $Cd^{II}$ ion in complex **3** is shown in Figure 7. Each $Cd^{II}$ center, which is located at an inversion center, is in an octahedral environment com-

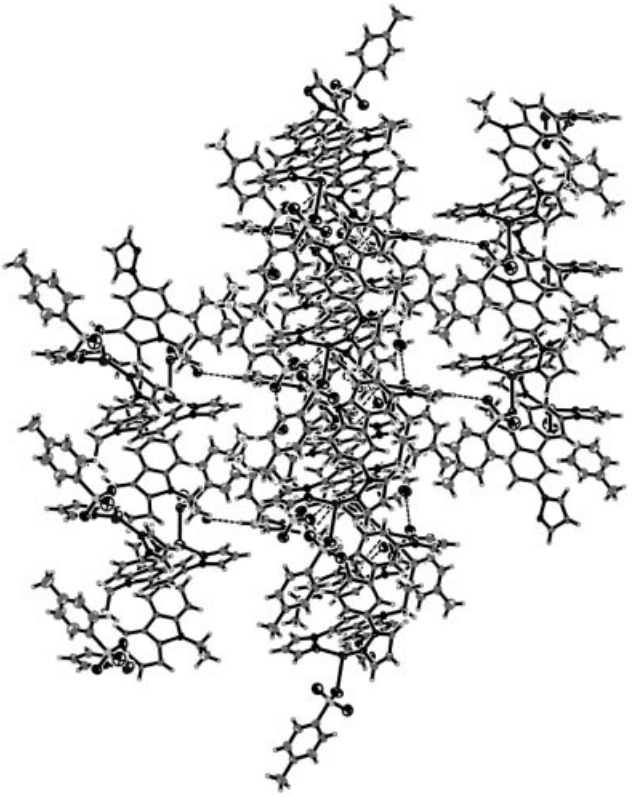

Figure 6. 2D network viewed along the *ab* plane in compound **2** showing the π–π stacking interactions and S–O···H and C–H···O interactions (dotted lines); the shortest H···O interaction is 2.455 Å.

posed of two nitrogen atoms from two $NCS^-$ groups in the axial positions and four imidazolyl nitrogen atoms from four $L^2$ molecules in the equatorial plane. The Cd–$N_{NCS}$ [2.347(3) Å] bond length is longer than Cd–$N_{im}$ [Cd–N(1) 2.345(2), Cd–N(5) 2.323(3) Å], and N–Cd–N bond angles with the same orientational fall in the range 88.59(12)–91.04(11)°. The two terminal $NCS^-$ groups are bent, with a

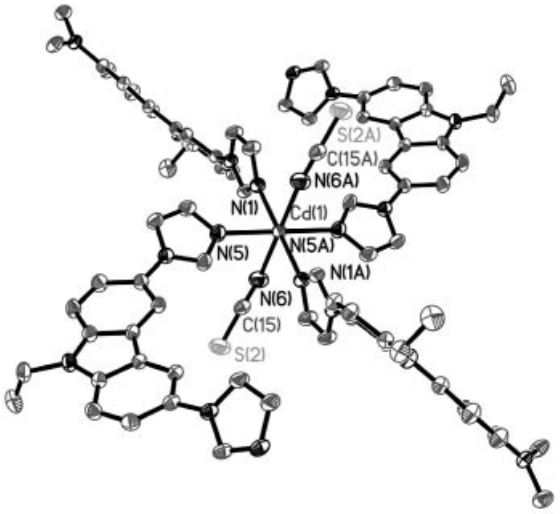


Figure 7. Octahedral coordination geometry around the cadmium center in **3**.

 © 2007 Wiley-VCH Verlag GmbH & Co. KGaA, Weinheim 

Cd(1)–N(6)–C(15) bond angle of 140.4(3)°, and are coordinated axially in opposite directions. The two imidazolyl rings within each ligand deviate from coplanarity, the dihedral angles between each terminal imidazolyl ring and the central carbazole unit being 139.8° and 31.4°.

The two imidazolyl rings of $L^2$ in complex **3** adopt the same orientation, the dihedral angle between two imidazolyl rings being 54.3°, and each one bridges two $Cd^{II}$ centers to form a 2D sheet containing $[Cd_4L^2_4]$ macrocycles as subunits. The $Cd^{II}$ atoms lie at the nodes of a rhombic grid in the undulating $[CdL^2_2(NCS)_2]_n$ layer, with ligand-bridging Cd···Cd distances of 23.744 and 12.769 Å (Figure 8). Each layer contains π–π interactions (the shortest distance between parallel carbazole rings is 3.89 Å), and these layers are stacked by C–H···S (H···S 2.913 Å) interactions along the *c* axis (Figure 9) to form a 3D network. Taking the van der Waals radii of H and S to be 1.00 and 2.05 Å, respectively, any H···S contact less than 3.05 Å can be considered significant. The H···S distance of 2.913 Å indicates the formation of C–H···S hydrogen bonds. C–H···S hydrogen-bonding interactions are very important in several novel supramolecular structures.[16]

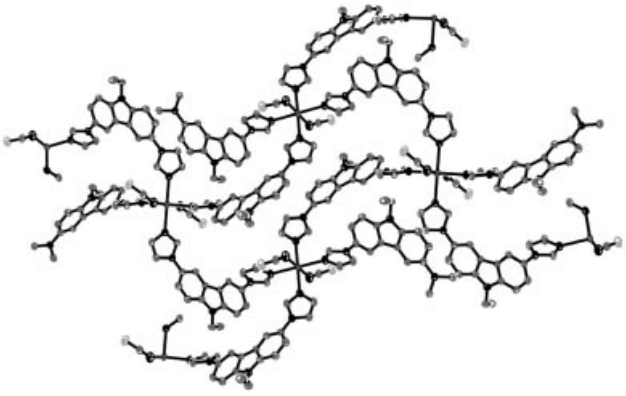

Figure 8. Two-dimensional grid structure of **3**.

### *Crystal Structure of $[CoL^2_2(NCS)_2(CHCl_3)_2]_n$ (4)*

The coordination environment of the $Co^{II}$ ion in **4** is shown in Figure 10. Each metal center is six-coordinate to two NCS groups and four $L^2$ ligands. The Co–N bond involving the NCS group [Co–$N_{NCS}$ 2.128(3) Å] is shorter than the other Co–N bonds [2.144(3) and 2.161(3) Å]. It is clear that each $Co^{II}$ center lies in the same octahedral coordination environment as complex **3**, and N–Co–N angles with the same orientation lie in the range 87.92(11)–92.08(11)°, similar to that for $Cd^{II}$. The oppositely oriented N–Co–N bond angles for $NCS^-$ and the $L^2$ ligands are 180°. The NCS ligands are coordinated axially in a terminal mode with angles of 180°. The two imidazolyl rings within each $L^2$ deviate by 50.2° and 140.7°, respectively, from the carbazole plane. The two imidazolyl rings of $L^2$ in complex **4** also adopt the same orientation and their dihedral angle is 65.0°. Selected bond lengths and angles for **4** are listed in Table 1.

Figure 11 shows the lamellar network of **4** in which the adjacent $Co^{II}$ centers are linked by a bridging $L^2$ ligand in two different directions to form large and nearly square repeating grids (the ligand-bridging Co···Co distances are 12.492 and 20.845 Å) in a 2D sheet. Each sheet contains weak π–π interactions[17] (the shortest distance between parallel carbazole rings is 4.225 Å), and these sheets are stacked by π–π (the shortest distance between parallel carbazole rings is 3.753 Å) and S···S (S···S 3.589 Å) interactions along the *a* axis (Figure 12) to form a 3D network. Taking the van der Waals radii of S to be 2.05 Å, any S···S contact less than 4.10 Å and C–S···S angle greater than 130° may therefore potentially be considered significant. The S···S distance of 3.589 Å and C–S···S angle of 153.2° in complex **4** indicate such an S···S interaction. In general, weak S···S interatomic interactions are often observed in multi-sulfur systems,[18] and these S···S weak interactions in complex **4** construct a novel supramolecular network structure. The shortest intersheet Co···Co distance is 13.139 Å. The coordination environment of the metal ions is similar

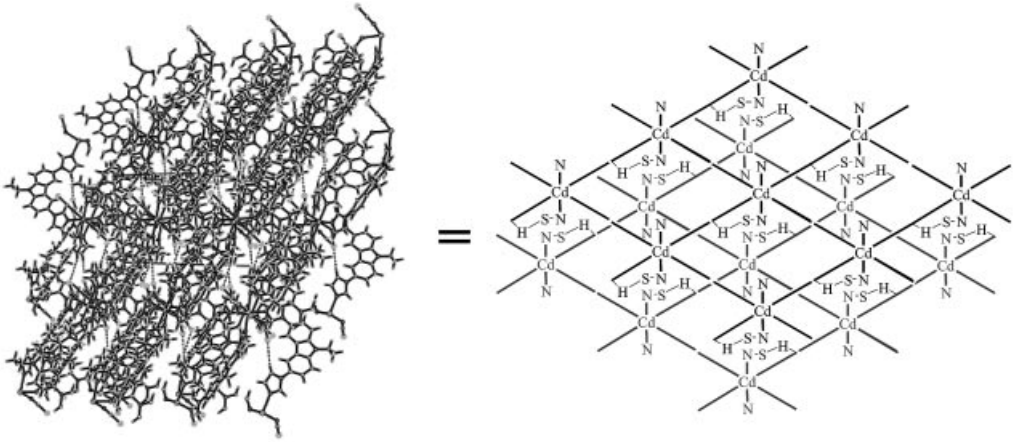

Figure 9. Molecular packing viewed along the *c* axis showing the intermolecular hydrogen bond C–H···S and π–π interactions.

 © 2007 Wiley-VCH Verlag GmbH & Co. KGaA, Weinheim 

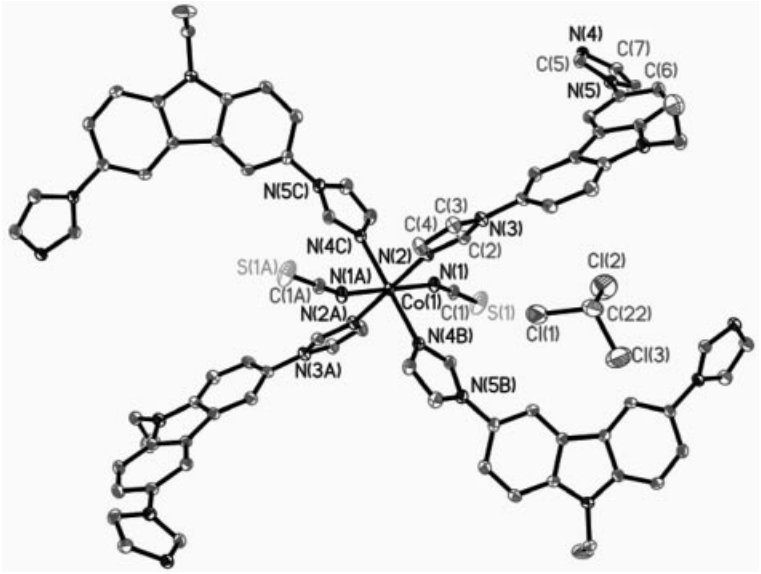


Figure 10. Octahedral coordination geometry around the cobalt center in **4**.

to that in complex **3**, but they adopt a different stacking arrangement due to the presence of different metal ions.

### *Crystal Structure of $[CdL^2_2(NO_3)_2(CH_3OH)_2]_n$ (5)*

The crystallographic analysis of complex **5** revealed that its structure is a 1D polymeric chain structure which is constituted by $[CdL^2_2(NO_3)_2]$ units. As shown in Figure 13, the $Cd^{II}$ atoms reside on crystallographic inversion centers and each has a slightly distorted octahedral $[CdN_4O_2]$ coordination geometry with the equatorial sites occupied by imidazolyl nitrogen donors from $L^2$; the axial positions are occupied by two monodentate nitrate counterions. The Cd–N and Cd–O bonds fall in the range of 2.307(7)–2.328(6) Å and 2.258(10) Å, respectively, which are very close to the corresponding bond lengths found in $[Cd(NO_3)_2(L)_2]$ [L = 2,5-bis(3-pyridyl)-3,4-diaza-2,4-hexadiene].[7] Two imidazolyl rings of $L^2$ also adopt the same orientation with a dihedral angle of 67.9°.

Compound **5** adopts a chain motif in the solid state with the $Cd^{II}$ centers linked by four crystallographically equiva-

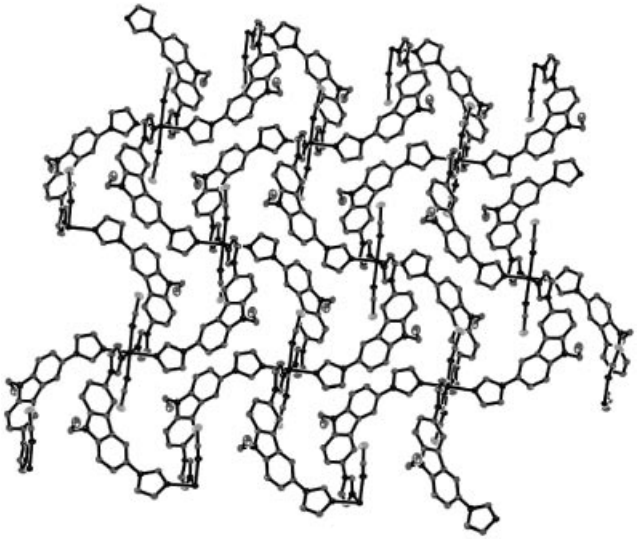

Figure 11. Two-dimensional grid structure of **4**.

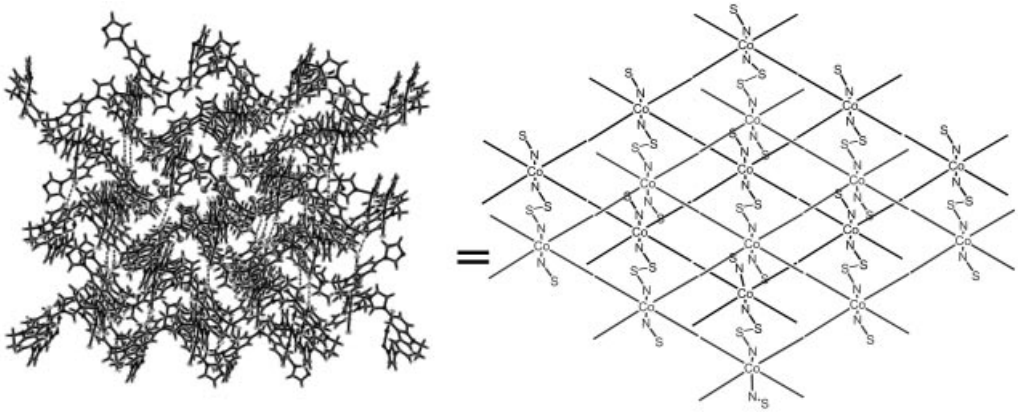

Figure 12. Molecular packing viewed along the *c* axis showing the intermolecular S···S and π–π interactions (dotted lines).

 © 2007 Wiley-VCH Verlag GmbH & Co. KGaA, Weinheim 

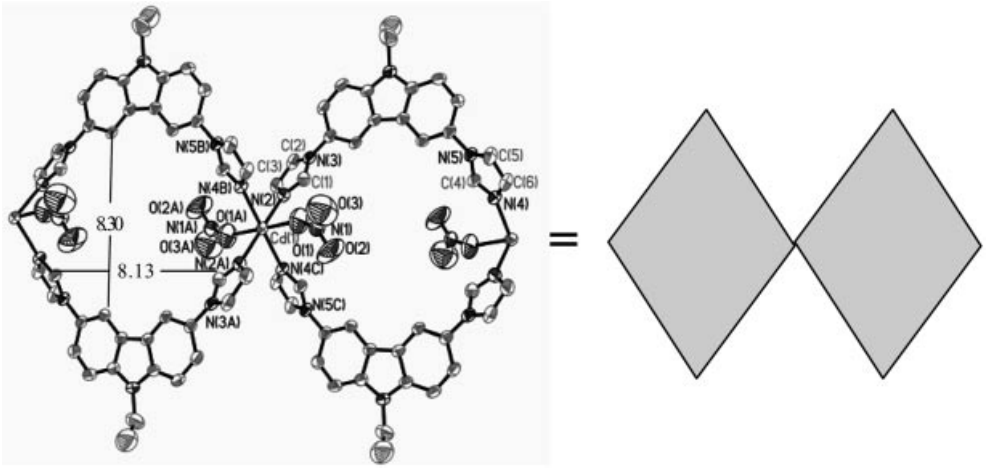


Figure 13. View of the basic box unit in the polymer chains of **5** (methanol molecules have been omitted for clarity).

lent $L^2$ ligands into an undulating one-dimensional chain running along the *b* axis (Figure 14). As shown in Figure 13, the individual "links" in the chain consist of $M_2L_2$ units, which a form 26-membered ring. The approximate (crystallographic) dimensions of the rings are $8.13 \times 8.30$ Å$^2$ (Figure 13). The intra- and interchain Cd···Cd distances are both 11.861 Å. Two crystallographically equivalent monodentate $NO_3^-$ ions are located above and below the $M_2L_2$ ring planes. In addition, hydrogen-bonding interactions between the chains, involving one uncoordinated O of the monodentate nitrate ion and H on the methyl and ethyl group of a ligand in an adjacent chain, are present in **5** (Figure 15). The O···H contacts are 2.498 and 2.534 Å. The existence and structural importance of weak C–H···O hydrogen-bonding interactions are now well established and they are present in many molecular and polymeric compounds.[19–22] O···H–C hydrogen bonds, although they are weak and are accompanied by π–π interactions (the shortest distance between parallel carbazolyl rings is 3.685 Å), contribute significantly to the structural organization of **5** in the crystalline phase, giving rise to a two-dimensional arrangement in which one-dimensional chains align together in a shoulder-to-shoulder fashion to generate a 2D sheet along the *a* axis. It is very interesting that these sheets are stacked to form a 3D structure along the *c* axis by intersheet hydrogen-bonding interactions and π–π interactions (the shortest distance between parallel carbazolyl rings is 3.4791 Å). Figure 16 shows that these sheets are overlapped vertically by the other uncoordinated O of the monodentate nitrate ion and two H atoms of the phenyl group of a ligand in the other sheet (the O···H contacts are 2.460 and 2.475 Å, respectively).

The metal ion in this complex is the same as in complex **3** but the anion is different, which indicates that the nature of the anion is a significant factor in controlling the structural topology of these metal-organic supramolecular architectures and offers the opportunity to control the coordination networks by changing the anion.

### *Crystal Structure of $[CoL^2{}_2(NO_3)_2(CH_3OH)_2]_n$ (6)*

In general, all the $Co^{II}$ centers in the coordination polymers generated from cobalt nitrate and *N*,*N*′-bidentate ligands adopt a $\{CoN_3O_4\}$ coordination environment.[22] zur Loye[19] reported the first $\{CoN_4O_2\}$ coordination sphere in coordination polymers. Compound **6** reported here also has a $\{CoN_4O_2\}$ coordination sphere and is similar to compound **5**. One of the Co–N bond lengths is 2.117(5) Å, which is significantly shorter than the corresponding Co–N bond lengths [2.210(2)–2.261(2) Å] in the $\{CoN_4N'_2\}$ coordination spheres but is consistent with the Co–N bond lengths in a $\{CoN_3O_4\}$ coordination sphere.[23] The two imidazolyl rings of the ligand also adopt the same orientation, with a dihedral angle of 69.4°.

Compound **6** is isostructural with **5** except that the $Cd^{II}$ centers are replaced by $Co^{II}$ atoms. The intra- and interchain Co···Co distances are both 11.72 Å. The same interchain hydrogen-bonding system is present in **6** (O···H 2.27, O···C 2.939 Å; O···H–C 125.9°) and π–π interactions

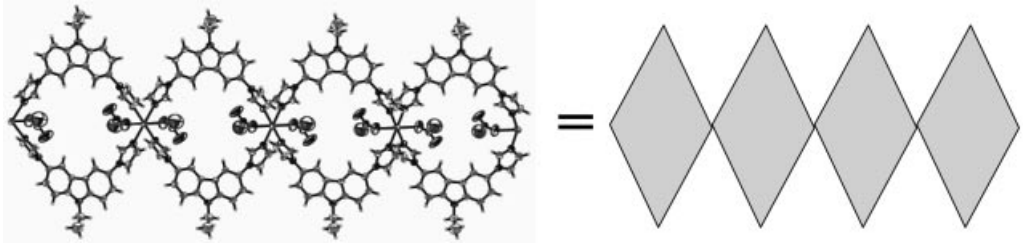

Figure 14. 1D chain in **5**.

 © 2007 Wiley-VCH Verlag GmbH & Co. KGaA, Weinheim 

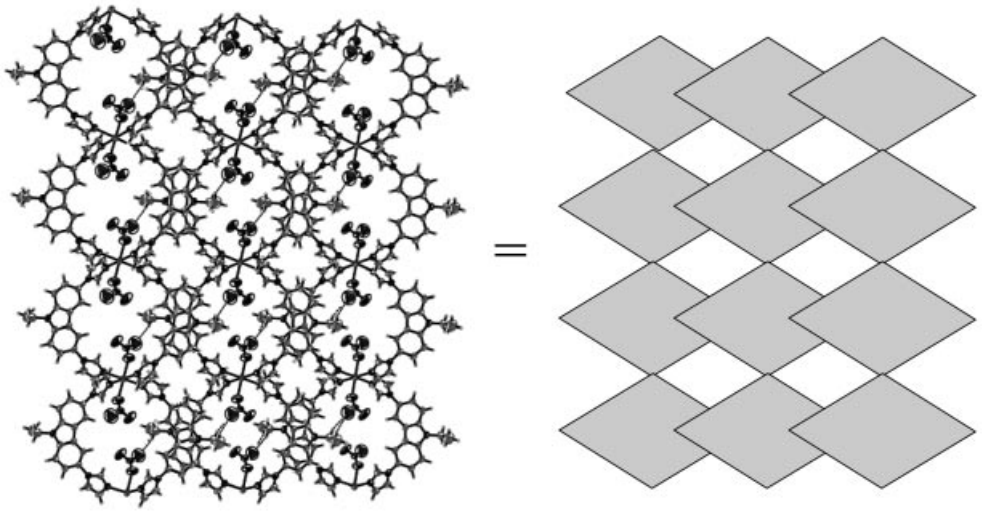

Figure 15. A view of the 2D networks formed by adjacent 1D chains in **5** showing the C–H···O hydrogen-bonding system and π–π interactions (dotted lines).

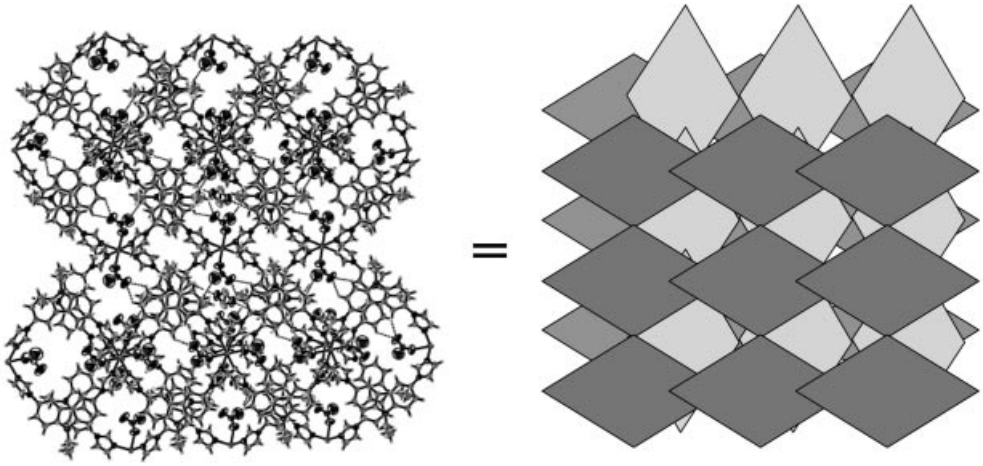

Figure 16. A view of the 3D network formed by interlayer C–H···O hydrogen bonding and π–π interactions (dotted lines).

(the shortest distance between parallel carbazolyl rings is 3.743 Å). The same intersheet hydrogen-bonding system is also present in **6** (O···H 2.56 and 2.514 Å; O···C 3.153 and 3.12 Å; O···H–C 122.0° and 123°) and π–π interactions (the shortest distance between parallel carbazolyl rings is 3.8135 Å). When compared with complex **4**, this complex again shows that the nature of the anion is a significant factor in controlling the structural topology of these metal-organic supramolecular architectures.

When the ligands of complexes **1**–**6** are compared, it can be seen that the two pyrazolyl rings of $L^1$ keep the same opposite orientation with a different dihedral angle during the complex formation (the dihedral angles of the two pyrazole rings are 64.1° for **1** and 71.4°, 73.9° for **2**) and the two imidazolyl rings of $L^2$ keep the same orientation with a different dihedral angle during the complex formation (the dihedral angles of the two imidazole rings are 54.3°, 65.0°, 67.9°, and 69.4° for **3**, **4**, **5**, and **6**, respectively). The opposite orientation and corresponding angle allow $L^1$ to coordinate the metal ion as a bidentate ligand using the nitrogen atom and form 1D helical chains, whereas the same orientation and corresponding angle allow $L^2$ to coordinate the metal ion as a bidentate ligand using the nitrogen atom and form a 2D grid or a 1D double chain. Finally, the intermolecular nonbonding weak interactions link low-dimensional entities into high-dimensional supramolecular frameworks.

In summary, two novel functional ligands and six coordination complexes (**1**–**6**) have been prepared and structurally characterized; the latter display metal-organic supramolecular architectures. As flexible bridging ligands can easily produce unique frameworks with useful properties due to their flexibility and orientational freedom,[24] we designed and synthesized conveniently two novel functional flexible ligands, namely 9-ethyl-3,6-dipyrazolylcarbazole and 9-ethyl-3,6-diimidazolylcarbazole, that are capable of coordinating to metal centers through their respective imidazolyl or pyrazolyl nitrogen atoms form novel 2D or 3D polymers. The results indicate that the metal ion, anion, and non-

 © 2007 Wiley-VCH Verlag GmbH & Co. KGaA, Weinheim 

Table 2. Crystallographic data and structure refinement for complexes **1**–**6**.

| Complex | **1** | **2** | **3** | **4** | **5** | **6** |
|---|---|---|---|---|---|---|
| Empirical formula | $C_{20}H_{17}CdI_2N_5$ | $C_{55}H_{54}Ag_2N_{10}O_8S_2$ | $C_{42}H_{34}CdN_{12}S_2$ | $C_{44}H_{36}Cl_6CoN_{12}S_2$ | $C_{42}H_{42}CdN_{12}O_8$ | $C_{42}H_{42}CoN_{12}O_8$ |
| Formula mass | 693.59 | 1262.95 | 883.33 | 1068.60 | 955.28 | 901.81 |
| Crystal system | orthorhombic | monoclinic | monoclinic | monoclinic | monoclinic | monoclinic |
| Space group | $P2_12_12_1$ | $P2_1/c$ | $P2_1/c$ | $P2_1/n$ | $C2/c$ | $C2/c$ |
| $a$ [Å] | 7.6381(13) | 28.199(7) | 11.1196(15) | 13.139(3) | 17.341(5) | 17.245(5) |
| $b$ [Å] | 17.050(3) | 10.677(3) | 12.7695(17) | 12.492(2) | 16.186(5) | 15.876(5) |
| $c$ [Å] | 17.623(3) | 19.036(4) | 14.711(2) | 14.902(3) | 15.353(5) | 15.436(4) |
| $\beta$ [°] | 90 | 102.798(13) | 103.001(2) | 95.838(3) | 107.148(4) | 106.503(4) |
| $V$ [Å$^3$] | 2295.0(7) | 5589(2) | 2035.3(5) | 2433.1(8) | 4118(2) | 4052.1(19) |
| $Z$ | 4 | 4 | 2 | 2 | 4 | 4 |
| $D_{calcd.}$ [g cm$^{-3}$] | 2.007 | 1.490 | 1.441 | 1.459 | 1.541 | 1.478 |
| $\theta_{range}$ [°] | 2.31–25.01 | 2.20–25.01 | 2.14–25.00 | 1.97–25.10 | 1.76–25.09 | 1.78–25.10 |
| Total data | 12094 | 13706 | 10390 | 12529 | 10037 | 9503 |
| Unique data | 4022 | 4811 | 3583 | 4321 | 3508 | 3371 |
| Number of refined parameters | 253 | 696 | 260 | 296 | 286 | 287 |
| $R_1$ | 0.0347 | 0.0295 | 0.0359 | 0.0560 | 0.0768 | 0.0769 |
| $wR_2$ | 0.0820 | 0.0782 | 0.0892 | 0.1336 | 0.1952 | 0.1803 |
| GOF | 1.024 | 1.003 | 1.035 | 1.002 | 1.043 | 1.014 |

bonding and π–π interactions are significant factors in controlling the structural topology of these metal-organic supramolecular architectures.

## Experimental Section

All chemicals and solvents were dried and purified by usual methods. Elemental analyses were performed with an Elmentar Vario EL-III analyzer. IR spectra were recorded with a Nicolet FT-IR Nexus 870 instrument in the range 4000–400 cm$^{-1}$ by using KBr pellets. $^1$H NMR spectra were recorded with a Bruker 600 MHz Ultrashield spectrometer and are reported in parts per million (ppm) from TMS ($\delta$). Melting points were recorded with a Perkin–Elmer Pris-1 DMDA-V1 analyzer under $N_2$ at a heating rate of 5 °C min$^{-1}$. The luminescent spectra were recorded for single crystals at room temperature using a Fluorolog-3-TAU steady-state/lifetime spectrofluorometer. The excitation slit and the emission slit were 2.5 nm.

**X-ray Crystallography:** Single-crystal X-ray diffraction measurements were performed with a Bruker Smart 1000 CCD diffractometer equipped with a graphite crystal monochromator situated in the incident beam for data collection at room temperature. Unit cell parameters and data collections were performed with Mo-$K_\alpha$ radiation ($\lambda$ = 0.71073 Å). Unit cell dimensions were obtained with least-squares refinements, and all structures were solved by direct methods using SHELXL-97.[26] The other non-hydrogen atoms were located in successive difference Fourier syntheses. The final refinement was performed by full-matrix least-squares methods with anisotropic thermal parameters for non-hydrogen atoms on $F^2$. The hydrogen atoms were added theoretically as riding on their parent atoms. Crystallographic crystal data and processing parameters for complexes **1**–**6** are given in Table 2. Selected bond lengths and bond angles are listed in Table 1.

CCDC-611826 (for **1**), -611825 (for **2**), -274291 (for **3**), -278330 (for **4**), -278332 (for **5**) and -278331 (for **6**) contain the supplementary crystallographic data for this paper. These data can be obtained free of charge from The Cambridge Crystallographic Data Centre via www.ccdc.cam.ac.uk/data_request/cif.

**Preparation of 9-Ethyl-3,6-dipyrazolylcarbazole ($L^1$):** CuI (0.27 g, 1.35 mmol), 1,10-phenanthroline (0.60 g, 3.02 mmol), and 3 mL of dmf were added to a three-necked flask equipped with a magnetic stirrer and a reflux condenser. This mixture was refluxed for 5 min in an oil bath at 120 °C, cooled to room temperature, and then pyrazole (3.65 g, 53.61 mmol), KO*t*Bu (6.05 g, 54.00 mmol), 9-ethyl-3,6-diiodocarbazole (3.00 g, 6.72 mmol),[11] and 18-crown-6 (little) were added and the mixture heated to 130 °C for 36 h. It was then cooled to room temperature and the residue was extracted with 150 mL of dichloromethane, washed three times with distilled water, and dried with anhydrous magnesium sulfate. It was then filtered and concentrated. Recrystallization from ethyl acetate produced light yellow crystals. Yield: 1.82 g (84%). M.p. 202–202.4 °C. $^1$H NMR (600 MHz, [D$_6$]DMSO): $\delta$ = 1.35 (t, $J$ = 7.20 Hz, 3 H, $CH_3$), 4.51 (q, $J$ = 7.20 Hz, 2 H, $CH_2$), 6.57 (s, 2 H, phenyl), 7.75 (d, $J$ = 8.40 Hz, 4 H, phenyl), 7.98 (d, $J$ = 7.2 Hz, 2 H, pyrazolyl), 8.53 (d, $J$ = 1.8 Hz, 2 H, pyrazolyl), 8.71 (d, $J$ = 0.6 Hz, 2 H, pyrazolyl) ppm. $C_{20}H_{17}N_5$ (327.39): calcd. C 73.37, H 5.23, N 21.39; found C 73.67, H 5.40, N 21.16. IR (KBr): $\tilde{\nu}$ = 3141 (w), 2973 (m), 2937 (w), 1636 (m), 1618 (m), 1584 (w), 1509 (vs), 1483 (vs), 1392 (m), 1316 (s), 1223 (m), 1195 (m), 1153 (m), 1085 (w), 1046 (m), 936 (m), 881 (m), 835 (w), 799 (m), 750 (s), 664 (m), 615 (m) cm$^{-1}$.

**Preparation of 9-Ethyl-3,6-diimidazolylcarbazole ($L^2$): $L^2$** was obtained by a similar method to **$L^1$**. Yield: 1.72 g (79%). M.p. 221–221.6 °C. $^1$H NMR (500 MHz, [D$_6$]DMSO): $\delta$ = 1.34 (t, $J$ = 7.04 Hz, 3 H, $CH_3$), 4.54 (q, $J$ = 6.98 Hz, 2 H, $CH_2$), 7.15 (s, 2 H, imidazolyl), 7.79 (d, $J$ = 8.72 Hz, 2 H, phenyl), 7.75 (t, $J$ = 5.12 Hz, 4 H, phenyl), 8.22 (s, 2 H, imidazolyl), 8.50 (d, $J$ = 1.36 Hz, 2 H, imidazolyl) ppm. $C_{20}H_{17}N_5$ (327.39): calcd. C 73.37, H 5.23, N 21.39; found C 73.30, H 5.19, N 21.07. IR (KBr): $\tilde{\nu}$ = 3104 (m), 2969 (w), 2863 (w), 1637 (m), 1620 (m), 1581 (m), 1506 (vs), 1380 (m), 1320 (m), 1260 (m), 1228 (m), 1105 (m), 1063 (m), 904 (m), 804 (m), 663 (m) cm$^{-1}$.

**Preparation of $[CdL^1I_2]_n$ (1):** 9-Ethyl-3,6-dipyrazolylcarbazole (**$L^1$**; 32.74 mg, 0.1 mmol) and $CdI_2$ (36.62 mg, 0.1 mmol) were dissolved in MeOH (10 mL). The mixture was refluxed for 2 h at 70 °C and then cooled to room temperature to give a clear colorless solution. Pale colorless crystals suitable for X-ray diffraction were obtained after two weeks by slow evaporation of the methanol solution at room temperature. Yield: 61.73 mg (89%). IR (KBr): $\tilde{\nu}$ = 3117 (m), 2971 (w), 2925 (w), 1632 (m), 1613 (m), 1519 (s), 1487 (s), 1403 (m), 1383 (m), 1230 (s), 1192 (m), 1149 (w), 1067 (m), 1038 (m),

 © 2007 Wiley-VCH Verlag GmbH & Co. KGaA, Weinheim 

958 (w), 894 (m), 874 (m), 805 (m), 746 (vs), 670 (w) $cm^{-1}$. $C_{20}H_{17}CdI_2N_5$ (693.59): calcd. C 34.63, H 2.47, N 10.10; found C 35.01, H 2.50, N 10.15.

**Preparation of $\{[AgL^1SO_3PhCH_3]_2(CH_3OH)(H_2O)\}_n$ (2):** Complex **2** was prepared by a procedure similar to that of **1** except that AgOTs (27.79 mg, 0.1 mmol) was dissolved in MeOH (10 mL) and $H_2O$ (0.5 mL). Colorless transparent cube-shaped crystals of **2** suitable for X-ray structure determination were obtained in 81% yield. $C_{55}H_{54}Ag_2N_{10}O_8S_2$ (1263.0): calcd. C 52.31, H 4.31, N 11.09; found C 52.74, H 4.08, N 11.30. IR (KBr): $\tilde{\nu}$ = 3131 (w), 2978 (w), 2920 (w), 1629 (m), 1581 (m), 1516 (s), 1487 (s), 1404 (m), 1382 (m), 1351 (w), 1317 (m), 1188 (s), 1119 (m), 1064 (m), 1034 (m), 1007 (m), 814 (m), 763 (m), 677 (s), 615 (m), 565 (s) $cm^{-1}$.

**Preparation of $[CdL^2_2(NCS)_2]_n$ (3):** A solution of $L^2$ (65.48 mg, 0.20 mmol) in 5 mL of $CHCl_3$ solution was layered onto a solution of $Cd(SCN)_2$ (22.86 mg, 0.10 mmol) in MeOH (10 mL) and allowed to stand for ten days to give pale-yellow single crystals. Yield: 85% (75.08 mg). $C_{42}H_{34}CdN_{12}S_2$ (883.33): calcd. C 57.11, H 3.88, N 19.03; found C 56.89, H 3.68, N 18.67. IR (KBr): $\tilde{\nu}$ = 3130 (m), 2976 (w), 2933 (w), 2088 (vs), 2034 (s), 1621 (m), 1587 (m), 1508 (vs), 1388 (m), 1332 (m), 1303 (m), 1269 (m), 1228 (s), 1122 (m), 1065 (s), 924 (m), 873 (m), 808 (s), 736 (s), 659 (s) $cm^{-1}$.

**Preparation of $[CoL^2_2(NCS)_2(CHCl_3)_2]_n$ (4):** Complex **4** was prepared by a procedure similar to that for **3** but with $Co(SCN)_2$ (17.48 mg, 0.1 mmol) in place of $Cd(SCN)_2$. Yield: 89% (95.11 mg). $C_{44}H_{36}Cl_6CoN_{12}S_2$ (1068.6): calcd. C 49.45, H 3.40, N 15.73; found C 49.87, H 3.60, N 15.36. IR (KBr): $\tilde{\nu}$ = 3131 (m), 2977 (w), 2930 (w), 2076 (vs), 2033 (s), 1614 (w), 1585 (m), 1508 (vs), 1380 (m), 1330 (m), 1268 (m), 1229 (m), 1152 (w), 1123 (w), 1090 (w), 1064 (s), 935 (m), 833 (m), 809 (m), 744 (s), 661 (s) $cm^{-1}$.

**Preparation of $[CdL^2_2(NO_3)_2(CH_3OH)_2]_n$ (5):** Complex **5** was prepared by a procedure similar to that for **3** but with $Cd(NO_3)_2$ (34.60 mg, 0.1 mmol) instead of $Cd(SCN)_2$. Yield: 80% (76.42 mg). $C_{42}H_{42}CdN_{12}O_8$ (955.28): calcd. C 52.81, H 4.43, N 17.60; found C 52.98, H 4.05, N 17.38. IR (KBr): $\tilde{\nu}$ = 3134 (m), 2977 (w), 2928 (w), 1640 (w), 1615 (m), 1585 (w), 1515 (vs), 1405 (m), 1385 (vs), 1317 (s), 1272 (m), 1230 (m), 1143 (w), 1115 (m), 1066 (s), 931 (m), 873 (w), 809 (m), 742 (m), 659 (m), 663 (s) $cm^{-1}$.

**Preparation of $[CoL^2_2(NO_3)_2(CH_3OH)_2]_n$ (6):** Complex **6** was prepared by a procedure similar to that for **3** but with $Co(NO_3)_2$ (33.10 mg, 0.1 mmol) instead of $Cd(SCN)_2$. Yield: 85% (76.65 mg). $C_{42}H_{42}CoN_{12}O_8$ (901.81): calcd. C 55.94, H 4.69, N 18.64; found C 56.31, H 4.26, N 18.79.. IR (KBr): $\tilde{\nu}$ = 3142 (w), 2977 (w), 2929 (w), 1633 (w), 1581 (w), 1510 (vs), 1385 (vs), 1334 (m), 1309 (m), 1260 (m), 1231 (s), 1148 (w), 1117 (m), 1086 (m), 1063 (s), 965 (w), 937 (m), 866 (m), 811 (s), 742 (m), 660 (s) $cm^{-1}$.

**Thermogravimetric Analysis:** Complexes **2**, **4**, **5**, and **6** are unstable in air. Complexes **1** and **3** are stable under ambient conditions, and thermogravimetric experiments were performed on single-crystalline samples. The TG-DSC measurements of complexes **1** and **3** were determined in the range 20–800 °C under nitrogen. TG data show that **1** is stable up to 223 °C and then loses weight from 223 to 298 °C, corresponding to decomposition of ligand $L^1$. The final weight loss occurs at 543 °C. The TG data of **2** show that it is also stable up to 245 °C and then keeps losing weight from 245 °C to 301 °C, corresponding to decomposition of ligand $L^2$. The final weight loss occurs at 568 °C.

**Luminescent Properties:** Metal complexes are promising luminescent materials with potential applications as light-emitting materials (LEDs) owing to their ability to enhance, shift, and quench luminescent emission of organic ligands by metal coordination. The solid-state emission spectra of $L^1$, **1**, $L^2$, and **3** are shown in Figure 17(a) and (b). The nanosecond range of the lifetime in the solid state at 298 K reveals that the emission is fluorescent in nature. A comparison of the fluorescence spectra of $L^1$, **1**, $L^2$, and **3** suggests their emission origin. The solid-state fluorescent analyses show that the complexes exhibit different properties. Free $L^1$ exhibits an emission maximum at 414 nm with a shoulder peak at about 435 nm, which is completely invariant upon excitation in the range 270–369 nm; complex **1** presents a broad strong emission band with a maximum at 470 nm upon excitation in the range 275–383 nm, which can be tentatively assigned to a MLCT based on a significant red shift from $L^1$ to **1** and literature studies.[25] Free $L^2$ exhibits an emission maximum at 396 nm with a shoulder peak at about 412 nm, which is completely invariant upon excitation in the range 260–312 nm; complex **3** presents a sharp strong emission band with a maximum at 400 nm upon excitation in the range 268–362 nm, which is largely characteristic of an intraligand fluorescent emission. It is obvious that insoluble **1** and **3** possess strong fluorescent intensity, which suggests they may have potential applications in solvent-resistant fluorescent materials.

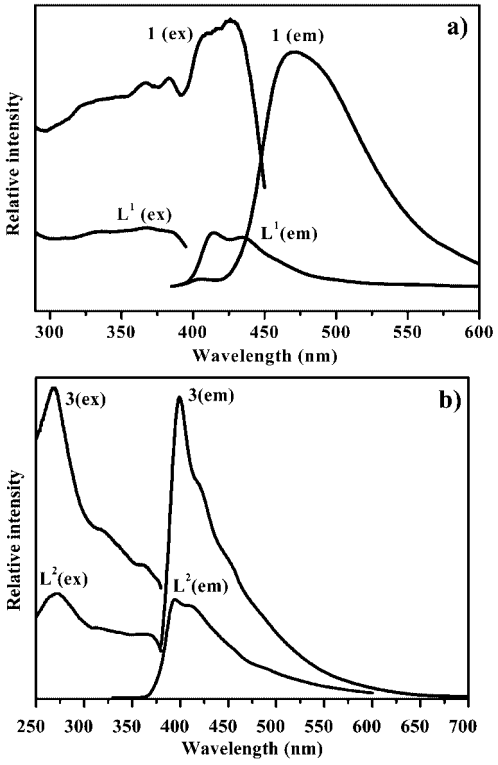


Figure 17. Fluorescent spectra of $L^1$ and complex **1** (a) and $L^2$ and complex **3** (b) in the solid state at room temperature.

## Acknowledgments

We thank the National Natural Science Foundation of China (50532030, 50325311, and 50335050), the Doctoral Program Foundation of the Ministry of Education of China, the Education Committee of Anhui Province (2006KJ032A and 2006KJ135B), the People with Ability Foundation of Anhui Province (2002Z021), the Team for Scientific Innovation Foundation of Anhui Province (2006KJ007TD), the Key Laboratory of Opto-Electronic Information Acquisition and Manipulation (Anhui University), and the

 © 2007 Wiley-VCH Verlag GmbH & Co. KGaA, Weinheim 

Ministry of Education, People with Ability Foundation of Anhui University for financial support.


[1] B. Moulton, M. J. Zaworotko, *Chem. Rev.* **2001**, *101*, 1629.

[2] a) M. J. Zaworotko, *Chem. Commun.* **2001**, 1; b) S. R. Batten, R. Robson, *Angew. Chem. Int. Ed.* **1998**, *37*, 1460; c) S. Kitagawa, M. Kondo, *Bull. Chem. Soc. Jpn.* **1998**, *71*, 1739; d) G. R. Desiraju, *Angew. Chem. Int. Ed. Engl.* **1995**, *34*, 2311.

[3] a) C. Janiak, *Angew. Chem. Int. Ed. Engl.* **1997**, *36*, 1431; b) C. Janiak, *Dalton Trans.* **2003**, 2781; c) O. M. Yaghi, H. Li, C. Davis, D. Richardson, T. L. Groy, *Acc. Chem. Res.* **1998**, *31*, 474.

[4] a) M. Eddaoudi, H. Li, O. M. Yaghi, *J. Am. Chem. Soc.* **2000**, *122*, 1391; b) H. Li, M. Eddaoudi, T. L. Groy, O. M. Yaghi, *J. Am. Chem. Soc.* **1998**, *120*, 8571; c) T. M. Reineke, M. Eddaoudi, M. Fehr, D. Kelley, O. M. Yaghi, *J. Am. Chem. Soc.* **1999**, *121*, 1651; d) N. L. Rosi, J. Eckert, M. Eddaoudi, D. T. Vodak, J. Kim, M. O'keeffe, O. M. Yaghi, *Science* **2003**, *300*, 1127; e) R. Kitaura, K. Seki, G. Akiyama, S. Kitagawa, *Angew. Chem. Int. Ed.* **2003**, *42*, 428; f) M. L. Tong, J. X. Shi, X. M. Chen, *New J. Chem.* **2002**, *26*, 814; g) W. B. Lin, L. Ma, O. R. Evans, *Chem. Commun.* **2000**, 2263; h) G. S. Matouzenko, G. Molnar, N. Brefuel, M. Perrin, A. Bousseksou, S. A. Borshch, *Chem. Mater.* **2003**, *15*, 550; i) V. Niel, A. L. Thompson, M. C. Muñoz, A. Galet, A. E. Goeta, J. A. Real, *Angew. Chem. Int. Ed.* **2003**, *42*, 3760; j) O. R. Evans, H. L. Ngo, W. Lin, *J. Am. Chem. Soc.* **2001**, *123*, 10395; k) J. S. Seo, D. Whang, H. Lee, S. I. Jun, J. Oh, Y. J. Jeon, K. Kim, *Nature* **2000**, *404*, 982; l) M. Fujita, Y. J. Kwon, S. Washizu, K. Ogura, *J. Am. Chem. Soc.* **1994**, *116*, 1151.

[5] a) O. M. Yaghi, G. M. Li, H. Li, *Nature* **1995**, *378*, 703; b) O. M. Yaghi, H. Li, T. L. Groy, *J. Am. Chem. Soc.* **1996**, *118*, 9096.

[6] a) C. Kirchner, B. Krebs, *Inorg. Chem.* **1987**, *26*, 3569; b) C. A. Hester, H. L. Collier, R. G. Baughman, *Polyhedron* **1996**, *15*, 4255; c) A. S. Abushamleh, H. A. Goodwin, *Aust. J. Chem.* **1979**, *32*, 513; d) U. Sakaguchi, A. W. Addison, *J. Chem. Soc., Dalton Trans.* **1979**, 600; e) A. Bendini, F. Mani, *Inorg. Chim. Acta* **1988**, *154*, 215; f) S. Fortin, A. L. Beauchamp, *Inorg. Chem.* **2000**, *39*, 4886; g) M. A. M. Lorente, F. Dahan, V. Petrouleas, A. Boussedsou, J.-P. Tuchagues, *Inorg. Chem.* **1995**, *34*, 5346; h) I. G. Dance, A. S. Abushamleh, H. A. Goodwin, *Inorg. Chim. Acta* **1980**, *43*, 217; i) A. D. Mighell, C. W. Reimann, F. A. Maucer, *Acta Crystallogr., Sect. B* **1969**, *25*, 60; j) J. Cancela, M. J. G. Garmendia, M. Quriós, *Inorg. Chim. Acta* **2001**, *313*, 156; k) R. Sang, M. Zhu, P. Yang, *Acta Crystallogr., Sect. E* **2002**, *58*, 172; l) B. H. Ye, F. Xue, G. Q. Xue, L. N. Ji, T. C. W. Mak, *Polyhedron* **1999**, *18*, 1785; m) C. A. Hester, R. G. Baughman, H. L. Collier, *Polyhedron* **1997**, *16*, 2893.

[7] a) S. W. Kaiser, R. B. Saillant, W. M. Butler, P. G. Rasmussen, *Inorg. Chem.* **1976**, *15*, 2681; b) S. W. Kaiser, R. B. Saillant, P. G. Rasmussen, *J. Am. Chem. Soc.* **1975**, *97*, 425; c) S. W. Kaiser, R. B. Saillant, W. M. Butler, P. G. Rasmussen, *Inorg. Chem.* **1976**, *15*, 2688; d) M. S. Haddad, D. N. Hendrickson, *Inorg. Chem.* **1978**, *17*, 2622; e) R. Usón, J. Gimeno, J. Forniés, F. Martínez, *Inorg. Chim. Acta* **1981**, *50*, 173; f) A. Maiboroda, G. Rheinwald, H. Lang, *Inorg. Chem. Commun.* **2001**, *4*, 381; g) P. Majumdar, S. M. Peng, S. Goswami, *J. Chem. Soc., Dalton Trans.* **1998**, 1569; h) R. Usón, L. A. Oro, J. Gimeno, M. A. Ciriano, J. A. Cabeza, *J. Chem. Soc., Dalton Trans.* **1983**, 323; i) A. P. Sadimenko, S. S. Basson, *Coord. Chem. Rev.* **1996**, *147*, 247.

[8] a) J. S. Casas, A. Castiñeiras, Y. Parajó, M. L. P. Parallé, A. Sánchez, A. S. González, J. Sordo, *Polyhedron* **2003**, *22*, 1113; b) A. S. Gonzalez, J. S. Casas, J. Sordo, U. Russo, M. I. Lareo, B. J. Regueiro, *J. Inorg. Biochem.* **1990**, *39*, 227; c) C. Lopez, A. Sanchez-Gonzalez, M. E. Garcia, J. S. Casas, J. Sordo, R. Graziani, U. Casellato, *J. Organomet. Chem.* **1992**, *434*, 261; d) B. J. Holliday, C. A. Mirkin, *Angew. Chem. Int. Ed.* **2001**, *40*, 2022; e) J. D. Watson, F. H. C. Crick, *Nature* **1953**, *171*, 737; f) P. A. Zoo, J. S. Casas, M. D. Couse, E. Freijanes, A. Furlani, V. Scarcial, J. Sordo, U. Russo, M. Varela, *Appl. Organomet. Chem.* **1997**, *11*, 963.

[9] a) M. Tadokoro, K. Isobe, H. Uekusa, Y. Ohashi, J. Toyoda, K. Tashiro, K. Nakasuji, *Angew. Chem. Int. Ed.* **1999**, *38*, 95; b) M. Tadokoro, H. Kanno, T. Kitajima, H. Shimada-Umemoto, N. Nakanishi, K. Isobe, K. Nakasuji, *Proc. Natl. Acad. Sci. USA* **2002**, *99*, 4950; c) M. Tadokoro, T. Shiomi, K. Isobe, K. Nakasuji, *Inorg. Chem.* **2001**, *40*, 5476; d) M. Tadokoro, K. Nakasuji, *Coord. Chem. Rev.* **2000**, *198*, 205; e) R. Atencio, M. Chacón, T. González, A. Briceño, G. Agrifoglio, A. Sierraalta, *Dalton Trans.* **2004**, 505; f) W. E. Allen, C. J. Fowler, V. M. Lynch, J. L. Sessler, *Chem. Eur. J.* **2001**, *7*, 721; g) L. Öhrström, K. Larsson, S. Borg, S. T. Norberg, *Chem. Eur. J.* **2001**, *7*, 4805; h) C. Pettinari, R. Pettinari, *Coord. Chem. Rev.* **2005**, *249*, 525.

[10] a) C. Y. Su, Y. P. Cai, C. L. Chen, M. D. Smith, W. Kaim, H. C. zur Loye, *J. Am. Chem. Soc.* **2003**, *125*, 8595; b) J. Fan, B. Sui, T. A. Okamura, W. Y. Sun, W. X. Tang, N. Ueyama, *J. Chem. Soc., Dalton Trans.* **2002**, 3868; c) H. K. Liu, W. Y. Sun, W. X. Tang, H. Y. Tan, H. X. Zhang, Y. X. Tong, X. L. Yu, B. Sh. Kang, *J. Chem. Soc., Dalton Trans.* **2002**, 3886; d) J. Fan, L. Gan, H. Kawaguchi, W. Y. Sun, K. B. Yu, W. X. Tang, *Chem. Eur. J.* **2003**, *9*, 3965; e) S. Y. Wan, Y. Z. Li, T. A. Okamura, J. Fan, W. Y. Sun, N. Ueyama, *Eur. J. Inorg. Chem.* **2003**, 3783; f) S. Y. Wan, J. Fan, T. A. Okamura, H. F. Zhu, X. M. Ouyang, W. Y. Sun, N. Ueyama, *Chem. Commun.* **2002**, 2520.

[11] a) H. P. Zhou, J. Zh. Zhang, D. M. Li, Y. M. Zhu, Zh. J. Hu, J. Y. Wu, Y. Xie, M. H. Jiang, X. T. Tao, Y. P. Tian, *J. Mol. Struct.* **2005**, *743*, 93; b) H. P. Zhou, Y. P. Tian, J. Y. Wu, J. Zh. Zhang, D. M. Li, Y. M. Zhu, Zh. J. Hu, X. T. Tao, M. H. Jiang, Y. Xie, *Eur. J. Inorg. Chem.* **2005**, 4976.

[12] F. D. Hager, *Org. Synthesis*, Col. Vol. 1, 2nd Ed. **1948**, 544.

[13] C. J. Horn, A. J. Blake, N. R. Champness, A. Garau, V. Lippolis, C. Wilson, M. Schröder, *Chem. Commun.* **2003**, 312.

[14] G. Barberà, C. Viñas, F. Teixidor, G. M. Rosair, A. J. Welch, *J. Chem. Soc., Dalton Trans.* **2002**, 3647.

[15] L. Y. Kong, Zh. H. Zhang, T. A. Okamura, M. J. Fei, W. Y. Sun, N. Ueyama, *Chem. Lett.* **2004**, *33*, 1572.

[16] a) F. H. Allen, C. M. Bird, R. S. Rowland, P. R. Raithby, *Acta Crystallogr., Sect. Sect. B* **1997**, *53*, 696; b) A. D. Bond, W. Jones, *J. Chem. Soc., Dalton Trans.* **2001**, 3045.

[17] H. F. Zhu, L. Y. Kong, T. A. Okamura, J. Fan, W. Y. Sun, N. Ueyama, *Eur. J. Inorg. Chem.* **2004**, 1465.

[18] Y. Zheng, M. Du, J. R. Li, R. H. Zhang, X. H. Bu, *Dalton Trans.* **2003**, 1509.

[19] Y. B. Dong, M. D. Smith, H. C. zur Loye, *Inorg. Chem.* **2000**, *39*, 4927.

[20] G. R. Desiraju, *Acc. Chem. Res.* **1996**, *29*, 441.

[21] I. Unamuno, J. M. Gutiérrez-Zorrilla, A. Luque, P. Román, L. Lezama, R. Calvo, T. Rojo, *Inorg. Chem.* **1998**, *37*, 6452.

[22] C. V. K. Sharma, R. D. Rogers, *Cryst. Eng.* **1998**, *1*, 19.

[23] a) K. N. Power, T. L. Hennigar, M. J. Zaworotko, *New J. Chem.* **1998**, *22*, 177; b) O. S. Jung, S. H. Park, K. M. Kim, H. G. Jang, *Inorg. Chem.* **1998**, *37*, 5781; c) P. Losier, M. J. Zaworotko, *Angew. Chem. Int. Ed. Engl.* **1996**, *35*, 2779; d) H. Gudbjartson, K. Biradha, K. M. Poirier, M. J. Zaworotko, *J. Am. Chem. Soc.* **1999**, *121*, 2599; e) L. Carlucci, G. Ciani, D. M. Proserpio, *J. Chem. Soc., Dalton Trans.* **1999**, 1799; f) Y. B. Dong, R. C. Layland, N. G. Pschirer, M. D. Smith, U. H. F. Bunz, H. C. zur Loye, *Chem. Mater.* **1999**, *11*, 1413.

[24] a) M. Du, X. H. Bu, Z. Huang, S. T. Chen, Y. M. Guo, C. Diaz, J. Ribas, *Inorg. Chem.* **2003**, *42*, 552; b) X. H. Bu, W. Chen, S. T. Lu, R. H. Zhang, D. Z. Liao, W. M. Bu, M. Shionoya, F. Brisse, J. Ribas, *Angew. Chem. Int. Ed.* **2001**, *40*, 3201; c) F. A. A. Paz, Y. Z. Khimyak, A. D. Bond, J. Rocha, J. Klinowski, *Eur. J. Inorg. Chem.* **2002**, 2823; d) Y. B. Dong, M. D. Smith, R. C. Layland, H. C. zur Loye, *Inorg. Chem.* **1999**, *38*, 5027.

[25] a) L. Y. Zhang, G. F. Liu, S. L. Zheng, B. H. Ye, X. M. Zhang, X. M. Chen, *Eur. J. Inorg. Chem.* **2003**, 2965; b) J. H. Luo,


 © 2007 Wiley-VCH Verlag GmbH & Co. KGaA, Weinheim 

M. C. Hong, R. H. Wang, R. Cao, L. Han, Z. Z. Lin, *Eur. J. Inorg. Chem.* **2003**, 2705; c) B. C. Tzeng, H. T. Yeh, *Z. Naturforsch., Teil B* **2004**, *59*, 1320; d) B. C. Tzeng, B. S. Chen, H. T. Yeh, G. H. Lee, S. M. Peng, *New J. Chem.* **2006**, *30*, 1087.

[26] G. M. Sheldrick, *SHELXL-97, Program for Crystal Structure Refinement*, University of Göttingen, Germany, **1997**.

Received: September 22, 2006
Published Online: March 20, 2007

 © 2007 Wiley-VCH Verlag GmbH & Co. KGaA, Weinheim 

DOI: 10.1002/ejic.200601002

# New Ternary Complexes of Copper(II) with 2,2′-Bipyridine (Bpy) and Phosphocholine ($PCh^-$) or the Quaternary 1-(2-Phosphonomethoxy)ethyl Derivative of 2,4-Diaminopyrimidine ($PMEDAPy^-$)

**Alfonso Fernández-Botello,[a] Albert Escuer,[a] Xavier Solans,[b] Mercè Font-Bardía,[b] Antonin Holý,[c] Helmut Sigel,[d] and Virtudes Moreno*[a]**

**Keywords:** Ternary complexes / Oxido bridges / Phosphonate bridges / Copper(II) / Magnetic properties

The polynuclear $Cu^{II}$ complexes $[Cu_4Cl_2(bpy)_4(PCh^-)_2](ClO_4)_4 \cdot H_2O$ (**1**) and $[Cu_6(bpy)_6(PMEAPy^-)_4](ClO_4)_8 \cdot 2H_2O$ (**2**), where bpy = 2,2′-bipyridine, $PCh^-$ = phosphocholine {[2-(phosphonooxy)ethyl]trimethylammonium} and $PMEDAPy^-$ = 1-[2-(phosphonomethoxy)ethyl]-2,4-diaminopyrimidine, have been synthesized and characterized by X-ray single-crystal analysis. Compound **1** crystallizes in the triclinic system (*P*-1 space group) and consists of tetranuclear $Cu^{II}$ units, which are threefoldly bridged by $\mu_3$-*O*,*O*′,*O*′′-phosphate groups in a square arrangement around the copper atoms. Complex **2** crystallizes in the monoclinic system ($P2_1/c$ space group) and consists of hexanuclear $Cu^{II}$ units containing the same kind of $\mu_3$-phosph(on)ate bridges like **1** and in addition $\mu_4$-*O*,*O*′,*O*′′,*O*′′-phosphonate bridges. The topology of compound **2** can be envisaged as two triangular subunits linked by means of a double Cu–O–Cu bridge provided by the $\mu_4$-phosphonate unit. Magnetic susceptibility measurements of the two complexes in the temperature range of 2–300 K show weak antiferromagnetic couplings mediated by the phosph(on)ate bridges.
(© Wiley-VCH Verlag GmbH & Co. KGaA, 69451 Weinheim, Germany, 2007)

## Introduction

Solid metal phosphates and phosphonates are receiving much attention[1,2] because of their interesting magnetic and electronic properties.[3] They also have promising potential for applications in different areas: supports for catalysts,[4] as sensors[5], and in nonlinear optics.[6] This diversity in applications is a reflection of their diversity in structure and composition which is characteristic for these compounds.

Moreover, the two phosph(on)ate ligands considered in this study are also of biological relevance: phosphocholine ($PCh^-$), also known as 2-(trimethylammonio)ethyl phosphate and [2-(phosphonooxy)ethyl]trimethylammonium (Figure 1), is a fundamental cell metabolite.[7] The quaternary 1-[2-(phosphonomethoxy)ethyl] derivative of 2,4-diaminopyrimidine (Figure 1) is also named 1-[2-(phosphonomethoxy)ethyl]-2,4-diaminopyrimidine ($PMEDAPy^-$)[8] to indicate its structural relationship to several other acyclic nucleotide analogues which show antiviral properties.[9–11] Metal ion complexes of both phosph(on)ate ligands (Figure 1), or at least close relatives, have already been studied in aqueous solution and their corresponding isomeric equilibria were quantified.[8,11,12] Indeed, for the ternary complexes of $PMEDAPy^-$ with $Cu^{2+}$ and 2,2′-bipyridine (bpy) or 1,10-phenanthroline (phen) intramolecular stacking interactions in solution could be established.[8] Knowledge of such weak interactions is important in order to understand biological interactions better, e.g. in structures of proteins, active-site cavities and in many low-molecular-weight

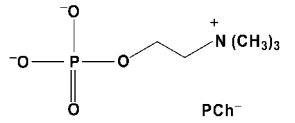


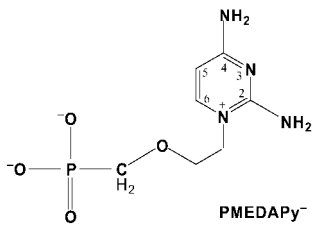


Figure 1. Chemical structures of the anions of phosphocholine ($PCh^-$) and 2,4-diamino-1-[2-(phosphonomethoxy)ethyl]pyrimidine ($PMEDAPy^-$; see also the second paragraph of the Introduction).

[a] Departament de Química Inorgànica, Universitat de Barcelona, Martí i Franqués 1–11, 08028 Barcelona, Spain
Fax: +34-93-4907725
E-mail: albert.escuer@qi.ub.es
virtudes.moreno@qi.ub.es
[b] Departament de Cristallografía, Mineralogia i Dipòsits Minerals, Universitat de Barcelona,
Martí Franqués s/n, 08028, Barcelona, Spain
[c] Academy of Sciences, Institute of Organic Chemistry and Biochemistry,
16610 Prague, Czech Republic
[d] Department of Chemistry, Inorganic Chemistry, University of Basel,
Spitalstrasse 51, 4056 Basel, Switzerland

 © 2007 Wiley-VCH Verlag GmbH & Co. KGaA, Weinheim 

mixed-ligand complexes,[13] also their relevance for the stability of DNA, which depends much on the stacking interactions of the nucleobases.[14]

Of course, the biological role of copper is nowadays well established: copper-containing enzymes and proteins are widely distributed in plants and animals,[15] the metal ion being present in the form of ternary or polynuclear complexes.[15,16] For example, exchange-coupled polynuclear $Cu^{II}$ complexes are of relevance in biological processes involving laccase, a metalloprotein which belongs to the family of multicopper oxidases. Laccase contains four copper ions which are coupled to four one-electron substrate oxidations, i.e. the reduction of dioxygen to water.[17,18]

For the various reasons indicated above, we studied ternary $Cu^{II}$ complexes of the phosph(on)ate ligands (Figure 1) in the solid state by employing 2,2′-bipyridine as the second ligand. The syntheses, X-ray crystal structure analyses and magnetic properties of two polynuclear $Cu^{II}$ complexes, $[Cu_4Cl_2(bpy)_4(PCh^-)_2](ClO_4)_4{\cdot}H_2O$ (**1**) and $[Cu_6(bpy)_6(PMEDAPy^-)_4](ClO_4)_8{\cdot}2H_2O$ (**2**), are now presented. In **1** $PCh^-$ acts as tridentate $\mu_3$-*O*,*O*′,*O*′′-bridging ligand, whereas in **2** one half of the $PMEDAPy^-$ ligands acts in a similar way, but the other half forms a tetradentate $\mu_4$-*O*,*O*′,*O*′′,*O*′′-phosphonate bridge. It needs to be emphasized that these coordination modes are quite unusual for phosph(on)ate bridges.

Complexes with large M–O–X–O–M bridges formed by tetrahedral anions like sulfate or phosphate show typically weak magnetic interactions[19] and indeed, compounds **1** and **2**, containing exclusively M–O–P–O–M phosph(on)ato bridges, show a moderately weak antiferromagnetic coupling. In the last few years there is a growing interest in this kind of structural units because of their ability to generate high nuclearity cages with a variety of first row transition cations. Phosph(on)ato ligands can bind up to six metallic centers and, combined with other bridges (mainly hydroxo or alkoxo derivatives), they are able to give high nuclearity systems containing, e.g. $Co_{13}$, $Mn_{12}$, $Fe_9$, $Co_8$ or $Mn_6$.[20] Interesting magnetic properties such as the single molecule magnet (SMM) response have been characterized for some of them.

## Results and Discussion

The reaction of $[Cu(ClO_4)_2]{\cdot}6H_2O$ with 2,2′-bipyridine (bpy) and phosphocholine ($PCh^-$) or 1-[2-(phosphonomethoxy)ethyl]-2,4-diaminopyrimidine ($PMEDAPy^-$) in water with addition of HCl afforded crystals of the complexes $[Cu_4Cl_2(bpy)_4(PCh^-)_2](ClO_4)_4{\cdot}H_2O$ (**1**) and $[Cu_6(bpy)_6(PMEDAPy^-)_4](ClO_4)_8{\cdot}2H_2O$ (**2**) after two or four weeks of evaporation at room temperature, respectively. The crystals were suitable to be studied by X-ray diffraction.

### Crystal Structures

#### *$[Cu_4Cl_2(bpy)_4(PCh^-)_2](ClO_4)_4{\cdot}H_2O$ (1)*

A labeled ORTEP plot of the structure is shown in Figure 2. Selected bond lengths and angles are reported in Table 1 and Table 2, respectively. The structure of the compound consists of a tetranuclear centrosymmetric ternary $Cu^{II}$ complex with bpy and $PCh^-$ as ligands. There are two nonequivalent complexes with the same structure and similar bond parameters in the asymmetric unit of **1**; the following description corresponds to one of them. The Cu1 atoms are pentacoordinated, with a polyhedral arrangement close to a square-pyramidal geometry, where the equatorial plane is defined by two nitrogen (bpy) atoms and two oxygen (phosphate) atoms; one chloride is in the apical position. For Cu2 the main plane is defined by two nitrogen (bpy), one chloride and one oxygen (phosphate) with a water molecule in the axial position. In both cases, the metal ion is above the equatorial plane (see Table 2 for bond angles). The equatorial bond lengths to the *O*-phosphate atoms lie within the short range between 1.899(5) and 1.960(4) Å.

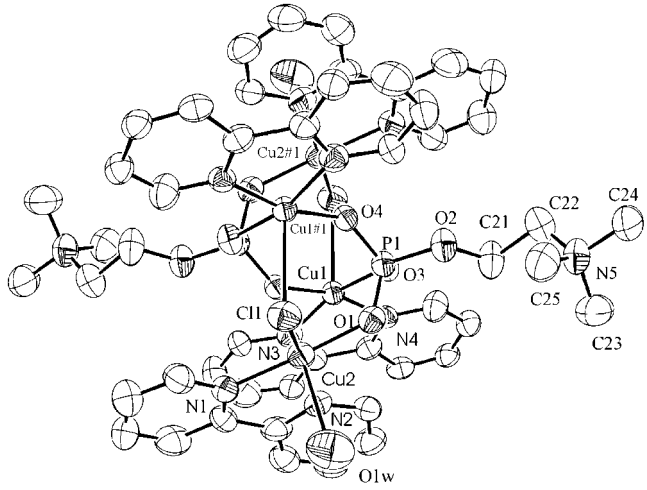


Figure 2. Labeled ORTEP plot (ellipsoid probability 30%) for one of the two nonequivalent units of $[Cu_4Cl_2(bpy)_4(PCh^-)_2](ClO_4)_4{\cdot}H_2O$ (**1**).

Table 1. Selected bond lengths [Å] $[Cu_4Cl_2(bpy)_4(PCh^-)_2](ClO_4)_4{\cdot}H_2O$ (**1**).[a]

| | | | |
|---|---|---|---|
| Cu1–N3 | 2.026(6) | Cu3–N7 | 2.021(6) |
| Cu1–N4 | 1.947(6) | Cu3–N6 | 1.974(6) |
| Cu1–O3 | 1.925(5) | Cu3–O7 | 1.911(5) |
| Cu1–O4#1** | 1.920(5) | Cu3–O8#2* | 1.960(4) |
| Cu1–Cl1#1** | 2.677(2) | Cu3–Cl2 | 2.666(2) |
| Cu2–N1 | 2.002(6) | Cu4–N8 | 1.977(6) |
| Cu2–N2 | 2.020(7) | Cu4–N9 | 1.982(6) |
| Cu2–O1 | 1.899(5) | Cu4–O5 | 1.926(5) |
| Cu2–Cl1 | 2.269(3) | Cu4–Cl2 | 2.319(2) |
| Cu2–O1w | 2.64(1) | Cu4–O8#2* | 2.350(5) |

[a] Symmetry transformations used to generate equivalent atoms: * $-x+1, -y, -z+1$; ** $-x+2, -y+1, -z$.

The four $Cu^{II}$ ions of the tetranuclear unit define a ring (Figure 3) which is held together by threefold bridged $\mu_3$-*O*,*O*′,*O*′′-phosphate groups. The Cu1···Cu1#1 distance is 4.9967(15) Å, whereas the side-ring distances are 3.8573(15) and 3.5830(13) Å, and thus smaller than the Cu···Cu distances in related dinuclear complexes.[21,22]

 © 2007 Wiley-VCH Verlag GmbH & Co. KGaA, Weinheim 

Table 2. Selected angles [°] for $[Cu_4Cl_2(bpy)_4(PCh^-)_2](ClO_4)_4 \cdot H_2O$ (**1**).[a]

| | | | |
|---|---|---|---|
| O3A–Cu2A–O4A* | 94.0(2) | C15A–N3A–Cu1A | 112.6(5) |
| O3A–Cu2A–N1A | 90.0(2) | C16A–N4A–Cu1A | 112.7(5) |
| O4A*–Cu2A–N1A | 172.8(3) | C20A–N4A–Cu1A | 126.9(5) |
| O3A–Cu2A–N2A | 166.2(3) | O4**–Cu1–O3 | 94.0(2) |
| O4A*–Cu2A–N2A | 94.1(2) | O4**–Cu1–N4 | 165.8(2) |
| N1A–Cu2A–N2A | 80.9(3) | O3–Cu1–N4 | 90.8(2) |
| O3A–Cu2A–Cl1A | 92.5(1) | O4**–Cu1–N3 | 91.9(2) |
| O4A*–Cu2A–Cl1A | 82.2(2) | O3–Cu1–N3 | 166.1(2) |
| N1A–Cu2A–Cl1A | 103.6(2) | N4–Cu1–N3 | 80.6(3) |
| N2A–Cu2A–Cl1A | 99.6(2) | O4**–Cu1–Cl1** | 100.4(2) |
| O1A–Cu1A–N3A | 170.2(2) | O3–Cu1–Cl1** | 86.4(1) |
| O1A–Cu1A–N4A | 91.2(2) | N4–Cu1–Cl1** | 93.3(2) |
| N3A–Cu1A–N4A | 81.3(3) | N3–Cu1–Cl1** | 104.9(2) |
| O1A–Cu1A–Cl1A | 94.0(1) | O1–Cu2–N1 | 170.9(3) |
| N3A–Cu1A–Cl1A | 95.5(2) | O1–Cu2–N2 | 92.7(3) |
| N4A–Cu1A–Cl1A | 153.0(2) | N1–Cu2–N2 | 82.2(3) |
| O1A–Cu1A–O4A* | 88.8(2) | O1–Cu2–Cl1 | 90.6(2) |
| N3A–Cu1A–O4A* | 90.2(2) | N1–Cu2–Cl1 | 96.1(2) |
| N4A–Cu1A–O4A* | 123.9(2) | N2–Cu2–Cl1 | 166.6(2) |
| Cl1A–Cu1A–O4A* | 82.7(1) | Cu2–Cl1–Cu1** | 92.5(9) |
| Cu1A–Cl1A–Cu2A | 84.1(7) | P1–O1–Cu2 | 126.8(3) |
| P1A–O1A–Cu1A | 129.7(3) | P1–O3–Cu1 | 125.9(3) |
| P1A–O3A–Cu2A | 126.5(3) | P1–O5–Cu1** | 135.9(3) |
| P1A–O4A–Cu2A* | 125.7(3) | C1–N1–Cu2 | 130.2(6) |
| P1A–O4A–Cu1A* | 121.3(2) | C5–N1–Cu2 | 111.5(5) |
| Cu2A*–O4A–Cu1A* | 101.5(2) | C6–N2–Cu2 | 116.4(6) |
| C1A–N1A–Cu2A | 123.0(5) | C10–N2–Cu2 | 124.2(5) |
| C5A–N1A–Cu2A | 114.0(5) | C15–N3–Cu1 | 115.3(5) |
| C6A–N2A–Cu2A | 113.5(5) | C11–N3–Cu1 | 125.7(6) |
| C10A–N2A–Cu2A | 123.9(5) | C20–N4–Cu1 | 127.4(6) |
| C11A–N3A–Cu1A | 126.2(5) | C16–N4–Cu1 | 115.7(5) |

[a] Symmetry transformations used to generate equivalent atoms: * $-x + 1, -y, -z + 1$ ** $-x + 2, -y + 1, -z$.

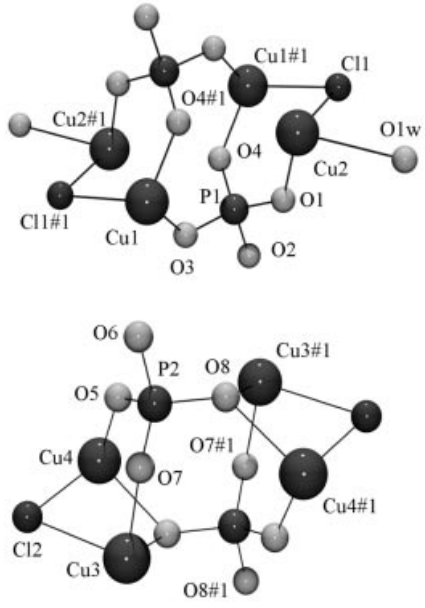


Figure 3. Plot of the $Cu_4$ arrangement for the core of the two nonequivalent units of **1**.

The distances between the two planes defined by the bipyridine ligands are in the range of 4.499(5) to 5.085(4) Å; this is longer than the distances for stacking interactions, which are usually between 3.3 and 3.8 Å.[23] Thus, the existence of a stacking interaction must be ruled out in this case. In Figure 3 a schematic representation of the four-copper atom core is shown for the two nonequivalent units.

### *$[Cu_6(bpy)_6(PMEDAPy^-)_4](ClO_4)_8 \cdot 2H_2O$ (2)*

A labeled ORTEP plot of the structure is shown in Figure 4. Selected bond lengths and angles are reported in Table 3 and Table 4, respectively. The structure of the compound consists of a hexanuclear $Cu^{II}$ ternary complex with bpy and $PMEDAPy^-$ as ligands. Two of the copper atoms are pentacoordinated, with a polyhedral arrangement close to a square-pyramidal geometry, where the equatorial positions are occupied by two nitrogen (bpy) and two oxygen (phosphonate) atoms, and the apical position by one oxygen (phosphonate) atom or one water molecule. The bond lengths for the equatorial position are in the range of 1.887(2)–1.993(2) Å (typical bond lengths), and the bond lengths for the apical position are 2.220(2) Å for Cu3–O8 and 2.486(4) Å for Cu2–O1w. In both cases, the copper

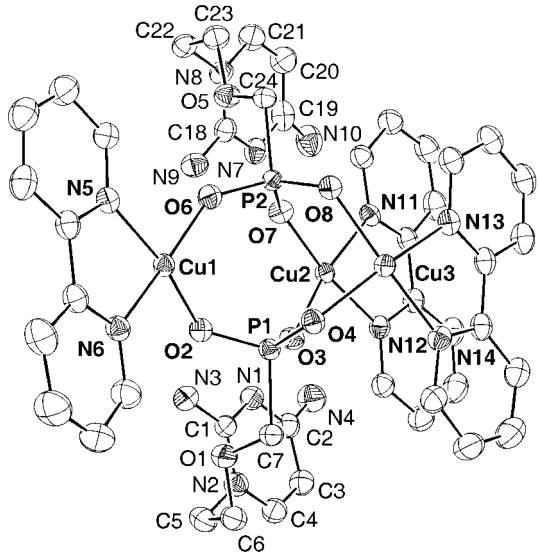


Figure 4. Labeled ORTEP plot (ellipsoid probability 30%) for the asymmetric unit of $[Cu_6(bpy)_6(PMEDAPy^-)_4](ClO_4)_8 \cdot 2H_2O$ (**2**). Oxygen atoms above Cu3 and Cu2 are omitted for clarity.

Table 3. Selected bond lengths [Å] for $[Cu_6(bpy)_6(PMEDAPy^-)_4](ClO_4)_8 \cdot 2H_2O$ (**2**).[a]

| | | | |
|---|---|---|---|
| Cu1–O6 | 1.887(2) | P1–O2 | 1.519(2) |
| Cu1–O2 | 1.919(2) | P1–O3 | 1.524(2) |
| Cu1–N6 | 1.986(3) | P1–O4 | 1.516(2) |
| Cu1–N5 | 1.990(3) | O1–C6 | 1.445(5) |
| Cu2–O3 | 1.917(2) | O1–C7 | 1.416(4) |
| Cu2–O7 | 1.918(2) | P2–O6 | 1.512(2) |
| Cu2–N12 | 1.997(6) | P2–O8 | 1.528(2) |
| Cu2–N11 | 2.003(2) | P2–O7 | 1.497(2) |
| Cu3–O4 | 1.941(2) | O5–C23 | 1.402(4) |
| Cu3–N14 | 1.977(3) | O5–C24 | 1.420(4) |
| Cu3–O8 | 1.993(2) | | |
| Cu3–N13 | 2.002(3) | | |
| Cu3–O8* | 2.220(2) | | |

[a] Symmetry transformations used to generate equivalent atoms: * $-x, -y, -z$.

 © 2007 Wiley-VCH Verlag GmbH & Co. KGaA, Weinheim 

atoms are always above the equatorial plane. Cu1 atom is placed in a distorted square planar environment.

Table 4. Selected angles [°] for $[Cu_6(bpy)_6(PMEDAPy^-)_4](ClO_4)_8 \cdot 2H_2O$ (**2**).[a]

| | | | |
|---|---|---|---|
| O6–Cu1–O2 | 96.09(10) | O8–Cu3–O8* | 84.54(08) |
| O6–Cu1–N6 | 165.97(12) | N13–Cu3–O8* | 101.50(09) |
| O2–Cu1–N6 | 94.53(11) | P1–O2–Cu1 | 128.14(15) |
| O6–Cu1–N5 | 89.84(11) | P1–O3–Cu2 | 135.76(15) |
| O2–Cu1–N5 | 169.39(10) | P1–O4–Cu3 | 124.86(13) |
| N6–Cu1–N5 | 81.16(11) | P2–O6–Cu1 | 142.93(16) |
| O3–Cu2–O7 | 93.79(10) | P2–O7–Cu2 | 143.31(15) |
| O3–Cu2–N12 | 91.14(11) | P2–O8–Cu3* | 136.44(13) |
| O7–Cu2–N12 | 171.26(10) | Cu3–O8–Cu3* | 95.46(08) |
| O3–Cu2–N11 | 170.44(11) | C8–N5–Cu1 | 125.00(02) |
| O7–Cu2–N11 | 93.81(11) | C12–N5–Cu1 | 115.70(02) |
| N12–Cu2–N11 | 80.61(11) | C17–N6–Cu1 | 127.10(03) |
| O4–Cu3–N14 | 92.14(11) | C13–N6–Cu1 | 113.60(02) |
| O4–Cu3–O8 | 92.02(09) | C29–N11–Cu2 | 114.40(02) |
| N14–Cu3–O8 | 170.80(10) | C25–N11–Cu2 | 125.00(02) |
| O4–Cu3–N13 | 159.69(10) | C34–N12–Cu2 | 126.20(02) |
| N14–Cu3–N13 | 80.38(12) | C30–N12–Cu2 | 114.20(02) |
| O8–Cu3–N13 | 92.97(10) | C39–N13–Cu3 | 113.90(02) |
| O4–Cu3–O8* | 98.57(08) | C35–N13–Cu3 | 125.30(02) |
| N14–Cu3–O8* | 102.94(10) | C40–N14–Cu3 | 115.70(02) |
| | | C44–N14–Cu3 | 125.40(03) |

[a] Symmetry transformations used to generate equivalent atoms: * $-x, -y, -z$.

The compound can be envisaged as two trinuclear subunits linked by means of a double oxido bridge. The Cu3···Cu3* distance is 3.1218(6) Å, whereas the distance between the metal ions Cu2 and Cu3 (see Figure 5) is 3.3268(6) Å; it means that this distance is shorter than the Cu···Cu distances in dinuclear complexes.[21,22] A schematic representation of the core environment for the six copper atoms of **2**, including the bridging phosphonate groups, is shown in Figure 5.

This compound exhibits both intra and intermolecular π–π interactions. Intramolecular stacking can be observed for the heteroaromatic rings including N11 and N13, where the distance between the centroids is 3.57 Å (see Figure 4); this distance is in the expected order.[13,24] Intermolecular interactions are found between the pyridine ring including

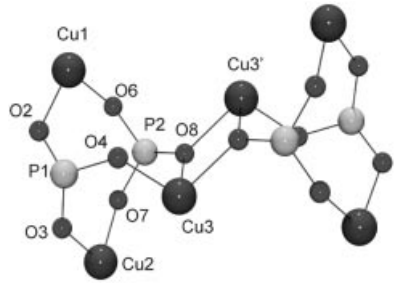


Figure 5. Plot of the core environment for the $Cu_6$ unit of compound **2**.

N6 and the diaminopyrimidine ring including N7/N8 of the neighboring hexanuclear unit with the distance between the centroids of 3.51 Å. These interactions give a supramolecular 1D arrangement of the $Cu_6$ molecules along the [010] direction (Figure 6). Hence, these observations in the solid state confirm the results obtained in aqueous solution for the ternary Cu(bpy)(PMEDAPy)$^+$ and Cu(phen)(PMEDAPy)$^+$ complexes; the formation degree of the intramolecular stacks amounts in these species in solution to about 69 and 77%, respectively.[8] It is not surprising that in the solid state stacking between bpy and the pyrimidine ring occurs in an inter- and not in an intramolecular fashion; crystal packing affects such weak interactions.[24] Indeed, similar differences between the stacking properties in solution and in the solid state have been observed before.[13,24]

## Magnetic Behavior

Experimental susceptibility data indicate that the $\chi_M \cdot T$ product for both compounds exhibits a quasi constant value between room temperature and 100 K. Below this temperature it decreases, approaching zero at very low temperatures, which indicates a weak antiferromagnetic coupling. For compound **1** the $\chi_M \cdot T$ value at room temperature is 1.73 $cm^3 \cdot K \cdot mol^{-1}$ and in good agreement with four isolated $Cu^{II}$ ions (the expected value for $g$ = 2.00 is

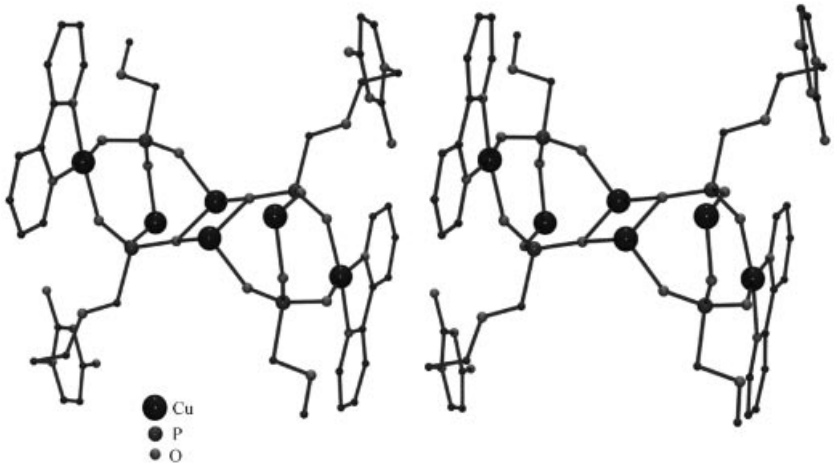


Figure 6. Plot of two $Cu_6$ units showing the π–π stacking between one of the bpy and one of the diaminopyrimidine rings. For clarity, the noninteracting aromatic rings are not plotted.

 © 2007 Wiley-VCH Verlag GmbH & Co. KGaA, Weinheim 

1.5 $cm^3 \cdot K \cdot mol^{-1}$). The $\chi_M$ vs. $T$ plot shows a maximum of susceptibility around 4 K (see Figure 7). The $\chi_M \cdot T$ value of 2.67 $cm^3 \cdot K \cdot mol^{-1}$ at room temperature for compound **2** is slightly greater than the spin only value of 2.25 $cm^3 \cdot K \cdot mol^{-1}$ expected for six $Cu^{II}$ ions (see Figure 8).

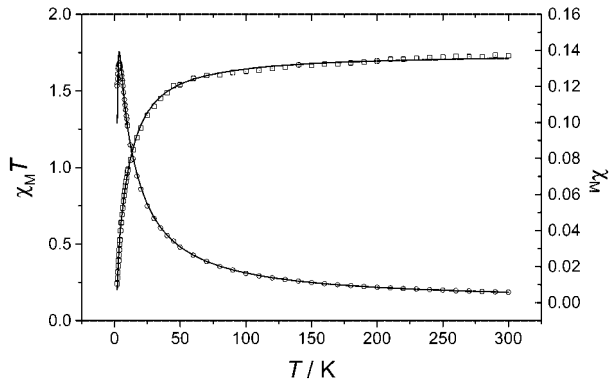


Figure 7. Plot of $\chi_M \cdot T$ vs. $T$ (open squares) and $\chi_M$ vs. $T$ (open circles) for compound $[Cu_4Cl_2(bpy)_4(PCh^-)_2](ClO_4)_4 \cdot H_2O$ (**1**). Solid lines show the best fit of the experimental data.

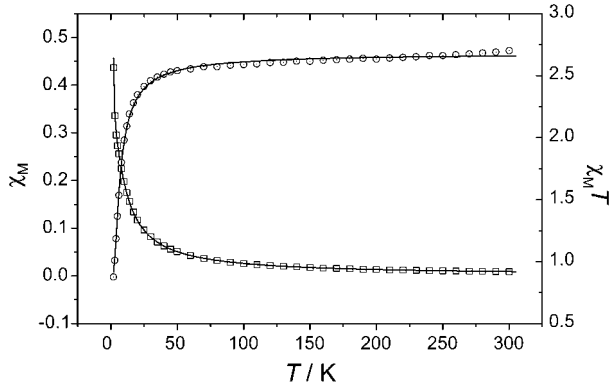


Figure 8. Plot of $\chi_M \cdot T$ vs. $T$ (open circles) and $\chi_M$ vs. $T$ (open squares) for compound $[Cu_6(bpy)_6(PMEDAPy^-)_4]$ $(ClO_4)_8 \cdot 2H_2O$ (**2**). Solid lines show the best fit obtained (see text).

A fit of the experimental susceptibility data for **1** was performed on the basis of the three coupling constants seen in the interaction Scheme 1.

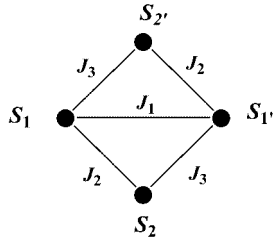


Scheme 1.

$J_1$ corresponds to the double OPO bridge with medium torsion angles, $J_2$ to the single bridge with low torsion angles, and $J_3$ to the single bridge with large torsion. The same Scheme is common for the two nonequivalent molecules present in the structure, which show only a minor difference in the torsion related to $J_2$. The best fit obtained by means of the CLUMAG program, based in the irreducible tensor operator formalism (ITO) on the Hamiltonian $H = -J_1(S_1 \cdot S_{1'}) - J_2(S_1S_2 + S_{1'} \cdot S_{2'}) - J_3(S_{1'} \cdot S_{2'} + S_{1'} \cdot S_2)$, gives the values $J_1 = -9.7$ $cm^{-1}$, $J_2 = -4.2$ $cm^{-1}$, $J_3 = -7.5$ $cm^{-1}$, and $g = 2.157$. A second fit performed assuming $J_2 = J_3$ gives a similar $J_1$ value ($J_1 = -8.7$ $cm^{-1}$) and an average value for $J_2 = J_3$ of 6.3 $cm^{-1}$.

The interaction Scheme for compound **2** consists of seven different interactions (Scheme 2). A negligible or very weak interaction can be expected for the superexchange pathway $J_4$ which relates the $Cu^{II}$ centers by means of an axial–equatorial double oxido bridge. Also, intermolecular interactions mediated by the π–π stacking should be negligible, because the rings involved in this interaction are placed far from the copper atoms.

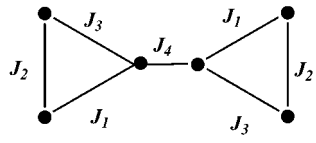


Scheme 2.

The three remaining interactions correspond to doubly Cu–$(OPO)_2$–Cu bridged fragments, which display large differences within the bond parameters, specially for the Cu–O–O–Cu torsion angles. Trying to fit a weakly coupled system (without susceptibility maximum) with four coupling constants does not make mathematical sense, because many local minima can be found in the least-squares process. Therefore, to avoid overparametrization the experimental data for this compound were fitted assuming an average $J$ value and neglecting the axial–equatorial interaction between the triangular units. The best fit under these conditions, performed by applying the Hamiltonian $H = -J(S_1S_2 + S_2S_3 + S_1S_3)$, gives the values $J = -4.1$ $cm^{-1}$ and $g = 2.180$. Fits including the interaction between the two triangular units gave negligible values for this constant, which is closer to the $\chi_M \cdot T$ value at low $T$ of two independent $Cu^{II}$ ions rather than an S = 0 ground state.

These results are in good agreement with related compounds containing the phosphonato ligand in its $\eta_3$-$O,O',O''$ coordination mode, for which superexchange interactions are typically in the range of –5 to –10 $cm^{-1}$.[25]

## Experimental Section

***Caution!*** *Perchlorate salts of metal complexes with organic ligands are potentially explosive. Only a small amount of the material should be prepared and it should be handled with extreme care.*

**$[Cu_4Cl_2(bpy)_4(PCh^-)_2](ClO_4)_4 \cdot H_2O$ (1):** $[Cu(ClO_4)_2] \cdot 6H_2O$ (1 mmol), 2,2′-bipyridine (1 mmol) and [2-(phosphonooxy)ethyl]-trimethylammonium chloride (= phosphocholine; $PCh^-$) (0.5 mmol), obtained from Fluka (Buchs, Switzerland), were mixed in distilled water (20 mL) and stirred for 48 h at room temperature. A few drops of 1 M HCl were then added to the solution. Single dark-blue crystals of **1** suitable for X-ray crystallography were formed by evaporation at room temperature after two weeks.

 © 2007 Wiley-VCH Verlag GmbH & Co. KGaA, Weinheim 

Table 5. Crystal data and summary of data collection and refinement for $[Cu_4Cl_2(bpy)_4(PCh^-)_2](ClO_4)_4 \cdot H_2O$ (**1**) and $[Cu_6(bpy)_6(PMEDAPy^-)_4](ClO_4)_8 \cdot 2H_2O$ (**2**).

| | **1** | **2** |
|---|---|---|
| Empirical formula | $C_{50}H_{60}C_{16}Cu_4N_{10}O_{25}P_2$ | $C_{88}H_{100}Cl_8Cu_6N_{28}O_{52}P_4$ |
| Wavelength [Å] | 0.71069 | 0.71073 |
| $T$ [K] | 293(2) | 293(2) |
| $\theta$ range [°] | 1.64 to 31.65 | 1.73 to 31.57 |
| $hkl$ ranges | –16 to 16, –15 to 13, 0 to 33 | –25 to 23, 0 to 17, 0 to 41 |
| Crystal system, space group | triclinic, $P\bar{1}$ | monoclinic, $P2_1/c$ |
| Crystal dimensions [mm] | $0.1 \times 0.1 \times 0.2$ | $0.1 \times 0.1 \times 0.2$ |
| $a$ [Å] | 12.4230(10) | 17.5970(10) |
| $b$ [Å] | 12.7080(10) | 13.2460(10) |
| $c$ [Å] | 22.7730(10) | 28.5280(10) |
| $\alpha$ [°] | 98.534(8) | 90 |
| $\beta$ [°] | 99.296(8) | 115.076(8) |
| $\delta$ [°] | 98.303(8) | 90 |
| Volume [Å$^3$] | 3456.1(4) | 6022.8(9) |
| Absorption coefficient [mm$^{-1}$] | 1.576 | 1.377 |
| Reflections collected/unique | 15246/9819 [$R$(int) = 0.0370] | 52896/17121 [$R$(int) = 0.0259] |
| Data/restraints/parameters | 9819/222/846 | 17121/0/839 |
| Goodness-of-fit on $F_2$ | 0.988 | 1.073 |
| Final $R$ indices [$I > 2\sigma(I)$] | $R_1$ = 0.0701, $wR_2$ = 0.2103 | $R_1$ = 0.0538, $wR_2$ = 0.1680 |
| $R$ indices (all data) | $R_1$ = 0.1271, $wR_2$ = 0.2353 | $R_1$ = 0.0746, $wR_2$ = 0.2244 |
| Extinction coefficient | 0.0034(10) | 0.0022(6) |
| Largest diff. peak and hole/e·Å$^{-3}$ | 0.633 and –0.554 | 0.794 and –0.744 |

(Yield: 64%). Calculated for $C_{50}H_{60}Cl_6Cu_4N_{10}O_{25}P_2$: C 34.68, N 8.09, H 3.47; found C 35.60, N 8.29, H 3.27%.

**$[Cu_6(bpy)_6(PMEDAPy^-)_4](ClO_4)_8 \cdot 2H_2O$ (2):** $[Cu(ClO_4)_2] \cdot 6H_2O$ (1 mmol), 2,2′-bipyridine (1 mmol) and 2,4-diamino-1-[2-(phosphonomethoxy)ethyl]pyrimidine·HCl (0.5 mmol), which was synthesized as described in the literature,[26] were mixed in distilled water and acetonitrile (15 mL:10 mL) and stirred for 24 h at room temperature. A few drops of 1 M HCl were then added to the solution. Single blue crystals of **2** suitable for X-ray crystallography were formed by evaporation at room temperature after four weeks. (Yield: 73%). Calculated for $C_{88}H_{100}Cl_8Cu_6N_{28}O_{52}P_4$: C 33.31, N 12.36, H 3.15; found C, 33.82, N 12.47, H 3.06%.

**Magnetic Measurements:** Magnetic susceptibility measurements were carried out for **1** and **2** on microcrystalline samples with a Quantum Design SQUID MPMS5 magnetometer working in the range of 2–300 K under magnetic fields of 7000 G. Application of Pascal's constant was used for diamagnetic corrections. The magnetic measurements were carried out by the Magnetochemistry Services of the University of Barcelona.

**Crystal-Structure Determination:** The X-ray single-crystal data for **1** and **2** were collected on a MAR345 diffractometer with an image plate detector. Crystal size: $0.1 \times 0.1 \times 0.2$ mm. The crystallographic data, conditions used for the intensity data collection, and some features of the structure refinement are listed in Table 5. Unit-cell parameters were determined from 8505 reflections ($3 < \theta < 30°$) in the case of complex **1** and 42513 reflections ($3 < \theta < 31°$) for complex **2**. Both cases were refined by the least-squares method. Intensities were collected with graphite-monochromatized Mo-$K_\alpha$ radiation. 15246 reflections were measured in the range $1.64 \leq \theta \leq 31.65$ and 52896 reflections were measured in the range $1.73 \leq \theta \leq 31.57$ for complex **1** and **2**, respectively. 9819 (complex **1**) and 17121 (complex **2**) reflections were nonequivalent by symmetry [$R$(int) (on $I$) = 0.037 and 0.025 for complex **1** and **2**, respectively]. For complex **1** 5385 reflections were assumed as observed applying the condition $I > 2\sigma(I)$. In the case of complex **2**, 13652 reflections were assumed as observed applying to the condition $I > 2\sigma(I)$. The Lorentz polarization was corrected but no absorption corrections were made in both cases.

The structures were solved by direct methods with the SHELXS computer program[27] and refined by the full-matrix least-squares method (SHELX97 program[27]) using 9819 reflections for complex **1** and 17121 reflections for complex **2** (very negative intensities were not assumed). The minimized function was $\Sigma w||F^o|^2 - |F_c|^2|^2$, where $w = [\sigma^2(I) + (0.1582P)^2]^{-1}$, and $P = (|F_o|^2 + 2|F_c|^2)/3$ in the case of complex **1**. For complex **2** $w = [\sigma^2(I) + (0.1630P)^2 + 1.6389P]^{-1}$, and $P = (|F_o|^2 + 2|F_c|^2)/3$. In both cases, $f$, $f'$, and $f''$ were taken from ref.[28].

All H atoms were computed and refined by a riding model, with an isotropic thermal parameter equal to 1.2 times the equivalent thermal parameter of the C linked to H. The final $R$ (on $F$) factor was 0.070 and 0.054, $wR$ (on $|F|^2$) = 0.210 and 0.168 and goodness of fit was 1.017 and 1.073 for complexes **1** and **2**, respectively, for all observed reflections. For complex **1**, the number of refined parameters was 846. As the ratio number of observed reflections/number of refined parameters was low, oxygen atoms of perchlorate ions were only refined isotropically with bond lengths and angles constrained to have the same value. Max. shift/esd. = 0.00, mean shift/esd. = 0.00. Max. and min. peaks in the final difference synthesis was 0.633 and –0.554 e·Å$^{-3}$, respectively. For complex **2**, the number of refined parameters was 839. Max. shift/esd. = 0.00, mean shift/esd = 0.00. Max. and min. peaks in the final difference synthesis was 0.794 and –0.744 e·Å$^{-3}$, respectively.

CCDC-624676 and -624677 contain the supplementary crystallographic data for this paper. These data can be obtained free of charge from the Cambridge Crystallographic Data Centre via www.ccdc.cam.ac.uk/data@request/cif.

## Acknowledgments

The authors thank COST D20 (Brussels and Bern), the Ministerio de Ciencia y Tecnología (MCYT) (ref. BQU-2002-00601) as well as

 © 2007 Wiley-VCH Verlag GmbH & Co. KGaA, Weinheim 

the University of Barcelona (grant to A. F. B.) and the University of Basel (grant to H. S.) for financial support.

[1] Y. Song, N. A. Chernova, P. Y. Zavalij, M. S. Whittingham, *Materials Research Society Symposium Proceedings* **2002**, *755*, 75–80.
[2] W. J. Chang, C. Y. Chen, K. H. Lii, *Solid State Chem.* **2003**, *172*, 6–11.
[3] J. E. Greedan, K. Reubenbauer, T. Birchall, M. Ehlert, D. R. Corbin, M. A. Subramanian, *Solid State Chem.* **1988**, *77*, 376–388.
[4] R. A. W. Johnstone, J. Y. Liu, L. Lu, D. Whittaker, *J. Mol. Catal. A J. Mol. Catal.* **2003**, *191*, 289–294.
[5] M. Shiotsuka, S. Takase, Y. Shimizu, *Chem. Sens.* **2001**, *17*, 381–383.
[6] S. B. Ungashe, W. L. Wilson, H. E. Katz, G. R. Scheller, T. M. Putvinski, *J. Am. Chem. Soc.* **1992**, *114*, 8717–8719.
[7] a) J. D. Rawn, *Biochemistry*, Patterson, Burlington, NC (USA), **1989**, pp. 213–216 and 541–544; b) L. Stryer, *Biochemie* (translated by B. Pfeiffer and J. Guglielmi from *Biochemistry*, W. H. Freeman & Co., New York, **1988**), Spektrum Akad. Verlag, Heidelberg, **1991**, pp. 296–299 and 574–577.
[8] A. Fernández-Botello, A. Holý, V. Moreno, H. Sigel, *Polyhedron* **2003**, *22*, 1067–1076.
[9] a) A. Holý, I. Votruba, M. Masojídková, G. Andrei, R. Snoeck, L. Naesens, E. De Clercq, J. Balzarini, *J. Med. Chem.* **2002**, *45*, 1918–1929; b) A. Holý, J. Günter, H. Dvořáková, M. Masojídková, G. Andrei, R. Snoeck, J. Balzarini, E. De Clercq, *J. Med. Chem.* **1999**, *42*, 2064–2086.
[10] A. Holý, *Curr. Pharm. Des.* **2003**, *9*, 2567–2592.
[11] H. Sigel, *Chem. Soc. Rev.* **2004**, *33*, 191–200.
[12] A. Fernández-Botello, R. B. Gómez-Coca, A. Holý, V. Moreno, H. Sigel, *Inorg. Chim. Acta* **2002**, *331*, 109–116.
[13] O. Yamauchi, A. Odani, H. Masuda, H. Sigel, *Met. Ions Biol. Syst.* **1996**, *32*, 207–270.
[14] T. J. Matray, E. T. Kool, *J. Am. Chem. Soc.* **1998**, *120*, 6191–6192.
[15] *Handbook on Metalloproteins* (Eds.: I. Bertini, A. Sigel, H. Sigel), M. Dekker, Inc., New York, **2001**, pp. 709–880.
[16] A. E. Palmer, R. K. Szilagyi, J. R. Cherry, A. Jones, F. Xu, E. I. Solomon, *Inorg. Chem.* **2003**, *42*, 4006–4017.
[17] E. I. Solomon, U. M. Sundaram, T. E. Machonkin, *Chem. Rev.* **1996**, *96*, 2563–2605.
[18] E. I. Solomon, P. Chen, S. K. Lee, M. Metz, A. E. Palmer, *Angew. Chem. Int. Ed.* **2001**, *40*, 4570–4590.
[19] E. W. Ainscough, A. M. Brodie, J. D. Ranford, J. M. Waters, *J. Chem. Soc., Dalton Trans.* **1997**, 1251–1256.
[20] a) S. J. Langley, M. Helliwell, R. Sessoli, P. Rosa, W. Wernsdorfer, R. E. P. Winpenny, *Chem. Commun.* **2005**, 5029–5031; b) H. C. Yao, J. J. Wang, Y. S. Ma, O. Waldmann, W. X. Du, Y. Song, Y. Z. Li, L. M. Zheng, S. Decurtins, X. Q. Xin, *Chem. Commun.* **2006**, 1745–1747; c) M. Shanmugam, M. Shanmugam, G. Chastanet, R. Sessoli, T. Mallah, W. Wernsdorfer, R. E. P. Winpenny, *J. Mater. Chem.* **2006**, *16*, 2576–2578.
[21] J. Pons, X. López, J. Casabó, F. Teixidor, A. Caubet, J. Rius, C. Miravitlles, *Inorg. Chim. Acta* **1992**, *195*, 6–66.
[22] J. Pons, A. Chadghan, A. Alvarez-Larena, J. F. Piniella, J. Ros, *Inorg. Chem. Commun.* **2001**, *4*, 610–612.
[23] C. Janiak, *J. Chem. Soc., Dalton Trans.* **2000**, 3885–3896.
[24] a) R. W. Gellert, R. Bau, *Met. Ions Biol. Syst.* **1979**, *8*, 1–55; b) K. Aoki, *Met. Ions Biol. Syst.* **1996**, *32*, 91–134.
[25] a) R. P. Doyle, P. E. Kruger, B. Moubaraki, K. S. Murray, M. Nieuwenhuyzen, *Dalton Trans.* **2003**, 4230–4237; b) S. Youngme, P. Phuengphai, N. Chaichit, G. A. van Albada, O. Roubeau, J. Reedijk, *Inorg. Chim. Acta* **2005**, *358*, 849–853.
[26] A. Holý, M. Buděšinský, J. Podlaha, I. Cisařová, *Collect. Czech. Chem. Commun.* **1999**, *64*, 242–256.
[27] G. M. Sheldrick, *A Computer Program for the Determination of Crystal Structures*, **1997**, University of Göttingen, Germany.
[28] *International Tables of X-ray Crystallography*, **1974**, Ed. Kynoch Press, vol. IV, pp 99–100 and 149.

Received: October 24, 2006
Published Online: March 16, 2007

 © 2007 Wiley-VCH Verlag GmbH & Co. KGaA, Weinheim 

DOI: 10.1002/ejic.200601012

# Receptor versus Counterion: Capability of *N*,*N*′-Bis(2-aminobenzyl)-diazacrowns for Giving Endo- and/or Exocyclic Coordination of $Zn^{II}$

**Lea Vaiana,[a] Carlos Platas-Iglesias,[a] David Esteban-Gómez,[a] Fernando Avecilla,[a] Andrés de Blas,*[a] and Teresa Rodríguez-Blas*[a]**

**Keywords:** Zinc / Macrocyclic ligands / Crown compounds / Coordination modes / Density functional calculations

The structure of $Zn^{II}$ complexes with receptors $L^1$ and $L^2$ [$L^1$ = *N*,*N*′-bis(2-aminobenzyl)-1,10-diaza-15-crown-5 and $L^2$ = *N*,*N*′-bis(2-aminobenzyl)-4,13-diaza-18-crown-6] was studied both in the solid state and in acetonitrile solution. Both receptors form mononuclear $Zn^{II}$ complexes in this solvent, while no evidence for the formation of dinuclear complexes was obtained. This is in contrast with previous investigations that demonstrated the formation of dinuclear complexes of $L^2$ with first-row transition metals such as $Ni^{II}$, $Co^{II}$ and $Cu^{II}$. Compounds of formula $[Zn(L^1)](ClO_4)_2$ (**1**), $[Zn(L^1)](NO_3)_2{\cdot}2CH_3CN$ (**2**), $[Zn(L^2)](ClO_4)_2$ (**3**) and $[Zn(L^2)(NO_3)_2]$ (**4**) were isolated and structurally characterised by X-ray diffraction analyses. $L^1$ forms seven-coordinate $Zn^{II}$ complexes in the presence of both nitrate and perchlorate anions, as a consequence of the good fit between the macrocyclic cavity and the ionic radius of the metal ion. The $Zn^{II}$ ion is deeply buried into the receptor cavity and the anions are forced to remain out of the metal coordination sphere. The cation $[Zn(L^1)]^{2+}$ present in **1** and **2** is one of the very few examples of seven-coordinate Zn complexes. Receptor $L^2$ provides a very rare example of a macrocyclic receptor allowing endocyclic and exocyclic coordination on the same guest cation, depending on the nature of the anion present. Thus, in **3** the $Zn^{II}$ ion is endocyclically coordinated, placed inside the crown hole coordinated to four donor atoms of the ligand in a distorted tetrahedral environment, whereas in **4**, the presence of a strongly coordinating anion such as nitrate results in an exocyclic coordination of $Zn^{II}$, which is directly bound only to the two primarily amine groups of $L^2$ and two nitrate ligands. Spectrophotometric titrations of $[Zn(L^2)]^{2+}$ with tetrabutylammonium nitrate in acetonitrile solution demonstrate the stepwise formation of 1:1 and 1:2 adducts with this anion in acetonitrile solution. The $[Zn(L^1)]^{2+}$, $[Zn(L^2)]^{2+}$ and $[Zn(L^2)(NO_3)_2]$ systems were characterised by means of DFT calculations (B3LYP model). The calculated geometries show an excellent agreement with the experimental structures obtained from X-ray diffraction analyses. Calculated binding energies of the macrocyclic ligands to $Zn^{II}$ are also consistent with the experimental data.

(© Wiley-VCH Verlag GmbH & Co. KGaA, 69451 Weinheim, Germany, 2007)

## Introduction

Since Pedersen reported the synthesis and cation complexing characteristics of the crown ethers, there has been increasing interest in these compounds as complexing agents. In particular, the cyclic framework of crown ethers affords an interesting platform for the complexation of metal ions, and the ability of crown ethers to selectively coordinate metal salts has made them attractive building blocks in supramolecular chemistry and material science.[1–6] Likewise, the relative ease with which crown ethers can be functionalised with pendant arm(s) containing additional donor atom(s) allows modification of the cation-binding ability and, in some cases, the selectivity of the parent crown ether.[7] Pendant-armed crowns, also known as lariat ethers, may be regarded as having a structural character intermediate to that of a flexible macrocyclic polyether and a relatively rigid macrobicyclic cage, and the presence of additional donor atoms in the side arms can be used to enhance their coordination potential and/or to build polynuclear structures.[8] Although the coordination chemistry of crowns and armed-crown receptors has been extensively studied over the last decades,[1–4] their coordination capability is not entirely predictable.

The lariat ethers $L^1$ and $L^2$ (Scheme 1) have been revealed as versatile receptors towards different metal ions. In some cases they impose their coordinative preferences whereas in others they adapt to steric and/or electronic requirements of the guest metal ion. In particular, we have found that whereas $L^1$ only forms mononuclear complexes with first-row transition-metal ions such as $Co^{II}$, $Ni^{II}$ and $Cu^{II}$,[9,10] imposing a pentagonal bipyramidal geometry and so dominating over the coordinative preferences of the particular ion guest, $L^2$ only forms dinuclear complexes with these cations and easily adapts to the coordinative preferences of these metal ions.[10,11] In this paper we report the

[a] Dpto. Química Fundamental, Facultade de Ciencias, Campus da Zapateira s/n, Universidade da Coruña,
15071 A Coruña, Spain
Fax: +34-981167065
E-mail: mayter@udc.es

Supporting information for this article is available on the WWW under http://www.eurjic.org or from the author.

 © 2007 Wiley-VCH Verlag GmbH & Co. KGaA, Weinheim 

coordinative properties of these two lariat ethers toward $Zn^{II}$. It is well known that coordination properties of transition-metal complexes are mainly related to the partly filled d orbitals of the metal ion and have common types of structures with specific coordination numbers, however, non-transition-metal complexes are able to take various coordination numbers and may show diverse structures because of the fact that d atomic orbitals of the metal centre are fully occupied. In particular, the geometries of $Zn^{II}$ complexes can vary from tetrahedral to octahedral through trigonal-bipyramidal and square-pyramidal, all of them frequently distorted. Likewise, although rare, coordination numbers higher than six may be reached by using high denticity polydentate ligands.

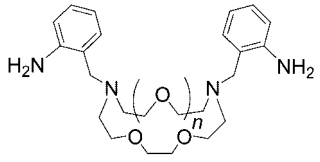


$L^1$: $n$ = 1
$L^2$: $n$ = 2

Scheme 1.

The study presented in this paper provides a very rare example of a macrocyclic receptor allowing endocyclic and exocyclic coordination on the same guest cation depending on the nature of the counterion present.

## Results and Discussion

### Synthesis and Solid-State Structure

The reaction of stoichiometric amounts of *N*,*N*′-bis(2-aminobenzyl)-1-10-diaza-15-crown-5 ($L^1$) or *N*,*N*′-bis(2-aminobenzyl)-4-13-diaza-18-crown-6 ($L^2$) with $Zn^{II}$ salts (perchlorates or nitrates) in ethanol or acetonitrile solution gives compounds of formula $[Zn(L^1)](ClO_4)_2$ (**1**), $[Zn(L^1)](NO_3)_2{\cdot}2CH_3CN$ (**2**), $[Zn(L^2)](ClO_4)_2$ (**3**) and $[Zn(L^2)(NO_3)_2]$ (**4**). The FAB-mass spectrum of each complex displays very intense peaks corresponding to the $[Zn(L\text{-}H)]^+$ and $[Zn(L)(X)]^+$ fragments (L = $L^1$ or $L^2$, X = $ClO_4^-$ or $NO_3^-$), thereby confirming the formation of the complexes. The IR spectra (KBr discs) of the perchlorate complexes **1** and **3** show bands corresponding to the $\nu_{as}$(Cl–O) stretching and $\delta_{as}$(O–Cl–O) bending modes of the perchlorate groups at about 1090 and 620 $cm^{-1}$. The absorption at about 620 $cm^{-1}$ clearly shows up without splitting, as befits an uncoordinated anion.[12] The spectrum of the nitrate complex **2** exhibits an intense band at 1384 $cm^{-1}$, as expected for the presence of ionic nitrate.[12]

The solid-state structures of the four compounds were determined by single-crystal X-ray diffraction analysis. Crystals of **1** and **2** contain the cation $[Zn(L^1)]^{2+}$ and two anions, perchlorate (**1**) or nitrate (**2**), involved in hydrogen-bonding interactions with the $-NH_2$ groups [compound **1**: N(4)···H(4B) 0.868(19) Å, H(4B)···O(9) 2.76(4) Å, N(4)···O(9) 3.209(6) Å, N(4)–H(4B)–O(9) 114(4)°; H(4B)···O(12) 2.18(2) Å, N(4)···O(12) 3.013(5) Å, N(4)–H(4B)–O(12) 162(4)°; N(3)···H(3A) 0.878(18) Å, H(3A)···O(6) 2.23(2) Å, N(3)···O(6) 3.112(7) Å, N(3)–H(3A)–O(6) 178(4)°. Compound **2**: N(2)···H(2N) 0.86(5) Å, H(2N)···O(3) 2.20(5) Å, N(2)···O(3) 2.965(5) Å, N(2)–H(2N)–O(3) 148(4)°; N(2)···H(1N) 0.79(5) Å, H(1N)···O(3) 2.56(5) Å, N(2)–H(1N)–O(3) 157(4)°]. Crystals of **2** also contain two acetonitrile molecules in the asymmetric unit. The structures of the cations present in **1** and **2** are shown in Figure 1, while selected bond lengths and angles are given in Table 1. The structures of both complex cations are very similar, although the one found in **2** is more symmetric and, in fact, the asymmetric unit of **2** only contains half a molecule of $[Zn(L^1)]^{2+}$. In both cases, the cation $[Zn(L^1)]^{2+}$ contains a $ZnN_4O_3$ core with the seven heteroatoms of $L^1$ coordinated to the $Zn^{II}$ ion. The metal ion resides in the macrocyclic cavity bound by the three ether oxygen atoms and the two pivotal nitrogen atoms of the azacrown moiety, while the donor atoms of the pendant arms coordinate apically. The Zn-crown ether oxygen bonds in compounds **1** and **2** are in line with those observed for a seven-coordinate $Zn^{II}$ complex of 15-crown-5, at an average of 2.30 Å.[13] The distances between the $Zn^{II}$ ion and the nitrogen atoms of the aniline groups are about 0.08 Å shorter than those observed for a six-coordinate $Zn^{II}$ complex derived from a triazamacrocycle containing three aniline pendants.[14] However, these distances are about 0.1 Å longer than those observed in the analogous $d^9$ complex $[Cu(L^1)]^{2+}$.[10] The N(3)–Zn–N(4) angle in **1** is 170.7(2)°, while the N(2)–Zn–N(2A) angle in **2** amounts to 175.8(2)°. Angles O(1)–Zn(1)–O(2), N(2)–Zn(1)–O(2), O(3)–Zn(1)–N(2), O(3)–Zn(1)–N(1) and N(1)–Zn(1)–O(1) in **1**, and angles O(1)–Zn(1)–N(1), O(2)–Zn(1)–N(1) and O(2)–Zn(1)–O(2A) in **2** take values close to 72° (Table 1). Thus, the coordination sphere of the zinc ion can be described as a distorted pentagonal bipyramid with an axial compression, as the apical distances between the zinc and the donor atoms of the pendant arms are significantly shorter than the equatorial bonds. The mean deviation from planarity of the plane containing the five equatorial donor atoms and the metal ion is relatively small, and amounts to 0.1668 Å in **1** and 0.1273 Å in **2**. In both compounds the arms of the bibracchial lariat ether $L^1$ are arranged on opposite sides with respect to the crown moiety, resulting in an *anti* conformation.

Both compounds **3** and **4** contain the larger receptor $L^2$, and unlike the analogous compounds containing $L^1$, the presence of different counterions (perchlorate or nitrate) results in dramatically different coordination environments around the $Zn^{II}$ ion. Crystals of **3** contain the $[Zn(L^2)]^{2+}$ cation and two perchlorate anions involved in hydrogen-bonding interactions with the $-NH_2$ groups [N(4)···H(2N) 0.846(19) Å, H(2N)···O(5) 2.27(4) Å, N(4)···O(5) 2.991(5) Å, N(4)–H(2N)–O(5) 171(4)°; N(3)···H(4N) 0.837(19) Å, H(4N)···O(10) 2.13(3) Å, N(3)···O(10) 2.897(6) Å, N(3)–H(4N)–O(10) 151(4)°], whereas the asymmetric unit of **4** contains a half $[Zn(L^2)(NO_3)_2]$ molecule. The structures of $[Zn(L^2)]^{2+}$ and $[Zn(L^2)(NO_3)_2]$ present in

 © 2007 Wiley-VCH Verlag GmbH & Co. KGaA, Weinheim 

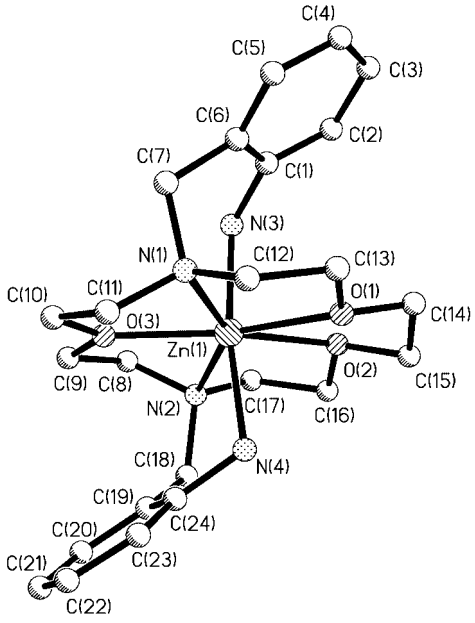


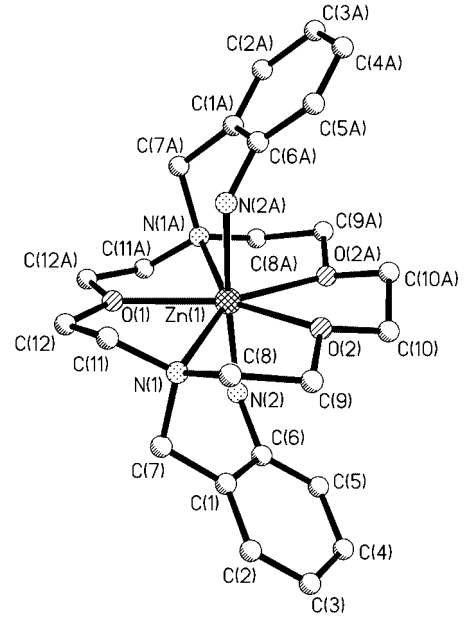


Figure 1. X-ray crystal structures of the cation $[Zn(L^1)]^{2+}$ present in compounds **1** (top) and **2** (bottom). Hydrogen atoms are omitted for simplicity. Symmetry transformations used to generate equivalent atoms in **2**: A: $-x + 1$, $y$, $-z + 3/2$.

**3** and **4**, respectively, are shown in Figure 2, while Table 2 summarises selected bond lengths and angles of the metal coordination environments. In $[Zn(L^2)]^{2+}$, the $Zn^{II}$ ion is endocyclically coordinated but only four of the eight available donor atoms of $L^2$ form part of the coordination sphere. Thus, the metal ion is directly bound to both aniline pendant arms [N(3) and N(4)], one of the pivotal nitrogen atoms, N(1), and an oxygen atom of the crown, O(2), while the remaining distances between the metal ion and the other heteroatoms of the crown are too long to be considered as bond lengths [Zn–O(1) 2.498 Å; Zn–O(3) 2.596 Å; Zn–O(4) 3.464 Å; Zn–N(2) 3.720 Å]. Receptor $L^2$ adopts an *anti* conformation and the coordination polyhedron around the zinc ion can be described as a distorted tetrahedron. Moreover, the $-NH_2$ group containing N(4) is involved in a hydrogen-bonding interaction with O(4) and N(2) [N(4)···H(1N) 0.80(4) Å, H(1N)···N(2) 2.27(4) Å, N(4)···N(2) 2.904(5) Å, N(4)–H(1N)–N(2) 137(3)°; N(4)···H(1N) 0.80(4) Å, H(1N)···O(4) 2.38(4) Å, N(4)···O(4) 3.063(4) Å, N(4)–H(1N)–O(4) 144(3)°].

Table 1. Selected bond lengths [Å] and angles [°] for **1** and **2**.

| **1** | | **2**[a] | |
|---|---|---|---|
| Zn(1)–N(3) | 2.151(4) | Zn(1)–N(2) | 2.150(3) |
| Zn(1)–N(4) | 2.157(4) | Zn(1)–N(2A) | 2.150(3) |
| Zn(1)–O(3) | 2.172(3) | Zn(1)–O(1) | 2.228(4) |
| Zn(1)–N(1) | 2.234(4) | Zn(1)–O(2) | 2.235(3) |
| Zn(1)–O(1) | 2.281(3) | Zn(1)–O(2A) | 2.235(3) |
| Zn(1)–N(2) | 2.323(4) | Zn(1)–N(1A) | 2.271(3) |
| Zn(1)–O(2) | 2.345(3) | Zn(1)–N(1) | 2.271(3) |
| N(3)–Zn(1)–N(4) | 170.97(2) | N(2)–Zn(1)–N(2A) | 175.8(2) |
| N(3)–Zn(1)–O(3) | 91.9(2) | N(2)–Zn(1)–O(1) | 92.1(1) |
| N(4)–Zn(1)–O(3) | 96.4(2) | N(2A)–Zn(1)–O(1) | 92.1(1) |
| N(3)–Zn(1)–N(1) | 87.3(2) | N(2)–Zn(1)–O(2) | 94.0(1) |
| N(4)–Zn(1)–N(1) | 99.0(2) | N(2A)–Zn(1)–O(2) | 82.6(1) |
| O(3)–Zn(1)–N(1) | 73.4(1) | O(1)–Zn(1)–O(2) | 144.8(1) |
| N(3)–Zn(1)–O(1) | 95.4(2) | N(2)–Zn(1)–O(2A) | 82.6(2) |
| N(4)–Zn(1)–O(1) | 79.9(1) | N(2A)–Zn(1)–O(2A) | 94.0(1) |
| N(1)–Zn(1)–O(1) | 74.8(1) | O(1)–Zn(1)–O(2A) | 144.8(1) |
| O(3)–Zn(1)–O(1) | 147.0(1) | O(2)–Zn(1)–O(2A) | 70.4(2) |
| N(3)–Zn(1)–N(2) | 95.5(2) | N(2)–Zn(1)–N(1A) | 95.0(1) |
| N(4)–Zn(1)–N(2) | 83.1(2) | N(2A)–Zn(1)–N(1A) | 86.4(1) |
| O(3)–Zn(1)–N(2) | 72.8(1) | O(1)–Zn(1)–N(1A) | 70.6(1) |
| N(1)–Zn(1)–N(2) | 146.1(1) | O(2)–Zn(1)–N(1A) | 142.9(2) |
| O(1)–Zn(1)–N(2) | 138.0(1) | O(2A)–Zn(1)–N(1A) | 75.2(2) |
| N(3)–Zn(1)–O(2) | 79.8(2) | N(2)–Zn(1)–N(1) | 86.4(1) |
| N(4)–Zn(1)–O(2) | 91.0(2) | N(2A)–Zn(1)–N(1) | 95.0(1) |
| O(3)–Zn(1)–O(2) | 144.5(1) | O(1)–Zn(1)–N(1) | 70.6(1) |
| N(1)–Zn(1)–O(2) | 139.6(1) | O(2)–Zn(1)–N(1) | 75.2(2) |
| O(1)–Zn(1)–O(2) | 68.5(1) | O(2A)–Zn(1)–N(1) | 142.9(2) |
| N(2)–Zn(1)–O(2) | 73.8(1) | N(1A)–Zn(1)–N(1) | 141.2(2) |

[a] Symmetry transformations used to generate equivalent atoms. A: $-x + 1$, $y$, $-z + 3/2$.

In the complex $[Zn(L^2)(NO_3)_2]$ present in **4**, the $Zn^{II}$ ion is exocyclically coordinated with the metal ion only directly bound to the two aniline groups of $L^2$, [N(2)] and [N(2)#1]. The $-NH_2$ groups are also involved in an intramolecular hydrogen-bonding interaction with the pivotal nitrogen atoms and an oxygen atom of the crown moiety [N(2)···H(2A) 0.90 Å, H(2A)···O(1) 2.16 Å, N(2)···O(1) 2.993(4) Å, N(2)–H(2A)–O(1) 153.9°; N(2)···H(2B) 0.90 Å, H(2B)···N(1) 2.04 Å, N(2)···N(1) 2.825(4) Å, N(2)–H(2B)–N(1) 144.7°]. As a consequence, $L^2$ adopts a *syn* arrangement with both aniline pendant arms disposed on the same side of the crown. Coordination number six is completed by two nitrate ligands in a bidentate fashion, as often observed for $Zn^{II}$ complexes with nitrate ligands.[15,16] The structure presents a disorder on one oxygen atom of a coordinated nitrate group and, as a result, the bidentate nitrate ion is coordinated in a nearly symmetrical fashion [Zn(1)–O(1SA) 2.336(13) Å, Zn(1)–O(3S) 2.371(5) Å] or in a clearly asymmetrical one [Zn(1)–O(1SB) 1.929(7) Å, Zn(1)–O(3S)

 © 2007 Wiley-VCH Verlag GmbH & Co. KGaA, Weinheim 

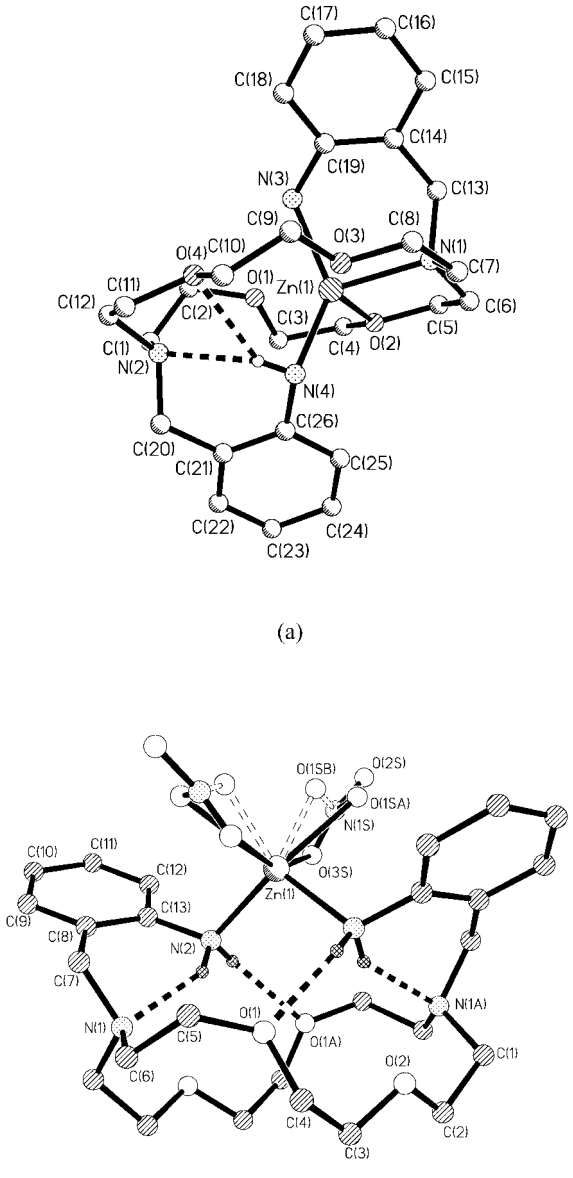


Figure 2. (a) X-ray crystal structure of the cation $[Zn(L^2)]^{2+}$ present in compound **3**; (b) X-ray crystal structure of compound **4**. Hydrogen atoms are omitted for simplicity. Symmetry transformations used to generate equivalent atoms in **4**: #1 $-x + 2$, $y$, $-z + 1/2$.

2.371(5) Å], depending on the occupation of sites O(1SA) or O(1SB).

A comparison of the bond lengths of the metal coordination environment in $[Zn(L^1)]^{2+}$ present in compounds **1** and **2** with those observed for $[Zn(L^2)]^{2+}$ present in **3** clearly shows a shortening of the bond lengths as the coordination number of the metal ion decreases. Likewise, the distances between the $Zn^{II}$ ion and the nitrogen atoms of the aniline groups in compounds **3** and **4** are close to those observed in four-coordinate $Zn^{II}$ complexes containing aniline groups.[17,18]

Table 2. Selected bond lengths [Å] and angles [°] for **3** and **4**.

| **3** | |
|---|---|
| Zn(1)–N(4) | 2.014(3) |
| Zn(1)–N(3) | 2.024(3) |
| Zn(1)–N(1) | 2.110(3) |
| Zn(1)–O(2) | 2.147(2) |
| N(4)–Zn(1)–N(3) | 131.0(2) |
| N(4)–Zn(1)–N(1) | 119.7(1) |
| N(4)–Zn(1)–O(2) | 103.7(1) |
| N(3)–Zn(1)–N(1) | 96.6(1) |
| N(3)–Zn(1)–O(2) | 114.8(1) |
| N(1)–Zn(1)–O(2) | 80.3(1) |
| **4**[a] | |
| Zn(1)–N(2) | 2.017(3) |
| Zn(1)–O(3S) | 2.371(5) |
| Zn(1)–O(1SA) | 2.336(13) |
| Zn(1)–O(1SB) | 1.929(7) |
| O(1SB)#1–Zn(1)–O(1SB) | 68.8(5) |
| O(1SB)–Zn(1)–N(2)#1 | 110.1(3) |
| O(1SB)–Zn(1)–N(2) | 134.2(2) |
| N(2)#1–Zn(1)–N(2) | 101.83(15) |
| N(2)–Zn(1)–O(1SA)#1 | 91.0(4) |
| N(2)–Zn(1)–O(1SA) | 137.5(3) |
| O(1SA)#1–Zn(1)–O(1SA) | 106.5(9) |
| O(1SB)–Zn(1)–O(3S)#1 | 108.2(3) |
| N(2)–Zn(1)–O(3S)#1 | 104.23(17) |
| O(1SA)–Zn(1)–O(3S)#1 | 116.5(4) |
| O(1SB)–Zn(1)–O(3S) | 52.2(2) |
| N(2)–Zn(1)–O(3S) | 89.09(16) |
| O(1SA)–Zn(1)–O(3S) | 48.4(3) |
| O(3S)#1–Zn(1)–O(3S) | 159.0(3) |

[a] Symmetry transformations used to generate equivalent atoms. #1: $-x + 2$, $y$, $-z + 1/2$.

### Solution Behaviour

The behaviour in [$D_3$]acetonitrile solution of compounds **1**–**4** was investigated by $^1H$ NMR spectroscopy. Significant changes in the chemical shifts, the structures of the signals and even the number of signals are observed in the $^1H$ NMR spectra upon coordination of the receptors to $Zn^{II}$. The most complicated region of the spectra is that where the ethylene and methylene proton signals are observed. The coordination to the metal ion increases the rigidity of the receptor, limiting conformational exchange processes, so that the geminal $CH_2$ protons are no longer equivalent. The aromatic region usually appears more clearly resolved in all complexes except for the nitrate complex **4** because of the presence of a conformational equilibrium between the different species present in solution (see Figure 3).

The $^1H$ NMR spectra of compounds **1** and **2** are identical, indicating that the presence of different counterions (perchlorate or nitrate) does not affect the structure of the $[Zn(L^1)]^{2+}$ cation in solution. The signals corresponding to the protons of the aromatic units are shifted downfield by about 0.4–0.6 ppm upon coordination to the metal ion, thereby confirming the coordination of the ligand to the metal ion in this solvent (Figures S1 and S2, Supporting Information). Conductivity measurements carried out in acetonitrile solution (281 $\Omega^{-1}cm^2mol^{-1}$ for **1** and 194 $\Omega^{-1}cm^2mol^{-1}$ for **2**) show that **1** and **2** behave as 2:1 electrolytes in this solvent,[19] confirming that the nature of

 © 2007 Wiley-VCH Verlag GmbH & Co. KGaA, Weinheim 

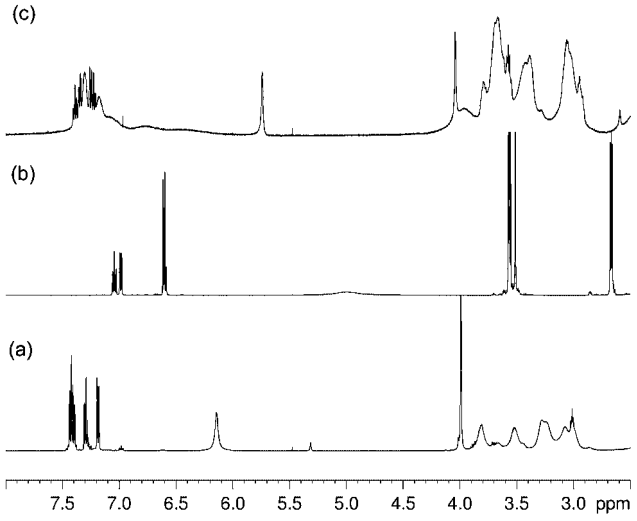


Figure 3. $^1$H NMR spectra recorded at 298 K on $10^{-3}$ M solutions of **3** (spectrum a), $L^2$ (spectrum b) and **4** (spectrum c).

the counterion has no influence in the coordination sphere of the metal ion, in agreement with their solid-state structures. The situation is quite different for compounds **3** and **4**. The molar conductivity measured for **3** in acetonitrile solution (287 $\Omega^{-1}$ cm$^2$ mol$^{-1}$) indicates that this compound behaves as a 2:1 electrolyte in this solvent, while the molar conductivity determined for a solution of **4** (prepared in situ by mixing stoichiometric amounts of $L^2$ and $Zn^{II}$ nitrate) is clearly lower (134 $\Omega^{-1}$ cm$^2$ mol$^{-1}$). These results are in agreement with the coordination of the $NO_3^-$ ligands to the metal ion. The interaction of $[Zn(L^2)]^{2+}$ is, however, relatively weak (vide infra), and therefore the conductivity measured experimentally is an average of the conductivity values of the different species in equilibrium. The $^1$H NMR spectra of **3** and **4** show that the signals of protons of the aromatic and amine groups are shifted downfield with respect to their position in the spectrum of the free receptor, indicating the coordination of the receptor to the metal ion in both compounds. However, while these signals are well resolved in the case of compound **3**, the spectrum of **4** shows broad resonances between 6.5 and 7.5 ppm (Figure 3). This is probably due to the presence in solution of exchange processes involving $[Zn(L^2)(NO_3)_2]$, $[Zn(L^2)(NO_3)]^+$ and $[Zn(L^2)]^{2+}$ complex species (vide infra). The spectra of **3** and **4** are very different (Figure 3), indicating a different structure of the complexes in solution, as also observed in the solid state. This is confirmed by a $^1$H NMR titration experiment, where tetrabutylammonium nitrate was added to a solution of compound **3** (Figure S3, Supporting Information). During the titration the aromatic proton signals gradually shifted upfield, giving rise to an identical spectral pattern to that observed for compound **4**. Upon addition of increasing amounts of $NO_3^-$, the intensity of the sharp signals due to the $[Zn(L^2)]^{2+}$ species gradually decrease as a new set of broad signals appear, in agreement with the formation of the $[Zn(L^2)(NO_3)_2]$ complex.

The UV/Vis spectra of $L^1$ and $L^2$ show two absorption bands at 240 and 290 nm, resulting from the $\pi \rightarrow \pi^*$ and $n \rightarrow \pi^*$ transitions on the aromatic subunits of the ligand. Upon addition of $Zn^{II}$ perchlorate both absorption bands show a blueshift while their intensity decreases. Figure 4 shows the spectral changes observed during the formation of the $Zn^{II}$ complexes of $L^1$ and $L^2$. The data display a single inflection point when the M/ligand molar ratio is close to 1, indicating a 1:1 reaction stoichiometry. The steep curvature of the titration profiles corresponds to an especially high equilibrium constant ($\log K > 7$). In particular, the *p* parameter (*p* = [concentration of complex]/[maximum possible concentration of complex]) was found to be higher than 0.8 in both cases, a condition that does not permit the determination of a reliable equilibrium constant.[20] A similar situation was observed for the $Mn^{II}$, $Co^{II}$ and $Ni^{II}$ complexes of $L^1$.[9] It is interesting to note that while $L^2$ is able to form dinuclear complexes with metal ions such as $Co^{II}$, $Ni^{II}$[11] and $Cu^{II}$[10] no evidence has been obtained in

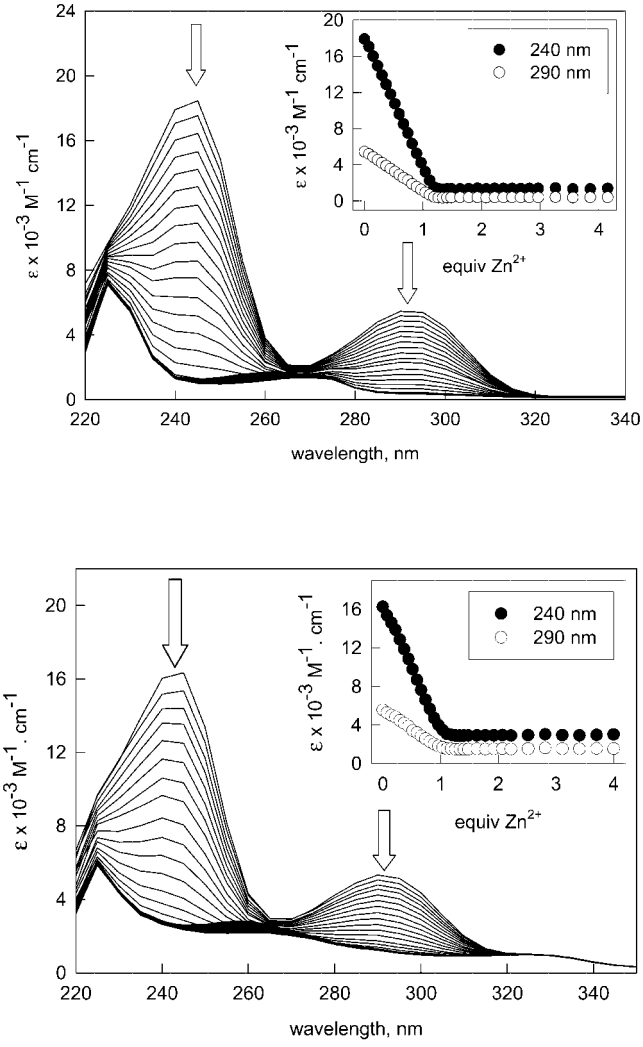


Figure 4. UV/Vis spectrum of $L^1$ (top) and $L^2$ (bottom) in acetonitrile solution and spectral changes upon addition of aliquots of a solution of $Zn(ClO_4)_2 \cdot 6H_2O$ in the same solvent.

 © 2007 Wiley-VCH Verlag GmbH & Co. KGaA, Weinheim 

this work for the formation of analogous dinuclear $Zn^{II}$ complexes at room temperature. The UV/Vis spectrum of **$L^2$** recorded in the presence of a 10 fold excess of $Zn^{II}$ does not change when the solution is heated to reflux for 24 h, indicating that no dinuclear species are formed even under these conditions.

The addition of tetrabutylammonium nitrate to a solution of $[Zn(L^2)]^{2+}$ provokes a substantial variation of the UV/Vis spectrum (Figure 5). Upon addition of $NO_3^-$ the intensity of the band that the complex shows at 290 nm increases. This is in agreement with the formation of the exocyclic complex because of the coordination of $NO_3^-$ to the metal ion. Indeed, the X-ray structure of **4** shows that the $Zn^{II}$ ion is not coordinated to the pivotal nitrogen atoms of the macrocycle, while at least one of the pivotal nitrogen atoms is involved in the coordination to $Zn^{II}$ in **3**. Thus, the decoordination of the pivotal nitrogen atoms appears to provoke an increase of the intensity of the band at 290 nm, in line with the spectral variations observed during the formation of complexes $[Zn(L^1)]^{2+}$ and $[Zn(L^2)]^{2+}$. The titration profile shown in the inset of Figure 5 indicates the formation of at least two complex species in solution.

$$[Zn(L^2)]^{2+} + NO_3^- \leftrightarrows [Zn(L^2)(NO_3)]^+ \quad \beta_{11}$$

$$[Zn(L^2)]^{2+} + 2\,NO_3^- \leftrightarrows [Zn(L^2)(NO_3)_2] \quad \beta_{12}$$

The best fit of the experimental data gives $\log\beta_{11}$ = 3.57(2) and $\log\beta_{12}$ = 8.5(1). These results indicate the stepwise formation of 1:1 and 1:2 adducts during the course of the titration. Figure 5 shows how the concentration of the species at the equilibrium, calculated from $\beta_{11}$ and $\beta_{12}$ values, varies upon nitrate addition. It can be seen that, because of the especially high value of $\beta_{12}$, the neutral complex $[Zn(L^1)(NO_3)_2]$ is formed in the early stages of titration. Notice also that under the conditions of the UV/Vis titration experiment the highest concentration of $[Zn(L^1)(NO_3)]^+$ is about 9%, reached after the addition of 1.6 equiv. of $NO_3^-$.

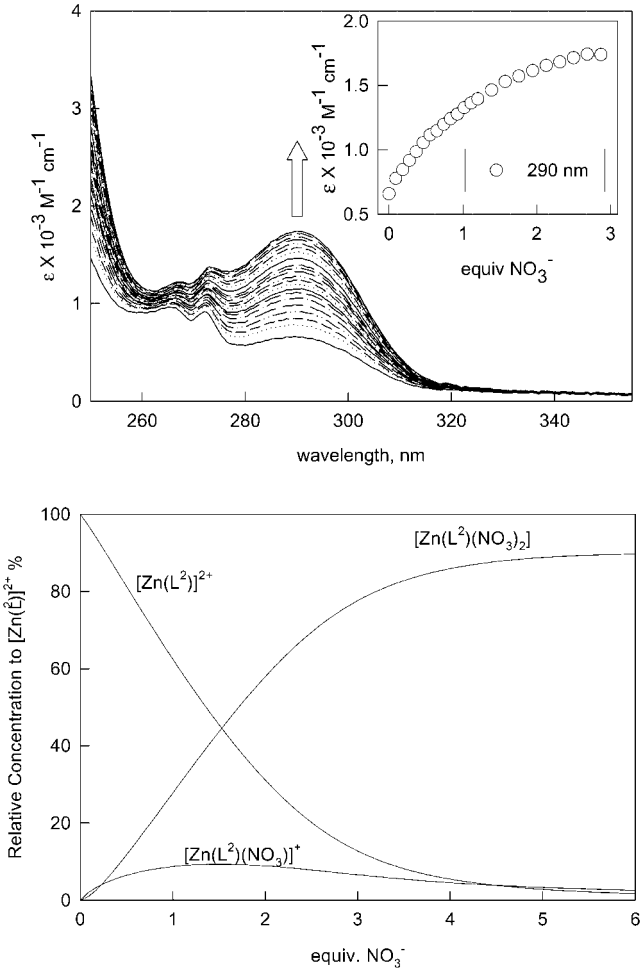


Figure 5. Top: UV/Vis spectrum of $[Zn(L^2)]^{2+}$ in acetonitrile solution and spectral changes upon addition of aliquots of a solution of tetrabutylammonium nitrate in the same solvent. Bottom: Species distribution diagram obtained from the best fit of the experimental data (see text).

## DFT Studies

Density functional theory (DFT) has emerged as the computational method of choice for the solution of many chemical problems. This is because DFT methods have relatively low computational cost, include a significant amount of the dynamic electron correlation and are applicable to a wide range of molecular types, including $Zn^{II}$ complexes.[21] In a recent paper we reported a theoretical study of the $[M(L^1)]^{2+}$ systems (M = Mn, Co or Ni) at the DFT (B3LYP) computational level.[9] The calculated geometries obtained from geometry optimisations for those systems show an excellent agreement with the experimental structures obtained by X-ray diffraction analyses. Moreover, a molecular orbital analysis on the calculated structures allowed us to gain insight into the electronic structure of this family of complexes. Aiming to understand if analogous calculations can reproduce the experimental structures reported in this paper, we have performed DFT calculations on the complexes reported in this work by using the B3LYP model. Full geometry optimisations of the $[Zn(L^1)]^{2+}$, $[Zn(L^2)]^{2+}$ and $[Zn(L^2)(NO_3)_2]$ systems were performed in vacuo by using the standard 6-31G(d) basis on the ligand atoms and Ahlrichs' valence triple-ζ (VTC) on Zn.[22] The latter basis has been shown to provide accurate molecular structures for several first-row transition-metal complexes.[23]

The most relevant geometrical parameters calculated for $[Zn(L^1)]^{2+}$, $[Zn(L^2)]^{2+}$ and $[Zn(L^2)(NO_3)_2]$ systems are given in Table S1 (Supporting Information). The calculated bond lengths for $[Zn(L^1)]^{2+}$ are in excellent agreement with those observed experimentally for compound **2**, as evidenced by the excellent agreement factor obtained (Table 3, $AF_i$ = $[\Sigma(\text{exp} - \text{calcd})^2/\Sigma(\text{exp})^2]^{1/2}$, where exp and calcd denote experimental and calculated values, respectively).[24,25] Calculated bond lengths of the metal coordination environment deviate from the experimental distances determined for **2**

 © 2007 Wiley-VCH Verlag GmbH & Co. KGaA, Weinheim 

by less than 0.07 Å, while calculated bond angles of the $Zn^{II}$ coordination environment deviate by less than 4.0° from the experimental values. Although no geometrical constraints were used during the geometry optimisation, the calculated structure of $[Zn(L^1)]^{2+}$ corresponds to a nearly undistorted $C_2$ symmetry that shows a slightly better agreement with the X-ray structure of **2** than with that of compound **1** (Table 3). The agreement factors between calculated and experimental geometrical parameters obtained for $[Zn(L^2)]^{2+}$ indicate that the experimental geometry is well reproduced at the B3LYP/6-31G(d) level, calculated bond lengths deviating from experimental values by less than 0.04 Å. For $[Zn(L^2)(NO_3)_2]$ our calculations provide a poorer agreement with experimental data than for $[Zn(L^1)]^{2+}$ and $[Zn(L^2)]^{2+}$ (Table 3). However, this is not surprising because the X-ray crystal structure of compound **4** shows that the coordinated nitrate anions are disordered, which suggests a rather shallow potential-energy surface for the variation of the Zn–O bond lengths. In the calculated structure the nitrate anions are coordinated in a nearly symmetrical fashion [Zn(1)–O(1S) 2.178 Å, Zn(1)–O(3S) 2.107 Å].

Table 3. Agreement factors ($AF_i$)[a] between exp./calcd. bond lengths and angles of the metal coordination environment for $[Zn(L^1)]^{2+}$, $[Zn(L^2)]^{2+}$ and $[Zn(L^2)(NO_3)_2]$, binding energies of the macrocyclic ligands [kcal mol$^{-1}$] and basis-set superposition error corrections [kcal mol$^{-1}$].

| | $[Zn(L^1)]^{2+}$ | $[Zn(L^2)]^{2+}$ | $[Zn(L^2)(NO_3)_2]$ |
|---|---|---|---|
| $AF_i$ (bond lengths) | 0.026[b]/0.021[c] | 0.016 | 0.083[d]/0.102[e] |
| $AF_i$ (bond angles) | 0.032[b]/0.018[c] | 0.067 | 0.093[d]/0.106[e] |
| Binding energy[f] | 412.5 | 405.9 | 50.5 |
| BSSE[f] | 7.8 | 7.3 | 20.6 |

[a] $AF_i = [\sum(\text{exp.} - \text{calcd.})^2/\sum(\text{exp.})^2]^{1/2}$. [b] Experimental data from the X-ray structure of **1**. [c] Experimental data from the X-ray structure of **2**. [d] Calculated by using O(1SA). [e] Calculated by using O(1SB). [f] Binding energies include corrections for basis-set superposition error (BSSE).

The metal cation–ligand binding energies are summarised in Table 3. In these calculations the basis-set superposition error (BSSE) was taken into account by the counterpoise method.[26] BSSE corrections are of similar magnitude for the three systems and do not change the calculated order of binding energies. The results predict a stronger interaction of the macrocyclic ligand with $Zn^{II}$ for $L^1$ than for $L^2$, in agreement with the results from the spectrophotometric titrations. This stronger interaction can be attributed to a better fit of the cation in the macrocyclic cavity of $L^1$ than in that of $L^2$. The lower coordination number of the metal ion in $[Zn(L^2)(NO_3)_2]$, where $Zn^{II}$ is exocyclically coordinated and only bound to the two nitrogen atoms of the aniline groups of the receptor $L^2$, results in a very low binding energy for this one (50.5 kcal mol$^{-1}$), while the binding energy of the two nitrate ligands is much higher (396.2 kcal mol$^{-1}$). These results indicate a strong interaction of the nitrate anions with $Zn^{II}$, while the interaction of the metal ion with the macrocyclic ligand appears to be very weak.

## Conclusions

$Zn^{II}$ binding by the lariat crown ethers $L^1$ and $L^2$ [$L^1$ = *N*,*N*′-bis(2-aminobenzyl)-1,10-diaza-15-crown-5 and $L^2$ = *N*,*N*′-bis(2-aminobenzyl)-4,13-diaza-18-crown-6] was analysed by spectrophotometric measurements in acetonitrile solution. Both receptors form stable mononuclear $Zn^{II}$ complexes in this solvent, while no evidence for the formation of dinuclear complexes was obtained. $L^1$ forms seven-coordinate $Zn^{II}$ complexes in the presence of both nitrate and perchlorate anions, as a consequence of the good fit between the macrocyclic cavity and the ionic radius of the metal ion. The $Zn^{II}$ ion is deeply buried in the receptor cavity and the anions are forced to remain out of the metal coordination sphere. The cation $[Zn(L^1)]^{2+}$ is one of the very few examples of seven-coordinate Zn complexes. In fact, a recent estimate based on the number of transition-metal σ-bonded complexes found in the Cambridge Structural Database reveals that seven-coordinate complexes represent 1.8% of the total number of structures reported and, even more, the distribution of seven-coordination throughout the first metal transition series is also quite irregular and it appears to be more common for manganese, iron and cobalt, than for zinc.

On the other hand, the cavity of $L^2$ is rather large for $Zn^{II}$, so that different coordination environments are observed for the metal cation depending on the coordinative properties of the counterion. The X-ray structure of the perchlorate salt **3** shows the metal ion placed inside the crown hole coordinated to four donor atoms of the ligand in a distorted tetrahedral environment, whereas the presence of a strongly coordinating anion such as nitrate results in an exocyclic coordination of $Zn^{II}$, which is directly bound only to the two primary amine groups of $L^2$. Spectrophotometric titrations of $[Zn(L^2)]^{2+}$ with $NO_3^-$ also indicate an exocyclic coordination of the metal ion in acetonitrile solution. DFT calculations performed at the B3LYP level reproduce the experimental structures of the $[Zn(L^1)]^{2+}$, $[Zn(L^2)]^{2+}$ and $[Zn(L^2)(NO_3)_2]$ systems obtained by X-ray diffraction analysis fairly well. They also predict a stronger binding of $L^1$ to $Zn^{II}$ compared to $L^2$.

The ability of a macrocyclic receptor to give endocyclic and exocyclic coordination on the same guest cation depending on the nature of the anion present in the medium is very rare. Although some examples with S-containing macrocycles and soft metals such as $Pd^{II}$ have been reported,[27] to the best of our knowledge compounds **3** and **4** reported here represent the first example of this with a pendant-armed crown and $Zn^{II}$.

## Experimental Section

**Materials and Synthesis:** *N*,*N*′-Bis(2-aminobenzyl)-1,10-diaza-15-crown-5 ($L^1$)[28] and *N*,*N*′-bis(2-aminobenzyl)-4,13-diaza-18-crown-6 ($L^2$)[10] were prepared as previously reported by us. All other chemicals were purchased from commercial sources and used without further purification. Solvents were of reagent grade purified by the usual methods.

 © 2007 Wiley-VCH Verlag GmbH & Co. KGaA, Weinheim 

***CAUTION!*** *Perchlorate salts combined with organic ligands are potentially explosive and should be handled in small quantities and with the necessary precautions.*[29]

**$[Zn(L^1)](ClO_4)_2$ (1):** A mixture of $L^1$ (0.100 g, 0.233 mmol) and $Zn(ClO_4)_2{\cdot}6H_2O$ (0.087 g, 0.233 mmol) in ethanol (23 mL) was stirred and heated to reflux over a period of 8 h. The white precipitate formed was isolated by filtration and air-dried (0.152 g, 94%). $C_{24}H_{36}Cl_2N_4O_{11}Zn$ (692.86): calcd. C 41.6, H 5.2, N 8.1; found C 41.3, H 5.1, N 8.0. FAB-MS: *m/z* (%BPI) = 591 (41) $[Zn(L^1)(ClO_4)]^+$, 491 (100) $[Zn(L^1 - H)]^+$. FTIR (KBr): $\tilde{\nu}$ = 3340 [$\nu_{as}(NH_2)$], 3250 [$\nu_s(NH_2)$], 1617 [$\delta(NH_2)$], 1586 [$\nu$(C=C)], 1078 [$\nu_{as}$(Cl–O)], 620 [$\delta_{as}$(Cl–O)] $cm^{-1}$. $\Lambda_M$ (acetonitrile, $cm^2\,\Omega^{-1}\,mol^{-1}$): 281 (2:1 electrolyte). Slow diffusion of diethyl ether into a solution of **1** in acetonitrile gave single crystals suitable for X-ray crystallography.

**$[Zn(L^1)](NO_3)_2{\cdot}2CH_3CN$ (2):** A mixture of $L^1$ (0.104 g, 0.243 mmol) and $Zn(NO_3)_2{\cdot}6H_2O$ (0.075 g, 0.253 mmol) in acetonitrile (20 mL) was stirred and heated to reflux over a period of 6 h. Slow diffusion of diethyl ether into the former solution at room temperature produced colourless crystals that were collected by filtration and air-dried (0.097 g, 57%). $C_{28}H_{42}N_8O_9Zn$ (700.07): calcd. C 48.0, H 6.1, N 15.6; found C 47.1, H 6.1, N 16.0. FAB-MS: *m/z* (%BPI) = 491 (28) $[Zn(L^1 - H)]^+$. FTIR (KBr): $\tilde{\nu}$ = 3268, 3225 [$\nu_{as}(NH_2)$], 3123, 3090 [$\nu_s(NH_2)$], 1618 [$\delta(NH_2)$], 1591 [$\nu$(C=C)], 1384 [$\nu(NO_3)$] $cm^{-1}$. $\Lambda_M$ (acetonitrile, $cm^2\,\Omega^{-1}\,mol^{-1}$): 194 (2:1 electrolyte). Slow diffusion of diethyl ether into a solution of **2** in acetonitrile gave single crystals suitable for X-ray crystallography.

**$[Zn(L^2)](ClO_4)_2$ (3):** The preparation of the white complex followed the same procedure as for **1** by using $L^2$ (0.107 g, 0.226 mmol) and $Zn(ClO_4)_2{\cdot}6H_2O$ (0.085 g, 0.228 mmol) in ethanol (23 mL) (0.125 g, 75%). $C_{26}H_{40}Cl_2N_4O_{12}Zn$ (736.91): calcd. C 42.4, H 5.5, N 7.6; found C 42.0, H 5.5, N 7.5. FAB-MS: *m/z* (%BPI) = 635 (28) $[Zn(L^2)(ClO_4)]^+$, 535 (58) $[Zn(L^2 - H)]^+$, 473 (100) $[L^2 + H]^+$. FTIR (KBr): $\tilde{\nu}$ = 3225 [$\nu(NH_2)$], 1614 [$\delta(NH_2)$], 1589 [$\nu$(C=C)], 1092 [$\nu_{as}$(Cl–O)], 622 [$\delta_{as}$(Cl–O)] $cm^{-1}$. $\Lambda_M$ (acetonitrile, $cm^2\,\Omega^{-1}\,mol^{-1}$): 287 (2:1 electrolyte). Slow diffusion of diethyl ether into a solution of **3** in acetonitrile gave single crystals suitable for X-ray crystallography.

**$[Zn(L^2)(NO_3)_2]$ (4):** Slow diffusion of diethyl ether into a solution of $Zn(NO_3)_2{\cdot}6H_2O$ (0.067 g, 0.225 mmol) and $L^2$ (0.105 g, 0.222 mmol) in acetonitrile (7 mL) gave some single crystals suitable for X-ray crystallography. Attempts to isolate more compound **4** were unsuccessful because it formed an intractable oily product when separated from the solvent.

**Physical Measurements:** Elemental analyses were carried out on a Carlo–Erba 1180 elemental analyser. FAB mass spectra were recorded with a Fisons Quatro mass spectrometer with a Cs ion gun using 3-nitrobenzyl alcohol as matrix. IR spectra were recorded, as KBr discs, using a Bruker Vector 22 spectrophotometer. Conductivity measurements were carried out at 20 °C with a Crison Micro CM 2201 conductimeter using $10^{-3}$ M solutions of the complexes in acetonitrile. $^1H$ NMR spectra were run on a Bruker AC 200 F or a Bruker WM-500 spectrometer. Proton NMR titration was performed on $5 \times 10^{-3}$ M solution of **3** and in [$D_3$]acetonitrile. Typically, aliquots of a fresh tetrabutylammonium nitrate solution (0.5 M) were added, and the $^1H$ NMR spectra of the samples were recorded.

**Spectrophotometric Titrations:** UV/Vis spectra were recorded with Hewlett–Packard 8452A or Perkin–Elmer Lambda 900 spectrophotometers, with a quartz cell (path length: 10 cm). The cell holder was thermostatted at 25.0 °C through circulating water. Spectrophotometric titrations were performed at 25 °C on $5.0 \times 10^{-5}$ M solutions of $L^1$ or $L^2$ in MeCN (polarographic grade). Typically, aliquots of a fresh $Zn(ClO_4)_2{\cdot}6H_2O$ standard solution were added and the UV/Vis spectra of the samples were recorded. The spectrophotometric titration of $[Zn(L^2)]^{2+}$ with tetrabutylammonium nitrate was performed on a $1 \times 10^{-5}$ M solution of the complex, which was titrated with a $1 \times 10^{-2}$ M solution of the tetrabutylammonium salt. All spectrophotometric titration curves were fitted with the HYPERQUAD program.[30]

**X-ray Crystallography:** Crystal data and details on data collection and refinement are summarised in Table 4. Three-dimensional X-

Table 4. Crystal data and structure refinement for compounds **1**–**4**.

| | **1** | **2** | **3** | **4** |
|---|---|---|---|---|
| Formula | $C_{24}H_{36}Cl_2N_4O_{11}Zn$ | $C_{28}H_{42}N_8O_9Zn$ | $C_{26}H_{40}Cl_2N_4O_{12}Zn$ | $C_{26}H_{40}N_6O_{10}Zn$ |
| Molecular weight ($g\,mol^{-1}$) | 692.84 | 700.07 | 736.89 | 662.01 |
| Crystal system | monoclinic | monoclinic | monoclinic | monoclinic |
| Space group | $P2_1/a$ | $C2/c$ | $P2_1$ | $C2/c$ |
| $a$ [Å] | 12.5098(13) | 12.1074(12) | 10.1909(2) | 23.327(5) |
| $b$ [Å] | 12.6196(13) | 16.0368(15) | 14.9591(3) | 9.081(5) |
| $c$ [Å] | 18.1259(18) | 16.9168(17) | 10.9007(2) | 17.325(5) |
| $\beta$ [°] | 92.263(2) | 91.604(2) | 108.7440(10) | 122.948(5) |
| Volume [$Å^3$] | 2859.3(5) | 3283.3(6) | 1573.64(5) | 3080(2) |
| $F$(000) | 1440 | 1472 | 768 | 1392 |
| $Z$ | 4 | 4 | 2 | 4 |
| Temperature [K] | 298(2) | 298(2) | 298(2) | 298(2) |
| $\lambda$(Mo-$K_\alpha$) [Å] | 0.71073 | 0.71073 | 0.71073 | 0.71073 |
| $\rho_{calcd}$ [$g\,cm^{-3}$] | 1.609 | 1.416 | 1.555 | 1.428 |
| $\mu$ [$mm^{-1}$] | 1.112 | 0.811 | 1.018 | 0.861 |
| $R_{int}$ | 0.1536 | 0.0341 | 0.0285 | 0.0701 |
| Measured reflections | 19748 | 10295 | 11076 | 10351 |
| Unique reflections | 7095 | 3900 | 7223 | 3804 |
| Observed reflections [$I > 2\sigma(I)$] | 2544 | 2355 | 5542 | 2089 |
| Goodness-of-fit on $F^2$ | 0.867 | 1.026 | 1.019 | 0.874 |
| $R_1$ [$I > 2\sigma(I)$][a] | 0.0632 | 0.0535 | 0.0447 | 0.0607 |
| $wR_2$ (all data)[b] | 0.1076 | 0.1640 | 0.1046 | 0.1748 |

[a] $R_1 = \Sigma||F_o| - |F_c||/\Sigma|F_o|$. [b] $wR_2 = \{\Sigma[w(|F_o|^2 - |F_c|^2)^2]/\Sigma[w(F_o^4)]\}^{1/2}$.

 © 2007 Wiley-VCH Verlag GmbH & Co. KGaA, Weinheim 

ray data for compounds **1**–**4** were collected on a Bruker SMART 1000 CCD diffractometer by the $\phi$-$\omega$ scan method. Reflections were measured from a hemisphere of data collected on frames each covering 0.3° in $\omega$. Data were corrected for Lorentz and polarisation effects and for absorption by semi-empirical methods.[31] Complex scattering factors were taken from the program package SHELXTL[32] as implemented on a Pentium® computer. The structures were solved by direct methods and refined by full-matrix least-squares on $F^2$. The hydrogen atoms were included in calculated positions and refined in riding mode, except for H(3A), H(3B), H(4A) and H(4B) in **1**, H(1N) and H(2N) in **2**, and H(1N), H(2N), H(3N) and H(4N) in **3**, which were first located in a Fourier difference density map and left to freely refine. Minimum and maximum final electron density of –0.370 and 0.474 Å$^{-3}$ for **1**, –0.310 and 0.526 Å$^{-3}$ for **2**, –0.508 and 0.343 Å$^{-3}$ for **3**, and –0.545 and 0.668 Å$^{-3}$ for **4** were found. The structure of **4** presents a disorder on an oxygen atom of the nitrate groups. The disorder has been resolved and two atomic sites have been observed and refined with isotropic atomic displacement parameters. The site occupancy factor was 0.546 for O(1SA).

CCDC-614190 to -614193 contain the supplementary crystallographic data for this paper. These data can be obtained free of charge from The Cambridge Crystallographic Data Center via http://www.ccdc.cam.ac.uk/data_request/cif.

**DFT Studies:** All calculations were performed using the Gaussian 03 (Revision C.01)[33] program package with the B3LYP[34,35] three-parameter hybrid density functional, unless otherwise stated. In vacuo geometry optimisations of the $[Zn(L^1)]^{2+}$, $[Zn(L^2)]^{2+}$ and $[Zn(L^2)(NO_3)_2]$ systems were performed without constraints by using the Ahlrichs' valence triple-ζ (VTC)[22] basis set on Zn and the standard 6-31G(d) basis set on C, H, N and O atoms. The X-ray crystal structures of compounds **1**, **3** and **4** were used as input for geometry optimisations. The stationary points found on the potential energy surfaces as a result of the geometry optimisations have been tested to represent energy minima rather than saddle points by frequency analysis. Binding energies of the macrocyclic ligands were calculated as $E_{bind} = E_{metal\ complex} - (E_{cation} + E_{free\ ligand})$, with the free ligand at the geometry found within the complex. Therefore, calculated binding energies are static and do not include energy contributions because of changes in ligand geometry. The binding energy (of the macrocyclic ligand) in $[Zn(L^2)(NO_3)_2]$ was calculated as $E_{bind} = E_{metal\ complex} - (E_{Zn(NO_3)_2} + E_{free\ ligand})$. Basis Set Superposition Errors (BSSEs) were calculated using the Counterpoise method.[26] BSSE is an undesirable consequence of using finite basis sets that leads to an overestimation of the binding energy.

**Supporting Information** (see also the footnote on the first page of this article): In vacuo optimised Cartesian Coordinates [Å], Table S1 listing experimental and calculated angles of the metal coordination environment for the $[Zn(L^1)]^{2+}$, $[Zn(L^2)]^{2+}$ and $[Zn(L^2)(NO_3)_2]$ systems, and Figures S1, S2 and S3.

## Acknowledgments

The authors thank Xunta de Galicia (PGIDIT03TAM10301PR) and Universidade da Coruña for generous financial support. The authors are indebted to Centro de Supercomputación of Galicia (CESGA) for providing the computer facilities.

[1] G. W. Gokel, *Crown Ethers and Cryptands*, RSC, Cambridge, **1991**.
[2] S. R. Cooper, *Crown Compounds: Toward Future Applications*, VCH Verlagsgesellschaft, Weinheim, **1992**.
[3] F. Vögtle, *Supramolecular Chemistry*, John Wiley & Sons, Chichester, **1991**.
[4] C. J. Pedersen, J.-M. Lehn, D. J. Cram, *Resonance* **2001**, *6*, 71–79.
[5] N. Steinke, W. Frey, A. Baro, S. Laschat, C. Drees, M. Nimtz, C. Haegele, F. Giesselmann, *Chem. Eur. J.* **2006**, *12*, 1026–1035.
[6] J. R. Pfeifer, P. Reiss, U. Koert, *Angew. Chem. Int. Ed.* **2006**, *45*, 501–504.
[7] a) G. W. Gokel, S. H. Korzeniowski in *Macrocyclic Polyether Synthesis*, Springer, Berlin, **1982**, pp. 6, 39; b) Y. Nakatsuji, T. Nakamura, M. Yometani, H. Yuya, M. Okahara, *J. Am. Chem. Soc.* **1988**, *110*, 531.
[8] G. W. Gokel, *Chem. Soc. Rev.* **1992**, *21*, 39–47 and references cited therein.
[9] C. Platas-Iglesias, L. Vaiana, D. Esteban-Gómez, F. Avecilla, J. A. Real, A. de Blas, T. Rodríguez-Blas, *Inorg. Chem.* **2005**, *44*, 9704–9713.
[10] C. Rodríguez-Infante, D. Esteban, F. Avecilla, A. de Blas, T. Rodríguez-Blas, J. Mahía, A. L. Macedo, C. F. G. C. Geraldes, *Inorg. Chim. Acta* **2001**, *317*, 190–198.
[11] L. Vaiana, C. Platas-Iglesias, D. Esteban-Gómez, F. Avecilla, J. M. Clemente-Juan, J. A. Real, A. de Blas, T. Rodríguez, *Dalton Trans.* **2005**, 2031–2037.
[12] K. Nakamoto, *Infrared and Raman Spectra of Inorganic and Coordination Compounds*, 3rd ed., John Wiley & Sons, New York, Chichester, Brisbane, Toronto, **1972**, pp. 142–154.
[13] K. M. Doxsee, J. R. Hagadorn, T. J. R. Weakley, *Inorg. Chem.* **1994**, *33*, 2600–2606.
[14] O. Schlager, K. Wieghardt, H. Grondey, A. Rufinska, B. Nuber, *Inorg. Chem.* **1995**, *34*, 6440–6448.
[15] K. R. Adam, S. P. H. Arshad, D. S. Baldwin, P. A. Duckworth, A. J. Leong, L. F. Lindoy, B. J. McCool, M. McPartlin, B. A. Tailor, P. A. Tasker, *Inorg. Chem.* **1994**, *33*, 1194–1200.
[16] A. Looney, G. Parkin, *Inorg. Chem.* **1994**, *33*, 1234–1237.
[17] C.-D. Wu, C.-Z. Lu, W.-B. Yang, H.-H. Zhuang, J.-S. Huang, *Inorg. Chem.* **2002**, *41*, 3302–3307.
[18] A. Kirkpatrick, W. T. A. Harrison, *Solid State Sci.* **2004**, *6*, 593–598.
[19] W. J. Weary, *Coord. Chem. Rev.* **1971**, *7*, 81–122.
[20] C. S. Wilcox, *Frontiers in Supramolecular Chemistry and Photochemistry*, VCH Verlagsgesellschaft, Weinheim, **1991**, 123–143.
[21] L. F. Lindoy, T. Rambusch, B. W. Skelton, A. H. White, *J. Chem. Soc., Dalton Trans.* **2001**, 1857–1862.
[22] A. Schäfer, H. Horn, R. Ahlrichs, *J. Chem. Phys.* **1992**, *97*, 2571–2577.
[23] A. A. Palacios, P. Alemany, S. Alvarez, *Inorg. Chem.* **1999**, *38*, 707–715.
[24] M. R. Willcott, R. E. Lenkinski, R. E. Davis, *J. Am. Chem. Soc.* **1972**, *94*, 1742–1744.
[25] R. E. Davis, M. R. Willcott, *J. Am. Chem. Soc.* **1972**, *94*, 1744–1745.
[26] S. F. Boys, F. Bernardi, *Mol. Phys.* **1970**, *19*, 553–566.
[27] I. Yoon, J. Seo, J.-E. Lee, K.-M. Park, J. S. Kim, M. S. Lah, S. S. Lee, *Inorg. Chem.* **2006**, *45*, 3487–3489.
[28] D. Esteban, D. Bañobre, A. de Blas, T. Rodríguez-Blas, R. Bastida, A. Macías, A. Rodríguez, D. E. Fenton, H. Adams, J. Mahía, *Eur. J. Inorg. Chem.* **2000**, 1445–1456.
[29] W. C. Wolsey, *J. Chem. Educ.* **1973**, *50*, A335–A337.
[30] P. Gans, A. Sabatini, A. Vacca, *Talanta* **1996**, *43*, 1739–1753.
[31] *SADABS Area-Detector Absorption Correction*, Siemens Industrial Automation, Inc., Madison, WI, **1996**.
[32] G. M. Sheldrick, *SHELXTL Bruker Analytical X-ray System*, release 5.1, Madison, WI, **1997**.
[33] M. J. Frisch, G. W. Trucks, H. B. Schlegel, G. E. Scuseria, M. A. Robb, J. R. Cheeseman, J. A. Montgomery Jr, T. Vreven, K. N. Kudin, J. C. Burant, J. M. Millam, S. S. Iyengar, J. Tomasi, V. Barone, B. Mennucci, M. Cossi, G. Scalmani, N. Rega, G. A. Petersson, H. Nakatsuji, M. Hada, M. Ehara, K. Toyota,

 © 2007 Wiley-VCH Verlag GmbH & Co. KGaA, Weinheim 

R. Fukuda, J. Hasegawa, M. Ishida, T. Nakajima, Y. Honda, O. Kitao, H. Nakai, M. Klene, X. Li, J. E. Knox, H. P. Hratchian, J. B. Cross, C. Adamo, J. Jaramillo, R. Gomperts, R. E. Stratmann, O. Yazyev, A. J. Austin, R. Cammi, C. Pomelli, J. W. Ochterski, P. Y. Ayala, K. Morokuma, G. A. Voth, P. Salvador, J. J. Dannenberg, V. G. Zakrzewski, S. Dapprich, A. D. Daniels, M. C. Strain, O. Farkas, D. K. Malick, A. D. Rabuck, K. Raghavachari, J. B. Foresman, J. V. Ortiz, Q. Cui, A. G. Baboul, S. Clifford, J. Cioslowski, B. B. Stefanov, G. Liu, A. Liashenko, P. Piskorz, I. Komaromi, R. L. Martin, D. J. Fox, T. Keith, M. A. Al-Laham, C. Y. Peng, A. Nanayakkara, M. Challacombe, P. M. W. Gill, B. Johnson, W. Chen, M. W. Wong, C. Gonzalez, J. A. Pople, Gaussian, Inc., Wallingford, CT, **2004**.

[34] A. D. Becke, *J. Chem. Phys.* **1993**, *98*, 5648–5652.

[35] C. Lee, W. Yang, R. G. Parr, *Phys. Rev. B* **1988**, *37*, 785–789.

Received: October 26, 2006
Published Online: March 20, 2007

 © 2007 Wiley-VCH Verlag GmbH & Co. KGaA, Weinheim 

DOI: 10.1002/ejic.200601131

# Hydrothermal Synthesis of Single Crystalline (K,Na)$NbO_3$ Powders

Ce Sun,[a] Xianran Xing,*[a,b] Jun Chen,[a] Jinxia Deng,[a] Lu Li,[a] Ranbo Yu,[a] Lijie Qiao,[c] and Guirong Liu[a]

**Keywords:** Hydrothermal synthesis / Crystal growth / Crystal morphology / Niobates

$(K_{1-x}Na_x)NbO_3$ (x = 0.01, 0.24, 0.89, 0.91, 0.99) single crystalline powders with perovskite structure were synthesized by a hydrothermal method with $Nb_2O_5$ in a mixed solution of KOH and NaOH at 220 °C for 24 h. XRD investigations showed that the structure of the synthesized $(K_{1-x}Na_x)NbO_3$ ceramics changed from a $KNbO_3$-type orthorhombic phase (space group *Bmm*2) to a $NaNbO_3$-type monoclinic phase (space group *Pm*) with the increase of Na content. The present results confirmed that $(K_{1-x}Na_x)NbO_3$ exhibited a morphotropic phase boundary (MPB) at around 50 %K separating the orthorhombic phase and monoclinic phase. FE-SEM images showed that the morphological structures of niobates were cubes and nanofingers. The TEM image and the selected area electron diffraction pattern of $(K_{0.01}Na_{0.99})NbO_3$ showed the as-synthesized powder was single crystalline and indexed to be monoclinic. The phase evolution of the products in the hydrothermal route revealed that the hydrothermal synthesis of $(K_{1-x}Na_x)NbO_3$ underwent two steps, where an intermediate product $(K_{8-8x}Na_{8x})Nb_6O_{19}{\cdot}nH_2O$ was found in the early stage and then pure $(K_{1-x}Na_x)NbO_3$ was obtained after another 30 min of hydrothermal treatment.

(© Wiley-VCH Verlag GmbH & Co. KGaA, 69451 Weinheim, Germany, 2007)

## Introduction

Alkaline niobates have captured considerable interest in the scientific community because of their excellent ferroelectric, piezoelectric, electromechanical, nonlinear optical, electricoptic, and ionic conductivity properties.[1–6] The alkaline niobate-based perovskite compounds without toxic elements show a high Curie temperature and low anisotropy. Among them, $(K_{0.5}Na_{0.5})NbO_3$ was considered a good candidate for lead-free piezoelectric ceramics because of its strong piezoelectricity and ferroelectricity.[2,7,8] $(K_{1-x}Na_x)NbO_3$ is a combination of ferroelectrics $KNbO_3$ and antiferroelectrics $NaNbO_3$, and forms a morphotropic phase boundary (MPB) at around 50%K separating two orthorhombic phases[7,9] or orthorhombic and tetragonal phases with the composition modification of Li and Sb.[10] The piezoelectric properties of $(K_{1-x}Na_x)NbO_3$ single crystals were first reported by Egerton et al.[7] and Cross.[11] The hot pressed $(K_{0.5}Na_{0.5})NbO_3$ ceramics have been reported to possess high phase transition temperature ($T_c \approx$ 420 °C), high remanent polarization ($P_r \approx 33\ \mu C/cm^2$), large piezoelectric longitudinal response ($d_{33} \approx 160$ pC/N), and planar coupling coefficients ($k_p \approx 45\%$).[12,13]

To date, several studies have been devoted to the fabricating processes and properties of $(K_{1-x}Na_x)NbO_3$. $(K_{1-x}Na_x)NbO_3$ powders are commonly synthesized by a solid-state method. Saito et al.[2] reported that a high $d_{33}$ (about 416 pC/N) constant was obtained in the textured $(K_{1-x}Na_x)NbO_3$-based ceramics close to a morphotropic phase boundary. Pithan et al.[14] and Zhang et al.[15] prepared $(K_{1-x}Na_x)NbO_3$ by microemulsion mediated and spark plasma sintering methods, respectively. Shiratori et al.[16] synthesized the monoclinic $(K_{0.5}Na_{0.5})NbO_3$ by a microemulsion mediated route. The hydrothermal synthesis method has been used to prepare perovskite-type $NaNbO_3$, $KNbO_3$, $KNb_3O_8$, and $K_4Nb_6O_{17}$ powders over the past decade.[1,17–20] However, synthesis of the complex of $(K_{1-x}Na_x)NbO_3$ has not involved a hydrothermal route.

In the present study, we synthesized single crystalline powders of $(K_{1-x}Na_x)NbO_3$ by a hydrothermal method under moderate conditions. The structural evolution during the reaction between $Nb_2O_5$ and concentrated aqueous NaOH and KOH mixed solution was investigated. The crystal structures of the obtained powders were identified by XRD. The morphology of the samples was studied by field-emission scanning electron microscopy (FE-SEM) and TEM, and elemental analyses for Nb, K, and Na were conducted by inductively coupled plasma (ICP) spectrometry.

[a] Department of Physical Chemistry, University of Science and Technology Beijing,
Beijing 100083, China
Fax: +86-10-6233-3477
E-mail: xing@ustb.edu.cn
[b] State Key Laboratory for Advanced Metals and Materials, University of Science and Technology Beijing,
Beijing 100083, China
[c] Key Laboratory of Environmental Fracture, Ministry of Education of China,
Beijing 100083, China

 InterScience © 2007 Wiley-VCH Verlag GmbH & Co. KGaA, Weinheim 

## Results and Discussion

The influence of the processing parameters of K/Na molar ratio in the aqueous mixed solution on the formation of $(K_{1-x}Na_x)NbO_3$ is summarized in Table 1. The elemental analysis for Na, K, and Nb was conducted by ICP spectrometry. Because the values of Na and Nb were more accurate than that of K, the stoichiometries of all products were calculated based on the measurements of Na and Nb. KOH/NaOH plays the role of $K^+/Na^+$ source and the alkalinity in the aqueous medium, which affects the nucleation and crystallization of the products. The K/Na molar ratio in the as-synthesized samples increased with the ratio in the mixed solution. However, there was a big jump from KNN2 (Na/K = 24:76) to KNN3 (Na/K = 89:11). This might be attributed to the larger ionic radii of $K^+$ compared to that of $Na^+$, leading to a sharp rise of the reaction activity of $Na^+$ in the solution.

Table 1. K/Na/Nb ratio and the possible formula of the sodium-potassium niobates.

| Sample No. | Concentration [mol/L] KOH | NaOH | K/Na/Nb ratio[a] | Formula |
|---|---|---|---|---|
| KNN1 | 9.0 | 1.0 | 96.2:1.3:100 | $K_{0.99}Na_{0.01}NbO_3$ |
| KNN2 | 8.0 | 2.0 | 76.9:24.4:100 | $K_{0.76}Na_{0.24}NbO_3$ |
| KNN3 | 7.0 | 3.0 | 7.6:88.7:100 | $K_{0.11}Na_{0.89}NbO_3$ |
| KNN4 | 6.0 | 4.0 | 7.8:91.3:100 | $K_{0.09}Na_{0.91}NbO_3$ |
| KNN5 | 5.0 | 5.0 | 3.5:99.4:100 | $K_{0.01}Na_{0.99}NbO_3$ |

[a] Measured by ICP.

The XRD patterns (Figure 1) showed that pure phase $(K_{1-x}Na_x)NbO_3$ powders were obtained in the 10 mol/L KOH and NaOH solution. This indicated that well-crystallized $(K_{1-x}Na_x)NbO_3$ powders were synthesized in the concentrated alkaline solution under mild conditions. $(K_{0.99}Na_{0.01})NbO_3$ and $(K_{0.76}Na_{0.24})NbO_3$ were indexed in orthorhombic symmetry (space group *Bmm*2), but $(K_{0.11}Na_{0.89})NbO_3$, $(K_{0.09}Na_{0.91})NbO_3$, and $(K_{0.01}Na_{0.99})NbO_3$ were indexed in monoclinic symmetry (space group *Pm*), the lattice parameters are labeled in Table 2. The increasing of Na content in (K,Na)$NbO_3$ resulted in the phase transition from a $KNbO_3$-type orthorhombic phase to a $NaNbO_3$-type monoclinic phase.[21] This further confirmed a morphotropic phase boundary at around 50%K separating orthorhombic and monoclinic phases, but not two orthorhombic phases[7,9] or orthorhombic and tetragonal phases with composition modification of Li and Sb[10] as reported before.

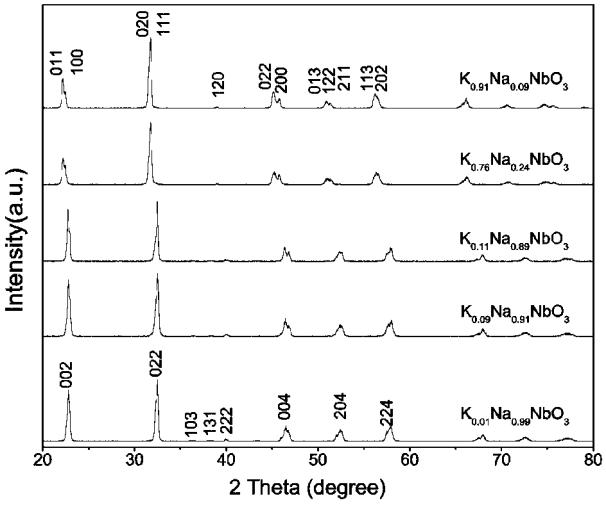


Figure 1. The XRD patterns of $(K_{1-x}Na_x)NbO_3$ prepared at 220 °C for 24 h.

Table 2. The crystal system and lattice parameters of the alkaline niobates.

| Sample | Syngony | Lattice parameters[a] *a* [Å] | *b* [Å] | *c* [Å] | *β* [°] |
|---|---|---|---|---|---|
| $K_{0.99}Na_{0.01}NbO_3$ | orthorhombic | 3.976(9) | 5.686(0) | 5.698(0) | – |
| $K_{0.76}Na_{0.24}NbO_3$ | orthorhombic | 3.970(6) | 5.675(5) | 5.687(1) | – |
| $K_{0.11}Na_{0.89}NbO_3$ | monoclinic | 7.773(8) | 7.838(2) | 7.849(8) | 89.901 |
| $K_{0.09}Na_{0.91}NbO_3$ | monoclinic | 7.781(0) | 7.825(6) | 7.867(6) | 89.624 |
| $K_{0.01}Na_{0.99}NbO_3$ | monoclinic | 7.789(3) | 7.819(9) | 7.866(3) | 89.717 |

[a] Lattice parameters were calculated by Powder X and TREOR software.

FE-SEM images of $(K_{0.99}Na_{0.01})NbO_3$ prepared by the hydrothermal treatment (220 °C, 24 h) are shown in Figure 2. Large-scale and well-crystallized $(K_{0.99}Na_{0.01})NbO_3$ cubes in microns were obtained (Figure 2, a), and a few nanofingers were also observed (Figure 2, b), which was confirmed by the previous work.[22] The aspect ratios (approximately length-to-width ratio) of the nanofingers are as high as 10 and their average width is about 60–75 nm.

The TEM images and the selected area electron diffraction (SAED) patterns of $(K_{0.01}Na_{0.99})NbO_3$ are displayed in Figure 3. The TEM image (see Figure 3, a) showed a club-shaped morphology for the $(K_{0.01}Na_{0.99})NbO_3$ single crystal. The SAED pattern (see Figure 3, b) revealed that $(K_{0.01}Na_{0.99})NbO_3$ was single crystalline and was indexed as monoclinic in structure, which was consistent with the present XRD investigation.

The phase evolution of $(K_{0.76}Na_{0.24})NbO_3$ (KNN2) via a hydrothermal synthesizing processing route was studied by XRD (see Figure 4). A series of XRD patterns of KNN2 were obtained at 220 °C and labeled KNN2-*n*, where *n* denoted the hydrothermal treatment time (in min). The raw material of $Nb_2O_5$ was mostly α-$Nb_2O_5$ with a few β-$Nb_2O_5$ as shown in Figure 4 (a). During the first 60 min $Nb_2O_5$ gradually reacted with the alkaline solution, and a new phase emerged as shown in Figure 4 (b,c). The XRD peaks of the new phase were isolated as $K_4Na_4Nb_6O_{19}{\cdot}9H_2O$.[23] However, the molar concentrations of $K^+$ and $Na^+$ were not equal in the final product KNN2 (see ICP result in Table 1), which suggested that the new phase would be $(K_{8-8x}Na_{8x})Nb_6O_{19}{\cdot}nH_2O$ but not $K_4Na_4Nb_6O_{19}{\cdot}9H_2O$. The dominant phases in KNN2–*90* were $(K_{8-8x}Na_{8x})Nb_6O_{19}{\cdot}nH_2O$ and $(K_{1-x}Na_x)NbO_3$ with minor $Nb_2O_5$ as shown in Figure 4 (d). After 120 min only one phase of KNN2 was observed (see Figure 4, e). This implied that the

 © 2007 Wiley-VCH Verlag GmbH & Co. KGaA, Weinheim 

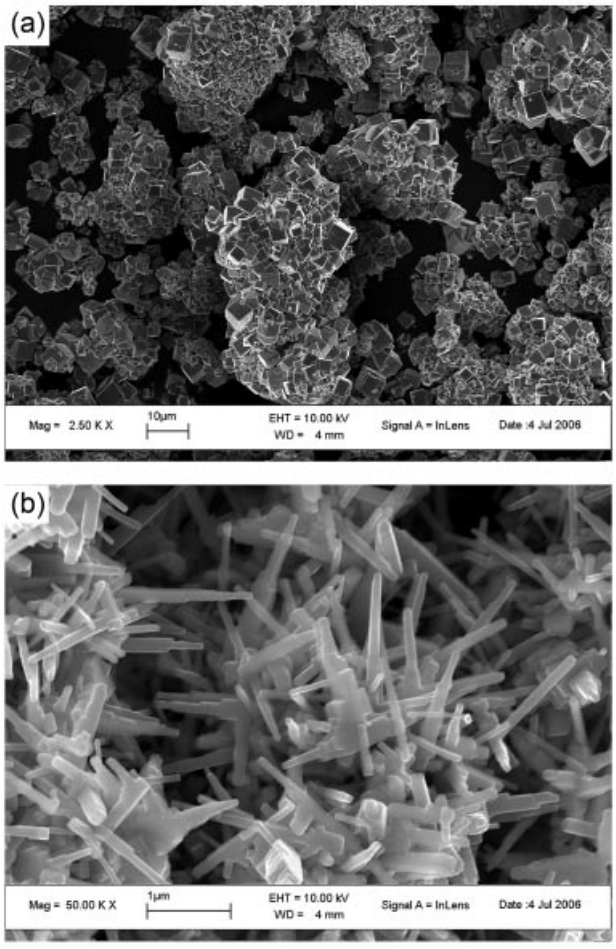


Figure 2. FE-SEM images of $(K_{0.99}Na_{0.01})NbO_3$ synthesized at 220 °C for 24 h: (a) cubes, (b) nanofingers.

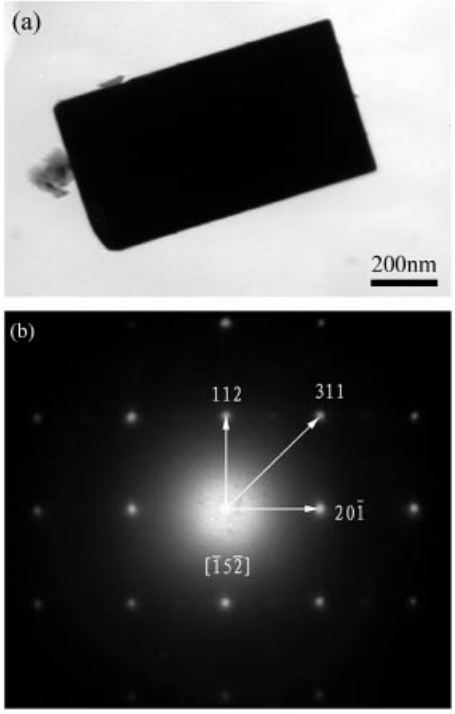


Figure 3. TEM images (a) and selected area electron diffraction (b) of the $(K_{0.01}Na_{0.99})NbO_3$ sample.

intermediate phase $(K_{8-8x}Na_{8x})Nb_6O_{19}{\cdot}nH_2O$ further reacted with $Nb_2O_5$ to form KNN2 powders. The KNN2–*150* sample was a well-crystallized phase of KNN2 (see part f in Figure 4). The same phase evolution was also observed for $(K_{0.09}Na_{0.91})NbO_3$ (KNN4) as shown in Figure 5, the intermediate product $(K_{8-8x}Na_{8x})Nb_6O_{19}{\cdot}nH_2O$ was found in the early stage and then pure $(K_{0.09}Na_{0.91})NbO_3$ was obtained after further hydrothermal treatment (see parts d,e in Figure 5).

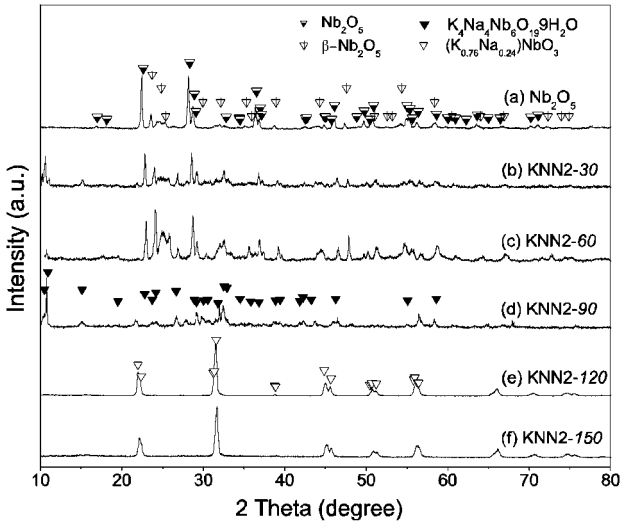


Figure 4. The XRD patterns of $(K_{0.76}Na_{0.24})NbO_3$ (KNN2) samples after various reaction periods (which were indicated in the figure) at 220 °C.

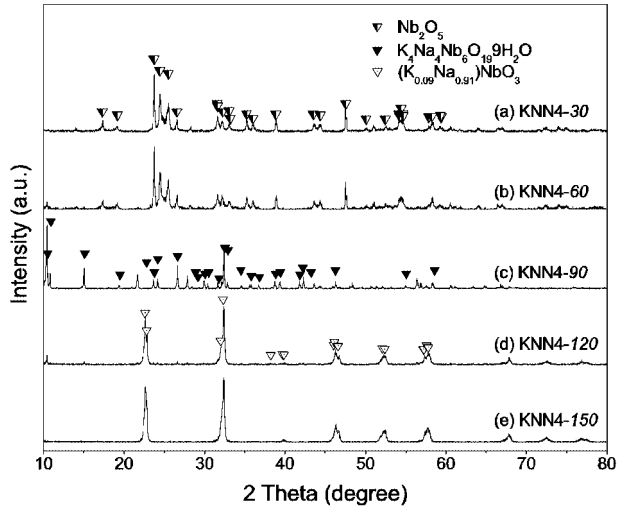


Figure 5. The XRD patterns of $(K_{0.09}Na_{0.91})NbO_3$ (KNN4) samples after various reaction periods (which were indicated in the figure) at 220 °C.

Hence, it was concluded that the formation of $(K_{1-x}Na_x)NbO_3$ occurred in two steps. The first step was that $Nb_2O_5$ reacted with MOH (M = Na, K) to form $(K_{8-8x}Na_{8x})Nb_6O_{19}{\cdot}nH_2O$ [Equation (1)].

 © 2007 Wiley-VCH Verlag GmbH & Co. KGaA, Weinheim 

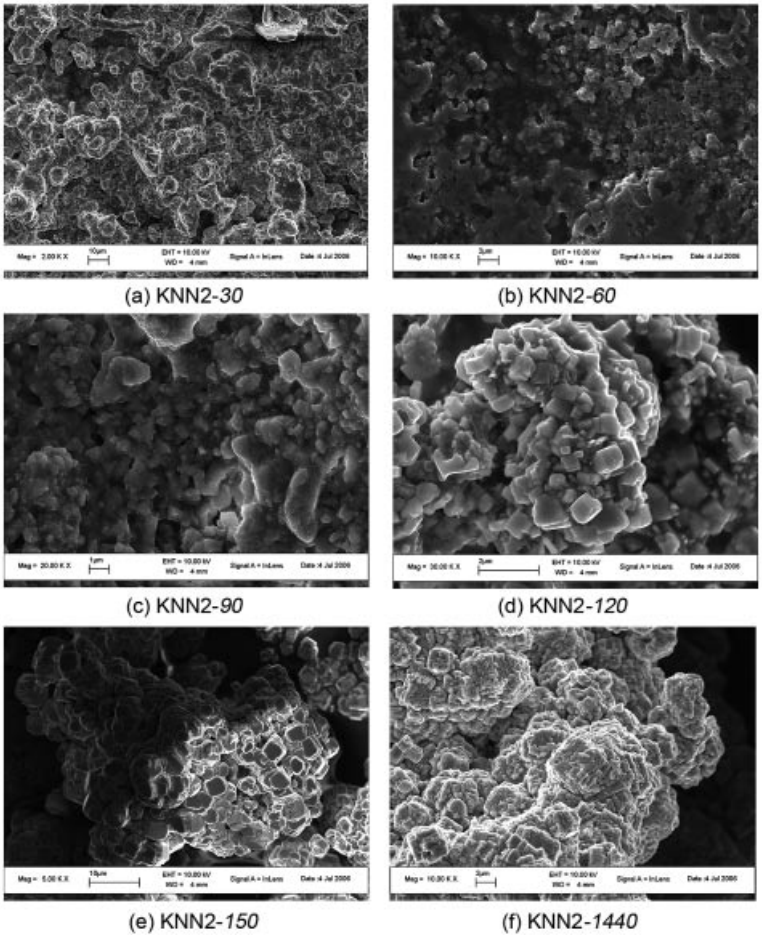


Figure 6. The morphological evolution of the $(K_{0.76}Na_{0.24})NbO_3$ (KNN2) samples during the reaction course by FE-SEM images: (a) KNN2–*30*, (b) KNN2–*60*, (c) KNN2–*90*, (d) KNN2–*120*, (e) KNN2–*150*, (f) KNN2–*1440*.

$$(8-8x)\ KOH + 8x\ NaOH + 3\ Nb_2O_5 + (n-4)\,H_2O = (K_{8-8x}Na_{8x})Nb_6O_{19}{\cdot}n\,H_2O \quad (1)$$

The second step was that $(K_{8-8x}Na_{8x})Nb_6O_{19}{\cdot}n\,H_2O$ reacted with $Nb_2O_5$ [Equation (2)].

$$(K_{8-8x}Na_{8x})Nb_6O_{19}{\cdot}n\,H_2O + Nb_2O_5 = 8\ (K_{1-x}Na_x)NbO_3 + n\,H_2O \quad (2)$$

The morphological evolution of $(K_{0.76}Na_{0.24})NbO_3$ was investigated by FE-SEM (see Figure 6). The reactants nearly kept the morphology of $Nb_2O_5$ in the first 30 min as shown in Figure 6 (a). But $Nb_2O_5$ gradually fluxed and reacted with the alkaline solution as shown in Figure 6 (b,c). After 120 min a small-scale cubic phase was formed. The KNN2–*150* sample was very pure potassium sodium niobate with a club-shaped morphology as shown in Figure 6 (e). The FE-SEM image and XRD pattern of KNN2–*1440* (KNN2 in Table 1) were similar to KNN2–*150*, and the XRD and ICP investigations demonstrated that it was $(K_{0.76}Na_{0.24})NbO_3$ crystal powder.

## Conclusions

$(K_{1-x}Na_x)NbO_3$ ($x$ = 0.01, 0.24, 0.89, 0.91, 0.99) single crystalline powders with perovskite structure were synthesized by a hydrothermal method with $Nb_2O_5$ in a mixed solution of KOH and NaOH at 220 °C for 24 h. The as-synthesized $(K_{1-x}Na_x)NbO_3$ powders showed that with the increase of Na content the crystal structure changed from a $KNbO_3$-type orthorhombic phase (space group *Bmm*2) to a $NaNbO_3$-type monoclinic phase (space group *Pm*). It further confirmed that $(K_{1-x}Na_x)NbO_3$ exhibited a morphotropic phase boundary at around 50%K separating the orthorhombic and monoclinic phases. The morphological structures of the niobates were cubes and nanofingers. The SAED pattern showed that $(K_{0.01}Na_{0.99})NbO_3$ was single crystalline and indexed as monoclinic in structure, which was consistent with the XRD investigation. We concluded that the hydrothermal synthesis of $(K_{1-x}Na_x)NbO_3$ underwent two steps, and had an intermediate phase as $(K_{8-8x}Na_{8x})Nb_6O_{19}{\cdot}n\,H_2O$. The first step was that $Nb_2O_5$ reacted with MOH (M = Na, K) to form $(K_{8-8x}Na_{8x})$-$Nb_6O_{19}{\cdot}n\,H_2O$. The second step was where $(K_{8-8x}Na_{8x})$-$Nb_6O_{19}{\cdot}n\,H_2O$ reacted with $Nb_2O_5$, and finally formed $(K_{1-x}Na_x)NbO_3$ single crystal powders.

## Experimental Section

**Synthetic Procedures:** KOH, NaOH, and $Nb_2O_5$ (all are analytic reagent grade) were used in the synthesis. In a typical synthesis

 © 2007 Wiley-VCH Verlag GmbH & Co. KGaA, Weinheim 

process, $Nb_2O_5$ (0.5 g) was added to a mixed solution of NaOH and KOH (30 mL), and stirred for half an hour. Then the white slurry was introduced into a Teflon-lined stainless steel autoclave and heated in a furnace at 220 °C for 24 h. After gradually cooling down to room temperature, the precipitates were filtered and washed with distilled water and ethanol, then dried at 80 °C.

**Measurements:** The morphologies of the samples were studied by field-emission scanning electron microscopy (FE-SEM, LEO1530) and transmission electron microscopy (TEM, JEM-100CXII). Elemental analysis for Nb, K, and Na was conducted by inductively coupled plasma (ICP, INC Profile) spectrometry.

**X-ray Structure:** The crystal structures of the obtained powders were identified by powder X-ray diffractometry, performed with a M21XVHF22 diffractometer (Japan) at room temperature. Cu-$K_\alpha$ radiation ($\lambda$ = 1.5418 Å) and a fixed power source (40 kV and 200 mA) were used. The samples were scanned at a rate of 8°/min over a range of 10–90°. The major diffraction peaks of the samples were indexed by Powder X and TREOR software.

## Acknowledgments

This work was financially supported by the National Natural Science Foundation of China (No. 50374009, 20571009, 20331030), and Funds of Ministry of Education of China for PCSIRT.

[1] H. Zhu, Z. Zheng, X. Gao, Y. Huang, Z. Yan, J. Zou, H. Yin, Q. Zou, S. H. Kable, J. Zhao, Y. Xi, W. N. Martens, R. L. Frost, *J. Am. Chem. Soc.* **2006**, *128*, 2373–2384.
[2] Y. Saito, H. Takao, T. Tani, T. Nonoyama, K. Takatori, T. Homma, T. Nagaya, M. Nakamura, *Nature* **2004**, *432*, 84–87.
[3] C. An, K. Tang, C. Wang, G. Shen, Y. Jin, Y. Qian, *Mater. Res. Bull.* **2002**, *37*, 1791–1796.
[4] G. Suyal, E. Colla, R. Gysel, M. Cantoni, N. Setter, *Nano Lett.* **2004**, *4*, 1339–1342.
[5] C.-R. Cho, I. Katardjiev, M. Grishin, A. Grishin, *Appl. Phys. Lett.* **2002**, *80*, 3171.
[6] M. Blomqvist, S. Khartsev, A. Grishin, A. Petraru, C. Buchal, *Appl. Phys. Lett.* **2003**, *82*, 439.
[7] L. Egerton, D. M. Dillon, *J. Am. Ceram. Soc.* **1959**, *42*, 438–442.
[8] E. Hollenstein, M. Davis, D. Damjanovic, N. Setter, *Appl. Phys. Lett.* **2005**, *87*, 182905.
[9] K. Kakimoto, I. Masuda, H. Ohsato, *Jpn. J. Appl. Phys. Part 1* **2003**, *42*, 6102–6105.
[10] G.-Z. Zang, J.-F. Wang, H.-C. Chen, W.-B. Su, C.-M. Wang, P. Qi, B.-Q. Ming, J. Du, L.-M. Zheng, S. Zhang, T. R. Shrout, *Appl. Phys. Lett.* **2006**, *88*, 212908.
[11] L. E. Cross, *Nature* **1958**, *181*, 178–179.
[12] R. E. Jeager, L. Egerton, *J. Am. Ceram. Soc.* **1962**, *45*, 208–213.
[13] G. H. Haertling, *J. Am. Ceram. Soc.* **1967**, *50*, 329–331.
[14] C. Pithan, Y. Shiratori, J. Dornseiffer, F.-H. Haegel, A. Magrez, R. Waser, *J. Cryst. Growth* **2005**, *280*, 191–200.
[15] B.-P. Zhang, J.-F. Li, K. Wang, H. Zhang, *J. Am. Ceram. Soc.* **2006**, *89*, 1605–1609.
[16] Y. Shiratori, A. Magrez, C. Pithan, *Chem. Phys. Lett.* **2004**, *391*, 288–292.
[17] J.-F. Liu, X.-L. Li, Y. D. Li, *J. Cryst. Growth* **2003**, *247*, 419–424.
[18] C. M. S. Santos, L. H. Loureiro, M. P. F. Silva, M. V. Cacaleiro, *Polyhedron* **2002**, *21*, 2009–2015.
[19] C.-H. Lu, S.-Y. Lo, H.-C. Lin, *Mater. Lett.* **1998**, *34*, 172–176.
[20] G. K. L. Goh, F. F. Lange, S. M. Haile, C. G. Levi, *J. Mater. Res.* **2003**, *18*, 338–345.
[21] a) A. W. Hewat, *J. Phys. C: Solid State Phys.* **1973**, *6*, 2559–2572; b) A. W. Hewat, *Ferroelectrics* **1974**, *7*, 83–85.
[22] E. Vasco, A. Magrez, L. Forró, N. Setter, *J. Phys. Chem. B* **2005**, *109*, 14331–14334.
[23] J. H. Kennedy, *J. Inorg. Nucl. Chem.* **1961**, *20*, 53–57.

Received: November 29, 2006
Published Online: March 20, 2007

 © 2007 Wiley-VCH Verlag GmbH & Co. KGaA, Weinheim 

DOI: 10.1002/ejic.200601132

# Protonolysis Reactions of $[(Me_3Si)_2N]_3Ln(\mu\text{-}Cl)Li(thf)_3$ with *t*BuSH or EtSH: Isolation, Structures and Catalytic Properties of Dinuclear Complexes $[\{(Me_3Si)_2N\}_2Ln(\mu\text{-}StBu)]_2$ and Tetranuclear Complexes $[Li(thf)_4][\{(Me_3Si)_2N\}_4Ln_4(\mu_4\text{-}SEt)(\mu\text{-}SEt)_8]$ (Ln = Pr, Sm)

**Mei-Ling Cheng,[a] Hong-Xi Li,[a] Wen-Hua Zhang,[a] Zhi-Gang Ren,[a] Yong Zhang,[a] and Jian-Ping Lang*[a,b]**

**Keywords:** Amidolanthanides / Alkylthiolates / Synthesis / Crystal structure / Ring-opening polymerization

Reactions of $[(Me_3Si)_2N]_3Ln(\mu\text{-}Cl)Li(thf)_3$ (**1**: Ln = Pr; **2**: Ln = Sm) with an equimolar amount of *t*BuSH or EtSH gave rise to four amidolanthanide alkylthiolate complexes $[\{(Me_3Si)_2N\}_2Ln(\mu\text{-}StBu)]_2$ (**3**: Ln = Pr; **4**: Ln = Sm) and $[Li(thf)_4][\{(Me_3Si)_2N\}_4Ln_4(\mu_4\text{-}SEt)(\mu\text{-}SEt)_8]$ (**5**: Ln = Pr; **6**: Ln = Sm). Compounds **3**–**6** were characterized by elemental analysis, IR and $^1H$ NMR spectroscopy and single-crystal X-ray diffraction, and their catalytic properties were also investigated. Compounds **3** and **4** are thiolate-bridged dimers in which each Ln atom adopts a distorted tetrahedral coordination. Compounds **5** and **6** contain a $Ln_4$ square plane, which is capped by a $\mu_4$-$SEt^-$ ligand. The edges of the square are bridged by four pairs of $SEt^-$ ligands on both sides of the $Ln_4$ plane. Each Ln atom has a distorted octahedral geometry.
(© Wiley-VCH Verlag GmbH & Co. KGaA, 69451 Weinheim, Germany, 2007)

## Introduction

In the past decades, synthesis of lanthanide chalcogenolates has attracted much attention due to their interesting structures[1] and their potential applications in advanced materials and catalytic processes.[2] Among these complexes, only a dozen of lanthanide alkylthiolate complexes[3] have been structurally characterized, though some lanthanide alkylthiolate complexes (e.g. $[Gd\{N(SiMe_3)_2\}(\mu\text{-}StBu)]_2$[4] and $[Cp_2Lu(\mu\text{-}StBu)_2Li(thf)_2]$[5]) were reported in 1985. These alkylthiolate complexes can be mainly classified into two types: mononuclear structures {e.g. $[Li(tmeda)]_3[Yb(StBu)_6]$; tmeda = $Me_2NCH_2CH_2NMe_2$},[3c] and dinuclear structures {e.g. $[Yb(StBu)_2(\mu\text{-}StBu)(bipy)]_2$}.[3a] Most of these compounds were prepared by metathesis of lanthanide halides or (substituted) cyclopentadienyl lanthanide complexes with alkali metal thiolates,[3b,3c,3g,4] by insertion reactions of $S_8$ into the Ln–carbon bond[3h] or by protonolysis reactions of (substituted) cyclopentadienyl lanthanide complexes with alkylthiols.[3a,3d–3f,5] It is noted that reactions of amidolanthanide complexes with alkylthiols appear to be less explored. Aspinall et al. reported the first amidolanthanide *tert*-butylthiolate complexes $[Ln\{N(SiMe_3)_2\}(\mu\text{-}StBu)]_2$ (Ln = Gd, Eu), which were prepared from protonolysis reactions of $[(Me_3Si)_2N]_3Ln$ with an equimolar amount of *t*BuSH in toluene/thf at –23 °C. However, these compounds readily decomposed into insoluble polymeric materials at ambient temperature.[4]

We are interested in the preparation of amidolanthanide benzenethiolate complexes from protonolysis reactions of bis(trimethylsilyl)amidolanthanide(III) chloride complexes, $[(Me_3Si)_2N]_3Ln(\mu\text{-}Cl)Li(thf)_3$, with benzenethiol.[6] For example, reactions of $[(Me_3Si)_2N]_3Nd(\mu\text{-}Cl)Li(thf)_3$ with an equimolar amount of benzenethiol gave rise to cationic tetranuclear complex $Li[\{(Me_3Si)_2N\}_4(\mu_4\text{-}Cl)Nd_4(\mu\text{-}SPh)_8]$. The facile formation of this complex and other previously reported related complexes could be attributed to the incorporation of lithium and chloride ions into their frameworks.[6a] In addition, these complexes exhibited good catalytic activity in the ring-opening polymerization (ROP) of ε-caprolactone. Therefore, if the benzenethiol that was used in the above reactions were to be replaced with different alkylthiols, would reactions between $[(Me_3Si)_2N]_3Ln(\mu\text{-}Cl)Li(thf)_3$ and the alkylthiols afford amidolanthanide thiolate complexes with different structural frameworks? Moreover, would the resulting complexes show better catalytic activity in the ROP of ε-caprolactone? With these questions in mind, we carried out reactions of $[(Me_3Si)_2N]_3Ln(\mu\text{-}Cl)Li(thf)_3$ (**1**: Ln = Pr; **2**: Ln = Sm)[7] with two common alkylthiols, *t*BuSH and EtSH, and two neutral binuclear complexes $[\{(Me_3Si)_2N\}_2Ln(\mu\text{-}StBu)]_2$ (**3**: Ln = Pr; **4**: Ln = Sm) and two cationic tetranuclear complexes $[Li(thf)_4][\{(Me_3Si)_2N\}_4Ln_4(\mu_4\text{-}SEt)(\mu\text{-}SEt)_8]$ (**5**: Ln = Pr; **6**: Ln =

[a] School of Chemistry and Chemical Engineering, Suzhou University,
Suzhou, 215123 Jiangsu, People's Republic of China
Fax: +86-512-65880089
E-mail: jplang@suda.edu.cn
[b] State Key Laboratory of Organometallic Chemistry, Shanghai Institute of Organic Chemistry, Chinese Academy of Sciences, 200032 Shanghai, People's Republic of China

 © 2007 Wiley-VCH Verlag GmbH & Co. KGaA, Weinheim 

Sm) were isolated therefrom. Compounds **3**–**6** did exhibit better catalytic activity in the ROP of ε-caprolactone than their benzenethiolate analogues. Herein, we report the synthesis, crystal structures and catalytic properties of **3**–**6**.

## Results and Discussion

Treatment of a thf solution of **1** with an equimolar amount of *t*BuSH in thf at ambient temperature led to a yellow solution. After removal of all the volatile species in vacuo, the residue was extracted with toluene and *n*-hexane, and the insoluble LiCl precipitate was filtered off. The filtrate was allowed to stand at 2 °C for three days, which resulted in the formation of yellow crystals of **3**·2(thf)$_{0.5}$ in 43% yield. Analogous reactions of **2** with an equimolar amount of *t*BuSH in thf gave rise to **4** in 40% yield (Scheme 1). Reactions of a thf solution of **1** or **2** in thf with an equimolar amount of EtSH at room temperature followed by a standard workup afforded **5**·0.5$C_7H_8$ in 21% yield or **6**·$C_6H_6$ in 17% yield, respectively (Scheme 1). The preparation of **5** and **6** was reproducible, though their yields were relatively low, which may be due to the formation of a large amount of insoluble material during the preparation. The yield of the two corresponding reactions decreased when **1** or **2** was treated with 2–3 equiv. of EtSH. Even at –20 °C, the formation of **5** or **6** was not observed, but a large amount of insoluble material was always isolated.

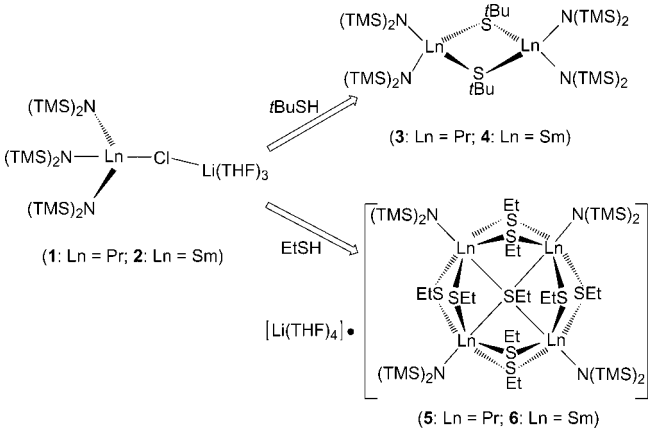


Scheme 1.

The protonolysis reactions of **1** and **2** with PhSH, *t*BuSH or EtSH deserve comments. Treatment of **1** or **2** with an equimolar amount of PhSH gave rise to a polymeric complex [{$(Me_3Si)_2N$}$_2$(μ-SPh)Pr(μ-SPh)Li(thf)$_2$]$_\infty$ and a tetranuclear wine-cup-shaped complex [{$(Me_3Si)_2N$}$_4$($\mu_4$-Cl)-$Sm_4$(μ-SPh)$_4$($\mu_3$-Cl)$_4$Li(thf)], respectively, whereas the reaction of **1** with *t*BuSH or EtSH produced binuclear complexes **3** and **4** or tetranuclear cationic complexes **5** and **6**. The remarkable difference in the outcome of these reactions may be related to the steric effects of the R organic group (*t*Bu > Ph > Et) bound to the S atom in the resulting structures. It is assumed that in the case of thiols that bear larger R groups (e.g. *t*Bu), the formation of a structure similar to that of the tetranuclear lanthanide thiolate complexes (e.g. **5** and **6**), described later in this paper, may cause the *t*Bu groups around the $Ln_4$ ring to become more crowded. Therefore, reactions of **1** or **2** with *t*BuSH seem to prefer the formation of smaller complexes **3** and **4**. Another reason for the formation of complexes with larger Ln nuclearity may be ascribed to the incorporation of $Li^+$ and/or $Cl^-$ ions into their structures.[6a] In the cases of **5** and **6**, the larger $[Li(thf)_4]^+$ cation that is incorporated into their structures may to some extent stabilize the larger [{$(Me_3Si)_2N$}$_4$-$Ln_4$($\mu_4$-SEt)(μ-SEt)$_8$]$^-$ anion by ionic interactions.

Compounds **3**–**6** are extremely air- and moisture-sensitive, and they are readily soluble in dme, thf and toluene; they are also slightly soluble in *n*-hexane. Elemental analyses of **3**–**6** are consistent with the proposed formulas. The $^1$H NMR spectra in $C_6D_6$ at room temperature shows the correct $(Me_3Si)_2N^-$/S*t*Bu$^-$ proton ratios for **3** and **4** and the correct $(Me_3Si)_2N^-$/SEt$^-$/thf proton ratio for **5**, though the proton signals of the $(Me_3Si)_2N^-$ and SEt$^-$ or S*t*Bu$^-$ ligands are shifted significantly upfield owing to the paramagnetism of these complexes. The $^1$H NMR spectrum of **6** contains broad uninterpretable signals that give no useful information about the solution behaviour of this paramagnetic complex. The identities of **3**–**6** were finally confirmed by X-ray crystallography.

Compound **3**·2(thf)$_{0.5}$ crystallizes in the triclinic space group $P\bar{1}$ and the asymmetric unit contains half of the [{$(Me_3Si)_2N$}$_2$Pr(μ-S*t*Bu)]$_2$ molecule and two halves of solvated thf molecules, whereas **4** crystallizes in the monoclinic space group $P2_1/c$ and the asymmetric unit contains half of the [{$(Me_3Si)_2N$}$_2$Sm(μ-S*t*Bu)]$_2$ molecule. As the molecular structures of **3** and **4** are very similar, only that of **3** is showed in Figure 1. Their selected bond lengths and angles are compared in Table 1.

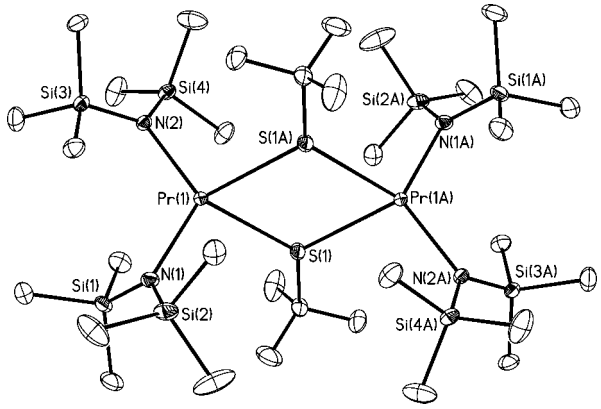


Figure 1. Perspective view of **3** with labelling scheme and 50% thermal ellipsoids. All hydrogen atoms are omitted for charity.

Compounds **3** or **4** consists of two {[$(Me_3Si)_2N$]$_2$Ln} moieties interconnected by a pair of μ-S*t*Bu anions to form a dimeric structure with a crystallographic centre of symmetry at the midpoint of the Ln(1) and Ln(1A) atoms. Although the $Pr_2S_2$ core structure in **3** is uncommon in Pr$^{III}$ thiolate complexes, the analogous $Sm_2S_2$ core structure in

 © 2007 Wiley-VCH Verlag GmbH & Co. KGaA, Weinheim 

Table 1. Selected bond lengths [Å] and angles [°] for **3** and **4**.[a]

| | Ln = Pr (**3**) | Ln = Sm (**4**) |
|---|---|---|
| Ln(1)–N(1) | 2.292(3) | 2.272(8) |
| Ln(1)–N(2) | 2.303(3) | 2.233(9) |
| Ln(1)–S(1) | 2.8704(17) | 2.786(3) |
| Ln(1)–S(1A) | 2.8579(13) | 2.844(3) |
| | | |
| N(1)–Ln(1)–N(2) | 114.43(13) | 113.7(3) |
| N(1)–Ln(1)–S(1A) | 131.27(10) | 137.1(2) |
| N(2)–Ln(1)–S(1A) | 103.28(9) | 103.9(2) |
| N(1)–Ln(1)–S(1) | 99.84(9) | 103.2(2) |
| N(2)–Ln(1)–S(1) | 135.75(9) | 121.9(2) |
| S(1A)–Ln(1)–S(1) | 69.61(5) | 71.54(9) |
| C(13)–S(1)–Ln(1A) | 119.97(15) | 128.6(4) |
| C(13)–S(1)–Ln(1) | 129.64(15) | 122.9(4) |
| Ln(1)–S(1)–Ln(1A) | 110.39(5) | 108.46(9) |

[a] Symmetry code: A: $-x+2, -y+2, -z+1$ for **3**; $-x, -y, -z+1$ for **4**.

**4** is found in some known dinuclear $Sm^{III}$ complexes such as $[(thf)_3I_2Sm(\mu\text{-}SC_6H_4(Me_2N)\text{-}4)]_2$,[8] $[(C_8H_8)Sm(\mu\text{-}SPh)(thf)_2]_2$,[9] $[Sm(C_8H_8)(thf)(\mu\text{-}SC_6H_2iPr_3\text{-}2,4,6)]_2$,[9] $[Sm(SC_6H_2iPr_3\text{-}2,4,6)(thf)_3(\mu\text{-}SC_6H_2iPr_3\text{-}2,4,6)]_2$[10] and $[Sm(SC_6F_5)_2(thf)(\mu\text{-}SC_6F_5)]_2$.[11] The Ln(1)···Ln(1A) separation within the dimer in **3** or **4** is 4.703 or 4.568 Å, respectively, which is too long to include any metal–metal interaction. Each Ln centre in **3** or **4** is coordinated by two S atoms from two μ-S*t*Bu$^-$ anions and two N atoms from two $[N(SiMe_3)_2]^-$ anions to form a distorted tetrahedral geometry.

In the $Pr_2S_2$ rhomb of **3**, the two Pr–S bond lengths are unsymmetrical with Pr(1)–S(1) of 2.870(17) Å and Pr(1)–S(1A) of 2.858(13) Å. The mean Pr–S bond length of 2.864(15) Å is comparable to that in $[\{(Me_3Si)_2N\}_2(\mu\text{-}SPh)Pr(\mu\text{-}SPh)Li(thf)_2]_n$ [2.831(5) Å].[6a] The mean Pr–N bond length [2.298(3) Å] is close to that in $[\{(Me_3Si)_2N\}_2(\mu\text{-}SPh)Pr(\mu\text{-}SPh)Li(thf)_2]_n$ [2.312(5) Å],[6a] but slightly shorter than those found in $[(Me_3Si)_2N]_3Pr(\mu\text{-}Cl)Li(thf)_3$ [2.359(3) Å][7b] and $[Pr\{N(SiMe_3)_2\}_4][K(thf)_6]$ [2.428(5) Å].[12]

In the $Sm_2S_2$ ring of **4**, the two Sm–S distances are also not equal [2.786(3) Å and 2.844(3) Å]. The average distance [2.815(3) Å] is close to those found in $[Li(tmeda)_2][Cp^*_2Sm(SC{\equiv}CPh)_2]$ [2.794(4) Å][5] and $\{(Cp_2Sm)_2Mo(\mu\text{-}S)_4\}(PPh_4)$ [2.785(3) Å],[13] but slightly shorter than that in $[Sm(C_8H_8)(thf)(\mu\text{-}SC_6H_2iPr_3\text{-}2,4,6)]_2$ [2.881(5) Å].[9] The mean Sm–N bond length [2.252(8) Å] is somewhat shorter than those in four-coordinate $Sm^{III}$ complexes $SmL[N(SiMe_3)_2]_2$ {2.350(3) Å, L = *N*-*tert*-butyl-*N*-[2-(*tert*-butylamino)ethyl]imidazolylidene}[14] and $Sm[N(SiMe_3)_2]_2(thf)_2$ [2.432(2) Å].[15]

Having a common chemical formula $[Li(thf)_4][\{(Me_3Si)_2N\}_4Ln_4(\mu_4\text{-}SEt)(\mu\text{-}SEt)_8]$, **5**·0.5$C_7H_8$ and **6**·$C_6H_6$ crystallize in the monoclinic space group $P2_1/c$ with half of one toluene solvated molecule (**5**), and one benzene solvated molecule (**6**). As the structures of the $[\{(Me_3Si)_2N\}_4Ln_4(\mu_4\text{-}SEt)(\mu\text{-}SEt)_8]^-$ anions in **5** and **6** are essentially identical, we only show the perspective view of the anion of **5** in Figure 2. The pertinent bond lengths and angles for **5** and **6** are compared in Table 2.

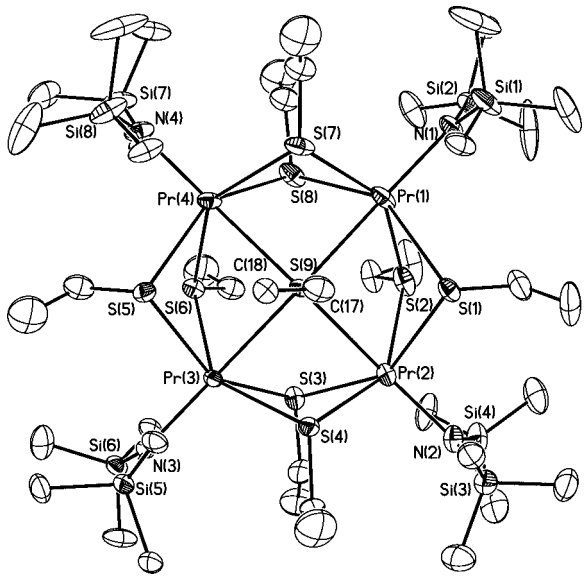


Figure 2. Perspective view of the anion of **5**, where only the disordered C(19)–C(20) atoms with a site occupancy factor of 0.45 are shown. The thermal ellipsoids are drawn at the 50% probability level and all hydrogen atoms are omitted for clarity.

The structures of the anions of **5** and **6** have a square-like $Ln_4$ array that is linked by four pairs of $SEt^-$ ligands and is capped by a $\mu_4$-$SEt^-$ ligand above the $Ln_4$ plane (0.919 Å for **5** and 0.953 Å for **6**). This structure resembles that of $[(thf)_6Yb_4(\mu_4\text{-}S)(\mu\text{-}\eta^2\text{:}\eta^2\text{-}S_2)_4(SC_6F_5)_2]$,[16a] $[(thf)_6Yb_4(\mu_4\text{-}S)(\mu\text{-}\eta^2\text{:}\eta^2\text{-}S_2)_4I_2]$[16b] and $Li[\{(Me_3Si)_2N\}_4Nd_4(\mu_4\text{-}Cl)(\mu\text{-}SPh)_8]\cdot C_6H_6$,[6a] which comprises a square array of $Ln^{III}$ ions connected by four $\mu\text{-}\eta^2\text{:}\eta^2\text{-}S_2$ ligands or four pairs of $SPh^-$ ligands and capped by a $\mu_4$-$S^{2-}$ or $\mu_4$-$Cl^-$ ion above the $Ln_4$ plane. It is noted that the symmetries of the structures of these compounds with the $Ln_4$ core are quite different owing to the different periphery bridging ligands and capping ligands. The structure of the anion of $Li[\{(Me_3Si)_2N\}_4Nd_4(\mu_4\text{-}Cl)(\mu\text{-}SPh)_8]\cdot C_6H_6$ shows an approximate $S_4$ symmetry whereas those of $[(thf)_6Yb_4(\mu_4\text{-}S)(\mu\text{-}\eta^2\text{:}\eta^2\text{-}S_2)_4(SC_6F_5)_2]$ and $[(thf)_6Yb_4(\mu_4\text{-}S)(\mu\text{-}\eta^2\text{:}\eta^2\text{-}S_2)_4I_2]$ have an approximate $C_{2v}$ symmetry. However, the symmetry of the anions of **5** and **6** is $C_2$ because of a $\mu_4$-$SEt^-$ ligand capping onto the $Ln_4$ core. Although thiolates serving as a quadruply bridging ligand are found in several transition- or main group metal–thiolate clusters such as $[\{Ag_8(\mu_4\text{-}SC_2H_4\text{-}NH_3)_6Cl_6\}Cl_2]_n$,[17a] $[Cu_7\{\mu_4\text{-}SCH_2CH_2NH(CH_3)_2\}_6(\mu_3\text{-}Cl)_2(\mu\text{-}Cl)_{13}Cl_2]_n$,[17b] $[Cu_4(\mu\text{-}dppm)_4(\mu\text{-}NS_2)(\mu_4\text{-}NS_2)]\cdot CH_2Cl_2$[17c] and $[\{Tl_7(\mu_4\text{-}Sthff)_6\}_2(PF_6)_2]_n$ (HSthff = tetrahydrofurfuryl-thiol),[17d] the existence of a $\mu_4$-$SEt^-$ ligand in **5** and **6** is unprecedented in the chemistry of lanthanide chalcogenolate complexes.

Each Ln centre in **5** and **6** is coordinated by one N atom from the $[N(SiMe_3)_2]^-$ anion and one $\mu_4$-S atom and four μ-S atoms from the $EtS^-$ ligands to form a distorted octahedral coordination geometry. The mean Ln–$\mu_4$-S bond length, 3.089(3) Å for **5** and 3.029(3) Å for **6**, is much longer than the corresponding Ln–μ-S bonds, which correlates with the number of bonding interactions at the Ln centres.

 © 2007 Wiley-VCH Verlag GmbH & Co. KGaA, Weinheim 

Table 2. Selected bond lengths [Å] and angles [°] for **5** and **6**.

| | Ln = Pr (**5**) | Ln = Sm (**6**) | | Ln = Pr (**5**) | Ln = Sm (**6**) |
|---|---|---|---|---|---|
| Ln(1)–N(1) | 2.317(10) | 2.271(10) | Ln(3)–S(3) | 2.895(3) | 2.813(5) |
| Ln(2)–N(2) | 2.314(12) | 2.262(13) | Ln(3)–S(4) | 2.916(3) | 2.831(4) |
| Ln(3)–N(3) | 2.303(9) | 2.280(11) | Ln(3)–S(5) | 2.871(3) | 2.795(4) |
| Ln(4)–N(4) | 2.316(12) | 2.304(13) | Ln(3)–S(6) | 2.860(3) | 2.846(5) |
| Ln(1)–S(1) | 2.892(4) | 2.828(4) | Ln(4)–S(5) | 2.859(4) | 2.819(5) |
| Ln(1)–S(2) | 2.865(5) | 2.861(4) | Ln(4)–S(6) | 2.872(3) | 2.842(4) |
| Ln(1)–S(7) | 2.892(5) | 2.822(4) | Ln(4)–S(7) | 2.902(4) | 2.809(4) |
| Ln(1)–S(8) | 2.865(4) | 2.807(4) | Ln(4)–S(8) | 2.869(4) | 2.818(4) |
| Ln(2)–S(1) | 2.870(3) | 2.794(4) | Ln(1)–S(9) | 3.057(3) | 3.013(3) |
| Ln(2)–S(2) | 2.866(4) | 2.835(4) | Ln(2)–S(9) | 3.163(3) | 3.092(4) |
| Ln(2)–S(3) | 2.851(3) | 2.809(4) | Ln(3)–S(9) | 3.079(3) | 3.012(3) |
| Ln(2)–S(4) | 2.894(3) | 2.820(4) | Ln(4)–S(9) | 3.058(3) | 2.998(3) |
| | | | | | |
| N(1)–Ln(1)–S(1) | 98.9(3) | 112.2(3) | S(5)–Ln(3)–S(9) | 74.58(9) | 82.98(10) |
| N(1)–Ln(1)–S(2) | 114.3(4) | 101.2(3) | S(6)–Ln(3)–S(3) | 80.07(10) | 147.81(12) |
| N(1)–Ln(1)–S(7) | 98.3(4) | 96.2(3) | S(6)–Ln(3)–S(4) | 138.74(9) | 111.83(12) |
| N(1)–Ln(1)–S(8) | 114.5(3) | 117.0(3) | S(6)–Ln(3)–S(5) | 70.06(10) | 77.01(14) |
| N(1)–Ln(1)–S(9) | 156.9(3) | 157.3(3) | S(6)–Ln(3)–S(9) | 77.69(8) | 68.16(10) |
| S(1)–Ln(1)–S(9) | 70.95(9) | 84.62(10) | S(8)–Ln(4)–S(9) | 81.65(11) | 79.63(10) |
| S(2)–Ln(1)–S(1) | 70.39(11) | 77.61(11) | N(4)–Ln(4)–S(5) | 95.4(3) | 114.4(4) |
| S(2)–Ln(1)–S(7) | 146.87(11) | 114.69(11) | N(4)–Ln(4)–S(6) | 120.1(3) | 97.7(3) |
| S(2)–Ln(1)–S(9) | 82.51(9) | 66.46(9) | N(4)–Ln(4)–S(7) | 98.0(3) | 95.6(4) |
| S(8)–Ln(1)–S(2) | 83.85(14) | 141.11(11) | N(4)–Ln(4)–S(8) | 115.2(3) | 118.5(3) |
| S(7)–Ln(1)–S(1) | 111.83(10) | 146.70(12) | N(4)–Ln(4)–S(9) | 156.0(3) | 155.6(3) |
| S(7)–Ln(1)–S(9) | 68.26(3) | 73.88(10) | S(5)–Ln(4)–S(6) | 70.05(9) | 76.69(14) |
| S(8)–Ln(1)–S(1) | 144.26(11) | 81.06(12) | S(5)–Ln(4)–S(7) | 115.85(11) | 146.42(13) |
| S(8)–Ln(1)–S(7) | 77.03(13) | 70.38(11) | S(5)–Ln(4)–S(8) | 145.65(12) | 81.66(13) |
| S(8)–Ln(1)–S(9) | 81.74(9) | 79.54(10) | S(5)–Ln(4)–S(9) | 75.07(9) | 82.84(12) |
| S(4)–Ln(2)–S(9) | 64.67(8) | 69.94(10) | S(8)–Ln(4)–S(7) | 76.81(12) | 70.41(11) |
| N(2)–Ln(2)–S(1) | 103.7(3) | 106.5(3) | S(6)–Ln(4)–S(7) | 141.31(12) | 115.55(12) |
| N(2)–Ln(2)–S(2) | 106.7(3) | 106.6(4) | S(6)–Ln(4)–S(9) | 77.85(8) | 68.41(10) |
| N(2)–Ln(2)–S(3) | 106.0(3) | 106.9(4) | S(7)–Ln(4)–S(9) | 68.10(9) | 74.31(10) |
| N(2)–Ln(2)–S(4) | 109.0(3) | 102.8(3) | S(8)–Ln(4)–S(6) | 80.69(11) | 143.12(13) |
| N(2)–Ln(2)–S(9) | 168.3(3) | 166.2(3) | Ln(1)–S(9)–Ln(4) | 84.90(7) | 85.98(9) |
| S(1)–Ln(2)–S(4) | 103.31(10) | 147.93(12) | Ln(3)–S(9)–Ln(2) | 83.08(7) | 84.47(9) |
| S(1)–Ln(2)–S(9) | 69.68(9) | 83.73(10) | Ln(1)–S(9)–Ln(3) | 146.84(10) | 144.39(11) |
| S(2)–Ln(2)–S(1) | 70.69(11) | 78.61(11) | Ln(4)–S(9)–Ln(3) | 86.41(8) | 84.16(8) |
| S(2)–Ln(2)–S(4) | 144.14(12) | 105.36(11) | Ln(1)–S(9)–Ln(2) | 85.35(8) | 82.68(8) |
| S(2)–Ln(2)–S(9) | 80.64(11) | 65.69(9) | Ln(4)–S(9)–Ln(2) | 143.93(9) | 142.21(11) |
| S(3)–Ln(2)–S(1) | 147.49(11) | 88.04(13) | N(3)–Ln(3)–S(5) | 95.8(2) | 113.1(3) |
| S(3)–Ln(2)–S(2) | 88.34(11) | 146.31(13) | N(3)–Ln(3)–S(9) | 158.7(2) | 156.9(3) |
| S(3)–Ln(2)–S(4) | 79.06(9) | 71.00(12) | S(3)–Ln(3)–S(4) | 77.99(9) | 70.80(12) |
| S(3)–Ln(2)–S(9) | 82.91(8) | 82.32(12) | S(3)–Ln(3)–S(9) | 83.69(9) | 83.72(11) |
| N(3)–Ln(3)–S(3) | 112.6(2) | 113.2(4) | S(4)–Ln(3)–S(9) | 65.54(8) | 71.00(10) |
| N(3)–Ln(3)–S(4) | 103.2(2) | 98.8(3) | S(5)–Ln(3)–S(3) | 146.00(10) | 84.54(15) |
| N(3)–Ln(3)–S(6) | 117.5(2) | 98.4(4) | S(5)–Ln(3)–S(4) | 114.51(10) | 145.53(12) |

The average Pr–μ-S bond length [2.877(3) Å] in **5** is the same as that in $Pr[S_2P(C_6H_{11})_2]_3$ [$S_2P(C_6H_{11})_2$ = dicyclohexyldithiophosphinate, 2.877(4) Å].[18] The mean Sm–μ-S bond length [2.822(4) Å] in **6** is comparable to those found in $[\{(Me_3Si)_2N\}_4(\mu_4\text{-Cl})Sm_4(\mu\text{-SPh})_4(\mu_3\text{-Cl})_4Li(thf)]$ [2.822(4) Å],[6a] $[(thf)Sm(SPh)_3]_{4n}$ [2.854(3) Å][19] and $[Sm\{O{=}P(NMe_2)_3\}(SPh)_3]$ [2.830(2) Å].[20] The mean Pr–N bond length [2.312(10) Å] in **5** is smaller than that reported in $Pr[Et_2NCH_2CH_2NC(Me)CHC(Me)NCH_2CH_2NEt_2]Cl_2$ [2.5702(3) Å],[21] whereas the length of the Sm–N bonds [2.279(12) Å] in **6** is between those of $[\{(Me_3Si)_2N\}_4(\mu_4\text{-Cl})Sm_4(\mu\text{-SPh})_4(\mu_3\text{-Cl})_4Li(thf)]$ [2.211(3) Å][6] and $[\{(Me_3Si)_2NSm(\mu\text{-Cl})_2Li(thf)_2\}(\mu\text{-Cl})]_2$ [2.284(4) Å].[22]

Weak coordination of a soft-base sulfur atom to a hard-acid Ln centre in lanthanide thiolate complexes is known to be the cause for their catalytic behaviour in the ROP of ε-caprolactone.[2j,6] Therefore, compounds **3**–**6** (Table 3) were employed to initiate the ROP of ε-caprolactone at ambient temperature. When the polymerization was performed in thf/toluene, a highly viscous product was observed to form in less than 10 min. After the resulting polymers were quenched by the addition of 1 M HCl in EtOH, the poly(ε-caprolactone)s were isolated as white solids and characterized by gel permeation chromatography. Compounds **3**–**6** were found to initiate the ROP of ε-caprolactone at room temperature to give relatively high molecular weight polymers ($M_n > 13400$) with narrow molecular weight distributions ($M_w/M_n$ = 1.17–1.56) in good yields within a few minutes. For comparison, Table 3 lists the results for the ROP of ε-caprolactone initiated by **1**–**6** along with two known $Pr^{III}$ and $Sm^{III}$ benzenethiolate complexes, $[\{(Me_3Si)_2N\}_4(\mu_4\text{-Cl})Sm_4(\mu\text{-SPh})_4(\mu_3\text{-Cl})_4Li(thf)]$ (**7**) and $[\{(Me_3Si)_2N\}_2$-

 © 2007 Wiley-VCH Verlag GmbH & Co. KGaA, Weinheim 

Table 3. Polymerization of ε-caprolactone catalyzed by **3**–**6**.

| Entry[a] | Catalyst | Time [min] | [Monomer]/[cat.] | Yield[b] | $M_n$ [$\times 10^4$ g mol$^{-1}$] | $M_w$ [$\times 10^4$ g mol$^{-1}$] | $M_w/M_n$[c] | Ref. |
|---|---|---|---|---|---|---|---|---|
| 1 | **1** | 20 | 400 | 59 | 2.71 | 5.55 | 2.05 | [6b] |
| 2 | **2** | 20 | 400 | 46 | 2.93 | 5.83 | 1.99 | [6b] |
| 3 | **3** | 1 | 400 | 100 | 6.31 | 9.12 | 1.44 | this work |
| 4 | **4** | 1 | 400 | 100 | 4.13 | 6.30 | 1.53 | this work |
| 5 | **4** | 2 | 100 | 100 | 1.77 | 2.76 | 1.56 | this work |
| 6 | **5** | 1 | 400 | 100 | 4.50 | 5.55 | 1.23 | this work |
| 7 | **5** | 2 | 800 | 100 | 1.34 | 1.70 | 1.27 | this work |
| 8 | **6** | 2 | 400 | 100 | 5.34 | 6.42 | 1.20 | this work |
| 9 | **6** | 9 | 600 | 100 | 2.42 | 2.83 | 1.17 | this work |
| 10 | **7** | 8 | 400 | 99 | 3.41 | 4.94 | 1.45 | [6a] |
| 11 | **7** | 15 | 600 | 75 | 3.33 | 5.09 | 1.53 | [6a] |
| 12 | **8** | 20 | 400 | 99 | 2.61 | 3.70 | 1.42 | [6a] |

[a] Temperature: 298 K; solvent: thf/toluene (1:4); $V_{\varepsilon\text{-caprolactone}}:V_{solvent}$ = 1:5. [b] Yield: weight of polymer obtained/weight of monomer used. [c] Determined by GPC analysis in thf, calibrated to a polystyrene standard.

$(\mu\text{-SPh})Pr(\mu\text{-SPh})Li(thf)_2]_n$ (**8**).[6a] Complexes **3**–**6** showed better catalytic activity than their precursors, **1** and **2**, which may be ascribed to the weak Ln–S bonds in **3**–**6**.[2g,2i,6] In addition, complexes **5** and **6** showed even better catalytic activity than complexes **3** and **4** under the same reaction conditions, which might be due to the fact that **3** and **4** have a less open coordination environment around the Ln metal (coordination number four) than **5** and **6**. Complex **3** and its $Pr^{III}$/benzenethiolate complex **8** had similar catalytic activity for the ROP of ε-caprolactone. In the case of [monomer]/[cat.] = 600, **6** initiated the polymerization of ε-caprolactone at a faster rate than its benzenethiolate analogue **7**. The former reaction was complete in 9 min with a 100% yield whereas the latter was complete in 15 min with a 75% yield. Therefore, we tentatively ascribed this difference to the fact that the $SEt^-$ anions may be more easily dissociated from the $Ln^{III}$ centres in **6** than the $SPh^-$ and $Cl^-$ anions in **7**.

## Conclusions

In summary, the protonolysis reaction of **1** or **2** with an equimolar amount of *t*BuSH or EtSH was studied and amidolanthanide alkylthiolate complexes **3**–**6** were isolated in reasonable yields. Compounds **3**–**6** were characterized by elemental analysis, IR spectroscopy and X-ray analysis. Compounds **3** and **4** contain a $Ln_2S_2$ core structure whereas **5** and **6** consist of a square $Ln_4$ array with one $SEt^-$ ligand capping above the mean $Ln_4$ plane. Occurrence of a $\mu_4$-$SEt^-$ ligand in the structures of **5** and **6** is rare in the chemistry of lanthanide chalcogenolate complexes. Compounds **3**–**6** showed better catalytic activity in the ROP of ε-caprolactone than their precursors **1** and **2** and their benzenethiolate analogues. It is anticipated that **1** or **2** could react with other thiols such as 1,2-diethanedithiol or cationic thiol $TabHPF_6$ [TabH = 4-(trimethylammonio)benzenethiol] to afford other lanthanide thiolate complexes with more interesting structural frameworks and better catalytic activities in the ROP of ε-caprolactone. Studies on these respects are underway in this laboratory.

## Experimental Section

All manipulations were carried out under an atmosphere of argon by using standard Schlenk techniques. All solvents were heated at reflux and distilled from sodium benzophenone ketyl under an atmosphere of argon prior to use. $[(Me_3Si)_2N]_3Ln(\mu\text{-}Cl)Li(thf)_3$ (**1**: Ln = Pr; **2**: Ln = Sm),[7] $LnCl_3$[23] and $LiN(SiMe_3)_2$[24] were prepared according to literature methods. *t*BuSH and EtSH were obtained from commercial sources and used as received. ε-Caprolactone, purchased from ACROS Com, was dried by stirring with $CaH_2$ for 8 d and then distilled under reduced pressure. $^1H$ NMR spectra were recorded at ambient temperature with a Varian UNITYplus-400 spectrometer. $^1H$ NMR chemical shifts were referenced to the solvent signal in $C_6D_6$. Elemental analyses for C, H and N were performed with a Carlo-Erbo CHNO-S microanalyzer. The IR spectra were recorded with a Nicolet MagNa-IR550 FTIR spectrometer (4000–400 cm$^{-1}$). Molecular weight and molecular weight distributions were determined against a polystyrene standard by gel permeation chromatography (GPC) with a Waters 1515 apparatus with three HR columns (HR-1, HR-2 and HR-4); thf was used as an eluent.

**$[\{(Me_3Si)_2N\}_2Pr(\mu\text{-}S\mathit{t}Bu)]_2$ (3):** A solution of *t*BuSH (2.09 mmol) in thf (1.65 mL) was slowly added to a solution of **1** (1.31 g, 2.09 mmol) in thf (20 mL). The mixture was stirred at room temperature for 2 h, and then the solution was concentrated to dryness in vacuo. The resulting solid was extracted with *n*-hexane (10 mL) and toluene (20 mL) and then filtered. Compound **3**·$2(thf)_{0.5}$ (1.05 g, 43%) was isolated as light yellow crystals by cooling the filtrate to 2 °C for 3 d. $^1H$ NMR (400 MHz, $C_6D_6$): $\delta$ = –7.17 [br. s, $w_{1/2}$ = 40 Hz, 18 H, $C(CH_3)_3$], –10.92 [br. s, $w_{1/2}$ = 200 Hz, 72 H, $Si(CH_3)_3$] ppm. IR (KBr disc): $\tilde{\nu}$ = 2960 (s), 2902 (m), 1635 (m), 1385 (m), 1260 (s), 1189 (s), 1079 (m), 938 (s), 845 (s), 608 (w) cm$^{-1}$. $C_{36}H_{98}N_4Pr_2S_2OSi_8$ (1173.86): calcd. C 36.83, H 8.42, N, 4.77; found C 36.56, H 8.01, N 4.43.

**$[\{(Me_3Si)_2N\}_2Sm(\mu\text{-}S\mathit{t}Bu)]_2$ (4):** Compound **4** (0.78 g, 40%) was isolated as light yellow crystals from the reaction of **2** (1.12 g, 1.75 mmol) with *t*BuSH (1.75 mmol) in thf followed by a similar workup to that used in the isolation of **3**. $^1H$ NMR (400 MHz, $C_6D_6$): $\delta$ = –0.90 [br. s, $w_{1/2}$ = 32 Hz, 18 H, $C(CH_3)_3$], –2.00 [br. s, $w_{1/2}$ = 9 Hz, 72 H, $Si(CH_3)_3$] ppm. IR: $\tilde{\nu}$ = 2962 (s), 2903 (m), 1632 (m), 1385 (m), 1258 (s), 1185 (s), 1084 (m), 938 (s), 848 (s), 613 (w) cm$^{-1}$. $C_{32}H_{90}N_4S_2Si_8Sm_2$ (1120.66): calcd. C 37.89, H 8.42, N 4.42; found C 37.56, H 8.01, N 4.93.

 © 2007 Wiley-VCH Verlag GmbH & Co. KGaA, Weinheim 

**$[Li(thf)_4][\{(Me_3Si)_2N\}_4Pr_4(\mu_4\text{-}SEt)(\mu\text{-}SEt)_8]$ (5):** A solution of EtSH (1.85 mmol) in thf (0.88 mL) was added dropwise to a solution of **1** (1.12 g, 1.85 mmol) in thf (20 mL). After stirring at room temperature for 3 h, the volatile species were removed in vacuo, and the crude product was extracted with toluene (20 mL) and then filtered. The filtrate was kept at 2 °C for one week, which resulted in the formation of light yellow crystals of **5**·0.5$C_7H_8$ (0.440 g, 21%). $^1$H NMR (400 MHz, $C_6D_6$): $\delta$ = 3.25 (s, 32 H, thf), 1.27 (br. s, $w_{1/2}$ = 20 Hz, 27 H, $CH_3$), 0.71 (br. s, $w_{1/2}$ = 36 Hz, 18 H, $CH_2$), –1.45 [br. s, $w_{1/2}$ = 40 Hz, 72 H, $Si(CH_3)_3$] ppm. IR: $\tilde{\nu}$ = 2961 (s), 2901 (m), 2184 (w), 1658 (m), 1520 (s), 1475 (s), 1385 (s), 1256 (s), 1179 (s), 1048 (m), 992 (m), 949 (s), 841 (s), 756 (m), 604 (s) cm$^{-1}$. $C_{61.5}H_{153}LiN_4O_4Pr_4S_9Si_8$ (2088.66): calcd. C 35.23, H 7.36, N 2.67; found C 35.58, H 7.42, N 2.19.

**$[Li(thf)_4][\{(Me_3Si)_2N\}_4Sm_4(\mu_4\text{-}SEt)(\mu\text{-}SEt)_8]$ (6):** A solution of EtSH (2.02 mmol) in thf (0.96 mL) was added dropwise to a solution of **2** (1.29 g, 2.02 mmol) in thf (20 mL). After stirring at room temperature for 3 h, the volatile species were removed in vacuo, and the crude product was extracted with benzene (20 mL) and then filtered. The filtrate was kept at 2 °C for one week, which resulted in the formation of light yellow crystals of **6**·$C_6H_6$ (0.368 g, 17%). The $^1$H NMR spectrum in $C_6D_6$ showed broad uninterpretable signals. IR: $\tilde{\nu}$ = 2962 (s), 2905 (m), 2183 (w), 1655 (m), 1518 (s), 1482 (s), 1385 (s), 1248 (s), 1181 (s), 1053 (m), 995 (m), 937 (s), 841 (s), 753 (m), 610 (s) cm$^{-1}$. $C_{64}H_{155}LiN_4O_4S_9Si_8Sm_4$ (2158.59): calcd. C 36.61, H 6.86, N 2.60; found C 37.06, H 7.21, N 2.43.

**Crystal Structure Determination and Refinement:** All measurements were recorded with a Rigaku Mercury CCD X-ray diffractometer (3 kV, sealed tube) at 193 K by using graphite monochromated Mo-$K_\alpha$ ($\lambda$ = 0.71070 Å) light. X-ray quality crystals of **3**·2(thf)$_{0.5}$, **4**, **5**·0.5$C_7H_8$ and **6**·$C_6H_6$ were obtained directly from the above preparations. A light yellow chunk of **3**·2(thf)$_{0.5}$ with dimensions 0.45 × 0.40 × 0.30 mm, a light yellow prism of **4** with dimensions 0.40 × 0.35 × 0.10 mm, a light yellow prism of **5**·0.5$C_7H_8$ with dimensions 0.22 × 0.47 × 0.30 mm and a light yellow prism of **6**·$C_6H_6$ with dimensions 0.14 × 0.50 × 0.30 mm were mounted in a sealed capillary, respectively. Diffraction data were collected with the $\omega$ mode with a detector distance of 35 mm to the crystals. A total of 720 oscillation images for each were collected in the range 6.04° < 2$\theta$ < 50.70° for **3**·2(thf)$_{0.5}$, 6.28° < 2$\theta$ < 50.70° for **4**, 6.10° < 2$\theta$ < 50.70° for **5**·0.5$C_7H_8$ and 6.18° < 2$\theta$ < 50.70° for **6**·$C_6H_6$. The collected data were reduced by using the program CrystalClear (Rigaku and MSC, ver. 1.3, 2001), and an absorption correction (multi-scan) was applied, which resulted in transmission factors ranging from 0.385 to 0.485 for **3**·2(thf)$_{0.5}$, from 0.406 to 0.799 for **4**, from 0.440 to 0.618 for **5**·0.5$C_7H_8$ and from 0.359 to 0.694 for **6**·$C_6H_6$. The reflection data were also corrected for Lorentz and polarization effects.

The structures of **3**·2(thf)$_{0.5}$, **4**, **5**·0.5$C_7H_8$, and **6**·$C_6H_6$ were solved by direct methods[25] and refined by full-matrix least-squares on $F^2$.[26] When crystals **3**·2(thf)$_{0.5}$ and **5**·0.5$C_7H_8$ were taken away from their mother liquors, rapid evaporation of part of the solvated molecules in these crystals was observed. Although we made numerous attempts, these crystals were always weakly diffracting, especially at high angles, which made the final R value relatively higher. In addition, in the structures of **3**·2(thf)$_{0.5}$, **5**·0.5$C_7H_8$ and **6**·$C_6H_6$, serious disorder problems derived from the solvated molecules and methyl groups from bis(trimethylsilyl)amide anions also contributed greatly to the high R value. Therefore, the thf and $C_7H_8$ molecules in **3**·2(thf)$_{0.5}$ and **5**·0.5$C_7H_8$ were fixed with constrained parameters and refined with an occupancy factor of 0.5. For **5**·0.5$C_7H_8$, three methyl groups bearing C(19), C(20) and C(21) atoms were found to be disordered over two positions with an occupancy ratio of 0.45:0.55 for C(19)/C(19A), C(20)/C(20A) and C(21)/C(21A). In the case of **6**·$C_6H_6$, a number of methyl groups were found to be disordered over two sites with an occupancy factor of 0.58:0.42 for C(12)/C(12A) and C(16)/C(16A) and 0.54:0.46 for C(19)/C(19A), C(25)/C(25A), C(28)/C(28A), C(31)/C(31A), C(34)/C(34A), C(35)/C(35A), C(36)/C(36A), C(38)/C(38A) and C(41)/C(41A). All non-hydrogen atoms, except for those from thf

Table 4. Summary of Crystallographic data for **3**·2(thf)$_{0.5}$, **4**, **5**·0.5$C_7H_8$ and **6**·$C_6H_6$.

| | **3**·2(thf)$_{0.5}$ | **4** | **5**·0.5$C_6H_5CH_3$ | **6**·$C_6H_6$ |
|---|---|---|---|---|
| Empirical formula | $C_{36}H_{98}N_4OPr_2S_2Si_8$ | $C_{32}H_{90}N_4S_2Si_8Sm_2$ | $C_{61.5}H_{145}LiN_4O_4Pr_4S_9Si_8$ | $C_{64}H_{147}LiN_4O_4S_9Si_8Sm_4$ |
| Formula mass | 1173.86 | 1120.66 | 2088.66 | 2158.59 |
| Crystal system | triclinic | monoclinic | monoclinic | monoclinic |
| Space group | $P\bar{1}$ | $P2_1/c$ | $P2_1/c$ | $P2_1/c$ |
| $a$ [Å] | 11.396(2) | 12.067(2) | 15.024(3) | 15.039(3) |
| $b$ [Å] | 12.160(2) | 11.313(2) | 25.455(5) | 25.445(5) |
| $c$ [Å] | 12.366(3) | 23.486(7) | 26.689(5) | 26.357(5) |
| $\alpha$ [°] | 109.74(3) | | | |
| $\beta$ [°] | 99.50(3) | 119.30(2) | 99.60(3) | 91.19(3) |
| $\gamma$ [°] | 99.763(3) | | | |
| $V$ [Å$^3$] | 1543.3(7) | 2790.0(12) | 10206(3) | 10084(3) |
| $Z$ | 1 | 2 | 4 | 4 |
| $D_{calcd.}$ [g cm$^{-3}$] | 1.263 | 1.331 | 1.359 | 1.422 |
| $F$(000) | 612 | 1156 | 4276 | 4392 |
| $\mu$ [Mo-$K_\alpha$ [cm$^{-1}$]] | 18.1 | 23.5 | 21.9 | 26.1 |
| Total no. of reflections | 14972 | 25926 | 99290 | 97851 |
| No. of unique reflections | 5595 ($R_{int}$ = 0.0206) | 5104 ($R_{int}$ = 0.0919) | 18652 ($R_{int}$ = 0.0779) | 18439 ($R_{int}$ = 0.0839) |
| No. of obsd. reflections | 5405 [$I > 2.00\sigma(I)$] | 4397 [$I > 2.00\sigma(I)$] | 13470 [$I > 2.00\sigma(I)$] | 12599 [$I > 2.00\sigma(I)$] |
| No. of variables | 249 | 217 | 726 | 706 |
| $R_1$[a] | 0.033 | 0.084 | 0.095 | 0.107 |
| $wR_2$[b] | 0.095 | 0.171 | 0.231 | 0.245 |
| $GOF$[c] | 0.987 | 1.178 | 1.089 | 1.437 |
| Residual peaks [e Å$^{-3}$] | 2.53, –1.21 | 2.72, –1.70 | 1.51, –2.03 | 2.16, –2.70 |

[a] $R = \Sigma||F_o| - |F_c||/\Sigma|F_o|$. [b] $R_w = \{w\Sigma(|F_o| - |F_c|)^2/\Sigma w|F_o|^2\}^{1/2}$. [c] $GOF = \{\Sigma w(|F_o| - |F_c|)^2/(n-p)\}^{1/2}$, where $n$ is the number of reflections and $p$ is total number of parameters refined.

 © 2007 Wiley-VCH Verlag GmbH & Co. KGaA, Weinheim 

solvent molecule in **3**·2(thf)$_{0.5}$, and those from $C_6H_6$ solvent molecule in **6**·$C_6H_6$, and those disordered C atoms in **5**·0.5$C_7H_8$, and part of disordered C atoms [C(12), C(16), C(19), C(25), C(28), C(31), C(38), C(41)] in **6**·$C_6H_6$ were refined anisotropically. Hydrogen atoms on C(43)–C(46) atoms in **5**·0.5$C_6H_5CH_3$ and C(43)–C(46) atoms in **6**·$C_6H_6$ were not located. All other hydrogen atoms were placed in geometrically idealized positions (C–H = 0.98 Å for methyl groups, C–H = 0.99 Å for methylene groups or C–H = 0.95 Å for phenyl groups) and constrained to ride on their parent atoms with $U_{iso}(H) = 1.2\ U_{eq}(C)$ or $1.5\ U_{eq}(C)$ for methyl groups. All the calculations were performed with a Dell workstation by using the CrystalStructure crystallographic software package (Rigaku and MSC, Ver.3.60, 2004). Crystal and data collection parameters for **3**·2(thf)$_{0.5}$, **4**, **5**·0.5$C_7H_8$ and **6**·$C_6H_6$ are summarized in Table 4.

CCDC-624794 (for **3**), -624795 (for **4**), -624796 (for **5**) and -624797 (for **6**) contain the supplementary crystallographic data for this paper. These data can be obtained free of charge from The Cambridge Crystallographic Data Centre via http://www.ccdc.cam.ac.uk/data_request/cif.

**A Typical Procedure for the ROP of ε-Caprolactone:** A 50-mL Schlenk flask equipped with a magnetic stir bar was charged with thf (0.33 mL), toluene (1.32 mL) and **5** (0.011 g). To this light yellow solution, ε-caprolactone (0.33 mL) was added at room temperature by using a syringe and with vigorous magnetic stirring. The stirring was ceased in a few minutes due to the viscosity. The reaction mixture was quenched by the addition of 1 M HCl in EtOH after a fixed interval. The solution was then poured into petroleum ether (20 mL) to precipitate the white oligomer. The resulting oligomer was washed with methanol three times, collected and dried in vacuo.

## Acknowledgments

This work was supported by the NNSF of China (Nos. 20271036 and 20525101), the NSF of Jiangsu Province (No. BK2004205), the Specialized Research Fund for the Doctoral Program of Higher Education (No. 20050285004), the Qin-Lan Project of Jiangsu Province and the State Key Laboratory of Organometallic Chemistry of SIOC (No. 06-26) in China.

[1] a) F. Nief, *Coord. Chem. Rev.* **1998**, *13*, 178–179; b) Z. M. Hou, Y. Wakatsuki, *Coord. Chem. Rev.* **2002**, *231*, 1–22; c) A. Kornienko, T. J. Emge, G. A. Kumar, R. E. Riman, J. G. Brennan, *J. Am. Chem. Soc.* **2005**, *127*, 3501–3505; d) H. X. Li, Y. J. Zhu, M. L. Cheng, Z. G. Ren, J. P. Lang, Q. Shen, *Coord. Chem. Rev.* **2006**, *250*, 2059–2092.

[2] a) E. Downing, L. Hesselink, J. Ralston, R. M. Macfarlane, *Science* **1996**, *273*, 1185–1189; b) A. Goldbach, M. L. Saboungi, *Acc. Chem. Res.* **2005**, *38*, 705–712; c) G. A. Kumar, R. E. Riman, L. A. D. Torres, O. B. Garcia, S. Banerjee, A. Kornienko, J. G. Brennan, *Chem. Mater.* **2005**, *17*, 5130–5135; d) G. S. Pomrenke, P. B. Klein, D. W. Langer, *Rare Earth Doped Semiconductors*: MRS Symposium, vol. 301, Materials Research Society, Pittsburgh, PA, **1993**; e) Q. Shen, H. R. Li, C. S. Yao, Y. M. Yao, L. L. Zhang, K. B. Yu, *Organometallics* **2001**, *20*, 3070–3073; f) J. Zhang, L. P. Ma, R. H. Cai, L. H. Weng, X. G. Zhou, *Organometallics* **2005**, *24*, 738–742; g) J. Y. Kim, T. Livinghouse, *Org. Lett.* **2005**, *7*, 1737–1739; h) Y. Nakayama, T. Shibahara, H. Fukumoto, A. Nakamura, K. Mashima, *Macromolecules* **1996**, *29*, 8014–8016; i) X. Y. Yu, G. X. Jin, N. H. Hu, L. H. Weng, *Organometallics* **2002**, *21*, 5540–5548; j) Z. Hou, Y. Zhang, H. Tezuka, P. Xie, O. Tardif, T. Koizumi, H. Yamazaki, Y. Wakatsuki, *J. Am. Chem. Soc.* **2000**, *122*, 10533–10543; k) D. R. Cary, G. E. Ball, J. Arnold, *J. Am. Chem. Soc.* **1995**, *117*, 3492–3501.

[3] a) H. C. Aspinall, S. A. Cunningham, *Inorg. Chem.* **1998**, *37*, 5396–5398; b) H. Sugiyama, Y. Hayashi, H. Kawaguchi, K. Tatsumi, *Inorg. Chem.* **1998**, *37*, 6773–6779; c) K. Tatsumi, T. Amemiya, H. Kawaguchi, K. Tani, *J. Chem. Soc., Chem. Commun.* **1993**, 773–774; d) S. D. Stults, R. A. Andersen, A. Zalkin, *Organometallics* **1990**, *9*, 1623–1629; e) Z. Z. Wu, W. W. Ma, Z. E. Huang, R. F. Cai, *Polyhedron* **1996**, *15*, 3427–3432; f) Z. Z. Wu, Z. E. Huang, R. F. Cai, X. G. Zhou, Z. Xu, X. Z. You, X. Y. Huang, *J. Organomet. Chem.* **1996**, *506*, 25–30; g) S. M. Cendrowski-Guillaume, G. L. Gland, M. Nierlich, M. Ephritikhine, *Organometallics* **2000**, *19*, 5654–5660; h) Y. R. Li, C. F. Pi, J. Zhang, X. G. Zhou, Z. X. Chen, L. H. Weng, *Organometallics* **2005**, *24*, 1982–1988.

[4] H. C. Aspinall, D. C. Bradley, M. B. Hursthouse, K. D. Sales, N. P. C. Walker, *J. Chem. Soc., Chem. Commun.* **1985**, 1585–1586.

[5] a) H. Schumann, I. Albrecht, E. Hahn, *Angew. Chem. Int. Ed. Engl.* **1985**, *24*, 985–986; b) H. Schumann, I. Albrecht, M. Gallagher, E. Hahn, *J. Organomet. Chem.* **1988**, *349*, 103–115.

[6] a) H. X. Li, Z. G. Ren, Y. Zhang, W. H. Zhang, J. P. Lang, Q. Shen, *J. Am. Chem. Soc.* **2005**, *127*, 1122–1123; b) H. X. Li, Z. G. Ren, M. L. Cheng, W. H. Zhang, J. P. Lang, Q. Shen, *Inorg. Chem.* **2006**, *45*, 1885–1887.

[7] a) S. L. Zhou, S. W. Wang, G. S. Yang, X. Y. Liu, E. H. Sheng, K. H. Zhang, L. Cheng, Z. X. Huang, *Polyhedron* **2003**, *22*, 1019–1024; b) M. H. Xie, X. Y. Liu, S. W. Wang, L. Liu, Y. Y. Wu, G. S. Yang, S. L. Zhou, E. H. Shen, Z. X. Huang, *Chin. J. Chem.* **2004**, *22*, 678–682.

[8] H. X. Li, Y. Zhang, Z. G. Ren, M. L. Cheng, J. Wang, J. P. Lang, *Chin. J. Chem.* **2005**, *23*, 1499–1502.

[9] K. Mashima, Y. Nakayama, N. Kanehisa, Y. Kai, A. Nakamura, *J. Chem. Soc., Chem. Commun.* **1993**, 1847–1848.

[10] K. Mashima, Y. Nakayama, H. Fukumoto, N. Kanehisa, Y. Kai, A. Nakamura, *J. Chem. Soc., Chem. Commun.* **1994**, 2523–2524.

[11] J. H. Melman, T. J. Emge, J. G. Brennan, *Inorg. Chem.* **2001**, *40*, 1078–1081.

[12] W. J. Evans, D. S. Lee, D. B. Rego, J. M. Perotti, S. A. Kozimor, E. K. Moore, J. W. Ziller, *J. Am. Chem. Soc.* **2004**, *126*, 14574–14582.

[13] W. J. Evans, M. A. Ansari, J. W. Ziller, S. I. Kham, *Organometallics* **1995**, *14*, 3–4.

[14] P. L. Arnold, S. A. Mungur, A. J. Blake, C. Wilson, *Angew. Chem. Int. Ed.* **2003**, *42*, 5981–5984.

[15] W. J. Evans, D. K. Drummond, H. M. Zhang, J. L. Atwood, *Inorg. Chem.* **1988**, *27*, 575–579.

[16] a) M. Fitzgerald, T. J. Emge, J. G. Brennan, *Inorg. Chem.* **2002**, *41*, 3528–3533; b) J. H. Melman, M. Fitzgerald, D. Freedman, T. J. Emge, J. G. Brennan, *J. Am. Chem. Soc.* **1999**, *121*, 10247–10248; c) A. Kornienko, L. Huebner, D. Freedman, T. J. Emge, J. G. Brennan, *Inorg. Chem.* **2003**, *42*, 8476–8480; d) D. Freedman, S. Sayan, T. J. Emge, M. Croft, J. G. Brennan, *J. Am. Chem. Soc.* **1999**, *121*, 11713–11719; e) A. Kornienko, J. H. Helman, T. J. Emge, J. G. Brennan, *Inorg. Chem.* **2002**, *41*, 121–126; f) A. Y. Kornienko, T. J. Emge, J. G. Brennan, *J. Am. Chem. Soc.* **2001**, *123*, 11933–11939; g) D. Freedman, T. J. Emge, J. G. Brennan, *Inorg. Chem.* **2002**, *41*, 492–500.

[17] a) W. P. Su, R. Cao, M. C. Hong, J. T. Chen, J. X. Lu, *Chem. Commun.* **1998**, 1389–1390; b) R. G. Prichard, R. V. Arish, Z. Salehi, *J. Chem. Soc., Dalton Trans.* **1999**, 243–250; c) H. Xu, J. H. K. Yip, *Inorg. Chem.* **2003**, *42*, 4492–4494; d) J. E. Barclay, D. J. Evans, S. C. Davies, D. L. Hughes, P. Sobota, *J. Chem. Soc., Dalton Trans.* **1999**, 1533–1534; e) X. J. Wang, T. Langetepe, D. Fenske, B. S. Z. Kang, *Z. Anorg. Allg. Chem.* **2002**, *628*, 1158–1167; f) M. D. Janssen, A. L. Spek, D. M. Grove, G. van Koten, *Inorg. Chem.* **1996**, *35*, 4078–4081; g) Y. Agnus, R. Louis, R. Weiss, *J. Chem. Soc., Chem. Commun.* **1980**, 867–

 © 2007 Wiley-VCH Verlag GmbH & Co. KGaA, Weinheim 

869; h) R. V. Parish, Z. Saleh, R. G. Pritchard, *Angew. Chem. Int. Ed. Engl.* **1997**, *36*, 251–253; i) K. L. Tang, T. B. Xia, X. L. Jin, Y. Q. Tang, *Polyhedron* **1993**, *12*, 2895–2898; j) B. Krebs, A. Brommelhaus, *Angew. Chem. Int. Ed. Engl.* **1989**, *28*, 16821683; k) B. Krebs, A. Brommelhaus, *Z. Anorg. Allg. Chem.* **1991**, *595*, 167–182.

[18] Y. Meseri, A. A. Pinkerton, G. Chapuis, *J. Chem. Soc., Dalton Trans.* **1977**, 725–729.

[19] J. Lee, D. Freedman, J. H. Melman, M. Brewer, L. Sun, T. J. Emge, F. H. Long, J. G. Brennan, *Inorg. Chem.* **1998**, *37*, 2512–2519.

[20] K. Mashima, Y. Nakayama, T. Shibahara, H. Fukumoto, A. Nakamura, *Inorg. Chem.* **1996**, *35*, 93–99.

[21] D. Neculai, H. W. Roesky, A. M. Neculai, J. Magull, H. G. Schmidt, M. Noltemeyer, *J. Organomet. Chem.* **2002**, *643*, 47–52.

[22] H. X. Li, Q. F. Xu, J. X. Chen, M. L. Cheng, Y. Zhang, W. H. Zhang, J. P. Lang, Q. Shen, *J. Organomet. Chem.* **2004**, *689*, 3438–3448.

[23] M. D. Taylor, C. P. Carter, *J. Inorg. Nucl. Chem.* **1962**, *24*, 387–393.

[24] J. S. Ghotra, M. B. Hursthouse, A. J. Welch, *J. Chem. Soc., Chem. Commun.* **1973**, 669–670.

[25] G. M. Sheldrick, *SHELXS-97: Program for the Solution of Crystal Structure*, University of Göttingen, Germany, **1997**.

[26] P. T. Beurskens, G. Admiral, G. Beurskens, W. P. Bosman, S. Garcia-Granda, R. O. Gould, J. M. M. Smits, C. Smykalla, *PATTY: The DIRDIF Program System*, Technical Report of the Crystallography Laboratory, University of Nijmegen, The Netherlands, **1992**.

Received: November 29, 2006
Published Online: March 22, 2007

 © 2007 Wiley-VCH Verlag GmbH & Co. KGaA, Weinheim 

DOI: 10.1002/ejic.200601218

# Order and Disorder in Cluster Phases – The Case of $La_{\approx 0.7}(Al_{\approx 0.1}I_{\approx 0.9})$

**Lorenz Kienle,*[a] Oliver Oeckler,[b] Thomas Weber,[c] Viola Duppel,[a] Hansjürgen Mattausch,[a] and Arndt Simon[a]**

**Keywords:** Electron microscopy / X-ray diffraction / Rare earth metal compounds / Clusters / Halides / Disorder

The structure of the new partially ordered cluster phase $La_{0.69(1)}(Al_{0.12(1)}I_{0.88(1)})$ was determined by a combined methodical approach of electron microscopy techniques and X-ray diffraction. The structure is derived from the $Gd_3CCl_3$-type and ca. 50 % of the cluster positions in this structure type are occupied. The majority of the clusters are condensed via common edges, however, the degree of cluster condensation is low. The arrangement of neighboring clusters is comparable to chemically related, but strongly disordered cluster phases.

(© Wiley-VCH Verlag GmbH & Co. KGaA, 69451 Weinheim, Germany, 2007)

## Introduction

Many low-valent compounds of rare earth metals (Ln) are composed of discrete or condensed clusters[1] of the $Ln_6ZX_{12}$-type (X = Cl, Br, I). Endohedral species Z (Z = B, C, $C_2$, etc.) centering the octahedral $Ln_6$ core stabilize the valence electron-poor clusters.[2] Most phases with isolated or condensed $Ln_6ZX_{12}$-type clusters show a topological relationship with the NaCl-type structure thus following the general remark that rocksalt is everywhere.[3] The Z atoms replace a fraction of the X atoms on the anion positions, whereas Ln atoms and voids are located on the cation positions, and all Z atoms are surrounded by six Ln neighbors. The ratio Ln/Z determines the degree of cluster condensation with the maximum value of 6 for phases with discrete $Ln_6ZX_{12}$ clusters as in $Zr_6CI_{12}$[4] and decreased ratios for the condensed cluster phases, e.g. Ln/Z = 5 for $La_{10}(C_2)_2I_{18}$[5] containing double octahedra. As a rule, neighboring $Ln_6$ octahedra are connected via edges both in ordered and disordered phases. Well-documented examples for the first are the triple $Ln_{14}$ octahedra in $Ln_{14}(C_2)_3I_{20}$ (Ln = La, Ce; Ln/Z = 4.67)[6] and the linear chain of octahedra found in $Sc_4CCl_6$ (Ln/Z = 4).[7] Examples for the latter are $Ln_{13}B_3Br_{18}$ (Ln = Gd, Tb)[8] and $Ce_{29}Al_{14}I_{28}$[9] where discrete $Ln_{10}$ double octahedra are ordered in layers which, however, exhibit stacking disorder. The disordered intergrowth phases $Ln_{4n+2}(C_2)_nI_{5n+5}$[10] contain layers of linear oligomers with distinct numbers (*n*) of condensed octahedra.

Recently, we analyzed the connectivity of clusters in the highly disordered phase $La_{0.70}(Al_{0.14}I_{0.86})$ (**1**)[11] with average NaCl-type structure. Here, we report on $La_{0.70}(Al_{0.12}I_{0.88})$ (**2**) which is the first partially ordered cluster phase occurring in the system La–Al–I. In the context of the following, the structure of $Gd_3CCl_3$[12] is of particular importance ($Ca_3PI_3$-type,[13] $I4_132$). Each octahedron of the latter is connected to three neighboring ones; see Figure 1, producing a characteristic quadratic or hexagonal pattern of clusters in projections along <100> and

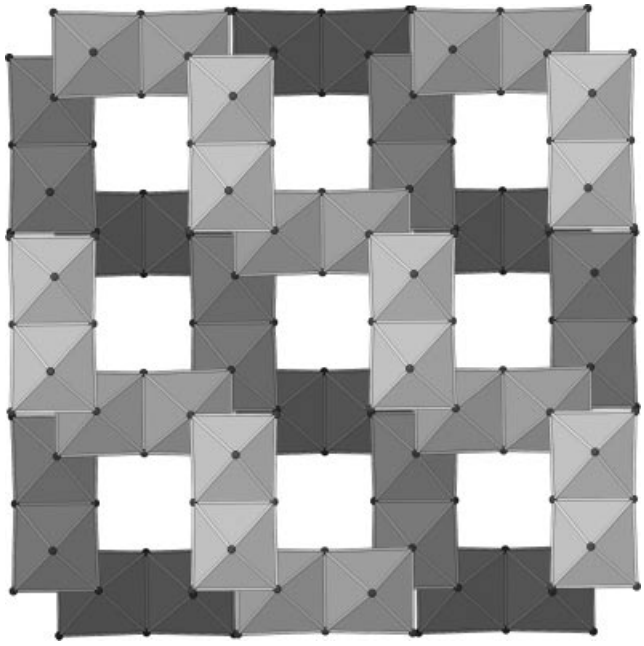

Figure 1. $CGd_6$ clusters in the structure of $Gd_3CCl_3$ along <100>, Cl atoms are omitted.

[a] Max-Planck-Institut für Festkörperforschung
Heisenbergstrasse 1, 70569 Stuttgart, Germany
Fax: +49-711-6891091
E-mail: L.Kienle@fkf.mpg.de
[b] Department Chemie und Biochemie der Ludwig-Maximilians-Universität
Butenandtstrasse 5–13(D), 81377 München, Germany
[c] Laboratorium für Kristallographie, ETH Hönggerberg
Wolfgang-Pauli-Strasse 10, 8093 Zürich, Switzerland

 © 2007 Wiley-VCH Verlag GmbH & Co. KGaA, Weinheim 

<111>, respectively. All known representatives of this structure type, including distorted ones,[14] are fully ordered.

## Results and Discussion

Despite the highly disordered real structure, neighboring clusters in **1** are far from a random arrangement. A structure refinement based on the intensity of the diffuse X-ray scattering had allowed the evaluation of relative cluster positions, indicating the presence of edge-condensed $La_6$ octahedra as expected from the ratio Ln/Z = 5, however, only as a small fraction. Crystals of **1** exhibit halo-shaped diffuse scattering around the Bragg reflections of electron and X-ray diffraction patterns. The new variant, **2** shows a segregation of the diffuse scattering into superstructure reflections indicating partial long-range ordering. The different degrees of structural disorder in **1** and **2** are exemplified by the SAED (selected area electron diffraction) patterns and electron micrographs of Figure 2. Both crystals were aligned along zone axis <111>, referring to the common NaCl-type subcell. The high resolution image for **1** (Figure 2, a) shows a strongly disordered, but non-random arrangement of dark and bright spots. The interpretation by simulated micrographs is based on the structural model derived from the diffuse X-ray scattering.[11] For $\Delta f \approx -70$ nm, low values of the projected potential produce dark spots, corresponding to the preferred cluster arrangement which leads to a superposition of Al atoms and voids along <111>, and bright spots represent high values of the projected potential resulting from <111> rows of La and I atoms. Following this analysis, **1** is characterized by pronounced correlations of the cluster positions. The interrelation of projected potential and image contrast is straightforward for all defocus values not only for Scherzer focus. The preferred cluster arrangement of **1** is imaged in the form of dark spots each surrounded by a hexagon of bright spots. Such hexagons can be seen in Figure 2 (a) bottom (see marks), however, they do not produce a periodic pattern due to the lack of perfect long range order in **1**. This contrasts the partially ordered crystallites of **2**, where ordering of the hexagons in {111} is observed, see Figure 2 (b) bottom. At the first glance, the HRTEM image seems to be entirely periodic, however, significant variations of the spot intensities are evident which disrupt the periodicity. In some cases, the partial order can also be demonstrated by faint diffuse intensities in Fourier transforms of HRTEM micrographs as seen in the electron-diffraction patterns (see Figure 2, b, top). SAED as well as corresponding zero layer X-ray patterns, like those along <100>, exhibit hardly any diffuse scattering. However, this observation does not unambiguously indicate long-range order of the 3D real structure, but a low significance of the disorder in the respective projection. A tilt from the precise zone axis orientation enables one to observe the diffuse intensity, and the existence of disorder becomes evident.

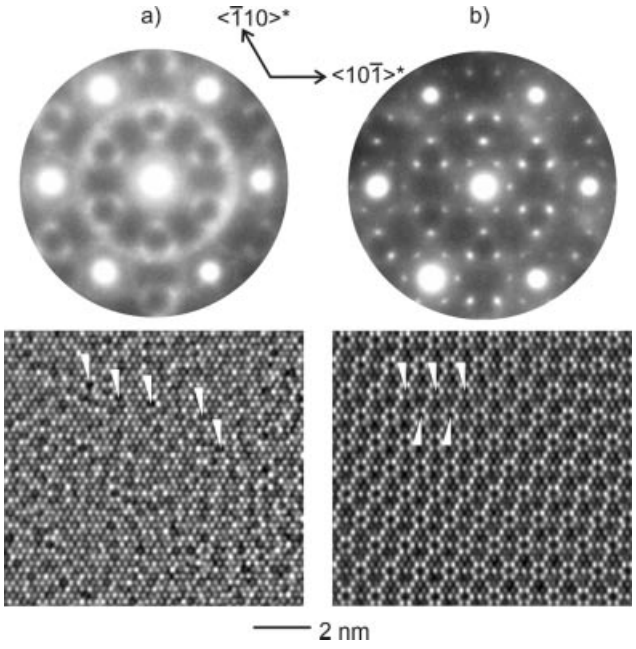


Figure 2. SAED pattern and HRTEM micrograph ($\Delta f \approx -70$ nm) for zone axis <111> recorded on a crystal of **1** (a), and **2** (b).

Such findings were the starting points for an interpretation of HRTEM micrographs and the corresponding SAED patterns of **2** in terms of the 3D structure, and they also entered the X-ray structure analysis. Two important aspects, the chemical composition and an average model need to be taken into account in order to derive a 3D structure of **2** before the real structure can be analyzed in detail. In order to elaborate the specific benefits, the information obtained by both approaches will be asserted separately first and then combined in the conclusion.

### Chemical Composition of 2

The chemical composition of **2** was determined by combining SAED and EDX. Both techniques allow nanoprobing and identification, whereas chemical analyses of probably inhomogeneous bulk samples are likely to fail due to averaging. The experimentally determined composition of $La_3I_3Al_2$,[15] taken as the standard, indicates only marginal correction factors as the average of 10 point measurements on 10 crystallites gave La 42.9(1.9) atom-%, Al 28.7(1.4) atom-% and I 28.4(1.0) atom-% (calculated values: 43.0 atom-%, 28.5 atom-%, 28.5 atom-%). For **2** we determined La 41.2(2.6) atom-%, Al 7.1(0.5) atom-% and I 51.7(2.9) atom-% (average of 7 point measurements on 7 crystallites), resulting in a composition $La_{0.70(4)}(Al_{0.12(1)}I_{0.88(5)})$. Point measurements on different regions of the same crystallite lead to variations of the composition within standard deviations.

### Symmetry of 2

X-ray measurements on single crystals of **2** yield an average unit cell with cubic metrics. A small amount of dif-

 © 2007 Wiley-VCH Verlag GmbH & Co. KGaA, Weinheim 

fuse scattering is present. The lattice parameter $a$ = 12.689(1) Å corresponds to a $2a2b2c$ supercell of the NaCl-type structure. This supercell has the Laue symmetry $m\bar{3}m$ and is body-centered. Reflections $h00$ are observed only for $h = 4n$, so the resulting space group is $I4_132$. As even small homogeneous selected areas of the crystallites yield tilting series of SAED patterns consistent with this symmetry, it is clear that the high symmetry is not due to twinning by (pseudo)-merohedry or reticular pseudo-merohedry (e.g. tetragonal with $c' = 2a$). Neither electron nor X-ray diffraction gave any indication of an even larger or not body-centered cell of **2**. Furthermore, the plane symmetry of electron micrographs ($p4mm$ for <100>, $p3m1$ for <111>, $p2mm$ for <110>, cf. Figure 5) in combination with the body-centered lattice is only allowed for the space groups $I432$ and $I4_132$.

### Structure Refinement from X-ray Data

For the structure refinement on the basis of X-ray data, diffuse scattering was not taken into account. As both the unit cell parameters and the space group $I4_132$ correspond to the $Gd_3CCl_3$ type,[12] initial refinements were started from an isotypic and hypothetical $La_3I_3Al$, although the chemical analysis contradicts this composition. The resulting $R$ value ($R_1$ = 0.21) was not convincing and the small displacement parameter of Al called for a mixed occupancy of this site by Al and I which was refined to an approximate ratio of 1. Hence, the structure contains only half the amount of $La_6Al$ units as compared to "$La_3I_3Al$". This does not necessarily lead to a lower La content, because all La atoms in the latter structure type belong to two $La_6$ octahedra. However, refining the occupancy of the La position yields a value of 87%. The model so far is only an approximation as residual electron density is found in the unoccupied octahedral voids of the $Gd_3CCl_3$ type, corresponding to ca. 15% occupancy with La. This means that a few cluster centers do not coincide with positions of the $Gd_3CCl_3$-type. Thus, the structure of **2** can be described as an approximately 50% thinned out variant of this structure type with many shared edges remaining and a few alternative cluster positions occupied. The $R$ values (e.g. $R_1$ = 0.044) for this structure model are satisfactory, in particular as the reflections to parameters ratio is 26 in spite of some disorder. The refinement in $Im\bar{3}m$ yields about the same $R$ values, however, the degree of disorder is higher and no centrosymmetric structure model can explain the $p3m1$ symmetry of electron micrographs for the <111> zone axis, where one would expect a $p6mm$ symmetry which is clearly absent, cf. Figure 5. For $I432$ which is consistent with the symmetry observed in HRTEM but not with all systematic absences, refinements yield a higher degree of disorder, too. Thus, the structure model derived from "$La_3I_3Al$" gives the best fit of the data with the highest degree of ordering. Based on the model assumptions, this refinement yields the chemical composition $La_{0.69}(I_{0.88}Al_{0.12})$ for **2** in good agreement with chemical analyses. Details are presented in Table 1, atomic parameters in Table 2.

Table 1. Crystal data of **2**.

| Formula | $La_{0.69(1)}(Al_{0.12(1)}I_{0.88(1)})$ |
|---|---|
| Formula weight | 210.75 [g mol$^{-1}$] |
| Crystal system | cubic |
| Space group | $I4_132$ (no. 214) |
| Diffractometer type | Stoe IPDS II |
| Radiation $\lambda$ | 0.71073 Å (Mo-$K_\alpha$) |
| Crystal size | 0.15 × 0.12 × 0.08 mm |
| Lattice parameter | $a$ = 12.689(1) Å |
| Cell volume | 2043.1(3) Å$^3$ |
| Formula units $Z$ | 32 |
| $\rho_{calcd.}$ | 5.481 g cm$^{-3}$ |
| $F(000)$ | 2800.7 |
| $\mu$ | 21.94 mm$^{-1}$ |
| Temperature | 295(2) K |
| $\theta$ range | 2.2°–30° |
| Reflections measured/observed [$F_o^2 \geq 2\sigma(F_o^2)$] | 10634/9055 |
| Independent reflections | 505 [$R_{int}$ = 0.062] |
| Absorption correction | numerical |
| Min./max. transmission | 0.086/0.293 |
| Number of refined parameters/restraints | 19/0 |
| Goodness of fit | 1.14 |
| $R_1/wR_2$ (all data) | 0.052/0.117 |
| $R_1/wR_2$ [$F_o^2 \geq 2\sigma(F_o^2)$] | 0.044/0.112 |

### Structure Information from Electron Microscopy

In an independent approach, the combination of HRTEM and SAED served to derive structure models and to analyze structural defects of **2**. Particularly for the <111> zone axes, the HRTEM micrographs indicate a separation into high and low values of the projected potential, see text above as well as Figure 3, consistent with a disordered arrangement of clusters in a thinned out $Gd_3CCl_3$-type structure. The triangles highlight regions with high and low cluster concentration, and the corresponding triangles

Table 2. Atom positions and displacement parameters (in Å$^2$) for **2** and comparison with the ordered $Gd_3CCl_3$ structure type.

| Atom | Wyck. | $x$ | $y$ | $z$ | Occ. | $U_{iso}$ | $U_{11}$ | $U_{22} = U_{33}$ | $U_{23}$ | $U_{13}$ | $U_{12}$ | Occ. in $Gd_3CCl_3$ |
|---|---|---|---|---|---|---|---|---|---|---|---|---|
| La1 | 24*g* | 1/8 | 0.11684(5) | $y$ + 1/4 | 0.870(4) | 0.0345(4) | 0.0301(4) | 0.0367(4) | –0.0114(4) | 0.0014(2) | $-U_{13}$ | 1 Gd |
| La2 | 8*b* | 7/8 | 7/8 | 7/8 | 0.15(1) | 0.104(9) | 0.104(9) | $U_{11}$ | 0.034(10) | $U_{23}$ | $U_{23}$ | 0 |
| I1 | 24*h* | 1/8 | 0.38225(5) | $-y$ + 1/4 | 1[a] | 0.0360(4) | 0.0293(4) | 0.0394(4) | 0.0065(4) | 0.0013(2) | $U_{13}$ | 1 I |
| I/Al | 8*a* | 1/8 | 1/8 | 1/8 | 0.525(8) I<br>0.475(8) Al | 0.0375(8) | 0.0375(8) | $U_{11}$ | –0.0123(6) | $U_{23}$ | $U_{23}$ | 1 C |

[a] Due to the presence of La2 atoms, a small fraction of this position is likely to be occupied by Al, however, this was not significant in refinements.

 © 2007 Wiley-VCH Verlag GmbH & Co. KGaA, Weinheim 

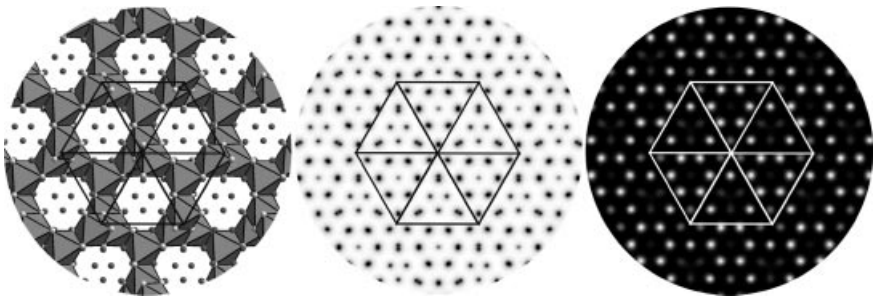

Figure 3. Correlation between projected potential based on the structure model of **2** (see text) and simulated micrograph for <111> ($\Delta f$ = –70 nm, $t$ = 3.5 nm). From left to right: projection of the structure model, projected potential, simulated micrograph. The triangles highlight regions with high and low cluster concentration.

in the projected potential and in the simulated micrograph give evidence for the experimental significance of such distribution.

In order to check the spatial 3D distribution of the clusters, all fundamental zone axes were investigated in an extended study. Neglecting faint diffuse intensities, experimental and calculated SAED patterns display a convincing agreement for different crystallites (see Figure 4). In addition tilting experiments performed on the same crystallite support the proposed model. As shown by simulations, aggregates of clusters could be identified by SAED and HRTEM; however, the lack of such correlations corresponds to the observed marginal diffuse intensity. Hypothetical structure models of a thinned out and ordered $Gd_3CCl_3$-type structure were also taken into account. Based on group-subgroup relations several ordering variants are possible, like a hypothetical phase $La_5AlI_7$ which would contain discrete clusters with edge-sharing double octahedral units. However, such orderings were never observed, even not in nanosized domains.

HRTEM gave additional evidence for the structure of **2**, as demonstrated by the simulated and experimental micrographs of Figure 5. However, a perfect match with simulations is impossible as the averaging is never complete for the transmittable regions of the crystallites. Of course, in very thin regions of the crystallites even an overall disordered distribution of clusters should separate into discernible aggregates. However, in the case of the extremely air-sensitive **2** those regions are already the subject of hydrolysis.

The real structure of **2** is further complicated by the presence of different domains. Firstly, **2** exhibits merohedrally twinned domains and antiphase boundaries, see relative positions of the high- and low intensity spots within the triangles of Figure 6. As the intensity of the spots correlates with the cluster concentration (cf. Figure 3 and Figure 5, bottom), domains with an inverted and shifted (bottom region of Figure 6) and a merely shifted arrangement of the clusters (top region of Figure 6) coexist. The diffraction patterns as well as Fourier transforms of HRTEM micrographs show a complete overlap of the reciprocal lattices for the different domains. Space-averaging of the cluster positions in different domains smaller than the X-ray coherence length could easily explain the detection of clusters on non-cluster positions of the thinned out $Gd_3CCl_3$-type as determined by XRD.

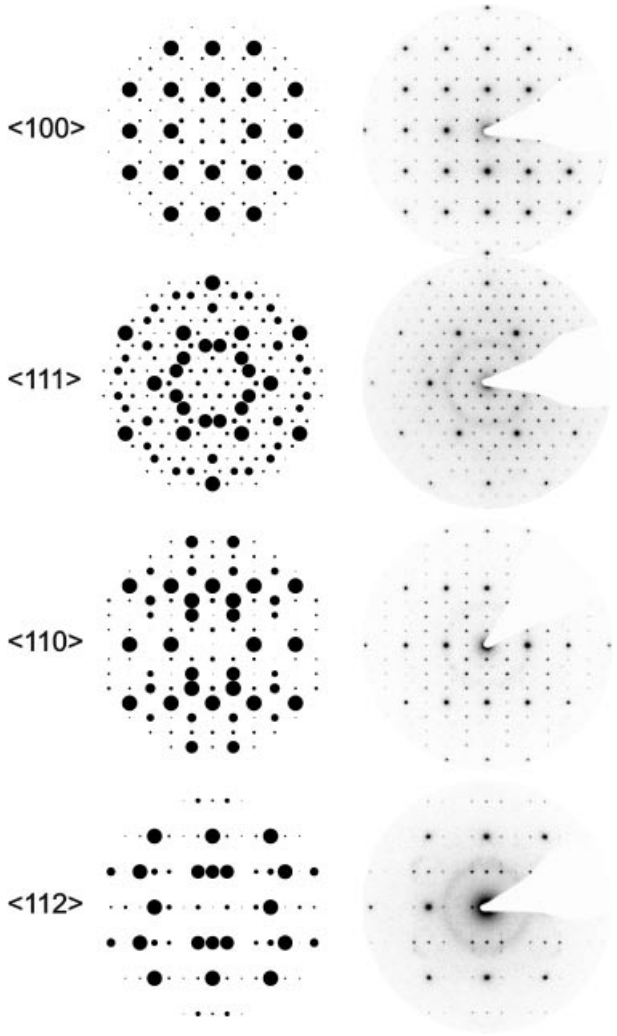


Figure 4. Calculated (left column) and experimental (right column) SAED patterns, zone axes are specified.

Secondly and more rarely, domains of **2** coexist with the domains of a byproduct. The intergrowth can easily by identified by sequentially recorded SAED patterns or the

 © 2007 Wiley-VCH Verlag GmbH & Co. KGaA, Weinheim 

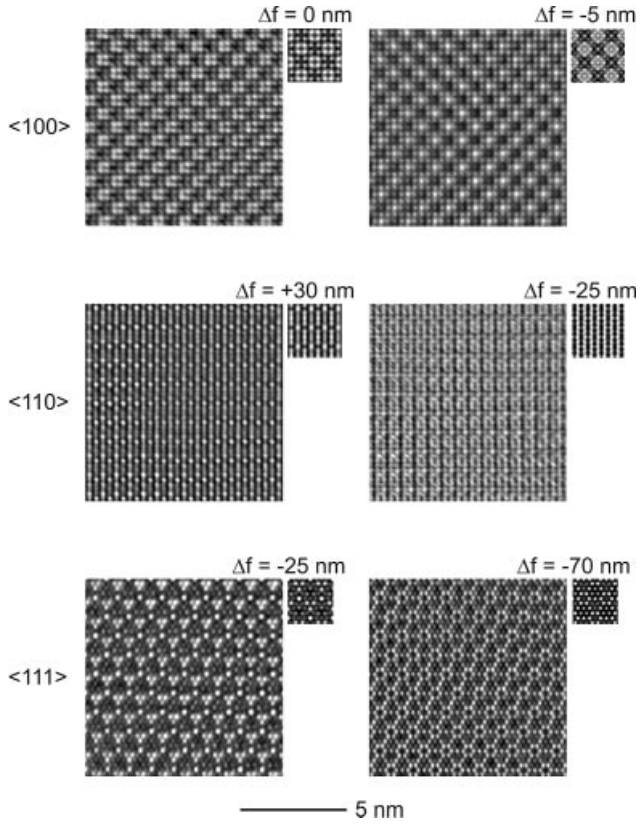


Figure 5. Experimental HRTEM micrographs with simulations for distinct zone axes and defocus values ($t$<100> = 6.3 nm, $t$<110> = 5.4 nm and $t$<111> = 4.4 nm).

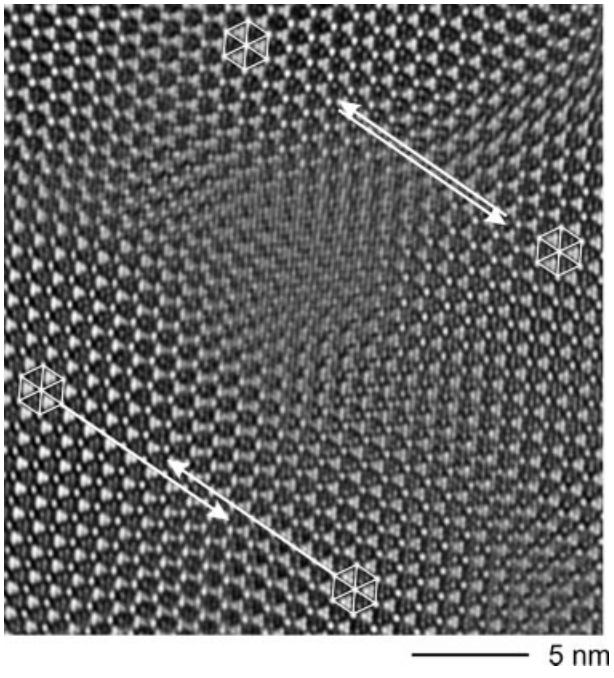


Figure 6. Twin domains (bottom region) and antiphase domains (top region) in **2**. The arrows indicate the shift of the domains.

corresponding superposition patterns, see Figure 7 (a). So far, the composition of the byproduct could not be analyzed reliably by EDX due to shading effects. The *d*-values and intensity distribution of the SAED patterns of the byproduct suggest a phase $La_{7+x}AlI_{12}$ related to $Sc_7CI_{12}$.[16] Furthermore, some crystallites of the byproduct exhibit the characteristic twinning frequently observed for phases $Ln_{7+x}ZX_{12}$, see superposition pattern in Figure 7 (b). In addition, an intergrowth of this phase and strongly disordered **1** occurs as demonstrated by the characteristic diffuse scattering in the SAED superposition pattern of Figure 7 (c). Hence, the byproduct forms intergrowth phases with both, the chemically related **1** and **2**.

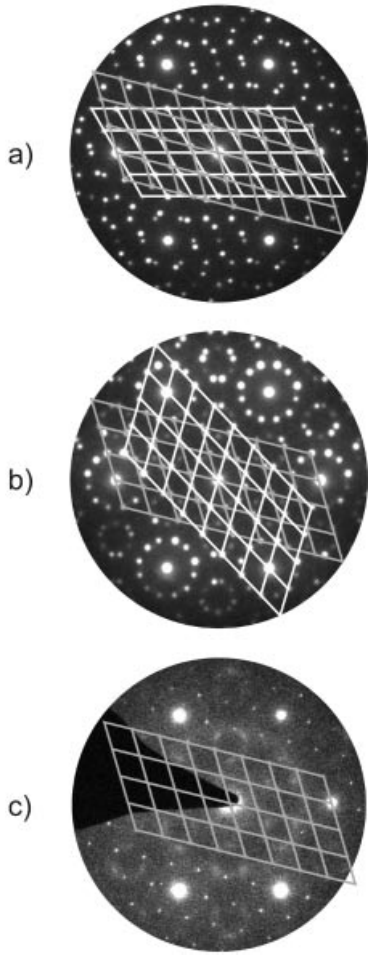


Figure 7. Distinct types of superposition patterns with the common zone axis <111> of **2**. a) Chemical intergrowth of **2** and the byproduct, b) twinning of the byproduct, c) intergrowth of the byproduct and **1**. The grey grids mark the unit cell of the byproduct.

## Conclusions

Conventional electron microscopy techniques allow the simultaneous determination of structure and composition of crystals on the nanoscale, however, they do not provide the precise localization of atoms as X-ray diffraction techniques do. Hence, a combined approach is of great value. The structural model for $La_{0.69(1)}(Al_{0.12(1)}I_{0.88(1)})$ determined from electron microscopy was used as the input for an accurate X-ray structure refinement. As X-ray data are

 © 2007 Wiley-VCH Verlag GmbH & Co. KGaA, Weinheim 

greatly influenced by averaging effects peculiarities of the refined model were then addressed and explained by local investigations in the electron microscope. The strongly disordered phase **1** and the partially ordered phase **2** are close in composition. As expected, they share certain structural properties, however, there are also distinctly different features. Both, the structures of **1** and **2** contain $La_6AlI_{12}$ clusters which are interconnected via I atoms in a rather defined way in spite of the disorder. **1** is arrived at by a systematic cation (La) depletion of a NaCl-type structure leaving the majority of $La_6$ units in an as far as possible distance from each other. One way of an ordered depletion follows the group-subgroup relation:

$Fm\bar{3}m$ ("Na": *4a*, "Cl": *4b*) $\xrightarrow{t2}$ $F432$ $\xrightarrow{k4}$ $P4_232$ $\xrightarrow{k4,\ a' = 2a}$ $I4_132$ (either La: *24h*, X: *24g*, □: *8a*, Z: *8b*, or La: *24g*, X: *24h*, □: *8b*, Z: *8a*) ending in the $Gd_3CCl_3$-type structure where close contacts between the metal atoms through edge-sharing of the $Ln_6$ units are still preserved. In the structure of **2**, this characteristic feature stays when the $Gd_3CCl_3$-type structure is further thinned out. Hence, the step from **1** via **2** to a $Gd_3CCl_3$-type structure marks a pathway from a discrete to a condensed cluster phase. As we were not able to change **1** into **2** by extended annealing, it still has to be elucidated which experimental parameters (composition, reaction temperature, etc.) lead along this pathway.

## Experimental Section

**Synthesis:** Powder samples of **2** were prepared by reaction of 500 mg $LaI_3$, 235 mg $AlI_3$ and 327 mg La (molar ratio La/Al/I = 18:3:24), pressed to pellets and heated 7 d at 870 °C in closed Ta-capsules.[17] After that the samples were ground and again heated at 900 °C for 8 d. From this batch the crystals were selected for X-ray and HRTEM investigations. All handlings were performed under inert (Ar) gas atmosphere.[18]

**X-ray Crystallography:** Powder diffractograms were recorded by modified Guinier technique[19] on fine powders sealed in glass capillaries (Cu-$K_{\alpha 1}$, Si as internal standard, Fuji™ film BAS-5000 image plate system). The lattice parameter of the NaCl-type subcell of **2** was determined to $a = 6.326(1)$ Å. Single-crystal X-ray data were collected on a STOE IPDS diffractometer (Mo-$K_\alpha$ radiation). The program package X-Area 1.18 (Stoe, Darmstadt, 2002) was used for data evaluation, SHELX97 was used for structure solution and refinement.[20] Further details of the crystal structure investigation can be obtained from the Fachinformationszentrum Karlsruhe, 76344 Eggenstein-Leopoldshafen, Germany (Fax: +49-7247-808-666; E-mail: crysdata@fiz-karlsruhe.de) on quoting the depository number CSD-417290.

**Electron Microscopy and Chemical Analysis:** HRTEM and SAED were performed with a Philips CM30ST microscope (300 kV, $LaB_6$ cathode, $C_S = 1.15$ mm). All manipulations for the preparation and transfer of the sample were carried out under dry argon by applying Schlenk techniques.[21] A perforated carbon/copper net served as support of the crystallites. Simulations of HRTEM images (multislice formalism) and of SAED patterns (kinematical approximation) were calculated with the EMS program package[22] (spread of defocus: 70 Å, illumination semiangle: 1.2 mrad). All images were recorded with a Gatan Multiscan CCD camera and evaluated (including Fourier filtering) with the program Digital Micrograph 3.6.1 (Gatan). Chemical analyses by EDX were performed in the nanoprobe and in the scanning mode of CM30ST with a Si/Li detector (Noran, Vantage System).

## Acknowledgments

The authors thank R. Eger for the preparation of many samples.

[1] A. Simon, *Angew. Chem.* **1981**, *93*, 23; *Angew. Chem. Int. Ed. Engl.* **1981**, *20*, 1.
[2] a) A. Simon, Hj. Mattausch, G. J. Miller, W. Bauhofer, R. K. Kremer, in: *Handbook on the Physics and Chemistry of Rare Earths*, vol. 15 (Eds.: K. A. Gschneidner, L. Eyring), Elsevier Science Publ., Amsterdam, London, New York, Tokyo, **1991**, p. 191; b) J. D. Corbett, *J. Chem. Soc., Dalton Trans.* **1996**, 575; c) G. Meyer, *Chem. Rev.* **1988**, *88*, 93–107; d) A. Simon, Hj. Mattausch, M. Ryazanov, R. K. Kremer, *Z. Anorg. Allg. Chem.* **2006**, *632*, 919.
[3] H. G. v. Schnering, *Angew. Chem.* **1981**, *93*, 44; *Angew. Chem. Int. Ed. Engl.* **1981**, *20*, 33.
[4] J. D. Smith, J. D. Corbett, *J. Am. Chem. Soc.* **1985**, *107*, 5704.
[5] E. Warketin, R. Masse, A. Simon, *Z. Anorg. Allg. Chem.* **1982**, *491*, 323.
[6] Hj. Mattausch, A. Simon, L. Kienle, C. Hoch, C. Zheng, R. Kremer, *Z. Anorg. Allg. Chem.* **2006**, *632*, 1661.
[7] S.-J. Hwu, J. D. Corbett, *J. Solid State Chem.* **1986**, *64*, 331.
[8] O. Oeckler, L. Kienle, Hj. Mattausch, A. Simon, *Angew. Chem.* **2002**, *114*, 4431; *Angew. Chem. Int. Ed.* **2002**, *41*, 4257.
[9] O. Oeckler, Hj. Mattausch, A. Simon, *Z. Anorg. Allg. Chem.* **2005**, *631*, 3013.
[10] a) L. Kienle, Hj. Mattausch, A. Simon, *Angew. Chem.* **2006**, paper accepted for publication; b) O. Oeckler, Hj. Mattausch, A. Simon, *Z. Anorg. Allg. Chem.* **2005**, *631*, 3013.
[11] O. Oeckler, T. Weber, L. Kienle, Hj. Mattausch, A. Simon, *Angew. Chem.* **2005**, *117*, 3985; *Angew. Chem. Int. Ed.* **2005**, *44*, 3917.
[12] E. Warkentin, A. Simon, *Rev. Chim. Min.* **1983**, *20*, 488.
[13] C. Hamon, R. Marchand, Y. Laurent, J. Lang, *Bull. Soc. Fr. Min. Crist.* **1974**, *97*, 6.
[14] C. Zheng, O. Oeckler, Hj. Mattausch, A. Simon, *Z. Anorg. Allg. Chem.* **2001**, *627*, 2151.
[15] Hj. Mattausch, O. Oeckler, C. Zheng, A. Simon, *Z. Anorg. Allg. Chem.* **2001**, *627*, 1523.
[16] D. S. Dudis, J. D. Corbett, S.-J. Hwu, *Inorg. Chem.* **1986**, *25*, 3434.
[17] Hj. Mattausch, W. Schramm, R. Eger, A. Simon, *Z. Anorg. Allg. Chem.* **1985**, *530*, 43.
[18] K. Ahn, B. J. Gibson, R. K. Kremer, Hj. Mattausch, A. Stolovitz, *J. Phys. Chem. B* **1999**, *103*, 5446.
[19] A. Simon, *J. Appl. Crystallogr.* **1979**, *3*, 11.
[20] G. M. Sheldrick, SHELX97, Program package for the solution and refinement of crystal structures, Release 97–2, University of Göttingen, Germany, **1997**.
[21] P. Jeitschko, A. Simon, R. Ramlau, Hj. Mattausch, *Eur. Microscopy Microanal.* **1997**, *46*, 21.
[22] P. A. Stadelmann, *Ultramicroscopy* **1987**, *21*, 131.

Received: December 20, 2006
Published Online: March 16, 2007

 © 2007 Wiley-VCH Verlag GmbH & Co. KGaA, Weinheim 

DOI: 10.1002/ejic.200700043

# Tungsten(VI) and Molybdenum(VI) Complexes with Soft Thioether Ligand Coordination – Synthesis, Spectroscopic and Structural Studies

**Martin F. Davis,[a] William Levason,[a] Mark E. Light,[a] Raju Ratnani,[b] Gillian Reid,*[a] Keerti Saraswat,[b] and Michael Webster[a]**

**Keywords:** Tungsten / Thioether / Molybdenum

Reaction of $WX_6$ (X = Cl or Br) with $O(SiMe_3)_2$ in $CH_2Cl_2$, followed by addition of MeCN and a further equivalent of $O(SiMe_3)_2$ in $CH_2Cl_2$ gives $[WO_2X_2(MeCN)_2]$ in situ, which subsequently react with the dithioethers $MeS(CH_2)_2SMe$, $iPrS(CH_2)_2SiPr$ or 1,4-dithiane to afford the first series of $W^{VI}$ thioether complexes, $[WO_2X_2(dithioether)]$. The very moisture-sensitive yellow complexes have been characterised by microanalysis, IR, $^1H$ and $^{13}C\{^1H\}$ NMR spectroscopy, which indicate *cis*-dioxido and *trans*-dihalide arrangements in the monomers with two thioether donor atoms completing the very distorted octahedral geometry (confirmed by a crystal structure of $[WO_2Cl_2\{iPrS(CH_2)_2SiPr\}]$). The strongly polymerised $WO_2X_2$ compounds themselves are not useful synthons for the preparation of the $W^{VI}$ thioether complexes and substitution of the dimethoxyethane ligand in $[WO_2Cl_2\{MeO(CH_2)_2OMe\}]$ by dithioethers is also incomplete. Molybdenum(VI) dioxidodichloride thioether complexes of the form $[MoO_2Cl_2(L)]$ (L = $iPrS(CH_2)_2SiPr$, 1,4-dithiane, $\kappa^2$-[15]ane$S_2O_3$, $\kappa^2$-[14]ane$S_4$ and $\kappa^2$-[12]ane$S_4$) ([15]ane$S_2O_3$ = 1,4-dithia-7,10,13-trioxacyclopentadecane, [14]ane$S_4$ = 1,4,8,11-tetrathiacyclotetradecane, [12]ane$S_4$ = 1,4,7,10-tetrathiacyclododecane) and the unusual dinuclear $[Mo_2O_4Cl_4\{o\text{-}C_6H_4(CH_2SMe)_2\}_2]$ are obtained by direct treatment of $MoO_2Cl_2$ with the appropriate ligand. The $[Mo_2O_4Cl_4\{o\text{-}C_6H_4(CH_2SMe)_2\}_2]$ adopts an unexpected metallocyclic structure with *cis*-$MoCl_2$ units and bridging bidentate dithioether (confirmed crystallographically). The structure of a new polymorph of $[WO_2Cl_2\{MeO(CH_2)_2OMe\}]$ is also described.

(© Wiley-VCH Verlag GmbH & Co. KGaA, 69451 Weinheim, Germany, 2007)

## Introduction

While thioether coordination chemistry is dominated by complexes involving late transition metals in medium oxidation states, we and others have shown that under appropriate experimental conditions these soft and modest σ-donor ligands can also form complexes with hard, medium and high oxidation state early transition metal ions,[1] including for example $Sc^{III}$,[2] $La^{III}$ and $U^{III}$ [3] complexes with the trithioether macrocycle [9]ane$S_3$, and $Ti^{IV}$, $Zr^{IV}$, $Hf^{IV}$, $V^{III,IV}$ and $Cr^{III}$ complexes with both acyclic and macrocyclic thioethers.[4–7] We have also established that the choice of chalcogenoether ligand architecture plays a very important role in facilitating the stabilisation of these hard/soft metal/ligand combinations, with dimethylene-linkages between the S atoms leading to increased stability, and macrocyclic frameworks further stabilising the complexes. Further, we have shown that reaction of $Ti^{IV}$, $Cr^{III}$ and $V^{III}$ precursors with mixed thia-oxa macrocyclic ligands involving $C_2$-linkages between adjacent heteroatoms results in preferential coordination via the softer S-donor groups – an observation we have attributed to destabilisation of the M–O(ether) coordination due to ring strain in the five-membered chelate rings.[8,9]

The coordination chemistry of molybdenum and tungsten continues to attract considerable interest owing to the roles that these elements play in biologically important species, the molybdo- and tungsto-enzymes,[10] and also due to the use of high oxidation state Mo and W species in ring-opening metathesis catalysis.[11] The chemistry of medium and high oxidation state Mo centres with neutral sulfur donor ligands remains little studied, with some examples of $Mo^{III,IV,V}$ thioether complexes.[12–19] In 2004 we reported the preparations and spectroscopic characterisation of the first examples of $Mo^{VI}$ complexes involving thioether and selenoether coordination, including crystal structure determinations of representative examples of the form $[MoO_2X_2\{RS(CH_2)_2SR\}]$ (X = Cl or Br; R = Me or Et) which confirmed *cis*-oxido ligands, *trans*-halides and bidentate chelating dithioether.[20] We found that these species form only for a very limited range of dichalcogenoether ligands – $Me_2S$, $MeS(CH_2)_3SMe$, MeSCH=CHSMe and even the $PhS(CH_2)_2SPh$ all lead to reduction of the metal and give no evidence for $Mo^{VI}$ thioether complexes. Medium and high oxidation state tungsten thioether complexes

[a] School of Chemistry, University of Southampton, Southampton SO17 1BJ, UK
E-mail: g.reid@soton.ac.uk
[b] Department of Pure and Applied Chemistry, M. D. S. University, Ajmer 305009, India

 © 2007 Wiley-VCH Verlag GmbH & Co. KGaA, Weinheim 

are even less explored than with molybdenum and, whereas direct reaction of $MoO_2X_2$ with the $RS(CH_2)_2SR$ (R = alkyl) in $CH_2Cl_2$ gives the requisite complexes, $WO_2X_2$ (X = Cl or Br) do not provide viable entries to this chemistry because they are unreactive and strongly polymerised.[21] We were interested in trying to extend the range of thioether and selenoether complexes of the hard, oxophilic $Mo^{VI}$ ion, to understand how the ligand donor properties and architecture influence the stability of the complexes, and also in developing synthetic routes to $W^{VI}$ analogues.

In order to investigate the chemistry of dioxidotungsten(VI) with thioether ligands and to widen the presently very limited range of thioether ligand types capable of coordinating to dioxidomolybdenum(VI), we report here the results of our studies on the preparations and properties of the first series of $W^{VI}$ dihalidedioxido complexes involving dithioether ligands and several new $Mo^{VI}$ dihalidedioxido complexes incorporating a range of ligand architectures and both thioether and mixed thia/oxa-macrocyclic ligands. The crystal structures of $[Mo_2O_4Cl_4\{o\text{-}C_6H_4(CH_2SMe)_2\}_2]$, $[WO_2Cl_2\{i\text{PrS}(CH_2)_2S i\text{Pr}\}]$ and a new polymorph of $[WO_2Cl_2\{MeO(CH_2)_2OMe\}]$ are reported and discussed.

## Results and Discussion

### Tungsten Thioether Complexes

Development of a synthetic route to give $W^{VI}$ complexes in respectable yields is much more difficult than for $Mo^{VI}$. The strongly polymerised nature of $WO_2Cl_2$[21] means that this is usually not a useful synthon for coordination complexes of $WO_2Cl_2$, hence alternative precursor compounds were sought. We have shown very recently that $WCl_6$ or $WBr_6$ react with two mol. equivs. of $O(SiMe_3)_2$ in $CH_2Cl_2$, followed by addition of two mol. equivs. of $OPR_3$ (R = Pr or Me) or one molar equivalent of $Ph_2P(O)(CH_2)_nP(O)Ph_2$ ($n$ = 1 or 2) or $o\text{-}C_6H_4(P(O)Ph_2)_2$, to give the distorted octahedral $[WO_2X_2(OPR_3)_2]$, $[WO_2X_2\{Ph_2P(O)(CH_2)_nP(O)Ph_2\}]$ or $[WO_2X_2\{o\text{-}C_6H_4(P(O)Ph_2)_2\}]$ respectively in good yields.[22] However, using this approach with $MeS(CH_2)_2SMe$ in place of the $OPR_3$ ligand gave mostly insoluble, polymeric $WO_2Cl_2$ (IR evidence) with only very weak bands in the IR spectrum corresponding to $[WO_2Cl_2(\text{dithioether})]$. We conclude from this that soft thioether ligands have less affinity for the hard $W^{VI}$ and are more dissociated in solution than the phosphane oxide complexes of $W^{VI}$, hence while the phosphane oxide "traps" the $WO_2Cl_2$ as a molecular complex, in the thioether ligand systems $(WO_2Cl_2)_n$ precipitates from the solution, removing it from the reaction.

Schulzke et al. have described the preparation of the only known thioether adduct of $W^{VI}$, $[WO_2Cl_2\{MeS(CH_2)_2SMe\}]$ by a closely related route, involving reaction of $WOCl_4$ with one molar equivalent of $O(SiMe_3)_2$ in $CH_2Cl_2$ solution, followed by addition of the dithioether. While the crystal structure of the distorted octahedral species was reported, no solution spectroscopic data were presented.[23] We have also investigated this reaction and in our hands it reproducibly leads to formation of a white solid which was very poorly soluble. While weak ν(W=O) and ν(W-Cl) bands consistent with the literature data were evident in the IR spectra of these products, strong, broad absorptions around 600–700 $cm^{-1}$ were also evident, which are indicative of polymeric $WO_2Cl_2$. The $^1H$ NMR spectra of the $CDCl_3$ soluble component of our reaction products from repeated attempts at this reaction consistently showed significant amounts of uncoordinated dithioether, and only very minor resonances for $[WO_2Cl_2\{MeS(CH_2)_2SMe\}]$ (ca. 10–15% by integration). Using $i\text{PrS}(CH_2)_2S i\text{Pr}$ gave similar results, although we were able to grow light yellow crystals of $[WO_2Cl_2\{i\text{PrS}(CH_2)_2S i\text{Pr}\}]$ by filtering the reaction mixture and cooling a $CH_2Cl_2$ solution of the complex in the freezer, however the yield based on tungsten was still very low. The crystal structure confirms the formation of the distorted octahedral $[WO_2Cl_2\{i\text{PrS}(CH_2)_2S i\text{Pr}\}]$ (Figure 1, Table 1) in which the W atom is bound to *cis*-oxido groups, *trans*-Cl ligands and the two S donor atoms of a chelating dithioether. An alternative description of the core geometry would be a distorted tetrahedral primary $O_2Cl_2$ coordination with additional weak $S_2$ coordination completing a very distorted six-coordination. The W–S bond lengths are 2.759(2) and 2.768(2) Å and compare with $d$(W–S) = 2.748 and 2.752 Å in $[WO_2Cl_2\{MeS(CH_2)_2SMe\}]$.[23] The complex adopts a DL configuration with the isopropyl substituents lying on opposite sides of the $WO_2S_2$ plane. The S–W–S chelate bite angle is 77.34(5)°, very similar to that in $[WO_2Cl_2\{MeS(CH_2)_2SMe\}]$ (77.4°) and $[MoO_2Cl_2\{RS(CH_2)_2SR\}]$; R = Me: 77.29(3)°; R = Et: 78.01(2)°.[20]

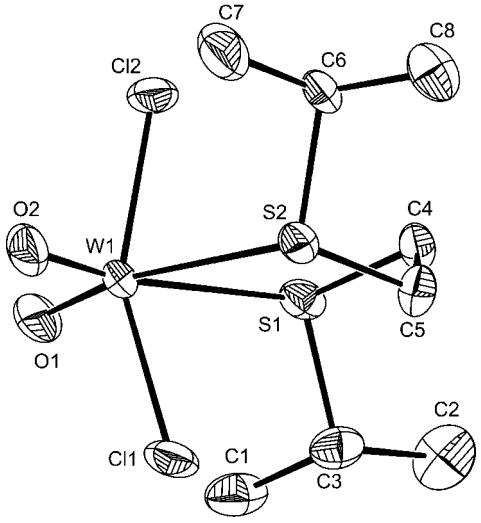


Figure 1. View of the structure of the $[WO_2Cl_2\{i\text{PrS}(CH_2)_2S i\text{Pr}\}]$ with numbering scheme adopted. Ellipsoids are drawn at 50% probability level and H atoms are omitted for clarity.

Small pale yellow crystals of the $Mo^{VI}$ analogue (below), $[MoO_2Cl_2\{i\text{PrS}(CH_2)_2S i\text{Pr}\}]$, were also obtained from $CH_2Cl_2$ solution. The structure determination shows that this compound is isostructural with the tungsten species ($C_8H_{18}Cl_2MoO_2S_2$, $MW$ = 377.18, $a$ = 11.838(2), $b$ = 13.034(2), $c$ = 18.951(3) Å, $\alpha = \beta = \gamma = 90°$, $V$ =

 © 2007 Wiley-VCH Verlag GmbH & Co. KGaA, Weinheim 

Table 1. Selected bond lengths [Å] and angles [°] for $[WO_2Cl_2\{i\text{PrS}(CH_2)_2\text{S}i\text{Pr}\}]$.

| | | | |
|---|---|---|---|
| W1–O1 | 1.726(6) | W1–O2 | 1.741(6) |
| W1–Cl1 | 2.345(2) | W1–Cl2 | 2.334(2) |
| W1–S1 | 2.768(2) | W1–S2 | 2.759(2) |
| O1–W1–O2 | 105.9(3) | O1–W1–Cl2 | 96.9(2) |
| O2–W1–Cl2 | 97.9(2) | O1–W1–Cl1 | 97.8(2) |
| O2–W1–Cl1 | 97.2(2) | Cl2–W1–Cl1 | 155.17(8) |
| O1–W1–S2 | 163.7(2) | O2–W1–S2 | 89.9(2) |
| Cl2–W1–S2 | 84.51(6) | Cl1–W1–S2 | 75.94(7) |
| O1–W1–S1 | 87.2(2) | O2–W1–S1 | 166.6(2) |
| Cl2–W1–S1 | 76.78(8) | Cl1–W1–S1 | 84.03(6) |
| S2–W1–S1 | 77.34(5) | | |

2924.3(8) Å$^3$, $Z$ = 8), although the crystal quality was poorer, giving rather high $R_1$ and $wR_2$ values ($R_1$ [$I_o > 2\sigma(I_o)$] = 0.0921, $wR_2$ [$I_o > 2\sigma(I_o)$] = 0.1814), with $d$(Mo–S) = 2.764(3), 2.783(4), $d$(Mo–O) = 1.673(12), 1.705(11), $d$(Mo–Cl) = 2.341(4), 2.345(4) Å and S1–Mo–S2 = 77.31(9)°.

The very poor yields from these tungsten reactions prompted further efforts to avoid formation of the insoluble by-products. We explored using the soluble and well-defined $[WO_2Cl_2\{MeO(CH_2)_2OMe\}]$,[24] however addition of the dithioether to a $CH_2Cl_2$ solution of this compound resulted in incomplete substitution of the dimethoxyethane, while treatment of $[WOCl_4]$ with one molar equivalent of $O(SiMe_3)_2$ in refluxing octane solution, followed by addition of dithioether gave light yellow insoluble, polymeric products with no evidence for thioether coordination. One route to $[WO_2X_2(\text{dithioether})]$ (X = Cl or Br) was via reaction of $[WOX_4]$ with $O(SiMe_3)_2$ in MeCN solution,[25] to give a colourless solution of $[WO_2X_2(MeCN)_2]$ in situ, followed by concentration of the solvent by ca. 50% in vacuo and addition of a solution of one molar equivalent of $RS(CH_2)_2SR$ (R = Me or *i*Pr) in anhydrous $CH_2Cl_2$. These reactions gave the desired compounds in good yields as yellow solids following removal of the solvent in vacuo and washing with hexane, with minimal polymer formation (and this could be removed by careful recrystallisation of the thioether complex from anhydrous $CH_2Cl_2$). The key to the success of this route is the clean formation of the molecular $[WO_2X_2(MeCN)_2]$ intermediates which seem to prevent the generation of the insoluble polymers. Using a similar approach we have found that the complexes may also be made in good yield from $WX_6$. Thus, reaction of $WX_6$ with one molar equivalent of $O(SiMe_3)_2$ in $CH_2Cl_2$ solution (to form $WOX_4$ in situ), followed by addition of ca. 0.5 mL MeCN, then another molar equivalent of $O(SiMe_3)_2$, and finally one equivalent of the dithioether gives yellow/brown solutions. Concentration of the solution in vacuo and cooling to ca. –15 °C (freezer) leads to deposition of the complexes as yellow (Cl) or yellow/brown (Br) precipitates. This approach was also used to obtain the 1,4-dithiane complexes, $[WO_2X_2(1,4\text{-dithiane})]$. We note that the dithiane complexes are relatively stable when stored as solids under a dry atmosphere, whereas the acyclic dithioether complexes are extremely moisture-sensitive and they also darken, turning blue-green over a few days, even when stored as powdered solids in the glove-box. The most sensitive is the light yellow $[WO_2Cl_2\{i\text{PrS}(CH_2)_2\text{S}i\text{Pr}\}]$ which develops an intense blue/green colour instantly on exposure to air and solutions of which become dark blue with trace water.

The IR spectra of the six $W^{VI}$ dithioether complexes show two strong ν(W=O) and one strong ν(W–X) bands, consistent with mutually *cis*-O and *trans*-X ligands. These are ca. 20–30 cm$^{-1}$ to high frequency of the corresponding Mo species.[20] This is typical of other series of $MO_2X_2$ compounds, e.g. $[MO_2X_2(OPR_3)_2]$ M = Mo or W,[23] although the difference is less in the phosphane oxide complexes. The higher frequency ν(M=O] for W is consistent with stronger metal-oxido bonds. The $^1$H and $^{13}$C{$^1$H} NMR spectra show small high frequency coordination shifts, although the patterns are indicative of fast pyramidal inversion. This was proven by obtaining spectra of representative examples at low temperature, whereupon resonances attributable to individual invertomers were observed. Samples containing added free ligand show resolved resonances for both coordinated and "free" ligand, demonstrating that intermolecular ligand exchange is slow on the NMR time scales at ambient temperatures.

In the course of our attempts to utilise $[WO_2Cl_2\{MeO(CH_2)_2OMe\}]$ as a molecular synthon for $W^{VI}$ thioether complexes we obtained colourless crystals. A structure analysis (120 K) revealed that these were in fact the $[WO_2Cl_2\{MeO(CH_2)_2OMe\}]$ precursor. A crystal structure of this species has been reported previously,[24] and while our cell is related to the published cell, we were unable to refine the structure using the published cell. Hence we conclude that this is a second polymorph. The new data refined very well, revealing (Figure 2, Table 2) a very similar distorted octahedral geometry based upon a W atom coordinated to *cis*-oxido groups, *trans*-Cl atoms and a chelating dimethoxyethane, giving a DL configuration. The bond lengths and angles are similar to those in the published structure.[24]

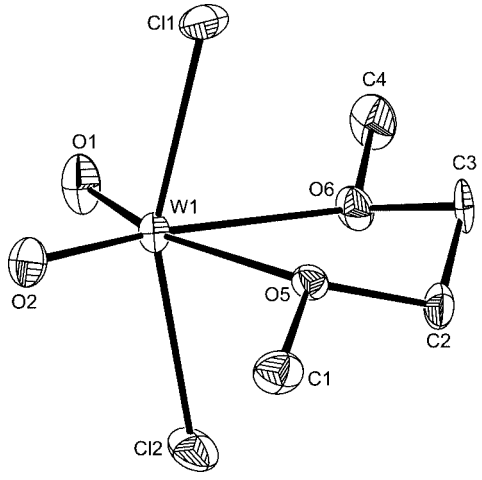


Figure 2. View of the structure of one of the two crystallographically independent $[WO_2Cl_2\{MeO(CH_2)_2OMe\}]$ molecules in the asymmetric unit with numbering scheme adopted. Ellipsoids are drawn at 50% probability level and H atoms are omitted for clarity. The second molecule is very similar.

 © 2007 Wiley-VCH Verlag GmbH & Co. KGaA, Weinheim 

Table 2. Selected bond lengths [Å] and angles [°] for $[WO_2Cl_2\{MeO(CH_2)_2OMe\}]$.

| | | | |
|---|---|---|---|
| W1–O2 | 1.705(3) | W1–O1 | 1.706(4) |
| W1–O5 | 2.274(3) | W1–O6 | 2.288(3) |
| W1–Cl2 | 2.3375(14) | W1–Cl1 | 2.3563(13) |
| W2–O4 | 1.707(4) | W2–O3 | 1.708(4) |
| W2–O7 | 2.260(3) | W2–O8 | 2.286(3) |
| W2–Cl3 | 2.3513(13) | W2–Cl4 | 2.3556(14) |
| O2–W1–O1 | 104.23(17) | O2–W1–O5 | 94.49(14) |
| O1–W1–O5 | 161.26(14) | O2–W1–O6 | 165.17(15) |
| O1–W1–O6 | 90.60(14) | O5–W1–O6 | 70.67(12) |
| O2–W1–Cl2 | 96.87(12) | O1–W1–Cl2 | 97.74(13) |
| O5–W1–Cl2 | 80.60(9) | O6–W1–Cl2 | 80.93(9) |
| O2–W1–Cl1 | 96.81(12) | O1–W1–Cl1 | 96.69(13) |
| O5–W1–Cl1 | 79.98(9) | O6–W1–Cl1 | 81.12(9) |
| Cl2–W1–Cl1 | 157.01(5) | O4–W2–O3 | 104.78(18) |
| O4–W2–O7 | 92.71(15) | O3–W2–O7 | 162.52(15) |
| O4–W2–O8 | 163.50(15) | O3–W2–O8 | 91.72(15) |
| O7–W2–O8 | 70.80(12) | O4–W2–Cl3 | 96.63(13) |
| O3–W2–Cl3 | 96.94(13) | O7–W2–Cl3 | 80.65(9) |
| O8–W2–Cl3 | 80.67(9) | O4–W2–Cl4 | 96.25(13) |
| O3–W2–Cl4 | 96.37(13) | O7–W2–Cl4 | 81.57(9) |
| O8–W2–Cl4 | 82.08(9) | Cl3–W2–Cl4 | 158.46(5) |

### Molybdenum Thioether Complexes

The very unusual and highly sensitive metallocyclic compound $[Mo_2O_4Cl_4\{o\text{-}C_6H_4(CH_2SMe)_2\}_2]$ was prepared by treatment of $MoO_2Cl_2$ with one molar equivalent of *o*-$C_6H_4(CH_2SMe)_2$ in anhydrous $CH_2Cl_2$ or $Et_2O$. The formulation as a dinuclear complex follows from the spectroscopic and structural data. Two distinct ν(Mo–Cl) bands at 389 and 355 $cm^{-1}$ are evident, consistent with *cis*-Cl atoms, contrasting with the structures previously determined for $[MoO_2X_2\{RS(CH_2)_2SR\}]$ (X = Cl or Br; R = Me or Et) which have *trans*-halides and *cis*-oxido ligands.[20] The room temperature $^1H$ NMR spectrum of the $MoO_2Cl_2$-*o*-$C_6H_4(CH_2SMe)_2$ system is simple and little different from the thioether ligand itself. Upon cooling to 183 K the spectrum becomes more complex with high frequency coordination shifts with three δ(Me) resonances evident at low temperature, consistent with the presence of stereoisomers, indicating that the compound is undergoing reversible ligand dissociation and fast pyramidal inversion under ambient conditions. In order to identify unambiguously the structure of this complex, light yellow crystals which were extremely air and moisture-sensitive, were obtained by cooling a solution containing the complex dissolved in $CH_2Cl_2$. The structure shows (Figure 3, Table 3) an unusual centrosymmetric dinuclear metallocyclic species in which each formally $Mo^{VI}$ is in a distorted octahedral geometry, coordinated to *cis*-oxido, *cis*-chlorido and *cis*-thioether groups. The *o*-$C_6H_4(CH_2SMe)_2$ ligands are not chelating, but instead function as bridging bidentates, with one S atom *trans* to O and one *trans* to Cl. This represents the first metallocyclic species incorporating the *o*-xylyl dithioether ligand. The different *trans* influences of these ligands are very clearly reflected in the disparate bond lengths within pairs of ligands, e.g. Mo–Cl 2.278(3), 2.423(3) Å, the longer bond being associated with the Cl *trans* to O. Even the Mo=O bond lengths are disparate due to the *trans* ligands; Mo–O 1.726(7), 1.777(7) Å. The Mo–S distances are *d*(Mo–S) = 2.604(3), 2.826(3) Å, with the exceptionally long Mo–S bond lying *trans* to the oxido ligand. These compare with *d*(Mo–S) = 2.73–2.77 Å in the other structurally characterised $Mo^{VI}$ thioether complexes.[20] The angles involving the mutually *cis* pairs of ligands also show considerable variation, O1–Mo–O2 105.3(4), Cl1–Mo–Cl2 91.21(12), S1–Mo–S2a 82.52(9)°, and the S–Mo–S angle is some 4–5° larger than in the chelate complexes $[MoO_2Cl_2\{RS(CH_2)_2SR\}]$ (R = Me or Et). This is the first $Mo^{VI}$ complex incorporating other than a dimethylene-linked dithioether ligand and follows from our earlier work which has shown that the *o*-$C_6H_4(CH_2EMe)_2$ (E = S, Se, Te) are remarkably effective ligands for a range of late transition metal ions.[26] The occurrence of a metallocyclic structure with bridging bidentate *o*-$C_6H_4(CH_2SMe)_2$ ligands in the case of the $Mo^{VI}$ species, may be a consequence of the sterically demanding *o*-xylyl linkage and the small radius of $Mo^{VI}$. We have shown previously that the E–M–E chelate angle in transition metal complexes involving the *o*-$C_6H_4(CH_2EMe)_2$ (E = S, Se or Te) ligands is invariably close to 100°.[26] In the dinuclear $[Mo_2O_4Cl_4\{o\text{-}C_6H_4(CH_2SMe)_2\}_2]$ the Me groups within a single dithioether ligand are *anti* (the SMe group coordinated to one Mo atom lies on the opposite side of the $MoO_2S_2$ coordination plane to that on the other Mo atom), while the coordinated SMe groups on each individual Mo atom are *syn* (Me substituents on a single Mo atom lie on the same side of the $MoO_2S_2$ plane) – Figure 3. A similar reaction using $MoO_2Cl_2$ with *o*-$C_6H_4(CH_2SeMe)_2$ led to reduction of the metal centre.

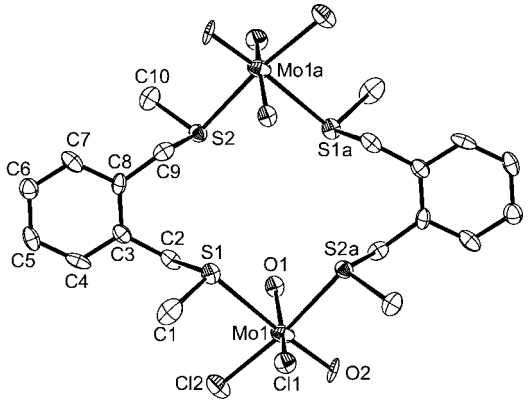


Figure 3. View of the structure of $[Mo_2O_4Cl_4\{o\text{-}C_6H_4(CH_2SMe)_2\}_2]$ with numbering scheme adopted. Ellipsoids are drawn at 50% probability level and H atoms are omitted for clarity. Symmetry operation *a* = 1 – *x*, 2 – *y*, –*z*.

The moisture-sensitive (macro)cyclic complexes of $Mo^{VI}$, $[MoO_2Cl_2(L)]$ (L = 1,4-dithiane, [15]ane$S_2O_3$, [12]ane$S_4$, [14]ane$S_4$), as well as $[MoO_2Cl_2\{iPrS(CH_2)_2SiPr\}]$ have been obtained similarly as light yellow solids in good yield. The isolated solids were stored in the glove box (<5 ppm $H_2O$) to prevent decomposition and have been characterised by microanalysis, IR, $^1H$ and $^{13}C\{^1H\}$ NMR spectroscopy. The IR spectra of these Mo species show evidence

 © 2007 Wiley-VCH Verlag GmbH & Co. KGaA, Weinheim 

Table 3. Selected bond lengths [Å] and angles [°] for $[Mo_2O_4Cl_4\{o\text{-}C_6H_4(CH_2SMe)_2\}_2]$.[a]

| | | | |
|---|---|---|---|
| Mo1–O1 | 1.726(7) | Mo1–O2 | 1.777(7) |
| Mo1–Cl1 | 2.423(3) | Mo1–Cl2 | 2.278(3) |
| Mo1–S1 | 2.826(3) | Mo1–S2a | 2.604(3) |
| O1–Mo1–O2 | 105.3(4) | O1–Mo1–Cl2 | 102.7(3) |
| O2–Mo1–Cl2 | 99.8(3) | O1–Mo1–Cl1 | 150.5(3) |
| O2–Mo1–Cl1 | 97.6(2) | Cl2–Mo1–Cl1 | 91.21(12) |
| O1–Mo1–S2a | 81.9(3) | O2–Mo1–S2a | 91.1(3) |
| Cl2–Mo1–S2a | 166.45(13) | Cl1–Mo1–S2a | 79.32(10) |
| O1–Mo1–S1 | 78.6(3) | O2–Mo1–S1 | 172.1(3) |
| Cl2–Mo1–S1 | 85.89(12) | Cl1–Mo1–S1 | 76.64(10) |
| S2a–Mo1–S1 | 82.52(9) | | |

[a] Symmetry operation: $a = 1 - x, 2 - y, -z$.

for coordinated thioether ligand, and two strong bands in the region 900–950 $cm^{-1}$ indicative is the *cis*-dioxido unit. For the mononuclear species one strong absorption at ca. 350–360 $cm^{-1}$, suggesting mutually *trans* Cl ligands (and confirmed crystallographically for $[MoO_2Cl_2\{i\text{PrS}(CH_2)_2\text{-}S i\text{Pr}\}]$ – above). The $^1H$ NMR spectrum of $[MoO_2Cl_2\{i\text{PrS}(CH_2)_2S i\text{Pr}\}]$ is simple, with resonances to high frequency of $i\text{PrS}(CH_2)_2S i\text{Pr}$, consistent with coordination of the dithioether ligand to Mo, and fast pyramidal inversion – similar to the behaviour observed previously for $[MoO_2X_2\{RS(CH_2)_2SR\}]$.[20] Molybdenum-95 NMR spectroscopy reveals a resonance at $\delta$ = 225 ppm, also in the same range as for $[MoO_2Cl_2\{RS(CH_2)_2SR\}]$ (R = Me or Et) described previously, and an X-ray structure determination showed that $[MoO_2Cl_2\{i\text{PrS}(CH_2)_2S i\text{Pr}\}]$ is isostructural with its W analogue (above), based upon distorted octahedral Mo with *cis*-oxido and *trans*-Cl ligands and a chelating dithioether ligand. The dithiane complex $[MoO_2Cl_2(\text{dithiane})]$ exhibits a singlet methylene resonance in the $^1H$ NMR spectrum at ambient temperatures, indicating either bridging dithiane or reversible chelate ring opening. However, this broadens and splits into complex multiplets at low temperature (183 K), consistent with chelation for which an AA′BB′ pattern is expected.[27]

For the complex $[MoO_2Cl_2([15]aneS_2O_3)]$, assuming six-coordination, the possible macrocycle coordination modes are $S_2$, SO or $O_2$. The former would give rise to a symmetrical pattern, and hence five distinct $CH_2$ resonances, whereas SO or $O_2$ coordination would lead to a less symmetrical species and hence a more complicated $^1H$ NMR pattern. In fact, the $^1H$ NMR spectrum of $[MoO_2Cl_2([15]aneS_2O_3)]$ clearly reveals five resonances, and comparison with the spectrum of the parent macrocycle is also consistent with $S_2$ coordination to molybdenum. The $^{95}Mo$ NMR spectrum of $[MoO_2Cl_2([15]aneS_2O_3)]$ shows a single resonance at $\delta$ = 194 ppm, slightly to low frequency of $[MoO_2Cl_2\{\text{MeS}(CH_2)_2\text{SMe}\}]$ ($\delta$ = 210 ppm) and $[MoO_2Cl_2\{\text{EtS}(CH_2)_2\text{-SEt}\}]$ ($\delta$ = 225 ppm).[20]

The poor solubilities of the yellow $[MoO_2Cl_2([n]aneS_4)]$ ($n$ = 12 or 14) in solvents which would not react with the complex hindered attempts to obtain solution spectroscopic data for these species. However, the IR spectra are consistent with a $Cl_2O_2S_2$ coordination sphere at $Mo^{VI}$ in $[MoO_2Cl_2([n]aneS_4)]$ ($n$ = 12 or 14), with *cis*-oxido ligands and *trans*-chlorines; microanalyses confirm the formulation. The reaction of $MoO_2Cl_2$ with [14]$aneS_4$ has been mentioned previously.[19]

## Conclusions

The first series of dioxidotungsten(VI) complexes with soft dithioethers has been prepared in good yield and characterised structurally and spectroscopically. Successful formation of these compounds is very sensitive to the precise reaction conditions, and they appear to be much more reactive than their $Mo^{VI}$ analogues, consistent with dioxidotungsten(VI) being harder than dioxidomolybdenum(VI). Several new examples of dioxidomolybdenum(VI) thioether complexes, including the unique dinuclear metallocyclic $[Mo_2O_4Cl_4\{o\text{-}C_6H_4(CH_2SMe)_2\}_2]$ which involves the rare *cis*-$MoCl_2$ unit, and examples containing the small cyclic 1,4-dithiane ligand and several macrocyclic thia- and mixed S/O-ligands have also been prepared and characterised. Work involving other $W^{VI}$ species with neutral sulfur ligands and related $M^{IV}$ and $M^V$ (M = Mo or W) complexes which may be relevant as redox models for the molybdo- and tungsto-enzymes, is underway.

## Experimental Section

Infrared spectra were recorded as Nujol nulls between CsI discs using a Perkin–Elmer 983G spectrometer over the range 4000–200 $cm^{-1}$. $^1H$ NMR spectra were recorded using a Bruker AV300 spectrometer. $^{13}C\{^1H\}$ and $^{95}Mo$ NMR spectra were recorded using a Bruker DPX400 spectrometer operating at 100.6 and 26.1 MHz, respectively, and are referenced to TMS and 1 mol $dm^{-3}$ $Na_2[MoO_4]$ respectively. Microanalyses were undertaken by the University of Strathclyde microanalytical service.

Solvents were dried prior to use and all preparations were undertaken using standard Schlenk techniques under a $N_2$ atmosphere. $MoO_2Cl_2$, $WCl_6$ and $W(CO)_6$ were obtained from Aldrich and used as received. $WBr_6$ was prepared by treating $W(CO)_6$ with $Br_2$.[28] The ligands $MeS(CH_2)_2SMe$, $i\text{PrS}(CH_2)_2S i\text{Pr}$, $o\text{-}C_6H_4(CH_2SMe)_2$, $MeSe(CH_2)_2SeMe$, [12]$aneS_2O_2$ and [15]$aneS_2O_3$ were prepared as described previously,[26,29,30] while 1,4-dithiane, [12]$aneS_4$ and [14]-$aneS_4$ were obtained from Aldrich and the solids dried by heating in vacuo for ca. 1 h before use.

**$[WO_2Cl_2\{MeS(CH_2)_2SMe\}]$. Method 1:** An acetonitrile solution of $(Me_3Si)_2O$ (0.049 g, 0.3 mmol in 5 mL of $CH_3CN$) was added dropwise at room temperature to a stirred suspension of $WOCl_4$ (0.103 g, 0.3 mmol) in acetonitrile (5 mL) over a period of 10 min. The $WOCl_4$ was consumed to give a clear, colourless solution, which was stirred for a further 10 min. The solution was then concentrated to half volume in vacuo and a $CH_2Cl_2$ solution of $MeS(CH_2)_2SMe$ (0.037 g, 0.3 mmol) was added dropwise. After stirring for ca. 30 min the solvent was removed in vacuo, leaving a yellow precipitate, which was washed with *n*-hexane and dried in vacuo. Yield 0.094 g, 76%.

**Method 2:** A suspension of $WCl_6$ (0.50 g, 1.25 mmol) in dry $CH_2Cl_2$ (10 mL) was treated dropwise with $(Me_3Si)_2O$ (0.20 g, 1.25 mmol) in $CH_2Cl_2$ (5 mL) and the mixture stirred for 10 min during which

 © 2007 Wiley-VCH Verlag GmbH & Co. KGaA, Weinheim 

orange $WOCl_4$ deposited from the solution. Dry MeCN (0.5 mL) was added, followed by dropwise addition of $(Me_3Si)_2O$ (0.20 g, 1.25 mmol) and the solution stirred for 30 min when it became colourless (or sometimes very faintly blue). $MeS(CH_2)_2SMe$ (0.16 g, 1.3 mmol) in $CH_2Cl_2$ solution (2 mL) was added producing a pale yellowish solution. The solution was stirred for 10 min and then concentrated in vacuo to ca. 2 mL, and refrigerated overnight. The yellow powder deposited was separated by decantation of the solvent and dried in vacuo. Yield 0.30 g, 58%.

Both methods gave the same product as confirmed by spectroscopic studies. $C_4H_{10}Cl_2O_2S_2W$ (409.0): calcd. C 11.7, H 2.5; found C 11.0, H 2.9. IR (Nujol): $\tilde{\nu}$ = 956, 918 (W=O), 343 (W–Cl) $cm^{-1}$. $^1H$ NMR ($CD_2Cl_2$, 300 K): $\delta$ = 3.24 (br. s, $CH_2S$, 4 H), 2.51 (br. s, Me, 6 H); (223 K): $\delta$ = 3.40–3.05 (m, $CH_2S$), 2.52 (s, Me, minor), 2.44 (s, Me, major). $^{13}C\{^1H\}$ ($CD_2Cl_2$, 300 K): br., ill-defined; (223 K): $\delta$ = 33.65 ($CH_2$), 18.1 (Me).

**[$WO_2Cl_2${*i*PrS$(CH_2)_2$S*i*Pr}]:** An acetonitrile solution of $(Me_3Si)_2O$ (0.048 g, 0.2 mmol in 5 mL of MeCN) was added dropwise at room temperature to a stirred suspension of $WOCl_4$ (0.102 g, 0.2 mmol) in acetonitrile (5 mL) over a period of 10 min to give a clear, colourless solution. After stirring for a further 10 min the solution was concentrated to half volume in vacuo and a $CH_2Cl_2$ solution of *i*PrS$(CH_2)_2$S*i*Pr (0.053 g, 0.2 mmol) was added dropwise at room temperature. The reaction mixture was stirred for ca. 30 min and then the solvent was evaporated to dryness in vacuo, leaving a yellow solid, which was washed with *n*-hexane and dried in vacuo. Yield 0.104 g, 75%. The compound was also prepared by method 2 used for [$WO_2Cl_2${$MeS(CH_2)_2SMe$}] above. Yield 55%. $C_8H_{18}Cl_2O_2S_2W{\cdot}CH_2Cl_2$ (550.0): calcd. C 19.6, H 3.7; found C 18.9, H 4.7. IR (Nujol): $\tilde{\nu}$ = 963, 923 (W=O), 338 (W–Cl) $cm^{-1}$. $^1H$ NMR ($CDCl_3$, 300 K): $\delta$ = 3.30 (br., CH, 2 H), 3.18 (br., $CH_2$, 4 H), 1.38 (br., $CHMe_2$, 12 H). $^{13}C\{^1H\}$ ($CDCl_3$, 300 K): $\delta$ = 36.6 (CH), 28.1($CH_2$), 23.2(Me).

**[$WO_2Cl_2$(1,4-dithiane)]:** A suspension of $WCl_6$ (0.50 g, 1.25 mmol) in dry $CH_2Cl_2$ (10 mL) was treated dropwise with $(Me_3Si)_2O$ (0.20 g, 1.25 mmol) in $CH_2Cl_2$ (5 mL) and the mixture stirred for 10 min. Dry MeCN (0.5 mL) was added to the orange suspension, followed by dropwise addition of $(Me_3Si)_2O$ (0.20 g, 1.25 mmol) and the solution stirred for 30 min when it became colourless. 1,4-Dithiane, which had been freshly sublimed in vacuo, (0.145 g, 1.2 mmol) in $CH_2Cl_2$ solution (5 mL) was added producing a pale yellowish solution. The solution was stirred for 10 min and then concentrated in vacuo to ca. 4 mL, and refrigerated for 48 h. The very fine yellow powder deposited was separated by decantation of the solvent and dried in vacuo. Yield 0.28 g, 55%. $C_4H_8Cl_2O_2S_2W$ (407.0): calcd. C 11.8, H 2.0; found C 11.5, H 2.9. IR (Nujol): $\tilde{\nu}$ = 940, 903 (W=O), 338 (W–Cl) $cm^{-1}$. $^1H$ NMR ($CDCl_3$, 300 K): $\delta$ = 2.91 (s, $CH_2$). $^{13}C\{^1H\}$ ($CDCl_3$, 300 K): $\delta$ = 29.3 ($CH_2$).

**[$WO_2Br_2${$MeS(CH_2)_2SMe$}]:** A suspension of $WBr_6$ (0.66 g, 1.0 mmol) in dry $CH_2Cl_2$ (10 mL) was treated dropwise with $(Me_3Si)_2O$ (0.16 g, 1.0 mmol) in $CH_2Cl_2$ (5 mL) and the mixture stirred for 10 min. Dry MeCN (0.5 mL) was added to the yellow-green suspension, followed by dropwise addition of $(Me_3Si)_2O$ (0.16 g, 1.0 mmol) and the solution stirred for 30 min when it became pale yellow-brown. $MeS(CH_2)_2SMe$ (0.12 g, 1.0 mmol) in $CH_2Cl_2$ solution (5 mL) was added producing a brown-yellow solution. The solution was stirred for 10 min and then concentrated in vacuo to ca. 5 mL, and refrigerated for 48 h. Only a small quantity of yellow-brown precipitate formed, so the solvent was removed in vacuo, and the residue stirred with hexane (10 mL). The powder deposited was separated by decantation of the solvent and dried in vacuo. Yield 0.3 g, 60%. $C_4H_{10}Br_2O_2S_2W$ (497.9): calcd. C 9.6, H 2.0; found C 10.2, H 1.3. IR (Nujol): $\tilde{\nu}$ = 965, 917 (W=O), 228 (W–Br) $cm^{-1}$. $^1H$ NMR ($CD_2Cl_2$, 300 K): $\delta$ = 2.90 (s, $CH_2S$, 4 H), 2.43 (s, Me, 6 H). $^{13}C\{^1H\}$ ($CDCl_3$, 300 K): $\delta$ = 33.4 ($CH_2$), 18.4 (Me).

**[$WO_2Br_2${*i*PrS$(CH_2)_2$S*i*Pr}]:** An acetonitrile solution of $(Me_3Si)_2O$ (0.038 g, 0.2 mmol in 5 mL of MeCN) was added dropwise at room temperature to a stirred suspension of $WOBr_4$ (0.123 g, 0.2 mmol) in MeCN (5 mL) over a period of 10 min. The reaction mixture changed to a green coloured solution which was stirred for a further 10 min. The solution was concentrated to half volume in vacuo and a $CH_2Cl_2$ solution of *i*PrS$(CH_2)_2$S*i*Pr (0.042 g, 0.2 mmol) was added dropwise and the mixture was stirred for ca. 30 min. At this point the solvent was removed in vacuo, leaving a yellow-brown solid which was stirred with *n*-hexane (10 mL), separated by decantation and dried in vacuo. Yield 0.093 g, 71%. The compound was also prepared by method 2 used for [$WO_2Cl_2${$MeS(CH_2)_2SMe$}] above. $C_8H_{18}Br_2O_2S_2W{\cdot}1/4C_6H_{14}$ (575.7): calcd. C 19.8, H 3.8; found C 19.9, H 4.0. IR (Nujol): $\tilde{\nu}$ = 962, 920 (W=O), 230 (W–Br) $cm^{-1}$. $^1H$ NMR ($CD_2Cl_2$, 300 K): $\delta$ = 3.48 (br. s, CH, 2 H) 3.30 (br. s, $CH_2$, 4 H), 1.46 (br. s, $CHMe_2$, 6 H); (223 K): $\delta$ = 3.01–3.53 (overlapping m, CH and $CH_2$), 1.43, 1.38 (s, Me). $^{13}C\{^1H\}$ ($CDCl_3$, 300 K): $\delta$ = 34.9 (CH), 30.7 ($CH_2$), 23.3 (Me).

**[$WO_2Br_2$(1,4-dithiane)]:** A suspension of $WBr_6$ (0.66 g, 1.0 mmol) in dry $CH_2Cl_2$ (10 mL) was treated dropwise with $(Me_3Si)_2O$ (0.16 g, 1.0 mmol) in $CH_2Cl_2$ (5 mL) and the mixture stirred for 10 min. Dry MeCN (0.5 mL) was added to the blue-green suspension, followed by dropwise addition of $(Me_3Si)_2O$ (0.16 g, 1.0 mmol) and the solution stirred for 30 min when it became pale yellow-brown. 1,4-Dithiane, which had been freshly sublimed in vacuo, (0.12 g, 1.0 mmol) in $CH_2Cl_2$ solution (5 mL) was added producing a brown-yellow solution. The solution was stirred for 10 min and then concentrated in vacuo to ca. 4 mL, and refrigerated for 48 h. The yellow-brown powder deposited was separated by decantation of the solvent, rinsed with dry hexane (5 mL) and dried in vacuo. Yield 0.35 g, 70%. $C_4H_8Br_2O_2S_2W$ (495.9): calcd. C 9.7, H 1.6; found C 9.0, H 1.7. IR (Nujol): $\tilde{\nu}$ = 961, 902 (W=O), 238 (W–Br) $cm^{-1}$. $^1H$ NMR ($CDCl_3$, 300 K): $\delta$ = 2.85 ($CH_2$). $^{13}C\{^1H\}$ ($CDCl_3$, 300 K): $\delta$ = 29.2 ($CH_2$).

**[$Mo_2O_4Cl_4${*o*-$C_6H_4(CH_2SMe)_2$}$_2$]:** A degassed ether solution of *o*-$C_6H_4(CH_2SMe)_2$ (0.104 g, 0.52 mmol) in 5 mL of $Et_2O$ was added dropwise at room temperature to a stirred solution of $MoO_2Cl_2$ (0.104 g, 0.52 mmol) in diethyl ether (10 mL) over a period of 5 min, giving a light yellow solution. The solution was stirred at room temperature for a further 30 min. The solution was then concentrated in vacuo by ca. 50% and placed in the freezer. This produced a yellow precipitate, which was collected by filtration and dried in vacuo. Yield 0.153 g, 74%. $C_{20}H_{28}Cl_4Mo_2O_4S_4$ (794.4): calcd. C 30.2, H 3.6; found C 29.2, H 3.8. IR (Nujol): $\tilde{\nu}$ = 933, 895 (Mo=O), 387, 355 (Mo–Cl) $cm^{-1}$. $^1H$ NMR ($CDCl_3$, 298 K): $\delta$ = 7.29 (br. s, *o*-$C_6H_4$, 4 H), 3.95 (br., $CH_2$, 4 H), 2.29 (br., Me, 6 H); (183 K): $\delta$ = 7.33–7.11 (m, *o*-$C_6H_4$, 4 H), 4.15, 3.74 (br., $CH_2$, 4 H), 2.64, 2.26, 1.94 (s, Me, 6 H). $^{13}C\{^1H\}$ NMR ($CDCl_3$, 298 K): no spectrum; (223 K): $\delta$ = 133.00 (*ipso*-C, *o*-$C_6H_4$), 132.67, 129.28 (*o*-$C_6H_4$), 37.21 ($CH_2$), 20.99 (Me).

**[$MoO_2Cl_2${*i*PrS$(CH_2)_2$S*i*Pr}]:** To a suspension of $MoO_2Cl_2$ (0.103 g, 0.52 mmol) in $CH_2Cl_2$ (20 mL) was added a $CH_2Cl_2$ solution (5 mL) of *i*PrS$(CH_2)_2$S*i*Pr (0.093 g, 0.52 mmol). Stirring the reaction mixture for ca. 15 min afforded a pale yellow solution which was reduced in vacuo to ca. 3 mL. Layering with anhydrous diethyl ether and storing the resulting mixture overnight at ca. –18 °C gave pale yellow crystals which were filtered, washed with diethyl ether and dried in vacuo. Yield 85%. $C_8H_{18}Cl_2MoO_2S_2$

 © 2007 Wiley-VCH Verlag GmbH & Co. KGaA, Weinheim 

(377.2): calcd. C 25.5, H 4.8; found C 25.3, H 5.1. IR (Nujol): $\tilde{\nu}$ = 944, 913 (Mo=O), 348 (Mo–Cl) $cm^{-1}$. $^1H$ NMR ($CD_2Cl_2$, 300 K): $\delta$ = 3.30 (sept, CH, 2 H), 3.08 (s, $CH_2$, 4 H), 1.47 (d, $CHMe_2$, 12 H). $^{13}C\{^1H\}$ NMR ($CH_2Cl_2/CDCl_3$, 300 K): $\delta$ = 38.25 (CH), 31.01 ($CH_2$), 21.99 ($CHMe_2$) ppm. $^{95}Mo$ NMR ($CH_2Cl_2/CDCl_3$): $\delta$ = 225.

**[$MoO_2Cl_2$(1,4-dithiane)]:** A degassed diethyl ether (5 mL) solution of 1,4-dithiane (0.072 g, 0.6 mmol) was added dropwise at room temperature to a stirred solution of $MoO_2Cl_2$ (0.120 g, 0.6 mmol) in diethyl ether (10 mL) over a period of 5 min, giving a light yellow precipitate. The reaction mixture was stirred at room temperature for a further 1 h. The yellow precipitate was collected by filtration and dried in vacuo. Yield 0.128 g, 67%. $C_4H_8Cl_2MoO_2S_2$ (319.1): calcd. C 15.1, H 2.5; found C 15.4, H 2.4. IR (Nujol): $\tilde{\nu}$ = 946, 916 (Mo=O), 362 (Mo–Cl) $cm^{-1}$. $^1H$ NMR ($CDCl_3$, 298 K): $\delta$ = 2.98 (s, $CH_2$); (183 K): $\delta$ = 3.53–2.69 (br. m, $CH_2$).

**[$MoO_2Cl_2$([15]ane$S_2O_3$)]:** A dry, degassed $CH_2Cl_2$ solution (5 mL) of [15]ane$S_2O_3$ (0.010 g, 0.4 mmol) was added dropwise at room temperature to a stirred solution of $MoO_2Cl_2$ (0.080 g, 0.4 mmol) in degassed diethyl ether (10 mL) over a period of 5 min, giving a light yellow precipitate. The reaction mixture was stirred at room temperature for a further 3 h. The yellow precipitate was collected by filtration and dried in vacuo. Yield 0.124 g, 68%. $C_{10}H_{20}Cl_2MoO_5S_2$ (451.2): calcd. C 26.6, H 4.5; found C 26.6, H 4.5. IR (Nujol): $\tilde{\nu}$ = 939, 908 (Mo=O), 355 (Mo–Cl) $cm^{-1}$. $^1H$ NMR ($CDCl_3$, 300 K): $\delta$ = 3.97 (br. s, $CH_2O$, 4 H), 3.84 (s, $CH_2O$, 4 H), 3.77 (s, $CH_2O$, 4 H), 3.15 (s, $CH_2S$, 4 H), 3.02 (s, $CH_2S$, 4 H). $^{95}Mo$ NMR ($CH_2Cl_2/CDCl_3$, 300 K): $\delta$ = 194.

**[$MoO_2Cl_2$([14]ane$S_4$)]:** Addition of a solution of $MoO_2Cl_2$ (0.075 g, 0.38 mmol) in dry diethyl ether (5 mL) dropwise via a bypass funnel at room temperature to a solution of [14]ane$S_4$ (0.102 g, 0.38 mmol) in dry $CH_2Cl_2$ (10 mL) over a period of 5 min, produced a light yellow precipitate. The reaction mixture was stirred at room temperature for a further 60 min, and the yellow precipitate was collected by filtration and dried in vacuo. Yield 0.135 g, 76%. $C_{10}H_{20}Cl_2MoO_2S_4$ (467.4): calcd. C 25.7, H 4.3; found C 25.9, H 4.5. IR (Nujol): $\tilde{\nu}$ = 939, 913 (Mo=O), 359 (Mo–Cl) $cm^{-1}$. $^1H$ NMR ($CDCl_3$, very poorly soluble, 300 K): $\delta$ = 2.72 (s, $SCH_2CH_2S$, 8 H), 2.61 (t, $SCH_2CH_2CH_2S$, 8 H), 1.88 (q, $SCH_2CH_2CH_2S$, 4 H) ([14]ane$S_4$).

**[$MoO_2Cl_2$([12]ane$S_4$)]:** Addition of a solution of $MoO_2Cl_2$ (0.084 g, 0.42 mmol) in dry diethyl ether (5 mL) dropwise via a bypass funnel at room temperature to a solution of [12]ane$S_4$ (0.102 g, 0.42 mmol) in dry $CH_2Cl_2$ (10 mL) over a period of 5 min, produced a light yellow precipitate. The reaction mixture was stirred at room temperature for a further 60 min. The yellow precipitate was collected by filtration and dried in vacuo. Yield 0.141 g, 76%. $C_8H_{16}Cl_2MoO_2S_4 \cdot CH_2Cl_2$ (524.2): calcd. C 20.6, H 3.5; found C 20.6, H 3.5. IR (Nujol): $\tilde{\nu}$ = 944, 919 (Mo=O), 358 (Mo–Cl) $cm^{-1}$. $^1H$ NMR ($CDCl_3$, very poorly soluble, 300 K): $\delta$ = 2.72 (s, $CH_2$) ([12]ane$S_4$).

**X-ray Crystallography:** Details of the crystallographic data collection and refinement parameters are given in Table 4. Yellow crystals of [$WO_2Cl_2${*i*PrS$(CH_2)_2$S*i*Pr}], [$Mo_2O_4Cl_4${*o*-$C_6H_4(CH_2SMe)_2$}$_2$] and a new polymorph of [$WO_2Cl_2${MeO$(CH_2)_2$OMe}] were obtained by liquid diffusion of diethyl ether into a $CH_2Cl_2$ solution of the complex. The crystals of [$Mo_2O_4Cl_4${*o*-$C_6H_4(CH_2SMe)_2$}$_2$] were extremely moisture-sensitive and some degradation occurred during transfer from the Schlenk flask to the diffractometer – the data presented are those from the best crystal from several different crystals examined. Nevertheless the quality was rather poor and hence the residuals are higher than usually expected. Data collection used a Nonius Kappa CCD diffractometer ($T$ = 120 K) and with graphite-monochromated Mo-$K_\alpha$ X-radiation ($\lambda$ = 0.71073 Å). Structure solution and refinement were routine.[31,32] with H atoms being placed in geometrically calculated positions. Selected bond lengths and angles are given in Table 1, Table 2, and Table 3.

CCDC-626755 (for W/S), -626756 (for W/O), -626754 and -626757 (for Mo) contain the supplementary crystallographic data for this paper. These data can be obtained free of charge from The Cambridge Crystallographic Data Centre via www.ccdc.cam.ac.uk/data_request/cif.

Table 4. Crystallographic parameters.[a]

| Compound | [$WO_2Cl_2${*i*PrS$(CH_2)_2$S*i*Pr}] | [$WO_2Cl_2${MeO$(CH_2)_2$OMe}] | [$(MoO_2Cl_2)_2${*o*-$C_6H_4(CH_2SMe)_2$}$_2$] |
|---|---|---|---|
| Formula | $C_8H_{18}Cl_2O_2S_2W$ | $C_4H_{10}Cl_2O_4W$ | $C_{20}H_{28}Cl_4Mo_2O_4S_4$ |
| $M$ | 465.09 | 376.87 | 794.34 |
| Crystal system | orthorhombic | monoclinic | monoclinic |
| Space group | *Pbca* (no. 61) | $P2_1/c$ (no. 14) | $P2_1/c$ (no. 14) |
| $a$ [Å] | 11.7823(16) | 14.248(3) | 7.4251(12) |
| $b$ [Å] | 12.964(2) | 11.216(3) | 23.984(4) |
| $c$ [Å] | 19.111(3) | 13.497(3) | 8.2293(14) |
| α [°] | 90 | 90 | 90 |
| $\beta$ [°] | 90 | 118.213(10) | 94.964(9) |
| $\gamma$ [°] | 90 | 90 | 90 |
| $U$ [Å$^3$] | 2919.2(8) | 1900.5(7) | 1460.0(4) |
| $Z$ | 8 | 8 | 2 |
| $\mu$(Mo-$K_\alpha$) [$mm^{-1}$] | 8.547 | 12.686 | 1.537 |
| Total number of reflections | 29514 | 11475 | 7617 |
| $R_{int}$ | 0.069 | 0.032 | 0.064 |
| Unique reflections | 3341 | 4179 | 2418 |
| Number of parameters | 136 | 203 | 154 |
| $R_1$ [$I_o > 2\sigma(I_o)$] | 0.0489 | 0.0282 | 0.0884 |
| $R_1$ [all data] | 0.0704 | 0.0391 | 0.1110 |
| $wR_2$ [$I_o > 2\sigma(I_o)$] | 0.0880 | 0.0536 | 0.2232 |
| $wR_2$ [all data] | 0.0959 | 0.0580 | 0.2411 |

[a] Common items: temperature = 120 K; wavelength (Mo-$K_\alpha$) = 0.71073 Å; $\theta$(max.) = 27.5°; $R_1 = \Sigma||F_o| - |F_c||/\Sigma|F_o|$; $wR_2 = [\Sigma w(F_o^2 - F_c^2)^2/\Sigma wF_o^4]^{1/2}$.

 © 2007 Wiley-VCH Verlag GmbH & Co. KGaA, Weinheim 

## Acknowledgments

We thank the Engineering and Physical Sciences Research Council (EPSRC) for funding, the Royal Society (RS), U.K., and Department of Science and Technology (DST), India, for the award of an overseas network grant and M. D. S. University, Ajmer, India for granting a leave of absence (R. R. and K. S.).

[1] W. Levason, G. Reid, *J. Chem. Res. (S)* **2002**, 467–472.
[2] C. S. Tredget, F. Bonnet, A. R. Cowley, P. Mountford, *Chem. Commun.* **2005**, 3301–3303.
[3] L. Karmazin, M. Mazzanti, J. Pécaut, *Chem. Commun.* **2002**, 654–655.
[4] a) W. Levason, B. Patel, G. Reid, V.-A. Tolhurst, M. Webster, *J. Chem. Soc., Dalton Trans.* **2000**, 3001–3006; b) P. J. McKarns, T. S. Lewkebandara, G. P. A. Yap, L. M. Liable-Sands, A. L. Rheingold, C. H. Winter, *Inorg. Chem.* **1998**, *37*, 418–424; c) P. J. Wilson, A. J. Blake, M. Schröder, *Chem. Commun.* **1998**, 1007–1008; d) W. Levason, B. Patel, G. Reid, *Inorg. Chim. Acta* **2004**, *357*, 2115–2120.
[5] R. Hart, W. Levason, B. Patel, G. Reid, *J. Chem. Soc., Dalton Trans.* **2002**, 3153–3159.
[6] a) H.-J. Küppers, K. Wieghardt, *Polyhedron* **1989**, *8*, 1770–1773; b) N. R. Champness, S. R. Jacob, G. Reid, C. S. Frampton, *Inorg. Chem.* **1995**, *34*, 396–398; c) S. J. A. Pope, N. R. Champness, G. Reid, *J. Chem. Soc., Dalton Trans.* **1997**, 1639–1644; d) G. J. Grant, K. E. Rogers, W. N. Setzer, D. G. VanDerveer, *Inorg. Chim. Acta* **1995**, *234*, 35–45.
[7] a) M. C. Durrant, S. Davies, D. L. Hughes, C. Le Floc'h, R. L. Richards, J. R. Sanders, N. R. Champness, S. J. Pope, G. Reid, *Inorg. Chim. Acta* **1996**, *251*, 13–14; b) S. C. Davies, M. C. Durrant, D. L. Hughes, C. Le Floc'h, S. J. A. Pope, G. Reid, R. L. Richards, J. R. Sanders, *J. Chem. Soc., Dalton Trans.* **1998**, 2191–2198; c) G. R. Willey, M. T. Lakin, N. W. Alcock, *J. Chem. Soc., Chem. Commun.* **1991**, 1414–1416.
[8] W. Levason, M. C. Popham, G. Reid, M. Webster, *Dalton Trans.* **2003**, 291–294.
[9] C. D. Beard, L. Carr, M. F. Davis, J. Evans, W. Levason, L. D. Norman, G. Reid, M. Webster, *Eur. J. Inorg. Chem.* **2006**, 4399–4406.
[10] J. M. Tunney, J. McMaster, C. D. Garner, in *Comprehensive Coordination Chemistry II* (Eds.: J. A. McCleverty, T. J. Meyer), Elsevier, Amsterdam, **2004**, vol. 8, p. 459.
[11] See for example A. H. Hoveyda, R. R. Schrock, in *Comprehensive Asymmetric Catalysis* (Eds.: E. N. Jacobsen, A. Pfaltz, H. Yamamoto), Springer, Heidelberg, **2004**, vol. 1, p. 207 and references cited therein.
[12] D. Sevdić, L. Fekete, *Polyhedron* **1985**, *4*, 1371–1378.
[13] W. Levason, C. A. McAuliffe, F. P. McCullough, S. G. Murray, C. A. Rice, *Inorg. Chim. Acta* **1977**, *22*, 227–231.
[14] D. Sellmann, L. Zapf, *J. Organomet. Chem.* **1985**, *289*, 57–59.
[15] T. Yoshida, T. Adachi, T. Ueda, M. Watanabe, M. Kaminaka, T. Higuchi, *Angew. Chem. Int. Ed. Engl.* **1987**, *26*, 1171–1172.
[16] T. Adachi, M. D. Durrant, D. L. Hughes, C. J. Pickett, R. L. Richards, J. Talarmin, T. Yoshida, *J. Chem. Soc., Chem. Commun.* **1992**, 1464–1467.
[17] F. A. Cotton, G. L. Powell, *J. Am. Chem. Soc.* **1984**, *106*, 3371–3372.
[18] F. A. Cotton, M. P. Diebold, C. J. O'Connor, G. L. Powell, *J. Am. Chem. Soc.* **1985**, *107*, 7438–7445.
[19] D. Sevdić, L. Fekete, *Inorg. Chim. Acta* **1982**, *57*, 111–117.
[20] M. D. Brown, M. B. Hursthouse, W. Levason, R. Ratnani, G. Reid, *Dalton Trans.* **2004**, 2487–2491.
[21] a) O. Jarchow, F. Schröder, H. Schulz, *Z. Anorg. Allgem. Chem.* **1968**, *363*, 58–71; b) I. Abrahams, J. L. Nowinski, P. G. Bruce, V. C. Gibson, *J. Sol. State Chem.* **1993**, *102*, 140–145.
[22] a) M. F. Davis, W. Levason, R. Ratnani, G. Reid, T. Rose, M. Webster, *Eur. J. Inorg. Chem.* **2007**, 306–313; b) M. B. Hursthouse, W. Levason, R. Ratnani, G. Reid, *Polyhedron* **2004**, *23*, 1915–1921.
[23] X. Ma, K. Starke, C. Schulzke, H.-G. Schmidt, M. Noltemeyer, *Eur. J. Inorg. Chem.* **2006**, 628–637.
[24] K. Dreisch, C. Andersson, C. Stalhandske, *Polyhedron* **1991**, *10*, 2417–2421.
[25] V. C. Gibson, T. P. Kee, A. Shaw, *Polyhedron* **1990**, *9*, 2293–2298.
[26] a) W. Levason, B. Patel, G. Reid, A. J. Ward, *J. Organomet. Chem.* **2001**, *619*, 218–225; b) W. Levason, M. Nirwan, R. Ratnani, G. Reid, N. Tsoureas, M. Webster, *Dalton Trans.* **2007**, 439–448.
[27] Y. Yamamoto, S. Sakamoto, Y. Ohki, A. Usuzawa, M. Fujita, T. Mochida, *Dalton Trans.* **2003**, 3534–3540.
[28] a) A. K. Brisdon, E. G. Hope, W. Levason, J. S. Ogden, *J. Chem. Soc., Dalton Trans.* **1989**, 313–316; b) P. C. Crouch, G. W. A. Fowles, R. A. Walton, *J. Inorg. Nucl. Chem.* **1970**, *32*, 329–333.
[29] F. R. Hartley, S. G. Murray, W. Levason, H. E. Soutter, C. A. McAuliffe, *Inorg. Chim. Acta* **1979**, *35*, 265–277.
[30] a) J. S. Bradshaw, J. Y. Hui, B. L. Haymore, J. J. Christensen, R. M. Izatt, *J. Heterocycl. Chem.* **1973**, *10*, 1–4; b) J. S. Bradshaw, J. Y. Hui, Y. Chan, B. L. Haymore, R. M. Izatt, J. J. Christensen, *J. Heterocycl. Chem.* **1974**, *11*, 45–49.
[31] G. M. Sheldrick, SHELXS-97, *Program for crystal structure solution*, University of Göttingen, Germany, **1997**.
[32] G. M. Sheldrick, SHELXL-97, *Program for crystal structure refinement*, University of Göttingen, Germany, **1997**.

Received: January 12, 2007
Published Online: March 16, 2007

 © 2007 Wiley-VCH Verlag GmbH & Co. KGaA, Weinheim 

DOI: 10.1002/ejic.200600995

# Synthesis, Characterization, and DFT Investigation of $Ir^{III}$ Tolylterpyridine Complexes

Naokazu Yoshikawa,*[a] Shinichi Yamabe,[b] Nobuko Kanehisa,[c] Yasushi Kai,[c] Hiroshi Takashima,[a] and Keiichi Tsukahara[a]

**Keywords:** Iridium / Terpyridine / Absorption / Emission / Density functional calculations

Three new polypyridine iridium(III) complexes $[Ir^{III}Cl(L)(tterpy)](PF_6)_2$ {L = phen (**1**), dpphen (**2**), and dmbpy (**3**)} were prepared. Reference complexes $[Ir^{III}Cl(bpy)(tterpy)](PF_6)_2$ (**4**) and $[Ir^{III}(L)_2](PF_6)_3$ {L = tterpy (**5**) and terpy (**6**)} were also prepared. Abbreviations of the ligands used here are phen = 1,10-phenanthroline, dpphen = 4,7-diphenyl-1,10-phenanthroline, bpy = 2,2′-bipyridine, dmbpy = 4,4′-dimethyl-2,2′-bipyridine, tterpy = 4′-(4-tolyl)-2,2′:6′,2′′-terpyridine, and terpy = 2,2′:6′,2′′-terpyridine. The syntheses, which were accomplished in typical reaction times of fifteen minutes by using a microwave oven, were easier than a previous method. The complexes were characterized by electrospray mass spectrometry, UV/Vis spectroscopy, and cyclic voltammetry (CV). The X-ray structures of the two complexes **5** and **6** were also obtained. Cyclic voltammograms of all the $[Ir^{III}Cl(L)(tterpy)]^{2+}$ complexes showed that the first reduction occurred at around –0.67 V, which is attributed to the reduction of the tterpy ligand in $[Ir^{III}Cl(L)(tterpy)]^{2+}$. The electronic properties of complexes **5** and **6** were studied by using B3LYP functional calculations, and their optimized geometries were compared to those of the experimentally observed ones. Excited triplet and singlet states are also examined by using time-dependent density functional theory (TDDFT). The calculated energies of the lowest singlet and triplet states in the two complexes are in good agreement with the experimental absorption and phosphorescence spectra. In this study, it was found that $[Ir^{III}Cl(L)(tterpy)]^{2+}$ emits an intense phosphorescence at room temperature. Since the lowest unoccupied molecular orbitals (LUMOs) of all $[Ir^{III}Cl(L)(tterpy)]^{2+}$ complexes are composed of the $\pi^*$-system contribution of the tterpy ligand, the spectroscopic and electrochemical results are discussed comparatively.
(© Wiley-VCH Verlag GmbH & Co. KGaA, 69451 Weinheim, Germany, 2007)

## Introduction

Polypyridine complexes of $d^6$ transition metals have been studied extensively because of their useful spectroscopic and photophysical properties. In recent years, much interest has been devoted to $Ir^{III}$ complexes.[1–4] These iridium(III) complexes are known to exhibit high triplet quantum yields due to the mixing of the singlet and triplet excited states through spin-orbital coupling,[5] leading to high phosphorescence efficiencies. The attractive luminescence properties of $[Ir(terpy)_2]^{3+}$, particularly the long lifetime under aerated ambient conditions, render it of interest as the light-emitting component in sensory systems.[6] Bis(terpyridine) complexes of iridium(III) incorporating *meta*- or *para*-*N*-methylpyridyl substituents at the terpyridine 4′ position display long-lived luminescence in solution.[6,7] In particular, $Ir^{III}$ cyclometalated complexes have attracted great attention because of their applications in photonic devices and light-emitting diode (LED) displays.[8,9]

In our previous work, we synthesized and crystallized $[IrCl_2L_2]PF_6$ complexes {L = bqn, phen, dpphen, bpy, and dmbpy} to reveal their long-lived excited states and good photoluminescence efficiencies.[10–13] Abbreviations of the ligands used here are bqn = 2,2′-biquinoline, phen = 1,10-phenanthroline, dpphen = 4,7-diphenyl-1,10-phenanthroline, bpy = 2,2′-bipyridine, and dmbpy = 4,4′-dimethyl-2,2′-bipyridine. Recently, we focused on $Ir^{III}$ complexes with a 2,2′:6′,2′′-terpyridine (terpy) and a polypyridine ligand.[14,15] These iridium complexes have intense phosphorescence at room temperature and remarkably high quantum yields close to unity.[16]

Computational methods were used to predict or confirm photophysical properties of metal complexes. More recently, we designed and synthesized new $[Ru(CH_3CN)(L)(terpy)]^{2+}$ {L = phen, dpbpy, and bpm} complexes, bearing a labile $CH_3CN$ ligand, and their reference complexes $[RuCl(L)(terpy)]^+$ {L = phen, dpbpy, and dpphen}.[17] The time-dependent-density-functional-theory

[a] Department of Chemistry, Faculty of Science, Nara Women's University,
Nara 630-8506, Japan
Fax: +81-742-20-3395
E-mail: naokazuu@dream.com
[b] Department of Chemistry, Nara University of Education, Nara 630-8528, Japan
[c] Department of Applied Chemistry, Graduate School of Engineering, Osaka University,
Osaka 565-0871, Japan
Supporting information for this article is available on the WWW under http://www.eurjic.org or from the author.

 © 2007 Wiley-VCH Verlag GmbH & Co. KGaA, Weinheim 

(TDDFT) approach provided a good agreement between the computed and the experimental absorption spectra of these ruthenium complexes.[18]

To elucidate the source of intense emission and the electrochemical behavior of the $Ir^{III}$ polypyridine complex and confirm the positions of the HOMO and LUMO in the iridium complexes by using DFT and TDDFT calculations, we tried to synthesize several $Ir^{III}$ complexes with matrixes of a 4′-(4-tolyl)-2,2′:6′,2′′-terpyridine (tterpy) and a polypyridine ligand and also investigate the relations between the structures of a tterpy and a polypyridine ligand and the singlet and triplet electronic states in the iridium complexes. We also report an X-ray crystal structure of $[Ir(tterpy)_2](PF_6)_3$, because crystal structures of $Ir^{III}$-terpy complexes are very rare.[19,20]

## Results and Discussion

### X-ray Crystallographic Results

The structural formulae of all the complexes used in this work are shown in Figure 1. The structure of **5**, viz. $[Ir(tterpy)_2](PF_6)_3$, was confirmed by X-ray crystallography (Table 7). The ORTEP view of **5** is shown in Figure 2, and its selected bond lengths and angles are given in Table 1. The crystal structure of a mononuclear iridium compound, **5**, consists of a discrete $[Ir(tterpy)_2]^{3+}$ cation and three hexa-

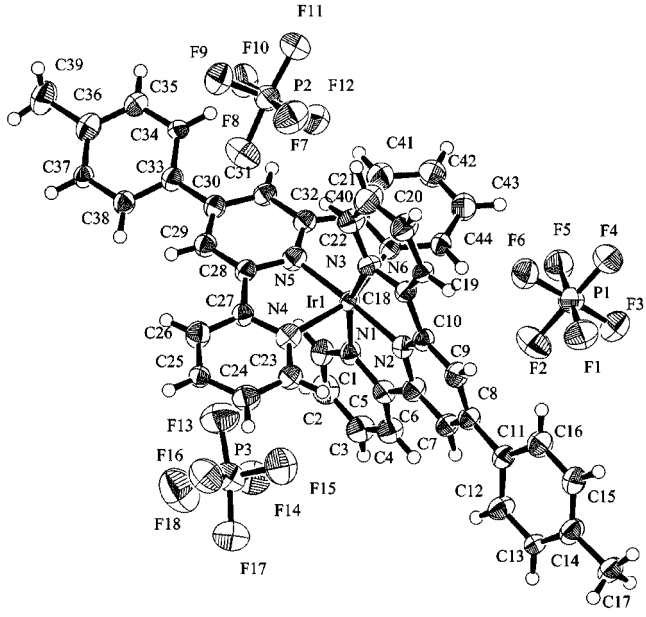


Figure 2. Molecular structure of $[Ir(tterpy)_2](PF_6)_3$ (**5**).

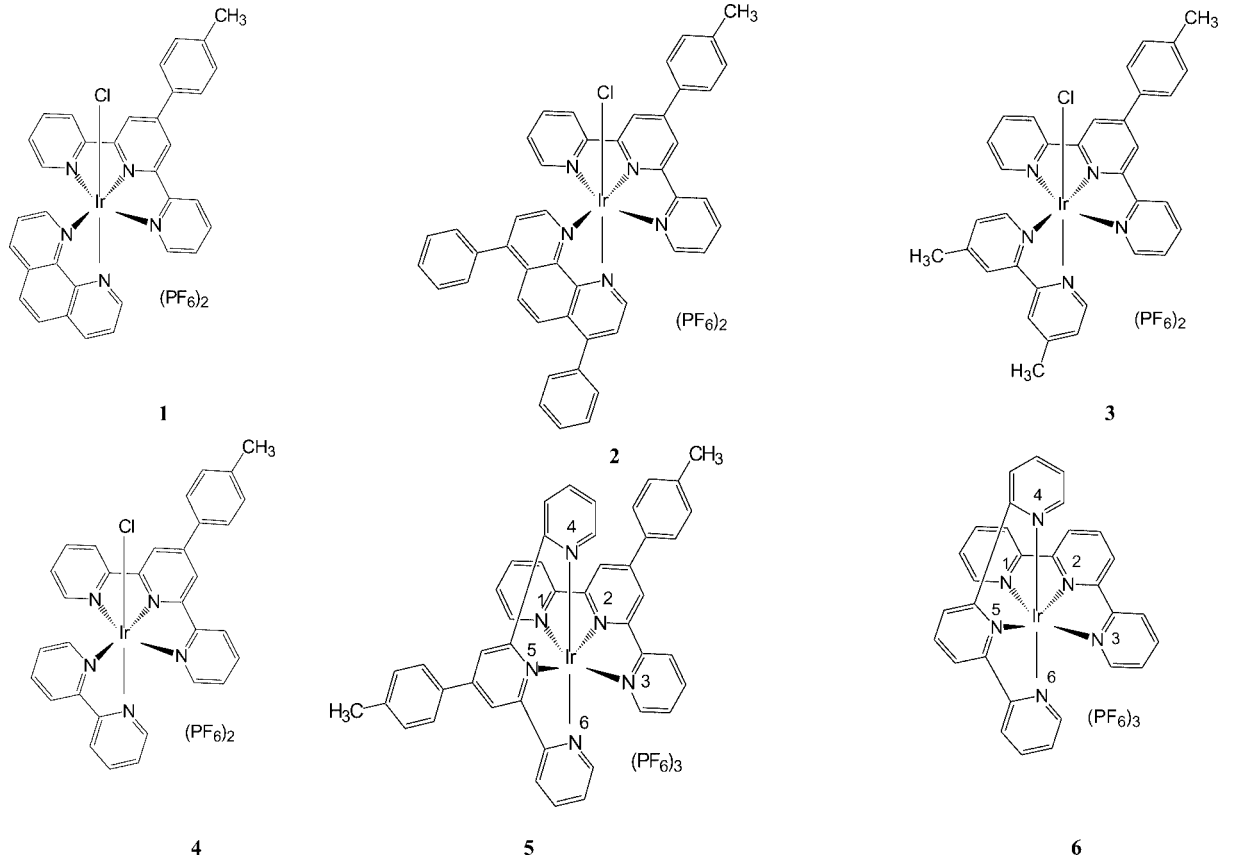


Figure 1. Structural formulae of iridium complexes.

 © 2007 Wiley-VCH Verlag GmbH & Co. KGaA, Weinheim 

fluorophosphate anions. The $Ir^{III}$ atom is located in a distorted octahedral environment formed by the two tterpy ligands. The Ir–N bond lengths are in the range 1.94(2)–2.09(3) Å and the three *trans* angles are in the range 159.1(7)–176.8(9)°, which are similar to the values of 1.978–2.058 Å and 160.2–177.8° reported for $[Ir(terpy)_2](PF_6)_3$.[19] The Ir cation is coordinated by six N atoms from a pair of chelating tterpy ligands. An equatorial plane is formed by atoms N2, N4, N5, and N6, where the largest deviation from the mean plane is 0.035(4) Å and the Ir atom is out of this plane by 0.013(3) Å. In the case of complex **5**, the axial positions are occupied by the tterpy N1 atom and another tterpy N3 atom. The $PF_6^-$ is not coordinated to the iridium metal atom but hydrogen bonded to ring protons. The average length of the Ir–N bonds is 2.035(2) Å and the average value of the ligand angles, N1–Ir–N2 and N2–Ir–N3 is 79.6(8)°, which compare well with the values of 2.026 Å and 79.1° reported for $[Ir(bpy)_3](ClO_4)_3$.[21]

Table 1. Selected bond lengths and angles for $[Ir(tterpy)_2](PF_6)_3$ (**5**).[a]

| Bond length [Å] | | | Angle [°] | | |
|---|---|---|---|---|---|
| Ir1–N1 | 2.04(2) | N1–Ir1–N2 | 78.5(8) | N3–Ir1–N4 | 92.3(10) |
| Ir1–N2 | 2.02(2) | N1–Ir1–N3 | 159.1(7) | N3–Ir1–N5 | 102.2(9) |
| Ir1–N3 | 2.09(2) | N1–Ir1–N4 | 91.2(9) | N3–Ir1–N6 | 91.1(9) |
| Ir1–N4 | 2.09(3) | N1–Ir1–N5 | 98.7(9) | N4–Ir1–N5 | 82.0(10) |
| Ir1–N5 | 1.94(2) | N1–Ir1–N6 | 92.6(9) | N4–Ir1–N6 | 160.2(9) |
| Ir1–N6 | 2.03(2) | N2–Ir1–N3 | 80.7(8) | N5–Ir1–N6 | 78.2(9) |
| N7–C45 | 1.24(4) | N2–Ir1–N4 | 96.6(9) | N7–C45–C46 | 167(3) |
| | | N2–Ir1–N5 | 176.8(9) | | |
| | | N2–Ir1–N5 | 103.3(9) | | |

[a] Standard deviations are given in parentheses.

## Absorption Properties

The electronic absorption spectra for iridium(III) polypyridyl complexes contain typical π–π* and n–π* bands in the ultraviolet region. The electronic absorption spectra for **1**, **2**, and **5** are shown in Figure 3, and the spectroscopic data for the complexes **1**–**6** and the tterpy and terpy ligands are tabulated in Table 2.[22] While the shapes of the spectra are similar, the absorption band at 282 nm for **2** is red shifted relative to that at 272 nm for **1** (Figure 3), owing to the two phenyl groups attached to complex **2**. The absorption band at 272 nm in **1** has been assigned as a phen(π)–phen(π*) transition.[14] Similarly, the bands at 282 nm in **2** could be assigned as dpphen(π)–dpphen(π*) transitions.[10] The absorption bands at 311 nm in both **1** and **2** have been assigned as tterpy(π)–tterpy(π*) transitions. On the other hand, the absorption spectrum of **4** with a bpy ligand is very similar to that of **3** with a dmbpy ligand. This indicates that the two methyl groups introduced in the bpy ligand did not affect the absorption spectra of **3** and **4**. The absorption bands at 252, 278, and 306 nm in the free tterpy are the same as those in **5** (Table 2) and have been assigned as tterpy(π)–tterpy(π*) transitions.[10] Although the free tterpy ligand does not absorb around 320–500 nm, **5** exhibits large absorption bands at 346 and 374 nm. As a consequence of complex formation, the electronic charges are delocalized, and thus the absorption bands at 346 and 306 nm in **5** can be assigned as tterpy(π)–tterpy(π*) transitions. The *para*-tolyl group attached to the terpy ring has the role of expanding the conjugation.

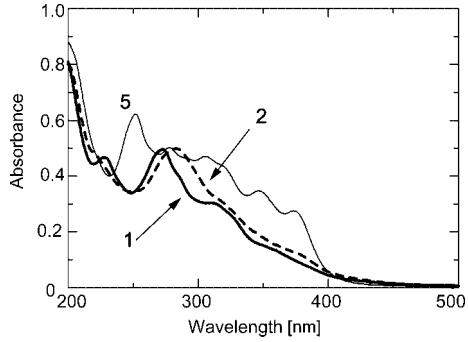


Figure 3. UV spectra of iridium complexes, **1**: $[IrCl(phen)(tterpy)]^{2+}$ (bold line), **2**: $[IrCl(dpphen)(tterpy)]^{2+}$ (broken line), and **5**: $[Ir(tterpy)_2]^{3+}$ (solid line) in $CH_3CN$ solution ($1.0 \times 10^{-5}$ M) at 25 °C.

## Electrochemistry

The electrochemical data obtained from cyclic voltammetry (CV) measurements are tabulated in Table 3. As for the complexes **5** and **6**, the first reductions occurred at the same potential (–0.67 V) and were assigned as tterpy/tterpy$^-$ and terpy/terpy$^-$ ligand-centered (LC) processes, respectively.[19] Two successive irreversible reductions of the ligand were then observed as shown in Figure 4. The similarity in

Table 2. Absorption properties for the complexes and ligands in $CH_3CN$ at 25 °C.

| | $\lambda_{max}$ [nm] ($\varepsilon$ [$10^3$ M$^{-1}$ cm$^{-1}$]) | | | | | |
|---|---|---|---|---|---|---|
| $[IrCl(phen)(tterpy)](PF_6)_2$ (**1**) | | 272(49.7) | 311(30.2) | 359(13.7) | | |
| $[IrCl(dpphen)(tterpy)](PF_6)_2$ (**2**) | | 282(54.6) | 311(37.2) | 375(17.3) | | |
| $[IrCl(dmbpy)(tterpy)](PF_6)_2$ (**3**) | 253(32.3) | 278(30.5) | 313(28.3) | | | |
| $[IrCl(bpy)(tterpy)](PF_6)_2$ (**4**) | 237(34.7) | 275(35.0) | 313(32.6) | | | |
| $[Ir(tterpy)_2](PF_6)_3$ (**5**) | 251(62.1) | 278(50.3) | 306(47.2) | 346(34.6) | 374(27.8) | |
| $[Ir(terpy)_2](PF_6)_3$ (**6**) | 251(27.6)[a] | 277(22.2)[a] | 313(11.4)[a] | 325(11.8)[a] | 352(5.8)[a] | 374(1.3)[a] |
| | | 273[0.2034][b] | 324[0.0794][b] | 329[0.1159][b] | 348[0.0618][b] | 385[0.0113][b] |
| tterpy | 252(43.2) | 278(52.0) | 306(13.3) | | | |
| terpy | 237(17.1) | 280(15.6) | | | | |
| | 248[0.3289][b] | 262[0.1924][b] | 275[0.1337][b] | 296[0.1569][b] | | |

[a] Ref.[19] [b] Obtained by RB3LYP/6-31+G*TD calculations. Oscillator strengths are shown in square brackets.

 © 2007 Wiley-VCH Verlag GmbH & Co. KGaA, Weinheim 

Table 3. Electrochemical properties of the complexes in DMF (V vs. Ag/AgCl).[a]

| | $E_{1pc}$ | $\Delta E_1$ | $E_{2pc}$ | $E_{3pc}$ | $\Delta E_3$ | $E_{4pc}$ | $\Delta E_4$ |
|---|---|---|---|---|---|---|---|
| [IrCl(phen)(tterpy)]$(PF_6)_2$ (**1**) | –0.78 | | –1.06 | –1.27 | 120 | –1.68 | 130 |
| [IrCl(dpphen)(tterpy)]$(PF_6)_2$ (**2**) | –0.78 | | –0.99 | –1.18 | 100 | –1.63 | 140 |
| [IrCl(dmbpy)(tterpy)]$(PF_6)_2$ (**3**) | –0.83 | | –1.06 | –1.41 | 150 | –1.70 | 160 |
| [IrCl(bpy)(tterpy)]$(PF_6)_2$ (**4**) | –0.78 | | –1.00 | –1.27 | 90 | –1.65 | 100 |
| $[Ir(tterpy)_2](PF_6)_3$ (**5**) | –0.67 | 70 | –0.80 | | | | |
| | –0.81[b] | | –0.91[b] | | | | |
| $[Ir(terpy)_2](PF_6)_3$ (**6**) | –0.67 | 70 | –0.80 | | | | |
| | –0.76[b] | | –0.91[b] | | | | |

[a] $E_{pc}$ means the reduction peak potential. $\Delta E$ is a peak separation between the anodic and cathodic peak potentials. [b] Ref.[19] Potentials are vs. SCE.

these successive reduction potentials between **5** and **6** indicates that both of the reductions occur on the terpyridine ligand frame. Similarly, the first reduction waves of **1** and **2** were at –0.78 V, but the second and third ones appeared at different potentials, –1.06 and –1.27 V for **1** and –0.99 and –1.18 V for **2**. The slightly positive shift in the reduction potential of **2** compared to those in **1** is probably due to the effect of the dpphen ligand (electron-withdrawing ligand). Complexes **3** and **4** gave the second reduction waves at –1.06 and –1.00 V, respectively, as a result of the effect of the electron-donating dmbpy. From these results, both the first and the second reduction waves are assigned as tterpy-centered reductions.[21] Using an electron-donating ligand dmbpy the third reduction potential in **3** was cathodically shifted relative to the reduction potential of **4**, i.e. 140 mV, they can therefore be assigned as polybipyridine-centered reductions. The fourth reduction waves of **1**, **2**, **3**, and **4** occurred at around –1.68, –1.63, –1.70, and –1.65 V, respectively. These processes have also been assigned as tterpy ligand-centered reductions.[10]

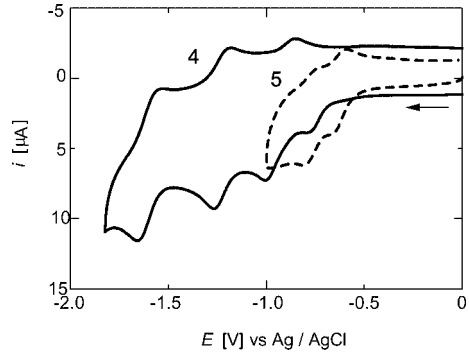


Figure 4. Cyclic voltammograms of **4**: $[IrCl(bpy)(tterpy)]^{2+}$ (bold line) and **5**: $[Ir(tterpy)_2]^{3+}$ (broken line) in $CH_3CN$ solution ($5.0 \times 10^{-4}$ M) at 25 °C with a scan rate of 100 mV $s^{-1}$.

The typical electrochemical behavior of iridium(III) polypyridine complexes are ligand-site oxidations and reductions. The highest occupied molecular orbital (HOMO) is localized on the ligand molecule, and the oxidative processes take place there. The six 5d lone-pair electrons on $Ir^{3+}$ are not involved in the HOMO, which leads to the absence of MLCT bands in the present six systems. The lowest unoccupied molecular orbital (LUMO) is also localized on the polypyridine ligand. In the case of the iridium complexes comprising a terpy and a bpy ligand, the LUMO is localized on the former ligand.[14]

## Emission Properties

The emission maxima and the excited-state lifetimes of the $[IrCl(L)(tterpy)]^{2+}$, $[Ir(tterpy)_2]^{3+}$, and $[Ir(terpy)_2]^{3+}$ systems are given in Table 4. Complex **1** has an intense phosphorescence band maximum at $\lambda_{em}$ = 537 nm ($\lambda_{ex}$ = 311 nm) in a solution at room temperature, whereas **2**, having a dpphen ligand, shows a slightly red shifted one at 539 nm (Figure 5). Complex **4** also displays strong phosphorescence at $\lambda_{em}$ = 542 nm ($\lambda_{ex}$ = 313 nm), whereas **3** with a dmbpy ligand exhibits a slight blue shift to 535 nm. It was found that the use of dpphen slightly extends the lifetime ($\tau$) of the $^3(\pi^*)$ excited state of the $Ir^{III}$ polypyridine complex ($\tau$ = 0.67 μs for **2**). However, in spite of the electron-withdrawing character of dpphen **2** gave a smaller emission quantum yield ($\phi$ = 0.096) relative to that of **1** ($\phi$ = 0.165). In complex **3**, the use of the dmbpy instead of the bpy ligand also resulted in the same lifetime as that of the π–π* transition in **3** ($\tau$ = 0.68 μs), and its emission quantum yield ($\phi$ = 0.110) was also similar to that of **4** ($\phi$ = 0.111). The emission spectrum of complex **5** shows a peak at 506 nm ($\lambda_{ex}$ = 305 nm) corresponding to the excited state of $^3$LC whenever the excitation is performed at 270 or 311 nm (Figure 5). This can be assigned to the phosphorescence from the tterpy* excited state (Table 4).[14]

Table 4. Emission properties and lifetimes of the $Ir^{III}$ complexes in $CH_3CN$ at 25 °C.

| | $\lambda_{ex}$ [nm] | $\lambda_{max}$ [nm] | $\tau$ [μs] | $\phi$[a] |
|---|---|---|---|---|
| [IrCl(phen)(tterpy)]$(PF_6)_2$ (**1**) | 311 | 537 | 0.63 | 0.165 |
| [IrCl(dpphen)(tterpy)]$(PF_6)_2$ (**2**) | 311 | 539 | 0.67 | 0.096 |
| [IrCl(dmbpy)(tterpy)]$(PF_6)_2$ (**3**) | 312 | 535 | 0.68 | 0.110 |
| [IrCl(bpy)(tterpy)]$(PF_6)_2$ (**4**) | 313 | 542 | 0.67 | 0.111 |
| $[Ir(tterpy)_2](PF_6)_3$ (**5**) | 305 | 506[b] | 2.4[b] | 0.029[b] |
| $[Ir(terpy)_2](PF_6)_3$ (**6**) | 313 | 458[b] | 1.2, 1.0[b] | 0.025[b] |

[a] The emission quantum yields were determined for nitrogen-equilibrated samples at 25 °C relative to that of the $[Ru(bpy)_3]^{2+}$ ($\phi$ = 0.062) solution with the same absorbance. [b] Ref.[19]

 © 2007 Wiley-VCH Verlag GmbH & Co. KGaA, Weinheim 

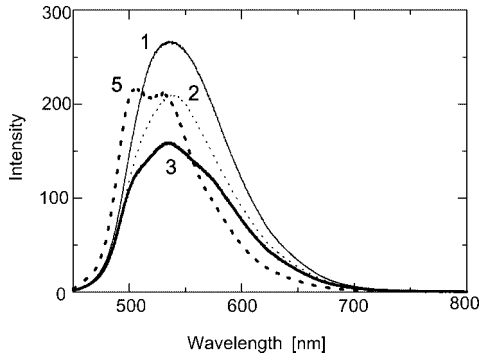


Figure 5. Emission spectra of iridium complexes in degassed $CH_3CN$ solution ($1.0 \times 10^{-5}$ M) at 25 °C. **1**: $[IrCl(phen)(tterpy)]^{2+}$ (bold line), **2**: $[IrCl(dpphen)(tterpy)]^{2+}$ (dotted line), **3**: $[IrCl(dpphen)(tterpy)]^{2+}$ (solid line), and **5**: $[Ir(tterpy)_2]^{2+}$ (broken line).

## DFT Calculations and Orbital Analyses

The experimental results obtained here suggest that the frontier orbitals (HOMO and LUMO) of the complexes are composed of the ligand π and π* components. The dπ components do not seem to be involved in the frontier orbitals. The absence of MLCT bands in Ir–terpyridine complexes has also been reported.[14,16] Apparently, the $Ir^{3+}$ cation works as a center of electrostatic stabilization in the complex, in addition to its role in spin-orbit coupling. In order to confirm the trend, DFT calculations were carried out for **5** and **6**. The geometries of $[Ir(tterpy)_2]^{3+}$ and $[Ir(terpy)_2]^{3+}$ were fully optimized in the closed-shell singlet and biradical triplet states. The calculated geometric values in the singlet state are comparable to the experimental ones determined in the present X-ray analyses (Table 5). Calculated metal–ligand bond lengths (angstroms) from singlet and triplet states (parentheses) for iridium complexes are shown in Figure S1. For instance, the calculated values for the Ir–N1 bond length (2.098 Å) and N1–Ir–N2 bond angle (80.2°) of **5** are comparable to the experimental values, 2.04 Å and 78.5°, determined from the X-ray structure, respectively. Calculated spin densities from the triplet state for iridium complexes are given in Figure S2. Table 6 exhibits the thirteen excited states of **6**, which result from low-energy one-electron transitions. The π–π* excitations occur between degenerate atomic orbitals of the tterpy ligand. The HOMO and HOMO–1 should be the frontier donor molecular orbitals, which were found not to be 5dπ but π MOs. The

Table 5. Comparison of the calculated bond lengths and angles from singlet and triplet states for complexes **5** and **6** with the present experimental values from X-ray diffraction.

| | Bond length [Å] | | | | Angle [°] | | |
|---|---|---|---|---|---|---|---|
| | | Calculated | | Experimental | | Calculated | Experimental |
| | | Singlet | Triplet | Singlet | | | |
| **5** | Ir–N1 | 2.098 | 2.095 | 2.04(2) | N1–Ir–N2 | 80.2 | 78.5(8) |
| | Ir–N2 | 2.003 | 2.010 | 2.02(2) | N1–Ir–N3 | 160.3 | 159.1(7) |
| | Ir–N3 | 2.098 | 2.095 | 2.09(2) | N1–Ir–N4 | 91.7 | 91.2(9) |
| | Ir–N4 | 2.098 | 2.095 | 2.09(3) | N1–Ir–N5 | 99.8 | 98.7(9) |
| | Ir–N5 | 2.003 | 1.985 | 1.94(2) | N1–Ir–N6 | 91.6 | 92.6(9) |
| | Ir–N6 | 2.098 | 2.095 | 2.03(2) | N2–Ir–N3 | 80.2 | 80.7(8) |
| **6** | Ir–N1 | 2.099 | 2.075 | 2.054[a] | N1–Ir–N2 | 80.4 | 80.3[a] |
| | Ir–N2 | 2.006 | 1.990 | 1.979[a] | N1–Ir–N3 | 160.7 | 160.2[a] |
| | Ir–N3 | 2.099 | 2.075 | 2.056[a] | N1–Ir–N4 | 91.6 | 92.4[a] |
| | Ir–N4 | 2.099 | 2.095 | 2.058[a] | N1–Ir–N5 | 99.7 | 100.4[a] |
| | Ir–N5 | 2.006 | 2.010 | 1.978[a] | N1–Ir–N6 | 91.6 | 91.4[a] |
| | Ir–N6 | 2.099 | 2.095 | 2.056[a] | N2–Ir–N3 | 80.4 | 80.0[a] |

[a] From ref.[19]

Table 6. Calculated low-energy excitations in complex **6**.[a]

| State | Assignment | *E* [eV] | λ [nm] | *f* |
|---|---|---|---|---|
| S1 | HOMO→LUMO (0.66); HOMO–1→LUMO (0.11); HOMO–2→LUMO (0.17) | 3.22 | 385.34 | 0.0113 |
| S2 | HOMO→LUMO+1 (0.66); HOMO–1→LUMO+1 (0.11); HOMO–2→LUMO+1 (0.17) | 3.22 | 385.33 | 0.0114 |
| S3 | HOMO→LUMO (0.14); HOMO–1→LUMO (0.67) | 3.56 | 348.41 | 0.0617 |
| S4 | HOMO→LUMO+1 (0.14); HOMO–1→LUMO+1 (0.67) | 3.56 | 348.40 | 0.0618 |
| S5 | HOMO→LUMO+2 (0.37); HOMO–3→LUMO+1 (0.33); HOMO–3→LUMO (0.22) HOMO–4→LUMO+1 (0.22); HOMO–4→LUMO (0.33); | 3.76 | 330.01 | 0.0020 |
| S6 | HOMO→LUMO (0.15); HOMO–2→LUMO (0.66) | 3.77 | 328.75 | 0.1159 |
| S7 | HOMO→LUMO+1 (0.15); HOMO–2→LUMO+1 (0.66) | 3.77 | 328.75 | 0.1159 |
| S8 | HOMO→LUMO+2 (0.52); HOMO–1→LUMO+3 (0.23); HOMO–2→LUMO+2 (0.18) HOMO–3→LUMO+1 (0.21); HOMO–3→LUMO (0.14); HOMO–4→LUMO+1 (0.14); HOMO–4→LUMO (0.21); | 3.83 | 323.61 | 0.0794 |
| S9 | HOMO–1→LUMO+3 (0.55); HOMO–2→LUMO+2 (0.39) | 4.13 | 300.46 | 0.0758 |
| S10 | HOMO→LUMO+5 (0.16); HOMO–3→LUMO+3 (0.39); HOMO–4→LUMO+3 (0.24) HOMO–4→LUMO+2 (0.46) | 4.16 | 298.33 | 0.1173 |
| S11 | HOMO→LUMO+6 (0.16); HOMO–3→LUMO+3 (0.24); HOMO–3→LUMO+2 (0.46) HOMO–4→LUMO+3 (0.39) | 4.16 | 298.30 | 0.1171 |
| S12 | HOMO→LUMO+4 (0.13); HOMO→LUMO+2 (0.21); HOMO–1→LUMO+3 (0.27) HOMO–2→LUMO+2 (0.53); HOMO–5→LUMO (0.11); HOMO–6→LUMO+1 (0.11) | 4.25 | 291.62 | 0.0879 |
| S13 | HOMO→LUMO+4 (0.46); HOMO–2→LUMO+4 (0.15); HOMO–5→LUMO+1 (0.19) HOMO–5→LUMO (0.24); HOMO–6→LUMO+1 (0.24); HOMO–6→LUMO (0.20) | 4.54 | 272.93 | 0.2034 |

[a] For each singlet state main electron configurations are displayed where absolute values of their coefficients are shown in parentheses.

 © 2007 Wiley-VCH Verlag GmbH & Co. KGaA, Weinheim 

LUMO, LUMO+1, and LUMO+2 are the expected ligand π* orbitals. Thus, the low-energy one-electron transitions should be mainly HOMO→LUMO, LUMO+1, LUMO+2 and HOMO–1→LUMO, LUMO+1, LUMO+2, which are actually shown in Table 6.

The free terpy and tterpy molecules are nonplanar; the N–C–C–N dihedral angles are 32.1° and 32.02°, respectively. In complexes **5** and **6**, these molecules are fixed to be planar. The forced planarity raises the HOMO energy [–0.246 a.u. (nonplanar) → –0.238 a.u. (planar), by RHF/LANL2MB] and lowers the LUMO energy [+0.194 a.u. (nonplanar) → +0.184 a.u. (planar)]. That is, the forced planarity leads to a smaller HOMO–LUMO energy gap (the larger conjugation) and consequently to a larger $\lambda_{max}$ value. The question as to why MLCT bands are absent in the $Ir(terpy)_2^{3+}$ complex is considered. In the nearly octahedral geometry of $Ir(terpy)_2^{3+}$ the $5d_{z^2-(x^2+y^2)}$ and $5d_{x^2-y^2}$ atomic orbitals of Ir along the *x*, *y*, and *z* axes are vacant and the $5d_{xy}$, $5d_{yz}$, and $5d_{xz}$ (5dπ orbitals) are lone-pair orbitals. These lone-pair orbitals are low-lying (–1.657 a.u. by RHF/LAN2MB), because the metal center is $Ir^{3+}$. Scheme 1 illustrates the orbital mixing of the 5dπ-containing occupied MOs. In the Cartesian coordinate shown in Scheme 1, the HOMO of the terpy ring may overlap with the $5d_{xz}$ orbital. The shape of the HOMO is shown in Scheme 2. However, the mixing is very small because the 2pπ coefficient of N3 and N1 is only 0.172 in the terpy HOMO. The HOMO–1 of the terpy ligand may overlap with the $5d_{yz}$ orbital. But the nodal property inside 5dπ orbital again makes the overlap small (Scheme 3). The HOMO–2 cannot overlap with the $5d_{xz}$ (Scheme 4), and the HOMO–3 may overlap with the $5d_{xz}$ orbital. However, the overlap again suffers partial cancellation of Scheme 3. Thus, the MLCT pattern is absent owing to the low orbital energy of $Ir^{3+}$ and the ineffective 5dπ–π orbital overlap.

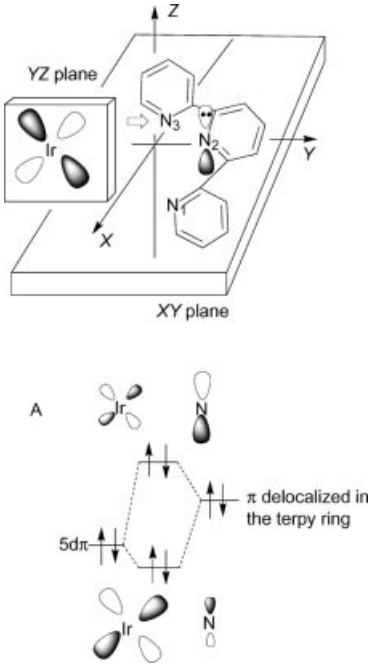


Scheme 1. One example of the orbital mixing that makes high-lying and 5dπ-containing occupied orbitals (A).

## Conclusions

Three new polypyridine iridium(III) complexes $[Ir^{II-I}Cl(L)(tterpy)](PF_6)_2$ were prepared {L = phen (**1**), dpphen (**2**), and dmbpy (**3**)}. Reference complexes $[Ir^{III}Cl(bpy)(tterpy)](PF_6)_2$ (**4**) and $[Ir^{III}(L)_2](PF_6)_3$ {L = tterpy (**5**) and terpy (**6**)} were also prepared and the X-ray structure of **5** was obtained. Cyclic voltammograms of all the $[Ir^{III}Cl(L)(tterpy)](PF_6)_2$ complexes showed that the first reduction occurred at around –0.67 V, which is attributed to the reduction of the tterpy ligand in $[Ir^{III}Cl(L)(tterpy)]^{2+}$. The electronic properties of complexes **5** and **6** were studied by using B3LYP functional calculations. Optimized geometries were compared to the experimentally observed structures. Excited singlet and triplet states were examined by using TDDFT. The calculated energies of the lowest singlet state of **6** are in good agreement with experimental absorption spectra. The LUMOs of all $[Ir^{III}Cl(L)(tterpy)]^{2+}$ complexes are composed of the π* system of the tterpy ligand. It was also found that $[Ir^{III}Cl(L)(tterpy)]^{2+}$ emits an intense phosphorescence at room temperature. The spectroscopic and electrochemical results were discussed comparatively. In the DFT calculations for the complexes **5** and **6** these molecules are fixed to be planar. The forced planarity raised the HOMO energy and lowered the LUMO energy, i.e., the forced planarity led to a smaller HOMO–LUMO energy gap (the larger conjugation) and consequently to a larger $\lambda_{max}$ value. However, the MLCT pattern was absent owing to the low orbital energy of $Ir^{3+}$ and the ineffective 5dπ–π orbital overlap.

## Experimental Section

**Reagents:** The materials used in the present experiments were of analytical reagent grade. The reagents are as follows: ammonium hexachloroiridate {$(NH_4)_3[IrCl_6]$, Aldrich}, bpy (Aldrich), dmbpy (Aldrich), phen (Aldrich), dpphen (Aldrich), tterpy (Aldrich), terpy (Aldrich), and potassium hexafluorophosphate ($KPF_6$, Wako). Tetrabutylammonium perchlorate {TBAP, $[(C_4H_9)_4N]ClO_4$, Aldrich} as a supporting electrolyte was purchased and used without further purification. $CH_3CN$ and *N*,*N*-dimethylformamide (DMF) used in spectroscopic and electrochemical studies were of spectroscopic grade obtained from Dojindo Laboratory. $[Ir(tterpy)_2](PF_6)_3$ (**5**) and $[Ir(terpy)_2](PF_6)_3$ (**6**) were prepared according to a previous method.[14] All other reagents and solvents were of guaranteed grade.

**Syntheses of the Mixed-Ligand Complexes $[IrCl(L)(tterpy)](PF_6)_2$ (1–4):** Syntheses of the complexes were undertaken by using a Mitsubishi Electric RR-12AF microwave oven (500 W, 2450 MHz) on medium-high power in a round-bottom flask fitted with a reflux condenser.[10,23] One target complex **3** (L = dmbpy), for example, was prepared by a sequential procedure with a ligand replacement. $(NH_4)_3[IrCl_6]$ (0.238 g, 0.500 mmol) and tterpy (0.161 g, 0.500 mmol) were mixed in ethylene glycol (15 mL). The suspended

 © 2007 Wiley-VCH Verlag GmbH & Co. KGaA, Weinheim 

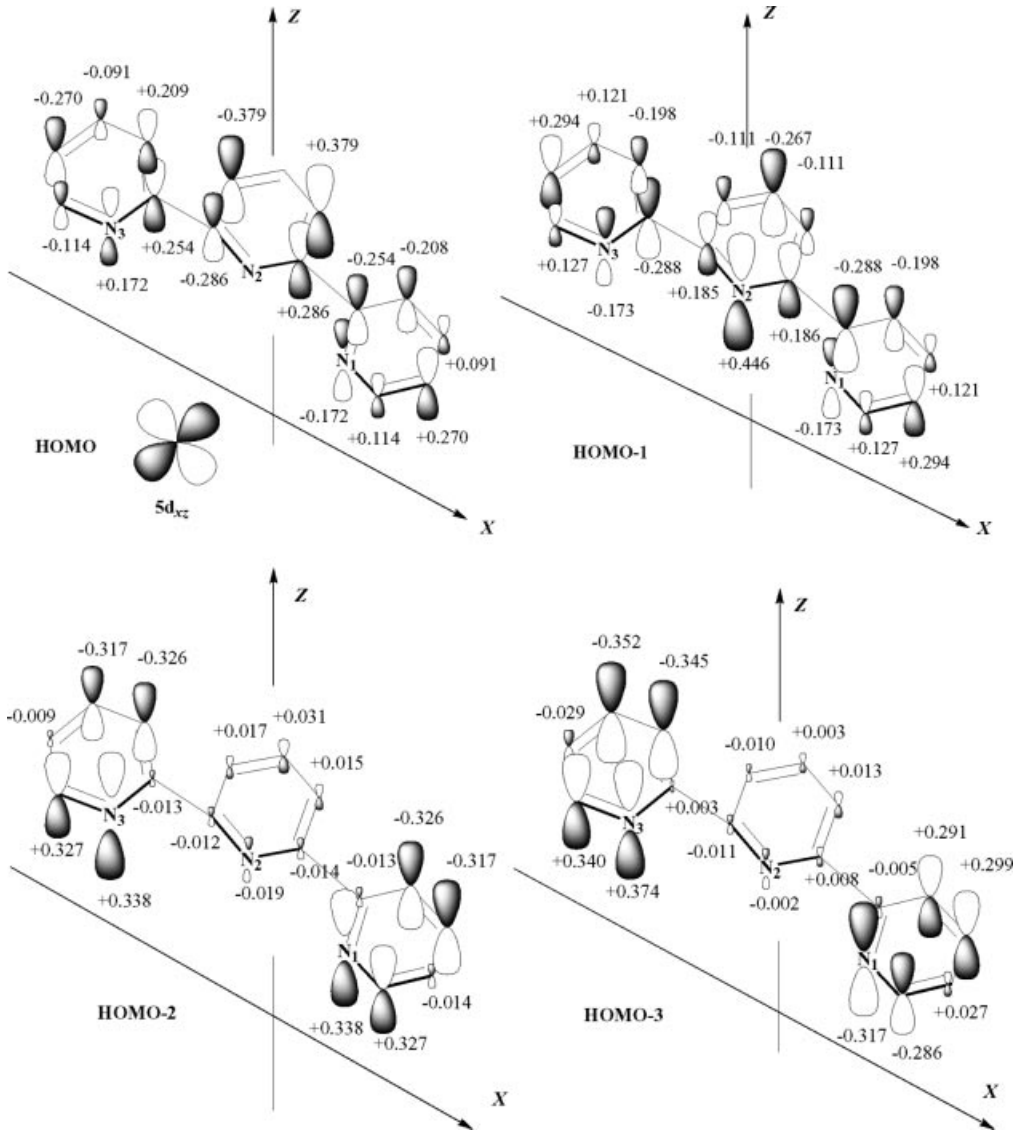


Scheme 2. MOs of the fixed planar terpyridine ligand.

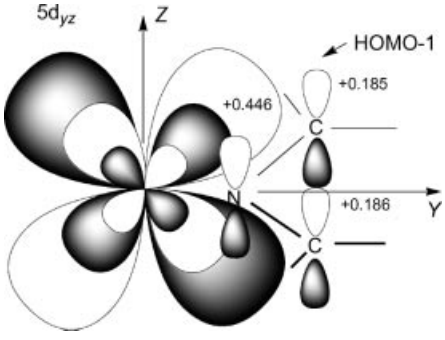


Scheme 3. The overlap between the 5d$_{yz}$ of $Ir^{3+}$ and the HOMO–1 of terpy. The outer white-white overlap in the $Y > 0$, $Z > 0$ region is diminished by the inner shaded-white overlap.

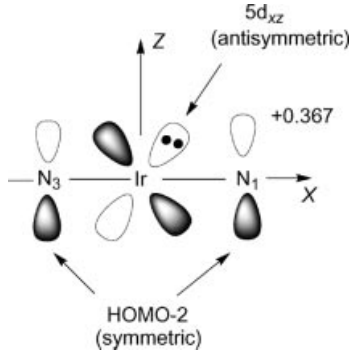


Scheme 4. The overlap between the HOMO–2 and 5d$_{xz}$ is zero (out of phase).

mixture was heated under reflux for 3 min in a microwave oven under a purging nitrogen atmosphere. Next, dmbpy (0.092 g, 0.500 mmol) was added to the mixture, and the refluxing was continued for 12 min. The mixture was then cooled to room temperature. A saturated aqueous solution of $KPF_6$ (20 mL) was added to provide the counterion $PF_6^-$, and a light yellow product **3** began to precipitate and was collected by vacuum filtration. The residue was dissolved in a minimal amount of $CH_3CN$ and immediately precipitated in diethyl ether. The product was separated by vacuum filtration and was dried under a vacuum. The purity of the yellow

 © 2007 Wiley-VCH Verlag GmbH & Co. KGaA, Weinheim 

complex was checked by thin-layer chromatography. Yield: 328 mg (63%). $C_{34}H_{29}ClF_{12}IrN_5P_2{\cdot}H_2O$ (1043.24): calcd. C 39.14, H 3.00, N 6.71; found C 39.47, H 3.15, N 6.30. $^1$H NMR ([D$_6$]DMSO): $\delta$ = 9.50 (s, 1 H, tterpy-H$_{3'}$), 9.31 (s, 1 H, tterpy-H$_{3''}$), 9.13 (d, $J$ = 7.6 Hz, 2 H, tterpy-H), 9.04 (d, $J$ = 8.4 Hz, 1 H, dmbpy-H), 8.87 (s, 1 H, dmbpy-H$_3$) 8.68 (s, 1 H, dmbpy-H$_{3'}$), 8.32 (m, 3 H, tterpy-H, dmbpy-H), 8.23 (d, $J$ = 7.6 Hz, 2 H, tterpy-H), 7.90 (d, $J$ = 7.6 Hz, 2 H, tterpy-H), 7.82 (d, $J$ = 4.8 Hz, 1 H, dmbpy-H), 7.61 (d, $J$ = 8.0 Hz, 1 H, dmbpy-H), 7.57–7.51 (m, 3 H, tterpy-H and tterpy-H), 2.52 (s, 6 H, dmbpy-CH$_3$), 2.04 (s, 3 H, tterpy-CH$_3$) ppm. ESI MS {[IrCl(dmbpy)(tterpy)](PF$_6$)$_2$ in CH$_3$CN, positive}: $m/z$ = 367.51 {[M – (PF$_6$)$_2$]$^{2+}$ requires 367.65}, 879.45 ([M – PF$_6$]$^+$ requires 880.26).

**[IrCl(phen)(tterpy)](PF$_6$)$_2$·H$_2$O (1):** Yield: 129 mg (22%). $C_{34}H_{25}ClF_{12}IrN_5P_2{\cdot}H_2O$ (1039.23): calcd. C 39.30, H 2.62, N 6.74; found C 39.10, H 2.92, N 6.78. $^1$H NMR ([D$_6$]DMSO): $\delta$ = 9.97 (d, $J$ = 5.2 Hz, 1 H, phen-H), 9.92 (d, $J$ = 5.2 Hz, 1 H, tterpy-H), 9.50 (s, 1 H, tterpy-H), 9.36 (s, 1 H, tterpy-H), 9.26 (dd, $J$ = 8.0 Hz, 1 H, phen-H), 9.13 (t, $J$ = 8.4 Hz, 1 H, tterpy-H), 9.05 (d, $J$ = 8.0 Hz, 1 H, tterpy-H), 8.78 (d, $J$ = 8.0 Hz, 1 H, phen-H), 8.72 (d, $J$ = 8.0 Hz, 1 H, tterpy-H), 8.56 (d, $J$ = 8.4 Hz, 1 H, phen-H), 8.46 (d, $J$ = 5.6 Hz, 1 H, tterpy-H), 8.35–8.26 (m, 3 H, phen-H, tterpy-H and tterpy-H), 8.04 (d, $J$ = 5.2 Hz, 1 H, tterpy-H), 7.91 (d, $J$ = 6.4 Hz, 1 H, phen-H), 7.74 (dd, $J$ = 5.2 Hz, 1 H, phen-H), 7.67–7.61 (m, 2 H, tterpy-H and tterpy-H), 7.58–7.48 (m, 3 H, phen-H, tterpy-H, and tterpy-H), 2.03 (s, 3 H, tterpy-CH$_3$) ppm. ESI MS {[IrCl(phen)(tterpy)](PF$_6$)$_2$ in CH$_3$CN, positive}: $m/z$ = 365.52 {[M – (PF$_6$)$_2$]$^{2+}$ requires 365.64}, 875.47 ([M – PF$_6$]$^+$ requires 876.25).

**[IrCl(dpphen)(tterpy)](PF$_6$)$_2$·2H$_2$O (2):** Yield: 108 mg (18%). $C_{46}H_{33}ClF_{12}IrN_5P_2{\cdot}2H_2O$ (1209.44): calcd. C 45.68, H 3.08, N 5.79; found C 45.94, H 3.46, N 5.59. $^1$H NMR ([D$_6$]DMSO): $\delta$ = 10.08 (dd, $J$ = 5.6 Hz, 1 H, dpphen-H), 9.45 (s, 1 H, tterpy-H), 9.37 (s, 1 H, tterpy-H), 9.19 (d, $J$ = 8.4 Hz, 1 H), 9.14 (d, $J$ = 8.4 Hz, 2 H, tterpy-H), 8.60 (d, $J$ = 5.6 Hz, 1 H, dpphen-H), 8.52 (d, $J$ = 5.6 Hz, 1 H), 8.48 (d, $J$ = 8.0 Hz, 1 H), 8.43–8.27 (m, 3 H, tterpy-H), 8.22 (d, $J$ = 9.2 Hz, 1 H), 7.93 (d, $J$ = 6.0 Hz, 1 H), 7.89 (dd, $J$ = 8.0 Hz, 2 H), 7.84–7.71 (m, 5 H, tterpy-H), 7.69–7.55 (m, 8 H, tterpy-H), 2.06 (s, 3 H, tterpy-CH$_3$) ppm. ESI MS {[IrCl(dpphen)(tterpy)](PF$_6$)$_2$ in CH$_3$CN, positive}: $m/z$ = 441.46 {[M – (PF$_6$)$_2$]$^{2+}$ requires 441.74}.

**[IrCl(bpy)(tterpy)](PF$_6$)$_2$·H$_2$O (4):** Yield: 249 mg (48%). $C_{32}H_{25}ClF_{12}IrN_5P_2{\cdot}H_2O$ (1015.20): calcd. C 37.86, H 2.68, N 6.90; found C 38.34, H 3.09, N 6.60. $^1$H NMR ([D$_6$]DMSO): $\delta$ = 9.73 (d, $J$ = 4.8 Hz, 1 H, bpy-H), 9.33 (s, 2 H, tterpy-H), 9.05 (d, $J$ = 8.0 Hz, 2 H, tterpy-H), 9.00 (d, $J$ = 7.2 Hz, 1 H, bpy-H), 8.80 (d, $J$ = 8.0 Hz, 1 H, bpy-H), 8.65 (t, $J$ = 8.0 Hz, 1 H, bpy-H), 8.32 (dd, $J$ = 7.6 Hz, 2 H, tterpy-H), 8.25–8.22 (m, $J$ = 8.8 Hz, 3 H, tterpy-H and bpy-H), 8.17 (t, $J$ = 7.2 Hz, 1 H, bpy-H), 7.97 (d, $J$ = 5.2 Hz, 1 H, bpy-H), 7.83 (d, $J$ = 5.6 Hz, 2 H, tterpy-H), 7.63 (t, $J$ = 6.4 Hz, 2 H, tterpy-H), 7.56 (d, $J$ = 8.0 Hz, 2 H, tterpy-H), 7.42 (t, $J$ = 7.2 Hz, 1 H, bpy-H), 2.52 (s, 3 H, tterpy-CH$_3$) ppm. ESI MS {[IrCl(bpy)(tterpy)](PF$_6$)$_2$ in CH$_3$CN, positive}: $m/z$ = 353.53 {[M – (PF$_6$)$_2$]$^{2+}$ requires 353.62}, 851.51 ([M – PF$_6$]$^+$ requires 852.22).

**Measurements:** Electronic absorption spectra were recorded at room temperature in CH$_3$CN solution with a Shimadzu UV-2550 spectrophotometer. ESI-MS spectra were obtained by an Applied Biosystems Mariner spectrometer. All NMR spectra were recorded with a JEOL JNM-AL400 FT spectrometer. $^1$H NMR chemical shift values are reported in ppm with reference to the internal standard TMS. Cyclic voltammograms were measured with an ALS-610B electrochemical analyzer fitted with a three-electrode system consisting of a glassy carbon working electrode, a platinum auxiliary electrode, and a Ag/AgCl reference electrode (0.21 V vs. NHE at 3.5 M KCl). CV experiments were performed on DMF solution of the complexes ($5.0 \times 10^{-4}$ M) and 0.050 M TBAP under nitrogen at 25 °C with a scan rate of 100 mV s$^{-1}$. The emission lifetimes were measured in nitrogen-equilibrated CH$_3$CN solutions using a Horiba single-photon counting system (NAES-500). The emission quantum yields for the iridium complexes were determined in CH$_3$CN at room temperature relative to those of a solution containing [Ru(bpy)$_3$]$^{2+}$ and having the same absorbance. The emission quantum yields for the iridium complexes were determined by comparing the integrated emission spectra and using $\phi$ = 0.062 for the standard.[24]

**Crystallographic Data Collection and Structure Determination of 5:** Crystals for the X-ray diffraction study were mounted on glass fibers. All of the measurements were made with a Rigaku R-Axis-Rapid Imaging Plate diffractometer with graphite monochromated Mo-$K_\alpha$ radiation (see Table 7).[25] Indexing was performed from three oscillations. The camera radius was 127.40 mm. Readout was performed in the 0.100 mm pixel mode. The structures were solved by direct methods and were refined on $F^2$ by full-matrix least-squares methods using SHELXL-97.[26] The non-hydrogen atoms were refined anisotropically by the full-matrix least-squares method. All hydrogen atoms were anisotropically refined. CCDC-619118 contains the supplementary crystallographic data for this paper. These data can be obtained free of charge from The Cambridge Crystallographic Data Centre via www.ccdc.cam.ac.uk/data_request/cif.

Table 7. Crystallographic data of the iridium complex.

| | |
|---|---|
| Empirical formula | $C_{48}H_{40}F_{18}IrN_8P_3$ (**5**) |
| Formula mass [g mol$^{-1}$] | 1356.01 |
| Crystal system | monoclinic |
| Space group | *Cc* |
| *a* [Å] | 14.7995(5) |
| *b* [Å] | 16.4658(5) |
| *c* [Å] | 21.5521(7) |
| $\beta$ [°] | 105.5450(8) |
| *Z* | 4 |
| $\lambda$(Mo-$K_\alpha$) [Å] | 0.71073 |
| $R_{int}$ | 0.101 |
| $\theta_{max}$ | 30.5 |
| *h* | –21 to 21 |
| *k* | –23 to 22 |
| *l* | –30 to 30 |
| Total reflections | 27453 |
| Unique reflections | 7614 |
| $\mu$ [mm$^{-1}$] | 2.852 |
| $D_c$ [Mg m$^{-3}$] | 1.780 |
| *T* [K] | 296 |
| *V* [Å$^3$] | 5059.8(3) |
| $R_1$ | 0.060 |
| $R_w$ | 0.140 |
| *S* | 1.19 |

**Computational Methods:** DFT calculations of **5** and **6** were performed using the Gaussian 98 program package.[27] The Becke three parameters hybrid exchange and the Lee–Yang–Parr correlation functionals (B3LYP) were used.[28,29] Geometries of **5** and **6** in the singlet closed-shell and triplet biradical states were optimized by the R(U)B3LYP/LANL2MB method.[30] Absorption spectra were computed as vertical excitations from the $S_0$ PES using the TDDFT approach as implemented in the Gaussian 98 program. A double-$\xi$ quality LANL2DZ basis was used for the iridium atom,[31] and

 © 2007 Wiley-VCH Verlag GmbH & Co. KGaA, Weinheim 

the other atoms were described by a split valence Pople basis plus one polarization and one diffuse function (6-31+G*).[32]

**Supporting Information** (see footnote on the first page of this article): A PDF file containing calculated parameters for the iridium complexes (**3**, **5**, and **6**).


[1] E. Baranoff, J.-P. Collin, J.-P. Sauvage, L. Flamigni, *Chem. Soc. Rev.* **2004**, *33*, 147.
[2] A. J. Wilkinson, A. E. Goeta, C. E. Foster, J. A. G. Williams, *Inorg. Chem.* **2004**, *43*, 6513.
[3] K. Dedeian, J. Shi, N. Shepherd, E. Forsythe, D. C. Morton, *Inorg. Chem.* **2005**, *44*, 4445.
[4] L. Flamigni, B. Venture, F. Barigelletti, E. Baranoff, J.-P. Collin, J.-P. Sauvage, *Eur. J. Inorg. Chem.* **2005**, 1312.
[5] A. B. Tamayo, B. D. Alleyne, P. I. Djurovich, S. Lamansky, I. Tsyba, N. H. Ho, R. Bau, E. Thompson, *J. Am. Chem. Soc.* **2003**, *125*, 7377.
[6] K. J. Arm, W. Leslie, J. A. G. Williams, *Inorg. Chim. Acta* **2006**, *359*, 1222.
[7] W. Goodall, J. A. G. Williams, *J. Chem. Soc., Dalton Trans.* **1985**, *82*, 299.
[8] S. Lamansky, P. Djurovich, D. Murphy, F. Abdel-Razzaq, H. E. Lee, C. Adachi, P. E. Burrows, S. R. Forrest, M. E. Thompson, *J. Am. Chem. Soc.* **2001**, *123*, 4304.
[9] M. K. Nazeeruddin, R. Humphry-Baker, D. Bemer, S. Rivier, L. Zuppiroll, M. Graetzel, *J. Am. Chem. Soc.* **2003**, *125*, 8790.
[10] N. Yoshikawa, J. Sakamoto, T. Matsumura-Inoue, H. Takashima, K. Tsukahara, N. Kanehisa, Y. Kai, *Anal. Sci.* **2004**, *20*, 711.
[11] N. Yoshikawa, J. Sakamoto, N. Kanehisa, Y. Kai, T. Matsumura-Inoue, H. Takashima, K. Tsukahara, *Acta Crystallogr., Sect. E* **2003**, *59*, m155.
[12] N. Yoshikawa, J. Sakamoto, N. Kanehisa, Y. Kai, T. Matsumura, H. Takashima, K. Tsukahara, *Acta Crystallogr., Sect. E* **2003**, *59*, m551.
[13] N. Yoshikawa, J. Sakamoto, N. Kanehisa, Y. Kai, T. Matsumura-Inoue, H. Takashima, K. Tsukahara, *Acta Crystallogr., Sect. E* **2003**, *59*, m972.
[14] N. Yoshikawa, T. Matsumura-Inoue, *Anal. Sci.* **2003**, *19*, 761.
[15] N. Yoshikawa, J. Sakamoto, N. Kanehisa, Y. Kai, T. Matsumura-Inoue, H. Takashima, K. Tsukahara, *Acta Crystallogr., Sect. E* **2003**, *59*, m832.
[16] T. Yutaka, S. Obara, S. Ogawa, K. Nozaki, N. Ikeda, T. Ohno, Y. Ishii, K. Sakai, M. Haga, *Inorg. Chem.* **2005**, *44*, 4737.
[17] N. Yoshikawa, S. Yamabe, N. Kanehisa, Y. Kai, H. Takashima, K. Tsukahara, *Inorg. Chim. Acta* **2006**, *359*, 4585.
[18] C. Yang, S. Li, Y. Chi, Y. Cheng, Y. Yeh, P. Chou, G. Lee, C. Wang, C. Shu, *Inorg. Chem.* **2005**, *44*, 7770.
[19] J.-P. Collin, I. M. Dixon, J.-P. Sauvage, J. A. G. Williams, F. Barigelletti, L. Flamigni, *J. Am. Chem. Soc.* **1999**, *121*, 5009.
[20] K. K.-W. Lo, C.-K. Chung, D. C.-M. Ng, N. Zhu, *New J. Chem.* **2002**, *26*, 81.
[21] A. C. Hazell, *Acta Crystallogr., Sect. C* **1984**, *40*, 806.
[22] N. P. Ayala, C. M. Flynn Jr, L. A. Sacksteder, J. N. Demas, B. A. DeGraff, *J. Am. Chem. Soc.* **1990**, *112*, 3837.
[23] P. A. Anderson, L. F. Anderson, M. Furue, P. C. Junk, F. R. Keene, B. T. Patterson, B. D. Yeomans, *Inorg. Chem.* **2000**, *39*, 2721.
[24] J. V. Casper, T. J. Meyer, *Inorg. Chem.* **1983**, *22*, 2444.
[25] N. Yoshikawa, A. Ichimura, N. Kanehisa, Y. Kai, H. Takashima, K. Tsukahara, *Acta Crystallogr., Sect. E* **2005**, *61*, m55.
[26] G. M. Sheldrick, *SHELXL 97*, University of Göttingen, Germany, **1997**.
[27] M. J. Frisch, G. W. Trucks, H. B. Schlegel, G. E. Scuseria, M. A. Robb, J. R. Cheeseman, V. G. Zakrzewski, J. A. Montgomery Jr, R. E. Stratmann, J. C. Burant, S. Dapprich, J. M. Millam, A. D. Daniels, K. N. Kudin, M. C. Strain, O. Farkas, J. Tomasi, V. Barone, M. Cossi, R. Cammi, B. Mennucci, C. Pomelli, C. Adamo, S. Clifford, J. Ochterski, G. A. Petersson, P. Y. Ayala, Q. Cui, K. Morokuma, D. K. Malick, A. D. Rabuck, K. Raghavachari, J. B. Foresman, J. Cioslowski, J. V. Ortiz, A. G. Baboul, B. B. Stefanov, G. Liu, A. Liashenko, P. Piskorz, I. Komaromi, R. Gomperts, R. L. Martin, D. J. Fox, T. Keith, M. A. Al-Laham, C. Y. Peng, A. Nanayakkara, C. Gonzalez, M. Challacombe, P. M. W. Gill, B. Johnson, W. Chen, M. W. Wong, J. L. Andres, C. Gonzalez, M. Head-Gordon, E. S. Replogle, J. A. Pople, *GAUSSIAN 98, Revision A.7*, Gaussian Inc., Pittsburgh PA, USA, **1998**.
[28] C. Lee, W. Yang, R. G. Parr, *Phys. Rev. B* **1988**, *37*, 785.
[29] A. D. Becke, *J. Chem. Phys.* **1993**, *98*, 5648.
[30] J. Hay, W. R. Wadt, *J. Chem. Phys.* **1985**, *82*, 299.
[31] T. H. Dunning Jr, P. J. Hay, *Modern Theoretical Chemistry* (Ed.: H. F. Schaefer III), Plenum, New York, **1976**, p. 1.
[32] M. M. Francl, W. J. Petro, W. J. Hehre, J. S. Binkley, M. H. Gordon, D. J. Defrees, J. A. Pople, *J. Chem. Phys.* **1982**, *77*, 3654.


Received: October 23, 2006
Published Online: March 14, 2007

 © 2007 Wiley-VCH Verlag GmbH & Co. KGaA, Weinheim 

DOI: 10.1002/ejic.200601050

# A Trinuclear Aqua Cyano-Bridged Ruthenium Complex $[\{(\eta^5\text{-}C_5H_5)(PPh_3)_2Ru(\mu\text{-}CN)\}_2RuCl_2(PPh_3)(H_2O)]PF_6$: Synthesis, Characterization and Crystal Structure

**Viatcheslav Vertlib,[a] João Figueira,[a] José Mesquita,[a] João Rodrigues,*[a] Kalle Nättinen,[b][‡] and Kari Rissanen*[b]**

**Keywords:** Ruthenium / Trinuclear complexes / Bridging ligands / X-ray structure / Metal–metal interactions / Chain structures

The organometallic trinuclear aqua cyano-bridged complex $[\{(\eta^5\text{-}C_5H_5)(PPh_3)_2Ru(\mu\text{-}CN)\}_2RuCl_2(PPh_3)(H_2O)]PF_6$ (**1**), in which the fragment $[RuCl_2(PPh_3)(H_2O)]$ acts as a bridge and an acceptor group between the two terminal cyclopentadienyl ruthenium cyano moieties, was isolated in moderate yield from the reaction of $[(\eta^5\text{-}C_5H_5)(PPh_3)_2RuCN]$ with $[RuCl_2(PPh_3)_3]$ in THF. To the best of our knowledge, compound **1** is one of the few examples of a trinuclear array of ruthenium fragments bridged by the nitrogen atom of the –C≡N– group (Ru–C≡**N**–Ru′–**N**≡C–Ru) with a Ru-coordinated water molecule. The new aqua complex was structurally characterized by FTIR, $^1H$, $^{13}C$, and $^{31}P$ NMR spectroscopy, mass spectrometry, elemental analysis, single-crystal X-ray diffraction, and cyclic voltammetry. The title complex crystallizes in a triclinic unit cell $a$ = 17.3477(6) Å, $b$ = 17.8551(5) Å, $c$ = 18.2460(7) Å, $\alpha$ = 95.693(2)°, $\beta$ = 111.648(2)°, and $\gamma$ = 97.839(2)° in the space group $P\bar{1}$ with $Z$ = 2.

(© Wiley-VCH Verlag GmbH & Co. KGaA, 69451 Weinheim, Germany, 2007)

## Introduction

Because of their interesting properties (such as conductivity, magnetic and spectral properties), di- and trinuclear complexes with bridging cyanide ligands have been widely studied and have been the object of a large number of publications in the last decades.[1] However, the number of trinuclear complexes reported is less than half of that reported for dinuclear cyanide-bridged complexes, because of difficulties in controlling the synthesis and the ease with which coordination polymers are formed.[2] The bonding characteristics of the cyanide anion make it a good donor at both its C and N atoms[3] – the C atom has a greater affinity for electron-rich metals (such as $M^{II}$), while the N atom for electron-deficient metals (such as $M^{III}$). The ability of the cyanide anion to bridge two metal centers and to mediate electronic communications between metal atoms (e.g. electron transfer)[4] led us recently to prepare and determine the X-ray structure of the dinuclear ruthenium cyano-bridged organometallic complex $[(\eta^5\text{-}C_5H_5)(PPh_3)_2Ru(\mu\text{-}CN)\text{-}Ru(PPh_3)_2(\eta^5\text{-}C_5H_5)]PF_6$.[5] As a natural extension of our previous work, we explored the properties of the –C≡N– bridging group in trinuclear complexes with linear arrays of ruthenium fragments (Ru–C≡**N**–Ru′–**N**≡C–Ru). Vahrenkamp et al.[4c,6] have systematically studied such trinuclear complexes, focusing mainly on the effects of the geometry and the oxidation state at the central metal and of the orientation of the bridges (cyanide vs. isocyanide) on the electronic communication between two terminal metallic fragments. Furthermore, while water is a very common ligand in classical Werner-type coordination chemistry, in 18-electron organometallic complexes coordinated water is relatively rare. This has two main reasons: (a) in organometallic compounds, the metal centers do not display either "hard" or "soft" character, (b) the oxygen atom has a hard donor capacity and binds weakly to most low-valent transition metals like $Ru^{II}$.[7] These labile complexes are frequently used as precursors for catalysts in organic reactions and in biological applications, viz. aqua complexes of ruthenium have proved to be effective for ring-opening metathesis polymerization (ROMP)[8] and as anti-tumor compounds.[9] In this paper, we report the preparation, structural characterization, and X-ray structure of a rare example of an organometallic trinuclear cyano-bridged ruthenium complex with Ru-coordinated water.

[a] Centro de Química da Madeira, LQCMM/MMRG, Departamento de Química da Universidade da Madeira, Campus de Penteada, 9000-390 Funchal, Portugal
E-mail: joaor@uma.pt
[b] Nanoscience Center, Department of Chemistry, University of Jyväskylä, P. O. Box 35, 40014 Jyväskylä, Finland
E-mail: krissane@cc.jyu.fi
[‡] Present address: VTT Processes, P. O. Box 1607, 33101 Tampere, Finland

Supporting information for this article is available on the WWW under http://www.eurjic.org or from the author.

 © 2007 Wiley-VCH Verlag GmbH & Co. KGaA, Weinheim 

## Results and Discussion

The title organometallic trinuclear aqua complex was readily synthesized by treatment of the electron rich $Ru^{II}$ precursor unit $[(\eta^5\text{-}C_5H_5)(PPh_3)_2RuCN]$ with 1 equiv. $[RuCl_2(PPh_3)_3]$ in THF in the presence of $NH_4PF_6$ to yield $[\{(\eta^5\text{-}C_5H_5)(PPh_3)_2Ru(\mu\text{-}CN)\}_2RuCl_2(PPh_3)(H_2O)]PF_6$ (**1**). During the reaction, $[RuCl_2(PPh_3)_3]$, a well-known ruthenium catalyst for hydrogenation catalysis and an important starting material for the preparation of different types of complexes, dissociated extensively in solution[10] and the labile phosphanes were substituted to the central ruthenium unit $[RuCl_2(PPh_3)(H_2O)]$ in complex **1**. The resulting air stable, dark green-blue solid was recrystallized from a mixture of *n*-pentane/dichloromethane/diethyl ether and yielded dark blue crystals suitable for X-ray analysis. The compound was successfully characterized by FTIR, $^1H$, $^{13}C$, and $^{31}P$ NMR spectroscopy, mass spectrometry, elemental analysis, and cyclic voltammetry.

The UV/Vis spectrum of **1** (ca. $2\times10^{-4}$ M) was obtained in dichloromethane, chloroform, and dimethylformamide at room temperature and shows intense absorptions in the 250–420 nm region that arise from d–d transitions in the ruthenium moieties that are overlapped by the expected transitions in the aromatic ligands in the UV region. The mono- and the dinuclear compound $[(\eta^5\text{-}C_5H_5)(PPh_3)_2RuCN]$[5] and $[(\eta^5\text{-}C_5H_5)(PPh_3)_2Ru(\mu\text{-}CN)Ru(PPh_3)_2(\eta^5\text{-}C_5H_5)]PF_6$,[5] respectively, as well as the starting material $[RuCl_2(PPh_3)_3]$[10b] also show these absorption bands in their spectra. Additionally, a new broad band in the upper limit of the visible region with a tail in the NIR and a maximum at 658 nm (15200 $cm^{-1}$, $\varepsilon_{max}$ = 3937 $M^{-1}cm^{-1}$) was also observed (see Figure 1). This was interpreted according to the solvent dependence, bandwidth at half height, shape, and Hush theoretical formalism ($\Delta\nu_{1/2}° = 5925\ cm^{-1}$)[11] as a metal-to-metal charge transfer (MMCT) transition of low intensity from the terminal units $[(\eta^5\text{-}C_5H_5)(PPh_3)_2RuCN]$ to the central ruthenium fragment $[RuCl_2(PPh_3)(H_2O)]$.[4a,6e] A similar assignment has been made by Matsui et al.[12] in a related trinuclear system $[(NC)(bpy)_2Ru\text{-}CN\text{-}Ru(H_2dcbpy)_2\text{-}NC\text{-}Ru(bpy)_2(CN)]^+$ (dcbpy = 4,4′-dicarboxy-2,2′-bipyridine).

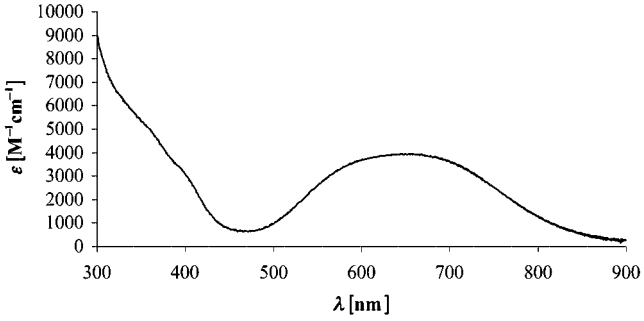


Figure 1. UV/Vis absorption spectrum of **1** (ca. $2\times10^{-4}$ M) recorded in $CH_2Cl_2$ at room temperature.

The IR spectrum shows two broad bands for the coordinated water at 3056 ($\upsilon_{OH}$) and 1635 $cm^{-1}$ ($\delta_{OH}$)[13] and two sharp bands for the counterion $PF_6^-$ at 841 and 520 $cm^{-1}$. As expected for a symmetrical cyanide arrangement in trinuclear complexes,[6d] compound **1** shows evidence of only one stretching frequency for the C≡N bonds in the IR spectrum at 2052 $cm^{-1}$, which occurs at a lower value than those for the mononuclear $[(\eta^5\text{-}C_5H_5)(PPh_3)_2RuCN]$ and dinuclear $[(\eta^5\text{-}C_5H_5)(PPh_3)_2Ru(\mu\text{-}CN)Ru(PPh_3)_2(\eta^5\text{-}C_5H_5)]PF_6$ complexes[5] (2072 and 2070 $cm^{-1}$, respectively). Usually a shift to higher frequency in the position of the $\nu_{CN}$ band is expected upon formation of the cyanide-bridged complex because of the kinematic effect (i.e. the restriction of the CN motion by simultaneous coordination of both N and C atoms).[6e] In the present case, a slight weakening of the CN bond can be observed with a band shift of about –20 $cm^{-1}$ relative to the mono- and dinuclear compounds. In spite of the fact that the central ruthenium fragment is a much stronger electron acceptor than the terminal ruthenium centers, this lowering of the position of the $\nu_{CN}$ band for the linear array Ru–C≡N–Ru′–N≡C–Ru is probably due to the π-back-donation from the terminal ruthenium to the CN-π* orbitals as well as due to the effect of the electron-donating aqua ligand bonded to the central ruthenium fragment, as was observed for the complex $[RuCl_2(PEt_3)_2(CO)(H_2O)]$.[14] In support of this observation, the $^1H$ NMR spectrum of the trinuclear complex **1** shows a general deshielding effect when compared with the mononuclear complex $[(\eta^5\text{-}C_5H_5)(PPh_3)_2RuCN]$; only one singlet of 10 protons for the two cyclopentadienyl ligands, which are deshielded by about 1 ppm, and a singlet at $\delta$ = 3.73 ppm for the coordinated water are observed in the spectrum of **1**. The $^{13}C\{^1H\}$ NMR spectrum shows a similar deshielding effect of about 5 ppm for the carbon signal of the CN bond. In the $^{31}P\{^1H\}$NMR spectrum, only two signals of different resonance intensities are observed; the four times more intense signal at $\delta$ = 30.0 ppm indicates the equivalency of the four phosphorus nuclei of the terminal ruthenium moieties, and the less intense signal at $\delta$ = 17.8 ppm is attributed to the phosphorus atom of the central ruthenium fragment and occurs more downfield relative to the signal arising from the basal $PPh_3$ group in the five-coordinate structure $[RuCl_2(PPh_3)_3]$ {$\delta(^{31}P)$ = 24.1 ppm}.[15] The NMR results show that the $[(\eta^5\text{-}C_5H_5)(PPh_3)_2RuCN]$ moieties are in a *trans* arrangement, which is also verified by the X-ray analysis (Figure 2). The redox behavior of complex **1** was investigated by cyclic voltammetry in the potential range 0–2.5 V (versus Ag/AgCl) with $CH_2Cl_2$ as solvent and *n*-$Bu_4NPF_6$ as the supporting electrolyte. No conclusive information was obtained because of the irreversible character of the observed processes (see Supporting Information).

The central ruthenium fragment is surrounded by six ligands in a slightly distorted octahedral coordination environment with O(48) *trans* to P(94) (Table 2, Figure 2). The Ru–Cl distances (2.327–2.348 Å) are in accordance with the normal, well-established range for $Ru^{III}$ chloride complexes.[16] The central Ru(2)–P(94) bond length (2.292 Å) is slightly shorter than the corresponding bond lengths at the terminal $Ru^{II}$ centers, which is expected for a relatively hard $Ru^{III}$ center. The Ru–$H_2O$ distance (2.215 Å) agrees well

 © 2007 Wiley-VCH Verlag GmbH & Co. KGaA, Weinheim 

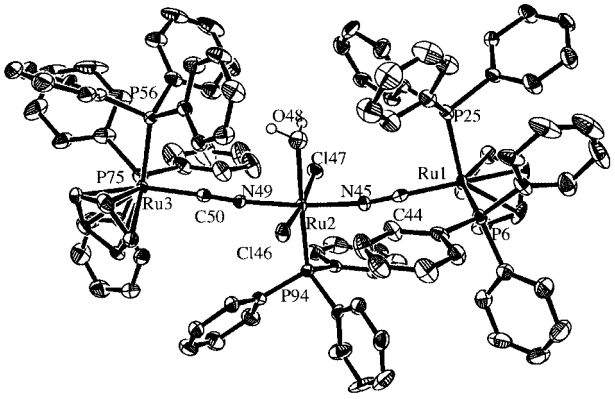


Figure 2. ORTEP[18] drawing at the 50% probability level for the cation of **1**. Solvent molecules and hydrogen atoms, except for the coordinated water, are omitted for clarity.

with the values in similar structural fragments.[16] The $H_2O$ ligand occupies a neat cavity formed by the bulky $PPh_3$ ligands [P(25) and P(56)]. One of the hydrogen atoms of water shows a weak O–H···π interaction, in which the H(48A)···C(68) distance is 2.52 Å. The Ru–C and Ru–N bond lengths in the terminal pseudo-tetrahedral ruthenium moieties are shorter than those in the dinuclear compound $[(\eta^5\text{-}C_5H_5)(PPh_3)_2Ru(\mu\text{-}CN)Ru(PPh_3)_2(\eta^5\text{-}C_5H_5)]PF_6$ and in the parent compound $[(\eta^5\text{-}C_5H_5)(PPh_3)_2RuCN]$, and are similar to those in the tetranuclear compound $Cl(CH_3CN)(PPh_3)Ru\{CNCuCl\}\{NCRu(PPh_3)_2Cp\}_2$.[17] A variation in the π-back-donation of the $[(\eta^5\text{-}C_5H_5)(PPh_3)_2$-Ru] unit can be observed on going from the mono- to the trinuclear complex. The two chlorine ligands are bent towards the water ligand with a Cl(47)–Ru(2)–Cl(46) angle of 171.39°. The cyclopentadienyl ligands are *trans* to each other, and the torsion angle [Ct(1)–Ru(1)–Ru(3)–Ct(2)] between the centroids of the cyclopentadienyl ligands and the metal centers is 123.8°. The most striking feature of the complex is the large deviation from linearity of the Ru–CN–Ru–NC–Ru chain; the Ru(1)–Ru(2)–Ru(3) angle is 164.8°. This is caused by the sterically bulky $PPh_3$ ligand that induces a steric strain on the other side of the complex – this strain is compensated by the curvature of the M–CN–M–NC–M chain (see Supporting Information). Crystallographic data for complex **1** are collected in Table 1, and the most relevant geometric parameters are shown in Table 2.

Table 1. Crystal data and structure refinement for **1**.

| | |
|---|---|
| Empirical formula | $C_{104.34}H_{91.67}F_6N_2P_6Ru_3Cl_{17.91}$ |
| Formula weight | 2273.10 |
| Crystal size [mm] | 0.15 × 0.15 × 0.20 |
| Temperature [K] | 173(2) |
| Wavelength [Å] | 0.71073 |
| Crystal system | triclinic |
| Space group | $P\bar{1}$ |
| Unit cell dimensions | |
| *a* [Å] | 17.3477(6) |
| *b* [Å] | 17.8551(5) |
| *c* [Å] | 18.2460(7) |
| α [°] | 95.693(2) |
| *β* [°] | 111.648(2) |
| *γ* [°] | 97.839(2) |
| Volume [Å$^3$] | 5134.8(3) |
| *Z* | 2 |
| Density (calculated) [mg/m$^3$] | 1.480 |
| Absorption coefficient [mm$^{-1}$] | 0.797 |
| *F*(000) | 2300 |
| *θ* range for data collection [°] | 1.54 to 24.70 |
| Index ranges | $-20 \le h \le 20$ |
| | $-20 \le k \le 19$ |
| | $-21 \le l \le 19$ |
| Reflections collected | 47358 |
| Independent reflections | 17423 [*R*(int) = 0.0849] |
| Absorption correction | none |
| Data/restraints/parameters | 17395/28/1194 |
| Goodness-of-fit on $F^2$ | 1.068 |
| Final *R* indices [$I > 2\sigma(I)$] | $R_1$ = 0.0590, $wR_2$ = 0.1446 |
| *R* indices (all data) | $R_1$ = 0.0996, $wR_2$ = 0.1681 |

Table 2. Selected bond lengths [Å] and angles [°] for **1**.

| Bond lengths | | Angles | |
|---|---|---|---|
| Ru(1)–C(44) | 1.972(7) | N(45)–C(44)–Ru(1) | 172.5(5) |
| Ru(1)–Ct(1) | 1.885(7) | N(49)–C(50)–Ru(3) | 172.6(5) |
| Ru(1)–P(6) | 2.346(2) | C(44)–N(45)–Ru(2) | 169.6(5) |
| Ru(1)–P(25) | 2.330(2) | C(50)–N(49)–Ru(2) | 171.6(5) |
| Ru(2)–N(45) | 2.021(5) | P(25)–Ru(1)–P(6) | 100.23(6) |
| Ru(2)–N(49) | 2.007(5) | N(49)–Ru(2)–N(45) | 174.3(2) |
| Ru(2)–P(94) | 2.292(2) | N(49)–Ru(2)–O(48) | 88.6(2) |
| Ru(2)–O(48) | 2.215(5) | N(45)–Ru(2)–O(48) | 85.8(2) |
| Ru(2)–Cl(47) | 2.327(2) | N(49)–Ru(2)–P(94) | 93.5(2) |
| Ru(2)–Cl(46) | 2.348(2) | N(45)–Ru(2)–P(94) | 92.1(2) |
| Ru(3)–C(50) | 1.974(7) | O(48)–Ru(2)–P(94) | 177.4(1) |
| Ru(3)–Ct(2) | 1.887(7) | N(49)–Ru(2)–Cl(47) | 89.0(2) |
| Ru(3)–P(56) | 2.312(2) | N(45)–Ru(2)–Cl(47) | 89.3(2) |
| Ru(3)–P(75) | 2.336(2) | O(48)–Ru(2)–Cl(47) | 84.5(1) |
| C(44)–N(45) | 1.159(8) | P(94)–Ru(2)–Cl(47) | 93.89(6) |
| C(50)–N(49) | 1.166(8) | N(49)–Ru(2)–Cl(46) | 88.6(2) |
| | | N(45)–Ru(2)–Cl(46) | 92.2(2) |
| | | O(48)–Ru(2)–Cl(46) | 87.2(1) |
| | | P(94)–Ru(2)–Cl(46) | 94.51(6) |
| | | Cl(47)–Ru(2)–Cl(46) | 171.39(6) |
| | | P(56)–Ru(3)–P(75) | 99.30(6) |
| | | H(48A)–O(48)–H(48B) | 99.49(14) |

## Conclusions

We have prepared and fully characterized the new organometallic trinuclear ruthenium aqua complex $[\{(\eta^5\text{-}C_5H_5)(PPh_3)_2Ru(\mu\text{-}CN)\}_2RuCl_2(PPh_3)(H_2O)]PF_6$ and isolated it in moderate yield by using a relatively simple synthetic strategy and trivial starting materials. The structure of the complex was determined by X-ray diffraction, confirming the structural assignments obtained from the spectroscopic data. The isolated organometallic trinuclear aqua compound represents one of the few examples of a Ru–C≡**N**–Ru′–**N**≡C–Ru array with a metal–metal interaction across the cyanide bridges and probably over more than one CN linkage. Because of the steric strain imposed by the large $PPh_3$ ligand at the central ruthenium, the complex shows a marked deviation from the expected linearity of the Ru–C≡**N**–Ru′–**N**≡C–Ru array. The lability of the aqua ligand can lead to a convenient synthetic route for the preparation of other tri- and tetranuclear cyanide-bridged com-

 © 2007 Wiley-VCH Verlag GmbH & Co. KGaA, Weinheim 

plexes. Further studies on this organometallic trinuclear ruthenium aqua complex are in progress in order to explore fundamental properties such as its reactivity in selected transformations, for example in ring-opening metathesis polymerization (ROMP).

## Experimental Section

**General:** All the experiments were carried out under vacuum or a nitrogen atmosphere by use of standard vacuum line Schlenk-tube techniques. All the solvents used were distilled and dried according to the usual published methods.[19] The compounds [($\eta^5$-$C_5H_5$)($PPh_3$)$_2$RuCN][5,20] (**2**) and [$RuCl_2(PPh_3)_3$][21] (**3**) were prepared following methods described in the literature, and the spectroscopic data (UV/Vis and/or NMR) agreed with that reported. The UV/Vis spectra were recorded with a GBC-Cintra 40 UV/Vis spectrometer using 1 cm optical path quartz cells with freshly prepared solutions (ca. $2 \times 10^{-4}$ M) in dichloromethane (dcm), chloroform, and dimethylformamide (dmf). The spectrum is presented as $\lambda_{max}$ or shoulder (sh.) [nm] ($\varepsilon_{max}$ [$M^{-1}cm^{-1}$]). The mass spectra (TOF-MS) were recorded with a Micromass LCT; peaks are reported as *m*/*z* (assignment, relative intensity). IR spectra were recorded by using a Nicolet Avatar 360 FTIR spectrometer, calibrated with polystyrene, with KBr pellets; only significant bands are cited in the text. $^1$H, $^{13}$C{$^1$H} and $^{31}$P{$^1$H} NMR spectra were recorded with a Bruker AM500 spectrometer at 500.13 MHz ($^1$H), 125.76 MHz ($^{13}$C), and 202.46 MHz ($^{31}$P); probe temperature (30 °C) in $CDCl_3$. The $^1$H chemical shifts ($\delta$), reported in parts per million (ppm) downfield, are referenced to residual chloroform ($\delta$ = 7.24 ppm). The $^{13}$C{$^1$H} chemical shifts are reported in ppm relative to the carbon resonance of the deuterated NMR solvent: $CDCl_3$ ($\delta$ = 77.00 ppm). The $^{31}$P{$^1$H} NMR spectra are reported in ppm downfield from the external standard 85% $H_3PO_4$ at $\delta$ = 0.00 ppm. Melting points were obtained on a Leica Gallen instrument and were not corrected.

**Preparation of [{($\eta^5$-$C_5H_5$)($PPh_3$)$_2$Ru(μ-CN)}$_2$$RuCl_2$($PPh_3$)($H_2O$)]-$PF_6$ (1)**: To a mixture of [($\eta^5$-$C_5H_5$)($PPh_3$)$_2$RuCN] (0.100 g, 0.14 mmol) and [$RuCl_2(PPh_3)_3$] (0.138 g, 0.14 mmol) in THF (30 mL) was added $NH_4PF_6$ (0.114 g, 0.7 mmol). The mixture was stirred at 60 °C for 3 h, then at 20 °C for 22 h. The color of the reaction mixture changed slowly from black-red to dark (almost black) green-blue. The solution was evaporated to dryness in vacuo. Dichloromethane (10 mL) was then added. The precipitate of ammonium salts was removed by cannula filtration, and the filtrate was evaporated to dryness and dried in vacuo. The resulting dark green-blue solid was recrystallized from a mixture of *n*-pentane/dichloromethane/diethyl ether (3 mL/6 mL/0.5 mL) to obtain dark blue crystals. Yield: 85 mg (59%). M.p. 184–187 °C. FTIR (KBr): $\upsilon_{OH}$ 3056 (br.), $\upsilon_{CN}$ 2052 (m), $\delta_{OH}$ 1635 (br.), $\upsilon_{PF6}$ 841 (s), 520 (s) $cm^{-1}$. $^1$H NMR (500 MHz, $CDCl_3$): $\delta$ = 7.57–7.30 (m, 75 H, Ph), 5.30 (s, 10 H, $C_5H_5$), 3.73 (s, $H_2O$) ppm. $^{13}$C{$^1$H} NMR (126 MHz, $CDCl_3$): $\delta$ = 146.7 (CN), 133.6–127.3 (Ph) ppm. $^{31}$P{$^1$H} NMR (202 MHz, $CDCl_3$): $\delta$ = 30.0 (s, 4 P, $PPh_3$), 17.8 (s, 1 P, $PPh_3$), –143.7 (m, $PF_6$) ppm. $C_{102}H_{87}Cl_2F_6N_2OP_6Ru_3$ (2030.74): calcd. C 60.3, H 4.3, N 1.4; found C 59.7, H 4.4, N 1.6. TOF-MS ($ES^+$): *m*/*z* (%) = calcd. 429.0, found 429.2 (84) [($\eta^5$-$C_5H_5$)$Ru(PPh_3)]^+$; calcd. 626.1, found 625.4 (100) $[Ru(PPh_3)_2]^+$; calcd. 1151.1, found 1151.7 (50) [($\eta^5$-$C_5H_5$)($PPh_3$)$_2$Ru(μ-CN)$RuCl_2(PPh_3)]^+$; calcd. 1868.2, found 1868.2 (75) $[M - PF_6 - H_2O]^+$; calcd. 1886.2, found 1886.2 (10) $[M - PF_6]^+$. UV/Vis ($CH_2Cl_2$): $\lambda_{max}$ ($\varepsilon_{max}$, $M^{-1}cm^{-1}$) = 658 (3937).

**Single Crystal X-ray Diffraction:** Data were recorded with a Nonius Kappa Apex II diffractometer by using graphite monochromatized Mo-$K_\alpha$ radiation [$\lambda$(Mo-$K_\alpha$) = 0.71073 Å] and a temperature of 173.0 ± 0.1 K. The data were processed with Denzo-SMN v0.97.638.[22] The structure was solved by direct methods (SHELXS-97),[23] and refinements based on $F^2$ were made by full-matrix least-squares techniques (SHELXL-97).[24] Graphics program ORTEP3 for Windows[18] was executed through the WinGX-suite.[25] The hydrogen atoms were calculated to their idealized positions with isotropic temperature factors (1.2 or 1.5 times the C temperature factor) and as riding atoms. The water hydrogen atoms were located from the difference Fourier map, but refined as riding atoms with isotropic temperature factors 1.5 times the O temperature factor.

In the structure, only one of the approximately 3.5 dichloromethane (dcm) molecules was found to be non-disordered and was refined with full occupancy, one full dcm molecule was disordered over four sites, and one dcm molecule was refined with a one third occupancy. Residual electron density showed high peaks, which could not be modeled with any chemically reasonable model (they probably arise because of severely disordered dcm molecules) and were treated as Cl atoms with partial occupancy.

CCDC-626456 for **1** contains the supplementary crystallographic data for this paper. These data can be obtained free of charge from The Cambridge Crystallographic Data Centre via www.ccdc.cam.ac.uk/data_request/cif.

**Supporting information** (see footnote on the first page of this article): The cyclic voltammogram and van der Waals and ball-and-stick representations of compound **1** are available.

## Acknowledgments

The presented research was supported by Fundação para a Ciência e a Tecnologia (Portugal) through a FEDER funded project POCTI/CTM/41495/2001 (V. V. and J. R.) and by the sabbatical research grant SFRH/BSAB/632/2006 (J. R.). J. R. thanks the University of Jyväskylä for supporting his stay as a visiting professor at the Nanoscience Center, Department of Chemistry. The Academy of Finland (Proj. no. 205729) is gratefully acknowledged for a research grant (K. R. and K. N.). We also wish to thank Spec. Lab. Technicians Mirja Lahtiperä and Reijo Kauppinen for their help in running the MS and NMR spectra.

[1] A search in the SciFinder 2006 retrieved 860 references for the keyword "cyanide-bridged".
[2] The number of di/trinuclear structures found in a Cambridge Structural Database (CSD) [CSD version 5.27 (August-2006 update)] search revealed 2091 hits for the dinuclear complexes of general formula M–CN–M, but only 932 hits for the trinuclear compounds of general formula M–CN–M′–NC–M.
[3] D. F. Sriver, *Struct. Bonding* **1966**, *1*, 32–58.
[4] For selected reviews in the field see: a) D. M. D′Alessandro, F. R. Keene, *Chem. Rev.* **2006**, *106*, 2270–2298; b) V. Balzani, A. Juris, M. Venturi, S. Campagna, S. Serroni, *Chem. Rev.* **1996**, *96*, 759–833; c) H. Vahrenkamp, A. Geiß, G. N. Richardson, *J. Chem. Soc., Dalton Trans.* **1997**, 3643–3651.
[5] C. Ornelas, C. Gandum, J. Mesquita, J. Rodrigues, M. H. Garcia, N. Lopes, M. Paula Robalo, K. Nättinen, K. Rissanen, *Inorg. Chim. Acta* **2005**, *358*, 2482–2488.
[6] a) T. Sheng, H. Vahrenkamp, *Eur. J. Inorg. Chem.* **2004**, 1198–1203; b) M.-L. Flay, H. Vahrenkamp, *Eur. J. Inorg. Chem.* **2003**, 1719–1726; c) R. Appelt, H. Vahrenkamp, *Inorg. Chim. Acta* **2003**, *350*, 387–398; d) A. Geiss, H. Vahrenkamp, *Inorg.*

 © 2007 Wiley-VCH Verlag GmbH & Co. KGaA, Weinheim 

*Chem.* **2000**, *39*, *40*29–4036; e) G. N. Richardson, U. Brand, H. Vahrenkamp, *Inorg. Chem.* **1999**, *38*, 3070–3079; f) N. Zhu, H. Vahrenkamp, *J. Organomet. Chem.* **1999**, *573*, 67–72 and references cited therein.

[7] a) M. F. Mahon, M. K. Wittlesey, P. T. Wood, *Organometallics* **1999**, *18*, 4068–4074 and references cited therein; b) J. P. Collman, L. S. Hegedus, J. R. Norton, R. G. Finke, *Principles and Applications of Organotransition Metal Chemistry*, University Science Books, Mill Valley, CA, **1987**.

[8] a) R. H. Grubbs, *Angew. Chem. Int. Ed.* **2006**, *45*, 3760–3765; b) D. M. Lynn, B. Mohr, R. H. Grubbs, *J. Am. Chem. Soc.* **1998**, *120*, 1627–1628.

[9] a) D. Chatterjee, A. Mitra, *Platinum Met. Rev.* **2006**, *50*, 2–12; b) P. V. Grundler, G. Laurenczy, A. E. Merbach, *Helv. Chim. Acta* **2001**, *84*, 2854–2867.

[10] a) P. R. Hoffman, K. G. Caulton, *J. Am. Chem. Soc.* **1975**, *97*, 4221–4228; b) B. R. James, L. D. Markham, *Inorg. Chem.* **1974**, *13*, 97–100; c) J. D. Gilbert, D. Rose, G. Wilkinson, *J. Chem. Soc. A* **1970**, 2765–2769; d) J. D. Gilbert, G. Wilkinson, *J. Chem. Soc. A* **1969**, 1749–1753.

[11] a) N. S. Hush, *Prog. Inorg. Chem.* **1967**, *8*, 391–444; b) N. S. Hush, *Electrochim. Acta* **1968**, *13*, 1005–1023.

[12] K. Matsui, M. K. Nazeeruddin, R. Humphry-Baker, M. Grätzel, K. Kalyanasundaram, *J. Phys. Chem.* **1992**, *96*, 10587–10590.

[13] J. Nakamoto, *Infrared and Raman Spectra of Inorganic and Coordination Compounds*, 3rd ed., Wiley, New York, **1978**, p. 226.

[14] Y. Sun, N. J. Taylor, A. J. Carty, *Inorg. Chem.* **1993**, *32*, 4457–4459.

[15] C. W. Jung, P. E. Garrou, P. R. Hoffman, K. G. Caulton, *Inorg. Chem.* **1984**, *23*, 726–729.

[16] L. R. Dinelli, A. A. Batista, K. Wohnrath, M. P. de Araujo, S. L. Queiroz, M. R. Bonfadini, G. Oliva, O. R. Nascimento, P. W. Cyr, K. S. MacFarlane, B. R. James, *Inorg. Chem.* **1999**, *38*, 5341–5345.

[17] V. Comte, H. Vahrenkamp, *J. Organomet. Chem.* **2001**, *627*, 153–1586.

[18] Ortep-3 for Windows: J. L. Farrugia, *J. Appl. Crystallogr.* **1997**, *30*, 565.

[19] D. D. Perrin, W. L. F. Amarego, D. R. Perrin, *Purification of Laboratory Chemical*, 2nd ed., Pergamon, New York, **1980**.

[20] G. J. Baird, S. G. Davies, *J. Organomet. Chem.* **1984**, *262*, 215–221.

[21] a) P. S. Hallman, T. A. Stephenson, G. Wilkinson, *Inorg. Synth.* **1970**, *12*, 237–240; b) S. J. Higgins, *J. Chem. Ed.* **2001**, *78*, 663–664.

[22] Z. Otwinowski, W. Minor, "Processing of X-ray Diffraction Data Collected in Oscillation Mode" in *Methods in Enzymology, Vol. 276: Macromolecular Crystallography*, *Part A* (Eds.: C. W. Carter Jr, R. M. Sweet), Academic Press, New York, **1997**, pp. 307–326.

[23] G. M. Sheldrick, *Acta Crystallogr., Sect. A* **1990**, *46*, 467–473.

[24] G. M. Sheldrick, *SHELXL97*, *A program for crystal structure refinement*, University of Göttingen, Germany, **1997**.

[25] WinGX: J. L. Farrugia, *J. Appl. Crystallogr.* **1999**, *32*, 837–838.

Received: November 9, 2006
Published Online: March 13, 2007

 © 2007 Wiley-VCH Verlag GmbH & Co. KGaA, Weinheim 

DOI: 10.1002/ejic.200601108

# Unusual T4(1) Water Chain Stabilized in the One-Dimensional Chains of a Copper(II) Coordination Polymer

Yi Jin,[a] Yunxia Che,[a] Stuart R. Batten,[b] Pangkuan Chen,[a] and Jimin Zheng*[a]

**Keywords:** Water chain / Self assembly / One dimensional / Coordination polymers

A novel T4(1) water chain in a new $Cu^{II}$ coordination polymer, $\{[Cu(C_4H_6N_2)_2(C_4H_2O_4)]\ (H_2O)_3\}_n$ (**1**, where $C_4H_6N_2$ = 2-methylimidazole, $C_4H_2O_4$ = maleate), has been synthesized and structurally characterized by single-crystal X-ray diffraction. Thermogravimetry, infrared spectroscopy, elemental analysis, and magnetic analysis have also been used to characterize **1**. Complex **1** crystallizes in the trigonal space group $P3_221$, and the 1-D chains composed of cyclic water tetramers play an important role in stabilizing the overall polymeric structure. Furthermore, this 1-D water chain presents an unusual association mode of water molecules.

(© Wiley-VCH Verlag GmbH & Co. KGaA, 69451 Weinheim, Germany, 2007)

## Introduction

Water in all its forms exhibits a mesmerizing collection of properties and functions. Because of its crucial role for life, its abundance in nature, and its importance in so many technological processes, many chemists, biochemists, and biologists study water in an attempt to achieve a comprehensive understanding of its properties.[1] The present upsurge in studying water clusters is aimed not only at understanding the "anomalous" behavior of bulk water but also in probing its possible roles in the stabilization and functioning of biomolecules[2] and in designing new materials.[3] Although considerable attention has been devoted to the theoretical and experimental investigation of water clusters, including a variety of oligomers and polymers consisting of the basis cyclic water subunits, they are still not fully understood. It is this realization that has prompted extensive investigations of water structures in recent years. Some discrete water clusters $(H_2O)_n$,[4–23] where $n$ = 2–10, 12, 16 and 18, in various crystal hosts at room temperature have been reported. Further attention has also been paid to the infinite one- and two-dimensional water morphologies, which structurally lie between small water clusters and bulk water/ice, while investigations of these clusters that are interlinked to form a larger network is much less[24–35] and infinite water chains consisting of cyclic water tetramers are rare.[26]

On the other hand, the investigations of novel metal–organic hybrid compounds have attracted considerable interest in recent years, not only because of their intriguing structural motifs and promising photochemical, electrochemical, and magnetic properties, but also their because of their potential applications in catalysis, medicine and host–guest chemistry.[36–42] It is noteworthy that the dicarboxylates such as malonate, fumarate, and 1,4-benzenedicarboxylate have been widely used in constructing novel different dimensional metal–organic hybrid compounds.[43] In contrast to the ligands mentioned above, maleate is rarely used. Of further interest is that few cases of such coordination polymers, especially those mixed with the other chelating N-donor imidazole ligands, have been document so far.

In this work we report the preparation, structural characterization, and properties of an unusual 1D water chain consisting of cyclic water tetramers in a new 1D dicarboxylate-bridged Cu(II) polymer, $\{[Cu(C_4H_2O_4)(C_4H_6N_2)_2](H_2O)_3\}_n$ (**1**, where $C_4H_6N_2$ = 2-methylimidazole, $C_4H_2O_4$ = maleate); the water chains are linked with the 1-D polymer through hydrogen-bonding interactions to form a 3D network structure. We believe that the water structure demonstrated herein brings to light yet another novel mode of the cooperative association of water molecules, and this discovery is helpful in improving the modeling of some of unexplained properties of water and in understanding better the structure and behavior of water molecules in biological systems.[25]

## Results and Discussion

### Crystal Structures

Single-crystal structure analysis reveals that compound **1** consists of a polymer $\{[Cu(C_4H_6N_2)_2(C_4H_2O_4)](H_2O)_3\}_n$, which crystallizes in the chiral space group $P3_221$. The asymmetric unit contains one $Cu^{II}$ ion, two 2-methylimid-

[a] Department of Chemistry, Nankai University, Tianjin 300071, People's Republic of China
Fax: +86-23508056
E-mail: jmzheng@public.tpt.tj.cn
[b] School of Chemistry, Monash University, P. O. Box 23, Clayton, Victoria, 3800, Australia

Supporting information for this article is available on the WWW under http://www.eurjic.org or from the author.

 © 2007 Wiley-VCH Verlag GmbH & Co. KGaA, Weinheim 

azole ligands, one maleate, and three independent water molecules (Figure 1). Each copper(II) ion lies on a twofold axis and exhibits a Jahn–Teller distorted $CuN_2O_4$ octahedral geometry. Two nitrogen atoms [N(2) and N(2A)] from two monodentate 2-methylimidazole groups and two carboxylate oxygen atoms [O(1) and O(1A)] from the maleate ligand occupy the equatorial sites, and the Cu–N bonds [1.9579(15) Å] are somewhat shorter than the Cu–O bonds [2.0283(12) Å]. The axial sites are occupied by the second carboxylate oxygen atom of each maleate [Cu(1)–O(2) = 2.4833(14) Å]; the chelating bite of the carboxylate group leads to a significant distortion from true octahedral geometry [O(2)–Cu(1)–Cu(2A) = 143.59(7)°]. The neighboring $Cu^{II}$ ions are connected through the dicarboxylate bridges to form a regular infinite 1D chain with a Cu···Cu distance of 6.977 Å (Figure 2). Simultaneously, the chains are interconnected though two types of hydrogen bonds to form a three-dimensional network, which involve the equatorial carboxyl oxygen atom O(1) of maleate and the O(3) atom of a water molecule [O(3)···O(1) = 2.879 Å] and the uncoordinated nitrogen atom N(1) from the 2-methylimidazole group and the carboxyl oxygen atom O(2) of maleate; the N(1)··· O(2) distance of 2.771 Å [$-x + y + 1$, $-x + 1$, $z + 1/3$] is shorter than those reported previously [N···O = 2.851(19) and 3.088(18) Å].[10a]

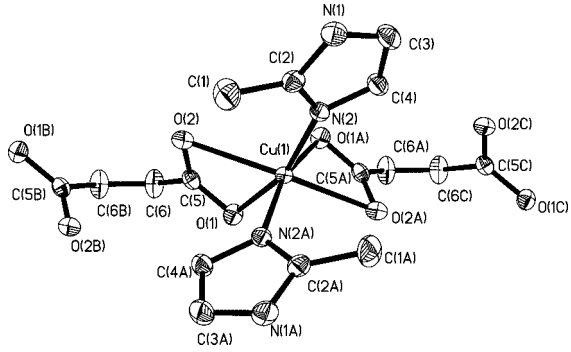


Figure 1. An ORTEP view of complex **1**, with selected atom numbering. The hydrogen atoms and uncoordinated water molecules are omitted for clarity.

Figure 2. Infinite 1D network of **1**. The hydrogen atoms and dissociated water molecules are omitted for clarity.

The most striking feature is that the structure contains extensive hydrogen bonding between the uncoordinated water molecules [O(3), O(4)] to form infinite 1D water chains containing cyclic water tetramers (Figure 3). The average O···O distance in the water chain is 2.790 Å, which is shorter than those observed in liquid water (2.854 Å) and comparable to those in the ice phase (2.77–2.84 Å).[32] However, this distance is a little longer than 2.768 Å[10a] and shorter than 2.95 Å[26] relative to the reported plane tetramer O···O distances.[26] The individual tetrameric clusters differ from the corner-sharing tetrameric and discrete tetrameric water clusters reported previously.[10,26] Two O(4) molecules form one side of the tetramer, and two O(3) molecules form the opposite side. The chains lie about the $3_2$ screw axes, and the tetramers are connected through the shared O(4) corners to give chains with a T4(1) symmetry[44] (Figure 4). The O(3) molecules lie on the periphery of the chain, and form hydrogen bonds with the coordinated O(1) carboxylate atoms of the coordination polymer chains (O···O = 2.879 Å); the $3_2$ screw axis means that each water chain is hydrogen bonded in this way to three adjoining coordination polymer chains. On a more local level, the two O(3) molecules within each tetramer bond to different coordination chains, whereas the two coordinated O(1) atoms in each Cu coordination environment form hydrogen bonds with the O(3) molecules belonging to two different (but adjoining) tetramers. Figure 5 displays the packing structure parallel to the *ab* plane of complex **1**. The water chains act as a "glue" to link the coordination polymer chains, forming an overall 3D structure.[32] Each water tetramer unit links two polymer chains, and each water chain links three 1D polymer chains through hydrogen bonds between the water molecules and the carboxyl groups. The T4(1) water chain is located in six polymer chains, and this plays a complementary role in stabilizing the network structure.

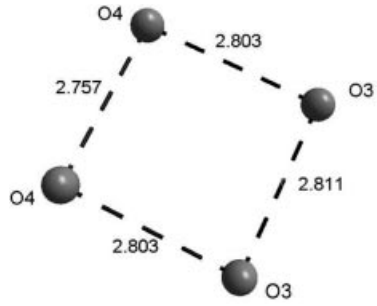


Figure 3. Tetrameric water cluster [O3···O3 = 2.811 Å, O4···O4 = 2.757 Å, O3···O4 = 2.803 Å].

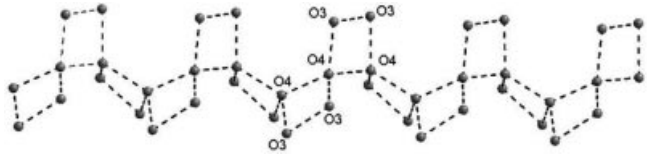


Figure 4. Hydrogen-bonding motif of the self-assembled infinite chain of water molecules.

The thermal stability of the water cluster was determined by thermogravimetric analysis (TGA) (see Figure S1 in the Supporting Information). TGA was performed at a heating rate of 10 °C/min with the single-crystal samples of **1**. Thermal analysis of the complex shows that the onset of water loss begins at 24 °C, and complete loss of water occurs within 200 °C. A 12.13-% weight loss was observed, which is almost equivalent to a loss of 2.7 water molecules – this value is lower than the calculated weight content of three water molecules (13.64%). In the infrared spectrum of **1**,

 © 2007 Wiley-VCH Verlag GmbH & Co. KGaA, Weinheim 

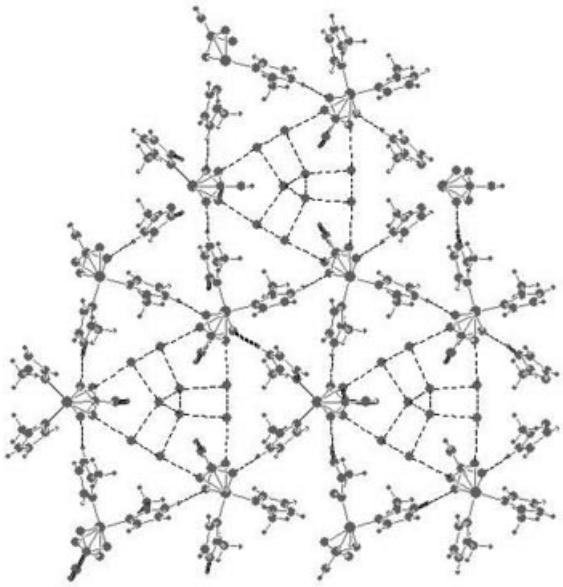

Figure 5. Packing diagram along the *c* axis of the supramolecular system for **1**.

the stretching frequency of the O–H bonds of the water cluster is observed as a band at about 3200 and 1631 $cm^{-1}$. The IR spectrum of ice shows the O–H stretching at 3220 $cm^{-1}$, while this stretching vibration in liquid water appears at 3490 and 3280 $cm^{-1}$.[16–18,29] This suggests that the water cluster in **1** shows an O–H stretching vibration similar to that of ice. It effectively proves that the O···O distance in the water chain is comparable to those in the ice phase (2.77–2.84 Å). In addition, there are several absorption bands observed at higher frequencies, 3133 $cm^{-1}$ and 3051.3 $cm^{-1}$, which are characteristic of the 2-MeIm groups. One strong peak corresponding to the $\nu(COO^-)$ vibration is observed at 1549 $cm^{-1}$ (see Figure S2 in the Supporting Information). The structural consistency and phase purity of compound **1** was confirmed by X-ray powder diffraction patterns (see Figure S3).

### Magnetic Properties

Magnetic measurement of **1** was carried out with a magnetic field of 500 Oe in the temperature range 2–300 K, and the results were presented in the form of a $\chi_M T$ vs. $T$ plot and $\chi_M^{-1}$ vs. $T$ plot (Figure 6), where $\chi_M$ is the corrected magnetic susceptibility per asymmetric $[Cu(C_4H_2O_4)(C_4H_6N_2)_2]$ unit.

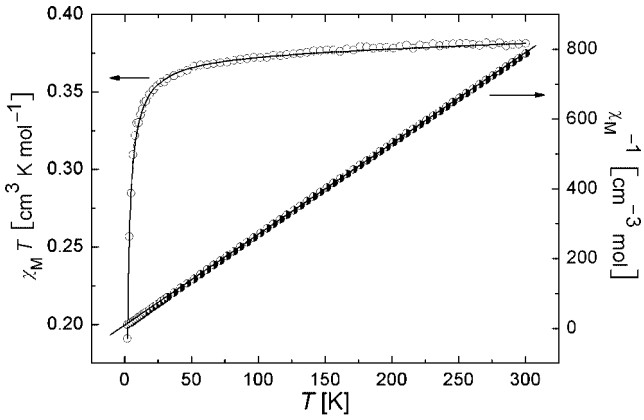


Figure 6. Plot of $\chi_M T$ vs. T and $\chi_M^{-1}$ vs. $T$ for **1**.

Magnetic susceptibility data per Cu unit for **1** can be fitted by the Curie–Weiss law: $\chi_M = C/(T - \theta)$ above 2 K, and this gives a Curie constant $C$ of 0.38 $cm^3 mol^{-1} K$ and a Weiss constant $\theta$ of –4.7 K. The $C$ value is slightly larger than that expected (0.375 $cm^3 mol^{-1} K$) for one $Cu^{II}$ ($S$ = 1/2) ion. The negative Weiss constant indicates that there are weak antiferromagnetic interactions between the $Cu^{II}$ ions through the maleate carboxyl bridge. The $\chi_M T$ value at room temperature is 0.38 $cm^3 mol^{-1} K$ and decreases gradually with decreasing temperature to a value of 0.35 $cm^3 mol^{-1} K$ at 25 K. The value then decreases sharply down to a minimum of 0.19 $cm^3 mol^{-1} K$ at 2 K, as shown Figure 6; this behavior is characteristic of an antiferromagnet.

The magnetic properties have been analyzed through the Bonner–Fisher result as shown in Equation (1), with $\chi = J/kT$ ($J$ is the intrachain magnetic coupling parameter). We take into account a proportion $\rho$ of a monomeric impurity, of which the susceptibility is assumed to follow the Curie law $Ng^2\beta^2S(S + 1)\rho/3kT$. The best fit obtained using a nonlinear regression analysis leads to $J$ = –1.54 $cm^{-1}$, $g$ = 2.05, $R = 7.105395 \times 10^{-5}$, and $\rho$ = 0.048; $R$ is the agreement factor defined as $\sum i[(\chi_M T)_{obs}(i) - (\chi_M T)_{calcd.}(i)]^2 / \sum[(\chi_M T)_{obs}(i)]^2$, $TIP$ is temperature-independent paramagnetism.

## Conclusions

An unusual 1D water chain with cyclic tetramers in a new 1D copper(II) coordination polymer chain has been successfully synthesized and structurally characterized. It is to be noted that the 1D water chain extends in an unusual association mode and is hydrogen bonded to surrounding 1D polymer chains to give a 3D network, thus highlighting

$$\chi = \frac{N g^2 \beta^2}{kT} \times \frac{0.25 + 0.074975x + 0.075235x^2}{1.0 + 0.9931x + 0.172135x^2 + 0.757825x^3} \times (1 - \rho) + Ng^2\beta^2 S(S+1)\rho / 3kT + TIP \quad (1)$$

 © 2007 Wiley-VCH Verlag GmbH & Co. KGaA, Weinheim 

the indispensable contribution to the stability of the coordination polymer frameworks. The unusual T4(1) water chain will enrich the water cluster family, and brings to light a novel mode for the cooperative association of water molecules and enhances the understanding of the 1D structural aspects of bulk water.

## Experimental Section

**Materials:** All reagents for syntheses were purchased from commercial sources and used as received.

**Physical Measurements:** Elemental analyses (C, H, N) were performed with an Elementar Vario EL instrument. Infrared spectra (KBr pellets) were measured on a MAGNA-IR 560 FTIR spectrometer in the 400–4000 $cm^{-1}$ region. Thermogravimetric analysis (TGA) was investigated with a standard TG-DTA analyzer under a flow of nitrogen at a heating rate of 10 °C$min^{-1}$ for all measurements. Magnetic studies were performed with MPMS SQUID and Maglab 2000 magnetometers in the temperature range 2–300 K. Powder diffraction data were collected with a Rigaku D/max-RC Diffractometer by using a Cu target ($\lambda$ = 1.54060 Å) operated at 45 KV and 180 mA.

**Synthesis of $\{[Cu(C_4H_2O_4)(C_4H_6N_2)_2](H_2O)_3\}_n$ (1):** $Cu(OAc)_2 \cdot H_2O$(0.20 g, 1 mmol), maleic acid (0.12 g, 1 mmol) and 2-methylimidazole (0.16 g, 2 mmol) in the molar ratio of 1:1:2 were dissolved in distilled water (25 mL). The pH value was then adjusted to about 7 with 2 M NaOH. The resulting solution was heated at 60 °C for 1 hr while stirring. The solvent was allowed to evaporate slowly at room temperature; small light blue single crystals appeared at the bottom of the cup. $C_{12}H_{20}CuN_4O_7$: C 36.41, H 5.09, N 14.15; found C 37.26, H 4.95, N 14.48%.

**X-ray Crystallography:** Single-crystal X-ray diffraction data for complex **1** was collected with a R-AXIS RAPID IP diffractometer, by using the $\omega$-scan technique with Mo-$K_\alpha$ radiation ($\lambda$ = 0.71073 Å). The structures were solved by direct methods and refined on $F^2$ by full-matrix least-squares with SHELXTL-97.[45] Non-hydrogen atoms were refined with anisotropic temperature parameters and the hydrogen atoms of the ligands were refined as rigid groups; the hydrogen atoms of water were not found or assigned. Crystal data of **1**: $M$ = 395.86 g$mol^{-1}$, trigonal, space group $P3_221$, $a$ = 14.868(3), $b$ = 14.868(3), $c$ = 6.9774(14) Å, $\gamma$ = 120°, $V$ = 1335.8(5) $Å^3$, $Z$ = 3, $R_1$ = 0.0223, $wR_2$ = 0.0592, $d_{calcd.}$ = 1.476 g$cm^{-3}$, $\mu$ = 1.266 $mm^{-1}$, $F(000)$ = 615. A total of 12859 reflections were collected, of which 2049 unique reflections were used. The selected bond lengths and angles of **1** are presented in Table 1.

Table 1. Selected bond lengths [Å] and angles [°] for **1**.[a]

| | | | |
|---|---|---|---|
| C(1)–C(2) | 1.486(3) | C(2)–N(2) | 1.330(2) |
| C(2)–N(1) | 1.333(3) | C(3)–C(4) | 1.350(3) |
| C(3)–N(1) | 1.375(3) | C(5)–O(2) | 1.248(2) |
| C(5)–O(1) | 1.267(2) | C(5)–C(6) | 1.489(3) |
| C(6)–C(6)#1 | 1.316(4) | Cu(1)–N(2) | 1.9579(15) |
| Cu(1)–N(2)#2 | 1.9579(15) | Cu(1)–O(1) | 2.0283(12) |
| Cu(1)–O(1)#2 | 2.0283(12) | Cu(1)–O(2) | 2.4833(14) |
| N(2)–C(2)–N(1) | 109.63(16) | N(2)–C(2)–C(1) | 126.79(18) |
| N(1)–C(2)–C(1) | 123.58(19) | C(4)–C(3)–N(1) | 106.21(18) |
| C(3)–C(4)–N(2) | 108.63(17) | O(2)–C(5)–O(1) | 121.77(16) |
| O(2)–C(5)–C(6) | 120.05(18) | O(1)–C(5)–C(6) | 118.14(17) |
| C(6)#1–C(6)–C(5) | 124.31(10) | N(2)–Cu(1)–N(2)#2 | 97.37(9) |
| N(2)–Cu(1)–O(1) | 161.91(6) | N(2)#2–Cu(1)–O(1) | 91.74(6) |
| O(1)–Cu(1)–O(1)#2 | 84.03(8) | O(2)–Cu(1)–O2)#2 | 143.59(7) |

[a] Symmetry codes for **1**: #1 $y$, $x$, $-z$; #2 $y$, $x$, $-z$ + 1.

CCDC-615376 (for **1**) contains the supplementary crystallographic data for this paper. These data can be obtained free of charge from the Cambridge Crystallographic Data Centre via www.ccdc.cam.ac.uk/data_request/cif.

**Supporting Information** (see footnote on the first page of this article): The TG curve, IR spectra, and XRD powder diffraction of **1** (Figure S1, Figure S2 and Figure S3).

## Acknowledgments

This work was supported by the National Natural Science Foundation of China (No. 50572040).

[1] a) R. Ludwig, *Angew. Chem. Int. Ed.* **2003**, *42*, 258–260; b) R. Ludwig, A. Appelhagen, *Angew. Chem. Int. Ed.* **2005**, *44*, 811–815.
[2] E. Westhoff (Eds.), *Water and Biological Macromolecules*, CRC Press, Boca Raton, FL, **1993**.
[3] J. D. Joannopoulos, *Nature* **2001**, *414*, 257–258.
[4] R. Ludwig, *Angew. Chem. Int. Ed.* **2001**, *40*, 1808–1827.
[5] J. Tao, Z. J. Ma, R. B. Huang, L. S. Zheng, *Inorg. Chem.* **2004**, *43*, 6133–6135.
[6] B. H. Ye, B. B. Ding, Y. Q. Weng, X. M. Chen, *Inorg. Chem.* **2004**, *43*, 6866–6868.
[7] R. J. Doedens, E. Yohannes, M. I. Khan, *Chem. Commun.* **2002**, 62–63.
[8] J. N. Moorthy, R. Natarajan, P. Venugopalan, *Angew. Chem. Int. Ed.* **2002**, *41*, 3417–3420.
[9] W. B. Blanton, S. W. Gordon-Wylie, G. R. Clark, K. D. Jordan, J. T. Wood, U. Geiser, T. J. Collins, *J. Am. Chem. Soc.* **1999**, *121*, 3551–3552.
[10] a) S. Supriya, S. K. Das, *New J. Chem.* **2003**, *27*, 1568–1574; b) S. Supriya, S. Manikumari, P. Raghavaiah, S. K. Das, *New J. Chem.* **2003**, *27*, 218–220.
[11] L. S. Long, Y. R. Wu, R. B. Huang, L. S. Zheng, *Inorg. Chem.* **2004**, *43*, 3798–3800.
[12] J. L. Atwood, L. J. Barbour, T. J. Ness, C. L. Raston, P. L. Raston, *J. Am. Chem. Soc.* **2001**, *123*, 7192–7193.
[13] S. K. Ghosh, P. K. Bharadwaj, *Inorg. Chem.* **2003**, *42*, 8250–8254.
[14] A. Michaelides, S. Skoulika, E. G. Bakalbassis, J. Mrozinski, *Cryst. Growth Des.* **2003**, *3*, 487–492.
[15] S. Neogi, G. Savitha, P. K. Bharadwaj, *Inorg. Chem.* **2004**, *43*, 3771–3773.
[16] S. K. Ghosh, P. K. Bharadwaj, *Inorg. Chem.* **2004**, *43*, 6887–6889.
[17] S. K. Ghosh, P. K. Bharadwaj, *Eur. J. Inorg. Chem.* **2005**, 4886–4889.
[18] J. Yang, J. F. Ma, Y. Y. Liu, J. C. Ma, H. Q. Jia, N. H. Hu, *Eur. J. Inorg. Chem.* **2006**, 1208–1215.
[19] U. Mukhopadhyay, I. Bernal, *Cryst. Growth Des.* **2005**, *5*, 1687–1689.
[20] K. Raghuraman, K. K. Katti, L. J. Barbour, N. Pillarsetty, C. L. Barmes, K. V. Katti, *J. Am. Chem. Soc.* **2003**, *125*, 6955–6961.
[21] S. K. Ghosh, P. K. Bharadwaj, *Eur. J. Inorg. Chem.* **2006**, 1341–1344.
[22] J. Fan, C. Slebodnick, B. E. Hanson, *Inorg. Chem. Commun.* **2006**, *9*, 103–106.
[23] U. Mukhopadhyay, I. Bernal, *Cryst. Growth Des.* **2006**, *6*, 363–365.
[24] A. Mukherjee, M. K. Saha, M. Nethaji, A. R. Chakravarty, *Chem. Commun.* **2004**, 716–717.
[25] S. Neogi, P. K. Bharadwaj, *Inorg. Chem.* **2005**, *44*, 816–818.
[26] S. Pal, N. B. Sankaran, A. Samanta, *Angew. Chem. Int. Ed.* **2003**, *42*, 1741–1743.
[27] P. S. Lakshminarayanan, E. Suresh, P. Ghosh, *J. Am. Chem. Soc.* **2005**, *127*, 13132–13133.

 © 2007 Wiley-VCH Verlag GmbH & Co. KGaA, Weinheim 

[28] X. J. Luan, Y. C. Chu, Y. Y. Wang, D. S. Li, P. Liu, Q. Z. Shi, *Cryst. Growth Des.* **2006**, *6*, 812–814.
[29] a) R. Custelcean, C. Afloroaei, M. Vlassa, M. Polverejan, *Angew. Chem. Int. Ed.* **2000**, *39*, 3094–3096; b) S. K. Ghosh, P. K. Bharadwaj, *Eur. J. Inorg. Chem.* **2005**, 4880–4885.
[30] N. S. Oxtoby, A. J. Blake, N. R. Champness, C. Wilson, *Chem. Eur. J.* **2005**, *11*, 4643–4654.
[31] J. M. Zheng, S. R. Batten, M. Du, *Inorg. Chem.* **2005**, *44*, 3371–3373.
[32] J. Lu, J. H. Yu, X. Y. Chen, P. Cheng, X. Zhang, J. Q. Xu, *Inorg. Chem.* **2005**, *44*, 5978–5980.
[33] G. Beobide, O. Castillo, A. Luque, U. Garcia-Couceriro, J. P. Garcia-Terán, P. Román, *Inorg. Chem.* **2006**, *45*, 5367–5382.
[34] Y. S. Jiang, G. H. Li, Y. Tian, Z. L. Liao, J. S. Chen, *Inorg. Chem. Commun.* **2006**, *9*, 595–598.
[35] D. L. Reger, R. F. Semeniue, C. Pettinari, F. Luna-Giles, M. D. Smith, *Cryst. Growth Des.* **2006**, *6*, 1068–1070.
[36] a) P. J. Stang, B. Olenyuk, *Acc. Chem. Res.* **1997**, *30*, 502–518; b) S. Leininger, B. Olenyuk, P. J. Stang, *Chem. Rev.* **2000**, *100*, 853–908; c) G. F. Swiegers, T. J. Malefetse, *Chem. Rev.* **2000**, *100*, 3483–3538; d) C. T. Chen, K. S. Suslick, *Coord. Chem. Rev.* **1993**, *128*, 293–322.
[37] a) P. J. Hagrman, D. Hagrman, J. Zubieta, *Angew. Chem. Int. Ed.* **1999**, *38*, 2638–2684; b) D. Hagrman, R. P. Hammond, R. Haushalter, J. Zubieta, *Chem. Mater.* **1998**, *10*, 2091–2100.
[38] a) X. M. Zhang, M. L. Tong, X. M. Chen, *Angew. Chem. Int. Ed.* **2002**, *41*, 1029–1031; b) G. F. Liu, B. H. Ye, Y. H. Ling, X. M. Chen, *Chem. Commun.* **2002**, 1442–1443; c) X. H. Bu, W. Chen, S. L. Lu, R. H. Zhang, D. Z. Liao, W. M. Bu, M. Shionoya, F. Brisse, J. Ribas, *Angew. Chem. Int. Ed.* **2001**, *40*, 3201–3203; d) X. H. Bu, W. Chen, W. F. Hou, M. Du, R. H. Zhang, F. Brisse, *Inorg. Chem.* **2002**, *41*, 3477–3482.
[39] a) W. Lin, O. R. Evans, R. G. Xiong, Z. Wang, *J. Am. Chem. Soc.* **1998**, *120*, 13272–13273; b) Y. Cui, O. R. Evans, H. L. Ngo, P. S. White, W. B. Lin, *Angew. Chem. Int. Ed.* **2002**, *41*, 1159–1162; c) Y. Cui, H. L. Ngo, W. Lin, *Inorg. Chem.* **2002**, *41*, 1033–1035.
[40] a) N. Takeda, K. Umemoto, K. Yamaguchi, M. Fujita, *Nature* **1999**, *398*, 794–796; b) A. Caneschi, D. Gatteschi, N. Lalioti, C. Sangregorio, R. Sessoli, G. Venturi, A. Vindigni, A. Rettori, M. G. Pini, M. A. Novak, *Angew. Chem. Int. Ed.* **2001**, *40*, 1760–1763; c) Y. Q. Tian, C. X. Cai, Y. Ji, X. Z. You, S. M. Peng, G. H. Lee, *Angew. Chem. Int. Ed.* **2002**, *41*, 1384–1386.
[41] a) Y. H. Wang, L. Y. Feng, Y. G. Li, C. W. Hu, E. B. Wang, N. H. Hu, H. Q. Jia, *Inorg. Chem.* **2002**, *41*, 6351–6357; b) Y. G. Li, N. Hao, Y. Lu, E. B. Wang, Z. H. Kang, C. W. Hu, *Inorg. Chem.* **2003**, *42*, 3119–3124; c) Y. G. Li, N. Hao, E. B. Wang, M. Yuan, C. Hu, N. Hu, H. Jia, *Inorg. Chem.* **2003**, *42*, 2729–2735.
[42] X. X. Xu, Y. Lu, E. B. Wang, Y. Ma, Y. Q. Guo, X. L. Bai, L. Xu, *J. Mol. Struct.* **2005**, *779*, 55–60.
[43] a) S. Konar, P. S. Mukherjee, E. Zangrando, F. Lloret, N. R. Chaudhuri, *Angew. Chem. Int. Ed.* **2002**, *41*, 1561–1563; b) P. S. Mukherjee, S. Dalai, G. Mostafa, E. Zangrando, T. H. Lu, G. Rogez, T. Mallah, N. Ray Chaudhuri, *Chem. Commun.* **2001**, 1346–1347; c) J. Sanchiz, Y. Rodriguez-Martin, C. Ruiz-Pérez, A. Mederos, F. Lloret, M. Julve, *New J. Chem.* **2002**, *26*, 1624–1628.
[44] a) M. Mascal, L. Infantes, J. Chisholm, *Angew. Chem. Int. Ed.* **2006**, *45*, 32–36; b) L. Infantes, J. Chisholm, S. Motherwell, *CrystEngComm* **2003**, *5*, 480–486; c) L. Infantes, S. Motherwell, *CrystEngComm* **2002**, *4*, 454–461.
[45] G. M. Sheldrick, *SHELXTL: Structure Determination Software Programs,* Bruker Analytical X-ray System Inc., Madison, WI, U.S.A, **1997**.

Received: January 19, 2006
Published Online: March 20, 2007

 © 2007 Wiley-VCH Verlag GmbH & Co. KGaA, Weinheim 

DOI: 10.1002/ejic.200601126

# The Iminophosphorane-Phosphane $Ph_2PC_6H_4OC_6H_4PPh_2$=NP(O)$(OPh)_2$: Synthesis, Reactivity, and Catalytic Activity in Suzuki Cross-Coupling and the Homogeneous Hydrogenation of Olefins

**Ramalingam Venkateswaran,[a] Maravanji S. Balakrishna,*[a] and Shaikh M. Mobin[b]**

**Keywords:** Monoimination / Monophosphane / Iminophosphorane-phosphane / Staudinger reaction / Suzuki cross-coupling

The iminophosphorane-phosphane ligand $Ph_2PC_6H_4OC_6H_4$-$PPh_2$=NP(O)$(OPh)_2$ (**1**) has been synthesized by partial imination of bis[2-(diphenylphosphanyl)phenyl] ether (DPEphos) with phosphoryl azide $(PhO)_2P(O)N_3$. A similar reaction in a 1:2 stoichiometry affords the bis(iminophosphorane) O-$\{C_6H_4PPh_2$=NP(O)$(OPh)_2\}_2$ (**2**). The chalcogen derivatives O$\{C_6H_4P(E)Ph_2\}_2$ [E = S (**3**) and Se (**4**)] and $Ph_2P(E)$-$C_6H_4OC_6H_4PPh_2$=NP(O)$(OPh)_2$ [E = S (**5**) and Se (**6**)] are also synthesized by treating DPEphos and **1** with elemental sulfur and selenium, respectively. The mononuclear complexes *trans*-[$MCl_2\{\kappa^1$-*P*-$Ph_2PC_6H_4OC_6H_4PPh_2$=NP(O)$(OPh)_2\}_2$] [M = Pt (**7**) Pd (**8**)] and *trans*-[Rh(CO)Cl{$\kappa^1$-*P*-$Ph_2PC_6$-$H_4OC_6H_4PPh_2$=NP(O)$(OPh)_2\}_2$] (**12**) are prepared by the reaction of **1** with $[Pt(COD)Cl_2]$, $[Pd(COD)Cl_2]$, and $[\{Rh(CO)_2$-$Cl\}_2]$, respectively. Treatment of **1** with $[Pd_2(dba_3)]$ (dba = dibenzylideneacetone) affords the mononuclear complex $[Pd^0\{\kappa^2$-*P,O*-$Ph_2PC_6H_4OC_6H_4PPh_2$=NP(O)$(OPh)_2\}_2]$ (**9**) in which ligand **1** coordinates through its P and O centers in a $\kappa^2$-*P,O* chelating fashion. The monocoordinated $Au^I$ complex [AuCl{$\kappa^1$-*P*-$Ph_2PC_6H_4OC_6H_4PPh_2$=NP(O)$(OPh)_2\}$] (**10**) has been prepared by the reaction of **1** and $[AuCl(SMe_2)]$ and its structure has been confirmed by X-ray crystallography. The reaction of **1** with $[\{Rh(COD)Cl\}_2]$ in the presence of AgOTf affords the cationic $Rh^I$ complex *cis*-[Rh(COD)$\{\kappa^2$-*P,O*-$Ph_2PC_6H_4OC_6H_4PPh_2$=NP(O)$(OPh)_2\}$][OTf] (**11**). The catalytic activity of the $Pd^0$ complex **9** has been investigated in Suzuki cross-coupling reactions. Homogeneous catalytic hydrogenation of olefins has also been studied using the cationic $Rh^I$ complex **11**.

(© Wiley-VCH Verlag GmbH & Co. KGaA, 69451 Weinheim, Germany, 2007)

## Introduction

There has been considerable interest in recent years in the chemistry of iminophosphorane-phosphane ligands due to their interesting coordination chemistry and applications in organic syntheses such as aza-Wittig reactions.[1] These iminophosphorane-phosphane ligands have been synthesized by selective imination of bis(phosphanes) in a Staudinger reaction.[2–4] Various types of organic azides have been employed for the synthesis of such ligands, including $R'_3SiN_3$ and $R'_2P(O)N_3$.[5–11] The monoimination of bis(phosphanes) with phosphoryl azide $R'_2P(O)N_3$ leads to the formation of the hemilabile iminophosphorane-phosphane ligands $R_2P$-X-P$\{$=NP(O)$R'_2\}R_2$ (X = divalent bridging group). These ligands have the ability to offer different coordination modes such as $\kappa^1$-*P*, $\kappa^2$-*P,N*, $\kappa^2$-*P,O*, and $\kappa^3$-*P,N,O*, and its hemilabile behavior has been successfully utilized in homogeneous catalysis such as hydrogenation of olefins,[12] olefin oligomerization,[13] transfer hydrogenation of ketones,[14,15] and cross-coupling of secondary amines with aryl halides.[16] Surprisingly, their involvement in Suzuki cross-coupling reaction still remains unexplored.

van Leeuwen and co-workers[17] and others[18] have extensively studied the coordination chemistry and the catalytic utility of the bis[2-(diphenylphosphanyl)phenyl] ether $Ph_2PC_6H_4OC_6H_4PPh_2$. The complexes of this large-bite bis(phosphane) are found to be very effective in catalyzing a variety of organic transformations.[19–21]As a continuation of our work in designing new phosphorus-based ligands in order to explore their coordination chemistry[22–29] and catalytic activity,[30–33] we report herein the synthesis, coordination chemistry, and catalytic activity of the iminophosphorane-phosphane $Ph_2PC_6H_4OC_6H_4PPh_2$=NP(O)$(OPh)_2$ (**1**) derived from $Ph_2PC_6H_4OC_6H_4PPh_2$.

[a] Phosphorus Laboratory, Department of Chemistry, Indian Institute of Technology Bombay,
Powai, Mumbai 400076, India
Fax: +91-22-2576-7152, -2572-3480
E-mail: krishna@chem.iitb.ac.in
[b] National Single Crystal X-ray Diffraction facility, Indian Institute of Technology Bombay,
Mumbai 400076, India

## Results and Discussion

### Synthesis of the Ligand and Chalcogen Derivatives

Reaction of the phosphoryl azide $(PhO)_2P(O)N_3$ with bis[2-(diphenylphosphanyl)phenyl] ether (DPEphos) (1:1 molar ratio) in thf at –78 °C affords the iminophos-

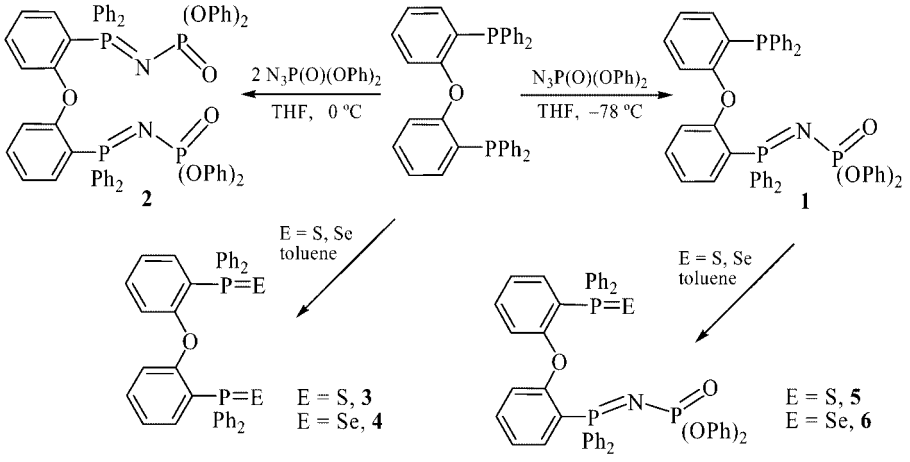


Scheme 1.

phorane-phosphane $Ph_2PC_6H_4OC_6H_4PPh_2{=}NP(O)(OPh)_2$ (**1**) in good yield. A similar reaction in a 2:1 molar ratio at 0 °C affords the bis(iminophosphorane) $O\{C_6H_4PPh_2{=}NP(O)(OPh)_2\}_2$ (**2**). Compounds **1** and **2** are moderately air stable and highly soluble in dichloromethane, diethyl ether, acetonitrile, and toluene.

The $^{31}P\{^1H\}$ NMR spectrum of ligand **1** shows three well-separated phosphorus signals with equal relative intensities. The terminal phosphoryl $P^V_{[O]}$ ($\delta$ = –10.5 ppm) and iminophosphorane $P^V_{[N]}$ ($\delta$ = 10.4 ppm) signals appear as simple doublets with a $^2J_{P,P}$ value of 37.7 Hz. The trivalent phosphorus appears as a singlet at $\delta$ = –20.1 ppm. The EI mass spectrum supports the structure as it shows the molecular ion peak at *m*/*z* 786.47 $[M + H]^+$. The $^{31}P\{^1H\}$ NMR spectrum of **2** shows two doublets of equal intensity [$\delta$ = 10.9 ($P^V_{[N]}$) and –10.6 ppm ($P^V_{[O]}$); $^2J_{P,P}$ = 40.4 Hz] with chemical shift values comparable to those described for analogous compounds of the type $[RNPPh_2NP(O)(OPh)_2]_2$.[8,10,11] The EI mass spectrum of compound **2** shows the molecular ion peak at *m*/*z* 1033.57 $[M + H]^+$. Treatment of DPEphos and **1** with elemental sulfur and selenium results in the isolation of the bis-chalcogenides $O\{C_6H_4P(E)Ph_2\}_2$ [E = S (**3**) and Se (**4**)] and the thio- and selenoyl derivatives $Ph_2P(E)$-$C_6H_4OC_6H_4PPh_2{=}NP(O)(OPh)_2$ [E = S (**5**) and Se (**6**)], respectively, in good yield. The $^{31}P\{^1H\}$ NMR spectra of compounds **3** and **4** show single resonances at $\delta$ = 39.1 and 29.4 ppm ($^1J_{Se,P}$ = 734.1 Hz), respectively. The EI mass spectrum of **4** shows the molecular ion peak at *m*/*z* 699.04 $[M + H]^+$. The $^{31}P\{^1H\}$ NMR spectra of **5** and **6** show three resonances, similar to the parent compound **1**. The $^{31}P$ resonances due to the chalcogenide phosphorus centers in **5** and **6** show a considerable downfield shift and appear at $\delta$ = 37.7 and 27.6 ppm, respectively, whereas the chemical shift values of the other two phosphorus centers are almost the same as those of compound **1**. The selenoyl derivative **6** shows a $^1J_{Se,P}$ coupling of 744 Hz. The mass spectra of compounds **5** and **6** support their structure, with molecular ion peaks at *m*/*z* 818.15 $[M + H]^+$ and 866.13 $[M + H]^+$, respectively (Scheme 1).

## Synthesis of Metal Complexes

The reactions of **1** with $[M(COD)Cl_2]$ (M = Pt, Pd), irrespective of the stoichiometry, afford the mononuclear complexes *trans*-$[MCl_2\{\kappa^1$-*P*-$Ph_2PC_6H_4OC_6H_4PPh_2{=}NP(O)(OPh)_2\}_2]$ [M = Pt (**7**) and Pd (**8**)]. These complexes were therefore prepared in good yield from the reagents in 2:1 molar ratio. The $^{31}P\{^1H\}$ NMR spectroscopic data are very diagnostic for characterizing the complexes. The $^{31}P$ chemical shift due to the coordinated $PPh_2$ group is shifted considerably downfield as a result of coordination whereas the resonances due to the $P^V_{[N]}$ and $P^V_{[O]}$ groups do not exhibit such a large change in their chemical shift and $^2J_{P,P}$ values, thereby indicating their non-involvement in the complex formation. The $^{31}P\{^1H\}$ NMR spectrum of complex **7** shows a singlet at $\delta$ = 10.3 ppm corresponding to the coordinated phosphorus with a $^1J_{Pt,P}$ value of 2642 Hz and two doublets at $\delta$ = 11.4 (P=N) and –10.6 ppm (P=O) with a $^2J_{P,P}$ value of 37.9 Hz. The low $^1J_{Pt,P}$ value suggests a *trans* geometry for complex **7**.[34] The EI mass spectrum of complex **7** shows the molecular ion peak at *m*/*z* 1838.01 $[M + H]^+$. The $^{31}P\{^1H\}$ NMR spectrum of complex **8** shows one singlet at $\delta$ = 14.2 ppm for the coordinated phosphorus and two doublets at $\delta$ = 11.7 and –10.6 ppm ($^2J_{P,P}$ = 38.1 Hz) for the other two phosphorus centers.

The reaction of **1** with $[Pd_2(dba)_3]$ in a 2:1 molar ratio in toluene affords the $Pd^0$ complex **9** in good yield (Scheme 2). The $^{31}P\{^1H\}$ NMR spectrum of $[Pd\{\kappa^2$-*P*,*O*-$Ph_2PC_6H_4OC_6H_4PPh_2{=}NP(O)(OPh)_2\}_2]$ (**9**) shows three resonances at $\delta$ = 23.6, 11.7, and –7.8 ppm for the $PPh_2$, $P^V_{[N]}$, and $P^V_{[O]}$ centers, respectively. The reaction of **1** with $[AuCl(SMe_2)]$ in $CH_2Cl_2$ affords $[AuCl\{\kappa^1$-*P*-$Ph_2PC_6H_4OC_6H_4PPh_2{=}NP(O)(OPh)_2\}]$ (**10**) in quantitative yield as a colorless crystalline solid. The $^{31}P\{^1H\}$ NMR spectrum of complex **10** shows three well-separated signals with equal intensities. The coordinated phosphorus center exhibits a singlet at $\delta$ = 19.0 ppm; there is no major change in the chemical shift values for the other two phosphorus centers with respect to ligand **1**. The elemental analysis and

 © 2007 Wiley-VCH Verlag GmbH & Co. KGaA, Weinheim 

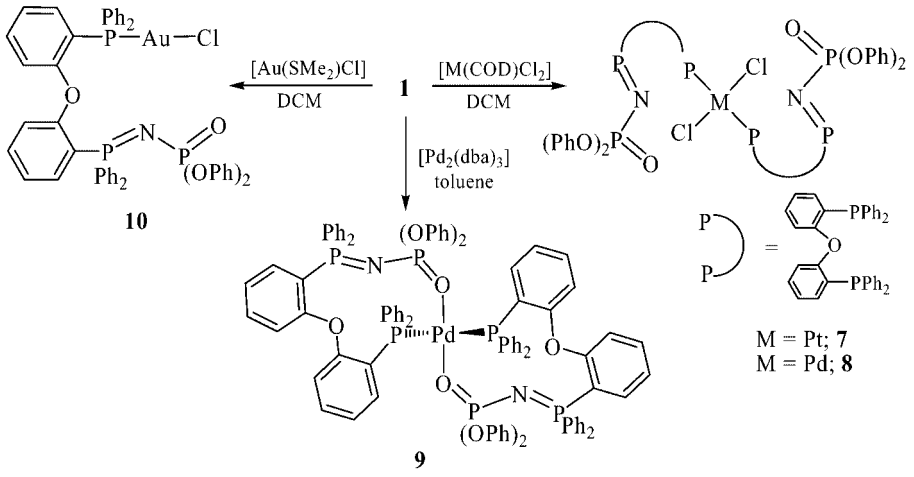


Scheme 2.

mass spectrum of complex **10** are in accordance with the proposed structure, which was further confirmed by single-crystal X-ray diffraction studies.

The mononuclear rhodium complex *cis*-[Rh(COD){κ²-*P*,*O*-$Ph_2PC_6H_4OC_6H_4PPh_2$=NP(O)$(OPh)_2$}][OTf] (**11**) was prepared by the reaction of **1** with [{Rh(COD)Cl}$_2$] followed by the addition of AgOTf in an equimolar ratio. The $^1$H NMR spectrum of **11** confirmed the presence of a cyclooctadiene group, which exhibits broad signals at around $\delta$ = 1.27–2.37 ppm for the four $CH_2$ groups and two doublets at $\delta$ = 2.90 and 5.13 ppm for the olefin protons with $^2J_{Rh,H}$ values of 119.2 and 115.6 Hz, respectively. The formation of an 11-membered chelate ring by binding of the P and O atoms of the phosphoryl group was confirmed by its $^{31}$P NMR spectroscopic data. The $^{31}$P{$^1$H} NMR spectrum of **11** consists of three resonances with equal intensities. The coordinated phosphorus appears as a doublet at $\delta$ = 12.9 ppm with a $^1J_{Rh,P}$ value of 149.3 Hz while the iminophosphorane and phosphoryl groups show mutually coupled doublets centered at $\delta$ = 8.8 and –11.1 ppm, respectively, with a $^2J_{P,P}$ value of 39 Hz. The doublet due to the phosphoryl group shows an additional $^2J_{Rh,P}$ coupling of 6.6 Hz, thus indicating the coordination of the phosphoryl oxygen to the rhodium center, similar to an analogous compound reported in the literature.[5b] The EI mass spectrum of cationic complex **11** shows the molecular ion peak at *m*/*z*

Table 1. Summary of $^{31}$P{$^1$H} NMR data for compounds **1**–**12** [$\delta$ in ppm and *J* in Hz].

| Compound | $\delta_{PPh_2}$ | $\delta_{Ph_2P=N}$ | $\delta_{(PhO)_2P=O}$ | $^2J_{P,P}$ |
|---|---|---|---|---|
| **1** | –20.1 (s) | 10.4 (d) | –10.5 (d) | 37.7 |
| **2** | | 10.9 (d) | –10.6 (d) | 40.4 |
| **3** | 39.1 (s) | | | |
| **4** | 29.4 (s), $^1J_{Se,P}$ = 734.1 | | | |
| **5** | 37.7 (s) | 10.8 (d) | –10.5 (d) | 38.9 |
| **6** | 27.6 (s), $^1J_{Se,P}$ = 744.0 | 10.8 (d) | –10.5 (d) | 39.0 |
| **7** | 10.3 (s), $^1J_{Pt,P}$ = 2642 | 11.4 (d) | –10.6 (d) | 37.9 |
| **8** | 14.2 (s) | 11.7 (d) | –10.6 (d) | 38.1 |
| **9** | 23.6 (s) | 11.7 (d) | –7.8 (d) | 39.5 |
| **10** | 19.0 (s) | 10.4 (d) | –10.5 (d) | 37.9 |
| **11** | 12.9 (d), $^1J_{Rh,P}$ = 149.3 | 8.8 (d) | –11.1 (dd), $^2J_{Rh,P}$ = 6.6 | 39.0 |
| **12** | 22.5 (d), $^1J_{Rh,P}$ = 140.3 | 11.3 (d) | –10.6 (d) | 37.9 |

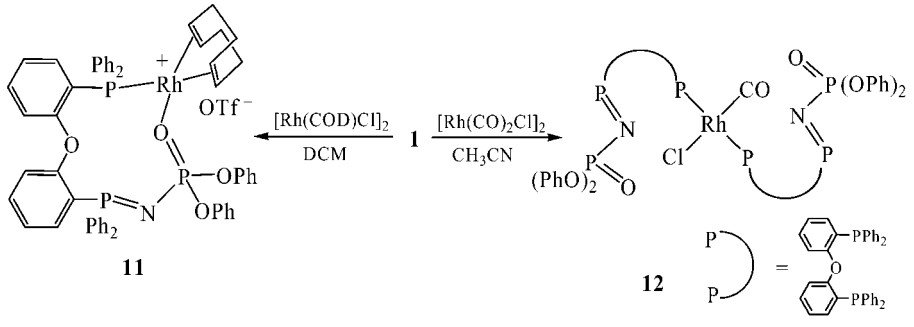


Scheme 3.

 © 2007 Wiley-VCH Verlag GmbH & Co. KGaA, Weinheim 

996.2 $[M - OTf]^+$. The reaction of $[\{Rh(CO)_2Cl\}_2]$ with **1** in a 1:2 molar ratio affords *trans*-$[Rh(CO)Cl\{\kappa^1$-*P*-$Ph_2PC_6H_4OC_6H_4PPh_2{=}NP(O)(OPh)_2\}_2]$ (**12**), as is evident from the $^{31}P\{^1H\}$ NMR, mass, and elemental analysis data. The $^{31}P\{^1H\}$ NMR spectrum of complex **12** consists of three doublets. The doublet at $\delta$ = 22.5 ppm with a $^1J_{Rh,P}$ coupling of 140 Hz is due to the coordinated phosphorus whereas the remaining two doublets at $\delta$ = 11.3 and –10.6 ppm are assigned to $P^V_{[N]}$ and $P^V_{[O]}$, respectively, with a $^2J_{P,P}$ coupling of 37.9 Hz. The mass spectrum of **12** exhibits the molecular ion peak at *m*/*z* 1701.1 $[M - Cl]^+$. The IR spectrum of **12** shows $\nu_{CO}$ at 1958 $cm^{-1}$ (Table 1 and Scheme 3).

## Crystal Structure of Complex 10

A perspective view of the molecular structure of complex **10** with the atom numbering scheme is shown in Figure 1. Crystal data and details of crystal structure determination are given in the Experimental Section, while the selected bond lengths [Å] and bond angles [°] are displayed in Table 2. The P(1)–Au(1)–Cl(1) bond angle of 177.81(7)° indicates that the gold is in a slightly distorted linear geometry. The Au(1)–Cl(1) and Au(1)–P(1) bond lengths are 2.284(1) and 2.230(1) Å, respectively, and are close to the reported values for $[O(C_6H_4PPh_2AuCl)_2]$.[18b] There is an intermolecular interaction between O(2_j) and H(34), as is evident from the bond length of 2.402 Å (less than the sum of the van der Waal's radii)[35] and the C(34)–H(34)–O(2_j) bond angle of 172°.

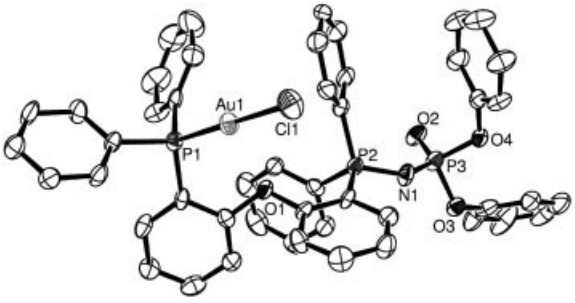


Figure 1. Molecular structure of $[AuCl\{\kappa^1$-*P*-$Ph_2PC_6H_4OC_6H_4PPh_2{=}NP(O)(OPh)_2\}]$ (**10**). All hydrogen atoms have been omitted for clarity. Thermal ellipsoids are drawn at the 50% probability level.

Table 2. Selected bond lengths [Å] and bond angles [°] for **10**.

| Bond lengths | | Bond angles | |
|---|---|---|---|
| Au(1)–Cl(1) | 2.284(1) | Au(1)–P(1)–C(1) | 112.90(2) |
| Au(1)–P(1) | 2.230(1) | P(1)–Au(1)–Cl(1) | 177.81(7) |
| P(2)–N(1) | 1.586(5) | N(1)–P(3)–O(2) | 122.40(3) |
| P(3)–N(1) | 1.570(5) | N(1)–P(3)–O(3) | 103.20(2) |
| P(3)–O(2) | 1.463(4) | P(2)–N(1)–P(3) | 135.40(3) |
| P(3)–O(3) | 1.605(4) | C(18)–O(1)–C(19) | 118.10(4) |
| P(3)–O(4) | 1.623(5) | C(34)–H(34)–O(2_j) | 172.00 |
| H(34)–O(2_j) | 2.402 | | |
| C(34)–O(2_j) | 3.325(7) | | |

## Catalytic Studies

### *Suzuki Cross-Coupling Reactions*

Although iminophosphorane-phosphane ligands have been employed in homogeneous catalysis, there are no re-

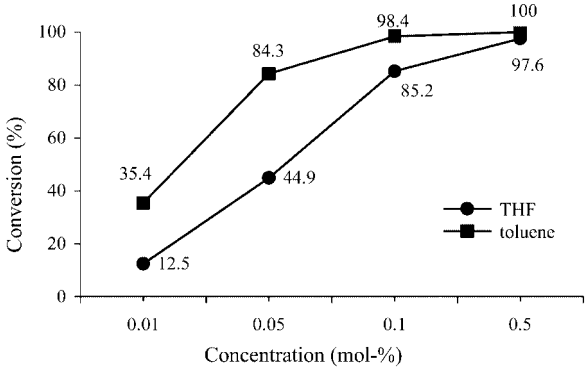


Figure 2. Influence of catalyst concentration on the coupling of 4-bromobenzaldehyde (1.0 mmol) and phenylboronic acid (1.5 mmol). Conditions: $K_3PO_4$ (2.0 mmol), toluene/thf (10 mL), *t* = 15 min, *T* = 70 °C.

Table 3. Effect of solvent on the coupling of 4-bromobenzaldehyde with phenylboronic acid.

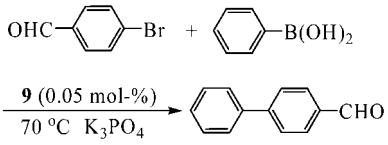


| Entry | Solvent | Base | Time [h] | Conversion [%][a] |
|---|---|---|---|---|
| 1 | tetrahydrofuran | $K_3PO_4$ | 2 | 84.6 |
| 2 | dioxane | $K_3PO_4$ | 2 | 63.2 |
| 3 | dimethylformamide | $K_3PO_4$ | 2 | 100 |
| 4 | toluene | $K_3PO_4$ | 2 | 100 |
| 5 | acetonitrile | $K_3PO_4$ | 2 | 63.7 |
| 6 | methanol | $K_3PO_4$ | 2 | 69.8 |

[a] Conversion to coupled product determined by GC, based on aryl halides; average of two runs.

Table 4. Effect of base on the coupling of 4-bromobenzaldehyde with phenylboronic acid.

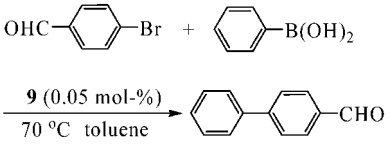


| Entry | Base | Solvent | Time [h] | Conversion [%][a] |
|---|---|---|---|---|
| 1 | $Cs_2CO_3$ | toluene | 2 | 100 |
| 2 | $K_3PO_4$ | toluene | 2 | 100 |
| 3 | $K_2CO_3$ | toluene | 2 | 97.1 |
| 4 | NaOH | toluene | 2 | 73.5 |
| 5 | TMEDA | toluene | 2 | 15.6 |
| 6 | none | toluene | 2 | 1.6 |

[a] Conversion to coupled product determined by GC, based on aryl halides; average of two runs.

 © 2007 Wiley-VCH Verlag GmbH & Co. KGaA, Weinheim 

ports of their application in Suzuki cross-coupling reactions. Interestingly, the iminophosphorane-phosphane ligand **1** shows excellent activity for Suzuki cross-coupling reactions with high turnover numbers at very low catalyst concentrations. The $Pd^0$ complex **9** effectively catalyzes the Suzuki cross-coupling reactions of a variety of aryl bromides and phenylboronic acids to afford the desired biaryls in remarkably high yields. These reactions were studied systematically to find the optimal conditions to afford biaryls in good yield. It is important to achieve good yields using minimum amounts of catalyst, therefore we examined the effect of catalyst loading on the coupling between 4-bromobenzaldehyde and phenylboronic acid (Figure 2 and Tables 3, 4, and 5). Complete conversion of the starting materials into 4-phenylbenzaldehyde was achieved with 0.5 mol-% of catalyst in 1 h or 0.05 mol-% in 2 h, therefore a concentration of 0.05 mol-% was selected as the optimal concentration for catalytic loading.

Table 5. Suzuki cross-coupling of aryl halides (1 mmol) with phenylboronic acid (1.5 mmol) catalyzed by **9** in the presence of $K_3PO_4$ (2 mmol) in toluene (10 mL).

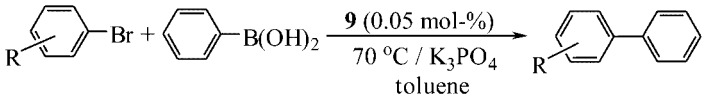


| Entry | Substrate | Product | Time (h) | Conversion[a] (%) | Yield (%) |
|---|---|---|---|---|---|
| 1 | 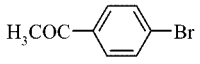 | 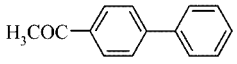 | 2 | 100 | 99 |
| 2 | 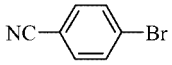 | 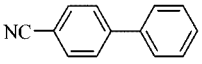 | 2 | 99.5 | 99 |
| 3 | 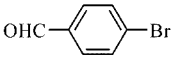 | 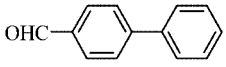 | 2 | 100 | 98 |
| 4 | 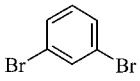 | 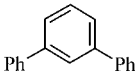 | 4 | 94.8 | 90 |
| 5 | 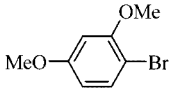 | 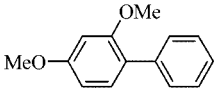 | 8 | 90.7 | 89 |
| 6 | 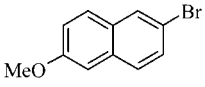 | 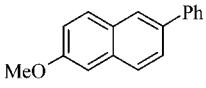 | 4 | 78.9 | 78 |
| 7 | 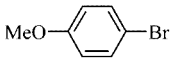 | 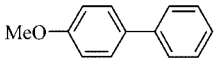 | 12 | 79.4 | 70 |
| 8 | | | 12 | 85.9 | 82 |
| 9 | 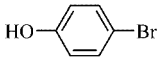 | 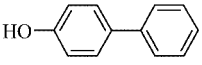 | 10 | 77.5 | 73 |
| 10 | 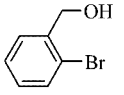 | 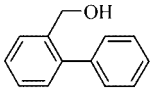 | 10 | 68.3 | 66 |
| 11 | 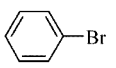 | 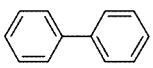 | 4 | 83.3 | 83 |
| 12 | | 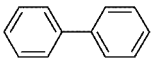 | 4 | 100 | 98 |

 © 2007 Wiley-VCH Verlag GmbH & Co. KGaA, Weinheim 

The above investigations showed that the reaction rate and the catalyst activity are significantly influenced by the base and the solvent employed. Various solvents were tested in the coupling reaction with $K_3PO_4$ as base. Toluene and dmf allowed complete conversion of 4-bromobenzaldehyde into 4-phenylbenzaldehyde. Considering the ease of separation of the product, toluene was chosen as the best solvent.

Inorganic bases such as $Cs_2CO_3$, $K_3PO_4$, $K_2CO_3$, and NaOH gave excellent yields whereas the reaction proceeded very slowly with TMEDA. Considering the high activity and cost effectiveness, $K_3PO_4$ was chosen as the base.

Under these optimized reaction conditions, a wide array of aryl bromides react with phenylboronic acid to provide the cross-coupling products in excellent yields (Table 5). The palladium(0) catalyst **9** is very effective in Suzuki cross-coupling reactions and exhibits remarkable tolerance towards both "deactivating" electron-donating substituents (Table 5, entries 7, 9 and 10) and sterically encumbering *ortho* substituents (Table 5, entry 5) on aryl bromides. The catalytic activity of **9** is found to be better than that of the catalyst $[Pd_2(dba)_3]$ + [1,1′-bis(diphenylphosphanyl)ferrocene (dppf)], which catalyzes the coupling of 4-bromoacetophenone and phenylboronic acid in toluene at 70 °C (2 h) in 86.5% yield,[36a] whereas it is similar to that of the parent compound DPEphos. However, DPEphos shows better activity only at higher temperature and higher catalytic loading.[36b]

### Catalytic Hydrogenation of Styrene

The cationic $Rh^I$ complex **11** was tested as a catalyst for the hydrogenation of styrene. The catalyst (0.0005 mol-%) shows effective conversions under mild conditions (4 atm of $H_2$ at room temperature). The conversion rate was monitored periodically by gas chromatography and the product formation was confirmed by $^1H$ NMR spectroscopy. The results are displayed in Figure 3.

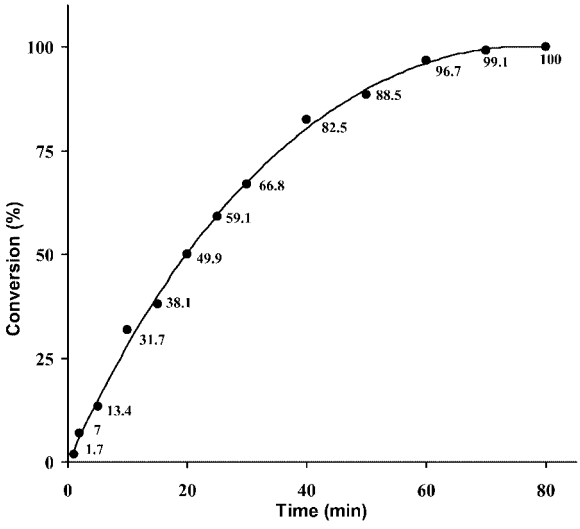


Figure 3. Hydrogenation of styrene. Conditions: styrene (1.0 mmol), $Et_3N$ (0.1 mmol), **11** (0.0005 mol-%), thf (20 mL); $H_2$ pressure: 4 atm; room temperature; stirring speed: 400 rpm.

The turnover number (TON) for the conversion of styrene to ethylbenzene was 200,000 and the turnover frequency (TOF) at 50% conversion was 300,000 $h^{-1}$. The TOF improved to 600,000 $h^{-1}$ when the pressure of $H_2$ was increased to 10 atm and the temperature to 70 °C. The catalytic activity was tested on other substrates such as α-methylstyrene, 4-methylstyrene, and phenylacetylene with a catalyst loading of 0.005 mol-%. The results are displayed in Table 6. Complex **11** was found to be more effective in homogeneous hydrogenation under mild conditions than $[RhCl(PPh_3)_3]$, for which complete conversion was observed under the following conditions: [styrene]/[catalyst] = 1200, $T$ = 80 °C, $t$ = 2 h, $H_2$ pressure: 28 atm.[37]

Table 6. Hydrogenation of olefins using complex **11**.[a]

| Entry | Substrate | Time [min] | Conversion [%] | TOF [$h^{-1}$] |
|---|---|---|---|---|
| 1 | styrene | 30 | 100 | 40,000 |
| 2 | α-methylstyrene | 40 | 100 | 30,000 |
| 3 | 4-methylstyrene | 30 | 100 | 40,000 |
| 4 | phenylacetylene | 70 | 100 | 17,143 |
| 5[b] | styrene | 20 | 100 | 600,000 |

[a] Conditions: olefin (1.0 mmol), $Et_3N$ (0.1 mmol), **11** (0.005 mol-%), thf (20 mL); $H_2$ pressure: 4 atm; room temp.; stirring speed: 400 rpm. [b] **11** (0.0005 mol-%), $H_2$ pressure: 10 atm; $T$: 70 °C.

## Summary

The hemilabile iminophosphorane-phosphane ligand **1** has been synthesized by monoimination of bis[2-(diphenylphosphanyl)phenyl] ether by a Staudinger reaction and its chalcogen derivatives **3**–**6** have been prepared and characterized. The imino-phosphorane shows both a monodentate and bidentate ($\kappa^2$-*P*,*O*) chelating coordination mode. The platinum(II), palladium(II), and rhodium(I) complexes **7**, **8**, and **12**, respectively, are obtained as *trans* isomers with simple monodentate coordination modes. The $Pd^0$ complex **9**, in which ligand **1** binds in a chelating ($\kappa^2$-*P*,*O*) fashion, has been synthesized by the reaction of **1** with $[Pd_2(dba)_3]$. The reaction of **1** with $[\{Rh(COD)Cl\}_2]$ and AgOTf affords the 11-membered macrocyclic square-planar complex **11** with the imino-phosphorane ligand showing a chelating bidentate mode of coordination. The cationic rhodium(I) complex **11** is catalytically active for the hydrogenation of olefins with a TON of $2\times10^5$ and a TOF of $6\times10^5$ $h^{-1}$. The $Pd^0$ complex **9** is catalytically active for Suzuki cross-coupling reactions of various aryl bromides and phenylboronic acid. A lower catalytic loading of 0.05 mol-% of **9** allows complete conversion of several aryl bromides into biaryls.

## Experimental Section

**Reagents and Techniques:** All manipulations were performed under an atmosphere of dry nitrogen using standard Schlenk techniques.

 © 2007 Wiley-VCH Verlag GmbH & Co. KGaA, Weinheim 

All the solvents were purified by conventional procedures and distilled under nitrogen prior to use. The compounds DPEphos,[17a] $[M(COD)Cl_2]$ (M = Pd, Pt),[38] $[\{Rh(COD)(\mu\text{-}Cl)\}_2]$,[39] $[\{Rh(CO)_2(\mu\text{-}Cl)\}_2]$,[40] $[Pd_2(dba)_3]$,[41] and $[AuCl(SMe_2)]$[42] were prepared according to published procedures. $(PhO)_2P(O)N_3$ was purchased from Lancaster and used as received. The $^1H$ and $^{31}P\{^1H\}$ NMR spectra ($\delta$ in ppm) were recorded with Varian 300 or 400 mercury plus spectrometers operating at the appropriate frequencies using TMS and 85% $H_3PO_4$ as internal and external references, respectively. Microanalyses were performed with a Carlo–Erba Model 1112 elemental analyzer. The IR spectra were recorded with a Nicolet Impact 400 FT-IR instrument as KBr disc. Electrospray ionization (EI) mass spectrometry experiments were carried out with a Waters Q-Tof micro-YA-105 spectrometer. Melting points were recorded in capillary tubes and are uncorrected. GC analyses were performed with a Perkin–Elmer Clarus 500 GC fitted with a packed column.

**Synthesis of $Ph_2PC_6H_4OC_6H_4PPh_2{=}NP(O)(OPh)_2$ (1):** A thf solution (20 mL) of $(PhO)_2P(O)N_3$ (0.153 g, 0.557 mmol) was added dropwise to a solution of DPEphos (0.300 g, 0.557 mmol) in thf (20 mL) at –78 °C. After stirring the mixture for 8 h at room temperature, all the solvents were removed under vacuum and the residue washed with petroleum ether (b.p. 60–80 °C), then extracted with $Et_2O$ (15 mL) and dried to give an analytically pure white solid. Yield: 85% (0.372 g); m.p. 76–78 °C. $C_{48}H_{38}NO_4P_3$ (785.7): calcd. C 73.37, H 4.87, N 1.78; found C 72.81, H 4.43, N 1.93. $^1H$ NMR (400 MHz, $CDCl_3$): $\delta$ = 5.93–8.18 (m, 38 H, Ph) ppm. $^{31}P\{^1H\}$ NMR (162 MHz, $CDCl_3$): $\delta$ = –20.1 (s, $P^{III}$), 10.4 (d, $^2J_{P,P}$ = 37.7 Hz, $P^V_{[N]}$), –10.5 (d, $^2J_{P,P}$ = 37.7 Hz, $P^V_{[O]}$) ppm. MS (EI): *m*/*z* 786.47 $[M + H]^+$.

**Synthesis of $O\{C_6H_4PPh_2{=}NP(O)(OPh)_2\}_2$ (2):** A solution of DPEphos (0.2 g, 0.371 mmol) in thf (10 mL) was added dropwise to a solution of $(PhO)_2P(O)N_3$ (0.204 g, 0.742 mmol) in thf (10 mL) at 0 °C. After stirring the mixture for 8 h at room temperature, all the solvents were removed under vacuum and the residue washed with petroleum ether, then extracted with $Et_2O$ (10 mL) and dried to give **2** as a white solid. Yield: 90% (0.350 g); m.p. 72–74 °C. $C_{60}H_{48}N_2O_7P_4$ (1032.9): calcd. C 69.77, H 4.68, N 2.71; found C 70.26, H 4.51, N 2.84. $^1H$ NMR (400 MHz, $CDCl_3$): $\delta$ = 6.12–7.65 (m, 48 H, Ph) ppm. $^{31}P\{^1H\}$ NMR (162 MHz, $CDCl_3$): $\delta$ = 10.9 (d, $^2J_{P,P}$ = 40.4 Hz, $P^V_{[N]}$), –10.6 (d, $^2J_{P,P}$ = 40.4 Hz, $P^V_{[O]}$) ppm. MS (EI): *m*/*z* 1033.57 $[M + H]^+$.

**Synthesis of $O\{C_6H_4P(S)Ph_2\}_2$ (3):** A mixture of DPEphos (0.200 g, 0.371 mmol) and sulfur (0.024 g, 0.093 mmol) was refluxed in toluene (10 mL) for 24 h with constant stirring to give a white precipitate of **3**. The solution was then cooled to room temperature, filtered, and recrystallized from hot $CHCl_3$. Yield: 92% (0.206 g); m.p. > 250 °C. $C_{36}H_{28}OP_2S_2$ (602.7): calcd. C 71.74, H 4.68, S 10.64; found C 71.62, H 4.81, S 10.88. $^1H$ NMR (400 MHz, $CDCl_3$): $\delta$ = 6.20–7.68 (m, 28 H, Ph) ppm. $^{31}P\{^1H\}$ NMR (162 MHz, $CDCl_3$): $\delta$ = 39.1 (s) ppm.

**Synthesis of $O\{C_6H_4P(Se)Ph_2\}_2$ (4):** A mixture of DPEphos (0.200 g, 0.371 mmol) and selenium (0.059 g, 0.742 mmol) was refluxed in toluene (10 mL) for 24 h with constant stirring to give a white precipitate of **4**. The solution was then cooled to room temperature, filtered, and recrystallized from hot $CHCl_3$. Yield: 90% (0.233 g); m.p. > 250 °C. $C_{36}H_{28}OP_2S_2$ (696.5): calcd. C 62.08, H 4.05; found C 62.45, H 4.26. $^1H$ NMR (400 MHz, $CDCl_3$): $\delta$ = 6.30–7.67 (m, 28 H, Ph) ppm. $^{31}P\{^1H\}$ NMR (162 MHz, $CDCl_3$): $\delta$ = 29.4 (s, $^1J_{Se,P}$ = 734.1 Hz) ppm. MS (EI): *m*/*z* 699.04 $[M + H]^+$.

**Synthesis of $Ph_2P(S)C_6H_4OC_6H_4PPh_2{=}NP(O)(OPh)_2$ (5):** A mixture of **1** (0.100 g, 0.127 mmol) and sulfur (0.003 g, 0.016 mmol) was refluxed in toluene (5 mL) for 24 h with constant stirring. The solution was then cooled to room temperature and petroleum ether (5 mL) was added to give white precipitate **5**. Yield: 93% (0.096 g); m.p. 98–100 °C. $C_{48}H_{38}P_3O_4NS$ (817.8): calcd. C 70.49, H 4.68, N 1.71, S 3.92; found C 70.52, H 4.44, N 1.82, S 4.09. $^1H$ NMR (400 MHz, $CDCl_3$): $\delta$ = 5.87–7.97 (m, 38 H, Ph) ppm. $^{31}P\{^1H\}$ NMR (162 MHz, $CDCl_3$): $\delta$ = 37.7 (s, $P^V_{[S]}$), 10.8 (d, $^2J_{P,P}$ = 38.9 Hz, $P^V_{[N]}$), –10.5 (d, $^2J_{P,P}$ = 38.9 Hz, $P^V_{[O]}$) ppm. MS (EI): *m*/*z* 818.15 $[M + H]^+$.

**Synthesis of $Ph_2P(Se)C_6H_4OC_6H_4PPh_2{=}NP(O)(OPh)_2$ (6):** A mixture of **1** (0.100 g, 0.127 mmol) and Se (0.010 g, 0.127 mmol) was refluxed in toluene (5 mL) for 24 h with constant stirring. The solution was then cooled to room temperature and petroleum ether (5 mL) was added to give a white microcrystalline solid of **6**. Yield: 98% (0.108 g); m.p. 120–122 °C. $C_{48}H_{38}NO_4P_3Se$ (864.7): calcd. C 66.67, H 4.42, N 1.61; found C 66.97, H 4.21, N 1.73. $^1H$ NMR (400 MHz, $CDCl_3$): $\delta$ = 5.89–7.92 (m, 38 H, Ph) ppm. $^{31}P\{^1H\}$ NMR (162 MHz, $CDCl_3$): $\delta$ = 27.6 (s, $^1J_{Se,P}$ = 744.0 Hz, $P^V_{[Se]}$), 10.8 (d, $^2J_{P,P}$ = 39.0 Hz, $P^V_{[N]}$), –10.5 (d, $^2J_{P,P}$ = 39.0 Hz, $P^V_{[O]}$) ppm. MS (EI): *m*/*z* 866.13 $[M + H]^+$.

**Synthesis of *trans*-$[PtCl_2\{\kappa^1\text{-}P\text{-}Ph_2PC_6H_4OC_6H_4PPh_2{=}NP(O)(OPh)_2\}_2]$ (7):** A solution of $[Pt(COD)Cl_2]$ (0.034 g, 0.091 mmol) in $CH_2Cl_2$ (5 mL) was added dropwise to a solution of **1** (0.144 g, 0.183 mmol) in $CH_2Cl_2$ (10 mL) at room temperature. The reaction mixture was stirred for 8 h to give a pale-yellow solution, which was concentrated to 5 mL. $Et_2O$ (10 mL) was added to give a pale-yellow precipitate of **7**, which was then filtered, washed, and dried. Yield: 87% (0.145 g); m.p. > 250 °C. $C_{96}H_{76}Cl_2N_2O_8P_6Pt$ (1837.5): calcd. C 62.75, H 4.16, N 1.52; found C 62.58, H 4.15, N 1.58. $^1H$ NMR (400 MHz, $CDCl_3$): $\delta$ = 5.87–8.21 (m, 76 H, Ph) ppm. $^{31}P\{^1H\}$ NMR (162 MHz, $CDCl_3$): $\delta$ = 10.3 (s, $^1J_{Pt,P}$ = 2642 Hz, $P_{[Pt]}$), 11.4 (d, $^2J_{P,P}$ = 37.9 Hz, $P^V_{[N]}$), –10.6 (d, $^2J_{P,P}$ = 37.9 Hz, $P^V_{[O]}$) ppm. MS (EI): *m*/*z* 1838.01 $[M + H]^+$.

**Synthesis of *trans*-$[PdCl_2\{\kappa^1\text{-}P\text{-}Ph_2PC_6H_4OC_6H_4PPh_2{=}NP(O)(OPh)_2\}_2]$ (8):** A solution of $[Pd(COD)Cl_2]$ (0.031 g, 0.109 mmol) in $CH_2Cl_2$ (10 mL) was added dropwise to a solution of **1** (0.170 g, 0.217 mmol) in $CH_2Cl_2$ (10 mL) at room temperature. The bright yellow solution was stirred for 8 h then concentrated to 5 mL. Addition of $Et_2O$ (10 mL) gave the mononuclear *trans* complex **8** as a yellow solid. Yield: 83% (0.158); m.p. 210–212 °C. $C_{96}H_{76}Cl_2N_2O_8P_6Pd$ (1748.8): calcd. C 65.93, H 4.38, N 1.60; found C 65.24, H 3.99, N, 1.75. $^1H$ NMR (300 MHz, $CDCl_3$): $\delta$ = 5.85–8.20 (m, 76 H, Ph) ppm. $^{31}P\{^1H\}$ NMR (121 MHz, $CDCl_3$): $\delta$ = 14.2 (s, $P_{[Pd]}$), 11.7 (d, $^2J_{P,P}$ = 38.1 Hz, $P^V_{[N]}$), –10.6 (d, $^2J_{P,P}$ = 38.1 Hz, $P^V_{[O]}$) ppm.

**Synthesis of $[Pd\{\kappa^2\text{-}P,O\text{-}Ph_2PC_6H_4OC_6H_4PPh_2{=}NP(O)(OPh)_2\}_2]$ (9):** A solution of $[Pd_2(dba)_3]$ (0.05 g, 0.048 mmol) in toluene (20 mL) was added dropwise to a stirring solution of **1** (0.152 g, 0.193 mmol) in toluene (10 mL) at room temperature. After 4 h the solution had turned yellow and all the solvents were removed in vacuo. The residual solid was washed several times with petroleum ether to remove dba and dried. Yield: 78% (0.126 g); m.p. 112 °C (dec). $C_{96}H_{76}N_2O_8P_6Pd$ (1677.9): calcd. C 68.72, H 4.57, N 1.67; found C 68.48, H 4.76, N 1.80. $^1H$ NMR (400 MHz, $CDCl_3$): $\delta$ = 5.93–8.30 (m, 38 H, Ph) ppm. $^{31}P\{^1H\}$ NMR (162 MHz, $CDCl_3$): $\delta$ = 23.6 (s, $P_{[Pd]}$), 11.7 (d, $^2J_{P,P}$ = 39.5 Hz, $P^V_{[N]}$), –7.8 (d, $^2J_{P,P}$ = 39.5 Hz, $P^V_{[O]}$) ppm.

**Synthesis of $[AuCl\{\kappa^1\text{-}P\text{-}Ph_2PC_6H_4OC_6H_4PPh_2{=}NP(O)(OPh)_2\}]$ (10):** A solution of $[AuCl(SMe_2)]$ (0.03 g, 0.102 mmol) in $CH_2Cl_2$ (5 mL) was added dropwise to a solution of **1** (0.08 g, 0.102 mmol)

 © 2007 Wiley-VCH Verlag GmbH & Co. KGaA, Weinheim 

in $CH_2Cl_2$ (10 mL) at room temperature. The reaction mixture was stirred for 12 h, then concentrated to 2 mL and layered with $Et_2O$ (5 mL) to give colorless crystals of analytical purity. Yield: 92% (0.095 g); m.p. 216–218 °C. $C_{48}H_{38}AuClNO_4P_3$ (1018.2): calcd. C 56.62, H 3.76, N 1.38; found C 56.64, H 3.79, N 1.38. $^1$H NMR (400 MHz, $CDCl_3$): $\delta$ = 6.15–7.88 (m, 38 H, Ph) ppm. $^{31}P\{^1H\}$ NMR (162 MHz, $CDCl_3$): $\delta$ = 19.0 (s, $P_{[Au]}$), 10.4 (d, $^2J_{P,P}$ = 37.9 Hz, $P^V_{[N]}$), –10.5 (d, $^2J_{P,P}$ = 37.9 Hz, $P^V_{[O]}$) ppm. MS (EI): *m*/*z* 982.49 $[M - Cl]^+$.

**Synthesis of *cis*-[Rh(COD){κ$^2$-*P*,*O*-$Ph_2PC_6H_4OC_6H_4PPh_2$=NP(O)-(OPh)$_2$}][OTf] (11):** A mixture of **1** (0.066 g, 0.083 mmol), [{Rh(COD)Cl}$_2$] (0.021 g, 0.042 mmol), and AgOTf (0.021, 0.083 mmol) in $CH_2Cl_2$ (10 mL) was stirred for 8 h at room temperature. The yellow solution was concentrated to 2 mL and $Et_2O$ (10 mL) added to give a yellow oily substance. The supernatant liquid was discarded and dried to give a yellow foamy substance **11**, which was washed with $Et_2O$ and dried. Yield: 78% (0.044 g, 0.025 mmol); m.p. 144–146 °C. $C_{57}H_{50}F_3NO_7P_3RhS$ (1145.9): calcd. C 59.74, H 4.39, N 1.22, S 2.80; found C 60.11, H 4.08, N 1.30, S 2.85. $^1$H NMR (400 MHz, $CDCl_3$): $\delta$ = 1.27–2.37 (br. m, 8 H, $CH_2$), 2.90 (br. d, $^2J_{Rh,H}$ = 119.2 Hz, 2 H, CH), 5.13 (br. d, $^2J_{Rh,H}$ = 115.6 Hz, 2 H, CH), 6.26–7.99 (m, 38 H, Ph) ppm. $^{31}P\{^1H\}$ NMR (162 MHz, $CDCl_3$): $\delta$ = 12.9 (d, $^1J_{Rh,P}$ = 149.3 Hz, $P_{[Rh]}$), 8.8 (d, $^2J_{P,P}$ = 39.0 Hz, $P^V_{[N]}$), –11.1 (dd, $^2J_{P,P}$ = 39.0, $^2J_{Rh,P}$ = 6.6 Hz, $P^V_{[O]}$) ppm. MS (EI): *m*/*z* 996.29 $[M - OTf]^+$.

**Synthesis of *trans*-[Rh(CO)Cl{κ$^1$-*P*-$Ph_2PC_6H_4OC_6H_4PPh_2$=NP-(O)(OPh)$_2$}$_2$] (12):** A $CH_3CN$ (8 mL) solution of [{$Rh(CO)_2Cl$}$_2$] (0.015 g, 0.039 mmol) was added dropwise to a solution of **1** (0.121 g, 0.154 mmol) in $CH_3CN$ (10 mL) at room temperature. The reaction mixture was stirred for 4 h to give the *trans* complex **12** as a yellow precipitate, which was then filtered, washed with $CH_3CN$ (2 mL), and dried. Yield: 88% (0.118 g, 0.068 mmol); m.p. 242–244 °C. $C_{97}H_{76}ClN_2O_9P_6Rh$ (1737.9): calcd. C 67.04, H 4.41, N 1.61; found C 66.37, H 4.80, N 1.82. $^1$H NMR (400 MHz, $CDCl_3$): $\delta$ = 6.77–8.12 (m, 76 H, Ph) ppm. $^{31}P\{^1H\}$ NMR (162 MHz, $CDCl_3$): $\delta$ = 22.5 (d, $^1J_{Rh,P}$ = 140.3 Hz, $P_{[Rh]}$), 11.3 (d, $^2J_{P,P}$ = 37.9 Hz, $P^V_{[N]}$), –10.6 (d, $^2J_{P,P}$ = 37.9 Hz, $P^V_{[O]}$) ppm. FT-IR (KBr disc): $\tilde{\nu}$ = 1958 cm$^{-1}$ [$\nu_{CO}$]. MS (EI): *m*/*z* 1701.70 $[M - Cl]^+$.

**Crystal Structure Determination:** Single crystals of **8** suitable for X-ray diffraction were grown by slow diffusion of diethyl ether into a dichloromethane solution and mounted on a glass fiber with epoxy resin. Unit cell determination and data collection of **8** were performed with an Oxford Diffraction XCALIBUR-S CCD system using Mo-$K_\alpha$ radiation ($\lambda$ = 0.71073 Å). The structure was solved and refined by full-matrix least-squares techniques on $F^2$ using the SHELX-97 (SHELXL program package).[43] The absorption corrections were done by multi-scan and all the data were corrected for Lorentz and polarization effects. The non-hydrogen atoms were refined with anisotropic thermal parameters. All the hydrogen atoms were geometrically fixed and allowed to refine using a riding model (Table 7).

CCDC-616229 (for **9**) contains the supplementary crystallographic data for this paper. These data can be obtained free of charge from The Cambridge Crystallographic Data Centre via www.ccdc.cam.ac.uk/data_request/cif.

**Suzuki Cross-Coupling Reactions of Aryl halides with Boronic Acids:** The appropriate amount of catalyst **9** (0.05 mol-%) was placed into a two-necked, round-bottomed flask under an atmosphere of nitrogen and 10 mL of toluene was added. After stirring for 15 min, aryl halide (1.0 mmol), arylboronic acid (1.5 mmol), and $K_2CO_3$ (2 mmol) were added. The mixture was stirred at 70 °C under an atmosphere of nitrogen until the conversion stopped (the course of the reaction was monitored by GC analysis). The solvent was then removed under reduced pressure. The resultant residual mixture was quenched with $H_2O$ (10 mL) and extracted twice with $Et_2O$ (2 × 10 mL). The combined organic fraction was dried ($MgSO_4$), the solvent removed under vacuum, and the residue dissolved in $CH_2Cl_2$ (5 mL). An aliquot of the solution was subjected to GC analysis. Yields were calculated with respect to aryl halides or dodecane as an internal standard.

**Catalytic Hydrogenation of Olefins:** A mixture of Rh$^I$ complex **11** (0.0005 or 0.005 mol-%), olefin (1.0 mmol), and triethylamine (0.1 mmol) was dissolved in 20 mL of thf and was introduced into a 50-mL glass vessel, which was placed into a steel autoclave and the reactor sealed. The vessel was purged three times with hydrogen and then the autoclave was pressurized with 4 atm of hydrogen. The reaction mixture was stirred at a room temperature for the required time. The extent of conversion was determined by periodic GC analysis until complete conversion was observed.

Table 7. Crystallographic data for complex **10**.

| | |
|---|---|
| Formula | $C_{48}H_{38}AuClNO_4P_3$ |
| Molecular weight | 1018.12 |
| Crystal system | monoclinic |
| Space group | $P2_1/c$ |
| *a* [Å] | 15.9417(14) |
| *b* [Å] | 10.9513(16) |
| *c* [Å] | 25.3394(18) |
| $\alpha$ [°] | 90 |
| $\beta$ [°] | 101.717(7) |
| $\gamma$ [°] | 90 |
| *V* [Å$^3$] | 4331.6(8) |
| *Z* | 4 |
| $\rho_{calc}$ [g cm$^{-3}$] | 1.561 |
| $\mu$ (Mo-$K_a$) [mm$^{-1}$] | 3.614 |
| *F*(000) | 2024 |
| Crystal size [mm$^3$] | 0.26 × 0.21 × 0.18 |
| *T* [K] | 150(2) |
| 2$\theta$ range [°] | 2.95–25.00 |
| Total number of reflections | 21719 [$R_{int}$ = 0.0702] |
| GOF [$F^2$] | 0.778 |
| $R_1$[a] | 0.0349 |
| $wR_2$[b] | 0.0563 |

[a] $R = \Sigma||F_o| - |F_c||/\Sigma|F_o|$. [b] $R_w = \{[\Sigma w(F_o^2 - F_c^2)/\Sigma w(F_o^2)^2]\}^{1/2}$; $w = 1/[\sigma^2(F_o^2) + (xP)^2]$, where $P = (F_o^2 + 2F_c^2)/3$.

## Acknowledgments

We are grateful to The Department of Science and Technology (DST) for financial support of this work through grant SR/S1/IC-05/2003. We would also like to thank the Sophisticated Analytical Instrument Facility (SAIF) IIT Bombay, Department of Chemistry IIT Bombay and National Single Crystal X-ray Diffraction Facility IIT Bombay for instrument facilities. R. V. is grateful to IIT Bombay for JRF and SRF Fellowships.

[1] G. Cami-Kobeci, J. M. J. Williams, *Chem. Commun.* **2004**, 1072–1073.
[2] H. Staudinger, J. Meyer, *Helv. Chim. Acta* **1919**, *2*, 635–646.
[3] Y. G. Gololobov, I. N. Zhmurova, L. F. Kasukhin, *Tetrahedron* **1981**, *37*, 437–472.
[4] Y. G. Gololobov, L. F. Kasukhin, *Tetrahedron* **1992**, *48*, 1353–1406.

 © 2007 Wiley-VCH Verlag GmbH & Co. KGaA, Weinheim 

[5] a) K. V. Katti, R. G. Cavell, *Inorg. Chem.* **1989**, *28*, 413–416; b) K. V. Katti, R. G. Cavell, *Organometallics* **1988**, *7*, 2236–2238.
[6] K. V. Katti, R. G. Cavell, *Comments Inorg. Chem.* **1990**, *10*, 53–73.
[7] M. S. Balakrishna, B. D. Santarsiero, R. G. Cavell, *Inorg. Chem.* **1994**, *33*, 3079–3084.
[8] R. G. Cavell, R. W. Reed, K. V. Katti, M. S. Balakrishna, P. W. Collins, V. Mozol, I. Bartz, *Phosphorus Sulfur Silicon Relat. Elem.* **1993**, *76*, 269–272.
[9] R. W. Reed, B. Santarsiero, R. G. Cavell, *Inorg. Chem.* **1996**, *35*, 4292–4300.
[10] M. S. Balakrishna, S. Teipel, A. A. Pinkerton, R. G. Cavell, *Inorg. Chem.* **2001**, *40*, 1802–1808.
[11] M. S. Balakrishna, R. M. Abhyankar, M. G. Walawalker, *Tetrahedron Lett.* **2001**, *42*, 2733–2734.
[12] D. J. Law, R. G. Cavell, *J. Mol. Catal.* **1994**, *91*, 175–186.
[13] R. G. Cavell, B. Creed, L. Gelmini, D. J. Law, R. McDonald, A. R. Sanger, A. Somogyvari, *Inorg. Chem.* **1998**, *37*, 757–763.
[14] V. Cadierno, P. Crochet, J. Garcia-Alvarez, S. E. Garcia-Garrido, J. Gimeno, *J. Organomet. Chem.* **2002**, *663*, 32–39.
[15] a) V. Cadierno, P. Crochet, J. Diez, J. Garcia-Alvarez, S. E. Garcia-Garrido, S. Garcia-Granda, J. Gimeno, M. A. Rodriguez, *Dalton Trans.* **2003**, 3240–3249; b) V. Cadierno, P. Crochet, J. Diez, J. Garcia-Alvarez, S. E. Garcia-Garrido, S. Garcia-Granda, J. Gimeno, M. A. Rodriguez, *Inorg. Chem.* **2003**, *10*, 3293–3307.
[16] P. Molina, A. Arques, A. Garcia, M. C. Ramirez de Arellano, *Tetrahedron Lett.* **1997**, *38*, 7613–7616.
[17] a) M. Kranenburg, Y. E. M. van der Burgt, P. C. J. Kamer, P. W. N. M. van Leeuwen, K. Goubitz, J. Fraanje, *Organometallics* **1995**, *14*, 3081–3089; b) M. A. Zuideveld, B. H. G. Swennenhuis, M. D. K. Boele, Y. Guari, G. P. F. van Strijdonck, J. N. H. Reek, P. C. J. Kamer, K. Goubitz, J. Fraanje, M. Lutz, A. L. Spek, P. W. N. M. van Leeuwen, *J. Chem. Soc., Dalton Trans.* **2002**, 2308–2317; c) R. J. van Haaren, E. Zuidema, J. Fraanje, K. Goubitz, P. C. J. Kamer, P. W. N. M. van Leeuwen, G. P. F. van Strijdonck, *C. R. Chim.* **2002**, *5*, 431–440.
[18] a) S. Kuang, D. G. Cuttell, D. R. McMillin, P. E. Fanwick, R. A. Walton, *Inorg. Chem.* **2002**, *41*, 3313–3322; b) A. Pintado-Alba, H. de la Riva, M. Nieuwhuyzen, D. Bautista, P. R. Raithby, H. A. Sparkes, S. J. Teat, J. M. Lopez-de-Luzuriaga, M. C. Lagunas, *Dalton Trans.* **2004**, 3459–3467; c) S.-M. Kuang, P. E. Fanwick, R. A. Walton, *Inorg. Chem.* **2002**, *41*, 405–412; d) D. Kim, B.-M. Park, J. Yun, *Chem. Commun.* **2005**, 1755–1757; e) M. L. Parr, C. Perez-Acosta, J. W. Faller, *New J. Chem.* **2005**, *29*, 613–619; f) J. Wilting, C. Muller, A. C. Hewat, D. D. Ellis, D. M. Tooke, A. L. Spek, D. Vogt, *Organometallics* **2005**, *24*, 13–15.
[19] a) P. W. N. M. van Leeuwen, P. C. J. Kamer, J. N. H. Reek, P. Dierkes, *Chem. Rev.* **2000**, *100*, 2741–2769; b) P. C. J. Kamer, P. W. N. M. van Leeuwen, J. N. H. Reek, *Acc. Chem. Res.* **2001**, *34*, 895–904.
[20] a) P. W. N. M. van Leeuwen, M. A. Zuideveld, B. H. G. Swennenhuis, Z. Freixa, P. C. J. Kamer, K. Goubitz, J. Fraanje, M. Lutz, A. L. Spek, *J. Am. Chem. Soc.* **2003**, *125*, 5523–5539; b) M. Tromp, J. A. van Bokhoven, R. J. van Haaren, G. P. F. van Strijdonck, A. M. J. van der Eerden, P. W. N. M. van Leeuwen, D. C. Koningsberger, *J. Am. Chem. Soc.* **2002**, *124*, 14814–14815; c) R. J. van Haaren, K. Goubitz, J. Fraanje, G. P. F. van Strijdonck, H. Oevering, B. Coussens, J. N. H. Reek, P. C. J. Kamer, P. W. N. M. van Leeuwen, *Inorg. Chem.* **2001**, *40*, 3363–3372.
[21] a) M. Ahmed, A. M. Seayad, R. Jackstell, M. Beller, *J. Am. Chem. Soc.* **2003**, *125*, 10311–10318; b) P.-E. Broutin, I. Cerna, M. Campaniello, F. Leroux, F. Colobert, *Org. Lett.* **2004**, *6*, 4419–4422; c) Y. Chen, X. P. Zhang, *J. Org. Chem.* **2003**, *68*, 4432–4438; d) R. Csuk, A. Barthel, C. Raschke, *Tetrahedron* **2004**, *60*, 5737–5750; e) G.-Y. Gao, A. J. Colvin, Y. Chen, X. P. Zhang, *Org. Lett.* **2003**, *5*, 3261–3264; f) Y. Kozawa, M. Mori, *J. Org. Chem.* **2003**, *68*, 3064–3067; g) R. Kuwano, Y. Kondo, Y. Matsuyama, *J. Am. Chem. Soc.* **2003**, *125*, 12104–12105; h) M. Ogasawara, H. Ikeda, T. Nagano, T. Hayashi, *Org. Lett.* **2001**, *3*, 2615–2617; i) C. H. Oh, V. R. Reddy, *Tetrahedron Lett.* **2004**, *45*, 5221–5224; j) M. C. Willis, D. Taylor, A. T. Gillmore, *Org. Lett.* **2004**, *6*, 4755–4757; k) J. P. Wolfe, M. A. Rossi, *J. Am. Chem. Soc.* **2004**, *126*, 1620–1621; l) M.-C. P. Yeh, W.-C. Tsao, L.-H. Tu, *Organometallics* **2005**, *24*, 5909–5915.
[22] M. S. Balakrishna, R. Panda, J. T. Mague, *J. Chem. Soc., Dalton Trans.* **2002**, 4617–4621.
[23] S. Priya, M. S. Balakrishna, S. M. Mobin, R. McDonald, *J. Organomet. Chem.* **2003**, *688*, 227–235.
[24] M. S. Balakrishna, R. Panda, J. T. Mague, *Polyhedron* **2003**, *22*, 587–593.
[25] M. S. Balakrishna, S. Priya, R. Panda, *Phosphorus Sulfur Silicon Relat. Elem.* **2004**, *179*, 911–914.
[26] P. Chandrasekaran, J. T. Mague, M. S. Balakrishna, *Inorg. Chem.* **2005**, *44*, 7925–7932.
[27] P. Chandrasekaran, J. T. Mague, M. S. Balakrishna, *Organometallics* **2005**, *24*, 3780–3783.
[28] P. Chandrasekaran, J. T. Mague, M. S. Balakrishna, *Inorg. Chem.* **2006**, *45*, 5893–5897.
[29] P. Chandrasekaran, J. T. Mague, M. S. Balakrishna, *Inorg. Chem.* **2006**, *45*, 6678–6683.
[30] S. Mohanty, B. Punji, M. S. Balakrishna, *Polyhedron* **2006**, *25*, 815–820.
[31] a) B. Punji, J. T. Mague, M. S. Balakrishna, *Dalton Trans.* **2006**, 1322–1330; b) B. Punji, J. T. Mague, M. S. Balakrishna, *Inorg. Chem.* **2006**, *45*, 9454–9464; c) R. Venkateswaran, J. T. Mague, M. S. Balakrishna, *Inorg. Chem.* **2007**, *46*, 809–817.
[32] B. Punji, C. Ganesamoorthy, M. S. Balakrishna, *J. Mol. Catal. A* **2006**, *259*, 78–83.
[33] B. Punji, J. T. Mague, M. S. Balakrishna, *J. Organomet. Chem.* **2006**, *691*, 4265–4272.
[34] I. M. Al-Najjar, *Inorg. Chim. Acta* **1987**, *128*, 93–104.
[35] A. Bondi, *J. Phys. Chem.* **1964**, *68*, 441–451.
[36] a) T. J. Colacot, H. Qian, R. Cea-Olivares, S. Hernandez-Ortega, *J. Organomet. Chem.* **2001**, *637–639*, 691–697; b) J. Yin, M. P. Rainka, X.-X. Zhang, S. L. Buchwald, *J. Am. Chem. Soc.* **2002**, *124*, 1162–1163.
[37] F. Lorenzini, K. T. Hindle, S. J. Craythorne, A. R. Crozier, F. Marchetti, C. J. Martin, P. C. Marr, A. C. Marr, *Organometallics* **2006**, *25*, 3912–3919.
[38] D. Drew, J. R. Doyle, *Inorg. Synth.* **1990**, *28*, 346–349.
[39] G. Giordano, R. H. Crabtree, *Inorg. Synth.* **1990**, *28*, 88–90.
[40] J. A. McCleverty, G. Wilkinson, *Inorg. Synth.* **1990**, *28*, 84–86.
[41] T. Ukai, H. Kawazura, Y. Ishii, J. J. Bonnet, J. A. Ibers, *J. Organomet. Chem.* **1974**, *65*, 253–266.
[42] M. Brandys, M. C. Jennings, R. J. Puddephatt, *J. Chem. Soc., Dalton Trans.* **2000**, 4601–4606.
[43] G. M. Sheldrick, *SHELXL-97, Program for the Refinement of Crystal Structures*, University of Göttingen, Germany, **1997**.

Received: November 28, 2006
Published Online: March 16, 2007

 © 2007 Wiley-VCH Verlag GmbH & Co. KGaA, Weinheim

**The EUChemSoc Societies have taken the significant step into the future by merging their traditional journals, to form two leading chemistry journals, the *European Journal of Inorganic Chemistry* and the *European Journal of Organic Chemistry.* Three further EUChemSoc Societies (Austria, Czech Republic and Sweden) are Associates of the two journals.**

## COVER PICTURE

**The cover picture shows** an apple snail (*Pomacea bridgesi*) and scanning electron micrographs of five different forms of calcium carbonate that were prepared in vitro (vaterite, calcite, monohydrocalcite, amorphous calcium carbonate, and aragonite). Details are discussed in the article by M. Neumann and M. Epple on p. 1953 ff.

 © 2007 Wiley-VCH Verlag GmbH & Co. KGaA, Weinheim 

# CONTENTS

## FULL PAPERS


### Biominerals

**M. Neumann, M. Epple* ..... 1953–1957**

Monohydrocalcite and Its Relationship to Hydrated Amorphous Calcium Carbonate in Biominerals

**Keywords:** EXAFS spectroscopy / Biomineralisation / Materials science / Monohydrocalcite / Bioinorganic chemistry

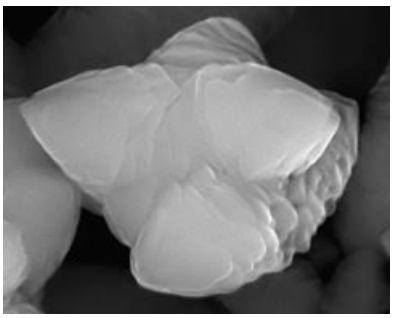

Hydrated amorphous calcium carbonate (ACC) is often postulated as an intermediate and final phase in biomineralisation. The crystalline phase monohydrocalcite ($CaCO_3 \cdot H_2O$) is prepared, characterised and compared to biogenic calcium carbonate phases.

### Chalcogen-Nitrogen Compounds

**K. Tersago, I. Yu. Bagryanskaya, Yu. V. Gatilov, S. A. Gromilov, A. Yu. Makarov, M. Mandado, C. Van Alsenoy, A. V. Zibarev,* F. Blockhuys* ..... 1958–1965**

Insight Into the Intermolecular Factors Responsible for the *Z*,*Z* Configuration of Ar–X–N=S=N–X–Ar (X = S, Se) Derivatives in the Solid State

**Keywords:** Chalcogen-nitrogen chains / Crystal packing / Density functional theory / Molecular configurations / X-ray diffraction

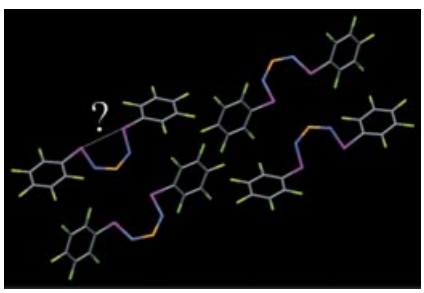


For derivatives of Ph–X–N=S=N–X–Ph (X = S, Se) the predominance of the *Z*,*Z* configuration in the solid state can not be explained by intramolecular stereoelectronic effects. Calculation of the packing energies and densities reveals that the crystal packing of the structures in the *Z*,*Z* configuration has a systematic preference over the corresponding packing in the *Z*,*E* configuration. As a result, packing forces are most likely responsible for the dominance of the *Z*,*Z* configuration in the crystal.

### CuO Nanostructures

**H.-M. Xiao, S.-Y. Fu,* L.-P. Zhu, Y.-Q. Li, G. Yang ..... 1966–1971**

Controlled Synthesis and Characterization of CuO Nanostructures through a Facile Hydrothermal Route in the Presence of Sodium Citrate

**Keywords:** Hydrothermal synthesis / Nanostructures / Sodium citrate / Copper complexes

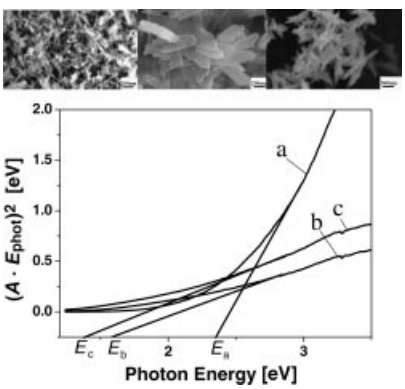


1D, 2D, and 3D CuO nanostructures have been synthesized by a hydrothermal process in the presence of sodium citrate. The bandgap energies of the nanostructures have been determined by ultraviolet absorption spectroscopy.

### Ferrimagnets

**A. Muñoz,* J. A. Alonso, M. J. Martínez-Lope, J. L. Martínez ..... 1972–1979**

Synthesis and Study of the Crystallographic and Magnetic Structure of $HoFeMnO_5$

**Keywords:** Ferrimagnetic structure / Superexchange interactions / Neutron diffraction / High oxygen pressure

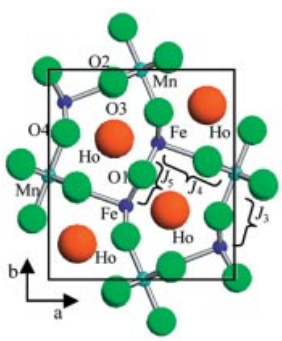


$HoFeMnO_5$ has been obtained by replacing $Mn^{3+}$ cations by $Fe^{3+}$ in $HoMn_2O_5$. $HoFeMnO_5$ adopts a collinear ferrimagnetic structure below $T_C \approx 153$ K; the magnetic moments are oriented along the *c* direction. There is a frustration concerning the long-range ordering of the $Ho^{3+}$ moments at low temperature.


 © 2007 Wiley-VCH Verlag GmbH & Co. KGaA, Weinheim 

## $^{27}$Al NMR Spectroscopy

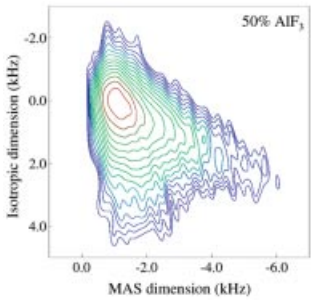

**M. Body,* C. Legein, J.-Y. Buzaré, G. Silly ..... 1980–1988**

The Relationship Between $^{27}$Al Quadrupolar Parameters and $AlF_6^{3-}$ Octahedron Connectivity in Crystalline and Glassy Fluoroaluminates

**Keywords:** Glasses / Fluorides / $^{27}$Al NMR spectroscopy / Quadrupolar parameters

Correlation of $^{27}$Al NMR results for glassy and crystalline phases enables an accurate picture to be gained of the glass network through the dependence of the quadrupolar parameters on the octahedron connectivity.

## Ligand Donor Properties

1 2a 3a

**T. I. Kückmann, F. Dornhaus, M. Bolte, H.-W. Lerner, M. C. Holthausen,* M. Wagner* ..... 1989–2003**

Broadening the Scope of Ancillary Phosphane-Type Ligands: A Systematic Comparison of $PR_3$, $PR_2BH_3^-$, and $SiR_3^-$ and Their Chalcogen Derivatives

**Keywords:** Isoelectronic analogs / P ligands / Si ligands / Ligand design / Boron

Phosphane derivatives are ubiquitous ligands in coordination chemistry. It is demonstrated that key properties of this ligand system can be further developed by using corresponding isolobal, negatively charged phosphanyl borohydride ($PR_2BH_3^-$) and silyl ($SiR_3^-$) derivatives to generate a broad spectrum of related species with smoothly varying donor capacities.

## Optical Limiting

The synthesis, structural characterization and optical limiting properties of a series of transition metal and lanthanide monoporphyrinate complexes functionalized with diphenylamino units are described. The performance of these optical power limiters is compared with those of benchmark materials.

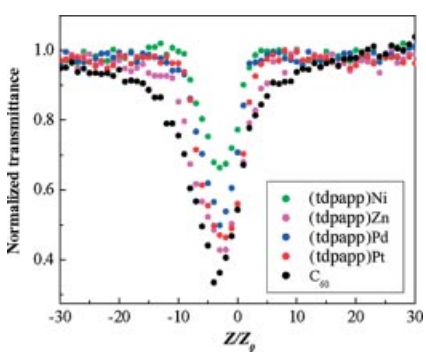


**S. Fu, X. Zhu, G.-J. Zhou, W.-Y. Wong, C. Ye, W.-K. Wong,* Z. Li* ..... 2004–2013**

Synthesis, Structures and Optical Power Limiting of Some Transition Metal and Lanthanide Monoporphyrinate Complexes Containing Electron-Rich Diphenylamino Substituents

**Keywords:** Lanthanides / Optical limiting / Photoluminescence / Porphyrins / Transition metals

## Ferrocene Amides

$^1$H NMR spectroscopic variation ratio analysis of asymmetrically substituted ferrocene derivatives suggests that an increase in the steric demand of the amino acid side chains favours conformations with hydrogen-bonded FnCO*NH*Me groups. CD spectroscopy of chiral derivatives reveals that (*P*)-helical conformations predominate in solution.

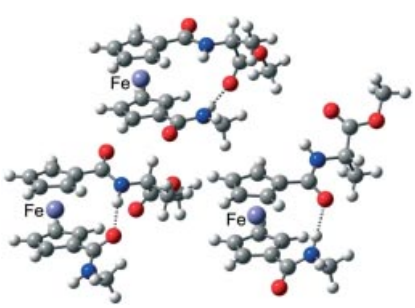


**J. Lapić, D. Siebler, K. Heinze,* V. Rapić* ..... 2014–2024**

Conformational Analysis of Heteroannularly Substituted Ferrocene Oligoamides

**Keywords:** Conformation analysis / Density functional calculations / Hydrogen bonds / Metallocenes / Molecular modelling

 © 2007 Wiley-VCH Verlag GmbH & Co. KGaA, Weinheim 

# CONTENTS

## Energetic Salts

**Y. Huang, H. Gao, B. Twamley, J. M. Shreeve* ..... 2025–2030**

Synthesis and Characterization of New Energetic Nitroformate Salts

**Keywords:** Nitroform / Energetic salt / Oxygen balance

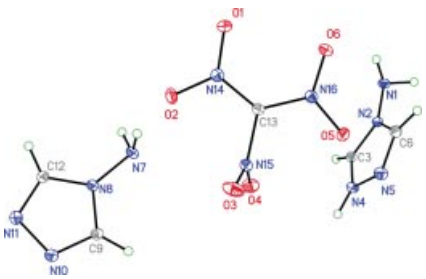


Energetic nitroformates with high-nitrogen cations were synthesized and characterized. Theoretical performance calculations indicate that these materials have properties which compare favorably with hydrazinium nitroformate, TNT and Tetryl suggesting potential applications as eco-friendly oxidizers.

## Mixed-Valent PtPd Chains

**S. Arai, M. Ochiai, K. Ishihara,* K. Matsumoto* ..... 2031–2039**

Mixed-Valent Linear Chain $Pt_2PdPt_2$ Complexes

**Keywords:** Platinum / Palladium / Chain structures / Metal–metal interactions / Mixed-valent compounds

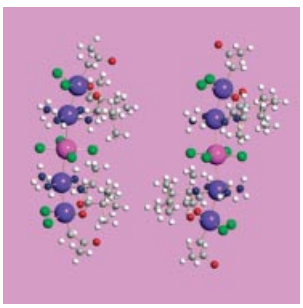

Pentanuclear linear-chain PtPd complexes composed of a monomeric $Pd^{II}$ complex sandwiched by two amidato-bridged dimeric $Pt^{III}$ units were synthesized. The PtPd complexes have either an arch or a sigmoid backbone structure, depending on the solvent used. The UV/Vis/NIR spectra clearly show the existence of quite rare charge transfer from Pd to Pt in the PtPd complexes.

## $Mn^{II}$ Ferrocenecarboxylato Complexes

**Z.-L. Chen, Y.-S. Ma, F.-P. Liang,* Z.-H. Zhou ..... 2040–2045**

Synthesis, Crystal Structure, and Magnetic Properties of Two Manganese(II) Polymers Bearing Ferrocenecarboxylato Ligands

**Keywords:** Manganese / Crystal structure / Ferrocenecarboxylato / Magnetic properties

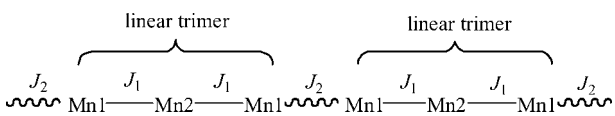


Two $Mn^{II}$ polymers bearing ferrocenecarboxylato ligands and having repeating linear trinuclear $-Mn-(\mu_2\text{-}COO)_n-Mn-(\mu_2\text{-}COO)-Mn-(\mu_2\text{-}COO)-Mn-(\mu_2\text{-}COO)_n-Mn-$ ($n$ = 4 and 2 for **1** and **2**, respectively) building blocks were prepared and characterized. Magnetic susceptibility measurements revealed a weak antiferromagnetic coupling for both complexes with an unprecedented $J_1-J_1-J_2$ (AF1–AF1–AF2) repeating sequence.

## Insertion Mechanisms

**S. Bi,* S. Zhu, Z. Zhang ..... 2046–2054**

Mechanisms of $H_2$, $H_2C{=}CH_2$, and $O{=}CH_2$ Insertion into $Cp_2Zr(\eta^2\text{-}SiMe_2{=}NtBu)(PMe_3)$

**Keywords:** Zirconium / Silanimines / Insertion / Mechanism

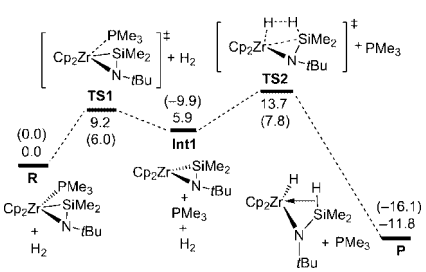


Mechanisms of $H_2$, $H_2C{=}CH_2$, and $O{=}CH_2$ insertion into $Cp_2Zr(\eta^2\text{-}SiMe_2{=}NtBu)(PMe_3)$ are theoretically investigated with the aid of DFT calculations. The regiochemistry for $O{=}CH_2$ insertion has been theoretically explored.

 © 2007 Wiley-VCH Verlag GmbH & Co. KGaA, Weinheim 

## Hydrogen Bonding

The new cluster compounds $[H_3O(Ph_3PO)_3]_2[Mo_6Cl_{14}]$ and $[H(Ph_3PO)_2]_2[Re_6S_6Br_8]$ have been studied by single-crystal X-ray diffraction and solid-state NMR and luminescence spectroscopy; strong hydrogen bonds are found in the complex cations.

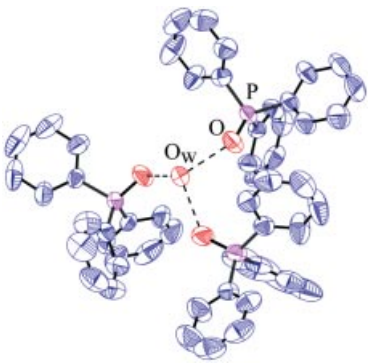


**Z. S. Kozhomuratova, Y. V. Mironov, M. A. Shestopalov, I. V. Drebushchak, N. K. Moroz, D. Y. Naumov, A. I. Smolentsev, E. M. Uskov, V. E. Fedorov* ..... 2055–2060**

Synthesis, Structures and Properties of Cluster Complexes $[H_3O(Ph_3PO)_3]_2[Mo_6Cl_{14}]$ and $[H(Ph_3PO)_2]_2[Re_6S_6Br_8]$

**Keywords:** Cluster compounds / Molybdenum / Rhenium / Triphenylphosphane oxide / Crystal structure / NMR spectroscopy / Hydrogen bonding

## MRI Contrast Agents

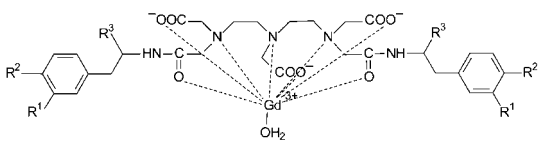


Three new potential MRI contrast agents, gadolinium complexes of DTPA-bis(tyramide), DTPA-bis(3-hydroxytyramide) and DTPA-bis(phenylalanine ethyl ester), were studied in vitro by $^{17}O$ NMR spectroscopy and by nuclear magnetic relaxation dispersion (NMRD) measurements. In view of the data, the best candidate is the Gd complex of DTPA-bis(tyramide).

**S. Laurent, T. N. Parac-Vogt,* K. Kimpe, C. Thirifays, K. Binnemans, R. N. Muller, L. Vander Elst* ..... 2061–2067**

Bis(phenylethylamide) Derivatives of Gd-DTPA as Potential Receptor-Specific MRI Contrast Agents

**Keywords:** Lanthanides / MRI contrast agents / N,O ligands / NMRD / $^{17}O$ NMR spectroscopy

## Layered Perovskites

An example of a noninteger member in the Ruddlesden–Popper series is found in a layered perovskite. The crystal is constituted by two structurally different domains; one corresponds to the $n = 1$ $Sr_4CoTaO_8$ Ruddlesden–Popper phase whereas the other corresponds to the $n = 1.5$ term and is associated to a chemical composition of $Sr_5(Co_{0.5}Ta_{0.5})_3O_{11}$.

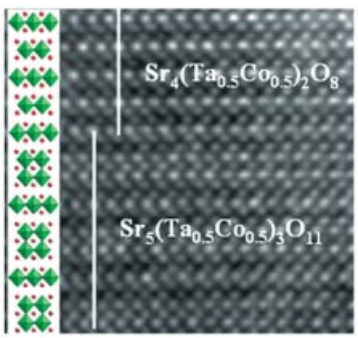


**K. Boulahya, M. Parras, J. M. González-Calbet* ..... 2068–2071**

Structural Chemistry of an $n = 1$ Member of the Ruddlesden–Popper $Sr_{n+1}(Co_{0.5}Ta_{0.5})_nO_{3n+1}$ Homologous Series: $Sr_4CoTaO_8$

**Keywords:** Electron diffraction / X-ray diffraction / Electron microscopy / Magnetic properties

## Hemilabile Ligands

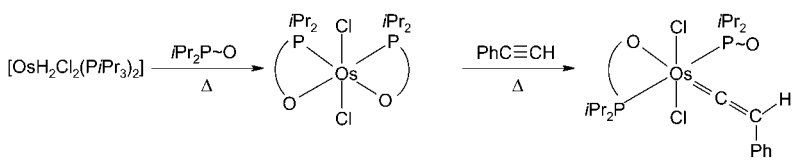


With the highly reactive dihydridoosmium(IV) compound $[OsH_2Cl_2(PiPr_3)_2]$ as the starting material, a series of osmium(II) and osmium(IV) complexes with phosphane–ethers, –esters, and –amines as mono- and bidentate ligands were prepared. The hemilabile nature of the functionalized phosphanes was illustrated by the reactions with CO, CN*t*Bu, and phenylacetylene, the latter yielding (vinylidene)-osmium(II) complexes, which in solution at room temperature are fluxional on the NMR timescale.

**B. Weber, H. Werner* ..... 2072–2082**

Osmium(II) and Osmium(IV) Complexes with Phosphane–Ethers, –Esters, and –Amines as Mono- and Bidentate Ligands

**Keywords:** Osmium / Phosphane–Ethers / Phosphane–Esters / Phosphane–Amines / Vinylidene complexes

 © 2007 Wiley-VCH Verlag GmbH & Co. KGaA, Weinheim 

# CONTENTS

## Ferromagnetic Dimers

**O. F. Ikotun, W. Ouellette, F. Lloret, M. Julve,* R. P. Doyle* ..... 2083–2088**

Synthesis, X-ray Structure, Thermal and Magnetic Behavior of $[(bipy)_2Ni_2(\mu\text{-}Cl)_2Cl_2(H_2O)_2]$: The First Neutral Ferromagnetically Coupled Six-Coordinate Dichlorido-Bridged Nickel(II) Dimer

**Keywords:** Crystal structures / Nickel complexes / Ferromagnetic coupling / Thermal analysis

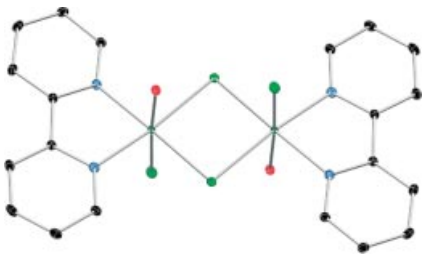

$[(bipy)_2Ni_2(\mu\text{-}Cl)_2Cl_2(H_2O)_2]$ (C = black; N = blue; Ni = green, small; Cl = green, large; O = red) exhibits the strongest ferromagnetism for a dichlorido-bridged dinuclear nickel(II) complex reported to date.

## Core-Shell Nanostructures

**S. V. Pol, V. G. Pol, I. Felner, A. Gedanken* ..... 2089–2096**

The Thermal Decomposition of Three Magnetic Acetates at Their Autogenic Pressure Yields Different Products. Why?

**Keywords:** Decomposition / Acetates / Magnetic properties / Core-shell nanostructures

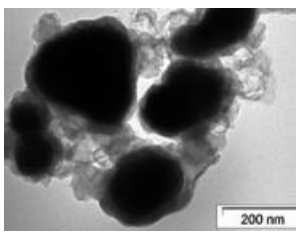


The reproducible and straightforward approach for the synthesis of fullerene-like Ni@C, Co@C and $Fe_3O_4$@C core-shell nanostructures is reported. Although identical reaction parameters are employed with the three acetate precursors, graphitic carbon is coated on nanosized metallic Ni and Co cores, while metallic Fe is not formed. $Fe_3O_4$ forms but maintains the same core-shell morphology.

**If not otherwise indicated in the article, papers in issue 13 were published online on April 16, 2007**

 © 2007 Wiley-VCH Verlag GmbH & Co. KGaA, Weinheim 

DOI: 10.1002/ejic.200601033

# Monohydrocalcite and Its Relationship to Hydrated Amorphous Calcium Carbonate in Biominerals

**Markus Neumann[a] and Matthias Epple*[a]**

**Keywords:** EXAFS spectroscopy / Biomineralisation / Materials science / Monohydrocalcite / Bioinorganic chemistry

Calcium carbonate monohydrate (monohydrocalcite) is prepared and structurally characterised by X-ray diffraction, X-ray absorption spectroscopy (EXAFS), thermal analysis, IR spectroscopy, and scanning electron microscopy. It is compared to hydrated phases of amorphous calcium carbonate (ACC) that have frequently been observed in biomineralisation. The crystal water is more strongly bound than in hydrated ACC phases, and monohydrocalcite can be distinguished from ACC by its IR spectrum. The EXAFS results suggest that monohydrocalcite is a suitable model for some biogenic and synthetic ACC phases, although not for all of them.
(© Wiley-VCH Verlag GmbH & Co. KGaA, 69451 Weinheim, Germany, 2007)

## Introduction

Monohydrocalcite, $CaCO_3 \cdot H_2O$, was first observed in 1930 during the dehydration of ikaite ($CaCO_3 \cdot 6H_2O$).[1] It was first observed in nature in 1959 in marine sediments,[2] and the first synthetic preparation was accomplished by Brooks et al. in 1950.[3] Under ambient conditions, this phase is metastable compared to the water-free calcium carbonate modifications calcite and aragonite, and upon dehydration, or at higher temperature, it transforms into these phases. Consequently, its solubility is higher than that of the water-free modifications (calcite, aragonite, vaterite).[4] Magnesium is generally incorporated into this phase in small quantities, therefore it is assumed that magnesium plays an important role during the crystallisation.[5–7] In nature, it is formed preferably in magnesium-rich marine locations.[8] The single crystal structure with trigonal symmetry (including a superstructure) was determined by Effenberger in 1981.[9]

Many living systems use inorganic minerals, for example for protection (shell, exoskeleton), as tools (teeth), for defence (spicule) or for internal stabilisation (bones forming an endoskeleton).[10–16] Calcium carbonate is the most prominent biomineral and is the main constituent of mollusc shells, crustacean cuticles, corals, skeletons of protozoa, etc.[17] In these cases, very delicate and often exceedingly mechanically stable structures are built by these organisms which (so far) cannot be mimicked in the laboratory. An exact control over the pathway of crystallisation lies at the centre of this process: There is a finely tuned interplay between the crystallising inorganic mineral and bio-organic compounds that control the crystallisation, both at the level of nucleation as well as during crystal growth.[10–17] The formation of mesocrystals has been proposed as a mechanism of how nanocrystals assemble into macroscopic crystals and aggregates.[18,19] In the case of calcium carbonate, there is increasing evidence that amorphous calcium carbonate (ACC) is first formed as a solid phase which then undergoes rearrangement/recrystallisation to one of the crystalline phases of calcium carbonate (calcite, aragonite and, much less frequently, vaterite). This is supported by studies of the mineral phase in developing organisms[20–32] and also by studies in vitro,[33–36] where ACC has been prepared synthetically. The role of ACC in biology was recently reviewed by Addadi et al.,[27] Meldrum,[17] and Weiner et al.[31] The thermodynamic[37] and structural[36] properties of synthetic ACC have been discussed by Günther et al.

When biogenic ACC is studied it usually contains some water, which suggests a hydrate-like structure. However, a distinction must be made between stable (permanent) forms of ACC and transient forms of ACC which transform into a crystalline phase. Addadi, Raz and Weiner have suggested that the stable forms are hydrated whereas the transient forms are not.[27] A water content of 15.7 wt.-% has been determined thermogravimetrically for hydrated ACC in the spicules of *Pyura pachydermatina*, which compares well to the stoichiometric formula for monohydrocalcite ($CaCO_3 \cdot H_2O$).[21] X-ray absorption spectroscopy (EXAFS) gave the best fit to the crystal structure of monohydrocalcite.[21] The monohydrocalcite EXAFS structure has also been found for ACC in cystoliths of *Ficus microcarpa* and *Ficus retusa*.[24]

We note here that all structural and thermal investigations that have suggested a similarity of hydrated ACC to monohydrocalcite refer only to literature data for monohydrocalcite, that is they use the crystal structure of monohy-

[a] Inorganic Chemistry, University of Duisburg-Essen, Universitätsstrasse 5–7, 45117 Essen, Germany
Fax: +49-201-183-2621
E-mail: matthias.epple@uni-due.de

 © 2007 Wiley-VCH Verlag GmbH & Co. KGaA, Weinheim 

drocalcite for EXAFS fits. Monohydrocalcite itself has never been studied by EXAFS spectroscopy. We therefore considered it appropriate to prepare this phase in pure form, to characterise it by modern methods and compare it to biogenic ACC.

## Result and Discussion

Monohydrocalcite was synthesised by adding potassium carbonate to artificial seawater. It was clearly identified by X-ray diffractometry in a phase-pure form (Figure 1). A sample stored for three months at room temperature in a closed vial showed the same diffractogram, which means that monohydrocalcite is completely stable over that period and does not lose its water of crystallisation.

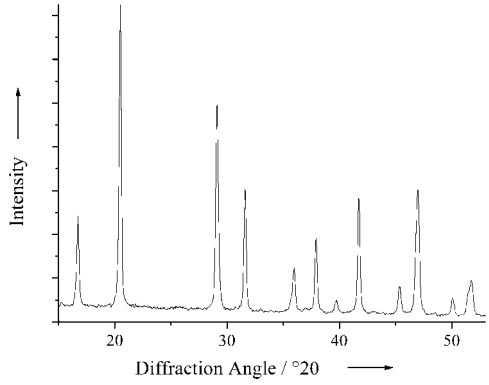


Figure 1. X-ray powder diffraction pattern of phase-pure monohydrocalcite.

The composition was studied by thermogravimetry, coupled with IR spectroscopic analysis of the released gases (Figure 2). A mass loss of 14.92 wt.-% from 140 to 205 °C was detected, which corresponds to the release of crystal water (theoretical value: 15.25 wt.-%). At higher temperatures (550 to 800 °C), decarboxylation occurred (observed mass loss: 36.44 wt.-%; theoretical value: 37.26 wt.-%). Released gaseous water and carbon dioxide, respectively, were detected in the connected IR spectrometer at the appropriate temperatures.

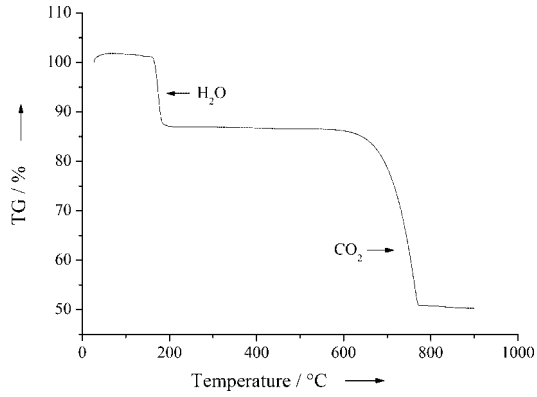


Figure 2. Thermogravimetric study of monohydrocalcite in a dynamic nitrogen atmosphere, showing first the dehydration and then the decarboxylation.

Synthetically prepared ACC has a water content of about 7.5 wt.-% (close to a hemihydrate), and about 1.5 wt.-% is released from 50–100 °C (loosely bound water) and about 6 wt.-% from 100–250 °C (structural water).[36] ACC from *Pyura pachydermatina* contains 15.7 wt.-% water (in good agreement with a monohydrate), which is released in the temperature range 20–200 °C.[21] We note that monohydrocalcite contains more strongly bound crystal water than ACC, a fact which is probably due to its higher crystallinity and its higher lattice energy.

Monohydrocalcite forms crystalline calcite after thermally induced loss of crystal water, as shown by X-ray powder diffraction (Figure 3). The fact that biogenic ACC can transform into calcite,[22,30,38] aragonite[20,26] and possibly vaterite[20] in vivo shows that there is a clear difference between a thermally induced dehydration and a biologically induced transformation at room temperature.

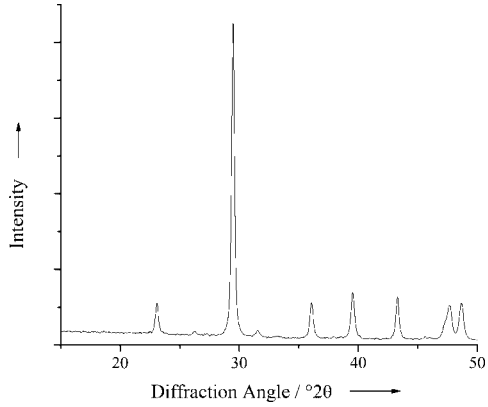


Figure 3. The X-ray powder diffractogram of monohydrocalcite after thermal dehydration (185 °C) shows only crystalline calcite.

The DSC curve shows an endothermal peak at 171.4 °C corresponding to the dehydration (Figure 4). The associated enthalpy change is +49.1 kJ mol$^{-1}$. Taking into account the enthalpy of evaporation of water [$\Delta_{vap}H_{373}°(H_2O)$ = 40.66 kJ mol$^{-1}$], the binding enthalpy of the water molecule is of the order of 8.5 kJ mol$^{-1}$.

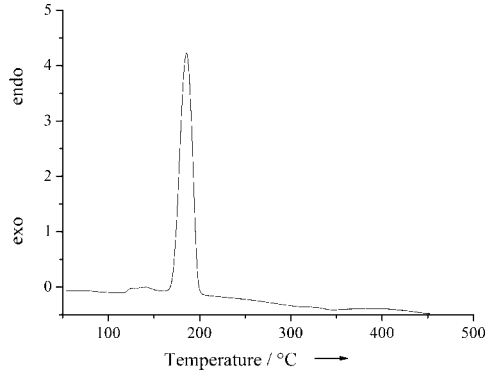


Figure 4. DSC curve of monohydrocalcite showing the endothermal peak associated with the dehydration. This is preceded by a broad endothermal peak which may be due to the release of water from disordered near-surface regions.

 © 2007 Wiley-VCH Verlag GmbH & Co. KGaA, Weinheim 

Monohydrocalcite was also characterised by IR spectroscopy (Figure 5). The asymmetric C–O stretching vibration is split (1408 and 1487 $cm^{-1}$). This is also observed for aragonite and vaterite, whereas calcite shows no splitting. In ACC from sternal deposits of the woodlouse *Porcellio scaber* we found an IR band at $\tilde{\nu}$ = 860 $cm^{-1}$ ($CO_3^{2-}$; $A_{2u}$).[28] The following values have been reported for this band in the literature: aragonite (860 $cm^{-1}$), calcite (876 $cm^{-1}$), and vaterite (877 $cm^{-1}$).[39] For biogenic ACC, a value of 866 $cm^{-1}$ has been reported.[27] Monohydrocalcite shows bands at 590 (lattice), 700/727 ($\nu_4$ of carbonate), 766 (lattice), 873 ($\nu_2$ of carbonate), 1068 ($\nu_1$ of carbonate), 1408/1487 ($\nu_3$ of carbonate), 1700 ($H_2O$ deformation), and 3235 $cm^{-1}$ (O–H stretch), in good agreement with the literature.[8,27,40,41] We therefore conclude that monohydrocalcite and ACC can be distinguished by IR spectroscopy by observing the carbonate band at around 870 $cm^{-1}$.

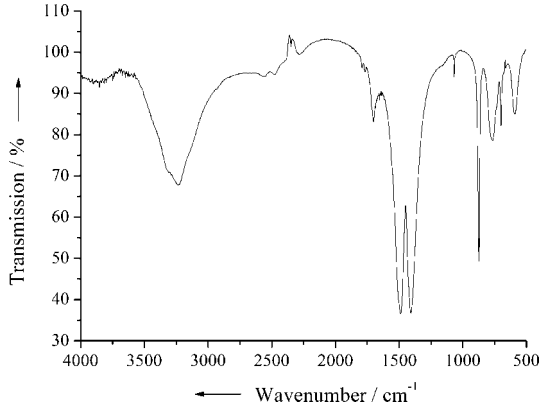


Figure 5. IR spectrum of monohydrocalcite.

The internal structure of monohydrocalcite was also studied by EXAFS, which examines the short-range order around Ca. Figure 6 shows the Fourier transform magnitude and the raw EXAFS data.

EXAFS is a versatile tool, especially for the analysis of amorphous materials which have short-range order but no long-range order. Investigations of amorphous calcium carbonates of different origin have shown that they differ in their short-range order.[27,36,43] The most stable forms of ACC contain one molecule of water per carbonate molecule, therefore monohydrocalcite has been suggested to be an appropriate model for hydrated ACC.[24,27] In the case of the ascidian *Pyura pachydermatina*, the best fit was actually obtained using monohydrocalcite as a model (see data in Table 1).[24] It is notable that no fit of the Ca–Ca coordination at around 4 Å was performed,[21] which shows that the disorder in ACC is much higher than in crystalline monohydrocalcite. The same situation has been observed for synthetic ACC, where only the first shell (Ca–O) could be fitted to the experimental data.[36] The transient amorphous calcium carbonate in the sternal deposits of the crustacean *Porcellio scaber* resembles either vaterite or monohydrocalcite.[28] Taylor et al. were the first to use EXAFS for the investigation of amorphous calcium carbonate from cystoliths of *Ficus retusa*. They showed that in the first coordination shell Ca is surrounded by eight O atoms, which is also the case for monohydrocalcite, and related it to ikaite ($CaCO_3 \cdot 6H_2O$).[42] However, this compound is very unstable and loses its crystal water even at 5 °C.[44] Note that the reference compound monohydrocalcite itself has never been studied by EXAFS until now, although its crystal structure has been used for EXAFS fits.[21,24,27] It must also be noted that the coordination number given by EXAFS is of limited accuracy due to its strong mathematical correlation with the Debye–Waller factor $\sigma^2$ and the amplitude reduction factor $S_0^2$.[45]

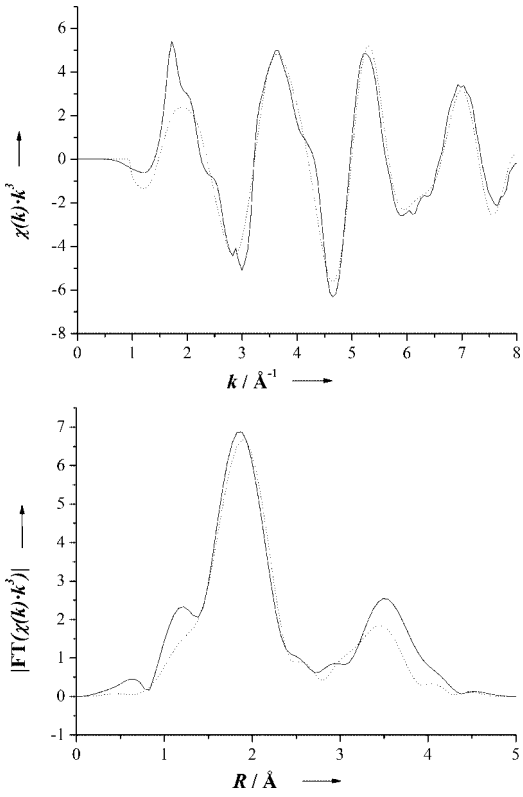


Figure 6. Ca *K*-edge EXAFS spectra of monohydrocalcite. Top: raw EXAFS data $\chi(k)$; bottom: Fourier transform magnitude. Solid line: experimental data; dotted line: fit data.

Crystallographically,[9] the environment of Ca in monohydrocalcite consists of eight oxygen atoms at distances of 2.41–2.49 Å (six from carbonate and two from hydrate water), two carbon atoms at a distance of 2.78–2.90 Å, two carbon atoms at a distance of 3.15–3.33 Å, one oxygen atom at a distance of 3.60 Å, and two calcium atoms at a distance of 3.86 Å. The higher coordination number in the first Ca–O shell (eight vs. six for calcite and vaterite, and nine for aragonite) and the lower coordination number in the outer Ca–Ca shell (two vs. six for calcite, aragonite and vaterite) distinguish monohydrocalcite from the water-free phases. The fact that the outer Ca–Ca shell in ACC is generally weak or not even present points to some similarity of monohydrocalcite to ACC, thus making it a useful structural model. An important difference, however, is the distance of the first Ca–O shell, which is very charac-

 © 2007 Wiley-VCH Verlag GmbH & Co. KGaA, Weinheim 

Table 1. Results reported in the literature for EXAFS spectra of X-ray-amorphous calcium carbonates (ACC) found naturally, together with crystalline phases. The entries are sorted by ascending distance of the first coordination shell of oxygen. Italicised values were kept constant during the EXAFS fit.

| | First shell: Ca–O | | | Second shell: Ca–C | | | Third shell: Ca–O | | | Fourth shell: Ca–Ca | | |
|---|---|---|---|---|---|---|---|---|---|---|---|---|
| | $R$ [Å] | $N$ | $\sigma^2 \cdot 10^3$ [Å$^2$] | $R$ [Å] | $N$ | $\sigma^2 \cdot 10^3$ [Å$^2$] | $R$ [Å] | $N$ | $\sigma^2 \cdot 10^3$ [Å$^2$] | $R$ [Å] | $N$ | $\sigma^2 \cdot 10^3$ [Å$^2$] |
| ACC in plant cystoliths of *Ficus microcarpa*[24] | 2.20<br>2.41 | 2.3<br>3.3 | 5<br>0.2 | 3.50 | *2* | 40 | –[a] | | | 3.79 | 4 | 13 |
| Calcite[28] | 2.34 | *6* | 9 | 3.30 | *6* | 35 | 3.64 | 6 | 16 | 4.05 | 6 | 9 |
| ACC in carapaces of *Homarus american*[24] | 2.23<br>2.41 | 1.9<br>3.9 | 5<br>3 | 3.47 | *4* | 13 | –[a] | | | 3.79 | *2* | 13 |
| ACC in plant cystoliths of *Ficus retusa*[42] | 2.35<br>2.43<br>2.44<br>2.73 | 2<br>2<br>2<br>2 | 17<br>29<br>34<br>47 | 3.20 | 1.5 | 31 | | –[a] | | | – | |
| Vaterite[28] | 2.37 | 6 | 7 | 3.09 | *2O*, *2C* | 21 | – | – | – | 4.24 | *6* | 15 |
| Cuticula of *Porcellio scaber* (calcite + ACC)[43] | 2.37 | 5.1 | 10 | 2.99 | 2.2 | 48 | 3.64 | 1.0 | 0 | 4.05 | *6* | 38 |
| Cuticula of *Armadillidum vulgare* (calcite + ACC)[43] | 2.37 | 6.6 | 12 | 3.00 | 2.4 | –23 | 3.64 | 0.8 | 0 | 4.02 | 6 | 35 |
| ACC in spicules of *Pyura Pachyderma tina*[21] | 2.37 | 7.4 | 9 | 3.03 | 1.5 | 7 | 3.36 | 3 | 0 | –[a] | | |
| ACC in sternal deposits of *Porcellio scaber*[28] | 2.38 | 3.8 | 14 | 3.00 | 1.4 | 7 | 3.72 | 0.4 | 1 | (3.89) | *6* | 109 |
| ACC prepared in vitro[36] | 2.41 | 5.3 | 11 | –[a] | | | –[a] | | | –[a] | | |
| Monohydrocalcite (this work) | 2.42 | 8.2 | 14 | 3.04 | *4* | 22 | –[a] | | | 3.83 | *2* | 5 |
| ACC in larval shells of *Biomphalaria glabrata*[20,29] | 2.44 | 9 | 31 | –[a] | | | –[a] | | | 3.92 | *6* | 47 |
| Aragonite[28] | 2.47 | *9* | 33 | 2.98 | *3* | 3 | 3.26 | 3 | 10 | 3.94 | *6* | 28 |

[a] Shell was not included in the fit.

teristic and can be determined with high accuracy by EXAFS. This shows that not all ACC phases that have been described have a short range like that of monohydrocalcite.

Scanning electron microscopy on monohydrocalcite showed that it consists of platelets that are aggregated into larger particles (Figure 7), whereas the ACC prepared by Faatz et al.[35] and Günther et al.[36] shows a spherical morphology with sub-micrometer-sized particles, therefore there is no similarity in the morphology of monohydrocalcite and ACC prepared in vitro.

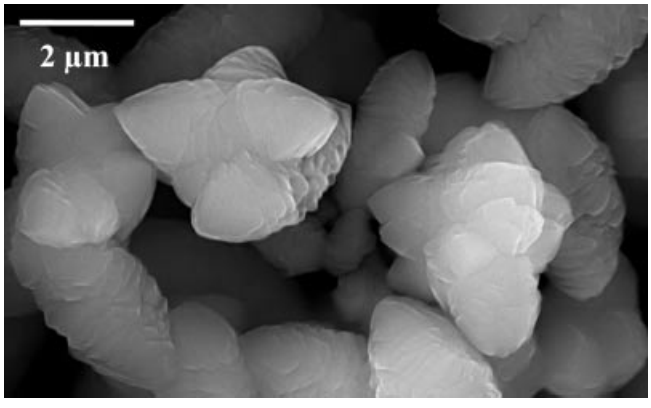


Figure 7. Scanning electron micrograph of synthetic monohydrocalcite.

## Conclusions

Monohydrocalcite as a stable hydrated phase of calcium carbonate is a suitable model for biogenic amorphous calcium carbonate (ACC) with regards to its composition (one water molecule per calcium carbonate unit). However, its microstructure, as determined by EXAFS, does not match the structure of all biogenic or synthetic ACC phases. This may be related to a higher degree of order in this crystalline phase, which also leads to a higher dehydration temperature compared to ACC. It may be assumed in the light of new theories on the formation of biominerals[18,19] that nanoscopic particles of hydrated calcium carbonate (resembling monohydrocalcite) assemble into water-containing ACC but do not crystallise (as shown by the fact that biogenic ACC is X-ray-amorphous), which means that the aggregates possess a higher energy than crystalline monohydrocalcite. Such biogenic assemblies always contain some organic material, which apparently prevents this ordering process. Unfortunately, no quantitative data on the content of organic matrix in biogenic ACC is available. The fact that many biogenic ACC phases are probably hydrated (although, to the best of our knowledge, this has only been quantified in one case by thermogravimetry[21] due to the small amount of sample material available) but structurally different[27,36,43] points to either different nanoscopic pre-

 © 2007 Wiley-VCH Verlag GmbH & Co. KGaA, Weinheim 

cursor particles or to a rearrangement during macroscopic assembly and ordering.

## Experimental Section

**Preparation of Monohydrocalcite:** Artificial seawater was prepared according to Kralj and Brecevic[4] by dissolving the following amounts of chemicals in 250 mL of doubly distilled water: 7.30 g of sodium chloride, 1.25 g of magnesium chloride, 0.370 g of calcium chloride dihydrate and 0.006 g of strontium chloride. Potassium carbonate (0.3 g) was then added and the solution was stirred until it had dissolved. The mixture was then placed in an ultrasonic bath for 10–15 s and left in a refrigerator at 6 °C overnight. The precipitate of monohydrocalcite obtained was filtered off and dried in air. Elemental analysis by combustion analysis (C, H) and atomic absorption spectroscopy (Ca, Mg) gave the following results: calcd. C 10.17, H 1.71, Ca 33.94, Mg 0; found C 10.06, H 1.83, Ca 33.67, Mg 0.32.

**Analytical Techniques:** Combined thermogravimetry/IR spectroscopy (TG-IR) was carried out with a Netzsch STA 209 TG-DTA/DSC instrument connected to a Bruker Vertex 70 IR spectrometer for gas analysis in situ. The sample was heated from 30 to 900 °C at a rate of 5 °C min$^{-1}$ under $N_2$ (50 mL min$^{-1}$). Scanning electron microscopy was carried out with a Zeiss DSM 962 instrument on Au-sputtered samples. X-ray powder diffractometry was carried out with a Stadi P instrument from STOE with Cu-$K_\alpha$ radiation. The DSC measurement was carried out with a Netzsch DSC 204 instrument. The sample was heated from 0 to 500 °C at a rate of 5 °C min$^{-1}$. Extended X-ray absorption fine structure (EXAFS) spectroscopy was carried out at beamline E4 at the Hamburger Synchrotronstrahlungslabor (HASYLAB) at the Deutsches Elektronen Synchrotron (DESY), Hamburg, Germany. The programs SPLINE/XFIT[46] and FEFF 6.01a[47] were used for quantitative data evaluation. The amplitude reduction factor $S_0^2$ was fixed to 0.8. Variation parameters were the bond lengths for all shells, the coordination numbers (only for the first shell), the Debye–Waller factors ($\sigma^2$) for all shells, and the zero-energy correction ($E_o$).


[1] F. Krauss, W. Schriever, *Z. Anorg. Chem.* **1930**, *188*, 259–273.
[2] D. G. Sapozhnikov, A. I. Zvetkov, *Dokl. Akad. Nauk SSSR* **1959**, *124*, 402–405.
[3] R. Brooks, L. M. Clark, E. F. Thurston, *Philos. Trans. R. Soc. London, A* **1950**, *243*, 1217–1219.
[4] D. Kralj, L. Brecevic, *Colloids Surf. A* **1995**, *96*, 287–293.
[5] D. J. J. Kinsman, H. D. Holland, *Geochim. Cosmochim. Acta* **1969**, *33*, 1–17.
[6] P. G. Malone, K. M. Towe, *Mar. Geol.* **1970**, *9*, 301–309.
[7] H. Hull, A. G. Turnbull, *Geochim. Cosmochim. Acta* **1973**, *37*, 685–694.
[8] M. M. Tlili, M. Ben Amor, C. Gabrielli, S. Joiret, G. Maurin, P. Rousseau, *J. Raman Spectrosc.* **2002**, *33*, 10–16.
[9] H. Effenberger, *Monatsh. Chem.* **1981**, *112*, 899–909.
[10] H. A. Lowenstam, S. Weiner, *On Biomineralisation*, Oxford University Press, New York, **1989**.
[11] S. Mann, *J. Mater. Chem.* **1995**, *5*, 935–946.
[12] S. Mann, *J. Chem. Soc., Dalton Trans.* **1997**, 3953–3961.
[13] E. Baeuerlein, *Biomineralisation*, Wiley-VCH, Weinheim, **2000**.
[14] S. Weiner, L. Addadi, H. D. Wagner, *Mater. Sci. Eng., C* **2000**, *11*, 1–8.
[15] S. Mann, *Biomineralisation*, Oxford University Press, Oxford, **2001**.
[16] E. Baeuerlein, *Biomineralisation. Progress in Biology, Molecular Biology and Applications*, Wiley-VCH, Weinheim, New York, **2004**.
[17] F. C. Meldrum, *Int. Mater. Rev.* **2003**, *48*, 187–224.
[18] S. Mann, H. Cölfen, *Angew. Chem. Int. Ed.* **2003**, *42*, 2350–2365.
[19] H. Cölfen, M. Antonietti, *Angew. Chem. Int. Ed.* **2005**, *44*, 5576–5591.
[20] B. Hasse, H. Ehrenberg, J. C. Marxen, W. Becker, M. Epple, *Chem. Eur. J.* **2000**, *6*, 3679–3685.
[21] Y. Levi-Kalisman, S. Raz, S. Weiner, L. Addadi, I. Sagi, *J. Chem. Soc., Dalton Trans.* **2000**, 3977–3982.
[22] S. Raz, S. Weiner, L. Addadi, *Adv. Mater.* **2000**, *12*, 38–42.
[23] J. Aizenberg, G. Lambert, S. Weiner, L. Addadi, *J. Am. Chem. Soc.* **2002**, *124*, 32–39.
[24] Y. Levi-Kalisman, S. Raz, S. Weiner, L. Addadi, I. Sagi, *Adv. Funct. Mater.* **2002**, *12*, 43–48.
[25] S. Raz, O. Testeniere, A. Hecker, S. Weiner, G. Luquet, *Biol. Bull.* **2002**, *203*, 269–274.
[26] I. M. Weiss, N. Tuross, L. Addadi, S. Weiner, *J. Exp. Zool.* **2002**, *293*, 478–491.
[27] L. Addadi, S. Raz, S. Weiner, *Adv. Mater.* **2003**, *15*, 959–970.
[28] A. Becker, U. Bismayer, M. Epple, H. Fabritius, B. Hasse, J. Shi, A. Ziegler, *Dalton Trans.* **2003**, 551–555.
[29] J. C. Marxen, W. Becker, D. Finke, B. Hasse, M. Epple, *J. Mollus. Stud.* **2003**, *69*, 113–121.
[30] S. Raz, P. C. Hamilton, F. H. Wilt, S. Weiner, L. Addadi, *Adv. Funct. Mater.* **2003**, *13*, 480–486.
[31] S. Weiner, I. Sagi, L. Addadi, *Science* **2005**, *309*, 1027–1028.
[32] X. Xu, J. T. Han, K. Cho, *Langmuir* **2005**, *21*, 4801–4804.
[33] R. J. Park, F. C. Meldrum, *J. Mater. Chem.* **2004**, *14*, 2291–2296.
[34] E. Loste, R. J. Park, J. Warren, F. C. Meldrum, *Adv. Funct. Mater.* **2004**, *14*, 1211–1220.
[35] M. Faatz, F. Gröhn, G. Wegner, *Adv. Mater.* **2004**, *16*, 996–1000.
[36] C. Günther, A. Becker, G. Wolf, M. Epple, *Z. Anorg. Allg. Chem.* **2005**, *631*, 2830–2835.
[37] G. Wolf, C. Günther, *J. Therm. Anal. Calorim.* **2001**, *65*, 687–698.
[38] E. Beniash, J. Aizenberg, L. Addadi, S. Weiner, *Proc. R. Soc. London, B* **1997**, *264*, 461–465.
[39] G. Falini, S. Albeck, S. Weiner, L. Addadi, *Science* **1996**, *271*, 67–69.
[40] L. Brecevic, A. E. Nielsen, *Acta Chem. Scand.* **1993**, *47*, 668–673.
[41] E. E. Coleyshaw, G. Crump, W. P. Griffith, *Spectrochim. Acta A* **2003**, *59*, 2231–2239.
[42] M. G. Taylor, K. Simkiss, G. N. Greaves, M. Okazaki, S. Mann, *Proc. R. Soc. London, B* **1993**, *252*, 75–80.
[43] A. Becker, A. Ziegler, M. Epple, *Dalton Trans.* **2005**, 1814–1820.
[44] A. Mikkelsen, A. B. Andersen, S. B. Engelsen, H. C. B. Hansen, O. Larsen, L. H. Skibstedt, *J. Agric. Food Chem.* **1999**, *47*, 911–917.
[45] M. Epple, M. Panthöfer, R. Walther, H. J. Deiseroth, *Z. Kristallogr.* **2000**, *215*, 445–453.
[46] P. J. Ellis, H. C. Freeman, *J. Synchrotron Radiat.* **1995**, *2*, 190–195.
[47] E. A. Stern, M. Newville, B. Ravel, Y. Yacoby, D. Haskel, *Physica B* **1995**, *208–209*, 117–120.


Received: November 3, 2006
Published Online: February 26, 2007

 © 2007 Wiley-VCH Verlag GmbH & Co. KGaA, Weinheim 

DOI: 10.1002/ejic.200601024

# Insight Into the Intermolecular Factors Responsible for the *Z*,*Z* Configuration of Ar–X–N=S=N–X–Ar (X = S, Se) Derivatives in the Solid State

**Karla Tersago,[a] Irina Yu. Bagryanskaya,[b] Yuri V. Gatilov,[b] Sergey A. Gromilov,[c] Alexander Yu. Makarov,[b] Marcos Mandado,[a] Christian Van Alsenoy,[a] Andrey V. Zibarev,*[b,d] and Frank Blockhuys*[a]**

*Dedicated to Prof. Dr. Dr. h. c. Rüdiger Mews on the occasion of his 65th birthday*

**Keywords:** Chalcogen-nitrogen chains / Crystal packing / Density functional theory / Molecular configurations / X-ray diffraction

The molecular and crystal structures of three new derivatives of Ph–S–N=S=N–S–Ph (**1**), with 2,4,6-(*tert*-$C_4H_9)_3C_6H_2$ (**4**), $C_6F_5$ (**5**) and 4-$CF_3C_6F_4$ (**6**) as peripheral rings, respectively, and one new derivative of Ph–Se–N=S=N–Se–Ph (**2**), with $C_6F_5$ (**7**) as peripheral rings, are reported and discussed in connection with those of the two parent structures **1** and **2** and those of the previously studied derivative of **1** containing 4-$ClC_6H_4$ (**3**) as peripheral rings. For these seven compounds the *Z*,*Z* configuration is the only one of the three theoretically possible configurations observed in the solid state and this configurational preference can not be explained by intramolecular stereoelectronic effects. Calculation of the packing energies and densities for the six most common space groups revealed that the crystal packing of the parent structure **1** in the *Z*,*Z* configuration has a systematic preference over the corresponding packing of **1** in the *Z*,*E* configuration by 0.3–4.9 kJ mol$^{-1}$. As a result, packing forces are most likely responsible for the dominance of the *Z*,*Z* configuration of the title compounds in the crystal.

(© Wiley-VCH Verlag GmbH & Co. KGaA, 69451 Weinheim, Germany, 2007)

## 1. Introduction

The molecular structures of chalcogen-nitrogen compounds are extremely diverse and continue to present a serious challenge to chemical theory in general.[1,2] Accurately predicting and rationalising these structures, both for isolated molecules and those arranged regularly in a crystal structure, remain of obvious fundamental interest.[3–5] This is particularly true when it comes to identifying and understanding the correlations that exist between molecular shape and the precise nature of the packing in the crystal. Within the family of chalcogen-nitrogen compounds, the oligomeric analogues of catenated sulfur nitride, $(SN)_x$, a metallic polymer and superconductor,[6] attract special attention due to possible applications as molecular wires in the field of molecular electronics. For this purpose, understanding the factors controlling molecular conformations is of the utmost importance.

Recently, we have shown[3] that the *Z*,*Z* configuration of $C_6H_5$–S–N=S=N–S–$C_6H_5$ (**1**)[7] and $C_6H_5$–Se–N=S=N–Se–$C_6H_5$ (**2**)[3] – and consequently that of 4-$ClC_6H_4$–S–N=S=N–S–$C_6H_4$Cl-4 (**3**)[8] – in the crystal can not be explained by the stabilising *intra*molecular interaction between the $X^{II}$ (X = S, Se) atoms, which had been suggested in the literature, and that *inter*molecular forces in the crystal must be the driving force behind the observed configuration. In particular, we have demonstrated that in the gas phase or in solution the *Z*,*Z* configuration is not stabilised to a greater extent than the *Z*,*E* configuration.

In this work we report the preparation and analysis of the crystal structures of four new substituted derivatives of **1** and **2**, including 2,4,6-(*tert*-$C_4H_9)_3C_6H_2$–S–N=S=N–S–$C_6H_2$(*tert*-$C_4H_9)_3$-2,4,6 (**4**), $C_6F_5$–S–N=S=N–S–$C_6F_5$ (**5**), 4-$CF_3C_6F_4$–S–N=S=N–S–$C_6F_4CF_3$-4 (**6**), and $C_6F_5$–Se–N=S=N–Se–$C_6F_5$ (**7**); see Figure 1 for structural formulas. For all these compounds only the *Z*,*Z* configuration is observed in the solid state.[9] Based on the results of quantum chemical calculations (i.e. energy differences, bond orders

[a] Department of Chemistry, University of Antwerp, Universiteitsplein 1, 2610 Wilrijk, Belgium
Fax: +32-3-820-23-10
E-mail: frank.blockhuys@ua.ac.be
[b] Institute of Organic Chemistry, Russian Academy of Sciences, 630090 Novosibirsk, Russia
Fax: +7-383-330-97-52
E-mail: zibarev@nioch.nsc.ru
[c] Institute of Inorganic Chemistry, Russian Academy of Sciences, 630090 Novosibirsk, Russia
[d] Department of Physics, Novosibirsk State University, 630090 Novosibirsk, Russia

 © 2007 Wiley-VCH Verlag GmbH & Co. KGaA, Weinheim 

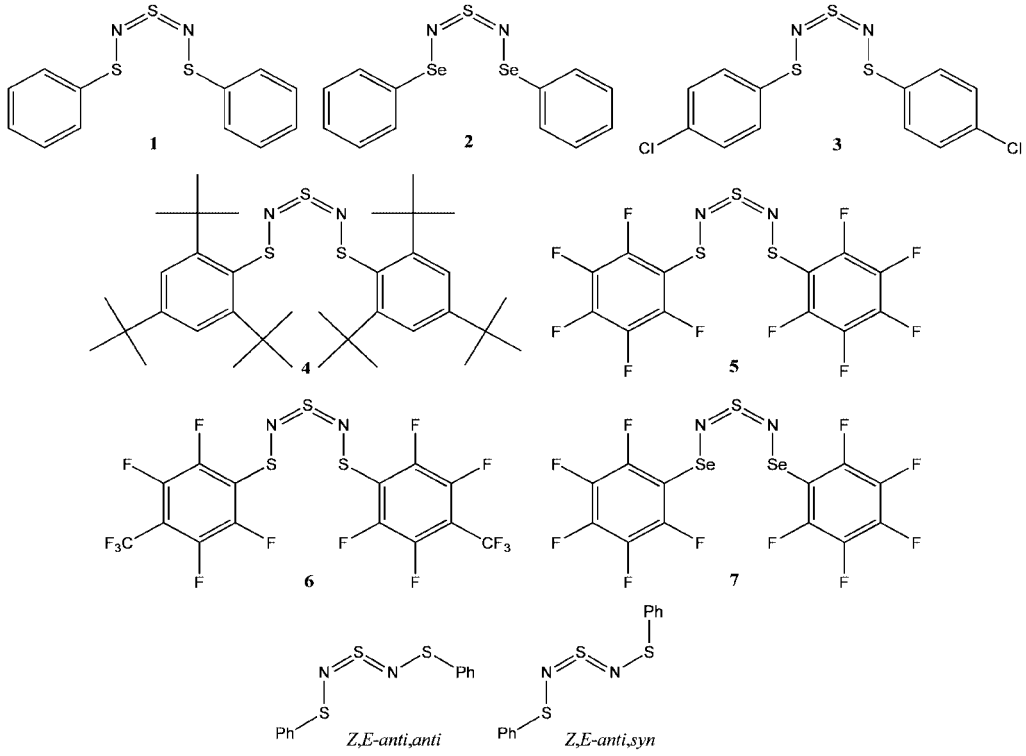


Figure 1. Structural formulas of the *Z*,*Z*-*anti*,*anti* conformers of the compounds under consideration; representative formulas of the *Z*,*E*-*anti*,*anti* and *Z*,*E*-*anti*,*syn* conformers have also been given.

and a topological analysis of the electron density) on 2,6-$(CH_3)_2C_6H_3$–S–N=S=N–S–$C_6H_3(CH_3)_2$-2,6 (**4′**) (as a model system for compound **4**) and **5**, using the same approach as we applied earlier,[3] *intra*molecular interactions can again be excluded as the reason for the observed *Z*,*Z* configurations. In order to shed more light on the possible *inter*molecular factors responsible for these observations, a number of simulations of the crystal packing of parent compound **1** were performed using the OPiX software.[10] The calculations show that for the six most common space groups ($P\bar{1}$, $P2_1/c$, $C2/c$, $Pbca$, $P2_1$, and $P2_12_12_1$) the crystal packing of **1** in the *Z*,*Z* configuration has a systematic preference over the packing of **1** in the *Z*,*E* configuration by 0.3–4.9 kJ mol$^{-1}$ and 0.010–0.025 g cm$^{-3}$ in energy and density, respectively. Based on this, we propose that the packing effects in the solid state are the driving force behind the observed *Z*,*Z* configuration of Ph–X–N=S=N–X–Ph (X = S, Se) and their derivatives.

## 2. Results and Discussion

### 2.1 Solid-State Molecular Structures

Previously, it was found that compounds **1**–**3** adopt the *Z*,*Z* configuration in the crystal.[3,7,8] This configuration features a virtually planar chalcogen-nitrogen fragment in which the $X^{II}\cdots X^{II}$ (X = S, Se) distance is significantly shorter than the sum of the van der Waals radii.[3,7,8] According to the XRD data we present here,[9] compounds **4**–**7** also exist in the *Z*,*Z* configuration in the crystal; see Figures 2, 3, 4, and 5 and Table 1 for geometrical data. For compound **4**, the –N=S=N– fragment is disordered over two sites (see Figure 2) in a ratio of 55:45. The chalcogen–nitrogen chain is planar to within ±0.012 and 0.032 Å for

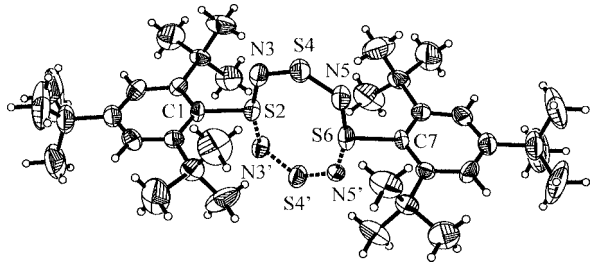


Figure 2. Molecular structure and partial numbering scheme of compound **4**. Displacement ellipsoids are at the 50% probability level; hydrogens are represented by spheres of arbitrary radius. Note that, for convenience, a unified numbering scheme has been used for compounds **4**–**7** in Figures 2, 3, 4, and 5; atoms S4 and S4′ of compound **4** actually lie on the $C_2$ symmetry axis.

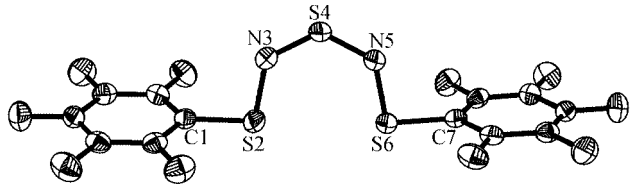


Figure 3. Molecular structure and partial numbering scheme of compound **5**. Displacement ellipsoids are at the 50% probability level.

 © 2007 Wiley-VCH Verlag GmbH & Co. KGaA, Weinheim 

Table 1. Selected solid-state geometrical data of compounds **4**–**6** (X = S) and **7** (X = Se); bond lengths in Å and angles in degrees.

| | **4**[a] | | **5**[b] | | **6** | **7** |
|---|---|---|---|---|---|---|
| C1–X2 | 1.777(4) | | 1.763(5) | 1.756(6) | 1.765(4) | 1.909(7) |
| X2–N3 | 1.816(6) | 1.845(7) | 1.668(5) | 1.683(5) | 1.684(3) | 1.830(8) |
| N3–S4 | 1.550(7) | 1.633(7) | 1.543(5) | 1.528(5) | 1.537(3) | 1.555(8) |
| S4–N5 | 1.550(7) | 1.633(7) | 1.525(5) | 1.536(5) | 1.537(3) | 1.519(9) |
| N5–X6 | 1.816(6) | 1.845(7) | 1.684(5) | 1.679(6) | 1.684(3) | 1.843(8) |
| X6–C7 | 1.777(4) | | 1.757(5) | 1.761(6) | 1.765(4) | 1.911(8) |
| X2···X6 | 3.274(2) | | 3.370(2) | 3.220(2) | 3.212(2) | 3.321(4) |
| C1–X2–N3 | 100.0(3) | 95.8(3) | 97.3(2) | 96.8(2) | 98.7(2) | 94.1(3) |
| X2–N3–S4 | 125.6(4) | 131.1(4) | 128.4(3) | 127.2(3) | 126.2(2) | 125.6(5) |
| N3–S4–N5 | 125.3(5) | 114.2(5) | 125.2(3) | 124.4(3) | 124.4(3) | 126.0(4) |
| S4–N5–X6 | 125.6(4) | 131.1(4) | 128.6(3) | 125.8(3) | 126.2(2) | 126.2(5) |
| N5–X6–C7 | 100.0(3) | 95.8(3) | 97.9(2) | 97.1(3) | 98.7(2) | 93.9(3) |
| C1–X2–N3–S4 | 159.1(4) | –154.1(4) | 174.0(5) | –169.6(5) | 175.7(3) | –146.9(7) |
| X2–N3–S4–N5 | –1.0(3) | –2.7(3) | –0.1(8) | 2.3(8) | –0.4(2) | –9.6(10) |
| N3–S4–N5–X6 | –1.0(3) | –2.7(3) | 0.6(8) | –0.1(8) | –0.4(2) | 2.4(10) |
| S4–N5–X6–C7 | 159.1(4) | –154.1(4) | 170.7(5) | –160.0(6) | 175.7(3) | –147.6(7) |

[a] The –N=S=N– fragment is disordered over two sites in a ratio of 55:45. The abnormally long S2–N3 bond lengths obtained are attributed to the disorder. [b] Two crystallographically independent molecules.

the two disordered molecules of **4**, ±0.004 and 0.017 Å for the two crystallographically independent molecules of **5**, ±0.005 Å for **6** and ±0.055 Å for **7**. The bond lengths and angles in compounds **4**–**7** given in Table 1 are typical[11] and quite similar to those found for compounds **1**–**3**.[3,7,8] The intramolecular $X^{II}\cdots X^{II}$ distances are again significantly shorter than the sums of corresponding van der Waals radii, which are 3.60 Å for the S···S and 3.80 Å for the Se···Se contacts.[12,13]

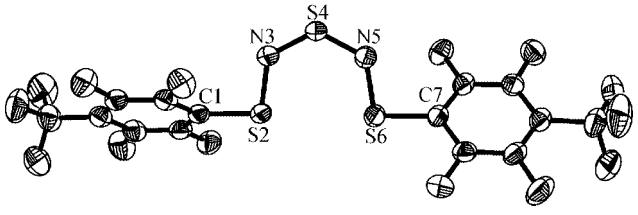


Figure 4. Molecular structure and partial numbering scheme of compound **6**. Displacement ellipsoids are at the 50% probability level.

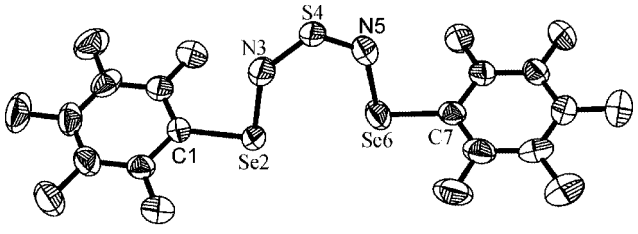


Figure 5. Molecular structure and partial numbering scheme of compound **7**. Displacement ellipsoids are at the 50% probability level.

Despite the fact that the seven compounds display the same *Z*,*Z* configuration, their particular molecular conformations are somewhat different. Molecules of compound **3** possess approximate $C_{2v}$ symmetry, while those of compound **1** display $C_2$ symmetry, since both phenyl rings are twisted away from the plane of the sulfur-nitrogen moiety by about 30°; the molecular conformation of **2** is very similar to that of **1**.[3] In contrast, the aromatic rings of compounds **4** and **5** are practically perpendicular to the plane of sulfur-nitrogen fragment: the corresponding dihedral angles in **4**, which displays $C_2$ symmetry, are 89.3(1)°. For the two crystallographically independent molecules of **5**, which possess $C_1$ symmetry, they are 79.9(1) and 76.6(1), and 73.7(1) and 71.5(1)°. For compound **6**, which also displays $C_2$ symmetry, the angles are 53.1(1)°, i.e. significantly smaller. The dihedral angles between the planes of the two aromatic rings are 10.6(1)° in **4**, 9.6(3)° and 9.3(3)° in **5**, and 10.4(5)° in **7**. Thus, the conformational changes observed on going from **2** to **7** are similar to those on going from **1** to **5**.

The above observations on compounds **1**–**7** provide clear evidence that the *Z*,*Z* configuration is the one which is generally favoured in the solid state, and that this configuration is stable towards intramolecular perturbations such as significant variations in the stereoelectronic demand of the terminal aromatic groups or the substitution of $S^{II}$ by $Se^{II}$ atoms. At the same time, the observed solid-state molecular conformations vary from practically coplanar to severely non-coplanar and it seems that these do depend greatly on the nature of the aromatic groups.

### 2.2 Gas-Phase Molecular Structures

The calculated relative energies of the three lowest-energy conformers [*Z*,*Z*-*anti*,*anti* ($C_2$), *Z*,*E*-*anti*,*anti* ($C_1$) and *Z*,*E*-*anti*,*syn* ($C_1$), see Figure 1] of compounds **4′** and **5** have been compiled in Table 2. We note that all other possible conformers have energies which are considerably higher ($> 20\ kJ\,mol^{-1}$), based on which they can be confidently excluded. The data in Table 2 indicate that the *Z*,*Z*-*anti*,*anti* conformer is the lowest-energy one; this is also the conformer that is found in the crystal. In analogy with the situation for the parent compounds **1** and **2**,[3] there are two *Z*,*E* conformers with an energy low enough so that they will be present in the gas phase (or in solution) at room

 © 2007 Wiley-VCH Verlag GmbH & Co. KGaA, Weinheim 

temperature. Based on the results of the calculations the equilibrium conformer compositions at 293 K are 87% $C_2$-*Z*,*Z*-*anti*,*anti*, 8% $C_1$-*Z*,*E*-*anti*,*anti* and 5% $C_1$-*Z*,*E*-*anti*,*syn* for compound **4′** and 73% $C_2$-*Z*,*Z*-*anti*,*anti*, 24% $C_1$-*Z*,*E*-*anti*,*anti*, and 3% $C_1$-*Z*,*E*-*anti*,*syn* for compound **5**.

Table 2. Calculated energies *E* [H] and relative energies Δ*E* [kJ mol$^{-1}$] of the three lowest-energy conformers [*Z*,*Z*-*anti*,*anti* ($C_2$), *Z*,*E*-*anti*,*anti* ($C_1$) and *Z*,*E*-*anti*,*syn* ($C_1$)] of compounds **4′** and **5** at the B3LYP/6-311+G* level of theory. See text for details.

| | Conformer | *E* | Δ*E* |
|---|---|---|---|
| **4′** | $C_2$-*Z*,*Z*-*a*,*a* | –1924.7753 | 0.00 |
| | $C_1$-*Z*,*E*-*a*,*a* | –1924.7731 | 5.98 |
| | $C_1$-*Z*,*E*-*a*,*s* | –1924.7727 | 6.87 |
| **5** | $C_2$-*Z*,*Z*-*a*,*a* | –2760.0944 | 0.00 |
| | $C_1$-*Z*,*E*-*a*,*a* | –2760.0934 | 2.65 |
| | $C_1$-*Z*,*E*-*a*,*s* | –2760.0914 | 7.78 |

The molecular geometries of the three conformers are given in Table 3. A comparison of the different calculated stable conformations of the two compounds reveals that when changing the conformation and/or configuration of the molecule the geometrical changes are quite substantial for the parameters directly involved in the change, i.e. S(4)–N(5), N(5)–S(6) and the three angles in the SNSNS fragment: differences of up to 0.056 Å for N(5)–S(6) and 15.7° for N(3)–S(4)–N(5) in **5** are found. These results are analogous to the ones found previously for the parent compounds **1** and **2**.[3] The changes in the non-bonded distances when going from one conformer to the other will be discussed in section 2.3. We note that conformational changes similar to the ones found in the solid state can be observed in the results of the calculations: while in the parent compounds **1** and **2** the benzene rings are twisted away from the plane of the XSNSX fragment by a mere 10.6 and 10.0°, respectively, for **4′** and **5** values of 70.1 and 69.1°, respectively, are found.

Comparing the XRD data of compounds **4** and **5** in Table 1 with those of the relevant gas-phase conformer (i.e. *Z*,*Z*-*anti*,*anti*) of compounds **4′** and **5** in Table 3 it is clear that the qualitative agreement between the calculated and experimental structures is quite good: the differences between single and double bonds are well reproduced, as are the different angles and torsion angles in the heteroatomic fragment. A quantitative comparison indicates that the calculations overestimate the bond lengths but this is mainly due to the fact that $r_{XRD}$ are $r_\alpha$-type distances while the $r_{calcd.}$ are $r_e$ distances by definition.[14,15]

Table 3. Selected calculated geometrical data of the three lowest-energy conformers of compounds **4′** and **5**; bond lengths in Å and angles in degrees.

| | **4′** | | | **5** | | |
|---|---|---|---|---|---|---|
| | *Z*,*Z*-*a*,*a* | *Z*,*E*-*a*,*a* | *Z*,*E*-*a*,*s* | *Z*,*Z*-*a*,*a* | *Z*,*E*-*a*,*a* | *Z*,*E*-*a*,*s* |
| C1–S2 | 1.795 | 1.797 | 1.796 | 1.781 | 1.783 | 1.781 |
| S2–N3 | 1.712 | 1.709 | 1.710 | 1.708 | 1.705 | 1.712 |
| N3–S4 | 1.570 | 1.574 | 1.574 | 1.568 | 1.564 | 1.569 |
| S4–N5 | 1.570 | 1.588 | 1.586 | 1.568 | 1.600 | 1.580 |
| N5–S6 | 1.712 | 1.728 | 1.705 | 1.708 | 1.744 | 1.692 |
| S6–C7 | 1.795 | 1.793 | 1.807 | 1.781 | 1.780 | 1.795 |
| S2···S6 | 3.509 | 4.702 | 4.678 | 3.424 | 4.667 | 4.619 |
| C1–S2–N3 | 99.7 | 98.5 | 98.5 | 98.1 | 96.8 | 96.6 |
| S2–N3–S4 | 129.1 | 119.8 | 120.2 | 128.4 | 119.6 | 119.4 |
| N3–S4–N5 | 125.8 | 110.8 | 111.1 | 124.9 | 109.2 | 110.8 |
| S4–N5–S6 | 129.1 | 119.6 | 124.8 | 128.4 | 113.9 | 127.0 |
| N5–S6–C7 | 99.7 | 99.0 | 107.1 | 98.1 | 99.2 | 107.5 |
| C1–S2–N3–S4 | 166.9 | 178.6 | –177.0 | 154.8 | 178.1 | –179.4 |
| S2–N3–S4–N5 | –2.2 | 0.2 | –0.2 | –1.2 | –0.5 | –0.1 |
| N3–S4–N5–S6 | –2.2 | 179.1 | –178.9 | –1.2 | –173.1 | 179.0 |
| S4–N5–S6–C7 | 166.9 | –179.5 | –4.9 | 154.8 | –120.4 | –1.1 |

### 2.3 Intramolecular S···S Interactions

As mentioned before, both in the crystal and in the lowest-energy conformer in the gas phase the distances between S(2) and S(6) [3.274(2) in **4** and 3.509 Å in **4′**, respectively, and 3.370(2)/3.220(2) and 3.424 Å in **5**, respectively] are well below the sum of the van der Waals radii (3.60 Å). This does suggest some sort of bonding interaction between those atoms. However, the energy difference between the conformer which has the interaction, i.e. $C_2$-*Z*,*Z*-*anti*,*anti*, and one which does not, e.g. $C_1$-*Z*,*E*-*anti*,*anti*, is only of the order of 5.98 kJ mol$^{-1}$ for **4′** and 2.65 kJ mol$^{-1}$ for **5** (Table 2). That the $C_1$-*Z*,*E*-*anti*,*anti* conformers do not display an interaction between S(2) and S(6) can be clearly seen from the S···S distances in Table 3 which are well above the sum of the van der Waals radii. These small energy differences suggest that the observed *Z*,*Z* configuration is not stabilised to a greater extent than the lowest-energy *Z*,*E* configuration and that the supposed S···S interactions do not play an important stabilising role.

Additional evidence comes from the calculated Hirshfeld bond orders of the different bonds in both molecules; the results are given in Table 4. The data reproduce the different types of bonding in the molecules equally well for the three conformers of **4′** and **5**: the XC bonds are clearly single while the S=N bonds are virtually double. The values for the S···S contacts are negative for all conformers of both compounds, which is a result of the scaling procedure,[16] and this indicates that the bond orders of these bonds are very small. The unscaled values for the *Z*,*Z*-*anti*,*anti* conformers of **4′** and **5** are 0.03 and 0.04, respectively, and these can be directly compared to the unscaled values for the XC bonds which are 0.38 and 0.39, respectively. The bonding in the S···S contacts is about thirteen and ten times lower, respectively, than in a regular single bond; the interaction between the two atoms must therefore be extremely

Table 4. Hirshfeld bond orders for the three lowest-energy conformers of compounds **4′** and **5**. See text for details.

| | **4′** | | | **5** | | |
|---|---|---|---|---|---|---|
| | *Z*,*Z*-*a*,*a* | *Z*,*E*-*a*,*a* | *Z*,*E*-*a*,*s* | *Z*,*Z*-*a*,*a* | *Z*,*E*-*a*,*a* | *Z*,*E*-*a*,*s* |
| C1–S2 | 1.02 | 1.01 | 1.01 | 1.09 | 1.07 | 1.08 |
| S2–N3 | 1.18 | 1.15 | 1.15 | 1.20 | 1.17 | 1.15 |
| N3–S4 | 1.83 | 1.76 | 1.77 | 1.83 | 1.80 | 1.79 |
| S4–N5 | 1.83 | 1.66 | 1.67 | 1.83 | 1.59 | 1.69 |
| N5–S6 | 1.18 | 1.11 | 1.25 | 1.20 | 1.07 | 1.30 |
| S6–C7 | 1.02 | 1.03 | 0.99 | 1.09 | 1.11 | 1.06 |
| S2···S6 | –0.53 | –0.68 | –0.68 | –0.51 | –0.68 | –0.68 |

 © 2007 Wiley-VCH Verlag GmbH & Co. KGaA, Weinheim 

weak. These values are of the same order of magnitude as for **1**, for which the scaled and unscaled bond orders are –0.52 and 0.04, respectively.[3]

Finally, a topological analysis of the total molecular electron density was performed using the Atoms In Molecules (AIM) theory.[17] The electron densities $\rho(r)$ of a number of relevant bond critical points (BCPs) and ring critical points (RCPs) of the three lowest-energy conformers of compounds **4′** and **5** were calculated and the results are given in Table 5. The topological analyses of **4′** and **5** show that there is an interaction between S(2) and S(6) but that this interaction is extremely weak. This conclusion is based on the fact that for **4′** the density in the BCP of the S···S bond is about 27 times lower than in the BCP of the SC single bond; for **5** this is 22 times. Moreover, the densities in the BCPs are 2.3 to 2.8 times lower than those found [calculated at the RI-BP86/TZVP level of theory] for the intermolecular S···S contacts (with a contact distance of about 3.0 Å) in a series of bis(thiocarbamoyl)disulfides.[18] The values of the density correlate well with those calculated for the parent compound **1**,[3] even though it seems that in compound **4′** the S···S interaction is slightly weaker than in **1** (0.0071 vs. 0.0078); in compound **5** the interaction seems slightly stronger (0.0087). The values of the RCPs confirm that the interaction should be very weak: the values of the phenyl rings are about three times larger those of the NSNS···S ring, for both compounds.

Table 5. Values of the electron density $\rho(r)$ (in au) of the relevant BCPs and RCPs for the three lowest-energy conformers of compounds **4′** and **5**. See text for details.

| | | **4′** | | | **5** | | |
|---|---|---|---|---|---|---|---|
| | | *Z,Z-a,a* | *Z,E-a,a* | *Z,E-a,s* | *Z,Z-a,a* | *Z,E-a,a* | *Z,E-a,s* |
| **BCP** | S2–C1 | 0.1887 | 0.1888 | 0.1889 | 0.1911 | 0.1911 | 0.1912 |
| | CH···N3 | 0.0081 | 0.0085 | 0.0086 | | | |
| | CH···N5 | 0.0081 | 0.0091 | | | | |
| | S2···S6 | 0.0071 | | | 0.0087 | | |
| **RCP** | $C_6Y_5$ | 0.0213 | 0.0213 | 0.0214 | 0.0192 | 0.0192 | 0.0193 |
| | SCCCH···N | 0.0080 | 0.0083 | 0.0082 | | | |
| | NSNS···S | 0.0064 | | | 0.0074 | | |

The combination of the above mentioned three criteria confirms the conclusion which was drawn for the parent compound: the proposed stabilising *intra*molecular interaction might not exist or at least be extremely weak, and *inter*molecular forces are the main cause of the observed *Z*,*Z* configuration in the solid.

### 2.4 Crystal Packing

Previously, it was hypothesized that in the crystal the *Z*,*Z* configuration of the title compounds allows a larger number of short intermolecular contacts per molecule, particularly via X···X (X = S, Se) contacts, than the corresponding *Z*,*E* configuration.[3] Naturally, this implies a closer packing. At present, though, the reliable ab initio prediction of a crystal packing remains practically very difficult, in particular for conformationally flexible molecules.[19–23] Still, we have been able to substantiate the idea that intermolecular (packing) forces are responsible for the preference of the *Z*,*Z* configuration, by performing simulations of the crystal packing of the parent compound **1** in both the *Z*,*Z* and *Z*,*E* configurations, using the OPiX software.[10] Starting from the atomic coordinates of a single molecule, this program generates[24–28] the solid-state packing for the six most common space groups ($P\bar{1}$, $P2_1/c$, $C2/c$, $Pbca$, $P2_1$, and $P2_12_12_1$), covering about 84% of the crystal structures deposited at the Cambridge Structural Database.[29,30] One limitation of the procedure, however, is the fact that the molecular geometry can not change during the optimization.[10] Even so, the energies of intermolecular interactions in molecular crystals are significantly smaller than the typical energies of intramolecular covalent interactions and, due to this, packing-induced molecular distortions are often limited.[31] Molecular structures calculated on higher levels of theory therefore often provide a good approximation to the structures observed in the crystal, and crystal structure predictions based on rigid calculated molecular structures is generally assumed to be reasonable.[32,33]

Also in the case of the parent Ph–S–N=S=N–S–Ph (**1**), the calculated gas-phase geometry of the *Z*,*Z-anti*,*anti* configuration seems to provide a useful model for the experimental geometry.[3] Therefore, the calculated molecular geometries of both configurations of **1** in the *anti,anti* conformation (i.e., *Z*,*Z-anti*,*anti* and *Z*,*E-anti*,*anti*, see Figure 1) were used in the OPiX calculations. However, to validate the simulation procedure and to investigate how well the method is able to reproduce experimentally observed unit cell dimensions, a first OPiX calculation was performed starting from the experimental geometry of **1** as it was reported by Leitch et al.[7] In the crystal (space group $C2/c$ and $Z = 4$) the molecules of **1** lie on $C_2$ axes. The OPiX software[10] allows using the corresponding subgroup which, in this case, is $P\bar{1}$. For this space group, the simulated unit cell of Ph–S–N=S=N–S–Ph (**1**) has a packing energy of –170.0 kJ mol$^{-1}$ and the following parameters: $a$ = 5.419 Å, $b$ = 7.584 Å, $c$ = 15.50 Å, $\alpha$ = 69.56°, $\beta$ = 79.94°, and $\gamma$ = 90.00°. The reduced unit cell parameters, calculated from the reported data,[7] are $a$ = 5.601(5) Å, $b$ = 7.792(8) Å, $c$ = 14.95(1) Å, $\alpha$ = 78.82(1)°, $\beta$ = 79.20(1)°, and $\gamma$ = 90.00°. As can be seen, there is a good agreement between calculated and experimental data.

The relevant results of the OPiX calculations performed using the molecular geometries of both the *Z*,*Z-anti*,*anti* and *Z*,*E-anti*,*anti* configurations of **1**, obtained from the quantum chemical calculations, are given in Table 6. From the packing energies and densities, given in Table 6, it can be seen that for all considered space groups the crystal packing of **1** in the *Z*,*Z* configuration has a systematic preference over the packing of **1** in the *Z*,*E* configuration by 0.3–4.9 kJ mol$^{-1}$ and 0.010–0.025 g cm$^{-3}$, respectively. In particular for the space group in which **1** crystallises, $C2/c$, the differences are 2.5 kJ mol$^{-1}$ and 0.012 g cm$^{-3}$ for the energy and density, respectively, in favour of the *Z*,*Z* configuration. It is interesting to note that for this space group the unit cell parameters simulated using the calculated *Z*,*Z*

 © 2007 Wiley-VCH Verlag GmbH & Co. KGaA, Weinheim 

geometry ($a$ = 6.113 Å, $b$ = 6.848 Å, $c$ = 15.466 Å, $\alpha$ = 77.25°, $\beta$ = 83.10°, $\gamma$ = 87.20°) are likewise acceptably close to the experimental values given above. Furthermore, the calculated packing energy of the crystal based on **1** in its experimental geometry is 10.0 kJ mol$^{-1}$ lower than that of the crystal based on **1** in its gas-phase geometry, at least for the $P\bar{1}$ space group (see Table 6); it is 8.8 kJ mol$^{-1}$ lower than the most favourable packing based on the gas-phase geometry, i.e. that in the $P2_12_12_1$ space group.

Table 6. Packing energies ($E$ in kJ mol$^{-1}$) and densities ($D$ in g cm$^{-3}$)[a] of the crystal structures simulated by the OPiX suite of programs for the $Z$,$E$ and $Z$,$Z$ configurations of Ph–S–N=S=N–S–Ph **1**.

| | $Z$,$Z$-$a$,$a$ | | $Z$,$E$-$a$,$a$ | |
|---|---|---|---|---|
| Space group | $E$ | $D$ | $E$ | $D$ |
| $P\bar{1}$ | –160.0 | 1.495 | –156.4 | 1.476 |
| $P2_1/c$ | –158.7 | 1.496 | –158.4 | 1.486 |
| $C2/c$ | –154.5 | 1.445 | –152.0 | 1.433 |
| $Pbca$ | –152.0 | 1.459 | –150.2 | 1.437 |
| $P2_1$ | –158.6 | 1.487 | –153.7 | 1.462 |
| $P2_12_12_1$ | –161.2 | 1.501 | –158.8 | 1.489 |

[a] The experimental value is 1.471 g cm$^{-3}$.[7]

These findings can be considered as the manifestation of a trend to approach a close-packing regime via the $Z$,$Z$ configuration. In turn, this very favourable way of organising the crystal structure must then be largely responsible for the observed $Z$,$Z$ configurations of the title compounds **1**–**7**. Indeed, our theoretical and experimental work on isolated molecules of Ar–X–N=S=N–X–Ar (X = S, Se, and their derivatives) – in this work and in ref.[3] – suggests that even in the absence of stabilizing stereoelectronic interactions between the X$^{II}$ atoms the $Z$,$Z$ configuration has a minor thermodynamic preference over the $Z$,$E$ configuration (at least for the method/basis set combination used). As a consequence, both configurations coexist in the corresponding equilibria in the gas phase and in solution, but in the solid state only the $Z$,$Z$ configuration exists. Our OPiX calculations then suggest that the crystal packing of the discussed derivatives in the $Z$,$Z$ configuration has a further minor thermodynamic preference over that of the compounds in the $Z$,$E$ configuration. Both the intramolecular and the intermolecular effects seemingly act in the same direction, i.e., towards the packing of Ar–X–N=S=N–X–Ar (X = S, Se) in the $Z$,$Z$ configuration. Whereas in the gas phase or in solution the energy differences between the different isomers allows for the presence of the less stable isomer, the intermolecular (packing) forces seem to be critically important for the total domination of the $Z$,$Z$ configuration in the solid state. The idea that rather than *intra*molecular factors *inter*molecular ones (i.e. packing forces) are the main driving force behind the experimentally observed configurations, which was until now based on the results of the quantum chemical calculations, has thus been strengthened by the simulations of the crystal packing.

## 3. Conclusions

For Ph–S–N=S=N–S–Ph (**1**) and Ph–Se–N=S=N–Se–Ph (**2**) and their derivatives **3**–**7** the $Z$,$Z$ configuration is the only one of the three theoretically possible configurations observed in the solid state and this configurational preference can not be explained by intramolecular stereoelectronic effects, which is shown by three theoretical arguments at the B3LYP/6-311+G* level of theory. The analysis of the properties of the simulated crystal structures of two conformers of the parent compound Ph–S–N=S=N–S–Ph (**1**) strengthens the idea that rather than *intra*molecular factors *inter*molecular ones (that is packing forces) are the main driving force behind the experimentally observed $Z$,$Z$ configurations.

## Experimental Section

Compounds **4**[34] and **5**[35] were synthesized from $(Me_3SiN=)_2S$ and the corresponding ArSCl as described before. $^{15}$N and $^{77}$Se NMR spectra were recorded on a Bruker DRX-500 spectrometer at frequencies of 50.68 and 95.38 MHz, respectively, with $NH_3$ (liq.) and $Me_2Se$ as standards. $^{19}$F NMR spectra were recorded on a Bruker AC-200 spectrometer at a frequency of 188.20 MHz with $C_6F_6$ as the standard (the chemical shift of $C_6F_6$ with respect to $CFCl_3$ is –162.2 ppm). High-resolution mass spectra (EI, 70 eV) were recorded on a Finnigan MAT MS-8200 instrument. UV/Vis spectra were recorded on a Hewlett–Packard 8453 spectrophotometer. Synthetic procedures were carried out under an argon atmosphere in dried solvents with stirring. The reagents were added dropwise and solvents were always distilled off under reduced pressure.

### Syntheses

**1,5-Bis(heptafluoro-4-methylphenyl)-2,4-diaza-1,3,5-trihia-2,3-pentadiene (6):** Over a period of 1 h, a solution of 4-$CF_3C_6F_4SCl$[36] (2.85 g, 0.01 mol) in $CH_2Cl_2$ (15 mL) was added to a solution of $(Me_3SiN=)_2S$[37] (1.03 g, 0.005 mol) in $CH_2Cl_2$ (10 mL) at –30 °C. The reaction mixture was slowly warmed up to 20 °C, the solvent was distilled off and the residue was recrystallized from hexane. Compound **6** was obtained as bright yellow crystals in a yield of 2.23 g (80%), m.p. 75–76 °C. MS $m/z$: 557.9022 [M$^+$, calculated for $C_{14}F_{14}N_2S_3$ 557.9000]. NMR ($C_6D_6$): $\delta$ = $^{19}$F 106.5, 31.1, 23.7 ppm. UV/Vis (heptane) $\lambda_{max}$ (nm) (log $\varepsilon$): 412 (3.97). $C_{14}F_{14}N_2S_3$ (558.34): calcd. C 30.12, F 47.64, N 5.01, S 17.23; found C 30.09, F 47.62, N 4.84, S 17.35.

**1,5-Bis(pentafluorophenyl)-2,4-diaza-3-thia-1,5-diselena-2,3-pentadiene (7):** Over a period of 1 h, a solution of $C_6F_5SeCl$[38] (0.90 g, 0.0032 mol) in hexane (10 mL) was added to a solution of $(Me_3SiN=)_2S$[37] (0.32 g, 0.0016 mol) in hexane (20 mL) at 20 °C. After an additional hour the solvent was distilled off and the residue was recrystallized from hexane. Compound **7** was obtained as orange crystals in a yield of 0.56 g (62%), m.p. 42–43 °C. MS $m/z$: 553.8034 [M$^+$, calculated for $C_{12}F_{10}N_2SSe_2$ 553.7952]. NMR ($CDCl_3$): $\delta$ = $^{15}$N 302.1; $^{19}$F 36.5, 13.7, 2.7; $^{77}$Se 775 (broad, cf. ref.[2]) ppm. UV/Vis (heptane) $\lambda_{max}$ (nm) (log $\varepsilon$): 422 (3.68, sh), 370 (3.92). $C_{12}F_{10}N_2SSe_2$ (552.11): calcd. C 26.11, F 34.41, N 5.07; found C 25.93, F 34.45, N 5.11.

### Crystallographic Analyses

The single-crystal X-ray structure determinations (Table 7) were carried out on a Bruker P4 for compound **4**, a Stoe Stadi4 for compound **5** and a Syntex $P2_1$ diffractometer for compounds **6** and **7**, with graphite-monochromated Mo-$K_\alpha$ ($\lambda$ = 0.71073 Å) or Cu-$K_\alpha$ ($\lambda$ = 1.54178 Å) radiation. The structures were solved by direct methods using SHELXS-97[39] and refined by least-squares methods in the full-matrix anisotropic (isotropic for hydrogen atoms)

 © 2007 Wiley-VCH Verlag GmbH & Co. KGaA, Weinheim 

Table 7. Crystal and refinement data of compounds **4**–**7**.

| | **4** | **5** | **6** | **7** |
|---|---|---|---|---|
| Formula | $C_{36}H_{58}N_2S_3$ | $C_{12}F_{10}N_2S_3$ | $C_{14}F_{14}N_2S_3$ | $C_{12}F_{10}N_2SSe_2$ |
| $M$ | 615.02 | 458.32 | 558.34 | 552.12 |
| $T$ [K] | 296 | 200 | 296 | 296 |
| $\lambda$ [Å] | 0.71073 | 0.71073 | 1.54178 | 1.54178 |
| Crystal system | orthorhombic | monoclinic | orthorhombic | monoclinic |
| Space group | *Ccca* | $P2_1/n$ | *Pbcn* | $P2_1/c$ |
| $a$ [Å] | 20.179(5) | 10.1269(6) | 6.086(2) | 4.531(4) |
| $b$ [Å] | 20.830(5) | 9.8234(6) | 9.550(2) | 10.791(7) |
| $c$ [Å] | 17.917(3) | 30.4702(14) | 31.650(10) | 31.96(2) |
| $\beta$ [°] | 90 | 92.422(5) | 90 | 91.26(14) |
| $U$ [Å$^3$] | 7531(3) | 3028.5(3) | 1839.5(9) | 1562(2) |
| $Z$ | 8 | 8 | 4 | 4 |
| $D_c$ [g cm$^{-3}$] | 1.085 | 2.010 | 2.016 | 2.348 |
| $\mu$ [mm$^{-1}$] | 0.222 | 0.604 | 5.107 | 8.291 |
| $F$(000) | 2688 | 1792 | 1088 | 1040 |
| Crystal size [mm] | $0.44\times0.41\times0.18$ | $1.04\times0.64\times0.16$ | $1.50\times0.40\times0.15$ | $0.60\times0.40\times0.25$ |
| $\theta$ range [°] | 1.81–25.00 | 2.09–25.01 | 2.79–69.94 | 2.77–69.92 |
| Index range | $0 \le h \le 23$ | $-12 \le h \le 12$ | $-7 \le h \le 0$ | $0 \le h \le 5$ |
| | $0 \le k \le 24$ | $0 \le k \le 11$ | $-2 \le k \le 11$ | $0 \le k \le 13$ |
| | $0 \le l \le 21$ | $0 \le l \le 36$ | $-2 \le l \le 38$ | $-38 \le l \le 38$ |
| Reflections collected | 3310 | 5409 | 1862 | 3312 |
| Independent reflections | 3310 | 5301 | 1746 | 2923 |
| | | [$R_{int}$ = 0.0239] | [$R_{int}$ = 0.0359] | [$R_{int}$ = 0.0417] |
| Completeness to $\theta$ (%) | 99.6 | 93.3 | 84.8 | 98.5 |
| Absorption correction | none | 0.63–0.76 | 0.85–1.00 | 0.06–0.25 |
| Refinement method | full-matrix least squares on $F^2$ | | | |
| Data/restraints/parameter | 3310/0/199 | 5301/0/488 | 1746/0/151 | 2923/0/245 |
| Goodness-of-fit on $F^2$ | 1.032 | 1.080 | 1.053 | 1.065 |
| Observed reflections | 1260 | 4126 | 1260 | 1903 |
| Final $R$ indices | $R_1$ = 0.0671 | $R_1$ = 0.0577 | $R_1$ = 0.0557 | $R_1$ = 0.0690 |
| [$I > 2\sigma(I)$] | $wR_2$ = 0.1616 | $wR_2$ = 0.1827 | $wR_2$ = 0.1435 | $wR_2$ = 0.1929 |
| $R$ indices (all data) | $R_1$ = 0.1434 | $R_1$ = 0.0770 | $R_1$ = 0.0774 | $R_1$ = 0.0928 |
| | $wR_2$ = 0.1703 | $wR_2$ = 0.2092 | $wR_2$ = 0.1601 | $wR_2$ = 0.2105 |
| Largest diff. peak | 0.737 | 1.063 | 0.326 | 1.154 |
| and hole [e Å$^{-3}$] | –0.263 | –0.804 | –0.411 | –0.588 |

approximation using SHELXL-97.[39] Hydrogen atoms were located geometrically.

CCDC-185941 (for **4**), -185939 (for **5**), -185940 (for **6**) and -604700 (for **7**) contain the supplementary crystallographic data for this paper. These data can be obtained free of charge from The Cambridge Crystallographic Data Centre via www.ccdc.cam.ac.uk/data_request/cif.

### Calculations

The DFT calculations were performed using Gaussian 03[40] applying standard gradient techniques at the B3LYP level of theory using the 6-311+G* basis set on all atoms; the basis set was used as it is implemented in the program. Calculations to determine the stability of the wave functions (or rather the mathematical constructions based on the Kohn–Sham orbitals) were performed using the same level and basis set and all wave functions were found to be stable. Force field calculations were used to ascertain whether the resulting structures were energy minima. All subsequent calculations of molecular properties were performed at the B3LYP/6-311+G* geometries. Bond orders (or rather overlap populations; see ref.[16]) were calculated according to the Hirshfeld Scheme.[16] QTAIM bond and ring properties were calculated using the AIMPAC suite of programs.[41] Crystal packing simulations were performed with the OPiX suite of programs[10] starting from the calculated (DFT/B3LYP/6-311+G*) geometries of the *Z*,*Z*-*anti,anti* and *Z*,*E*-*anti,anti* conformers of **1** (Figure 1). Initially, the recommended parameters were used in the optimizations, but in subsequent calculations these values were modified. In particular, the *energy threshold* parameter was lowered from the recommended value of 0.5 to 0.3 to obtain more detailed results. In the case of the *Pbca* space group the recommended values of the *energy threshold* and *step resolution* parameters were modified to 0.9 and 0.7, and 0.7 and 0.5 for the *Z*,*E* and *Z*,*Z* configurations, respectively.

## Acknowledgments

The authors are grateful to Prof. Angelo Gavezzotti for kindly providing the OPiX suite of programs, and to one referee for his or her valuable comments. The Novosibirsk authors are grateful to Dr. Vladimir V. Shcherbukhin for performing preliminary DFT calculations on the discussed compounds, to Mr. Mikhail K. Kovalev for his assistance in the syntheses, and to the Russian Foundation for Basic Research for financial support of their work (grant 06-03-32229).

[1] T. Chivers, *A Guide to Chalcogen-Nitrogen Chemistry*, World Scientific, **2005**, pp. 340.
[2] N. N. Greenwood, A. Earnshow, *Chemistry of the Elements*, Butterworth-Heinemann, **1997**, 1340 pp.
[3] K. Tersago, M. Mandado, C. Van Alsenoy, I. Yu. Bagryanskaya, M. K. Kovalev, A. Yu. Makarov, Yu. V. Gatilov, M. M. Shakirov, A. V. Zibarev, F. Blockhuys, *Chem. Eur. J.* **2005**, *11*, 4544–4551.

 © 2007 Wiley-VCH Verlag GmbH & Co. KGaA, Weinheim 

[4] F. Blockhuys, S. L. Hinchley, A. Yu. Makarov, Yu. V. Gatilov, A. V. Zibarev, J. D. Woollins, D. W. H. Rankin, *Chem. Eur. J.* **2001**, *7*, 3592–3602.
[5] A. R. Turner, F. Blockhuys, C. Van Alsenoy, H. E. Robertson, S. L. Hinchley, A. V. Zibarev, A. Yu. Makarov, D. W. H. Rankin, *Eur. J. Inorg. Chem.* **2005**, 572–581.
[6] A. J. Banister, I. B. Gorrell, *Adv. Mater.* **1998**, *10*, 1415–1429.
[7] J. Leitch, S. C. Nyburg, D. A. Armitage, M. J. Clark, *J. Cryst. Mol. Struct.* **1973**, *3*, 337–342.
[8] F. P. Olsen, J. C. Barrick, *Inorg. Chem.* **1973**, *12*, 1353–1355.
[9] The *Z*,*Z* statistics are even more impressive since it was recently shown by XRD that the 2,2′-dinitro derivative of compound **1** also has the *Z*,*Z* configuration in the solid state. E. Lork, A. Yu. Makarov, R. Mews, A. V. Zibarev, manuscript in preparation.
[10] A. Gavezzotti, *OPiX, a computer program package for the calculation of intermolecular interactions and crystal energies, May 2006 version*, Dipartimento di Chimica Strutturale e Stereochimica Inorganica, Università di Milano, Milano, Italy.
[11] I. Yu. Bagryanskaya, Yu. V. Gatilov, A. V. Zibarev, *J. Struct. Chem.* **1997**, *38*, 829–845.
[12] A. Bondi, *J. Phys. Chem.* **1964**, *68*, 441–451.
[13] R. S. Rowland, R. Taylor, *J. Phys. Chem.* **1996**, *100*, 7384–7391.
[14] K. Kuchitsu, S. J. Cyvin, *Molecular Structures and Vibrations* (Ed.: S. J. Cyvin), Elsevier: Amsterdam, The Netherlands, **1972**.
[15] E. A. V. Ebsworth, D. W. H. Rankin, S. Cradock, *Structural Methods in Inorganic Chemistry*, Blackwell: Oxford, **1991**.
[16] J. Oláh, F. Blockhuys, T. Veszprémi, C. Van Alsenoy, *Eur. J. Inorg. Chem.* **2006**, 69–77.
[17] R. F. W. Bader, *Atoms in Molecules: A quantum theory*; Oxford University Press: Oxford, **1990**.
[18] J. Saczewski, A. Frontera, M. Gdaniec, Z. Brzozowski, F. Saczewski, P. Tabin, D. Quinonero, P. M. Deya, *Chem. Phys. Lett.* **2006**, *422*, 234–239.
[19] G. M. Day, W. D. S. Motherwell, H. L. Ammon, S. X. M. Boerrigter, R. G. Della Valle, E. Venuti, A. Dzyabchenko, J. D. Dunitz, B. Schweizer, B. P. Van Eijck, P. Erk, J. C. Facelli, V. E. Bazterra, M. B. Ferraro, D. W. M. Hofmann, F. J. J. Leusen, C. Liang, C. C. Pantelides, P. G. Karamertzanis, S. L. Price, T. C. Lewis, H. Nowell, A. Torrisi, H. A. Scheraga, Y. A. Arnautova, M. U. Schmidt, P. Verwer, *Acta Crystallogr. Sect. B* **2005**, *61*, 511–527.
[20] W. D. S. Motherwell, H. L. Ammon, J. D. Dunitz, A. Dzyabchenko, P. Erk, A. Gavezzotti, D. W. M. Hofmann, F. J. J. Leusen, J. P. M. Lommerse, W. T. M. Mooij, S. L. Price, H. Scheraga, B. Schweizer, M. U. Schmidt, B. P. van Eijck, P. Verwer, D. E. Williams, *Acta Crystallogr. Sect. B* **2002**, *58*, 647–661.
[21] J. P. M. Lommerse, W. D. S. Motherwell, H. L. Ammon, J. D. Dunitz, A. Gavezzotti, D. W. M. Hofmann, F. J. J. Leusen, W. T. M. Mooij, S. L. Price, B. Schweizer, M. U. Schmidt, B. P. van Eijck, P. Verwer, D. E. Williams, *Acta Crystallogr. Sect. B* **2000**, *56*, 697–714.
[22] J. D. Dunitz, *Chem. Commun.* **2003**, 545–548.
[23] A. Gavezzoti, *Acc. Chem. Res.* **1994**, *27*, 309–314.
[24] A. Gavezzotti, *J. Am. Chem. Soc.* **1991**, *113*, 4622–4629.
[25] A. Gavezzotti, G. Filippini, *J. Am. Chem. Soc.* **1996**, *118*, 7153–7157.
[26] J. D. Dunitz, G. Filippini, A. Gavezzotti, *Helv. Chim. Acta* **2000**, *83*, 2317–2335.
[27] A. Gavezzotti, *Cryst. Eng. Commun.* **2002**, *4*, 343–347.
[28] J. D. Dunitz, A. Gavezzotti, *Cryst. Growth Des.* **2005**, *5*, 2180–2189.
[29] F. H. Allen, O. Kennard, *Chem. Des. Autom. News* **1993**, *8*, 31–37.
[30] *Cambridge Structural Database*, *Version 5.27*, University of Cambridge, Cambridge, UK.
[31] F. H. Allen, S. E. Harris, R. Taylor, *J. Comput.-Aided Mol. Des.* **1996**, *10*, 247–254.
[32] P. G. Karamertzanis, S. L. Price, *J. Chem. Theory Comput.* **2006**, *2*, 1184–1199.
[33] A. J. Cruz Cabeza, G. M. Day, W. D. S. Motherwell, W. Jones, *Cryst. Growth Des.* **2006**, *6*, 1858–1866.
[34] R. Mayer, D. Decker, S. Bleisch, G. Domschke, *J. Prakt. Chem.* **1987**, *329*, 81–86.
[35] A. V. Zibarev, S. N. Konchenko, G. G. Furin, M. A. Fedotov, *Bull. Acad. Sci. USSR Div. Chem. Sci. (Engl. Transl.)* **1986**, *35*, 1915–1919.
[36] A. Yu. Makarov, I. Yu. Bagryanskaya, F. Blockhuys, C. Van Alsenoy, Yu. V. Gatilov, V. V. Knyazev, A. M. Maksimov, T. V. Mikhalina, V. E. Platonov, M. M. Shakirov, A. V. Zibarev, *Eur. J. Inorg. Chem.* **2003**, 77–88.
[37] I. Yu. Bagryanskaya, Yu. V. Gatilov, A. O. Miller, M. M. Shakirov, A. V. Zibarev, *Heteroat. Chem.* **1994**, *5*, 561–565.
[38] A. Yu. Makarov, K. Tersago, K. Nivesanond, F. Blockhuys, C. Van Alsenoy, M. K. Kovalev, I. Yu. Bagryanskaya, Yu. V. Gatilov, M. M. Shakirov, A. V. Zibarev, *Inorg. Chem.* **2006**, *45*, 2221–2228.
[39] G. M. Sheldrick, *SHELX-97 – Programs for Crystal Structure Analysis (Release 97–2)*, Institute for Inorganic Chemistry, University of Goettingen, Goettingen, Germany.
[40] M. J. Frisch, G. W. Trucks, H. B. Schlegel, G. E. Scuseria, M. A. Robb, J. R. Cheeseman, J. A. Montgomery Jr, T. Vreven, K. N. Kudin, J. C. Burant, J. M. Millam, S. S. Iyengar, J. Tomasi, V. Barone, B. Mennucci, M. Cossi, G. Scalmani, N. Rega, G. A. Petersson, H. Nakatsuji, M. Hada, M. Ehara, K. Toyota, R. Fukuda, J. Hasegawa, M. Ishida, T. Nakajima, Y. Honda, O. Kitao, H. Nakai, M. Klene, X. Li, J. E. Knox, H. P. Hratchian, J. B. Cross, C. Adamo, J. Jaramillo, R. Gomperts, R. E. Stratmann, O. Yazyev, A. J. Austin, R. Cammi, C. Pomelli, J. W. Ochterski, P. Y. Ayala, K. Morokuma, G. A. Voth, P. Salvador, J. J. Dannenberg, V. G. Zakrzewski, S. Dapprich, A. D. Daniels, M. C. Strain, O. Farkas, D. K. Malick, A. D. Rabuck, K. Raghavachari, J. B. Foresman, J. V. Ortiz, Q. Cui, A. G. Baboul, S. Clifford, J. Cioslowski, B. B. Stefanov, G. Liu, A. Liashenko, P. Piskorz, I. Komaromi, R. L. Martin, D. J. Fox, T. Keith, M. A. Al-Laham, C. Y. Peng, A. Nanayakkara, M. Challacombe, P. M. W. Gill, B. Johnson, W. Chen, M. W. Wong, C. Gonzalez, J. A. Pople, *Gaussian 03, Revision B.05*, Gaussian, Inc., Pittsburgh PA, **2003**.
[41] R. F. W. Bader et al., *AIMPAC: A suite of programs for the AIM theory*, McMaster University, Hamilton, Ontario, Canada.

Received: October 31, 2006
Published Online: March 28, 2007

 © 2007 Wiley-VCH Verlag GmbH & Co. KGaA, Weinheim 

DOI: 10.1002/ejic.200601029

# Controlled Synthesis and Characterization of CuO Nanostructures through a Facile Hydrothermal Route in the Presence of Sodium Citrate

**Hong-Mei Xiao,[a,b] Shao-Yun Fu,*[a] Lu-Ping Zhu,[a,b] Yuan-Qing Li,[a,b] and Guo Yang[a,b]**

**Keywords:** Hydrothermal synthesis / Nanostructures / Sodium citrate / Copper complexes

The controlled synthesis of one-dimensional, two dimensional, and three-dimensional CuO nanostructures has been achieved by a hydrothermal process in the presence of sodium citrate (SC) by simply controlling the reaction conditions. When the molar ratio of sodium citrate to $CuSO_4 \cdot 5H_2O$ (represented by SC/$Cu^{2+}$) is below 1.0, 1D CuO nanorods with 30–40 nm diameters and 100–200 nm lengths are formed. In the absence of citrate, 2D flakelike CuO nanostructures with 150–200 nm widths and 300–400 nm lengths are obtained. When the SC/$Cu^{2+}$ ratio is more than 1.0, 3D branchlike CuO nanostructures with lengths of hundreds of nanometers and diameters of 20–100 nm are attained. On the basis of the morphology and X-ray diffraction patterns of the samples, a possible growth mechanism for the CuO nanostructures is proposed. Moreover, it is shown that the optical bandgap energy ($E_g$) of resulting CuO nanostructures can be tuned through morphological control of the CuO nanostructures. Ultraviolet absorption measurements reveal that the estimated bandgap energy of the 1D rodlike, 2D flakelike, and 3D branchlike CuO nanostructures is 2.36, 1.60, and 1.40 eV, respectively.

(© Wiley-VCH Verlag GmbH & Co. KGaA, 69451 Weinheim, Germany, 2007)

## Introduction

Copper monoxide based materials are well known because of their relevance in high-temperature superconductivity and semiconducting antiferromagnetism.[1] CuO is a narrow bandgap ($E_g$ = 1.2 eV) *p*-type semiconductor and has been recognized as an industrially important material for a variety of practical applications, such as catalysis, solar energy conversion, gas sensing and field emission, in batteries, and in magnetic storage media.[2–14] Nanosized CuO may exhibit unique properties that can be significantly different from those of their bulk counterparts, for example, unusual optical, electrical, and catalytic properties, etc.[15a] Therefore, the synthesis and study of CuO nanostructures is both of practical and fundamental importance. In the last two decades, great efforts have been made to synthesize CuO nanostructures with various morphologies by a variety of wet chemical methods.[15–27] Among the various methods developed for fabrication of nanostructured CuO materials, the hydrothermal process has been considered as the most promising route because it is simple and can operate at low-temperatures and in a large scale.[16,19]

Besides the great interest in synthetic methods of the CuO nanostructures, there is a growing interest in the morphological control of CuO nanostructures.[18a,18d,28,29] Wet chemical methods, in which a water/ethanol mixture was used, were reported for the controlled synthesis of 1D CuO nanostructures, namely nanorods and nanoribbons, by controlling reagent concentrations.[18a] Controlled synthesis of CuO nanostructures such as nanoplatelets, nanoleaflets and nanowires was also realized by thermal dehydration of the as-prepared $Cu(OH)_2$ nanostructures in solution or in the solid state.[18d] CuO nanosheets and nanowhiskers were successfully obtained by controlling the liquid–solid reaction on copper surfaces under alkaline and oxidative conditions.[28] As mentioned above, the hydrothermal method is advantageous as it is simple and can operate at low temperatures and in a large scale, and hence should be more promising route for the controlled synthesis of CuO nanostructures, but this has not been reported previously.

It was claimed that semiconductors with bandgap energies in the range from 1 to 3 eV have important applications in solid-state photonic devices.[30] Various CuO nanostructures with different bandgap energies were reported.[15d,27b,29,31] A bandgap of 2.1 eV was reported for CuO nanoparticles,[15d] 2.78 eV for needle-shaped CuO nanocrystals,[31] 3.02 eV for CuO nanoplatelets,[27b] and 2.05 and 2.47 eV for CuO nanoellipsoids and nanosheets, respectively.[29] Moreover, the bandgap energy of CuO nanofibrils was estimated to be 1.67 eV.[32] Obviously, the bandgap energy depends on the morphology of CuO nanostructures. Thus, it can be expected that the bandgap energy of CuO nanostructures can be tuned by controlling the morphology of CuO nanostructures.

[a] Technical Institute of Physics and Chemistry, Chinese Academy of Sciences,
Beijing 100080, China
Fax: +86-10-82543752
E-mail: syfu@cl.cryo.ac.cn
syfu@mail.ipc.ac.cn
[b] Graduate School, Chinese Academy of Sciences,
Beijing 100039, P. R. China

 © 2007 Wiley-VCH Verlag GmbH & Co. KGaA, Weinheim 

It is well known that sodium citrate (SC) is an important biological ligand for metal ions. It has been widely employed as a reductant and capping agent in the synthesis of elemental Ag, Au, and Ag–Au alloy nanoparticles.[33] It also serves as shape controller and stabilizer in the synthesis of $Ni(OH)_2$, calcite, coated CdSe colloids, doughnut-shaped ZnO microparticles, calcium phosphate and CuI crystals.[34] In this study, sodium citrate was employed for the first time for the controllable synthesis of CuO nanostructures with various morphologies using the hydrothermal process.

The controlled synthesis of nanostructured CuO samples with various morphologies was realized using the facile hydrothermal process through changing the molar ratio of sodium citrate to $CuSO_4 \cdot 5H_2O$ only. On the basis of the morphology and X- ray diffraction patterns of the samples, a possible growth mechanism for the CuO nanostructures was proposed. Moreover, UV absorption measurements show that CuO nanostructures display a blue shift of the bandgap relative to bulk CuO material and that the bandgap energy of the CuO nanostructures is tunable by controlling the morphology of the CuO nanostructures.

## Results and Discussion

### The Role of SC on Crystal Structure and Morphology

The control of the phase of the products through the hydrothermal route is shown in Figure 1. Figure 1a presents the XRD pattern of the product obtained without the addition of sodium citrate, and all peaks in the XRD patterns of the sample are consistent with the JCPDS (5–0661) data of copper oxide with a monoclinic phase.[35] When the SC/$Cu^{2+}$ ratio is 1.0, the XRD diffraction peaks can be indexed as the monoclinic phase of CuO (Figure 1b). The atomic ratio of Cu to O was estimated to be 1:1 by SEM-EDS elemental analysis (inset in Figure 1). However, when the SC/$Cu^{2+}$ is increased to 1.3, the XRD pattern of the obtained sample shows that the sample is no longer pure monoclinic CuO – a weak peak of cubic $Cu_2O$ also appears (Figure 1c). The above results indicate that citrate is very important in controlling the phase of the products during the hydrothermal process.

The influence of sodium citrate on the morphology of the CuO products was examined by scanning electron microscopy (SEM) and transmission electron microscopy (TEM). Figure 2a,b shows that the 2D flakelike CuO nanostructures with a width of 150–200 nm and a length of 300–400 nm were obtained by the hydrothermal process without citrate. Moreover, the 1D CuO nanorods with diameters of 30–40 nm and lengths of 100–120 nm were formed when the SC/$Cu^{2+}$ ratio was 1.0, as shown in Figure 2c,d. Figure 2e,f shows the 3D branchlike CuO nanostructures at a SC/$Cu^{2+}$ ratio of 1.3. The branchlike CuO nanostructures consist of sub-branched nanorods with diameters of about 20–100 nm, which radiate from the sides of the main stem of the branchlike CuO nanostructures.

The electron diffraction (ED) patterns of 1D (inset in Figure 2d), 2D (inset in Figure 2b), and 3D (inset in Figure 2f) CuO show that they are all single crystals.

### Formation Mechanism

Figure 3a shows the molecular structure of sodium citrate with three carbonyl groups and one hydroxy group. After the addition of sodium citrate to $CuSO_4 \cdot 5H_2O$, $Cu^{2+}$ and sodium citrate form a complex. Daniele et al. reported that the main component of citrate solutions of $Cu^{2+}$ in the

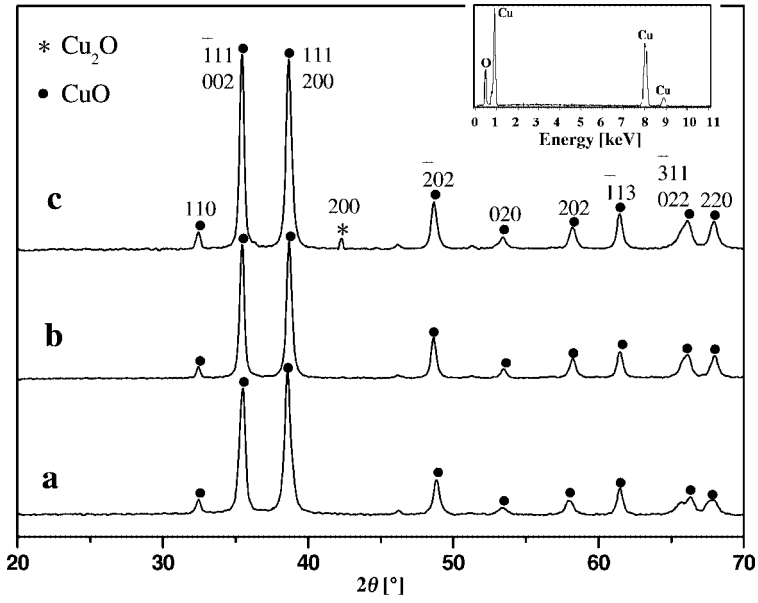


Figure 1. XRD patterns of the samples prepared by the hydrothermal route: (a) without sodium citrate, (b) SC/$Cu^{2+}$ = 1.0, and (c) SC/$Cu^{2+}$ = 1.3. The inset presents the SEM-EDS elemental analysis of the sample with SC/$Cu^{2+}$ = 1.0.

 © 2007 Wiley-VCH Verlag GmbH & Co. KGaA, Weinheim 

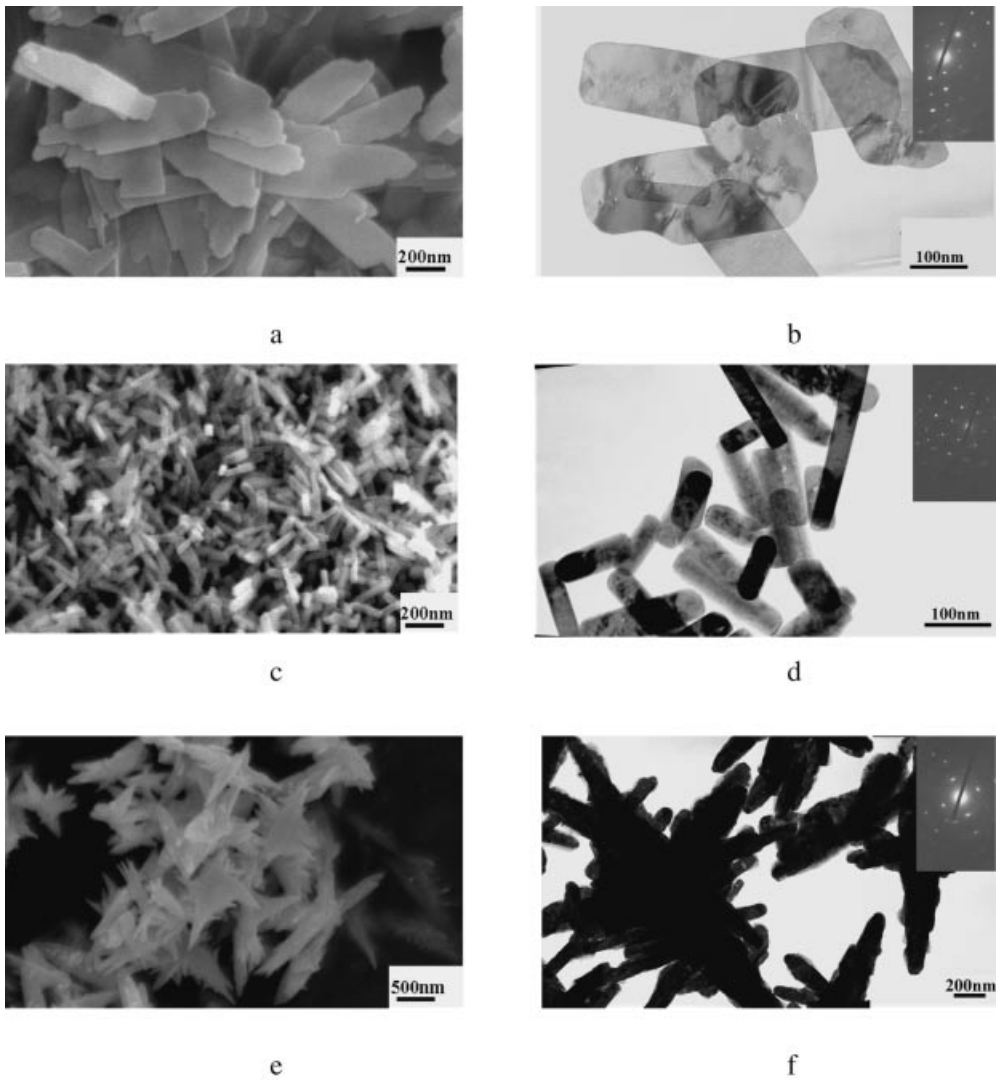


Figure 2. SEM images (a, c, e) and TEM images (b, d, f) of flakelike CuO (a and b, without sodium citrate), rodlike CuO (c and d, $SC/Cu^{2+}$ = 1.0), and branchlike CuO (e and f, $SC/Cu^{2+}$ = 1.3). The corresponding ED patterns of CuO are shown in the insets of the TEM images.

pH range 5–10 is the dimer $[Cu_2(cit)_2]^{4-}$ ($cit^{4-}$ = $[C_6H_4O_7]^{4-}$).[36] When the $SC/Cu^{2+}$ ratio is ≤1.0, the possible molecular structure of the citrate complex of $Cu^{2+}$ (complex **1**) is shown in the Figure 3b. Two $Cu^{2+}$ ions can form two six-membered rings and two seven-membered rings with two $cit^{4-}$ ions. As the $SC/Cu^{2+}$ ratio increases, the amount of complex **1** increases. Upon addition of NaOH solution, the formation of complex **1** delays the formation of $Cu(OH)_2$ nanoparticles and the crystal growth of $Cu(OH)_2$. Furthermore, the formation of complex **1** allows the elongation of the $Cu(OH)_2$ crystals in the direction perpendicular to the principal plane of the complex and elongation is inhibited in other directions. Therefore, the $Cu(OH)_2$ nanoparticles grow preferentially by the oriented attachment of the primary nanoparticles, which is coupled with coordination self-assembly thereby resulting in polycrystalline $Cu(OH)_2$ nanorods. With hydrothermal treatment the $Cu(OH)_2$ nanorods are transformed into CuO nanorods.

When the $SC/Cu^{2+}$ ratio is more than 1.0, another citrate complex of $Cu^{2+}$ (complex **2**, shown in the Figure 3c) appears. One $Cu^{2+}$ ion forms two six-membered rings with two $cit^{4-}$ ions. Strong H-bonds form between the carbonyl group ($-COO^-$) and the hydroxy group (–OH) in complex **2**. As the $SC/Cu^{2+}$ ratio increases, the amount of complex **2** also increases. Upon adding NaOH solution, the H-bonds in complex **2** attacks the hydroxy ion in complex **1** that protrudes out of the edge of the orthorhombic $Cu(OH)_2$ with the corrugated layer structure. Consequently, the orthorhombic $Cu(OH)_2$ is activated, and the dehydrated reaction takes place more easily at the positions attacked by complex **2**. With hydrothermal treatment, the preferential growth of CuO occurs easily in the direction of attack by complex **2**, and branched CuO therefore forms. The XRD patterns of the branched CuO samples show that they are not pure monoclinic CuO samples – a weak peak of cubic $Cu_2O$ also appears (Figure 1c). The appearance of the

 © 2007 Wiley-VCH Verlag GmbH & Co. KGaA, Weinheim 

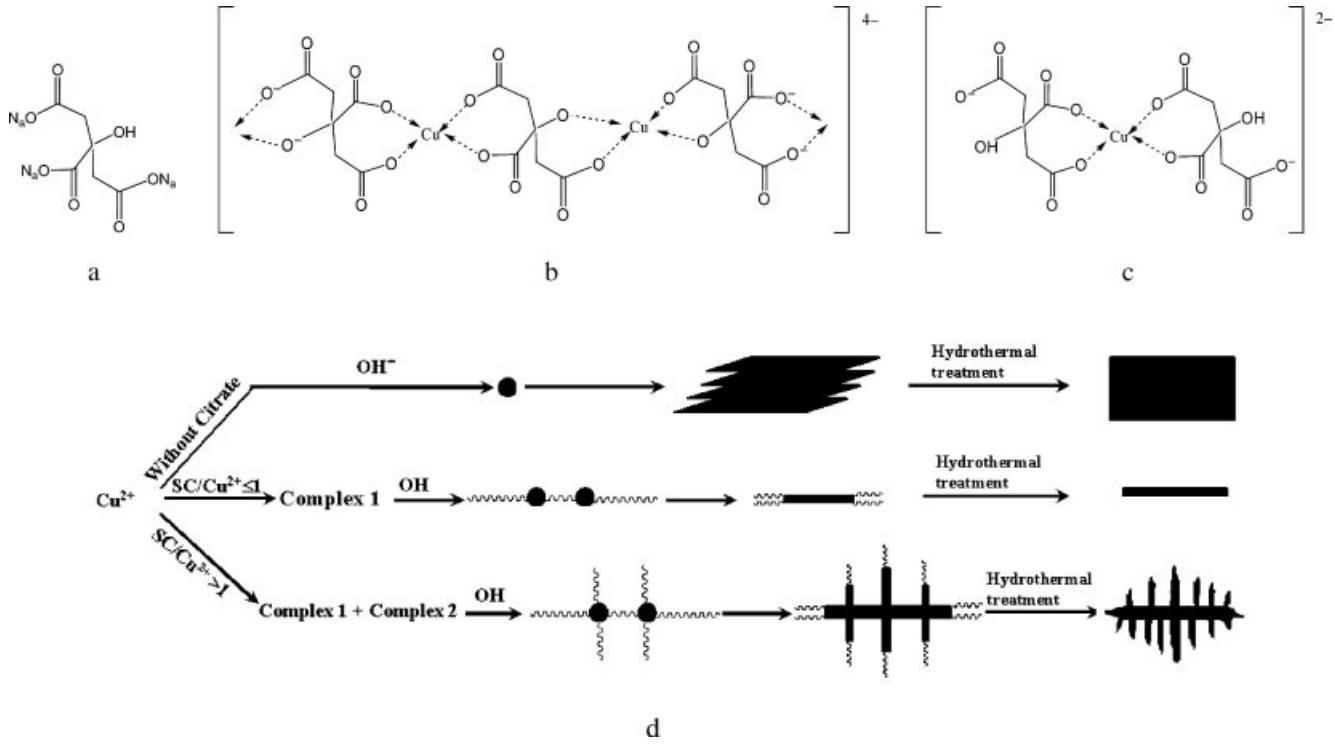


Figure 3. Molecular structures of (a) sodium citrate, (b) complex **1**, and (c) complex **2**, and (d) schematic illustration of the formation process for the as-prepared CuO nanostructures.

$Cu_2O$ phase shows that citrate has a reducing capability. The above-mentioned results indicate that citrate, which acts as a modifying and reducing agent, plays a critical role in the determination of the morphology and in the control of the phase of the CuO nanostructures during the hydrothermal process. Yang et al. reported a similar result in the presence of ethylene glycol.[19]

A schematic diagram of the proposed growth mechanism is shown in Figure 3d. The formation of the flakelike CuO nanostructures without sodium citrate is determined by the internal crystallographic structure of the $Cu(OH)_2$ precursor.[28] After the addition of $OH^-$, orthorhombic $Cu(OH)_2$ first precipitates in solution. The orthorhombic $Cu(OH)_2$ consists of chains in the (001) planes, which are oriented along [100] and characterized by the square-planar coordination of the $Cu^{2+}$ ions with strong H-bonds. By edge-sharing, a sheet of distorted $Cu(OH)_6$ octahedra is formed. The 2D layers of these sheets parallel to the (010) plane are connected through H-bonds. With hydrothermal treatment, orthorhombic $Cu(OH)_2$ transforms into flakelike, monoclinic CuO nanostructures by a dehydration reaction in which the interplanar H-bonds are broken. When the $SC/Cu^{2+}$ ratio is $\leq 1.0$, the formation of complex **1** leads to the formation of the rodlike CuO. When the $SC/Cu^{2+}$ ratio is $\geq 1.0$, the coexistence of complex **1** and complex **2** results in the appearance of branchlike CuO.

## Optical Properties

The UV/Vis absorption spectrum of the CuO samples dispersed in distilled water (the concentration was about 0.02 $mgmL^{-1}$) is presented in Figure 4, which shows a broad absorption peak centered at about 335 nm. In principle, the optical bandgap energy for a semiconductor can be estimated by Equation (1),[37] where $A$ is the absorbance, $K$ is a constant, and $m$ equals 1 for a direct transition.

$$A = \frac{K(hv - E_g)^{m/2}}{hv} \quad (1)$$

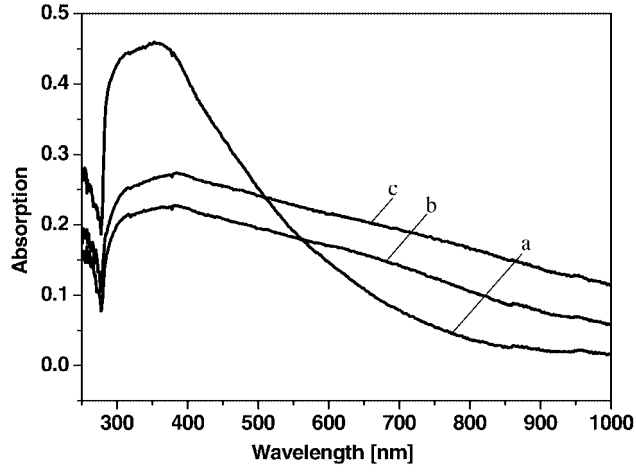


Figure 4. UV/Vis absorption spectrum of (a) rodlike CuO, (b) flakelike CuO, and (c) branchlike CuO.

Figure 5 shows a plot of $(A \cdot E_{phot})^2$ vs. photon energy ($E_{phot}$) for a direct transition. Extrapolation to $A = 0$ gives an absorption edge energy that corresponds to the bandgap energy $E_g$.[38] The bandgap energies of the 1D rodlike, 2D

 © 2007 Wiley-VCH Verlag GmbH & Co. KGaA, Weinheim 

flakelike, and 3D branchlike CuO samples were estimated to be 2.36, 1.60, and 1.40 eV, respectively, which are all larger than that reported for bulk CuO ($E_g$ = 1.2 eV).[18d] The result shows that the bandgap of the CuO samples strongly depends on the morphology of the CuO products. A large enhancement of the bandgap energy of the CuO nanorods is attributed to the well-known quantum size effect for nanostructured semiconductors.[39] In addition, the different values of the bandgap energy of the CuO nanostructures with various morphologies indicates that the bandgap can be tuned by controlling the morphology of the CuO nanostructures.

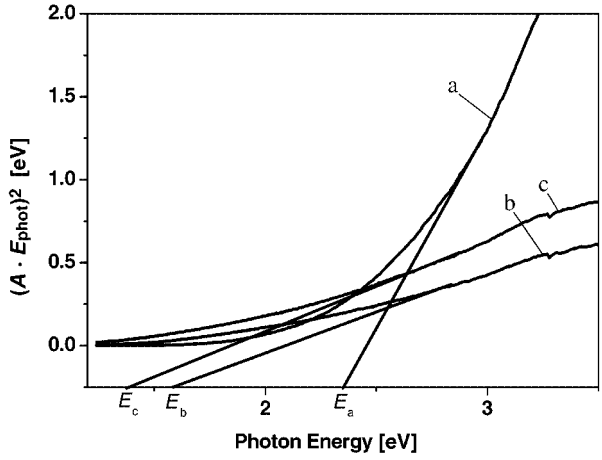


Figure 5. Plot of $(A \cdot E_{phot})^2$ vs. $E_{phot}$ for a direct transition for (a) 1D rodlike CuO, (b) 2D flakelike CuO, and (c) 3D branchlike CuO.

## Conclusions

The controlled synthesis of different nanostructured CuO samples has been achieved by a hydrothermal process in the presence of sodium citrate. It was found that the morphology of the CuO samples was affected by the SC/$Cu^{2+}$ ratio. When the SC/$Cu^{2+}$ ratio was below 1.0, 1D CuO nanorods with 30–40 nm diameters and 100–200 nm lengths were formed. In the absence of citrate, 2D flakelike CuO nanostructures were obtained. However, 3D branchlike CuO nanostructures were attained when the SC/$Cu^{2+}$ ratio was more than 1.0. It is proposed that the formation of different nanostructured CuO is influenced by the different citrate complex of $Cu^{2+}$ formed. The bandgap energies of the 1D rodlike, 2D flakelike, and 3D branchlike CuO nanostructures was estimated to be 2.36, 1.60, and 1.40 eV, respectively, which are all larger than that reported ($E_g$ = 1.2 eV) for bulk CuO material.

## Experimental Section

The chemical reagents including $CuSO_4 \cdot 5H_2O$, sodium citrate ($C_6H_5O_7Na_3 \cdot 2H_2O$), and sodium hydroxide were of analytical grade and used without further purification.

CuO nanostructures were synthesized by a hydrothermal process in the presence of sodium citrate. A typical synthesis of the CuO nanostructures is described as follows: $CuSO_4 \cdot 5H_2O$ (1.3 mmol) and a chosen amount of sodium citrate were dissolved in distilled water (40 mL), and the solution was constantly stirred for 15 min. NaOH (5.3 mmol) was then added to the above solution mixture. After 2.5 h of constant stirring, the final solution was transferred to a 50-mL Teflon-lined autoclave. The autoclave was then sealed in a stainless steel tank and kept at 160 °C for 12 h. The reactor was then naturally cooled to room temperature. The resulting samples were collected and washed with deionized water and dried at 50 °C in air. In order to investigate the influence of sodium citrate on the morphology of the final product, the molar ratio of sodium citrate to $CuSO_4 \cdot 5H_2O$ was changed from 0.1 to 1.5.

X-ray diffraction patterns [RINT 2000 Wilder-angel goniometer with Cu-$K_\alpha$ radiation ($\lambda$ = 1.5406 Å)] and UV/Vis absorption spectra (Lambda 900 spectrometer) were used to characterize the as-obtained CuO nanostructures. The morphology of the CuO nanostructures was studied using transmission electron microscopy (Hitachi H-600 with an accelerating voltage of 200 kV) and scanning electron microscopy (Hitachi S-4300 microscope). The electron diffraction patterns were recorded with a JEOL JEM-2010 transmission electron microscope at an accelerating voltage of 200 kV.

## Acknowledgments

Financial support of this work by the Overseas Outstanding Scholar Foundation of the Chinese Academy of Sciences (Grant Nos.: 2005–1-3 and 2005–2-1) and the National Natural Science Foundation of China (Grant No. 50573090) is gratefully acknowledged.

[1] M. K. Wu, J. R. Ashburn, C. J. Torng, P. H. Hor, R. L. Meng, L. Gao, Z. J. Huang, Y. Q. Wang, C. W. Chu, *Phys. Rev. Lett.* **1987**, *58*, 908–910.
[2] a) J. B. Reitz, E. I. Solomon, *J. Am. Chem. Soc.* **1998**, *120*, 11467–11478; b) K. B. Zhou, R. P. Wang, B. Q. Xu, Y. D. Li, *Nanotechnology* **2006**, *17*, 3939–3943.
[3] F. Lanza, R. Feduzi, J. Fuger, *J. Mater. Res.* **1990**, *5*, 1739–1744.
[4] M. Frietsch, F. Zudock, J. Goschnick, M. Bruns, *Sens. Actuators B* **2000**, *65*, 379–381.
[5] T. Maruyama, *Sol. Energy Mater. Sol. Cells* **1998**, *56*, 85–92.
[6] Y. Jiang, S. Decker, C. Mohs, K. J. Klabunde, *J. Catal.* **1998**, *180*, 24–35.
[7] B. Ao, L. Kummerl, K. Haarer, *Adv. Mater.* **1995**, *7*, 495–499.
[8] C. T. Hsieh, J. M. Chen, H. H. Lin, H. C. Shih, *Appl. Phys. Lett.* **2003**, *83*, 3383–3385.
[9] J. A. Switzer, H. M. Kothari, P. Poizot, S. Nakanishi, E. W. Bohannan, *Nature* **2003**, *425*, 490–493.
[10] A. Chowdhuri, V. Gupta, K. Sreenivas, R. Kumar, S. Mozumdar, P. K. Patanjali, *Appl. Phys. Lett.* **2004**, *84*, 1180–1182.
[11] X. P. Gao, J. L. Bao, G. L. Pan, H. Y. Zhu, P. X. Huang, F. Wu, D. Y. Song, *J. Phys. Chem. B* **2004**, *108*, 5547–5551.
[12] J. Chen, S. Deng, N. Xu, W. Zhang, X. Wen, S. Yang, *Appl. Phys. Lett.* **2003**, *83*, 746–748.
[13] P. Samarasekara, N. T. R. N. Kumara, N. U. S. Yapa, *J. Phys.: Condens. Mater.* **2006**, *18*, 2417–2420.
[14] J. T. Zhang, J. F. Liu, Q. Peng, X. Wang, Y. D. Li, *Chem. Mater.* **2006**, *18*, 867–871.
[15] a) Z. S. Hong, Y. Cao, J. F. Deng, *Mater. Lett.* **2002**, *52*, 34–38; b) S. H. Lee, Y. S. Her, E. Matijevic, *J. Colloid Interface Sci.* **1997**, *186*, 193–202; c) R. Yang, L. Gao, *Chem. Lett.* **2004**, *33*, 1194–1195; d) R. V. Kumar, R. Elgamiel, Y. Diamant, A. Gedanken, *Langmuir* **2001**, *17*, 1406–1410.
[16] a) D. Chen, G. Z. Shen, K. B. Tang, Y. T. Qian, *J. Cryst. Growth* **2003**, *254*, 225–228; b) Y. G. Zhang, S. T. Wang, X. B.

 © 2007 Wiley-VCH Verlag GmbH & Co. KGaA, Weinheim 

Li, L. Y. Chen, Y. T. Qian, Z. D. Zhang, *J. Cryst. Growth* **2006**, *291*, 196–201.
[17] a) C. K. Xu, Y. K. Liu, G. D. Xu, G. G. Wang, *Mater. Res. Bull.* **2002**, *37*, 2365–2372; b) D. Ghoshal, T. K. Maji, T. Mallah, T. H. Lu, G. Mostafa, N. R. Chaudhuri, *Inorg. Chim. Acta* **2005**, *358*, 1027–1033; c) T. Yu, F. C. Cheong, C. H. Sow, *Nanotechnology* **2004**, *15*, 1732–1736; d) W. Wang, Z. Liu, Y. Liu, C. Xu, C. Zheng, G. *Wang*, *Appl. Phys. A* **2003**, *76*, 417–420; e) C. H. Lo, T. T. Tsung, L. C. Chen, *J. Vac. Sci. Technol. B* **2005**, *23*, 2394–2397; f) Q. Liu, Y. Y. Liang, H. J. Liu, J. M. Hong, Z. Xu, *Mater. Chem. Phys.* **2006**, *98*, 519–522.
[18] a) Y. Chang, H. C. Zeng, *Cryst. Growth Des.* **2004**, *4*, 397–402; b) C. L. Zhu, C. N. Chen, L. Y. Hao, Y. Hu, Z. Y. Chen, *J. Cryst. Growth* **2004**, *263*, 473–479; c) C. L. Zhu, C. N. Chen, L. Y. Hao, Y. Hu, Z. Y. Chen, *Solid State Commun.* **2004**, *130*, 681–686; d) C. H. Lu, L. M. Qi, J. H. Yang, D. Y. Zhang, N. Z. Wu, J. M. Ma, *J. Phys. Chem. B* **2004**, *108*, 17825–17831; e) H. W. Hou, Y. Xie, Q. Li, *Cryst. Growth Des.* **2005**, *5*, 201–205.
[19] S. Z. Li, H. Zhang, Y. J. Ji, D. R. Yang, *Nanotechnology* **2004**, *15*, 1428–1432.
[20] a) Z. H. Liang, Y. J. Zhu, *Chem. Lett.* **2005**, *34*, 214–215; b) R. Yang, L. Gao, *Solid State Commun.* **2005**, *134*, 729–733; c) W. W. Wang, Y. J. Zhu, G. F. Cheng, Y. H. Huang, *Mater. Lett.* **2006**, *60*, 609–612; d) Q. Liu, H. J. Liu, Y. Y. Liang, Z. Xu, G. Yin, *Mater. Res. Bull.* **2006**, *41*, 697–702.
[21] a) X. Y. Song, S. X. Sun, W. M. Zhang, H. Y. Yu, W. L. Fan, *J. Phys. Chem. B* **2004**, *108*, 5200–5205; b) M. H. Cao, Y. H. Wang, C. X. Guo, Y. J. Qi, C. W. Hu, E. B. Wang, *J. Nanosci. Nanotechnol.* **2004**, *4*, 824–828; c) Y. D. Huh, S. S. Kweon, *Bulletin Korean Chem. Society* **2005**, *26*, 2054–2056.
[22] M. H. Cao, C. W. Hu, Y. H. Wang, Y. H. Guo, C. X. Guo, E. B. Wang, *Chem. Commun.* **2003**, *15*, 1884–1885.
[23] a) G. H. Du, G. V. Tendeloo, *Chem. Phys. Lett.* **2004**, *393*, 64–69; b) X. Y. Song, H. Y. Yu, S. X. Sun, *J. Colloid Interface. Sci.* **2005**, *289*, 588–591.
[24] Y. Y. Xu, D. R. Chen, X. L. Jiao, *J. Phys. Chem. B* **2005**, *109*, 13561–13566.
[25] L. Z. Zhang, J. C. Yu, A. W. Xu, Q. Li, K. W. Kwong, S. H. Yu, *J. Cryst. Growth* **2004**, *266*, 545–551.
[26] B. Liu, H. C. Zeng, *J. Am. Chem. Soc.* **2004**, *126*, 16744–16746.
[27] a) Z. H. Liang, Y. J. Zhu, *Chem. Lett.* **2004**, *33*, 1314–1315; b) G. F. Zou, H. Li, D. W. Zhang, K. Xiong, C. Dong, Y. T. Qian, *J. Phys. Chem. B* **2006**, *110*, 1632–1637.
[28] W. X. Zhang, X. G. Wen, S. H. Yang, *Inorg. Chem.* **2003**, *42*, 5005–5014.
[29] J. P. Liu, X. T. Huang, Y. Y. Li, K. M. Sulieman, X. He, F. L. Sun, *Cryst. Growth Des.* **2006**, *6*, 1690–1696.
[30] A. J. Heeger, *J. Phys. Chem. B* **2001**, *105*, 8475–8491.
[31] J. W. Zhu, H. Q. Chen, H. B. Liu, X. J. Yang, L. D. Lu, X. Wang, *Mater. Sci. Eng., A* **2004**, *384*, 172–176.
[32] H. H. Lin, C. Y. Wang, H. C. Shih, *J. Appl. Phys.* **2004**, *95*, 5889–5895.
[33] a) Z. S. Pillai, P. V. Kamat, *J. Phys. Chem. B* **2004**, *108*, 945–951; b) K. R. Brown, D. G. Walter, M. Natan, *Chem. Mater.* **2000**, *12*, 306–313; c) M. P. Mallin, C. Murphy, *Nano Lett.* **2002**, *2*, 1235–1237; d) G. J. Zhou, M. K. Lu, Z. S. Yang, H. P. Zhang, Y. Y. Zhou, S. M. Wang, S. F. Wang, A. Y. Zhang, *J. Cryst. Growth* **2006**, *289*, 255–259.
[34] a) M. Meyer, A. Bée, D. Talbot, V. Cabuil, J. M. Boyer, B. Répetti, R. Garrigos, *J. Colloid Interface Sci.* **2004**, *277*, 309–315; b) F. C. Meldrum, S. T. Hyde, *J. Cryst. Growth* **2001**, *231*, 544–558; c) Y. Wang, Z. Y. Tang, M. A. Correa-Duarte, I. Pastoriza-Santos, M. Giersig, N. A. Kotov, L. M. Liz-Marzan, *J. Phys. Chem. B* **2004**, *108*, 15461–15469; d) J. B. Liang, J. W. Liu, Q. Xie, S. Bai, W. C. Yu, Y. T. Qian, *J. Phys. Chem. B* **2005**, *109*, 9463–9467; e) Q. Y. Zhang, Y. Leng, H. J. Fan, J. Y. Chen, X. D. Zhang, *Key Eng. Mater.* **2006**, *309–311*, 387–390; f) L. P. Zhang, F. Guo, X. Z. Liu, *Mater. Res. Bull.* **2006**, *41*, 905–908.
[35] Joint Committee on Powder Diffraction Standards. Diffraction Data File No. 5–661; JCPDS International Center for Diffraction Data, Pennsylvania, **1991**.
[36] P. G. Daniele, G. Ostacoli, O. Zerbinati, S. Sammartano, *Transition Met. Chem.* **1988**, *13*, 87–91.
[37] B. Subramanian, C. Sanjeeviraja, M. Jayachandran, *J. Cryst. Growth* **2002**, *234*, 421–426.
[38] S. Tsunekawa, T. Fukuda, A. Kasuya, *J. Appl. Phys.* **2000**, *87*, 1318–1321.
[39] J. P. Yang, F. C. Meldrum, J. H. Fendler, *J. Phys. Chem.* **1995**, *99*, 5500–5504.

Received: November 2, 2006
Published Online: March 30, 2007

 © 2007 Wiley-VCH Verlag GmbH & Co. KGaA, Weinheim 

DOI: 10.1002/ejic.200601144

# Synthesis and Study of the Crystallographic and Magnetic Structure of $HoFeMnO_5$

**Angel Muñoz,*[a] José A. Alonso,[b] María J. Martínez-Lope,[b] and José L. Martínez[b]**

**Keywords:** Ferrimagnetic structure / Superexchange interactions / Neutron diffraction / High oxygen pressure

A new oxide of stoichiometry $HoFeMnO_5$ has been obtained by replacing $Mn^{3+}$ cations by $Fe^{3+}$ in the parent oxide $HoMn_2O_5$. The crystallographic and magnetic structures have been analyzed by neutron powder diffraction (NPD), which complements susceptibility and magnetization measurements. $HoFeMnO_5$ is orthorhombic, belonging to the *Pbam* space group like the parent compound. The crystal structure contains infinite chains of edge-sharing $Mn^{4+}O_6$ octahedra, interconnected by dimer units of $Fe^{3+}O_5$ square pyramids. In comparison with $HoMn_2O_5$, containing elongated $Mn^{3+}O_6$ pyramids, the $Fe^{3+}O_5$ units are flattened. The magnetization measurements show that $HoFeMnO_5$ presents a long-range magnetic order below $T_C \approx 153$ K. An NPD study shows that $HoFeMnO_5$ adopts a collinear ferrimagnetic structure: each of the $Mn^{4+}$ and $Fe^{3+}$ sublattices are ferromagnetically coupled, and the coupling between the two sublattices is antiferromagnetic; the magnetic moments are oriented along the *c* direction. The $Ho^{3+}$ cations also order below $T_C$, but with a very small magnetic moment; the $Ho^{3+}$ moments are parallel to the $Fe^{3+}$ magnetic sublattice. At $T = 2.7$ K, the ordered magnetic moments for the $Mn^{4+}$, $Fe^{3+}$ and $Ho^{3+}$ ions are 1.31(6), 3.20(10) and 0.36(7) $\mu_B$, respectively. In comparison with $ErFeMnO_5$, where $Er^{3+}$ cations are fully ordered at low temperatures, in $HoFeMnO_5$ there is a frustration concerning the long-range order of the $Ho^{3+}$ cations, which remain virtually paramagnetic over the whole temperature range.

(© Wiley-VCH Verlag GmbH & Co. KGaA, 69451 Weinheim, Germany, 2007)

## Introduction

In the last years, the interest in some rare-earth manganese oxide families such as $RMn_2O_5$ (R = rare earth, Y or Bi) has been revitalized, as different studies have shown a strong coupling between magnetism and ferroelectricity, also in the oxides that are in the select club of magnetoferroelectric materials.[1–6] For instance, in $TbMn_2O_5$, the application of an oscillating magnetic field can reverse the direction of the electrical polarization.[2,3,6] As it has been demonstrated for $(Tb,Dy,Ho)Mn_2O_5$,[5,6] an external magnetic field also gives rise to a strong increase in the dielectric constant near the order temperature $T_N$.

$RMn_2O_5$ compounds crystallize in an orthorhombic crystallographic structure having space group *Pbam*. The 4*f* and 4*h* sites are occupied by the $Mn^{4+}$ and $Mn^{3+}$ cations, respectively.[7–11] The structure contains infinite chains of edge-sharing $Mn^{4+}O_6$ octahedra arranged along the *c* axis; the chains are corner-linked by pairs of $Mn^{3+}O_5$ edge-sharing pyramids. Below $T_N$, in the temperature interval 39–45 K, most of the $RMn_2O_5$ compounds become magnetically ordered according to an incommensurate magnetic structure[12,13] defined by the propagation vector $\mathbf{k} = (k_x,0,k_z)$, with $k_x \approx 0.5$. A few compounds of this family present a commensurate magnetic structure such as $BiMn_2O_5$, $\mathbf{k} = (1/2,0,1/2)$,[14] and $LaMn_2O_5$, $\mathbf{k} = (0,0,1/2)$.[15] A few degrees below $T_N$, the onset of a ferroelectric transition takes place, with the polarization vector **P** oriented along the *b* axis. Very recently, it has been reported that $(Ho,Tb,Er,Y)Mn_2O_5$ presents a magnetic transition to a commensurate structure at the ferroelectric transition temperature $T_C$. Furthermore, on decreasing temperature, another magnetic transition to an incommensurate structure happens, which coincides with an anomaly in the dielectric constant.[4,16–19]

Recently, a new series of rare-earth manganese oxides has been derived from $RMn_2O_5$ by replacing $Mn^{3+}$ by $Fe^{3+}$ cations. The crystallographic structure and the magnetic behaviour of $YFeMnO_5$ and $ErFeMnO_5$ have already been reported.[20,21] The sample preparation requires a high-oxygen-pressure treatment, in order to stabilize $Mn^{4+}$ cations into the crystal structure. These novel $RFeMnO_5$ compounds keep the orthorhombic structure (space group *Pbam*) of the parent $RMn_2O_5$ oxides. However, important changes are observed in the magnetic behaviour, as both $YFeMnO_5$ and $ErFeMnO_5$ display ferrimagnetic behaviour below $T_C \approx 165$ K. The magnetic moments of the $Mn^{4+}$ and $Fe^{3+}$ cations are antiferromagnetically coupled along the *c* direction.

[a] Dpto. de Física Aplicada, EPS, Universidad Carlos III, Avda. Universidad 30, 28911, Leganés-Madrid, Spain
E-mail: angel.munoz@uc3m.es
[b] Instituto de Ciencia de Materiales de Madrid, CSIC, 28049, Cantoblanco-Madrid, Spain

 © 2007 Wiley-VCH Verlag GmbH & Co. KGaA, Weinheim 

In this paper we describe a new phase of this family, $HoFeMnO_5$, for which we report the crystallographic structure and the magnetic properties, analyzed by neutron powder diffraction (NPD); the magnetic behaviour is also investigated by macroscopic magnetization measurements.

## Results

### Sample Preparation

Stoichiometric amounts of analytical grade $Ho_2O_3$, $FeC_2O_4{\cdot}2H_2O$ and $MnCO_3$ were dissolved in citric acid; the solvent was slowly evaporated, and the obtained organic resin was dried at 120 °C and slowly decomposed at temperatures up to 600 °C in air. High-oxygen-pressure treatments were performed in a VAS furnace. About 2 g of the precursor powder were placed in a gold can during the oxygenation process. The sample was slowly heated up to 900 °C at a final pressure of 200 bar and held at this temperature for 12 h. The product was finally cooled, under pressure, at 300 °C/h, down to room temperature. Finally, the oxygen pressure was slowly released.

### Magnetic Susceptibility and Magnetization

The magnetic measurements were performed in a commercial SQUID magnetometer from Quantum Design. The dc magnetic susceptibility was measured both in zero-field cooling (ZFC) and field cooling (FC) conditions in the temperature intervals $1.8 < T < 400$ K and $1.8 < T < 328$ K, respectively, under a magnetic field of 1 kOe. Ac magnetic susceptibility measurements were also carried out in the temperature range 50–250 K, the frequencies of the transversal oscillating magnetic field being 0.32, 7, 33, 321 and 997 Hz. As regards the isothermal magnetization curves, different hysteresis cycles were obtained at $T$ = 3, 50 and 225 K for a magnetic field ranging from –50 kOe to 50 kOe.

### Neutron Diffraction Data

The NPD experiments were carried out at the Institut Laue-Langevin, Grenoble (France). For the study of the crystallographic structure, two patterns, one at room temperature and one at 10 K were collected with the high-resolution D2B diffractometer, at a wavelength of 1.594 Å. For the magnetic structure resolution and the study of its thermal evolution, a set of NPD patterns were acquired with the high-flux D20 diffractometer at $\lambda$ = 2.418 Å and in the temperature interval $2.7 < T < 267$ K. The refinement of the different NPD diagrams was performed by the Rietveld method[22] with the Fullprof program.[23] A pseudo-Voigt function was used for the simulation of the profile of the Bragg peaks and a fifth-degree polynomial function was used for the fitting of the background. The coherent scattering lengths for Ho, Fe, Mn and O were 8.01, 9.45, –3.73 and 5.803 fm, respectively.

### Results of Magnetic Measurements

The ZFC and FC curves of the dc susceptibility are presented in Figure 1. Both curves coincide at high temperature, but below $T_C \approx 153$ K the two curves split at the onset of a magnetic ordering process. Below $T_C$, the ZFC susceptibility curve steadily increases and exhibits a maximum at $T$ = 100 K, which suggests the presence of antiferromagnetic interactions, and then a minimum at around 50 K, where a new change in the slope of the ZFC susceptibility indicates the presence of a remnant magnetization. The FC susceptibility curve continuously increases below $T_C$, also displaying a change in the slope at around 50 K. In the isothermal magnetization curves represented in Figure 2, a narrow hysteresis loop is observed at $T$ = 50 K and $T$ = 2 K with a remnant magnetization of 0.11 and 0.32 $\mu_B$ per formula, respectively. A maximum magnetization of 6.5 $\mu_B$/f.u. is reached for the maximum applied field of 5 T. The presence of a remnant magnetization is in good agreement with the thermal behaviour of the dc susceptibility below $T_C$ and with the ferrimagnetic order determined from the neutron diffraction data. At $T$ = 225 K, the isothermal magnetization curve presents linear behaviour, as it corresponds to a paramagnetic state.

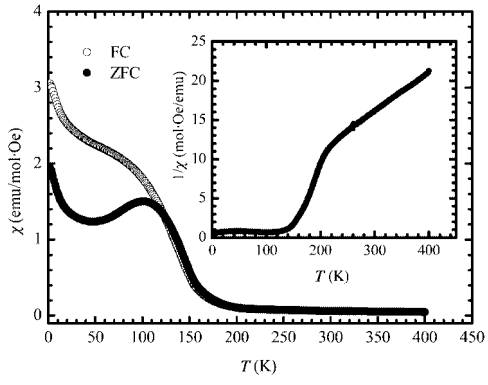


Figure 1. Thermal evolution of the field cooling (FC) and zero-field cooling (ZFC) dc susceptibility. Inset: inverse of the susceptibility (ZFC data).

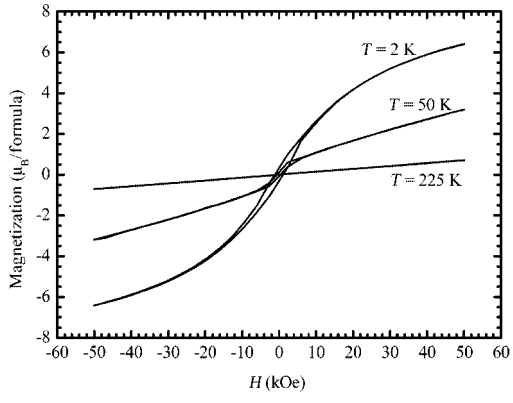


Figure 2. Magnetization vs. magnetic field isotherms at $T$ = 2, 50 and 225 K.

 © 2007 Wiley-VCH Verlag GmbH & Co. KGaA, Weinheim 

As it can be seen in the inset of Figure 1, the inverse of the susceptibility shows linear behaviour at high temperature; in the temperature interval $263 < T < 395$ K, the reciprocal susceptibility is fitted to a Curie–Weiss law, yielding a paramagnetic temperature $\Theta_P = -28.5(5)$ K and an effective paramagnetic moment of 12.16(1) $\mu_B$/f.u. The theoretical effective magnetic moment can be estimated by considering the expression $\mu_{eff} = [\mu_B(Mn^{4+})^2 + \mu_B(Fe^{3+})^2 + \mu_B(Ho^{3+})^2]^{1/2}$; the effective magnetic moments for spin-only $Mn^{4+}$, high-spin $Fe^{3+}$ and $Ho^{3+}$ ($^5I_8$ ground state configuration) are 3.87, 5.92 and 10.60 $\mu_B$, respectively, which implies an effective magnetic moment of 12.74 $\mu_B$, in good agreement with the experimental value.

The thermal evolution of the ac susceptibility is shown in Figure 3 for temperatures ranging from 50 to 250 K at different frequencies. $\chi'$ and $\chi''$ represent the real (in-phase) and imaginary (out-of-phase) components of the susceptibility, respectively. Both $\chi'$ and $\chi''$ present only one maximum at around the long-range ordering temperature $T_C \approx 153$ K, and the height of the peak decreases with increasing frequency; in both cases, the position of the maximum does not seem to shift upon varying the frequency.

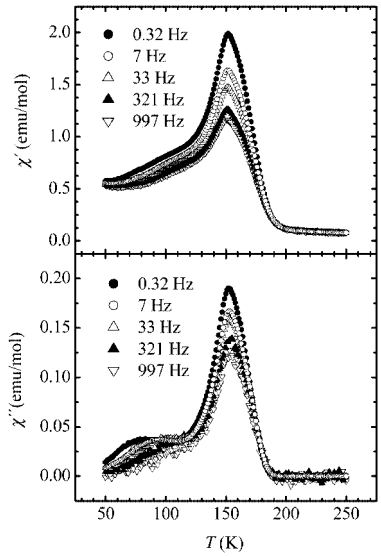


Figure 3. Thermal evolution of the real and imaginary parts of the ac susceptibility.

## Crystallographic Structure from Neutron Powder Diffraction

For the refinement of the crystallographic structure, two high-resolution NPD patterns, one acquired at room temperature and the other at $T = 10$ K, with $\lambda = 1.594$ Å were used. In the refinement carried out with the room temperature NPD pattern, all the Bragg peaks of the diagram could be indexed in the orthorhombic space group *Pbam*. Firstly, it was assumed that the Mn and Fe atoms occupy the 4*f* (*0*,1/2,*z*) and 4*h* (*x*,*y*,1/2) sites, respectively; however, a better fit was obtained if a certain anti-site disorder was allowed between Mn and Fe atoms. The lattice parameters obtained in the refinement and the corresponding discrepancy factors are shown in Table 1. In Table 2, the atomic positions and the occupancy of the Mn/Fe cations are presented. At room temperature, the 4*f* site is occupied at 94(2)% by the Mn atoms [6(2)% of Fe atoms]; in contrast, in the 4*h* site the disorder is slightly higher, since it is occupied at 86(2)% and 14(2)% by Fe and Mn atoms, respectively. Since a high oxygen pressure was necessary for the sample preparation, the possible deficiency in oxygen has also been checked by refining the oxygen occupancy at room temperature. As it is shown in Table 2, a small oxygen deficiency seems to ex-

Table 1. Lattice parameters and reliability factors of the Rietveld refinements from NPD data with $\lambda = 1.594$ Å.

| | Room temp. | $T = 10$ K |
|---|---|---|
| *a* (Å) | 7.2793(4) | 7.2652(5) |
| *b* (Å) | 8.5060(4) | 8.4938(5) |
| *c* (Å) | 5.6921(3) | 5.6851(3) |
| Vol. (Å$^3$) | 352.44(3) | 350.82(4) |
| $R_P$ (%) | 2.7 | 3.1 |
| $R_{wp}$ (%) | 3.4 | 4.0 |
| $R_B$ (%) | 6.5 | 8.0 |
| $\chi^2$ | 1.4 | 1.8 |

Table 2. Atomic parameters after the refinement of the crystallographic structure from NPD data with $\lambda = 1.594$ Å. Sites: Ho and O2 in 4*g* (*x*,*y*,0), Mn in 4*f* (0,1/2,*z*), Fe and O3 in 4*h* (*x*,*y*,1/2), O1 in 4*e* (0,0,*z*) and O4 in 8*i* (*x*,*y*,*z*).

| | | Room temp. | $T = 10$ K |
|---|---|---|---|
| Ho | *x* | 0.1353(5) | 0.1350(6) |
| | *y* | 0.1704(4) | 0.1701(4) |
| | *B* (Å$^2$) | 0.48(6) | 0.19(5) |
| | z | 0.264(2) | 0.272(2) |
| Mn/Fe′ | *B* (Å$^2$) | 0.3(2) | 0.19(5) |
| | Occup. (%) | 0.94(2)/0.06(2) | 0.98(2)/0.02(2) |
| | *x* | 0.3892(4) | 0.3905(5) |
| Fe/Mn′ | *y* | 0.3543(4) | 0.3546(4) |
| | *B* (Å$^2$) | 0.32(8) | 019(5) |
| | Occup. (%) | 0.86(2)/0.14(2) | 0.88(2)/0.12(2) |
| | *z* | 0.2660(13) | 0.259(2) |
| O1 | *B* (Å$^2$) | 0.44(8) | 0.78(4) |
| | Occup. (%) | 92(2) | 92(2) |
| | *x* | 0.1598(8) | 0.1623(8) |
| O2 | *z* | 0.4449(5) | 0.4461(6) |
| | *B* (Å$^2$) | 1.13(10) | 0.78(4) |
| | Occup. (%) | 99(2) | 99(2) |
| | *x* | 0.1465(8) | 0.1456(9) |
| O3 | *y* | 0.4322(6) | 0.4349(6) |
| | *B* (Å$^2$) | 0.99(9) | 0.78(4) |
| | Occup. (%) | 92(2) | 92(2) |
| | *x* | 0.3939(4) | 0.3932(5) |
| O4 | *y* | 0.2046(4) | 0.2057(4) |
| | *z* | 0.2413(6) | 0.2397(7) |
| | *B* (Å$^2$) | 1.07(6) | 0.78(4) |
| | Occup. (%) | 96(2) | 96(2) |

 © 2007 Wiley-VCH Verlag GmbH & Co. KGaA, Weinheim 

ist, which is as high as 8(2)% for the O1 and O3 atoms. The crystallographic formula refined from NPD data is $HoFe_{0.92(2)}Mn_{1.08(2)}O_{4.74(10)}$, yielding a slightly Mn-rich compound with respect to the nominal stoichiometry. The most characteristic interatomic distances and bond angles are presented in Table 3. The good agreement between the experimental and calculated NPD patterns in the final Rietveld fit can be observed in Figure 4a.

Table 3. Selected interatomic distances (Å) and bond angles (°).

| | Room temp. | $T$ = 10 K |
|---|---|---|
| Mn–O2 (×2) | 1.955(11) | 1.999(9) |
| Mn–O3 (×2) | 1.811(11) | 1.761(9) |
| Mn–O4 (×2) | 1.908(3) | 1.921(4) |
| <Mn–O> | 1.891(9) | 1.894(7) |
| Fe–O1 (×2) | 1.9906(6) | 2.000(9) |
| Fe–O3 | 1.887(7) | 1.904(7) |
| Fe–O4 (×2) | 1.947(4) | 1.947(4) |
| <Fe–O> | 1.952(5) | 1.968(7) |
| Ho···O1 (×2) | 2.316(6) | 2.284(7) |
| Ho···O2 | 2.341(6) | 2.353(6) |
| Ho···O2 | 2.430(6) | 2.406(7) |
| Ho···O4 (×2) | 2.348(4) | 2.339(5) |
| Ho···O4 (×2) | 2.471(4) | 2.460(5) |
| <Ho···O> | 2.383(5) | 2.373(6) |
| Mn···Mn | 3.00(2) | 3.10(2) |
| Mn···Mn | 2.69(2) | 2.59(2) |
| Fe···Fe | 2.956(5) | 2.938(5) |
| Fe–O1–Fe | 95.9(3) | 94.0(4) |
| Mn–O2–Mn | 100.2(9) | 101.5(8) |
| Mn–O3–Mn | 96.0(9) | 94.6(9) |
| Mn–O3–Fe | 131.5(5) | 132.3(5) |
| Mn–O4–Fe | 123.6(4) | 121.4(3) |

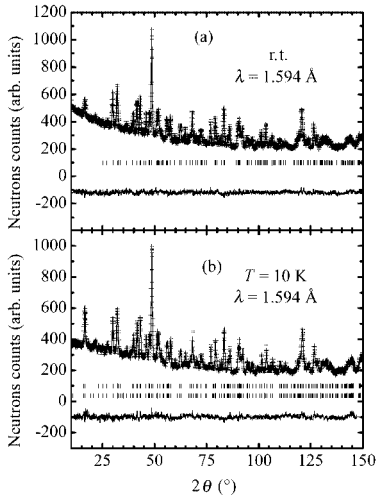


Figure 4. Comparison of the experimental (crosses), calculated (solid line) and difference (at the bottom) NPD patterns. (a) At room temperature; the tick marks correspond to the positions of the allowed Bragg reflections. (b) At $T$ = 10 K; the first and second rows of tick marks correspond to the nuclear and magnetic reflections, respectively.

The crystallographic structure at $T$ = 10 K has also been refined from high-resolution NPD data in the same orthorhombic space group *Pbam*. At this temperature $HoFeMnO_5$ is magnetically ordered; therefore, the magnetic contribution to the NPD pattern was taken into consideration. After including the magnetic structure described below, the refinement yielded the lattice parameters, atomic positions and discrepancy factors also included in Table 1 and Table 2; the most important interatomic distances and bond angles are listed in Table 3. As it can be observed in Table 2, the anti-site disorder between the Fe and Mn cations is very similar to that found at room temperature. The experimental and calculated NPD patterns are compared in Figure 4b.

In Figure 5, a projection of the crystallographic structure along the *c* axis is presented. $Mn^{4+}$ cations (4*f* site) are at the centre of $Mn^{4+}O_6$ octahedra which share edges via the equatorial O2 and O3 oxygen atoms, forming infinite chains along the *c* axis. The $Fe^{3+}$ cations (4*h* site) are coordinated to five closer neighbouring oxygen atoms in a pyramidal configuration; in the $Fe^{3+}O_5$ pyramids the O3 oxygen atom is in the axial position and the O1 and O4 oxygen atoms are in the equatorial plane. Two $Fe^{3+}O_5$ pyramids, doubly linked by O1 oxygen atoms, form a dimer unit $Fe_2O_{10}$. In this way, four $Mn^{4+}O_6$ octahedral chains are linked by these dimer units through the O3 and O4 oxygen atoms.

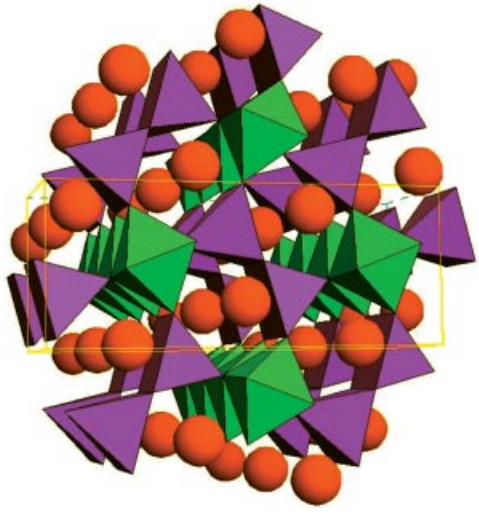

Figure 5. View of the crystallographic structure of $HoFeMnO_5$ along the *c* axis. Octahedra and tetragonal pyramids correspond to $Mn^{4+}O_6$ and $Fe^{3+}O_5$ polyhedra, respectively. The octahedra share edges, forming infinite chains along the *c* axis. The pyramids form dimer units, linking together the chains of octahedra. The spheres represent the Ho atoms.

### Determination of the Magnetic Structure

The determination of the magnetic structure and the analysis of its thermal evolution was carried out from a set of NPD patterns acquired in the temperature range from 267.0 to 2.7 K. The thermal evolution of the different NPD patterns is displayed in Figure 6; upon cooling below 153 K, the intensities of some Bragg peaks start to increase, indicating the onset of a magnetic order, in good agreement with the magnetization measurements. The magnetic struc-

 © 2007 Wiley-VCH Verlag GmbH & Co. KGaA, Weinheim 

ture is defined by the propagation vector **k** = 0, since there are no magnetic peaks outside the permitted Bragg positions. The thermal evolution of the integrated intensity for some Bragg reflections is shown in Figure 7; in the thermal evolution of the intensity, no changes are observed that could suggest a variation in the magnetic arrangement.

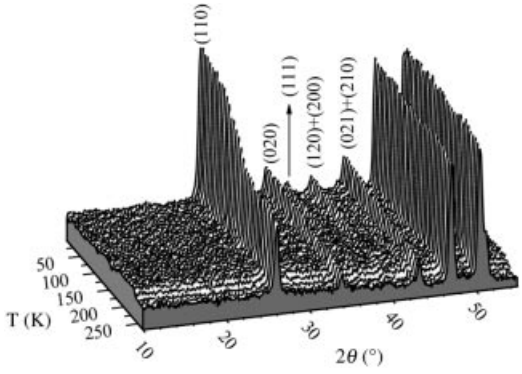


Figure 6. Thermal dependence of the NPD patterns collected with $\lambda$ = 2.418 Å.

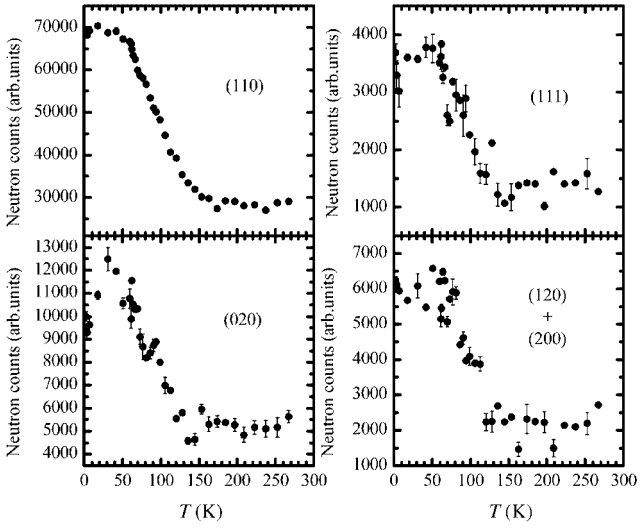


Figure 7. Thermal evolution of the integrated intensity of some magnetic reflections.

The different magnetic structure models, compatible with the crystallographic structure of the compound, have been determined from the representation analysis technique of group theory, by following the method described by Bertaut.[24] The possible magnetic structures corresponding to Mn (4*f* site), Fe (4*h* site) and Ho (4*g* site) atoms are those given in ref.[20]. The Mn atoms are labelled as 1(0,1/2,*z*), 2(1/2,0,–*z*), 3(0,1/2,–*z*) and 4(1/2,0,*z*); the notation for the Fe atoms is 5(*x*,*y*,1/2), 6(–*x*,–*y*,1/2), 7(–*x* + 1/2,*y* + 1/2,1/2) and 8(*x* + 1/2, –*y* + 1/2,1/2); the notation for the Ho atoms is 9(*x*,*y*,0), 10(–*x*,–*y*,0), 11(–*x* + 1/2,*y* + 1/2,0) and 12(*x* + 1/2, –*y* + 1/2,0).

After checking the different magnetic structure models, the solution that gives a better agreement with the experimental results corresponds to the basis vectors (0,0,$F_z$), (0,0,$F'_z$), and (0,0,$F''_z$) for the $Mn^{4+}$, $Fe^{3+}$ and $Ho^{3+}$ ions, respectively. For the $Fe^{3+}$ and $Ho^{3+}$ cations, the moments are oriented along the positive *z* direction, whereas for $Mn^{4+}$cations, the magnetic moments are directed along the negative *z* direction, in a global ferrimagnetic structure. At *T* = 2.7 K the magnetic moment values for $Mn^{4+}$, $Fe^{3+}$ and $Ho^{3+}$ ions are 1.31(6), 3.20(1) and 0.36(7) $\mu_B$, respectively (see Table 4). The good agreement between the experimental and calculated NPD patterns after the fitting of the magnetic structure at *T* = 2.7 K is shown in Figure 8; the discrepancy factors of the refinement are displayed in Table 4. A schematic plot of the ferrimagnetic order is presented in Figure 9. The thermal evolution of the magnetic moments for the magnetic ions is displayed in Figure 10; according to this figure, all the magnetic ions become ordered at the same temperature, but the magnetic moment of the $Ho^{3+}$ cations remains nearly constant (around 0.40 $\mu_B$) over the whole temperature range. As regards the magnetic moments of the $Mn^{4+}$ and $Fe^{3+}$ cations, they seem to reach saturation at around 60 K.

Table 4. Results obtained in the refinement of the magnetic structure at *T* = 2.7 K (angular range $2\Theta$ = 8–86°). Discrep. factors: $R_B$ = 3.9%, $R_{Mag}$ = 9.9%, $\chi^2$ = 3.1.

| | $Mn^{4+}$ | $Fe^{3+}$ | $Ho^{3+}$ |
|---|---|---|---|
| Solution | (0,0,$F_z$) | (0,0,$F'_z$) | (0,0,$F''_z$) |
| *z* Component ($\mu_B$) | –1.31(6) | 3.20(10) | 0.36(7) |

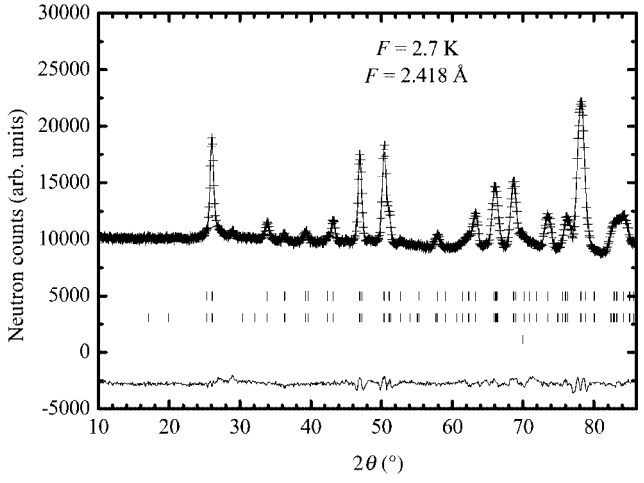


Figure 8. Experimental (crosses) and calculated (solid line) NPD patterns at *T* = 2.7 K. The first row of tick marks corresponds to the nuclear Bragg reflections and the second one to the magnetic reflections.

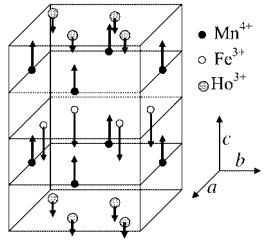


Figure 9. A view of the magnetic structure.

 © 2007 Wiley-VCH Verlag GmbH & Co. KGaA, Weinheim 

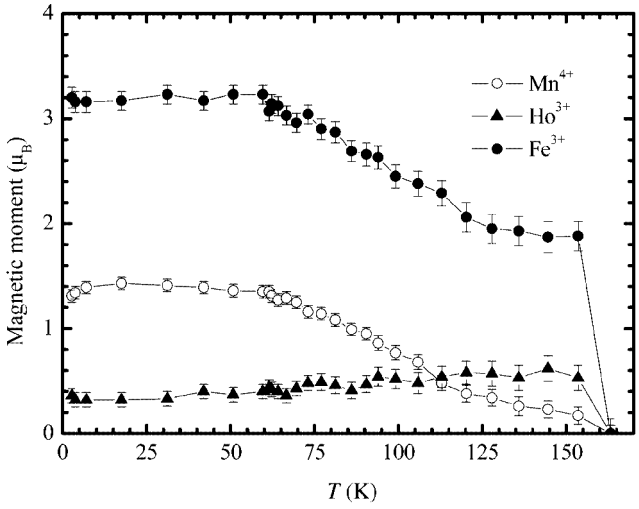


Figure 10. Thermal evolution of the module of the magnetic moments.

The thermal evolution of the lattice parameters has also been determined; as shown in Figure 11, the unit-cell volume progressively shrinks down to 130 K, and in the magnetically ordered regime, the volume remains nearly constant. The three lattice parameters *a*, *b* and *c* (not shown here) present a similar thermal variation.

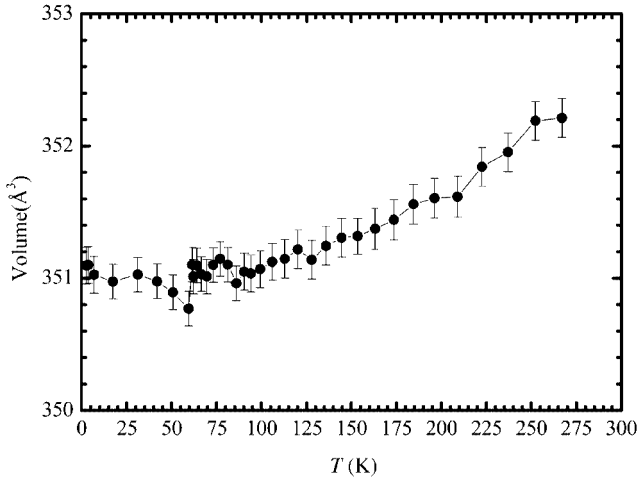


Figure 11. Thermal evolution of the volume of the unit cell.

## Discussion

The analysis of the crystallographic structure of $HoFeMnO_5$ by neutron diffraction indicates that this new oxide keeps the crystallographic structure of the parent $HoMn_2O_5$ oxide[11] (space group *Pbam*). Despite the fact that the ionic radii of the $Fe^{3+}$ and $Mn^{3+}$cations are very similar (0.645 Å in sixfold coordination and high-spin state[25]), some distinct features have been found both in the lattice parameters and in the interatomic distances of the $Mn^{4+}O_6$, $Fe^{3+}O_5$ and $Ho^{3+}O_8$ polyhedra. A comparison of the room-temperature lattice parameters of $HoMn_2O_5$,[11] *a* = 7.2643(3), *b* = 8.4768(3) and *c* = 5.6700(2) Å, with those of $HoFeMnO_5$, shows that the substitution of the $Mn^{3+}$ cations by $Fe^{3+}$ gives rise to an expansion of the unit-cell parameters. The changes in the interatomic distances in the $Mn^{4+}O_6$ octahedra are not very significant; the average bond length is 1.902(2) Å in $HoMn_2O_5$ and 1.891(9) Å in $HoFeMnO_5$. In both cases the $Mn^{4+}O_6$ octahedral are flattened, because the three Mn–O distances are different; the Mn–O3 and Mn–O2 bonds in the equatorial plane correspond to the shorter and longer bonds, respectively. In the tetragonal pyramids, the substitution of $Mn^{3+}$ by $Fe^{3+}$ causes a shortening of the axial bond length Fe–O3 and an elongation of the equatorial bond lengths Fe–O4 and Fe–O1, with a slight average expansion of the pyramidal units: the average bond length is 1.933(3) Å in $HoMn_2O_5$ and 1.947(4) Å in $HoFeMnO_5$. The changes observed in the tetragonal pyramids cannot be related to the ionic radii, because $Mn^{3+}$ and $Fe^{3+}$ have the same tabulated value. The changes are very possibly linked to the Jahn–Teller character of the $Mn^{3+}$ cations, which favour the lengthening of the axial interatomic distance in order to remove the degeneracy of the $t_{2g}$ and $e_{2g}$ energy levels; the $Fe^{3+}$ cations do not show such a Jahn–Teller character. Finally, in the $Ho^{3+}O_8$ polyhedron, although some slight variations in the individual Ho···O interatomic distances are observed, the average Ho···O distances are very similar, 2.381(2) Å in $HoMn_2O_5$ and 2.383(5) Å in $HoFeMnO_5$.

The magnetic structure of $HoFeMnO_5$ is similar to the magnetic structure of the previously described members of the $RFeMnO_5$ family, with R = Y and Er; the magnetic moments within the $Mn^{4+}$ and $Fe^{3+}$ sublattices are ferromagnetically coupled, and the two sublattices couple antiferromagnetically, giving rise to a global ferrimagnetic structure in such a way that the magnetic unit cell coincides with the crystallographic one. In all the mentioned compounds the magnetic moments are oriented along the *z* direction. However, $HoFeMnO_5$ presents certain features that distinguish it from other members of the series containing paramagnetic $R^{3+}$ cations, namely $ErFeMnO_5$. Firstly, the ordered magnetic moments of the $Mn^{4+}$ and $Fe^{3+}$ cations at 2 K, 1.31(6) and 3.20(10) $\mu_B$, respectively, are relatively small in comparison with the theoretical values of 3 and 5 $\mu_B$. Secondly, the ordered magnetic moment of $Ho^{3+}$ is very small relative to the magnetic moment reached by $Er^{3+}$ in $ErFeMnO_5$,[21] 8.59(7) $\mu_B$; in fact, it can be said that the $Ho^{3+}$ moments undergo a weak long-range magnetic order. The different magnetic behaviour of the $Er^{3+}$ and $Ho^{3+}$ sublattices is clearly exhibited by the different thermal evolution presented by the magnetic reflections (110) and (020): although in $ErFeMnO_5$[21] these magnetic reflections undergo a sharp increase below 75 K, in $HoFeMnO_5$ the integrated intensity of the mentioned reflections increase monotonically below $T_C \approx 153$ K, reaching saturation at around 50 K, much like the situation in $YFeMnO_5$.

The magnetic ordering of the $Mn^{4+}$ and $Fe^{3+}$ sublattices is defined by the superexchange interactions that appear between the $Mn^{4+}$···$Mn^{4+}$, $Mn^{4+}$···$Fe^{3+}$ and $Fe^{3+}$···$Fe^{3+}$ cations. The magnetic interactions between the $Mn^{4+}$···$Mn^{4+}$

 © 2007 Wiley-VCH Verlag GmbH & Co. KGaA, Weinheim 

cations are characterized by the $J_1$ and $J_2$ superexchange interactions, which are associated with the $Mn^{4+}$–O2–$Mn^{4+}$ and $Mn^{4+}$–O3–$Mn^{4+}$ paths, with bond angles of 101.5(8)° and 94.6(9)°, respectively, at $T$ = 10 K. The Goodenough–Kanamori rules[26,27] for a 90° cation($d^3$)–anion–cation($d^3$) interaction indicate the presence of ferromagnetic (FM) and antiferromagnetic (AFM) interactions, the AFM interactions being mainly associated with a direct overlap of the $t_{2g}$ orbitals of the two cations, which strongly depends on the interatomic distance between the two cations. This subtle equilibrium between AFM and FM interactions along the chains of the $MnO_6$ octahedra, which in the case of the parent $RMn_2O_5$ compounds gives rise to incommensurate magnetic structures, is clearly broken by the presence of Fe at the pyramidal positions via strong Fe–O–Fe FM interactions followed by AFM Fe–O–Mn coupling, giving rise to positive $J_1$ and $J_2$ superexchange interactions along the chains of the octahedra.

It seems reasonable to think that the strong superexchange Fe–O–Fe interactions within the dimer $Fe_2O_{10}$ units trigger the onset of the magnetic ordering of the $Fe^{3+}$ spins immediately below $T_C$. There is an abrupt change in the reciprocal dc susceptibility at 220 K, as displayed in the inset of Figure 1, which plausibly coincides with the onset of Fe–O–Fe short-range interactions. In each dimer, the two $Fe^{3+}$ cations are linked through the O1 oxygen with a bond angle at $T$ = 10 K of 94.0(4)°. We can define $J_5$ as the superexchange interaction across the $Fe^{3+}$–O1–$Fe^{3+}$ path (Figure 12). On considering the Goodenough–Kanamori rules[26,27] for a 90° cation($d^5$)–anion–cation($d^5$) interaction, the coupling between the $Fe^{3+}$···$Fe^{3+}$ cations via O1 oxygen atoms would be FM ($J_5 > 0$), in accord with Hund's rule applied to the $p_x$ and $p_y$ orbitals of the central O1 oxygen, forming strong σ chemical bonds with the $d_{z^2-y^2}$ orbitals of neighbouring Fe atoms.

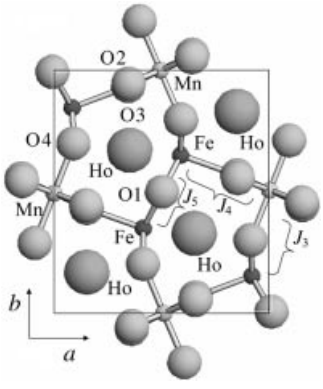


Figure 12. A view of the crystallographic structure along the [001] direction.

As it can be seen in Figure 12, the $Mn^{4+}$···$Fe^{3+}$ interactions are characterized by the superexchange $Fe^{3+}$–O4–$Mn^{4+}$ ($J_3$) and $Fe^{3+}$–O3–$Mn^{4+}$ ($J_4$) paths, whose bond angles are 121.4(3)° and 132.3(5)°, respectively, at $T$ = 10 K. The Goodenough–Kanamori rules[26,27] indicate that for a 180° cation($d^5$)–anion–cation($d^3$) interaction, the superexchange interactions are predominantly FM, whereas for a 90° bond there are FM and AFM interactions, the AFM interactions being more important. As the bond angles are closer to 90°, it seems that the superexchange interaction in the $Fe^{3+}$–O4–$Mn^{4+}$ and $Fe^{3+}$–O3–$Mn^{4+}$ bonds are mainly AFM ($J_3 < 0$, $J_4 < 0$). These interactions define the global AFM coupling between the Fe and Mn sublattices, giving rise to a ferrimagnetic structure.

As regards the ordering of the $Ho^{3+}$ sublattice, the experimental results suggest that the $Ho^{3+}$ moments are weakly polarized by the molecular field of the $Fe^{3+}$ magnetic sublattice immediately below $T_C$, giving rise to FM and AFM alignments with the $Fe^{3+}$ and $Mn^{4+}$ sublattices, respectively. In principle, a weak direct superexchange interaction is expected between the $Ho^{3+}$ cations via the $Ho^{3+}$···O1···$Ho^{3+}$, $Ho^{3+}$···O2···$Ho^{3+}$ and $Ho^{3+}$···O4···$Ho^{3+}$ paths (see Figure 12); therefore, the observed magnetic order at relatively high temperatures should be caused by the interaction with the $Mn^{4+}$ and $Fe^{3+}$ cations. The superexchange interactions would take place via the $Ho^{3+}$···O1–$Fe^{3+}$ ($J_6$), $Ho^{3+}$···O4–$Fe^{3+}$ ($J_7$), $Ho^{3+}$···O2–$Mn^{4+}$ ($J_8$) and $Ho^{3+}$···O4–$Mn^{4+}$ ($J_9$) paths; the interaction through the Ho···O1–Fe path involves the indirect interaction with the two $Fe^{3+}$ cations of the dimer. Besides, around the O1 oxygen there are two Ho atoms linked by an inversion centre and the $\mathbf{r} = \mathbf{a} + \mathbf{b}$ lattice translation; so, independently of the sign of $J_6$, both $Ho^{3+}$ cations must be ferromagnetically coupled. However, according to the magnetic structure, the interactions between $Ho^{3+}$ and the two $Fe^{3+}$ cations of the dimer are FM; therefore, $J_6$ is positive. In contrast, the coupling with the $Mn^{4+}$ cations is AFM, so $J_8$ and $J_9$ are negative. As regarding the sign of $J_7$ associated with the $Ho^{3+}$···O4–$Fe^{3+}$ path, it is very possible that $J_7$ is negative in contrast with the sign of $J_6$; it would contribute to the frustration of the long-range magnetic order of the $Ho^{3+}$ sublattice. In $ErFeMnO_5$, the scenario for the $Er^{3+}$ sublattice can be similar, but in this compound the <Er···O> interatomic distances are slightly shorter [2.363(2) Å at room temp.], so it seems that the direct Er···O···Er superexchange interactions play a more important role in the establishment of the long-range magnetic order. In $HoFeMnO_5$, with longer Ho···O interatomic distances, the participation of the direct superexchange interactions Ho···O···Ho in the long-range magnetic order seems to be much less important.

## Conclusions

By following a singular synthesis process that includes a thermal treatment under high oxygen pressure, it has been possible to obtain $HoFeMnO_5$. The crystallographic structure, investigated by NPD, is similar to that of $HoMn_2O_5$ (orthorhombic, space group *Pbam*), and can be described as infinite chains of edge-sharing $Mn^{4+}O_6$ octahedra running along the *c* axis; the chains are corner-linked by pairs of $Fe^{3+}O_5$ edge-sharing pyramids; the $Ho^{3+}$ cations are arranged in voids with eightfold oxygen coordination. A certain cationic disorder has been found over the 4*f* and 4*h* sites, ideally occupied by the $Mn^{4+}$ and $Fe^{3+}$ cations, respec-

 © 2007 Wiley-VCH Verlag GmbH & Co. KGaA, Weinheim 

tively: the crystallographic formula can be rewritten as $Ho(Fe_{0.86(2)}Mn_{0.14(2)})_{4h}(Mn_{0.94(2)}Fe_{0.06(2)})_{4f}O_{4.74(10)}$. In contrast with $HoMn_2O_5$, showing elongated $Mn^{3+}O_5$ pyramids, the $Fe^{3+}O_5$ units in $HoFeMnO_5$ are flattened; this difference is ascribed to the Jahn–Teller character of the $Mn^{3+}$ cations.

Magnetization and NPD data show that $HoFeMnO_5$ is a ferrimagnet with $T_C \approx 153$ K; the magnetic structure is characterized by $\mathbf{k} = 0$, consisting of an AFM arrangement of $Fe^{3+}$ and $Mn^{4+}$ spins, aligned along the *c* axis. $Ho^{3+}$ moments become slightly polarized below $T_C$, ferromagnetically coupled to the $Fe^{3+}$ sublattice and antiferromagnetically coupled to the $Mn^{4+}$ sublattice. At $T = 2.7$ K, the magnetic moment values for the $Mn^{4+}$, $Fe^{3+}$ and $Ho^{3+}$ ions are 1.31(6), 3.20(10) and 0.36(7) $\mu_B$, respectively. In contrast with the full long-range magnetic ordering of $Er^{3+}$ cations in $ErFeMnO_5$, where the initial polarization of Er moments immediately below $T_C$ is completed at lower temperatures by direct Er···O···Er interactions, in the present case it seems that the participation of direct Ho···O···Ho superexchange interactions in the long-range magnetic order is insignificant and the $Ho^{3+}$ moments remain in a quasi-paramagnetic state down to 2 K in $HoFeMnO_5$.

## Acknowledgments

We thank CICyT for the financial support of the project MAT2004-0479 and CAM for financing the project GR/MAT/0427/2004, and we are grateful to ILL for making all facilities available.

[1] Y. F. Popov, A. M. Kadomtseva, S. S. Krotov, G. P. Vorob'ev, M. M. Lukina, *Ferroelectrics* **2002**, *279*, 147.
[2] T. Kimura, T. Goto, H. Shintani, K. Ishizaka, T. Arima, Y. Tokura, *Nature* **2003**, *426*, 55.
[3] N. Hur, S. Park, P. A. Sharma, J. Ahn, S. Guha, S.-W. Cheong, *Nature* **2004**, *429*, 392.
[4] L. C. Chapon, G. R. Blake, M. J. Gutmann, S. Park, N. Hur, P. G. Radaelli, S.-W. Cheong, *Phys. Rev. Lett.* **2004**, *93*, 177402.
[5] N. Hur, S. Park, P. A. Sharma, S. Guha, S.-W. Cheong, *Phys. Rev. Lett.* **2004**, *93*, 107207.
[6] R. Valdés Aguilar, A. B. Sushkov, S. Park, S.-W. Cheong, H. D. Drew, *Phys. Rev. B* **2006**, *74*, 184404.
[7] S. Quezel-Ambrunaz, E. F. Bertaut, G. Buisson, *C. R. Acad. Sci.* **1964**, *258*, 3025.
[8] E. F. Bertaut, G. Buisson, A. Durif, A. Mareschal, M. C. Montmory, S. Quezel-Ambrunaz, *Bull. Soc. Chim. Fr.* **1965**, 1132.
[9] E. F. Bertaut, G. Buisson, A. Durif, A. Mareschal, M. C. Montmory, S. Quezel-Ambrunaz, *Bull. Soc. Chim. Fr.* **1965**, 1132.
[10] J. A. Alonso, M. T. Casais, M. J. Martínez-Lope, I. Rasines, *J. Solid State Chem.* **1997**, *129*, 105.
[11] J. A. Alonso, M. T. Casais, M. J. Martínez-Lope, J. L. Martínez, M. T. Fernández-Díaz, *J. Phys.: Condens. Matter* **1997**, *9*, 8515.
[12] G. Buisson, *Phys. Status Solidi A* **1973**, *16*, 533.
[13] G. Buisson, *Phys. Status Solidi A* **1973**, *17*, 191.
[14] A. Muñoz, J. A. Alonso, M. T. Casais, M. J. Martínez-Lope, J. L. Martínez, M. T. Fernández-Díaz, *Phys. Rev. B* **2002**, *65*, 144423.
[15] A. Muñoz, J. A. Alonso, M. T. Casais, M. J. Martínez-Lope, J. L. Martínez, M. T. Fernández-Díaz, *Eur. J. Inorg. Chem.* **2005**, 685.
[16] G. R. Blake, L. C. Chapon, P. G. Radaelli, S. Park, N. Hur, S.-W. Cheong, J. Rodríguez-Carvajal, *Phys. Rev. B* **2005**, *71*, 214402.
[17] S. Kobayashi, T. Osawa, H. Kimura, Y. Noda, I. Kagomiya, K. Khon, *J. Phys. Soc. Jpn.* **2004**, *73*, 1031.
[18] S. Kobayashi, T. Osawa, H. Kimura, Y. Noda, I. Kagomiya, K. Khon, *J. Phys. Soc. Jpn.* **2004**, *73*, 1593.
[19] L. C. Chapon, P. G. Radaelli, G. R. Blake, S. Park, S.-W. Cheong, *Phys. Rev. Lett.* **2006**, *96*, 097601.
[20] A. Muñoz, J. A. Alonso, M. J. Martínez-Lope, J. L. Martínez, *Chem. Mater.* **2004**, *16*, 4087–4094.
[21] A. Muñoz, J. A. Alonso, M. J. Martínez-Lope, J. L. Martínez, *Phys. Rev. B* **2005**, *72*, 184402.
[22] H. M. Rietveld, *J. Appl. Crystallogr.* **1969**, *2*, 65.
[23] J. Rodríguez-Carvajal, *Physica B* **1993**, *192*, 55.
[24] E. F. Bertaut, *Magnetism* (Eds.: G. T. Rado, H. Shull), Academic Press, New York, **1963**, vol. III, ch. 4.
[25] R. D. Shanon, *Acta Crystallogr., Sect. A* **1976**, *32*, 751.
[26] J. B. Goodenough, *Magnetism and the Chemical Bond*, Interscience Publishers, New York, **1963**.
[27] J. Kanamori, *J. Phys. Chem. Solids* **1959**, *10*, 87.

Received: December 4, 2006
Published Online: March 28, 2007

 © 2007 Wiley-VCH Verlag GmbH & Co. KGaA, Weinheim 

DOI: 10.1002/ejic.200601148

# The Relationship Between $^{27}Al$ Quadrupolar Parameters and $AlF_6^{3-}$ Octahedron Connectivity in Crystalline and Glassy Fluoroaluminates

**Monique Body,*[a] Christophe Legein,[b] Jean-Yves Buzaré,[a] and Gilles Silly[c]**

*This paper is dedicated to Professor Neil Bartlett on the occasion of his 75th birthday*

**Keywords:** Glasses / Fluorides / $^{27}Al$ NMR spectroscopy / Quadrupolar parameters

$^{27}Al$ SATRAS and MQ-MAS spectra were recorded for eight crystalline compounds, from the $CaF_2$–$AlF_3$ and $BaF_2$–$AlF_3$ binary and $BaF_2$–$CaF_2$–$AlF_3$ ternary systems, and four glass compositions with different $CaF_2$/$BaF_2$/$AlF_3$ contents. For the crystalline phases, the reconstruction of the spectra leads to the precise determination of the NMR parameters. For the glassy phases, the $^{27}Al$ SATRAS spectra have been reconstructed using quadrupolar parameter distributions. The main finding of this study is the dependence of the quadrupolar frequency on the type of $AlF_6^{3-}$ octahedron connectivity. For crystalline phases the experimental $\nu_Q$ values range between 75 kHz and 510 kHz for structures built up from isolated octahedra, and are between 560 kHz and 1250 kHz for structures built up from isolated chains of *cis*-connected octahedra, and are between 1530 kHz and 1580 kHz for structures built up from isolated chains of *trans*-connected octahedra. In the glassy phases the maximum of the quadrupolar frequency distribution shifts toward larger values and its width increases with increasing $AlF_3$ content, and subsequently with the number of connected octahedra. The range of the $\nu_Q$ values seems to indicate that when the octahedra are connected, *cis* connections occur most frequently.
(© Wiley-VCH Verlag GmbH & Co. KGaA, 69451 Weinheim, Germany, 2007)

## Introduction

The use of $^{27}Al$ NMR can provide important structural information relating to the local order around aluminium atoms in crystalline and disordered compounds. Numerous $^{27}Al$ NMR studies have been performed on a wide range of chemical systems. Oxide minerals have been particularly well studied. The isotropic chemical shifts observed in the spectra for these materials have been used to determine the nature of the Al coordination, and for obtaining information about the chemical environments of the Al atoms.

As aluminium atoms have a quadrupolar nucleus ($I$ = 5/2), other valuable structural information may also be obtained through the quadrupolar interactions. Actually, the $^{27}Al$ NMR spectra are broadened by this interaction even under Magic Angle Spinning (MAS) conditions. This hinders the precise determination of the quadrupolar parameters, especially when several crystallographically independent Al sites are present in the compound. However, the development of techniques such as SAtellite TRAnsition Spectroscopy (SATRAS),[1,2] and Multiple Quantum Magic Angle Spinning (MQ-MAS),[3] which are able to average first- and second-order broadenings, have allowed high-resolution $^{27}Al$ NMR spectra to be recorded from which the quadrupolar parameters in crystalline compounds,[4–20] and their distributions in disordered phases,[16,21–30] can be accurately determined.

In this paper we present a $^{27}Al$ NMR study of crystalline and glassy fluoride phases that are built up from $AlF_6^{3-}$ octahedra. The compounds under investigation are crystalline fluoridoaluminates of the $BaF_2$–$AlF_3$ (α-, β- and γ-$BaAlF_5$, $Ba_3Al_2F_{12}$, and $Ba_3AlF_9$-Ib) and $CaF_2$–$AlF_3$ binary systems (α-$CaAlF_5$, $Ca_2AlF_7$), α-$BaCaAlF_7$, and glassy phases of the corresponding $BaF_2$–$CaF_2$–$AlF_3$ ternary system ($50CaF_2$–$15BaF_2$–$35AlF_3$, $35CaF_2$–$25BaF_2$–$40AlF_3$, $35CaF_2$–$20BaF_2$–$45AlF_3$, and $35CaF_2$–$15BaF_2$-$50AlF_3$). We have already investigated β-$CaAlF_5$ and β-$Ba_3AlF_9$ by $^{27}Al$ NMR spectroscopy.[18,19] The crystalline compounds belonging to these systems that are not included in this study are as follows: $Ba_5AlF_{13}$ and $Ba_5Al_3F_{19}$, the crystal structures of which are unknown,[31] δ-$BaAlF_5$[32] which, to the best of our knowledge, cannot

[a] Laboratoire de Physique de l'Etat Condensé, CNRS UMR 6087, Institut de Recherche en Ingénierie Moléculaire et Matériaux Fonctionnels, CNRS FR 2575, Université du Maine, Avenue Olivier Messiaen, 72085 Le Mans Cedex 9, France
Fax: +33-2-43833518
E-mail: monique.body@univ-lemans.fr
[b] Laboratoire des Oxydes et Fluorures, CNRS UMR 6010, Institut de Recherche en Ingénierie Moléculaire et Matériaux Fonctionnels, CNRS FR 2575, Université du Maine, Avenue Olivier Messiaen, 72085 Le Mans Cedex 9, France
[c] Laboratoire de Physicochimie de la Matière Condensée, CNRS UMR 5617, Institut Charles Gerhardt, CNRS FR 1878, Université de Montpellier II, Place Eugène Bataillon, C.C. 03, 34095 Montpellier Cedex 5, France

 InterScience® © 2007 Wiley-VCH Verlag GmbH & Co. KGaA, Weinheim 

be obtained by a solid-state reaction, and $Ba_3AlF_9$-Ia, which we were unable to synthesize.[33] SATRAS experiments were carried out for all the studied samples. For multi-site crystalline phases and glasses, MQ-MAS spectra were also recorded. The reconstruction of the NMR spectra leads to the determination of the quadrupolar parameters for the crystalline compounds. These quadrupolar parameters are then classified according to the $AlF_6^{3-}$ octahedron connectivities.

The reconstructions of the SATRAS spectra for the $BaF_2$–$CaF_2$–$AlF_3$ glassy phases lead to a determination of the quadrupolar parameter distributions in relation to the $AlF_3$ content. These results are discussed in the light of a recent $^{19}$F NMR study on the same glassy phases,[34] which led to the experimental determination of the mean number, $\beta$, of fluorine atoms per $AlF_6^{3-}$ octahedron. It was shown that the $\beta$ value is between 6 and 5 for the studied glasses, and is dependent on the amount of $AlF_3$ in the glass (35–50%). For $\beta$ = 6, the $AlF_6^{3-}$ octahedra are isolated, and $\beta$ = 5 may correspond to the presence of infinite chains of octahedra in the glass. Correlation of $^{27}$Al NMR results for glassy and crystalline phases with $^{19}$F NMR spectroscopic data analyses of the glassy phases enables an accurate picture to be gained of the glass network through the dependence of the quadrupolar parameters on the octahedron connectivity.

## Results

### $^{27}$Al Quadrupolar Parameters in Crystalline Compounds

All the compounds under investigation are built up from a framework of $AlF_6^{3-}$ octahedra. In α- and β-$CaAlF_5$[35,18] only infinite isolated chains of $AlF_6^{3-}$ octahedra sharing *trans*-fluorine atoms are present, as shown in Figure 1a. The chains are corrugated, and the F–Al–F angles are equal to 157.5° and 155.8° in α- and β-$CaAlF_5$, respectively. In α-,[36] β-, and γ-$BaAlF_5$[37], the octahedra share corners at the *cis* position to form infinite isolated chains as shown in Figure 1b. The Al–F–Al angles show small variations: 146.2° in α-$BaAlF_5$, 145.9° and 145.6° in β-$BaAlF_5$, and 144.5° and 139.5° in γ-$BaAlF_5$.

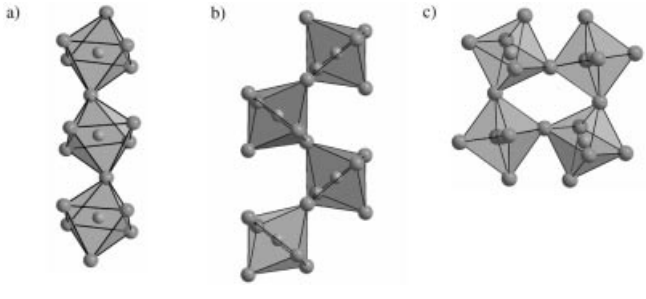


Figure 1. The different connectivities of the $AlF_6^{3-}$ octahedra encountered in the investigated crystalline phases: isolated chains of (a) *trans*-connected octahedra, (b) *cis*-connected octahedra and (c) tetrameric group of *cis*-connected octahedra.

There is only one unique aluminium site present in the α-$CaAlF_5$[35] and α-$BaAlF_5$[36] structures. Accordingly, for both compounds, the central transitions of the SATRAS spectra (Figure 2) correspond to one Al site. These central transitions present singularities that are characteristic of high quadrupolar frequency values. However, the line shape of the α-$CaAlF_5$ central transition is typical of an $\eta_Q$ value that is nearly equal to 1, whereas the central transition in the α-$BaAlF_5$ spectrum corresponds to a small $\eta_Q$ value. The method for extracting the NMR parameters has been described in detail for β-$CaAlF_5$;[16] an initial estimation of the quadrupolar parameters $\nu_Q$ and $\eta_Q$ is obtained from the reconstruction of the central transition line shape (Figure 2), and then precise values are given by the reconstruction of the overall spinning sideband envelope shape. $AlF_3$ is present as an impurity in α-$CaAlF_5$ and its contribution has been included in the reconstructed spectrum with a relative intensity of 0.5%, using the relevant NMR parameters previously determined by Silly et al.[15]. The NMR parameters leading to the best simulations are summarized in Table 1. $^{27}$Al MAS NMR spectra were previously recorded by Sakida et al.[38] for α-$CaAlF_5$ and α-$BaAlF_5$. However, these authors did not determine the quadrupolar parameter values, and they did not give the $\delta_{iso}$ value for α-$CaAlF_5$. However, they found $\delta_{iso}$ = –13.4 ppm for α-$BaAlF_5$, which is significantly different from our value. Their value is questionable since the experimental spectrum was not recon-

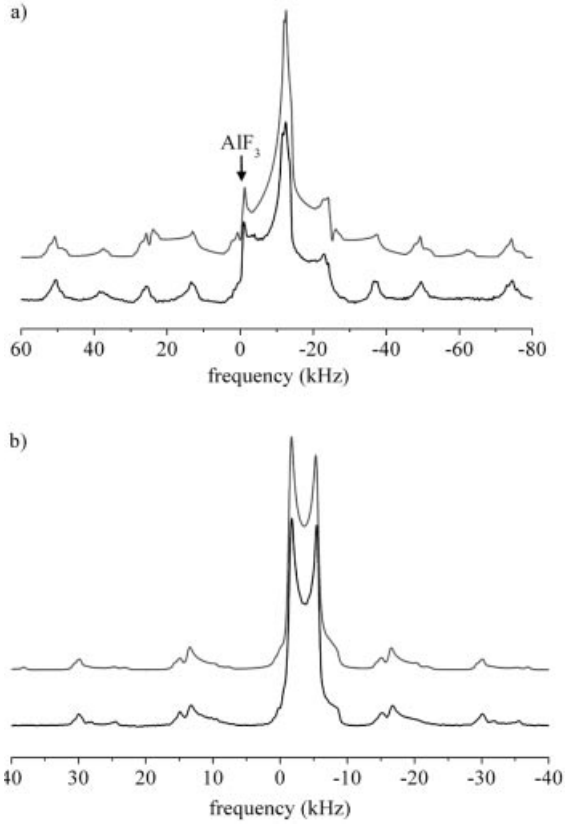


Figure 2. Experimental (bottom) and reconstructed (top) central transitions in the $^{27}$Al SATRAS NMR spectra for (a) α-$CaAlF_5$ (25 kHz) and (b) α-$BaAlF_5$ (15 kHz).

 © 2007 Wiley-VCH Verlag GmbH & Co. KGaA, Weinheim 

structed. We suggest that our results are more reliable as the experimental spectra were reconstructed taking into account all the interactions up to the second order.

Table 1. $AlF_6^{3-}$ octahedron connections, compounds, isotropic chemical shifts, $\delta_{iso}$ (ppm), quadrupolar frequencies, $\nu_Q$ (kHz), and asymmetry parameters, $\eta_Q$, from the reconstructions of the $^{27}Al$ NMR spectra.

| Connection | Compound | $\delta_{iso}$ (± 2) | $\nu_Q$ (± 5%) | $\eta_Q$ (± 0.05) |
|---|---|---|---|---|
| *trans* | α-$CaAlF_5$ | –6 | 1580 | 0.95 |
| | β-$CaAlF_5$[a] | –7 | 1530 | 0.10 |
| *cis* | α-$BaAlF_5$ | –3 | 1000 | 0.09 |
| | β-$BaAlF_5$ | –0.5 | 750 | 0.10 |
| | | –2 | 550 | 0.45 |
| | γ-$BaAlF_5$ | 1 | 1250 | 0.15 |
| | | –3 | 900 | 0.15 |
| | $Ba_3Al_2F_{12}$ | –2 | 560 | 0.30 |
| Isolated | $Ca_2AlF_7$ | –6 | 340 | 0.95 |
| | $Ba_3AlF_9$-Ib | 0 | 75 | 0.50 |
| | | 0 | 510 | 0.07 |
| | β-$Ba_3AlF_9$[b] | 1 | 140 | 0.50 |
| | | –2 | 210 | 0.85 |
| | α-$BaCaAlF_7$ | –0.5 | 190 | 0.80 |

[a] From ref.[18] [b] From ref.[19]

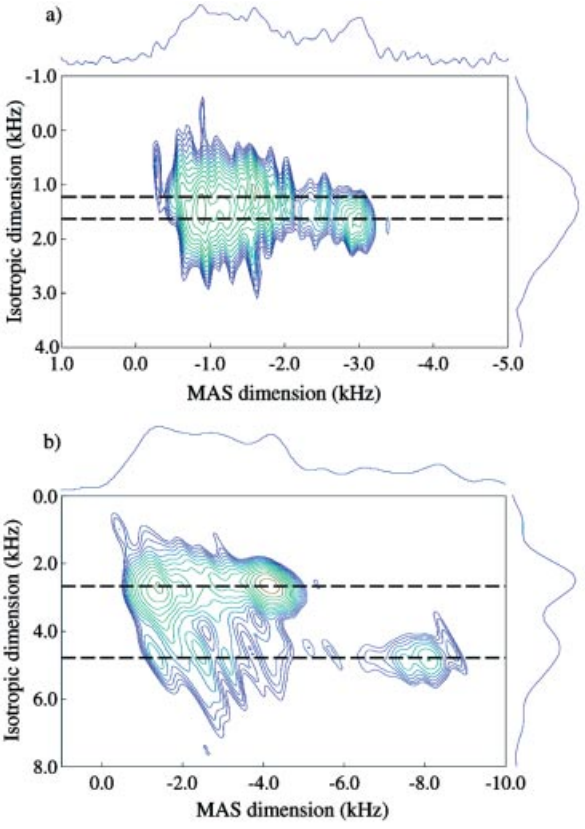


Figure 3. Experimental $^{27}Al$ 3Q-MAS NMR spectra for (a) β-$BaAlF_5$ and (b) γ-$BaAlF_5$ at 25 kHz. The curves at the top and to the right of the spectra are the projections of the spectra on to the MAS (*F2*) and isotropic (*F1*) axes, respectively. The dashed lines indicate the *F1* slices used for preliminary estimation of the NMR parameters.

Both the β- and γ-$BaAlF_5$ structures contain two symmetry-independent aluminium sites.[37] For these two compounds two aluminium sites can be resolved along the *F1* dimension in the 3Q-MAS spectra, as shown in Figure 3. As previously done for β-$Ba_3AlF_9$,[19] an initial estimation of the NMR parameters is given by the reconstruction of the *F1* slices. Then a precise determination of the NMR parameters is obtained from the reconstruction of the whole $^{27}Al$ SATRAS spectra. Two contributions of equal intensity are needed for the reconstruction of the β-$BaAlF_5$ SATRAS spectrum. Similarly, the two contributions used for the reconstruction of the γ-$BaAlF_5$ SATRAS spectrum have the same relative intensity. For both compounds the corresponding NMR parameters are listed in Table 1. The experimental and reconstructed central transitions are presented in Figure 4. In both compounds the Al sites have the same multiplicities, therefore ab initio calculations are required before any of these parameters can be attributed to the symmetry-independent Al atoms.

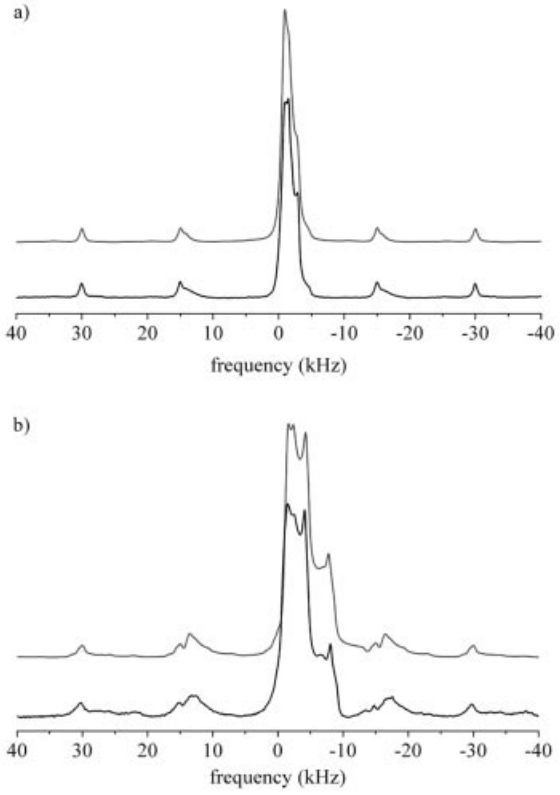


Figure 4. Experimental (bottom) and reconstructed (top) central transitions of the $^{27}Al$ SATRAS NMR spectra for (a) β-$BaAlF_5$ and (b) γ-$BaAlF_5$ at 15 kHz.

$Ba_3Al_2F_{12}$ comprises tetramers formed by four $AlF_6^{3-}$ octahedra sharing corners at the *cis* position,[39,40] as shown in Figure 1c. These tetrameric groups are separated from each other by barium and "free" fluorine ions (i.e. not linked to Al). Similarly, the NMR parameters were determined by first reconstructing the central transition, and then the whole experimental $^{27}Al$ SATRAS spectrum. These NMR parameters are given in Table 1. Experimental and reconstructed central transition and SATRAS spectra

 © 2007 Wiley-VCH Verlag GmbH & Co. KGaA, Weinheim 

are presented in Figure 5. Sakida et al.[38] determined an isotropic chemical shift value of $\delta_{iso}$ = –11.7 ppm for this compound. The comments made above with respect to α-$BaAlF_5$ hold for this compound as well.

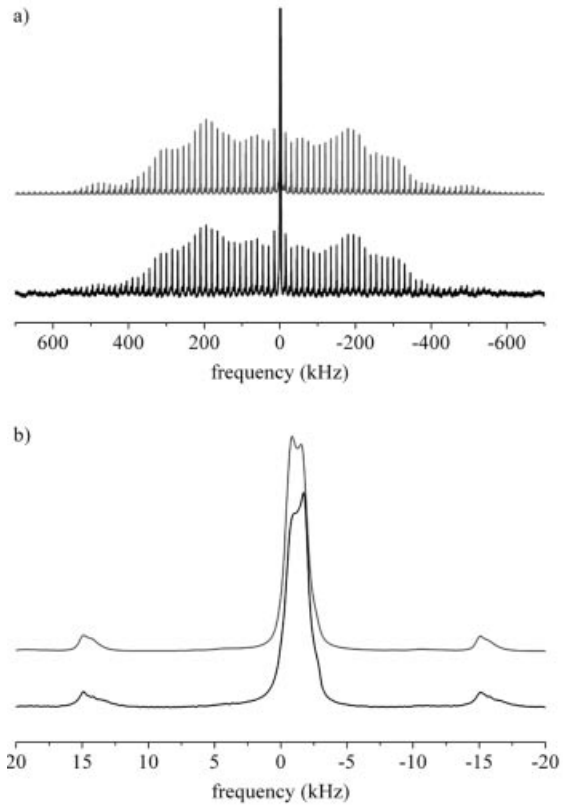


Figure 5. Experimental (bottom) and reconstructed (top) spectra: (a) $^{27}$Al SATRAS NMR spectra and (b) central transitions for $Ba_3Al_2F_{12}$ at 15 kHz. In the full SATRAS spectra the central transitions are truncated to improve the visiblity of the spinning sidebands.

$Ca_2AlF_7$,[41] $Ba_3AlF_9$-Ib,[42] β-$Ba_3AlF_9$,[43] and α-$BaCaAlF_7$[44] contain isolated $AlF_6^{3-}$ octahedra. $Ba_3AlF_9$-Ib and β-$Ba_3AlF_9$ are structurally quite different, even though they are both characterized by isolated $AlF_6^{3-}$ octahedra and $FBa_4^{7+}$ tetrahedra. β-$Ba_3AlF_9$ contains three aluminium sites; their corresponding NMR parameters have already been determined, and are reported in ref.[19] $Ca_2AlF_7$, $Ba_3AlF_9$-Ib, and α-$BaCaAlF_7$ contain one aluminium site, as confirmed by the $^{27}$Al SATRAS spectra presented in Figure 6. For these three spectra the central transitions are shapeless, and are therefore not shown. The shapeless central transitions, and the overall SATRAS spectrum expansions, may be related to low quadrupolar frequencies. The comparison between these three spectra indicates that $Ca_2AlF_7$ has the highest quadrupolar frequency, whereas $Ba_3AlF_9$-Ib has the lowest value. The NMR parameters leading to the best simulations are provided in Table 1. The $^{27}$Al MAS NMR spectrum of $Ca_2AlF_7$ previously recorded by Sakida et al.[38] presents two "split peaks" that we do not observe in our SATRAS spectrum.

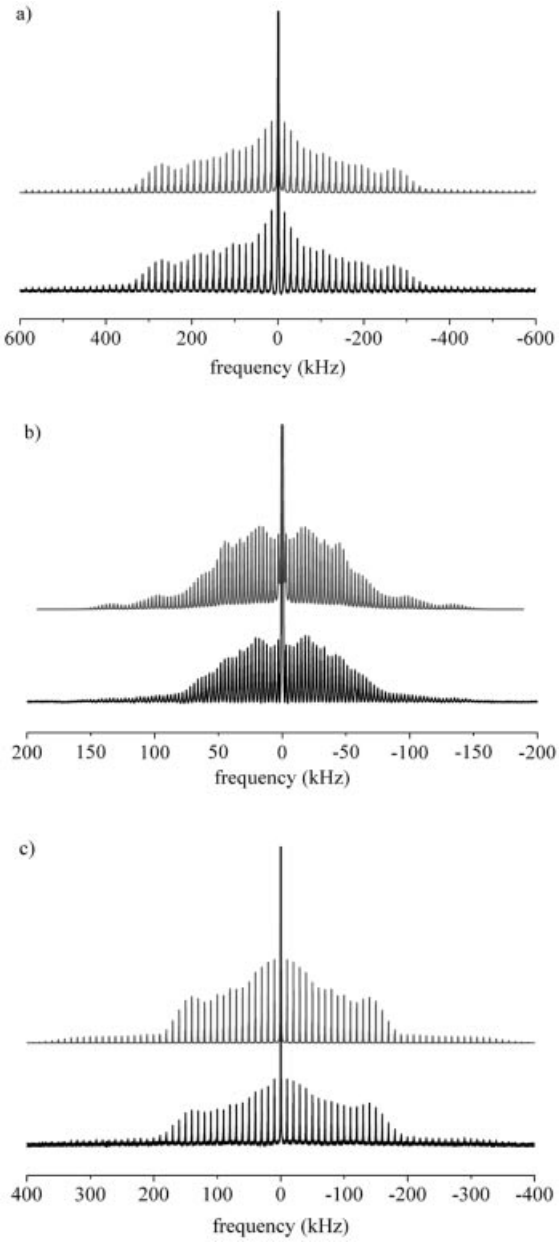


Figure 6. Experimental (bottom) and reconstructed (top) $^{27}$Al SATRAS NMR spectra for (a) $Ca_2AlF_7$ (15 kHz), (b) $Ba_3AlF_9$-Ib (3 kHz) and (c) α-$BaCaAlF_7$ (10 kHz). The central transitions are truncated to improve the visiblity of the spinning sidebands.

The previously published results for β-$CaAlF_5$[16] and β-$Ba_3AlF_9$[19] have been added to Table 1.

## Quadrupolar Parameters in Glassy Phases

For the $BaF_2$–$CaF_2$–$AlF_3$ ternary system several glass compositions have been synthesized in a previous study.[34] Four of these compositions have been chosen for this study, and contain 35–50% $AlF_3$. The selected glass compositions are given in Table 2.

 © 2007 Wiley-VCH Verlag GmbH & Co. KGaA, Weinheim 

Table 2. Glass compositions (mol fractions), isotropic chemical shifts, $\delta_{iso}$ (ppm), $\sigma$ parameters (kHz), and $\beta$ parameters for the studied glasses.

| Composition | $\delta_{iso}$ (± 2) | $\sigma$ (±20) | $\beta$[a] |
|---|---|---|---|
| $50CaF_2$–$15BaF_2$–$35AlF_3$ | –3 | 370 | 6 |
| $35CaF_2$–$25BaF_2$–$40AlF_3$ | –4 | 420 | 5.76 |
| $35CaF_2$–$20BaF_2$–$45AlF_3$ | –3 | 440 | 5.44 |
| $35CaF_2$–$15BaF_2$–$50AlF_3$ | –7 | 470 | 5 |

[a] From ref.[34]

The $^{27}$Al 3Q-MAS spectra clearly show only one Al contribution, and are presented in Figure 7. These spectra are similar to the those reported by Chan and Eckert for a related glass composition.[45] A striking feature of the data is the broadening of the 3Q-MAS spectra, which is expected to mirror the broadening of the quadrupolar parameter distribution with increasing $AlF_3$ glass content.

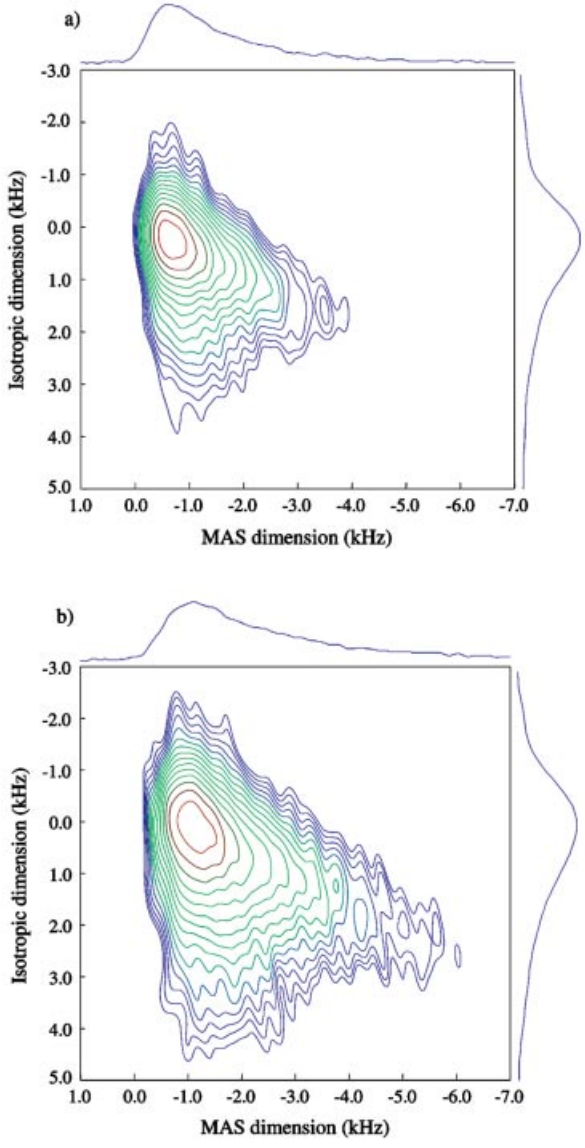


Figure 7. Experimental $^{27}$Al 3Q-MAS NMR spectra for (a) $50CaF_2$–$15BaF_2$–$35AlF_3$ and (b) $35CaF_2$–$15BaF_2$–$50AlF_3$ glasses at 25 kHz. The curves at the top and to the right of the spectra are the projections of the spectra on to the MAS (*F2*) and isotropic (*F1*) axes, respectively.

The $^{27}$Al SATRAS spectra, shown in Figure 8, were reconstructed using the Czjzek-like distribution[46,47] of the electric field gradients (EFG) [Equation (1)], where $\nu_Q = [3eQV_{zz}]/[2I(2I-1)h]$, $\eta_Q = [V_{xx} - V_{yy}]/V_{zz}$, $Q$ is the nuclear quadrupole moment, and $V_{ii}$ are the principal elements of the EFG tensor defined as $|V_{zz}| \geq |V_{yy}| \geq |V_{xx}|$.

$$P(\nu_Q, \eta_Q) = \frac{1}{\sqrt{2\pi}\sigma^d} \nu_Q^{d-1} \cdot \eta_Q \left(1 - \frac{\eta_Q^2}{9}\right) \cdot \exp\left(-\frac{\nu_Q^2\left(1 + \frac{\eta_Q^2}{3}\right)}{2\sigma^2}\right) \quad (1)$$

In Equation (1), $\sigma$ and $d$ are two adjustable parameters. The parameter $\sigma$ characterizes the strength of the quadrupolar interaction. When the five components of the quadrupolar tensor are independent, $d = 5$. In this case the distribution corresponds to the Gaussian Isotropic Model[48] in which the electric field gradient (EFG) distribution is assumed to correspond to statistical disorder.[28] Values of $d < 5$ account for local geometrical constraints.[47] Several tests have been performed for different $d$ values while assuming a unique value of the isotropic chemical shift. The best agreements between the experimental and reconstructed spectra were obtained with $d = 3$ and a line width equal to 350 Hz. This $d$ value is in agreement with previous studies on disordered and glassy aluminium and gallium phases, where good reconstructions of the $^{27}$Al and $^{69,71}$Ga NMR spectra were obtained with $d = 3$ corresponding to the metal atoms residing in octahedral environments.[26,49–51] The relevant parameters ($\delta_{iso}$, and $\sigma$) are given in Table 2. The $\delta_{iso}$ values are within the same range observed for the crystalline compounds, i.e. between –7 ppm and –2 ppm. The experimental and reconstructed $^{27}$Al SATRAS spectra for the glasses with lowest and highest $AlF_3$ contents are compared in Figure 8. The asymmetry of the central transitions is satisfactorily reproduced. The corresponding distributions $P(\nu_Q, \eta_Q)$ used for the reconstruction of these two spectra are shown in Figure 9. Most $\nu_Q$ values are within the range of 100–900 kHz for the 35% $AlF_3$ glass composition ($\sigma$ = 370 kHz and $d$ = 3), with a maximum around 450 kHz. For the 50% $AlF_3$ glass composition ($\sigma$ = 470 kHz and $d$ = 3), the distribution is enlarged, and most of the $\nu_Q$ values are between 100 kHz and 1200 kHz, with a maximum around 600 kHz. Moreover, these quadrupolar parameter distributions are nil when $\nu_Q$ and/or $\eta_Q$ are equal to zero. Therefore, high symmetrical EFGs are prohibited, as would be expected for materials exhibiting the level of disorder present in glassy phases.

 © 2007 Wiley-VCH Verlag GmbH & Co. KGaA, Weinheim 

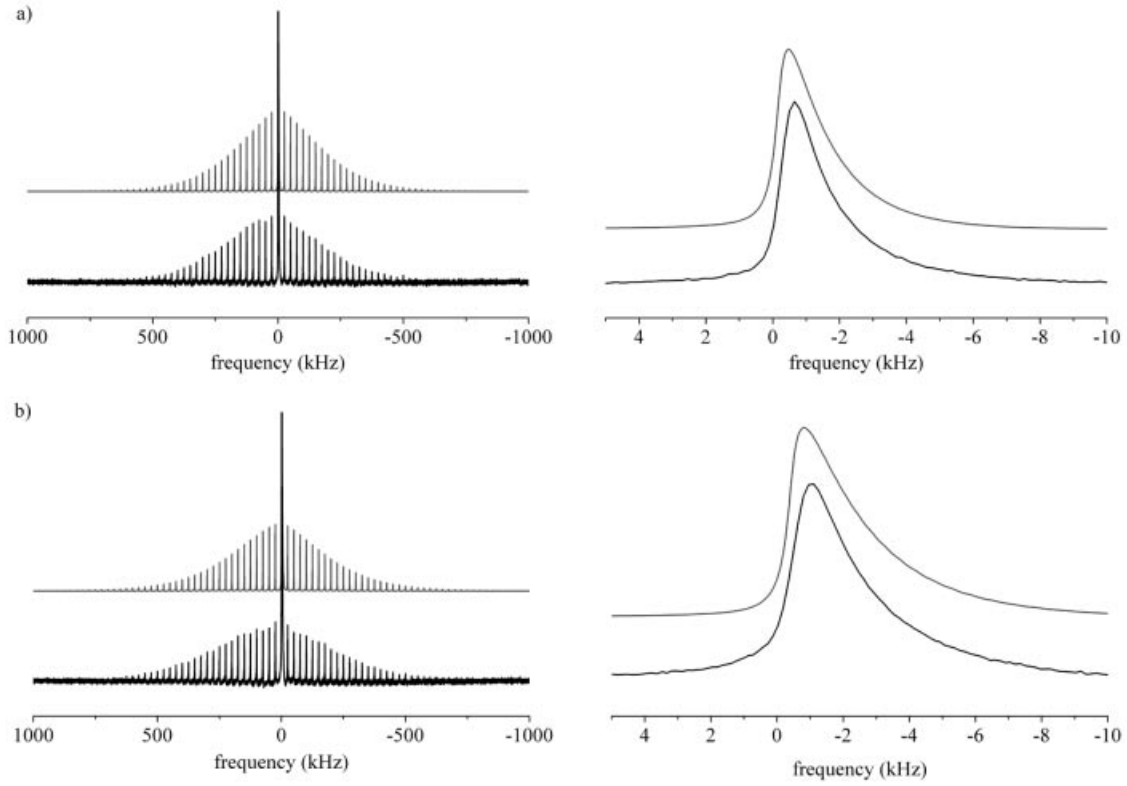


Figure 8. Experimental (bottom) and reconstructed (top) $^{27}$Al SATRAS spectra (left) and central transitions (right) for (a) $50CaF_2$–$15BaF_2$–$35AlF_3$, and (b) $35CaF_2$–$15BaF_2$–$50AlF_3$ glasses at 25 kHz. In the full SATRAS spectra the central transitions are truncated to improve the visiblity of the spinning sidebands.

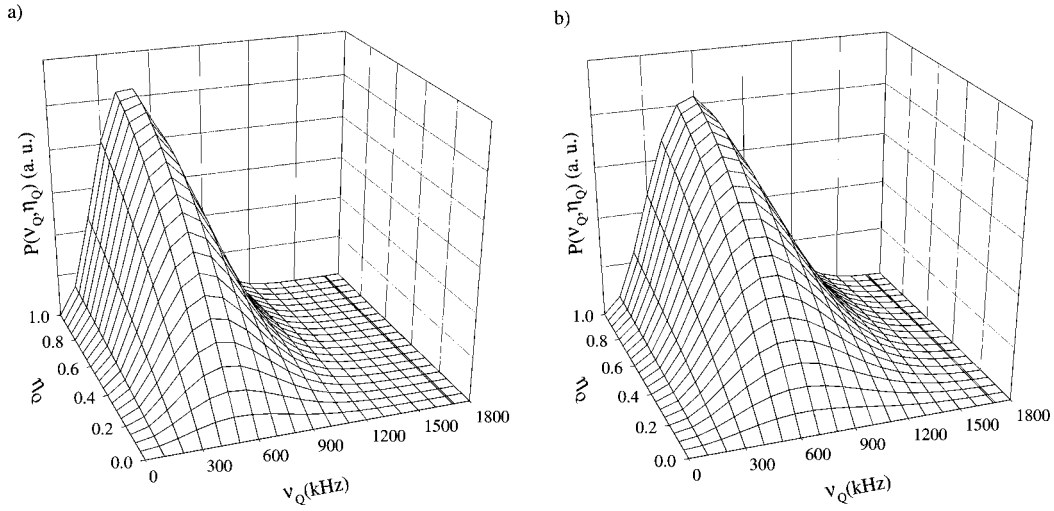


Figure 9. Quadrupolar parameter distributions, $P(\nu_Q, \eta_Q)$, for (a) $\sigma$ = 370 kHz and $d$ = 3; (b) $\sigma$ = 470 kHz and $d$ = 3.

## Discussion

For all the crystalline and glassy phases investigated, the isotropic chemical shift values are between –7 ppm and 1 ppm (Tables 1 and 2), which are typical $\delta_{iso}$ values for $Al^{3+}$ ions in $AlF_6^{3-}$ octahedra. The $\eta_Q$ values deviate from zero, which indicates that the $AlF_6^{3-}$ octahedra are rhombically distorted, in agreement with the crystal data.

For α- and β-$CaAlF_5$ the $\nu_Q$ values are equal to 1580 kHz and 1530 kHz, respectively. Both structures are built up by *trans*-connected $AlF_6^{3-}$ octahedra. The structures of α-, β- and γ-$BaAlF_5$, and $Ba_3Al_2F_{12}$ contain $AlF_6^{3-}$ octahedra that are *cis*-connected at the corners, and the $\nu_Q$ values are between 550 kHz and 1250 kHz. Isolated octahedra are encountered only in $Ca_2AlF_7$, $Ba_3AlF_9$-Ib, β-$Ba_3AlF_9$ and α-

 © 2007 Wiley-VCH Verlag GmbH & Co. KGaA, Weinheim 

$BaCaAlF_7$, and the $\nu_Q$ values range from 75 kHz to 510 kHz (Table 1).

It is well known that a bond involving a shared F ligand is usually longer than one involving an unshared F ligand. For example, in α-$CaAlF_5$[35] the Al-shared F distance is equal to 1.873 Å, and the Al-unshared F distances are equal to 1.806 Å and 1.749 Å. For *trans*-connected octahedron structures these bonds lie in opposite directions and the experimental $\nu_Q$ values are the highest of those measured. The charge distribution is expanded along the longest bond axis, which may correspond to the main *z* axis of the EFG. In the case of the *cis*-connected octahedron structures, the angle formed by the two longest bonds is around 90°, and the experimental $\nu_Q$ values are smaller than those measured for the *trans*-connected structures. We may assume that in this case the charge distribution is expanded along a direction that bisects the two longest bonds; as a result, the axial character of the charge distribution around the aluminium atom in the *cis*-connected octahedra is less pronounced than in the case of the *trans*-connected octahedra. For isolated octahedra the experimental $\nu_Q$ values are the smallest values measured, so in this case the axial character of the charge distributions around the Al atoms is even less pronounced than in the two previous cases, which may be related to smaller differences between the Al–F bond lengths. From these results it appears that the $\nu_Q$ value, which is related to the largest component of the EFG, could account for the way in which the $AlF_6^{3-}$ octahedra are connected i.e. in a *trans*, *cis* or isolated manner.

The main results for the glassy phases are as follows: (i) the low $\delta_{iso}$ values indicate that the $Al^{3+}$ ions are six-fold coordinated; (ii) the quadrupolar parameter distributions have $\nu_Q$ values that are usually encountered in cases where *cis*-connected and isolated octahedra are present in crystalline phases; (iii) the width of the $\nu_Q$ distribution increases with increasing $AlF_3$ content. In a previous $^{19}F$ NMR study[34] the $\beta$ parameter, which gives the mean number of F atoms per octahedron, was found to equal 6 for the glass with 35% $AlF_3$ content. Therefore, it can be stated that the glassy structure contains isolated $AlF_6^{3-}$ octahedra only. The reconstruction of the corresponding SATRAS spectrum indicates that most of the $\nu_Q$ values are between 100 kHz and 900 kHz (Figure 9). It is noticeable that these values appear to be slightly larger than for the crystalline phases containing isolated $AlF_6^{3-}$ octahedra (Table 1). Conversely, for the glass with a 50% $AlF_3$ content, the $\beta$ parameter was found to equal 5, which indicates that, on average, all octahedra are connected at two corners. The $\nu_Q$ range is enlarged to 1200 kHz, and accordingly the maximum $\nu_Q$ value increases from ca. 450 kHz to ca. 600 kHz (Figure 9). This increase in the $\nu_Q$ values with increasing $AlF_3$ content is in agreement with the previous observation based on the crystalline structures. The quadrupolar parameter distributions determined for the intermediate compositions confirm that the ratio of connected octahedra increases along with the $AlF_3$ content. In the glassy samples most of the $\nu_Q$ values range from 100 kHz to 1200 kHz, so we may infer that the *cis* connection is the favoured mode of bonding as far as the octahedra are connected. However, since low $\nu_Q$ values are observed for all the glasses investigated, we may infer that they contain isolated octahedra ($\beta$ = 6). For the glass comprising 50% $AlF_3$, we should assume the presence of ramified chains ($\beta < 5$) rather than infinite chains ($\beta$ = 5), as previously deduced from our $^{19}F$ NMR study.[34]

## Conclusion

$^{27}Al$ SATRAS and 3Q-MAS spectra (for compounds with several Al sites) were recorded for eight crystalline compounds from binary $CaF_2$–$AlF_3$ and $BaF_2$–$AlF_3$ and ternary $BaF_2$–$CaF_2$–$AlF_3$ systems, and four glass compositions with different $CaF_2/BaF_2/AlF_3$ contents.

For the crystalline phases the reconstruction of the spectra leads to the precise determination of the NMR parameters ($\delta_{iso}$, $\nu_Q$ and $\eta_Q$). For the glassy phases the $^{27}Al$ SATRAS spectra have been reconstructed using Czjzek distributions, and the relevant parameters ($\delta_{iso}$ and $\sigma$) were determined.

In agreement with the crystalline and glassy structures, the experimental $\delta_{iso}$ values are typical for $Al^{3+}$ ions in $AlF_6^{3-}$ octahedra. The measured $\eta_Q$ values are not equal to zero, which indicates that the $AlF_6^{3-}$ octahedra are rhombically distorted. It should be noted that despite of the precise determination of the quadrupolar parameters, it was impossible to relate these values to the two Al sites in β- and γ-$BaAlF_5$ both of which have the same multiplicity.

The most interesting finding from this study is the dependence of the quadrupolar frequency on the $AlF_6^{3-}$ octahedron connectivity. For crystalline phases the $\nu_Q$ values are measured between 75 kHz and 510 kHz for structures built up from isolated $AlF_6^{3-}$ octahedra, between 560 kHz and 1250 kHz for structures built up from isolated chains of *cis*-connected $AlF_6^{3-}$ octahedra, and between 1530 kHz and 1580 kHz for structures built up from isolated chains of *trans*-connected $AlF_6^{3-}$ octahedra. In the glassy phases the maximum of the quadrupolar frequency distribution is shifted towards larger values, and its width increases with increasing $AlF_3$ content and therefore the number of connected octahedra. The range of the $\nu_Q$ values seems to indicate that when the octahedra are connected, the most encountered connections are of the *cis* type.

In order to gain a deeper understanding of the dependence of the $\nu_Q$ values on the $AlF_6^{3-}$octahedron network connectivity, ab initio EFG calculations of $^{27}Al$ in crystalline phases are in progress. These calculations will provide important structural information about the sign and the orientation of the EFG tensors with respect to the crystallographic axes. They should also enable us to relate the quadrupolar parameters to the Al sites in the case of multi-site compounds such as β- and γ-$BaAlF_5$.

## Experimental Section

**Sample Preparation:** Owing to the fact that the fluoride compounds are moisture-sensitive, all weighting, mixing and grinding opera-

 © 2007 Wiley-VCH Verlag GmbH & Co. KGaA, Weinheim 

tions were done under anhydrous nitrogen. Before heating, the mixtures were introduced into Pt tubes sealed under anhydrous conditions. The crystalline compounds were synthesized as powders by solid-state reaction of mixtures containing the fluorides $AlF_3$, $CaF_2$ and/or $BaF_2$; the synthesis conditions are detailed in ref.[33] The purity and crystallinity of the phases were monitored by powder X-ray diffraction analysis. The glassy phases were obtained by heating $BaF_2/CaF_2/AlF_3$ mixtures at 1000 °C over a period of 1 h, followed by quenching in cold water. The glass formation was checked by powder X-ray diffraction (the XRD spectra should be featureless). Information regarding the glass formation area is reported in ref.[34]

**High-Resolution Solid-State NMR:** The high-resolution $^{27}$Al NMR spectra were recorded at 78.2 MHz with a Bruker Avance 300 spectrometer. CP MAS probes with 4 mm and 2.5 mm rotors were used for low and high spinning speeds, respectively. The $^{27}$Al isotropic chemical shifts were referenced to a 1 M aqueous solution of $Al(NO_3)_3$. $^{27}$Al SATRAS spectra[1,2] were recorded for all samples. To ensure a linear response regime[52] we chose the pulse duration and the RF field strength to equal 1 μs and 26 kHz, respectively. The recycle delay was set at 1 s. Under these experimental conditions the relative peak intensities are quantitative. The reconstructions of these spectra were achieved using an in-house FORTRAN 95 code based on the theoretical treatment developed by Skibsted et al.,[1,53] and including a correction for the second-order frequency shift, the formula for which is given in ref.[54,26] The adjustable parameters for the crystalline compounds are the quadrupolar frequency, $\nu_Q$, the asymmetry parameter, $\eta_Q$, and the chemical shift tensor, $\delta$. For the glassy phases the SATRAS spectra were reconstructed using the distributions of the quadrupolar parameters ($\nu_Q$, $\eta_Q$) implemented in the FORTRAN 95 code. For the crystalline multi-site compounds and for the glasses MQ-MAS experiments[3] were also carried out using a high-speed CP MAS probe with a 2.5 mm rotor. In the present case 3Q-MAS experiments were performed using a *z*-filter sequence without decoupling. The magnetic field strength was 188 kHz for the two hard pulses, and 8 kHz for the soft pulse. The pulse lengths were equal to 2.7 μs, 0.95 μs, and 10 μs, respectively. A two-dimensional Fourier transformation followed by a shearing[55] transformation gave 2D absorption spectra. For crystalline multi-site compounds an estimation of the quadrupolar parameters and chemical shift values of each contribution was obtained by simulating the corresponding *F1* slices with the DMFit[56] software.

## Acknowledgments

We thank A. Le Bail and A.-M. Mercier, from the Laboratoire des Oxydes et Fluorures, CNRS UMR 6010, who kindly supplied us with the three $BaAlF_5$ structural forms.

[1] J. Skibsted, N. C. Nielsen, H. J. Bildsoe, H. J. Jakobsen, *J. Magn. Reson.* **1991**, *95*, 88–117.
[2] C. Jäger in *Solid State NMR II* (Ed.: B. Blümich), Springer-Verlag, Berlin, **1994**, pp. 133–170.
[3] L. Frydman, J. S. Harwood, *J. Am. Chem. Soc.* **1995**, *117*, 5367–5368.
[4] P. Faucon, J.-C. Petit, T. Charpentier, J. F. Jacquinot, F. Adenot, *J. Am. Ceram. Soc.* **1999**, *82*, 1307–1312.
[5] L. B. Alemany, R. L. Callender, A. R. Barron, S. Steuernagel, D. Iuga, A. P. M. Kentgens, *J. Phys. Chem. B* **2000**, *104*, 11612–11616.
[6] T. Vosegaard, D. Massiot, P. J. Grandinetti, *Chem. Phys. Lett.* **2000**, *326*, 454–460.
[7] C. Gervais, K. J. D. MacKenzie, M. E. Smith, *Magn. Reson. Chem.* **2001**, *39*, 23–28.
[8] S. Ding, C. A. McDowell, *Chem. Phys. Lett.* **2001**, *333*, 413–418.
[9] O. H. Han, C.-S. Kim, S. B. Hong, *Angew. Chem.* **2002**, *114*, 487–490.
[10] M. Capron, F. Fayon, J. Coutures, D. Massiot, A. Douy, *J. Solid State Chem.* **2002**, *169*, 53–59.
[11] J.-P. Amoureux, C. Huguenard, F. Engelke, F. Taulelle, *Chem. Phys. Lett.* **2002**, *356*, 497–504.
[12] U. G. Nielsen, A. Boisen, M. Brorson, C. J. H. Jacobsen, H. J. Jakobsen, J. Skibsted, *Inorg. Chem.* **2002**, *41*, 6432–6439.
[13] M. Capron, F. Fayon, D. Massiot, A. Douy, *Chem. Mater.* **2003**, *15*, 575–579.
[14] S. Ganapathy, K. U. Gore, R. Kumar, J.-P. Amoureux, *Solid State Nucl. Magn. Reson.* **2003**, *24*, 184–195.
[15] G. Silly, C. Legein, J.-Y. Buzaré, F. Calvayrac, *Solid State Nucl. Magn. Reson.* **2004**, *25*, 241–251.
[16] R. Stösser, G. Scholz, J.-Y. Buzaré, G. Silly, M. Nofz, D. Schultze, *J. Am. Ceram. Soc.* **2005**, *88*, 2913–2922.
[17] J. Jiao, J. Kanellopoulos, W. Wang, S. S. Ray, H. Foerster, D. Freude, M. Hunger, *Phys. Chem. Chem. Phys.* **2005**, *7*, 3221–3226.
[18] M. Body, G. Silly, C. Legein, J.-Y. Buzaré, *J. Solid State Chem.* **2005**, *178*, 3655–3661.
[19] M. Body, G. Silly, C. Legein, J.-Y. Buzaré, *Chem. Phys. Lett.* **2006**, *424*, 321–326.
[20] C. Martineau, M. Body, C. Legein, G. Silly, J.-Y. Buzaré, F. Fayon, *Inorg. Chem.* **2006**, *45*, 10215–10223.
[21] D. Iuga, S. Simon, E. De Boer, A. P. M. Kentgens, *J. Phys. Chem. B* **1999**, *103*, 7591–7598.
[22] V. Montouillot, D. Massiot, A. Douy, J. P. Coutures, *J. Am. Ceram. Soc.* **1999**, *82*, 3299–3304.
[23] F. Angelli, T. Charpentier, P. Faucon, J.-C. Petit, *J. Phys. Chem. B* **1999**, *103*, 10356–10364.
[24] J. A. van Bokhoven, A. L. Roest, D. C. Koningsberger, J. T. Miller, G. H. Nachtegaal, A. P. M. Kentgens, *J. Phys. Chem. B* **2000**, *104*, 6743–6754.
[25] P. J. Chupas, M. F. Ciraolo, J. C. Hanson, C. P. Grey, *J. Am. Chem. Soc.* **2001**, *123*, 1694–1702.
[26] G. Scholz, R. Stösser, J. Klein, J.-Y. Buzaré, G. Silly, Y. Laligant, B. Ziemer, *J. Phys.: Condens. Matter* **2002**, *14*, 2101–2117.
[27] M. Fechtelkord, H. Behrens, F. Holtz, J. L. Bretherton, C. A. Fyfe, L. A. Groat, M. Raudsepp, *Am. Mineral.* **2003**, *88*, 1046–1054.
[28] D. R. Neuville, L. Cormier, D. Massiot, *Geochim. Cosmochim. Acta* **2004**, *68*, 5071–5079.
[29] D. Iuga, C. Morais, Z. Gan, D. R. Neuville, L. Cormier, D. Massiot, *J. Am. Chem. Soc.* **2005**, *127*, 11540–11541.
[30] F. Prescuitti, D. Capitani, A. Sgamellotti, B. G. Brunetti, F. Costantino, S. Viel, A. Segre, *J. Phys. Chem. B* **2005**, *109*, 22147–22158.
[31] A. de Kozak, M. Samouël, J. Renaudin, G. Férey, *Z. Anorg. Allg. Chem.* **1992**, *613*, 98–104.
[32] M. Weil, E. Zobetz, F. Werner, F. Kubel, *Solid State Sci.* **2001**, *3*, 441–453.
[33] M. Body, G. Silly, C. Legein, J.-Y. Buzaré, *Inorg. Chem.* **2004**, *43*, 2474–2485.
[34] M. Body, C. Legein, G. Silly, J.-Y. Buzaré, to be published in *J. Non-Cryst. Solids.*
[35] A. Hémon, G. Courbion, *Acta Crystallogr., Sect. C* **1991**, *47*, 1302–1303.
[36] R. Domesle, R. Hoppe, *Z. Anorg. Allg. Chem.* **1982**, *495*, 16–26.
[37] A. Le Bail, G. Férey, A.-M. Mercier, A. de Kozak, M. Samouël, *J. Solid State Chem.* **1990**, *89*, 282–291.
[38] S. Sakida, M. Shojiya, Y. Kawamoto, *J. Fluorine Chem.* **2000**, *106*, 127–131.
[39] R. Domesle, R. Hoppe, *Z. Anorg. Allg. Chem.* **1982**, *195*, 27–38.
[40] V. Kaiser, D. Babel, *Z. Anorg. Allg. Chem.* **2004**, *630*, 794–798.
[41] R. Domesle, R. Hoppe, *Z. Kristallogr.* **1980**, *153*, 317–328.

 © 2007 Wiley-VCH Verlag GmbH & Co. KGaA, Weinheim 

[42] J. Renaudin, G. Férey, A. de Kozak, M. Samouël, *Eur. J. Solid State Inorg. Chem.* **1991**, *28*, 373–381.
[43] A. Le Bail, *J. Solid State Chem.* **1993**, *103*, 287–291.
[44] F. Werner, M. Weil, *Acta Crystallogr., Sect. E* **2003**, *59*, i17–i19.
[45] J. C. C. Chan, H. Eckert, *J. Non-Cryst. Solids* **2001**, *284*, 16–21.
[46] G. Czjzek, J. Fink, F. Götz, H. Schmidt, J. M. D. Coey, J.-P. Rebouillat, A. Liénard, *Phys. Rev. B* **1981**, *23*, 2513–2530.
[47] G. Czjzek, *Phys. Rev. B* **1982**, *25*, 4908–4910.
[48] G. Le Caër, R. A. Brand, *J. Phys.: Condens. Matter* **1998**, *10*, 10715–10774.
[49] B. Bureau, G. Silly, J.-Y. Buzaré, C. Legein, D. Massiot, *Solid State Nucl. Magn. Reson.* **1999**, *15*, 129–138.
[50] B. Bureau, H. Guérault, G. Silly, J.-Y. Buzaré, J.-M. Grenèche, *J. Phys.: Condens. Matter* **1999**, *11*, L423–L431.
[51] B. Bureau, G. Silly, J.-Y. Buzaré, B. Boulard, C. Legein, *J. Phys.: Condens. Matter* **2000**, *12*, 5775–5788.
[52] M. E. Smith, E. R. H. van Eck, *Prog. Nucl. Magn. Reson. Spectrosc.* **1999**, *34*, 159–201.
[53] J. Skibsted, N. C. Nielsen, H. Bildsoe, H. J. Jakobsen, *Chem. Phys. Lett.* **1992**, *188*, 405–412.
[54] S. Ding, C. A. McDowell, *Chem. Phys. Lett.* **2001**, *333*, 413–418.
[55] R. Ernst, G. Bodenhausen, A. Wokaun, *Principles of Nuclear Magnetic Resonance in One and Two Dimensions*, Oxford University Press, New York, **1987**.
[56] D. Massiot, F. Fayon, M. Capron, I. King, S. Le Calvé, B. Alonso, J.-O. Durand, B. Bujoli, Z. Gan, G. Hoatson, *Magn. Reson. Chem.* **2002**, *40*, 70–76.

Received: December 5, 2006
Published Online: March 28, 2007

 © 2007 Wiley-VCH Verlag GmbH & Co. KGaA, Weinheim 

DOI: 10.1002/ejic.200601207

# Broadening the Scope of Ancillary Phosphane-Type Ligands: A Systematic Comparison of $PR_3$, $PR_2BH_3^-$, and $SiR_3^-$ and Their Chalcogen Derivatives

**Theresa I. Kückmann,[a] Franz Dornhaus,[a] Michael Bolte,[a] Hans-Wolfram Lerner,[a] Max C. Holthausen,*[a] and Matthias Wagner*[a]**

**Keywords:** Isoelectronic analogs / P ligands / Si ligands / Ligand design / Boron

This work describes a systematic experimental and theoretical study of the properties of two series of isoelectronic and largely isosteric ligands, namely $PPh_2Me$, $PPh_2BH_3^-$, and $SiPh_2Me^-$ and $SPtBu_3$, $SPtBu_2BH_3^-$, and $SSitBu_3^-$. In addition, we have also investigated the oxo derivatives $OPPh_2BH_3^-$ and $OSiPh_2Me^-$. Based on X-ray crystal structure determinations (Fe–CO and C–O bond lengths) as well as NMR [e.g. $\delta(^{13}CO)$] and IR [$\nu$(CO)] spectroscopic investigations of the corresponding $[CpFe(CO)_2]^+$ complexes, we can conclude that, with respect to electron donor strength, phosphanyl borohydrides occupy an intermediate position between phosphanes (weakest donors) and silyl ligands (strongest donors). The same is true for the thio derivatives, although the differences are smaller. In the reaction with $[CpFe(CO)_2]^+$, the oxo derivative $OPPh_2BH_3^-$ transfers a hydride ion rather than forming a stable $[CpFe(CO)_2(OPPh_2BH_3)]$ complex. The tendency to undergo hydride-transfer reactions was studied by density functional calculations for the series $PtBu_2BH_3^-$, $OPtBu_2BH_3^-$, and $SPtBu_2BH_3^-$. The results reveal that $OPtBu_2BH_3^-$ is the strongest and $SPtBu_2BH_3^-$ the weakest hydride donor, in accordance with the experimental observations. Theoretical analysis indicates that the three derivatives $PPh_2Me$, $PPh_2BH_3^-$, and $SiPh_2Me^-$ are truly isolobal species despite variations in their charge distributions.
(© Wiley-VCH Verlag GmbH & Co. KGaA, 69451 Weinheim, Germany, 2007)

## Introduction

The performance of a homogeneous catalyst depends critically on the steric and electronic properties of its ligands.[1,2] Intense research has therefore been devoted to the development of donor molecules specifically designed for the assembly of a particular catalyst with a well-defined purpose. As a result, homogeneous catalysis with transition-metal complexes has enjoyed enormous success, and catalyst research continues to gain momentum.[3] A wealth of information has been gathered on numerous individual ligand classes, which now must be compared in order to establish their relationship to one another. The goal is to create versatile toolboxes of ligands with smoothly varying donor properties so that the most suitable derivative can easily be selected for the rational de novo design of efficient catalysts.

We have a long-standing interest in the development of boron-based N-donor ligand systems [e.g. mono- and ditopic bis- and tris(pyrazol-1-yl)borates] for applications both in materials science and catalysis.[4–10] In order to extend the range of accessible complexes, we are presently broadening our focus to include negatively charged boron-based P-donor ligands and their isoelectronic silyl analogs. The purpose of this paper is to reveal the underlying relationship between two representatives of these ligand classes, namely phosphanyl borohydrides $PR_2BH_3^-$ and triorganylsilanides $SiR_3^-$, and to compare them with the well established phosphane ligands $PR_3$.

A generic methyldiorganylphosphane **A** is shown in Figure 1. On moving to the phosphanyl borohydride **B**, the phosphane methyl group is replaced by a $BH_3$ moiety. This leaves the central atom unchanged but results in a negatively charged ligand. The substitution pattern is conserved in the corresponding silyl compound **C** but the central phosphorus atom is replaced by silicon, which again introduces a negative charge. The same relationship holds true for the chalcogen derivatives of these compounds (**D**–**F**; Figure 1), which have been the subject of two recent studies.[11,12] We are interested in investigating the similarities as well as the fundamental differences between these three related species. We commence with a brief review of selected literature relevant to this pursuit.

Phosphanes are ubiquitous ligands in coordination chemistry due to their σ-donating and π-accepting properties.[13,14] The degree to which these σ and π components influence the overall coordination characteristics of a given phosphane depends on the phosphorus-bound substituents. The π-acceptor strength of $PF_3$, for example, is comparable to that of CO, which is often considered the archetypical π-

[a] Institut für Anorganische Chemie, Johann Wolfgang Goethe-Universität Frankfurt am Main,
Max-von-Laue-Straße 7, 60438 Frankfurt, Germany
Fax: +49-69-798-29260
E-mail: Matthias.Wagner@chemie.uni-frankfurt.de
Supporting information for this article is available on the WWW under http://www.eurjic.org or from the author.

 © 2007 Wiley-VCH Verlag GmbH & Co. KGaA, Weinheim 

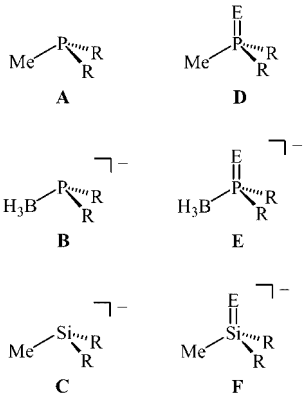


Figure 1. Isoelectronic phosphanes, phosphanyl borohydrides, and silanides, and their chalcogen derivatives.

acceptor ligand. Trialkylphosphanes, on the other hand, are primarily σ-donors and participate to only a small degree in π-backbonding.

Transition metal complexes with silyl ligands, while not as widespread as phosphane complexes, have also received significant attention in the literature.[15,16] Such studies have focused primarily on the reactivity of the Si–M bond, for example in transition-metal-catalyzed hydrosilylation or C–Si bond formation.[15,17] Recently, silyl derivatives have also generated increasing interest as ancillary ligands.[18] Indeed, it has been suggested that silyl ligands might enhance the performance of soluble catalytic systems for hydrogenation or hydroformylation reactions.[19] Silyl ligands are strongly electron-releasing with comparatively poor π-accepting properties and display a pronounced *trans* effect, which makes them potentially complementary ligands to phosphanes.[18,20–22] It is clear, however, that the properties of formally isoelectronic silyl and phosphane ligands differ significantly and that this difference is too large to be considered a gradual transition.

Phosphanyl borohydrides $PR_2BH_3^-$ are intermediate species in which the donor phosphorus atom remains as in phosphanes, but which contain a negative charge, as do silyl ligands. To date, these anionic phosphane analogues have mainly been generated in situ and used as building blocks for the preparation of chiral organophosphanes.[23–26] However, there is a growing number of phosphanyl borohydride transition metal complexes in the literature. Manners et al., for example, have exploited the regioselective insertion of the $Pt(PEt_3)_2$ fragment into the P–H bond of $PPhBH_3(H)_2$ or $PPh_2BH_3(H)$ in order to prepare the platinum phosphanyl borohydride complexes *trans*-[PtH(PPhRBH$_3$)-$(PEt_3)_2$] (R = H, Ph).[27] Other examples of structurally characterized phosphanyl borohydride complexes include the compounds $[(dppp)Pd(C_6F_5)(PPh_2BH_3)]$[28] and $[(C_5Me_5)Fe(CO)_2(PPh_2BH_3)]$.[29] In a 1996 paper, Fu and co-workers described diphenylphosphidoboratabenzene, $PPh_2(BC_5H_5)^-$, as the anionic analog of triphenylphosphane and investigated its coordination chemistry.[30]

While not as common as the parent phosphanes, phosphane oxides also play an important role as ancillary ligands in coordination chemistry,[13] especially in the form of bidentate bisphosphane monooxides [P(O)–P] or P(O)–O and P(O)–N type ligands, which form part of efficient catalytic systems for rhodium- and cobalt-catalyzed hydroformylation reactions.[31–33]

Transition metal siloxide complexes have also been investigated.[34–38] For example, rhodium siloxides are active in catalytic hydrosilylation reactions,[34,39] and titanium, niobium, and tantalum siloxide systems have been used to investigate C–H activation[37] and olefin-to-alkylidene rearrangement.[38]

The corresponding chalcogen derivatives of phosphanyl borohydrides, $EPR_2BH_3^-$ (E = O–Te), have only recently been reported in the literature,[12] and their application as ligands for transition metals has yet to be explored.

In order to shed more light on the relative importance of donor atom and electronic structure for the ligand properties of phosphanes, phosphanyl borohydrides, and silanides, we have investigated two series of isoelectronic, isosteric compounds (Figure 2). In the case of the non-chalcogen species, the diphenyl derivatives **1**, **2a**, and **3a** were chosen for detailed study. In order to still be able to evaluate the effect of increased steric demand, P*t*Bu$_2$BH$_3^-$ (**2b**) was also investigated. For the chalcogen derivatives, both the phenyl and *tert*-butyl systems **4**–**8** were studied.

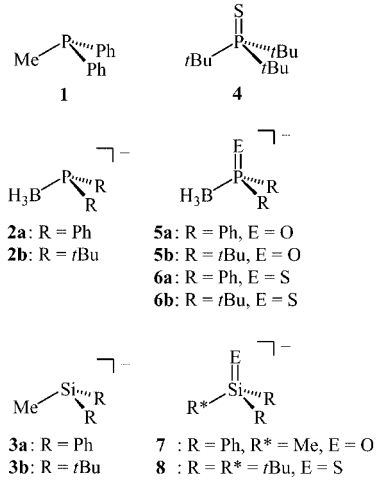


Figure 2. Ligand numbering scheme for isoelectronic species **1**–**3** and **4**–**8**.

For the transition metal site, we chose the cyclopentadienidoiron dicarbonyl fragment $[CpFe(CO)_2]^+$ (in future referred to as $Fp^+$) as a model system. This fragment is an ideal candidate for our pursuit because it has a single vacant coordination site (often occupied by halides or donor solvent molecules in its isolable derivatives) and all of the ligands in question can be expected to coordinate to it in a similar fashion, regardless of whether the result is a neutral or cationic complex. In addition, its electronic properties can be related to the carbonyl IR stretching frequencies[40] as well as to the $^{13}C$ NMR shifts of the carbonyl[41] and cyclopentadienido[42] carbon atoms.

 © 2007 Wiley-VCH Verlag GmbH & Co. KGaA, Weinheim 

Terminal, unbridged phosphane complexes of the $Fp^+$ fragment are well known in the literature, with one of two synthetic routes generally being applied. The first involves treating $Fp^+$ complexes containing labile ligands such as thf or $I^-$ with phosphanes.[43–46] In the second, $Fp_2$ is oxidized in the presence of phosphane ligand, typically with ferrocenium or cobaltocenium ions.[47–49] Using a different approach, Malisch has succeeded in isolating $[(C_5Me_5)Fe(CO)_2(PPh_2Me)]I$, which was prepared by reaction of the corresponding diphenylphosphido complex with MeI and characterized spectroscopically.[29]

To the best of our knowledge, no structurally characterized monomeric $FpSiR_3$ complexes in which the silyl ligand bears only alkyl and/or aryl substituents R have been previously reported. Nevertheless, there are a number of silyl complexes with known molecular structures where the silicon atom is bound to electron-withdrawing functional groups.[50–53] Complexes of $Fp^+$ bearing silyl ligands with solely aryl and/or alkyl substituents have, however, been spectroscopically characterized and are typically obtained by treating NaFp with a triorganylsilyl chloride.[54–57]

The σ-donor properties of the phosphanyl borohydride **2a** (Figure 2) towards selected main group Lewis acids have already been explored.[58] It was found that **2a** forms stronger Lewis acid–base adducts than the related phosphane $PPh_2Me$ (**1**). Transition metal complexes of phosphanyl borohydrides are rare in the literature, with only a handful of structurally characterized complexes {e.g. $[FpPPh_2(BC_5H_5)]$ and $[(C_5Me_5)Fe(CO)_2(PPh_2BH_3)]$}.[27–30] The complex $[FpPPh_2BH_3]$ was prepared from $FpPPh_2$ and $BH_3$·thf and was characterized spectroscopically.[59]

The few examples of Fp-phosphane chalcogenide complexes with trialkyl- and triarylphosphane chalcogenides $EPR_3$ (R = *i*Pr, *t*Bu, Ph; E = O, S, Se) were prepared by reaction with $[Fp(thf)]BF_4$ and characterized spectroscopically[60] and, in part, by cyclic voltammetry.[61] The same synthetic route can be followed for silyl thiolates, and a small number of complexes of the type $FpSSiR_3$ have been isolated.[62] The coordination of chalcogenated phosphanyl borohydrides to the $Fp^+$ fragment has not been described previously.

## Results and Discussion

### Synthesis

In order to conduct a detailed comparison of transition metal complexes of the non-chalcogen ligands, compounds $[FpPPh_2Me]I$ (**11I**), $[FpPPh_2BH_3]$ (**12a**), $[FpPtBu_2BH_3]$ (**12b**), and $[FpSiPh_2Me]$ (**13**) were synthesized (Scheme 1). Compound **11I** was prepared from FpI (**9**), $LiPPh_2$, and MeI in thf. Reports of the synthesis of this complex directly from FpI and $PPh_2Me$ (**1**) describe impurities due to the CO-substitution product $[CpFe(CO)(PPh_2Me)I]$.[63] In contrast, the procedure followed here produces the product as a yellow solid in high purity and good yield. Complex **11I** is, however, sensitive to light, and photochemical decomposition can be observed, which proceeds more quickly in solution than in the solid state. When the solid is stored under inert atmosphere and protected from light, the compound is stable for several months. X-ray quality crystals can be obtained by gas-phase diffusion of diethyl ether into an acetonitrile solution of the complex.

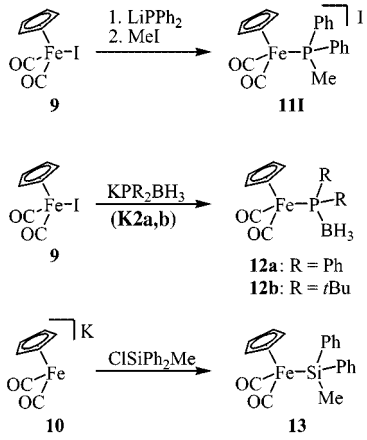


Scheme 1. Complexes of a phosphane and its isoelectronic analogues, **11I**–**13**.

Preparation of the phosphanyl borohydride homologue **12a** in an analogous reaction using $BH_3$·thf instead of MeI has been reported.[59] However, the general utility of phosphanyl borohydrides as ligands can best be achieved if it is possible to form metal complexes by introducing the preformed ligands, rather than assembling them with the phosphorus atom connected to a metal fragment. With this goal in mind, FpI was treated with $KPPh_2BH_3$ (**K2a**) in thf, which resulted in nearly quantitative formation of the desired compound **12a**. It also proved possible to synthesize $[FpPtBu_2BH_3]$ (**12b**) by the same method. Both complexes were isolated as X-ray quality crystals by gas-phase diffusion of pentane into a concentrated toluene solution of **12a** or **12b**. The yellow solids can be handled in air for short periods of time but decompose upon longer exposure.

Considering the similarities between silanides and phosphanyl borohydrides, it would be desirable to apply the same synthetic route used for complexes of the latter to the preparation of complexes of the former. The sodium silanides $NaSiPh_2Me$[64] (**Na3a**) and $NaSitBu_2Me$[65] (**Na3b**) are both known in the literature, although the former has been characterized only by boiling point determination of the corresponding silane after hydrolysis. The di-*tert*-butyl species **Na3b** is well documented, but the synthesis of the donor-free compound as described by Sekiguchi, which involves reduction of the bromosilane with elemental sodium in boiling heptane, results in a significant amount of disilane impurity.[65] Another common synthesis of sterically hindered sodium silanides, in this case donor-supported, involves the reduction of the corresponding bromosilanes with sodium metal in thf.[66] Biphenyl can be used as a redox catalyst to allow lower reaction temperatures. In an effort to avoid unnecessary and unwanted by-products, this method was used to prepare $(thf)_xNaSitBu_2Me$. The NMR

 © 2007 Wiley-VCH Verlag GmbH & Co. KGaA, Weinheim 

chemical shifts ($^1$H, $^{13}$C, $^{29}$Si) of the sodium silanide produced by this route were in good agreement with the published values. Slight variations can be attributed to the fact that the procedure reported here results in a donor-supported silanide, while the literature describes the synthesis of the donor-free compound. Unfortunately, this synthetic method led to unexpected side products. In an attempt to grow crystals of the silanide, dark green blocks of the silylated biphenyl radical [(18-crown-6)(thf)$_2$Na][4,4′-(Si*t*Bu$_2$Me)$_2$(C$_6$H$_4$)$_2$] were isolated.[67] In light of this result and the poor characterization of NaSiPh$_2$Me in the literature, no further attempts to synthesize [FpSiR$_2$Me] (R = Ph, *t*Bu) from Fp$^+$ and SiR$_2$Me$^-$ were undertaken.

As described above, a number of [FpSiR$_3$] complexes have been reported in the literature. Due to the low electronegativity of silicon, these reactions generally proceed with silyl chlorides. This, in essence, represents the umpolung of the procedure used with phosphanyl borohydrides **2a** and **2b**. The synthesis of [FpSiPh$_2$Me] (**13**) by this method has been described.[57] When KFp (**10**) is treated with ClSiPh$_2$Me in thf, the desired complex is formed in nearly quantitative yield (Scheme 1). Impurities can be removed by filtration through silica gel using hexane/CH$_2$Cl$_2$ (2:1) as the eluent. Recrystallization from hexane at –25 °C yields the complex as light-brown plates.

Considering the success achieved with the parent compounds, it was logical to explore the behavior of the chalcogen derivatives KOPPh$_2$BH$_3$ (**K5a**), NaOSiPh$_2$Me (**Na7**), and KSPPh$_2$BH$_3$ (**K6a**) with the Fp$^+$ fragment (the silyl thiolate NaSSiPh$_2$Me is not readily accessible).

When FpI was treated with **K5a** in thf, a colorless solid was slowly deposited over the course of several days. NMR analysis of the resulting mixture revealed conversion of FpI to Fp$_2$ and the appearance of unidentified components in the $^{31}$P and $^{11}$B NMR spectra. Upon closer inspection of the hydride region of the $^1$H NMR spectrum, a small amount of FpH[68] could be identified, which is known to be an unstable intermediate that decomposes to Fp$_2$ and H$_2$.[69,70] This finding suggests that rather than forming an Fe–O bond, the iron atom interacts with the borohydride moiety of the ligand, ultimately resulting in hydride transfer. Although the fate of the ligand after hydride transfer remains unclear, it seems likely that oligomeric or polymeric compounds of the type [OPPh$_2$BH$_2$]$_n$ are formed.

The observation of a hydride-transfer product with **K5a** is particularly interesting in light of a comparison with the siloxide **Na7**, since it is unlikely that the methyl moiety would engage in the same kind of behavior. However, when a thf solution of FpI is treated with **Na7**, Fp$_2$ is the only Cp-containing product. In the $^{29}$Si NMR spectrum, O(SiPh$_2$Me)$_2$ can be identified as the major silicon-containing product (its $^1$H, $^{13}$C, and $^{29}$Si NMR shifts correspond to an authentic sample prepared from ClSiPh$_2$Me and NaOSiPh$_2$Me).[71–73] A similar reaction to that with FpI was observed when the alternative starting material [Fp(thf)]PF$_6$ was treated with **K5a** and **Na7**. However, in the latter case a significant amount of ferrocene was formed in addition to Fp$_2$.

The reaction of KSPPh$_2$BH$_3$ (**K6a**) with [Fp(thf)]PF$_6$ (**14PF$_6$**) was more successful. Thus, when the reactants were combined in CH$_2$Cl$_2$ at –78 °C and warmed to room temperature overnight, a colorless precipitate (KPF$_6$) formed. Changing the solvent to toluene with subsequent filtration through a plug of silica gel on a frit allowed the product complex [FpSPPh$_2$BH$_3$] (**16a**, Scheme 2) to be isolated as an orange oil. Although the NMR and IR data clearly indicate the formation of the complex, attempts to obtain single crystals of **16a** failed.

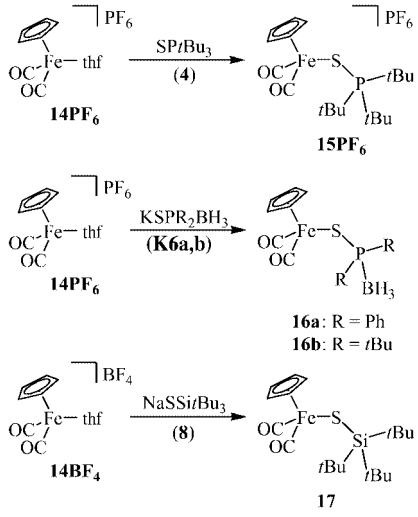


Scheme 2. Complexes of a phosphane sulfide and its isoelectronic analogs, **15PF$_6$**–**17**.

In the hope of isolating a crystalline product, the same reaction was carried out using the *tert*-butyl derivative **K6b** rather than the phenyl derivative **K6a**. In this case, filtration of the crude product through silica gel and recrystallization from benzene yielded orange X-ray quality needles of [FpSP*t*Bu$_2$BH$_3$] (**16b**).

Since the isosteric silyl thiolate NaSSi*t*Bu$_2$Me is not easily accessible, we turned to the sterically more hindered NaSSi*t*Bu$_3$ (**Na8**). This compound reacts readily with [Fp(thf)]BF$_4$ (**14BF$_4$**) in CH$_2$Cl$_2$ at room temperature to give the desired complex [FpSSi*t*Bu$_3$] (**17**; Scheme 2). Recrystallization from a concentrated pentane solution yielded X-ray quality crystals.

The complex of the analogous phosphane sulfide **4**, [FpSP*t*Bu$_3$]BF$_4$ (**15BF$_4$**), has been described in the literature.[60] Using the PF$_6^-$ salt **14PF$_6$**, we were able to isolate X-ray quality crystals of the compound by gas-phase diffusion of pentane into a solution of [FpSP*t*Bu$_3$]PF$_6$ (**15PF$_6$**) in CHCl$_3$ (Scheme 2).

It was thus possible to prepare two series of three isoelectronic compounds each in which all six compounds were characterized by X-ray crystal structure analysis and NMR and IR spectroscopy. Complexes **11I**, **12a**, and **13** are derived from the phosphane PPh$_2$Me, while complexes **15PF$_6$**, **16b**, and **17** are related to the phosphane sulfide SP*t*Bu$_3$. A comparison of these two sets of isoelectronic complexes grants insight into the electronic differences between the ligands.

 © 2007 Wiley-VCH Verlag GmbH & Co. KGaA, Weinheim 

### Structural and Spectroscopic Comparison of 11I, 12a, 12b, and 13

Selected bond lengths and angles for **11I**, **12a**, **12b**, and **13** are compiled in Table 1. Details of the X-ray crystal structure analyses of these compounds are summarized in Table 5.

Table 1. Selected bond lengths [Å] for compounds **11I**–**13**; calculated values in italics.

| | Fe–P/Si | Fe–CO (av.) | C–O (av.) |
|---|---|---|---|
| **11I** | 2.236(2) | 1.779(9) | 1.146(10) |
| *calc.* | *2.338* | *1.787* | *1.158* |
| **12a** | 2.2705(6) | 1.772(2) | 1.141(2) |
| *calc.* | *2.367* | *1.772* | *1.163* |
| **12b** | 2.3404(6) | 1.756(3) | 1.142(3) |
| **13** | 2.3353(5) | 1.755(2) | 1.160(3) |
| *calc.* | *2.389* | *1.757* | *1.168* |

Phosphane compound **11I** crystallizes in the triclinic space group $P\bar{1}$ with well-separated complex cations and iodide anions (Figure 3). The Fe–P bond [2.236(2) Å] is in the range of Fe–P distances found for other $[FpPR_3]^+$ complex cations.[74]

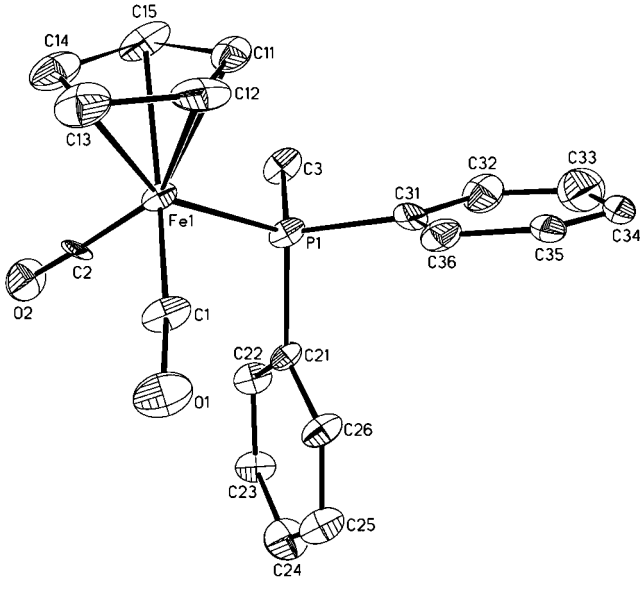


Figure 3. Solid-state structure of the complex cation of **11I**. Thermal ellipsoids are drawn at the 50% probability level. H atoms have been omitted for clarity.

Both phosphanyl borohydride complexes **12a** and **12b** crystallize in the orthorhombic space group $P2_12_12_1$ (Figures 4 and 5, respectively). Their structural parameters are similar, although **12b** shows signs of the higher steric demand of the *tert*-butyl substituents: the Fe–P bond [2.3404(6) Å] is somewhat longer than in the diphenyl derivative **12a** [2.2705(6) Å]. The Fe–CO bonds, on the other hand, are slightly shorter in **12b** (Table 1). Furthermore, the B–P–Fe–COG torsion angles (COG = center of gravity of the Cp ring) differ significantly: the torsion angle is 56.8° for **12a** and –175.9° for **12b**. The only other structurally characterized Fp complex with an anionic phosphorus/boron ligand was reported by Fu and co-workers and contains coordinated diphenylphosphidoboratabenzene.[30] This complex has an Fe–P bond of 2.276(2) Å, which is similar to that in **12a** [2.2705(6) Å]. The Fe–CO distances in Fu's compound [av. 1.742(10) Å] are slightly shorter than in **12a** [av. 1.772(2) Å] but similar to those in **12b** [av. 1.756(3) Å]. The C–O distances [av. 1.169(9) Å] are longer than in both of the phosphanyl borohydride complexes [**12a**: av. 1.141(2) Å; **12b**: av. 1.142(3) Å].

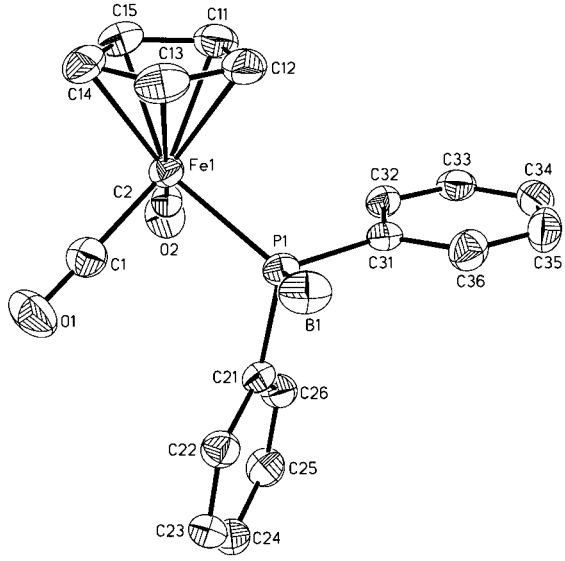


Figure 4. Solid-state structure of **12a**. Ellipsoids are drawn at the 50% probability level. H atoms have been omitted for clarity.

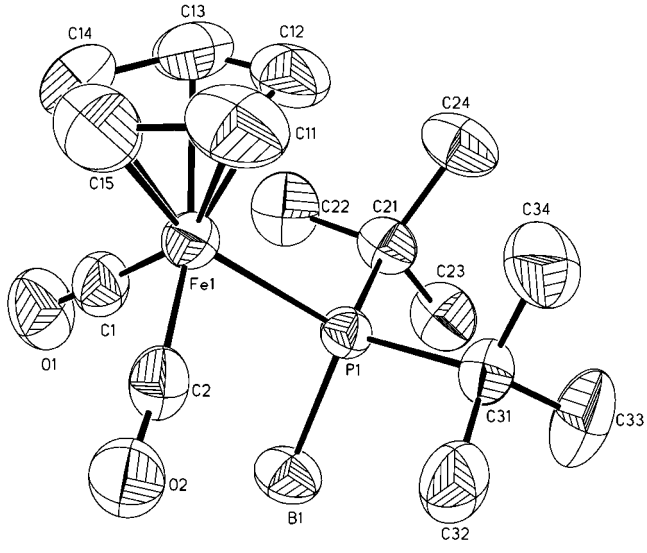


Figure 5. Solid-state structure of **12b**. Ellipsoids are drawn at the 50% probability level. H atoms have been omitted for clarity.

 © 2007 Wiley-VCH Verlag GmbH & Co. KGaA, Weinheim 

Complex **13** (orthorhombic, $P2_12_12_1$; Figure 6) has the longest Fe–Si bond [2.3353(5) Å] of the structurally characterized Fp-silyl complexes in the literature, with the exception of those complexes with donor silicon atoms bound to silyl residues without electron-withdrawing substituents (cf. $[FpSiMe_2SiPh_3]$: Fe–Si = 2.346(1) Å;[75] $[FpSiPh(SiMe_3)_2]$: Fe–Si = 2.366(1) and 2.355(1) Å in two crystallographically independent molecules[76]). The Fe–Si bond in **13** cannot, of course, be compared directly to the Fe–P bonds in complexes **11I**, **12a**, and **12b**. However, the difference between the Fe–P bond length in **12a** and the Fe–Si bond length in **13** is roughly equivalent to the difference in the covalent radii[71] of P and Si. The Fe–CO distances in **13** are comparable to those found in other Fp-silyl complexes[74] but shorter than those in complexes **11I** and **12a** (Table 1). The C–O bonds found in silyl complex **13** [av. 1.160(3) Å] are roughly 0.015 Å longer than in the complexes **11I** and **12**. This indicates that the π-backbonding from the iron center to the CO ligands is most pronounced in the silyl complex and suggests that **3a** is the strongest donor of the isoelectronic series **1**, **2a**, and **3a**.

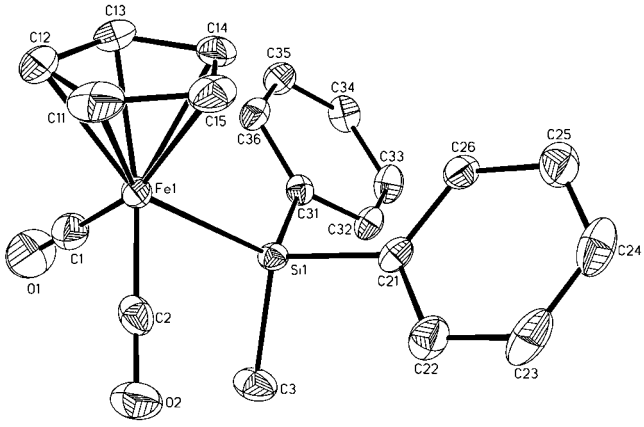


Figure 6. Solid-state structure of **13**. Ellipsoids are drawn at the 50% probability level. H atoms have been omitted for clarity.

This interpretation of relative donor strengths is supported by the $^{13}C$ NMR chemical shifts of the carbonyl carbon atoms. A summary of spectroscopic data can be found in Table 2. It has been shown in the literature that an increase in the donor capacity of an ancillary ligand in a carbonyl complex leads to a shift of the carbonyl carbon atom resonance to lower field.[41,49,77] The carbonyl carbon atom of silyl complex **13** resonates at $\delta$ = 215.8 ppm. The corresponding signals for **12a** and **11I** are found at $\delta$ = 213.5 and 210.4 ppm, respectively. The $^{13}C$ NMR chemical shifts of the cyclopentadienido ligands in metal carbonyl complexes also correlate to the electron density at the metal center, although in this case higher electron density corresponds to a shift to higher field.[42,49,77] Phosphane complex **11I** contains the Cp ring with the most deshielded carbon nuclei ($\delta$ = 89.1 ppm). The cyclopentadienido ring of **12a** resonates at $\delta$ = 86.8 ppm (**12b**: $\delta$ = 86.5 ppm), and the corresponding signal for silyl complex **13** can be seen at $\delta$ = 84.4 ppm. In summary, the NMR spectroscopic data also support the conclusion that the following trend can be established for the donor strengths of the isoelectronic, isosteric ligands: **3a** > **2a** > **1**.

In the $^{31}P$ NMR spectrum, the resonance of the P atom in **12b** is found at $\delta$ = 81.4 ppm, a shift to considerably lower field compared to **11I** ($\delta$ = 48.6 ppm) and **12a** ($\delta$ = 34.3 ppm). This is attributable to the difference in steric demand between the two complexes. This effect has already been observed for potassium phosphanyl borohydrides **K2a** and **K2b**[78] as well as for the parent phosphanes $PPh_3$ and $PtBu_3$.[79] The $^1J_{P,C}$ coupling constants can be correlated to the degree of s character in the P–C bonding orbital.[79] For the two isosteric compounds **11I** and **12a**, $^1J_{P,C}$ (C-*i*) is significantly larger for the phosphane complex (**11I**: 52.9 Hz; **12a**: 27.8 Hz), thereby indicating a larger degree of s character in the P–C-*i* bonding orbital of **11I**. A similar relationship between the $^1J_{P,C}$ values is observed for the free ligands and can easily be explained by Bent's rule.[58,80]

Comparison of the carbonyl IR stretching frequencies is, of course, also an important measure of donor strength in carbonyl complexes (Table 2). In accordance with the interpretation of the $^{13}C$ NMR spectra, complex **11I** is found to have the highest CO stretching frequencies (2055 and 2011 $cm^{-1}$ in MeCN solution). These values compare favorably with those found in the literature for similar complexes.[81–83] Introduction of the $BH_3$ moiety and consequently of a negative charge in **12a** leads to a marked decrease in the frequencies of these vibrations to 2030 and 1982 $cm^{-1}$ (MeCN solution). The relatively low-energy bands found for complex **13** (1994 and 1938 $cm^{-1}$; MeCN

Table 2. Selected spectroscopic parameters for compounds **11I**–**13**; calculated values in italics.

| | $\tilde{\nu}$(CO)[a] [$cm^{-1}$] | $\delta$($^{13}C$) (CO)[b] ($^2J_{P,C}$ [Hz]) | $\delta$($^{13}C$) (Cp)[b] | $\delta$($^{13}C$) (C-*i*)[b] ($^1J_{P,C}$ [Hz]) | $\delta$($^{31}P$/$^{29}Si$)[b] |
|---|---|---|---|---|---|
| **11I** | 2055, 2011 (2033) | 210.4 (24.2) | 89.1 | 134.1 (52.9) | 48.6 |
| *calc.* | *2029*[c] | *205.7* | *89.1* | *128.9* | – |
| **12a** | 2030, 1982 (2006) | 213.5 (18.0) | 86.8 | 140.2 (27.8) | 34.3 |
| *calc.* | *2002*[c] | *208.6* | *88.6* | *139.2* | – |
| **12b** | 2029, 1982 | 215.5 (17.0) | 86.5 | – | 81.4 |
| **13** | 1994, 1938 (1966) | 215.8 | 84.4 | 144.6 | 35.1 |
| *calc.* | *1977*[c] | *208.5* | *85.6* | *142.9* | – |

[a] In MeCN; ($\tilde{\nu}_{as}$ + $\tilde{\nu}_{s}$)/2 given in parentheses. [b] **11I** in $CD_3CN$ and **12**–**13** in $C_6D_6$. [c] ($\tilde{\nu}_{as}$ + $\tilde{\nu}_{s}$)/2 scaled by 0.9884 to correct for systematic errors.

 © 2007 Wiley-VCH Verlag GmbH & Co. KGaA, Weinheim 

Table 3. Selected bond lengths [Å] and angles [°] for compounds **15PF$_6$**, **16b**, and **17**; calculated values in italics.

| | Fe–S | S–P/Si | Fe–CO (av.) | C–O (av.) | OC–Fe–CO | Fe–S–P/Si |
|---|---|---|---|---|---|---|
| **15PF$_6$** | 2.3469(4) | 2.0473(5) | 1.799(2) | 1.139(3) | 93.35(9) | 127.88(2) |
| *calc.* | *2.434* | *2.072* | *1.791* | *1.158* | *95.3* | *129.4* |
| **16b** | 2.3125(8) | 2.087(1) | 1.784(3) | 1.144(4) | 98.0(2) | 115.86(4) |
| *calc.* | *2.399* | *2.104* | *1.784* | *1.159* | *97.0* | *118.6* |
| **17** | 2.345(2) | 2.147(2) | 1.776(5) | 1.151(6) | 93.1(2) | 129.01(7) |
| *calc.* | *2.387* | *2.194* | *1.774* | *1.162* | *94.6* | *127.9* |

solution) are consistent with the NMR spectroscopic data, which indicate that the silyl ligand is the strongest donor of the three.

When moving from **1** to **2a** to **3a** within the $Fp^+$ system, it is also interesting to consider the effect of exchanging the Cp ligand for Cp* (Cp* = $C_5Me_5^-$) while leaving the other ligands unchanged. While the Cp* silyl complex has not been described in the literature, both the phosphane and phosphanyl borohydride adducts have been reported by Malisch and co-workers.[29] In $CH_2Cl_2$ solution, the CO stretching frequencies are observed at 2029 and 1987 $cm^{-1}$ for the phosphane complex [Cp*Fe(CO)$_2$(PPh$_2$Me)]I, thereby demonstrating that the effect of exchanging Cp for Cp* is comparable to exchanging the phosphane ligand for the corresponding phosphanyl borohydride. Bands attributable to the CO ligands in [Cp*Fe(CO)$_2$(PPh$_2$BH$_3$)], on the other hand, are found at 2007 and 1959 $cm^{-1}$ ($CH_2Cl_2$ solution). These frequencies lie above those seen for complex **13**, thus indicating that moving from the phosphanyl borohydride to the silyl ligand has a more dramatic effect on the electronic structure of the compound than replacing Cp with Cp*. Taken together, these results suggest that, when viewed electronically, the difference between the phosphane and phosphanyl borohydride ligands is somewhat smaller than between the phosphanyl borohydride and silyl ligands.

### Structural and Spectroscopic Comparison of 15PF$_6$, 16b, and 17

Selected bond lengths and angles for **15PF$_6$**, **16b**, and **17** are compiled in Table 3. Details of the X-ray crystal structure analyses of these compounds are summarized in Table 6.

The three iron–sulfur complexes [FpSP*t*Bu$_3$]PF$_6$ (**15PF$_6$**; orthorhombic, $P2_12_12_1$, Figure 7), [FpSP*t*Bu$_2$BH$_3$] (**16b**; orthorhombic, *Pbca*, Figure 8) and [FpSSi*t*Bu$_3$] (**17**; triclinic, $P\bar{1}$, Figure 9) all adopt the expected structure with monodentate, end-on coordination of the sulfide ligands. Separated ion pairs are found in **15PF$_6$**. The effect of the increased steric bulk of **15PF$_6$** and **17** compared to **16b** is most noticeable in the Fe–S–P/Si bond angle, which is nearly 130° in the tri-*tert*-butyl derivatives **15PF$_6$** [127.88(2)°] and **17** [129.01(7)°], compared to 115.86(4)° in **16b**. The Fe–S bond is also affected by the steric strain: **15PF$_6$** and **17** possess the longest reported Fe–S bonds of all Fp complexes with terminal sulfur ligands [2.3469(4) and 2.345(2) Å, respectively].[74] The less sterically hindered complex **16b**, on the other hand, has an Fe–S bond of 2.3125(8) Å. This complex also displays an OC–Fe–CO angle of 98.0(2)°, nearly 5° larger than those found for the two related complexes with three *t*Bu residues.

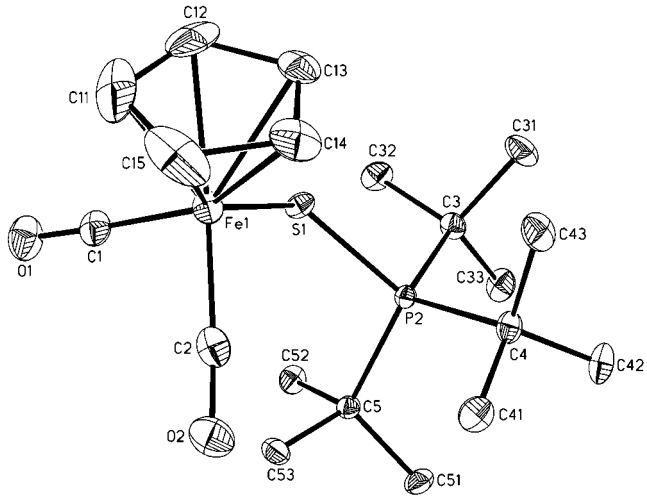


Figure 7. Solid-state structure of the complex cation of **15PF$_6$**. Ellipsoids are drawn at the 50% probability level. H atoms have been omitted for clarity.

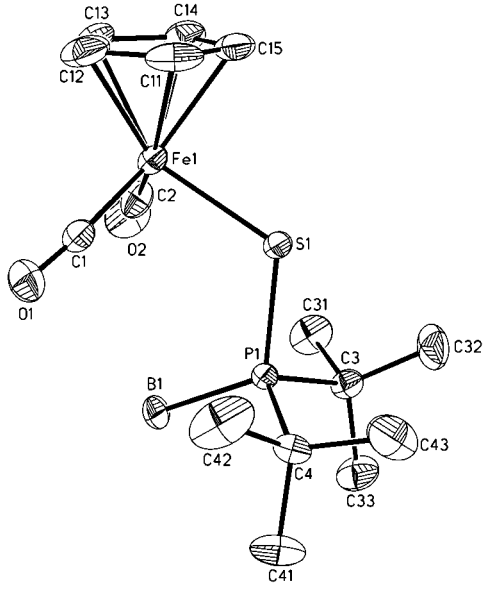


Figure 8. Solid-state structure of **16b**. Ellipsoids are drawn at the 50% probability level. H atoms have been omitted for clarity.

The iron–carbonyl bond lengths and the C–O distances in the carbonyl ligands, however, seem to follow trends that are independent of steric hindrance. Of complexes **15PF$_6$**,

 © 2007 Wiley-VCH Verlag GmbH & Co. KGaA, Weinheim 

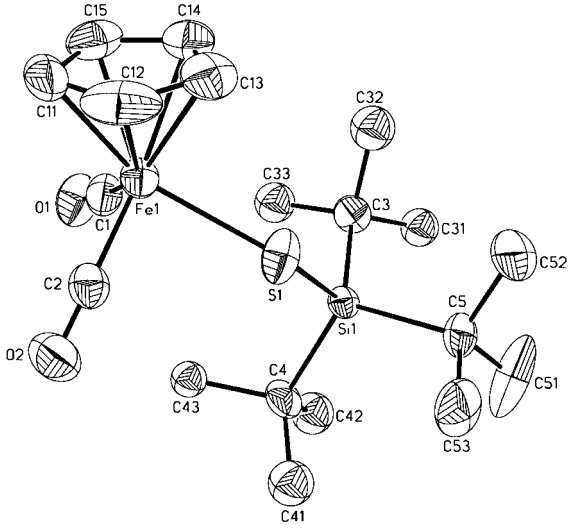


Figure 9. Solid-state structure of **17**. Ellipsoids are drawn at the 50% probability level. H atoms have been omitted for clarity.

**16b**, and **17**, for example, $[FpSPtBu_3]PF_6$ (**15PF$_6$**) displays the longest Fe–CO and the shortest C–O distances [an average of 1.799(2) and 1.139(3) Å, respectively]. The equally sterically hindered silyl thiolate complex **17**, on the other hand, has the shortest Fe–CO and the longest C–O bond [an average of 1.776(5) and 1.151(6) Å, respectively], although the individual C–O distances for this complex are quite different [1.139(6) and 1.163(6) Å]. The phosphanyl borohydride sulfide complex **16b** displays intermediate average bond lengths of 1.784(3) (Fe–CO) and 1.144(4) Å (C–O). These results indicate that the donor-strength trends observed for the non-chalcogen complexes **11I**–**13** also hold true for the thio derivatives. The silyl thiolate **8** appears to be the strongest donor, causing increased Fe–CO backbonding, which leads to a shortening of the Fe–CO bonds and lengthening of the C–O bonds, followed by **6b** and finally phosphane sulfide **4**.

This general trend is also supported by the chemical shifts of the CO carbon atoms in the $^{13}C$ NMR spectra (Table 4). As explained above, a more deshielded CO carbon atom correlates to a stronger donor ligand being attached to the same metal center.[41,42,49,77] The silyl thiolate complex **17** has the furthest downfield CO signal ($\delta$ = 215.1 ppm), while the carbonyl ligands of **16b** and **15PF$_6$** resonate at $\delta$ = 213.1 and 211.5 ppm, respectively (cf. $[FpSSiiPr_3]$: $\delta$ = 214.7;[62] $[FpSPPh_3]PF_6$: $\delta$ = 211.3 ppm[61]). In contrast to complexes **11I**–**13**, the differences in the chemical shifts of the carbon atoms in the Cp rings of complexes **15PF$_6$**–**17** are too small to discern any meaningful trends.

When considering the IR data (Table 4), silyl thiolate complex **17** is found to have CO vibrations at 2030 and 1982 cm$^{-1}$, compared to 2040 and 1994 cm$^{-1}$ for **16b** and 2054 and 2010 cm$^{-1}$ for **15BF$_4$**. The steric influence on the IR stretching frequencies appears to be minimal, as $[FpSPPh_2BH_3]$ (**16a**) displays bands at 2042 and 1998 cm$^{-1}$, which vary only slightly from those of the corresponding *tert*-butyl species **16b**. These results correspond well with published data.[60,62] It can thus be concluded that the CO stretching frequencies in the IR spectra clearly indicate that the silyl thiolate is the strongest donor of the three, while the phosphane sulfide is the weakest.

In summary, X-ray, IR, and NMR spectroscopic data indicate that differences in the electron densities of the non-chalcogen complexes **11I**–**13** on the one hand and the thio complexes **15PF$_6$**–**17** on the other follow the same qualitative trend. However, the differences found for **15PF$_6$**–**17** are less than half as large as those for **11I**–**13**.

## Quantum Chemical Calculations

The experimental studies described thus far were augmented by quantum chemical calculations in order to learn more about qualitative differences in the charge density distribution between formally isoelectronic ligands as well as between the $[CpFe(CO)_2]^+$ complexes of these ligands and also about the hydride-donor capacities of phosphanyl borohydrides compared to their chalcogen derivatives. The latter computations were inspired by the experimental observation that the parent phosphanyl borohydride $PtBu_2BH_3^-$ (**2b**) and the corresponding thio derivative **6b** react with the $CpFe(CO)_2$ fragment with formation of a coordinative Fe–P and Fe–S bond, respectively. In contrast, the oxo derivative $OPPh_2BH_3^-$ (**5a**) does not form stable complexes. Instead, we identified the hydride species FpH in the reaction mixture, which is most likely generated by hydride transfer from the $BH_3$ group.

For the calculation of complex structures and vibrational frequencies, we employed the BP86 functional in combination with the SVP valence double-zeta basis of Ahlrichs and

Table 4. Selected spectroscopic parameters for compounds **15PF$_6$**–**17**; calculated values in italics.[a]

| | $\tilde{\nu}$(CO) [cm$^{-1}$] | $\delta$($^{13}$C) (CO) ($^3J_{P,C}$ [Hz]) | $\delta$($^{13}$C) (Cp) | $\delta$($^{13}$C) (*C*Me$_3$) ($^1J_{P,C}$ [Hz]) | $\delta$($^{31}$P/$^{29}$Si) |
|---|---|---|---|---|---|
| **15PF$_6$** | 2054, 2010[60] (2032) | 211.5(2.3) | 87.4 | 44.1(24.4) | 93.8 |
| *calc.* | *2028*[b] | *211.1* | *89.5* | – | – |
| **16a** | 2042, 1998 | 212.1(4.4) | 86.3 | – | 48.3 |
| **16b** | 2040, 1994 (2017) | 213.1(3.1) | 86.5 | 36.8(20.7) | 86.8 |
| *calc.* | *2022*[b] | *212.6* | *87.5* | – | – |
| **17** | 2030, 1982 (2006) | 215.1 | 86.9 | 25.3 | 29.2[c] |
| *calc.* | *2004*[b] | *213.0* | *88.4* | – | – |

[a] IR spectra measured in $CH_2Cl_2$; NMR spectra measured in $CD_2Cl_2$ unless otherwise noted; ($\tilde{\nu}_{as}$ + $\tilde{\nu}_s$)/2 given in parentheses. [b] ($\tilde{\nu}_{as}$ + $\tilde{\nu}_s$)/2 scaled by 0.9884 to correct for systematic errors. [c] In $C_6D_6$.

 © 2007 Wiley-VCH Verlag GmbH & Co. KGaA, Weinheim 

co-workers.[84] The good agreement between computed and experimental values for key geometric data (cf. Tables 1 and 3), as well as for characteristic spectroscopic parameters (cf. Tables 2 and 4) validates this level of density functional theory for an adequate description of electronic structures of the class of compounds studied here.[85,86] For the computation of thermodynamic data for the hypothetical hydride transfer reaction sketched in Scheme 3, we employed the more reliable B3LYP functional in combination with the TZVP valence triple-zeta basis set of Ahlrichs et al.[87] All computations were performed with the Gaussian03 program.[88] Electrostatic potential surfaces were obtained from analogous computations employing the SPARTAN program.[89]

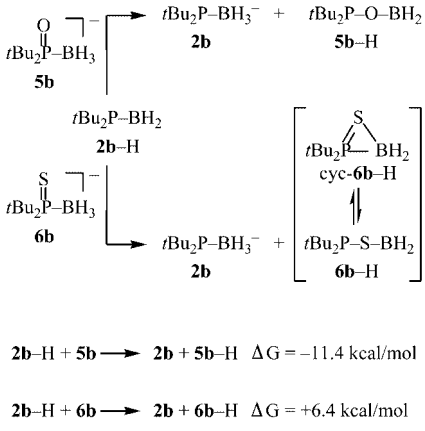


Scheme 3. Isodesmic reactions to assess the relative hydride donor strengths of P*t*Bu$_2$BH$_3^-$ (**2b**), OP*t*Bu$_2$BH$_3^-$ (**5b**), and SP*t*Bu$_2$BH$_3^-$ (**6b**).

An inspection of the electrostatic potential surfaces of PPh$_2$BH$_3^-$ (**2a**) and SiPh$_2$Me$^-$ (**3a**; Figure 10) clearly reveals an accumulation of negative charge concentrated on the BH$_3$ fragment for the phosphanyl borohydride and on the silicon atom for the silyl ligand. In contrast, all of the chalcogen derivatives OP*t*Bu$_2$BH$_3^-$ (**5b**), SP*t*Bu$_2$BH$_3^-$ (**6b**), OSi*t*Bu$_3^-$, and SSi*t*Bu$_3^-$ (**8**) bear the bulk of their negative charge on the chalcogen atom (Figure 10).

Given this qualitative background, it is at first glance surprising to see that **2a** and **2b** react with FpI to give complexes **12a** and **12b**, respectively, whereas treatment of FpI with **5a** leads to hydride transfer and formation of FpH and ultimately of Fp$_2$. The reactivities of **2a/2b** and **5a** with respect to FpI are obviously not governed simply by electrostatic attraction between the positively charged iron center and the most negatively charged part of the ligand molecule; other factors appear to play an important role. We suspected that in the case of ligand **5a**, a neighboring group effect might be responsible for the facile hydride abstraction, because the resulting borane OPPh$_2$BH$_2$ (**5a**-H) can stabilize itself by intramolecular O–B adduct formation leading to a three-membered P–O–B ring. In the case of PR$_2$BH$_2$, the electron deficiency of the boron atom can only be alleviated by P–B pπ–pπ bonding, which is not very efficient.[90]

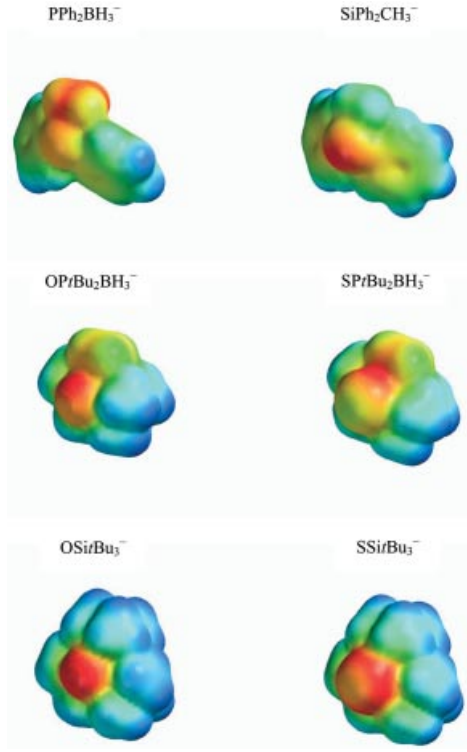


Figure 10. Electrostatic potential surfaces of the anionic ligands PPh$_2$BH$_3^-$ (**2a**), SiPh$_2$Me$^-$ (**3a**), OP*t*Bu$_2$BH$_3^-$ (**5b**), SP*t*Bu$_2$BH$_3^-$ (**6b**), OSi*t*Bu$_3^-$, and SSi*t*Bu$_3^-$ (**8**); color code: red = negative potential; blue = positive potential.

To test the relevance of a possible neighboring group effect, we calculated the molecular structures of the monomeric products of hydride abstraction from P*t*Bu$_2$BH$_3^-$ (**2b**), OP*t*Bu$_2$BH$_3^-$ (**5b**), and SP*t*Bu$_2$BH$_3^-$ (**6b**) (Scheme 3). After geometry optimization, the P–B length in P*t*Bu$_2$BH$_2$ (**2b**-H; 1.818 Å) indicates very little double-bond character between the two atoms. In the case of the oxo derivative OP*t*Bu$_2$BH$_2$, an interesting rearrangement is observed computationally which leads to a migration of the BH$_2$ fragment from phosphorus to oxygen via the anticipated three-membered P–O–B ring (Scheme 3). In the resulting isomer *t*Bu$_2$P–O–BH$_2$ (**5b**-H), pronounced O–B π-bonding aids in the stabilization of the BH$_2$ fragment (O–B = 1.352 Å). To assess the relative stabilities of P*t*Bu$_2$BH$_2$ and *t*Bu$_2$P–O–BH$_2$, we computed the free reaction energy for the isodesmic reaction P*t*Bu$_2$BH$_2$ + OP*t*Bu$_2$BH$_3^-$ → P*t*Bu$_2$BH$_3^-$ + *t*Bu$_2$P–O–BH$_2$ and obtained a value of –11.4 kcal mol$^{-1}$ (Scheme 3). A neighboring group effect similar to the one suggested for hydride-transfer reactions of **5b** may also be operative in the thio derivative **6b**. This in turn raises the question as to why this ligand reacts with [Fp(thf)]$^+$ to form [FpSP*t*Bu$_2$BH$_3$] (**16b**) rather than [FpH]. To address this point, we also calculated the molecular structure of SP*t*Bu$_2$BH$_2$ and found two minima, one containing a three-membered P–S–B ring and the other being the open-chain isomer (Scheme 3). Both isomers are similar in energy, with cyc-**6b**-H being less stable than the open chain species **6b**-H by merely 2.6 kcal mol$^{-1}$. We interpret this result as fol-

 © 2007 Wiley-VCH Verlag GmbH & Co. KGaA, Weinheim 

lows: due to poor orbital overlap, S–B π-bonding is less favorable than O–B π-bonding, and consequently S–B σ-donation becomes competitive, even though the resulting cyclic structure suffers from severe Baeyer strain. As before, we computed the free reaction energy for the isodesmic reaction $PtBu_2BH_2 + SPtBu_2BH_3^- \rightarrow PtBu_2BH_3^- + tBu_2P–S–BH_2$ (Scheme 3). Contrary to our results for the O-containing analogs, we found this process to be endergonic by +6.4 kcal mol$^{-1}$ relative to the more stable open-chain isomer. Hence, we conclude that hydride abstraction from $OPtBu_2BH_3^-$ (**5b**) is significantly more facile (by 17.8 kcal mol$^{-1}$) than from $SPtBu_2BH_3^-$ (**6b**). These theoretical findings agree very well with our experimental observations.

In all three compounds [**11**]$^+$, **12a**, and **13**, the CpFe(CO)$_2$ fragment bears a positive charge $q$ (obtained from NPA analyses) which is largest in the cationic phosphane complex [**11**]$^+$ ($q$ = + 0.486), intermediate in the phosphanyl borohydride complex **12a** [$q$ = +0.302; $\Delta q$([**11**]$^+$ – **12a**) = 0.184], and smallest in the silyl complex **13** [$q$ = +0.072; $\Delta q$(**12a** – **13**) = 0.230]. This finding supports the conclusion drawn from inspection of the IR and NMR spectroscopic data that silyl ligand **3a** is a significantly stronger electron donor than phosphanyl borohydride ligand **2a**. A similar trend is also visible for the series of complexes [**15**]$^+$ ($q$ = +0.576), **16b** [$q$ = +0.435; $\Delta q$([**15**]$^+$ – **16b**) = 0.141], and **17** [$q$ = +0.353; $\Delta q$(**16b** – **17**) = 0.082], even though the differences in the computed NPA charges on the three CpFe(CO)$_2$ fragments are less pronounced with a sulfur atom between the iron center and the P/Si atom. Again, these results are nicely reflected by the changes of the CO stretching frequencies: The highest wavenumbers are found for [**15**]$^+$, while a shift to lower wavenumbers is observed for **17** (Table 4), although this difference is much smaller than in the case of [**11**]$^+$ and **13** (Table 2). An inspection of the HOMOs of the three isoelectronic ligands **1**, **2a**, and **3a** reveals very similar topologies, all of which correspond to the lone pair being located on the donor atoms P or Si (Figure 11). This finding provides convincing evidence that the interaction of these ligands with transition metal ions will be of essentially the same nature and implies that these ligands are truly isolobal species. Quantitatively, however, the degree of charge transfer is different for the different ligand classes, with phosphanes being the weakest and silyl ligands being the strongest donors.

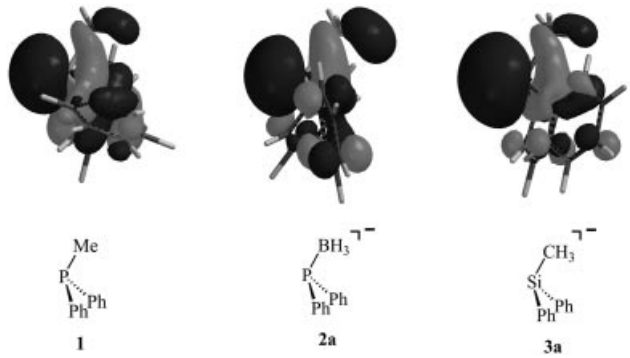


Figure 11. HOMOs of the series of isoelectronic ligands $PPh_2Me$ (**1**), $PPh_2BH_3^-$ (**2a**), and $SiPh_2Me^-$ (**3a**).

## Conclusions

A series of isoelectronic and isosteric iron complexes [CpFe(CO)$_2$(EPh$_2$XH$_3$)]$^{n+}$ (E = Si, X = C; E = P, X = C, B; $n$ = 0, 1) **11I**, **12a**, and **13** has been synthesized and characterized by X-ray crystallography and $^1$H and heteronuclear NMR and IR spectroscopy. A comparison of the structural and spectroscopic properties of compounds **11I**–**13** indicates that the silyl ligand **3a** displays the highest propensity towards electron donation, followed by the anionic phosphanyl borohydride ligand **2a**. The phosphane ligand **1** is the weakest donor.

In addition, the reactivity of phosphane chalcogenides, phosphanyl borohydride chalcogenides, and silyl chalcogenolates with the [CpFe(CO)$_2$]$^+$ fragment has been investigated. A second series of isoelectronic complexes [CpFe(CO)$_2$(SE*t*Bu$_2$XH$_3$)]$^{n+}$ (E = Si, X = C; E = P, X = C, B; $n$ = 0, 1) **15PF$_6$**–**17** has been isolated with *tert*-butyl rather than phenyl residues and fully characterized. The conclusion that the silyl species is the strongest donor of the sulfur-containing ligands can be drawn, but this effect, now mediated by the sulfur atom, is not as pronounced as for the non-chalcogen species **11I**–**13**, and the differences in the CO stretching frequencies in the IR spectra and the $^{13}$C NMR resonances of the CO carbon atoms are about half as large in **15PF$_6$**–**17** as in **11I**–**13**. The molecular structures of all crystallographically characterized compounds as well as key spectroscopic parameters have been calculated by DFT. Overall, an excellent agreement was found between experimentally and theoretically derived data. In the reaction with [CpFe(CO)$_2$]$^+$, the oxo derivative $OPPh_2BH_3^-$ transfers a hydride ion rather than forming a stable [CpFe(CO)$_2$(OPPh$_2$BH$_3$)] complex. The tendency to undergo hydride transfer reactions has been studied by DFT calculations for the series $PtBu_2BH_3^-$, $OPtBu_2BH_3^-$, and $SPtBu_2BH_3^-$. The results reveal that $OPtBu_2BH_3^-$ is the strongest and $SPtBu_2BH_3^-$ the weakest hydride donor, in agreement with experimental observations. Further theoretical analysis indicates that the three derivatives $PPh_2Me$, $PPh_2BH_3^-$, and $SiPh_2Me^-$ are truly isolobal species, despite variations in their charge distributions.

## Experimental Section

**General Considerations:** All reactions and manipulations of air-sensitive compounds were carried out under an atmosphere of dry nitrogen using standard Schlenk techniques. Solvents were freshly distilled under argon from sodium/benzophenone (thf, diethyl ether, toluene, $C_6D_6$) or sodium-lead alloy (pentane, hexane) prior to use. MeCN, $CD_3CN$, $CH_2Cl_2$, $CD_2Cl_2$, and $CDCl_3$ were dried with molecular sieves (4 Å) and degassed. NMR spectra were recorded with Bruker AMX 250, DPX 250, Avance 300, or Avance 400 spectrometers. $^1$H and $^{13}$C chemical shifts are reported relative to tetramethylsilane and were referenced against residual solvent

 © 2007 Wiley-VCH Verlag GmbH & Co. KGaA, Weinheim 

peaks ($C_6D_5H$: $\delta$ = 7.16; $C_6D_6$: $\delta$ = 128.06; $CHCl_3$: $\delta$ = 7.26; $CDCl_3$: $\delta$ = 77.16 ppm).[91] $^{11}B$ NMR spectra were referenced against external $BF_3{\cdot}OEt_2$. $^{31}P$ NMR spectra are reported relative to external $H_3PO_4$ (85%). $^{29}Si$ NMR spectra were referenced against external TMS and recorded using the INEPT pulse sequence with empirically optimized parameters for polarization transfer from the methyl and phenyl substituents (**13**) or the *t*Bu substituents (**Na3b** and **17**). Abbreviations: Fp = $CpFe(CO)_2$, n.r. = multiplet expected but not resolved. IR spectra were recorded with a Perkin–Elmer 1650 FTIR spectrophotometer or a Jasco FT/IR-420 spectrophotometer. Elemental analyses were performed by the microanalytical laboratory of the J. W. Goethe University, Frankfurt(Main).

**Materials:** Li, Na, KH, *n*BuLi solution (ca. 1.6 M in hexane), $BH_3$·thf solution (1 M in thf), $PPh_3$, $ClSiPh_2Me$, biphenyl, FpI, and MeI were obtained from commercial sources (Aldrich, Fluka, Acros or Chemetall) and used as received. $HPPh_2$ was obtained by reductive cleavage of $PPh_3$ with Li powder in thf and subsequent hydrolysis and distillation, as described by Bianco and Doronzo.[92] Deprotonation of $HPPh_2$ with *n*BuLi yields $LiPPh_2$;[93] employing hexane leads to precipitation of solvent-free $LiPPh_2$. Bromination of $HSitBu_2Me$[94] according to the literature method[95] yields $BrSitBu_2Me$. KFp (**10**),[96] $KPPh_2BH_3$ (**K2a**),[12,58] and $KPtBu_2BH_3$ (**K2b**)[12,58] were prepared by literature methods. $[Fp(thf)]PF_6$ (**14PF$_6$**) was obtained by treating $[Cp_2Fe]PF_6$ with $Fp_2$ as reported by Catheline and Astruc.[97] $[Fp(thf)]BF_4$ (**14BF$_4$**) was prepared from FpI and $AgBF_4$.[98]

**Synthesis of (thf)$_x$NaSi*t*Bu$_2$Me (Na3b):** Na (2.0 g, 87.0 mmol) and biphenyl (1.29 g, 8.4 mmol) were stirred overnight in thf (20 mL) to give a dark green solution surrounding blocks of unreacted sodium. A solution of $BrSitBu_2Me$ (3.38 g, 14.2 mmol) in thf (15 mL) was then added dropwise to this mixture over 2.5 h. After stirring for 16 h, all volatiles were removed in vacuo, and the dark brown residue was extracted with pentane (25 mL). After filtration, the filter cake was washed with pentane (10 mL). Volatiles were removed in vacuo overnight from the dark brown filtrate, and the resulting brown residue was dissolved in thf (30 mL) to give a 0.305 M solution of the product in thf (9.15 mmol, 64%). $^1H$ NMR ($C_6D_6$, 250.13 MHz): $\delta$ = 0.33 (s, 3 H, $SiCH_3$), 1.35 ppm (s, 18 H, $CCH_3$). $^{13}C\{^1H\}$ NMR ($C_6D_6$, 62.90 MHz): $\delta$ = 0.3 ($SiCH_3$), 21.3 ($CCH_3$), 32.2 ppm (s, $CCH_3$). $^{29}Si\{^1H\}$ NMR ($C_6D_6$, 49.7 MHz): $\delta$ = 14.4 ppm.

**Synthesis of [FpPPh$_2$Me]I (11I):** A solution of $LiPPh_2$ (0.147 g, 0.77 mmol) in thf (6 mL) was added with stirring to a solution of FpI (**9**, 0.233 g, 0.77 mmol) in thf (8 mL) at –78 °C. Slowly warming to ambient temperature overnight resulted in a color change from black to dark red and the formation of a colorless precipitate (LiI). The mixture was filtered and the filtrate treated with a solution of MeI (0.112 g, 0.79 mmol) in thf (3 mL). The resulting dark yellow precipitate was washed with thf (2 × 5 mL) and dried in vacuo. Yield: 0.243 g (63%). X-ray quality crystals were obtained by gas-phase diffusion of diethyl ether into a solution of **11I** in MeCN. $^1H$ NMR ($CD_3CN$, 400.13 MHz): $\delta$ = 2.38 (d, $^2J_{P,H}$ = 10.5 Hz, 3 H, $CH_3$), 5.38 (d, $^3J_{P,H}$ = 1.6 Hz, 5 H, Cp), 7.50–7.64 ppm (m, 10 H, H-*o,m,p*). $^{13}C\{^1H\}$ NMR ($CD_3CN$, 100.63 MHz): $\delta$ = 19.5 (d, $^1J_{P,C}$ = 35.4 Hz, $CH_3$), 89.1 (d, $^2J_{P,C}$ = 0.5 Hz, Cp), 130.4 (d, $^3J_{P,C}$ = 11.0 Hz, C-*m*), 132.3 (d, $^2J_{P,C}$ = 10.2 Hz, C-*o*), 132.9 (d, $^4J_{P,C}$ = 2.8 Hz, C-*p*), 134.1 (d, $^1J_{P,C}$ = 52.9 Hz, C-*i*), 210.4 ppm (d, $^2J_{P,C}$ = 24.2 Hz, CO). $^{31}P\{^1H\}$ NMR ($CD_3CN$, 161.98 MHz): $\delta$ = 48.6 ppm (s). IR (MeCN): $\tilde{\nu}$ = 2055, 2011 $cm^{-1}$ (CO). $C_{20}H_{18}FeIO_2P$ (504.06): calcd. C 47.65, H 3.60; found C 47.46, H 3.65.

**Synthesis of [FpPPh$_2$BH$_3$] (12a):** A solution of $KPPh_2BH_3$ (**K2a**; 0.239 g, 1.00 mmol) in thf (10 mL) was added with stirring to a solution of FpI (**9**, 0.304 g, 1.00 mmol) in thf (10 mL) at –78 °C. Slowly warming to ambient temperature overnight resulted in a color change from black to light brown and formation of a colorless precipitate (KI). The mixture was filtered and the solvent removed from the filtrate in vacuo. The resulting brown solid residue was washed with pentane (5 mL) and extracted with toluene (10 mL). The toluene was removed from the filtrate in vacuo to give the product as a yellow crystalline material. Yield: 0.274 g (73%). X-ray quality crystals were obtained by gas-phase diffusion of pentane into a solution of **12a** in toluene. $^1H$ NMR ($C_6D_6$, 250.13 MHz): $\delta$ = 2.3 (m, 3 H, $BH_3$), 4.16 (d, $^3J_{P,H}$ = 1.6 Hz, 5 H, Cp), 6.97–7.16 (m, 6 H, H-*m,p*), 7.93–8.02 ppm (m, 4 H, H-*o*). $^{11}B\{^1H\}$ NMR ($C_6D_6$, 128.37 MHz): $\delta$ = –28.0 ppm (d, $^1J_{P,B}$ = 44 Hz). $^{13}C\{^1H\}$ NMR ($C_6D_6$, 62.90 MHz): $\delta$ = 86.8 (n.r., Cp), 128.3 (d, $^3J_{P,C}$ = 8.7 Hz, C-*m*), 129.3 (d, $^4J_{P,C}$ = 2.3 Hz, C-*p*), 133.3 (d, $^2J_{P,C}$ = 8.0 Hz, C-*o*), 140.2 (d, $^1J_{P,C}$ = 27.8 Hz, C-*i*), 213.5 ppm (d, $^2J_{P,C}$ = 18.0 Hz, CO). $^{31}P\{^1H\}$ NMR ($C_6D_6$, 161.98 MHz): $\delta$ = 34.3 ppm (m). IR (MeCN): $\tilde{\nu}$ = 2030, 1982 $cm^{-1}$ (CO). $C_{19}H_{18}BFeO_2P$ (375.96): calcd. C 60.74, H 4.83; found C 60.58, H 4.73.

**Synthesis of [FpP*t*Bu$_2$BH$_3$] (12b):** A solution of $KPtBu_2BH_3$ (**K2b**, 0.291 g, 1.47 mmol) in thf (10 mL) was added with stirring to a solution of FpI (**9**, 0.446 g, 1.47 mmol) in thf (10 mL) at –78 °C. Slowly warming to ambient temperature overnight resulted in a color change from black to yellow and formation of a colorless precipitate (KI). The mixture was filtered and the solvent removed from the filtrate in vacuo. The resulting brown solid residue was washed with pentane (5 mL) and extracted with toluene (10 mL). The toluene was removed from the filtrate in vacuo to give the product as a yellow crystalline material. Yield: 0.355 g (72%). X-ray quality crystals were obtained by gas-phase diffusion of pentane into a solution of **12b** in toluene. $^1H$ NMR ($C_6D_6$, 250.13 MHz): $\delta$ = 1.35 (d, $^3J_{P,H}$ = 11.9 Hz, 18 H, $CH_3$), 1.60 (q, $^1J_{B,H}$ = 93.6 Hz, 3 H, $BH_3$), 4.33 ppm (s, 5 H, Cp). $^{11}B\{^1H\}$ NMR ($C_6D_6$, 128.37 MHz): $\delta$ = –30.0 ppm (d, $^1J_{P,B}$ = 49 Hz). $^{13}C\{^1H\}$ NMR ($C_6D_6$, 62.90 MHz): $\delta$ = 31.2 (d, $^2J_{P,C}$ = 2.0 Hz, $CH_3$), 37.4 (d, $^1J_{P,C}$ = 6.6 Hz, $CCH_3$), 86.5 (n.r., Cp), 215.5 ppm (d, $^2J_{P,C}$ = 17.0 Hz, CO). $^{31}P\{^1H\}$ NMR ($C_6D_6$, 161.98 MHz): $\delta$ = 81.4 ppm (m). IR (MeCN): $\tilde{\nu}$ = 2029, 1982 $cm^{-1}$ (CO). $C_{15}H_{26}BFeO_2P$ (335.99): calcd. C 53.62, H 7.80; found C 53.48, H 7.69.

**Synthesis of [FpSiPh$_2$Me] (13):** A solution of $ClSiPh_2Me$ (0.33 mL, 0.367 g, 1.57 mmol) in thf (8 mL) was added dropwise to a suspension of KFp (0.307 g, 1.42 mmol) in thf (10 mL). After stirring overnight, volatiles were removed in vacuo, then the brown residue was extracted with pentane (4 × 10 mL) and filtered. Removal of the solvent yielded the crude product as a brown oil (0.392 g, 74%). The crude product was purified by filtration through silica gel under an inert atmosphere using hexane/$CH_2Cl_2$ (2:1) as the eluent, which yielded the product as a yellow solid after removal of the volatiles in vacuo. X-ray quality crystals were obtained from hexane solution at –25 °C. $^1H$ NMR (300.0 MHz, $C_6D_6$): $\delta$ = 0.95 (s, 3 H, $CH_3$), 3.97 (s, 5 H, Cp), 7.21, 7.69 ppm (2 × m, 6 H, 4 H, H-*o,m,p*). $^{13}C\{^1H\}$ NMR (75.4 MHz, $C_6D_6$): $\delta$ = 5.5 ($CH_3$), 84.4 (s, Cp), 128.0 (C-*m* or C-*o*), 128.4 (s, C-*p*), 134.6 (C-*m* or C-*o*), 144.6 (C-*i*), 215.8 ppm (CO). $^{29}Si\{^1H\}$ NMR (59.6 MHz, $C_6D_6$): $\delta$ = 35.1 ppm. IR (MeCN): $\tilde{\nu}$ = 1994, 1938 $cm^{-1}$ (CO). $C_{20}H_{18}FeO_2Si$ (374.28): calcd. C 64.18, H 4.85; found C 64.14, H 4.88.

**Reaction of KOPPh$_2$BH$_3$ (K5a) with FpI (9):** An NMR tube was charged with **K5a** (0.05 g, 0.2 mmol), FpI (**9**; 0.06 g, 0.2 mmol), and [D$_8$]thf (0.6 mL), and the tube was flame-sealed and shaken

 © 2007 Wiley-VCH Verlag GmbH & Co. KGaA, Weinheim 

until all the solids had dissolved. Slow deposition of a colorless precipitate (KI) took place over several days. Analysis by NMR spectroscopy showed slow formation of $Fp_2$ and several unidentified phosphorus- and boron-containing products. The integrals of the $^1H$ NMR Cp resonances of $Fp_2$ and FpI account for over 95% of the total Cp region integral. Main phosphorus-containing product, approx. 60% yield by $^{31}P$ NMR: $^{31}P\{^1H\}$ NMR ([D$_8$]thf, 161.98 MHz): $\delta$ = 80.8 ppm (m); $^{11}B$ NMR ([D$_8$]thf, 128.37 MHz): $\delta$ = –37.5 ppm (m). Analysis of the hydride region of the $^1H$ NMR spectrum showed small amounts of FpH at $\delta$ = –11.7 ppm.[68]

**Reaction of $NaOSiPh_2Me$ (Na7) with FpI (9):** A Schlenk flask was charged with FpI (**9**; 0.220 g, 0.72 mmol) in thf (5 mL), cooled to –78 °C, and a solution of **Na7** (0.170 g, 0.72 mmol) in thf (5 mL) was added dropwise to this solution. The mixture was then warmed to room temperature overnight. All volatiles were removed in vacuo, and the brown residue was extracted with toluene and filtered. The only major Cp-containing product in the filtrate was $Fp_2$ and the only major Si-containing product $O(SiPh_2Me)_2$, both of which were identified by comparison with authentic samples. Red crystals of $[(NaOSiPh_2Me)_4(Fp_2)_2]$ were isolated by removing toluene from the filtrate, washing the residue with benzene, and recrystallizing from toluene. It should be noted that the solubility of the adduct is significantly higher in toluene than in benzene. IR $[(NaOSiPh_2Me)_4(Fp_2)_2]$ (KBr): $\tilde{\nu}$ = 2005 (m), 1957 (s), 1932 (m), 1756 (m), 1735 (s) cm$^{-1}$ (CO).

**Synthesis of $[FpSPtBu_3]PF_6$ (15PF$_6$):** The synthesis and NMR and IR data of the complex cation as its $BF_4$ salt have been reported by Kuhn and Schumann (data given in Table 4 are for the $PF_6$ salt).[60] We modified their procedure by using $[Fp(thf)]PF_6$ instead of the $BF_4^-$ salt, as described in the literature.[97] X-ray quality crystals were obtained by gas-phase diffusion of pentane into a solution of **15PF$_6$** in $CHCl_3$. $C_{19}H_{32}F_6FeO_2P_2S$ (556.30): calcd. C 41.02, H 5.80; found C 40.97, H 5.81.

**Synthesis of $[FpSPPh_2BH_3]$ (16a):** A solution of $KSPPh_2BH_3$ (**K6a**; 0.098 g, 0.36 mmol) in thf (3 mL) was added to a solution of $[Fp(thf)]PF_6$ (**14PF$_6$**; 0.143 g, 0.36 mmol) in $CH_2Cl_2$ (30 mL) with stirring at –78 °C. As the mixture warmed to ambient temperature overnight, the color lightened from dark red to orange. The solvent was removed in vacuo and the resulting red-brown solid residue washed with pentane (2 × 5 mL) and extracted with toluene (2 × 10 mL). The extracts were filtered through silica gel, and the toluene was removed from the filtrate in vacuo to give the product as an orange oil. Yield: 0.106 g (72%). $^1H$ NMR ($CD_2Cl_2$, 300.03 MHz): $\delta$ = 1.25 (br. m, 3 H, $BH_3$), 5.08 (s, 5 H, Cp), 7.1–7.9 ppm (m, 10 H, H-*o,m,p*). $^{11}B\{^1H\}$ NMR ($CD_2Cl_2$, 96.26 MHz): $\delta$ = –33.8 ppm (d, $^1J_{P,B}$ = 55 Hz). $^{13}C\{^1H\}$ NMR ($CD_2Cl_2$, 75.45 MHz): $\delta$ = 86.3 (s, Cp), 128.5 (d, $^3J_{P,C}$ = 9.9 Hz, C-*m*), 130.6 (d, $^4J_{P,C}$ = 2.5 Hz, C-*p*), 132.0 (d, $^2J_{P,C}$ = 9.9 Hz, C-*o*), 136.2 (d, $^1J_{P,C}$ = 46.4 Hz, C-*i*), 212.1 ppm (d, $^3J_{P,C}$ = 4.4 Hz, CO). $^{31}P\{^1H\}$ NMR ($CD_2Cl_2$, 121.46 MHz): $\delta$ = 48.3 ppm (br. m). IR ($CH_2Cl_2$): $\tilde{\nu}$ = 2042, 1998 cm$^{-1}$ (CO). A correct elemental analysis could not be obtained due to residual solvent and an unidentified impurity that could not be removed.

**Synthesis of $[FpSPtBu_2BH_3]$ (16b):** A solution of $KSPtBu_2BH_3$ (**K6b**; 0.137 g, 0.60 mmol) in thf (3 mL) was added to a solution of $[Fp(thf)]PF_6$ (**14PF$_6$**; 0.185 g, 0.47 mmol) in $CH_2Cl_2$ (40 mL) with stirring at –78 °C. As the mixture warmed to ambient temperature overnight, the color lightened from dark red to orange, and a colorless precipitate ($KPF_6$) formed. The solvent was removed in vacuo and the resulting red-brown semi-solid residue was extracted with pentane (2 × 10 mL). The extracts were filtered through silica gel (approx. 1 cm) on a Schlenk frit. The product adsorbed completely on the silica gel and was subsequently washed with 30 mL of pentane. It was eluted with benzene, and all volatiles were removed in vacuo to give a dark red oil. Upon standing overnight, fine orange needles of **16b** formed in X-ray quality. Yield: 0.100 g (58%). $^1H$

Table 5. Crystallographic data for compounds **11I**–**13**.

| | **11I** | **12a** | **12b** | **13** |
|---|---|---|---|---|
| Empirical formula | $C_{20}H_{18}FeIO_2P$ | $C_{19}H_{18}BFeO_2P$ | $C_{15}H_{26}BFeO_2P$ | $C_{20}H_{18}FeO_2Si$ |
| Formula mass | 504.06 | 375.96 | 335.99 | 374.28 |
| Color, shape | orange, block | yellow, block | yellow, block | light-brown, plate |
| Temperature [K] | 173(2) | 203(2) | 293(2) | 173(2) |
| Crystal system | triclinic | orthorhombic | orthorhombic | orthorhombic |
| Space group | $P\bar{1}$ | $P2_12_12_1$ | $P2_12_12_1$ | $P2_12_12_1$ |
| *a* [Å] | 9.768(1) | 8.488(1) | 7.7785(5) | 7.2717(6) |
| *b* [Å] | 12.026(2) | 13.727(2) | 14.802(1) | 15.532(1) |
| *c* [Å] | 18.416(3) | 15.195(2) | 14.991(1) | 16.055(1) |
| *α* [°] | 108.78(1) | 90 | 90 | 90 |
| *β* [°] | 98.99(1) | 90 | 90 | 90 |
| *γ* [°] | 91.41(1) | 90 | 90 | 90 |
| *V* [Å$^3$] | 2016.6(5) | 1770.4(4) | 1725.9(2) | 1813.3(3) |
| *Z* | 4 | 4 | 4 | 4 |
| $D_{calcd.}$ [g cm$^{-3}$] | 1.660 | 1.411 | 1.293 | 1.371 |
| *F*(000) | 992 | 776 | 712 | 776 |
| $\mu$ [mm$^{-1}$] | 2.368 | 0.949 | 0.964 | 0.906 |
| Crystal size [mm] | 0.19 × 0.15 × 0.14 | 0.32 × 0.22 × 0.19 | 0.48 × 0.45 × 0.34 | 0.32 × 0.26 × 0.11 |
| Reflections collected | 15825 | 29550 | 17282 | 9046 |
| Independent reflns ($R_{int}$) | 7125 (0.0792) | 3679 (0.0583) | 3246 (0.0590) | 3321 (0.0292) |
| Data/restraints/parameters | 7125/0/451 | 3679/0/217 | 3246/0/182 | 3321/0/218 |
| GOOF on $F^2$ | 1.108 | 0.857 | 0.973 | 1.005 |
| $R_1$, $wR_2$ [$I > 2\sigma(I)$] | $R_1$ = 0.0666, $wR_2$ = 0.0631 | $R_1$ = 0.0215, $wR_2$ = 0.0440 | $R_1$ = 0.0270, $wR_2$ = 0.0650 | $R_1$ = 0.0223 $wR_2$ = 0.0512 |
| $R_1$, $wR_2$ (all data) | $R_1$ = 0.1274, $wR_2$ = 0.0684 | $R_1$ = 0.0271, $wR_2$ = 0.0448 | $R_1$ = 0.0307, $wR_2$ = 0.0662 | $R_1$ = 0.0259 $wR_2$ = 0.0522 |
| Largest difference peak/hole [e Å$^{-3}$] | 1.613/–2.791 | 0.290/–0.150 | 0.188/–0.162 | 0.187/–0.195 |

 © 2007 Wiley-VCH Verlag GmbH & Co. KGaA, Weinheim 

Table 6. Crystallographic data for compounds **15PF$_6$**, **16b**, and **17**.

| | **15PF$_6$** | **16b** | **17** |
|---|---|---|---|
| Empirical formula | $C_{19}H_{32}F_6FeO_2P_2S$ | $C_{15}H_{26}BFeO_2PS$ | $C_{19}H_{32}FeO_2SSi$ |
| Formula mass | 556.30 | 368.05 | 408.45 |
| Color, shape | red, plate | orange, needle | orange, plate |
| Temperature [K] | 173(2) | 173(2) | 173(2) |
| Crystal system | orthorhombic | orthorhombic | triclinic |
| Space group | $P2_12_12_1$ | *Pbca* | $P\bar{1}$ |
| *a* [Å] | 8.3294(3) | 12.3927(8) | 8.671(1) |
| *b* [Å] | 14.2375(5) | 15.1586(8) | 8.707(1) |
| *c* [Å] | 20.7808(9) | 19.310(1) | 16.215(2) |
| $\alpha$ [°] | 90 | 90 | 86.25(1) |
| $\beta$ [°] | 90 | 90 | 88.78(1) |
| $\gamma$ [°] | 90 | 90 | 62.46(1) |
| *V* [Å$^3$] | 2464.4(2) | 3627.5(4) | 1083.0(3) |
| *Z* | 4 | 8 | 2 |
| $D_{calcd.}$ [g cm$^{-3}$] | 1.499 | 1.348 | 1.252 |
| *F*(000) | 1152 | 1552 | 436 |
| $\mu$ [mm$^{-1}$] | 0.885 | 1.035 | 0.856 |
| Crystal size [mm] | 0.34 × 0.23 × 0.12 | 0.17 × 0.09 × 0.08 | 0.18 × 0.15 × 0.08 |
| Reflections collected | 45095 | 31420 | 10454 |
| Independent reflns ($R_{int}$) | 6885 (0.0563) | 3330 (0.0622) | 3997 (0.0996) |
| Data/restraints/parameters | 6885/0/281 | 3330/0/191 | 3997/60/213 |
| GOOF on $F^2$ | 1.053 | 0.934 | 0.952 |
| $R_1$, $wR_2$ [$I > 2\sigma(I)$] | $R_1$ = 0.0295, $wR_2$ = 0.0789 | $R_1$ = 0.0397, $wR_2$ = 0.0742 | $R_1$ = 0.0699, $wR_2$ = 0.1704 |
| $R_1$, $wR_2$ (all data) | $R_1$ = 0.0303, $wR_2$ = 0.0794 | $R_1$ = 0.0671, $wR_2$ = 0.0805 | $R_1$ = 0.0986, $wR_2$ = 0.1888 |
| Largest difference peak/hole [e Å$^{-3}$] | 0.447/–0.323 | 0.325/–0.521 | 0.530/–0.744 |

NMR ($CD_2Cl_2$, 300.03 MHz): $\delta$ = 0.68 (m, 3 H, $BH_3$), 1.27 (d, $^3J_{P,H}$ = 13.2 Hz, 18 H, $CH_3$), 5.12 ppm (s, 5 H, Cp). $^{11}B\{^1H\}$ NMR ($CD_2Cl_2$, 96.26 MHz): $\delta$ = –37.1 ppm (d, $^1J_{P,B}$ = 55 Hz). $^{13}C\{^1H\}$ NMR ($CD_2Cl_2$, 75.45 MHz): $\delta$ = 28.4 (d, $^2J_{P,C}$ = 2.3 Hz, $CH_3$), 36.8 (d, $^1J_{P,C}$ = 20.7 Hz, *C*$CH_3$), 86.5 (s, Cp), 213.1 ppm (d, $^3J_{P,C}$ = 3.1 Hz, CO). $^{31}P\{^1H\}$ NMR ($CD_2Cl_2$, 121.46 MHz): $\delta$ = 86.8 ppm (br. m). IR ($CH_2Cl_2$): $\tilde{\nu}$ = 2040, 1994 cm$^{-1}$ (CO). $C_{15}H_{26}BFeO_2PS$ (368.05): calcd. C 48.95, H 7.12; found C 48.06, H 7.12.

**Synthesis of [FpSSi*t*Bu$_3$] (17):** Solid $(thf)_2NaSSitBu_3$ (**Na8**, 0.155 g, 0.39 mmol) was added in one portion to a solution of $[Fp(thf)]BF_4$ (**14BF$_4$**; 0.131 g, 0.39 mmol) in $CH_2Cl_2$ (12 mL). After 4 h stirring, the volatiles were removed from the reaction mixture and the brown residue was extracted with pentane (5 mL) and filtered through Celite® on a frit. The filter cake was then washed with pentane (2 × 5 mL). Slow concentration of the filtrate yielded a dark brown, microcrystalline solid. Yield: 0.156 g (98%). Recrystallization from pentane yielded X-ray quality crystals. $^1H$ NMR ($C_6D_6$, 400.13 MHz): $\delta$ = 1.39 (s, 27 H, $CH_3$), 4.11 ppm (s, 5 H, Cp). $^{13}C\{^1H\}$ NMR ($C_6D_6$, 100.63 MHz): $\delta$ = 25.5 (*C*$CH_3$), 31.6 ($CH_3$), 86.2 (Cp), 215.1 ppm (CO). $^{29}Si\{^1H\}$ NMR ($C_6D_6$, 59.6 MHz): $\delta$ = 29.2 ppm. $^1H$ NMR ($CD_2Cl_2$, 300.0 MHz): $\delta$ = 1.13 (s, 27 H, $CH_3$), 5.02 ppm (s, 5 H, Cp). $^{13}C\{^1H\}$ NMR ($CD_2Cl_2$, 75.4 MHz): $\delta$ = 25.3 (*C*$CH_3$), 31.3 ($CH_3$), 86.9 (Cp), 215.1 ppm (CO). IR (hexane): $\tilde{\nu}$ = 2035 (s), 1988 (s) cm$^{-1}$ (CO). IR ($CH_2Cl_2$): $\tilde{\nu}$ = 2030 (s), 1982 (s) cm$^{-1}$ (CO). $C_{19}H_{32}FeO_2SSi$ (408.45): calcd. C 55.87, H 7.90; found C 54.59, H 7.85.

**X-ray Structural Characterization:** Data were collected with a Stoe IPDS-II two circle diffractometer with graphite-monochromated Mo-$K_\alpha$ radiation. Empirical absorption corrections were performed with the MULABS option[99] in the program PLATON.[100] Equivalent reflections were averaged. The structures were solved by direct methods[101] and refined with full-matrix least-squares on $F^2$ using the program SHELXL-97.[102] Hydrogen atoms were placed at ideal positions and refined with fixed isotropic displacement parameters using a riding model. Complex **17**: Two of the three *t*Bu substituents are disordered over two sites and were refined isotropically. In order to keep the geometric parameters in reasonable ranges, similarity restraints were applied for bond lengths and bond angles. Details of the X-ray crystal structure analyses of compounds **11I**, **12a**, **12b**, and **13** are summarized in Table 5 and compounds **15PF$_6$**, **16b**, and **17** in Table 6.

CCDC-628090 (**11I**), -628087 (**12a**), -628088 (**12b**), -628091 (**13**), -628094 (**15PF$_6$**), -628093 (**16b**), -628092 (**17**), and -628089 ([(18-crown-6)$(thf)_2$Na][4,4′-$(SitBu_2Me)_2(C_6H_4)_2$]) contain the supplementary crystallographic data for this paper. These data can be obtained free of charge from The Cambridge Crystallographic Data Center via www.ccdc.cam.ac.uk/data_request/cif.

**Supporting Information** (see footnote on the first page of this article): Calculated molecular structures of compounds **2b**, **2b**-H, **5b**, **5b**-H, **6b**, and **6b**-H (Figure S1).

## Acknowledgments

The authors are grateful to the Deutsche Forschungsgemeinschaft (DFG) and the Fonds der Chemischen Industrie (FCI) for financial support and to Chemetall for the donation of *t*BuLi. We gratefully acknowledge computer time provided by the Frankfurt Center for Scientific Computing.

[1] C. A. Tolman, *Chem. Rev.* **1977**, *77*, 313–348.
[2] S. Trofimenko, *Scorpionates: The Coordination Chemistry of Polypyrazolylborate Ligands*, Imperial College Press, **1999**.
[3] B. Cornils, W. A. Herrmann, *Applied Homogeneous Catalysis with Organometallic Compounds*, Wiley-VCH, Weinheim, **1996**.
[4] A. Haghiri Ilkhechi, J. M. Mercero, I. Silanes, M. Bolte, M. Scheibitz, H.-W. Lerner, J. M. Ugalde, M. Wagner, *J. Am. Chem. Soc.* **2005**, *127*, 10656–10666.

 © 2007 Wiley-VCH Verlag GmbH & Co. KGaA, Weinheim 

[5] S. Bieller, M. Bolte, H.-W. Lerner, M. Wagner, *Chem. Eur. J.* **2006**, *12*, 4735–4742.
[6] S. Bieller, M. Bolte, H.-W. Lerner, M. Wagner, *Inorg. Chem.* **2005**, *44*, 9489–9496.
[7] S. Bieller, M. Bolte, H.-W. Lerner, M. Wagner, *J. Organomet. Chem.* **2005**, *690*, 1935–1946.
[8] A. Haghiri Ilkhechi, M. Bolte, H.-W. Lerner, M. Wagner, *J. Organomet. Chem.* **2005**, *690*, 1971–1977.
[9] S. Bieller, F. Zhang, M. Bolte, J. W. Bats, H.-W. Lerner, M. Wagner, *Organometallics* **2004**, *23*, 2107–2113.
[10] A. Haghiri Ilkhechi, S. Guo, M. Bolte, M. Wagner, *Dalton Trans.* **2003**, 2303–2307.
[11] T. I. Kückmann, M. Hermsen, M. Bolte, M. Wagner, H.-W. Lerner, *Inorg. Chem.* **2005**, *44*, 3449–3458.
[12] F. Dornhaus, M. Bolte, H.-W. Lerner, M. Wagner, *Eur. J. Inorg. Chem.* **2006**, 5138–5147.
[13] T. S. Lobana, in *Coordination Chemistry of Phosphane Chalcogenides and Their Analytical and Catalytic Applications*, *Vol. 2* (Ed.: F. R. Hartley), John Wiley & Sons, Chichester, **1992**, pp. 409–566.
[14] L. H. Gade, *Koordinationschemie*, Wiley-VCH, Weinheim, **1998**.
[15] T. D. Tilley, in *The Chemistry of Organic Silicon Compounds*, *Vol. 1* (Eds.: S. Patai and Z. Rappoport), John Wiley & Sons, New York, **1989**, pp. 1415–1477.
[16] J. Y. Corey, J. Braddock-Wilking, *Chem. Rev.* **1999**, *99*, 175–292.
[17] H. Nakazawa, K. Kamata, M. Itazaki, *Chem. Commun.* **2005**, 4004–4006.
[18] M. Okazaki, S. Ohshitanai, M. Iwata, H. Tobita, H. Ogino, *Coord. Chem. Rev.* **2002**, *226*, 167–178.
[19] R. D. Brost, G. C. Bruce, F. L. Joslin, S. R. Stobart, *Organometallics* **1997**, *16*, 5669–5680.
[20] D. L. Lichtenberger, A. Rai-Chaudhuri, *J. Am. Chem. Soc.* **1991**, *113*, 2923–2930.
[21] J. Chatt, C. Eaborn, S. Ibekwe, *Chem. Commun. (London)* **1966**, 700–701.
[22] H. Tobita, K. Hasegawa, J. J. G. Minglana, L.-S. Luh, M. Okazaki, H. Ogino, *Organometallics* **1999**, *18*, 2058–2060.
[23] J.-M. Camus, J. Andrieu, P. Richard, R. Poli, C. Darcel, S. Jugé, *Tetrahedron: Asymmetry* **2004**, *15*, 2061–2065.
[24] B. Wolfe, T. Livinghouse, *J. Am. Chem. Soc.* **1998**, *120*, 5116–5117.
[25] T. Miura, H. Yamada, S.-I. Kikuchi, T. Imamoto, *J. Org. Chem.* **2000**, *65*, 1877–1880.
[26] B. Wolfe, T. Livinghouse, *J. Org. Chem.* **2001**, *66*, 1514–1516.
[27] H. Dorn, C. A. Jaska, R. A. Singh, A. J. Lough, I. Manners, *Chem. Commun.* **2000**, 1041–1042.
[28] A.-C. Gaumont, M. B. Hursthouse, S. J. Coles, J. M. Brown, *Chem. Commun.* **1999**, 63–64.
[29] W. Angerer, W. S. Sheldrick, W. Malisch, *Chem. Ber.* **1985**, *118*, 1261–1266.
[30] D. A. Hoic, W. M. Davis, G. C. Fu, *J. Am. Chem. Soc.* **1996**, *118*, 8176–8177.
[31] V. V. Grushin, *Chem. Rev.* **2004**, *104*, 1629–1662.
[32] R. Weber, U. Englert, B. Ganter, W. Keim, M. Möthrath, *Chem. Commun.* **2000**, 1419–1420.
[33] C. Abu-Gnim, I. Amer, *J. Organomet. Chem.* **1996**, *516*, 235–243.
[34] B. Marciniec, H. Maciejewski, *Coord. Chem. Rev.* **2001**, *223*, 301–335.
[35] S. E. Denmark, J. D. Baird, *Chem. Eur. J.* **2006**, *12*, 4954–4963.
[36] P. T. Wolczanski, *Polyhedron* **1995**, *14*, 3335–3362.
[37] J. L. Bennett, P. T. Wolczanski, *J. Am. Chem. Soc.* **1994**, *116*, 2179–2180.
[38] K. F. Hirsekorn, A. S. Veige, M. P. Marshak, Y. Koldobskaya, P. T. Wolczanski, T. R. Cundari, E. B. Lobkovsky, *J. Am. Chem. Soc.* **2005**, *127*, 4809–4830.
[39] B. Marciniec, P. Krzyzanowski, E. Walczuk-Gusciora, W. Duczmal, *J. Mol. Catal. A* **1999**, *144*, 263–271.
[40] F. A. Cotton, C. S. Kraihanzel, *J. Am. Chem. Soc.* **1962**, *84*, 4432–4438.
[41] P. S. Braterman, D. W. Milne, E. W. Randall, E. Rosenberg, *J. Chem. Soc., Dalton Trans.* **1973**, 1027–1031.
[42] B. E. Mann, B. F. Taylor, *$^{13}C$ NMR Data for Organometallic Compounds*, Academic Press, London, **1981**, p. 326.
[43] P. M. Treichel, D. A. Komar, *J. Organomet. Chem.* **1981**, *206*, 77–88.
[44] H. Schumann, L. Eguren, *J. Organomet. Chem.* **1991**, *403*, 183–193.
[45] E. E. Isaacs, W. A. G. Graham, *J. Organomet. Chem.* **1976**, *120*, 407–421.
[46] M. L. Brown, J. L. Cramer, J. A. Ferguson, T. J. Meyer, N. Winterton, *J. Am. Chem. Soc.* **1972**, *94*, 8707–8710.
[47] A. S. Goldman, D. R. Tyler, *Inorg. Chem.* **1987**, *26*, 253–258.
[48] E. Louattani, A. Lledós, J. Suades, *Organometallics* **1995**, *14*, 1053–1060.
[49] H. Schumann, *J. Organomet. Chem.* **1987**, *320*, 145–162.
[50] U. Schubert, G. Kraft, E. Walther, *Z. Anorg. Allg. Chem.* **1984**, *519*, 96–106.
[51] W. Malisch, H. Jehle, S. Möller, G. Thum, J. Reising, A. Gbureck, V. Nagel, C. Fickert, W. Kiefer, M. Nieger, *Eur. J. Inorg. Chem.* **1999**, 1597–1605.
[52] W. Malisch, H. Jehle, D. Schumacher, M. Binnewies, N. Söger, *J. Organomet. Chem.* **2003**, *667*, 35–41.
[53] J. S. McIndoe, B. K. Nicholson, *J. Organomet. Chem.* **2002**, *648*, 237–245.
[54] T. S. Piper, D. Lemal, G. Wilkinson, *Naturwissenschaften* **1956**, *43*, 129.
[55] W. Malisch, M. Kuhn, *Chem. Ber.* **1974**, *107*, 979–995.
[56] R. J. P. Corriu, W. E. Douglas, *J. Organomet. Chem.* **1973**, *51*, C3–C4.
[57] G. Cerveau, E. Colomer, R. Corriu, W. E. Douglas, *J. Organomet. Chem.* **1977**, *135*, 373–386.
[58] F. Dornhaus, M. Bolte, H.-W. Lerner, M. Wagner, *Eur. J. Inorg. Chem.* **2006**, 1777–1785.
[59] H. Nakazawa, Y. Ueda, K. Nakamura, K. Miyoshi, *Organometallics* **1997**, *16*, 1562–1566.
[60] N. Kuhn, H. Schumann, *J. Organomet. Chem.* **1986**, *304*, 181–193.
[61] M. Morán, I. Cuadrado, C. Pascual, J. R. Masaguer, J. Losada, *Inorg. Chim. Acta* **1987**, *132*, 257–262.
[62] I. Kovács, F. Bélanger-Gariépy, A. Shaver, *Inorg. Chem.* **2003**, *42*, 2988–2991.
[63] N. J. Coville, E. A. Darling, A. W. Hearn, P. Johnston, *J. Organomet. Chem.* **1987**, *328*, 375–385.
[64] F. W. G. Fearon, H. Gilman, *J. Organomet. Chem.* **1967**, *9*, 403–411.
[65] A. Sekiguchi, T. Fukawa, M. Nakamoto, V. Y. Lee, M. Ichinohe, *J. Am. Chem. Soc.* **2002**, *124*, 9865–9869.
[66] N. Wiberg, K. Amelunxen, H.-W. Lerner, H. Schuster, H. Nöth, I. Krossing, M. Schmidt-Amelunxen, T. Seifert, *J. Organomet. Chem.* **1997**, *542*, 1–18.
[67] Crystallographic data for [(18-crown-6)(thf)$_2$Na][4,4′-(Si*t*Bu$_2$Me)$_2$(C$_6$H$_4$)$_2$]: empirical formula $C_{58}H_{106}NaO_{10}Si_2$; formula mass 1042.60; green block; $T$ = 173(2) K, crystal system monoclinic; space group $P2_1/c$; unit cell dimensions $a$ = 13.1292(8), $b$ = 18.3379(8), $c$ = 14.4381(8) Å, $\beta$ = 113.233(4)°; $V$ = 3194.3(3) Å$^3$; $Z$ = 2; $D_{calcd.}$ = 1.084 g cm$^{-3}$; $\mu$ = 0.112 mm$^{-1}$; $F(000)$ = 1146; crystal size 0.40 × 0.23 × 0.22 mm; reflections collected = 40036; independent reflections = 5846 [$R$(int)= 0.0665]; data/restraints/parameters = 5846/12/318; GOOF on $F^2$ = 1.086; final R [$I > 2\sigma(I)$]: $R_1$ = 0.0999, $wR_2$ = 0.2692; R (all data): $R_1$ = 0.1169, $wR_2$ = 0.2834; largest diff. peak and hole 0.716 and –0.528 e Å$^{-3}$. The solvent thf molecule is disordered over two positions and was refined isotropically. In order to keep the geometric parameters in reasonable ranges, bond length restraints of C–O = 1.40(1) and C–C = 1.50(1) Å as well as restraints of 2.5(1) Å for 1,3-distances were applied.

 © 2007 Wiley-VCH Verlag GmbH & Co. KGaA, Weinheim 

[68] T. H. Whitesides, J. Shelly, *J. Organomet. Chem.* **1975**, *92*, 215–226.
[69] S. B. Fergusson, L. J. Sanderson, T. A. Shackleton, M. C. Baird, *Inorg. Chim. Acta* **1984**, *83*, L45–L47.
[70] M. L. H. Green, C. N. Street, G. Wilkinson, *Z. Naturforsch., Teil B* **1959**, *14*, 738.
[71] A. F. Holleman, N. Wiberg, *Lehrbuch der Anorganischen Chemie*, Walter de Gruyter, Berlin, **1995**, p. 2033.
[72] It appears that rather than attacking the iron atom, the nucleophilic siloxide reacts with the iodide ligand to form an $[Fp]^-$ fragment and intermediate $IOSiPh_2Me$. The complex iron anion subsequently reacts with one equivalent of FpI to give $Fp_2$. We speculate that the intermediate silicon-containing species reacts with one equivalent of siloxide ligand to give disiloxane $O(SiPh_2Me)_2$ and NaIO. The disiloxane is also the major product when **Na7** is treated with $I_2$. This can be thought of as analogous to the reaction of $I_2$ with $OH^-$, which results in $IO_3^-$, $I^-$, and $H_2O$.[71] When the same reaction is carried out using FpBr rather than FpI, an identical outcome is observed. However, the formation of $Fp_2$ and $O(SiPh_2Me)_2$ from **Na7** and FpI is slow, with about 50% of the starting material left after stirring for two weeks at room temperature. This slow reaction rate allows for the isolation of an adduct of **Na7** and $Fp_2$ in which the siloxide sodium atoms are supported by donor–acceptor interactions with the oxygen atoms of the bridging carbonyl ligands in $Fp_2$. The details of this adduct formation have been discussed recently in another context.[73]
[73] T. I. Kückmann, M. Bolte, H.-W. Lerner, M. Wagner, *Z. Anorg. Allg. Chem.* **2007**, *633*, 290–297.
[74] F. H. Allen, *Acta Crystallogr., Sect. B* **2002**, *58*, 380–388) (Cambridge Crystallographic Database, CSD Version 5.27, November 2005; update August 2006).
[75] L. Párkányi, K. H. Pannell, C. Hernandez, *J. Organomet. Chem.* **1983**, *252*, 127–132.
[76] R. West, E. K. Pham, *J. Organomet. Chem.* **1991**, *402*, 215–220.
[77] N. Kuhn, H. Schumann, *J. Organomet. Chem.* **1984**, *276*, 55–66.
[78] L. D. Quin, *A Guide to Organophosphorus Chemistry*, John Wiley and Sons, Inc., New York, **2000**, p. 394.
[79] S. Berger, S. Braun, H.-O. Kalinowski, *$^{31}$P-NMR-Spektroskopie*, Thieme Verlag, Stuttgart, **1993**.
[80] H. A. Bent, *Chem. Rev.* **1961**, *61*, 275–311.
[81] P. M. Treichel, W. K. Dean, W. M. Douglas, *J. Organomet. Chem.* **1972**, *42*, 145–158.
[82] M. Green, D. J. Westlake, *J. Chem. Soc. A.* **1971**, 367–371.
[83] P. M. Treichel, R. L. Shubkin, K. W. Barnett, D. Reichard, *Inorg. Chem.* **1966**, *5*, 1177–1181.
[84] A. Schäfer, H. Horn, R. Ahlrichs, *J. Chem. Phys.* **1992**, *97*, 2571–2577.
[85] A comparison of the averaged computed harmonic CO stretching frequencies [obtained as $(\tilde{\nu}_{as} + \tilde{\nu}_s)/2$] with the averaged experimentally determined frequencies revealed a systematic deviation. A scaling factor of 0.9884 was therefore employed to improve the overall agreement.
[86] W. Koch, M. C. Holthausen, *A Chemist's Guide to Density Functional Theory*, Wiley-VCH, Weinheim, **2001**.
[87] A. Schäfer, C. Huber, R. Ahlrichs, *J. Chem. Phys.* **1994**, *100*, 5829–5835.
[88] M. J. Frisch, G. W. Trucks, H. B. Schlegel, G. E. Scuseria, M. A. Robb, J. R. Cheeseman, J. J. A. Montgomery, T. Vreven, K. N. Kudin, J. C. Burant, J. M. Millam, S. S. Iyengar, J. Tomasi, V. Barone, B. Mennucci, M. Cossi, G. Scalmani, N. Rega, G. A. Petersson, H. Nakatsuji, M. Hada, M. Ehara, K. Toyota, R. Fukuda, J. Hasegawa, M. Ishida, T. Nakajima, Y. Honda, O. Kitao, H. Nakai, M. Klene, X. Li, J. E. Knox, H. P. Hratchian, J. B. Cross, C. Adamo, J. Jaramillo, R. Gomperts, R. E. Stratmann, O. Yazyev, A. J. Austin, R. Cammi, C. Pomelli, J. W. Ochterski, P. Y. Ayala, K. Morokuma, G. A. Voth, P. Salvador, J. J. Dannenberg, V. G. Zakrzewski, S. Dapprich, A. D. Daniels, M. C. Strain, O. Farkas, D. K. Malick, A. D. Rabuck, K. Raghavachari, J. B. Foresman, J. V. Ortiz, Q. Cui, A. G. Baboul, S. Clifford, J. Cioslowski, B. B. Stefanov, G. Liu, A. Liashenko, P. Piskorz, I. Komaromi, R. L. Martin, D. J. Fox, T. Keith, M. A. Al-Laham, C. Y. Peng, A. Nanayakkara, M. Challacombe, P. M. W. Gill, B. Johnson, W. Chen, M. W. Wong, C. Gonzalez, J. A. Pople, *Gaussian 03, Revision B.3*, Gaussian, Inc., Pittsburgh, PA, **2003**.
[89] *Spartan 06.1*, Wavefunction, Inc., Irvine, CA, **2006**.
[90] It is reasonable to assume that the final products of hydride abstraction for both the oxide **5b** and the phosphanyl borohydride **2b** will be cyclic dimers or polymers of the corresponding boranes. Nonetheless, the first intermediates following hydride abstractions are key species along the reaction pathways, and these are likely to be as described above.
[91] H. E. Gottlieb, V. Kotlyar, A. Nudelman, *J. Org. Chem.* **1997**, *62*, 7512–7515.
[92] V. D. Bianco, S. Doronzo, *Inorg. Synth.* **1976**, *16*, 161–163.
[93] G. Stieglitz, B. Neumüller, K. Dehnicke, *Z. Naturforsch. Teil B* **1993**, *48*, 156–160.
[94] T. J. Barton, C. R. Tully, *J. Org. Chem.* **1978**, *43*, 3649–3653.
[95] N. Wiberg, C.-K. Kim, *Chem. Ber.* **1986**, *119*, 2980–2994.
[96] T. Ohishi, Y. Shiotani, M. Yamashita, *J. Org. Chem.* **1994**, *59*, 250.
[97] D. Catheline, D. Astruc, *Organometallics* **1984**, *3*, 1094–1100.
[98] D. L. Reger, C. Coleman, *J. Organomet. Chem.* **1977**, *131*, 153–162.
[99] R. H. Blessing, *Acta Crystallogr., Sect. A* **1995**, *51*, 33–38.
[100] A. L. Spek, *Acta Crystallogr., Sect. A* **1990**, *46*, C34.
[101] G. M. Sheldrick, *Acta Crystallogr., Sect. A* **1990**, *46*, 467–473.
[102] G. M. Sheldrick, *SHELXL-97, A Program for the Refinement of Crystal Structures*, Universität Göttingen, Germany, **1997**.

Received: November 21, 2006
Published Online: April 4, 2007

 © 2007 Wiley-VCH Verlag GmbH & Co. KGaA, Weinheim 

DOI: 10.1002/ejic.200601190

# Synthesis, Structures and Optical Power Limiting of Some Transition Metal and Lanthanide Monoporphyrinate Complexes Containing Electron-Rich Diphenylamino Substituents

**Shitao Fu,[a,b] Xunjin Zhu,[b] Guijiang Zhou,[b] Wai-Yeung Wong,[b] Cheng Ye,[c] Wai-Kwok Wong,*[b] and Zaoying Li*[a]**

**Keywords:** Lanthanides / Optical limiting / Photoluminescence / Porphyrins / Transition metals

Transition metal and lanthanide monoporphyrinate complexes based on 5,10,15,20-tetrakis[*p*-(diphenylamino)-phenyl]-21*H*,23*H*-porphine ($H_2$tdpapp) have been synthesized and characterized and the X-ray crystal structures of the palladium and platinum analogues [M(tdpapp)] (M = Pd, Pt) determined. Experimental investigations of the nonlinear optical transmittance characteristics at 532 nm show that most of these new metalated porphyrinate complexes are excellent optical limiters with performances comparable or superior to those of the benchmark reverse saturable absorption dyes such as fullerene $C_{60}$ and (phthalocyanine)metal complexes. The nonlinear optical measurements reveal that the optical-limiting effects of porphyrins can be enhanced greatly by incorporation of lanthanide ions and covalent attachment of the electron-donating diphenylamino moieties to the parent porphyrinate ring. The optical-limiting thresholds for these lanthanide monoporphyrinate complexes range from 0.09 to 0.30 J cm$^{-2}$ at 82 % linear transmittance, which makes them attractive candidates as optical-limiting materials for the protection of various optical devices.
(© Wiley-VCH Verlag GmbH & Co. KGaA, 69451 Weinheim, Germany, 2007)

## Introduction

With the rapid development of laser technology, the damage to human eyes, optical sensors, and optical components caused by exposure to sudden, intense laser pulses has driven the search for effective optical limiters that display fast response speeds and relatively high linear transmissions.[1,2] Optical limiters are materials that are transparent at normal light intensities but opaque to very bright light.[3–5] Over the last decade, interest has focused on materials with weak ground-state absorption and strong excited-state absorption, which typically achieve optical limiting by a mechanism known as reverse saturable absorption (RSA). An ideal material would have a low ground-state absorption over a wide spectral bandwidth and strong excited-state absorption across the same region.[6]

At present, the materials employed for optical power limiting (OPL) are mainly composed of small molecules, such as fullerene ($C_{60}$),[7,8] phthalocyanines,[9,10] diacetylenes,[11] nanotubes,[12] and organometallic compounds.[13,14] Some conjugated organic polyynes also exhibit good optical-limiting capabilities.[15] Metalloporphyrins are among the most effective optical limiters[6,16–20] because their ground-state absorption is mostly confined to a few narrow regions (Soret and Q-bands), which allows high transmission in the spectral window between these bands. In addition, these macrocycles present a highly developed π-conjugation system which contributes to strong excited-state absorption, high triplet yields, long excited line-like spectra, and long luminescence lifetimes. Porphyrins and metalloporphyrins are known to exhibit RSA at 532 nm. Molecular modifications, for example by incorporating functional groups on the porphyrin ring or inserting metal ions in the ring, are commonly adopted to improve their OPL properties.

Recent investigations on the use of metalloporphyrins for optical limiting have focused on the transition metals,[16] phosphorus(V),[17] and group III and IV metals.[6,18] Wang and co-workers, for example, have reported a series of pentaazadentate porphyrin-like metal complexes with potential uses as optical-limiting materials where the metal ion is $Sm^{3+}$ or $Gd^{3+}$.[19] A europium(III) tetraphenylporphyrinate complex with OPL capability has also been reported by Kuznetsova et al.[20] It is well known that insertion of the lanthanide ion into the porphyrin core allows the energy of the ligand's triplet state to transfer efficiently to the excited state of the lanthanide ion, thus enabling this ion to emit light.[21] While triarylamine-derived organic materials have been investigated extensively because of their potential applications in various areas of optoelectronic devices,[22] there are only a few reports of porphyrin/triarylamine hybrids.[23] In this paper, we describe the synthesis and charac-

[a] Department of Chemistry, Wuhan University, Wuhan 430072, Hubei, P. R. China
[b] Department of Chemistry and Centre for Advanced Luminescence Materials, Hong Kong Baptist University, Kowloon Tong, Hong Kong, P. R. China
[c] Center for Molecular Sciences, Institute of Chemistry, Chinese Academy of Sciences, Beijing 100080, P. R. China

 © 2007 Wiley-VCH Verlag GmbH & Co. KGaA, Weinheim 

terization of a series of lanthanide monoporphyrinate complexes [(tdpapp)Ln($L_{OMe}$)] {Ln = Yb, Er, and Gd; $L_{OMe}^-$ = ($\eta^5$-$C_5H_5$)Co[P(=O)(OMe)$_2$]$^-$, $H_2$tdpapp = 5,10,15,20-tetrakis[*p*-(diphenylamino)phenyl]-21*H*,23*H*-porphine} and their late transition metal analogues [M(tdpapp)] (M = Ni, Zn, Pd, Pt) which show large optical-limiting capabilities; the mechanisms pertaining to their nonlinear optical behavior are critically discussed.

## Results and Discussion

### Synthesis and Characterization

Scheme 1 shows the chemical structures and the synthetic strategies of the metal monoporphyrinate complexes discussed in the present study. The porphyrin free-base ($H_2$tdpapp) containing diphenylamino (DPA) units was prepared according to a literature procedure.[24] When the molar ratio of pyrrole/DDQ (DDQ = 2,3-dichloro-5,6-dicyano-1,4-benzoquinone) was set at 4:3, the synthetic yield improved by up to 52%. The precursor complex Ln[N(SiMe$_3$)$_2$]$_3$·*x*[LiCl(thf)$_3$] (Ln = Yb, Er, and Gd) was generated from the reaction of anhydrous $LnCl_3$ with 3 equiv. of Li[N(SiMe$_3$)$_2$] in thf. An excess of the precursor complex was treated with the porphyrin free-base under nitrogen, and the mixture was refluxed in toluene for 12 h. Excess $NaL_{OMe}$ was then added to the reaction mixture at room temperature. This procedure gave green crystals of [(tdpapp)Ln($L_{OMe}$)] [Ln = Yb (**1**), Er (**2**), Gd (**3**)] in about 80% yield. These lanthanide complexes are thermally and air-stable, and could be purified by column chromatography, which indicates that the tripodal anion is capable of stabilizing labile normal lanthanide(III) porphyrinate complexes by effectively encapsulating the lanthanide(III) ion and thereby shielding it from interactions with the environment. The transition metal porphyrinate complexes [M(tdpapp)] [M = Ni (**4**), Zn (**5**), Pd (**6**), Pt (**7**)] were synthesized by refluxing the porphyrin free-base with 1 equiv. of the metal salts in an appropriate solvent. Purification was effected by preparative thin layer chromatography (TLC) with high isolated yields of 87–96%. All of these metal monoporphyrinate complexes were characterized by accurate mass spectrometric and spectroscopic techniques. The electrospray ionization high-resolution (ESI-HR) mass spectra of **1**–**3** exhibit the $[M + 1]^+$ or $[M]^+$ peak at *m*/*z* = 1906.4548, 1899.4461, and 1890.4455, respectively, which deviate by less than 5 ppm from the theoretical values of 1906.4627, 1899.4488, and 1890.2683; their isotopic distribution patterns match the theoretical fittings very well. The $^{31}$P NMR spectra (vs. 85% $H_3PO_4$) of **1** and **2** display a single peak at $\delta$ = 68.29 and –166.01 ppm, respectively.

The solid-state structures of complexes **6** and **7** were also confirmed by X-ray crystallographic studies. Perspective drawings of **6** and **7** are displayed in Figure 1, and Table 1 lists selected bond lengths and angles. There is only half of the molecule per asymmetric unit in the unit cell in each case, and the porphyrin framework is essentially planar. The group 10 metal ion is coordinated to the four pyrrolic nitrogen atoms, as is typical of other normal metalated porphyrinates. The bond lengths and angles in the porphyrin ring are also similar to those observed in the 5,10,15,20-tetraarylporphyrin system.[25,26]

The absorption spectra of all the new complexes were also measured and, in general, show a bathochromic shift in the absorption features after adding the diphenylamino chromophores (see Exp. Sect.). For example, complexes **1**–**3** show typical Soret and Q-bands for the lanthanide monoporphyrinate complexes at about 441, 564, and 607 nm, which are redshifted by at least 10 nm compared to those of the unsubstituted lanthanide tetraphenylporphyrinate (TPP) complexes. The large red shifts of both the Soret and Q-bands indicate a decreased energy gap between the HOMO and LUMOs as a consequence of the expanded π-conjugation. This can be attributed to the strong electron-donating ability of the DPA substituents, which produces a profound perturbation of the ground-state properties of the porphyrin TPP.

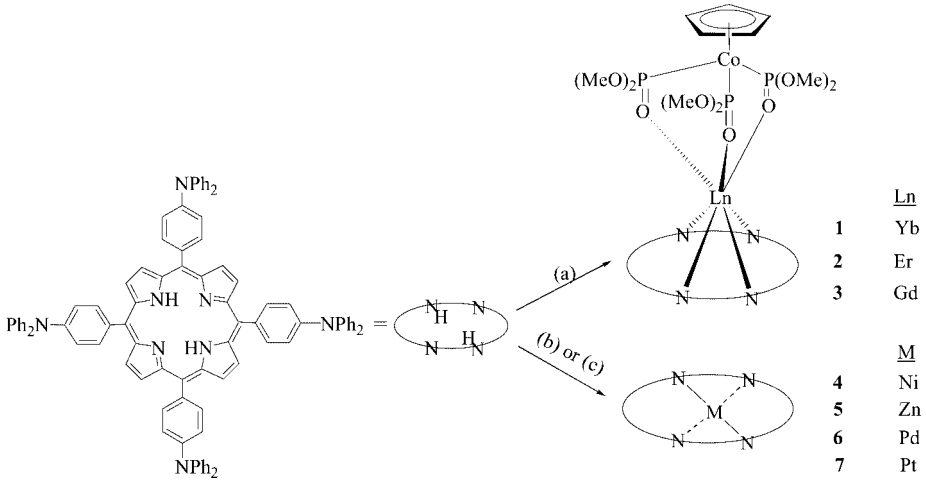


Scheme 1. Synthesis of lanthanide and transition metal monoporphyrinate complexes: (a) Ln[N(SiMe$_3$)$_2$]$_3$·*x*[LiCl(thf)], reflux in toluene, then $NaL_{OMe}$; (b) M(OAc)$_2$, $CHCl_3$/MeOH (M = Ni, Zn, Pd); (c) [$PtCl_2$(PhCN)$_2$], reflux in PhCN.

 © 2007 Wiley-VCH Verlag GmbH & Co. KGaA, Weinheim 

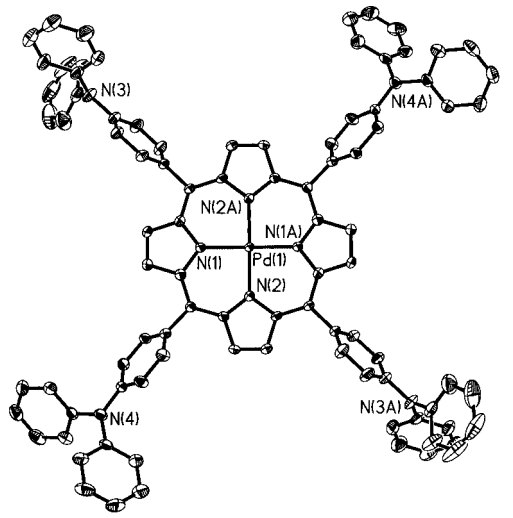


(a)

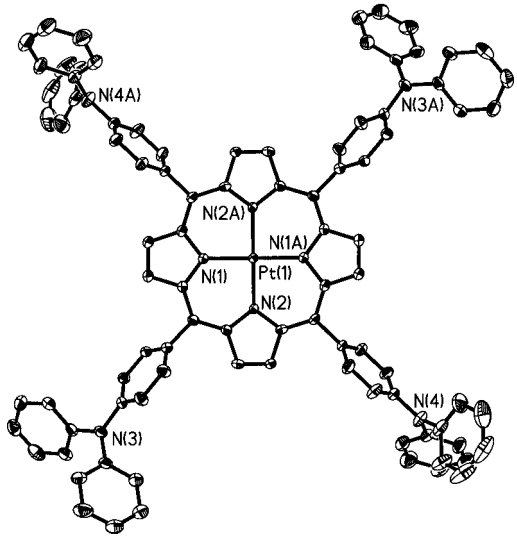


(b)

Figure 1. Perspective views of the crystal structures of **6** (a) and **7** (b). Hydrogen atoms and the labels on all carbon atoms have been omitted for clarity.

Table 1. Selected bond lengths [Å] and angles [°] for **6** and **7**.

| | **6** [M = Pd] | **7** [M = Pt] |
|---|---|---|
| M(1)–N(1) | 2.015(3) | 2.008(4) |
| M(1)–N(2) | 2.015(3) | 2.012(3) |
| C(5)–C(6) | 1.491(5) | 1.507(6) |
| N(3)–C(9) | 1.429(5) | 1.423(6) |
| N(3)–C(12) | 1.416(6) | 1.410(6) |
| N(3)–C(18) | 1.398(6) | 1.423(6) |
| C(28)–C(29) | 1.496(5) | 1.504(6) |
| N(4)–C(32) | 1.406(5) | 1.423(6) |
| N(4)–C(35) | 1.416(5) | 1.425(7) |
| N(4)–C(41) | 1.426(5) | 1.418(7) |
| N(1)–M(1)–N(2) | 89.89(12) | 90.21(14) |
| C(9)–N(3)–C(12) | 120.2(4) | 120.8(4) |
| C(9)–N(3)–C(18) | 120.8(4) | 121.3(4) |
| C(32)–N(4)–C(35) | 121.1(3) | 121.7(5) |
| C(32)–N(4)–C(41) | 121.5(4) | 119.6(5) |

## Optical-Limiting Properties of Lanthanide Monoporphyrinate Complexes

All the samples are stable toward air and laser light under our experimental conditions. In order to characterize the OPL properties at 532 nm excitation, the materials should show weak ground-state absorption at this wavelength. The UV/Vis spectra of the complexes in toluene at room temperature are shown in Figure 2; there is clearly a transparent window at 532 nm for the lanthanide monoporphyrinate complexes.

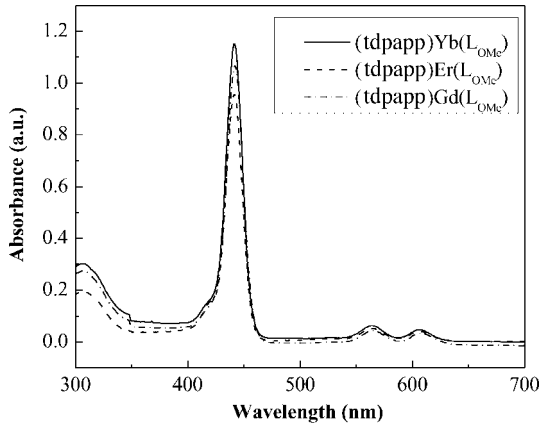


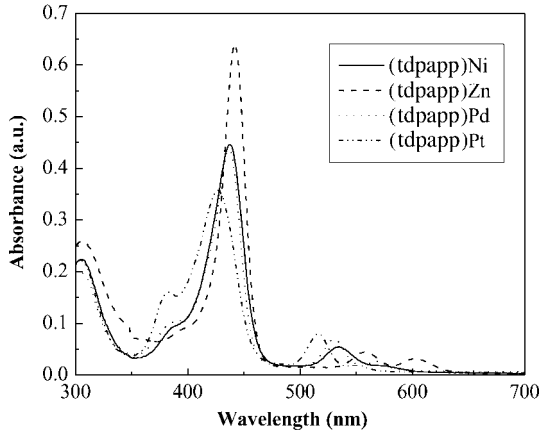


Figure 2. UV/Vis linear-absorption spectra of all the complexes in dilute toluene solution at room temperature.

According to the *Z*-scan curves for all the complexes measured in $CH_2Cl_2$ (Figure 3), the three lanthanide monoporphyrinate complexes show excellent OPL behavior relative to the benchmark material $C_{60}$, while the effect is only moderate for the transition metal complexes. Experiments with $CH_2Cl_2$ alone showed no detectable OPL effect, which indicates that there is a negligible contribution of solvent. When each sample is far from the focus ($Z/Z_0 = 0$) and the incident irradiance upon it is weak, the transmittance of the sample remains almost constant and shows a linear behavior (obeying Beer's law). When the sample is close to the focus, however, and the incident irradiance is strong, the transmittance of the sample decreases rapidly and an OPL

 © 2007 Wiley-VCH Verlag GmbH & Co. KGaA, Weinheim 

effect appears. It is clear that complex **2** shows the strongest optical-limiting capability, superior even to that of $C_{60}$, which is generally regarded as an excellent optical limiter. Complexes **1** and **3** also exhibit good OPL properties similar to those of $C_{60}$. As anticipated, compound **4** with the lighter nickel ion only showed a relatively weaker OPL response among **4**–**7**. On the other hand, we observe that incorporation of DPA units to the porphyrin ring leads to enhanced OPL responses (Figure 4), indicative of strong electronic interaction between the porphyrin and DPA moieties in the present system.

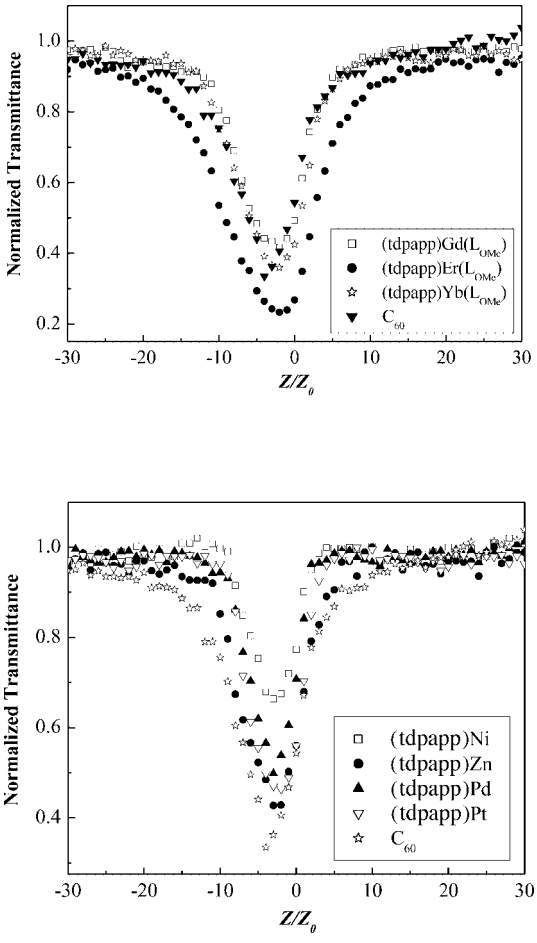


Figure 3. Open-aperture *Z*-scan results for the metal monoporphyrinate complexes and $C_{60}$ solutions at $T_o$ = 82%.

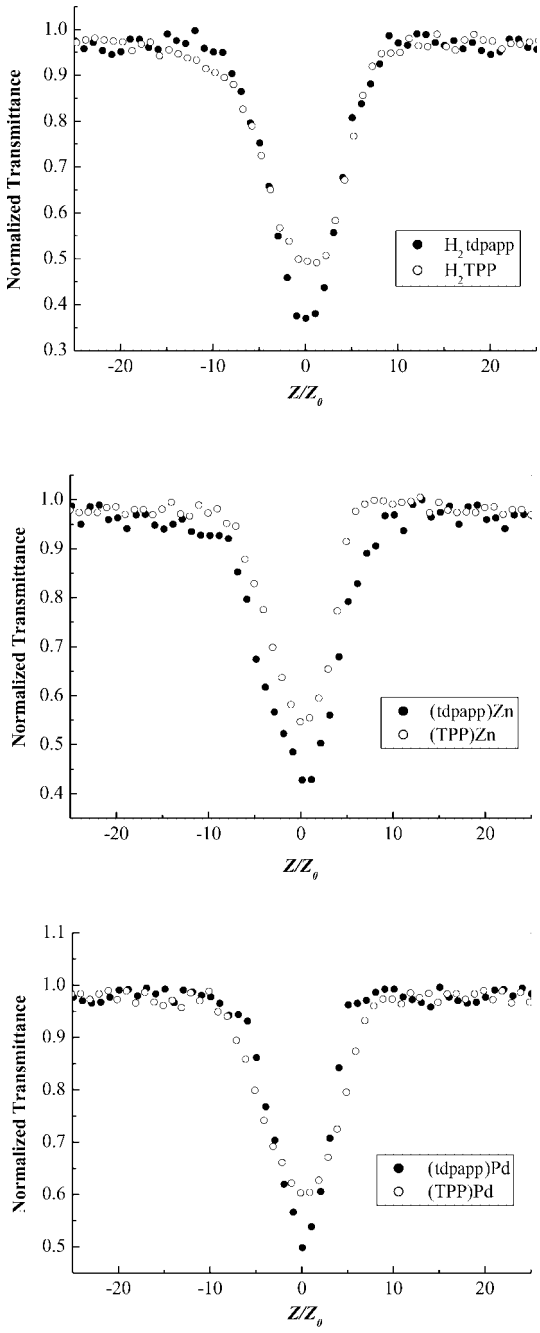


Figure 4. The effect of diphenylamino groups on the open-aperture *Z*-scan results for the free porphyrin and its metal complexes at $T_o$ = 82%.

In order to explain the *Z*-scan data obtained, we must consider the optical-limiting mechanism. According to the five-level model for the RSA mechanism (see Figure 5),[27] the molecules in the ground state ($S_0$) initially absorb optical energy and are excited to the first singlet state ($S_1$). After the $S_1$ state reaches a certain population, it can absorb optical energy strongly and leap to a higher singlet state ($S_n$), where it can induce an optical-limiting effect or undergo intersystem crossing (ISC) to the first triplet state ($T_1$). This can then also absorb optical energy strongly to reach a higher triplet state ($T_n$), which leads to optical-limiting action. Owing to the short lifetime (<10 ns) of the singlet state (see Table 2), it is the triplet-state absorption that contributes to the nanosecond optical-limiting process.[15b,27] To support this, the photoluminescence (PL) spectra for the singlet and triplet states of all complexes were measured (see Figures 6, 7, 8, and 9). At 77 K, the PL spectrum for **3** shows an obvious triplet emission at 815 nm with a measured triplet lifetime of 109 ms. The singlet-state lifetime for **3** is 3.23 ns. Since the pulse lengths are shorter than the lifetime of the triplet state, it acts as an accumulation site. This could confirm that the OPL effect of **3** is mainly induced by the triplet-state absorption. While a more complicated discussion may be invoked for the other

 © 2007 Wiley-VCH Verlag GmbH & Co. KGaA, Weinheim 

two lanthanide porphyrinate complexes, there is no apparent triplet emission for **1** and **2**, even at 77 K (Figure 6a and b), which suggests that the OPL effects of the Er and Yb complexes are not induced by the triplet-state absorption of the ligands. It is well known that there are efficient energy-transfer processes from the triplet state of the porphyrinate ligand to the excited states of the central lanthanide ions, thus enabling the ion to emit light. The energy absorption that accompanies the transition processes from the lower excited states of the lanthanide ion to the higher energy ones will therefore contribute to the OPL effect of the lanthanide complexes. Owing to the presence of its multiple excited states, the porphyrinate ligand will provide more possible energy absorption transitions in **2** than its Yb counterpart **1**. Complex **2** therefore shows a much better optical-limiting performance than **1**. It can be concluded that the OPL effects of **1** and **2** are predominantly caused by the excited state absorption of the central lanthanide ion. As trivalent lanthanide ions, $Yb^{3+}$ and $Er^{3+}$ should show strong near-infrared (NIR) emission bands.[21a,28] To support this, the NIR PL spectra of **1** and **2** (Figure 7) were measured. Our previous PL studies on related lanthanide porphyrinate complexes have shown that the excitation of $Yb^{3+}$ is due to the $\pi \rightarrow \pi^*$ transitions of the porphyrinate antenna, and that the porphyrinate antenna transfers its absorbed visible energy of the Q-bands to the excited state of the lanthanide ion, which then relaxes through emission in the NIR region.[21a,28b] A strong emission due to the $^2F_{5/2} \rightarrow {}^2F_{7/2}$ transition is observed at 995 nm for the $Yb^{3+}$ complex **1**, whereas for the $Er^{3+}$ complex **2**, the emission at 1529 nm can be assigned to the $^4I_{13/2} \rightarrow {}^4I_{15/2}$ transition. The NIR lifetime of **1** in toluene at room temperature is 30 μs, which also confirms that the excited state of the $Yb^{3+}$ ion should play a major role in the OPL effect of **1**. However, we were unable to measure the NIR lifetime of **2** due to the limitations of the instrument. Unlike **1** and **2**, the OPL effect of **3** should be due to the triplet state of the ligand which can be corroborated by the observation of an obvious triplet emission at 77 K (Figure 6c). Furthermore, the absence of an NIR emission for the $Gd^{3+}$ ion will also preclude the involvement of the excited state of the central Gd ion in the OPL phenomenon. In other words, the OPL effect of **3** is likely dominated by the triplet excited state absorption of the ligand. In view of these factors, complex **3** can be anticipated to show an inferior OPL effect than the free ligand.

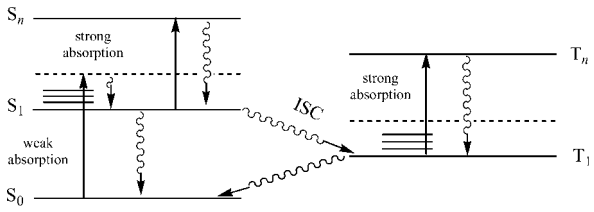


Figure 5. RSA mechanism for the lanthanide monoporphyrinate complexes.

Table 2. Lifetime of the $S_1$ state for the lanthanide monoporphyrinate complexes.

| Complex | Lifetime [ns][a] |
|---|---|
| [(tdpapp)Yb($L_{OMe}$)] | 1.43 |
| [(tdpapp)Er($L_{OMe}$)] | 3.55 |
| [(tdpapp)Gd($L_{OMe}$)] | 3.23 |
| [Ni(tdpapp)] | < 0.50 |
| [Zn(tdpapp)] | 2.66 |
| [Pd(tdpapp)] | 1.76 |
| [Pt(tdpapp)] | 5.88 |

[a] Measured at room temperature in toluene solution with an excitation wavelength of 337 nm.

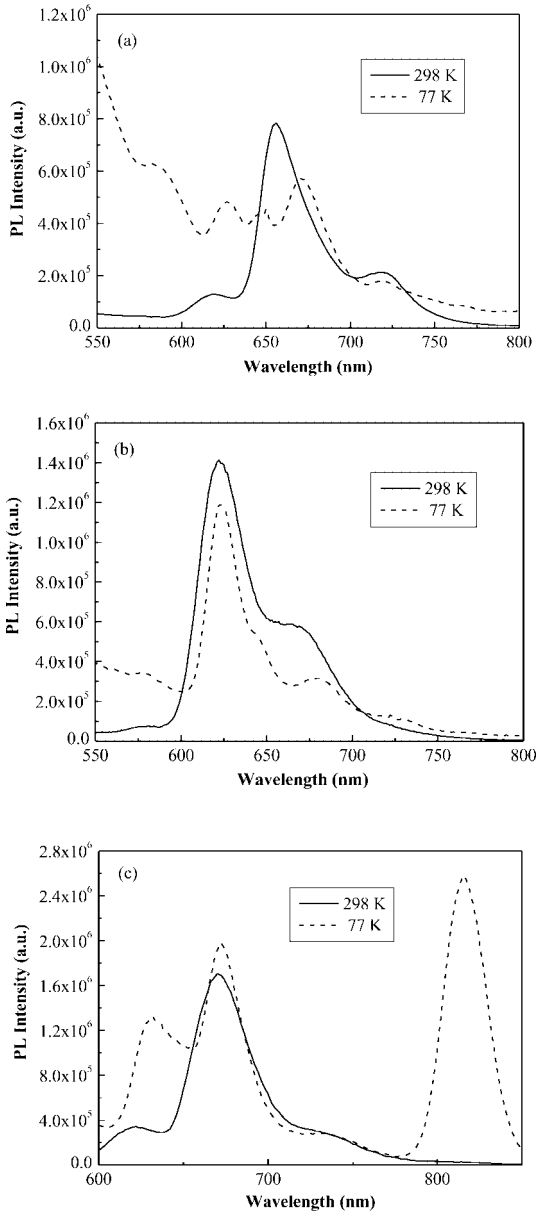


Figure 6. PL spectra for **1** (a), **2** (b), and **3** (c) at 298 and 77 K in toluene.

The OPL effect of $H_2$tdpapp and **4**–**7** is induced mainly by the strong absorption of the triplet states of the ligand induced by spin-orbital coupling effect, which can be de-

 © 2007 Wiley-VCH Verlag GmbH & Co. KGaA, Weinheim 

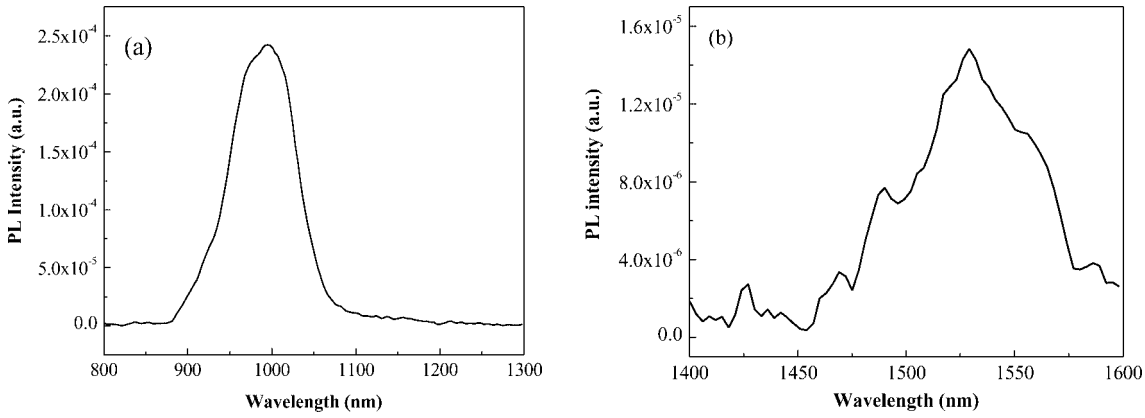


Figure 7. NIR photoluminescence spectra of **1** (a) and **2** (b) in toluene at room temperature.

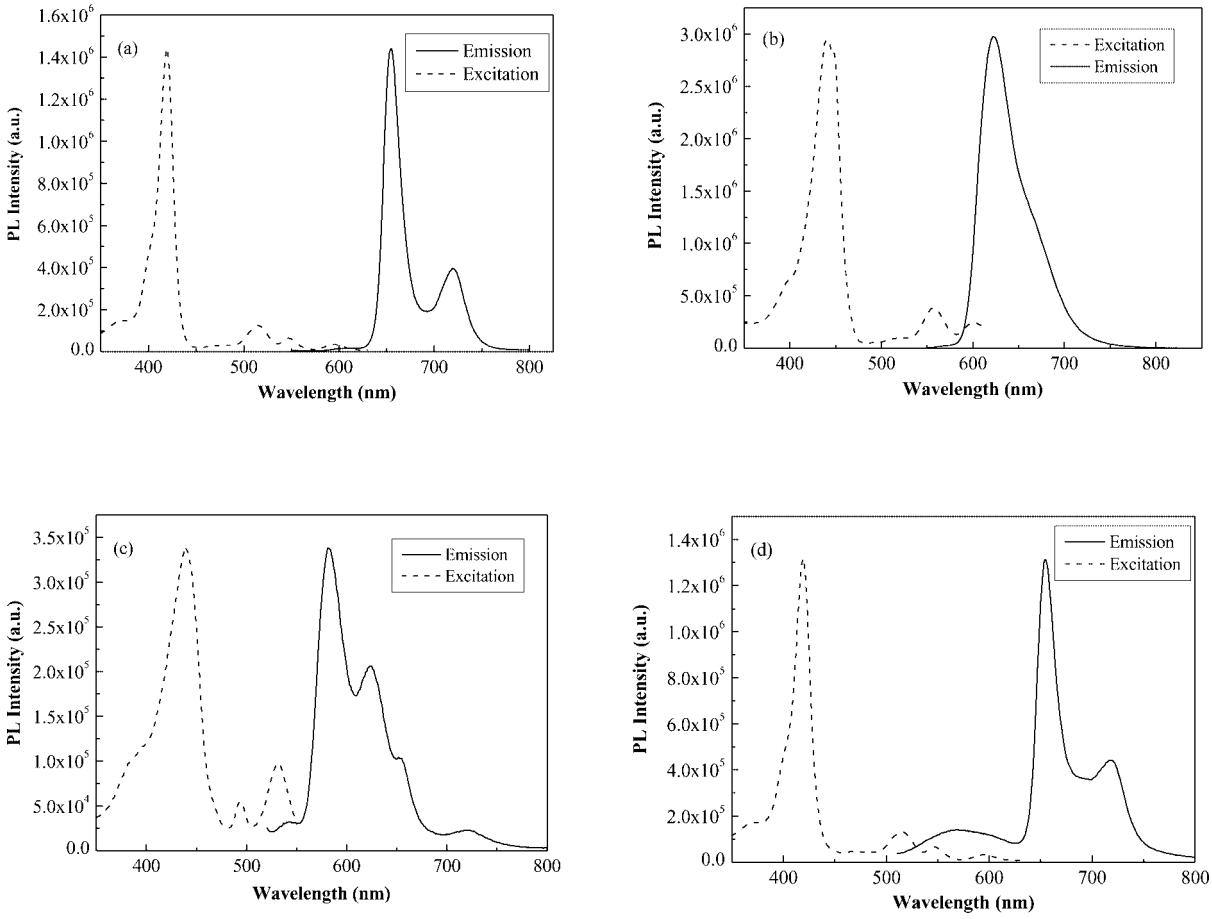


Figure 8. PL spectra for **4** (a), **5** (b), **6** (c), and **7** (d) at 298 K in toluene.

scribed by the typical RSA mechanism (Figure 5) and is typical of other known transition metal porphyrins reported in the literature. The PL spectra of **4**–**7** in toluene at 298 and 77 K are depicted in Figures 8 and 9, respectively. Owing to the much stronger triplet emission at 77 K for **6** ($\lambda_{em}$ = 723 nm) and **7** ($\lambda_{em}$ = 689 nm) and their long lifetimes (890 and 80 μs, respectively), both of them show a stronger OPL effect than **4** according to the RSA mechanism stated above. As complex **4** contains the light Ni ion, it is not phosphorescent even at 77 K. The observation of a reasonably strong OPL response for **5**, which also shows no triplet emission at 77 K but only a singlet emission at 630 nm with a lifetime of 7.78 ns at 77 K, can be ascribed to its higher transparency at 532 nm compared with that of other three transition metal complexes (as revealed clearly from the UV/Vis spectra shown in Figure 2). In view of its better transparency, the Zn complex **5** should possess a higher concentration than the others when the OPL signal is measured at the same linear transmittance. As there should be more molecules contributing to its OPL effect,

 © 2007 Wiley-VCH Verlag GmbH & Co. KGaA, Weinheim 

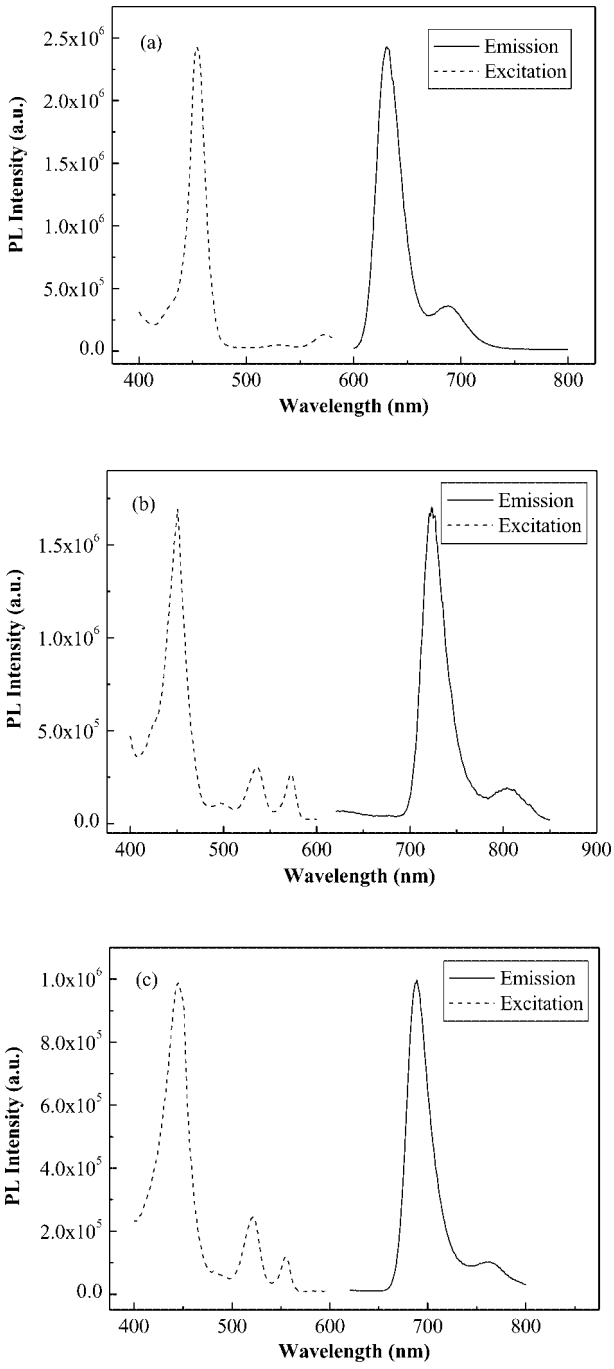


Figure 9. PL spectra for **5** (a), **6** (b), and **7** (c) at 77 K in toluene.

this will compensate for the loss in contribution due to the triplet-state absorption. Hence, despite its low triplet yield, complex **5** can still show an OPL close to those of **6** and **7**.

Figure 10 shows a simple, widely accepted photophysical model of the sensitization process in some (Por)Ln($L_{OMe}$)-type compounds (Por = porphyrinate anion).[28c,28d,29] In this process, the porphyrin absorbs light and is excited to its singlet state ($S_1$). The energy is then transferred to its triplet state ($T_1$), which is, in part, transferred to the excited state of the lanthanide ion ($Ln^{3+}$)* to produce the final luminescence. The $Er^{3+}$ ion is clearly able to introduce more low-lying states in the HOMO–LUMO gap to perturb the ring π-electron system,[16f] which might explain why **2** has the strongest optical-limiting yield of the three lanthanide monoporphyrinate complexes.

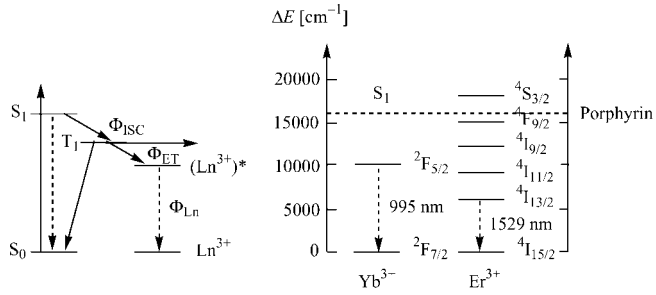


Figure 10. Schematic energy diagram of (Por)Ln($L_{OMe}$) complexes. The arrows indicate the excitation mechanism of lanthanide ions by the porphyrin sensitizer ($S_0 \rightarrow S_1$ transition followed by intersystem crossing and energy transfer).

Table 3 lists the optical-limiting thresholds of the three lanthanide monoporphyrinate complexes, which is an important parameter in characterizing the merit of these optical limiters. All three complexes possess low optical-limiting thresholds at 82% linear transmittance. Complex **2** shows a lower optical-limiting threshold than fullerene $C_{60}$ that is even comparable to those of some state-of-the-art phthalocyanine dyes. The optical-limiting thresholds of the transition metal analogues **4**–**7** are, however, less attractive than the lanthanide congeners. Hence, the OPL effects of the functionalized porphyrin $H_2$tdpapp can be enhanced greatly by the incorporation of trivalent lanthanide ions.

## Concluding Remarks

We have reported a series of new lanthanide monoporphyrinate complexes that exhibit excellent optical-limiting capabilities for a nanosecond laser pulse at 532 nm and display optical-limiting thresholds comparable to or lower than those reported for optical-limiting materials currently in use. Experimental investigations on their photophysics suggest that these complexes show optical-limiting effects following the standard five-level RSA mechanism. The optical-limiting effects of porphyrins can be enhanced greatly by the addition of electron-rich $Ph_2N$ groups and the incorporation of lanthanide ions, which can make the energy of the porphyrin triplet state transfer efficiently to the excited state of the lanthanide ions. We have shown that the three monoporphyrinate lanthanide complexes have an excellent optical-limiting performance and are very promising candidates for practical use as optical-limiting materials for the protection of optical devices. Solid films are desirable for many optical power-limiting applications, therefore further work will be carried out to determine the response of polymer films to an optical pulse for use in practical devices.

 © 2007 Wiley-VCH Verlag GmbH & Co. KGaA, Weinheim 

Table 3. Comparison of the optical-limiting performance of **1**–**7** with some reported materials.

| Compound | Optical limiting threshold [J cm$^{-2}$][b] | $T_o$ [%][c] | Sample thickness [mm] | $\sigma_{ex}/\sigma_o$[a] | Reference |
|---|---|---|---|---|---|
| PbPc(β-CP)$_4$ | 0.070 | 62 | [d] | [d] | [30] |
| CuPcR$_8$[e] | 0.30 | 68 | 10 | 4.18 | [31] |
| MPc; M = Si, Ge, etc | 0.10 | 84 | 10 | [d] | [32] |
| $C_{60}$ | 0.18 | 55 | 2 | [d] | [33] |
| $C_{60}$ | 0.19 | 84 | 1 | 5.74 | this work |
| $H_2$tdpapp | 0.27 | 82 | 1 | 5.35 | this work |
| [(tdpapp)Yb($L_{OMe}$)] | 0.17 | 82 | 1 | 5.42 | this work |
| [(tdpapp)Er($L_{OMe}$)] | 0.093 | 82 | 1 | 7.35 | this work |
| [(tdpapp)Gd($L_{OMe}$)] | 0.30 | 82 | 1 | 4.80 | this work |
| [Ni(tdpapp)] | 1.99[f] | 82 | 1 | 2.67 | this work |
| [Zn(tdpapp)] | 0.38 | 82 | 1 | 4.69 | this work |
| [Pd(tdpapp)] | 0.69 | 82 | 1 | 3.95 | this work |
| [Pt(tdpapp)] | 0.46 | 82 | 1 | 4.39 | this work |

[a] $\sigma_{ex}/\sigma_o = \ln T_{sat}/\ln T_o$, where $\sigma_{ex}$ is the effective excited-state absorption cross-section, $\sigma_o$ is the ground-state absorption cross-section, and $T_{sat}$ is the transmittance at the saturation fluence. [b] The optical-limiting threshold is defined as the input light fluence at which the output light fluence is 50% of that predicted by linear transmittance. [c] Linear transmittance. [d] Not reported. [e] R = pentyloxy. [f] Predicted by theoretical fitting.

## Experimental Section

**General:** All reactions were carried out under dry nitrogen. Solvents were dried by standard procedures, distilled, and degassed prior to use. All chemicals used were purchased from Aldrich or Acros. 4-(Diphenylamino)benzaldehyde was prepared according to a literature method by formylation of triphenylamine with dmf and $POCl_3$.[34] 5,10,15,20-Tetrakis[*p*-(diphenylamino)phenyl]-21*H*,23*H*-porphine ($H_2$tdpapp) was also prepared according to a literature method by condensing pyrrole and 4-(diphenylamino)benzaldehyde.[24] NMR spectra were measured in $CDCl_3$ with a JEOL EX270 or a Varian Inova 400 MHz FT-NMR spectrometer, with the $^1$H NMR chemical shifts quoted relative to $SiMe_4$ and the $^{31}$P NMR chemical shifts relative to 85% $H_3PO_4$ as external standard. Electrospray ionization high-resolution mass spectra were recorded with a QSTAR mass spectrometer. The electronic absorption spectra in the UV/Vis region were obtained with a Hewlett Packard 8453 spectrophotometer. The photoluminescent properties and lifetimes of the complexes were determined with a Photon Technology International (PTI) spectrophotometer. NIR emission was detected by a liquid-nitrogen-cooled InSb IR detector (EG & G) with a preamplifier, and recorded by a lock-in amplifier system. The third harmonic of the 355-nm line of an Nd:YAG laser (Quantel Brilliant B) was used as the excitation light source. Infrared spectra were obtained with a Nicolet Magna 550 series II FTIR spectrometer in KBr pellets.

**Optical-Limiting Measurements:** To study the optical-limiting properties, intensity-dependent transmittance and *Z*-scan measurements were performed with a Q-switched Nd:YAG laser at a repetition rate of 10 Hz. The laser frequency was doubled with an output wavelength of 532 nm and a 10-ns pulse width for the Gaussian mode by a frequency double crystal. The laser beam was then split into two by a beam splitter. One was used as the reference beam, which was received by a detector ($D_1$), and the other was used for the sample measurement, and was focused with a lens ($f$ = 20 cm). After transmitting through the sample, the light beam entered another detector ($D_2$). The sample to be measured was moved along a rail to change the incident irradiance on it. The incident and transmitted energies were detected simultaneously by the two detectors $D_1$ and $D_2$ (LPE-1A). The performance of each sample was measured as an 82% transmitting solution at 532 nm in $CH_2Cl_2$ in a 1-mm quartz cell.

**Preparation of Precursor Complexes:** Stock solutions of the precursor complexes, Ln[N(SiMe$_3$)$_2$]$_3$·*x*[LiCl(thf)$_3$] (Ln = Yb$^{3+}$, Er$^{3+}$ and Gd$^{3+}$), were prepared in a similar manner. A detailed description is given for the Yb$^{3+}$ complex.

**Yb[N(SiMe$_3$)$_2$]$_3$·*x*[LiCl(thf)$_3$] (Solution A):** HN(SiMe$_3$)$_2$ (5.06 mL, 0.024 mol) was dissolved in thf (10 mL) in an ice bath, then *n*BuLi (1.6 M in hexane; 15.0 mL, 0.024 mol) was added slowly over a period of 30 min. The resulting solution was magnetically stirred for 12 h until a clear pale yellow solution was obtained. The solution was then transferred slowly into a Schlenk flask containing $YbCl_3$ (2.24 g, 0.008 mol) suspended in thf (20 mL). The resulting mixture was magnetically stirred for 24 h until all of the solid $YbCl_3$ had disappeared. The resulting solution A contains Yb[N(SiMe$_3$)$_2$]$_3$·*x*[LiCl(thf)] (*x* = 3–5).

**Er[N(SiMe$_3$)$_2$]$_3$·*x*[LiCl(thf)$_3$] (Solution B):** Er[N(SiMe$_3$)$_2$]$_3$·*x*[LiCl(thf)$_3$] was prepared by the same method as for solution A except that HN(SiMe$_3$)$_2$ (5.06 mL, 0.024 mol), *n*BuLi (1.6 M in hexane; 15.0 mL, 0.024 mol), and $ErCl_3$ (2.18 g, 0.008 mol) in thf were used.

**Gd[N(SiMe$_3$)$_2$]$_3$·*x*[LiCl(thf)$_3$] (Solution C):** Gd[N(SiMe$_3$)$_2$]$_3$·*x*[LiCl(thf)$_3$] was prepared similarly as for solution A except that HN(SiMe$_3$)$_2$ (5.06 mL, 0.024 mol), *n*BuLi (1.6 M in hexane; 15.0 mL, 0.024 mol), and $GdCl_3$ (2.11 g, 0.008 mol) in thf were used.

**Synthesis of Complexes 1–3:** Compounds **1**–**3** were prepared according to the same procedure. A typical procedure is given for **1**. We used the tripodal anion $L_{OMe}^-$ {$L_{OMe}^-$ = ($\eta^5$-$C_5H_5$)Co[P(=O)(OMe)$_2$]$_3^-$} to stabilize labile normal lanthanide(III) porphyrinate complexes.

**[(tdpapp)Yb($L_{OMe}$)] (1):** Solution A (2.0 mL, 0.32 mmol) was transferred into a Schlenk flask and the solvent was removed under vacuum. Dichloromethane (10 mL) was then added to precipitate LiCl. The mixture was centrifuged and the clear layer was transferred to another Schlenk flask containing dry $H_2$tdpapp (50 mg, 0.039 mmol) dissolved in toluene (15 mL). The progress of the reaction was monitored by UV/Vis spectroscopy. The resulting solution was refluxed for 12 h until most of the free base had coordinated to the metal ion. Upon cooling of the reaction mixture to room temperature, solid $NaL_{OMe}$ (0.1 g, 0.22 mmol) was added and the resultant solution was magnetically stirred for another 24 h. The

 © 2007 Wiley-VCH Verlag GmbH & Co. KGaA, Weinheim 

solvent was removed in vacuo, and the residue was dissolved in chloroform, filtered, and chromatographed on silica gel using chloroform/petroleum ether (1:1, v/v) as the eluent. Complex **1** was obtained in 75% yield (56 mg). IR (KBr): $\tilde{\nu}$ = 3445 m, 2940 m, 1591 s, 1490 s, 1276 m, 1143 s, 1006 m, 752 m, 696 m cm$^{-1}$. $^1$H NMR ($CDCl_3$): $\delta$ = 16.39 (s, 4 H, Ar), 15.57 (s, 8 H, β-H), 10.30 (s, 4 H, Ar), 8.58–8.56 (m, 24 H, Ar), 8.11–8.07 (m, 16 H, Ar), 7.63–7.61 (m, 8 H, Ar), 6.44 (s, 18 H, OMe), –4.71 (s, 5 H, $\eta^5$-$C_5H_5$) ppm. $^{31}$P NMR ($CDCl_3$): $\delta$ = 68.29 (s) ppm. UV/Vis (toluene, 20 °C): $\lambda_{max}$ (log$\varepsilon$) = 307 (5.18), 441 (5.76), 564 (4.50), 607 (4.38 M$^{-1}$cm$^{-1}$) nm. ESI-HRMS ($CHCl_3$): *m*/*z* = 1906.4548 [M + H]$^+$.

**[(tdpapp)Er($L_{OMe}$)] (2):** Solution B (2.0 mL, 0.32 mmol), $H_2$tdpapp (100 mg, 0.078 mmol), and $NaL_{OMe}$ (0.1 g, 0.22 mmol) were used. Yield: 81% (120 mg). IR (KBr): $\tilde{\nu}$ = 3445 m, 2940 m, 1591 s, 1490 s, 1277 s, 1141 s, 1006 s, 796 m, 752 m, 696 m cm$^{-1}$. $^1$H NMR ($CDCl_3$): $\delta$ = 45.59 (s, 4 H, Ar), 35.09 (s, 8 H, β-H), 20.64–19.99 (m, 24 H, Ar), 12.56 (s, 18 H, OMe), 12.14 (s, 4 H, Ar), 10.39 (s, 16H, Ar), 9.43 (s, 8 H, Ar), –34.16 (s, 5 H, $\eta^5$-$C_5H_5$) ppm. $^{31}$P NMR ($CDCl_3$): $\delta$ = –166.01 (s) ppm. UV/Vis (toluene, 20 °C): $\lambda_{max}$ (log$\varepsilon$) = 307 (4.99), 441 (5.68), 564 (4.41), 606 (4.31 M$^{-1}$cm$^{-1}$) nm. ESI-HRMS ($CHCl_3$): *m*/*z* = 1899.4461 [M]$^+$.

**[(tdpapp)Gd($L_{OMe}$)] (3):** Solution C (2.0 mL, 0.32 mmol), $H_2$tdpapp (100 mg, 0.078 mmol), and $NaL_{OMe}$ (0.1 g, 0.22 mmol) were used. Yield: 76% (112 mg). IR (KBr): $\tilde{\nu}$ = 3449 m, 2940 m, 1591 s, 1491 s, 1277 m, 1137 s, 1006 m, 752 m, 696 m cm$^{-1}$. UV/Vis (toluene, 20 °C): $\lambda_{max}$ (log$\varepsilon$) = 307 (5.14), 442 (5.73), 566 (4.35), 608 (4.24 M$^{-1}$cm$^{-1}$) nm. ESI-HRMS ($CHCl_3$): *m*/*z* = 1890.4455 [M + H]$^+$.

**Synthesis of Complexes 4–7:** Transition metal porphyrinate complexes **4**–**7** were prepared by refluxing the porphyrin free-base with 1 equiv. of the metal salts in an appropriate solvent. The typical procedure is described in detail for **4**.

**[Ni(tdpapp)] (4):** $Ni(OAc)_2$·$4H_2O$ (100 mg, 0.4 mmol) dissolved in MeOH (8 mL) was added to a solution of $H_2$tdpapp (50 mg, 0.039 mmol) in $CHCl_3$ (30 mL). The mixture was then refluxed until the reaction was complete, as revealed by TLC. The product was purified on silica gel using chloroform/petroleum ether (2:1, v/v) as the eluent. The title product was obtained in 92% yield (48 mg). IR (KBr): $\tilde{\nu}$ = 3444 m, 3029 w, 1591 s, 1491 s, 1280 s, 1177 w, 1002 m, 800 m, 753 m, 695 m cm$^{-1}$. $^1$H NMR ($CDCl_3$): $\delta$ = 8.81 (s, 8 H, β-H), 7.78 (d, *J* = 8.4 Hz, 8 H, Ar), 7.34–7.28 (m, 40 H, Ar), 7.06–7.01 (m, 8 H, Ar) ppm. UV/Vis (toluene, 20 °C): $\lambda_{max}$ (log$\varepsilon$) = 304 (5.05), 437 (5.35), 534 (4.44 M$^{-1}$cm$^{-1}$) nm. ESI-HRMS ($CHCl_3$): *m*/*z* = 1339.4674 [M]$^+$.

**[Zn(tdpapp)] (5):** $H_2$tdpapp (50 mg, 0.039 mmol) and $Zn(OAc)_2$·$2H_2O$ (50 mg, 0.23 mmol) were used. Yield: 96% (50 mg). IR (KBr): $\tilde{\nu}$ = 3446 m, 3027 w, 1590 s, 1489 s, 1279 s, 1176 w, 999 m, 798 m, 753 m, 695 m cm$^{-1}$. $^1$H NMR ($CDCl_3$): $\delta$ = 9.03 (s, 8 H, β-H), 8.01 (d, *J* = 8.4 Hz, 8 H, Ar), 7.40–7.33 (m, 40 H, Ar), 7.07–7.04 (m, 8 H, Ar) ppm. UV/Vis (toluene, 20 °C): $\lambda_{max}$ (log$\varepsilon$) = 306 (5.11), 442 (5.51), 558 (4.35), 603 (4.20 M$^{-1}$cm$^{-1}$) nm. ESI-HRMS ($CHCl_3$): *m*/*z* = 1346.4536 [M]$^+$.

**[Pd(tdpapp)] (6):** $H_2$tdpapp (50 mg, 0.039 mmol) and $Pd(OAc)_2$ (50 mg, 0.22 mmol) were used. Yield: 89% (48 mg). IR (KBr): $\tilde{\nu}$ = 3443 m, 3029 w, 1591 s, 1491 s, 1278 s, 1175 w, 1014 m, 805 w, 751 m, 695 m cm$^{-1}$. $^1$H NMR ($CDCl_3$): $\delta$ = 8.90 (s, 8 H, β-H), 7.96 (d, *J* = 8.4 Hz, 8 H, Ar), 7.39–7.33 (m, 40 H, Ar), 7.09–7.07 (m, 8 H, Ar) ppm. UV/Vis (toluene, 20 °C): $\lambda_{max}$ (log$\varepsilon$) = 307 (4.99), 437 (5.34), 530 (4.54), 569 (4.13 M$^{-1}$cm$^{-1}$) nm. ESI-HRMS ($CHCl_3$): *m*/*z* = 1386.4327 [M]$^+$.

**[Pt(tdpapp)] (7):** A solution of $H_2$tdpapp (100 mg, 0.078 mmol) and $PtCl_2(PhCN)_2$ (74 mg, 0.156 mmol) in benzonitrile (10 mL) was heated at reflux to afford **7** in 87% yield (100 mg).[35] IR (KBr): $\tilde{\nu}$ = 3444 m, 3029 w, 1591 s, 1491 s, 1281 s, 1177 w, 1021 m, 803 w, 753 m, 695 m cm$^{-1}$. $^1$H NMR ($CDCl_3$): $\delta$ = 8.85 (s, 8 H, β-H), 7.93 (d, *J* = 8.1 Hz, 8 H, Ar), 7.38–7.33 (m, 40 H, Ar), 7.08–7.06 (m, 8 H, Ar) ppm. UV/Vis (toluene, 20 °C): $\lambda_{max}$ (log$\varepsilon$) = 305 (5.16), 428 (5.25), 516 (4.58), 551 (3.94 M$^{-1}$cm$^{-1}$) nm. ESI-HRMS ($CHCl_3$): *m*/*z* = 1476.4990 [M]$^+$.

**X-ray Crystallography:** Crystals of **6**·$2CHCl_3$ and **7**·$2CHCl_3$ suitable for X-ray diffraction were grown by slow concentration of chloroform solutions of these compounds in air. Because of severe solvent loss, the selected crystals were mounted in sealed capillary tubes for diffraction experiments. The intensity data were collected at 293 K with a Bruker AXS SMART 1000 CCD area-detector diffractometer using graphite-monochromated Mo-$K_\alpha$ radiation ($\lambda$ = 0.71073 Å). The collected frames were processed with proprietary software (SAINT[36]) and an absorption correction was applied (SADABS[37]) to the collected reflections. The structures of these molecules were solved by direct methods and expanded by standard difference Fourier syntheses using the software SHELXTL.[38] Structure refinements were made on $F^2$ using the full-matrix least-squares technique. All non-hydrogen atoms were refined with anisotropic displacement parameters. Hydrogen atoms were placed in their idealized positions and allowed to ride on the respective carbon atoms. Pertinent crystallographic data and other experimental details are summarized in Table 4. CCDC-628463 (**6**) and -628464 (**7**) contain the supplementary crystallographic data for this paper. These data can be obtained free of charge from The Cambridge Crystallographic Data Centre via www.ccdc.cam.ac.uk/data_request/cif.

Table 4. Crystal data and refinement for compounds **6** and **7**.

| | **6**·$2CHCl_3$ | **7**·$2CHCl_3$ |
|---|---|---|
| Empirical formula | $C_{94}H_{66}N_8Cl_6Pd$ | $C_{94}H_{66}N_8Cl_6Pt$ |
| Formula mass | 1626.65 | 1715.34 |
| Crystal system | monoclinic | monoclinic |
| Space group | $P2_1/n$ | $P2_1/n$ |
| *a* [Å] | 17.4493(10) | 17.441(2) |
| *b* [Å] | 9.4600(6) | 9.4752(12) |
| *c* [Å] | 24.3486(14) | 24.345(3) |
| $\beta$ [°] | 104.8050(10) | 104.778(2) |
| *V* [Å$^3$] | 3885.8(4) | 3890.2(9) |
| Z | 2 | 2 |
| *F*(000) | 1668 | 1732 |
| $D_{calcd.}$ [g cm$^{-3}$] | 1.390 | 1.464 |
| $\mu$(Mo-$K_\alpha$) [mm$^{-1}$] | 0.500 | 2.064 |
| Reflections collected | 18533 | 18744 |
| Unique reflections | 6800 | 6810 |
| Observed reflections | 4139 | 4462 |
| GOF on $F^2$ | 1.009 | 1.056 |
| $R_1$, $wR_2$ [$I > 2\sigma(I)$] | 0.0657, 0.1718 | 0.0436, 0.1145 |
| $R_1$, $wR_2$ (all data) | 0.1174, 0.2082 | 0.0776, 0.1304 |

## Acknowledgments

We thank the Hong Kong Baptist University (FRG/03-04/II-52) and Hong Kong Research Grants Council (HKBU 2021/03P) for their financial support.

[1] L. W. Tutt, T. F. Boggess, *Prog. Quantum Electron.* **1993**, *17*, 299.
[2] D. G. Mclean, R. L. Sutherland, M. C. Brant, D. M. Brandelick, P. A. Fleitz, T. Potten, *Opt. Lett.* **1993**, *18*, 858.

 © 2007 Wiley-VCH Verlag GmbH & Co. KGaA, Weinheim 

[3] W. Blau, H. Byrne, W. M. Dennis, J. M. Kelly, *Opt. Commun.* **1985**, *56*, 25.
[4] G. De La Torre, P. Vázquez, F. Agulló-López, T. Torres, *J. Mater. Chem.* **1998**, *8*, 1671.
[5] G. L. Wood, M. J. Miller, A. G. Mott, *Opt. Lett.* **1995**, *20*, 973.
[6] A. Krivokapic, H. L. Anderson, G. Bourhill, R. Ives, S. Clark, K. J. McEwan, *Adv. Mater.* **2001**, *13*, 652.
[7] M. Cha, N. S. Sariciftci, A. J. Hegger, J. C. Hummelen, F. Wudl, *Appl. Phys. Lett.* **1995**, *67*, 3850.
[8] L. C. Song, G. A. Yu, H. T. Wang, F. H. Su, Q. M. Hu, Y. L. Song, Y. C. Gao, *Eur. J. Inorg. Chem.* **2004**, 866.
[9] N. V. Kamanina, I. Y. Denisyuk, *Opt. Spectrosk.* **2004**, *96*, 77.
[10] Y. Chen, S. O'Flaherty, M. Fujitsuka, M. Hanack, L. R. Subramanian, O. Ito, W. J. Blau, *Chem. Mater.* **2002**, *14*, 5163.
[11] P. Zhu, C. Yu, J. Liu, Y. Song, C. Li, *Proc. SPIE-Int. Soc. Opt. Eng.* **1996**, *2879*, 289.
[12] K. P. Loh, H. Zhang, W. Z. Chen, W. Ji, *J. Phys. Chem. B* **2006**, *110*, 1235.
[13] M. Pittman, P. Plaza, M. M. Martin, Y. H. Meyer, *Opt. Commun.* **1998**, *158*, 201.
[14] A. Baev, O. Rubio-Pons, F. Gel'mukhanov, H. Ågren, *J. Phys. Chem. A* **2004**, *108*, 7406.
[15] a) G.-J. Zhou, S. Zhang, P.-J. Wu, C. Ye, *Chem. Phys. Lett.* **2002**, *363*, 610; b) G.-J. Zhou, W.-Y. Wong, D. M. Cui, C. Ye, *Chem. Mater.* **2005**, *17*, 5209; c) G.-J. Zhou, W.-Y. Wong, Z. Lin, C. Ye, *Angew. Chem. Int. Ed.* **2006**, *45*, 6189.
[16] a) K. Sendhil, C. Vijayan, M. P. Kothiyal, *Opt. Mater.* **2005**, *27*, 1606; b) X. H. Zhong, Y. Y. Feng, S. L. Ong, J. Y. Hu, W. J. Ng, Z. M. Wang, *Chem. Commun.* **2003**, *15*, 1882; c) G. Y. Yang, S. G. Ang, L. L. Chng, Y. W. Lee, W. P. Lau, K. S. Lai, H. G. Ang, *Chem. Eur. J.* **2003**, *9*, 900; d) K. J. McEwan, G. Bourhill, J. M. Robertson, H. L. Anderson, *J. Nonlinear Opt. Phys. Mater.* **2000**, *9*, 451; e) B. Dupuis, C. Michaut, I. Jouanin, J. Delaire, P. Robin, P. Feneyrou, V. Dentan, *Chem. Phys. Lett.* **1999**, *300*, 169; f) K. Kandasamy, S. J. Shetty, P. N. Puntambekar, T. S. Srivastava, T. Kundu, B. P. Singh, *J. Porphyrins Phthalocyanines* **1999**, *3*, 81.
[17] a) P. P. Kiran, D. R. Reddy, B. G. Maiya, A. K. Dharmadhikari, G. R. Kumar, N. R. Desai, *Appl. Opt.* **2002**, *41*, 7631; b) K. P. Prem, R. D. Raghunath, B. G. Maiya, R. D. Narayana, *Opt. Mater.* **2003**, *21*, 565.
[18] R. B. Martin, H. P. Li, L. R. Gu, S. Kumar, C. M. Sanders, Y. P. Sun, *Opt. Mater.* **2005**, *27*, 1340.
[19] a) D. Y. Wang, W. F. Sun, S. M. Dong, J. H. Si, C. F. Li, *Mater. Res. Soc. Symp. Proc.* **1997**, *479*, 41; b) W. F. Sun, C. C. Byeon, C. M. Lawson, G. M. Gray, D. Y. Wang, *Appl. Phys. Lett.* **1999**, *74*, 3254; c) D. Y. Wang, W. F. Sun, C. F. Wang, F. Q. Guo, Y. H. Zou, *Proc. SPIE-Int. Soc. Opt. Eng.* **1998**, *3472*, 53.
[20] R. T. Kuznetsova, T. N. Kopylova, G. V. Mayer, L. G. Samsonova, V. A. Svetlichnyi, A. V. Vasil'ev, D. N. Filinov, E. N. Tel'minov, N. S. Kabotaeva, N. V. Svarovskaya, V. M. Podgaetskii, A. V. Reznichenko, *Quantum Electron.* **2004**, *34*, 139.
[21] a) H.-S. He, J.-P. Guo, Z.-X. Zhao, W.-K. Wong, W.-Y. Wong, W.-K. Lo, K.-F. Li, L. Luo, K.-W. Cheah, *Eur. J. Inorg. Chem.* **2004**, 837; b) M. P. Oude Wolebers, F. C. J. M. Van Veggel, B. H. M. Snellink-Ruel, J. W. Hofstraat, F. A. J. Geurts, D. N. Reinhoudt, *J. Chem. Soc., Perkin Trans. 2* **1998**, 2141.
[22] a) P. Strohriegl, J. V. Grazulevicius, *Adv. Mater.* **2002**, *14*, 1439; b) R. D. Hreha, C. P. George, A. Haldi, B. Domercq, M. Malagoli, S. Barlow, J.-L. Brédas, B. Kippelen, S. R. Marder, *Adv. Funct. Mater.* **2003**, *13*, 967; c) P. Kunda, K. R. Justin Thomas, J. T. Lin, Y.-T. Tao, C.-H. Chien, *Adv. Funct. Mater.* **2003**, *13*, 445; d) L. A. Majewski, R. Schroeder, M. Grell, *Adv. Funct. Mater.* **2005**, *15*, 1017; e) N. Satoh, T. Nakashima, K. Yamamoto, *J. Am. Chem. Soc.* **2005**, *127*, 13030; f) W.-Y. Wong, G.-J. Zhou, X.-M. Yu, H.-S. Kwok, B.-Z. Tang, *Adv. Funct. Mater.* **2006**, *16*, 838; g) X.-M. Yu, H.-S. Kwok, W.-Y. Wong, G.-J. Zhou, *Chem. Mater.* **2006**, *18*, 5097.
[23] a) B. Li, X. Xu, M. Sun, Y. Fu, G. Yu, Y. Liu, Z. Bo, *Macromolecules* **2006**, *39*, 456; b) M. J. Frampton, R. Beavington, J. M. Lupton, I. D. W. Samuel, P. L. Burn, *Synth. Met.* **2001**, *121*, 1671; c) J.-C. Chang, C.-J. Ma, G.-H. Lee, S.-M. Peng, C.-Y. Yeh, *Dalton Trans.* **2005**, 1504; d) T.-G. Zhang, Y. Zhao, K. Song, I. Asselberghs, A. Persoons, K. Clays, M. J. Therien, *Inorg. Chem.* **2006**, *45*, 9703.
[24] C. W. Huang, K. Y. Chiu, S. H. Cheng, *Dalton Trans.* **2005**, 2417.
[25] W.-N. Yen, S.-S. Lo, M.-C. Kuo, C.-L. Mai, G.-H. Lee, S.-M. Peng, C.-Y. Yeh, *Org. Lett.* **2006**, *8*, 4239.
[26] a) C. K. Schauer, O. P. Anderson, S. S. Eaton, G. R. Eaton, *Inorg. Chem.* **1985**, *24*, 4082; b) W. R. Scheidt, M. E. Kastner, K. Hatano, *Inorg. Chem.* **1978**, *17*, 706.
[27] S. V. Rao, D. N. Rao, J. A. Akkara, B. S. DeCristifano, D. V. G. L. N. Rao, *Chem. Phys. Lett.* **1998**, *297*, 491.
[28] a) A. Beeby, R. S. Dickins, S. Faulkner, D. Parker, J. A. G. Williams, *Chem. Commun.* **1997**, 1401; b) W.-K. Wong, A.-X. Hou, J.-P. Guo, H.-S. He, L.-L. Zhang, W.-Y. Wong, K.-F. Li, K.-W. Cheah, F. Xue, T. C.-W. Mak, *J. Chem. Soc., Dalton Trans.* **2001**, 3092; c) W. D. Horrocks Jr, J. P. Bolender, W. D. Smith, R. M. Supkowski, *J. Am. Chem. Soc.* **1997**, *119*, 5972; d) G. A. Hebbink, L. Grave, L. A. Woldering, D. N. Reinhoudt, F. C. J. M. Van Veggel, *J. Phys. Chem. A* **2003**, *107*, 2483.
[29] a) M. H. V. Werts, J. W. Hofstraat, F. A. J. Geurts, J. W. Verhoeven, *Chem. Phys. Lett.* **1997**, *276*, 196; b) G. F. De Sá, O. L. Malta, C. De Mello Donegá, A. M. Simas, R. L. Longo, P. A. Santa-Cruz, E. F. Da Silva Jr, *Coord. Chem. Rev.* **2000**, *196*, 165; c) F. R. G. Silva, O. L. Malta, C. Reinhard, H. U. Güdel, C. Piguet, J. E. Moser, J. C. G. Bünzli, *J. Phys. Chem. A* **2002**, *106*, 1670.
[30] J. S. Shirk, R. G. S. Pong, S. R. Flom, F. J. Bartoli, M. E. Boyle, A. W. Snow, *Pure Appl. Opt.* **1996**, *5*, 701.
[31] T. C. Wen, I. D. Lian, *Synth. Met.* **1996**, *83*, 111.
[32] J. W. Perry, K. Mansour, S. R. Marder, K. J. Perry, D. Alvarez Jr, I. Choong, *Opt. Lett.* **1994**, *19*, 625.
[33] Y. P. Sun, J. E. Riggs, B. Liu, *Chem. Mater.* **1997**, *9*, 1268.
[34] J. Ostrauskaite, V. Voska, J. Antulis, V. Gaidelis, V. Jankauskas, J. V. Glazulevicius, *J. Mater. Chem.* **2002**, *12*, 3469.
[35] S. W. Lai, Y. J. Hou, C. M. Che, H. L. Pang, K. Y. Wong, C. K. Chang, N. Y. Zhu, *Inorg. Chem.* **2004**, *43*, 3724.
[36] *SAINT+*, ver. 6.02a, Bruker Analytical X-ray System, Inc., Madison, WI, **1998**.
[37] G. M. Sheldrick, *SADABS, Empirical Absorption Correction Program*, University of Göttingen, Germany, **1997**.
[38] G. M. Sheldrick, *SHELXTL™, Reference manual*, ver. 5.1, Madison, WI, **199**.


Received: December 15, 2006
Published Online: April 4, 2007

 © 2007 Wiley-VCH Verlag GmbH & Co. KGaA, Weinheim 

DOI: 10.1002/ejic.200601230

# Conformational Analysis of Heteroannularly Substituted Ferrocene Oligoamides

Jasmina Lapić,[a] Daniel Siebler,[b] Katja Heinze,*[b] and Vladimir Rapić*[a]

**Keywords:** Conformation analysis / Density functional calculations / Hydrogen bonds / Metallocenes / Molecular modelling

The main conformer of symmetrical conjugates of ferrocene-1,1′-dicarboxylic acid with natural amino acids – Fn(CO–$AA_{1–2}$–$OMe)_2$ (type I, Fn = ferrocene-1,1′-diyl, AA = L-α-amino acid) – is supported by two hydrogen bonds between the peptide substituents. To compare intramolecular hydrogen bond patterns of type I conjugates with related asymmetrically substituted derivatives, type II (MeNHCO–Fn–CO–AA–OMe) and type III conjugates (MeNHCO–Fn–CO–AA–NHMe) were prepared in moderate-to-good yields in a few steps starting from 1′-(methoxycarbonyl)ferrocene-1-carboxylic acid by using the HOBt/EDC method (AA = Gly, Ala, Val). $^1$H NMR spectroscopic variation ratio analysis suggests that an increase in the steric demand of the amino acid side chains favours conformations with hydrogen-bonded FnCO*NH*Me groups. CD spectroscopy of chiral derivatives reveals that (*P*)-helical conformations predominate in solution. The experimental findings are in accordance with DFT calculations.
(© Wiley-VCH Verlag GmbH & Co. KGaA, 69451 Weinheim, Germany, 2007)

## Introduction

Symmetrically substituted bioconjugates of ferrocene-1,1′-dicarboxylic acid − Fn(CO–$AA_n$–$OMe)_2$ (Fn = ferrocene-1,1′-diyl, AA = L-α-amino acid, $n$ = 1–2) (type I conjugates) − have been extensively studied, especially with the focus on applications as turn mimetica. Depending on the amino acid employed, these molecules adopt different conformations, A, B or C in the solid state, as well as in solution (Scheme 1).

In the solid state, the majority of type I conjugates form two intramolecular hydrogen bonds, which results in two 10-membered rings (conformation A, β-turn, "Herrick conformation"). If these intramolecular hydrogen bonds are sufficiently strong, conformation A is even retained in chloroform solution.[1–11] The bis(phenylalanine) derivative Fn(CO–Phe–$OMe)_2$ crystallises in asymmetrical form B characterised by a single seven-membered intramolecular hydrogen-bonded ring (γ-turn, "van Staveren conformation"), whereas conformation A presumably predominates in solution.[12] The derivatives Fn(CO–AA–$OMe)_2$ (AA = Pro, Cys(Bzl), Val) provide examples of open "Xu conformations" C in the solid state.[13–16] However, conformations found in the solid state can be substantially different from solution conformations as intermolecular hydrogen bonds are usually additionally present in the solid state. Therefore, with respect to chemical reactivity, the conformations adopted in solution are of importance. A systematic description of the structural motifs and a suitable nomenclature of 1,1′-disubstituted ferrocenes has been recently put forward.[17]

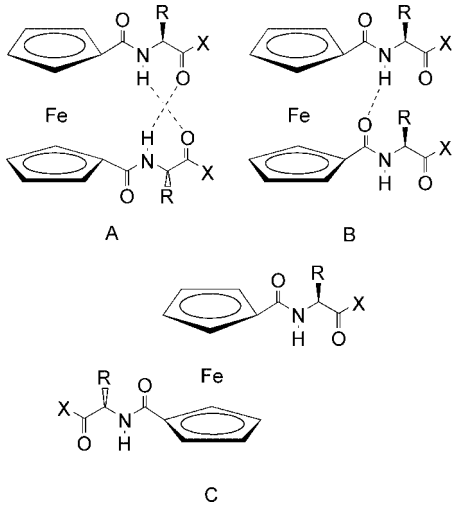


Scheme 1. Intramolecular hydrogen bond patterns in symmetrical ferrocene peptides (type I) [X = OMe, L–AA–OMe].

Having in mind the conformational characteristics of type I conjugates, we aimed to investigate the hydrogen bonding patterns of related asymmetrically substituted derivatives of ferrocene-1,1′-dicarboxylic acid belonging to

[a] Department of Chemistry and Biochemistry, Faculty of Food Technology and Biotechnology,
Pierottijeva 6, 10000 Zagreb, Croatia
Fax: +385-4836-082
E-mail: vrapic@pbf.hr
[b] Department of Inorganic Chemistry, University of Heidelberg,
Im Neuenheimer Feld 270, 69120 Heidelberg, Germany
Fax: +49-6221-545707
E-mail: katja.heinze@urz.uni-heidelberg.de
Supporting information for this article is available on the WWW under http://www.eurjic.org or from the author.


© 2007 Wiley-VCH Verlag GmbH & Co. KGaA, Weinheim

type II (MeNHCO–Fn–CO–AA–OMe) and type III (MeNHCO–Fn–CO–AA–NHMe) (AA = Gly, L-Ala, L-Val) to understand individual conformational preferences in solution with respect to the amino acid employed (i.e. the size of their side chains). Here we describe the conformational analyses based on a combined experimental (NMR, IR and CD spectroscopy) and theoretical approach (DFT calculations).

## Results and Discussion

Scheme 2 depicts three possible hydrogen bonded conformations, D, E and F, with (*P*)-helical stereochemistry at the ferrocene as well as an open form of type II conjugates. The corresponding (*M*)-helical diastereomeric conformations can be derived from the mirror images and by changing the resulting D-configuration of the amino acid to L. Descriptor "1-" denotes the amino acid containing the substituent and descriptor "1′-" denotes the CONHMe part of the compounds. Conformations D and E can be described by seven-membered "van Staveren"-like intramolecular hydrogen bonds (Scheme 1, B), whereas form F is stabilised by a 10-membered intramolecular hydrogen bonded ring, which can be considered as half of a "Herrick's" motive (Scheme 1, A). These patterns represent γ- and β-turn structures, and it is expected that their relative population depends on the

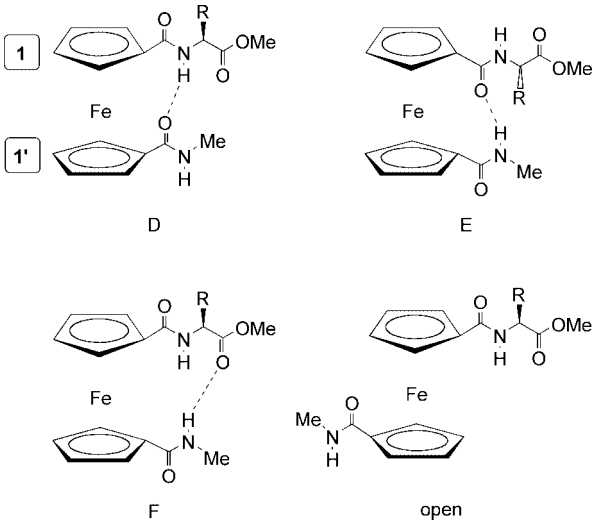


Scheme 2. Possible intramolecular hydrogen bond patterns in diamide esters (type II).

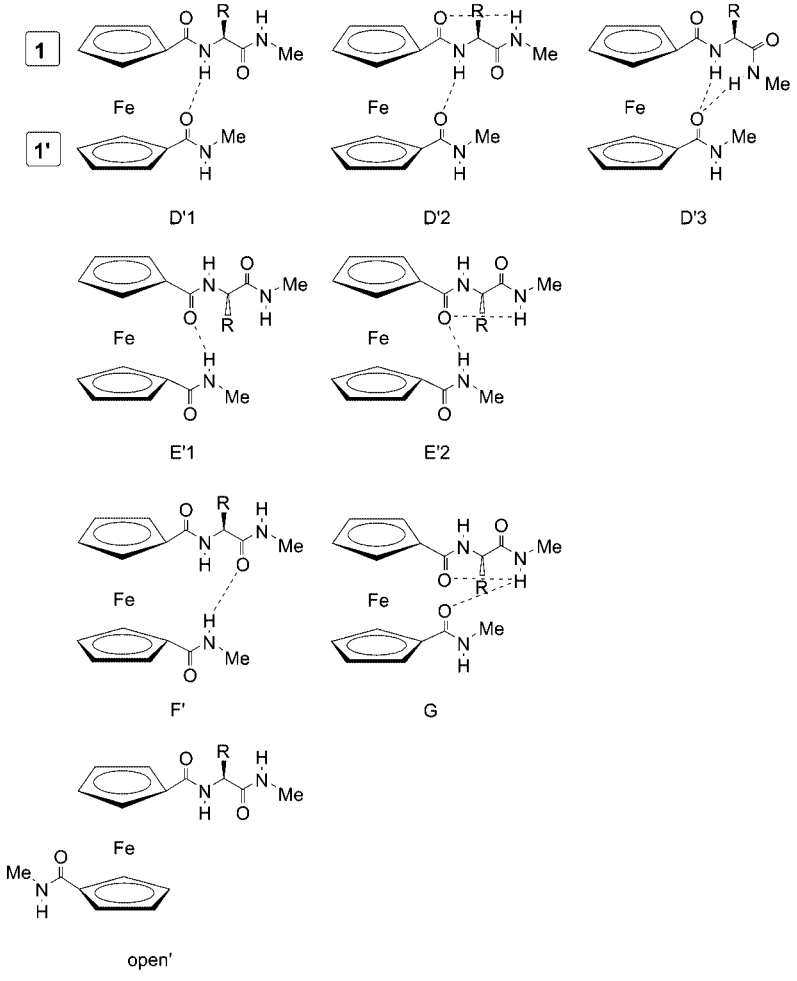


Scheme 3. Possible intramolecular hydrogen bond patterns in triamides (type III).

 © 2007 Wiley-VCH Verlag GmbH & Co. KGaA, Weinheim 

steric demand of the amino acid side chain (R). Conformation E was recently observed in the solid state and in a $CDCl_3$ solution of 1′-(butylcarbamoyl)-*N*-morpholinoferrocene-1-carboxamide.[18]

Intramolecular hydrogen bonding patterns possible in type III conjugates are shown in Scheme 3. Three conformations are analogous to forms D, E and F of amide esters and for clarity, they are denoted as D′, E′ and F′. However, owing to the additional 1-NHMe group, a further hydrogen bond between 1-NHMe and 1-CO in D′2, E′2 and F′ or between 1-NHMe and 1′-CO in D′3 is possible. In theoretically possible conformation G, a 10-membered hydrogen bonded ring between 1′-CO and 1-NHMe occurs together with an intrachain hydrogen bond between 1-NHMe and 1-CO. Thus, the conformational space of type III conjugates is considerably expanded relative to type II conjugates.

## Synthesis of Type II and Type III Conjugates

The syntheses of diamide esters **9**–**11** and triamides **15**–**17** are depicted in Scheme 4. The starting compound, 1′-(methoxycarbonyl)ferocene-1-carboxylic acid (**6**), was prepared according to a previously described procedure.[30] Activation of acid **6** with HOBt/EDC (HOBt = 1-hydroxybenzotriazole, EDC = *N*-(3-dimethylaminopropyl)-*N*′-ethylcarbodiimide hydrochloride) in $CH_2Cl_2$ solution, followed by treatment with $NH_2Me$ (obtained from $NH_2Me{\cdot}HCl$ and $NEt_3$) gave 45% of methyl 1′-(methylcarbamoyl)ferrocene-1-carboxylate (**7**). Amide ester **7** was hydrolysed with $NaOH/H_2O$ in MeOH to give 1′-(methylcarbamoyl)ferrocene-1-carboxylic acid (**8**) (97% yield). Acid **8** was activated by HOBt/EDC and coupled with Gly–OMe, L-Ala–OMe, D-Ala–OMe and L-Val–OMe (obtained from AA–OMe·HCl by treatment with $NEt_3$), which resulted in the formation of diamide esters **9** (42%), **10** (60%), **10a** (54%) and **11** (46%), respectively. Hydrolysis of diamide esters **9**–**11** gave MeNHCO–Fn–CO–AA–OH in good yields [**12** (94%), **13** (81%) and **14** (94%)] which were subsequently transformed into triamides **15** (24%) **16** (56%) and **17** (20%), respectively, in a manner analogous to that described for the preparation of **7**. Unexpectedly, compounds **16** and **17** thus obtained had racemized during hydrolysis as they displayed only a negligible Cotton effect (in contrast to **10** and **11**, Table 6). Therefore, **8** was directly coupled with AA–NHMe (AA = Gly, L-Ala, L-Val) to give triamide **15** (45%), as well as optically pure triamides **16** (45%) and **17** (34%).

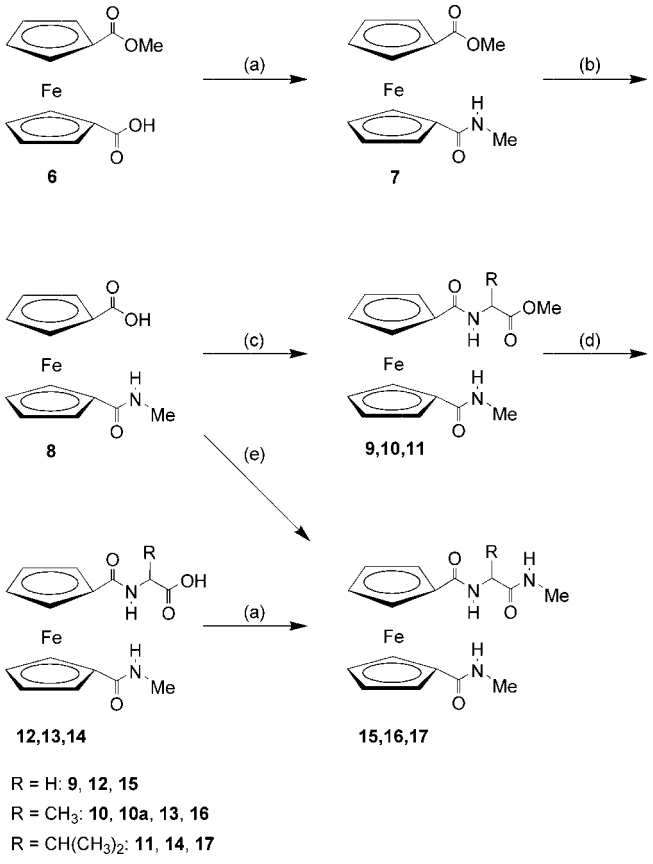


Scheme 4. Synthesis of $Fn(COOH)_2$-derived oligoamides. a) 1. HOBt/EDC, $CH_2Cl_2$, 2. $NH_2Me{\cdot}HCl$, $NEt_3$, $CH_2Cl_2$; b) $NaOH/H_2O$, MeOH; c) 1. HOBt/EDC, $CH_2Cl_2$, 2. L-AA–OMe·HCl, $NEt_3$, $CH_2Cl_2$; d) $NaOH/H_2O$, dioxane; e) 1. HOBt/EDC, $CH_2Cl_2$, 2. L-AA–NHMe·HCl, $NEt_3$, $CH_2Cl_2$.

## Spectroscopy of Type II and Type III Conjugates

Intramolecular hydrogen bonds found in the solid state often undergo cleavage even in weakly coordinating solvents (e.g. chloroform, dichloromethane) with competitive formation of hydrogen-bond-free states and species with hydrogen bonded rings of different sizes. The conformational equilibria are usually fast on the NMR timescale, which results in time-averaged and population-weighted chemical shifts, but in some cases, barriers are high enough to allow the detection of individual conformers or conformer groups.[19] On the faster IR timescale, however, absorptions for NH and CO stretching vibrations are detected for each conformer present in solution (unfortunately with severe overlap, which often precludes detailed assignment).[20] In chiroptical experiments (CD spectroscopy) the measured signal represents the sum of signals for all species present in solution.

To elucidate the conformational equilibria of **9**–**11** and **15**–**17** in solution and to probe the influence of the amino acid side chain [R = H, $CH_3$, $CH(CH_3)_2$], we used IR and CD spectroscopy, NMR spectroscopy (solvent-dependent, temperature-dependent) and DFT calculations (B3LYP, LanL2DZ[19,21–24]).

IR spectra of **7**, **9**–**11** and **15**–**17** were measured in $CH_2Cl_2$ solution at different concentrations (Table 1). The characteristic signals (NH, CO) were unchanged in the concentration range $0.5\times10^{-2}$ to $2.5\times10^{-2}$ M, which confirms

 © 2007 Wiley-VCH Verlag GmbH & Co. KGaA, Weinheim 

that intermolecular interactions are absent under these conditions. Signals for non-hydrogen-bonded NH groups as well as hydrogen bonded NH groups are observed. For **7**, the low-energy $CO_{ester}$ absorption indicates a quite strong hydrogen bond from 1′-NH to the ester carbonyl group, which corresponds to the only possible hydrogen bonded conformation E. Thus, **7** exists in solution as conformer E in equilibrium with the open form.

Table 1. IR data [$cm^{-1}$] for **7**, **9**–**11** and **15**–**17** in $CH_2Cl_2$ ($c$ = $10^{-2}$ M).

| | $\nu_{NH}$ (free) | $\nu_{NH}$ (assoc.) | $\nu_{CO}$ (ester) | $\nu_{CO}$ (amide I) |
|---|---|---|---|---|
| **7** | 3462 | 3373 | 1712 | 1659 |
| **9** | 3446, 3391 | 3259 | 1742 | 1650 |
| **10** | 3451 | 3271 | 1740 | 1650 |
| **11** | 3453, 3418 | 3293 | 1736 | 1665 |
| **15** | 3449 | 3341 | – | 1655 |
| **16** | 3449 | 3363, 3327 | – | 1653 |
| **17** | 3451 | 3342, 3326 | – | 1657 |

Chiral amide esters **10** and **11** display Cotton effects at about 350 (300 nm), –275 (348 nm), –155 (411 nm), and 395° $M^{-1}cm^{-1}$ (470 nm) in acetonitrile. For chiral triamides **16** and **17**, the following Cotton effects were observed: 825 (305 nm), –410 (352 nm), –230 (417 nm) and 470° $M^{-1}cm^{-1}$ (480 nm) (Experimental Section, Table 6). The spectra are very similar to those of type I derivatives with "Herrick conformations" (Scheme 1, A). A positive Cotton effect around the ferrocene absorption ($\lambda_{max} \approx 440$ nm; Experimental Section, Table 6) was previously interpreted as being indicative of (*P*)-enantiomers of the helically ordered ferrocenes.[9,17] However, the CD intensities of **10**, **11**, **16** and **17** are one order of magnitude lower than those found for type I (*P*)-helical "Herrick conformations" (Scheme 1, A; $M_\theta \approx$ 5000° $M^{-1}cm^{-1}$) with two intramolecular hydrogen bonds between the L-amino acid side arms. Thus, CD spectroscopy of L-amino acid derivatives suggests that (*P*)-helical conformations are present in slight excess over (*M*)-helical and open conformations, whereas (*M*)-helical conformations are slightly preferred for D-Ala derivative **10a** (Figure 1, Experimental Section, Table 6). As expected, CD spectra of amide esters **10** and **10a** derived from L- and D-Ala, respectively, are mirror images of each other (Figure 1). Interestingly, the positive Cotton effects increase for amide esters **10** and **11** from 360 to 430° $M^{-1}cm^{-1}$ (470 nm) as well as for triamides **16** and **17** from 410 to 530° $M^{-1}cm^{-1}$ (480 nm). This slight enhancement could be attributed to an increased amount of (*P*)-helical ferrocenes present in solution, which results from an increase in the size of the amino acid side chain from R = $CH_3$ to R = $CH(CH_3)_2$.

To address the engagement of specific NH protons (1-NH, 1′-NH, 1-NHMe) in hydrogen bonding by $^1H$ NMR spectroscopy, all the NH proton signals have to be correctly assigned. NOE spectroscopy allowed all NH proton signals to be distinguished as specific NOE cross peaks are observed to cyclopentadienyl protons and $CH_\alpha$ of the amino acid as shown exemplarily for **16** in Figure 2. NH protons

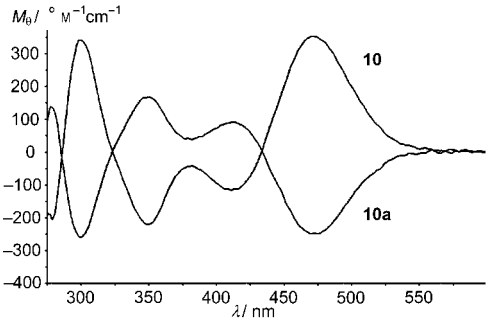


Figure 1. CD spectra of **10** and **10a** in $CH_3CN$.

adjacent to ferrocene carbonyl (1-NH, 1′-NH) display NOE cross peaks to two Cp protons, while 1-NHMe shows an NOE contact to $CH_\alpha$.

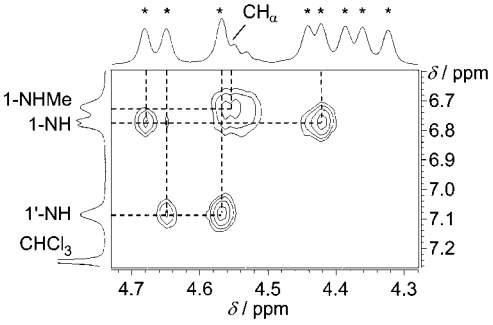


Figure 2. Part of the NOESY spectrum of **16**, which indicates NOE contacts between NH protons and Cp-H and $CH_\alpha$ (* denotes Cp-H).

To address the question as to which NH group preferentially participates in hydrogen bonds, NH chemical shifts were measured in different solvents ["variation ratio" (v.r.) method][25] and at different temperatures (VT $^1H$ NMR spectroscopy). For interpretation of the observed $\delta_{NH}$ values, it has proven useful to compare them to those of standard (reference) compounds. The standard compounds possess NH groups in a comparable chemical environment but without any intramolecular hydrogen bonds (non-hydrogen-bonded reference state) in noncoordinating solvents (e.g. $CDCl_3$). The fully hydrogen-bonded reference state is simulated by measuring the $^1H$ NMR spectrum in the strongly coordinating solvent [$D_6$]DMSO (Experimental Section, Tables 4 and 5).

Chemical shift variation from [$D_6$]DMSO to $CDCl_3$ ($\Delta\delta_{NH}$) provides a measure of the extent to which an amide proton takes part in an intramolecular hydrogen bond. If the shift variation of a particular NH proton is distinctly smaller than that of the hydrogen-bond-free reference, the NH proton is considered to be intramolecularly hydrogen bonded in $CDCl_3$ solution. The variation ratio v.r. = $\Delta\delta_{NH}$(substrate)/$\Delta\delta_{NH}$(reference) describes the involvement of the considered proton in an intramolecular hydrogen bond. Small v.r. values indicate strong hydrogen bonds whereas larger v.r. values suggest weak hydrogen bonds.[25] We, and others, have previously synthesised a number of peptides derived from 1′-aminoferrocene-1-carboxylic acid

 © 2007 Wiley-VCH Verlag GmbH & Co. KGaA, Weinheim 

Table 2. $^1$H NMR spectroscopic data for **7**, **9**–**11**, **15**–**17** and standard (reference) compounds ($c = 5\times10^{-3}$ to $2\times10^{-4}$ M).[a]

| | $\delta_{NH}$ / ppm ($CDCl_3$)[b] | | | $\delta_{NH}$ / ppm ([$D_6$]DMSO)[b] | | | $\Delta\delta$ / ppm ([$D_6$]DMSO/$CDCl_3$) | | | v.r. (standard) | | | $-\Delta\delta/T$[c] / ppb K$^{-1}$ | | |
|---|---|---|---|---|---|---|---|---|---|---|---|---|---|---|---|
| **1** | 5.43 | | | 7.71 | | | 2.37 | | | | | | | | |
| **2** | 6.08 | | | 8.25 | | | 2.17 | | | | | | | | |
| **3** | 6.02 | | | 8.23 | | | 2.21 | | | | | | | | |
| **4** | 5.90 | | | 8.08 | | | 2.18 | | | | | | | | |
| **5** | 5.73 | | | 7.73 | | | 2.00 | | | | | | | | |
| **7** | 6.10 | | | 7.75 | | | 1.65 | | | 0.83 (**5**) | | | | | |
| **9** | 6.72 | 7.39 | | 7.73 | 8.40 | | 1.01 | 1.01 | | 0.51 (**5**) | 0.47 (**2**) | | 7.0 | 16.0 | |
| **10** | 6.88 | 7.03 | | 7.75 | 8.24 | | 0.87 | 1.21 | | 0.44 (**5**) | 0.55 (**3**) | | 7.0 | 8.4 | |
| **11** | 7.03 | 6.63 | | 7.66 | 7.88 | | 0.63 | 1.25 | | 0.32 (**5**) | 0.57 (**4**) | | [d] | | |
| **15** | 6.89 | 7.15 | 6.86 | 7.98 | 8.17 | 7.85 | 1.09 | 1.02 | 0.99 | 0.55 (**5**) | 0.47 (**2**) | 0.42 (**1**) | 6.1 | 0.4 | 8.9 |
| **16** | 7.08 | 6.77 | 6.71 | 7.97 | 7.88 | 7.91 | 0.89 | 1.11 | 1.20 | 0.45 (**5**) | 0.50 (**3**) | 0.51 (**1**) | 18.9 | 7.9 | 11.5 |
| **17** | 7.20 | 6.52 | 6.55 | 7.88 | 7.65 | 8.01 | 0.68 | 1.13 | 1.46 | 0.34 (**5**) | 0.52 (**4**) | 0.62 (**1**) | 11.8 | 2.6 | 10.9 |

[a] All values are given in the sequence 1′-NH, 1-NH and 1-NHMe. [b] $\delta_{NH}$ ($CDCl_3$) and $\delta_{NH}$ ([$D_6$]DMSO) for compounds **1**–**5** are taken from refs.[25,26] [c] $1.0\times10^{-4}$ M in $CDCl_3$. [d] Sample precipitates under these conditions.

(Fca)[21,27] and natural amino acids.[19,24,26,28,29] In this context, we have successfully employed the v.r. method in the estimation of intramolecular hydrogen bond strengths and conformer populations in Fca–AA conjugates.[24,26]

Suitable reference compounds for amide esters **9**–**11** are Ac–AA–OEt (AA = Gly, Ala, Val; **2**–**4**) for the amino acid containing substituent in position 1- and *N*-methylferrocenecarboxamide Fc–CONHMe (**5**) for the 1′-NHMe part. For the 1-NHMe moiety of triamides **15**–**17**, *N*-methylacetamide (MeCONHMe, **1**) is used as a reference compound. As mentioned above, the reference compounds are unable to engage in intramolecular hydrogen bonds and exhibit chemical shifts of the amide protons at positions well below $\delta = 7$ ppm in $CDCl_3$. In [$D_6$]DMSO solution, the signals are shifted to lower field ($\delta \approx 8$ ppm), which indicates intermolecular hydrogen bonds to the solvent ($\Delta\delta_{NH} \geq 2.0$ ppm, Table 2).

To exemplify this approach, v.r. calculations for ester amide **9** will be described. In $CDCl_3$ solution, compound **9** exhibits amide resonances at $\delta = 6.72$ ppm for 1′-NH and $\delta = 7.39$ ppm for 1-NH groups (unambiguously assigned by NOESY experiments and coupling patterns). In [$D_6$]-DMSO, the corresponding resonances appear at $\delta = 7.73$ ppm and $\delta = 8.40$ ppm (Figure 3). The difference in the chemical shifts of the two amide protons in the two solvents is $\Delta\delta = 1.01$ ppm for both protons. A suitable standard (reference) for 1′-NH is FcCONHMe (**5**) with $\Delta\delta = 2.00$ ppm, and for 1-NH Ac–Gly–OEt (**2**) with $\Delta\delta = 2.17$ ppm was chosen. Thus, v.r. (1′-NH) = 0.51 and v.r. (1-NH) = 0.47 can be calculated for **9**, and these values indicate medium–strong hydrogen bonds for both protons. This finding can only be explained by the presence of several conformations which are in equilibrium in solution. As only conformer D possesses a hydrogen bonded 1-NH group, this species is surely present in solution, whereas the v.r. data do not discriminate between conformations E and F as both possess 1′-NH involved in hydrogen bonds (Scheme 2).

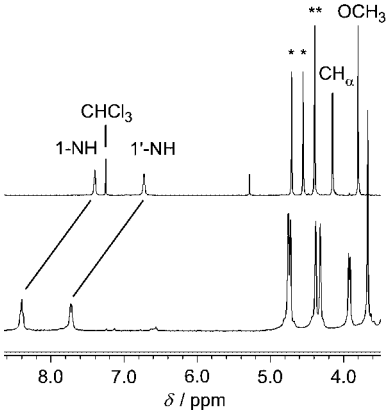


Figure 3. Part of the $^1$H NMR spectra of **9** in $CDCl_3$ (top) and [$D_6$]DMSO (bottom) (* denotes Cp-H).

In the sequence **9**, **10**, **11**, a monotonous lowering of v.r. values of the 1′-NH protons occurred ($0.51 > 0.44 > 0.32$), which indicates an enrichment of conformations E and/or F displaying 1′-NH···O bonds. Concomitantly, conformations with 1-NH···O bonds (D) are less populated (v.r. values: $0.47 < 0.55 < 0.57$). Similar to amide esters **9**–**11**, in the order **15**, **16**, **17**, v.r. values for 1′-NH protons decrease ($0.55 > 0.45 > 0.34$) and increase for 1-NH protons ($0.47 < 0.50 < 0.52$). 1-NHMe protons show increasing v.r. values ($0.34 < 0.52 < 0.62$). Once again, these findings indicate enrichment of E′ and/or F′ forms at the expense of conformers D′ and G (Scheme 3).

Additionally, variable temperature NMR experiments were undertaken in $CDCl_3$ solution (Figure 4). However, valine derivative **11** visibly precipitates upon cooling (presumably by association through intermolecular hydrogen bonds). For **9** and **16**, the large temperature shifts $\Delta\delta/T$ of NH protons are indicative of beginning intermolecular hydrogen bonding upon cooling (Table 2). Thus, temperature shifts $\Delta\delta/T$ of **9**, **16** and **17** are clearly not interpretable in

 © 2007 Wiley-VCH Verlag GmbH & Co. KGaA, Weinheim 

terms of intramolecular hydrogen bonding. Thus, for **10** and **15**, it should also be considered that intermolecular interactions (especially through 1′-NH and 1-NHMe) are highly probable at lower temperatures.

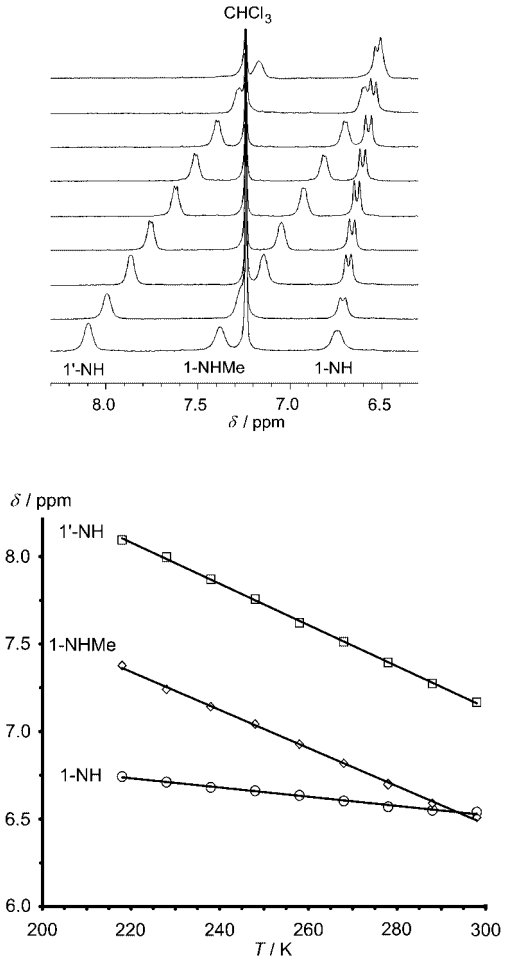


Figure 4. Partial VT $^1$H NMR spectra of **17** in $CDCl_3$ (top) and $\delta$ versus $T$ plot of the amide protons.

The combined experimental data can be summarised as follows: (1) chiral L-amino acid conjugates form predominantly (*P*)-helical conformations in solution for both type II and III conjugates, (2) all NH protons are involved in intramolecular hydrogen bonding in the ensemble, (3) according to NH v.r. values for types II and III, increasing the steric bulk of the amino acid side chain (R) results in a larger fraction of conformers with 1′-NH···O hydrogen bonds and a smaller fraction of conformers with 1-NH···O hydrogen bonds, (4) for type III conjugates, an increase in the steric bulk of the amino acid side chain (R) leads to a depletion of conformers with 1-NHMe···O hydrogen bonds in the ensemble.

## DFT Calculations

To gain deeper insight into the possible conformations, the geometries of compounds **9**–**11** and **15**–**17** were optimised by DFT calculations without symmetry constraints (B3LYP, LanL2DZ) in different conformations, that is, with respect to hydrogen bonding patterns (D, E, F, open, D′, E′, F′, G′ and open′) and ferrocene helicity (*P*, *M*) (Table 3, Figures 5 and 6). In all cases, the open form is calculated to be higher in energy by 13–19 kJ mol$^{-1}$ relative to the calculated minimum geometry. Type II compounds **9**–**11** with two hydrogen-donors and three hydrogen-acceptors will be discussed before type III conjugates **15**–**17** with three donors and three acceptors are addressed.

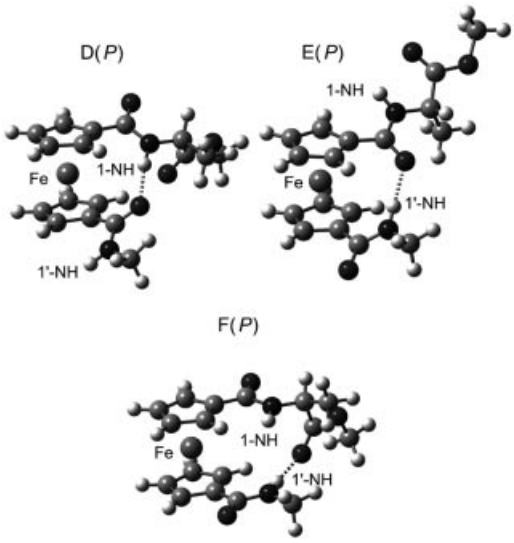


Figure 5. DFT-calculated (*P*)-helical minimum structures of **10**.

For glycine derivative **9**, all conformations D, E and F are local minima with marginal energy differences, which confirms that no conformation is especially preferred over the others and also substantiates conclusion (2) above. In sterically more demanding conjugates **10** and **11**, conformations D(*M*) and F(*M*) are destabilised by the larger substituent R (Figure 7). Thus, less (*M*)-helical ferrocenes equalling more (*P*)-helical conformers are present in the ensemble in accordance with conclusion (1) above. According to the calculations, the ensemble is enriched in E conformers as D(*M*) and F(*M*) are energetically unfavourable for **10** and **11**. Conformers E exhibit 1′-NH···O hydrogen bonds, which accounts for conclusion (3). Additionally, F(*P*) becomes the most stable conformation for **11**, which also shows 1′-NH···O hydrogen bonds and furthermore explains the lower $C{=}O_{ester}$ stretching vibration frequency of **11** relative to that of **9** (Table 1).

Type III conjugates show a more complicated behaviour as the number of possible conformations with hydrogen bonds has doubled relative to type II compounds. No stable minimum structure could be obtained for the G conformation shown in Scheme 3 as the 1-NHMe···1′-CO hydrogen bond is disrupted, which leaves only the intrachain hydrogen bond between 1-NHMe and 1-CO. This conformation is almost as high in energy as the open form and rules out a significant contribution (Table 3). Glycine conjugate **15** shows no conformational preference as does its type II counterpart **9**, that is, all conformations D′1, D′2, D′3, E′1, E′2 and F′ with (*P*) and (*M*) helical ferrocenes are present

 © 2007 Wiley-VCH Verlag GmbH & Co. KGaA, Weinheim 

Table 3. DFT calculated relative energies and (N)H···O distances of hydrogen bonds of conformers for **9**–**11** and **15**–**17**.

| | $E_{rel}$ / kJ mol$^{-1}$ | (N)H···O / Å (interchain) | (N)H···O / Å (intrachain) |
|---|---|---|---|
| 9D | 0.6 | 1.87 | – |
| 9E | 0.0 | 1.93 | – |
| 9F | 3.9 | 2.00 | – |
| 9-open | 13.4 | – | – |
| 10D(*P;M*) | 0.0; 12.0 | 1.89; 1.87 | –; – |
| 10E(*P;M*) | 0.4; 0.7 | 1.93; 1.93 | –; – |
| 10F(*P;M*) | 3.7; 17.2 | 1.99; 1.97 | –; – |
| 10-open | 13.6 | – | – |
| 11D(*P;M*) | 7.8; 25.6 | 1.96; 1.87 | – |
| 11E(*P;M*) | 1.7; 2.4 | 1.93; 1.93 | –; – |
| 11F(*P;M*) | 0.0; 25.5 | 2.00; 2.16 | –; – |
| 11-open | 15.0 | – | – |
| 15D′1 | 7.3 | 1.86 | – |
| 15D′2 | 0.0 | 1.85 | 1.93 |
| 15D′3 | 9.1 | 2.17, 1.90 | – |
| 15E′1 | 1.9 | 1.91 | – |
| 15E′2 | 5.5 | 1.97 | 2.03 |
| 15F′ | 7.0 | 1.99 | (2.45) |
| 15G | 16.2 | – | 1.97 |
| 15open′ | 17.1 | – | – |
| 16D′1(*P;M*) | –; – | –; – | –; – (both converged to 16D′2) |
| 16D′2(*P;M*) | 0.0; 8.7 | 1.87; 1.85 | 1.94; 1.84 |
| 16D′3(*P;M*) | 10.6; 13.1 | 2.16, 1.92; 1.96, 1.94 | – |
| 16E′1(*P;M*) | 6.6; 6.4 | 1.92; 1.92 | – |
| 16E′2(*P;M*) | 1.7; 18.5 | 1.94; 1.96 | 2.03; 1.90 |
| 16F′(*P;M*) | 5.9; 18.9 | 1.98; 1.93 | (2.60); (3.06) |
| 16G(*P;M*) | 14.4; 30.9 | –; – | 2.01; 1.92 |
| 16open′ | 16.7 | – | – |
| 17D′1(*P;M*) | 13.5; – | 1.99; – | –; – (the latter converged to 17D′2(M) |
| 17D′2(*P;M*) | 0.0; 5.0 | 1.86; 1.85 | 2.00; 1.84 |
| 17D′3(*P;M*) | 12.7; 15.7 | 2.13, 1.92; 1.97, 1.93 | – |
| 17E′1(*P;M*) | 7.6; 6.3 | 1.93; 1.92 | –; – |
| 17E′2(*P;M*) | 3.4; 12.4 | 1.95; 1.96 | 2.10; 1.91 |
| 17F′(*P;M*) | 2.9; 14.7 | 1.97; 2.05 | (2.48); 2.06 |
| 17G(*P;M*) | 17.0; 44.6 | –; – | 1.89; 1.89 |
| 17open′ | 19.4 | – | – |

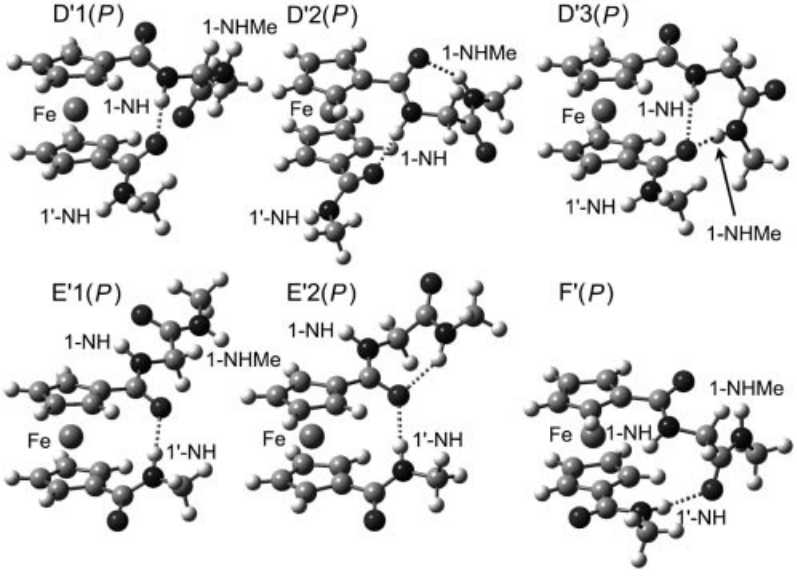


Figure 6. DFT-calculated (*P*)-helical minimum structures of **15**.

in the ensemble (Figure 7). An increase in the size of R in the L-amino acid destabilises conformations D′1(*P*), D′1(*M*), D′3(*P*), D′3(*M*), E′2(*M*) and F′(*M*). Thus, in the ensemble, conformers D′2(*P*), D′2(*M*), E′1(*P*), E′1(*M*), E′2(*P*) and F′(*P*) are still present, which results in an excess of (*P*)-helical ferrocenes for **16** and **17** and corroborates

 © 2007 Wiley-VCH Verlag GmbH & Co. KGaA, Weinheim 

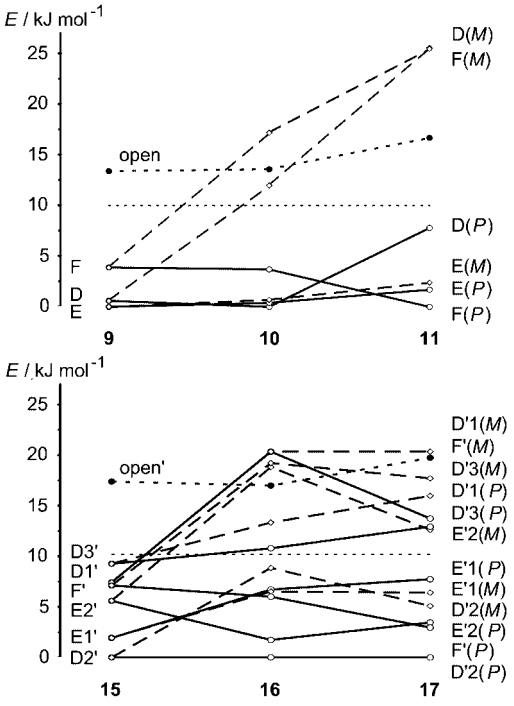


Figure 7. Relative energies of conformations of type II conjugates **9**–**11** (top) and of conformations of type III conjugates **15**–**17** (bottom) [for 16D′1(*P*), 16D′1(*M*) and 17D′1(*M*), the relative energy must be arbitrarily set to 20 kJ mol$^{-1}$; the dotted lines at 10 kJ mol$^{-1}$ are a guide for the eye].

conclusion (1) above. Analogously to type II conjugates, the ensembles of **16** and **17** contain more E conformers relative to the ensemble of glycine derivative **15**. This confirms conclusion (3), which states that a larger fraction of conformers with 1′-NH···O hydrogen bonds exists for derivatives with larger R substituents. As for type II derivatives, F′(*P*) conformations (with 1′-NH···O hydrogen bonds) are increasingly stabilised by larger R side chains.

Interchain 1-NHMe hydrogen bonds are only present in conformations D′3 and G (Scheme 3), which are quite high in energy. Thus, 1-NHMe hydrogen bonds are mainly intrachain in nature and occur in conformations D′2, E′2 and 17F′(*M*) (Table 3). As E′2(*M*) and F′(*M*) are destabilised for **16** and **17**, the number of conformations with 1-NHMe hydrogen bonds is reduced relative to the ensemble of **15**. This accounts for the observed weakening of 1-NHMe hydrogen bonds [conclusion (4) above].

## Conclusions

It was shown that ferrocene-1,1′-dicarboxylic acid conjugates of types II and III form an ensemble of conformations in weakly coordinating solvents without a preference for one specific conformer. However, an increase in the steric demand of the L-amino acid side chain reduces the number of conformations [especially with respect to (*M*)-helical ferrocenes] in solution, which provides an explanation for the observed positive Cotton effect at the ferrocene absorption in the CD spectra. Furthermore, large amino acid side chains favour conformations with 1′-NH···O hydrogen bonds (conformations E/E′ and F/F′) as shown by NMR spectroscopic techniques (v.r. method) and DFT calculations.

A single hydrogen bond spanning the 1- and 1′-substituents already provides an explanation for the preference of (*P*)-helical ferrocenes in asymmetrical type II and III conjugates with one L-amino acid attached. This effect is even more pronounced in symmetrically substituted type I conjugates with two L-amino acids and two hydrogen bonds between the ferrocene substituents. For Fn(CO–Ala–OMe)$_2$, the energy difference between (*P*)- and (*M*)-"Herrick" conformers was calculated as 17.3 kJ mol$^{-1}$ by DFT methods.[22] However, in these systems, an increase in the number of L-amino acids has no further stabilising effect.

On the basis of the results obtained in this study, it is expected that an increase in the size of the amino acid side chains adjacent to the ferrocene carbonyl might be a means to further stabilise chiral secondary structures, for example, turn motifs.

## Experimental Section

**General:** The syntheses were carried out under an atmosphere of argon. $CH_2Cl_2$ that was used for syntheses and FTIR spectroscopy was dried ($P_2O_5$), distilled from $CaH_2$ and stored over molecular sieves (4 Å). EDC, HOBt (Aldrich) and amino acid esters and amides (Merck) were used as received. NMR spectroscopic data for compounds **1**–**5** were taken from refs.[25,26]. Products were purified by preparative thin layer chromatography on silica gel (Merck, Kieselgel 60 $HF_{254}$) by using $CH_2Cl_2$/EtOAc or $CH_2Cl_2$/MeOH. Melting points were determined with a Buechi apparatus. IR spectra were recorded as $CH_2Cl_2$ solutions with a Bomem MB 100 mid FTIR spectrophotometer. $^1$H- and $^{13}$C{$^1$H}-NMR spectra were recorded with a Varian EM 360 or Varian Gemini 300 spectrometer in $CDCl_3$ and [$D_6$]DMSO solutions with $Me_4Si$ as the internal standard or with a Varian Unity Plus 400 spectrometer. ESI mass spectra were recorded with a Finnigan TSQ 700 spectrometer. High resolution FAB mass spectra were recorded with a JEOL JMS-700. CD spectra were recorded as $CH_3CN$ solutions with CD spectrophotometer Jasco-810. 1′-(Methoxycarbonyl)ferrocene-1-carboxylic acid (**6**) was prepared according to a literature procedure.[30]

**Computational Method:** Density functional calculations were carried out with the Gaussian03/DFT[31] series of programs. The B3LYP formulation of density functional theory was used by employing the LanL2DZ basis set.[31] All points were characterised as minima ($N_{imag}$ = 0) by frequency analysis.

**Methyl 1′-(methylcarbamoyl)ferrocene-1-carboxylate (7):** EDC (1.7 g, 9.1 mmol) and HOBt (1.2 g, 9.1 mmol) were added to a suspension of 1′-(methoxycarbonyl)ferrocene-1-carboxylic acid (**6**; 2 g, 7 mmol) in dry dichloromethane (20 mL), and the solution was stirred for 1 h at room temp. $MeNH_2$·HCl (682.5 mg, 10.5 mmol) was suspended in dichloromethane (5 mL) at 0 °C and dissolved by the addition of dry $NEt_3$ until ca. pH 8. This solution was added to the solution of activated **6**. After stirring for 1 h at room temp., the reaction mixture was washed with saturated aqueous $NaHCO_3$ and water. The organic layer was dried with $Na_2SO_4$ and evaporated in vacuo. TLC purification of the crude product with $CH_2Cl_2$/EtOAc (10:1) gave 900 mg (45%) of orange crystals. M.p. 135–

 © 2007 Wiley-VCH Verlag GmbH & Co. KGaA, Weinheim 

137 °C. $^1$H NMR (300 MHz, $CDCl_3$): $\delta$ = 6.16 (br. s, 1 H, NH), 4.77 (pt, 2 H, $H^{2,5}$), 4.59 (pt, 2 H, $H^{2',5'}$), 4.46 (pt, 2 H, $H^{3,4}$), 4.37 (pt, 2 H, $H^{3',4'}$), 3.85 (s, 3 H, $COOCH_3$), 2.98 (d, $^3J_{HH}$ = 4.9 Hz, 3 H, $NHCH_3$) ppm. $^1$H NMR (300 MHz, [$D_6$]-DMSO): $\delta$ = 7.75 (br. q, 1 H, NH), 4.80 (s, 2 H, $H^{2,5}$), 4.71 (s, 2 H, $H^{2',5'}$), 4.44 (s, 2 H, $H^{3,4}$), 4.36 (s, 2 H, $H^{3',4'}$), 3.71 (s, 3 H, $COOCH_3$), 2.32 (d, $^3J_{HH}$ = 4.5 Hz, 3 H, $NHCH_3$) ppm. $^{13}$C NMR, APT (75 MHz, $CDCl_3$): $\delta$ = 172.0 (s, $COOCH_3$), 169.72 (s, C=O), 78.66 (s, $C^{1'}$), 71.99 (s, $C^1$), 72.64 (s, $C^{2,5}$), 71.84 (s, $C^{2',5'}$), 71.31 (s, $C^{3,4}$), 70.06 (s, $C^{3',4'}$), 51.96 (s, $OCH_3$), 26.55 (s, $NHCH_3$) ppm. IR ($CH_2Cl_2$): $\tilde{\nu}$ = 3462 (s, NH, free), 3373 (vw, NH, assoc.), 1712 (s, $CO_{ester}$), 1659 (s, amide I) 1606 (m), 1530 (s, amide II) cm$^{-1}$.

**1′-(Methylcarbamoyl)ferrocene-1-carboxylic acid (8):** A solution of NaOH (140 mg, 3.5 mmol) in water (5 mL) was added to a solution of amide ester **7** (900 mg, 3 mmol) in methanol (20 mL). After heating to 80 °C for 50 min, the reaction mixture was extracted with $CH_2Cl_2$. The alkaline aqueous layer was treated with conc. HCl (pH = 1–2), extracted with EtOAc and washed with water. The organic layer was dried with $Na_2SO_4$ and evaporated in vacuo to afford 840 mg (97%) of orange crystals. M.p. 146–149 °C. IR (KBr): $\tilde{\nu}$ = 3334 (s, NH), 3089 (s, OH), 1676 (s, $CO_{acid}$), 1637 (s, amide I), 1550 (s, amide II) cm$^{-1}$.

**MeNHCO–Fn–CO–AA–OMe (9–11):** Compound **8** (200 mg, 0.7 mmol) was activated by using EDC/HOBt (as described for the preparation of **7**). The solution was cooled to 0 °C and AA–OMe (obtained from AA–OMe·HCl by treatment with $NEt_3$ in $CH_2Cl_2$, pH ca. 8) was added. The reaction mixture was stirred for 1 h at room temp., washed thrice with a saturated aqueous solution of $NaHCO_3$, 10% aqueous solution of citric acid, and $H_2O$. After drying over $Na_2SO_4$ and evaporating in vacuo, the crude products were TLC-purified with EtOAc as eluent. **9** (AA = Gly): Yield: 110 mg (42%), orange crystals. M.p. 149–152 °C. $^{13}$C NMR, APT (75 MHz, $CDCl_3$): $\delta$ = 170.49 (s, $CONHCH_3$), 170.48 (s, $COOCH_3$), 170.44 (s, C=O), 78.07 (s, $C^{1'}$), 76.62 (s, $C^1$), 70.69 (s, $C^{2,5}$), 70.59 (s, $C^{2',5'}$), 70.40 (s, $C^{3,4}$), 70.29 (s, $C^{3',4'}$), 51.85 (s, $OCH_3$), 40.85 (s, $CH_{2Gly}$), 26.07 (s, $NHCH_3$) ppm. IR ($CH_2Cl_2$): $\tilde{\nu}$ = 3446 (m, NH, free), 3259 (w, NH, assoc.), 1742 (s, $CO_{ester}$) 1650 (s, amide I), 1609 (m), 1535 (s, amide II) cm$^{-1}$. IR (KBr): $\tilde{\nu}$ = 3401 (s, NH, free), 3273 (s, NH, assoc.), 1737 (s, $CO_{ester}$), 1634 (s, amide I), 1540 (s, amide II) cm$^{-1}$. MS (ESI+, $CH_3CN$): *m*/*z* (%) = 359.3 (100) [M + H]$^+$, 381.3 (7) [M + Na]$^+$, 397.2 (5) [M + K]$^+$, 717.3 (14) [2M + H]$^+$, 739.3 (4) [2M + Na]$^+$, 755.3 (2) [2M + K]$^+$. HRMS (FAB): calcd. for $C_{16}H_{18}FeN_2O_4$ 358.0616; found 358.0619. **10** (AA = L-Ala): Yield: 157 mg (61%), orange resin. $^{13}$C NMR, APT (75 MHz, $CDCl_3$): $\delta$ = 174.25 (s, $COOCH_3$), 170.82 (s, $CONHCH_3$), 170.39 (s, C=O), 78.54 (s, $C^{1'}$), 76.75 (s, $C^1$), 71.37 (s, $C^2$), 71.32 (s, $C^5$), 71.28 (s, $C^{2'}$), 71.26 (s, $C^{5'}$), 70.89 (s, $C^3$), 70.83 (s, $C^4$), 70.77 (s, $C^{3'}$), 70.09 (s, $C^{4'}$), 52.57 (s, $OCH_3$), 48.39 (s, $CH_{Ala}$), 26.58 (s, $NHCH_3$), 17.71 (s, $CH_{3Ala}$) ppm. IR ($CH_2Cl_2$): $\tilde{\nu}$ = 3451 (m, NH, free), 3271 (w, NH, assoc.), 1740 (s, $CO_{ester}$), 1650 (s, amide I), 1534 (s, amide II) cm$^{-1}$. MS (ESI+, $CH_3CN$): *m*/*z* (%) = 373.3 (100) [M + H]$^+$, 395.3 (18) [M + Na]$^+$, 411.3 (21) [M + K]$^+$, 745.3 (8) [2M + H]$^+$, 767.3 (14) [2M + Na]$^+$, 783.2 (6) [2M + K]$^+$. HRMS (FAB): calcd. for $C_{17}H_{20}FeN_2O_4$ 372.0773; found 372.0766. **10a** (AA = D-Ala): Yield: 54%, orange resin. NMR and IR spectra of **10a** were similar to those of **10**. **11** (AA = L-Val): Yield: 130 mg (46%), orange resin. $^{13}$C NMR, APT (75 MHz, $CDCl_3$): $\delta$ = 173.28 (s, $COOCH_3$), 170.72 (s, $CONHCH_3$), 170.57 (s, C=O), 78.69 (s, $C^{1'}$), 76.81 (s, $C^1$), 71.51 (s, $C^2$), 71.38 (s, $C^{2',5}$), 71.12 (s, $C^{3,5'}$), 70.83 (s, $C^4$), 70.25 (s, $C^{3'}$), 70.07 (s, $C^{4'}$), 57.53 (s, $CH\alpha_{Val}$), 52.34 (s, $OCH_3$), 30.73 (s, $CH\beta_{Val}$), 26.55 (s, $NHCH_3$), 19.20 (s, $CH_{3Val}$), 18.19 (s, $CH_{3Val}$) ppm. IR ($CH_2Cl_2$): $\tilde{\nu}$ = 3453, 3418 (m, NH, free), 3293 (w, NH, assoc.), 1736 (s, $CO_{ester}$), 1665 (s, amide I), 1520 (s, amide II) cm$^{-1}$. MS (ESI+, $CH_3CN$): *m*/*z* (%) = 401.3 (100) [M + H]$^+$, 423.3 (28) [M + Na]$^+$, 439.3 (18) [M + K]$^+$, 801.4 (5) [2M + H]$^+$, 823.3 (17) [2M + Na]$^+$, 839.2 (7) [2M + K]$^+$. HRMS (FAB): calcd. for $C_{19}H_{24}FeN_2O_4$ 400.1085; found 400.1073.

**MeNHCO–Fn–CO–AA–OH (12–14):** MeNHCO–Fn–CO–AA–OMe (**9**–**11**, 0.3 mmol) was dissolved in a mixture of dioxane (10 mL) and water (10 mL). After cooling to 10 °C and the ad-

Table 4. $^1$H NMR chemical shifts for **9**–**11** and **15**–**17** in $CDCl_3$.

| | **9** | **10** | **11** | **15** | **16** | **17** |
|---|---|---|---|---|---|---|
| 1-N*H* | 7.39 (1 H, br. t) | 7.03 (d, 1 H, *J* = 7.0 Hz) | 6.63 (d, 1 H, *J* = 8.4 Hz) | 7.15 (1 H, br. t) | 6.77 (d, 1 H, *J* = 6.8 Hz) | 6.52 (1 H, br. d, *J* = 7.9 Hz) |
| 1′-N*H* | 6.72 (1 H, br. q) | 6.88 (1 H, br. q) | 7.03 (1 H, br. q) | 6.89 (1 H, br. q) | 7.08 (1 H, br. q) | 7.20 (1 H, br. q) |
| 1-N*H*$CH_3$ | – | – | – | 6.86 (1 H, br. q) | 6.71 (1 H, br. q) | 6.55 (1 H, br. q) |
| C*Hα* | 4.13 (d, 2 H, *J* = 5.8 Hz) | 4.62 (m, 1 H) | 4.61 (m, 1 H) | 4.03 (d, 2 H, *J* = 5.8 Hz) | 4.55 (m, 1 H) | 4.32 (m, 1 H) |
| Cp-*H* | 4.69 (2 H, pt)<br>4.53 (2 H, pt)<br>4.38 (4 H, pt) | 4.73 (1 H, pt)<br>4.63 (1 H, pt)<br>4.58 (1 H, pt)<br>4.44 (1 H, pt)<br>4.39 (m, 2 H)<br>4.36 (1 H, pt)<br>4.33 (1 H, pt) | 4.62 (1 H, pt)<br>4.60 (m, 2 H)<br>4.43 (1 H, pt)<br>4.41 (1 H, pt)<br>4.38 (1 H, pt)<br>4.36 (1 H, pt)<br>4.32 (1 H, pt) | 4.64 (2 H, pt)<br>4.59 (2 H, pt)<br>4.40 (2 H, pt)<br>4.37 (2 H, pt) | 4.68 (1 H, pt)<br>4.65 (1 H, pt)<br>4.57 (1 H, pt)<br>4.44 (1 H, pt)<br>4.42 (1 H, pt)<br>4.39 (1 H, pt)<br>4.36 (1 H, pt)<br>4.32 (1 H, pt) | 4.69 (m, 2 H)<br>4.51 (1 H, pt)<br>4.48 (1 H, pt)<br>4.41 (1 H, pt)<br>4.36 (1 H, pt)<br>4.35 (1 H, pt)<br>4.31 (1 H, pt) |
| 1′-NHC*H*$_3$ | 2.91 (d, 3 H, *J* = 4.8 Hz) | 2.91 (d, 3 H, *J* = 4.8 Hz) | 2.95 (d, 3 H, *J* = 4.7 Hz) | 2.90 (d, 3 H, *J* = 4.7 Hz) | 2.95 (d, 3 H, *J* = 4.7 Hz) | 2.94 (d, 3 H, *J* = 4.7 Hz) |
| OC*H*$_3$/ 1-NHC*H*$_3$ | 3.78 (s, 3 H) | 3.78 (s, 3 H) | 3.82 (s, 3 H) | 2.86 (d, 3 H, *J* = 4.7 Hz) | 2.87 (d, 3 H, *J* = 4.7 Hz) | 2.87 (d, 3 H, *J* = 4.7 Hz) |
| R | – | 1.51 (d, 3 H, *J* = 7.3 Hz) | 2.11 (m, 1 H)<br>1.04 (d, 3 H, *J* = 6.7 Hz)<br>1.02 (d, 3 H, *J* = 6.7 Hz) | – | 1.47 (d, 3 H, *J* = 6.8 Hz) | 2.16 (m, 1 H)<br>1.01 (d, 3 H, *J* = 6.7 Hz)<br>1.00 (d, 3 H, *J* = 6.7 Hz) |

 © 2007 Wiley-VCH Verlag GmbH & Co. KGaA, Weinheim 

Table 5. $^1$H NMR chemical shifts for **9**–**11** and **15**–**17** in [D$_6$]DMSO.

| | **9** | **10** | **11** | **15** | **16** | **17** |
|---|---|---|---|---|---|---|
| 1-N*H* | 8.40 (1 H, br. t, *J* = 5.2 Hz) | 8.24 (d, 1 H, *J* = 6.9 Hz) | 7.88 (d, 1 H, *J* = 7.9 Hz) | 8.17 (t, 1 H, *J* = 5.9 Hz) | 7.88 (1 H, br. d, *J* = 7.4 Hz) | 7.65 (1 H, br. d, *J* = 8.6 Hz) |
| 1′-N*H* | 7.73 (1 H, br. q) | 7.75 (1 H, br. q) | 7.66 (1 H, br. q) | 7.98 (1 H, br. q) | 7.97 (1 H, br. q) | 7.88 (1 H, br. q) |
| 1-N*H*CH$_3$ | – | – | – | 7.85 (1 H, br. q) | 7.91 (1 H, br. q) | 8.01 (1 H, br. q) |
| C*Ha* | 3.92 (d, 2 H, *J* = 5.7 Hz) | 4.35 (m, 1 H) | 4.26 (1 H, pt, *J* = 7.6 Hz) | 3.74 (d, 2 H, *J* = 5.9 Hz) | 4.32 (m, 1 H) | 4.11 (pt, 1 H, *J* = 8.0 Hz) |
| Cp-*H* | 4.76 (s, 2 H)<br>4.73 (s, 2 H)<br>4.38 (s, 2 H)<br>4.31 (s, 2 H) | 4.78 (s, 1 H)<br>4.76 (s, 1 H)<br>4.71 (s, 2 H)<br>4.38–4.31 (m, 4 H) | 4.77 (m, 3 H)<br>4.71 (s, 1 H)<br>4.34 (m, 2 H)<br>4.30 (m, 2 H) | 4.73 (s, 2 H)<br>4.70 (s, 2 H)<br>4.38 (s, 2 H)<br>4.34 (s, 2 H) | 4.78 (s, 1 H)<br>4.72 (m, 3 H)<br>4.36 (s, 2 H)<br>4.32 (s, 2 H) | 4.81 (s, 1 H)<br>4.79 (s, 1 H)<br>4.70 (s, 1 H)<br>4.68 (s, 1 H)<br>4.33 (s, 1 H)<br>4.31 (s, 1 H)<br>4.28 (s, 2 H) |
| 1′-NHC*H*$_3$ | 2.69 (d, 3 H, *J* = 4.2 Hz) | 2.70 (d, 3 H, *J* = 4.5 Hz) | 2.72 (d, 3 H, *J* = 4.6 Hz) | 2.69 (d, 3 H, *J* = 4.5 Hz) | 2.71 (d, 3 H, *J* = 4.5 Hz) | 2.70 (d, 3 H, *J* = 4.1 Hz) |
| OC*H*$_3$/ 1-NHC*H*$_3$ | 3.67 (s, 3 H) | 3.66 (s, 3 H) | 3.67 (s, 3 H) | 2.64 (d, 3 H, *J* = 4.5 Hz) | 2.63 (d, 3 H,*J* = 4.5 Hz) | 2.61 (d, 3 H, *J* = 4.2 Hz) |
| R | – | 1.39 (d, 3 H, *J* = 7.3 Hz) | 2.18 (m, 1 H)<br>1.01 (d, 3 H, *J* = 6.8 Hz)<br>0.96 (d, 3 H, *J* = 6.8 Hz) | – | 1.30 (d, 3 H, *J* = 7.2 Hz) | 2.07 (m, 1 H)<br>0.94 (d, 3 H, *J* = 6.6 Hz)<br>0.89 (d, 3 H, *J* = 6.7 Hz) |

dition of NaOH (23 mg, 0.6 mmol), the reaction mixture was stirred at room temp. for 10 min. The solution was treated with conc. HCl to pH = 2–3, extracted with EtOAc, washed with saturated aqueous $NaHCO_3$ and water. The organic layer was dried with $Na_2SO_4$ and evaporated in vacuo. Compounds **12**–**14** were used without purification for further transformation. **12** (AA = Gly): Yield: 100 mg (94%), orange crystals. M.p. 115–117 °C. IR (KBr): $\tilde{\nu}$ = 3458 (m, NH, free), 3092 (s, OH), 1630 (s, amide I), 1534 (s, amide II) cm$^{-1}$. **13** (AA = L-Ala): Yield: 94 mg (81%), orange resin. IR ($CH_2Cl_2$): $\tilde{\nu}$ = 3450 (m, NH, free), 3100 (s, OH), 1655 (s, amide I), 1534 (s, amide II) cm$^{-1}$. **14** (AA = L-Val): Yield: 96 mg (94%), orange resin. IR ($CH_2Cl_2$): $\tilde{\nu}$ = 3453 (m, NH, free), 3110 (s, OH), 1650 (s, amide I), 1534 (s, amide II) cm$^{-1}$.

**MeNHCO–Fn–CO–AA–NHMe (15–17). Procedure A:** MeNHCO–Fn–CO–AA–OH (**12**–**14**; 0.25 mmol) was activated (as described for **7**) and reacted with $MeNH_2$·HCl (cf. preparation of **9**–**11**). The crude products were purified by TLC using EtOAc as the eluent to give orange resins **15** (24%), **16** (56%) and **17** (20%), respectively. **Procedure B:** Acid amide **8** (150 mg, 0.526 mmol) was activated by using EDC/HOBt as described for **7** and reacted with AA–NHMe (obtained from AA–NHMe·HCl similarly as in preparation of **9**–**11**). The products were purified by TLC using EtOAc as the eluent to give orange resins **15** (45%), **16** (45%), **17** (34%). The compounds prepared by these alternative procedures display identical NMR and IR spectra. **15** (AA = Gly): orange resin. $^{13}$C NMR, APT (75 MHz, $CDCl_3$): $\delta$ = 170.31 (s, $CONHCH_3$), 170.22 (s, $CONHCH_3$), 169.72 (s, C=O), 77.75 (s, C$^{1'}$), 76.25 (s, C$^1$), 70.93 (s, C$^{2,5}$), 70.75 (s, C$^{2',5'}$), 70.12 (s, C$^{3,4}$), 69.92 (s, C$^{3',4'}$), 43.01 (s, $CH_{2Gly}$), 26.08 (s, $NHCH_3$), 25.85 (s, $NHCH_3$) ppm. IR ($CH_2Cl_2$): $\tilde{\nu}$ = 3449 (m, NH, free), 3341 (w, NH, assoc.), 1655 (s, amide I), 1607 (s), 1534 (s, amide II) cm$^{-1}$. MS (ESI+, $CH_3CN$): *m*/*z* (%) = 358.4 (100) [M + H]$^+$, 380.4 (5) [M + Na]$^+$, 715.3 (4) [2M + H]$^+$, 737.5 (3) [2M + Na]$^+$. HRMS (EI): calcd. for $C_{16}H_{19}FeN_3O_3$ 357.0776; found 357.0754. **16** (AA = L-Ala): orange resin. $^{13}$C NMR, APT (75 MHz, $CDCl_3$): $\delta$ = 173.80 (s, $CONHCH_3$), 170.69 (s, $CONHCH_3$), 170.32 (s, C=O), 78.16 (s, C$^{1'}$), 76.40 (s, C$^1$), 71.59 (s, C$^2$), 71.38 (s, C$^5$), 71.34 (s, C$^{2'}$) 71.01 (s, C$^{5'}$), 70.65 (s, C$^3$), 70.62 (s, C$^4$), 70.58 (s, C$^{3'}$), 70.19 (s, C$^{4'}$), 49.47 (s, $CH_{Ala}$), 26.62 (s, $NHCH_3$), 26.48 (s, $NHCH_3$), 18.18 (s, $CH_{3Ala}$) ppm. IR ($CH_2Cl_2$): $\tilde{\nu}$ = 3449 (m, NH, free), 3363, 3327 (m, NH, assoc.), 1653 (s, amide I), 1536 (s, amide II) cm$^{-1}$. MS (ESI+, $CH_3CN$): *m*/*z* (%) = 372.3 (100) [M + H]$^+$, 394.3 (2) [M + Na]$^+$, 410.4 (4) [M + K]$^+$, 743.3 (21) [2M + H]$^+$, 765.2 (5) [2M + Na]$^+$, 781.2 (3) [2M + K]$^+$. HRMS (FAB): calcd for $C_{17}H_{21}FeN_3O_3$ 371.0932; found 371.0965. **17** (AA = L-Val): orange resin. $^{13}$C NMR, APT (75 MHz, $CDCl_3$): $\delta$ = 172.68 (s, $CONHCH_3$), 170.65 (s, $CONHCH_3$), 170.60 (s, C=O), 78.13 (s, C$^{1'}$), 76.8 (s, C$^1$), 71.67 (s, C$^2$) 71.39 (s, C$^5$), 71.31 (s, C$^{2',5'}$), 71.15 (s, C$^3$) 70.91 (s, C$^4$), 69.87 (s, C$^{3'}$) 69.74 (s, C$^{4'}$), 59.34 (s, $CH_{Val}$), 30.74 (s, $CH_{Val}$), 26.64 (s, $NHCH_3$), 26.40 (s, $NHCH_3$), 19.51 (s, $CH_{3Val}$), 18.53 (s, $CH_{3Val}$) (Tables 4, 5 and 6) ppm. IR ($CH_2Cl_2$): $\tilde{\nu}$ = 3451 (m, NH, free), 3342, 3326 (m, NH, assoc.), 1657 (s, amide I), 1605 (m), 1532 (s, amide II) cm$^{-1}$. MS (ESI+, $CH_3CN$): *m*/*z* (%) = 400.4 (100) [M + H]$^+$, 422.4 (24) [M + Na]$^+$, 438.3 (4) [M + K]$^+$, 799.4 (9) [2M + H]$^+$, 821.3 (4) [2M + Na]$^+$, 837.3 (2) [2M + K]$^+$. HRMS (FAB): calcd for $C_{19}H_{25}FeN_3O_3$ 399.1245; found 399.1227.

Table 6. UV/Vis and CD data for **10**, **11**, **16** and **17** in $CH_3CN$.

| | $\lambda_{max}$ / nm | $\lambda_{max}$ / nm ($M_\theta$ / °M$^{-1}$cm$^{-1}$) |
|---|---|---|
| **10** | 452 | 299 (340), 349 (–220), 411 (–120), 471 (360) |
| **10a** | 442 | 300 (–260), 350 (170), 413 (90), 475 (–250) |
| **11** | 439 | 301 (360), 347 (–330), 411 (–190), 470 (430) |
| **16** | 452 | 305 (810), 352 (–340), 419 (–190), 483 (410) |
| **17** | 444 | 305 (860), 352 (–480), 415 (–270), 479 (530) |

**Supporting Information** (see footnote on the first page of this article): DFT calculated cartesian coordinates for all conformers of **9**, **10**, **11**, **15**, **16** and **17**.

## Acknowledgments

The authors are grateful to Ph. D. Dinko Žiher, GlaxoSmithKline Research Centre Zagreb, Ltd., for the CD measurements. We thank

 © 2007 Wiley-VCH Verlag GmbH & Co. KGaA, Weinheim 

the Ministry for Science, Education and Sport of Croatia for support through a grant and the German Science Foundation for a Heisenberg fellowship (to K. H.).

[1] S. Chowdhury, D. A. R. Sanders, G. Schatte, H.-B. Kraatz, *Angew. Chem.* **2006**, *118*, 765–768; *Angew. Chem. Int. Ed.* **2006**, *45*, 751–754.
[2] T. Moriuchi, T. Nagai, T. Hirao, *Org. Lett.* **2005**, *7*, 5265–5268.
[3] S. I. Kirin, D. Wissenbach, N. Metzler-Nolte, *New J. Chem.* **2005**, *29*, 1168–1173.
[4] S. Chowdhury, G. Schatte, H.-B. Kraatz, *Dalton Trans.* **2004**, 1726–1730.
[5] F. E. Appoh, T. C. Sutherland, H.-B. Kraatz, *J. Organomet. Chem.* **2004**, *689*, 4669–4677.
[6] T. Moriuchi, K. Yoshida, T. Hirao, *Org. Lett.* **2003**, *5*, 4285–4288.
[7] T. Moriuchi, A. Nomoto, K. Yoshida, T. Hirao, *Organometallics* **2001**, *20*, 1008–1013.
[8] T. Moriuchi, A. Nomoto, K. Yoshida, A. Ogawa, T. Hirao, *J. Am. Chem. Soc.* **2001**, *123*, 68–75.
[9] T. Moriuchi, A. Nomoto, K. Yoshida, T. Hirao, *J. Organomet. Chem.* **1999**, *589*, 50–58.
[10] A. Nomoto, T. Moriuchi, S. Yamazaki, A. Ogawa, T. Hirao, *Chem. Commun.* **1998**, 1963–1964.
[11] R. S. Herrick, R. M. Jarret, T. P. Curran, D. R. Dragoli, M. B. Flaherty, S. E. Lindyberg, R. A. Slate, L. C. Thornton, *Tetrahedron Lett.* **1996**, *37*, 5289–5292.
[12] D. R. van Staveren, T. Weyhermüller, N. Metzler-Nolte, *Dalton Trans.* **2003**, 210–220.
[13] X. de Hatten, T. Weyhermüller, N. Metzler-Nolte, *J. Organomet. Chem.* **2004**, *689*, 4856–4867.
[14] Y. Xu, P. Saweczko, H.-B. Kraatz, *J. Organomet. Chem.* **2004**, *689*, 4669–4677.
[15] Y. Xu, P. Saweczko, H. B. Kraatz, *J. Organomet. Chem.* **2001**, *637–639*, 335–342.
[16] M. Oberhoff, L. Duda, J. Karl, R. Mohr, G. Erker, R. Fröhlich, M. Grehl, *Organometallics* **1996**, *15*, 4005–4011.
[17] S. I. Kirin, H.-B. Kraatz, N. Metzler-Nolte, *Chem. Soc. Rev.* **2006**, *35*, 348–354.
[18] A. Kuik, R. Skoda-Földes, A. C. Benyei, G. Rangits, L. Kollar, *J. Organomet. Chem.* **2006**, *691*, 3037–3042.
[19] K. Heinze, M. Beckmann, *Eur. J. Inorg. Chem.* **2005**, 3450–3457.
[20] E. Vass, M. Hollósi, F. Besson, R. Buchet, *Chem. Rev.* **2003**, *103*, 1917–1954.
[21] K. Heinze, M. Schlenker, *Eur. J. Inorg. Chem.* **2004**, 2974–2988.
[22] S. I. Kirin, U. Schatzschneider, X. de Hatten, T. Weyhermüller, N. Metzler-Nolte, *J. Organomet. Chem.* **2006**, *691*, 3451–3457.
[23] K. Heinze, M. Beckmann, *J. Organomet. Chem.* **2006**, *691*, 5588–5596.
[24] K. Heinze, U. Wild, M. Beckmann, *Eur. J. Inorg. Chem.* **2007**, 617–623.
[25] Y. Jin, K. Tonan, S. Ikawa, *Spectrochim. Acta Part A* **2002**, *58*, 2795–2802.
[26] L. Barišić, M. Čakić, K. A. Mahmoud, Y. Liu, H.-B. Kraatz, H. Pritzkow, S. I. Kirin, N. Metzler-Nolte, V. Rapić, *Chem. Eur. J.* **2006**, *12*, 4965–4980.
[27] L. Barišić, V. Rapić, V. Kovač, *Croat. Chem. Acta* **2002**, *75*, 199–210.
[28] a) L. Barišić, M. Dropučić, V. Rapić, H. Pritzkow, S. I. Kirin, N. Metzler-Nolte, *Chem. Commun.* **2004**, 2004–2005; b) S. Chowdhury, G. Schatte, H.-B. Kraatz, *Angew. Chem.* **2006**, *118*, 7036–7038; *Angew. Chem. Int. Ed.* **2006**, *45*, 6882–6884.
[29] L. Barišić, V. Rapić, N. Metzler-Nolte, *Eur. J. Inorg. Chem.* **2006**, 4019–4021.
[30] A. Sonda, I. Martini, *J. Organomet. Chem.* **1971**, *26*, 133–140.
[31] M. J. Frisch, G. W. Trucks, H. B. Schlegel, G. E. Scuseria, M. A. Robb, J. R. Cheeseman, J. A. Montgomery Jr, T. Vreven, K. N. Kudin, J. C. Burant, J. M. Millam, S. S. Iyengar, J. Tomasi, V. Barone, B. Mennucci, M. Cossi, G. Scalmani, N. Rega, G. A. Petersson, H. Nakatsuji, M. Hada, M. Ehara, K. Toyota, R. Fukuda, J. Hasegawa, M. Ishida, T. Nakajima, Y. Honda, O. Kitao, H. Nakai, M. Klene, X. Li, J. E. Knox, H. P. Hratchian, J. B. Cross, C. Adamo, J. Jaramillo, R. Gomperts, R. E. Stratmann, O. Yazyev, A. J. Austin, R. Cammi, C. Pomelli, J. W. Ochterski, P. Y. Ayala, K. Morokuma, G. A. Voth, P. Salvador, J. J. Dannenberg, V. G. Zakrzewski, S. Dapprich, A. D. Daniels, M. C. Strain, O. Farkas, D. K. Malick, A. D. Rabuck, K. Raghavachari, J. B. Foresman, J. V. Ortiz, Q. Cui, A. G. Baboul, S. Clifford, J. Cioslowski, B. B. Stefanov, G. Liu, A. Liashenko, P. Piskorz, I. Komaromi, R. L. Martin, D. J. Fox, T. Keith, M. A. Al-Laham, C. Y. Peng, A. Nanayakkara, M. Challacombe, P. M. W. Gill, B. Johnson, W. Chen, M. W. Wong, C. Gonzalez, J. A. Pople, *Gaussian 03*, Revision B.03, Gaussian, Inc., Pittsburgh PA, **2003**.

Received: December 22, 2006
Published Online: March 23, 2007

 © 2007 Wiley-VCH Verlag GmbH & Co. KGaA, Weinheim 

DOI: 10.1002/ejic.200601228

# Synthesis and Characterization of New Energetic Nitroformate Salts

Yangen Huang,[a] Haixiang Gao,[a] Brendan Twamley,[a] and Jean'ne M. Shreeve*[a]

**Keywords:** Nitroform / Energetic salt / Oxygen balance

New energetic nitroformate salts that contain high-nitrogen cations were synthesized by taking advantage of the relatively high acidity of nitroform. All of the new salts have been characterized by elemental, spectral, and thermal analyses. Single-crystal X-ray analysis of **2** shows that it is a co-crystal of a neutral 4-amino-1,2,4-triazole molecule with the 4-amino-1,2,4-triazolium nitroformate ion pair. The presence of the neutral molecule appears to lend stability to the salt. The structure of 3,6-diguanidino-1,2,4,5-tetrazinium nitroformate (**10**) was also confirmed by single-crystal X-ray analysis. Theoretical performance calculations indicate that these materials have properties which compare favorably with hydrazinium nitroformate, TNT and Tetryl suggesting potential applications as eco-friendly oxidizers.
(© Wiley-VCH Verlag GmbH & Co. KGaA, 69451 Weinheim, Germany, 2007)

## Introduction

On the basis of their special properties such as lower vapor pressures and higher densities than their atomically similar non-ionic analogues, the synthesis of energetic salts as a unique class of high energetic materials has attracted considerable interest over the past decade.[1] Recently, the syntheses of new members of heterocyclic-based energetic, low-melting salts were reported.[2] Some of them display attractive energetic properties including high positive heats of formation and high density, e.g., the salt of 3-amino-6-(nitroamino)tetrazine (ANAT) with 3,6-diguanidinotetrazine exhibits a heat of formation of +1089 kJ mol$^{-1}$.[2a] Due to its high oxygen content and labile hydrogen atom which facilitates the preparation of nitroformate derivatives, nitroform (trinitromethane) is a very valuable compound for use in the preparation of ingredients with good explosive and propellant properties. A number of nitroform derivatives including those with potassium, silver, pyridinium, piperidinium, ammonium, guanidinium, aminoguanidinium, diaminoguanidinium, triaminoguanidinium, and hydrazinium cations have been reported.[3] Among them, hydrazinium nitroformate (HNF) has received considerable attention as an effective oxidizer.[4]

High-energy solid oxygen oxidizers which possess useful propellant properties such as high density, good thermal stability and high impact resistance continue to be sought. Ammonium nitrate (AN) and ammonium perchlorate (AP) are two oxidizers widely used in military and civilian applications. HNF has a higher heat of formation than AP ($\Delta H_f$ = –71 kJ mol$^{-1}$ compared to –292.88 kJ mol$^{-1}$), is relatively dense (1.86 g cm$^{-3}$) and is more environmentally friendly making it a suitable substitute. Because of its rather high thermal stability ($T_d$ = 123 °C),[4c] HNF is in the minority relative to most nitroform salts which often decompose rapidly at ≤25 °C. However, hydrazine hydrate, the precursor to HNF, is a probable human carcinogen. Therefore, it was worthwhile to attempt to design benign energetic salts with trinitromethanide as the anion. With respect to this need, we have prepared several high-nitrogen energetic salts with the highly oxidizing trinitromethanide anion, two of which appear to exhibit considerable promise.

## Results and Discussion

The key synthon, nitroform (NF), was prepared from acetic anhydride through a three-step process in 38% overall yield (Scheme 1)[5] (m.p. 22 °C; reported m.p. 15–26 °C mainly due to the degree of purity of the product)[4c,6] (see Supporting Information).

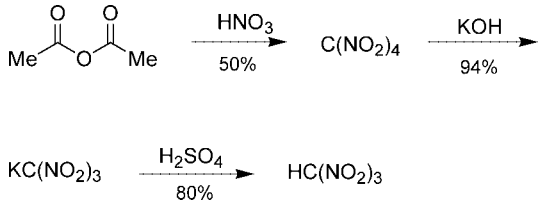


Scheme 1.

Due to the high acidity of nitroform (p$K_a$ = 0),[4c] which is comparable to mineral acids, a series of nitrogen-rich compounds were protonated in methanol or water at 25 °C or below (Scheme 2). All of the nitroform salts **1**, **3**–**11** are formed in nearly quantitative yields and in high purity.

[a] Department of Chemistry, University of Idaho,
Moscow, Idaho 83843-2343, USA
Fax: +1-208-885-9146
E-mail: jshreeve@uidaho.edu
Supporting information for this article is available on the WWW under http://www.eurjic.org or from the author.

 © 2007 Wiley-VCH Verlag GmbH & Co. KGaA, Weinheim 

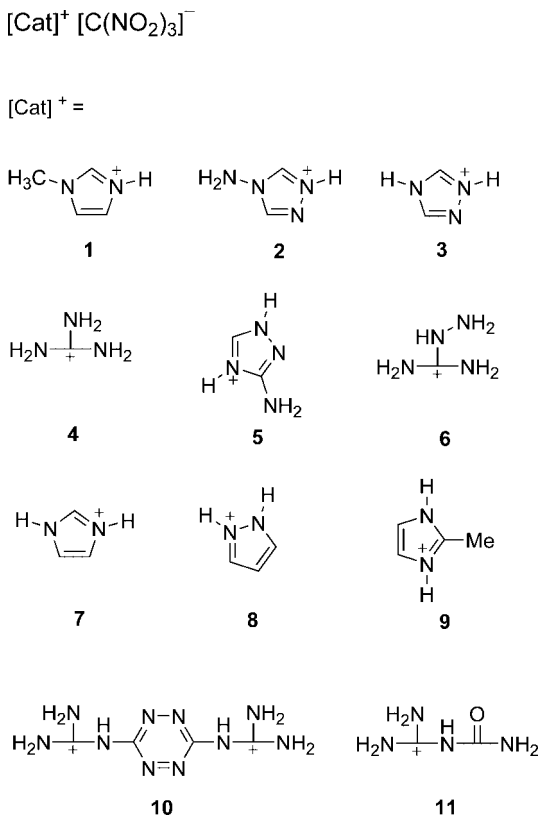


Scheme 2.

While attempting to synthesize 4-amino-1,2,4-triazolium nitroformate, the product which was obtained after recrystallization from methanol and diethyl ether was found to be molecular 4-amino-1,2,4-triazole combined with the 4-amino-1,2,4-triazolium nitroformate in a novel co-crystal **2**. The same product was obtained even after a prolonged reaction time (36 h) or by increasing the equivalent ratio of nitroform from 1 to 5 and reaction temperature from 25 °C to 50 °C. Using water as solvent did not affect the results. However, the expected 1:1 salt **5** was obtained when the 3-amino isomer, 3-amino-1,2,4-triazole, and nitroform were reacted. Guanylurea nitroformate (**11**) was synthesized by reaction of guanylurea carbonate with nitroform in methanol. Meanwhile, all attempts to isolate the corresponding nitroformate salts with 5-amino-1*H*-tetrazole (**12**) and 3,6-dihydrazinotetrazine (**13**) were unsuccessful due to their extremely low thermal stability. The reaction mixture foamed dramatically even at 0 °C which suggested that the desired product decomposed immediately (Scheme 3).

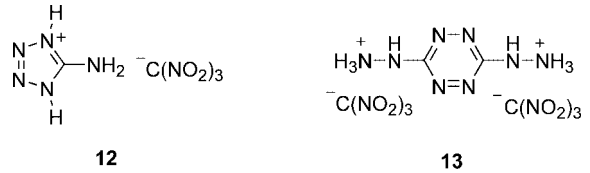


Scheme 3.

All the new salts, namely, 1-methylimidazolium, 3-amino-1,2,4-triazolium, 1,2,4-triazolium, guanidinium, 4-amino-1,2,4-triazolium, aminoguanidinium, imidazolium, pyrazolium, 2-methylimidazolium, 3,6-diguanidino-1,2,4,5-tetrazinium and *N*-guanylurea nitroformate (**1**–**11**) were characterized by IR, and $^{1}H$ and $^{13}C$ NMR spectral and elemental analyses. The IR spectra of these salts exhibit absorption bands in the range 1510–1590 $cm^{-1}$ which are attributed to the presence of nitro groups. The several main absorption bands in the range 3100–3430 $cm^{-1}$ can be assigned to the N–H bonds. It was not possible to locate the $^{13}C$ NMR signal of the nitroformate anion in **1**–**11**.

Crystals suitable for single-crystal X-ray analysis were obtained by crystallization from methanol and diethyl ether for **2** and water for **10**. The structure of **2** (Figure 1) consists of a co-crystal of a neutral 4-amino-1,2,4-triazole with the 4-amino-1,2,4-triazolium nitroformate ion pair. The tetrahedral geometry and bond length [1.412(1) Å] of the amino group of the triazolium cation indicates little interaction by the N1 lone pair and the triazolium ring pi system, similar to other triazolium species.[2b,7] However, there are many strong hydrogen bonds which stabilize this structure and assist with charge delocalization. The extended structure of

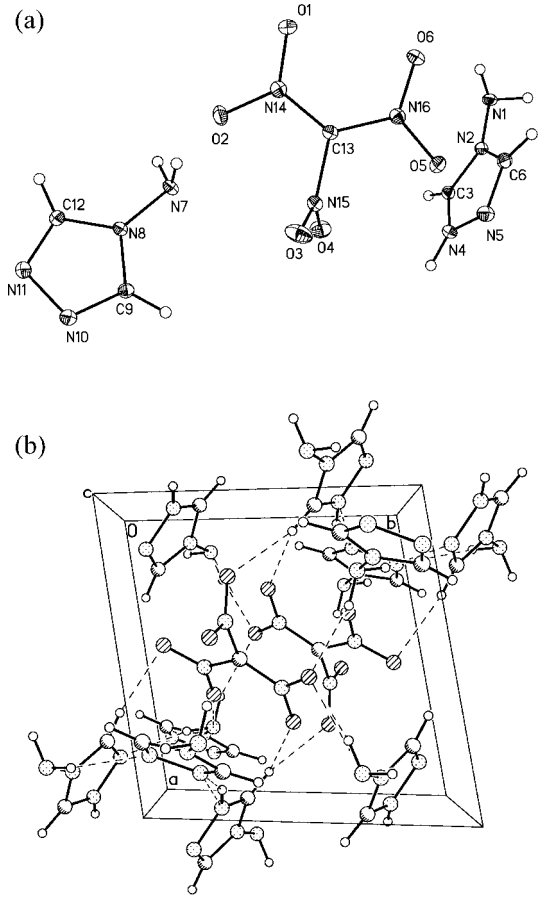


Figure 1. (a) Thermal ellipsoid plot (30%) and labeling scheme for 4-amino-1,2,4-triazolium nitroformate (**2**). Hydrogen atoms included but are unlabelled for clarity. (b) Ball and stick packing diagram of **2** viewed down the *c* axis. Dashed lines indicate strong hydrogen bonding.

 © 2007 Wiley-VCH Verlag GmbH & Co. KGaA, Weinheim 

**2** (Figure 1, b) shows some of these strong hydrogen bonds and indicates the layer structure formed by alternating nitroformate anions and cationic triazolium/neutral triazole. The triazolium/neutral triazole pair hydrogen bond into an oblique square which stacks to form a four-sided channel with an approximate diameter of 3.8 Å. Although an anhydrous salt of **10** could be obtained by dehydration in vacuo at room temperature (confirmed by elemental analyses), the structure of **10** (Figure 2) is a dihydrate and consists of a 3,6-diguanidino-1,2,4,5-tetrazinium dication with two nitroformate anions.

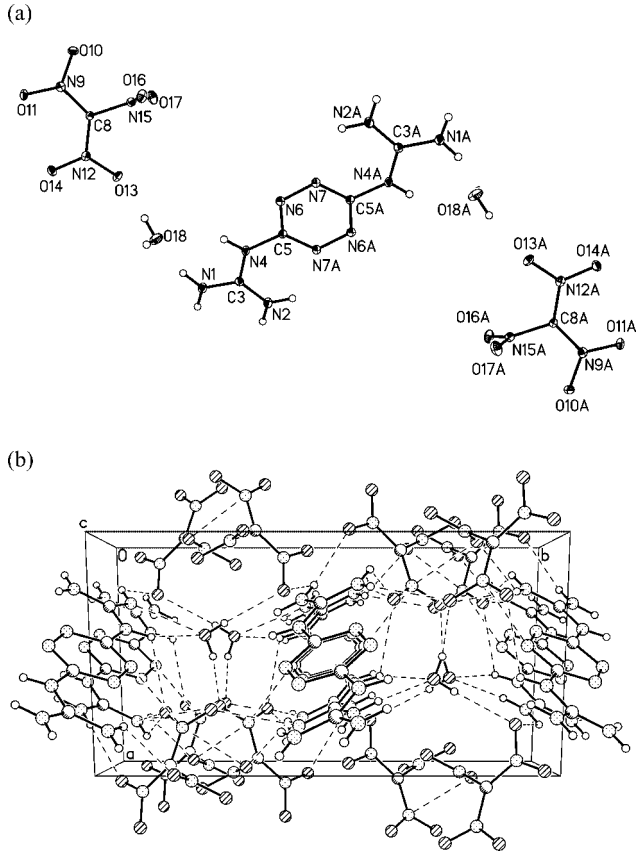


Figure 2. (a) Thermal ellipsoid plot (30%) and labeling scheme for 3,6-diguanidino-1,2,4,5-tetrazinium nitroformate (**10**). Hydrogen atoms included but are unlabelled for clarity. (b) Ball and stick packing diagram of **10** viewed down the *c* axis. Dashed lines indicate strong hydrogen bonding.

In this structure, the guanidine moieties are planar with an 8.7° dihedral angle to the central tetrazinium ring. This indicates a stabilization of the cation via delocalization of the charge over the entire diguanidino tetrazinium moiety. The extended structure also forms a strongly hydrogen-bonded network with alternating anionic nitroformate/water and cationic tetrazinium layers parallel to the *a* axis (Figure 2, b). There are few known nitroformate structures.[7a,8] In **2** and **10**, one nitro group is ca. 73° and 85° degrees, respectively, to the main plane of the anion. This angle varies in the other published structures from planar[8b] to 90°.[8d]

Densities and thermochemical data for **1**–**11** are summarized in Table 1. DSC and TGA were used to evaluate the relative thermal stabilities of **1**–**11** and are measured under comparable conditions. In the DSC thermograms, most of the salts (**1**, **3**–**11**) decomposed at their melting points except for **2** which melted sharply at 92 °C. The results from DSC are consistent with those obtained using TGA. The decomposition temperatures of **1**–**11** occur over the range of 74–167 °C with **2** displaying the highest decomposition temperature (167 °C). The results indicate that the neutral 4-amino-1,2,4-triazole contained in the 4-amino-1,2,4-triazolium nitroformate crystal may have a stabilizing effect on the product. Comparison of guanylurea nitroformate (**11**) with guanylurea dinitramide (FOX-12),[9] showed that the stability of **11** is slightly lower than FOX-12 ($T_d$ = 153 °C vs. 216 °C), but they have essentially the same density, detonation pressure and detonation velocity (Table 2). The low decomposition temperature of nitroform salts **1**, **3**–**11** and HNF ($T_d$ = 120–153 °C) confirmed further that the thermal stability of compounds with the trinitromethanide anion is low.

Table 1. Densities and thermochemical results for nitroformate salts at 298.15 K.

| Compd. | $d$[a] | $T_d$[b] | $OB$[c] | $\Delta_f H_m$[d] | $I_{sp}$[e] | $P$[f] | $D$[g] |
|---|---|---|---|---|---|---|---|
| **1** | 1.60 | 83 | –51.48 | –91.7 | 222.1 | 22.1 | 7399 |
| **2** | 1.62 | 167 | –17.01 | 163.5 | 267.6 | 26.6 | 8079 |
| **3** | 1.70 | 90 | –14.54 | 47.6 | 262.3 | 28.3 | 8261 |
| **4** | 1.79 | 126 | –7.62 | –233.7 | 251.5 | 32.4 | 8984 |
| **5** | 1.74 | 74 | –17.01 | 24.4 | 255.2 | 28.6 | 8365 |
| **6** | 1.80 | 107 | –10.66 | –124.5 | 257.0 | 33.9 | 9145 |
| **7** | 1.77 | 104 | –32.86 | –81.8 | 240.5 | 27.5 | 7977 |
| **8** | 1.63 | 86 | –32.86 | 40.5 | 253.9 | 23.9 | 7582 |
| **9** | 1.53 | 98 | –51.48 | –120.1 | 218.9 | 19.6 | 7117 |
| **10** | 1.79 | 100 | –16.06 | 207.6 | 256.6 | 31.0 | 8660 |
| **11** | 1.74 | 153 | –15.80 | –421.9 | 228.5 | 26.0 | 8174 |

[a] Density [g cm$^{-3}$]. [b] Decomposition temperature (°C). [c] $OB$ = Oxygen balance (%) for $C_aH_bO_cN_d$: 1600 ($c - 2a - b/2$)/$MW$, $MW$ = molecular weight of salt. [d] Heat of formation [kJ mol$^{-1}$]. [e] Specific impulse (s). [f] Detonation pressure (GPa). [g] Detonation velocity (m s$^{-1}$).

Table 2. Comparison of salts **2** and **10** with conventional explosives.[a]

| Compound | $MW$ | $OB$ [%] | $D$ [m/s] | $P$ [GPa] | $d$ [g/cm$^3$] |
|---|---|---|---|---|---|
| HNF | 183 | +13.1 | 8902 | 46.9 | 1.86 |
| RDX | 222 | –21.61 | 8800 | 36.5 | 1.77 |
| TNT | 227 | –73.96 | 6660 | 19.3 | 1.66 |
| Tetryl | 287 | –47.35 | 7770 | 27.3 | 1.75 |
| FOX-12 | 209 | –19.1 | 8210 | 25.7 | 1.75 |
| **2** | 235 | –17.01 | 8079 | 26.6 | 1.69 |
| **10** | 498 | –16.06 | 8660 | 31.0 | 1.79 |

[a] Ref.[4c], ref.[9] for FOX-12.

As one of the important physical properties of energetic salts, the densities of **1**–**10** were measured by using helium displacement methods to yield results shown in Table 1. All of the compounds had densities > 1.50 g/cm$^3$ with **10** exhibiting a density of 1.79 g/cm$^3$ which is comparable with HNF (1.86 g/cm$^3$). The performance of a high explosive is

 © 2007 Wiley-VCH Verlag GmbH & Co. KGaA, Weinheim 

measured by its detonation velocity, $vD$ (m/s), detonation pressure, $P$ (Gpa), and specific impulse $I_{sp}$ (s).[10] These parameters are directly related to oxygen balance (OB), density, and heat of formation. The detonation pressure and velocity (based on traditional Chapman–Jouget thermodynamic detonation theory) and specific impulse ($I_{sp}$) were obtained by using Cheetah 4.0 (Table 1).[11]

For the compounds **1**–**11** the calculated detonation pressures lie in the range between $P$ = 19.6 GPa (**9**) and $P$ = 33.9 GPa (**6**). Detonation velocities are distributed from $D$ = 7230 m s$^{-1}$ (**8**) to $D$ = 9145 m s$^{-1}$ (**6**). Substituents on the nitrogen-containing heterocycle lower the density and detonation performance of the corresponding nitroform salts (**2** to **3**, **1** to **7**). Aminoguanidinium nitroformate (**6**) has the highest density and best performance among these salts; however, it decomposes within 36 h at 25 °C with loss of color. The salts **2** and **10** show the best stability being storable at 25 °C for several weeks. In addition, the performance potential of salts **2** and **10** are superior to the conventional explosives TNT and Tetryl as shown in Table 2.

## Conclusions

In conclusion, several energetic salts with the nitroformate anion have been synthesized and characterized. The neutral molecule contained in the crystalline salt **2** exhibits a stabilizing effect on the corresponding ion pair. This may offer a new way to stabilize energetic salts by designing co-crystals. In addition, thermal computations indicate that the performance potentials of **2** and **10** are better than the conventional explosives, TNT and Tetryl, which suggests their potential as eco-friendly oxidizers.

## Experimental Section

***Caution:*** Although none of the compounds described herein has exploded or detonated in the course of this research, these materials should be handled with extreme care using the best safety practices because their shock and impact sensitivities have not been determined. All nitroform salts should be stored at lower temperatures (–18 °C) to preclude decomposition.

**General Methods:** $^1$H and $^{13}$C NMR spectra were recorded with a 300-MHz NMR spectrometer operating at 300.13, and 75.48 MHz, respectively, using $CD_3CN$ as solvent unless otherwise indicated. Chemical shifts were reported relative to $Me_4Si$. The melting and decomposition points were recorded with a differential scanning calorimeter (DSC) and a thermogravimetric analyzer (TGA) at a scan rate of 10 °C/min, respectively. IR spectra were recorded using KBr pellets for solids. Densities were measured at room temperature using a Micromeritics Accupyc 1330 gas pycnometer. Elemental analyses were obtained by with a CE-440 elemental analyzer (EAI Exeter Analytical).

**Computational Details:** Computations were performed with the Gaussian03 (Revision D.01) suite of programs.[12] The geometric optimization of the structures based on single-crystal structures, where available, and frequency analyses are carried out using B3-LYP functional with 6-31+G** basis set,[13] and single energy points were calculated at the $MP_2$(full)/6-311++G** level. All of the optimized structures were characterized to be true local energy minima on the potential energy surface without imaginary frequencies.

On the basis of Born–Haber energy cycles, the heat of formation of an ionic salt can be simplified by the formula:

$\Delta H_f°$(ionic salt, 298 K) = $\Delta H_f°$(cation, 298 K) + $\Delta H_f°$(anion, 298 K) – $\Delta H_L$

where $\Delta H_L$ is the lattice energy of the ionic salts which could be predicted by the formula suggested by Jenkins et al.[14] as:

$\Delta H_L = U_{POT} + [p(nM/2 - 2) + q(nX/2 - 2)]RT$ (**A**)

where $n_M$ and $n_X$ depend on the nature of the ions $M_p^+$ and $Xq^-$, respectively, and are equal to **3** for monatomic ions, **5** for linear polyatomic ions, and **6** for nonlinear polyatomic ions. The equation for lattice potential energy $U_{POT}$ (Equation **B**) has the form:

$U_{POT}$/kJ mol$^{-1}$ = $\gamma$ $(\rho_m/M_m)^{1/3}$ + $\delta$ (**B**)

where $\rho_m$/g cm$^{-3}$ is the density, $M_m$ is the chemical formula mass of the ionic material, values for $g$ and the coefficients $\gamma$/kJ mol$^{-1}$ cm and $\delta$/kJ mol$^{-1}$ were taken from ref.[14]

The remaining task is to determine the heat of formation of the cation, which is computed using the method of isodesmic reactions.[2c] The enthalpy of reaction ($\Delta H_r°_{298}$) is obtained by combining the MP2(full)/6-311++G** energy difference for the reaction, the scaled zero point energies, and other thermal factors. Thus, the heat of formation of the cation being investigated can be readily extracted.

With the value of the heats of formation and density of energetic salts, the expected detonation pressures ($P$) and detonation velocities ($D$) were calculated based on the traditional Chapman–Jouget thermodynamic detonation theory.[11a]

**X-ray Analyses:** Crystals of compound **2** (**10**) were removed from the flask, a suitable crystal selected, attached to a glass fiber, and data were collected at 90(2) K with a Bruker/Siemens SMART APEX instrument (Mo-$K_\alpha$ radiation, $\lambda$ = 0.71073 Å) equipped with a Cryocool NeverIce low-temperature device. Data were measured using omega scans 0.3° (0.5°) per frame for 5 (20) s, and a full sphere of data was collected. A total of 2400 (1065) frames were collected with a final resolution of 0.83 Å. Cell parameters were retrieved using SMART[15] (APEX2)[16] software for **2** (**10**), and refined using SAINTPlus[17] on all observed reflections. Data reduction and correction for Lp and decay were performed using SAINTPlus software. Absorption corrections were applied using SADABS.[18] The structures were solved by direct methods and refined by least-squares method on $F^2$ using the SHELXTL program package.[19] Structure were solved in the space group $P\bar{1}$ and $P2_1/c$ for compounds **2** and **10**, respectively, by analysis of systematic absences. All non-hydrogen atoms were refined anisotropically. Hydrogen atoms were located and refined independently for the amino groups in **2**. No decomposition was observed during data collection. CCDC-628775 and -628776 contain the supplementary crystallographic data for **2** and **10**. These data can be obtained free of charge from The Cambridge Crystallographic Data Centre via www.ccdc.cam.ac.uk/data_request/cif.

**Synthesis of Nitroform:** The synthesis of nitroform is carried out as described in the literature (Supporting Information).[5]

**General Procedure for the Preparation of Nitroformate Salts. 1-Methylimidazolium Nitroformate (1):** A solution of nitroform (151 mg, 1.0 mmol) in methanol (2 mL) was slowly added to a solution of 1-methylimidazole (82 mg, 1.0 mmol) in methanol (2 mL) at 25 °C with stirring. After stirring for 3 h at room temperature,

 © 2007 Wiley-VCH Verlag GmbH & Co. KGaA, Weinheim 

the solvent was removed in vacuo to leave the desired product **1** (233 mg, 96%) as a yellow crystalline solid. IR (KBr): $\tilde{\nu}$ = 3415, 3150, 1584, 1535, 1484, 1277, 1153, 805 $cm^{-1}$. $^1H$ NMR: $\delta$ = 8.48 (s, 1 H), 7.39 (s, 2 H), 3.88 (s, 3 H) ppm. $^{13}C$ NMR: $\delta$ = 136.2, 124.2, 120.5, 36.6 ppm. $C_5H_7N_5O_6$ (233.14): calcd. C 25.76, H 3.03, N 30.04; found C 25.81, H 2.67, N 30.05.

**4-Amino-1,2,4-triazolium Nitroformate (2):** IR (KBr): $\tilde{\nu}$ = 3418, 3131, 1628, 1532, 1486, 1272, 1155, 617 $cm^{-1}$. $^1H$ NMR: $\delta$ = 8.68 (s, 4 H), 7.42 (br., 4 H) ppm. $^{13}C$ NMR: $\delta$ = 145.3, 151.2 ppm. $C_5H_9N_{11}O_6$ (319.07): calcd. C 18.81, H 2.84, N 48.27; found C 18.88, H 2.71, N 48.32.

**1,2,4-Triazolium Nitroformate (3):** IR (KBr): $\tilde{\nu}$ = 3424, 3130, 2793, 1572, 1536, 1404, 1335, 1159, 825 $cm^{-1}$. $^1H$ NMR: $\delta$ = 8.92 (br., 2 H) ppm. $^{13}C$ NMR: $\delta$ = 143.3, 39.8 ppm. $C_3H_4N_6O_6$ (220.11): calcd. C 16.37, H 1.83, N 38.18; found C 16.55, H 2.21, N 38.53.

**Guanidinium Nitroformate (4):** IR (KBr): $\tilde{\nu}$ = 3398, 1642, 1533, 1495, 1409, 1283, 868, 787 $cm^{-1}$. $^1H$ NMR: $\delta$ = 6.0 (br., 6 H) ppm. $C_2H_6N_6O_6$ (210.11): calcd. C 11.43, H 2.88, N 40.00; found C 11.49, H 2.72, N 39.27.

**3-Amino-1,2,4-triazolium Nitroformate (5):** IR (KBr): $\tilde{\nu}$ = 3360, 3152, 2765, 1686, 1561, 1482, 1284, 1153, 951, 785 $cm^{-1}$. $^1H$ NMR: $\delta$ = 10.12 (br., 4 H), 8.66 (s, 1 H) ppm. $^{13}C$ NMR: $\delta$ = 143.3 ppm. $C_3H_5N_7O_6$ (235.12): calcd. C 15.33, H 2.14, N 41.70; found C 15.44, H 1.94, N 41.72.

**Aminoguanidinium Nitroformate (6):** IR (KBr): $\tilde{\nu}$ = 3406, 3277, 3168, 1678, 1554, 1484, 1315, 1157, 787 $cm^{-1}$. $^1H$ NMR: $\delta$ = 7.41 (br., 1 H), 6.51 (br., 2 H), 5.92 (br., 2 H), 4.14 (br., 2 H) ppm. $C_2H_7N_7O_6$ (225.12): calcd. C 10.67, H 3.13, N 43.55; found C 10.80, H 2.87, N 43.01.

**Imidizolium Nitroformate (7):** IR (KBr): $\tilde{\nu}$ = 3398, 3150, 2983, 1587, 1537, 1484, 1370, 1285, 1157, 829 $cm^{-1}$. $^1H$ NMR: $\delta$ = 10.75 (br., 2 H), 8.57 (s, 1 H), 7.45 (s, 2 H) ppm. $^{13}C$ NMR: $\delta$ = 135.0, 120.2 ppm. $C_4H_5N_5O_6$ (219.11): calcd. C 21.93, H 2.30, N 31.96; found C 22.27, H 2.39, N 31.32.

**Pyrazolium Nitroformate (8):** IR (KBr): $\tilde{\nu}$ = 3131, 3061, 2839, 1763, 1561, 1391, 1245, 1040, 825 $cm^{-1}$. $^1H$ NMR: $\delta$ = 8.00 (s, 2 H), 6.65 (s, 1 H) ppm. $^{13}C$ NMR: $\delta$ = 135.0, 107.7 ppm. $C_4H_5N_5O_6$ (219.11): calcd. C 21.93, H 2.30, N 31.96; found C 21.88, H 2.11, N 31.83.

**2-Methylimidazolium Nitroformate (9):** IR (KBr): $\tilde{\nu}$ = 3403, 3121, 2993, 2721, 1625, 1537, 1483, 1269, 1157, 756 $cm^{-1}$. $^1H$ NMR: $\delta$ = 7.28 (s, 2 H), 2.61 (s, 3 H) ppm. $^{13}C$ NMR: $\delta$ = 119.4, 11.7 ppm. $C_5H_7N_5O_6$ (233.14): calcd. C 25.76, H 3.03, N 30.04; found C 25.54, H 2.70, N 29.86.

**3,6-Diguanidino-1,2,4,5-tetrazinium Nitroformate (10):** IR (KBr): $\tilde{\nu}$ = 3400, 3345, 3281, 2945, 2872, 1703, 1592, 1417, 947 $cm^{-1}$. $^1H$ NMR: $\delta$ = 7.79 (br., 10 H) ppm. $^{13}C$ NMR: $\delta$ = 159.6, 155.9 ppm. $C_6H_{10}N_{16}O_{12}$ (498.24): calcd. C 14.46, H 2.02, N 44.98; found C 14.26, H 2.18, N 45.64.

***N*-Guanylurea Nitroformate (11):** IR (KBr): $\tilde{\nu}$ = 3400, 3345, 3281, 2945, 2872, 1703, 1592, 1417, 947 $cm^{-1}$. $^1H$ NMR: $\delta$ = 7.29 (br., 5 H), 5.90 (br., 2 H) ppm. $^{13}C$ NMR: $\delta$ = 156.7, 154.7 ppm. $C_3H_7N_7O_7$ (253.13): calcd. C 14.23, H 2.79, N 38.73; found C 14.22, H 2.59, N 37.94.

**Supporting Information** (see also the footnote on the first page of this article): Synthesis of nitroform.

## Acknowledgments

We gratefully acknowledge the support of Air Force Office of Scientific Research (AFOSR) (F49620-03-1-0209), National Science Foundation (NSF) (CHE0315275), and Office of Naval Research (ONR) (N00014-06-1-1032). We appreciate the work of Drs. Gary Knerr and Alex Blumenfeld for mass spectra and NMR analyses, respectively. The Bruker (Siemens) SMART APEX diffraction facility was established at the University of Idaho with the assistance of the NSF-EPSCoR program and the M. J. Murdock Charitable Trust, Vancouver, WA.

[1] a) K. E. Gutowski, J. D. Holbrey, R. D. Rogers, D. A. Dixon, *J. Phys. Chem. B* **2005**, *109*, 23196–23208; b) R. P. Singh, R. D. Verma, D. T. Meshri, J. M. Shreeve, *Angew. Chem. Int. Ed.* **2006**, *45*, 3584–3601; c) G. Drake, T. Hawkins, A. Brand, L. Hall, V. A. Mckay, I. Ismail, *Propellants Explos. Pyrotech.* **2003**, *28*, 174–180.

[2] a) H. Gao, R. Wang, B. Twamley, M. A. Hiskey, J. M. Shreeve, *Chem. Commun.* **2006**, 4007–4009; b) H. Xue, Y. Gao, B. Twamley, J. M. Shreeve, *Chem. Mater.* **2005**, *17*, 191–198; c) M. W. Schmidt, M. S. Gordon, J. A. Boatz, *J. Phys. Chem. A* **2005**, *109*, 7285–7295; d) H. Xue, Y. Gao, B. Twamley, J. M. Shreeve, *J. Mater. Chem.* **2005**, *15*, 3459–3465.

[3] a) T. S. Konkova, Y. N. Matyushin, *Russ. Chem. Bull.* **1998**, *47*, 2371–2374; b) E. Schmidt, H. Fischer, *Ber. Dtsch. Chem. Ges.* **1920**, *53*, 1529–1537; c) A. M. Krishnan, P. Sjoberg, P. Politzer, J. H. Boyer, *J. Chem. Soc., Perkin Trans. 2* **1989**, 1237–1242; d) V. I. Slovetskii, V. M. Brusnikina, L. A. Khmel′nitskii, O. V. Lebedev, S. S. Novikov, *Khim. Geterotsikl. Soedin.* **1996**, *3*, 448–452; e) M. Goebel, T. M. Klapötke, P. Mayer, *Z. Anorg. Allg. Chem.* **2006**, *632*, 1043–1050; f) M. Goebel, T. M. Klapötke, P. C. Thumbs, *New Trends in Research of Energetic Materials, Proceedings of the Seminar, 9th,* Pardubice, Czech Republic, Apr. 19–21, **2006** (**2006**), (Pt. 1), 127–134.

[4] a) H. F. R. Schöyer, A. J. Schnorhk, P. A. O. G. Korting, P. J. Van Lit, J. M. Mul, G. M. H. J. L. Gadiot, J. J. Meulenbrugge, *J. Propul. Power* **1995**, *11*, 856–869; b) H. F. R. Schöyer, *J. Propul. Power* **2002**, *18*, 131–137; c) H. S. Jadhav, M. B. Talawar, D. D. Dhavale, S. N. Asthana, V. N. Krishnamurthy, *Indian J. Chem. Technol.* **2005**, *12*, 187–192; d) C. Laurence, A. Dan, R. Sylvie, K. Charles, *Appl. Catal., B* **2006**, *62*, 217–225; e) P. S. Dendage, D. B. Sarwade, A. B. Mandale, S. N. Asthana, *J. Energ. Mater.* **2003**, *21*, 167–183.

[5] a) P. Liang, *Org. Synth.* **1955**, *3*, 803–809; b) F. G. Borgardt, A. K. Seller, P. J. Nobel, *Org. Chem.* **1966**, *31*, 2806–2811; c) H. Shechter, H. L. Cates, *J. Org. Chem.* **1961**, *26*, 51–53.

[6] a) K. V. Auwers, L. Harres, *Ber. Dtsch. Chem. Ges.* **1929**, *62*, 2296; b) A. Hantzsch, K. Rinckenberger, *Ber. Dtsch. Chem. Ges.* **1899**, *32*, 628–641.

[7] a) N. V. Podberezskaya, N. V. Pervukhina, V. P. Doronina, *Zh. Strukt. Khim* **1991**, *32*, 34–39; b) C. Ye, J.-C. Xiao, B. Twamley, J. M. Shreeve, *Chem. Commun.* **2005**, 2750–2752.

[8] a) N. V. Grigor'eva, N. V. Margolis, I. N. Shokhor, V. V. Mel'nikov, *Zh. Strukt. Khim.* **1966**, *7*, 278–280; b) K. D. Scherfise, F. Weller, K. Dehnicke, *Z. Naturforsch., Teil B* **1985**, *40*, 906–912; c) B. Dickens, *J. Res. Natl. Bur. Stand.* **1970**, *A74*, 309–318; d) H. L. Ammon, C. S. Choi, A. Bashir-Hashemi, R. M. Moriarty, *Acta Crystallogr., Sect. C* **1989**, *45*, 319–321; e) N. I. Golovina, L. O. Atovmyan, *Zh. Strukt. Khim.* **1967**, *8*, 307–311; f) N. V. Grigor'eva, N. V. Margolis, I. N. Shokhor, I. V. Tselinskii, V. V. Mel'nikov, *Zh. Strukt. Khim.* **1968**, *9*, 550–552; g) H. L. Ammon, C. S. Choi, R. S. Damvarapu, S. Iyer, J. Alster, *Acta Crystallogr., Sect. C* **1990**, *46*, 295–298; h) H. Bock, T. Hauck, C. Naether, Z. Z. Havlas, *Naturforsch., Teil B* **1994**, *49*, 1012–1020.

[9] H. Östmark, U. Bemm, H. Bergman, A. Langlet, *Thermochim. Acta* **2002**, *384*, 253–259.

[10] a) P. Politzer, J. S. Murray, M. E. Grice, *Chem. Energ. Mater.*, Academic Press, San Diego, CA, **1991**, p. 77; b) R. Mayer, *Explosives*, VCH, Weinheim, W. Germany, **1987**, p. 243.

[11] a) L. E. Fried, K. R. Glaesemann, W. M. Howard, P. C. Souers, **2004**. *CHEETAH 4.0 User's Manual*, Lawrence Livermore

 © 2007 Wiley-VCH Verlag GmbH & Co. KGaA, Weinheim 

National Laboratory; b) J. P. Lu, *Evaluation of the Thermochemical Code – CHEETAH 2.0 for Modelling Explosives Performance*, DSTO-TR-1199, DSTO, Edinburgh, **2001**.
[12] M. J. Frisch, G. W. Trucks, H. B. Schlegel, G. E. Scuseria, M. A. Robb, J. R. Cheeseman, J. A. Montgomery Jr, T. Vreven, K. N. Kudin, J. C. Burant, J. M. Millam, S. S. Iyengar, J. Tomasi, V. Barone, B. Mennucci, M. Cossi, G. Scalmani, N. Rega, G. A. Petersson, H. Nakatsuji, M. Hada, M. Ehara, K. Toyota, R. Fukuda, J. Hasegawa, M. Ishida, T. Nakajima, Y. Honda, O. Kitao, H. Nakai, M. Klene, X. Li, J. E. Knox, H. P. Hratchian, J. B. Cross, V. Bakken, C. Adamo, J. Jaramillo, R. Gomperts, R. E. Stratmann, O. Yazyev, A. J. Austin, R. Cammi, C. Pomelli, J. W. Ochterski, P. Y. Ayala, K. Morokuma, G. A. Voth, P. Salvador, J. J. Dannenberg, V. G. Zakrzewski, S. Dapprich, A. D. Daniels, M. C. Strain, O. Farkas, D. K. Malick, A. D. Rabuck, K. Raghavachari, J. B. Foresman, J. V. Ortiz, Q. Cui, A. G. Baboul, S. Clifford, J. Cioslowski, B. B. Stefanov, G. Liu, A. Liashenko, P. Piskorz, I. Komaromi, R. L. Martin, D. J. Fox, T. Keith, M. A. Al-Laham, C. Y. Peng, A. Nanayakkara, M. Challacombe, P. M. W. Gill, B. Johnson, W. Chen, M. W. Wong, C. Gonzalez, J. A. Pople, *Gaussian 03*, Revision D.01, Gaussian, Inc., Wallingford CT, **2004**.
[13] R. G. Parr, W. Yang, *Density Functional Theory of Atoms and Molecules*, Oxford University Press, New York, **1989**.
[14] H. D. B. Jenkins, D. Tudeal, L. Glasser, *Inorg. Chem.* **2002**, *41*, 2364–2367.
[15] *SMART*, version 5.632, Bruker AXS, Madison, WI, **2005**.
[16] *APEX2*, version 2.1-RC12, Bruker AXS, Madison, WI, **2006**.
[17] *SAINTPlus*, version 7.23a, Data Reduction and Correction Program, Bruker AXS, Madison, WI, **2004**.
[18] *SADABS*, version 2004/1, an empirical absorption correction program, Bruker AXS Inc., Madison, WI, **2004**.
[19] G. M. Sheldrick, *SHELXTL*, version 6.14, Structure Determination Software Suite, Bruker AXS Inc., Madison, WI, **2004**.
Received: December 22, 2006
Published Online: March 23, 2007

 © 2007 Wiley-VCH Verlag GmbH & Co. KGaA, Weinheim 

DOI: 10.1002/ejic.200601247

# Mixed-Valent Linear Chain $Pt_2PdPt_2$ Complexes

Saiko Arai,[a] Masahiko Ochiai,[a] Koji Ishihara,*[a,b] and Kazuko Matsumoto*[a]

**Keywords:** Platinum / Palladium / Chain structures / Metal–metal interactions / Mixed-valent compounds

Pentanuclear linear-chain PtPd complexes $\{[Pt_2(NH_3)_2X_2(\mu\text{-pivalamidato})_2(CH_2COCH_3)]_2[PdX'_4]\}\cdot 2CH_3COCH_3$ (X = X′ = Cl (**1a**), X = Cl, X′ = Br (**1b**), X = Br, X′ = Cl (**1c**), X = X′ = Br (**1d**)) composed of a monomeric $Pd^{II}$ complex sandwiched by two amidato-bridged dimeric $Pt^{III}$ units were synthesized from the reaction between the acetonyl dinuclear $Pt^{III}$ complexes having equatorial halide ligands $[Pt_2(NH_3)_2X_2(\mu\text{-pivalamidato})_2(CH_2COCH_3)]X''$ (X = Cl (**2a**), Br (**2b**), X″ = $NO_3^-$, $CH_3C_6H_4SO_3^-$) and $K_2[PdX'_4]$ (X′ = Cl, Br). The X-ray crystallographic analysis of **1a**–**1d** shows that the complexes have metal–metal bonded linear $Pt_2PdPt_2$ structures. The pentanuclear PtPd complexes have either an arch backbone structure or a sigmoid backbone structure, depending on the solvent of crystallization. The UV/Vis/NIR spectra clearly show the existence of a rare charge-transfer band from Pd to Pt in the pentanuclear PtPd complexes.
(© Wiley-VCH Verlag GmbH & Co. KGaA, 69451 Weinheim, Germany, 2007)

## Introduction

Discrete metal chains composed of direct metal–metal interactions are of current interest from both theoretical and practical points of view.[1] One of the synthetic methods for this class of compounds is based on ligand-assisted metal–metal bond formation reactions by using polydentate ligands.[2,3] In this case, the number of the available coordination atoms of the ligand determines the length of the metal–metal chain. One of the representative cases is the family of metal string complexes supported by oligo-α-pyridylamido ligands.[2] A second approach involves the formation of metal–metal bonds by oxidation of $d^8$ square-planar complexes or by reduction of $d^7$ octahedral complexes, in which mixed-valent metal chain complexes are formed, such as platinum,[4–6] rhodium, and iridium blues.[7] The latter approach recently successfully extended the chain length to infinity, and allowed the isolation of the rare rhodium[8] and platinum one-dimensional mixed-valence compounds.[9,10] One-dimensional infinite platinum chain compounds,[11–13] such as Magnus' green salt[12] are another well known class of compounds, in which the metal–metal bond interactions rely upon self-stacking of square-planar complexes. Apart from these approaches, we previously reported pentanuclear Pt chain complexes $\{[Pt_2(NH_3)_2X_2(\mu\text{-pivalamidato})_2(CH_2COCH_3)]_2[PtX'_4]\}\cdot n CH_3COCH_3$ (X = X′ = Cl, $n$ = 2 (**3a**), X = Cl, X′ = Br, $n$ = 1 (**3b**), X = Br, X′ = Cl, $n$ = 2 (**3c**), X = X′ = Br, $n$ = 1 (**3d**))[14] having Pt–Pt···Pt···Pt–Pt structures with strong $Pt^{III}$···$Pt^{II}$ interactions between the $Pt^{III}$ dinuclear and $[PtX'_4]^{2-}$ units. The pentanuclear structures are maintained even in solution.

The number of $Pd^{III}$ complexes that have been isolated and characterized is very limited, compared to the number of the mixed-valence Pt(II,III) chain species such as platinum blues.[4–6] Although paddlewheel compounds are known for most of the transition elements, there are only two types of structurally characterized Pd compounds having $Pd^{III}_2$ cores.[15] Palladium hardly makes a $Pd^{III}$–$Pd^{III}$ σ bond based on the $d_{z^2}$–$d_{z^2}$ overlap; if any it would be hard to observe experimentally.[15c] Attempts to generate a seemingly less difficult heterodinuclear $Pt^{III}Pd^{III}$ system have so far failed; oxidation of the dinuclear $Pt^{II}Pd^{II}$ complex $[(X_2)Pt(1\text{-MeU})_2Pd(Y_2)]Z$ ($X_2$, $Y_2$ = $(NH_3)_2$, en, or bpy; Z = $(NO_3)_2$, $(ClO_4)_2$, or $SO_4$) resulted in cleavage of the dinuclear complex into mononuclear $Pt^{IV}$ and $Pd^{II}$ complexes.[16] The dinuclear $Pt^{II}Pd^{II}$ complexes with Pt→Pd dative bonds, *trans*-$[(RNH_2)_2Pt(amidato)_2PdCl]^+$ (R = H, $CH_3$) or *trans*-$[(RNH_2)_2Pt(amidato)_2Pd(NH_3)]^{2+}$ (R = H, $CH_3$), have been reported, in which the coordination planes of Pt and Pd are perpendicular to each other and Pd is coordinated by Pt.[17] Only two trinuclear $Pt^{II}Pd^{III}Pt^{II}$ complexes with charge transfer from Pt to Pd have been reported, in which Pt–Pd σ bonds by the $d_{z^2}$–$d_{z^2}$ overlap are involved.[18]

We report here the synthesis of the novel pentanuclear PtPd complexes $\{[Pt_2(NH_3)_2X_2(\mu\text{-pivalamidato})_2(CH_2COCH_3)]_2[PdX'_4]\}\cdot 2CH_3COCH_3$ (X = X′ = Cl (**1a**), X = Cl, X′ = Br (**1b**), X = Br, X′ = Cl (**1c**), X = X′ = Br (**1d**)) and $\{[Pt_2(NH_3)_2Cl_2(\mu\text{-pivalamidato})_2(CH_2COCH_3)]_2[PdCl_4]\}\cdot H_2O$ (**1a′**) having Pt–Pt–Pd–Pt–Pt structures with strong Pt–Pd interactions maintained by novel charge transfer from Pd to Pt (Scheme 1).

[a] Department of Chemistry, Advanced Research Center for Science and Engineering, Waseda University,
Okubo, Shinjuku-ku, Tokyo 169-8555, Japan
[b] Advanced Research Institute for Science and Engineering, Waseda University,
Okubo, Shinjuku-ku, Tokyo 169-8555, Japan
Supporting information for this article is available on the WWW under http://www.eurjic.org or from the author.

 © 2007 Wiley-VCH Verlag GmbH & Co. KGaA, Weinheim 

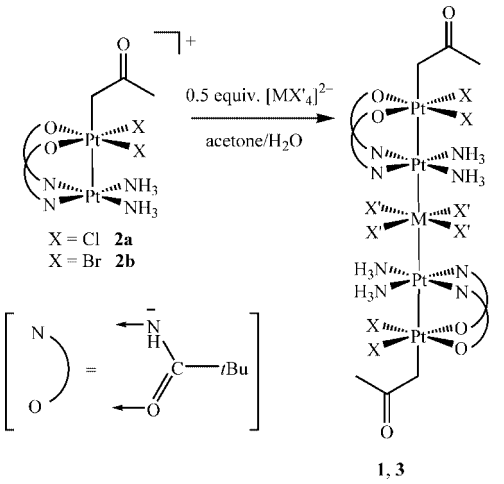


Scheme 1.

## Results and Discussion

### Synthesis and Characterization

The pivalamidato-bridged pentanuclear linear chain $Pt_2PdPt_2$ complexes **1a**–**1d** were synthesized in the same way as **3a**–**3d**[14a] from the reaction of 2 equiv. of **2a** or **2b** with 1 equiv. of $K_2[PdX'_4]$ (X′ = Cl, Br). The FAB-MS spectra of **1a**–**1d** showed the presence of molecular ions of **1a**–**1d**. Considering the fact that weak bonds such as ionic bonds are usually fragmented in FAB-MS spectra, the Pt···Pd interactions between the dinuclear units and the mononuclear unit seem to be substantially strong. The $^{195}Pt\{^1H\}$ NMR spectroscopic data of **1a**, **1d**, and related compounds including **3a** and **3d** are listed in Table 1. In Table 1, only one signal was observed for **1d**, and the satellite signals due to Pt–Pt coupling were not observed for **3a**, whereas all the signals were observed for **1a** and **3d**. The $^{195}Pt$ NMR spectra of **1a** and **3d** are shown in Figure 1. For **1a** and **3d**, the least-shielded signals at $\delta$ = 269 ppm (**1a**) and –230 ppm (**3d**) can be assigned to the $Pt(X_2O_2)$ atom (the elements in the parenthesis are coordination atoms), while the more- and most-shielded signals at $\delta$ = –2173 ppm (**1a**) and –2254 ppm (**3d**), and –2689 ppm (**3d**) can be assigned to the $Pt(N_4)$ and the $Pt(Br_4)$, according to the results of the $^{195}Pt$ NMR measurements for the related amidato-bridged $Pt^{III}$ dinuclear complexes.[14,19] In fact, the peaks at $\delta$ = –2173 ppm (**1a**) and –2254 ppm (**3d**), and –2689 ppm (**3d**) are broader than those at $\delta$ = 269 ppm (**1a**) and –230 ppm (**3d**), and would be caused by quadrupole moments of the N atom and Br atoms [the nuclear spin quantum numbers (*I*) of $^{14}N$ and $^{81}Br$ are 1 and 3/2, respectively] coordinated to the Pt atom. The assignment of the broad peaks at $\delta$ = –2173 ppm (**1a**) and –2254 ppm (**3d**) is also supported by the fact that the $Pt(N_4)$ peak is split and most broadened because of the Pt–Pd (**1a**) or Pt–Pt (**3d**) coupling in addition to the Pt–N coupling. In **1d**, the peak of the $Pt(N_4)$ was more broadened than the corresponding $Pt(N_4)$ peak in **3d** because of the coupling with the Pd atom ($^{105}Pd$, $I$ = 5/2).

Table 1. The $^{195}Pt$ NMR chemical shifts of the pentanuclear complexes and related compounds.

| Complexes[a] | Coordinated atoms | $\delta(^{195}Pt)$ [ppm] |
|---|---|---|
| **1a**[b] | $Cl_2O_2$ | 269 |
| | $N_4$ | –2173 |
| | $Cl_4$ | ND |
| **1d**[b] | $Br_2O_2$ | –231 |
| | $N_4$ | ND |
| | $Br_4$ | ND |
| **3a**[b] | $Cl_2O_2$ | 268 |
| | $N_4$ | –2208 |
| | $Cl_4$ | –1888 |
| **3d**[b] | $Br_2O_2$ | –230 |
| | $N_4$ | –2254 |
| | $Br_4$ | –2689 |
| **2a**[c] | $Cl_2O_2$ | 253 |
| | $N_4$ | –2080 |
| **2b**[c] | $Br_2O_2$ | –241 |
| | $N_4$ | –2122 |
| $K_2[Pt^{II}Cl_4]$[d] | $Cl_4$ | –1623 |
| $K_2[Pt^{II}Br_4]$[d] | $Br_4$ | –2672 |

[a] PVM: $(CH_3)_3CCONH$; X′′′ = $p$-$CH_3C_6H_4SO_3^-$, $NO_3^-$. [b] Measured in $[D_6]$acetone/$D_2O$ (9:1), and locked with $D_2O$ in an inner tube. [c] Measured in $[D_6]$acetone, and locked with $D_2O$ in an inner tube. [d] Measured in $D_2O$.

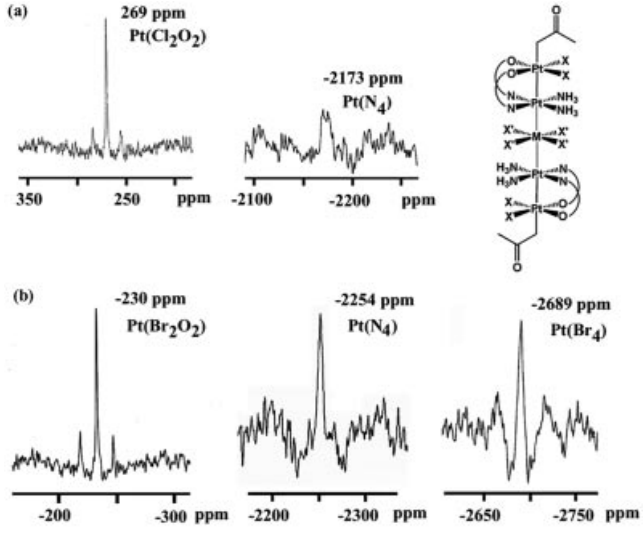


Figure 1. The $^{195}Pt$ NMR spectra of the pentanuclear PtPd complex (**1a**) and the pentanuclear Pt complex (**3d**): (a) $\{[Pt_2(NH_3)_2Cl_2(\mu\text{-pivalamidato})_2(CH_2COCH_3)]_2[PdCl_4]\}\cdot 2CH_3COCH_3$ (**1a**), (b) $\{[Pt_2(NH_3)_2Br_2(\mu\text{-pivalamidato})_2(CH_2COCH_3)]_2[PdBr_4]\}\cdot 2CH_3COCH_3$ (**3d**).

The broadenings caused by the couplings suggest that the $Pt_2MPt_2$ (M = Pt, Pd) backbones are retained even in solution. The UV/Vis/NIR spectra also showed the formation of the $Pt_2PdPt_2$ structures in the reaction solutions (see below).

Gradual evaporation of acetone from the reaction solution of **1a** gave two types of complexes from the same reaction solution, one with the arch structure (**1a**) and another

 © 2007 Wiley-VCH Verlag GmbH & Co. KGaA, Weinheim 

with the sigmoid structure (**1a′**). Crystallization of **1b** gave only one product as orange microcrystals because **1b** was quickly evaporated to avoid decomposition to black precipitate. The FAB-MS spectrum of the orange microcrystals showed the presence of molecular ions, and the elemental analysis approximately corresponded to **1b** with two molecules of acetone solvent. Crystallizations of **1c** and **1d** were carried out similarly to **1a**, however, **1c** and **1d** gave complexes of the arch structure and the sigmoid structure, respectively. In the case of **1d**, black precipitate was also obtained.

### Crystal Structures

The X-ray structures of **1a** and **1a′** are shown in Figure 2. The structural parameters of **1a**, **1a′**, **1c**, **1d**, and **4b** are listed in Table 2. We have already reported that the equatorial halide ligands in the dimer units of **3a**–**3d** polarize the $R–Pt^{III}–Pt^{III}$ (R is acetonyl) in the amidato-bridged dimer approximately to $R–Pt^{IV}–Pt^{II}$ and induce the electron transfer from the monomer unit to the dimer units having the axial acetonyl ligands to stabilize the Pt–Pt bonds between the dimer and monomer units.[14,20] The same polarization of the Pt–Pt bonds in the dimer units of **1a**, **1a′**, **1c**, and **1d** is considered to work similarly in the pentanuclear structures of **1a**, **1a′**, **1c**, and **1d**. Such polarization of the Pt–Pt bonds in the dimer units is proved by the $^{195}Pt$ NMR spectra of both PtPd and PtPt complexes.

Two types of PtPd backbones, the arch structure (**1a**) and the sigmoid structure (**1a′**), were obtained from the same mother liquor as mentioned above. We previously reported that **3a** also had both arch and sigmoid backbones,[14a] but they were obtained from different mother liquors. In the present case, **1a**, which has two acetone molecules of crystallization, is formed preferentially from the mother liquor when acetone is moderately evaporated, while **1a′** is preferentially formed when the evaporation of acetone is either depressed or very rapid. In the crystals of **1a** two molecules of the arch PtPd complex exist facing each other probably by hydrophobic interaction. In the crystals of **1a** the pentanuclear $Pt_4Pd$ molecules are regularly arranged by both intermolecular hydrophobic and hydrophilic interactions. As will be mentioned later, once-separated and redissolved solutions of **1a** and **1a′** showed the same spectral and chemical behavior. So the formation of **1a** and **1a′** would be explained as follows. The symmetrical sigmoid structure of **1a′** would be energetically favored and exist predominantly in the acetone-rich aqueous solution, because **1a′** would be favorably solvated by the moderately polar solvent, acetone in acetone-rich aqueous solution. So **1a′** crystallizes out by itself when the evaporation of acetone does not occur or occurs rapidly. On the other hand, in view of the fact that solubilities of **1a** and **1a′** into water are very low, **1a′** cannot gain such solvation energy in acetone-poor aqueous solution, so that **1a′** transforms into **1a** to gain stabilization energy from intermolecular interaction. Thus, when acetone evaporates gradually to make

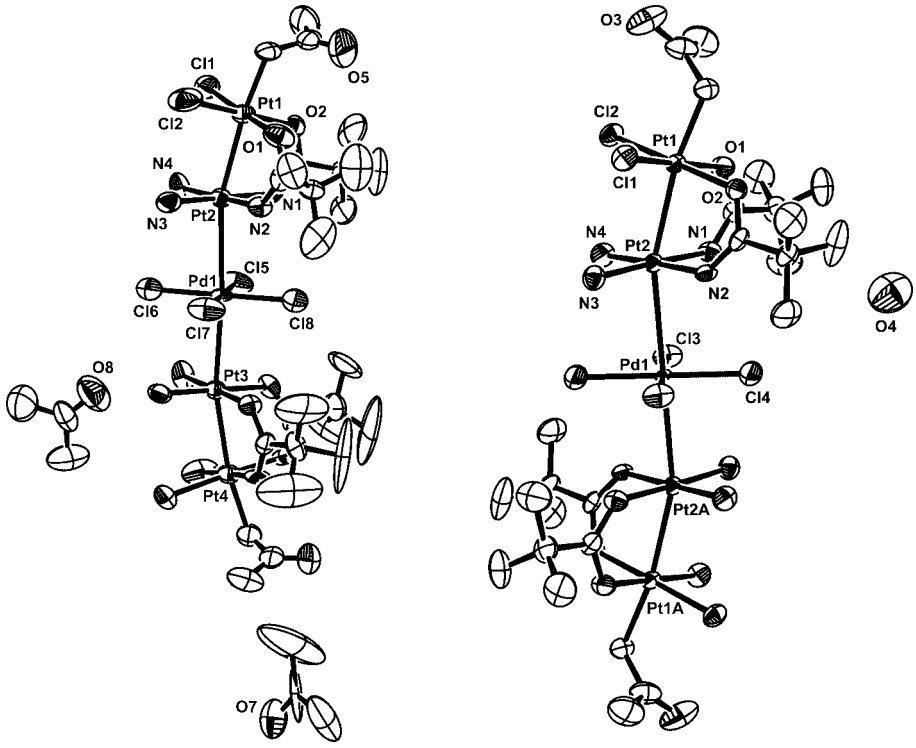


Figure 2. Crystal structures of the arch PtPd backbone complex (**1a**) and the sigmoid PtPd backbone complex (**1a′**): (a) $\{[Pt_2(NH_3)_2Cl_2(\mu\text{-pivalamidato})_2(CH_2COCH_3)]_2[PdCl_4]\}\cdot 2CH_3COCH_3$ (**1a**), (b) $\{[Pt_2(NH_3)_2Cl_2(\mu\text{-pivalamidato})_2(CH_2COCH_3)]_2[PdCl_4]\}\cdot H_2O$ (**1a′**). H atoms are omitted for clarity.

 © 2007 Wiley-VCH Verlag GmbH & Co. KGaA, Weinheim 

Table 2. Selected structural parameters of **1a**, **1a′**, **1c**, **1d**, and **4b**.[a]

| | **1a** | **1a′** | **1c** | **1d** | **4b** |
|---|---|---|---|---|---|
| Bond lengths [Å] | | | | | |
| Pt1–Pt2 | 2.6895(19) | 2.6924(11) | 2.7188(19) | 2.7100(9) | 2.7182(10) |
| Pt2–$M_{monomer}$ | 3.030(2) | 3.0319(14) | 3.061(3) | 3.1424(7) | 3.3818(10) |
| Pt1–X1 | 2.280(7) | 2.292(2) | 2.413(3) | 2.410(2) | 2.4180(19) |
| Pt1–X2 | 2.270(8) | 2.299(3) | 2.423(3) | 2.4113(17) | 2.4034(19) |
| Pt1–$C_{axial}$ | 2.08(2) | 2.092(9) | 2.10(2) | 2.089(12) | 2.083(15) |
| $M_{monomer}$–$L_{av}$[b] | 2.291(7) | 2.312(3) | 2.325(6) | 2.4458(18) | 2.072(14) |
| Bond angles [°] | | | | | |
| Pt1–Pt2–$M_{monomer}$ | 164.53(5) | 162.724(17) | 165.42(5) | 162.79(2) | 164.99(3) |
| Form[c] | A | S | A | S | A |

[a] The parameters for Pt4 and Pt5 are close to those of Pt1 and Pt2, and therefore are omitted. [b] L = Cl (**1a**, **1a′**, and **1c**), Br (**1d**), $NO_2$ (**4b**). [c] The Pt backbone: arch (A), sigmoid (S).

the acetone-rich aqueous solution into an acetone-poor aqueous solution, **1a** comes out.

In the previous paper, it was concluded that the charges of the Pt atoms in **3a**–**3d** are not delocalized as in the platinum blues[4–6] but are localized approximately to $Pt^{III}_2Pt^{II}Pt^{III}_2$. The distances of $Pt(N_4)$–$Pt(X_4)$ [3.0054(11)–3.1109(15) Å] in **3a**–**3d** are significantly shorter than the $Pt(N_4)$–$Pt(Cl_4)$ distance (3.24 Å)[9] in Magnus' green salt, so the interactions between $Pt(N_4)$ and $Pt(X_4)$ are stronger in **3a**–**3d**, though the distances are slightly longer than a typical Pt–Pt single bond. However, it was found in the present study that the charges of the Pt atoms in **1a**, **1a′**, **1c**, **1d**, **4b**, and **3a**–**3d** are much more delocalized through the Pt backbones, as shown by the UV/Vis/NIR spectra (see below).

The X-ray structure of $[Pt_2(NH_3)_2Br_2(\mu\text{-pivalamidato})_2(CH_2COCH_3)]_2[Pt(NO_2)_4]$ (**4b**) is shown in Figure S3 (Supporting Information). The structural parameters of **4b** are listed in Table 2. The distances of $Pt(N_4)$–$Pt(X_4)$ in **4b** are too long to be a significant Pt–Pt interaction, so **4b** would not have a Pt–Pt bond between the monomer unit and the dimer units (see below).

## Observation of Charge Transfers with UV/Vis/NIR Measurements

Long-wavelength absorption bands are known for the mixed-valence species such as tetranuclear platinum blues ($\lambda_{max}$ = about 500 nm and 680–750 nm)[5] and the octanuclear platinum blue ($\lambda_{max}$ = 540 nm and 1140 nm).[6] In these platinum blues, the latter bands are assigned to intervalence excitation from the inner Pt–Pt σ orbital to the inner Pt–Pt σ* orbital.[5c,6c] The present pentanuclear $Pt_4Pd$ complexes **1a**–**1d** also have the intervalence charge transfer (IVCT) bands, which are similar to those of **3a**–**3d** (Table 3).

The absorption spectra of **2a** and $K_2[PdCl_4]$ are shown in Figure 3. The broad band ($\lambda_{max}$ = 423 nm) in the $K_2[PdCl_4]$ spectrum is assigned to Cl → Pd LMCT transitions.[21] Complex **2a** has two strong absorption bands at $\lambda_{max}$ = 325 and 434 nm. The former band is assigned to Pt → Pt MMCT transitions as judged from the comparison with other amidato-bridged $Pt^{III}$ dinuclear complexes,[22] and the latter is assigned to Cl → Pt LMCT transitions. Obviously, there is no absorption band above 650 nm in the spectra. Figure 4 shows the time course of the UV/Vis/NIR spectral change during the reaction between **2a** and $K_2[PdCl_4]$ in aqueous acetone solution. The spectral change shows the process of **1a** formation. Little occurred until about 7 h after mixing, when the reaction started with a gradual rise of the IVCT absorption band at $\lambda_{max}$ = 735 nm, and was complete after about 10 h. This absorption band was also observed when the crystals of **1a** or **1a′** were dissolved into the aqueous acetone solvent, and both solutions of **1a** and **1a′** showed an identical spectrum.

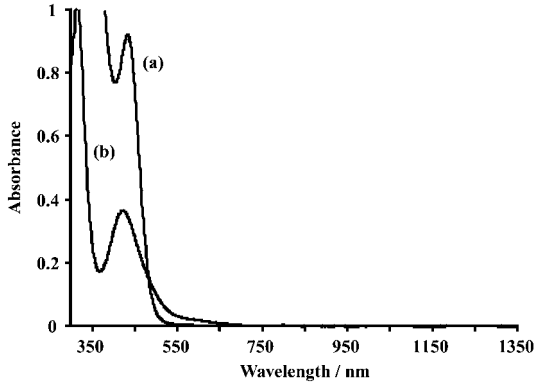


Figure 3. The UV/Vis/NIR spectra of **2a** and $K_2[PdCl_4]$: (a) acetone/water (9:1) solution of **2a** ($4.5 \times 10^{-4}$ M), (b) aqueous solution of $K_2[PdCl_4]$ ($2.5 \times 10^{-3}$ M).

Table 3. Absorption bands of **1a**–**1d** and **3a**–**3d** at various conditions.[a]

| | **1a**, **1a′** | **1b** | **1c** | **1d** | **3a** | **3b** | **3c** | **3d** |
|---|---|---|---|---|---|---|---|---|
| Solution | 735 | 763 | 724 | 808, 1014 | 770 | 810 | 792 | 835 |
| Crystal (arch) | 780 | | | 801 | 847 | | 801 | 825 |
| Crystal (sigmoid) | 808 | | | | | 844 | | |

[a] All values are displayed as $\lambda_{max}$ (nm).

 © 2007 Wiley-VCH Verlag GmbH & Co. KGaA, Weinheim 

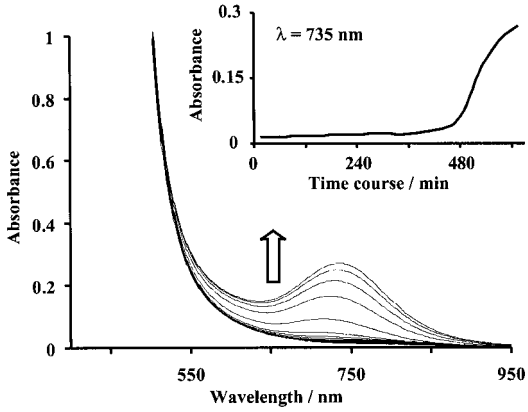


Figure 4. The time-course UV/Vis spectra for the pentanuclear PtPd backbone formation of **1a**. Spectra were recorded every 30 min after mixing solutions (a) and (b) in a quartz cell with 5-mm pathlength at room temperature. (a) 1.8 mL of the acetone solution of **2a** ($1.0 \times 10^{-2}$ M), (b) 0.2 mL of the aqueous solution of $K_2[PdCl_4]$ ($4.5 \times 10^{-2}$ M).

After reaction completion, the solution of **1a** was several-fold diluted and the spectrum was measured as shown in Figure 5. It is obvious that the original absorption bands at $\lambda_{max}$ = 382 and 735 nm remain up to about 30-fold dilution. It is noteworthy that the Pt–Pd σ bonds are kept even in such a dilute solution of $1.5 \times 10^{-4}$ M.

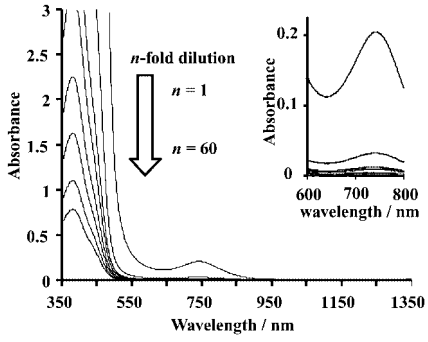


Figure 5. The UV/Vis/NIR spectra of **1a** with different concentrations. The acetone/water (9:1) solution of **1a** ($4.5 \times 10^{-3}$ M) was *n*-fold diluted with acetone/water (9:1) mixed solvent: $n$ = 1 (no dilution), 5, 10, 15, 20, 30, 40, and 60.

Similar measurements were carried out for **1b**–**1d** and **3a**–**3d**, and similar results were obtained (see Figures S4–S17, Supporting Information).

The diffuse reflectance spectra of the microcrystals of **1a** and **1a′** in the range of 200–2000 nm were measured, and are shown in Figure 6 along with the spectra of **2a** and $K_2[PtCl_4]$. Figure 6 clearly shows the IVCT absorption band at around 850 nm. Complexes **3a**–**3d** and **1b**–**1d** also show the IVCT bands, as shown in Figures S18 and S19.

Recently, sensitivity of diffuse reflectance spectroscopy has greatly improved. We used the Kubelka–Munk transformation,[23] which can convert a reflectance spectrum into a spectrum similar to a conventional absorption spectrum for solution samples, to compare the reflectance and absorption spectra to each other. According to the Kubelka–Munk theory,[23] the Kubelka–Munk function $F(R_\infty)$ is

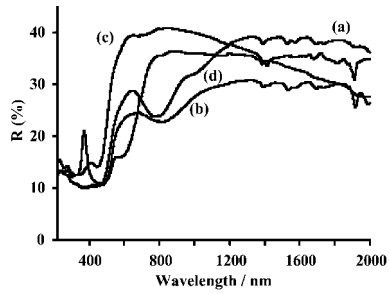


Figure 6. The diffuse reflectance spectra of **3a**, **2a**, $K_2PtCl_4$, and **1a**: (a) red-orange crystals of **3a**, (b) yellow powders of **2a**, (c) pale red powders of $K_2[PtCl_4]$, (d) yellow-orange crystals of **1a**.

given by the following equation for "infinitely thick" layers. In the equation $R_\infty$ is the absolute reflectance for an infinitely thick sample and $k$ is the absorption coefficient of the layer at a given wavelength,

$$F(R_\infty) = \frac{(1-R_\infty)^2}{2R_\infty} = \frac{k}{S} = \frac{\varepsilon c}{S}$$

$S$ is the scattering coefficient (depending on the size and form of the particles), $\varepsilon$ is the molar extinction coefficient of the analyte, and $c$ is the molar concentration. The converted Kubelka–Munk spectra and the absorption spectra of **1a** and **1a′** in solution are shown in Figure 7 (see also Figures S20, S21 in the Supporting Information).

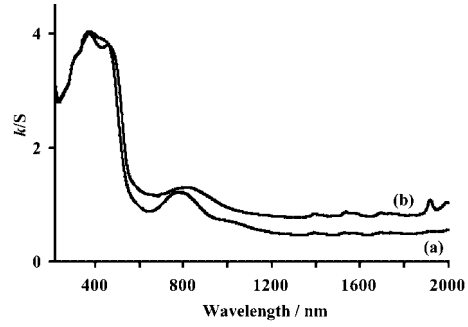


Figure 7. The transformed diffuse reflectance spectra of **1a** and **1a′**: (a) the arch PtPd backbone structure of **1a**, (b) the sigmoid PtPd backbone structure of **1a′**.

The band of the sigmoid backbone structure **1a′** in Figure 7 appeared at a longer wavelength than the arch one (**1a**), probably because the overlaps of $d_{z^2}$ orbitals of Pt and Pd in **1a′** are more linear and therefore more efficient than in **1a**. The close similarity of the spectra in Figures 7 and 5 supports the assumption that the pentanuclear $Pt_2MPt_2$ structure is maintained, even in dilute solution.

### Synthetic Elucidation of the Charge Transfer

In our previous article[14a] it was shown by the DFT calculation for **3a**–**3d** that the Pt···Pt interactions consist of the electron transfer from the monomer to the dimers. In the present study we prepared several pentanuclear $Pt_4Pd$ complexes with different mononuclear complexes to examine

 © 2007 Wiley-VCH Verlag GmbH & Co. KGaA, Weinheim 

whether the same electron transfer as in **3a**–**3d** exists in **1a**–**1d** or not.

According to the DFT calculation of **3a**–**3d**, the p orbitals of halide ligands of the monomer unit, especially $p_y$ orbital, donate electrons to the $Pt(X_4)$, and the $d_{z^2}$ orbital of the $Pt(X_4)$ donates electrons to the Pt dimeric units.[14a] The π donor ability of the halide ligands would play a role in the electron flows through the Pt chains.

At first, we tried to prepare the pentanuclear analogues by using $[M(dmit)_2]^{2-}$ (M = Pt, Pd; dmit = 2-thioxo-1,3-dithiole-4,5-dithiolate) as a monomer complex, in which dmit is a σ donor and weak π acceptor contrary to halide ligands.[24] The metal complexes with dmit ligand are used to prepare charge transfer (CT) complexes similar to the organic CT compounds, such as BEDT-TTF, a well-known molecular metal and molecular superconductor.[25] As a result, pentanuclear complexes could not be synthesized, because dmit is a weak π acceptor.

In another attempt, we used $[M(CN)_4]^{2-}$ (M = Pt, Pd) as a monomer complex. $CN^-$ is a weaker σ donor and weaker π acceptor than dmit.[24] The monomeric complex $K_2[Pt(CN)_4]$ is used to prepare the well-known Krogmann salt (KCP).[11] No pentanuclear complex was synthesized from the reaction of **2a** or **2b** with $[M(CN)_4]^{2-}$ (M = Pt, Pd), as shown in the VIS/NIR spectra (Figure S22).

Further, we used the $NO_2^-$ ligand, which is a weaker σ donor and weaker π acceptor than the $CN^-$ ligand.[24] Arch-like poor crystals of **4a** and needle crystals of **4b** were obtained. The former crystals would be $[Pt_2(NH_3)_2Cl_2(\mu\text{-pivalamidato})_2(CH_2COCH_3)]_2[Pt(NO_2)_4]$ (**4a**), though the structure could not be confirmed by X-ray analysis because of their poor crystallinity. The latter was $[Pt_2(NH_3)_2Br_2(\mu\text{-pivalamidato})_2(CH_2COCH_3)]_2[Pt(NO_2)_4]$ (**4b**), as confirmed by X-ray analysis. The distances of $Pt(N_4)$–$Pt(X_4)$ in **4b** are too long to be significant Pt–Pt interactions (about 3.4 Å), and correspondingly the reaction solutions did not show any absorption bands in the NIR region (Figures S23 and S24). The relative bulkiness of $NO_2^-$ compared with halide would not be responsible for the long $Pt(N_4)$–$Pt(X_4)$ distance, because the coordination planes of the dimer units and the monomer unit are rotated to each other in a staggered form, as in all other pentanuclear complexes, to avoid steric hindrance among the coordinating ligands (Figure 8). The FAB-MS spectrum of the saturated solution of **4b** shows the small peaks of its molecular ion.

Thus, it seems that $[PtX'_4]^{2-}$, as well as other mononuclear complexes with ligands having considerable π donor ability, can form pentanuclear complexes, and the electron flow from the $Pd(X_4)$ to the $Pt(N_4)$ creates a strong $Pt_{dimer}$–$Pd_{monomer}$ interaction in **1a**–**1d**, which is similar to the interaction of $Pt_{dimer}$–$Pt_{monomer}$ in **3a**–**3d**.

## Concluding Remarks

Novel linear pentanuclear complexes having $Pt_2PdPt_2$ chain backbones have been synthesized from the reaction between the amidato-bridged $Pt^{III}$ dimer complexes and $[PdX_4]^{2-}$. The pentanuclear complexes are composed of two units of the amidato-bridged $Pt^{III}$ dimer complexes sandwiching one unit of $[PdX_4]^{2-}$. The interactions between the $Pt^{III}$ dimer units and the $Pd^{II}$ monomer unit are strong enough to hold the linear pentanuclear chain structure retained in solution. The UV/Vis/NIR spectra clearly showed the charge transfer from the π donor chloride ligands of the Pd or Pt monomer unit to the $Pt^{III}$ dinuclear units with axial acetonyl ligands. Such charge transfer from Pd to Pt is quite rare, and in fact multinuclear complexes involving a Pd→Pt dative bond are not known. It is noteworthy that the Pd–Pt bond is maintained even in highly diluted solution.

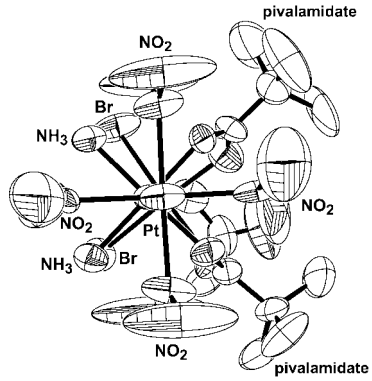


Figure 8. The structure of $[Pt_2(NH_3)_2Br_2(\mu\text{-pivalamidato})_2(CH_2COCH_3)]_2[Pt(NO_2)_4]$ (**4b**) viewed along the Pt axis from the monomer unit to the dimer unit.

## Experimental Section

**Materials and Methods:** All the reactions and manipulations were performed in air and in the dark. Solvents were used as received. All the reagents were purchased from commercial sources and used as received. The complexes, $[Pt_2(NH_3)_2X_2\{(CH_3)_3CCONH\}_2(CH_2COCH_3)]X''$ (X = Cl, X'' = $NO_3^-$ or $CH_3C_6H_4SO_3^-$ (**2a**), X = Br, X'' = $NO_3^-$ or $CH_3C_6H_4SO_3^-$ (**2b**)), $[\{Pt_2(NH_3)_2X_2\{(CH_3)_3CCONH\}_2(CH_2COCH_3)]_2\}][PtX'_4]\cdot n CH_3COCH_3$ (X = X' = Cl, *n* = 2 (**3a**), X = Cl, X' = Br, *n* = 1 (**3b**), X = Br, X' = Cl, *n* = 2 (**3c**), X = X' = Br, *n* = 1 (**3d**)), and $K_2[Pt(NO_2)_4]$, were prepared as reported.[14,26]

Elemental analyses were carried out on a Perkin–Elmer PE 2400II. The $^1H$ NMR spectra were recorded with a JEOL Lambda 270 spectrometer and a Bruker AVANCE 400 spectrometer operating at 270 MHz and 400 MHz for $^1H$, respectively. The $^{195}Pt\{^1H\}$ NMR spectra were recorded with a JEOL Lambda 500 spectrometer operating at 107.3 MHz for $^{195}Pt$. Chemical shifts are in $\delta$ unit (parts per million, ppm) referenced to $(CD_3)_2CO$ at $\delta$ = 2.04 ppm for $^1H$ and to $H_2[PtCl_6]$ (external reference, 0 ppm) or $K_2[PtCl_4]$ (external reference, –1622 ppm) for $^{195}Pt$. The mass spectra were measured with a JEOL JMS-SX102A spectrometer (FAB) and Thermo Quest LCQ-Deca spectrometer (ESI). The UV/Vis/NIR absorption spectra were measured with a JASCO Ubest V-570 with a cell holder for 5-mm pathlength. The diffuse reflectance spectra were measured with a JASCO Ubest V-570 with the custom-tailored integrating sphere unit.

 © 2007 Wiley-VCH Verlag GmbH & Co. KGaA, Weinheim 

**Preparation of {[$Pt_2(NH_3)_2Cl_2$(μ-pivalamidato)$_2(CH_2COCH_3)$]$_2$-[$PdCl_4$]}·$2CH_3COCH_3$ (1a):** A solution of **2a** (0.02 mmol) in acetone (2.0 mL) was added into an aqueous solution of $K_2[PdCl_4]$ (6.52 mg, 0.02 mmol, in 0.4 mL of water). The color of the reaction solution immediately changed from yellow to red. Yellow-orange crystals were obtained by slow evaporation of acetone in the dark. Yield: 8.49 mg, 45% (as crystals). $C_{32}H_{74}Cl_8N_8O_8PdPt_4$ (1869.3): C 20.56, H 3.99, N 5.99; found C 20.48, H 3.67, N 5.54. $^1$H NMR (400 MHz, [D$_6$]acetone, 23 °C): $\delta$ = 5.20 (s, 4 H, $CH_2$), 2.25 (s, 6 H, $CH_3$), 1.16 (s, 36 H, $CH_3$). FAB-MS (positive) 1753.1 (molecule + $H^+$).

**Preparation of {[$Pt_2(NH_3)_2Cl_2$(μ-pivalamidato)$_2(CH_2COCH_3)$]$_2$-[$PdCl_4$]}·$H_2O$ (1a′):** Dark orange crystals of **1a′** were obtained from the mother solution of **1a**. The evaporation conditions to sort the conformation of the PtPd backbones are shown in the text. Yield: 9.61 mg, 54% (as crystals). $C_{26}H_{64}Cl_8N_8O_7PdPt_4$ (1771.2): C 17.63, H 3.64, N 6.33; found C 17.65, H 3.43, N 6.05. $^1$H NMR (400 MHz, [D$_6$]acetone, 23 °C): $\delta$ = 5.20 [s, $^2J$(Pt,H) = 78.8 Hz, 4 H, $CH_2$], 2.26 (s, 6 H, $CH_3$), 1.17 (s, 36 H, $CH_3$) ppm.

**Preparation of {[$Pt_2(NH_3)_2Cl_2$(μ-pivalamidato)$_2(CH_2COCH_3)$]$_2$-[$PdBr_4$]}·$2CH_3COCH_3$ (1b):** The reaction solution of complex **1b** was prepared by the reaction of **2a** with $K_2[PdBr_4]$ (10.08 mg, 0.02 mmol). Orange microcrystals were obtained by speedy evaporation with a rotary evaporator to avoid decomposition. Yield 10.17 mg, 53%. $C_{32}H_{74}Br_4Cl_4N_8O_8PdPt_4$ (2047.1): C 18.77, H 3.64, N 5.47; found C 18.74, H 3.17, N 4.89. $^1$H NMR (400 MHz, [D$_6$]-acetone, 23 °C): $\delta$ = 5.22 (s, 4 H, $CH_2$), 2.26 (s, 6 H, $CH_3$), 1.21 (s, 36 H, $CH_3$). FAB-MS (positive) 1931.9 (molecule + $H^+$).

**Preparation of {[$Pt_2(NH_3)_2Br_2$(μ-pivalamidato)$_2(CH_2COCH_3)$]$_2$-[$PdCl_4$]}·$2CH_3COCH_3$ (1c):** Complex **1c** was prepared in the same way as **1a** by the reaction of **2b** with $K_2[PdCl_4]$ (6.52 mg, 0.02 mmol), and was obtained as yellow-orange crystals. Yield 8.88 mg, 43% (as crystals). $C_{32}H_{74}Br_4Cl_4N_8O_8PdPt_4$ (2047.1): C 18.77, H 3.64, N 5.47; found C 18.82, H 3.69, N 5.19. $^1$H NMR (400 MHz, [D$_6$]acetone, 23 °C): $\delta$ = 5.27 [s, $^2J$(Pt,H) = 84.0 Hz, 4 H, $CH_2$], 2.28 (s, 6 H, $CH_3$), 1.17 (s, 36 H, $CH_3$). FAB-MS (positive) 1932.0 (molecule + $H^+$).

**Preparation of {[$Pt_2(NH_3)_2Br_2$(μ-pivalamidato)$_2(CH_2COCH_3)$]$_2$-[$PdBr_4$]}·$2CH_3COCH_3$ (1d):** Complex **1d** was prepared in the same way as **1a** by the reaction of **2b** with $K_2[PdBr_4]$ (10.08 mg, 0.02 mmol), and was obtained as red-orange crystals. Yield 5.27 mg, 24% (as crystals). $C_{32}H_{74}Br_8N_8O_8PdPt_4$ (2224.9): C 17.27, H 3.35, N 5.04; found C 17.02, H 3.28, N 4.85. $^1$H NMR (400 MHz, [D$_6$]acetone, 23 °C): $\delta$ = 5.30 (s, 4 H, $CH_2$), 2.28 (s, 6 H, $CH_3$), 1.19 (s, 36 H, $CH_3$). FAB-MS (positive) 2109.3 (molecule + $H^+$).

**Preparation of [$Pt_2(NH_3)_2Cl_2$(μ-pivalamidato)$_2(CH_2COCH_3)$]$_2$-[$Pt(NO_2)_4$] (4a):** Complex **4a** was prepared in the same way as **1a** by the reaction of **2a** with $K_2[Pt(NO_2)_4]$ (2.29 mg, 0.005 mmol), and was obtained as poor yellow arch crystals. Yield 1.26 mg, 13% (as poor crystals).

**Preparation of {[$Pt_2(NH_3)_2Br_2$(μ-pivalamidato)$_2(CH_2COCH_3)$]$_2$-[$Pt(NO_2)_4$]}·$2CH_3COCH_3$ (4b):** Complex **4b** was prepared in the same way as **1a** by the reaction of **2b** with $K_2[Pt(NO_2)_4]$ (4.57 mg, 0.01 mmol). $C_{29}H_{68}Br_4N_{12}O_{15}Pt_5$ (2178.0): C 16.43, H 3.23, N 7.93; found C 16.79, H 3.13, N 7.19. FAB-MS (positive) 2062.8 (molecule + $H^+$).

**X-ray Structure Determination:** The data were collected on a Bruker SMART 1000 CCD diffractometer. The cell parameters were determined by using the programs SMART[27] and R-LATT.[28] Data reduction and integration were performed with the software package SAINT,[29] whereas the absorption collection was applied by using the program SADABS.[30] The structures were solved by full-matrix least-squares on $F^2$, and were refined with SHELXTL.[31] Hydrogen atoms were added in the idealized positions. Non-hydrogen atoms were refined with anisotropic temperature parameters. The crystal data are given in Table 4.

CCDC-631866 (for **1a**), -631865 (for **1a′**), -631867 (for **1c**), -631868 (for **1d**), and -631869 (for **4b**) contain the supplementary crystallographic data for this paper. These data can be obtained free of charge from The Cambridge Crystallographic Data Centre via www.ccdc.cam.ac.uk/data_request/cif.

**Supporting Information** (see also the footnote on the first page of this article): Full tables of the data collection parameters, anisotropic temperature factors, and bond lengths and angles for **1a**, **1a′**, **1c**, **1d**, and **4b**. Crystal structures of **1b**, **1c**, and **1d** are included. The UV/Vis/NIR spectra are also available.

## Acknowledgments

We wish to express our thanks for financial support from the 21COE "Practical Nano-Chemistry" project from MEXT, Japan and from a Waseda University Grant for Special Research Projects.

Table 4. Crystallographic data for **1a**, **1a′**, **1c**, **1d**, and **4b**.

| | **1a** | **1a′** | **1c** | **1d** | **4b** |
|---|---|---|---|---|---|
| Empirical formula | $C_{32}H_{74}Cl_8N_8O_8PdPt_4$ | $C_{26}H_{62}Cl_8N_8O_8PdPt_4$ | $C_{32}H_{74}Br_4Cl_4N_8O_8PdPt_4$ | $C_{32}H_{74}Br_8N_8O_8PdPt_4$ | $C_{32}H_{74}Br_8N_8O_8Pt_5$ |
| $M_r$ | 1869.35 | 1785.20 | 2047.19 | 2225.03 | 2178.12 |
| Crystal system | orthorhombic | monoclinic | orthorhombic | monoclinic | monoclinic |
| Space group | $Pca2_1$ | $P2_1/n$ | $Pca2_1$ | $P2_1/c$ | $P2_1/c$ |
| $a$ [Å] | 24.291(17) | 13.021(7) | 24.663(18) | 11.286(2) | 16.052(4) |
| $b$ [Å] | 15.362(11) | 12.158(6) | 15.531(12) | 23.260(5) | 15.546(4) |
| $c$ [Å] | 15.478(11) | 15.949(8) | 15.568(11) | 11.185(2) | 25.731(7) |
| $\beta$ [°] | | 97.731(9) | | 92.22(3) | 106.072(4) |
| $V$ [Å$^3$] | 5776(7) | 2502(2) | 5963(8) | 2934.1(10) | 6170(3) |
| $Z$ | 4 | 2 | 4 | 2 | 4 |
| $\rho_{calcd.}$ [g cm$^{-3}$] | 2.150 | 2.370 | 2.280 | 2.519 | 2.345 |
| $T$ [K] | 296(2) | 296(2) | 296(2) | 296(2) | 296(2) |
| $\mu$ Mo-$K_\alpha$ [mm$^{-1}$] | 10.375 | 11.970 | 12.551 | 15.296 | 13.949 |
| Gof | 1.042 | 1.044 | 1.023 | 0.995 | 0.950 |
| $R_1$, $wR_2$ | 0.0507, 0.0919 | 0.0292, 0.0729 | 0.0567, 0.1305 | 0.0540, 0.1143 | 0.0562, 0.1242 |

 © 2007 Wiley-VCH Verlag GmbH & Co. KGaA, Weinheim 

[1] a) J. K. Bera, K. R. Dunbar, *Angew. Chem. Int. Ed.* **2002**, *41*, 4453–4457 and references cited therein; b) P. Pyykkö, *Chem. Rev.* **1997**, *97*, 597–636; c) J. S. Miller (Ed.), *Extended Linear Chain Compounds*, Plenum Press, New York, **1982**, vols. 1–3.

[2] Selected references: a) J. F. Berry in *Multiple Bonds Between Metal Atoms*, 3rd ed. (Eds.: F. A. Cotton, C. A. Murillo, R. A. Walton), Springer Science and Business Media, Inc., New York, **2005**, pp. 669–706; b) I.-W. P. Chen, M.-D. Fu, W.-H. Tseng, J.-Y. Yu, S.-H. Wu, C.-J. Ku, C.-H. Chen, S.-M. Peng, *Angew. Chem. Int. Ed.* **2006**, *45*, 5814–5818.

[3] a) E. Goto, R. A. Begum, S. Zhan, T. Tanase, K. Tanigaki, K. Sakai, *Angew. Chem. Int. Ed.* **2004**, *43*, 5029–5032; b) T. Murahashi, M. Fujimoto, M. Oka, Y. Hashino, T. Uemura, Y. Tatsumi, Y. Nakao, A. Ikeda, S. Sakaki, H. Kurosawa, *Science* **2006**, *313*, 1104–1107; c) B. Osukui, W. S. Sheldrick, *Eur. J. Inorg. Chem.* **1999**, 1325–1333; d) B. Osukui, M. Mintert, W. S. Sheldrick, *Inorg. Chim. Acta* **1999**, *287*, 72–81; e) R. Usón, A. Laguna, M. Laguna, J. Jiménez, P. G. Jones, *Angew. Chem. Int. Ed. Engl.* **1991**, *30*, 198–199; f) A. Laguna, M. Laguna, J. Jiménez, F. J. Lahoz, E. Olmos, *Organometallics* **1994**, *13*, 253–257; g) T. Tanase, *Bull. Chem. Soc. Jpn.* **2002**, *75*, 1407–1422.

[4] a) S. J. Lippard, *Science* **1982**, *218*, 1075–1082; b) K. Matsumoto in *Cisplatin Chemistry and Biochemistry of a Leading Anticancer Drug* (Ed.: B. Lippert), Wiley-VCH, New York, **1999**, pp. 455–475; c) K. Matsumoto, K. Sakai, *Adv. Inorg. Chem.* **1999**, *49*, 375–427 and references cited therein.

[5] a) J. K. Barton, H. N. Rabinowitz, D. J. Szalda, S. J. Lippard, *J. Am. Chem. Soc.* **1977**, *99*, 2827–2829; b) J. K. Barton, C. Caravana, S. J. Lippard, *J. Am. Chem. Soc.* **1979**, *101*, 7269–7277; c) A. P. Ginsberg, T. V. O'Halloran, P. E. Fanwick, L. S. Hollis, S. J. Lippard, *J. Am. Chem. Soc.* **1984**, *106*, 5430–5439; d) T. V. O'Halloran, P. K. Mascharak, I. D. Williams, M. M. Roberts, S. J. Lippard, *Inorg. Chem.* **1987**, *26*, 1261–1270; e) K. Sakai, Y. Tanaka, Y. Tsuchiya, K. Hirata, T. Tsubomura, S. Iijima, A. Bhattacharjee, *J. Am. Chem. Soc.* **1998**, *120*, 8366–8379.

[6] a) K. Sakai, K. Matsumoto, *J. Am. Chem. Soc.* **1989**, *111*, 3074–3075; b) K. Sakai, K. Matsumoto, K. Nishio, *Chem. Lett.* **1991**, 1081–1084; c) K. Matsumoto, K. Sakai, K. Nishio, Y. Tokisue, R. Ito, T. Nishide, Y. Shichi, *J. Am. Chem. Soc.* **1992**, *114*, 8110–8118.

[7] a) C. Tejel, M. A. Ciriano, B. E. Villarroya, J. A. López, F. J. Lahoz, L. A. Oro, *Angew. Chem. Int. Ed.* **2003**, *42*, 529–532; b) C. Tejel, M. A. Ciriano, L. A. Oro, *Chem. Eur. J.* **1999**, *5*, 1131–1135 and references cited therein; c) B. E. Villarroya, C. Tejel, M.-M. Rohmer, L. A. Oro, M. A. Ciriano, M. Bénard, *Inorg. Chem.* **2005**, *44*, 6536–6544.

[8] a) G. M. Finniss, E. Canadell, C. Campana, K. R. Dunbar, *Angew. Chem. Int. Ed. Engl.* **1996**, *35*, 2772–2774; b) M. E. Prater, L. E. Pence, R. Clérac, G. M. Finniss, C. Campana, P. Auban-Senzier, D. Jérome, E. Canadell, K. R. Dunbar, *J. Am. Chem. Soc.* **1999**, *121*, 8005–8016; c) M. P. Doyle, T. Ren, *Prog. Inorg. Chem.* **2001**, *49*, 113–168; d) F. A. Cotton, E. V. Dikarev, M. A. Perukhina, *J. Organomet. Chem.* **2000**, *596*, 130–135; e) F. A. Cotton, E. V. Dikarev, M. A. Perukhina, *J. Chem. Soc., Dalton Trans.* **2000**, 4241–4243; f) F. P. Pruchnik, P. Jakimowicz, Z. Ciunik, K. Stanislawek, L. A. Oro, C. Tejel, M. A. Ciriano, *Inorg. Chem. Commun.* **2001**, *4*, 19–22.

[9] a) K. Sakai, E. Ishigami, Y. Konnno, T. Kajiwara, T. Ito, *J. Am. Chem. Soc.* **2002**, *124*, 12088–12089; b) K. Sakai, M. Takeshita, Y. Tanaka, T. Ue, M. Yanagisawa, M. Kosaka, T. Tsubomura, M. Ato, T. Nakano, *J. Am. Chem. Soc.* **1998**, *120*, 11353–11363.

[10] a) K. Uemura, K. Fukui, H. Nishikawa, S. Arai, K. Matsumoto, *Angew. Chem. Int. Ed.* **2005**, *44*, 5459–5464; b) K. Uemura, K. Fukui, K. Yamasaki, K. Matsumoto, *Sci. Technol. Adv. Mater.* **2006**, *7*, 461–467; c) W. Chen, F. Liu, D. Xu, K. Matsumoto, S. Kishi, M. Kato, *Inorg. Chem.* **2006**, *45*, 5552–5560.

[11] a) K. Krogmann, *Angew. Chem. Int. Ed. Engl.* **1969**, *8*, 35–42; b) J. S. Williams, A. J. Schultz, A. E. Underhill, K. Carneiro in *Extended Linear Chain Compounds* (Ed.: J. S. Miller), Plenum Press, New York, **1982**, vol. 1, pp. 73–118; c) S. Yamada, *Bull. Chem. Soc. Jpn.* **1951**, *24*, 125–127.

[12] a) M. Atoji, J. W. Richardson, R. E. Rundle, *J. Am. Chem. Soc.* **1957**, *79*, 3017–3020; b) J. R. Miller, *J. Chem. Soc.* **1965**, 713–720; c) H. J. Keller, in *Extended Linear Chain Compounds* (Ed.: J. S. Miller), Plenum Press, New York, **1982**, vol. 1, pp. 357–407; d) J. Bremi, W. R. Caseri, P. Smith, *J. Mater. Chem.* **2001**, *11*, 2593–2596; e) W. Caseri, *Platinum Met. Rev.* **2004**, *48*, 91–100 and references cited therein.

[13] a) M. Yamashita, S. Takaishi, A. Kobayashi, H. Kitagawa, H. Matsuzaki, H. Okamoto, *Coord. Chem. Rev.* **2006**, *250*, 2335–2346 and references cited therein; b) K. Otsubo, A. Kobayashi, H. Kitagawa, M. Hedo, Y. Uwatoko, H. Sagayama, Y. Wakabayashi, H. Sawa, *J. Am. Chem. Soc.* **2006**, *128*, 8140–8141; c) H. Kitagawa, T. Mitani, *Coord. Chem. Rev.* **1999**, *190–192*, 1169–1184; d) J. Ohara, S. Yamamoto, *Phys. Rev. B* **2006**, *73*, 045122-1-7.

[14] a) K. Matsumoto, S. Arai, M. Ochiai, W. Chen, A. Nakata, H. Nakai, S. Kinoshita, *Inorg. Chem.* **2005**, *44*, 8552–8560; b) F. Liu, W. Chen, D. Wang, *Dalton Trans.* **2006**, 3445–3453.

[15] a) F. A. Cotton, I. O. Koshevoy, P. Lahuerta, C. A. Murillo, M. Sanaú, M. A. Ubeda, Q. Zhao, *J. Am. Chem. Soc.* **2006**, *128*, 13674–13675; b) F. A. Cotton, J. Gu, C. A. Murillo, D. Timmons, *J. Am. Chem. Soc.* **1998**, *120*, 13280–13281; c) J. F. Berry, E. Bill, E. Bothe, F. A. Cotton, N. S. Dalal, S. A. Ibragimov, N. Kaur, C. Y. Liu, C. A. Murillo, S. Nellutla, J. M. North, D. Villagrán, *J. Am. Chem. Soc.* **2007**, *129*, 1393–1401; d) J. F. Berry, F. A. Cotton, S. A. Ibragimov, C. A. Murillo, X. Wang, *Inorg. Chem.* **2005**, *44*, 6129–6137.

[16] a) W. Micklitz, J. Riede, B. Huber, G. Müller, B. Lippert, *Inorg. Chem.* **1988**, *27*, 1979–1986; b) K. Matsumoto, H. Urata, *Chem. Lett.* **1993**, 2061–2064.

[17] a) C. Mealli, F. Pichierri, L. Randaccio, E. Zangrando, M. Krumm, D. Holtenrich, B. Lippert, *Inorg. Chem.* **1995**, *34*, 3418–3424; b) M. Krumm, B. Lippert, B. L. Randaccio, E. Zangrando, *J. Am. Chem. Soc.* **1991**, *113*, 5129–5130; c) M. Krumm, E. Zangrando, L. Randaccio, S. Menzer, B. Lippert, *Inorg. Chem.* **1993**, *32*, 700–712.

[18] a) W. Micklitz, G. Müller, J. Riede, B. Lippert, *J. Chem. Soc., Chem. Commun.* **1987**, 76–78; b) W. Micklitz, G. Müller, B. Huber, J. Riede, F. Rashwan, J. Heinze, B. Lippert, *J. Am. Chem. Soc.* **1988**, *110*, 7084–7092; c) A. Hegmans, E. Zangrando, E. Freisinger, F. Pichierri, L. Randaccio, C. Mealli, M. Gerdan, A. X. Trautweon, B. Lippert, *Chem. Eur. J.* **1999**, *5*, 3010–3018.

[19] a) S. Iwatsuki, E. Isomura, A. Wada, K. Ishihara, K. Matsumoto, *Eur. J. Inorg. Chem.* **2006**, 2484–2490; b) R. Z. Pellicani, F. P. Intini, L. Meresca, E. Mesto, C. Pacifico, G. Natile, *Eur. J. Inorg. Chem.* **2006**, 1635–1642; c) M. Sterzel, J. Autshbach, *Inorg. Chem.* **2006**, *45*, 3316–3324; d) W. Brüning, I. Ascaso, E. Freisinger, M. Sabat, B. Lippert, *Inorg. Chim. Acta* **2002**, *339*, 400–410; e) T. G. Appleton, K. A. Byriel, J. M. Garrett, J. R. Hall, C. H. L. Kennard, M. T. Mathieson, R. Stranger, *Inorg. Chem.* **1995**, *34*, 5646–5655.

[20] a) K. Matsumoto, M. Ochiai, *Coord. Chem. Rev.* **2002**, *231*, 229–238; b) M. Ochiai, K. Fukui, S. Iwatsuki, K. Ishihara, K. Matsumoto, *Organometallics* **2005**, *24*, 5528–5536; c) N. Saeki, N. Nakamura, T. Ishibashi, M. Arime, H. Sekiya, K. Ishihara, K. Matsumoto, *J. Am. Chem. Soc.* **2003**, *125*, 3605–3616; d) M. Ochiai, Y.-S. Lin, J. Yamada, H. Misawa, S. Arai, K. Matsumoto, *J. Am. Chem. Soc.* **2004**, *126*, 2536–2545; e) M. Arime, K. Ishihara, K. Matsumoto, *Inorg. Chem.* **2004**, *43*, 309–316; f) M. Ochiai, K. Matsumoto, *Chem. Lett.* **2002**, 270–271; g) Y.-S. Lin, H. Misawa, J. Yamada, K. Matsumoto, *J. Am. Chem. Soc.* **2001**, *123*, 569–575; h) Y.-S. Lin, S. Takeda, K. Matsumoto, *Organometallics* **1999**, *18*, 4897–4899; i) K. Matsumoto, Y. Nagai, J. Matsunami, K. Mizuno, T. Abe, R. Somazawa, J.


 © 2007 Wiley-VCH Verlag GmbH & Co. KGaA, Weinheim 

Kinoshita, H. Shimura, *J. Am. Chem. Soc.* **1998**, *120*, 2900–2907; j) K. Matsumoto, J. Matsunami, K. Mizuno, H. Uemura, *J. Am. Chem. Soc.* **1996**, *118*, 8959–8960.

[21] a) D. S. Martin Jr, in *Extended Linear Chain Compounds* (Ed.: J. S. Miller), Plenum Press, New York, **1982**, vol. 1, pp. 409–451; b) F. A. Cotton, G. Wilkinson, C. A. Murillo, M. Bochmann, *Advanced Inorganic Chemistry*, 6th ed., John Wiley & Sons, New York, **1999**.

[22] a) S. Iwatsuki, K. Ishihara, K. Matsumoto, *Sci. Technol. Adv. Mater.* **2006**, *7*, 411–424; b) S. Iwatsuki, C. Mizushima, N. Morimoto, S. Muranaka, K. Ishihara, K. Matsumoto, *Inorg. Chem.* **2005**, *44*, 8097–8104; c) K. Shimazaki, H. Sekiya, H. Inoue, N. Saeki, K. Ishihara, K. Matsumoto, *Eur. J. Inorg. Chem.* **2003**, 1785–1793; d) N. Saeki, Y. Hirano, Y. Sasamoto, I. Sato, T. Toshida, S. Ito, N. Nakamura, K. Ishihara, K. Matsumoto, *Eur. J. Inorg. Chem.* **2001**, 2081–2088; e) N. Saeki, Y. Hirano, Y. Sasamoto, I. Sato, T. Toshida, S. Ito, N. Nakamura, K. Ishihara, K. Matsumoto, *Bull. Chem. Soc. Jpn.* **2001**, *74*, 861–868.

[23] a) M. P. Fuller, P. R. Griffiths, *Anal. Chem.* **1978**, *50*, 1906–1910; b) S. A. Yeboah, S. Wang, P. R. Griffiths, *Appl. Spectrosc.* **1984**, *38*, 259–264; c) E. Péré, H. Cardy, O. Cairon, M. Simon, S. Lacombe, *Vib. Spectrosc.* **2001**, *25*, 163–175.

[24] a) R. H. Crabtree, *The Organometallic Chemistry of the Transition Metals*, 4th ed., Wiley-Interscience, **2005**; b) F. A. Cotton, C. A. Murillo, R. A. Walton, *Multiple Bonds between Metal Atoms*, 3rd ed., Springer Science and Business Media, Inc., New York, **2005**; c) G. Aullón, S. Alvarez, *Inorg. Chem.* **1996**, *35*, 3137–3144; d) T. Yamaguchi, F. Yamazaki, T. Ito, *J. Am. Chem. Soc.* **1999**, *121*, 7405–7406; e) T. Yamaguchi, F. Yamazaki, T. Ito, *J. Am. Chem. Soc.* **2001**, *123*, 743–744.

[25] P. Cassoux, L. Valde, H. Kobayashi, A. Kobayashi, R. A. Clark, A. E. Underhill, *Coord. Chem. Rev.* **1991**, *110*, 115–160.

[26] M. Vézes, *Bull. Soc. Chim. Fr.* **1899**, *21*, 481–487.

[27] *SMART for WindowsNT/2000*, *Version 5.625*, Bruker Advanced X-ray Solutions, Inc., Madison, WI, **2001**.

[28] *R-LATT*, *Reciprocal Lattice Viewer*, *Version 3.0*, Bruker Advanced X-ray Solutions, Inc., Madison, WI, **2000**.

[29] *SAINT*, *Data Reduction Software*, *Version 6.22*, Bruker Advanced X-ray Solutions, Inc., Madison, WI, **2001**.

[30] *SADABS*, *Area Detector Absorption and other Corrections Software*, *Version 2.03*, Bruker Advanced X-ray Solutions, Inc., Madison, WI, **2000**.

[31] G. M. Sheldrick, *SHELXTL*, *Version 5.1*, Bruker Advanced X-ray Solutions, Inc., Madison, WI, **1998**.

Received: December 26, 2006
Published Online: April 10, 2007

 © 2007 Wiley-VCH Verlag GmbH & Co. KGaA, Weinheim 

DOI: 10.1002/ejic.200600868

# Synthesis, Crystal Structure, and Magnetic Properties of Two Manganese(II) Polymers Bearing Ferrocenecarboxylato Ligands

Zilu Chen,[a] Yunsheng Ma,[a] Fupei Liang,*[a] and Zhaohui Zhou[b]

**Keywords:** Manganese / Crystal structure / Ferrocenecarboxylato / Magnetic properties

Reactions of $Mn(ClO_4)_2{\cdot}6H_2O$ with $FcCO_2Na$ [Fc = ($\eta^5$-$C_5H_4$)Fe($\eta^5$-$C_5H_5$)] in methanol solution gave $[Mn_3(FcCO_2)_6(CH_3OH)_4]_n$ (**1**), and, in the presence of 4,4′-bipyridine (4,4′-bpy), $[Mn_3(FcCO_2)_6(H_2O)_2(4,4'\text{-bpy})]_n$ (**2**). Both complexes have the similar chains with a sequence of –Mn–($\mu_2$-COO)$_n$–Mn–($\mu_2$-COO)–Mn–($\mu_2$-COO)–Mn–($\mu_2$-COO)$_n$–Mn– ($n$ = 4 and 2 for complex **1** and **2**, respectively), which are constructed alternatively from mononuclear [$Mn^{II}$] units and dinuclear $[Mn_2(FcCO_2)_4]$ units by $\mu_2$-ferrocenecarboxylato-$O,O'$ bridging. The two $Mn^{II}$ ions in the dinuclear $[Mn_2(FcCO_2)_4]$ units of complex **1** are connected by four ferrocenecarboxylato ligands to form a swastika-like shaped skeleton, which is rare in metallocenecarboxylato complexes. However, the two $Mn^{II}$ ions in the dinuclear $[Mn_2(FcCO_2)_4]$ units of complex **2** are bridged only by two carboxylato ligands, and the other two ferrocenecarboxylato ligands in this unit bind in a chelating mode. The chains in complex **2** are further interconnected by the coordinated 4,4′-bipyridine molecules to form two-dimensional coordination sheets. Magnetic susceptibility measurements revealed a weak antiferromagnetic coupling for both complexes. A model Heisenberg chain comprising classical spins coupled through alternating exchange interactions $J_1$–$J_1$–$J_2$ (AF1–AF1–AF2) is proposed to describe the magnetic behavior.
(© Wiley-VCH Verlag GmbH & Co. KGaA, 69451 Weinheim, Germany, 2007)

## Introduction

The chemistry of polynuclear manganese complexes has drawn significant research interest in the recent years due to their intriguing network topologies and their potential use as precursors for molecule-based magnetic materials.[1] To elucidate the fundamental relationship between the structures and the magnetic properties, a number of polynuclear manganese(II) complexes with various types of ligands have been synthesized and characterized in addition to the theoretical treatment provided in this paper.[2] Many factors govern the assembly process, and it is desirable to select the appropriate extended bridging ligands that can transmit magnetic interactions and bind several metal centers through various bonding modes and also to introduce some chelating or linear ditopic ancillary ligands to tune the composition and structure.[3,4] Carboxylato ligands have been widely used because they can exist in diverse coordination modes such as terminal monodentate, chelating to one metal center, and bridging bidentate, in a *syn-syn*, *syn-anti*, or *anti-anti* configuration to two metal centers.[5,6] However, most of the work has been focused on organic carboxylates such as oxalate, malonate, succinate, fumarate, maleate, terephthalate, 1,3,5-benzenetricarboxylate, and reports on organometallic carboxylates are limited. From the viewpoint of constructing functional manganese compounds, it may be interesting to incorporate the carboxyl group with the ferrocene moiety, for it was thought that, in addition to the electronic factors that are operative, the ferrocene moiety might introduce steric restrictions which might affect the nature of the adducts formed. Furthermore, the multicentered adducts may present opportunities for studying electronic interactions between the manganese center and the ferrocenyl groups. Ferrocenes not only show good redox activity but also play important roles in the field of materials science, as components of catalysts, molecular magnets, and nonlinear optical materials.[7] To the best of our knowledge, only three papers have been published on manganese complexes with ferrocene-involving carboxylate groups as ligands.[8–10] Among them, only the study reported by Hou, et al. includes some investigation of the magnetic properties of the manganese complex with a *p*-ferrocenylbenzoato ligand.[9] In the other two cases, Tian, et al.[8] and Kondo et al.[10] described the redox properties of a dinuclear complex cation $[Mn_2(phen)_4(FCA)_2]^{2+}$ (FCA = dianion of 3-ferrocenyl-2-crotonic acid, phen = 1,10-phenanthroline) and a manganese supercubane $[Mn_{13}O_8(OCH_3)_6(fcdc)_6]{\cdot}8H_2O{\cdot}2CH_3OH{\cdot}2(CH_3)_2CO$ (fcdc = 1, 1′-ferrocenedicarboxylato), respectively. This information led us to pursue the design and synthesis of manganese complexes with the participa-

[a] College of Chemistry and Chemical Engineering, Guangxi Normal University,
Yucai Road 15, Guilin, 541004, China
Fax: +86-773-5832294
E-mail: fliangoffice@yahoo.com
[b] Department of Chemistry, College of Chemistry and Chemical Engineering and State Key Laboratory of Physical Chemistry of Solid Surfaces, Xiamen University,
Xiamen 361005, China

 InterScience © 2007 Wiley-VCH Verlag GmbH & Co. KGaA, Weinheim 

tion of ferrocene-involving carboxylato ligands and to investigate the magnetic properties of the compounds formed.

In this work, we chose ferrocenecarboxylato as the main ligand with the aim of investigating its ability to tune the structure and magnetic properties of $Mn^{II}$ complexes. We present here the synthesis and characterization of two antiferromagnetic manganese coordination polymers, $[Mn_3(FcCO_2)_6(CH_3OH)_4]_n$ (**1**) and $[Mn_3(FcCO_2)_6(H_2O)_4(4,4'\text{-bpy})]_n$ (**2**). Both exhibit similar antiferromagnetic chains with a $J_1$–$J_1$–$J_2$ (AF1–AF1–AF2) repeating sequence, which is unprecedented in $Mn^{II}$–carboxylato complexes. The only reported $Mn^{II}$–carboxylato complexes with a $J_1$–$J_1$–$J_2$ repeating sequence exhibit ferrimagnetic properties with an AF–AF–F repeating sequence.[11]

## Results and Discussion

### Description of the Structure of Complexes 1 and 2

The X-ray diffraction analysis of complex **1** reveals an infinite 1D chain structure (Figure 1) with repeating linear trinuclear units $[Mn_3(FcCO_2)_6(CH_3OH)_4]$. It is shown in the structure that there are two kinds of coordination modes for the $Mn^{II}$ ions. The $Mn2^{II}$ ion is six-coordinate in a distorted octahedral geometry and is coordinated by four oxygen atoms from four methanol molecules and two oxygen atoms from two ferrocenecarboxylato ligands (Figure 1). However, a distorted square-pyramidal coordination mode is established for the $Mn1^{II}$ ion, which is coordinated by five oxygen atoms from five ferrocenecarboxylato ligands. The Mn–O bond lengths of complex **1** are in the range 2.035(2)–2.227(3) Å (Table 1), which is comparable to those in related complexes.[3,12] The O–Mn–O angles range from 83.18 to 180.0° (Table 1). An interesting feature is the construction of the $[Mn_2(FcCO_2)_4]$ building block as shown in Figure 2. Two $Mn1^{II}$ ions are connected by four *syn-syn* $\mu_2$-ferrocenecarboxylato ligands with a Mn···Mn separation of 3.0767(1) Å, and each ferrocenyl group points away from its neighbor. This gives a swastika-like shaped skeleton for the dimer structure when viewed down the Mn···Mn axis. To the best of our knowledge, only a few structures with Cu, Zn, Ru, and Mo were reported to have this kind of dimer skeleton with four $\mu_2$-metallocenecarboxylato ligands.[13] This is the first report of such a structure for a $Mn^{II}$–metallocenecarboxylato complex. The short intradimer Mn···Mn separation is comparable to those reported for dinuclear $Mn^{II}$ complexes bridged by four organic carboxylato ligands,[14] suggesting a nonbonding interaction between two $Mn^{II}$ ions. Each $Mn1^{II}$ ion of the $[Mn_2(FcCO_2)_4]$ building block are connected to a $Mn2^{II}$ ion by one *syn-anti* ferrocenecarboxylato ligand with a Mn···Mn separation of 4.7884(3) Å, which is much larger than the intradimer Mn···Mn separation in the $[Mn_2(FcCO_2)_4]$ building block. A 1D infinite chain with repeating linear $[Mn_3(FcCO_2)_6(CH_3OH)_4]$ trinuclear units is thus formed along the *b* axis, in which both the $Mn2^{II}$ ion and the midpoint of the two $Mn1^{II}$ ions in the $[Mn_2(FcCO_2)_4]$ building block are located on the centers of symmetry. It is easy to see that all of the ferrocenecarboxylato ligands in the complex act as $\mu_2$-bridges.

Table 1. Selected bond lengths [Å] and angles [°] for **1**.[a]

| | | | |
|---|---|---|---|
| Mn2–O2 | 2.132(3) | Mn1–O4 | 2.108(3) |
| Mn2–O8 | 2.183(3) | Mn1–O5B | 2.124(3) |
| Mn2–O7 | 2.227(3) | Mn1–O6 | 2.197(3) |
| Mn1–O3B | 2.097(3) | Mn1–O1 | 2.035(2) |
| | | | |
| O2A–Mn2–O2 | 180.00(15) | O1–Mn1–O4 | 108.53(12) |
| O2–Mn2–O8A | 91.44(13) | O3B–Mn1–O4 | 155.66(13) |
| O2–Mn2–O8 | 88.56(13) | O1–Mn1–O5B | 112.47(11) |
| O8A–Mn2–O8 | 180.00(17) | O3B–Mn1–O5B | 89.09(13) |
| O2–Mn2–O7A | 92.33(11) | O4–Mn1–O5B | 88.62(12) |
| O8–Mn2–O7A | 91.75(11) | O1–Mn1–O6 | 91.56(10) |
| O2–Mn2–O7 | 87.67(11) | O3B–Mn1–O6 | 89.19(13) |
| O8–Mn2–O7 | 88.25(11) | O4–Mn1–O6 | 83.18(12) |
| O7A–Mn2–O7 | 180.0 | O5B–Mn1–O6 | 155.96(11) |
| O1–Mn1–O3B | 94.71(13) | | |

[a] Symmetry operations: (A) $-x + 2, -y + 1, -z$, (B) $-x + 2, -y + 2, -z$.

Complex **2** is different from complex **1**, and it displays a 2D layered structure parallel to the *ab* plane with the composition $[Mn_3(FcCO_2)_6(H_2O)_2(4,4'\text{-bpy})]_n$, as depicted in Figure 3. The coordination modes of the $Mn^{II}$ ions in complex **2** (Figure 4) are similar to those in complex **1**. The $Mn2^{II}$ ion is coordinated in a distorted octahedral geometry by two oxygen atoms from water molecules, two nitrogen atoms from two 4,4′-bpy ligands, and two oxygen atoms from two ferrocenecarboxylato ligands. The $Mn1^{II}$ ion is in a distorted square-pyramidal environment and is coordinated by five oxygen atoms from four ferrocenecarboxylato ligands. Thus, there are two kinds of coordination modes (chelating and *syn-anti* $\mu_2$-bridging) for the ferrocenecarboxylato ligands in complex **2**. The Mn–O bond lengths are in the range 2.056(5)–2.257(5) Å, and the O–Mn–O bond angles vary from 58.50(19) to 180.0° (Table 2). Two $Mn1^{II}$ ions of complex **2** are bridged by two *syn-anti* $\mu_2$-ferrocenecarboxylato ligands to form a dimer building block $[Mn_2(FcCO_2)_4]$ with a Mn···Mn separation of 3.7757(2) Å, which is shorter than those for the reported dimers with two $\mu_2$-carboxylato-*O*,*O*′ ligands.[15–17] It is noteworthy that

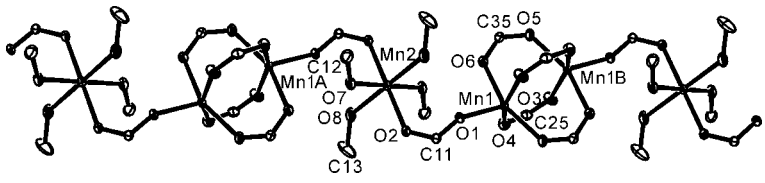


Figure 1. 1D infinite chain of complex **1** showing 30% probability ellipsoids. For clarity, ferrocenyl groups and hydrogen atoms are omitted. Symmetry operations: (A) $-x + 2, -y + 1, -z$, (B) $-x + 2, -y + 2, -z$.

 © 2007 Wiley-VCH Verlag GmbH & Co. KGaA, Weinheim 

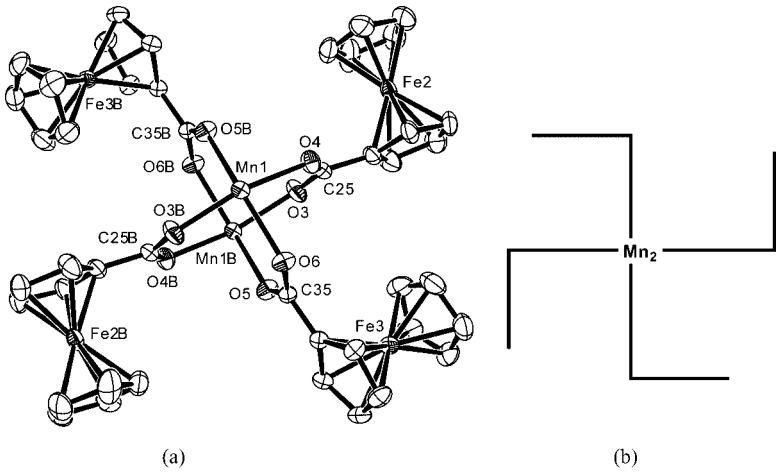


Figure 2. (a) The $[Mn_2(FcCO_2)_4]$ building block of complex **1**. Symmetry operations: (B) $-x + 2, -y + 2, -z$. (b) The skeletal swastika-like shape of $[Mn_2(FcCO_2)_4]$ of complex **1** when viewed down the Mn···Mn axis.

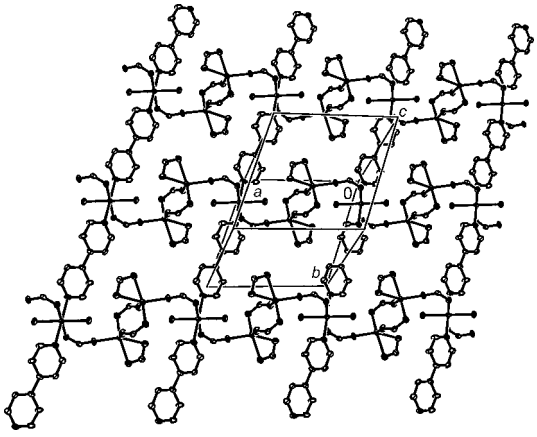


Figure 3. 2D network of complex **2**. Ferrocenyl groups and hydrogen atoms are omitted for clarity.

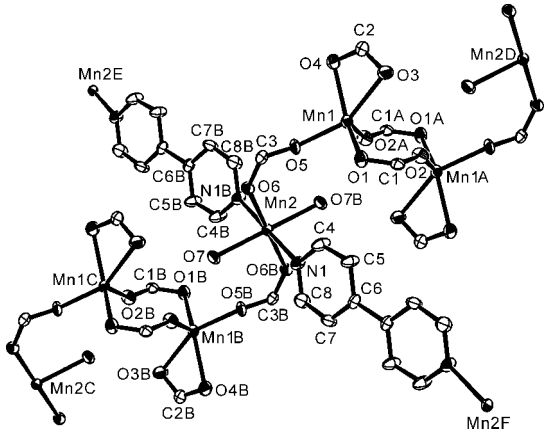


Figure 4. ORTEP drawing of complex **2** showing 30% probability ellipsoids. For clarity, ferrocenyl groups and hydrogen atoms are omitted and only selected atoms are labeled. Symmetry operations: (A) $-1 - x, 1 - y, 1 - z$, (B) $-x, 1 - y, 1 - z$, (C) $1 + x, y, z$, (D) $-1 + x, y, z$, (E) $x, 1 + y, z$, (F) $x, -1 + y, z$.

the dimer building blocks in complex **1** and **2** have the same composition but different structures. All of the ferrocenecarboxylato ligands in the dimer of complex **1** behave as *syn-syn* $\mu_2$-bridging ligands to bridge the two $Mn^{II}$ ions. However, only two ferrocenecarboxylato ligands in the dimer of **2** act as *syn-anti* $\mu_2$-bridging ligands, the other two chelate to $Mn^{II}$ ions. This results in a much shorter Mn···Mn separation for complex **1** than that for complex **2**. Each $Mn1^{II}$ ion of the dimer building block in complex **2** is further connected to one $Mn2^{II}$ ion by one *syn-anti* $\mu_2$-ferrocenecarboxylato bridge with a Mn···Mn separation of 5.1268(3) Å. This leads to the formation of an infinite 1D chain along the *a* axis, which has linear trimer repeating units of $[Mn_3(FcCO_2)_6(H_2O)_2]$. The 1D chains are further connected by the coordination of 4,4′-bpy molecules to $Mn2^{II}$ ions from adjacent chains with an interchain Mn···Mn separation of 11.493 Å, resulting in the construction of a 2D coordination sheet in the *ab* plane, as shown in Figure 3. The two pyridine rings of the 4,4′-bpy molecule are parallel to each other. In the structure of complex **2**, both the $Mn2^{II}$ ion and the midpoint of two $Mn1^{II}$ ions in the dimer are located on the centers of symmetry.

Table 2. Selected bond lengths [Å] and angles [°] for **2**.[a]

| | | | |
|---|---|---|---|
| Mn1–O2A | 2.056(5) | Mn1–O3 | 2.275(5) |
| Mn1–O5 | 2.070(5) | Mn2–O6 | 2.166(4) |
| Mn1–O1 | 2.128(5) | Mn2–O7 | 2.195(5) |
| Mn1–O4 | 2.179(5) | Mn2–N1 | 2.257(5) |
| | | | |
| O2A–Mn1–O5 | 87.61(19) | O6B–Mn2–O7B | 84.23(18) |
| O2A–Mn1–O1 | 116.9(2) | O6–Mn2–O6B | 180.00(9) |
| O5–Mn1–O1 | 96.7(2) | O6–Mn2–O7B | 95.77(18) |
| O2A–Mn1–O4 | 100.8(2) | O6–Mn2–O7 | 84.23(18) |
| O5–Mn1–O4 | 100.4(2) | O7B–Mn2–O7 | 180.0 |
| O1–Mn1–O4 | 139.1(2) | O6–Mn2–N1 | 91.5(2) |
| O2A–Mn1–O3 | 110.3(2) | O7–Mn2–N1 | 92.8(2) |
| O5–Mn1–O3 | 153.8(2) | O6–Mn2–N1B | 88.5(2) |
| O1–Mn1–O3 | 92.1(2) | O7–Mn2–N1B | 87.2(2) |
| O4–Mn1–O3 | 58.50(19) | N1–Mn2–N1B | 180.0(3) |

[a] Symmetry operations: (A) $-x - 1, -y + 1, -z + 1$, (B) $-x, -y + 1, -z + 1$.

 © 2007 Wiley-VCH Verlag GmbH & Co. KGaA, Weinheim 

It is of great interest that both compounds have similar chains constructed from alternately repeating mononuclear [$Mn^{II}$] units and dinuclear [$Mn_2(FcCO_2)_4$] units. The big difference is that the two $Mn^{II}$ ions in the dinuclear [$Mn_2(FcCO_2)_4$] units of compound **2** are bridged only by two *syn-anti* carboxylato ligands; the other two carboxylato ligands in this unit act as chelating ligands. However, the two $Mn^{II}$ ions in the dinuclear [$Mn_2(FcCO_2)_4$] units of compound **1** are connected by four *syn-syn* carboxylato ligands, that is to say, all of the ferrocenecarboxylato ligands in the dinuclear unit of compound **1** behave as $\mu_2$-bridging ligands. Another difference is that the chains in compound **2** are further interconnected by the coordinated 4,4′-bipyridine molecules to form two-dimensional coordination sheets.

## Magnetic Properties

The magnetic properties of complexes **1** and **2** were investigated by solid-state magnetic susceptibility ($\chi_m$) measurements in the 2.0–300 K range in a DC field of 2000 Oe; the resulting data are shown in Figure 5 and Figure 6 as $\chi_m$ and $\chi_mT$ vs. $T$ plots. The $\chi_m$ value decreases monotonously with $T$ for both compounds. Its values at 300 K and 2 K are 0.03274 and 1.8322 $cm^3 mol^{-1}$, respectively, for compound **1**, and 0.04101 and 1.331 $cm^3 mol^{-1}$, respectively, for compound **2**. The values of $\chi_mT$ at 300 K for compounds **1** and **2** are 9.82 and 12.30 $cm^3 mol^{-1}$ K, respectively, which are lower than that (13.1 $cm^3 mol^{-1}$ K) expected for three magnetically isolated high-spin $Mn^{II}$ ions. This indicates the presence of antiferromagnetic coupling. With decreasing temperature, the $\chi_mT$ of **1** and **2** gradually decrease, reaching 3.66 and 2.66 $cm^3 mol^{-1}$ K, respectively, at 2.0 K. The shapes of these curves are also characteristic of weak antiferromagnetic interactions between the $Mn^{II}$ centers.

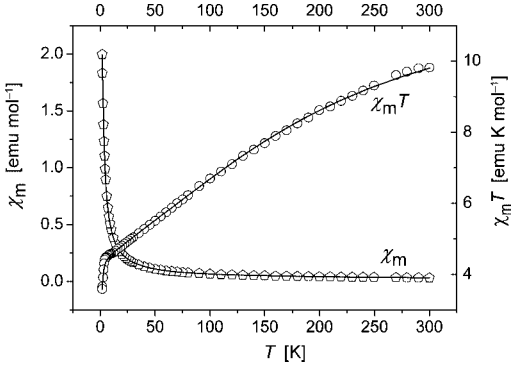


Figure 5. Plot of $\chi_m$ and $\chi_mT$ vs. $T$ for **1**. Solid lines show the best fit of the data according to the proposed model.

There are two sets of magnetic exchange pathways within the chain in both compounds. One consists of one *syn-anti* $\mu_2$-1,3-carboxylato bridge. The other mainly consists of four *syn-syn* $\mu_2$-1,3-carboxylato bridges for compound **1** and two *syn-anti* $\mu_2$-1,3-carboxylato bridges for compound **2**. The interactions alternate according to a $J_1$–$J_1$–$J_2$ repeating sequence to yield an antiferromagnetic chain (AF1–AF1–AF2) as shown in Scheme 1. This unprecedented antiferromagnetic chain is different from the reported AF–AF–F ferrimagnetic chains.[11,18] The ground state is $S$ = 5/2 for each trinuclear $Mn_3$ unit.

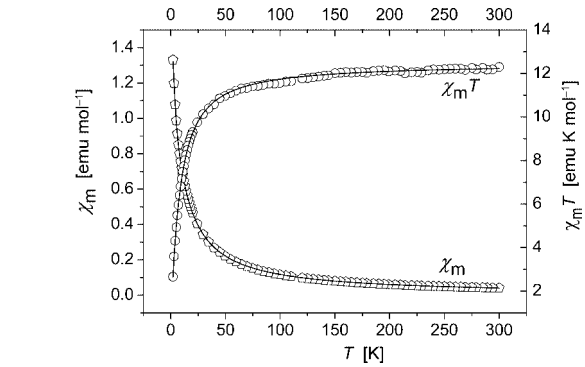


Figure 6. Plot of $\chi_m$ and $\chi_mT$ vs. $T$ for **2**. Solid lines show the best fit of the data according to the proposed model.

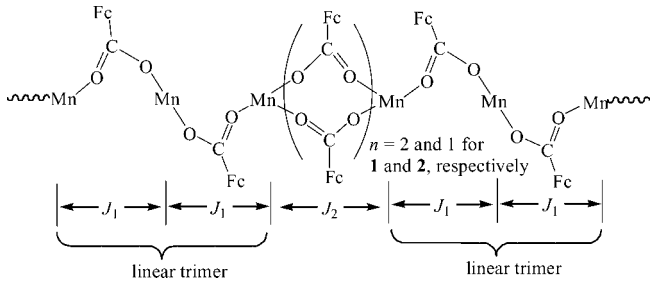


Scheme 1.

The theoretical expression proposed by Escuer and Ribas et al.[11,18] was employed to fit the observed magnetic data for complexes **1** and **2**:

$$H = -J_1\Sigma(S_{3i}\cdot S_{3i+1} + S_{3i+1}\cdot S_{3i+2}) - J_2\Sigma S_{3i-1}\cdot S_{3i}$$

$$\chi_{chain} = \frac{Ng^2\mu_B^2}{3kT}\,\frac{3(1-\mu_1^4\mu_2^2)+4\mu_1(1-\mu_1^2\mu_2^2)+2\mu_2(1+\mu_1)^2(1-\mu_1^2)+2\mu_1^2(1-\mu_2^2)}{(1-\mu_1^2\mu_2)^2}$$

where $\mu_1 = \coth(J_1/kT) - kT/J_1$, $\mu_2 = \coth(J_2/kT) - kT/J_2$, $J_i = J_iS(S + 1)$ and $g_i = g_i[S(S + 1)]^{1/2}$. The best fitting parameters obtained for **1** are $J_1$ = –0.15 $cm^{-1}$, $J_2$ = –29.56 $cm^{-1}$, and $g$ = 2.00 with $R = 3.73\times10^{-4}$.

For complex **2**, the fitting was carried out by employing a molecular field approximation, assuming that there is an interchain interaction ($zJ'$) through the 4,4′-bpy bridge. With this assumption, the final susceptibilities for **2** are shown below:

$$\chi_M = \frac{\chi_{chain}}{1-(zJ'/Ng^2\beta^2)\chi_{chain}}$$

The best fitting parameters for **2** were found to be $J_1$ = –0.27 $cm^{-1}$, $J_2$ = –1.28 $cm^{-1}$, $zJ'$ = –0.081 $cm^{-1}$, $g$ = 1.95 with $R = 1.32\times10^{-5}$. This fit gives a nice agreement factor $R$. It was revealed that the 4,4′-bpy ligand (between the chains) mediates a very weak antiferromagnetic interaction ($zJ'$ = –0.081 $cm^{-1}$), in agreement with the large Mn···Mn separation (11.493 Å).

 © 2007 Wiley-VCH Verlag GmbH & Co. KGaA, Weinheim 

These $J$ values are comparable to those of compounds with similar bridging modes and also confirm the dependence of $J$ on the nature of the carboxylato bridges.[19,20] The adjacent trinuclear units of **1** are bridged by four *syn-syn* $\mu_2$-1,3-carboxylato ligands which are much more efficient pathways for superexchange than *syn-anti* $\mu_2$-1,3-carboxylato bridges. Thus, they induce a much larger $|J|$ ($J_2$ = –29.56 cm$^{-1}$) than that ($J_1$ = –0.15 cm$^{-1}$) in the trimer of **1** and those ($J_1$ = –0.27 cm$^{-1}$, $J_2$ = –1.28 cm$^{-1}$) in **2**. The intratrimer $J$ ($J_1$ = –0.27 cm$^{-1}$) and intertrimer $J$ ($J_2$ = –1.28 cm$^{-1}$) of **2** are in the range reported for one *syn-anti* carboxylato bridge (–0.1 to –0.4 cm$^{-1}$)[5,17,21] and two *syn-anti* carboxylato bridges (–0.9 to –1.7 cm$^{-1}$),[16,17,20] respectively. This confirms again that the magnitude of $|J|$ increases with the number of carboxylato bridges.

## Conclusions

Two manganese(II) complexes bearing the organometallic ligand ferrocenecarboxylato have been synthesized and characterized crystallographically and magnetically. Both complexes have similar chains constructed by $\mu_2$-ferrocenecarboxylato-*O*,*O*′ bridging from alternately repeating mononuclear [Mn$^{II}$] units and dinuclear [$Mn_2(FcCO_2)_4$] units. The dinuclear [$Mn_2(FcCO_2)_4$] unit of complex **1** presents a swastika-like shaped skeleton, which is rare in metallocenecarboxylato complexes. Both compounds show antiferromagnetic interactions with a $J_1$–$J_1$–$J_2$ repeating sequence. To the best of our knowledge, this is the first AF1–AF1–AF2 antiferromagnetic chain with an organometallic carboxylato bridge. The analysis of the magnetic properties also confirms that the exchange coupling through the carboxylato bridge is highly dependent on the conformation modes of the bridge between the metal atoms. The *syn-syn* mode usually induces a much larger $|J|$ value than the *syn-anti* mode, and the magnitude of $|J|$ increases with the number of carboxylato bridges.

## Experimental Section

**General:** Sodium ferrocenecarboxylate was prepared according to the literature method.[22] The other starting materials were commercially available and were used without further purification. Elemental analyses (C, H, and N) were performed with a Vario EL analyzer. Infrared spectra were recorded with KBr pellets by using a Nicolet 360 FT-IR spectrometer in the region 400–4000 cm$^{-1}$. Variable-temperature magnetic susceptibility data were obtained with a SQUID magnetometer (MPMS XL-5) in the temperature range 2–300 K with an applied magnetic field of 2000 Oe.

**CAUTION:** Although no problems were encountered in this work, perchlorate salts are potentially explosive. They should be prepared in small quantities and handled with great care.

**Preparation of $[Mn_3(FcCO_2)_6(CH_3OH)_4]_n$ (1):** A methanol solution (5 mL) of $FcCO_2Na$ (0.0251 g; 0.1 mmol) was added dropwise to a methanol solution (5 mL) of $Mn(ClO_4)_2{\cdot}6H_2O$ (0.0362 g; 0.1 mmol). The resulting mixture was stirred at room temperature for 10 h and filtered. The filtrate was allowed to condense at ambient temperature to give orange crystals. Yield: 0.0584 g (70%). $C_{70}H_{70}Fe_6Mn_3O_{16}$ (1667.18): calcd. C 50.38, H 4.20; found C 50.67, H 4.24. IR (KBr): $\tilde{\nu}$ = 3431 (m), 1533 (s), 1391 (s), 1360 (s), 1105 (w), 1001 (w), 816 (m), 506 (m), 486 (m) cm$^{-1}$.

**Preparation of $[Mn_3(FcCO_2)_6(H_2O)_2(4,4'\text{-bpy})]_n$ (2):** A methanol solution (5 mL) of $FcCO_2Na$ (0.0251 g; 0.1 mmol) was added dropwise to a methanol solution (10 mL) of 4,4′-bpy (0.0156 g, 0.1 mmol) and $Mn(ClO_4)_2{\cdot}6H_2O$ (0.0362 g; 0.1 mmol). The resulting solution was stirred at ambient temperature for 10 h and filtered. The filtrate was allowed to condense at ambient temperature to give orange crystals. Yield: 0.0519 g (60%). $C_{76}H_{66}Fe_6Mn_3N_2O_{14}$ (1731.23): calcd. C 52.68, H 3.81, N 1.61; found C 53.01, H 3.97, N 1.47. IR (KBr): $\tilde{\nu}$ = 3431 (m), 1607 (w), 1577 (s), 1531 (s), 1391 (s), 1359 (s), 1218 (w), 1105 (w), 1002 (w), 811 (m), 508 (m), 487 (w) cm$^{-1}$.

**X-ray Crystallography:** All the data for complexes **1** and **2** were collected with a Bruker APEX CCD diffractometer by using graphite monochromatic Mo-$K_\alpha$ radiation ($\lambda$ = 0.71073 Å). A prismatic single crystal was mounted on a glass fiber. The data were collected at 296(2) K. Absorption effects were corrected by semi-empirical methods. The structure was solved by direct methods with the program SHELXS-97[23] and refined by full-matrix least-squares methods on all $F^2$ data with SHELXL-97.[24] The non-hydrogen atoms were refined anisotropically. Hydrogen atoms of water molecules and hydroxyl groups were located in a difference Fourier map and refined isotropically in the final refinement cycles. Other hydrogen atoms were placed in calculated positions and refined by using a riding model. The final cycle of full-matrix least-squares refinement was based on observed reflections and variable parameters. The molecular illustrations were drawn with the program XP.[25] All cal-

Table 3. Crystal data and refinement details of complexes **1** and **2**.

| | **1** | **2** |
|---|---|---|
| Formula | $C_{70}H_{70}Fe_6Mn_3O_{16}$ | $C_{76}H_{66}Fe_6Mn_3N_2O_{14}$ |
| $M$ [g mol$^{-1}$] | 1667.18 | 1731.23 |
| $T$ [K] | 296(2) | 296(2) |
| Wavelength [Å] | 0.71073 | 0.71073 |
| Crystal system | triclinic | triclinic |
| Space group | $P\bar{1}$ | $P\bar{1}$ |
| $a$ [Å] | 11.9256(7) | 10.9802(7) |
| $b$ [Å] | 12.0542(7) | 11.4929(7) |
| $c$ [Å] | 13.0976(8) | 14.8800(9) |
| $\alpha$ [°] | 88.4100(10) | 82.3570(10) |
| $\beta$ [°] | 78.9410(10) | 83.4290(10) |
| $\gamma$ [°] | 63.5120(10) | 65.9560(10) |
| $V$ [Å$^3$] | 1650.30(17) | 1695.84(18) |
| $Z$ | 1 | 1 |
| $D_{calcd.}$ [g cm$^{-3}$] | 1.678 | 1.695 |
| $\mu$, Mo-$K_\alpha$ [mm$^{-1}$] | 1.901 | 1.852 |
| $F$(000) | 849 | 879 |
| Crystal size [mm] | 0.27 × 0.11 × 0.08 | 0.25 × 0.15 × 0.05 |
| $\theta$ range for data | 1.59–25.90° | 1.38–25.01° |
| Reflections collected | 9069 | 10094 |
| Unique reflections ($R_{int}$) | 6284 (0.0597) | 5917 (0.0548) |
| Completeness to $\theta_{max}$ | 98.0% | 98.9% |
| Max. and min. transmission | 0.8628 and 0.6279 | 0.9131 and 0.6546 |
| Data/restraints/parameters | 6284–2–431 | 5917–3–463 |
| Goodness of fit on $F^2$ | 0.993 | 1.279 |
| Final $R$ indices[a] [$I > 2\sigma(I)$] | $R_1$ = 0.0531 | $R_1$ = 0.0863 |
| Final $wR_2$ indices[a] | $wR_2$ = 0.1352 | $wR_2$ = 0.1522 |
| Final $R$ (for all data)[a] | $R_1$ = 0.0639, | $R_1$ = 0.0982 |
| Final $wR_2$ (for all data)[a] | $wR_2$ = 0.1421 | $wR_2$ = 0.1575 |
| Largest diff. peak and hole [e Å$^{-3}$] | 0.858 and –0.933 | 0.724 and –0.624 |

[a] $R_1(F_o) = \Sigma||F_o| - |F_c||/\Sigma|F_o|$, $wR_2(F_o^2) = [\Sigma w(F_o^2 - F_c^2)^2/\Sigma w(F_o^2)^2]^{1/2}$.

 © 2007 Wiley-VCH Verlag GmbH & Co. KGaA, Weinheim 

culations were performed with the WinGX System 1.64.05.[26] Crystallographic data for compounds **1** and **2** are given in Table 3. Selected bond lengths and bond angles are given in Table 1 and Table 2.

CCDC-621075 and CCDC-621076 (for complexes **1** and **2**, respectively) contain the supplementary crystallographic data for this paper. These data can be obtained free of charge from The Cambridge Crystallographic Data Centre via www.ccdc.cam.ac.uk/datarequest/cif.

## Acknowledgments

The authors thank the National Natural Science Foundation of China (No.20461001) and the Education Department of Guangxi Province, China for financial support.

[1] a) M. Murugesu, W. Wernsdorfer, K. A. Abboud, G. Christou, *Angew. Chem. Int. Ed.* **2005**, *44*, 892–896; b) C. Dendrinou-Samara, M. Alexiou, C. M. Zaleski, J. W. Kampf, M. L. Kirk, D. P. Kessissoglou, V. L. Pecoraro, *Angew. Chem. Int. Ed.* **2003**, *42*, 3763–3766; c) H. Miyasaka, N. Matsumoto, H. Okawa, N. Re, E. Gallo, C. Floriani, *J. Am. Chem. Soc.* **1996**, *118*, 981–994; d) H. O. Stumpf, L. Ouahab, Y. Pei, D. Grandjean, O. Kahn, *Science* **1993**, *261*, 447–449; e) M. Murugesu, M. Habrych, W. Wernsdorfer, K. A. Abboud, G. Christou, *J. Am. Chem. Soc.* **2004**, *126*, 4766–4767; f) H. Miyasaka, K. Nakata, K. Sugiura, M. Yamashita, R. Clérac, *Angew. Chem. Int. Ed.* **2004**, *43*, 707–711; g) J. M. Lim, Y. Do, J. Kim, *Eur. J. Inorg. Chem.* **2006**, 711–717; h) S. Martín, M. G. Barandika, L. Lezama, J. L. Pizarro, Z. E. Serna, J. I. Ruiz de Larramendi, M. I. Arriortua, T. Rojo, R. Cortés, *Inorg. Chem.* **2001**, *40*, 4109–4115.

[2] a) D. Huang, W. Wang, X. Zhang, C. Chen, F. Chen, Q. Liu, D. Liao, L. Li, L. Su, *Eur. J. Inorg. Chem.* **2004**, 1454–1464; b) M. A. Youssef, A. Escuer, M. A. S. Goher, F. A. Mautner, R. Vicente, *J. Chem. Soc., Dalton Trans.* **2000**, 413–416; c) F. Bonadio, M.-C. Senna, J. Ensling, A. Sieber, A. Neels, H. Stoeckli-Evans, S. Decurtins, *Inorg. Chem.* **2005**, *44*, 969–978; d) J. Tao, Y.-Z. Zhang, Y.-L. Bai, O. Sato, *Inorg. Chem.* **2006**, *45*, 4877–4879; e) M. Ferbinteanu, H. Miyasaka, W. Wernsdorfer, K. Nakata, K.-I. Sugiura, M. Yamashita, C. Coulon, R. Clérac, *J. Am. Chem. Soc.* **2005**, *127*, 3090–3099; f) C. Ma, C. Chen, Q. Liu, F. Chen, D. Liao, L. Li, L. Sun, *Eur. J. Inorg. Chem.* **2003**, 2872–2879; g) J. S. Miller, M. Drilon, *Magnetism: Molecules to Materials I–IV*, Wiley-VCH, Weinheim, Germany, **2002**; h) R. D. Willet, D. Gatteschi, O. Kahn, *Magneto Structural Correlations in Exchange Coupled Systems, NATO ASI Series C140*, Reidel, Dordrecht, The Netherlands, **1985**.

[3] C. Ma, C. Chen, Q. Liu, F. Chen, D. Liao, L. Li, L. Sun, *Eur. J. Inorg. Chem.* **2004**, 3316–3325.

[4] C.-Y. Sun, S. Gao, L.-P. Jin, *Eur. J. Inorg. Chem.* **2006**, 2411–2421.

[5] C. Policar, F. Lambert, M. Cesario, I. Morgenstern-Badarau, *Eur. J. Inorg. Chem.* **1999**, 2201–2207.

[6] E. Colacio, J. M. Domínguez-Vera, M. Ghazi, R. Kivekäs, M. Klinga, J. M. Moreno, *Eur. J. Inorg. Chem.* **1999**, 441–445.

[7] a) P. Jutzi, N. Lenze, B. Neumann, H.-G. Stammler, *Angew. Chem. Int. Ed.* **2001**, *40*, 1423–1427; b) H. Plenio, C. Aberle, Y. A. Shihadeh, J. M. Lloris, R. Martínez-Máñez, T. Pardo, J. Soto, *Chem. Eur. J.* **2001**, *7*, 2848–2861; c) T. Farrell, T. Meyer-Friedrichsen, M. Malessa, D. Haase, W. Saak, I. Asselberghs, K. Wostyn, K. Clays, A. Persoons, J. Heck, A. R. Manning, *J. Chem. Soc., Dalton Trans.* **2001**, 29–36; d) A. Togni, T. Hayashi, *Ferrocenes: Homogeneous Catalysis, Organic Synthesis Materials Science*, VCH, Weinheim, **1995**; e) J. S. Miller, A. J. Epstein, W. M. Reiff, *Acc. Chem. Res.* **1988**, *21*, 114–120.

[8] Z. Zhang, Q.-L. Liu, J.-X. Yang, J.-Y. Wu, Y.-P. Tian, B.-K. Jin, H.-K. Fun, S. Chantrapromma, A. Usman, *Transition Met. Chem.* **2003**, *28*, 930–934.

[9] H. Hou, L. Li, Y. Zhu, Y. Fan, Y. Qiao, *Inorg. Chem.* **2004**, *43*, 4767–4774.

[10] M. Kondo, R. Shinagawa, M. Miyazawa, M. K. Kabir, Y. Irie, T. Horiba, T. Naito, K. Maeda, S. Utsuno, F. Uchida, *Dalton Trans.* **2003**, 515–516.

[11] R. Wang, E. Gao, M. Hong, S. Gao, J. Luo, Z. Lin, L. Han, R. Cao, *Inorg. Chem.* **2003**, *42*, 5486–5488.

[12] V. Tangoulis, D. A. Malamatari, K. Soulti, V. Stergiou, C. P. Raptopoulou, A. Terzis, T. A. Kabanos, D. P. Kessissoglou, *Inorg. Chem.* **1996**, *35*, 4974–4983.

[13] a) F. A. Cotton, L. R. Falvello, A. H. Reid Jr, J. H. Tocher, *J. Organomet. Chem.* **1987**, *319*, 87–97; b) M. R. Churchill, Y. J. Li, D. Nalewajek, P. M. Schaber, J. Dorfman, *Inorg. Chem.* **1985**, *24*, 2684–2687; c) M. W. Cooke, C. A. Murphy, T. S. Cameron, J. C. Swarts, M. A. S. Aquino, *Inorg. Chem. Commun.* **2000**, *3*, 721–725; d) M. W. Cooke, T. S. Cameron, K. N. Robertson, J. C. Swarts, M. A. S. Aquino, *Organometallics* **2002**, *21*, 5962–5971; e) G. Li, B.-Y. Chen, L.-K. Li, H.-W. Hou, Y. Zhu, Y.-T. Fan, *J. Coord. Chem.* **2003**, *56*, 877–884.

[14] a) I. G. Fomina, G. G. Aleksandrov, A. A. Sidorov, V. M. Novotortsev, Y. V. Rakitin, Z. V. Dobrokhotova, V. N. Ikorskii, Y. G. Shvedenkov, I. L. Eremenko, I. I. Moiseev, *Inorg. Chem. Commun.* **2005**, *8*, 89–93; b) M. Nakashima, H. Maruo, T. Hata, T. Tokii, *Chem. Lett.* **1999**, *28*, 1277–1278; c) E. V. Amel′chenkova, T. O. Denisova, S. E. Nefedov, *Mendeleev Commun.* **2004**, *14*, 103–104.

[15] a) C. Ma, W. Wang, X. Zhang, C. Chen, Q. Liu, H. Zhu, D. Liao, L. Li, *Eur. J. Inorg. Chem.* **2004**, 3522–3532; b) P.-R. Wei, Q. Li, W.-P. Leung, T. C. W. Mak, *Polyhedron* **1997**, *16*, 897–902; c) M. U. Triller, W. Y. Hsieh, V. L. Pecoraro, A. Rompel, B. Krebs, *Inorg. Chem.* **2002**, *41*, 5544–5554; d) P. S. Mukherjee, K. S. Min, A. M. Arif, P. J. Stang, *Inorg. Chem.* **2004**, *43*, 6345–6350; e) J. Chai, H. Zhu, H. W. Roesky, C. He, H. G. Schmidt, M. Noltemeyer, *Organometallics* **2004**, *23*, 3284–3289.

[16] B. Albela, M. Corbella, J. Ribas, I. Castro, J. Sletten, H. Stoeckli-Evans, *Inorg. Chem.* **1998**, *37*, 788–798.

[17] H. Oshio, E. Ino, I. Mogi, T. Ito, *Inorg. Chem.* **1993**, *32*, 5697–5703.

[18] a) M. A. M. Abu-Youssef, M. Drillon, A. Escuer, M. A. S. Goher, F. A. Mautner, R. Vicente, *Inorg. Chem.* **2000**, *39*, 5022–5027; b) M. A. M. Abu-Youssef, A. Escuer, M. A. S. Goher, F. A. Mautner, G. J. Reiss, R. Vicente, *Angew. Chem. Int. Ed.* **2000**, *39*, 1624–1626; c) A. K. Ghosh, D. Ghoshal, E. Zangrando, J. Ribas, N. R. Chaudhuri, *Inorg. Chem.* **2005**, *44*, 1786–1793.

[19] a) T. K. Maji, S. Sain, G. Mostafa, T.-H. Lu, J. Ribas, M. Monfort, N. R. Chaudhuri, *Inorg. Chem.* **2003**, *42*, 709–716; b) S. Durot, C. Policar, G. Pelosi, F. Bisceglie, T. Mallah, J.-P. Mahy, *Inorg. Chem.* **2003**, *42*, 8072–8080.

[20] R. Wang, D. Yuan, F. Jiang, L. Han, S. Gao, M. Hong, *Eur. J. Inorg. Chem.* **2006**, 1649–1656.

[21] a) X. M. Xen, Y. X. Tong, Z. T. Xu, T. C. W. Mak, *J. Chem. Soc., Dalton Trans.* **1995**, 4001–4004; b) V. Tangoulis, G. Psomas, C. Dendrinou-Samara, C. P. Raptopoulou, A. Terzis, D. P. Kessissoglou, *Inorg. Chem.* **1996**, *35*, 7655–7660; c) H. Iikura, T. Nagata, *Inorg. Chem.* **1998**, *37*, 4702–4711.

[22] *Gemlin Handbuch der Anorganische Chemie. Eisen Organische Verbindungen, Vol. A3*, Springer-Verlag, Berlin, **1976**, p. 58.

[23] G. M. Sheldrick, *Acta Crystallogr., Sect. A* **1990**, *46*, 467–473.

[24] G. M. Sheldrick, PC Version, University of Göttingen, Germany, **1997**.

[25] A. Bruker, *XP-Interactive Molecular Graphics*, Vers. 5.1, **1998**.

[26] L. J. Farrugia, *J. Appl. Crystallogr.* **1999**, *32*, 837–838.

Received: September 16, 2006
Published Online: March 30, 2007

 © 2007 Wiley-VCH Verlag GmbH & Co. KGaA, Weinheim 

DOI: 10.1002/ejic.200601139

# Mechanisms of $H_2$, $H_2C{=}CH_2$, and $O{=}CH_2$ Insertion into $Cp_2Zr(\eta^2\text{-}SiMe_2{=}NtBu)(PMe_3)$

**Siwei Bi,*[a] Shufen Zhu,[a] and Zhenwei Zhang[a]**

**Keywords:** Zirconium / Silanimines / Insertion / Mechanism

In this paper, the mechanisms for the insertion of $H_2$, $H_2C{=}CH_2$, and $O{=}CH_2$ into the Zr–Si bond of $Cp_2Zr(\eta^2\text{-}SiMe_2{=}NtBu)(PMe_3)$ (**R**) are theoretically investigated with the aid of density functional theory (DFT) calculations. The structure of the $H_2$ insertion product **P** is discussed on the basis of our calculations, and its bonding features are rationalized in terms of molecular orbital theory. The regiochemistry for insertion of $O{=}CH_2$ has also been theoretically investigated. It is found that the relative stabilities of the three insertion products of **R** are in the order $\mathbf{P} < \mathbf{P}' < \mathbf{P}''$. For the reactions of **R** with $H_2$ and $CH_2{=}CH_2$, the rate-determining steps are the insertions of $H_2$ and $CH_2{=}CH_2$ into the Zr–Si bond of $Cp_2Zr(\eta^2\text{-}SiMe_2{=}NtBu)$ (**Int1**), whereas $PMe_3$ dissociation is the rate-determining step for the reaction of **R** with $O{=}CH_2$. Only the precursor **Int2**′′, formed by the coordination of $O{=}CH_2$ to the Zr atom, is located; those formed by the coordination of $H_2$ and $CH_2{=}CH_2$ to **Int1** are not found.

(© Wiley-VCH Verlag GmbH & Co. KGaA, 69451 Weinheim, Germany, 2007)

## 1. Introduction

Free unsaturated silicon substrates are very reactive and usually exhibit unsaturation at the Si atom. However, they can be stabilized by coordination to transition metals. Metal complexes of silicon analogs of common carbon-based ligands such as silylenes and silaolefins were prepared, but remained quite rare despite their unusual reactivity in chemical transformations, their proposed role in metal-catalyzed transformations at silicon, and their potential utility in the selective formation of silicon-based polymers. Transition-metal complexes of unsaturated silicon compounds such as silenes ($R_2Si{=}CR'_2$), disilenes ($R_2Si{=}SiR_2$), and silanimines ($R_2Si{=}NR'$) are important candidates for experimental and theoretical investigation. The reactions of these complexes with a range of organic and inorganic reagents afford interesting products and provide further insight into the role of such species in catalytic reactions. Remarkable progress has been made over more than ten years in the synthesis of stable transition-metal complexes of unsaturated silicon ligands. In 1988, Tilley and co-workers reported the first stable unsaturated silene complex, $(C_5Me_5)Ru(PR_3)(H)(\eta^2\text{-}R'_2Si{=}CH_2)$.[1,2] Stable mononuclear and binuclear complexes of disilenes were subsequently prepared.[3–8] Okazaki and co-workers prepared a three-membered silametallacyclic complex, $Cp^*Fe(CO)\{\kappa^2(Si,P)\text{-}SiMe_2PPh_2\}$ and studied its reactivity toward MeOH.[9] We have theoretically investigated the mechanisms of formation of the ring-opening products of this reaction.[10] Berry introduced the first unsaturated silanimine complex, $Cp_2Zr(\eta^2\text{-}SiMe_2{=}NtBu)(PMe_3)$,[11] and investigated some chemical reactivity experimentally in 1991. As depicted in Scheme 1, $Cp_2Zr(\eta^2\text{-}SiMe_2{=}NtBu)L$ (L = $PMe_3$, CO) can react with $H_2$ by α-bond metathesis, and with olefins, alkynes, aldehydes, or ketones[11,12] by unsaturated bond insertion leading to ring expansion. For these reactions, only the structures of the complexes $Cp_2Zr(\eta^2\text{-}SiMe_2{=}NtBu)(PMe_3)$ and $Cp_2Zr(\eta^2\text{-}SiMe_2{=}NtBu)(CO)$ were determined by single-crystal X-ray diffraction analyses.[11,13] For the complex $Cp_2Zr(\eta^2\text{-}SiMe_2{=}NtBu)(CO)$, the origin of π-back-bonding to the carbonyl ligand directly from an orbital on the adjacent silicon atom has been theoretically investigated by ZINDO molecular orbital calculations.[13] To the best of our knowledge, theoretical studies on the reactions of $Cp_2Zr(\eta^2\text{-}SiMe_2{=}NtBu)(PMe_3)$ with $H_2$, olefins, alkynes, and aldehydes or ketones have been very limited. For example, the reaction of $[Cp_2ZrHCl]_n$ with $LiNtBuSiMe_2H{\cdot}THF$ in benzene yields $Cp_2ZrH(NtBuSiMe_2H)$, whose structure was characterized by single-crystal X-ray diffraction. The same molecular formalism was afforded by $H_2$ insertion into the Zr–Si bond of $Cp_2Zr(\eta^2\text{-}SiMe_2{=}NtBu)(PMe_3)$; the product of this reaction has not been analyzed by single-crystal X-ray diffraction. Are the two products obtained from these two reactions the same or different? What structural and bonding features are involved in the product obtained by $H_2$ insertion? For the reaction of $Cp_2Zr(\eta^2\text{-}SiMe_2{=}NtBu)(PMe_3)$ with $CH_2{=}O$, chemoselectivity clearly appears. Why does the O atom, and not the C atom, of $CH_2{=}O$ bind to the Zr center? In addition, it is necessary to study the reactions in

[a] College of Chemistry Science, Qufu Normal University, Qufu, Shandong, 273165, P. R. China
Fax: +86-537-4456305
E-mail: siweibi@126.com

 © 2007 Wiley-VCH Verlag GmbH & Co. KGaA, Weinheim 

more detail in order to gain an insight into the mechanisms on these reactions. In this work, theoretical calculations based on the B3LYP DFT have been carried out to examine the structural, bonding, and energetic aspects related to these reaction pathways.

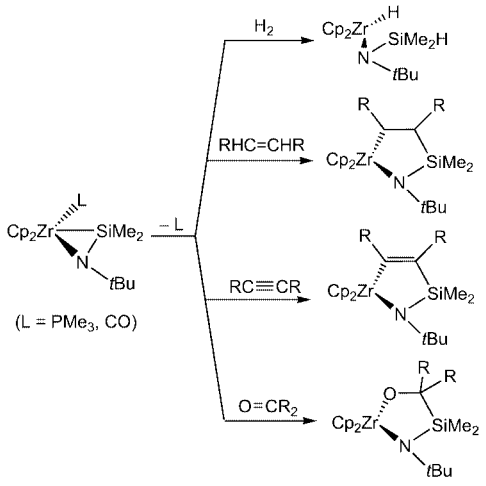


Scheme 1.

As known, the bonding of the silanimine fragment to the metal falls between two resonance extremes. One is a metallacycle in which Si has $sp^3$ hybridization ($X_2$ type), and the other is a π-donor complex in which Si has $sp^2$ hybridization (L type) as shown in the diagram. We will give further evidence for the bonding of the silanimine fragment to the metal on the basis of the results of our calculations.

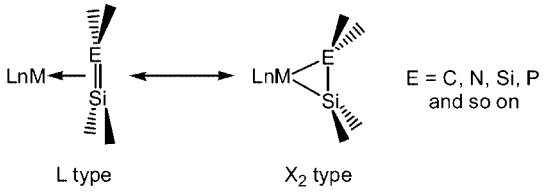


## 2. Computational Details

All molecular geometries were optimized at the Becke-3LYP (B3LYP) level of DFT.[14–16] Frequency calculations at the same level of theory have also been performed to identify all stationary points as minima (zero imaginary frequencies) or transition states (one imaginary frequency). The transition states involved were checked by IRC (Intrinsic Reaction Coordinate) analysis.[17,18] The effective core potentials (ECPS) of Hay and Wadt with double-ζ valence basis sets (LanL2DZ) were used to describe Zr, Si, and P atoms, while the standard 6-31G basis set was used to describe C, N, and H atoms. Polarization functions were added for P(ζ $d$ = 0.34), Si(ζ $d$ = 0.262), N(ζ $d$ = 0.8), and those atoms directly involved in bond-forming and bond-breaking processes, C(ζ $d$ = 0.8), H(ζ $p$ = 0.11). All the calculations were performed with the Gaussian 98 software package.[19]

For examining the feasibility of the B3LYP level of DFT, the computed geometrical structure of the reactant **R** was compared to the original X-ray diffraction structure. Selected calculated and experimental (in brackets) bond lengths are shown in Figure 2. The calculated values and the geometrical parameters obtained from X-ray diffraction are close enough, indicating that our calculations at the B3LYP level of DFT are reliable. We have also used this computational method to investigate other organometallic systems.[20–23]

## 3. Results and Discussion

For investigating the mechanisms, the structures, and the bonding features involved in the reactions mentioned above, we chose $H_2$, $H_2C{=}CH_2$, and $O{=}CH_2$ as substrates to react with $Cp_2Zr(\eta^2\text{-}SiMe_2{=}N\mathit{t}Bu)(PMe_3)$ (**R**). The mechanisms for the three reactions are theoretically proposed as shown in Scheme 2. Since the reactant **R** is coordinatively saturated, it is proposed that **R** first loses the phosphane ligand, $PMe_3$, through a transition state **TS1**, to form a 16-electron intermediate **Int1**. In reaction (1), **Int1** reacts with $H_2$ to yield the product **P** via a transition state **TS2**. In reaction (2), **Int1** reacts with ethylene to give the product **P′** via a transition state **TS2′**. In reaction (3), **Int1** reacts with formaldehyde to afford the product **P′′** via a transition state **TS2′′**.

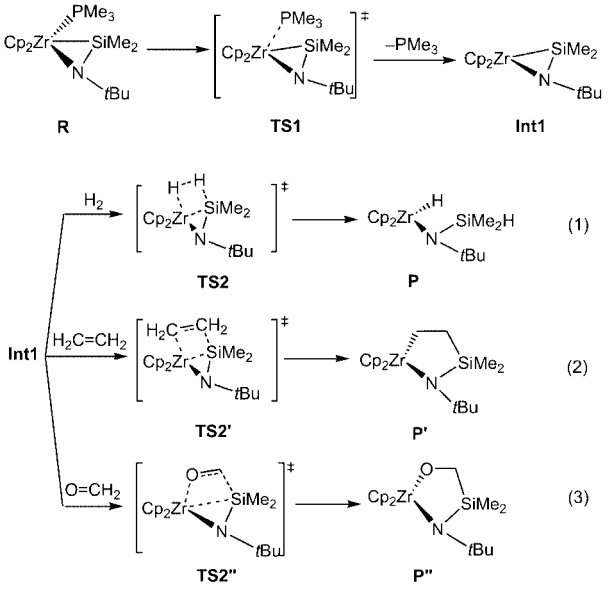


Scheme 2.

### 3.1 Insertion of $H_2$

Figure 1a shows the calculated potential energy profile corresponding to the reaction of **R** with $H_2$ by the mechanism shown in Scheme 2. Figure 2 shows all the B3LYP-optimized geometrical structures with selected structural parameters. The first step is the dissociation of $PMe_3$. In **R**

 © 2007 Wiley-VCH Verlag GmbH & Co. KGaA, Weinheim 

and **TS1**, the calculated Zr–P bond lengths are 2.76 and 3.73 Å, respectively, indicating that the $PMe_3$ leaves from the metal center. Table 1 indicates that the Zr–Si and Zr–N bond lengths decrease and the Si–N bond length increases in going from **R** via **TS1** to **Int1**. This means that, with the dissociation of $PMe_3$, the $Me_2SiNtBu$ unit tends to be closer to the Zr center, and correspondingly the interaction between the $Me_2SiNtBu$ unit and Zr is enhanced. The Si–N bond is then weakened with the increasing interaction of the Zr center with the $Me_2SiNtBu$ unit, and hence the Si–N bond length increases in going from **R** via **TS1** to **Int1**, as shown in Table 1. Also, as the $Me_2SiNtBu$ unit approaches the Zr atom, the increasing strain in the Zr–Si–N ring in going from **R** to **Int1** can make the Si–N bond longer. Clearly, this structural variation results from the loss of the $PMe_3$ ligand. The activation energy for the step from **R** to **Int1** is calculated to be 9.2 kcal/mol. **Int1** is higher than **R** in energy by 5.9 kcal/mol, indicating that this step is thermodynamically unfavorable. The reason for the instability of **Int1** compared with **R** is the transformation from the 18-electron species **R** to the 16-electron species **Int1**.

Table 1. Zr–N, Zr–Si, and Si–N bond lengths [Å] in all the species involved in the reaction mechanism shown in Figure 1a.

| | Zr–N | Zr–Si | Si–N |
|---|---|---|---|
| **R** | 2.16 | 2.67 | 1.72 |
| **TS1** | 2.09 | 2.62 | 1.76 |
| **Int1** | 2.07 | 2.60 | 1.77 |
| **TS2** | 2.09 | 2.62 | 1.75 |
| **P** | 2.20 | 2.94 | 1.71 |

As for step two (**Int1** to **P**), the results of our calculations indicate that insertion of $H_2$ into the Zr–Si bond becomes energetically accessible as shown in Figure 1a. The H–H bond length in free $H_2$ is calculated to be 0.74 Å. In **TS2**, the calculated H1–H2, Zr–Si, Zr–H1, and Si–H2 bond lengths are 0.76, 2.62, 2.72, and 2.89 Å, respectively. As $H_2$ approaches the metal center in **TS2**, the H1–H2 and Zr–Si bonds are elongated with respect to their values in **Int1**. The activation energy for the step is calculated to be 7.8 kcal/mol. In the product **P**, the H1–H2 and Zr–Si bonds are broken, and Zr–H1 and Si–H2 σ bonds are formed. As shown in Table 1, the Zr–Si bond length increases in going from **Int1** via **TS2** to **P** as a result of the insertion of $H_2$. The Si–N bond strength is enhanced as a result of the decrease in the π-back-donation from the metal center to the Si–N unit and the release of the ring strain. As indicated in Table 1, the Si–N bond length decreases in going from **Int1** via **TS2** to **P**. The Zr–N bond length increases slightly as shown in Table 1, which arises mainly from two factors. One is the decrease in the π-back-donation, which weakens the Zr–N bond. The other is the increasing steric hindrance of the *t*Bu group attached to the N atom by the two Cp rings because of the increase in the Zr–N–Si bond angle. The energy difference for the step is calculated to be –17.7 kcal/mol, indicating that this step is very much favored thermodynamically.

Examining carefully the structure of **P**, we predict the presence of an agostic interaction between the Si–H bond and the metal center. Evidence offered by our calculations is as follows: (i) The Zr, N, Si, and C1 atoms are coplanar, and hence the N atom has $sp^2$ hybridization. Thus, the Zr–N–Si bond angle could be predicted to be about 120°. However, this angle is calculated to be 96.4°, supporting the occurrence of an interaction between the Zr atom and the Si–H bond. (ii) The Si atom has $sp^3$ hybridization, and hence the N–Si–H2 bond angle could be predicted to be about 109°. In fact, the bond angle is calculated to be 95.2°, also providing evidence for the agostic interaction. (iii) The Si–H2 bond length is calculated to be 1.54 Å. This bond could be expected to be longer in the absence of an agostic interaction. For investigating the Si–H2 bond length, we designed a model complex, **A**, as shown in Figure 2. **A** is derived from the product **P** by the replacement of the two methyl groups attached to the Si atom by two hydrogen atoms. The Si–H3 and Si–H4 bond lengths in **A** are calculated to be 1.49 Å, and the Si–H2 bond length in **A** is 1.52 Å. Clearly, the Si–H2 bond is longer than both the Si–H3 and the Si–H4 bonds, implying the presence of an agostic interaction between the Si–H2 bond and the Zr atom in **A**, and further supporting the prediction of an agostic interaction in **P**. Even though Zr has $d^0$ configuration, meaning that little back-donation from Zr to the σ* orbital of Si–H is present, the agostic interaction is still present. The greater stability of **P** compared with **Int1** has two main reasons. One is the release of the strain in the Zr–N–Si three-membered ring. The other is the presence of the agostic interaction mentioned above. The agostic interaction helps the complex achieve a formal 18-electron configuration, and hence makes some contribution to the stability of **P**. To the best of our knowledge, the structure of **P** has not been characterized by single-crystal X-ray diffraction. However, the structure of an isomer of **P**, represented by **P**-isomer in this paper, was analyzed by single-crystal X-ray diffraction.[24] **P**-isomer was prepared from the reaction of $[Cp_2ZrHCl]_n$ with $LiNtBuSiMe_2H{\cdot}THF$ in benzene as shown in Scheme 3. The structure of **P**-isomer is optimized at the same level of B3LYP, which is illustrated in Figure 2 with selected bond lengths. The calculated Zr–N and N–Si bond lengths (2.17, 1.72 Å, respectively) are close to the experimental observations (2.14, 1.71 Å). The results of our calculations are consistent with the experimental analysis results that an agostic interaction between Zr and the Si–H bond is present in the compound. The Zr···H1 distance and the N–Si–H1 angle in **P**-isomer are calculated to be 2.29 Å and 95.7°, respectively; these values are similar to those in **P** (2.20 Å, 95.2°). The calculated Zr–N–Si bond angle is 98.8°, which is close to that in **P** (96.4°) and to the experimental result (95.1°).[24] On the basis of the structural parameters above, we can also theoretically support the presence of the β-agostic interaction mentioned above. **P**-isomer is calculated to be more stable than **P** by –2.0 kcal/mol. The weaker steric hindrance in **P**-isomer compared with that in **P** may be responsible for its relative stability. Theoretically, **P** could be converted into the more stable **P**-isomer by rota-

 © 2007 Wiley-VCH Verlag GmbH & Co. KGaA, Weinheim 

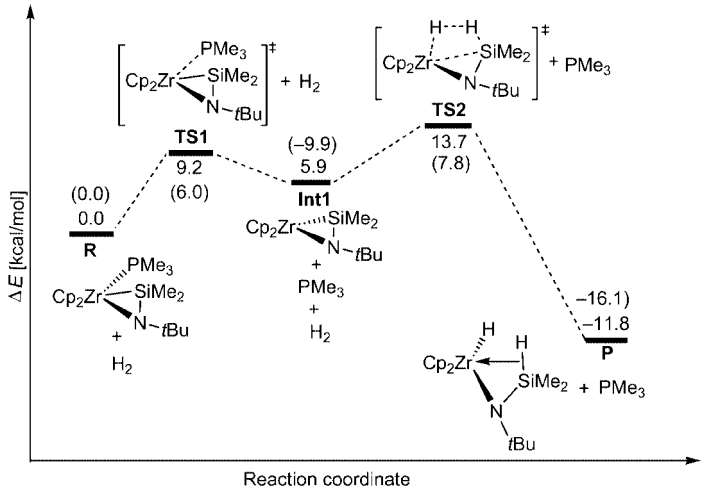


(a)

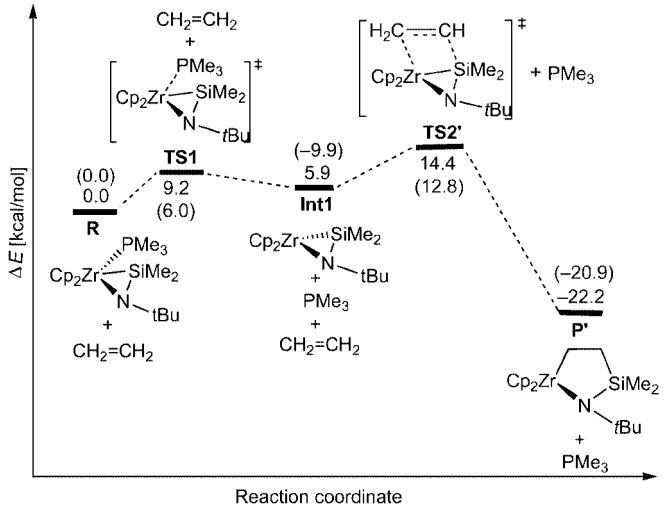


(b)

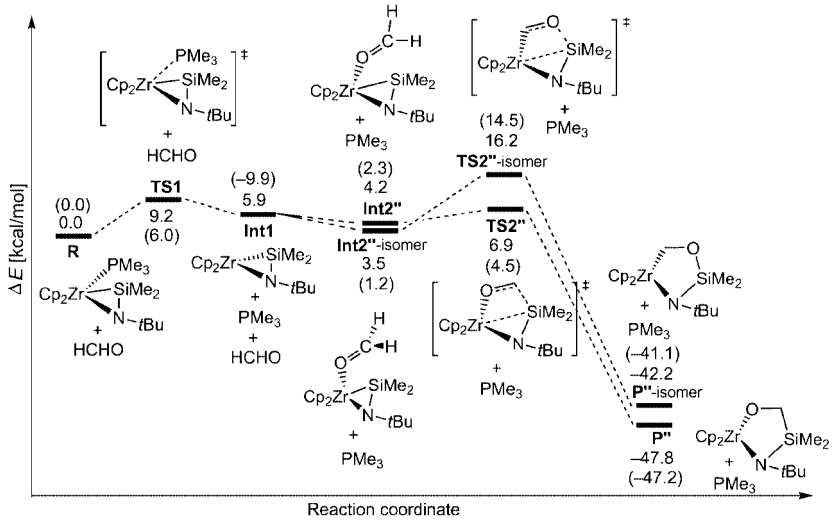


(c)

Figure 1. (a) Energy profile for the insertion reaction of $H_2$ into $Cp_2Zr(\eta^2\text{-}SiMe_2{=}NtBu)(PMe_3)$. (b) Energy profile for the insertion reaction of ethylene into $Cp_2Zr(\eta^2\text{-}SiMe_2{=}NtBu)(PMe_3)$. (c) Energy profile for the insertion reaction of formaldehyde into $Cp_2Zr(\eta^2\text{-}SiMe_2{=}NtBu)(PMe_3)$. The relative energies and free energies (in parentheses) are given in kcal/mol.

 © 2007 Wiley-VCH Verlag GmbH & Co. KGaA, Weinheim 

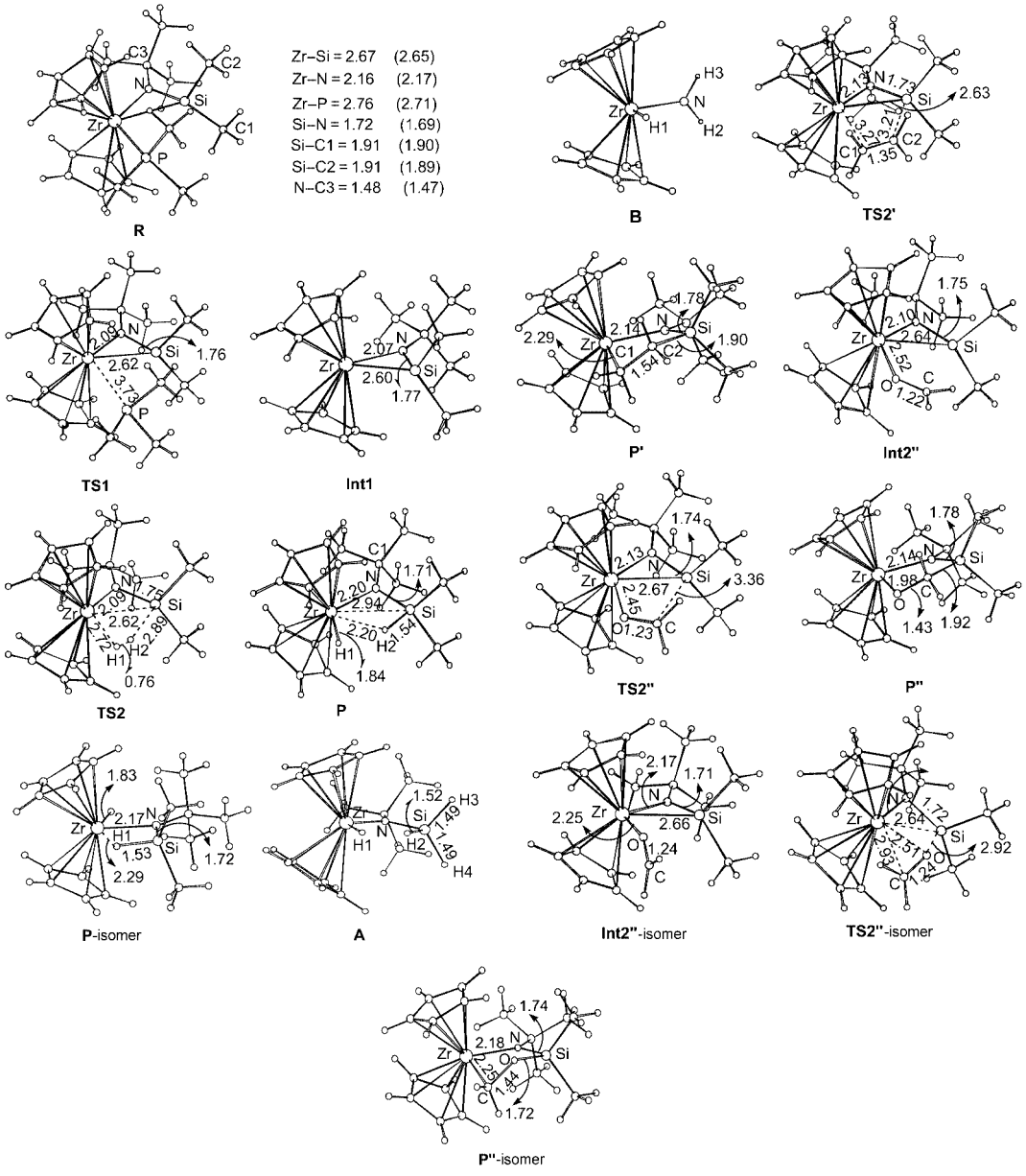


Figure 2. B3LYP-optimized structures of all related compounds with selected structural parameters. The experimental data are given in brackets. Bond lengths are in Å.

tion of –N(*t*Bu)($SiMe_2H$) about the Zr–N axis. However, the conversion through rotation is very difficult because of the agostic interaction and the steric hindrance as mentioned above. So, we suggest theoretically that the final product for reaction (1) in Scheme 2 is **P** but not **P**-isomer.

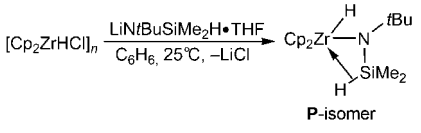


Scheme 3.

It is interesting to further discuss the structure of the product **P** and the bonding features involved. If the *t*Bu and $SiHMe_2$ groups are substituted by two hydrogen atoms, the B3LYP-optimized structure of the derived model complex, $Cp_2ZrH(NH_2)$ (**B**), shown in Figure 2, is different from that of **P**. The Zr, N, H2, and H3 atoms are coplanar, meaning that the N atom has $sp^2$ hybridization, and one lone pair is on the p orbital of the N atom perpendicular to the Zr–N–H2–H3 plane. The H1–Zr–N–H2 and H1–Zr–N–H3 dihedral angles are calculated to be equal (89.4°). In other words, the H2–N–H3 plane is perpendicular to the H1–Zr–N plane in **B**, whereas H1, Zr, N, C1, and Si are coplanar in **P**. The structural difference between **P** and **B** is worth to explore in terms of molecular orbital interactions. For the model complex $Cp_2ZrH(NH_2)$, only if the H2–N–H3 plane is perpendicular to the H1–Zr–N plane can the lone pair on the N atom have the same symmetry with one

 © 2007 Wiley-VCH Verlag GmbH & Co. KGaA, Weinheim 

LUMO ($1a_1$) of the fragment $Cp_2M$, as shown in Scheme 4.[25] Thus, the π interaction between $1a_1$ and the p orbital takes effect, and the Zr–N bond is further stabilized. Therefore, the π interaction between the $1a_1$ orbital of the fragment $Cp_2M$ and the p orbital on the N atom is responsible for the orientation of the H2–N–H3 plane. In contrast, the C1–N–Si plane in **P** is wedged into the two Cp rings. Clearly, the π interaction mentioned above is not present in **P**, since the LUMO ($1a_1$) is not symmetric to the p orbital on the N atom. Other factors play a dominant role in controlling the geometrical structure. One is the agostic interaction between Zr and the Si–H bond, which prevents the rotation of the C1–N–Si plane around the Zr–N axis. Another is the steric hindrance of the two Cp rings, affecting the bulky *t*Bu and $SiHMe_2$ groups, which also blocks the rotation of the C1–N–Si plane around the Zr–N axis. Only when the C1–N–Si plane is wedged into the two Cp rings can the steric effect be reduced to the least possible amount.

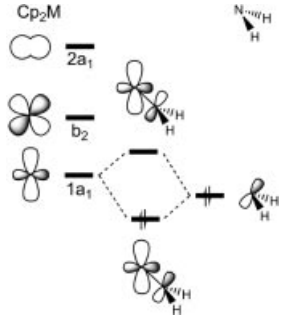


Scheme 4.

Figure 1a shows that the rate-determining step is the insertion of $H_2$ into the Zr–Si bond. The reaction activation energy is calculated to be 13.7 kcal/mol. The product **P** is lower in energy than the reactant **R** by 11.8 kcal/mol, indicating that the reaction is thermodynamically favorable. The high stability of the product **P** relative to the reactant **R** arises mainly from the release of the strong ring strain in going from **R** to **P**, the formation of the relatively strong Zr–H bond, and the agostic interaction of the Si–H bond with the metal center.

The bonding between Zr and the Si–N is also worth discussing. As mentioned in the introduction, there are two extremes for the structure of the Zr–Si–N three-membered ring, the L type and the $X_2$ type. What we want to know is which one is the major type in the reactant **R**. First, we take a look at the structure of the product **P**. The Si atom in **P** has $sp^3$ hybridization, and hence the Si–N bond is a σ bond. The bond length is calculated to be 1.71 Å. In the reactant **R**, both N and Si atoms bind to the metal, and the Si–N bond length is calculated to be 1.72 Å, which is even slightly longer than that in **P**, suggesting that the Zr–Si–N unit has $X_2$-type bonding. This is a result of the fact that the remaining $d^2$ electrons in the fragment $Cp_2Zr$ are very reactive, and hence the $Cp_2Zr$ fragment is a very good π base. The two methyl groups attached to the Si atom are bent far away from the metal, which is also consistent with the $X_2$-type structure. The Zr–N bond in **P** is a σ bond, which is longer than that in **R** only by 0.04 Å, also suggesting that the Zr–N bond in **R** is a σ bond.

### 3.2 Insertion of $CH_2{=}CH_2$

Reaction (2) in Scheme 2 is the insertion of ethene into the Zr–Si bond. Figure 1b shows the energy profile corresponding to the reaction mechanism. Related geometrical structures with selected structural parameters are also illustrated in Figure 2. The first step is the same as that in reaction (1). The second step is the insertion of the C=C double bond into the Zr–Si bond. In **TS2′**, the calculated Zr···C1 and Si···C2 distances are 3.27 and 3.21 Å, respectively. The Zr–Si bond length is 2.63 Å, which is slightly larger than that in **Int1** (2.60 Å). The C1–C2 bond length (1.35 Å) is almost the same as the free ethylene C–C bond length, indicating that the C1 and C2 atoms keep nearly $sp^2$ hybridization. Clearly, **TS2′** is a very early transition state. IRC analysis confirms that **TS2′** directly connects to **Int1** and the product **P′**. In other words, along the reaction coordinate, no precursor in which ethylene is coordinated to the metal center can be located as a minimum on the potential energy profile. The reason is probably that the $d^0$ metal center cannot stabilize an olefin complex because of lack of back-donation. The activation energy for the step is calculated to be 8.5 kcal/mol. When the ethylene ligand is inserted into the Zr–Si bond, a five-membered metallacycle is formed in the product **P′**. The hybridizations of C1 and C2 are changed from $sp^2$ to $sp^3$, which is supported by change in the C1–C2 bond length from 1.35 Å in **TS2′** to 1.54 Å in **P′**. No agostic interaction between C–H and Zr is found because of the formation of the metallacycle. The energy difference for the step is calculated to be –28.1 kcal/mol, indicating that this step is thermodynamically very favorable . The high stability of **P′** relative to **Int1** is a result of the chelating effect involved and the releasing of ring strain.

As shown in Figure 1b, the rate-determining step is the insertion of ethylene into the Zr–Si bond. The reaction activation energy is calculated to be 14.4 kcal/mol, which is slightly higher than that for $H_2$ insertion. The reaction energy difference is –22.2 kcal/mol. Although the reactant **R** is an 18-electron species, **R** is much less stable than the 16-electron product **P′**. The reasons for the energy difference are the releasing of ring strain from **R** to **P′** and the chelating effect involved in **P′**.

### 3.3 Insertion of $CH_2{=}O$

Figure 1c shows the energy profile for the reaction of **R** with the substrate formaldehyde. Related B3LYP geometrical structures are illustrated in Figure 2. In contrast to the insertion of $H_2$ and ethylene, a precursor, **Int2′′**, is located for the insertion of formaldehyde. In the structure of **Int2′′** shown in Figure 2, the Zr–O bond length is calculated to be 2.52 Å. The C–O bond length in the coordinated $CH_2O$ is 1.22 Å, while that in free $CH_2O$ is 1.21 Å, calculated at

 © 2007 Wiley-VCH Verlag GmbH & Co. KGaA, Weinheim 

the same level of theory, which supports the coordination of $CH_2O$ to the metal center. The calculated distance between the Zr atom and the C atom of $CH_2$=O is 3.44 Å, indicating that the O atom is coordinated to the metal center rather than the $CH_2$=O π bond. This means that the binding of the terminal oxygen coordination is stronger than that of the side C=O coordination. The reason for the different binding ability is that the metal center $Zr^{IV}$ is a hard acid and the O atom is a hard base, which can form a relatively strong σ coordination bond to afford an 18-electron intermediate. **Int2′′** is more stable than **Int1** by 1.7 kcal/mol. The coordination of $CH_2O$ to the metal to achieve an 18-electron species may be responsible for the relatively high stability of **Int2′′** relative to **Int1**. The coordination abilities of the substrates studied in this paper to the Zr center are in the order $PMe_3$ > $CH_2O$ > $CH_2$=$CH_2$ > $H_2$. The calculated results show that **R** is more stable than **Int2′′**, whereas the precursors formed by the coordination of ethylene and dihydrogen to the Zr atom are not present.

Ring expansion from **Int2′′** to **P′′** results from the insertion of the C=O bond of $CH_2$=O into the Zr–Si bond. Obviously, the regiochemistry of the C=O insertion could occur in two modes: one would be the binding of the Zr with the O atom and Si with the C atom, and the other would be the binding of the Zr with the C atom and Si with the O atom. Experiments confirmed that the O atom is coordinated to the Zr atom to afford a five-membered metallacycle in **P′′**. This results from the fact that the $Zr^{IV}$ is a hard acid and the O atom is a hard base in terms of the so-called "hard soft acid base theory", leading to the relatively strong interaction between the Zr and O atoms.

In the calculated insertion transition state **TS2′′**, the calculated Zr–O bond length is 2.45 Å, and the Si···C distance is 3.36 Å. IRC calculations confirmed that **TS2′′** directly connects to **Int2′′** and **P′′**. The longer Zr–N and Zr–Si bond lengths than those in **Int2′′** indicate a decrease in π-back-donation from the metal to the Si–N unit. Consequently, the Si–N bond becomes slightly shorter than that in **Int2′′**. The C–O bond length in **TS2′′** is calculated to be 1.23 Å, which is larger than that in **Int2′′**. The longer Zr–Si and C–O bonds and shorter Zr–O and Si–C bonds imply stronger interaction between the latter two bonds relative to that in **Int2′′**. In the structure of **P′′**, a five-membered ring containing the metal center is formed. The Si atom is far away from the metal center, and the three σ bonds (Zr–O, O–C, and C–Si) are formed; this can be confirmed by the structural parameters of **P′′** shown in Figure 2. The activation energy for the step is calculated to be 2.7 kcal/mol, indicating the insertion of formaldehyde is kinetically much favorable. The energy difference for the step is calculated to be –52.0 kcal/mol. In contrast to the insertion of $H_2$ and ethylene, the rate-determining step of Reaction (3) in Scheme 2 is theoretically predicted to be the dissociation of the phosphane ligand $PMe_3$ and not the insertion of C=O into the Zr–Si bond. The strong interaction between the Zr and O atoms plays a crucial role in stabilizing the transition state **TS2′′**. The reaction energy is calculated to be –47.8 kcal/mol, indicating that this reaction is much favorable thermodynamically. Releasing of ring strain and the chelating effect due to the formation of the five-membered metallacycle are responsible for the favored thermodynamics.

Clearly, there is regioselectivity in the insertion of O=$CH_2$. The metal could be attacked by the O atom of O=$CH_2$ or by the C atom. As shown in Figure 1c, the transition state **TS2′′**-isomer is located, which connects an intermediate **Int2′′**-isomer and a proposed product **P′′**-isomer. In this step, the C atom is bound to Zr and the O atom bound to Si. Calculations show that **Int2′′**-isomer is more stable than **Int2′′** by 0.7 kcal/mol. This arises from the stronger Zr–O bond in **Int2′′**-isomer than that in **Int2′′**, since the Zr–O bond length is shorter in the former (2.25 Å) than in the latter (2.52 Å). The **TS2′′**-isomer is calculated to be higher in energy than **TS2′′** by 9.3 kcal/mol. The reason for this energy difference can be understood by an energy-decomposition analysis of reaction barriers.[26,27] As shown in Scheme 5, $\Delta E_1$ and $\Delta E_2$ represent the binding energies between **TS2′′**-frag and **TS2′′**, and **TS2′′**-isomer-frag and **TS2′′**-isomer, respectively. $\Delta E_3$ is the energy difference between the two kinds of fragments. $\Delta E_4$ is the activation energy difference between **TS2′′** and **TS2′′**-isomer. It can be seen in Scheme 5 that $\Delta E_4 = (\Delta E_1 - \Delta E_2) - \Delta E_3$ = –5.9–3.5 = –9.4 (kcal/mol). The binding energy difference (–5.9 kcal/mol) plays a dominant role in the difference between the activation energies. Clearly, the stronger Zr–O bond in **TS2′′** relative to the Zr–C bond in **TS2′′**-isomer is responsible for the activation energy difference. The isomer of **P′′**, **P′′**-isomer, is 5.6 kcal/mol higher in energy than **P′′**. The driving force from **Int2′′** to **P′′**, but not to **P′′**-isomer is still the strong interaction of the O atom with the metal center.

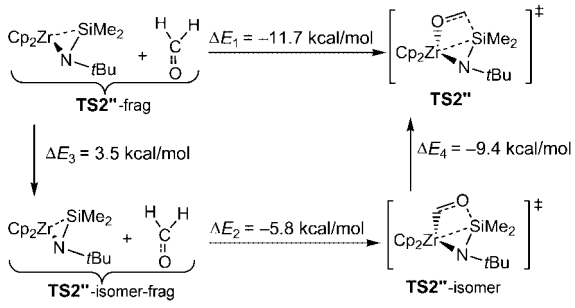


Scheme 5.

### 3.4 Comparison of the Insertions of $H_2$, $CH_2$=$CH_2$, and $CH_2$=O

In a comparison of the three reactions, insertion of $H_2$ can be regarded as a σ-bond metathesis, while insertion of ethylene and formaldehyde are processes of ring expansion. The reactant **R** is an 18-electron species, so we propose that the first step is the dissociation of $PMe_3$ to give a 16-electron intermediate. Among the insertions of the three substrates, only that of formaldehyde involves a precursor formed by the coordination of formaldehyde to the Zr cen-

 © 2007 Wiley-VCH Verlag GmbH & Co. KGaA, Weinheim 

ter as a result of the strong interaction between the so-called "hard acid" $Zr^{IV}$ center and the so-called "hard base" O atom of $CH_2$=O. The precursors formed by coordination of $H_2$ and $CH_2$=$CH_2$ are theoretically predicted to be nonexistent, mainly owing to the lack of back-donation, as the Zr center has $d^0$ configuration. As for the three transition states, **TS2**, **TS2′**, and **TS2′′**, the former two are relatively close to each other. $H_2$ has a higher bond energy than the ethylene π bond, indicating that the H–H σ bond is more difficult to break than the C=C π bond. However, ethylene engages in a larger steric repulsive interaction as it approaches the metal center, while $H_2$ can easily reach the metal center with its much less bulky structure. These two factors lead to similar activation energies for the two insertions. In comparison, the transition state **TS2′′** for the insertion of formaldehyde is much lower than **TS2** and **TS2′** in energy, and even lower than the dissociation barrier of $PMe_3$, as a result of the strong interaction between the Zr and O atoms. Therefore, in contrast to the insertion of $H_2$ and ethylene, the rate-determining step for reaction (3) in Scheme 2 becomes the dissociation of $PMe_3$ and not the insertion of formaldehyde. Figure 1 indicates that the relative stability of the three products with respect to the reactant **R** is in the order **P** < **P′** < **P′′**. A chelating effect due to the formation of the five-membered metallacycle in **P′** and **P′′** leads to the higher stability of **P′** and **P′′** relative to **P**. For early transition metals, M–X (X is a heteroatom) bonds are much stronger than M–C bonds.[28] For example, calculated results show that the bonding energy difference between Ta–OH and Ta–C bonds is about 53.1 kcal/mol, and the difference between Ta–Cl and Ta–C bonds is about 35.6 kcal/mol. For late transition metals, M–X bonds are a little stronger than M–C bonds. For example, the bond dissociation energy of a Pt–Cl bond is estimated to be only about 10.0 kcal/mol larger than that of a Pt–C bond.[29,30] The energy of **P′** is calculated to be –22.2 kcal/mol, while that of **P′′** is –47.8 kcal/mol with respect to the reactant **R**. **P′′** is much more stable than **P′**. Clearly, the reason for the higher stability of **P′′** is the formation of the strong Zr–O σ bond.

## 4. Conclusions

Metal complexes of silanimines ($R_2Si{=}NR'$) exhibit unusual reactivity in chemical transformations. The reactions of these complexes with a range of organic and inorganic reagents yield interesting products and provide further insight into the role of such species in catalytic reactions. Three typical insertion reactions, those of $H_2$, $CH_2$=$CH_2$, and $CH_2$=O into the Zr–Si bond of $Cp_2Zr(\eta^2\text{-}SiMe_2{=}NtBu)(PMe_3)$ were chosen to investigate their reaction mechanisms and the structural and bonding features involved in these reactions. The product of $H_2$ insertion, **P**, is structurally discussed, and we find that a Zr···H–Si agostic interaction is present. The bonding feature in **P** is analyzed in comparison to the designed model complex $Cp_2Zr(NH_2)H$ (**B**). The geometrical structural difference between **P** and **B** results from their different bonding properties and steric environments. We also predict that the $H_2$ insertion product, **P**, is different from **P**-isomer, the product obtained from the reaction of $[Cp_2ZrHCl]_n$ with $LiNtBuSiMe_2H{\cdot}THF$. The results of our calculations also confirm that the product of $CH_2$=O insertion contains the Zr–O bond and not the Zr–C bond as a result of the stronger interaction of Zr with the O atom than with the C atom.

The reaction mechanisms are confirmed theoretically to comprise two steps, dissociation of $PMe_3$ and insertion of $H_2$, $CH_2$=$CH_2$, and $CH_2$=O. Theoretical findings are: (i) the relative stabilities of the three insertion products of **R** are in the order **P** < **P′** < **P′′**; (ii) the rate-determining step is $H_2$ insertion in reaction (1) and $CH_2$=$CH_2$ insertion in reaction (2), whereas it is $PMe_3$ dissociation in reaction (3); (iii) only the precursor **Int2′′** is located, while those formed by the coordination of $H_2$ and $CH_2$=$CH_2$ to **Int1** are not found.

## Acknowledgments

This work was supported by the National Science Foundation of China (No.: 20473047).

[1] B. K. Campion, R. Heyn, T. D. Tilley, *J. Am. Chem. Soc.* **1988**, *110*, 7558.
[2] B. K. Campion, R. Heyn, T. D. Tilley, *J. Am. Chem. Soc.* **1990**, *112*, 4079.
[3] E. K. Pham, R. West, *J. Am. Chem. Soc.* **1989**, *111*, 7667–7668.
[4] E. K. Pham, R. West, *Organometallics* **1990**, *9*, 1517.
[5] D. H. Berry, J. H. Chey, H. S. Zipin, P. J. Carroll, *J. Am. Chem. Soc.* **1990**, *112*, 452.
[6] E. A. Zarate, C. A. Tessier-Youngs, W. J. Youngs, *J. Am. Chem. Soc.* **1988**, *110*, 4068–4070.
[7] E. A. Zarate, C. A. Tessier-Youngs, W. J. Youngs, *J. Chem. Soc., Chem. Commun.* **1989**, 577–578.
[8] A. E. Anderson, P. Shiller, E. A. Zarate, C. A. Tessier-Youngs, W. J. Youngs, *Organometallics* **1989**, *8*, 2320.
[9] M. Okazaki, K. A. Jung, H. Tobita, *Organometallics* **2005**, *24*, 659–664.
[10] X. Zhu, B. Zhao, B. Wang, Y. Zhao, S. Bi, *Chem. Phys. Lett.* **2006**, *422*, 6–10.
[11] L. J. Procopio, P. J. Carroll, D. H. Berry, *J. Am. Chem. Soc.* **1991**, *113*, 1870–1872.
[12] L. J. Procopio, P. J. Carroll, D. H. Berry, *Organometallics* **1993**, *12*, 3087–3093.
[13] L. J. Procopio, P. J. Carroll, D. H. Berry, *Polyhedron* **1995**, *14*, 45–55.
[14] C. S. Cramer, *Essentials of Computational Chemistry, Theories and Models*, John Wiley & Sons, New York, **2002**.
[15] C. Lee, W. Yang, G. Parr, *Phys. Rev. B* **1988**, *37*, 785.
[16] A. D. Becke, *J. Chem. Phys.* **1993**, *98*, 5648.
[17] C. Gonzalez, H. B. Schlegel, *J. Chem. Phys.* **1989**, *90*, 2154.
[18] C. Gonzalez, H. B. Schlegel, *J. Chem. Phys.* **1990**, *94*, 5523.
[19] M. J. Frisch, G. W. Trucks, H. B. Schlegel, G. E. Scuseria, M. A. Robb, J. R. Cheeseman, V. G. Zakrzewski, J. A. Montgomery Jr, R. E. Stratmann, J. C. Burant, S. Dapprich, J. M. Millam, A. D. Daniels, K. N. Kudin, M. C. Strain, O. Farkas, J. Tomasi, V. Barone, M. Cossi, R. Cammi, B. Mennucci, C. Pomelli, C. Adamo, S. Clifford, J. Ochterski, G. A. Petersson, P. Y. Ayala, Q. Cui, K. Morokuma, D. K. Malick, A. D. Rabuck, K. Raghavachari, J. B. Foresman, J. Cioslowski, J. V. Otitz, B. B. Stefanov, G. Liu, A. Liashenko, P. Piskorz, I. Komaromi,

 © 2007 Wiley-VCH Verlag GmbH & Co. KGaA, Weinheim 

R. Gomperts, R. L. Martin, D. J. Fox, T. Keith, M. A. Al-Laham. C. Y. Peng, A. Nanayakkara, C. Gonzales, M. Challacombe, P. M. W. Gill, B. Johnson, W. Chen, M. W. Wong, J. L. Andres, M. Head-Gordon, E. S. Replogle, and J. A. Pople, *Gaussian 98 Revision A.5*, Gaussian, Inc., Pittsburgh, PA, **1998**.
[20] S. Bi, Z. Lin, R. F. Jordan, *Organometallics* **2004**, *23*, 4882–4890.
[21] S. Bi, A. Ariafard, G. Jia, Z. Lin, *Organometallics* **2005**, *24*, 680–686.
[22] S. Bi, B. Wang, Y. Zhao, Z. Zhang, S. Zhu, *Chem. Phys. Lett.* **2006**, *426*, 192–196.
[23] A. Ariafard, S. Bi, Z. Lin, *Organometallics* **2005**, *24*, 2241–2244.
[24] L. J. Procopio, P. J. Carroll, D. H. Berry, *J. Am. Chem. Soc.* **1994**, *116*, 177–185.
[25] T. A. Albright, J. K. Burdett, M.-H. Whangbo, *Orbital Interactions in Chemistry*, John Wiley & Sons, New York, **1985**, pp. 394–398.
[26] T. Ziegler, A. Rauk, *Theor. Chim. Acta* **1977**, *46*, 1.
[27] J. Zhu, G. Jia, Z. Lin, *Organometallics* **2006**, *25*, 1812–1819.
[28] T. R. Cundari, C. D. Taylor, *Organometallics* **2003**, *22*, 4047.
[29] G. Altakhin, H. A. Skinner, A. A. Zaki, *J. Chem. Soc., Dalton Trans.* **1984**, 371.
[30] S. R. Foley, R. A. Stockland, H. Shen, R. F. Jordan, *J. Am. Chem. Soc.* **2003**, *125*, 4350.

Received: December 1, 2006
Published Online: April 10, 2007

 © 2007 Wiley-VCH Verlag GmbH & Co. KGaA, Weinheim 

DOI: 10.1002/ejic.200601158

# Synthesis, Structures and Properties of Cluster Complexes $[H_3O(Ph_3PO)_3]_2[Mo_6Cl_{14}]$ and $[H(Ph_3PO)_2]_2[Re_6S_6Br_8]$

**Zhyldyz S. Kozhomuratova,[a] Yuri V. Mironov,[a] Michael A. Shestopalov,[a] Irina V. Drebushchak,[a] Nikolay K. Moroz,[a] Dmitry Y. Naumov,[a] Anton I. Smolentsev,[a] Evgenii M. Uskov,[a] and Vladimir E. Fedorov*[a]**

**Keywords:** Cluster compounds / Molybdenum / Rhenium / Triphenylphosphane oxide / Crystal structure / NMR spectroscopy / Hydrogen bonding

New cluster compounds $[H_3O(Ph_3PO)_3]_2[Mo_6Cl_{14}]$ (**I**) and $[H(Ph_3PO)_2]_2[Re_6S_6Br_8]$ (**II**) have been prepared by the reaction of a acetonitrile solution of triphenylphosphane oxide $Ph_3PO$ with octahedral cluster complexes of molybdenum $(H_3O)_2Mo_6Cl_{14}\cdot 6H_2O$ and rhenium $K_2Re_6S_6Br_8$, respectively, (with addition of several drops of HBr). The structures and properties of the products were studied by single-crystal X-ray diffraction and NMR and luminescence spectroscopic methods. The compounds studied are characterized by strong hydrogen bonds with O–O distances of 2.45–2.51 Å (**I**) and 2.34–2.41 Å (**II**); unusual H-bonded cationic trimers, $[H_3O(Ph_3PO)_3]^+$, were found in compound **I**.
(© Wiley-VCH Verlag GmbH & Co. KGaA, 69451 Weinheim, Germany, 2007)

## Introduction

The reactions of triphenylphosphane oxide ($Ph_3PO$) with various acids give molecular compounds of different types. Compounds with the stoichiometry $Ph_3PO$/acid = 1:1 are formed for the reactions with $HNO_3$,[1] HF,[2] HCl,[3] HBr,[4] $CCl_3COOH$.[5] Compounds with a $Ph_3PO$/acid ratio of 2:1 are also found – $(Ph_3PO)_2\cdot H_2O\cdot HBr$,[6] $(Ph_3PO)_2\cdot(CH_3)_2C(COOH)$,[7] $(Ph_3PO)_2\cdot HAuCl_4$,[8] $(Ph_3PO)_2\cdot HClO_4$.[9] The compounds that form from triphenylphosphane oxide and acids can be separated into three main groups depending on the nature of the interaction between the acidic protons and the $Ph_3PO$ molecules.[9] The first group includes compounds in which the hydrogen atoms belong more to the acid than to the $Ph_3PO$ molecule, as, for example, in the case of $Ph_3PO\cdot CCl_3COOH$. In such compounds, the lengths of the P=O bonds are close to those observed in the free $Ph_3PO$ molecule (1.487 Å).[10] In the second group, on the contrary, the proton lies more towards $Ph_3PO$, which results in a remarkable lengthening of the P=O bond. Such compounds can be considered as ionic pairs (e.g. $[Ph_3POH]^+Cl^-$), and their formation is typical of non-oxygen acids. The third group combines the compounds in which the $Ph_3PO$ molecules are bound together by strong symmetrical or non-symmetrical hydrogen bonds, but the anions do not participate in the hydrogen bonding. A typical example of such compounds is $(Ph_3PO)_2HClO_4$, where the two triphenylphosphane oxide fragments are bound together by very short (2.41 Å) hydrogen bonds to form a dimer cation $[Ph_3PO\cdots H\cdots OPPh_3]^+$.[9]

The interaction of chloromolybdenic(II) acid $(H_3O)_2Mo_6Cl_{14}$ with triphenylphosphane oxide was first studied by Sheldon,[11] but the reaction products were not described thoroughly enough and their structure was not studied.

In this paper we present the synthesis of two novel cluster compounds containing $Ph_3PO$ molecules: $[H_3O(Ph_3PO)_3]_2[Mo_6Cl_{14}]$ (**I**) and $[H(Ph_3PO)_2]_2[Re_6S_6Br_8]$ (**II**). In the frame of the above classification, these compounds can be assigned to the third group, since their triphenylphosphane oxide molecules are connected by strong hydrogen bonds to form large cationic complexes: dimers $[H(Ph_3PO)_2]^+$ (in **II**) and unusual trimers $[H_3O(Ph_3PO)_3]^+$ (in **I**). Inspection of the Cambridge crystallographic database showed that the trimeric cation, namely tris(oxotriphenylphosphane)-oxonium, has not been mentioned in the literature so far. Therefore, it is interesting to consider its structure in detail. The structures of the H-bonded complexes **I** and **II** were solved by single-crystal X-ray diffraction and examined by solid-state NMR spectroscopy.

## Results and Discussion

The interaction of the cluster acid $(H_3O)_2Mo_6Cl_{14}$ and triphenylphosphane oxide gives a complex compound $[H_3O(Ph_3PO)_3]_2[Mo_6Cl_{14}]$ (**I**). The unit cell of compound **I** contains one centrosymmetrical and two noncentrosymmetrical $[Mo_6Cl_{14}]^{2-}$ anions formed by slightly distorted $Mo_6$ octahedrons with Mo–Mo distances of 2.594–2.608 Å (Table 1, Figure 1, Figure 2). The lengths of the Mo–Cl

[a] Nikolaev Institute of Inorganic Chemistry, Siberian Branch of Russian Academy of Sciences,
3, Akad. Lavrentiev prospect, Novosibirsk, 630090, Russia
E-mail: fed@che.nsk.su

 © 2007 Wiley-VCH Verlag GmbH & Co. KGaA, Weinheim 

Table 1. Crystallographic data for compounds **I** and **II**.

| | **I** | **II** |
|---|---|---|
| Chemical formula | $C_{108}H_{96}Cl_{14}Mo_6O_8P_6$ | $C_{72}H_{62}Br_8O_4P_4Re_6S_6$ |
| Formula weight | 2779.61 | 3063.94 |
| Crystal size [mm] | $0.40 \times 0.40 \times 0.40$ | $0.12 \times 0.10 \times 0.08$ |
| Crystal system | triclinic | triclinic |
| Space group | $P\bar{1}$ | $P\bar{1}$ |
| $a$ [Å] | 13.5625(10) | 13.2357(4) |
| $b$ [Å] | 22.6936(17) | 18.1285(6) |
| $c$ [Å] | 29.316(2) | 18.7516(6) |
| $\alpha$ [°] | 103.240(2) | 94.5280(10) |
| $\beta$ [°] | 99.354(2) | 104.9130(10) |
| $\gamma$ [°] | 91.857(2) | 105.6660(10) |
| $V$ [Å$^3$] | 8643.4(11) | 4132.6(2) |
| $Z$ | 3 | 2 |
| $D_{calcd.}$ [Mg/m$^3$] | 1.602 | 2.462 |
| Diffractometer | Bruker Nonius X8Apex | Bruker Nonius X8Apex |
| Temperature [K] | 293(2) | 298(2) |
| $\mu$(Mo-$K_\alpha$) [mm$^{-1}$] | 1.094 | 12.894 |
| $\theta$ range for data collection [°] | 1.30 to 25.68 | 1.50 to 28.26 |
| Absorption correction | multiscan (SADABS; Bruker 2004) | multiscan (SADABS; Bruker 2004) |
| Goodness-of-fit on $F^2$ | 0.965 | 0.953 |
| Reflections collected/unique | 46022/32128 [$R_{int}$ = 0.0200] | 34098/20065 [$R_{int}$ = 0.0431] |
| Final $R$ indices [$I > 2\sigma(I)$] | $R_1$ = 0.0440, $wR_2$ = 0.0871 | $R_1$ = 0.0480, $wR_2$ = 0.0992 |
| $R$ indices (all data) | $R_1$ = 0.0939, $wR_2$ = 0.1018 | $R_1$ = 0.1054, $wR_2$ = 0.1132 |
| $\Delta\rho$(max; min) [e Å$^{-3}$] | 0.476; –0.710 | 1.941; –1.558 |

bonds, 2.421(8) Å and 2.472(5) Å for terminal and bridged ligands, respectively, are typical of those observed in related clusters.[12–14] The formation of the unusual cationic complex ion $[H_3O(Ph_3PO)_3]^+$ (Figure 3) is a distinctive feature of the structure. Such structures consist of three triphenylphosphane oxide molecules that are H-bonded to a central oxygen atom ($O_W$) to form a trigonal pyramid $\{O_3O_W\}$ (see the inset in Figure 3). The O–$O_W$ lengths (Table 2) range between 2.449 Å and 2.504 Å, which indicates relatively strong hydrogen bonding. The angles O–$O_W$–O are within the range 99.1–110.4°. However, as is evident from Table 2, the H-bonding does not lead to considerable deformation of the P=O bonds. Relative to unbound $Ph_3PO$,[10,15] the bonds are approximately 0.01 Å longer. This fact might be indicative of a shift in the positions of the protons towards the central oxygen atom to form the $H_3O^+$ ion as a cation–complex core.

We studied the H-bond geometry by $^1$H NMR wide-line spectroscopy. The NMR spectrum of the compound **I** (Figure 4) is determined mainly by magnetic dipole–dipole interactions of the $C_6H_5$ ring protons, whereas the protons involved in the hydrogen bonds, which are closer together and therefore coupled more strongly, are represented as very feeble tails at the absorption edges. In this regard, we considered the spectral domains at frequencies $|\Delta f|$ = (25 – 60) kHz where the influence of the aromatic protons is not overwhelming. The spectra recorded below 200 K were chosen for analysis since higher temperatures result in significant narrowing of the NMR spectra because of increased proton mobility. The simulation of the spectrum was performed by an approach outlined in the Experimental Section. The best fits to the experimental spectra were obtained for a three-spin configuration close to equilateral (the distortion of the triangle sides does not exceed 2%), with an average proton–proton distance of 1.76(1) Å. On the basis of these assessments and by supposing the linearity of the

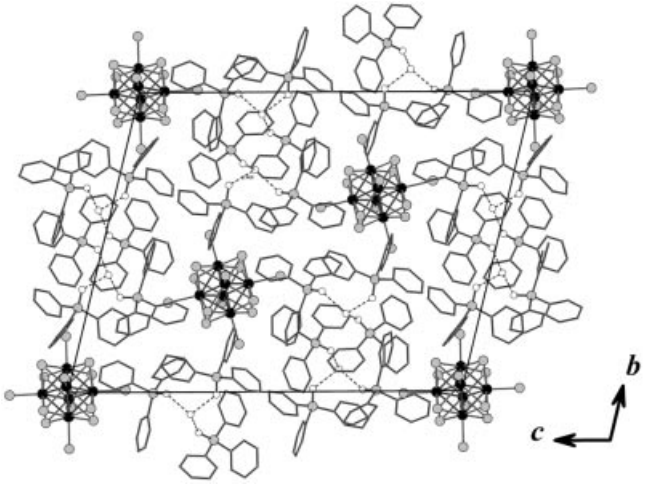


Figure 1. Packing in the crystal structure of $[H_3O(OPPh_3)_3]_2[Mo_6Cl_{14}]$.

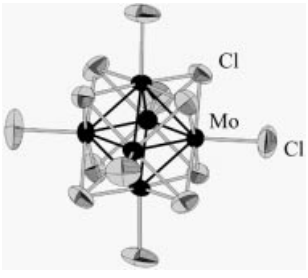


Figure 2. The structure of the cluster anion $[Mo_6Cl_{14}]^{2-}$ in compound **I**. Displacement ellipsoids are drawn at the 50% probability level.

 © 2007 Wiley-VCH Verlag GmbH & Co. KGaA, Weinheim 

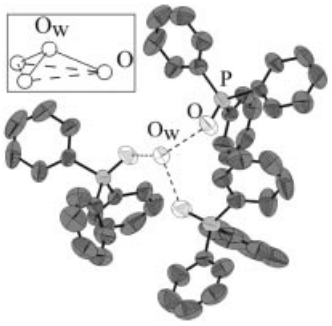


Figure 3. The structure of the cation $[H_3O(OPPh_3O)_3]^+$ in compound **I**. Displacement ellipsoids are drawn at the 50% probability level.

Table 2. Interatomic distances [Å] for the hydrogen bonds in compound **I**.

| | $O_W\cdots O^{[a]}$ | $O–H^{[b]}$ | $H\cdots O^{[b]}$ | $\cdots O=P^{[a]}$ |
|---|---|---|---|---|
| Cation 1 | | | | |
| O1W–H···O5 | 2.489(4) | 1.09 | 1.40 | 1.497(3) |
| O1W–H···O7 | 2.461(4) | 1.11 | 1.35 | 1.494(3) |
| O1W–H···O8 | 2.518(5) | 1.11 | 1.40 | 1.491(3) |
| Cation 2 | | | | |
| O2W–H···O1 | 2.470(6) | 1.17 | 1.30 | 1.495(4) |
| O2W–H···O2 | 2.486(5) | 1.12 | 1.37 | 1.495(3) |
| O2W–H···O3 | 2.478(5) | 1.11 | 1.37 | 1.504(3) |
| Cation 3 | | | | |
| O3W–H···O4 | 2.481(5) | 1.11 | 1.38 | 1.491(3) |
| O3W–H···O6 | 2.487(5) | 1.09 | 1.40 | 1.502(3) |
| O3W–H···O9 | 2.492(5) | 1.12 | 1.37 | 1.489(3) |

[a] Values obtained from crystal structure determination. [b] Values estimated from NMR spectroscopic data (no corrections for the $H_3O$ librations were made).

O–H···O bonds, we estimated the proton positions in the hydrogen bonds. On the whole, the obtained proton arrangement (Table 2) corresponds to asymmetrical H-bonding with the mean distances of 1.11(2) and 1.37(3) Å for $O_W$–H and H···O, respectively, which are in satisfactory agreement with the experimental correlation of O–H vs. H···O found for the oxonium ions in inorganic crystals.[16] Therefore, the discussed complex ion can be named *tris-(oxotriphenylphosphane)oxonium*.

The complex $[H_3O(Ph_3PO)_3]_2[Mo_6Cl_{14}]$ is brightly luminescent in the red and near infrared regions of the emission spectrum (Figure 5). It is interesting to note that the intensity of its emission is almost twice as high as that for the initial compound $(H_3O)_2Mo_6Cl_{14}\cdot 6H_2O$. Recently we observed similar luminescence behaviour in some related complexes $[Ca(DMF)_6][Mo_6Cl_{14}]$ and $[Ca(Ph_3PO)_4][Mo_6Cl_{14}]$;[15] the emission intensities for these two complexes are four and six times higher than that for $(H_3O)_2Mo_6Cl_{14}\cdot 6H_2O$.

We tried to find a similar cationic complex ion (as in **I**) in the related rhenium system containing the isoelectronic cluster complex $[Re_6S_6Br_8]^{2-}$ with similar geometric characteristics. The interaction of the rhenium complex $K_2Re_6S_6Br_8$ with triphenylphosphane oxide was carried out in acetonitrile solution with the addition of several drops of HBr. Indeed, we succeeded in obtaining a similar complex

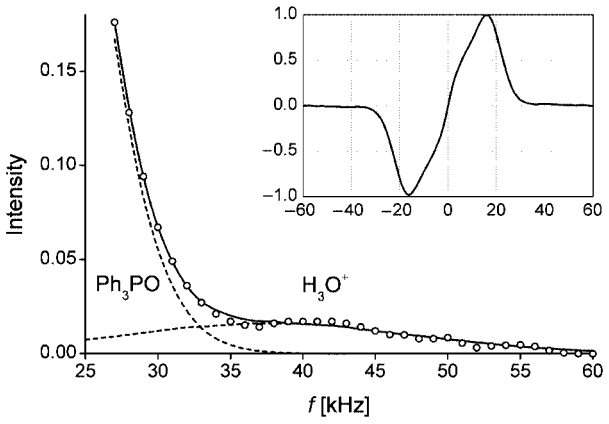


Figure 4. Fragment of the $^1H$ NMR absorption derivative for $[H_3O(Ph_3PO)_3]_2[Mo_6Cl_{14}]$ at 180 K (○) (the complete spectrum is illustrated in the inset). The best fit to the experimental spectrum is shown as a solid line. The dashed curves correspond to the contributions of the $H_3O^+$ and the $Ph_3PO$ protons.

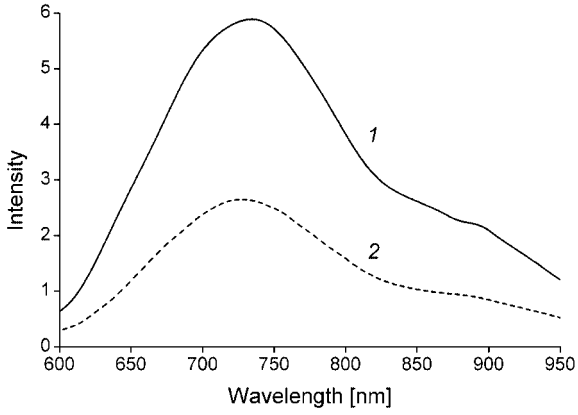


Figure 5. Luminescence spectrum of $[H_3O(OPPh_3)_3]_2[Mo_6Cl_{14}]$ (1) and $(H_3O)_2Mo_6Cl_{14}\cdot 6H_2O$ (2).

$[H_3O(Ph_3PO)_3]_2[Re_6S_6Br_8]$ (**III**) with unit-cell parameters [$a$ = 13.699(3) Å, $b$ = 22.731 Å, $c$ = 29.596(5) Å, $\alpha$ = 102.889(8)°, $\beta$ = 99.129(5)°, $\gamma$ = 92.202(5)°] similar to those observed for **I** (Table 1). Unfortunately, compound **III** crystallized with a very small yield, and several crystals that were isolated had poor quality and were therefore unsuitable for single-crystal X-ray analysis.

In the $K_2Re_6S_6Br_8$–$Ph_3PO$–HBr system, another new complex with the composition $[H(Ph_3PO)_2]_2[Re_6S_6Br_8]$ (**II**) was obtained in a high yield (Table 1, Figure 6). In **II**, there are two types of cluster anions, $[Re_6S_2(S_{2/3}Br_{1/3})_6Br_6]^{2-}$ and $[Re_6S_4(S_{1/2}Br_{1/2})_4Br_6]^{2-}$, with different distributions of the $\mu_3$ ligands (Figure 7). In $[Re_6S_2(S_{2/3}Br_{1/3})_6Br_6]^{2-}$, four sulfur and two bromine atoms alternatively occupy six corners of a cube; in $[Re_6S_4(S_{1/2}Br_{1/2})_4Br_6]^{2-}$, two sulfur and two bromine atoms are distributed over four positions. The interatomic distances for both isomers are summarized in Table 3. The observation of similar cluster isomers among octahedral cluster complexes is not unexpected. In particular, it was shown[17] that in the related complex $[\{Re_6Se_6Br_2\}Br_6]^{2-}$, the cluster core $[Re_6Se_6Br_2]^{4+}$ is repre-

 © 2007 Wiley-VCH Verlag GmbH & Co. KGaA, Weinheim 

sented by three isomers that can be identified in solution by $^{77}Se$ NMR spectroscopy.

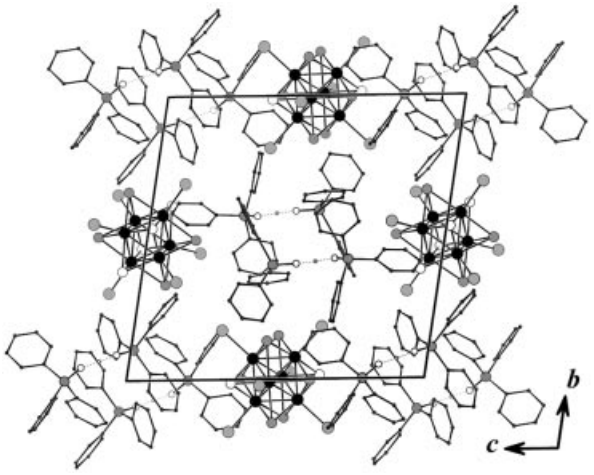


Figure 6. Packing in the crystal structure of $[H(Ph_3PO)_2]_2$-$[Re_6S_6Br_8]$.

In compound **II**, the triphenylphosphane oxide molecules are integrated into H-bonded dimers $[H(OPPh_3)_2]^+$ (Figure 8) with very short O–O distances of 2.34(1) Å and 2.41(1) Å for the two structurally nonequivalent dimers in the unit cell. Note that one of these distances is even less than the known limit (2.39 Å) usually associated with the formation of the symmetric O–H–O bond.[16] The P=O bond lengths are essentially different in each of the dimers: 1.483(8) and 1.549(7) Å, 1.488(10) and 1.523(8) Å. This difference might possibly be explained by the asymmetric proton positions in the hydrogen bonds, i.e. the protons are shifted from the bond centres towards the oxygen atoms with longer P=O contacts.[9] In this regard, of interest is the MAS $^1H$ NMR spectrum (Figure 9): the protons involved in H-bond formation give rise to a diffuse peak with a chemical shift $\delta$ of 17.5(5) ppm. The observed $\delta$ value differs noticeably from the shift of 21.6 ppm expected for a symmetrical bond.[18] On the basis of the various experimental correlations between the chemical shift and hydrogen-bond geometry,[18,19] the proton displacements from the bond

Table 3. Bond lengths [Å] in the cluster anions $[Re_6S_6Br_8]^{2-}$ of compound **II**.[a]

| $[Re_6S_2(S_{2/3}Br_{1/3})_6Br_6]^{2-}$ | | $[Re_6S_4(S_{1/2}Br_{1/2})_4Br_6]^{2-}$ | |
|---|---|---|---|
| **Re–Re** | | **Re–Re** | |
| Re(1)–Re(2) | 2.5978(5) | Re(4)–Re(6)#2 | 2.5959(6) |
| Re(1)–Re(2)#1 | 2.6101(6) | Re(4)–Re(6) | 2.5964(6) |
| Re(1)–Re(3)#1 | 2.6112(6) | Re(4)–Re(5) | 2.6005(6) |
| Re(1)–Re(3) | 2.5929(6) | Re(4)–Re(5)#2 | 2.6055(5) |
| Re(2)–Re(3)#1 | 2.6114(6) | Re(6)–Re(5)#2 | 2.5886(6) |
| Re(2)–Re(3) | 2.5996(6) | Re(6)–Re(5) | 2.6071(5) |
| **Re–S** | | **Re–S** | |
| Re(1)–S(1) | 2.408(3) | Re(4)–S(6) | 2.454(2) |
| Re(2)–S(1) | 2.416(3) | Re(4)–S(7) | 2.455(2) |
| Re(3)–S(1) | 2.407(3) | Re(5)–S(6)#2 | 2.440(2) |
| **Re–Q$^i$ (S, Br)** | | Re(5)–S(7) | 2.434(3) |
| Re(1)–Q(2) | 2.498(2) | Re(6)–S(6) | 2.447(3) |
| Re(1)–Q(3) | 2.5226(19) | Re(6)–S(7)#2 | 2.447(2) |
| Re(1)–Q(4) | 2.522(2) | **Re–Q$^i$ (S, Br)** | |
| Re(2)–Q(2)#1 | 2.493(2) | Re(4)–Q(5) | 2.493(2) |
| Re(2)–Q(3) | 2.536(2) | Re(4)–Q(8) | 2.514(2) |
| Re(2)–Q(4)#1 | 2.510(2) | Re(5)–Q(5) | 2.507(2) |
| Re(3)–Q(2) | 2.478(2) | Re(5)–Q(8)#2 | 2.511(2) |
| Re(3)–Q(3)#1 | 2.5297(19) | Re(6)–Q(5) | 2.521(2) |
| Re(3)–Q(4)#1 | 2.5006(19) | Re(6)–Q(8)#2 | 2.522(2) |
| **Re–Br** | | **Re–Br** | |
| Re(1)–Br(1) | 2.5234(11) | Re(4)–Br(9) | 2.5358(13) |
| Re(2)–Br(5) | 2.5368(12) | Re(5)–Br(10) | 2.5336(11) |
| Re(3)–Br(6) | 2.5401(13) | Re(6)–Br(11) | 2.5180(13) |

[a] Symmetry transformations used to generate equivalent atoms: #1 $-x+1, -y, -z+1$; #2 $-x+1, -y-1, -z$.

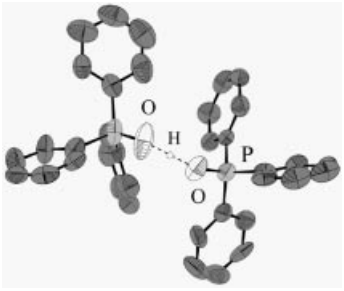


Figure 8. The structure of cation $[(Ph_3PO)_2H]^+$ in compound **II**. Displacement ellipsoids are drawn at the 50% probability level.

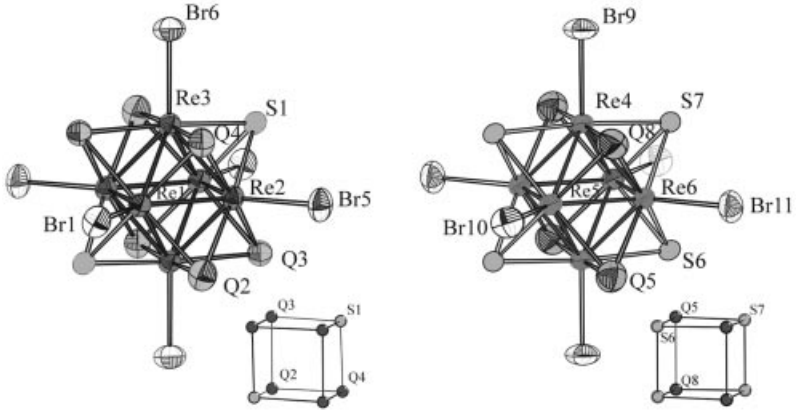


Figure 7. The structures of the cluster anions $[Re_6S_6Br_8]^{2-}$ in compound **II**. Q – mixed S/Br positions. Displacement ellipsoids are drawn at the 50% probability level.

 © 2007 Wiley-VCH Verlag GmbH & Co. KGaA, Weinheim 

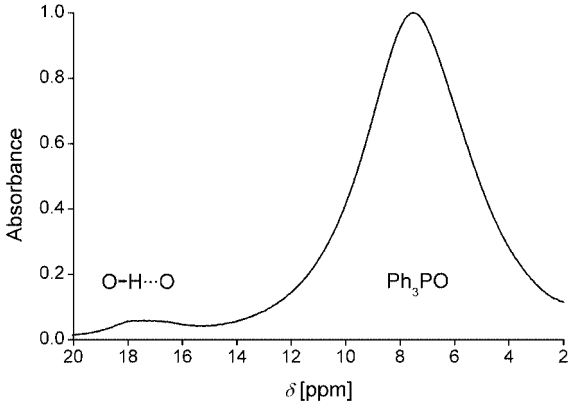


Figure 9. MAS $^1$H NMR spectrum of $[H(Ph_3PO)_2]_2[Re_6S_6Br_8]$.

centre were estimated to fall in the range from 0.13 to 0.17 Å.

The obtained experimental results together with those cited in the literature allow us to predict that triphenylphosphane oxide in acid solutions is able to form several protonated complex ions, namely $[HOPPh_3]^+$, $[H(OPPh_3)_2]^+$, $[(H_3O)(OPPh_3)_2]^+$ and $[(H_3O)(OPPh_3)_3]^+$, which can exist simultaneously in chemical equilibrium with each other. The question "What forms can be isolated in proper complexes?" can be answered differently depending on the specific chemical system to be studied. The oxonium ion $H_3O^+$ plays a key role in the formation of cationic trimeric complex ion $[H_3O(OPPh_3)_3]^+$ (a single proton involved in the formation of $[HOPPh_3]^+$ or $[H(OPPh_3)_2]^+$ is obviously not able to interact with a third oxygen atom). In solids containing $OPPh_3$ and large cluster anions, we have discovered the cationic complex ion $[H(OPPh_3)_2]^+$ (observed earlier[9]) and a novel complex ion $[H_3O(OPPh_3)_3]^+$. These complex ions resemble well-known protonated complexes inherent to hydrated systems (Zundel complex $[H_5O_2]^+$[20] and Eigen complex $[H_9O_4]^+$[21] in which the $H_2O$ molecules are replaced by $OPPh_3$) owing to the type of solvation observed in these complexes.

## Experimental Section

**Materials and Methods:** Starting compounds were prepared by known methods described in the literature. $Mo_6Cl_{12}$ was synthesized by the method described previously.[22] $(H_3O)_2Mo_6Cl_{14}\cdot 6H_2O$ was prepared by dissolution of $Mo_6Cl_{12}$ in hot concentrated HCl. The solution was filtered and $(H_3O)_2Mo_6Cl_{14}\cdot 6H_2O$ was crystallized by cooling of the solution. The precipitate was washed with cold water and dried in air. $K_2[Re_6S_6Br_8]$ was synthesized as described previously.[23] Other reagents were purchased from Aldrich and used as received without additional treatment. Elemental analyses (Carlo Erba Instrument EA1106) were performed by the laboratory of microanalysis at the Vorozhtsov Institute of Organic Chemistry, Siberian Branch of Russian Academy of Sciences.

**Synthesis of $[H_3O(Ph_3PO)_3]_2[Mo_6Cl_{14}]$ (I):** $(H_3O)_2Mo_6Cl_{14}\cdot 6H_2O$ (100 mg, 0.08 mmol) was dissolved in acetonitrile (10 mL), and $Ph_3PO$ (300 mg, 1.1 mmol) was dissolved in acetonitrile (10 mL). The solutions obtained were mixed, boiled for 5 min and evaporated until a crystalline precipitate began to form. Then the solution was cooled. The crystals were filtered and washed with diethyl ether (5 mL). Yield: 170 mg (61%). Single crystals for X-ray diffraction analysis were separated from the precipitate. The XPD pattern of solid **I** agreed well with the pattern calculated from the single-crystal parameters. $C_{108}H_{96}Cl_{14}Mo_6O_8P_6$ (2779.61): calcd. C 46.67, H 3.48; found C 46.61, H 3.60%.

**Synthesis of $[H(Ph_3PO)_2]_2[Re_6S_6Br_8]$ (II):** $K_2Re_6S_6Br_8$ (100 mg, 0.04 mmol) was dissolved in acetonitrile (10 mL), and $Ph_3PO$ (100 mg, 0.36 mmol) was dissolved in acetonitrile (10 mL). The solutions obtained were mixed, a drop of HBr was added and the solution boiled for 2–3 min. The solution was filtered, and the filtrate was evaporated to a volume of 10 mL, after which diffusion was carried out using ether. Bright red vinous crystals precipitated, which were collected. Single crystals for X-ray diffraction analysis were separated from the precipitate manually. Yield 95 mg (63%). A further amount of the compound could be obtained from the mother liquor by evaporation. The XPD pattern of solid **II** agreed with the pattern calculated from the single-crystal parameters. $C_{72}H_{62}Br_8O_4P_4Re_6S_6$ (3063.94): calcd. C 28.22, H 2.04; found C 28.39, H 2.18%.

**Crystallography:** The structures of complexes **I** and **II** were solved by X-ray diffraction analysis of single crystals. The diffraction data were collected on a Bruker-Nonius X8APEX CCD diffractometer by using Mo-$K_\alpha$ (0.71073 Å) radiation and a graphite monochromator. The absorption corrections were semiempirical using the intensities of equivalent reflections and the SADABS software.[24] The structures were solved by direct methods and refined by full-matrix least-squares on $F^2$; anisotropic approximation for non-hydrogen atoms using the program package SHELXL.[25] The crystallographic and experimental details are given in Table 1. CCDC 614149 (**I**) and 614150 (**II**) contain the supplementary crystallographic data for this paper. These data can be obtained free of charge from The Cambridge Crystallographic Data Centre via www.ccdc.cam.ac.uk/data_request/cif.

**NMR Spectroscopy:** MAS $^1$H NMR measurements for **II** were performed at room temperature with a Bruker Advance 400 spectrometer at 400.13 MHz. The π/2 rf-pulse width and the recycle delay were 10 μs and 60 s, respectively. The spectra were recorded at rotation frequencies in the range 10–20 kHz using a 4-mm $ZrO_2$ rotor. The powder sample was prepared by several synthesis cycles described above. The $^1$H chemical shift was measured relative to the resonance of TMS. The wide-line $^1$H NMR spectrum of **I** was recorded in the form of the first derivative of the NMR absorption line by sweeping the frequency in the neighbourhood of 25 MHz in the temperature range 180–350 K with a home-made NMR spectrometer with signal accumulation. For the analyzed spectra, the signal/noise ratio reached about $3\times10^3$. The $H_3O^+$ spectra, as a function of the proton–proton distances $r_1$, $r_2$ and $r_3$, were simulated with a known three-spin approximation.[26,27] The contribution of the aromatic protons in the analyzed frequency region was approximated by a rectangle-Gaussian convolution function[28] determined by two parameters: $a$ and $b$ for the rectangle and Gaussian, respectively. This gives the NMR absorption derivative for a powder in the form:

$$F(f) \sim -c/(4\pi\beta^3)\int\sum J_i(f-\delta_i)\exp[-(f-\delta_i)^2/2\beta^2]d\Omega$$

$$+ (1-c)/(2ab)\{\exp[-(f+a)^2/2b^2] - \exp[-(f-a)^2/2b^2]\}$$

where $J_i$ and $\delta_i$ are corresponding intensities and line positions of the $H_3O^+$ NMR septet,[27] which depend on $r_i$ and the orientation (Ω) of the proton triangle with respect to the external magnetic field; $\beta$ is the parameter of the spectral broadening due to the di-

 © 2007 Wiley-VCH Verlag GmbH & Co. KGaA, Weinheim 

polar interactions of the $H_3O^+$ group with surrounding protons; $c$ is the concentration of the $H_3O^+$ protons. In the frequency ranges $|\Delta f| = (25 - 60)$ kHz, the discrepancy between the experimental spectra and the best fits obtained with this equation is about 2.5%.

**Luminescence Spectroscopy:** Luminescence spectra were recorded at room temperature by using the spectrometer SDL-1 with the photoelectron multiplier PEM-62. The excitation source was a mercury lamp of type DRSH-250 with a 365-nm filter. The measured samples had the shape of square pellets of equal size.

## Acknowledgments

This work was supported by the Russian Foundation for Basic Research, projects no. 05–03–32123, 05–03–08090 and 06–03–89503-HHC. The authors thank Prof. O. Lapina and Dr. K. Romanenko for recording MAS $^1$H NMR spectra.

[1] D. Hadzi, *J. Chem. Soc.* **1962**, 5128–5138.
[2] D. Thierbach, F. Huber, *Z. Anorg. Allg. Chem.* **1979**, *451*, 137–142.
[3] H. J. Haupt, F. Huber, C. Kruger, H. Preut, D. Thierbach, *Z. Anorg. Allg. Chem.* **1977**, *436*, 229–236.
[4] H. P. Lane, C. A. McAuliffe, R. G. Pritchard, *Acta Crystallogr., Sect. C* **1992**, *48*, 2002–2004.
[5] L. Golic, V. Kaucic, *Cryst. Struct. Commun.* **1976**, *5*, 319–324.
[6] D. Thierbach, F. Huber, *Z. Anorg. Allg. Chem.* **1979**, *457*, 189–196.
[7] J. P. Declercq, G. Germain, J. P. Putzeys, S. Rona, M. van Meerssche, *Cryst. Struct. Commun.* **1974**, *3*, 579–582.
[8] P. G. Jones, G. M. Sheldrick, *Acta Crystallogr., Sect. B* **1978**, *34*, 1353–1355.
[9] M. Yu. Antipin, A. E. Kalinin, Yu. T. Struchkov, E. I. Matrosov, M. I. Kabachnik, *Kristallographiya* **1980**, *25*, 514–524 (in Russian).
[10] J. A. Thomas, T. A. Hamor, *Acta Crystallogr., Sect. C* **1993**, *49*, 355–357.
[11] J. C. Sheldon, *J. Chem. Soc.* **1961**, 750–752.
[12] W. Preetz, G. Peters, D. Bublitz, *Chem. Rev.* **1996**, *96*, 977–1025.
[13] N. Prokopuk, D. F. Shriver, *Adv. Inorg. Chem.* **1999**, *46*, 1–49.
[14] T. G. Gray, *Coord. Chem. Rev.* **2003**, *243*, 213–235.
[15] Z. S. Kozhomuratova, Y. V. Mironov, M. A. Shestopalov, Ya, M. Gaifulin, N. V. Kutatieva, E. M. Uskov, V. E. Fedorov, *Russ. J. Coord. Chem.* **2007**, *33*, 1–6.
[16] Th. Steiner, W. Saenger, *Acta Crystallogr., Sect. B* **1994**, *50*, 348–357.
[17] S. S. Yarovoi, S. F. Solodovnikov, S. V. Tkachev, Yu. V. Mironov, V. E. Fedorov, *Russ. Chem. Bull.* **2003**, *52*, 68–72.
[18] Th. Emmler, S. Gieschler, H. H. Limbach, G. Buntkowsky, *J. Mol. Struct.* **2004**, *700*, 29–38.
[19] E. Brunner, U. Sternberg, *Prog. Nucl. Magn. Reson. Spectrosc.* **1998**, *32*, 21–57.
[20] G. Zundel, H. Metzger, *Z. Phys. Chem., Neue Folge* **1968**, *58*, 225–245.
[21] E. Wicke, M. Eigen, T. Ackerman, *Z. Phys. Chem., Neue Folge* **1954**, *1*, 340–364.
[22] A. V. Nikolaev, A. A. Opalovsky, V. E. Fedorov, in *Thermal Analysis*, Academic Press. Inc. New York, **1969**, vol. 2, p. 793–810.
[23] A. Slougui, S. Ferron, A. Perrin, M. Sergent, *J. Cluster Sci.* **1997**, *8*, 349–359.
[24] *SADABS* (Version 2.11), Bruker Advanced X-ray Solutions, Bruker AXS Inc., Madison, Wisconsin, USA, **2004**.
[25] *SHELXTL* (Version 6.12), Bruker Advanced X-ray Solutions, Bruker AXS Inc., Madison, Wisconsin, USA, **2004**.
[26] E. R. Andrew, B. Bersohn, *J. Chem. Phys.* **1950**, *18*, 159–161.
[27] E. R. Andrew, N. D. Finch, *Proc. Phys. Soc.* **1957**, *70B*, 980–990.
[28] A. Abragam, *The Principles of Nuclear Magnetism*, Clarendon Press, Oxford, **1961**.

Received: December 8, 2006
Published Online: March 30, 2007

 © 2007 Wiley-VCH Verlag GmbH & Co. KGaA, Weinheim 

DOI: 10.1002/ejic.200601170

# Bis(phenylethylamide) Derivatives of Gd-DTPA as Potential Receptor-Specific MRI Contrast Agents

**Sophie Laurent,[a] Tatjana N. Parac-Vogt,*[b] Kristof Kimpe,[b] Coralie Thirifays,[a] Koen Binnemans,[b] Robert N. Muller,[a] and Luce Vander Elst*[a]**

**Keywords:** Lanthanides / MRI contrast agents / N,O ligands / NMRD / $^{17}O$ NMR spectroscopy

DTPA-bis(amide) derivatives bearing phenyl, phenol or catechol groups that mimic side chains of naturally occurring amino acids, such as phenylalanine, tyrosine or dopamine, were synthesized and characterized by elemental analysis, electrospray mass spectrometry, NMR spectroscopy and IR spectroscopy. The gadolinium(III) complexes of the ligands DTPA-bis(tyramide) [DTPA-$(TA)_2$], DTPA-bis(3-hydroxytyramide) [DTPA-$(HTA)_2$] and DTPA-bis(phenylalanine ethyl ester) [DTPA-$(PAE)_2$], were prepared and then studied in vitro by $^{17}O$ NMR spectroscopy and by nuclear magnetic relaxation dispersion (NMRD) measurements. The residence time of the coordinated water in gadolinium(III) complexes was obtained from $^{17}O$ NMR relaxometric $T_2$ measurements. At 310 K, the following $\tau_M$ values were obtained: Gd-DTPA-$(TA)_2$ 582 ns, Gd-DTPA-$(HTA)_2$ 372 ns and Gd-DTPA-$(PAE)_2$ 809 ns. As shown by the analysis of the proton NMRD profiles, the larger proton relaxivities of the gadolinium(III) complexes at 310 K relative to that of the parent Gd-DTPA complex are mainly because of the increase in the rotational correlation time.
(© Wiley-VCH Verlag GmbH & Co. KGaA, 69451 Weinheim, Germany, 2007)

## Introduction

Magnetic resonance imaging (MRI) is a powerful diagnostic technique which is used for obtaining images of internal organs and tissues.[1] Nowadays, an increasing number of MRI scans are performed employing contrast agents, which are able to greatly increase the contrast between tissues in magnetic resonance images.[2] The efficiency of contrast agents is related to their ability to enhance the proton relaxation of water tissues. This property, called *relaxivity*, depends on different factors such as the molecular mobility of the contrast agent, the water dynamics and the noncovalent binding of the contrast agent to endogenous proteins.[3,4] In recent years, new developments in molecular imaging applications have prompted the development of a novel class of contrast agents characterized by a higher contrasting ability and improved targeting capabilities.

Several strategies have been explored in order to slow down the rotational motion of the gadolinium(III)-based contrast agents and thus to increase their relaxation efficiency. These approaches include (i) the synthesis of covalently or noncovalently bound macromolecular gadolinium(III) chelates such as dendrimers, linear polymers or proteins;[5–7] (ii) the synthesis of amphiphilic gadolinium(III) complexes which can self-assemble to micelles;[8,9] (iii) lipophilic gadolinium(III) complexes incorporated in supramolecular systems with a better control of the size such as mixed micelles;[10–12] and (iv) incorporation of amphipathic gadolinium(III) complexes into the membranes of liposomes.[13–17]

The properties of the contrast agents that are important for the tissue specificity include molecular size, charge and lipophilicity. Since most of the specific cell-cell interactions or recognitions are regulated by special proteins, receptor targeting can be attained by mimicking signal peptides. For example, adhesive proteins present in extracellular matrices and in blood, such as fibrinogen and collagens, contain the tripeptide arginine–glycine–aspartic acid as the cell recognition site.[18] Using this binding domain or similar sequences, small peptides can be designed to target receptors.[19] Additionally, some receptors have an affinity for certain classes of substrates such as amino acids or catechol amines.[20] These receptors may also bind molecules that resemble the substrate, for example, a derivative of an amino acid that is present in a peptide substrate or an amide derivative of a naturally occurring catechol amine such as dopamine. The coupling of these potential recognition groups to high relaxivity moieties such as $[Gd(DTPA)(H_2O)]^{2-}$ could thus lead to tissue specificity of the contrast agent.

In this paper we report on ligands based on bis(amide) derivatives of DTPA bearing phenyl, phenol or catechol groups that mimic the side chains of naturally occurring

[a] Department of General, Organic and Biomedical Chemistry, NMR and Molecular Imaging Laboratory, University of Mons-Hainaut,
7000 Mons, Belgium
Fax: +32-65-373520
E-mail: Luce.VanderElst@umh.ac.be
[b] Department of Chemistry, Katholieke Universiteit Leuven, Celestijnenlaan 200F, 3001 Leuven, Belgium
Fax: +32-16-327992
E-mail: Tatjana.Vogt@chem.kuleuven.be

 © 2007 Wiley-VCH Verlag GmbH & Co. KGaA, Weinheim 

amino acids such as phenylalanine, tyrosine and dopamine. The gadolinium(III) complexes of these ligands were synthesized and then studied in vitro. The residence time of the coordinated water molecule was studied by means of $^{17}O$ NMR spectroscopy, and nuclear magnetic relaxation dispersion (NMRD) measurements were performed in order to test the efficiency of these complexes as potential MRI contrast agents.

## Results and Discussion

### Ligands and Complexes

The ligands DTPA-bis(tyramide) [DTPA-$(TA)_2$], DTPA-bis(3-hydroxytyramide) [DTPA-$(HTA)_2$] and DTPA-bis-(phenylalanine ethyl ester) [DTPA-$(PAE)_2$] were synthesized by the reaction between DTPA-bis(anhydride) and the corresponding amine in DMF. In pyridine, the ligands readily formed complexes with gadolinium(III) ions (Scheme 1). Infrared absorption data of all ligands show strong absorptions in the region 1630–1650 $cm^{-1}$, corresponding to the CO stretching modes.[21] Shifts of ca. 10 to 20 $cm^{-1}$ to lower wavenumber were observed for the carbonyl stretching frequencies upon complexation. This indicates amide oxygen coordination to the gadolinium(III) ion. These findings are consistent with previous studies which have shown that DTPA-bis(amide) derivatives coordinate to trivalent lanthanide ions by three acetate oxygen atoms, three nitrogen atoms and two carbonyl oxygen atoms of the amide groups, while the ninth coordination site is occupied by a water molecule.[22–25] In the case of DTPA-$(TA)_2$ and DTPA-$(HTA)_2$ ligands, no evidence for the coordination of phenol oxygen to gadolinium(III) was observed. Positive-mode electrospray ionization mass spectroscopy (ESI-MS) of the Gd-DTPA-$(TA)_2$, Gd-DTPA-$(HTA)_2$ and Gd-DTPA-$(PAE)_2$ complexes indicate the presence of fully complexed species in the solution (see Experimental Section and Scheme 1).

### Estimation of $\tau_M$: $^{17}O$ NMR and Proton Relaxometric Measurements

The value of the residence time of the coordinated water molecule, $\tau_M$, was classically obtained by analysis of the temperature dependence of the reduced transverse relaxation rate of the water $^{17}O$ nucleus in solutions containing the gadolinium(III) complexes. The procedure has been described previously.[26,27] As expected for bis(amide) derivatives of Gd-DTPA,[28] the curves representing the reduced transverse relaxation rates versus the reciprocal of the tem-

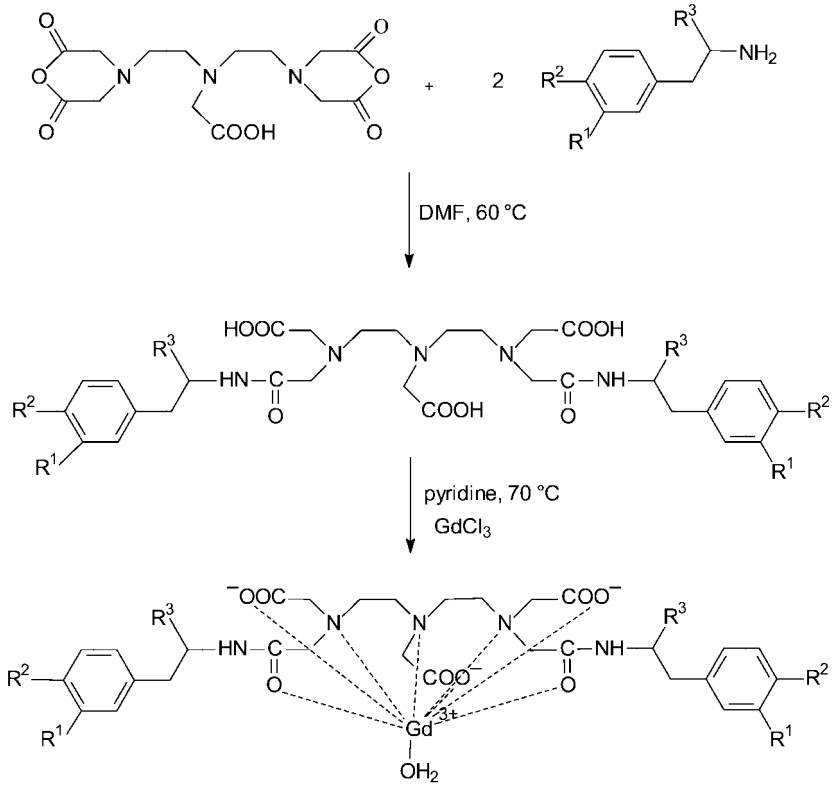


Scheme 1. Synthesis of the ligands and corresponding gadolinium(III) complexes.

 © 2007 Wiley-VCH Verlag GmbH & Co. KGaA, Weinheim 

perature are closer to the data obtained for Gd-DTPA-BMA than to those of Gd-DTPA (Figure 1). Theoretical adjustment of these experimental data was performed as described previously, assuming the presence of one water molecule in the first coordination sphere.[26,27] This procedure allows for the determination of (i) $A/\hbar$, the hyperfine coupling constant between the oxygen nucleus of bound water molecules and the gadolinium(III) ion; (ii) the parameters describing the electronic relaxation times of gadolinium(III), that is, the correlation time modulating the electronic relaxation, $\tau_V$, its activation energy, $E_v$, and a parameter related to the mean-square of the zero-field splitting energy, $B$ ($B = 2.4\Delta^2$); and (iii) parameters related to the water exchange, that is, the enthalpy ($\Delta H^{\#}$) and entropy ($\Delta S^{\#}$) of the process. A second fitting was performed with the value of $A/\hbar$ set to $-3.8 \times 10^6$ rad s$^{-1}$. Similar values of $\tau_M$ were obtained by both procedures. At 310 K, the water residence time of Gd-DTPA-$(PAE)_2$ [$\tau_M{}^{310}$ = (809 ± 46) or (811 ± 72) ns], is quite similar to that reported[28] for the bis(methylamide) derivative of Gd-DTPA, Gd-DTPA-BMA [$\tau_M{}^{310}$ = (967 ± 36) ns], whereas smaller values are obtained for the two other complexes [$\tau_M{}^{310}$ = (582 ± 149) or (545 ± 24) ns for Gd-DTPA-$(TA)_2$ and $\tau_M{}^{310}$ = (372 ± 18) or (404 ± 18) ns for Gd-DTPA-$(HTA)_2$] (Table 1). The presence of an ethyl ester group on the ethylene chain of the amide substituent seems thus to have a harmful effect on the water exchange rate. This could be related to the steric hindrance and the hydrophobicity of the ethyl chains and/or to the possible formation of hydrogen bonds between the ester function and the coordinated water molecule leading to stabilization of the hydrated state and thus to a slowing down of the water exchange. On the other hand, the presence of two hydroxy groups on the aromatic ring has a beneficial effect on the water exchange rate.

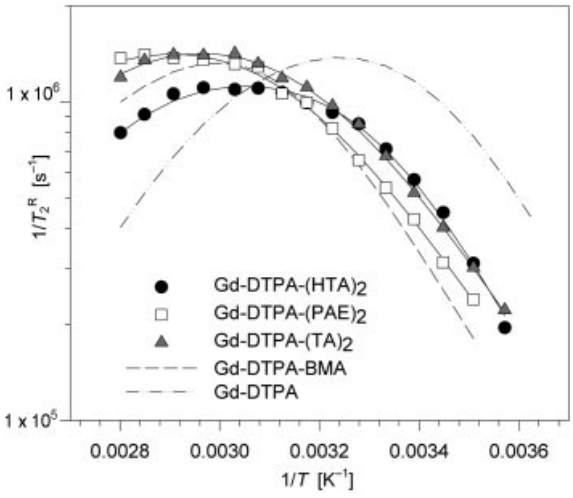


Figure 1. $^{17}$O transverse reduced relaxation rate ($1/T_2{}^R$ = 55.55/{$T_2{}^P$[Gd complex]}) of aqueous solutions of the gadolinium(III) complexes as a function of the reciprocal of temperature.

Such values of $\tau_M$ are not expected to significantly influence the relaxivity of small complexes at 310 K and 20 MHz, but at lower temperatures the relaxivity should be quenched. This is confirmed by the similarity of the proton relaxivities measured at 298 and 278 K (Figure 2) and their very small variations (less than 10%) observed in the temperature range extending between 310 and 278 K.

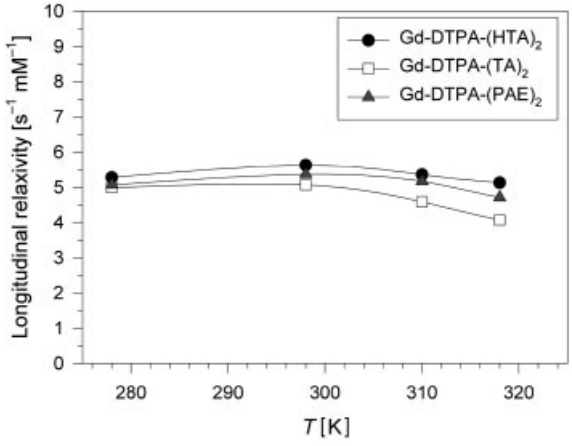


Figure 2. Evolution of the proton longitudinal relaxivity of Gd-DTPA-$(TA)_2$, Gd-DTPA-$(HTA)_2$ and Gd-DTPA-$(PAE)_2$ as a function of the temperature ($B$ = 0.47 T).

It should be pointed out that such $\tau_M$ values are unfavourable in the context of the design of tracers for molecular imaging if covalent coupling of the chelate to a vector is considered.

Table 1. Parameters obtained from the theoretical fitting of the $^{17}$O NMR spectroscopic data.[a]

| Parameter | Gd-DTPA-$(TA)_2$ | Gd-DTPA-$(HTA)_2$ | Gd-DTPA-$(PAE)_2$ |
|---|---|---|---|
| $\tau_V{}^{298}$ [ps] | 12.9 ± 2.7 (22.0 ± 0.5) | 21.1 ± 0.5 (24.1 ± 0.5) | 12.9 ± 0.4 (20.5 ± 1.6) |
| $B$ [$10^{20}$ s$^{-2}$] | 2.85 ± 0.57 (6.22 ± 0.15) | 1.36 ± 0.03 (9.50 ± 0.2) | 3.57 ± 0.10 (4.70 ± 0.40) |
| $E_v$ [kJ mol$^{-1}$] | 1.8 ± 4.5 (0.1 ± 18.8) | 0.1 ± 3.0 (0.1 ± 12.4) | 4.8 ± 3.7 (3.8 ± 2.6) |
| $\tau_{SO}{}^{310}$ [ps][b] | 54 ± 22 (15 ± 1) | 70 ± 3 (9 ± 0.4) | 43 ± 3 (21 ± 4) |
| $A/\hbar$ [$10^6$ rad s$^{-1}$] | –3.6 ± 0.7 (–3.8) | –4.5 ± 1.4 (–3.8) | –4.2 ± 0.4 (–3.8) |
| $\Delta H^{\#}$ [kJ mol$^{-1}$] | 44.6 ± 0.4 (46.1 ± 0.1) | 55.8 ± 0.1 (53.3 ± 0.1) | 43.6 ± 0.1 (42.2 ± 0.2) |
| $\Delta S^{\#}$ [J mol$^{-1}$ K$^{-1}$] | 18.2 ± 1.0 (23.4 ± 0.2) | 58.1 ± 0.2 (49.2 ± 0.2) | 12.2 ± 0.3 (7.6 ± 0.3) |
| $\tau_M{}^{310}$ [ns] | 582 ± 149 (545 ± 24) | 372 ± 18 (404 ± 18) | 809 ± 46 (811 ± 72) |

[a] The values in parentheses correspond to the second type of fitting ($A/\hbar$ fixed to $-3.8 \times 10^6$ rad s$^{-1}$), whereas the other values correspond to the first type of fitting ($A/\hbar$ fitted). [b] Values calculated using the equation: $\tau_{S0} = (5B\tau_v)^{-1}$.

 © 2007 Wiley-VCH Verlag GmbH & Co. KGaA, Weinheim 

### Influence of pH on Proton Relaxivity

In a pH range extending from 4 to 8, no significant change in the proton relaxivity at 20 MHz and 310 K was noticed ($r_1$ varies by less than 8%). These results show that no decomplexation occurs in this pH range and that the possible acceleration of the exchange rate of the water protons in acidic or basic media induce no or very little change in the proton relaxivity of the complexes. Since the hydrogen bonding is pH dependent, the absence of pH dependence of the Gd-DTPA-$(PAE)_2$ proton relaxivity could suggest the absence of a hydrogen bond between the ester function and the coordinated water molecule.[29] However, one can not exclude the existence of this hydrogen bond, since it has been established that the hydrogen bonding between neutral groups is usually insensitive to pH over the wide range in which no protonation or deprotonation of the hydrogen-bond acceptor or donor occurs.[29]

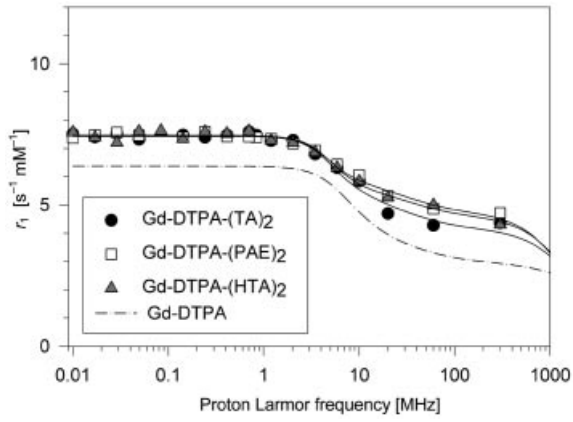


Figure 3. Proton NMRD profiles of the relaxivity of Gd-DTPA-$(TA)_2$, Gd-DTPA-$(HTA)_2$ and Gd-DTPA-$(PAE)_2$ at 37 °C. [Gd-DTPA-$(TA)_2$] = 3.22 mM, [Gd-DTPA-$(HTA)_2$] = 3.65 mM and [Gd-DTPA-$(PAE)_2$] = 2.84 mM. The NMRD profile of Gd-DTPA was added for comparison.[34]

### Proton NMRD Measurements

The proton NMRD relaxivities of the three gadolinium(III) complexes recorded at 310 K are quite similar and 20 to 36% larger than that for Gd-DTPA at 20 MHz (Figure 3, Table 2). The fittings of the proton NMRD profiles were performed as described in the Exp. Sect. and include both inner-sphere and outer-sphere interactions.[30–32] Some parameters were fixed during the fitting procedure: *d*, the distance of closest approach for the outer-sphere contribution was set at 0.36 nm, *D*, the relative diffusion constant was set to $3.3 \times 10^{-9}$ m$^2$ s$^{-1}$,[33] $\tau_M^{310}$ values were those obtained by $^{17}$O NMR spectroscopy, and the number of water molecules in the first coordination sphere of gadolinium(III) was set to one. $\tau_V^{310}$ and $\tau_{S0}^{310}$ (the electronic relaxation time at zero field) were optimized for the outer-sphere and the inner-sphere contributions simultaneously. The distance *r* between the protons of the coordinated water molecule and the gadolinium(III) ion was set to 0.31 nm.

The fitting of the experimental data of the three complexes gave values of $\tau_{S0}$ and $\tau_V$ close to those of Gd-DTPA. However, the $\tau_{S0}$ values calculated from the $^{17}$O NMR spectroscopic data or obtained from the fitting of the proton NMRD profiles are quite different. This can be related to the fact that $^{17}$O data are obtained at high magnetic field where $\tau_{S1}$ values are quite large (of the order of $10^{-8}$ s), whereas the $\tau_{S0}$ values estimated from the proton relaxometric NMRD data of small complexes are predominantly determined from the low-field data (where $\tau_{S1}$ values are of the order of $10^{-10}$ s). The rotational correlation times $\tau_R$ are, as expected, somewhat larger (Table 2) than the value found for Gd-DTPA and agree with the increase in molecular weight on going from Gd-DTPA-$(TA)_2$ to Gd-DTPA-$(PAE)_2$.

### Transmetallation

The transmetallation by zinc(II) ions was assessed in order to test the stability of the complexes. The procedure is based on the very low solubility of gadolinium(III) ions in phosphate solution and on the subsequent decrease of the proton paramagnetic relaxation rate during the transmetallation process. The data are shown in Figure 4 and are compared to those of Gd-DTPA and Gd-DTPA-BMA. The "ratio index" is defined as the time ($t$) required to reach a ratio $R_1^P(t)/R_1^P(0) = 80\%$,[34] and is larger for the three complexes than that of the commercial Gd-DTPA-BMA. After 50 hours, the ratio $R_1^P(t = 3000)/R_1^P(0)$ of Gd-DTPA-$(TA)_2$ and Gd-DTPA-$(PAE)_2$ is still better or similar to that of Gd-DTPA-BMA, whereas for Gd-DTPA-$(HTA)_2$ a

Table 2. Experimental proton longitudinal relaxivity at 20 MHz and 37 °C, and parameters obtained from the theoretical fitting of the proton NMRD data.

| Parameter | $r_1$ at 0.41 T [s$^{-1}$ mM$^{-1}$] | $r_1$ at 1.4 T [s$^{-1}$ mM$^{-1}$] | $\tau_R^{310}$ [ps] | $\tau_{S0}^{310}$ [ps] | $\tau_V^{310}$ [ps] | $\tau_M^{310}$ [ns][c] |
|---|---|---|---|---|---|---|
| Gd-DTPA[d] | 3.8[a] | 3.4[a] | 54 ± 1 | 87 ± 3 | 25 ± 3 | 143 ± 25 |
| Gd-DTPA-$(TA)_2$ | 4.8[a] | 4.5[a] | 99 ± 2 | 96 ± 2 | 34 ± 4 | 582 ± 149 |
| | 6.8[b] | 6.0[b] | | | | |
| Gd-DTPA-$(HTA)_2$ | 5.3[a] | 5.0[a] | 111 ± 2 | 83 ± 2 | 31 ± 2 | 372 ± 18 |
| | 5.4[b] | – | | | | |
| Gd-DTPA-$(PAE)_2$ | 5.3[a] | 4.8[a] | 127 ± 2 | 90 ± 1 | 36 ± 3 | 809 ± 46 |
| | 6.9[b] | 6.2[b] | | | | |

[a] Relaxivity in water. [b] Apparent relaxivity in 4% HSA (i.e., paramagnetic relaxation rate of 1 mM solution of the complex in 4% HSA). [c] Obtained from $^{17}$O relaxometry. [d] From ref.[34]

 © 2007 Wiley-VCH Verlag GmbH & Co. KGaA, Weinheim 

lower ratio is obtained. The complexes reported in the present work thus undergo a slower transmetallation than Gd-DTPA-BMA within the first five hours. However, after 50 hours the extent of the transmetallation process is more pronounced for Gd-DTPA-$(HTA)_2$ (Figure 4).

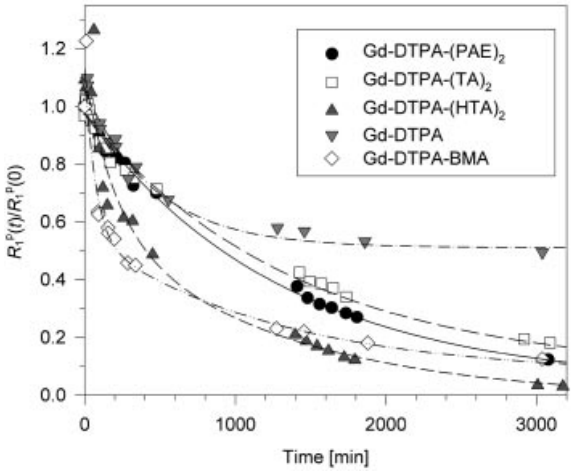


Figure 4. Evolution of $R_1^P(t)/R_1^P(0)$ vs. time for Gd-DTPA-$(TA)_2$, Gd-DTPA-$(HTA)_2$, Gd-DTPA-$(PAE)_2$, Gd-DTPA and Gd-DTPA-BMA (initial concentrations of Gd complexes and $ZnCl_2$ are 2.5 mM in phosphate buffer pH = 7, $T$ = 37 °C, $B$ = 0.47 T).

### Interaction with Human Serum Albumin

The interaction of a small gadolinium(III) complex with human serum albumin (HSA) increases its rotational correlation time and subsequently enhances its paramagnetic relaxation rate and its vascular remanence. A quick insight into the strength of the interaction can be obtained by the measurement of the paramagnetic relaxation rate of a solution (1 mM) of the complex in the presence of HSA (4%) at 20 MHz. An increase in the relaxation rate larger than 60% attests to a significant interaction between the gadolinium complex and the protein.[34] Such experiments performed with all three complexes showed maximum increases of 40% at 0.41 T and smaller values of the paramagnetic relaxation rate at 1.4 T (Table 2), testifying to the absence of a significant binding of these complexes with HSA.

## Conclusions

DTPA-bis(amide) derivatives bearing phenyl, phenol or catechol groups were synthesized in high yields and complexed to gadolinium(III) ions. As expected for bis(amide) derivatives of Gd-DTPA, the residence time of the coordinated water, as obtained from $^{17}O$ NMR relaxometric $T_2$ data, is longer than that for the parent Gd-DTPA complex. Surprisingly, a significantly longer residence time of the coordinated water was observed for the complex bearing an ethyl ester substituent. This could be caused by the existence of a hydrogen bond between the ester function and the water molecule, which can result in the stabilization of the hydrated state, or by the steric hindrance and the hydrophobicity of the ethyl groups. The larger proton relaxivity of all three complexes relative to that of Gd-DTPA is mainly because of the increase in the rotational correlation time. The stability of these new paramagnetic complexes tested in the presence of zinc(II) ions is better than that of Gd-DTPA-BMA within the first five hours. Taking into account the water residence time and the stability compared with zinc(II) transmetallation, the best candidate as a potential MRI contrast agent is thus Gd-DTPA-$(TA)_2$. The lack of significant interaction with HSA could be favourable to their use as receptor-specific contrast agents. In a next step, these contrast agents should be tested in the presence of catechol receptors and characterized in vivo in animal models.

## Experimental Section

**Chemicals:** Reagents were obtained from Aldrich Chemical Co. Inc., Acros Organics and Fluka, and were used without further purification. DTPA-bis(anhydride) was prepared by the published procedure.[35]

**Instruments:** Elemental analysis was performed with a CE Instruments EA-1110 elemental analyzer. $^1H$- and $^{13}C$ NMR spectra were recorded with a Bruker AMX-300 spectrometer, operating at 7.05 T. For $^{13}C$ NMR spectra, methanol was used as the internal reference. IR spectra were measured with a FTIR spectrometer Bruker IFS66, using KBr discs. Mass spectra were recorded with a Q-tof 2 (Micromass, Manchester UK). Samples for the mass spectra were prepared as follows. The complex (2 mg) was dissolved in methanol (1 mL). A sample of this solution (200 μL) was added to a 50:50 water/methanol solution (800 μL). The resulting solution was injected with a flow rate of 5 μL min$^{-1}$.

**Synthesis of the Ligands:** Ligands DTPA-$(PAE)_2$, DTPA-$(TA)_2$ and DTPA-$(HTA)_2$ were synthesized by the following general procedure. To a solution of DTPA-bis(anhydride) (0.357 g, 1 mmol) in dry DMF (30 mL) was added the corresponding amine (2.5 mmol), and the reaction mixture was heated overnight at 60 °C under nitrogen.[35] For the ligand DTPA-$(HTA)_2$, a small amount of ascorbic acid (50 mg) was added to the mixture to prevent oxidation. After the removal of the solvent, the product was re-dissolved in ethanol and precipitated by addition of diethyl ether. The precipitate was filtered off and dried in vacuo overnight.

#### Analytical Data for the Ligands

**DTPA-$(PAE)_2$:** Yield: 89% (661 mg). $C_{34}H_{49}N_5O_{12}$ (743.81): calcd. C 58.12, H 6.64, N 9.42; found C 58.55, H 6.61, N 9.40. $^1H$ NMR ([D$_6$]dmso): $\delta$ = 1.10 (t, 6 H, $CH_3$), 2.72 (m, 4 H, 2 × N–$CH_2$), 2.81 (m, 4 H, 2 × N–$CH_2$), 3.01 (m, 2 H, N–$CH_2$), 3.25 (s, 4 H, 2 × N–$CH_2$), 3.32 (s, 4 H, 2 × N–$CH_2$), 3.48 (d, 4 H, 2 × $CH_2$–Ph), 4.05 (q, 4 H, $CH_2$–O), 4.52 (m, 2 H, 2 × CH), 7.19–7.43 (m, 10 H, Ph), 8.32 (d, 2 H, 2 × NH) ppm. $^{13}C$ NMR ([D$_6$]dmso): $\delta$ = 172.8, 171.5, 170.7, 168.9, 137.4, 129.3, 128.4, 126.7, 60.8, 56.6, 56.2, 52.2, 48.7, 45.5, 38.9, 35.9, 14.0 ppm. IR: $\tilde{\nu}$ = 2972, 2952, 2876 (CH alkyl), 1733 (CO ester), 1677 (CO acid), 1633 (CO amide I), 1534 (CO amide II) cm$^{-1}$. ESI-MS(+) ($C_{36}H_{49}N_5O_{12}$: $M_{calcd.}$ = 743): $m/z$ = 744 [M + H]$^+$, 766 [M + Na]$^+$.

**DTPA-$(TA)_2$:** Yield: 85% (536 mg). $C_{30}H_{41}N_5O_{10}$ (631.68): calcd. C 57.04, H 6.54, N 11.09; found C 57.36, H 6.68, N 11.38. $^1H$ NMR ($D_2O$): $\delta$ = 2.64 (t, 4 H, 2 × N–$CH_2$), 2.97 (t, 4 H, 2 × N–$CH_2$), 3.11 (m, 4 H, 2 × $CH_2$–NH–CO), 3.35 (m, 4 H, 2 × $CH_2$–

 © 2007 Wiley-VCH Verlag GmbH & Co. KGaA, Weinheim 

Ph), 3.50 (s, 2 H, $CH_2$–COOH), 3.57 (s, 4 H, 2 × $CH_2$–COOH), 3.69 (s, 4 H, 2 × $CH_2$–CO–NH), 6.60–6.92 (AA′BB′, 8 H, 2 × Ph) ppm. $^{13}$C NMR ($D_2O$): $\delta$ = 173.2, 172.1, 169.4, 154.4, 131.2, 130.6, 115.7, 57.2, 54.7, 51.9, 51.4, 51.3, 40.8, 33.9 ppm. IR: $\tilde{\nu}$ = 1635 (CO amide I), 1510 (CO amide II) cm$^{-1}$. ESI-MS(+) ($C_{30}H_{41}N_5O_{10}$: $M_{calcd.}$ = 631): $m/z$ = 632 [M + H]$^+$, 654 [M + Na]$^+$.

**DTPA-(HTA)$_2$:** Yield: 79% (630 mg). $C_{30}H_{38}N_5O_{12}Na_3(H_2O)$ (747.64): calcd. C 48.18, H 5.39, N 9.37; found C 48.63, H 5.60, N 8.97. $^1$H NMR ($D_2O$): $\delta$ = 2.61 (t, 4 H, 2 × N–$CH_2$), 2.95 (t, 4 H, 2 × N–$CH_2$), 3.10 (m, 4 H, 2 × $CH_2$–NH–CO), 3.37 (m, 4 H, 2 × $CH_2$–Ph), 3.50 (s, 2 H, $CH_2$–COOH), 3.56 (s, 4 H, 2 × $CH_2$–COOH), 3.68 (s, 4 H, 2 × $CH_2$–CO–NH), 6.56–6.82 (m, 6 H, Ph) ppm. $^{13}$C NMR ($D_2O$): $\delta$ = 179.6, 174.4, 171.4, 152.3, 149.5, 128.9, 117.5, 116.7, 115.7, 59.4, 57.8, 52.1, 48.1, 46.5, 40.9, 35.5 ppm. IR: $\tilde{\nu}$ = 1740 (CO acid), 1647 (CO amide I), 1521 (CO amide II) cm$^{-1}$. ESI-MS(+) ($C_{30}H_{41}N_5O_{12}$: $M_{calcd.}$ = 663): $m/z$ = 664 [M + H]$^+$, 686 [M + Na]$^+$.

**Synthesis of the Gadolinium(III) Complexes:** All complexes were synthesized according to the following general procedure. A solution of hydrated $GdCl_3$ salt (1 mmol) in $H_2O$ (1 mL) was added to the ligand (1 mmol) dissolved in pyridine (30 mL), and the mixture was heated at 70 °C for 3 h. Because of the basicity of pyridine, the addition of extra base for the deprotonation of the ligand was not necessary.The solvents were evaporated under reduced pressure, and the crude product was then refluxed in ethanol for 1 h. After cooling to room temp., the complex was filtered off and dried in vacuo. The absence of free gadolinium(III) ions was checked with xylenol orange indicator.[36]

**Analytical Data for the Gadolinium(III) Complexes**

**Gd-DTPA-(PAE)$_2$:** Yield: 35% (315 mg). IR: $\tilde{\nu}$ = 1733 (CO ester), 1622 (CO amide I), 1589 ($COO^-$ asym. stretch), 1388 ($COO^-$ sym. stretch) cm$^{-1}$. ESI-MS(+) ($C_{36}H_{46}GdN_5O_{12}$: $M_{calcd.}$ = 897): $m/z$ = 898 [M + H]$^+$.

**Gd-DTPA-(TA)$_2$:** Yield: 53% (417 mg). IR: $\tilde{\nu}$ = 1627 (CO amide I), 1595 ($COO^-$ asym. stretch), 1399 ($COO^-$ sym. stretch) cm$^{-1}$. ESI-MS(+) ($C_{30}H_{38}GdN_5O_{10}$: $M_{calcd.}$ = 785): $m/z$ = 786 [M + H]$^+$, 809 [M + Na]$^+$.

**Gd-DTPA-(HTA)$_2$:** Yield: 95% (770 mg). IR: $\tilde{\nu}$ = 2923, 2852 (CH alkyl), 1628 (CO amide I), 1602 ($COO^-$ asym. stretch), 1408 ($COO^-$ sym. stretch) cm$^{-1}$. ESI-MS(+) ($C_{30}H_{38}GdN_5O_{12}$: $M_{calcd.}$ = 817): $m/z$ = 840 [M + Na]$^+$.

**Sodium and Potassium Ion Content Measurements:** The potassium and sodium ion content of the solutions was checked by flame photometry (IL 943, Instrumentation Laboratories, Massachusetts, USA). $Na^+$ content (mmol per mol of the complex): Gd-DTPA-(PAE)$_2$: 0.7; Gd-DTPA-(TA)$_2$: 0.0; Gd-DTPA-(HTA)$_2$: 0.0. $K^+$ content: no $K^+$ could be detected in any of the complexes.

**Proton $T_1$ Measurements:** Proton nuclear magnetic relaxation dispersion (NMRD) profiles were recorded at 310 K between 0.24 mT and 0.24 T with a Field Cycling Relaxometer (Stelar Spinmaster FFC-2000, Stelar S. R. L., Mede, Italy) on solutions (0.6 mL) contained in 10-mm o.d. tubes. Proton relaxation rates were also measured at 0.47, 1.5 and 7.05 T on Minispec PC-120, mq-60 and AMX-300 spectrometers (Bruker, Karlsruhe, Germany), respectively. $^1$H NMRD data were fitted according to the theoretical inner-sphere model described by Solomon[30] and Bloembergen[31] and to the outer-sphere contribution described by Freed.[32] Calculations were performed with a previously described software.[26]

**$^{17}$O NMR Measurements:** $^{17}$O NMR measurements of solutions were performed on samples (2 mL) contained in 10-mm external diameter tubes with a Bruker AMX-300 spectrometer. The temperature was regulated by air or nitrogen flow controlled by a BVT 2000 unit. No field frequency lock was used. $^{17}$O transverse relaxation times of distilled water (pH = 6.5–7) were measured using a CPMG sequence and a subsequent two-parameter fit of the data points. The 90° and 180° pulse lengths were 25 and 50 μs, respectively. $^{17}$O $T_2$ values of water in complex solution were obtained from line-width measurement. Concentrations of the samples were less than 25 mM {[Gd-DTPA-(TA)$_2$] = 20.1 mM, [Gd-DTPA-(HTA)$_2$] = 20.0 mM and [Gd-DTPA-(PAE)$_2$] = 20.3 mM}. The data were treated as described elsewhere.[26–28,34]

**Transmetallation Kinetics:** The technique is based on the measurement of the evolution of the water proton paramagnetic longitudinal relaxation rate ($R_1^P$) of a buffered solution ([$KH_2PO_4$] = 0.026 mol L$^{-1}$, [$Na_2HPO_4$] = 0.041 mol L$^{-1}$, pH = 7) containing the gadolinium(III) complex (2.5 mM) and $ZnCl_2$ (2.5 mM).[37] The measurements were performed with a spin analyzer Minispec PC-120 (Bruker, Karlsruhe, Germany) at 20 MHz and 310 K. The samples (0.3 mL) were contained in 7-mm o.d. Pyrex™ tubes and kept at 310 K in a dry block between measurements (up to 4 d).

## Acknowledgments

T. N. P.-V., K. K. and K. B. thank the K. U. Leuven for financial support (VIS/01/006.01/20002-06/2004 and GOA 03/03). T. N. P.-V. acknowledges the F. W. O.-Flanders (Belgium) for a Postdoctoral Fellowship. C,H,N microanalyses were performed by Mrs. Petra Bloemen. This work was supported by the ARC Program (contracts number 95/00-194 and 00-05/258) of the French Community of Belgium. L. V. E., S. L., C. T. and R. N. M. kindly acknowledge the support and sponsorship concerted by COST Action D18 "Lanthanide Chemistry for Diagnosis and Therapy", and the EMIL NoE of the FP6 of the EC.

[1] P. A. Rinck, *Magnetic Resonance in Medicine*, Blackwell Scientific Publications, Oxford, UK, **1993**.
[2] A. E. Merbach, É. Tóth, *The Chemistry of Contrast Agents in Medical Magnetic Resonance Imaging*, John Wiley & Sons, Chichester, UK, **2001**.
[3] P. Caravan, J. J. Ellison, T. J. McMurry, R. B. Lauffer, *Chem. Rev.* **1999**, *99*, 2293–2352.
[4] T. N. Parac-Vogt, K. Kimpe, S. Laurent, C. Piérart, L. Vander Elst, C. Burtea, F. Chen, Y. Ni, A. Verbruggen, R. N. Muller, K. Binnemans, *Chem. Eur. J.* **2005**, *11*, 3077–3086.
[5] É. Tóth, D. Pubanz, S. Vauthey, L. Helm, A. E. Merbach, *Chem. Eur. J.* **1996**, *2*, 1607–1615; V. C. Pierre, M. Botta, K. N. Raymond, *J. Am. Chem. Soc.* **2005**, *127*, 504–505.
[6] M. Spanoghe, D. Lanens, R. Dommisse, A. Van der Linden, F. Alderweireldt, *J. Magn. Reson. Imaging* **1992**, *10*, 913–917; V. S. Vexler, O. Clement, H. Schmitt-Willich, R. C. Brasch, *J. Magn. Reson. Imaging* **1994**, *4*, 381–388; T. S. Desser, D. L. Rubin, H. H. Muller, F. Qing, S. Khodor, G. Zanazzi, S. U. Young, L. Ladd, J. A. Wellons, K. E. Kellar, J. L. Toner, R. A. Snow, *J. Magn. Reson. Imaging* **1994**, *4*, 467–472; É. Tóth, L. Helm, K. E. Kellar, A. E. Merbach, *Chem. Eur. J.* **1999**, *5*, 1202–1211.
[7] É. Tóth, F. Connac, L. Helm, K. Adzamli, A. E. Merbach, *J. Biol. Inorg. Chem.* **1998**, *3*, 606–613; S. Aime, M. Botta, M. Fasano, E. Terreno, *Chem. Soc. Rev.* **1998**, *27*, 19–29.
[8] K. Binnemans, C. Görller-Walrand, *Chem. Rev.* **2002**, *102*, 2303–2345.
[9] J. P. André, É. Tóth, H. Fischer, A. Seelig, H. R. Mäcke, A. E. Merbach, *Chem. Eur. J.* **1999**, *5*, 2977–2983.
[10] P. L. Anelli, L. Lattuada, V. Lorusso, M. Schneider, H. Tourner, F. Uggeri, *Magn. Reson. Mater. Phys.* **2001**, *12*, 114–

 © 2007 Wiley-VCH Verlag GmbH & Co. KGaA, Weinheim 

120; H. Tournier, R. Hyacinthe, M. Schneider, *Acad. Radiol.* **2002**, 9 (suppl. 1), S20–S28.
[11] K. Kimpe, T. N. Parac-Vogt, S. Laurent, C. Piérart, L. Vander Elst, R. N. Muller, K. Binnemans, *Eur. J. Inorg. Chem.* **2003**, 3021–3027; T. N. Parac-Vogt, K. Kimpe, S. Laurent, C. Piérart, L. Vander Elst, R. N. Muller, K. Binnemans, *Eur. J. Inorg. Chem.* **2004**, 3538–3543.
[12] T. N. Parac-Vogt, L. Vander Elst, K. Kimpe, S. Laurent, C. Burtea, F. Chen, R. Van Deun, Y. Ni, R. N. Muller, K. Binnemans, *Contrast Med. Mol. Imaging* **2006**, *1*, 267–278.
[13] G. W. Kabalka, E. Buonocore, K. Hubner, M. Davis, L. Huang, *Magn. Reson. Med.* **1988**, *8*, 89–95.
[14] C. W. Grant, S. Karlik, E. Florio, *Magn. Reson. Med.* **1989**, *11*, 236–243.
[15] V. J. Caride, H. D. Sostman, R. J. Winchell, J. C. Gore, *Magn. Reson. Imaging* **1984**, *2*, 107–112.
[16] E. C. Unger, P. Macdougall, P. Cullis, C. Tilcock, *Magn. Reson. Imaging* **1989**, *7*, 417–423.
[17] T. N. Parac-Vogt, K. Kimpe, S. Laurent, C. Piérart, L. Vander Elst, R. N. Muller, K. Binnemans, *Eur. Biophys. J.* **2006**, *35*, 136–144.
[18] E. Ruoslahti, M. D. Pierschbacher, *Science* **1987**, *238*, 491–497.
[19] L. O. Johansson, A. Bjornerud, H. K. Ahlstrom, D. L. Ladd, D. K. Fujii, *J. Magn. Reson. Imaging* **2001**, *13*, 615–618.
[20] R. D. O'Brien (Ed.), *The Receptors: A Comprehensive Treatise*, Plenum Press, New York, **1979**, vol. 1.
[21] E. Pretsch, T. Clerc, J. Seibl, W. Simon, *Tabellen zur Strukturaufklärung organischer Verbindungen mit spektroskopischen Methoden*, Springer, Berlin, **1976**.
[22] L. Ehnebom, B. F. Pedersen, *Acta Chem. Scand.* **1992**, *46*, 126–130.
[23] S. W. A. Bligh, A. H. M. S. Chowdhury, M. McPartlin, T. J. Scowen, R. A. Bulman, *Polyhedron* **1995**, *14*, 567–569.
[24] S. Aime, F. Benetollo, G. Bombieri, S. Colla, M. Fasano, S. Paoletti, *Inorg. Chim. Acta* **1997**, *254*, 63–70.
[25] Y.-M. Wang, Y.-J. Wang, R.-S. Sheu, G.-C. Lin, W.-C. Lin, J.-H. Liao, *Polyhedron* **1999**, *18*, 1147–1152.
[26] L. Vander Elst, F. Maton, S. Laurent, F. Seghi, F. Chapelle, R. N. Muller, *Magn. Reson. Med.* **1997**, *38*, 604–614.
[27] S. Laurent, L. Vander Elst, S. Houzé, N. Guérit, R. N. Muller, *Helv. Chim. Acta* **2000**, *83*, 394–406.
[28] F. Botteman, G. M. Nicolle, L. Vander Elst, S. Laurent, A. E. Merbach, R. N. Muller, *Eur. J. Inorg. Chem.* **2002**, 2686–2693.
[29] J. L. Wood, *Biochem. J.* **1974**, *143*, 775–777.
[30] I. Solomon, *Phys. Rev.* **1955**, *99*, 559–565.
[31] N. Bloembergen, *J. Chem. Phys.* **1957**, *27*, 572–573.
[32] J. H. Freed, *J. Chem. Phys.* **1978**, *68*, 4034–4037.
[33] L. Vander Elst, A. Sessoye, S. Laurent, R. N. Muller, *Helv. Chim. Acta* **2005**, *88*, 574–587.
[34] S. Laurent, L. Vander Elst, R. N. Muller, *Contrast Media Mol. Imaging* **2006**, *1*, 128–137.
[35] T. N. Parac-Vogt, K. Kimpe, K. Binnemans, *J. Alloy Compd.* **2004**, *374*, 325–329.
[36] A. Barge, G. Cravotto, E. Gianolio, F. Fedeli, *Contrast Media Mol. Imaging* **2006**, *1*, 184–188.
[37] S. Laurent, L. Vander Elst, F. Copoix, R. N. Muller, *Invest Radiol.* **2001**, *36*, 115–122.

Received: December 11, 2006
Published Online: March 28, 2007

 © 2007 Wiley-VCH Verlag GmbH & Co. KGaA, Weinheim 

DOI: 10.1002/ejic.200700047

# Structural Chemistry of an $n = 1$ Member of the Ruddlesden–Popper $Sr_{n+1}(Co_{0.5}Ta_{0.5})_nO_{3n+1}$ Homologous Series: $Sr_4CoTaO_8$

**Khalid Boulahya,[a] Marina Parras,[a] and José María González-Calbet*[a]**

**Keywords:** Electron diffraction / X-ray diffraction / Electron microscopy / Magnetic properties

A layered perovskite related compound with the $Sr_4CoTaO_8$ composition was isolated. This material constitutes the $n = 1$ member of the recently reported $[Sr_{n+1}(Co_{0.5}Ta_{0.5})_nO_{3n+1}]$ Ruddlesden–Popper series. XRPD, SAED and HREM reveal that this compound crystallizes as a $K_2NiF_4$-type with space group $I4/mmm$. The structure is formed by one $Sr_2CoTaO_6$ perovskite block that intergrows with one SrO rock salt layer; no ordering between the Co and Ta cations was established. (© Wiley-VCH Verlag GmbH & Co. KGaA, 69451 Weinheim, Germany, 2007)

## Introduction

Main-layered perovskites and their derivatives are characterized by an excess of anions relative to the ideal perovskite, and they constitute homologous series that are defined on the basis of the interslab composition and orientation of the layer plane relative to the aristotype cubic lattice. When this layer is parallel to the (001) plane of the cubic perovskite, the $(ABO_3)_nAO$ Ruddlesden–Popper (RP) series[1] arises. Most of the RP phases described up to now contain B cations of the first transition series, such as Ti, Ni, Cu, ...; however, structures related to the $n = 2$ member of this series, $Sr_3Co_2O_{7-\delta}$, which involves the substitution of Co by other metals of the later transition series, have been recently reported.[2] Indeed, a broad range of complex tantalum oxides have been reported to exhibit very high photocatalytic activities for the decomposition of water into $H_2$ and $O_2$; this is one of the most promising pathways for the conversion of photon energy into chemical energy.[3] For instance, $A_2SrTa_2O_7$ (A = H, K, Rb)[4] is the $n = 2$ member of the RP-layered series whose structure is built up of two cubic perovskite blocks that intergrow with a SrO rock-salt-type layer. The substitution of a monovalent cation by a divalent cation in the A sublattice must be accompanied by the partial substitution of Ta by other metals that stabilize lower oxidation states. In an attempt to stabilize homologous series with cations of later transition-metal series, and taking into account the versatility of cobalt, we recently isolated the $n = 2$ and $n = \infty$ members of the $Sr_{n+1}(CoTa)_nO_{3n+1}$[5] family with a Co/Ta ratio of 1:1.

Cobalt-containing systems present a particular behaviour when compared with other RP series, and this difference in behaviour is related to the difficulty in stabilizing the $n = 1$ term. In fact, $Sr_2CoO_4$ can only be stabilized under high pressure conditions[6] whereas the upper $n$ terms can be easily prepared under atmospheric pressure. In a somewhat similar way, the high temperatures used to stabilize the different members of the $Sr_{n+1}(CoTa)_nO_{3n+1}$ series were not adequate to isolate the first member ($n = 1$) because disordered intergrowths of upper members ($n > 1$) were usually obtained. Lower synthetic temperatures combined with longer annealing times allowed us to successfully stabilize, for the first time, this $n = 1$ member. In this paper, we describe the synthetic conditions and microstructural characterization of the $n = 1$ member of this series, which possesses the composition $Sr_2(Co_{0.5}Ta_{0.5})O_4$ (i.e. $Sr_4CoTaO_8$). This is the end, in the absence of tilting, members of the series belong to the $I4/mmm$ $K_2NiF_4$ structural type with the layer sequence ($ABO_3$) perovskite-(AO) rock salt. To fully determine the structural details and physical properties of the series, X-ray powder diffraction (XRPD), selected area electron diffraction (SAED), high resolution electron microscopy (HREM) and magnetic properties were investigated.

## Results and Discussion

The synthetic pathway to $Sr_4CoTaO_8$ was followed by XRPD. After annealing for three days, the XRPD pattern can be indexed on the basis of a single $A_2BO_4$, $n = 1$ RP single phase. As it is well known, different members of the RP series ranging from $n = 1$ to $n = \infty$ (the $ABO_3$ perovskite structure) can be isolated. However, the presence of disorder in the stacking of the perovskite and SrO blocks is not unusual and it is not always detected by powder X-ray diffraction, and therefore, careful microstructural study of these phases is always advisable. In fact, the microstructural study of $Sr_4CoTaO_8$ by HREM confirms that most of the

[a] Departamento de Química Inorgánica, Facultad de Químicas, Universidad Complutense de Madrid
28040 Madrid, Spain
Fax: +34-91-394-4352
E-mail: jgcalbet@quim.ucm.es

 © 2007 Wiley-VCH Verlag GmbH & Co. KGaA, Weinheim 

crystals are constituted by intergrowth of $n = 1$ and $n = \infty$ members of the RP series.

Actually, in the [010] zone image (Figure 1), $n = 1$ regions, $A_2BO_4$ structural blocks intergrow with isolated lamellae of the cubic perovskite $n = \infty$ member of the mentioned series. Moreover, in some crystals, the intergrowth of the $n = 1$ member with other related superstructures, which correspond to other terms of the RP series, is apparent. The presence of this type of disorder was attributed to kinetic reasons. In fact, sintering times play an important role in the stabilization of single phases and, usually, long times are necessary to avoid intergrowths of different members of the series. Therefore, to attain a long range ordered material, the sample was reannealed. After seven days at 1000 °C, a fully ordered $Sr_4CoTaO_8$ single phase was isolated as revealed by XRPD, SAED and HREM.

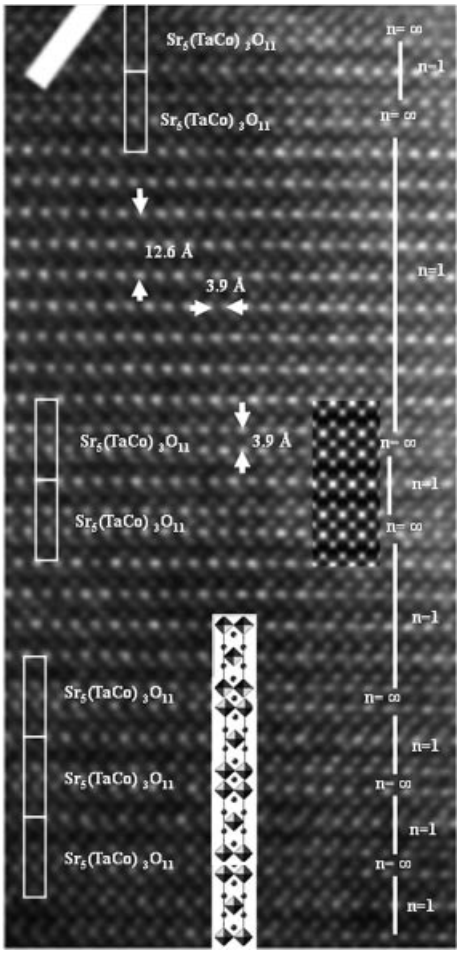


Figure 1. HRTEM image along the [010] zone axis that corresponds to a sample with nominal composition $Sr_4CoTaO_8$ after 3 d annealing. $Sr_5(CoTa)_3O_{11}$ ($n = 1.5$) member of $Sr_{n+1}(Co_{0.5}Ta_{0.5})_nO_{3n+1}$ series intergrows in a disordered way with $n = 1$ regions. Ideal structural model of $Sr_5(CoTa)_3O_{11}$ and calculated image from the model are shown in the inset.

The whole XRPD pattern (Figure 2) can be indexed on the basis of a tetragonal unit cell with lattice parameters $a = b = 3.8991(1)$ and $c = 12.6264(8)$ Å, no extra reflections are detected. SAED was used to fully reconstruct the reciprocal space. The most relevant zone axes, [001] and [010], are depicted in Figure 3. The diffraction spots are always sharp; streaking or diffuse intensity, which are indicative of some disorder, are not observed. All reflections can be indexed on the basis of the above tetragonal unit cell. Besides, the reflection conditions are compatible with the *I*4/*mmm* (139) space group, which was previously proposed for other $n = 1$ members of the RP family.[9]

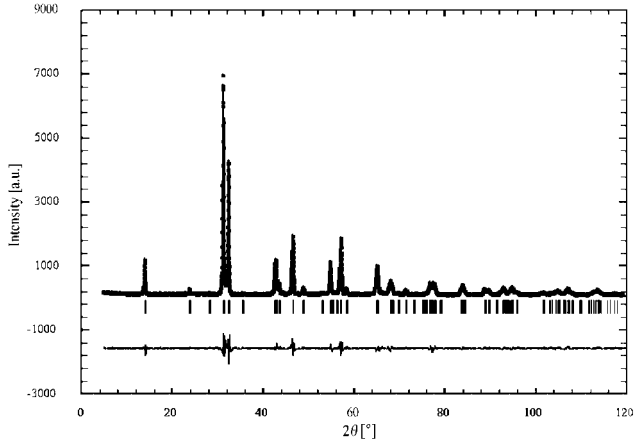


Figure 2. Graphic results of the fitting of the XRPD powder data of $Sr_4CoTaO_8$: experimental (points), calculated (solid line) and difference (bottom).

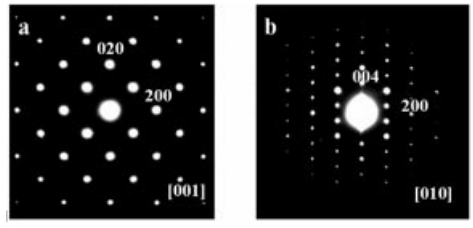


Figure 3. SAED patterns corresponding to $Sr_4CoTaO_8$ along (a) [001] and (b) [010] zone axes.

The [010] HREM image (Figure 4) corresponds to an apparently well-ordered material that shows *d*-spacing of 3.9 Å and 12.6 Å, which corresponds to $d_{100}$ and $d_{001}$, respectively. The contrast variation in this image corresponds to two layers with black dots that are marked by an arrow, which can be associated to Sr atoms of the rock salt blocks; these layers are separated by one layer with less intense dots that are marked by a dashed arrow, which correspond to Co/Ta atoms of the perovskite blocks. This configuration is shown in the enlarged image of Figure 4 and corresponds to the structural model depicted in Figure 5. Fourier transform was performed on the HREM micrograph to look for the existence of different domains that could indicate the presence of additional Co/Ta ordering in the structure. However, the whole crystal is homogeneous and no additional ordering was observed. Therefore, from the corresponding ideal atomic coordinates, an image calculation was performed. The simulated image fits nicely to the experimental one for $\Delta f = -50$ nm and $\Delta t = 6$ nm (see Figure 4).

 © 2007 Wiley-VCH Verlag GmbH & Co. KGaA, Weinheim 

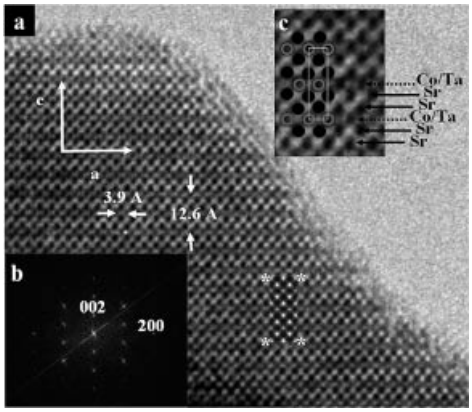


Figure 4. (a) HRTEM image of $Sr_4CoTaO_8$ along the [010] zone axis. Calculated image is shown in the inset. (b) Corresponding optical Fourier transform (FT). (c) Image magnification where metal atoms are superimposed.

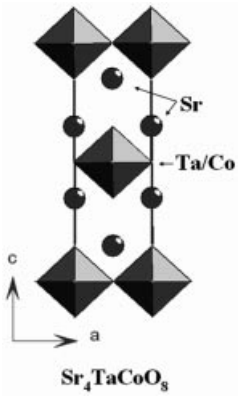


Figure 5. Structural model of $Sr_4CoTaO_8$ along the *b* axis.

B-site ordering for Co compounds has only been reported in $K_2NiF_4$-related materials when monovalent and trivalent cations occupy this site. For instance, Abou-Warda et al.[10] suggest that ordering of Co and Li in $La_2Li_{0.5}Co_{0.5}O_4$ is due to size rather than charge differences [$^{VI}r_{Li^+}$ = 0.76 Å; $^{VI}r_{Co^{3+}}$ = 0.545 Å (low-spin)]. In our case, the smaller difference between the $Co^{3+}$ and $Ta^{5+}$ radii ($^{VI}r_{Ta^{5+}}$ = 0.76 Å) could justify the disorder between the $[CoO]_6$ and $[TaO]_6$ octahedra.

According to the above results, an X-ray profile refinement of $Sr_4CoTaO_8$ was performed. The structure was solved in the *I*4/*mmm* space group by taking the crystallographic data corresponding to an $n$ = 1 member of this layered family as a starting point.[11] Because no evidence for the presence of Co/Ta order in the B sublattice was detected, both cations were randomly distributed over the octahedral sites in a first stage. Peak shapes were described by pseudo-Voigt functions. Figure 2 shows the graphic results of the fitting of the experimental X-ray diffraction pattern and the difference between observed and calculated data. The refinement was stable, and it was possible to refine the positions of the oxygen atoms provided that a temperature factor for each type of atom was used. Structure refinement confirms isotypism with $Sr_2TiO_4$.[11] The final structural parameters are collected in Table 1, and Table 2 shows some selected interatomic distances.

Table 1. Final structural parameters of $Sr_4CoTaO_8$.[a]

| Atom | *x*/*a* | *y*/*b* | *z*/*c* | $B_{iso}$ | *Occ* |
|---|---|---|---|---|---|
| Sr1 | 0.50000 | 0.5000 | 01466(1) | 1.68(4) | 1.00000 |
| Ta/Co1 | 0.00000 | 0.00000 | 0.00000 | 1.53(5) | 1.00000 |
| O1 | 0.50000 | 0.00000 | 0.00000 | 1.85(13) | 1.00000 |
| O2 | 0.00000 | 0.00000 | 0.1684(8) | 1.85(13) | 1.00000 |

[a] S.G. *I*4/*mmm* (139), $a$ = 3.8991(1) Å, $a$ = 12.6264(8) Å, $V$ = 191.962(2) Å$^3$. $R_{wp}$ = 0.118, $R_{exp}$ = 0.070, $R_B$ = 0.038, $\chi^2$ = 2.6.

Table 2. Selected interatomic distances [Å] in $Sr_4CoTaO_8$.

| | |
|---|---|
| Sr1–O1: 2.688(1) × 4 | Co/Ta–O1: 1.950(0) × 4 |
| Sr1–O2: 2.336(1) | Co/Ta–O2: 2.126(1) × 2 |
| Sr1–O2: 2.771(1) × 4 | |

Refinement of the XRPD pattern confirms that $Sr_4TaCoO_8$ constitutes a new example of an $n$ = 1 term of the layered RP family. The structure consists of layers of corner-sharing $[Co/TaO_6]$ octahedra running perpendicular to the *c* axis and separated by Sr atoms. Adjacent sets of layers are staggered as shown in Figure 5. The observed Co/Ta–O(1) and Co/Ta–O(2) bond lengths of 1.950(0) and 2.126(1) Å indicate that the octahedra are tetragonally distorted along the *c* axis. These interatomic Co/Ta–O distances fit well with those of analogous oxides as $K_2SrTa_2O_7$[12] [distances Ta–O, 2.102(1)–1.812(1) Å] or $Sr_3Co_2O_{7-\delta}$[2] where the Co–O interatomic distances range from 1.92 to 2.00(1) Å. Finally, the Sr–O [2.771(1)–2.336(1) Å] distances are similar to those observed in other Sr oxides. At this point, it is worth remembering that the analogous $Sr_2CoO_4$ phase is only stabilized under high pressure. The partial substitution of Co by $Ta^V$ reduces the oxidation state of Co from IV to III in $Sr_4CoTaO_8$, which allows their stabilization under ambient pressure.

Figure 6 shows the temperature dependence of the magnetic susceptibility for $Sr_4CoTaO_8$ in the temperature range from 150 to 300 K. $Sr_4CoTaO_8$ exhibits a small and flat

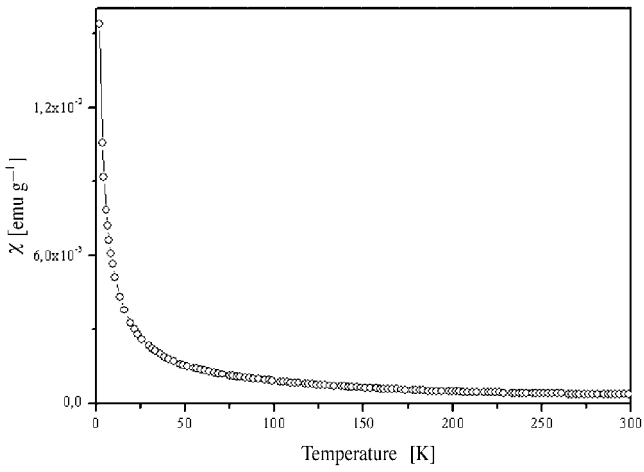


Figure 6. Magnetic susceptibility versus temperature plot corresponding to $Sr_4CoTaO_8$.

 © 2007 Wiley-VCH Verlag GmbH & Co. KGaA, Weinheim 

susceptibility, with a significant increase only at low temperatures. This low-temperature tail is usually attributed to spurious local paramagnetic moments. A similar behaviour was reported for $NaCoO_2$,[13] with all Co as low spin $Co^{III}$.

## Conclusions

The $n = 1$ member of the $[Sr_{n+1}(Co_{0.5}Ta_{0.5})_nO_{3n+1}]$ Ruddlesden–Popper series was successfully isolated. Large annealing times were necessary because SAED and HREM show that the first stage of the synthesis of $Sr_4CoTaO_8$ requires the initial formation of intergrowths of different members of the series. In this case, $Sr_4CoTaO_8$ intergrowths with the $n = \infty$ term is observed in most of the crystals.

A very interesting point of this work arises from this result. From the micrograph shown in Figure 1 it is clear that the existence of a new stable term of the series, formed by the ordered stacks of one $Sr_4CoTaO_8$ and one $SrCo_{0.5}Ta_{0.5}O_3$ structural block is possible and this corresponds to a chemical composition of $Sr_5(Co_{0.5}Ta_{0.5})_3O_{11}$. This recurrent intergrowth constitutes the $n = 1.5$ term, and this is the first example of a noninteger member of a RP series. This result opens the route to the research of new members of this series. We are currently investigating the synthetic conditions necessary to stabilize this new series member, and we hope to publish the results of this study in the near future.

## Experimental Section

Polycrystalline $Sr_4CoTaO_8$ was synthesized by heating stoichiometric amounts of $SrCO_3$ (Aldrich 99.98%), $Co_3O_4$ (Aldrich 99.9%) and $Ta_2O_5$ (Aldrich 99+%) at 1000 °C for 7 d. Annealing at higher temperatures does not lead to an ordered situation. In fact, the microstructural study shows that most parts of the crystals are constituted by disordered intergrowths of different members of the RP series, which results from the loss of SrO layers. X-ray powder diffraction (XRPD) patterns were collected by using Cu-$K_\alpha$ radiation ($\lambda$ = 1.5418 Å) at room temperature with a PHILIPS X'PERT diffractometer equipped with a graphite monochromator. Diffraction data were analyzed by the Rietveld method[7] with the use of the Fullprof program.[8] The sample was characterized by selected area electron diffraction (SAED) and high resolution electron microscopy (HREM) with a JEOL 3000 FEG electron microscope, fitted with a double tilting goniometer stage (±20°, ±20°). Local composition was analyzed by energy-dispersive X-ray spectroscopy (EDS) with an Oxford analyzer system attached to the above-described electron microscope. Magnetization was measured with a SQUID Quantum Design MPMS magnetometer, in a temperature range from 2 to 300 K, and magnetic field of 1000 Oe.

## Acknowledgments

Financial support through research projects MAT2004-01248, MAT/0627/2004 and CAM/S-0505/PPQ0316 is acknowledged. K. B. thanks the MCYT (Spain) for financial support under the "Ramón y Cajal" Program.

[1] S. N. Ruddlesden, P. Popper, *Acta Crystallogr.* **1958**, *11*, 54–55.
[2] S. E. Dann, M. T. Weller, *J. Solid State Chem.* **1995**, *115*, 499–507.
[3] K. Domen, J. N. Kondo, M. Hara, T. Takata, *Bull. Chem. Soc. Jpn.* **2000**, *73*, 1307–1331.
[4] K. Shimizu, Y. Tsuji, T. Hatamachi, K. Toda, T. Kodama, M. Sato, Y. Kitayama, *Phys. Chem. Chem. Phys.* **2004**, *6*, 1064–1069.
[5] K. Boulahya, M. Parras, J. M. González-Calbet, *Chem. Eur. J.* **2007**, *13*, 910–915.
[6] X. L. Wang, E. Takayama-Muromachi, *Phys. Rev. B* **2005**, *72*, 064401(1–7).
[7] H. V. Rietveld, *Appl. Crystallogr.* **1969**, *2*, 65–71.
[8] J. Rodríguez-Carvajal, *Physica* **1993**, *B192*, 55–69.
[9] P. Ganguly, C. N. R. Rao, *J. Solid State Chem.* **1984**, *53*, 193–216.
[10] S. Abou-Warda, W. Pietzuch, G. Berghöfer, U. Kesper, W. Massa, D. Reinen, *J. Solid State Chem.* **1998**, *138*, 18–31.
[11] S. N. Ruddlesden, P. Popper, *Acta Crystallogr.* **1957**, *10*, 538–539.
[12] T. A. Kodenkandath, J. B. Wiley, *Mater. Res. Bull.* **2000**, *35*, 1737–1742.
[13] G. Lang, J. Bobroff, H. Alloul, P. Mendels, N. Blanchard, G. Collin, *Phys. Rev. B* **2005**, *72*, 094404 (1–7).

Received: January 15, 2007
Published Online: March 28, 2007

 © 2007 Wiley-VCH Verlag GmbH & Co. KGaA, Weinheim 

DOI: 10.1002/ejic.200700134

# Osmium(II) and Osmium(IV) Complexes with Phosphane–Ethers, –Esters, and –Amines as Mono- and Bidentate Ligands

**Birgit Weber[a] and Helmut Werner*[a]**

*Dedicated to Professor Max Herberhold on the occasion of his 70th birthday*

**Keywords:** Osmium / Phosphane–Ethers / Phosphane–Esters / Phosphane–Amines / Vinylidene complexes

The six-coordinate dihydridoosmium(IV) complex $[OsH_2Cl_2(PiPr_3)_2]$ (**1**) reacted with the hemilabile chelating phosphanes $iPr_2PCH_2CH_2OMe$ and $iPr_2PCH_2CO_2R$ (R = Me, Et) at room temperature to give the substitution products $[OsH_2Cl_2(iPr_2PCH_2CH_2OMe)_2]$ (**2**) and $[OsH_2Cl_2\{\kappa^2(P,O)\text{-}iPr_2PCH_2C(=O)OR\}\{\kappa(P)\text{-}iPr_2PCH_2CO_2R\}]$ (**3**, **4**) in good to excellent yields. Treatment of **1** with $iPr_2PCH_2CH_2NMe_2$ led to the displacement of only one $PiPr_3$ ligand and gave $[OsH_2Cl_2(PiPr_3)(iPr_2PCH_2CH_2NMe_2)]$ (**5**). The reaction of **1** with $iPr_2PCH_2CH_2OMe$ and $iPr_2PCH_2CO_2R$ (R = Me, Et) at elevated temperature afforded the osmium(II) complexes $[OsCl_2\{\kappa^2(P,O)\text{-}iPr_2PCH_2CH_2OMe\}_2]$ (**6**) and $[OsCl_2\{\kappa^2(P,O)\text{-}iPr_2PCH_2C(=O)OR\}_2]$ (**7**, **8**), which were also obtained on heating the osmium(IV) precursor **3** or the labile 1:1 adducts of **3** and **4** with ethene in benzene under reflux. The dihydrido compounds **2** and **3** reacted with CO at room temperature to give initially the octahedral all-*cis*-configured complexes $[OsCl_2(CO)_2\{\kappa(P)\text{-}iPr_2PCH_2CH_2OMe\}_2]$ (**11a**) and $[OsCl_2(CO)_2\{\kappa(P)\text{-}iPr_2PCH_2CO_2Me\}_2]$ (**12a**), which rearrange to the more stable *cis*,*cis*,*trans* isomers **11b** and **12b** in benzene under reflux. The all-*trans* isomer **11c** and the monocarbonyl complexes *trans*,*trans*-$[OsCl_2(CO)\{\kappa^2(P,O)\text{-}iPr_2PCH_2C(=O)OR\}\{\kappa(P)\text{-}iPr_2PCH_2CO_2R\}]$ (**13**, **14**) were prepared by passing CO through a solution of **6**–**8** in benzene or toluene/dichloromethane at room temperature. While the osmium(IV) compounds **3**, **4** as well as the osmium(II) complexes **7**, **8** reacted with CN*t*Bu to give the neutral complexes *cis*,*cis*,*trans*-$[OsCl_2(CNtBu)_2\{\kappa(P)\text{-}iPr_2PCH_2CO_2R\}_2]$ (**15**, **16**), treatment of **5** with CN*t*Bu afforded the ionic product $[OsHCl(CNtBu)_2(PiPr_3)(iPr_2PCH_2CH_2NHMe_2)]Cl$ (**17**). The reaction of **7** with $Ph_2CN_2$ did not lead to the formation of a (carbene)osmium(II) compound but gave the dinitrogen complex *trans*,*trans*-$[OsCl_2(N_2)\{\kappa^2(P,O)\text{-}iPr_2PCH_2C(=O)OMe\}(\kappa(P)\text{-}iPr_2PCH_2CO_2Me)]$ (**18**) instead. The structurally related vinylidene complexes *trans*,*trans*-$[OsCl_2(=C=CHPh)\{\kappa^2(P,O)\text{-}iPr_2PCH_2CH_2OMe\}\{\kappa(P)\text{-}iPr_2PCH_2CH_2OMe\}]$ (**19a**) and *trans*,*trans*-$[OsCl_2(=C=CHPh)\{\kappa^2(P,O)\text{-}iPr_2PCH_2C(=O)OR\}\{\kappa(P)\text{-}iPr_2PCH_2CO_2R\}]$ (**20**, **21**) were prepared from **6**–**8** and PhC≡CH as starting materials. The *cis*,*cis*-configured compound $[OsCl_2(=C=CHPh)(PiPr_3)\{\kappa^2(P,N)\text{-}iPr_2PCH_2CH_2NMe_2\}]$ (**22**) was obtained analogously from **5** and phenylacetylene.

(© Wiley-VCH Verlag GmbH & Co. KGaA, 69451 Weinheim, Germany, 2007)

## Introduction

In the context of our investigations to prepare highly reactive transition-metal complexes with coordinatively unsaturated metal centers, we reported the synthesis of the dichloridodihydridoosmium(IV) compounds $[OsH_2Cl_2(PR_3)_2]$ ($PR_3$ = $PiPr_3$, $PtBu_2Me$, $PCy_3$), in which the osmium atom, although six-coordinate, has only 16 instead of 18 electrons in its valence shell.[1,2] We as well as Esteruelas, Caulton and co-workers showed that these compounds have a diverse chemistry which opened the gate not only to (carbyne)- but also to (vinylidene)osmium complexes.[3,4]

The aim of the present work was to find out whether dichloridodihydridoosmium(IV) compounds containing hemilabile, potentially chelating phosphane ligands were also accessible and could be converted into the osmium(II) compounds $[OsCl_2(P\text{–}X)_2]$ (P–X = $iPr_2PCH_2CH_2OR$, $iPr_2PCH_2CO_2R$, $iPr_2PCH_2CH_2NMe_2$). Previous attempts in our laboratory to prepare the corresponding phosphane–ether complex $[OsCl_2(P\text{–}O)_2]$ (P–O = $iPr_2PCH_2CH_2OMe$) from $[OsCl_2(PPh_3)_3]$ and $iPr_2PCH_2CH_2OMe$ led unexpectedly to the formation of the (carbene)osmium complex $[OsCl_2\{\kappa^2(P,C)\text{-}(=CHOCH_2CH_2PiPr_2)\}\{\kappa^2(P,O)\text{-}iPr_2PCH_2CH_2OMe\}]$ by double metalation of the methoxy group of the phosphane.[5] The phosphane–amine $iPr_2PCH_2CH_2NMe_2$ behaves similarly.

In this paper we describe the synthesis of a series of osmium(II) and osmium(IV) compounds with hemilabile phosphane ligands which, as expected, are highly reactive and can serve as starting materials for the preparation of new carbonyl-, (isocyanide)- and (vinylidene)osmium(II) complexes.[6]

[a] Institut for Anorganische Chemie, Universität Würzburg
Am Hubland, 97974 Würzburg, Germany
Fax: +931-888-4623
E-mail: helmut.werner@mail.uni-wuerzburg.de

 © 2007 Wiley-VCH Verlag GmbH & Co. KGaA, Weinheim 

## Results and Discussion

The reactions of the dichloridodihydridoosmium(IV) complex $[OsH_2Cl_2(PiPr_3)_2]$ (**1**) with the phosphane–ether $iPr_2PCH_2CH_2OMe$ and the phosphane–esters $iPr_2PCH_2CO_2R$ (R = Me, Et) in pentane or hexane at room temperature proceed smoothly and give the substitution products **2**–**4** in good to excellent yields (Scheme 1). These compounds are pale-yellow or colorless, only moderately air-sensitive solids, for which correct elemental analyses were obtained. The $^1H$ and $^{13}C$ NMR spectra of **2**–**4** in $CDCl_3$ or $C_6D_6$ display at room temperature only one set of signals for the protons and carbon atoms of the phosphane ligands, indicating that these are stereochemically equivalent under those conditions. The $^{31}P$ NMR spectra of **2**–**4** show in each case one singlet which, due to $^1H,^{31}P$ coupling, becomes a triplet in off-resonance.

The IR spectra of the phosphane–ester complexes **3** and **4** display two equally strong ν(C=O) stretching modes at 1720 and 1630 $cm^{-1}$ (for **3**) and 1755 and 1665 $cm^{-1}$ (for **4**), of which those at higher wavenumbers are assigned in analogy to the data of the phosphane–esters $iPr_2PCH_2CO_2R$ (R = Me, Et) to a free, noncoordinated C=O unit.[7] This indicates that in the ground state of compounds **3** and **4** one phosphane ligand is coordinated in a monodentate and the other in a bidentate fashion. In agreement with this proposal, the singlets observed in the room-temperature $^{31}P$ NMR spectra of **3** and **4** are split at –90 °C into two slightly broadened resonances at $\delta$ = 18.0 and 9.7 ppm (for **3**) and $\delta$ = 19.0 and 9.8 ppm (for **4**) of about equal intensity. The small $^{31}P,^{31}P$ coupling is consistent with a *cis* position of the $iPr_2PCH_2CO_2R$ ligands. The $^1H$ NMR spectrum of **3** at –90 °C in $[D_8]$toluene shows two singlets for the methoxy protons of the ester functionality, which supports the proposed different coordination mode of the phosphanes. It is conceivable that not only the phosphane–ester complexes **3** and **4** but also the phosphane–ether analogue **2** is fluxional on the NMR time scale in solution at room temperature.

In contrast to $iPr_2PCH_2CH_2OMe$ and $iPr_2PCH_2CO_2R$, the phosphane–amine $iPr_2PCH_2CH_2NMe_2$ reacts with the starting material **1** at room temperature to give compound **5**, which still contains one $PiPr_3$ ligand. Even with an excess of the phosphane–amine, the coordinated triisopropylphosphane could not be displaced. Treatment of **1** with $iPr_2PCH_2CH_2NMe_2$ in refluxing hexane or benzene did also not lead to the formation of $[OsH_2Cl_2(iPr_2PCH_2CH_2NMe_2)_2]$ or $[OsCl_2(iPr_2PCH_2CH_2NMe_2)_2]$, but afforded the aminocarbene complex $[OsCl_2\{\kappa^2(C,N)\text{-}(=CHN(Me)CH_2CH_2PiPr_2)\}\{\kappa^2(P,N)\text{-}iPr_2PCH_2CH_2NMe_2\}]$, probably via $[OsCl_2(iPr_2PCH_2CH_2NMe_2)_2]$ as the intermediate.[5] The $^{31}P$ NMR spectrum of **5** displays two broadened resonances at $\delta$ = 30.8 and 14.2 ppm, which indicates the coordination of two different phosphane ligands. The $^1H$ NMR spectrum of **5** shows a sharp triplet for the two hydrido ligands, the chemical shift of which ($\delta$ = –12.22 ppm) is nearly identical to that of the hydrido signal of **2** ($\delta$ = –12.39 ppm). Therefore, it is likely that the stereochemistry of compounds **2** and **5** is the same.

The reaction of **1** with $iPr_2PCH_2CH_2OMe$ and $iPr_2PCH_2CO_2R$ (R = Me, Et) in hexane at 110 °C in a closed vessel gave instead of the osmium(IV) compounds **2**–**4** the osmium(II) complexes **6**–**8** by elimination of dihydrogen. They are probably formed via the osmium(IV)

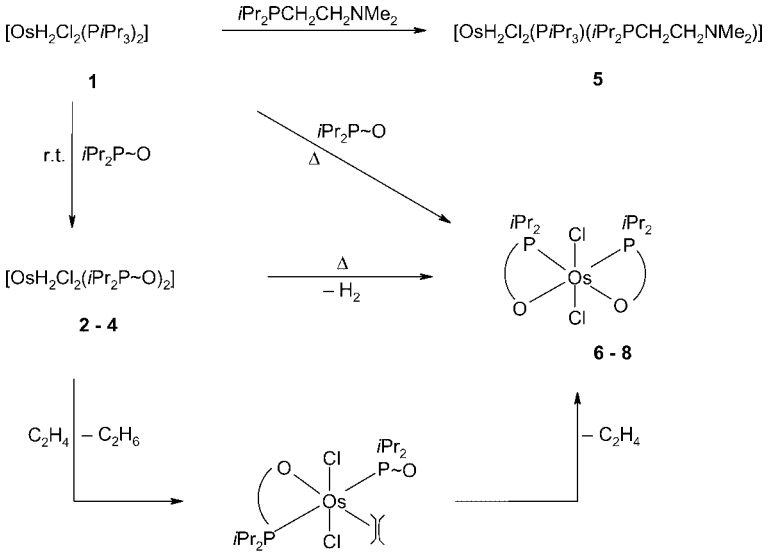


| | P~O |
|---|---|
| **2, 6** | $PCH_2CH_2OMe$ |
| **3, 7, 9** | $PCH_2CO_2Me$ |
| **4, 8, 10** | $PCH_2CO_2Et$ |

Scheme 1.

 © 2007 Wiley-VCH Verlag GmbH & Co. KGaA, Weinheim 

compounds **2**–**4**, as was shown by the thermal conversion of **3** to **6** in benzene under reflux. An alternative method of synthesis of **6**–**8** consists of the reaction of **2**–**4** in benzene in the presence of ethene, which affords the required osmium(II) complexes in nearly quantitative yield. If the conversion was carried out in $C_6D_6$ in an NMR tube, ethane could be detected as a by-product. Under these conditions it was also possible to observe the formation of the ethene derivatives **9** and **10** as intermediates. Similar to the IR spectra of **3** and **4**, those of **9** and **10** also display two ν(C=O) stretching modes at 1710 and 1605 $cm^{-1}$ (for **9**) and 1705 and 1610 $cm^{-1}$ (for **10**), which is consistent with the coordination of one monodentate and one bidentate $iPr_2PCH_2CO_2R$ ligand. This proposal is supported by the $^{31}P$ NMR spectra of **9** and **10**, in which two signals corresponding to an AB spin system are observed. The large $^{31}P,^{31}P$ coupling constants of 324.0 Hz (for **9**) and 325.6 Hz (for **10**) suggest that the two phosphorus atoms are *trans*-disposed. The $^1H$ NMR spectra of **9** and **10** show in each case a single resonance at $\delta$ = 4.01 ppm (for **9**) and $\delta$ = 4.05 ppm (for **10**), which is split into a triplet due to $^1H,^{31}P$ coupling. Since for a rigid structure two signals for the ethene protons should be observed, we assume that a rapid rotation of the ethene ligand around the metal–olefin axis occurs, making these protons equivalent. With regard to the stereochemistry of the six-coordinate osmium(II) complexes **6**–**8**, we favor a *cis*,*cis*,*trans* configuration (see Scheme 1), which is not only consistent with the spectroscopic data but also with the molecular structure of the related ruthenium(II) compound $[RuCl_2\{\kappa^2(P,O)\text{-}Ph_2PCH_2CH_2OMe\}_2]$.[8]

Similar to $[OsH_2Cl_2(PtBu_2Me)_2]$,[1] the osmium(IV) complexes **2** and **3** react with CO at room temperature within a few minutes by elimination of $H_2$. While with **2** as starting material the all-*cis* isomer **11a** (Scheme 2) is exclusively formed, in the case of **3** a mixture of **12a** (all-*cis*) and **12b** (*cis*,*cis*,*trans*) is generated under these conditions. Typical spectroscopic features for **11a** are two CO stretching modes in the IR spectrum, two doublet resonances in the $^{31}P$ NMR spectrum, two singlets for the methoxy protons in the $^1H$ NMR spectrum, and two signals for the carbon atoms of the stereochemically different CO ligands in the $^{13}C$ NMR spectrum. One of these $^{13}C$ NMR signals is split into a triplet and assigned to the carbonyl ligand *trans* to the chlorido ligand, while the other is split into a doublet of doublets and assigned to the carbonyl ligand *cis*-disposed to one and *trans*-disposed to the other phosphorus atom. The $^1H$ and $^{31}P$ NMR spectroscopic data of **12a** are very similar to those of **11a**.

If a solution of **11a** in benzene is stirred under reflux for 3 h, a complete conversion of the all-*cis* to the *cis*,*cis*,*trans* isomer **11b** occurs. The related complex **12b** is obtained upon heating a solution of the isomeric mixture of **12a** and **12b** in refluxing benzene for 5 h. Like the dibromidoosmium(II) compounds all-*trans*-$[OsBr_2(CO)_2\{\kappa(P)\text{-}R_2PCH_2CH_2OMe\}_2]$ (R = Ph, Cy), prepared by Lindner and co-workers,[9] the stereochemically different dichlorido complexes **11a**,**12a** and **11b**,**12b** are white solids, which are air-stable and readily soluble in benzene, toluene and chlorinated aliphatic hydrocarbons. In contrast to **11a** and **12a**, the $^{31}P$ NMR spectra of **11b** and **12b** display only one resonance for the equivalent phosphorus atoms and the $^1H$ NMR spectra of **11b** and **12b** only one signal for the methoxy protons. The IR spectra of **11b** and **12b** show two CO stretching modes, which is in agreement with a *cis* disposition of the carbonyl ligands.

In addition to **11a** and **11b** a third isomer **11c** of the general composition $[OsCl_2(CO)_2\{\kappa(P)\text{-}iPr_2PCH_2CH_2OMe\}_2]$ was obtained by passing a slow stream of CO through a solution of **6** in benzene at room temperature. The proposed all-*trans* configuration of **11c** is supported by the appearance of only one ν(C=O) band in the IR spectrum and of a single resonance in the $^{31}P$ NMR spectrum. The $^{31}P,^{187}Os$ coupling constant of 162.8 Hz is also in agreement with the *trans* position of the phosphorus atoms.[10]

In contrast to **6**, the corresponding phosphane–ester complexes **7** and **8** react with CO in toluene/dichloromethane at room temperature to give the monocarbonyl compounds **13** and **14** as yellow, air-stable solids in about 75% yield. Even if the solutions are stirred under CO for 12 h,

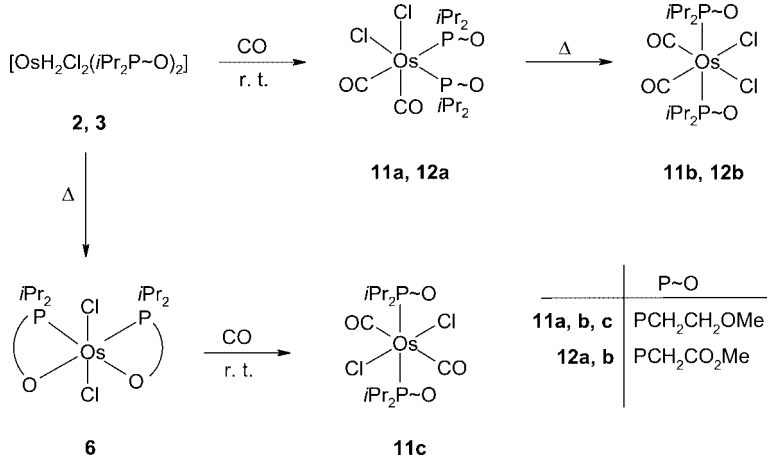


Scheme 2.

 © 2007 Wiley-VCH Verlag GmbH & Co. KGaA, Weinheim 

the expected dicarbonyl complexes, structurally related to **11a**, **11b** or **11c**, are not formed. The IR spectra of **13** and **14** display besides the strong ν(CO) band for the carbonyl ligand at 1915 $cm^{-1}$ (for **13**) and 1905 $cm^{-1}$ (for **14**) two ν(C=O) stretching modes for the free and the coordinated C=O ester function at 1710 and 1615 $cm^{-1}$ (for **13**) and 1705 and 1610 $cm^{-1}$ (for **14**). The observation of an AB spin system in the $^{31}P$ NMR spectra supports the different bonding mode of the $iPr_2PCH_2CO_2R$ ligands and the size of the $^{31}P,^{187}Os$ coupling constant the *trans* position of the phosphorus atoms. If we take this (and the supposed octahedral structure) into consideration, there remain two alternatives for the coordination site of the carbonyl ligand: it could be *trans* to the chlorido ligand or *trans* to the oxygen atom of the C=O ester group. Since the splitting pattern of the signals of the $CHCH_3$ protons and the $CHCH_3$ carbon atoms in the $^1H$ and $^{13}C$ NMR spectra of **13** and **14** indicate the presence of a mirror plane in the molecules, the second alternative, shown in Scheme 3, should be correct.

Under the same conditions, under which the monocarbonyl complexes **13** and **14** are obtained, the osmium(II) precursors **7** and **8** react with *tert*-butyl isocyanide to afford the disubstituted compounds **15** and **16**. Based on the NMR spectroscopic data, we assume that exclusively the *cis*,*cis*,*trans* isomers are formed. In analogy to the structurally related dicarbonyl derivatives **11b** and **12b**, the $^{31}P$ NMR spectra of **15** and **16** display one singlet for the equivalent phosphorus atoms, while the IR spectra show two ν(C≡N) stretching modes in the expected region. We note that prior to our work on the reactivity of the osmium(II) compounds **7** and **8**, we found that the analogous ruthenium(II) complex $[RuCl_2\{\kappa^2(P,O)\text{-}iPr_2PCH_2CO_2Me\}_2]$ reacts with CO to give the monocarbonyl compound $[RuCl_2(CO)\{\kappa(P)\text{-}iPr_2PCH_2CO_2Me\}\{\kappa^2(P,O)\text{-}iPr_2PCH_2CO_2Me\}]$ whereas with *t*BuNC the bis(isocyanide) complex $[RuCl_2(CNtBu)_2\{\kappa(P)\text{-}iPr_2PCH_2CO_2Me\}_2]$ (having in contrast to **15** the all-*trans* configuration) was obtained. The corresponding 1:1 adduct $[RuCl_2(CNtBu)\{\kappa(P)\text{-}iPr_2PCH_2CO_2Me\}\{\kappa^2(P,O)\text{-}iPr_2PCH_2CO_2Me\}]$ was isolated as an intermediate.[11]

The dihydridoosmium(IV) compounds **3** and **4** behave similarly to **7** and **8** and upon treatment with excess *t*BuNC in benzene at room temperature give the bis(isocyanide) complexes **15** and **16** in good to excellent yield. In contrast, the reaction of the phosphane–amine complex **5** with *tert*-butyl isocyanide in benzene under reflux led to the formation of the ionic product **17**, the conductivity of which in nitromethane is in agreement with that of a 1:1 electrolyte.

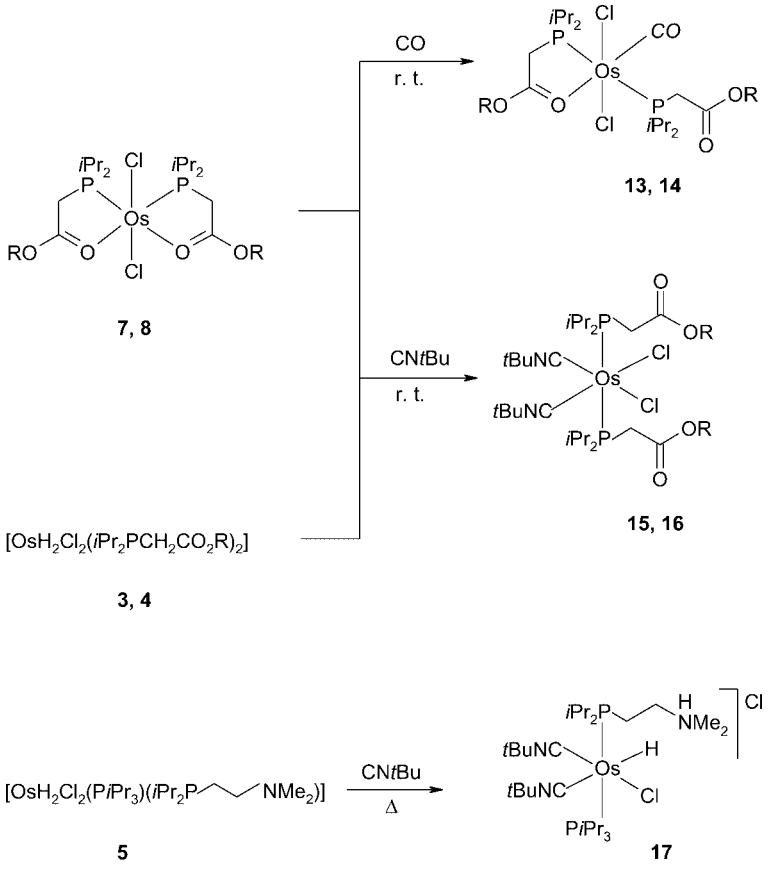


Scheme 3.

 © 2007 Wiley-VCH Verlag GmbH & Co. KGaA, Weinheim 

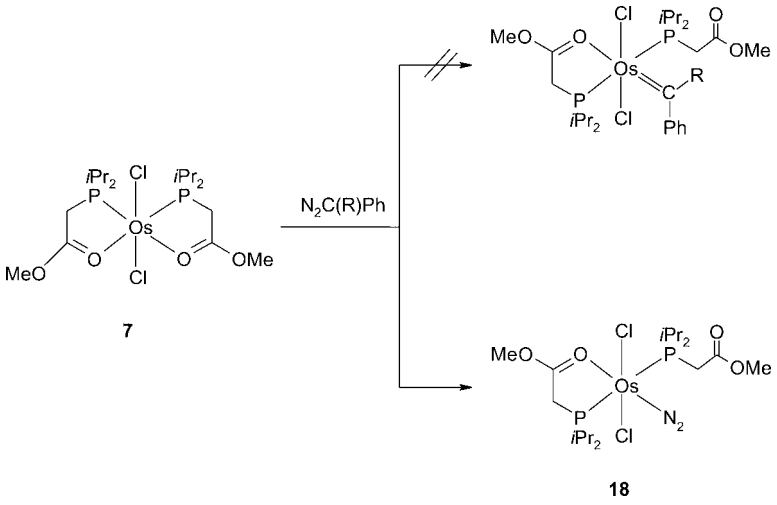


Scheme 4.

The $^1$H NMR spectrum of **17** displays for the hydrido ligand a resonance at $\delta$ = –7.48 ppm, which due to the coupling with two different $^{31}$P nuclei is split into a doublet of doublets. The presence of the OsH unit is also indicated by the {$^1$H}-decoupled $^{31}$P NMR spectrum, in which the two singlet signals of the AB spin system are split into doublets. The large $^{31}$P,$^{31}$P coupling constant of 245.8 Hz supports the *trans* position of the two phosphane ligands.

Attempts to prepare a (carbene)osmium(II) complex [$OsCl_2$(=CRPh){κ(*P*)-*i*$Pr_2PCH_2CO_2Me$}{κ$^2$(*P*,*O*)-*i*$Pr_2PCH_2CO_2Me$}] (R = H, Ph) from **6** and phenyl- or diphenyldiazomethane led unexpectedly to the formation of the dinitrogen compound **18** (see Scheme 4). A similar observation was already made in the course of studies on the reactivity of the dimer [RhCl(P*i*$Pr_3)_2]_2$, which upon treatment with $PhCHN_2$ gave the mononuclear complex *trans*-[RhCl($N_2$)(P*i*$Pr_3)_2$].[12] As we failed to separate **18** from organic by-products by column chromatography or fractional crystallization, the dinitrogenosmium(II) compound was characterized spectroscopically. Diagnostic for the coordination of the $N_2$ ligand is the N–N stretching mode at 2060 cm$^{-1}$ in the IR spectrum, which appears at a similar position as for the complexes [$OsCl_2(N_2)(L_3)$] (L = $PMe_2Ph$, $PEt_2Ph$, $PEt_3$)[13] and is consistent with an "end-on" coordination of the dinitrogen molecule.[14] Since the IR spectrum of **18** displays two ν(C=O) stretching modes at almost the same wavenumbers as for the monocarbonyl complex **13**, and since also the $^1$H, $^{13}$C and $^{31}$P NMR spectroscopic data of the two compounds are quite similar, we assume that the two chlorido ligands, the two phosphorus atoms, and the ester C=O group and the $N_2$ ligand are *trans*-disposed.

The reactions of the bis(chelate) osmium(II) precursors **6**–**8** with phenylacetylene in benzene under reflux gave the six-coordinate vinylidene complexes **19a**, **20** and **21** in 48–95% yield (Scheme 5). They are possibly formed via the isomeric alkyne- and alkynyl(hydrido) compounds as intermediates, although in contrast to the reactions of [RhCl{κ(*P*)-*i*$Pr_2PCH_2CH_2OMe$}{κ$^2$(*P*,*O*)-*i*$Pr_2PCH_2CH_2OMe$}] and [IrCl($C_2H_4$){κ(*P*)-*i*$Pr_2PCH_2CO_2Me$}$_2$] with phenylacetylene,[15,16] species with an Os(PhC≡CH) or OsH(C≡CPh) unit could not be observed. The most characteristic spectroscopic features of **19a**, **20** and **21** are (1) the signal of the =C*H*Ph proton at $\delta \approx$ 2.0–2.6 ppm in the $^1$H NMR spectra and (2) the low-field resonances at $\delta$ = 291.8 and 108.9 ppm (for **19a**), 297.1 and 109.3 ppm (for **20**), and 297.3 and 108.3 ppm (for **21**) in the $^{13}$C NMR spectra. The latter are assigned to the α-C and β-C vinylidene carbon atoms. The chemical shifts of the $^1$H and $^{13}$C NMR signals are quite similar to those of the related five-coordinate phenylvinylidene complexes [$OsCl_2$(=C=CHPh)(P*i*$Pr_3)_2$][17] and [$OsCl_2$(=C=CHPh)($PPh_3)_2$].[18]

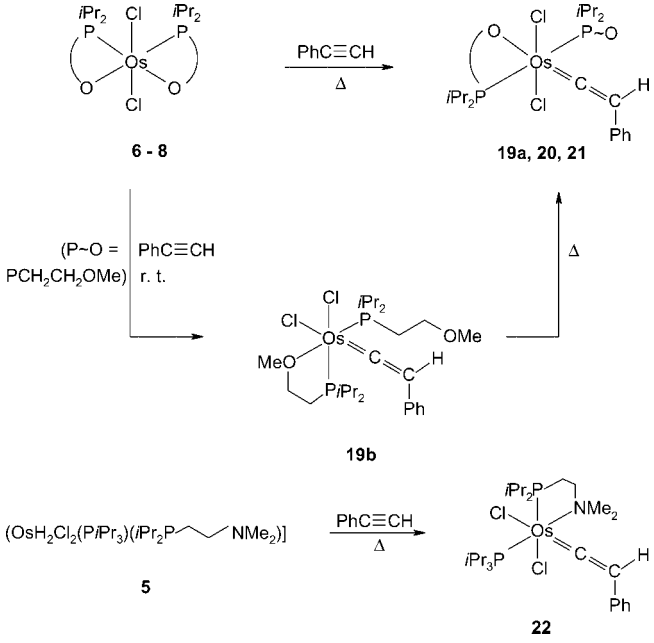


Scheme 5.

At room temperature, compounds **19a**, **20** and **21** are fluxional in solution, as can be seen by the appearance of one broad singlet in the $^{31}$P NMR spectra. The dynamic

 © 2007 Wiley-VCH Verlag GmbH & Co. KGaA, Weinheim 

process is frozen out at low temperature, and thus in the spectra of **19a** (in $CDCl_3$ at –90 °C), **20** (in $C_6D_5CD_3$ at –80 °C), and **21** (in $C_6D_5CD_3$ at –20 °C) the typical pattern of an AB spin system is observed. The large $^{31}P,^{31}P$ coupling constants of about 320–333 Hz are consistent with the *trans* position of the phosphorus atoms. From the coalescence temperatures and the difference in the chemical shifts of the two signals $\Delta G^{\neq}$ values of approximately 40 kJ mol$^{-1}$ (for **19a**), 51 kJ mol$^{-1}$ (for **20**), and 54 kJ mol$^{-1}$ (for **21**) can be calculated. The observed phenomenon is reversible and explained by a rapid exchange in the chelating behavior of the two phosphane ligands. It is interesting to note that neither the monocarbonyl complexes **13** and **14** nor the dinitrogen derivative **18** are fluxional in solution at room temperature.

The proposed stereochemistry of **20** with the phosphanes and the chlorido ligands in *trans* disposition was confirmed by a single-crystal X-ray diffraction investigation.[19] The Os–C–C unit is almost linear [176.7(5)°] and the Os–C bond length [1.802(6) Å] slightly shorter than in some other (vinylidene)osmium(II) complexes such as $[OsCl_2(=C=CHPh)(P\textit{i}Pr_3)\{\kappa^2(\textit{P},\textit{N})\text{-}\textit{i}Pr_2PCH_2CH_2NMe_2\}]$ [1.82(1) Å],[3b] $[OsCl(=C=CHSiMe_3)(CH=CHSiMe_3)(P\textit{i}Pr_3)_2]$ [1.82(3) Å],[20] $[OsCl(=C=CHPh)(PPh_3)\{1,3\text{-}(PPh_2CH_2)_2C_6H_4\}]$ [1.819(6) Å],[21] and $[OsCl_2(=C=CHPh)(H_2O)(PPh_3)_2]$ [1.812(7) Å].[18] The smallest corner–center–corner angle of the octahedron is found for P–Os–O (80.0(1)°], which is probably due to the ring strain in the five-membered $OsPC_2O$ chelating system.

If the reaction of **6** with phenylacetylene in benzene was carried out at room temperature instead of under reflux, the red, moderately air-stable *cis,cis*-configured compound **19b** was generated (see Scheme 5). Under the same conditions, **7** and **8** are inert towards PhC≡CH. Upon heating, **19b** rearranges quickly to the thermodynamically preferred isomer **19a**. In contrast to **19a**, the $^{31}P$ NMR spectrum of **19b** displays two sharp doublets at room temperature, which indicates that in solution the molecule is non-fluxional on the NMR time scale under these conditions. The chemical shift of the two doublets ($\delta$ = 19.0 and –10.4 ppm) and the $^{31}P,^{31}P$ coupling constant (9.2 Hz) are similar to those of the phenylvinylidene complex **22** ($\delta$ = 15.4 and –11.2 ppm, $^2J_{P,P}$ = 6.7 Hz), which was prepared from **5** and excess phenylacetylene in benzene under reflux and characterized crystallographically.[3b] The X-ray crystal structure analysis of **22** revealed a slightly distorted octahedral geometry with the phosphorus atoms and the chlorido ligands in *cis* disposition and bond angles Cl–Os–Cl and P–Os–P of 85.10(9)° and 105.80(9)°, respectively. The P–Os–N angle of the chelate ring amounts to 82.4(1)° and is thus similar to the corresponding P–Os–O angle of **20**.

## Conclusion

The present work has shown that osmium(II) complexes of the general composition $[OsCl_2(P\text{–}O)_2]$ with the phosphane–ether $\textit{i}Pr_2PCH_2CH_2OMe$ and the phosphane–esters $\textit{i}Pr_2PCH_2CO_2R$ (R = Me, Et) as chelate ligands are accessible from dichloridodihydridoosmium(IV) compounds as precursors. Due to the lability of the Os–O bond, the osmium(II) complexes react smoothly with carbon monoxide and *tert*-butyl isocyanide by partial opening of the chelate ring. Depending on the reaction conditions, different isomers of the dicarbonyl compounds $[OsCl_2(CO)_2(\textit{i}Pr_2PCH_2CH_2OMe)_2]$ and $[OsCl_2(CO)_2(\textit{i}Pr_2PCH_2CO_2Me)_2]$ are formed. The monocarbonyl complexes $[OsCl_2(CO)(\textit{i}Pr_2PCH_2CO_2R)_2]$ and the dinitrogen derivative $[OsCl_2(N_2)(\textit{i}Pr_2PCH_2CO_2Me)_2]$, each of them containing one monodentate and one bidentate phosphane ligand, have also been obtained. The reactions of the chelate compounds $[OsCl_2(P\text{–}O)_2]$ with phenylacetylene afford the phenylvinylidene complexes $[OsCl_2(=C=CHPh)(P\text{–}O)_2]$, which in solution at room temperature are fluxional on the NMR time scale. The phosphane–amine complex $[OsCl_2(=C=CHPh)(P\textit{i}Pr_3)(\textit{i}Pr_2PCH_2CH_2NMe_2)]$ was prepared from $[OsH_2Cl_2(P\textit{i}Pr_3)(\textit{i}Pr_2PCH_2CH_2NMe_2)]$ and phenylacetylene and characterized crystallographically.

## Experimental Section

**General:** All operations were carried out under argon using Schlenk techniques. The osmium complex **1**[1] and the phosphane derivatives $\textit{i}Pr_2PCH_2CH_2OMe$,[16] $\textit{i}Pr_2PCH_2CH_2NMe_2$,[16] and $\textit{i}Pr_2PCH_2CO_2R$ (R = Me, Et)[7] were prepared as described in the literature. NMR: Bruker AC 200 and AMX 400. IR: Perkin–Elmer 397 and 1320. MS: Varian CH 7 MAT (70 eV). The molar conductivity $\Lambda_M$ was determined in nitromethane. Melting points were determined by DTA. Abbreviations used: s: singlet; d: doublet; t: triplet; q: quartet; m: multiplet; vt: virtual triplet; br.: broad signal; $N = {}^3J_{P,H} + {}^5J_{P,H}$ or ${}^2J_{P,C} + {}^4J_{P,C}$.

**1. Preparation of $[OsH_2Cl_2(\textit{i}Pr_2PCH_2CH_2OMe)_2]$ (2):** A suspension of **1** (145 mg, 0.25 mmol) in pentane (10 mL) was treated with $\textit{i}Pr_2PCH_2CH_2OMe$ (142 μL, 0.75 mmol) and stirred at room temperature for 24 h. A pale-yellow solid precipitated, which was filtered, washed three times with 5-mL portions of pentane and dried; yield 144 mg (94%); m.p. 65 °C (decomp.). MS: *m*/*z* ($I_r$) = 614 (0.4) [$M^+$], 578 (2.8) [$M^+$ – HCl], 542 (2.4) [$M^+$ – 2 HCl]. IR (KBr): $\tilde{\nu}$ = 2225 [ν(OsH)] cm$^{-1}$. $^1H$ NMR (400 MHz, $CDCl_3$): $\delta$ = 3.65 (m, 4 H, $OCH_2$), 3.49 (s, 6 H, $OCH_3$), 2.53 (m, 4 H, $PCHCH_3$), 1.99 (m, 4 H, $PCH_2$), 1.24 (dd, $^3J_{P,H}$ = 16.2, $^3J_{H,H}$ = 7.1 Hz, 12 H, $PCHCH_3$), 1.23 (dd, $^3J_{P,H}$ = 13.9, $^3J_{H,H}$ = 7.0 Hz, 12 H, $PCHCH_3$), –12.39 (t, $^2J_{P,H}$ = 26.8 Hz, 2 H, $OsH_2$) ppm. $^{13}C$ NMR (50.3 MHz, $C_6D_6$): $\delta$ = 72.4 (s, $OCH_2$), 60.5 (s, $OCH_3$), 28.0 (d, $^1J_{P,C}$ = 35.7 Hz, $PCHCH_3$), 27.3 (d, $^1J_{P,C}$ = 33.7 Hz, $PCH_2$), 19.2, 18.8 (2 s, $PCHCH_3$) ppm. $^{31}P$ NMR (81.0 MHz, $C_6D_6$): $\delta$ = 25.2 (s, t in off-resonance) ppm. $C_{18}H_{44}Cl_2O_2OsP_2$ (615.7): calcd. C 35.11, H 7.20; found C 35.38, H 7.32.

**2. Preparation of $[OsH_2Cl_2\{\kappa^2(\textit{P},\textit{O})\text{-}\textit{i}Pr_2PCH_2C(=O)OMe\}\{\kappa(\textit{P})\text{-}\textit{i}Pr_2PCH_2CO_2Me\}]$ (3):** This compound was prepared as described for **2**, with **1** (134 mg, 0.29 mmol) and $\textit{i}Pr_2PCH_2CO_2Me$ (135 μL, 0.69 mmol) as starting materials and hexane (10 mL) as solvent. Colorless solid; yield 106 mg (72%); m.p. 80 °C (decomp.). IR (KBr): $\tilde{\nu}$ = 2140 [ν(OsH)], 1720, 1630 [ν(C=O)] cm$^{-1}$. $^1H$ NMR (400 MHz, $CDCl_3$): $\delta$ = 3.75 (s, 6 H, $OCH_3$), 3.31 (d, $^2J_{P,H}$ = 9.9 Hz, 4 H, $PCH_2$), 2.38 (m, 4 H, $PCHCH_3$), 1.29 (dd, $^3J_{P,H}$ = 15.9, $^3J_{H,H}$ = 7.0 Hz, 12 H, $PCHCH_3$), 1.13 (dd, $^3J_{P,H}$ = 14.5, $^3J_{H,H}$ = 6.7 Hz, 12 H, $PCHCH_3$), –9.97 (t, $^2J_{P,H}$ = 18.2 Hz, 2 H, $OsH_2$)

 © 2007 Wiley-VCH Verlag GmbH & Co. KGaA, Weinheim 

ppm. $^{13}$C NMR (100.6 MHz, $C_6D_6$): $\delta$ = 177.4 (s, *C*$O_2$Me), 53.9 (s, $OCH_3$), 31.8 (d, $^1J_{P,C}$ = 25.0 Hz, $PCH_2$), 27.8 (d, $^1J_{P,C}$ = 32.7 Hz, P*C*HCH$_3$), 18.8, 18.5 (2 s, PCH*C*H$_3$) ppm. $^{31}$P NMR (36.2 MHz, $C_6D_6$, 295 K): $\delta$ = 15.8 (s, t in off-resonance) ppm. $^{31}$P NMR (36.2 MHz, $C_6D_5CD_3$, 183 K): $\delta$ = 18.0, 9.7 (2 br., $J_{P,P}$ not resolved) ppm. $C_{18}H_{40}Cl_2O_4OsP_2$ (643.6): calcd. C 33.59, H 6.26; found C 33.54, H 6.22.

**3. Preparation of [OsH$_2$Cl$_2${κ$^2$(*P*,*O*)-*i*Pr$_2$PCH$_2$C(=O)OEt}{κ(*P*)-*i*Pr$_2$PCH$_2$CO$_2$Et}] (4):** This compound was prepared as described for **2**, with **1** (98 mg, 0.17 mmol) and *i*Pr$_2$PCH$_2$CO$_2$Et (120 μL, 0.51 mmol) as starting materials and hexane (10 mL) as solvent. Colorless solid; yield 99 mg (88%); m.p. 112 °C (decomp.). IR (KBr): $\tilde{\nu}$ = 2140 [ν(OsH)], 1755, 1665 [ν(C=O)] cm$^{-1}$. $^1$H NMR (200 MHz, $CDCl_3$): $\delta$ = 4.25 (q, $J$ = 4 H, $^3H_{H,H}$ = 7.1 Hz, OC*H*$_2$CH$_3$), 3.29 (d, $^2J_{P,H}$ = 9.8 Hz, 4 H, $PCH_2$), 2.32 (m, 4 H, PC*H*CH$_3$), 1.28 (dd, $^3J_{P,H}$ = 16.4, $^3J_{H,H}$ = 7.0 Hz, 12 H, PCHC*H*$_3$), 1.26 (t, $^3J_{H,H}$ = 7.1 Hz, 6 H, OCH$_2$C*H*$_3$), 1.11 (dd, $^3J_{P,H}$ = 14.3, $^3J_{H,H}$ = 6.9 Hz, 12 H, PCHC*H*$_3$), –9.90 (t, $^2J_{P,H}$ = 18.3 Hz, 2 H, OsH$_2$) ppm. $^{31}$P NMR (36.2 MHz, $C_6D_6$, 295 K): $\delta$ = 15.5 (s, t in off-resonance) ppm. $^{31}$P NMR (36.2 MHz, $C_6D_5CD_3$, 183 K): $\delta$ = 19.0, 9.8 (2 br., $J_{P,P}$ not resolved) ppm. $C_{20}H_{44}Cl_2O_4OsP_2$ (671.6): calcd. C 35.77, H 6.60; found C 35.43, H 6.63.

**4. Preparation of [OsH$_2$Cl$_2$(P*i*Pr$_3$)(*i*Pr$_2$PCH$_2$CH$_2$NMe$_2$)] (5):** This compound was prepared as described for **2**, with **1** (200 mg, 0.35 mmol) and *i*Pr$_2$PCH$_2$CH$_2$NMe$_2$ (218 μL, 1.03 mmol) as starting materials and benzene (8 mL) as solvent. Time of reaction 3 h. Pale-yellow solid; yield 185 mg (88%); m.p. 98 °C (decomp.). MS: *m*/*z* ($I_r$) = 576 (17.6) [M$^+$ – HCl)], 540 (0.8) [M$^+$ – 2 HCl]. IR (KBr): $\tilde{\nu}$ = 2180, 2140 [ν(OsH)] cm$^{-1}$. $^1$H NMR (400 MHz, $CDCl_3$): $\delta$ = 2.80 (s, 6 H, $NCH_3$), 2.71, 2.57, 2.53 (3 m, 7 H, C*H*$_2$NMe$_2$ and PC*H*CH$_3$), 1.78 (m, 2 H, $PCH_2$), 1.30 (dd, $^3J_{P,H}$ = 13.2, $^3J_{H,H}$ = 7.2 Hz, 12 H, PCHC*H*$_3$ of P*i*Pr$_3$), 1.24 (dd, $^3J_{P,H}$ = 13.2, $^3J_{H,H}$ = 7.1 Hz, 6 H, PCHC*H*$_3$ of P*i*Pr$_2$), 1.21 (dd, $^3J_{P,H}$ = 14.5, $^3J_{H,H}$ = 7.2 Hz, 6 H, PCHC*H*$_3$ of P*i*Pr$_2$), –12.22 (dd, $^2J_{P,H}$ = $^2J_{P',H}$ = 18.2 Hz, 2 H, OsH$_2$) ppm. $^{13}$C NMR (50.3 MHz, $CDCl_3$): $\delta$ = 63.3 (s, $NCH_2$), 54.0 (s, $NCH_3$), 30.2 (d, $^1J_{P,C}$ = 33.5 Hz, P*C*HCH$_3$ of P*i*Pr$_2$), 26.4 (d, $^1J_{P,C}$ = 31.5 Hz, P*C*HCH$_3$ of P*i*Pr$_3$), 20.9 (d, $^1J_{P,C}$ = 27.7 Hz, $PCH_2$), 19.7 (s, PCH*C*H$_3$ of P*i*Pr$_3$), 18.7, 18.6 (2 s, PCH*C*H$_3$ of P*i*Pr$_2$) ppm. $^{31}$P NMR (162.0 MHz, $CDCl_3$, 295 K): $\delta$ = 30.8, 14.2 (2 br. s, both t in off-resonance) ppm. $C_{19}H_{47}Cl_2NOsP_2$ (612.6): calcd. C 37.25, H 7.73, N 2.29; found C 37.03, H 7.75, N 2.25.

**5. Preparation of [OsCl$_2${κ$^2$(*P*,*O*)-*i*Pr$_2$PCH$_2$CH$_2$OMe}$_2$] (6). (a)** A suspension of **1** (305 mg, 0.52 mmol) in hexane (70 mL) was treated dropwise with *i*Pr$_2$PCH$_2$CH$_2$OMe (351 μL, 1.57 mmol) and heated at 110 °C in a closed vessel for 4 h. After the reaction mixture was cooled to room temperature, an orange solid precipitated. The solution was concentrated to ca. 2 mL, the yellow precipitate was filtered, washed twice with 5-mL portions of pentane (0 °C) and dried; yield 154 mg (48%). **(b)** A stream of ethene was passed through a solution of **2** (206 mg, 0.34 mmol) in benzene (10 mL) for 1 min and, after the ethene was replaced by argon, the solution was stirred under reflux for 30 min. After the reaction mixture was cooled to room temperature, the solvent was evaporated. The remaining oily residue was suspended in pentane (5 mL, 0 °C) and the suspension was stirred until an orange solid precipitated. The isolation of the product was analogous to the one described in (a); yield 156 mg (76%); m.p. 96 °C (decomp.). $^1$H NMR (200 MHz, $C_6D_6$): $\delta$ = 3.60 (s, 6 H, $OCH_3$), 3.56 (m, 4 H, $OCH_2$), 2.78 (m, 4 H, PC*H*CH$_3$), 1.84 (m, 4 H, $PCH_2$), 1.21 (dvt, PCHC*H*$_3$, $^3J_{H,H}$ = 7.3 Hz, 12 H, $N$ = 13.2 Hz), 1.19 (dvt, PCHC*H*$_3$, $^3J_{H,H}$ = 7.4 Hz, 12 H, $N$ = 13.0 Hz) ppm. $^{13}$C NMR (50.3 MHz, $C_6D_6$): $\delta$ = 75.0 (s, $CH_2O$), 62.6 (s, $OCH_3$), 29.0 (X part of an ABX spin system, $J_{A,X}$ = 28.6 Hz, P*C*HCH$_3$), 26.3 (X part of an ABX spin system, $J_{A,X}$ = 23.0 Hz, $PCH_2$), 20.7, 20.5 (2 s, PCH*C*H$_3$) ppm. $^{31}$P NMR (81.0 MHz, $C_6D_6$): $\delta$ = –0.6 (s, $^1J_{Os,P}$ = 361.8 Hz) ppm. $C_{18}H_{42}Cl_2O_2OsP_2$ (613.6): calcd. C 35.23, H 6.86; found C 35.22, H 6.90.

**6. Preparation of [OsCl$_2${κ$^2$(*P*,*O*)-*i*Pr$_2$PCH$_2$C(=O)OMe}$_2$] (7). (a)** A suspension of **1** (119 mg, 0.20 mmol) in hexane (15 mL) was treated dropwise with *i*Pr$_2$PCH$_2$CO$_2$Me (120 μL, 0.16 mmol) and heated at 110 °C in a closed vessel for 4 h. The reaction mixture was worked up as described for **6**; yield 118 mg (90%). **(b)** A stream of ethene was passed through a solution of **3** (515 mg, 0.80 mmol) in benzene (20 mL) for 1 min and, after the ethene was replaced by argon, the solution was stirred under reflux for 1 h. After the reaction mixture was cooled to room temperature, the solvent was evaporated. The remaining oily residue was dissolved in benzene (20 mL) and the solution refluxed again for 1 h. After the solution was cooled and the solvent removed, the residue was suspended in pentane (5 mL, 0 °C) and the suspension was stirred until an orange solid precipitated; yield 467 mg (91%). **(c)** A suspension of **3** (101 mg, 0.17 mmol) in benzene (20 mL) was heated under reflux for 12 h. The hot reaction mixture was filtered, the filtrate was brought to drynes in vacuo, and the oily residue worked up as described for **6**. Orange microcrystalline solid; yield 96 mg (87%); m.p. 69 °C (decomp.). IR (KBr): $\tilde{\nu}$ = 1630 [ν(C=O)] cm$^{-1}$. $^1$H NMR (400 MHz, $C_6D_6$): $\delta$ = 3.41 (s, 6 H, $OCH_3$), 3.13 (d, $^2J_{P,H}$ = 9.1 Hz, 4 H, $PCH_2$), 2.43 (m, 4 H, PC*H*CH$_3$), 1.21 (dd, $^3J_{P,H}$ = 14.3, $^3J_{H,H}$ = 7.1 Hz, 12 H, PCHC*H*$_3$), 1.15 (dd, $^3J_{P,H}$ = 13.6, $^3J_{H,H}$ = 7.1 Hz, 12 H, PCHC*H*$_3$) ppm. $^{13}$C NMR (100.6 MHz, $C_6D_6$): $\delta$ = 185.3 (s, *C*$O_2$Me), 55.0 (s, $OCH_3$), 35.7 (X part of an ABX spin system, $J_{A,X}$ = 23.7 Hz, $PCH_2$), 28.3 (X part of an ABX spin system, $J_{A,X}$ = 29.5 Hz, P*C*HCH$_3$), 19.1, 18.8 (2 s, PCH*C*H$_3$) ppm. $^{31}$P NMR (162.0 MHz, $C_6D_6$): $\delta$ = 2.8 (s, $^1J_{Os,P}$ = 341.4 Hz) ppm. $C_{18}H_{38}Cl_2O_4OsP_2$ (641.5): calcd. C 33.70, H 5.97; found C 34.02, H 6.15.

**7. Preparation of [OsCl$_2${κ$^2$(*P*,*O*)-*i*Pr$_2$PCH$_2$C(=O)OEt}$_2$] (8). (a)** A suspension of **1** (353 mg, 0.61 mmol) in hexane (60 mL) was treated dropwise with *i*Pr$_2$PCH$_2$CO$_2$Et (434 μL, 1.82 mmol) and heated at 110 °C in a closed vessel for 4 h. The reaction mixture was worked up as described for **6**; yield 180 mg (44%). **(b)** A stream of ethene was passed through a solution of **4** (150 mg, 0.22 mmol) in benzene (10 mL) for 1 min and, after the ethene was replaced by argon, the solution was stirred under reflux for 1 h. The reaction mixture was worked up as described for **6**. Orange microcrystalline solid; yield 133 mg (89%); m.p. 56 °C (decomp.). IR (KBr): $\tilde{\nu}$ = 1630 [ν(C=O] cm$^{-1}$. $^1$H NMR (200 MHz, $C_6D_6$): $\delta$ = 4.05 (q, $^3J_{H,H}$ = 7.1 Hz, 4 H, OC*H*$_2$CH$_3$), 3.14 (d, $^2J_{P,H}$ = 9.1 Hz, 4 H, $PCH_2$), 2.43 (m, 4 H, PC*H*CH$_3$), 1.22 (dvt, PCHC*H*$_3$, $^3J_{H,H}$ = 7.7 Hz, 12 H, $N$ = 14.6 Hz), 1.15 (dvt, PCHC*H*$_3$, $^3J_{H,H}$ = 6.8 Hz, 12 H, $N$ = 13.9 Hz), 0.88 (t, $^3J_{H,H}$ = 7.1 Hz, 6 H, OC*H*$_2$CH$_3$) ppm. $^{13}$C NMR (50.3 MHz, $C_6D_6$): $\delta$ = 185.3 (t, $^2J_{P,C}$ = 3.3 Hz, *C*$O_2$Et), 65.4 (s, O*C*H$_2$CH$_3$), 36.6 (X part of an ABX spin system, $J_{A,X}$ = 23.1 Hz, $PCH_2$), 30.0 (X part of an ABX spin system, $J_{A,X}$ = 29.6 Hz, P*C*HCH$_3$), 19.8, 19.6 (2 s, PCH*C*H$_3$), 14.5 (s, $OCH_2CH_3$) ppm. $^{31}$P NMR (81.0 MHz, $C_6D_6$): $\delta$ = 3.2 (s, $^1J_{Os,P}$ = 341.4 Hz) ppm. $C_{20}H_{42}Cl_2O_4OsP_2$ (669.6): calcd. C 35.87, H 6.32; found C 36.26, H 6.85.

**8. Generation of [OsCl$_2$(C$_2$H$_4$){κ$^2$(*P*,*O*)-*i*Pr$_2$PCH$_2$C(=O)OMe}-{κ(*P*)-*i*Pr$_2$PCH$_2$CO$_2$Me}] (9):** A slow stream of ethene was passed through a solution of **3** (40 mg, 0.06 mmol) in $C_6D_6$ (1 mL) in an NMR tube for 1 min. The ethene was replaced by argon, and the solution was stirred at 70 °C for 5 min. After it was cooled to room

 © 2007 Wiley-VCH Verlag GmbH & Co. KGaA, Weinheim 

temperature, the $^1H$ NMR spectrum indicated that a 1:1 mixture of **7** and **9** had formed. Attempts to separate the two compounds by chromatography or fractional crystallization failed. Data for **9**: IR ($CH_2Cl_2$): $\tilde{\nu}$ = 1710, 1605 [ν(C=O)], 1590 [ν(C=C)] $cm^{-1}$. $^1H$ NMR (200 MHz, $C_6D_6$): $\delta$ = 4.01 (t, $^3J_{P,H}$ = 3.7 Hz, 4 H, $C_2H_4$), 3.60 (br. d, $^2J_{P,H}$ = 6.6 Hz, 2 H, $PCH_2$), 3.29 (s, 6 H, $OCH_3$), 2.90, 2.61 (2 m, 2 H each, $PCHCH_3$), 2.89 (br. d, $^2J_{P,H}$ = 9.1 Hz, 2 H, $PCH_2$), 1.45, 1.15 (2 m, 12 H each, $PCHCH_3$) ppm. $^{31}P$ NMR (81.0 MHz, $C_6D_6$): AB spin system: $\delta_A$ = –0.1, $\delta_B$ = –15.3 ($^2J_{P,P}$ = 324.0 Hz) ppm.

**9. Generation of [$OsCl_2(C_2H_4)$\{κ²(*P*,*O*)-*i*$Pr_2PCH_2C(=O)OEt$\}-\{κ(*P*)-*i*$Pr_2PCH_2CO_2Et$\}] (10):** This compound was generated as described for **9**, with **4** (38 mg, 0.05 mmol) and ethene as starting materials. The $^1H$ NMR spectrum indicated that a 2:1 mixture of **8** and **10** had formed. Attempts to separate the two compounds by chromatography or fractional crystallization failed. Data for **10**: IR ($CH_2Cl_2$): $\tilde{\nu}$ = 1705, 1610 [ν(C=O)], 1585 [ν(C=C)] $cm^{-1}$. $^1H$ NMR (200 MHz, $C_6D_6$): $\delta$ = 4.05 (t, $^3J_{P,H}$ = 3.1 Hz, 4 H, $C_2H_4$), 3.64 (d, $^2J_{P,H}$ = 7.2 Hz, 2 H, $PCH_2$), 2.95, 2.64 (2 m, 2 H each, $PCHCH_3$), 2.93 (br. d, $^2J_{P,H}$ = 9.0 Hz, 2 H, $PCH_2$), 1.50, 1.08 (2 m, 12 H each, $PCHCH_3$), 0.97 (t, $^3J_{H,H}$ = 7.2 Hz, 3 H, $OCH_2CH_3$) ppm. $^{31}P$ NMR (81.0 MHz, $C_6D_6$): AB spin system: $\delta_A$ = –0.5, $\delta_B$ = –15.4 ($^2J_{P,P}$ = 325.6 Hz) ppm.

**10. Preparation of all-*cis*-[$OsCl_2(CO)_2$\{κ(*P*)-*i*$Pr_2PCH_2CH_2OMe$\}$_2$] (11a):** A slow stream of CO was passed through a solution of **2** (96 mg, 0.16 mmol) in a 5:1 mixture of toluene and dichloromethane (12 mL) at room temperature for 10 min. The solvent was evaporated in vacuo and the oily residue dissolved in a 1:10 mixture of acetone/diethyl ether (5 mL). After the solution had been stored at –78 °C for 12 h, colorless crystals precipitated, which were washed twice with 2-mL portions of hexane and dried; yield 48 mg (46%); m.p. 102 °C (decomp.). IR (KBr): $\tilde{\nu}$ = 2005, 1940 [ν(CO)] $cm^{-1}$. $^1H$ NMR (200 MHz, $CDCl_3$): $\delta$ = 3.76 (m, 4 H, $OCH_2$), 3.40, 3.38 (2 s, 3 H each, $OCH_3$), 3.02, 2.82, 2.64, 2.56 (4 m, 8 H, $PCH_2$ and $PCHCH_3$), 1.50–1.22 (br. m, 24 H, $PCHCH_3$) ppm. $^{13}C$ NMR (50.3 MHz, $C_6D_6$): $\delta$ = 175.2 (t, $^2J_{P,C}$ = 8.9 Hz, OsCO *trans* to Cl), 174.8 (dd, $^2J_{P,C}$ = 100.5 and 8.9 Hz, OsCO *trans* to P), 68.8, 68.7 (2 s, $OCH_2$), 59.0, 58.9 (2 s, $OCH_3$), 28.6 (d, $^1J_{P,C}$ = 25.4 Hz, $PCHCH_3$), 27.9 (d, $^1J_{P,C}$ = 28.0 Hz, $PCHCH_3$), 26.8 (d, $^1J_{P,C}$ = 29.2 Hz, $PCH_2$), 25.0, 23.7 (2 d, $^1J_{P,C}$ = 25.4 Hz, $PCHCH_3$), 21.5 (d, $^1J_{P,C}$ = 22.9 Hz, $PCH_2$), 20.2, 20.0, 19.7, 19.3, 18.9 (5 s, $PCHCH_3$), 19.1 (br., $PCHCH_3$) ppm. $^{31}P$ NMR (81.0 MHz, $CDCl_3$): $\delta$ = 2.3 (d, $^2J_{P,P}$ = 14.5, $^1J_{Os,P}$ = 222.0 Hz), –12.3 (d, $J_{P,P}$ = 14.5, $J_{Os,P}$ = 151.3 Hz) ppm. $C_{20}H_{42}Cl_2O_4OsP_2$ (669.6): calcd. C 35.88, H 6.32; found C 36.20, H 6.47.

**11. Preparation of *cis*,*cis*,*trans*-[$OsCl_2(CO)_2$\{κ(*P*)-*i*$Pr_2PCH_2CH_2OMe$\}$_2$] (11b):** A solution of **11a** (48 mg, 0.07 mmol) in benzene (10 mL) was stirred under reflux for 3 h. After the solution had cooled to room temperature, the solvent was evaporated in vacuo. The oily residue was treated with a small quantity of hexane (ca. 2 mL) and stirred until small crystals precipitated. The crystallization was completed while the mixture was stored at –78 °C for 12 h. The colorless solid was filtered, washed twice with 2-mL portions of hexane and dried; yield 45 mg (94%); m.p. 98 °C (decomp.). IR (KBr): $\tilde{\nu}$ = 2000, 1940 [ν(CO)] $cm^{-1}$. $^1H$ NMR (200 MHz, $CDCl_3$): $\delta$ = 3.73 (m, 4 H, $OCH_2$), 3.31 (s, 6 H, $OCH_3$), 2.74, 2.67 (2 m, 4 H each, $PCH_2$ and $PCHCH_3$), 1.31 (m, 24 H, $PCHCH_3$) ppm. $^{13}C$ NMR (50.3 MHz, $C_6D_6$): $\delta$ = 176.4 (t, $^2J_{P,C}$ = 7.4 Hz, OsCO), 69.0 (s, $OCH_2$), 59.1 (s, $OCH_3$), 25.3 (vt, *N* = 13.8 Hz, $PCH_2$), 20.8 (vt, *N* = 13.4 Hz, $PCHCH_3$), 19.4, 19.1 (2 s, $PCHCH_3$) ppm. $^{31}P$ NMR (81.0 MHz, $CDCl_3$): $\delta$ = 3.6 (s, $^1J_{Os,P}$ = 149.7 Hz) ppm. $C_{20}H_{42}Cl_2O_4OsP_2$ (669.6): calcd. C 35.88, H 6.32; found C 36.14, H 6.53.

**12. Preparation of all-*trans*-[$OsCl_2(CO)_2$\{κ(*P*)-*i*$Pr_2PCH_2CH_2OMe$\}$_2$] (11c):** A slow stream of CO was passed through a solution of **6** (50 mg, 0.08 mmol) in benzene (10 mL) at room temperature for 5 min. The solvent was evaporated in vacuo and the oily residue worked up as described for **11b**. Pale-orange crystals; yield 34 mg (63%); m.p. 105 °C (decomp.). IR (KBr): $\tilde{\nu}$ = 1960 [ν(CO)] $cm^{-1}$. $^1H$ NMR (200 MHz, $CDCl_3$): $\delta$ = 3.71 (m, 4 H, $OCH_2$), 3.32 (s, 6 H, $OCH_3$), 2.66 (m, 4 H, $PCH_2$), 2.48 (m, 4 H, $PCHCH_3$), 1.32 (m, 24 H, $PCHCH_3$) ppm. $^{31}P$ NMR (81.0 MHz, $CDCl_3$): $\delta$ = –4.7 (s, $^1J_{Os,P}$ = 162.8 Hz) ppm. $C_{20}H_{42}Cl_2O_4OsP_2$ (669.6): calcd. C 35.88, H 6.32; found C 35.41, H 6.65.

**13. Preparation of a Mixture of all-*cis*- and *cis*,*cis*,*trans*-[$OsCl_2(CO)_2$\{κ(*P*)-*i*$Pr_2PCH_2CO_2Me$\}$_2$] (12a,b):** A slow stream of CO was passed through a solution of **3** (46 mg, 0.07 mmol) in a 1:1 mixture of toluene/dichloromethane (4 mL) at room temperature for 10 min. The solvent was evaporated in vacuo, and the oily residue dissolved in diethyl ether (1 mL). After the solution had been stored at –78 °C for 24 h, a colorless solid precipitated which was filtered, washed twice with 2-mL portions of pentane and dried. According to the NMR spectroscopic data, the product consisted of a mixture of **12a** and **12b** in a ratio of 7:3; yield 32 mg (65%). IR (KBr): $\tilde{\nu}$ = 2060, 1965 [ν(CO)], 1725, 1715 [ν(C=O)] $cm^{-1}$. $^1H$ NMR (400 MHz, $C_6D_6$): $\delta$ = 4.11 (dd, $^2J_{P,H}$ = 15.1, $^4J_{H,H}$ = 12.2 Hz, $PCH_2$ of **12a**), 3.81 (m, $PCH_2$ of **12a/b**), 3.25 (dd, $^2J_{P,H}$ = 14.6, $^4J_{H,H}$ = 9.4 Hz, $PCH_2$ of **12a**), 3.17, 3.16, 3.15 (3 s, $OCH_3$), 2.83, 2.51, 2.33 (3 m, $PCHCH_3$ of **12a**), 2.74 (m, $PCHCH_3$ of **12b**), 1.49 (dd, $^3J_{P,H}$ = 15.4, $^3J_{H,H}$ = 7.2 Hz, $PCHCH_3$ of **12a**), 1.48 (dd, $^3J_{P,H}$ = 14.1, $^3J_{H,H}$ = 7.0 Hz, $PCHCH_3$ of **12a**), 1.32 (dvt, *N* = 16.1 Hz, $^3J_{H,H}$ = 7.3 Hz, $PCHCH_3$ of **12b**), 1.17 (dvt, *N* = 14.6 Hz, $^3J_{H,H}$ = 7.5 Hz, $PCHCH_3$ of **12b**), 1.18–0.96 (br. m, $PCHCH_3$ of **12a**) ppm. $^{31}P$ NMR (162.0 MHz, $C_6D_6$): $\delta$ = 6.2 (s, P of **12b**), 4.9, –9.0 (2 d, $^2J_{P,P}$ = 15.2 Hz, P of **12a**) ppm. $C_{20}H_{38}Cl_2O_6OsP_2$ (697.6): calcd. C 34.44, H 5.49; found C 34.12, H 5.15.

**14. Preparation of *cis*,*cis*,*trans*-[$OsCl_2(CO)_2$\{κ(*P*)-*i*$Pr_2PCH_2CO_2Me$\}$_2$] (12b):** A solution of **12a**,**b** (32 mg, 0.05 mmol) in benzene (3 mL) was stirred under reflux for 5 h. After the solution had cooled to room temperature, the solvent was evaporated in vacuo, and the oily residue layered with diethyl ether (1 mL). The mixture was vigorously stirred until a colorless solid precipitated. The precipitate was filtered, washed twice with 2-mL portions of pentane and dried; yield 12 mg (39%); m.p. 85 °C (decomp). IR (KBr): $\tilde{\nu}$ = 2020, 1945 [ν(CO)], 1710 [ν(C=O)] $cm^{-1}$. $^1H$ NMR (400 MHz, $C_6D_6$): $\delta$ = 3.81 (vt, 4 H, *N* = 9.5 Hz, $PCH_2$), 3.15 (s, 6 H, $OCH_3$), 2.74 (m, 4 H, $PCHCH_3$), 1.32 (dvt, $PCHCH_3$, $^3J_{H,H}$ = 7.3 Hz, 12 H, *N* = 16.1 Hz), 1.17 (dvt, $PCHCH_3$, $^3J_{H,H}$ = 7.5 Hz, 12 H, *N* = 14.6 Hz) ppm. $^{31}P$ NMR (162.0 MHz, $C_6D_6$): $\delta$ = 6.2 (s, $^1J_{Os,P}$ = 151.6 Hz) ppm. $C_{20}H_{38}Cl_2O_6OsP_2$ (697.6): calcd. C 34.44, H 5.49; found C 33.99, H 5.43.

**15. Preparation of *trans*,*trans*-[$OsCl_2(CO)$\{κ²(*P*,*O*)-*i*$Pr_2PCH_2C(=O)OMe$\}\{κ(*P*)-*i*$Pr_2PCH_2CO_2Me$\}] (13):** A slow stream of CO was passed through a solution of **7** (52 mg, 0.08 mmol) in a 3:2 mixture of toluene/dichloromethane (10 mL) at room temperature for 10 min. A change of color from orange to yellow occurred. The solvent was evaporated in vacuo, the remaining yellow oil was dissolved in methanol (2 mL) and the solution was layered with diethyl ether (4 mL). After the mixture had been stored at –78 °C for 12 h, a lemon-yellow microcrystalline solid precipitated, which was filtered, washed twice with 2-mL portions of diethyl ether and dried; yield 42 mg (77%); m.p. 116 °C (decomp.). IR ($CH_2Cl_2$): $\tilde{\nu}$ = 1915 [ν(CO)], 1710, 1615 [ν(C=O)] $cm^{-1}$. $^1H$ NMR (400 MHz, $C_6D_5CD_3$): $\delta$ = 3.83 (d, $^2J_{P,H}$ = 8.4 Hz, 2 H, $PCH_2$), 3.53, 3.52 (2 s, 3 H each, $OCH_3$), 3.31, 2.97 (2 m, 2 H each, $PCHCH_3$), 2.94 (d,

 © 2007 Wiley-VCH Verlag GmbH & Co. KGaA, Weinheim 

$^2J_{P,H}$ = 9.0 Hz, 2 H, $PCH_2$), 1.67 (dd, $^3J_{P,H}$ = 16.0, $^3J_{H,H}$ = 7.1 Hz, 6 H, PCHC$H_3$), 1.56 (dd, $^3J_{P,H}$ = 13.4, $^3J_{H,H}$ = 7.3 Hz, 6 H, PCHC$H_3$), 1.50 (dd, $^3J_{P,H}$ = 16.3, $^3J_{H,H}$ = 7.4 Hz, 6 H, PCHC$H_3$), 1.31 (dd, $^3J_{P,H}$ = 14.1, $^3J_{H,H}$ = 9.3 Hz, 6 H, PCHC$H_3$) ppm. $^{13}$C NMR (22.5 MHz, $CDCl_3$): $\delta$ = 186.9 [dd, $^2J_{P,C}$ = 14.5, $^3J_{P',C}$ = 6.0 Hz, *C*(=O)OMe], 177.7 (dd, $^2J_{P,C}$ = $^2J_{P',C}$ = 8.5 Hz, OsCO), 170.8 (d, $^2J_{P,C}$ = 8.5 Hz, *C*$O_2$Me), 55.8 (s, $OCH_3$), 30.7 (d, $^2J_{P,C}$ = 22.2 Hz, $PCH_2$), 23.0 (d, $^2J_{P,C}$ = 12.8 Hz, $PCH_2$), 22.7 (dd, $^1J_{P,C}$ = 23.9, $^3J_{P',C}$ = 3.4 Hz, P*C*HCH$_3$), 21.3 (dd, $^1J_{P,C}$ = 23.0, $^3J_{P',C}$ = 3.4 Hz, P*C*HCH$_3$), 18.6 (d, $^2J_{P,C}$ = 2.6 Hz, PCH*C*H$_3$), 18.0 (s, PCH*C*H$_3$), 16.5 (d, $^2J_{P,C}$ = 2.6 Hz, PCH*C*H$_3$), 16.2 (s, PCH*C*H$_3$) ppm. $^{31}$P NMR (36.2 MHz, $CDCl_3$): AB spin system: $\delta_A$ = 24.8, $\delta_B$ = 9.6 ($^2J_{P,P}$ = 290.2 Hz) ppm.

**16. Preparation of *trans*,*trans*-[OsCl$_2$(CO){κ$^2$(*P*,*O*)-*i*Pr$_2$PCH$_2$C(=O)OEt}{κ(*P*)-*i*Pr$_2$PCH$_2$CO$_2$Et}] (14):** This compound was prepared as described for **13**, with **8** (45 mg, 0.07 mmol) and CO as starting materials. Yellow solid; yield 34 mg (73%); m.p. 108 °C (decomp.). IR (KBr): $\tilde{\nu}$ = 1905 [ν(CO)], 1705, 1610 [ν(C=O)] cm$^{-1}$. $^1$H NMR (400 MHz, $CDCl_3$): $\delta$ = 4.40, 4.13 (2 q, $^3J_{H,H}$ = 7.2 Hz, OC$H_2$CH$_3$, 2 H each), 3.35, 3.13 (2 d, $^2J_{P,H}$ = 8.8 Hz, $PCH_2$, 2 H each), 2.94 (m, 4 H, PC*H*CH$_3$), 1.40 (m, 12 H, PCHC$H_3$), 1.38–1.32 (br. m, 15 H, PCHC$H_3$ and OCH$_2$C$H_3$), 1.27 (t, $^3J_{H,H}$ = 7.2 Hz, OCH$_2$C$H_3$) ppm. $^{31}$P NMR (81.0 MHz, $CDCl_3$): AB spin system: $\delta_A$ = 24.1, $\delta_B$ = 11.2 ($^2J_{P,P}$ = 289.1 Hz) ppm. $C_{21}H_{42}Cl_2O_5OsP_2$ (697.6): calcd. C 36.16, H 6.07; found C 36.39, H 6.33.

**17. Preparation of *cis*,*cis*,*trans*-[OsCl$_2$(CN*t*Bu)$_2${κ(*P*)-*i*Pr$_2$PCH$_2$CO$_2$Me}$_2$] (15). (a)** A solution of **3** (62 mg, 0.10 mmol) in benzene (10 mL) was treated with *tert*-butyl isocyanide (200 μL, 1.77 mmol) and stirred at room temperature for 10 min. The solvent was evaporated in vacuo, and the oily residue layered with hexane (1 mL). The mixture was vigorously stirred until a pale-yellow solid precipitated. The precipitate was filtered, washed twice with 1-mL portions of pentane (0 °C) and dried; yield 64 mg (83%). **(b)** Similarly as described for (a), but with **7** (65 mg, 0.10 mmol) as starting material; yield 63 mg (77%); m.p. 87 °C (decomp.). IR (KBr): $\tilde{\nu}$ = 2065, 2025 [ν(CN)], 1715 [ν(C=O)] cm$^{-1}$. $^1$H NMR (200 MHz, $CDCl_3$): $\delta$ = 3.57 (s, 6 H, $OCH_3$), 3.23 (vt, 4 H, *N* = 7.2 Hz, $PCH_2$), 2.73 (m, 4 H, PC*H*CH$_3$), 1.44 (s, 18 H, CNCCH$_3$), 1.32–1.14 (br. m, 24 H, PCHC$H_3$) ppm. $^{13}$C NMR (50.3 MHz, $CDCl_3$): $\delta$ = 172.7 (vt, *N* = 6.6 Hz, *C*$O_2$Me), 138.6 (br. s, *C*NCCH$_3$), 56.9 (s, CN*C*CH$_3$), 51.9 (s, $OCH_3$), 25.1 (vt, *N* = 11.0 Hz, $PCH_2$), 24.4 (vt, *N* = 25.0 Hz, P*C*HCH$_3$), 18.3, 17.6 (2 s, PCH*C*H$_3$) ppm. $^{31}$P NMR (81.0 MHz, $CDCl_3$): $\delta$ = –2.9 (s, $^1J_{Os,P}$ = 187.1 Hz) ppm. $C_{28}H_{56}Cl_2N_2O_4OsP_2$ (807.8): calcd. C 41.63, H 6.99, N 3.47; found C 42.05, H 7.18, N 3.35.

**18. Preparation of *cis*,*cis*,*trans*-[OsCl$_2$(CN*t*Bu)$_2${κ(*P*)-*i*Pr$_2$PCH$_2$CO$_2$Et}$_2$] (16):** This compound was prepared as described for **15**, either with **4** (50 mg, 0.07 mmol) or **8** (59 mg, 0.09 mmol) and *tert*-butyl isocyanide (200 μL, 1.77 mmol) as starting materials. Pale-yellow solid; yield 50 mg (81%) using **3** as starting material, or 56 mg (76%) using **8** as starting material; m.p. 95 °C (decomp.). IR (KBr): $\tilde{\nu}$ = 2065, 2040 [ν(CN)], 1705 [ν(C=O)] cm$^{-1}$. $^1$H NMR (200 MHz, $CDCl_3$): $\delta$ = 3.99 (q, $^3J_{H,H}$ = 6.9 Hz, 4 H, OC$H_2$CH$_3$), 3.17 (vt, 4 H, *N* = 7.4 Hz, $PCH_2$), 2.71 (m, 4 H, PC*H*CH$_3$), 1.42 (s, 18 H, CNCCH$_3$), 1.31–1.11 (br. m, 30 H, PCHC$H_3$ and OCH$_2$C$H_3$) ppm. $^{31}$P NMR (81.0 MHz, $CDCl_3$): $\delta$ = –2.9 (s) ppm. $C_{30}H_{60}Cl_2N_2O_4OsP_2$ (835.9): calcd. C 43.11, H 7.23, N 3.35; found C 43.50, H 7.38, N 3.54.

**19. Preparation of [OsHCl(CN*t*Bu)$_2$(P*i*Pr$_3$)(*i*Pr$_2$PCH$_2$CH$_2$NHMe$_2$)]Cl (17):** A solution of **5** (60 mg, 0.10 mmol) in benzene (15 mL) was treated with *tert*-butyl isocyanide (33 μL, 0.29 mmol) and stirred under reflux for 10 min. After the solution had cooled to room temperature, the solvent was evaporated in vacuo, and the oily residue layered with hexane (3 mL). The mixture was vigorously stirred until a white solid precipitated. The precipitate was filtered, washed twice with 1-mL portions of hexane and dried; yield 60 mg (78%); m.p. 122 °C (decomp.); $\Lambda_M$ = 65 Ω$^{-1}$cm$^2$mol$^{-1}$. IR (KBr): $\tilde{\nu}$ = 3400 [ν(NH)], 2160 [ν(OsH)], 2110, 2010 [ν(CN)] cm$^{-1}$. $^1$H NMR (400 MHz, $CDCl_3$): $\delta$ = 11.86 (br. s, 1 H, N*H*Me$_2$), 3.62, 3.48 (2 m, 1 H each, C$H_2$NHMe$_2$), 2.73 (s, 6 H, $NCH_3$), 2.52 (m, 3 H, PC*H*CH$_3$ of P*i*Pr$_3$), 2.39 (m, 2 H, PC*H*CH$_3$ of P*i*Pr$_2$), 1.23, 2.08 (2 m, 1 H each, $PCH_2$), 1.43 (s, 9 H, CNCCH$_3$), 1.26 (dd, $^3J_{P,H}$ = 12.5, $^3J_{H,H}$ = 7.3 Hz, 18 H, PCHC$H_3$ of P*i*Pr$_3$), 1.19 (s, 9 H, CNCCH$_3$), –7.48 (dd, $^2J_{P,H}$ = 24.4, $^2J_{P',H}$ = 21.9 Hz, 1 H, OsH); signal for PCHC$H_3$ protons of of P*i*Pr$_2$, and second signals for PCHC$H_3$ protons of P*i*Pr$_3$ and for CNCCH$_3$ protons of CN*t*Bu overlap and could not be exactly located. $^{31}$P NMR (162.0 MHz, $CDCl_3$): AB spin system: $\delta_A$ = 28.4, $\delta_B$ = 24.5 ($^2J_{P,P}$ = 245.8 Hz, 2 d in off-resonance) ppm. $C_{29}H_{65}Cl_2N_3OsP_2$ (778.9): calcd. C 44.72, H 8.41, N 5.39; found C 44.28, H 8.69, N 5.52.

**20. Generation of *trans*,*trans*-[OsCl$_2$(N$_2$){κ$^2$(*P*,*O*)-*i*Pr$_2$PCH$_2$C(=O)OMe}{κ(*P*)-*i*Pr$_2$PCH$_2$CO$_2$Me}] (18):** A solution of **7** (84 mg, 0.13 mmol) in dichloromethane (10 mL) was treated with diphenyldiazomethane (26 mg, 0.13 mmol) and stirred at room temperature for 30 min. The solvent was evaporated in vacuo, and the red residue was extracted with diethyl ether (5 mL). The extract was dried in vacuo and the residue was recrystallized from dichloromethane/diethyl ether/hexane (1:2:10). After the solution had been stored at –30 °C for 12 h, a red solid precipitated, which was filtered, washed twice with 2-mL portions of hexane and dried. According to the $^1$H NMR spectrum, the precipitate contained besides compound **18** some organic by-products, which could not be separated neither by fractional crystallization nor column chromatography. A similar mixture of products was obtained from **7** and excess of phenyldiazomethane in benzene. Data for **18**: IR (KBr): $\tilde{\nu}$ = 2060 [ν(N$_2$)], 1725, 1620 [ν(C=O)] cm$^{-1}$. $^1$H NMR (400 MHz, $C_6D_6$): $\delta$ = 3.77 (d, $^2J_{P,H}$ = 8.0 Hz, 2 H, $PCH_2$), 3.38, 3.22 (2 s, 3 H each, $OCH_3$), 3.30, 2.98 (2 m, 2 H each, PC*H*CH$_3$), 2.70 (d, $^2J_{P,H}$ = 8.5 Hz, 2 H, $PCH_2$), 1.55 (dd, $^3J_{P,H}$ = 15.6, $^3J_{H,H}$ = 6.6 Hz, 6 H, PCHC$H_3$), 1.48 (dd, $^3J_{P,H}$ = 13.0, $^3J_{H,H}$ = 6.6 Hz, 6 H, PCHC$H_3$), 1.40 (dd, $^3J_{P,H}$ = 15.6, $^3J_{H,H}$ = 6.5 Hz, 6 H, PCHC$H_3$), 1.20 (dd, $^3J_{P,H}$ = 13.8, $^3J_{H,H}$ = 5.4 Hz, 6 H, PCHC$H_3$) ppm. $^{13}$C NMR (100.6 MHz, $C_6D_6$): $\delta$ = 189.5 [dd, $^2J_{P,C}$ = 15.3, $^3J_{P',C}$ = 5.1 Hz, *C*(=O)OMe], 171.3 (dd, $^2J_{P,C}$ = 10.2, $^2J_{P',C}$ = 3.2 Hz, *C*$O_2$Me), 56.6, 51.4 (2 s, $OCH_3$), 31.7 (d, $^2J_{P,C}$ = 22.9 Hz, $PCH_2$), 23.9 (d, $^1J_{P,C}$ = 21.6 Hz, P*C*HCH$_3$), 22.6 (d, $^1J_{P,C}$ = 22.9 Hz, P*C*HCH$_3$), 22.3 (d, $^2J_{P,C}$ = 30.5 Hz, $PCH_2$), 19.5, 18.6, 17.5, 17.3 (4 s, PCH*C*H$_3$) ppm. $^{31}$P NMR (162.0 MHz, $C_6D_6$): AB spin system: $\delta_A$ = 15.1, $\delta_B$ = 1.4 ($^2J_{P,P}$ = 316.0 Hz) ppm.

**21. Preparation of *trans*,*trans*-[OsCl$_2$(=C=CHPh){κ$^2$(*P*,*O*)-*i*Pr$_2$PCH$_2$CH$_2$OMe}{κ(*P*)-*i*Pr$_2$PCH$_2$CH$_2$OMe}] (19a):** A solution of **6** (54 mg, 0.16 mmol) in benzene (10 mL) was treated with phenylacetylene (20 μL, 0.18 mmol) and stirred under reflux for 3 h. After the solution had cooled to room temperature, the solvent was evaporated in vacuo. The oily residue was recrystallized from a 1:5 mixture of diethyl ether/pentane (3 mL) to give an orange microcrystalline solid. This was filtered, washed twice with 2-mL portions of pentane and dried; yield 29 mg (48%); m.p. 170 °C (decomp.). IR ($CH_2Cl_2$): $\tilde{\nu}$ = 1610 [ν(C=C)] cm$^{-1}$. $^1$H NMR (200 MHz, $CDCl_3$): $\delta$ = 7.00, 6.77, 6.59 (3 m, 5 H, $C_6H_5$), 3.75 (m, 4 H, $OCH_2$), 3.33 (s, 6 H each, $OCH_3$), 2.76 (m, 4 H, PC*H*CH$_3$), 2.04 (m, 4 H, $PCH_2$), 1.97 (t, $^4J_{P,H}$ = 3.1 Hz, 1 H, =C*H*Ph), 1.24 (m, 24 H, PCHC$H_3$) ppm. $^{13}$C NMR (50.3 MHz, $CDCl_3$): $\delta$ = 291.8 (t, $^2J_{P,C}$ = 10.2 Hz, =*C*=CHPh), 130.7 (s, *i*-C of $C_6H_5$), 127.4, 124.5,

 © 2007 Wiley-VCH Verlag GmbH & Co. KGaA, Weinheim 

122.3 (3 s, $C_6H_5$), 108.9 (s, =C=*C*HPh), 71.1 (s, $OCH_2$), 60.6 (s, $OCH_3$), 22.9 (vt, *N* = 26.6 Hz, P*C*HCH$_3$), 21.4 (vt, *N* = 24.1 Hz, $PCH_2$), 19.0, 18.7 (2 s, PCH*C*H$_3$) ppm. $^{31}$P NMR (36.2 MHz, $CDCl_3$, 298 K): $\delta$ = –4.1 (br.) ppm. $^{31}$P NMR (36.2 MHz, $CDCl_3$, 183 K): AB spin system: $\delta_A$ = 7.9, $\delta_B$ = –15.7 ($^2J_{P,P}$ = 319.5 Hz) ppm. $C_{26}H_{48}Cl_2O_2OsP_2$ (715.7): calcd. C 43.63, H 6.76; found C 43.26, H 6.51.

**22. Preparation of *cis*-(*P*)-[OsCl$_2$(=C=CHPh){κ$^2$(*P*,*O*)-*i*Pr$_2$PCH$_2$-CH$_2$OMe}{κ(*P*)-*i*Pr$_2$PCH$_2$CH$_2$OMe}] (19b):** A solution of **6** (42 mg, 0.07 mmol) in benzene (2 mL) was treated with phenylacetylene (16 μL, 0.14 mmol) and slowly stirred at room temperature for 30 min. The solvent was evaporated in vacuo and pentane (5 mL) added to the oily residue. The mixture was stirred until a red solid precipitated. The solid was filtered, washed twice with 2-mL portions of pentane and dried; yield 24 mg (48%); m.p. 164 °C (decomp.). IR ($CH_2Cl_2$): $\tilde{\nu}$ = 1600 [ν(C=C)] cm$^{-1}$. $^1$H NMR (200 MHz, $CDCl_3$): $\delta$ = 7.20, 6.78 (2 m, 5 H, $C_6H_5$), 3.83, 3.26 (2 s, 3 H each, $OCH_3$), 3.80, 3.62 (2 m, 2 H each, $OCH_2$), 2.84, 2.71, 2.60, 2.32, 1.98 (5 m, 8 H, $PCH_2$ and PC*H*CH$_3$), 1.79 (br. s, 1 H, =C*H*Ph), 1.31 (m, 24 H, PCHC*H*$_3$) ppm. $^{31}$P NMR (36.2 MHz, $CDCl_3$): $\delta$ = 19.0, –10.4 (2 d, $^2J_{P,P}$ = 9.2 Hz) ppm. $C_{26}H_{48}Cl_2O_2OsP_2$ (715.7): calcd. C 43.63, H 6.76; found C 43.38, H 6.45.

**23. Preparation of *trans*,*trans*-[OsCl$_2$(=C=CHPh){κ$^2$(*P*,*O*)-*i*Pr$_2$PCH$_2$C(=O)OMe}{κ(*P*)-*i*Pr$_2$PCH$_2$CO$_2$Me}] (20):** A solution of **7** (304 mg, 0.47 mmol) in benzene (20 mL) was treated with phenylacetylene (104 μL, 0.95 mmol) and stirred under reflux for 3 h. After the solution had cooled to room temperature, the solvent was evaporated in vacuo. The oily residue was disolved in benzene (3 mL) and the solution was chromatographed on $Al_2O_3$ (neutral, activity grade V, length of column 5 cm). With benzene, a red fraction was eluted which was dried in vacuo. The residue was recrystallized from pentane (3 mL) to give a salmon-red microcrystalline solid. This was filtered, washed twice with 2-mL portions of pentane (0 °C) and dried; yield 333 mg (95%); m.p. 154 °C (decomp.). MS: *m*/*z* (*I*$_r$) = 743 (6.3) [M$^+$]. IR (KBr): $\tilde{\nu}$ = 1715, 1640 [ν(C=O)] cm$^{-1}$. $^1$H NMR (400 MHz, $C_6D_5CD_3$, 60 °C): $\delta$ = 7.38, 6.95 (2 m, 5 H, $C_6H_5$), 3.52 (br. s, 10 H, $OCH_3$ and $PCH_2$), 3.20 (m, 4 H, PC*H*CH$_3$), 2.64 (t, $^4J_{P,H}$ = 5.9 Hz, 1 H, =C*H*Ph), 1.55 (dvt, PCHC*H*$_3$, $^3J_{H,H}$ = 7.2 Hz, 12 H, *N* = 14.5 Hz), 1.52 (dvt, PCHC*H*$_3$, $^3J_{H,H}$ = 7.0 Hz, 12 H, *N* = 14.6 Hz) ppm. $^{13}$C NMR (22.5 MHz, $C_6D_6$): $\delta$ = 297.1 (t, $^2J_{P,C}$ = 11.0 Hz, Os=*C*=CHPh), 129.7, 128.2, 125.2, 123.5 (4 s, $C_6H_5$), 109.3 (t, $^3J_{P,C}$ = 6.1 Hz, Os=C=*C*HPh), 53.3 (s, $OCH_3$), 27.5 (br. s, $PCH_2$), 23.4 (vt, *N* = 25.6 Hz, P*C*HCH$_3$), 18.5, 18.3 (2 s, PCH*C*H$_3$) ppm; signal for *C*O$_2$CH$_3$ could not be exactly located. $^{31}$P NMR (36.2 MHz, $C_6D_5CD_3$, 313 K): $\delta$ = 2.6 (s) ppm. $^{31}$P NMR (36.2 MHz, $C_6D_5CD_3$, 193 K): AB spin system: $\delta_A$ = 9.5, $\delta_B$ = –2.9 ($^2J_{P,P}$ = 331.9 Hz) ppm. $C_{26}H_{44}Cl_2O_4OsP_2$ (743.5): calcd. C 42.00, H 5.93; found C 42.34, H 5.72.

**24. Preparation of *trans*,*trans*-[OsCl$_2$(=C=CHPh){κ$^2$(*P*,*O*)-*i*Pr$_2$PCH$_2$C(=O)OEt}{κ(*P*)-*i*Pr$_2$PCH$_2$CO$_2$Et}] (21):** This compound was prepared as described for **20**, with **8** (74 mg, 0.11 mmol) and phenylacetylene (36 μL, 0.33 mmol) as starting materials. Red microcrystalline solid; yield 69 mg (81%); m.p. 152 °C (decomp.). IR (KBr): $\tilde{\nu}$ 1700, 1635 [ν(C=O)] cm$^{-1}$. $^1$H NMR (200 MHz, $C_6D_6$): $\delta$ = 7.32, 7.22, 6.77 (3 m, 5 H, $C_6H_5$), 3.82 (q, $^3J_{H,H}$ = 7.0 Hz, 4 H, C*H*$_2$CH$_3$), 3.42, 3.05 (2 m, 4 H each, $PCH_2$ and PC*H*CH$_3$), 2.58 (t, $^4J_{P,H}$ = 5.9 Hz, 1 H, =C*H*Ph), 1.40 (dvt, PCHC*H*$_3$, $^3J_{H,H}$ = 7.2 Hz, 12 H, *N* = 14.5 Hz), 1.30 (m, 12 H, PCHC*H*$_3$), 0.82 (t, $^3J_{H,H}$ = 7.0 Hz, 6 H, CH$_2$C*H*$_3$) ppm. $^{13}$C NMR (50.3 MHz, $C_6D_5CD_3$, 253 K): $\delta$ = 297.3 (t, $^2J_{P,C}$ = 11.1 Hz, Os=*C*=CHPh), 185.4 [dd, $^2J_{P,C}$ = 12.1, $^2J_{P',C}$ = 3.2 Hz, *C*(=O)OEt], 170.6 (d, $^2J_{P,C}$ = 6.6 Hz, *C*O$_2$Et), 131.3, 128.3, 125.3, 123.3 (4 s, $C_6H_5$), 108.3 (s, Os=C=*C*HPh), 65.2, 60.4 (2 s, *C*H$_2$CH$_3$), 32.4 (d, $^1J_{P,C}$ = 22.8 Hz, $PCH_2$), 23.1 (m, P*C*HCH$_3$), 18.9 (d, $^1J_{P,C}$ = 22.9 Hz, $PCH_2$), 17.4 (br. s, PCH*C*H$_3$), 13.7, 13.5 (2 s, CH$_2$*C*H$_3$) ppm. $^{31}$P NMR (36.2 MHz, $C_6D_5CD_3$, 333 K): $\delta$ = 8.0 (s) ppm. $^{31}$P NMR (36.2 MHz, $C_6D_5CD_3$, 253 K): AB spin system: $\delta_A$ = 13.2, $\delta_B$ = 4.4 ($^2J_{P,P}$ = 333.1 Hz) ppm. $C_{28}H_{48}Cl_2O_4OsP_2$ (771.7): calcd. C 43.58, H 6.27; found C 43.68, H 6.53.

**25. Preparation of *cis*,*cis*-[OsCl$_2$(=C=CHPh)(P*i*Pr$_3$){κ$^2$(*P*,*N*)-*i*Pr$_2$PCH$_2$CH$_2$NMe$_2$}] (22):** This compound was prepared as described for **20**, method (a), with **5** (80 mg, 0.13 mmol) and phenylacetylene (43 μL, 0.39 mmol) as starting materials. Pale-red microcrystalline solid; yield 77 mg (82%); m.p. 170 °C (decomp.). MS: *m*/*z* (*I*$_r$) = 710 (0.1) [M$^+$]. $^1$H NMR (400 MHz, $CDCl_3$): $\delta$ = 7.11, 7.00, 6.66 (3 m, 5 H, $C_6H_5$), 3.46 (m, 2 H, $PCH_2$ or $NCH_2$), 2.76 (br. s, 4 H each, $NCH_3$ and =C*H*Ph), 2.57 (s, 3 H, $NCH_3$), 2.46, 2.33, 2.09, 2.02 (4 m, 7 H, $PCH_2$ or $NCH_2$ and PC*H*CH$_3$), 1.38 (dd, $^3J_{P,H}$ = 12.6, $^3J_{H,H}$ = 6.9 Hz, 6 H, PCHC*H*$_3$), 1.30 (br. m, 12 H, PCHC*H*$_3$), 1.23 (dd, $^3J_{P,H}$ = 12.7, $^3J_{H,H}$ = 7.1 Hz, 6 H, PCHC*H*$_3$), 1.17 (dd, $^3J_{P,H}$ = 13.5, $^3J_{H,H}$ = 7.3 Hz, 6 H, PCHC*H*$_3$) ppm. $^{13}$C NMR (100.6 MHz, $CDCl_3$): $\delta$ = 294.0 (dd, $^2J_{P,C}$ = $^2J_{P',C}$ = 12.3 Hz, Os=*C*=CHPh), 129.3, 128.8, 126.0, 124.2 (4 s, $C_6H_5$), 114.5 (s, Os=C=*C*HPh), 62.8 (s, $NCH_2$), 54.8, 49.2 (2 s, $NCH_3$), 28.6 (d, $^1J_{P,C}$ = 26.9 Hz, P*C*HCH$_3$), 28.2 (d, $^1J_{P,C}$ = 32.9 Hz, $PCH_2$), 25.7 (d, $^1J_{P,C}$ = 26.2 Hz, P*C*HCH$_3$), 20.2 (d, $^1J_{P,C}$ = 28.8 Hz, P*C*HCH$_3$), 21.9, 21.8, 20.8, 20.6, 20.1, 20.0 (6 s, PCH*C*H$_3$) ppm. $^{31}$P NMR (81.0 MHz, $CDCl_3$): $\delta$ = 15.4 (d, $^2J_{P,P}$ = 6.7, $J_{Os,P}$ = 239.1 Hz), –11.2 (d, $^2J_{P,P}$ = 6.7, $J_{Os,P}$ = 252.5 Hz) ppm. $C_{27}H_{51}Cl_2NOsP_2$ (712.8): calcd. C 45.50, H 7.21, N 1.97; found C 44.98, H 7.05, N 1.97.


[1] M. Aracama, M. A. Esteruelas, F. J. Lahoz, J. A. Lopez, U. Meyer, L. A. Oro, H. Werner, *Inorg. Chem.* **1991**, *30*, 288–293.

[2] H. Werner, S. Jung, B. Weberndörfer, J. Wolf, *Eur. J. Inorg. Chem.* **1999**, 951–957.

[3] Carbyne complexes: a) J. Espuelas, M. A. Esteruelas, F. J. Lahoz, L. A. Oro, N. Ruiz, *J. Am. Chem. Soc.* **1993**, *115*, 4683–4689; b) B. Weber, P. Steinert, B. Windmüller, J. Wolf, H. Werner, *J. Chem. Soc., Chem. Commun.* **1994**, 2595–2596; c) G. J. Spivak, J. N. Coalter, M. Oliván, O. Eisenstein, K. G. Caulton, *Organometallics* **1998**, *17*, 999–1001.

[4] Vinylidene complexes: a) M. A. Esteruelas, L. A. Oro, N. Ruiz, *Organometallics* **1994**, *13*, 1507–1509; b) M. Bourgault, A. Castillo, M. A. Esteruelas, E. Oñate, N. Ruiz, *Organometallics* **1997**, *16*, 636–645; c) P. Crochet, M. A. Esteruelas, A. M. López, M.-P. Matrinez, M. Oliván, E. Oñate, N. Ruiz, *Organometallics* **1998**, *17*, 4500–4509.

[5] H. Werner, B. Weber, O. Nürnberg, J. Wolf, *Angew. Chem.* **1992**, *104*, 1105–1107; *Angew. Chem. Int. Ed. Engl.* **1992**, *31*, 1025–1027.

[6] For reviews on transition metal complexes with hemilabile phosphanes, see: a) A. Bader, E. Lindner, *Coord. Chem. Rev.* **1991**, *108*, 27–110; b) E. Lindner, S. Pautz, M. Haustein, *Coord. Chem. Rev.* **1996**, *155*, 145–162; c) C. S. Slone, D. A. Weinberger, C. A. Mirkin, *Prog. Inorg. Chem.* **1999**, *48*, 233–350; d) P. Braunstein, F. Naud, *Angew. Chem.* **2001**, *113*, 702–722; *Angew. Chem. Int. Ed.* **2001**, *40*, 680–699.

[7] W. Wolfsberger, W. Burkart, S. Bauer, A. Hampp, J. Wolf, H. Werner, *Z. Naturforsch., Teil B* **1994**, *49*, 1659–1673.

[8] E. Lindner, U. Schober, R. Fawzi, W. Hiller, U. Englert, P. Wegner, *Chem. Ber.* **1987**, *120*, 1621–1628.

[9] E. Lindner, H. Rothfuß, R. Fawzi, W. Hiller, *Chem. Ber.* **1992**, *125*, 541–550.

[10] R. Benn, H. Brenneke, E. Joussen, H. Lehmkuhl, F. L. Ortiz, *Organometallics* **1990**, *9*, 756–761.


 © 2007 Wiley-VCH Verlag GmbH & Co. KGaA, Weinheim 

[11] H. Werner, A. Stark, P. Steinert, C. Grünwald, J. Wolf, *Chem. Ber.* **1995**, *128*, 49–62.
[12] H. Werner, N. Mahr, M. E. Schneider, M. Bosch, J. Wolf, *Polyhedron* **2004**, *23*, 2645–2657.
[13] J. Chatt, G. J. Leigh, R. L. Richards, *J. Chem. Soc. A* **1970**, 2243–2246.
[14] J. Chatt, J. R. Dilworth, R. L. Richards, *Chem. Rev.* **1978**, *78*, 589–625.
[15] H. Werner, A. Hampp, K. Peters, E. M. Peters, L. Walz, H. G. von Schnering, *Z. Naturforsch., Teil B* **1990**, *45*, 1548–1558.
[16] P. Steinert, H. Werner, *Organometallics* **1994**, *13*, 2677–2681.
[17] R. Castarlenas, M. A. Esteruelas, E. Gutiérrez-Puebla, E. Oñate, *Organometallics* **2001**, *20*, 1545–1554.
[18] T. B. Wen, W. Y. Hung, Z. Y. Zhou, M. F. Lo, I. D. Williams, G. Jia, *Eur. J. Inorg. Chem.* **2004**, 2837–2846.
[19] O. Nürnberg, Dissertation, Universität Würzburg **1993**.
[20] D. Huang, M. Oliván, J. C. Huffman, O. Eisenstein, K. G. Caulton, *Organometallics* **1998**, *21*, 4700–4706.
[21] T. B. Wen, Y. K. Cheung, J. Yao, W.-T. Wong, Z. Y. Zhou, G. Jia, *Organometallics* **2000**, *19*, 3803–3809.
Received: January 30, 2007
Published Online: March 30, 2007

 © 2007 Wiley-VCH Verlag GmbH & Co. KGaA, Weinheim 

DOI: 10.1002/ejic.200700179

# Synthesis, X-ray Structure, Thermal and Magnetic Behavior of $[(bipy)_2Ni_2(\mu\text{-}Cl)_2Cl_2(H_2O)_2]$: The First Neutral Ferromagnetically Coupled Six-Coordinate Dichlorido-Bridged Nickel(II) Dimer

**Oluwatayo F. Ikotun,[a] Wayne Ouellette,[a] Francesc Lloret,[b] Miguel Julve,*[b] and Robert P. Doyle*[a]**

**Keywords:** Crystal structures / Nickel complexes / Ferromagnetic coupling / Thermal analysis

$NiCl_2 \cdot 6H_2O$ and 2,2′-bipyridine (bipy) (1:1) were allowed to react under ambient conditions in dimethyl sulfoxide in the presence of acetylacetone (Hacac). The resulting green solution was concentrated in vacuo, and a green solid was isolated by precipitation with cold acetone. X-ray quality crystals of $[(bipy)_2Ni_2(\mu\text{-}Cl)_2(Cl)_2(H_2O)_2]$ (**1**) were grown by subsequent vapor/liquid diffusion of acetonitrile into a methanolic solution for one week. The structure of **1** consists of a dimeric nickel system with each metal atom in an octahedral geometry. Both equatorial bridging and axial chlorine atoms are present in this neutral species. The nickel–nickel distance (3.441 Å) is the shortest reported to date for this class of complexes and the bridging chlorido angles at 91.5° are the most acute. Variable-temperature magnetic susceptibility measurements reveal the complex to have the strongest ferromagnetic interaction reported to date ($J$ = +16.8 $cm^{-1}$, the Hamiltonian being defined as $H = -JS_A \cdot S_B$) for this family of complexes.

(© Wiley-VCH Verlag GmbH & Co. KGaA, 69451 Weinheim, Germany, 2007)

## Introduction

Multimetallic nickel(II) species occupy an important position in modern inorganic and materials chemistry. They are ubiquitous in nature as active sites in a variety of metallo-enzymes and this recognition has fuelled the development of numerous low molecular weight model compounds.[1] In addition, they have been investigated from the viewpoint of magnetochemistry, in particular in the prediction of superexchange coupling between paramagnetic centers.[2] In this field the seminal work on structure/function correlation remains that by Hatfield and Hodgson who found a linear correlation between the strength and sign of the magnetic interaction and the bridging angle, $\theta$, for eight, essentially planar, di-μ-hydroxidodicopper(II) complexes.[3] This was further expanded by Ruiz et al. to include the effects of the out-of-plane dispersion of the hydroxido hydrogen atom resulting in a highly successful predictor of magnetic behaviour in this class of compounds.[1] Such a correlation, with clear predictors, has yet to be established for five- and six-coordinate di-μ-chloridodinickel(II) complexes. Reedijk et al. have produced a comprehensive review of such structures and their magnetic behaviour[4] but attempts to produce a structure/function correlation have been hampered by the dearth of such complexes in the literature, especially complexes that are unique or extreme in geometry, bridging angle, nickel–nickel distance, charge, etc. Goodenough, Kanamori, and Anderson predicted that with an octahedral geometry and an M–X–M bridging angle close to 90°, a ferromagnetic coupling between two $d^8$ metal ions would be observed.[5] Theoretical studies by Barraclough and Brookes[6] and work by Gatteschi et al.[7] have also concluded that close proximity of the bridging Ni–Cl–Ni angle to 90° was a strong predictor of a ferromagnetic interaction. They also noted, however, that distortions about the octahedral metal ion would increase antiferromagnetic character by mixing d orbitals, and this sensitivity would make predicting the coupling strength and sign difficult for such systems. A search of the literature revealed only six ferromagnetic di-μ-chloridodinickel(II) complexes that have been both magnetically and structurally characterized with the most acute bridging angle noted to date between the Ni–Cl–Ni atoms being 93.03°.[8] Two of the six complexes with intramolecular ferromagnetic coupling are five-coordinate, distorted trigonal-bipyramidal with the remaining four having octahedral geometry. Both the five-coordinate structures show a high degree of distortion from perfect square-pyramidal geometry (as measured by $\tau$ and compared to analogous complexes displaying antiferromagnetic behaviour).[9] Reedijk et al. have noted this may be the

[a] Department of Chemistry, Syracuse University, Syracuse, NY 13244-4100, USA
E-mail: rpdoyle@syr.edu
[b] Department of Química Inorgànica/Instituto de Ciencia Molecular, Universitat de València, Polígono La Coma s/n, 46980 Paterna (València), Spain
E-mail: miguel.julve@uv.es

Supporting information for this article is available on the WWW under http://www.eurjic.org or from the author.

 © 2007 Wiley-VCH Verlag GmbH & Co. KGaA, Weinheim 

source of the strengthening of the ferromagnetic coupling in five-coordinate structures (again distortion playing an important role).[4] All the octahedral ferromagnetic complexes are charged and no such neutral structures have been characterized. Such a structure, devoid of counterion-induced distortions, that exhibits close proximity to 90°, would be an intriguing result, because current predictors would charge that this structure be strongly ferromagnetic (certainly stronger than any such value of ferromagnetic coupling reported to date). In this paper we present a new octahedral dichlorido-bridged nickel(II) dimer, $[(bipy)_2Ni_2(\mu\text{-}Cl)_2(Cl)_2(H_2O)_2]$ (**1**), with the most acute Ni–Cl–Ni bridging angle (91.5°) and the shortest intramolecular Ni···Ni distance (3.44 Å) observed to date. These extremes and the fact that it is the first neutral octahedral complex in this family, makes this structure somewhat of a "missing link" for such di-μ-chloridodinickel(II) complexes.

## Results and Discussion

### Synthesis of $[(bipy)_2Ni_2(\mu\text{-}Cl)_2(Cl)_2(H_2O)_2]$ (1)

The compound was synthesized from nickel(II) chloride hexahydrate and 2,2′-bipyridine (bipy) in a stoichiometric ratio of 1:1 in the presence of acetylacetone (Hacac). Interestingly, attempts to obtain **1** without the presence of Hacac failed, instead producing a blue solid for which a crystal structure is currently being sought. Our desire to follow this reaction stems from our observation that in reactions involving attempts to incorporate pyrophosphate ($P_2O_7^{4-}$) into $(bipy)Ni^{II}$ systems, dichlorido "impurities" were observed when the chloride salt was used. We wanted to know if we could prepare this complex directly and subsequently conduct full structural and functional characterization.

### Characterization of 1

The IR spectrum of **1** is consistent with the presence of coordinated 2,2′-bipyridine.[17] Electrospray mass spectrometry revealed the presence of Cl isotopes and is consistent with the presence of **1** as the monocationic acetonitrile solvate $\{[(bipy)_2Ni_2(\mu\text{-}Cl)_2Cl(H_2O)_2]\cdot MeCN\}^+$. Elemental analysis (C, H, N) is also consistent with the formula of **1**. The extinction coefficient ($H_2O$) was calculated to be 3.4 $M^{-1}\,cm^{-1}$ for both $Ni^{II}$ atoms, a value, which is indicative of the presence of an octahedral structure in solution.

### Description of the Crystal Structure of 1

The structure of **1** consists of neutral $(bipy)NiCl_2(H_2O)$ units, which are related by the crystallographic center of symmetry, as shown in Figure 1.

The crystallographically independent unit consists of an $Ni^{II}$ ion, octahedrally surrounded by two N atoms from the bipyridine ligand [Ni(1)–N(1) = 2.048 Å and Ni(1)–N(2) = 2.053 Å], one coordinated water molecule [Ni(1)–O(90) = 2.14 Å], and three chlorine atoms (one axial chlorido group [Ni(1)–Cl(2)] and two bridging equatorial chlorido groups [Ni(1)–Cl(1) and Ni(1)–Cl(1a)]). The *trans*-axial bridging angles [Cl(2)–Ni(1)–O(90)] show only a slight deviation from linearity at 176°. The Ni–Cl–Ni bridging unit is practically planar and the dimer is located on an inversion center.

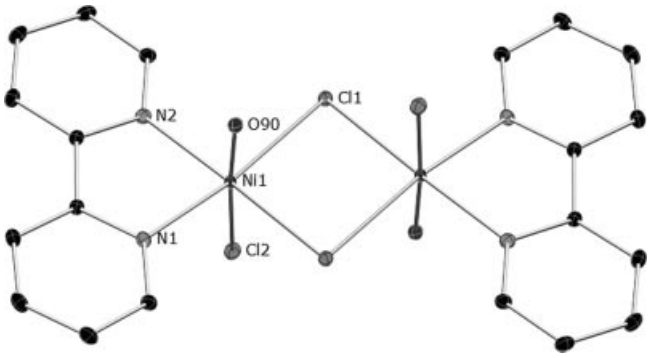


Figure 1. ORTEP plot of **1** with the atom labeling scheme; hydrogen atoms have been removed for clarity; the unlabeled atoms are generated by an inversion center. Thermal ellipsoids are plotted at 50% probability level.

Table 1. Comparison between structural and magnetic data of di-μ-chloridodinickel(II) complexes.[a]

| Compound | Ni–Cl–Ni [°] | Ni···Ni [Å] | Ni–$Cl_{bridge}$ [Å] | Ni–$Cl_{bridge}$ [Å] | Space group | $J$ [$cm^{-1}$] | Ref. |
|---|---|---|---|---|---|---|---|
| Square-pyramidal or trigonal-bipyramidal | | | | | | | |
| $[Ni(biq)Cl_2]_2$ | 96.68(2) | 3.563(1) | 2.372(1) | 2.400(1) | $\bar{P}$ | –7.74 | [10] |
| $[Ni(dmp)Cl_2]_2$ | 97.4(1) | 3.600(1) | 2.378(1) | 2.414(1) | $\bar{P}$ | –5.1 | [10] |
| $[Ni(qnqn)Cl_2]_2$ | 98.23(5) | 3.652(1) | 2.408(2) | 2.422(2) | $\bar{P}$ | –4.4 | [11,12] |
| $[NiCl_2(pqo)]_2$ | 95.84(8) | – | 2.337(2) | 2.387(2) | $P2_1/n$ | –0.632 | [13] |
| $[NiCl_2\{CH_2(dmpz)_2\}]_2$ | 97.36(4) | 3.587(2) | 2.318(1) | 2.456(1) | $\bar{P}$ | +2.58 | [2a] |
| $[NiCl_2(tbz)_2]_2\cdot 2C_2H_6O$ | 97.23(6) | 3.5891(12) | 2.3556(17) | 2.4275(16) | $P2_1/c$ | +2.5 | [4] |
| Octahedral | | | | | | | |
| $[Ni(en)_2Cl]_2Cl_2$ | 94.1 | 3.67 | 2.461(3) | 2.551(3) | $P2_1/n$ | +9 | [14] |
| $[Ni(en)_2Cl]_2(ClO_4)_2$ | 95.4 | – | 2.461(3) | 2.512(3) | $P2_1/n$ | +8.9 | [14] |
| $[Ni(EG)_2Cl]_2Cl_2$ | 93.03(5) | 3.458(1) | 2.383(1) | 2.383(1) | $C2/m$ | +5.5 | [8] |
| $(PDA)_2[NiCl_4(H_2O)]_2$ | 95.05(5) | 3.606(2) | 2.430(2) | 2.459(1) | $C2/c$ | +8.2 | [15,16] |

[a] Abbreviations: biq = 2,2′-biquinolyl, dmp = 2,9-dimethyl-1,10-phenanthroline, qnqn = *trans*-2-(2′-quinolyl)methylene-3-quinuclidinone, pqo = 2-(pyrid-2-yl)quinoxaline, dmpz = 3,5-dimethylpyrazolyl, tbz = 2-benzimidazolyl, EG = ethyleneglycol, PDA = 1,3-propylenediammonium. Table adapted from ref.[4]

 © 2007 Wiley-VCH Verlag GmbH & Co. KGaA, Weinheim 

The separation between the Ni ions is 3.441 Å and the Ni–Cl–Ni angle is 91.5°, both are extreme values for this family of complexes (see Table 1). The interior Cl(1)–Ni(1)–Cl(1a) angle is 88.4° with Cl(1)···Cl(1a) intramolecular distance being 3.348 Å. Further selected bond lengths and angles are given in Table 2.

Table 2. Selected bond lengths [Å] and angles [°] for **1**.

| | | | |
|---|---|---|---|
| Ni(1)–N(1) | 2.0483(12) | N(1)–Ni(1)–N(2) | 79.60(5) |
| Ni(1)–N(2) | 2.0535(11) | N(1)–Ni(1)–Cl(1) | 95.90(3) |
| Ni(1)–O(90) | 2.1394(10) | O(90)–Ni(1)–Cl(1) | 84.60(3) |
| Ni(1)–Cl(1) | 2.3957(4) | O(90)–Ni(1)–Cl(2) | 176.04(3) |
| Ni(1)–Cl(1a) | 2.4048(4) | Cl(1)–Ni(1)–Cl(2) | 91.532(13) |
| Ni(1)–Cl(2) | 2.4383(4) | Ni(1)–Cl(1)–Ni(1a) | 91.564(13) |
| Torsion angles: | | | |
| N(2)–N(1)–Cl(2)–Cl(2) | 1.62 | | |
| N(2)–N(1)–Ni(1)–Cl(2) | 54.75 | | |

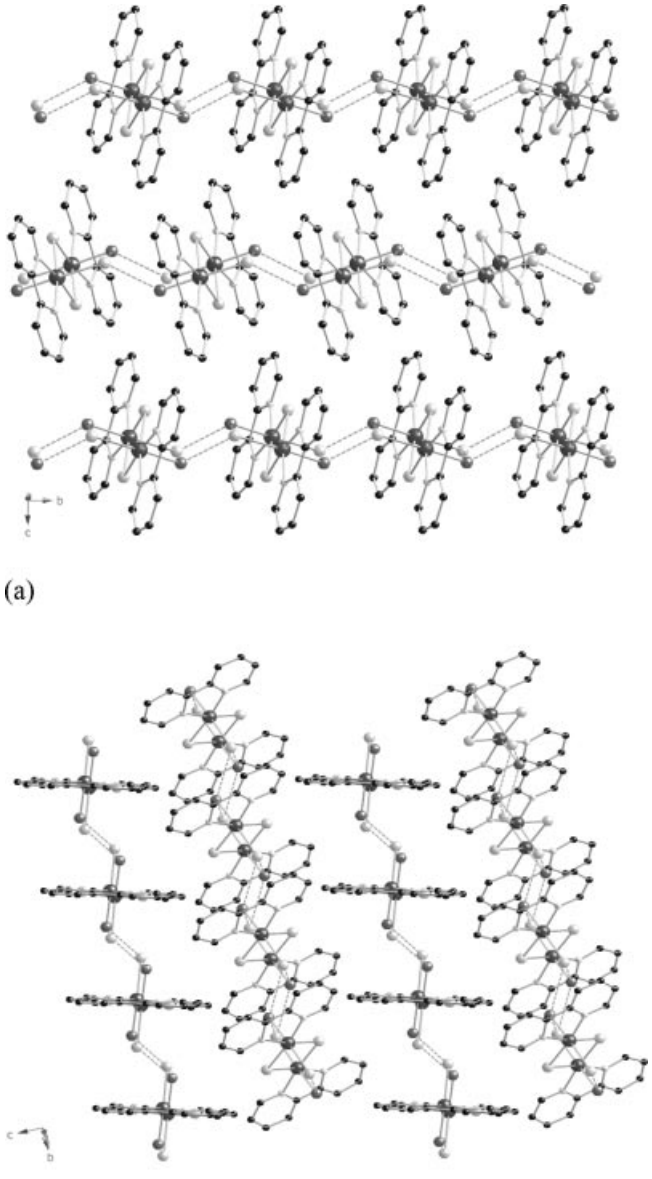

Figure 2. (a) Packing diagram of **1** looking along the crystallographic *b* axis; note the alternating arrangement of intermolecular hydrogen bonds. (b) Looking along the crystallographic *c* axis. Hydrogen atoms have been omitted for clarity.

Average carbon–carbon and carbon–nitrogen bond lengths of the coordinated 2,2′- bipyridine are close to those reported for the free molecule.[18] The significant deviation of the N(1)–Ni–N(2) angle [79.60(5)°] from the ideal value (90°) is due to steric requirements of a bipyridine ring ligand. Interestingly, complex **1** packs to produce 1-dimensional alternating ABAB layers of asymmetric units along the crystallographic *b* axis. Within each individual layer the asymmetric units are connected through intermolecular hydrogen bonds between the coordinated water and chlorine atoms of adjacent dimers. The intermolecular $O_w$···Cl distance of 3.195 Å is typical of an O–H···Cl interaction (range of 2.95–3.30 Å). The torsional angle between intralayer bipyridine rings is ca. 180°, indicating a near perfect parallel alignment within each layer. Closest distance between such bipyridine rings, however, is ca. 6.4 Å indicating that intralayer π–π stacking is not present in **1**. Interlayer distances, however, approach 3.7 Å with the phenanthroline rings interleaving such that the edge of one ring interacts with the face of another, both consistent with *phenyl embraces*.[19] Certainly, the complex packs to produce clear hydrophobic and hydrophilic regions, and their combination helps to explain the "twist" between layers in **1** as shown in Figure 2 (b).

### Magnetic Behavior of 1

Variable-temperature magnetic susceptibility studies were carried out on a powdered sample of the crystalline complex **1** over the temperature range 1.9–300 K. The magnetic behavior of **1** is shown in Figure 3 in the form of a $\chi_M T$ vs. $T$ plot [$\chi_M$ being the magnetic susceptibility per two nickel(II) ions]. The value of $\chi_M T$ at room temperature, ca. 2.30 $cm^3 mol^{-1}$ K, is as expected for two single-ion triplet states magnetically isolated ($\chi_M T$ = 2.31 $cm^3 mol^{-1}$ K with $g$ = 2.15). This value continuously increases upon cooling to reach a maximum of 4.10 $cm^3 mol^{-1}$ K at 5.0 K and then further decreases to 3.68 $cm^3 mol^{-1}$ K at 1.9 K. The shape of this curve is typical of a significant ferromagnetic coupling in **1**, the decrease of $\chi_M T$ at low temperatures being due to zero-field splitting effects and/or intermolecular interactions. In addition, the fact that $\chi_M T$ at low temperatures reaches values larger than 3.50 $cm^3 mol^{-1}$ K (the calculated value for a magnetically isolated quintet spin state with $g$ = 2.09) supports the occurrence of interdimer ferromagnetic interactions in **1**. Most likely, the hydrogen bonds, which link the dimers to afford a chain of dinuclear nickel(II) units along the crystallographic *a* axis [see Figure 2 (a)] provide the exchange pathway for this additional ferromagnetic interaction.

Keeping in mind the dinuclear structure of **1** and the fact that the ground state for a nickel(II) ion in an octahedral environment is orbitally nondegenerate, it is possible to represent the intradimer magnetic interaction $J$ with the iso-

 © 2007 Wiley-VCH Verlag GmbH & Co. KGaA, Weinheim 

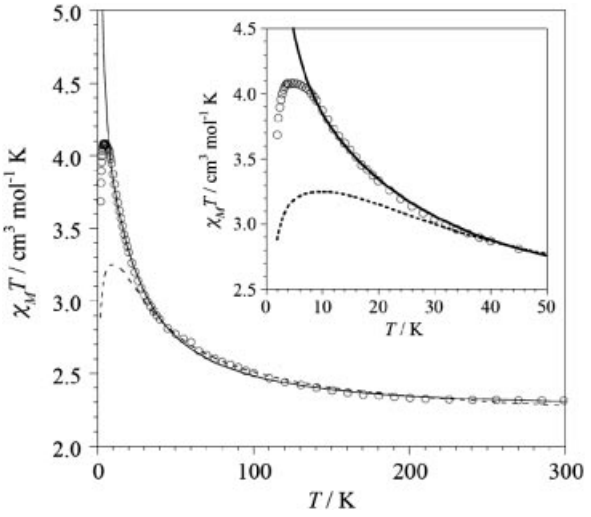


Figure 3. $\chi_M T$ vs. $T$ plot for **1**: experimental data (circles); best-fit curve for a nickel(II) dimer with $J$, $g$ and $D$ as variable parameters (dashed line); best-fit curve for a uniform chain of nickel(II) dimers (solid line) (see text). The inset shows the low-temperature region in detail.

tropic spin Hamiltonian $H = -JS_A \cdot S_B$. This approach works well for the cases where a relatively strong antiferromagnetic coupling is involved. However, when a weak antiferromagnetic interaction occurs or when the coupling is ferromagnetic (as in **1**), the effect of $D$ [zero-field splitting of the octahedral nickel(II) ion] has to be taken into account to describe the magnetic behaviour at low temperatures.[20]

We have then analyzed the magnetic susceptibility data of **1** in the high-temperature range by the corresponding expression derived through the Hamiltonian of Equation (1).[20]

$$H = -JS_A \cdot S_B + D(S_{zA}^2 + S_{zB}^2) \quad (1)$$

The best-fit values are: $J = +16.8$ cm$^{-1}$, $g = 2.09$ and $D = 3.5$ cm$^{-1}$. The calculated plot corresponds to the dashed line in Figure 3. The theoretical curve reproduces the experimental data from room temperature to $T = 40$ K. At $T < 40$ K, there is a clear mismatch between the experimental data and the theoretical plot, the former being above the calculated curve. This is in agreement with the additional ferromagnetic interaction between the nickel(II) dimers through the hydrogen bonds mentioned above. As the spin of the ferromagnetically coupled nickel(II) dimer at $T \leq 40$ K is large enough ($S \approx 2.0$) to be considered as a classic one, the magnetic data of **1** in the low-temperature range could be modelled through a uniform chain of hydrogen-bonded nickel(II) dimers (denoted $P$) with an interdimer ferromagnetic coupling $j_{eff}$, the Hamiltonian being defined by Equation (2).

$$H_{eff} = -j_{eff} \Sigma_i (S_{P,i} \cdot S_{P,i+1}) \quad (2)$$

The value of the spin of each $P$ unit ($S_P$) is given by Equation (3), where $\chi_P$ is the magnetic susceptibility for the nickel(II) dimer derived through Equation (1)[19] and $g_P$ is the $g$ factor for the ground spin sate of the dimer which is the local $g$ factor of the nickel(II) ion.

$$S_P(S_P + 1) = 8\chi_P T/g_P \quad (3)$$

In such an approach of a classical spin Heisenberg chain model,[21] the expression for the magnetic susceptibility per $P$ unit is given by Equations (4), (5) and (6).

$$\chi_P = [N\beta^2 g_P^2 S_P(S_P + 1)/3kT]\{[1 + u(K)]/[1 - u(K)]\} \quad (4)$$

$$u(K) = \coth(K - 1)/K \quad (5)$$

$$K = j_{eff} S_P(S_P + 1)/kT \quad (6)$$

This approach allowed us to fit the magnetic data of **1** from room temperature to $T = 8.0$ K (solid line in the inset of Figure 3), the values of the best-fit parameters being $J_P = +16.8$ cm$^{-1}$, $g_P = 2.09$, $D = 3.5$ cm$^{-1}$ and $j_{eff} = +0.37$ cm$^{-1}$. The previous values of $J$, $g$ and $D$ remain unchanged in the new fit and the weak ferromagnetic coupling ($j_{eff}$) between the nickel(II) dimers through the hydrogen bonds is evaluated. The very small $j_{eff}/J_P$ ratio (ca. 0.02) supports the validity of the perturbational model used here.

Such an approach was successfully used by some of us in other magnetic systems.[22–26] The mismatch between the calculated curve and the experimental data at $T < 8.0$ K for **1** in Figure 3 is most likely due to weak interchain antiferromagnetic interactions, which certainly would cause a decrease of the magnetic moment in the very-low-temperature region. We should also note that although the simulation of the magnetisation ($M$) vs. the applied magnetic field ($H$) plots for a discrete molecule with $J$ (magnetic coupling) and $D$ (zero-field splitting) as variable parameters is possible for a discrete molecule, it cannot be used for a chain (as is the case here). Consequently, $M$ vs. $H$ plots for **1** were discarded. Finally, the decrease of the $\chi_M T$ product being due to saturation phenomena (Zeeman level depopulation effects) was also discarded because the plots for three $H$ values less than 500 G (that is 250, 100 and 50 G) provided the same susceptibility curve.

## Conclusion

We report the first neutral octahedral di-μ-chloridodinickel(II) complex with the most acute Ni–Cl–Ni bridging angle to date. The complex exhibits the strongest intramolecular ferromagnetic interaction for this family, as expected given the acute bridging angle and quasi-planarity of the bridging unit, and is an important addition to this family of complexes.

## Experimental Section

**General:** Solvents and chemicals were of laboratory grade and were used as received except dimethyl sulfoxide, which was dried with molecular sieves (4 Å) under dry dinitrogen. Electrospray mass spectrometry was performed with a Shimadzu LCMS-2010 A system at a cone voltage of 5 kV. Infrared spectra were recorded with a

 © 2007 Wiley-VCH Verlag GmbH & Co. KGaA, Weinheim 

Nicolet Magna-IR 850 Series II spectrophotometer as KBr pellets. Thermal analysis was performed with a TA instruments TGA Q500 using 2–6 mg samples placed on platinum pans and ran under nitrogen (40 mL/min). The temperature was ramped from ca. 25 to 500 °C at a rate of 10 °C/min. Analysis was performed using the TA instruments Universal Analysis 2000 software program. Elemental analysis (C, H, N) was performed by Quantitative Technologies Inc., Whitehouse, NJ. Water was distilled and deionized to 18.6 MΩ using a Barnstead Diamond RO Reverse Osmosis machine coupled to a Barnstead Nano Diamond ultrapurification machine. Variable-temperature magnetic susceptibility measurements were performed with a Quantum design SQUID susceptometer in the temperature range 1.9–300 K with an applied magnetic field of $H$ = 1000 G ($T \geq 100$ K) and 50 G ($T < 100$ K). Crystalline samples were obtained directly from the reaction mixture, air-dried and powdered in a mortar. Diamagnetic corrections for the constituent atoms were estimated using Pascal's constants and corrections for the sample holder and the temperature-independent paramagnetism were also performed. Electronic absorption spectra were obtained with a Varian Cary 50 Bio spectrophotometer in 1-mL Quartz cuvettes between 200 and 800 nm at ambient temperature.

**Synthesis and Characterization of $[(bipy)_2Ni_2(\mu\text{-}Cl)_2(Cl)_2(H_2O)_2]$ (1):** $NiCl_2$ (0.48 g, 2.0 mmol) was suspended in dimethyl sulfoxide (DMSO) (10 mL). To this was added acetylacetone (10 mL, 99.3%) and then 2,2′-bipyridine (0.31 g; 2.0 mmol) was added as a 10-mL solution in DMSO. The volume of the solution was reduced in vacuo to approximately 5 mL, and a green solid was precipitated with chilled acetone. The precipitate was subsequently dissolved in a minimum amount of methanol and filtered (0.45 μm Fisher). Crystallization was conducted by an acetonitrile/methanol diffusion performed under ambient conditions. Green block-shaped crystals grew over ca. 8 d. Yield 0.941 g (41% based on $Ni^{II}$). $C_{20}H_{20}Cl_4N_4Ni_2O_2$ (607.6): calcd. C 39.50, H 3.32, N 9.22; found C 39.24, H 3.18, N 9.06. $\lambda_{max}$ ($H_2O$) = 612 nm (3.4 $M^{-1}cm^{-1}$). FT-IR (KBr): $\tilde{\nu}$ = 1598 (s), 1475 (s), 1445 (s), 1313 (m), 1115 (w), 1057 (w), 1027 (w), 775 (s), 736 (m), 654 (w) $cm^{-1}$. ES-MS (90% MeOH/10% $H_2O$): $m/z$ = 612 $\{[(bipy)_2Ni_2(\mu\text{-}Cl)_2(Cl)(H_2O)_2]\cdot MeCN\}^+$.

**Crystal-Structure Determination and Refinement for 1:** Structural measurements were performed with a Bruker-AXS SMART-CCD diffractometer at low temperature (90 K) using graphite-monochromated Mo-$K_\alpha$ radiation ($\lambda$ = 0.71073 Å). Absorption correction was applied using SADABS and SHELXTL and the structure was solved by direct methods and refined using the SHELXTL program package.[27] Key crystallographic data are given in Table 3. CCDC-631084 contains the supplementary crystallographic data for this paper. These data can be obtained free of charge from The Cambridge Crystallographic Data Centre via www.ccdc.cam.ac.uk/data_request/cif.

Table 3. Crystal data for $[(bipy)_2Ni_2(\mu\text{-}Cl)_2(Cl)_2(H_2O)_2]$ (**1**).

| | |
|---|---|
| Empirical formula | $C_{20}H_{20}Cl_4N_4Ni_2O_2$ |
| Formula mass | 607.602 |
| Crystal system | monoclinic |
| Space group | $P2_1/n$ |
| $\mu$ (Mo-$K_\alpha$) [$mm^{-1}$] | 2.173 |
| $a$ [Å] | 11.0985(9) |
| $b$ [Å] | 6.7873(6) |
| $c$ [Å] | 14.9609(12) |
| $\beta$ [°] | 91.900(2) |
| $V$ [Å$^3$] | 1126.37(16) |
| $Z$ | 2 |
| $D_{calcd.}$ [$gcm^{-3}$] | 1.792 |
| $F$[000] | 616 |
| $T$ [K] | 175 |
| $\theta_{max}$ | 28.07 |
| $R$, $wR_2$ [$I > 2\sigma(I)$] | 0.0202, 0.0510 |
| $R$, $wR_2$ (all data) | 0.0211, 0.0516 |
| Total data, total unique data | 11216, 2733 |
| Observed data [$I > 2\sigma(I)$] | 2733 |
| No. of final reflections, parameters | 2733, 185 |
| Final $R_1$, $wR_2$ | 0.0202, 0.0510 |

**Supporting Information** (see footnote on the first page of this article): Thermal analysis of **1**.

## Acknowledgments

Thanks are due to Promega Corporation (Madison, WI, USA), the iLEARN Program, Syracuse University and the Ministerio Español de Ciencia y Tecnología (Project BQU2004-03633) for funding.

[1] a) E. Ruiz, P. Alemany, S. Alvarez, J. Cano, *Inorg. Chem.* **1997**, *36*, 3683; b) E. Ruiz, P. Alemany, S. Alvarez, J. Cano, *J. Am. Chem. Soc.* **1997**, *119*, 1297.
[2] a) J. C. Jansen, H. van Koningsveld, J. A. C. van Ooijen, J. Reedijk, *Inorg. Chem.* **1980**, *19*, 170; b) J. Reedijk, J. Verbiest, *Transition Met. Chem.* **1978**, *3*, 51; c) R. P. Doyle, P. E. Kruger, M. Nieuwenhuyzen, B. Moubaraki, K. S. Murray, *Dalton Trans.* **2003**, 4230; d) P. E. Kruger, G. D. Fallon, B. Moubaraki, K. J. Berry, K. S. Murray, *Inorg. Chem.* **1995**, *34*, 4808; e) R. P. Doyle, P. E. Kruger, M. Julve, F. Lloret, M. Nieuwenhuyzen, *Dalton Trans.* **2006**, 2081; f) R. P. Doyle, M. Nieuwenhuyzen, P. E. Kruger, *Dalton Trans.* **2005**, 3745; g) R. P. Doyle, P. E. Kruger, M. Julve, F. Lloret, M. Nieuwenhuyzen, *CrystEngComm* **2002**, *4*, 13; h) R. P. Doyle, P. E. Kruger, M. Julve, F. Lloret, M. Nieuwenhuyzen, *Inorg. Chem.* **2001**, *40*, 1726.
[3] V. H. Crawford, H. W. Richardson, J. R. Wasson, D. J. Hodgson, W. E. Hatfield, *Inorg. Chem.* **1976**, *15*, 2107.
[4] G. A. Van Albada, J. J. A. Kolnaar, W. J. J. Smeets, A. L. Spek, J. Reedijk, *Eur. J. Inorg. Chem.* **1998**, *9*, 1337.
[5] a) J. B. Goodenough, *Phys. Rev.* **1955**, *100*, 564; b) J. Kanamori, *J. Phys. Chem. Solids* **1959**, *10*, 87; c) P. W. Anderson, *Phys. Rev.* **1959**, *115*, 2.
[6] C. G. Barraclough, R. W. Brookes, *J. Chem. Soc., Faraday Trans.* **1974**, *2*, 1364.
[7] A. Bencini, D. Gatteschi, *Inorg. Chim. Acta* **1978**, *31*, 11.
[8] B. M. Antti, *Acta Chem. Scand. Ser. A* **1975**, *29*, 76.
[9] A. W. Addison, T. N. Rao, J. Reedijk, J. Van Rijn, G. C. Verschoor, *J. Chem. Soc., Dalton Trans.* **1984**, 1349.
[10] R. J. Butcher, E. Sinn, *Inorg. Chem.* **1977**, *16*, 2334.
[11] E. J. Laskowski, T. R. Felthouse, D. N. Hendrickson, G. J. Long, *Inorg. Chem.* **1976**, *15*, 2908.
[12] G. J. Long, E. O. Schlemper, *Inorg. Chem.* **1974**, *13*, 279.
[13] C. Shao, W. Sun, Y. Chen, R. Wang, C. Xi, *Inorg. Chem. Commun.* **2002**, *5*, 667.
[14] G. A. Bottomley, L. G. Glossop, C. L. Raston, A. H. White, A. C. Willis, *Aust. J. Chem.* **1978**, *31*, 285.
[15] C. P. Landee, R. D. Willett, *Inorg. Chem.* **1981**, *20*, 2521.
[16] D. Knetsch, W. L. Groeneveld, *Inorg. Nucl. Chem. Lett.* **1976**, *12*, 27.
[17] K. Nakamoto, *Infrared Spectra of Inorganic and Coordination Compounds*, John Wiley & Sons, Inc., New York, **1963**.
[18] L. L. Merrit, E. D. Schroeder, *Acta Crystallogr.* **1956**, *9*, 801.
[19] I. Dance, M. Scudder, *J. Chem. Soc., Chem. Commun.* **1995**, 1039.
[20] G. De Munno, M. Julve, F. Lloret, A. Derory, *J. Chem. Soc., Dalton Trans.* **1993**, 1179.
[21] M. E. Fisher, *Am. J. Phys.* **1964**, *32*, 343.
[22] F. Lloret, M. Julve, R. Ruiz, Y. Journaux, K. Nakatani, O. Kahn, J. Sletten, *Inorg. Chem.* **1993**, *32*, 27.

 © 2007 Wiley-VCH Verlag GmbH & Co. KGaA, Weinheim 

[23] F. Lloret, R. Ruiz, M. Julve, J. Faus, Y. Journaux, I. Castro, M. Verdaguer, *Chem. Mater.* **1992**, *4*, 1150.
[24] F. Lloret, R. Ruiz, B. Cervera, I. Castro, M. Julve, J. Faus, J. A. Real, F. Sapiña, Y. Journaux, J. C. Colin, M. Verdaguer, *J. Chem. Soc., Chem. Commun.* **1994**, 2615.
[25] L. K. Thompson, S. S. Tandon, F. Lloret, M. Julve, J. Cano, *Inorg. Chem.* **1997**, *36*, 3301.
[26] Y. Rodríguez-Martin, C. Ruiz-Pérez, J. Sanchiz, F. Lloret, M. Julve, *Inorg. Chim. Acta* **2001**, *318*, 159.
[27] *SHELXTL PC*, version 6.1, Bruker-AXS, Inc., Madison, WI, USA, **2002**.

Received: February 6, 2007
Published Online: March 27, 2007

 © 2007 Wiley-VCH Verlag GmbH & Co. KGaA, Weinheim 

DOI: 10.1002/ejic.200700146

# The Thermal Decomposition of Three Magnetic Acetates at Their Autogenic Pressure Yields Different Products. Why?

**Swati V. Pol,[a] Vilas G. Pol,[a] Israel Felner,[b] and Aharon Gedanken*[a]**

**Keywords:** Decomposition / Acetates / Magnetic properties / Core-shell nanostructures

We report on the one-stage, reproducible, solvent-free, competent and straightforward approach for the synthesis of fullerene-like Ni@C, Co@C, and $Fe_3O_4$@C core-shell nanostructures that can be scaled up. The single precursor reactions of low cost acetates of Fe, Co and Ni are separately conducted at a relatively low temperature (700 °C) in a closed Swagelok reactor, as compared to other methods for the formation of graphitic layers. It is worth mentioning that although identical reaction parameters are employed, using the three acetate precursors, the graphitic carbon is coated on nanosized metallic Ni and Co cores, while Fe tends to form $Fe_3O_4$, maintaining the same core-shell morphology. The systematic morphological, compositional, structural characterization and the room temperature magnetic susceptibility measurements of the as-made particles are carried out on a vibrating sample magnetometer. The plausible mechanism is based on the comparison between the dissociation products of three acetate precursors, their obtained experimental data, and calculations on the enthalpy and free energy changes.

(© Wiley-VCH Verlag GmbH & Co. KGaA, 69451 Weinheim, Germany, 2007)

## Introduction

The studies of magnetic nanoparticles and nanostructures combine a broad range of synthetic and investigative techniques from physics, chemistry, and materials science. Ultra fine magnetic particles have been the subject of intense scientific research in recent years with respect to their novel properties and commercially-potential valuable applications.[1] The application of the encapsulated magnetic nanomaterials ranges from magnetic inks, magnetic recording media, toners for xerography, and ferrofluids for biomedical applications, such as contrast agents in magnetic resonance imaging.[2] Single- and multi-walled carbon nanotubes filled with ferromagnetic materials (Fe, Co, Ni) showed significant potential in data storage.[3] The ferromagnetic nanosized Fe, Ni, or Co coated with carbon constitute a group of especially interesting magnetic nanomaterials. This is because of their fascinating magnetic properties, and the carbon coating that protects the magnetic nanoparticles against environmental degradation.[3] The discovery of fullerenes and carbon-coated materials accelerated extensive investigation on nanoparticles, carbon-coated nanomaterials, and a wide range of carbon-based materials.[4] Some of the standard problems encountered in the synthesis of nanoparticles are those of good control of composition, particle size and morphology, a narrow monodisperse size distribution, and stabilization against oxidation in the case of reactive metals.

Various synthetic methods of magnetic nanoparticles have been reported in recent times, e.g., wet chemical processes,[5–6] inert gas condensation,[7] ultra-rapid quenching and vacuum-based deposition.[8] Carbon nanotubes and filled carbon nanostructures such as onions, wires, and rods, have been prepared by the pyrolysis of metallocene.[9–10] Using Ni(acac) and Cu(acac) as catalyst precursors, carbon nanotubes and onions from carbon monoxide were produced previously.[11] An arc-discharge process[12] was employed for the preparation of ferromagnetic carbon-coated Fe, Co, and Ni nanoparticles. The major problem with the synthesis of graphite-encapsulated nanocrystals by using the standard arc method has been the production of large amounts of unwanted carbonaceous debris.[13] This causes the reduction of particle-exchange coupling, which is an important issue in the ongoing attempt to synthesize high density magnetic recording media.[14a] Vivekchand et al. recently developed a new method for the preparation of metal nanowires by the nebulized spray pyrolysis of precursors.[14b] The arc evaporation method is also successfully demonstrated for the encapsulation of ferromagnetic metals (iron, cobalt, and nickel) nanoparticles in graphitic carbon.[14c] Chemical vapor synthesis (CVS) is becoming increasingly important because of its potential for producing nanomaterials in a controlled and scalable way with a low degree of agglomeration.[15] Each technique has its own advantages and disadvantages. However, most of the techniques require a high energy input and are not suitable for

[a] Department of Chemistry and Kanbar Laboratory for Nanomaterials at the Bar-Ilan University Center for Advanced Materials and Nanotechnology, Bar-Ilan University, Ramat-Gan, 52900, Israel
E-mail: gedanken@mail.biu.ac.il
[b] Rakah Institute of Physics, Hebrew University, Jerusalem, 91904, Israel

 © 2007 Wiley-VCH Verlag GmbH & Co. KGaA, Weinheim 

mass production because of the low yield and the complicated process control. The research community is seeking methods for producing carbon nanomaterials with specific properties and on an industrial scale. Thus, further experimental research on their synthesis is needed.

Herein, we report on a one-stage, reproducible, solvent-free, competent, and straightforward approach for the synthesis of fullerene-like Ni@C, Co@C, and $Fe_3O_4$@C core-shell nanostructures that can be scaled up. The single precursor reactions of low-cost acetates of Fe, Co and Ni are conducted separately at a relatively low temperature (700 °C) in a closed Swagelok reactor, as compared to other methods for the formation of graphitic layers. It is worth mentioning that although identical reaction parameters are employed, using the three acetate precursors, graphitic carbon-coated nanosize metals are obtained for Ni and Co, while Fe tends to form $Fe_3O_4$, maintaining the same core-shell morphology. Early results on a similar reaction of $Ni(AcAc)_2$ have been reported.[16] This publication extends this report and also includes a comparison between $Fe^{II}$, $Ni^{II}$, and $Co^{II}$ acetates, which yield different products. This manuscript also attempts to account for and explain the formation of different products. The systematic morphological, compositional, structural characterization and room temperature magnetic susceptibility measurements of the as-made particles are measured by using a vibrating sample magnetometer. The suggested mechanism is supported by the obtained experimental data and calculations on enthalpy, as well as free energy changes.

## Results and Discussion

### 1. C, H, N, S, and O Analysis, X-ray Diffraction, Mössbauer, and BET Surface Area Measurements

Here we present and compare the results related to the three metal acetates that produce core/shell structures of metal/metal oxide surrounded by carbon. The carbon and hydrogen content in the product/carbonaceous material is determined by elemental analysis measurements (Table 1). The calculated element percentages of carbon in Ni, Co and Fe acetates are 27.2, 27.1, and 27.6%, while the element percentages of hydrogen are 3.4, 3.4, and 3.5%, respectively. The measured percentage of carbon in Ni@C, Co@C, and $Fe_3O_4$@C products are 11.78, 15.25, and 22.3 wt.-%, while the percentages of hydrogen are 0.18, 0.1, and 0.12%, respectively. The calculated oxygen percentage for Ni, Co, and Fe acetates is almost the same (ca. 36 wt.-%). The measured oxygen percentages are 0.2, 0.3, and 21.43 wt.-% for Ni@C, Co@C, and $Fe_3O_4$@C products, respectively. The calculated weight of metal Ni, Co, and Fe is 332 mg, 333 mg, and 321 mg in 1 g of nickel(II) acetate, cobalt(II) acetate, and iron(II) acetate precursors, while 337 mg, 339 mg, and 315 mg account for the 382 mg, 400 mg, and 560 mg of the Ni@C, Co@C, and $Fe_3O_4$@C products, respectively. It is obvious that the products show less carbon than the reactants, while the percent of hydrogen is almost negligible. This means that some of the carbon is bonded to the hydrogen in the form of hydrocarbons and/or to oxygen to form carbon oxides. Furthermore, the reduction in the transition metal is observed in both Ni@C and Co@C. This reduction might have occurred due to carbon monoxide. Jesus et al. reported on the thermal decomposition[17] process of the nickel acetate precursor under inert atmosphere. Our obtained coupled TGA-Mass spectroscopy analysis data for Ni acetate salt are in agreement with this. The TGA spectra of all the three acetates are shown in Figure 1.

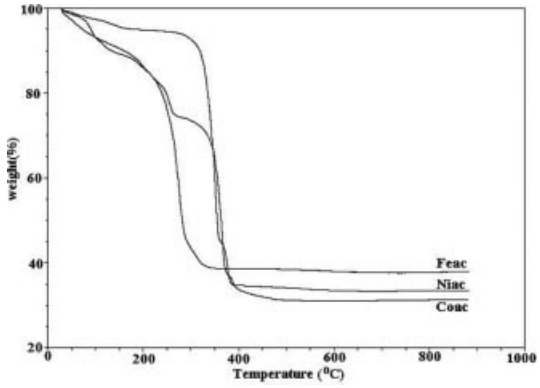


Figure 1. The TGA curve of Fe, Co, and Ni acetates.

The complete decomposition of all the acetates is observed at about 400 °C. The higher weight loss is observed for Ni and Co acetates (68%), while early (ca. 300 °C) and less weight loss (60%) accounts for Fe acetate. The residual weight of about 32% corresponds to the metallic Ni and Co for the related acetates, while the 40% for Fe acetate corresponds to FeO. The gaseous content of the dissociation products of these acetates at 350 °C is monitored by an MS. The gases detected by the instrument are acetone, $CH_3COCH_3$ ($m/z$ = 58), acetic acid, $CH_3COOH$ (60), $CO_2$ (44), CO (28), $CH_4$ (16), $C_2H_6$ (30), and $C_2H_2$ (26).

Conducting the RAPET reaction of all three acetates at 650 °C does not lead to any crystalline products, and only amorphous products are obtained, based on XRD mea-

Table 1. The obtained products, % yield, morphology, crystal structure, percent of carbon, hydrogen and oxygen and BET surface area are illustrated.

| Sample name | % Yield | XRD | Morphology (TEM) | wt.-% C | wt.-% H | wt.-% O | BET Surface area $m^2/g$ |
|---|---|---|---|---|---|---|---|
| Ni@C | 38.2 | Ni | core-shell | 11.78 | 0.18 | 0.2 | 1 |
| Co@C | 40 | Co | core-shell | 15.25 | 0.10 | 0.3 | 3 |
| $Fe_3O_4$@C | 56 | $Fe_3O_4$ | core-shell | 22.3 | 0.12 | 21.43 | 2 |

 © 2007 Wiley-VCH Verlag GmbH & Co. KGaA, Weinheim 

surements. The first crystalline products for the RAPET of the acetates appear at 700 °C. The RAPET of Ni and Co acetates in a closed cell at 700 °C yields 38.2% and 40% of products containing metallic Ni and Co, respectively coated with carbon. The dissociation of Fe acetate in a closed RAPET system confirms the weight loss of 44%, keeping about 56% of a solid product consisting of $Fe_3O_4$ and carbon. The rest of the weight loss is due to the formation of hydrocarbons and carbon oxides. In the case of the RAPET of Fe acetate, the reactant possesses a +2 oxidation state, while the product has a 2.66 oxidation state. This means that unlike Co and Ni ions, which undergo a reduction to the corresponding metals, the $Fe^{+2}$ is partially oxidized to $Fe_3O_4$ before being coated by carbon. Since the particles are densely coated with graphitic carbon, the oxidation of the product due to handling under air atmosphere is impossible. It is noticeable that the Fe is more facile to oxidation than Ni and Co. The measured surface areas for the Ni@C, Co@C and $Fe_3O_4$@C products are 1, 3, and 2 $m^2/g$, respectively.

The XRD pattern of the as-prepared Ni@C sample is presented in Figure 2 (top). The diffraction peaks, observed at $2\theta$ = 44.49, 51.85, and 76.38, are assigned as (111), (200), and (220) reflection lines of the face-centered cubic phase of Ni (space group: *Fm-3m*). These values are in good agreement with the diffraction peaks, peak intensities and cell parameters of crystalline Ni (PDF No. 87-712). The diffraction patterns of the as-prepared Co@C sample (middle) can be indexed to fcc (space group: *Fm-3m*) Co, and matches well with PDF No. 89-4307. The diffraction peaks observed at $2\theta$ = 44.22, 51. 35, and 75.86 are assigned as (111), (200), and (220) reflection lines. The XRD pattern of the as-prepared $Fe_3O_4$@C sample is presented at the bottom of Figure 2. The major diffraction peaks are observed at $2\theta$ = 30.10, 35.45, 37.08, 43.08, 53.45, 56.98, 62.57, and 74.02 and are assigned as (220), (311), (222), (400), (422), (511), (440) and (533) reflection lines. These values are in good agreement with the diffraction peaks, peak intensities and cell parameters of crystalline $Fe_3O_4$ (PDF No. 65-3107). However, since the XRD of $\gamma$-$Fe_2O_3$ is very similar to that of magnetite, we also used Mössbauer spectroscopy to further substantiate our assignment. In none of the three cases is a carbide phase detected. The small diffraction peak at $2\theta$ = 26.6°, assigned to graphitic carbon, is only detected for Co@C, and is suppressed in Ni and $Fe_3O_4$.

The Mössbauer spectra of $Fe_3O_4$ at 298 K are shown in Figure 3. The spectra show two hyperfine magnetic splits, which are clear evidence for the existence of $Fe_3O_4$ (magnetite). In the transmission spectrum, the hyperfine split arises due to a nuclear quadrupole interaction. This indicates that there is some departure from the cubic symmetry of the electric field due to the existence of an electric field gradient at the nucleus. It means that the $^{57}Fe$ excited level ($I = {}^3/_2$) has split, whereas the ground state ($I = {}^1/_2$) remains whole/intact. The difference in energy levels is only due to different electronic densities of the Fe atoms at the source, and the absorber. $Fe_3O_4$ can be written as $[(Fe^{3+})(Fe^{2+}Fe^{3+})]O_4$. The magnetic hyperfine fields of 455 and 487 kOe and the

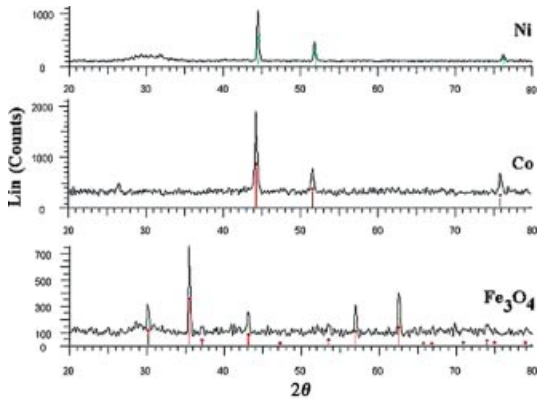


Figure 2. XRD patterns of as-prepared Ni@C (top), Co@C (middle), and $Fe_3O_4$@C (bottom) samples.

two isomer shift values, 0.67 and 0.37 mm/s, correspond to site A ($Fe^{3+}$) ions and to site B ($Fe^{2+}$, $Fe^{3+}$) ions, respectively. The high isomer shift for the B site is typical for $Fe^{2+}$. The resultant parameters are given in Table 2.

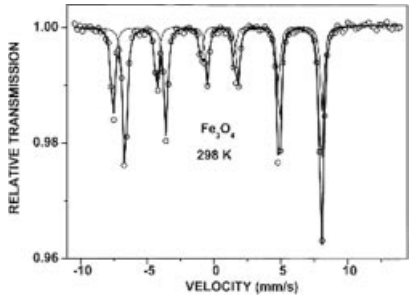


Figure 3. The Mössbauer spectrum of a $Fe_3O_4$@C sample at room temperature.

Table 2. The Mössbauer parameters of $Fe_3O_4$@C sample: isomeric shift (mm/s), quadrupole moment (mm/s) and effective field (kOe) for site A and site B.

| | I.S. (mm/s) | eQ (mm/s) | $H_{eff}$ (kOe) |
|---|---|---|---|
| Site A | 0.67 | 0.028 | 455 |
| Site B | 0.37 | – | 487 |

The nature of the coated carbon for all of three samples is also studied by employing Raman spectroscopy and HR-TEM measurements.

## 2. TEM, SEM, EDS, Raman, and HR-TEM Measurements

The morphology of all the samples is studied by TEM measurements. The transmission electron micrograph of Ni@C core-shell structures is shown in part a of Figure 4. The thermal dissociation of Ni acetate favors the formation of the dark particles of Ni, which are coated with carbon layers. We assume that the thermal decomposition of $Ni(CH_3COO)_2$, leads to dissociation into carbon, hydrogen, oxygen and nickel atoms at 700 °C. The Ni atoms forms the Ni core. The particle diameters range from 20 nm to 160 nm. The high resolution image (Figure 4b) taken on a

 © 2007 Wiley-VCH Verlag GmbH & Co. KGaA, Weinheim 

single particle revealed that the 25 nm dark core of Ni is encapsulated in 5–10 nm carbon layers. Using the SAEDS technique, the identification of the dark cores as Ni, Co and iron oxide, which are covered by carbon, is confirmed for all the three products of (Ni, Co, and Fe) acetates. The TEM image of the Co@C sample demonstrates (Figure 4c) that the particles, whose diameters range from 30 to 230 nm, are covered with in situ formed carbon layers after the dissociation of cobalt acetate. The central 110 nm diameter cobalt particle is uniformly surrounded by a 20 nm carbon layer (Figure 4d). Thus, a similar trend is observed for the thermal decomposition of $Co(CH_3COO)_2$ and $Ni(CH_3COO)_2$, resulting in a metallic core and a carbon shell structure. Part e of Figure 4 shows that the 5 to 20 nm particles of $Fe_3O_4$ are densely covered with carbon. The HR-TEM image (Figure 4f) of a 10 nm $Fe_3O_4$ particle is surrounded by a thick layer of carbon. The thermal dissociation of Fe acetate favors the formation of a $Fe_3O_4$ core, which is coated with carbon layers after the decomposition of $Fe(CH_3COO)_2$. This means that the produced carbon, hydrogen, oxygen and FeO facilitate the FeO to react with oxygen to form $Fe_3O_4$, thus hindering the reduction.

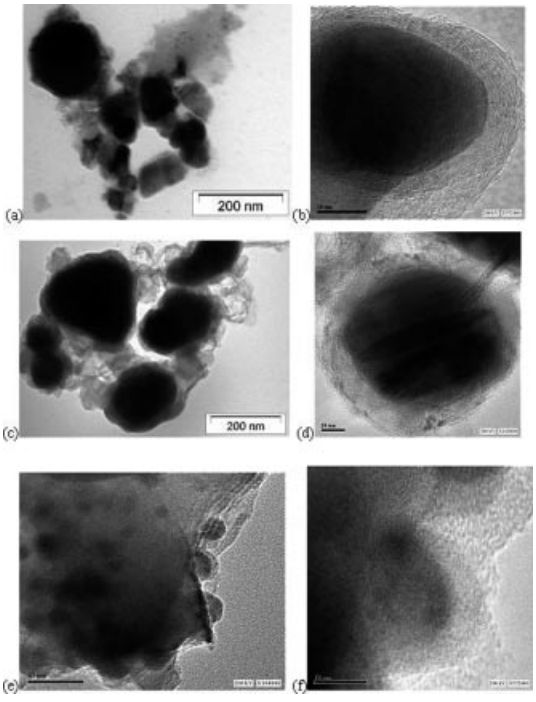


Figure 4. Transmission electron micrographs of (a) Ni@C sample, (b) single Ni@C particle at high resolution, (c) Co@C sample, (d) single Co@C particle at high resolution, (e) $Fe_3O_4$@C sample, and (f) single $Fe_3O_4$@C particle at high resolution.

The SEM image shown in Figure 5a indicates the spherical morphology of the Ni@C. The Ni-C particles have a tendency to form a few agglomerates, which are observed in addition to the individual particles. The aggregation is attributed to their magnetic nature. The diameters of the separated individual particles are in the range of 40–160 nm. The EDS of the Ni@C particles is presented in Figure 5b, and confirms the presence of Ni and C. No additional peak is detected, which verifies the purity of the Ni@C sample.

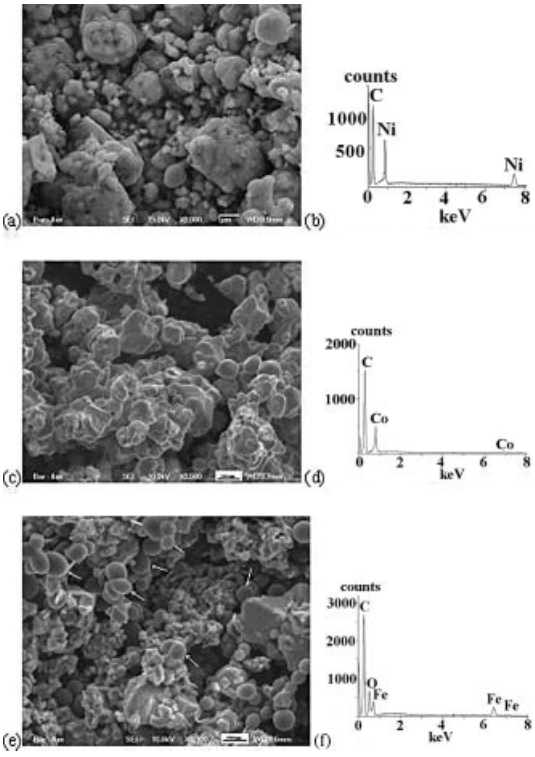


Figure 5. Scanning electron micrographs of (a) Ni@C sample, (b) EDS of Ni@C sample, (c) Co@C sample, (d) EDS of Co@C sample, (e) $Fe_3O_4$@C sample [arrow indicates egg-like carbon entities], and (f) EDS of $Fe_3O_4$@C sample.

The SEM image of the Co@C sample demonstrates (Figure 5c) that the particle diameter ranges from 50 to 200 nm. In addition, the obvious aggregating tendency of magnetic Co@C particles is observed. The EDS analysis of the Co@C sample (Figure 5d) detected only the presence of cobalt and carbon, without additional impurities. Negligible amounts of oxygen are detected in Ni@C and Co@C samples.

The $Fe_3O_4$@C sample possesses an oval shaped mixture of about 400 nm and aggregates of about 100 nm particles (Figure 5e). The SAEDS confirm that the oval shaped particles, indicated by an arrow, are composed solely of carbon, while the smaller particles are composed of $Fe_3O_4$ and carbon. The core-shell nature of $Fe_3O_4$ surrounded by C is substantiated by TEM measurements. The excess of carbon might have lead to the formation of egg-like carbon entities in the $Fe_3O_4$@C sample. The bulk EDS analysis of the $Fe_3O_4$@C sample is shown in part f of Figure 5, presented Fe, O, and carbon occurrence. The formation of $Fe_3O_4$ and carbon without additional impurities is confirmed by the EDS spectrum shown in Figure 5f.

The nature of the carbon shell is investigated by Raman spectroscopy. The Raman spectra (Figure 6) are the charac-

 © 2007 Wiley-VCH Verlag GmbH & Co. KGaA, Weinheim 

teristics of disordered graphitic carbon with nanosized graphitic crystals. The first D peak, located at ca. 1330 $cm^{-1}$, originates from the in-plane lattice vibrations. The second G peak is located at ca. 1595 $cm^{-1}$, and only occurs when small, crystal-size graphitic particles are present.[18] The D band is associated with graphitic edge-planes and defects in the graphitic lattice. The relative intensity of the D and G bands is generally used to estimate the size of graphitic clusters in the hexagonal plane, *La*. Although all the samples are prepared at 700 °C, the intensity of graphitic carbon is much higher than the disordered carbon for the Ni@C sample. Almost the same intensity is observed for the Co@C and $Fe_3O_4$@C samples. The results indicate that Ni is the best catalyst for the preparation of high order graphitic planes. This is also manifested in the relatively low temperature that the graphitic layers reach.

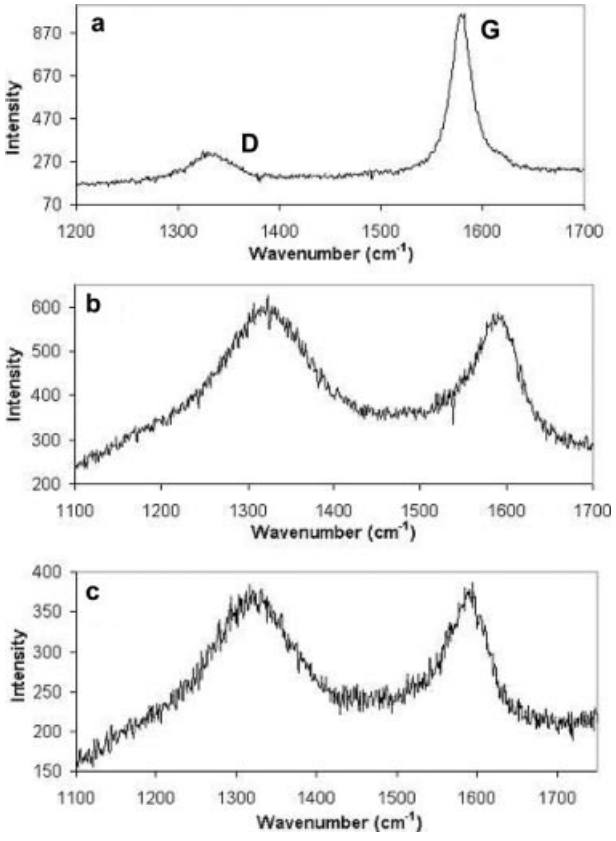


Figure 6. Raman spectra of a) Ni@C, b) Co@C, and c) $Fe_3O_4$@C samples.

In order to understand the graphitization of formed carbon layers around the cores, HR-TEM measurements of the carbon-shells are carried out for the Ni@C, Co@C, and $Fe_3O_4$@C samples. The measured interlayer spacings between these graphitic planes are 0.345, 0.337, and 0.341 nm for Ni@C (Figure 7a), Co@C (Figure 7b), and $Fe_3O_4$@C (Figure 7c) samples, respectively, which are very close to that of the graphitic layers. It should be noted that the graphitic ordering is much better in Ni than in the Co and $Fe_3O_4$.

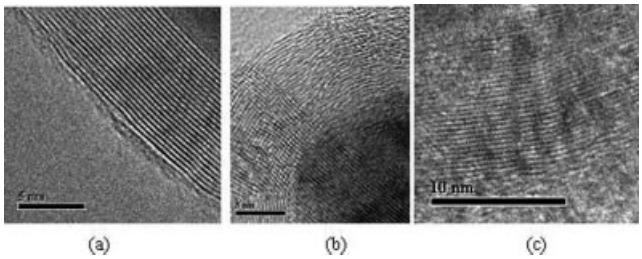


Figure 7. HR-TEM images of a) carbon layer coated on the Ni core, b) carbon coated on the Co core, and c) carbon layer on the surface of $Fe_3O_4$ core.

To summarize, the few points that need further clarification and discussion on the results reported for the decomposition of all three acetates (Co, Ni, and Fe) are: 1) The cores of Co, Ni, and iron oxide are surrounded by graphitic carbon (interlayer spacing ≈ 0.34 nm). 2) A wide particle size distribution is observed. 3) The thickness of the carbon coating around the cores is proportional to the percentage of carbon present in the product (see Table 1). 4) Although the graphitic carbon encapsulates the cores, nanosize Ni and Co are obtained in metallic form, while Fe tends to form $Fe_3O_4$ (confirmed by XRD, EDS, and SAEDS), maintaining the core-shell morphology. The three-dimensionality of the onion-like structures of Ni@C, Co@C, and $Fe_3O_4$@C products is confirmed by tilting the TEM grid during HR-TEM measurements, when the pictures remained unchanged.

## 3. Magnetic Properties

A room temperature magnetic susceptibility measurement of Ni@C, Co@C, and $Fe_3O_4$@C samples is conducted by employing a vibrating sample magnetometer. A small amount of material, ca. 20 mg, is inserted into a plastic capsule. Cotton wool is placed on the top of the sample and the capsule is sealed. This prevents the particles from any movement caused by the vibration of a VSM sample holder rod, or by a variation in the applied magnetic field during measurements. The magnetization vs. magnetic field curves are measured for all the samples (Figure 8a–c) in the range of –15800 to 16000 Oe.

The Ni@C sample exhibits typical hysteresis with a saturation magnetization of 21.7 emu/g (Figure 8a). Taking into account the fact that the sample contains 11.78% carbon and the remaining 88.22% Ni, this yields a value of 24.6 emu/g for 100% Ni. A 151 Oe coercive field is obtained for the Ni@C sample. The Co@C sample shows a saturation magnetization of 21.87 emu/g (Figure 8b). When considering that the sample contains 84.75% of Co, this gives a value of 25.81 emu/g for 100% Co. This sample shows the coercivity of 97 Oe with a remanent magnetization of 2.6 emu/g. Figure 8c shows the magnetization curve of the $Fe_3O_4$@C sample. Unlike the ferromagnetic behavior detected for Ni@C and the Co@C, the characteristic behavior of superparamagnetic particles is detected for $Fe_3O_4$@C. The magnetization curve does not show hysteresis and does

 © 2007 Wiley-VCH Verlag GmbH & Co. KGaA, Weinheim 

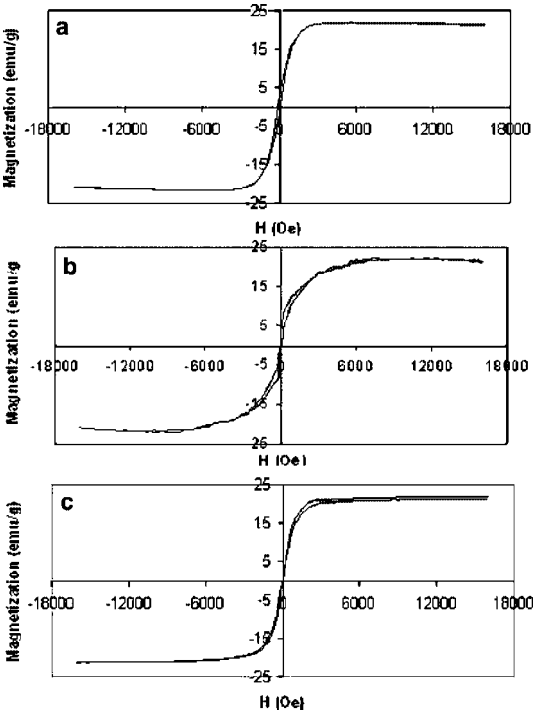


Figure 8. Magnetization vs. magnetic field curves for a) Ni@C, b) Co@C, and c) $Fe_3O_4$@C samples.

not saturate (a small increase in magnetization is measured between 12–16 kOe), even at 16 kOe. This is due to the $Fe_3O_4$ core, which is comprised of small 5–20 nm crystallites (shown in the TEM measurements). The magnetization of ferromagnetic materials is very sensitive to the microstructure of a sample. If a specimen consists of small particles, its total magnetization decreases with decreasing particle size due to the increased dispersion in the exchange integral,[19] finally reaching the superparamagnetic state, when each particle acts as a big 'spin' with suppressed exchange interaction between the particles, which is more hindered because of the presence of the carbon shell. Nanomagnetic particles are expected to exhibit reduced magnetization due to the large percentage of surface spins with disordered magnetization orientation.[20] In fact, the magnetization is smaller than the bare particles, indicating that there is no magnetic proximity effect between the magnetic (Ni, Co, or $Fe_3O_4$) particles and carbon, which is consistent with recent experiments.[21]

The main question remaining now is why are Ni and Co obtained in the metallic form, while Fe tends to form $Fe_3O_4$, maintaining a carbon shell in all three cases. The thermal decomposition of $Ni(CH_3COO)_2$ at 350 °C[17] leads to dissociation into nickel oxide and oxygenates like acetone and acetic acid, as perceived by TGA coupled with MS. It is worth mentioning that both, Jesus et al.[17] and our own TGA + MS results show that CO is one of the intermediates in the decomposition of the Ni acetate. We attribute the reduction of nickel oxide to carbon monoxide. The product of the reduction is the Ni atom, forming the Ni core, while the oxygenate molecule decomposes to hydrocarbon, and further to carbon. In our previous RAPET reactions of various organic or organometallic materials, we observed the appearance of carbon above 550 °C.[22–24]

The decomposition of $Co(ac)_2$ and $Ni(ac)_2$ results in a metallic core and carbon shell structures, while the thermal dissociation of Fe acetate favors the formation of a $Fe_3O_4$ core, which is coated with graphitic and disordered carbon layers. It should be noted that the only source of oxygen is the acetate ion, and its quantity in all three acetates is almost the same (36 wt.-%).

Based on the obtained MS data, we propose the dissociation of acetates as follows:

$$M(CH_3COO)_2 \rightarrow MCO_3 + CH_3COCH_3 \quad (1)$$

$$MCO_3 \rightarrow MO + CO_2 \quad (2)$$

$$CH_3COCH_3 \rightarrow CO + C_2H_6 \quad (3)$$

$$MO + CO \rightarrow M + CO_2 \quad (4)$$

where M = Ni, Co, Fe.

The formation of the first oxygenated product, acetone, occurs by Equation (1). The metal carbonate,[17,25] which is a short-lived intermediate, immediately decarboxylates to give a metal oxide at 350 °C. This metal oxide, in the case of Ni and Co acetates, gets reduced by carbon monoxide, while the Fe atoms prefer to stay as FeO. It further is oxidized to form $Fe_3O_4$ and then coated by carbon to form the core-shell structure during solidification. This can be explained by the reduction potential values of Ni, Co, and Fe. The well-known standard reduction potentials[26] at 25 °C for Ni, Co and Fe are –0.25, –0.27, and –0.44 V, respectively, for the metal–metal ion equilibrium. These numbers indicate that iron is less favorably reduced than cobalt and nickel.

Thus, all three acetates decompose into their corresponding oxides, which further get reduced by carbon monoxide to a metallic form. The values for the enthalpy change, $\Delta H^0$, and free energy change, $\Delta G^0$, are calculated to form the respective metals from the corresponding oxide[27] in the presence of carbon monoxide at 700 K. Since the cases of Ni and Co are similar, the values are calculated for the representative Co@C case and, for simplicity, are compared with the case of $Fe_3O_4$@C.

$FeO(s) + CO(s) \rightarrow Fe_{(s)} + CO_2(g)$
$\Delta H^0$ = –14.7 kJ/mol at 700 K
$\Delta G^0$ = +3.55 kJ/mol at 700 K
$CoO(s) + CO(s) \rightarrow Co(s) + CO_2(g)$
$\Delta H^0$ = –49.89 kJ/mol at 700 K
$\Delta G^0$ = –37.61 kJ/mol at 700 K

The positive value obtained for the $\Delta G^0$ of formation of Fe from $Fe^{II}$ acetate, unlike Ni and Co, indicates that thermodynamically, the reduction to the metallic state is not favorable. Therefore, the alternative is its partial oxidation and the kinetically-controlled coating by the carbon surrounding it, forming the $Fe_3O_4$@C. On the other hand, the $\Delta G^0$ value is negative for the formation of metallic cobalt and Ni, and we assume that the reaction is also fast. Thus the core of metallic Co or Ni is formed in this way in Co@C and Ni@C particles.

 © 2007 Wiley-VCH Verlag GmbH & Co. KGaA, Weinheim 

## Conclusions

In summary, using low cost, transition metal acetate precursors and employing identical reaction parameters, graphitic carbon-coated nanosize Ni, Co are obtained in the metallic form. Metallic Fe is not obtained, and instead it forms $Fe_3O_4$, maintaining the core-shell morphology. A broad particle size distribution is observed. Graphite-encapsulated Ni, Co, and $Fe_3O_4$ fullerene-like core-shell nanostructures could be obtained at a relatively low temperature (700 °C) in a closed Swagelok reactor, as compared to other methods for the formation of graphitic layers. The one-stage, reproducible, solvent-free, competent and straightforward approach for the synthesis of Ni@C, Co@C, and $Fe_3O_4$@C core-shell nanostructures can be scaled up.

## Experimental Section

**Synthesis of Fullerene-like Ni@C, Co@C and $Fe_3O_4$@C Core-Shell Nanostructures:** Acetates of $Fe^{II}$ (Aldrich), $Co^{II}$ (Aldrich) and $Ni^{II}$ (Alfa Aesar), were purchased with > 99% purity and used as received. In the fabrication of Ni@C, Co@C, and $Fe_3O_4$@C core-shell nanostructures, 1 g of the acetate of Ni, Co and Fe are introduced separately into a 3 mL stainless steel reactor at room temperature in a nitrogen-filled glove box. The filled Swagelok reactors are closed tightly with the other plug.[22] The temperature of the tube furnace is raised to 700 °C at a rate of 10 °C/min, and the temperature is maintained at 700 °C for 3 h. The Swagelok-reactors heated at 700 °C are gradually cooled (ca. 6 h) to room temperature and opened. A black powders of Ni@C (0.382 g), Co@C (0.400 g) and $Fe_3O_4$@C (0.560 g) is obtained. The obtained products, their morphology, crystal structure, carbon percent are shown in Table 1. Earlier, such a one-stage, efficient, and the simplest economic RAPET (Reactions under Autogenic Pressure at Elevated Temperature) technique was employed for the fabrication of various interesting nanostructures.[22–24]

**Characterization:** Various analytical techniques are used to identify and characterize the as-prepared RAPET products of the Ni, Co and Fe acetate reactions. To understand the purity of the crystal structure (the interatomic distance, and angle) of the as-prepared products, the X-ray diffraction patterns are measured with a Bruker AXS D* Advance Powder X-ray diffractometer [$\lambda$(Cu-$K_a$) = 1.5418 Å]. Since all the acetate contains C, H, and O, in addition to metal, C, H, N, S and O analyses are carried out for the as-prepared products on an Eager 200 C,H,N,S analyzer and an EA1110, oxygen analyzer, respectively. The morphology, grain size, and chemical composition in a selected area are measured for the fullerene-like Ni@C, Co@C, and $Fe_3O_4$@C core-shell nanostructures by employing transmission electron microscopy (TEM) (JEM-1200EX) and high-resolution transmission electron microscopy (HRTEM) (JOEL 2010), working at acceleration voltages of 80 kV and 200 kV, respectively. The morphology and energy dispersive X-ray analysis (EDX) of the materials are investigated by high resolution scanning electron microscopy (HR-SEM, JSM, 7000 F). The Mössbauer spectroscopy (MS) studies are carried out at room temp. using a conventional constant acceleration spectrometer. The $^{57}$Fe MS are measured with a 50 mCi $^{57}$Co:Rh source and the spectra were least square fitted with two sub spectra. The isomer shift (IS) values are relative to Fe metal at 300 K. A Micromeritics (Gemini 2375) surface area analyzer is used to measure the surface area of the samples. An Olympus BX41 (Jobin–Yvon–Horiba) Raman spectrometer is employed, using the 514.5 nm line of an Ar ion laser as the excitation source to analyze the nature of the carbon present in the samples. A vibrating sample magnetometer (VSM-Oxford-3001) is used for the magnetic susceptibility measurements for Ni@C, Co@C, and $Fe_3O_4$@C samples at room temperature.


[1] W. Krätschmer, L. D. Lamb, K. Fostiropoulos, D. R. Huffman, *Nature* **1990**, *347*, 354.
[2] T. Hayashi, S. Hirono, M. Tomita, S. Umemura, *Nature* **1996**, *381*, 772.
[3] A. Leonhardt, M. Ritschel, R. Kozhuharova, A. Graff, T. Muhl, R. Huhle, I. Monch, D. Elefant, C. M. Schneider, *Diamond Relat. Mater.* **2003**, *12*, 790–793.
[4] H. W. Kroto, J. R. Keath, S. C. O'Brien, R. F. Curl, R. E. Smalley, *Nature* **1985**, *318*, 162–165.
[5] L. Guo, Q. J. Huang, X. Y. Li, S. H. Yang, *Phys. Chem. Chem. Phys.* **2001**, *3*, 1661.
[6] T. Hyeon, *Chem. Commun.* **2003**, *8*, 927.
[7] S. Gangopadhyay, G. C. Hadjipanayis, B. Dale, C. M. Sorensen, K. J. Klabunde, V. Papaefthymiou, A. Kostikas, *Phys. Rev. B* **1992**, *45*, 9778.
[8] R. Sen, A. Govindaraj, C. N. R. Rao, *Chem. Phys. Lett.* **1997**, *267*, 276.
[9] C. N. R. Rao, R. Sen, B. C. Satishkumar, A. Govindaraj, *Chem. Commun.* **1998**, 1525.
[10] B. K. Pradhan, T. Kyotani, A. Tomita, *Chem. Commun.* **1999**, 1317.
[11] A. G. Nasibulin, A. Moisala, D. P. Brown, E. I. Kauppinen, *Carbon* **2003**, *41*, 2711–2724.
[12] J. Jiao, S. Seraphin, X. Wang, J. C. Withers, *J. Appl. Phys.* **1996**, *1*, 80.
[13] J. J. Host, J. A. Block, K. Parvin, V. P. Dravid, J. L. Alpers, T. Sezen, R. LaDuca, *J. Appl. Phys.* **1998**, *2*, 83.
[14] a) T. Yogi, T. Nguyen, *IEEE Trans. Magn.* **1993**, *29*, 307; b) S. R. C. Vivekchand, G. Gundiah, A. Govindaraj, C. N. R. Rao, *Adv. Mater.* **2004**, *16*, 1842; c) S. R. Sen, R. Subbanna, G. N. Kannan, C. N. R. Rao, *Chem. Phys. Lett.* **1995**, *31*, 308.
[15] S. Klein, M. Winterer, H. Hahn, *Chem. Vap. Deposition* **1998**, *4*, 143.
[16] S. V. Pol, V. G. Pol, A. Frydman, G. N. Churilov, A. Gedanken, *J. Phys. Chem. B* **2005**, *109*, 9495.
[17] J. C. De Jesus, I. Gonzalez, A. Quevedo, T. Puerta, *J. Mol. Catal. A* **2005**, *228*, 283.
[18] Y. Lifshitz, *Diamond Relat. Mater.* **1999**, *8*, 1659.
[19] S. R. Elliott, *Physics of Amorphous Materials*, Longman, London, New York, **1984**, p. 350.
[20] H. R. Kodoma, A. E. Berkovitz, E. J. Mcniff Jr, S. Foner, *Phys. Rev. Lett.* **1996**, *77*, 394.
[21] R. Hohne, M. Ziese, P. Esquinazi, *Carbon* **2004**, *42*, 3109.
[22] S. V. Pol, V. G. Pol, A. Gedanken, *Chem. Eur. J.* **2004**, *10*, 4467–4473.
[23] a) V. G. Pol, S. V. Pol, A. Gedanken, *J. Phys. Chem. B* **2005**, *109*, 6121; b) S. V. Pol, V. G. Pol, V. G. Kessler, G. A. Seisenbaeva, M. Sung, S. Asai, A. Gedanken, *J. Phys. Chem. B* **2004**, *108*, 6322; c) V. G. Pol, S. V. Pol, B. Markovsky, J. M. Calderon-Moreno, A. Gedanken, *Chem. Mater.* **2006**, *18*, 1512; d) S. V. Pol, V. G. Pol, A. Gedanken, *Adv. Mater.* **2006**, *18*, 2023.
[24] a) S. V. Pol, V. G. Pol, G. Seisenbaeva, V. G. Kessler, A. Gedanken, *Chem. Mater.* **2004**, *16*, 1793; b) V. G. Pol, S. V. Pol, A. Gedanken, *Chem. Mater.* **2005**, *17*, 1797; c) S. V. Pol, V. G. Pol, V. G. Kessler, G. A. Seisenbaeva, L. A. Solovyov, A. Gedanken, *Inorg. Chem.* **2005**, *44*, 9938; d) V. G. Pol, S. V. Pol, A. Gedanken, S. H. Lim, Z. Zhong, J. Lin, *J. Phys. Chem. B* **2006**, *110*, 11237.
[25] G. A. M. Hussein, A. K. H. Nohman, K. A. M. Attiya, *J. Therm. Anal.* **1994**, *42*, 1155.


 © 2007 Wiley-VCH Verlag GmbH & Co. KGaA, Weinheim 

[26] A. J. Bard, R. Parsons, J. Jordan, *Standard Potentials in Aqueous Solutions*, IUPAC, Marcel Dekker, New York, USA, **1985**.
[27] M. W. Chase Jr, C. A. Davies, J. R. Downey Jr, D. J. Frurip, R. A. McDonald, A. N. Syverud, *JANAF Thermochemical Tables*, 3rd ed., part I–III, ACS and Chemical Institute of Physics for the National Bureau of Standards, J. Phys. and Chem. Reference data, 14, **1985**, supplement no. 1.

Received: December 8, 2006
Published Online: April 10, 2007

 © 2007 Wiley-VCH Verlag GmbH & Co. KGaA, Weinheim 

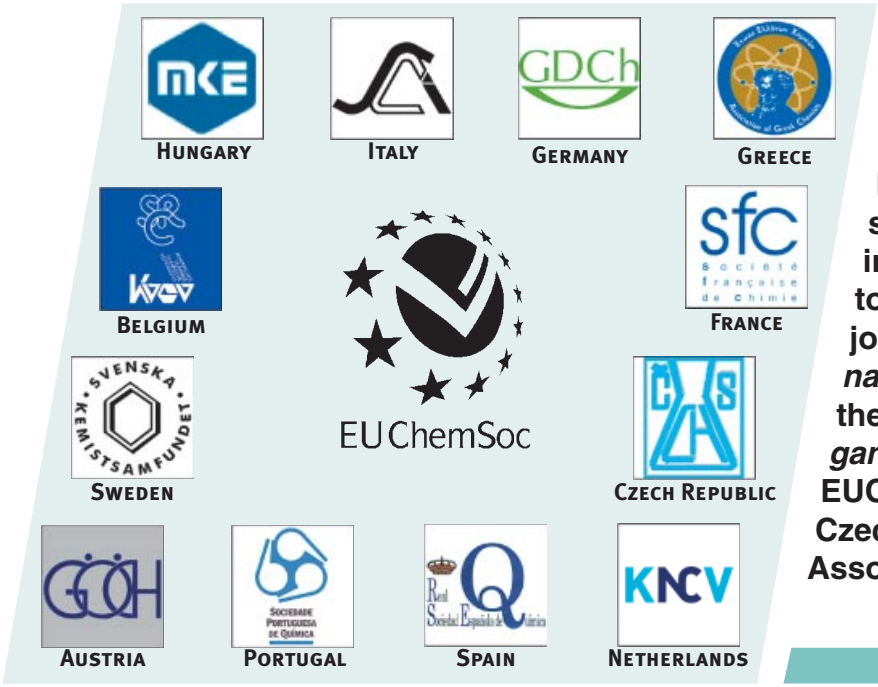


**The EUChemSoc Societies have taken the significant step into the future by merging their traditional journals, to form two leading chemistry journals, the *European Journal of Inorganic Chemistry* and the *European Journal of Organic Chemistry.* Three further EUChemSoc Societies (Austria, Czech Republic and Sweden) are Associates of the two journals.**

## COVER PICTURE

**The cover picture shows,** with the help of a heteroditopic tpy-pincer building block, the preparation of heterodimetallic complexes through the "complex as ligand" approach. Even with such small building blocks the construction of large molecular assemblies will eventually be possible. A beautiful example of small building blocks leading to large constructions is the Aquaduct Segovia, a masterpiece of classical Roman architecture. Details of the synthesis and structures of the heterodimetallic complexes are described in the article by G. van Koten et al. on p. 2111 ff.

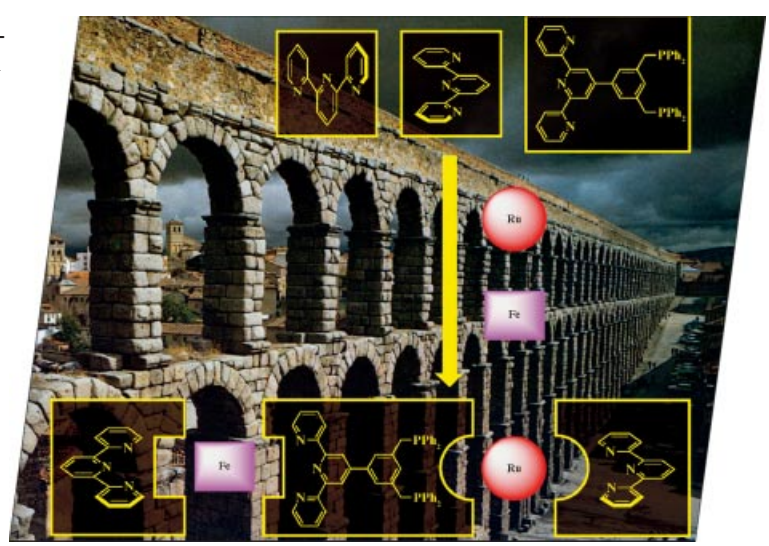


 © 2007 Wiley-VCH Verlag GmbH & Co. KGaA, Weinheim 

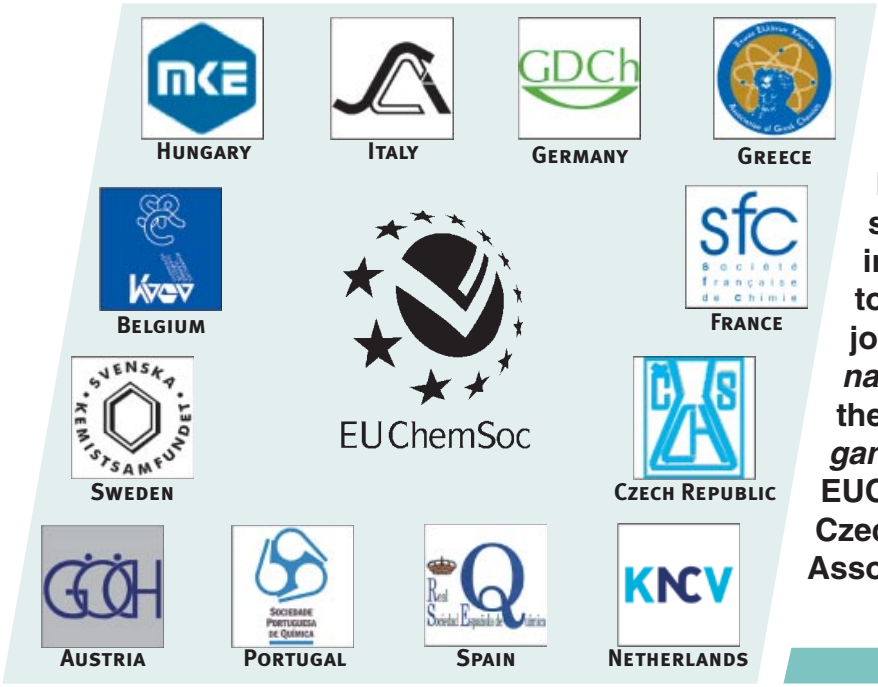


**The EUChemSoc Societies have taken the significant step into the future by merging their traditional journals, to form two leading chemistry journals, the *European Journal of Inorganic Chemistry* and the *European Journal of Organic Chemistry.* Three further EUChemSoc Societies (Austria, Czech Republic and Sweden) are Associates of the two journals.**

## COVER PICTURE

**The cover picture shows,** with the help of a heteroditopic tpy-pincer building block, the preparation of heterodimetallic complexes through the "complex as ligand" approach. Even with such small building blocks the construction of large molecular assemblies will eventually be possible. A beautiful example of small building blocks leading to large constructions is the Aquaduct Segovia, a masterpiece of classical Roman architecture. Details of the synthesis and structures of the heterodimetallic complexes are described in the article by G. van Koten et al. on p. 2111 ff.

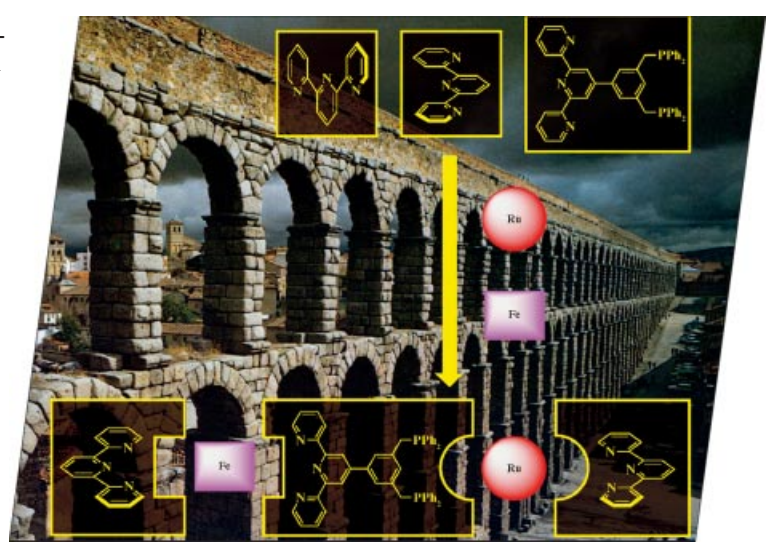


 © 2007 Wiley-VCH Verlag GmbH & Co. KGaA, Weinheim 

# CONTENTS

## FULL PAPERS

### Pincer Ligands

**M. Gagliardo, J. Perelaer, F. Hartl, G. P. M. van Klink, G. van Koten* ..... 2111–2120**

Mono- and Heterodimetallic $Fe^{II}$ and $Ru^{II}$ Complexes Based on a Novel Heteroditopic 4′-{Bis(phosphanyl)aryl}-2,2′:6′,2′′-terpyridine Ligand

**Keywords:** Ruthenium / Iron / Terpyridine ligands / Pincer ligands / Spectroelectrochemistry

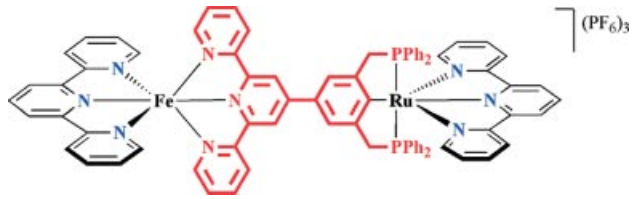


The redox and spectroscopic properties of the mono- and dimetallic complexes of the heteroditopic ligand 4′-{$C_6H_3(CH_2PPh_2)_2$-3,5}-2,2′:6′,2′′-terpyridine have been investigated in detail. The degree of electronic communication between the $Ru^{II}$ and $Fe^{II}$ centres in the heterodimetallic complex was probed. The electronic interaction between the metal centres appears to be very limited.

### Photosensitizers

**F. A. Al-mutlaq, P. G. Potvin,* A. I. Philippopoulos, P. Falaras ..... 2121–2128**

Catechol-Bearing Dipyrazinylpyridine Complexes of Ruthenium(II)

**Keywords:** Ruthenium / Tridentate ligands / Photosensitizers / Electron transfer / Energy conversion

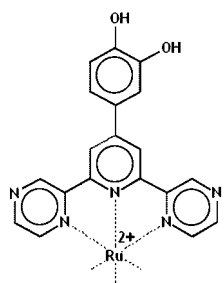


Homoleptic and heteroleptic dipyrazinylpyridine complexes of $Ru^{II}$ with one or two peripheral catechol groups were prepared via protected forms. They were characterized by electronic spectra and cyclic voltammetry, then assessed as photosensitizers in homogeneous solutions and in photovoltaic devices.

### Hexagonal Perovskite Oxides

**L. Miranda, J. Ramírez-Castellanos, M. Hernando, A. Varela, J. M. González-Calbet, M. Parras* ..... 2129–2135**

Structural Chemistry of a New 10H Hexagonal Perovskite: $BaMn_{0.4}Fe_{0.6}O_{2.73}$

**Keywords:** Hexagonal perovskites / Magnetic properties / Mn polytypes / High-resolution electron microscopy

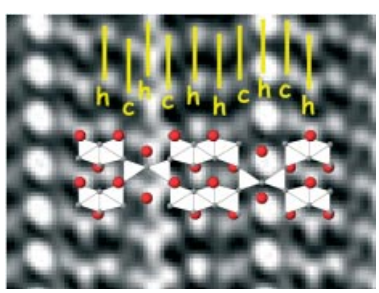


A new 10H polytype has been stabilized in the $BaMn_{1-x}Fe_xO_{3-y}$ system with the composition $BaMn_{0.4}Fe_{0.6}O_{2.73}$. The anionic composition has been established by a reduction and re-oxidation cycle in the stability range of this phase. The structure can be described by the stacking of cubic (c) and hexagonal (h) $BaO_3$ layers with oxygen-deficient hexagonal (h′) $BaO_{2-y}$ layers according to the sequence $(hch'ch)_2$.

### Phosphanylboranes

**A. Adolf, M. Zabel, M. Scheer* ..... 2136–2143**

Main Group Lewis Acid/Base-Stabilised Phosphanylboranes

**Keywords:** Boron / Phosphorus / Hydrides / Lewis acids / Lewis bases

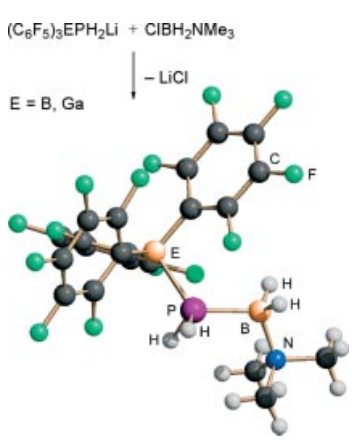


The synthesis of the novel parent compounds of the phosphanylboranes stabilised by Lewis acid/Lewis base is described, where the perfluorinated main group moieties $B(C_6F_5)_3$ and $Ga(C_6F_5)_3$, respectively, were used as Lewis acids for the first time. These are stable compounds which do not show any tendency of dehydrocoupling to form polymerisation products.

 © 2007 Wiley-VCH Verlag GmbH & Co. KGaA, Weinheim 

## Markovnikov Addition

A simple but efficient method for synthesizing stable azaplatinacyclobutanes containing platinum(II) is reported together with two crystal structures. The influence of the substituents on the parent complexes on the molar ratios of the anti-Markovnikov/Markovnikov isomers formed is highlighted and interpreted in terms of electronic and steric factors. These reactions can serve as models for metal-catalyzed amination of alkenes.

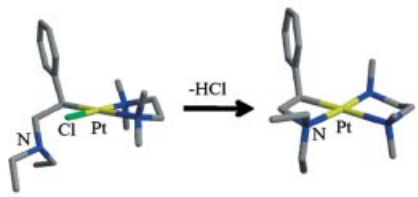


**G. Lorusso, C. R. Barone, N. G. Di Masi, C. Pacifico, L. Maresca,* G. Natile ..... 2144–2150**

Aiding Factors in the Formation of Azaplatinacyclobutane Rings – X-ray and Crystal Structure of [Pt{CH(Ph)$CH_2$$NEt_2$-κC,κN}(*N*,*N*,*N*′,*N*′-tetramethylethylenediamine)]$^+$ and of Its Open-Chain Precursor

**Keywords:** Chelates / Metallacycles / N ligands / Nucleophilic addition / Platinum

## Aromatization of $C_5$ Rings

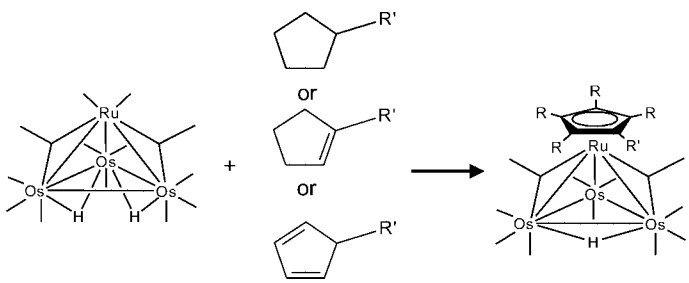


The reaction of $RuOs_3(\mu\text{-}H)_2(CO)_{13}$ with saturated and unsaturated $C_5$ rings led to the aromatization of the rings to afford the clusters $RuOs_3(\mu\text{-}H)(CO)_9(\mu\text{-}CO)_2(\eta^5\text{-}C_5R_4R')$. However, the reaction with cyclopentene gave the cluster $RuOs_3(\mu\text{-}H)_3(CO)_{11}(\mu,\eta^1\text{:}\eta^2\text{-}C_5H_7)$ via C–H activation of an $sp^2$ carbon instead. Thermolysis of two of the products led to their isomerization to butterfly clusters.

**Y. L. K. Tan, W. K. Leong* ..... 2151–2160**

The Aromatization of $C_5$ Rings on a Heteronuclear Cluster

**Keywords:** Heterometallic complexes / Ruthenium / Osmium / Carbocyclic rings / Cyclopentadienyl ligands

## Magnetic Dinuclear Complexes

The dinuclear $M^{II}_2$ complexes (M = Ni, Cu) show steroelectronic preference of metal ions. Magnetic measurments reveal the existence of strong antiferromagnetic coupling for both complexes. Coulometric oxidation of the dinickel(II) complex generates mixed-valence $Ni^{II}$-$Ni^{III}$ species with interesting redox properties.

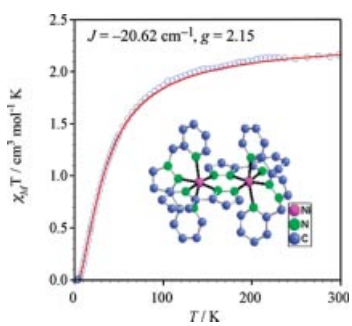


**V. Mishra, F. Lloret, R. Mukherjee* ..... 2161–2170**

Bis-μ-pyrazolate-Bridged Dinickel(II) and Dicopper(II) Complexes: An Example of Stereoelectronic Preference of Metal Ions and Stabilization of Mixed-Valence $Ni^{III}$-$Ni^{II}$ Species

**Keywords:** Nickel / Copper / Dinuclear complexes / Pyrazolate bridge / $Ni^{III}$-$Ni^{II}$ species

## Black Dye

Ruthenium(II) "black dye" complexes are investigated by DFT and TD-DFT methods. In the calculated absorption spectra, the first four bands have MLCT/LLCT nature, whereas the fifth band, the one with the strongest intensity, arises from an intraligand tricarboxyterpyridine π → π* charge transfer (ILCT) with some LLCT character.

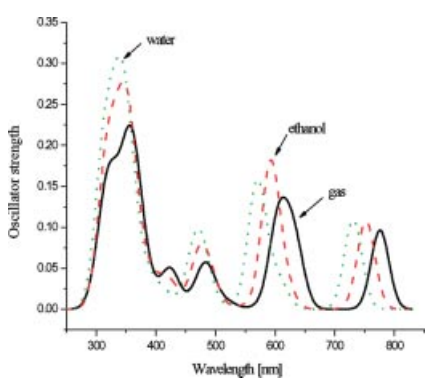


**M.-X. Li, H.-X. Zhang,* X. Zhou, Q.-J. Pan, H.-G. Fu, C.-C. Sun ..... 2171–2180**

Theoretical Studies of the Electronic Structure and Spectroscopic Properties of $[Ru(Htcterpy)(NCS)_3]^{3-}$

**Keywords:** Black dyes / Electronic structure / Spectroscopic properties / Solvent effects

 © 2007 Wiley-VCH Verlag GmbH & Co. KGaA, Weinheim 

# CONTENTS


## Weak Transition-Metal Interactions

**X. Zhou, H.-X. Zhang,* Q.-J. Pan, M.-X. Li, Y. Wang, C.-M. Che ..... 2181–2188**

Electronic Structures and Spectroscopic Properties of $[Pt(CNMe)_2(CN)_2]_n$ ($n$ = 1–4): A Theoretical Exploration of Promising Phosphorescent Materials

**Keywords:** Ab initio calculations / DFT calculations / Luminescence / Excited states / Platinum(II) oligomer

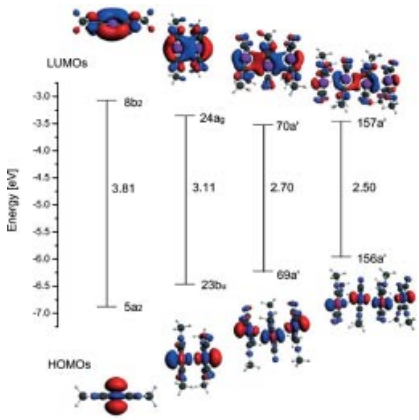


Platinum(II) oligomers were investigated by ab initio and DFT methods. The $^3B_u \rightarrow {}^1A_g$ transition in the dimer corresponds to the experimental higher-energy emission at 530 nm in $CH_3CN$ solution, while the $^3A' \rightarrow {}^1A'$ transitions in the trimer and tetramer at 557 and 650 nm, respectively, are responsible for the low-energy emission at 584 nm.

## Heterometallic Selenium Clusters

**Z. Yu, Q.-F. Zhang,* Y. Song, W.-Y. Wong, A. Rothenberger, W.-H. Leung ..... 2189–2197**

Syntheses, Structures and Optical Nonlinearities of Heteroselenometallic W–Se–Cu Cluster Compounds Containing Bridging Phosphane Ligands

**Keywords:** Heterometallic complexes / Copper / Selenium / Nonlinear optical properties / Cluster compounds

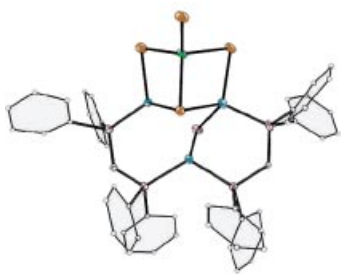

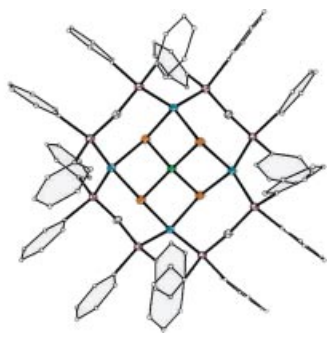

Two types of heterometallic selenium cluster compounds with bridging phosphane ligands have been synthesized and structurally characterized and their nonlinear optical properties investigated [W (green, Se (gold), Cu (blue), P (purple), C (grey)].

## Metal Ion Complementarity

**M. Regueiro-Figueroa, D. Esteban-Gómez, C. Platas-Iglesias, A. de Blas,* T. Rodríguez-Blas* ..... 2198–2207**

Metal Ion Complementarity: Effect of Ring-Size Variation on the Conformation and Stability of Lead(II) and Cadmium(II) Complexes with Pendant-Armed Crowns

**Keywords:** Lead / Cadmium / Macrocycles / N,O ligands / Density functional calculations

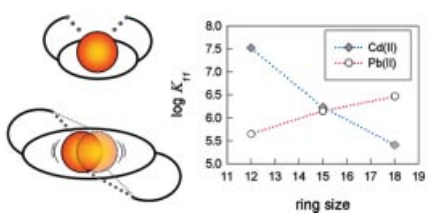


A detailed structural and stability study of series of $Cd^{II}$ and $Pb^{II}$ complexes with *N*,*N*′-bis(benzimidazol-2-ylmethyl)-diaza-crowns, where the crown ether ring size is systematically varied, shows that increasing the crown size induces a conformational change in the series of $Cd^{II}$ complexes, whereas no such change was observed for the corresponding $Pb^{II}$ complexes.

## Dinuclear Yttrium Complexes

**S. Mishra,* S. Daniele,* L. G. Hubert-Pfalzgraf, E. Jeanneau ..... 2208–2215**

Hydrolysis of a (2-Propanol)yttrium Triiodide Complex in the Presence of Glymes: Synthesis and X-ray Structures of Hydroxo-Bridged Dinuclear Yttrium Complexes and Their Applications in Materials Science

**Keywords:** Yttrium / Iodine / Glymes / Structure / Dinuclear complexes

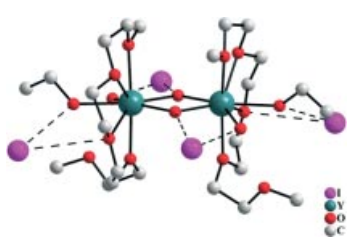

The reactions of $Y(i\text{PrOH})_4I_3$ with stoichiometric amounts of water in the presence of di-, tri-, and tetraglyme yield a facile synthetic route to hydroxo-bridged, centrosymmetric dimeric yttrium complexes. The utility of these ionic derivatives as potential sources of yttrium oxide in high $T_c$ superconductors is also evaluated.


 © 2007 Wiley-VCH Verlag GmbH & Co. KGaA, Weinheim 

## Polyoxometalates

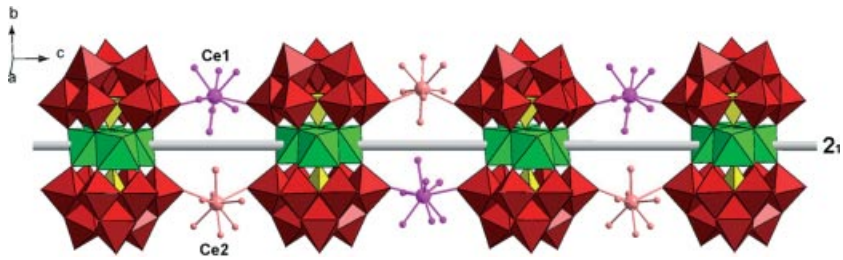


**W. Chen, Y. Li, Y. Wang, E. Wang* ..... 2216–2220**

An Inorganic Aggregate Based on a Sandwich-Type Polyoxometalate with Lanthanide and Potassium Cations: From 1D Chiral Ladder-Like Chains to a 3D Open Framework

**Keywords:** Polyoxometalates / Sandwich complexes / Lanthanides / Chirality / Open framework

$K_4Na_2[\{Ce(H_2O)_7\}_2Mn_4Si_2W_{18}O_{68}(H_2O)_2]\cdot 21.5H_2O$ (**1**) represents the first inorganic aggregate composed of sandwich-type polyanions and lanthanide cation linkers. Complex **1** comprises novel chiral ladder-like chains based on sandwich-type polyanions and two different lanthanide linkers, which are further connected by K cations into a 3D open framework.

## Heterocyclic Carbenes

**J.-c. Shi,* N. Lei, Q. Tong, Y. Peng, J. Wei, L. Jia ..... 2221–2224**

Synthesis of Chiral Imidazolinium Carbene from a Carbohydrate and Its Rhodium(I) Complex

**Keywords:** Nitrogen heterocycles / Carbenes / Rhodium / Carbohydrates / Chirality

A chiral imidazolinium salt with two bulky carbohydrate subunits and its corresponding NHC-coordinated Rh complex **5** were synthesized and characterized. A water adduct of the corresponding N-heterocyclic carbene was also isolated.

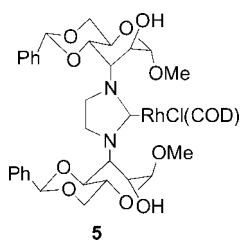


**5**

**If not otherwise indicated in the article, papers in issue 14 were published online on April 20, 2007**

 © 2007 Wiley-VCH Verlag GmbH & Co. KGaA, Weinheim 

DOI: 10.1002/ejic.200600928

# Mono- and Heterodimetallic $Fe^{II}$ and $Ru^{II}$ Complexes Based on a Novel Heteroditopic 4′-{Bis(phosphanyl)aryl}-2,2′:6′,2′′-terpyridine Ligand

**Marcella Gagliardo,[a] Jolke Perelaer,[a] František Hartl,[b] Gerard P. M. van Klink,[a] and Gerard van Koten*[a]**

**Keywords:** Ruthenium / Iron / Terpyridine ligands / Pincer ligands / Spectroelectrochemistry

In the search for a versatile building block that allows the preparation of heteroditopic tpy-pincer bridging ligands, the synthon {4′-[$C_6H_3(CH_2Br)_2$-3,5]-2,2′:6′,2′′-terpyridine} was synthesized. Facile introduction of diphenylphosphanyl groups in this synthon gave the ligand {4′-[$C_6H_3(CH_2PPh_2)_2$-3,5]-2,2′:6′,2′′-terpyridine} ([**tpyPC(H)P**]). The asymmetric mononuclear complex [Fe(tpy){**tpyPC(H)P**}]$(PF_6)_2$, prepared by selective coordination of [$Fe(tpy)Cl_3$] to the tpy moiety of [**tpyPC(H)P**], was used for the synthesis of the heterodimetallic complex [Fe(tpy)(**tpyPCP**)Ru(tpy)]$(PF_6)_3$, which applies the "complex as ligand" approach. Coordination of the ruthenium centre at the PC(H)P-pincer moiety of [Fe(tpy){**tpyPC(H)P**}]$(PF_6)_2$ has been achieved by applying a transcyclometallation procedure. The ground-state electronic properties of both complexes, investigated by cyclic and square-wave voltammetries and UV/Vis spectroscopy, are discussed and compared with those of $[Fe(tpy)_2](PF_6)_2$ and [Ru(PCP)(tpy)]Cl, which represent the mononuclear components of the heterodinuclear species. An in situ UV/Vis spectroelectrochemical study was performed in order to localize the oxidation and reduction steps and to gain information about the $Fe^{II}$–$Ru^{II}$ communication in the heterodimetallic system [Fe(tpy)(**tpyPCP**)Ru(tpy)]$(PF_6)_3$ mediated by the bridging ligand [**tpyPCP**]. Both the voltammetric and spectroelectrochemical results point to only very limited electronic interaction between the metal centres in the ground state.
(© Wiley-VCH Verlag GmbH & Co. KGaA, 69451 Weinheim, Germany, 2007)

## Introduction

In the past decades, much attention was devoted to the field of coordination chemistry of substituted terpyridines. Currently, a significant amount of research is devoted to the preparation of mononuclear terpyridine complexes bearing an externally oriented vacant binding site. A huge potential is concealed in these compounds with tuneable redox and photophysical properties, which can be used as building blocks for the construction of molecular devices,[1] metal-containing dendrimers[2] and one-dimensional polymers.[3]

Only a few examples have been reported in which metal–tpy and organometallic subunits are incorporated into a single molecule.[4] Bridging ligands based on 2,2′:6′,2′′-terpyridine (tpy) functionalized at the 4′-position with a cyclometallating unit proved to have a high potential for linking chromophoric Ru–tpy centres and robust organometallic units containing a stable M–C σ-bond.[1b,5] Recently, we described the synthesis of the heteroditopic ligand 4′-{4-Br-$C_6H_3(CH_2NMe_2)_2$-3,5}-2,2′:6′,2′′-terpyridine [**tpyNCNBr** (**1**)], which combines the properties of the tpy and NCNBr-pincer {$BrC_6H_3(CH_2NMe_2)$-2,6} ligands.[6] It was shown that selective metallation and coordination of the NCNBr and tpy moieties, respectively, affords monometallic species that can be further used as building blocks for the construction of heterodi- and trimetallic complexes containing covalently linked photosensitizing octahedral $[Ru(tpy)_2]^{2+}$ and cyclometalated NCN–$Pd^{II}$ domains.[6]

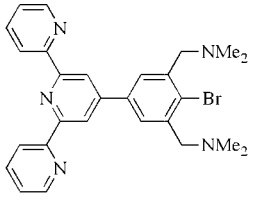


**1**

Metallation of the NCNBr moiety in **1** can be performed only by oxidative addition of the C–Br bond to transition-metal salts.[7] For a broader application in template-directed synthesis of multimetallic systems based on metal–tpy binding domains containing aryl pincer components, we extended our studies to the preparation of the versatile tpy-pincer building block 4′-{$C_6H_3(CH_2Br)_2$-3,5}-2,2′:6′,2′′-terpyridine (**5**). Interestingly, **5** can be used as a precursor for several tpy-pincer ligand systems because the bromo

[a] Faculty of Science, Organic Chemistry and Catalysis, University of Utrecht,
Padualaan 8, 3584 CH Utrecht, The Netherlands
Fax: +31-30-252-3615
E-mail: g.vankoten@chem.uu.nl
[b] Van't Hoff Institute for Molecular Sciences, Homogeneous and Supramolecular Catalysis, University of Amsterdam,
Nieuwe Achtergracht 166, 1018 WV Amsterdam, The Netherlands

 © 2007 Wiley-VCH Verlag GmbH & Co. KGaA, Weinheim 

substituents at the benzylic arms can be easily converted into $ER_2$ groups, where E = N, P, S, O and R = alkyl or aryl.[8] In the pincer moiety, several parameters (e.g. nature of the donor atoms, size and electron-withdrawing or releasing character of the donor substituents) can readily be varied. This allows for fine-tuning of the target ligand depending on its envisaged application.[9] Moreover, incorporation of a wider range of transition metals into the pincer moiety can at the same time be achieved through C–H activation,[10] transmetallation[11] and transcyclometallation[12] procedures.

In our previous work, we described a heterometallic system with weak electronic interactions between the $Ru^{II}$ and $Pd^{II}$ centres mediated by tpy-pincer ligand **1**.[6] However, this study was hampered by the low redox activity of the $Pd^{II}$ centre and by the instability of the NCN–Pd pincer moiety upon electrochemical reduction.[6] Aimed at continuing these physicochemical investigations and with synthon **5** in hand, we focused our attention on its derivatization to form the heteroditopic ligand 4′-{$C_6H_3(CH_2PPh_2)_2$-3,5}-2,2′:6′,2′′-terpyridine {[**tpyPC(H)P**] (**7**, see Scheme 1} containing P-donor atoms. Facile attachment of redox active $Fe^{II}$ and $Ru^{II}$ centres to the tpy and PCP-pincer moieties of **7**, respectively, led to the formation of the heterodimetallic complex [Fe(tpy)(**tpyPCP**)Ru(tpy)]$(PF_6)_3$ (**11**). For the purpose of comparison, the mononuclear complex [Fe(tpy){**tpyPC(H)P**}]$(PF_6)_2$ (**9**) was also prepared. Our main goal was to investigate the spectroelectrochemical behaviour of **11** and the known reference complexes [Fe(tpy)$_2$]$^{2+}$[13] and [Ru(PCP)(tpy)]Cl (PCP = [$C_6H_3(CH_2PPh_2)_2$-2,6]$^-$)[14] to probe the degree of intramolecular electronic interaction between the metal centres in the novel dinuclear species mediated by the **tpyPCP** bridging ligand.

## Results and Discussion

### Synthesis of the [tpyPC(H)P] Ligand

The starting point for the synthesis of the building block 4′-{$C_6H_3(CH_2Br)_2$-3,5}-2,2′:6′,2′′-terpyridine (**5**) (Scheme 1) is the preparation of the stannane pincer compound {$C_6H_3(CH_2OMe)_2$-3,5}-$SnMe_3$ (**3**). Chemoselective lithiation of 3,5-bis(methoxymethyl)iodobenzene **2**[15] at the C–I position was achieved by reaction of **2** with 2 equiv. of *t*BuLi in $Et_2O$ at –100 °C. Subsequent quenching with $Me_3SnCl$ followed by slow warming of the reaction mixture to room temperature resulted in the formation of **3** in good yield. Pd-catalyzed Stille cross-coupling[16] of **3** with 4′-triflato-2,2′:6′,2′′-terpyridine[17] gave **4** in moderate yield after chromatographic purification.

First attempts to replace the methoxy groups in **4** with bromide substituents by using $BF_3{\cdot}EtO_2$/AcBr in $CH_2Cl_2$[18] mainly resulted in the formation of unwanted side products and only small amounts of **5**. However, **5** was conveniently prepared by treatment of **4** with an excess amount of HBr·AcOH in dichloromethane.

Subsequently, a two-step procedure was employed for the preparation of **7**. First, treatment of **5** with 2 equiv. of in situ prepared $LiPPh_2{\cdot}BH_3$ afforded **6**. Deprotection of the diphenylphopshine–$BH_3$ moieties with $Et_2NH$ yielded **7** as

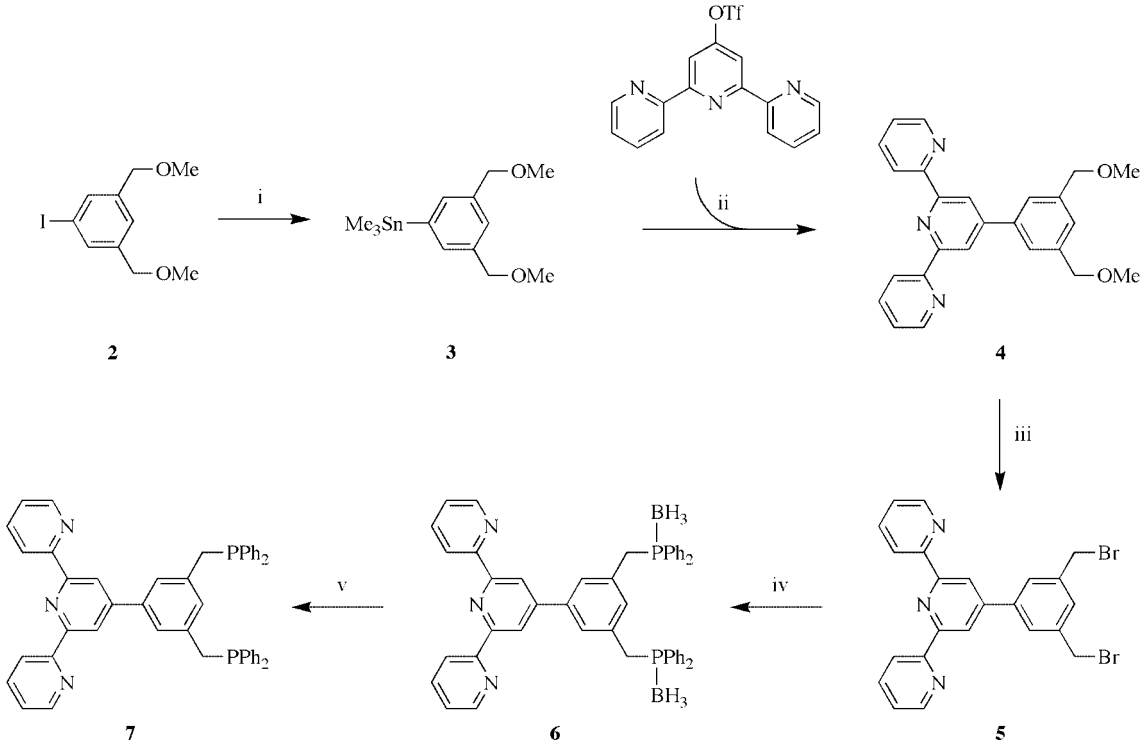


Scheme 1. Synthesis of [**tpyPC(H)P**] ligand **7**. Reagents and conditions: i) (a) 2 equiv. *t*BuLi, $Et_2O$, –100 °C, 0.5 h. (b) $Me_3SnCl$, $Et_2O$, –100 °C→ room temp., 15 h. ii) LiCl, [$PdCl_2(PPh_3)_2$], toluene, reflux, 20 h. iii) (a) HBr·AcOH, $CH_2Cl_2$, room temp., 15 h. (b) aq. $NaHCO_3$. iv) $HPPh_2{\cdot}BH_3$, *n*BuLi, THF, –78 °C → room temp., 20 h. v) (a) $Et_2NH$, room temp., 2 h. (b) aq. $NaHCO_3$.

 © 2007 Wiley-VCH Verlag GmbH & Co. KGaA, Weinheim 

an air- and moisture-sensitive sticky white solid. Notably, both the tpy and PCP-pincer moieties of **7** proved to be stable both in acidic and basic media during the entire synthetic procedure. All the intermediates and ligand **7** have been fully characterized by analytical and spectroscopic methods. The $^1H$ and $^{13}C$ NMR spectra of **7** show the characteristic coupling between the benzylic proton and carbon atoms, of the $PPh_2$ groups, respectively. The $^{31}P\{^1H\}$ NMR spectrum exhibits a signal at $\delta$ = –8.5 ppm typical for the diphenylphosphanyl groups.

### Syntheses of Mono- and Heterodimetallic Complexes

Previous work carried out by Constable and coworkers[19] showed the high potential of the phosphane-functionalized terpyridine ligand 4′-($PPh_2$)-2,2′:6′,2′′-terpyridine to link $M^{II}$ coordination centres (M = Fe, Ru) and organometallic units through the N,N,N- and P-donor domains, respectively. Because it was demonstrated that reaction of ruthenium(III) chloro complexes with this ligand leads to partial or complete oxidation of the $PPh_2$ group,[19a] it was decided to employ different ruthenium starting materials to produce the (**tpyPCP**)Ru-containing species. The use of $[RuCl_2(PPh_3)_3]$ gave a mixture of N,N,N- and P-bound compounds. Confident that a selective and quantitative transfer of the $RuClPPh_3$-moiey into the PCP-pincer unit of **7** could be achieved by a transcyclometallation (TCM) procedure developed in our laboratories for the synthesisofmulti(pincer–metal)complexes,[12,20]wereactedthe ruthenium precursor $[RuCl(NCN)(PPh_3)]$[21] (NCN = $[C_6H_3(CH_2NMe_2)_2$-2,6$]^-$) (**8**, Scheme 2) with **7** in refluxing benzene. Resonances of free **7** or unreacted **8** (singlet at $\delta$ = 90.2 ppm) were subsequently not detected in the $^{31}P\{^1H\}$ NMR spectrum. The main signals present in the spectrum, a triplet at $\delta$ = 83.2 ppm ($PPh_3$, $^2J_{PP}$ = 31.8 Hz) and a doublet at $\delta$ = 37.9 ppm (PCP, $^2J_{PP}$ = 31.8 Hz), together with a large amount of free $PPh_3$, are consistent with the incorporation of the ruthenium centre into the PCP-pincer unit by TCM.[12a] However, the presence of a singlet at $\delta$ = 41.82 ppm indicated that an unwanted reaction concomitant to the TCM procedure occurred. The ruthenium centre of the {(PCP)$RuCl(PPh_3)$} moiety partly reacted with the tpy site of another molecule of the bridging ligand, which produced an oligonuclear species containing the unit [(PCP)Ru(**tpyPCP**)$RuCl(PPh_3)$]. The nature of this material was not investigated in detail. However, fine-tuning of the reaction conditions, as well as the introduction of solubilizing substituents at the phosphorus atoms, may give rise to the formation of soluble redox- and photoactive organometallic molecular wires. Because the synthesis of mononuclear complexes incorporating **7** failed as a result of the affinity of both PCP-pincer and tpy sites for ruthenium, we decided to choose a different approach: to first coordinate an iron centre to the tpy unit in **7**, and then to bind the ruthenium centre at the PCP-site through a TCM reaction.

The reaction of equivalent amounts of $[Fe(tpy)Cl_3]$[22] and **7** in refluxing methanol resulted in the formation of an intensely purple-coloured solution, from which the cation $[Fe\{\mathbf{tpyPC(H)P}\}(tpy)]^{2+}$ could be isolated as the diamagnetic $PF_6$-salt **9** (Scheme 2). Similarly to what was found for **7**, complex **9** is highly air and moisture-sensitive and has to be handled under strictly anaerobic conditions. This sensitivity hampered the removal of small amounts of tpy-containing impurities by chromatography. Attempts to obtain single-crystals suitable for X-ray diffraction analysis were, unfortunately, also unsuccessful. However, complex **9** was sufficiently characterized by NMR spectroscopy and high-resolution ESI-MS analysis. In the ESI-MS spectrum of **9**, the highest mass peak at $m/z$ = 497.20 corresponds to $[M - 2\ PF_6]^{2+}$, which shows the correct isotopic pattern for this formulation. The resonances in the aromatic region of the $^1H$ NMR spectrum could be unequivocally assigned to the protons of the complexed tpy moieties. A single resonance

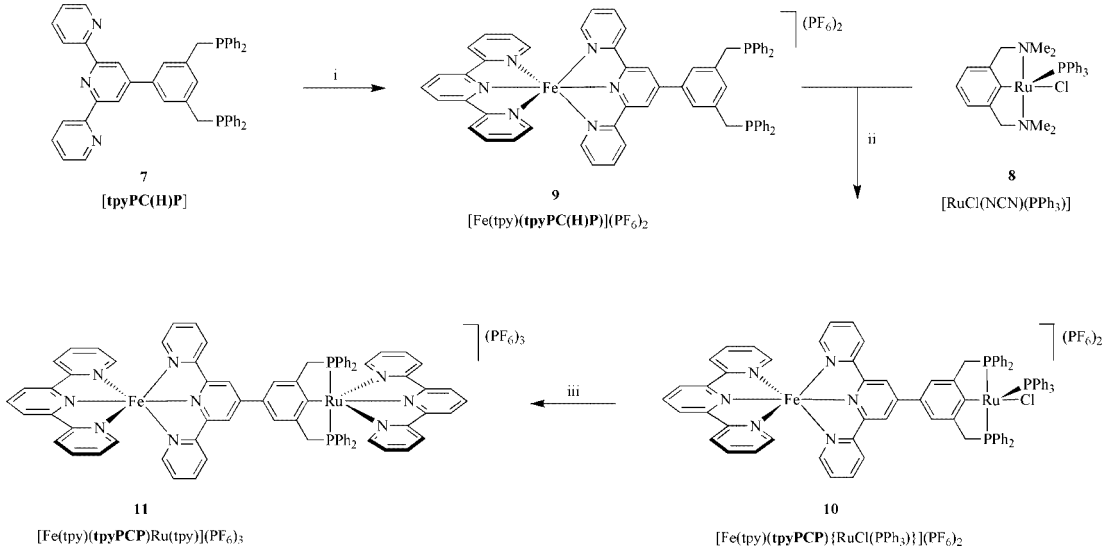


Scheme 2. Synthesis of **9** and heterodimetallic **11**. Reagents and conditions: i) (a) 1 equiv. $[Fe(tpy)Cl_3]$, MeOH, reflux, 4 h. (b) Excess $NH_4PF_6$. ii) **8**, THF/MeCN, reflux, 2 d. iii) (a) tpy, MeOH. (b) Excess $NH_4PF_6$.

 © 2007 Wiley-VCH Verlag GmbH & Co. KGaA, Weinheim 

in the $^{31}P\{^1H\}$ NMR spectrum ($\delta$ = –4.9 ppm in $CD_3CN$) for the equivalent diphenylphosphanyl groups clearly indicates that the iron centre is selectively coordinated to the tpy moiety.

Ruthenation of the PCP-pincer unit of **9** was achieved by the TCM procedure: the reaction of **9** with an equivalent amount of **8** in refluxing THF/MeCN (8:3 v/v). Removal of the volatiles gave intermediate species **10** (Scheme 2) that was subsequently treated with tpy in refuxing methanol. Addition of aqueous $NH_4PF_6$ to the red–purple methanolic solution resulted in the precipitation of **11** as a wine-red solid.

The presence of the $PPh_2$ groups and three nonequivalent tpy ligands results in a complicated $^1H$ NMR spectrum in the aromatic region. Nevertheless, the resonances of **11** could be assigned by comparison with the data obtained for **9** and [Ru(PCP)(tpy)]Cl.[14] The $^1H$ and $^{31}P\{^1H\}$ NMR spectra reveal a high degree of symmetry for the {(PCP)-Ru(tpy)} unit in **11**, with the geometry in solution probably very close to that of [Ru(PCP)(tpy)]Cl. The aliphatic region of the $^1H$ NMR spectrum shows a singlet resonance for the equivalent benzylic hydrogens, which is indicative of a molecular mirror plane containing the benzylic carbon atoms. These data, together with the peak at $\delta$ = 41.82 ppm in the $^{31}P\{^1H\}$ NMR spectrum for the equivalent phosphorus nuclei, suggest an octahedral geometry of the ruthenium coordination sphere, with both the PCP-pincer and tpy ligands coordinated in a meridional fashion. The ESI-MS spectrum of **11** displays $[M - 3PF_6]^{3+}$ ($m/z$ = 442.75) and $[M - 2PF_6]^{2+}$ ($m/z$ = 736.67) for the heterodinuclear complex with good isotopic matching to the simulated spectrum.

### Redox Behaviour and Electronic Absorption Spectra

The electrochemical and spectroscopic properties of the prepared compounds were studied with the aim to estimate the extent of the $Fe^{II}$–$Ru^{II}$ interactions within **11**, mediated by bridging ligand **7**. The redox behaviour of **9** and **11** was investigated by cyclic and square-wave voltammetries (CV and SWV) in MeCN at room temperature. Pertinent electrochemical data are collected in Table 1. Literature data for $[Fe(tpy)_2](PF_6)_2$[13] and [Ru(PCP)(tpy)]Cl[14] have been included for reference purposes.

Table 1. Electrochemical data for complexes **9** and **11**, and reference compounds.[a]

| Complex | $E_{1/2}$ [V] (oxidation) | $E_{1/2}$ [V] (reduction) |
|---|---|---|
| $[Fe(tpy)_2](PF_6)_2$[b] | 0.74 | –1.64, –1.82 |
| [Ru(PCP)(tpy)]Cl[c] | 0.17 | –1.95 |
| [Fe(tpy){**tpyPC(H)P**}]$(PF_6)_2$ (**9**) | 0.74 | –1.59; –1.69 |
| [Fe(tpy)(**tpyPCP**)Ru(tpy)]$(PF_6)_3$ (**11**) | 0.16 | –1.93 |
| | 0.71 | –1.62; –1.77 |

[a] Measured in MeCN containing $10^{-1}$ M TBAH at 298 K. Electrode potentials are given in Volt versus $Fc/Fc^+$. Scan rate = 100 mV $s^{-1}$. [b] Ref.[13] [c] Ref.[14]

It is well known that redox processes for common $Ru^{II}$–polypyridine complexes are mainly localized either on the metal centres (oxidations) or the ligands (reductions).[23] According to experimental results previously reported,[13a,13b] oxidation of the $Fe^{II}$-tpy complexes can be assigned as metal-localized.[13c] However, DFT calculations performed on the complexes $[Fe(tpy)_2]^{2+}$ and $[Fe(B\text{-}ptpy)_2]^{2+}$ {B-ptpy = 4′-(*tert*-butyl-phenyl)-2,2′:6′,2′′-terpyridine} showed that the highest molecular orbital (HOMO) of these compounds is not solely iron-based.[13c] In fact, the HOMO of the complex $[Fe(tpy)_2]^{2+}$ resides mainly on one of the tpy ligands and partly on the iron. Introduction of a substituted phenyl group at the 4′-position of the terpyridine ligands in $[Fe(B\text{-}ptpy)_2]^{2+}$ significantly changes the HOMO character relative to that of $[Fe(tpy)_2]^{2+}$, which has a stronger metal dπ component, with a contribution from the phenyl π orbitals.[13c] The lowest unoccupied molecular orbital (LUMO) of $[Fe(tpy)_2]^{2+}$ is localized on both tpy ligands, whereas the LUMO of $[Fe(B\text{-}ptpy)_2]^{2+}$ is mainly localized on only one of the B-ptpy ligands and partly on the metal.[13c]

The redox potentials determined for **9** and **11** are close to those reported for other $Fe^{II}$–tpy complexes (Table 1). This indicates that the oxidation and reduction of these species involve frontier orbitals having comparable energy and probably also similar character to those calculated for $[Fe(B\text{-}ptpy)_2]^{2+}$. Thus, the reversible anodic wave at $E_{1/2}$ = 0.74 V ($\Delta E_p$ = 0.60 mV) in the cyclic voltammogram of **9** corresponds to a one-electron oxidation of the $Fe^{II}$–tpy moiety. In the cathodic region, two reversible one-electron waves at –1.59 V ($\Delta E_p$ = 0.58 mV) and –1.69 V ($\Delta E_p$ = 0.54 mV) belong to the sequential reduction of the tpy ligands. By comparison with $[Fe(tpy)_2]^{2+}$,[13b] we assign the first and second reduction steps in **9** to the pincer-substituted and terminal tpy ligands, respectively. The electron-withdrawing character of the phenyl moiety renders the substituted tpy less electron rich, thereby decreasing its reduction potential. The anodic potential region of the heterodimetallic complex **11** exhibits two reversible, one-electron anodic waves due to the $Ru^{II}$ centre at $E_{1/2}$ = 0.16 V ($\Delta E_p$ = 0.56 mV) and the $Fe^{II}$–tpy moiety at $E_{1/2}$ = 0.71 V, respectively. These values are nearly identical with the electrode potentials of the $Fe^{II}$–tpy and $Ru^{II}$-based oxidations of complex **9** and [Ru(PCP)(tpy)Cl], respectively. Apparently, the electronic communication between the metal centres is very limited. In the cathodic region, complex **11** undergoes three ligand-centred reduction processes. The first two cathodic waves lie at –1.62 V and –1.77 V. The initial reduction is fully reversible ($\Delta E_p$ = 0.54 mV). The second cathodic step, however, is characterized by slower electron transfer as indicated by decreased peak currents in both voltammetric (CV and SWV) records. More information about this behaviour has been obtained from the corresponding spectroelectrochemical experiments (see below). According to the reference data in Table 1, these reductions are localized at the terminal and substituted tpy ligands that are coordinated to the iron centre, respectively. The third cathodic step at –1.92 V ($\Delta E_p$ = 0.60 mV), which is fully reversible, can be readily assigned to the reduction of the terminal tpy ligand bound to the ruthenium centre. The reduction

 © 2007 Wiley-VCH Verlag GmbH & Co. KGaA, Weinheim 

potential is only slightly less negative than that of the tpy ligand in [Ru(PCP)(tpy)]Cl (Table 1). These observations are consistent with a negligible electronic communication between the Ru(tpy) and the doubly reduced (tpy)Fe(**tpyPCP**) moieties.

The electronic absorption spectra of **9** and **11** were recorded in MeCN solution at room temperature. Absorption maxima ($\lambda_{max}$) and molar absorption coefficients ($\varepsilon_{max}$) for both compounds are listed in Table 2, together with the reference data for $[Fe(tpy)_2](PF_6)_2$[13] and [Ru(PCP)(tpy)]Cl.[14] The UV/Vis spectra of **9** and **11** show features typical for other $Fe^{II}$– and $Ru^{II}$–tpy compounds,[13,23] in particular intense $\pi\rightarrow\pi^*$ intraligand (IL) transitions in the UV region, 320 and 280 nm for **9**, and at 308, 319 and 275 nm for **11**. In the visible spectral region, complexes **9** and **11** exhibit moderately intense visible absorption bands (Figure 1) that are tentatively attributed to electronic transitions having a mixed $\pi$(tpy)$\rightarrow\pi^*$(tpy) IL and d$\pi$(Ru)$\rightarrow\pi^*$(ph) MLCT character by comparison with literature data on the basis of the TD-DFT calculations performed on the complexes $[Fe(tpy)_2]^{2+}$ and $[Fe(B\text{-}ptpy)_2]^{2+}$ (B-ptpy = 4′-(*n*-butylphenyl)-2,2′:6′,2′′-terpyridine) (vide supra).[13c,23] The small shift in the lowest absorption of **9** and **11** (Figure 1) to a lower energy relative to $[Fe(tpy)_2](PF_6)_2$ is consistent with the electrochemical results. The lowest transition of **9** is only slightly affected by the incorporation of the ruthenium centre into the PCP-pincer unit (Table 2).

Table 2. UV/Vis absorption maxima ($\lambda_{max}$) and molar absorption coefficients ($\varepsilon_{max}$) of complexes **9** and **11**, and reference compounds.[a]

| Compound | $\lambda_{max}$ [nm] ($\varepsilon_{max}$ $10^{-4}$ [$M^{-1}$ $cm^{-1}$]) |
|---|---|
| $[Fe(tpy)_2](PF_6)_2$[b] | 548 (1.4) |
| [Ru(PCP)(tpy)]Cl[c] | 275 (3.7), 305 (3.9), 479 (0.8) |
| $[Fe(tpy)\{(tpyPC(H)P\})](PF_6)_2$ (**9**) | 280 (5.9), 320 (5.6), 563 (1.0) |
| $[Fe(tpy)(tpyPCP)Ru(tpy)](PF_6)_3$ (**11**) | 275 (5.1), 308 (4.1), 319 (4.0), 489 (0.8), 563 (1.0) |

[a] Measured at 298 K in MeCN. [b] Ref.[13] [c] Ref.[14]

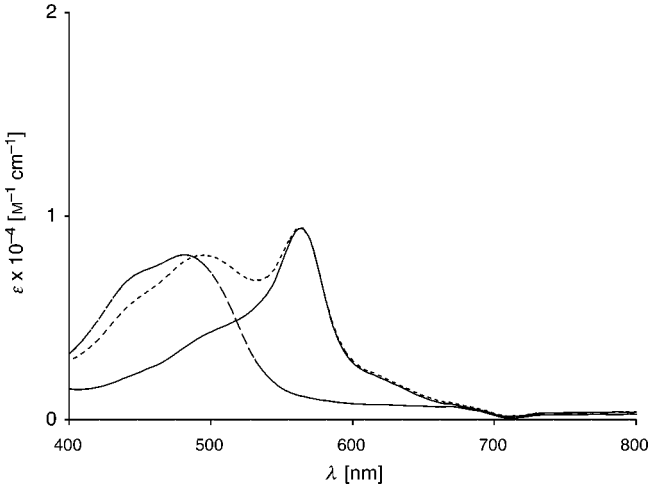


Figure 1. Visible region of the absorption spectra of complexes [Ru(PCP)(tpy)]Cl (– – –), **9** (——), and **11** (-----) recorded in MeCN at 298 K.

For the ruthenium centre in [Ru(PCP)(tpy)]Cl, it is expected that the lowest MLCT excited state involves the coordinated tpy ligands rather than the strongly donating cyclometallated PCP-pincer ligand.[14] The Ru-to-tpy CT band of complex **11** at 489 nm is only slightly shifted to a lower energy relative to the mononuclear [Ru(PCP)(tpy)]Cl (Table 2). This shift, although small, is in agreement with the less positive oxidation and less negative reduction potentials of the Ru(tpy) moiety in the latter complex (Table 1), that is, with a slightly larger HOMO – LUMO gap: $\Delta E$ = 0.03 eV. These results again reveal that the electronic communication between the **tpyPCP**-bridged Ru(tpy) and Fe(tpy) moieties in complex **11** is very limited. A large dihedral angle between the tpy and the PCP-pincer units of the bridging ligand is the most likely reason for the lack of electronic coupling between the two motifs.[24]

However, it cannot be excluded that stabilization of the ruthenium orbitals by $\pi$-back donation to the $PPh_2$ moieties to some extent contributes to a decrease in the mixing between the d$\pi$(Ru)- and the bridging ligand-based orbitals, and thus, the metal-coupling in the studied heterodimetallic complex.

### UV/Vis Spectroelectrochemistry

UV/Vis spectroelectrochemical studies of heterodimetallic complex **11** were performed in MeCN at room temperature within an optically-transparent thin-layer electrochemical (OTTLE)[25] cell. These investigations were mainly aimed at gaining more information about the degree of the $Fe^{II}$–$Ru^{II}$ interaction mediated by the twisted bridging ligand [**tpy(PCP)**]. In addition, the spectral changes recorded during the oxidation and reduction steps help to more accurately appoint their assignment in the preceding section.

Electrochemical oxidation of **11** to $\mathbf{11}^+$ at 0.16 V caused flattening of the band at 500 nm (Figure 2), consistent with

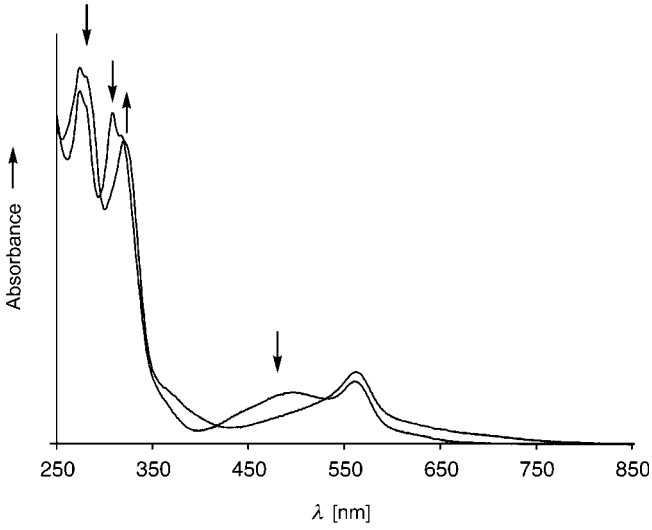


Figure 2. UV/Vis spectra recorded during one-electron oxidation of the $Ru^{II}$ centre in complex **11**. Conditions: OTTLE cell, MeCN/$10^{-1}$ M TBAH, 293 K.

 © 2007 Wiley-VCH Verlag GmbH & Co. KGaA, Weinheim 

its assignment to the MLCT transition in the {Ru(tpy)} moiety. Further oxidation of $\mathbf{11}^{+}$ to $\mathbf{11}^{2+}$ at 0.70 V then resulted in disappearance of the composed absorption band at 565 nm (Figure 3), which agrees with the oxidation of the Fe(tpy) moiety. The formation of $\mathbf{11}^{+}$ and $\mathbf{11}^{2+}$ is also accompanied by stepwise disappearance of the π→π* absorption bands at 308 and 319 nm, respectively. Accordingly, they can be attributed to intraligand Ru(tpy) and Fe(tpy) transitions, respectively. This assignment, supported also by the reference data ([Ru(PCP)(tpy)]Cl and complex **9** in Table 2), is also important for the discussion of the cathodic steps (see below). Reduction of $\mathbf{11}^{2+}$ at 0.16 V led to full recovery of the electronic absorption spectrum of **11**.

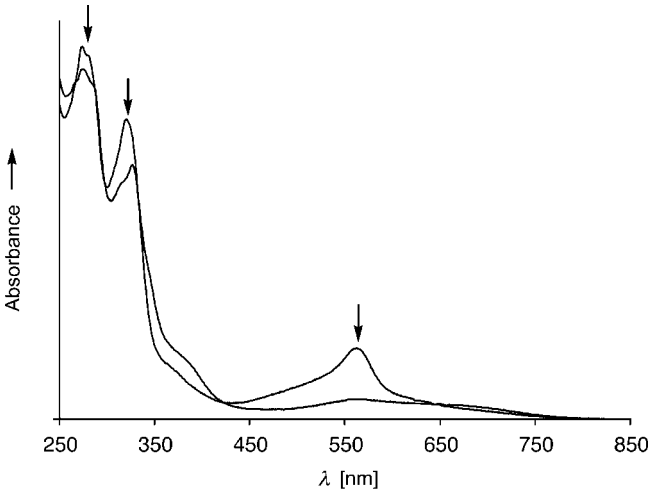


Figure 3. UV/Vis spectra recorded during one-electron oxidation of complex $\mathbf{11}^{+}$, which is probably localized at the Fe(tpy) moiety.[13c] The preceding anodic step is depicted in Figure 2. Conditions: OTTLE cell, MeCN/$10^{-1}$ M TBAH, 293 K.

The spectroscopic changes observed during one-electron reduction of the heterodinuclear complex **11** to $\mathbf{11}^{-}$ were very similar to those observed in the UV/Vis spectra of the singly and doubly reduced complex $[Fe(tpy)_2]^{2+}$.[13b] Reduction of **11** at –1.73 V led to the disappearance of the mixed IL/MLCT band at 565 nm (Figure 4). New low-lying absorption bands due to π*→π*($tpy^{-}$) transitions[13b] arose at 641, 736 and 905 nm (Figure 4). The persisting Ru-to-tpy CT transition of $\mathbf{11}^{-}$ at 498 nm, as well as the unaffected intraligand Ru(tpy) transition at 308 nm also prove that the first reduction step is localized on the terminal tpy ligand coordinated at the iron(II) centre. The slightly decreased intensity of the band at 498 nm in the UV/Vis spectrum of $\mathbf{11}^{-}$ is most probably caused by the disappearance of the underlying shoulder of the composed IL/MLCT Fe(tpy)-band (Figure 1).[13c] Unlike that reported for $[Fe(tpy)_2]^{2+}$,[13b] the addition of the second electron did not result in a shift of the π*→π*($tpy^{-}$) transitions to lower energies. Instead, the formation of $\mathbf{11}^{2-}$ resulted in the increasing intensity of the broad π*→π* absorption between 550–900 nm, with the main absorption maximum at 732 nm (Figure 4).

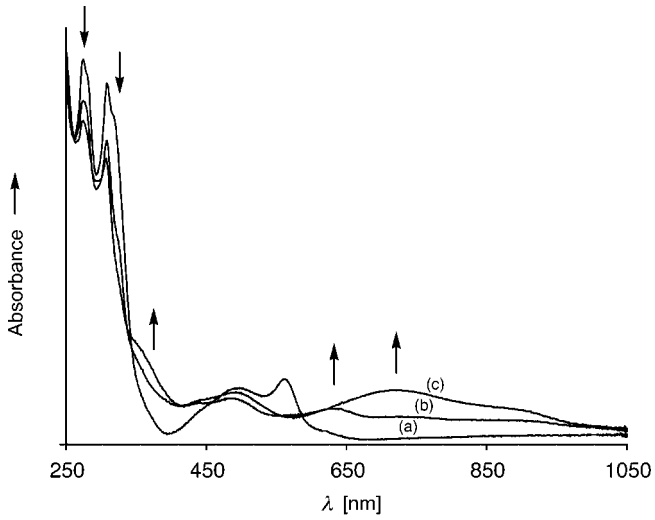


Figure 4. UV/Vis spectral changes accompanying reduction of complex **11** (a) to $\mathbf{11}^{-}$ (b) and $\mathbf{11}^{2-}$ (c) in two tpy(Fe)-localized steps. Conditions: OTTLE cell, MeCN/$10^{-1}$ M TBAH, 293 K.

Importantly, the Ru-to-tpy CT and π→π* Ru(tpy) bands also do not change during the second cathodic step, which indicates that this step is localized on the substituted tpy part of the bridging [**tpyPCP**] ligand. These findings again reveal only a weak communication between the two metal centres through the **tpyPCP** bridge. The qualitatively different changes in the visible spectral region upon the formation of $\mathbf{11}^{2-}$ compared with the doubly reduced reference $[Fe(tpy)_2]$[13b] may reflect some involvement of the phenyl ring of the pincer part of the bridging ligand in the occupied π* system, possibly due to some variation in the central twist angle caused by the second reduction. This observation may explain the slower voltammetric response to the second electron transfer than the first, electrochemically reversible cathodic step of **11**. The third one-electron reduction producing $\mathbf{11}^{3-}$ caused flattening of the Ru-to-tpy CT band. The π→π* Ru(tpy) absorption band at 308 nm

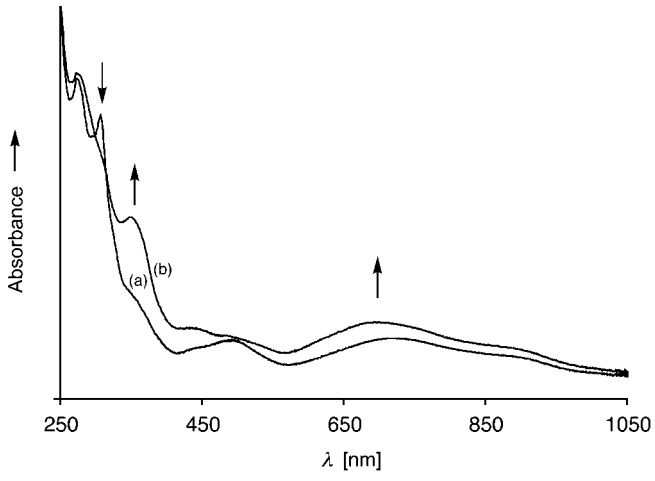


Figure 5. UV/Vis spectrum of $\mathbf{11}^{3-}$ (b) formed from $\mathbf{11}^{2-}$ (a) in the third, tpy(Ru)-localized cathodic step. Conditions: OTTLE cell, MeCN/$10^{-1}$ M TBAH, 293 K.

 © 2007 Wiley-VCH Verlag GmbH & Co. KGaA, Weinheim 

also became affected (Figure 5). Importantly, a new $\pi^*\rightarrow\pi^*(tpy^{-})$ absorption appeared around 550 nm.

Similar spectral changes are characteristic for the one-electron reduction of the reference complex [Ru(PCP)(tpy)]Cl (Figure 6), which confirms that the third reduction step of complex **11** involves occupation of the lowest $\pi^*$ orbital that is essentially localized on the Ru-bound terminal terpyridine ligand, tpy(Ru).

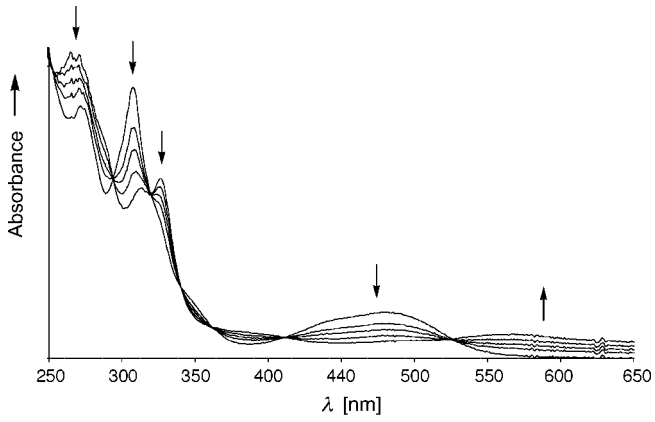


Figure 6. UV/Vis spectral changes accompanying the tpy-localized one-electron reduction of the reference complex [Ru(PCP)(tpy)]Cl. Conditions: OTTLE cell, MeCN/$10^{-1}$ M TBAH, 293 K.

Reoxidation of all three one-electron-reduced species, $\mathbf{11}^{n-}$ ($n$ = 1, 2, 3), fully regenerated the UV/Vis spectrum of parent **11**. It is clear that the reduction steps are largely tpy-localized. The stability of the Ru–C σ-bond during the second and third cathodic steps is remarkable and is a consequence of this localization. In fact, significant delocalization of the added electron density over the PCP-pincer moiety would most likely break the Ru–C σ-bond.[6]

## Conclusions

In this work, the synthesis of novel building block 4′-{$C_6H_3(CH_2Br)_2$-3,5}-2,2′:6′,2′′-terpyridine is presented, which can be used as a precursor for bridging ligands containing an N,N,N-domain and an E,C,E-coordination (E = N, P, S, O) motive. Heteroditopic tpy-pincer ligands are interesting from different viewpoints. In particular, electronic and steric properties of the pincer moiety, in which several transition metals can be incorporated by applying various metallation procedures, can easily be tuned.

Incorporation of diphenylphosphanyl groups gave the 4′-{$C_6H_3(CH_2PPh_2)_2$-3,5}-2,2′:6′,2′′-terpyridine [**tpyPC(H)P**] ligand. The asymmetric complex [Fe(tpy){**tpyPC(H)P**}]-$(PF_6)_2$, prepared by reaction of [**tpyPC(H)P**] with 1 equiv. of [Fe(tpy)$Cl_3$], was used for the construction of the heterodimetallic complex [Fe(tpy)(**tpyPCP**)Ru(tpy)]$(PF_6)_3$, which follows the "complex as ligand" approach.

For both complexes, the oxidation and reduction processes have been assigned by comparison with literature data reported for related $Fe^{II}$–tpy compounds and with [Ru(PCP)(tpy)]Cl, which was extensively studied in this work. The redox potentials do not significantly change on passing from the mononuclear $Fe^{II}$ to the heterodimetallic $Fe^{II}$–$Ru^{II}$ complex. UV/Vis spectroelectrochemical studies of the heterodimetallic complex confirm the voltammetric results. The spectral changes allow the stepwise $Ru^{II}$– and $Fe^{II}$–tpy oxidations to be distinguished. The first and second reduction steps are localized at the terminal and pincer-substituted tpy ligands coordinated at the iron centre, respectively. The third reduction resides at the tpy ligand coordinated at the ruthenium centre.

Apparently, despite the relatively moderate internuclear separation, only a very weak electronic interaction exists between the {Fe(tpy)$_2$} and {(PCP)Ru(tpy)} fragments. This can be rationalized in terms of the very limited ability of the nonplanar (twisted) [**tpyPCP**] bridging ligand to mediate electronic communication between the metal centres. However, stabilization of the dπ(Ru) orbitals as a result of the π-accepting properties of the $PPh_2$ moieties may also cause a decrease in the Fe–Ru coupling by limiting the overlap between the ruthenium orbitals and the bridging ligand orbitals. Connection of the {Fe(tpy)$_2$} and {(PCP)Ru(tpy)} fragments through a bridge capable of achieving a more effective aromatic conjugation would be highly desirable.[26]

## Experimental Section

**General:** All experiments were carried out under a dry nitrogen atmosphere by using standard Schlenk techniques. Benzene, toluene, pentane, hexane and diethyl ether ($Et_2O$) were distilled from sodium/benzophenone. Dichloromethane and methanol were dried with $CaH_2$ and magnesium, respectively. All solvents were freshly distilled under a nitrogen atmosphere prior to use. 1D NMR spectra were recorded with a Varian Inova 300 MHz spectrometer. Chemical shifts are given in ppm relative to the residual solvent signal ($^1$H and $^{13}$C NMR spectra) or 85% $H_3PO_4$ external reference ($^{31}P\{^1H\}$ NMR spectra). EtOAc and all reagents were purchased from Acros or Aldrich and used as received. Compounds **2**,[15] 4′-trifluoromethylsulfonato-2,2′:6′,2′′-terpyridine,[17] **8**[21] and [Fe(tpy)$Cl_3$][22] were synthesized according to literature procedures. Elemental analyses were performed by Dornis und Kolbe, Mikroanalytisches Laboratorium, Mülheim a. d. Ruhr, Germany. Electron spray ionization (ESI) mass spectra were recorded with a Micromass LC-TOF mass spectrometer by the Department of Biomolecular Mass Spectrometry, Utrecht University.

**Electrochemical Measurements:** Cyclic and square-wave voltammetric scans were performed with a gas-tight single compartment cell under a dry nitrogen atmosphere. The cell was equipped with a Pt microdisk working electrode (apparent surface area of 0.42 mm$^2$), Pt wire auxiliary electrode and a Ag wire pseudoreference electrode. The working electrode was carefully polished with a 0.25 μm-grain diamond paste between scans. The potential control was achieved with a PAR Model 283 potentiostat. All redox potentials are reported against the ferrocene–ferrocenium ($Fc/Fc^+$) redox couple used as an internal standard[27] ($E_{1/2}$ = +0.63 V versus NHE[28]). All electrochemical samples were $5\times10^{-4}$ M in the studies complexes and $10^{-1}$ M in $Bu_4NPF_6$ used as the supporting electrolyte.

**Electronic Spectroscopic Measurements:** UV/Vis absorption spectra were obtained with a Varian Cary 1 spectrophotometer by using matched 1 cm cells and operating with a 0.5 nm spectral resolution. Peak positions are given within 0.5 nm accuracy.

 © 2007 Wiley-VCH Verlag GmbH & Co. KGaA, Weinheim 

**UV/Vis Spectroelectrochemical Measurements:** All the experiments were performed with an optically transparent thin-layer electrochemical (OTTLE)[25] cell, equipped with a Pt minigrid working electrode and quartz optical windows. The controlled-potential electrolyses were carried out with a PA4 potentiostat (EKOM, Polná, Czech Republic). All electrochemical samples were $5 \times 10^{-4}$ M in the studied complex and $10^{-1}$ M in $Bu_4NPF_6$. UV/Vis spectra were recorded with a Hewlett Packard 8453 diode-array spectrophotometer.

**[$C_6H_3(CH_2OMe)_2$-3,5]-$SnMe_3$ (3):** A solution of *t*BuLi (13.0 mL, 1.5 M in pentane, 19.52 mmol) was added dropwise to a solution of **2** (3.00 g, 10.27 mmol) in $Et_2O$ (75 mL) at –100 °C with vigorous stirring. After 0.5 h, a solution of $Me_3SnCl$ (3.07 g, 15.41 mmol) in $Et_2O$ (35 mL) was slowly added. The resulting pale yellow coloured suspension was warmed to room temperature and stirring was continued for another 15 h. Subsequently, water was added, and the obtained mixture was treated with a NaOH solution (0.1 M, $2 \times 50$ mL). The $Et_2O$ layer was separated, and the water layer was washed with $Et_2O$ ($2 \times 50$ mL). The organic layers were combined, washed with brine, dried with $MgSO_4$, filtered and concentrated to afford **3** as a colourless oil. Yield: 2.95 g, 85%. $^1$H NMR (300 MHz, $CDCl_3$): $\delta$ = 7.37 (s, 2 H, Ar), 7.26 (s, $^2J_{Sn,H}$ = 21.7 Hz, 1 H, Ar), 4.43 (s, 4 H, $OCH_2$), 3.34 (s, 6 H, $OCH_3$), 0.29 [s, $^2J_{Sn,H}$ = 27.0 Hz, 9 H, $Sn(CH_3)_3$] ppm. $^{13}$C NMR (75 MHz, $CDCl_3$): $\delta$ = 142.9 ($^1J_{Sn,C}$ = 228.3 and 451 Hz), 137.9 ($^2J_{Sn,C}$ = 18.3 Hz), 134.7 ($^2J_{Sn,C}$ = 22.3 Hz, ArH), 127.5, 75.0 ($OCH_3$), 58.4 [$CH_2$, Sn-$(CH_3)_3$], –9.3 [$^1J_{Sn,C}$ = 171.5 Hz, $Sn(CH_3)_3$] ppm. ESI-MS: *m*/*z* 331.05 $[M - H]^+$. $C_{13}H_{22}O_2Sn$ (329.02): calcd. C 47.46, H 6.74; found C 47.55, H 6.62.

**4′-{$C_6H_3(CH_2OMe)_2$-3,5}-2,2′:6′,2″-terpyridine (4):** 4′-Trifluoromethylsulfonato-2,2′:6′,2″-terpyridine (2.66 g, 6.99 mmol), **3** (2.315 g, 6.99 mmol), $[PdCl_2(PPh_3)_2]$ (0.41 g, 0.58 mmol) and dried LiCl (1.72 g, 40.6 mmol) were heated at reflux in dry toluene (100 mL) for 20 h in a 100-mL round-bottomed flask under a nitrogen atmosphere. Subsequently, the solvent was removed in vacuo, and the residue was redissolved in $CH_2Cl_2$. The $CH_2Cl_2$ solution was washed with water, filtered through Celite and dried with $MgSO_4$. The crude product was obtained as a light yellow oil after removal of the solvent as purified by silica gel column chromatography (EtOAc/MeOH 8:1). The fractions containing **4** were collected, concentrated and cooled to –30 °C. Product **4** precipitated as a white crystalline solid and was collected and dried in vacuo. Yield: 1.02, g, 40%. $^1$H NMR (300 MHz, $CDCl_3$): $\delta$ = 8.75 [s, 2 H, tpy(3′, 5′)], 8.73 [d, $J_{H,H}$ = 4.3 Hz, 2 H, tpyH(6, 6″)], 8.67 [d, $J_{H,H}$ = 9.0 Hz, 2 H, tpyH(3, 3″)], 7.88 [td, $J_{H,H}$ = 7.89, 1.61 Hz, 2 H, tpyH(4, 4″)], 7.80 (s, 2 H, ArH), 7.43 (s, 1 H, Ar), 7.35 [m, 2 H, tpyH(5, 5″)], 4.57 (s, 4 H, $CH_2$), 3.44 (s, 12 H, $OCH_3$) ppm. $^{13}$C NMR (75 MHz, $CDCl_3$): $\delta$ = 156.4, 156.0, 150.4, 149.2, 139.6, 139.0, 137.3, 127.8, 126.2, 124.0, 121.7, 119.3, 74.6 ($OCH_3$), 58.5 ($CH_2$) ppm. $C_{25}H_{23}N_3O_2$ (397.47): calcd. C 75.54, H 5.83, N 10.57; found C 75.63, H 5.88, N 10.62.

**4′-{$C_6H_3(CH_2Br)_2$-3,5}-2,2′:6′,2″-tpy (5)**: Compound **4** (0.25 g, 0.7 mmol) was dissolved in dry $CH_2Cl_2$ (20 mL) under a nitrogen atmosphere. The temperature of the solution was lowered with an ice bath and excess HBr·AcOH (110 mL, 33%) was slowly added. The mixture was then stirred at room temperature for 15 h and then cooled to 0 °C. Subsequently, aqueous 6 M $K_2CO_3$ was slowly added until the solution reached a pH of 8. The organic layer was then collected, washed with water and brine, dried with $MgSO_4$, filtered and concentrated to ca. 5 mL. Addition of hexane caused the precipitation of **5** as a white crystalline material. The crystals were collected by filtration, washed with cold hexane and dried in vacuo. Yield: 0.31 g, 64%. $^1$H NMR (300 MHz, $CDCl_3$): $\delta$ = 8.75 [d, $J_{H,H}$ = 4.8 Hz, 2 H, tpyH(6, 6″)], 8.73 [s, 2 H, tpy(3′, 5′)], 8.69 [d, $J_{H,H}$ = 8.1 Hz, 2 H, tpy(3, 3″)], 7.90 [td, $J_{H,H}$ = 7.80, 1.60 Hz, 2 H, tpy(4, 4″)], 7.85 (s, 2 H, ArH), 7.53 (s, 1 H, Ar), 7.38 [t, $J_{HH}$ = 6.13 Hz, 2 H, tpy(5, 5″)], 4.58 (s, 4 H, $CH_2$) ppm. $^{13}$C NMR (75 MHz, $CDCl_3$): $\delta$ = 156.3, 156.1, 149.3, 149.2, 139.9, 139.5, 137.2, 130.5, 128.1, 124.2, 121.7, 118.9, 32.7 ($CH_2$) ppm. Because of its toxicity, elemental and ESI analyses were not carried out. *Caution: Substituted benzyl bromides can be powerful lachrymators and should be used with adequate ventilation and precaution against skin contact or ingestion.*

**4′-{$C_6H_3\{CH_2P(BH_3)Ph_2\}_2$-3,5}-2,2′:6′,2″-terpyridine ([tpyPC(H)P]·$2BH_3$, 6):** *n*BuLi (0.8 mL, 1.34 mmol) was added to $HPPh_2{\cdot}BH_3$ (0.27 g, 1.34 mmol) in dry THF (30 mL) at –78 °C. The temperature was allowed to rise to room temperature and stirring was continued overnight. A solution of **5** (0.32 g, 0.67 mmol) in dry THF (20 mL) was then added at –78 °C. The mixture was warmed to room temperature and stirred for ca. 20 h. All volatiles were then removed in vacuo, and the obtained residue was dissolved in $CH_2Cl_2$. The organic layer was washed with water and brine and dried with $MgSO_4$. Product **6** was obtained after evaporation of $CH_2Cl_2$ as a white solid that was washed with hot EtOH and hexane and dried in vacuo. Yield: 0.63 g, 64%. $^1$H NMR (300 MHz, $CDCl_3$): $\delta$ = 8.77 [d, $J_{H,H}$ = 4.0 Hz, 2 H, tpyH(6, 6″)], 8.60 [d, $J_{H,H}$ = 7.8 Hz, 2 H, tpyH(3, 3″)], 8.19 [s, 2 H, PyrH(3′, 5′)], 7.86 [td, $J_{H,H}$ = 7.8, 1.6 Hz, 2 H, tpyH(4, 4″)], 7.63 (m, 8 H, *meta*-H PAr), 7.47 (m, 12 H, *ortho*- and *para*-H PAr), 7.35 [t, $J_{H,H}$ = 6.13 Hz, 2 H, tpyH(5, 5″)], 7.15 (s, 2 H, ArH), 6.95 (s, 1 H, Ar), 3.58 (d, $^2J_{H,P}$ = 11.0 Hz, 4 H, $CH_2$), 0.90 (br. m, 6 H, $BH_3$) ppm. $^{13}$C NMR (75 MHz, $CDCl_3$): $\delta$ = 156.3, 155.9, 149.8, 149.0, 138.3, 137.2, 133.3, 132.9 (d, $^1J_{C,P}$ = 8.5 Hz, $C_{quat.}$, PAr), 131.7, 129.0 (d, $^2J_{C,P}$ = 9.2 Hz, PAr), 128.2, 128.0, 124.0, 121.7, 119.2, 34.2 (d, $^1J_{C,P}$ = 31.7 Hz, $CH_2$) ppm. $^{31}$P{$^1$H} NMR: $\delta$ = (121.4 MHz, $CDCl_3$): $\delta$ = 19.3 (br. m) ppm. $C_{35}H_{33}B_2N_3P$ (548.25): calcd. C 76.97, H 5.91, N 5.73, B 2.95, P 8.45; found C 76.78, H 6.10, N 5.59, B 3.01, P 8.50.

**4′-{$C_6H_3(CH_2PPh_2)_2$-3,5}-2,2′:6′,2″-terpyridine ([tpyPC(H)P], 7):** Freshly distilled $Et_2NH$ (5 mL) was added to a solution of **6** in $CH_2Cl_2$. The mixture was stirred at reflux for 4 h. All the volatiles were removed in vacuo, and the obtained white solid was redissolved in dry $CH_2Cl_2$ (10 mL). The organic layer was collected, washed with degassed water and brine and dried with $MgSO_4$. After evaporation of the $CH_2Cl_2$ in vacuo, product **7** was obtained as an extremely air- and moisture-sensitive white sticky solid. This product was used without further purification. Yield: 0.54 g, 88%. $^1$H NMR (300 MHz, $CDCl_3$): $\delta$ = 8.76 [d, $J_{H,H}$ = 3.0 Hz, 2 H, tpyH(6, 6″)], 8.75 [d, $J_{H,H}$ = 3.0 Hz, 2 H, tpyH(3, 3″)], 8.38 [s, 2 H, tpyH(3′, 5′)], 7.86 [td, $J_{H,H}$ = 7.5, 1.6 Hz, 2 H, tpyH(4, 4″)], 7.37 [m, 2 H, tpyH(5, 5″) and PAr], 7.18 (s, 2 H, ArH), 6.93 (s, 1 H, Ar), 3.39 (s, 4 H, $CH_2$) ppm. $^{13}$C NMR (75 MHz, $CDCl_3$): $\delta$ = 156.6, 155.9, 150.6, 149.2, 138.3, 138.2, 136.9, 133.2 (d, $^1J_{C,P}$ = 18.0 Hz, $C_{quat.}$, PAr), 131.2, 129.0, 128.6 (d, $^2J_{C,P}$ = 6.0 Hz, PAr), 126.4, 123.9, 121.6, 119.2, 36.2 (d, $^1J_{C,P}$ = 16.0 Hz, $CH_2$) ppm. $^{31}$P{$^1$H} NMR (121.4 MHz, $CDCl_3$): $\delta$ = –8.5 (s) ppm.

**[Fe(tpy){tpyPC(H)P}]$(PF_6)_2$ (9):** Ligand **7** (0.17 g, 0.25 mmol) and $[Fe(tpy)Cl_3]$ (0.095 g, 0.25 mmol) were heated at reflux in dry MeOH for 4 h. The yellow mixture rapidly turned purple upon heating. The solution was then cooled down to room temperature, filtered and excess $NH_4PF_6$ in degassed water was added. The formed deep purple precipitate was filtered off, washed with degassed water and dried in vacuo. Yield: 0.10 g, 40%. Removal of a small amount of a tpy-containing impurity by chromatography

 © 2007 Wiley-VCH Verlag GmbH & Co. KGaA, Weinheim 

could not be carried out because of the high sensitivity to air and moisture of the $PPh_2$ moieties. Complex **9** was used in the next reaction without further purification. $^1H$ NMR (300 MHz, $CD_3CN$): $\delta$ = 8.96 [d, $J_{H,H}$ = 7.8 Hz, 2 H, tpyA(3′, 5′)], 8.70 [t, $J_{H,H}$ = 8.1 Hz, 1 H, tpyA(4′)], 8.51 [d, $J_{H,H}$ = 8.4 Hz, 4 H, tpyA(3, 3′′) + tpyA(3, 3′′)], 7.98 [s, 2 H, tpyB(3′, 5′)], 7.91–7.86 [m, 4 H, tpyA(4, 4′′) + tpyA(4, 4′′)], 7.71 [d, $J_{HH}$ = 7.8 Hz, 2 H, tpyA(6, 6′′)], 7.61 [d, $J_{H,H}$ = 8.0 Hz, 2 H, tpyB(6, 6′′)], 7.43–7.39 (m, 12 H, *para*-H + *meta*-H PAr), 7.34–7.28 [m, 6 H, Ar + tpyA(5, 5′′) + tpyA(5, 5′′)], 7.09 (m, 9 H, Ar + *ortho*-H PAr), 2.7 (s, 4 H, $CH_2$) ppm. $^{31}P\{^1H\}$ NMR (121.4 MHz, $CD_3CN$): $\delta$ = –4.9 (s, 2 P), –143.28 (sept, $^1J_{P,F}$ = 705 Hz, $[PF_6]^-$) ppm. ESI-MS: *m/z* = 497.20 $[M - 2\ PF_6]^{2+}$.

**$[Fe(tpy)(tpyPCP)Ru(tpy)](PF_6)_3$ (11):** Compounds **8** (0.10 g, 0.08 mmol) and **9** (0.05 g, 0.08 mmol) were dissolved in THF/MeCN (2:1, 30 mL). The solution was stirred at reflux for 10 h. The solvent was evaporated in vacuo. The deep purple residue was washed several times with hexane until no more free bis(amino)-arene (NCN) ligand could be detected by $^1H$ NMR spectroscopy, and then dried in vacuo. The obtained deep purple solid (**10**), characterized only by NMR spectroscopy, was added to 2,2′:6′,2′′-terpyridine (0.02 g, 0.08 mmol) dissolved in dry MeOH (25 mL). The mixture was heated at reflux for 2 d. Subsequently, the methanolic solution was cooled to room temperature, filtered, and concentrated until a small residual amount remained. Addition of aqueous $NH_4PF_6$ resulted in the precipitation of **11** as an air-stable red–purple solid that was collected by filtration, washed with water, hexane and dried in vacuo. The crude product was purified by column chromatography on silica gel (MeCN/water/saturated $NaNO_3$ solution 70:25:5). The major fraction was dried to afford **11** as a red-purple solid. Yield: 0.07 g, 52%. $^1H$ NMR (300 MHz, $CD_3COCD_3$): $\delta$ = 9.07 [d, $J_{H,H}$ = 8.1 Hz, 2 H, tpyC(3′, 5′)], 8.86 [d, $J_{H,H}$ = 8.1 Hz, 2 H, tpyA(3′, 5′)], 8.82–8.70 [m, 3 H, tpyA(4′) + tpyC(3, 3′′)], 8.58 [t, $J_{H,H}$ = 8.5 Hz, 1 H, tpyC(4′)], 8.48 [d, $J_{H,H}$ = 8.1 Hz, 4 H, tpyA(3, 3′′) + tpyB(3, 3′′)], 8.09 [s, 2 H, tpyB(3′, 5′)], 8.06–8.00 [m, 8 H, Ar + tpyA(4, 4′′) + tpyB(4, 4′′) + tpyC(4, 4′′)], 7.69 [d, $J_{H,H}$ = 5.4 Hz, 2 H, tpyC(6, 6′′)], 7.42 [d, $J_{H,H}$ = 5.1 Hz, 4 H, tpyA(6, 6′′) + tpyA(6, 6′′)], 7.64–7.53 [m, 6 H, tpyA(5, 5′′) + tpyB(5, 5′′) + tpyC(5, 5′′)], 7.35–6.77 (m, 20 H, PAr) ppm. $^{31}P\{^1H\}$ NMR (121.4 MHz, $CD_3CN$): $\delta$ = 41.82 (s, 2 P), –142.92 (sept, $^1J_{P,F}$ = 705 Hz, $[PF_6]^-$) ppm. ESI-MS: *m/z* = 442.75 $[M - 3\ PF_6]^{3+}$, 736.67 $[M - 2\ PF_6]^{2+}$.

## Acknowledgments

This work was financially supported by the Council for Chemical Sciences of the Netherlands Organization of Scientific Research (CW-NWO).

[1] a) E. C. Constable in *Electronic Materials: The Oligomer Approach*, Wiley-VCH, Weinheim, **1998**; b) J.-P. Collin, P. Graviña, V. Heitz, J.-P. Sauvage, *Eur. J. Inorg. Chem.* **1998**, 1–14; c) E. A. Harriman, R. Ziessel, *Coord. Chem. Rev.* **1998**, *171*, 331–339; d) R.-A. Fallahpour, *Synthesis* **2003**, 155–184; e) H. Hofmeier, U. S. Schubert, *Coord. Chem. Rev.* **2004**, *33*, 373–399; f) R. T. F. Jukes, V. Adamo, F. Hartl, P. Belser, L. De Cola, *Coord. Chem. Rev.* **2005**, *249*, 1327–1335.

[2] a) E. C. Constable, A. M. W. Cargill Thompson, P. Harverson, L. Macko, M. Zehnder, *Chem. Eur. J.* **1995**, *1*, 360–367; b) S. Serroni, S. Campagna, F. Puntoriero, C. Di Pietro, N. D. McClenaghan, F. Loiseau, *Chem. Soc. Rev.* **2001**, *30*, 367–375.

[3] a) B. G. G. Lohmeijer, U. S. Schubert, *Angew. Chem. Int. Ed.* **2002**, *41*, 3825–3829; b) B. G. G. Lohmeijer, U. S. Schubert, *J. Polym. Sci., Part A: Polym. Chem.* **2003**, *41*, 1413–1427; c) H. Hofmeier, A. El-Ghayoury, A. P. H. J. Schenning, U. S. Schubert, *Chem. Commun.* **2004**, *3*, 318–319.

[4] V. W.-W. Yam, W. W. Lee, K. K. Cheung, *Organometallics* **1997**, *16*, 2833–2841.

[5] E. A. Medlycott, G. S. Hannan, *Chem. Soc. Rev.* **2005**, *34*, 133–142.

[6] M. Gagliardo, G. Rodríguez, H. H. Dam, M. Lutz, A. L. Spek, R. W. A. Havenith, P. Coppo, L. De Cola, F. Hartl, G. P. M. van Klink, G. van Koten, *Inorg. Chem.* **2006**, *45*, 2143–2155.

[7] a) B. R. Steele, K. Vrieze, *Transition Met. Chem.* **1977**, *2*, 140–144; b) D. M. Grove, G. van Koten, H. J. C. Ubbels, R. Zoet, A. L. Spek, *Organometallics* **1984**, *3*, 1003–1009; c) J. A. M. van Beek, G. van Koten, M. J. Ramp, N. C. Coenjaarts, D. M. Grove, K. Goublitz, M. C. Zoutberg, C. H. Stam, W. J. J. Smeets, A. L. Spek, *Inorg. Chem.* **1991**, *30*, 3059–3068; d) A. J. Canty, J. Patel, B. W. Skelton, A. H. White, *J. Organomet. Chem.* **2000**, *607*, 194–202; e) G. Rodríguez, M. Albrecht, J. Schoenmaker, A. Ford, M. Lutz, A. L. Spek, G. van Koten, *J. Am. Chem. Soc.* **2002**, *124*, 5127–5138.

[8] H. P. Dijkstra, P. Steenwinkel, D. M. Grove, M. Lutz, A. L. Spek, G. van Koten, *Angew. Chem. Int. Ed.* **1999**, *38*, 2186–2188.

[9] Representative examples of aryl pincer complexes applied as liquid crystalline materials, optical and electro-optical devices, sensors and catalysts: a) B. Donnio, D. W. Bruce in *Structure and Bonding* (*Liquid Crystals II*) (Ed.: D. M. P. Mingos), Springer, **1999**; b) M. Ghedini, G. Pucci, A. Crispini, I. Aiello, F. Barigelletti, A. Gessi, O. Francescangeli, *Appl. Organomet. Chem.* **1999**, *13*, 565–581; c) P. Espinet, E. Garcia-Orodea, J. A. Miguel, *Inorg. Chem.* **2000**, *39*, 3645–3651; d) L. Omnes, B. A. Timini, T. Gelbrich, M. B. Hursthouse, G. R. Luckhurst, D. W. Bruce, *Chem. Commun.* **2001**, 2248–2249; e) M. Albrecht, G. van Koten, *Angew. Chem. Int. Ed.* **2001**, *40*, 3750–3781; f) I. Aiello, D. Dattilo, M. Ghedini, A. Bruno, R. Termine, A. Golemme, *Adv. Mater.* **2002**, *14*, 1233–1236; g) M. Talarico, G. Barberio, D. Pucci, M. Ghedini, A. Golemme, *Adv. Mater.* **2003**, *15*, 1374–1377; h) M. E. van der Boom, D. Milstein, *Chem. Rev.* **2003**, *103*, 1759–1792; i) J. T. Singleton, *Tetrahedron* **2003**, *59*, 1837–1857; j) J. K. Szabó, *Synlett* **2006**, 811–824.

[10] a) C. Moulton, B. L. Shaw, *J. Chem. Soc., Dalton Trans.* **1976**, 1020–1024; b) F. Gorla, L. M. Venanzi, A. Albinati, *Organometallics* **1994**, *13*, 43–54; c) A. Weisman, M. Gozin, H.-B. Kraatz, D. Milstein, *Inorg. Chem.* **1996**, *35*, 1792–1797; d) G. Jia, H. M. Lee, I. D. Williams, *J. Organomet. Chem.* **1997**, *534*, 173–180; e) M. E. van der Boom, S.-Y. Liou, Y. Ben-David, L. J. W. Shimon, D. Milstein, *J. Am. Chem. Soc.* **1998**, *120*, 6531–6541; f) M. E. van der Boom, H.-B. Kraatz, L. Hassner, Y. Ben-David, D. Milstein, *Organometallics* **1999**, *18*, 3873–3884; g) P. Dani, M. Albrecht, G. P. M. van Klink, G. van Koten, *Organometallics* **2000**, *19*, 4468–4476; h) D. G. Gusev, M. Madott, F. M. Dolgushin, K. A. Lyssenko, M. Y. Antipin, *Organometallics* **2000**, *19*, 1734–1739; i) R. M. Gauvin, H. Rozenberg, L. J. W. Shimon, D. Milstein, *Organometallics* **2001**, *20*, 1719–1724; j) M. W. Haenel, S. Oevers, K. Angermund, W. C. Kaska, H.-J. Fan, M. B. Hall, *Angew. Chem. Int. Ed.* **2001**, *40*, 3596–3600; k) D. Morales-Morales, R. E. Cramer, C. M. Jensen, *J. Organomet. Chem.* **2002**, *654*, 44–50.

[11] a) P. Steenwinkel, S. L. James, D. M. Grove, N. Veldman, A. L. Spek, G. van Koten, *Chem. Eur. J.* **1996**, *2*, 1440–1445; b) A. Pape, M. Lutz, G. Müller, *Angew. Chem.* **1994**, *106*, 2375–2377; c) P. Steenwinkel, H. Kooijman, W. J. J. Smeets, A. L. Spek, D. M. Grove, G. van Koten, *Organometallics* **1998**, *17*, 5411–5426; d) M. Mehring, M. Schürmann, K. Jurkschat, *Organometallics* **1998**, *17*, 1227–1236; e) M. Albrecht, B. M. Kocks, A. L. Spek, G. van Koten, *J. Organomet. Chem.* **2001**, *624*, 271–286; f) H. P. Dijkstra, M. Q. Slagt, A. McDonald, C. A. Kruithof, R. Kreiter, A. M. Mills, M. Lutz, A. L. Spek, W. Klopper, G. P. M. van Klink, G. van Koten, *Eur. J. Inorg. Chem.* **2003**, 830–838.

 © 2007 Wiley-VCH Verlag GmbH & Co. KGaA, Weinheim 

[12] a) P. Dani, T. Karlen, R. A. Gossage, W. J. J. Smeets, A. L. Spek, G. van Koten, *J. Am. Chem. Soc.* **1997**, *119*, 11317–11318; b) M. Albrecht, P. Dani, M. Lutz, A. L. Spek, G. van Koten, *J. Am. Chem. Soc.* **2000**, *122*, 11822–11833.
[13] a) E. C. Constable, G. Baum, E. Bill, R. Dyson, R. van Eldik, D. Fenske, S. Kaderli, D. Morris, A. Neubrand, M. Neuburger, D. R. Smith, K. Wieghardt, M. Zehnder, A. D. Zuberbühler, *Chem. Eur. J.* **1999**, *5*, 498–508; b) P. S. Braterman, J.-L. Song, R. D. Peacock, *Inorg. Chem.* **1992**, *31*, 555–559; c) X. Zhou, A.-M. Ren, J.-K. Feng, *J. Organomet. Chem.* **2005**, *690*, 338–347.
[14] M. Gagliardo, H. P. Dijkstra, P. Coppo, L. De Cola, M. Lutz, A. L. Spek, G. P. M. van Klink, G. van Koten, *Organometallics* **2004**, *23*, 5833–5840.
[15] H. P. Dijkstra, M. D. Meijer, J. Patel, R. Kreiter, G. P. M. van Klink, M. Lutz, A. L. Spek, A. J. Canty, G. van Koten, *Organometallics* **2001**, *20*, 3159–3168.
[16] a) J. K. Stille, *Pure Appl. Chem.* **1985**, *57*, 1171–1780; b) M. Heller, U. S. Schubert, *J. Org. Chem.* **2002**, *67*, 8269–8272.
[17] K. T. Potts, D. Konwar, *J. Org. Chem.* **1991**, *56*, 4815–4816.
[18] K.-H. Duchêne, F. Vögtle, *Synthesis* **1986**, 659–661.
[19] a) E. C. Constable, C. E. Housecroft, M. Neuburger, A. G. Schneider, M. Zehnder, *J. Chem. Soc., Dalton Trans.* **1997**, 2427–2434; b) E. C. Constable, C. E. Housecroft, A. G. Schneider, *J. Organomet. Chem.* **1999**, *573*, 101–108; c) E. C. Constable, C. E. Housecroft, M. Neuburger, A. G. Schneider, B. Springler, M. Zehnder, *Inorg. Chim. Acta* **2000**, *300–302*, 49–55.
[20] H. P. Dijkstra, M. Albrecht, G. van Koten, *Chem. Commun.* **2002**, 126–127.
[21] J.-P. Sutter, S. L. James, P. Steenwinkel, T. Karlen, D. M. Grove, N. Veldman, W. J. J. Smeets, A. L. Spek, G. van Koten, *Organometallics* **1996**, *15*, 941–948.
[22] D. J. Hathcock, K. Stone, J. Madden, S. J. Slattery, *Inorg. Chim. Acta* **1998**, *282*, 131–135.
[23] J.-P. Sauvage, J.-P. Collin, J.-C. Chambron, S. Guillerez, C. Coudret, V. Balzani, F. Barigelletti, L. De Cola, L. Flamigni, *Chem. Rev.* **1994**, *94*, 993–1019.
[24] a) P. Lainé, F. Bedioui, P. Ochsenbein, V. Marvaud, M. Bonin, E. Amouyal, *J. Am. Chem. Soc.* **2002**, *124*, 1364–1377.
[25] a) M. Krejčík, M. Daněk, M. F. Hartl, *J. Electroanal. Chem. Interfacial Electrochem.* **1991**, *317*, 179–187; b) F. Hartl, H. Luyten, H. A. Nieuwenhuis, G. C. Schoemaker, *Appl. Spectrosc.* **1994**, *48*, 1522–1528.
[26] S. Barlow, D. O'Hare, *Chem. Rev.* **1997**, *97*, 637–669.
[27] V. V. Pavlishchuk, A. W. Addison, *Inorg. Chim. Acta* **2002**, *298*, 97–102.
[28] G. Gritzner, J. Kůta, *Pure Appl. Chem.* **1984**, *56*, 461–466.

Received: October 2, 2006
Published Online: February 14, 2007

 © 2007 Wiley-VCH Verlag GmbH & Co. KGaA, Weinheim 

DOI: 10.1002/ejic.200600772

# Catechol-Bearing Dipyrazinylpyridine Complexes of Ruthenium(II)

**Fahad A. Al-mutlaq,[a] Pierre G. Potvin,*[a] Athanassios I. Philippopoulos,[b] and Polycarpos Falaras[b]**

**Keywords:** Ruthenium / Tridentate ligands / Photosensitizers / Electron transfer / Energy conversion

The new tridentate ligand 4-(3,4-methylenedioxyphenyl)-2,6-dipyrazinylpyridine (**2**) was prepared in good yield in a one-pot reaction. The $Ru^{II}$ complexes $[Ru(\mathbf{2})_2](PF_6)_2$ and $[Ru(\mathbf{1})(\mathbf{2})](PF_6)_2$ [**1** is 2,6-dipyrazinyl-4-(4-tolyl)pyridine] were prepared in good yields and tested as photosensitizers against $[Ru(\mathbf{1})_2](PF_6)_2$ and $[Ru(ttpy)_2](PF_6)_2$ [ttpy is 4′-(4-tolyl)-2,2′:6′,2′′-terpyridine]. The photosensitization ability follows the order $[Ru(\mathbf{1})_2](PF_6)_2 > [Ru(\mathbf{1})(\mathbf{2})](PF_6)_2 > [Ru(\mathbf{2})_2](PF_6)_2 >> [Ru(ttpy)_2](PF_6)_2$, which is explainable in terms of mechanism and driving force. Hydrolysis of the methylene acetal function affords the catechol-appended complexes $[Ru(\mathbf{3})_2](PF_6)_2$ and $[Ru(\mathbf{1})(\mathbf{3})](PF_6)_2$ [**3** is 4-(3,4-dihydroxyphenyl)-2,6-dipyrazinylpyridine] in excellent yields. These insoluble, paramagnetic precipitates when tested as photosensitizers in homogeneous solution and in one case adsorbed on titania are able to generate photocurrents in a photovoltaic cell, albeit more weakly compared to the so-called N719 dye.
(© Wiley-VCH Verlag GmbH & Co. KGaA, 69451 Weinheim, Germany, 2007)

## Introduction

$Ru^{II}$ complexes of polypyridine-type ligands continue to enjoy great interest as photosensitizers,[1,2] owing to strong absorption of visible light, favourable redox potentials, appreciable excited state lifetimes and the ability of the excited states to transfer an electron to acceptor molecules or electrodes.[3–5] We have a long-standing interest in discovering non-stereogenic ligands that promote these properties. The present work arises from a desire to incorporate three promising phenomena into the design of a new ligand.

Firstly, we devised sometime ago a new tridentate ligand family with promising features. The first member of the dipyrazinylpyridine (dpp) family of ligands, the 4-*p*-tolyl derivative **1** (Scheme 1), was prepared in a remarkable one-step reaction of commercial materials, in excellent yield and without purification.[6] We have since used this procedure to prepare other dpp examples,[7–9] and extended it to terpyridine synthesis, although those reactions were slower.[9,10] Besides their easier syntheses, the homoleptic $Ru^{II}$ complex $[Ru(\mathbf{1})_2]^{2+}$ revealed an additional advantage of dpp ligands over other tridentates: a longer excited-state lifetime, $\tau$ (18 ns at room temperature),[6] compared to that of the analogous terpyridine complex $[Ru(ttpy)_2]^{2+}$ [0.95 ns,[11] ttpy is 4′-(4-tolyl)-2,2′:6′,2′′-terpyridine], a result which can be attributed to the electron-withdrawing effect of the additional nitrogen atoms in stabilizing the ligand π* orbital relative to metal-centred orbitals. At the same time, its absorption (498 nm) and emission (667 nm) were only of slightly lower energy (cf. 490 nm[12] and 640 nm,[11] respectively, for the ttpy analogue), and the shift is the direction favouring the more efficient harvesting of visible light. The $Ru^{III/II}$ oxidation potential was comparatively very high (1.62 V vs. SCE; cf. 1.25 V[13] for the ttpy analogue), again because of the additional nitrogens. This enabled the operation of an electrostatically advantaged reductive quenching mechanism in photosensitization experiments using other dpp complexes.[9]

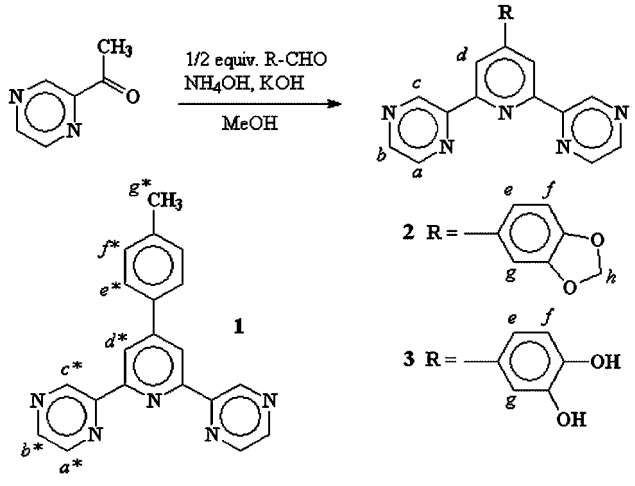


Scheme 1.

Secondly, we recently demonstrated the significant benefit conferred by peripheral carboxylate groups in establishing a binding site for a cationic electron acceptor during oxidative quenching in organic solvents.[14] We wished to

[a] Department of Chemistry, York University, Toronto, ON, Canada M3J 1P3
E-mail: pgpotvin@yorku.ca
[b] Institute of Physical Chemistry, NCSR "Demokritos", Aghia Paraskevi, 15310 Attiki, Greece

 © 2007 Wiley-VCH Verlag GmbH & Co. KGaA, Weinheim 

gauge the extent of this benefit during reductive quenching with dpp complexes, and to explore the utility of peripheral catecholate groups in supramolecularly binding an electron acceptor.

Thirdly, we knew that catechols form relatively stable complexes with $Ti^{IV}$.[15–17] As mesoporous $TiO_2$ is the anchoring substrate for carboxylated $Ru^{II}$ sensitizers on nanocrystalline solar cells,[3] we reasoned that catechol groups would enable stronger, more covalent anchoring to the surface. Indeed, catechol is known to chemisorb to particulate $TiO_2$[18,19] and Rice et al. have indeed found stronger and faster grafting with catechol-bearing terpyridine complexes on $TiO_2$-coated electrodes.[20]

Therefore, this paper reports the preparation of a ligand with a dpp core and a peripheral catechol group, the synthesis of its $Ru^{II}$ complexes in both homo- and heteroleptic forms, and an assessment of the photosensitization ability of its $Ru^{II}$ complexes both in solution and while attached to an electrode surface in a photovoltaic cell.

## Results

### Synthesis

As with the terpyridine analogues,[21] the catechol function was introduced in protected form and deprotected after binding to the metal, this time using the methylene acetal for a less harsh deprotection. As shown in Scheme 1, methylenedioxy ligand **2** was prepared from commercial materials (piperonal, acetylpyrazine and ammonia) in a remarkable one-pot reaction from which it precipitated in good yield (75%, after recrystallization). This compares very favourably with the two-step preparation of the (dimethoxyphenyl)terpyridine analogue in 21–36% overall yield.[21]

The complex $[Ru(\mathbf{2})_2]^{2+}$ was prepared by three procedures with varying results. The direct reaction of $RuCl_3$ with two equiv. of **2** in hot ethylene glycol, followed by isolation of the product by precipitation as the $PF_6^-$ salt using aqueous $NH_4PF_6$, proceeded in 55–65% yields, but the product contained unacceptable amounts of unidentified impurities. If, instead, the intermediate $Ru(\mathbf{2})Cl_3$ was first prepared in $CH_3CN$ from one equiv. of **2** and $RuCl_3$, then treated with 3 equiv. of $AgBF_4$ to precipitate AgCl and activate the $Ru^{III}$ centre for substitution with a second equiv. of **2** in ethylene glycol, the final $[Ru(\mathbf{2})_2](PF_6)_2$ product was isolated in better yields (65–75%) with less impurity, even though this three-step procedure was more tedious. In a shortened variant, $RuCl_3$ was activated in $CH_3CN$ with 3 equiv. of $AgBF_4$ before reaction with two equiv. of **2** in ethylene glycol, followed by treatment with $NH_4PF_6$, for a final yield of 75–85% of the purest product yet.

The mixed-ligand species $[Ru(\mathbf{1})(\mathbf{2})]^{2+}$ was also prepared with and without $Ag^+$ activation.

The $Ru(\mathbf{2})Cl_3$ intermediate was prepared as before, then treated with **1** in ethylene glycol to afford, after the usual work-up, $[Ru(\mathbf{1})(\mathbf{2})](PF_6)_2$ in 45–50% yields, but this product of direct reaction was even less pure than in the homoleptic case. Treatment of $Ru(\mathbf{2})Cl_3$ with 3 equiv. of $AgBF_4$ in ethylene glycol, followed by reaction with one equiv. of **1** in the same solvent and precipitation of the $PF_6^-$ salt, produced $[Ru(\mathbf{1})(\mathbf{2})](PF_6)_2$ in purer form and in better yields (65–70%).

Deprotection of the acetal function proved to be incomplete and slow with plain aqueous acid. Heating with HBr in HOAc afforded complete deprotection in 3–4 d, and proceeded in very high yields (90–95% for $[Ru(\mathbf{3})_2](PF_6)_2$ and 85–90% for $[Ru(\mathbf{1})(\mathbf{3})](PF_6)_2$, after anion exchange with $NH_4PF_6$).

Despite repeated crystal growth attempts with the four new complexes, only microcrystals or powders were obtained. Upon prolonged standing in $CH_3CN$ solutions, the deprotected salts tended to lose the elements of $HPF_6$ and form amorphous precipitates that resisted redissolution with heat, but these were easily rescued by redissolving with a small excess of 60% aqueous $HPF_6$, then diluting with water to re-precipitate the original salts.

### Proofs of Identity

$^1H$ NMR spectroscopy was able to verify the identities of the new complexes. While three aromatic signals in free **2** were fortuitously overlapped, they were well separated in the complexes of **2** and **3**. COSY spectra were used in the assignments but, in the heteroleptic cases, many of the signals from one ligand were unfortunately overlapped with the corresponding signals from the other ligand, making individual assignments impossible.

The coordinating nitrogen atoms of heteroaromatic bi- and tridentate ligands are actually in *anti* conformations to minimize dipole–dipole repulsions.[22] Complexation causes a change to *syn* binding conformations and, commonly, the signals adjoining the coordinated nitrogen atoms on the end rings are shifted upfield owing to magnetic anisotropy from the ring current of the perpendicular ligand, while other signals are shifted downfield due to the electron-withdrawing effect of the metal ion. In the present case, the fine doublets due to 5-H and 6-H of the pyrazine rings (which often appeared as broad singlets) were shifted upfield (by 0.8 and 0.3 ppm, respectively) upon complexation, and remained so upon deprotection. However, deprotection predictably caused the disappearance of the distinctive methylene singlets at 6.1–6.2 ppm.

Mass spectrometry confirmed the complex formulations. ES-MS of $[Ru(\mathbf{2})_2]^{2+}$ showed two high-mass clusters, one at *m*/*z* 406 corresponding to the dicationic molecular ion, and a smaller one at *m*/*z* 400 due to partial hydrolysis of the protecting group. With $[Ru(\mathbf{1})(\mathbf{2})]^{2+}$, there was a similar pair of clusters at *m*/*z* 391 and 385. LDI-TOF was used with the deprotected complexes, and both $[Ru(\mathbf{3})_2]^{2+}$ and $[Ru(\mathbf{1})(\mathbf{3})]^{2+}$ showed monocationic molecular ions at *m*/*z* 788 and 769, respectively. While this was the base peak in the former case, a fragment ion dominated the spectrum of the latter (at M-17). In all cases, the mass distributions within each cluster of peaks owing to isotopic diversity was well matched by computed spectra.

 © 2007 Wiley-VCH Verlag GmbH & Co. KGaA, Weinheim 

Finally, the formulae of all of the new materials were also confirmed by elemental analyses.

### UV/Vis Spectroscopy

The UV/Vis spectrum of free **2** showed only n→π* and π→π* transitions in the 200–300 nm range, as is usual with polypyridine-type ligands, but with extended tailing into the visible region. In addition to this same sort of transition, all four complexes showed a similar metal-to-ligand charge transfer (MLCT) band at $\lambda_{max}$ 500–502 nm (Table 1), as well as a much smaller feature near 405 nm. The MLCT bands were typical of complexes of this type and virtually the same as that of the analogous $[Ru(\mathbf{1})_2]^{2+}$.[6] The influence of the oxygen functionalities is apparently weak, shifting the peak positions only slightly toward the red, in agreement with their π-donating character. The only significant difference between them was that the catechol forms were more strongly absorbing than were the protected forms, with a molar extinction coefficient ($\varepsilon$) value 37% larger with one catechol unit, and 53% larger with two. The terpyridine analogues[21] behaved differently in that deprotection to the catechol forms caused 8 nm red shifts in $\lambda_{max}$ and much larger increases in $\varepsilon$ (by 133% and 57% for homo- and heteroleptic varieties, respectively) than with our complexes.

We also explored the effect of deprotonation of the catechol units on the MLCT transitions, using sample solutions of the two deprotected complexes prepared at various [$Et_3N$]:[Ru] ratios in $CH_3CN$. The effect was mild: the red color of the pure complexes changed to a light brown, as the MLCT $\lambda_{max}$ drifted slightly with $[Ru(\mathbf{3})_2]^{2+}$ (from 502 to 506 nm with 0–6 equiv. of $Et_3N$) but held steady at 500 nm with $[Ru(\mathbf{1})(\mathbf{3})]^{2+}$ (with 0–4 equiv. of base), while the band tails lengthened toward the red and the $\varepsilon$ values at $\lambda_{max}$ decreased gently in lock-step with increasing [$Et_3N$]:[Ru].

### Cyclic Voltammetry

Cyclic voltammograms were obtained for all four complexes in degassed $CH_3CN$ and DMF (Figure 1 is representative). Oxidation was only detected in $CH_3CN$ but was irreversible in all cases. Limited-range scans did not improve the reversibility. Some of the features in the negative range appeared only after first scanning positive, so were probably reductions of oxidation products having undergone subsequent chemical transformations. Therefore DPV scans were employed to help determine $E_{1/2}$ values. Except for more positive potentials owing to the electron-poorer pyrazine rings, the results (Table 1) mimicked the behaviour

Table 1. Spectroscopic, electrochemical and photochemical data in $CH_3CN$ solutions.

| Complex | $\lambda_{max}$, nm [$\varepsilon$, $10^4$ M$^{-1}$ cm$^{-1}$] | $E_{1/2}(Ru^{III/II})$[a] V vs. SCE | $E_{1/2}(L^{+/0})$ V vs. SCE | $E_{1/2}(L^{0/-})$ V vs. SCE | $k_f$ $10^{-5}$ s$^{-1}$ |
|---|---|---|---|---|---|
| $[Ru(\mathbf{2})_2]^{2+}$ | 502 (1.65) | 1.56 | 1.85 | –0.86 | 4.68(6) |
| $[Ru(\mathbf{1})(\mathbf{2})]^{2+}$ | 500 (1.53) | 1.60 | 1.70 | –0.77 | 4.82(5) |
| $[Ru(\mathbf{3})_2]^{2+}$ | 502 (2.52) | (1.80) | 1.34 | –0.80 | – |
| $[Ru(\mathbf{1})(\mathbf{3})]^{2+}$ | 500 (2.09) | 1.65 | – | –0.85 | – |
| $[Ru(\mathbf{1})_2]^{2+}$ [6] | 498 (1.66) | 1.62 | – | –0.85 | 8.9(5)[b] |
| $[Ru(ttpy)_2]^{2+}$ | 490 (1.55)[12] | 1.25[13] | – | –1.24[13] | 0.936(4)[23] |

[a] In parentheses, $E_{pa}$. [b] This work.

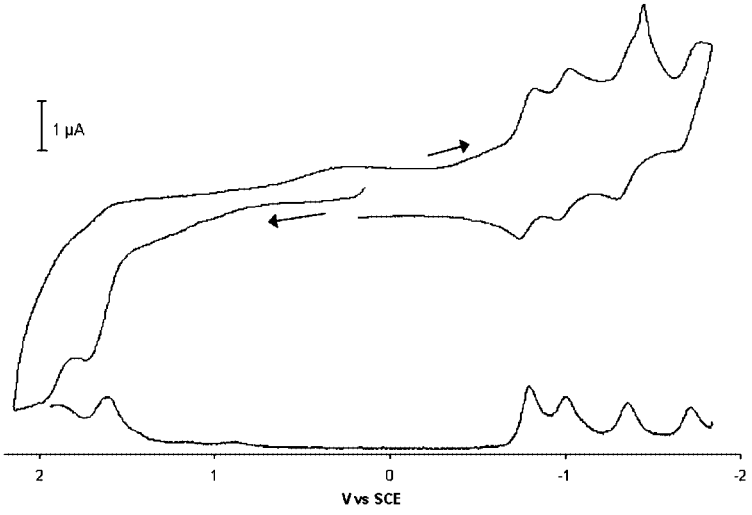


Figure 1. Cyclic voltammogram (upper plot) and differential pulse voltammogram (DPV, lower plot) of $[Ru(\mathbf{1})_2](PF_6)_2$ in $CH_3CN$ containing 0.1 M $Bu_4NPF_6$.

 © 2007 Wiley-VCH Verlag GmbH & Co. KGaA, Weinheim 

of the terpyridine analogues,[21] in that metal oxidation was followed by a more positive ligand oxidation when in protected form, and a less positive one after deprotection to catechol forms. Both metal oxidation and first ligand reduction potentials occurred near those previously measured for the dpp complex $[Ru(\mathbf{1})_2]^{2+}$ lacking a catechol unit,[6] and up to three further reduction waves occurred at 100–340 mV intervals.

### Photosensitization

Samples of all four new complexes were submitted to the assessment protocol[23] that we have used several times to gauge photosensitizer ability[9,12,14,24,25] by monitoring the rate of accumulation of the methyl viologen cation radical ($MV^{\cdot+}$) arising by electron transfer from the photo-excited state to methyl viologen ($MV^{2+}$) in the presence of a sacrificial reductant, triethanolamine (TEOA), which is used to reduce the $Ru^{III}$ photoproduct back to the starting $Ru^{II}$ state. When a mixture of $[Ru(\mathbf{3})_2]^{2+}$, $MV(PF_6)_2$ and TEOA in $CH_3CN$ was irradiated at 400–600 nm, the Ru complex quantitatively formed a dark precipitate and very little $MV^{\cdot+}$ accumulated in the supernatant, as judged by the absorption spectrum. This precipitation recurred with repeated trials. The precipitate was isolated by filtration, but the material was insoluble in most solvents, including $CH_3CN$ and DMF. It was soluble in TFA, but it was NMR-silent in [D]TFA, suggesting that it was paramagnetic. Its LDI-TOF mass spectrum was very noisy and generally uninformative, showing very few peaks and these were not attributable to any reasonable formulation. No further characterization was carried out, but control experiments revealed that the three chemical components, the $Ru^{II}$ complex, $MV^{2+}$ and TEOA, were all required to produce the precipitation. We also found that no precipitation occurred in the dark; light – even sunlight through a window – was required. This precipitation behaviour was also noted with $[Ru(\mathbf{1})(\mathbf{3})]^{2+}$, but we did not carry out control experiments in that case.

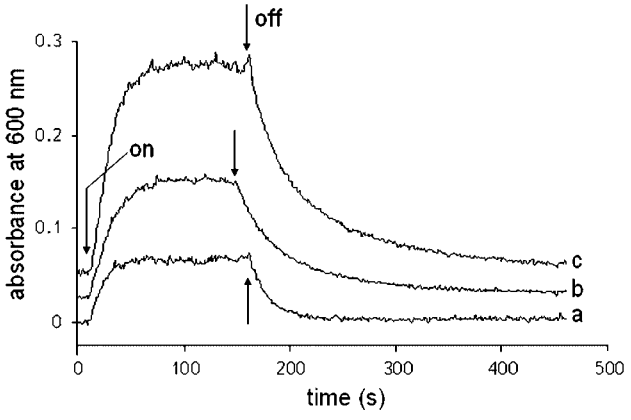


Figure 2. Plots of absorbance at 600 nm over time for (a) $[Ru(\mathbf{3})_2]^{2+}$, (b) $[Ru(\mathbf{1})(\mathbf{3})]^{2+}$, offset by 0.025 absorbance units, and (c) $[Ru(\mathbf{1})_2]^{2+}$, offset by 0.05 absorbance units. Arrows indicate the start and end of irradiation.

In contrast, the protected forms, $[Ru(\mathbf{2})_2]^{2+}$and $[Ru(\mathbf{1})(\mathbf{2})]^{2+}$, behaved normally, showing the same pattern as had been seen with other sensitizers (Figure 2): a rapid, steady rise in absorbance at 600 nm owing to $MV^{\cdot+}$, followed by a levelling off and, after turning off the light, a slow aerobic decay back to the starting absorbance. For comparison, $[Ru(\mathbf{1})_2]^{2+}$ was assessed in the same manner. The data were treated as before,[23] and the first-order rate constants $k_f$ for $MV^{\cdot+}$ accumulation are reported in Table 1. These clearly show that all three species were significantly better sensitizers than was the terpyridine complex $[Ru(ttpy)_2]^{2+}$, and that $[Ru(\mathbf{1})_2]^{2+}$ was a better sensitizer than the catechol-containing species.

### Photovoltaic Performance

A photovoltaic cell was assembled for each of the two catechol-bearing complexes. The sensitizer was adsorbed from a $CH_3CN$ solution onto a titania-coated conductive glass plate. A solid-state electrolyte film was sandwiched between this and a platinized counter-electrode. The current and potential between the electrodes were monitored while the assembly was irradiated using a "standard" light source approximating the sun's spectrum and density (per unit area) at the Earth's surface. Another assembly was similarly prepared using the so-called N719 dye, the bis(tetrabutylammonium) salt of *cis*-bis(2,2′-bipyridyl-4,4′-dicarboxylic acid)bis(thiocyanato)ruthenium(II), to serve as a comparison. The results are presented in Table 2 in terms of the four quantities of importance for solar cells: the open-circuit potential $V_{oc}$, the short-circuit current density $I_{sc}$, the "fill factor" (*FF*), which is the maximum or peak power ($V \times I$) divided by $V_{oc}$ and by $I_{sc}$, and the photon-to-electron conversion efficiency $\eta$.

Table 2. Photovoltaic characteristics.

| Sensitizer | $I_{sc}$ [mA cm$^{-2}$] | $V_{oc}$ [mV] | *FF* | $\eta$ [%] |
|---|---|---|---|---|
| $[Ru(\mathbf{3})_2]^{2+}$ | 0.297 | 337 | 0.52 | 0.05 |
| $[Ru(\mathbf{1})(\mathbf{3})]^{2+}$ | 1.006 | 348 | 0.52 | 0.19 |
| N719 | 9.29 | 583 | 0.53 | 2.87 |

Gratifyingly, the new catechol dyes both were able to generate a current when irradiated under these conditions. However, they showed significantly lower efficiencies ($\eta$) than the well studied N719 dye, which generated a stronger $V_{oc}$ and a much larger $I_{sc}$ under the same conditions, while *FF* was virtually the same for all three sensitizers. Interestingly, it appears that the asymmetric catechol complex is about four times more efficient than the symmetrical bis(catechol) one, in spite of the latter's ability to absorb more light (higher $\varepsilon$). Two catechol-bearing terpyridine complexes have previously been tested in photovoltaic cells, with moderately good results.[20] The cell constitution was different in that a liquid electrolyte was used, and the results are not directly comparable to ours, but the $\eta$ values were also

 © 2007 Wiley-VCH Verlag GmbH & Co. KGaA, Weinheim 

significantly lower than for carboxylated sensitizers like the N719 dye, in spite of the determination that the surface grafting was superior and faster with catechol than with carboxylate groups.

## Discussion

The weak base-dependence of the position and intensity of the MLCT absorption of the two catechol-bearing complexes, and the similarity in the $E_{1/2}(Ru^{II/I})$ values of all dpp complexes is consistent with the LUMO in dpp complexes being centred over a pyrazine ring. This is reasonable, since pyrazine rings are the most electron-poor and are π-disconnected from each other and from the 4-substituent on the central pyridine ring. Moreover, pyrazine rings on the less π-rich ligand **1** are expected to be of lower energy than those of the oxygenated **2** or **3**. In contrast, the LUMO of a tpy ligand is likely centred over the central pyridine ring, more strongly influenced, therefore, by a 4′-substituent on that ring, as demonstrated by the MLCT absorptions of the tpy analogues.[21]

According to its very positive $E_{1/2}(Ru^{III/II})$ value, $[Ru(\mathbf{1})_2]^{2+}$ can undergo reductive quenching, and the other dpp complexes should also have been capable of reductive quenching. However, they would not benefit from the same driving force. In comparison with the *p*-tolyl groups in $[Ru(\mathbf{1})_2]^{2+}$, the methylenedioxy group in **2** is much more strongly electron-donating in character. Since electron-donating substituents destabilize the metal-centered orbitals to a greater degree than they destabilize the pyrazine-centered LUMO, and especially since the electron-donating substituents are π-disconnected from the pyrazines, $E(Ru^{III/II})$ should be much more affected than $E(Ru^{II/I})$ and shifted to less positive values. Consequently, both absorption and emission (and $E_{00}$) will shift to lower energies, as the gaps between the ground state and $^1$MLCT or $^3$MLCT states become narrower as a result. Since both $E(Ru^{III/II})$ and $E_{00}$ will be depressed by the same HOMO destabilization, $E(Ru^{III/II*}) = E(Ru^{III/II}) - E_{00}$ will be little changed and oxidative quenching will remain impossible. However, $E(Ru^{II*/I}) = E_{00} + E(Ru^{II/I})$ will decrease. While this decrease may not be sufficient to prevent reductive quenching from occurring, it will certainly reduce the driving force for the initial reaction of the excited state with TEOA. According to Marcus–Hush theory, that driving force determines the rate of the electron transfer reaction.[26] This then explains the stronger photosensitization in the order $[Ru(\mathbf{1})_2]^{2+} > [Ru(\mathbf{1})(\mathbf{2})]^{2+} > [Ru(\mathbf{2})_2]^{2+}$.

Yet all three dpp complexes were better than $[Ru(ttpy)_2]^{2+}$. We can identify two reasons for this. Firstly, we can expect enhanced steady-state concentrations of the excited states with dpp sensitizers, owing to three factors: the absorption bands are more centred in the 400–600 nm irradiation window, there is increased light absorption (higher ε values) and, because $[Ru(\mathbf{1})_2]^{2+}$ was previously found to have a higher τ value than had $[Ru(ttpy)_2]^{2+}$, as mentioned earlier, it is reasonable to expect similarly higher values for the other dpp complexes. Secondly, and perhaps most importantly, the dpp-containing complexes are expected to follow a reductive quenching mechanism while $[Ru(ttpy)_2]^{2+}$ can only undergo oxidative quenching. As the crucial step involves a reaction of the excited state with the neutral TEOA in reductive quenching, or with the dicationic $MV^{2+}$ during oxidative quenching, reductive quenching is electrostatically advantaged.

In light of this, we can postulate a reason for precipitate formation during irradiation of the complexes of **3**. With the additional nitrogens present, catechol oxidation would have occurred at a slightly more positive potential with these than that measured for the *tpy* analogues (1.21 V vs. SCE),[21] but this would probably still remain below $E(Ru^{III/II})$ (as exemplified by the *p*-tolyl case). However, under the basic conditions provided by TEOA, the catechol groups had probably ionized – even more likely because of the additional nitrogens – since this would have served to balance the metal charge and would have constituted a binding site for $MV^{2+}$. The catecholate oxidation would then have occurred at a less positive potential. It is therefore probable that catecholate groups served as internal quenchers of the excited states of our deprotected complexes. This is illustrated in Scheme 2, where a possible mechanism for precipitate formation is compared to "normal" photo-catalytic cycles. Just as with other $Ru^{II}$ complexes of this type, the $^3$MLCT excited state **B** can undergo "normal" non-radiative decay (path *a*). In our case, it can also undergo non-radiative decay from an internally quenched state **D** (path *b*), or "normal" reductive quenching by TEOA to **C** followed by electron transfer to $MV^{2+}$ and regenerating the ground state **A** (path *c*). Alternatively, the internally quenched state **D** can feasibly be reduced by TEOA to **C** in an "abnormal" reductive quenching (path *d*), or oxidized by $MV^{2+}$ (path *e*) in "abnormal" oxidative quenching to produce a radical product **E**. But $E(TEOA^{\cdot+/0})$ is 0.81 V vs. SCE,[27] i.e. below the catechol oxidation potential. Hence, as depicted, **D** should have been able to oxidize TEOA and path *d* should have been followed. At the same time, oxidative quenching of **D** (path *e*) might also have occurred and the cation radical product **E** should have been reduced by TEOA to regenerate **A** (path *f*). In both cases, $MV^{\cdot+}$ would have accumulated and no insoluble paramagnetic species should have formed by path *g*.

With TEOA acting as a base instead, catecholates would result. If their lower oxidation potentials indeed lie below $E(TEOA^{\cdot+/0})$, then paths *d* and *f* would be obviated and **E** would accumulate by path *e*. (The amount of $MV^{\cdot+}$ so formed could not have exceeded the amount of Ru complex initially present; it would have been too small to observe and would have quickly decayed aerobically.) The fates of the resulting radicals **E** are unknown, but deprotonation (by TEOA) and dimerization by phenolic coupling are likely outcomes, eventually resulting in the paramagnetic precipitates that were observed.

There are several possible reasons for the better photovoltaic behaviour of the N719 dye. Its MLCT band at 534 nm extends well beyond 700 nm,[28] although the ε

 © 2007 Wiley-VCH Verlag GmbH & Co. KGaA, Weinheim 

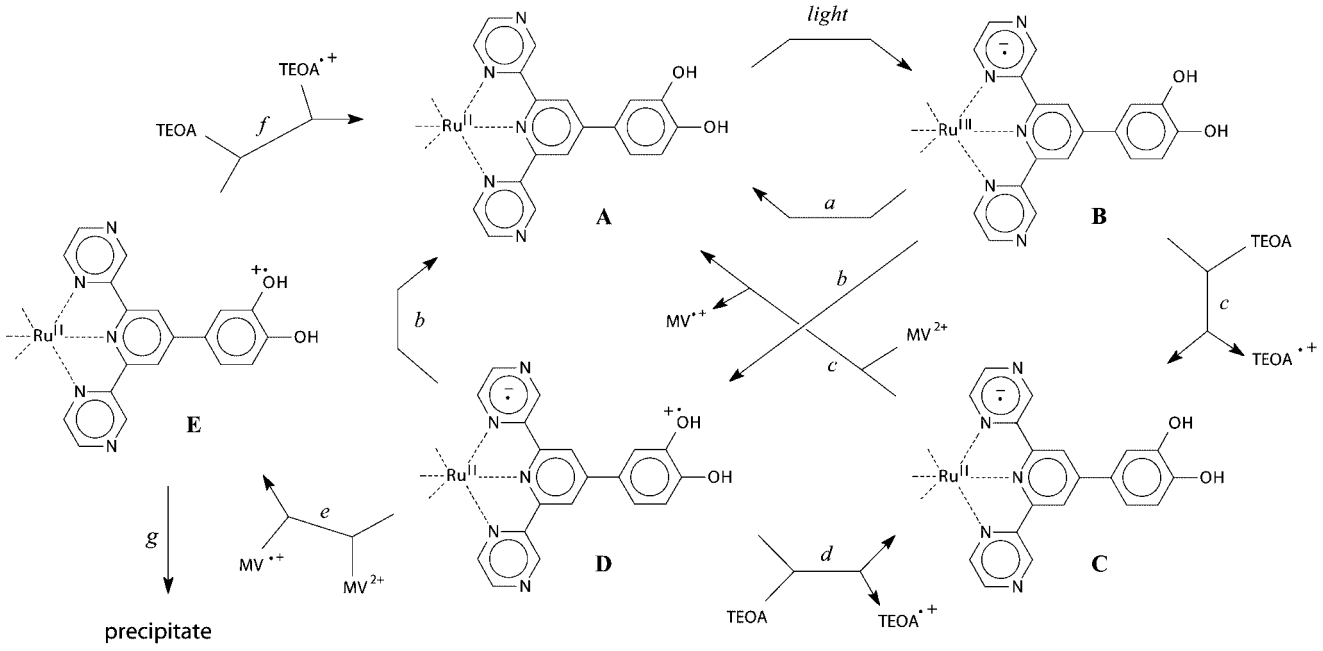


Scheme 2.

value at $\lambda_{max}$ is actually a little weaker ($1.42 \times 10^4$ M$^{-1}$ cm$^{-1}$) than with our materials. Its $\tau$ value (50 ns)[28] is also larger than that of $[Ru(\mathbf{1})_2]^{2+}$. Photovoltaic sensitizers normally have $E(Ru^{III/II})$ well below 1 V vs. SCE (0.85 V for N719 itself,[28] 0.61 V[29] for $[Ru(tpy)(SCN)_3]^0$), much less positive than in dpp complexes, so that the driving force for electron injection is much weaker with dpp complexes. Internal quenching by catechol groups could short-circuit the photoconduction process by constituting a second, "abnormal", non-radiative decay path (path *b* in Scheme 2) for the excited state, and thereby decrease the solar conversion efficiency. This would need to occur at a rate competitive with electron injection, but the literature suggests that electron injection is exceedingly fast (on sub-ps or even fs timescales)[30–32] and it occurs even with sensitizers having exceedingly short $\tau$ values.[33]

Finally, another contributing factor may have been the state of aggregation on the surface. In multilayer assemblies, the outer layers may be too distant from the surface for an efficient photo-induced transfer of an electron to the surface, and may insulate the inner layers from the $I^-/I_3^-$ of the bulk phase, preventing the photo-produced $Ru^{III}$ state from returning to the ground $Ru^{II}$ state, and thereby effectively slowing down or stopping the catalytic cycle. Rice et al. report using cholic acid derivatives to inhibit aggregation,[20] but no such treatment was applied in our experiments.

Overall, the differences in photovoltaic behaviour between the three complexes tested may be due to a combination of factors, including differences in the complexes' photophysical properties once anchored to the electrode surface, the driving force for electron injection and the state of aggregation at the surface. It may be possible to address each of these factors in new sensitizer designs.

## Experimental Section

**General:** Samples of **1** and $[Ru(\mathbf{1})_2](PF_6)_2$ were prepared according to Liegghio et al.[6]

All NMR spectra were obtained with a Bruker AMX-400 spectrometer at 300 K. Signal assignments are given using the position labels of Scheme 1. Electron-impact mass spectrometry (EI-MS) was performed by Dr. Alex Young of the University of Toronto on a Micromass 70S-250 sector instrument at 70 eV. Laser Desorption Ionization-Time of Flight mass spectra (LDI-TOF-MS) were obtained on a Voyager DE STR instrument, while electrospray mass spectra were obtained on a Sciex-TAGA 600E instrument. Elemental analyses were performed by Guelph Chemical Laboratories, Guelph, ON, Canada.

Electronic spectroscopy was performed on a HP 8452A instrument. Stock solutions that were $5 \times 10^{-4}$ M in Ru were prepared. Aliquots (0.5 mL) were diluted with 2 mL of $CH_3CN$ in a disposable polymethacrylate cuvette (spectral range: 275–800 nm) to achieve a final concentration of $1 \times 10^{-4}$ M. Acetonitrile in a matching cuvette was used for baseline correction. The cuvettes were maintained at 25 °C by a Peltier block controlled by a HP 89090A controller. To explore the effect of deprotonation, 2 mL aliquots of the Ru stock were combined with 0–2 mL of an $8 \times 10^{-4}$ M stock solution of $Et_3N$ in $CH_3CN$, and the resulting mixture was diluted to 4 mL with $CH_3CN$. Samples were also prepared with 2.25–3 mL $Et_3N$ without further dilution, and the increased volume was taken into account. The position of the MLCT $\lambda_{max}$ was monitored and the nominal $\varepsilon$ values were computed.

Cyclic voltammetry was performed with an Obbligato Objectives Faraday MP potentiometer, using a graphite working electrode, a Pt wire counter electrode, and a Ag/AgCl *quasi*-reference electrode, which was prepared by immersing a virgin Ag wire in 1 M HCl and rinsing with $H_2O$ and absolute ethanol. Sample solutions in either $CH_3CN$ or DMF were assembled by combining 5 mL of a $5 \times 10^{-3}$ M Ru stock solution and 5 mL of a 0.1 M stock solution of tetrabutylammonium hexafluorophosphate (TBAH), then degassed

 © 2007 Wiley-VCH Verlag GmbH & Co. KGaA, Weinheim 

by bubbling with Ar for 2–3 min. For the last scan at the end of an experiment, 5 mL of a $5 \times 10^{-3}$ M ferrocene (Fc, $E°$ = 0.40 V in $CH_3CN$ containing TBAH vs. SCE)[34] stock solution was added.

For photosensitizer assessments, the equipment, sample preparation, data acquisition and data treatment were exactly as described earlier.[23]

For the photovoltaic measurements, titania films were prepared on commercial Pilkington TEC 8 conductive glass plates according to a standard procedure,[28,35] using the scalpel technique. The films were sintered and stored in a dessicator in the dark. Before impregnating the films, they were heat-treated at 450 °C for 30 min. While still hot at ca. 100 °C, they were immersed in sensitizer solutions, where they remained for grafting for 3 d. The sensitizers were dissolved in dry acetonitrile (distilled over $P_2O_5$) giving a ca. $1 \times 10^{-4}$ M solution of $[Ru(\mathbf{3})_2](PF_6)_2$ and a ca. $2 \times 10^{-4}$ M solution of $[Ru(\mathbf{1})(\mathbf{3})](PF_6)_2$, both of which were stored in the dark. A solid-state polyethylene oxide/titania/$I^-/I_3^-$ composite electrolyte[36,37] was used in the course of the experiments. The electrolyte was sandwiched between the photoelectrode and the platinized counterelectrode. Current–voltage (I–V) characteristics were obtained by connecting the cell to a variable resistor together with a micro-amperemeter in series and a voltmeter in parallel. Illumination was provided by a 300-W Xe light source (Oriel). A cut-off filter was used to exclude wavelengths less than 400 nm so as to prevent the generation of electron-hole pairs through direct $TiO_2$ bandgap excitation. Through accurate positioning of the cell assembly, all measurements were obtained under global air mass 1.5 (AM 1.5) solar irradiation conditions[38] (power density 1000 W $m^{-2}$). The experiments were repeated four times for each complex and a mean value was taken. *cis*-Bis(2,2′-bipyridyl-4,4′-dicarboxylato)bis(thiocyanato)ruthenium(II) bis(tetrabutylammonium) salt (N719 dye), purchased from Solaronix s.a., was used for comparison.

**4-(3,4-Methylenedioxyphenyl)-2,6-dipyrazinylpyridine (2):** Acetylpyrazine (0.20 g, 1.6 mmol) and piperonal (0.12 g, 0.8 mmol) were dissolved in a mixture of concentrated $NH_4OH$ (0.5 mL), 15% aq. KOH (5.2 mL), and methanol (5.7 mL), giving a canary yellow solution. The mixture turned beige over a period of 4 d at room temperature, and had formed a precipitate. This was isolated by filtration, rinsing with MeOH/$H_2O$ (1:1), then heated in hot acetone for 3 h to dissolve. The solution was cooled, then filtered. The solid was washed with acetone and ether, and then left to dry in a 70–80 °C oven, providing **2** in 75% yield (0.28 g). $^1$H NMR (400 MHz, $CDCl_3$, 300 K): $\delta$ = 9.90 (s, 1 H, *c*), 8.73 (3s, 3 H, *a*, *b* & *d*), 7.39 (d, 1 H, *e*), 7.28 (s, 1 H, *g*), 6.99 (d, 1 H, *f*), 6.09 (s, 2 H, *h*) ppm. EI–MS: *m*/*z* = 355. $C_{20}H_{13}N_5O_2$ (355.4): calcd. C 67.60, H 3.70, N 19.71; found C 67.54, H 3.75, N 19.58.

**$[Ru(\mathbf{2})_2](PF_6)_2$:** $RuCl_3 \cdot 3H_2O$ (0.10 g, 0.38 mmol) and $AgBF_4$ (0.20 g, 1.2 mmol) were heated in acetonitrile at reflux for 3 h, then filtered free of AgCl, affording a deep green solution. The solvent was then removed and replaced with fresh ethylene glycol. Ligand 2 (0.28 g, 0.76 mmol) was added, and the mixture was heated to reflux overnight, changing to a deep red colour. The Ru complex was precipitated by adding two equivalents of aqueous $NH_4PF_6$ (0.12 g, 0.76 mmol), collected by filtration, rinsed with ether and left to dry overnight in a 60–80 °C oven. Yield 0.94 g (85%). $^1$H NMR (400 MHz, $CD_3CN$, 300 K): δ = 9.76 (s, 2 H, c), 9.13 (s, 2 H, d), 8.40 (d, 2 H, b), 7.82 (d, 1 H, e), 7.78 (s, 1 H, g), 7.54 (d, 2 H, a), 7.27 (d, 1 H, f), 6.23 (s, 2 H, h) ppm. ES-MS: m/z = 406. $C_{40}H_{26}N_{10}O_4Ru^{2+}$ requires 406. $C_{40}H_{26}F_{12}N_{10}O_4P_2Ru$ (1101.7): calcd. C 43.61, H 2.38, N 12.71; found C 43.96, H 2.29, N 12.69.

**$[Ru(\mathbf{1})(\mathbf{2})](PF_6)_2$:** $RuCl_3 \cdot 3H_2O$ (0.10 g, 0.38 mmol) and ligand **2** (0.14 g, 0.38 mmol) were dissolved in acetonitrile and the mixture was left to reflux for 3 h, whence the reaction mixture became deep brown. Then, $AgBF_4$ (0.2 g, 1.2 mmol) was added, and heating continued for an additional 3 h, developing a deep green colour. This mixture was filtered free of AgCl, the filtrate was freed of solvent, then diluted with fresh ethylene glycol. Ligand **1** (0.12 g, 0.38 mmol) was then added and the mixture was heated to reflux overnight, changing to a deep red. The complex was precipitated by addition of aqueous $NH_4PF_6$ (0.12 g, 0.76 mmol), collected by filtration, and washed with diethyl ether, then left to dry overnight in a 60–80 °C oven. Yield 0.75 g (70%). $^1$H NMR (400 MHz, $CD_3CN$, 300 K): $\delta$ = 9.76 (2s, 2 H, *c* & *c**), 9.19 (s, 1 H, *d*), 9.12 (s, 1 H, *d**), 8.40 (m, 2 H, *b* & *b**), 8.17 (d, 2 H, *e**), 7.82 (d, 1 H, *e*), 7.78 (s, 1 H, *g*), 7.66 (d, 2 H, *f**), 7.55 (m, 2 H, *a* & *a**), 7.27 (d, 1 H, *f*), 6.23 (s, 1 H, *h*), 2.58 (s, 3 H, *g**) ppm. ES-MS: *m*/*z* = 391.0. $C_{40}H_{28}N_{10}O_2Ru^{2+}$ calcd. 390.9. $C_{40}H_{28}F_{12}N_{10}O_2P_2Ru$ (1071.7): calcd. C 44.83, H 2.63, N 13.07; found C 44.67, H 2.54, N 12.96.

**$[Ru(\mathbf{3})_2](PF_6)_2$:** $[Ru(\mathbf{2})_2](PF_6)_2$ (0.10 g, 0.91 mmol) was dissolved in 30–45% HBr in acetic acid (40 mL) and heated to just below reflux temperature for 3–4 d, whence the colour turned deep brown. The solvent was removed in vacuo and the residue was dissolved in a minimal amount of $CH_3CN$. The product was precipitated with 2 M aqueous $NH_4PF_6$ (30 mL), collected by filtration and washed with diethyl ether, then was left to dry overnight in a 50–60 °C oven. Yield 1.02 g (95%). $^1$H NMR (400 MHz, $CD_3CN$, 300 K): $\delta$ = 9.77 (s, 2 H, *c*), 9.13 (s, 2 H, *d*), 8.38 (d, 2 H, *b*), 7.79 (s, 2 H, *g*), 7.70 (d, 1 H, *e*), 7.54 (d, 2 H, *a*), 7.22 (d, 1 H, *f*) ppm. LDI-TOF-MS: *m*/*z* = 788.1. $C_{40}H_{28}N_{10}O_2Ru^+$ requires 788.1. $C_{38}H_{26}N_{10}O_4P_2F_{12}Ru$ (1077.7): calcd. C 43.65, H 2.51, N 13.40; found C 43.47, H 2.43, N 13.36.

**$[Ru(\mathbf{1})(\mathbf{3})](PF_6)_2$:** The procedure used to generate $[Ru(\mathbf{3})_2](PF_6)_2$ was applied to $[Ru(\mathbf{1})(\mathbf{2})](PF_6)_2$ (0.10 g, 0.93 mmol). Yield 0.95 g (90%). $^1$H NMR (400 MHz, $CD_3CN$, 300 K): $\delta$ = 9.79 (2s, 2 H, *c* & *c**), 9.19 (2s, 2 H, *d* & *d**), 8.39 (m, 2 H, *b* & *b**), 8.17 (d, 2 H, *e**), 7.87 (s, 1 H, *g*), 7.71 (d, 1 H, *e*), 7.64 (d, 2 H, *f**), 7.53 (m, 2 H, *a* & *a**), 7.22 (d, 1 H, *f*), 2.58 (s, 3 H, *g**) ppm. LDI-TOF-MS: *m*/*z* = 768.7. $C_{39}H_{27}N_{10}O_2Ru^+$ requires 768.3. $C_{39}H_{27}N_{10}O_2P_2F_{12}Ru$ (1058.7): calcd. C 44.25, H 2.57, N 13.23; found C 44.14, H 2.51, N 13.19.

## Acknowledgments

F. A. and P. G. P. thank the Natural Sciences and Engineering Research Council of Canada for financial support.

[1] V. Balzani, P. Ceroni, B. Ferrer, *Pure Appl. Chem.* **2004**, *76*, 1887–1901.
[2] A. Islam, H. Sugihara, H. J. Arakawa, *Photochem. Photobiol. A* **2003**, *158*, 131–138.
[3] M. Grätzel, *Pure Appl. Chem.* **2001**, *73*, 459.
[4] C. Klein, M. K. Nazeeruddin, P. Liska, D. Di Censo, N. Hirata, E. Palomares, J. R. Durrant, M. Grätzel, *Inorg. Chem.* **2005**, *44*, 178–180.
[5] P. Wang, C. Klein, R. Humphry-Baker, S. M. Zakeeruddin, M. Grätzel, *J. Am. Chem. Soc.* **2005**, *127*, 808–809.
[6] R. Liegghio, P. G. Potvin, A. B. P. Lever, *Inorg. Chem.* **2001**, *40*, 5485.
[7] T. Manivannan, P. G. Potvin, manuscript in preparation.
[8] M. Abboud, P. G. Potvin, manuscript in preparation.
[9] S. Vaduvescu, P. G. Potvin, *Eur. J. Inorg. Chem.* **2004**, 1763–1769.
[10] S. Vaduvescu, P. G. Potvin, *Acta Crystallogr., Sect. E* **2003**, *59*, o483–484.

 © 2007 Wiley-VCH Verlag GmbH & Co. KGaA, Weinheim 

[11] F. Barigelletti, L. Flamigni, V. Balzani, J.-P. Collin, J.-P. Sauvage, A. Sour, E. C. Constable, A. M. W. Cargill Thompson, *J. Chem. Soc., Chem. Commun.* **1993**, 942.
[12] C. Mikel, P. G. Potvin, *Polyhedron* **2002**, *21*, 49.
[13] K. Kalyanasundaram, M. K. Nazeeruddin, M. Grätzel, G. Viscardi, P. Savarino, E. Barini, *Inorg. Chim. Acta* **1992**, *198*, 831.
[14] P. G. Potvin, P. U. Luyen, J. Bräckow, *J. Am. Chem. Soc.* **2003**, *125*, 4894–4906.
[15] B. A. Borgias, S. R. Cooper, Y. B. Koh, K. N. Raymond, *Inorg. Chem.* **1984**, *23*, 1009–1016.
[16] K. Gigant, A. Rammal, M. Henry, *J. Am. Chem. Soc.* **2001**, *123*, 11632–11637.
[17] M. Albrecht, M. Napp, M. Schneider, P. Weis, R. Fröhlich, *Chem. Eur. J.* **2001**, *7*, 3966–3975.
[18] R. Rodriguez, M. A. Blesa, A. E. Regazzoni, *J. Colloid Interface Sci.* **1996**, *177*, 122–131.
[19] P. A. Connor, K. D. Dobson, A. J. McQuillan, *Langmuir* **1995**, *11*, 4193–4195.
[20] C. R. Rice, M. D. Ward, M. K. Nazeeruddin, M. Grätzel, *New J. Chem.* **2000**, *24*, 651–652.
[21] B. Whittle, N. S. Everest, C. Howard, M. D. Ward, *Inorg. Chem.* **1995**, *34*, 2025–2032.
[22] J. Zadykowicz, P. G. Potvin, *J. Coord. Chem.* **1999**, *47*, 395–407.
[23] P. G. Potvin, P. U. Luyen, F. A. Al-mutlaq, *New J. Chem.* **2001**, *25*, 839.
[24] C. M. Chamchoumis, P. G. Potvin, *Inorg. Chim. Acta* **2001**, *325*, 1–8.
[25] F. A. Al-mutlaq, P. G. Potvin, *J. Combin. Chem.* **2005**, in press.
[26] R. A. Marcus, N. Sutin, *Biochim. Biophys. Acta* **1985**, *811*, 265.
[27] K. Tokumaru, *J. Porphyrins Phthalocyanines* **2001**, *5*, 77–86.
[28] M. K. Nazeeruddin, A. Kay, I. Rodicio, R. Humphry-Baker, E. Muller, P. Liska, N. Vlachopoulos, M. Grätzel, *J. Am. Chem. Soc.* **1993**, *115*, 6382–6390.
[29] M. K. Nazeeruddin, P. Pechy, T. Renouard, S. M. Zakeeruddin, R. Humphry-Baker, P. Comte, P. Liska, L. Cevey, E. Costa, V. Shklover, L. Spiccia, G. B. Deacon, C. A. Bignozzi, M. Grätzel, *J. Am. Chem. Soc.* **2001**, *123*, 1613–1624.
[30] R. Eichberger, F. Willig, *Chem. Phys.* **1990**, *141*, 159–173.
[31] J. M. Rehm, G. L. McLendon, Y. Nagasawa, K. Yoshihara, J. Moser, M. Grätzel, *J. Phys. Chem.* **1996**, *100*, 9577–9578.
[32] Y. Tachibana, J.-E. Moser, M. Grätzel, D. R. Klug, J. R. Durrant, *J. Phys. Chem.* **1996**, *100*, 20056–20062.
[33] S. Ferrere, B. A. Gregg, *J. Am. Chem. Soc.* **1998**, *120*, 843–844.
[34] N. G. Connelly, W. E. Geiger, *Chem. Rev.* **1996**, *96*, 877.
[35] I. M. Arabatzis, T. Stergiopoulos, G. Katsaros, M. C. Bernard, D. Labou, S. G. Neofytides, P. Falaras, *Appl. Catal. B* **2003**, *42*, 187–201.
[36] G. Katsaros, T. Stergiopoulos, I. M. Arabatzis, K. G. Papdokostaki, P. Falaras, *J. Photochem. Photobiol. A* **2002**, *149*, 191–198.
[37] T. Stergiopoulos, G. Arabatzis, P. Katsaros, P. Falaras, *Nano Lett.* **2002**, *2*, 1259–1261.
[38] R. Hulstrom, R. Bird, C. Riordan, *Solar Cells* **1985**, *15*, 365–391.

Received: August 18, 2006
Published Online: April 11, 2007

 © 2007 Wiley-VCH Verlag GmbH & Co. KGaA, Weinheim 

DOI: 10.1002/ejic.200601173

# Structural Chemistry of a New 10H Hexagonal Perovskite: $BaMn_{0.4}Fe_{0.6}O_{2.73}$

**Laura Miranda,[a] Julio Ramírez-Castellanos,[a] María Hernando,[a,b] Aurea Varela,[a] José M. González-Calbet,[a] and Marina Parras*[a]**

**Keywords:** Hexagonal perovskites / Magnetic properties / Mn polytypes / High-resolution electron microscopy

A new 10H polytype has been stabilized in the $BaMn_{1-x}Fe_xO_{3-y}$ system with the composition $BaMn_{0.4}Fe_{0.6}O_{2.73}$. The anionic composition has been established by a reduction and re-oxidation cycle in the stability range of this phase. The structural characterization was carried out by high-resolution electron microscopy (HREM), electron diffraction, and X-ray diffraction. The structure is closely related to the ideal $(hch'ch)_2$ 10H polytype with two oxygen-deficient hexagonal (h′) $BaO_{2-y}$ layers per unit formula. This framework gives rise to blocks of three octahedra sharing faces linked by corners to two corner-sharing tetrahedra.

(© Wiley-VCH Verlag GmbH & Co. KGaA, 69451 Weinheim, Germany, 2007)

## Introduction

The perovskite family is one of the series of oxides most widely studied in the field of solid state chemistry. The compositional flexibility of a perovskite is reflected in the ability of its structure to accommodate a large variety of cations into the oxygen framework due, in part, to the huge range of structurally related polymorphs which can be adopted. The crystal structures of perovskites, $ABO_3$, can be considered to consist of stacks of pseudo-close-packed layers $AO_3$; the smaller B cations occupy the oxygen octahedral holes between the layers. When all the $AO_3$ layers stack in a cubic close-packed structure (ABC sequence), the $[BO_6]$ octahedra form the three-dimensional, corner-sharing network of the well-known cubic perovskite of the 3C structural type. On the contrary, if all the $AO_3$ layers are in a hexagonal close-packing structure (AB sequence), the octahedra sharing faces and the one-dimensional 2H structural type (hexagonal perovskite) is obtained. In general, the hexagonal perovskites are less common than the cubic ones because of unfavorable electrostatic cation repulsion associated with the much shorter B–B distance between adjacent face-sharing octahedra.

Between hexagonal and cubic perovskites, a wide range of hexagonal polytypes has been described, whose structures arise from different cubic (c) and hexagonal (h) periodic mixed sequences of the $AO_3$ layers. These polytypes are usually referred to by the symbols $n$H or $n$R, where $n$ corresponds to the number of layers per unit cell, while H and R denote the hexagonal and rhombohedral symmetry, respectively, of the corresponding unit cell.

Many compounds with a hexagonal perovskite-type structure have been reported during the last years. The cation size, the electronic configuration of the B cations, and the oxygen stoichiometry are factors that strongly influence the stabilization of a particular polytype for a given composition. $BaMnO_3$[1] crystallizes in the 2H hexagonal type (**…**hhh**…** sequence). In this system, the introduction of anionic vacancies leads to the stabilization of a large number of anion-deficient $BaMnO_{3-y}$ hexagonal polytypes containing 100–50% hexagonal stacking.[2–5] This behavior is also observed in the $BaFeO_{3-y}$ system, which has been extensively studied in the $0 < y \leq 0.5$ compositional range.[6–10] This system is characterized by a large structural variety; in particular, three different hexagonal polytypes are stabilized for the more oxidized samples. Unlike in the Ba-Mn-O system, stoichiometric $BaFeO_3$ has not been stabilized up to now, but the closest anionic composition, $BaFeO_{2.95}$, adopts the 6H hexagonal polytype with a $(hcc)_2$ stacking arrangement containing only 33% hexagonal layers,[11] that is, much less than $BaMnO_3$. This feature can be related to the bigger size of $Fe^{IV}$ relative to that of $Mn^{IV}$, both of which are in an octahedral oxygen environment ($r_{Fe}^{IV}$ = 0.585 Å, $r_{Mn}^{IV}$ = 0.550 Å).[12] Actually, in general, an increase of the cubic layers per unit cell occurs when the $r_A/r_B$ ratio decreases, because of the increase of the cationic repulsion in the face-sharing octahedra.

Similarly, different structural modifications have been reported within more complex systems where two or more cations of different chemical nature occupy the B position of the perovskite. Taking into account the great number of polytypes that can be stabilized in the above-mentioned Ba-Mn-O and Ba-Fe-O systems, a diverse structural chemistry may be expected for the $BaMn_{1-x}Fe_xO_{3-y}$ system. This fact,

[a] Dpto. de Química Inorgánica, Facultad de Químicas, Universidad Complutense de Madrid,
28040 Madrid, Spain
Fax: +34-91-394-43-52
E-mail: mparras@quim.ucm.es
[b] Institut Laue Langevin
BP 156X, 38042 Grenoble, France

 © 2007 Wiley-VCH Verlag GmbH & Co. KGaA, Weinheim 

besides the current interest in the physical properties of Mn-containing perovskites, provides a significant motivation for investigating the effects of substituting Fe for Mn in $BaMnO_3$. Previous work in $BaMn_{1-x}Fe_xO_{3-y}$ involved the stabilization of a 6H polytype (hhhchc sequence) for the $0 \leq x \leq 0.3$ compositional range.[13] All the samples are oxygen-deficient. In view of the sensitivity of the structural chemistry to cation size or redox chemistry, it seems reasonable that changes in the cationic distribution of the B sites are accompanied by structural changes. Therefore, we have investigated this system and we have identified a new single phase adopting a 10H hexagonal polytype. We report in this paper the synthesis and the structural study, of $BaMn_{0.4}Fe_{0.6}O_{3-y}$, carried out by using X-ray diffraction, selected area electron diffraction (SAED), and high-resolution electron microscopy (HREM).

## Results and Discussion

### Microstructural Characterization

The initial characterization of $BaMn_{0.4}Fe_{0.6}O_{3-y}$ by X-ray diffraction suggests that it is a hexagonal single-phase material with unit cell dimensions corresponding to a 10H polytype. There are twelve stacking sequences of the $BaO_3$ layers which can result in a 10H cell. Three of them correspond to a $P6_3/mmc$ space group whereas the other nine correspond to space groups without systematic extinctions ($P\bar{6}m2$, $P\bar{3}m1$ and $P3m1$).

The SAED patterns along the most relevant zone axes [001], [010], and [1$\bar{1}$0], are shown in Figure 1a, b, and c, respectively. The diffraction spots are always sharp, and no streaking or diffuse intensity is observed. All the reflections appearing in these patterns can be indexed on the basis of a hexagonal unit cell of lattice parameters close to $a$ = 5.7, $c$ = 24.7 Å. In addition, as it can be observed in the SAED pattern in Figure 1b, the reflection conditions are compatible with a $P6_3/mmc$ space group. By tilting 30° around the $c^*$ axis (Figure 1c), all the spots due to multiple diffraction are visible. According to these results, three stacking sequences are possible for this 10H structure: $(ccccch)_2$, $(hhhcc)_2$, and $(hchch)_2$. The first one presents a much greater proportion of cubic layers than the other two; this sequence has been found in $SrMn_{0.7}Fe_{0.3}O_{2.87}$.[14] The bigger size of the barium atom allows the stabilization of polytypes with a large component of hexagonal perovskite; therefore, one of the other two sequences (containing a 60% of hexagonal layers) seems to be more probable.

Electron microscopy is a very efficient tool for determining the layer-stacking sequence along the $c$ axis. Figure 2a corresponds to the HREM along the [010] axis. In this zone, the structure is viewed parallel to the columns of close-packed Ba–O rows, and therefore the sequence of the layers is directly revealed. In fact, in the hexagonal polytypes, the image contrast along the [010] projection consists of lines of dots in which the straight segments correspond to adjacent cubic (c) layers, whereas every change of slope is associated to the presence of hexagonal (h) layers. Ac-

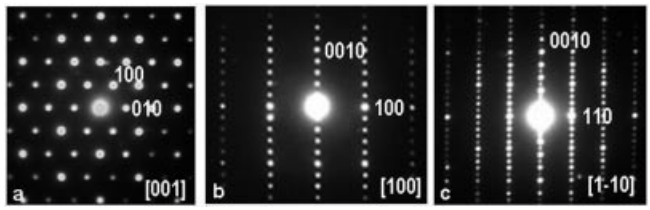


Figure 1. SAED patterns corresponding to $BaMn_{0.4}Fe_{0.6}O_{2.73}$ along (a) [001], (b) [010] and (c) [1$\bar{1}$0].

cording to this, the observed contrast of the image (see Figure 2b) can be interpreted as corresponding to a $(hchch)_2$ layer arrangement. Therefore, from the ideal atomic coordinates corresponding to this 10H sequence, an image calculation was performed. The simulated image (inset of Figure 2a) nicely fits the experimental one for $\Delta t$ = 70 Å, $\Delta f$ = –500 Å. This result shows that $BaMn_{0.6}Fe_{0.4}O_{3-y}$ either actually exhibits this hexagonal 10H structure or has a closely related structural type. In this structure (Figure 3a), blocks of three face-sharing octahedra are linked by their terminal corners to blocks of two face-sharing octahedra. It is worth mentioning that this hexagonal polytype is stable in both the Ba-Mn-O and the Ba-Fe-O systems for the compositions $BaMnO_{2.90}$[2] and $BaFeO_{2.80}$,[9,10] respectively.

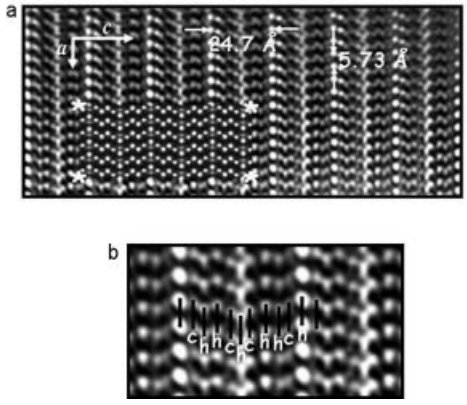


Figure 2. (a) HRTEM image of $BaMn_{0.4}Fe_{0.6}O_{2.73}$ along [010]; the calculated image is shown in the inset. ($\Delta t$ = 70 Å, $\Delta f$ = –500 Å) (b) Enlarged image showing the stacking sequence of the $BaO_3$ layers along the $c$ axis.

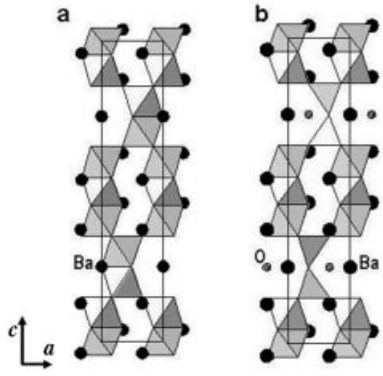


Figure 3. Structural models corresponding to: (a) the 10H-$ABO_3$ polytype; (b) 10H-$BaFeO_{2.80}$ (according to ref.[10]). Only the Ba and nonbonding O atoms are marked.

 © 2007 Wiley-VCH Verlag GmbH & Co. KGaA, Weinheim 

### Compositional Characterization

The cationic composition was determined by energy-dispersive X-ray spectroscopy (EDS). In order to ensure the chemical homogeneity of the sample, the analysis was performed not only on several dozens of crystallites, but also in different crystal zones. Initially, the absence of Al (from crucible material) in the crystals was confirmed by a preliminary search of all the elements present in the studied samples. Once the lack of additional elements was confirmed, the Ba/Mn/Fe ratio was obtained from the relative intensity of the Ba-$L_\alpha 1$ (4.466 eV), Mn-$K_\alpha 1$ (5.899 eV), and Fe-$K_\alpha 1$ (6.404 eV) lines in the EDS spectra. The obtained result, $Ba_{1.00(2)}Mn_{0.39(3)}Fe_{0.61(1)}O_x$, is in agreement with the nominal composition.

The sample is rather insoluble and we were unable to perform a volumetric analysis to determine the oxygen content. Therefore, in order to establish the anionic stoichiometry, we have undertaken a thermogravimetric study of the sample. First, the sample was reduced under a 300-mbar $H_2$/200-mbar He atmosphere and heated at 3 °C/min up to 700 °C (Figure 4). Under these experimental conditions, the weight loss is close to 7.1%, BaO, MnO, FeO, and Fe metal being identified by XRD as final products of the reduction. However, since the FeO/Fe ratio in the final products is not known, it is not possible to obtain the oxygen content of the studied sample from this experiment. Unfortunately, even for the most reductive conditions, a FeO/Fe mixture was always obtained. Therefore, in order to estimate the oxygen content, it was necessary to design a different reduction pathway.

In this context, the oxygen content of the above sample can be obtained by thermogravimetric analysis if its anionic compositional range is known. In fact, $BaFeO_{2.80}$[9] adopts the same 10H structural type as the anionic vacancies located in the hexagonal layers on the dimer structural units, changing its anionic composition from $BaO_3$ to $BaO_2$ (Figure 3b). The remaining two oxygen atoms rearrange in such a way that only one of them is bonded to the two Fe atoms adjacent to the layer, thus leading to a dimer of corner-sharing tetrahedra. The other oxygen is a nonbonding atom. For lower oxygen content, this nonbonding oxygen is partially removed, and this results in a hexagonal $BaO_{2-y}$ layer.[10] On the basis of the crystallochemical analysis of this phase, we propose that, in a similar way, the anionic range of the stability of the 10H-$BaMn_{0.4}Fe_{0.6}O_{3-y}$ phase varies from 2.80 to 2.60, which corresponds to the range from an h-$BaO_2$ down to an h-BaO layer from one to zero nonbonding oxygen atoms, respectively. According to this assumption, the anionic composition of $BaMn_{0.4}Fe_{0.6}O_{3-y}$ can be obtained from a reduction and re-oxidation cycle of the sample.

Let us go back now to the reduction curve in Figure 4. In inset (a), a slight change in the slope is visible at 375 °C, corresponding to a weight loss close to 0.9%, that could indicate the existence of a stable phase with lower oxygen content. Therefore, in order to stabilize this reduced phase, we have carried out a partial reduction of the starting material under a 100-mbar $H_2$/400-mbar He atmosphere by heating at 2 °C/min up to 280 °C for 12 h to ensure oxygen homogeneity in the final product. This reduction process is represented in Figure 5. The lost weight between the starting and the final points amounts to 0.88%. In addition, the X-ray data shows that the reduced phase maintains the basic structural features of the 10H phase. Taking into account the above considerations, if we assume that the stabilized phase corresponds to the lowest limit of the 10H anionic stability range, i.e., $BaMn_{0.4}Fe_{0.6}O_{2.60}$, $BaMn_{0.4}Fe_{0.6}O_{2.73}$ should be the composition of the starting material.

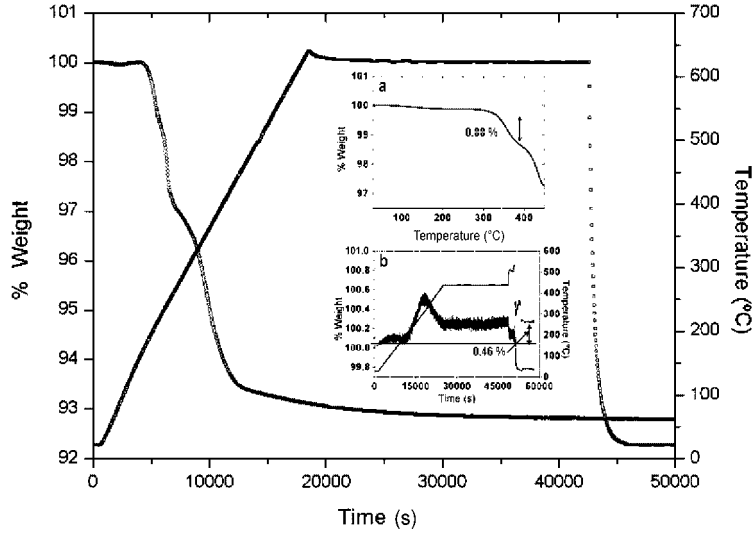


Figure 4. Thermogravimetric analysis of $BaMn_{0.4}Fe_{0.6}O_{3-y}$. The experiment was carried out in a 300-mbar $H_2$/200-mbar He atmosphere. Inset (a): The temperature dependence of the weight loss. Inset (b): Thermogravimetric curve corresponding to the oxidation of $BaMn_{0.4}Fe_{0.6}O_{3-y}$.

 © 2007 Wiley-VCH Verlag GmbH & Co. KGaA, Weinheim 

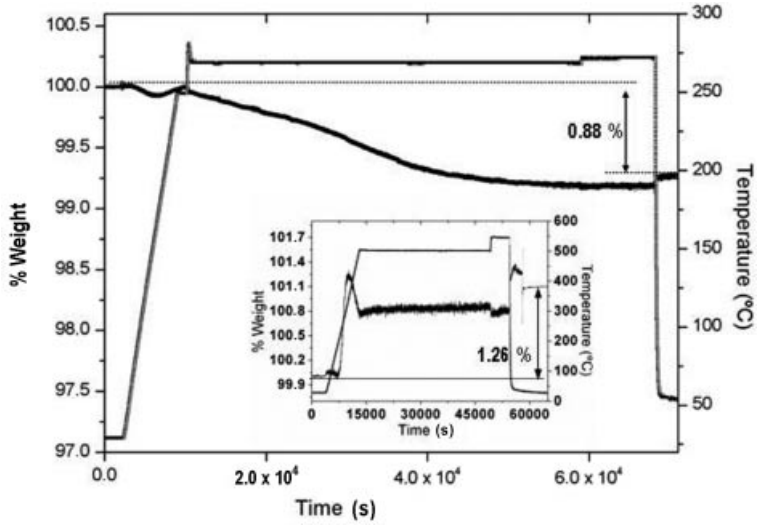


Figure 5. Thermogravimetric curve corresponding to the reduction process (100-mbar $H_2$/400-mbar He; 2 °C/min up to 270 °C) from the starting material, $BaMn_{0.4}Fe_{0.6}O_{3-y}$, up to a composition of $BaMn_{0.4}Fe_{0.6}O_{2.60}$. The re-oxidation process is shown in the inset.

On the other hand, the starting material was also heated at 2 °C/min up to 400 °C under 1 atm $O_2$ in a CAHN electrobalance. As shown in inset (b) of Figure 4, the weight of the sample increases slightly with temperature up to a gain of 0.46%. The low stability of the equipment (CAHN electrobalance) used for data collection when working at a static gas pressure of 1 atm gives rise to high data dispersion, which is reflected in the thickness of the oxidation line. However, this experimental aspect does not influence the reliability of the determined oxygen content since both initial and final weight are measured at 0.5-mbar He in a static atmosphere. The XRD pattern of the final product shows that the oxidized sample also maintains the 10H structure of the starting phase. Taking into account the above considerations, this process should be associated to the oxidation from the starting material up to the most oxidized 10H sample, i.e., according to previous results, to the reaction: $BaMn_{0.4}Fe_{0.6}O_{2.73} + O_2 \rightarrow BaMn_{0.4}Fe_{0.6}O_{2.80}$. For this process, the theoretical weight gain corresponds to 0.47%, which nicely fits with the experimental one of 0.46%.

Finally, we have completed this cycle by the re-oxidation of the reduced $BaMn_{0.4}Fe_{0.6}O_{2.60}$ sample (see inset of Figure 5). In this process, the sample weight increases up to 1.26%, in agreement with the $BaMn_{0.4}Fe_{0.6}O_{2.60} + O_2 \rightarrow BaMn_{0.4}Fe_{0.6}O_{2.80}$ reaction (theoretical value: 1.36%). This result supports the previous ones; therefore, from this thermogravimetric study, the anionic stoichiometry of the studied sample is $BaMn_{0.4}Fe_{0.6}O_{2.73}$.

### Structural Refinement

According to the above results, $BaMn_{0.4}Fe_{0.6}O_{2.73}$ adopts a structure based on a 10H-$(hch'ch)_2$ sequence. A structural study by X-ray profile refinement has been performed by taking as starting model the structural parameters of the hexagonal 10H-$BaFeO_{2.80-y}$ in the space group $P6_3/mmc$.[9]

Because of their similar scattering factors, Mn and Fe are indistinguishable by XRD; therefore, both metals were randomly distributed over the two crystallographically different octahedral sites, the tetrahedral one is fully occupied by Fe, since neither $Mn^{III}$ nor $Mn^{IV}$ are stable in this oxygen coordination. In addition, the determined anionic stoichiometry indicates the presence of oxygen vacancies in the structure, which, according to the above considerations, have been located into the hexagonal h′-$BaO_2$ up to a $BaO_{1.65}$ anionic composition; the nonbonding oxygen position (2c) being 65% occupied. This structural feature will be confirmed by neutron diffraction.

The refinement was stable, and it was possible to refine the positions of the oxygen atoms and the isotropic temperature factor for each type of atom (Ba, Mn/Fe, O). Figure 6 shows the graphical results of the fitting of the experimental X-ray diffraction pattern and the difference between observed and calculated data. The final structural parameters are given in Table 1; Table 2 shows selected interatomic distances.

A schematic representation of the structure is depicted in Figure 7. The octahedron at the center of the trimer, $M_3O_6$, is regular with six identical M–O bonds of length 1.918 Å. This value is in excellent agreement with Mn–O bond lengths observed for $Mn^{IV}$ in the same environment as 2H-$BaMnO_3$ (1.9044 Å),[15] and it is also close to that found in 10H-$BaFeO_{2.8-y}$ for $Fe^{III}$ in octahedral coordination ($d_{average}$ = 2.01 Å).[9,10] In contrast, the $M1O_6$ octahedron is quite distorted, with three long and three short M–O bonds (see Table 2), indicating that metals in this position are displaced from the center toward the oxygen atoms in the cubic layer (O1), i.e., to the neighboring tetrahedra sharing a corner, and hence away from the shared face. As a consequence, with respect to the ideal structure, the M3···M1 distance increases, reducing the electrostatic repulsion between cations in adjacent face-sharing polyhedra. This feature is shown by other polytypes with structural

 © 2007 Wiley-VCH Verlag GmbH & Co. KGaA, Weinheim 

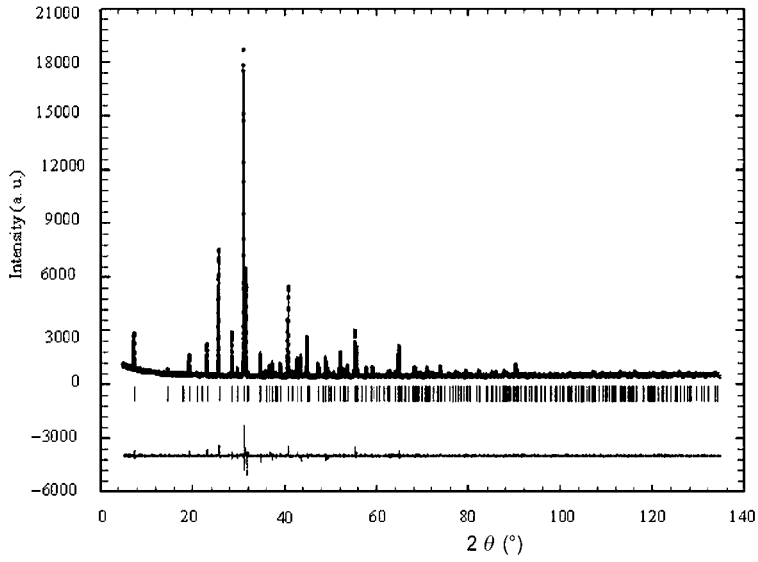


Figure 6. Experimental, calculated, and difference X-ray diffraction patterns corresponding to $BaMn_{0.4}Fe_{0.6}O_{2.73}$.

Table 1. Final structural parameters of $BaMn_{0.4}Fe_{0.6}O_{2.73}$.[a]

| Atom | Site | *x*/*a* | *y*/*b* | *z*/*c* | $B_{iso}$(Å$^2$) | Occ. |
|---|---|---|---|---|---|---|
| Ba1 | 2*b* | 0 | 0 | 0.25 | 0.47(3) | 1 |
| Ba2 | 4*f* | 1/3 | 2/3 | 0.36627(6) | 0.47(3) | 1 |
| Ba3 | 4*f* | 1/3 | 2/3 | 0.95936(7) | 0.47(3) | 1 |
| M1 | 4*e* | 0 | 0 | 0.60771(1) | 0.94(6) | 1 |
| Fe2 | 4*f* | 1/3 | 2/3 | 0.82148(2) | 0.94(6) | 1 |
| M3 | 2*a* | 0 | 0 | 0 | 0.94(6) | 1 |
| O1 | 12*k* | 0.319(2) | 0.1596(8) | 0.3501(3) | 1.1(1) | 1 |
| O2 | 12*k* | 0.696(1) | 0.8479(8) | 0.4510(3) | 1.1(1) | 1 |
| O3 | 2*d* | 1/3 | 2/3 | 0.75 | 1.1(1) | 1 |
| O4 | 2*c* | 1/3 | 2/3 | 0.25 | 1.1(1) | 0.648[b] |

[a] Space group: $P6_3/mmc$ $a$ = 5.74644(4) Å, $c$ = 24.0433(2); $R_B$ = 6.81, $R_{exp}$ = 4.31, $R_{wp}$ = 5.82, $\chi^2$ = 1.82; M = Mn and Fe cations. [b] The O4 occupancy factor has been fixed.

Table 2. Selected interatomic distances (Å) in $BaMn_{0.4}Fe_{0.6}O_{2.73}$.

| | |
|---|---|
| Ba1–O1 2.883(7) × 6 | M1–O1 1.886(5) × 3 |
| Ba1–O3 3.318(3) × 3 | M1–O2 2.069(6) × 3 |
| Ba1–O4 3.318(3) × 3 | |
| | M2–O1 1.860(5) × 3 |
| | M2–O3 1.718(4) |
| Ba2–O1 2.900(6) × 6 | M2–O4 3.672(1) |
| Ba2–O2 2.721(6) × 3 | |
| Ba2–O4 2.796(1) | M3–O2 1.918(6) × 6 |
| | |
| Ba3–O1 3.146(6) × 3 | M1–M2 3.729(2) |
| Ba3–O2 2.883(6) × 6 | M1–M3 2.589(4) |
| Ba3–O2 2.811(6) × 3 | M2–M2 3.437(1) |

octahedral trimers like 9R-$BaIr_xMn_{1-x}O_3$.[16] In addition, these M–O octahedral bond lengths [$d_{average}(M2O_6)$ = 1.97 Å] agree with those of the Ba-Mn/Fe-O polytypes, for instance, in 6H-$BaMn_{0.767}Fe_{0.233}O_{2.87}$ the Mn/Fe–O bond lengths range from 1.94 to 2.14 Å, whereas the Fe–O bond lengths in 10H-$BaFeO_{2.8-y}$[9,10] range from 1.94 to 1.859 Å; both are in octahedral coordination.

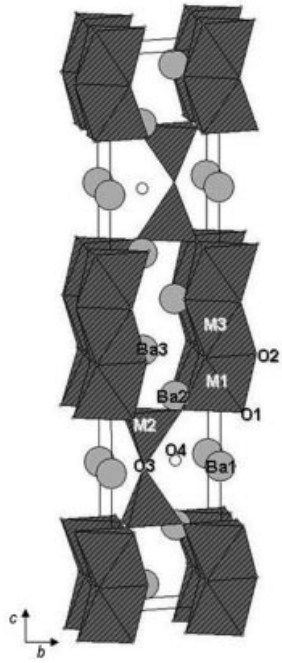


Figure 7. Structural model corresponding to $BaMn_{0.4}Fe_{0.6}O_{2.73}$.

The $Fe2O_4$ tetrahedra are quite distorted with three long Fe2–O1 bonds (1.860 Å) and one short Fe2–O3 bond (1.71 Å). These values are close to those observed in the 10H-$BaFeO_{2.8-y}$[9,10] (1.83 and 1.76 Å, respectively). Finally, as in $BaFeO_{2.8-y}$, the long Fe2–O4 distance obtained (3.672 Å) is not within the bonding distance of the M2 cation.

 © 2007 Wiley-VCH Verlag GmbH & Co. KGaA, Weinheim 

As we have already mentioned, from the XRD data we are unable to discern between the two metals; however, we can propose a tentative cationic distribution over the different sites. In this sense, it is well known that the presence of Mn stabilizes strings of various face-sharing octahedra in such a way that $Mn^{IV}$ shows a strong preference for occupying the central one of these units. Therefore, we can assume that Mn should be located mainly in the center of the trimers. This fact is well in accordance with the high symmetry of this M3 site. The units of tetrahedra sharing corners involve only Fe (probably in the III oxidation state); therefore, according to the Mn/Fe experimental cationic ratio of 0.4:0.6, Mn/Fe should occupy the outer octahedra of the trimer units in a ratio close to 50:50. If Mn is stabilized as $Mn^{IV}$, the oxidation state of the Fe remaining in this polyhedron should be close to 3.3; this fact indicates the presence of $Fe^{IV}$ in this polyhedron, whose high-spin configuration should be stabilized by the large distortion of the M1 site. The large contrast between the scattering lengths of Mn and Fe makes neutron scattering a particularly sensitive tool in this case. Therefore, in order to confirm these crystallochemical considerations, a neutron diffraction study is in progress.

We would like to emphasize that, from single-crystal XRD analysis, an orthorhombic deformation is found in 10H-$BaFeO_{2.80}$ (*Cmcm* space group).[10] This lower symmetry seems to be caused by a displacement of barium and oxygen atoms in the $BaO_2$ layers from hexagonal special positions, changing the symmetry from hexagonal to orthorhombic. We have also performed the refinement of the 10H-$BaMn_{0.4}Fe_{0.6}O_{2.73}$ structure by using the orthorhombic description reported for the 10H-$BaFeO_{2.8}$ polytype. However, even though a similar displacement of the barium into the $BaO_2$ layers seems occur, we are unable to draw any meaningful conclusion in relation to this symmetry change, since it is not possible to obtain accurate atomic positions of the oxygen atoms from powder X-ray diffraction analysis.

### Magnetic Properties

The magnetic properties of 10H-$BaMn_{0.4}Fe_{0.6}O_{2.73}$ have also been explored. Figure 8 shows the temperature dependence of the magnetic susceptibility as measured in a field of 1000 Oe. A very slight divergence between the zero-field-cooled (ZFC) and field-cooled (FC) data opens up below 150 K. Besides, low values, close to $2.4 \times 10^{-3}$ emu/mol, and weak temperature dependence of the magnetic susceptibility are observed above 100 K. These features suggest the presence of strong interactions between magnetic cations in this temperature range; the negative temperature intercept shown in the inverse magnetic susceptibility plot can indicate that these interactions are antiferromagnetic. Analogous behavior has been evidenced in other Mn polytypes, as in 4H-$SrMnO_{3-x}$[17] where only short-range antiferromagnetic coupling between the $Mn^{4+}$ cations in the $Mn_2O_9$ face-sharing octahedra is detected. In a similar way, it can be considered that short-range antiferromagnetic coupling takes place between the $Mn^{4+}$ cations in the $Mn_3O_9$ structural units in $BaMn_{0.4}Fe_{0.6}O_{2.73}$. However, long-range interactions do not occur, since it is no indication of 3D magnetic order in the susceptibility data at low temperatures. Because of these short-range interactions, we cannot obtain the oxidation state of Mn/Fe cations from the magnetic susceptibility curve. Nevertheless, according to the anionic stoichiometry of the sample and on the basis of crystallochemical considerations, the following formulation $Ba[(Mn_{0.2}^{IV})(Fe_{0.14}^{III}Fe_{0.06}^{IV})]_{Oh1}[Mn_{0.2}^{IV}]_{Oh3}[Fe_{0.4}^{III}]_{td}O_{2.73}$ can be proposed for the investigated sample.

## Experimental Section

The black polycrystalline sample of $BaMn_{0.4}Fe_{0.6}O_{3-y}$ was prepared from a well-ground stoichiometric mixture of $BaCO_3$ (Aldrich, 99.98%), $MnCO_3$ (Aldrich, 99%), and $Fe_2O_3$ (Aldrich, 99.98%). The mixture was heated in an $Al_2O_3$ crucible at 900 °C in air for 48 h. Then, the sample was treated at 1200 °C for one

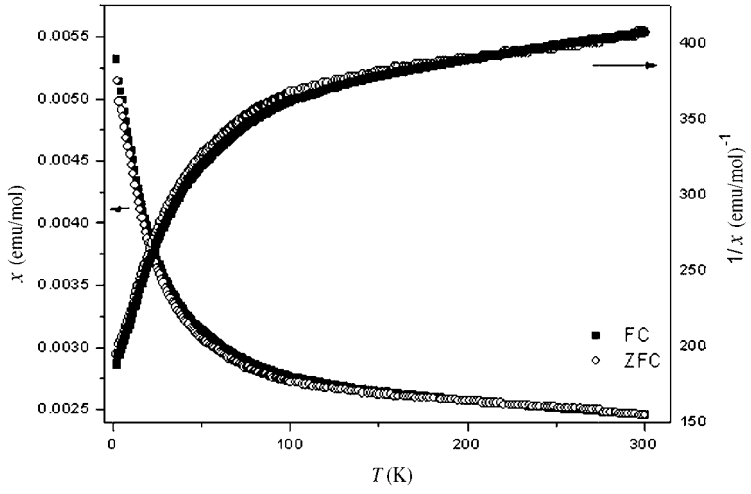


Figure 8. Temperature dependence of the magnetic susceptibility under an applied magnetic field of 1000 Oe.

 © 2007 Wiley-VCH Verlag GmbH & Co. KGaA, Weinheim 

day and then quenched to room temperature. This process was repeated four times with intermediate grinding in order to ensure homogeneity.

The average cationic composition was determined by Inductively Coupled Plasma (ICP) analysis, whereas the local composition was analyzed by EDS with an INCA analyzer system attached to a JEOL 3000 FEG electron microscope. The overall oxygen content was determined by thermogravimetric analysis with a thermobalance based on a CAHN D-200 electrobalance, which allows the determination of variations of the oxygen content within $\pm 1 \times 10^{-3}$ on a sample of about 100 mg when working under an atmosphere of 500 mbar gas.

Powder XRD patterns were collected by using Cu-$K_\alpha$ radiation ($\lambda$ = 1.5418 Å) at room temperature with a PHILIPS X′PERT PRO MPD diffractometer equipped with a germanium monochromator. Diffraction data were analyzed by the Rietveld method[18] using the Fullprof program.[19]

SAED and HREM were performed with a JEOL 3000 FEG electron microscope fitted with a double-tilting goniometer stage ($\pm$ 22°, $\pm$ 22°). Simulated HREM images were calculated by the multislice method with the MacTempas software package.

## Acknowledgments

Financial support by MEC (Spain) through research project MAT2004–01248 is acknowledged.

[1] A. Hardy, *Acta Crystallogr.* **1962**, *15*, 179–181.
[2] T. Negas, R. S. Roth, *J. Solid State Chem.* **1971**, *3*, 323–339.
[3] M. Parras, J. M. González-Calbet, J. Alonso, M. Vallet-Regí, *J. Solid State Chem.* **1994**, *113*, 78–87.
[4] J. M. González-Calbet, M. Parras, J. Alonso, M. Vallet-Regí, *J. Solid State Chem.* **1994**, *111*, 202–207.
[5] M. Parras, J. Alonso, J. M. González-Calbet, M. Vallet-Regí, *J. Solid State Chem.* **1995**, *117*, 21–29.
[6] A. J. Jacobson, *Acta Crystallogr., Sect. B* **1976**, *32*, 1087–1090.
[7] J. M. González-Calbet, M. Parras, M. Vallet-Regí, J. C. Grenier, *J. Solid State Chem.* **1990**, *86*, 149–159.
[8] Z. Zou, S. Hovmoller, M. Parras, J. M. González-Calbet, M. Vallet-Regí, J. C. Grenier, *Acta Crystallogr. A* **1993**, *49*, 27–35.
[9] M. I. Gómez, G. Lucotti, J. A. de Moran, P. J. Aymonino, S. Pagola, P. Stephens, R. E. Carbonio, *J. Solid State Chem.* **2001**, *160*, 17–24.
[10] J. D. Delattre, A. m. Stacy, T. Siegrist, *J. Solid State Chem.* **2004**, *177*, 928–935.
[11] I. Muro, M. Isausti, L. Lezama, T. Rojo, *J. Solid State Chem.* **2005**, *178*, 1712–1719.
[12] R. D. Shannon, *Acta Crystallogr., Sect. A* **1976**, *32*, 751–767.
[13] V. Caignaert, M. Hervieu, B. Domengès, N. Nguyen, J. Pannetier, B. Raveau, *J. Solid State Chem.* **1988**, *73*, 107–117.
[14] P. D. Battle, C. M. Davison, T. C. Gibbs, J. F. Vente, *J. Mater. Chem.* **1996**, *6*, 1187–1190.
[15] E. J. Cussen, P. D. Battle, *Chem. Mater.* **2000**, *12*, 831–838.
[16] N. A. Jordan, P. D. Battle, *J. Mater. Chem.* **2003**, *9*, 2220–2226.
[17] P. D. Battle, T. C. Giba, C. W. Jones, *J. Solid State Chem.* **1988**, *74*, 60–66.
[18] H. M. Rietveld, *J. Appl. Crystallogr.* **1969**, *2*, 65–71.
[19] J. Rodríguez-Carvajal, *Physica B* **1993**, *192*, 55–69.

Received: December 11, 2006
Published Online: April 10, 2007

 © 2007 Wiley-VCH Verlag GmbH & Co. KGaA, Weinheim 

DOI: 10.1002/ejic.200601186

# Main Group Lewis Acid/Base-Stabilised Phosphanylboranes

**Ariane Adolf,[a] Manfred Zabel,[a] and Manfred Scheer*[a]**

*Dedicated to Professor Michael Binnewies on the occasion of his 60th birthday*

**Keywords:** Boron / Phosphorus / Hydrides / Lewis acids / Lewis bases

The parent compounds of phosphanylboranes of the type $(LA)H_2P–BH_2(LB)$ (LA = Lewis acid, LB = Lewis base) stabilised by Lewis acid/Lewis base have been synthesised by using perfluorinated main-group Lewis acids. The Lewis acid–phosphane adducts $(C_6F_5)_3BPH_3$, $(C_6F_5)_3BPPhH_2$ and $(C_6F_5)_3GaPPhH_2$ (**3**) were used as starting materials, which upon lithiation with *n*BuLi react with the chlorinated Lewis base borane adduct $ClBH_2NMe_3$. The LA/LB stabilised phosphanylboranes $(C_6F_5)_3BPH_2BH_2NMe_3$ (**1**), $(C_6F_5)_3BPPhHBH_2NMe_3$ (**4**) and $(C_6F_5)_3GaPPhHBH_2NMe_3$ (**5**), were obtained via salt elimination reactions. $(C_6F_5)_3GaPH_2BH_2NMe_3$ (**2**) was not accessible using this method due to the unavailability of an efficient synthetic route to $(C_6F_5)_3GaPH_3$. The synthesis of **2** could be achieved quantitatively via reaction of $PH_2BH_2NMe_3$ with $(C_6F_5)_3Ga{\cdot}Et_2O$. All products were comprehensively characterised by spectroscopic methods and X-ray crystallography. Additionally, the intermediate products $(C_6F_5)_3BPH_2Li$ and $(C_6F_5)_3GaPPhH_2$ (**3**) were spectroscopically characterised.

(© Wiley-VCH Verlag GmbH & Co. KGaA, 69451 Weinheim, Germany, 2007)

## Introduction

Phosphanylboranes $(R_2P–BR'_2)_n$ have attracted much attention since the beginning of the 90's.[1] However, attempts to isolate the parent compound of this class $(H_2P–BH_2)$ (**A**) (Scheme 1) have been futile, and only theoretical investigations on **A** have been performed.[2] Oligophosphanylboranes with the general formula $(HRP–BH_2)_n$ can be synthesised via dehydrocoupling reactions at elevated temperatures[3] or catalysed by either $Rh^I$ complexes (R = Ph)[4] or $B(C_6F_5)_3$ (R = H).[5] Experimentally accessible monomeric phosphanylboranes are mostly stabilised by sterically demanding substituents to avoid intermolecular oligomerisation.[1] Our approach to the parent compounds of phosphanylboranes was to stabilise them by the coordination of Lewis acids and Lewis bases as type **B** compounds. By this way the lone pair of the pnicogen is occupied by a Lewis acid (LA) and the Group 13 element is coordinated by a Lewis base (LB) (**B**).[6] Recently we were able to synthesise the first phosphanylborane **C**, which is stabilised only by a Lewis base.[7]

The Lewis acid stabilised phosphanylboranes that we synthesised carry transition metal carbonyls as the Lewis acid.[6] In contrast, less is known about main group Lewis acid stabilised group 13/15 compounds.[5,7,8] A disadvantage of transition metal carbonyls as Lewis acids is their influence on the reactivity of the phosphanylboranes [Equation (1)]. For example, photolysis of compound **D** leads to a dimer with elimination of CO and $H_2$.[6] Furthermore, the reaction of **D** with iodine leads to oxidation of the tungsten atom with concomitant loss of CO and not, as expected, to halogenation of the phosphorus atom.[9]

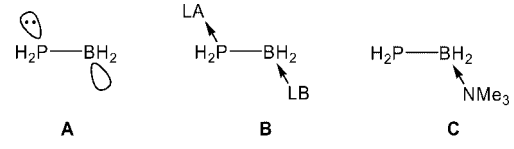


Scheme 1.

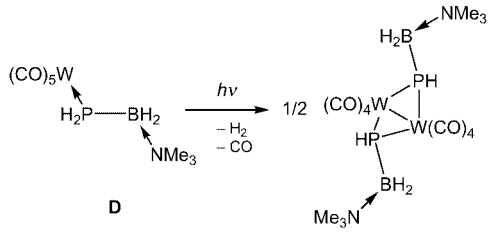


(1)

In order to circumvent the problem of CO elimination reactions, we decided to use main group Lewis acids for the synthesis of LA/LB stabilised phosphanylboranes.

[a] Institut für Anorganische Chemie der Universität Regensburg, 93040 Regensburg, Germany
Fax: +49-941-9434439
E-mail: manfred.scheer@chemie.uni-regensburg.de


© 2007 Wiley-VCH Verlag GmbH & Co. KGaA, Weinheim

Herein we report on the synthesis and characterisation of hydrogen substituted LA/LB stabilised phosphanylboranes with $B(C_6F_5)_3$ and $Ga(C_6F_5)_3$ as main group Lewis acids.[10] Furthermore, the synthesis of the LA/LB stabilised phosphanylboranes is described which are substituted with a phenyl group at the phosphorus atom.

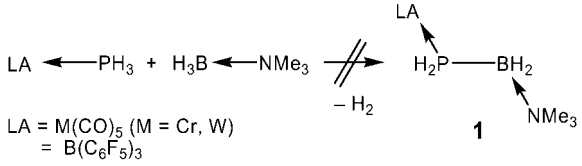


(2)

## Results and Discussion

### Synthesis and Spectroscopic Characterisation of the Lewis Acid/Base-Stabilised Phosphanylboranes

For the synthesis of the type **B** compounds containing transition metal carbonyls as the LA, the salt elimination method was chosen as a general synthetic route since the $H_2$ elimination had failed. The same behaviour was found for the main group LA containing compounds [Equation (2)].

Thus, for the synthesis of the LA/LB stabilised phosphanylborane **1** [Equation (3)] $(C_6F_5)_3BPH_3$ was metallated in toluene with *n*BuLi. The $^{31}P$ NMR spectrum of the in situ generated $[(C_6F_5)_3BPH_2Li]$ in $[D_8]$THF exhibits a multiplet of triplets at $\delta$ = –165.1 ppm (Figure 1). The strongly upfield shifted resonance of the phosphorus nucleus of $[(C_6F_5)_3BPH_2Li]$ can be attributed to the formation of a negatively charged phosphanido complex. The $^1J_{P,H}$ value of 180 Hz of $[(C_6F_5)_3BPH_2Li]$ is comparable with the coupling constant in $BH_3PH_2Li$ ($^1J_{P,H}$ = 175).[11] By treating $[(C_6F_5)_3BPH_2Li]$ with $ClBH_2NMe_3$, $(C_6F_5)_3BPH_2BH_2NMe_3$ (**1**) is formed [Equation (3)].

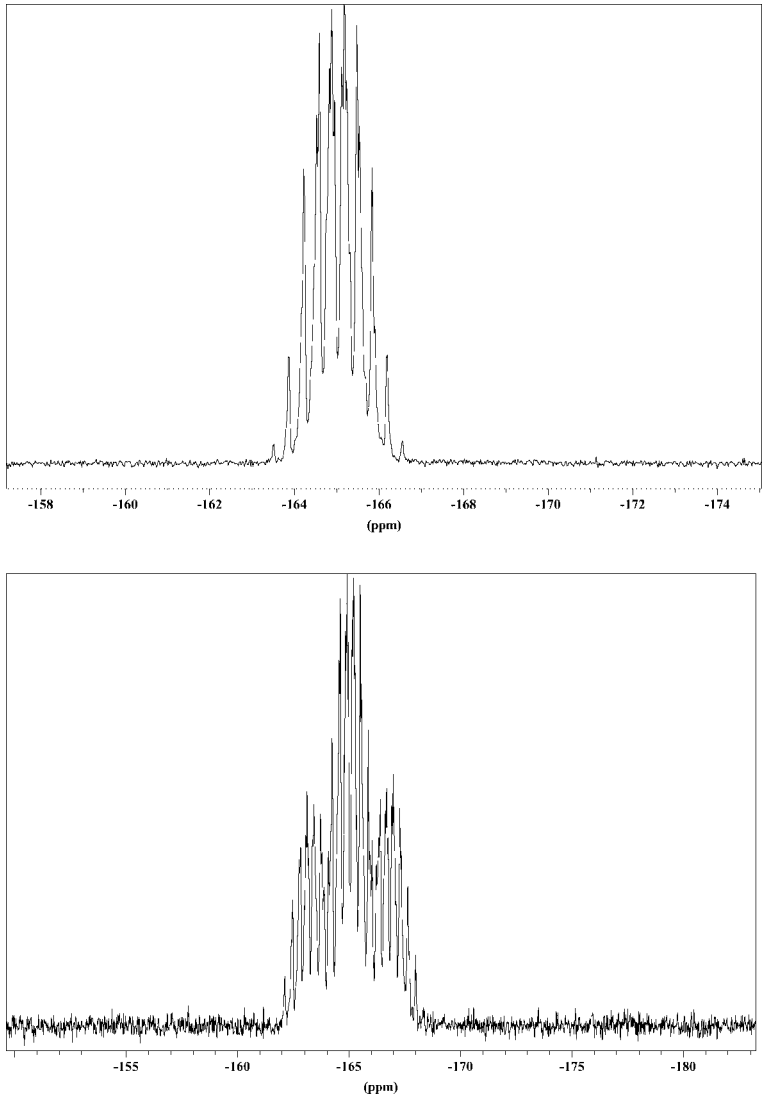


Figure 1. $^{31}P\{^1H\}$ (top) and $^{31}P$ NMR spectra (bottom) of $[(C_6F_5)_3BPH_2Li]$.

 © 2007 Wiley-VCH Verlag GmbH & Co. KGaA, Weinheim 

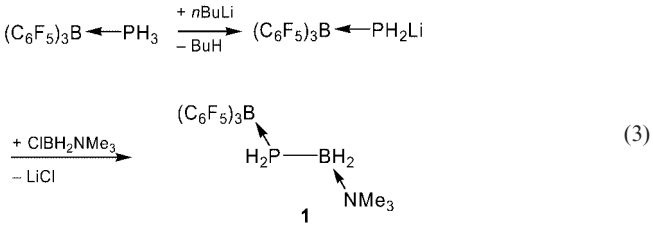


(3)

Since $(C_6F_5)_3GaPH_3$ could not be synthesised in sufficient amounts, the LiCl-elimination route is unsuitable.[12] An elegant way to obtain $(C_6F_5)_3GaPH_2BH_2NMe_3$ (**2**) in quantitative yields is the reaction of $(C_6F_5)_3Ga{\cdot}OEt_2$[13] with $PH_2BH_2NMe_3$ **C** in toluene according to Equation (4).

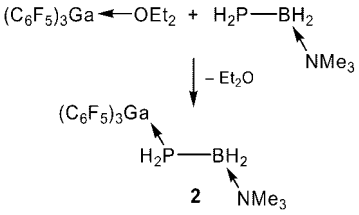


(4)

Furthermore, the synthesis of the LA/LB stabilised phosphanylboranes bearing a phenyl substituent at the P atom was of interest. This additional stabilisation could be helpful in subsequent investigations concerning the abstraction of the Lewis base.

Since $(C_6F_5)_3BPPhH_2$[5] was already described in the literature, the unknown Ga analogue $(C_6F_5)_3GaPPhH_2$ (**3**) was synthesised in almost quantitative yield by adding $PPhH_2$ to a solution of $(C_6F_5)_3Ga{\cdot}OEt_2$ in toluene [Equation (5)].

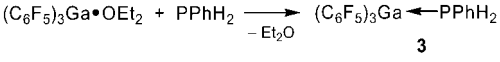


(5)

The $^1H$ NMR spectrum of **3** shows a doublet at $\delta$ = 4.53 ppm ($^1J_{P,H}$ = 369 Hz) attributable to the $PH_2$ protons. The phenyl protons are detected as multiplets between 6.65 and 6.85 ppm. The $^{31}P\{^1H\}$ NMR spectrum reveals a resonance at $\delta$ = –81.4 ppm which is detected as a triplet ($^1J_{P,H}$ = 369 Hz).

$(C_6F_5)_3GaPPhH_2$ (**3**) crystallises as colourless prisms in the triclinic space group $P\bar{1}$. The Ga–P bond length (2.477(1) Å] is within the normal range for Ga–P single bonds, which may vary from 2.256(3) Å to 2.462(3) Å.[1b,14] A π-stacking interaction between the phenyl ring at the P atom and one of the perfluorinated phenyl rings of $(C_6F_5)_3Ga$ is observed (Figure 2) with a distance of 3.851(1) Å between the ring centres, which is longer than the interlayer distance in graphite (3.354 Å). The angle between the planes of these two phenyl rings was determined to be 24.04°. These results are in good agreement with known aryl–perfluoroaryl π-interactions, where the distances and angles between the aromatic rings are in the range of 3.3 to 3.8 Å and 20°, respectively.[15–17]

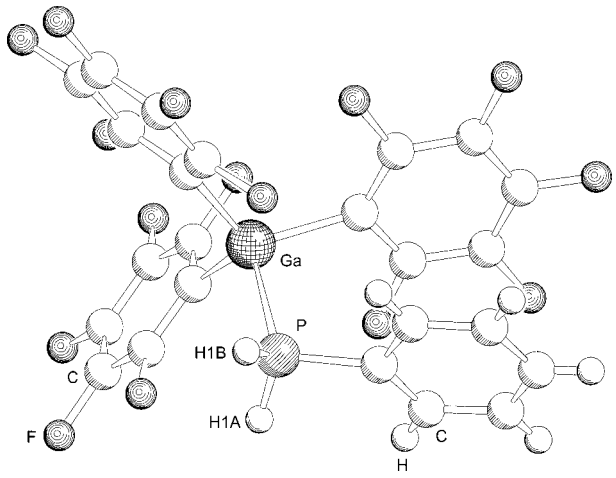


Figure 2. Molecular structure of $(C_6F_5)_3GaPPhH_2$ (**3**) in the crystal.

Metalation of $(C_6F_5)_3GaPPhH_2$ **3** as well as of $(C_6F_5)_3BPPhH_2$ with *n*BuLi leads to $[(C_6F_5)_3EPPhHLi]$ which were then treated with $ClBH_2NMe_3$ to yield colourless crystals of $(C_6F_5)_3BPPhHBH_2NMe_3$ (**4**) and $(C_6F_5)_3GaPPhHBH_2NMe_3$ (**5**), respectively [Equation (6)].

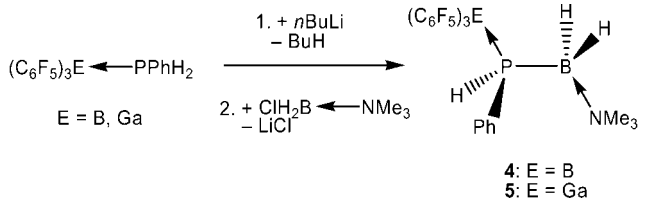


(6)

Only in the mass spectrum of **5** is the molecular ion peak detected. In the case of **1**, **4** and **5** the highest peak is that of the Lewis acid $[E(C_6F_5)_3]^+$. Furthermore, in the mass spectrum of **2** a peak corresponding to $[PH_2BH_2NMe_3]^+$ was found. The IR spectra of the compounds **1**, **2**, **4** and **5** reveal absorptions in the range of 2410 $cm^{-1}$ to 2460 $cm^{-1}$ for the B–H stretching modes and the P–H stretching frequencies appear between 2320 $cm^{-1}$ and 2440 $cm^{-1}$. The $^{19}F$ NMR spectra of the products show the three separated resonances for *ortho*-, *meta*- and *para*-fluorine atoms. The *ortho* and the *meta* resonances of **1** are slightly upfield shifted compared to the corresponding resonances of free $(C_6F_5)_3B$.[18] The *para*-fluorine resonance of **1**, in which the boron atom of the Lewis acid is in a tetrahedral environment, is shifted downfield by about 10 ppm relative to that of free $(C_6F_5)_3B$ in which the boron atom possesses a trigonal planar geometry.

In the $^1H$ NMR spectrum of **1** a singlet is detected at $\delta$ = 2.11 ppm for the trimethylamine group, and a doublet at $\delta$ = 4.0 ppm ($^1J_{P,H}$ = 345 Hz) arising from the $PH_2$ protons. The $^{31}P\{^1H\}$ NMR spectrum of **1** shows a broadened singlet at $\delta$ = –109.8 ppm, while the proton-coupled spectrum reveals a broad triplet ($^1J_{P,H}$ = 345 Hz). Also, the $^{11}B\{^1H\}$ NMR spectrum shows a broad resonance at $\delta$ = –0.4 ppm

 © 2007 Wiley-VCH Verlag GmbH & Co. KGaA, Weinheim 

for the $BH_2$ moiety, which splits into a broad triplet with a boron–hydrogen coupling constant of $^1J_{B,H}$ = 133 Hz when the spectrum is measured with proton coupling. In comparison with the trigonal planar surrounded boron atom of free $B(C_6F_5)_3$, which can be detected in its $^{11}B$ NMR spectrum at $\delta$ = 59.6 ppm, the resonance of the boron atom of the LA in compound **1**, which is in a tetrahedral environment, is shifted strongly upfield and appears at $\delta$ = –18.3 ppm as a broad singlet.

The chemical shift for the methyl protons of the Lewis base of **2** is detected at $\delta$ = 1.48 ppm in the $^1H$ NMR spectrum and the $PH_2$ protons show a broad doublet at $\delta$ = 2.85 ppm ($^1J_{P,H}$ = 318 Hz). The $^{31}P$ NMR spectrum of **2** shows a broad triplet at $\delta$ = –161.1 ppm ($^1J_{P,H}$ = 321.8 Hz) and a broad singlet in the case of the $^{31}P\{^1H\}$ NMR spectrum. In the $^{11}B\{^1H\}$ NMR spectrum the resonance for the boron nucleus is detected at $\delta$ = –10.81 ppm as a broad singlet, with no discernible fine structure. Acquisition of the proton-coupled spectrum only leads to broadening of this signal.

The $^1H$ NMR spectrum of **4** shows a singlet at $\delta$ = 1.33 ppm which can be assigned to the $NMe_3$ group, a resonance for the P–H proton, which splits into a doublet at $\delta$ = 5.44 ppm ($^1J_{P,H}$ = 353 Hz), and multiplets for the aromatic protons between 6.8 and 7.0 ppm. The $^{31}P\{^1H\}$ NMR spectrum shows a resonance at $\delta$ = –51.5 ppm, which is detected in the $^{31}P$ NMR as a doublet ($^1J_{P,H}$ = 352 Hz). The boron atom of the Lewis acid $(C_6F_5)_3B$ can be detected in the $^{11}B$ NMR and $^{11}B\{^1H\}$ NMR spectra ($\delta$ = –14.7 ppm) as can that of the $BH_2$ group ($\delta$ = –10.8 ppm). The latter signal is only revealed as a broad singlet, displaying no splitting into a triplet when a proton-coupled spectrum of **4** is recorded.

The $^1H$ NMR spectrum of **5** shows a broadened doublet at $\delta$ = 4.53 ppm arising from the PH unit ($^1J_{P,H}$ = 328 Hz). The $NMe_3$ resonance is detected at $\delta$ = 1.34 ppm and the protons of the phenyl group are split into a multiplet between 6.8 and 6.9 ppm. The $^{31}P\{^1H\}$NMR spectrum of **5** shows a resonance at $\delta$ = –77.9 ppm, which is detected as a triplet ($^1J_{P,H}$ = 328 Hz) in the $^{31}P$ NMR spectrum. The $^{11}B\{^1H\}$ NMR spectrum shows a broad signal at $\delta$ = –9.7 ppm, which reveals slightly broadening in the proton-coupled spectrum.

## X-ray Structural Characterisation of the Lewis Acid/Base-Stabilised Phosphanylboranes

The compounds **1**–**5** crystallise as colourless prisms from a mixture of toluene and *n*-hexane. The structures were confirmed by X-ray diffraction studies (Table 2). Selected bond lengths and angles of the compounds **1**, **2**, **4** and **5** are listed in Table 1.

**1**, **2**, **4** and **5** show the same HRP–$BH_2$ structural motif [**1**, **2**: R = H (Figure 3); **4**, **5**: R = Ph (Figure 4)] in the solid state. This moiety is coordinated to the Lewis acid (**1**, **4**: $B(C_6F_5)_3$; **2**, **5**: $Ga(C_6F_5)_3$) by the lone pair of the phosphorus atom, so that the phosphorus is surrounded by four substituents. The boron atom is in a tetrahedral environment due to coordination of the Lewis base $NMe_3$. The Lewis acid (**1**, **4**: $B(C_6F_5)_3$; **2**, **5**: $Ga(C_6F_5)_3$) and the Lewis base $NMe_3$ adopt a *trans* arrangement and the substituents around the P–B bond are arranged in a slightly staggered geometry. The compounds **1** and **2** are isostructural and crystallise in the centrosymmetric space group $P\bar{1}$ revealing

Table 1. Selected bond lengths [Å] and angles [°] of the phosphanylboranes **1**, **2**, **4** and **5**.

| | **1** | **2** | **4** | **5** |
|---|---|---|---|---|
| $LA_B$–P | 2.047(3) | – | 2.046(3) | – |
| $LA_{Ga}$–P | – | 2.393(1) | – | 2.424(1) |
| P–B | 1.989(4) | 1.992(2) | 1.974(3) | 1.963(2) |
| B–N | 1.601(4) | 1.586(3) | 1.604(4) | 1.606(3) |
| LA–P–B | 122.98(13) | 116.55(8) | 111.02(10) | 114.17(9) |
| P–B–N | 112.2(2) | 113.36(14) | 116.05(16) | 115.06(16) |
| Torsion angles | | | | |
| LA–P–B–N | 150.781(26) | 154.24(14) | 170.18(16) | 175.61(12) |

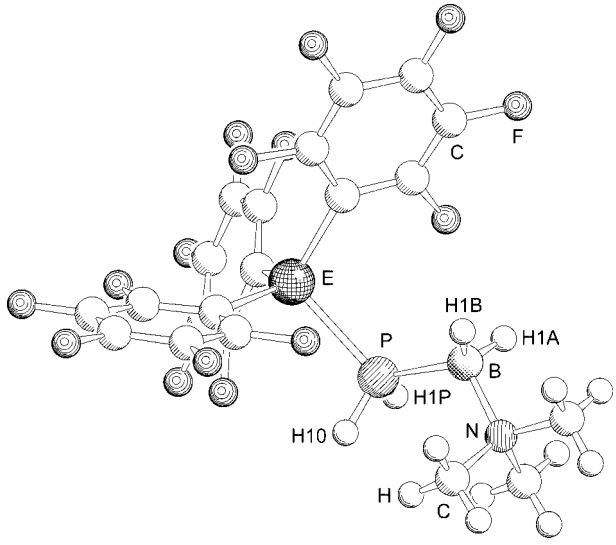


Figure 3. Molecular structures of **1** (E = B) and **2** (E = Ga) in the crystal.

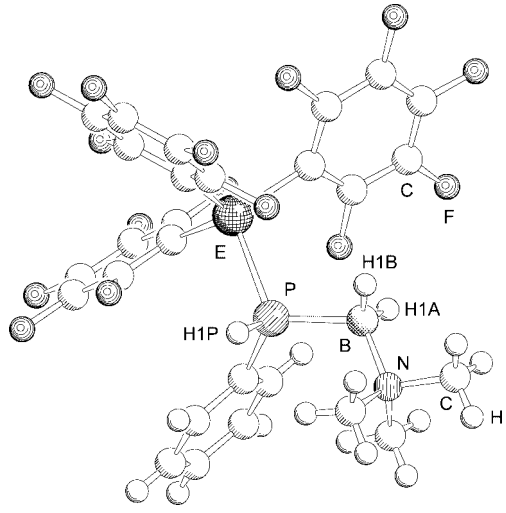


Figure 4. Molecular structure of **4** (E = B) and **5** (E = Ga), respectively in the crystal.

 © 2007 Wiley-VCH Verlag GmbH & Co. KGaA, Weinheim 

the same staggered geometry around the P–B core as both enantiomers show which are present in the solid state (Figure 5, a).

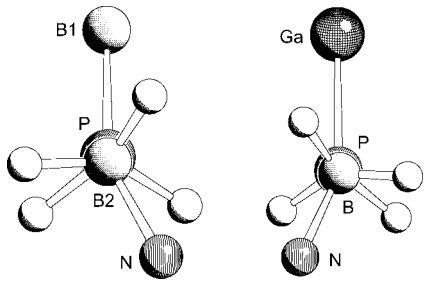


Figure 5. Staggered conformation around the B–P bonds in **1** (left, E = B) and **2** (right, E = Ga).

Besides the LA and LB, **1** and **2** are only substituted by hydrogen atoms. The P–B bond distances of **1** [(1.989(4) Å] and **2** [(1.992(2) Å] agree well with usual P–B single-bond distances, which range from 1.90 Å to 2.0 Å.[1] A comparison with the P–B bond length in $[W(CO)_5PH_2BH_2NMe_3]$ **D** [(1.955(2) Å] shows that compounds **1** and **2** possess slightly longer P–B bond distances. The P–B bond distance in the calculated LA and LB free compound **A** is with 1.90 Å[2b] (1.905 Å[2c]) slightly shortened due to a small P–B π-bond contribution in **A**, which is absent in the LA/LB stabilised molecules **1** and **2**. Whereas the P–B–N angles of **1** [(112.2(2)°] and **2** [(113.36(14)°] are very similar, the LA–P–B angles differ significantly [**1**: 122.98(13)°; **2**: 116.55(8)°], revealing the different valence radii of the boron and gallium atoms in the LA.

Compounds **4** and **5**, which possess a phenyl substituent at the phosphorus atom, show similar structures, although they do not crystallise in the same space group. The values of their P–B bond distances do not differ much. Their P–B–N angles are very similar [**4**: 116.05(16); **5**: 115.06(16)°], as are their LA–P–B angles [**4**: 111.02(10)°; **5**: 114.17(9)°]. The substituents around the P–B core in **4** and **5** adopt a staggered geometry (Figure 6).

Whereas the Ga containing LA substituted compound **5** shows some π-stacking interaction between one of the perfluorinated phenyl rings of the LA and the phenyl substituent at the phosphorus atom (Figure 7), no π-stacking interaction is noticeable in **4**. The center-to-center distance of the phenyl rings in **5** is 4.082 Å, which is longer than the distance between the fluoroaryl and the aryl groups in **3** (3.851 Å). The angle formed by the two planes of the staggered phenyl rings is 29°.

In comparison with the bond distance of the B–P core of the phosphanylboranes the boron containing LA–P bond distances in **1** and **4** are slightly elongated [**1**: 2.076(3) Å; **4**: 2.046(3) Å]. The Ga–P bond distance in compound **5** [2.424(1) Å] shows nearly the same length as that that is found in the starting material **3** [2.477(1) Å], and is in the normal range for a Ga–P single bond, which varies between 2.256(3) Å and 2.462(3) Å.[1b,14] The value of the Ga–P bond length of compound **2** [2.393(1) Å] also lies within this range.

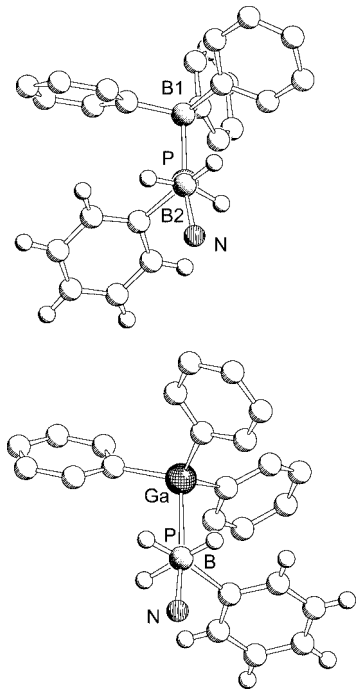


Figure 6. Staggered geometries of **4** (top, E = B) and **5** (bottom, E = Ga). F atoms and Me groups are omitted for clarity.

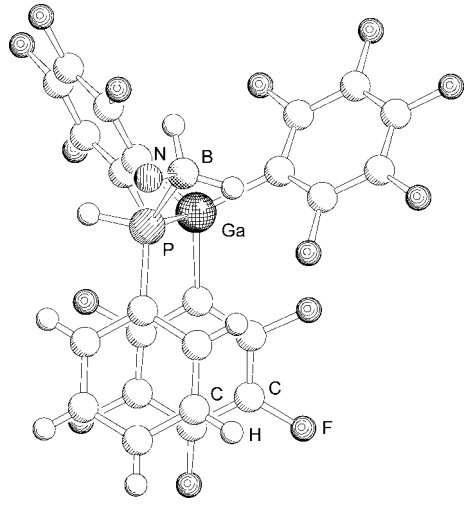


Figure 7. π-stacking interaction in **5**.

In 2003 Denis et al. reported on the dehydrocoupling between $(C_6F_5)_3BPH_2R$ (R = H or Ph) and $BH_3/SMe_2$ to form $(C_6F_5)_3BPH_2BH_2SMe_2$ and $(C_6F_5)_3BPH(Ph)$-$BH_2SMe_2$.[5] They described a subsequent polymerization at 20 °C in the case of the phenyl-substituted derivative and at 110 °C for 3 h in the case of the hydrogen substituted derivative, which led to the formation of the polymers $[PHRBH_2]_n$ (R = H or Ph) and $(C_6F_5)_3BSMe_2$, as confirmed by NMR studies. In contrast the $NMe_3$-substituted LA/LB-stabilised phosphanylboranes **1**, **2**, **4**, and **5**, which we report herein, show a very high thermal stability up to 150 °C, without any signs of decomposition or dehydrocoupling to form polymerisation products.

 © 2007 Wiley-VCH Verlag GmbH & Co. KGaA, Weinheim 

## Conclusions

The results reported herein have shown that we were able to use perfluorinated main group Lewis acids to prepare LA/LB-stabilised phosphanylboranes. The parent compound $H_2P–BH_2$ can be stabilised with $NMe_3$ as the Lewis base and $B(C_6F_5)_3$ (**1**) or $Ga(C_6F_5)_3$ (**2**) as the main group Lewis acid. Furthermore the synthesis of the phenyl-substituted LA/LB stabilised phosphanylboranes **4** and **5** was achieved. In the solid state, the substituents in all products show a staggered geometry around the central P–B core. In the Ga containing compounds **3** and **5**, π-stacking interactions between one of the perfluorinated phenyl rings of the LA and the phenyl substituent at the phosphorus atom contribute to their stability. These compounds do not show any tendency to polymerise in contrast to previously reported $SMe_2$-substituted compounds.[5] Furthermore we expect that removal of the Lewis base from the synthesised compounds will yield stable derivatives stabilised only by a Lewis acid. These investigations are in progress.

## Experimental Section

**General Techniques:** All manipulations were performed under an atmosphere of dry nitrogen using standard Glovebox and Schlenk techniques. Solvents were purified and degassed by standard procedures. The compounds $B(C_6F_5)_3$,[13] $(C_6F_5)_3GaOEt_2$,[13] $(C_6F_5)_3BPH_3$,[19] $(C_6F_5)_3BPPhH_2$,[5] $PH_2BH_2NMe_3$,[7] $ClBH_2NMe_3$[20] and $PPhH_2$[21] were prepared according to the literature procedures. *n*BuLi (Fluka, 1.6 molar solution in *n*-hexane) was used as received.

The NMR spectra were recorded on either a Bruker 300 or Avance 400 spectrometer with $\delta$ referenced to external $SiMe_4$ ($^1H$), $H_3PO_4$ ($^{31}P$), $BF_3–Et_2O$ ($^{11}B$) and $CFCl_3$ ($^{19}F$). IR spectra were measured on a DIGILAB (FTS 800) FT-IR spectrometer. All mass spectra were recorded on a Finnigan MAT 95 (FD) or a Finnigan MAT SSQ 710 A (EI, 70 eV) instrument.

**Synthesis of $(C_6F_5)_3BPH_2BH_2NMe_3$ (1):** To a solution of $(C_6F_5)_3BPH_3$ (170 mg, 0.31 mmol) in toluene (20 mL), *n*BuLi (0.19 mL, 0.31 mmol) is added dropwise at 0 °C. After stirring the solution at room temperature for 3 h, the formation of $(C_6F_5)_3BPH_2Li$ is confirmed by $^{31}P$ NMR ([D$_8$]THF, 101.256 MHz, $\delta$ = –165.14, mt, $^1J_{P,H}$ = 180 Hz, $PH_2$). $ClBH_2NMe_3$ (33 mg, 0.31 mmol) is then added and the mixture is stirred at room temperature for 18 h. The LiCl precipitate is filtered through a plug of Celite and the resulting solution is concentrated to 2 mL in vacuo. Colourless crystals of **1** are obtained as prisms by slow diffusion of *n*-hexane into this solution of **1** at room temperature. Yield 163 mg (85%). $^1H$ NMR ($C_6D_6$, 25 °C, 250 MHz): $\delta$ = 2.11 (s, 9 H, $N(CH_3)_3$), 4.0 (dm, $^1J_{P,H}$ = 345 Hz, 2 H, $PH_2$) ppm. $^{31}P$ NMR ($C_6D_6$, 25 °C, 101.3 MHz): $\delta$ = –109.66 (br. t, $^1J_{P,H}$ = 345 Hz, $PH_2$) ppm. $^{31}P\{^1H\}$ NMR: $\delta$ = –109.81 (br. s, $PH_2$) ppm. $^{11}B$ NMR ($C_6D_6$, 25 °C, 96.3 MHz): $\delta$ = –0.42 (br. t, $^1J_{B,H}$ = 133 Hz, $BH_2$), –18.27 (br. s, $B(C_6F_5)_3$) ppm. $^{11}B\{^1H\}$ NMR: $\delta$ = –0.4 (br. s, $BH_2$), –18.27 (br. s, $B(C_6F_5)_3$) ppm. $^{19}F$ NMR ($C_6D_6$, 25 °C, 282.4 MHz): $\delta$ = –130.8 (br. s, 6 F, *o*-F), –157.52 (t, $^3J_{F,F}$ = 20.8 Hz, 3 F, *p*-F), –164.03 (m, 6 F, *m*-F) ppm. EI-MS (70eV, 180 °C): *m*/*z* (%) = 512 (100) $[(C_6F_5)_3B]^+$, 168 (52) $[C_6F_5H]^+$, 58 (64) $[NMe_3–H]^+$. Raman (Solid): $\tilde{\nu}$ = 3027 (s, CH), 2973 (s, CH), 2956 (s, CH), 2871 (s, CH), 2471 (br. m, BH), 2433 (s, PH), 2394 (vs, PH), 1647 (s, CF), 1377 (m), 975 (br. m), 850 (s), 595 (m), 581 (s), 490 (s), 472 (m), 448 (s), 394 (s) cm$^{-1}$. IR (KBr): $\tilde{\nu}$ = 3026 (s, CH), 2962 (s, CH), 2925 (m, CH), 2853 (w, CH), 2463 (s, BH), 2433 (s, BH), 2394 (w, PH), 2324 (vw, PH), 1647 (vs, CF), 1601 (w), 1518 (vs), 1464 (vs), 1376 (s), 1281 (s), 1130 (s), 1110 (vs), 1085 (s), 1071 (w, sh), 982 (s), 966 (s), 868 (m), 826 (m), 784 (s), 772 (s), 736 (m), 709 (m), 674 (s), 670 (s, sh), 624 (m), 575 (m), 472 (br. m) cm$^{-1}$. $C_{21}H_{13}B_2F_{15}NP$ (616.9): calcd. C 40.88, H 2.12, N 2.27; found C 41.25, H 2.38, N 2.28.

**Synthesis of $(C_6F_5)_3GaPH_2BH_2NMe_3$ (2):** $(C_6F_5)_3GaOEt_2$ (356 mg, 0.552 mmol) is added to a solution of $PH_2BH_2NMe_3$ (0.058 mg, 0.552 mmol) in toluene (25 mL). After stirring for 18 h, the solution is concentrated to ca. 4 mL in vacuo. Colourless crystals of **2** are obtained by slow diffusion of *n*-hexane into this solution at room temperature. Yield 401 mg (97%). $^1H$ NMR ($C_6D_6$, 25 °C, 300 MHz): $\delta$ = 1.48 (s, 9 H, $N(CH_3)_3$), 2.85 (br. d, $^1J_{P,H}$ = 318 Hz, 2 H, $PH_2$) ppm. $^{31}P$ NMR ($C_6D_6$, 25 °C, 121.5 MHz): $\delta$ = –161.13 (br. t, $^1J_{P,H}$ = 321.8 Hz, $PH_2$) ppm. $^{31}P\{^1H\}$ NMR: $\delta$ = –161.14 (s, $PH_2$) ppm. $^{11}B$ NMR ($C_6D_6$, 25 °C, 128.4 MHz): $\delta$ = –10.94 (br. s, $BH_2$) ppm. $^{11}B\{^1H\}$ NMR: $\delta$ = –10.81 (br. s, $BH_2$) ppm. $^{19}F$ NMR ($C_6D_6$, 25 °C, 282.4 MHz): $\delta$ = –122.7 (d, $^3J_{F,F}$ = 18.5 Hz, 6 F, *o*-F), –154.4 (t, $^3J_{F,F}$ = 19.6 Hz, 3 F, *p*-F), –161.9 (m, 6 F, *m*-F) ppm. EI-MS (70 eV): *m*/*z* (%) = 570 (21) $[[(C_6F_5)_3Ga]^+]$, 403 (43) $[[(C_6F_5)_2Ga]^+]$, 168 (100) $[[C_6F_5H]^+]$, 105 (12) $[[PH_2BH_2NMe_3]^+]$. IR (KBr): $\tilde{\nu}$ = 3026 (s, CH), 2961 (s, CH), 2925 (m, CH), 2853 (br. m, CH), 2454 (s, BH), 2424 (s, BH), 2374 (br. m, PH), 2318 (m, PH), 1643 (vs, CF), 1613 (w), 1556 (w, sh), 1511 (vs), 1467 (vs), 1445 (m, sh), 1411 (m), 1363 (s), 1268 (s), 1243 (m), 1160 (s), 1126 (s), 1066 (vs), 1015 (m), 960 (vs), 863 (s), 798 (m), 756 (m), 740 (w), 720 (w), 700 (m), 608 (m), 490 (m) cm$^{-1}$. $C_{21}H_{13}BF_{15}GaNP$ (675.8): calcd. C 37.32, H 1.94, N 2.07; found C 37.21, H 2.01, N 2.02.

**Synthesis of $(C_6F_5)_3GaPPhH_2$ (3):** $PhPH_2$ (0.852 mL, 0.853 g, 7.75 mmol) is added slowly to a solution of $(C_6F_5)_3GaOEt_2$ (5 g, 7.75 mmol) in toluene (70 mL) at 0 °C. After stirring the solution for 18 h at room temperature the solvent is removed in vacuo and the residue is washed with *n*-hexane (3 × 20 mL) leaving $(C_6F_5)_3GaPPhH_2$ as a white powder. Single crystals of **3** can be obtained by recrystallisation from a mixture of toluene and *n*-hexane as colourless prisms. Yield 5.06 g (91%). $^1H$ NMR ($C_6D_6$, 25 °C, 400 MHz): $\delta$ = 4.53 (d, $^1J_{P,H}$ = 369 Hz, 2 H, $PH_2$), 6.65–6.85 (m, 5 H, Ph) ppm. $^{31}P$ NMR ($C_6D_6$, 25 °C, 162 MHz): $\delta$ = –81.44 (t, $^1J_{P,H}$ = 369 Hz, $PH_2$) ppm. $^{31}P\{^1H\}$ NMR: $\delta$ = –81.44 (s, $PH_2$) ppm. $^{19}F$ NMR ($C_6D_6$, 25 °C, 376.5 MHz): $\delta$ = –122.89 (d, $^3J_{F,F}$ = 17 Hz, 6 F, *o*-F), –151.73 (t, $^3J_{F,F}$ = 20 Hz, 3 F, *p*-F), –160.46 (m, 6 F, *m*-F) ppm. $^{13}C\{^1H\}$ NMR ($C_6D_6$, 25 °C, 75.5 MHz): $\delta$ = 129.19 (d, $^3J_{C,P}$ = 9 Hz, *m*-C ($C_6H_5$)), 130.74 (s, *p*-C ($C_6H_5$)), 133.79 (d, $^2J_{C,P}$ = 12 Hz, *o*-C ($C_6H_5$)), 137.42 (br. d, $^1J_{C,F}$ = 250 Hz, *p*-C, $Ga(C_6F_5)_3$), 142.06 (br. d, $^1J_{C,F}$ = 254 Hz, *m*-C, $Ga(C_6F_5)_3$), 148.97 (br. d, $^1J_{C,F}$ = 235 Hz, *o*-C, $Ga(C_6F_5)_3$) ppm. EI-MS (70 eV, toluene): *m*/*z* (%) = 570 (15) $[Ga(C_6F_5)_3]^+$, 168 (100) $[C_6F_5H]^+$. IR (KBr): $\tilde{\nu}$ = 3067 (m, CH), 2968 (w, CH), 2916 (w, CH), 2880 (w, CH), 2405 (m, PH), 2323 (m, PH), 1639 (s, CF), 1613 (w), 1576 (w), 1555 (w, sh), 1510 (vs), 1468 (vs), 1443 (s, sh), 1365 (s), 1271 (s), 1221 (m), 1127 (m), 1086 (s, sh), 1068 (vs), 1024 (m), 999 (m), 962 (vs), 844 (s), 799 (m), 738 (s), 719 (w), 691 (m), 611 (m), 582 (w), 491 (m), 460 (w), 412 (m) cm$^{-1}$. $C_{24}H_7F_{15}GaP$ (681): calcd. C 42.33, H 1.04; found C 42.17, H 1.12.

**Synthesis of $(C_6F_5)_3BPPhHBH_2NMe_3$ (4):** To a solution of $(C_6F_5)_3BPPhH_2$ (298 mg, 0.479 mmol) in toluene (25 mL), *n*BuLi (0.3 mL, 0.48 mmol) is added slowly at 0 °C. After stirring the solution at room temperature for 1 h, $ClBH_2NMe_3$ (51 mg, 0.475 mmol) is added and the solution is stirred overnight at room

 © 2007 Wiley-VCH Verlag GmbH & Co. KGaA, Weinheim 

temperature. Filtration of the reaction mixture over a bed of Celite followed by concentration of the filtrate to ca. 2 mL and layering with *n*-hexane yields **4** as colourless prisms. Yield 266 mg (81%). $^{1}$H NMR ($C_6D_6$, 25 °C, 400 MHz): $\delta$ = 1.33 (s, 9 H, $N(CH_3)_3$), 5.44 (dm, $^{1}J_{P,H}$ = 353 Hz, 1 H, PH), 6.8–7.0 (m, 5 H, $C_6H_5$) ppm. $^{31}$P NMR ($C_6D_6$, 25 °C, 162 MHz): $\delta$ = –51.5 (d, $^{1}J_{P,H}$ = 352 Hz, PH) ppm. $^{31}$P{$^{1}$H} NMR: $\delta$ = –51.5 (s, PH) ppm. $^{11}$B NMR ($C_6D_6$, 25 °C, 128.4 MHz): $\delta$ = –14.66 (br. s, $(C_6F_5)_3B$), –10.83 (br. s, $BH_2$) ppm. $^{11}$B{$^{1}$H} NMR: $\delta$ = –14.66 [s, $(C_6F_5)_3B$], –10.83 (s, $BH_2$) ppm. $^{19}$F NMR ($C_6D_6$, 25 °C, 376.5 MHz): $\delta$ = –128.15 (s, 6 F, *o*-F), –158.25 (t, $^{3}J_{F,F}$ = 20 Hz, 3 F, *p*-F), –164.45 (t, $^{3}J_{F,F}$ = 19 Hz, 6 F, *m*-F) ppm. $^{13}$C{$^{1}$H} NMR ($C_6D_6$, 25 °C, 100.6 MHz): $\delta$ = 52 ppm. 96 (d, $^{3}J_{C,P}$ = 4.8 Hz, $N(CH_3)_3$), 128.73 (d, $^{3}J_{C,P}$ = 9.2 Hz, *m*-C, $C_6H_5$), 130.75 (d, $^{4}J_{C,P}$ = 2.7 Hz, *p*-C, $C_6H_5$), 133.52 (d, $^{2}J_{C,P}$ = 5.9 Hz, *o*-C, $C_6H_5$), 137.56 (br. d, $^{1}J_{C,F}$ = 248 Hz, *p*-C, $Ga(C_6F_5)_3$), 140.03 (br. d, $^{1}J_{C,F}$ = 231 Hz, *m*-C, $Ga(C_6F_5)_3$), 148.7 (br. d, $^{1}J_{C,F}$ = 242 Hz, *o*-C, $Ga(C_6F_5)_3$) ppm. FI/FD-MS (toluene): *m*/*z* (%) = 512 (100), $[(C_6F_5)_3B]^+$, 361.5 (26), $[M^+ - 2\ C_6F_5]$). IR (KBr):[22] $\tilde{\nu}$ = 3079 (br. m, CH), 3028 (s, CH), 3010 (s, CH), 2954 (s, CH), 2924 (w, b, CH), 2846 (s, CH), 2462 (s, BH), 2419 (s, BH), 1645 (vs, CF), 1602 (w), 1518 (vs), 1469 (vs), 1409 (m), 1382 (s), 1372 (w, sh), 1317 (w), 1284 (s), 1158 (m), 1129 (s), 1094 (vs), 1025 (m), 980 (vs), 849 (s, br), 789 (s), 773 (m), 759 (s), 744 (m), 705 (m), 677 (s), 605 (m), 575 (m), 502 (m), 468 (m), 430 (m), 419 (w) cm$^{-1}$. $C_{27}H_{17}B_2F_{15}NP$ (693.00): calcd. C 46.79, H 2.47, N 2.02; found C 46.96, H 2.52, N 1.98.

**Synthesis of $(C_6F_5)_3GaPPhHBH_2NMe_3$ (5):** *n*BuLi (0.3 mL, 0.48 mmol) is added dropwise to a solution of $(C_6F_5)_3GaPPhH_2$ (327 mg, 0.48 mmol) in toluene (25 mL) at 0 °C. The solution is stirred for 1 h at room temperature and then $ClBH_2NMe_3$ (52 mg, 0.484 mmol) is added. After filtration through Celite, the solution is concentrated to ca. 2 mL and layered with *n*-hexane. Crystals of **5** are obtained as colourless prisms which are washed with *n*-hexane (3 × 20 mL). Yield 311 mg (86%). $^{1}$H NMR ($C_6D_6$, 25 °C, 400 MHz): $\delta$ = 4.53 (br. d, $^{1}J_{P,H}$ = 328 Hz, 1 H, PH), 1.34 (s, 9 H, $N(CH_3)_3$), 6.8–6.9 (m, 5 H, $C_6H_5$) ppm. $^{31}$P NMR ($C_6D_6$, 25 °C, 162 MHz): $\delta$ = –77.9 (br. d, $^{1}J_{P,H}$ = 328 Hz, PH) ppm. $^{31}$P{$^{1}$H} NMR: $\delta$ = –77.9 (br. s, PH) ppm. $^{11}$B NMR ($C_6D_6$, 25 °C, 128.4 MHz): $\delta$ = –9.69 (br. m, $BH_2$) ppm. $^{11}$B{$^{1}$H} NMR: $\delta$ = –9.69 (br. s, $BH_2$) ppm. $^{19}$F NMR ($C_6D_6$, 25 °C, 376.5 MHz): $\delta$ = –121.9 (d, $^{3}J_{F,F}$ = 17 Hz, 6 F, *o*-F), –154.4 (t, $^{3}J_{F,F}$ = 20 Hz, 3 F, *p*-F), –161.94 (m, 6 F, *m*-F) ppm. $^{13}$C{$^{1}$H} NMR ($C_6D_6$, 25 °C, 100.6 MHz): $\delta$ = 52.58 (d, $^{3}J_{C,P}$ = 4.9 Hz, $N(CH_3)_3$), 129.03 (d, $^{3}J_{C,P}$ = 10 Hz, *m*-C, $C_6H_5$), 129.9 (s, *p*-C, $C_6H_5$), 132.36 (d, $^{2}J_{C,P}$ = 8 Hz, *o*-C, $C_6H_5$), 137.37 (br. d, $^{1}J_{C,F}$ = 252 Hz, *p*-C, $Ga(C_6F_5)_3$), 141.4 (br. d, $^{1}J_{C,F}$ = 250 Hz, *m*-C, $Ga(C_6F_5)_3$), 149.39 (br. d, $^{1}J_{C,F}$ = 235 Hz, *o*-C, $Ga(C_6F_5)_3$) ppm. FI/FD-MS (toluene): *m*/*z* = 750 (1%, $[M^+ - H]$), 570 (100%, $[(C_6F_5)_3Ga]^+$). IR (KBr):[22] $\tilde{\nu}$ = 3065 (w, CH), 3014 (br. s, CH), 2958 (br. s, CH), 2926 (w, CH), 2451 (br. s, BH), 2416 (br. s, BH), 2318 (w, PH), 1639 (vs, CF), 1612 (w), 1556 (w), 1510 (vs), 1484 (m, sh), 1464 (vs), 1446 (s, sh), 1412 (m), 1361 (s), 1328 (w), 1267 (s), 1243 (m), 1155 (m), 1126 (s), 1076 (vs), 1066 (vs), 1016 (m), 959 (vs), 887 (w), 857 (m), 818 (w), 794 (m), 745 (m), 720 (w), 701 (w, sh), 695 (m), 660 (w), 609 (m), 582 (w), 490 (m) (cm$^{-1}$) cm$^{-1}$. $C_{27}H_{17}BF_{15}GaNP$ (751.9): calcd. C 43.13, H 2.28, N 1.86; found C 42.76, H 2.22, N 1.86.

**Crystal Structure Analyses:** The crystal structure analyses of **1**, **3**, **4** and **5** (Table 2) were performed on a STOE IPDS diffractometer with Mo-$K_\alpha$ radiation ($\lambda$ = 0.71073 Å). The crystal structure analysis of **2** was performed on an Oxford Diffraction Gemini Ultra

Table 2. Crystallographic data for compounds **1**–**5**.

| | **1** | **2** | **3** | **4** | **5** |
|---|---|---|---|---|---|
| Empirical formula | $C_{21}F_{15}H_{13}B_2PN$ | $C_{21}F_{15}H_{13}GaPBN$ | $C_{24}F_{15}H_7GaP$ | $C_{27}H_{17}F_{15}B_2PN$ | $C_{27}H_{17}F_{15}GaPBN$ |
| Formula mass [g mol$^{-1}$] | 616.91 | 675.82 | 680.99 | 693.01 | 751.92 |
| $\lambda$ [Å] | 0.71073 | 0.71073 | 0.71073 | 0.71073 | 0.71073 |
| Crystal system | triclinic | triclinic | triclinic | monoclinic | monoclinic |
| Collection temp. [K] | 100(1) | 123(1) | 123(1) | 173(1) | 173(1) |
| Space group | $P\bar{1}$ | $P\bar{1}$ | $P\bar{1}$ | $P2_1/c$ | $P2_1/n$ |
| *a* [Å] | 9.5020(19) | 9.8314(5) | 7.6898(7) | 9.0723(8) | 14.0153(14) |
| *b* [Å] | 11.544(2) | 11.6007(6) | 10.9916(10) | 14.5892(9) | 12.6649(8) |
| *c* [Å] | 11.592(2) | 11.98837(16) | 14.1418(12) | 21.3383(18) | 17.2272(15) |
| $\alpha$ [°] | 70.93(3) | 70.792(7) | 84.309(11) | 90 | 90 |
| $\beta$ [°] | 76.51(3) | 75.442(7) | 89.773(11) | 93.773(11) | 95.067(11) |
| $\gamma$ [°] | 77.44(3) | 77.731(4) | 77.249(11) | 90 | 90 |
| V [Å$^3$] | 1157(4) | 1236.6(2) | 1159.89(19) | 2818.2(4) | 3045.9(5) |
| Z | 2 | 2 | 2 | 4 | 4 |
| $D_{calcd.}$ [g cm$^{-3}$] | 1.774 | 1.815 | 1.95 | 1.633 | 1.64 |
| $\mu$ [mm$^{-1}$] | 0.254 | 1.303 | 1.39 | 0.218 | 1.068 |
| *F*(000) | 612 | 664 | 664 | 1384 | 1488 |
| 2 $\theta$ range | 3.78–54.08 | 6.20–58.04 | 4.56–53.7 | 3.38–51.64 | 3.60–51.72 |
| Index ranges | $-11 \le h \le 12$ | $-11 \le h \le 13$ | $-9 \le h \le 9$ | $-11 \le h \le 11$ | $-17 \le h \le 17$ |
| | $-14 \le k \le 14$ | $-15 \le k \le 15$ | $-13 \le k \le 13$ | $-17 \le k \le 17$ | $-15 \le k \le 15$ |
| | $-14 \le l \le 14$ | $-16 \le l \le 15$ | $-17 \le l \le 17$ | $-26 \le l \le 26$ | $-21 \le l \le 21$ |
| Reflections collected | 8413 | 14488 | 12608 | 21292 | 29999 |
| Independent reflections | 4688 | 5537 | 4609 | 5374 | 5850 |
| Goodness-of-fit on $F^2$ | 0.942 | 1.094 | 1.078 | 0.844 | 0.942 |
| $R_{int}$ | 0.0714 | 0.0210 | 0.0283 | 0.0462 | 0.043 |
| Parameters | 380 | 376 | 378 | 439 | 427 |
| $R_1$[a] [$I > 2s(I)$] | 0.0485 | 0.0293 | 0.0247 | 0.0366 | 0.0324 |
| $wR_2$[b] (all data) | 0.1309 | 0.0797 | 0.0644 | 0.0893 | 0.0838 |
| max./min. $\Delta\rho$ [e·Å$^{-3}$] | 0.255/–0.494 | 0.515/–0.459 | 0.415/–0.233 | 0.313/–0.203 | 0.454/–0.293 |

[a] $R_1 = \Sigma||F_0|-|F_c||/\Sigma|F_0|$. [b] $wR_2 = \sqrt{\Sigma[w(F_0^2 - F_c^2)^2]}/\sqrt{\Sigma[w(F_0^2)^2]}$.

 © 2007 Wiley-VCH Verlag GmbH & Co. KGaA, Weinheim 

diffractometer with Mo-$K_\alpha$ radiation ($\lambda$ = 0.71073 Å). The structures were solved by direct methods with the program SHELXS-97,[23a] and full-matrix least-squares refinement on $F^2$ in SHELXL-97[23b] was performed with anisotropic displacements for non-H atoms. Hydrogen atoms at the carbon atoms were located in idealised positions and refined isotropically according to the riding model. The hydrogen atoms at the phosphorus and boron atoms could be localised by residual electron density and freely refined. CCDC-630846 (for **1**), -630849 (for **2**), -630847 (for **3**), -630850 (for **4**), and -630848 (for **5**) contain the supplementary crystallographic data for this paper. These data can be obtained free of charge from the Cambridge Crystallographic Data Centre via www.ccdc.cam.ac.uk/data_request/cif.

## Acknowledgments

This work was comprehensively supported by the Deutsche Forschungsgemeinschaft and the Fonds der Chemischen Industrie.

[1] a) R. T. Paine, H. Nöth, *Chem. Rev.* **1995**, *95*, 343–379; b) P. P. Power, *Chem. Rev.* **1999**, *99*, 3463–3503.
[2] a) T. L. Allen, W. H. Fink, *Inorg. Chem.* **1992**, *31*, 1703–1705; b) T. L. Allen, A. C. Scheiner, H. F. Schaefer, *Inorg. Chem.* **1990**, *29*, 1930–1936; c) M. B. Coolidge, W. T. Borden, *J. Am. Chem. Soc.* **1990**, *112*, 1704–1706.
[3] a) R. I. Wagner, F. F. Caserio, *J. Inorg. Nucl. Chem.* **1959**, *11*, 259; b) A. B. Burg, *J. Inorg. Nucl. Chem.* **1959**, *11*, 258.
[4] a) H. Dorn, R. A. Singh, J. A. Massey, A. J. Lough, I. Manners, *Angew. Chem.* **1999**, *111*, 3540–3543; *Angew. Chem. Int. Ed.* **1999**, *38*, 3321–3323; b) H. Dorn, R. A. Singh, J. A. Massey, J. M. Nelson, C. A. Jaska, A. J. Lough, I. Manners, *J. Am. Chem. Soc.* **2000**, *122*, 6669–6678.
[5] J.-M. Denis, H. Forintos, H. Szelke, L. Toupet, T.-N. Pham, P.-J. Madec, A.-C. Gaumont, *Chem. Commun.* **2003**, *1*, 54–55.
[6] U. Vogel, P. Hoemensch, K.-C. Schwan, A. Y. Timoshkin, M. Scheer, *Chem. Eur. J.* **2003**, *9*, 515–519.
[7] K.-C. Schwan, A. Y. Timoskin, M. Zabel, M. Scheer, *Chem. Eur. J.* **2006**, *12*, 4900–4908.
[8] F. Thomas, S. Schulz, H. Mansikkamaeki, M. Nieger, *Organometallics* **2003**, *22*, 3471–3477.
[9] K.-C. Schwan, Ph. D. Thesis, University of Regensburg, **2006**.
[10] W. E. Pier, T. Chivers, *Chem. Soc. Rev.* **1997**, *26*, 345–354; K. Ishihara, H. Yamamoto, *Eur. J. Org. Chem.* **1999**, 527–538.
[11] E. Mayer, *Inorg. Chem.* **1971**, *10*, 2259–2262.
[12] Usually, to synthesise the LA phosphane adducts, $PH_3$ was bubbled through a solution of the corresponding Lewis acid. Whereas Lewis base-free $B(C_6F_5)_3$ can be used as the starting material to synthesise $B(C_6F_5)_3PH_3$, $Ga(C_6F_5)_3$ is only available as a diethyl ether adduct, which hinders the preparation of $Ga(C_6F_5)_3PH_3$ in an acceptable yield per time scale.
[13] J. L. W. Pohlmann, F. E. Brinckmann, *Z. Naturforsch. Teil B* **1965**, *20*, 5–11.
[14] M. Westerhausen, T. Rotter, Ch. Pfaller, A. N. Kneifel, A. Schulz, *Inorg. Chim. Acta* **2005**, *358*, 4253–4260.
[15] C. Janiak, *J. Chem. Soc. Dalton Trans.* **2000**, 3885–3896.
[16] J. H. Williams, *Acc. Chem. Res.* **1993**, *26*, 593–598.
[17] J. C. Collings, K. P. Roscoe, E. G. Robins, A. S. Batsanov, L. M. Stimons, J. A. K. Howard, S. J. Clark, T. B. Marder, *New J. Chem.* **2002**, *26*, 1740–1746.
[18] A. G. Massey, A. J. Park, *J. Organomet. Chem.* **1966**, *5*, 218–225.
[19] D. C. Bradley, M. B. Hursthouse, M. Motevalli, Z. Dao-Hong, *J. Chem. Soc. Chem. Commun.* **1991**, *1*, 7–8.
[20] G. E. Ryschkewitsch, J. W. Wiggins, *Inorg. Synth.* **1970**, *12*, 116–126.
[21] K. Bourumeau, A.-C. Gaumont, J.-M. Denis, *J. Organomet. Chem.* **1997**, *529*, 205–213.
[22] The assignment of the P–H stretching frequencies was difficult, because the $CO_2$ vibration frequencies, which occur in the same region, could not be completely excluded due to the spectrometer settings.
[23] a) G. M. Sheldrick, *SHELXS-97*, University of Göttingen, **1996**; b) G. M. Sheldrick, *SHELXL-97*, University of Göttingen, **1997**.

Received: December 13, 2006
Published Online: April 10, 2007

 © 2007 Wiley-VCH Verlag GmbH & Co. KGaA, Weinheim 

DOI: 10.1002/ejic.200601219

# Aiding Factors in the Formation of Azaplatinacyclobutane Rings – X-ray and Crystal Structure of [Pt{CH(Ph)$CH_2$$NEt_2$-κC,κN}(*N*,*N*,*N*′,*N*′-tetramethylethylenediamine)]$^+$ and of Its Open-Chain Precursor

**Giuseppe Lorusso,[a] Carmen R. Barone,[a] Nicola G. Di Masi,[a] Concetta Pacifico,[a] Luciana Maresca,*[a] and Giovanni Natile[a]**

**Keywords:** Chelates / Metallacycles / N ligands / Nucleophilic addition / Platinum

The addition products **2** of a secondary amine to a coordinated olefin, in the cationic complexes [PtCl(η$^2$-$CH_2$=CHR)(tmeda)]$^+$ (tmeda = *N*,*N*,*N*′,*N*′-tetramethylethylenediamine; R = Me, **1a**; Ph, **1b**, H, **1c**), undergo in basic medium an intramolecular nucleophilic substitution with elimination of the chlorido ligand and formation of an azaplatinacyclobutane ring **3**. The ring-closing process occurs notwithstanding the absence of a labilizing ligand *trans* to the leaving chlorido ligand and of bulky substituents on the amino–ethanide chain. If the addition product **2** is a mixture of Markovnikov and anti-Markovnikov isomers, the ring-closing reaction is faster for the anti-Markovnikov form, and this leads to an increase of the relative amount of the anti-Markovnikov isomer in the cyclized species **3**. The difference in the rate of formation of the azaplatinacyclobutane ring between the two isomers has been interpreted on the basis of a more favorable stereochemistry in the case of the anti-Markovnikov form. The X-ray crystal structures of [Pt{CH(Ph)$CH_2$$NEt_2$-κC,κN}(tmeda)]$^+$ (**3bn**) and of its open-chain precursor, [PtCl{CH(Ph)$CH_2$$NHEt_2$}(tmeda)]$^+$ (**2bn**) fully support this hypothesis.

(© Wiley-VCH Verlag GmbH & Co. KGaA, 69451 Weinheim, Germany, 2007)

## Introduction

A number of azametallacyclobutanes have been reported in the literature; in some cases they have been isolated and fully characterized, while in other cases they have only been detected in solution, or proposed as key intermediates in catalytic processes concerned with the hydroamination of olefins and allenes.[1–8]

The reaction sequence leading to their formation is very much dependent upon the nature of the metal involved. In the case of early transition metals, the azametallacyclobutanes are generated by [2+2] cycloaddition of an olefin to a metalla-imido moiety (M=NR).[1] The reaction is generally reversible, and in the specific case of [$Cp_2$(THF)Zr(=*N*-*t*Bu)] reacting with norbornene, the formed azazirconacyclobutane was also structurally characterized.[1b]

A different and more complex reaction pathway was proposed for the formation of an azatungstacyclobutane. The allenyl precursor, $Cp(CO)_3W$–CH=C=$CH_2$, underwent methylamine addition both at a carbonyl ligand (which was transformed into a carbamoyl group) and at the β-carbon atom of the allenyl ligand (across the terminal double bond), accompanied by a regiospecific coupling of the amido group with the α-carbon atom of the allenyl ligand and the coordination of the amine to the tungsten metal center.[2]

Also in the case of late transition metals, several procedures have been reported to lead to the formation of azametallacyclobutanes. For instance, in the iridium-catalyzed hydroamination of norbornene, reported by Calabrese et al., a very reactive 14-electron iridium complex first undergoes oxidative addition with aniline followed by [2+2] cycloaddition of the formed metalla-amido moiety to norbornene to form an azairidacyclobutane complex.[3] An azairidacyclobutane is also formed by a ring-closing reaction (with elimination of HCl) of an iridium 2-aminoethanide complex obtained by the photolysis of an iridium hydride species in the presence of *tert*-butylamine.[4]

More recently, Puddephatt has reported a platinum(IV) complex containing an azaplatinacyclobutane ring obtained through oxidative addition of a protonated tethered imine group present on a platinum(II)-coordinated amine (the azaplatinacyclobutane ring resulting from the coordination of the imine carbon and the nitrogen atom of a 2-pyridyl substituent present on the imine carbon atom to the platinum atom).[5]

More often, 2-aminoethanide species are formed through nucleophilic addition of an amine to a coordinated olefin followed by a ring-closing process.[6–8] By this procedure stable azaplatinacyclobutane complexes have been prepared since the early 1980's. Their isolation was strictly dependent

[a] Dipartimento Farmaco-Chimico, Università di Bari,
Via E. Orabona, 4, 70125 Bari, Italia
Fax: +390805442230
E-mail: maresca@farmchim.uniba.it


InterScience
© 2007 Wiley-VCH Verlag GmbH & Co. KGaA, Weinheim

upon the nature of the ancillary ligands and the presence of substituents on the metal-coordinated olefin and on the attacking amine.[6,7] Starting from a complex such as *cis*-[$PtCl_2(L)(\eta^2$-alkene/allene)], the addition to the olefin of a secondary amine leads to a zwitterionic species (formal negative charge on the platinum atom and positive charge on the nitrogen ammonium group), which can eliminate HCl and form an azaplatinacyclobutane ring. The reaction occurs readily when L is a *trans*-labilizer (phosphorus or sulfur donor ligand).[6,7] When L is a N-donor ligand, the ring-closing reaction is observed only in the case of olefins bearing substituents on the α and/or β carbon atoms.[7] Azaplatinacyclobutanes formed in the case of L = triphenylphosphane have also been characterized by X-ray crystallography.[6]

We have recently reconsidered the amination reaction of platinum-coordinated olefins in some cationic complexes and observed a facile ring closing of the 2-ammonium ethanide species obtained therefrom, with the ready formation of azaplatinacyclobutane rings. The results, hereafter described, have allowed us to gain new insights into factors governing this reaction (for a preliminary account see ref.[10]).

## Results and Discussion

The cationic complexes [$PtCl(\eta^2$-olefin)(tmeda)]$^+$ (**1**)[9] (tmeda = *N*,*N*,*N*′,*N*′-tetramethylethylenediamine; olefin = alkyl or aryl-substituted ethene such as propene, **1a**, or styrene, **1b**) react quickly and smoothly with secondary amines (such as dimethylamine, **m**, and diethylamine, **n**) to give the corresponding $\eta^1$-2-ammonium ethanide species **2** (see Scheme 1). Species of type **2** exist as equilibrium mixtures of Markovnikov (**M**) and anti-Markovnikov (**anti-M**) forms; the interconversion process most likely requires the detachment and re-addition of the amine as illustrated in Scheme 1. The thermodynamically determined isomeric ratio is largely in favor of the Markovnikov form in the case of **2an** and in favor of the anti-Markovnikov isomer in the case of **2bm**,**n**.[10]

Under basic conditions, the product of amination (**2** in Scheme 1) undergoes deprotonation followed by displacement of the *cis* chlorido ligand by the amine nitrogen atom and formation of an azaplatinacyclobutane species (**3** in Scheme 1). We have found that the **M/anti-M** ratio decreases on going from the linear addition product to the ring-closed species. Therefore, the linear addition product **2an**, containing at equilibrium a **M/anti-M** ratio of 95:5, yields, upon ring-closing, compound **3an**, in which the **M/anti-M** ratio decreases to 75:25. Similarly, the linear addition product **2bm**, in which at equilibrium the **M/anti-M** ratio was 30:70, gives, after the ring-closing process, compound **3bm**, in which the anti-Markovnikov isomer is the exclusive form. This behavior can be explained with a greater propensity of the linear anti-Markovnikov addition product to undergo the ring-closing reaction.

The cyclization reaction of **2an** and **2bm** (leading to **3an** and **3bm**, respectively), performed in an NMR tube under basic conditions, did show the formation of trace amounts of byproducts that were probably due to the reaction of species **1a** and **1b**, which are intermediates in the Markovnikov/anti-Markovnikov isomerization of **2a** and **2b**, with the base.[11] However, by operating on millimolar quantities and after work-up procedures, the species of type **3** were obtained in almost pure form (> 95%).

The structures of species **3** could be unequivocally determined by NMR techniques (1D and 2D $^1H$, $^1H/^{13}C$, APT). The Markovnikov and anti-Markovnikov isomers could be easily distinguished through the different patterns of connectivities in the metallacyclobutane ring. The separation of the Markovnikov and anti-Markovnikov isomers of **3an** (**3bm**,**n** are essentially formed as the **anti-M** isomer)[13] has not been attempted at this stage of the work.

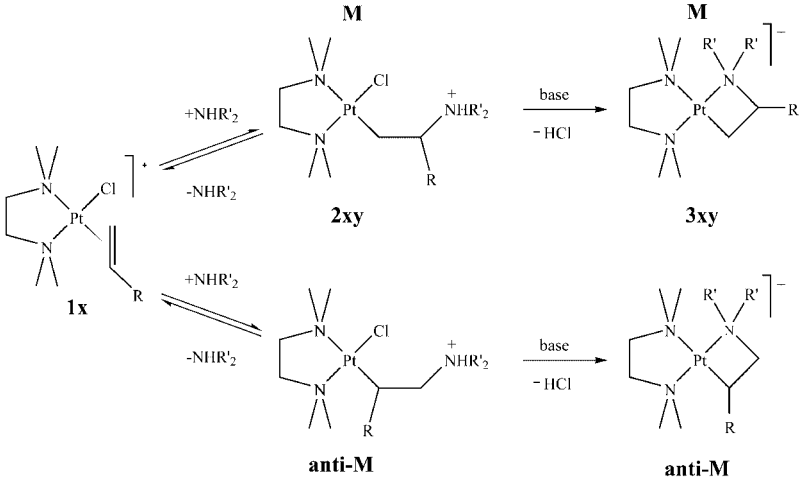


**x** = **a** (R = $CH_3$), **b** (R = $C_6H_5$), **c** (R = H); **y** = **m** (R' = $CH_3$), **n** (R' = $CH_2CH_3$)

**M** = Markovnikov; **anti-M** = anti-Markovnikov

Scheme 1.

 © 2007 Wiley-VCH Verlag GmbH & Co. KGaA, Weinheim 

Some significant differences can be observed between the NMR parameters of the open-chain species **2** and the ring-closed species **3**. In particular, Cα is more shielded in **3** than in **2** while Cβ is more shielded in **2** than in **3** [for the pairs of compounds: **M-2an/M-3an**, **anti-M-2bm/anti-M-3bm**, and **anti-M-2bn/anti-M-3bn**; $\Delta\delta$(Cα) and $\Delta\delta$(Cβ) values are –17.8 and +6.3, –22.7 and +15.6, and –22.1 and +13.7 ppm, respectively]. Similarly to the carbon atom, the protons on the β carbon are also considerably less shielded in the cyclized species **3** than in the linear addition product **2** ($\Delta\delta$ in the range 0.6–1.9 ppm). The deshielding of the β protons was taken by Green et al. as an indicator for the occurrence of the ring-closing process[7] (although in that work the reaction stereochemistry and the possible formation of Markovnikov and anti-Markovnikov isomers were not discussed in detail). Another highly distinctive NMR feature of species **3** is the value of $^{3}J_{Pt,H}$ for the β protons, which can nearly reach 100 Hz, well above the observed values for the corresponding coupling in the linear compounds. It is worth noting that in the **anti-M** isomer, where there are two β protons, these protons are diastereotopic with a dispersion which can be as large as 1 ppm. Moreover, only for one of these protons (that at lower field), the $^{3}J_{Pt,H}$ is very high (78, 99, and 95 Hz for **anti-M-3an**, **anti-M-3bm**, and **anti-M-3bn**, respectively), while for the other proton (that at higher field) the $^{3}J_{Pt,H}$ is much smaller and ill-defined. Finally we have found that, on going form **2** to **3**, the resonance of the $^{195}$Pt nucleus shifts downfield by more than 300 ppm ($\Delta\delta$ = +354.4 and +415.7 ppm for **M-2an/M-3an** and **anti-M-2bn/anti-M-3bn**, respectively).

Crystals suitable for X-ray analysis were obtained for the **anti-M** isomers of **2bn** and **3bn**. The structures of **2bn** and **3bn**, together with the numbering scheme, are depicted in Figure 1 (bond lengths and angles are in Table 1). In both cases, the coordination around the platinum atom is roughly square planar, considering the four metal-linked atoms: the tmeda nitrogen atoms, the carbon, and the chlorine (**2bn**) or the nitrogen atom of the four-membered chelate (**3bn**). The maximum deviation from the mean plane through the four donor atoms applies to N1 in **2bn** and to C8 in **3bn** [–0.019(6) and –0.026(4) Å, respectively]; moreover, the displacement exhibited by the platinum atom is 0.0141(2) and –0.0214(1) Å for **2bn** and **3bn**, respectively. Bond lengths for Pt–C8, Pt–N1, and Pt–N2 fall in the usual range. A significant difference (0.09 and 0.12 Å, for **2bn** and **3bn**, respectively) is found between the two Pt–N bonds pertaining to the tmeda ligand, as a result of the stronger *trans* influence of the carbon atom with respect to the chlorine or nitrogen donor atoms. The penta-atomic ring, resulting from chelation of the tmeda ligand to the platinum atom, is puckered with displacements of the C1 and C2 carbon atoms on opposite sides of the plane defined by Pt, N1, and N2 [–0.44(1) and 0.24(1) Å for **2bn** and 0.398(6) and –0.310(6) Å for **3bn**].[14] In **2bn**, the C9–C8–C7–N3 torsion angle of –172.5(4)° indicates an antiperiplanar disposition of the phenyl and amine substituents on the ethanide chain. This brings the amine group in a synclinal disposition with respect to the platinum atom with a Pt–C8–C7–N3 torsion angle of –45.9(5)°. The proximity of the amine group to the chlorido ligand sets the nitrogen in a suitable position to undergo chlorido substitution and ring-closing reaction.

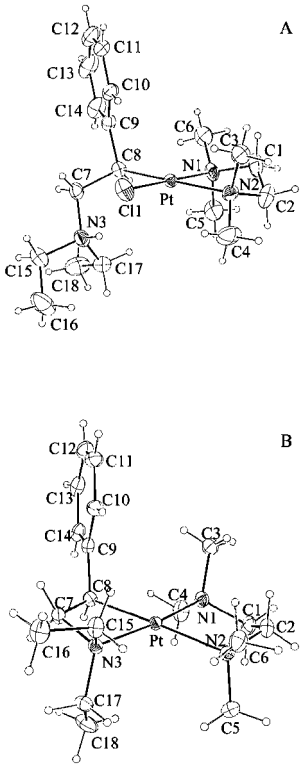


Figure 1. (A) ORTEP drawing of the complex cation [PtCl{CH(Ph)$CH_2NHEt_2$}(tmeda)]$^+$; the ellipsoids enclose 20% probability. (B) ORTEP drawing of the complex cation [Pt{CH(Ph)$CH_2NEt_2$-κC,κN}(tmeda)]$^+$; the ellipsoids enclose 20% probability.

Table 1. Selected bond lengths [Å] and angles [°] for **2bn** and **3bn**.

| | **2bn** | **3bn** |
|---|---|---|
| Pt–C8 | 2.062(4) | 2.053(4) |
| Pt–N1 | 2.081(6) | 2.084(3) |
| Pt–N2 | 2.174(4) | 2.209(3) |
| Pt–N3 | | 2.085(3) |
| Pt–Cl1 | 2.312(2) | |
| N3–C7 | | 1.516(5) |
| C7–C8 | | 1.522(6) |
| C8–Pt–N1 | 91.5(2) | 100.3(2) |
| C8–Pt–N3 | | 70.4(2) |
| N1–Pt–N2 | 85.2(2) | 83.3(2) |
| N3–Pt–N2 | | 106.0(2) |
| N3–C7–C8 | | 103.5(3) |
| C8–Pt–Cl1 | 93.1(1) | |
| N2–Pt–Cl1 | 90.1(2) | |
| C7–C8–Pt | | 93.1(2) |

In **3bn**, the cyclobutane metallacycle is rather strained and "quasi" planar; as a consequence, the substituents on adjacent atoms of the aminoethanide chain are placed in eclipsed positions. Notwithstanding the large deviation from theoretical values of bond angles, bond lengths within the four-member metallacycle are rather normal and in agreement with values found in the analogous

 © 2007 Wiley-VCH Verlag GmbH & Co. KGaA, Weinheim 

[Pt($CH_2CH_2NMe_2$-κC,κN)Cl($PPh_3$)] complex, in which, however, the ethanide chain had no substituents and the Pt–N bond was *ca*. 0.04 Å longer because of the *trans* influence of phosphane.[6] The steric interaction between substituents on *cis* ligands [particularly C9···C3 = 3.426(8) and C6···C15 = 3.548(8) Å] can fully explain the pyramidal distortion of the platinum coordination center. Moreover, it can be noted that, in both compounds (**2bn** and **3bn**), the phenyl ring angle centered on the *ipso* carbon is smaller than all the others [C10–C9–C14 = 117.3(5)° and 117.3(4)° for **2bn** and **3bn**, respectively]. The distortion of benzene rings has been the object of careful studies by Domenicano et al., who have rationalized the deviations from a regular geometry in terms of electronegativity, resonance, and steric effects of the substituent. An angle that is less than 120° is indicative of the accumulation of negative charge on the *ipso* carbon induced by an electron-donor substituent (electron-withdrawing substituents produce the opposite effect).[15] Therefore, the platinum-bonded carbon atom behaves like an electron donor towards the *ipso* carbon atom of the phenyl ring, and the electronic characteristics of this carbon atom are rather similar for the two compounds.

Azaplatinacyclobutanes, analogous to those here described,[6,7] were already reported in the literature; however, all of them were characterized by the presence of a labilizing ligand *trans* to the ligand displaced in the ring-closing process (usually a chlorido), and/or by having substituents on the ethanide chain (the Thorpe–Ingold effect of these substituents promoting the chelate ring formation).[12] However, the ring-closing reaction readily occurs in our systems notwithstanding the absence of a labilizing ligand *trans* to the leaving chlorido ligand. Moreover, although compounds **2an** and **2bm**,**n** contain a substituent (a methyl and a phenyl, respectively) on the ethanide chain, we could prove that compound [PtCl($\eta^1$-$CH_2CH_2NHEt_2$)(tmeda)]($ClO_4$), **2cn**, which has no substituents on the ethanide chain, can also easily undergo a ring-closing process. In particular, **2cn** in chloroform solution, treated with a slight excess of $NHEt_2$, affords a new complex species that is characterized, with respect to the NMR parameters of **2cn**, by a considerable downfield shift of the $^{195}$Pt resonance ($\Delta\delta$ = +440 ppm), a shielding of the C and H atoms in the α position ($\Delta\delta$ = –20 and –0.6 ppm, respectively), and a deshielding of the C and H atoms in the β position ($\Delta\delta$ = +10 and +1.3 ppm, respectively). All these features are characteristic of a ring-closed species. Moreover, the ESI mass spectrum of the reaction solution did show, besides a peak at 447.9, due to residual **2cn**, another intense peak at 411.5 corresponding to the elimination of HCl from **2cn** (the absence of chlorine was also confirmed by the peak isotopic pattern).

The cyclized species **3** of this work are closely related to the metallacycles proposed by Hartwig for the rhodium-catalyzed **anti-M** amination of vinylarenes.[16] Our findings prove that the formation of such intermediates is very likely, and the greater propensity of the **anti-M** isomer to undergo a ring-closing reaction may be the reason for the **anti-M** selectivity observed in the Hartwig reaction.

It can also be noted that, in spite of its strained structure, compound **3** appears to have considerable stability. To account for such stability, the concept of geometrical rigidity (steric constraints disfavor the reorganization of the metal orbital, which is necessary for a reaction pattern to take place) can be invoked. The same concept has been proposed by Zetterberg for justifying the lack of β-hydrogen elimination in azapalladacyclobutane species.[8c]

## Conclusions

In the systems under consideration, neither the *trans*-labilization of the ligand to be displaced by the entering nitrogen, nor the presence of substituents on the ethanide chain (which facilitates cyclization by the Thorpe–Ingold effect) are necessary for the ring-closing reaction to take place. The main difference between our substrates and those previously investigated[6,7] is the absence of a formal negative charge on the aminoethanide compound undergoing cyclization (deprotonated **2**). Therefore, a greater electrophilicity of the metal center (which is deprived of formal negative charge) could be the aiding factor promoting the ring-closing process.

Another outcome of the present investigation is the greater propensity of the anti-Markovnikov isomer of **2**, as compared with the Markovnikov one, to undergo ring-closing reaction. The **anti-M** isomer of **2** differs from the **M** isomer in that it has the two substituents (the methyl or phenyl group and the amine) on different carbon atoms of the ethanide chain. Steric repulsion between the two substituents will set them in an antiperiplanar conformation. As a consequence, the amine group is brought in a synclinal conformation with respect to the platinum atom and therefore in a suitable position to undergo chlorido substitution and ring-closing. This aiding effect is not present in the Markovnikov isomer, for which the hydrocarbon and the amine substituents are on the same carbon atom of the ethanide chain. The X-ray structure of compound **2bn** has fully confirmed this prevision. The phenyl ring and the amine substituents on the ethanide chain are in antiperiplanar disposition, which brings the amine group in a synclinal position with respect to the platinum atom and close to the chlorido ligand, which can therefore be easily displaced.

## Experimental Section

**General Methods:** All reagent-grade chemicals were purchased from Aldrich and used without purification. Elemental analyses were performed by using an Elemental Analyzer 1106 Carlo Erba instrument. $^1$H NMR spectra were recorded with a DPX300 Advance Bruker instrument equipped with a probe for inverse detection and with *z* gradient for gradient-accelerated spectroscopy. $^1$H and $^{13}$C spectra were referenced to TMS; the residual proton signal of the solvent was used as internal standard. For $^{195}$Pt spectra $K_2PtCl_4$ was used as external standard (–1643.00 ppm). $^1$H/$^{13}$C inversely detected gradient-sensitivity-enhanced heterocorrelated 2D NMR spectra for normal coupling (INVIEAGSSI) were acquired by

 © 2007 Wiley-VCH Verlag GmbH & Co. KGaA, Weinheim 

using standard Bruker automation programs and pulse sequences. APT spectra were recorded on a 300-MHz Mercury Varian instrument equipped with *z* gradient. All spectra were acquired in $CDCl_3$ and at 298 K. ESI mass spectra were obtained through a direct injection (10 μL/min) of micromolar methanol solutions of all the compounds into an Agilent 1100 Series LC-MSD Trap System VL instrument.

**Synthesis**

Alkene complexes [PtCl($\eta^2$-$CH_2$=CHX)(tmeda)]($ClO_4$) (X = $CH_3$, **1a**. $C_6H_5$, **1b**) were prepared by ethene exchange on the cationic complex [PtCl($\eta^2$-$C_2H_4$)(tmeda)]($ClO_4$) (**1c**) by following a reported procedure.[17]

Amine addition compounds **2xy** were prepared by reaction of the alkene complex **1** (0.4 mmol), suspended in dichloromethane (8 mL), with a slight excess of the amine ($NHMe_2$, **m**; $NHEt_2$, **n**; 1.2-fold the stoichiometric amount). After stirring for 3 h at room temperature, complete dissolution of the solid was observed. The solution was filtered, the solvent evaporated under reduced pressure, and the oily residue, after trituration with diethyl ether, afforded a white solid which was identified as the amine addition product. The isolated yield, referred to platinum, was ca. 95% for all the compounds.

**2an($ClO_4$):** $C_{13}H_{33}Cl_2N_3O_4Pt$ (561.40): calcd. C 27.81, H 5.92, N 7.48; found C 27.62, H 5.81, N 7.38. NMR (tmeda signals are given first) **M-2an:** $^1$H NMR $\delta$ = 2.65 (s, 3 H), 2.67 (s, 3 H), 2.81 (s, 3 H), and 2.87 (s, 3 H), C$H_3$N; 2.56 (1 H) and 2.73 (1 H), 2.82 (1 H) and 3.02 (1 H), -C$H_2$N; 1.26 (d, 1 H), Pt-$CH_2$CH(C$H_3$)-NH($CH_2CH_3$)$_2$; 1.46 (dd, 1 H) and 1.59 (dd, 1 H), Pt-C$H_2$CH-($CH_3$)NH($CH_2CH_3$)$_2$; 3.59 (m, 1 H), Pt-$CH_2$C*H*($CH_3$)NH-($CH_2CH_3$)$_2$; 1.43 (m, 3 H) and 1.49 (m, 3 H), Pt-C$H_2$CH($CH_3$)NH-($CH_2$C$H_3$)$_2$; 2.77 (m, 1 H) and 3.34 (m, 1 H), 3.05 (m, 1 H) and 3.28 (m, 1 H), Pt-$CH_2$CH($CH_3$)NH(C$H_2CH_3$)$_2$ ppm. $^{13}$C NMR $\delta$ = 47.4, 49.1, 51.1, and 52.2, *C*$H_3$N; 59.9 and 66.1, -*C*$H_2$N; 1.0, Pt-*C*$H_2$CH($CH_3$)NH($CH_2CH_3$)$_2$; 15.5, Pt-$CH_2$CH(*C*$H_3$)NH-($CH_2CH_3$)$_2$; 62.6, Pt-$CH_2$*C*H($CH_3$)NH($CH_2CH_3$)$_2$; 10.9 and 10.6, Pt-$CH_2$CH($CH_3$)NH($CH_2$*C*$H_3$)$_2$; 42.8 and 46.8, Pt-$CH_2$CH($CH_3$)-NH(*C*$H_2CH_3$)$_2$ ppm. $^{195}$Pt NMR $\delta$ = –3384.0 ppm. **anti-M-2an:** $^1$H NMR $\delta$ = 0.95 (d, 3 H), Pt-CH(C$H_3$)$CH_2$NH($CH_2CH_3$)$_2$; 1.39 (m, 1 H), Pt-C*H*($CH_3$)$CH_2$NH($CH_2CH_3$)$_2$; 2.34 (dd, 1 H) and 3.21 (dd, 1 H), Pt-CH($CH_3$)C$H_2$NH($CH_2CH_3$)$_2$ ppm.

**2bm($ClO_4$):** $C_{16}H_{31}Cl_2N_3O_4Pt$ (595.42): calcd. C 32.27, H 5.25, N 7.06; found C 32.03, H 5.11, N 6.98. NMR (tmeda signals are given first) **anti-M-2bm:** $^1$H NMR $\delta$ = 2.46 (s, 3 H), 2.69 (s, 3 H), 2.85 (s, 3 H), and 2.98 (s, 3 H), C$H_3$N; 2.48 (1 H), 2.68 (2 H), and 2.98 (1 H), -C$H_2$N; 2.76 (dd, $^2J_{Pt,H}$ = 76.2, 1 H), Pt-C*H*(Ph)$CH_2$NH-($CH_3$)$_2$; 2.32 (1 H) and 3.79 (1 H), Pt-CH(Ph)C$H_2$NH($CH_3$)$_2$; 3.02 (3 H) and 3.12 (3 H), Pt-CH(Ph)$CH_2$NH(C$H_3$)$_2$; 7.12 (1 H, *para*), 7.19 (2 H, *meta*), and 7.40 (2 H, *ortho*), Pt-CH(*Ph*)$CH_2$NH($CH_3$)$_2$ ppm. $^{13}$C NMR $\delta$ = 48.9, 49.0, and 52.0, *C*$H_3$N; 59.8 and 66.8, -*C*$H_2$N; 16.5 ($^1J_{Pt,C}$ = 846 Hz), Pt-*C*H(Ph)$CH_2$NH($CH_3$)$_2$; 67.6, Pt-CH(Ph)*C*$H_2$NH($CH_3$)$_2$; 42.7 and 45.2, Pt-CH(Ph)$CH_2$NH(*C*$H_3$)$_2$; 125.3 (*para*), 128.4 (*meta*), and 129.2 (*ortho*), Pt-CH(*Ph*)-$CH_2$NH($CH_3$)$_2$ ppm. **M-2bm:** $^1$H NMR $\delta$ = 1.77 (dd, 1 H) and 2.08 (dd, 1 H), Pt-C$H_2$CH(Ph)NH($CH_3$)$_2$; 4.64 (1 H), Pt-$CH_2$C*H*(Ph)-NH($CH_3$)$_2$; 7.40 (3 H, *meta* and *para*) and 7.57 (2 H, *ortho*), Pt-$CH_2$CH(*Ph*)NH($CH_3$)$_2$ ppm. $^{13}$C NMR $\delta$ = –0.6, Pt-*C*$H_2$CH(Ph)-NH($CH_3$)$_2$; 74.5, Pt-$CH_2$*C*H(Ph)NH($CH_3$)$_2$; 129.0 (*meta* and *para*) and 129.6 (*ortho*), Pt-$CH_2$CH(*Ph*)NH($CH_3$)$_2$ ppm.

**2bn($ClO_4$):** $C_{18}H_{35}Cl_2N_3O_4Pt$ (623.47): calcd. C 34.68, H 5.66, N 6.74; found C 34.39, H 5.56, N 6.84. NMR (tmeda signals are given first) **anti-M-2bn:** $^1$H NMR $\delta$ = 2.42 (s, 3 H), 2.68 (s, 3 H), 2.78 (s, 3 H), and 2.94 (s, 3 H), C$H_3$N; 2.47 (1 H), 2.62 (1 H), 2.64 (1 H), and 3.02 (1 H), -C$H_2$N; 2.85 (dd, 1 H), Pt-C*H*(Ph)$CH_2$NH-($CH_2CH_3$)$_2$; 2.52 (1 H) and 3.46 (1 H), Pt-CH(Ph)C$H_2$NH-($CH_2CH_3$)$_2$; 1.36 (3 H) and 1.38 (3 H), Pt-CH(Ph)$CH_2$NH-($CH_2$C$H_3$)$_2$; 3.23 (4 H), 3.49 (2 H), and 3.63 (2 H), Pt-CH(Ph)-$CH_2$NH(C$H_2CH_3$)$_2$; 7.13 (1 H, *para*), 7.21 (2 H, *meta*), and 7.59 (2 H, *ortho*), Pt-CH(*Ph*)$CH_2$NH($CH_2CH_3$)$_2$ ppm. $^{13}$C NMR $\delta$ = 48.9 and 51.8, *C*$H_3$N; 59.8 and 66.6, -*C*$H_2$N; 14.8, Pt-*C*H(Ph)-$CH_2$NH($CH_2CH_3$)$_2$; 61.1, Pt-CH(Ph)*C*$H_2$NH($CH_2CH_3$)$_2$; 7.8 and 9.5, Pt-CH(Ph)$CH_2$NH($CH_2$*C*$H_3$)$_2$; 44.2 and 48.3, Pt-CH(Ph)-$CH_2$NH(*C*$H_2CH_3$)$_2$; 125.9 (*para*), 128.2 (*meta*), and 129.0 (*ortho*), Pt-CH(*Ph*)$CH_2$NH($CH_2CH_3$)$_2$ ppm. $^{195}$Pt NMR $\delta$ = –3294.4 ppm. **M-2bn:** $^1$H NMR $\delta$ = 1.69 (dd, 1 H) and 2.25 (dd, 1 H), Pt-C$H_2$CH(Ph)NH($CH_2CH_3$)$_2$; 4.66 (1 H), Pt-$CH_2$C*H*(Ph)NH-($CH_2CH_3$)$_2$ ppm.

Azaplatinacyclobutane complexes **3xy** were prepared by treatment of a dichloromethane solution of the amine addition product **2xy** (0.2 mmol in 0.4 mL solvent) with a water solution of KOH (1.2 times the stoichiometric amount in 0.4 mL solvent). The mixture was kept under vigorous stirring for 48 h at room temperature. The organic phase was then removed, washed twice with water (1 mL), dried with $Na_2SO_4$, and submitted to solvent evaporation under vacuum. The oily residue, triturated with diethyl ether, afforded a white solid, which was separated by filtration of the solvent and dried. It was identified as the azaplatinacyclobutane complex. The isolated yield, referred to platinum, was ca. 90% for all compounds.

**3an($ClO_4$):** $C_{13}H_{32}ClN_3O_4Pt$ (524.94): calcd. C 29.74, H 6.14, N 8.00; found C 29.44, H 6.03, N 7.92. NMR (tmeda signals are given first) **M-3an:** $^1$H NMR $\delta$ = 2.79 (s, 6 H), 2.80 (s, 6 H), C$H_3$N; 2.35–3.30 (m, 4 H), -C$H_2$N; 1.04 (d, 3 H), Pt{$CH_2$CH(C$H_3$)-N($CH_2CH_3$)$_2$-κC,κN}; 0.71 (dd, $^2J_{Pt,H}$ = 87.8 Hz, 1 H) and 1.23 (dd, 1 H), Pt{C$H_2$CH($CH_3$)N($CH_2CH_3$)$_2$-κC,κN}; 4.35 (m, 1 H), Pt{$CH_2$C*H*($CH_3$)N($CH_2CH_3$)$_2$-κC,κN}; 1.26 (t, 3 H) and 1.64 (t, 3 H), Pt{$CH_2$CH($CH_3$)N($CH_2$C$H_3$)$_2$-κC,κN}; 2.58 (m, 1 H) and 2.79 (m, 1 H), 2.92 (m, 1 H) and 3.08 (m, 1 H), Pt{$CH_2$CH($CH_3$)-N(C$H_2CH_3$)$_2$-κC,κN} ppm. $^{13}$C NMR $\delta$ = 50.1 and 52.7, *C*$H_3$N; –16.08 ($^1J_{Pt,c}$ = 583.7 Hz), Pt{*C*$H_2$CH($CH_3$)N($CH_2CH_3$)$_2$-κC,κN}; 21.8, Pt{$CH_2$CH(*C*$H_3$)N($CH_2CH_3$)$_2$-κC,κN}; 73.5, Pt{$CH_2$*C*H-($CH_3$)N($CH_2CH_3$)$_2$-κC,κN}; 11.7 and 16.2, Pt{$CH_2$CH($CH_3$)-N($CH_2$*C*$H_3$)$_2$-κC,κN}; 57.4 and 57.6, Pt{$CH_2$CH($CH_3$)-N(*C*$H_2CH_3$)$_2$-κC,κN} ppm. $^{195}$Pt NMR $\delta$ = –3029.6 ppm. **anti-M-3an:** $^1$H NMR $\delta$ = 0.63 (d, $^3J_{Pt,H}$ = 64.4 Hz, 3 H), Pt{CH(C$H_3$)-$CH_2$N($CH_2CH_3$)$_2$-κC,κN}; 1.39 (m, 1 H), Pt{C*H*($CH_3$)-$CH_2$N($CH_2CH_3$)$_2$-κC,κN}; 3.79 (dd, 1 H) and 4.71 (dd, $^3J_{Pt,H}$ = 78.0 Hz, 1 H), Pt{CH($CH_3$)C$H_2$N($CH_2CH_3$)$_2$-κC,κN} ppm.

**3bm($ClO_4$):** $C_{16}H_{30}ClN_3O_4Pt$ (558.96): calcd. C 34.38, H 5.41, N 7.52; found C 34.13, H 5.49, N 7.44. NMR (tmeda signals are given first) **anti-M-3bm:** $^1$H NMR $\delta$ = 1.90 (s, 3 H), 2.69 (s, 3 H), 2.82 (s, 3 H), and 2.84 (s, 3 H), C$H_3$N; 2.43 (1 H), 2.56 (1 H), 2.64 (1 H), and 2.80 (1 H), -C$H_2$N; 2.85 (dd, $^2J_{Pt,H}$ = 105.4 Hz, 1 H), Pt{C*H*(Ph)$CH_2$N($CH_3$)$_2$-κC,κN}; 4.24 (1 H) and 5.21 ($^3J_{Pt,H}$ = 99.4 Hz, 1 H), Pt{CH(Ph)C$H_2$N($CH_3$)$_2$-κC,κN}; 2.85 (3 H) and 2.89 (3 H), Pt{CH(Ph)$CH_2$N(C$H_3$)$_2$-κC,κN}; 7.14 (1 H, *para*), 7.20 (2 H, *meta*), and 7.44 (2 H, *ortho*), Pt{CH(*Ph*)$CH_2$N($CH_3$)$_2$-κC,κN} ppm. $^{13}$C NMR $\delta$ = 49.8, 50.5, 51.1, and 53.2, *C*$H_3$N; 60.5 and 64.8, -*C*$H_2$N; –6.2 ($^1J_{Pt,C}$ = 564.4 Hz), Pt{*C*H(Ph)$CH_2$-N($CH_3$)$_2$-κC,κN}; 83.2 ($^2J_{Pt,C}$ = 188.2 Hz), Pt{CH(Ph)*C*$H_2$-N($CH_3$)$_2$-κC,κN}; 53.0 and 52.4, Pt{CH(Ph)$CH_2$N(*C*$H_3$)$_2$-κC,κN}; 124.6 (*para*), 128.4 (*meta*), and 127.8 (*ortho*), Pt{CH(*Ph*)-$CH_2$N($CH_3$)$_2$-κC,κN} ppm. **M-3bm:** (not isolated in the solid state but detected in solution by performing the ring-closing reaction in an NMR tube) $^1$H NMR $\delta$ = 1.44 (dd, 1 H) and 1.65 (dd, 1 H),

 © 2007 Wiley-VCH Verlag GmbH & Co. KGaA, Weinheim 

Pt{C$H_2$CH(Ph)N(C$H_3$)$_2$-κC, κN}; 5.20 (1 H), Pt{C$H_2$C$H$(Ph)N(C$H_3$)$_2$-κC,κN} ppm.

**3bn(ClO$_4$):** $C_{18}H_{34}ClN_3O_4Pt$ (587.01): calcd. C 36.83, H 5.83, N 7.16; found C 36.54, H 5.73, N 7.08. NMR (tmeda signals are given first) **anti-M-3bn:** $^1$H NMR $\delta$ = 1.91 (s, 3 H), 2.68 (s, 3 H), 2.80 (s, 3 H), and 2.83 (s, 3 H), C$H_3$N; 2.48 (1 H), 2.56 (1 H), 2.62 (1 H), and 2.80 (1 H), -C$H_2$N; 2.57 (dd, $^2J_{Pt,H}$ = 98.0 Hz, 1 H), Pt{C$H$(Ph)CH$_2$N(CH$_2$CH$_3$)$_2$-κC,κN}; 4.28 (1 H) and 5.09 ($^3J_{Pt,H}$ = 94.8 Hz, 1 H), Pt{CH(Ph)C$H_2$N(CH$_2$CH$_3$)$_2$-κC,κN}; 1.49 (3 H) and 1.75 (3 H), Pt{CH(Ph)CH$_2$N(CH$_2$C$H_3$)$_2$-κC,κN}; 2.62 (1 H), 2.89 (1 H), 2.90 (1 H), and 3.34 (1 H), Pt{CH(Ph)CH$_2$N-(C$H_2$CH$_3$)$_2$-κC,κN}; 7.13 (1 H, *para*), 7.19 (2 H, *meta*), and 7.42 (2 H, *ortho*), Pt{CH(*Ph*)CH$_2$N(CH$_2$CH$_3$)$_2$-κC,κN} ppm. $^{13}$C NMR $\delta$ = 49.9, 50.8, 51.2, and 52.7, *C*H$_3$N; 60.7 and 65.1, -*C*H$_2$N; –7.2 ($^1J_{Pt,C}$ = 564.4 Hz), Pt{*C*H(Ph)CH$_2$N(CH$_2$CH$_3$)$_2$-κC,κN}; 74.8 ($^2J_{Pt,C}$ = 188.2 Hz), Pt{CH(Ph)*C*H$_2$N(CH$_2$CH$_3$)$_2$-κC,κN}; 11.1 and 13.8, Pt{CH(Ph)CH$_2$N(CH$_2$*C*H$_3$)$_2$-κC,κN}; 56.4 and 57.7, Pt{CH(Ph)CH$_2$N(*C*H$_2$CH$_3$)$_2$-κC,κN}; 124.8 (*para*), 127.8 (*ortho*), and 128.7 (*meta*), Pt{CH(*Ph*)CH$_2$N(CH$_2$CH$_3$)$_2$-κC,κN} ppm. $^{195}$Pt NMR $\delta$ = –2878.7 ppm.

In the case of unsubstituted ethene compounds **2cn/3cn**, the reaction was only performed in an NMR tube, and the species were identified and characterized by ESI-MS and NMR spectroscopy. NMR (tmeda signals are given first) **2cn:** $^1$H NMR $\delta$ = 2.72 (s, 6 H) and 2.93 (s, 6 H), C$H_3$N; 2.59 (2 H) and 2.84 (2 H), -C$H_2$N; 1.62 (m, $^2J_{Pt,H}$ = 93.6 Hz, 2 H), Pt-C$H_2$CH$_2$NH(CH$_2$CH$_3$)$_2$; 3.13 (m, 2 H), Pt-CH$_2$C$H_2$NH(CH$_2$CH$_3$)$_2$; 1.32 (t, 6 H), Pt-CH$_2$CH$_2$NH(CH$_2$C$H_3$)$_2$; 3.18 (q, 4 H), Pt-CH$_2$CH$_2$NH-(C$H_2$CH$_3$)$_2$ ppm. $^{13}$C NMR $\delta$ = 48.8 and 52.5, *C*H$_3$N; 59.9 and 66.1, -*C*H$_2$N; –9.3 ($^1J_{Pt,C}$ = 752.5 Hz), Pt-*C*H$_2$CH$_2$NH(CH$_2$CH$_3$)$_2$; 57.4, Pt-CH$_2$*C*H$_2$NH(CH$_2$CH$_3$)$_2$; 8.8, Pt-CH$_2$CH$_2$NH(CH$_2$*C*H$_3$)$_2$; 44.9, Pt-CH$_2$CH$_2$NH(*C*H$_2$CH$_3$)$_2$ ppm. $^{195}$Pt NMR $\delta$ = –3336.0 ppm. **3cn:** $^1$H NMR $\delta$ = 2.80 (s, 6 H) and 2.81 (s, 6 H), C$H_3$N; 2.68 (2 H) and 2.73 (2 H), -C$H_2$N; 0.98 (m, $^2J_{Pt,H}$ = 91.2 Hz, 2 H), Pt{C$H_2$CH$_2$N(CH$_2$CH$_3$)$_2$-κC,κN}; 4.46 (m, $^3J_{Pt,H}$ = 58.4 Hz, 2 H), Pt{CH$_2$C$H_2$N(CH$_2$CH$_3$)$_2$-κC,κN}; 1.49 (t, 6 H), Pt{CH$_2$CH$_2$N-(CH$_2$C$H_3$)$_2$-κC,κN}; 2.60 (m, 2 H) and 2.90 (m, 2 H), Pt{CH$_2$CH$_2$N(C$H_2$CH$_3$)$_2$-κC,κN} ppm. $^{13}$C NMR $\delta$ = 50.5 and 52.4, *C*H$_3$N; 61.0 and 64.1, -*C*H$_2$N; –29.2 ($^1J_{Pt,C}$ = 517.4 Hz), Pt{*C*H$_2$CH$_2$N(CH$_2$CH$_3$)$_2$-κC,κN}; 67.4 ($^2J_{Pt,C}$ = 188.1 Hz), Pt{CH$_2$*C*H$_2$N(CH$_2$CH$_3$)$_2$-κC,κN}; 12.5, Pt{CH$_2$CH$_2$N(CH$_2$-*C*H$_3$)$_2$-κC,κN}; 56.7, Pt{CH$_2$CH$_2$N(*C*H$_2$CH$_3$)$_2$-κC,κN} ppm. $^{195}$Pt NMR $\delta$ = –2895.3 ppm.

### X-ray Crystallography

X-ray data were collected for the crystals **2bn**(ClO$_4$) and **3bn**(ClO$_4$) with a Bruker AXS X8 APEX CCD system equipped with a four-circle Kappa goniometer and a 4-K CCD detector (Mo-$K_\alpha$ radiation). The crystal-to-detector distance was 40 mm. The SAINT-IRIX package was employed for data reduction and unit-cell refinement.[18] All reflections were indexed, integrated, and corrected for Lorentz, polarization, and absorption effects by using the program SADABS.[19]

For compound **2bn**(ClO$_4$), which was crystallized from CHCl$_3$/pentane, a total of 33622 reflections ($\Theta_{max}$ = 37.00°) were collected. The number of independent reflections was 11082. The unit-cell dimensions were calculated from all reflections. The structure was solved by direct methods in the *Cc* space group. The model was refined by full-matrix least-squares methods. Anisotropic thermal parameters were applied for all non-hydrogen atoms. H atoms were located in difference maps, and were included in the full-matrix least-squares cycles with isotropic thermal parameters ($U$) fixed at 1.2 and 1.5 (for methyl group) times the values of $U$ of the corresponding carbon atoms. The perchlorate counterion is disordered. The final difference-Fourier map showed electron-density peaks (up to 1.839 e Å$^{-3}$) lying near the Pt atoms.

For compound **3bn**(ClO$_4$), also crystallized from CHCl$_3$/pentane, a total of 25934 reflections ($\Theta_{max}$ = 41.00°) were collected. The number of independent reflections was 12990. The unit-cell dimensions were calculated from all reflections. The structure was solved by direct methods in the $P2_1/c$ space group. The model was refined by full-matrix least-squares methods. Anisotropic thermal parameters were applied for all non-hydrogen atoms. H atoms were located in difference maps, and the parameters were freely refined. The final difference-Fourier map showed electron-density peaks (up to 3.432 e Å$^{-3}$) lying near the Pt atoms.

The crystallographic data are listed in Table 2. All calculations and molecular graphics were carried out by using the SIR2004,[20] SHELXL97,[21] PARST97,[22] WinGX,[23] or ORTEP-3 for Windows packages.[24] CCDC-624564 (**2bn**) and CCDC-269917 (**3bn**) contain the supplementary crystallographic data for this paper. These data can be obtained free of charge from The Cambridge Crystallographic Data Centre via www.ccdc.cam.ac.uk/data_request/cif.

Table 2. Crystal data and structure refinement parameters for **2bn**(ClO$_4$) and **3bn**(ClO$_4$).

| | **2bn**(ClO$_4$) | **3bn**(ClO$_4$) |
|---|---|---|
| Empirical formula | $C_{18}H_{35}Cl_2N_3O_4Pt$ | $C_{18}H_{34}ClN_3O_4Pt$ |
| Formula weight | 623.48 | 587.02 |
| Crystal system | monoclinic | monoclinic |
| Space group | *Cc* | $P2_1/c$ |
| $a$ [Å] | 13.4927(3) | 10.1870(5) |
| $b$ [Å] | 13.7925(3) | 15.6315(7) |
| $c$ [Å] | 13.1851(3) | 14.1576(7) |
| $\beta$ [°] | 97.424(1) | 95.348(1) |
| $V$ [Å$^3$] | 2433.2(1) | 2244.6(2) |
| $Z$ | 4 | 4 |
| $\rho_{calc}$[g cm$^{-3}$] | 1.702 | 1.737 |
| $\mu$[mm$^{-1}$] | 6.013 | 6.397 |
| $F$(000) | 1232 | 1160 |
| $\theta$ Range | 7.11–36.84 | 1.95–41.21 |
| Reflections collected | 33622 | 25934 |
| Data/restraints/parameters | 11082/2/263 | 12990/0/380 |
| Goodness-of-fit on $F^2$ | 1.029 | 1.041 |
| $R_1$, $wR_2$[$F^2 > 2\sigma(F^2)$] | 0.0311, 0.0682 | 0.0471, 0.0914 |
| $R_1$, $wR_2$ (all data) | 0.0452, 0.0732 | 0.0888, 0.1080 |

## Acknowledgments

We are grateful to Prof. Emanuela Schingaro and Prof. Ferdinando Scordari (University of Bari) for data collection; we thank Dr. Francesco Cannito (Consorzio Interuniversitario di Ricerca in Chimica dei Metalli nei Sistemi Biologici, C.I.R.C.M.S.B.) for assistance in the preparation of the manuscript. The financial support of the University of Bari (Contribution ex 60%) and of the Italian Ministero dell'Università e Ricerca (MIUR, Rome – PRIN 2005032730) is also gratefully acknowledged.

[1] a) J. L. Polse, R. A. Andersen, R. G. Bergman, *J. Am. Chem. Soc.* **1998**, *120*, 13405–13414; b) P. J. Walsh, F. J. Hollander, R. G. Bergman, *Organometallics* **1993**, *12*, 3705–3723; c) J. S. Johnson, R. G. Bergman, *J. Am. Chem. Soc.* **2001**, *123*, 2923–2924.

[2] a) T.-W. Tseng, I.-Y. Wu, Y.-C. Lin, M.-C. Chen, Y.-J. Tsai, M.-C. Chen, Y. Wang, *Organometallics* **1991**, *10*, 43–45; b) T.-W.

 © 2007 Wiley-VCH Verlag GmbH & Co. KGaA, Weinheim 

Tseng, I.-Y. Wu, Y.-C. Lin, M.-C. Chen, Y.-J. Tsai, M.-C. Chen, Y. Wang, *Organometallics* **1994**, *13*, 3963–3971.
[3] A. L. Casalnuovo, J. C. Calabrese, D. Milstein, *J. Am. Chem. Soc.* **1988**, *110*, 6738–6744.
[4] D. P. Klein, J. C. Hayes, R. G. Bergman, *J. Am. Chem. Soc.* **1988**, *110*, 3704–3706.
[5] C. R. Baar, L. P. Carbray, M. C. Jennings, R. J. Puddephatt, *J. Am. Chem. Soc.* **2000**, *122*, 177–177.
[6] A. De Renzi, B. Di Blasio, G. Morelli, A. Vitagliano, *Inorg. Chim. Acta* **1982**, *63*, 233–241 and references quoted therein.
[7] a) M. Green, J. K. K. Sarhan, I. M. Al-Najjar, *J. Chem. Soc.* **1981**, 1565–1571; b) J. K. K. Sarhan, M. Green, I. M. Al-Najjar, *J. Chem. Soc.* **1984**, 771–777; c) M. Green, J. K. K. Sarhan, I. M. Al-Najjar, *Organometallics* **1984**, *3*, 520–524.
[8] a) L. S. Hegedus, B. Akemark, K. Zetterberg, L. F. Olsson, *J. Am. Chem. Soc.* **1984**, *106*, 7122–7126; b) R. Arnek, K. Zetterberg, *Organometallics* **1987**, *6*, 1230–1235; c) L. Zhang, K. Zetterberg, *Organometallics* **1991**, *10*, 3806–3813.
[9] L. Maresca, G. Natile, *Comments Inorg. Chem.* **1994**, *16*, 95–112 and references quoted therein.
[10] G. Lorusso, N. G. Di Masi, L. Maresca, C. Pacifico, G. Natile, *Inorg. Chem. Commun.* **2006**, *9*, 500–503.
[11] a) F. P. Fanizzi, L. Maresca, G. Natile, C. Pacifico, *Gazz. Chim. Ital.* **1994**, *124*, 137–142; b) G. Bandoli, A. Dolmella, F. P. Fanizzi, N. G. Di Masi, L. Maresca, G. Natile, *Organometallics* **2002**, *21*, 4595–4603.
[12] a) R. M. Beesley, C. K. Ingold, J. F. J. Thorpe, *J. Chem. Soc.* **1915**, 1080–1106; b) C. K. Ingold, *J. Chem. Soc.* **1921**, 305–329; c) S. W. Smith, M. S. Newman, *J. Am. Chem. Soc.* **1968**, *90*, 1253–1257.
[13] In the case of **3bm**, by performing the ring-closing reaction in an NMR tube, it was possible to observe a spin system assignable to the Markovnikov isomer, which, however, was formed in a yield not higher than ≈ 5%. The NMR spectroscopic data are included in the Experimental Section.
[14] G. Gervasio, S. A. Mason, L. Maresca, G. Natile, *Inorg. Chem.* **1986**, *25*, 2207–2211.
[15] a) A. Domenicano, P. Mazzeo, A. Vaciago, *Tetrahedron Lett.* **1976**, *17*, 1029–1032; b) A. R. Campanelli, A. Domenicano, F. Ramondo, *J. Phys. Chem. A* **2003**, *107*, 6429–6440; c) A. R. Campanelli, A. Domenicano, F. Ramondo, I. Hargittai, *J. Phys. Chem. A* **2004**, *108*, 4940–4948.
[16] M. Utsonomiya, R. Kuwano, M. Kawatsura, J. F. Hartwig, *J. Am. Chem. Soc.* **2003**, *125*, 5608–5609.
[17] G. Lorusso, G. Boccaletti, N. G. Di Masi, F. P. Fanizzi, L. Maresca, G. Natile, *Eur. J. Inorg. Chem.* **2004**, 4751–4754.
[18] Bruker: *SAINT-IRIX*, Bruker AXS Inc., Madison, Wisconsin, USA, **2003**.
[19] G. M. Sheldrick, *SADABS*, Program for Empirical Absorption Correction of Area Detector Data, University of Göttingen, Germany, **1996**.
[20] M. C. Burla, R. Caliandro, M. Camalli, B. Carrozzini, G. L. Cascarano, L. De Caro, C. Giacovazzo, G. Polidori, R. Spagna, *J. Appl. Crystallogr.* **2005**, *38*, 381–388.
[21] *Programs for Crystal Structure Analysis* (Release 97-2), G. M. Sheldrick, Institut für Anorganische Chemie der Universität Göttingen, Göttingen, Germany, **1998**.
[22] a) M. Nardelli, *Comput. Chem.* **1983**, *7*, 95–97; b) M. Nardelli, *J. Appl. Crystallogr.* **1995**, *28*, 659.
[23] L. J. Farrugia, *J. Appl. Crystallogr.* **1999**, *32*, 837–838.
[24] L. J. Farrugia, *J. Appl. Crystallogr.* **1997**, *30*, 565.

Received: December 20, 2006
Published Online: April 4, 2007

 © 2007 Wiley-VCH Verlag GmbH & Co. KGaA, Weinheim 

DOI: 10.1002/ejic.200700072

# The Aromatization of $C_5$ Rings on a Heteronuclear Cluster

Yong Leng Kelvin Tan[a] and Weng Kee Leong*[a]

**Keywords:** Heterometallic complexes / Ruthenium / Osmium / Carbocyclic rings / Cyclopentadienyl ligands

The reaction of the heteronuclear cluster $RuOs_3(\mu\text{-}H)_2(CO)_{13}$ with saturated and unsaturated $C_5$ rings led to the aromatization of the rings to afford the clusters $RuOs_3(\mu\text{-}H)(CO)_9(\mu\text{-}CO)_2(\eta^5\text{-}C_5R_4R')$. However, the reaction with cyclopentene gave the cluster $RuOs_3(\mu\text{-}H)_3(CO)_{11}(\mu,\eta^1\text{:}\eta^2\text{-}C_5H_7)$ via C–H activation of an $sp^2$ carbon instead. Thermolysis of two of the products, $RuOs_3(\mu\text{-}H)(CO)_9(\mu\text{-}CO)_2(\eta^5\text{-}Cp')$ and $RuOs_3(\mu\text{-}H)(CO)_9(\mu\text{-}CO)_2(\eta^5\text{-}C_5H_4SiMe_3)$, led to their isomerization to butterfly clusters.

(© Wiley-VCH Verlag GmbH & Co. KGaA, 69451 Weinheim, Germany, 2007)

## Introduction

Carbocyclic ligands such as cyclopentadienyls are ubiquitous in organometallic chemistry, and many of their compounds are important as catalysts. Furthermore, these ligands have an important role in many catalytic processes, and establishing the nature of the ligand–metal interaction is important to an understanding of the catalytic reaction.[1] Transition-metal clusters incorporating unsaturated organic molecules can serve as useful models for comprehending these processes due to the similarities between ligand–cluster and absorbate–surface interactions. This has resulted in a well-developed chemistry of this class of compounds, and several reviews have been published.[2] In contrast to the extensive reports on the reactivity of homonuclear clusters with carbocyclic ligands, few examples exist for heteronuclear clusters. The synergistic effect of having different adjacent metals in heteronuclear clusters may offer higher activity, greater selectivity, and better stability than their homonuclear counterparts. We had earlier developed a high-yield synthetic route to the hetero group 8 tetranuclear cluster $RuOs_3(\mu\text{-}H)_2(CO)_{13}$ (**1**) and have initiated a series of investigations into the chemistry of **1** and its derivatives.[3,4] It is with an exploration of the reactivity of a heteronuclear cluster with $C_5$ carbocyclic rings in mind that we would like to report here the results of our investigations into the reaction of **1** with a number of representative saturated and unsaturated $C_5$ rings, particularly in relation to their binding and transformation on the cluster.

## Results and Discussion

With the notable exception of cyclopentene, we have found that the reaction of **1** with a variety of cyclopentanes, cyclopentenes, and cyclopentadienes at 120 °C afforded tetrahedral clusters of the general formula $RuOs_3(\mu\text{-}H)(CO)_9(\mu\text{-}CO)_2(\eta^5\text{-}C_5R_4R')$ (**2**) in moderate to high yields; this is depicted in Scheme 1. Although aromatization of cyclohexene and cyclohexadiene on tetraosmium clusters are known,[5] this appears to be the first time that aromatization of $C_5$ rings, including even saturated ones, on clusters have been observed. All the clusters **2** have been characterized completely and, with the exception of **2c**, also by single-crystal X-ray crystallography. The synthesis of **2a** by the ionic coupling of $[Ru(C_5H_5)(MeCN)_3]^+$ with $[Os_3H(CO)_{11}]^-$ and its X-ray crystal structure have also been previously reported;[6] we are reporting our results here to minimize instrumental variations for purposes of comparison.

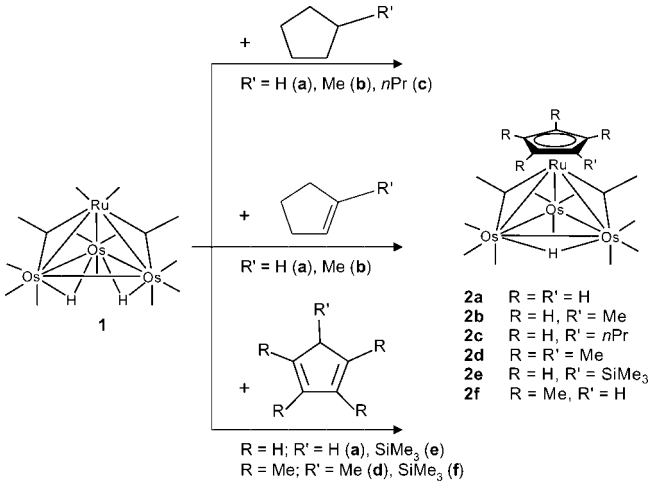


Scheme 1.

The ORTEP diagrams for **2d** and **2e** are shown in Figure 1, and a common atomic numbering scheme and selected bond parameters for the clusters **2** are given in Table 1. The clusters consist of a tetrahedral arrangement

[a] Department of Chemistry, National University of Singapore, Kent Ridge, 119260 Singapore

 © 2007 Wiley-VCH Verlag GmbH & Co. KGaA, Weinheim 

of metal atoms; the three osmium atoms form the triangular basal plane and are capped by a ruthenium atom at the apex. The tetrahedral metal core with six metal–metal bonds is consistent with the valence electron count of 60 for the molecules. The longest metal–metal edge found in all of the clusters is bridged by a hydride ligand;[7] the Os(1)–Os(2) bond length ranges from 2.9413(6) to 3.0056(10) Å; the other metal–metal bond lengths in the clusters range from 2.7709(7) to 2.9060(12) Å. There are two asymmetric bridging carbonyl groups which span the Os(1)–Ru(4) and Os(2)–Ru(4) edges; the bond to the ruthenium atom [average 1.97(2) Å] is shorter than that to the osmium atom [average 2.26(4) Å]. Bridging carbonyl groups are better π-acceptors than terminal CO groups, and their presence helps to disperse the additional electron density contributed by the electron-rich Ru(η$^5$-cyclopentadienyl) fragment.[8]

The organic moiety in **2** is coordinated to the cluster at the apical ruthenium atom via the conventional η$^5$-cyclopentadienyl bonding mode. It is noted that cyclopentadienyl ligand substitution occurs overwhelmingly at the ruthenium vertex, in line with previous reports of group 15 derivatives of cluster **1**.[3] There is no evidence for the presence of an isomer with the carbocyclic ligand ligating an osmium ver-

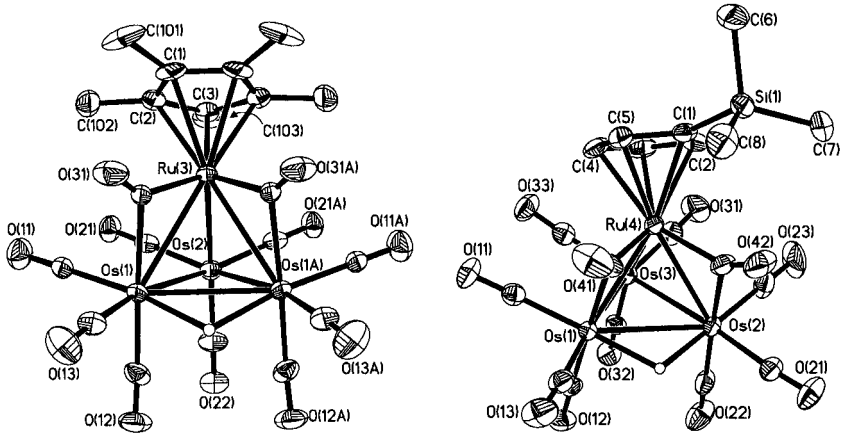


Figure 1. ORTEP diagram (50% probability thermal ellipsoids, organic hydrogen atoms omitted) for **2d** (left) and **2e** (right).

Table 1. Common atomic numbering scheme and selected bond parameters for **2**.

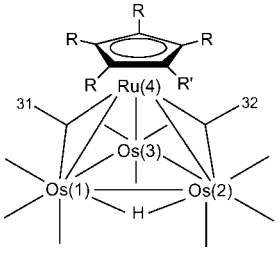


**2a** R = R' = H
**2b** R = H, R' = Me
**2c** R = H, R' = $CH_2CH_2CH_3$
**2d** R = R' = Me
**2e** R = H, R' = $SiMe_3$
**2f** R = Me, R' = H

| | **2a** Molecule A | Molecule B | **2b** | **2d** | **2e** | **2f** |
|---|---|---|---|---|---|---|
| Bond lengths [Å] | | | | | | |
| Os(1)–Os(2) | 2.9458(6) | 2.9470(6) | 2.9428(4) | 2.9413(6) | 2.9425(3) | 3.0056(10) |
| Os(1)–Os(3) | 2.7853(7) | 2.7789(7) | 2.7872(3) | 2.7781(4) | 2.7848(3) | 2.8434(7) |
| Os(1)–Ru(4) | 2.7933(10) | 2.8292(11) | 2.8168(5) | 2.8571(7) | 2.8278(4) | 2.9060(12) |
| Os(2)–Os(3) | 2.7709(7) | 2.7907(7) | 2.7872(3) | 2.7781(4) | 2.7732(3) | 2.8434(7) |
| Os(2)–Ru(4) | 2.8319(10) | 2.8042(10) | 2.8168(5) | 2.8571(7) | 2.8322(4) | 2.9060(12) |
| Os(3)–Ru(4) | 2.7705(10) | 2.7693(10) | 2.7721(6) | 2.8055(9) | 2.7906(4) | 2.8609(13) |
| Os(1)–C(31) | 2.187(11) | 2.253(13) | 2.315(5) | 2.244(8) | 2.253(5) | 2.297(11) |
| Ru(4)–C(31) | 2.007(12) | 1.971(13) | 1.965(5) | 1.960(7) | 1.967(6) | 1.997(11) |
| Os(2)–C(32) | 2.254(12) | 2.228(13) | 2.231(5) | 2.244(8) | 2.272(5) | 2.297(11) |
| Ru(4)–C(32) | 1.947(14) | 1.967(13) | 1.965(5) | 1.960(7) | 1.946(5) | 1.997(11) |
| Ru(4)–Cp(centroid) | 1.918(18) | 1.923(18) | 1.905(17) | 1.925(8) | 1.896(5) | 1.948(11) |
| Bond angles [°] | | | | | | |
| Os(1)–C(31)–Ru(4) | 83.4(5) | 83.8(5) | 84.1(2) | 84.4(3) | 83.8(2) | 84.9(4) |
| Os(2)–C(32)–Ru(4) | 84.4(5) | 83.6(4) | 84.1(2) | 84.4(3) | 84.0(2) | 84.9(4) |

 © 2007 Wiley-VCH Verlag GmbH & Co. KGaA, Weinheim 

tex. This preference for substitution at a ruthenium vertex is electronic; it cannot be statistical since that would lead to a 3:1 preference for substitution at an osmium vertex.

As has been observed for $Os_4(\mu\text{-H})(CO)_9(\mu\text{-CO})_2(\eta^5\text{-Cp*})$, one of the methyl carbon atoms in **2d** [C(103) in the ORTEP diagram] is displaced out of the plane of the central carbon ring of the pentacyclopentadienyl ligand by 18°. The displacement of the other methyl carbon atoms from the carbon ring plane for this cluster averages 7°. This bending of the methyl carbon atom has been ascribed to the steric interaction of the methyl group with the nearest carbonyl groups.[9] The presence of bridging carbonyl ligands results in a reduction of the distance as well as an increase in the nonbonding interaction between the oxygen atom of the CO ligand and any bulky substituents on the cyclopentadienyl ring, giving rise to bridging carbonyl-substituted cyclopentadienyl ring repulsion. This can be seen in **2e**, where the bulky trimethylsilyl group is placed directly above and between the two bridging carbonyl ligands to minimize steric strain, while the cyclopentadienyl ring is tilted at an angle of 36° with respect to the triosmium basal plane.

Steric reasons may also account for the fact that the cluster $RuOs_3(\mu\text{-H})(CO)_9(\mu\text{-CO})_2(\eta^5\text{-}C_5Me_4SiMe_3)$ was not isolated in the reaction of **1** with trimethyl(2,3,4,5-tetramethyl-2,4-cyclopentadien-1-yl)silane. Instead the major products isolated from the reaction were **2f**, in which the trimethylsilyl group was lost, and another species $RuOs_3(\mu\text{-H})_3(CO)_8(\mu\text{-CO})(\eta^5\text{-}C_5Me_4SiMe_3)$ (**4**) (see below). The steric crowding around the $C_5Me_4H$ ring in **2f** is reflected by the out-of-plane displacement of the methyl groups (average 6°) away from the $RuOs_3$ core. The cyclopentadienyl ring is also tilted at an angle of 36° with respect to the triosmium basal plane. The presence of an additional bulky trimethylsilyl substituent would have resulted in an even larger displacement of the silicon and methyl carbon atoms out of the plane of the cyclopentadienyl ring. This steric strain may similarly account for our observation that prolonged thermolysis of pentaphenylcyclopentadiene with **1** failed to give the expected product $RuOs_3(\mu\text{-H})(CO)_9(\mu\text{-CO})_2(\eta^5\text{-}C_5Ph_5)$, but resulted in the recovery of **1**.

The clusters appear to retain their solid-state structures in solution. The singlet resonance in the high-field region for the hydride shows a systematic downfield shift with increasing number of electron donating groups (such as methyl) on the cyclopentadienyl ring. Furthermore, a comparison of the hydride chemical shift for **2d** ($\delta$ = –18.34 ppm) with that reported for the tetraosmium analogue, $Os_4(\mu\text{-H})(CO)_9(\mu\text{-CO})_2(\eta^5\text{-Cp*})$ ($\delta$ = –20.71 ppm),[9] shows that replacement of the osmium atom at the apex of the tetrahedron with the relatively more electronegative ruthenium atom results in a decrease in electron density at the hydride.[10]

Some of the reactions with the $C_5$ carbocyclic rings also afforded other minor products other than **2**. The reaction of **1** with propylcyclopentane afforded, after TLC separation, unreacted **1**, $Os_3(\mu\text{-H})_2(CO)_{10}$ (a decomposition product of **1**), **2c**, and another novel cluster $Ru_2Os_3(\mu\text{-H})_2(CO)_{13}(\mu\text{-CO})(\mu_3,\eta^5\text{:}\sigma^2\text{-}C_5H_3C_3H_7)$ (**3**). Clusters **2c** and **3** could not be separated by chromatographic methods although NMR integration suggested that they were present in a ratio of 5:2. We managed to obtain some pure samples by fractional crystallization. Cluster **3** has been completely characterized, also by a single-crystal X-ray crystallographic study; the ORTEP diagram showing the molecular structure of **3** is depicted in Figure 2, together with selected bond parameters.

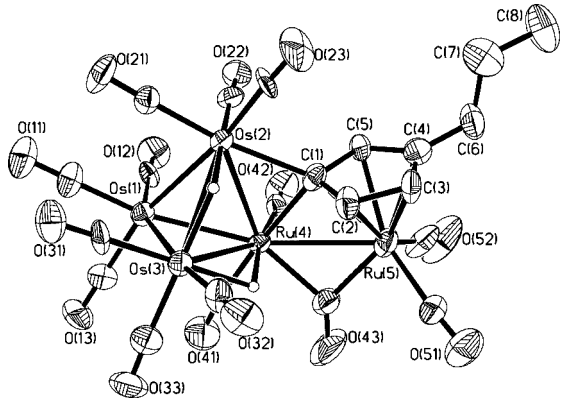


Figure 2. ORTEP diagram (50% probability thermal ellipsoids, organic hydrogen atoms omitted) and selected bond lengths [Å] and angles [°] for **3**. Os(1)–Os(2) = 2.8420(11); Os(1)–Os(3) = 2.7746(11); Os(1)–Ru(4) = 2.7729(17); Os(2)–Os(3) = 2.9572(11); Os(2)–Ru(4) = 2.8291(16); Os(3)–Ru(4) = 2.9571(17); Ru(4)–Ru(5) = 2.933(2); Os(2)–C(1) = 2.217(19); Ru(4)–C(1) = 2.30(2); Ru(5)–Cp(centroid) = 1.90(2); Ru(4)–C(43) = 2.08(2); Ru(5)–C(43) = 2.09(2); Os(2)–C(1)–Ru(4) = 77.5(7); Ru(4)–C(43)–Ru(5) = 89.5(9).

The metal framework in **3** consists of a ruthenium-spiked $RuOs_3$ tetrahedron. In metal carbonyl chemistry the spiked tetrahedron metal framework has been rarely reported. Amongst the few known clusters with this arrangement are $Os_6(\mu\text{-H})(\eta^2\text{-}C_6F_5NNNC_6F_5)(\mu\text{-CO})(CO)_{19}$,[11] $ReOs_4(\mu\text{-H})(\mu\text{-CO})(CO)_{17}$,[12] $RuOs_4(\mu\text{-H})_3(\mu_3\text{-}\eta^6\text{-}C_6H_5)(CO)_{12}[P(OMe)_3]$[13] and $Ru_2Os_3(\mu\text{-H})(\mu_3\text{-}\eta^5\text{-}C_5H_4)(\eta^5\text{-}C_5H_5)(CO)_{11}[P(OMe)_3]$.[14] The spike Ru(4)–Ru(5) edge at 2.933(2) Å in **3** is long despite its being bridged by a carbonyl group; usually the shortest metal–metal distance is associated with a bridging CO. For the metal tetrahedron, the two longest metal–metal bonds are bridged by metal hydrides [Os(2)–Os(3) and Os(3)–Ru(4), at 2.9572(11) and 2.9571(11) Å, respectively], whereas the other metal–metal vectors are significantly shorter [2.7729(11)–2.8420(11) Å]. The propylcyclopentadienylidene ligand is bonded to Os(2), Ru(4), and Ru(5) via an uncommon $\mu_3,\eta^5\text{:}\sigma^2$ mode; the ligand caps Ru(5) in a $\eta^5$-cyclopentadienyl manner, and C(1) is also asymmetrically bound to Os(2) [2.217(19) Å] and Ru(4) [2.30(2) Å]. The C(1) carbon acts as a one-electron donor, and the coordination of this atom to the Os(2)–Ru(4) edge can be considered as a "three-center-two-electron" bond. This gives **3** a cluster valence electron count of 76, consistent with the observed spiked tetrahedron metal core.[15] Cluster **3** can be envisaged as having been formed by the addition of a "$Ru(\eta^5\text{-}C_5H_4C_3H_7)(CO)_2$" fragment, from decomposition of **2c**, to **1** followed by oxidative addition of the substituted cyclopentadienyl group; the reaction of **1** with **2c** indeed afforded **3**.

 © 2007 Wiley-VCH Verlag GmbH & Co. KGaA, Weinheim 

The $^1$H NMR spectrum, in the hydride region, of **3** indicated the presence of three species, together with **2c**. The major species exhibited a broad singlet at –19.54 ppm (I); the two other sets comprised singlets at –20.73 and –21.70 ppm (II) and at –20.74 and –21.62 ppm (III). We were unable to obtain a pure sample of **3** free of **2c**, and the relative intensities of the other resonances remained unchanged across repeated recrystallizations. Integration of the spectrum taken at 198 K indicated the ratio I/II/III to be 4.6:2.7:1.0. Below 233 K, the signals due to I appeared as two sharp singlets at –19.06 and –20.12 ppm; the other signals showed no variation except for minor changes in chemical shifts due to temperature. The major resonances (I) can be attributed to the solid-state structure, and the EXSY spectrum at 198 K confirmed the chemical exchange between the two hydride resonances. The identities of the species giving rise to the other two sets of resonances are uncertain, but there was an absence of crosspeaks involving these resonances, and the chemical shift ranges indicated that these hydrides may be bridging Os–Os bonds.[16]

As already mentioned above, besides **2f**, the reaction with trimethyl(2,3,4,5-tetramethyl-2,4-cyclopentadien-1-yl)silane also afforded $RuOs_3(\mu\text{-}H)_3(CO)_9(\mu\text{-}CO)(\eta^5\text{-}C_5Me_4SiMe_3)$ (**4**), which has also been completely characterized, also by a single-crystal X-ray diffraction analysis; the ORTEP plot together with selected bond parameters is shown in Figure 3.

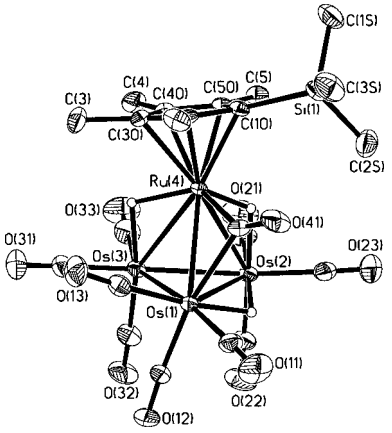


Figure 3. ORTEP diagram (50% probability thermal ellipsoids, organic hydrogen atoms omitted) and selected bond lengths [Å] and angles [°] for **4**. Os(1)–Os(2) = 2.9454(3); Os(1)–Os(3) = 2.8153(3); Os(1)–Ru(4) = 2.8292(4); Os(2)–Os(3) = 2.7988(3); Os(2)–Ru(4) = 2.9612(4); Os(3)–Ru(4) = 2.9626(4); Os(1)–C(41) = 2.208(5); Ru(4)–C(41) = 1.949(5); Ru(4)–Cp(centroid) = 1.840(5); Ru(4)–C(41)-Os(1) = 85.53(19).

The silicon atom of the $C_5Me_4SiMe_3$ ligand is displaced by 9°, while the four methyl groups are displaced at an average of 5°, out of the plane of the central carbon ring. These indicate that the replacement of a carbonyl ligand with two bridging hydrides enabled the cyclopentadienyl ring to coordinate to the metal tetrahedron with less steric strain, and may explain why the $SiMe_3$ group was retained, unlike in **2f**.

The ambient temperature $^1$H NMR spectrum in the hydride region of **4** comprised a sharp singlet at –18.46 ppm. At 183 K, this was replaced by broad resonances centered at –16.95 ppm (A), –18.62 (B), and –20.75 (C), as well as a relatively sharper resonance at –21.07 ppm (D), in an integration ratio A/B/C/D of 8:2:1:4. These resonances may be ascribed to two inter-converting isomers existing in a 4:1 ratio; their proposed structures and tentative assignments are given in Figure 4. It is assumed that the major isomer has the structure as that in the X-ray crystallographic study, and that the resonances due to the two hydrides bridging the Ru–Os edges have collapsed into one broad resonance even at 183 K. The proposed structure of the minor isomer is based on the reported structures of $WM_3(\mu\text{-}H)_3(CO)_{11}(\eta^5\text{-}L)$ (M = Os or Ru, L = $C_5H_5$ or $C_5Me_5$).[17] The poor solubility of **4** at low temperatures precluded any attempt at studying the hydride exchange pathways further.

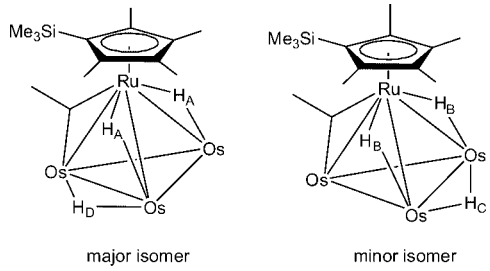


Figure 4. Proposed structures and tentative $^1$H NMR assignments (hydride region) for **4**.

Among the reactions giving rise to clusters **2**, however, the most interesting was that involving the reaction with cyclopentene. The yield of **2a** from this reaction in refluxing octane was rather low (10%). In contrast, the reaction carried out at 120 °C in a Carius tube with hexane as solvent afforded an orange product in essentially quantitative yield, which was identified as the novel cluster $RuOs_3(\mu\text{-}H)_3(CO)_{11}(\mu,\eta^1\text{:}\eta^2\text{-}C_5H_7)$ (**5**). Attempts at purification by TLC on silica led to decomposition. Cluster **5** has been completely characterized, also by a single-crystal X-ray crystallographic analysis. An ORTEP plot of **5** showing the atomic numbering scheme, together with selected bond parameters, is given in Figure 5.

The crystal structure exhibits disorder of the metal framework, with ruthenium occupancies on the M(4) and M(1) positions refined to about 0.88 and 0.12, respectively. The cyclopentenyl ligand bridges one of the metal–metal edges in a $\mu,\eta^1\text{:}\eta^2$ manner. This bonding mode has been previously encountered, for example, in $Os_4(\mu\text{-}H)_3(CO)_{11}(\mu,\eta^1\text{:}\eta^2\text{-}C_6H_9)$,[2b,18] $Os_4(\mu\text{-}H)_3(CO)_{11}(\mu,\eta^1\text{:}\eta^2\text{-}CHCHPh)$,[19] $Os_3(\mu\text{-}H)(CO)_{10}(\mu,\eta^1\text{:}\eta^2\text{-}CHCHCH_2CH_3)$, $Os_3(\mu\text{-}H)(CO)_{10}(\mu,\eta^1\text{:}\eta^2\text{-}CHCH_2)$, and $Os_3(\mu\text{-}H)(CO)_{10}(\mu,\eta^1\text{:}\eta^2\text{-}CHCHPh)$.[20] The alkene C=C bond [1.392(9) Å], is elongated with respect to the typical alkene bond length of 1.33 Å,[21] consistent with a decrease in the bond order. The hydrides were placed by potential energy calculations[22] and are consistent with the elongation of the bridged metal–metal bonds.[23] Moreover, the M–M–C angles for CO ligands adjacent to, and in the same plane as, the bridging hydrides are observed to be abnormally large, ranging from 116 to 122°, relative to usual M–M–C angles of 70 to

 © 2007 Wiley-VCH Verlag GmbH & Co. KGaA, Weinheim 

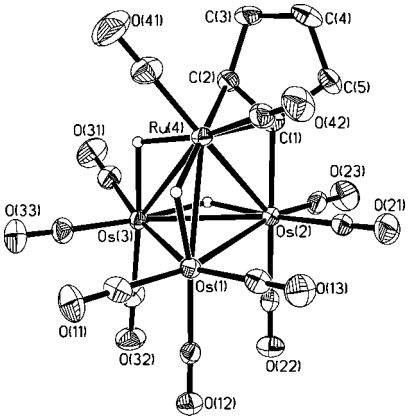


Figure 5. ORTEP diagram (50% probability thermal ellipsoids) and selected bond lengths [Å] and angles [°] for **5**. Os(1)–Os(2) = 2.9252(3); Os(1)–Os(3) = 2.7903(4); Os(1)–Ru(4) = 2.8020(5); Os(2)–Os(3) = 2.9763(4); Os(2)–Ru(4) = 2.7974(5); Os(3)–Ru(4) = 2.9452(5); Os(2)–C(1) = 2.112(7); Ru(4)–C(1) = 2.172(6); Ru(4)–C(2) = 2.307(7); C(1)–C(2) = 1.392(9); Os(2)–C(1)–Ru(4) = 81.5(2).

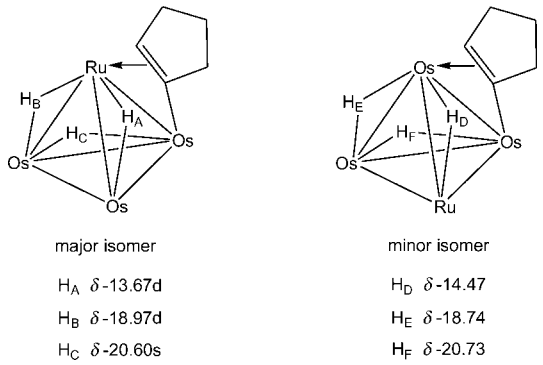


Figure 6. Proposed solution structures (carbonyl groups omitted) for the isomers of **5** and tentative NMR assignments for the bridging hydrides.

95°. This provides additional evidence for the location of the bridging hydride ligands. As has been observed in the case of $Os_4(\mu\text{-}H)_3(CO)_{11}(\mu,\eta^1\text{:}\eta^2\text{-}C_6H_9)$ and $Os_4(\mu\text{-}H)_3(CO)_{11}(\mu,\eta^1\text{:}\eta^2\text{-}CHCHPh)$,[18b] one of the longer metal–metal bonds is not bridged [Os(1)–Os(2) = 2.9252(3) Å].

The $^1H$ resonances for the organic moiety have been tentatively assigned with the aid of COSY and NOESY experiments, and the coupling constants have been determined by selective decoupling experiments. The $^1H$ NMR spectrum in the high-field region suggested the presence of two isomers in a 9:1 ratio, consistent with the disorder ratio observed in the solid-state crystal structure. The major set of resonances consists of doublets at –13.67 and –18.97 ppm, and a singlet at –20.60 ppm. The H–H coupling has been confirmed by COSY and selective decoupling experiments. The resonances of the minor isomer were very low in intensity and appeared as singlets. We have tentatively assigned the resonances as shown in Figure 6. The assignments were corroborated by a NOESY spectrum which showed a crosspeak between the resonances at –18.97 and –20.60 ppm, indicating spatial proximity of the hydrides giving rise to them.

In addition to the two sets of resonances described above, the $^1H$ NMR spectrum of **5** at ambient temperature displayed two broad signals at –19.70 and –21.20 ppm, suggesting the presence of another fluxional species. A variable-temperature experiment showed that at 213 K, three singlet resonances at –19.33, –20.41, and –21.41 ppm resulted. An EXSY experiment (213 K and 343 K) indicated exchange crosspeaks between the first two resonances, but no intermolecular exchange was observed between this species and either isomer of **5**. Together with the rather different chemical shifts for these hydrides relative to the others, this species may be unrelated to **5**, although at this point in time a structure cannot be unambiguously assigned.

The EXSY experiment at 343 K also indicated hydride fluxionality in each of the two isomers of **5** but no isomerization between them. Two fluxional processes that can account for the exchange crosspeaks in the major isomer are depicted in Scheme 2. Both processes involve rapid reorientation of the cyclopentenyl moiety about the Ru–Os edge; a similar process has earlier been proposed for the norbornene triosmium cluster $Os_3(\mu\text{-}H)(CO)_{10}(\mu,\eta^1\text{:}\eta^2\text{-}C_7H_9)$.[24] In process I, the flipping of $H_C$ from one Os–Os edge to another, coupled with the reorientation of the cyclopentenyl ligand interchanges $H_A$ and $H_B$. The movement of the organic moiety together with simultaneous flipping of all three hydrides in process II exchanges $H_A$ with $H_C$. Process I is expected to occur at a faster rate than II, and this is supported by the variable-temperature NMR spectra, which show that the signals ascribable to $H_A$ and $H_B$ broaden more rapidly than that attributable to $H_C$. This is further supported by the more intense exchange crosspeak between $H_A$ and $H_B$; the weaker intensity of the exchange crosspeak between $H_B$ and $H_C$ may be attributed to a combination of processes I and II.

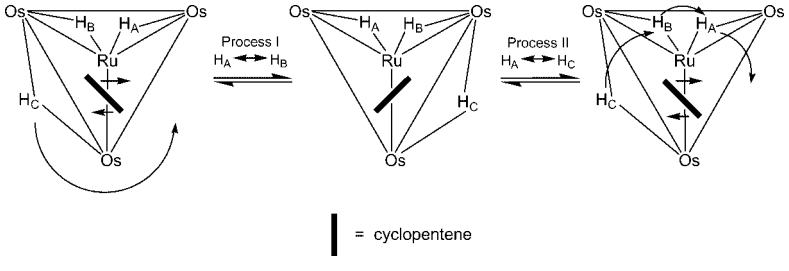


Scheme 2.

 © 2007 Wiley-VCH Verlag GmbH & Co. KGaA, Weinheim 

The interesting question is why the reaction of **1** with cyclopentene should afford only **5**. This is particularly in contrast with the reaction with methylcyclopentene, which afforded **2b** in comparatively good yield. Furthermore, no methylcyclopentenyl analogue of **5** could be identified spectroscopically despite attempts to decrease the reaction time or temperature. It is tempting to view cluster **5** as a possible precursor to **2a**; indeed, heating a sample of **5** in hexane for 12 h afforded **2a**. However, the low yield (20%) and the great number of side products obtained from this thermolysis seem to indicate that this is not so. The transformation of **5** to **2a** would require not only dehydrogenation but also the rehydrogenation of the metallated carbon atom. This situation is similar to that in the related tetraosmium cluster $Os_4(\mu\text{-}H)_3(CO)_{11}(\mu,\eta^1\text{:}\eta^2\text{-}C_6H_9)$,[18c] which was determined not to be an active intermediate in the dehydrogenation of the cluster-bound cyclohexa-1,3-diene to give $Os_4(\mu\text{-}H)_2(CO)_{10}(\eta^6\text{-}C_6H_6)$.[2c] We believe that **5** was formed preferentially because of faster C–H activation of an $sp^2$ carbon than an allylic $sp^3$ carbon;[25] the latter is what would be required for aromatization to **2a**.

The reason why methylcyclopentene failed to give an analogue to **5** is probably steric; the hydrogen atom on C(2) (which is where the methyl substituent would be) points towards CO(31) in **5** (Figure 5). In the case of the dienes, presumably the fact that one C–H activation at an $sp^3$ carbon would be sufficient to bring about aromatization may have tilted the balance against the formation of an analogue of **5**. This is corroborated by the observation that to date, only $Os_3(CO)_{10}(\eta^4\text{-}C_5H_6)$, obtained in the reaction of $Os_3(CO)_{10}(MeCN)_2$ with cyclopentadiene in dichloromethane, has been successfully characterized by infrared spectroscopy; in the absence of excess cyclopentadiene the cluster decomposed rapidly.[26]

The clusters **2** have also been subjected to thermolysis in cyclohexane. While **2a**, **2d**, and **2f** were found to be thermally stable, **2b** and **2e** afforded the novel products $RuOs_3(\mu\text{-}H)_2(CO)_{11}(\mu,\eta^5\text{:}\eta^1\text{-}C_5H_3Me)$(**6b**)and$RuOs_3(\mu\text{-}H)_2(CO)_{11}(\mu,\eta^5\text{:}\eta^1\text{-}C_5H_3SiMe_3)$ (**6e**) respectively. Both **6b** and **6e** have been completely characterized by spectroscopic, elemental, and single-crystal X-ray crystallographic analyses. An ORTEP plot of the molecular structure of **6e** is displayed in Figure 7; selected bond parameters for **6b** and **6e** are given in Table 2, together with a common atomic numbering scheme. There were two molecules in the asymmetric unit of **6b**.

Clusters **6b** and **6e** are isomers of **2b** and **2e**, respectively, in which it may be considered that oxidative addition of a C–H bond of the cyclopentadienyl across a metal–metal bond has occurred, so that the resulting ligand bridges the wingtip metal atoms of a butterfly cluster core. The cluster valence electron count of 62 for these clusters is consistent with the butterfly structure. The dihedral angle between the two "wings" of the butterfly – the Ru(4)–Os(1)–Os(3) and Os(1)–Os(2)–Os(3) planes – is 87.8° for **6b** and 88.6° for **6e**. While the Os(1)–Os(3) bonds in **6b** [3.0488(5) Å, molecule A; 3.0451(5) Å, molecule B] as well as **6e** [3.0212(3) Å] show the lengthening associated with a metal–metal vector bridged by a hydride ligand,[7] the hinge bond [2.7948(5)–2.8004(3) Å] is short despite the presence of a bridging hydride. Similar behavior has been observed for the tetraosmium butterfly clusters $Os_4(\mu\text{-}H)_2(CO)_{13}(PMe_3)$ and $Os_4(\mu\text{-}H)(CO)_{12}(Cp^*)$,[27,28] and this has been attributed to the different coordination numbers of the metal atoms; without exception, the osmium atoms linked to only three terminal ligands in these tetraosmium clusters are associated with shorter metal–metal bond lengths.

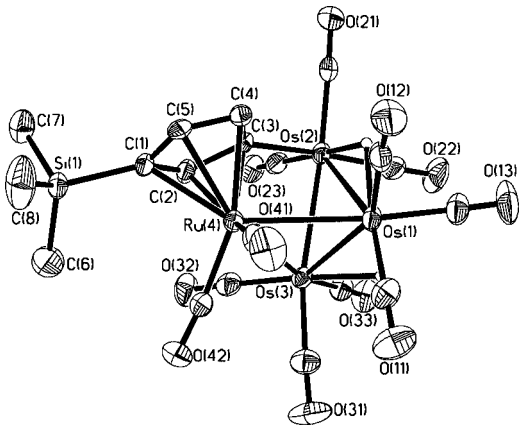


Figure 7. ORTEP diagram (50% probability thermal ellipsoids, organic hydrogen atoms omitted) for **6e**.

Table 2. Common atomic numbering scheme and selected bond parameters for **6b** and **6e**.

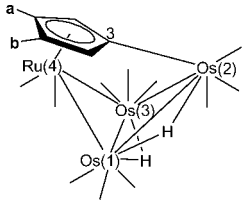


| | **a** | **b** |
|---|---|---|
| **6b** | H | Me |
| **6e** | $SiMe_3$ | H |

| Bond lengths [Å] | **6b** (Molecule A) | **6b** (Molecule B) | **6e** |
|---|---|---|---|
| Os(1)–Os(2) | 3.0488(5) | 3.0451(5) | 3.0212(3) |
| Os(1)–Os(3) | 2.7953(5) | 2.7948(5) | 2.8009(3) |
| Os(1)–Ru(4) | 2.9043(10) | 2.9111(10) | 2.9172(5) |
| Os(2)–Os(3) | 2.8289(5) | 2.8335(5) | 2.8527(3) |
| Os(3)–Ru(4) | 2.9469(9) | 2.9367(9) | 2.9393(4) |
| Os(2)–C(3) | 2.122(11) | 2.120(12) | 2.096(5) |
| Ru(4)–Cp(centroid) | 1.880(11) | 1.880(11) | 1.886(5) |
| Bond angles [°] | | | |
| Os(2)–C(3)–Cp(centroid) | 168.55 | 167.16 | 169.67 |

The $^1H$ NMR spectrum for **6e** indicated that the solid-state structure persisted in solution. In contrast, the ambient-temperature $^1H$ NMR spectrum of **6b** showed a broad singlet at –17.05 ppm. On prolonged standing in solution, the compound isomerized to **2b**, as well as decomposing into some unidentified products. On cooling **6b** to 183 K, we observed three sets of resonances, which may be attributed to the presence of three isomers. However, it is not possible to assign solution-state structures for these isomers unambiguously.

 © 2007 Wiley-VCH Verlag GmbH & Co. KGaA, Weinheim 

## Concluding Remarks

Our investigations show that thermolysis of **1** with both saturated and unsaturated $C_5$ rings led to ring aromatization via C–H activation and/or loss of a trimethylsilyl moiety, resulting in the formation of clusters **2**; binding of the resulting cyclopentadienyl moiety was specifically at the ruthenium vertex. Loss of the trimethylsilyl group appeared to be dictated by steric factors, so that two products were formed in the reaction with trimethyl(2,3,4,5-tetramethyl-2,4-cyclopentadien-1-yl)silane, viz., **2f** via loss of the silyl group, or **4** via loss of a carbonyl. The reaction with cyclopentene gave, in high yields, the unusual cluster **5** via C–H activation at an $sp^2$ carbon rather than aromatization of the cyclopentene via activation of an allylic $sp^3$ carbon, and again steric reason seemed to explain the fact that an analogue was not observed in the case of 1-methylcyclopentene. Under prolonged thermolysis, cluster fragmentation and condensation can occur, and this accounts for the low yields of **2** observed in some of the reactions.

## Experimental Section

**General Procedures:** All reactions and manipulations were carried out under nitrogen by using standard Schlenk techniques. Solvents were purified, dried, distilled, and stored under nitrogen prior to use. The products were separated by thin layer chromatography (TLC), using plates coated with silica gel 60 F254 of 0.25 or 0.5 mm thickness and extracted with dichloromethane. Routine NMR spectra were acquired with a Bruker ACF300 NMR spectrometer, while decoupling, variable-temperature and 2D NMR spectra were obtained with a Bruker Avance DRX500 or Bruker AMX500 machine. EXSY spectra were recorded with a mixing time of 0.5 s unless otherwise stated. The solvent used was deuterated chloroform unless otherwise stated. $^1$H chemical shifts reported are referenced against the residual proton of the solvents. Mass spectra were obtained with a Finnigan MAT95XL-T spectrometer in an *m*-nitrobenzyl alcohol matrix. Microanalyses were carried out by the microanalytical laboratory at the National University of Singapore. The preparation of cluster **1** appears in our earlier report.[3a] All other reagents were from commercial sources and used as supplied.

**Reactions of $RuOs_3(\mu\text{-}H)_2(CO)_{13}$ (1) with $C_5$ Rings:** In a typical reaction, to a solution of **1** in the solvent in a Carius tube was added an excess of the substrate. The solution was degassed by three freeze-pump-thaw cycles and heated. The solvent was removed under reduced pressure, and the residue so obtained was redissolved in the minimum of dichloromethane and chromatographed on TLC plates with hexane/dichloromethane (3:2, v/v) as the mobile phase. The reaction conditions and yields are summarized in Table 3, and the spectroscopic and analytical data for the products are in Table 4 and Table 5.

**Reaction of 1 with Cyclopentene:** To a Carius tube containing **1** (20.5 mg, 0.020 mmol) and hexane (30 mL) was added cyclopentene (0.1 mL). The reaction mixture was degassed by three freeze-pump-thaw cycles and stirred at 120 °C for 12 h, after which the solvent was removed under reduced pressure. Recrystallization of the red solid in hexane/dichloromethane gave dark orange crystals of **5** as the sole product (19.7 mg, 95%).

**Thermolysis of $RuOs_3(\mu\text{-}H)_3(CO)_{11}(\mu,\eta^1\text{:}\eta^2\text{-}C_5H_7)$ (5):** To a Carius tube containing hexane (30 mL) was added **5** (10.1 mg, 0.010 mmol). The reaction mixture was degassed by three freeze-pump-thaw cycles and stirred at 120 °C for 12 h, after which the solvent was removed under reduced pressure. The residue so obtained was redissolved in the minimum of dichloromethane and chromatographed on TLC plates. Elution with hexane/dichloromethane (7:3, v/v) gave a plethora of products, amongst which **2a** was identified (2.1 mg, 20%).

**Reaction of 1 with 2c:** To a Carius tube containing hexane (30 mL) was added **1** (8.2 mg, 0.079 mmol) and **2c** (5.1 mg, 0.047 mmol). The reaction mixture was degassed by three freeze-pump-thaw cycles and stirred at 120 °C for 24 h, after which the solvent was removed under reduced pressure. The residue so obtained was redissolved in the minimum of dichloromethane and chromatographed on TLC plates. Elution with hexane/dichloromethane (7:3,

Table 3. Reaction conditions and yields for the reaction of **1** with $C_5$ rings.

| Amount of **1** | Substrate (volume) | Conditions | Prod. | $R_f$ | Color | Yield |
|---|---|---|---|---|---|---|
| 16.7 mg 0.016 mmol | cyclopentane (20 mL) | 120 °C, 24 h | **2a** | 0.56 | dark brown | 7.5 mg (45%) |
| 18.2 mg, 0.018 mmol | cyclopentene (0.1 mL) | octane (20 mL), reflux, 12 h | **2a** | 0.56 | dark brown | 1.9 mg (10%) |
| 20.7 mg, 0.020 mmol | cyclopentadiene (0.1 mL) | hexane (30 mL), 120 °C, 12 h | **2a** | 0.56 | dark brown | 13.7 mg (66%) |
| 7.5 mg, 0.008 mmol | 1-methyl-1-cyclopentane (5.0 mL) | 120 °C, 24 h | **2b** | 0.44 | dark brown | 6.3 mg (74%) |
| 20.6 mg, 0.020 mmol | 1-methyl-1-cyclopentene (0.1 mL) | hexane (30 mL), 120 °C, 12 h | **6b** | 0.48 | dark brown | 4.4 mg (14%) |
| | | | **2b** | 0.44 | dark brown | 8.2 mg (39%) |
| 20.2 mg, 0019 mmol | propylcyclopentane (0.1 mL) | cyclohexane (30 mL), 120 °C, 40 h | **3** | 0.46 | orange | 8.3 mg (40%) |
| | | | **2c** | 0.46 | orange | (**2c**/**3** = 5:2) |
| 23.6 mg, 0.023 mmol | pentamethylcyclopentadiene (0.1 mL) | hexane (30 mL), 120 °C, 12 h | **2d** | 0.63 | dark brown | 17.0 mg (67%) |
| 21.2 mg, 0.020 mmol | (trimethyl silyl)cyclopentadiene (0.5 mL) | cyclohexane (30 mL), 120 °C, 20 h | **6e** | 0.56 | orange | 8.5 mg (42%) |
| | | | **2e** | 0.36 | orange | 9.0 mg (45%) |
| 30.1 mg, 0.029 mmol | trimethyl[2,3,4,5-tetramethyl-2,4-cyclopentadien-1-yl]-silane (0.5 mL) | hexane (30 mL), 120 °C, 20 h | **4** | 0.56 | dark red | 7.8 mg (23%) |
| | | | **2f** | 0.47 | dark red | 8.1 mg (25%) |

 © 2007 Wiley-VCH Verlag GmbH & Co. KGaA, Weinheim 

Table 4. Infrared spectroscopy and elemental analysis data for **2**–**6**.

| Cluster | IR ($CH_2Cl_2$) $\nu$(CO) [$cm^{-1}$] | Elemental analysis [%] found (calculated) |
|---|---|---|
| **2a** | 2089m, 2062s, 2034s, 2007m, 1952w(br), 1830w(br) | – |
| **2b** | 2086m, 2062s, 2032s, 2004m, 1950w(br), 1825w(br) | $C_{17}H_8O_{11}Os_3Ru$: C 19.43 (19.26), H 0.89 (0.76) |
| **2c** | 2088m, 2061s, 2033s, 2004m, 1950w(br), 1830w(br) | $C_{19}H_{12}O_{11}Os_3Ru.CH_2Cl_2$: C 20.35(20.46), H 1.01(1.19)[a] |
| **2d** | 2084m, 2058s, 2027s, 1998m, 1943w(br), 1821w(br) | $C_{21}H_{16}O_{11}Os_3Ru$: C 22.52 (22.60), H 1.30 (1.44) |
| **2e** | 2088m, 2061s, 2033s, 2004m, 1951w(br), 1839w(br) | $C_{19}H_{14}O_{11}Os_3RuSi$: C 20.58 (20.41), H 0.83 (1.26) |
| **2f** | 2084m, 2058s, 2028s, 2000m, 1942w(br), 1828w(br) | $C_{20}H_{14}O_{11}Os_3Ru{\cdot}1.5C_6H_{14}$: C 28.50 (28.27), H 3.21 (2.84)[b] |
| **3** | 2084m, 2064s, 2032m, 2019m, 2004m, 1948w(br) | $C_{22}H_{12}O_{14}Os_3Ru_2{\cdot}0.5C_6H_{14}$: C 22.98 (22.81), H 1.25 (1.45)[b] |
| **4** | 2082m, 2055ms, 2026s, 2002m, 1948w(br) | $C_{22}H_{24}O_{10}Os_3RuSi$: C 22.84 (22.99), H 2.33 (2.09) |
| **5** | 2098vw, 2082w, 2066vs, 2051s, 2043m, 2021m, 2001w | $C_{16}H_{10}O_{11}Os_3Ru$: C 18.05 (18.30), H 0.87 (0.96) |
| **6b** | 2111w, 2100w, 2080m, 2070ms, 2043s, 2017m, 2000m, 1968w | $C_{17}H_8O_{11}Os_3Ru$: C 19.39 (19.26), H 0.58 (0.76) |
| **6e** | 2111w, 2100w, 2074m, 2070ms, 2043s, 2016mw, 2000mw, 1968w | $C_{19}H_{14}O_{11}Os_3RuSi$: C 20.44 (20.41), H 1.26 (1.26) |

[a] $^1$H NMR confirmed the presence of dichloromethane in the sample. [b] $^1$H NMR confirmed the presence of hexane in the sample.

Table 5. $^1$H NMR spectroscopy and MS data for **2**–**6**.

| Cluster | $^1$H NMR, $\delta$ [ppm] | MS, *m*/*z* found (calculated) for $M^+$ |
|---|---|---|
| **2a** | 5.56 (s, 5 H, Cp), –21.81 (s, 1 H, Os*H*Os) | 1045 (1045) |
| **2b** | 5.62 (m, 2 H, γ-H), 5.46 (m, 2 H, β-H), 1.88 (s, 3 H, Me), –21.60 (s, 1 H, Os*H*Os) | 1061 (1060) |
| **2c** | 4.85 (m, 2 H, γ-H), 4.73 (m, 2 H, β-H), 1.67 (t, $^3J_{HH}$ = 7.5 Hz, 2 H, $CH_2$), 1.01 (quintet, $^3J_{HH}$ = 7.5 Hz, 2 H, $CH_2$), 0.58 (t, 3 H, Me, $^3J_{HH}$ = 7.5 Hz), –21.53 (s, 1 H, Os*H*Os)[a] | 1088 (1088) |
| **2d** | 1.25 (s, 15 H, Me), –18.34 (s, 1 H, Os*H*Os) | 1116 (1116) |
| **2e** | 6.15 (m, 2 H, γ-H), 4.99 (m, 2 H, β-H), 0.32 (s, 9 H, Me), –21.21 (s, 1 H, Os*H*Os) | 1118 (1118) |
| **2f** | 5.92 (s, 1 H, Cp), 1.97 (s, 12 H, Me), –20.78 (s, 1 H, Os*H*Os) | 1102 (1102) |
| **3** | 4.78 (m, 1 H), 4.29 (m, 1 H), 4.05 (m, 1 H), 1.18 (m, 2 H), 0.95 (m, 2 H), 0.71 (m, 3 H), –19.54 (br. s, 2 H)[a] | 1273 (1273) |
| **4** | 1.98 (s, 6 H), 1.96(s, 6 H), 0.38 (s, 9 H), –18.46 (s, 3 H) | 1147 (1148) |
| **5** | 4.56 (d, $^3J_{H1H2}$ = 3.2 Hz, 1 H, $H^1$), 2.93 (dd, $^3J_{H7H6}$ = 15.3 Hz, $^3J_{H7H5}$ = 7.1 Hz, 1 H, $H^7$), 2.36 (ddd, $^3J_{H2H1}$ = 3.2 Hz, $^3J_{H2H3}$ = 12.2 Hz, $^3J_{H2H4}$ = 6.9 Hz, 1 H, $H^2$), 2.33 (dd, $^3J_{H3H2}$ = 12.2 Hz, $^3J_{H3H5}$ = 8.2 Hz, 1 H, $H^3$), 2.17 (ddd, $^3J_{H6H4}$ = 6.9 Hz, $^3J_{H6H5}$ = 11.2 Hz, $^3J_{H6H7}$ = 15.3 Hz, 1 H, $H^6$), 2.02 (ddd, $^3J_{H4H2}$ = 6.9 Hz, $^3J_{H4H5}$ = 13.0 Hz, $^3J_{H4H6}$ = 8.2 Hz, 1 H, $H^4$), 1.21 (dddd, $^3J_{H5H3}$ = 8.2 Hz, $^3J_{H5H4}$ = 13.0 Hz, $^3J_{H5H6}$ = 11.2 Hz, $^3J_{H5H7}$ = 7.1 Hz, 1 H, $H^5$)<br>Major isomer: –13.67 (d, $^2J_{HH}$ = 2.5 Hz, 1 H), –18.97 (d, 1 H), –20.60 (s, 1 H)<br>Minor isomer: –14.47 (s, 1 H), –18.74 (s, 1 H) and –20.73 (s, 1 H) | 1049 (1050) |
| **6b** | 5.21 (s, 1 H), 5.08 (s, 1 H), 4.96 (s, 1 H), 2.13 (s, 3 H), –17.05 (s, br) | 1060 (1060) |
| **6e** | 5.21 (m, 1 H), 5.12 (m, 1 H), 5.04 (m, 1 H), 0.22 (s, 9 H), –17.06 (s, 1 H, Os*H*Os), –17.10 (s, 1 H, Os*H*Os) | 1118 (1118) |

[a] In $C_6D_6$.

v/v) gave unreacted **1** (4.1 mg), $Os_3(\mu\text{-}H)_2(CO)_{10}$ (1.3 mg), and a mixture of **2c** and **3** (5.9 mg; **2c**/**3** : 1.3:1.0).

**Thermolysis of 2b:** To a Carius tube containing cyclohexane (30 mL) was added **2b** (20.2 mg, 0.019 mmol). The reaction mixture was degassed by three freeze-pump-thaw cycles and stirred at 120 °C for 18 h, after which the solvent was removed on the vacuum line. The residue so obtained was redissolved in the minimum of dichloromethane and chromatographed on TLC plates. Elution with hexane/dichloromethane (3:2, v/v) yielded two bands, identified as **6b** (3.6 mg, 18%) and unreacted **2b** (16.2 mg), respectively.

**Thermolysis of 2e:** To a Carius tube containing cyclohexane (30 mL) was added **2e** (10.7 mg, 0.010 mmol). The reaction mixture was degassed by three freeze-pump-thaw cycles and stirred at 120 °C for 20 h, after which the solvent was removed on the vacuum line. The residue so obtained was redissolved in the minimum of dichloromethane and chromatographed on TLC plates. Elution with hexane/dichloromethane (3:2, v/v) yielded two bands, identified as **6e** (1.5 mg, 14%) and unreacted **2e** (8.7 mg), respectively.

**X-ray Crystal Structure Determinations**

Crystals were mounted on quartz fibers. X-ray data were collected on a Bruker AXS APEX system, using Mo-$K_\alpha$ radiation, at 223 K with the SMART suite of programs.[29] Data were processed and corrected for Lorentz and polarization effects with SAINT[30] and for absorption effects with SADABS.[31] Structural solution and refinement were carried out with the SHELXTL suite of programs.[32] Crystal and refinement data are summarized in Table 6 and Table 7.

The structures were solved by direct methods to locate the heavy atoms, followed by difference maps for the light, non-hydrogen atoms. There were two molecules in the asymmetric unit for **2a** and **6b**. The hydrides were either located in low-angle difference electron density maps or were placed by potential energy calculations with the program XHYDEX,[22] given fixed isotropic thermal parameters, and were either refined freely, with restraints on the M–H bond lengths, or with a riding model. Organic hydrogen atoms were placed in calculated positions and refined with a riding model. All non-hydrogen atoms were generally given anisotropic displacement parameters in the final model.

Cluster **5** exhibited disorder of the heavy atom positions; the ruthenium atom was modeled as disordered over two sites – M(1) and M(4). The disordered atoms at the same site were given the same coordinate and shifts and thermal parameters, and the Ru occupancy refined and restrained to add up to unity; the refined occupancies were 0.12 and 0.88 for M(1) and M(4), respectively.

 © 2007 Wiley-VCH Verlag GmbH & Co. KGaA, Weinheim 

Table 6. Crystal data for **2a**, **2b**, **2d**, **2e**, and **2f**.

| Compound | **2a** | **2b** | **2d** | **2e** | **2f** |
|---|---|---|---|---|---|
| Formula | $C_{16}H_6O_{11}Os_3Ru$ | $C_{17}H_8O_{11}Os_3Ru$ | $C_{21}H_{16}O_{11}Os_3Ru$ | $C_{19}H_{14}O_{11}Os_3RuSi$ | $C_{20}H_{14}O_{11}Os_3Ru$ |
| FW | 1045.88 | 1059.90 | 1116.01 | 1118.06 | 1101.98 |
| Crystal system | orthorhombic | monoclinic | orthorhombic | triclinic | monoclinic |
| Space group | $P2_12_12_1$ | $P2_1/m$ | *Pnma* | $P\bar{1}$ | $P2_1/m$ |
| Unit cell dimensions | | | | | |
| $a$ [Å] | 8.67370(10) | 8.4734(3) | 19.0091(3) | 8.8293(5) | 8.940(2) |
| $b$ [Å] | 13.9557(2) | 14.4955(5) | 14.7068(2) | 9.0592(5) | 15.324(4) |
| $c$ [Å] | 33.1562(5) | 8.6127(3) | 8.81410(10) | 17.5325(9) | 9.186(2) |
| $\alpha$ [°] | 90 | 90 | 90 | 90.960(1) | 90 |
| $\beta$ [°] | 90 | 95.4930(10) | 90 | 91.866(1) | 96.021(6) |
| $\gamma$ [°] | 90 | 90 | 90 | 117.198(1) | 90 |
| Volume [Å$^3$] | 4013.48(10) | 1053.01(6) | 2464.10(6) | 1245.85(12) | 1251.6(5) |
| $Z$ | 8 | 2 | 4 | 2 | 2 |
| $\rho_c$ [Mg m$^{-3}$] | 3.462 | 3.343 | 3.008 | 2.980 | 2.924 |
| $\mu$(Mo-$K_\alpha$) [mm$^{-1}$] | 19.731 | 18.803 | 16.079 | 15.946 | 15.826 |
| $F$(000) | 3696 | 940 | 2008 | 1004 | 988 |
| Crystal size [mm$^3$] | $0.09\times0.26\times0.36$ | $0.20\times0.18\times0.10$ | $0.04\times0.32\times0.38$ | $0.34\times0.26\times0.02$ | $0.19\times0.14\times0.02$ |
| $\theta$ range [°] | 2.35 to 30.49 | 2.38 to 30.02 | 2.55 to 26.37 | 2.33 to 29.97 | 2.23 to 26.37 |
| Reflections collected | 34822 | 15665 | 21261 | 18903 | 14131 |
| Independent reflections ($R_{int}$) | 11607 [$R$(int) = 0.0557] | 3125 (0.0417) | 2612 (0.0968) | 7057 (0.0427) | 2653 (0.0636) |
| Completeness%, (to $\theta$ [°]) | 97.2 (30.49) | 98.3 (30.02) | 100.0 (26.37) | 97.1 (29.97) | 99.5 (26.37) |
| Transmission range | 0.266–0.115 | 0.255–0.117 | 0.528–0.130 | 0.741–0.074 | 0.743–0.153 |
| Data/restraints/parameters | 11607/0/559 | 3125/0/169 | 2612/0/176 | 7057/0/319 | 2653/0/170 |
| Goodness-of-fit on $F^2$ | 0.984 | 1.146 | 1.074 | 1.060 | 1.212 |
| Final $R$ indices [$I>2\sigma(I)$] | $R_1$ = 0.0459 | $R_1$ = 0.0275 | $R_1$ = 0.0394 | $R_1$ = 0.0294 | $R_1$ = 0.0503 |
| | $wR_2$ = 0.0878 | $wR_2$ = 0.0592 | $wR_2$ = 0.1036 | $wR_2$ = 0.0731 | $wR_2$ = 0.1207 |
| $R$ indices (all data) | $R_1$ = 0.0520 | $R_1$ = 0.0302 | $R_1$ = 0.0415 | $R_1$ = 0.0336 | $R_1$ = 0.0549 |
| | $wR_2$ = 0.0897 | $wR_2$ = 0.0601 | $wR_2$ = 0.1052 | $wR_2$ = 0.0751 | $wR_2$ = 0.1234 |
| Absolute structure parameter | 0.003(8) | – | – | – | – |
| Largest diff. peak and hole [e Å$^{-3}$] | 4.114 and –2.175 | 1.647 and –2.500 | 2.612 and –4.167 | 1.421 and –1.450 | 5.023 and –1.303 |

Table 7. Crystal data for **3**, **4**, **5**, **6b**, and **6e**.

| Compound | **3** | **4** | **5** | **6b** | **6e** |
|---|---|---|---|---|---|
| Formula | $C_{22}H_{12}O_{14}Os_3Ru_2$ | $C_{22}H_{24}O_{10}Os_3RuSi$ | $C_{16}H_{10}O_{11}Os_3Ru$ | $C_{17}H_8O_{11}Os_3Ru$ | $C_{19}H_{14}O_{11}Os_3RuSi$ |
| FW | 1273.06 | 1148.17 | 1049.91 | 1059.90 | 1118.06 |
| Crystal system | monoclinic | monoclinic | triclinic | monoclinic | triclinic |
| Space group | $C2/c$ | $P2_1/n$ | $P\bar{1}$ | Cc | $P\bar{1}$ |
| Unit cell dimensions | | | | | |
| $a$ [Å] | 14.5019(8) | 12.2261(3) | 7.7946(3) | 8.9642(4) | 9.1646(5) |
| $b$ [Å] | 12.9211(7) | 14.5775(3) | 9.0192(4) | 16.7004(7) | 12.0684(6) |
| $c$ [Å] | 30.7798(17) | 15.9292(3) | 15.4979(7) | 29.4309(13) | 12.3927(6) |
| $\alpha$ [°] | 90 | 90 | 94.9330(10) | 90 | 83.407(1) |
| $\beta$ [°] | 95.998(1) | 93.4830(10) | 95.9450(10) | 93.6030(10) | 88.641(1) |
| $\gamma$ [°] | 90 | 90 | 97.3720(10) | 90 | 69.804(1) |
| Volume [Å$^3$] | 5736.0(5) | 2833.75(11) | 1069.24(8) | 4397.3(3) | 1277.69(11) |
| $Z$ | 8 | 4 | 2 | 8 | 2 |
| $\rho_c$ [Mg m$^{-3}$] | 2.948 | 2.691 | 3.261 | 3.202 | 2.906 |
| $\mu$(Mo-$K_\alpha$) [mm$^{-1}$] | 14.337 | 14.023 | 18.515 | 18.011 | 15.549 |
| $F$(000) | 4576 | 2088 | 932 | 3760 | 1004 |
| Crystal size [mm$^3$] | $0.34\times0.20\times0.16$ | $0.38\times0.34\times0.18$ | $0.10\times0.17\times0.36$ | $0.28\times0.18\times0.16$ | $0.38\times0.24\times0.05$ |
| $\theta$ range [°] | 2.12 to 26.37 | 2.04 to 30.02 | 2.29 to 30.51 | 2.44 to 29.55 | 2.31 to 30.00 |
| Reflections collected | 43335 | 23997 | 15556 | 16172 | 19422 |
| Independent reflections ($R_{int}$) | 5861 (0.0423) | 8098 (0.0346) | 6282 (0.0462) | 8336 (0.0257) | 7215 (0.0353) |
| Completeness%, (to $\theta$ [°]) | 100.0 (26.37) | 97.6 (30.02) | 96.2 (30.51) | 91.4 (29.55) | 96.8 (30.00) |
| Transmission range | 0.208–0.085 | 0.187–0.076 | 0.266–0.122 | 0.161–0.081 | 0.510–0.067 |
| Data/restraints/parameters | 5861/0/370 | 8098/0/344 | 6282/6/309 | 8336/2/579 | 7215/0/331 |
| Goodness-of-fit on $F^2$ | 1.434 | 1.053 | 1.015 | 1.061 | 1.051 |
| Final $R$ indices [$I>2\sigma(I)$] | $R_1$ = 0.0702 | $R_1$ = 0.0311 | $R_1$ = 0.0332 | $R_1$ = 0.0274 | $R_1$ = 0.0290 |
| | $wR_2$ = 0.1561 | $wR_2$ = 0.0717 | $wR_2$ = 0.0683 | $wR_2$ = 0.0706 | $wR_2$ = 0.0701 |
| $R$ indices (all data) | $R_1$ = 0.0727 | $R_1$ = 0.0398 | $R_1$ = 0.0405 | $R_1$ = 0.0286 | $R_1$ = 0.0338 |
| | $wR_2$ = 0.1569 | $wR_2$ = 0.0747 | $wR_2$ = 0.0705 | $wR_2$ = 0.0712 | $wR_2$ = 0.0751 |
| Largest diff. peak and hole [e Å$^{-3}$] | 2.251 and –2.606 | 2.237 and –2.123 | 2.196 and –1.747 | 1.430 and –1.422 | 1.555 and –1.668 |

 © 2007 Wiley-VCH Verlag GmbH & Co. KGaA, Weinheim 

CCDC-634245 to CCDC-634254 contain the supplementary crystallographic data for this paper. These data can be obtained free of charge from The Cambridge Crystallographic Data Centre via www.ccdc.cam.ac.uk/data_request/cif.

## Acknowledgments

This work was supported by the National University of Singapore (Research Grant No. R143–000–190–112) and one of us (Y. L. K. T.) thanks the University for a Research Scholarship.

[1] B. F. G. Johnson, J. Lewis, C. E. Housecroft, M. A. Gallop, M. Martinelli, D. Braga, F. Grepioni, *J. Mol. Catal.* **1992**, *74*, 61–72.
[2] a) E. L. Muetterties, T. L. Rhoden, E. Band, C. F. Bruker, W. R. Pretrzer, *Chem. Rev.* **1979**, *79*, 91–137; b) H. Wadepohl, *Angew. Chem. Int. Ed. Engl.* **1992**, *31*, 247–262; c) B. F. G. Johnson, M. A. Gallup, Y. V. Roberts, *J. Mol. Catal.* **1994**, *86*, 51–69; d) B. F. G. Johnson, *J. Organomet. Chem.* **1994**, *475*, 31–43; e) P. J. Dyson, J. S. McIndoe, *Transition Metal Carbonyl Cluster Chemistry*, Gordon and Breach, The Netherlands, **2000**.
[3] a) L. Pereira, W. K. Leong, S. Y. Wong, *J. Organomet. Chem.* **2000**, *609*, 104–109; b) L. J. Pereira, K. S. Chan, W. K. Leong, *J. Organomet. Chem.* **2005**, *690*, 1033–1043; c) L. J. Pereira, W. K. Leong, *J. Organomet. Chem.* **2006**, *691*, 1941–1944; d) L. J. Pereira, W. K. Leong, *J. Organomet. Chem.* **2006**, *691*, 2448–2456; e) L. J. Pereira, W. K. Leong, *Polyhedron* **2006**, *25*, 2392–2400.
[4] a) Y. L. K. Tan, W. K. Leong, *J. Organomet. Chem.* **2006**, *691*, 2048–2054; b) Y. L. K. Tan, C. W. A. Koh, T. B. Lim, W. K. Leong, *J. Cluster Sci.* **2006**, *17*, 509–516; c) Y. L. K. Tan, W. K. Leong, *J. Organomet. Chem.* **2007**, *692*, 768–772.
[5] a) H. Wadepohl, S. Gebert, H. Pritzkow, *J. Organomet. Chem.* **2000**, *614–5*, 158–167; b) P. J. Dyson, B. F. G. Johnson, C. M. Martin, *Coord. Chem. Rev.* **1996**, *155*, 69–86; c) M. Castiglioni, R. Giordano, E. Sappa, *J. Organomet. Chem.* **1995**, *491*, 111–120; d) B. F. G. Johnson, *J. Organomet. Chem.* **1994**, *475*, 31–43.
[6] R. Buntem, J. Lewis, C. A. Morewood, P. R. Raithby, M. C. R. de Arellano, G. P. Shields, *J. Chem. Soc., Dalton Trans.* **1998**, 1091–1096.
[7] a) M. R. Churchill, B. G. DeBoer, F. J. Rotella, *Inorg. Chem.* **1976**, *15*, 1843–1853; b) R. Bau, R. G. Teller, S. W. Kirtley, T. F. Koetzle, *Acc. Chem. Res.* **1979**, *12*, 176–186; c) D. J. Elliot, J. J. Vittal, R. J. Puddephatt, D. G. Holah, A. N. Hughes, *Inorg. Chem.* **1992**, *31*, 1247–1250; d) R. D. Adams, J. P. Selegue in *Comprehensive Organometallic Chemistry* (Eds.: G. Wilkinson, F. G. A. Stone, E. W. Abel), Pergamon, **1982**, vol. 4.
[8] a) J. Lewis, C. A. Morewood, P. R. Raithby, M. C. R. de Arellano, *J. Chem. Soc., Dalton Trans.* **1996**, 4509–4510; b) J. Lewis, C. A. Morewood, P. R. Raithby, M. C. R. de Arellano, *J. Chem. Soc., Dalton Trans.* **1997**, 3335–3342.
[9] W. Wang, H. B. Davis, F. W. B. Einstein, R. K. Pomeroy, *Organometallics* **1994**, *13*, 5113–5121.
[10] J. A. Iggo, *NMR Spectroscopy in Inorganic Chemistry*, Oxford University Press, Oxford, **1999**.
[11] H. G. Ang, L. L. Koh, G. Y. Yang, *J. Chem. Soc., Dalton Trans.* **1996**, 1573–1581.
[12] M. R. A. Al-Mandhary, J. Lewis, P. R. Raithby, *J. Organomet. Chem.* **1997**, *530*, 247–250.
[13] J. P. Canal, G. P. A. Yap, R. K. Pomeroy, *Organometallics* **2003**, *22*, 3439–3447.
[14] R. Buntem, J. F. Gallagher, J. Lewis, P. R. Raithby, M. A. Rennie, G. P. Shields, *J. Chem. Soc., Dalton Trans.* **2000**, 4297–4303.
[15] R. K. Pomeroy in *Comprehensive Organometallic Chemistry II* (Eds.: G. Wilkinson, F. G. A. Stone, E. W. Abel), Pergamon Press, **1995**, vol. 7, ch. 15.
[16] a) J. R. Fox, W. L. Gladfelter, T. G. Wood, J. A. Smegal, T. K. Foreman, G. L. Geoffroy, I. Tavanaipour, V. W. Day, C. S. Day, *Inorg. Chem.* **1981**, *20*, 3214–3224; b) W. L. Gladfelter, G. L. Geoffroy, *Inorg. Chem.* **1980**, *19*, 2579–2585.
[17] Y. Chi, C.-Y. Cheng, S.-L. Wong, *J. Organomet. Chem.* **1989**, *378*, 45–56.
[18] a) H. Chen, B. F. G. Johnson, J. Lewis, D. Braga, F. Grepioni, E. Parasini, *J. Chem. Soc., Dalton Trans.* **1991**, 215–219; b) S. Bhaduri, B. F. G. Johnson, J. W. Kelland, J. Lewis, P. R. Raithby, S. Rehani, G. M. Sheldrick, K. Wong, M. McPartlin, *J. Chem. Soc., Dalton Trans.* **1979**, 562–568; c) B. F. G. Johnson, A. J. Blake, C. M. Martin, D. Braga, E. Parasini, H. Chen, *J. Chem. Soc., Dalton Trans.* **1994**, 2167–2175.
[19] B. F. G. Johnson, J. Lewis, A. G. Orpen, P. R. Raithby, K. D. Rouse, *J. Chem. Soc., Dalton Trans.* **1981**, 788–792.
[20] a) J. J. Guy, B. E. Reichert, G. M. Sheldrick, *Acta Crystallogr., Sect. B* **1976**, *32*, 3319–3320; b) A. G. Orpen, D. Pippard, G. M. Sheldrick, K. D. Rouse, *Acta Crystallogr., Sect. B* **1978**, *34*, 2466–2472; c) R. J. Goudsmit, B. F. G. Johnson, J. Lewis, P. R. Raithby, *Acta Crystallogr., Sect. B* **1982**, *38*, 2689–2691.
[21] M. B. Smith, J. March, *March's Advanced Organic Chemistry*, 5th ed., Wiley, New York, **2001**.
[22] A. G. Orpen, *XHYDEX*, School of Chemistry, University of Bristol, UK, **1997**.
[23] a) M. R. Churchill, B. G. DeBoer, *Inorg. Chem.* **1977**, *16*, 878–884; b) B. F. G. Johnson, J. Lewis, P. R. Raithby, G. M. Sheldrick, K. Wong, M. McPartlin, *J. Chem. Soc., Dalton Trans.* **1978**, 673–676.
[24] D. B. Brown, B. F. G. Johnson, C. M. Martin, A. E. H. Wheatley, *J. Chem. Soc., Dalton Trans.* **2000**, 2055–2060.
[25] a) R. Della Pergola, L. Garlaschelli, M. Manassero, M. Sansoni, A. Sironi, D. Strumolo, *J. Organomet. Chem.* **2005**, *690*, 4768–4772; b) Y.-C. Liu, W.-Y. Yeh, G.-H. Lee, S.-M. Peng, *J. Organomet. Chem.* **2004**, *689*, 1944–1948; c) J. B. Keister, J. R. Shapley, *J. Am. Chem. Soc.* **1976**, *98*, 1056–1057; d) A. J. Deeming, M. Underhill, *J. Chem. Soc., Dalton Trans.* **1974**, 1415–1419; e) B. F. G. Johnson, J. W. Kelland, J. Lewis, S. K. Rehani, *J. Organomet. Chem.* **1976**, *113*, C42–44.
[26] M. A. Gallop, B. F. G. Johnson, J. Lewis, P. R. Raithby, *J. Chem. Soc., Chem. Commun.* **1986**, *9*, 706–708.
[27] L. R. Martin, F. W. B. Einstein, R. K. Pomeroy, *Inorg. Chem.* **1988**, *27*, 2986–2989.
[28] W. Wang, F. W. B. Einstein, R. K. Pomeroy, *Organometallics* **1993**, *12*, 3079–3086.
[29] *SMART* version 5.628, Bruker AXS Inc., Madison, Wisconsin, USA, **2001**.
[30] *SAINT+* version 6.22a, Bruker AXS Inc., Madison, Wisconsin, USA, **2001**.
[31] G. M. Sheldrick, *SADABS*, **1996**.
[32] *SHELXTL* version 5.1, Bruker AXS Inc., Madison, Wisconsin, USA, **1997**.

Received: January 22, 2007
Published Online: April 10, 2007

 © 2007 Wiley-VCH Verlag GmbH & Co. KGaA, Weinheim 

DOI: 10.1002/ejic.200700004

# Bis-μ-pyrazolate-Bridged Dinickel(II) and Dicopper(II) Complexes: An Example of Stereoelectronic Preference of Metal Ions and Stabilization of Mixed-Valence $Ni^{III}Ni^{II}$ Species

**Vibha Mishra,[a] Francesc Lloret,[b] and Rabindranath Mukherjee*[a]**

**Keywords:** Nickel / Copper / Dinuclear complexes / Pyrazolate bridge / $Ni^{III}$-$Ni^{II}$ species

New dimeric nickel(II) and copper(II) complexes $[(L)Ni(\mu\text{-}L')]_2[ClO_4]_2$ **1** and $[(L)Cu(\mu\text{-}L')]_2[ClO_4]_2$ **2**, [2-[3-(2′-pyridyl)-pyrazol-1-ylmethyl]pyridine (L) and 3-(2-pyridyl)pyrazole (HL′)] have been synthesized, structurally characterized, and their absorption, magnetic, EPR and redox properties investigated. The crystal structure of **1**·MeCN reveals a planar $\{Ni_2(\mu\text{-}L')_2\}^{2+}$ core [Ni···Ni separation: 4.0765(10) Å] in which each distorted octahedral $Ni^{II}$ ions is terminally coordinated by a tridentate ligand L and bridged by two HL′ units, in their deprotonated form. The structural analysis of **2**·2MeCN reveals two five-coordinate $Cu^{II}$ ions, each terminally coordinated by adopting only a bidentate coordination mode of L, in which the $-CH_2$py arm remains uncoordinated. A similar bridging [Cu···Cu separation: 3.9382(24) Å] as in **1**·MeCN is observed. Thus stereoelectronic preferences of $Ni^{II}$ and $Cu^{II}$ are clearly revealed. Closer inspection of crystal packing diagram of **1**·MeCN reveals the formation of 2-D network structure assembled solely via C–H···π interaction [pyridyl C–H (4-position) of pyridylpyrazole unit of L and π cloud of pyridine of bridging deprotonated L′ unit]. In **2**·2MeCN, however, π···π interactions between uncoordinated pyridyl arms are observed. Variable-temperature magnetic studies on both complexes indicate the existence of strong antiferromagnetic coupling between the two metal ions (singlet-triplet energy separation, $J = -20\ cm^{-1}$ for **1** and $-200\ cm^{-1}$ for **2**). When investigated by cyclic voltammetry complex **1** displays two quasi-reversible electron-transfer reactions at $E_{1/2}$ = 1.36 V ($\Delta E_p$ = 110 mV) and 1.79 V ($\Delta E_p$ = 120 mV) vs. SCE, due to $Ni^{III}Ni^{II}/Ni^{II}{}_2$ and $Ni^{III}{}_2/Ni^{III}Ni^{II}$ redox processes, respectively. Constant potential electrolysis at 1.50 V vs. SCE leads to the generation of dark green mixed-valence $Ni^{III}Ni^{II}$ species, which is stable enough to be subjected to characterization by UV/Vis and EPR spectroscopy. Compound **2** exhibits only irreversible reductions (cathodic peak potential, $E_{pc}$ = –0.28 V and –0.50 V vs. SCE).

(© Wiley-VCH Verlag GmbH & Co. KGaA, 69451 Weinheim, Germany, 2007)

## Introduction

There has been continuing interest in the investigation of the magneto-structural properties of symmetrical dibridged metal(II) dimers.[1] As part of our continued involvement in the exploration of interesting coordination chemistry of pyridyl/pyrazole-based chelating ligands,[2] we have investigated the magneto-structural properties of a large variety of dinuclear/trinuclear/polymeric complexes with a varied combinations of endogenous/exogenous and solely exogenous bridging ligands (alkoxo/pyrazolato,[3] acetato/pyrazolato,[4] carbonato,[5] diacetato,[4,6] dichloro,[7] dihydroxo,[4,8] monohydroxo,[9] oxo/bis-acetato,[10,11] phenoxo/chloro,[12] phenoxo/hydroxo,[8,13] diphenoxo[14]).

Among the diverse bridging ligands/ligand frameworks that have been employed in holding two metal centers for efficient mediation of magnetic exchange interactions, pyrazolates are extensively explored, due to their coordination flexibility, versatility and potential to fine-tune metal–metal distance over a wide range of 2.4–4.6 Å affording oligo- and polymetallic compounds.[15]

This work finds impetus from the fact that a combination of carefully designed chelating ligands and judicious choice of metal ions with stereoelectronic preference can lead to the synthesis of metal complexes with interesting molecular and electronic structural properties.[16,17] The choice of terminal ligands of this work stems from our continued activity in the coordination chemistry of nonplanar pyridyl/pyrazole ligands toward transition metal ions.[2,4,6,7,18,19] Specifically, in the present work our target has been to synthesize and structurally characterize dimetal(II) complexes, satisfying the following requirements. (i) The metal ions should show stereoelectronic preference in their coordination. (ii) The terminal coordination of the metal ions should be provided by tridentate ligand L and bridging coordination by deprotonated form of 3-(2-pyridyl)pyrazole

[a] Department of Chemistry, Indian Institute of Technology Kanpur,
Kanpur 208 016, India
Fax: +91-2597436
E-mail: rnm@iitk.ac.in
[b] Departament de Química Inorgànica/Instituto de Ciencia Molecular (ICMOL),
Facultat de Química de la Universitat de València,
Dr Moliner, 46100 Burjassot (València), Spain

Supporting information for this article is available on the WWW under http://www.eurjic.org or from the author.

 © 2007 Wiley-VCH Verlag GmbH & Co. KGaA, Weinheim 

(HL′).[16,17,20] (iii) The magneto-structural behavior should be investigated. Thus we report here the synthesis, crystal structure of bis-μ-pyrazolate-bridged dimetal(II) complexes $[(L)M^{II}(\mu\text{-}L')]_2[ClO_4]_2$ (M = Ni **1**, Cu **2**), and investigation of their spectroscopic, magnetic, and redox properties.

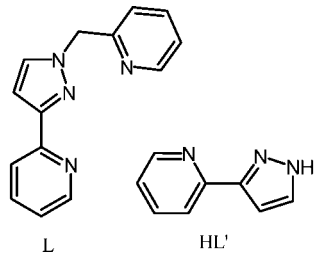


## Results and Discussion

### Synthesis and General Characterization

The designed synthesis of two complexes $[\{(L)M^{II}(\mu\text{-}L')\}_2][ClO_4]_2$ (M = Ni **1**, Cu **2**) are based on the following considerations: (i) L is a potential tridentate ligand,[18d] (ii) 3-(2-pyridyl)pyrazole (HL′)[20] can assume several coordination modes and the one adopted in the complex formation is governed by the reaction conditions.[21] Notably, it can act as a terdentate bridging ligand via deprotonation of the pyrazolyl NH group and coordination of the pyrazolyl N atom to a second metal ion, and (iii) The $Cu^{II}$ ion is well-known to produce variable and distorted coordination geometries[22] and the $Ni^{II}$ ion is expected to produce six-coordinate geometry with the given combination of ligands L and deprotonated L′. Keeping these points in mind a common synthetic strategy was followed for preparing the two complexes. The metal salt $Ni(OAc)_2{\cdot}4H_2O$/$[Cu(H_2O)_6][ClO_4]_2$ and L (1:1) were allowed initially to react in MeOH, addition of 1 equiv. of HL′, followed by addition of $Et_3N$ led to the formation/isolation of the complexes.

As expected, both complexes behave as 1:2 electrolytes in MeCN solution.[23] IR spectra show the characteristic bands at ca. 1100 $cm^{-1}$ and ca. 620 $cm^{-1}$ for ionic perchlorate vibrations. Elemental analysis, IR, and solution electrical conductivity data are in excellent agreement with the above formulations of the two new complexes.

### Crystal Structure of $[\{(L)Ni(\mu\text{-}L')\}_2][ClO_4]_2$ (1·MeCN)

A perspective view of the cation of **1**·MeCN with atom numbering scheme is shown in Figure 1 and selected metric parameters are given in Table 1. Each $Ni^{II}$ ion is in six-coordinate geometry with coordination by two bridging pyrazolate nitrogen atoms [N(6) and N(14) to Ni1; N(7) and N(13) to Ni2], a terminal pyridyl coordination from 3-(2-pyridyl)pyrazole units N(5) to Ni1 and N(12) to Ni2. Two additional coordinations are achieved by pyrazole nitrogen of ligand L: N(2) to Ni1 and N(9) to Ni2. Two long axial coordinations are achieved by the pyridyl nitrogen atoms of L: N(1) and N(4) for Ni1; N(8) and N(11) for Ni2. Both $Ni^{II}$ ions are bridged by the deprotonated 3-(2-pyridyl)pyrazole unit, leading to a Ni···Ni separation of 4.0765(10) Å. In essence, it is a bis(μ-pyrazolate)-bridged six-coordinate dinickel(II) complex. Metric parameters indicate that the coordination geometry deviates from regular octahedron. While the *trans* angles vary in the range 160–175° the *cis* angle variation is in the range 77–101° (Table 1).

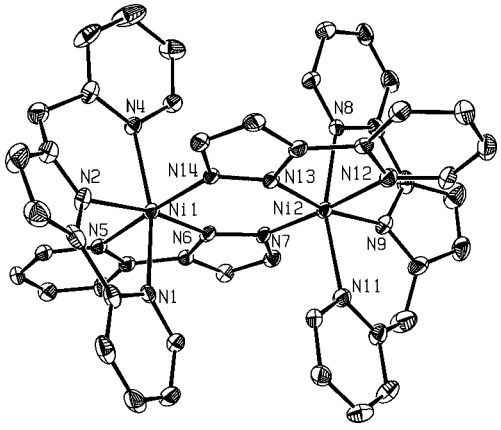


Figure 1. View of the dication $[(L)_2Ni_2(\mu\text{-}L')_2]^{2+}$ in complex **1**·MeCN, showing the atom numbering scheme. Atoms are drawn at 30% probability level. All hydrogen atoms are excluded for clarity.

The two nickel(II) ions deviate from the mean plane passing through bridging pyrazolate units by only 0.1482 Å and 0.0765 Å (Ni1 and Ni2, respectively). Dihedral angle between the plane of pyrazolate ring of {Ni1(μ-L′)} unit and {Ni2(μ-L′)} is 5.529(172)°. In this structure there are three types of donor atoms: pyrazole nitrogen and two types of pyridyl nitrogen atoms. Average distances for Ni–$N_{py}$ (directly attached pyridyl ring), Ni–$N_{py}$ (pyridyl ring with $CH_2$-spacer), and Ni–$N_{pz}$ (pyrazole ring) are 2.1575(4), 2.173(4) and 2.0333(4) Å, respectively. It is found that pyrazole rings from terminal ligands are more strongly bonded to the $Ni^{II}$ ions than the bridging ones. In fact, the observed Ni–$N_{py}$ (N5/N12) (bridging pyrazolate) distances are shorter than Ni–$N_{py}$ (N1/N8) bond lengths from terminally coordinated L ligand [2.128(4) and 2.152(4) Å vs. 2.160(4) and 2.189(4) Å]. The present complex is amongst relatively few structurally characterized bis(μ-pyrazolate)-bridged dinickel(II) complexes.[2a,24,25]

### Crystal Structure of $[\{(L)Cu(\mu\text{-}L')\}_2][ClO_4]_2{\cdot}2MeCN$ (2·2MeCN)

A perspective view of the cation of **2**·2MeCN is displayed in Figure 2, along with the atom-numbering scheme. The structural analysis reveals that crystallographic asymmetric unit consists of a binuclear dipyrazolate-bridged copper(II) cation, two perchlorate ions, and two MeCN molecules. The dication sits on a crystallographically imposed inversion center and hence only half of the dimeric unit is unique and the other half is symmetry-related. Each $Cu^{II}$ ion is in five-coordinate geometry with coordination by two bridging pyrazolate nitrogen atoms [N(6) and N(7) for Cu1;

 © 2007 Wiley-VCH Verlag GmbH & Co. KGaA, Weinheim 

Table 1. Selected bond lengths [Å] and angles [°] of **1**·MeCN and **2**·2MeCN.

| **1**·MeCN | | **2**·2MeCN | |
|---|---|---|---|
| Ni(1)–N(1) | 2.160(4) | Cu(1)–N(1) | 2.040(6) |
| Ni(1)–N(2) | 2.014(4) | Cu(1)–N(2) | 2.302(7) |
| Ni(1)–N(4) | 2.178(4) | Cu(1)–N(5) | 2.054(6) |
| Ni(1)–N(5) | 2.128(4) | Cu(1)–N(6) | 1.940(6) |
| Ni(1)–N(6) | 2.033(3) | Cu(1)–N(7)$^{i}$ | 1.971(6) |
| Ni(1)–N(14) | 2.064(4) | | |
| Ni(2)–N(7) | 2.037(4) | | |
| Ni(2)–N(8) | 2.189(4) | | |
| Ni(2)–N(9) | 2.017(4) | | |
| Ni(2)–N(11) | 2.168(4) | | |
| Ni(2)–N(12) | 2.152(4) | | |
| Ni(2)–N(13) | 2.035(3) | | |
| N(1)–Ni(1)–N(2) | 77.16(15) | N(2)–Cu(1)–N(1) | 76.5(2) |
| N(1)–Ni(1)–N(4) | 162.53(14) | N(2)–Cu(1)–N(5) | 91.9(2) |
| N(1)–Ni(1)–N(5) | 89.26(13) | N(2)–Cu(1)–N(6) | 108.8(2) |
| N(1)–Ni(1)–N(6) | 97.80(14) | N(2)–Cu(1)–N(7)$^{i}$ | 96.1(2) |
| N(1)–Ni(1)–N(14) | 91.58(14) | N(1)–Cu(1)–N(5) | 90.7(2) |
| N(2)–Ni(1)–N(4) | 85.38(15) | N(1)–Cu(1)–N(6) | 169.8(2) |
| N(2)–Ni(1)–N(5) | 92.11(15) | N(1)–Cu(1)–N(7)$^{i}$ | 89.9(2) |
| N(2)–Ni(1)–N(6) | 169.96(16) | N(5)–Cu(1)–N(6) | 80.6(3) |
| N(2)–Ni(1)–N(14) | 92.47(15) | N(5)–Cu(1)–N(7)$^{i}$ | 171.9(3) |
| N(4)–Ni(1)–N(5) | 91.92(14) | N(6)–Cu(1)–N(7)$^{i}$ | 98.0(2) |
| N(4)–Ni(1)–N(6) | 99.54(14) | | |
| N(4)–Ni(1)–N(14) | 88.62(14) | | |
| N(5)–Ni(1)–N(6) | 79.04(14) | | |
| N(5)–Ni(1)–N(14) | 175.42(14) | | |
| N(6)–Ni(1)–N(14) | 96.38(14) | | |
| N(7)–Ni(2)–N(8) | 96.22(14) | | |
| N(7)–Ni(2)–N(9) | 93.04(15) | | |
| N(7)–Ni(2)–N(11) | 92.87(15) | | |
| N(7)–Ni(2)–N(12) | 175.12(14) | | |
| N(7)–Ni(2)–N(13) | 96.42(14) | | |
| N(8)–Ni(2)–N(9) | 77.66(15) | | |
| N(8)–Ni(2)–N(11) | 160.88(14) | | |
| N(8)–Ni(2)–N(12) | 83.01(14) | | |
| N(8)–Ni(2)–N(13) | 94.52(14) | | |
| N(9)–Ni(2)–N(11) | 85.11(15) | | |
| N(9)–Ni(2)–N(12) | 91.50(15) | | |
| N(9)–Ni(2)–N(13) | 168.34(16) | | |
| N(11)–Ni(2)–N(12) | 89.29(15) | | |
| N(11)–Ni(2)–N(13) | 101.16(14) | | |
| N(12)–Ni(2)–N(13) | 78.86(15) | | |

Symmetry code: (i) = $-x + 2, -y + 1, -z + 1$

N(6′) and N(7′) for Cu1′], a terminal pyridyl coordination N(5)/N(5′) from 3-(2-pyridyl)pyrazole units, and a pyridyl nitrogen atom N(1)/N(1′) from the ligand L in the equatorial plane. Axial coordination is achieved by the pyrazole nitrogen atom [Cu–N(2): 2.302(7) Å] of ligand L. A noteworthy feature of this structure is that in each ligand L the methyl pyridine arm remains uncoordinated. Thus the $Cu^{II}$ center has square-pyramidal geometry [precisely it is slightly distorted ($\tau = 0.035$)],[26] which is achieved by having the two potentially tridentate chelating units of L acting as bidentate ligands. The preference of the $Cu^{II}$ ion for five-coordination over six, is a consequence of Jahn–Teller distortion.[18c] The Cu(1) atom lies above the equatorial plane by 0.118 Å towards pyrazole nitrogen N(2) of terminally coordinated L. The sum of four angles provided by the equatorial nitrogen donors is 359.2°, consistent with a small displacement of the copper atom from the equatorial plane. The two $Cu^{II}$ ions are bridged by the deprotonated 3-(2-pyridyl)pyrazole unit, leading to a Cu···Cu separation of 3.9382(24) Å. In essence, it is a bis(μ-pyrazolate)-bridged dicopper(II) complex in which a planar $\{Cu_2(\mu\text{-}L')_2\}^{2+}$ core is terminally coordinated by two L ligands, in which methyl-pyridine arms remain uncoordinated. The Cu···Cu distance is on the higher end of distances reported for complexes with similar structural motif.[2,21,27–29]

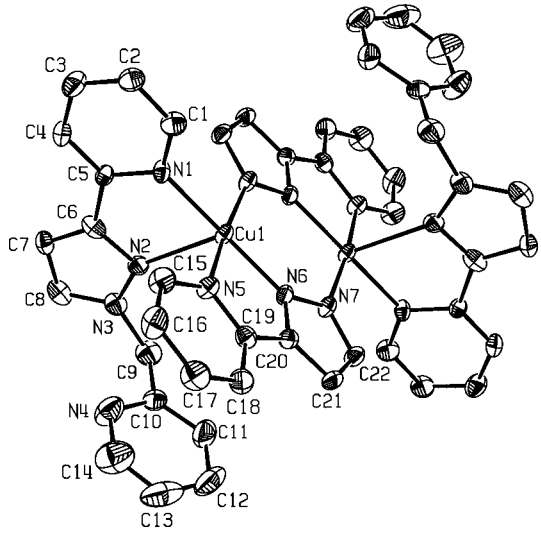


Figure 2. View of the dication $[(L)_2Cu_2(\mu\text{-}L')_2]^{2+}$ in complex **2**·2MeCN, showing the atom numbering scheme. Atoms are drawn at 30% probability level. All hydrogen atoms are excluded for clarity.

### Noncovalent Interactions

A closer inspection of the crystal packing diagram of **1**·MeCN reveals that the cations are engaged in an extensive intermolecular C–H···π interactions[18f,30a,30b] involving *para*-C–H of coordinating pyridine ring of pyridylpyrazole unit of L with the π-electron cloud of pyridine ring of bridging 3-(2-pyridylpyrazole) unit. Interaction parameters are given in Table 2. These C–H···π interactions led to the formation of linear one-dimensional chains (Figure 3, a). These chains are interconnected via neighboring molecules of adjacent chain through another C–H···π interaction involving *para*-C–H of pyridine ring of bridging 3-(2-pyridyl)pyrazole unit with the π-electron cloud of coordinating pyridine ring of pyridylpyrazole unit of L. This resulted in the formation of 2D network (Figure 3, b). This is rather interesting that

Table 2. Hydrogen-bonding (C–H···π) parameters for $[(L)_2Ni_2(\mu\text{-}L')_2]^{2+}$ in **1**·MeCN.

| *D*–H···π | H···π /Å | *D*···π /Å | *D*–H···π |
|---|---|---|---|
| C3–H3···Ct1 | 2.4737$^{i}$ | 3.47866(3)$^{i}$ | 173.2°$^{i}$ |
| C16–H16···Ct2 | 2.7767$^{ii}$ | 3.6668(3)$^{ii}$ | 147.4°$^{ii}$ |
| C25–H25···Ct3 | 2.5490$^{iii}$ | 3.5127(3)$^{iii}$ | 159.96°$^{iii}$ |

(i) $-x, 1-y, 1-z$; (ii) $-x, 1-y, -z$; (iii) $-x, -y, 2-z$

 © 2007 Wiley-VCH Verlag GmbH & Co. KGaA, Weinheim 

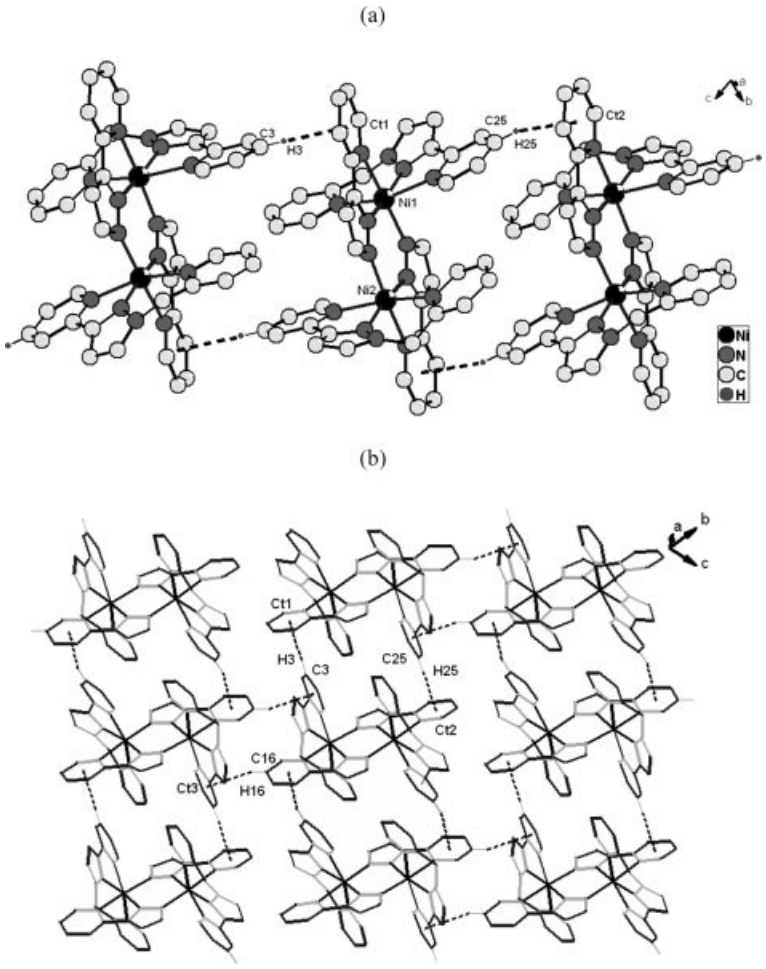


Figure 3. (a) A perspective view of the formation of a linear chain and (b) Formation of 2D-network solely via C–H···π interactions in the dication $[(L)_2Ni_2(\mu\text{-}L')_2]^{2+}$ of complex **1**·MeCN. All hydrogen atoms except those involved in hydrogen-bonding are excluded for clarity.

such 2D architecture has formed solely via C–H···π interactions.

The molecular packing in the crystal structure of **2**·2MeCN does not reveal C–H···π interactions, as observed for **1**·MeCN. However, it is realized that uncoordinated pyridine arm of L is involved in intermolecular π-π stacking,[19a,30c] leading to the formation of staircase-like arrangement of molecules (see Figure S1 in the electronic Supporting Information). The π···π stacking parameters are as follows: centroid–centroid distance: 3.9570(17) Å; perpendicular distance between two $CH_2$-py arm: 3.5682 Å; dihedral angle between the planes is 0.0°; displacement angle $\beta$ = 25.60°.[18f,30] The difference in the nature of noncovalent interactions observed for **1**·MeCN and **2**·2MeCN must have originated from dissimilar nature of metal coordination mode of ligand L. While for the former complex the potential tridentate ligand L acts as a tridentate ligand in the case of the latter complex it acts as a bidentate ligand leaving the $CH_2$py arm uncoordinated. This effect caused by stereoelectronic geometric preference of metal ions is manifested in the observed noncovalent interactions for these two structures.

We present here a rationalization of observed secondary interactions. C–H···π interactions observed in **1**·MeCN is facilitated due to *meridional* coordination of L which forces the ligand L to attain planar and perpendicular orientation to the bridging 3-(2-pyridylpyrazole) unit (Figure 1). Hence we believe that the relative disposition of L and bridging 3-(2-pyridylpyrazole) unit in **1**·MeCN favors the formation of 2D network via extensive C–H···π interactions. Such a situation is absent in **2**·2MeCN due to uncoordinated $CH_2$-py arm of L (Figure 2) and therefore C–H···π interaction is not observed in **2**·2MeCN. In **2**·2MeCN, however, the uncoordinated $CH_2$-py arms are suitably placed away from the metal center and remains almost parallel to the pyridine ring of the bridging 3-(2-pyridylpyrazole) unit. This in turn triggers to engage in weak intermolecular π-π stacking interactions (Figure S1) involving $CH_2$-py arm of L.

## Absorption Spectra

Absorption spectra for both complexes in MeCN are displayed in Figure S2. Purplish-green solutions of complex **1**

 © 2007 Wiley-VCH Verlag GmbH & Co. KGaA, Weinheim 

exhibit crystal-field transitions at 966 nm and 526 nm, which could be assigned as $^3A_{2g}\rightarrow{}^3T_{2g}$ and $^3A_{2g}\rightarrow{}^3T_{1g}$ (in octahedral coordination environment), respectively. A spin forbidden transition could be identified at 800 nm ($^3A_{2g}\rightarrow{}^1E_g$).[31] Compound **2** exhibits a crystal-field transition at 640 nm with a shoulder at 850 nm, typical of square-pyramidal $Cu^{II}$ stereochemistry.[22] An intense transition occurs as a shoulder at ca. 300 nm probably due to pyrazolate $\rightarrow Cu^{II}$ charge-transfer. Absorptions at higher energy originate in the intraligand.

### Magnetic Properties

Complexes **1** and **2** have the same planar $[M^{II}(\mu\text{-}L')]_2$ (M = Ni and Cu) binuclear entities, with the $Ni^{II}$ ion having distorted octahedral and $Cu^{II}$ ion assuming square-pyramidal geometry. From the magnetic point of view these complexes are clearly of interest and give us a unique opportunity to compare their magnetostructural behavior. The magnetic behavior of **1** (Figure 4) deserves special attention owing to the status of this complex as one among very few examples of bis(μ-pyrazolate)-bridged $Ni^{II}$ dimers.[2a,24,25] The temperature-dependence of the magnetic behavior is shown in Figure 4 in the form of $\chi_M T$ and $\chi_M$ vs. $T$ plots. The observed $\chi_M T$ value of 2.16 $cm^3 mol^{-1} K$ (2.94 $\mu_B$/Ni) at room temperature is indicative of $S = 1$ system. The value of $\chi_M T$ decreases very smoothly when cooling and it is 1.87 $cm^3 mol^{-1} K$ at 100 K (2.73 $\mu_B$/Ni). Below this temperature $\chi_M T$ decreases rapidly and it vanishes when $T$ tends to zero. The $\chi_M$ curve shows a maximum at 30 K. It clearly reveals the presence of antiferromagnetically coupled $Ni^{II}$ ions in **1**. According to the dinuclear nature of the complex, the experimental data were modeled through the Hamiltonian $H = -J\hat{S}_1\hat{S}_2 + D(\hat{S}_{z1}^2 + \hat{S}_{z2}^2)$ (with $\hat{S}_1 = \hat{S}_2 = 1$)[32] in the range from 298 K to 2.1 K. In this case, the magnetic susceptibility for a $Ni^{II}$ dimer is given by Equation (1).

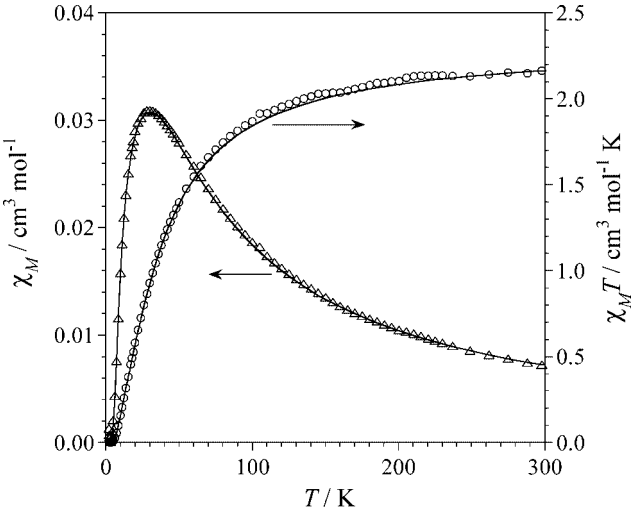


Figure 4. Temperature-dependence of the $\chi_M$ and $\chi_M T$ product for powdered sample of $[(L)_2Ni_2(\mu\text{-}L')_2][ClO_4]_2$ (**1**). The solid lines represent the best theoretical fit using the equation described in the text.

$$\chi_M = \frac{2N\beta^2 g^2}{3\alpha}\left(\frac{F_1}{kT} + \frac{2F_2}{D} + \frac{6a^2F_3}{3J-\Delta} + \frac{6b^2F_4}{3J+\Delta}\right)$$

$$F_1 = 1 + \exp(2x) + 4\exp(2x+y)$$

$$F_2 = -1 + 2\exp(2x+y) + \exp(y) - 2\exp(2x)$$

$$F_3 = \exp(2x) - \exp(\frac{x}{2} + z)$$

$$F_4 = \exp(2x) - \exp(\frac{x}{2} - z)$$

$$\alpha = 2 + \exp(y) + \exp(\frac{x}{2} - z) + \exp(\frac{x}{2} + z) + \ldots$$
$$\ldots\ 2\exp(2x) + 2\exp(2x+y)$$

$$x = \frac{J}{kT};\quad y = \frac{D}{kT};\quad z = \frac{\Delta}{kT};\quad \Delta = \left[(3J+D)^2 - 8JD\right]^{1/2}$$

$$a = \frac{9J - D + 3\Delta}{\left[(9J - D + 3\Delta)^2 + 8D^2\right]^{1/2}}$$

$$b = \frac{2\sqrt{2D}}{\left[(9J - D + 3\Delta)^2 + 8D^2\right]^{1/2}} \qquad (1)$$

To reduce the number of variables the $D$ (zero-field splitting parameter) and g values were considered to be identical for the two nickel(II) ions. A satisfactory fit was obtained with the set of parameters $J = -20.6\ cm^{-1}$, $|D| = 1.2\ cm^{-1}$ and $g = 2.15$ [$R = 1.3\times10^{-5}$, $R = \Sigma(\chi_M{}^{obs} - \chi|_M{}^{calc})^2/\Sigma(\chi_M{}^{obs})^2$], confirming the intramolecular antiferromagnetic coupling between nickel(II) centers. The temperature-independent paramagnetism, TIP, was observed to be 90 $cm^3 mol^{-1}$ for each $Ni^{II}$ ion, which was corrected on the magnetic curve of Figure 4. No paramagnetic impurities were observed. The magnitude of the exchange interaction is comparable to that observed for closely similar compounds.[25]

Generally, the dicopper(II) complexes with pyrazolate-bridge show a very strong antiferromagnetic coupling.[2,21,27–29] Variable-temperature (5–300 K) magnetic studies were done on powdered samples in order to determine the magnitude of the magnetic coupling of **2**. In fact, compound **2** shows a subnormal magnetic moment at room temperature ($\mu_{eff}$/Cu = 1.58 $\mu_B$). The $\chi_M T$ value decreases gradually upon cooling and it reaches a plateau below 50 K. A plot of $\chi_M T$ vs. $T$ for **2** (Figure 5) is typical of a moderate antiferromagnetically coupled dicopper(II) complex. The experimentally observed $\chi_M$ values (per dimer) were fitted to the modified[3,4,8b,9,12–14] Bleaney–Bowers equation based on the Heisenberg spin Hamiltonian, $H = -JS_1 \cdot S_2$ [Equation (2)], allowing for the presence of monomeric copper(II) impurity behaving as a Curie paramagnet, where $\rho$ is the mole fraction of such an impurity and $N_\alpha$ is the temperature-independent paramagnetism per $Cu^{II}$ ion; other symbols have their usual meaning. Keeping $g$ and $N_\alpha$ fixed at 2.1 [obtained from the EPR spectrum of the complex, Figure S3 {typical value for a tetragonal $Cu^{II}$[4]}] and $60\times10^{-6}\ cm^3 mol^{-1}$, the $J$ and $\rho$ parameters

 © 2007 Wiley-VCH Verlag GmbH & Co. KGaA, Weinheim 

were determined by minimizing $R = \Sigma(\chi_M^{obs} - \chi_M^{calc})^2/\Sigma(\chi_M^{obs})^2$ using Equation (2) gave good data fits. As shown by the trace in Figure 5, an excellent simulation (non-linear regression analyses) of the data could be attained with the following parameters: $J = -200\ cm^{-1}$ and $\rho = 0.86\%$. $R = 1.84 \times 10^{-7}$ for **2**. The magnitude of the exchange interaction is similar to that observed for other bis(μ-pyrazolate)-bridged[28,29] and the related bis(μ-$N^1$,$N^2$)triazole-bridged[33] dinuclear $Cu^{II}$ complexes. Solution-state $\mu_{eff}$/Cu value for **2** at 298 K is 1.4 $\mu_B$, slightly lower than that obtained as a solid.

$$\chi_M = 2N\beta^2g^2/3kT\,[1 + 1/3\exp(-J/kT)]^{-1}(1-\rho) + (N\beta^2g^2/2kT)\rho + 2N\alpha \quad (2)$$

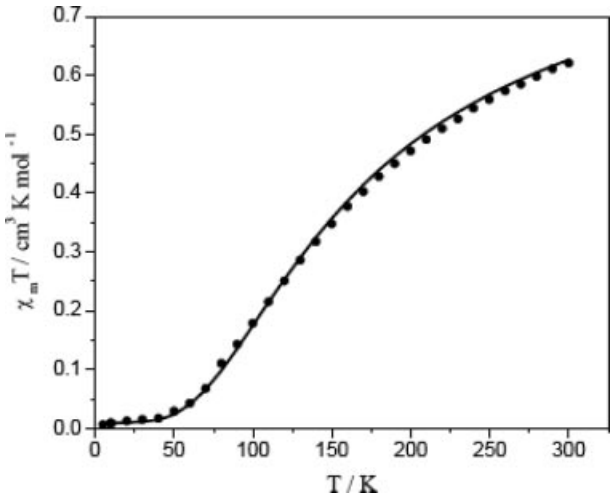


Figure 5. Temperature dependence of the $\chi_M T$ product for powdered samples of $[(L)_2Cu_2(\mu\text{-}L')]_2[ClO_4]_2$ (**2**). The solid lines represent the best theoretical fit using the equation described in the text.

In these complexes the pathway for magnetic exchange is propagated through the bridging pyrazolate ligands. From the molecular structure of **2**, one can conclude that the unpaired electron in each metal center is clearly described by $d_{x^2-y^2}$ magnetic orbital, which is coplanar with the pyrazolate skeleton (see part a of Scheme 1). The significant overlap between these magnetic orbitals accounts for the strong antiferromagnetic coupling observed.

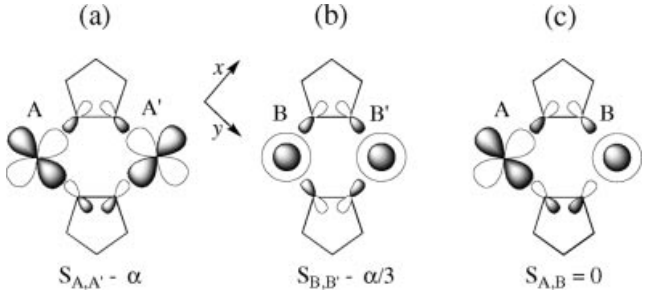


Scheme 1.

It is interesting to observe that the value of $J$ for $Ni^{II}$ dimer (ca. $-20\ cm^{-1}$) is much lower than the corresponding value for the $Cu^{II}$ dimer (ca. $-200\ cm^{-1}$).[34] In **1**, the $Ni^{II}$ ion has two magnetic orbitals, $d_{x^2-y^2}$ and $d_{z^2}$ (see Scheme 1). In order to evaluate both magnetic exchange pathways, we can describe the unpaired electrons on each $Ni^{II}$ ion by the orbitals $\Psi_A$ and $\Psi_B$ [Equations (3) and (4)], where &πηι;$_L$ is the orbital of the bridging ligand.[35] The participation of the peripheral ligands is neglected and the same energy for both metal orbitals was assumed (the same mixing coefficient $a$).

$$\Psi_A = N(d_{x^2-y^2} - a\phi_L) \quad (3)$$

$$\Psi_B = N(d_{z^2} - \frac{a}{\sqrt{3}}\ \phi_L) \quad (4)$$

In the frame of Kahn's orbital model[36] it is found that $J$ varies as $S_{u,v}^2$ ($S_{u,v}$ being the overlap integral between the magnetic orbitals $u$ and $v$). The values of $S_{u,v}$ can be approximated to be $S_{A,A'} = \langle\Psi_A|\Psi_{A'}\rangle \propto a^2$ and $S_{B,B'} = \langle\Psi_B|\Psi_{B'}\rangle \propto \frac{a^2}{3}$, where the prime refers to the second magnetic orbital in the dimer. In this approach, our prediction concerning the relative magnitudes of both pathways is $\frac{J_{x^2-y^2,x^2-y^2}}{J_{z^2,z^2}} \approx \frac{S_{A,A'}^2}{S_{B,B'}^2} \approx 9$, showing the greater magnetic exchange through the $d_{x^2-y^2}$ pathway.[35]

When the metal ion has more than one unpaired electron, the experimental $J$ parameter must be decomposed into a sum of individual contributions, $J_{uv}$, concerning each pair of magnetic orbitals involved in the exchange phenomenon [Equation (5)], where $n_A$ and $n_B$ are the number of unpaired electrons associated with the transition metal ions A and B, respectively.[36,37] Equations (5), (6), and (7) show how the magnitude of the antiferromagnetic interaction is not properly described by $J$ but by $n_An_BJ$. In the present case ca. $-80\ cm^{-1}$ for $Ni^{II}$ ($n_A = n_B = 2$) respect to ca. $-200\ cm^{-1}$ for $Cu^{II}$ dimer ($n_A = n_B = 1$), values which are still too different.

$$J = \frac{1}{n_An_B}\sum_{u=1}^{n_A}\sum_{v=1}^{n_B} J_{uv} \quad (5)$$

$$J_{CuCu} = J_{x^2-y^2,x^2-y^2} \approx -200\ cm^{-1} \quad (6)$$

$$J_{NiNi} = \frac{1}{4}(J_{x^2-y^2,x^2-y^2} + J_{z^2,z^2} + J_{x^2-y^2,z^2}) \approx -20\ cm^{-1} \quad (7)$$

The low value for the $Ni^{II}$ dimer can be attributed to the existence of ferromagnetic terms between the magnetic orbitals $d_{x^2-y^2}$ and $d_{z^2}$ (strict orthogonality, Scheme 1, c), which can be important when the distance between paramagnetic centers is short (cases of mono- and diatomic bridges).[38] Assuming a similar energy and bond lengths for $Ni^{II}$ and $Cu^{II}$ complexes and taking into account that $J_{x^2-y^2,x^2-y^2} \approx 9J_{z^2,z^2} \approx -200\ cm^{-1}$ (see above), a rough value of $J_{x^2-y^2,z^2} \approx +70\ cm^{-1}$ can be inferred from Equation (7), which is of the same order as that observed for diatomic bridges such as oximes.[37]

 © 2007 Wiley-VCH Verlag GmbH & Co. KGaA, Weinheim 

### Redox Properties

The redox behavior of these complexes has been investigated by cyclic voltammetry (CV) in MeCN at a platinum electrode (scan rate 100 mV s$^{-1}$). Complex **1** exhibits both oxidative as well as reductive redox behavior. In the potential range 0.0 to 2.0 V it undergoes two one-electron quasi-reversible oxidations (Figure 6) at [$E_{1/2}$ = +1.36 V ($\Delta E_p$ = 110 mV)] and [$E_{1/2}$ = +1.79 V ($\Delta E_p$ = 120 mV) vs. SCE], respectively. The two processes are tentatively assigned to the formation of $Ni^{III}Ni^{II}$ and $Ni^{III}Ni^{III}$ species. During negative scan 0.0 to –2.0 V it exhibits an irreversible response at –1.52 V vs. SCE. Such oxidative redox behavior is similar to other dinickel(II) complexes reported in the literature.[39] Notably, the difference between the successive redox processes in **1** is sufficient (ca. 450 mV) to stabilize the mixed-valence $Ni^{III}Ni^{II}$ species. Controlled-potential electrolysis of **1** at an applied potential of +1.50 V vs. SCE in MeCN solution consumed $n = 0.95 \pm 0.02$ e$^-$/complex (mean value of three independent measurements) and produced dark green solutions. Such solutions display the same CV response as that of $Ni^{II}Ni^{II}$ species. However, this time the response at 1.36 V is reductive, as expected (Figure S4). Re-reduction of such solutions at 0.0 V caused a transfer of 85% of the charge that passed during oxidation, attesting reasonable stability of the oxidized mixed-valence $Ni^{III}Ni^{II}$ species. Absorption spectra of dark green solutions (Figure 7) display a characteristic broad band at 755 nm ($\varepsilon$ = 930 M$^{-1}$ cm$^{-1}$). No other absorption is noted. In more likelihood this has happened either due to superposition of the spectra of individual $Ni^{II}$ and $Ni^{III}$ ions or due to strong delocalization (X-ray structure of **1**·MeCN), properties of the component species have been replaced by a new delocalized species. However, the high molar extinction coefficient value than that expected for a d-d band indicates it to be an IVCT band. The dark green color of the oxidized solution is similar to those of similar $Ni^{III}$-$Ni^{II}$ mixed-valence species reported in the literature.[40]

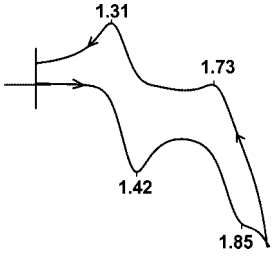


Figure 6. Cyclic voltammogram (100 mV s$^{-1}$) of [$(L)_2Ni_2$ ($\mu$-L′)$_2$]-[$ClO_4$]$_2$ (**1**) at a Pt electrode in MeCN (ca. 0.1 dm$^3$ mol$^{-1}$ in TBAP). Indicated potentials (in V) are vs. SCE.

To throw more light on the nature of this supposedly mixed-valence species the dark green solution has been further characterized by EPR spectral measurements. The EPR spectrum of coulometrically generated solutions recorded at 120 K is shown in Figure 8. The spectrum is characteristics of $S$ = 3/2 system with $g$ values 2.08, 3.20, and 5.29, arising out of spin-exchange coupling between $S$ = 1 $Ni^{II}$ state and $S$ = 1/2 $Ni^{III}$ state.[39] The $Ni^{III}$ ion is considered to be low-spin since all known $Ni^{III}$ complexes to date are low-spin.[41] To strengthen our hypothesis we measured solution-state magnetic susceptibility of the green solution. The $\mu_{eff}$ value of 4.33 $\mu_B$ at 293 K (Evans method),[42] for two independent measurements, confirm our claim that it is a $S$ = 3/2 system.

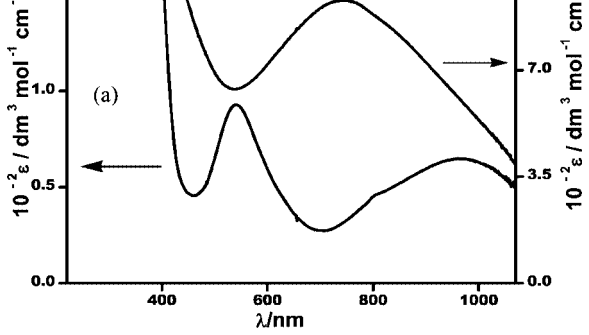


Figure 7. UV/Vis spectra in the range 400–1100 nm (in MeCN) of (a) [{$(L)_2Ni_2(\mu\text{-}L')$}$_2$][$ClO_4$]$_2$ (**1**) and (b) coulometrically oxidized green solution (1.67 mM) at 1.50 V vs. SCE.

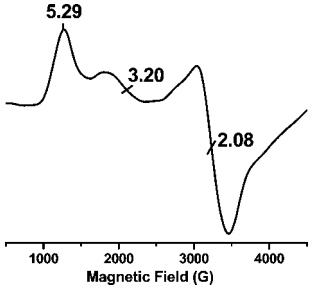


Figure 8. EPR spectrum at 120 K of coulometrically generated green solution of $[(L)_2Ni_2(\mu\text{-}L')_2]^{3+}$ in MeCN.

Dicopper(II) complex **2** displays two cathodic responses with $E_{pc}$ values of –0.28 V and –0.50 V vs. SCE (Figure S5), due to $Cu^{II}{}_2$/$Cu^{II}Cu^{I}$ and $Cu^{II}Cu^{I}$/$Cu^{I}{}_2$ redox processes, respectively. On reversal scan, only one anodic response at 0.24 V vs. SCE was observed. This behavior is indicative of an unstable mixed-valence $Cu^{II}Cu^{I}$ and $Cu^{I}{}_2$ species. Given the planarity of the $\{Cu(\mu\text{-}L')\}_2{}^{2+}$ unit, this result is understandable, as $Cu^{I}$ would prefer to assume tetrahedral geometry.

### Concluding Remarks

In this report designed synthesis of bis(μ-pyrazolate)-bridged dinickel(II) and dicopper(II) complexes has been achieved with a simple potentially tridentate ligand L and bridging ligand 3-(2-pyridyl)pyrazole. Structural proof for the complexes illustrates a neat example of stereoelectronic geometric requirement of $M^{II}$ ion: $Ni^{II}$ preferring six- and $Cu^{II}$ preferring five-coordination. The outcome of stereoelectronic preference is manifested in the observed noncovalent interactions: C–H···π in the case of **1**·MeCN and

 © 2007 Wiley-VCH Verlag GmbH & Co. KGaA, Weinheim 

π···π for **2**·MeCN, dictated by the spatial disposition of L around $M^{II}$ ion. Temperature-dependent magnetic studies reveal the presence of antiferromagnetic coupling in both, the extent of coupling is more in the case $Cu^{II}$ dimer than in the case of $Ni^{II}$ dimer. Generation and stabilization of mixed-valence $Ni^{III}$-$Ni^{II}$ species presented in this work encourage the synthesis of other variety of pyrazolate-bridged nickel(II) complexes in order to gain a better understanding of redox chemistry of dinickel(II) systems.

## Experimental Section

**General:** All chemicals were obtained from commercial sources and used as received. Solvents were purified/dried following standard procedures.[3–14] The ligand L was prepared as before.[18d] 3-(2-pyridyl)pyrazole (HL′) was synthesized following a reported procedure.[20] Tetra-*n*-butylammonium perchlorate (TBAP), was prepared/purified as before.[11]

**Syntheses**

**Preparation of [{(L)Ni(μ-L′)}$_2$][ClO$_4$]$_2$ (1):** To a stirred solution of $Ni(OAc)_2{\cdot}4H_2O$ (0.052 g, 0.212 mmol) in MeOH (3 cm$^3$), L (0.050 g, 0.212 mmol) was added in small portions. After stirring for 30 min, HL′ (0.031 g, 0.212 mmol) was added and the resulting mixture was stirred for 5 min, followed by addition of $Et_3N$ (0.021 g, 0.212 mmol). The reaction mixture was then allowed to stir for a further 30 min. Solid sodium perchlorate (0.052 g, 0.424 mmol) was added to it and the mixture was kept in air for slow evaporation, which led to the precipitation of a purple microcrystalline solid. It was filtered, washed with MeOH and dried in vacuo (yield: 0.052 g, ca. 45%). $C_{44}H_{36}Cl_2N_{14}Ni_2O_8$ (1077.98): calcd. C 49.02, H 3.36, N 18.19%; found C 48.95, H 3.41, N 17.83%. Molar conductance, $\Lambda_M$ (MeCN, 298 K) = 240 Ω$^{-1}$cm$^2$mol$^{-1}$ (expected range[23] for 1:2 electrolytes: 220–300 Ω$^{-1}$cm$^2$mol$^{-1}$). UV/Vis (MeCN), $\lambda_{max}$/nm ($\varepsilon$/M$^{-1}$cm$^{-1}$): 966 (65), 800 (sh) (48), 526 (93), 315 (sh) (20 000), 290 (sh) (33 200), 254 (44 729). $\mu_{eff}$/Ni: 2.94 $\mu_B$ (solid, 298 K) and 3.20 $\mu_B$ (in MeCN, 298 K). Diffraction quality single crystals containing a molecule of MeCN as a solvent of crystallization (**1**·MeCN) were grown by diffusion of diethyl ether into a MeCN solution of the complex.

**Preparation of [{(L)Cu(μ-L′)}$_2$][ClO$_4$]$_2$ (2):** To a stirred solution of L (0.050 g, 0.212 mmol) in MeOH (3 cm$^3$) $[Cu(H_2O)_6][ClO_4]_2$ (0.079 g, 0.212 mmol) was added in small portions. After stirring for 30 min, HL′ (0.031 g, 0.212 mmol) was added and the resulting mixture was refluxed for one and half hour. Addition of $Et_3N$ (0.021 g, 0.212 mmol) led to the precipitation of a bluish green microcrystalline solid. It was filtered, washed with a minimum amount of MeOH and dried in vacuo. Recrystallization was achieved by diffusion of diethyl ether (5 cm$^3$) into a MeCN solution (3 cm$^3$) of the complex (yield: 0.052 g, ca. 45%). $C_{44}H_{36}Cl_2Cu_2N_{14}O_8$ (1086.84): calcd. C 48.62, H 3.34, N 18.04%; found C 48.95, H 3.41, N 17.83%. Molar conductance, $\Lambda_M$ (MeCN, 298 K) = 226 Ω$^{-1}$cm$^2$mol$^{-1}$. UV/Vis (MeCN), $\lambda_{max}$/nm ($\varepsilon$/M$^{-1}$cm$^{-1}$): 770 (sh) (70), 640 (120), 300 (sh) (19 400), 290 (sh) (22 700), 253 (46 550). $\mu_{eff}$/Cu: 1.58 $\mu_B$ (solid, 299 K) and 1.40 $\mu_B$ (in MeCN, 298 K). Diffraction quality single crystals containing two molecules of MeCN as solvent of crystallization (**2**·2MeCN) were grown by diffusion of diethyl ether into a MeCN solution of the complex.

***Caution:*** *Perchlorate salts of compounds containing organic ligands are potentially explosive!*

**Physical Measurements:** Elemental analyses (C, H, N) were obtained at the Microanalytical Laboratory at this Department. Infrared spectra were recorded on a Bruker Vector 22 spectrophotometer using KBr discs. Electronic spectra were recorded using Agilent 8453 diode-array spectrophotometer. $^1$H NMR spectral measurements were performed on a Bruker WP 80 (80 MHz) NMR spectrometer. Solution electrical conductivity measurements (298 K) were carried out with an Elico (Hyderabad, India) Type CM-82 T conductivity bridge. X-band EPR were obtained on a Bruker EMX 1444 EPR spectrometer operating at 9.455 GHz (fitted with a quartz Dewar for measurements at 120 K). The spectra were calibrated with diphenylpicrylhydrazyl, DPPH ($g$ = 2.0037).

**Magnetism:** Magnetic susceptibility measurements on polycrystalline sample of **1** were performed in the temperature range of 2–298 K with a Quantum Design SQUID magnetometer [(Model MPMSXL-5) Valencia, Spain]. For **2** variable temperature magnetic susceptibility measurements in the range 5–300 K was obtained in the solid state using a Quantum Design (Model MPMSXL-5) SQUID (Kanpur, India) magnetic susceptometer operating at a magnetic field of 0.5 T. Magnetic susceptibility measurements in MeCN solution were obtained by Evans's method[42] using a PMX-60 JEOL (60 MHz) NMR spectrometer. Susceptibilities were corrected for diamagnetic contributions, by using literature values.[32] Effective magnetic moments were calculated from $\mu_{eff} = 2.828\,[\chi_M T]^{1/2}$, where $\chi_M$ is the corrected molar susceptibility.

**Cyclic Voltammetry:** Cyclic voltammograms were recorded at 298 K on PAR model 370 electrochemistry system consisting of model 174A polarographic analyzer and model 175 universal programmer. A standard three-electrode cell was employed with a Beckman M-39273 platinum-inlay working electrode, a platinum-wire auxiliary electrode and a saturated calomel electrode (SCE) as reference; no correction was made for junction potentials.

**Crystallography:** For complex **1**·MeCN diffracted intensities were collected on a Bruker SMART APEX CCD diffractometer, with graphite-monochromated Mo-$K_\alpha$ ($\lambda$ = 0.71073 Å) radiation at 100(2) K. For data reduction 'Bruker Saint Plus' program was used. Data for **2**·2MeCN were collected at 293 K on a Enraf Nonius MACH2 diffractometer, equipped with graphite-monochromated Mo-$K_\alpha$ radiation ($\lambda$ = 0.71073 Å). Data were corrected for absorption and the Lorentz and polarization effects. The structures were solved with SIR-92 and refined with the SHELXL-97 package incorporated in WinGX 1.64 crystallographic collective package.[43] Anisotropic refinements were performed by full-matrix least-squares procedure on $F^2$. The positions of the hydrogen atoms were calculated assuming ideal geometries, but not refined. The data-set of **1**·MeCN was treated with the SQUEEZE filter of PLATON[44] due to the presence of severely disordered solvent molecule(s) (probably acetonitrile, water) which could not be modeled satisfactorily. PLATON estimated the electron count to be 15 electron/cell in a volume of 398.0 Å$^3$ out of a unit volume of 4307.0 Å$^3$ (9.2%). Pertinent crystallographic parameters are summarized in Table 3. Intermolecular contacts of the C–H···π and π···π stacking were examined with the DIAMOND package.[45] C–H distances were normalized along the same vectors to the neutron derived values of 1.083 Å.[46]

CCDC-632189 (for **1**·MeCN) and -240140 (for **2**·2MeCN) contain the supplementary crystallographic data for this paper. These data can be obtained free of charge from The Cambridge Crystallographic Data Centre via www.ccdc.cam.ac.uk/data_request/cif.

**Supporting Information** (see also the footnote on the first page of this article): Figure S1 presents the intermolecular π-π stacking leading to the formation of staircase-like arrangement of molecules

 © 2007 Wiley-VCH Verlag GmbH & Co. KGaA, Weinheim 

Table 3. Data collection and structure refinement parameters for **1**·MeCN and **2**·2MeCN.

| | **1**·MeCN | **2**·2MeCN |
|---|---|---|
| Molecular formula | $C_{46}H_{39}Cl_2Ni_2N_{15}O_8$ | $C_{48}H_{42}Cl_2Cu_2N_{16}O_8$ |
| $M_r$ | 1118.24 | 1168.96 |
| Temperature /K | 100(2) | 293(2) |
| Radiation used ($\lambda$ /Å) | Mo-$K_\alpha$ (0.71073) | Mo-$K_\alpha$ (0.71073) |
| Crystal system | triclinic | triclinic |
| Space group | $P\bar{1}$ (no. 2) | $P\bar{1}$ (no. 2) |
| $a$ /Å | 12.6720(12) | 10.630(9) |
| $b$ /Å | 15.1890(14) | 11.689(2) |
| $c$ /Å | 16.1269(15) | 12.510(4) |
| $\alpha$ /° | 69.082(2) | 109.78(2) |
| $\beta$ /° | 83.528(2) | 102.64(5) |
| $\gamma$ /° | 69.395(2) | 110.46(3) |
| $V$ /Å | 2713.7(4) | 1266.3(12) |
| $Z$ | 2 | 1 |
| $D_c$ /g cm$^{-3}$ | 1.369 | 1.533 |
| $\mu$ /mm$^{-1}$ | 0.855 | 1.016 |
| Crystal size /mm | 0.20 × 0.10 × 0.10 | 0.20 × 0.10 × 0.10 |
| Unique reflections, $R_{int}$ | 12895, 0.0328 | 3315, 0.0329 |
| Observed reflections [$I > 2\sigma(I)$] | 6959 | 2457 |
| Refined parameters | 662 | 344 |
| $R^{[a]}(R_w)^{[b]}$ | 0.0767 (0.1837) | 0.0768 (0.2208) |
| $R^{[a]}(R_w)^{[b]}$ (all data) | 0.1364 (0.2068) | 0.1182 (0.2407) |
| Goodness-of-fit on $F^2$ | 0.950 | 1.050 |

[a] $R(F) = \Sigma(||F_o| - |F_c||)/\Sigma|F_o|$. [b] $R_w(F^2) = \{\Sigma[w(|F_o|^2 - |F_c|^2)^2]/\Sigma[w(|F_o|^2)^2]\}^{1/2}$.

in complex **2**·2MeCN. Figure S2 shows absorption spectral features for both complexes in MeCN. Figure S3 shows the EPR spectra of complex **2** at 293 K and Figure S4 the CV response of electrochemically generated green solution from complex **1**. Figure S5 deals with the CV response of complex **2**.

## Acknowledgments

Financial assistance received from the Department of Science and Technology (DST) and the Council of Scientific & Industrial Research (CSIR), Government of India is gratefully acknowledged. We acknowledge the National Single Crystal Diffractometer Facility at the Department of Chemistry, Indian Institute of Technology Kanpur, for data collection of **1**·MeCN. We acknowledge Prof. M. S. Hundal and Dr. G. Hundal (Guru Nanak Dev University, Amritsar, India) for data collection of **2**·2MeCN. We sincerely thank Dr. Jhumpa Mukherjee for variable-temperature magnetic data analysis of complex **2** and Mr. Haritosh Mishra for analysis of noncovalent interactions in the crystal structures. Comments of the reviewers at the revision stage were very helpful.

[1] a) H. van Crawford, H. W. Richardson, J. R. Wasson, D. J. Hodgson, W. E. Hatfield, *Inorg. Chem.* **1976**, *15*, 2107–2110; b) O. Kahn, *Angew. Chem. Int. Ed. Engl.* **1985**, *24*, 834–850; c) T. Kawata, M. Yamanaka, S. Ohba, Y. Nishida, M. Nagamatsu, T. Tokii, M. Kato, O. W. Steward, *Bull. Chem. Soc. Jpn.* **1992**, *65*, 2739–2747; d) S. Meenakumari, S. K. Tiwari, A. R. Chakravarty, *J. Chem. Soc., Dalton Trans.* **1993**, 2175–2181; e) L. K. Thompson, S. K. Mandal, S. K. Tandon, J. N. Bridson, M. K. Park, *Inorg. Chem.* **1996**, *35*, 3117–3125.

[2] a) R. Mukherjee, *Coord. Chem. Rev.* **2000**, *203*, 151–218; b) R. Mukherjee, in *Comprehensive Coordination Chemistry-II: From Biology to Nanotechnology*, Vol. 6 (Eds.: J. A. McCleverty, T. J. Meyer; Volume Ed.: D. E. Fenton), Chapter on Copper, Elsevier/Pergamon, Amsterdam, **2004**, pp. 747–910.

[3] R. Gupta, R. Hotchandani, R. Mukherjee, *Polyhedron* **2000**, *19*, 1429–1435.

[4] J. Mukherjee, R. Mukherjee, *Dalton Trans.* **2006**, 1611–1621.

[5] J. Mukherjee, R. Gupta, T. Mallah, R. Mukherjee, *Inorg. Chim. Acta* **2005**, *358*, 2711–2717.

[6] V. Mishra, F. Lloret, R. Mukherjee, *Inorg. Chim. Acta* **2006**, *359*, 4053–4062.

[7] R. Gupta, R. Mukherjee, *Polyhedron* **2000**, *19*, 719–724.

[8] a) D. Ghosh, T. K. Lal, S. Ghosh, R. Mukherjee, *Chem. Commun.* **1996**, 13–14; b) D. Ghosh, R. Mukherjee, *Inorg. Chem.* **1998**, *37*, 6597–6605.

[9] A. K. Patra, M. Ray, R. Mukherjee, *Polyhedron* **2000**, *19*, 1423–1428.

[10] a) S. Mahapatra, N. Gupta, R. Mukherjee, *J. Chem. Soc., Dalton Trans.* **1992**, 3041–3045; b) J. Mukherjee, V. Balamurugan, R. Gupta, R. Mukherjee, *Dalton Trans.* **2003**, 3686–3692.

[11] a) S. Mahapatra, P. Das, R. Mukherjee, *J. Chem. Soc., Dalton Trans.* **1993**, 217–220; b) T. K. Lal, R. Mukherjee, *Inorg. Chem.* **1998**, *37*, 2373–2382 and references cited therein.

[12] S. P. Foxon, D. Utz, J. Astner, S. Schindler, F. Thaler, F. W. Heinemann, G. Liehr, J. Mukherjee, V. Balamurugan, D. Ghosh, R. Mukherjee, *Dalton Trans.* **2004**, 2321–2328.

[13] S. Mandal, R. Mukherjee, *Inorg. Chim. Acta* **2006**, *359*, 4019–4026.

[14] R. Gupta, S. Mukherjee, R. Mukherjee, *J. Chem. Soc., Dalton Trans.* **1999**, 4025–4030.

[15] a) S. Trofimenko, *Prog. Inorg. Chem.* **1986**, *34*, 115–210; b) G. La Monica, G. A. Ardizzoia, *Prog. Inorg. Chem.* **1997**, *46*, 151–238; c) J. Vela, S. Vaddadi, S. Kingsley, C. J. Flaschenriem, R. J. Lachicotte, T. R. Cundari, P. L. Holland, *Angew. Chem. Int. Ed.* **2006**, *45*, 1607–1611.

[16] M. D. Ward, J. A. McCleverty, J. C. Jeffery, *Coord. Chem. Rev.* **2001**, *222*, 251–272.

[17] a) R. L. Paul, S. M. Couchman, J. C. Jeffery, J. A. McCleverty, Z. R. Reeves, M. D. Ward, *J. Chem. Soc., Dalton Trans.* **2000**, 845–851; b) D. A. McMorran, P. J. Steel, *Chem. Commun.* **2002**, 2120–2121; c) D. A. McMorran, P. J. Steel, *Inorg. Chem. Commun.* **2003**, *6*, 43–47; d) R. L. Paul, Z. R. Bell, J. C. Jeffery, L. P. Harding, J. McCleverty, M. D. Ward, *Polyhedron* **2003**, *22*, 781–787; e) B. A. Leita, B. Moubaraki, K. S. Murray, J. P. Smith, J. D. Cashion, *Chem. Commun.* **2004**, 156–157; f) S. P. Argent, H. Adams, L. P. Harding, T. Riis-Johannessen, J. C. Jefferey, M. D. Ward, *New J. Chem.* **2005**, *29*, 904–911; g) T. K. Ronson, H. Adams, M. D. Ward, *Eur. J. Inorg. Chem.* **2005**, 4533–4549; h) S. P. Argent, H. Adams, T. Riis-Johannessen, J. C. Jefferey, L. P. Harding, W. Clegg, R. W. Harrington, M. D. Ward, *Dalton Trans.* **2006**, 4996–5013.

[18] a) R. Gupta, R. Mukherjee, *Polyhedron* **2001**, *20*, 2545–2549; b) S. Mahapatra, R. J. Butcher, R. Mukherjee, *Indian J. Chem.* **2001**, *40A*, 973–975; c) R. Gupta, T. K. Lal, R. Mukherjee, *Polyhedron* **2002**, *21*, 1245–1253; d) S. Singh, V. Mishra, J. Mukherjee, N. Seethalekshmi, R. Mukherjee, *Dalton Trans.* **2003**, 3392–3397; e) C. Enachescu, J. Linares, F. Varret, K. E. Codjovi, S. G. Salunke, R. Mukherjee, *Inorg. Chem.* **2004**, *43*, 4880–4888; f) H. Mishra, R. Mukherjee, *J. Organomet. Chem.* **2006**, *691*, 3545–3555.

[19] a) V. Balamurugan, M. S. Hundal, R. Mukherjee, *Chem. Eur. J.* **2004**, *10*, 1683–1690; b) V. Balamurugan, W. Jacob, J. Mukherjee, R. Mukherjee, *CrystEngComm* **2004**, *6*, 396–400; c) V. Balamurugan, R. Mukherjee, *CrystEngComm* **2005**, *7*, 337–341; d) V. Balamurugan, R. Mukherjee, *Inorg. Chim. Acta* **2006**, *359*, 1376–1382.

[20] A. J. Amoroso, A. M. C. Thompson, J. C. Jeffery, P. L. Jones, J. A. McCleverty, M. D. Ward, *J. Chem. Soc., Chem. Commun.* **1994**, 2751–2752.

[21] T.-L. Hu, J.-R. Li, C.-S. Liu, X.-S. Shi, J.-N. Zhou, X.-H. Bu, J. Ribas, *Inorg. Chem.* **2006**, *45*, 162–173 and references cited therein.

 © 2007 Wiley-VCH Verlag GmbH & Co. KGaA, Weinheim 

[22] B. J. Hathaway, in *Comprehensive Coordination Chemistry* (Eds.: G. Wilkinson, R. D. Gillard, J. A. McCleverty), Pergamon, Oxford, **1987**, vol. *5*, pp. 533–774.
[23] W. J. Geary, *Coord. Chem. Rev.* **1971**, *7*, 81–122.
[24] J. Casabó, J. Pons, K. S. Siddiqi, F. Teixidor, E. Molins, C. Miravitlles, *J. Chem. Soc., Dalton Trans.* **1989**, 1401–1403.
[25] a) F. Meyer, E. Kaifer, P. Kircher, K. Heinze, H. Pritzkow, *Chem. Eur. J.* **1999**, *5*, 1617–1630; b) L. Siegfried, T. A. Kaden, F. Meyer, P. Kircher, H. Pritzkow, *J. Chem. Soc., Dalton Trans.* **2001**, 2310–2315; c) J. C. Röder, F. Meyer, E. Kaifer, H. Pritzkow, *Eur. J. Inorg. Chem.* **2004**, *10*, 1646–1660 and references cited therein.
[26] A. W. Addison, T. N. Rao, J. Reedijk, J. van Rijn, G. C. Verschoor, *J. Chem. Soc., Dalton Trans.* **1984**, 1349–1356 (square pyramidal geometry $\tau = 0$; trigonal bipyramidal geometry $\tau = 1$).
[27] S. Tanase, I. A. Koval, E. Bouwman, R. de Gelder, J. Reedijk, *Inorg. Chem.* **2005**, *44*, 7860–7865.
[28] a) T. Kamiusuki, H. Ōkawa, N. Matsumoto, S. Kida, *J. Chem. Soc., Dalton Trans.* **1990**, 195–198; b) T. Kamiusuki, H. Ōkawa, K. Inoue, N. Matsumoto, M. Kodera, S. Kida, *J. Coord. Chem.* **1991**, *23*, 201–211; c) F. Degang, W. Guoxiong, Z. Zongyuan, Z. Xiangge, *Transition Met. Chem.* **1994**, *19*, 592–594; d) E. Spodine, A. M. Atria, J. Valenzuela, J. Jalocha, J. Manzur, A. M. García, M. T. Garland, O. Peña, J.-Y. Saillard, *J. Chem. Soc., Dalton Trans.* **1999**, 3029–3034; e) L. Lamarque, P. Navarro, C. Miranda, V. J. Arán, C. Ochoa, F. Escartí, E. García-España, J. Latorre, S. V. Luis, J. F. Miravet, *J. Am. Chem. Soc.* **2001**, *123*, 10560–10570; f) M. J. Hallam, C. A. Kilner, M. A. Halcrow, *Acta Crystallogr., Sect. C* **2002**, *58*, m445–m446.
[29] a) M. Munakata, L. P. Wu, M. Yamamoto, T. Kuroda-Sowa, M. Maekawa, S. Kawata, S. Kitagawa, *J. Chem. Soc., Dalton Trans.* **1995**, 4099–4103; b) C. Miranda, F. Escartí, L. Lamarque, E. García-España, P. Navarro, J. Latorre, F. Lloret, H. R. Jiménez, M. J. R. Yunta, *Eur. J. Inorg. Chem.* **2005**, 189–208.
[30] a) D. L. Reger, J. R. Gardinier, R. F. Semeniuc, M. D. Smith, *Dalton Trans.* **2003**, 1712–1718; b) D. L. Reger, R. F. Semeniuc, M. D. Smith, *Cryst. Growth Des.* **2005**, *5*, 1181–1190; c) C. Janiak, *J. Chem. Soc., Dalton Trans.* **2000**, 3885–3896.
[31] F. A. Cotton, G. Wilkinson, C. A. Murillo, M. Bochmann, *Advanced Inorganic Chemistry*, Wiley, New York, 6th ed., **1999**.
[32] G. De Munno, M. Julve, F. Lloret, A. Derory, *J. Chem. Soc., Dalton Trans.* **1993**, 1179–1184.
[33] E. Aznar, S. Ferrer, J. Borrás, F. Lloret, M. Liu-González, H. Rodríguez-Prieto, S. García-Granda, *Eur. J. Inorg. Chem.* **2006**, 5115–5125.
[34] F. Lloret, J. Sletten, R. Ruiz, M. Julve, J. Faus, M. Verdaguer, *Inorg. Chem.* **1992**, *31*, 778–784.
[35] I. Castro, J. Sletten, M. L. Calatayud, M. Julve, J. Cano, F. Lloret, A. Caneschi, *Inorg. Chem.* **1995**, *34*, 4903–4909.
[36] O. Kahn, *Molecular Magnetism,* VCH Publishers, New York, **1993**.
[37] R. Ruiz, F. Lloret, M. Julve, M. C. Muñoz, C. Bois, *Inorg. Chim. Acta* **1994**, *219*, 179–186.
[38] R. Ruiz, F. Lloret, M. Julve, J. Faus, M. C. Muñoz, X. Solans, *Inorg. Chim. Acta* **1993**, *213*, 261–268.
[39] a) T. R. Holman, M. P. Hendrich, L. Que Jr, *Inorg. Chem.* **1992**, *31*, 937–939; b) B. Kersting, D. Siebert, *Inorg. Chem.* **1998**, *37*, 3820–3828.
[40] a) F. Meyer, H. Kozlowski, *Comprehensive Coordination Chemistry* II: *From Biology to Nanotechnology*, Pergamon, **2004**, *6*, 247–554; b) K. Nag, A. Chakravorty, *Coord. Chem. Rev.* **1980**, *33*, 87–147; c) R. I. Haines, A. McAuley, *Coord. Chem. Rev.* **1981**, *39*, 77–119; d) A. G. Lappin, A. McAuley, *Adv. Inorg. Chem.* **1988**, *32*, 241–295.
[41] A. K. Patra, R. Mukherjee, *Inorg. Chem.* **1999**, *38*, 1388–1393.
[42] D. F. Evans, *J. Chem. Soc.* **1959**, 2003–2004.
[43] L. J. Farrugia, *WinGX ver. 1.64*, An Integrated Systems of Windows Programs for the Solution, Refinement and Analysis of Single-Crystal X-ray Diffraction Data, Department of Chemistry, University of Glasgow, **2003**.
[44] PLATON: A. L. Spek, *J. Appl. Crystallogr.* **2003**, *36*, 7–13.
[45] *DIAMOND ver 2.1c*, Crystal Impact GbR, Bonn, Germany, **1999**.
[46] T. Steiner, *Angew. Chem. Int. Ed.* **2002**, *41*, 48–76.

Received: January 3, 2007
Published Online: April 4, 2007

 © 2007 Wiley-VCH Verlag GmbH & Co. KGaA, Weinheim 

DOI: 10.1002/ejic.200601052

# Theoretical Studies of the Electronic Structure and Spectroscopic Properties of $[Ru(Htcterpy)(NCS)_3]^{3-}$

**Ming-Xia Li,[a,b] Hong-Xing Zhang,*[a] Xin Zhou,[a] Qing-Jiang Pan,[b] Hong-Gang Fu,[b] and Chia-Chung Sun[a]**

**Keywords:** Black dyes / Electronic structure / Spectroscopic properties / Solvent effects

The ground- and excited-state structures of $[Ru(Htcterpy)(NCS)_3]^{3-}$ (**1H**) (tcterpy = 4,4′,4′′-tricarboxy-2,2′:6′,2′′-terpyridine) are optimized by the DFT and CIS methods, respectively. Absorption and emission spectra in the gas phase and in solution (ethanol and water) are predicted at the TD-DFT/B3LYP level. Experimental spectra are roughly reproduced by our calculated results. In ethanol solution, the HOMOs of the absorption spectra are dominated by d orbitals of the ruthenium atom and thiocyanate ligands, and the LUMOs possess π*(tcterpy) character with considerable carboxyl contribution. In the theoretically simulated absorption spectra, the first four bands are attributed to Ru/NCS→π*(tcterpy) charge-transfer (MLCT/LLCT) transitions, whereas the fifth one with the strongest intensity arises from intraligand tcterpy π→π* charge transfer (ILCT) mixed with some $O(p_z)$→terpy charge transfer (LLCT). Our calculations reveal that the MLCT/LLCT absorption bands in water are blue-shifted with respect to those in ethanol, agreeing with experimental observations. This can be rationalized by a decreased dipole moment in the excited state. The phosphorescent emissions are calculated to occur at 724, 711, and 691 nm in the gas phase, in ethanol, and in water, respectively, all with the same $^3$LMCT/$^3$LLCT character.

(© Wiley-VCH Verlag GmbH & Co. KGaA, 69451 Weinheim, Germany, 2007)

## 1. Introduction

In recent years, dye-sensitized solar cells (DSSCs) have attracted considerable interest for the conversion of sunlight into electricity because of their low cost and high efficiency.[1–4] The DSSCs comprise four major parts: a nanocrystalline metal oxide semiconductor film, a dye sensitizer, a redox electrolyte, and a counter electrode. Undoubtedly, one of the key components of these cells is the dye sensitizer, which is used to sensitize the semiconductor electrode. An efficient solar cell sensitizer should fulfill several requirements: (1) it must be strongly adsorbed onto the semiconductor surface to ensure device stability and good electronic coupling for charge injection; (2) it should exhibit intense absorption in the visible part of the spectrum and form long-lived excited states with energies matching those of the conduction band of the semiconductor substrate;[3] (3) its redox potential should be sufficiently high, so that it can be regenerated rapidly by electron donation from the electrolyte or a hole conductor.

In the search for a promising sensitizer, a considerable number of complexes have been synthesized and analyzed.[4–10] Among these dyes, *cis*-dithiocyanatobis(2,2′-bipyridyl-4,4′-dicarboxylate)ruthenium(II) (hereafter referred to as N3 or red dye)[5] and trithiocyanato(4,4′,4′′-tricarboxy-2,2′:6′,2′′-terpyridine)ruthenium(II) (black dye)[6] are the most well-known. The N3 dye has been regarded as an efficient photosensitizer because of its broad range of visible light absorption, relatively long-lived excited states, and high thermal stability; moreover, the presence of terminal acidic carboxyl group allows stable anchoring of the dye to the semiconductor surface.[11–15] The incident photon to current conversion efficiency (IPCE) values are reported to be nearly 80% in the range 400–600 nm. However, the main drawback of this sensitizer is its lack of absorption in the red region of the visible spectrum. Numerous attempts to synthesize superior sensitizers[16–19] failed to improve the efficiency and to enhance the spectral response in the red and infrared region until 1997. In 1997, Grätzel and co-workers[20] reported a terpyridine–$Ru^{II}$ complex, the "black dye", with visible absorption extending into the near-IR region up to 920 nm, yielding over 80% IPCE, and producing an overall efficiency of 10.4%.

Black dyes having different degrees of protonation have been fully characterized by Grätzel and co-workers.[6,20–22] It is conceived that the absorption spectra of the black dyes are dominated by metal-to-ligand-charge-transfer (MLCT) transitions. For example, the absorption spectrum of the

[a] State Key Laboratory of Theoretical and Computational Chemistry, Institute of Theoretical Chemistry, Jilin University, Changchun 130023, China
Fax: +86-431-88945942
E-mail: zhanghx@mail.jlu.edu.cn
[b] College of Chemistry and Chemical Engineering, Heilongjiang University,
Haerbin 150080, China

Supporting information for this article is available on the WWW under http://www.eurjic.org or from the author.

 © 2007 Wiley-VCH Verlag GmbH & Co. KGaA, Weinheim 

monoprotonated black dye complex (hereafter named **1H**) in ethanol exhibits three MLCT bands in the visible region centered at 610, 536, and 411 nm, and a high-energy $\pi\rightarrow\pi^*$ band at about 340 nm. It shows a strong negative solvatochromism, resulting in a red-shift of the UV/Vis absorption bands from 570 nm (in $H_2O$) to 620 nm (in γ-butyrolactone).[6] The observed emission of the complex **1H** (854 nm) has been assigned as arising from the Ru→tcterpy CT excited state.[6] Similarly, the emissions of the complex **1H** in different solvents also show a strong solvent dependence.

Since the spectroscopic properties of the dye are crucial in determining its long-term stability, the light-harvesting efficiency of the DSSCs, and the charge-transfer dynamics at the semiconductor interface,[16,23] a full understanding of its electronic properties, especially in the excited state, is very essential. In contrast to the numerous experimental studies, only a few theoretical calculations have been performed for dye molecules.[23–30] Most of these investigations are focused on the calculations of the N3 dye.[25–30] To date, one investigation for the fully protonated black dye is limited to the gas-phase calculations of molecular structure and absorption spectrum.[23] Another theoretical investigation focuses on the comparative study of ground-state properties (such as energies, geometries, and population analysis in molecular orbitals) and the absorption spectra of the black dye complex and its linkage isomers.[24] These theoretical calculations all focus on the fully protonated black dye complex. However, the photovoltaic performance of the monoprotonated black dye, **1H**, is superior to the other three black dye complexes. Moreover, no theoretical study was conducted on the geometry and electronic structure of the excited states and the emission properties of the black dye. In addition, in the solar cell, the dye sensitizer is adsorbed on the semiconductor electrode on one hand and interacts with the redox electrolyte on the other hand; therefore, it may not be possible to directly apply calculations excluding environment effects. Thus, in this paper, we employed DFT, the CIS method, and the TD-DFT approach to study the electronic structure, spectroscopic properties, and solvatochromic properties of the monoprotonated black dye **1H**. The solvent effects are seriously considered by using the conductor-like polarizable continuum model (CPCM). These results will provide a direct insight into the origins of the observed transitions and their possible role in dye–sensitized solar cell injection dynamics as well as the design of new and more efficient solar cell sensitizers.

## 2. Computational Details and Theory

In this work, $C_s$ symmetry was adopted to set the conformation of $[Ru(Htcterpy)(NCS)_3]^{3-}$ (**1H**) in both the ground and the excited states. The geometry of the ground-state structure is fully optimized by using the density functional theory (DFT) with the B3LYP functional (Becke's three-parameter functional and the Lee–Yang–Parr functional),[31] while the geometry of the excited-state structure is fully optimized by the single-excitation configuration interaction (CIS) method.[32,33] With such calculations, the spectroscopic properties related to absorption and emission are obtained by the time-dependent density functional theory (TD-DFT),[34] and the conductor-like polarizable continuum model (CPCM)[35] is employed to account for the effects of the solvent molecules water and ethanol.

It is well-known that for excited states, the CIS method is most similar to the HF method for the ground state. However, through the use of analytic gradients and methods properly by including the effects of electronic correlation, this method gives bond lengths, frequencies, and dipole moments well in line with the experimental values. In addition, the application of the method to very large molecules is possible.[32] Although a reasonable excited-state structure can be obtained by the CIS method, the predicted transition energies deviate from experimental values commonly by about 1 eV or more. In the recent years, the TD-DFT methods have been successfully used to calculate singlet–singlet and singlet–triplet transitions in many reports.[36] More electronic correlations are involved in the TD-DFT (B3LYP) approach, which then yields more accurate excitation energies than the CIS method. This approach overcomes many of the problems encountered in vertical energies with the CIS method, providing accurate excitation energies of valence and Rydberg states. Therefore, on the basis of CIS optimized structures, we have employed the TD-DFT method to calculate the emission energies.

In the calculations, quasi-relativistic pseudopotentials of the Ru, C, N, and S atoms proposed by Hay and Wadt[37] with 16, 4, 5, and 6 valence electrons, respectively, are employed, and the LanL2DZ basis sets associated with the pseudopotential are adopted. Here, the basis sets are taken as Ru(8s7p6d/6s5p3d), S(3s3p1d/2s2p1d), N(10s5p/3s2p), C(10s5p/3s2p), and H(4s/2s). Thus, 361 basis functions and 262 electrons are included for the complex **1H**. All the calculations were accomplished by using the Gaussian (Revision B.03) program package[38] on an Origin/3900 server.

## 3. Results and Discussion

### 3.1 The Ground- and Excited-State Structures of 1H

The DFT optimization on **1H** indicates that the complex has a $^1A'$ ground state with the $[101(a'^2)30(a''^2)]$ electronic configuration. The geometry of the structure is depicted in Figure 1, and the main optimized geometry parameters in the gas phase are listed in Table 1 together with the X-ray crystal structure data of $(NBu_4^+)_2[Ru(H_2tcterpy)(NCS)_3]^{2-}$.[22] As shown in Figure 1, complex **1H** has a slightly distorted octahedral coordination with $C_s$ symmetry. The geometry of the structure of complex **1H** displays a RuN6 central core derived from three nitrogen atoms of the terpyridine ligand and three nitrogen atoms of the isothiocyanate ligands. The coordination axis is also shown in Figure 1; the tcterpy-Ru-N1C1S1 moiety lies on the *xy* plane, and the other two isothiocyanate ligands are slightly tilted with respect to the *z* axis. As shown in Table 1,

 © 2007 Wiley-VCH Verlag GmbH & Co. KGaA, Weinheim 

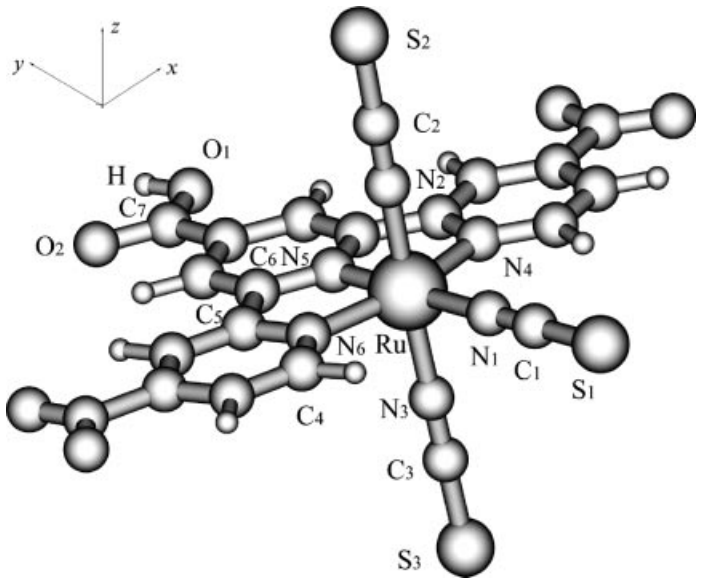


Figure 1. Ground-state structure of $[Ru(Htcterpy)(NCS)_3]^{3-}$ (**1H**) optimized by DFT(B3LYP).

the optimized geometrical parameters are in excellent agreement with the available X-ray data, and consistent with those calculated by Aiga and co-workers[23] by the PBE0 approach.[39] The N–C bond lengths in the terpyridine rings are about 1.38 Å and are much shorter than a normal N–C single-bond length of 1.48 Å, indicating that there is some delocalization of the lone pairs of the nitrogen atoms. It is noted that there exits an extended π bonding between the central pyridine (nitrogen p orbitals), the Ru atom (d π orbitals), and the N1C1S1 ligand (π electrons). The effective π bonding makes the bond lengths of Ru–N1 and Ru–N5 quite similar. Therefore, the Ru–N5 bond length (1.939 Å) is ca. 0.16 Å shorter than that of Ru–N4 (or Ru–N6), whereas the Ru–N1 bond length is ca. 0.05 Å longer than that of Ru–N2 (or Ru–N3). In addition to the bond lengths, the important bond angles are also accurately reproduced.

On the basis of the optimized ground-state structure, the CIS method is used to optimize the geometry of the excited-state structure of the **1H** complex, and the lowest-energy triplet excited state with $^3A'$ symmetry is obtained. The main geometry parameters of the excited state are presented in Table 1. Three conclusions can be drawn from the excited-state results: (1) The coordination geometry of Ru in the $^3A'$ excited state still keeps the quasi-octahedral structure similar to the ground state. (2) A general elongation of all the metal–ligand bonds is observed. For example, the Ru–N bond lengths in the excited state are elongated by ca. 0.04–0.07 Å relative to the ground-state ones. (3) The most nonmetallic bonds (N–C, C–C, C–O, and O–H) of tcterpy in the triplet excited state are shorter than those in the ground state, on the contrary, the C–S bond lengths for the NCS ligands are slightly longer upon excitation. It is noteworthy that the comparison of the bond lengths is between the ground state and the excited state obtained with two different methods (DFT/B3LYP for the ground state and CIS for the excited state). So the conclusions drawn from those comparisons are only used as relative results. However, this has no impact on the nature of the charge-transfer transition related to the emissions for the complex **1H**.

Table 1. Optimized geometry parameters for the $^1A'$ ground state calculated by DFT and for the $^3A'$ triplet excited state calculated by CIS for $[Ru(Htcterpy)(NCS)_3]^{3-}$ (**1H**), together with the experimental data.

| Parameters | Ground state ($^1A'$) | Triplet excited state ($^3A'$) | Exp.[a] |
|---|---|---|---|
| Bond lengths [Å] | | | |
| Ru–N1 | 2.107 | 2.147 | 2.032 |
| Ru–N2 | 2.057 | 2.098 | 2.052 |
| Ru–N5 | 1.939 | 1.995 | 1.936 |
| Ru–N6 | 2.099 | 2.174 | 2.090 |
| N1–C1 | 1.192 | 1.159 | |
| N2–C2 | 1.191 | 1.160 | |
| N5–C6 | 1.382 | 1.354 | |
| N6–C4 | 1.357 | 1.341 | |
| N6–C5 | 1.384 | 1.365 | |
| C1–S1 | 1.696 | 1.709 | 1.672 |
| C2–S2 | 1.694 | 1.703 | 1.613 |
| C7–O1 | 1.320 | 1.292 | |
| H1–O1 | 0.982 | 0.954 | |
| Bond angles [°] | | | |
| N6–Ru–N5 | 80.2 | 78.7 | 81.1 |
| N6–Ru–N4 | 160.3 | 157.5 | 161.6 |
| N2–Ru–N3 | 177.1 | 179.8 | 177.4 |
| N1–Ru–N5 | 180.0 | 180.0 | 177.6 |
| N1–Ru–N6 | 99.9 | 101.3 | 101.4 |
| H1–O1–C7 | 109.8 | 113.5 | |

[a] Ref.[22]

### 3.2. Absorption Spectra

#### *3.2.1. Electronic Structures*

On the basis of the optimized ground-state geometry, the electronic structure of the excited state and the absorption

 © 2007 Wiley-VCH Verlag GmbH & Co. KGaA, Weinheim 

properties of **1H** in ethanol solution are obtained by the combination of the TD-DFT and CPCM methods. The frontier orbitals play a relevant role in complex **1H**, because they rule the electronic excitations and the transition character. The following assignment for each molecular orbital was made according to its composition (Table 2) and by visual inspection of its three-dimensional representation (e.g. Figure 2). Some lower-lying occupied molecular orbitals (such as 95a′, 26a′′, 96a′, and 27a′′) are centered on the carboxyl groups. The $COO^-$ character of the lower-lying HOMOs was already found in the bipyridine–$Ru^{II}$ complex by De Angelis et al.[40,41] The HOMO(30a′′) and HOMO-1(29a′′), lying within 0.02eV, are a set of quasi-degenerate orbitals arising from the antibonding combinations of ruthenium d orbitals ($d_{xz}$ and $d_{yz}$, respectively) with sulfur p orbitals and nitrogen lone pairs of the two NCS ligands which are perpendicular to the tcterpy ring. HOMO-2(101a′), lying ca. 0.23 eV below the HOMO, is characterized by the antibonding combination nature between the ruthenium $d_{xy}$ orbital and the NCS π orbital of the thiocyanate ligand that is in the plane of the tcterpy ligand. The HOMO-3(100a′) and HOMO-4(99a′), lying 0.46 and 0.47 eV below the HOMO, respectively, are mainly localized on the $COO^-$ ligands which are attached to the peripheral pyridines, and have vanishing metal character. The HOMO-5(28a′′), HOMO-6(98a′), and HOMO-7(97a′), lying 0.51, 0.64, and 0.66 eV below the HOMO, respectively, are all pure NCS π orbitals. This significant thiocyanate character in the HOMOs was already found in the N3 dye[29,30] and seems to play an important role in the regeneration of dye-sensitized solar cells.[30]

The five lowest LUMOs of the **1H** complex, lying 1.92 eV above the HOMO within a range of ca. 1.86 eV, are π* orbitals localized over the pyridine ligands with considerable contributions arising from the carboxyl groups. In particular, the LUMO(31a′′) is localized on the central pyridine, while LUMO+3(34a′′) and LUMO+4(35a′′) are localized on the two peripheral pyridine groups. LUMO+1(32a′′) and LUMO+2(33a′′) are completely delo-

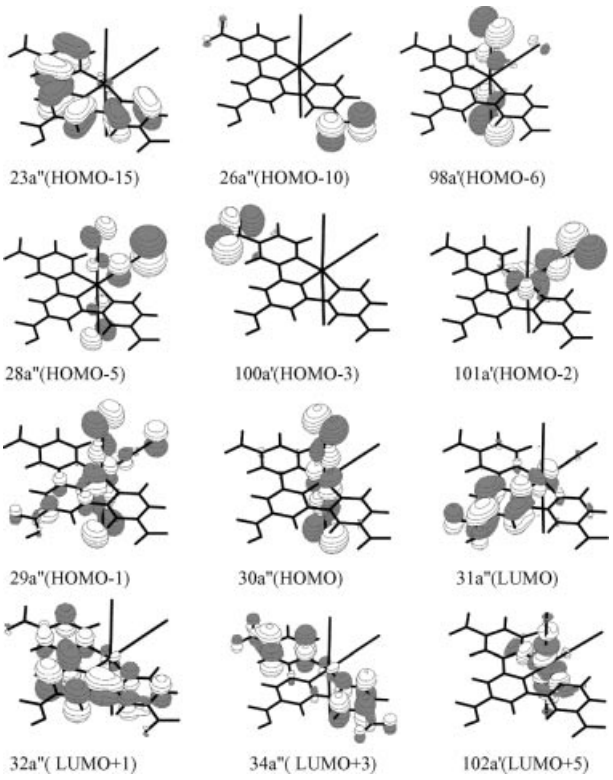


Figure 2. Electron-density diagrams of the frontier molecular orbitals involved in absorption for $[Ru(Htcterpy)(NCS)_3]^{3-}$ (**1H**) in ethanol calculated by TD-DFT.

Table 2. Partial molecular orbital compositions of $[Ru(Htcterpy)(NCS)_3]^{3-}$ (**1H**) in ethanol calculated by TD-DFT.

| MO | Energy [eV] | Compositions [%] | | | | Ru components [%] | | | Orbital assignment |
|---|---|---|---|---|---|---|---|---|---|
| | | Ru | terpy | $COO^-$ | NCS | s | p | d | |
| 102a′ | 1.4727 | 44.5 | 26.5 | | 28.3 | 5.8 s | 3.2$p_y$ | 28.0 $d_{z^2}$,7.5 $d_{x^2-y^2}$ | $d_{z^2}/d_{x^2-y^2}$(Ru)-π*(NCS) |
| 35a′′ | 0.1075 | | 91.4 | 7.4 | | | | | π*(tcterpy) |
| 34a′′ | –0.0215 | | 89.8 | 6.9 | | | | 3.2 $d_{xz}$ | π*(tcterpy) |
| 33a′′ | –0.5646 | | 76.6 | 21.5 | | | | | π*(tcterpy) |
| 32a′′ | –1.0830 | | 97.2 | | | | | | π*(tcterpy) |
| 31a′′(L) | –1.7777 | 14.5 | 57.8 | 23.7 | 4.0 | | | 14.4 $d_{yx}$ | π*(tcterpy) |
| 30a′′(H) | –3.6970 | 40.6 | 5.1 | | 53.9 | | | 40.6 $d_{xz}$ | $d_{xz}$ (Ru)–π*(NCS) |
| 29a′′ | –3.7160 | 30.5 | | | 49.8 | | | 29.9 $d_{yz}$ | $d_{yz}$ (Ru)–π*(NCS) |
| 101a′ | –3.9226 | 35.3 | | | 50.9 | | | 35.0 $d_{xy}$ | $d_{xy}$ (Ru)–π*(NCS) |
| 100a′ | –4.1549 | | | 81.4 | | | | | $p_x/p_y(COO^-)$ |
| 99a′ | –4.1656 | | | 81.4 | | | | | $p_x/p_y(COO^-)$ |
| 28a′′ | –4.2077 | | | | 99.0 | | | | π*(NCS) |
| 98a′ | –4.3419 | | | | 94.7 | | | | π*(NCS) |
| 97a′ | –4.3555 | | | | 98.2 | | | | π*(NCS) |
| 27a′′ | –4.4447 | | | 98.2 | | | | | $p_z(COO^-)$ |
| 96a′ | –4.4458 | | | 62.3 | | | | | $p_x/p_y(COO^-)$ |
| 26a′′ | –4.4551 | | | 98.2 | | | | | $p_z(COO^-)$ |
| 95a′ | –4.4594 | | | 62.3 | | | | | $p_x/p_y(COO^-)$ |
| 25a′′ | –5.0224 | 43.5 | | | 35.8 | | | 43.5 $d_{xz}$ | $d_{xz}$(Ru)–π*(NCS) |
| 94a′ | –5.0584 | 50.7 | | | 28.4 | | | 50.2 $d_{xy}$ | $d_{xy}$(Ru)–π*(NCS) |
| 24a′′ | –5.2227 | 40.5 | | | 41.3 | | | 40.0 $d_{yz}$ | $d_{yz}$(Ru)–π*(NCS) |
| 23a′′ | –5.8665 | | 97.1 | | | | | | π(tcterpy) |

 © 2007 Wiley-VCH Verlag GmbH & Co. KGaA, Weinheim 

calized over the full tcterpy ring ligands. Such a contribution from the carboxyl groups to the π* LUMOs should favor the electron injection process from the dye excited state to the semiconductor surface, because the carboxyl units serve as anchoring groups to the $TiO_2$ semiconductor surface.[2,3] Moreover, another role of the terminal carboxyl groups is to ensure intimate electronic coupling between the donor energy level of the excited dye and the acceptor $TiO_2$ conduction band.

### *3.2.2. Absorption Spectra in Ethanol*

The absorption spectra of the complex **1H** are simulated with Gaussian curves based on the transitions with oscillator strength $f > 0$ in ethanol solution calculated by TD-DFT/CPCM. The fitting absorption curve is depicted as oscillator strength vs. wavelength in Figure 3; the most representative calculated optical transitions are collected in Table 3. Within the considered energy range, the absorption spectrum of **1H** shows five bands, labeled I, II, III, IV, and V in order of decreasing wavelength; band V is more intense than other bands.

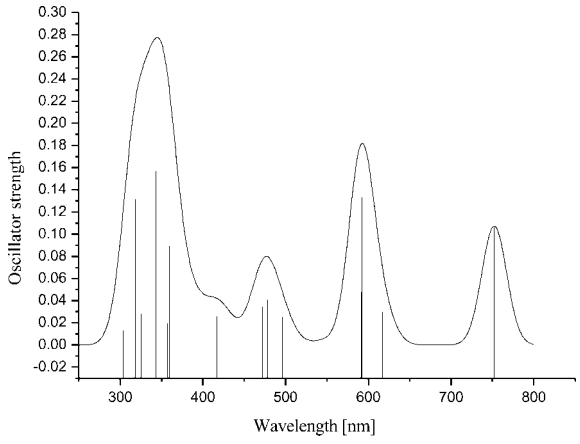


Figure 3. Absorption spectra and excited states of $[Ru(Htcterpy)(NCS)_3]^{3-}$ (**1H**) in ethanol calculated by TD-DFT.

The peak of the lowest-energy band, I, which results from one transition and has the oscillator strength 0.1073, is calculated to be at 752 nm. As shown in Table 3, the transition is mainly contributed by the excitations 29a′′(HOMO-1)→31a′′(LUMO) and 30a′′(HOMO)→32a′′(LUMO+1) with CI coefficients of ca. 0.58 and 0.25, respectively. It has been mentioned in the above section that the HOMO and HOMO-1 are antibonding combinations of the d orbitals ($d_{xz,yz}$) of the ruthenium atom with the π orbitals of the NCS ligand. The LUMO and LUMO+1 are π* orbitals localized over the tcterpy ring ligand. Therefore, we assign the lowest-energy band as a mixed Ru–NCS-to-tcterpy-charge-transfer (MLCT/LLCT) transition. The absorption band at 752 nm is not observed in the experimental absorption spectra. We calculated the maximum of band II to be at 592 nm, whose position is in excellent agreement with the experimental value of 610 nm. This band is caused by three transitions calculated at 617, 592, and 591 nm. As depicted in Table 2 and Table 3, band II is assigned as a mixed Ru–NCS-to-tcterpy charge transfer (MLCT/LLCT) with a little LMCT character. The dominating transition in this band, at 592 nm with an oscillator strength of 0.1300, is mainly contributed by the 28a′′(HOMO-5)→31a′′(LUMO) and 30a′′(HOMO)→32a′′(LUMO+1) configurations with CI coefficients of about 0.48 and 0.42, respectively. The molecular orbital 28a′′(HOMO-5) is localized on three NCS ligands up to 99% in composition, and the molecular orbital 31a′′(LUMO) is composed of $Ru(d_{yz})$ (15%), and tcterpy (82%). So we attribute the 592 nm absorption band to NCS→tcterpy charge transfer (LLCT), NCS→$Ru(d_{yz})$ charge transfer (LMCT), and $Ru(d_{xz})$→tcterpy charge transfer (MLCT) transitions. The maximum of band III is calculated at ca. 478 nm, which is only 58 nm blue-shifted with respect to the experimental datum of 536 nm, and has a multitransition character and involves excitations from the 25a′′(HOMO-12), 29a′′(HOMO-1), and 30a′′(HOMO) to the 31a′′(LUMO) and 33a′′(LUMO+2). This set of HOMOs have ruthenium-d-orbital nature (44%, 31%, and 41%, respectively) with sizeable contribution from the orbitals of the NCS ligand (36%, 50%, and 54%, respectively), while the LUMO and LUMO+2 are localized on the tcterpy ligands. Therefore, in the same way as for band I, the origin of band III is assigned to be the Ru–NCS to tcterpy charge transfer (MLCT/LLCT) transitions. Band IV, with the smallest oscillator strength, is calculated to have its maximum at 417 nm, which is in close accord with the experimental data of 411 nm. This band arises from one transition with a small oscillator strength of 0.0228, which mainly comes from the combination of 24a′′(HOMO-14)→31a′′(LUMO) and 30a′′(HOMO)→34a′′(LUMO+3) configurations with CI coefficients of around 0.50 and 0.42, respectively. In Table 2 and Figure 2, the 24a′′ orbital and 30a′′ orbital are both the antibonding combinations of Ru(d) orbitals and the NCS π orbitals, whereas the 31a′′ orbital and 34a′′ orbital are localized on tcterpy ring ligands. So the 417-nm band is unambiguously attributed to a mixed Ru–NCS to tcterpy charge transfer (MLCT/LLCT) transition. At the highest energy, the strongest band V, appears to be composed of multitransitions spanning the range 360–300 nm. The dominating transition in this band, at about 343 nm ($f$ = 0.1536), is mainly contributed by the 23a′′(HOMO-15)→31a′′(LUMO) and 24a′′(HOMO-14)→32a′′(LUMO+1) configurations with CI coefficients of around 0.46 and 0.47, respectively. As show in Table 2 and Figure 2, we can see that the 23a′′ orbital (HOMO-15) and 31a′′ orbital (LUMO) are π combinations and π* combinations, respectively, localized on the tcterpy ligands. Thus the 343 nm absorption is attributed to the intraligand tcterpy π→π* charge transfer (ILCT) involved in a mixed Ru–NCS to tcterpy charge transfer (MLCT/LLCT) transition. The next most intense transition, at about 318 nm ($f$ = 0.1283), arises from the combination of 25a′′(HOMO-12)→33a′′(LUMO+2), 26a′′(HOMO-10)→34a′′(LUMO+3), and 26a′′(HOMO-10)→35a′′(LUMO+4) configurations with CI coefficients of around 0.53, 0.32, and 0.21, respectively. The 25a′′ orbital (HOMO-12) is the anti-

 © 2007 Wiley-VCH Verlag GmbH & Co. KGaA, Weinheim 

Table 3. Excitation energies and oscillator strengths for the optical transitions with $f > 0.01$ for the absorptions of [Ru(Htcterpy)-$(NCS)_3]^{3-}$ (**1H**) in ethanol calculated by TD-DFT.

| State | Excitation (CI coef.) | $\lambda$ [nm] ($E$ [eV]) | Oscillator strength | Character |
|---|---|---|---|---|
| 3A′ | 28a′′→31a′′(0.12) | 752 (1.65) | 0.1073 | MLCT/LLCT |
| | 29a′′→31a′′(0.58) | | | |
| | 30a′′→32a′′(0.25) | | | |
| 6 A′ | 29a′′→32a′′(0.69) | 617 (2.01) | 0.0268 | MLCT/LLCT |
| 9 A′ | 28a′′→31a′′(0.48) | 592 (2.09) | 0.1300 | MLCT/LLCT/LMCT |
| | 29a′′→31a′′(0.19) | | | |
| | 30a′′→32a′′(0.42) | | | |
| 10A′′ | 97a′→31a′′(0.70) | 591 (2.10) | 0.0443 | LLCT/LMCT |
| 16 A′ | 25a′′→31a′′(0.58) | 496 (2.50) | 0.0221 | MLCT/LLCT |
| | 30a′′→31a′′(0.13) | | | |
| | 30a′′→33a′′(0.40) | | | |
| 20 A′ | 25a′′→31a′′(0.37) | 478 (2.60) | 0.0375 | MLCT/LLCT |
| | 30a′′→33a′′(0.59) | | | |
| 21 A′ | 29a′′→33a′′(0.68) | 472 (2.63) | 0.0310 | MLCT/LLCT |
| 32 A′ | 24a′′→31a′′(0.50) | 417 (2.98) | 0.0228 | MLCT/LLCT |
| | 30a′′→34a′′(0.42) | | | |
| 46 A′ | 23a′′→31a′′(0.47) | 360 (3.45) | 0.0181 | π→π*/MLCT/LLCT |
| | 24a′′→32a′′(0.49) | | | |
| 47 A′ | 24a′′→31a′′(0.27) | 359 (3.45) | 0.0864 | MLCT/LLCT |
| | 25a′′→32a′′(0.53) | | | |
| 51 A′ | 26a′′→33a′′(0.66) | 357 (3.47) | 0.0164 | $O(p_z)$→tcterpy |
| 52 A′ | 23a′′→31a′′(0.46) | 343 (3.61) | 0.1536 | π→π*/MLCT/LLCT |
| | 24a′′→32a′′(0.47) | | | |
| 57 A′ | 94a′→102a′(0.22) | 325 (3.81) | 0.0248 | d→d/LLCT |
| | 94a′→103a′(0.21) | | | |
| | 101a′→102a′(0.41) | | | |
| | 101a′→103a′(0.32) | | | |
| 64 A′ | 25a′′→33a′′(0.25) | 318 (3.90) | 0.0125 | $O(p_z)$→tcterpy/MLCT/LLCT |
| | 26a′′→34a′′(0.39) | | | |
| | 26a′′→35a′′(0.34) | | | |
| | 27a′′→34a′′(0.32) | | | |
| 66 A′ | 25a′′→33a′′(0.53) | 318 (3.91) | 0.1283 | $O(p_z)$→tcterpy/MLCT/LLCT |
| | 26a′′→34a′′(0.32) | | | |
| | 26a′′→35a′′(0.21) | | | |
| 70 A′ | 24a′′→33a′′(0.67) | 304 (4.08) | 0.0100 | MLCT/LLCT |

bonding combination of the Ru($d_{xz}$) orbital and the NCS π orbitals, and the 26a′′ orbital (HOMO-10) is mainly composed of O($p_z$) from the $COO^-$ group. However, the 33a′′, 34a′′, and 35a′′ orbitals are all localized on tcterpy ligands. So the 318 nm transition is assigned as a mixed Ru–NCS-to-tcterpy charge transfer (MLCT/LLCT) and O($p_z$)→terpy charge transfer (LLCT) transition. We also notice that a few weak ($f$ = 0.0248) d–d transitions, at 325 nm, contribute to band V.

In experiments, the 610–400 nm regions have been assigned as the Ru-to-tcterpy-charge-transfer bands, while the 360–300 nm absorptions are attributed to the π→π* charge transfer transitions.[6] By comparing this experimental spectrum with the absorption spectrum of **1H** calculated in ethanol solution, we notice that our calculation is in rough agreement with experimental observations. However, there are some differences between the theoretical calculation and the experimental investigation. As mentioned above, we assign the low energy bands I–IV to mixed Ru–NCS-to-tcterpy charge transfer (MLCT/LLCT) rather than to pure metal–ligand-charge-transfer (MLCT) transitions, results from a set of Ru–NCS d-π* orbitals, while the highest energy band V, arises from intraligand tcterpy π→π* charge transfer (ILCT) and is involved in a sizeable O($p_z$)→terpy charge transfer (LLCT) transition. Furthermore, the calculated absorption spectra have two peaks at long wavelengths around 600–800 nm, while the experimental spectra[6] have one peak. The calculated absorption peak at 752 nm is not observed in experiment. Moreover, the calculated absorption spectra have lesser intense bands at short wavelengths around 500–350 nm than those at longer wavelengths between 500–700 nm, but the experimental spectra have the reverse trend. Our calculation overestimates the intensity of band II (500–700) and underestimates that of band III (350–500 nm). This is perhaps not surprising, since from a comparison between TD-DFT and the more expansive CASPT2 method, the results of Full et al. show that TD-DFT oscillator strengths diverge from the CASPT2 values.[42] In addition, a similar comparison by Tozer et al. show that TD-DFT has difficulty distributing intensity properly;[43] it is thus possible that intensity is erroneously shifted from band III to band II in our calculation.

### *3.2.3. Solvent Effects*

To check the solvent dependence of spectroscopic properties, we also calculated the absorptions of **1H** in the gas phase and in water solution, and the results are listed in Tables S1 and S2 (see Supporting Information). A compari-

 © 2007 Wiley-VCH Verlag GmbH & Co. KGaA, Weinheim 

son of the molecular orbital energy levels of the absorptions for complex **1H** in the gas phase, in ethanol and in water is presented in Figure 4. From Figure 4, we can see that the solvent effect leads to a sizeable change of the molecular orbital energies. However, the occupied and unoccupied orbitals maintain similar compositions in the gas phase and in solution (ethanol and water). In ethanol, the HOMOs (from HOMO to HOMO-7) are significantly stabilized by about 5.1 eV with respect to the corresponding values computed in the gas phase, while they maintain a similar composition. In the same way as the HOMOs, the five lowest LUMOs are stabilized by ca. 5.0–5.1 eV with respect to the corresponding values computed in the gas phase, even though they maintain similar compositions based on terpyridine and carboxyl group contributions. The LUMO+5 of the absorption in the gas phase has the C7–O1 π-bonding properties from the carboxyl group which is attached to the central pyridine, while in ethanol, the LUMO+5 orbital shows a higher contribution of d orbitals of the ruthenium atom (45%) mixed with π orbitals of the NCS ligand (28%). Altogether, the presence of the solvent leads to a slight increase of the HOMO–LUMO gap, which changes from 1.80 eV in the gas phase to 1.92 eV in ethanol. Moreover, the electronic structure of the absorption for complex **1H** in water is rather similar to that found in ethanol. The LUMOs and HOMOs are further stabilized, resulting in a HOMO–LUMO gap of 2.0 eV, namely 0.08 eV larger than that computed in ethanol.

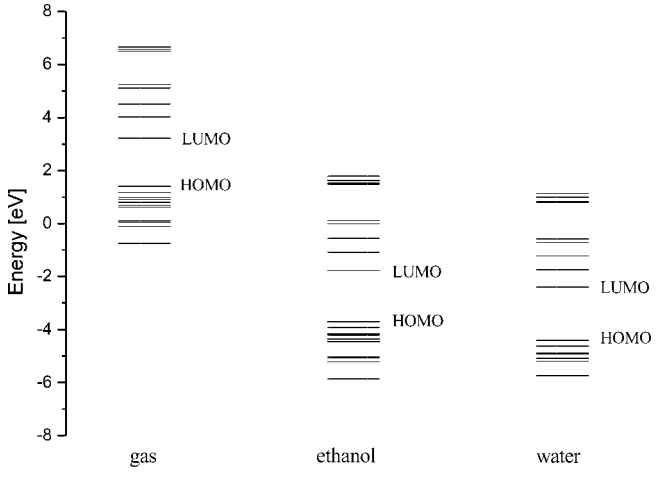


Figure 4. Energy-level diagrams of the orbitals involved in absorption for $[Ru(Htcterpy)(NCS)_3]^{3-}$ (**1H**) in the gas phase, in ethanol, and in water calculated by TD-DFT.

The calculated absorption spectra of complex **1H** in the gas phase, in ethanol and in water are shown in Figure 5. With the inclusion of seventy excitation states, all of these spectra exhibit five bands. As listed in Table 3 and Table S2, the CI configurations, oscillator strengths, and transition characters calculated in ethanol and water are rather similar. In both solvents, the four low-lying absorption bands have a mixed Ru–NCS-to-tcterpy charge transfer (MLCT/LLCT) character, whereas the high-lying absorption band V with the greatest intensity is attributed to the intraligand π→π* charge transfer mixed with $O(p_z)$→terpy charge transfer transitions. In the gas phase, the compositions of the transitions show a small variation relative to those in ethanol and water. As depicted in Table 2 and Table S1, we can see that the $O(p_z)$→terpy charge transfer character already appears in band VI in the gas phase. In the first two lowest-energy absorption bands, the wavelengths are blue-shifted by about 20 and 45 nm in ethanol and water with respect to those for the gas phase.

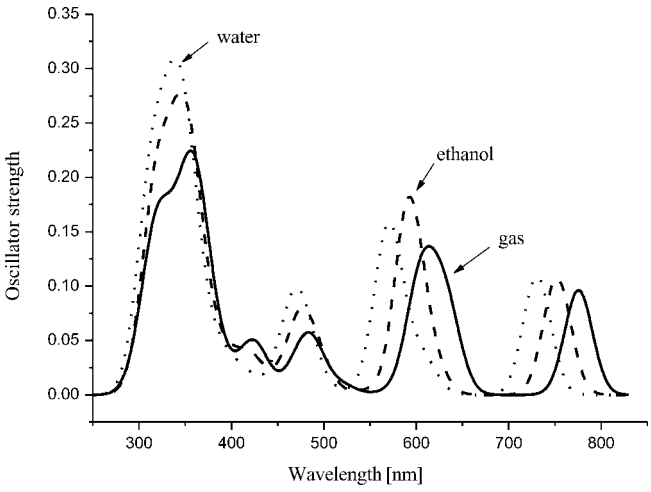


Figure 5. The simulated absorption spectra for $[Ru(Htcterpy)(NCS)_3]^{3-}$ (**1H**) in the gas phase, in ethanol, and in water.

As shown in Figure 5, negative solvatochromism is observed in the MLCT/LLCT band ($\lambda$ = 400–800 nm) of complex **1H**. With increasing solvent polarity from ethanol to water, the wavelengths are blue-shifted by about 20 nm. In addition, we find that the π→π* band is only weakly affected by the change in solvent polarity. The calculated values are in excellent agreement with the experimental data. There is a factor that can be responsible for the observed blue-shift from ethanol to water: the electrostatic interaction between the solvent water and the NCS ligand is stronger than that between the solvent ethanol and the NCS ligand.

To get an insight into the origin of the negative solvatochromism of the MLCT/LLCT bands, it is useful to keep in mind the dipole moments of the complexes. As discussed above, the MLCT/LLCT transitions involve displacement of the electron charge from the Ru center and the NCS ligand toward the tcterpy π* orbitals. Thus, to approximately evaluate the dipole moment in the excited states, we considered the electronic state in which one electron is promoted from the HOMO(30a′′) to the LUMO(31a′′). The excited-state dipole moments in the gas phase, in ethanol and in water are predicted at the B3LYP/LAN2DZ level on the basis of the optimized ground-state geometry. Table S3 gives the dipole moments of complex **1H** in the ground and excited states in the gas phase, in ethanol, and in water. From Table S3, we can see that the dipole moments are apparently reduced from the ground state to the excited state. That is to say, the excited state should be less stabilized by polar solvents than the ground state. For instance,

 © 2007 Wiley-VCH Verlag GmbH & Co. KGaA, Weinheim 

in ethanol, the dipole moment in the excited state is 3.95 D, with a reduction $\Delta\mu$ = 5.81 D with respect to the dipole moment in the ground state (9.76 D). Similarly, in water, the dipole moment in the excited state is 2.96 D, with a reduction $\Delta\mu$ = 7.76 D with respect to the dipole moment in the ground state (10.72 D). The small increase in $\Delta\mu$ with increasing solvent polarity from ethanol to water correlates well with the calculated negative solvatochromism in the MLCT/LLCT band. It is noted that the definition of the dipole moment for neutral systems is independent of the choice of the origin of the reference system, while the dipole moment of charged systems will change as the molecule is shifted. However, in the present paper, the ground state and excited state exist as ions in the solvents. In addition, as discussed above, the excited-state dipole moments are predicted on the basis of the optimized ground-state geometry. So the center of coordinates of the ground and excited state do not change. Thus, though the complex **1H** is a charged molecule, we think it is reliable to discuss solvent effects in terms of the variation of dipole moment between the ground and excited states.

### 3.3. Emission Spectra

In view of obtaining a feasible emissive energy on the basis of the excited-state structures optimized by the CIS method, the emission spectrum of complex **1H** in ethanol is calculated by the TD-DFT approach at the B3LYP level associated with the CPCM model. The corresponding emissions of **1H** in the gas phase, in ethanol, and in water are listed in Table 4, associated with the emissive energies, transition assignments, and experimental values. To conveniently discuss the transition properties of the emissions, we present the partial compositions of the frontier molecular orbitals related to the emissions in Table 5.

The calculated lowest-energy emission for complex **1H** occurs at 711 nm in ethanol solution with a transition of $^3A'\rightarrow{}^1A'$ nature. As shown in Table 4, the phosphorescence is mainly from the transitions of 32a′′(LUMO+1)→24a′′(HOMO-14) and 32a′′(LUMO+1)→30a′′(HOMO) configuration with CI coefficients of 0.12 and 0.71, respectively. Furthermore, as seen in Table 4 and Table 5, this emission has tcterpy→Ru ($^3$LMCT) and tcterpy→NCS ($^3$LLCT)

Table 4. The lowest-energy phosphorescent emission of $[Ru(Htcterpy)(NCS)_3]^{3-}$ (**1H**) in the gas phase, in ethanol, and in water calculated by TD-DFT, together with experimental values.

| Medium | Transition | Config.(CI coef.) | $\lambda$ [nm] ($E$ [eV]) | Character | Exp.[a] |
|---|---|---|---|---|---|
| gas | $^3A'\rightarrow{}^1A'$ | 32a′′→24a′′(0.12)<br>32a′′→29a′′(0.16)<br>32a′′→30a′′(0.69) | 724 (1.71) | $^3$LMCT/$^3$LLCT | |
| $CH_3CH_2OH$ | $^3A'\rightarrow{}^1A'$ | 32a′′→24a′′(0.11)<br>32a′′→30a′′(0.71) | 711 (1.74) | $^3$LMCT/$^3$LLCT | 854 |
| $H_2O$ | $^3A'\rightarrow{}^1A'$ | 32a′′→24a′′(0.11)<br>32a′′→30a′′(0.71) | 690 (1.80) | $^3$LMCT/$^3$LLCT | 829 |

[a] From ref.[6]

Table 5. Partial molecular orbital compositions in the lowest-energy $^3A'$ excited state of $[Ru(Htcterpy)(NCS)_3]^{3-}$ (**1H**) in ethanol calculated by TD-DFT.

| MO | Energy [eV] | Compositions [%] | | | | Ru components [%] | | | Orbital assignment |
|---|---|---|---|---|---|---|---|---|---|
| | | Ru | terpy | $COO^-$ | NCS | s | p | d | |
| 35a′′ | 0.1442 | | 92.8 | 6.2 | | | | | π*(terpy) |
| 34a′′ | –0.0063 | | 90.9 | 6.4 | | | | | π*(terpy) |
| 33a′′ | –0.4756 | | 76.8 | 21.7 | | | | | π*(terpy) |
| 32a′′ | –1.1889 | | 98.0 | | | | | | π*(terpy) |
| 31a′′(LUMO) | –1.7459 | 11.3 | 62.0 | 24.0 | 2.6 | | | 11.2 $d_{yx}$ | π*(terpy) |
| 30a′′(HOMO) | –3.6578 | 32.9 | 12.2 | | 52.7 | | | 32.4 $d_{yz}$ | $d_{yz}$ (Ru)–π*(NCS) |
| 29a′′ | –3.6698 | 40.3 | | | 55.8 | | | 40.3 $d_{xz}$ | $d_{xz}$ (Ru)–π*(NCS) |
| 101a′ | –3.8499 | 34.9 | | | 52.8 | | | 34.7 $d_{xy}$ | $d_{xy}$ (Ru)–π*(NCS) |
| 28a′′ | –4.1098 | | | | 99.6 | | | | π*(NCS) |
| 100a′ | –4.1490 | | | 80.8 | | | | | $p_x/p_y(COO^-)$ |
| 99a′ | –4.1615 | | | 80.8 | | | | | $p_x/p_y(COO^-)$ |
| 98a′ | –4.2230 | | | | 94.7 | | | | π*(NCS) |
| 97a′ | –4.2330 | | | | 98.2 | | | | π*(NCS) |
| 96a′ | –4.4409 | | 38.0 | 61.5 | | | | | $p_x/p_y(COO^-)$ |
| 95a′ | –4.4562 | | 38.0 | 61.5 | | | | | $p_x/p_y(COO^-)$ |
| 27a′′ | –4.4771 | | | 98.1 | | | | | $p_z(COO^-)$ |
| 26a′′ | –4.4894 | | | 98.1 | | | | | $p_z(COO^-)$ |
| 94a′ | –4.8562 | 53.1 | | | 26.9 | | | 52.7 $d_{xy}$ | $d_{xy}$(Ru)–π*(NCS) |
| 25a′′ | –5.9095 | 51.0 | | | 34.4 | | | 51.0 $d_{xz}$ | $d_{xz}$(Ru)–π*(NCS) |
| 24a′′ | –5.0747 | 47.8 | 12.1 | | 38.6 | | | 47.3 $d_{yz}$ | $d_{yz}$(Ru)–π*(NCS) |

 © 2007 Wiley-VCH Verlag GmbH & Co. KGaA, Weinheim 

character. The electron density diagrams of the frontier molecular orbitals for the 711 nm emission in Figure 6 provide intuitive evidence for the above assignment. As shown in Table 5 and Figure 6, the electron density mainly focuses around the tcterpy ligands: about 98% in the 32a′′(LUMO+1) orbital. The 24a′′(HOMO-14) and 30a′′(HOMO) orbitals are both composed of $Ru^{II}$ and NCS ligands. The former is composed of 48% Ru($d_{yz}$), 39% NCS ligands, and 12% tcterpy ligand, while the latter comprises 33% Ru($d_{yz}$), 53% NCS ligands, and 12% tcterpy ligands.

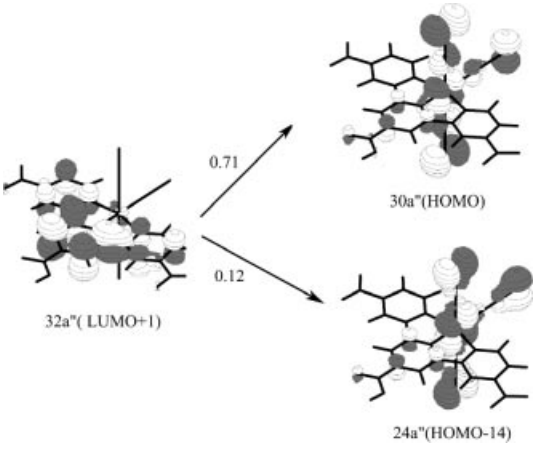


Figure 6. Single-electron transitions with |CI coefficient| > 0.1 calculated by TD-DFT for the 711-nm emission of $[Ru(Htcterpy)(NCS)_3]^{3-}$ (**1H**) in ethanol.

On the basis of the optimized $^3A'$ excited state, the 724- and 691-nm phosphorescence in the gas phase and in water solution are calculated by the TD-DFT method and the TD-DFT/CPCM method, respectively; these bands also have tcterpy→Ru/NCS-charge-transfer ($^3$LMCT/$^3$LLCT) character. The electron density diagrams of the frontier molecular orbitals related to the 724- and 691-nm emissions displayed in Figures S1–S2 can help us intuitively understand the nature of the transitions causing the emissions. The emission spectroscopic data of complex **1H** calculated in ethanol and water solution show a certain solvent dependence. In water, the emission maximum is blue-shifted (20 nm) relative to that in ethanol solution, because the electrostatic interaction between the solvent water and the NCS ligand is stronger than that between the solvent ethanol and the NCS ligand.

## 4. Conclusions

The electronic structure and spectroscopic properties of $[Ru(Htcterpy)(NCS)_3]^{3-}$ (**1H**) are investigated theoretically. We predict absorption and emission spectra in the gas phase and in solution by using the TD-DFT method without and with the solvent-effect CPCM model, respectively. The analysis of electronic structure in ethanol solution shows that the HOMOs are composed of d orbitals of the ruthenium atom and the thiocyanate ligands and the LUMOs are the admixture of π* orbitals localized on the terpyridine ring ligand and the carboxyl groups. The contributions of the thiocyanate and carboxyl group to the HOMOs and LUMOs, respectively, are believed to play an important role in the regeneration and electron-injection performance of dye-sensitized $TiO_2$ solar cells.

The calculated absorption spectra in ethanol solution are in rough agreement with the experimental data. The theoretically simulated spectra based on TD-DFT calculations contain four intense peaks and a shoulder. The calculated absorption peak at 752 nm is not observed in experiment. We assign four lower-energy bands as d(Ru) and NCS-to-tcterpy-charge-transfer (MLCT and LLCT) transitions, different from a previous assignment of pure MLCT transitions.[6] The fifth absorption band with the greatest intensity is attributed to a π→π* transition localized on the tcterpy ligand mixed with some O($p_z$)→tcterpy charge transfer. Furthermore, our calculation overestimates the intensity of band II and underestimates that of band III.

To explore the effect of solvents on the spectra, we also calculated the absorptions of **1H** in the gas phase and in solution. The results quantitatively reproduce the negative solvatochromism (the MLCT/LLCT electronic transition energies of complex **1H** decrease upon increasing solvent polarity). We find that the MLCT/LLCT absorption bands are blue-shifted by about 20 nm in going from ethanol solvent to water solvent. The appearance of negative solvatochromism is closely related to a negative change of dipole moment in the excited state with respect to the ground state, which results in a higher stabilization of the ground state in solvents with increasing polarity.

TD-DFT predicts phosphorescent emissions at 724, 711, and 691 nm in the gas phase, in ethanol, and in water, respectively. We attribute them to tcterpy→Ru/NCS charge transfer ($^3$LMCT/$^3$LLCT) transitions.

**Supporting Information** (see footnote on the first page of this article): Figures S1 and S2 are the diagrams of the single-electron transitions for the emissions in the gas phase and in water solution, respectively. Tables S1 and S2 present the calculated absorptions of **1H** in the gas phase and in water. The calculated dipole moments of the ground and excited states of **1H** in the gas phase, in ethanol, and in water are given in Table S3.

## Acknowledgments

This work is supported by the Natural Science Foundation of China (20173021, 20333050, and 20573042).

[1] B. O'Regan, M. Grätzel, *Nature* **1991**, *353*, 737–740.
[2] A. Hagfeldt, M. Grätzel, *Acc. Chem. Res.* **2000**, *33*, 269–277.
[3] M. Grätzel, *Nature* **2001**, *414*, 338–344.
[4] K. Kalyanasundaram, M. Grätzel, *Coord. Chem. Rev.* **1998**, *177*, 347–414.
[5] M. K. Nazeeruddin, A. Kay, I. Rodicio, R. Humphry-Baker, E. Müeller, P. Liska, N. Vlachopoulos, M. Grätzel, *J. Am. Chem. Soc.* **1993**, *115*, 6382–6390.
[6] M. K. Nazeeruddin, P. Péchy, T. Renouard, S. M. Zakeeruddin, R. Humphry-Baker, P. Comte, P. Liska, L. Cevey, E. Costa, V. Shklover, L. Spiccia, G. B. Deacon, C. A. Bignozzi, M. Grätzel, *J. Am. Chem. Soc.* **2001**, *123*, 1613–1624.

 © 2007 Wiley-VCH Verlag GmbH & Co. KGaA, Weinheim 

[7] S. M. Zakeeruddin, M. K. Nazeeruddin, R. Humphry-Baker, P. Péchy, P. Quagliotto, C. Barolo, G. Visvardi, M. Grätzel, *Langmuir* **2002**, *18*, 952–954.
[8] M. K. Nazeeruddin, F. D. Angelis, S. Fantacci, A. Selloni, G. Viscardi, P. Liska, S. Ito, B. Taleru, M. Grätzel, *J. Am. Chem. Soc.* **2005**, *127*, 16835–16847.
[9] Z.-S. Wang, T. Yamaguchi, H. Sugihara, H. Arakawa, *Langmuir* **2005**, *21*, 4272–4276.
[10] C. Barolo, M. K. Nazeeruddin, S. Fantacci, D. D. Censo, P. Comte, P. Liska, G. Viscard, P. Quagliotto, F. D. Angelis, S. Ito, M. Grätzel, *Inorg. Chem.* **2006**, *45*, 4642–4653.
[11] V. Shklover, M. K. Nazeeruddin, S. M. Zakeeruddin, C. Barbè, A. Kay, T. Haibach, W. Steurer, R. Hermann, H.-U. Nissen, M. Grätzel, *Chem. Mater.* **1997**, *9*, 430–439.
[12] V. Shklover, Yu. E. Ovchinnikov, L. S. Graginsky, S. M. Zakeeruddin, M. Grätzel, *Chem. Mater.* **1998**, *10*, 2533–2541.
[13] M. K. Nazeeruddin, S. M. Zakeeruddin, R. Humpry-Baker, S. I. Gorelsky, A. B. P. Lever, M. Grätzel, *Coord. Chem. Rev.* **2000**, *208*, 213–225.
[14] Md. K. Nazeeruddin, S. M. Zakeeruddin, R. Humpry-Baker, M. Jirousek, P. Liska, N. Vlachopoulos, V. Shklover, C.-H. Fisher, M. Grätzel, *Inorg. Chem.* **1999**, *38*, 6298–6305.
[15] S. M. Zakeeruddin, Md. K. Nazeeruddin, R. Humpry-Baker, M. Grätzel, *Inorg. Chim. Acta* **1999**, *296*, 250–253.
[16] M. K. Nazeeruddin, E. Muller, R. Humphry-Baker, N. Vlachopoulos, M. Grätzel, *J. Chem. Soc., Dalton Trans.* **1997**, *23*, 4571–4578.
[17] S. M. Zakeeruddin, M. K. Nazeeruddin, P. Pechy, F. P. Rotzinger, R. Humphry-Baker, K. Kalyanasundaram, M. Grätzel, V. Shklover, T. Haibach, *Inorg. Chem.* **1997**, *36*, 5937–5946.
[18] S. Ruile, O. Kohle, P. Péchy, M. Grätzel, *Inorg. Chim. Acta* **1997**, *261*, 129–140.
[19] C. Klein, M. K. Nazeeruddin, P. Liska, D. D. Censo, N. Hirata, E. Palomares, J. R. Durrant, M. Grätzel, *Inorg. Chem.* **2005**, *44*, 178–180.
[20] M. K. Nazeeruddin, P. Péchy, M. Grätzel, *Chem. Commun.* **1997**, 1705–1706.
[21] Y. V. Zubavichus, Y. L. Slovokhotov, M. K. Nazeeruddin, S. M. Zakeeruddin, M. Grätzel, V. Shklover, *Chem. Mater.* **2002**, *14*, 3556–3563.
[22] V. Shklover, M. K. Nazeeruddin, M. Grätzel, Y. E. Ovchinnikov, *Appl. Organomet. Chem.* **2002**, *16*, 635–642.
[23] F. Aiga, T. Tada, *J. Mol. Struct.* **2003**, *658*, 25–32.
[24] S. Ghosh, G. K. Chaitanya, K. Bhanuprakash, M. K. Nazeeruddin, M. Grätzel, P. Y. Reddy, *Inorg. Chem.* **2006**, *45*, 7600–7611.
[25] H. Rensmo, S. Södergren, L. Patthey, K. Westmark, L. Vayssieres, O. Khole, P. A. Brühwiler, A. Hagfeldt, H. Siegbahn, *Chem. Phys. Lett.* **1997**, *274*, 51–57.
[26] F. Cecchet, A. M. Gioacchini, M. Marcaccio, F. Paolucci, S. Roffia, M. Alebbi, C. A. Bignozzi, *J. Phys. Chem. B* **2002**, *106*, 3926–3932.
[27] A. Broo, P. Lincoln, *Inorg. Chem.* **1997**, *36*, 2544–2553.
[28] S. I. Gorelsky, E. S. Dodsworth, A. B. P. Lever, A. A. Vlcek, *Coord. Chem. Rev.* **1998**, *174*, 469–494.
[29] J. E. Monat, J. H. Rodriguez, J. K. McCusker, *J. Phys. Chem. A* **2002**, *106*, 7399–7406.
[30] S. Fantacci, F. D. Angelis, A. Selloni, *J. Am. Chem. Soc.* **2003**, *125*, 4381–4387.
[31] A. D. Becke, *J. Chem. Phys.* **1993**, *98*, 5648–5652.
[32] a) J. F. Stanton, J. Gauss, N. Ishikawa, M. Head-Gordon, *J. Chem. Phys.* **1995**, *103*, 4160–4174; b) J. B. Foreman, M. Head-Gordon, A. Pople, *J. Phys. Chem.* **1992**, *96*, 135–149; c) V. A. Waiters, C. M. Hadad, Y. Thiel, S. D. Colson, K. B. Wibergy, P. M. Johnson, J. B. Foresmanl, *J. Am. Chem. Soc.* **1991**, *113*, 4782–4791.
[33] a) H. X. Zhang, C. M. Che, *Chem. Eur. J.* **2001**, *7*, 4887–4893; b) Q. J. Pan, H. X. Zhang, *J. Chem. Phys.* **2003**, *119*, 4346–4352; c) Q. J. Pan, H. X. Zhang, *J. Phys. Chem. A* **2004**, *108*, 3650–3661; d) Q. J. Pan, H. X. Zhang, *Eur. J. Inorg. Chem.* **2003**, 4202–4210; e) Q. J. Pan, H. X. Zhang, *Inorg. Chem.* **2004**, *43*, 593–601.
[34] a) M. E. Casida, C. Jamorski, K. C. Casida, D. R. Salahub, *J. Chem. Phys.* **1998**, *108*, 4439–4449; b) R. E. Stratmann, G. E. Scuseria, *J. Chem. Phys.* **1998**, *109*, 8218–8224; c) N. N. Matsuzawa, A. Ishitani, *J. Phys. Chem. A* **2001**, *105*, 4953–4962.
[35] a) V. Barone, M. Cossi, *J. Phys. Chem. A* **1998**, *102*, 1995–2001; b) M. Cossi, N. Rega, G. Scalmani, V. Barone, *J. Comput. Chem.* **2003**, *24*, 669–681.
[36] a) R. Bauernschmitt, R. Ahlrichs, *Chem. Phys. Lett.* **1996**, *256*, 454–464; b) A. Rosa, E. J. Baerends, S. J. A. V. Gisbergen, E. Lenthe, J. A. Groeneveld, J. G. Snijders, *J. Am. Chem. Soc.* **1999**, *121*, 10356–10365.
[37] a) W. R. Wadt, P. J. Hay, *J. Chem. Phys.* **1985**, *82*, 284–298; b) P. J. Hay, W. R. Wadt, *J. Chem. Phys.* **1985**, *82*, 299–310.
[38] M. J. Frisch, G. W. Trucks, H. B. Schlegel, G. E. Scuseria, M. A. Robb, J. R. Cheeseman, J. A. Montgomery Jr, T. Vreven, K. N. Kudin, J. C. Burant, J. M. Millam, S. S. Iyengar, J. Tomasi, V. Barone, B. Mennucci, M. Cossi, G. Scalmani, N. Rega, G. A. Petersson, H. Nakatsuji, M. Hada, M. Ehara, K. Toyota, R. Fukuda, J. Hasegawa, M. Ishida, T. Nakajima, Y. Honda, O. Kitao, H. Nakai, M. Klene, X. Li, J. E. Knox, H. P. Hratchian, J. B. Cross, C. Adamo, J. Jaramillo, R. Gomperts, R. E. Stratmann, O. Yazyev, A. J. Austin, R. Cammi, C. Pomelli, J. W. Ochterski, P. Y. Ayala, K. Morokuma, G. A. Voth, P. Salvador, J. J. Dannenberg, V. G. Zakrzewski, S. Dapprich, A. D. Daniels, M. C. Strain, O. Farkas, D. K. Malick, A. D. Rabuck, K. Raghavachari, J. B. Foresman, J. V. Ortiz, Q. Cui, A. G. Baboul, S. Clifford, J. Cioslowski, B. B. Stefanov, G. Liu, A. Liashenko, P. Piskorz, I. Komaromi, R. L. Martin, D. J. Fox, T. Keith, M. A. Al-Laham, C. Y. Peng, A. Nanayakkara, M. Challacombe, P. M. W. Gill, B. Johnson, W. Chen, M. W. Wong, C. Gonzalez, J. A. Pople, *Gaussian 03*, Revision B.03, Gaussian, Inc., Pittsburgh, PA, **2003**.
[39] C. Adamo, G. E. Scuseria, V. Barone, *J. Chem. Phys.* **1999**, *111*, 2889–2899.
[40] F. De Angelis, S. Fantacci, A. Selloni, *Chem. Phys. Lett.* **2004**, *389*, 204–208.
[41] F. De Angelis, S. Fantacci, A. Selloni, M. L. Nazeeruddin, *Chem. Phys. Lett.* **2005**, *415*, 115–120.
[42] J. Full, L. Gonzalez, C. Daniel, *J. Phys. Chem. A* **2001**, *105*, 184–189.
[43] D. J. Tozer, R. D. Amos, N. C. Handy, B. O. Roos, L. Serrano-Andres, *Mol. Phys.* **1999**, *97*, 859–868.

Received: November 10, 2006
Published Online: April 10, 2007

 © 2007 Wiley-VCH Verlag GmbH & Co. KGaA, Weinheim 

DOI: 10.1002/ejic.200700128

# Electronic Structures and Spectroscopic Properties of $[Pt(CNMe)_2(CN)_2]_n$ ($n$ = 1–4): A Theoretical Exploration of Promising Phosphorescent Materials

**Xin Zhou,[a] Hong-Xing Zhang,*[a] Qing-Jiang Pan,[b] Ming-Xia Li,[a,b] Yue Wang,[c] and Chi-Ming Che[d]**

**Keywords:** Ab initio calculations / DFT calculations / Luminescence / Excited states / Platinum(II) oligomer

The structures of $[Pt(CNMe)_2(CN)_2]_n$ ($n$ = 1–4) in the ground states ($S_0$) and lowest-energy triplet excited states ($T_1$) were calculated by using the second-order Møller–Plesset perturbation (MP2) and density functional theory (DFT) methods, respectively. The MP2 results show that the formation of the dimer causes a significant red shift in emission energy, and the frequency calculations reveal that a weak metal–metal interaction exists in the $S_0$ state, which is greatly enhanced in the $^3[d_\sigma \cdot p_\sigma]$ excited state. The aggregation of $[Pt(CNMe)_2(CN)_2]_n$ ($n$ = 1–4) was explored by using the slate-type VWN functional in the DFT method. The $^3B_u \rightarrow {}^1A_g$ transition in the dimer at 509 nm corresponds to the experimental higher-energy emission at 530 nm in $CH_3CN$ solution, while the $^3A' \rightarrow {}^1A'$ transitions in the trimer and tetramer at 557 and 650 nm, respectively, are responsible for the low-energy emission at 584 nm observed experimentally. The analyses of the Wiberg bond indices for the Pt–Pt bond indicate that the dimer may be the most stable form in solution and that the oligomer species ($n$ = 3 and 4) can be treated as a special dimer in which the excess z electron ligand is bonded to the Pt atoms of the central dimer.

(© Wiley-VCH Verlag GmbH & Co. KGaA, 69451 Weinheim, Germany, 2007)

## Introduction

In the past three decades, there has been a continuous interest in luminescent platinum(II) complexes. The distinctive molecular and electronic structures that occur in $d^8$ platinum(II) systems give rise to some unusual and potentially useful excited-state properties, in particular, those containing weak $d^8$–$d^8$ interaction in the range of 2.7–3.5 Å.[1] Generally, $Pt^{II}$–$Pt^{II}$ contacts exist not only in the solid state but also in solution. Unusual colors and strong emissions, as well as highly anisotropic properties, are often the result of such stacking interactions. Platinum(II) complexes having a weak Pt–Pt interaction are classified into two types: (a) dimers with bridging ligands connecting two platinum(II) atoms[2] and (b) one-dimensional (1D) linear-chain platinum(II) oligomers with a zigzag Pt–Pt–Pt chain stacked equidistantly.[3]

Platinum(II) dimers have been extensively investigated in the last century. For example, $[Pt_2(pop)_4]^{4-}$ ($pop^{2-}$ = $P_2O_5H_2^{2-}$) with rich photophysical and photochemical properties greatly motivated the study of binuclear $d^8$ complexes.[2a,2b,4–11] The light-induced $^3A_{2u}$ excited state of $[Pt_2(pop)_4]^{4-}$ is highly reactive. It reacts with a wide range of quenchers by mechanisms that involve the platinum complex as an oxidant, reductant, or atom-transfer reagent. Coppens[12a] and Rillema[12b] have investigated $[Pt_2(pop)_4]^{4-}$ by DFT, and the featured absorptions and emissions were attributed to the metal-localized $\sigma^*(d) \rightarrow \sigma(p)$ transition. Another case is the well-studied *trans*-$[Pt_2(CN)_4(PR_2CH_2PR_2)_2]$ (R = Me and cyclohexyl) and *trans*-$[Pt_2(CN)_4(PPh_2CH_2PPh_2)_2]$ complexes.[2c–2f] These platinum(II) dimers exhibit an intense emission both in the solid state and in solution at room temperature in the visible region, which has been assigned to a $\sigma(p) \rightarrow \sigma^*(d)$ (metal-centered, MC) transition. Recently, a great interest in 1D platinum(II) linear structures has developed because they are expected to play a critical role in the fabrication of nanodevices with novel electrical, magnetic, and optical properties. The most-investigated 1D platinum(II) complex with a linear-chain structure is platinum(II) polypyridine.[3] Compounds with polypyridyl ligands show intense luminescence and typically exhibit $\pi^*(L) \rightarrow d_{\sigma^*}$ (Pt) emission from a metal-metal-to-ligand-charge-transfer (MMLCT) excited state. Furthermore, the nature and lifetime of the excited

[a] State Key Laboratory of Theoretical and Computational Chemistry, Institute of Theoretical Chemistry, Jilin University, Changchun 130023, China
Fax: +86-431-8945942
E-mail:zhanghx@jlu.edu.cn
[b] School of Chemistry and Materials Science, Heilongjiang University, Haerbin 150080, China
[c] Key Laboratory for Supramolecular Structure and Materials of the Ministry of Education College of Chemistry, Jilin University Changchun 130012, China
[d] Department of Chemistry and HKU-CAS Joint Laboratory on New Materials, University of Hong Kong, Pokfulam Road, Hong Kong SAR, China

Supporting information for this article is available on the WWW under http://www.eurjic.org or from the author.

 © 2007 Wiley-VCH Verlag GmbH & Co. KGaA, Weinheim 

state of these complexes can be changed greatly through modifying the ligands.

In our previous works, Wang and Che et al. found that $[Pt(CNtBu)_2(CN)_2]$[13] can form 1D luminescent nanowires through weak Pt–Pt interactions, which are rare in the reported self-assembly 1D architectures. As suggested, the metal-localized $5d_{\sigma^*} \rightarrow 6p_{\sigma}$ transition of $[Pt(CNtBu)_2(CN)_2]_2$ can lead to the effective construction of 1D functional nanomaterials and intense green emission; the oligomerization of the monomers does impact on the luminescence behavior and the electronic structures. In fact, similar neutral platinum(II) complexes with the general formulas $[Pt(CNR)_4][Pt(CN)_4]$ and $[Pt(CNR)_2(CN)_2]_2$ (R = alkyl and aryl) have been extensively studied by Mann and coworkers.[14] However, their investigation was limited to their application towards chemical sensors and their vapochromic behavior, and there was little discussion on their luminescence properties and the effect of oligomerization on the luminescence and the electronic structures. Furthermore, to the best of our knowledge, the luminescent properties for oligomerized $[Pt(CNtBu)_2(CN)_2]_n$ have not been theoretically investigated for the platinum(II) complexes.

In this paper, we have examined the ground- and excited-state properties of $[Pt(CNMe)_2(CN)_2]_n$ ($n$ = 1–4) by using ab initio and DFT calculations. We aimed at elucidating three points: (1) the ground- and excited-state geometrical and electronic structures of $[Pt(CNMe)_2(CN)_2]_n$ ($n$ = 1–4), (2) the relationship between the weak $Pt^{II}$–$Pt^{II}$ interaction and the electronic structure as well as the luminescence properties, (3) whether the oligomerization of the platinum(II) chain will strengthen the weak inter- and/or intra-interaction in solution and lower the emission energies. Here we present the study of the electronic structures, geometrical structures, and spectroscopic properties.

## Computational Details

$[Pt(CNMe)_2(CN)_2]$ was used as the computational model to represent the real complex $[Pt(CNtBu)_2(CN)_2]$. This strategy was employed in our previous work to save computational cost, and it proved to be suitable for reproducing the experimental results.[15]

The electronic structures and emission spectra of monomer $[Pt(CNMe)_2(CN)_2]$ (**1**) and dimer $[Pt(CNMe)_2(CN)_2]_2$ (**2**) were carried out with the Gaussian 03 program package (G03).[16] Full optimizations on the ground state ($S_0$) and lowest-energy triplet excited state ($T_1$) were performed at the second-order Møller–Plesset perturbation (MP2) and UMP2 levels of theory, respectively.[17] On the basis of the optimized $T_1$ geometries of the complexes, we employed the time-dependent density functional theory (TDDFT)[18] method at the PBE0 functional level[19] to predict the emission spectra. By considering the differences in the emission spectra in gas and solution, the solvent effect of acetonitrile was taken into account by using the polarizable continuum model (PCM).[20] The above calculations were performed by using the LanL2DZ basis sets with effective core potentials (ECPs) for the Pt atom proposed by Hay and Wadt.[21] To describe the Pt–Pt interaction and the molecular properties precisely, one additional function was implemented for the Pt atom ($\alpha_f$ = 0.14).[22]

One of the objectives of this paper is to discuss whether the formation of oligomers can affect the electronic structure and emission energy of $[Pt(CNMe)_2(CN)_2]_n$. However, to achieve these goals with ab initio calculations will require very long computational resources, because we are dealing with large oligomers containing rather heavy atoms, the modeling of which requires an extremely large number of basis functions. Therefore, in order to pursue these goals, we performed DFT calculations with relativistic effects by using the Amsterdam Density Functional (ADF2005.01) program.[23] As concluded by Pyykkö,[24] the weakly- or non-overlapping systems are not reasonably calculated by the DFT method, because the dispersion interaction of $R^{-6}$ is not explicitly included in the present DFT method. Nevertheless, in some recent papers, it was reported that the experimental results of weak metal–metal bonding can be reproduced by a simple local density functional (such as SVWN or Xα), rather than the gradient corrected density functionals (DFs) [B3LYP, BLYP, BP86, and PBE0].[25] Although the intrinsic reason is not yet clear, the application of the DFT approach to study large oligomers seems to be feasible. Similar $[AuCN_2^-]_n$ oligomers have been studied with Extended Hückel calculations, and the corresponding results were satisfactory.[26]

In the ADF calculations, the geometrical structures of $[Pt(CNMe)_2(CN)_2]_n$ ($n$ = 1–4) in the $S_0$ and $T_1$ states were optimized by spin-restricted and spin-unrestricted Vosko–Wilk–Nusair (VWN) calculations, respectively.[27] The valence atomic orbitals of the platinum, nitrogen, carbon, and hydrogen atoms were described by the TZP basis sets. The cores (1s2s2p3s3p4s4p for Pt and 1s for C, N and O) were kept frozen. Relativistic effects were included by means of the Zero Order Regular Approximation (ZORA).[28] TDDFT (PBE0) calculations were performed on the equilibrium excited-state geometries of $[Pt(CNMe)_2(CN)_2]_n$. The conductor-like screening model (COSMO)[29] was used to simulate the solvent effects, as implemented in the ADF code. In order to describe the asymptotic behavior well, a combination of the local VWN and the Becke–Perdew (BP86)[30] gradient correction term was employed.

## Results and Discussion

### The Monomer and Dimer in the $S_0$ State

In this work, $C_{2v}$ symmetry is assigned to monomer **1**, with the two mutually *cis* CN ligands. For dimer **2**, the initial $C_1$ symmetry is adopted with a torsion angle C1–Pt1–Pt2–C3 of 55°, as indicated in the X-ray results. The torsion angle is subjected to geometry optimization and decreases by ca. 0.2° for the dimer, the framework of which is close to $C_{2h}$ symmetry. Such a big difference in the torsion angle results from the replacement of *tert*-butyl groups used experimentally by methyl groups used in the calculation. As

 © 2007 Wiley-VCH Verlag GmbH & Co. KGaA, Weinheim 

a result, the steric repulsion between the bulky *tert*-butyl groups is eliminated, and the torsion angle is greatly reduced. Therefore, the $C_{2h}$ symmetry for the dimer is adopted throughout this paper. The optimized $S_0$ structures of the platinum(II) monomer and dimer, with the coordination axis, are depicted in Figure 1, and the corresponding important parameters are listed in Table 1. As shown in Table 1, the geometrical parameters for the monomer and dimer are very close and agree well with most of the experimental values for $[Pt(CN)_4^{2-}]$ ions and for double salts such as $[Pt(CNR)_4(CN)_4]$ (R = toluene),[14] which indicates that the eclipsed structures do not have an impact on the geometrical structure of the monomer. The Pt–C1 and C1≡N1 bonds are ca. 0.017 and 0.023 Å longer than the Pt–C2 and C2≡N2 bonds. The small increase in length results from the different electronic structures of the *iso*cyanide and cyanide ligands as discussed in most textbooks. The C1≡N1 and C2≡N2 bonds are slightly long, but fall in the range of C≡N distances generally measured experimentally for these types of complexes. The deviations are thought to arise because the experimental values are measured with rather large uncertainties and because smaller basis sets are applied to the C and N atoms. To test the dependence of the Pt–C and C≡N bond lengths on the basis sets, we optimized **1** at the MP2 level with different basis sets (Table S1). The results suggest that with the increase in the size of the basis sets (BS I–VII), the lengths of the Pt–C and C≡N bonds decrease greatly and are much closer to the experimental values. Because the Pt–Pt bond is obviously shortened, a definite hydrogen bond between the N (CN) and H (Me) atoms is formed and the N1–H1 bond length is 2.468 Å, which falls within the normal range of hydrogen bond lengths. Further, the stacking of $[Pt(CNMe)_2(CN)_2]_2$ may be partially stabilized by hydrogen bonds in the solid state and in solution. In addition, the formation of the hydrogen bond gives rise to a tilted angle of 9.6° for the Pt–Pt vector relative to the *z* axis, which is in accordance with that observed experimentally.

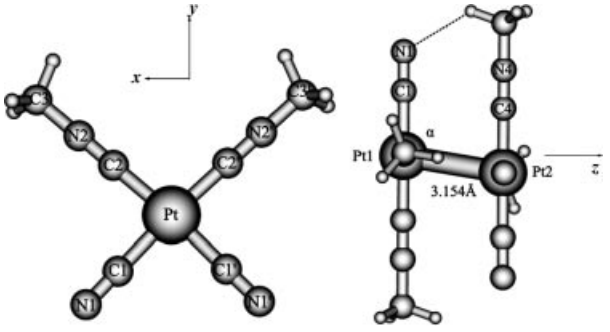


Figure 1. Optimized $S_0$ structures for **1**–**2** determined by MP2 methods.

The most important Pt–Pt bond length was calculated to be 3.154 Å, which falls in the usual range for most platinum(II) dimers (2.7–3.5 Å) and is comparable to those calculated previously for the $[Pt_2(pop)_4]^{4-}$ and $[Pt_2(pop)_4]^{4-}$ ions[15c] and for the neutral molecule $[Pt_2(CN)_4(PH_2CH_2PH_2)_2]$.[31] The slightly shorter Pt–Pt distance than the van der Waals contact of 3.2 Å indicates the presence of a possible weak bonding interaction between the two $Pt^{II}$ centers in **2**. It should also be noted that the calculated Pt–Pt bond length is ca. 0.2 Å shorter than that determined by X-ray diffraction. This is because excess electron correlation effects are included in the MP2 calculation (which considerably shortens the Pt–Pt bond length) and because methyl groups are used in the calculation. To evaluate the interaction strength between the two monomers, the interaction energy is obtained by taking into account the counterpoise (CP) correction; these results are summarized in Table 1. The calculated interaction energy after CP correction is ca. 35 kJ/mol, comparable to that of hydrogen bonds. The interaction energy should result from three contributions. In addition to the contribution from the metallophilic interaction between Pt–Pt and from the hydrogen bond of N1–H1, the attraction between the π-electron clouds of $CN^-$ and *iso*-$CN^-$ also partially contributes to the interaction energy. To further understand the Pt–Pt bonding nature, the frequency calculation was preformed on the dimer (Table 1). Table 1 shows that the stretching vibration of Pt–Pt is 87 $cm^{-1}$ and the force constant is 0.309 mDyne/A. The two values agree well with those in systems in which there are weak $Au^I$–$Au^I$ interactions,[26] and suggest the presence of Pt–Pt bonding. The MO diagram of **2**, represented in Figure 2, is used to elucidate the formation of the Pt–Pt bond. The fully occupied $5d_{z^2}$ atomic orbitals of adjacent platinum centers split to give $d_\sigma$ bonding and $d_{\sigma^*}$ antibonding molecular orbitals, as has been reported in other papers.[32] Similarly, the unoccupied $6p_z$ atomic orbitals split to give $p_\sigma$ and $p_{\sigma^*}$ molecular orbitals. There exist two kinds of

Table 1. Optimized $S_0$ and $T_1$ geometrical parameters for **1**–**2** determined by MP2 calculations.

| | Bond length [Å] | | | | | | Bond angle [°] | | | | Frequency | | $\Delta E$ |
|---|---|---|---|---|---|---|---|---|---|---|---|---|---|
| | Pt–Pt | Pt–C1 | Pt–C2 | C1≡N1 | C2≡N2 | N1–H1 | C1–Pt–C2 | C2–Pt–C2′ | C1–Pt–C2′ | α | $\nu_{Pt-Pt}$ [$cm^{-1}$] | $k$(Pt–Pt) [mDyne/A] | [kJ $mol^{-1}$][a] |
| monomer | | | | | | | | | | | | | |
| $^1A_1$ | – | 2.014 | 1.995 | 1.219 | 1.198 | – | 87.6 | 95.5 | 176.9 | – | – | – | – |
| $^3B_2$ | – | 2.011 | 2.036 | 1.156 | 1.191 | – | 91.3 | 90.0 | 178.7 | – | – | – | – |
| dimer | | | | | | | | | | | | | |
| $^1A_g$ | 3.154 | 2.013 | 1.998 | 1.220 | 1.195 | 2.468 | 89.1 | 98.0 | 178.4 | 105.4 | 87.7 | 0.3090 | 32 |
| (Exp.) | (3.354) | | | | | (2.66) | | | | | | | |
| $^3B_u$ | 2.830 | 2.022 | 2.014 | 1.167 | 1.186 | 2.696 | 91.0 | 89.9 | 173.5 | 101.1 | 115.6 | 0.4522 | 176 |

[a] Interaction energy between two monomers after counterpoise correction.

 © 2007 Wiley-VCH Verlag GmbH & Co. KGaA, Weinheim 

bonding interactions between two platinum(II) atoms: the first interaction is a four-electron repulsion between the $d_{z^2}$ orbitals that prevents the two platinum(II) atoms from approaching one another, and the second interaction is a bonding donor–acceptor interaction between the $d_{z^2}$ and $p_z$ orbitals. The combination of the two interactions can account for the weak Pt–Pt bonding.

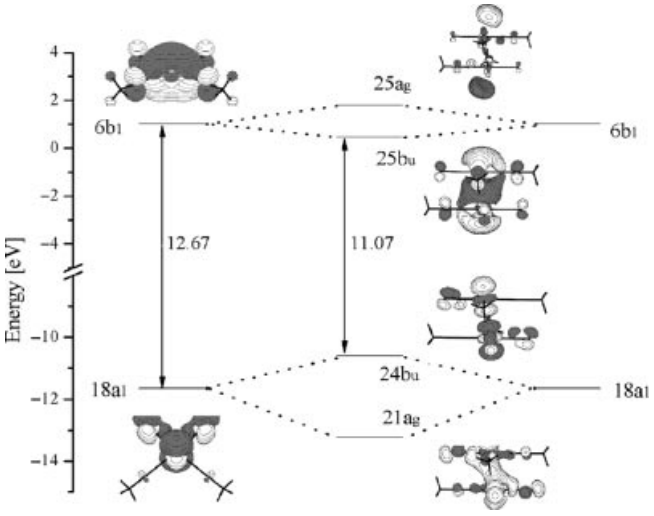


Figure 2. Energy level of **2**.

### Monomer and Dimer in the $T_1$ State and Lowest-Energy Emission Spectra

The structures of **1** and **2** in the $T_1$ states were determined by the UMP2 method. Optimizations on **1** and **2** predict that their $T_1$ states have $^3B_2$ and $^3B_u$ symmetry, respectively. Selected structural parameters are listed in Table 1. The $T_1$ geometries of the monomer and dimer are found to differ from those in the $S_0$ state. Both the Pt–C1 and Pt–C2 bonds are elongated slightly in the $T_1$ state. The formation of Pt–Pt single bond in the $T_1$ state weakens the Pt–C covalent bonds and Pt←C dative bonds, which can account for the elongation of the Pt–C bond. The C1–N1 and C2–N2 bonds are shorter in the $S_0$ state than in the $T_1$ state, in particular, the C1–N1 bond length is reduced by roughly 5.0%. For the dimer, the Pt–Pt distance decreases by ca. 0.324 Å on going from the $S_0$ state to the $T_1$ state, while the N1–H1 distance increases by ca. 0.23 Å. The opposite trend for the Pt–Pt and N1–H1 bond lengths implies that the hydrogen bonding of N1–H1 only plays a secondary role in the stabilization of the dimer. Upon excitation, the coordination geometry of the platinum(II) atom is much closer to the regular square-planar structure, as indicated by the C1–Pt–C2 and C2–Pt–C2′ bond angles of ca. 90°. The tilted angle $\alpha$ for **2** decreases by ca. 4°, which suggests that the complex has a straighter chain in the $T_1$ state. We performed the frequency calculation for the optimized geometry of $T_1$ at the UMP2 level for **2** in order to further characterize the Pt–Pt bonding in the excited state (Table 1). Table 1 shows that Pt–Pt stretching frequency undergoes a moderate increase from ca. 87.7 to 116 $cm^{-1}$, and the force constant increases by ca. 0.15, which is consistent with a single electron that is promoted from the $d_{\sigma^*}$ antibonding to $p_\sigma$ bonding orbital and with the formation of Pt–Pt single bond in the excited state. In addition, the calculated overlap population between the two Pt atoms is 0.0278 and 0.0169 for the $^3B_u$ excited state and $^1A_g$ ground state, respectively. From such calculated frequencies and overlap populations between the two Pt atoms, it can easily be seen that the Pt–Pt interaction in the former is stronger. This suggests that there may be some electron transfer to the 6p bonding orbitals of the Pt atoms. More evidence for the enhancement of the Pt–Pt bonding is the increased interaction energy between the two monomers. UMP2 calculations show that the interaction energy is ca. 176 kJ $mol^{-1}$, which is of the same order of magnitude as that for the covalent bonding energy. All of the above results illustrate the obvious contraction of Pt–Pt bond that results from the formation of single bond between the two platinum(II) atoms. The conclusion is in agreement with other weakly interacting systems involving heavy transition metals such as $Au^I$ and $Pt^{II}$ etc.[12,26,33]

According to the Franck–Condon vertical transition principle, the emission properties of **1** and **2** were calculated on the basis of their corresponding $T_1$ geometries. Complexes **1** and **2** give rise to the lowest-energy phosphorescent emissions at 301 and 512 nm (Table 2), which mainly originate from the excited states with the transitions $^3B_1 \rightarrow {}^1A_1$ and $^3B_u \rightarrow {}^1A_g$, respectively. Table 3 gives the partial MO compositions for the two complexes in the phosphorescence, the results from which can be used to further shed light on the emission nature. With respect to the $^3B_1 \rightarrow {}^1A_1$ transition of **1**, the $19a_1 \rightarrow 6b_1$ configuration has the largest CI coefficient of ca. 0.72. As shown in Table 3, the MO $19a_1$ (HOMO) results largely from the contributions of the Pt $d_{z^2}$ orbital (83.6%), whereas the MO $6b_1$ (LUMO) is localized on the Pt $p_z$ and *iso*-$CN^-$ π* orbital. Therefore, the calculation shows that the $^3B_1$ excited state of **1** can give rise to the $p_z/\pi^*(iso\text{-}CN^-) \rightarrow d_{z^2}$ phosphorescent emission. With regard to the $^3B_u \rightarrow {}^1A_g$ transition of **2**, the configuration of $24b_u \rightarrow 25a_g$ corresponds to the largest CI coefficient of ca. 0.72. Analyses of the wavefunctions of the $^3B_u$ excited state of **2** indicate that the $24b_u$ orbital (HOMO) is a σ* antibonding orbital that results from the Pt $5d_{z^2}$ atomic orbital, and the $25a_g$ orbital (LUMO) has bonding charac-

Table 2. Emissions of **1** and **2** in $CH_3CN$ solution determined by TD-DFT (PBE0) calculations.

| | Transition | Configuration (CI coefficients) | *E* [eV] (λ [nm]) Calcd. | Exp. | Assignment |
|---|---|---|---|---|---|
| monomer | $^3B_1 \rightarrow {}^1A_1$ | $19a_1 \rightarrow 6b_1$(0.72) | 4.12(301) | – | $d_{z^2} \rightarrow p_z$ |
| dimer | $^3B_u \rightarrow {}^1A_g$ | $24b_u \rightarrow 25a_g$(0.72) | 2.42 (512) | 2.29 (542) | $5d_{\sigma^*} \rightarrow 6p_\sigma$ |

 © 2007 Wiley-VCH Verlag GmbH & Co. KGaA, Weinheim 

ter that arises mainly from the Pt $6p_z$ atomic orbital. Thus, we assign the 512 nm phosphorescence as a $\sigma[p_z(Pt_2)]\rightarrow\sigma^*[d_{z^2}(Pt_2)]$ transition from the triplet to the singlet $S_0$ state, which is comparable to the 542 nm phosphorescence observed experimentally.

Table 3. HOMO and LUMO compositions (%) of the phosphorescent emissions for **1** and **2** in $CH_3CN$ solution.

| Orbital | *E* [eV] | Composition [%] Pt s | Pt p | Pt d | CN | *Iso*-CN | $CH_3$ |
|---|---|---|---|---|---|---|---|
| monomer | | | | | | | |
| $6b_1$[a] | –2.0033 | – | $24.1p_z$ | 2.3 | 11.4 | 54.9 | 0.3 |
| $19a_1$[b] | –7.5441 | 11.0 | – | $83.6d_{z^2}$ | 3.5 | 1.9 | – |
| dimer | | | | | | | |
| $25a_g$[a] | –3.2651 | 1.2 | $27.2p_z$ | 4.2 | 14.6 | 46.4 | 0.6 |
| $24b_u$[b] | –5.8108 | 5.4 | $3.0p_z$ | $76.2d_{z^2}$ | 8.4 | 6.0 | 0.4 |

[a] LUMO. [b] HOMO.

### The $[Pt(CNMe)_2(CN)_2]_n$ ($n$ = 1–4) in the $S_0$ and $T_1$ States

In previous experimental work,[13] it was found that the emission of $[Pt(CNtBu)_2(CN)_2]$ at 542 nm can be resolved into two bands at 530 and 584 nm, which suggests that two different emissions originate from $[Pt(CNtBu)_2(CN)_2]_n$ oligomers with different values of $n$ in $CH_3CN$ solution. Similar split bands have also been observed in most platinum(II) dimers that exhibit rich excited states such as $^{1,3}$MLCT, $^{1,3}$ILCT, and $^3\pi$–$\pi$ transition. However, the various excited states are mostly dominated by the different ligands not by the stacking of the oligomers. Thus, our interest is in whether oligomerization might occur in $CH_3CN$ solution and in the consequent change in geometry and luminescence behavior. In fact, the photophysics of $[Pt(CN)_4^{2-}]_n$[34] with $n$ = 1–5 has been experimentally investigated by Schindler and co-workers in detail; different absorption bands were attributed to the $^1[5d_{\sigma^*},6p_\sigma]$ and $^3[5d_{\sigma^*},6p_\sigma]$ excited states for different values of $n$. Nevertheless, to the best of our knowledge, there is no theoretical study on the electronic structure and luminescence for similar platinum(II) compounds that are affected by the degree of oligomerization.

The DF approach was employed to obtain the geometrical and electronic structures for $[Pt(CNMe)_2(CN)_2]_n$ ($n$ = 1–4, **1**–**4**). Because the choice of functional is very important for the reproduction of the weak interaction for multiplatinum(II) complexes, the optimization of dimer $[Pt(CNMe)_2(CN)_2]_2$ was carried out with several different versions of the exchange-correlation DF (BP86, PBE0, BLYP, and VWN) to test which DF is better suited to the $[Pt(CNMe)_2(CN)_2]_n$ species. Table S2 presents the partial geometrical parameters of the $[Pt(CNMe)_2(CN)_2]_2$ species. The results show that, analogous to those found in $Au^I$ clusters,[25] the most important Pt–Pt distance was reproduced well by the VWN DF (3.257 Å) but not by the DF involving the gradient-corrected (GGA) exchange potential (BLYP: 3.631 Å, BP86: 3.505 Å, PBE0: 3.498 Å). Therefore, all the $[Pt(CNMe)_2(CN)_2]_n$ ($n$ = 1–4) species were investigated by using the local VWN DF. The Pt–Pt parameters for **1**–**4** are shown in Table 4, and the complete data are tabulated in Table S3. As depicted in Table 4, the Pt–Pt bond lengths are sensitive to $n$, and all compounds show stronger Pt–Pt bonding in the $T_1$ state than in the $S_0$ state, which is reflected by the shorter Pt–Pt equilibrium distances. The Pt–C bond length of **1** and **2** (Table S3) is in agreement with those obtained by the MP2 calculations, but the C≡N bond length is ca. 0.06 Å shorter than those obtained by the MP2 calculations with small basis sets (BS I) and compares to those from calculations with the largest basis set (BS VII). This result is not surprising because the MP2 method is known to be unreliable in the prediction of triple bond lengths.[31]

Table 4. Optimized $S_0$ and $T_1$ geometrical parameters in **2**–**4** determined by DFT (VWN) calculations.

| | | Pt1–Pt2 [Å] | Pt2–Pt3 [Å] | Pt1–Pt2–Pt3 [°] | $\alpha$ [°] |
|---|---|---|---|---|---|
| dimer | $^1A_g$ | 3.257 | – | – | 104.8 |
| | $^3B_u$ | 2.819 | – | – | 99.6 |
| trimer | $^1A'$ | 3.225 | 3.260 | 130.8 | 107.9 |
| | $^3A'$ | 2.954 | 3.000 | 142.0 | 105.7 |
| tetramer | $^1A'$ | 3.282 | 3.187 | 135.3 | 106.1 |
| | $^3A'$ | 3.091 | 2.936 | 156.9 | 100.5 |

A scheme of the geometric structures of the $[Pt(CNMe)_2(CN)_2]_n$ ($n$ = 2–4) species in the $S_0$ and $T_1$ state is presented in Figure 3 to intuitively understand the geometry change upon oligomerization. Three points can be drawn from Figure 3. (1) The chain of the complexes is straighter in the $T_1$ state than in the $S_0$ state, as reflected by the smaller $\alpha$ angles and larger Pt–Pt–Pt bond angles. (2) In the dimer, a larger reduction (ca. 13%) of the Pt–Pt distance on going from the $S_0$ state to the $T_1$ state is observed, whereas a smaller reduction of 6–8% occurs in the trimer and tetramer. This larger contraction in the dimer implies that the dimer in the triplet excited state may be the most stable species in $[Pt(CNMe)_2(CN)_2]_n$. This conclusion is in agreement with that by Rillima et al.[33] for the platinum(II) diphenyl dicarbonyl complex. (3) With respect to the trimer in both the $S_0$ and $T_1$ state, the distance between one pair of adjacent monomers is smaller than that between the other pair. The case is different for the tetramer; the distance between the central two monomers (Pt2–Pt3) is much smaller than that between the other adjacent pairs (Pt1–Pt2 and Pt3–Pt4). In fact, there are two different interactions in the trimer and tetramer, e.g. intramolecular and intermolecular interactions. In **2**–**4**, the Pt1–Pt2 interactions of **2** and **3** and the Pt2–Pt3 interactions of **4** are intramolecular contacts (d1), while the Pt2–Pt3 interactions of **3** and the Pt1–Pt2 and Pt3–Pt4 interactions of **4** are of the intermolecular type (d2). We can see that the d1 distances are moderately shorter than the d2 distances, and d1 gradually decreases on going from the trimer to tetramer. With reference to previous remarks by Novoa et al.,[35] in platinum(II) dimers, four electrons in one Pt–Pt bond contribute to the excess electrons in the $z$ direction. If the trimer or tetramer can be treated as a special dimer in which a monomer is bonded

 © 2007 Wiley-VCH Verlag GmbH & Co. KGaA, Weinheim 

to the axial positions, the attacked $Pt^{II}$ unit could act as a base and could contribute two $d_{z^2}$ electrons to bind in the axial direction in a face-to-face fashion. Therefore, the forming of two or three bonds with a total of six or eight $d_{z^2}$ electrons will result in a greater excess of *z* electron density and enhance the interactions of the stacked complexes. Preliminary extended Hückel calculations[36] on the corresponding $d^8$–$d^8$ dimers suggested that binding of Lewis acid and/or base to metal atoms at the axial positions has an increasing effect on the M–M bond strength. Our results are in agreement with these conclusions, and excess electrons in the axial direction can account for the variation in the Pt–Pt distance.

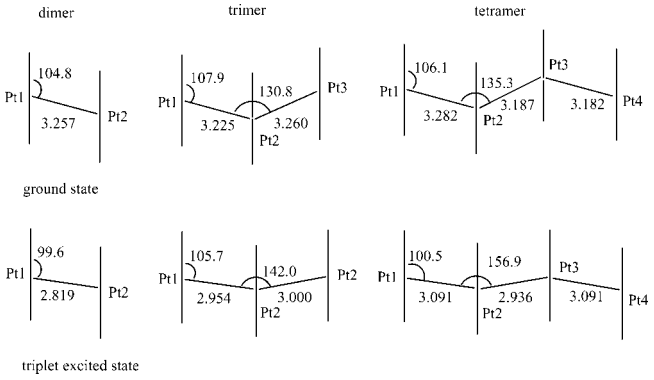


Figure 3. Schematic representation of the $S_0$ and $T_1$ structures for **2**–**4**.

The above description is based on only a qualitative analysis, quantitative proof must be obtained with the bond order indices. Bond order is a measure of the number of bonding electron pairs between atoms. Here, we use bond order to qualitatively compare the relative strength of the Pt–Pt bond in **2**–**4**. As suggested previously in the literature,[12a,12b] the Pt–Pt bonding of such complexes is mainly determined by the electrons in the $\sigma[d_{z^2}(Pt_2)]$ and $\sigma^*[d_{z^2}(Pt_2)]$ orbitals. We investigated the Pt–Pt bonding for **2**–**4** by using the Wiberg bond indices (WBIs)[37] in the Natural Bond Orbital (NBO 5.0) program;[38] the details of the WBIs are presented in Table 5. As seen from Table 5, the Pt–Pt WBIs in **2**–**4** are 0.0141 (**2**), 0.0157 and 0.0149 (**3**), and 0.0139, 0.0199, and 0.0139 (**4**), respectively, and they are one magnitude order less than that of an ordinary single bond (for example: Pt1–C3 WBI in **2** is 0.5445), which implies that the Pt–Pt bond is weak. There is a correlation between Pt–Pt WBIs and Pt–Pt bond lengths – the shorter the bond length, the higher the WBI. Therefore, the largest WBI (Pt2–Pt3, 0.0199 in **4**) results in the shortest Pt–Pt contact in **2**–**4**. From another point of view, the proportion of $\sigma[d_{z^2}(Pt_2)]$ orbitals relative to $\sigma^*[d_{z^2}(Pt_2)]$ orbitals in Pt2–Pt3 of **4** is the largest.

We have analyzed the effect of aggregation on the Pt–Pt distances, we will now further discuss the effect on the HOMO–LUMO gap for the $[Pt(CNMe)_2(CN)_2]_n$ ($n$ = 1–4) species. Figure 4 shows the trend in the HOMO–LUMO gap as the value of $n$ increases. A progressive reduction in the HOMO–LUMO gap is observed upon aggregation. The

Table 5. Wiberg bond orders of **2**–**4** calculated by the program NBO 5.0.

| | | Pt1–Pt2 | Pt2–Pt3 | Pt3–Pt4 |
|---|---|---|---|---|
| **2** | Bond length [Å] | 3.257 | – | – |
| | WBI | 0.0141 | – | – |
| **3** | Bond length [Å] | 3.225 | 3.260 | – |
| | WBI | 0.0157 | 0.0149 | – |
| **4** | Bond length [Å] | 3.282 | 3.187 | 3.182 |
| | WBI | 0.0139 | 0.0199 | 0.0139 |

HOMOs for **2**–**4** are all of the $d_{\sigma^*}(d_{z^2}$–$d_{z^2})$ type, while the LUMOs are mainly localized on the mixed $p_\sigma(p_z$–$p_z)$ and *iso*-$CN^-$ π orbital. The reduction in the HOMO–LUMO gap due to 1D aggregation is a result of concomitant destabilization of the HOMOs and stabilization of the LUMOs. It is noticeable that the decrease in the energy of the LUMOs is more gentle than the increase in energy of the HOMOs, which implies that aggregation has a greater impact on $d_{\sigma^*}(d_{z^2}$–$d_{z^2})$ than on $p_\sigma(p_z$–$p_z)$. This observation is in agreement with the results predicted by other calculations. We do not consider 2D aggregation similar to that observed in $[Au(CN)^-]_n$, because 2D aggregation is prohibited from the square-planar geometry of the $Pt^{II}$ atom.

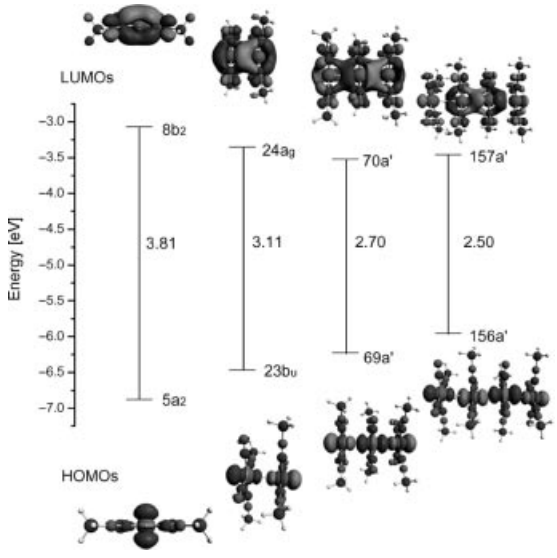


Figure 4. The HOMO and LUMO energy levels for **1**–**4** in the $S_0$ state.

On the basis of the optimized $T_1$ geometry for the $[Pt(CNMe)_2(CN)_2]_n$ ($n$ = 1–4) species, the emission spectra were determined by the TD-DFT method embedded in the ADF2005.01 package (see Table 6). As shown in Figure 4, the emissions are all attributed to the excitation of HOMO→LUMO, and the emission energies decrease in the order **1** > **2** > **3** > **4**, in accordance with the sequence of the HOMO–LUMO gap. The emission energies of **1** and **2** calculated by VWN DF are close to those calculated by the MP2 method, which shows the relative reliability of the DFT approach. With respect to the four lowest-energy excite states, $^3B_2$, $^3B_u$, $^3A'$, and $^3A'$, the excitation configura-

 © 2007 Wiley-VCH Verlag GmbH & Co. KGaA, Weinheim 

tion of HOMO→LUMO contributes the largest weight of ca. 0.99 and should be responsible for the character of the emissions. According to above description, the emissions of **1** and **2** are identical to those predicted by the MP2 method and arise from the $d_{z^2}$→$p_z$/*iso*-$CN^-$ transitions (MC and MLCT) for **1** and $d_{\sigma^*}$→$p_\sigma$/*iso*-$CN^-$ transitions (MC and MLCT) for **2**. It should be noted that the emission energies for **3** and **4** are red-shifted by ca. 0.21 and 0.53 eV relative to **2**, respectively. Although the Pt–Pt intramolecular distances for **3** and **4** are shorter than that for **2**, the contraction of intramolecular contacts alone cannot account for the distinctive red-shift. For example, our previous work showed that the Pt–Pt distance in $[Pt_2(pop)_4]^{4-}$ is ca. 0.08 Å shorter than that in $[Pt_2(pcp)_4]^{4-}$ (pop = $P_2O_5H_2^{2-}$ and pcp = $P_2O_4CH_4^{2-}$), but the difference in their emission energies is only 0.07 eV. Thus, we conceive that the intermolecular $5d_{z^2}$–$5d_{z^2}$ interactions also play an important role in the red-shift of the emission energy. The 557 and 650 nm emissions for **3** and **4** are attributed to the combination of intermolecular and intramolecular $d_{\sigma^*}$→$p_\sigma$/*iso*-$CN^-$ transitions (intra/inter MC and MLCT). This can be intuitively understood from the electron density diagram (Figure 4). This assignment also indicates that the 584 nm emission observed experimentally may arise from the combined contribution of the trimer and tetramer oligomers.

Table 6. Emissions of **1**–**4** in $CH_3CN$ solution determined by TD-DFT (VWN/BP86) calculations.

| | Excited state | Configuration (contribution weight) | *E* [eV] ($\lambda$ [nm]) Calcd. | Exp. |
|---|---|---|---|---|
| monomer | $^3B_2$ | $16a_2$→$8b_2$ (0.99) | 3.81 (326) | – |
| dimer | $^3B_u$ | $23b_u$→$24a_g$(0.99) | 2.44 (509) | 2.34 (530)[a] |
| trimer | $^3A'$ | 69a′→70a′(0.99) | 2.23 (557) | 2.13 (584)[a] |
| tetramer | $^3A'$ | 156a′→157a′(0.99) | 1.91 (650) | 2.13 (584)[a] |

[a] Ref.[13]

## Conclusions

We explored the electronic properties of the $S_0$ and $T_1$ states of $[Pt(CNMe)_2(CN)_2]_n$ ($n$ = 1–2) complexes at the MP2 and UMP2 levels. The geometrical parameters of the monomer and dimer are in agreement with that observed experimentally. In the $S_0$ state, the calculated Pt–Pt distance of the dimer is 3.154 Å. The shorter Pt–Pt distance than the van der Waals distance of 3.2 Å indicates the presence of a weak interaction between the two platinum(II) atoms, and the frequency calculations further prove that there is a weak bonding interaction. In the $T_1$ state, the Pt–Pt distance undergoes a significant reduction, which results from the promotion of an electron from the σ*[$Pt(d_{z^2})$] to σ[$Pt(p_z)$] orbital. As a consequence, a red-shift in the emission energy is observed from monomer to dimer, and the luminescence arises from the $^3[d_{\sigma^*}p_\sigma]$ excited state.

The slate type VWN functional in the DF method was used to predict the impact of oligomerization on $[Pt(CNMe)_2(CN)_2]_n$ ($n$ = 1–4). In the calculation, the dimer is proposed to be the most stable form in the solid state and in solution. The trimer and tetramer can be treated as a special dimer in which the donor ligand is bonded to the central Pt atoms of the dimer. The excess $z$ electrons increase the electron density localized on the Pt–Pt bond and hence enhance the strength of the Pt–Pt bonding. The Pt–Pt distance in the tetramer (3.187 Å) is the shortest, which is consistent with the highest WBI in the investigated Pt–Pt bond.

The experimentally observed lower- and higher-energy emission bands result from the different oligomers in solution. The emission at 530 nm mainly originates from the dimer, while the lower-energy emission at 584 nm derives from the associated contribution of the trimer and tetramer. It should be noted that, aside from intramolecular Pt–Pt interactions, intermolecular Pt–Pt contacts also plays an important role in the red-shift of the emission energy.

## Acknowledgments

This work is supported by the Natural Science Foundation of China (20173021, 20333050, 20573042), Natural Science Foundation of Heilongjiang Province of China (No. B200601), and Science Foundation for Excellent Youth of Heilongjiang University of China (No. JC2006L2).

[1] a) H. Yersin, *J. Chem. Phys.* **1978**, *68*, 4707–4713; b) W. A. Fordyce, J. G. Brummer, G. A. Crosby, *J. Am. Chem. Soc.* **1981**, *103*, 7061–7064; c) C. Bellitto, A. Flamini, O. Piovesana, P. F. Zanazzi, *Inorg. Chem.* **1980**, *19*, 3632–3636; d) P. Stein, M. K. Dickson, D. M. Roundhill, *J. Am. Chem. Soc.* **1983**, *105*, 3489–3494; e) V. M. Miskowski, V. H. Houlding, *Inorg. Chem.* **1991**, *30*, 4446–4452.

[2] a) A. P. Zipp, *Coord. Chem. Rev.* **1988**, *84*, 47–83; b) D. M. Roundhill, H. B. Gray, C. M. Che, *Acc. Chem. Res.* **1989**, *22*, 55–61; c) B.-H. Xia, C.-M. Che, D. L. Phillips, K.-H. Leung, *Inorg. Chem.* **2002**, *41*, 3866–3875; d) C.-M. Che, V.-W.-W. Yam, W.-T. Wong, T.-F. Lai, *Inorg. Chem.* **1989**, *28*, 2908–2910; e) B.-H. Xia, C.-M. Che, Z.-Y. Zhou, *Chem. Eur. J.* **2003**, *9*, 3055–3064; f) H.-K. Yip, T.-F. Lai, C.-M. Che, *J. Chem. Soc., Dalton Trans.* **1991**, 1639–1641.

[3] a) R. Büchner, C. T. Cunningham, J. S. Field, R. J. Haines, D. R. McMillin, G. Summerton, *J. Chem. Soc., Dalton Trans.* **1999**, 711–718; b) W. B. Connick, R. E. Marsh, W. P. Schaefer, H. B. Gray, *Inorg. Chem.* **1997**, *36*, 913–922; c) E. M. Ratilla, B. K. Scott, M. S. Moxness, N. M. Kostic, *Inorg. Chem.* **1990**, *29*, 918–926; d) Y. Chen, J. W. Merkert, Z. Murtaza, C. Woods, D. P. Rillema, *Inorg. Chim. Acta* **1995**, *240*, 41–47.

[4] W. A. Fordyce, J. G. Brummer, G. A. Grosby, *J. Am. Chem. Soc.* **1981**, *103*, 7061–7064.

[5] a) C.-M. Che, L. G. Butler, H. B. Gray, *J. Am. Chem. Soc.* **1981**, *103*, 7796–7797; b) S. F. Rice, H. B. Gray, *J. Am. Chem. Soc.* **1983**, *105*, 4571–4575.

[6] a) W. B. Heuer, M. D. Totten, G. S. Rodman, E. J. Hebert, H. J. Tracy, J. K. Nagle, *J. Am. Chem. Soc.* **1984**, *106*, 1163–1164; b) J. R. Peterson, K. Kalyanasundaram, *J. Phys. Chem.* **1985**, *89*, 2486–2492; c) M. S. Herman, J. L. Goodman, *Inorg. Chem.* **1991**, *30*, 1147–1149.

[7] a) D. M. Roundhill, *J. Am. Chem. Soc.* **1985**, *107*, 4354–4356; b) D. M. Roundhill, S. J. Atherton, *Inorg. Chem.* **1986**, *25*, 4071–4072; c) D. M. Roundhill, Z. P. Shen, S. J. Atherton, *Inorg. Chem.* **1987**, *26*, 3833–3835.

[8] a) A. Vlcek Jr, H. B. Gray, *Inorg. Chem.* **1987**, *26*, 1997–2001; b) E. L. Harvey, A. E. Stiegman, A. Vlcek Jr, H. B. Gray, *J. Am. Chem. Soc.* **1987**, *109*, 5233–5235; c) C.-M. Che, W.-M.

 © 2007 Wiley-VCH Verlag GmbH & Co. KGaA, Weinheim 

Lee, K.-C. Cho, P. D. Harvey, H. B. Gray, *J. Phys. Chem.* **1989**, *93*, 3095–3099; d) R. J. Sweeney, E. L. Harvey, H. B. Gray, *Coord. Chem. Rev.* **1990**, *105*, 23–24.

[9] a) W. A. Kalsbeck, N. Grover, H. H. Thorp, *Angew. Chem. Int. Ed. Engl.* **1991**, *30*, 1517–1518; b) W. A. Kalsbeck, D. M. Gingell, J. E. Malinsky, H. H. Thorp, *Inorg. Chem.* **1994**, *33*, 3313–3316; c) S. A. Ciftan, H. H. Thorp, *J. Am. Chem. Soc.* **1998**, *120*, 9995–10000.

[10] M. K. Dickson, S. K. Pettee, D. M. Roundhill, *Anal. Chem.* **1981**, *53*, 2159–2160.

[11] D. M. Roundhill, *Sol. Energy* **1986**, *36*, 297–299.

[12] a) I. V. Novozhilova, A. V. Volkov, P. Coppens, *J. Am. Chem. Soc.* **2003**, *125*, 1079–1087; b) S. R. Stoyanov, J. M. Villegas, D. P. Rillema, *J. Phys. Chem. B* **2004**, *108*, 12175–12180.

[13] Y.-H. Sun, K.-Q. Ye, H.-Y. Zhang, J.-H. Zhang, L. Zhao, B. Li, G. D. Yang, B. Yang, Y. Wang, S.-W. Lai, C.-M. Che, *Angew. Chem. Int. Ed.* **2006**, *45*, 5610–5613.

[14] a) C. E. Buss, C. E. Anderson, M. K. Pomije, C. M. Lutz, D. Britton, K. R. Mann, *J. Am. Chem. Soc.* **1998**, *120*, 7783–7790; b) C. E. Buss, K. R. Mann, *J. Am. Chem. Soc.* **2002**, *124*, 1031–1039; c) C. L. Exstrom, J. R. Sowa Jr, C. A. Daws, D. Janzen, K. R. Mann, *Chem. Mater.* **1995**, *7*, 15–17; d) C. A. Daws, C. L. Exstrom, J. R. Sowa Jr, K. R. Mann, *Chem. Mater.* **1997**, *9*, 363–368; e) C. L. Exstrom, M. K. Pomije, K. R. Mann, *Chem. Mater.* **1998**, *10*, 942–945.

[15] a) H.-X. Zhang, C.-M. Che, *Chem. Eur. J.* **2001**, *7*, 4887–4893; b) Q.-J. Pan, H.-X. Zhang, *Organometallics* **2004**, *23*, 5198–5209; c) Q.-J. Pan, H.-G. Fu, H.-T. Yu, H.-X. Zhang, *Inorg. Chem.* **2006**, *45*, 8729–8735.

[16] M. J. Frisch, G. W. Trucks, H. B. Schlegel, G. E. Scuseria, M. A. Robb, J. R. Cheeseman, J. A. Montgomery Jr, T. Vreven, K. N. Kudin, J. C. Burant, J. M. Millam, S. S. Iyengar, J. Tomasi, V. Barone, B. Mennucci, M. Cossi, G. Scalmani, N. Rega, G. A. Petersson, H. Nakatsuji, M. Hada, M. Ehara, K. Toyota, R. Fukuda, J. Hasegawa, M. Ishida, T. Nakajima, Y. Honda, O. Kitao, H. Nakai, M. Klene, X. Li, J. E. Knox, H. P. Hratchian, J. B. Cross, C. Adamo, J. Jaramillo, R. Gomperts, R. E. Stratmann, O. Yazyev, A. J. Austin, R. Cammi, C. Pomelli, J. W. Ochterski, P. Y. Ayala, K. Morokuma, G. A. Voth, P. Salvador, J. J. Dannenberg, V. G. Zakrzewski, S. Dapprich, A. D. Daniels, M. C. Strain, O. Farkas, D. K. Malick, A. D. Rabuck, K. Raghavachari, J. B. Foresman, J. V. Ortiz, Q. Cui, A. G. Baboul, S. Clifford, J. Cioslowski, B. B. Stefanov, G. Liu, A. Liashenko, P. Piskorz, I. Komaromi, R. L. Martin, D. J. Fox, T. Keith, M. A. Al-Laham, C. Y. Peng, A. Nanayakkara, M. Challacombe, P. M. W. Gill, B. Johnson, W. Chen, M. W. Wong, C. Gonzalez, and J. A. Pople, *Gaussian 03, Revision B.03*, Gaussian, Inc. Pittsburgh PA, **2003**.

[17] C. Møller, M. S. Plesset, *Phys. Rev.* **1934**, *46*, 618–622.

[18] a) M. E. Casida, C. Jamorski, K. C. Casida, D. R. Salahub, *J. Chem. Phys.* **1998**, *108*, 4439–4449; b) C. Jamorski, M. E. Casida, D. R. Salahub, *J. Chem. Phys.* **1996**, *104*, 5134–5147; c) R. E. Statmann, G. E. Scuseria, *J. Chem. Phys.* **1998**, *109*, 8218–8224; d) R. Bauernschmitt, R. Ahlrichs, *Chem. Phys. Lett.* **1996**, *256*, 454–464; e) N. Matsuzawa, N. A. Ishitani, D. Dixon, A. T. Uda, *J. Phys. Chem. A* **2001**, *105*, 4953–4962.

[19] J. P. Perdew, K. Burke, M. Ernzerhof, *Phys. Rev. Lett.* **1996**, *77*, 3865–3868.

[20] a) S. Miertuš, E. Scrocco, J. Tomasi, *Chem. Phys.* **1981**, *55*, 117; b) E. Cancès, B. Mennucci, J. Tomasi, *J. Chem. Phys.* **1997**, *107*, 3032–3041; c) V. Barone, M. Cossi, J. Tomasi, *J. Comput. Chem.* **1998**, *19*, 404–417.

[21] a) W. R. Wadt, P. J. Hay, *J. Chem. Phys.* **1985**, *82*, 284–298; b) P. J. Hay, W. R. Wadt, *J. Chem. Phys.* **1985**, *82*, 299–310.

[22] P. Pyykkö, F. Mendizabal, *Inorg. Chem.* **1998**, *37*, 3018–3025.

[23] a) G. Te Velde, F. M. Bickelhaupt, S. J. A. van Gisbergen, C. Fonseca Guerra, E. J. Baerends, J. G. Snijders, T. Ziegler, *J. Comput. Chem.* **2001**, *22*, 931–967; b) C. Fonseca Guerra, J. G. Snijders, G. Te Velde, E. J. Baerends, *Theor. Chem. Acc.* **1998**, *99*, 391–403; c) *Vrije ADF 2005.01*, SCM, Amsterdam, **2005**.

[24] a) P. Pyykkö, N. Runerberg, *Chem. Phys. Lett.* **1994**, *218*, 133; b) P. Pyykkö, Y. F. Zhao, *Angew. Chem. Int. Ed. Engl.* **1991**, *30*, 604–605; c) P. Pyykkö, N. Runerberg, F. Mendizabal, *Chem. Eur. J.* **1997**, *3*, 1451–1456.

[25] S.-G. Wang, W. H. Eugen Schwarz, *J. Am. Chem. Soc.* **2004**, *126*, 1266–1276.

[26] a) M. A. Rawashdeh-Omary, M. A. Omary, H. H. Patterson, *J. Am. Chem. Soc.* **2000**, *122*, 10371–10380; b) M. A. Rawashdeh-Omary, M. A. Omary, H. H. Patterson, J. P. Fackler Jr, *J. Am. Chem. Soc.* **2001**, *123*, 11237–11247.

[27] S. H. Vosko, L. Wilk, M. Nusair, *Can. J. Phys.* **1980**, *58*, 1200–1210.

[28] a) T. Ziegler, J. G. Snijders, E. J. Baerends, *J. Chem. Phys.* **1981**, *74*, 1271–1281; b) E. van Lenthe, E. J. Baerends, J. G. Snijders, *J. Chem. Phys.* **1994**, *101*, 9783–9792; c) E. van Lenthe, E. J. Baerends, J. G. Snijders, *J. Chem. Phys.* **1993**, *99*, 4597–4610; d) E. van Lenthe, R. van Leeuwen, E. J. Baerends, J. G. Snijders, *Int. J. Quantum Chem.* **1996**, *57*, 281–293; e) E. van Lenthe, A. E. Ehlers, E. J. Baerends, *J. Chem. Phys.* **1999**, *110*, 8943–8953.

[29] F. Eckert, A. Klamt, *AIChE J.* **2002**, *48*, 369–385.

[30] a) A. D. Becke, *Phys. Rev. A* **1988**, *38*, 3098–3100; b) J. P. Perdew, *Phys. Rev. B* **1986**, *33*, 8822–8824.

[31] Q.-J. Pan, H.-X. Zhang, X. Zhou, H.-G. Fu, H.-T. Yu, *J. Phys. Chem. A* **2007**, *111*, 287–294.

[32] W. B. Connick, R. E. Marsh, W. P. Schaefer, H. B. Gray, *Inorg. Chem.* **1997**, *36*, 913–922.

[33] S. R. Stoyanov, J. M. Villegas, D. P. Rillema, *Inorg. Chem.* **2003**, *42*, 7852–7860.

[34] J. W. Schindler, R. C. Fukuda, A. W. Adamson, *J. Am. Chem. Soc.* **1982**, *104*, 3596–3600.

[35] J. J. Novoa, G. A. Pere Alemany, S. Alvarez, *J. Am. Chem. Soc.* **1995**, *117*, 7169–7171.

[36] K. R. Mann, J. G. Gordon, H. B. Gray, *J. Am. Chem. Soc.* **1975**, *97*, 3553–3555.

[37] C. M. Breneman, K. B. Wiberg, *J. Comput. Chem.* **1990**, *11*, 361–373.

[38] E. D. Glendening, . J. K. Badenhoop, A. E. Reed, J. E. Carpenter, J. A. Bohmann, C. M. Morales, F. Weinhold, *NBO 5.0*, Theoretical Chemistry Institute, University of Wisconsin, Madison, WI, **2001**.

Received: January 8, 2007
Published Online: April 10, 2007

 © 2007 Wiley-VCH Verlag GmbH & Co. KGaA, Weinheim 

DOI: 10.1002/ejic.200601114

# Syntheses, Structures and Optical Nonlinearities of Heteroselenometallic W–Se–Cu Cluster Compounds Containing Bridging Phosphane Ligands

**Zhan Yu,[a] Qian-Feng Zhang,*[a] Yinglin Song,[b] Wai-Yeung Wong,[c] Alexander Rothenberger,[d] and Wa-Hung Leung[e]**

*Dedicated to Professor Dieter Fenske on the occasion of his 65th birthday*

**Keywords:** Heterometallic complexes / Copper / Selenium / Nonlinear optical properties / Cluster compounds

Treatment of $[Et_4N]_2[WSe_4]$ with the trinuclear trigonal-bipyramidal copper(I) complexes $[Cu_3(\mu_3\text{-}X)_2(\mu\text{-}L)_3]X$ [X = I, L = bis(diphenylphosphanyl)methane (dppm) (**1a**); X = Cl, L = bis(diphenylphosphanyl)amine (dppa) (**1b**)] affords the tetranuclear cluster compounds $[(\mu_3\text{-}WSe_4)Cu_3(\mu\text{-}X)(\mu\text{-}L)_2]$ [X = I, L = dppm (**2a**); X = Cl, L = dppa (**2b**)], which exhibit an open butterfly configuration. Interaction of $[Et_4N]_2[WSe_4]$ with $[Cu(MeCN)_4][PF_6]$ and L gives the pentanuclear cluster compounds $[(\mu_4\text{-}WSe_4)Cu_4(\mu\text{-}L)_4][PF_6]_2$ [L = dppm (**3a**), dppa (**3b**)] which contain an open co-planar $WCu_4$ core. The solid-state structures of cluster compounds **2a**, **2b**, and **3a** have been established by X-ray crystallography. The nonlinear optical properties of **2a** and **3a** have been examined by z-scan techniques with 7-ns pulses at 532 nm. The pentanuclear co-planar cluster **3a** exhibits a large optical limiting effect (the limiting threshold is about 0.40 J cm$^{-2}$).
(© Wiley-VCH Verlag GmbH & Co. KGaA, 69451 Weinheim, Germany, 2007)

## Introduction

The coordination chemistry of $[MS_4]^{2-}$ anions (M = Mo, W) with transition metal ions has been well developed owing to their relevance to biological systems,[1–3] special optical properties,[4–6] and rich structural variations.[7] However, analogous heterometallic complexes with $[MSe_4]^{2-}$ anions have not been well explored. Heterometallic selenium complexes are of significance, in part, due to their interesting nonlinear optical and electronic properties.[8–10] Studies of the interaction of $[MSe_4]^{2-}$ with the coinage-metal cations, namely $Cu^+$, $Ag^+$, and $Au^+$, have resulted in the isolation of a series of heterometallic selenium clusters with various structural types, including linear, cubane, incomplete cubane, co-planar T-frame and open cross-frame, crown, cage, and pin-wheel shapes, and polymeric frameworks.[11–19] We have a long-standing interest in heterometallic selenium cluster compounds based on the $[MSe_4]^{2-}$ anions.[20] It is noteworthy that the structure of coinage-metal/$[MSe_4]^{2-}$ clusters is closely related to the number of coinage metal ions coordinated to the six $MSe_2$ edges of the tetrahedral $[MSe_4]^{2-}$ moiety, which depends upon the reaction conditions, especially the M′/$[MSe_4]^{2-}$ (M′ = coinage metal) ratio, and the peripheral ligands.[21] In this context, we report here the synthesis of two types of heterometallic selenium W–Se–Cu cluster compounds, namely tetranuclear butterfly-like $[(\mu_3\text{-}WSe_4)Cu_3(\mu\text{-}I)(\mu\text{-}L)_2]$ [L = dppm (**2a**), dppa (**2b**)] and pentanuclear open co-planar $[(\mu_4\text{-}WSe_4)Cu_4(\mu\text{-}L)_4][PF_6]_2$ [L = dppm (**3a**), dppa (**3b**)], from reactions of tetraselenotungstate anion with copper species in the presence of the bridging phosphane ligands bis(diphenylphosphanyl)methane (dppm) and bis(diphenylphosphanyl)amine (dppa). The nonlinear optical data of the newly prepared heterometallic selenium clusters have been investigated to provide some evidence regarding the structure/property relationships of this class of cluster compounds.

[a] Department of Applied Chemistry, Anhui University of Technology,
Ma'anshan, Anhui 243002, P. R. China
E-mail: zhangqf@ahut.edu.cn
[b] Department of Physics, Harbin Institute of Technology, Harbin 150001, P. R. China
[c] Department of Chemistry, Hong Kong Baptist University, Waterloo Road, Kowloon Tang, Hong Kong, P. R. China
[d] Institut für Anorganische Chemie, Universität Karlsruhe (TH), 76128 Karlsruhe, Germany
[e] Department of Chemistry, The Hong Kong University of Science and Technology,
Clear Water Bay, Kowloon, Hong Kong, P. R. China

## Results and Discussion

### Syntheses and Spectral Characterizations

It has been reported previously that reactions of copper halides with dppm give a series of trinuclear trigonal-bipyramidal complexes $[Cu_3(\mu_3\text{-}X)_2(\mu\text{-dppm})_3]X$ (X = Cl,[22] Br,[23] I[24]). Similarly, treatment of [CuCl] powder with

 © 2007 Wiley-VCH Verlag GmbH & Co. KGaA, Weinheim 

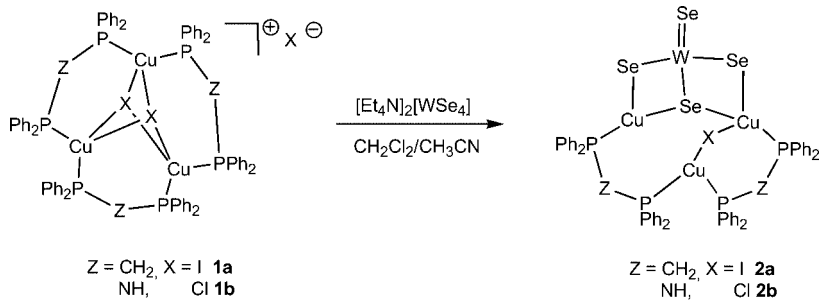


Scheme 1.

1 equiv. of dppa in $CH_2Cl_2$ affords the complex $[Cu_3(\mu_3\text{-}Cl)_2(\mu\text{-}dppa)_3]Cl$ (**1b**) in nearly quantitative yield. It is therefore not surprising to find a similar behavior between the bridging ligands dppa and dppm in their reaction with copper halides. A similar reaction in thf solution results in the formation of the same cationic complex but with a $[Cu^ICl_2]^-$ anion, which seems to be easily formed in thf.[25] The $^{31}P\{^1H\}$ NMR spectrum of **1b** shows one singlet at $\delta$ = 38.2 ppm assignable to the dppa ligands.

The reaction of $[Et_4N]_2[WSe_4]$ with **1a** and **1b** affords the neutral tetranuclear cluster compounds $[(\mu_3\text{-}WSe_4)Cu_3(\mu\text{-}I)(\mu\text{-}dppm)_2]$ (**2a**) and $[(\mu_3\text{-}WSe_4)Cu_3(\mu\text{-}Cl)(\mu\text{-}dppa)_2]$ (**2b**), respectively (Scheme 1). This implies that the formation of **2a** and **2b** involves the metathesis of $[Cu_3(\mu_3\text{-}X)_2(\mu\text{-}L)_3]^+$ (L = dppm and dppa) with the $[WSe_4]^{2-}$ anion. It seems that the displacement of one halide ion and one L molecule from $[Cu_3(\mu_3\text{-}X)_2(\mu\text{-}L)_3]^+$ gives an unsaturated intermediate $[Cu_3(\mu_3\text{-}X)(\mu\text{-}L)_2]^{2+}$, which subsequently coordinates to $[WSe_4]^{2-}$. The trigonal $Cu_3$ core in these compounds is maintained after the cluster formation, as confirmed by X-ray crystallography (see below). The treatment of $[Et_4N]_2[WSe_4]$ with $[Cu(MeCN)_4][PF_6]$ in the presence of the bidentate phosphane ligands dppm and dppa affords the cationic pentanuclear cluster compounds $[(\mu_4\text{-}WSe_4)Cu_4(\mu\text{-}dppm)_4][PF_6]_2$ (**3a**) and $[(\mu_4\text{-}WSe_4)Cu_4(\mu\text{-}dppa)_4][PF_6]_2$ (**3b**), respectively (Scheme 2). In this reaction, dppm and dppa act as bridging ligands for the construction of a dinuclear $[Cu_2(L)]^{2+}$ species obtained from the 1:1 mixture of $[Cu(MeCN)_4]^-$ and L.[26] Formation of the pentanuclear cluster **3** is not surprising for a co-planar $WCu_4$ core because the four faces of the tetrahedral $[WSe_4]^{2-}$ anion are equally capable of coordinating to $Cu^I$ species in polar dmf solution. A similar cluster compound $[(\mu_4\text{-}WSe_4)Cu_4(\mu\text{-}dppm)_4][ClO_4]_2$ has been reported previously.[27]

The IR and electronic spectra for **2** and **3** are in agreement with those observed for other known $[WSe_4]^{2-}$ anion derivatives.[11–13,16–19] The W–Se stretching modes of the clusters can be identified as sharp peaks in the low-wavenumber region below 400 $cm^{-1}$.[11,20,28] The terminal W–$Se_t$ absorptions at 316 $cm^{-1}$ for **2a** and 319 $cm^{-1}$ for **2b** appear at higher wavenumber than the ν(W–Se) absorption (305 $cm^{-1}$ in the $[WSe_4]^{2-}$ anion).[1] The bridging W–Se vibrations are observed in the range 285–300 $cm^{-1}$, at lower wavenumbers relative to that of $[WSe_4]^{2-}$.[1] The strong absorption at 2011 $cm^{-1}$ in the IR spectrum of **2b** may be attributed to the C≡N stretching vibration of the co-crystallization acetonitrile solvent. The electronic absorption spectrum of each cluster shows several intense bands in the UV region with weaker bands in the visible region (see Figure 1). These bands are not of the d-d type but probably arise from ligand-to-metal charge transfer. Band assignments for heterometallic selenium complexes containing the $[WSe_4]^{2-}$ anion have been reported in the literature.[11–19,28,29] The patterns for both the intense and weaker bands can be assigned to the internal Se-to-W charge-transfer transition of the $[WSe_4]^{2-}$ moiety and a relatively weak ligand $[WSe_4]^{2-}$-to-copper interaction, respectively. It is interesting to note that the $[WSe_4]^{2-}\rightarrow$Cu charge-transfer transition peaks at 470–478 nm in the present clusters are blueshifted by around 20 nm with respect to the $[WSe_4]^{2-}\rightarrow$Ag charge-transfer transition peaks (450–460 nm) in the argentoselenotungstate clusters, while the

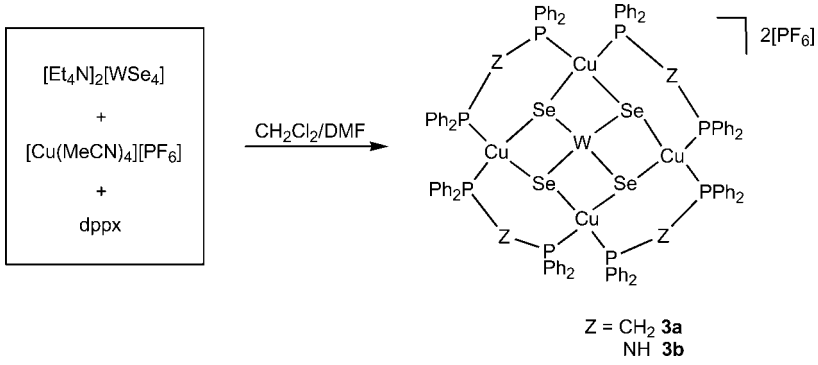


Scheme 2. dppx = dppm for **3a** and dppa for **3b**.

 © 2007 Wiley-VCH Verlag GmbH & Co. KGaA, Weinheim 

Se→W charge-transfer peaks at 310–325 nm are less influenced by the different coinage metals in the heteroselenotungstate clusters containing phosphane ligands.[11,18]

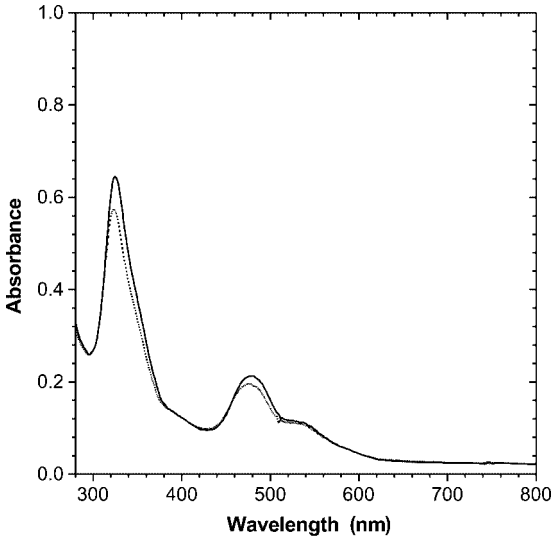


Figure 1. Electronic absorption (UV/Vis) spectra of **2a** (dash) and **2b** (solid), both as $2.75 \times 10^{-4}$ M $CH_2Cl_2$ solutions. The optical path is 1 cm.

The $^{31}P\{^1H\}$ NMR spectrum of **2a** shows two singlets at $\delta$ = 6.34 and 9.16 ppm, which suggests that there are two magnetically inequivalent phosphorus atoms in the open butterfly cluster. Similarly, two singlets at $\delta$ = 41.6 and 47.2 ppm in the $^{31}P$ NMR spectrum of **2b** may be ascribed to the two phosphorus atoms with different coordination environments. Two $^{31}P$ signals at $\delta$ = 2.57 and –142.5 ppm for **3a** are assigned to the phosphorus atoms of the dppm ligand and $[PF_6]^-$ anion, respectively. Similar $^{31}P$ signals at $\delta$ = 34.3 and –141.2 ppm are observed in the $^{31}P$ NMR spectrum of **3b**. The $FAB^+$ mass spectra of compounds **2** and **3** exhibit molecular ions corresponding to $[M^+ + 1]$ and $[M^+ - 2\ [PF_6]^-]$, respectively, with the appropriate isotopic distribution patterns.

## Crystal Structures

The structure of **1b**·0.5$CH_2Cl_2$ comprises a well-separated cation and anion along with the lattice solvent. The molecular structure of the $[Cu_3(\mu_3\text{-}Cl)_2(\mu\text{-}dppa)_3]^+$ cation in **1b** is illustrated in Figure 2, and selected bond lengths and angles are listed in Table 1. Similar to the structures of $[Cu_3(\mu_3\text{-}X)_2(\mu\text{-}dppm)_3]^+$ (X = Cl, Br, I),[22–24] two chloride ions cap the triangle from both sides to form a $[Cu_3Cl_2]$ trigonal bipyramid. Each dppa bidentate ligand bridges one Cu···Cu edge to give a roughly planar $[Cu_3P_6]$ structure. The average distance between two copper atoms in **1b**·0.5$CH_2Cl_2$ [2.988(2) Å] is slightly shorter than those observed in $[Cu_3(\mu_3\text{-}X)_2(\mu\text{-}dppm)_3]^+$ [X = Cl 3.210(4),[22] Br 3.081(3),[23] I 3.214(2) Å[24]], possibly due to the relatively stronger phosphorus σ-donor of dppa (amide) vs. dppm (methane).[25]

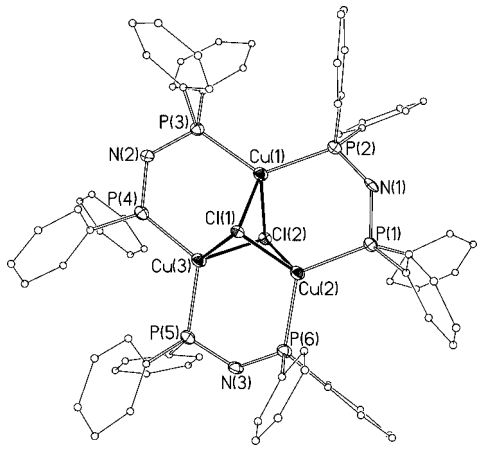


Figure 2. Molecular structure of the $[Cu_3(\mu_3\text{-}Cl)_2(\mu\text{-}dppa)_3]^+$ cation in **1b**.

Table 1. Selected bond lengths [Å] and angles [°] for **1b**·0.5$CH_2Cl_2$.

| | | | |
|---|---|---|---|
| Cu(1)–P(2) | 2.265(3) | Cu(1)–P(3) | 2.274(3) |
| Cu(2)–P(1) | 2.239(3) | Cu(2)–P(6) | 2.248(3) |
| Cu(3)–P(4) | 2.236(4) | Cu(3)–P(5) | 2.252(3) |
| Cu(1)–Cl(1) | 2.529(3) | Cu(1)–Cl(2) | 2.528(3) |
| Cu(2)–Cl(1) | 2.500(3) | Cu(2)–Cl(2) | 2.470(3) |
| Cu(3)–Cl(1) | 2.533(2) | Cu(3)–Cl(2) | 2.465(3) |
| Cu(1)···Cu(2) | 3.040(2) | Cu(2)···Cu(3) | 2.937(2) |
| P(2)–Cu(1)–P(3) | 125.49(12) | P(2)–Cu(1)–Cl(2) | 107.32(11) |
| P(3)–Cu(1)–Cl(2) | 113.31(11) | P(2)–Cu(1)–Cl(1) | 109.86(11) |
| P(3)–Cu(1)–Cl(1) | 104.50(11) | P(1)–Cu(2)–P(6) | 119.64(13) |
| P(1)–Cu(2)–Cl(2) | 108.02(11) | P(6)–Cu(2)–Cl(2) | 114.71(11) |
| P(1)–Cu(2)–Cl(1) | 112.07(11) | P(6)–Cu(2)–Cl(1) | 106.45(11) |
| P(4)–Cu(3)–P(5) | 119.97(12) | P(4)–Cu(3)–Cl(2) | 108.40(11) |
| P(5)–Cu(3)–Cl(2) | 111.05(12) | P(4)–Cu(3)–Cl(1) | 108.80(11) |
| P(5)–Cu(3)–Cl(1) | 112.98(11) | Cl(2)–Cu(1)–Cl(1) | 90.68(9) |
| Cl(2)–Cu(2)–Cl(1) | 92.71(9) | Cl(2)–Cu(3)–Cl(1) | 92.03(9) |
| Cu(2)–Cl(1)–Cu(1) | 74.40(8) | Cu(2)–Cl(1)–Cu(3) | 71.39(7) |
| Cu(1)–Cl(1)–Cu(3) | 74.84(7) | Cu(3)–Cl(2)–Cu(2) | 73.06(8) |
| Cu(3)–Cl(2)–Cu(1) | 76.05(8) | Cu(2)–Cl(2)–Cu(1) | 74.93(8) |

The structures of **2a** and **2b**·$CH_3CN$ were also determined by X-ray diffraction. The molecular structures of **2a** and **2b** are shown in Figures 3 and 4, respectively, and selected bond lengths and angles are listed in Tables 2 and 3, respectively. The structural frameworks in both neutral compounds **2a** and **2b** have an open butterfly configuration. The structures of **2a** and **2b**·$CH_3CN$ consist of trigonal $[Cu_3(\mu\text{-}I)(\mu\text{-}dppm)_2]^{2+}$ and $[Cu_3(\mu\text{-}Cl)(\mu\text{-}dppa)_2]^{2+}$ fragments, respectively, that are bound to a tetrahedral $[WSe_4]^{2-}$ moiety. The coordination geometry of the W atom in **2a** or **2b** remains nearly tetrahedral with the Se–W–Se angles ranging from 107.10(12)° to 114.60(15)° in **2a** and from 108.05(8)° to 110.92(10)° in **2b**. The W–Se bond lengths fall into three categories: the W–$Se_t$, W–μ-Se, and W–$\mu_3$-Se bond lengths are 2.254(3), 2.310(3) (av.), and 2.479(3) Å, respectively, in **2a** [2.251(3), 2.325(3) (av.), and 2.429(2) Å, respectively, in **2b**]. There are three different types of copper atoms in **2**: one has a tetrahedral geometry (bonded to two selenium atoms, one halide ion, and one phosphorus atom) and the other two have a trigonal-planar geometry (one is bonded to two selenium atoms and one

 © 2007 Wiley-VCH Verlag GmbH & Co. KGaA, Weinheim 

phosphorus atom, and the other to two phosphorus atoms and one halide ion). The Cu–Se distances in **2** are slightly influenced by the coordination modes of Se and Cu. For example, the Cu–Se distances involving μ-Se and three-coordinate Cu, μ-Se and four-coordinate Cu, $\mu_3$-Se and three-coordinate Cu, and $\mu_3$-Se and four-coordinate Cu are 2.369(4), 2.391(4), 2.396(4), and 2.430(4) Å, respectively, in **2a**. A similar situation is observed in **2b** (see Table 3). The Cu(3)–Se(3) bond in **2a** [2.702(4) Å] and the Cu(3)–Se(4) bond in **2b** [2.742(2) Å] are much longer than those observed in related systems such as $[Cu_4(dppm)_4(\mu_4\text{-Se})][PF_6]_2$ [Cu–$\mu_4$-Se: 2.384(3)–2.387(3) Å][30] and $[Cu_8(\mu_8\text{-Se})\{Se_2P(OiPr)_2\}_6]$ [Cu–$\mu_8$-Se: 2.539(3)–2.624(3) Å],[31] which is indicative of no bonding between the $\mu_3$-Se and $Cu(XP_2)$ moieties. The W···Cu separations for the three-coordinate copper atom [2.718(3) Å in **2a** and 2.698(3) Å in **2b**] are obviously shorter than those for their four-coordinate counterparts [2.779(4) Å in **2a** and 2.780(3) Å in **2b**]. The Cu(1)···Cu(3)···Cu(2) angles of 66.62(11)° in **2a** and 69.30(8)° in **2b** are more obtuse than those in **1a** [60.36(2)°] and **1b** [61.91(5)°], respectively; such an enlargement of the trigonal $Cu_3$ angles is due to the coordination of $[Cu_3(\mu\text{-}X)(\mu\text{-}L)_2]^{2+}$ species to the $[WSe_4]^{2-}$ anion. Accordingly, the Cu(1)···Cu(3) separations bridged by the halide ion [2.763(4) Å in **2a** and 2.795(3) Å in **2b**] are much shorter than those in **1a** [3.214(2) Å][24] and **1b** [2.988(2) Å], which is suggestive of weak metal–metal interactions between the $[Cu_2(\mu\text{-}X)]$ moieties of the present clusters. The Cu(1)–I(1)–Cu(3) bond angle in **2a** [61.23(10)°] is more acute than the Cu(1)–Cl(1)–Cu(3) bond angle in **2b** [68.95(10)°], whereas the average Cu–I bond in **2a** [2.709(3) Å] is longer than the average Cu–Cl bond in **2b** [2.465(3) Å].

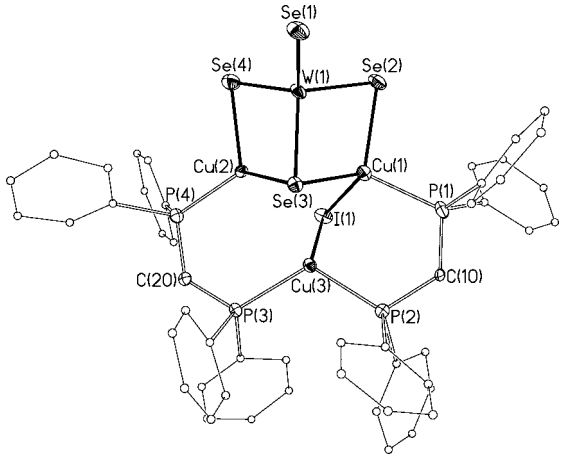


Figure 3. Molecular structure of the $[(\mu_3\text{-}WSe_4)Cu_3(\mu\text{-}I)(\mu\text{-}dppm)_2]$ cation in **2a**.

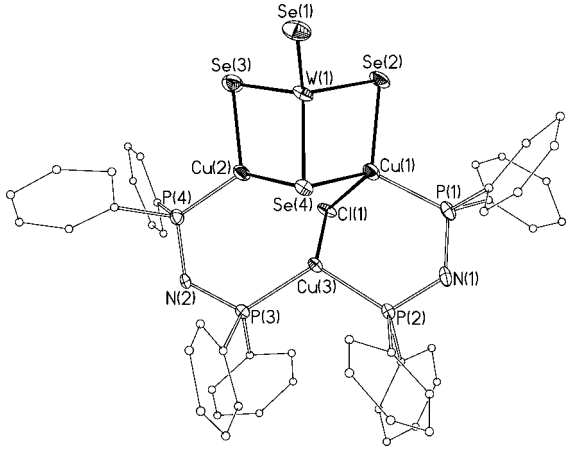


Figure 4. Molecular structure of the $[(\mu_3\text{-}WSe_4)Cu_3(\mu\text{-}Cl)(\mu\text{-}dppa)_2]$ cation in **2b**.

Table 2. Selected bond lengths [Å] and angles [°] for **2a**.

| | | | |
|---|---|---|---|
| W(1)–Se(1) | 2.254(3) | W(1)–Se(2) | 2.334(3) |
| W(1)–Se(3) | 2.479(3) | W(1)–Se(4) | 2.287(4) |
| Cu(1)–Se(2) | 2.391(4) | Cu(2)–Se(3) | 2.396(4) |
| Cu(1)–Se(3) | 2.430(4) | Cu(3)–Se(3) | 2.702(4) |
| Cu(2)–Se(4) | 2.369(4) | Cu(1)–I(1) | 2.788(4) |
| Cu(3)–I(1) | 2.630(3) | Cu(1)–P(1) | 2.214(8) |
| Cu(2)–P(4) | 2.196(7) | Cu(3)–P(3) | 2.263(6) |
| Cu(3)–P(2) | 2.271(7) | W(1)···Cu(1) | 2.779(4) |
| W(1)···Cu(2) | 2.718(3) | Cu(1)···Cu(3) | 2.763(4) |
| Cu(2)···Cu(3) | 3.020(4) | | |
| Se(1)–W(1)–Se(4) | 114.60(15) | Se(1)–W(1)–Se(2) | 107.25(12) |
| Se(4)–W(1)–Se(2) | 111.40(14) | Se(1)–W(1)–Se(3) | 107.10(12) |
| Se(4)–W(1)–Se(3) | 108.53(10) | Se(2)–W(1)–Se(3) | 107.67(11) |
| W(1)–Se(2)–Cu(1) | 72.04(11) | W(1)–Se(3)–Cu(2) | 67.73(10) |
| W(1)–Se(3)–Cu(1) | 68.95(11) | W(1)–Se(3)–Cu(3) | 121.46(11) |
| Cu(2)–Se(3)–Cu(3) | 72.36(11) | Cu(1)–Se(3)–Cu(3) | 64.88(11) |
| P(1)–Cu(1)–Se(2) | 107.7(2) | P(1)–Cu(1)–Se(3) | 119.1(2) |
| Se(2)–Cu(1)–Se(3) | 107.44(16) | P(1)–Cu(1)–I(1) | 106.3(2) |
| Se(2)–Cu(1)–I(1) | 111.88(15) | Se(3)–Cu(1)–I(1) | 104.50(13) |
| P(4)–Cu(2)–Se(4) | 112.8(2) | P(4)–Cu(2)–Se(3) | 128.8(2) |
| Se(4)–Cu(2)–Se(3) | 108.65(16) | P(3)–Cu(3)–P(2) | 117.2(3) |
| P(3)–Cu(3)–I(1) | 107.49(19) | P(2)–Cu(3)–I(1) | 113.03(19) |
| P(3)–Cu(3)–Se(3) | 109.30(19) | P(2)–Cu(3)–Se(3) | 107.10(19) |
| I(1)–Cu(3)–Se(3) | 101.60(12) | Cu(3)–I(1)–Cu(1) | 61.23(10) |
| Cu(1)···Cu(3)···Cu(2) | 66.62(11) | | |

Table 3. Selected bond lengths [Å] and angles [°] for **2b**·$CH_3CN$.

| | | | |
|---|---|---|---|
| W(1)–Se(1) | 2.251(3) | W(1)–Se(2) | 2.332(2) |
| W(1)–Se(3) | 2.318(3) | W(1)–Se(4) | 2.429(2) |
| Cu(1)–Se(2) | 2.377(3) | Cu(2)–Se(3) | 2.350(3) |
| Cu(2)–Se(4) | 2.348(3) | Cu(1)–Se(4) | 2.425(3) |
| Cu(3)–Se(4) | 2.742(2) | Cu(1)–P(1) | 2.194(5) |
| Cu(2)–P(4) | 2.170(5) | Cu(3)–P(3) | 2.245(4) |
| Cu(3)–P(2) | 2.264(4) | Cu(1)–Cl(1) | 2.570(4) |
| Cu(3)–Cl(1) | 2.359(3) | W(1)···Cu(1) | 2.780(3) |
| W(1)···Cu(2) | 2.698(3) | Cu(1)···Cu(3) | 2.795(3) |
| Cu(2)···Cu(3) | 3.036(3) | | |
| Se(1)–W(1)–Se(3) | 109.58(12) | Se(1)–W(1)–Se(2) | 109.98(11) |
| Se(3)–W(1)–Se(2) | 109.52(10) | Se(1)–W(1)–Se(4) | 110.92(10) |
| Se(3)–W(1)–Se(4) | 108.76(7) | Se(2)–W(1)–Se(4) | 108.05(8) |
| Se(1)–W(1)–Cu(2) | 133.90(12) | W(1)–Se(2)–Cu(1) | 72.36(8) |
| W(1)–Se(3)–Cu(2) | 70.61(9) | W(1)–Se(4)–Cu(3) | 120.42(7) |
| W(1)–Se(4)–Cu(2) | 68.75(8) | W(1)–Se(4)–Cu(1) | 69.86(7) |
| Cu(2)–Se(4)–Cu(1) | 88.17(11) | Cu(2)–Se(4)–Cu(3) | 72.76(9) |
| Cu(1)–Se(4)–Cu(3) | 65.15(8) | P(1)–Cu(1)–Se(2) | 112.04(15) |
| P(1)–Cu(1)–Se(4) | 118.68(15) | Se(2)–Cu(1)–Se(4) | 106.70(11) |
| P(1)–Cu(1)–Cl(1) | 106.89(17) | Se(2)–Cu(1)–Cl(1) | 111.27(13) |
| Se(4)–Cu(1)–Cl(1) | 100.69(12) | P(4)–Cu(2)–Se(4) | 132.35(17) |
| P(4)–Cu(2)–Se(3) | 112.42(16) | Se(4)–Cu(2)–Se(3) | 110.49(12) |
| P(3)–Cu(3)–P(2) | 115.27(16) | P(3)–Cu(3)–Cl(1) | 112.95(16) |
| P(3)–Cu(3)–Se(4) | 109.76(13) | P(2)–Cu(3)–Se(4) | 105.33(12) |
| P(2)–Cu(3)–Cl(1) | 114.02(16) | Cl(1)–Cu(3)–Se(4) | 97.62(11) |
| Cu(3)–Cl(1)–Cu(1) | 68.95(10) | Cu(1)···Cu(3)···Cu(2) | 69.30(8) |

 © 2007 Wiley-VCH Verlag GmbH & Co. KGaA, Weinheim 

The structure of the $[(\mu_4\text{-}WSe_4)Cu_4(\mu\text{-}dppm)_4]^{2+}$ cluster cation in **3a** is shown in Figure 5, and selected bond lengths and angles are listed in Table 4. Similar core structures have been found previously in pentanuclear clusters with a coplanar $WCu_4$ core, such as the anionic cluster $[Et_4N]_2[(\mu_4\text{-}WSe_4)(CuS_2CNMe_2)_4]$,[32] the neutral cluster $[(\mu_4\text{-}WSe_4)Cu_4Cl_6(py)_4]$[33] (py = pyridine), and the cationic cluster $[(\mu_4\text{-}WSe_4)Cu_4(\mu\text{-}dppm)_4][ClO_4]_2$.[27] The W atom is at the center of a slightly distorted tetrahedral $WSe_4$ unit with an average W–Se bond length of 2.347(1) Å and Se–W–Se angles in the range 105.44(3)–111.85(3)°. Four copper atoms are almost symmetrically bound to the four $WSe_2$ edges of the tetrahedral $[WSe_4]^{2-}$ anion. Four distorted chair-type six-membered $CP_2Cu_2Se$ rings around the $[WSe_4]^{2-}$ anion enhance the structural stability of the cationic cluster **3a**. The five metal atoms in the $WCu_4$ core are nearly coplanar with deviations of not more than 0.01 Å from the least-squares plane. The average W–Cu distance of 2.820(1) Å in **3a** is similar to those in $[(\mu_4\text{-}WSe_4)Cu_4(\mu\text{-}dppm)_4][ClO_4]_2$ [2.815(2) Å][27] and $(\mu_2\text{-}WSe_4)[Cu(PMe_2Ph)_2]_2$ [2.873(2) Å], which contain σ-donor phosphane ligands,[11] but clearly longer than those in $[Et_4N]_2[(\mu_3\text{-}WSe_4)(CuS_2CNEt_2)_3]$ [av. 2.737(2) Å] and $[Et_4N]_2[(\mu_4\text{-}WSe_4)(CuS_2CNMe_2)_4]$ [av. 2.707(2) Å], which contain π-conjugated dithiocarbamate ligands.[32]

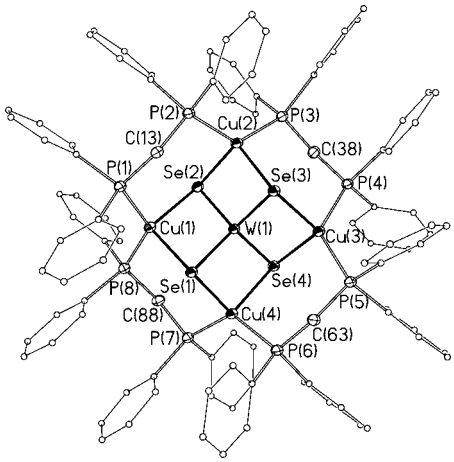


Figure 5. Molecular structure of the $[(\mu_4\text{-}WSe_4)Cu_4(\mu\text{-}dppm)_4]^{2+}$ cation in **3a**.

Table 4. Selected bond length [Å] and angles [°] for **3a**.

| | | | |
|---|---|---|---|
| W(1)–Se(1) | 2.3490(8) | W(1)–Se(2) | 2.3490(12) |
| W(1)–Se(3) | 2.3456(9) | W(1)–Se(4) | 2.3457(8) |
| Cu(1)–Se(1) | 2.4594(14) | Cu(1)–Se(2) | 2.4461(10) |
| Cu(2)–Se(2) | 2.4617(12) | Cu(2)–Se(3) | 2.4520(14) |
| Cu(3)–Se(3) | 2.4523(10) | Cu(3)–Se(4) | 2.4458(11) |
| Cu(4)–Se(4) | 2.4560(10) | Cu(4)–Se(1) | 2.4317(10) |
| Cu(1)–P(1) | 2.2763(16) | Cu(1)–P(8) | 2.2667(18) |
| Cu(2)–P(2) | 2.2697(16) | Cu(2)–P(3) | 2.2676(17) |
| Cu(3)–P(4) | 2.2663(16) | Cu(3)–P(5) | 2.2656(18) |
| Cu(4)–P(6) | 2.2662(19) | Cu(4)–P(7) | 2.2729(18) |
| W(1)···Cu(1) | 2.8096(12) | W(1)···Cu(2) | 2.8357(14) |
| W(1)···Cu(3) | 2.8075(12) | W(1)···Cu(4) | 2.8285(14) |
| Se(3)–W(1)–Se(4) | 111.77(4) | Se(3)–W(1)–Se(1) | 105.44(3) |
| Se(4)–W(1)–Se(1) | 110.81(4) | Se(3)–W(1)–Se(2) | 111.24(4) |
| Se(4)–W(1)–Se(2) | 105.85(3) | Se(1)–W(1)–Se(2) | 111.85(3) |
| W(1)–Se(1)–Cu(4) | 72.53(4) | W(1)–Se(1)–Cu(1) | 71.47(3) |
| W(1)–Se(2)–Cu(1) | 71.70(3) | W(1)–Se(2)–Cu(2) | 72.19(4) |
| W(1)–Se(3)–Cu(2) | 72.43(4) | W(1)–Se(3)–Cu(3) | 71.59(4) |
| W(1)–Se(4)–Cu(3) | 71.70(4) | W(1)–Se(4)–Cu(4) | 72.14(4) |
| Cu(4)–Se(1)–Cu(1) | 108.15(4) | Cu(1)–Se(2)–Cu(2) | 109.89(4) |
| Cu(2)–Se(3)–Cu(3) | 108.75(4) | Cu(3)–Se(4)–Cu(4) | 108.97(4) |
| Se(2)–Cu(1)–Se(1) | 104.98(4) | Se(3)–Cu(2)–Se(2) | 104.10(4) |
| Se(4)–Cu(3)–Se(3) | 104.92(4) | Se(1)–Cu(4)–Se(4) | 104.49(4) |
| P(8)–Cu(1)–P(1) | 132.26(7) | P(8)–Cu(1)–Se(2) | 105.80(5) |
| P(1)–Cu(1)–Se(2) | 107.49(6) | P(8)–Cu(1)–Se(1) | 104.86(5) |
| P(1)–Cu(1)–Se(1) | 98.46(5) | P(3)–Cu(2)–P(2) | 131.77(6) |
| P(3)–Cu(2)–Se(3) | 106.99(5) | P(2)–Cu(2)–Se(3) | 103.06(5) |
| P(3)–Cu(2)–Se(2) | 104.64(5) | P(2)–Cu(2)–Se(2) | 103.49(6) |
| P(5)–Cu(3)–P(4) | 128.05(7) | P(5)–Cu(3)–Se(4) | 105.33(6) |
| P(4)–Cu(3)–Se(4) | 105.81(6) | P(5)–Cu(3)–Se(3) | 108.20(5) |
| P(4)–Cu(3)–Se(3) | 102.56(5) | P(6)–Cu(4)–P(7) | 127.67(6) |
| P(6)–Cu(4)–Se(1) | 105.65(5) | P(7)–Cu(4)–Se(1) | 105.17(6) |
| P(6)–Cu(4)–Se(4) | 103.06(6) | P(7)–Cu(4)–Se(4) | 108.76(5) |

## NLO Properties

The nonlinear absorption component of cluster compounds **2a** and **3a** was evaluated by a *z*-scan experiment in an open-aperture configuration (see Figure 6). Although the detailed mechanism is still not clear, it is interesting to note that the NLO absorption data obtained under the conditions used in this study can be well described by Equations (1) and (2), which describe a third-order NLO process, where $\alpha_0$ and $\alpha_2^{eff}$ are the linear and effective third-order NLO absorptivities, respectively.[34,35]

$$T(Z) = \{1/[\pi^{1/2}q(Z)]\}\int_{-\infty}^{\infty}\ln[1 + q(Z)]e^{-\tau^2}d\tau \quad (1)$$

$$q(Z) = \alpha_2^{eff}I_0[(1 - e^{-\alpha_0 L})/\alpha_0] \quad (2)$$

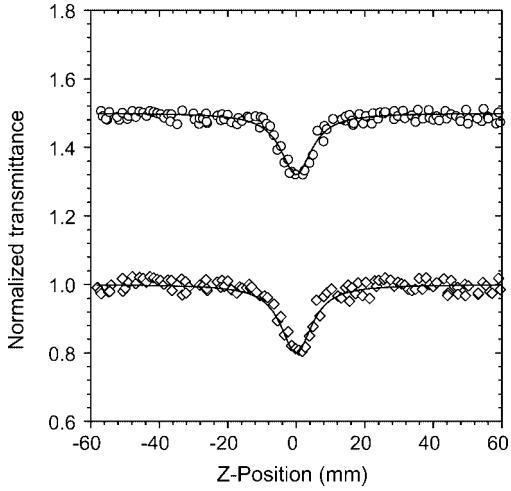


Figure 6. *z*-Scan data of cluster compounds **2a** (circle) and **3a** (diamond) in $2.75 \times 10^{-4}$ M $CH_2Cl_2$ solution. The data were collected in an open-aperture configuration. The solid curves are fits based on theoretical calculations.

The best fit of the theoretical curve (the solid curve in Figure 6) to the experimental data clearly illustrates that the absorption increases as the incident light irradiance arises, which is characteristic of a reverse saturable absorption (RSA) process.[34] The origin of the observed RSA in cluster

 © 2007 Wiley-VCH Verlag GmbH & Co. KGaA, Weinheim 

compounds **2a** and **3a** can be attributed to excited-state absorption. Figure 7 shows the *z*-scan data measured with the aperture and indicates that the two cluster compounds **2a** and **3a** have a negative sign for the refractive nonlinearity, which gives rise to self-defocusing. The measurements confirm that the observed NLO effects are effectively third-order in nature, which implies that both the absorption coefficient and refractive index should be expressed as $\alpha = \alpha_0 + \alpha_2 I$ and $n = n_0 + n_2 I$, respectively, where $\alpha_0$ and $\alpha_2$ are the linear and nonlinear absorption coefficients and $n_0$ and $n_2$ are the linear and nonlinear refractive indices, respectively, and $I$ is the irradiance of the laser beam within the sample. By applying the *z*-scan theory, the solid curves in Figures 6 and 7 can be fitted to the experimental data. The best fits reveal that $\alpha_2 = 1.74 \times 10^{-6}\ m\,W^{-1}\,M^{-1}$ and $n_2 = -5.32 \times 10^{-13}\ m^2\,W^{-1}\,M^{-1}$ for cluster **2a**, and $\alpha_2 = 2.56 \times 10^{-6}\ m\,W^{-1}\,M^{-1}$ and $n_2 = -1.54 \times 10^{-12}\ m^2\,W^{-1}\,M^{-1}$ for cluster **3a**.

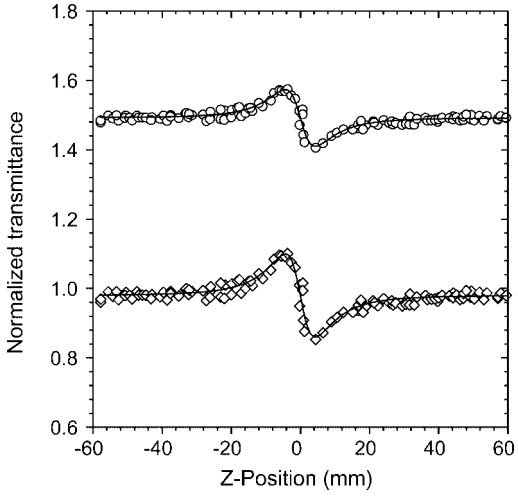


Figure 7. *z*-Scan data of cluster compounds **2a** (circle) and **3a** (diamond) in $2.75 \times 10^{-4}$ M $CH_2Cl_2$ solution. The data were obtained by dividing the normalized *z*-scan data obtained in a closed-aperture configuration by the normalized *z*-scan data obtained in an open-aperture configuration. The solid curves are fits based on theoretical calculations.

The optical limiting effects of cluster compounds **2a** and **3a** are depicted in Figure 8. At very low fluences, they respond linearly to the incident light and therefore obey Beer's law. Deviation from the linear response takes place when the incident fluence reaches about 0.35 $J\,cm^{-2}$ for **2a** and 0.12 $J\,cm^{-2}$ for **3a**. The cluster materials become increasingly less transparent as the light fluence rises. Experiments with the solvents alone showed no detectable optical limiting effect. These observations indicate that solvent contributions are negligible. The limiting threshold, which is defined as the incident fluence at which the actual transmittance falls to 55% of the corresponding linear transmittance, was found to be 1.2 $J\,cm^{-2}$ for **2a** and 0.4 $J\,cm^{-2}$ for **3a**. Cluster **2a**, which has a butterfly configuration, therefore has a higher threshold than that of cluster **3a**, which has an open co-planar $WCu_4$ core, an obvious indication of the influence of structural types on the non-linear optical properties. The butterfly-shaped clusters have two different types of coordinated selenium atoms, therefore the electronic interactions between μ-Se- and $\mu_3$-Se-bridged metal atoms may result in different electron delocalization in the cluster molecule, which needs a higher pump energy to generate the plasma and further leads to degradation of the limiting effect.[36] Similar to the butterfly-shaped clusters, the clusters of other structural types, including incomplete cubane-like, T-frame, and nest-shapes with non-equivalent bridging selenium or sulfur atoms, have lower optical limiting effects.[32,37,38] Previous reports have shown that cluster compounds with an open co-planar cross $MCu_4$ (M = Mo, W) core, for example the neutral clusters $[(\mu_4\text{-}MS_4)Cu_4(SCN)_2(py)_6]$ (0.3 $J\,cm^{-2}$)[39] and $[(\mu_4\text{-}MS_4)Cu_4(CN)_2(py)_6]$ (0.1 $J\,cm^{-2}$),[40] the anionic clusters $[\{Et_4N\}_2\{(\mu_4\text{-}MS_4)Cu_4(CN)_4\}]_n$ (0.2 $J\,cm^{-2}$)[41] and $[\{Et_4N\}_2\{(\mu_4\text{-}WSe_4)Cu_4(CN)_4\}]_n$ (0.3 $J\,cm^{-2}$),[18] and the cationic clusters $[(\mu_4\text{-}WSe_4)Cu_4(\mu\text{-}dppm)_4][ClO_4]_2$ (0.35 $J\,cm^{-2}$), have a large optical limiting effect.[27] These clusters have four equivalent $\mu_4$-Se atoms, therefore the plasma in the polarized nanosecond pulses may be generated at a lower pump energy, and lower limiting thresholds are therefore found for this class of clusters.[42] The lower limiting threshold of cluster compound **3a** (0.40 $J\,cm^{-2}$) may provide effective proof for this class of clusters that possess an open co-planar structure.

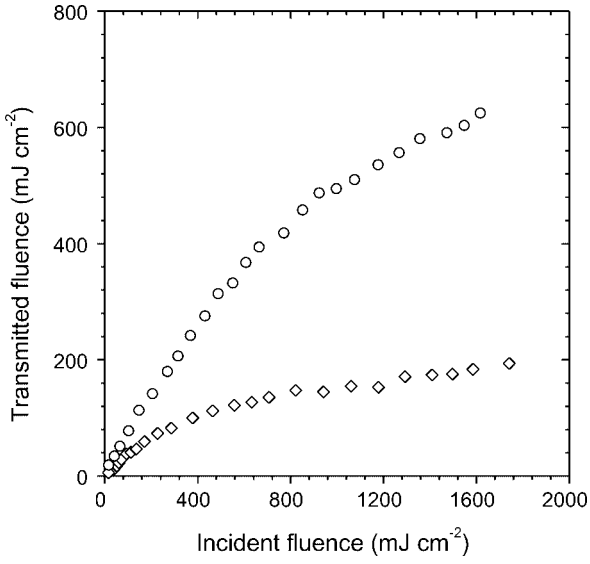


Figure 8. Optical limiting effect of cluster compounds **2a** (circle) and **3a** (diamond) in $2.75 \times 10^{-3}$ M $CH_2Cl_2$ solution.

## Conclusion

We have investigated the reaction of the anion $[WSe_4]^{2-}$ with copper(I) species in the presence of bridging phosphane ligands dppm and dppa and have isolated two types of heterometallic selenium cluster compounds, namely tetranuclear, butterfly-like $[(\mu_3\text{-}WSe_4)Cu_3(\mu\text{-}X)(\mu\text{-}L)_2]$ and pentanuclear, open co-planar $[(\mu_4\text{-}WSe_4)Cu_4(\mu\text{-}L)_4][PF_6]_2$ (X = Cl, I; L = dppm, dppa). The open co-planar cluster with a $WCu_4$ core structure has a relatively large optical

 © 2007 Wiley-VCH Verlag GmbH & Co. KGaA, Weinheim 

limiting effect and therefore may be considered as a promising candidate for a nonlinear optical limiting cluster material. We are currently investigating the design and synthesis of new heterometallic selenium clusters with strong NLO properties.

## Experimental Section

**General:** All reactions were performed using Schlenk techniques under nitrogen. $[Et_4N]_2[WSe_4]$[43] and $[Cu_3(\mu_3\text{-}I)_2(\mu\text{-}dppm)_3]I$[24] (**1a**) were prepared according to literature methods. $[Cu(MeCN)_4][PF_6]$ was synthesized by the reaction of $Cu_2O$ powder with $HPF_6$ in acetonitrile.[44] Bis(diphenylphosphanyl)amine (dppa) was synthesized by the reaction of $Ph_2PCl$ with $(Me_3Si)NH(SiMe_3)$ in toluene.[45] CuI and bis(diphenylphosphanyl)methane (dppm) were purchased from Aldrich Ltd. and used without further purification. IR spectra were recorded with a Digilab FTS-40 spectrophotometer. Electronic spectra were recorded with a Hitachi U-3410 spectrophotometer. NMR spectra were recorded with a Bruker ALX 300 spectrometer operating at 300 and 121.5 MHz for $^1H$ and $^{31}P$, respectively; chemical shifts ($\delta$ in ppm) are quoted relative to $SiMe_4$ ($^1H$) and $H_3PO_4$ ($^{31}P$). Mass spectra were recorded with a Finnigan TSQ 7000 spectrometer. All elemental analyses were performed with a Perkin–Elmer 2400 CHN analyzer.

**$[Cu_3(\mu_3\text{-}Cl)_2(\mu\text{-}dppa)_3]Cl$ (1b):** A mixture of CuCl powder (150 mg, 0.15 mmol) and dppa (578 mg, 0.15 mmol) in $CH_2Cl_2$ (20 mL) was stirred at room temperature overnight. The resulting colorless solution was filtered and the volume of filtrate was reduced to about 10 mL. Colorless block crystals of $[Cu_3(\mu_3\text{-}Cl)_2(\mu\text{-}dppa)_3]Cl$ (**1b**) were obtained by layering hexane on top of the filtrate at room temperature. Yield: 746 mg (96%). IR (KBr): $\tilde{\nu}$ = 3335 [br ν(N–H)]; 531 (s), 509 (s), 492 (m) [ν(P–C)] $cm^{-1}$. $^1H$ NMR ($CDCl_3$): $\delta$ = 8.05 (br., 3 H, N*H*), 7.21–7.52 (m, 60 H, Ph) ppm. $^{31}P\{^1H\}$ NMR ($CDCl_3$): $\delta$ = 37.2 (s) ppm. MS (FAB): *m*/*z* = 1414 $[Cu_3(\mu_3\text{-}Cl)_2(\mu\text{-}dppa)_3]^+$, 512 $[[Cu_2(\mu\text{-}dppa)]^+ - 1]$. $C_{72}H_{63}Cl_2Cu_3N_3P_6\cdot 0.5CH_2Cl_2$ (1495.5): calcd. C 58.2, H 4.28, N 2.81; found C 57.7, H 4.15, N, 2.78.

**$[(\mu_3\text{-}WSe_4)Cu_3(\mu\text{-}I)(\mu\text{-}dppm)_2]$ (2a):** A solution of **1a** (346 mg, 0.25 mmol) in $CH_2Cl_2$ (15 mL) was added to a solution of $[Et_4N]_2[WSe_4]$ (152 mg, 0.20 mmol) in dmf (5 mL). After stirring at room temperature for 45 min, the mixture was filtered through a filter paper to provide an orange filtrate. Slow addition of $Et_2O$ resulted in the formation of orange block crystals suitable for single-crystal X-ray diffraction analysis, which were subsequently identified as **2a**. Yield: 183 mg (52%). UV/Vis ($CH_2Cl_2$): $\lambda_{max}$ ($\varepsilon$) = 315 ($6.94\times10^{-3}$), 475 ($2.91\times10^{-3}$ $M^{-1}cm^{-1}$) nm. IR (KBr): $\tilde{\nu}$ = 312 (s), 295 (m), 291 (w) [ν(W–Se)] $cm^{-1}$. $^1H$ NMR ($CDCl_3$): $\delta$ = 7.33–7.51 (m, 40 H, Ph), 5.42 (s, 4 H, $CH_2$) ppm. $^{31}P$ NMR ($CDCl_3$): $\delta$ = 6.34, 9.16 ppm. MS (FAB): *m*/*z* = 1587 $[M^+ + 1]$. $C_{50}H_{44}Cu_3I_2P_4Se_4W$ (1585.9): calcd. C 37.8, H 2.77; found C 37.3, H 2.76.

**$[(\mu_3\text{-}WSe_4)Cu_3(\mu\text{-}Cl)(\mu\text{-}dppa)_2]$ (2b):** This compound was prepared similarly to **2a** but using **1b** (291 mg, 0.20 mmol) instead of **1a**. It was recrystallized from $CH_2Cl_2$/MeCN/$Et_2O$. Yield: 168 mg (46%). UV/Vis ($CH_2Cl_2$): $\lambda_{max}$ ($\varepsilon$) = 318 ($5.63\times10^{-3}$), 472 ($3.04\times10^{-3}$ $M^{-1}cm^{-1}$) nm. IR (KBr): $\tilde{\nu}$ = 311 (s), 298 (m), 292 (w) [ν(W–Se)] $cm^{-1}$. $^1H$ NMR ($CDCl_3$): $\delta$ = 7.84 (br., 2 H, N*H*), 7.23–7.45 (m, 40 H, Ph) ppm. $^{31}P$ NMR ($CDCl_3$): $\delta$ = 41.6, 47.2 ppm. MS (FAB): *m*/*z* = 1496 $[M^+ + 1]$. $C_{48}H_{41}ClCu_3N_2P_4Se_4W\cdot CH_3CN$ (1536.5): calcd. C 39.0, H 2.86, N 2.73; found C 38.1, H 2.74, N 2.71.

**$[(\mu_4\text{-}WSe_4)Cu_4(\mu\text{-}dppm)_4][PF_6]_2$ (3a):** A mixture of $[Cu(MeCN)_4][PF_6]$ (300 mg, 0.80 mmol) and dppm (320 mg, 0.80 mmol) in $CH_2Cl_2$ (20 mL) was added to a solution of $[Et_4N]_2[WSe_4]$ (152 mg, 0.20 mmol) in dmf (10 mL). After stirring at room temperature for 45 min, the mixture was filtered through a filter paper to provide an orange-red filtrate. Slow addition of $Et_2O$ afforded red block-shaped crystals suitable for a single-crystal X-ray diffraction analysis, which were subsequently identified as **3a**. Yield: 279 mg (73%). UV/Vis ($CH_2Cl_2$): $\lambda_{max}$ ($\varepsilon$) = 324 ($6.62\times10^{-3}$), 478 ($3.06\times10^{-3}$ $M^{-1}cm^{-1}$) nm. IR (KBr): $\tilde{\nu}$ = 312 (s), 297 (m), 290 (w) [ν(W–Se)] $cm^{-1}$. $^1H$ NMR ($CDCl_3$): $\delta$ = 7.16–7.52 (m, 80 H, Ph), 5.42 (s, 8 H, C*H*$_2$) ppm. $^{31}P$ NMR ($CDCl_3$): $\delta$ = 2.57, –142.5 ppm. MS (FAB): *m*/*z* 2291 $[M^+ - 2\ PF_6]$. $C_{100}H_{88}Cu_4F_{12}P_{10}Se_4W$ (2581.3): calcd. C 46.5, H 3.41; found C 46.2, H 3.37.

**$[(\mu_4\text{-}WSe_4)Cu_4(\mu\text{-}dppa)_4][PF_6]_2$ (3b):** This compound was prepared similarly to **3a** but using dppa (320 mg, 0.80 mmol) instead of dppm. It was recrystallized from $CH_2Cl_2$/MeCN/$Et_2O$. Yield: 184 mg (49%). UV/Vis ($CH_2Cl_2$): $\lambda_{max}$ ($\varepsilon$) = 319 ($6.82\times10^{-3}$), 473 ($2.75\times10^{-3}$ $M^{-1}cm^{-1}$) nm. IR (KBr): 313 (s), 298 (m), 294 (w) [ν(W–Se)] $cm^{-1}$. $^1H$ NMR ($CDCl_3$): $\delta$ = 8.06 (br., 4 H, N*H*), 7.32–7.57 (m, 80 H, Ph) ppm. $^{31}P$ NMR ($CDCl_3$): $\delta$ = 34.3, –141.2 ppm. MS (FAB): *m*/*z* = 2290 $[M^+ - 2\ PF_6]$. $C_{96}H_{84}Cu_4F_{12}N_4P_{10}Se_4W$ (2585.2): calcd. C 44.6, H 3.25, N 2.17; found C 44.2, H 3.18, N 2.13.

**Crystal Structure Determination:** Data for **1b**·$0.5CH_2Cl_2$ were collected at 293 K with a Bruker SMART-CCD area detector diffractometer with a graphite monochromator using Mo-$K_\alpha$ radiation ($\lambda$ = 0.71073 Å). Data for **2a**, **2b**·$CH_3CN$, and **3a** were collected at 153 K with a Siemens Stoe-IPDS diffractometer (Mo-$K_\alpha$ radiation; $\lambda$ = 0.71073 Å) equipped with an imaging plate area detector and a rotating anode. The intensities were corrected for Lorentz, polarization, and absorption effects. The structures were solved by direct methods using the SHELXTL software package.[46] The positions of all W, Se, Cu, I (Cl), and P atoms were revealed on the first refinement. Other non-hydrogen atoms were located from subsequent difference Fourier syntheses. The structures were refined by full-matrix least-squares methods on $F^2$. All non-hydrogen atoms were refined anisotropically. Hydrogen atoms were included but not refined. Two of the phenyl rings of the dppm ligands in **2b**·$CH_3CN$ were refined with bond-length restraints due to disorder. Further details of the structure analyses are given in Table 5. CCDC-628300 (**1b**·$0.5CH_2Cl_2$), -628301 (**2a**), -628302 (**2b**·$CH_3CN$), and -628303 (**3a**) contain the supplementary crystallographic data for this paper. These data can be obtained free of charge from The Cambridge Crystallographic Data Centre via www.ccdc.cam.ac.uk/data_request/cif.

**Optical Measurements:** A $CH_2Cl_2$ solution of cluster **2a** or **3a** was placed in a 1-mm quartz cuvette for nonlinear optical measurements, which were performed with linearity polarized 7-ns pulses at 532 nm generated from a Q-switched frequency-doubled Nd:YAG laser. Both clusters are stable toward air and laser light under these conditions. The spatial profiles of the pulsed laser were focused on the sample cell with a 30-cm focal length mirror. The spot radius of the laser beam was measured to be 55 μm (half-width at $1/e^2$ maximum). The incident and transmitted pulse energies were measured simultaneously with two energy detectors (Laser Precision Rjp-735), which were linked to a computer by an IEEE interface.[34,35] The NLO properties of the samples were manifested by moving the samples along the axis of the incident laser irradiance beam (*z*-direction) with respect to the focal point and with the incident laser irradiance kept constant (*z*-scan methods). The closed-aperture curves are normalized to the open-aperture curves. An

 © 2007 Wiley-VCH Verlag GmbH & Co. KGaA, Weinheim 

Table 5. Crystal data and structure refinement for $[Cu_3(\mu_3\text{-}Cl)_2(\mu\text{-}dppa)_3]Cl\cdot 0.5CH_2Cl_2$ (**1b**·$0.5CH_2Cl_2$), $[(\mu_3\text{-}WSe_4)Cu_3(\mu\text{-}I)(\mu\text{-}dppm)_2]$ (**2a**), $[(\mu_3\text{-}WSe_4)Cu_3(\mu\text{-}Cl)(\mu\text{-}dppa)_2]\cdot CH_3CN$ (**2b**·$CH_3CN$), and $[(\mu_4\text{-}WSe_4)Cu_4(\mu\text{-}dppm)_4][PF_6]_2$ (**3a**).

| Compound | **1b**·$0.5CH_2Cl_2$ | **2a** | **2b**·$CH_3CN$ | **3a** |
|---|---|---|---|---|
| Formula | $C_{72.5}H_{64}N_3Cl_4P_6Cu_3$ | $C_{50}H_{44}P_4ICu_3Se_4W$ | $C_{50}H_{44}N_3ClP_4Cu_3Se_4W$ | $C_{100}H_{88}F_{12}P_{10}Cu_4Se_4W$ |
| Formula weight | 1495.51 | 1585.94 | 1536.52 | 2581.25 |
| Crystal system | triclinic | monoclinic | monoclinic | triclinic |
| Space group | $P\bar{1}$ | $P2_1/c$ | $P2_1/c$ | $P\bar{1}$ |
| $a$ [Å] | 13.5358(17) | 18.878(4) | 18.094(4) | 15.048(3) |
| $b$ [Å] | 14.4773(18) | 14.238(3) | 14.237(3) | 15.268(3) |
| $c$ [Å] | 20.357(3) | 21.255(4) | 21.249(4) | 25.010(5) |
| $\alpha$ [°] | 76.984(7) | 90 | 90 | 78.97(3) |
| $\beta$ [°] | 75.046(7) | 108.90(3) | 103.82(3) | 83.64(3) |
| $\gamma$ [°] | 87.325(7) | 90 | 90 | 62.96(3) |
| $V$ [Å$^3$] | 3754.9(8) | 5405.1(19) | 5315.4(18) | 5021.3(17) |
| $Z$ | 2 | 4 | 4 | 2 |
| $D_{calcd.}$ [g cm$^{-3}$] | 1.323 | 1. 949 | 1.920 | 1.707 |
| Temperature [$K$] | 293(2) | 153(2) | 153(2) | 153(2) |
| $F$(000) | 1530 | 3016 | 3128 | 2544 |
| $\mu$(Mo-$K_\alpha$) [mm$^{-1}$] | 1.153 | 6.075 | 6.288 | 3.652 |
| No. reflections measured | 47388 | 41609 | 35233 | 40271 |
| No. unique reflections | 13181 | 11652 | 10417 | 20409 |
| No. observed reflections | 7262 | 9239 | 7779 | 16200 |
| No. parameters | 806 | 568 | 551 | 1180 |
| $R_{int}$ | 0.0722 | 0.0571 | 0.0605 | 0.0687 |
| $R_1$,[a] $wR_2$[b] [$I \geq 2\sigma(I)$] | 0.0753, 0.1342 | 0.0618, 0.0901 | 0.0690, 0.0956 | 0.0480, 0.1297 |
| $R_1$,[a] $wR_2$[b] (all data) | 0.0971, 0.2133 | 0.0828, 0.1455 | 0.1021, 0.1549 | 0.0624, 0.1450 |
| GoF[c] | 1.097 | 1.012 | 1.043 | 1.073 |
| Final diff. peaks [e Å$^{-3}$] | +1.015, –1.060 | +1.778, –1.669 | +1.147, –1.229 | +1.946, –1.493 |

[a] $R_1 = ||F_o| - |F_c||/|F_o|$. [b] $wR_2 = [w(|F_o^2| - |F_c^2|)^2/w|F_o^2|^2]^{1/2}$. [c] GoF = $[w(|F_o| - |F_c|)2/(N_{obs} - N_{param})]^{1/2}$.

aperture of 0.2 mm radius was placed in front of the detector to measure the transmitted energy when assessment of laser beam distortion was needed. To eliminate scattering effects, a lens was mounted after the samples to collect the scattered light.

## Acknowledgments

This project was supported by the Natural Science Foundation of China (project number 90301005) and the Hong Kong Research Grants Council (project number 601506). Q.-F. Z. would like to thank the Science and Technological Fund of Anhui Province for Outstanding Youth (06046100) and the Research Fund for the Returned Overseas Talents of Anhui Province (2006Z041).

[1] A. Müller, E. Diemann, R. Jostes, H. Bögge, *Angew. Chem. Int. Ed. Engl.* **1981**, *20*, 934–954.
[2] D. Coucouvanis, *Acc. Chem. Res.* **1991**, *24*, 1–73.
[3] R. H. Holm, *Adv. Inorg. Chem.* **1992**, *38*, 1–71.
[4] S. Shi, W. Ji, S. H. Tang, J. P. Lang, X. Q. Xin, *J. Am. Chem. Soc.* **1994**, *116*, 3615–3616.
[5] C.-M. Che, B.-H. Xia, J.-S. Huang, C.-K. Chan, Z.-Y. Zhou, K.-K. Cheung, *Chem. Eur. J.* **2001**, *7*, 3998–4006.
[6] B. J. Coe, in *Comprehensive Coordination Chemistry II* (Eds.: J. A. McCleverty, T. J. Meyer), Elsevier Pergamon, Oxford, U.K., **2004**, vol. 9, pp. 621–687.
[7] X. T. Wu, P. C. Chen, S. W. Du, Z. Y. Zhu, J. X. Lu, *J. Cluster Sci.* **1994**, *5*, 265–276.
[8] Q. F. Zhang, Y. N. Xiong, T. S. Lai, W. Ji, X. Q. Xin, *J. Phys. Chem. B* **2000**, *104*, 3476–3479.
[9] B. J. Coe, N. R. M. Curati, *Comments Inorg. Chem.* **2004**, *25*, 147–184.
[10] J. Wachter, *Eur. J. Inorg. Chem.* **2004**, 1367–1378.
[11] C. C. Christuk, M. A. Ansari, J. A. Ibers, *Inorg. Chem.* **1992**, *31*, 4365–4369.
[12] R. J. Salm, J. A. Ibers, *Inorg. Chem.* **1994**, *33*, 4216–4220.
[13] Q. M. Wang, X. T. Wu, Q. Huang, T. L. Sheng, P. Lin, *Polyhedron* **1997**, *16*, 1439–1443.
[14] M. C. Hong, M. H. Wu, X. Y. Huang, F. L. Jiang, R. Cao, H. Q. Liu, J. X. Lu, *Inorg. Chim. Acta* **1997**, *260*, 73–77.
[15] M. C. Hong, Q. F. Zhang, R. Cao, D. X. Wu, J. T. Chen, W. J. Zhang, H. Q. Liu, J. X. Lu, *Inorg. Chem.* **1997**, *36*, 6251–6260.
[16] C. C. Christuk, M. A. Ansari, J. A. Ibers, *Angew. Chem. Int. Ed. Engl.* **1992**, *31*, 1477–1478.
[17] Q. F. Zhang, Z. Yu, J. Ding, Y. Song, A. Rothenberger, D. Fenske, W. H. Leung, *Inorg. Chem.* **2006**, *45*, 5187–5195.
[18] Q. F. Zhang, J. Ding, Z. Yu, Y. Song, A. Rothenberger, D. Fenske, W. H. Leung, *Inorg. Chem.* **2006**, *45*, 8638–8647.
[19] Q. F. Zhang, W. H. Leung, X. Q. Xin, H. K. Fun, *Inorg. Chem.* **2000**, *39*, 417–516.
[20] Q. F. Zhang, W. H. Leung, X. Q. Xin, *Coord. Chem. Rev.* **2002**, *224*, 35–49.
[21] Y. Y. Niu, H. G. Zheng, H. W. Hou, X. Q. Xin, *Coord. Chem. Rev.* **2004**, *248*, 169–183.
[22] N. Bresciani, N. Marsich, G. Nardin, L. Randaccio, *Inorg. Chim. Acta* **1974**, *10*, L5–L6.
[23] J. K. Bera, M. Nethaji, A. G. Samuelson, *Inorg. Chem.* **1999**, *38*, 218–228.
[24] W. B. Zhou, Z. C. Dong, J. L. Song, H. Y. Zeng, R. Cao, G. C. Guo, J. S. Huang, J. Li, *J. Cluster Sci.* **2002**, *13*, 119–136.
[25] Q. F. Zhang, Z. Yu, A. Rothenberger, D. Fenske, W. H. Leung, *Inorg. Chim. Acta* **2007**, *360*, 1568–1574.
[26] J. Diaz, M. P. Gamasa, J. Gimeno, A. Tirpicchio, M. T. Camellini, *J. Chem. Soc., Dalton Trans.* **1987**, 1275–1278.
[27] Q. F. Zhang, S. S. S. Raj, H. K. Fun, X. Q. Xin, *Chem. Lett.* **1999**, 619–620.
[28] M. A. Ansari, C.-N. Chau, C. H. Mahler, J. A. Ibers, *Inorg. Chem.* **1989**, *28*, 650–654.
[29] M. A. Ansari, C. H. Mahler, G. S. Chorghade, Y.-J. Lu, J. A. Ibers, *Inorg. Chem.* **1990**, *29*, 3832–3839.
[30] V. W.-W. Yam, K. K. W. Lo, K. K. Cheung, *Inorg. Chem.* **1996**, *35*, 3459–3462.
[31] C. W. Liu, I. J. Shang, J. C. Wang, T. J. Keng, *Chem. Commun.* **1999**, 995–996.

 © 2007 Wiley-VCH Verlag GmbH & Co. KGaA, Weinheim 

[32] Q. F. Zhang, M. T. Bao, M. C. Hong, R. Cao, Y. L. Song, X. Q. Xin, *J. Chem. Soc., Dalton Trans.* **2000**, 605–610.
[33] C. C. Christuk, J. A. Ibers, *Inorg. Chem.* **1993**, *37*, 5105–5108.
[34] M. Sheik-Bahae, A. A. Said, T. H. Wei, D. J. Hagan, E. W. van Stryland, *IEEE J. Quantum Electron.* **1990**, *26*, 760–769.
[35] M. Sheik-Bahae, A. A. Said, E. W. van Stryland, *Opt. Lett.* **1989**, *14*, 955–957.
[36] S. Shi, Z. Lin, Y. Mo, X. Q. Xin, *J. Phys. Chem.* **1996**, *100*, 10696–10701.
[37] Z. R. Chen, H. W. Hou, X. Q. Xin, K. B. Yu, S. Shi, *J. Phys. Chem.* **1995**, *99*, 8717–8721.
[38] H. G. Zheng, Y. Xiao, Y. X. Wang, M. H. Ma, Y. Cai, A. Usman, H. K. Fun, Y. L. Song, X. Q. Xin, *Inorg. Chim. Acta* **2003**, *351*, 63–68.
[39] M. K. M. Low, H. W. Hou, H. G. Zheng, W. T. Wong, G. X. Jin, X. Q. Xin, W. Ji, *Chem. Commun.* **1998**, 505–506.
[40] C. Zhang, Y. L. Song, B. M. Fung, Z. L. Xue, X. Q. Xin, *Chem. Commun.* **2000**, 843–844.
[41] C. Zhang, Y. L. Song, Y. Xu, H. K. Fun, G. Y. Fang, Y. X. Wang, X. Q. Xin, *J. Chem. Soc., Dalton Trans.* **2000**, 2823–2829.
[42] C. Zhang, Y. L. Song, F. E. Kühn, Y. X. Wang, X. Q. Xin, W. A. Herrmann, *Adv. Mater.* **2002**, *14*, 818–822.
[43] S. C. O'Neal, J. W. Kolis, *J. Am. Chem. Soc.* **1988**, *110*, 1971–1972.
[44] G. J. Kubas, *Inorg. Synth.* **1996**, *28*, 68–70.
[45] F. T. Wang, J. Najzionek, K. L. Leneker, H. Wasserman, D. M. Braitsch, *Inorg. Synth. Met.-Org. Chem.* **1978**, *8*, 119–125.
[46] G. M. Sheldrick, *SHELXTL-97 Version 5.1*, Software Reference Manual, Bruker AXS, Inc., Madison, Wisconsin, USA, **1997**.

Received: November 25, 2006
Published Online: April 4, 2007

 © 2007 Wiley-VCH Verlag GmbH & Co. KGaA, Weinheim 

DOI: 10.1002/ejic.200601220

# Metal Ion Complementarity: Effect of Ring-Size Variation on the Conformation and Stability of Lead(II) and Cadmium(II) Complexes with Pendant-Armed Crowns

**Martín Regueiro-Figueroa,[a] David Esteban-Gómez,[a] Carlos Platas-Iglesias,[a] Andrés de Blas,*[a] and Teresa Rodríguez-Blas*[a]**

**Keywords:** Lead / Cadmium / Macrocycles / N,O ligands / Density functional calculations

The binding tendencies of the pendant-armed crown ethers $L^1$–$L^3$ [$L^1$ = *N*,*N*′-bis(benzimidazol-2-ylmethyl)-1,7-diaza-12-crown-4, $L^2$ = *N*,*N*′-bis(benzimidazol-2-ylmethyl)-1,10-diaza-15-crown-5) and $L^3$ = *N*,*N*′-bis(benzimidazol-2-ylmethyl)-4,13-diaza-18-crown-6] towards $Pb^{II}$ and $Cd^{II}$ have been investigated. The X-ray crystal structure of $[Cd(L^3)](ClO_4)_2$·EtOH shows that, in the solid state, the $Cd^{II}$ ion is eight-coordinate and fits quite well into the crown hole, favouring an *anti* arrangement of the organic receptor. NMR measurements recorded in acetonitrile solution indicate that increasing the crown size induces a conformational change in the series of $Cd^{II}$ complexes. The conformation goes from a *syn* arrangement for $L^1$ to an *anti* arrangement for $L^3$, passing through a *syn* ⇆ *anti* equilibrium in the complex derived from $L^2$. On the contrary, no conformational change was observed for the corresponding $Pb^{II}$ complexes, which have a *syn* conformation in all cases. These results have been confirmed by means of density functional theory (DFT) calculations performed by using the B3LYP model. The binding constants obtained from UV/Vis titration experiments in DMSO solution demonstrate that a decrease in the crown size provokes a $10^2$-fold enhancement of the stability for this series of $Cd^{II}$ complexes, whereas for $Pb^{II}$ a gradual decrease of the binding constants is observed. Receptor $L^1$ shows a certain degree of selectivity for $Cd^{II}$ over $Pb^{II}$, with a selectivity factor $> 10^2$.
(© Wiley-VCH Verlag GmbH & Co. KGaA, 69451 Weinheim, Germany, 2007)

## Introduction

Rational ligand design for selective complexation of metal ions is a field of great interest for chemists. Indeed, selective complexation of metal ions is a condition required for practical applications in many research areas such as the design of ligands as therapeutic reagents for the treatment of metal intoxication, design of antibiotics that owe their antibiotic action to specific metal complexation, design of complexes for imaging agents in the body or design of functional groups for chelating ion-exchange materials, selective metal extractants and metal ion sequestering agents, among others. Some interesting papers and reviews have been written on this subject.[1] Ligand design essentially consists of selecting appropriate donor atoms for the target metal ion and connecting them in an architecture that satisfies the geometric and electronic requirements of the metal ion. Two important concepts must be taken into account for ligand design: preorganization[2] and complementarity.[3] The former may be considered as an entropic effect[4] related to the different conformational states that the ligand can adopt in the free and bound form. Complementarity corresponds to the degree of structural correspondence between the binding sites offered by the ligand structure and the binding sites required by the metal ion. One of the criteria for optimal complementarity is that the metal ion should be able to contact all the donor atoms of the ligand at an optimal metal–donor distance, and therefore the concept of size-match (matching the size of the ligand cavity to the size of the metal ion) must be taken into account in ligand design. Commonly, this has been used as the key concept for the design of complementary ligand architecture; however, many examples have pointed out that when size-match is the sole criterion for the design, the results are often undesired.[1e,5] From the examples given in the literature, it follows that although size-match is a necessary condition for complementarity, it is not sufficient, and that there are other structural factors that must be considered in assessing the degree of metal ion complementarity, in particular the spatial distribution of donor atoms around the metal ion and the orientation of the donor groups.[1e] The application of the complementarity concept is not only restricted to the interaction between a ligand and a given metal ion, but it can also be generalized to any kind of host–guest interaction (i.e. supramolecular assemblies).[6]

[a] Dpto. Química Fundamental, Facultade de Ciencias, Campus da Zapateira s/n, Universidade da Coruña,
15071 A Coruña, Spain
Fax: +34-167065
E-mail: mayter@udc.es
Supporting information for this article is available on the WWW under http://www.eurjic.org or from the author.

 © 2007 Wiley-VCH Verlag GmbH & Co. KGaA, Weinheim 

In this paper, we report the binding tendencies of the pendant-armed crown ethers $L^1$–$L^3$ [$L^1$ = *N*,*N*′-bis(benzimidazol-2-ylmethyl)-1,7-diaza-12-crown-4, $L^2$ = *N*,*N*′-bis(benzimidazol-2-ylmethyl)-1,10-diaza-15-crown-5) and $L^3$ = *N*,*N*′-bis(benzimidazol-2-ylmethyl)-4,13-diaza-18-crown-6; see Scheme 1] towards $Pb^{II}$ and $Cd^{II}$. The cyclic framework of crown ethers affords an interesting platform for the complexation of metal ions, and they have been commonly used for studying metal ion complementarity. On the other hand, $Pb^{II}$ and $Cd^{II}$ have been selected by taking into account their ionic radius and particular coordination properties. $Pb^{II}$ exhibits the "inert pair effect" and has variable coordination numbers and geometries.[7] The so-called "inert pair effect" refers to the resistance of the pair of outer electrons on $Pb^{II}$ to removal or to participation in covalent bond formation, and it has been explained as a relativistic effect causing the 6s orbital to contract, thereby increasing the energy required to remove or interact with the 6s lone pair of electrons. Likewise, $Cd^{II}$ is capable of considerable plasticity in the lengths of its bonds, and recently Hancock et al.[5] have proved that this metal ion shows an unusual ability to complex almost equally strongly with 12-crown-4, 15-crown-5 and 18-crown-6, in spite of the very different metal ion size requirements of these crown ethers. These authors attribute this behaviour to relativistic effects.

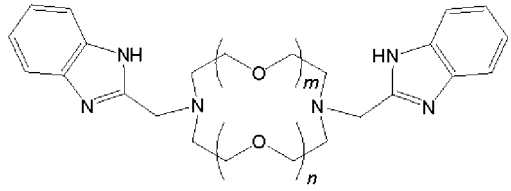


$L^1$: *m* = 1, *n* = 1
$L^2$: *m* = 1, *n* = 2
$L^3$: *m* = 2, *n* = 2

Scheme 1.

## Results and Discussion

### Synthesis and Characterization of Complexes

The reaction of receptors $L^1$, $L^2$ or $L^3$ (Scheme 1) with $Cd^{II}$ or $Pb^{II}$ perchlorates in absolute ethanol or acetonitrile led to compounds of formula $[Cd(L^1)](ClO_4)_2 \cdot EtOH$ (**1**), $[Pb(L^1)](ClO_4)_2 \cdot 2H_2O$ (**2**), $[Cd(L^2)](ClO_4)_2 \cdot CH_3CN \cdot EtOH$ (**3**), $[Pb(L^2)](ClO_4)_2$ (**4**), $[Cd(L^3)](ClO_4)_2 \cdot EtOH$ (**5**) and $[Pb(L^3)](ClO_4)_2 \cdot EtOH$ (**6**) in good yields (66–76%). The IR spectra (KBr disks) show bands at ca. 1540 and 1120 $cm^{-1}$ due to the ν(C=C) and ν(C–O) stretching frequencies of the benzimidazole and ether groups, respectively. These bands are shifted by 10–15 $cm^{-1}$ to higher wavenumbers with respect to their position in the spectra of the free receptors. The spectra also show absorption bands at ca. 1090 and 625 $cm^{-1}$ attributable to the asymmetric $\nu_{as}$(Cl–O) stretching and $\delta_{as}$(O–Cl–O) bending modes of the perchlorate groups. These bands appear without splitting, as befit uncoordinated anions. The FAB mass spectra of each complex shows intense peaks corresponding to the fragments $[M(L^n)(ClO_4)]^+$ and $[M(L^n–H)]^+$ ($L^n$ = $L^1$, $L^2$ or $L^3$), which confirms the formation of the complexes. Conductivity measurements were carried out in ca. $10^{-3}$ M acetonitrile solutions at 20 °C. The molar conductivity values revealed that all complexes behave as 2:1 electrolytes in this solvent.[8]

### X-ray Crystal Structures

The structure of the uncoordinated receptor $L^1$ was determined by X-ray diffraction analysis. The receptor crystallizes in the $P2_1/n$ monoclinic space group. The arms of the lariat ether are arranged on the same side of the crown moiety, resulting in a *syn* conformation (Figure 1), with the lone pairs of both pivotal nitrogen atoms directed into the receptor cavity in an *endo-endo* arrangement. The conformation of the receptor is conditioned by two strong intramolecular hydrogen-bonding interactions between the NH groups of the benzimidazole subunits and the oxygen atoms of the crown moiety [N2···O1 2.936(3) Å, N2···H2 0.88(2) Å, O1···H2 2.07(3) Å, N2–H2–O1 166(2)°; N6···O2 2.911(2) Å, N6···H6 0.91(2) Å, O2···H6 2.02(2) Å, N6–H6–O2 = 166(2)°]. The *syn* conformation brings the two benzimidazole units close together, so that intramolecular π–π interactions are possible.[9–11] The distance between the centres of the two rings is 3.681 Å, while the C5–C19 distance amounts to 3.371(3) Å, and the angle between the least-squares planes of the two benzimidazole units is 13.77(7)°.

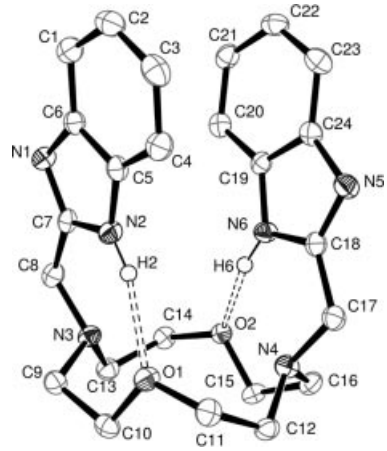


Figure 1. X-ray crystal structure of receptor $L^1$ with atom labelling; hydrogen atoms are omitted for simplicity; the ORTEP plot is drawn at the 50% probability level.

The solid-state structure of compound **5** was also determined by single-crystal X-ray diffraction analysis. Crystals contain the cation $[Cd(L^3)]^{2+}$, two perchlorate anions and one ethanol molecule. The compound crystallizes in the centrosymmetric $P2_1/c$ monoclinic space group. One of the perchlorate anions and the ethanol molecule are quite disordered: the site occupancy factor is 0.776(5) for the perchlorate group [Cl1A, O10A, O11A, O12A and O13A], and 0.641(9) for the ethanol molecule [O100, C100 and C101].

 © 2007 Wiley-VCH Verlag GmbH & Co. KGaA, Weinheim 

Table 1 summarizes selected bond lengths of the metal coordination environment, while Figure 2 displays a view of the structure of the cation. The complex cation $[Cd(L^3)]^{2+}$ contains a $CdN_4O_4$ core in which the eight heteroatoms of $L^3$ are coordinated to the metal ion. The organic receptor $L^3$ adopts an *anti* arrangement in which both benzimidazole pendant arms are disposed on opposite sides of the crown moiety. The $Cd^{II}$ ion is asymmetrically placed inside the macrocyclic ring, being closer to the donor atoms O2 and O3 [Cd1–O2: 2.585(2) Å; Cd1–O3: 2.526(2) Å] than to O1 and O4 [Cd1–O1: 2.594(2) Å; Cd1–O4: 2.604(2) Å]. The distances between $Cd^{II}$ and the two pivotal nitrogen atoms differ by ca. 0.1 Å [Cd1–N3: 2.516(3) Å and Cd1–N4: 2.627(3) Å], whereas the distances between $Cd^{II}$ and nitrogen atoms of the benzimidazole groups are similar and fall within the range reported for Cd–N distances in complexes with ligands containing benzimidazole groups.[12,13] On the other hand, the distances between the metal ion and nitrogen pivotal atoms and oxygen atoms of the crown moiety are ca. 0.2 Å longer than those observed in a cadmium(II) cryptate derived from 1,10-diaza-15-crown-5 containing a pyridinyl Schiff base spacer, where the metal ion is seven-coordinate.[14] The Cd–O bond lengths are also ca. 0.2 Å longer than those observed for $Cd^{II}$ complexes of 12-crown-4[15] and 15-crown-5,[16] but similar to those observed for different $Cd^{II}$ complexes of 18-crown-6.[16] These data reflect the ability of $Cd^{II}$ to change Cd–O bond lengths to meet the requirements of crown ethers of different size, which has been attributed to relativistic effects.[5] Relativistic effects lower the energy of the valence shell s orbital next in energy to a filled d orbital in heavy $d^{10}$ metal ions, which leads to a tendency to sp hybridization and the formation of more covalent M–L bonds.[17] In the case of compound **5**, the presence of two axial nitrogen donor atoms of the benzimidazole groups [N1 and N5] causes a distortion toward linear coordination geometry with long equatorial Cd–O bonds.

Table 1. Selected bond lengths [Å] and angles [°] of the metal coordination environment in $[Cd(L^3)]^{2+}$.

| | | | |
|---|---|---|---|
| Cd1–N1 | 2.287(2) | Cd1–O3 | 2.526(2) |
| Cd1–N5 | 2.245(2) | Cd1–O4 | 2.604(2) |
| Cd1–O1 | 2.594(2) | Cd1–N3 | 2.516(3) |
| Cd1–O2 | 2.585(2) | Cd1–N4 | 2.627(3) |
| N5–Cd1–N1 | 158.78(8) | O2–Cd1–O1 | 64.18(7) |
| N5–Cd1–N3 | 111.85(9) | N5–Cd1–O4 | 80.91(7) |
| N1–Cd1–N3 | 74.01(8) | N1–Cd1–O4 | 119.22(7) |
| N5–Cd1–O3 | 121.09(8) | N3–Cd1–O4 | 66.64(8) |
| N1–Cd1–O3 | 76.91(7) | O3–Cd1–O4 | 64.10(7) |
| N3–Cd1–O3 | 96.35(8) | O2–Cd1–O4 | 157.23(7) |
| N5–Cd1–O2 | 78.04(8) | O1–Cd1–O4 | 122.98(7) |
| N1–Cd1–O2 | 82.85(8) | N5–Cd1–N4 | 71.32(9) |
| N3–Cd1–O2 | 129.99(8) | N1–Cd1–N4 | 109.83(8) |
| O3–Cd1–O2 | 120.95(7) | N3–Cd1–N4 | 161.82(8) |
| N5–Cd1–O1 | 86.05(8) | O3–Cd1–N4 | 68.16(7) |
| N1–Cd1–O1 | 77.30(7) | O2–Cd1–N4 | 68.00(7) |
| N3–Cd1–O1 | 67.73(8) | O1–Cd1–N4 | 130.26(7) |
| O3–Cd1–O1 | 152.65(7) | O4–Cd1–N4 | 97.07(7) |

The coordination polyhedron around the $Cd^{II}$ ion can be described as a distorted square antiprism composed of two

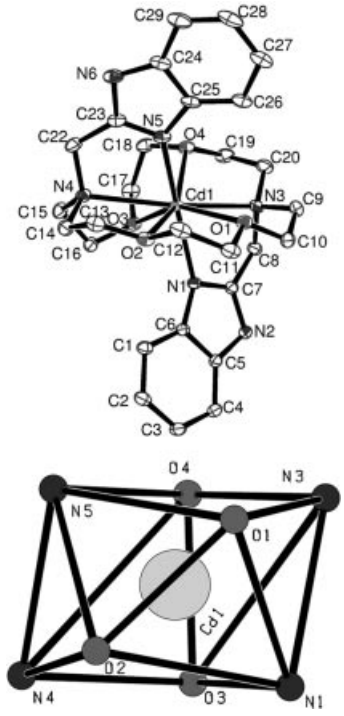


Figure 2. Top: X-ray crystal structure of the cation $[Cd(L^3)]^{2+}$ in compound **5** with atom labelling; hydrogen atoms are omitted for simplicity; the ORTEP plot is drawn at the 30% probability level. Bottom: Coordination polyhedron around $Cd^{II}$ in compound **5**.

parallel pseudoplanes (see Figure 2): O1, O4, N3 and N5 define the upper pseudoplane (mean deviation from planarity 0.0889 Å), while O2, O3, N4 and N1 define the lower pseudoplane (mean deviation from planarity 0.0982 Å). The angle between the two least-squares planes is 9.14°. The mean twist angle, $\omega$,[18] between these nearly parallel squares is 26.0°, showing a deformation of the coordination polyhedron from a square antiprism (ideal value 45°) toward a square prism (ideal value 0°) by ca. 19°.

## Solution Structure

The behaviour of compounds **1** to **6** in [$D_3$]acetonitrile solution was investigated by $^1H$ and $^{13}C$ NMR spectroscopy. The spectra were assigned on the basis of two-dimensional COSY, HSQC and HMBC experiments. Significant changes in the chemical shifts, the structures of the signals and even the number of signals are observed in the $^1H$ NMR spectra upon coordination of the ligands to the metal ions (Tables S1–S3, Supporting Information). The most complicated region of the spectra is the part where the ethylene and methylene proton signals are observed. The coordination to the metal ion increases the rigidity of the ligand, limiting conformational exchange processes, so that the geminal $CH_2$ protons are no longer equivalent. Since assignments to specific axial/equatorial $CH_2$ protons were not possible on the basis of the 2D NMR spectra, they were carried out by using the stereochemical dependence of their shifts on the polarization of the C–H bonds derived from

 © 2007 Wiley-VCH Verlag GmbH & Co. KGaA, Weinheim 

the coordination of the metal ion.[19] This polarization results in a deshielding of the equatorial protons, which point away from the metal ion. The aromatic region appears to be usually more clearly resolved for metal ion complexes than for free ligands. This is due to the presence in the latter of exchange processes involving the NH and N positions of the benzimidazole groups that are prevented by coordination to the metal ion.

The $^{13}C$ NMR spectra of **1** and **2** display ten resonances for the 24 proton nuclei present in the ligand backbone, in agreement with an effective $C_{2v}$ symmetry for both complexes in solution. Upon coordination to the metal ion, the signals corresponding to the ethylene and methylene protons shift downfield (Figure 3), confirming the coordination of the ligand in the complexes. The ethylene protons at the five-membered chelate rings formed by the coordination of the ligand to the metal ion give an AA′XX′ spectrum, where the equatorial protons are more deshielded by the electric field effect of the cation (Figure 3). The methylene proton signals of the pendant arms in the $^1H$ NMR spectra of **1** and **2** show satellites attributable to proton coupling to the naturally abundant $^{113}Cd$ ($I$ = 1/2) and $^{207}Pb$ ($I$ = 1/2), respectively, reflecting kinetic inertness in the complexes as well as a degree of covalence in the interaction with the nearby donor atom. So, the signals at $\delta$ = 4.28 ppm for **1** and $\delta$ = 4.51 ppm for **2** appear as a singlet flanked by the satellites, with a $^3J(H_8–^{113}Cd)$ of 9.96 Hz and $^3J(H_8–^{207}Pb)$ of 10.10 Hz. A $^3J(H–^{113}Cd)$ of 8.00 Hz has been reported for the methylene protons of a $Cd^{II}$ complex with a multidentate nitrogen receptor, for which a Cd–N bond length of 2.53 Å was found in the solid state,[20] while $^3J(H–^{207}Pb)$ values of 14.30 and 17.00 Hz have been observed for $[Pb(EDTA–N_4)]^{2+}$, where the Pb–N bond length in the solid state was found to be 2.61 Å.[21]

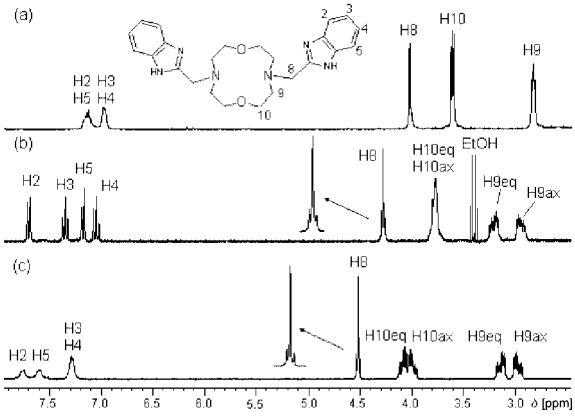


Figure 3. $^1H$ NMR spectra of (a) $L^1$, (b) compound **1** and (c) compound **2** as recorded in [$D_3$]acetonitrile solution at 298 K.

The $^1H$ NMR spectrum of **3** shows two different resonances with different intensities for the NH groups of the benzimidazole subunits, which suggests the presence of two different isomers of **3** in acetonitrile solution. The spectrum recorded at 298 K displays broad resonances for the signals of the aromatic protons, but the signals become better resolved upon decreasing the temperature below 233 K. A detailed analysis of the $^1H$ and $^{13}C$ NMR spectra at this temperature clearly confirms the presence of two complex species in solution that are in equilibrium. The signals corresponding to both species were fully assigned with the aid of two-dimensional COSY, HSQC and HMBC spectra (Table S2, Supporting Information). The $^1H$ NMR spectrum of **3** recorded at 233 K is shown in Figure 4a. The spectrum of the major species shows 26 resonances in the $^{13}C$ NMR spectrum, indicating $C_1$ symmetry in solution, while the minor species shows 13 resonances, which indicates an effective $C_2$ symmetry of the complex where the benzimidazole pendant arms are equivalent. In a previous work, we reported a similar situation for lanthanide complexes with lariat ethers derived from 1,10-diaza-15-crown-5 containing salicylaldimine groups, which show a *syn* conformation with a $C_1$ symmetry.[11] A striking feature of the $^1H$ NMR spectrum of the species with $C_1$ symmetry is the unusually large low-frequency shift found for the signal of the H5′ protons ($\delta$ =6.18 ppm, Figure 4a). Similar shielding effects have been observed in lanthanide complexes with lariat ethers having a *syn* conformation, which have been explained by the observation that these protons are directed toward the aromatic ring current of the neighbouring pendant arm.[22] On this basis, we assign the major species of $[Cd(L^2)]^{2+}$ in solution, which shows $C_1$ symmetry, to a complex with a *syn* arrangement of the pendant arms, while the minor species (with an effective $C_2$ symmetry in solution) is assigned to an *anti* isomer. An equilibrium in solution between the *syn* and *anti* conformations has been previously reported for $Ba^{II}$ complexes with pendant-armed crowns derived from 4,13-diaza-18-crown-6.[23] The smaller $Cd^{II}$ ion fits quite well inside the crown moiety hole of $L^2$, which makes possible an equilibrium between *syn* and *anti* isomers in acetonitrile solution. To confirm this we have performed DFT calculations at the B3LYP level on the $[Cd(L^2)]^{2+}$ system. Our calculations provide two minimum-energy conformations for $[Cd(L^2)]^{2+}$, which correspond to the *syn* and *anti* isomers (Figure 5). The calculated geometry for the *syn*

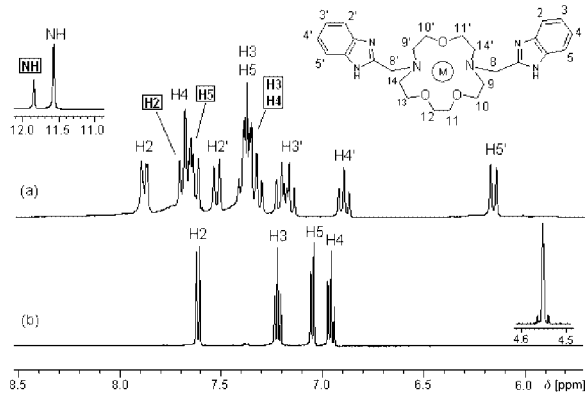


Figure 4. (a) Partial $^1H$ NMR spectrum of compound **3** recorded in [$D_3$]acetonitrile at 233 K. The labels within rectangles correspond to the signals of the *anti* isomer (effective $C_2$ symmetry), while the remaining ones denote signals of the *syn* one ($C_1$ symmetry). (b) Partial $^1H$ NMR spectrum of compound **4** recorded in [$D_3$]acetonitrile at 298 K.

 © 2007 Wiley-VCH Verlag GmbH & Co. KGaA, Weinheim 

isomer shows the H5′ proton placed above the plane of the benzimidazole group of the neighbour pendant arm, in agreement with the high-field shift observed for this proton in the NMR spectrum.

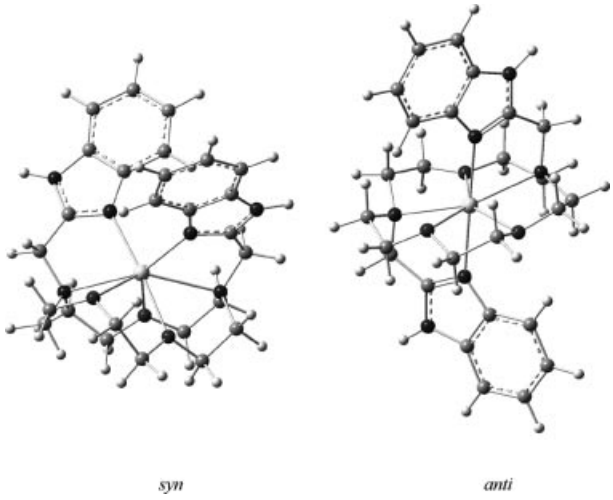


Figure 5. Structures of the two isomers of $[Cd(L^2)]^{+2}$ obtained from DFT calculations at the B3LYP level.

The equilibrium between the *syn* and *anti* isomers of $[Cd(L^2)]^{2+}$ is shown in Equation (1).

$$[Cd(L^2)]^{2+}_{syn} \leftrightarrows [Cd(L^2)]^{2+}_{anti} \quad (1)$$

The equilibrium constant defined by Equation (1), $K_{eq}$, was determined at several temperatures between 233 to 294 K from the relative integrations of the $^1$H NMR signals due to the NH protons of the benzimidazole groups. The ratio between the intensity of the peaks corresponding to the *syn* and *anti* species was found to be constant within experimental error in the range of temperatures studied. This indicates that $\Delta S^0 \approx 0$ for the interconversion process described by Equation (1), in agreement with an intramolecular rearrangement. From the $^1$H NMR in acetonitrile solution, we obtain $K_{eq} = 0.33 \pm 0.02$, pointing out that the *syn* isomer predominates in acetonitrile solution at any temperature.

The $^1$H NMR spectrum of the $Pb^{II}$ derivative **4** (Figure 4b) is clearly more simple than that of the corresponding $Cd^{II}$ analogue. In this case, a single species with an effective $C_s$ symmetry in solution is observed. This is confirmed by the $^{13}$C NMR spectrum, which shows 13 signals for the 26 nuclei of the ligand backbone (Table S2, Supporting information). DFT calculations predict a *syn* conformation for the receptor in the $[Pb(L^2)]^{2+}$ system, where the metal ion is placed over the crown moiety interacting with all the donor atoms present in the receptor (Figure S1, Supporting Information). An identical situation has been observed in complexes with lariat ethers derived from 1,10-diaza-15-crown-5.[14] It may be surprising to observe an effective $C_s$ symmetry for $[Pb(L^2)]^{2+}$ while the analogous $[Cd(L^2)]^{2+}$ *syn* isomer displays a $C_1$ symmetry in solution. This can be explained if one considers the smaller size of $Cd^{II}$ compared to $Pb^{II}$, which allows the two benzimidazole pendants to adopt a face-to-face conformation (Figure 6). In $[Pb(L^2)]^{2+}$ the two pendant arms adopt a more open conformation (see Figure 5 and Figure S1, Supporting Information), which allows an easy interconversion between the two optical isomers ($\Delta$ and $\Lambda$) characteristic of the *syn* conformation.[24] When this interconversion is fast enough on the $^1$H NMR time scale, an effective $C_s$ symmetry in solution is observed (Figure 6).

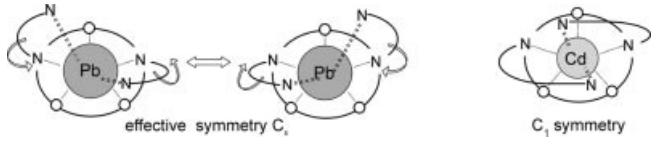


Figure 6. Schematic representation of the different *syn* conformations adopted by lariat ethers derived from 1,10-diaza-15-crown-5 depending on the size of the metal ion.

As observed for the complex of $L^1$, the $^1$H NMR spectrum of $[Pb(L^2)]^{2+}$ shows the singlet due to the H8 protons at $\delta = 4.52$ ppm flanked by satellites with a $^3J(H_8–^{207}Pb)$ of 20.40 Hz (Figure 4b), reflecting a strong interaction between $Pb^{II}$ and the coordinated nitrogen pivot atoms of the receptor. This value is much higher than that observed for the analogous complex derived from $L^1$ (10.10 Hz, vide supra), suggesting that a greater crown size favours a better fit between the $Pb^{II}$ ions and the macrocyclic cavity.

The $^{13}$C NMR spectrum of **5** displays eleven resonances for the 28 carbon nuclei present in the ligand backbone, in agreement with an effective $C_{2h}$ symmetry in solution. This is consistent with an *anti* arrangement of the pendant arms in the complex, as observed in the solid-state structure of this compound described above. In the $^1$H NMR spectra (Figure 7), the signals corresponding to the ethylene protons are again complicated because of the coordination to the metal ion. The signal of the methylene protons of the pendant arms appears as a singlet flanked by the satellites attributable to proton coupling to the naturally abundant $^{113}$Cd ($I = 1/2$) at $\delta = 4.25$ ppm with a $^3J(H_8–^{113}Cd)$ of 7.41 Hz. If we compare this value with that found for **1** (9.96 Hz) we can conclude that, for $Cd^{II}$, increasing the crown size weakens the interaction between the metal ion and the coordinated pivotal nitrogen atoms.

Unlike the $Cd^{II}$ analogue, the $^1$H NMR and the $^{13}$C NMR spectra of the lead(II) complex **6**, (Figure 7b) registered at 233 K are in agreement with an effective $C_2$ symmetry of the complex in solution. The $^1$H-$^1$H COSY spectrum clearly shows a coupling between protons H11 and H12 (see the labelling scheme in Figure 7), which indicates that the $C_2$ axis of the complex is perpendicular to the pseudoplane formed by the donor atoms of the crown moiety. This result indicates a *syn* arrangement of the receptor in the complex.[24] The H8 protons appear as an AB spin system ($^2J_{8a,8b} = 18.40$ Hz) in the spectrum of **6**, while a singlet is observed for the H8 protons in the $Cd^{II}$ analogue **5**. These results are in agreement with a *syn* conformation of the $Pb^{II}$ complex with the pendant arms adopting a face-to-face conformation, as observed for $[Cd(L^2)]^{2+}$.

 © 2007 Wiley-VCH Verlag GmbH & Co. KGaA, Weinheim 

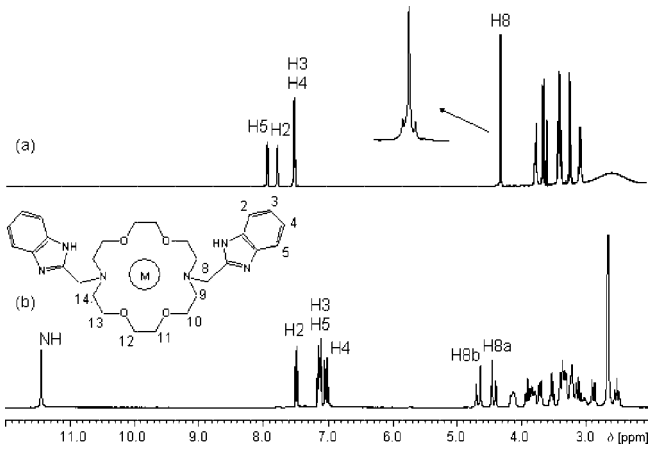


Figure 7. $^1$H NMR spectra of compounds (a) **5** and (b) **6** recorded in [$D_3$]acetonitrile at 298 K.

In order to obtain structural information on this complex in solution we performed geometry optimizations of the $[Pb(L^3)]^{2+}$ system. Our DFT calculations predict two minimum-energy conformations corresponding to a *syn* and an *anti* conformation (Figure S2, Supporting Information). From the conformational energies of the *syn* and *anti* isomers of $[Pb(L^3)]^{2+}$ we have calculated an in vacuo relative free energy, $\Delta G°_{298K} = G°_{anti} - G°_{syn}$, of 3.54 kcal mol$^{-1}$. Likewise, from the results obtained in acetonitrile solution (COSMORS model) we have obtained a relative free energy, $\Delta G^{sol} = G^{sol}_{anti} - G^{sol}_{syn}$, of 4.79 kcal mol$^{-1}$. Thus, our quantum mechanical calculations predict that the *syn* isomer is the most stable one both in vacuo and in solution. These results confirm that the complex adopts a *syn* conformation in solution. This situation contrasts that observed for a related lead(II) complex derived from the same crown moiety and containing aniline pendants, for which an *anti* arrangement of the receptor was found.[25] In that complex, the aniline pendants form six-membered chelate rings upon coordination to the metal ion, which probably favour an *anti* arrangement of the macrocyclic receptor in the complex.

### Stability of the Complexes in Solution

The binding of $Cd^{II}$ and $Pb^{II}$ by the three receptors was investigated by means of spectrophotometric titrations in DMSO solution. The electronic spectra of the free ligands show two typical absorption bands in the near UV attributable to the benzimidazole groups, which can be assigned as $\pi^* \leftarrow \pi$ singlet–singlet transitions[26] ($^1L_a \leftarrow S_0$ and $^1L_b \leftarrow S_0$, where the two excited states are labelled by $^1L_a$ and $^1L_b$ following the suggestion of Platt).[27] Addition of the metal ion salt causes appreciable modification of the spectral patterns. In particular, metal ion addition induces blue shifts of the bands centred at 277 and 284 nm as their intensity increases. These results indicate the coordination of the benzimidazole groups to the metal ion in this solvent. In the course of the titration of $Cd^{II}$ with $L^3$, the development of a weak band centred at ca. 330 nm is also observed. The family of UV/Vis spectra recorded over the course of the titrations of $L^1$ and $L^3$ with $Cd^{II}$ are shown in Figure 8. Nonlinear least-squares analysis of the titration profiles (absorbance against the number of equivalents of $Cd^{II}$, see insets of Figure 8) clearly indicates the formation of 1:1 complexes in every case; the association constants are summarized in Table 2. In all cases, the three ligands form stable complexes with both $Cd^{II}$ and $Pb^{II}$ ($\log K > 5$, Table 2). For $[Cd(L^1)]^{2+}$ the steep curvature of the profile at the addition of 1 equiv. prevents a safe determination of the binding constant, and a lower threshold value of $\log K > 7.5$ can be estimated (Figure 8).

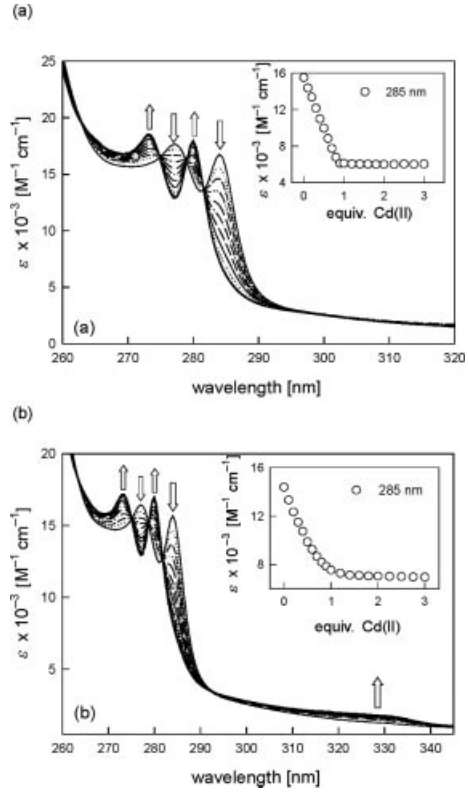


Figure 8. Spectra recorded over the course of the titration of a $10^{-4}$ M solution of (a) $L^1$ and (b) $L^3$ with a standard solution of cadmium(II) perchlorate. Insets: titration profiles at selected wavelengths.

Table 2. Binding constants of the $Cd^{II}$ and $Pb^{II}$ complexes with $L^1$, $L^2$ and $L^3$ obtained from spectrophotometric titrations in DMSO solutions at 25 °C. Log $K$ refers to $L^n + M^{2+} \leftrightarrows [ML^n]^{2+}$.[a]

| Ligand | Ring size | $\log K_{Cd^{II}}$ | $\log K_{Pb^{II}}$ |
|---|---|---|---|
| $L^1$ | 12 | >7.5[b] | 5.65(5) |
| $L^2$ | 15 | 6.23(3) | 6.15(5) |
| $L^3$ | 18 | 5.41(1) | 6.63(9) |

[a] The errors given correspond to one statistical deviation; the experimental errors are estimated to be ±0.2 log $K$ units. [b] The complex is too stable to allow a safe determination of the binding constant.

The log $K$ values obtained show different trends in the binding of $Cd^{II}$ and $Pb^{II}$ on changing the macrocyclic ring size. For $Cd^{II}$, a gradual decrease of the binding constants is observed as the macrocyclic ring size increases, while the $Pb^{II}$ complexes show the opposite behaviour. As a result,

 © 2007 Wiley-VCH Verlag GmbH & Co. KGaA, Weinheim 

receptor $L^1$ shows a certain degree of selectivity for $Cd^{II}$ over $Pb^{II}$, with a selectivity factor $> 10^2$. It is interesting to note that the stability of $Cd^{II}$ complexes with crown ethers such as 18-crown-6, 15-crown-5 or 12-crown-4 increases as the macrocyclic cavity is enlarged.[5] Thus, the introduction of pendant arms into the framework of these crown ethers appears to reverse this trend, revealing the complementarity of $L^1$ and $Cd^{II}$.

The binding affinity trend of the above ligand series toward $Pb^{II}$ is probably the result of a better size-match of the ligand for this metal ion as the size of the crown moiety increases. Moreover, $Pb^{II}$ usually prefers higher coordination numbers than $Cd^{II}$, and therefore one expects an increasing stability of the $Pb^{II}$ complexes with this series of ligands as the number of oxygen atoms of the crown moiety increases. The introduction of an oxygen atom into the crown moiety increases the stability of the corresponding $Pb^{II}$ complex by ca. 0.5 $\log K$ units. The $Pb^{II}$ complex of $L^3$ is more stable than the $Cd^{II}$ analogue by ca. 1 $\log K$ units. A similar difference in the $\log K$ values has been previously reported for $Pb^{II}$ and $Cd^{II}$ complexes of a bibracchial lariat ether derived from diaza-18-crown-6 containing 5-chloro-8-methoxyquinoline pendants ($\log K_{Pb}$ = 7.0 and $\log K_{Cd}$ = 6.1 in MeOH).[28] The binding tendencies discussed above for the $Pb^{II}$ and $Cd^{II}$ complexes described in this work parallel the $^3J(H_8–^{113}Cd)$ and $^3J(H_8–^{207}Pb)$ coupling constants observed in the $^1H$ NMR spectra recorded in acetonitrile solution (vide supra), which are related to the strength of the interaction between the cation and the pivotal nitrogen atoms of the ligand.

## Conclusions

The pendant-armed macrocycles $L^1$, $L^2$ and $L^3$ ($L^1$ = *N*,*N*′-bis(benzimidazol-2-ylmethyl)-1,7-diaza-12-crown-4, $L^2$ = *N*,*N*′-bis(benzimidazol-2-ylmethyl)-1,10-diaza-15-crown-5) and $L^3$ = *N*,*N*′-bis(benzimidazol-2-ylmethyl)-4,13-diaza-18-crown-6) form mononuclear complexes with both $Cd^{II}$ and $Pb^{II}$. NMR measurements recorded in acetonitrile solution indicate that increasing the crown size induces a conformational change in the series of cadmium(II) complexes that goes from a *syn* arrangement for $L^1$ to an *anti* arrangement for $L^3$, passing through a *syn* ⇆ *anti* equilibrium in the complex derived from $L^2$. The X-ray structure of the $[Cd(L^3)]^{2+}$ complex confirms the *anti* arrangement observed in acetonitrile solution. On the contrary, no conformational change was observed for the corresponding lead(II) complexes, which show a *syn* conformation in all cases. DFT calculations (B3LYP model) support the results of the conformational analyses performed on the basis of the NMR spectroscopic data. The binding constants obtained from UV/Vis titration experiments in DMSO solution indicate that a diminution of the crown moiety size provokes a $> 10^2$-fold enhancement of the stability for this series of $Cd^{II}$ complexes, whereas for $Pb^{II}$ a smooth decrease of the binding constants is observed. Receptor $L^1$ shows a certain degree of selectivity for $Cd^{II}$ over $Pb^{II}$, with a selectivity factor $> 10^2$.

## Experimental Section

**General Considerations:** All chemicals were purchased from commercial sources and used without further purification. Solvents were of reagent grade and were purified by the usual methods. *N*,*N*′-Bis(benzimidazol-2-ylmethyl)-4,13-diaza-18-crown-6 ($L^3$) was prepared according to the literature method.[29] ***Caution!*** Although we have experienced no difficulties with perchlorate salts, these should be regarded as potentially explosive and handled with care.[30]

Elemental analyses were carried out with a Carlo Erba 1108 elemental analyzer. FAB mass spectra were recorded by using a FISONS QUATRO mass spectrometer with Cs ion gun in a 3-nitrobenzyl alcohol matrix. $^1H$ and $^{13}C$ NMR spectra were recorded with a Bruker AMX300 or a Bruker WM-500 spectrometer. IR spectra were recorded, as KBr discs, by using a Bruker Vector 22 spectrometer. Conductivity measurements were carried out at 20 °C with a Crison Micro CM 2201 conductimeter by using ca.$10^{-3}$-M solutions of the complexes in acetonitrile. UV/Vis spectra were recorded with a Perkin–Elmer Lambda 900 spectrophotometer, in quartz cells (path length: 1 cm). The cell holder was thermostatted at 25.0 °C with circulating water. Spectrophotometric titrations were performed at 25 °C on $10^{-4}$-M solutions of the ligand in DMSO (polarographic grade). Typically, aliquots of a fresh standard solution of the envisaged perchlorate salt (Pb or Cd, $10^{-2}$ M) were added and the UV/Vis spectra of the samples were recorded. All spectrophotometric titration curves were fitted with the HYPERQUAD program.[31]

**Preparation of the Ligands**

***N*,*N*′-Bis(benzimidazol-2-ylmethyl)-1,7-diaza-12-crown-4 ($L^1$):** 1,7-Diaza-12-crown-4 (1.0 g, 5.7 mmol), *N*,*N*-diisopropylethylamine (4.0 mL, 23.1 mmol) and 2-(chloromethyl)benzimidazole (2.1 g, 12.7 mmol) in acetonitrile (200 mL) were heated under reflux for 12 h and cooled to room temperature. The reaction mixture was concentrated in a rotary evaporator and after being kept at –4 °C for 24 h, a brown precipitate was filtered off and the filtrate was concentrated under vacuum. The resulting yellow oily residue was extracted with $CH_2Cl_2$/water, and the organic phase was dried with anhydrous $MgSO_4$ and concentrated in vacuo. Addition of cold diethyl ether to the oily residue led to the deposition of a light yellow precipitate, which was purified by column chromatography on $Al_2O_3$ with a $CH_2Cl_2$/MeOH 2% mixture as eluent to give a brown solid (1.7229 g, 65%). $C_{24}H_{30}N_6O_2{\cdot}0.5CH_3CN{\cdot}0.5H_2O$ (475.08): calcd. C 64.70, H 7.06, N 19.62; found C 65.32, H 7.83, N 19.36. M.p. 190 °C. $^1H$ NMR (300 MHz, $CDCl_3$, 25 °C): $\delta$ = 2.90 (t, $^3J_{H,H}$ = 4.6 Hz, 8 H), 3.66 (t, $^3J_{H,H}$ = 4.6 Hz, 8 H), 4.10 (s, 4 H), 7.14–7.08 (m, 4 H), 7.66 (br., 4 H), 11.56 (br., 2 H) ppm. $^{13}C$ NMR (75.5 MHz, $CDCl_3$, 25 °C): $\delta$ = 53.8, 55.4, 69.0, 122.6, 153.8 ppm. MS (FAB): *m*/*z* (%BPI) = 435 (100) $[C_{24}H_{30}N_6O_2]^+$. IR (KBr): $\tilde{\nu}$ = 1623 [ν(C=N)], 1531 [ν(C=C)], 1443 [δ(N–H)], 1428 [$\delta(C–H)_{ar}$], 1355, 1274 [$\delta(C–H)_{crown}$], 1104 [ν(C–O)], [ν(C–N) and ν(C–C)], 744 [π(C–H) and π(N–H)] $cm^{-1}$. Single crystals of $L^1$ suitable for X-ray diffraction were grown by recrystallization from acetonitrile.

***N*,*N*′-Bis(benzimidazol-2-ylmethyl)-1,10-diaza-15-crown-5 ($L^2$):** 1,10-Diaza-15-crown-5 (1.0 g, 4.7 mmol), *N*,*N*-diisopropylethyl amine (3.2 mL, 18.4 mmol) and 2-(chloromethyl)benzimidazole (1.7 g, 10.1 mmol) in acetonitrile (200 mL) were heated under reflux for 12 h and cooled to room temperature. The reaction mixture was concentrated in a rotary evaporator and after being kept at –4 °C overnight, the precipitate formed was filtered and air-dried to give a brown solid (1.2411 g, 52%). $C_{26}H_{34}N_6O_3{\cdot}0.5CH_3CN{\cdot}H_2O$

 © 2007 Wiley-VCH Verlag GmbH & Co. KGaA, Weinheim 

(507.81): calcd. C 62.71, H 7.31, N 17.61; found C 63.41, H 7.73, N 17.63. M.p. 228 °C. $^1$H NMR (300 MHz, $CDCl_3$, 25 °C): $\delta$ = 2.84 (t, $^3J_{H,H}$ = 4.7 Hz, 4 H), 2.96 (t, $^3J_{H,H}$ = 4.7 Hz, 4 H), 3.40 (t, $^3J_{H,H}$ = 4.7 Hz, 4 H), 3.58–3.53 (m, 8 H), 4.03 (s, 4 H), 7.22–7.16 (m, 4 H), 7.55 (br., 4 H) ppm. $^{13}$C NMR (75.5 MHz, $CDCl_3$, 25 °C): $\delta$ = 54.1, 56.8, 57.0, 68.5, 69.7, 121.9, 154.7 ppm. MS (FAB): *m/z* (%BPI) = 479 (100) $[C_{26}H_{34}N_6O_3]^+$. IR (KBr): $\tilde{\nu}$ = 1621 [ν(C=N)], 1520 [ν(C=C)], 1455 [δ(N–H)], 1422 [δ(C–H)$_{ar}$], 1346, 1273 [δ(C–H)$_{crown}$], 1106 [ν(C–O)], [ν(C–N) and ν(C–C)], 752 [π(C–H) and π(N–H)] cm$^{-1}$.

**Preparation of the Lead(II) and Cadmium(II) Complexes**

**General Procedure:** A stoichiometric amount (1:1) of the corresponding metal salt was added to a stirred solution of ligand (0.100 g) in absolute ethanol or acetonitrile (50 mL). The mixture was vigorously stirred and heated for 4 h, and the resulting pale-yellow solution was filtered while hot. Quantities of reactants, isolation procedures and characterization of the compounds are described below for each compound.

**[Cd(L$^1$)](ClO$_4$)$_2$·EtOH (1):** Solvent: absolute ethanol. Cd(ClO$_4$)$_2$·3H$_2$O (0.096 g, 0.230 mmol). Slow diffusion of diethyl ether into the former solution at room temperature produced pale-yellow crystals that were collected by filtration and air-dried (0.113 g, 62%). $C_{26}H_{36}CdCl_2N_6O_{11}$ (791.91): calcd. C 39.43, H 4.58, N 10.61; found C 39.88, H 4.58, N 10.90. $\Lambda_M$ (acetonitrile) = 264 cm$^2$Ω$^{-1}$mol$^{-1}$ (2:1 electrolyte). MS (FAB): *m/z* (%BPI) = 647 (70) $[Cd(L^1)(ClO_4)]^+$, 547 (100) $[Cd(L^1–H)]^+$. IR (KBr): $\tilde{\nu}$ = 1622 [ν(C=N)], 1542 [ν(C=C)], 1456 [δ(N–H) δ(C–H)$_{ar}$], 1339, 1277 [δ(C–H)$_{crown}$], 1113 [ν(C–O)], 758 [π(C–H)], 1090 [ν$_a$(Cl–O)], 623 [δ$_a$(O–Cl–O)] cm$^{-1}$.

**[Pb(L$^1$)](ClO$_4$)$_2$·2H$_2$O (2):** Solvent: absolute ethanol. Pb(ClO$_4$)$_2$·3H$_2$O (0.106 g, 0.230 mmol). Slow diffusion of diethyl ether into the former solution at room temperature produced pale-yellow crystals that were collected by filtration and air-dried (0.132 g, 66%). $C_{24}H_{34}Cl_2PbN_6O_{12}$ (876.67): calcd. C 32.88, H 3.91, N 9.59; found C 32.80, H 4.13, N 9.54. $\Lambda_M$ (acetonitrile): 276 cm$^2$Ω$^{-1}$mol$^{-1}$ (2:1 electrolyte). MS (FAB): *m/z* (%BPI) = 741 (100) $[Pb(L^1)(ClO_4)]^+$, 641 (85) $[Pb(L^1–H)]^+$. IR (KBr): $\tilde{\nu}$ = 1621 [ν(C=N)], 1536 [ν(C=C)], 1481 [δ(N–H)], 1452 [δ(C–H)$_{ar}$], 1340, 1274 [δ-(C–H)$_{crown}$], 1118 [ν(C–O)], 762 [π(C–H)], 1086 [ν$_a$(Cl–O)], 625 [δ$_a$(O–Cl–O)] cm$^{-1}$.

**[Cd(L$^2$)](ClO$_4$)$_2$·CH$_3$CN·EtOH (3):** Solvent: acetonitrile. Cd(ClO$_4$)$_2$·3H$_2$O (0.109 g, 0.259 mmol). The reaction mixture was concentrated in a rotary evaporator and addition of cold diethyl ether to the residue led to the deposition of a brown precipitate that was filtered and air-dried (0.155 g, 72%). $C_{30}H_{43}CdCl_2N_7O_{12}$ (877.02): calcd. C 41.08, H 4.94, N 11.18; found C 41.73, H 4.95, N 11.20. $\Lambda_M$ (acetonitrile) = 251 cm$^2$Ω$^{-1}$mol$^{-1}$ (2:1 electrolyte). MS (FAB): *m/z* (%BPI) = 691 (15) $[Cd(L^2)(ClO_4)]^+$, 591 (65) $[Cd(L^2–H)]^+$. IR (KBr): $\tilde{\nu}$ = 1622 [ν(C=N)], 1539 [ν(C=C)], 1452 [δ(N–H) δ(C–H)$_{ar}$], 1333, 1273 [δ(C–H)$_{crown}$], 1117 [ν(C–O)], 752 [π(C–H)], 1088 [ν$_a$(Cl–O)], 626 [δ$_a$(O–Cl–O)] cm$^{-1}$.

**[Pb(L$^2$)](ClO$_4$)$_2$ (4):** Solvent: absolute ethanol. Pb(ClO$_4$)$_2$·3H$_2$O (0.108 g, 0.235 mmol). Slow evaporation of the filtrate produced white crystals that were collected by filtration and air-dried (0.145 g, 70%). $C_{26}H_{34}Cl_2PbN_6O_{11}$ (884.69): calcd. C 35.30, H 3.87, N 9.50; found C 35.16, H 4.10, N 9.52. $\Lambda_M$ (acetonitrile): 300 cm$^2$Ω$^{-1}$mol$^{-1}$ (2:1 electrolyte). MS (FAB): *m/z* (%BPI) = 785 (80) $[Pb(L^2)(ClO_4)]^+$, 685 (100) $[Pb(L^2–H)]^+$. IR (KBr): $\tilde{\nu}$ = 1621 [ν(C=N)], 1536 [ν(C=C)], 1452 [δ(N–H) δ(C–H)$_{ar}$], 1337, 1272 [δ(C–H)$_{crown}$], 1121 [ν(C–O)], 752 [π(C–H)], 1090 [ν$_a$(Cl–O)], 621 [δ$_a$(O–Cl–O)] cm$^{-1}$.

**[Cd(L$^3$)](ClO$_4$)$_2$·EtOH (5):** Solvent: absolute ethanol. Cd(ClO$_4$)$_2$·3H$_2$O (0.086 g, 0.191 mmol). Slow evaporation of the filtrate produced pale-brown crystals that were collected by filtration and air-dried (0.107 g, 64%). $C_{30}H_{44}CdCl_2N_6O_{13}$ (880.02): calcd. C 40.94, H 5.04, N 9.55; found C 41.09, H 5.27, N 9.76. $\Lambda_M$ (acetonitrile): 282 cm$^2$Ω$^{-1}$mol$^{-1}$ (2:1 electrolyte). MS (FAB): *m/z* (%BPI) = 735 (20) $[Cd(L^3)(ClO_4)]^+$, 635 (100) $[Cd(L^3–H)]^+$. IR (KBr): $\tilde{\nu}$ = 1624 [ν(C=N)], 1540 [ν(C=C)], 1471 [δ(N–H)], 1453 [δ(C–H)$_{ar}$], 1345, 1269 [δ(C–H)$_{crown}$], 752 [π(C–H)], 1090 [ν$_a$(Cl–O)], 625 [δ$_a$(O–Cl–O)] cm$^{-1}$. Single crystals of formula [Cd(L$^3$)](ClO$_4$)$_2$·EtOH suitable for X-ray diffraction were grown by slow diffusion of diethyl ether into solutions of the complex in acetonitrile.

**[Pb(L$^3$)](ClO$_4$)$_2$·EtOH (6):** Solvent: absolute ethanol. Pb(ClO$_4$)$_2$·3H$_2$O (0.088 g, 0.191 mmol). Slow evaporation of the filtrate produced pale-brown crystals that were collected by filtration and air-dried (0.112 g, 60%). $C_{30}H_{44}Cl_2PbN_6O_{13}$ (974.81): calcd. C 36.96, H 4.55, N 8.62; found C 36.83, H 4.65, N 8.72. $\Lambda_M$ (acetonitrile): 304 cm$^2$Ω$^{-1}$mol$^{-1}$ (2:1 electrolyte). MS (FAB) = *m/z* (%BPI): 829 (50) $[Pb(L^3)(ClO_4)]^+$, 729 (100) $[Pb(L^3–H)]^+$. IR (KBr): $\tilde{\nu}$ = 1621 [ν(C=N)], 1535 [ν(C=C)], 1464 [δ(N–H)], 1448 [δ(C–H)$_{ar}$], 1343, 1270 [δ(C–H)$_{crown}$], 1116 [ν(C–O)], 754 [π(C–H)], 1091 [ν$_a$(Cl–O)], 626 [δ$_a$(O–Cl–O)] cm$^{-1}$.

**Crystal Structure Determination**

Crystal data and details of data collection and refinement are summarized in Table 3. Three-dimensional X-ray data were collected with a Bruker SMART 1000 CCD diffractometer by the *&πη;-ω* scan method. Reflections were measured from a hemisphere of data collected of frames each covering 0.3° in *ω*. Of the 26720 reflections measured for L$^1$ and the 33146 measured for compound **5**, all were corrected for Lorentz and polarization effects and for absorption by semiempirical methods[32] on the basis of symmetry-equivalent and repeated reflections. Of the 4825 independent reflections measured for the receptor L$^1$ and 8645 for compound **5**, 2734 and 7598 reflections, respectively, exceeded the significance level $I > 2\sigma I$. Complex scattering factors were taken from the program SHELX97[33] included in the WinGX program system[34] as implemented on a Pentium® computer. The structure of L$^1$ was solved by direct methods (SHELX97), whereas the structure of **5** was solved by Patterson methods (DIRDIF99).[35] Both structures were refined by full-matrix least-squares methods on $F^2$. The hydrogen

Table 3. Crystal data and structure refinement for L$^1$ and **5**.

| | L$^1$ | **5** |
|---|---|---|
| Empirical formula | $C_{24}H_{30}N_6O_2$ | $C_{30}H_{44}CdCl_2N_6O_{13}$ |
| Formula mass | 434.54 | 880.01 |
| Space group | $P12_1/n1$ | $P2_1/c$ |
| Crystal system | monoclinic | monoclinic |
| *a* [Å] | 15.0205(12) | 10.760(2) |
| *b* [Å] | 10.7111(8) | 24.614(5) |
| *c* [Å] | 15.1438(12) | 13.688(3) |
| *β* [°] | 115.412(2) | 97.166(4) |
| *V* [Å$^3$] | 2200.7(3) | 3596.9(13) |
| *Z* | 4 | 4 |
| *T* [K] | 100.0(2) | 293(2) |
| *λ* [Å] (Mo-$K_\alpha$) | 0.71073 | 0.71073 |
| $D_{calcd.}$ [g cm$^{-3}$] | 1.312 | 1.625 |
| *μ* [mm$^{-1}$] | 0.087 | 0.828 |
| $R_{int}$ | 0.1263 | 0.0265 |
| Reflections measured | 26720 | 33146 |
| Reflections observed | 4825 | 8645 |
| $R_1$[a] | 0.0583 | 0.0392 |
| $wR_2$ (all data)[b] | 0.1252 | 0.0992 |

[a] $R_1 = \Sigma||F_0| - |F_c||/\Sigma|F_0|$. [b] $wR_2 = \{\Sigma[w(||F_0|^2-|F_c|^2)^2]/\Sigma[w(F_0^4)]\}^{1/2}$.

 © 2007 Wiley-VCH Verlag GmbH & Co. KGaA, Weinheim 

atoms were included in calculated positions and refined by using a riding mode, except for the hydrogen atoms H2 and H6 of $L^1$, which were freely refined. Refinement converged with allowance for thermal anisotropy of all non-hydrogen atoms.

CCDC 623182 and 623183 contain the supplementary crystallographic data for the structures included in this paper. These data can be obtained free of charge from The Cambridge Crystallographic Data Centre via http://www.ccdc.cam.ac.uk/datarequest/cif.

**Computational Methods:** The $[M(L^n)]^{2+}$ (M = Cd or Pb, $n$ = 2 or 3) systems were fully optimized in vacuo by using the B3LYP density functional model[36,37] and the Gaussian 03 package (Revision C.01).[38] In these calculations, we used the 6-31G(d) basis set for ligand atoms, while for Cd and Pb the LanL2DZ valence and effective core potential functions were used.[39,40] The stationary points found on the potential energy surfaces as a result of the geometry optimizations have been tested by frequency analysis to represent energy minima rather than saddle points. The relative free energies of the two isomers of $[Pb(L^3)]^{2+}$ were calculated in vacuo at the same computational level, and they include nonpotential energy contributions (that is, zero-point energy and thermal terms) obtained by frequency analysis. Relative free energies of the two isomers of $[Pb(L^3)]^{2+}$ were also calculated in acetonitrile solution (COSMO-RS model).[41] Final free energies include both electrostatic and nonelectrostatic contributions.

**Supporting Information** (see footnote on the first page of this article): Figures S1 and S2 showing the B3LYP optimized structures of the $[Pb(L^2)]^{2+}$ and $[Pb(L^3)]^{2+}$ systems, Tables S1–S3 reporting $^1H$ and $^{13}C$ NMR spectroscopic data of the ligands and $Cd^{II}$ and $Pb^{II}$ complexes and in vacuo optimized Cartesian coordinates [Å] for the $[M(L^2)]^{2+}$ and $[M(L^3)]^{2+}$ systems (M = Cd or Pb).

## Acknowledgments

The authors thank Xunta de Galicia (PGIDIT03TAM10301PR and PGIDIT06TAM10301PR) for generous financial support. The authors are indebted to Centro de Supercomputación of Galicia (CESGA) for providing the computer facilities.

[1] See, for instance: a) R. D. Hancock, A. E. Martell, *Chem. Rev.* **1989**, *89*, 1875–1914; b) R. D. Hancock, *Perspectives in Coordination Chemistry* (Eds.: A. F. Williams, C. Floriani, A. Merbach), Verlag HCA, Basel, **1992**, p. 129; c) R. D. Hancock, A. E. Martell, *Supramol. Chem.* **1996**, *6*, 401–407; d) R. D. Hancock, H. Maumela, A. S. de Sousa, *Coord. Chem. Rev.* **1996**, *148*, 315–347; e) B. P. Hay, R. D. Hancock, *Coord. Chem. Rev.* **2001**, *212*, 61–78.
[2] D. J. Cram, *Science* **1988**, *240*, 760–767.
[3] D. J. Cram, J.-M. Lehn, *J. Am. Chem. Soc.* **1985**, *107*, 3657–3658.
[4] A. E. Martell, R. D. Hancock, R. J. Motekaitis, *Coord. Chem. Rev.* **1994**, *133*, 39–65.
[5] J. M. Harrington, S. B. Jones, P. H. White, R. D. Hancock, *Inorg. Chem.* **2004**, *43*, 4456–4463.
[6] a) U. Hahn, M. Elhabiri, A. Trabolsi, H. Herschbach, E. Leize, A. Van Dorsselaer, A.-M. Albrecht-Gary, J.-F. Nierengarten, *Angew. Chem. Int. Ed.* **2005**, *44*, 5338–5341; b) E. C. Constable, C. E. Housecroft, J. N. Lambert, D. A. Malarek, A. Dan, *Chem. Commun.* **2005**, 3739–3741.
[7] L. Shimoni-Livny, J. P. Glusker, C. P. Bock, *Inorg. Chem.* **1998**, *37*, 1853–1867.
[8] W. J. Geary, *Coord. Chem. Rev.* **1971**, *7*, 81–122.
[9] a) X. X. Zhang, A. V. Boedunov, J. S. Bradshaw, N. K. Dalley, X. Kou, R. M. Izatt, *J. Am. Chem. Soc.* **1995**, *117*, 11507–11511; b) D. Ranganathan, V. Haridas, R. Gilardi, I. L. Karle, *J. Am. Chem. Soc.* **1998**, *120*, 10793–10800.
[10] S. Lahiri, J. L. Thompson, J. S. Moore, *J. Am. Chem. Soc.* **2000**, *122*, 11315–11319.
[11] M. González-Lorenzo, C. Platas-Iglesias, F. Avecilla, C. F. G. C. Geraldes, D. Imbert, J.-C. G. Bünzli, A. de Blas, T. Rodríguez-Blas, *Inorg. Chem.* **2003**, *42*, 6946–6954.
[12] E. Quiroz-Castro, S. Bernes, N. Barba-Behrens, R. Tapia-Benavides, R. Contreras, H. Noth, *Polyhedron* **2000**, *19*, 1479–1484.
[13] J.-M. Grevy, F. Tellez, S. Bernes, H. Noth, R. Contreras, N. Barba-Behrens, *Inorg. Chim. Acta* **2002**, *339*, 532–542.
[14] D. Esteban, D. Bañobre, A. de Blas, T. Rodríguez-Blas, R. Bastida, A. Macías, A. Rodríguez, D. E. Fenton, H. Adams, J. Mahía, *Eur. J. Inorg. Chem.* **2000**, 1445–1456.
[15] a) H. Zhang, X. Wang, H. Zhu, W. Xiao, B. K. Teo, *J. Am. Chem. Soc.* **1997**, *119*, 5463–5464; b) P. C. Junk, M. K. Smith, J. W. Steed, *Polyhedron* **2001**, *20*, 2979–2988.
[16] A. H. Bond, R. D. Rogers, *J. Chem. Crystallogr.* **1998**, *28*, 521–527.
[17] N. Kaltsoyannis, *J. Chem. Soc., Dalton Trans.* **1997**, 1–11.
[18] a) C. Piguet, J.-C. G. Bünzli, G. Bernardinelli, C. G. Bochet, P. Froidevaux, *J. Chem. Soc., Dalton Trans.* **1995**, 83–97; b) M. Elhabiri, R. Scopelliti, J.-C. G. Bünzli, C. Piguet, *J. Am. Chem. Soc.* **1999**, *121*, 10747–10762.
[19] a) R. K. Harris, *Nuclear Magnetic Resonance Spectroscopy: A Physicochemnical View*, Pitman, London, **1983**; b) D. Esteban-Gómez, C. Platas-Iglesias, T. Enríquez-Pérez, F. Avecilla, A. de Blas, T. Rodríguez-Blas, *Inorg. Chem.* **2006**, *45*, 5407–5416.
[20] D. C. Bebout, S. W. Stokes, R. J. Butcher, *Inorg. Chem.* **1999**, *38*, 1126–1133.
[21] E. S. Claudio, M. A. ter Horst, C. E. Forde, C. L. Stern, M. K. Zart, H. A. Godwin, *Inorg. Chem.* **2000**, *39*, 1391–1397.
[22] M. González-Lorenzo, C. Platas-Iglesias, F. Avecilla, S. Faulkner, S. J. A. Pope, A. de Blas, T. Rodríguez-Blas, *Inorg. Chem.* **2005**, *44*, 4254–4262.
[23] C. Platas-Iglesias, D. Esteban, V. Ojea, F. Avecilla, A. de Blas, T. Rodríguez-Blas, *Inorg. Chem.* **2003**, *42*, 4299–4307.
[24] C. Platas, F. Avecilla, A. de Blas, T. Rodríguez-Blas, R. Bastida, A. Macias, A. Rodriguez, H. Adams, *J. Chem. Soc., Dalton Trans.* **2001**, 1699–1705.
[25] D. Esteban, C. Platas-Iglesias, F. Avecilla, J. Mahía, A. de Blas, T. Rodríguez-Blas, *Inorg. Chem.* **2002**, *41*, 4337–4347.
[26] G. Berden, W. L. Meerts, E. Jalviste, *J. Chem. Phys.* **1995**, *103*, 9596–9606, and references therein.
[27] J. R. Platt, *J. Chem. Phys.* **1951**, *19*, 101–118.
[28] L. Prodi, M. Montalti, N. Zaccheroni, J. S. Bradshaw, R. M. Izatt, P. B. Savage, *Tetrahedron Lett.* **2001**, *42*, 2941–2944.
[29] N. Su, J. S. Bradshaw, X. X. Zhang, P. B. Savage, K. E. Krakowiak, R. M. Izatt, *J. Heterocycl. Chem.* **1999**, *36*, 771–775.
[30] W. C. Wolsey, *J. Chem. Educ.* **1973**, *50*, A335–A337.
[31] P. Gans, A. Sabatini, A. Vacca, *Talanta* **1996**, *43*, 1739–1753.
[32] *SADABS Area-Detector Absorption Correction*, Siemens Industrial Automation, Inc., Madison, WI, **1996**.
[33] G. M. Sheldrick, *SHELX97* [Includes *SHELXS97*, *SHELXL97*, *CIFTAB*] - Programs for Crystal Structure Analysis (Release 97–2), Institut für Anorganische Chemie der Universität, Tammanstrasse 4, D-3400 Göttingen, Germany, **1998**.
[34] *WinGX*, MS-Windows system of programs for solving, refining and analyzing single-crystal X-ray diffraction data for small molecules, L. J. Farrugia, *J. Appl. Crystallogr.* **1999**, *32*, 837–838.
[35] P. T. Beurskens, G. Beurskens, R. de Gelder, S. Garcia-Granda, R. O. Gould, R. Israel, J. M. M. Smits, *DIRDIF99 Program System*, Crystallography Laboratory, University of Nijmegen, The Netherlands, **1999**.
[36] A. D. Becke, *J. Chem. Phys.* **1993**, *98*, 5648–5652.
[37] C. Lee, W. Yang, R. G. Parr, *Phys. Rev. B* **1988**, *37*, 785–789.
[38] M. J. Frisch, G. W. Trucks, H. B. Schlegel, G. E. Scuseria, M. A. Robb, J. R. Cheeseman, J. A. Montgomery Jr, T. Vreven,

 © 2007 Wiley-VCH Verlag GmbH & Co. KGaA, Weinheim 

K. N. Kudin, J. C. Burant, J. M. Millam, S. S. Iyengar, J. Tomasi, V. Barone, B. Mennucci, M. Cossi, G. Scalmani, N. Rega, G. A. Petersson, H. Nakatsuji, M. Hada, M. Ehara, K. Toyota, R. Fukuda, J. Hasegawa, M. Ishida, T. Nakajima, Y. Honda, O. Kitao, H. Nakai, M. Klene, X. Li, J. E. Knox, H. P. Hratchian, J. B. Cross, C. Adamo, J. Jaramillo, R. Gomperts, R. E. Stratmann, O. Yazyev, A. J. Austin, R. Cammi, C. Pomelli, J. W. Ochterski, P. Y. Ayala, K. Morokuma, G. A. Voth, P. Salvador, J. J. Dannenberg, V. G. Zakrzewski, S. Dapprich, A. D. Daniels, M. C. Strain, O. Farkas, D. K. Malick, A. D. Rabuck, K. Raghavachari, J. B. Foresman, J. V. Ortiz, Q. Cui, A. G. Baboul, S. Clifford, J. Cioslowski, B. B. Stefanov, G. Liu, A. Liashenko, P. Piskorz, I. Komaromi, R. L. Martin, D. J. Fox, T. Keith, M. A. Al-Laham, C. Y. Peng, A. Nanayakkara, M. Challacombe, P. M. W. Gill, B. Johnson, W. Chen, M. W. Wong, C. Gonzalez, J. A. Pople, *Gaussian 03*, Gaussian Inc., Wallingford CT, **2004**.

[39] P. J. Hay, W. R. Wadt, *J. Chem. Phys.* **1985**, *82*, 270–283.

[40] A description of the basis sets and theory level used in this work can be found in the following: J. B. Foresman, A. E. Frisch, *Exploring Chemistry with Electronic Structure Methods*, 2nd ed., Gaussian Inc., Pittsburgh, PA, **1996**, ch. 5.

[41] F. Eckert, A. Klamt, *AlChE J.* **2002**, *48*, 369–385.

Received: December 20, 2006
Published Online: April 4, 2007

 © 2007 Wiley-VCH Verlag GmbH & Co. KGaA, Weinheim 

DOI: 10.1002/ejic.200601232

# Hydrolysis of a (2-Propanol)yttrium Triiodide Complex in the Presence of Glymes: Synthesis and X-ray Structures of Hydroxo-Bridged Dinuclear Yttrium Complexes and Their Applications in Materials Science

**Shashank Mishra,*[a] Stéphane Daniele,*[a] Liliane G. Hubert-Pfalzgraf,[a][†] and Erwann Jeanneau[b]**

**Keywords:** Yttrium / Iodine / Glymes / Structure / Dinuclear complexes

The reactions of (2-propanol)yttrium triiodide, $Y(i\text{PrOH})_4I_3$, with stoichiometric amounts of water in the presence of di-, tri-, and tetraglyme yield a facile synthetic route to hydroxo-bridged, centrosymmetric dimeric yttrium complexes. These ionic derivatives, $[Y_2L_2(\mu\text{-}OH)_2(H_2O)_x(ROH)_y]I_4$ [**1**: L = triglyme, x = 2, y = 2, R = *i*Pr; **2**: L = tetraglyme, x = 2, y = 0; **3**·2EtOH: L = diglyme, x = 2, y = 4, R = Et; **4**·2EtOH: L = triglyme, x = 4, y = 0; **5**: L = tetraglyme, x = 2, y = 2, R = Et] have been characterized by elemental analysis, IR and $^1$H NMR spectroscopy, as well as by single-crystal X-ray diffraction for **3**, **4**, and **5**. Preliminary results on the utility of these ionic derivatives as potential sources of yttrium oxide in high $T_c$ superconductors are also presented.

(© Wiley-VCH Verlag GmbH & Co. KGaA, 69451 Weinheim, Germany, 2007)

## Introduction

Yttrium triiodide is an attractive alternative to yttrium trifluoroacetate derivatives as a source of yttrium oxide in chemical routes to $YBa_2Cu_3O_{7-x}$ (YBCO) high $T_c$ superconductors, because it does not form corrosive hydrofluoric acid during decomposition.[1] Hydroxo ligands are of interest in yttrium and lanthanide chemistry as reaction sites for condensation to bridged oxides[2] and as nucleophiles in RNA cleavage as well as in the catalytic hydrolysis of phosphate diesters.[3] It is generally accepted that the catalysis of phosphate diester cleavage involves substrate activation by a dinuclear lanthanide core followed by nucleophilic attack by an activated hydroxide (Scheme 1).[3] Hydroxo complexes are also often proposed as intermediates in the degradation pathways of f-element organometallic and coordination compounds.[4] Polynuclear oxo and/or hydroxo complexes of lanthanides with $[Ln_4(\mu_3\text{-}OH)_4]^{8+}$,[5] $[Ln_6(\mu_6\text{-}O)(\mu_3\text{-}OH)_8(H_2O)_{24}]^{8+}$,[6] or $[Ln_{15}(\mu_3\text{-}OH)_{20}(\mu_5\text{-}X)]^{24+}$[7] (X = halide) cores have been obtained by direct hydrolysis of lanthanide nitrates, perchlorates, or halides (chloride and iodide) in aqueous media. However, the high charge and polarizing power of lanthanides as well as the absence of any organic auxiliary ligands result in a high tendency to readily hydrolyze, thus making it difficult to control oligomerization of rare-earth centers.[8] A common synthetic strategy for controlling the advancement of hydrolysis is to introduce auxiliary ligands such as carboxylates, polyketonates, polyamines, polyols, pyridonates, alkoxides, and amino acids in the metal coordination sphere (ligand-controlled hydrolysis).[9] We have previously reported octa- and nonanuclear oxo-hydroxo yttrium species, namely $[Y_8(\mu_4\text{-}O)_2(\mu_3\text{-}OH)_4(\mu,\eta^2\text{-}AAA)_4(\eta^4\text{-}AAA)_6(\mu\text{-}OEt)_4(\mu_3\text{-}OEt)_2]$[10] and $[Y_9O_2(OH)_8(\mu,\eta^2\text{-}AAA)_8(\eta^2\text{-}AAA)_8]^-$,[11] using allylacetatoacetate $MeCOCH_2COOCH_2CH{=}CH_2$ (HAAA) as an auxiliary ligand.

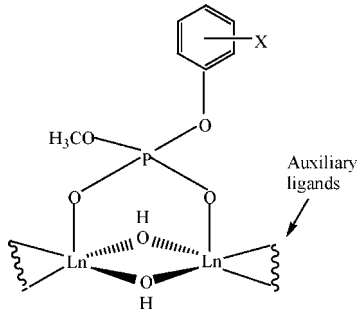


Scheme 1. A possible mechanism for the activation and cleavage of a phosphate diester substrate by a hydroxo-bridged dinuclear lanthanide species.

Although a few examples of hydroxo-bridged yttrium and lanthanide complexes with chelating ligands exist in the literature (Table 1), they have mostly been obtained from nonaqueous solutions as the result of serendipitous hydrolysis and include N-donor ligands.[12–21] The reaction conditions that lead to hydroxo formation in nonaqueous solvents have rarely been elucidated, and general synthetic pro-

[a] Université Lyon1, IRCELYON,
2 av. A. Einstein, 69626 Villeurbanne Cédex, France
Fax: +33-4-72445399
E-mail: mishrashashank74@rediffmail.com
[b] Université Lyon1, Centre de Diffractométrie,
69629 Villeurbanne Cédex, France
[†] Deceased

 © 2007 Wiley-VCH Verlag GmbH & Co. KGaA, Weinheim 

Table 1. X-ray crystallographically characterized dinuclear yttrium and lanthanide complexes with N- and/or O-donor ligands containing a $[Ln_2(\mu\text{-}OH)_2]$ core.

| Entry | Compound[a] | Coordination environment | Ln–O(μ-OH) [Å] | Ln···Ln in dimer [Å] | Ln–μ-OH–Ln [°] | Reference |
|---|---|---|---|---|---|---|
| 1 | $[Y_2(\mu\text{-}OH)_2(H_2O)_2(\eta^6\text{-}L)_2](NO_3)_4\cdot 6H_2O$ | $N_6O_3$ | 2.235(9) | 3.709(3) | 112.1(4) | [3b] |
| 2 | $[La_2(\mu\text{-}OH)_2(\mu,\eta^1\text{:}\eta^1\text{-}OTf)(\eta^6\text{-tpen})_2](OTf)_3\cdot 3MeCN$ | $N_6O_3$ | 2.415(2)–2.421(2) | 3.988(1) | 111.5(8) | [21] |
| 3 | $[Yb_2(\mu\text{-}OH)_2(\eta^3\text{-bmp})_2](ClO_4)_4(HClO_4)_{0.5}(MeCN)_{7.32}(bmp)_{0.5}$ | $N_6O_2$ | 2.231(4)–2.235(5) | 3.656(5) | [b] | [14] |
| 4 | $[Er_2(\mu\text{-}OH)_2(\text{hexacyclen})_2](OTf)_4$ | $N_6O_2$ | 2.246(2)–2.275(2) | 3.802(1) | 112.0(1) | [15] |
| 5 | $[Ce_2(\mu\text{-}OH)_2(MeCN)_2(H_2O)_2(\eta^4\text{-tpa})_2]I_4$ | $N_5O_3$ | 2.324(7)–2.337(7) | 3.829(2) | 110.5(3) | [20] |
| 6 | $[Sm_2(\mu\text{-}OH)_2(N\text{-MeIm})_{10}]I_4$ | $N_5O_2$ | 2.287(3)–2.309(3) | [b] | 111.0(1) | [13] |
| 7 | $[Eu_2(\mu\text{-}OH)_2(\eta^4\text{-tpa})_2(OTf)_4]$ | $N_4O_4$ | 2.228(2)–2.298(2) | 3.715(8) | 110.4(1) | [20] |
| 8 | $[Y_2(\mu\text{-}OH)_2(H_2O)_4(\eta^2\text{-phen})_4][Cl]_4\cdot 2(phen)\cdot MeOH$ | $N_4O_4$ | 2.218(3)–2.233(3) | 3.651(2) | 110.2(2) | [12] |
| 9 | $[Tm_2(\mu\text{-}OH)_2(H_2O)_2(\eta^2\text{-phen})_4](NO_3)_4\cdot 2phen$ | $N_4O_4$ | 2.204(6)–2.226(6) | 3.647(1) | 110.8(2) | [19] |
| 10 | $[Yb_2(\mu\text{-}OH)_2(H_2O)_2(\eta^2\text{-phen})_4](NO_3)_4\cdot 2phen$ | $N_4O_4$ | 2.207(4)–2.211(4) | 3.636(1) | 110.7(2) | [19] |
| 11 | $[Er_2(\mu\text{-}OH)_2(H_2O)_4(\eta^2\text{-phen})_4](NO_3)_4\cdot 2phen$ | $N_4O_4$ | 2.224(3)–2.247(3) | 3.672(1) | 110.4(1) | [18] |
| 12 | $[Lu_2(\mu\text{-}OH)_2(H_2O)_4(\eta^2\text{-phen})_4](NO_3)_4\cdot 2phen$ | $N_4O_4$ | 2.201(3)–2.210(3) | 3.632(1) | 110.9(1) | [18] |
| 13 | $[Yb_2(\mu\text{-}OH)_2(H_2O)_2(\eta^4\text{-tmpp})_2]$ | $N_4O_3$ | 2.247(7)–2.255(5) | 3.724(1) | [b] | [16] |
| 14 | $[Yb_2(\mu\text{-}OH)_2(H_2O)_6(\eta^3\text{-paphy})_2]Cl_4\cdot 4H_2O$ | $N_3O_5$ | 2.19(1)–2.22(1) | 3.608(1) | 110.0(3) | [17] |
| 15 | $[Y_2(\mu\text{-}OH)_2(H_2O)_2(EtOH)_4(\eta^3\text{-diglyme})_2]I_4\cdot 2EtOH$ | $O_8$ | 2.223(6)–2.246(6) | 3.684(1) | 111.0(2) | this work |
| 16 | $[Y_2(\mu\text{-}OH)_2(H_2O)_4(\eta^4\text{-triglyme})_2]I_4\cdot 2EtOH$ | $O_8$ | 2.237(4)–2.262(4) | 3.719(1) | 111.5(2) | this work |
| 17 | $[Y_2(\mu\text{-}OH)_2(H_2O)_2(EtOH)_2(\eta^4\text{-tetraglyme})_2]I_4$ | $O_8$ | 2.209(7)–2.247(6) | 3.710(1) | 112.7(3) | this work |

[a] Abbreviations: bmp = 2,6-bis(1-methylbenzimidazol-2-yl)pyridine; hexacyclen = 1,4,7,10,13,16-hexaazacyclooctadecane; L = an 18-membered hexaaza macrocycle ligand; *N*-MeIm = *N*-methylimidazole; OTf = trifluoromethanesulfonate (triflate); paphy = pyridine-2-carboxaldehyde 2′-pyridylhydrazone; phen = *o*-phenanthroline; $tmppH_2$ = 5,10,15,20-tetrakis(*p*-methoxyphenyl)porphyrin; tpa = tris(2-pyridylmethyl)amine; tpen = *N*,*N*,*N*′,*N*′-tetrakis(2-pyridylmethyl)ethylenediamine. [b] Not mentioned in the literature.

cedures for the preparation of dinuclear hydroxo complexes are lacking. In continuation of our earlier studies on the reactivity of $Y(i\text{PrOH})_4I_3$,[22,23] we wish to report in this manuscript its hydrolytic reactions in the presence of glymes. The obtained compounds **1**–**5** are the first examples of hydroxo-bridged dimeric yttrium (or lanthanide) complexes with an all-oxygen environment (Table 1). These compounds are potentially good starting materials for the synthesis of larger yttrium oxo/hydroxo clusters.[24] In addition, their utility as sources of yttrium oxide for high $T_c$ superconductors has also been evaluated, and the preliminary results are presented in this paper.

## Results and Discussion

The hydrolytic reactions of (2-propanol)yttrium triiodide, $Y(i\text{PrOH})_4I_3$, with stoichiometric amounts of water in the presence of glymes have been evaluated by using different solvents. Reactions of $Y(i\text{PrOH})_4I_3$ in toluene with triglyme or tetraglyme containing two to three equivalents of water proceed with an immediate precipitation of compounds **1** and **2** as yellow solids in good yield. The same compounds were obtained when 2-propanol was used as the reaction medium, though in lower yields because of the moderate solubility of these compounds in 2-propanol. Crystallization of these compounds from an EtOH/*n*-pentane (1:1) or EtOH/$Et_2O$ (1:2) solution gave ethanol-solvated, hydroxo-bridged, ionic dimeric yttrium compounds **3**–**5** (Scheme 2), as established by X-ray crystallography. Similar ethanol-solvated, hydroxo-bridged dinuclear compounds were isolated in better yields by using ethanol as the reaction medium. The stability of a dinuclear $Y_2(OH)_2$ core in complexes **1**–**5** is reflected by the fact that the yttrium/glyme ratio always remained at 1:1 even if glymes were added in excess (up to 2.5 equiv.; IR and $^1H$ NMR evidence), the remaining coordination sites of eight-coordinated yttrium centers being filled by water and/or alcohol molecules.

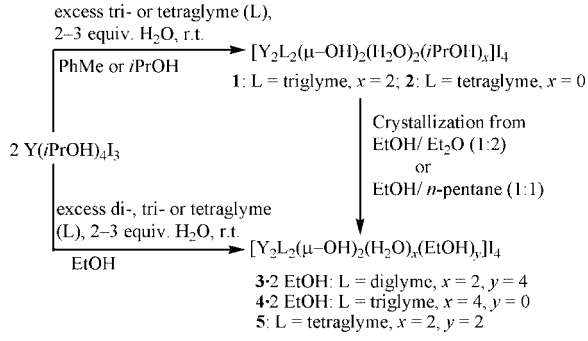


Scheme 2. Hydrolysis of $Y(i\text{PrOH})_4I_3$ in the presence of glymes.

### Spectroscopic Characterization

The FT-IR spectra of **1**–**5** show the presence of alcohol functionalities as well as glyme ligands in the metal coordination sphere (Table 2). A broad strong IR absorption at 3100–3350 $cm^{-1}$ due to ν(OH) and a weak-to-medium-intensity band at 1600–1630 $cm^{-1}$ due to δ(OH) confirm the presence of the hydroxy functionality in **1**–**5**, the ν(Y–O) frequency appearing as medium-intensity bands in the region 400–700 $cm^{-1}$. The presence of di-, tri-, or tetraglyme is also confirmed by their characteristic IR absorptions. $^1H$ NMR spectra of compounds **1**–**5** at ambient temperature are independent of concentration and are consistent with a single-ligand environment. These spectra show peaks for the polydentate glymes, bridging hydroxy groups, and coordinated water and/or alcohol molecules in the expected

 © 2007 Wiley-VCH Verlag GmbH & Co. KGaA, Weinheim 

Table 2. $^1$H NMR and IR spectroscopic data for compounds **1**–**5**.

| Comp. | $^1$H NMR ($CD_3CN$) $\delta$ [ppm][a] | | | | IR (Nujol) $\tilde{\nu}$ [cm$^{-1}$] |
|---|---|---|---|---|---|
| | μ-OH | $H_2O$ | di-, tri-, or tetraglyme moiety | *i*PrOH/EtOH | |
| **1** | 6.40 (s, 2 H) | 5.2 (s, 4 H) | 3 43 (s, 6 H, OMe), 3.83 (m, 14 H, $OCH_2$ of tetraglyme + CH of 2-propanol) | 1.14 (d, $J$ = 7.0 Hz, 12 H, Me), 3.83 (m, 14 H, $OCH_2$ of tetraglyme + CH of 2-propanol) | 3340br ν(OH), 1610m δ(OH), 1346m, 1281m, 1249m, 1198m, 1111s, 1096s, 1077s, 1057s, 1018m, 996s, 936s, 875m, 860s, 833s, 722w, 630w, 537w, 454w ν(Y–O) |
| **2** | 5.45 (s, 2 H) | 5.22 (s, 4 H) | 3.54 (s, 6 H, OMe), 3.80 (s, H, $OCH_2$), 3.90 (s, H, $OCH_2$) | – | 3333 br ν(OH), 1458s, 1377m, 1302w, 1260m, 1194w, 1095m, 1034m, 951w, 870w, 851w, 800m, 722w, 674w, 620w, 571w, 444w ν(Y–O) |
| **3** | 6.20 (s, 2 H) | 5.50 (s, 4 H) | 3.80 (s, 12 H, OMe), 3.85 (m, $J$ = 7.0 Hz, 16 H, $OCH_2$) | 1.24 (t, $J$ = 7.0 Hz, 18 H, Me), 3.62 (m, $J$ = 7.0 Hz, 12 H, $CH_2$), 2.60 (br., 6 H, OH) | 3306 br ν(OH), 1631s, 1607s δ(OH), 1454s, 1398w, 1373w, 1349w, 1291m, 1242m, 1198m, 1078s, 1037s, 935s, 870s, 828m, 780w, 643m, 575m, 536m, 517m, 459m ν(Y–O) |
| **4** | 5.40 (br., 2 H) | 5.15 (s, 8 H) | 3. 60 (br. m, 16 H, OMe of triglyme + $OCH_2$ of ethanol) 3.89 (br., 24 H, $OCH_2$) | 1.18 (t, $J$ = 7.0 Hz, 6 H, Me), 2.55 (br., 2 H, OH), 3. 60 (br. m, 16 H, OMe of triglyme + $OCH_2$ of ethanol) | 3251 br ν(OH), 1617m δ(OH), 1464s, 1377m, 1349m, 1274m, 1239m, 1196m, 1090s, 1067s, 1019s, 993s, 946s, 876m, 833m, 718w, 632m, 456w ν(Y–O) |
| **5** | 5.23, 5.35 (s, 2 H) | 4.95 (br., 4 H) | 3.60 (s, 12 H, OMe), 3.95 (m, $J$ = 7.0 Hz, 32 H, $OCH_2$) | 1.10 (t, $J$ = 7.0 Hz, 6 H, Me), 2.61 (t, $J$ = 7.0 Hz, 2 H, OH), 3.45 (m, $J$ = 7.0 Hz, 4 H, $CH_2$) | 3300, 3100 br ν(OH), 1602.2 m δ(OH), 1458s, 1377m, 1297m, 1273m, 1243m, 1201m, 1116s, 1091s, 1076s, 1027s, 950s, 910m, 875m, 853m, 792m, 718m, 679m, 625m, 571m, 454m ν(Y–O) |

[a] $^1$H NMR spectrum of **3** in $CD_2Cl_2$.

multiplicities and integrated intensity ratios (Table 2). The bridging hydroxo groups exhibit the greatest downfield shifting and appear as a singlet at $\delta$ = 5.40–6.40 ppm for compounds **1**–**4** but as two singlets (1:1) at $\delta$ = 5.23 and 5.35 ppm for compound **5**, probably as a result of some asymmetric interactions with the pendant oxygen atoms O5 and O5$^i$ of the tetraglyme ligands in solution. The signals due to the coordinated water molecules appear as a relatively broad singlet in the region $\delta$ = 4.95–5.50 ppm. The signals of the methylene groups of glyme and coordinated ethanol are well resolved in the spectra of compounds **3** and **5** and show two distinct multiplets ($J$ = 7 Hz) at $\delta$ = 3.85–3.95 and 3.45–3.62 ppm, respectively, while they appear as overlapping multiplets centered at $\delta$ = 3.60 ppm in the spectrum of complex **4**.

It is worth noting that some hydroxo-bridged dinuclear metal complexes have been shown to form dinuclear/mononuclear equilibrium mixtures in solution on the basis of their concentration-dependent NMR spectra.[25,26] The driving force for the formation of monomer units usually involves either the coordination of an additional Lewis base (e.g. $R_3P$) to the metal center[25] or the formation of new, stronger secondary hydrogen-bond interactions with the terminal metal hydroxide moiety.[26] Concentration-independent $^1$H NMR spectra of **1**–**5** suggest that none of above-mentioned driving forces are important in the present case and indicate that the dimeric structure is probably retained upon dissolution.

### Molecular Structures of $[Y_2(\mu\text{-}OH)_2(H_2O)_2(EtOH)_4(\eta^3\text{-diglyme})_2]I_4\cdot 2EtOH$ (3), $[Y_2(\mu\text{-}OH)_2(H_2O)_4(\eta^4\text{-triglyme})_2]I_4\cdot 2EtOH$ (4), and $[Y_2(\mu\text{-}OH)_2(H_2O)_2(EtOH)_2(\eta^4\text{-tetraglyme})_2]I_4$ (5)

The selected interatomic bond lengths and angles for compounds **3**, **4**, and **5** are given in Table 3, 4, and 5, respectively, whereas intramolecular hydrogen bond lengths are summarized in Table 6. All three structures are based on a centrosymmetric $Y_2(\mu\text{-}OH)_2$ diamond core (Figure 1). The oxygen atoms of the di-, tri-, or tetraglymes, ethanol and/or water molecules complete the eight-coordinate environment about each yttrium center in **3**–**5**. All iodides act as noncoordinating counteranions. Although all the yttrium centers in **3**–**5** are eight-coordinate, their stereochemistry is different. The geometry around yttrium in the $[Y_2(\mu\text{-}OH)_2(H_2O)_2(EtOH)_4(\eta^3\text{-diglyme})_2]^{4+}$ cation of (**3**·2EtOH) can best be described as a square antiprism, which is slightly distorted towards dodecahedral geometry (Figure 2).[27]

Table 3. Selected bond lengths and angles for $[Y_2(\mu\text{-}OH)_2(H_2O)_2(EtOH)_4(\eta^3\text{-diglyme})_2]I_4\cdot 2EtOH$ (**3**).

| Bond lengths [Å] | | | |
|---|---|---|---|
| Y1–O6$^i$ | 2.246(6) | Y1–O6 | 2.223(6) |
| Y1–O7 | 2.425(6) | Y1–O2 | 2.364(6) |
| Y1–O3 | 2.471(6) | Y1–O5 | 2.494(6) |
| Y1–O4 | 2.440(6) | Y1–O1 | 2.386(6) |
| **Bond angles [°]** | | | |
| O6$^i$–Y1–O7 | 146.3(2) | O6$^i$–Y1–O5 | 85.8(2) |
| O6$^i$–Y1–O3 | 135.2(2) | O7–Y1–O5 | 67.7(2) |
| O7–Y1–O3 | 73.3(2) | O3–Y1–O5 | 102.5(2) |
| O6$^i$–Y1–O4 | 80.0(2) | O4–Y1–O5 | 65.0(2) |
| O7–Y1–O4 | 105.2(1) | O6–Y1–O5 | 143.7(2) |
| O3–Y1–O4 | 65.0(2) | O2–Y1–O5 | 136.1(2) |
| O6$^i$–Y1–O6 | 69.0(2) | O6$^i$–Y1–O1 | 74.7(2) |
| O7–Y1–O6 | 143.9(2) | O7–Y1–O1 | 79.7(2) |
| O3–Y1–O6 | 80.3(2) | O3–Y1–O1 | 150.0(2) |
| O4–Y1–O6 | 84.6(2) | O4–Y1–O1 | 136.8(2) |
| O6$^i$–Y1–O2 | 121.6(2) | O6–Y1–O1 | 116.8(2) |
| O7–Y1–O2 | 72.3(2) | O5–Y1–O1 | 78.6(2) |
| O3–Y1–O2 | 82.1(2) | O2–Y1–O1 | 77.3(2) |
| O4–Y1–O2 | 145.7(2) | Y1$^i$–O6–Y1 | 111.0(2) |
| O6–Y1–O2 | 80.1(2) | | |

Symmetry codes: (i) 2 –$x$, 1–$y$, 1–$z$.

 © 2007 Wiley-VCH Verlag GmbH & Co. KGaA, Weinheim 

The tridentate diglyme (O3, O4, and O5) and a water molecule (O7) occupy four adjacent corners of the square antiprism, the remaining sites being occupied by two ethanol molecules (O1 and O2) and the two bridging hydroxides (O6 and O6$^{i}$). The stereochemistry around the yttrium atoms in $[Y_2(\mu\text{-}OH)_2(H_2O)_4(\eta^4\text{-triglyme})_2]I_4\cdot 2EtOH$ (**4**) is slightly distorted dodecahedral (Figure 3).[27] The oxygen atoms of two bridging hydroxides (O5 and O5$^{i}$) and two water molecules (O6 and O7) form four corners of the first trapezoid, whereas the second trapezoid consists of four oxygen atoms, O1, O2, O3, and O4, of a triglyme ligand.

Table 4. Selected bond lengths and angles for $[Y_2(\mu\text{-}OH)_2(H_2O)_4(\eta^4\text{-triglyme})_2]I_4\cdot 2EtOH$ (**4**).

| Bond lengths [Å] | | | |
|---|---|---|---|
| Y1–O5$^{i}$ | 2.262(4) | Y1–O2 | 2.447(4) |
| Y1–O5 | 2.237(4) | Y1–O3 | 2.500(4) |
| Y1–O7 | 2.386(4) | Y1–O4 | 2.387(4) |
| Y1–O6 | 2.372(4) | Y1–O1 | 2.420(4) |
| **Bond angles [°]** | | | |
| O5$^{i}$–Y1–O5 | 68.51(2) | O5$^{i}$–Y1–O4 | 87.89.8(1) |
| O1$^{i}$–Y1–O7 | 176.15(1) | O5–Y1–O4 | 98.98(1) |
| O5$^{i}$–Y1–O7 | 143.62(1) | O7–Y1–O4 | 88.61(1) |
| O5–Y1–O7 | 147.62(1) | O6–Y1–O4 | 81.29(2) |
| O5$^{i}$–Y1–O6 | 74.32(1) | O5$^{i}$–Y1–O1 | 83.46(1) |
| O5–Y1–O6 | 142.77(1) | O5–Y1–O1 | 90.1(1) |
| O7–Y1–O6 | 6936(1) | O2–Y1–O4 | 128.72(1) |
| O5$^{i}$–Y1–O2 | 136.49(1) | O3–Y1–O4 | 65.21(1) |
| O5–Y1–O2 | 81.61(1) | O2–Y1–O1 | 65.12(1) |
| O7–Y1–O2 | 69.43(1) | O3–Y1–O1 | 129.44(1) |
| O6–Y1–O2 | 127.14(1) | O4–Y1–O1 | 164.3(1) |
| O5$^{i}$–Y1–O3 | 135.1(1) | O6–Y1–O1 | 83.77(1) |
| O5–Y1–O3 | 80.5(1) | O2–Y1–O3 | 64.38(1) |
| O7–Y1–O3 | 74.2(1) | Y1$^{i}$–O5–Y1 | 111.49(2) |
| O6–Y1–O3 | 130.49(1) | | |

Symmetry codes: (i) $-x$, $1-y$, $1-z$.

Table 5. Selected bond lengths and angles for $[Y_2(\mu\text{-}OH)_2(H_2O)_2(EtOH)_2(\eta^4\text{-tetraglyme})_2]I_4$ (**5**).

| Bond lengths [Å] | | | |
|---|---|---|---|
| Y1–O6$^{i}$ | 2.247(6) | Y1–O2 | 2.472(7) |
| Y1–O6 | 2.209(7) | Y1–O1 | 2.402(8) |
| Y1–O3 | 2.428(7) | Y1–O8 | 2.376(8) |
| Y1–O4 | 2.392(8) | Y1–O7 | 2.369(8) |
| **Bond angles [°]** | | | |
| O6$^{i}$–Y1–O6 | 67.3(3) | O6$^{i}$–Y1–O1 | 82.2(3) |
| O6$^{i}$–Y1–O3 | 139.3(3) | O6–Y1–O1 | 104.3(3) |
| O6–Y1–O3 | 79.2(2) | O3–Y1–O1 | 129.8(3) |
| O6$^{i}$–Y1–O4 | 90.8(3) | O4–Y1–O8 | 87.3(3) |
| O3–Y1–O4 | 66.0(3) | O2–Y1–O1 | 65.6(2) |
| O6–Y1–O4 | 89.9(3) | O1–Y1–O7 | 80.7(3) |
| O6$^{i}$–Y1–O2 | 126.5(3) | O8–Y1–O7 | 68.0(3) |
| O6–Y1–O2 | 80.4(3) | O1–Y1–O8 | 88.0(3) |
| O3–Y1–O2 | 65.8(2) | O2–Y1–O7 | 132.0(3) |
| O2–Y1–O8 | 77.4(3) | O4–Y1–O7 | 79.6(3) |
| O6$^{i}$–Y1–O7 | 77.6(3) | O4–Y1–O1 | 160.1(3) |
| O6$^{i}$–Y1–O8 | 145.4(3) | Y1$^{i}$–O3–Y1 | 112.7(3) |
| O3–Y1–O7 | 125.9(3) | O6–Y1–O8 | 147.2(3) |
| O3–Y1–O8 | 69.8(3) | O6–Y1–O7 | 143.2(2) |
| O4–Y1–O2 | 131.8(2) | Y1$^{i}$–O6–Y1 | 112.7(3) |

Symmetry codes: (i) $-x$, $y$, $3/2-z$.

The yttrium centers in the complex $[Y_2(\mu\text{-}OH)_2(H_2O)_2(EtOH)_2(\eta^4\text{-tetraglyme})_2]I_4$ (**5**) have a bicapped trigonal prismatic geometry.[27] The six corners of the trigonal prism are occupied by the O1, O2, O4 (tetraglyme), O6, O6$^{i}$ (bridging hydroxide), and O8 (ethanol) atoms, whereas O3 (tetraglyme) and O7 (water) atoms occupy the two capping positions (Figure 4).

Table 6. Intramolecular hydrogen bond lengths [Å] in **3**–**5**.

| Compound **3** | | | |
|---|---|---|---|
| I1$^{ii}$···O1 | 3.444(7) | I2···O2 | 3.437(5) |
| I1$^{ii}$···O6$^{i}$ | 3.513(8) | I2···O7 | 3.501(8) |
| I1$^{ii}$···O3$^{i}$ | 3.934(8) | I2···O8$^{iv}$ | 3.470(1) |
| **Compound 4** | | | |
| I1···O6 | 3.443(5) | I2···O5 | 3.798(5) |
| I1···O7 | 3.505(5) | I2···O6$^{i}$ | 3.415(5) |
| **Compound 5** | | | |
| I1···O6$^{i}$ | 3.875(6) | I2···O3 | 3.761(7) |
| I1···O7 | 3.412(8) | I2···O8 | 3.441(8) |

Symmetry codes, **3**: (i) $2-x$, $1-y$, $1-z$; (ii) $2-x$, $-y$, $-z$; (iv) $1-x$, $1-y$, $-z$. **4**: (i) $-x$, $1-y$, $1-z$. **5**: (i) $-x$, $y$, $3/2-z$.

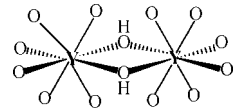

Figure 1. Coordination environment around yttrium centers in complexes **1**–**5**.

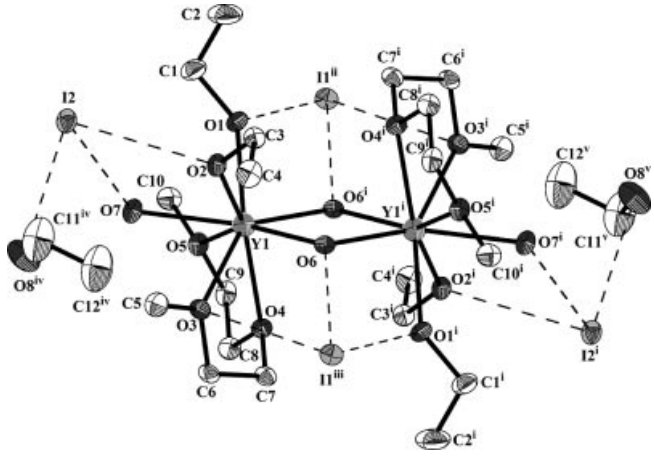


Figure 2. Molecular structure of $[Y_2(\mu\text{-}OH)_2(H_2O)_2(EtOH)_4(\eta^3\text{-diglyme})_2]I_4\cdot 2EtOH$ (**3**) with 30% ellipsoids. Hydrogen atoms have been omitted for clarity. Intramolecular hydrogen bonds are shown as broken lines (-----). Symmetry codes: (i) $2-x$, $1-y$, $1-z$; (ii) $2-x$, $-y$, $-z$; (iii) $x$, $1+y$, $1+z$; (iv) $1-x$, $1-y$, $-z$; (v) $1+x$, $y$, $1+z$.

Other than the stereochemistry, the structures of **3**–**5** appear to be affected only minimally by the change in the chelating glyme ligand. The average Y–O(glyme) bond lengths, decreasing slightly in the order diglyme (2.46 Å) > triglyme (2.44 Å) > tetraglyme (2.42 Å), are comparable with those in other yttrium complexes with glymes.[28] As expected, the average Y–O(μ-OH) length, 2.24 Å, is shorter than that of terminal Y–O ($H_2O$/EtOH), 2.38 Å. These values are consistent with those in the literature.[3b,12] Overall,

 © 2007 Wiley-VCH Verlag GmbH & Co. KGaA, Weinheim 

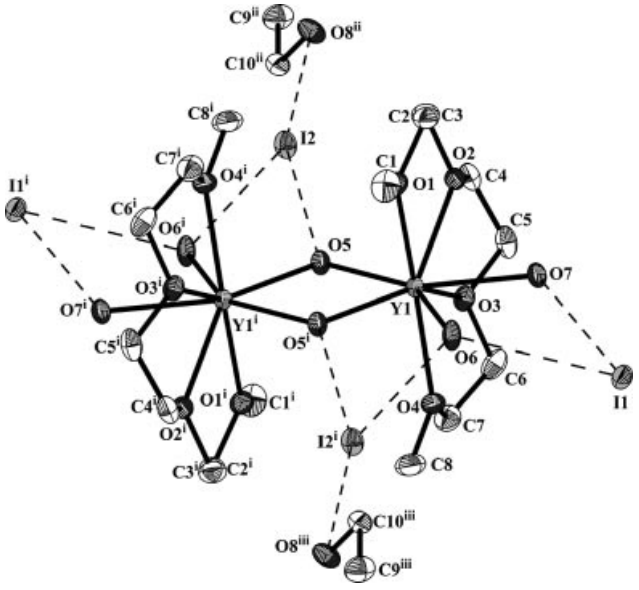


Figure 3. Molecular structure of $[Y_2(\mu\text{-}OH)_2(H_2O)_4(\eta^4\text{-triglyme})_2]I_4\cdot 2EtOH$ (**4**) with 30% ellipsoids. Hydrogen atoms have been omitted for clarity. Intramolecular hydrogen bonds are shown as broken lines (-----). Symmetry codes: (i) $-x, 1-y, 1-z$; (ii) $1-x, 1-y, 2-z$; (iii) $-1+x, y, -1+z$.

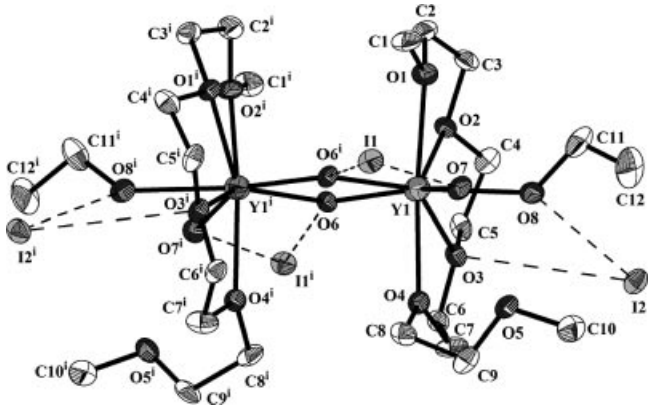


Figure 4. Molecular structure of $[Y_2(\mu\text{-}OH)_2(H_2O)_2(EtOH)_2(\eta^4\text{-tetraglyme})_2]I_4$ (**5**) with 30% ellipsoids. Hydrogen atoms have been omitted for clarity. Intramolecular hydrogen bonds are shown as broken lines (-----). Symmetry code: (i) $-x, y, 3/2-z$.

the Y–O bond lengths vary from 2.209(7) to 2.500(4) Å, the order of variation being Y–O(μ-OH) < Y–O($H_2O$) ≈ Y–O(EtOH) < Y–O(glyme). The tetraglyme ligands in **5** are coordinated through four of their five oxygen atoms, the oxygen atoms, O5 and O5$^i$, lie too far away [4.116(9) Å] to interact with yttrium atoms (Figure 4). These pendant oxygen atoms, O5 and O5$^i$, are also far from the bridging hydroxide groups [4.811(1) Å]. The potentially pentadentate tetraglyme ligand has previously been shown to bind the metal centers in the $\eta^3$ or $\eta^4$ manner as well, depending upon steric considerations and the nature of metals.[29] The Y···Y distances [3.684(1)–3.719(1) Å] are also comparable with those reported for other hydroxo-bridged dinuclear yttrium complexes.[3b,12] In fact, a perusal of structural data for hydroxo-bridged dinuclear yttrium and lanthanide complexes with O- and N-donor ligands (Table 1) reveals that, despite differences in coordination number (7, 8, or 9), coordinating atoms (O and N), or central lanthanide atoms among these complexes, the dimensions of the $Ln_2(\mu\text{-}OH)_2$ diamond core vary little, as indicated by the small range of Ln···Ln [3.608(1)–3.988(1) Å] and Ln–μ-OH [2.19(1)–2.421(2) Å] distances as well as Ln–O–Ln angles [110.2(2)–112.7(3)°]. One additional feature of the $Y_2(\mu\text{-}OH)_2$ diamond core in the structures reported here is the presence of intramolecular hydrogen bonds between iodide anions and bridging hydroxide groups and coordinated water/ethanol molecules; the I···O distances vary in the range 3.412(8)–3.934(8) Å (Table 6). These distances are in agreement with those reported for hydrogen bonding involving iodides.[23]

### $YBa_2Cu_3O_{7-x}$ (YBCO) Powder from $[Y_2(\mu\text{-}OH)_2(H_2O)_2(EtOH)_2(\eta^4\text{-tetraglyme})_2]I_4$ (5), $[Ba(tetraglyme)_2]I_2\cdot C_7H_8$, and CuI by Metal Organic Decomposition (MOD)

Iodides of yttrium, barium, and copper have been shown to be among the most attractive precursors for the formation of YBCO, since they do not form stable $BaCO_3$ during the decomposition.[1,30] However, formation of ionic Y-Cu clusters was recently reported by us from an all-iodide solution in DMF and 2-isopropoxyethanol.[23] This results in an inhomogeneous solution, which is inappropriate for MOD. The use of hydroxo-bridged dinuclear complex **5** instead of yttrium triiodide successfully suppressed this tendency, because of the presence of chelating glymes in the coordination sphere and also fewer iodide atoms than required for Y-Cu clusters. Another advantage of using derivatives $[Y_2(\mu\text{-}OH)_2(H_2O)_2(EtOH)_2(\eta^4\text{-tetraglyme})_2]I_4$ (**5**) and $[Ba(tetraglyme)_2]I_2\cdot C_7H_8$[31] as precursors is that they provide, as a result of their ionic nature, good solubility in ionic liquids (ILs). We then carried out the MOD process in high-boiling 1-butyl(methylimidazolium) bis[(trifluoromethyl)-sulfonyl]amide (IL) as the medium for the decomposition of an all-iodide solution containing $[Y_2(\mu\text{-}OH)_2(H_2O)_2(EtOH)_2(\eta^4\text{-tetraglyme})_2]I_4$ (**5**), $[Ba(tetraglyme)_2]I_2\cdot C_7H_8$, and CuI in the ratio 0.5:2:3. The as-prepared powder, after 1 h at 260 °C, was analyzed by FT-IR spectroscopy, TGA-DTA, and XRD. FT-IR data of the as-prepared powder show the presence of the tetraglyme ligand (1457m, 1351s, 1197s, 1138s, 791m $cm^{-1}$) and other absorption bands corresponding to ν(OH) (3470br $cm^{-1}$) and ν(Y–O) (678m, 572m, 514m $cm^{-1}$). No absorption bands characteristic of the IL could be observed. The TGA and DTA patterns (Figure 5) of this powder showed a two-step decomposition process in the range 270–420 °C associated with strong exothermic peaks corresponding to the combustion of the remaining organics. The total weight loss was 65.5%. The as-prepared powder was amorphous, and crystallization of the $YBa_2Cu_3O_{6.35}$ phase started after annealing in air at only 500 °C. This temperature is much lower than that reported for YBCO powder/films obtained from trifluoroacetate derivatives.[32] XRD analysis of the sample annealed at 900 °C showed the well-crystallized $YBa_2Cu_3O_{6.35}$ phase (Fig-

 © 2007 Wiley-VCH Verlag GmbH & Co. KGaA, Weinheim 

ure 6), though some additional peaks indexing as $YBa_2Cu_4O_8$ were also observed. Crystallite sizes of 25–44 nm were calculated by using the Debye–Scherrer formula. To the best of our knowledge, this is the first report of the use of a neat ionic liquid for synthesis of a high $T_c$ superconductor material.[33]

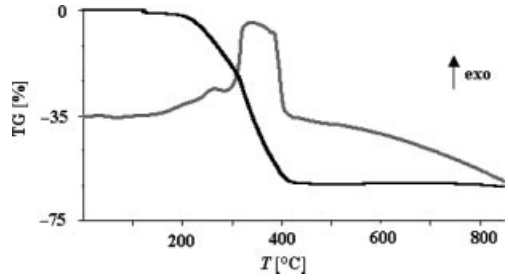


Figure 5. TGA-DTA curve of the powder obtained from the MOD of $[Y_2(\mu\text{-}OH)_2(H_2O)_2(EtOH)_2(\eta^4\text{-tetraglyme})_2]I_4$ (**5**), $[Ba(tetraglyme)_2]I_2{\cdot}C_7H_8$, and CuI.

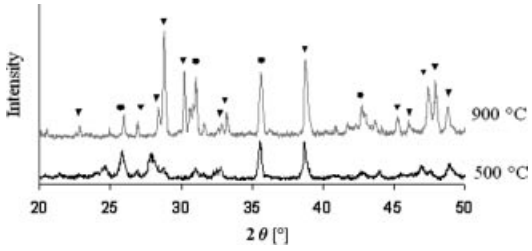


Figure 6. XRD of the powder obtained from the MOD of **5**, $[Ba(tetraglyme)_2]I_2{\cdot}C_7H_8$, and CuI (▼ = $YBa_2Cu_3O_{6.35}$ phase; ■ = $YBa_2Cu_4O_8$ phase).

## Conclusion

We described here a facile synthetic route to ionic, centrosymmetric, hydroxo-bridged, dimeric yttrium iodide complexes with glymes. It is the first report of hydroxo-bridged dimeric yttrium (or lanthanide) complexes with an all-oxygen environment. Such dimeric hydroxo species are potentially good starting materials for the synthesis of larger yttrium oxo/hydroxo clusters. Unlike yttrium triiodide, use of these dinuclear yttrium hydroxo iodide species in an all-iodide solution for high $T_c$ superconductors successfully suppresses the formation of ionic Y–Cu species and thus provides a homogeneous solution for MOD. Preliminary studies show that the $YBa_2Cu_3O_{6.35}$ phase starts after annealing the as-prepared powder in air at 500 °C, though some additional peaks indexing as $YBa_2Cu_4O_8$ were also observed. Further studies are now in progress to obtain the desired $YBa_2Cu_3O_{7-x}$ phase only.

## Experimental Section

All reactions were carried out under argon by using Schlenk tubes and vacuum line techniques. $Y(i\text{PrOH})_4I_3$[22] and $[Ba(tetraglyme)_2]I_2{\cdot}C_7H_8$[31] were prepared as reported, whereas CuI was purchased from Aldrich Co. and used as received. Solvents were purified by standard methods. Di-, tri-, and tetraglyme (Aldrich) were stored over molecular sieves. The ionic liquid 1-butyl(methylimidazolium) bis[(trifluoromethyl)sulfonyl]amide was purchased from Solvionic and used without purification. $^1$H NMR spectra were registered with a Bruker AC-300 spectrometer. FT-IR spectra of **1**–**5** were recorded as Nujol mulls with a Perkin–Elmer Paragon 500 spectrometer, whereas IR spectra of YBCO powder were recorded as KBr pellets with a Bruker Vector-22 spectrometer. TGA/DTA data were collected with a Setaram 92 system in air (thermal ramp 10 °C/min, 20–900 °C). XRD were obtained with a Bruker (Siemens) D 500 diffractometer by using Cu-$K_\alpha$ radiation. Analytical data were obtained from the Service Central d′Analyses du CNRS.

### Synthesis of Compounds 1–5

**$[Y_2(\mu\text{-}OH)_2(H_2O)_2(i\text{PrOH})_2(\text{triglyme})_2]I_4$ (1):** Addition of a toluene solution (5 mL) of triglyme (0.5 mL) and $H_2O$ (47 μL, 2.65 mmol) to a suspension of $Y(i\text{PrOH})_4I_3$ (0.94 g, 1.32 mmol) in toluene (3 mL) led to an immediate precipitation of a yellow-orange solid. After the mixture was stirred at room temp. for 6 h, the precipitate was separated by filtration and washed twice with *n*-hexane. Crystallization by slow cooling of a hot 2-propanol solution of this solid gave needle-shaped crystals, which were unsuitable for X-ray crystallography (0.62 g, 77%). $C_{22}H_{58}I_4O_{14}Y_2$ (1231.4): calcd. C 21.43, H 4.71; found C 21.82, H 4.54.

**$[Y_2(\mu\text{-}OH)_2(H_2O)_2(\text{tetraglyme})_2]I_4$ (2):** With the same procedure, **2** was obtained from $Y(i\text{PrOH})_4I_3$ (0.99 g, 1.38 mmol), tetraglyme (0.3 mL) and $H_2O$ (50 μL, 2.78 mmol) in toluene (10 mL) as a yellow solid and crystallized by slow cooling of its hot 2-propanol solution (0.61 g, 73%). $C_{20}H_{25}I_4O_{14}Y_2$ (1199.4): calcd. C 20.01, H 4.16; found C 19.17, H 4.16.

**$[Y_2(\mu\text{-}OH)_2(H_2O)_2(EtOH)_4(\eta^3\text{-diglyme})_2]I_4{\cdot}2EtOH$ (3):** An ethanol (5 mL) solution of diglyme (0.4 mL) and $H_2O$ (27 μL, 1.49 mmol) was added to a solution of $Y(i\text{PrOH})_4I_3$ (0.55 g, 0.77 mmol) in EtOH (5 mL), and the resulting solution was stirred at room temp. for 6 h. Removal of solvents under vacuum afforded **3** as a yellow solid, which was crystallized from EtOH/*n*-pentane (1:1) at room temp. (0.74 g, 74%). $C_{24}H_{70}I_4O_{16}Y_2$ (1300.3): calcd. C 22.15, H 5.38; found C 21.93, H 5.27.

**$[Y_2(\mu\text{-}OH)_2(H_2O)_4(\eta^4\text{-triglyme})_2]I_4{\cdot}2EtOH$ (4):** This compound was obtained as yellow solid by using the same procedure from $Y(i\text{PrOH})_4I_3$ (0.71 g, 1.0 mmol), triglyme (0.5 mL), and $H_2O$ (55 μL, 3.05 mmol) in ethanol (5 mL) followed by crystallization from EtOH/*n*-pentane (1:1) at –20 °C (0.81 g, 68%). $C_{20}H_{54}I_4O_{14}Y_2$ (1238.1): calcd. C 19.90, H 4.47; found C 19.78, H 4.41. Compound **4** was also obtained by crystallization of **1** from EtOH/*n*-pentane (1:1) at –20 °C in 60% yield.

**$[Y_2(\mu\text{-}OH)_2(H_2O)_2(EtOH)_2(\eta^4\text{-tetraglyme})_2]I_4$ (5):** In a similar procedure, the reaction of $Y(i\text{PrOH})_4I_3$ (0.69 g, 0.97 mmol) with tetraglyme (0.5 mL) and $H_2O$ (35 μL, 1.94 mmol) in ethanol (5 mL) followed by crystallization from EtOH/$Et_2O$ (1:2) at –20 °C afforded $[Y_2(\mu\text{-}OH)_2(H_2O)_2(EtOH)_2(\eta^4\text{-tetraglyme})_2]I_4$ (**5**) as a pale yellow crystalline solid (0.87 g, 70%). $C_{24}H_{62}I_4O_{16}Y_2$ (1292.2): calcd. C 22.29, H 4.79; found C 22.11, H 4.72. Compound **5** was also obtained by crystallization of **2** from EtOH/$Et_2O$ (1:2) at –20 °C in 57% yield.

Compounds **1**–**5** are yellow or orange-yellow solids, insoluble in aliphatic or aromatic hydrocarbons but soluble in acetonitrile and ethanol. They are only moderately soluble in 2-propanol and dichloromethane.

**Preparation of $YBa_2Cu_3O_{7-x}$ (YBCO) Powder from $[Y_2(\mu\text{-}OH)_2(H_2O)_2(EtOH)_2(\eta^4\text{-tetraglyme})_2]I_4$, $[Ba(tetraglyme)_2]I_2{\cdot}C_7H_8$, and CuI by Metal Organic Decomposition**

 © 2007 Wiley-VCH Verlag GmbH & Co. KGaA, Weinheim 

$[Y_2(\mu\text{-}OH)_2(H_2O)_2(EtOH)_2(\eta^4\text{-tetraglyme})_2]I_4$ (0.54 g, 0.42 mmol) and $[Ba(tetraglyme)_2]I_2{\cdot}C_7H_8$ (1.55 g, 1.66 mmol) were each dissolved in ethanol (5 mL). Dissolution of CuI (0.47 g, 2.50 mmol) in ethanol (5 mL) was achieved by using a solution of $NH_4I$ in ethanol (3.4 M, 3 mL). Mixing of these solutions gave an orange-yellow clear solution. After addition of the ionic liquid 1-butyl-(methylimidazolium) bis[(trifluoromethyl)sulfonyl]amide (10 mL) into this solution, ethanol was removed under vacuum to give a yellow pasty liquid. After this solution was heated at 260 °C for 1 h, the brownish-black powder was precipitated by adding methanol (30 mL). This powder was then removed by centrifugation and washed twice with hexane (0.36 g).

**X-ray Crystallography**

Suitable crystals of **3**–**5** were obtained from EtOH/pentane (1:1, room temp. or –20 °C) or EtOH/$Et_2O$ (1:2, –20 °C) solutions and mounted on a Nonius Kappa CCD diffractometer with Mo-$K_\alpha$ radiation ($\lambda$ = 0.71073 Å). Crystallographic and refinement data for **3**–**5** are given in Table 7. Intensities were collected at 150 K by means of the program COLLECT.[34] Reflection indexing, Lorentz-polarization correction, peak integration, and background determination were carried out with the DENZO program.[35] Frame scaling and refinement of unit-cell parameters were carried out with the program SCALEPACK.[35] Absorption correction was achieved with the program DIFABS.[36] The starting structure was solved by direct methods with SIR92.[37] The remaining non-hydrogen atoms were located by successive difference Fourier map analyses. The structure refinement was carried out with CRYSTALS.[38] The H atoms were placed geometrically and refined with riding constraints.

Table 7. Crystallographic and refinement data for **3**–**5**.

| Compound | **3** | **4** | **5** |
|---|---|---|---|
| Empirical formula | $C_{24}H_{70}I_4O_{16}Y_2$ | $C_{20}H_{56}I_4O_{16}Y_2$ | $C_{24}H_{62}I_4O_{16}Y_2$ |
| Formula weight | 1300.3 | 1238.1 | 1292.2 |
| Crystal system | triclinic | triclinic | monoclinic |
| Space group | $P\bar{1}$ | $P\bar{1}$ | $C2/c$ |
| $a$ [Å] | 11.04(5) | 9.88(5) | 23.48(5) |
| $b$ [Å] | 11.08(5) | 10.62(5) | 12.00(5) |
| $c$ [Å] | 1I.54(5) | 11.45(5) | 15.89(5) |
| $\alpha$ [°] | 111.91(5) | 64.96(5) | 90 |
| $\beta$ [°] | 95.77(5) | 85.22(5) | 88.51(5) |
| $\gamma$ [°] | 111.86(5) | 72.15(5) | 90 |
| Volume [Å$^3$] | 1167.8(9) | 1035.9(8) | 4477(3) |
| $Z$ | 1 | 1 | 4 |
| Absorption coefficient [mm$^{-1}$] | 5.17 | 5.82 | 5.39 |
| Temperature [K] | 150 | 150 | 150 |
| Measured reflections | 15019 | 12822 | 15104 |
| Independent reflections | 5567 | 4918 | 3974 |
| $R_{int}$ | 0.139 | 0.070 | 0.147 |
| Data/restrains/parameters | 3467/7/208 | 3233/0/190 | 2123/0/208 |
| Goodness of fit | 1.11 | 1.08 | 1.10 |
| $R_1$ [$I$>2(σ)] | 0.0347 | 0.0350 | 0.0602 |
| $R_1$ (all data) | 0.0665 | 0.0556 | 0.1292 |
| $wR_2$ [$I$>2(σ)] | 0.0389 | 0.0416 | 0.0492 |
| $wR_2$ (all data) | 0.0574 | 0.0543 | 0.0742 |
| Residual electron density [e Å$^{-3}$] | –1.98 to 2.57 | –1.33 to 1.13 | –0.92 to 1.26 |

CCDC-628903–628905 contain the supplementary crystallographic data for **3**–**5**. These data can be obtained free of charge from The Cambridge Crystallographic Data Centre via www.ccdc.cam.ac.uk/data_request/cif.

## Acknowledgments

S. M. is grateful to the region Rhone Alpes for a postdoctoral fellowship (project Superflex).

[1] a) R. H. Baney, D. F. Bergstrom, B. H. Justice, *Chem. Mater.* **1992**, *4*, 984–987; b) I. Matsubara, M. Paranthaman, A. Singhal, C. Vallet, D. F. Lee, P. M. Martin, R. D. Hunt, R. Feenstra, C. Y. Yang, S. E. Babcock, *Physica C* **1999**, *319*, 127–132.
[2] L. G. Hubert-Pfalzgraf, *New J. Chem.* **1987**, *11*, 663–675.
[3] See for example: a) S. J. Oh, K. H. Song, D. Whang, K. Kim, T. H. Yoon, H. Moon, J. W. Park, *Inorg. Chem.* **1996**, *35*, 3780–3785; b) S. W. A. Bligh, N. Choi, E. G. Evagorou, M. McPartlin, K. N. White, *J. Chem. Soc., Dalton Trans.* **2001**, 3169–3172; c) F. Aguilar-Perez, P. Gomez-Tagle, E. Collado-Fregoso, A. K. Yatsimirsky, *Inorg. Chem.* **2006**, *45*, 9502–9517.
[4] A. Domingos, M. R. J. Elsegood, A. C. Hillier, G. Lin, S. Y. Liu, I. Lopes, N. Marques, G. Maunder, R. McDonald, A. Sella, J. W. Steed, J. Takats, *Inorg. Chem.* **2002**, *41*, 6761–6768.
[5] R. Wang, H. Liu, M. D. Carducci, T. Jin, C. Zheng, Z. Zheng, *Inorg. Chem.* **2001**, *40*, 2743–2750.
[6] a) R. Wang, M. D. Carducci, Z. Zheng, *Inorg. Chem.* **2000**, *39*, 1836–1837; b) N. Mahe, O. Guillou, C. Daiguebonne, Y. Gerault, A. Caneschi, C. Sangregorio, J. Y. Chane-Ching, P. E. Car, T. Roisnel, *Inorg. Chem.* **2005**, *44*, 7743–7750; c) A.-V. Mudring, T. Timofte, A. Babai, *Inorg. Chem.* **2006**, *45*, 5162–5166.
[7] R. Wang, H. D. Selby, H. Liu, M. D. Carducci, T. Jin, Z. Zheng, J. W. Anthis, R. J. Staples, *Inorg. Chem.* **2002**, *41*, 278–286.
[8] R. Anwander, *Angew. Chem. Int. Ed.* **1998**, *37*, 599–602.
[9] Z. Zheng, *Chem. Commun.* **2001**, 2521–2529.
[10] L. G. Hubert-Pfalzgraf, L. Cauro-Gamet, A. Brethon, S. Daniele, P. Richard, *Inorg. Chem. Commun.* **2007**, *10*, 143–147.
[11] L. G. Hubert-Pfalzgraf, N. Miele-Pajot, R. Papienik, J. Vaissermann, *J. Chem. Soc., Dalton Trans.* **1999**, 4127–4130.
[12] M. D. Grillone, F. Benetollo, G. Bombieri, *Polyhedron* **1991**, *10*, 2171–2177.
[13] W. J. Evans, G. W. Rabe, J. W. Ziller, *Inorg. Chem.* **1994**, *33*, 3072–3078.
[14] S. Petoud, J.-C. G. Bünzli, F. Renaud, C. Piguet, K. J. Schenk, G. Hopfgartner, *Inorg. Chem.* **1997**, *36*, 5750–5760.
[15] R. Wang, J. Zhao, T. Jin, G. Xu, Z. Zhou, X. Zhou, *Polyhedron* **1998**, *17*, 43–47.
[16] W.-K. Wong, L. Zhang, F. Xue, T. C. W. Mak, *J. Chem. Soc., Dalton Trans.* **1999**, 3053–3062.
[17] E. Baraniak, R. S. L. Bruce, H. C. Freeman, N. J. Hair, J. James, *Inorg. Chem.* **1976**, *15*, 2226–2230.
[18] Y.-Q. Zheng, L.-X. Zhou, J.-L. Lin, S.-W. Zhang, *Z. Anorg. Allg. Chem.* **2001**, *627*, 2425–2429.
[19] D.-Y. Wei, Y.-Q. Zheng, J.-L. Lin, *Z. Naturforsch., Teil B* **2002**, *57*, 625–630.
[20] L. Natrajan, J. Pécaut, M. Mazzanti, C. LeBrun, *Inorg. Chem.* **2005**, *44*, 4756–4765.
[21] L. Natrajan, J. Pécaut, M. Mazzanti, *Dalton Trans.* **2006**, 1002–1005.
[22] S. Mishra, L. G. Hubert-Pfalzgraf, M. Rolland, H. Chermette, *Inorg. Chem. Commun.* **2007**, *10*, 15–19.
[23] S. Mishra, L. G. Hubert-Pfalzgraf, E. Jeanneau, H. Chermette, *Dalton Trans.* **2007**, 410–413.
[24] W. Teng, M. Guino-o, J. Hitzbleck, U. Englich, K. Ruhlandt-Senge, *Inorg. Chem.* **2006**, *45*, 9531–9539.
[25] V. V. Grushin, H. Alper, *Organometallics* **1996**, *15*, 5242–5245.
[26] R. A. Allred, S. A. Huefner, K. Rudzka, A. M. Arif, L. M. Berreau, *Dalton Trans.* **2007**, 351–357.
[27] a) C. W. Haigh, *Polyhedron* **1995**, *14*, 2871–2878; b) C. W. Haigh, *Polyhedron* **1996**, *15*, 605–643.

 © 2007 Wiley-VCH Verlag GmbH & Co. KGaA, Weinheim 

[28] a) S. R. Drake, M. B. Hursthouse, K. M. A. Malik, S. A. S. Miller, D. J. Otway, *Inorg. Chem.* **1993**, *32*, 4464–4471; b) K. D. Pollard, J. J. Vittal, G. P. A. Yap, R. J. Puddephatt, *J. Chem. Soc., Dalton Trans.* **1998**, 1265–1267; c) G. Malandrino, R. L. Nigro, I. L. Fragala, C. Benelli, *Eur. J. Inorg. Chem.* **2004**, 500–509.
[29] a) S. R. Drake, S. A. S. Miller, D. J. Williams, *Inorg. Chem.* **1993**, *32*, 3227–3235; b) M. E. Fragala, G. Malandrino, O. Puglist, C. Benelli, *Chem. Mater.* **2000**, *12*, 290–293.
[30] L. C. Pathak, S. K. Mishra, *Supercond. Sci. Technol.* **2005**, *18*, R67–R89.
[31] S. Mishra, L. G. Hubert-Pfalzgraf, E. Jeanneau, *Polyhedron* **2007**, *26*, 66–72.
[32] T. Araki, I. Hirabayashi, *Supercond. Sci. Technol.* **2003**, *16*, R71–R94.
[33] A. Taubert, Z. Li, *Dalton Trans.* **2007**, 723–727.
[34] B. V. Nonius, *COLLECT*, Delft, The Netherlands, **1997**–2001.
[35] Z. Otwinowski, W. Minor, *Methods in Enzymology* (Eds.: C. W. Carter Jr, R. M. Sweet), New York, Academic Press, **1997**, vol. 276, pp. 307–326.
[36] N. Walker, D. Stuart, *Acta Crystallogr., Sect. A* **1983**, *39*, 158–166.
[37] A. Altomare, M. C. Burla, M. Camalli, G. L. Cascarano, C. Giacovazzo, A. Guagliardi, A. G. G. Moliterni, G. Polidori, R. Spagna, *J. Appl. Crystallogr.* **1999**, *32*, 115–119.
[38] P. W. Betteridge, J. R. Carruthers, R. I. Cooper, K. Prout, D. J. Watkin, *J. Appl. Crystallogr.* **2003**, *36*, 1487.

Received: December 22, 2006
Published Online: April 4, 2007

 © 2007 Wiley-VCH Verlag GmbH & Co. KGaA, Weinheim 

DOI: 10.1002/ejic.200601245

# An Inorganic Aggregate Based on a Sandwich-Type Polyoxometalate with Lanthanide and Potassium Cations: From 1D Chiral Ladder-Like Chains to a 3D Open Framework

**Weilin Chen,[a] Yangguang Li,[a] Yonghui Wang,[a] and Enbo Wang*[a]**

**Keywords:** Polyoxometalates / Sandwich complexes / Lanthanides / Chirality / Open framework

The reaction of sandwich-type polyanion $[Mn_4Si_2W_{18}O_{68}(H_2O)_2]^{12-}$, ceric sulfate, and potassium citrate in an acidic aqueous solution led to the isolation of a new compound $K_4Na_2[\{Ce(H_2O)_7\}_2Mn_4Si_2W_{18}O_{68}(H_2O)_2]\cdot 21.5H_2O$ (**1**), which crystallizes in the space group $P2_12_12_1$ with $a$ = 12.040(2) Å, $b$ = 26.094(5) Å, $c$ = 30.043(6) Å, $V$ = 9439(3) Å$^3$, $Z$ = 4, and flack parameter $x$ = 0.63(1). X-ray diffraction analysis reveals that **1** consists of novel chiral ladder-like chains based on sandwich-type polyanions and lanthanide cations, which are further connected into a three-dimensional open framework by potassium cations.

(© Wiley-VCH Verlag GmbH & Co. KGaA, 69451 Weinheim, Germany, 2007)

## Introduction

The use of polyoxometalates (POMs) as basic building blocks to construct novel extended materials by means of different cationic linkers is of great interest and stems not only from their intriguing variety of architectures and topologies, but also from their numerous potential applications in catalysis, sorption, nonlinear optics, magnetic materials, and bioinorganic pharmaceuticals.[1] In this field, lanthanide cations ($Ln^{3+/4+}$) are popular linkers due to their high coordination numbers and oxyphilic activities, as well as their multiple physicochemical properties.[2] To date, a series of POM-based extended aggregates linked by lanthanide ions have been extensively reported as follows: (1) Keggin[3] polyanions and their monovacant derivatives are linked by $Ln^{3+/4+}$ ions to form one-dimensional zigzag chains, such as $[Ln_n(SiW_{11}O_{39})]$,[4a] $[Ln(SiW_{11}O_{39})_2]^{13-}$,[4b] and $[Ce_2(BW_{11}O_{39})_2(H_2O)_6]^{12-}$,[4d] a two-dimensional layer $[\varepsilon\text{-}PMo_{12}O_{36}(OH)_4\{La(H_2O)_4\}_4]^{5-}$,[4e] and a three-dimensional framework $[Gd(H_2O)_3]_3[GdMo_{12}O_{42}]$.[4i] Further, a series of trivacant Keggin polyanions can be self-assembled with $Ln^{3+/4+}$ ions to form nanoscale inorganic aggregates, such as $[Ln_{16}As_{12}W_{148}O_{524}(H_2O)_{36}]^{76-}$,[4g] $[(PM_2W_{10}O_{38})_4(W_3O_{14})]^{30-}$ (M = Eu, Y),[4h] and $[K\subset\{Eu(H_2O)_2(\alpha\text{-}AsW_9O_{33})\}_6]^{35-}$.[4f] (2) Wells–Dawson[5] polyanions and their monovacant congeners[6] are another kind of popular building blocks[7] assembled with lanthanide ions. A current report in this family is $[Ln(H_2O)_2(\alpha_2\text{-}P_2W_{17}O_{61})]_n^{7n-}$,[7b] which displays a series of extended structures with 1D chains and 2D layers. (3) Recently, Anderson-type polyanions have become a new class of precursors for the construction of extended inorganic aggregates,[8] such as $[La(H_2O)_7CrMo_6H_6O_{24}]^{2-}$[8a] and $[\{(C_6H_5NO_2)_2Ln(H_2O)_4\}_2\{IMo_6O_{24}\}]$.[8b] (4) Various isopolyoxoanion units connected with $Ln^{3+/4+}$ ions have also been reported,[9] exemplified by $[Ce(H_2O)(DMF)_6(W_{10}O_{32})]$,[9a] $[La(W_5O_{18})_2]^{9-}$,[9b] and $[\{Ln(H_2O)_5\}_2(H_2M_{12}O_{42})\}]^{2-}$ (M = Mo, W).[9c] (5) A series of large molybdenum and vanadium clusters have also been linked by lanthanide ions, which led to a series of infinite chains and networks.[10] As a continuation of the exploration of novel extended POM-based aggregates in this subfield with the "property-adding" feature, transition-metal-substituted POMs should be suitable precursors owing to their optical, electronic, and magnetic properties, which are largely dependent on the changeable transition metal centers.[11] In this aspect, the sandwich-type POMs with tetranuclear transitional-metal centers are an ideal class of candidates. However, no such extended inorganic aggregates based on sandwich-type POMs and lanthanide linkers have been reported. Because the pH stability ranges for sandwich-type POMs in aqueous solutions are different from those of lanthanide ions, together with the obvious reactive activity between the highly negative polyanions and strongly oxyphilic lanthanide cations,[12] most reactions between such two units result in immediate precipitates but not crystals. Thus, it is still a challenge to explore suitable synthetic conditions that would enable the acquisition of novel inorganic aggregates that are based on

[a] Key Laboratory of Polyoxometalate Science of Ministry of Education, Department of Chemistry, Northeast Normal University,
Ren Min Street No. 5268, Changchun, Jilin 130024, P. R. China
Fax: +86-431-85098787
E-mail: wangenbo@public.cc.jl.cn
wangeb889@nenu.edu.cn

Supporting information for this article is available on the WWW under http://www.eurjic.org or from the author.

 InterScience © 2007 Wiley-VCH Verlag GmbH & Co. KGaA, Weinheim 

these two building blocks. Nevertheless, some current efforts indicate that the introduction of organic N- and O-donor ligands or solvents during the preparation could somewhat stabilize the lanthanide cations, reduce the reactivity between POMs and lanthanide linkers, and improve the solubility of the final products. Therefore, the use of multidentate O-donor ligands (such as citrate, tartrate, and EDTA salts) were fully considered during our preparation of novel inorganic aggregates based on sandwich-type POMs and lanthanide cations. Although most of the sandwiching POMs possess lower symmetry in the crystal form, if they were to coordinate to different linkers they may present chirality and improve their functionality. On the basis of the above consideration, we synthesized a new compound with the assistance of citrate ligands, $K_4Na_2[\{Ce(H_2O)_7\}_2Mn_4Si_2W_{18}O_{68}(H_2O)_2]\cdot 21.5H_2O$ (**1**), which represents the first extended inorganic aggregate composed of sandwich-type POMs and lanthanide linkers. The structure of **1** possesses a chiral ladder-like chain based on $[Mn_4Si_2W_{18}O_{68}(H_2O)_2]^{12-}$ polyanions and cerium cations. These chains are further connected into a 3D open framework by potassium cation linkers.

## Results and Discussion

### Syntheses

Compound **1** was synthesized by boiling a mixed aqueous solution of $K_4Na_6Mn[Mn_4Si_2W_{18}O_{68}(H_2O)_2]\cdot\approx 33H_2O$, $Ce(SO_4)_2\cdot 4H_2O$ and potassium citrate for 2 h. Yellow block crystals were isolated after the filtrate stood at room temperature for one week. The precursor $K_4Na_6Mn[Mn_4Si_2W_{18}O_{68}(H_2O)_2]\cdot\approx 33H_2O$ was synthesized according to the published procedure.[13] Two important problems must be fully considered during the synthesis. Firstly, the pH value of the reaction system should be carefully controlled so as to stabilize the structure of the sandwich-type polyanions and avoid early precipitation of cerium cations. However, a series of reports indicate that the surface oxygen atoms of POMs are rather active to react with the oxyphilic lanthanide ions,[12] and in most cases precipitation instead of crystallization occurs. Thus, a multidentate O-donor ligand of potassium citrate was used to stabilize the cerium ions or maybe reduce the reactivity of cerium ions owing to the high coordination ability of such organic ligand with metal ions. Although the citrate ligand was not observed in the final structure of **1**, it is definitely necessary during the preparation of **1**. It is also noteworthy that there are two obvious color changes during the reaction. At the beginning of the reaction, the yellow aqueous solution of $K_4Na_6Mn[Mn_4Si_2W_{18}O_{68}(H_2O)_2]$ immediately changed to brown when the mixed solution of $Ce(SO_4)_2\cdot 4H_2O$ and potassium citrate was added. However, the brown color changed back to yellow after boiling for 2 h. It is presumed that the redox reactions between $Mn^{2+}$ and $Ce^{4+}$ ions in the first step led to the formation of $Mn^{3+}$ and $Ce^{3+}$ ions, which exhibit the brown color. After boiling for 2 h, the disproportionation reaction of the metastable $Mn^{3+}$ ions occurred, which resulted in the transformation of $Mn^{3+}$ into $Mn^{2+}$; thus, the brown solution changed back to yellow.

### Structure Description

Single-crystal X-ray diffraction analysis revealed that **1** consists of a novel chiral ladder-like chain based on sandwich-type $[Mn_4Si_2W_{18}O_{68}(H_2O)_2]^{12-}$ polyanions and cerium cation linkers. In **1**, the well-known sandwich-type polyanion (as shown in Figures 1 and S1) consists of two trivacant $[B\text{-}\alpha\text{-}SiW_9O_{34}]^{10-}$ Keggin moieties sandwiching a central symmetric rhomb-like $[Mn_4O_{16}(H_2O)_2]$ segment through the W–O–Mn and Si–O–Mn connecting modes. All the W and Mn centers exhibit an octahedral coordination environment. The bond lengths of W–O are in the range 1.664(2)–2.471(2) Å, whereas the bond lengths of Mn–O are between 2.107(2) and 2.250(2) Å. It is interesting that two cerium cations are coordinated directly to the surface oxygen atoms (O45, O27, O14, O47) of the sandwich-type polyanion (see Figures 1 and S1). The bond lengths of the four Ce–O bond lengths are 2.541(2) Å, 2.492(2) Å, 2.519(2) Å, and 2.578(2) Å, respectively. The residual coordination sites of two nona-coordinated cerium cations are fulfilled by coordinated water molecules. The distances of Ce–Ow vary from 2.394(14) Å to 2.68(3) Å. Further, these Ce cations can be viewed as $\mu_2$-bridges that link the sandwich-type polyanions into an infinite ladder-like chain along the *c* axis (Figure 2). It is also noteworthy that the central symmetric sandwich-type polyanions change into asymmetric moieties as a result of the connection with two different $[Ce(H_2O)_7]$ linkers. On the basis of the space group $P2_12_12_1$ of **1**, it is considered that a $2_1$ screw axis passes through the central part of the ladder-like chain (as shown in Figure 2) and the whole chain possesses the chirality. However, the flack parameter

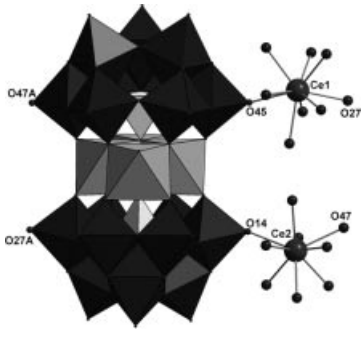


Figure 1. Polyhedral and ball-and-stick representation of the sandwich-type polyanion and the cerium cations of **1**.

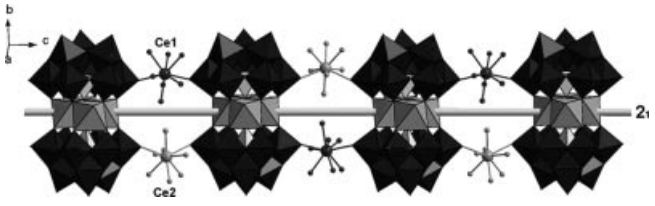


Figure 2. View of the 1D chiral ladder-like chain of **1**.

 © 2007 Wiley-VCH Verlag GmbH & Co. KGaA, Weinheim 

[0.63(1)] indicates that **1** is just a twin crystal containing two enantiomers simultaneously with the content of ca. 63 and 37%, respectively.[14]

In the unit cell of **1**, there are four independent potassium cations that exhibit a hepta-coordinated environment with six O atoms derived from the three different polyanions and one solvent water molecule (Figure S2). The bond lengths of K–$O_{POM}$ are in the range 2.680(2)–3.073(2) Å, whereas the distances of K–Ow is in the range 2.710(3)–2.860(5) Å. Thus, all the potassium cations can be viewed as $\mu_3$-bridges and each of them links with three polyanion moieties (Figure S3). On the *ac* plane, adjacent ladder-like chains are connected by the four types of potassium cations to form a two-dimensional framework (Figure 3a). Interestingly, adjacent four polyanions together with four cerium linkers and four potassium linkers constitute a relatively closed space with the total volume of ca. 124.7 $Å^3$ estimated with PLATON software (Figures 3b and S4). The entrances of the closed space seem to be somewhat small with the size of ca. 7.7 × 8.0 Å (along the *a* axis) and ca. 6.2 × 12.3 Å (along the *c* axis) based on the distances among cerium, potassium, and tungsten centers. However, all the lattice water molecules and sodium cations are sealed in these "containers" during the self-assembly process of **1** (Figure S4). Furthermore, these 2D porous layers are linked by potassium cations in a stagger way to form a 3D open framework (Figures 4 and S5).

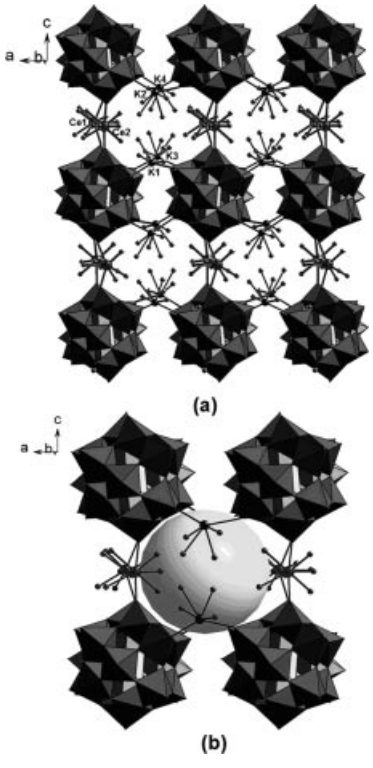


Figure 3. (a) View of the 2D double porous framework on the *ac* plane. (b) View of the simulated closed-space based on four polyanions, four $[Ce(H_2O)_7O_2]$, and four $[K(H_2O)O_6]$ linkers. The sodium cations and crystal water molecules are omitted for clarity.

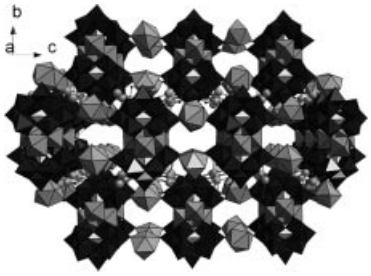


Figure 4. Polyhedral and ball-and-stick view of the 3D open framework along the *a* axis.

The oxidation states of Si, W, Mn, and Ce sites are +4, +6, +2, and +3, respectively, on the basis of the bond lengths and angles, charge balance consideration, and bond valence sum calculations.[15]

## Spectroscopic and Electrochemical Analyses

The IR spectrum of **1** (Figure S6) shows the characteristic bands at 946, 905, 873, 770, 722, 536, 511, and 489 $cm^{-1}$, which are similar to the IR peaks of $[Mn_4Si_2W_{18}O_{68}(H_2O)_2]$[11–13] except for some slight shifts owing to the influence of coordinated cerium cations on polyanions in the range 450–1000 $cm^{-1}$. This similarity indicates that the polyanion of **1** still keeps the basic sandwich-type structure, which is consistent with the result of single-crystal X-ray diffraction analysis.

The UV/Vis spectrum of **1** (Figure S7) was recorded in a solution of $H_2SO_4/Na_2SO_4$ at pH = 3.5 and shows absorbance bands between 200 and 400 nm, which can be attributed to the characteristics of charge-transfer bands of terminal oxygen and bridging oxygen atoms to tungsten centers, respectively.

To investigate the solution properties of **1**, the cyclic voltammogram (CV) (Figure S8) was recorded for 1 mM solutions of **1** in 0.5 M $H_2SO_4/Na_2SO_4$ at pH = 3.50. The voltammogram shows two similar quasi reversible peaks at $E_{1/2}$ = –1.09 and –0.76 V [$E_{1/2} = (E_{pa} + E_{pc})/2$] that can be attributed to two two-electron redox cycles of $W^{6+}$ and one quasi reversible peak at $E_{1/2}$ = +0.68 V that indicates a one-electron redox process of $Ce^{3+}$ to $Ce^{4+}$. The redox peaks of $Mn^{2+}$ are too weak to be assigned.[16] (Figures S8 and S9). The blurry redox peaks and quasi reversible CV feature of **1** probably result from slow electron transfer rather than chemical irreversibility.

## TG and XRPD Analyses

Thermogravimetric (TG) analysis of compound **1** was carried out with a Perkin–Elmer TGA7 instrument under an $N_2$ atmosphere. The TG curve (Figure 5) exhibits a continuous weight loss step from 35 to 250 °C, attributed to the loss of all lattice and coordinated water molecules. The weight loss is about 11.51%, in correspondence with the calculated value of 11.57%. Then, no weight loss occurs in the temperature range 250–650 °C. There is another minor

 © 2007 Wiley-VCH Verlag GmbH & Co. KGaA, Weinheim 

weight loss of 1.8% in the temperature range 650–800 °C, which might be attributable to the loss of oxygen atoms from the residual metal oxides.

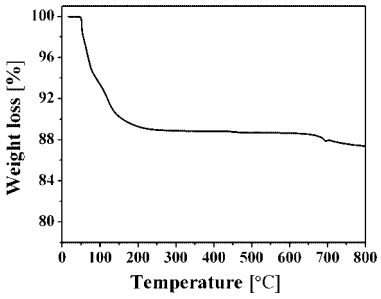


Figure 5. TG curve of **1**.

To check the stability of the open framework of **1**, the X-ray powder diffraction (XRPD) of **1** was checked at 20, 70, and 120 °C. As shown in Figure 6, the peak positions of the simulated and experimental XRPD pattern at 20 °C are in agreement with each other, which indicates the good phase purity of the compound. The differences in intensity may be due to the preferred orientation of the crystalline powder samples. The main peaks of the XRPD pattern at 20 and 70 °C are also similar to each other except for the minor differences in peak intensity, which are due to the loss of some crystal water molecules; this indicates that the open framework of **1** is still stable below 70 °C. However, most peaks of the XRPD pattern of **1** disappeared at 120 °C, which suggests that compound **1** is not in the crystalline state. This could be ascribed to a collapsed framework resulting from the loss of most of the coordinated water molecules from the cerium and potassium cation linkers.

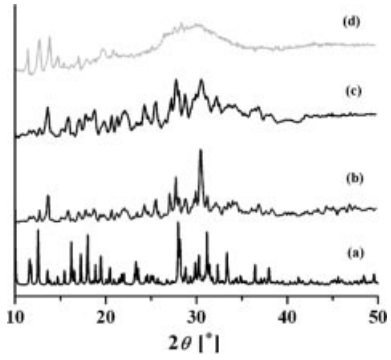


Figure 6. Stimulated and experimental XRPD patterns of **1**. (a) Stimulated XRPD; (b) XRPD at 20 °C; (c) XRPD at 70 °C; (d) XRPD at 120 °C.

## Conclusions

A new compound, $K_4Na_2[\{Ce(H_2O)_7\}_2Mn_4Si_2W_{18}O_{68}(H_2O)_2]\cdot 21.5H_2O$ (**1**), was successfully synthesized with the assistance of a citrate ligand, and this complex represents the first extended inorganic aggregate composed of sandwich-type POMs and lanthanide cations. Compound **1** consists of novel chiral ladder-like chains based on $[Mn_4Si_2W_{18}O_{68}(H_2O)_2]^{12-}$ polyanions and two different $[Ce(H_2O)_7]^{3+}$ linkers, which are further connected by potassium cations into a 3D open framework with a space volume of ca. 124.7 Å$^3$ per unit cell. TG and XRD analyses indicate that the porous framework of **1** is stable (around 70 °C) just before losing most of its coordinated water molecules. The successful synthesis of **1** suggests a new model for the construction of POM-based extended frameworks. The properties and functionalities of such compounds might be adjusted by the choice of different transition-metal ions in the sandwich sites and lanthanide cation linkers. More work in this field is underway.

## Experimental Section

**Materials:** All chemicals purchased were of reagent grade and used without further purification.

**Physical Methods:** Elemental analyses W, Mn, and Ce were determined with a Leaman inductively coupled plasma (ICP) spectrometer. IR spectra were recorded in the range of 400–4000 cm$^{-1}$ with an Alpha Centaurt FT/IR Spectrophotometer with pressed KBr pellets. UV/Vis absorption spectra were obtained with the use of a 752 PC UV/Vis spectrophotometer. TG analyses were performed with a Perkin–Elmer TGA7 instrument in flowing $N_2$ with a heating rate of 10 °C min$^{-1}$. The electrochemical measurement was carried out with a CHI 660 electrochemical workstation at room temperature (25–30 °C). X-ray powder diffractometry (XRPD) studies of **1** were performed with a NETZSCH STA 449C instrument, with a Panalytical X-Pert pro diffractometer and Cu-$K_\alpha$ radiation.

**Compound 1:** The precursor $K_4Na_6Mn[Mn_4Si_2W_{18}O_{68}(H_2O)_2]\cdot\approx 33H_2O$ was synthesized according to the published procedure.[13] The molecular formula was presumed by elemental analysis and thermogravimetric analysis. An aqueous solution (15 mL, pH = 4.5) of $Ce(SO_4)_2\cdot 4H_2O$ (0.16 g, 0.4 mmol) and potassium citrate (0.12 g, 0.4 mmol) was added to an aqueous solution (15 mL) of $K_4Na_6Mn[\{SiMn_2W_9O_{34}(H_2O)\}_2]\cdot 33H_2O$ (1.12 g, 0.2 mmol) with stirring. The color changed from yellow to brown. The solution was then heated to boiling for 2 h, and the color changed again from brown to yellow. After cooling to room temperature, the final yellow suspension was filtered, and the pH value of the filtrate was ca. 3.5. The filtrate was slowly evaporated at room temperature. The yellow columnar crystals of **1** were isolated after 10 d (yield 60% based on W). $H_{79}Ce_2K_4Mn_4Na_2O_{105.5}Si_2W_{18}$ (5835.49): calcd. Ce 4.80, Mn 3.77, W 56.71; found Ce 4.71, Mn 3.87, W 56.85.

**X-ray Crystallography:** Crystallographic data for **1** was collected at 298 K with a Rigaku R-axis Rapid IP diffractometer with the use of graphite monochromatic Mo-$K_\alpha$ radiation ($\lambda$ = 0.71073 Å) and IP technique. The structure was solved by direct methods and refined by the full-matrix least-squares method on $F^2$ by using the SHELXTL-97 crystallographic software package.[17] Anisotropic thermal parameters were used to refine all atoms on polyanions, cerium, potassium, and sodium cations. All the water molecules were refined isotropically. Non-hydrogen atoms were included. Some crystal water molecules were disordered. Their occupancies were determined by fixing the atomic displacement parameter factors (0.08) at the beginning, and then occupancy numbers were fixed to refine their atomic displacement parameter factors. Atoms with occupancies lower than 0.25 were ignored. Further details of the X-ray structural analysis are given in Table 1. Further details of the crystal-structure investigation may be obtained from the

 © 2007 Wiley-VCH Verlag GmbH & Co. KGaA, Weinheim 

Table 1. Crystal Data and Structure Refinement for **1**.

| | |
|---|---|
| Chemical formula | $H_{79}Ce_2K_4Mn_4Na_2O_{105.5}Si_2W_{18}$ |
| Formula weight | 5835.49 |
| Crystal system | orthorhombic |
| Space group | $P2_12_12_1$ |
| $a$ [Å] | 12.040(2) |
| $b$ [Å] | 26.094(5) |
| $c$ [Å] | 30.043(6) |
| $\alpha$ [°] | 90 |
| $\beta$ [°] | 90 |
| $\gamma$ [°] | 90 |
| $V$ [Å$^3$] | 9439(3) |
| $Z$ | 4 |
| $D$ [mg m$^{-3}$] | 4.107 |
| $T$ [K] | 293(2) |
| Reflections collected | 85946 |
| Reflections unique | 21490 |
| Goodness of fit on $F^2$ | 0.947 |
| $R_1$[a] | 0.0618 |
| $wR_2$[b] | 0.1074 |

[a] $R_1 = \Sigma||F_o| - |F_C||/\Sigma|F_o|$. [b] $wR_2 = \Sigma[w(F_o^2 - F_C^2)^2]/\Sigma[w(F_o^2)^2]^{1/2}$.

Fachinformationszentrum Karlsruhe, 76344 Eggenstein-Leopoldshafen, Germany, on quoting the depository number CSD-417468.

**Supporting Information** (see footnote on the first page of this article): Ball-and-stick view of the structure of **1**, view of the coordination environments of potassium cations, view of the packing arrangement of **1**. IR and UV/Vis spectra of **1**, selected bond lengths and angles of **1**.

## Acknowledgments

This work was supported by the National Science Foundation of China (No. 20371011).

[1] a) M. T. Pope, *Heteropoly and Isopoly Oxometalates*, Springer, Berlin, **1983**; b) M. T. Pope, A. Müller, *Polyoxometalates: From Platonic Solids to Anti-Retroviral Activity*, Kluwer, Dordrecht, **1993**; c) C. L. Hill, *Chem. Rev.* **1998**, *98*, 1–357; d) T. Yamase, M. T. Pope, *Polyoxometalate Chemistry for Nano-Composite Design*, Kluwer, Dordrecht, **2002**.

[2] J. Bartis, S. Sukal, M. Dankova, E. Kraft, R. Kronzon, M. Blumenstein, L. C. Francesconi, *J. Chem. Soc., Dalton Trans.* **1997**, *11*, 1937–1944.

[3] J. F. Keggin, *Nature* **1933**, *131*, 908–909.

[4] a) P. Mialane, L. Lisnard, D. Vivien, F. Sécheresse, *Inorg. Chem.* **2003**, *42*, 2102–2108; b) M. Sadakane, M. H. Dickman, M. T. Pope, *Angew. Chem. Int. Ed.* **2000**, *39*, 2914–2916; c) J. P. Wang, X. Y. Duan, X. D. Du, J. Y. Niu, *Cryst. Growth Des.* **2006**, *6*, 2266–2270; d) F. L. Sousaa, F. A. Almeida Paz, C. M. C. E. Grnadeiro, A. M. V. Cavaleiro, J. Rocha, J. Klinowski, H. I. S. Nogueira, *Inorg. Chem. Commun.* **2005**, *8*, 924–927; e) P. Mialane, A. Dolbecq, L. Lisnard, A. Mallard, J. Marrot, F. Sécheresse, *Angew. Chem. Int. Ed.* **2002**, *41*, 2398–2401; f) K. Fukaya, T. Yamase, *Angew. Chem. Int. Ed.* **2003**, *42*, 654–658; g) K. Wassermann, M. H. Dickman, M. T. Pope, *Angew. Chem. Int. Ed.* **1997**, *36*, 1445–1448; h) R. C. Howell, F. G. Perez, S. Jain, W. D. Horrocks Jr, A. L. Rheingold, L. C. Francesconi, *Angew. Chem. Int. Ed.* **2001**, *40*, 4031–4034; i) C. D. Wu, C. Z. Lu, H. H. Zuang, J. S. Huang, *J. Am. Chem. Soc.* **2002**, *124*, 3836–3837.

[5] B. Dawson, *Acta Crystallogr.* **1953**, *6*, 113–126.

[6] A. P. Ginsbergh, *Inorganic Syntheses*, Wiley, New York, **1990**, vol. 27, pp. 107–110.

[7] a) J. Y. Niu, D. J. Guo, J. P. Wang, J. W. Zhao, *Cryst. Growth Des.* **2004**, *4*, 241–247; b) Y. Lu, Y. Xu, Y. G. Li, E. B. Wang, X. X. Xu, Y. Ma, *Inorg. Chem.* **2006**, *45*, 2055–2060; c) M. Sadakane, M. H. Dickman, M. T. Pope, *Inorg. Chem.* **2001**, *40*, 2715–2719; d) Q. Luo, R. C. Howell, J. Bartis, M. Dankova, W. D. J. Horrocks, A. Rheingold, L. Francesconi, *Inorg. Chem.* **2002**, *41*, 6112–6117; e) Q. H. Luo, R. C. Howell, M. Dankova, J. Bartis, C. W. Williams, W. D. J. Horrocks, V. G. J. Young, A. L. Rheingold, L. C. Francesconi, M. R. Antonio, *Inorg. Chem.* **2001**, *40*, 1894–1901; f) X. K. Fang, T. M. Anderson, C. Benelli, C. L. Hill, *Chem. Eur. J.* **2005**, *11*, 712–718.

[8] a) H. Y. An, Y. Lan, Y. G. Li, E. B. Wang, N. Hao, D. R. Xiao, L. Y. Duan, L. Xu, *Inorg. Chem. Commun.* **2004**, *7*, 356–358; b) H. Y. An, Y. G. Li, D. R. Xiao, E. B. Wang, C. Y. Sun, *Cryst. Growth Des.* **2006**, *6*, 1107–1112; c) H. Y. An, E. B. Wang, D. R. Xiao, Y. G. Li, L. Xu, *Inorg. Chem. Commun.* **2005**, *8*, 267–270; d) H. Y. An, D. R. Xiao, E. B. Wang, C. Y. Sun, *J. Mol. Struct.* **2005**, *743*, 117–123; e) H. Y. An, D. R. Xiao, E. B. Wang, Y. G. Li, X. L. Wang, L. Xu, *Eur. J. Inorg. Chem.* **2005**, 854–859; f) B. Gao, S. X. Liu, L. H. Xie, M. Yu, C. D. Zhang, C. Y. Sun, H. Y. Cheng, *J. Solid State Chem.* **2006**, *179*, 1681–1689.

[9] a) C. Liu, F. Luo, N. Liu, Y. Cui, X. Wang, E. B. Wang, J. Chen, *Cryst. Growth Des.* **2006**, *6*, 2658–2660; b) F. A. A. Paz, M. S. S. Balula, A. M. V. Cavaleiro, J. Klinowski, H. I. S. Nogueiraa, *Acta Crystallogr. Sect. E* **2005**, *61*, i28–i31; c) X. T. Zhang, D. Q. Wang, J. M. Dou, S. S. Yan, X. X. Yao, J. Z. Jiang, *Inorg. Chem.* **2006**, *45*, 10629–10635; d) H. Zhang, L. Y. Duan, Y. Lan, E. B. Wang, C. W. Hu, *Inorg. Chem.* **2003**, *42*, 8053–8058.

[10] a) S. X. Liu, D. H. Li, L. H. Xie, H. Y. Cheng, X. Y. Zhao, Z. M. Su, *Inorg. Chem.* **2006**, *45*, 8036–8040; b) N. V. Izarova, M. N. Sokolov, D. G. Samsonenko, A. Rothenberger, D. Yu. Naumov, D. Fenske, V. P. Fedin, *Eur. J. Inorg. Chem.* **2005**, *24*, 4985–4996; c) G. Liu, Y. G. Wei, Q. Yu, Q. Liu, S. W. Zhang, *Inorg. Chem. Commun.* **1999**, *2*, 434–437.

[11] a) F. B. Xin, M. T. Pope, *J. Am. Chem. Soc.* **1996**, *118*, 7731–7736; b) A. Müller, A. M. Todea, H. Bögge, J. V. Slageren, M. Dressel, A. Stammler, M. Rusu, *Chem. Commun.* **2006**, 3066–3068; c) B. S. Bassil, M. H. Dickman, U. Kortz, *Inorg. Chem.* **2006**, *45*, 2394–2396; d) S. S. Mal, U. Kortz, *Angew. Chem. Int. Ed.* **2005**, *44*, 3777–3780; e) X. K. Fang, T. M. Anderson, C. L. Hill, *Angew. Chem. Int. Ed.* **2005**, *44*, 3540–3544.

[12] a) P. Mialane, A. Dolbecq, F. Sécheresse, *Chem. Commun.* **2006**, 3477–3485; b) P. Mialane, A. Dolbecq, E. Riviére, J. Marrot, F. Sécheresse, *Eur. J. Inorg. Chem.* **2004**, *1*, 33–36; c) U. Kortz, *J. Cluster Sci.* **2003**, *14*, 205–214; d) C. D. Wu, C. Z. Lu, H. H. Zuang, J. S. Huang, *J. Am. Chem. Soc.* **2002**, *124*, 3836–3837; e) H. Zhang, L. Y. Duan, Y. Lan, E. B. Wang, C. W. Hu, *Inorg. Chem.* **2003**, *42*, 8053–8058; f) P. Gouzerh, A. Proust, *Chem. Rev.* **1998**, *98*, 77–111.

[13] U. Kortz, S. Isber, M. H. Dickman, D. Ravot, *Inorg. Chem.* **2000**, *39*, 2915–2922.

[14] H. D. Flack, G. Bernardinelli, *Acta Crystallogr. Sect. A* **1999**, *55*, 908–915.

[15] I. D. Brown, D. Altermatt, *Acta Crystallogr. Sect. B* **1985**, *41*, 244–247.

[16] Actually, the redox peaks of $Mn^{2+}$ were concealed by the relatively strong peaks of $Ce^{3+}$. The detailed explanation is in the supporting information. a) X. Y. Zhang, G. B. Jameson, C. J. O'Connor, M. T. Pope, *Polyhedron* **1996**, *15*, 917–922; b) J. F. Liu, F. Ortéga, P. Sethuraman, D. E. Katsoulis, C. E. Costello, M. T. Pope, *J. Chem. Soc., Dalton Trans.* **1992**, 1901–1906.

[17] a) G. M. Sheldrick, *SHELXL97, Program for Crystal Structure Refinement*, University of Göttingen, Germany, **1997**; b) G. M. Sheldrick, *SHELXS97, Program for Crystal Structure Solution*, University of Göttingen, Germany, **1997**.

Received: December 26, 2006
Published Online: April 11, 2007

 © 2007 Wiley-VCH Verlag GmbH & Co. KGaA, Weinheim 

DOI: 10.1002/ejic.200700027

# Synthesis of Chiral Imidazolinium Carbene from a Carbohydrate and Its Rhodium(I) Complex[‡]

**Ji-cheng Shi,*[a,b] Ni Lei,[b,c] Qingsong Tong,[a] Yiru Peng,[a] Junfa Wei,[b] and Li Jia[a]**

**Keywords:** Nitrogen heterocycles / Carbenes / Rhodium / Carbohydrates / Chirality

A chiral imidazolinium salt with two bulky carbohydrate subunits, *N*,*N*′-1,3-bis(methyl 4,6-*O*-benzylidene-3-deoxy-α-D-altropyrano-3-yl)imidazolinium chloride (**4**), was synthesized in high yield. Deprotonation of **4** with sodium *tert*-butoxide in the presence of $[RhCl(COD)]_2$ produced NHC-coordinated rhodium complex **5** along with water adduct **6** to a lesser extent depending on the moisture content of the reaction mixture. These compounds were fully characterized by IR, MS, and $^1H$ and $^{13}C\{^1H\}$ NMR spectroscopy.

(© Wiley-VCH Verlag GmbH & Co. KGaA, 69451 Weinheim, Germany, 2007)

## 1. Introduction

Since the isolation and characterization of stable N-heterocyclic carbenes (NHCs) by Arduengo in 1991,[1] these compounds have generated considerable interest in catalysis reactions, both as a transition metal ligand[2] and directly as a nucleophilic catalyst.[3] The strong σ-donating character of NHCs combined with their poor π-accepting properties generate metal centers that are electron-rich relative to the corresponding phosphane-coordinated complexes.[4] Consequently, these carbene ligands do not appear to dissociate from the metal centers, and their complexes tend to be highly active in oxidative addition steps.[5] These properties of NHCs have led to significant improvements in some reactions that originally used phosphane-coordinated catalysts, such as Ru-catalyzed olefin metathesis[6] and Pt-catalyzed olefin hydrosilylation.[7]

Chiral phosphanes have been widely used in asymmetric catalysis, and the advances achieved have had a significant impact on both academic and industrial research. It was therefore a logical extension to similarly modify NHCs with a chiral moiety.[8] An advantage of chiral NHCs is that an excess of the ligand is not necessary as a result of its low propensity to dissociate from the metal center. Recently, high levels of enantiomeric excess were reported in several catalysis reactions using chiral NHCs. These reactions include the iridium-catalyzed asymmetric hydrogenation of aryl alkenes,[9] Ru-catalyzed symmetry-breaking olefin metathesis,[10] Rh-catalyzed hydrogenation of α,β-unsaturated esters,[11] and the hydrosilylation of methyl ketones.[12] In addition to these examples of bidentate NHC ligands, a monodentate NHC ligand with two bulky chiral [2,2]-paracyclophane groups was reported to give excellent enantiomeric excess in the rhodium-catalyzed enone addition.[13] These examples highlight the potential and promise of chiral NHC ligands in asymmetric catalysis. However, when compared to chiral phosphanes, the field of asymmetric catalysis with chiral NHCs remains in its infancy and further work in the area, primarily the synthesis of new chiral NHCs, is well justified.

Carbohydrates are a diverse and widely available source of chirality. Chiral phosphanes derived from carbohydrates have been used in the commercial synthesis of optically pure products; however, there have been no reports of chiral NHCs prepared from carbohydrates so far. Previously, we have selectively incorporated diphenylphosphanyl groups into the C-2 and C-3 positions of a pyrano rings in high yields through an epoxide ring-opening reaction.[14] The resulting chiral phosphanes were found to be versatile ligands in the coordination of late transition metals[15] and were successfully applied in nickel-catalyzed asymmetric hydrovinylation reactions.[16] Herein we wish to report the synthesis of a chiral imidazolinium salt with two bulky subunits derived from D-glucose, as well as the synthesis of a rhodium complex from the corresponding chiral N-heterocyclic carbene ligand.

## 2. Results and Discussion

Methyl 2,3-anhydro-4,6-*O*-benzylidene-α-D-mannopyranoside (**1**) can be easily prepared from D-glucose on a large

[‡] Chiral Ligands Derived from Carbohydrates, 19. Part 18: Ref.[15a]

[a] College of Chemistry and Materials Science, Fujian Normal University,
Fuzhou 350007, China
Fax: +86-591-63053129
E-mail: jchshi@fjnu.edu.cn
[b] Department of Chemistry, Shanxi Normal University,
Xi'an 710062, China
[c] Dalian Institute of Chemical Physics, Chinese Academy of Sciences,
Dalian, Liaonin 116023, China

Supporting information for this article is available on the WWW under http://www.eurjic.org or from the author.

 © 2007 Wiley-VCH Verlag GmbH & Co. KGaA, Weinheim 

scale, and it is also commercially available (Scheme 1).[17] Our initial synthetic approach to the imidazolium salt by the co-condensation of methyl 3-deoxy-3-amino-4,6-benzylidene-α-D-altropyranoside (**2**), made from ammonolysis of epoxide **1**,[18] with glyoxal and formaldehyde was unsuccessful.[19] The failure of this approach seemed to result from the hydrolysis of the protecting groups in **1** and with difficulties in the isolation of the desired product. Therefore, an alternative route was pursued that used ethane-1,2-diamine instead of ammonia.

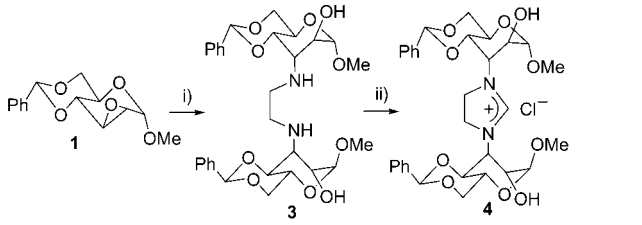


[a] Conditions: i) ethane-1,2-diamine, MeOH, 140 °C; ii) $NH_4Cl$, $CH(OEt)_3$, 110 °C.

Scheme 1. Synthesis of an imidazolinium chloride.[a]

By raising the reaction temperature to 140 °C, an 86% yield of diamine **3** was readily obtained. The higher reaction temperature that was necessary for this reaction was attributed to the steric hindrance in the reaction of the second epoxide with the diamine. By heating **3** at 110 °C for 3 h in neat triethylorthoformate in the presence of $NH_4Cl$, imidazolinium salt **4** was produced in 92% yield as a precipitate upon cooling the reaction mixture. Crude **4** was pure enough to be used directly in the next step. It is worth noting that when the reaction was conducted with $NH_4BF_4$ instead of $NH_4Cl$, which is more frequently used for the ring-closure of imidazolinium salts,[20] several side products resulted, which made isolation of the desired imidazolium salt tedious. At the present time, the reason for this is uncertain, but we speculate that $NH_4BF_4$ may be unstable at high temperature and that it may generate trace amounts of acid that hydrolyze the protecting groups in **1**. Compounds **3** and **4** were fully characterized by IR, MS, and $^1H$ and $^{13}C\{^1H\}$ NMR spectroscopy (see Supporting Information). The $^1H$ and $^{13}C\{^1H\}$ NMR spectra of chiral products **3** and **4** are indicative of a $C_2$-symmetric product, and the presence of only one set of signals also suggests that no racemization occurred in the synthesis of **4**. The signal at $\delta$ = 8.83 ppm in the $^1H$ NMR spectrum of **4** is characteristic of the NCHN proton in the imidazolinium salt.[21]

We next examined the coordination properties of the chiral N-heterocyclic carbene generated from **4**. Deprotonation of **4** with sodium *tert*-butoxide in a THF solution of $[RhCl(COD)]_2$ at 45 °C for 48 h afforded NHC-coordinated Rh complex **5** in 76% yield. The extent of dryness of imidazolinium salt **4** was found to be crucial to the yield of **5**; if **4** was not carefully dried with $P_2O_5$ under vacuum, the yield of **5** dropped significantly to 20–50%, and the water adduct of the carbene, compound **6**, could be seen at approximately 20% yield (Scheme 2). The fact that nearly no reaction occurred at room temperature suggests that steric hindrance around the carbene hampered its coordination to rhodium. This would further suggest that the carbene reaction with water to yield **6** is faster than its complexation to yield **5**, as our observations would indicate. Evidence for a highly steric environment around rhodium can be seen in the $^1H$ and $^{13}C\{^1H\}$ NMR spectrum. The $C_2$-symmetry seen in **4** disappeared in **5**, and in **6** as well. The loss of $C_2$-symmetry in **6**, with its relatively small hydroxy group in the imidazolidine ring, is indicative of a carbene center surrounded by two bulky chiral substituents. It would be interesting to evaluate the chiral induction ability of the NHC-coordinated rhodium complex with its two large carbohydrate subunits. The assignments of **5** and **6** are based on MS and NMR spectroscopic data. The HRMS measurement of 809.2529 $[M - Cl]^+$ for NHC-coordinated Rh complex **5** is consistent with the calculated value of 809.2520. A peak at 617 $[M + 1]^+$ in the MS of **6** suggests that it is an $H_2O$ adduct of the carbene derived from **4**.

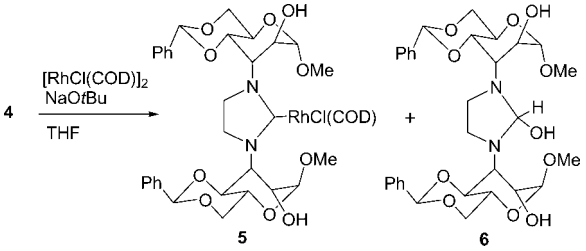


Scheme 2. Synthesis of NHC-coordinated $Rh^I$ complex.

In conclusion, we have synthesized the first example of a chiral imidazolinium salt with two bulky carbohydrate subunits and its corresponding rhodium complex. The reaction conditions for the rhodium complex and the NMR signals suggest that the carbene center is highly encumbered by the two bulky chiral subunits. Future studies will focus on (1) the use of rhodium complex **5** in asymmetric catalysis, (2) the deprotection of **5** to form a polyhydroxy complex as a potential water-soluble asymmetric catalyst, and (3) the synthesis of more chiral N-heterocyclic carbenes from carbohydrates and their corresponding transition-metal complexes.

## 3. Experimental Section

**General Procedures.** All reactions and manipulations involving air- and/or moisture-sensitive compounds were carried out by using standard Schlenk techniques under an atmosphere of nitrogen. NMR spectra were recorded with a BRUKER DRX 400 MHz or Varian INOVA 400 MHz spectrometer. Chemical shifts are reported in $\delta$ relative to $CDCl_3$. High-resolution mass spectra (HRMS, ESI) were obtained with a Micromass Q-Tof Micro (Micromass Inc., Manchester, England). THF was distilled from sodium benzophenone ketyl under an atmosphere of nitrogen. NaO*t*Bu was used as received. $[RhCl(COD)]_2$ and methyl 2,3-anhydro-4,6-*O*-benzylidene-α-D-mannopyranoside (**1**)[17] were prepared according to the literature methods, respectively.

 © 2007 Wiley-VCH Verlag GmbH & Co. KGaA, Weinheim 

***N*,*N*′-Bis(methyl 4,6-*O*-benzylidene-3-deoxy-α-D-altropyrano-3-yl)-1,2-diaminoethane (3):** A mixture of methyl 2,3-anhydro-4,6-*O*-benzylidene-α-D-mannopyranoside (**1**; 4.1 g, 15.5 mmol) and ethane-1,2-diamine (0.4 g, 6.67 mmol) in methanol (60 mL) was stirred in an autoclave at 140 °C for 12 h. After cooling the reaction mixture, the solvent was evaporated, and the residue was purified by chromatography (3–10% methanol in dichloromethane) to afford the product. Yield: 3.4 g (86%). M.p. 91–93 °C. $[\alpha]_D^{21}$ = +112.2 (*c* = 1.0, ethanol). $^1$H NMR (400 MHz, $CDCl_3$): $\delta$ = 7.50–7.30 (m, 10 H), 5.47 (s, 2 H), 4.52 (s, 2 H), 4.30–4.25 (m, 2 H), 4.10–4.00 (m, 2 H), 3.95–3.90 (m, 2 H), 3.91 (br., 2 H), 3.80–3.70 (m, 2 H), 3.34 (s, 6 H), 3.22 (br., 2 H), 3.10–3.05 (m, 2 H), 2.90–2.85 (m, 2 H), 2.65–2.55 (m, 2 H) ppm. $^{13}$C NMR (100 MHz, $CDCl_3$): $\delta$ = 137.64 129.06 128.38 (2 C), 126.21 (2 C), 102.05 (2 C), 77.86, 70.80, 69.50, 58.69, 57.10, 55.47, 47.08, 46.11 ppm. IR (KBr): $\tilde{\nu}$ = 3440, 2907, 1637, 1457, 1380, 1105, 1067, 1044, 974, 755, 670 cm$^{-1}$. MS (ES): *m*/*z* (%) = 589 (100) $[M + 1]^+$.

***N*,*N*′-1,3-Bis(methyl 4,6-*O*-benzylidene-3-deoxy-α-D-altropyrano-3-yl)imidazolinium chloride (4):** A mixture of diaminoethane **3** (2.0 g, 3.4 mmol) and $NH_4Cl$ (0.3 g, 5.6 mmol) in triethylorthoformate (40 mL) was stirred at 110 °C for 3 h. Upon cooling of the reaction mixture to room temperature, ashen solids appeared and were collected by filtration and washed with hexane. The solid was dissolved in dichloromethane and purified through a short column to remove excess $NH_4Cl$. Yield: 2.0 g (92%). M.p. 153–154 °C. $[\alpha]_D^{20}$ = +127.9 (*c* = 1.0, ethanol). $^1$H NMR (400 MHz, $CDCl_3$): $\delta$ = 8.83 (s, 1 H), 7.40–7.15 (m, 10 H), 5.88 (br., 2 H), 5.50 (s, 2 H), 4.57 (s, 2 H), 4.30–4.05 (m, 8 H), 3.90 (br., 2 H), 3.75–3.60 (m, 4 H), 3.10 (s, 6 H), 3.06 (s, 2 H) ppm. $^{13}$C NMR (100 MHz, $CDCl_3$): $\delta$ = 157.29, 136.96, 129.44, 128.45 (2 C), 126.12 (2 C), 102.55, 100.70, 74.51, 69.30, 66.86, 58.66, 58.22, 55.43, 50.09 ppm. IR (KBr): $\tilde{\nu}$ = 3440, 3257, 2930, 1642, 1459, 1409, 1262, 1138, 1104, 995, 964, 772, 707 cm$^{-1}$. MS (ESI): *m*/*z* (%) = 599 (100) $[M - Cl]^+$.

**NHC-Coordinated Rh complex 5:** A mixture of dried imidazolinium salt **4** (1.35 g, 2.15 mmol), $[RhCl(COD)]_2$ (0.40 g, 0.82 mmol), and NaO*t*Bu (0.31 g, 3.2 mmol) was stirred in THF (20 mL) at 45 °C for 48 h. The reaction mixture was filtered through celite, evaporated, and the residue was then purified by silica gel chromatography (2% methanol in dichloromethane). Yield: 1.06 g (77%). M.p. 157–159 °C. $^1$H NMR (400 MHz, $CDCl_3$): $\delta$ = 7.60–7.20 (m, 11 H), 6.60–6.62 (m, 1 H), 5.80 (br., 1 H), 5.71 (s, 1 H), 5.64 (s, 1 H), 5.05–4.90 (m, 2 H), 4.69 (d, *J* = 3.2 Hz, 1 H), 4.66 (s, 1 H), 4.42 (br., 1 H), 4.35–4.25 (m, 3 H), 4.11 (br., 2 H), 4.05–3.98 (m, 1 H), 3.92–3.81 (m, 2 H), 3.80–3.65 (m, 5 H), 3.64–3.55 (m, 2 H), 3.46 (s, 3 H), 3.39 (br., 1 H), 3.27 (s, 3 H), 2.55–2.42 (m, 2 H), 2.35–2.22 (m, 2 H), 2.10–1.98 (m, 2 H), 1.82–1.67 (m, 4 H) ppm. $^{13}$C NMR (100 MHz, $CDCl_3$): $\delta$ = 137 ppm. 65, 137.42, 129.00, 128.56, 128.40, 128.04, 126.30, 126.01, 102.31, 101.40, 101.21, 74.70, 73.80, 71.67, 70.22, 69.94, 69.04, 68.90, 62.41, 61.72, 59.38, 58.52, 55.48, 55.09, 49.23, 47.41, 34.18, 31.68, 29.96, 27.96. IR (KBr): $\tilde{\nu}$ = 3421, 2933, 2875, 1486, 1452, 1378, 1266, 1133, 1112, 1087, 972, 819, 754, 689 cm$^{-1}$. MS (ESI): *m*/*z* (%) = positive 809 (100) $[M - Cl^-]$; negative 879 (100) $[M + Cl^-]$. HRMS: calcd. for $C_{39}H_{50}N_2O_{10}Rh$ $[M - Cl]^+$ 809.2520; found 809.2529.

***N*,*N*′-1,3-Bis(methyl 4,6-*O*-benzylidene-3-deoxy-α-D-altropyrano-3-yl)-2-hydroxyimidazolidine (6):** The compound was isolated as a side product in the preparation of **5**; its yield is around 5–20% depending on the dryness of imidazolinium salt **4** used. $^1$H NMR (400 MHz, $CDCl_3$): $\delta$ = 8.35 (s, 1 H), 7.50–7.30 (m, 10 H), 5.55 (s, 1 H), 5.44 (s, 1 H), 4.65–4.60 (m, 2 H), 4.35–4.25 (m, 2 H), 4.15–4.10 (m, 2 H), 4.07–4.00 (m, 2 H), 3.95–3.91 (m, 2 H), 3.90–3.77 (m, 4 H), 3.68–3.60 (m, 2 H), 3.51–3.40 (m, 8 H), 3.38–3.10 (m, 3 H) ppm. $^{13}$C NMR (100 MHz, $CDCl_3$): $\delta$ = 165.28, 137.38, 137.07, 129.17, 128.36, 128.29, 126.46, 126.31, 126.08, 102.51, 102.33, 102.03, 101.88, 77.40, 75.80, 69.88, 69.68, 69.49, 69.08, 61.74, 59.55, 58.92, 58.66, 55.60, 55.54, 47.16, 45.51 ppm. IR (KBr): $\tilde{\nu}$ = 3409, 3257, 2934, 1654, 1455, 1380, 1136, 1107, 1049, 974, 756, 700 cm$^{-1}$. MS (ESI): *m*/*z* (%) = 617 (20) $[M + 1]^+$.

**Supporting Information** (see footnote on the first page of this article): Full characterization of compounds **3**–**6**.

## Acknowledgments

This work was financially supported by the National Natural Science Foundation of China (20473089), the National Basic Research Program of China (2003CB61615803), and Fujian Normal University.

[1] a) A. J. Arduengo III, R. L. Harlow, M. Kline, *J. Am. Chem. Soc.* **1991**, *113*, 361; b) A. J. Arduengo III, *Acc. Chem. Res.* **1999**, *32*, 913; c) W. A. Herrmann, C. Köcher, *Angew. Chem. Int. Ed. Engl.* **1997**, *36*, 2162.
[2] a) W. A. Herrmann, *Angew. Chem. Int. Ed.* **2002**, *41*, 1290; b) M. C. Perry, K. Burgess, *Tetrahedron: Asymmetry* **2003**, *14*, 951.
[3] D. Enders, T. Balensiefer, *Acc. Chem. Res.* **2004**, *37*, 534.
[4] a) J. Huang, H.-J. Schanz, E. D. Stevens, S. P. Nolan, *Organometallics* **1999**, *18*, 2370; b) W. A. Herrmann, M. Elison, J. Fischer, C. Köcher, G. R. J. Artus, *Angew. Chem. Int. Ed. Engl.* **1995**, *34*, 2371; c) P. Bazinet, G. P. A. Yap, D. S. Richeson, *J. Am. Chem. Soc.* **2003**, *125*, 13314.
[5] a) H. Yu, J.-C. Shi, H. Zhang, P. Yang, X. Wang, Z. Jin, *J. Mol. Catal. A* **2006**, *250*, 15; b) J.-C. Shi, P. Yang, Q. Tong, Y. Wu, Y. Peng, *J. Mol. Catal. A* **2006**, *259*, 7; c) J.-C. Shi, X. Cao, Y. Zheng, L. Jia, *Chin. J. Org. Chem.* **2007**, *27*, in press.
[6] a) T. Weskamp, F. J. Kohl, W. Heiringer, D. Gleich, W. A. Herrmann, *Angew. Chem. Int. Ed.* **1999**, *38*, 2416; b) S. Blechert, H. Wakamatsu, *Angew. Chem. Int. Ed.* **2002**, *41*, 794; c) T. M. Trnka, R. H. Grubbs, *Acc. Chem. Res.* **2001**, *34*, 18.
[7] I. E. Marko, S. Sterin, O. Buisine, G. Mignani, P. Branlard, B. Tinant, J.-P. Declercq, *Science* **2002**, *298*, 204.
[8] a) W. A. Herrmann, L. J. Goossen, C. Köcher, G. R. J. Artus, *Angew. Chem. Int. Ed. Engl.* **1996**, *35*, 2805; b) D. Enders, H. Gielen, G. Raabe, J. Runsink, J. H. Teles, *Chem. Ber.* **1996**, *129*, 1483; c) M. Scholl, S. Ding, C. W. Lee, R. H. Grubbs, *Org. Lett.* **1999**, *1*, 953; d) J. Pytkowicz, S. Roland, P. Mangeney, G. Meyer, A. Jutand, *J. Organomet. Chem.* **2003**, *678*, 166; e) L. G. Bonnet, R. E. Douthwaite, B. M. Kariuki, *Organometallics* **2003**, *22*, 4187; f) L. G. Bonnet, R. E. Douthwaite, R. Hodgson, *Organometallics* **2003**, *22*, 4384; g) M. Alcarazo, S. J. Roseblade, E. Alonso, R. Fernández, E. Alvarez, F. J. Lahoz, J. M. Lassaletta, *J. Am. Chem. Soc.* **2004**, *126*, 13242.
[9] M. C. Perry, X. Cui, M. T. Powell, D.-R. Hou, J. H. Reibenspies, K. Burgess, *J. Am. Chem. Soc.* **2003**, *125*, 113.
[10] A. O. Larsen, W. Leu, C. N. Oberhuber, J. E. Campbell, A. H. Hoveyda, *J. Am. Chem. Soc.* **2004**, *126*, 11130.
[11] E. Bappert, G. Helmchen, *Synlett* **2004**, 1789.
[12] W.-L. Duan, M. Shi, G.-B. Rong, *Chem. Commun.* **2003**, 2916.
[13] Y. Ma, C. Song, C. Ma, Z. Sun, Q. Chai, M. B. Andrus, *Angew. Chem. Int. Ed.* **2003**, *42*, 5871.
[14] a) J.-C. Shi, M.-C. Hong, D. Wu, Q. Liu, B. S. Kang, *Chem. Lett.* **1995**, 685; b) J.-C. Shi, T. Weng, D. Wu, M. C. Hong, Q. Liu, B. S. Kang, H. Wang, S. Lu, *Chin. J. Chem.* **1996**, *14*, 455.
[15] a) J.-C. Shi, H. Chao, W. Fu, S. M. Peng, C.-M. Che, *J. Chem. Soc., Dalton Trans.* **2000**, 3128; b) J.-C. Shi, C.-H. Yueng, D. Wu, Q. Liu, B. S. Kang, *Organometallics* **1999**, *18*, 3796; c) J.-C. Shi, X. Huang, D. Wu, Q. Liu, B. S. Kang, *Inorg. Chem.* **1996**, *35*, 2742; d) J.-C. Shi, L. Chen, X. Huang, D. Wu, B. S. Kang, *J. Organomet. Chem.* **1997**, *535*, 17; e) J.-C. Shi, D. Wu,

 © 2007 Wiley-VCH Verlag GmbH & Co. KGaA, Weinheim 

T. Weng, M. C. Hong, Q. Liu, B. S. Kang, *J. Chem. Soc., Dalton Trans.* **1996**, 2911; f) J.-C. Shi, Y. Zheng, D. Wu, X. Huang, Q. Liu, B. S. Kang, *Inorg. Chim. Acta* **1999**, *290*, 121.
[16] G. Franció, F. Faraone, W. Leitner, *J. Am. Chem. Soc.* **2002**, *124*, 736.
[17] L. Coodman, J. E. Christensen, *J. Org. Chem.* **1963**, *28*, 158.
[18] M. A. Brown, P. J. Cox, R. A. Howie, O. A. Melvinh, O. J. Taylor, J. L. Wardell, *J. Organomet. Chem.* **1995**, *498*, 275.
[19] W. A. Herrmann, L. J. Goossen, C. Köcher, G. R. Artus, *Angew. Chem. Int. Ed. Engl.* **1995**, *35*, 2805.
[20] C. C. Scarborough, M. J. W. Grady, I. A. Guzei, B. A. Gandhi, E. E. Bunel, S. S. Stahl, *Angew. Chem. Int. Ed.* **2005**, *44*, 2.
[21] S. Dastgir, K. S. Coleman, A. R. Cowley, M. L. H. Green, *Organometallics* **2006**, *25*, 300.

Received: January 10, 2007
Published Online: April 16, 2007

 © 2007 Wiley-VCH Verlag GmbH & Co. KGaA, Weinheim

**The EUChemSoc Societies have taken the significant step into the future by merging their traditional journals, to form two leading chemistry journals, the *European Journal of Inorganic Chemistry* and the *European Journal of Organic Chemistry.* Three further EUChemSoc Societies (Austria, Czech Republic and Sweden) are Associates of the two journals.**

## COVER PICTURE

**The cover picture shows** three types of nickel complexes that are stabilized by 1,1′-bis(phosphanyl)-ferrocene ligands, which can be considered as model complexes for the hypothetical metal-mediated reaction between $CO_2$ and ethylene to form acrylic acid. The (acrylic acid)nickel(0) complexes are of particular interest as they represent the first stable combination between $Ni^0$ and this strong acid as a ligand. These complexes form hydrogen-bonded dimers in the solid state and are surprisingly stable. Details of their synthesis and reactivity along with the description of the other complexes are discussed in the article by D. Walther et al. on p. 2257ff. The artwork was created by Ulf Walther.

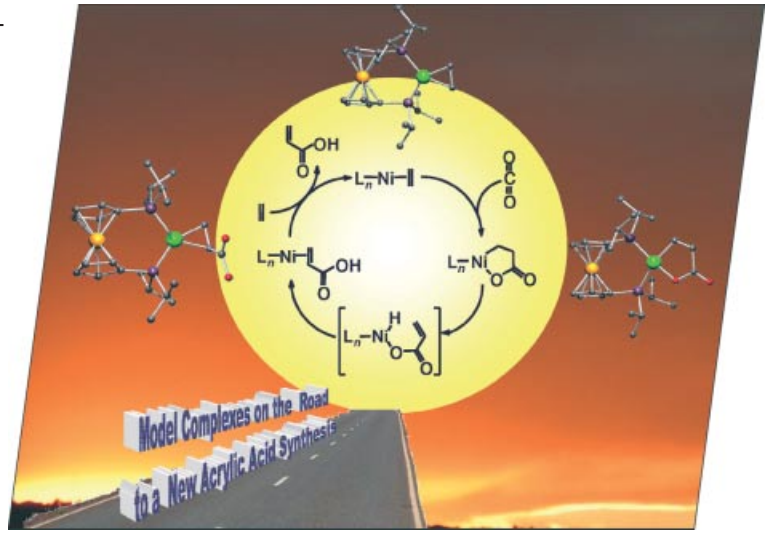


 © 2007 Wiley-VCH Verlag GmbH & Co. KGaA, Weinheim

**The EUChemSoc Societies have taken the significant step into the future by merging their traditional journals, to form two leading chemistry journals, the *European Journal of Inorganic Chemistry* and the *European Journal of Organic Chemistry.* Three further EUChemSoc Societies (Austria, Czech Republic and Sweden) are Associates of the two journals.**

## COVER PICTURE

**The cover picture shows** three types of nickel complexes that are stabilized by 1,1′-bis(phosphanyl)-ferrocene ligands, which can be considered as model complexes for the hypothetical metal-mediated reaction between $CO_2$ and ethylene to form acrylic acid. The (acrylic acid)nickel(0) complexes are of particular interest as they represent the first stable combination between $Ni^0$ and this strong acid as a ligand. These complexes form hydrogen-bonded dimers in the solid state and are surprisingly stable. Details of their synthesis and reactivity along with the description of the other complexes are discussed in the article by D. Walther et al. on p. 2257ff. The artwork was created by Ulf Walther.

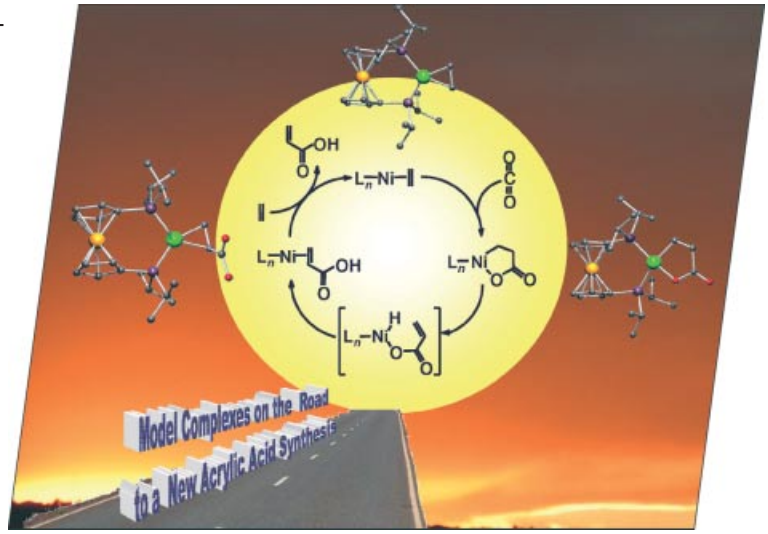


 © 2007 Wiley-VCH Verlag GmbH & Co. KGaA, Weinheim 

# CONTENTS

## MICROREVIEW


### Catalytic Hydroamination

**A. V. Lee, L. L. Schafer* ..... 2243–2255**

Modular *N,O*-Chelating Ligands: Group-4 Amidate Complexes for Catalytic Hydroamination

**Keywords:** Amidate ligands / Group-4 metal complexes / Hydroamination / Homogeneous catalysis / Asymmetric catalysis

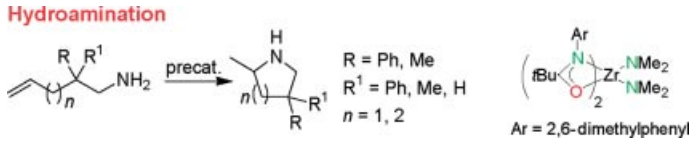


This microreview of transition metal amidate complexes and their applications in catalysis focuses on a new family of easily prepared, modular group 4 complexes for use in alkyne, allene and alkene hydroamination catalysis.


## FULL PAPERS


### Acrylic Acid $Ni^0$ Complexes

**J. Langer, R. Fischer, H. Görls, D. Walther* ..... 2257–2264**

Low-Valent Nickel and Palladium Complexes with 1,1′-Bis(phosphanyl)ferrocenes: Syntheses and Structures of Acrylic Acid and Ethylene Complexes

**Keywords:** Alkene ligands / Chelates / Nickel / Palladium / P ligands

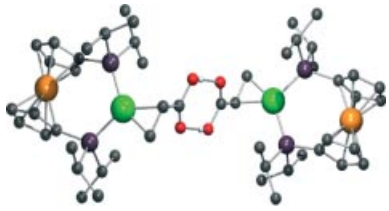

$Ni^0$ complexes of the type [(L)Ni($\eta^2$-$CH_2$=CH-COOH)] [L = 1,1′-bis(phosphanyl)-ferrocenes] containing acrylic acid as olefinic ligand are hydrogen bonded dimers in the solid state. Their isomers [(L)Ni($CH_2CH_2COO$)] can not be interconverted into the acrylic acid complexes, but undergo reductive decoupling to form complexes of the type (L)Ni($\eta^2$-$CH_2$=$CH_2$).

### Biomimetic Nanomaterials

**Q. Dong, H. Su,* W. Cao, D. Zhang, Q. Guo, F. Zhang ..... 2265–2273**

Assembly and Formation of Biomorphic Tin Dioxide by a Biomimetic Sol–Gel Approach Involving Glycoprotein

**Keywords:** Biomimetic synthesis / Colloids / Hierarchy / Nanotubes / Sol–gel processes

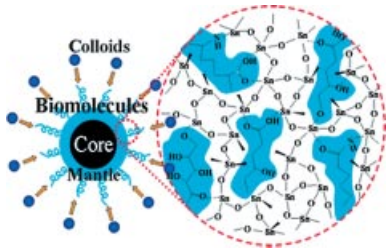


The eggshell membrane (ESM) plays a crucial role as the physical substrate and functional macromolecule template in achieving the synthesis of hierarchical $SnO_2$ through an interfacial sol–gel approach combined with calcination treatment. The formation mechanism is attributed to a protein-directed sol–gel process.


 © 2007 Wiley-VCH Verlag GmbH & Co. KGaA, Weinheim 

## Chiral Ferrocene-Based Ligands

A novel (phosphanylalkyl)ferrocenecarboxylic acid with combined planar and central chirality and its selected derivatives modified at both the phosphane and carboxyl groups have been prepared and used as ligands in palladium and rhodium complexes. These complexes are applied in enantioselective rhodium-catalysed hydrogenation and in palladium-catalysed allylic alkylation reactions.

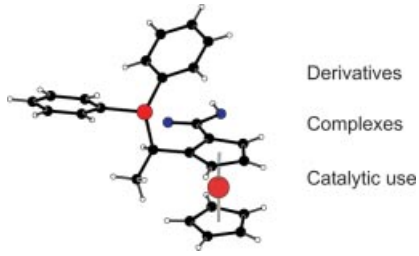


**M. Lamač, I. Císařová, P. Štěpnička* ..... 2274–2287**

Synthesis, Coordination and Catalytic Utility of Novel Phosphanyl–ferrocenecarboxylic Ligands Combining Planar and Central Chirality

**Keywords:** Asymmetric catalysis / Ferrocene ligands / Rhodium / Palladium / Allylic alkylation

## $Ce^{IV}$ Calixarene Complexes

The synthesis of $Ce^{IV}$ calixarene complexes is performed by two different synthetic approaches; the direct reaction of the Ce–β-diketonate with the calix[4]arene ligand and a complex modification of a bromination reaction. XPS studies revealed X-ray-induced changes in the effective Ce oxidation state of the two complexes in question.

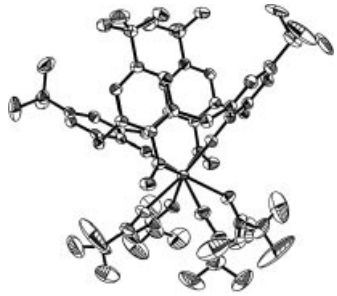

**J. Gottfriedsen,* R. Hagner, M. Spoida, Y. Suchorski ..... 2288–2295**

Synthesis, Structure, and Reactivity of Cerium(IV) Calix[4]arene Complexes

**Keywords:** Cerium / Calixarenes / Photoelectron spectroscopy

## Boratoheterocycles

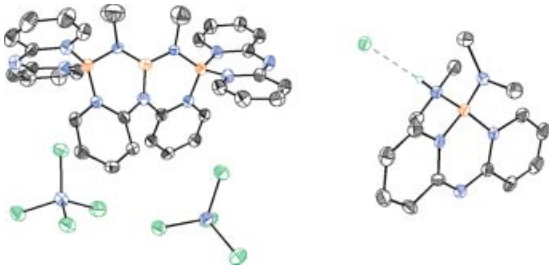

Transamination of di(pyrid-2-yl)amine with $B(NMe_2)_3$ yields a cyclic *B*-bis(dimethylamino)boratoheterocycle, which reacts with $CHCl_3$ to give the corresponding boronium chloride. With $AlCl_3$, the first diboronium salt is formed in a complex reaction and is isolated as its bis(tetrachloro)aluminate.

**U. Braun, H. Nöth* ..... 2296–2302**

Synthesis and Structures of Two New Types of Boronium Salts

**Keywords:** Boronium Cations / Transamination / X-ray structures

## Polymer-Anchored Complexes

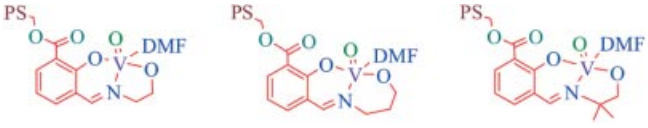


Three polymer-anchored oxidovanadium(IV) complexes were synthesized and their catalytic applications for the oxidation of styrene and cumene were studied.

**M. R. Maurya,* U. Kumar, P. Manikandan ..... 2303–2314**

Synthesis and Characterisation of Polymer-Anchored Oxidovanadium(IV) Complexes and Their Use for the Oxidation of Styrene and Cumene

**Keywords:** Vanadium(IV) complexes / Polymer support / Heterogeneous catalysts / Oxidations

 © 2007 Wiley-VCH Verlag GmbH & Co. KGaA, Weinheim 

# CONTENTS


## Lanthanide Complexes

**L. N. Puntus, A.-S. Chauvin, S. Varbanov, J.-C. G. Bünzli* ..... 2315–2326**

Lanthanide Complexes with a Calix[8]-arene Bearing Phosphinoyl Pendant Arms

**Keywords:** Lanthanides / Calixarenes / Europium / Luminescence

The phosphinoyl-substituted *p-tert*-butyl-calix[8]arene $B_8bL^8$ reacts with $Ln^{III}$ ions to form predominantly 1:1 complexes, but also 2:1 complexes. The final coordination environment of the ligand depends on the counterion. Optical electronegativity can be used to predict the charge transfer energies.

## Cationic Zirconocenes

**J. Saßmannshausen,* A. Track, T. A. D. S. Dias ..... 2327–2333**

Synthesis, Reactivity and DFT Investigation of a Cationic Zirconocene Benzyl Compound with an Appended Phenyl Group

**Keywords:** Density functional calculations / NMR spectroscopy / Polymerisation

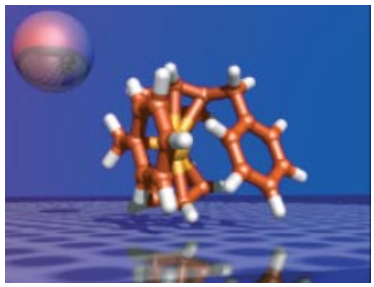

The reaction of $[\eta^5\text{-}C_5H_5\text{-}(\eta^5\text{-}C_5H_4CMe_2C_6H_4Me)Zr(CH_2Ph)_2]$ with $B(C_6F_5)_3$ was studied by multinuclear NMR spectroscopy and density functional theory (DFT). Detailed DFT calculations of the product explain the unusual chemical shift of the coordinated *ortho* atom of the tolyl moiety; the coordination was further elaborated by Bader and NBO analysis.

## Tetradentate Ligands

**E. Safaei, T. Weyhermüller, E. Bothe, K. Wieghardt, P. Chaudhuri* ..... 2334–2344**

A Magnetostructural and Electrochemical Study of $Cu^{II}$ and $Fe^{III}$ Complexes Containing a Tetradentate Aminebis(phenolate) Ligand with a Pendent Tetrahydrofuran Group

**Keywords:** Iron / Copper / Aminebis(phenol) / Electrochemistry / Magnetism

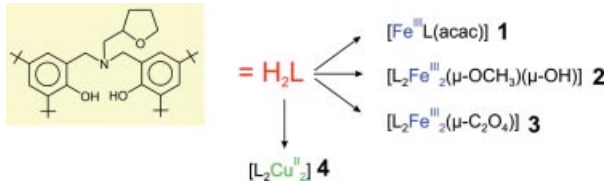


The tetradentate ligand $H_2L$ yields complexes **1**–**4**, which were characterized by various physical techniques, including X-ray diffraction, Mössbauer, electrochemical and magnetic susceptibility (2–290 K) measurements. Electrochemical oxidations are ligand-centered, the formation of phenoxyl radicals occurs from the coordinated phenolates.

## Partially Brominated Corroles

**S. Nardis, F. Mandoj, R. Paolesse,* F. R. Fronczek, K. M. Smith, L. Prodi, M. Montalti, G. Battistini ..... 2345–2352**

Synthesis and Functionalization of Germanium Triphenylcorrolate: The First Example of a Partially Brominated Corrole

**Keywords:** Corrole / Bromination / Regioselectivity / Porphyrinoid

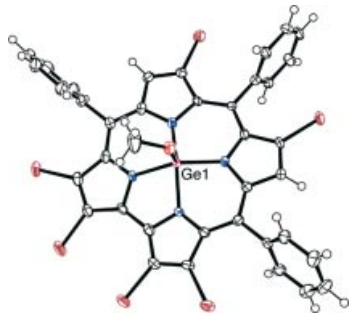


Ge complexes of 5,10,15-triphenylcorrole were prepared using $GeCl_4$ as the metal source. By reaction with $Br_2$ under a variety of reaction conditions, the first examples of partially brominated corroles have been obtained.. Photophysical characterization of Ge corrolates confirmed the high fluorescence quantum yield of such complexes, and also led to the first observation of phosphorescence emissions from corrole complexes.


 © 2007 Wiley-VCH Verlag GmbH & Co. KGaA, Weinheim 

## Photochemistry of $Ru^{II}$ Complexes

**M. Brindell, G. Stochel,* V. Bertolasi, R. Boaretto, S. Sostero 2353–2359**

Photochemistry of *trans*- and *cis*-$[RuCl_2(dmso)_4]$ in Aqueous and Non-aqueous Solutions

**Keywords:** Ruthenium / Photochemistry / Photolabilization / Photoisomerization / Antitumor agents

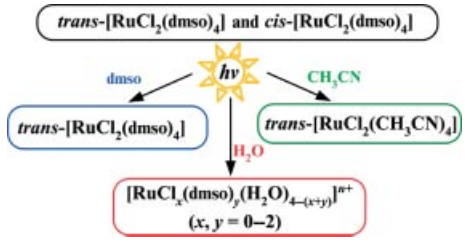


The *cis* to *trans* isomerization and the substitution of the dmso ligand by solvent are the two main photoreactions observed for the $[RuCl_2(dmso)_4]$ complex in nonaqueous solutions, whereas in aqueous solution, additionally $Cl^-$ ligand dissociation takes place in the secondary photochemical processes.

**If not otherwise indicated in the article, papers in issue 15 were published online on May 8, 2007**

 © 2007 Wiley-VCH Verlag GmbH & Co. KGaA, Weinheim 

# SPOTLIGHTS …

*Phosphine Ligands*

A. Ochida, M. Sawamura*

**Phosphorus Ligands with a Large Cavity: Synthesis of Triethynylphosphines with Bulky End Caps and Application to the Rhodium-Catalyzed Hydrosilylation of Ketones**

*Chem. Asian J.*
DOI: **10.1002/asia.200700006**

**Holey phosphines!** The end capping of triethynylphosphine with bulky groups results in the creation of ligands with a large cavity in which the phosphorus lone-pair electrons are located. The novel coordination properties of these ligands lead to a rate-accelerating effect in the rhodium-catalyzed hydrosilylation of ketones. cod = 1,5-cyclooctadiene.

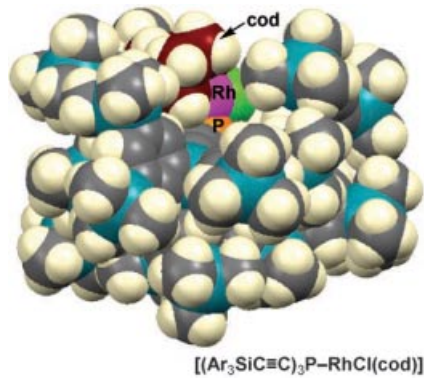


*Biosynthesis*

Z. D. Aron, P. D. Fortin, C. T. Calderone, C. T. Walsh*

**FenF: Servicing the Mycosubtilin Synthetase Assembly Line *in trans***

*ChemBioChem*
DOI: **10.1002/cbic.200600575**

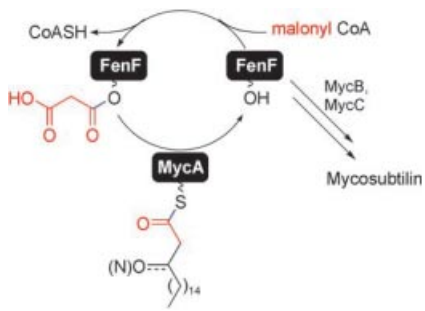


**AT your service**. We report the expression and characterization of FenF from mycosubtilin biosynthesis. This work represents the first kinetic and selectivity studies performed on an *in trans* AT domain servicing a polyketide synthase (PKS), and revealed a strong acyl-group specificity and broad promiscuity toward substrate carrier proteins. The lack of specificity in FenF-mediated malonyl transfer suggests that this protein might prove a powerful tool for combinatorial biosynthesis.

*Electrochemistry*

C. Amatore,* E. Maisonhaute, B. Schöllhorn, J. Wadhawan

**Ultrafast Voltammetry for Probing Interfacial Electron Transfer in Molecular Wires**

*ChemPhysChem*
DOI: **10.1002/cphc.200600774**

**Up to speed**: Electron transfer in self-assembled monolayers of complex redox-active oligophenylenevinylene molecular wires is examined by ultrafast cyclic voltammetry. If the redox center is buried within long hydrophobic diluents, counterion movement towards the redox entity becomes rate-limiting. This effect is examined for superexchange and electron-hopping mechanisms (see picture).

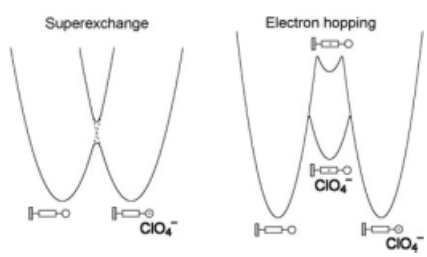


*Programmable Enzymes*

N. C. Gianneschi, M. R. Ghadiri*

**Design of Molecular Logic Devices Based on a Programmable DNA-Regulated Semisynthetic Enzyme**

*Angew. Chem. Int. Ed.*
DOI: **10.1002/anie.200700047**

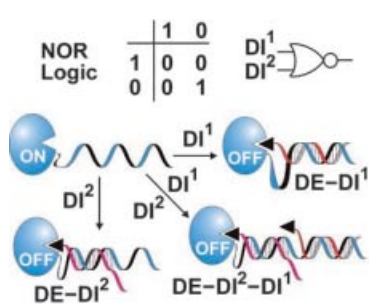


**Informed decisions**: Logic operations (AND, OR, NOR) can be performed with an enzyme by tagging it and its inhibitor with single-strand DNA. By adding appropriate single-strand DNA, the activity of the enzyme complex can be switched ON and OFF (see picture for NOR logic; **DE**: DNA-tagged enzyme; **DI**$^1$, **DI**$^2$: DNA-tagged inhibitors), or it can be used as a sensitive PCR-independent gene-diagnostic probe.

 © 2007 Wiley-VCH Verlag GmbH & Co. KGaA, Weinheim 

# … ON OUR SISTER JOURNALS

**A series of chiral** 4-chlorophenoxyacetic acid analogues was synthesized and tested for activity toward both PPARα and PPARγ. Some derivatives were potent PPARα agonists as well as PPARγ agonists. Docking experiments were performed to explain the influence of the absolute configuration on PPARα activity.

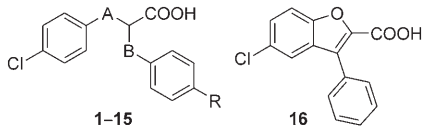


A = NH, O, S
B = alkyl or alkyloxy chain
R = H, Cl

### *PPAR Agonists*

G. Fracchiolla, A. Laghezza, L. Piemontese, G. Carbonara, A. Lavecchia,* P. Tortorella, M. Crestani, E. Novellino, F. Loiodice*

**Synthesis, Biological Evaluation, and Molecular Modeling Investigation of Chiral Phenoxyacetic Acid Analogues with PPARα and PPARγ Agonist Activity**

*ChemMedChem*
DOI: **10.1002/cmdc.200600307**

---

**Glycosidic prodrugs**: A novel class of β-D-galactosidic prodrugs based on the cytotoxic antibiotics CC-1065 and the duocarmycins were synthesized for an antibody directed enzyme prodrug therapy (ADEPT) for a selective treatment of cancer. Subsequent in vitro cytotoxicity tests of the illustrated β-D-galactosidic prodrug against the human bronchial carcinoma cell line A549 show an excellent $QIC_{50}$ value thus exceeding all prodrugs of this type prepared to date by us and others.

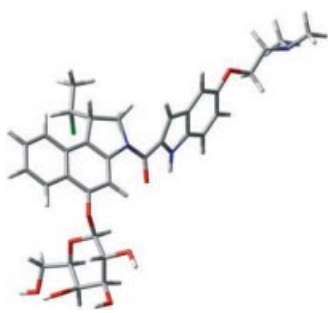

### *Antitumor Agents*

L. F. Tietze,* F. Major, I. Schuberth, D. A. Spiegl, B. Krewer, K. Maksimenka, G. Bringmann, J. Magull

**Selective Treatment of Cancer: Synthesis, Biological Evaluation and Structural Elucidation of Novel Analogues of the Antibiotic CC-1065 and the Duocarmycins**

*Chem. Eur. J.*
DOI: **10.1002/chem.200700113**

---

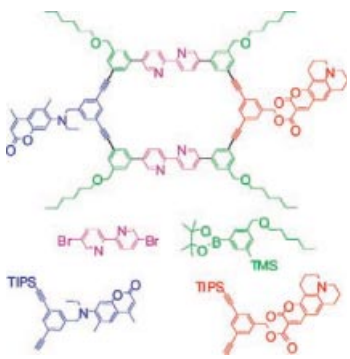


A flexible route to shape-persistent macrocycles based upon a collection of building blocks is reported. An easy introduction of several different functional units at predetermined positions as well as the obtainment of cycles in high isolated yields were accomplished by copper-free Sonogashira cross-coupling reactions and gel-permeation chromatography.

### *Shape-Persistent Macrocycles*

J. Sakamoto, A. D. Schlüter*

**Shape-Persistent Macrocycles: A Synthetic Strategy that Combines Easy and Site-Specific Decorations with Improved Cyclization Efficiency**

*Eur. J. Org. Chem.*
DOI: **10.1002/ejoc.200700118**

---

On these pages, we feature a selection of the excellent work that has recently been published in our sister journals. If you are reading these pages on a computer, click on any of the items to read the full article. Otherwise please see the DOIs for easy online access through Wiley InterScience.

 © 2007 Wiley-VCH Verlag GmbH & Co. KGaA, Weinheim 

DOI: 10.1002/ejic.200700036

# Modular *N*,*O*-Chelating Ligands: Group-4 Amidate Complexes for Catalytic Hydroamination

**Alison V. Lee[a] and Laurel L. Schafer*[a]**

**Keywords:** Amidate ligands / Group-4 metal complexes / Hydroamination / Homogeneous catalysis / Asymmetric catalysis

Amidate ligands have been used as a modular ligand set for early transition-metal complexes, and have been found to exhibit high reactivity in the catalytic hydroamination of alkynes, allenes, and alkenes. This microreview focuses on coordination metal complexes containing amidate functionality including their bonding, structure and reactivity trends. The synthesis and characterization of a number of different group-4 metal complexes is presented, and their applications in both hydroamination and organic synthesis are discussed.

(© Wiley-VCH Verlag GmbH & Co. KGaA, 69451 Weinheim, Germany, 2007)

## Introduction

Investigations involving cyclopentadienyl (Cp) complexes have been widespread, and their application in many catalytic and stoichiometric synthetic transformations is well established.[1] However, there are several limitations associated with the modification of Cp, leading to extensive research into broadly applicable non-Cp-based ligand sets in which ligand tuning is more easily accomplished.[2,3] Examples of these classes of ligands have included, but are not restricted to, amidinates,[4–8] troponiminates,[9,10] guanidinates,[11–13] sulfonamides,[14,15] nitrogen-based ligands[16–18] and chelating nitrogen and oxygen ligand sets.[19–21] In surveying the literature, it became apparent that while many elaborate ligand classes have been studied, a very simple group of *N*,*O*-chelating molecules, namely deprotonated organic amides (amidates), has been largely overlooked.

Amides are readily synthesized and the starting materials are widely available. Amidate steric and electronic properties are easily varied, resulting in the modular synthesis of a simple, tunable ligand set. An existing limitation of this class of ligands is the variable coordination modes that amidates can adopt when binding to a metal (Figure 1). Poss-

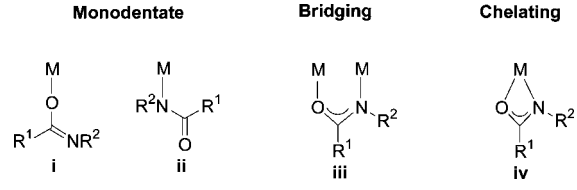


Figure 1. Some of the possible bonding modes of amidate ligands.

[a] Department of Chemistry, The University of British Columbia, Vancouver, British Columbia, Canada

*Alison Lee obtained her Bachelor's of Science (Honours) degree from Queen's University, in Kingston, Ontario, Canada in 2002 where she majored in chemistry. She then moved to Vancouver to attend the University of British Columbia and pursue her doctorate degree, with scholarship support from NSERC, under the supervision of Dr. Laurel Schafer. Her research has been focused on both catalyst development for hydroamination, and methodology development for regioselective C–N and C–C bond forming. She plans to finish her degree in the summer of 2007.*

*Laurel Schafer completed her undergraduate and graduate degrees in Canada at the University of Guelph (1993) and University of Victoria (1999), respectively. Upon completion of her doctoral work she joined the laboratories of Prof. T. Don Tilley at the University of California – Berkeley as an NSERC Postdoctoral Fellow. In 2001 she joined the faculty at the University of British Columbia with the support of an NSERC University Faculty Award. In 2004 she received the Boehringer Ingelheim (Canada) Young Investigator Award for Organic Synthesis and more recently in 2007 she was named a Sloan Fellow. Her research program investigating the synthesis, structure and reactivity of early transition metal and lanthanide amidate complexes has resulted in the development of a new family of catalysts for the hydroamination of alkynes, allenes and alkenes.*

 © 2007 Wiley-VCH Verlag GmbH & Co. KGaA, Weinheim 

ibly it is the numerous potential coordination isomers in resultant complexes that has kept amidates from being fully exploited as auxiliary ligands.

A survey of the literature shows that most characterized examples of amidate metal complexes fall into one of the following four categories: i) monodentate, *O*-bound, ii) mondentate, *N*-bound, iii) bridging and iv) chelating. Examples of several complexes that are used for bioinorganic[22–24] and lanthanide coordination chemistry display these coordination modes,[25,26] however, these are outside the scope of this review, and only a few select examples will be discussed. Also, there are several examples of catalytically relevant complexes with coordinated neutral amides as ligands,[22,27,28] which will be largely excluded from our discussion. In summary, this microreview highlights recent contributions that have used the modular amidate ligand framework to advantage in the facile synthesis of catalytically active complexes. Recent results have shown that with a chelating ligand motif (bonding mode iv) a new family of catalytically active group-4 complexes can be prepared and used for hydroamination. The structure, bonding and reactivity trends observed in this easily synthesized class of compounds will be summarized here.

## Monodentate

There are several examples of amidate ligands coordinating to a metal center in a monomeric fashion through either the oxygen (**i**) or the nitrogen (**ii**). In general, coordination occurs through the more basic oxygen with "hard" metals (**1**),[29] but through the nitrogen to "soft" metals (**2**).[30,31] Most examples are reported as either type **i** or type **ii**, without reference to isomerism between the two. Furthermore, if the amide is in its neutral form, typically the ligand coordinates through the oxygen to the metal center (eg. **1**), (Figure 2).

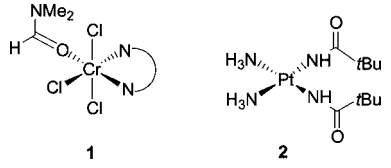


Figure 2. Examples of complexes that are bound through the amide oxygen, or the amidate nitrogen without further donation from another atom in the same ligand.

Typically, ligands that bind to a metal center solely through the amidate nitrogen have a constrained geometry such that donation through the carbonyl is unfavorable. For example, the diamidate chelating ligands in **3** and **4** in Figure 3 both have other donor atoms in their backbone that restrict the coordination environment. Complexes **3** and **4** were investigated as models for the interaction between metalloenzymes and amides of peptides in biological chemistry[23] and in medicinal inorganic chemistry,[32,33] respectively.

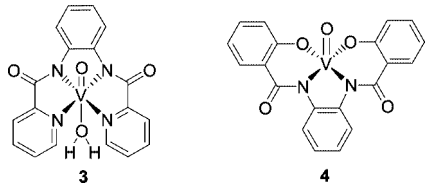


Figure 3. Examples of constrained bis(amidate) ligands that bind the metal through both the amidate nitrogen, and other atoms in the molecule.

Variations of **4** have been made with $Cu^{II}$, $Ni^{II}$, $Zn^{II}$, $Cr^{III}$, $Fe^{III}$, and $Bi^{III}$ metal centers and were used for catalytic investigations in the selective liquid-phase hydroxylation of phenol.[34,35]

While many examples in coordination chemistry investigations have monodentate binding modes of amidates, few examples of well characterized complexes for catalytic applications have been reported. The few examples included here illustrate the aspects of ligand design which must be considered in preparing well-defined complexes with discrete binding modes for use in further applications.

## Bridging

One of the most common bonding motifs observed with amidates is bonding type **iii** in which the amidate ligand bridges two metal centers. Many of these examples use very simple amidate ligands, to form complexes that have been investigated for their interesting structural features (Figure 4) and stoichiometric reactivity (Figure 5). For example, in 1979 the first Cr (**5**) and Mo complexes containing metal–metal bonds and bridging amidates were reported.[36]

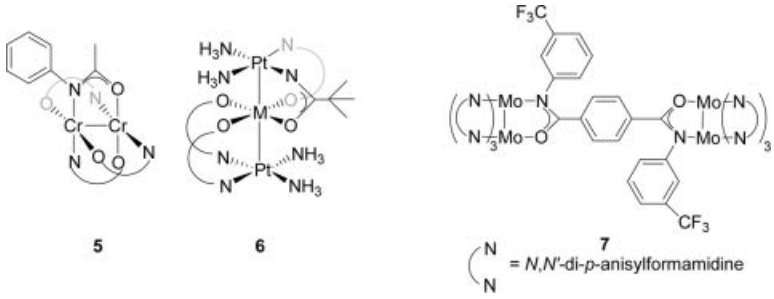


Figure 4. Examples of structurally investigated bridging amidate complexes. Complex **5** showed a very short Cr–Cr bond. Complex **6** is a heterotrimetallic complex in which amidate ligands are bridging two different metal centers, M = Cu, Co, Mn, Cd, In, Ni. Complex **7** is a tetranuclear complex with bridging amidate ligands.

 © 2007 Wiley-VCH Verlag GmbH & Co. KGaA, Weinheim 

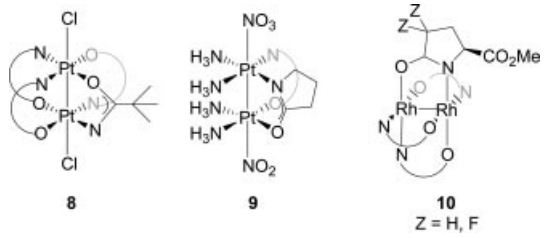


Figure 5. Bridging amidates forming lantern-type Pt dimers (**8**) or head-to-head complexes (**9**). Dirhodium(II) carboxamidates (**10**) used in metal carbene transformations.

Another example of type **iii** bonding is seen in complex **6**. These heterotrimetallic complexes contain two platinum atoms and a Cu, Co, Mn, Cd, In, or Ni atom and have been formed with various amidate ligands in which the amidate ligands bridge two metal centers (**6**).[37] Finally, structurally interesting tetranuclear complexes with bridging amidate ligands have been reported with both Mo[38] (**7**) and Re[39] metal centers.

While the aforementioned examples have been used for structural chemistry studies, similar complexes have also been used to probe stoichiometric reactivity and catalysis (Figure 5). For example, bridging amidate complexes involving Pt, as seen in **8** and **9** have been reported,[31,40–42] and their reactivity has been been investigated,[43–45] including their application in catalytic olefin functionalization.[46]

Notably, the group of Doyle and co-workers have made a series of dirhodium(II) carboxamidates of the type shown in complex **10**. These compounds have shown important reactivity in a wide variety of metal carbene transformations[47,48] and as catalysts for enantioselective hetero-Diels–Alder reactions.[49]

## Chelating

Of particular interest to this review are examples of amidates that chelate through nitrogen and oxygen to a single metal center (bonding type **iv**), which have been more rarely reported in the literature. In one example, simple amidates, such as *N*-*tert*-butylbenzamidate and substituted derivatives have been investigated in conjunction with organoaluminum compounds, such as $AlMe_3$. They have been used for the synthesis of aluminum deketiminates.[27] Furthermore, tris(amidate) aluminum(III) compounds have been synthesized and identified as the catalyst resting state in $Al^{III}$-catalyzed transamidation of carboxamides.[50]

Many of the examples of amidates chelating to metal centers have resulted from organometallic compounds reacting with isocyanates. For example, Nb and Ta complexes of the sort $M(Me)_xCl_y$ readily insert phenyl or methyl isocyanates, resulting in the methyl group adding to the carbon of the newly formed amidate chelate [Equation (1)].[51]

$$M(Me)_3Cl_2 \xrightarrow{RNCO} M(Me)Cl_2(NRC(O)Me)_2 \quad (1)$$

M = Nb, Ta
R = Ph, Me

Analogous reactions occur with $[Cp_2ZrMe_2]$[52] and $Cp_2TiR$[51] complexes and various isocyanates to give complexes of the type **12** (Figure 6).

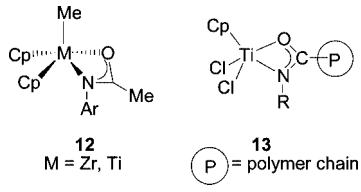


Figure 6. Amidate complex resulting from reactions with isocyanates.

With respect to polymerization catalysis, complexes like **12** are relevant to more recent examples using $TiCl_3OCH_2CF_3$ and $CpTiCl_2L$ [L = $–OCH_2CF_3$, $–N(CH_3)_2$, $–CH_3$] as catalysts for the living polymerization of isocyanates.[53] It was proposed, based on IR spectroscopic analysis, that the propagating endgroup during chain growth is an amidate-Ti complex, **13** (Figure 6), with a chelating bonding motif.[53]

There have only been a few reports of titanium amidate chelates that were not formed as intermediates in organometallic reactions. One example includes the use of caprolactam as a precursor to form the titanium complex **14** (Figure 7), which is postulated to be an intermediate in the ring-opening polymerization of lactams to form polyamides.[54]

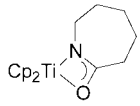


Figure 7. Example of a chelating lactamidate on titanium.

Another example of a sterically congested Cp*–Ti complex was synthesized by Stahl and co-workers, **15** (Figure 8), during investigations of $Ti^{IV}$-catalyzed transamidation.[55]

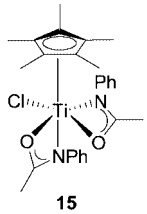


Figure 8. Chelating amidate complexes in transamidation investigations.

Finally, an example of a Ti complex with chelating amidates that did not contain any Cp ligands was described in 2001 by the Arnold group.[56] They employed a diamide proligand (Figure 9, left), which reacted cleanly with homoleptic titanium amides to generate a crystalline bimetallic complex **16** which maintained the chelating bonding motif.

 © 2007 Wiley-VCH Verlag GmbH & Co. KGaA, Weinheim 

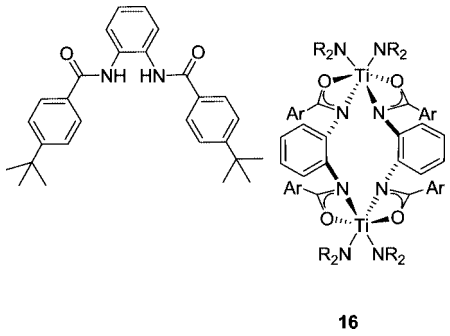

16

Figure 9. Proligand and resultant bimetallic bis(amidate) complex.

The two reactive $NR_2$ groups on each Ti are oriented in a *cisoid* fashion to one another, and bond lengths indicate delocalization of the amidate double bond. These compounds were screened and showed modest activity for the polymerization of ethylene with methylalumoxane activation.[56]

While a large variety of amidate structures using different metal centers and bonding motifs have been reported in the literature, it is clear that little work has been disclosed using neutral amides as easily synthesized and readily modified precursors to amidate auxiliary ligands. In particular, the variation of electronic and steric effects within the amidate backbone and their impacts on the structural properties of early transition metal complexes had not been investigated, previous to our work in the area. Most importantly, the catalytic potential of these tunable complexes were largely unexplored. The remainder of this microreview will focus on our contributions in the area of amidate-supported group-4 complexes and their applications in hydroamination catalysis.

## Monomeric Chelating Amidate Complexes of Early Transition Metals

### Proligands

Amides are easily synthesized with a variety of steric and electronic properties as the starting materials, acid chlorides and amines, are inexpensive, and commercially available. Once deprotonated, the monoanionic amidate ligand can adopt a conformation to bind the metal in a chelating fashion, in which the anion is delocalized throughout the N,C,O backbone. The hard nature of both the donor atoms in combination with early transition metals suggests that the bonding in these complexes will be largely ionic in character.

The steric nature of both the groups on the carbonyl and on the nitrogen affects the resultant metal complex as the smaller the degree of steric bulk, the greater the possibility of synthesizing dimers and oligomers. Consequently, to minimize this possibility, a certain degree of steric bulk must be maintained in the ligand design.

There are five possible geometric isomers that can result from the formation of monomeric bis(amidate) complexes, as shown in Figure 10. This large number of potential isomers complicates spectral assignments and could be a reason why amidates have been largely overlooked as auxiliary ligands.

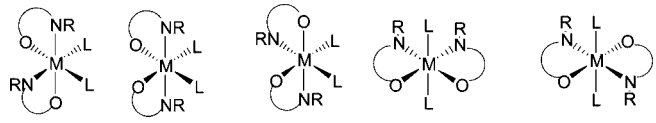

Figure 10. Possible coordination isomers of bis(amidate) complexes; L = chloro, alkyl, amido.

## Coordination Chemistry

### Bis(amidate) Dichloro Complexes

With several proligands in hand, we set out to make bis(amidate)metal dichloride complexes using group-4 metals such as titanium and zirconium. Metal chlorides of titanium and zirconium are inexpensive and readily available, making them attractive starting materials for the preparation of amidate supported organometallic complexes. However, we found salt metathesis with amide proligands to be very base dependent. For example, use of typical bases such as *n*BuLi, NaH, or KH resulted in only insoluble powders, while the Arnold group reported limited success with lithium bis(trimethylsilylamide).[56] However, use of sodium bis(trimethylsilylamide) resulted in a more general route for forming titanium dichlorides with several amidate ligands; see Equation (2) and Figure 11.[57]

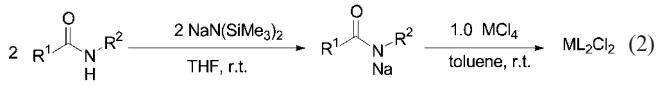

(2)

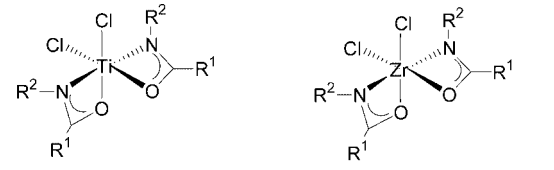

**16a**: $R^1$ = Ph, $R^2$ = 2,6-di*i*Pr-$C_6H_3$
**16b**: $R^1$ = *t*Bu, $R^2$ = 2,6-diMe-$C_6H_3$
**16c**: $R^1$ = $C_6F_5$, $R^2$ = 2,6-di*i*Pr-$C_6H_3$
**16d**: $R^1$ = Ph, $R^2$ = 2,6-di*i*Pr-$C_6H_3$
**16e**: $R^1$ = *t*Bu, $R^2$ = adamantyl

Figure 11. Bis(amidate)titanium and -zirconium dichlorides formed through salt metathesis with $NaN(SiMe_3)_2$.

The sodium amidate salts, though isolated as crude materials, are used immediately without any further purification.

Many of these complexes have been crystallographically characterized[57] and an example (**16a**) is shown in Figure 12.

 © 2007 Wiley-VCH Verlag GmbH & Co. KGaA, Weinheim 

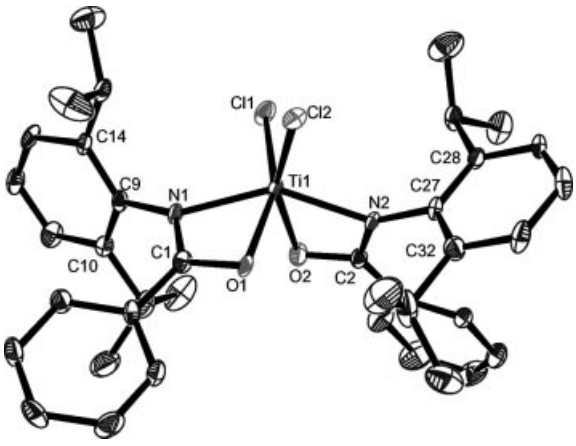


Figure 12. ORTEP plot of bis(amidate)titanium dichloride complex **16a**. Hydrogen atoms have been removed for clarity. Selected bond lengths [Å] and angles [°]: Ti–O(1) 2.025(4), Ti–N(1) 2.087(5), Ti–Cl(1) 2.2479(19), O(1)–C(1) 1.313(7), N(1)–C(1) 1.304(8), Ti–N(1)–C(2) 121.6(2), O(1)–C(1)–N(1) 111.7(6).

Complex **16** is pseudo-octahedral and $C_2$ symmetric. The C–O and the C–N bond lengths in the amidate backbone are nearly identical [1.313(7) Å and 1.304(8) Å, respectively] suggesting significant electron delocalization. The Ti–O bond length [2.025(4) Å] is only slightly shorter then the Ti–N bond length [2.087(5) Å]. The Ti–Cl bond lengths of 2.2479(19) Å are typical.[8] The bulky diisopropyl-substituted aryl substituents of the *N*-groups on the amidate backbone are *trans* to one another.

### Bis(amidate) Bis(alkyl) Complexes

While transition metal dichloride complexes are flexible starting materials for the preparation of many different organometallic complexes, an alternative route into organometallic compounds is to start with a homoleptic alkyl metal complex in a protonolysis reaction. Synthesis of group-4 bis(alkyl) complexes with the amidate ligand is easily achieved using this reaction. For example, a protonolysis reaction between *N*-(2,6-dimethylphenyl)benzamide and $Hf(Bn)_4$ [Equation (3)] led to the fully characterized bis(amidate)-dibenzylhafnium complex **17**.[58]

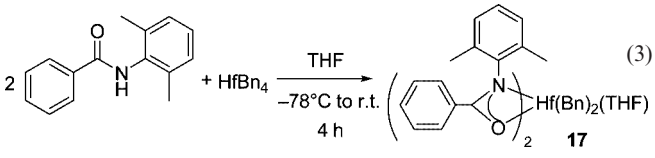


(3)

Complex **17** exhibits pseudo-$C_{2v}$ symmetry in a slightly distorted pentagonal bipyramidal geometry. A THF molecule occupies the final equatorial coordination site, which, while bound in the solid state, is labile in solution phase. This complex is stable to heat and light, though sensitive to moisture, such that exposure of **17** to a small amount of adventious moisture led to the formation of an interesting tetrametallic bridged oxo species, in which the amidates adopted both a chelating and a bridging mode of metal coordination.[58] An analogous protonolysis reaction led to the bis(amidate)-dibenzyl-$Zr^{IV}$ complex **18** (Figure 13).

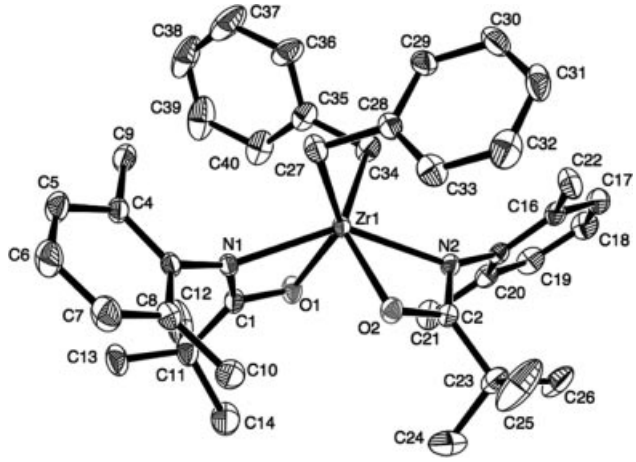


Figure 13. ORTEP plot of bis(amidate)-dibenzyl-zirconium complex (**18**). Selected bond lengths [Å] and angles [°]: Zr–O(1) 2.0988(13), Zr–O(2) 2.1080(13), Zr–N(1) 2.2836(14), Zr–N(2) 2.875(13), Zr–C(27) 2.2440(13), Zr–C(34) 2.2390(19), N(1)–C(1) 1.286(2), C(1)–O(1) 1.307(2), O(2)–Zr–N(2) 58.39(5), C(27)–Zr–C(34) 97.18, N(2)–C(2)–O(2) 112.29(14).

In contrast to the 7-coordinate **17**, **18** is a $C_2$-symmetric, slightly distorted octahedral compound that does not have a bound THF molecule in the solid state.

### Bis(amidate) Bis(amido) Complexes

The most widely synthesized and studied metal complexes in our laboratories are bis(amidate) bis(amido)-titanium and -zirconium complexes. These complexes are both precursors to other organometallic compounds and catalytically active species for synthetic transformations such as hydroamination. Bis(amidate) bis(amido) complexes of titanium and zirconium are easily synthesized in high yields by a protonolysis reaction as shown in Equation (4).

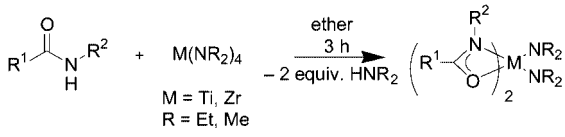


(4)

A wide variety of organic amides have been used for making these bis(amidate) bis(amido) complexes.[59] In general, amides containing alkyl groups on both the carbonyl and the nitrogen yield metal complexes that are oily and difficult to purify. A simple switch to a phenyl group on either the nitrogen or the carbonyl yields crystalline metal complexes suitable for X-ray analysis (**19**, Figure 14).

 © 2007 Wiley-VCH Verlag GmbH & Co. KGaA, Weinheim 

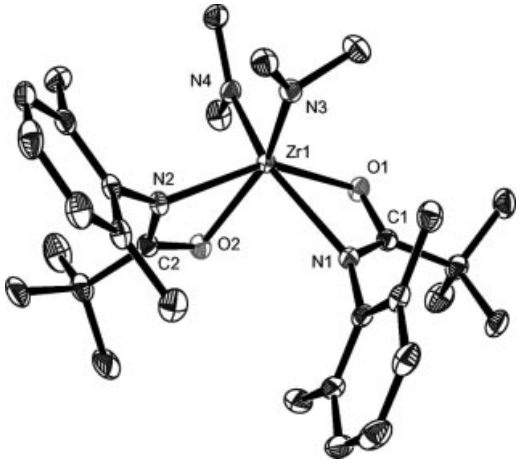


Figure 14. ORTEP plot of bis(amidate) bis(amido)-zirconium complex **19**. Hydrogen atoms have been removed for clarity. Selected bond lengths [Å] and angles [°]: Zr–O(1) 2.1524(19), Zr–O(2) 2.201(2), Zr–N(1) 2.403(2), Zr–N(2) 2.3055(19), Zr–N(3) 2.038(3), Zr–N(4) 2.044(2), O(1)–Zr–N(1) 57.25(8), O(1)–C(1)–N(1) 113.8(3).

This $C_2$-symmetric compound **19** exhibits pseudo-octahedral geometry with the dimethylamido ligands oriented in a *cisoid* fashion, which is advantageous for catalytic applications. A switch to proligand *N*-*tert*-butylbenzamide yielded bis(amido) complexes of both titanium and zirconium as different geometric isomers, although the amido ligands remain *cis* to one another. A subsequent investigation kept the phenyl substituent on the carbonyl constant, and varied the steric properties of the nitrogen substituent as shown in Figure 15.[60]

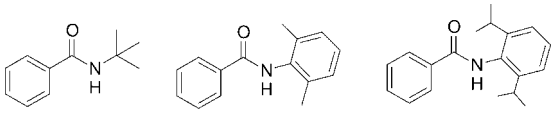

**20** **21** **22**

Figure 15. Proligands with varying degrees of steric bulk on the nitrogen.

Bis(amidate) bis(amido)-titanium complexes were formed using **20**–**22**, and characterized by X-ray crystallography. The steric properties of the proligand affect the geometric isomer observed in the solid state, such that the bulky substituent of **22** ensured that the *N*-substituents are *trans* to each other, in contrast to **20**, where the *N*-substituents are *cis*-oriented. DFT calculations were performed on these complexes in order to better understand the different possible coordination geometries and bonding interactions.[60] The calculations predicted the lowest energy isomers for proligands **20** and **22**, which also matched the structures observed in the solid state. However, in NMR spectroscopic investigations, fluxional behavior is observed suggesting that there is an interconversion between low-energy isomers.

## Bis(amidate) Imido Complexes

As the bis(amidate) bis(amido)-metal complexes proved to be easily accessed with this ligand set, we extended this chemistry further to synthesize bis(amidate) imido complexes. As well as exhibiting interesting coordination chemistry, these complexes are implicated as model systems of mechanistic intermediates (vide infra). The first reported characterized amidate-supported titanium–imido complex **23** was synthesized; see Equation (5).[61]

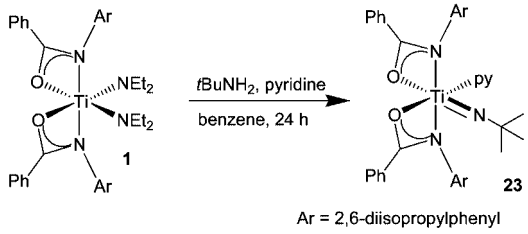


(5)

This reaction is general to this class of complexes and other terminal imido compounds **24** have been prepared using amidate auxiliary ligands (Figure 16).

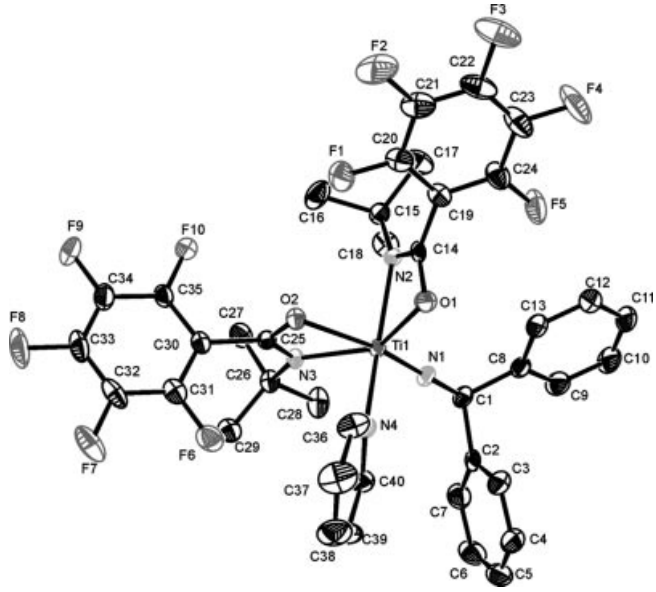


Figure 16. Solid-state molecular structure of bis(amidate) imido-titanium complex **24**. Hydrogen atoms are removed for clarity. Selected bond lengths [Å] and angles [°]: Ti–N(5) 1.705(3), Ti–O(3) 2.259(2), Ti–O(4) 2.111(2), Ti–N(6) 2.125(3), Ti–N(7) 2.165(3), Ti–N(8) 2.214(3), C(41)–N(5)–Ti 176.3(2), O(3)–C(54)–N(6) 117.9(3).

These group-4 imido complexes can also be trapped with triphenylphosphane oxide as shown in Equation (6).

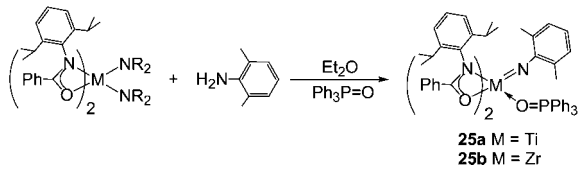


(6)

 © 2007 Wiley-VCH Verlag GmbH & Co. KGaA, Weinheim 

The solid-state molecular structure of the Zr-imido complex **25b** is of distorted pentagonal-pyramidal geometry where both the amidate and the TPPO ligands are pseudo-equatorial and the imido is in the axial position.[62]

Amidates are a modular ligand set and they have been used in the synthesis of a wide variety of metal complexes. The ease with which both the proligand and the metal complexes are synthesized makes this auxiliary ligand set very desirable for catalytic investigations. As both the steric and the electronic properties of the system can be readily varied, there is enormous potential for tuning of catalytic reactivity.

## Hydroamination Catalysis

One area in which early transition metal bis(amido) complexes have found wide-spread catalytic application is in hydroamination. Hydroamination is the addition of nitrogen and hydrogen across a carbon–carbon multiple bond such as an alkyne (shown), allene or alkene; see Equation (7).

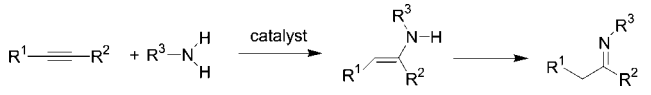


(7)

This leads to the formation of enamines, imines, and amines, which are important building blocks in pharmaceuticals, detergents, and dyes.[63] Furthermore, as many procedures for the synthesis of amines are multi-step and inefficient,[64] catalytic hydroamination has the potential to greatly improve existing methodology. There are no side products in this reaction, thus hydroamination can be used in a tandem reaction sequence, utilizing the imine as an in situ intermediate.[65–68] Following an initial report of titanium catalyzed hydroamination by Rothwell and coworkers,[69] research into hydroamination catalysis has also followed the trend of focusing on Cp-based ligand systems and then moving onto non-Cp-based catalysts. A variety of systems have been developed for hydroamination reactions including work from the groups of Bergman,[15,64,70–73] Livinghouse,[74,75] Odom,[67,76–81] Beller,[65,82–86] Doye,[87–94] ourselves,[59,61,62,95,96] and others.[11,97–105] The low toxicity, low cost, and high availability of group-4 metals make them attractive systems for catalytic applications.[106] To this end, we have established amidate complexes of Ti as tunable catalytic systems for highly reactive and regioselective hydroamination.

### Alkyne Hydroamination

Initial investigations into catalytic hydroamination began using three different proligands: *N*-*tert*-butyl-2-methylpropanamide (**26**), *N*-*tert*-butylbenzamide (**27**), and *N*-*tert*-butylperfluorophenylamide (**28**). Bis(amidate) bis(amido)-titanium and -zirconium complexes were synthesized and the tunable reactivity accessible through modification of the metal and electronic properties of the ligand is shown in Table 1 and Equation (8).

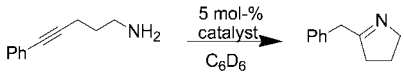


(8)

Table 1. Results for intramolecular hydroamination of alkynes.

| Entry | Proligand | Metal | *T* [°C] | *t* [h] | % Yield[a] |
|---|---|---|---|---|---|
| 1 | **27** | Zr | 60 | 24 | 95 |
| 2 | **28** | Zr | 60 | 7 | 98 |
| 3 | **26** | Ti | 25 | 14 | 99 |
| 4 | **27** | Ti | 25 | 3.5 | 98 |
| 5 | **28** | Ti | 25 | 0.25 | 97 |
| 6 | CpH | Ti | 110 | 4 | 90[b] |
| 7 | $HNMe_2$ | Ti | 25 | 0.5 | quant.[64] |

[a] NMR conversion vs. 1,3,5-trimethoxybenzene. [b] Reported yield for the isolated amine product after reduction of imine.

The titanium-based complexes were more active than the corresponding zirconium complexes. It is also apparent that electron-withdrawing substituents enhance the catalytic activity of the complex. Moreover, the most active species (Entry 5) is more active then both the corresponding Cp complex, and $Ti(NMe_2)_4$. As a further comparison to $Ti(NMe_2)_4$, a more challenging intramolecular substrate was attempted; see Equation (9).

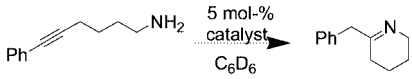


(9)

In this case our system went to completion within 3 h at 40 °C whereas use of $Ti(NMe_2)_4$ only went to 30% completion in the same time period.

Encouraged by these initial findings, we set out to screen a number of our bis(amidate) bis(amido)-titanium complexes, particularly to see how steric bulk on the nitrogen would affect the catalytic activity. Furthermore, we wanted to investigate the more challenging intermolecular hydroamination reaction. This transformation can lead to the formation of two regioisomers and thus regioselectivity is also an important concern; see Equation (10) and Table 2.

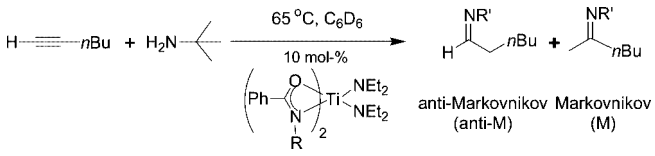


(10)

Table 2. Intermolecular hydroamination with tunable bis(amidate) bis(amido)-titanium precatalysts.

| Entry | R | *t* [h] | % Yield (*anti*-M:M)[a] |
|---|---|---|---|
| 1 | *i*Pr | 24 | no reaction |
| 2 | *t*Bu | 24 | 71 (5:1) |
| 3 | Ph | 24 | 55 (99:1) |
| 4 | 2,6-dimethylphenyl | 10 | 78 (>99:1) |
| 5 | 2,6-diisopropylphenyl | 6 | 82 (>99:1) |

[a] Yields were determined by $^1$H NMR with an internal standard (1,3,5-trimethoxybenzene). Ratio confirmed by GCMS after hydrolysis.

 © 2007 Wiley-VCH Verlag GmbH & Co. KGaA, Weinheim 

The complex derived from the proligand with the bulkiest substituent on the nitrogen (Entry 5) was the most effective, giving the highest yield, the lowest reaction time and excellent regioselectivity. Most importantly, this complex **29** affected regioselective hydroamination, in high yield, with a broad range of substrates including the most challenging benzylamine substrate.[65] The wide range of alkynes and functional groups tolerated is illustrated in Table 3.

Table 3. Hydroamination of various terminal alkynes with alkylamines.

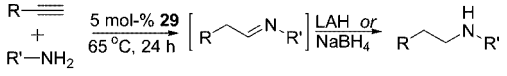


| Entry | Alkyne | Amine | % Yield[a] |
|---|---|---|---|
| 1 | | $BnNH_2$ | 88 |
| 2 | | $iPrNH_2$ | 88 |
| 4 | | $BnNH_2$ | 87 |
| 5 | | $iPrNH_2$ | 89 |
| 7 | | $BnNH_2$ | 95 |
| 8 | | $iPrNH_2$ | 82 |
| 9 | | $BnNH_2$ | 87 |
| 10 | | $iPrNH_2$ | 86 |
| 11 | MeO | $BnNH_2$ | 83 |
| 12 | Cl | $BnNH_2$ | 93 |
| 13 | TBDMSO | $BnNH_2$ | 76 |
| 14 | O, O | $BnNH_2$ | 80 |

[a] Isolated yield.

In our initial investigations into hydroamination, it was noted that secondary amines did not lead to hydroamination products and only unreacted starting materials were recovered. This suggests that our system mediates alkyne hydroamination via an imido intermediate as elucidated by Bergman and co-workers in the early 90's (Figure 17).[73]

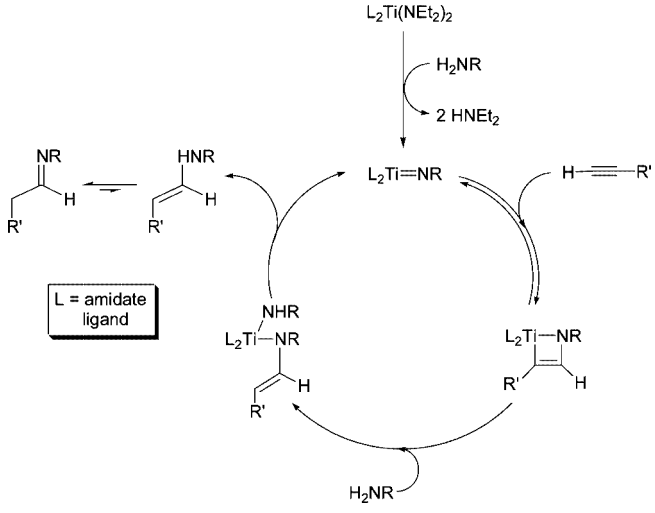


Figure 17. Proposed simplified catalytic cycle for alkyne hydroamination.

The bis(amido) precatalyst reacts with the primary amine to form the requisite titanium–imido complex. Coordination by the alkyne to this electrophilic metal center, followed by cycloaddition leads to the formation of titanaazacyclobutene. Protonation of the Ti–C bond by another equivalent of primary amine gives the enamide-amide complex, which then undergoes α-elimination to give the hydroamination product and regenerate the catalytically active imido species.

We have been successful in synthesizing titanium–imido complexes through reactions of the amido complexes with a stoichiometric amount of primary amine (vide supra). Our system forms the imido species very quickly such that when two hydroamination reactions are carried out side by side, one with the bis(amidate) bis(amido)-titanium precatalyst and the other with the bis(amidate) imido-titanium precatalyst, both show 50% product formation after approximately 50 min.[61] This is in contrast to many literature reports that state that there is a significant induction period required for conversion to the catalytically active imido complex.[70] We propose that the polarization of the M–N bonds and highly electrophilic metal center of the amidate complexes affects both the rate of conversion from the precatalyst to the imido complex, and the subsequent reactivity of this imido species. It is important to note that during all of the aforementioned reactions we have not observed any loss of the amidate ligands.

## Applications in Synthesis

The hydroamination of terminal alkynes with precatalyst **29** leads to the formation of synthetically useful aldimines. These often unstable intermediates are useful in organic chemistry for synthesizing other more complex molecules. For example, catalytic hydroamination has been combined with the Strecker reaction, to give a tandem C–N, C–C bond forming sequence for the synthesis of α-cyano amines; see Equation (11).[66]

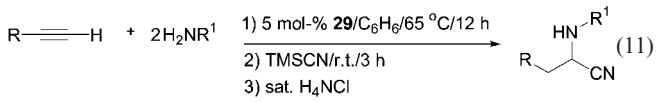


α-Cyano amines are useful molecules for the synthesis of diamines, amino acids, amino acid derivatives and amino alcohols. This methodology has been applied to the synthesis of a number of amino methyl esters that were synthesized in good overall yields (Table 4).

Precatalyst **29** has also been applied toward the synthesis of a number of biologically important molecules. For example substituted tetrahydroisoquinolines (THIQs), molecules that have promising biological and pharmacological properties, can be synthesized using hydroamination as a key step.[61] Hydroamination can also be used to construct the more complex tricyclic benzo[*a*]quinolizine framework in three tandem reactions (Figure 18).

 © 2007 Wiley-VCH Verlag GmbH & Co. KGaA, Weinheim 

Table 4. Yields of synthesized α-amino esters.

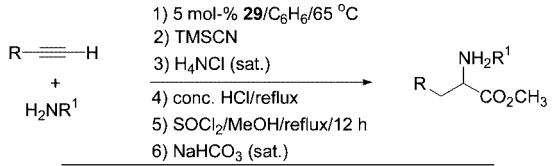


| α-Amino ester | $R^1$ | % Yield[a] |
|---|---|---|
| 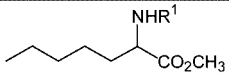 | Bn | 58 |
| | *i*Pr | 61 |
| 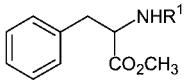 | Bn | 58 |
| | *i*Pr | 54 |
| 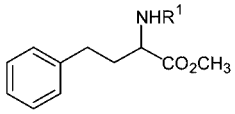 | Bn | 58 |
| | *i*Pr | 69 |

[a] Isolated yield calculated from terminal alkyne.

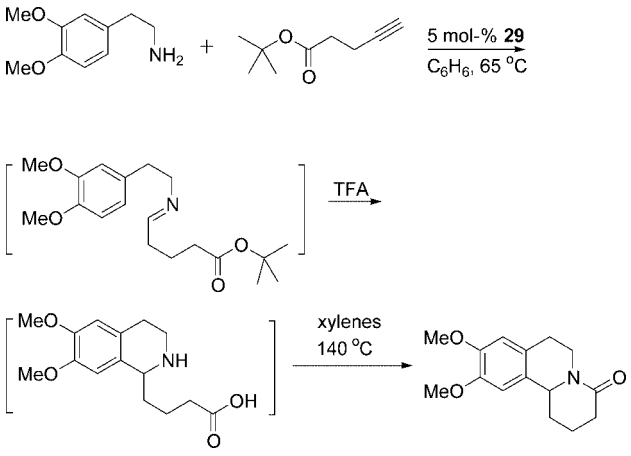


Figure 18. One pot synthesis of tricyclic benzo[*a*]quinolizine framework using hydroamination.

## Allene Hydroamination

The intermolecular hydroamination of allenes is notably more challenging then both the intramolecular hydroamination of allenes and the intermolecular hydroamination of alkynes.[15,64] This reaction can result in the formation of three regioisomers as shown in Figure 19.

While this transformation has received limited attention in the literature, in general it has been found that with early transition metals it is usually regioisomer **30** that is formed (in both the *E* and *Z* isomers).[15,70,73,98,104] With late transition metals, on the other hand, it is regioisomers **31** and **32** that are reported, and the double hydroamination side-product is also observed.[107–111] To begin our investigations into the hydroamination of allenes, we used our most active alkyne hydroamination catalyst, **29**, and investigated the hydroamination of aryl and alkyl allenes with a variety of amines (Table 5).

While these reactions were slower then the corresponding alkyne reactions, the products were formed in 7–24 h at 85–90 °C. In all cases, regioisomer **30** was observed as both the *E* and *Z* isomers. These first examples of intermolecular allene hydroamination with alkylamines require higher temperatures, but are compatible with primary amines of varying steric bulk.[112] The ketimine products isolated here contrast with the aldimine products obtained from terminal al-

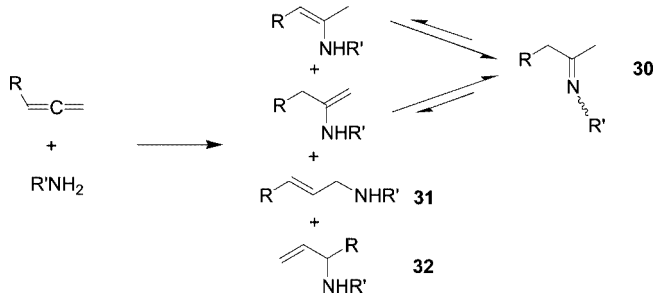


Figure 19. Possible regioisomers resulting from intermolecular allene hydroamination.

Table 5. Intermolecular hydroamination of alkyl- and arylallenes with arylamines (Ar = 2,6-dimethylaniline.).

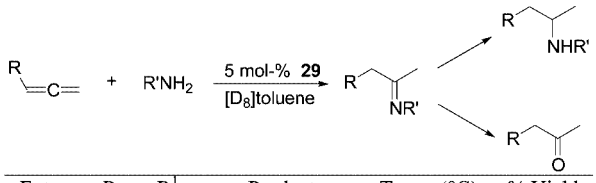


| Entry | R | $R^1$ | Product | Temp. (°C) | % Yield |
|---|---|---|---|---|---|
| 1 | Ph | Bn | 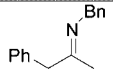 | 120 | 75[a] |
| 2 | Ph | *i*Pr | 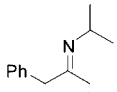 | 120 | 65[a] |
| 3 | Ph | *t*Bu | 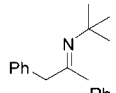 | 120 | 60[a] |
| 4 | Ph | Ph | 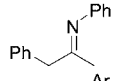 | 90 | 76[b] |
| 5 | Ph | Ar | 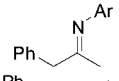 | 90 | 64[b] |
| 6 | Bn | Bn | 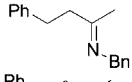 | 120 | 85[a] |
| 7 | Bn | *i*Pr | 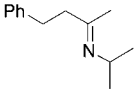 | 120 | 91[a] |
| 8 | Bn | *t*Bu | 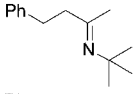 | 120 | 71[a] |
| 9 | Bn | Ph | 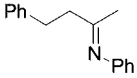 | 85 | 83[b] |
| 10 | Bn | Ar | 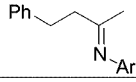 | 85 | 93[b] |

[a] Isolated yield of corresponding ketone product. [b] Isolated yield of the corresponding secondary amine.

 © 2007 Wiley-VCH Verlag GmbH & Co. KGaA, Weinheim 

kyne hydroamination. Interestingly, the allene substrates used here were prepared from terminal alkyne substrates.[111] Therefore, by judicious selection of the hydroamination substrate either the ketimine or the aldimine products can be selectively obtained with precatalyst **29**.

### Alkene Hydroamination

Alkene hydroamination is more challenging then both alkyne and allene hydroamination, and thus initial investigations have focused on the intramolecular hydroamination of aminoalkenes. In general, examples of group-4 metal complexes for alkene hydroamination are much less numerous than alkyne hydroamination. There have been a few reports of cationic group-4 complexes that can catalyze the hydroamination of secondary aminoalkenes.[113,114] These reactions are thought to proceed through a σ-bond insertion mechanism, analogous to the established mechanism for the isovalent lanthanide catalysts.[115,116] Furthermore, these cationic group-4 complexes are unable to catalyze the cyclization of primary aminoalkenes, an observation that was attributed to the formation of catalytically inactive imido complexes. Very recently there have been a few reported examples of neutral group-4 metal complexes for the hydroamination of primary aminoalkenes.[117,118] In light of these results, we wanted to investigate our bis(amidate) bis(amido) complexes for this reaction.[62] Intramolecular reactions can be carried out as shown in Equation (12).

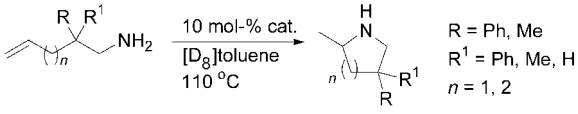


(12)

Both the Ti complex **29** and the Zr analogue can catalyze this reaction, although the Zr complex is the more active. In order to probe the application of Zr-imido complexes for alkene hydroamination, we tested the bis(amidate) imidometal complexes **25a**,**b** for this desirable hydroamination reaction. Again, both were active in this cyclization, and the Zr complex **25b** was more active then the Ti analogue **25a**. These are the first examples of isolable group-4 imido complexes for the hydroamination of alkenes. Kinetic experiments revealed that the reaction is first-order in catalyst, and first order in substrate. It was also shown that there was no appreciable difference in the half-lives for the bis(amido) and imido precatalysts, implying that both precatalysts share a common catalytically active species. Most importantly, there was no observed activity when these catalysts were used with secondary aminoalkenes. This further supports the imido complex as being the catalytically active species. Preliminary substrate scope investigations showed that both substituted pyrrolidine and piperidine complexes could be formed with this system.[62]

Catalytic asymmetric alkene hydroamination is an extremely attractive goal as it leads to the generation of enantioenriched α-chiral amines. To date, there is no general catalyst that can perform this reaction. Most breakthroughs in this area have been with rare-earth metal catalysts.[119–127] There have also been some chiral late-transition metals that have been investigated for enantioselective intermolecular hydroamination with activated alkene and alkyne substrates.[128–134] The cationic group-4 complexes that were mentioned in the preceding section are capable of asymmetric hydroamination of secondary aminoalkenes, albeit with modest enantioselectivities.[114] Very recently, Bergman and co-workers reported a number of neutral bis(amido)zirconium precatalysts for the asymmetric hydroamination of aminoalkenes which displayed *ee* values of up to 80%.[135] Our efforts in this area include the synthesis of tethered bis(amidate) ligands using 2,2′-diamino-6,6′-dimethylbiphenyl as the diamine backbone to control both the coordination isomerism and the chirality. Three different bis(amides) **33a**–**c** were synthesized with mesityl, naphthyl, and adamantyl substituents on the carbonyl; see Equation (13).

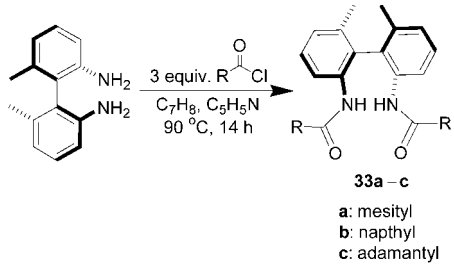


(13)

After synthesis of the proligands, neutral κ⁴-tethered bis(amidate) bis(amido)-zirconium complexes were made to give precatalysts **34a**–**c** which were screened for catalytic activity in the test reaction shown below (Table 6).

Table 6. Screening for asymmetric hydroamination with precatalysts **34a**–**c**.

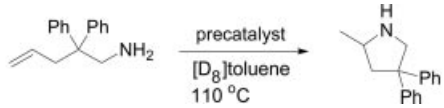


| Entry | Precatalyst | mol-% | *t* [h] | % Conversion[a] | % *ee*[b] |
|---|---|---|---|---|---|
| 1 | (+)-**34a** | 10 | 1.25 | >98 (93)[c] | 74 (*R*)[d] |
| 2 | (+)-**34b** | 10 | 18 | >98 | 31 |
| 3 | (+)-**34c** | 10 | 3 | >98 | 39 |
| 4 | (–)-**34a** | 10 | 1.25 | >98 (93)[c] | 72 (*S*)[d] |
| 5 | (+)-**34a** | 5 | 2.5 | >98 | 74 |

[a] Measured by $^1$H NMR spectroscopy. [b] Enantiomeric excess based on $^1$H NMR spectroscopy of the product following derivatization with (+)-(*S*)-α-methoxy-α-trifluoromethylphenylacetyl chloride. [c] Isolated yield. [d] Absolute stereochemistry assigned based on $^{19}$F NMR of the (+)-(*S*)-α-methoxy-α-trifluoromethylphenylacetyl chloride derivative.

The zirconium complex **34a** gave the highest *ee* values (74%) for this reaction. Comparable *ee* values could be obtained with the other enantiomer of the proligand (72%). When this optimized catalyst is used with the commonly

 © 2007 Wiley-VCH Verlag GmbH & Co. KGaA, Weinheim 

tested dimethyl-substituted substrate [Equation (14)], a remarkable enantioselectivity of 93% was observed.[96] This complex was then fully characterized, and a solid-state molecular structure of the $HNMe_2$ adduct is shown in Figure 20.

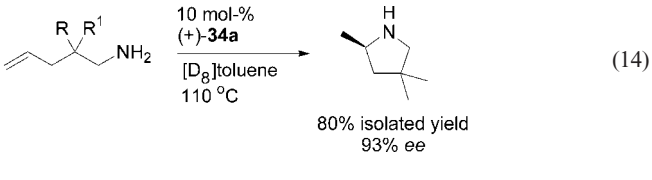


(14)

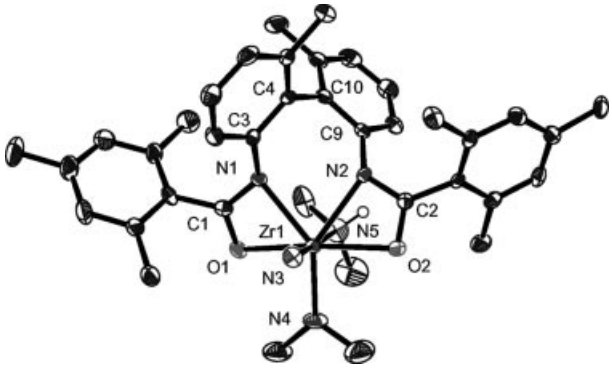


Figure 20. The ORTEP plot of (+)-**34a** (-$CH_3$ substituents omitted from the N4 dimethylamido ligand for clarity).

This is a seven-coordinate monomeric complex with distorted pentagonal-bipyramidal geometry.[96]

Investigations into the mechanism of this reaction are ongoing. As we understand more about how this reaction progresses, we can modify our ligand set to optimize reactivity and enantioselectivity. Ultimately, the goal is to design a precatalyst that would be capable of performing intermolecular alkene hydroamination leading to the general synthesis of enantioenriched α-chiral amines.

## Conclusions

As has been shown in this review, amidates are an excellent class of modular ligands for the synthesis of a wide variety of metal complexes, including catalytically active Group-4 compounds. Most importantly, the bis(amidate) bis(amido) and imido complexes have shown excellent catalytic reactivity for the hydroamination of alkynes, allenes, and alkenes. The ease of synthesis of the proligands has led to the facile tuning of catalytic reactivity and ready evaluation of structure–activity relationships. These catalytic systems show promise for the development of new catalysts that can be used for the synthesis of complex molecules with enantiomerically enriched α-chiral amines.

[1] R. L. Halterman, *Chem. Rev.* **1992**, *92*, 965.
[2] R. Kempe, *Angew. Chem. Int. Ed.* **2000**, *39*, 468.
[3] G. J. P. Britovsek, V. C. Gibson, D. F. Wass, *Angew. Chem. Int. Ed.* **1999**, *38*, 428.
[4] P. J. Stewart, A. J. Blake, P. Mountford, *Organometallics* **1998**, *17*, 3271.
[5] J. R. Hagadorn, J. Arnold, *J. Am. Chem. Soc.* **1996**, *118*, 893.
[6] J. R. Hagadorn, J. Arnold, *Inorg. Chem.* **1997**, *36*, 2928.
[7] J. R. Hagadorn, J. Arnold, *Organometallics* **1998**, *17*, 1355.
[8] A. Littke, N. Sleiman, C. Bensimon, D. S. Richeson, *Organometallics* **1998**, *17*, 446.
[9] M. R. Burgstein, H. Berberich, P. W. Roesky, *Organometallics* **1998**, *17*, 1452.
[10] H. V. R. Dias, W. Jin, Z. Wang, *Inorg. Chem.* **1996**, *35*, 6074.
[11] T. Ong, G. P. A. Yap, D. S. Richeson, *Organometallics* **2002**, *21*, 2839.
[12] M. P. Coles, P. B. Hitchcock, *Organometallics* **2003**, *22*, 5201.
[13] P. Bazinet, D. Wood, G. P. A. Yap, D. S. Richeson, *Inorg. Chem.* **2003**, *42*, 6225.
[14] S. Pritchett, P. Gantzel, P. J. Walsh, *Organometallics* **1999**, *18*, 823.
[15] L. Ackermann, R. G. Bergman, R. N. Loy, *J. Am. Chem. Soc.* **2003**, *125*, 11956.
[16] L. H. Gade, *Chem. Commun.* **2000**, 173.
[17] F. Basuli, B. C. Bailey, J. C. Huffman, D. J. Mindiola, *Chem. Commun.* **2003**, 1554.
[18] F. Basuli, J. Tomaszweski, J. C. Huffman, D. J. Mindiola, *J. Am. Chem. Soc.* **2003**, *125*, 10170.
[19] R. Baumann, W. M. Davis, R. R. Schrock, *J. Am. Chem. Soc.* **1997**, *119*, 3830.
[20] R. Duchateau, T. Tuinstra, E. A. C. Brussee, A. Meetsma, P. T. van Duijnen, J. H. Teuben, *Organometallics* **1997**, *16*, 3511.
[21] L. Liang, R. R. Schrock, W. M. Davis, *Organometallics* **2000**, *19*, 2526.
[22] H. Maumela, R. D. Hancock, L. Carlton, J. H. Reibenspies, K. P. Wainwright, *J. Am. Chem. Soc.* **1995**, *117*, 6698.
[23] A. T. Vlahos, E. I. Tolis, C. P. Raptopoulou, A. Tsohos, M. P. Sigalas, A. Terzis, T. A. Kabanos, *Inorg. Chem.* **2000**, *39*, 2977.
[24] H. J. Kruger, G. Peng, R. H. Holm, *Inorg. Chem.* **1991**, *30*, 734.
[25] H. F. Brito, O. L. Malta, M. C. F. C. Felinto, E. E. S. Teotonio, J. F. S. Menezes, C. F. B. Silva, C. S. Tomiyama, C. A. A. Carvalho, *J. Alloys Compd.* **2002**, *344*, 293.
[26] X. Zhou, L. Zhang, M. Zhu, R. Cai, L. Weng, *Organometallics* **2001**, *20*, 5700.
[27] Y. Huang, B. Huang, B. Ko, C. Lin, *J. Chem. Soc., Dalton Trans.* **2001**, 1359.
[28] A. Honda, K. M. Waltz, P. J. Carroll, P. J. Walsh, *Chirality* **2003**, *15*, 615.
[29] J. A. Broomhead, J. Evans, W. D. Grumley, M. Sterns, *J. Chem. Soc., Dalton Trans.* **1977**, 173.
[30] D. P. Fairlie, P. M. Angus, M. D. Fenn, W. G. Jackson, *Inorg. Chem.* **1991**, *30*, 1564.
[31] W. Chen, K. Matsumoto, *Inorg. Chim. Acta* **2003**, *342*, 88.
[32] A. D. Keramidas, A. B. Papaioannou, A. Vlahos, T. A. Kabanos, G. Bonas, A. Makriyannis, C. P. Raptopoulou, A. Terzis, *Inorg. Chem.* **1996**, *35*, 357.
[33] A. S. Borovik, T. M. Dewey, K. N. Raymond, *Inorg. Chem.* **1993**, *32*, 413.
[34] M. R. Maurya, S. J. J. Titinchi, S. Chand, *Catal. Lett.* **2003**, *89*, 219.
[35] M. R. Maurya, S. J. J. Titinchi, S. Chand, *J. Mol. Catal. A* **2004**, *214*, 257.
[36] A. Bino, F. A. Cotton, W. Kaim, *Inorg. Chem.* **1979**, *18*, 3030.
[37] W. Chen, F. Liu, T. Nishioka, K. Matsumoto, *Eur. J. Inorg. Chem.* **2003**, 4234.
[38] F. A. Cotton, L. M. Daniels, J. P. Donahue, C. Y. Liu, C. A. Murillo, *Inorg. Chem.* **2002**, *41*, 1354.
[39] K. J. Nelson, R. W. McGaff, D. R. Powell, *Inorg. Chim. Acta* **2000**, *304*, 130.
[40] T. N. Fedotova, G. N. Kuznetsova, K. L. Minacheva, I. B. Baranovskii, *Russ. J. Inorg. Chem.* **1997**, *42*, 1838.
[41] A. Dolmella, F. P. Intini, C. Pacifico, G. Padovano, G. Natile, *Polyhedron* **2002**, *21*, 275.
[42] T. Abe, H. Moriyama, K. Matsumoto, *Inorg. Chem.* **1991**, *30*, 4198.

 © 2007 Wiley-VCH Verlag GmbH & Co. KGaA, Weinheim 

[43] K. Matsumoto, J. Matsunami, K. Mizuno, H. Uemura, *J. Am. Chem. Soc.* **1996**, *118*, 8959.
[44] Y. Lin, S. Takeda, K. Matsumoto, *Organometallics* **1999**, *18*, 4897.
[45] Y. Lin, H. Misawa, J. Yamada, K. Matsumoto, *J. Am. Chem. Soc.* **2001**, *123*, 569.
[46] K. Matsumoto, Y. Nagai, J. Matsunami, K. Mizuno, T. Abe, R. Somazawa, J. Kinoshita, H. Shimura, *J. Am. Chem. Soc.* **1998**, *120*, 2900.
[47] D. J. Timmons, M. P. Doyle, *J. Organomet. Chem.* **2001**, *617–618*, 98.
[48] M. P. Doyle, S. B. Davies, W. Hu, *Org. Lett.* **2000**, *2*, 1145.
[49] M. P. Doyle, I. M. Phillips, W. Hu, *J. Am. Chem. Soc.* **2001**, *123*, 5366.
[50] J. M. Hoerter, K. M. Otte, S. H. Gellman, S. S. Stahl, *J. Am. Chem. Soc.* **2006**, *128*, 5177.
[51] P. Braunstein, D. Nobel, *Chem. Rev.* **1989**, *89*, 1927.
[52] S. Gambarotta, S. Strologo, C. Floriani, A. Chiesi-Villa, C. Guastini, *Inorg. Chem.* **1985**, *24*, 654.
[53] T. E. Patten, B. M. Novak, *J. Am. Chem. Soc.* **1996**, *118*, 1906.
[54] P. Arndt, C. Lefeber, R. Kempe, A. Tillack, U. Rosenthal, *Chem. Ber.* **1996**, *129*, 1281.
[55] D. A. Kissounko, I. A. Guzei, S. H. Gellman, S. S. Stahl, *Organometallics* **2005**, *24*, 5208.
[56] G. R. Giesbrecht, A. Shafir, J. Arnold, *Inorg. Chem.* **2001**, *40*, 6069.
[57] Manuscript in preparation.
[58] R. K. Thomson, B. O. Patrick, L. L. Schafer, *Can. J. Chem.* **2005**, *83*, 1037.
[59] C. Li, R. K. Thomson, B. Gillon, B. O. Patrick, L. L. Schafer, *Chem. Commun.* **2003**, 2462.
[60] R. K. Thomson, F. E. Zahariev, Z. Zhang, B. O. Patrick, Y. A. Wang, L. L. Schafer, *Inorg. Chem.* **2005**, *44*, 8680.
[61] Z. Zhang, D. C. Leitch, M. Lu, B. O. Patrick, L. L. Schafer, *Chem. Eur. J.* **2007**, *13*, 2012.
[62] K. T. Thomson, J. A. Bexrud, L. L. Schafer, *Organometallics* **2006**, *25*, 4069.
[63] P. W. Roesky, T. E. Muller, *Angew. Chem. Int. Ed.* **2003**, *42*, 2708.
[64] L. Ackermann, R. G. Bergman, *Org. Lett.* **2002**, *4*, 1475.
[65] A. Tillack, I. G. Castro, C. G. Hartung, M. Beller, *Angew. Chem. Int. Ed.* **2002**, *41*, 2541.
[66] A. V. Lee, L. L. Schafer, *Synlett* **2006**, 2973.
[67] C. Cao, Y. Shi, A. L. Odom, *Org. Lett.* **2002**, *4*, 2853.
[68] L. Ackermann, L. T. Kaspar, C. J. Gschrei, *Chem. Commun.* **2004**, 2824.
[69] J. E. Hill, R. D. Profilet, P. E. Fanwick, I. P. Rothwell, *Angew. Chem. Int. Ed. Engl.* **1990**, *29*, 664.
[70] J. S. Johnson, R. G. Bergman, *J. Am. Chem. Soc.* **2001**, *123*, 2923.
[71] L. L. Anderson, J. Arnold, R. G. Bergman, *J. Am. Chem. Soc.* **2005**, *127*, 14542.
[72] A. M. Baranger, P. J. Walsh, R. G. Bergman, *J. Am. Chem. Soc.* **1993**, *115*, 2753.
[73] P. J. Walsh, A. M. Baranger, R. G. Bergman, *J. Am. Chem. Soc.* **1992**, *114*, 1708.
[74] P. L. McGrane, M. Jensen, T. Livinghouse, *J. Am. Chem. Soc.* **1992**, *114*, 5459.
[75] D. FairFax: , M. Stein, T. Livinghouse, M. Jensen, *Organometallics* **1997**, *16*, 1523.
[76] Y. Li, Y. Shi, A. L. Odom, *J. Am. Chem. Soc.* **2004**, *126*, 1794.
[77] B. Ramanathan, A. J. Keith, D. Armstrong, A. L. Odom, *Org. Lett.* **2004**, *6*, 2957.
[78] C. Cao, J. T. Ciszewski, A. L. Odom, *Organometallics* **2001**, *20*, 5011.
[79] A. L. Odom, *Dalton Trans.* **2005**, 225.
[80] C. Cao, Y. Li, Y. Shi, A. L. Odom, *Chem. Commun.* **2004**, 2002.
[81] Y. Shi, C. Hall, J. T. Ciszewski, C. Cao, A. L. Odom, *Chem. Commun.* **2003**, 586.
[82] A. Tillack, V. Khedkar, M. Beller, *Tetrahedron Lett.* **2004**, *45*, 8875.
[83] V. Khedkar, A. Tillack, M. Beller, *Org. Lett.* **2003**, *5*, 4767.
[84] I. G. Castro, A. Tillack, C. G. Hartung, M. Beller, *Tetrahedron Lett.* **2003**, *44*, 3217.
[85] A. Tillack, H. Jiao, I. G. Castro, C. G. Hartung, M. Beller, *Chem. Eur. J.* **2004**, *10*, 2409.
[86] F. Pohlki, I. Bytschkov, H. Siebeneicher, A. Heutling, W. A. Konig, S. Doye, *Eur. J. Org. Chem.* **2004**, 1967.
[87] K. Marcsekova, B. Wegener, S. Doye, *Eur. J. Org. Chem.* **2005**, 4843.
[88] A. Heutling, F. Pohlki, S. Doye, *Chem. Eur. J.* **2004**, *10*, 3059.
[89] F. Pohlki, A. Heutling, I. Bytschkov, T. Hotopp, S. Doye, *Synlett* **2002**, *5*, 799.
[90] F. Pohlki, S. Doye, *Angew. Chem. Int. Ed.* **2001**, *40*, 2305.
[91] E. Haak, H. Siebeneicher, S. Doye, *Org. Lett.* **2000**, *2*, 1935.
[92] E. Haak, I. Bytschkov, S. Doye, *Angew. Chem. Int. Ed.* **1999**, *38*, 3389.
[93] I. Bytschkov, S. Doye, *Eur. J. Org. Chem.* **2001**, 4411.
[94] I. Bytschkov, S. Doye, *Tetrahedron Lett.* **2002**, *43*, 3715.
[95] Z. Zhang, L. L. Schafer, *Org. Lett.* **2003**, *5*, 4733.
[96] M. C. Wood, D. C. Leitch, C. S. Yeung, J. A. Kozak, L. L. Schafer, *Angew. Chem. Int. Ed.* **2007**, *46*, 354.
[97] C. Lorber, R. Choukroun, L. Vendier, *Organometallics* **2004**, *23*, 1845.
[98] J. M. Hoover, J. R. Petersen, J. H. Pikul, A. R. Johnson, *Organometallics* **2004**, *23*, 4614.
[99] L. Ackermann, L. T. Kaspar, C. J. Gschrei, *Org. Lett.* **2004**, *6*, 2515.
[100] L. Ackermann, *Organometallics* **2003**, *22*, 4367.
[101] M. A. Esteruelas, A. M. Lopez, A. C. Mateo, E. Onate, *Organometallics* **2006**, *25*, 1448.
[102] E. Smolensky, M. Kapon, M. S. Eisen, *Organometallics* **2005**, *24*, 5495.
[103] H. Wang, H. Chan, Z. Xie, *Organometallics* **2005**, *24*, 3772.
[104] J. R. Petersen, J. M. Hoover, W. S. Kassel, A. L. Rheingold, A. R. Johnson, *Inorg. Chim. Acta* **2005**, *358*, 687.
[105] B. D. Ward, A. Maisse-Francois, P. Mountford, L. H. Gade, *Chem. Commun.* **2004**, *6*, 704.
[106] I. Bytschkov, S. Doye, *Eur. J. Org. Chem.* **2003**, 935.
[107] D. Lathbury, T. Gallagher, *J. Chem. Soc., Chem. Commun.* **1986**, 114.
[108] S. Arseniyadis, J. Sartoretti, *Tetrahedron Lett.* **1985**, *26*, 729.
[109] L. Besson, J. Gore, B. Cazes, *Tetrahedron Lett.* **1995**, *36*, 3857.
[110] M. Al-Masum, M. Meguro, Y. Yamamoto, *Tetrahedron Lett.* **1997**, *38*, 6071.
[111] M. Meguro, Y. Yamamoto, *Tetrahedron Lett.* **1998**, *39*, 5421.
[112] R. O. Ayinla, L. L. Schafer, *Inorg. Chim. Acta* **2006**, 3097.
[113] D. V. Gribkov, K. C. Hultzsch, *Angew. Chem. Int. Ed.* **2004**, *43*, 5442.
[114] P. D. Knight, I. Munslow, P. N. O'Shaughnessy, P. Scott, *Chem. Commun.* **2004**, 894.
[115] S. Hong, T. J. Mark, *Acc. Chem. Res.* **2004**, *37*, 673.
[116] M. R. Gagne, T. J. Mark, *J. Am. Chem. Soc.* **1989**, *111*, 4108.
[117] J. A. Bexrud, J. D. Beard, D. C. Leitch, L. L. Schafer, *Org. Lett.* **2005**, *7*, 1959.
[118] H. Kim, P. H. Lee, T. Livinghouse, *Chem. Commun.* **2005**, 5205.
[119] N. Meyer, A. Zulys, P. W. Roesky, *Organometallics* **2006**, *25*, 4179.
[120] D. V. Gribkov, K. C. Hultzsch, F. Hampel, *J. Am. Chem. Soc.* **2006**, *128*, 3748.
[121] D. Riegert, J. Collin, A. Meddour, E. Schulz, A. Trifonov, *J. Org. Chem.* **2006**, *71*, 2514.
[122] K. C. Hultzsch, D. V. Gribkov, F. Hampel, *J. Organomet. Chem.* **2005**, *690*, 4441.
[123] J. Y. Kim, T. Livinghouse, *Org. Lett.* **2005**, *7*, 1737.
[124] J. Collin, J. Daran, O. Jacquet, E. Schulz, A. Trifonov, *Chem. Eur. J.* **2005**, *11*, 3455.

 © 2007 Wiley-VCH Verlag GmbH & Co. KGaA, Weinheim 

[125] S. Hong, S. Tian, M. V. Metz, T. J. Mark, *J. Am. Chem. Soc.* **2003**, *125*, 14768.
[126] P. N. O'Shaughnessy, P. D. Knight, C. Morton, K. M. Gillespie, P. Scott, *Chem. Commun.* **2003**, 1770.
[127] P. N. O'Shaughnessy, P. Scott, *Tetrahedron: Asymmetry* **2003**, *14*, 1979.
[128] K. K. Hii, *Pure Appl. Chem.* **2006**, *78*, 341.
[129] N. T. Patil, L. M. Lutete, H. Wu, N. K. Pahadi, I. D. Gridnev, Y. Yamamoto, *J. Org. Chem.* **2006**, *71*, 4270.
[130] L. M. Lutete, I. Kadota, Y. Yamamoto, *J. Am. Chem. Soc.* **2004**, *126*, 1622.
[131] S. Gischig, A. Togni, *Eur. J. Inorg. Chem.* **2005**, 4745.
[132] L. Fadini, A. Togni, *Chem. Commun.* **2003**, 30.
[133] O. Loeber, M. Kawatsura, J. F. Hartwig, *J. Am. Chem. Soc.* **2001**, *123*, 4366.
[134] R. Dorta, P. Egli, F. Zurcher, A. Togni, *J. Am. Chem. Soc.* **1997**, *119*, 10857.
[135] D. A. Watson, M. Chiu, R. G. Bergman, *Organometallics* **2006**, *25*, 4731

Received: January 11, 2007
Published Online: May 4, 2007

 © 2007 Wiley-VCH Verlag GmbH & Co. KGaA, Weinheim 

DOI: 10.1002/ejic.200601051

# Low-Valent Nickel and Palladium Complexes with 1,1′-Bis(phosphanyl)-ferrocenes: Syntheses and Structures of Acrylic Acid and Ethylene Complexes

Jens Langer,[a] Reinald Fischer,[a] Helmar Görls,[a] and Dirk Walther*[a]

**Keywords:** Alkene ligands / Chelates / Nickel / Palladium / P ligands

Thermally stable acrylic acid complexes with low-valent nickel or palladium of the type [(L)M($\eta^2$-$CH_2$=CH-COOH)] [**1a**: M = Ni, L = 1,1′-bis(diphenylphosphanyl)ferrocene (dppf), **1b**: M = Ni, L = 1,1′-bis(diisopropylphosphanyl)ferrocene (dippf), **1c**: M = Pd, L = dippf] were obtained by reaction of [Ni(cod)$_2$] or [(L)Pd(nb)] with acrylic acid in the presence of the phosphane ligands. X-ray diffraction analysis of **1a** and **1c**, respectively display that only the olefin part is coordinated. Hydrogen bonds between two carboxyl groups result in dimers in the solid state. The isomeric nickela-cyclic carboxylates of the type [(L)Ni($CH_2CH_2COO$)] are stable complexes in case of **2a** (L = dppf) and **2b** (L = dippf) whereas the unstable compound **2c** [L = 1,1′-bis(di-*tert*-butylphosphanyl)-ferrocene (dtbpf)] undergoes fast reductive decoupling to form $CO_2$ and the ethylene complex [(dtbpf)Ni(ethylene)] (**3c**). The related complex [(dippf)Ni(ethylene)] (**3b**) was prepared from nickel(0) complexes by ligand exchange reaction. **3b** and **3c** were characterized by elemental analyses, NMR spectroscopy and X-ray structure analysis of single crystals.

(© Wiley-VCH Verlag GmbH & Co. KGaA, 69451 Weinheim, Germany, 2007)

## Introduction

Recently we have described some model complexes of the hypothetical catalytic reactions between ethylene and $CO_2$ to form acrylic acid or its derivatives.[1] In connection with these investigations we have also tried to synthesize the hitherto unknown nickel(0) complexes with $\eta^2$-coordinated acrylic acid which are assumed to be model compounds of the final intermediate of the catalytic cycle. However, such complexes could not be obtained with N-donor ligands or phosphanes of the type $R_2P(CH_2)_nPR_2$.

In this paper we report that some 1,1′-bis(phosphanyl)-ferrocenes (L) are able to form surprisingly stable complexes of the type [(L)M($\eta^2$-acrylic acid)]. Furthermore, we have isolated the isomeric form of [(dippf)Ni(acrylic acid)], the metallacycle [(dippf)Ni($CH_2CH_2COO$)], and we also succeeded in obtaining ethylene nickel(0) complexes with bis(phosphanyl)ferrocene ligands which are also hitherto unknown. These three types of complexes may also be considered as model compounds for intermediates of the metal-mediated reaction between ethylene and $CO_2$ to form acrylic acid.

Generally, the low-valent nickel chemistry with 1,1′-bis-(phosphanyl)ferrocene ligands L is rather limited. To the best of our knowledge the only isolated nickel(0) compounds are some carbonyl complexes[2,3] and [(dppf)-Ni(cod)].[4] The compound [(dppf)$_2$Ni] was only prepared in situ.[5,6] This is somewhat surprising since low-valent nickel complexes with 1,1′-bis(phosphanyl)ferrocene ligands are known to be intermediates in numerous homogeneous catalytic reactions.[7–13] In addition, they may serve as precursors for new catalysts and for the study, in a stoichiometric manner, of key steps in the catalytic reactions.

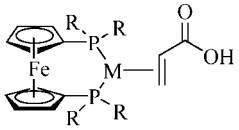

R = Ph, M = Ni (**1a**)
R = *i*Pr, M = Ni (**1b**)
R = *i*Pr, M = Pd (**1c**)

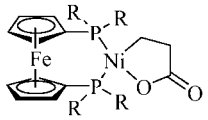

R = Ph (**2a**)
R = *i*Pr (**2b**)

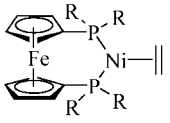

R = *i*Pr (**3b**)
R = *t*Bu (**3c**)

## Results and Discussion

### Nickel(0) and Palladium(0) Complexes with Acrylic Acid

The acrylic acid complexes **1a** and **1b** were obtained by reacting a mixture of [Ni(cod)$_2$], dppf or dippf and acrylic acid in a solution of THF at 0 °C according to Scheme 1.

[a] Institute of Inorganic and Analytical Chemistry, Friedrich-Schiller University Jena,
Lessingstraße 8, 07743 Jena, Germany
Fax: +49-3641-948102
E-mail: dirk.walther@uni-jena.de

 © 2007 Wiley-VCH Verlag GmbH & Co. KGaA, Weinheim 

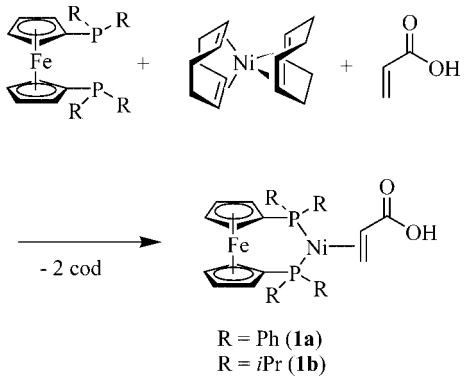


Scheme 1. Formation of nickel complexes with acrylic acid.

**1a** was isolated in good yields (71%) as red crystalline compound. NMR spectroscopic data showed that both phosphorus donor atoms coordinate to the nickel in a different chemical environment ($^{31}P\{^1H\}$ NMR ([D$_8$]THF): 26.7 and 32.6 ppm). In the $^1H$ NMR spectrum ([D$_8$]THF) the proton signals of the olefinic $CH_2$ group appeared at $\delta$ = 1.95 and 2.25 ppm and the resonance of the olefinic CH group was found at $\delta$ = 2.98 ppm. A broad signal for the COOH proton appeared at $\delta$ = 9.64 ppm. Furthermore, six different signals of the cp groups integrating together to eight protons were observed, and the 20 protons of phenyl groups appeared between 7.28 and 7.80 ppm. The $^{13}C$ NMR spectrum also confirmed the olefin-like coordination of the acrylic acid with the two signals for the olefinic carbons at $\delta$ = 43.9 and 49.8 ppm and the signal of the COOH group at $\delta$ = 175.9 ppm.

Single crystals of **1a** were grown from a solution of THF and an X-ray diffraction analysis (Figure 1) showed the nickel atom, surrounded by two phosphorus atoms and the two carbon atoms C1 and C2 of the alkene group. Since the angle between the P1,P2,Ni plane and the C1,C2,Ni plane is only 6.24°, the coordination geometry around the metal centre can be considered as essentially planar. The COOH group is not coordinated. Complex **1a** forms a dimer in the solid state since two carboxylic groups are connected by the typical hydrogen bond pattern of carboxylic acids. As expected, the bond length between C1 and C2 of the olefin group [1.417(4) Å] is slightly enlarged compared with the uncoordinated state of acrylic acid. Other relevant bond lengths and angles (see caption of Figure 1) are within the normal range and need therefore no further discussion.

The reaction between [Ni(cod)$_2$], dippf und acrylic acid in THF resulted in a mixture of the acrylic acid complex **1b** as main product and traces of a second compound, suspected to be the isomeric nickela-cyclic carboxylate [(dippf)-Ni($CH_2CH_2COO$)] (**2b**, see below) according to the signals in the $^{31}P$ NMR spectrum of the mother liquor.

The pure complex **1b** was isolated upon crystallisation from a solution of THF or DMF in good yields. $^1H$ NMR spectroscopy of **1b** revealed that the compound has a similar structure as found for **1a**: The proton signals of the coordinated $CH_2$=CH- group at 2.57 and 2.88 are only slightly downfield shifted compared with those of **1a**, and

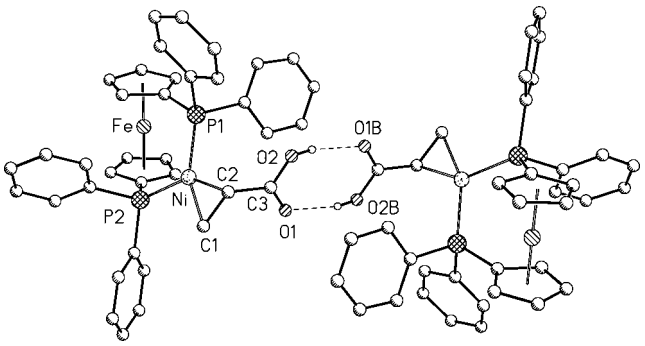


Figure 1. Molecular structure of **1a** (H atoms except the one at O2 are omitted for clarity, cocrystallized THF not shown). Selected bond lengths [Å] and angles [°]: Ni–C1 1.945(2), Ni–C2 1.993(3), Ni–P1 2.1781(7), Ni–P2 2.1411(8), C1–C2 1.417(4), C2–C3 1.446(4), C3–O1 1.275(4), C3–O2 1.291(4), P1–Ni–P2 109.71(3), P1–Ni–C2 111.55(9), P2–Ni–C1 109.71(3), C1–Ni–C2 42.2(1), plane(P1,P2,Ni)-plane(Ni,C1,C2) 6.24.

the resonance of the COOH proton appeared at $\delta$ = 10.35 ppm. The $^{13}C$ resonances of **1b** for the olefin group were found at 32.7 (=$CH_2$) and 42.7 (=CH) ppm and the signal of the COOH group was observed at $\delta$ = 177.7 ppm confirming the olefin-like coordination of the acrylic acid ligand as well. In addition, X-ray structure of single crystals (not depicted) showed that **1b** has essentially the same solid-state structure as **1a** with the $\eta^2$ coordination of the acrylic acid ligand and hydrogen bonds between two acrylic acid ligands resulting in a dimer.

Reaction between acrylic acid and nickel(0) complexes in the presence of $Cy_3P$ was already investigated by Yamamoto et al.[14] In this case, however, no stable nickel(0) complex of acrylic acid was formed, instead the interconversion into the isomeric nickela-cyclic carboxylate [($Cy_3P$)-Ni($CH_2CH_2COO$)]$_n$ was observed. This clearly demonstrates the strong influence of the supporting ligands on the following equilibrium (Scheme 2).

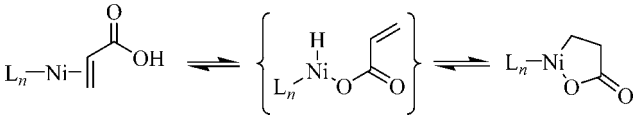

Scheme 2. Equilibrium between L$_n$Ni($CH_2$=CH-COOH)) and [(L$n$)Ni($CH_2CH_2COO$)].

**1a** is surprisingly thermally stable in THF as well in the solid state. Even heating the complex for 3 h in refluxing THF did not result in any reaction. This demonstrates that the isomerization into the nickela-cyclic carboxylate (see Scheme 2) is in this case an energetically unfavourable pathway.

So far, only the metal(0) acrylic acid complex [(acrylic acid)Fe(CO)$_4$] was described.[15] Furthermore, the dimeric $Cu^I$ compound [ClCu(acrylic acid)]$_2$ with $\eta^2$ coordinated acrylic acid has been prepared.[16] In addition, Carmona has found that acrylate hydrido molybdenum(II) and tungsten(II) complexes were formed by reaction of ethylene and $CO_2$ at an electron-rich Mo(0) or $W^0$ fragment.[17] In contrast, acrylic ester complexes with $Ni^0$ or $Pd^0$ have been

 © 2007 Wiley-VCH Verlag GmbH & Co. KGaA, Weinheim 

found to be stable[18,19] due to the lack of the reactive COOH group.

To demonstrate that the ability of 1,1′-bis(phosphanyl)-ferrocene ligands in stabilizing acrylic acid complexes is not restricted to nickel(0) we also prepared the related $Pd^0$ complex [(dippf)Pd(acrylic acid)] **1c** by reacting of [(dippf)-Pd(nb)] (nb = norbornene) with an excess of acrylic acid in THF [Equation (1)].

$$[(\text{dippf})\text{Pd(nb)}] + \text{HOOC–CH=CH}_2 \rightarrow [(\text{dippf})\text{Pd}(\eta^2\text{-CH}_2\text{=CH–COOH})]\ (\mathbf{1c}) + \text{nb} \quad (1)$$

Isolation of the orange solid and recrystallisation from diethyl ether resulted in orange single crystals. To confirm the structure in the solid state, the X-ray crystal structure analysis of **1c** was carried out. Figure 2 reveals the molecule structure which shows that **1c** has the same arrangement of the ligands as the related nickel(0) acrylic acid complexes with the olefin part of acrylic acid being coordinated at $Pd^0$ centre and with a C=C bond lengths of 1.419(3) Å. Also, the other bond lengths and angles lie within a typical range. The angle between the plane (P1,P2,Pd) and the (Pd, C1,C2) is only 2.27° which undoubtedly shows that the $Pd^0$ centre is in a planar environment formed by the two P donor atoms and the carbons C1 and C2 of the olefinic part of the acrylic acid ligand. **1c** forms also a dimer in the solid state in which two carboxylic groups are connected by hydrogen bonds.

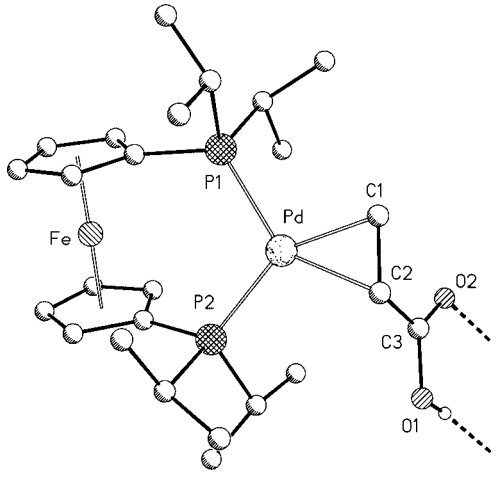


Figure 2. Molecular structure of **1c** (the formation of hydrogen bonds analogously to fig. 1 is indicated by the dotted lines indicating the points at which the dimer is formed; H atoms except the one at O1, and cocrystallized THF have been omitted clarity). Selected bond lengths [Å] and angles [°]: Pd–C1 2.100(2), Pd–C2 2.154(2), Pd–P1 2.3116(7), Pd–P2 2.3215(8), C1–C2 1.419(3), C2–C3 1.457(3), C3–O1 1.327(3), C3–O2 1.237(3), P1–Pd–P2 105.98(3), P1–Pd–C1 104.35(7), P2–Pd–C2 110.67(7), C1–Pd–C2 38.95(9), plane (P1,P2,Pd)-plane(Pd, C1,C2) 2.27.

### Nickela-Cyclic Carboxylates of the Type [(L)NiCH$_2$CH$_2$COO] (L = dppf, dippf)

In order to proof whether the isomers of **1**, the nickela-cyclic carboxylates of the type [(L)Ni($CH_2CH_2COO$)] (L: dppf, dippf, dtbpf) (**2**) are stable compounds, we reacted [$(py)_2$Ni($CH_2CH_2COO$)] with these ligands in DMF at room temperature. This pyridine complex is a labile ligand complex which serves as precursor for many other reactions.[20–22] Scheme 3 displays that, depending on the bis-(phosphanyl)ferrocene ligands, different products were formed.

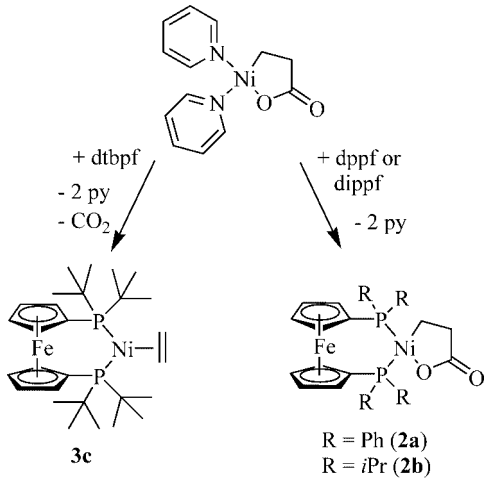


Scheme 3. Reactions of bis(phosphanyl)ferrocene ligands with a nickela-lactone.

In contrast to the formation of the thermally unstable complex **2a** from dppf and [$(py)_2$Ni($CH_2CH_2COO$)], the reaction with dippf resulted in the formation of the thermally stable nickela-cyclic carboxylate **2b** which was isolated as orange crystals in high yields (85%). **2b** was fully characterized by elemental analyses, IR, and NMR spectroscopy, and by X-ray analysis of single crystals. In the $^1$H NMR spectrum of **2b** in [$D_8$]THF the Ni-$CH_2$ protons were observed at $\delta$ = 0.96 ppm and those of the $CH_2COO$ unit resonated at $\delta$ = 1.96 ppm; each of these signals correspond to two protons. The signals of the $CH_3$ groups appeared at 1.23–1.54 ppm, the signals of the CH groups were found at 2.20–2.47 ppm and the cp protons were observed as singlets at $\delta$ = 4.40 and 4.44 ppm. In addition, the $^{13}$C NMR spectrum showed the expected simple pattern of signals for the Ni–$CH_2$ group at 12.4 and for the $CH_2$-COO- fragment at $\delta$ = 37.2 ppm, besides the resonances for the ligand carbons, and in the $^{31}P\{^1H\}$ NMR spectrum in [$D_7$]DMF the $^{31}$P signals appeared at $\delta$ = 36.4 and 44.7 ppm. In the IR spectrum the ν(C=O) band was found at 1634 cm$^{-1}$.

Single crystals were grown from DMF at –20 °C and the crystal structure of **2b** has been solved by X-ray diffraction analysis. Its molecule structure is displayed in Figure 3 and shows it to be very similar to the starting complex [$(py)_2$Ni($CH_2CH_2COO$)][22] and other closely related nickela-cyclic carboxylates.[1,21] However, due to the disorder of the nickela-cylopentanone unit a closer comparison with other nickela-cyclic carboxylates is not possible.

 © 2007 Wiley-VCH Verlag GmbH & Co. KGaA, Weinheim 

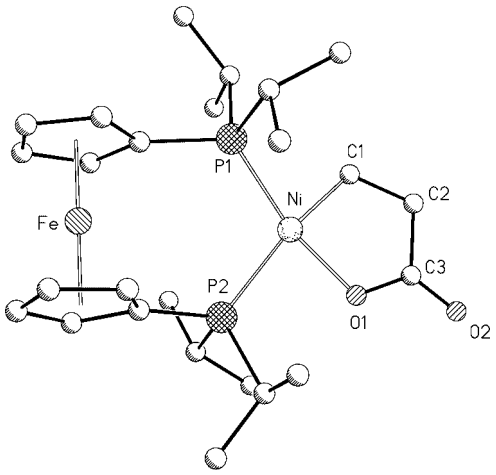


Figure 3. Molecular structure of **2b** (H atoms have been omitted for clarity).

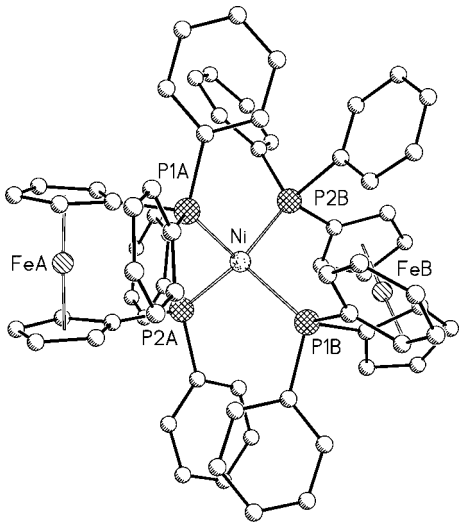


Figure 4. Molecular structure of **4** (H atoms have been omitted for clarity). Selected bond lengths [Å] and angles [°]: Ni–P1A 2.269(2), Ni–P2A 2.238(2), Ni–P1B 2.243(2), Ni–P2B 2.237(2), P1A–Ni–P1B 120.93(4), P1A–Ni–P2A 106.28(5), P1A–Ni–P2B 115.62(4), P1B–Ni–P2A 106.47(5), P1B–Ni–P2B 101.64(4), P2A–Ni–P2B 115.62(4).

**2a** is extremely sparingly soluble in organic solvents preventing complete characterization by NMR spectroscopy. The compound shows the typical ν(C=O) band for a nickela-cyclic carboxylate at 1642 $cm^{-1}$ in nujol suspension. Furthermore, $^{31}P$ NMR measurements in [$D_7$]DMF at 25 °C gave two signals for the coordinated P atoms in a different chemical environment at $\delta$ = 19.4 and 39.0 ppm. In addition, in the $^1H$ NMR spectrum the two resonances of the coordinated $CH_2CH_2COO$ fragment were observed at $\delta$ = 0.64 ppm (as a multiplet of the Ni-$CH_2$ group) and at $\delta$ = 1.93 ppm. The latter appears as a triplet and is assigned to the $CH_2COO$ protons. Comparison of these data with those of the nickela-cyclic carboxylate **2b** suggest that **2a** is also the expected nickela-cyclic carboxylate according to Scheme 3.

**2a** is a thermally unstable compound. Even at 40 °C in DMF the complex decomposes into a mixture of compounds. One product isolated from the reaction mixture was the nickel(0) complex [$(dppf)_2Ni$] (**4**). This compound was already generated in situ either by reaction of $NiBr_2$, dppf and Zn or by reduction of [$Ni(acac)_2$] using DIBAL-H in the presence of dppf,[5,6] however to the best of our knowledge it has not been isolated so far. Complex **4** was characterized by elemental analyses, $^1H$ and $^{13}C$ NMR spectroscopy and by a single crystal structure analysis. Figure 4 shows its molecule structure and contains the most relevant bond lengths and angles in the caption.

The nickel centre is in the tetrahedral environment of four P donor atoms with typical Ni–P bond lengths. In the dppf ligand A the two cp ligands have a synclinal staggered conformation with a torsion angle $\tau$ of 43.9°. This conformation is the most common one found for dppf in its metal complexes (characteristic values: 18° < $\tau$ < 54°).[23] In the other ligand B, however, the torsion angle is only 15.0° and the cp ligands have a synperiplanar eclipsed conformation (characteristic region: 0° < $\tau$ < 18°).[23] This different arrangement results in different bite angles (106.3° for P1A–Ni–P2A and 101.6° for P1B–Ni–P2B).

### Complexes of the Type [(L)Ni(ethylene)] [L: dtbpf, (dippf)]

The steric bulky ligand dtbpf yielded in the reaction with [$(py)_2Ni(CH_2CH_2COO)$] under similar conditions a different product compared to the dippf complex. In this case reductive decoupling of the $NiCH_2CH_2COO$- unit was observed resulting in the formation of the nickel(0) ethylene complex [(dtbpf)Ni(ethylene)] **3c** and $CO_2$ (Scheme 1). This demonstrates how sensitive the reactivity can be influenced by the steric demand of the ligands. **3c** was characterized by NMR spectroscopy in [$D_7$]DMF and by an X-ray analysis of single crystals grown from DMF. When the nickelacycle **2b** was heated at 80 °C, reductive decoupling was observed as well, resulting in the formation of [(dippf)Ni(ethylene)] (**3b**) in good yields.

As expected for a symmetrical structure in solution, the $^{31}P\{^1H\}$ NMR spectrum of **3c** in [$D_7$]DMF at room temperature showed only one signal at $\delta$ = 65.6 ppm. In the $^1H$ NMR spectrum the ethylene protons appeared at $\delta$ = 1.86 ppm. The methyl protons of the *tert*-butyl group resonated at $\delta$ = 1.35 ppm and the singlets at $\delta$ = 4.06 and 4.21 ppm (each integrating to four protons) were assigned the cp ring protons. Single crystals of **3c** were grown from DMF suitable for X-ray structure determination, and its molecule structure is shown in Figure 5.

The nickel(0) centre is in the distorted tetrahedral environment of the two P donor groups and the carbons of the ethylene ligand with typical bond lengths for the Ni–P and Ni–C bonds. As expected, the double bond of the coordinated ethylene ligand [C(1)–C(2) 1.399(4) Å] is significantly elongated compared to free ethylene.

It is noteworthy, that the hitherto unknown ethylene complexes with 1,1′-bis(phosphanyl)ferrocene ligands can also be formed by other methods. For example, the ethylene

 © 2007 Wiley-VCH Verlag GmbH & Co. KGaA, Weinheim 

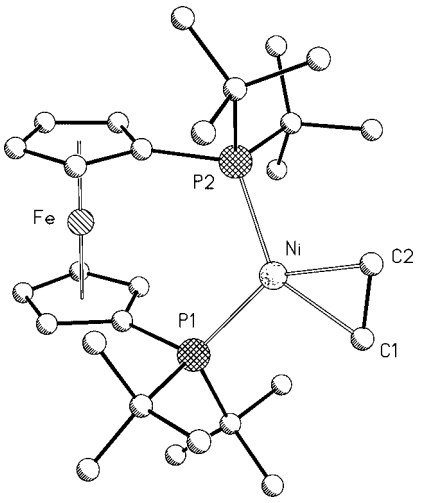


Figure 5. Molecular structure of **3c** (H atoms have been omitted for clarity). Selected bond lengths [Å] and angles [°]: Ni–C1 1.980(3), Ni–C2 1.984(3), Ni–P1 2.1893(6), Ni–P2 2.1908(6), C1–C2 1.399(4), P1–Ni–P2 111.95(3), P1–Ni–C1 103.96(9), P2–Ni–C2 104.03(9), C1–Ni–C2 41.3(2), plane (P1,P2,Ni)-plane(Ni,C1,C2) 15.71.

complex **3b** was additionally prepared by ligand displacement from (cyclododeca-1,5,9-triene)nickel(0) [Equation (2)].

$$[Ni(cdt)] + dippf + C_2H_4 \rightarrow [(dippf)Ni(C_2H_4)] + cdt \quad (2)$$

NMR spectroscopic data are very similar to those of the dtbpf complex **3c**, and the crystal structure of single crystals of **3b** (not depicted) is also comparable with that of the closely related complex **3c** and need therefore no further discussion.

## Conclusions

Complexes of the type [(L)M($\eta^2$-$CH_2$=CH-COOH)] (**1a**–**1c**) are the first Ni- and $Pd^0$ complexes with acrylic acid as olefin-like ligand. Due to the rigidity and the bulkiness of the ferrocenyl-bisphosphane ligands these complexes are surprisingly stable and do not thermally interconvert into the isomeric nickela-lactones of the type [(L)Ni($CH_2CH_2$-COO)] (**2**) which could be independently prepared by ligand exchange from [$(py)_2$Ni($CH_2CH_2COO$)] as thermally stable compounds. The nickela-lactones **2b** and **2c** react at heating under reductive decoupling to yield the new ethylene complexes of the type **3**, however, the isomerization of the complexes of the type **2** to form the acrylic acid complexes **1** was not observed.

## Experimental Section

**General:** Infrared spectra were recorded using a Perkin–Elmer 2000 FT-IR; $^1$H-NMR spectra were recorded on a Bruker 400 MHz/200 MHz spectrophotometer. The mass spectra were recorded using a SSQ 170, Finnigan Mat. Electro spray mass spectra were recorded on a Finnnigan MAT, MAT 95 XL. Values for *m*/*z* are for the most intense peak of isotope envelope.

All manipulations were carried out by using modified Schlenk techniques under an atmosphere of argon. Prior to use, THF, benzene and diethyl ether were dried with potassium hydroxide and distilled from sodium/benzophenone. DMF was dried with $CaH_2$.

dppf, dippf, and dtbpf were prepared in analogy to known procedures by reaction of *n*BuLi/tmeda with ferrocene, followed by addition of the chlorodiphenylphoshane, chlorodiisopropylphosphane or chlorodi-*tert*-butylphosphane.[24–27] [Ni(cod)$_2$],[28] [$(py)_2$-Ni($C_2H_4COO$)][22] and [Pd($\eta^2$-$C_7H_{10}$)$_3$][29] were prepared according to literature procedures.

**[(dppf)Ni($\eta^2$-$CH_2$=CH-COOH)] (1a):** A solution of dppf (2.67 g, 4.82 mmol) in THF (30 mL) was added to solid [Ni(cod)$_2$] (1.32 g, 4.80 mmol). The suspension was stirred until all solids had dissolved. Afterwards the stirred solution was cooled to 0 °C and acrylic acid (0.37 g, 5.13 mmol) was added, resulting in formation of a yellow precipitate. This solid was isolated by filtration and dried in a vacuum. Yield: 2.83 g (71%). Suitable crystals of (**1a**)·2THF for X-ray measurement were obtained by slowly cooling a saturated solution in THF from room temperature to 5 °C. In a similar manner, crystals of [(dppf)Ni($\eta^2$-$CH_2$=CH-COOH)]·1.5DMF were obtained from a solution of DMF. Those crystals were used for elemental analysis. $C_{41.5}H_{42.5}FeN_{1.5}NiO_{3.5}P_2$ (794.8) calcd. C 62.71, H 5.39, N 2.64; found C 62.11, H 5.54, N 2.53. $^1$H NMR ([D$_8$]THF, 25 °C): $\delta$ = 1.95 (m, 1 H, $CH_2$=), 2.25 (m, 1 H, $CH_2$=), 2.98 (m, 1 H, CH=), 3.89 (s, 1 H, CH cp), 4.07 (s, 1 H, CH cp), 4.22 (s, 2 H, CH cp), 4.26 (s, 1 H, CH cp), 4.29 (s, 1 H, CH cp), 4.35 (s, 2 H, CH cp), 7.28–7.80 (m, 20 H, CH ph), 9.64 (br., 1 H, COOH). $^{13}$C{$^1$H} NMR ([D$_8$]THF, 25 °C): 43.9 (d, $J_{P,C}$ = 19.6 Hz, $CH_2$=). 49.8 (d, $J_{P,C}$ = 11.6 Hz, CH=), 71.1 (dd, $J_{P,C}$ = 7.3 Hz, $J_{P,C}$ = 4.1 Hz, CH cp), 72.9 (d, $J_{P,C}$ = 6.4 Hz, CH cp), 74.4 (dd, $J_{P,C}$ = 20.0 Hz, $J_{P,C}$ = 6.0 Hz, CH cp), 75.3 (dd, $J_{P,C}$ = 17.5 Hz, $J_{P,C}$ = 13.8 Hz, CH cp), 81.9 (dd, $J_{P,C}$ = 40.4 Hz, $J_{P,C}$ = 5.1 Hz, C cp), 82.2 (dd, $J_{P,C}$ = 40.4 Hz, $J_{P,C}$ = 5.1 Hz, C cp), 128.4 (dd, $J_{P,C}$ = 7.5 Hz, $J_{P,C}$ = 2.9 Hz, CH), 128.7 (d, $J_{P,C}$ = 9.3 Hz, CH), 129.3 (d. $J_{P,C}$ = 8.3 Hz, CH), 130.2 (d, $J_{P,C}$ = 20.1 Hz, CH), 134.0 (dd, $J_{P,C}$ = 12.2 Hz, $J_{P,C}$ = 5.9 Hz, CH), 135.5 (dd, $J_{P,C}$ = 49.6 Hz, $J_{P,C}$ = 15,2 Hz, CH), 137.2 (d, $^1J_{P,C}$ = 37.8 Hz, C), 137.2 (d, $^1J_{P,C}$ = 37.8 Hz, C), 175.9 (COOH). $^{31}$P{$^1$H} NMR ([D$_8$]THF, 25 °C): $\delta$ = 26.7 (d, $^2J_{P,P}$ = 21.9 Hz), 32.6 (d, $^2J_{P,P}$ = 21.9 Hz).

**[(dippf)Ni($\eta^2$-$CH_2$=CH-COOH)] (1b):** A solution of dippf (2.21 g, 5.28 mmol) in THF (30 mL) was added to [Ni(cod)$_2$] (1.45 g, 5.27 mmol). The mixture was stirred until all solids had dissolved and then cooled to 0 °C. At this temperature acrylic acid (0.38 g, 5.27 mmol) was added drop wise. The resulting reaction mixture was stored at 5 °C overnight. Afterwards the solvent was removed by distillation under reduced pressure and ether was added to the remaining residue, resulting in the formation of a yellow precipitate. This solid was isolated by filtration and dried in a vacuum. Suitable crystals for X-ray measurement were obtained by layering a saturated solution of **1b** in DMF with ether. Yield: 1.76 g (60.6%). $C_{25}H_{40}FeNiO_2P_2$ (549.0) calcd. C 54.68, H 7.34; found C 54.36, H 7.53. $^1$H NMR ([D$_8$]THF): $\delta$ = 0.65 (dd, $J$ = 10.3 Hz, $J$ = 3.6 Hz, 3 H, $CH_3$), 0.74 (m, 3 H, $CH_3$), 0.65 (dd, $J$ = 10.3 Hz, $J$ = 3.6 Hz, 3 H, $CH_3$), 1.03 (dd, $J$ = 15.6 Hz, $J$ = 7.1 Hz, 3 H, $CH_3$), 1.15 (dd, $J$ = 13.7 Hz, $J$ = 6.9 Hz, 3 H, $CH_3$), 1.27–1.56 (m, 12 H, $CH_3$), 1.85 [m, 2 H, C*H*($CH_3$)$_2$], 1.97 [m, 2 H, C*H*($CH_3$)$_2$], 2.57 (br., 1 H, =$CH_2$), 2.88 (br., 1 H, CH=), 3.94 (s, 2 H, CH cp), 3.99 (s, 1 H, CH cp), 4.01 (s, 1 H, CH cp), 4.03 (s, 2 H, CH cp), 4.16 (s, 1 H, CH cp), 4.29 (s, 1 H, CH cp), 10.35 (br., 1 H, COOH). $^{13}$C{$^1$H} NMR ([D$_8$]THF): $\delta$ = 17.7 ($CH_3$), 17.8 ($CH_3$), 19.2 ($CH_3$), 19.4 ($CH_3$), 20.5 (d, $^2J_{P,C}$ = 7.3 Hz, $CH_3$), 21.2 ($CH_3$), 22.5 (d, $^2J_{P,C}$ = 9.2 Hz, $CH_3$), 22.6 (d, $^2J_{P,C}$ = 8.7 Hz, $CH_3$), 26.3 (d, $^1J_{P,C}$ =

 © 2007 Wiley-VCH Verlag GmbH & Co. KGaA, Weinheim 

38.6 Hz, 2×CH-P), 26.7 (d, $^1J_{P,C}$ = 23.5 Hz, 2×CH-P), 32.7 (br., =$CH_2$), 42.7 (br., =CH), 69.3 (CH, cp), 69.4 (CH, cp), 71.0 (2×CH, cp), 72.4 (CH, cp), 72.7 (CH, cp), 73.8 (d, $J_{P,C}$ = 4.0 Hz, CH, cp), 73.9 (d, $J_{P,C}$ = 4.7 Hz, CH, cp), 83.8 (dd, $^1J_{P,C}$ = 23.7 Hz, $^3J_{P,C}$ = 5.1 Hz, C-P, cp), 84.7 (d, $^1J_{P,C}$ = 25.4 Hz, C-P, cp), 177.7 (br., COOH). $^{31}P\{^1H\}$ NMR ([$D_8$]THF, 25 °C): $\delta$ = 46.9 (d, $^2J_{P,P}$ = 15.3 Hz), 39.3 (d, $^2J_{P,P}$ = 15.3 Hz).

**[(dippf)Pd(nb)]:** A solution of dippf (0.36 g, 0.86 mmol) in THF (20 mL) was cooled to –30 °C and added to solid [$(nb)_3$Pd] (0.30 g, 0.77 mmol) at this temperature. The stirred solution was allowed to slowly warm to room temperature. Afterwards half of the solvent was distilled of under reduced pressure. The remaining orange coloured solution was stored at –20 °C for several days, resulting in the formation of orange red crystals. These crystals were separated by filtration and dried in a vacuum. From the mother liquor a second crop of product was obtain by further reduction of the volume and layering with diethyl ether. Yield: 120 mg (25%). $C_{29}H_{46}P_2FePd$ (618.9) calcd. C 56.28, H 7.49; found C 56.12, H 7.52. $^1H$ NMR ([$D_8$]THF, 25 °C): $\delta$ = 0.58 (d, $^2J_{H,H}$ = 7.6 Hz, 1 H, C*H*H′ bridge), 1.05–1.30 (m, 15 H, 4×$CH_3$, 2×C*H*H′, CH*H*′ bridge), 1.52 (m, 2 H, 2×CH*H*′), 2.19 (m, $^2J_{H,P}$ = 6.0 Hz, 4 H, CH *i*Pr), 2.88 (s, 2 H, CH), 2.99 (d, $^2J_{H,P}$ = 6.0 Hz, 2 H, CH), 4.23 (s, 2 H, CH cp), 4.28 (s, 6 H, CH cp). $^{13}C\{^1H\}$ NMR ([$D_8$]THF): $\delta$ = 20.0 (t, $^2J_{C,P}$ = 5.0 Hz, 4×$CH_3$ *i*Pr), 20.4 (br., 4×$CH_3$ *i*Pr), 26.9 (t, $^1J_{C,P}$ = 6.3 Hz, 2×CH *i*Pr), 27.0 (t, $^1J_{C,P}$ = 7.6 Hz, 2×CH *i*Pr), 29.9 (t, $^4J_{CP}$ = 5.0 Hz, 2×CHH′), 43.4 (s, CHH′), 45.6 (s, 2×CH), 64.2 (pseudo-dt, 2×= CH-), 69.8 (s, 4×CH cp), 73.7 (t, $^2J_{C,P}$ = 3.8 Hz, 4×CH cp), 85.3 (t, $^1J_{C,P}$ = 9.5 Hz, 2×C cp). $^{31}P\{^1H\}$ NMR (81 MHz, [$D_8$]THF, 25 °C): $\delta$ = 36.4 (s).

**[(dippf)Pd($\eta^2$-$CH_2$=CH-COOH)] (1c):** Acrylic acid (0.03 mL, 0.44 mmol) was added to a solution of [(dippf)Pd(nb)] (40 mg, 0.065 mmol) in THF (1 mL) at 0 °C with rapid stirring. The resulting mixture was warmed to room temperature and stirred for additional 30 min. Afterwards the solvent was completely removed by distillation under reduced pressure. The remaining orange red sticky oil was treated with diethyl ether (2 mL) and stirred for 20 min. The resulting suspension was filtered and the clear yellow solution was stored at –20 °C. The isolated solid was redissolved in a few drops of THF and that solution was kept at 5 °C for several days. From both solutions, suitable crystals for X-ray measurement were obtained; [(dippf)Pd($\eta^2$-$CH_2$=CH-COOH)] from ether, [[(dippf)Pd($\eta^2$-$CH_2$=CH-COOH)]·THF from THF]. The yield was not determined.

**[(dppf)Ni($C_2H_4$-COO)] (2a):** Yellow dppf (0.77 g, 1.39 mmol) was added to a suspension of green [$(py)_2$Ni($C_2H_4$COO)] (0.40 g, 1.38 mmol) in DMF (8 mL) at 0 °C. The solution was allowed to slowly warm to room temperature, while the starting materials dissolved and a yellow precipitate was formed. To remove liberated pyridine, 2 mL of DMF was distilled of under reduced pressure at room temperature. Afterwards the yellow solid was isolated by filtration, washed with diethyl ether and dried in a vacuum. Yield: 0.91 g (96%) yellow powder. $^1H$ NMR ([$D_7$]DMF, 25 °C): $\delta$ = 0.64 (m, 2 H, Ni-$CH_2$), 1.93 (t, $J$ = 6.9 Hz, 2 H, $CH_2$-COO), 4.45 (s, 4 H, CH cp), 7.45–8.00 (m, 20 H Phenyl). $^{31}P\{^1H\}$ NMR ([$D_7$]DMF, 25 °C): $\delta$ = 19.4 (br), 39.0 (br). IR (nujol): $\tilde{\nu}$ = (C=O) 1642 $cm^{-1}$.

**[(dippf)Ni($C_2H_4$-COO)] (2b):** A solution of dippf (0.83 g, 1.98 mmol) in DMF (4 mL) was added to a suspension of green [$(py)_2$Ni($C_2H_4$COO)] (0.49 g, 1.70 mmol) in DMF (4 mL) at room temperature. The resulting solution was stirred for 1 h. Meanwhile an orange yellow precipitate was formed. The solid was afterwards collected by filtration and dried in a vacuum. Suitable crystals for X-ray measurement were obtained from a saturated solution of the complex in DMF at room temp. und subsequent cooling to –20 °C. Yield: 0.8 g (85%). $C_{25}H_{40}P_2O_2FeNi$ (549.08) calcd. C 54.69, H 7.34; found. C 54.21, H 7.39. $^1H$ NMR ([$D_8$]THF, 25 °C): $\delta$ = 0.96 (tdd, $^3J_{H,H}$ = 6.9 Hz, $^3J_{P,H}$ = 4.0 Hz, $^3J_{P,H}$ = 8.7 Hz, 2 H, Ni–$CH_2$), 1.23–1.54 (m, 24 H, $CH_3$), 1.96 (tdd, $^3J_{H,H}$ = 7.0 Hz, $^4J_{P,H}$ = 5.1 Hz, $^4J_{P,H}$ = 7.2 Hz, 2 H, $CH_2$-COO), 2.20–2.47 (m, 4 H, CH), 4.40 (m, 4 H, CH cp), 4.44 (m, 4 H, CH cp). $^{13}C\{^1H\}$ NMR ([$D_8$]THF, 25 °C): $\delta$ = 12.4 (dd, $J$ = 31.6 Hz, $J$ = 59.9 Hz, Ni-$CH_2$), 19.8 (d, $J$ = 11.5 Hz, $CH_3$), 20.6 (d, $J$ = 5.7 Hz, $CH_3$), 37.2 (dd, $J$ = 2.7 Hz, $J$ = 4.6 Hz, *C*$H_2$-COO), 71.1 (d, $J$ = 4.5 Hz, CH cp), 71.9 (d, $J$ = 3.9 Hz, CH′ cp), 73.3 (d, $J$ = 6.3 Hz, CH cp), 73.5 (d, $J$ = 6.2 Hz, CH′ cp), 82.2 (d, $J$ = 10.7 Hz, C cp), 82.8 (d, $J$ = 10.7 Hz, C′ cp), 185.5 (m, COO). The signals for CH groups of the isopropyl substituents overlap with the signals of the used solvent and were therefore not detected. $^{31}P\{^1H\}$ NMR ([$D_7$]DMF, 25 °C): $\delta$ = 36.5 (d, $J_{P,P}$ = 14.4 Hz), 44.7 (d, $J_{P,P}$ = 14.4 Hz). IR (nujol): $\tilde{\nu}$ = (C=O) 1634 $cm^{-1}$ (s).

**[(dippf)Ni($\eta^2$-$C_2H_4$)] (3b):** a) A suspension of [(dippf)Ni($C_2H_4$-COO)] (**2b**) (200 mg, 0.36 mmol) in DMF (5 mL) was heated to 80 °C. The resulting clear solution was stirred at this temperature for additional 3 h. Upon slow cooling to room temperature orange coloured crystals were formed overnight. These crystals were collected by filtration and dried in a vacuum. A second crop of product was obtained by storing the mother liquor at 0 °C for 3 d. Yield: 130 mg (70%). $C_{24}H_{40}FeNiP_2$ (505.06) calcd. C 57.07, H 7.98; found 57.17, H 8.16. $^1H$ NMR ($C_6D_6$, 25 °C): $\delta$ = 1.13 (sext, $J$ 6.8 Hz, 24 H, $CH_3$), 2.05 (m, 4 H, CH *i*Pr), 2.19 (br., 4 H, $C_2H_4$), 4.06 (br., 4 H, CH cp), 4.21 (br., 4 H, CH cp). $^{13}C\{^1H\}$ NMR ($C_6D_6$, 25 °C): $\delta$ = 19.9 (t, $^2J_{P,C}$ = 3.2 Hz, $CH_3$), 20.1 (t, $^2J_{P,C}$ = 3.2 Hz, $CH_3$), 26.0 (t, $^1J_{P,C}$ = 10.6 Hz, CH *i*Pr), 34.7 (t, $^2J_{P,C}$ = 7.3 Hz, $CH_2$), 69.3 (br., CH, cp), 72.7 (t, $^2J_{P,C}$ = 2.9 Hz, CH cp), 86.4 (t, $^1J_{P,C}$ = 12.6 Hz, C cp). $^{31}P\{^1H\}$ NMR ($C_6D_6$, 25 °C): $\delta$ = 42.4 (s).

**[(dtbpf)Ni($\eta^2$-$C_2H_4$)] (3c):** A solution of dtbpf (0.50 g, 1.05 mmol) in DMF (3 mL) was added to a suspension of green [$(py)_2$Ni($C_2H_4$-COO)] (0.29 g, 1.00 mmol) in DMF (3 mL) at room temperature. The resulting orange brown solution was stirred for 2 h and afterwards 3 mL of DMF were distilled of under reduced pressure at room temperature. The resulting orange coloured precipitate was collected by filtration and dried in a vacuum. Suitable crystals for X-ray measurement were obtained from a saturated solution of the complex in DMF at room temp. und subsequent cooling. Yield: 0.3 g (50%). $C_{28}H_{48}P_2FeNi$ (561.18). $^1H$ NMR ([$D_7$]DMF, 25 °C): $\delta$ = 1.35 (d, $^3J_{H,P}$ = 11.5 Hz, 36 H, $CH_3$ *t*Bu), 1.80 (s, 4 H, $CH_2$), 4.40 (m, 4 H, CH cp), 4.45 (br., 4 H, CH cp). $^{13}C\{^1H\}$ NMR ([$D_8$]-THF, 25 °C): $\delta$ = 32.0 (s, $CH_3$ *t*Bu), 36.6 (t, $^2J_{C,P}$ = 7.0 Hz, $C_2H_4$), 37.3 (t, $^1J_{C,P}$ = 6.2 Hz, C *t*Bu), 69.6 (s, CH cp), 75.4 (s, CH cp), 87.0 (t, $^1J_{C,P}$ = 8.4 Hz, C cp). $^{31}P\{^1H\}$ NMR ([$D_7$]DMF, 25 °C): $\delta$ = 65.6 (s).

**[$(dppf)_2$Ni] (4):**[5,6] A suspension of **2a** in THF was heated to 40 °C and DMF was added with rapid stirring until nearly all solids have dissolved. The resulting solution was filtered through celite and stored for 2 weeks at 5 °C. During this period, some precipitate was formed and afterwards removed by decantation. The remaining solution was concentrated in vacuo until all THF was removed. The residual orange brown coloured solution in DMF was stored for several weeks at –20 °C, after which orange red crystals had occurred. These crystals were collected by filtration and dried in a vacuum. The yield was not determined. $C_{68}H_{60}P_4Fe_2Ni$ (1171.51) calcd. C 69.72, H 5.16; found C 69.82, H 5.09. $^1H$NMR ([$D_8$]THF, 25 °C): $\delta$ = 3.97 (s, 8 H, CH cp), 4.10 (s, 8 H, CH cp), 6.84 (pt, $J$ = 7.4 Hz, 16 H, *o*-CH ph), 7.01 (pt, $J$ = 7.2 Hz, 8 H, *p*-CH ph),

 © 2007 Wiley-VCH Verlag GmbH & Co. KGaA, Weinheim 

7.45–7.55 (m, 16 H, *m*-CH ph). $^{13}C\{^1H\}$ NMR ([D$_8$]THF, 25 °C): $\delta$ = 70.5 (s, 8 × CH cp), 75.2 (s, 8 × CH cp), 87.5 (m, 4 × C cp), 127.4 (s, 16 × *m*-CH ph), 128.1 (s, 8 × *p*-CH ph), 135.1 (pt, $J_{C,P}$ = 7.5 Hz, 16 × *o*-CH ph), 142.0 (m, 8 × C ph).

**X-ray Crystallographic Studies:** The intensity data for the compounds were collected on a Nonius KappaCCD diffractometer by using graphite-monochromated Mo-$K_\alpha$ radiation. Data were corrected for Lorentz and polarization effects, but not for absorption effects.[30,31] The structures were solved by direct methods (SHELXS[32]) and refined by full-matrix least-squares techniques against $F_o^2$ (SHELXL-97[33]). All hydrogen atoms were included at calculated positions with fixed thermal parameters. All non-hydrogen atoms were refined anisotropically.[4] XP (SIEMENS Analytical X-ray Instruments, Inc.) was used for structure representations.

**Crystal Data for 1a·1.5DMF:**[34] $C_{37}H_{32}FeNNiO_2P_2 \cdot 1.5C_3H_7ON$, *Mr* = 795.78 g mol$^{-1}$, orange prism, size 0.12 × 0.12 × 0.10 mm$^3$, monoclinic, space group $P2_1/n$, *a* = 14.5426(3), *b* = 13.9250(6), *c* = 19.0968(7) Å, $\beta$ = 108.237(2)°, *V* = 3673.0(2) Å$^3$, *T* = –90 °C, *Z* = 4, $\rho_{calcd.}$ = 1.439 g cm$^{-3}$, $\mu$ (Mo-$K_\alpha$) = 10.38 cm$^{-1}$, *F*(000) = 1660, 12426 reflections in *h*(–18/18), *k*(–18/16), *l*(–24/24), measured in the range 1.55° ≤ $\Theta$ ≤ 27.60°, completeness $\Theta_{max}$ = 93%, 7921 independent reflections, $R_{int}$ = 0.0553, 4887 reflections with $F_o > 4\sigma(F_o)$, 441 parameters, 0 restraints, $R_{1obs}$ = 0.0743, $wR_{2obs}$ = 0.2116, $R_{1all}$ = 0.1110, $wR_{2all}$ = 0.2206, GOOF = 1.058, largest difference peak and hole: 0.815/–0.499 e·Å$^{-3}$.

**Crystal Data for 1a·2THF:**[34] $C_{37}H_{32}FeNiO_2P_2 \cdot 2C_4H_8O$, *Mr* = 829.33 g mol$^{-1}$, orange prism, size 0.18 × 0.12 × 0.08 mm$^3$, triclinic, space group $P\bar{1}$, *a* = 11.1233(7), *b* = 12.7648(6), *c* = 14.696(1) Å, *a* = 87.660(4), $\beta$ = 79.684(3), $\gamma$ = 77.065(3)°, *V* = 2000.8(2) Å$^3$, *T* = –90 °C, *Z* = 2, $\rho_{calcd.}$ = 1.377 g cm$^{-3}$, $\mu$ (Mo-$K_\alpha$) = 9.55 cm$^{-1}$, *F*(000) = 868, 13225 reflections in *h*(–14/14), *k*(–16/16), *l*(–19/18), measured in the range 1.64° ≤ $\Theta$ ≤ 27.49°, completeness $\Theta_{max}$ = 95.6%, 8782 independent reflections, $R_{int}$ = 0.0588, 5591 reflections with $F_o > 4\sigma(F_o)$, 484 parameters, 0 restraints, $R_{1obs}$ = 0.0447, $wR_{2obs}$ = 0.0980, $R_{1all}$ = 0.0746, $wR_{2all}$ = 0.1036, GOOF = 0.901, largest difference peak and hole: 0.719/–0.765 e·Å$^{-3}$.

**Crystal Data for 1b:**[34] $C_{25}H_{40}FeNiO_2P_2$, *Mr* = 549.07 g mol$^{-1}$, orange prism, size 0.12 × 0.12 × 0.10 mm$^3$, triclinic, space group $P\bar{1}$, *a* = 10.2600(4), *b* = 10.8590(4), *c* = 12.7729(3) Å, *a* = 84.885(2), $\beta$ = 73.799(2), $\gamma$ = 68.3570(10)°, *V* = 1270.07(7) Å$^3$, *T* = –90 °C, *Z* = 2, $\rho_{calcd.}$ = 1.436 g cm$^{-3}$, $\mu$ (Mo-$K_\alpha$) = 14.58 cm$^{-1}$, *F*(000) = 580, 8596 reflections in *h*(–12/13), *k*(–14/12), *l*(–16/14), measured in the range 2.40° ≤ $\Theta$ ≤ 27.48°, completeness $\Theta_{max}$ = 96.6%, 5633 independent reflections, $R_{int}$ = 0.0549, 4352 reflections with $F_o > 4\sigma(F_o)$, 304 parameters, 0 restraints, $R_{1obs}$ = 0.0341, $wR_{2obs}$ = 0.0920, $R_{1all}$ = 0.0458, $wR_{2all}$ = 0.0949, GOOF = 1.002, largest difference peak and hole: 0.553/–0.532 e·Å$^{-3}$.

**Crystal Data for 1c·THF:**[34] $C_{25}H_{40}FeO_2P_2Pd \cdot C_4H_8O$, *Mr* = 668.86 g mol$^{-1}$, yellow prism, size 0.05 × 0.05 × 0.05 mm$^3$, monoclinic, space group $P2_1/n$, *a* = 10.242(2), *b* = 15.994(3), *c* = 18.487(4) Å, $\beta$ = 96.18(3)°, *V* = 3010.8(10) Å$^3$, *T* = –90 °C, *Z* = 4, $\rho_{calcd.}$ = 1.476 g cm$^{-3}$, $\mu$ (Mo-$K_\alpha$) = 12.13 cm$^{-1}$, *F*(000) = 1392, 20354 reflections in *h*(–10/13), *k*(–20/20), *l*(–23/23), measured in the range 1.69° ≤ $\Theta$ ≤ 27.47°, completeness $\Theta_{max}$ = 99.6%, 6871 independent reflections, $R_{int}$ = 0.0232, 6267 reflections with $F_o > 4\sigma(F_o)$, 349 parameters, 0 restraints, $R_{1obs}$ = 0.0291, $wR_{2obs}$ = 0.0789, $R_{1all}$ = 0.0327, $wR_{2all}$ = 0.0820, GOOF = 0.983, largest difference peak and hole: 1.891/–0.850 e·Å$^{-3}$.

**Crystal Data for 1c:**[34] $C_{25}H_{40}FeO_2P_2Pd$, *Mr* = 596.76 g mol$^{-1}$, yellow prism, size 0.06 × 0.04 × 0.04 mm$^3$, monoclinic, space group *C*2/*c*, *a* = 19.7868(7), *b* = 10.0423(4), *c* = 27.6093(9) Å, $\beta$ = 106.060(2)°, *V* = 5272.0(3) Å$^3$, *T* = –90 °C, *Z* = 8, $\rho_{calcd.}$ = 1.504 g cm$^{-3}$, $\mu$ (Mo-$K_\alpha$) = 13.73 cm$^{-1}$, *F*(000) = 2464, 15456 reflections in *h*(–24/25), *k*(–13/9), *l*(–35/34), measured in the range 2.14° ≤ $\Theta$ ≤ 27.50°, completeness $\Theta_{max}$ = 97.4%, 5901 independent reflections, $R_{int}$ = 0.1058, 4654 reflections with $F_o > 4\sigma(F_o)$, 300 parameters, 0 restraints, $R_{1obs}$ = 0.0537, $wR_{2obs}$ = 0.1336, $R_{1all}$ = 0.0736, $wR_{2all}$ = 0.1471, GOOF = 1.028, largest difference peak and hole: 0.847/–0.871 e·Å$^{-3}$.

**Crystal Data for 2b:**[34] $C_{25}H_{40}FeNiO_2P_2$, *Mr* = 549.07 g mol$^{-1}$, yellow-green prism, size 0.10 × 0.10 × 0.02 mm$^3$, monoclinic, space group $P2_1/c$, *a* = 17.3484(9), *b* = 8.7957(6), *c* = 16.7547(8) Å, $\beta$ = 96.382(4)°, *V* = 2540.8(2) Å$^3$, *T* = –90 °C, *Z* = 4, $\rho_{calcd.}$ = 1.435 g cm$^{-3}$, $\mu$ (Mo-$K_\alpha$) = 14.57 cm$^{-1}$, *F*(000) = 1160, 9791 reflections in *h*(–22/22), *k*(–10/11), *l*(–21/21), measured in the range 2.36° ≤ $\Theta$ ≤ 27.45°, completeness $\Theta_{max}$ = 99.4%, 5774 independent reflections, $R_{int}$ = 0.0555, 3696 reflections with $F_o > 4\sigma(F_o)$, 288 parameters, 0 restraints, $R_{1obs}$ = 0.0740, $wR_{2obs}$ = 0.1567, $R_{1all}$ = 0.1260, $wR_{2all}$ = 0.1807, GOOF = 1.066, largest difference peak and hole: 1.321/–0.610 e·Å$^{-3}$.

**Crystal Data for 3b:**[34] $C_{24}H_{40}FeNiP_2$, *Mr* = 505.06 g mol$^{-1}$, orange prism, size 0.10 × 0.09 × 0.08 mm$^3$, triclinic, space group $P\bar{1}$, *a* = 8.7665(2), *b* = 9.0021(2), *c* = 17.1663(3) Å, *a* = 87.0310(10), $\beta$ = 82.8390(10), $\gamma$ = 65.4730(10)°, *V* = 1222.86(4) Å$^3$, *T* = –90 °C, *Z* = 2, $\rho_{calcd.}$ = 1.372 g cm$^{-3}$, $\mu$ (Mo-$K_\alpha$) = 15.02 cm$^{-1}$, *F*(000) = 536, 9447 reflections in *h*(–10/11), *k*(–11/11), *l*(–22/22), measured in the range 2.74° ≤ $\Theta$ ≤ 27.43°, completeness $\Theta_{max}$ = 99.5%, 5557 independent reflections, $R_{int}$ = 0.0345, 4870 reflections with $F_o > 4\sigma(F_o)$, 277 parameters, 0 restraints, $R_{1obs}$ = 0.0343, $wR_{2obs}$ = 0.0894, $R_{1all}$ = 0.0416, $wR_{2all}$ = 0.0950, GOOF = 1.016, largest difference peak and hole: 0.374/–0.557 e·Å$^{-3}$.

**Crystal Data for 3c:**[34] $C_{28}H_{48}FeNiP_2$, *Mr* = 561.16 g mol$^{-1}$, orange prism, size 0.10 × 0.08 × 0.07 mm$^3$, orthorhombic, space group *Pbca*, *a* = 16.0359(2), *b* = 11.61920(10), *c* = 29.9821(4) Å, *V* = 5586.39(11) Å$^3$, *T* = –90 °C, *Z* = 8, $\rho_{calcd.}$ = 1.334 g cm$^{-3}$, $\mu$ (Mo-$K_\alpha$) = 13.22 cm$^{-1}$, *F*(000) = 2400, 11956 reflections in *h*(–20/20), *k*(–15/15), *l*(–38/38), measured in the range 2.88° ≤ $\Theta$ ≤ 27.48°, completeness $\Theta_{max}$ = 99.4%, 6363 independent reflections, $R_{int}$ = 0.0422, 4695 reflections with $F_o > 4\sigma(F_o)$, 317 parameters, 0 restraints, $R_{1obs}$ = 0.0368, $wR_{2obs}$ = 0.0784, $R_{1all}$ = 0.0630, $wR_{2all}$ = 0.0863, GOOF = 0.985, largest difference peak and hole: 0.376/–0.447 e·Å$^{-3}$.

**Crystal Data for 4:**[34] $C_{68}H_{56}Fe_2NiP_4$, *Mr* = 1167.42 g mol$^{-1}$, orange prism, size 0.03 × 0.03 × 0.02 mm$^3$, triclinic, space group $P\bar{1}$, *a* = 12.9787(5), *b* = 13.8150(6), *c* = 15.2711(7) Å, *a* = 86.939(2), $\beta$ = 89.940(2), $\gamma$ = 87.033(2)°, *V* = 2730.5(2) Å$^3$, *T* = –90 °C, *Z* = 2, $\rho_{calcd.}$ = 1.420 g cm$^{-3}$, $\mu$ (Mo-$K_\alpha$) = 10.26 cm$^{-1}$, *F*(000) = 1208, 18086 reflections in *h*(–16/15), *k*(–16/17), *l*(–19/19), measured in the range 2.10° ≤ $\Theta$ ≤ 27.50°, completeness $\Theta_{max}$ = 95.8%, 11986 independent reflections, $R_{int}$ = 0.0487, 7647 reflections with $F_o > 4\sigma(F_o)$, 676 parameters, 0 restraints, $R_{1obs}$ = 0.0629, $wR_{2obs}$ = 0.1086, $R_{1all}$ = 0.1191, $wR_{2all}$ = 0.1295, GOOF = 1.045, largest difference peak and hole: 0.444/–0.472 e·Å$^{-3}$.

## Acknowledgments

This research was supported by a grant from the Deutsche Bundesstiftung Umwelt and by the Deutsche Forschungsgemeinschaft (DFG) (SFB 436).

[1] R. Fischer, J. Langer, A. Malassa, D. Walther, H. Görls, G. Vaughan, *Chem. Commun.* **2006**, 2510–2512.

 © 2007 Wiley-VCH Verlag GmbH & Co. KGaA, Weinheim 

[2] G. Vasapollo, L. Toniolo, G. Cavinato, F. Bigoli, M. Lanfranchi, M. A. Pellinghelli, *J. Organomet. Chem.* **1994**, *481*, 173–178.
[3] S. Ekici, M. Nieger, R. Glaum, E. Niecke, *Angew. Chem.* **2003**, *115*, 451–454; *Angew. Chem. Int. Ed.* **2003**, *42*, 435–438.
[4] J. Pawlas, Y. Nakao, M. Kawatsura, J. F. Hartwig, *J. Am. Chem. Soc.* **2002**, *124*, 3669–3679.
[5] K. Takagi, *Chem. Lett.* **1987**, *11*, 2221–2224.
[6] M.-T. Lee, B. M. Foxman, M. Rosenblum, *Organometallics* **1985**, *4*, 539–547.
[7] Z.-Y. Tang, S. Spinella, Q.-S. Hu, *Tetrahedron Lett.* **2006**, *47*, 2427–2430.
[8] C. A. Busacca, M. C. Eriksson, R. Fiaschisi, *Tetrahedron Lett.* **1999**, *40*, 3101–3104.
[9] K. Park, K. Yuan, W. Scott, *J. Org. Chem.* **1993**, *58*, 4866–4870.
[10] K. Yuan, W. J. Scott, *Tetrahedron Lett.* **1991**, *32*, 189–192.
[11] K. Takagi, *Chem. Lett.* **1987**, 2221–2224.
[12] T. Hayashi, K. Kabeta, M. Kumada, *Tetrahedron Lett.* **1984**, *25*, 1499–1500.
[13] T. Hayashi, K. Konishi, K. Yokota, M. Kumada, *J. Chem. Soc., Chem. Commun.* **1981**, 313–314.
[14] T. Yamamoto, K. Igarasi, S. Komiya, A. Yamamoto, *J. Am. Chem. Soc.* **1980**, *102*, 7448–7456.
[15] E. Weiss, K. Stark, J. E. Lancaster, H. D. Murdoch, *Helv. Chim. Acta* **1963**, *46*, 288–297.
[16] P. Y. Zavalii, V. S. Fundamenskii, M. G. Myskiv, E. I. Gladyshevskii, *Kristallografiy* **1982**, *27*, 911–915.
[17] R. Alvarez, E. Carmona, A. Galindo, E. Gutlérez, J. M. Marin, A. Monge, M. L. Poveda, C. Ruiz, J. M. Savariault, *Organometallics* **1989**, *8*, 2430–2439.
[18] S. D. Ittel, *Inorg. Chem.* **1977**, *16*, 2589–2596.
[19] A. Jutand, K. K. Hii, M. Thornton-Pett, J. M. Brown, *Organometallics* **1999**, *18*, 5367–5374.
[20] J. Langer, H. Görls, R. Fischer, D. Walther, *Organometallics* **2005**, *24*, 272–279.
[21] J. Langer, H. Görls, G. Gillies, D. Walther, *Z. Anorg. Allg. Chem.* **2005**, *631*, 2719–2726.
[22] J. Langer, R. Fischer, H. Görls, D. Walther, *J. Organomet. Chem.* **2004**, *689*, 2952–2962.
[23] For a review see: G. Bandoli, A. Dolmella, *Coord. Chem. Rev.* **2000**, *209*, 161–196.
[24] M. Fild, O. Stelzner, R. Schmutzler, G. O. Doak, *Inorg. Synth.* **1973**, *14*, 4–9.
[25] J. J. Bishop, A. Davison, M. L. Katcher, W. D. Lichtenberg, R. E. Merrill, J. C. Smart, *J. Organomet. Chem.* **1971**, *27*, 241–249.
[26] W. R. Cullen, F. W. Eisenstein, T. Jones, T. J. Kim, *Organometallics* **1983**, *2*, 714–719.
[27] R. J. de Lang, J. van Soolingen, H. D. Verkruijsse, L. Brandsma, *Synth. Commun.* **1995**, *25*, 2989–2991.
[28] G. Wilke, B. Bogdanovic, M. Körner, *Justus Liebigs Ann. Chem.* **1966**, *699*, 1–23.
[29] M. Green, J. A. K. Howard, J. L. Spencer, F. G. A. Stone, *J. Chem. Soc., Dalton Trans.* **1977**, 271–277.
[30] COLLECT, Data Collection Software, Nonius B. V., The Netherlands, **1998**.
[31] Z. Otwinowski, W. Minor, *Processing of X-ray Diffraction Data Collected*, in: *Oscillation Mode*, in *Methods in Enzymology*, vol. 276, *Macromolecular Crystallography, Part A* (Eds.: C. W. Carter, R. M. Sweet), p. 307–326, Academic Press, San Diego, **1997**.
[32] G. M. Sheldrick, *Acta Crystallogr., Sect. A* **1990**, *46*, 467–473.
[33] G. M. Sheldrick, SHELXL-97 (Release 97-2), University of Göttingen, Germany, **1997**.
[34] CCDC-623548 (for **1a**·1.5DMF), -623549 (for **1a**·2THF), -623550 (for **1b**), -623551 (for **1c**·THF), -623552 (for **1c**), -623553 (for **2b**), -623554 (for **3b**), -623555 (for **3c**), and -623556 (for **4**) contain the supplementary crystallographic data for this paper. These data can be obtained free of charge from The Cambridge Crystallographic Data Centre via www.ccdc.cam.ac.uk/data_request/cif.

Received: November 9, 2006
Published Online: February 21, 2007

 © 2007 Wiley-VCH Verlag GmbH & Co. KGaA, Weinheim 

DOI: 10.1002/ejic.200601176

# Assembly and Formation of Biomorphic Tin Dioxide by a Biomimetic Sol–Gel Approach Involving Glycoprotein

Qun Dong,[a] Huilan Su,*[a] Wei Cao,[a] Di Zhang,[a] Qixin Guo,[b] and Fangying Zhang[c]

**Keywords:** Biomimetic synthesis / Colloids / Hierarchy / Nanotubes / Sol–gel processes

Three diverse layers of eggshell membrane (ESM) were introduced in a biogenic sol–gel technique for the synthesis of hierarchical $SnO_2$ nanomaterials with corresponding configurations. Typically, the biomorphic replication of the interwoven inner eggshell membrane was systematically investigated by controlling synthesis conditions such as pH value, dipping time, and calcination temperature. The as-prepared $SnO_2$ tubes consisting of interconnected 5-nm nanocrystallite units were successfully interwoven into ESM-morphic films. Herein, the biomaterial ESM served both as the physical substrate and the functional macromolecule template to realize the precision replication, by the interactions between ESM macromolecules (containing carboxyl, hydroxy, amino groups, etc.) and Sn colloid ingredients. Moreover, some biomacromolecules also acted as the surfactant to yield small-scaled and well-distributed $SnO_2$ nanocrystallites based on the strong bondage of short-chained amino acids within ESM glycoprotein with $SnO_2$ nuclei. This technique can be attributed to a biomimetic sol–gel process and is widely applicable to the synthesis of other functional material systems.
(© Wiley-VCH Verlag GmbH & Co. KGaA, 69451 Weinheim, Germany, 2007)

## Introduction

Lately, nanoscale functional materials have attracted much attention because of their potentially excellent and fascinating properties. In the progressive stage, the assembly of the nanoscale units into a hierarchical architecture would be required to obtain higher functionality and performance. Nevertheless, there are few feasible reports on the construction of hierarchical nanomaterials, especially practical and functional metal or metal oxide nanocomposites. Notably, natural organisms or biological structures that have evolved as a result of highly complex and elegant mechanisms[1] are a great inspiration for materials scientists and chemists in the imitation of the hierarchical structures. The work in this field is based on the premise that amphiphilic and bioorganic macromolecules could be utilized for tailoring elaborate structures through the self-assembly of nanoscale units[2] to engender new functional properties.[3] Quite a few biological species have been utilized to construct hierarchical inorganic materials: the list includes DNA,[4] viruses,[5] diatoms and skeletal plates,[6] butterfly wings,[7] shell membrane,[8] silk fiber,[9] hair,[10] wood,[11] and other plants (leaves, paper, pollen grains),[7,12] etc.

Recently, mimicking vital functions in aqueous systems has been noteworthy as a promising nanofabrication technique for functional materials.[3a,13] These biomimetic techniques enable the construction of hierarchical architectures including macro- and nanostructures by growing inorganic crystals with coexisting biospecies under ambient conditions. Quoting from Cook et al.,[7] "the synthetic replication of evidently useful biological structures by a simple casting process is expected to introduce some of the superb properties of biological structures into man-made materials." The most feasible method of attaining this goal at a high level seems to be the aqueous sol–gel technique.[14] The colloid components could interact with some biomacromolecules and undergo surface-preferred gelation to form the coats on the biomaterials, even to veraciously replicate the biotemplate frameworks down to the nanoscale. Moreover, the sol–gel process offers several advantages over other methods, including simplicity of procedure, lower processing temperature, and better homogeneity. Commonly, metallic alkoxides are used as starting materials to prepare fine-scaled metallic oxides by the sol–gel processes. However, metallic alkoxides are both expensive and extremely sensitive to moisture, heat, and light, implying that the process is relatively difficult to control and not economical. Therefore, various metal salts[15] are preferred as the precursors. Once biomaterials are introduced to the reformative sol–gel techniques, a series of intricate hydrolysis and condensation reactions happen in the sol–gel process. It seems to be a process that would enable the easy preparation of hierarchical

[a] State Key Lab of Metal Matrix Composites, Shanghai Jiaotong University,
Shanghai 200030, P. R. China
[b] Department of Electrical and Electronic Engineering, Saga University,
Saga 840-8502, Japan
[c] National Key Lab of Surface Physics, Fudan University,
Shanghai 200433, P. R. China
Fax: +86-21-62822012
E-mail: hlsu@sjtu.edu.cn
Supporting information for this article is available on the WWW under http://www.eurjic.org or from the author.

 © 2007 Wiley-VCH Verlag GmbH & Co. KGaA, Weinheim 

metal oxides, such as $TiO_2$, $SiO_2$, ZnO, $ZrO_2$, and so on. Therefore, biomimetic synthesis associated with the sol–gel technique would be an ideal approach for the design and fabrication of functional materials with predetermined physical and chemical properties.

Having a large bandgap of 3.6 eV at 300 K, a high achievable carrier concentration of up to $6 \times 10^{20}$ $cm^{-3}$, and an expected exciton Bohr radius of about 2.4 nm,[16] nanocrystalline tin oxide is of great technological and scientific interest as a key functional semiconductor that is used extensively for photovoltaic devices,[17] transparent conductive electrodes,[18] gas sensors,[19] antistatic coatings,[20] dye-sensitized solar cells,[21] etc. It has also been demonstrated that, when such ultrafine nanocrystallites are arrayed into a macroscale hierarchical structure (such as tubes, hollow spheres, etc), these materials sometimes exhibit novel properties.[22] However, fresh tin gel has a hydrous skeleton and is either amorphous or pseudocrystalline. To achieve well-crystallized $SnO_2$, further calcination treatment at a higher temperature would be advisable to remove organic substrates and improve the stability and the purity of the target materials. As the growth of particles is controlled by the motion of the boundaries between the particles, calcination usually results in the increase and wider distribution of particle size.[23] Therefore, the growth inhibition of $SnO_2$ nanocrystallites was recently implemented with the addition of heterogeneous particles or in-situ secondary-phase particle generation. However, this solution may result in interface poisoning or poor purity. It has been discovered that, in biological systems such as diatoms and sponges, the formation of solid silica nanostructures with precisely controlled morphologies is the function of proteins and polysaccharides.[24] These biomacromolecules could direct and bind the nucleation and the growth of inorganic particles. Attracted by this bioinspiration, we introduce a convenient biomaterial, the eggshell membrane (ESM), in combination with a tin salt precursor, with the intent of synthesizing hierarchical $SnO_2$ semiconductors by suitable vehicles of special protein structures and functional residues of ESM biomacromolecules in a sol–gel process. In contrast to the metallic alkoxide precursors used by Yang et al.,[8] we attempted to employ a trilayer bio-scaffold in tin nitrate solution as a template for the structure of $SnO_2$. The natural trilayer ESM composed of the outer shell membrane (OSM), the inner shell membrane (ISM), and the limiting membrane (LM) with dissimilar hierarchical structures and morphologies, has been faithfully reproduced from the macroscopic to the nanometer scale by $SnO_2$ nanosemiconductors. Additionally, the reaction mechanism involving a biomimetic sol–gel process was explored. This method provides a simple but efficient and universal route to the biomimetic synthesis of advanced functional materials.

## Results and Discussion

### Overview of ESM Hierarchical Structures

The avian eggshell is composed of multilayered membranes and a calcified extracellular matrix, which are sequentially assembled during the motion of the egg along the oviduct.[25] The examination of cross-fractured eggshell by FESEM, shown in Figure 1a, reveals that the calcified shell is composed of an inner mammillary layer (ML) and an outer palisade layer (PL) resting upon the shell membranes. In fact, ESM consists of the organic OSM, ISM, and LM, which are nonmineralized, collagen-based matrices interposed between the egg white and the mineralized shell. From the images of ESM shown in Figure 1b, the three layers are readily distinguished. Sparsely deposited on the outer layer of the shell membranes are the mammillary knobs for penetrating into the tips of the mammillary cones. In addition, the interwoven and coalescing nature of the shell membrane fibers with an average width ranging from 500 nm to 2 μm is evident both in the OSM and the ISM. Furthermore, some of the broader fibers have a longitudinally striated appearance, where two or more narrower fibers join each other for part of their length. The amorphous LM shows an undulant appearance, which is due to a layer of spherical protein granules formed between the ISM and the LM. In this work, the distinct membranes were utilized as biotemplates for the synthesis of hierarchical $SnO_2$.

### Characterization of Biomorphic Tin Dioxide

The calcination process was traced by conducting TGA and DTA surveys to follow the formation of hierarchical

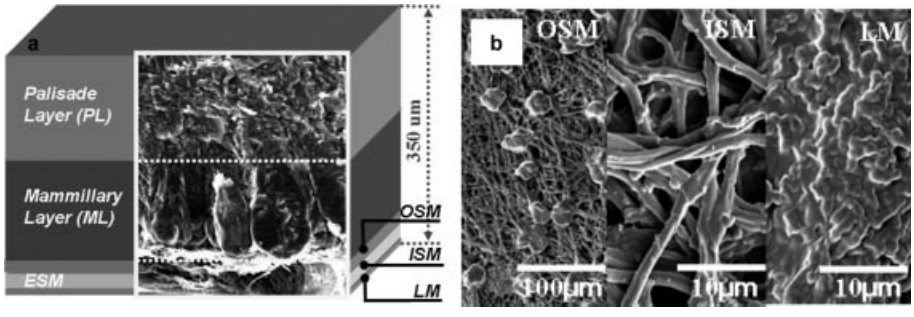


Figure 1. (a) FESEM images of eggshell and eggshell membrane and the corresponding schematic illustration of eggshell structures. (b) FESEM images of OSM, ISM, and LM.

 © 2007 Wiley-VCH Verlag GmbH & Co. KGaA, Weinheim 

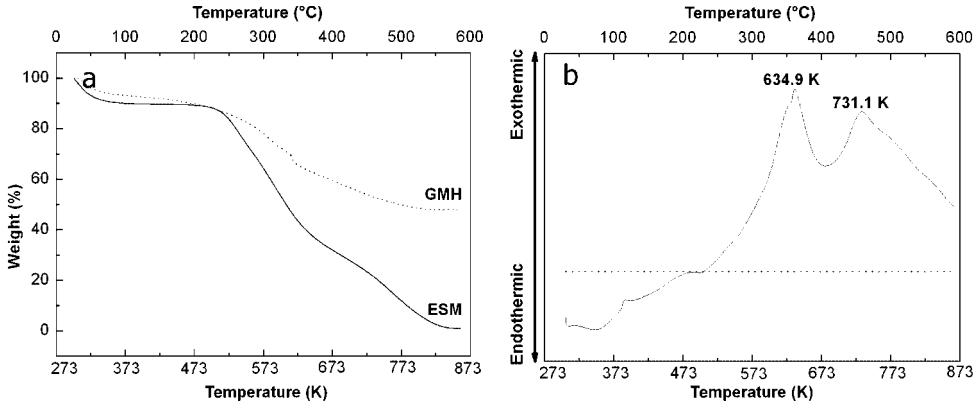


Figure 2. (a) TGA curves of the natural ESM and the intergradation of GMH; (b) DTA curve of GMH.

$SnO_2$. The corresponding curves for the natural ESM and gel–membrane hybrids (GMH) are shown in Figure 2. It is evident that the ESM starts pyrolyzing at 473 K and is absolutely decomposed by 823 K. Although GMH are also decomposed around 473 K, they can preserve up to 47.2% (by mass) inorganic matter at 823 K, at which temperature the organic ESM is completely removed. As seen from the differential curve, when GMH are heated from room temperature to 473 K, the weight loss of 9.8 wt-% is due to the removal of adsorbed water, and above 473 K they experience a two-step weight loss. Congruously, the DTA curve shows two peaks at 635 K and 731 K, which should represent the decomposition of Sn–ligand hybrids and organic ESM components, respectively.

To clarify the crystalline structure, the XRD patterns of the ESM and GMH as well as the corresponding sinters at 673 K and 823 K are shown in Figure 3. It can be seen that the natural ESM and GMH are totally amorphous. After calcination at 673 K, the amorphous hybrids are found to be crystallized. However, according to the TGA and DTA results, the ESM is not thoroughly decomposed at this temperature: although the intensities of some peaks are enhanced, there are new diffraction peaks accompanying the complete pyrolysis of ESM, indicating the well-established crystallization process at 823 K. All these diffraction peaks can be indexed to tetragonal $SnO_2$ with a rutile structure (JCPDS 41–1445), which indicates that the specimens consist of pure single tetragonal $SnO_2$. The fairly broadened diffraction peaks are assigned to $SnO_2$ nanocrystallites with very small dimensions. The average crystallite sizes of about 2.8 nm at 673 K and 5.2 nm at 823 K, are estimated according to the line-width analysis of the diffraction peaks based on the Scherrer formula. The chemical states of tin and oxygen during the sol–gel process were investigated by XPS analysis (Supporting Information, Figure S1). The corrected XPS spectra of the O1s emissions are different, where the peak with binding energy around 532.3 eV corresponds to the hydroxyl bonds of GMH, while the weaker peak around 531.1 eV corresponds to the Sn–O–Sn bonds of the sinters.[26] Moreover, GMH appear as a spin-orbit doublet at 487.9 ($3d_{5/2}$) and 496.4 eV ($3d_{3/2}$) in the Sn3d emission spectra with an area ratio of 1.5:1. Thus, the chemical state of the element tin in as-prepared GMH corresponds to $Sn^{IV}$, but not to $Sn^{II}$ or $Sn^{III}$.

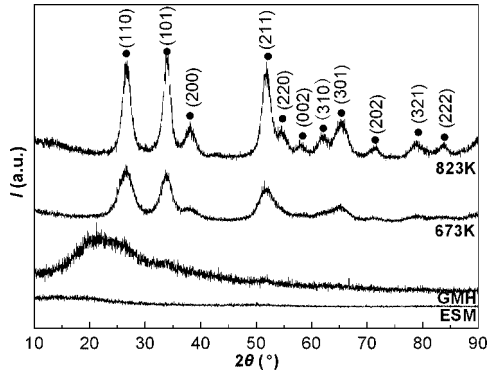


Figure 3. XRD patterns of the sinters calcined at 673 K and 823 K, compared with those of ESM and GMH.

It has been demonstrated that the interfacial sol–gel process is a facile chemical method to deposit ultrathin metal oxide layers with molecular precision.[27] This process is usually based on the chemical adsorption of metal alkoxides or metallic salts from the colloid medium onto the substrate surface to form a covalently bound monolayer, followed by hydrolysis to give a new hydroxylated gel layer for the successive film deposition. Organic molecules of the substrate can be readily incorporated as second components if they are reactive toward the as-deposited amorphous gel layer, thus the configuration and structure of the substrate can be accurately traced by the metal oxide network.[28] Here, the three diverse layers of organic ESM have the same ingredients containing amine, amide, and carboxyl surface functional groups, which may lead to complicated reactions to achieve the duplication of ESM configuration during the interfacial sol–gel process.

Representative FESEM images of as-prepared $SnO_2$ with various morphologies calcined at 823 K are shown in Figure 4a, 4b, and 4c. A comparison with the original OSM, ISM, and LM (insets) suggests that the refined reprography of the natural ESM hierarchy is achieved, although there

 © 2007 Wiley-VCH Verlag GmbH & Co. KGaA, Weinheim 

exists modest shrinkage. Analysis with energy-dispersive X-ray spectroscopy reveals that the atomic ratio Sn/O is close to 1:2, further confirming the stoichiometry of the replicas as $SnO_2$, in agreement with XRD results. As shown in Figure 4a, the obtained $SnO_2$ is composed of interwoven fibers and sparse crunodes depositing on the ceramic fibers with an average interval of about 18 μm. The interval is smaller than the original spacing of 30 μm as a result of heat shrinkage. Moreover, the refined meshworks of the natural OSM are also duplicated in addition to the larger intersectional crunodes. Figure 4b shows the interwoven and coalescing $SnO_2$ fibers ranging from 200 to 500 nm in diameter in comparison with the original ISM fibers. When using LM as the template, a lumpy layer of $SnO_2$ composed of consecutive ravines is obtained (Figure 4c). These special silkworm-like structures may come into being and array according to the spherical protein granules under the ultrathin LM. Therefore, it can be concluded that hierarchical $SnO_2$ accurately replicates the hierarchy of the biotemplate ESM from the OSM to the innermost LM. However, a shrinkage rate of nearly 55% is sometimes observed during the calcination treatment. By repeating the immersing manipulation, heat constringency in size could be lowed to below 30%, and up to 47.2% of the mass of the sinters was preserved without changes in configuration and structure.

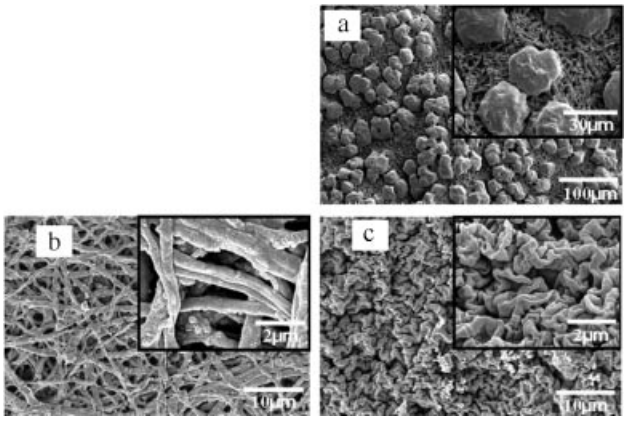


Figure 4. FESEM images of (a) OSM-based, (b) ISM-based, and (c) LM-based $SnO_2$. Insets show the corresponding detailed morphologies of the original OSM, ISM, and LM.

Figure 5a and 5b show the relative location of the hierarchical $SnO_2$ replicated from the three diverse membranes. It is clearly seen in Figure 5a that the LM-based one has been sheltered by the upper layers composed of the ISM-based and OSM-based $SnO_2$ layers. However, the replica of the LM layer can be identified when the other side of this sheet is observed (Figure 5b). The configuration of the intermeshed ISM consisting of interwoven fibers is intact, whereas the LM-based layer (denoted by an arrow) is curled up thoroughly. Moreover, the thickness of the obtained $SnO_2$ film can be tuned by removing the multilayers of the ISM. Thus, an $SnO_2$ film with a continuous thickness up to 20 μm can be achieved by varying the original thickness of remnant ISM layers (see Supporting Information, Figure S2). Figure 5c and 5d display higher magnifications of the cross section and the vertical section of these $SnO_2$ interwoven fibrous films, respectively. The tubular structures have an inner-diameter range from 100 nm to 300 nm and an average wall thickness of less than 90 nm. These $SnO_2$ tubes are rather uniform, and the hollow cores are glabrous and continuous throughout their length. Notably, these interwoven tubular structures are actually interconnected at junctions. A special kind of tube wrapping several smaller collateral cannulations is also observed, which likewise reproduces the original structures of the membrane fibers (see Supporting Information, Figure S3). To further investigate the replication process, we selected the organic ISM as a typical template to achieve the synthesis of hierarchical biomorphic $SnO_2$ under different experimental conditions.

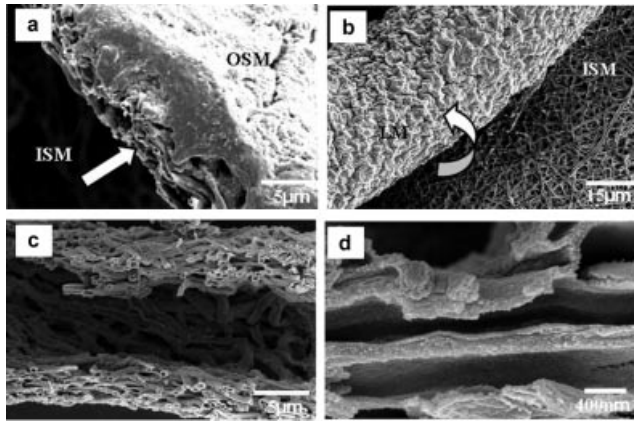


Figure 5. (a), (b) Typical FESEM images of as-prepared ISM-morphic $SnO_2$ revealing relative locations of the three distinct layers of the original ESM. (c), (d) FESEM images showing the cross-section and the vertical section of the ISM-based $SnO_2$, respectively.

### Controllable Synthesis of ISM-Morphic $SnO_2$ Tubes

Figure 6 shows the micrographs of $SnO_2$ tubes synthesized at different calcination temperatures (823 to 1073 K). All the replicas have similar microscopic features and preserve the interwoven tubular structures of the natural ISM, but their building blocks, $SnO_2$ nanocrystallites, may grow with the increase in calcination temperature. The surface of $SnO_2$ tubes synthesized below 973 K looks more glazed in virtue of the smaller particle units, which was further proved by TEM results. Above 1073 K, the tubular structure is apparently composed of a network of interconnected $SnO_2$ particles, and it may collapse down into zonary form at 1273 K. On the contrary, if the calcination temperature is lowered to 673 K, characteristic tubular structures appear partially, and some look puffy, which may be caused by the organic remnants (see Supporting Information, Figure S4). It is reasonable that some residues of organic ESM remain at 673 K even though $SnO_2$ nanocrystallites have formed, which is in agreement with the TGA and XRD results.

 © 2007 Wiley-VCH Verlag GmbH & Co. KGaA, Weinheim 

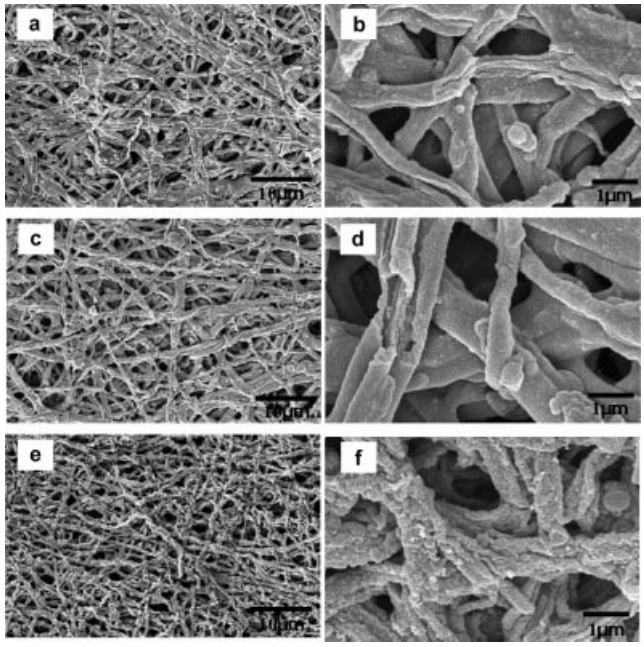


Figure 6. FESEM images of as-prepared ISM-morphic $SnO_2$ at different temperatures: (a) 823 K, (c) 973 K, and (e) 1073 K. Images (b), (d), and (f) show relevant higher magnifications of (a), (c), and (e), respectively.

Figure 7 gives the XRD patterns of the samples calcined at various temperatures between 823 and 1273 K for 1.5 h. All the diffraction peaks are assigned to the tetragonal rutile structure of $SnO_2$. It is found that the XRD peaks gradually become sharper with increasing temperature, indicating that the $SnO_2$ nanocrystallites grow larger. The crystallite sizes determined from the Scherrer equation are 5.2, 9.5, 10.3, and 20 nm, which have also been supported by the TEM results.

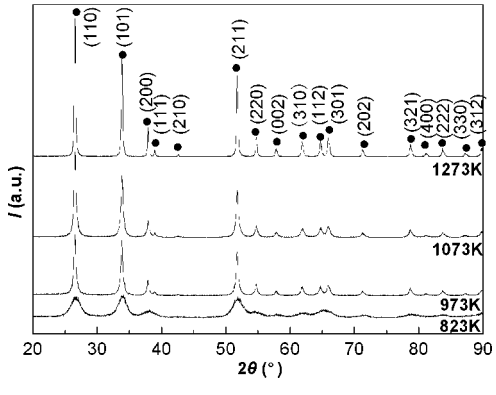


Figure 7. XRD patterns of ISM-based $SnO_2$ calcined at 823, 973, 1073, and 1273 K.

The TEM images in Figure 8a further reveal the tubular interwoven character of ISM-based $SnO_2$. The hollow tubular structure is clearly identified, and the wall thickness (50–60 nm) is found to be uniform along its entire length. This indicates that at 1073 K each tube has been transformed from a dense structure with a smooth surface into a highly porous structure consisting of interconnected nanocrystallites of ca. 10 nm in size (bottom inset in Figure 8a). In addition, the SAED patterns (top inset in Figure 8a) show that nanoscaled $SnO_2$ at 1073 K has polycrystalline tetragonal rutile structure (cassiterite) due to the uniform central and diffraction spots, and the diffraction rings are indexed to the (110), (101), (200), (211), and (301) diffractions of rutile-phase $SnO_2$. There are other supporting TEM data (see Supporting Information, Figure S5) supporting the construction of $SnO_2$ nanotubes by nanocrystallites calcined at different temperatures. Although the sinters at 673 K contain some impurities from ESM residues, the characteristic crystalline structure of tetragonal $SnO_2$ is observed in the electron diffraction image. This can be explained by the exothermic reactions occurring during the removal of the ESM: oxidation of the organic biomaterial emits heat locally, causing an increase in the temperature around the adsorbed Sn colloids, thereby accelerating the gelation and bringing on nanocrystalline $SnO_2$. These nanoparticles are ultrafine below 823 K while growing more quickly above 1073 K, and the average sizes of the nanoparticles are coincident with the crystallite sizes calculated from the XRD analyses by the Scherrer equation. As the nanoparticles grow with the increase in calcination temperatures, the diffraction patterns gradually transform from ring (nanoscale) to spot (bulk scale). This indicates that accurately defined, size-controlled $SnO_2$ nanoparticles in the range 2 to 20 nm are obtained to enable the construction of hierarchical nanomaterials at the corresponding calcination temperatures.

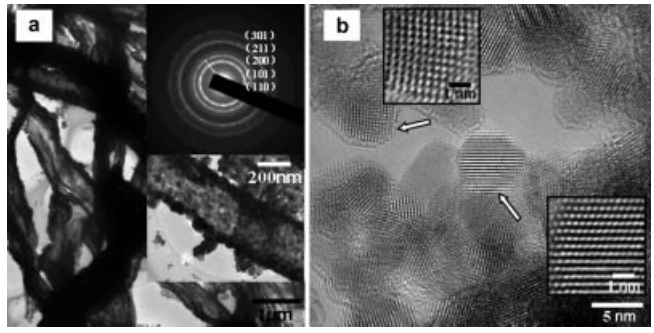


Figure 8. (a) TEM images of ISM-based $SnO_2$ synthesized at 1073 K and pH 1. Insets in (a) show an individual $SnO_2$ tube and the corresponding SAED pattern. (b) HRTEM image of ISM-based $SnO_2$ obtained at 823 K and pH 1. Insets in (b) correspond to the tetragonal $SnO_2$ (101) plane (top left) and the (110) plane (bottom right).

Figure 8b shows the typical HRTEM images of $SnO_2$ nanocrystallite units calcined at 823 K for 1.5 h. The lattice image can be clearly seen as a result of phase contrast. The distances between the adjacent lattice fringes correspond to the interplanar distances of the tetragonal $SnO_2$ (101) and (110), $d_{101}$ = 0.264 nm and $d_{110}$ = 0.335 nm, respectively. Considering that each domain having parallel lattice fringes is a single crystal of $SnO_2$, the average crystallite size is

 © 2007 Wiley-VCH Verlag GmbH & Co. KGaA, Weinheim 

observed to be 5 nm. The HRTEM results are in accord with the XRD analysis. A careful look at the images also reveals that the present $SnO_2$ is characterized by larger "nanostructured" particles consisting of nanocrystalline domains with structural defects such as twins.

### Mechanism of the Biomimetic Sol–Gel Approach

To understand the multilevel interactions between the Sn colloids and the ESM biomacromolecules during the biomimetic sol–gel process, FTIR spectroscopic analysis was carried out on the original ESM, the GMH and the sinters. Figure 9 presents the typical FTIR spectra of GMH before and after calcination at 823 K compared with those of the original ISM. The spectrum of the original ISM shows the diagnostic peaks at 1641, 1532, and 1234 $cm^{-1}$, which are assigned to the amide I, amide II, and amide III bands of the proteins from the natural ISM, respectively. After interaction with the sol precursor, the red shift to 1630 $cm^{-1}$ of the peak in the spectrum of GMH may be partly attributed to the superposition of the bending mode of water with the broad band around 3450 $cm^{-1}$ (not 3400 $cm^{-1}$). The peak at 3430 to 3450 $cm^{-1}$ is believed to be caused by adsorbed water. In general, the absorption band centered at 1630 $cm^{-1}$, as well as the one at 3450 $cm^{-1}$, is also ascribed to water adsorbed on the surface of the samples. Here, there would be no other corresponding peaks of amide I after immersion in the sol medium, if the peak at 1630 $cm^{-1}$ (near 1620 $cm^{-1}$) in the spectrum of GMH were only due to the bending mode of water. The spectrum shows an increase in intensity of the amide I band relative to that of the amide II band. It does confirm the presence of a water deformation mode. Actually, the red shift of the amide I peak is probably overlapped by the above-mentioned water bending-mode peak. This red shift indicates that the C=O bonds in the peptide chains may be weakened because of the formation of new chelate bonds between C=O bonds and Sn colloids. This can be further corroborated by the NMR spectroscopic results (Supporting Information, Figure S6). It is also detected that the peak corresponds to the Sn–OH vibration band at around 3400 $cm^{-1}$,[29] which is superimposed on the underlying C–H stretching signals of the polypeptides at 3290 $cm^{-1}$ and close to the hydroxy bands of the water. As mentioned above, the bands of the sinters observed at around 3450 and 1630 $cm^{-1}$ are assigned to the hydroxy bands of the adsorbed water. Below 700 $cm^{-1}$, the intense bands appearing both in GMH and the sinters at lower frequencies around 600 $cm^{-1}$ are typical of the Sn–O–Sn antisymmetric and symmetric vibrations.[30] In addition, the bands appearing in the range between 850 and 1350 $cm^{-1}$ are assigned to the bending mode of different types of surface hydroxy groups, which goes well with the previous research results.[31] The surface of the GMH could be terminated with the–OH groups after the ESM was dipped in the Sn sol medium. However, the calcination treatment would bring on weak IR bands between 850 and 1350 $cm^{-1}$, contributed by the decomposition of Sn–OH hydrate compounds into tin oxides. Accordingly, the interactions between Sn colloids and ESM macromolecules are mostly ascribed to the coordination of carboxyl, hydroxy, and other groups.

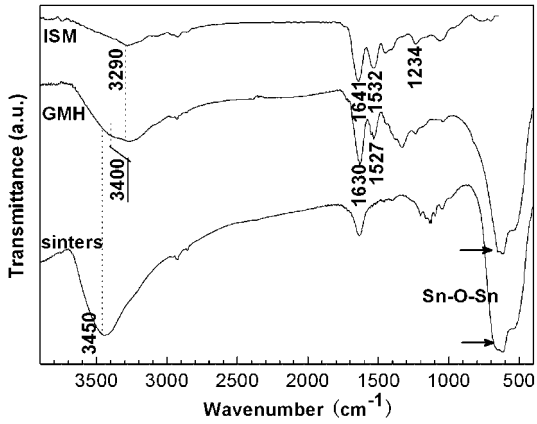


Figure 9. FTIR spectra of the original ISM, the corresponding GMH, and the relevant sinters at 823 K.

As we know, the shell membranes are nonmineralized, collagen-based matrices consisting of type I, V, and X collagens located in the core of each fiber. Each fiber is composed of a collagenous core surrounded by a glycoprotein mantle. It has been documented that the core is predominantly composed of collagen and osteopontin proteins, while the mantle is rich in polyanions exhibiting a variety of keratan sulfate (KS) epitopes and dermatan sulfate (DS).[25,32] Lysozyme and clusterin are also present at high levels in ESMs, and both have been detected within the membrane fibers, distributed discontinuously with no apparent partitioning between the core and the mantle. It is considered that the cationic lysozyme is bound to the anionic sites of DS and particularly those of KS in the membrane.[32b] Elegant studies[33] with clusterin have demonstrated that it exerts a powerful chaperone-like activity on lysozyme, as well as other purified proteins. Herein, the interfacial sol–gel process is presumably based on the adsorption of cationic groups from the colloid medium into the glycoprotein mantle of the ESM fiber containing an abundance of carboxylic, hydroxy, and amino residues; subsequently a series of complicated reactions proceed to give hierarchical $SnO_2$ films composed of ultrafine nanoparticles. The formation of $SnO_2$ can be denoted as follows:

$$Sn^0 \rightarrow Sn^{IV} \text{ ions (hydrate ions)} \rightarrow Sn^{IV} \text{ colloids} \rightarrow Sn^{IV} \text{oxo species (Sn-gel)} \rightarrow \text{amorphous } SnO_2 \rightarrow \text{nanocrystalline } SnO_2$$

The cationic $Sn^{IV}$ species in the sol system are prone to interaction with the residues of the ESM glycoprotein, as proved by FTIR- and NMR spectroscopic results (Supporting Information, Figure S6). The formation of amorphous Sn colloid/glycoprotein hybrids arises from the strong binding affinity of some residues that involves multiple hydrogen bonds, van der Waals interactions, and the ordering of surface polypeptide loops. The Sn colloids are bound to the

 © 2007 Wiley-VCH Verlag GmbH & Co. KGaA, Weinheim 

amino groups of the glycoprotein in the biotemplate ESM and to the –OH and $–NH_2$ groups of the sugar chains linked to polypeptides. Amorphous Sn–O networks can be derived from these reactions, and indeed an amorphous $SnO_2$ film located in the mantle is obtained without changing the original morphologies at room temperature. The $Sn^{IV}$ oxo species are assumed to be intermediates consisting of partly dehydrated polymeric $Sn^{IV}$ hydroxides.

Amorphous $SnO_2$ ripens into well-defined nanocrystallites during the calcination treatment. Heat treatment frequently causes agglomeration and enlargement. However, $SnO_2$ nanocrystallites in our work have small size and good crystallization as well as a narrow size distribution (Supporting Information, Figure S7). This can probably be ascribed to some short-chained amino acids of glycoprotein, which function as capping agents, since the binding is strong enough for controlling the growth of tin dioxide nuclei.[34] For comparison, a blank sample is synthesized through a similar sol–gel approach and calcination treatment at 823 K only without using the biomaterials. $SnO_2$ nanoparticles in the blank sample are disorganized and have an average size of 21 nm, while the ESM-based $SnO_2$ nanocrystallites with an average size of 5 nm are arranged into orderly hierarchical structures. This observation proves the significance of the biotemplate and supports the above analysis. It is also concluded that the ESM peptidoglycan functioning as the surfactant may play a key role in the aggregation and further crystallization of tin oxide nanoparticles. In addition, electrostatic forces assist the biomimetic sol–gel process. Because of the higher acidity of the system (with ample $H^+$ ions), the tin oxide clusters in the colloid are likely to be positively charged at the surface by reference to the isoelectric point of cassiterite $SnO_2$ (7.3).[26] By electrostatic force, they would preferably attach onto the negatively charged $DS^–$ ions on the surface of the membrane. As surface coating is always dependent on surfactant concentration, it is difficult and complicated to determine the precise dosage. However, in our work the "surfactant molecules" could be released systematically by the dissociation and reforming of ESM biomolecules. With the aid of "surfactant molecules", the construction of biostructure hierarchy can be achieved to synthesize subtle biomorphic functional nanomaterials, which is similar to biomolecule-micelle systems.

Notably, a completely morphologic conversion from $SnO_2$ tubes to $SnO_2$ belts occurred as a result of tuning the pH value of the sol media. As lysozyme is a kind of protein that is unstable in alkaline medium, it is clear that the mantle of ESM fiber containing lysozyme is prone to dissociation, its glucide contents not in the collagenous core end up in the colloid system. Therefore, the resultant morphologies of the $SnO_2$ products might have an inherent affiliation with the structures and constituents of the glycoprotein mantle. It is observed that the mantle can exist as a steady covering layer at $pH < 2$, while the distortions and dissociations of this protein layer occur as the pH value is elevated. The mantle protein seems to flow and reform evidently when $pH > 3$, as depicted in Supporting Information (Figure S8). Under these circumstances, lysozyme is most active, and it functions as a kind of enzyme leading to the dissociation and disintegration of the peptidoglycan-based mantle layer. These protein chains then interact with the Sn colloids. Simultaneously, the proteins formerly carrying tubular hybrids start to dissociate and stretch into planar fibers as a result of decreased acidity as illustrated in Scheme 1. Moreover, it is revealed that clusterin, exhibiting powerful chaperone-like action on lysozyme, binds to and stabilizes aggregating proteins, thus leading to irreversible precipitation by preferentially recognizing partially folded protein conformations.[33] This process conduces to the stabilization of the final structures of $SnO_2$. The special layer thus makes it possible for $SnO_2$ fibers to transform from tubular to solid fibrous structures. However, the interaction of the strongly cationic lysozyme with the collagenous matrix may

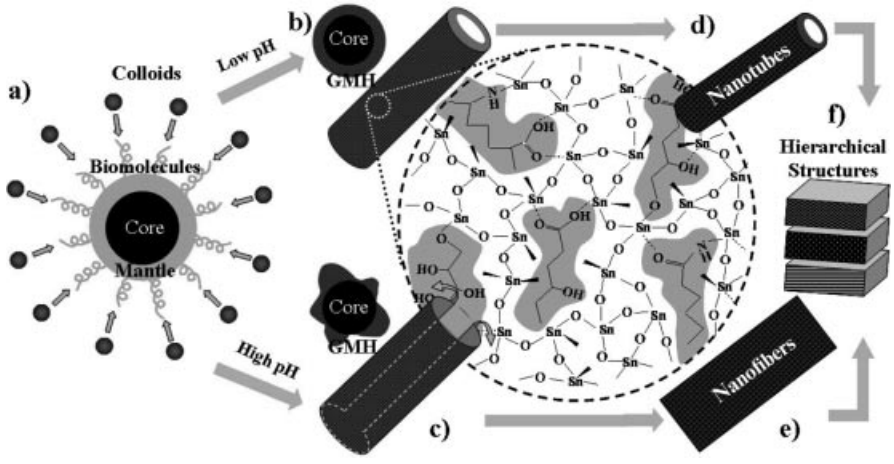


Scheme 1. Schematic depiction of hierarchical $SnO_2$ synthesized through the ESM-directed interfacial sol–gel process: (a) the cross-fractured ESM fiber showing its biomolecules interacting with Sn colloids; (b), (c) the stages of the mantle being immersed in the Sn sol media at different pH; the inset in (b) illustrates the interaction between the sol ingredients and the functional residues of ESM macromolecules after the removal of the ESM, (d) tubular $SnO_2$ and (e) $SnO_2$ fibrous belts; (f) hierarchical $SnO_2$ achieved by nanotube or nanobelt arrays.

 © 2007 Wiley-VCH Verlag GmbH & Co. KGaA, Weinheim 

be mediated by proteoglycans.[35] It is difficult for Sn colloids to interact with the core matrix under the current concentrations. Accordingly, hollow tubes form under higher acidity, while fibrous structures are obtained at lower acidity after the ESM is removed.

Prompted by their porous appearance and small-scale nanocrystalline units, we speculate that as-prepared hierarchical ESM-based $SnO_2$ must be useful in fabricating semiconducting sensors. When the grain size is reduced to a scale comparable to the space-charge length (for $SnO_2$, this value is 6 nm), the sensitivity could be exponentially enhanced.[23c,36] As an n-type semiconductor, $SnO_2$ has been extensively exploited in applications related to gas sensing. Most of these studies have focused on polycrystalline films made of small $SnO_2$ particles.[37] In contrast to some sensors made of individual single crystalline nanostructures or polycrystalline films, hierarchical nanostructured $SnO_2$ in our work, assembled by the small-scale, well-crystallized nanocrystallite units into tubular or zonary $SnO_2$ fibers with porous conformations and interconnected fibrous meshworks, would allow the sensors to be operated in the most sensitive, grain-controlled mode.

## Conclusions

Hierarchical biomorphic $SnO_2$ has been successfully synthesized, by utilizing the biomaterial ESM as template, through a biomimetic sol–gel approach. The detailed configurations of three ESM layers from the outermost OSM to the ISM, then to the innermost LM, are duplicated with their typical mammillary knobs, interwoven fibers, and silkworm-like structures, respectively. Notably, the average size of $SnO_2$ nanocrystallite units could be tuned in the range 2 to 20 nm by the control over synthesis temperatures and could be restricted to an average size about 5 nm even at 823 K. It has been revealed that some functional groups such as the carboxyl, hydroxy, and amido groups of ESM macromolecules and the specific colloid medium as well as the relationship between them predominantly determine the formation of biomorphic $SnO_2$. ESM provides both a physical substrate and an inductive template for the interfacial sol–gel process to direct the chemical reactions between the sol ingredients and functional residues of ESM macromolecules. Moreover, on the basis of the "surfactant" action of short-chain amino acids of the ESM glycoprotein, the precision assembly from the nanoscale to the micrometer scale could be further realized. As-prepared hierarchical nanostructured films consisting of interwoven tubular $SnO_2$ with inner interconnectivity may be valuable gas-sensing materials in view of their intrinsically small grain size and high surface-to-volume ratios, allowing them to be operated in the most sensitive, grain-controlled mode. As a mild, green, and universal technique, biomimetic sol–gel synthesis is a versatile and feasible route to functional inorganic hierarchical materials. We envisage that, inspired by natural biostructures, the design and assembly of inorganic materials with predetermined structures and properties would lead to a new family of advanced functional systems.

## Experimental Section

### Preparation of the Biotemplates

Commercial eggs were gently broken and cleaned up. The eggshells were washed with distilled water, then the LM and the ISM were manually and successively removed. After the remaining eggshell was immersed in HCl solution (0.5 M) for 5 min, the OSM was separated from the $CaCO_3$ shell. All three layers of fresh membranes were washed with distilled water and subsequently dried by blast at room temperature. They were finally conserved in a vacuum desiccator for the following synthesis.

### Synthesis of $SnO_2$ Hierarchical Nanomaterials

In a typical procedure, Sn powder (ca. 1.45 g) was added stepwise into $HNO_3$ solution (50 mL, 2 M) and stirred for 2 h. Then, distilled water (30 mL) was added slowly within 10 min to promote the hydrolysis of tin ions. It could be observed that a clear solution was obtained incipiently. It then turned into a slightly yellow colloid after being filtered. The pH values of the colloid media were generally kept at 1. For comparison, NaOH solution (1 M) was also added to modify the pH value of the media to 2 and 3. Then the OSM, the ISM, and the LM were immersed in the above-mentioned colloid systems for 13 h at room temperature. The GMH obtained were rinsed with distilled water and directly dried under air flow. Finally, the dry GMH were subjected to calcination treatments in air at 673 K, 823 K, 973 K, 1073 K, and 1273 K for 1.5 h. In all cases, white sheets were obtained and stored in vacuo for characterization.

### Characterization

The morphology and composition were investigated with an FEI Sirion 200 field emission gun scanning electron microscope (FESEM) attached to an X-ray microanalyzer. Transmission electron microscopy (TEM) and high-resolution transmission electron microscopy (HRTEM) images were obtained as bright-field images and were examined by selected area electron diffraction (SAED), conducted with a JEOL JEM-2010 instrument and a JEOL JEM-2100F instrument, respectively. X-ray diffraction (XRD) measurements of the samples were carried out with a Rigaku Dmax 2550V instrument operating at a voltage of 40 kV and a current of 200 mA with Cu-$K_\alpha$ radiation ($\lambda$ = 1.5406 Å) in the range 10–90°. X-ray photoelectron spectroscopy (XPS) was carried out with a VG Microlab 310F using Mg radiation to analyze the chemical states of tin oxide before and after calcination. Thermogravimetric analysis (TGA) and differential thermal analysis (DTA) were conducted to trace the calcination process with a TA 2050 thermoanalyzer and a TA 1600 thermal analysis system, respectively. For Fourier-transform infrared (FTIR) spectroscopy measurements, the spectra of the samples were recorded with a Bruker EQUINOX55 instrument at a resolution of 0.5 $cm^{-1}$ and in a spectral range 4000–400 $cm^{-1}$.

**Supporting Information** (see footnote on the first page of this article): (1) XPS spectra of GMH and the sinters, (2) FESEM image of the biomorphic $SnO_2$ hierarchy, (3) FESEM images of tubular $SnO_2$ compared with the natural membrane fibers, (4) FESEM images of the interwoven ISM-based $SnO_2$ synthesized at 673 K and 1273 K, (5) TEM images of templated $SnO_2$ nanocrystallites synthesized at various temperatures, (6) MAS solid-state NMR spectra of original ESM and GMH, (7) TEM images of ISM-based $SnO_2$ nanocrystallites compared with the corresponding as-synthesized $SnO_2$ nanoparticles without template introduced through the same process, (8) FESEM images of GMH prepared at different pH values, (9) FESEM images of as-prepared intersectant $SnO_2$ fibers, and (10) nitrogen adsorption-desorption isotherms and

 © 2007 Wiley-VCH Verlag GmbH & Co. KGaA, Weinheim 

pore-size-distribution plots of ISM-templated $SnO_2$ and samples prepared without the biotemplate.

## Acknowledgments

Financial support from NSFC (no. 50371055) and Shanghai Science and Technology Committee (nos. 04DZ14002, 0352nm051, 05nm05020) are gratefully acknowledged.

[1] a) S. A. Wainwright, *Mechanical Design in Organisms*, John Wiley & Sons, New York, **1976**; b) H. A. Lowenstam, *On Biomineralization*, Oxford University Press, Oxford, **1989**; c) S. Kamat, X. Su, R. Ballarini, A. H. Heuer, *Nature* **2000**, *405*, 1036–1040; d) M. Rubner, *Nature* **2003**, *423*, 925–926.
[2] a) H. Colfen, S. Mann, *Angew. Chem. Int. Ed.* **2003**, *42*, 2350–2365; b) M. Antonietti, G. A. Ozin, *Chem. Eur. J.* **2004**, *10*, 29–41.
[3] a) S. Mann, *Biomimetic Materials Chemistry*, VCH, Weinheim, **1996**; b) P. Vukusic, J. R. Sambles, *Nature* **2003**, *424*, 852–855; c) A. Sellinger, P. M. Weiss, A. Nguyen, Y. F. Lu, R. A. Assink, W. L. Gong, C. J. Brinker, *Nature* **1998**, *394*, 256–260.
[4] R. C. Mucic, J. J. Storhoff, C. A. Mirkin, R. L. Letsinger, *J. Am. Chem. Soc.* **1998**, *120*, 12674–12675.
[5] S. W. Lee, C. B. Mao, C. E. Flynn, A. M. Belcher, *Science* **2002**, *296*, 892–895.
[6] M. R. Weatherspoon, S. M. Allan, E. Hunt, Y. Cai, K. H. Sandhage, *Chem. Commun.* **2005**, 651–653.
[7] G. Cook, P. L. Timms, C. G. Spickermann, *Angew. Chem. Int. Ed.* **2003**, *42*, 557–559.
[8] a) D. Yang, L. M. Qi, J. M. Ma, *Adv. Mater.* **2002**, *14*, 1543–1546; b) D. Yang, L. M. Qi, J. M. Ma, *J. Mater. Chem.* **2003**, *13*, 1119–1123; c) D. Y. Zhang, L. M. Qi, *Chem. Commun.* **2005**, 2735–2737.
[9] Q. Dong, H. L. Su, D. Zhang, *J. Phys. Chem. B* **2005**, *109*, 17429–17434.
[10] Y. Kim, *Biomacromolecules* **2003**, *4*, 908–913.
[11] C. R. Rambo, H. Sieber, *Adv. Mater.* **2005**, *17*, 1088–1091.
[12] J. G. Huang, T. Kunitake, *J. Am. Chem. Soc.* **2003**, *125*, 11834–11835.
[13] a) S. Mann, *Biomineralization: Principles and Concepts in Bioinorganic Materials Chemistry*, Oxford University Press, New York, **2001**; b) R. A. Caruso, *Angew. Chem. Int. Ed.* **2004**, *43*, 2746–2748.
[14] R. A. Caruso, M. Antonietti, *Chem. Mater.* **2001**, *13*, 3272–3282.
[15] a) N. Shirahata, W. Shin, N. Murayama, A. Hozumi, Y. Yokogawa, T. Kameyama, Y. Masuda, K. Koumoto, *Adv. Funct. Mater.* **2004**, *14*, 580–588; b) B. Cheng, J. M. Russell, W. S. Shi, L. Zhang, E. T. Samulski, *J. Am. Chem. Soc.* **2004**, *126*, 5972–5973; c) G. S. Pang, S. G. Chen, Y. Koltypin, A. Zaban, S. H. Feng, A. Gedanken, *Nano Lett.* **2001**, *1*, 723–726.
[16] S. Ferrere, A. Zaban, B. A. Gregg, *J. Phys. Chem. B* **1997**, *101*, 4490–4493.
[17] D. A. Gaal, J. T. Hupp, *J. Am. Chem. Soc.* **2000**, *122*, 10956–10963.
[18] D. S. Ginley, C. Bright, *Mater. Res. Soc. Bull.* **2000**, *25*, 15–18.
[19] a) G. J. Li, X. H. Zhang, S. Kawi, *Sens. Actuators B* **1999**, *60*, 64–70; b) A. Kolmakov, Y. X. Zhang, G. S. Cheng, M. Moskovits, *Adv. Mater.* **2003**, *15*, 997–1000.
[20] H. Ogawa, A. Abe, M. Nishikawa, S. Hayakawa, *J. Electrochem. Soc.* **1981**, *128*, 2020–2025.
[21] Z. W. Pan, Z. R. Dai, Z. L. Wang, *Science* **2001**, *291*, 1947–1949.
[22] Y. L. Wang, X. C. Jiang, Y. N. Xia, *J. Am. Chem. Soc.* **2003**, *125*, 16176–16177.
[23] a) Y. M. Chiang, *Physical Ceramics: Principles for Ceramic Science and Engineering*, John Wiley & Sons, New York, **1997**; b) C. J. Brinker, *Sol–Gel Science: The Physics and Chemistry of Sol–Gel Processing*, Academic Press, San Diego, **1990**; c) N. L. Wu, S. Y. Wang, I. A. Rusakova, *Science* **1999**, *285*, 1375–1377.
[24] J. N. Cha, G. D. Stucky, D. E. Morse, T. J. Deming, *Nature* **2000**, *403*, 289–292.
[25] M. S. Fernandez, M. Araya, J. L. Arias, *Matrix Biol.* **1997**, *16*, 13–20.
[26] C. H. Liang, Y. Shimizu, T. Sasaki, N. Koshizaki, *J. Phys. Chem. B* **2003**, *107*, 9220–9225.
[27] a) I. Ichinose, H. Senzu, T. Kunitake, *Chem. Mater.* **1997**, *9*, 1296–1298; b) W. Jones, *Supramolecular Organization and Materials Design*, Cambridge University Press, Cambridge, **2002**.
[28] a) I. Ichinose, T. Kawakami, T. Kunitake, *Adv. Mater.* **1998**, *10*, 535–539; b) T. Kunitake, S. W. Lee, *Anal. Chim. Acta* **2004**, *504*, 1–6.
[29] P. Salas, J. G. Hernandez, J. A. Montoya, J. Navarrete, J. Salmones, I. Schifter, J. Morales, *J. Mol. Catal. A: Chem.* **1997**, *123*, 149–154.
[30] V. M. Jimenez, A. Caballero, A. Fernandez, J. P. Espinos, M. Ocana, A. R. Gonzalez-Elipe, *Solid State Ionics* **1999**, *116*, 117–127.
[31] D. N. Srivastava, S. Chappel, O. Palchik, A. Zaban, A. Gedanken, *Langmuir* **2002**, *18*, 4160–4164.
[32] a) M. Wong, M. J. C. Hendrix, K. VonderMark, C. Little, R. Stern, *Dev. Biol.* **1984**, *104*, 28–36; b) M. T. Hincke, J. Gautron, M. Panheleux, J. Garcia-Ruiz, M. D. McKee, Y. Nys, *Matrix Biol.* **2000**, *19*, 443–453.
[33] a) K. Mann, J. Gautron, Y. Nys, M. D. McKee, T. Bajari, W. J. Schneider, M. T. Hincke, *Matrix Biol.* **2003**, *22*, 397–407; b) S. Poon, M. S. Rybchyn, S. B. Easterbrook-Smith, J. A. Carver, G. J. Pankhurst, M. R. Wilson, *J. Biol. Chem.* **2002**, *277*, 39532–39540.
[34] D. C. Pan, N. N. Zhao, Q. Wang, S. C. Jiang, X. L. Ji, L. J. An, *Adv. Mater.* **2005**, *17*, 1991–1995.
[35] J. M. Moss, M. P. I. VanDamme, W. H. Murphy, P. G. Stanton, P. Thomas, B. N. Preston, *Arch. Biochem. Biophys.* **1997**, *339*, 172–182.
[36] A. Dieguez, A. Romano-Rodriguez, J. R. Morante, J. Kappler, N. Barsan, W. Gopel, *Sens. Actuators B* **1999**, *60*, 125–137.
[37] a) D. F. Zhang, L. D. Sun, C. J. Jia, Z. G. Yan, L. P. You, C. H. Yan, *J. Am. Chem. Soc.* **2005**, *127*, 13492–13493; b) Y. Wang, J. Y. Lee, H. C. Zeng, *Chem. Mater.* **2005**, *17*, 3899–3903.

Received: December 12, 2006
Published Online: April 13, 2007

 © 2007 Wiley-VCH Verlag GmbH & Co. KGaA, Weinheim 

DOI: 10.1002/ejic.200700093

# Synthesis, Coordination and Catalytic Utility of Novel Phosphanyl–ferrocenecarboxylic Ligands Combining Planar and Central Chirality

Martin Lamač,[a] Ivana Císařová,[a] and Petr Štěpnička*[a]

**Keywords:** Asymmetric catalysis / Ferrocene ligands / Rhodium / Palladium / Allylic alkylation

The chiral ferrocene derivative ($R,R_p$)-2-[1-(diphenylphosphanyl)ethyl]ferrocenecarboxylic acid (**1**) is prepared together with selected derivatives resulting from modification at the phosphane moiety [*P*-oxide (**5**) and *P*-sulfide (**4**)] and the carboxyl group {amides bearing benzyl (**6**) and (*R*)- or (*S*)-1-phenylethyl substituents [(*R*)-**7** and (*S*)-**7**] at the amide nitrogen atom}. Acid **1** and amide **6** are studied as ligands in rhodium and palladium complexes. Bridge cleavage of the dimer [{Rh(μ-Cl)Cl($\eta^5$-$C_5Me_5$)}$_2$] with **1** gives [RhCl$_2$($\eta^5$-$C_5Me_5$)(**1**-κ*P*)] (**9**) containing P-monodentate **1**, which undergoes smooth conversion to the (phosphanylalkyl)ferrocenecarboxylato complex [RhCl($\eta^5$-$C_5Me_5$){Fe($\eta^5$-$C_5H_5$)($\eta^5$-$C_5H_3$-1-CH(Me)PPh$_2$-2-COO-κ$^2$*O*,*P*}] (**10**) upon treatment with silica gel or alumina. Yet another *O*,*P*-chelate complex, [Rh{Fe($\eta^5$-$C_5H_5$)($\eta^5$-$C_5H_3$-1-CH(Me)PPh$_2$-2-COO-κ$^2$*O*,*P*}(CO)(PCy$_3$)] (**11**; Cy = cyclohexyl) is obtained directly by an acid-base reaction between the acetylacetonato complex [Rh(acac)(CO)(PCy$_3$)] and **1**. Amide **6** reacts with [{Pd(μ-Cl)($\eta^3$-$C_3H_5$)}$_2$] to give the expected phosphane complex [PdCl($\eta^3$-$C_3H_5$)(**6**-κ*P*)] (**12**), while the replacement of the cyclooctadiene (cod) ligand in [PdCl(Me)(cod)] affords the chelate complex [PdCl(Me)(**6**-κ$^2$*O*,*P*)] (**13**). All compounds are characterised by spectroscopic methods and the solid-state structures of **5**, **9**, **11**, **13**, ($R,S_p$)-2-[1-(diphenylphosphoryl)-ethyl]-1-[*N*-(*R*)-(1-phenylethyl)carbamoyl]ferrocene [(*R*)-**8**; phosphane oxide from (*R*)-**7**], and the synthetic precursors ($R,S_p$)-1-bromo-2-[1-(diphenylphosphanyl)ethyl]ferrocene (**2**) and ($R,S_p$)-1-bromo-2-[1-(diphenylthiophosphoryl)ethyl]ferrocene (**3**) determined by single-crystal X-ray diffraction. The catalytic properties of **1** and the amides are probed in enanatioselective rhodium-catalysed hydrogenation and palladium-catalysed asymmetric allylic alkylation.
(© Wiley-VCH Verlag GmbH & Co. KGaA, 69451 Weinheim, Germany, 2007)

## Introduction

The chemistry of ferrocene has attracted a great deal of attention ever since its discovery in the early 1950s.[1] Ferrocene derivatives have become some of the most frequently studied organometallic compounds, finding applications in organometallic synthesis, materials science, bioorganometallic chemistry and, above all, in catalysis.[2,3] To date an enormous number of chiral and achiral ligands derived from ferrocene have been reported and utilised as donors in the preparation of various coordination compounds[2a] and as catalyst components in transition metal-mediated reactions on both a laboratory and industrial scale.[2a,4]

We have focused our research mainly on phosphanyl–ferrocenecarboxylic donors. The first ligand of this kind, 1′-(diphenylphosphanyl)ferrocenecarboxylic acid (Hdpf), was reported in 1996,[5] and since then we have synthesised several other phosphanyl–ferrocenecarboxylic ligands (see Scheme 1) and studied their structural and coordination properties. More recently, we have extended our interest towards the utilisation of these phosphane–carboxylic acids and their derivatives as organometallic synthons and catalyst components.[6]

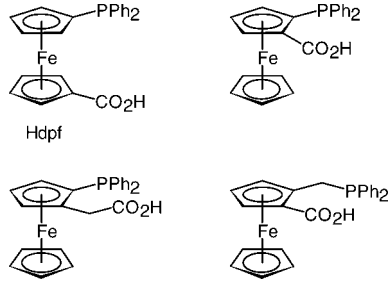


Scheme 1.

In this contribution we report the synthesis of a novel phosphanyl–ferrocenecarboxylic ligand combining planar and central chirality, namely ($R,R_p$)-2-[1-(diphenylphosphanyl)ethyl]ferrocenecarboxylic acid (**1**), which is a homologue of *rac*-2-[(diphenylphosphanyl)methyl]ferrocenecarboxylic acid.[7] We also describe the preparation of selected derivatives of **1** modified at both the phosphanyl and carboxyl groups, and use of the acid and amides thereof as ligands in rhodium and palladium complexes and as catalyst components in enantioselective rhodium-catalysed hydrogenation and palladium-catalysed allylic alkylation reactions.

[a] Department of Inorganic Chemistry, Faculty of Natural Science, Charles University
Hlavova 2030, 12840 Prague, Czech Republic
E-mail: stepnic@natur.cuni.cz
Supporting information for this article is available on the WWW under http://www.eurjic.org or from the author.

 © 2007 Wiley-VCH Verlag GmbH & Co. KGaA, Weinheim 

## Results and Discussion

### Preparation and Structural Characterisation of the Ligands

The key compound in this study, ($R$,$R_p$)-2-[1-(diphenylphosphanyl)ethyl]ferrocenecarboxylic acid (**1**), was synthesised from the known chiral precursor ($R$,$S_p$)-1-bromo-2-[1-(diphenyphosphanyl)ethyl]ferrocene (**2**)[8] by lithiation and subsequent carboxylation with carbon dioxide (Scheme 2). Alternatively, **1** was prepared first in its *P*-protected form **4** according to a similar methodology and the bromo-substituted phosphane sulfide **3** as the precursor. Following desulfurisation of **4** with $P(NMe_2)_3$/methyl triflate[9] afforded acid **1**. The structures of the bromo precursors **2** and **3**, including their absolute configuration, have been determined by X-ray crystallography (see Figure 1, Figure S1 in the Supporting Information and Table 1).

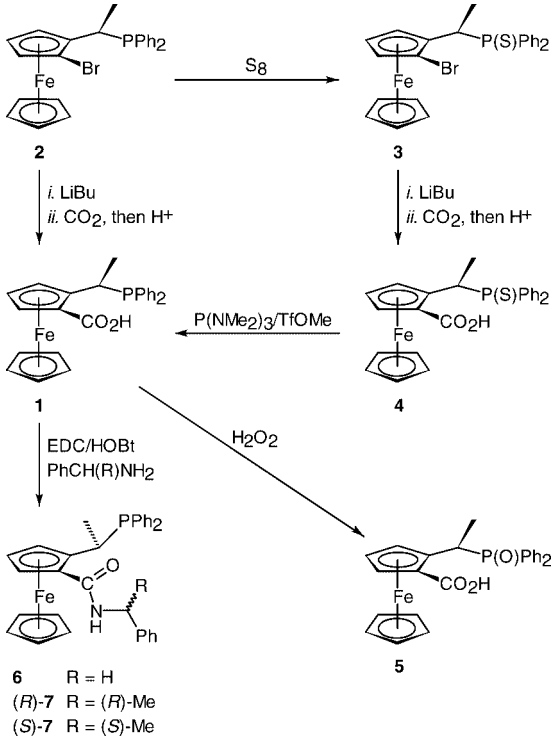


Scheme 2.

Acid **1** was further converted into its corresponding phosphane oxide **5** by treatment with aqueous hydrogen peroxide in acetone. A small amount of crystalline **5** was unintentionally obtained during the attempted crystallisation of **1** from ethyl acetate/hexane and its structure was established by single-crystal X-ray diffraction (see below). All compounds have been characterised by spectroscopic methods and elemental analysis. The $^1H$ and $^{13}C$ NMR spectra of **1**, **4** and **5** are in agreement with their formulations and show signals due to phosphorus-coupled ethane-1,1-diyl and phenyl groups and a 1,2-disubstituted ferrocene unit. The $^{31}P$ NMR chemical shifts follow the expected trend [$\delta_P$ = 11.1 (**1**), 36.5 (**5**) and 54.7 ppm (**4**)],[10] with the $^1J_{P,C}$ coupling constants of the $C_{ipso}$ carbon atoms within the cyclopentadienido and phenyl rings increasing in the same order (**1** < **5** < **4**).[11] In addition, the NMR spectra of **2**–**5** indicate the presence of only one diastereoisomeric form for each compound.

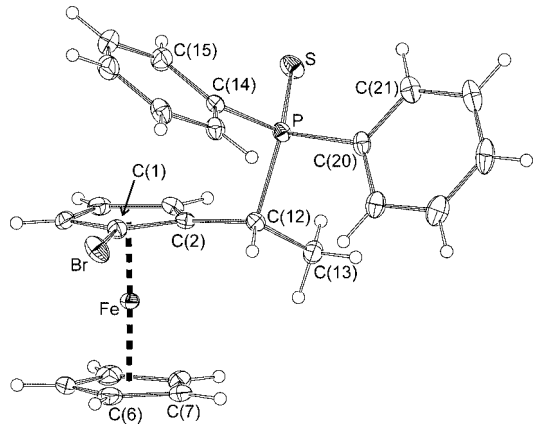


Figure 1. PLATON view of the molecular structure of **3** showing displacement ellipsoids with 30% probability. Note: a structural drawing of the corresponding phosphane **2** is available as Supporting Information (Figure S1).

Table 1. Selected bond lengths [Å] and angles [°] for **2** and **3**.[a]

| | **2** | **3** |
|---|---|---|
| Fe–Cg(1) | 1.6499(8) | 1.6387(1) |
| Fe–Cg(2) | 1.655(1) | 1.650(1) |
| ∠Cp(1),Cp(2) | 5.6(1) | 3.2(2) |
| C(1)–Br | 1.887(2) | 1.888(2) |
| C(2)–C(12) | 1.499(3) | 1.502(3) |
| C(12)–C(13) | 1.528(3) | 1.532(3) |
| P–C(12) | 1.885(2) | 1.852(3) |
| P–C(14) | 1.842(2) | 1.813(3) |
| P–C(20) | 1.838(2) | 1.819(3) |
| P–S | – | 1.957(1) |
| C(2)–C(12)–P | 108.5(1) | 110.2(2) |
| C–P–C[b] | 101.3(1)–103.20(9) | 104.9(1)–105.9(1) |
| S–P–C[c] | – | 112.73(8)–113.74(8) |

[a] The ring planes are defined as follows: Cp(1) = C(1–5); Cp(2) = C(6–10). Cg(1) and Cg(2) denote the respective ring centroids. [b] Range of C(12)–P–C(14,20) and C(14)–P–C(20) angles. [c] Range of S–P–C(12,14,20) angles.

Acids **1**, **4** and **5** display characteristic carbonyl stretching bands in their IR spectra, the position of which varies with substitution at the phosphorus atom. Thus, whereas phosphane **1** and phosphane sulfide **4** show similar $\nu_{C=O}$ frequencies (1667 and 1663 $cm^{-1}$, respectively), the $\nu_{C=O}$ band of phosphane oxide **5** is shifted to higher energy (1685 $cm^{-1}$). This difference probably reflects different hydrogen-bonding patterns in the solid samples.[6]

The crystal structure of **5** (Figure 2a, Table 2) confirms both the expected connectivity and configuration [i.e., ($R$,$R_p$)-**5**]. The geometry of the ferrocene unit is quite regular except for a slight torsion at the substituted cyclopentadienido (Cp) ring, as indicated by the torsion angle C(11)–C(1)–C(2)–C(12) of –11.5(4)°. This can be accounted for by steric interactions between the sterically demanding ferrocene substituents and intermolecular interactions (see below). Nonetheless, the substituents bind symmetrically to

 © 2007 Wiley-VCH Verlag GmbH & Co. KGaA, Weinheim 

the ferrocene unit, the C(11)–C(1)–C(2/5) and C(12)–C(2)–C(1/3) angles being similar. The carboxyl group [C(11)O(1) O(2)] is rotated from the Cp(1) plane (see Table 2) by 6.4(3)°, while the phosphorus-substituted side arm is oriented above the Cp(1) plane, with an angle between the C(12)–P bond and the Cp(1) plane of 78.0(1)°. The P=O bond is directed outward the carboxyl group [torsion angle C(2)–C(12)–P–O(3) 61.1(2)°], which brings the P=O(3) and C(12)–C(13) bonds into a synclinal orientation [C(13)–C(12)–P–O(3) –63.1(2)°]. Such an arrangement, as well as the individual geometric parameters, compares favourably with those of racemic 2-[(diphenylphosphoryl)methyl]ferrocenecarboxylic acid.[7]

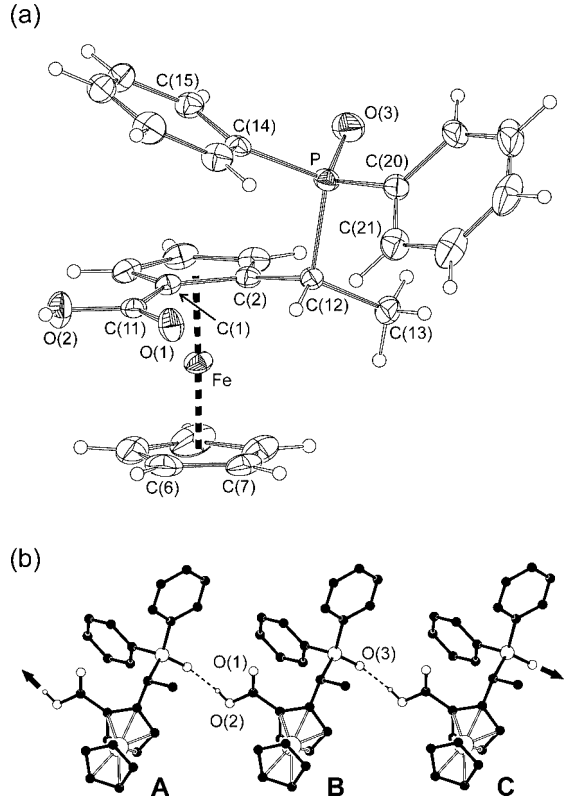


Figure 2. (a) Molecular structure of **5**. Displacement ellipsoids are shown at the 30% probability level. (b) Section of the infinite hydrogen-bonded chain in the structure of **5** showing the hydrogen bonds as dashed lines. Symmetry operations: A ($x$, 1 + $y$, $z$), B ($x$, $y$, $z$), C ($x$, $y$ – 1, $z$).

Individual molecules in the crystal of **5** are linked into infinite chains along the crystallographic $b$ axis by means of hydrogen bonds between the carboxylic OH group and the phosphoryl oxygen atom [O(2)–H(90)···O(3$^{i}$): O(2)···O(3$^{i}$) 2.517(3) Å (i: $x$, 1 + $y$, $z$); angle at H: 162(4)°; Figure 2b]. Similar hydrogen-bonding patterns have been found in the crystal structures of 1′-(diphenylphosphoryl)-ferrocenecarboxylic acid [O···O 2.588(4) Å][12] and ($S_p$)-2-(diphenylphosphoryl)ferrocenecarboxylic acid [O···O 2.556(4) Å].[13]

For the purpose of catalytic testing we prepared a series of *N*-benzylamides without (**6**) and with [(*R*)- and (*S*)-**7**] additional asymmetric centres (Scheme 2). The amides were

Table 2. Selected bond lengths [Å] and angles [°] for **5** and (*R*)-**8**.[a]

| | **5** | (*R*)-**8**[d] |
|---|---|---|
| E | O(2) | N |
| Fe–Cg(1) | 1.648(1) | 1.650(1) |
| Fe–Cg(2) | 1.646(2) | 1.654(1) |
| ∠Cp(1),Cp(2) | 3.2(2) | 2.0(2) |
| C(1)–C(11) | 1.491(4) | 1.495(3) |
| C(11)–O(1) | 1.205(3) | 1.229(2) |
| C(11)–E | 1.300(4) | 1.352(2) |
| C(2)–C(12) | 1.492(3) | 1.497(3) |
| C(12)–C(13) | 1.544(4) | 1.534(3) |
| C(12)–P | 1.837(2) | 1.835(2) |
| P–C(14) | 1.808(2) | 1.813(2) |
| P–C(20) | 1.808(3) | 1.808(2) |
| P=O(3 or 2) | 1.469(2) | 1.471(2) |
| O(1)–C(11)–E | 125.5(3) | 122.3(2) |
| C(2)–C(12)–P | 107.3(2) | 108.6(2) |
| C(2)–C(12)–C(13) | 114.2(2) | 114.0(2) |
| P–C(12)–C(13) | 109.1(2) | 107.9(1) |
| C–P=O[b] | 108.1(1)–114.1(1) | 112.0(1)–114.4(1) |
| C–P–C[c] | 104.7(1)–108.1(1) | 103.0(1)–107.32(9) |

[a] The ring planes are defined as for **2** and **3**; see Table 1. [b] Range of O(3)–P–C(12,14,20) (**5**) or O(2)–P–C(12,14,20) [(*R*)-**8**] angles. [c] Range of C(12)–P–C(14,20) and C(14)–P–C(20) angles. [d] Further data: N–C(26) 1.465(3), C(26)–C(27) 1.513(3), C(26)–C(28) 1.526(4) Å; C(11)–N–C(26) 122.4(2), N–C(26)–C(27) 109.1(2), N–C(26)–C(28) 111.0(2)°.

obtained in very good yields by standard amidation of **1** with the appropriate amine in the presence of 1-hydroxybenzotriazole (HOBt) and *N*-[3-(dimethylamino)propyl]-*N*′-ethylcarbodiimide (EDC),[14] and characterised by spectroscopic methods. An independent confirmation of the structures came from the structure determination of the ferrocene amide–phosphane oxide (*R*)-**8** (Figure 3, Table 2), which was obtained in small amounts during prolonged recrystallisation of (*R*)-**7** from ethyl acetate/hexane under aerobic conditions.

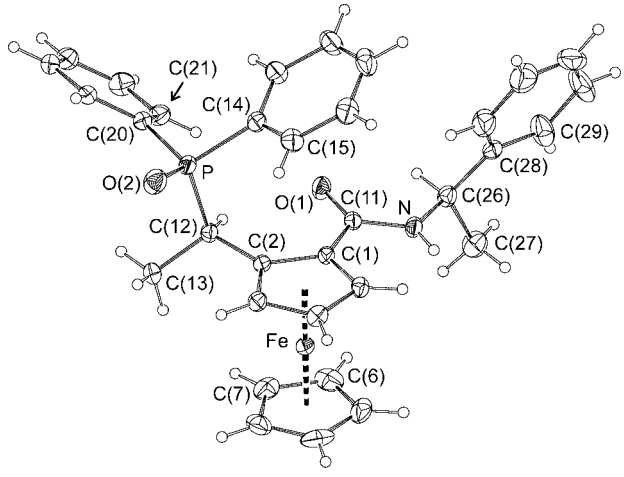


Figure 3. Molecular structure of (*R*)-**8**. Displacement ellipsoids are shown at the 30% probability.

Again, the structure confirms the expected configuration at the stereogenic elements, with the (*R*)-1-phenylethyl group acting as the reference chirality centre. The molecular geometry and conformation, including the mutual orienta-

 © 2007 Wiley-VCH Verlag GmbH & Co. KGaA, Weinheim 

tion of the functional groups, are similar to those in **5**. The C(12)–P vector points above the Cp(1) plane, intersecting the latter at an angle of 74.8(1)°, whilst the substituents at the P–C(12) bond adopt a conformation similar to **5**, departing slightly from the ideal staggered arrangement [cf. C(2)–C(12)–P–O(2) 74.0(2)° and C(13)–C(12)–P–O(2) –49.9(2)°]. Finally, the amide moiety [C(11)O(1)N] is rotated from the Cp(1) plane by 9.5(2)° and adopts a *syn* geometry [C(26)–N–C(11)–O(1) –1.2(3)°], with the phenyl group oriented away from the ferrocene plane [the dihedral angle between the C(26)–C(28) bond and the C(28–33) ring is 49.0(2)°]. In the crystal, the molecules of (*R*)-**8** associate through N–H(90)···O(2$^{ii}$) (ii: 1 – *x*, –1/2 + *y*, 1/2 – *z*) hydrogen bonds [N···O(2) 3.066(2) Å; angle at H(90): 158°] to form infinite angular chains parallel to the crystallographic *b* axis. The crystal assembly is further supported by relatively weaker C–H···O(2) interactions.

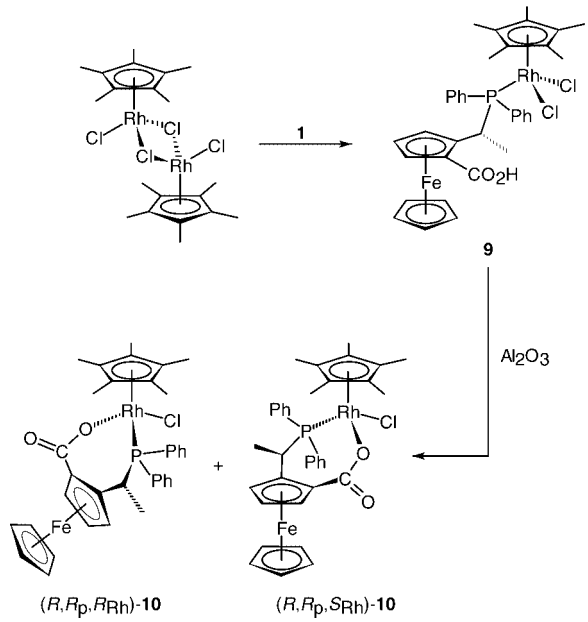


Scheme 3.

## Coordination Studies: Rhodium Complexes

With the aim of using these newly prepared ferrocene-linked phosphane–carboxylate donors in rhodium- and palladium-catalysed reactions, we first tested the coordination ability of acid **1** and amide **6** towards these metal ions. Thus, the reaction between **1** and di-μ-chlorobis[chloro(η$^5$-pentamethylcyclopentadienido)rhodium(III)] gave the expected product of bridge cleavage (**9**; Scheme 3). When treated with chromatography grade alumina or silica gel (during column chromatography or in a batch mode), complex **9** underwent clean dehydrohalogenation to give phosphane–carboxylato complex **10** as a mixture of diastereoisomers that differ in their configuration at the newly formed stereogenic centre (Rh atom). The diastereoisomeric ratio of about 1:9 determined by NMR spectroscopy clearly indicates that the ferrocene phosphane–carboxylato ligand provides a pronounced steric bias during the chelate formation.

The P-monodentate coordination of **1** in compound **9** is reflected mainly in a low-shift of the $^{31}$P NMR signal [cf. the coordination shift, $\Delta_P = \delta_P$(complex) – $\delta_P$(ligand) = 23.2 ppm for **9**] and its splitting into a $^{103}$Rh-coupled doublet ($^1J_{Rh,P}$ = 140 Hz). On the contrary, the carboxyl $^{13}$C NMR signal and the $\nu_{C=O}$ band of the IR spectrum differ only slightly from those in the free ligand. On going from **9** to **10**, the $^{31}$P NMR resonance shifts to even lower fields ($\Delta_P$ = 40.9/38.7 ppm for the major/minor diastereoisomer) while coordination of the deprotonated carboxyl group is clearly manifested by characteristic carboxylate bands in the IR spectrum (1581 and 1307 cm$^{-1}$; cf. 1664 cm$^{-1}$ for **9** and 1321 cm$^{-1}$ for **11**).

It is noteworthy that complex **9** shows markedly broad $^1$H NMR resonances at +25 °C, particularly those due to the CH*Me* and $C_5H_3$ protons, which sharpen upon both heating to 50 °C and cooling to 0 °C. Such behaviour is indicative of a hindered intramolecular motion, which most likely results from steric interaction between the bulky (η$^5$-$C_5Me_5$)Rh unit and the ligand. The motion apparently becomes slow at low temperature, where the "equilibrium" shifts in favour of the preferred (low-energy) conformer, while higher temperatures result in a fast molecular motion and, hence, signal averaging. The expected nature of the observed dynamic behaviour is supported by the $^{31}$P NMR spectra, which show a rather minor shift of the main signal over the whole temperature range monitored ($\delta_P$ = 34.9 ppm at 50 °C, and 34.0 ppm at 0 °C; $^1J_{Rh,P} \approx$ 145 Hz in both cases), thus excluding that chemically different forms are involved in the equilibrium.

The structure of **9** was corroborated by X-ray crystallography. The unit cell of **9** comprises two crystallographically distinct, but structurally very similar, molecules (Figure 4a, Table 3). This multiplication of otherwise almost identical moieties within the asymmetric unit apparently results from the crystal packing. The independent molecules aggregate into familiar dimers through double hydrogen bonds between their carboxyl groups [(C=O···H–O)$_2$ with O···O 2.652(4)/2.541(4) Å; Figure 4b]. However, such a bonding pattern requires two appropriately oriented carboxyl groups which, in a *chiral* space group, necessitates multiplication of the "repeating" units (instead of the crystallographically imposed symmetry typically observed in centrosymmetric space groups). Indeed, the most notable difference between the two independent molecules is the orientation of their carboxyl groups, which are mutually rotated by 180°. The hydrogen-bonded dimers further assemble into columnar stacks through π···π interactions between the non-substituted ferrocene and Rh-bonded cyclopentadienido rings [Cg(12)···Cg(13) 3.455(3) Å, tilt 2.5°; Cg(22)···Cg(23) 3.460(3) Å, tilt 7.5°; see Table 3 for definitions].

The different steric demands of the donors around the rhodium atom in **9** naturally result in angular deformation of the coordination environment (see the interligand angles

 © 2007 Wiley-VCH Verlag GmbH & Co. KGaA, Weinheim 

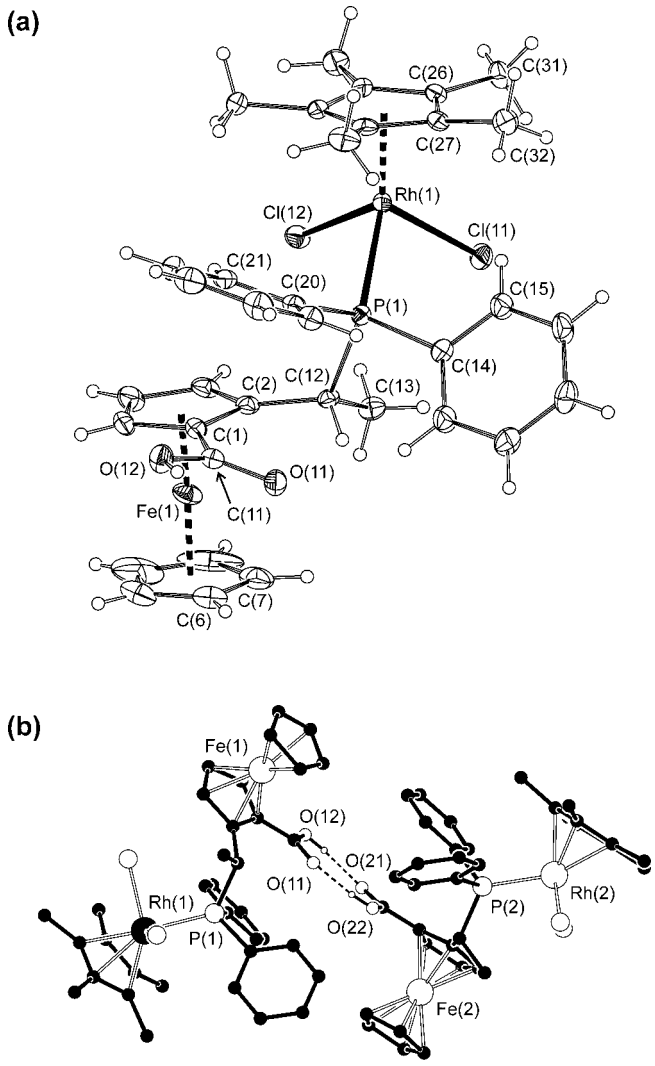


Figure 4. (a) PLATON view of molecule 1 in the crystal structure of complex **9**. Displacement ellipsoids are drawn with 30% probability. Molecule 2 is very similar and its labelling scheme is strictly analogous: On going from molecule 1 to molecule 2, the non-carbon, heavy atoms change the first digit in their atom labels to 2 while the atom labels for the carbon atoms are obtained by adding 40 to the respective atom label in molecule 1. (b) Dimeric motif in the crystal of **9**. Hydrogen bonds are shown as dashed lines.

Table 3. Selected bond lengths [Å] and angles [°] for **9**.[a]

| | Molecule 1 ($n$ = 1) | Molecule 2 ($n$ = 2) |
|---|---|---|
| Rh($n$)–Cl($n$1/$n$2) | 2.4069(9)/2.392(1) | 2.420(1)/2.402(1) |
| Rh($n$)–P($n$) | 2.3621(9) | 2.3558(9) |
| Rh–Cg($n$3) | 1.838(2) | 1.828(2) |
| Cl($n$1)–Rh($n$)–Cl($n$2) | 91.40(3) | 94.12(4) |
| P($n$)–Rh($n$)–Cl($n$1/$n$2) | 89.77(3)/89.42(3) | 88.92(4)/90.62(4) |
| Cg($n$3)-Rh($n$)–Cl($n$1/$n$2) | 122.26(5)/118.65(6) | 119.93(6)/119.38(7) |
| Cg($n$3)-Rh($n$)–P($n$) | 133.97(6) | 133.76(7) |
| Fe–Cg($n$1) | 1.644(2) | 1.653(2) |
| Fe–Cg($n$2) | 1.653(2) | 1.659(2) |
| ∠Cp($n$1),Cp($n$2) | 2.8(3) | 0.8(3) |
| C=O[b] | 1.258(3) | 1.262(4) |
| C–OH[c] | 1.277(4) | 1.275(4) |
| O–C=O[d] | 123.9(3) | 123.1(3) |
| P–C[e] | 1.834(4)–1.893(2) | 1.830(3)–1.907(4) |
| C–P–C[f] | 101.2(1)–104.3(2) | 100.4(2)–103.4(2) |

[a] Definitions: Cp(11) = C(1–5), Cp(12) = C(6–10), Cp(21) = C(41–45), Cp(22) = C(46–50), Cp(13) = C(26–30), and Cp(23) = C(66–70). Cg($n$1,$n$2,$n$3) represent the respective centroids. For a note on the atom labelling scheme, see Figure 4. [b] C(11)–O(11) (molecule 1) or C(51)–O(21) (molecule 2). [c] C(11)–O(12) (molecule 1) or C(51)–O(22) (molecule 2). [d] O(11)–C(11)–O(12) (molecule 1) or O(21)–C(51)–O(22) (molecule 2). [e] Range of P(1)–C(12,14,20) (molecule 1) or P(2)–C(52,54,60) (molecule 2) distances. [f] Range of C(12)–P(1)–C(14,20) and C(14)–P(1)–C(20) (molecule 1) or C(52)–P(2)–C(54,60) and C(54)–P(2)–C(60) (molecule 2) angles.

in Table 3), albeit without any significant slanting of the three-legged piano-stool geometry, as evidenced by the dihedral angles of the basal [Cl($n$1),Cl($n$2),P($n$)] and Cp($n$3) planes of 8.1(2)° and 7.0(2)° for molecules 1 and 2 (≡ $n$), respectively. The overall molecular geometry is similar to that of the analogous complex with P-monodentate 2-[(diphenylphosphanyl)methyl]ferrocenecarboxylic acid.[7] The P-monodentate phosphane–carboxylic ligand is oriented such that its ferrocene and phenyl groups are kept clear of the ($\eta^5$-$C_5Me_5$)Rh moiety while the methyl group of the ethane-1,1-diyl linker is located approximately below the rhodium atom [cf. Rh(1)–P(1)–C(12)–C(2/13) and Rh(2)–P(2)–C(52)–C(42/53) torsion angles of –85.9(3)/45.6(3)° and –85.4(3)/44.9(3)°, respectively]. The Cp($n$1) and Cp($n$3) rings are nearly parallel in both molecules, the respective dihedral angles being 7.3(2)° [Cp(11)/Cp(13) in molecule 1] and 8.2(2)° [Cp(21)/Cp(23) in molecule 2]. This arrangement obviously corresponds with the π···π stacking interactions mentioned above.

Similarly to other ferrocene-based phosphane–carboxylic acids,[6,7,15] **1** reacts with [Rh(acac)(CO)($PCy_3$)] (Hacac = pentane-2,5-dione, Cy = cyclohexyl) to give a complex with *O*,*P*-chelating phosphane–carboxylate (**11**, Scheme 4) by replacement of the acetylacetonate and concomitant proton transfer. Compound **11** shows characteristic strong bands due to $\nu_{C\equiv O}$ at 1959 $cm^{-1}$ and carboxylate vibrations at 1612 and 1321 $cm^{-1}$ in its IR spectrum. The presence of two different phosphane donors in *trans* positions is best manifested in the $^{31}P$ NMR spectrum, which shows two doublets of doublets at $\delta_P$ = 40.9 and 46.5 ppm with typical coupling constants ($^1J_{Rh,P} \approx 125$, $^2J_{P,P}$ = 319 Hz),[7,15,16] and further by $^{31}P$-$^{13}C$ coupling patterns in the $^{13}C$ NMR spectrum (e.g., by a doublet of triplets at $\delta_C$ = 190.20 ppm with $^1J_{Rh,C}$ = 73 and $^2J_{P,C}$ = 16 Hz for Rh-*C*O).

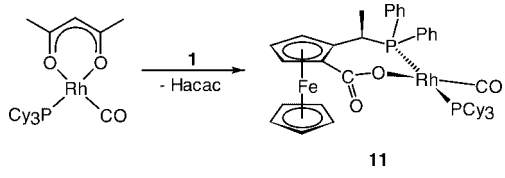


Scheme 4.

As revealed by X-ray diffraction analysis (Figure 5, Table 4), the coordination environment of the rhodium atom in **11** is almost planar with the phosphane moieties in *trans* positions. The maximum deviation of the donor atoms and the metal atom from the mean coordination plane [Rh]

 © 2007 Wiley-VCH Verlag GmbH & Co. KGaA, Weinheim 

(see Table 4 for definitions) is much less than 0.1 Å. Likewise, the interligand angles differ only marginally from 90° which, together with their sum of 360.4°, rules out any tetrahedral deformation of the coordination polyhedron.

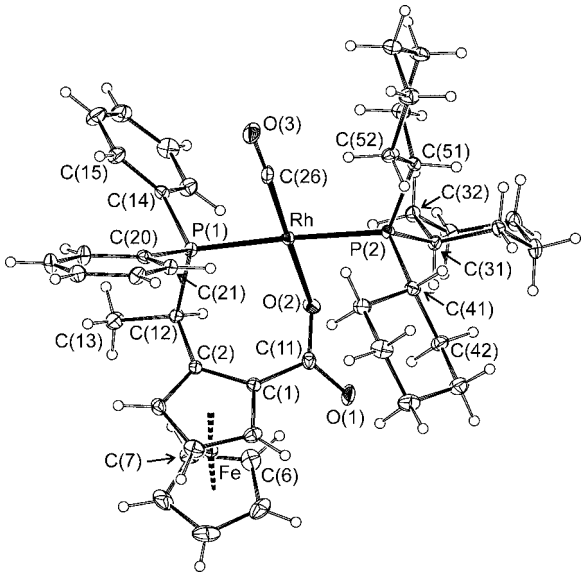


Figure 5. PLATON view of the molecular structure of **11** showing displacement ellipsoids at the 30% probability level.

On the whole, the coordination geometry compares favourably with that in similar complexes featuring 2-[(diphenylphosphanyl)methyl]ferrocenecarboxylate[7] and 1′-(diphenylphosphanyl)ferrocenecarboxylate as the *O*,*P*-chelating ligands.[15a] The pendant phosphane and, consequently, the [Rh] plane in **11** are directed above the ferrocene framework such that the [Rh] and Cp(1) planes subtend a dihedral angle of about 73° (see Table 4 for definition of the ring planes). The methyl and rhodium "substituents" at the P(1)–C(12) bond are arranged in an antiperiplanar manner [C(13)–C(12)–P(1)–Rh 169.3(2)°] whilst the ferrocene unit and the rhodium atom are close to synperiplanar [C(2)–C(12)–P(1)–Rh –62.3(2)°]. In such an arrangement, the formation of the Rh–O(2) bonds leads to a rotation of the carboxyl group from its parent Cp(1) plane by about 33° (note that the carboxyl and [Rh] planes are rotated by about 53°). The overall conformation is similar to the 2-[(diphenylphosphanyl)methyl]ferrocenecarboxylato complex mentioned above from which **11** differs only by substitution at the phosphanyl side chain (methyl vs. H). Similarly to the mentioned complex, the "$PC_3$" moieties of the phosphane donors in **11** appear staggered when looking in the P(1)–P(2) direction and all cyclohexyl rings adopt a chair conformation,[17] binding the phosphorus atom in equatorial positions.

### Palladium Complexes

When studying palladium(II) complexes we focused on amide **6** due to its expected ability to ligate metal centres in different ways. First, we turned to (allyl)palladium species as they are relevant to palladium-mediated allylic alkylation reactions (see below). The reaction of [{Pd(μ-Cl)($\eta^3$-$C_3H_5$)}$_2$] with **6** in a 1:2 molar ratio was monitored in situ. A single "product" **12** was detected in the $^1$H NMR spectrum, which shows two sets of broad signals at room temperature (25 °C). Heating to 50 °C resulted in the coalescence of most signals (see Experimental Section). On the other hand, cooling to 0 °C and below caused the broad resonances to sharpen and split into two distinct sets of signals attributable to isomers due to a fluxional $\eta^3$-allyl moiety.[18] The $^{31}$P NMR spectra are in agreement with these observations, showing two narrow-spaced signals ($\delta_P$ = 34.8 and 34.6 ppm at 0 °C), which collapse into a sharp singlet at higher temperature ($\delta_P$ = 35.3 ppm at 50 °C). The $^{31}$P NMR shift and unaffected $\nu_{C=O}$ band in the IR spectrum allowed us to formulate **12** as a fluxional complex with P-monodentate **6**, i.e. [PdCl($\eta^3$-$C_3H_5$)(**6**-κ*P*)], which results from a simple bridge-cleavage reaction. Support for this formulation was obtained from the ESI mass spectrum, which shows a peak at *m*/*z* = 678 attributable to [($\eta^3$-$C_3H_5$)-Pd(**6**)]$^+$.

The chelating, non-fluxional palladium(II) complex **13** was obtained from the reaction of **6** with [PdCl(Me)(cod)] (cod = $\eta^2$:$\eta^2$-cycloocta-1,5,-diene; Scheme 5). The spectro-

Table 4. Selected bond lengths [Å] and angles [°] for **11**.[a]

| | | | |
|---|---|---|---|
| Rh–P(1) | 2.3041(9) | P(1)–Rh–O(2) | 93.12(6) |
| Rh–P(2) | 2.3692(8) | P(1)–Rh–C(26) | 86.5(1) |
| Rh–O(2) | 2.064(2) | P(2)–Rh–O(2) | 85.24(6) |
| Rh–C(26) | 1.793(3) | P(2)–Rh–C(26) | 95.5(1) |
| C(26)–O(3) | 1.155(4) | Rh–C(26)–O(3) | 175.8(3) |
| Fe–Cg(1) | 1.643(2) | ∠Cp(1),Cp(2) | 5.9(2) |
| Fe–Cg(2) | 1.652(2) | ∠Cp(1),[COO] | 33.3(4) |
| C(1)–C(11) | 1.506(4) | ∠[Rh],[COO] | 53.3(4) |
| C(11)–O(1) | 1.229(4) | ∠[Rh],Cp(1) | 73.3(1) |
| C(11)–O(2) | 1.288(4) | O(1)–C(11)–O(2) | 124.1(3) |
| C(2)–C(12) | 1.500(4) | C(2)–C(12)–P | 107.8(2) |
| C(12)–C(13) | 1.537(5) | C(2)–C(12)–C(13) | 113.9(3) |
| P(1)–C[b] | 1.815(3)–1.867(3) | C–P(1)–C[c] | 102.0(1)–108.6(2) |
| P(2)–C[d] | 1.855(3)–1.875(3) | C–P(2)–C[e] | 102.6(1)–105.5(1) |

[a] Definitions: Ring planes: Cp(1) = C(1–5), Cp(2) = C(6–10); Cg(1,2) denote the respective ring centroids. [Rh] = {Rh, P(1), P(2), O(2), C(26)}, [COO] = {C(11), O(1), O(2)}. [b] Range of P–C(12,14,20) distances. [c] Range of C(12)–P–C(14,20) and C(14)–P(1)–C(20) angles. [d] Range of P–C(31,41,51) distances. [e] Range of C(31)–P–C(41,51) and C(41)–P(2)–C(51)angles.

 © 2007 Wiley-VCH Verlag GmbH & Co. KGaA, Weinheim 

scopic data of **13** clearly indicate the formation of only one of all possible isomers that differ in the coordination mode of the amide ligand (*P,O* vs. *P,N*) *and* configuration (*trans*-P,Cl and *trans*-P,C) in solution. Whereas the P-coordination was clearly inferred from the shift of the $^{31}P$ NMR resonance to lower fields ($\Delta_P$ = 44.0 ppm), the shift of the $\nu_{C=O}$ (amide I) band to lower energies and a low-field shift of the C=O resonance in the $^{13}C$ NMR spectrum ($\Delta_C$ = 5.3 ppm) suggested coordination through the amide oxygen atom. A *trans*-P,Cl configuration was proposed on the basis of a comparison of $^3J_{P,H}$ values for the palladium-bonded methyl group obtained from the $^1H$ NMR spectrum with literature data.[19,20]

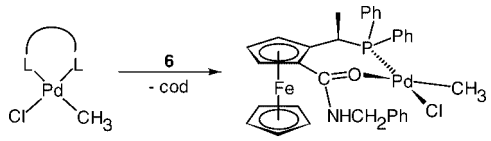


**13**

Scheme 5. Preparation of complex **13** (L–L is cycloocta-1,5-diene).

The crystal structure of **13** (Figure 6, Table 5) confirmed both the anticipated coordination mode of **6** and the *trans*-P,Cl disposition of the donors. The palladium atom and its four donor atoms are coplanar within 0.1 Å; the sum of the interligand angles is 360.15°. The Pd–donor distances are rather unexceptional, comparing well with those in [PdCl($C_6F_5$){2-$Ph_2PC_6H_4CONHCHMe_2$-$\kappa^2$*O,P*}] [Pd–Cl 2.3691(4), Pd–P 2.2114(4), Pd–O 2.098(1) Å],[21] [PdCl(Me)(L-$\kappa^2$*P,P′*)] (L = various chiral ferrocene-derived diphosphanes of the type [Fe{$\eta^5$-$C_5H_3$($PR_2$-1)[CH(Me)-$PR'_2$-2]}($\eta^5$-$C_5H_5$)]; Pd–C 2.081–2.141 Å)[20a,22] and bis{μ-[2-(diphenylphosphanyl)ferrocenyl]carboxylato-*O,O′,P*}bis-{methylpalladium(II)}] [Pd–C 2.013(3) Å], for example.[23]

The structural data of the related amido phosphane oxide (*R*)-**8** enable an inspection of the changes in the amide group geometry upon coordination. On going from (*R*)-**8** to **13**, for example, the C=O bond elongates by about 0.03 Å while the C(11)–N/C(1) bond lengths decrease by about 0.02 Å. This is consistent with donation from the amide oxygen atom and a corresponding electron density shift towards C11. As usual, the amide moiety is almost

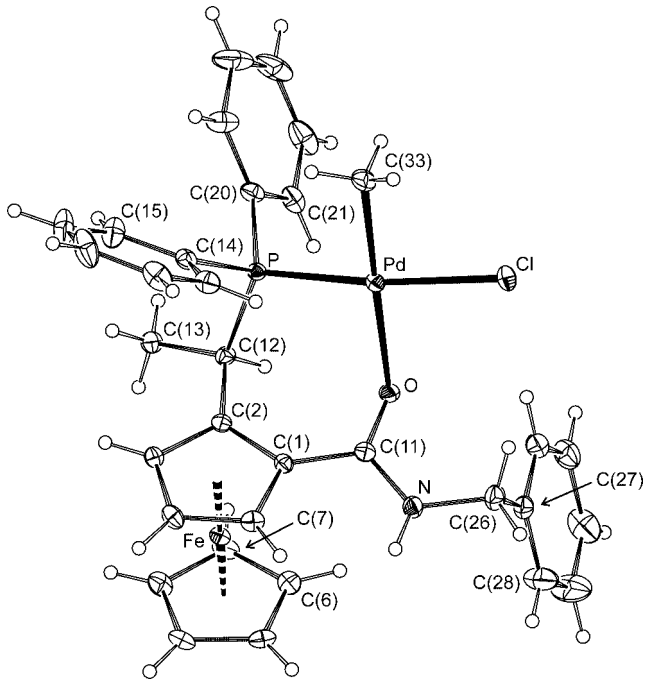


Figure 6. PLATON view of the molecular structure of **13** showing 30% probability displacement ellipsoids.

planar [τ(O–C(11)–N–C(26) 7.0(4)°] but is rotated from the Cp1 plane by 16.8(3)° along the C1–C11 bond, which brings the O atom above the ferrocene unit and in the vicinity of the palladium atom. The geometry of the ferrocene unit remains practically unaffected: the Fe–Cg distances are nearly the same as in (*R*)-**8** and the cyclopentadienido ligands show a tilt of 3.7(2)°. However, a minor deformation, not detectable in (*R*)-**8**, can be found at the amide-linking bond C(1)–C(11), which is bent away from the phosphanylalkyl chain. The C(11)–C(1)–C(2/5) angles differ by as much as 18° [125.9(2)/107.9(2)°] whereas the difference between the C(12)–C(2)–C(1/3) angles is only 2.5°. Such a distortion of the valence angles can be attributed to *O,P*-chelate coordination, making the donor sites more distant.

In the solid state, the molecules of **13** interact predominantly through N–H(90)···Cl$^{iii}$ bonds [N–H(90)···Cl$^{iii}$ (iii: 1 – *x*, 1/2 + *y*, 2 – *z*) 3.281(2) Å; angle at H(90) 160°], which

Table 5. Selected bond lengths [Å] and angles [°] for **13**.[a]

| | | | |
|---|---|---|---|
| Pd–Cl | 2.3781(8) | Cl–Pd–O | 89.97(6) |
| Pd–P | 2.2028(6) | Cl–Pd–C(33) | 88.92(9) |
| Pd–O | 2.171(2) | P–Pd–O | 93.76(6) |
| Pd–C(33) | 2.029(3) | P–Pd–C(33) | 87.50(8) |
| Fe–Cg(1) | 1.647(1) | ∠Cp(1),Cp(2) | 3.7(2) |
| Fe–Cg(2) | 1.657(1) | ∠[Pd],[CON] | 55.8(3) |
| C(1)–C(11) | 1.478(4) | ∠[Pd],Cp(1) | 67.2(1) |
| C(11)–O | 1.257(4) | O–C(11)–N | 119.7(3) |
| C(11)–N | 1.334(4) | C(11)–N–C(26) | 121.6(2) |
| N–C(26) | 1.468(4) | C(2)–C(12)–P | 108.6(2) |
| C(26)–C(27) | 1.506(5) | C(2)–C(12)–C(13) | 112.9(2) |
| P–C[b] | 1.815(3)–1.865(3) | C–P–C[c] | 105.5(1)–109.4(1) |

[a] Definitions: Ring planes are defined as follows: Cp(1) = C(1–5), Cp(2) = C(6–10); Cg(1,2) are the respective ring centroids. [Pd] = {Pd,Cl,P,O,C(33)}, [CON] = {C(11),O,N}. [b] Range of P–C(12,14,20) distances. [c] Range of C(12)–P–C(14,20) and C(14)–P(1)–C(20) angles.

 © 2007 Wiley-VCH Verlag GmbH & Co. KGaA, Weinheim 

gives rise to infinite helical chains running along the crystallographic $2_1$ screw axis.

### Catalytic Tests

In order to probe the catalytic performance of this newly synthesised family of ligands derived from **1**, we first chose the rhodium-catalysed hydrogenation of methyl β-acetamidocinnamate.[24] Somewhat unexpectedly, the reductions performed under standard conditions (see Experimental Section) did not proceed at all. As the next step, we turned to palladium-mediated asymmetric allylic alkylation,[25] which is a widely used benchmark test that often allows a direct comparison with other chiral ferrocene-based ligands.

When performing allylic substitutions (Scheme 6) we used 1,3-diphenylprop-2-en-1-yl acetate as the substrate, dimethyl malonate/*N*,*O*-bis(trimethylsilyl)acetamide/potassium acetate as the nucleophile source, and pre-catalysts formed in situ from [{Pd(μ-Cl)(η$^3$-$C_3H_5$)}$_2$] and a slight excess of the appropriate ligand. All reactions were carried out in dichloromethane at room temperature. The results are summarised in Table 6.

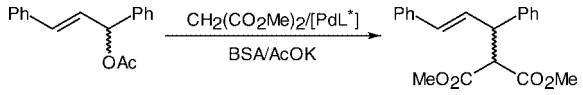


Scheme 6.

Table 6. Application of **1** and its amides in palladium-catalysed enantioselective allylic alkylation.[a]

| Entry | Ligand | Conv. (isolated yield) [%][b] | *ee* [%] (config.)[c] |
|---|---|---|---|
| 1 | **1** | 100 (94) | 10 (*S*) |
| 2 | **6** | 55 | 41 (*R*) |
| 3 | (*R*)-**7** | 42 | 43 (*R*) |
| 4 | (*S*)-**7** | 22 | 35 (*R*) |

[a] See Experimental Section for conditions. [b] Conversion determined by $^1$H NMR spectroscopy. [c] Absolute configuration assigned by comparison of the sign of the optical rotation with the literature data.

The reaction in the presence of the catalyst obtained from **1** proceeded with the highest rate (conversion) but with disappointingly low enantioselectivity (Table 6, Entry 1). Replacement of the carboxy group with a carbamoyl moiety resulted in lower chemical yields and higher *ee* values, although with an *opposite* configuration of the major product (Table 6, Entries 2–4). This change of configuration of the preferred alkylated product can be attributed to a changed donor ability of the ligands (P,O for **1** vs. P,N or P,O for the amides) or to a changed access for the nucleophile towards the η$^3$-allyl intermediate. A comparison of the results obtained with amides that differ only in their *N*-substituents (type and chirality) indicates that the nature of the benzylic group has only a small influence on the course of the catalytic reaction in terms of enantioselectivity while changing the reaction rate. Our observations correspond with previous attempts to clarify the role of individual chirality elements in ferrocene-based donors possessing both central and planar chirality, which clearly showed that the reaction course is governed not only by both chirality elements but also by their *mutual* matching.[26]

Despite the numerous reports concerning the use of ferrocene-based donors in allylic alkylations, there seems to be no example available in the literature relating directly to the compounds under study (same reaction, similar ligands). Most reports involving phosphanyl–ferrocenecarboxylic acids and their amides deal, with varying success, with reactions involving *cyclic* allylic acetates.[27,28] Nonetheless, acid **1** and its amides show *ee* values inferior to those reported for the chemically related (phosphanylferrocenyl)oxazolines[4b,26d,29] and for *meso*-1,1′-bis(diphenylphosphanyl)-2,2′-bis{*N*-(ω-hydroxyalkyl)carbamoyl}ferrocenes, which combine *two* phosphane and amide moieties.[30] Even so, the catalytic performance observed for **1** and the related amido phosphanes is lower than that of Josiphos-type ligands[31] where, however, a stronger ligand–palladium interaction can be expected due to the presence of two phosphane moieties.

## Conclusions

We have reported the preparation of a novel, enantiopure phosphanyl–ferrocenecarboxylic ligand combining planar and central chirality elements, namely (*R*,*R*$_p$)-2-[1-(diphenylphosphanyl)ethyl]ferrocenecarboxylic acid (**1**), and its derivatives modified at both the phosphorus (**4** and **5**) and carboxyl groups [amides **6**, (*S*)-**7** and (*R*)-**7**]. A study of the representative phosphanes as ligands for rhodium (**1**→**9**, **10**, **11**) and palladium(II) (**6**→**12** and **13**) clearly has shown their coordination versatility and the potentially multidentate nature of these phosphanyl–ferrocenecarboxylic donors. Based on these results, we have also investigated the catalytic performance of the modified phosphanes in enantioselective rhodium-catalysed hydrogenation and asymmetric palladium-catalysed allylic alkylation. Whereas the former reaction gave disappointing results, not proceeding with any of the ligands tested [**1**, **6**, (*R*)-**7**, and (*S*)-**7**], the latter proved more successful, thereby providing an insight into the role of the individual molecular parts on the reaction rate and stereodiscrimination.

## Experimental Section

**Materials and Methods:** All syntheses were performed under argon with exclusion of direct daylight. Tetrahydrofuran was dried by refluxing with potassium/benzophenone ketyl and distilled. Toluene was dried with sodium metal and distilled. Dichloromethane and chloroform were predried by standing over anhydrous potassium carbonate and then distilled from calcium hydride. Butan-2-one was dried with phosphorus pentaoxide and distilled prior to use. (*R*,*S*$_p$)-1-Bromo-2-[1-(diphenylphosphanyl)ethyl]ferrocene (**2**), [{(μ-Cl)RhCl(η$^5$-$C_5Me_5$)}$_2$],[32] [Rh(acac)(CO)(PCy$_3$)][15c] and [PdCl(Me)(cod)][33] were prepared according to the literature procedures. Other chemicals (Lachema, Fluka) and solvents used for crystallisations (Lach-Ner) were used without further purification. NMR

 © 2007 Wiley-VCH Verlag GmbH & Co. KGaA, Weinheim 

spectra were recorded with a Varian Unity Inova spectrometer ($^1$H: 399.95; $^{13}$C: 100.58; $^{31}$P: 161.90 MHz) at 25 °C unless indicated otherwise. Chemical shifts ($\delta$) are given relative to internal tetramethylsilane ($^{13}$C and $^1$H) or to external 85% aqueous $H_3PO_4$ ($^{31}$P). IR spectra were recorded with an FT IR Nicolet Magna 650 spectrometer. Positive ion electron impact (EI) and fast atom bombardment (FAB) mass spectra [including high resolution (HR) measurements] were obtained with a ZAB SEQ spectrometer. Electrospray (ESI) mass spectra were recorded with a Micromass Q-TOF spectrometer (acetonitrile solvent). Optical rotations were measured with an automatic polarimeter Autopol III (Rudolph Research) at room temperature.

**Preparation of ($R$,$R_p$)-2-[1-(Diphenylphosphanyl)ethyl]ferrocenecarboxylic Acid (1):** Butyllithium (2.1 mL, 2.5 M in hexanes, 5.3 mmol) was added dropwise to a stirred solution of **2** (1.91 g, 4.0 mmol) in thf (50 mL) at –78 °C. After stirring at –78 °C for 1 h, the reaction solution was poured onto crushed solid $CO_2$ (approx. 50 g) and allowed to stand at room temperature overnight. The mixture was then diluted with water and diethyl ether (approx. 30 mL each), and washed with saturated aqueous NaCl solution (2 × 30 mL). The organic phase was dried with anhydrous $MgSO_4$ and the solvents were evaporated under vacuum. The residue was purified by chromatography on silica gel, eluting with dichloromethane/methanol (20:1). A minor band of (*R*)-[1-(diphenylphosphanyl)ethyl]ferrocene eluted first, followed by the band of the product, which, after evaporation of the solvent, afforded **1** as an orange solid foam. Yield: 1.482 g (84%). $^1$H NMR ($CDCl_3$): $\delta$ = 1.55 (dd, $^3J_{H,H}$ = 7.1, $^3J_{P,H}$ = 13.9 Hz, 3 H, CHC*H*$_3$), 4.21 (s, 5 H, $C_5H_5$), 4.28 (qd, $^3J_{H,H}$ = 7.1, $^2J_{P,H}$ = 5.7 Hz, 1 H, C*H*CH$_3$), 4.36 (m, 1 H, $C_5H_3$), 4.40 (apparent t, $J \approx$ 2.7 Hz, 1 H, $C_5H_3$), 4.68 (m, 1 H, $C_5H_3$), 7.01–7.64 (m, 10 H, P*Ph*$_2$) ppm. $^{13}$C{$^1$H} NMR ($CDCl_3$): $\delta$ = 18.49 (d, $^2J_{P,C}$ = 19 Hz, CH*C*H$_3$), 28.90 (d, $^1J_{P,C}$ = 15 Hz, *C*HCH$_3$), 67.44 (d, $^3J_{P,C}$ = 2 Hz, $C_5H_3$ *C*-CO$_2$H), 69.95 ($C_5H_3$ *C*H), 69.97 ($C_5H_3$ *C*H), 70.32 ($C_5H_5$), 70.85 (d, $J_{P,C}$ = 5 Hz, $C_5H_3$ *C*H), 95.82 (d, $^2J_{P,C}$ = 16 Hz, $C_5H_3$ *C*-CH), 127.48 (d, $^3J_{P,C}$ = 6 Hz, PPh$_2$ *C*H$_m$), 128.07 (PPh$_2$ *C*H$_p$), 128.31 (d, $^3J_{P,C}$ = 6 Hz, PPh$_2$ *C*H$_m$), 129.09 (PPh$_2$ *C*H$_p$), 133.23 (d, $^2J_{P,C}$ = 18 Hz, PPh$_2$ *C*H$_o$), 134.40 (d, $^2J_{P,C}$ = 20 Hz, PPh$_2$ *C*H$_o$), 135.78, 136.69 (2 × d, $^1J_{P,C}$ = 16 Hz, PPh$_2$ *C*$_{ipso}$), 178.06 (*C*O$_2$H) ppm. $^{31}$P{$^1$H} NMR ($CDCl_3$): $\delta$ = 11.1 (s) ppm. IR (Nujol): $\tilde{\nu}$ = 1667 (s), 1303 (m), 1227 (m), 1157 (w), 1088 (w), 1000 (vw), 958 (vw), 821 (w), 742 (m), 697 (m), 496 (w), 479 (w) cm$^{-1}$. MS (EI+): *m*/*z* (%) = 442 (13) [M]$^{+\cdot}$, 257 (59) [M – PPh$_2$]$^+$, 239 (6), 213 (8), 186 (51), 183 (34) [PPh$_2$ – 2 H]$^+$, 152 (12), 138 (22), 121 (27) [$C_5H_5Fe$]$^+$, 119 (63), 108 (100). HR MS calcd. for $C_{25}H_{23}{}^{56}FeO_2P$ [M]$^{+\cdot}$ 442.0785; found 442.0782. [$a$]$_D$ = –56.5 ($c$ = 1.0, $CHCl_3$).

**Preparation of ($R$,$R_p$)-2-[1-(Diphenylthiophosphoryl)ethyl]ferrocenecarboxylic Acid (4):** A solution of **1** (115 mg, 0.26 mmol) and sulfur (13 mg, 0.41 mmol) in toluene (10 mL) was heated at reflux for 1.5 h. After cooling to room temperature, the reaction solution was concentrated to dryness and the residue purified by column chromatography (silica gel, dichloromethane/methanol, 10:1). Subsequent evaporation of the solvent gave **4** as an orange solid foam. Yield: 111 mg (90%). $^1$H NMR ($CDCl_3$): $\delta$ = 1.67 (dd, $^3J_{H,H}$ = 7.0, $^3J_{P,H}$ = 18.6 Hz, 3 H, CHC*H*$_3$), 4.24 (s, 5 H, $C_5H_5$), 4.52 (apparent t, $J \approx$ 2.7 Hz, 1 H, $C_5H_3$), 4.61 (m, 1 H, $C_5H_3$), 4.80 (dq, $^3J_{H,H}$ = 7.0, $^2J_{P,H}$ = 8.3 Hz, 1 H, C*H*CH$_3$), 4.92 (m, 1 H, $C_5H_3$), 7.08–8.22 (m, 10 H, P*Ph*$_2$) ppm. $^{13}$C{$^1$H} NMR ($CDCl_3$): $\delta$ = 16.43 (CH*C*H$_3$), 32.61 (d, $^1J_{P,C}$ = 48 Hz, *C*HCH$_3$), 67.34 (d, $^2J_{P,C}$ = 2 Hz, $C_5H_3$ *C*-CO$_2$H), 70.01 ($C_5H_3$ *C*H), 70.57 ($C_5H_5$), 70.67 ($C_5H_3$ *C*H), 72.82 (d, $^3J_{P,C}$ = 2.5 Hz, $C_5H_3$ *C*H), 90.07 ($C_5H_3$ *C*-CH), 127.23, 128.66 (2 × d, $^3J_{P,C}$ = 12 Hz, PPh$_2$ *C*H$_m$), 130.23 (d, $^1J_{P,C}$ = 75 Hz, PPh$_2$ *C*$_{ipso}$), 130.77 (d, $^4J_{P,C}$ = 3 Hz, PPh$_2$ *C*H$_p$), 131.60 (d, $^1J_{P,C}$ = 79 Hz, PPh$_2$ *C*$_{ipso}$), 131.68 (d, $^4J_{P,C}$ = 3 Hz, PPh$_2$ *C*H$_p$), 131.95, 132.31 (2 × d, $^2J_{P,C}$ = 9 Hz, PPh$_2$ *C*H$_o$), 177.10 (*C*O$_2$H) ppm. $^{31}$P{$^1$H} NMR ($CDCl_3$): $\delta$ = 54.7 (s) ppm. IR (Nujol): $\tilde{\nu}$ = 1663 (s), 1437 (sh), 1300 (m), 1227 (m), 1158 (w), 1100 (m), 1028 (w), 999 (w), 824 (w), 752 (m), 729 (s), 708 (m), 690 (m), 651 (m), 588 (w), 511 (w), 486 (m) cm$^{-1}$. MS (EI+): *m*/*z* (%) = 474 (39) [M]$^+$, 442 (4) [M – S]$^{+\cdot}$, 338 (8), 275 (100) [M – Ph$_2$PS]$^+$, 218 (25), 186 (16), 183 (18), 138 (12), 119 (39), 108 (28). HR MS calcd. for $C_{25}H_{23}{}^{56}FeO_2PS$ [M]$^{+\cdot}$ 474.0506; found 474.0518. [$a$]$_D$ = 39 ($c$ = 1.0, $CHCl_3$).

**Preparation of ($R$,$R_p$)-2-[1-(Diphenylphosphoryl)ethyl]ferrocenecarboxylic Acid (5):** In air, hydrogen peroxide (0.3 mL 30%, 2.5 mmol) was added to a solution of acid **1** (93 mg, 0.21 mmol) in acetone (5 mL) whilst stirring and cooling in an ice bath. The cooling bath was removed after 5 min and stirring was continued at room temperature for 30 min. A saturated aqueous solution of $Na_2S_2O_3$ (5 mL) was added to remove the excess of $H_2O_2$ and, after an additional 10 min, acetone was removed under reduced pressure, the residue diluted with water (10 mL) and extracted with dichloromethane (3 × 10 mL). The combined extracts were washed with saturated aqueous NaCl solution (20 mL), dried with $MgSO_4$, and the solvents were evaporated under vacuum. The residue was immediately purified by column chromatography (silica gel, dichloromethane/methanol mixture, 10:1) to yield **4** as a yellow solid foam after solvent evaporation. Yield: 48 mg (50%); the reaction is accompanied by decomposition, which results in the formation of a dark material that remains adsorbed at the top of the chromatographic column. $^1$H NMR ($CDCl_3$): $\delta$ = 1.71 (dd, $^3J_{H,H}$ = 7.3, $^3J_{P,H}$ = 15.7 Hz, 3 H, CHC*H*$_3$), 4.23 (s, 5 H, $C_5H_5$), 4.43 (apparent t, $J \approx$ 2.7 Hz, 1 H, $C_5H_3$), 4.46 (dq, $^3J_{H,H} \approx {}^2J_{P,H} \approx$ 7.5 Hz, 1 H, C*H*CH$_3$), 4.66 (m, 2 H, 2 × $C_5H_3$), 7.12–8.02 (m, 10 H, P*Ph*$_2$) ppm. $^{13}$C{$^1$H} NMR ($CDCl_3$): $\delta$ = 15.21 (d, $^2J_{P,C}$ = 2 Hz, CH*C*H$_3$), 31.91 (d, $^1J_{P,C}$ = 65 Hz, *C*HCH$_3$), 68.67 ($C_5H_3$ *C*-CO$_2$H), 70.31 ($C_5H_3$ *C*H), 70.49 ($C_5H_5$), 70.51 ($C_5H_3$ *C*H), 71.84 (d, $J_{P,C}$ = 2 Hz, $C_5H_3$ *C*H), 89.79 ($C_5H_3$ *C*-CH), 127.58, 128.59 (2 × d, $^3J_{P,C}$ = 12 Hz, PPh$_2$ *C*H$_m$), 130.32, (d, $^1J_{P,C}$ = 52 Hz, PPh$_2$ *C*$_{ipso}$), 131.27 (d, $^1J_{P,C}$ = 57 Hz, PPh$_2$ *C*$_{ipso}$), 131.29 (d, $^4J_{P,C}$ = 2.5 Hz, PPh$_2$ *C*H$_p$), 131.41, 131.68 (2 × d, $^2J_{P,C}$ = 9 Hz, PPh$_2$ *C*H$_o$), 131.89 (d, $^4J_{P,C}$ = 2 Hz, PPh$_2$ *C*H$_p$), 175.99 (*C*O$_2$H) ppm. $^{31}$P{$^1$H} NMR ($CDCl_3$): $\delta$ = 36.5 (s) ppm. IR (Nujol): $\tilde{\nu}$ = 1685 (s), 1281 (m), 1215 (m), 1153 (s), 1118 (m), 1105 (m), 1083 (m), 1027 (w), 1000 (w), 820 (w), 742 (m), 723 (s), 696 (m), 541 (m), 497 (m), 472 (w) cm$^{-1}$. MS (EI+): *m*/*z* (%) = 458 (7) [M]$^{+\cdot}$, 393 (2) [M – $C_5H_5$]$^+$, 368 (5), 322 (4). HR MS calcd. for $C_{25}H_{23}{}^{56}FeO_3P$ [M]$^{+\cdot}$ 458.0734; found 458.0750. [$a$]$_D$ = 30.5 ($c$ = 1.0, $CHCl_3$).

**Preparation of ($R$,$S_p$)-1-bromo-2-[1-(diphenylthiophosphoryl)ethyl]ferrocene (3):** A solution of **2** (382 mg, 0.80 mmol) and sulfur (32 mg, 1.0 mmol) in toluene (10 mL) was heated at reflux for 1 h and then stirred at room temperature overnight. The solvent was evaporated under vacuum, and the residue was purified by column chromatography (silica gel; diethyl ether/hexane, 1:1). Subsequent concentration afforded the product as an orange solid. Yield: 359 mg (88%). $^1$H NMR ($CDCl_3$): $\delta$ = 1.66 (dd, $^3J_{H,H}$ = 7.1, $^3J_{P,H}$ = 18.4 Hz, 3 H, CHC*H*$_3$), 3.80 (dq, $^3J_{H,H} \approx {}^2J_{P,H} \approx$ 7.5 Hz, 1 H, C*H*CH$_3$), 4.19 (s, 5 H, $C_5H_5$), 4.22 (apparent t, $J \approx$ 2.6 Hz, 1 H, $C_5H_3$), 4.26 (m, 1 H, $C_5H_3$), 4.68 (m, 1 H, $C_5H_3$), 7.10–8.16 (m, 10 H, P*Ph*$_2$) ppm. $^{13}$C{$^1$H} NMR ($CDCl_3$): $\delta$ = 17.01 (CH*C*H$_3$), 33.72 (d, $^1J_{P,C}$ = 49 Hz, *C*HCH$_3$), 66.38 (s, 2 C, 2 × $C_5H_3$ *C*H), 68.76 ($C_5H_3$ *C*H), 71.00 ($C_5H_5$), 80.93 (d, $^3J_{P,C}$ = 2 Hz, $C_5H_3$ *C*-Br), 86.04 ($C_5H_3$ *C*-CH), 127.54, 128.67 (2 × d, $^3J_{P,C}$ = 12 Hz, PPh$_2$ *C*H$_m$), 129.79 (d, $^1J_{P,C}$ = 74 Hz, PPh$_2$ *C*$_{ipso}$), 131.03, 131.78 (2 × d, $^4J_{P,C}$ = 3 Hz, PPh$_2$ *C*H$_p$), 131.91 (d, $^1J_{P,C}$ = 80 Hz, PPh$_2$ *C*$_{ipso}$), 132.00, 132.36 (2 × d, $^2J_{P,C}$ = 9 Hz, PPh$_2$ *C*H$_o$) ppm. $^{31}$P{$^1$H} NMR

 © 2007 Wiley-VCH Verlag GmbH & Co. KGaA, Weinheim 

($CDCl_3$): $\delta$ = 53.5 (s) ppm. MS (EI+): *m*/*z* (%) = 510 (40)/508 (40) $[M]^+$, 445 (3)/443 (3) $[M - C_5H_5]^+$, 363 (9), 338 (8), 308 (67), 293 (97)/291 (100) $[M - Ph_2PS]^+$, 260 (13), 217 (18) $[Ph_2PPS]^+$, 196 (14), 185 (16), 183 (30) $[Ph_2P - 2\ H]^+$, 155 (25), 153 (18), 139 (26), 121 (21) $[C_5H_5Fe]^+$. HR MS calcd. for $C_{24}H_{22}{}^{56}FePS^{79}Br$ $[M]^{+\cdot}$ 507.9713; found 507.9703. $C_{24}H_{22}Br^{56}FePS$ (509.2): calcd. C 56.61, H 4.35; found C 56.29, H 4.34. $[\alpha]_D$ = 55.5 (*c* = 1.0, $CHCl_3$).

**Alternative Preparation of 1:** The reaction was performed as described above for the preparation of **1**, starting from bromide **3** (280 mg, 0.55 mmol in 10 mL of thf) and butyllithium (0.3 mL, 2.5 M in hexanes, 0.75 mmol). Purification of the crude product by column chromatography (silica gel; dichloromethane/methanol, 10:1) afforded **4** as an orange glassy solid. Yield: 138 mg (53%). In the next step, phosphane sulfide **4** (58 mg, 0.12 mmol) was dissolved in dichloromethane (5 mL) and MeOTf (0.05 mL, 0.44 mmol) was added. The mixture was stirred at room temperature for 3 h. The solvent was removed under reduced pressure, the residue immediately dissolved in dichloromethane (5 mL), and treated with $P(NMe_2)_3$ (0.06 mL, 0.33 mmol). After stirring the resulting mixture at room temperature overnight, the volatiles were removed under vacuum and the residue was purified by column chromatography (silica gel, dichloromethane/methanol, 20:1). Concentration of the appropriate fraction gave acid **1** as an orange glassy solid. Yield: 23 mg (43%).

**General Procedure for the Preparation of Amides:** 1-Hydroxybenzotriazole (HOBt) was added to a solution of acid **1** in dichloromethane (15 mL) and the reaction mixture was stirred at 0 °C for 5 min (some HOBt, which is used in excess, remained undissolved). *N*-(3-Dimethylaminopropyl)-*N*′-ethylcarbodiimide (EDC) was then added dropwise and the formed solution was stirred at 0 °C for another 30 min, during which time the colour of the solution turned from orange to red. Finally, the appropriate amine (neat) was added and stirring was continued at room temperature for an additional 20 h. The mixture was then extracted with 3 M HCl (10 mL), twice with saturated aqueous $NaHCO_3$ (10 mL), and brine (10 mL). The organic phase was dried with $MgSO_4$, and the solvents were evaporated under vacuum. The residual orange oil was purified by column chromatography on silica gel, eluting with dichloromethane/methanol (20:1).

***N*-Benzyl-(*R*,*R*$_p$)-2-[1-(diphenylphosphanyl)ethyl]ferrocenecarboxamide (6):** Starting from **1** (221 mg, 0.50 mmol), HOBt (78 mg, 0.56 mmol), EDC (0.1 mL, 0.6 mmol) and benzylamine (57 mg, 0.53 mmol), the above procedure gave **6** as an orange solid foam. Yield: 195 mg (73%). $^1H$ NMR ($CDCl_3$): $\delta$ = 1.55 (dd, $^3J_{H,H}$ = 7.1, $^3J_{P,H}$ = 14.9 Hz, 3 H, CHC*H*$_3$), 3.99 (dd, *J* = 5.0, *J* = 14.9 Hz, 1 H, NHC*H*$_2$Ph), 4.18 (s, 5 H, $C_5H_5$), 4.19 (m, 1 H, $C_5H_3$), 4.22 (apparent t, *J* ≈ 2.6 Hz, 1 H, $C_5H_3$), 4.26 (m, 1 H, $C_5H_3$), 4.47 (dq, $^3J_{H,H} \approx {}^2J_{P,H} \approx 7$ Hz, 1 H, C*H*CH$_3$), 4.48 (dd, $^3J_{H,H}$ = 5.0, $^2J_{H,H}$ = 14.9 Hz, 1 H, NHC*H*$_2$Ph), 5.38 (t, $^3J_{H,H}$ = 5.5 Hz, 1 H, CON*H*), 6.85–7.65 (m, 15 H, P*Ph*$_2$ and CH$_2$*Ph*) ppm. $^{13}C\{^1H\}$ NMR ($CDCl_3$): $\delta$ = 18.62 (d, $^2J_{P,C}$ = 20 Hz, CH*C*H$_3$), 28.47 (d, $^1J_{P,C}$ = 13 Hz, *C*HCH$_3$), 43.33 (NH*C*H$_2$Ph), 65.41 ($C_5H_3$ *C*H), 67.81 ($C_5H_3$ *C*H), 69.13 (d, $J_{P,C}$ = 6 Hz, $C_5H_3$ *C*H), 70.04 ($C_5H_5$), 75.65 ($C_5H_3$ *C*-CONH), 95.06 (d, $^2J_{P,C}$ = 18 Hz, $C_5H_3$ *C*-CH), 127.30 (d, $^3J_{P,C}$ = 6 Hz, PPh$_2$ *C*H$_m$), 127.30 (CH$_2$Ph *C*H$_p$), 127.68 (br. s, PPh$_2$ *C*H$_p$), 127.69 (CH$_2$Ph *C*H$_o$), 128.33 (d, $^3J_{P,C}$ = 6 Hz, PPh$_2$ *C*H$_m$), 128.60 (CH$_2$Ph *C*H$_m$), 129.14 (br. s, PPh$_2$ *C*H$_p$), 133.50 (d, $^2J_{P,C}$ = 18 Hz, PPh$_2$ *C*H$_o$), 134.45 (d, $^2J_{P,C}$ = 20 Hz, PPh$_2$ *C*H$_o$), 138.72 (CH$_2$Ph $C_{ipso}$), 170.11 (*C*ONH) ppm; (PPh$_2$ $C_{ipso}$) signals not observed. $^{31}P\{^1H\}$ NMR ($CDCl_3$): $\delta$ = 10.3 (s) ppm. IR (Nujol): $\tilde{\nu}$ = 1635 (s), 1520 (s), 1303 (w), 1266 (w), 1232 (w), 1106 (w), 1027 (w), 1001 (w), 819 (w), 742 (m), 697 (m), 480 (w) $cm^{-1}$. MS (EI+): *m*/*z* (%) = 531 (58) $[M]^{+\cdot}$, 440 (4) $[M - C_7H_7]^+$, 374 (3), 346 (56) $[M - PPh_2]^+$, 255 (12) $[M - C_7H_7 - PPh_2]^+$, 238 (32), 212 (43), 183 (37) $[PPh_2 - 2\ H]^+$, 121 (40) $[C_5H_5Fe]^+$, 91 (100) $[C_7H_7]^+$. HR MS calcd. for $C_{32}H_{30}{}^{56}FeNOP$ $[M]^{+\cdot}$ 531.1414; found 531.1430. $[\alpha]_D$ = –156.5 (*c* = 1.0, $CHCl_3$).

**(*R*,*R*$_p$)-2-[1-(Diphenylphosphanyl)ethyl]-*N*-[(*R*)-1-(phenylethyl)]ferrocenecarboxamide [(*R*)-7]:** According to the general procedure with **1** (221 mg, 0.50 mmol), HOBt (78 mg, 0.56 mmol), EDC (0.1 mL, 0.6 mmol) and (*R*)-(1-phenylethyl)amine (64 mg, 0.53 mmol) gave amide (*R*)-**7** as an orange solid foam. Yield: 218 mg (80%). $^1H$ NMR ($CDCl_3$): $\delta$ = 1.49 [d, $^3J_{H,H}$ = 6.8 Hz, NHCH(C*H*$_3$)Ph], 1.53 (dd, $^3J_{H,H}$ = 7.2, $^3J_{P,H}$ = 14.0 Hz, 3 H, PCHC*H*$_3$), 4.18 (s, 5 H, $C_5H_5$), 4.19 (m, 1 H, $C_5H_3$), 4.21 (apparent t, *J* ≈ 2.6 Hz, 1 H, $C_5H_3$), 4.27 (m, 1 H, $C_5H_3$), 4.39 (dq, $^3J_{H,H}$ = 7.2, $^2J_{P,H}$ = 5.2 Hz, 1 H, PC*H*CH$_3$), 5.00 [dq, $^3J_{H,H} \approx {}^3J_{H,H} \approx 7$ Hz, 1 H, NHC*H*(CH$_3$)Ph], 5.60 (d, $^3J_{H,H}$ = 7.1 Hz, 1 H, CON*H*), 6.90–7.58 [m, 15 H, P*Ph*$_2$ and CH(CH$_3$)*Ph*] ppm. $^{13}C\{^1H\}$ NMR ($CDCl_3$): $\delta$ = 18.57 (d, $^2J_{P,C}$ = 19 Hz, PCH*C*H$_3$), 21.87 [NHCH(*C*H$_3$)Ph], 28.58 (d, $^1J_{P,C}$ = 12 Hz, P*C*HCH$_3$), 48.76 [NH*C*H(CH$_3$)Ph], 66.44 ($C_5H_3$ *C*H), 67.95 ($C_5H_3$ *C*H), 69.44 (d, $J_{P,C}$ = 5 Hz, $C_5H_3$ *C*H), 70.12 ($C_5H_5$), 75.04 ($C_5H_3$ *C*-CONH), 94.52 (d, $^2J_{P,C}$ = 16 Hz, $C_5H_3$ *C*-CH), 126.52 (CHPh *C*H$_o$), 127.34 (CHPh *C*H$_p$), 127.45 (d, $^3J_{P,C}$ = 7 Hz, PPh$_2$ *C*H$_m$), 127.88 (PPh$_2$ *C*H$_p$), 128.31 (d, $^3J_{P,C}$ = 7 Hz, PPh$_2$ *C*H$_m$), 128.60 (CHPh *C*H$_m$), 129.25 (PPh$_2$ *C*H$_p$), 133.11 (d, $^2J_{P,C}$ = 17 Hz, PPh$_2$ *C*H$_o$), 134.56 (d, $^2J_{P,C}$ = 20 Hz, PPh$_2$ *C*H$_o$), 143.12 (CHPh $C_{ipso}$), 169.41 (*C*ONH) ppm; (PPh$_2$ $C_{ipso}$) signals not observed. $^{31}P\{^1H\}$ NMR ($CDCl_3$): $\delta$ = 10.1 (s) ppm. IR (Nujol): $\tilde{\nu}$ = 1632 (s), 1493 (s), 1305 (w), 1262 (w), 1225 (w), 1105 (w), 1000 (w), 820 (m), 742 (s), 697 (s), 480 (m) $cm^{-1}$. MS (EI+): *m*/*z* (%) = 545 (33) $[M]^{+\cdot}$, 440 (3) $[M - PhCHMe]^+$, 398 (4), 360 (24) $[M - PPh_2]^+$, 255 (11) $[M - PhCHMe - PPh_2]^+$, 238 (10), 213 (40), 186 (19), 183 (17) $[PPh_2 - 2\ H]^+$, 121 (19) $[C_5H_5Fe]^+$, 108 (32), 105 (34) $[C_8H_9]^+$, 85 (67), 83 (100). HR MS calcd. for $C_{33}H_{32}{}^{56}FeNOP$ $[M]^{+\cdot}$ 545.1571; found 545.1557. $[\alpha]_D$ = –69 (*c* = 1.0, $CHCl_3$).

**(*R*,*R*$_p$)-2-[1-(Diphenylphosphanyl)ethyl]-*N*-[(*S*)-1-(phenylethyl)]ferrocenecarboxamide [(*S*)-7]:** According to the general procedure with **1** (221 mg, 0.50 mmol), HOBt (78 mg, 0.56 mmol), EDC (0.1 mL, 0.6 mmol) and (*S*)-(1-phenylethyl)amine (64 mg, 0.53 mmol) gave (*S*)-**7** as an orange solid foam. Yield: 200 mg (73%). $^1H$ NMR ($CDCl_3$): $\delta$ = 1.34 [d, $^3J_{H,H}$ = 7.1 Hz, NHCH(C*H*$_3$)Ph], 1.52 (dd, $^3J_{H,H}$ = 7.2, $^3J_{P,H}$ = 15.0 Hz, 3 H, PCHC*H*$_3$), 4.07 (s, 5 H, $C_5H_5$), 4.20–4.22 (2 × m, 2 H, $C_5H_3$), 4.26 (m, 1 H, $C_5H_3$), 4.52 (dq, $^3J_{H,H} \approx {}^2J_{P,H} \approx 7$ Hz, 1 H, PC*H*CH$_3$), 4.89 [dq, $^3J_{H,H} \approx {}^3J_{H,H} \approx 7$ Hz, 1 H, NHC*H*(CH$_3$)Ph], 5.40 (d, $^3J_{H,H}$ = 7.1 Hz, 1 H, CON*H*), 6.99–7.65 [m, 15 H, P*Ph*$_2$, and CH(CH$_3$)*Ph*] ppm. $^{13}C\{^1H\}$ NMR ($CDCl_3$): $\delta$ = 18.53 (d, $^2J_{P,C}$ = 21 Hz, PCH*C*H$_3$), 22.20 [NHCH(*C*H$_3$)Ph], 28.30 (d, $^1J_{P,C}$ = 12 Hz, P*C*HCH$_3$), 48.48 [NH*C*H(CH$_3$)Ph], 65.32 ($C_5H_3$ *C*H), 67.79 ($C_5H_3$ *C*H), 69.33 (d, $J_{P,C}$ = 6 Hz, $C_5H_3$ *C*H), 69.98 ($C_5H_5$), 75.11 ($C_5H_3$ *C*-CONH), 95.24 (d, $^2J_{P,C}$ = 16 Hz, $C_5H_3$ *C*-CH), 125.80 (CHPh *C*H$_o$), 127.08 (CHPh *C*H$_p$), 127.36 (d, $^3J_{P,C}$ = 7 Hz, PPh$_2$ *C*H$_m$), 127.80 (PPh$_2$ *C*H$_p$), 128.35 (d, $^3J_{P,C}$ = 7 Hz, PPh$_2$ *C*H$_m$), 128.58 (CHPh *C*H$_m$), 129.18 (PPh$_2$ *C*H$_p$), 133.63 (d, $^2J_{P,C}$ = 18 Hz, PPh$_2$ *C*H$_o$), 134.49 (d, $^2J_{P,C}$ = 20 Hz, PPh$_2$ *C*H$_o$), 144.27 (CHPh $C_{ipso}$), 169.32 (*C*ONH) ppm; (PPh$_2$ $C_{ipso}$) signals not observed. $^{31}P\{^1H\}$ NMR ($CDCl_3$): $\delta$ = 10.4 (s) ppm. IR (Nujol): $\tilde{\nu}$ = 1631 (s), 1495 (s), 1308 (w), 1262 (w), 1228 (w), 1105 (w), 1000 (w), 820 (w), 742 (s), 697 (s), 485 (br. m) $cm^{-1}$. MS (EI+): *m*/*z* (%) = 545 (100) $[M]^+$, 480 (5) $[M - C_5H_5]^+$, 440 (9) $[M - PhCHMe]^+$, 360 (66) $[M - PPh_2]^+$, 333 (6), 255 (28) $[M - PhCHMe - PPh_2]^+$, 238 (26), 212 (43), 186 (36), 183 (19) $[PPh_2 - 2\ H]^+$, 121 (25) $[C_5H_5Fe]^+$, 108 (54), 105 (50) $[C_8H_9]^+$. HR MS calcd. for $C_{33}H_{32}{}^{56}FeNOP$ $[M]^{+\cdot}$ 545.1571; found 545.1579. $[\alpha]_D$ = –173 (*c* = 1.0, $CHCl_3$).

 © 2007 Wiley-VCH Verlag GmbH & Co. KGaA, Weinheim 

**Preparation of Dichlorido{(*R*,$R_p$)-2-[1-(diphenylphosphanyl-κ*P*)ethyl]ferrocenecarboxylic acid}(η$^5$-pentamethylcyclopentadienido)rhodium(III) (9):** A solution of acid **1** (90 mg, 0.20 mmol) in chloroform (5 mL) was added to a solution of [{(μ-Cl)RhCl(η$^5$-$C_5Me_5$)}$_2$] (62 mg, 0.10 mmol) in the same solvent (5 mL) and the resulting clear mixture was stirred at room temperature overnight. The solution was filtered through a PTFE syringe filter (0.45 μm pore size) and the solvents were evaporated to dryness under vacuum to give the product as a red glassy solid in practically quantitative yield (150 mg) according to NMR spectroscopy. $^1$H NMR ($CDCl_3$): δ = 1.18 (br. s, 15 H, $C_5Me_5$), 1.89 (br. dd, $^3J_{H,H}$ = 7.5, $^3J_{P,H}$ = 18.6 Hz, 3 H, CHC$H_3$), 4.08 (br. s, 1 H, $C_5H_3$), 4.13 (s, 5 H, $C_5H_5$), 4.24 (apparent t, $J \approx 2.7$ Hz, 1 H, $C_5H_3$), 4.58 (m, 1 H, $C_5H_3$), 4.86 (dq, $^3J_{H,H} \approx {}^2J_{P,H} \approx 7.5$ Hz, 1 H, C*H*CH$_3$), 7.28–8.12 (m, 10 H, P*Ph*$_2$) ppm. $^{13}$C{$^1$H} NMR ($CDCl_3$): δ = 8.43 ($C_5Me_5$), 20.30 (br. s, CH*C*H$_3$), 37.28 (br. s, *C*HCH$_3$), 67.81 ($C_5H_3$ *C*-COOH), 69.40 ($C_5H_3$ *C*H), 69.60 ($C_5H_3$ *C*H), 71.06 ($C_5H_5$), 74.81 ($C_5H_3$ *C*H), 94.19 (br. s, $C_5H_3$ *C*-CH), 98.77 (dd, $^1J_{Rh,C}$ = 7, $^2J_{P,C}$ = 2 Hz, *C*$_5$Me$_5$), 127.00, 127.81 (2 × d, $^3J_{P,C}$ = 10 Hz, PPh$_2$ *C*H$_m$), 130.43, 130.71 (2 × s, PPh$_2$ *C*H$_p$), 134.22, 136.84 (2 × d, $^2J_{P,C}$ = 9 Hz, PPh$_2$ *C*H$_o$), 176.96 (br. s, *C*OOH) ppm; (PPh$_2$ $C_{ipso}$) signals not observed. $^{31}$P{$^1$H} NMR ($CDCl_3$): δ = 34.3 (br. d, $^1J_{Rh,P}$ = 140 Hz) ppm. IR (Nujol): ν̃ = 1664 (composite s), 1299 (m), 1216 (m), 1157 (m), 1095 (m), 1021 (w), 1000 (w), 823 (w), 747 (s), 699 (m), 610 (w), 491 (m) cm$^{-1}$. HR MS (ESI–): calcd. for $C_{35}H_{37}{}^{35}Cl_2{}^{56}Fe^{103}RhO_2P$ [M – H$^+$]$^-$ 749.0313; found 749.0402; the observed isotopic distribution matched the calculated one.

**Preparation of Chlorido{(*R*,$R_p$)-2-[1-(diphenylphosphanyl)ethyl]-ferrocenecarboxylato-κ$^2$*O*,*P*}(η$^5$-pentamethylcyclopentadienido)rhodium(III) (10):** Chloroform solutions (5 mL each) of **1** (90 mg, 0.20 mmol) and [{(μ-Cl)RhCl(η$^5$-$C_5Me_5$)}$_2$] (62 mg, 0.10 mmol) were mixed and the mixture was stirred at room temperature for 2 h. Neutral chromatography grade alumina (ca. 2 g) was added to the solution and stirring was continued overnight. The alumina was then filtered off and washed thoroughly with chloroform. The liquid phase was concentrated under vacuum to give the product as a red glassy solid. Yield: 134 mg (94%). According to the NMR spectra, the product was an approximately 9:1 mixture of diastereoisomers. Note: An identical product mixture was formed when the solution containing in situ generated **9** was filtered through a short silica gel column. IR (Nujol): ν̃ = 1581 (s), 1307 (s), 1234 (w), 1171 (w), 1095 (m), 1044 (vw), 1025 (w), 999 (w), 816 (m), 746 (vs), 699 (s), 662 (w), 526 (s), 496 (m), 460 (m) cm$^{-1}$. HR MS (ESI+): calcd. for $C_{35}H_{38}{}^{35}Cl^{56}Fe^{103}RhO_2P$ [M + H]$^+$ 715.0702; found 715.0713. Major isomer: $^1$H NMR ($CDCl_3$): δ = 1.46 (d, $^2J_{Rh,H}$ = 3.3 Hz, 15 H, $C_5Me_5$), 1.52 (dd, $^3J_{H,H}$ = 7.3, $^3J_{P,H}$ = 13.9 Hz, 3 H, CHC$H_3$), 3.22 (m, 1 H, $C_5H_3$), 3.72 (apparent t, $J \approx 2.6$ Hz, 1 H, $C_5H_3$), 4.07 (s, 5 H, $C_5H_5$), 4.67 (dq, $^3J_{H,H} \approx {}^2J_{P,H} \approx 7.5$ Hz, 1 H, C*H*CH$_3$), 4.76 (m, 1 H, $C_5H_3$), 7.16–7.98 (m, 10 H, P*Ph*$_2$) ppm. $^{13}$C{$^1$H} NMR ($CDCl_3$): δ = 9.02 (d, $^2J_{Rh,C} \approx 1$ Hz, $C_5Me_5$), 14.16 (d, $^2J_{P,C}$ = 7 Hz, CH*C*H$_3$), 33.90 (d, $^1J_{P,C}$ = 18 Hz, *C*HCH$_3$), 67.89 (d, $J \approx$ 1 Hz, $C_5H_3$, *C*H), 68.18 ($C_5H_3$ *C*H), 70.17 ($C_5H_5$), 72.09 ($C_5H_3$ *C*H), 77.61 (d, $^3J_{P,C}$ = 2.5 Hz, $C_5H_3$ *C*-COO), 88.18 (d, $^2J_{P,C}$ = 5 Hz, $C_5H_3$ *C*-CH), 98.25 (dd, $^1J_{Rh,C}$ = 7, $^2J_{P,C}$ = 3 Hz, *C*$_5$Me$_5$), 125.20 (d, $^1J_{P,C}$ = 41 Hz, PPh$_2$ $C_{ipso}$), 127.14, 127.48 (2 × d, $^3J_{P,C}$ = 10 Hz, PPh$_2$ *C*H$_m$), 130.22 (d, $^4J_{P,C}$ = 2 Hz, PPh$_2$ *C*H$_p$), 130.84 (d, $^1J_{P,C}$ = 38 Hz, PPh$_2$ $C_{ipso}$), 131.04 (d, $^4J_{P,C}$ = 2 Hz, PPh$_2$ *C*H$_p$), 133.93, 135.30 (2 × d, $^2J_{P,C}$ = 9 Hz, PPh$_2$ *C*H$_o$), 180.14 (*C*OO) ppm. $^{31}$P{$^1$H} NMR ($CDCl_3$): δ = 52.0 (d, $^1J_{Rh,P}$ = 148 Hz) ppm. Minor isomer: $^{31}$P{$^1$H} NMR ($CDCl_3$): δ = 49.8 (d, $^1J_{Rh,P}$ = 146 Hz) ppm.

**Preparation of (*SP*-4-2)-Carbonyl{(*R*,$R_p$)-2-[1-(diphenylphosphanyl)ethyl]ferrocenecarboxylato-κ$^2$*O*,*P*}(tricyclohexylphosphane)rhodium(I) (11):** A solution of acid **1** (45 mg, 0.10 mmol) in butan-2-one (3 mL) was added to a solution of [Rh(acac)(CO)(PCy$_3$)] (51 mg, 0.10 mmol) in butan-2-one (5 mL) and the mixture was heated at reflux for 5 min. The reaction solution was cooled to room temperature and volatiles were removed under vacuum to afford **11** as a yellow solid in quantitative yield (85 mg). $^1$H NMR ($CDCl_3$): δ = 1.12–2.24 (m, 34 H, P*Cy*$_3$ and CHC$H_3$), 3.31 (m, 1 H, $C_5H_3$), 3.96 (apparent t, $J \approx 2.5$ Hz, 1 H, $C_5H_3$), 4.16 (s, 5 H, $C_5H_5$), 4.20 (dq, $^3J_{H,H} \approx {}^2J_{P,H} \approx 7$ Hz, 1 H, C*H*CH$_3$), 4.72 (m, 1 H, $C_5H_3$), 7.31–7.69 (m, 10 H, P*Ph*$_2$) ppm; the CHC$H_3$ signal is obscured by those of P*Cy*$_3$. $^{13}$C{$^1$H} NMR ($CDCl_3$): δ = 13.91 (dd, $^2J_{P,C}$ = 2, $^3J_{Rh,C}$ = 6 Hz, CH*C*H$_3$), 26.57 (s, PCy$_3$ γ-*C*H$_2$), 27.56 (dd, $^2J_{P,C}$ = 2, $^3J_{Rh,C}$ = 10 Hz, PCy$_3$ α-*C*H$_2$), 29.12 (dd, $^1J_{P,C}$ = 14, $^2J_{Rh,C}$ = 3 Hz, *C*HCH$_3$), 30.18 (d, $^3J_{P,C}$ = 37 Hz, PCy$_3$ β-*C*H$_2$), 33.36 (d, $^1J_{P,C}$ = 19 Hz, PCy$_3$ *C*H), 66.01 ($C_5H_3$ *C*H), 66.72 (d, $J_{P,C} \approx 1$ Hz, $C_5H_3$ *C*H), 70.44 ($C_5H_5$), 71.71 ($C_5H_3$ *C*H), 84.27 (d, $^3J_{P,C}$ = 9 Hz, $C_5H_3$ *C*-COO), 85.90 (d, $^2J_{P,C}$ = 2 Hz, $C_5H_3$ *C*-CH), 127.43, 128.75 (2 × d, $^3J_{P,C}$ = 9 Hz, PPh$_2$ *C*H$_m$), 128.92 (ddd, $^1J_{P,C}$ = 38, $^2J_{Rh,C} = {}^3J_{P,C} \approx 3$ Hz, PPh$_2$ $C_{ipso}$), 129.45, 130.75 (2 × d, $^4J_{P,C}$ = 2 Hz, PPh$_2$ *C*H$_p$), 131.53 (d, $^2J_{P,C}$ = 10 Hz, PPh$_2$ *C*H$_o$), 132.67 (dd, $^1J_{P,C}$ = 32, $J$ = 2 Hz, PPh$_2$ $C_{ipso}$), 135.76 (d, $^2J_{P,C}$ = 12 Hz, PPh$_2$ *C*H$_o$), 175.14 (*C*OO), 190.20 (dt, $^1J_{Rh,C}$ = 73, $^2J_{P,C}$ = 16 Hz, *C*≡O) ppm. $^{31}$P{$^1$H} NMR ($CDCl_3$): δ = 40.9 (dd, $^1J_{Rh,P}$ = 125, $^2J_{P,P}$ = 319 Hz, *P*Ph$_2$), 46.5 (dd, $^1J_{Rh,P}$ = 127, $^2J_{P,P}$ = 319 Hz, *P*Cy$_3$) ppm. IR (Nujol): ν̃ = 1959 (vs), 1612 (s), 1321 (s), 1244 (w), 1174 (w), 1101 (w), 997 (w), 815 (w), 785 (w), 745 (m), 721 (m), 708 (m), 694 (w), 593 (w), 532 (m) cm$^{-1}$. MS (FAB+): *m*/*z* = 853 [M + H]$^+$, 824 [M – CO]$^+$. HR MS calcd. for $C_{44}H_{56}{}^{56}Fe^{103}RhO_3P_2$ [M + H]$^+$ 853.2109; found 853.2079.

**(η$^3$-Allyl)palladium Complexes with 6. An in situ NMR Study:** Amide **6** (11 mg, 0.02 mmol) was added to a solution of [{Pd(μ-Cl)(η$^3$-$C_3H_5$)}$_2$] (3.7 mg, 0.01 mmol) in $CDCl_3$ (1 mL). The mixture was stirred in the dark for 1 h, then filtered through a PTFE syringe filter (0.45 μm) and the filtrate used directly for NMR measurements. The sample used for IR measurements was obtained by concentrating the reaction mixture under vacuum. $^1$H NMR ($CDCl_3$, 50 °C): δ = 1.83 (dd, $^3J_{P,H}$ = 18.0, $^3J_{H,H}$ = 7.2 Hz, 3 H, CHC$H_3$), 4.00 (dd, $^2J_{H,H}$ = 14.8, $^3J_{H,H}$ = 4.9 Hz, 1 H, C$H_2$Ph), 4.16 (s, 5 H, $C_5H_5$), 4.21 (m, 1 H, $C_5H_3$), 4.31 (m, 1 H, $C_5H_3$), 4.46 (dd, $^2J_{H,H}$ = 14.8, $^3J_{H,H}$ = 6.6 Hz, 1 H, C$H_2$Ph), 5.01 (dq, $^3J_{H,H} \approx {}^2J_{P,H} \approx 7$ Hz, 1 H, C*H*CH$_3$), 5.47 (br. t, $^3J_{H,H} \approx 6$ Hz, 1 H, N*H*), 7.06–7.94 (m, 15 H, P*Ph*$_2$ and CH$_2$*Ph*) ppm; the remaining three signals of the allyl moiety and one $C_5H_3$ resonance are observed as broad bands between δ = 2.1 and 3.1 ppm and at δ ≈ 4.93 and 5.40 ppm. $^{31}$P{$^1$H} NMR ($CDCl_3$, 50 °C): δ = 35.3 (s) ppm. IR (Nujol): ν̃ = 3314 (m br.), 1639 (s), 1522 (s), 1302 (m), 1266 (m), 1234 (m), 1104 (m), 1099 (m), 1003 (m), 821 (m), 746 (m), 697 (vs), 609 (m), 514 (m), 482 (s), 460 (m) cm$^{-1}$. MS (ESI+): *m*/*z* = 678 [M – Cl]$^+$; the isotopic envelope agrees with the calculated one.

**Preparation of (*SP*-4-2)-{(*R*,$R_p$)-*N*-Benzyl-2-[1-(diphenylphosphanyl)ethyl]ferrocenecarboxamido-κ$^2$*O*,*P*}chloro(methyl)palladium(II) (13):** A solution of amide **6** (64 mg, 0.12 mmol) in dichloromethane (5 mL) was added to a solution of [PdCl(Me)(cod)] (33 mg, 0.12 mmol) in the same solvent (5 mL) and the mixture was stirred in the dark for 20 h. The reaction solution was then filtered through a PTFE syringe filter (0.45 μm). The product crystallised upon diffusion of diethyl ether to afford **12** as an orange crystalline solid, which was filtered off and dried in vacuo. Yield: 60 mg (70%). $^1$H NMR ($CDCl_3$): δ = 0.60 (d, $^3J_{P,H}$ = 2.8 Hz, 3 H, PdC$H_3$), 1.41 (dd, $^3J_{P,H}$ = 11.5, $^3J_{H,H}$ = 7.2 Hz, 3 H, CHC$H_3$), 3.43 (m, 1 H, $C_5H_3$), 4.04 (s, 5 H, $C_5H_5$), 4.05 (m, 1 H, $C_5H_3$), 4.16 (dq, $^3J_{H,H} \approx {}^2J_{P,H} \approx 7.5$ Hz, 1 H, C*H*CH$_3$), 4.68 (dd, $^2J_{H,H}$ = 14.4, $^3J_{H,H}$ = 5.1 Hz, 1 H, C$H_2$Ph), 4.99 (m, 1 H, $C_5H_3$), 5.14 (dd, $^2J_{H,H}$ = 14.4, $^3J_{H,H}$ = 6.5 Hz, 1 H, C$H_2$Ph), 7.15 (br. t, $^3J_{H,H} \approx 6$ Hz, 1 H,

 © 2007 Wiley-VCH Verlag GmbH & Co. KGaA, Weinheim 

N*H*), 7.28–7.72 (m, 15 H, P*Ph*$_2$ and CH$_2$*Ph*) ppm. $^{13}$C{$^1$H} NMR ($CDCl_3$): $\delta$ = –1.26 (Pd*C*H$_3$), 14.53 (d, $^2J_{P,C}$ = 6 Hz, CH*C*H$_3$), 31.21 (d, $^1J_{P,C}$ = 20 Hz, *C*HCH$_3$), 45.11 (*C*H$_2$Ph), 68.42 (C$_5$H$_3$ *C*H), 69.93 (C$_5$H$_3$ *C*H), 70.38 (C$_5$H$_5$), 70.45 (C$_5$H$_3$ *C*H), 73.06 (d, $^3J_{P,C}$ = 2 Hz, C$_5$H$_3$ *C*-CONH), 88.38 (d, $^2J_{P,C}$ = 9 Hz, C$_5$H$_3$ *C*-CH), 125.11 (d, $^1J_{P,C}$ = 48 Hz, PPh$_2$ *C*$_{ipso}$), 127.65 (CH$_2$Ph *C*H$_p$), 127.66 (d, $J_{P,C}$ = 11 Hz, PPh$_2$ *C*H), 128.78 (CH$_2$Ph *C*H$_o$), 128.83 (CH$_2$Ph *C*H$_m$), 128.89 (d, $J_{P,C}$ = 9 Hz, PPh$_2$ *C*H), 130.11 (d, $^4J_{P,C}$ = 2 Hz, PPh$_2$ *C*H$_p$), 130.67 (d, $^1J_{P,C}$ = 40 Hz, PPh$_2$ *C*$_{ipso}$), 131.23 (d, $^4J_{P,C}$ = 2 Hz, PPh$_2$ *C*H$_p$), 131.40 (d, $J_{P,C}$ = 10 Hz, PPh$_2$ *C*H), 136.23 (d, $J_{P,C}$ = 12 Hz, PPh$_2$ *C*H), 138.35 (CH$_2$Ph *C*$_{ipso}$), 175.45 (*C*ONH) ppm. $^{31}$P{$^1$H} NMR ($CDCl_3$): $\delta$ = 54.3 (s) ppm. IR (Nujol): $\tilde{\nu}$ = 3262 (m, N–H), 1573 and 1545 (vs, C=O), 1439 (s), 1408 (w), 1352 (m), 1307 (s), 1207 (w), 1178 (m), 1106 (s), 1059 (w), 1000 (m), 820 (m), 750 (m), 743 (s), 700 (s), 693 (s), 627 (w), 537 (m), 499 (m) cm$^{-1}$. $C_{33}H_{33}ClFeNOPPd$ (688.5): calcd. C 57.58, H 4.83, N 2.04; found C 57.27, H 4.62, N 1.95.

**Catalytic Experiments. Rhodium-Catalysed Hydrogenation:** Hydrogenation of methyl (*Z*)-acetamidocinnamate was performed as described in ref.[34] using [Rh(cod)$_2$]BF$_4$ or [{(μ-Cl)Rh(cod)}$_2$] as the metal source and **1**, **6**, (*R*)-**7** and (*S*)-**7** as the ligands. However, no reaction occurred even after 1 d. Racemic *N*,*N*-dimethyl{[2-(diphenylphosphanyl)ferrocenyl]methyl}amine[35] utilized as the ligand in a parallel run showed 80% conversion under otherwise identical conditions.

**Allylic Substitution. General Procedure:**[36] Ligand (25 μmol) and [{Pd($\eta^3$-C$_3$H$_5$)Cl}$_2$] (4.8 mg, 13 μmol) were dissolved in dry dichloromethane (3 mL). The solution was stirred at room temperature for 10 min and then added to a mixture of *rac*-1,3-diphenyl-2-propenyl acetate (126 mg, 0.5 mmol), potassium acetate (5 mg, 0.05 mmol) and dichloromethane (3 mL). After stirring for another 5 min, *N*,*O*-bis(trimethylsily)acetamide (BSA; 0.37 mL, 1.5 mmol), and dimethyl malonate (0.17 mL, 1.5 mmol) were added successively and the reaction mixture was stirred at room temperature for 20 h. The reaction solution was then washed with saturated aqueous $NH_4Cl$ solution (2 × 5 mL), the organic layer was dried with $MgSO_4$ and the solvents were evaporated in vacuo. Purification by column chromatography (silica gel, hexane/ethyl acetate, 3:1) afforded the product mixture (in the case of an incomplete conversion, mixtures with the starting allyl acetate were collected). Enantiomeric excesses were determined from $^1$H NMR spectra recorded in $C_6D_6$ in the presence of chiral lanthanide shift reagent tris(3-trifluoroacetyl-*d*-camphorato)europium(III), Eu(facam)$_3$, while the configuration of the major component was assigned on the basis of optical rotation of the mixture.[37]

**X-ray Crystallography:** Crystals suitable for single-crystal X-ray diffraction analysis were selected directly from the reaction batch (**2**: orange prism, 0.13 × 0.20 × 0.28 mm) or grown by recrystallisation from hot hexane (**3**: yellow prism, 0.09 × 0.13 × 0.28 mm), ethyl acetate/hexane (**9**: dark red prism, 0.13 × 0.20 × 0.33 mm; **11**: yellow plate, 0.08 × 0.15 × 0.38 mm), or chloroform/diethyl ether (**13**: orange prism, 0.10 × 0.13 × 0.25 mm). X-ray quality crystals of phosphane oxides **5** and (*R*)-**8** formed during prolonged recrystallisation of the respective phosphanes from ethyl acetate/hexane (**5**: orange block, 0.18 × 0.25 × 0.35 mm; (*R*)-**8**: red-brown block, 0.08 × 0.25 × 0.45 mm). Full-set diffraction data ($\pm h \pm k \pm l$; $2\theta \leq 55°$ for **2**, **3**, **9**, **11**, and **13**; $2\theta \leq 54°$ for **5**) were collected with a Nonius KappaCCD diffractometer equipped with a Cryostream Cooler (Oxford Cryosystems) at 150(2) K using graphite-monochromated Mo-$K_\alpha$ radiation ($\lambda$ = 0.71073 Å) and analysed with the HKL program package.[38] When appropriate, the data were corrected for absorption by using the Gaussian absorption correction incorporated in the diffractometer software; the transmission factor ranges are given in Table 7. The structures were solved by direct methods (SIR97[39]) and refined by weighted full-matrix least-squares procedure on $F^2$ (SHELXL97[40]). All non-hydrogen atoms were refined with anisotropic thermal motion parameters, whilst the hydrogen atoms were included in their calculated positions and refined as riding atoms with $U_{iso}$(H) assigned to a multiple of $U_{eq}$ of their bonding atom. Selected crystallographic data are given in

Table 7. Crystallographic data and data collection and structure refinement parameters for **2**, **3**, **5**, (*R*)-**8**, **9**, **11** and **13**.

| | **2** | **3** | **5** | (*R*)-**8** | **9** | **11** | **13** |
|---|---|---|---|---|---|---|---|
| Empirical formula | $C_{24}H_{22}BrFeP$ | $C_{24}H_{22}BrFePS$ | $C_{25}H_{23}FeO_3P$ | $C_{33}H_{32}FeNO_2P$ | $C_{35}H_{38}Cl_2FeO_2PRh$ | $C_{44}H_{55}FeO_3P_2Rh$ | $C_{33}H_{33}ClFeNOPPd$ |
| $M$ [g mol$^{-1}$] | 477.15 | 509.21 | 458.25 | 561.42 | 751.28 | 852.58 | 688.27 |
| Crystal system | orthorhombic | orthorhombic | monoclinic | orthorhombic | orthorhombic | monoclinic | monoclinic |
| Space group | $P2_12_12_1$ (no. 19) | $P2_12_12_1$ (no. 19) | $P2_1$ (no. 4) | $P2_12_12_1$ (no. 19) | $P2_12_12_1$ (no. 19) | $P2_1$ (no. 4) | $P2_1$ (no. 4) |
| $T$ [K] | 150(2) | 150(2) | 150(2) | 150(2) | 150(2) | 150(2) | 150(2) |
| $a$ [Å] | 7.2823(2) | 7.0056(1) | 11.3855(3) | 7.6157(2) | 12.8470(1) | 11.1809(2) | 10.0973(3) |
| $b$ [Å] | 7.3882(1) | 17.5052(3) | 7.7313(2) | 16.1930(3) | 16.3555(1) | 10.3941(3) | 11.1269(2) |
| $c$ [Å] | 38.7068(8) | 17.6365(3) | 12.4535(3) | 22.2013(4) | 30.6572(2) | 17.2950(4) | 13.2474(3) |
| $\beta$ [°] | | | 100.742(2) | | | 99.552(1) | 94.703(1) |
| $V$ [Å$^3$] | 2082.55(8) | 2162.84(6) | 1077.01(5) | 2737.8(1) | 6441.66(8) | 1982.08(8) | 1483.36(6) |
| $Z$ | 4 | 4 | 2 | 4 | 8 | 2 | 2 |
| $D_{calcd.}$ [g mL$^{-1}$] | 1.522 | 1.564 | 1.413 | 1.362 | 1.549 | 1.429 | 1.541 |
| $\mu$(Mo-$K_\alpha$) [mm$^{-1}$] | 2.725 | 2.723 | 0.798 | 0.641 | 1.209 | 0.902 | 1.266 |
| $T$[a] | 0.506–0.705 | 0.379–0.865 | –[b] | –[b] | 0.702–0.906 | 0.812–0.948 | 0.753–0.925 |
| Total relections, $R_{int}$ [%][c] | 21276, 3.42 | 27159, 4.71 | 16974, 4.1 | 35364, 4.7 | 99821, 4.82 | 30126, 4.79 | 25673, 4.02 |
| Unique/observed[d] reflections | 4731/4487 | 4952/4369 | 4727/4297 | 6239/5801 | 14752/13499 | 9082/7984 | 6798/6228 |
| $R$ (observed data) [%][e] | 2.10 | 2.81 | 3.52 | 3.16 | 3.46 | 3.42 | 2.82 |
| $R$, $wR$ (all data) [%][e] | 2.40, 4.62 | 3.74, 5.70 | 4.20, 8.15 | 3.65, 7.48 | 4.14, 8.56 | 4.66, 6.60 | 3.46, 5.79 |
| Flack's parameter | –0.006(5) | –0.008(6) | –0.00(2) | 0.04(1) | –0.02(2) | –0.01(1) | –0.03(1) |
| $\Delta\rho$ [e Å$^{-3}$] | 0.35, –0.24 | 0.24, –0.47 | 0.45, –0.44 | 0.20, –0.28 | 1.76,[f] –1.06 | 0.58, –0.60 | 0.58, –0.64 |
| CCDC reference no. | 633611 | 633612 | 633613 | 633614 | 633615 | 633616 | 633617 |

[a] Range of transmission coefficients. [b] Not corrected. [c] $R_{int} = \Sigma|F_o^2 - F_o^2(\text{mean})|/\Sigma F_o^2$, where $F_o^2$(mean) is the average intensity for symmetry-equivalent reflections. [d] Reflections with $I_o > 2\sigma(I_o)$. [e] $R = \Sigma||F_o| - |F_c||/\Sigma|F_o|$, $wR = [\Sigma\{w(F_o^2 - F_c^2)^2\}/\Sigma w(F_o^2)^2]^{1/2}$. [f] Residual positive electron density in the vicinity of the rhodium atom.

 © 2007 Wiley-VCH Verlag GmbH & Co. KGaA, Weinheim 

Table 7. Geometric parameters and structural drawings were obtained with a recent version of Platon.[41] CCDC-633611 to -633617 (for compounds **2**, **3**, **5**, **8**, **9**, **11** and **13**, respectively) contain the supplementary crystallographic data for this paper. These data can be obtained free of charge from The Cambridge Crystallographic Data Centre via www.ccdc.cam.ac.uk/data_request/cif.

**Supporting Information** (see footnote on the first page of this article): View of the crystal structure of **2** (Figure S1).

## Acknowledgments

This work was supported financially by the Grant Agency of Charles University (grant no. 318/2005/B-CH/PrF) and forms part of the project "Centre for Structure and Synthetic Application of Transition Metal Complexes" from the Ministry of Education, Youth and Sports of the Czech Republic (project no. LC 06070).

[1] a) T. J. Kealy, P. L. Pauson, *Nature* **1951**, *168*, 1039–1040; b) S. A. Miller, J. A. Tebboth, J. F. Tremaine, *J. Chem. Soc.* **1952**, 632–635.

[2] a) *Ferrocenes: Homogeneous Catalysis, Organic Synthesis, Materials Science* (Eds.: A. Togni, T. Hayashi), VCH, Weinheim, **1995**; b) E. G. Perevalova, M. D. Reshetova, K. Y. Grangberg, *Metody elementoorganicheskoy khimii, Ferrocen*, Nauka, Moscow, **1973**.

[3] Bioorganometallic chemistry: D. R. van Staveren, N. Metzler-Nolte, *Chem. Rev.* **2004**, *104*, 5931–5985.

[4] a) A. Togni, "New Chiral Ferrocenyl Ligands for Asymmetric Catalysis", in *Metallocenes* (Eds.: A. Togni, R. L. Halterman), Wiley-VCH, Weinheim, **1998**, vol. 2, chapter 11, p. 685–721; b) C. J. Richards, A. J. Locke, *Tetrahedron: Asymmetry* **1998**, *9*, 2377–2407; c) T. J. Colacot, *Chem. Rev.* **2003**, *103*, 3101–3118; d) R. C. J. Atkinson, V. C. Gibson, N. J. Long, *Chem. Soc. Rev.* **2004**, *33*, 313–328; e) R. G. Arrayás, J. Adrio, J. C. Carretero, *Angew. Chem. Int. Ed.* **2006**, *45*, 7674–7715.

[5] J. Podlaha, P. Štěpnička, I. Císařová, J. Ludvík, *Organometallics* **1996**, *15*, 543–550.

[6] P. Štěpnička, *Eur. J. Inorg. Chem.* **2005**, 3787–3803.

[7] M. Lamač, I. Císařová, P. Štěpnička, *J. Organomet. Chem.* **2005**, *690*, 4285–4301.

[8] P. Barbaro, C. Bianchini, G. Giambastiani, *Synthesis* **2005**, 2445–2448.

[9] J. Omelanczuk, M. Mikolajczyk, *Tetrahedron Lett.* **1984**, *25*, 2493–2496.

[10] *CRC Handbook of Phosphorus-31 Nuclear Magnetic Resonance Data* (Ed.: J. C. Tebby), CRC Press, Boca Raton, **1991**.

[11] H.-O Kalinowski, S. Berger, S. Braun, *$^{13}$C-NMR-Spektroskopie*, Thieme, Stuttgart, **1984**, chapter 4, section 6, pp. 530–538.

[12] J. Podlaha, P. Štěpnička, I. Císařová, J. Ludvík, *Organometallics* **1996**, *15*, 543–550.

[13] P. Štěpnička, *New J. Chem.* **2002**, *26*, 567–575.

[14] H.-B. Kraatz, *J. Inorg. Organomet. Polym.* **2005**, *15*, 83–106.

[15] a) P. Štěpnička, I. Císařová, *J. Chem. Soc., Dalton Trans.* **1998**, 2807–2811. (Diphenylphosphanyl)acetic acid reacts similarly: b) A. Jegorov, B. Kratochvíl, V. Langer, J. Podlahová, *Inorg. Chem.* **1984**, *23*, 4288–4291; c) A. Jegorov, J. Podlaha, J. Podlahová, F. Tureček, *J. Chem. Soc., Dalton Trans.* **1990**, 3259–3263.

[16] P. S. Pregosin, R. W. Kunz, in *$^{31}$P and $^{13}$C NMR of Transition Metal Phosphane Complexes*, vol. 16 of *NMR Basic Principles and Progress* (Eds.: P. Diehl, E. Fluck, R. Kosfeld), Springer, Heidelberg, **1979**, part G, pp. 110–123, and references cited therein.

[17] This is best indicated by the ring puckering parameters for the cyclohexyl rings: C(31–36): $Q$ = 0.579(4) Å, $\theta$ = 176.5(4)°; C(41–46): $Q$ = 0.583(4) Å, $\theta$ = 0.4(4)°; C(51–56): $Q$ = 0.558(4) Å, $\theta$ = 5.2(4)°. Note: An ideal envelope requires $\theta$ = 0 or 180°. For reference, see: D. Cremer, J. A. Pople, *J. Am. Chem. Soc.* **1975**, *97*, 1354–1358.

[18] For examples of fluxional ($\eta^3$-allyl)palladium(II)complexes with ferrocene-based donors, see: a) C. Breutel, P. S. Pregosin, R. Salzmann, A. Togni, *J. Am. Chem. Soc.* **1994**, *116*, 4067–4068; b) H. C. L. Abbenhuis, U. Burckhardt, V. Gramlich, C. Köllner, P. S. Pregosin, A. Togni, *Organometallics* **1995**, *14*, 759–766; c) P. S. Pregosin, R. Salzmann, A. Togni, *Organometallics* **1995**, *14*, 842–847; d) U. Bruckhardt, V. Gramlich, P. Hofman, R. Nesper, P. S. Pregosin, R. Salzman, A. Togni, *Organometallics* **1996**, *15*, 3496–3503; e) R. Fernández-Galán, F. A. Jalón, B. R. Manzano, J. Rodríguez-de la Fuente, M. Vrahani, B. Jedlicka, W. Weissensteiner, G. Jogl, *Organometallics* **1997**, *16*, 3758–3768; f) F. Gómez-de la Torre, F. A. Jalón, A. López-Agenjo, B. R. Manzano, A. Rodríguez, T. Sturm, W. Weissensteiner, M. Martínez-Ripoll, *Organometallics* **1998**, *17*, 4634–4644; g) A. Farrell, R. Goddard, P. J. Guiry, *J. Org. Chem.* **2002**, *67*, 4209–4217; h) M. Ogasawara, K. Takizawa, T. Hayashi, *Organometallics* **2002**, *21*, 4853–4861.

[19] Due to a different *trans* influence, the $^3J_{P,H}$ coupling constants differ for *cis*- and *trans*-P,C isomers [$^3J$(*trans*-P,H) > $^3J$(*cis*-P,H)]. See, for instance: a) K. Nozaki, N. Sato, Y. Tonumura, M. Yasutomi, H. Takaya, T. Hiyama, T. Matsubara, N. Koga, *J. Am. Chem. Soc.* **1997**, *119*, 12779–12795; b) P. Braunstein, M. D. Fryzuk, M. Le Dall, F. Naud, S. J. Rettig, F. Speiser, *J. Chem. Soc., Dalton Trans.* **2000**, 1067–1074.

[20] Complexes [PdCl(Me)(L-κ$^2$*P*,*P*′)], where L are various chiral ferrocene-based diphosphanes [Fe{$\eta^5$-$C_5H_3$($PR_2$-1)[CH(Me)$PR'_2$-2}($\eta^5$-$C_5H_5$)], show clearly distinct $^3J$(*trans*-P,H) and $^3J$(*cis*-P,H) values: a) C. Gambs, G. Consiglio, A. Togni, *Helv. Chim. Acta* **2001**, *84*, 3105–3126; b) M. C. Carrión, F. A. Jalón, A. López-Agenjo, B. R. Manzano, W. Weissensteiner, K. Mereiter, *J. Organomet. Chem.* **2006**, *691*, 1369–1381.

[21] G. Sánchez, J. García, D. Meseguer, J. L. Serrano, L. García, J. Pérez, G. López, *Inorg. Chim. Acta* **2006**, *359*, 1650–1658.

[22] The bond lengths were retrieved from the Cambridge Structural Database (version 5.27 of November **2005** with updates from January, May, and August 2006).

[23] P. Štěpnička, I. Císařová, *Z. Anorg. Allg. Chem.* **2004**, *630*, 1321–1325.

[24] a) H. Takaya, T. Ohta, R. Noyori, "Asymmetric Hydrogenation", in *Catalytic Asymmetric Synthesis* (Ed.: I. Ojima), VCH, New York **1993**, chapter 1, pp. 1–39; b) H.-U. Blaser, C. Malan, B. Pugin, F. Spindler, H. Steiner, M. Studer, *Adv. Synth. Catal.* **2003**, *345*, 103–151.

[25] a) T. Hayashi, "Asymmetric Allylic Substitution and Grignard Cross-Coupling" in *Catalytic Asymmetric Synthesis* (Ed.: I. Ojima), VCH, New York **1993**, chapter 7.1, pp. 325–365; b) B. M. Trost, D. L. Van Vranken, *Chem. Rev.* **1996**, *96*, 395–422; c) B. M. Trost, M. L. Crawley, *Chem. Rev.* **2003**, *103*, 2921–2943; d) B. M. Trost, *J. Org. Chem.* **2004**, *69*, 5813–5837.

[26] a) W.-P. Deng, X.-L. Hou, L.-X. Dai, Y.-H. Yu, W. Xia, *Chem. Commun.* **2000**, 285–286; b) W.-P. Deng, S.-L. You, X.-L. Hou, L.-X. Dai, Y.-H. Yu, W. Xia, J. Sun, *J. Am. Chem. Soc.* **2001**, *123*, 6508–6519; c) S.-L. You, X.-L. Hou, L.-X. Dai, Y.-H. Yu, W. Xia, *J. Org. Chem.* **2002**, *67*, 4684–4695. See also the following review article: d) X. L. Hou, S. L. You, T. Tu, W. P. Deng, X. W. Wu, M. Li, K. Yuan, T. Z. Zhang, L. X. Dai, *Top. Catal.* **2005**, *35*, 87–103.

[27] ($S_p$)-2-(Diphenylphosphanyl)ferrocenecarboxylic acid: S.-L. You, Y.-M. Luo, W.-P. Deng, X.-L. Hour, L.-X. Dai, *J. Organonomet. Chem.* **2001**, *637–639*, 845–849.

[28] Chiral *N*,*N*′-bis(phosphanyl)ferrocenyl-substituted diamides: a) J. M. Longmire, B. Wang, X. Zhang, *Tetrahedron Lett.* **2000**, *41*, 5435–5439; b) S.-L. You, X.-L. Hou, L.-X. Dai, *J. Organonomet. Chem.* **2001**, *637–639*, 762–766.

[29] O. B. Sutcliffe, M. R. Bryce, *Tetrahedron: Asymmetry* **2003**, *14*, 2297–2325.

[30] W. Zhang, T. Shimanuki, T. Kida, Y. Nakatsuji, I. Ikeda, *J. Org. Chem.* **1999**, *64*, 6247–6251.

 © 2007 Wiley-VCH Verlag GmbH & Co. KGaA, Weinheim 

[31] a) A. Togni, C. Breutel, A. Schnyder, F. Spindler, F. Landert, A. Tijani, *J. Am. Chem. Soc.* **1994**, *116*, 4062–4066; b) H.-U. Blaser, W. Brieden, B. Pugin, F. Spindler, M. Studer, A. Togni, *Top. Catal.* **2002**, *19*, 3–16.
[32] C. White, D. Yates, P. M. Maitlis, in *Inorganic Syntheses* (Ed.: R. N. Grimes), Wiley, New York, **1992**, vol. 29, pp. 228–234.
[33] R. E. Rülke, J. M. Ernsting, A. L. Spek, C. J. Elsevier, P. W. N. M. van Leeuwen, K. Vrieze, *Inorg. Chem.* **1993**, *32*, 5769–5778.
[34] G. Argouarch, O. Samuel, H. B. Kagan, *Eur. J. Org. Chem.* **2000**, 2885–2891.
[35] G. Marr, T. Hunt, *J. Chem. Soc. C* **1969**, 1070–1072.
[36] a) W. Zang, Y. Yoneda, T. Kida, Y. Nakatsuji, I. Ikeda, *Tetrahedron: Asymmetry* **1998**, *9*, 3371–3380; b) D. Drahoňovský, I. Císařová, P. Štěpnička, H. Dvořáková, P. Maloň, D. Dvořák, *Collect. Czech. Chem. Commun.* **2001**, *66*, 588–604.
[37] T. Hayashi, A. Yamamoto, T. Hagihara, Y. Ito, *Tetrahedron Lett.* **1986**, *27*, 191–194.
[38] Z. Otwinowski, W. Minor, *HKL Denzo and Scalepack Program Package*, Nonius BV, Delft, The Netherlands. For reference, see: Z. Otwinowski, W. Minor, *Methods Enzymol.* **1997**, *276*, 307–326.
[39] A. Altomare, M. C. Burla, M. Camalli, G. L. Cascarano, C. Giacovazzo, A. Guagliardi, A. G. G. Moliterni, G. Polidori, R. Spagna, *J. Appl. Crystallogr.* **1999**, *32*, 115–119.
[40] G. M. Sheldrick, *SHELXL97. Program for Crystal Structure Refinement from Diffraction Data*, University of Göttingen, Germany, **1997**.
[41] A. L.Spek, *Platon – A multipurpose crystallographic tool*, Utrecht University, Utrecht, The Netherlands, **2003** and updates. Available via the Internet at http://www.cryst.chem.uu.nl/platon/.

Received: January 24, 2007
Published Online: April 25, 2007

 © 2007 Wiley-VCH Verlag GmbH & Co. KGaA, Weinheim 

DOI: 10.1002/ejic.200601004

# Synthesis, Structure, and Reactivity of Cerium(IV) Calix[4]arene Complexes

Jochen Gottfriedsen,*[a] Reimo Hagner,[a] Marlies Spoida,[a] and Yuri Suchorski[a]

**Keywords:** Cerium / Calixarenes / Photoelectron spectroscopy

The equimolar reaction of $Ce(hfac)_4$ (**1**) (hfac = 1,1,1,5,5,5-hexafluoropentanedionato) with *p*-*t*Bu-calix[4](OMe)$_2$(OH)$_2$ in toluene gave the new cerium(IV) calix[4]arene complex {*p*-*t*Bu-calix[4](OMe)$_2$(O)$_2$}Ce(hfac)$_2$ (**2**). The single-crystal X-ray structure shows the cone geometry of the calixarene ligand with the methoxy groups coordinated to the cerium; it shows slightly longer cerium–oxygen (acetylacetonate ligand) bond lengths than the corresponding bonds in the analogous nonfluorinated complex {*p*-*t*Bu-calix[4](OMe)$_2$(O)$_2$}Ce(acac)$_2$ (**3**). The bromination reaction of **3** gave the bisbrominated complex {*p*-*t*Bu-calix[4](OMe)$_2$(O)$_2$}Ce(Br-acac)$_2$ (**4**). $^1$H NMR spectroscopic studies and a single-crystal X-ray structure of **4** revealed that the bromination took place in the 3-position of the acac ligand. Furthermore, the first X-ray photoelectron spectroscopy (XPS) evaluation of the Ce oxidation state in cerium calix[4]arene complexes **2** and **3** is presented, and X-ray induced changes of $Ce_{ox}$ in these complexes are detected.
(© Wiley-VCH Verlag GmbH & Co. KGaA, 69451 Weinheim, Germany, 2007)

## Introduction

The coordination chemistry of cerium in the oxidation state +4 is dominated by its alkoxy and β-diketonate complexes. β-Diketonate complexes of cerium(IV) are well established as precursors in MOCVD (metal organic chemical vapor deposition) or ALE (atomic layer epitaxy) processes. The deposition of $CeO_2$ films as buffer layers for YBCO high temperature super conductor devices[1] were studied, and doped $Ce_{1-x}M_xO_{2-y}$ (M = Sm, Y, Gd) materials, which exhibit high oxygen ion conductivity, have been presented. These compounds are considered to be promising materials for solid oxide fuel cells, oxygen pumps, and methane conversion reactors.[2] Furthermore, the application of $Ce(tmhd)_4$ (tmhdH = 2,2,6,6-tetramethyl-3,5-heptanedione) as a dopant in SrS and $CaGa_2S_4$ thin films has been examined owing to the fact that cerium doping in these materials can produce blue–green and blue electroluminescent (EL) phosphors.[3] In addition to the studies on $Ce(tmhd)_4$,[1b,4] the suitabilities of the following other volatile β-diketonate complexes were investigated: $Ce(fdh)_4$ (fdhH = 6,6,6-trifluoro-2,2-dimethyl-3,5-hexanedione),[5] $Ce(fod)_4$ (fodH = 1,1,1,2,2,3,3-heptafluoro-7,7-dimethyloctane-4,6-dione),[6] $Ce(tmod)_4$ (tmodH = 2,2,7-trimethyl-3,5-octanedione),[7] and $Ce(txhd)_4$ (txhdH = 2,2,6-trimethyl-3,6-heptanedione).[7]

The high synthetic potential of $Ce^{IV}$ β-diketonate complexes remains largely unexplored. Recently, literature reports indicated the synthesis of double-decker tetrapyrrole cerium complexes starting from $Ce(acac)_3(H_2O)_n$,[8] and our group reported the synthesis of {*p*-*t*Bu-calix[4](OMe)$_2$(O)$_2$}Ce(acac)$_2$ (**3**) from $Ce(acac)_4$.[9] A variety of methods have been used to study the valency of Ce in cerium complexes. Theoretical calculations[10] and XANES (X-ray absorption near-edge spectroscopy)[11] experiments, as well as studies of their magnetic properties,[11b] have been used to study the oxidation states of cerium COT (COT = cyclooctatetraenyl) and substituted COT complexes in detail,[12] which led to the conclusion that cerium is trivalent in these complexes. XANES studies of a series of double-decker tetrapyrrole cerium complexes[8a] also suggest partial delocalization of the ligand π electrons into a cerium 4f orbital, which results in a valency of 3.59 to 3.68. The XPS data of [Ce(Pc)$_2$] (Pc = phthalocyaninate) complexes revealed a valency that is neither tri- nor tetravalent, but a mixed valent state of them.[13] Calix[4]arene ligand systems are widely used to form complexes with almost all metal ions.[14] Complexes with cerium are still rare and mainly focused on $Ce^{III}$ {e.g. cerium(III) calix[4]arene complexes [Ce(LH$_{-2}$)(MeOH)$_2$A]HA (L = 5,11,17,23-tetra-*tert*-butyl-25,27-bis(diethylcarbamoylmethoxy)-26,28-dihydroxycalix[4]arene, HA = picric acid)[15] and Ce(H$_2$O)$_5$(*p*-sulfonatocalix[4]arene + H$^+$)}.[16] Studies of the coordination behavior of *p*-*tert*-butylcalix[*n*]arene (*n* = 4–6) with tetravalent cerium in solution have also been performed.[17]

Here we present the synthesis of novel calix[4]arene complexes of $Ce^{IV}$ using two different synthetic approaches. In addition to the synthesis starting from a homoleptic cerium β-diketonato complex, the reaction of {*p*-*t*Bu-calix[4](OMe)$_2$(O)$_2$Ce(acac)$_2$} (**3**) with $Br_2$ will be described to demonstrate its high synthetic potential in this class of cerium

[a] Chemisches Institut der Otto-von-Guericke, Universität Magdeburg,
Universitätsplatz 2, 39106 Magdeburg, Germany
Fax: +49-391-67-12933
E-mail: jochen.gottfriedsen@vst.uni-magdeburg.de

 © 2007 Wiley-VCH Verlag GmbH & Co. KGaA, Weinheim 

complexes. In addition to the standard characterization methods, NMR spectroscopy, MS, and single-crystal X-ray determination studies, we performed XPS experiments for two of the cerium calix[4]arene complexes to obtain the effective oxidation state of Ce in these complexes.

## Results and Discussion

The equimolar reaction of $Ce(hfac)_4$ (**1**) (hfac = 1,1,1,5,5,5-hexafluoropentanedionato) with *p*-*t*Bu-calix[4](OMe)$_2$(OH)$_2$ in boiling toluene gave an immediate color change upon reaching the boiling point. After workup, the new cerium(IV) calix[4]arene complex {*p*-*t*Bu-calix[4](OMe)$_2$(O)$_2$}Ce(hfac)$_2$ (**2**) could be isolated as blue crystalline blocks (Scheme 1). Complex **2** is highly soluble in nonpolar organic solvents such as hexane, pentane, and toluene as well as in the polar solvents diethyl ether, THF, dichloromethane, and chloroform.

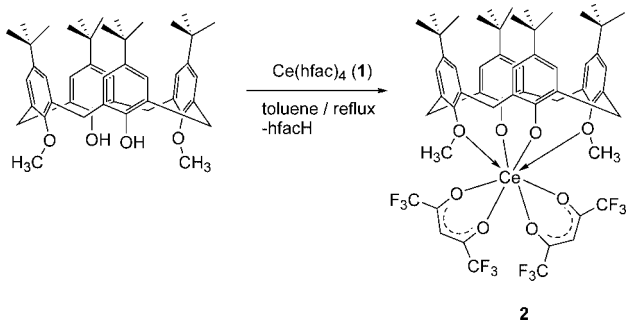


Scheme 1. Synthesis of **2**.

The reaction of the corresponding nonfluorinated Ce calix[4]arene complex {*p*-*t*Bu-calix[4](OMe)$_2$(O)$_2$}Ce(acac)$_2$ (**3**) with bromine in a 1:2 ratio in diethyl ether resulted in bromination of the acac ligand in the 3-position with formation of the bisbrominated complex {*p*-*t*Bu-calix[4](OMe)$_2$(O)$_2$}Ce(Br-acac)$_2$ (**4**) (Br-acac = 3-bromo-pentanedionato) (Scheme 2).

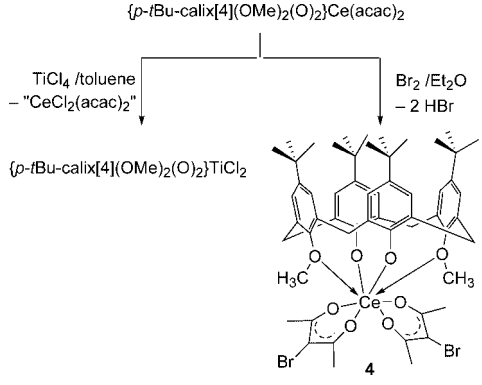


Scheme 2. Reactivity of **3** towards $Br_2$ and $TiCl_4$.

The reaction of **3** with bromine in a 1:1 ratio produced a monobrominated species which was detected by $^1$H NMR spectroscopy but not isolated or further studied. Complex **4** exhibits the same solubility as that of **2** and the same blue color. The bromination of $Ce(acac)_4$ was described previously[18] by using NBS (*N*-bromosuccinimide) to yield $Ce(Br\text{-}acac)_4$. A ligand transfer to $TiCl_4$ was investigated to further elucidate the reactivity of complex **3**. Red crystals were obtained after crystallization from toluene, which where characterized by NMR spectroscopy and shown to be the known titanium complex {*p*-*t*Bu-calix[4](OMe)$_2$(O)$_2$}$TiCl_2$.[19] $^1$H and $^{13}$C NMR spectroscopic studies revealed the typical cone geometry of the calix[4]arene ligands for both complexes **2** and **4** in benzene solution. The $^1$H NMR (Table 1) spectroscopic data show that the chemical shifts of the calix[4]arene ligand of brominated complex **4** are basically identical with those of starting material **3**, whereas the chemical shifts of **2** are significantly different, which is due to the electron-withdrawing fluorine substituents. The resonances of the methoxy group of complexes **2**, **3**, and **4** show the highest change in their chemical shifts compared with the corresponding ones of the free calix[4]arene ligand. Resonances of the methoxy group in all three complexes are shifted downfield by nearly 1.5 ppm for **2**, 1.25 ppm for **3**, and approximately 1 ppm for **4** relative to the chemical shift of the free ligand ($\delta$ =3.47 ppm). This is due to the electron-withdrawing fluorine atoms that induce a decrease in the electron density on the cerium atom, which is compensated by the coordinated methoxy group thus deshielding the $CH_3$ group. Doublets at 5.11 and 3.27 ppm for **2** and 5.04 and 3.35 ppm for **4** in the $^1$H NMR spectra are attributable to the *endo* and *exo* protons of the $CH_2$ bridges of the calix[4]arene ligand. Whereas the chemical shifts of the *endo* protons are shifted downfield (nearly 0.7 ppm for **2** and 0.6 ppm for **4**) relative to the free calix[4]arene ligand, the resonances for the *exo* protons are not influenced by coordination to the cerium center. Two sets of signals for the aromatic hydrogens and the substituted tertiary butyl groups were found for each new complex, **2** and **4**, by assigning the two different ring systems of the calix[4]arene ligands (Table 1). The $^{13}$C NMR spectra also show the two unequally substituted phenyl groups of the calixarene ligand in **2** and **4**. The different coordinationenvironments that are adopted by **1** (–76.51 ppm), **2** (–75.93 ppm), and 1,1,1,5,5,5-hexafluoropentanedione (–77.40 ppm) are made apparent in their $^{19}$F NMR spectra,

Table 1. $^1$H NMR spectroscopic data of complexes **2**, **3**, and **4** in $C_6D_6$ at 25 °C ($\delta$ in ppm).

| | **2** | **3** | **4** |
|---|---|---|---|
| (s, 4 H, Ar*H*) | 7.11 | 7.23 | 7.22 |
| (s, 4 H, Ar*H*) | 6.85 | 6.97 | 6.96 |
| (d, *endo*-C*H*$_2$) | 5.11 | 5.04 | 5.04 |
| (d, *exo*-C*H*$_2$) | 3.27 | 3.35 | 3.35 |
| (s, 6 H, OC*H*$_3$) | 4.93 | 4.72 | 4.58 |
| (s, 18 H, CC*H*$_3$) | 1.27 | 1.39 | 1.34 |
| (s, 18 H, CC*H*$_3$) | 0.90 | 0.98 | 0.97 |
| (s, 2 H, COC*H*) | 5.8 | 4.96 | no signal |
| (s, 12 H, COC*H*$_3$) | no signal | 1.76 | 2.19 |

 © 2007 Wiley-VCH Verlag GmbH & Co. KGaA, Weinheim 

which shows a small influence of the $CF_3$ groups on the chemical shift for this β-diketone. Mass spectrometric data of complexes **2** and **4** show the molecular ions as the signals with the highest mass. The signals with the highest abundance can be interpreted as the molecular ions reduced by the mass of the corresponding β-diketonate.

### X-ray Structure Determinations

A single-crystal X-ray structure determination of the starting material $Ce(hfac)_4$ (**1**), which crystallized from toluene as dark brown crystals, was carried out. The molecular structure exhibits an eight-coordinate cerium in a distorted square antiprismatic coordination sphere (Figure 1).

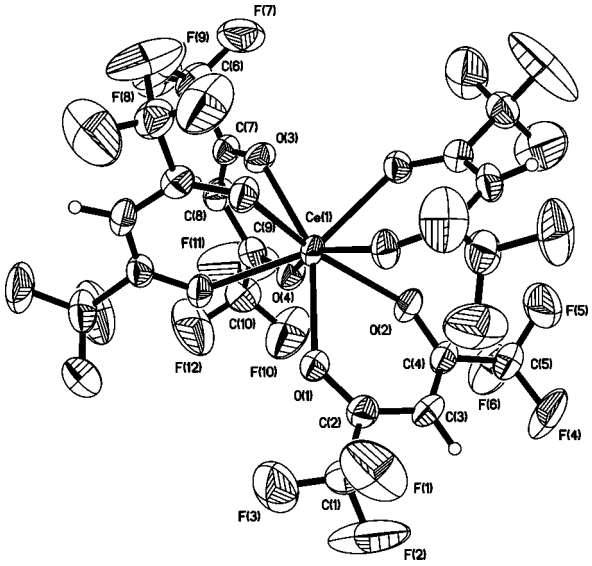


Figure 1. ORTEP plot of the molecular structure of **1**. Thermal ellipsoids are drawn with 50% probability. Hydrogen atoms are omitted for clarity.

The Ce–O bond lengths of the O,O′-bidentate hexafluoropentanedionato ligands range from 2.325(3) to 2.346(3) Å, which is in good agreement with similar distances found for cerium acetylacetonato complexes {e.g. α-$Ce(acac)_4$,[20a,20b] β-$Ce(acac)_4$,[20c] and $[Ce(acac)_4]\cdot 10H_2O$[21]}, which have a mean distance of 2.32 Å. Other cerium β-diketonato complexes display Ce–O distances between 2.24 Å and 2.36 Å [e.g. $Ce(fda)_4$, $Ce(tmhd)_4$, $Ce(txhd)_4$, and $Ce(tmod)_4$].

{*p*-*t*Bu-calix[4]$(OMe)_2(O)_2$}$Ce(hfac)_2$ (**2**) was crystallized from toluene at 5 °C and single crystals of the brominated complex {*p*-*t*Bu-calix[4]$(OMe)_2(O)_2$}$Ce(Br\text{-}acac)_2$ (**4**) were obtained from $CH_2Cl_2$ at 5 °C. The single-crystal X-ray structures of both complexes showed the typical cone geometry of the calixarene ligand with the methoxy groups coordinated to the cerium, which gave an eight coordinate cerium center with square antiprismatic coordination spheres (Figures 2 and 3).

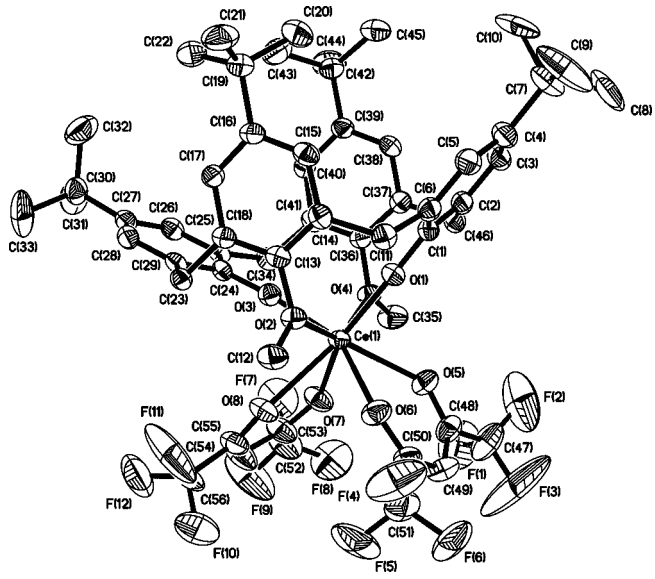


Figure 2. ORTEP plot of the molecular structure of **2**. Thermal ellipsoids are drawn with 50% probability. Hydrogen atoms are omitted for clarity.

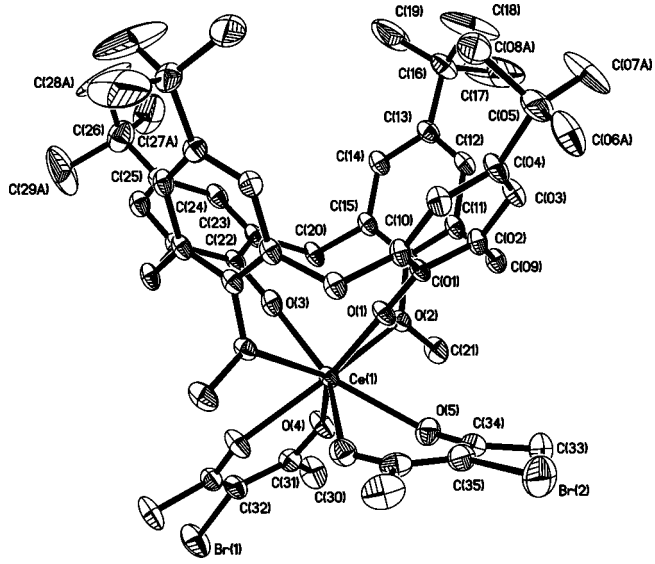


Figure 3. ORTEP plot of the molecular structure of **4**. Thermal ellipsoids are drawn with 50% probability. Hydrogen atoms are omitted for clarity.

The Ce–O phenoxy bond lengths in **2** [2.069(3)/2.089(3) Å] are slightly shorter than the corresponding distances in **4** [2.111(4)/2.134(5) Å], which are equal to the ones found for {*p*-*t*Bu-calix[4]$(OMe)_2(O)_2$}$Ce(acac)_2$ (**3**) (2.130 Å average)[9] (Table 2). They are in the same range as those in other cerium alkoxides {e.g. the hexafluoroisopropoxide (hfip) adducts $Ce(hfip)_4(TMEDA)$ and $Ce(hfip)_4$(diglyme) (2.13 Å average)M,[22] the terminal Ce–OR alkoxide groups in $Ce_2(O\text{i}Pr)_8(\text{i}PrOH)_2$ (2.088 Å average),[23] $Ce(O\text{t}Bu)_2(NO_3)_2(HO\text{t}Bu)_2$ (2.088 Å average),[24] and $Ce(O\text{t}Bu)_2(\mu\text{-}O\text{t}Bu)_2(\mu_3\text{-}O\text{t}Bu)_2Na_2(dme)_2$ [2.136–2.146 Å for the terminal (O*t*Bu) ligands]},[24] although they are longer than those observed for $Cp_3Ce^{IV}(O\text{t}Bu)$ (2.045 Å).[24] The

 © 2007 Wiley-VCH Verlag GmbH & Co. KGaA, Weinheim 

Table 2. Selected bond lengths [Å] and angles [°].

| **1** | | **2** | | **4** | |
|---|---|---|---|---|---|
| Ce(1)–O(1) | 2.346(3) | Ce(1)–O(3) | 2.069(3) | Ce(1)–O(1) | 2.111(4) |
| Ce(1)–O(2) | 2.325(3) | Ce(1)–O(1) | 2.089(3) | Ce(1)–O(3) | 2.134(5) |
| Ce(1)–O(3) | 2.334(3) | Ce(1)–O(7) | 2.408(3) | Ce(1)–O(4) | 2.365(3) |
| Ce(1)–O(4) | 2.339(3) | Ce(1)–O(6) | 2.409(4) | Ce(1)–O(4)[a] | 2.365(3) |
| | | Ce(1)–O(5) | 2.426(3) | Ce(1)–O(5) | 2.372(3) |
| | | Ce(1)–O(8) | 2.461(3) | Ce(1)–O(5)[a] | 2.372(3) |
| | | Ce(1)–O(4) | 2.560(3) | Ce(1)–O(2)[a] | 2.581(3) |
| | | Ce(1)–O(2) | 2.577(3) | Ce(1)–O(2) | 2.581(3) |
| O(1)–Ce(1)–O(1)[a] | 132.52(14) | O(3)–Ce(1)–O(1) | 102.07(12) | O(1)–Ce(1)–O(3) | 94.11(16) |
| O(2)–Ce(1)–O(1) | 70.98(11) | O(3)–Ce(1)–O(7) | 85.38(13) | O(1)–Ce(1)–O(4) | 145.84(7) |
| O(2)–Ce(1)–O(3) | 126.42(11) | O(1)–Ce(1)–O(7) | 146.66(11) | O(3)–Ce(1)–O(4) | 87.30(13) |
| O(2)–Ce(1)–O(4) | 74.44(10) | O(3)–Ce(1)–O(6) | 144.93(11) | O(1)–Ce(1)–O(4)[a] | 145.84(7) |
| O(2)–Ce(1)–O(3)[a] | 126.23(11) | O(1)–Ce(1)–O(6) | 93.22(13) | O(3)–Ce(1)–O(4)[a] | 87.30(13) |
| O(2)–Ce(1)–O(4)[a] | 153.33(11) | O(7)–Ce(1)–O(6) | 98.95(13) | O(4)–Ce(1)–O(4)[a] | 68.31(15) |
| O(2)–Ce(1)–O(1)[a] | 72.80(11) | O(3)–Ce(1)–O(5) | 143.00(12) | O(1)–Ce(1)–O(5) | 82.72(13) |
| O(2)[a]–Ce(1)–O(2) | 78.92(16) | O(1)–Ce(1)–O(5) | 85.51(11) | O(3)–Ce(1)–O(5) | 145.17(8) |
| O(2)[a]–Ce(1)–O(3) | 126.23(11) | O(7)–Ce(1)–O(5) | 70.52(12) | O(4)–Ce(1)–O(5) | 77.09(12) |
| O(3)–Ce(1)–O(1) | 153.61(11) | O(6)–Ce(1)–O(5) | 68.77(12) | O(4)[a]–Ce(1)–O(5) | 114.41(11) |
| O(3)–Ce(1)–O(1)[a] | 73.86(10) | O(3)–Ce(1)–O(8) | 80.58(12) | O(1)–Ce(1)–O(5)[a] | 82.72(13) |
| O(3)–Ce(1)–O(3)[a] | 79.77(15) | O(1)–Ce(1)–O(8) | 144.67(12) | O(3)–Ce(1)–O(5)[a] | 145.17(8) |
| O(3)[a]–Ce(1)–O(1) | 73.86(10) | O(7)–Ce(1)–O(8) | 68.32(11) | O(4)–Ce(1)–O(5)[a] | 114.41(11) |
| O(3)–Ce(1)–O(4) | 71.18(11) | O(6)–Ce(1)–O(8) | 69.16(12) | O(4)[a]–Ce(1)–O(5)[a] | 77.09(12) |
| O(3)[a]–Ce(1)–O(4) | 72.61(11) | O(5)–Ce(1)–O(8) | 113.72(11) | O(5)–Ce(1)–O(5)[a] | 69.09(16) |
| O(4)–Ce(1)–O(1) | 99.27(11) | O(3)–Ce(1)–O(4) | 76.17(10) | O(1)–Ce(1)–O(2)[a] | 76.98(7) |
| O(4)–Ce(1)–O(1)[a] | 99.50(11) | O(1)–Ce(1)–O(4) | 79.56(11) | O(3)–Ce(1)–O(2)[a] | 75.80(7) |
| O(4)–Ce(1)–O(4)[a] | 132.22(15) | O(7)–Ce(1)–O(4) | 70.67(11) | O(4)–Ce(1)–O(2)[a] | 135.76(10) |
| | | O(6)–Ce(1)–O(4) | 138.20(10) | O(4)[a]–Ce(1)–O(2)[a] | 70.29(9) |
| | | O(5)–Ce(1)–O(4) | 69.63(11) | O(5)–Ce(1)–O(2)[a] | 135.80(10) |
| | | O(8)–Ce(1)–O(4) | 133.98(11) | O(5)[a]–Ce(1)–O(2)[a] | 69.68(10) |
| | | O(3)–Ce(1)–O(2) | 81.08(11) | O(1)–Ce(1)–O(2) | 76.98(7) |
| | | O(1)–Ce(1)–O(2) | 77.15(10) | O(3)–Ce(1)–O(2) | 75.80(7) |
| | | O(7)–Ce(1)–O(2) | 136.15(10) | O(4)–Ce(1)–O(2) | 70.29(9) |
| | | O(6)–Ce(1)–O(2) | 71.74(10) | O(4)[a]–Ce(1)–O(2) | 135.76(10) |
| | | O(5)–Ce(1)–O(2) | 135.59(11) | O(5)–Ce(1)–O(2) | 69.68(10) |
| | | O(8)–Ce(1)–O(2) | 68.40(10) | O(5)[a]–Ce(1)–O(2) | 135.80(10) |
| | | O(4)–Ce(1)–O(2) | 143.03(9) | O(2)[a]–Ce(1)–O(2) | 139.56(11) |

[a] Atoms that are generated by using the symmetry transformation $-x + 1, y, -z + 1$ (**1**), and $x, -y, z$ (**4**), respectively.

Ce–O bond lengths for the two coordinated methoxy groups Ce(1)–O(2) and Ce(1)–O(4) in **2** [2.560(3)/2.577(3) Å] and Ce(1)–O(2) and Ce(1)–O(2)# in **4** [2.581(3) Å] are in the typical range of Ce–O coordination bonds[22] and fit well with the corresponding bonds in {*p*-*t*Bu-calix[4](OMe)$_2$(O)$_2$}Ce(acac)$_2$ (**3**) (2.604 Å average).[9] The Ce–O distances of the O,O′-bidentate hexafluoropentanedionato ligands in **2** range from 2.408(3) to 2.461(3) Å and are thus slightly longer than the distances found for starting material **1** [2.325(3) to 2.346(3) Å] and the Ce–O bonds of the two O,O′-bidentate acetylacetonate ligands in the analogous nonfluorinated complex {*p*-*t*Bu-calix[4](OMe)$_2$(O)$_2$}Ce(acac)$_2$ (**3**) (2.338 to 2.371 Å).[9] The corresponding Ce–O distances of the O,O′-bidentate 3-bromo-2,4-pentanedionato ligands to cerium in **4** [2.365(3) and 2.372(3) Å] match well with the ones of complex **3**. The Ce–O (β-diketonato) lengths of complexes **2** and **4** are only slightly longer than the Ce–O lengths found for the homoleptic cerium β-diketonate complexes. However, they are in good agreement with these lengths {e.g. α-Ce(acac)$_4$,[20a,20b] β-Ce(acac)$_4$,[20c] and [Ce(acac)$_4$](H$_2$O)$_{10}$,[21] with a mean distance of 2.32 Å, as well as Ce(fda)$_4$, Ce(tmhd)$_4$, Ce(txhd)$_4$, and Ce(tmod)$_4$, which exhibit Ce–O distances between 2.24 Å and 2.36 Å}.

The four donor atoms of the calixarene in **2**, **3**, and **4** define a mean O$_4$ plane with a rms deviation of 0.2464 Å in **2**, 0.2549 Å in **3**, and 0.2774 Å in **4** and the cerium atom is located at 1.0607(14) Å from this mean plane in **2**, 1.1641(10) Å in **3**, and 1.1686(20) Å in **4**. The macrocycles in new complexes **2** and **4**, as well as in **3**,[9] are in a distorted cone conformation, with dihedral angles between the four aromatic rings and the O$_4$ plane of 39.50(16), 89.50(11), 34.66(8), and 83.31(11)° in **2** [46.16(24), 71.72(9), 37.45(13), and 72.02(11)° in **4**]. The dihedral angles of the cone in **2** are similar to the ones in **3** [38.09(7), 83.86(7), 36.90(13), and 84.02(7)°], and to those found in [UCl$_2$(Me$_2$-calix)(THF)$_2$], [UCl$_2$(Me$_2$calix)(py)$_2$], and [U(acac)$_2$(Me$_2$calix)(THF)$_2$].[25] The slightly different values of the homologous angles in **4** might be due to crystal packing effects.

## XPS Studies

High-resolution XPS spectra of complexes **2** and **3** were obtained by using monochromatic X-ray excitation. From

 © 2007 Wiley-VCH Verlag GmbH & Co. KGaA, Weinheim 

this spectra we determined the effective oxidation state of Ce (in the sense of an effective charge state of the Ce atoms in the ground state of the solid), $Ce_{ox}$. The $Ce_{ox}$ value does not necessary represent the integral "formal valence" of Ce (in compounds with largely covalent character the formal valence does not approximate the actual ionic charge), but it reflects objectively the electronic structure of the studied materials. The direct use of established techniques, such as the commonly used deconvolution of high-resolution XPS spectra to evaluate the $Ce_{ox}$ in coordination complexes, is still difficult despite a great effort devoted to the electronic structure of ceria and similar compounds. The main uncertainties are associated with the complex features in the Ce3d XPS-spectra and result from the variable occupancy of the Ce4f level, redistribution of the levels as a result of the core hole creation, and changed hybridization at different oxidation states.[26] Therefore, the interpretation of the spectra is not always unambiguous and can even be contradictory. In addition, artifacts created merely by the X-ray exposure have to be considered.[27] In the present work we evaluated $Ce_{ox}$ in **2** and **3** by correlation of the XPS data for the studied samples with those of reference samples with a known oxidation state.

Ar-sputtered $CeO_2$ was used as the reference sample where the preferential release of oxygen atoms in the surface region, as a result of the impact of $Ar^+$ ions in ultrahigh vacuum (UHV), allows the creation of $Ce_xO_y$ oxides in the top surface layers with continuously variable artificial $Ce_{ox}$ in the range from 4 to 3.4. The details of the $Ce_{ox}$ evaluation are published elsewhere.[28] A similar method was recently applied by us for the determination of the oxidation state of vanadium in vanadium oxide and vanadium/phosphate oxide catalysts.[29] The measurements of samples of both the studied complexes revealed an X-ray induced "photoreduction", an effect in principle known (but not entirely understood) for some rare earth containing materials such as, for example, $Sm^{3+}$-doped fluoroaluminate glasses[30] or for the pure $CeO_2$.[31] Thorough long-time studies of the X-ray-induced evolution of the $Ce_{ox}$ revealed its exponential decay with increasing irradiation time (from 3.60 to 3.28 for **2** and from 3.62 to 3.27 for **3**) (Figure 4), where the extrapolation to "zero irradiation" (zero exposure) allows the determination of the initial oxidation state in the freshly synthesized complexes (3.61 for **2** and 3.65 for **3**). It has to be noted that in contrast to vanadium-containing oxide compounds, no UHV-induced modification of the cerium oxidation state was observed in the present study, that is, the observed effect is a pure X-ray-induced "photoreduction". The X-ray modified $Ce_{ox}$ of cerium remained also stable after exposure to air at room temperature. Concerning the interpretation of the observed "photoreduction", we noted that the local irradiation-induced heating, proposed as a reduction mechanism for ceria,[31] cannot explain our observation as no significant increase in the surface temperature was observed. Apparently, alternative mechanisms such as the electron-hole pair formation and Auger decay have to be taken into account.[32] Another possible mechanism, associated with an impact of the numerous low-energy electrons,[33] which could cause desorption due to their large cross-section seems to be less probable, as was proven by low-energy electron bombardment from an external electron gun. Furthermore, a possible reason for the decrease in $Ce_{ox}$ might be due to decomposition processes that are induced by the X-ray radiation, which leads to the formation of a mixture of cerium centers in the oxidation state 3 and 4. It should also be noted that the attenuation length of the Al $K_\alpha$ photons exceeds the XPS information depth of ≈ 2.5 nm, by at least three orders of magnitude, in the present case. Therefore, the irradiation-caused changes in the Ce oxidation state may extend to a significant depth.

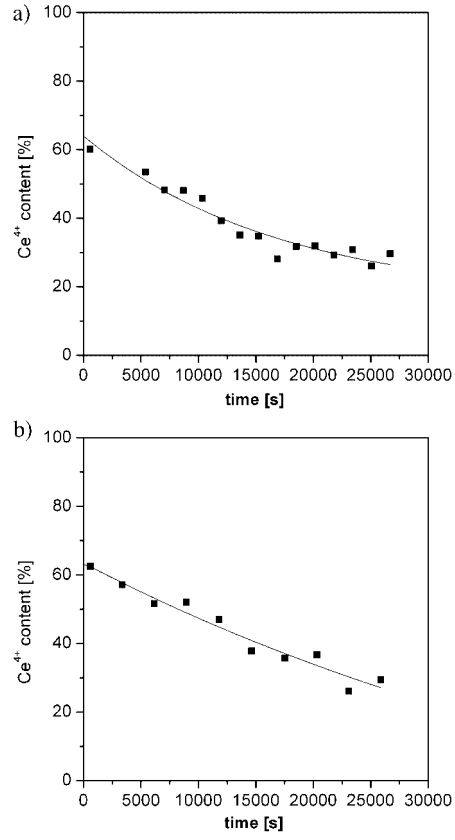


Figure 4. Dependencies of the $Ce^{4+}$ content for **2** and **3**, respectively, on the X-ray exposure. Extrapolation to "zero irradiation" provides the initial values of $Ce_{ox}$.

## Conclusions

Two novel cerium calix[4]arene complexes could be synthesized by using two different synthetic approaches. {*p*-*t*Bu-calix[4](OMe)$_2$(O)$_2$}Ce(hfac)$_2$ (**2**) was generated starting from a homoleptic cerium β-diketonato complex Ce(hfac)$_4$ (**1**). However, {*p*-*t*Bu-calix[4](OMe)$_2$(O)$_2$}Ce(Br-acac)$_2$ (**4**) was obtained from the reaction of {*p*-*t*Bu-calix[4](OMe)$_2$(O)$_2$}Ce(acac)$_2$ (**3**) with $Br_2$; thus, the high synthetic potential of this class of cerium complexes was demonstrated. Furthermore, we detected X-ray-induced changes in the effective Ce oxidation state in cerium calix-

 © 2007 Wiley-VCH Verlag GmbH & Co. KGaA, Weinheim 

[4]arene complexes **2** and **3**, and performed the first evaluation of $Ce_{ox}$ in these complexes.

## Experimental Section

**General:** All reactions were carried out under an inert atmosphere of dry nitrogen by using standard dry box and Schlenk techniques. Melting points were determined in a sealed capillary without correction. NMR spectra were recorded with a Bruker DPX 400 or AVANCE 600 NMR spectrometer. Chemical shifts (all reported in ppm) are referenced to tetramethylsilane as internal standard. Chemical shifts of the $^{13}C$ NMR were assigned to the corresponding carbons by using HSQC, HMBC, and NOSY techniques. In turn, chemical shifts of the $^{19}F$ NMR spectra are referenced to trifluorotoluene as external standard. The single-crystal X-ray diffraction studies were performed with a Bruker CCD SMART (**2**, **4**) or Stoe IPDS (**1**) diffractometer. Crystal data are given in Table 3. The structures were solved by Patterson methods (SHELXS-97).[34] Refinements were carried out by using full-matrix least-squares techniques on $F^2$ with the SHELXL-97 program.[35] CCDC-624482 (for **1**), -616674 (for **2**), and -624481 (for **4**) contain the supplementary crystallographic data for this paper. These data can be obtained free of charge from The Cambridge Crystallographic Data Centre via www.ccdc.cam.ac.uk/data_request/cif. Mass spectra (EI, 70 eV) were obtained with a Finnigan SSQ 7000 or a Finnigan MAT 95 (70 eV). Only characteristic fragments containing the isotopes of the highest abundance are listed. The starting materials *p*-*t*Bu-calix[4](OMe)$_2$(OH)$_2$[36] and {*p*-*t*Bu-calix[4](OMe)$_2$(O)$_2$}Ce(acac)$_2$[9] were produced according to a published procedure. Ce(hfac)$_4$ was synthesized by using a slightly modified procedure.[37] Elemental analyses were performed with a LECO CHNS932 apparatus. Hexafluoroacetylacetone and $(NH_4)_4[Ce(SO_4)_4]\cdot 2H_2O$ were purchased from Aldrich Chemical Co. and used as received. X-ray photoelectron spectra were obtained from the dry powders of **2** and **3**, which were carefully grinded and fixed on Mo sample-carrier plates under an argon atmosphere in a glove box and transferred inertly to the multipurpose UHV surface analysis apparatus (SPECS, Germany) where the XPS analyses were performed. To avoid the vacuum-induced reduction of the samples, a "fast transfer" XPS mode[29] was used: the SPECS load-lock and transfer systems allows sample-transfer times of less than 5 min between the start of the evacuation of the load lock and the first XPS spectrum at a pressure better than $5\times10^{-9}$ mbar. The monochromatic X-ray source (FOCUS-500, SPECS, excitation energy 1253.74 eV, Al-$K_\alpha$, linewidth after monochromatization $<$ 0.3 eV) was used. High-resolution spectra (pass energy 10 eV, step size 0.1–0.2 eV) were recorded at room temperature with a hemispherical energy analyzer (PHOIBOS-150, SPECS), which provides the possibility of simultaneous photo-electron detection on nine channels, and allows fast data acquisition times (0.5 s per data point) with a satisfactory signal-to-noise ratio.

**Ce(hfac)$_4$ (1):** $(NH_4)_4[Ce(SO_4)_4]\cdot 2H_2O$ (3.8 g, 6 mmol) in $H_2O$ (200 mL) and 1,1,1,5,5,5-hexafluoro-2,4-pentanedione (5.0 g, 24 mmol) in toluene (100 mL) were mixed and stirred for 15 min, which resulted in a fast color change in the organic layer to dark brown. The two phases were separated, and toluene was removed under vacuum to leave a brown solid that was recrystallized from dry toluene (15 mL) to yield dark brown crystal blocks in 35% yield (2.03 g). $^1H$ NMR (400 MHz, $C_6D_6$, 25 °C): $\delta$ = 6.05 (s, 4 H, C*H*) ppm. $^{19}F$ NMR (376.5 MHz, $C_6D_6$, 25 °C): $\delta$ = –76.51 ppm. UV/Vis (250–800 nm, $CHCl_3$): $\lambda$ = 275.6 nm.

**{*p*-*t*Bu-calix[4](OMe)$_2$(O)$_2$}Ce(hfac)$_2$ (2):** Ce(hfac)$_4$ (1.0 g, 1.03 mmol) and *p*-*t*Bu-calix[4](OMe)$_2$(OH)$_2$ (0.7 g, 1.03 mmol) were dissolved in toluene (50 mL), stirred at reflux temperature for 2 h, and another 12 h at room temperature. The reaction mixture was dried under vacuum ($10^{-2}$ mbar) at 40 °C, and the resulting

Table 3. Crystal data and structural refinement for complexes **1**, **2**, and **4**.

| | **1** | **2** | **4** |
|---|---|---|---|
| Empirical formula | $C_{20}H_4CeF_{24}O_8$ | $C_{63}H_{68}CeF_{12}O_8$ | $C_{60}H_{65}Br_2CeCl_4O_9$ |
| Formula weight | 968.35 | 1321.29 | 1371.86 |
| Temperature [K] | 180(2) | 200(2) | 180(2) |
| Wavelength [Å] | 0.71073 | 0.71073 | 0.71073 |
| Crystal system | monoclinic | triclinic | monoclinic |
| Space group | *I*2/*a* | $P\bar{1}$ | *C*2/*m* |
| *a* [Å] | 16.511(3) | 13.3831(10) | 28.049(6) |
| *b* [Å] | 11.081(2) | 14.3193(10) | 15.198(3) |
| *c* [Å] | 16.519(3) | 16.9920(12) | 16.611(3) |
| $\alpha$ [°] | 90 | 102.0560(10) | 90 |
| $\beta$ [°] | 90.42(3) | 98.3980(10) | 118.84(3) |
| $\gamma$ [°] | 90 | 94.188(2) | 90 |
| Volume [Å$^3$] | 3022.3(10) | 3132.2(4) | 6203(2) |
| *Z*, calcd. density [mg m$^{-3}$] | 4, 2.128 | 2, 1.401 | 4, 1.469 |
| Abs coeff [mm$^{-1}$] | 1.698 | 0.814 | 2.246 |
| *F*(000) | 1848 | 1352 | 2772 |
| Crystal size [mm] | $0.50\times0.50\times0.20$ | $0.50\times0.40\times0.20$ | $0.60\times0.50\times0.10$ |
| $\theta$ range for data coll. [°] | 2.47 to 27.96 | 2.01 to 29.29 | 3.54 to 27.96 |
| Reflections collected | 14035 | 21948 | 29279 |
| Unique reflections | 3583 ($R_{int}$ = 0.0819) | 12975 ($R_{int}$ = 0.0268) | 7645 ($R_{int}$ = 0.0877) |
| Absorption correction | face indexed | SADABS | face indexed |
| Data/rest./parameters | 3583/0/248 | 12975/0/928 | 7645/0/395 |
| GOF on $F^2$ | 0.945 | 1.248 | 1.101 |
| Final *R* indices [$I>2\sigma(I)$] | $R_1$ = 0.0445 | $R_1$ = 0.0595 | $R_1$ = 0.0576 |
| | $wR_2$ = 0.1064 | $wR_2$ = 0.1411 | $wR_2$ = 0.1409 |
| *R* indices (all data) | $R_1$ = 0.0572 | $R_1$ = 0.0659 | $R_1$ = 0.0716 |
| | $wR_2$ = 0.1094 | $wR_2$ = 0.1447 | $wR_2$ = 0.1480 |

 © 2007 Wiley-VCH Verlag GmbH & Co. KGaA, Weinheim 

blue powder was dissolved in toluene (10 mL). Crystallization at 5 °C gave dark blue crystals in 79% yield (1.08 g, calculated as toluene solvate). M.p. 295 °C. $^1$H NMR (400 MHz, $C_6D_6$, 25 °C): $\delta$ = 7.13 (m, 2 H, toluene), 7.11 (s, 4 H, Ar*H*), 7.05–7.0 (m, 3 H, toluene), 6.85 (s, 4 H, Ar*H*), 5.8 (s, 2 H, COC*H*), 5.11 [d, $^1J(^1H,^1H)$ = 12.6 Hz, *endo*-C$H_2$], 4.93 (s, 6 H, OC$H_3$), 3.27 [d, $^1J(^1H,^1H)$ = 12.6 Hz, *exo*-C$H_2$], 2.11 (s, 3 H, toluene), 1.27 (s, 18 H, CC$H_3$), 0.90 (s, 18 H, CC$H_3$) ppm. $^{13}$C NMR (100.6 MHz, $C_6D_6$, 25 °C): $\delta$ = 177.57 ($CF_3C$-O), 173.57 [*C*(Ar)OCe], 152.54 [*C*(Ar)OCH$_3$], 148.53 (*t*Bu*C*), 145.92 (*t*Bu*C*), 133.45 (*C*CH$_2$), 133.4 (*C*CH$_2$), 129.30 (toluene), 128.31 (toluene), 126.29 [*C*H(Ar)], 125.66 (toluene), 122.19 [*C*H(Ar)], 118.5 (*C*F$_3$CO), 93.09 (CO*C*HCO), 67.96 (O*C*H$_3$), 34.02 (CH$_3$*C*), 33.48 (CH$_3$*C*), 32.46 (C*C*H$_3$), 31.31 (*C*H$_2$), 30.94 (C*C*H$_3$), 21.40 (toluene) ppm. $^{19}$F NMR (376.5 MHz, $C_6D_6$, 25 °C): $\delta$ = –75.93 ppm. MS (EI, $^{140}$Ce): *m*/*z* (%) = 1228 (5) $[M]^{+\cdot}$, 1021 (100) $[M - hfac]^+$, 1021 (40) $[M - hfac - CH_3]^+$. UV/Vis (250–800 nm, $CHCl_3$): $\lambda$ = 276.8 nm. $C_{56}H_{60}CeF_{12}O_8C_7H_8$ (1321.31): calcd. C 57.27, H 5.19; found C 57.24, H 5.22.

**{*p*-*t*Bu-calix[4](OMe)$_2$(O)$_2$}Ce(Br-acac)$_2$ (4):** {*p*-*t*Bu-calix[4](OMe)$_2$(O)$_2$}Ce(acac)$_2$ (0.31 g, 0.31 mmol) was dissolved in diethyl ether (30 mL), and $Br_2$ (0.098 g, 0.62 mmol) was added by syringe at room temperature. The reaction mixture was heated under reflux for 3 h. The color of the solution changed from deep purple to deep blue. The solvent was removed under vacuum at 40 °C to give a blue powder, which was solved in dichloromethane (5 mL) and recrystallized at 5 °C to yield small cube-like crystals in 45% yield (0.16 g). M.p. 310 °C. $^1$H NMR (400 MHz, $C_6D_6$, 25 °C): $\delta$ = 7.22 (s, 4 H, Ar*H*), 6.96 (s, 4 H, Ar*H*), 5.04 [d, $^1J(^1H,^1H)$ = 12.1 Hz, *endo*-C$H_2$], 4.58 (s, 6 H, OC$H_3$), 3.35 [d, $^1J(^1H,^1H)$ = 12.1 Hz, *exo*-C$H_2$], 2.19 (s, 12 H, COC$H_3$), 1.34 (s, 18 H, CC$H_3$), 0.97 (s, 18 H, CC$H_3$) ppm. $^{13}$C NMR (100.6 MHz, $C_6D_6$, 25 °C): $\delta$ = 187.72 (CH$_3$*C*-O), 170.57 [*C*(Ar)OCe], 153.71 [*C*(Ar)OCH$_3$], 147.56 (*t*Bu*C*), 141.39 (*t*Bu*C*), 133.17 (*C*CH$_2$), 132.39 (*C*CH$_2$), 125.94 (*C*H), 123.49 (*C*H), 100.66 (CO*C*BrCO), 66.79 (O*C*H$_3$), 34.01 (CH$_3$*C*), 33.82 (CH$_3$*C*), 32.43 (*C*H$_2$), 32.32 (C*C*H$_3$), 31.13 (C*C*H$_3$), 28.82 (*C*H$_3$CO) ppm. MS (EI, $^{140}$Ce): *m*/*z* (%) = 1170 (5) $[M]^{+\cdot}$, 993 (100) $[M - (Br\text{-}acac)]^+$, 912 (60) $[M - (Br\text{-}acac) - Br]^+$. UV/Vis (250–800 nm, $CHCl_3$): $\lambda$ = 289.8 nm. $C_{56}H_{70}Br_2CeO_8$ (1171.07): calcd. C 57.43, H 6.02; found C 57.23, H 6.04.

**Synthesis of {*p*-*t*Bu-calix[4](OMe)$_2$(O)$_2$}TiCl$_2$ from {*p*-*t*Bu-calix[4](OMe)$_2$(O)$_2$}Ce(acac)$_2$ and TiCl$_4$:** {*p*-*t*Bu-calix[4](OMe)$_2$(O)$_2$-Ce(acac)$_2$} (1.7 g, 1.7 mmol) was dissolved in toluene (50 mL) and $TiCl_4$ (0.096 g, 1.7 mmol) was added by syringe at room temperature, which caused the color of the solution to change to red. Subsequent stirring for another 12 h and removal of the solvent under vacuum gave a red–brown powder that was recrystallized from toluene (10 mL) to afford deep red crystals. $^1$H NMR (400 MHz, $C_6D_6$, 25 °C): $\delta$ = 7.17 (s, 4 H, Ar*H*), 6.82 (s, 4 H, Ar*H*), 4.61 [d, $^1J(^1H,^1H)$ = 13.4 Hz, *endo*-C$H_2$], 4.18 (s, 6 H, OC$H_3$), 3.18 [d, $^1J(^1H,^1H)$ = 13.4 Hz, *exo*-C$H_2$], 1.38 (s, 18 H, CC$H_3$), 0.69 (s, 18 H, CC$H_3$) ppm.

## Acknowledgments

The authors thank Dr. S. Blaurock for solving the X-ray structures, Prof. Krautscheid (University of Leipzig, Germany) for providing the single-crystal X-ray facilities, and Prof. Frank T. Edelmann for helpful discussions, as well, R. Wrobel and B. Strzelczyk are thanked for the performance of the XPS studies. This work was financially supported by the Otto-von-Guericke-University of Magdeburg.

[1] a) X. D. Wu, R. C. Dye, R. E. Muenchausen, S. R. Foltyn, M. Maley, A. D. Rollett, A. R. Garcia, N. S. Nogar, *Appl. Phys. Lett.* **1991**, *58*, 2165; b) Z. Lu, R. Hiskes, S. A. DiCarolis, A. Nel, R. K. Route, R. S. Feigelson, *J. Cryst. Growth* **1995**, *156*, 227.
[2] a) F. Eguchi, T. Setoguchi, T. Inoue, H. Arai, *Solid State Ionics* **1992**, *52*, 165; b) D. L. Maricle, T. E. Swarr, S. Karavolis, *Solid State Ionics* **1992**, *52*, 173.
[3] a) P. Soininen, L. Niinistö, E. Nykänen, M. Leskelä, *Appl. Surf. Sci.* **1994**, *75*, 99; b) D. Endisch, K. Barth, J. Lau, G. Peterson, A. E. Kaloyeros, D. Tuenge, C. N. King, *Mater. Res. Soc. Symp. Proc.* **1997**, *471*, 269; c) J. E. Lau, K. W. Barth, G. G. Peterson, D. Endisch, A. Topol, A. E. Kaloyeros, R. T. Tuenge, M. J. DelaRosa, C. N. King, *J. Electrochem. Soc.* **1998**, *145*, 4271; d) T. S. Moss, R. C. Dey, D. C. Smith, J. A. Samuels, M. J. DelaRosa, C. F. Schaus, *Mater. Res. Soc. Symp. Proc.* **1996**, *415*, 21; e) T. S. Moss, R. C. Dey, M. J. DelaRosa, C. F. Schaus, *Proc. Electrochem. Soc.* **1996**, *96–5*, 396.
[4] a) H. Song, Y. Jiang, C. Xia, G. Meng, D. Peng, *J. Cryst. Growth* **2003**, *250*, 423–430; b) M. Pan, H. W. Meng, C. S. Chen, D. K. Peng, Y. S. Lin, *Thin Solid Films* **1998**, *324*, 89; c) H. Z. Song, H. B. Wang, J. Zhang, D. K. Peng, G. Y. Meng, *Mater. Res. Bull.* **2002**, *37*, 1487.
[5] a) M. Becht, K.-H. Dahmen, V. Gramlich, A. Marteletti, *Inorg. Chim. Acta* **1996**, *248*, 27; b) M. Becht, T. Gerfin, K.-H. Dahmen, *Chem. Mater.* **1993**, *5*, 137–144.
[6] J. McAleese, J. C. Plakatourras, B. C. H. Steele, *Thin Solid Films* **1996**, *280*, 152.
[7] M. J. DelaRosa, K. S. Bousman, J. T. Welch, P. J. Toscano, *J. Coord. Chem.* **2002**, *55*, 781.
[8] a) Y. Bian, J. Jiang, Y. Tao, M. T. M. Choi, R. Li, A. C. H. Ng, P. Zhu, N. Pan, X. Sun, D. P. Arnold, Z.-Y. Zhou, H.-W. Li, T. C. W. Mak, D. K. P. Ng, *J. Am. Chem. Soc.* **2003**, *125*, 12257; b) J. Jiang, W. Liu, K.-W. Poon, D. Du, D. P. Arnold, D. K. P. Ng, *Eur. J. Inorg. Chem.* **2000**, 205.
[9] J. Gottfriedsen, D. Dorokhin, *Z. Anorg. Allg. Chem.* **2005**, *631*, 2928.
[10] M. Dolg, P. Fulde, H. Stoll, H. Preuss, A. Chang, R. M. Pitzer, *Chem. Phys.* **1995**, *195*, 71.
[11] a) N. M. Edelstein, P. G. Allen, J. J. Bucher, D. K. Shuh, C. D. Sofield, *J. Am. Chem. Soc.* **1996**, *118*, 13115; b) C. H. Booth, M. D. Walter, M. Daniel, W. W. Lukens, R. A. Andersen, *Phys. Rev. Lett.* **2005**, *95*, 267202.
[12] a) For a recent review of Ce$^{IV}$ [8]annulene complexes, see: F. T. Edelmann, D. M. M. Freckmann, H. Schumann, *Chem. Rev.* **2002**, *102*, 1851; b) A. Streitwieser, S. A. Kinsley, C. H. Jenson, J. T. Rigsbee, *Organometallics* **2004**, *23*, 5169; c) H.-D. Amberger, H. Reddmann, F. T. Edelmann, *J. Organomet. Chem.* **2005**, *690*, 2238.
[13] H. Isago, M. Shimoda, *Chem. Lett.* **1992**, 147.
[14] P. Thuéry, M. Nierlich, J. Harrowfield, M. Ogden, *Calixarenes 2001* (Eds.: Z. Asfari, V. Böhmer, J. Harrowfield, J. Vicens), Kluwer, Dordrecht, **2001**, ch. 30, p. 561 and references cited therein.
[15] P. D. Beer, M. G. B. Drew, A. Grieve, M. I. Ogden, *J. Chem. Soc., Dalton Trans.* **1995**, 3455.
[16] J. L. Atwood, L. J. Barbour, S. Dalgarno, C. L. Raston, H. R. Webb, *J. Chem. Soc., Dalton Trans.* **2002**, 4351.
[17] Z. Yawen, Y. Chunhua, M. Yoshitaka, *J. Rare Earths* **2002**, *20*, 41.
[18] G. Shankar, S. K. Ramalingam, *Transition Met. Chem.* **1984**, *9*, 449.
[19] a) U. Radius, A. Friedrich, *Z. Anorg. Allg. Chem.* **1999**, *625*, 2154; b) A. Zanotti-Gerosa, E. Solari, L. Giannini, C. Floriani, N. Re, A. Chiesi-Villa, C. Rizzoli, *Inorg. Chim. Acta* **1998**, *270*, 298.
[20] a) B. Matković, D. Grdenić, *Acta Crystallogr.* **1963**, *16*, 456; b) H. Titze, *Acta Chem. Scand. A* **1974**, *28*, 1079; c) H. Titze, *Acta Chem. Scand.* **1969**, *23*, 399.

 © 2007 Wiley-VCH Verlag GmbH & Co. KGaA, Weinheim 

[21] T. Behrsing, A. M. Bond, G. B. Deacon, C. M. Forsyth, M. Forsyth, K. J. Kamble, B. W. Skelton, A. H. White, *Inorg. Chim. Acta* **2003**, *352*, 229.
[22] S. Daniele, L. G. Hubert-Pfalzgraf, M. Perrin, *Polyhedron* **2002**, *21*, 1985.
[23] B. A. Vaartstra, J. C. Huffman, P. S. Gradeff, L. G. Hubert-Pfalzgraf, J. C. Daran, S. Parraud, K. Yunlu, K. G. Caulton, *Inorg. Chem.* **1990**, *29*, 3126.
[24] W. J. Evans, T. J. Deming, J. M. Olofson, J. W. Ziller, *Inorg. Chem.* **1989**, *28*, 4027.
[25] L. Salmon, P. Thuéry, Z. Asfari, M. Ephritikhine, *Dalton Trans.* **2006**, 3006–3014.
[26] a) A. Pfau, K. D. Schierbaum, *Surf. Sci.* **1994**, *321*, 71; b) E. Wuilloud, B. Delley, W.-D. Schneider, Y. Baer, *Phys. Rev. Lett.* **1984**, *53*, 202; c) D. R. Mullins, S. H. Overbury, D. R. Huntley, *Surf. Sci.* **1998**, *409*, 307.
[27] L. El Fallah, L. Hilaire, B. Romeo, F. Le Normand, *J. Electron. Spectrosc. Relat. Phenom.* **1995**, *73*, 89.
[28] Y. Suchorski, J. Gottfriedsen, R. Wrobel, B. Strzelczyk, H. Weiss, *Solid State Phenom.* **2007**, *128*, 115–122.
[29] Y. Suchorski, L. Rihko-Struckmann, F. Klose, Y. Ye, M. Alandjiyska, K. Sundmacher, H. Weiss, *Appl. Surf. Sci.* **2005**, *249*, 231.
[30] J. Qiu, K. Nouch, K. Miura, T. Mitsuyu, K. Hirao, *J. Phys.: Condens. Matter* **2000**, *12*, 5061.
[31] E. Paparazzo, G. M. Ingo, *J. Electron. Spectrosc. Relat. Phenom.* **1998**, *95*, 301.
[32] a) J. Cazaux, *J. Electron. Spectrosc. Relat. Phenom.* **1999**, *105*, 155; b) S. P. Chenakin, R. Prada Silvy, N. Kruse, *Catal. Lett.* **2005**, *102*, 39.
[33] a) R. G. Copperthwhite, J. Lloyd, *Nature* **1978**, *271*, 141; b) D. E. Ramaker, C. T. White, J. S. Murday, *J. Vac. Sci. Technol.* **1981**, *18*, 74.
[34] G. M. Sheldrick, *SHELXS-97, Program of Crystal Structure Solution*, University of Göttingen, Göttingen, Germany, **1997**.
[35] G. M. Sheldrick, *SHELXL-97, Program of Crystal Structure Refinement*; University of Göttingen: Göttingen, Germany, **1997**.
[36] A. Arduini, A. Casnati in *Macrocycle Synthesis* (Ed.: O. Parker), Oxford University Press, New York, **1996**, ch. 7.
[37] T. Yoshimura, C. Miyake, S. Imoto, *Bull. Chem. Soc. Jpn.* **1973**, *46*, 2096–2101.

Received: October 24, 2006
Published Online: April 17, 2007

 © 2007 Wiley-VCH Verlag GmbH & Co. KGaA, Weinheim 

DOI: 10.1002/ejic.200601075

# Synthesis and Structures of Two New Types of Boronium Salts[‡]

Ulrike Braun[a] and Heinrich Nöth*[a]

**Keywords:** Boronium Cations / Transamination / X-ray structures

Transamination of di(pyrid-2-yl)amine (**1**) with $B(NMe_2)_3$ leads to the isomeric heterocyclic bis(dimethylamino)boryl compound **4** and not to bis(dimethylamino)di(pyrid-2-yl)aminoborane (**2**). $B(NMe_2)_3$ reacts with aniline (1:2 ratio) to yield a 1:1 mixture of $B(NHPh)_3$ and $(Me_2N)_2BNHPh$. Transamination of this mixture with **1** yields the anilinodimethylamino analogue of **4** (compound **7**). Compound **4** reacts with $CHCl_3$ to generate the boronium salt **5** by the abstraction of HCl from $CHCl_3$ and addition of HCl to one of the dimethylamino groups. Compound **5** crystallizes with 4 molecules of $CHCl_3$. Compound **4** is attacked by $AlCl_3$ in toluene to give a mixture of unidentified products from which the tetrachloroaluminate of a new type of spirocyclic diboronium cation, **8**, was isolated and characterized by X-ray crystallography.
(© Wiley-VCH Verlag GmbH & Co. KGaA, 69451 Weinheim, Germany, 2007)

## Introduction

The cationic chemistry of boron started in 1955.[1] At that time, there was a lively discussion on the structure of the so-called diammoniate of diborane $B_2H_6{\cdot}2NH_3$. Two structures were favored, $[NH_4][H_3B{-}NH_2{-}BH_3]$[1] and $[H_2B(NH_3)_2]BH_4$.[2] The classical papers by Parry and Shore[2–7] revealed that the latter structure is correct. Since then, many cations with tri- and di-coordinated boron atoms have been characterized in addition to those with tetra-coordinated boron atoms. A recent review summarizes the present status in this field.[8] The interest in gaseous cations, such as $BF_2^+$ or $BMe_2^+$, as reagents has also grown.[9] In spite of these advances, the cationic chemistry of boron, over the last decade, is still a somewhat neglected part of boron chemistry.

Here we present a study that was actually not directed towards the synthesis of new boron cations, but that resulted from reactions aimed at the preparation of aminoboranes suitable for *N*-lithiation.[10]

### Transamination of $B(NMe_2)_3$ with Di(pyrid-2-yl)amine and Formation of a New Type of Heterocyclic Boronium Salt

*N*-lithiation of tris(pyridylamino)borane leads to an interesting cluster structure.[10] For this reason, the unknown bis(phenylamino)di(pyrid-2-yl)aminoborane (**3**) appeared as a potential candidate for *N*-lithiation. We tried to achieve its synthesis in a two step reaction as shown in Equation (1). The transamination of di(pyrid-2-yl)amine (**1**) with tris(dimethylamino)borane was expected to yield bis(dimethylamino)di(pyrid-2-yl)aminoborane (**2**), which on further transamination with aniline should have given the target compound **3**.

However, the $^{11}B$ NMR spectrum definitely excludes the formation of **2**. The solution obtained shows intense yellow fluorescence and a sharp $^{11}B$ NMR signal at 5.0 ppm in its spectrum, which is typical for a tetra-coordinated boron atom. The elemental analysis corresponds with the composition expected for **2**. However, in the $^1H$ NMR spectrum, no signal for an NH proton is observed, and all NMR spectroscopic data are in accord with the structure of **4**, as shown in Equation (2). The position of attack of the boron atom of $B(NMe_2)_3$ is at one of the pyridine N atoms of **1** and not at the NH nitrogen atom, as shown in Equation (3). Elimination of $Me_2NH$ is expected to be favored because of the formation of an N–H···N hydrogen bridge bond. Rotation about the N–C bond of the non-coordinated pyridyl unit allows the formation of a six-membered ring.

The hydrogen atoms on the *o*-positions of the pyridine rings of **4** give rise to an $^1H$ NMR signal at 7.64 ppm, and the carbon atoms at the *o*-positions to a $^{13}C$ NMR signal at 138.4 ppm. These nuclei are better shielded than those in **1** (8.23 and 147.6 ppm). This can be compared with the corresponding $^1H$ and $^{13}C$ NMR signals for pyridine (8.59 and 149.8 ppm) and pyridine *N*-oxide (8.36 and 138.5 ppm), which carries, like **4**, a formal positive charge at the N atom.[11] In addition, the $^1H$ resonance for the dimethylamino groups of **4** are found at slightly higher field ($\delta$ =2.36 ppm) relative to those of $B(NMe_2)_3$ ($\delta$ =2.48 ppm). The coordination mode in compound **4** is similar to that in pyrazaboles **A**[12] or in the boron biguanidine complexes **B**.[13] The structures of pyrazaboles have been extensively investigated,[14–16] although no species is yet known in

[‡] Contribution to the Chemistry of Boron 265. Contribution 264: R. Jetzfellner, H. Nöth, R. T. Paine, *Z. Anorg. Allg. Chem.*, in press.

[a] Department of Chemistry, University of Munich, Butenandt-Str. 5–13, 81377 München, Germany
E-mail: H. Noeth@lrz.uni-muenchen.de

 InterScience © 2007 Wiley-VCH Verlag GmbH & Co. KGaA, Weinheim 

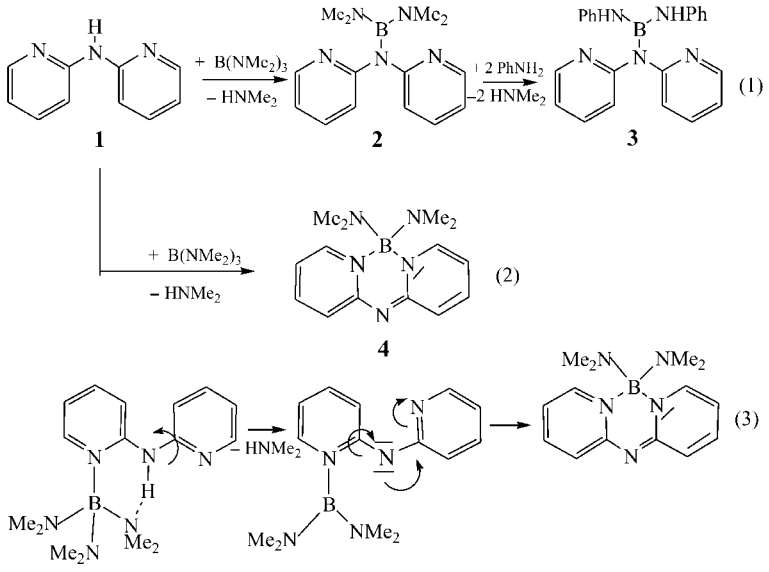


which the boron atoms of the pyrazaboles carry two exocyclic amino groups at the boron atoms; however, CNDO calculations on a *N*,*N*′-dimethylethylenediamino species have been performed.[17]

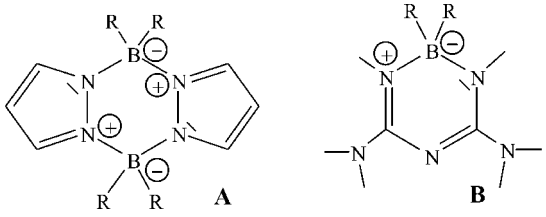


In order to prove the structure of compound **4**, we attempted to obtain single crystals of this compound; but, only polycrystalline material separated from various solvents. Single crystals, however, did form from a 1:1 mixture of chloroform and pentane at –78 °C. The X-ray structure determination of a monoclinic crystal (space group $P2_1/n$, $Z = 4$) shows that the investigated species is not compound **4**, but rather its hydrochloride. The crystals have the composition $C_{14}H_{20}BN_5 \cdot HCl \cdot 4CHCl_3$. The molecular structure of **4·HCl** (**5**) is depicted in Figure 1.

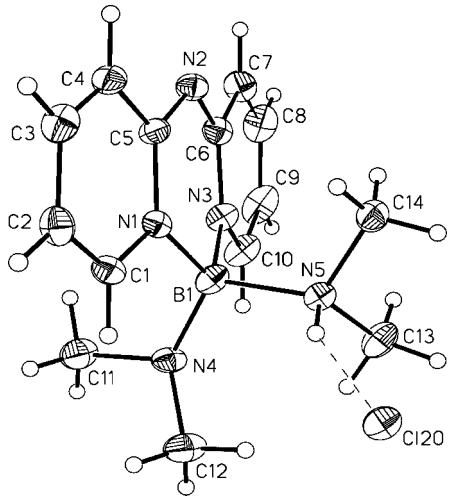


Figure 1. ORTEP plot of the molecular structure **5**. Selected bond lengths [Å]: B1–N1 1.566(8), B1–N3 1.565(8), B1–N4 1.453(9), B1–N5 1.636(8), N4–C12 1.461(7), N4–C11, 1.463(8), N5–C13 1.492(7), N5–C14 1.481(8), N5–H1 0.86 Cl20–H1 2.307. Selected bond angles [°]: C1–N1–B1 118.5(5), C5–N1–B1 122.7(5), C10–N3–B1 118.3(5), C6–N3–B1 121.7(5), C12–N4–B1 126.5(5), C11–N4–B1 117.0(5), B11–N4–C12 111.0(5), C13–N5–C14 108.0(5), C14–N5–B1 115.7(5), C13–N5–B1 114.2(5), N3–B1–N4 112.5(5), N1–B1–N4 115.6(5), N1–B1–N3 105.0(5), N4–B1–N5 110.6(5), N3–B1–N5 106.5(5), N1–B1–N5 106.1(5), N1–C5–N2 122.7(5), N2–C6–N3 123.7(5).

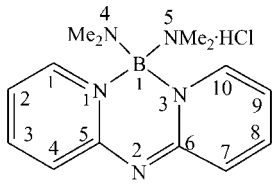


**5**

Its $N_3C_2B$ ring adopts a tub-shape conformation. Atoms C6, C5, and N1 lay almost in a plane (interplanar angle C6-C5-N1/N1-N3-C6 = 1.1°). The N3-B1-N1 plane forms an interplanar angle of 18.3° with the C6-C5-N3-N1 plane and 7.7° with the C6-N2-C5 plane. The N2 atom sits only 0.095 Å above the N3-B1-N1 plane. Therefore, it is incorporated into the π-system of the heterocycle. This is also shown by the presence of short C–N bonds. The annulated six-membered rings are bent backwards from the central ring. Their interplanar angles with the C6-C5-N3-N1 plane is 13.4°. The two endocyclic B–N bonds, B1–N1 and B1–N3, have the same lengths, while the two exocyclic B–N bonds are different [B1–N4 = 1.453(9) Å and B1–N5 = 1.636(8) Å]. The N4 atom has an almost planar environment (Σ = 354.4°), in contrast to the tetra-coordinated N5 atom with its significantly longer B–N bond. Bond angles at the tri-coordinated N4 atom range from 111.0(5) to 126.5(5)°. Similarly, bond angles at the tetra-coordinated N5 atom span from 108.0(5) to 115.7(5)°. It is obvious that

 © 2007 Wiley-VCH Verlag GmbH & Co. KGaA, Weinheim 

most of the positive charge is located at the tetra-coordinated N5 atom. Its H1 atom forms a hydrogen bond to the chloride ion as shown by the bond lengths of 0.98 Å for N5–H1 and 2.307 Å for H1···Cl20. This H···Cl distance is shorter than the NH···Cl bond in 2,2,4,4-tetramethylpiperidinium chloride [2.232(5) Å].[18] The N5–H1–Cl2 bond angle is 154.0°.

Figure 2 represents a stereoplot of the unit cell of compound **5** that shows that the chloroform molecules fill the spaces between the atoms of the boronium salt. The H atom of the chloroform molecules interact either with the chloride ions or with *p*-N atoms of the heterocycles.

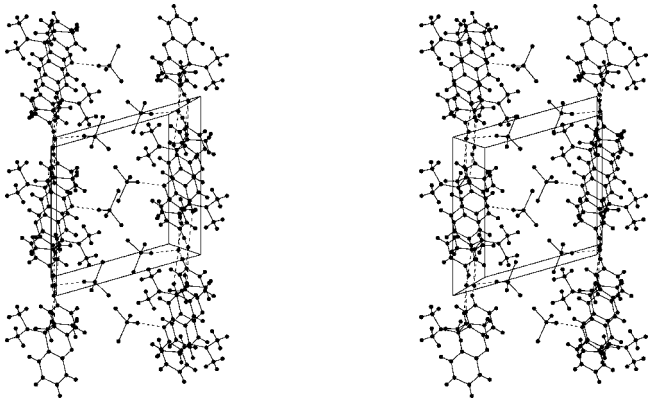

Figure 2. Stereoplot of the unit cell of compound **5**·$(CHCl_3)_4$. View down the *b* axis. The chloroform molecules are "lined" up between two strands of **5** molecules.

It is obvious that HCl is necessary to form **5**, and chloroform is the HCl source. It is known that strong bases can be protonated by $CHCl_3$, with subsequent removal of HCl to form dichlorocarbene as an intermediate. Compound **4** possesses a high proton affinity as was already demonstrated for the ready synthesis of the related 2,2′-dipyridylbis(dimethylamino)boronium salt.[19]

A possible alternative synthesis for compound **2** is shown in Equation (4). The components, **6** and $ClB(NMe_2)_2$, react readily with the formation of chlorotrimethylsilane, but again the product is **4** [Equation (5)]. This shows that the chlorobis(dimethylamino)borane attacks also at a pyridine nitrogen atom of **1**. Another possible route is to first synthesize dianilinodimethylaminoborane followed by transamination with **1**. However, treatment of $B(NMe_2)_3$ with 2 mol of aniline resulted in a 1:1 mixture of $B(NHPh)_3$ and $(Me_2N)_2BNHPh$ as shown in Equation (6). Two $^{11}B$ NMR signals at $\delta$ = 24.9 and 23.6 ppm of equal intensity are observed in the solution. The latter signal is assigned to $B(NHPh)_3$[10] and the former to bis(dimethylamino)organylaminoborane.[20] Treatment of the mixture of $B(NHPh)_3$ and $(Me_2N)_2BNHPh$ with **1** produced a solution with resonances in the $^{11}B$ NMR spectrum at 23.7 and 2.0 ppm ($h_{1/2}$ = 83 Hz). Obviously, $B(NHPh)_3$ remained untouched, while $(Me_2N)_2BNHPh$ reacted with the di(pyrid-2-yl)amine with elimination of $Me_2NH$ and formation of **7** [see Equation (7)]. $B(NHPh)_3$ precipitated from the concentrated solution, and it was possible to isolate compound **7** from the red-brown fluorescent filtrate. Compound **7** was characterized by NMR spectroscopy and elemental analysis.

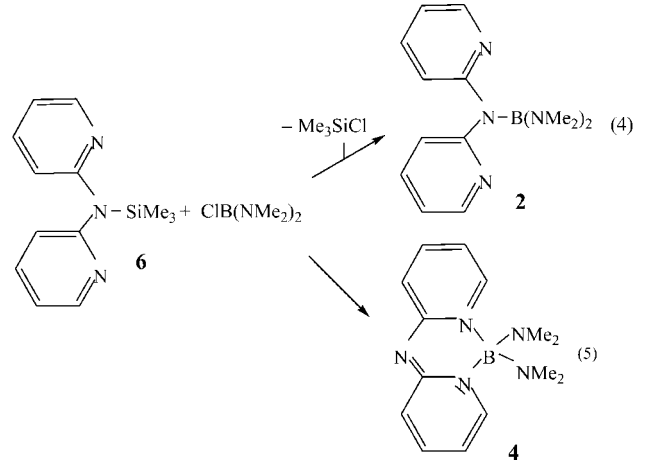


$$2\ B(NMe_2)_3 + 4\ PhNH_2 \rightarrow (Me_2N)_2BNHPh + B(NHPh)_3 + 4\ HNMe_2 \quad (6)$$

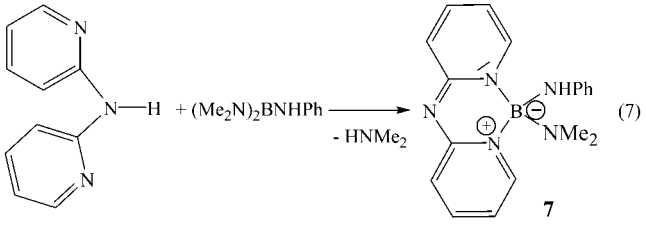


## The Formation of a Spirocyclic Diboronium Cation as Its Tetrachloroaluminate

While the HCl adduct of **4** is a boronium salt with a tetra-coordinated boron atom, compound **4** may also be the source for a boronium cation with a tri-coordinated boron atom. The first boronium salts with tri-coordinated boron atoms were reported in 1962.[21] In this case, the pyridine adduct of $Ph_2BCl$ was treated with $AgClO_4$ to generate $(pyBPh_2)ClO_4$. It was also reported later[22] that the abstraction of a chloride ion from $Ph_2BCl$ by $AlCl_3$ would produce the di-coordinated boron cation $BPh_2^+$. But because all these reactions were performed in solvents like nitromethane or ethylmethyl ketone, it is more likely that adducts with the solvents were formed. None of these cations could be isolated as salts. Their existence was, therefore, disputed.[22,23] Today, sterically and electronically stabilized cations of boron are readily accessible.[9] In particular, suitable anion acceptors have been widely used for hydride or halide abstraction from base adducts $L{\cdot}BY_2X$ (X = H, Hal; Y = organyl, OR, $NR_2$).[24–26] Compound **4** could form a cation with a tri-coordinated boron atom because this cation should be stabilized by electron delocalization as shown in formula **C**.

 © 2007 Wiley-VCH Verlag GmbH & Co. KGaA, Weinheim 

To generate this cation we treated **4** with $AlCl_3$ in a 1:1 ratio in toluene. No reaction occurs at ambient temperature, but after keeping the mixture at reflux, a yellow-green precipitate and a yellow solution forms. The $^{11}B$ NMR spectrum of the solution shows an intense signal at 26.5 ppm and a very weak multiplet around 0.7 ppm. The intense signal indicates the presence of a triaminoborane[27] or a triaminoborane cation.[28] The $^{27}Al$ NMR spectrum of the solution shows signals at 68.0 and 31.9 ppm (broad) as well as a group of signals with peaks at 80.4, 92.2, and 104.4 ppm. The sharp signal at 104.4 ppm arises from $AlCl_4^-$.[29] The others are indicative of a mixture of $AlCl_{4-n}(NMe_2)_n^-$ anions. Signals in the range 80–108 ppm have been observed for these anions.[30,31] Most likely, the first anion formed is $AlCl_3NMe_2^-$, followed by redistribution of the substituents, a well-known phenomenon in the chemistry of mixed tetrahaloaluminate anions.[32]

The yellow solid that remains after evaporation of toluene from the filtrate was almost insoluble in all common solvents, and this was also observed for the precipitate. Only $CH_2Cl_2$ proved to be a suitable solvent. The spectrum of the dissolved part of the precipitate shows a $^{27}Al$ NMR signal at $\delta$ = 106.4 ppm ($h_{1/2}$ = 25 Hz), which is typical for $AlCl_4^-$, and a broad weak signal around 26.8 ppm, which is due to a hexacoordinate Al species.$^{11}B$ NMR signals were observed at 1.1 and 0.36 ppm and also at 26.5 ppm. These data show that the reaction between **4** and $AlCl_3$ is rather complex.

Fortunately, yellow single crystals could be obtained from a $CH_2Cl_2$ solution at –20 °C. They are monoclinic and crystallize in the space group $P2_1/c$ with $Z$ = 4. The X-ray structure determination shows the presence of a new kind of spiroheterocyclic molecular cation **8** containing two tetra-coordinated boron atoms and one tri-coordinated boron atom. It crystallizes as a bis(tetrachloroaluminate) with the composition [**8**][$AlCl_4$]$_2$($CH_2Cl_2$)$_2$ (Figure 3 shows the atoms in the asymmetric unit).

The central part of the molecule is a naphthalene-like $B_3N_5C_2$ ring with formal positive charges that reside preferably on the four pyridine nitrogen atoms N1, N3, N9 and N11, while the boron atoms B1 and B2 are formally negatively charged. The ring B–N bond lengths in the tricyclic rings are comparatively long and range from 1.542(7) to 1.569(7) Å. On the other hand, the B1–N5 and B2–N7 bonds are shorter (1.472 and 1.467 Å). The bonds B1–N4 and B2–N8 [1.610(8) and 1.603(8) Å] to the di(pyrid-2-yl)-amino group are much longer despite the fact that these two N atoms are tri-coordinate. By taking the B–N bond lengths as a criterion, these two bonds have to be considered as coordinative B–N bonds.

A tub-shaped conformation is observed for the central ring of the two heteroanthracene groups. The C5-N1-N3 plane is almost coplanar with the N3-C6-C5 plane (1.3°), and the interplanar angle of the C5-C6-N1-N3 plane to the N3-B1-N1 plane is 19.9°, but 29.6° to the C6-N3-C10 plane. Analogous interplanar angles between C25-C26-N9-N11 and N9-B2-N11 or C25-N11-C21 are 11.7° and 5.7°, respectively. N2–C6–C7–C8 and N10–C25–C24–C23 torsion angles are 3.5° and 1.1°. The central B3 atom is present in a trigonal-planar environment (Σ = 360.1°) with a wide N5–B3–N7 bond angle of 126.7(5)°. This open angle is a steric consequence of the interaction between the two NMe groups, because the B3-N5-C31 plane is twisted against the B3-N5-B1 plane by 27.8° but is almost coplanar with the B3-N7-C32 plane. The B3–N5 and B3–N7 bond lengths are 1.382(7) and 1.401(7) Å. This is in the typical range for B–N π-bonding. A significantly longer B–N bond with less double bond character is observed for B3–N6 with a length of 1.455(7) Å. Although the C15–N6–C16 bond angle is 118.7(4)°, this plane is twisted against the N5-B3-N7 plane by 31.3°. The respective $N_2B$ planes N5-B1-N4 and N7-B2-N8 stand almost perpendicular to the C31-N5-B3 and B3-N7-C32 planes (94.3° and 97.3°, respectively), while the N7-B2-N8 plane forms an interplanar angle with the N5-B1-N4 plane of only 3.5°. The semichair conformation of the central two six-membered rings is typical of what is usually observed.

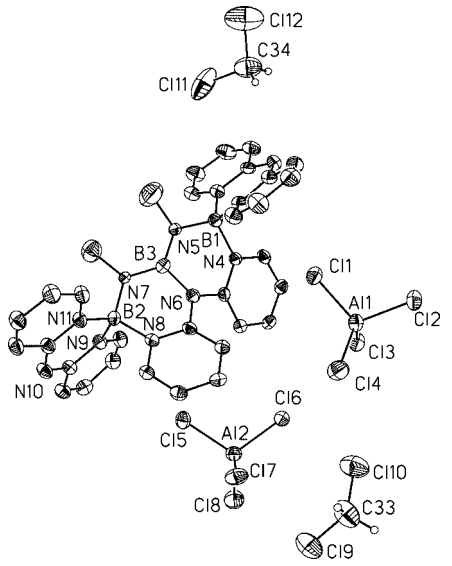


Figure 3. ORTEP plot of the contents of the asymmetric unit in the cell of **8**($AlCl_4$)$_2$·2$CH_2Cl_2$. Hydrogen atoms of cation **8** are omitted for clarity.Selected bond lengths [Å]: N1–B1 1.561(7), N3–B1 1.543(8), N4–B1 1.610(8), N8–B2 1.603(8), N5–B3 1.382(7), N5–B1 1.472(7), N6–B3 1.455(7), N7–B3 1.401(7), N5–C31 1.495(9). Selected bond angles [°]: N1–B1–N5 111.4(5), N5–B1–N4 114.3(5), N3–B1–N1 106.8(5), N5–B1–N4 108.1(5), N3–B1–N4 108.9(4), N1–B1–N4 107.0(4), N5–B3–N7 126.7(5), N7–B3–N6 116.5(5), N4–C15–N6 115.8(5), N8–C16–C6 116.3(5), C15–N6–B3 120.5(4), C15–N6–C16 118.7(4), C16–N6–B3 120.7(4), C11–N3–B1 120.3(4), C11–Ne4C15 117.5(4), C15–N4–B1 122.1(4).

In spite of the NMR spectroscopic data, the route from **4** to **8** remains speculative because not all of the $^{27}Al$ NMR signals could be unequivocally assigned. For instance, the signal at 68 ppm might result form $AlCl_3$·2$NMe_3$ (71 ppm),[30] but it seems unlikely that $AlCl_3$ would first form $AlCl_3$·$NMe_3$ during its attack on **4**, which then must attack a second molecule of **4** in order to form $AlCl_3$·2$NMe_3$. It is more likely that $AlCl_3$ removes a $Me_2N$ group by BN cleavage to form a cation of type **C**, which then attacks another molecule of **4**. Too little information

 © 2007 Wiley-VCH Verlag GmbH & Co. KGaA, Weinheim 

can be extracted from the NMR spectroscopic data to suggest a route from **4** to **8**. However, it should be noted that **8** contains a di(pyrid-2-yl)amino group. This suggests that isomer **2** is generated during the process.

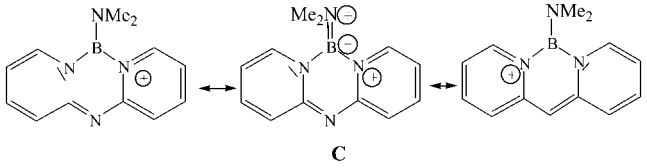

**C**

## Discussion

Transamination of 2-aminopyridine with $B(NMe_2)_3$ led to 2-aminopyridine(dimethylamino)boranes $(pyNH)_nB(NMe_2)_{3-n}$,[10] amongst which $B(HNpy)_3$ is most readily isolated. In contrast, di(pyrid-2-yl)amine (**1**) reacts in a different manner. This is due to the different basicity of the $NH_2$/NH groups as well as to the sterically more shielded NH group. In addition, the driving force for the formation of **4** is not only a consequence of steric factors, but also because of greater electron delocalization, as shown by the formulae **D/E**. In principle, **1** might exist in two forms, **D/E** and **F**. The structure of the isomer **D/E** is said to remain intact on reaction with $Me_3N{\cdot}BH_2I$, which generates the boronium iodide **9** [see Equation (8)].

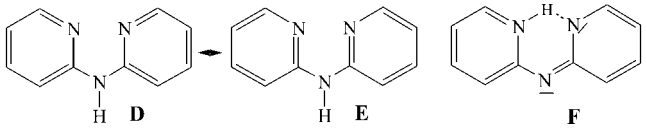

**D** **E** **F**

Since the proton of **1** can be readily removed in strong basic solutions,[33] it is surprising that compound **9** is stable. One would expect that this compound would readily loose hydrogen gas, as shown in Equation (9), with formation of a tri-coordinate borenium salt **10** or the intramolecular iodoborane dipyrid-2-yl complex **11**.

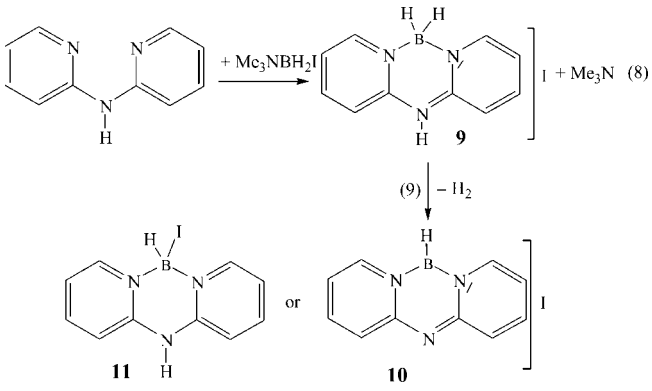

**11** **10**

Although we have only studied the transamination of $B(NMe_2)_3$ with **1** in a 1:1 ratio, it would be interesting to also perform the transamination reaction with 2 and 3 mol of this amine in order to see whether the 1:3 transamination product $B(Npy'_2)_3$ contains structural elements in analogy to those in **4** or whether it is a "normal" triaminoborane $B(Npy'_2)_3$. In this context, one should note that cation **8** contains a di(pyrid-2-yl)amino group, an indication that isomers **2** and **4** may interconvert.

The transamination of $B(NMe_2)_3$ with aniline leads to a mixture of $(Me_2N)_2BNHPh$ and $B(NHPh)_3$. This is in accord with earlier observations,[34] although it has been reported that $(Me_2N)_2BNHPh$ and $Me_2NB(NHPh)_2$ can be prepared by transamination.[35] We did not find any $^{11}B$ NMR evidence for the formation of the latter compound.

The removal of a $Me_2N$ anion from compound **4** by $AlCl_3$ leads finally to the heterocyclic boronium dication in the salt $[\mathbf{8}][AlCl_4]_2$ (Figure 4). As far as we know, this is the first example of a diboronium cation and the second example[25] in which a cationic boron species has been generated from a triaminoborane. Particularly surprising is the fact that, in the course of this reaction, the dimethylamino groups are transformed by loss of a methyl group into NMe

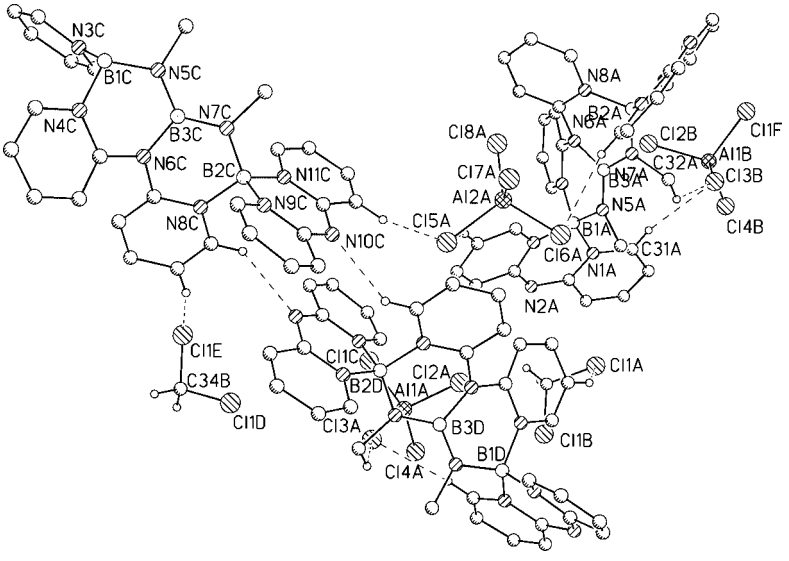


Figure 4. Section representing three cations of **8**, three $AlCl_4$ anions, and two $CH_2Cl_2$ molcules. Cl···HC distances are in the order of 2.7(0.2) Å, and CHN distances in the order of 2.1 Å. Only relevant H atoms are shown.

 © 2007 Wiley-VCH Verlag GmbH & Co. KGaA, Weinheim 

units. As far as we know, this N–C bond cleavage is rather unusual, although this step must occur in order to reasonably explain the formation of **8**. Obviously, aminoboron halides are better suited[8] to generate borenium cations than triaminoborane systems. However, there is no doubt that this result opens up new aspects for the chemistry of cationic boron compounds. Reactions that take unexpected routes are certainly more interesting than those that occur along a "normal" route, and this example shows that BN chemistry still offers surprises.

## Experimental Section

All experiments have been performed under anhydrous conditions using $N_2$ or Ar as protective gases. All compounds were freshly crystallized or distilled. Solvents were dried by conventional methods. NMR spectroscopy: Bruker ACP-200 and Jeol EX 400. Standards for $^{11}B$, $^{14}N$ and $^{27}Al$: external $BF_3{\cdot}OEt_2$, nitromethane, and 1 M $AlCl_3$ in water, respectively. UV/Vis Spectroscopy: Varian Cray 60 CONC spectrometer. Elemental analysis: microanalytical laboratory of the department. X-ray structure determinations: Bruker P4 four circle diffractometer equipped with an area detector and a LT2 cooling device; Mo-$K_\alpha$ radiation, graphite monochromator. Thermal ellipsoids are represented at a 25% probability level.

**Compound 4:** To a stirred solution of **1** (1.59 g, 9.3 mmol) in toluene (40 mL) was added tris(dimethylamino)borane (1.6 mL, 9.3 mmol). After heating to reflux for 20 h, a bright yellow fluorescing solution formed, which presented an $^{11}B$ NMR signal at 4.7 ppm ($h_{1/2}$ = 57 Hz). The solvent was removed, and a yellow powder of **4** remained. Yield: 2.3 g (91%). $C_{14}H_{20}BN_5$ (269.22): calcd. C 63.46, H 7.48, N 26.02; found C 61.87, H 7.53, N 25.92. $^1H$ NMR (270 MHz, $C_6D_6$): $\delta$ = 2.36 (N–*Me*)$_2$ ppm. $^{13}C$ NMR (100 MHz): $\delta$ = 39.5 (N–*Me*)$_2$ ppm, as well as the resonances listed for **5**. $^{11}B$ NMR (64 MHz): $\delta$ = 4.7 ($h_{1/2}$ = 57 Hz) ppm.

**Compound 5:** The yellow solid that remained after evaporation of the solvent from **4** was dissolved in $CHCl_3$ (30 mL). After 10 d, addition of pentane (20 mL) to the top of the solution led to the formation of only a few very small crystals in two days. A few days later, the homogeneous solution was cooled to –78 °C. Yellow fluorescing crystals of **5**·$(CHCl_3)_4$ separated. On drying the crystals in vacuo, they turned turbid as they lost weight. Yield: 2.19 g (83%). M.p. 180 °C. $C_{14}H_{21}BClN_5$ (305.62): calcd. C 55.02, H 6.93, N 22.92, Cl 11.60; found C 54.12, H 6.88, N 21.75, Cl 10.74. $^1H$ NMR (400 MHz, $C_6D_6$): $\delta$ = 2.54 (s, 6 H, HN–*Me*), 5.47 (br. s, 1 H, N–*H*), 6.06 [td, $^3J$ ($^1H^1H$) = 6.6 Hz, $^4J$ ($^1H^1H$) = 1.2 Hz, 2 H, C2–*H*], 6.81 [td, $^3J$ ($^1H^1H$) = 8.3 Hz, $^4J$ ($^1H^1H$) = 3.1 Hz, 2 H, C3–*H*], 7.06 [br. d, $^3J$ ($^1H^1H$) = 8.7 Hz, 2 H, C4–*H*], 7.64 [dd, $^3J$ ($^1H^1H$) = 6.4, $^4J$ ($^1H^1H$) = 1.7 Hz, 2 H, C1–*H*] ppm. $^{13}C$ NMR (100 MHz): $\delta$ = 48.7 (N–*Me*$_2$), 111.7 (py-*C*2), 121.9 (py-*C*4), 131.8 (py-*C*3), 138.4 (py-*C*1), 156.5 (py-*C*5) ppm. $^{11}B$ NMR (64 MHz): $\delta$ = 5.0 ppm. $^{14}N$ NMR (28.9 MHz): $\delta$ = –92.5 (py-*N*), –203.8 (*N*–H), –356.2 (*N*–Me$_2$, H*N*–Me$_2$) ppm. UV/Vis (toluene): $\lambda_{max}$ = 320, 393 cm$^{-1}$.

**Compound 7:** A mixture of $B(NMe_2)_3$ (3.45 mL, 20 mmol) and aniline (3.65 mL, 40 mmol) in toluene (150 mL) was kept at reflux for 20 h. After cooling the solution, $^{11}B$ NMR signals (1:1 intensity) at 24.9 ppm for $(Me_2N)_2BNHPh$[10] and at 23.6 ppm for $B(NHPh)_3$ were observed in the spectrum.[6] **1** (3.42 g, 20 mmol) was added to the reaction mixture, which was kept at reflux for another 20 h. The $^{11}B$ NMR spectrum showed a signal for $B(NHPh)_3$ in addition to one at 2.0 ppm. On cooling the mixture to –20 °C, most of the $B(NHPh)_3$ separated as a solid, which was removed by filtration. The filtrate exhibited red brown fluorescence. It was then reduced in volume to 20 mL. At –50 °C, only a few additional crystals of $B(NHPh)_3$ separated, which were removed by filtration. All the volatile material from the filtrate was then evaporated under vacuum to leave behind a light brown powder of **7**. $C_{18}H_{20}BN_5$ (317.18): calcd. C 68.10, H 6.35, N 22.07; found C 68.29, H 5.22, N 22.20. $^1H$ NMR (400 MHz, $C_6D_6$): $\delta^1$ = 2.11 (N–*Me*$_2$), 2.82 (br., N–*H*), 6.42, 6.70, 6.72, 6.96, 7.63, 7.97 (Ar-*H*, Ph-*H*) ppm. $^{11}B$ NMR (64 MHz, toluene): $\delta$ = 2.0 ppm ($h_{1/2}$ = 83 Hz).

**Di(pyrid-2-yl)aminotrimethylsilane (6):** To a solution of **1** (1.712 g, 10.1 mmol) in toluene (80 mL) was added a solution of *n*BuLi (6.4 mmol, 1.56 M, 10 mmol) at –78 °C. A precipitate of $(py')_2NLi$ formed immediately. At room temperature, the suspension was treated with $Me_3SiCl$ (1.3 mL, 10 mmol). After stirring for 2 h, the insoluble material (LiCl) was removed by filtration, and the filtrate reduced in volume to about 15 mL. White needles of **6** separated over a week by keeping the solution at 0 °C. Yield: 1.97 g (81%). $C_{13}H_{17}N_3Si$ (243.59): calcd. C 64.17, H 6.99, N 17.28; found C 66.18, H 7.06, N 17.88. $^1H$ NMR (400 MHz, $C_6D_6$): $\delta$ = 0.44 (s, 9 H, Si–*Me*$_3$), 6.38 [br. d, $^3J$($^1H^1H$) = 8.5 Hz, 2 H, py-C3–*H*], 6.48 [ddd, $^3J$($^1H^1H$) = 6.5 Hz, $^3J$($^1H^1H$) = 5.6 Hz, $^4J$($^1H^1H$) = 1.3 Hz, 2 H, py-C5–*H*], 7.02 [ddd, $^3J$($^1H^1H$) = 7.0 Hz, $^4J$($^1H^1H$) = 1.1 Hz, 2 H, py-C4–*H*], 8.27 [dd, br, $^3J$($^1H^1H$) = 5.4 Hz, $^4J$($^1H^1H$) = 2.1 Hz, 2 H, py-C6–*H*] ppm. $^{13}C$ NMR (100 MHz, $C_6D_6$): $\delta$ = 1.3 (Si–*Me*$_3$), 116.9 (py-*C*5), 117.7 (py-*C*3), 137.6 (py-*C*4), 149.0 (py-*C*6), 160.0 (py-*C*2) ppm. $^{29}Si$ NMR (80 MHz, $C_6D_6$): $\delta$ = 6.8 ppm. $^{14}N$ NMR (28.9 MHz, toluene): $\delta$ = –85.9 (py-*N*), –266.6 (*N*–Si) ppm.

**Reaction of 6 with Chlorobis(dimethylamino)borane:** A solution of **6** (2.44 g, 10 mmol) in toluene (40 mL) was cooled to 0 °C. $(Me_2N)_2BCl$ (1.35 mL, 10 mmol) in toluene (20 mL) was then added. After stirring the solution for several hours and warming to ambient temperature, a single $^{11}B$ NMR signal at 4.7 ppm was observed in the spectrum, which shows a quantitative conversion to **4**. All other NMR spectroscopic data were identical to those found for **4**. Yield: 2.6 g of **4** (97%).

**Diboroniumbis(tetrachloroaluminate) 8$(AlCl_4)_2$:** To a solution of **4** (2.05 g, 7.6 mmol) in toluene (70 mL) was added $AlCl_3$ powder (1.00 g, 7.6 mmol). The suspension was stirred for 1 d. The $^{11}B$ NMR spectrum shows that no reaction had occurred. The mixture was then kept at reflux for 20 h. During this period, a green-yellow precipitate formed. The yellow solution presented a $^{11}B$ NMR signal at $\delta$ = 26.5 ppm (70%) and a multiplet at 0.7 ppm (≈30%). Two signals were observed in the $^{27}Al$ NMR spectrum at 80.4 and 68 ppm, in addition to overlapping bands in the range 92–104 ppm. After filtration, the solid material was dried and treated with $CH_2Cl_2$. Only part of the material dissolved. The concentrated solution was then cooled to –20 °C. Fairly large yellow-orange crystals with an octahedral shape formed over a few days. As revealed by the X-ray structure determination, the crystals have the composition **8**$(AlCl_4)_2{\cdot}2CH_2Cl_2$. Yield: not determined. M.p. 200 °C. $C_{34}H_{34}Al_2B_3Cl_{12}N_{11}$ (1108.51): calcd. C 36.81, H 3.07, N 13.90, Cl 38.38; found C 36.00, H 2.78, N 12.84, Cl 37.89. $^1H$ NMR (400 MHz, $CH_2Cl_2/C_6D_6$): $\delta$ = 2.13 (s, C–*Me*) ppm. $^{13}C$ NMR (100 MHz, $CH_2Cl_2/C_6D_6$): $\delta$ = 21.2 (N–*Me*) ppm. $^{11}B$ NMR (64 MHz): $\delta$ = 2.0, –26.5 ppm. $^{27}Al$ NMR: $\delta$ = 106.4 ($AlCl_4^-$, $h_{1/2}$ = 20 Hz) ppm.

**X-ray Structure Determinations:** Single crystals were suspended in perfluoro ether oil, and a suitable crystal was selected, fixed on a glass fibre and mounted on the goniometer head flushed with nitrogen gas cooled to –80 °C. The unit cell was determined from the reflections recorded on 5 sets of 15 different exposures each. Data

 © 2007 Wiley-VCH Verlag GmbH & Co. KGaA, Weinheim 

collection was performed in the hemisphere mode. Data were reduced with the program SMART.[36] For the structure solution, the SHELXTL program system[37] was used. Hydrogen atoms bound to N atoms were taken from the Fourier maps as well as those in $CH_2Cl_2$ and $CHCl_3$. All other hydrogen atoms were placed in calculated positions. Crystallographic data and structural parameters are summarized in Table 1. CCDC-626869 and -626870 contains the supplementary crystallographic data for this paper. These data can be obtained free of charge from The Cambridge Crystallographic Data Centre via www.ccdc.cam.ac.uk/data_request/cif.

Table 1. Crystallographic data and structure refinement parameters.

| Compound | **5**·4$CHCl_3$ | **8**$(AlCl_4)_2$·2$CH_2Cl_2$ |
|---|---|---|
| Chemical formula | $C_{18}H_{25}BCl_{13}N_5$ | $C_{34}H_{34}Al_2B_3Cl_{12}N_{11}$ |
| Formula weight | 783.09 | 1108.51 |
| Crystal size [mm] | 0.10 × 0.10 × 0.10 | 0.30 × 0.40 × 0.40 |
| Crystal system | monoclinic | monoclinic |
| Space group | $P2_1/n$ | $P2_1/n$ |
| $a$ [Å] | 11.1059(8) | 15.674(1) |
| $b$ [Å] | 27.428(2) | 18.123(1) |
| $c$ [Å] | 11.719(1) | 18.194(1) |
| $\alpha$ [°] | 90 | 90 |
| $\beta$ [°] | 105.866(1) | 110.709(1) |
| $\gamma$ [°] | 90 | 90 |
| $V$ [Å$^3$] | 3433.8(5) | 4834.3(6) |
| Z | 4 | 4 |
| $\rho$(calcd.) [Mgm$^{-3}$] | 1.515 | 1.523 |
| $\mu$ [mm$^{-1}$] | 1.065 | 0.765 |
| $F$(000) | 1576 | 2240 |
| Index range | $-14 < h < 10$ | $-18 < h < 18$ |
| | $-35 < k < 35$ | $-23 < k < 23$ |
| | $-14 < l < 15$ | $-22 < l < 22$ |
| $2\theta$ [°] | 58.46 | 58.86 |
| Temperature [K] | 193(2) | 193(2) |
| Reflections collected | 19865 | 28240 |
| Reflections unique | 6586 | 9522 |
| Reflections observed (4σ) | 3029 | 3680 |
| $R$(int.) | 0.0743 | 0.0700 |
| No. variables | 342 | 561 |
| Weight scheme[a] $x/y$ | 0.1034/3.4764 | 0.1451/0.000 |
| GOOF | 1.044 | 0.837 |
| Final $R$ (4σ) | 0.0788 | 0.0719 |
| Final $wR_2$ | 0.1947 | 0.1959 |
| Largest residual peak [eÅ$^{-3}$] | 0.953 | 1.530 |

[a] $w^{-1} = \Sigma^2 F_o^2 + (xP)^2 + yP$; $P = (F_o^2 + 2F_c^2)/3$.

## Acknowledgments

We are grateful for support from the University of Munich, Wacker GmbH, and Fonds der Chemischen Industrie. We also like to thank Dr. M. Suter and Dr. T. Habereder for collecting the X-ray data sets.

[1] For a review see: *Gmelin Handbook of Inorganic Chemistry, Boron Compounds*; Springer Publishers, Berlin, Heidelberg, New York, **1976**, vol. 37, pp. 37–42.
[2] S. G. Shore, R. W. Parry, *J. Am. Chem. Soc.* **1955**, *77*, 6084–6085.
[3] D. R. Schultz, R. W. Parry, *J. Am. Chem. Soc.* **1958**, *80*, 4–8.
[4] S. G. Shore, R. W. Parry, *J. Am. Chem. Soc.* **1958**, *80*, 8–12.
[5] S. G. Shore, R. W. Parry, *J. Am. Chem. Soc.* **1958**, *80*, 12–15.
[6] R. W. Parry, S. G. Shore, *J. Am. Chem. Soc.* **1958**, *80*, 15–20.
[7] S. G. Shore, P. R. Giradot, R. W. Parry, *J. Am. Chem. Soc.* **1958**, *80*, 20–24.
[8] W. E. Piers, S. C. Bourke, K. D. Conroy, *Angew. Chem.* **2005**, *117*, 5142–5163; *Angew. Chem. Int. Ed.* **2005**, *44*, 5016–5036.
[9] T. D. Ranatunga, H. I. Kenttämaa, *J. Am. Chem. Soc.* **1992**, *114*, 8600–8604.
[10] U. Braun, T. Habereder, H. Nöth, H. Pietrowsky, M. Warchhold, *Eur. J. Inorg. Chem.* **2002**, 1132–1145.
[11] M. Hesse, H. Meier, B. Zeeh, *Spektroskopische Methoden in der Organischen Chemie*, 3rd ed., Thieme Publishers, Stuttgart, New York, **1987**.
[12] H. Binder, J. Palmtag, *Z. Naturforsch.* **1979**, *34b*, 179–187.
[13] K. B. Anderson, R. A. Franich, H. W. Kroese, R. Meder, E. F. Rickard, *Polyhedron* **1995**, *14*, 1149–1153.
[14] N. W. Alcock, J. F. Sawyer, *Acta Crystallogr., Sect. B* **1974**, *30*, 2899–2901.
[15] C. P. Brock, K. Niedenzu, E. Hanecker, H. Nöth, *Acta Crystallogr., Sect. C* **1985**, *41*, 1458–1463.
[16] J. Bielawski, M. K. Das, E. Hanecker, K. Niedenzu, H. Nöth, S. Trofimenko, *Inorg. Chem.* **1986**, *25*, 87–90.
[17] A. L. Companion, F. Liu, K. Niedenzu, *Inorg. Chem.* **1985**, *24*, 1738–1740.
[18] U. Braun, PhD Thesis, University of Munich, **2000**.
[19] M. A. Kruck, G. Urry, *J. Am. Chem. Soc.* **1966**, *88*, 426–431.
[20] J. M. Davidson, C. M. French, *J. Chem. Soc. (London)* **1962**, 2264.
[21] J. M. Davidson, C. M. French, *J. Chem. Soc. (London)* **1958**, 114.
[22] R. B. Moodie, B. Elliel, T. M. Conner, *Chem. Ind. (London)* **1966**, 767.
[23] D. R. Armstrong, P. G. Perkins, *J. Chem. Soc. A* **1966**, 1026.
[24] H. Nöth, *Nachr. Chem. Techn. Labor* **1984**, *32*, 958–959.
[25] H. Nöth, S. Weber, B. Rasthofer, C. K. Narula, A. Konstantinov, *Pure Appl. Chem.* **1983**, *55*, 1453–1461.
[26] D. J. Brauer, H. Bürger, G. Pawelke, W. Weuter, J. Wilke, *J. Organomet. Chem.* **1987**, *329*, 293–304.
[27] H. Nöth, B. Wrackmeyer, *Nuclear Magnetic Resonance of Boron Compounds* (Eds.: P. Diehl, E. Fluck, R. Kosfeld), Springer Publishers, Berlin, Heidelberg, New York, **1978**.
[28] B. Rasthofer; PhD Thesis, University of Munich, **1984**.
[29] R. K. Harris, B. E. Mann, *NMR and the Periodic Table*, Academic Press, London, New York, San Francisco, **1978**.
[30] I. Krossing, PhD Thesis, University of Munich, **1997**.
[31] P. Wolfgardt, PhD Thesis, University of Munich, **1975**.
[32] J. C. Lockhart, *Redistribution Reactions,* Academic Press, New York, London, **1970**.
[33] B. K. Abate, PhD Thesis, University of Florida, Gainesville, **1972**.
[34] Ya. M. Pushkin, I. S. Panidi, L. A. Platoova, *Dokl. Akad. Nauk SSR* **1964**, *157/159*, 1233–1235.
[35] R. J. Brotherton, T. Buckman, *Inorg. Chem.* **1963**, *2*, 424–425.
[36] *SMART*, Bruker AG, Madison, Version 5.1, **1995**.
[37] *SHELXTL*, Bruker AG, Madison, Version 5.2, **1995**.

Received: December 19, 2006
Published Online: April 23, 2007

 © 2007 Wiley-VCH Verlag GmbH & Co. KGaA, Weinheim 

DOI: 10.1002/ejic.200601130

# Synthesis and Characterisation of Polymer-Anchored Oxidovanadium(IV) Complexes and Their Use for the Oxidation of Styrene and Cumene

**Mannar R. Maurya,*[a] Umesh Kumar,[a] and P. Manikandan[b]**

**Keywords:** Vanadium(IV) complexes / Polymer support / Heterogeneous catalysts / Oxidations

The Schiff bases $H_2$fsal-ea (**I**), $H_2$fsal-pa (**II**) and $H_2$fsal-amp (**III**), derived from 3-formylsalicylic acid and 2-aminoethanol, 3-aminopropanol and 2-amino-2-methylpropanol, respectively, have been connected, by means of covalent bonds, to chloromethylated polystyrene cross-linked with 5% divinylbenzene. On treatment with [VO(acac)$_2$] in dimethylformamide (DMF), these polymer-anchored ligands PS-$H_2$fsal-ea (**IV**), PS-$H_2$fsal-pa (**V**) and PS-$H_2$fsal-amp (**VI**) gave the oxidovanadium(IV) complexes, PS-[VO(fsal-ea)·DMF] (**4**), PS-[VO(fsal-pa)·DMF] (**5**) and PS-[VO(fsal-amp)·DMF] (**6**), respectively. The corresponding neat complexes [VO(fsal-ea)]$_2$ (**1**), [VO(fsal-pa)]$_2$ (**2**) and [VO(fsal-amp)]$_2$ (**3**) have also been similarly prepared. These complexes all exhibit a medium intensity band between 964 and 993 cm$^{-1}$ in their IR spectra resulting from the V=O stretch. The EPR spectra of the polymer-anchored complexes are characteristics of monomeric $V^{IV}$ centres with a simple $S = ½$ electronic spin and with an axial pattern typical of square pyramidal geometry. Broad features for the neat complexes along with magnetic susceptibility studies suggest the presence of antiferromagnetic exchange interactions between two vanadium centres in close proximity. These catalysts have been tested for the oxidation of styrene and cumene and were found to be efficient. Styrene gives five reaction products namely styrene epoxide, benzaldehyde, 1-phenylethane-1,2-diol, benzoic acid and phenylacetaldehyde, whereas cumene gives acetophenone, 2-phenylpropanal, α-methyl styrene epoxide, 2-phenyl-2-propanol, 2-isopropyl-1,4-benzoquinone and α-methyl styrene. The polymer-anchored heterogeneous catalysts are recyclable. The catalytic activities of the neat complexes have also been examined and compared with the corresponding anchored analogues.
(© Wiley-VCH Verlag GmbH & Co. KGaA, 69451 Weinheim, Germany, 2007)

## Introduction

Advances in the coordination chemistry of vanadium with multidentate ligands stem from the discovery of the vanadium containing enzymes, namely vanadate-dependent haloperoxidases,[1] vanadium nitrogenases[2] and vanadium containing nitrate reductases.[3] Vanadate-dependent haloperoxidases catalyse the peroxide mediated oxidation of halides to hypohalous acid which further halogenates hydrocarbons in a non-enzymatic process.[4] Many vanadium complexes provide a suitable structural and/or functional model for these enzymes.[5,6] Oxidations of aliphatic as well as aromatic substrates including (prochiral) organic sulfides to (chiral) sulfoxides, catalysed by vanadium complexes, have also been achieved in excellent yield.[7,8]

The catalytic potential of [VO(sal-ohyba)] and [K(H$_2$O)][-VO$_2$(sal-ohyba)] ($H_2$sal-ohyba = Schiff base derived from salicylaldehyde and *o*-hydroxybenzylamine) for the oxidation and oxidative bromination of organic substrates has been recently investigated in our group.[9] The stability and potential of these complexes to be recycled were improved remarkably by immobilizing them onto a polymer support. For the development of industrial processes, such modifications to homogeneous catalysts would be very important and this, in addition, would lead to operational flexibility of the catalyst as well.[10] Recently, Ando et al. reported oxidovanadium(IV) complexes covalently bonded to Merrifield resin as a heterogeneous catalysts for the oxidation of organic sulfide selectively.[11]

In continuation of our efforts on the development of polymeric supported/anchored vanadium complexes and their catalytic potential, we report herein the preparation and characterisation of polymer-anchored oxidovanadium(IV) complexes of ligands **I**, **II** and **III**, Scheme 1, along with their neat complexes. The catalytic potential of these complexes has been demonstrated by studying the oxidation of styrene and cumene.

[a] Department of Chemistry, Indian Institute of Technology Roorkee,
Roorkee 247667, India
E-mail: rkmanfcy@iitr.ernet.in
[b] Catalysis and Inorganic Chemistry Division, National Chemical Laboratory,
Pune 411008, India
Supporting information for this article is available on the WWW under http://www.eurjic.org or from the author.

 © 2007 Wiley-VCH Verlag GmbH & Co. KGaA, Weinheim 

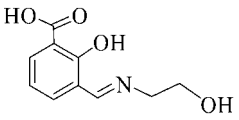

**I**: $H_2$fsal-ea

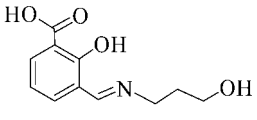

**II**: $H_2$fsal-pa

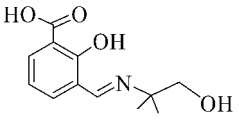

**III**: $H_2$fsal-amp

Scheme 1.

## Results and Discussion

### Synthesis, Reactivity and Solid-State Characteristics

The elemental and spectroscopic data (IR, $^1$H and $^{13}$C NMR) of the ligands $H_2$fsal-ea (**I**), $H_2$fsal-pa (**II**) and $H_2$fsal-amp (**III**) used in the present study, described in the experimental section, confirm the structures of ligands. The chloromethylated polystyrene, cross-linked with 5% divinylbenzene, reacts with these ligands in DMF in the presence of triethylamine to give the polymer-anchored ligands PS-$H_2$fsal-ea(IV), PS-$H_2$fsal-pa (**V**) and PS-$H_2$fsal-amp (**VI**), respectively. During this process the -COOH group of 3-formylsalicylic acid reacts with the -$CH_2Cl$ group of polystyrene. Covalent bonding through the -COOH group of the ligand has been further demonstrated by treating benzylchloride with $H_2$fsal-ea (**I**) under the above reaction conditions. Scheme 2 depicts the structures of the ligands isolated; a representative synthetic procedure for **IV** is also shown. The remaining chlorine content of 1.7% (0.49 mmol Cl/g of resin) in PS-$H_2$fsal-ea, 1.8% (0.51 mmol Cl/g of resin) in PS-$H_2$fsal-pa and 2.2% (0.62 mmol Cl/g of resin) in PS-$H_2$fsal-amp suggested roughly a 90% load of the ligands.

These anchored ligands react with [VO(acac)$_2$] in DMF at ca. 90 °C to give the polymer-anchored oxidovanadium(IV) complexes PS-[VO(fsal-ea)·DMF] (**4**), PS-[VO(fsal-pa)·DMF] (**5**) and PS-[VO(fsal-amp)·DMF] (**6**) which are dark green in colour. Equation (1) represents the synthetic procedure.

$$\text{PS-H}_2\text{fsal-ea} + [\text{VO(acac)}_2] \xrightarrow{\text{DMF}} \text{PS-[V}^{\text{IV}}\text{O(fsal-ea)·DMF]} + 2\ \text{Hacac} \quad (1)$$

**4**

Similarly, the reaction of [VO(acac)$_2$] with an equimolar amount of the neat ligands **I**, **II** and **III** in acetonitrile at reflux yields the neat oxidovanadium(IV) complexes [VO(fsal-ea)]$_2$ (**1**), [VO(fsal-pa)]$_2$ (**2**) and [VO(fsal-amp)]$_2$ (**3**), respectively. The neat complexes exhibit effective magnetic moments of 1.31 (for **1**), 1.34 (for **2**) and 1.49 $\mu_B$ (for **3**) at 298 K which are lower than the expected value of 1.73 $\mu_B$ for a $d^1$ ($S$ = ½) system. We have also studied the magnetic susceptibilities of these complexes as a function of temperature in the 298–90 K range. Figure 1 shows a plot of the magnetic susceptibility $\chi_M^{corr}$ as a function of temperature for **1**. The $\chi_M^{corr}$ values show a slight dependence on temperature, the observed magnetic moment values varied in the range 1.31–1.15 $\mu_B$ and the Curie–Weiss plot [$1/\chi_M^{corr}$ vs. $T$], as shown in Figure 2, was found to be a straight line with a Weiss constant of –40. Similarly, the magnetic moment values of **2** and **3** varied in the ranges 1.34–1.10 and 1.49–1.23 $\mu_B$, respectively, with Weiss constant values of ca. –50. These data all indicate an antiferromagnetic interaction possibly due to dimerisation of the complexes.[12,13] Based on the variations in magnetic moments with temperature and the spectroscopic studies of, for example, complexes [VO(X-sal-ea)]$_2$ (where X-sal-ea = Schiff bases derived from salicylaldehyde and 2-aminoethanol or 3-aminopropanol, X = 5-Cl, 5-Br, 5-$NO_2$, 3-$NO_2$,

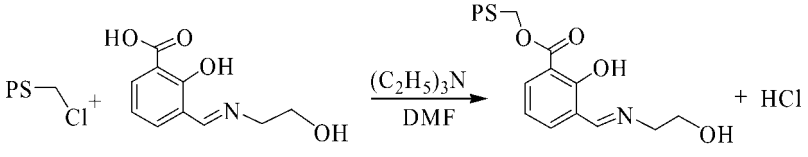

$H_2$fsal-ea **I**

PS-$H_2$fsal-ea **IV**

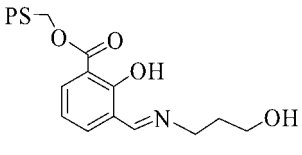

PS-$H_2$fsal-pa **V**

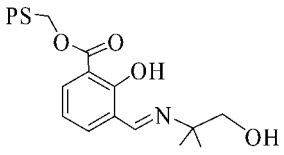

PS-$H_2$fsal-amp **VI**

Scheme 2. Synthetic procedure for **IV** only; PS represents the backbone of chloromethylated polystyrene.

 © 2007 Wiley-VCH Verlag GmbH & Co. KGaA, Weinheim 

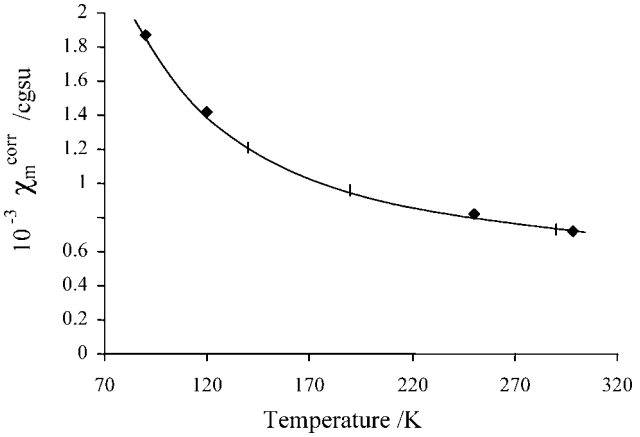


Figure 1. Plot of the magnetic susceptibility $\chi_m^{corr}$ vs. temperature for $[VO(fsal\text{-}ea)]_2$ (**1**).

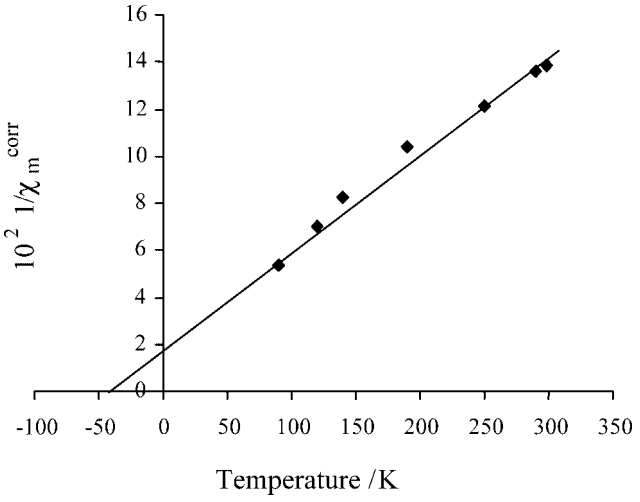


Figure 2. Curie–Weiss plot $[1/\chi_m^{corr}$ vs. $T]$ for $[VO(fsal\text{-}ea)]_2$ (**1**).

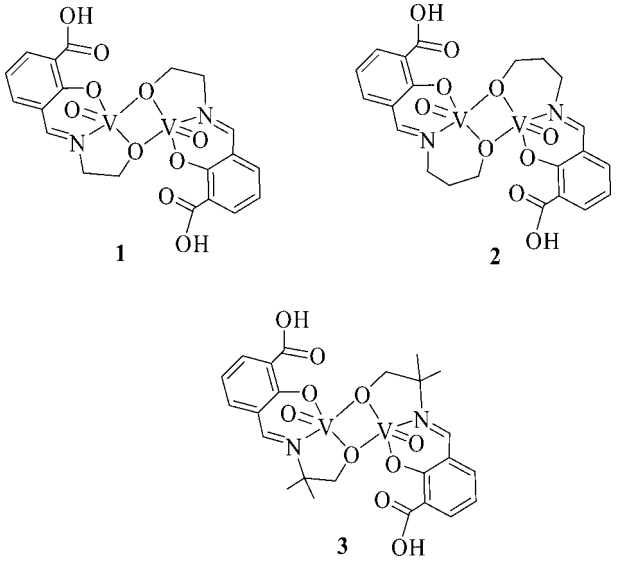


Scheme 3. Proposed structure for neat oxidovanadium(IV) complexes.

5-OMe, 3-OMe), Syamal et al. suggested antiferromagnetic exchange interactions along with a dimeric structure.[14] Thus, the dimeric structure as shown in Scheme 3 for the neat complexes may also be proposed here. A dimeric structure for $[VO(sal\text{-}ea)]_2$ has been confirmed by a single-crystal X-ray diffraction study.[15]

### Scanning Electron Micrograph

Scanning electron micrographs (SEM) for a single bead of pure chloromethylated polystyrene, the polymer-anchored ligand and the polymer-anchored vanadium complexes were recorded in order to observe the morphological changes. Images of PS-$H_2$fsal-ea (**IV**) and PS-[VO(fsal-ea)·DMF] (**4**) are reproduced in Figure 3. As expected, the pure polystyrene bead has a smooth and flat surface while the anchored ligands and complexes show a very slight roughening of the top layer. This roughening is relatively greater in the complexes possibly due to the interaction of vanadium with the anchored ligand which resulted in the formation of complexes with a fixed geometry. Accurate information on the morphological changes in terms of the exact orientation of the ligands coordinated to the metal ion has not been possible due to poor loading of the metal complex.

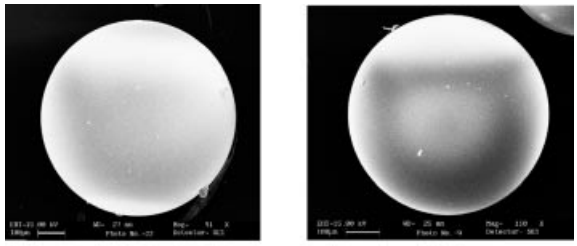


Figure 3. Scanning Electron Micrographs (SEM) of PS-$H_2$fsal-ea (**IV**) and PS-[VO(fsal-ea)·DMF] (**4**); magnification ca. ×200.

### TGA Study

Thermogravimetric analyses in an oxygen atmosphere showed good stabilities for polymer-anchored complexes **4**, **5** and **6** up to ca. 175 °C. The first weight loss starting just above 175 °C is possibly due to the loss of coordinated DMF. The complexes, thereafter, decompose in multiple steps. Quantitative measurement of weight loss at various stages was not possible due to the overlapping nature of the decompositions. However, the stabilities of the final residues at ca. 700 °C suggest the formation of $V_2O_5$. The metal content calculated from the final residue in each case was close to that recorded by atomic absorption spectroscopy.

### IR Spectroscopic Study

The experimental section contains a partial list of the IR spectroscopic data of all ligands and complexes. The chloromethylated polystyrene exhibits strong peaks at 1264 and

 © 2007 Wiley-VCH Verlag GmbH & Co. KGaA, Weinheim 

673 $cm^{-1}$ due to $CH_2Cl$ group and the absence of these peaks in the polymer-anchored ligands suggests covalent bonding of the chloromethylated polystyrene to the ligands.[16] A sharp band due to ν(C=O) of the carboxylate group appears at 1670–1676 $cm^{-1}$ in the polymer-anchored ligands and complexes. In the corresponding neat ligands and complexes, this band appears at either the same or a slightly lower wavenumber. The ν(C=N) (azomethine) stretch of the neat ligands mostly appears along with the ν(C=O). However, a sharp peak due to the ν(C=N) (azomethine) stretch is observable in the spectra of the corresponding complexes at a lower wavenumber. The polymer-anchored ligands show a medium intensity band at 1630–1635 $cm^{-1}$ and this band shifts to a lower wavenumber by ca. 30 $cm^{-1}$ in the complexes thereby indicating the coordination of the azomethine nitrogen atom. The coordination of phenolic oxygen could not be assigned unequivocally in most complexes because of the appearance of a weak broad band in the 3400 $cm^{-1}$ region. Similarly, coordination of DMF in **4**, **5** and **6** could not be possible because of the strong ν(C=O) absorption band of the carboxylate in the same region. In addition to this, all the complexes exhibit a sharp ν(V=O) band in the 964–993 $cm^{-1}$ region.[6]

### Electronic and Fluorescence Spectroscopic Studies

The electronic spectra of the neat and anchored complexes in Figure S1 and relevant data in Table S2 are given in the Supporting Information (see also the footnote on the first page of this article). The spectroscopic patterns shown by the neat as well as the supported ligands are essentially the same except for the broadness of the bands in nujol. The expected charge-transfer band at ca. 400 nm could not be distinguished due to the appearance of an n→π* transition in the same region. In addition, two additional weak bands at ca. 570 and 690 nm were observed for neat complexes in DMF due to d-d transitions thus indicating the presence of a vanadium(IV) ion at the centre.

The fluorescence excitation and emission spectra of $10^{-6}$ M methanolic solution of oxidovanadium(IV) complexes **1**, **2** and **3** were recorded at room temperature and are presented in Figure 4. All neat complexes have approximately the same chromophore units and exhibit similar spectroscopic patterns. On excitation at 257 nm (in the UV region) complex **1** exhibited a strong band at $\lambda_{max}$ = 483 nm (in the visible region) with a shoulder band at 556 nm and, on excitation at 387.5 nm, exhibited a broad peak with $\lambda_{max}$ = 501 nm. In the case of complexes **2** and **3**, excitation at 258 (in **2**) and 255 (in **3**) nm gave emission bands at 464 and 466 nm, respectively, along with weak shoulder bands at 517 and 554 nm. Similarly, broad peaks at 503 (in **2**) and 502 nm (in **3**) were obtained with excitation at 382 and 385.5 nm, respectively. As, expected, the overtone at ca. 510 nm was observed as a sharp band in all complexes. All these spectroscopic patterns hint towards the photo-catalytic utility of these complexes.

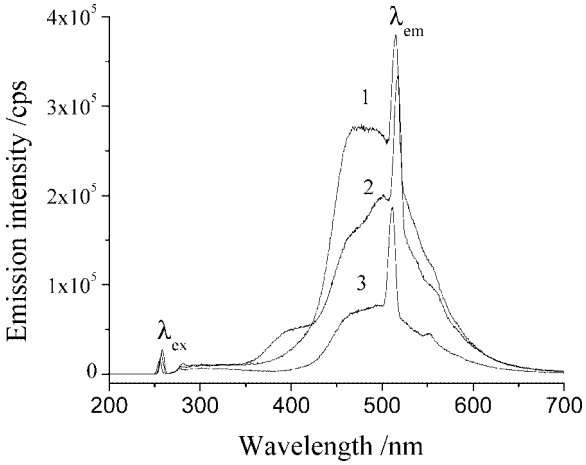


Figure 4. Emission spectra of complexes $[VO(fsal\text{-}ea)]_2$ (**1**), $[VO(fsal\text{-}pa)]_2$ (**2**) and $[VO(fsal\text{-}amp)]_2$ (**3**) recorded in methanol at ambient temperature.

### EPR Spectroscopic Study

The room temperature X-band EPR spectra of the polymer-anchored samples are reproduced in Figure 5. They are characteristics of monomeric $V^{IV}$ centres with a simple $S$ = ½ electronic spin and a typical axial pattern for a possible square pyramidal geometry, Scheme 4. The hyperfine features are well resolved in both the parallel and perpendicular regions. These resolved hyperfine features reflect the fact that the vanadium centres are well separated by the polymer backbones which causes least dipolar vanadium–vanadium coupling. Such arrangements generally broaden the EPR pattern. The hyperfine lines are typical for an interaction of the unpaired electron of the vanadium(IV) ion with its nucleus, $^{51}V$ having a high abundance of 99.75% and a nuclear

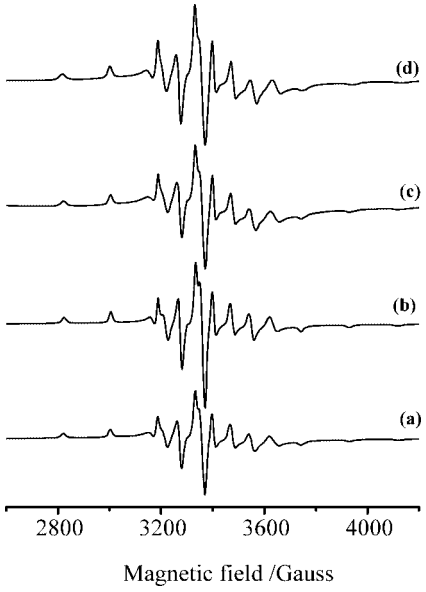


Figure 5. Room temperature EPR spectra of polymer-anchored complexes (a) PS-[VO(fsal-ea)·DMF] (**4**), (b) PS-[VO(fsal-pa)·DMF] (**5**), (c) PS-[VO(fsal-amp)·DMF] (**6**) and (d) PS-[VO(fsal-pa)·DMF] (**5**) (recovered); the microwave frequency was 9.4458 GHz.

 © 2007 Wiley-VCH Verlag GmbH & Co. KGaA, Weinheim 

spin $I = {}^{7}/_{2}$. The anisotropic EPR spectrum of the $V^{IV}$ ion with $g_{\|} < g_{\perp}$ and $A_{\|} > A_{\perp}$ is characteristic of square pyramidal complexes with possible $C_{4v}$ symmetry in which the V=O bond is along the $z$ axis and the other four coordinating atoms are along the $x$ and $y$ axes.[17] Simulation of the EPR spectra was carried to extract the Hamiltonian parameters and the resultant parameters are given in Table 1. As seen in the table and Figure 5, the Hamiltonian parameters are more or less the same for the all three polymer-anchored samples indicating that local symmetry and environments around the V centres are more or less the same.

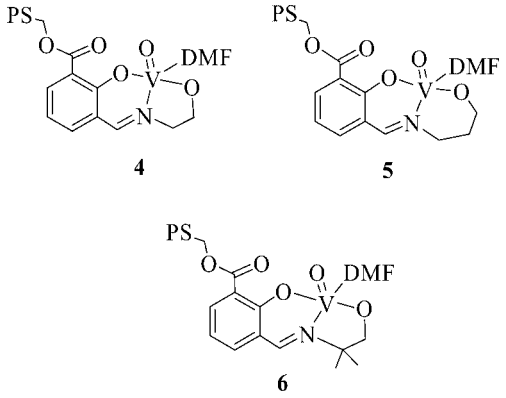


Scheme 4. Possible structure for polymer-anchored complexes.

After carrying out the catalytic reactions, the polymer-anchored catalysts were filtered, washed with acetonitrile and dried. The EPR spectra were then recorded under identical conditions. The EPR spectrum for one of the recovered catalysts, PS-[VO(fsal-amp)·DMF] (**6**), is also reproduced in Figure 5 as a representative example. The EPR spectra of the recovered (spent) samples were only slightly different from the fresh samples indicating the environment and coordination geometry of the vanadium centres is retained to the maximum extent after the catalytic reaction. A slight increase in the $A_{\|}$ component for the recovered catalyst can be observed from 18.6 mT to 18.8 mT. A higher $A_{\|}$ value is generally due to reduced delocalisation of the paramagnetic electron density of the V centre indicating a slight displacement in the coordinating atom of the ligand. In other words, the vanadium–nitrogen bond is slightly weaker than that in the neat compound.

The EPR spectra for the neat compounds were also recorded and are reproduced in Figure 6. The broad spectroscopic features are typical for dimeric or polymeric species with dipolar interactions or exchange interactions with $V^{4+}$–$V^{4+}$ pairs with spin $S = 1$.[18] In the absence of any hyperfine features, the spectra could be best fitted by superimposing features of at least two $V^{4+}$–$V^{4+}$ pairs having slightly different environments with different zero-field splitting parameters, $D$ and $E$, and the resultant parameters are given in Table 1. As seen in the table, one of the $V^{4+}$–$V^{4+}$ pairs has a $D$ value in the range 1850–1900 MHz and an $E$ value of 500 MHz indicating a strong rhombic distortion site. The other species could be fitted with $D$ in the range 1250–1350 MHz with no $E$ splitting thus indicating less distortion. The broad features in the EPR spectra for the complexes $[VO(X\text{-sal-ea})]_2$ (X = 5-Cl, 5-Br, 5-$NO_2$, 5-OMe, 3-OMe) have also been noted previously and interpreted on the basis of the presence of antiferromagnetic exchange interactions between two vanadium centres in close proximity.[12–14]

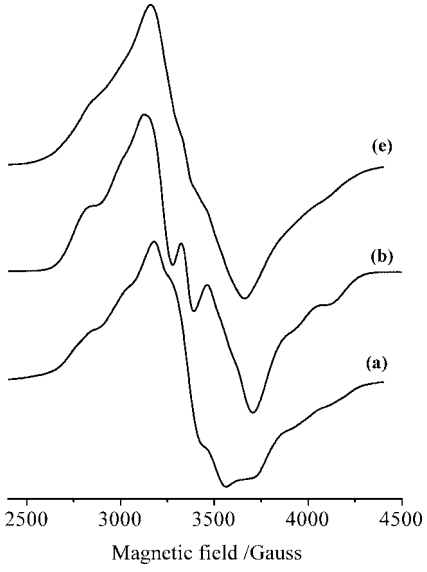


Figure 6. Room temperature EPR spectra of neat complexes (a) $[VO(fsal\text{-}ea)]_2$ (**1**), (b) $[VO(fsal\text{-}pa)]_2$ (**2**) and (c) $[VO(fsal\text{-}amp)]_2$ (**3**).

Table 1. Spin Hamiltonian parameters for the calculated EPR spectra: $g$-tensors ($g_{\|}$, $g_{\perp}$), hyperfine tensors ($A_{\|}$, $A_{\perp}$), zero-field splitting parameters ($D$, $E$).

| Compound | Spectrum | $g_{\|}$ ($g_{iso}$) | $g_{\perp}$ | $A_{\|}$ ($A_{iso}$) (mT) | $A_{\perp}$ (mT) | $D$ (MHz) | $E$ (MHz) |
|---|---|---|---|---|---|---|---|
| PS-[VO(fsal-ea)·DMF] (**4**) | 1 | 1.945 | 1.999 | 18.6 | 7 | – | – |
| PS-[VO(fsal-pa))·DMF] (**5**) | 1 | 1.945 | 1.999 | 18.4 | 7 | – | – |
| PS-[VO(fsal-amp))·DMF] (**6**) | 1 | 1.945 | 1.999 | 18.6 | 7 | – | – |
| PS-[VO(fsal-pa))·DMF] (**5**) (recovered) | 1 | 1.943 | 1.999 | 18.8 | 7 | – | – |
| $[VO(fsal\text{-}ea)]_2$ (**1**) | 1 | 1.955 | – | – | – | 1250 | 0 |
| | 2 | 1.940 | – | – | – | 1190 | 500 |
| $[VO(fsal\text{-}pa)]_2$ (**2**) | 1 | 1.975 | – | – | – | 1150 | 0 |
| | 2 | 1.940 | – | – | – | 1850 | 500 |
| $[VO(fsal\text{-}amp)]_2$ (**3**) | 1 | 1.975 | – | – | – | 1350 | 0 |
| | 2 | 1.940 | – | – | – | 1850 | 500 |

 © 2007 Wiley-VCH Verlag GmbH & Co. KGaA, Weinheim 

### Catalytic Activity Study

The catalytic potential of the polymer-anchored as well as the neat complexes were studied for the oxidation of styrene and cumene.

#### *Oxidation of Styrene*

Oxidation of styrene catalysed by the polymer-anchored complexes PS-[VO(fsal-ea)·DMF] (**4**), PS-[VO(fsal-pa)·DMF] (**5**) and PS-[VO(fsal-amp)·DMF] (**6**) gave styrene oxide, benzaldehyde, benzoic acid, phenylacetic acid and 1-phenylethane-1,2-diol as indicated in Scheme 5. These reaction products are common and have also been identified earlier by other workers.[19–21]

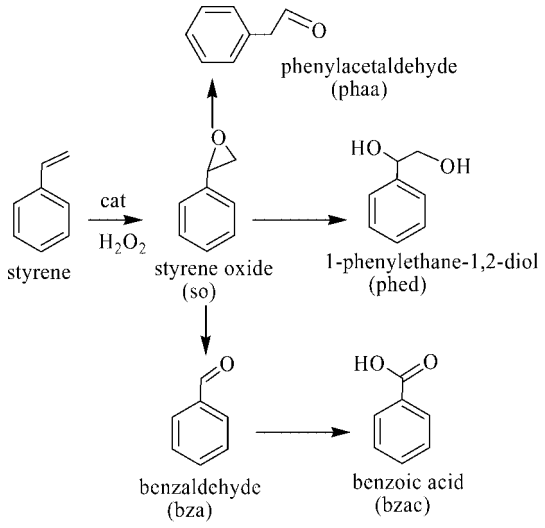


Scheme 5.

Complex **5** was taken as a representative amongst these catalysts and its catalytic activity was studied as a function of the amount of $H_2O_2$ (mol of $H_2O_2$ per mol of styrene) and catalyst as well as the temperature of the reaction mixture. These parameters were varied in order to obtain suitable reaction conditions for the maximum oxidation of styrene. Reactions were carried out with three different molar ratios of 1:1, 1:1.5 and 1:2 of styrene to aqueous 30% $H_2O_2$ for a fixed amount of styrene (1.04 g, 10 mmol) and catalyst (0.040 g) in $CH_3CN$ (10 mL) at 80 °C. The results were analysed periodically for up to 6 h. As illustrated in Figure 7, a maximum conversion of 42% was achieved in 6 h with a styrene to $H_2O_2$ molar ratio of 1:1. On increasing the ratio to 1:1.5 the conversion was improved to 65% while a 1:2 molar ratio showed a maximum conversion of 95%. No further improvement in the oxidation was observed on increasing the molar ratio to 1:3 (not shown in Figure) which suggests that a large amount of oxidant is not an essential condition for improving the oxidation of styrene. In another experiment, three different catalyst loadings, viz. 0.030, 0.040 and 0.070 g, were varied at styrene to $H_2O_2$ ratios of 1:2 under the above reaction conditions and the results are shown in Figure 8. As seen in the figure, 0.030 g of catalyst gave only a 52.5% conversion while catalyst loadings of 0.040 and 0.070 g showed maximum conversions of 95 and 97.3%, respectively, at the end of the 6 h. Thus, at the expense of $H_2O_2$, 0.040 g of catalyst was found to be sufficient to carry out the reaction. The temperature of the reaction mixture also influenced the performance of the catalyst. Figure 9 shows the effect of the reaction temperature on the performance of the catalysts and at 80 °C a much better conversion was achieved.

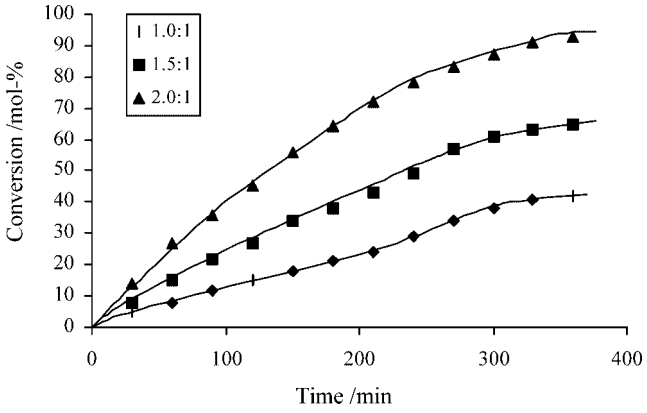


Figure 7. Effect of amount of $H_2O_2$ on the oxidation of styrene. Reaction conditions: styrene (1.04 g, 10 mmol), PS-[VO(fsal-pa)·DMF] (**5**) (0.040 g), $CH_3CN$ (10 mL) and temp. (80 °C).

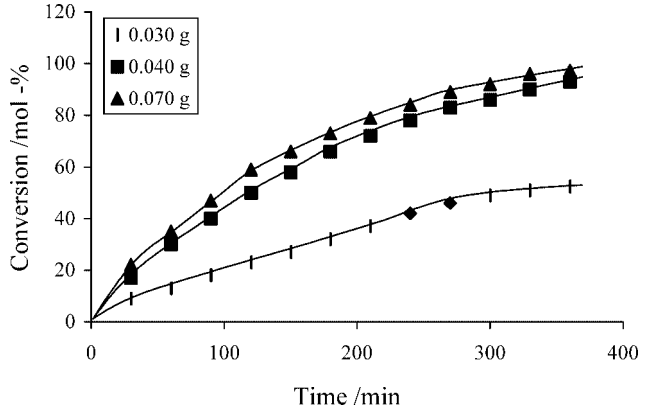


Figure 8. Effect of amount of catalyst on the oxidation of styrene. Reaction conditions: styrene (1.04 g, 10 mmol), $H_2O_2$ (2.27 g, 20 mmol), $CH_3CN$ (10 mL) and temp. (80 °C).

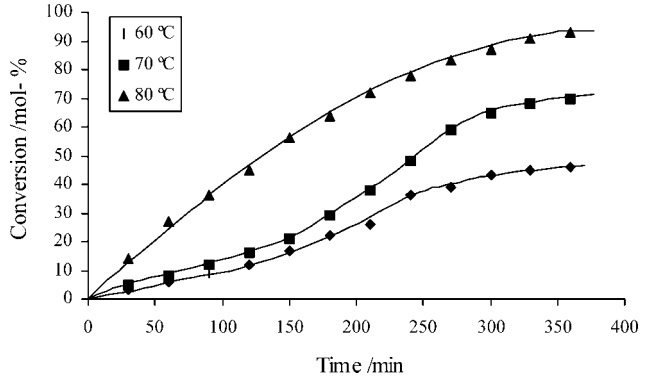


Figure 9. Effect of temperature on the oxidation of styrene. Reaction conditions: styrene (1.04 g, 10 mmol), PS-[VO(fsal-pa)·DMF] (**5**) (0.040 g), $H_2O_2$ (2.27 g, 20 mmol) and $CH_3CN$ (10 mL).

 © 2007 Wiley-VCH Verlag GmbH & Co. KGaA, Weinheim 

Other catalysts e.g. **4** and **6** were tested under the reaction conditions as optimised above. Thus, for 10 mmol of substrate, aqueous 30% $H_2O_2$ (20 mmol) and catalyst (0.040 g) were added in $CH_3CN$ (10 mL) and the reaction was carried out at 80 °C. Table 2 shows a comparison of percent conversion of styrene and the selectivity of various reaction products along with the turnover frequency of the catalysts. Catalyst **4** exhibits a 90% conversion of styrene while **6** exhibits only an 82% conversion. Thus, the performances of these catalysts follow the order: **5** (95%) > **4** (90%) > **6** (82%). The good performance of these catalysts is possibly due to easy formation of peroxo species in the presence of $H_2O_2$ (vide infra) as well as the ease in transferring oxygen from the intermediate peroxo species to the substrate.

We also tested the catalytic activity of the neat complexes for the oxidation of styrene. Their performances after 6 h are also presented in Table 2. Figure 10 provides conversion percentages for each catalyst as a function of time. For 0.020 g of each the neat vanadium complexes **1**, **2** and **3**, and with reaction conditions fixed as above, the obtained conversions were 65, 70 and 62%, respectively. Their calculated turnover frequencies vary in the range 15.3–17.6 $h^{-1}$. Thus, the catalytic performances of the neat complexes are also good. However, in the light of special features e.g. easy recovery, no leaching and the ability of the polymer-anchored complexes to be recycled, it may be concluded that polymer-anchored vanadium complexes are better catalysts.

The product selectivity for the polymer-anchored complexes follows the order: benzaldehyde > 1-phenylethane-1,2-diol > benzoic acid > styrene oxide > phenylacetaldehyde while for the neat complexes the order is: benzaldehyde > benzoic acid >1-phenylethane-1,2-diol > styrene oxide > phenylacetaldehyde. The formation of benzaldehyde in the highest yield is possibly due to a nucleophilic attack of $H_2O_2$ on styrene oxide formed in the first step followed by a cleavage of the intermediate hydroperoxystyrene as shown in Scheme 6. Benzaldehyde formation may also be facilitated by direct oxidative cleavage of the styrene side chain double bond by a radical mechanism.[19] Formation of other products such as benzoic acid from benzaldehyde is rather slow in all reactions. Similarly the formation of phenylacetaldehyde, a product formed by isomerisation of styrene oxide, is less in all cases. Water present in $H_2O_2$ is probably responsible for the hydrolysis of styrene oxide to 1-phenylethane-1,2-diol to some extent. Low formation of styrene oxide, an important product, is understandable because of its further conversion into other products.

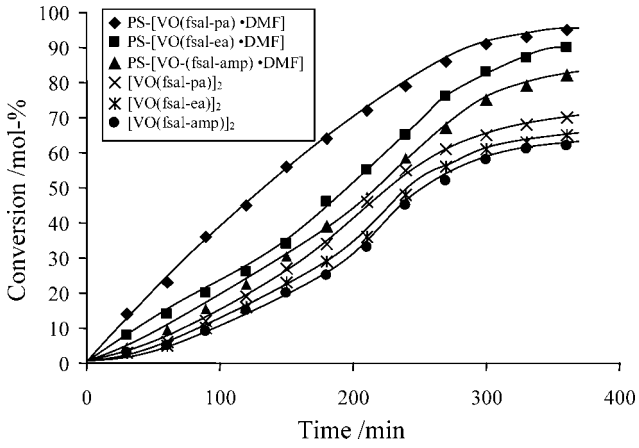


Figure 10. Catalytic comparison of polymer-anchored and neat complexes for the oxidation of styrene. Reaction conditions: styrene (1.04 g, 10 mmol), catalyst (0.040 g for polymer anchored and 0.020 g for neat complexes), $H_2O_2$ (1.27 g, 20 mmol), $CH_3CN$ (10 mL) and temp. (80 °C).

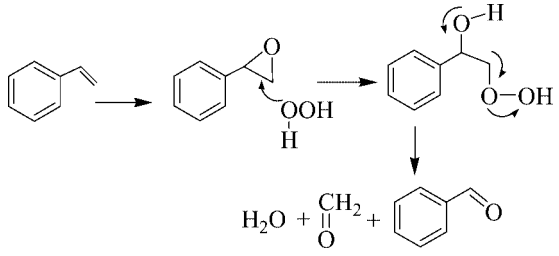


Scheme 6.

Several other polymer-anchored oxidovanadium(IV) complexes e.g. PS-[VO(hmbmz)$_2$] [where PS-Hhmbmz = polymer-anchored 2-(α-hydroxymethyl)benzimidazole],[22] PS-K[VO(O$_2$)$_2$(2-pybzm)] [where 2-pybzm = 2-(2-pyridyl)-benzimidazole][20] and PS-[VO(sal-ohyba)·DMF][9] have been used as catalysts in our laboratory for the oxidation of styrene. Though all these catalysts gave all five products with nearly similar selectivity patterns, the conversions with the catalysts reported here are higher.

Table 2. Turn over frequencies of various catalysts, percent conversion of styrene and product selectivities.

| Catalyst | Conv. /mol-% | TOF /$h^{-1}$ | Selectivity /mol-% | | | | | |
|---|---|---|---|---|---|---|---|---|
| | | | so[a] | phaa[b] | bza[c] | bzac[d] | phed[e] | Others |
| [VO(fsal-ea)]$_2$ (**1**) | 65 | 15.3 | 3.9 | 3.1 | 61.7 | 18.3 | 8.8 | 4.3 |
| [VO(fsal-pa)]$_2$ (**2**) | 70 | 16.4 | 3.6 | 3.8 | 62.5 | 17.2 | 8.8 | 4.2 |
| [VO(fsal-amp)]$_2$ (**3**) | 62 | 17.6 | 3.9 | 3.4 | 60.4 | 18.8 | 8.9 | 4.6 |
| PS-[VO(fsal-ea)·DMF (**4**) | 90 | 22.5 | 4.1 | 2.9 | 58.4 | 7.6 | 23.5 | 3.5 |
| PS-[VO(fsal-pa)·DMF] (**5**) | 95 | 25.5 | 3.8 | 3.5 | 62.8 | 8.7 | 17.3 | 3.8 |
| PS-[VO(fsal-amp)·DMF] (**6**) | 82 | 24.0 | 4.3 | 3.9 | 60.6 | 9.0 | 18.3 | 4.0 |

[a] Styrene epoxide. [b] Phenylacetaldehyde. [c] Benzaldehyde. [d] Benzoic acid. [e] 1-Phenylethane-1,2-diol. Reaction conditions as mentioned in Figure 10.

 © 2007 Wiley-VCH Verlag GmbH & Co. KGaA, Weinheim 

### *Oxidation of Cumene*

Oxidation of cumene by the polymer-anchored complexes **4**, **5** and **6** gave acetophenone, 2-phenylpropanal, α-methylstyrene epoxide, 2-phenyl-2-propanol, 2-isopropyl-1,4-benzoquinone and α-methylstyrene, as indicated in Scheme 7.

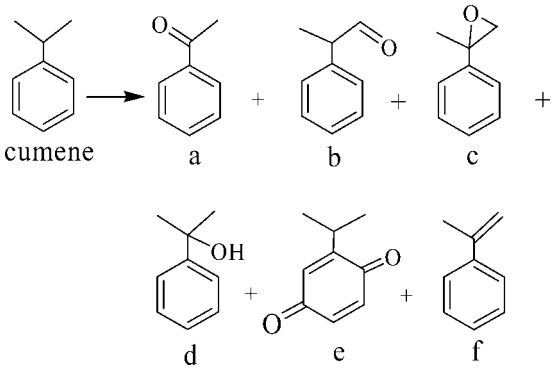


Scheme 7. a = acetophenone, b = 2-phenylpropanal, c = α-methylstyrene epoxide, d = 2-phenyl-2-propanol, e = 2-isopropyl-1,4-benzoquinone and f = α-methylstyrene.

In order to achieve suitable reaction conditions for the maximum oxidation of cumene, complex **5** was taken as a representative catalyst and three different parameters were varied, viz. the amounts of $H_2O_2$ (mol of $H_2O_2$ per mol of cumene) and catalyst as well as the temperature of the reaction mixture. The effect of $H_2O_2$ concentration on the oxidation of cumene is illustrated in Figure 11. A conversion of about 13% was achieved at a cumene to 30% $H_2O_2$ molar ratio of 1:1 in 6 h when cumene (1.20 g, 10 mmol), 30% $H_2O_2$ (1.14 g, 10 mmol) and catalyst (0.060 g) were placed in acetonitrile (10 mL) and the reaction was carried out at 80 °C. This conversion improved to ca. 18% on increasing the ratio to 1:1.5 and to 41% at a cumene to 30% $H_2O_2$ molar ratio of 1:2. This oxidation remained nearly constant on further increasing the amount of oxidant which suggests that a 1:2 (cumene to oxidant) ratio is sufficient enough to maximise the oxidation of cumene.

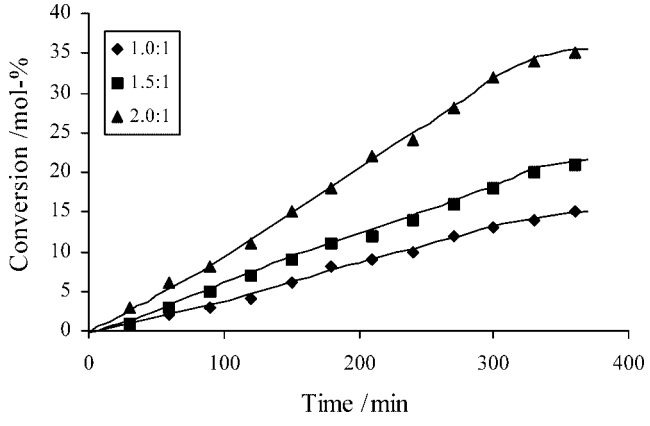


Figure 11. Effect of amount of $H_2O_2$ on the oxidation of cumene. Reaction conditions: cumene (1.20 g, 10 mmol), PS-[VO(fsal-pa)·DMF] (**5**) (0.060 g), $CH_3CN$ (10 mL) and temp. (80 °C).

Similarly, for a cumene to $H_2O_2$ ratio of 1:2, three different amounts of catalyst were used, viz. 0.040, 0.060 and 0.080 g, under above reaction conditions and the results are summarised in Figure 12. An amount of 0.040 g of catalyst gave only a 29% conversion while 0.060 g and 0.080 g of catalyst showed maximum conversions of 41 and 44%, respectively. Since the conversion is not significantly higher using 0.080 g of catalyst, an amount of 0.060 g of catalyst can be considered sufficient to carry out the oxidation. Moreover, the turnover rates of the catalyst for the catalytic conversions using 0.060 g and 0.080 g are comparable (7.32 $h^{-1}$ for 0.060 g and 5.9 $h^{-1}$ for 0.080 g). As observed in the case of styrene oxidation, a temperature of at least 80 °C was required to carry out the above reaction effectively. Moreover, time required in achieving the maximum conversion was also reduced on carrying out the reaction at 80 °C.

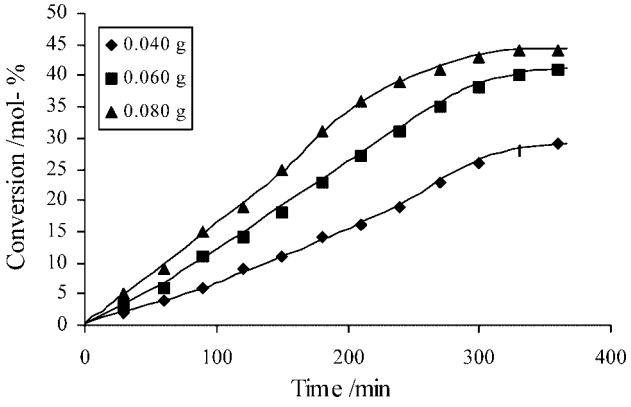


Figure 12. Effect of amount of catalyst PS-[VO(fsal-pa)·DMF] on the oxidation of cumene. Reaction conditions: cumene (1.20 g, 10 mmol), $H_2O_2$ (2.27 g, 20 mmol), $CH_3CN$ (10 mL) and temp. (80 °C).

Thus, suitable reaction conditions for the maximum oxidation of cumene were fixed as follows: cumene (1.20 g, 10 mmol), 30% $H_2O_2$ (2.27 g, 20 mmol), catalyst (0.060 g), acetonitrile (10 mL) and a temperature of 80 °C. Catalysts **4** and **6** were also tested under the above optimised reaction conditions and results are summarised in Table 3. Figure 13 shows a comparison of the percentage conversions of all three catalysts as a function of time. The conversion percentages of cumene after 6 h follow the order: **5** (41%) > **4** (39%) > **6** (35%). Independent of the type of catalyst, the percent yield of various products follow the order: acetophenone > 2-phenyl-2-propanal > α-methylstyrene epoxide > 2-phenylpropanol > 2-isopropyl-1,4-benzoquinone ≈ α-methylstyrene.

We have also compared the catalytic activity of these polymer-anchored complexes with their respective neat ones. Table 3 shows a comparison of the percentage conversion of cumene as well as product selectivity of various catalysts obtained after a reaction time of 6 h. For 0.030 g of each of the neat vanadium complexes and keeping other reaction conditions fixed as above, oxidation of cumene in

 © 2007 Wiley-VCH Verlag GmbH & Co. KGaA, Weinheim 

Table 3. Percent conversion of cumene and selectivity of various oxidation products.

| Catalyst | Conv. /mol-% | TOF /$h^{-1}$ | Selectivity /mol-% | | | | | | |
|---|---|---|---|---|---|---|---|---|---|
| | | | a[a] | b | c | d | e | f | Others |
| $[VO(fsal\text{-}ea)]_2$ (**1**) | 25 | 3.92 | 62 | 18 | 10 | 4 | 3 | 2 | 1 |
| $[VO(fsal\text{-}pa)]_2$ (**2**) | 27 | 4.46 | 63 | 19 | 9 | 3 | 2 | 2 | 2 |
| $[VO(fsal\text{-}amp)]_2$ (**3**) | 21 | 3.52 | 66 | 17 | 8 | 3 | 2 | 3 | 1 |
| PS-[VO(fsal-ea)·DMF (**4**) | 39 | 6.50 | 60 | 13 | 17 | 3 | 2 | 3 | 3 |
| PS-[VO(fsal-pa)·DMF] (**5**) | 41 | 7.32 | 63 | 13 | 14 | 4 | 2 | 2 | 1 |
| PS-[VO(fsal-amp)·DMF] (**6**) | 35 | 6.83 | 59 | 12 | 17 | 3 | 3 | 2 | 3 |

[a] a = acetophenone, b = 2-phenylpropanal, c = α-methylstyrene epoxide, d = 2-phenyl-2-propanol, e = 2-isopropyl-1,4-benzoquinone, f = α-methylstyrene.

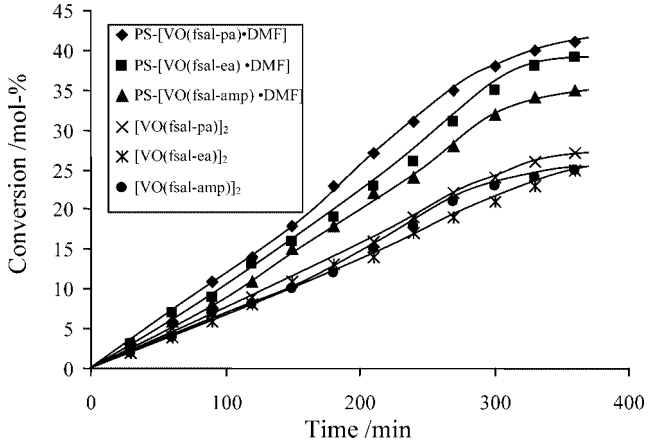


Figure 13. Catalytic comparison of catalysts for the oxidation of cumene. Reaction conditions: cumene (1.20 g, 10 mmol), catalyst (0.060 g), $H_2O_2$ (2.27 g, 20 mmol), $CH_3CN$ (10 mL), temp. (80 °C).

the 21–27% range was observed which is less than the corresponding values recorded for the anchored complexes. The percentage yields of various products follow the order: acetophenone > 2-phenylpropanal > α-methylstyrene epoxide > 2-phenyl-2-propanol ≈ 2-isopropyl-1,4-benzoquinone ≈ α-methylstyrene. Thus, the yield of α-methylstyrene epoxide is slightly better than 2-phenyl-2-propanal in the case of the neat complexes. However, the selectivity as well as the yield of the major product acetophenone is comparable in all cases.

Homogeneous catalysts such as metal complexes[23] and metalloporphyrins,[24] and heterogeneous catalysts such as platinum metals,[25] metal oxides,[26] metal oxides supported on alumina[27] and metals or metal oxides supported MCM-41[28] have been used for the oxidation of cumene. Only limited literature deals with the oxidation of cumene using polymer-supported catalysts e.g. metal salts[29] and $[Fe(phen)_2]^{2+}$ (phen = phenanthroline)[30] supported on a polymer. Catalytic activity of the complexes reported here compares well with the literature data. However, cumene hydroperoxide, in most cases, has been reported to be the major product amongst the various products formed whereas we observed the formation of acetophenone with a selectivity of 59–66%. This difference is possibly due to the use of different oxidants as well as different metal centres in catalysts.

**Proposed Mechanism**

As observed earlier, the reaction of cumene proceeds by means of a radical mechanism if molecular oxygen is used as the oxidant. The cumene radical, formed by abstracting the tertiary hydrogen of the cumene by a metal ion, reacts with molecular oxygen to produce an alkyl peroxide, which in turn abstracts hydrogen from cumene to form hydroperoxide (Scheme 8).[28,31] The oxidant $H_2O_2$ is likely to form peroxidovanadium(V) species with the oxidovanadium(IV) complexes reported here, which finally transfer oxygen to the substrate to give the various products. As cumene hydroperoxide was not observed among the reaction products, the reaction pathway either does not follow any secondary mechanism, e.g. through radical formation, or the cumene hydroperoxide, if formed at all, decomposes catalytically to yield acetophenone and other products.

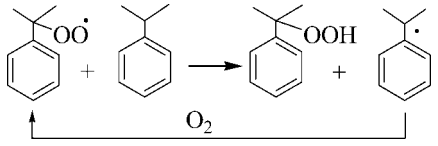


Scheme 8.

Similarly, the formation of styrene oxide may proceed through the transfer of oxygen from oxidoperoxidovanadium(V) species to styrene. The oxidoperoxido species is finally converted to dioxidovanadium(V) and the catalytic cycle moves through these intermediates. These are the most common species observed during the catalytic action of oxidovanadium(IV)/dioxidovanadium(V) complexes for most oxidation reactions carried out in the presence of peroxide.[5a,7b] As the recovered species is EPR active, it seems that dioxidovanadium(V) species are slowly converted to oxidovanadium(IV) during the washing and drying processes and exhibit EPR spectroscopic patterns similar to that of the neat oxidovanadium(IV) complex (cf. Figure 5).

To support the reaction mechanism through peroxidovanadium(V) species formation, we tried the isolation of neat peroxidovanadium(V) complexes with ligands **I**, **II** and **III** but were unsuccessful possibly due to their poor stability at ambient temperature. Nevertheless, the generation of the oxido-monoperoxidovanadium(V) complex, $[VO(O_2)(fsal\text{-}pa)]^-$ has been established in methanol by electronic absorption spectroscopy. In a typical reaction, 10 mL of a ca.

 © 2007 Wiley-VCH Verlag GmbH & Co. KGaA, Weinheim 

$1 \times 10^{-4}$ M solution of $[VO(fsal\text{-}pa)]_2$ (**2**) was treated with one drop portions of 30% $H_2O_2$ dissolved in methanol and the resultant spectroscopic changes are presented in Figure 14 Thus, the intensity of the 390 nm band increases slowly along with a corresponding shift to 399 nm by dropwise addition of $H_2O_2$ dissolved in methanol. The shoulder band at 279 nm does not change its position but undergoes an increase in intensity. Two other bands centred at 255 and 212.5 nm remain constant while a shoulder band at 223 nm slowly appears. We have interpreted this result in terms of the formation of the oxidoperoxidovanadium(V) complex $[VO(O_2)(sal\text{-}pa)]^-$.

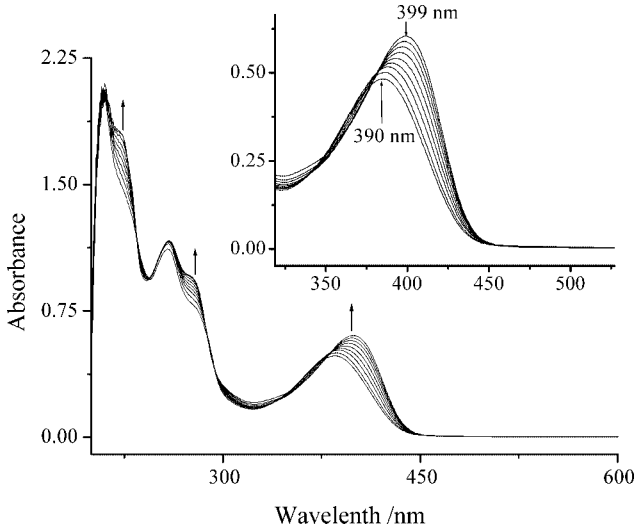


Figure 14. Titration of $[VO(fsal\text{-}pa]_2$ (**2**) with 30% $H_2O_2$; the spectra were recorded after the successive addition of 1-drop portions of $H_2O_2$ dissolved in methanol to 10 mL of ca. $10^{-4}$ M solution of **2** in methanol.

Similar spectroscopic patterns were also observed for complexes **1** and **3**. Oxidoperoxidovanadium(V) complexes have also been generated previously on treatment of, for example, complexes [VO(sal-ohyba)][9] and $K[VO_2(sal\text{-}inh)(H_2O)]$[32] with $H_2O_2$ in methanol.

### Leaching and Heterogeneity of the Catalytic Reaction and Potential of the Catalyst to be Recycled

The polymer-anchored complexes **4**, **5** and **6** have been tested for their ability to be recycled. The reaction mixture was filtered after a contact time of 6 h. The catalysts separated from the reaction mixture after catalytic action in all three cases were washed with acetonitrile, dried and subjected to further catalytic reactions under similar conditions. No appreciable loss in the activity in all cases suggests that catalysts were active even after the first cycle. During catalytic oxidation of styrene and cumene, the solid catalyst was separated from the reaction mixture by filtration after 2 h and the reaction was continued for a further 4 h. The gas chromatographic analyses showed barely a 1% increment in the conversion. This confirms no leaching of the catalyst during the catalytic reaction. No further oxidation of substrates on removal of the solid catalysts is consistent with a heterogeneous process.

## Conclusions

Polymer-anchored oxidovanadium(IV) complexes with polymer-anchored ligand PS-$H_2$fsal-ea, PS-$H_2$fsal-pa and PS-$H_2$fsal-amp, having potential catalytic activities for the oxidation of styrene and cumene, have been isolated and characterised. The oxidation of styrene follows the order: PS-[VO(fsal-pa)·DMF] (95%) > PS-[VO(fsal-ea)·DMF] (90%) > PS-[VO(fsal-amp)·DMF] (82%) where the selectivity of the five different products follows the order: benzaldehyde > 1-phenylethane-1,2-diol > benzoic acid > phenylacetaldehyde > styrene oxide. The oxidation of cumene gives at least six different products with the following order of selectivity: acetophenone > 2-phenyl-2-propanal > α-methylstyrene epoxide > 2-phenylpropanol > 2-isopropyl-1,4-benzoquinone and α-methylstyrene. The good performance of these catalysts is possibly due to the facile formation of peroxido species in the presence of $H_2O_2$ as well as the ease in transferring oxygen from the intermediate peroxido species to the substrate. However, complexes slowly convert back to the oxidovanadium(IV) species since the recycled species exhibit similar EPR spectroscopic patterns. The catalytic activities of these complexes have also been compared with the corresponding neat complexes and it was observed that the neat complexes are, however, good catalyst but exhibit less catalytic activity than the anchored ones. The easy separation of the polymer anchored complexes from the reaction mixture and their ability to be recycled makes them better catalyst compared wit the neat ones. They can pass through up to three cycles without significant loss in their catalytic activities.

## Experimental Section

**Materials:** Analytical reagent grade $V_2O_5$, (Loba Chemie, India), salicylaldehyde, acetylacetone (Ranbaxy, India), styrene, cumene, 3-aminopropanol (Acros organics, USA), 2-aminoethanol, 2-amino-2-methylpropanol (S.D. Fine Chemicals, India), aqueous 30% $H_2O_2$ (Qualigens, India) were used as obtained. Other chemicals and solvents were of AR grade. Chloromethylated polystyrene [18.9% Cl (5.3 mmol Cl per gram of resin)] cross-linked with 5% divinylbenzene was obtained as gift from Thermax limited, Pune, India. $[VO(acac)_2]$[33] and 3-formylsalicylic acid[34] were prepared following the methods reported in the literature.

**Methods:** Elemental analyses of the ligands and complexes were obtained using an Elementar model Vario-EI-III instrument. IR spectra were recorded as KBr pellets on a Nicolet NEXUS Aligent 1100 FT-IR spectrometer. Electronic spectra of the polymer-anchored compounds were recorded in Nujol on a Shimadzu1601 UV/Vis spectrophotometer by layering a mull of the sample inside one of the cuvettes while keeping other one layered with Nujol as a reference. The spectra of other ligands and complexes were recorded in methanol or DMF. $^1$H NMR spectra were obtained using a Bruker 500 NMR spectrometer in $[D_6]$DMSO. EPR spectra were

 © 2007 Wiley-VCH Verlag GmbH & Co. KGaA, Weinheim 

recorded at room temperature on a Bruker EMX X-band spectrometer operating at 100-kHz field modulation at room temperature. The microwave frequency was calibrated using a frequency counter of the Microwave Bridge ER 041 XG-D. The Bruker Simfonia software package was used in the spectroscopic simulations and to calculate hyperfine coupling constant. The magnetic susceptibilities of simple oxidovanadium(IV) complexes were measured at 298 K with a Vibrating Sample Magnetometer model 155, using nickel as a standard. Diamagnetic corrections were carried out using Pascal's increments.[35] Thermogravimetric analyses of the complexes were carried out using a Perkin–Elmer (Pyris Diamond) instrument. Scanning Electron Micrographs (SEM) of polymer anchored ligands and complexes were recorded on a Leo instrument model 435 VP. The samples were coated with a thin film of gold to prevent the surface changing and to protect the surface material from thermal damage by the electron beam.

### Preparations

**$H_2$fsal-ea (I):** A stirred solution of 2-aminoethanol (0.61 g, 10 mmol) in acetonitrile (10 mL) was added to a solution of 3-formylsalicylic acid (1.66 g, 10 mmol) in hot acetonitrile (30 mL) and the reaction mixture was heated to reflux on a water bath for 5 h. After reducing the solvent volume to ca. 10 mL, the flask was kept at room temperature. A yellow solid of **I** slowly separated out overnight. This was filtered, washed with petroleum ether and dried in vacuo. Yield 72%. $C_{10}H_{11}NO_4$ (209.2): calcd. C 57.40, H 5.30, N 5.70; found C 57.43, H 5.32, N 5.68. IR (KBr): $\tilde{\nu}_{max}$ = 1658 ($\nu_{C=O}$) $cm^{-1}$. $^1H$ NMR ([D$_6$]DMSO): $\delta$ = 12.89 (br., 1 H, carboxylic –OH), 5.20 (br., 1 H, phenolic OH), 8.37 (s, 1 H, –CH=N–), 8.09 (d, 1 H, aromatic), 7.69 (d, 1 H, aromatic), 6.75 (t, 1 H, aromatic), 3.77 (s, 2 H, –$CH_2$–), 3.70 (s, 2 H, –$CH_2$–) ppm. $^{13}C$ NMR ([D$_6$]DMSO): $\delta$ = 190.1 (carboxyl), 175.2 (azomethine), 168.4 (phenolic), 141.1, 139.9, 119.5, 116.1, 114.2 (aromatic), 59.3, 54.2 (alkyl chain) ppm.

**$H_2$fsal-pa (II) and $H_2$fsal-amp (III):** These ligands were prepared following the above procedure using 3-formylsalicylic acid (1.66 g, 10 mmol) and 3-aminopropanol (0.89 g, 10 mmol) or 2-amino-2-methylpropanol (0.89 g, 10 mmol).

**Data for II:** Yield 55%. $C_{11}H_{13}NO_4$ (223.2): calcd. C 59.17, H 5.87, N 6.28; found C 59.39, H 5.84, N 6.23. IR (KBr): $\tilde{\nu}_{max}$ = 1657 ($\nu_{C=O}$) $cm^{-1}$. $^1H$ NMR ([D$_6$]DMSO): $\delta$ = 12.09 (br., 1 H, carboxylic –OH), 4.80 (br., 1 H, phenolic –OH), 8.76 (s, 1 H, –CH = N–), 8.08 (d, 1 H, aromatic), 7.65 (d, 1 H, aromatic), 6.67 (t, 1 H, aromatic), 3.81 (t, 2 H, –$CH_2$–), 3.53 (t, 2 H, –$CH_2$–), 1.89 (quin, 2 H, –$CH_2$) ppm. $^{13}C$ NMR ([D$_6$]DMSO): $\delta$ = 190.8 (carboxyl), 175.2 (azomethine), 168.4 (phenolic), 141.0, 139.8, 119.5, 116.1, 114.1 (aromatic), 58.4, 49.7, 32.1 (alkyl chain) ppm.

**Data for III:** Yield 60%. $C_{12}H_{15}NO_4$ (237.2): calcd. C 60.73, H 6.38, N 5.91; found C 60.60, H 6.31, N 5.94. IR (KBr): $\tilde{\nu}_{max}$ = 1680 ($\nu_{C=O}$) $cm^{-1}$. $^1H$ NMR ([D$_6$]DMSO): $\delta$ = 13.57 (br., 1 H, carboxylic –OH), 5.57 (br., 1 H, phenolic –OH), 8.81 (s, 1 H, –CH = N–), 8.84 (d, 1 H, aromatic), 7.79 (d, 1 H, aromatic), 6.71 (t, 1 H, aromatic), 3.49 (s, 2 H, –$CH_2$–), 1.42 (s, 3 H, –$CH_3$), 1.17 (s, 3 H, –$CH_3$) ppm. $^{13}C$ NMR ([D$_6$]DMSO): $\delta$ = 190.1 (carboxyl), 168.2 (azomethine), 165.7 (phenolic), 141.2, 139.7, 119.4, 116.2, 114.2 (aromatic), 68.0, 61.2 (alkyl chain), 23.2 (methyl) ppm.

**PS-$H_2$fsal-ea (IV):** The polymer-anchored ligand PS-$H_2$fsal-ea was prepared following the procedure developed by Syamal et al.[36] Chloromethylated polystyrene (3.0 g) was allowed to swell in DMF (30 mL) for 2 h. A solution of $H_2$fsal-ea (9.96 g, 45 mmol) in DMF (30 mL) was added to the above suspension followed by triethylamine (4.50 g, 45 mmol) in ethyl acetate (50 mL). The reaction mixture was heated in an oil bath at 80 °C for 20 h with mechanical stirring. After cooling to room temperature, the yellow resins were filtered, washed thoroughly with hot DMF followed by hot methanol and dried in an air oven at 120 °C. Found: C 70.76, H 8.64, N 3.16. IR (KBr): $\tilde{\nu}_{max}$ = 1675 ($\nu_{C=O}$), 1635 ($\nu_{C=N}$) $cm^{-1}$.

**PS-$H_2$fsal-pa (V) and PS-$H_2$fsal-amp (VI):** The ligands PS-$H_2$fsal-pa and PS-$H_2$fsal-amp were prepared by following the procedure out lined for PS-$H_2$fsal-ea.

**Data for V:** Found: C 71.58, H 8.63, N 3.25. IR (KBr): $\tilde{\nu}_{max}$ = 1675 ($\nu_{C=O}$), 1637 ($\nu_{C=N}$) $cm^{-1}$.

**Data for VI:** Found: C 69.21, H 7.43, N 3.05. IR (KBr): $\tilde{\nu}_{max}$ = 1673 ($\nu_{C=O}$), 1630 ($\nu_{C=N}$) $cm^{-1}$.

**[VO(fsal-ea)]$_2$ (1):** A stirred solution of $H_2$fsal-ea (1.05 g, 5 mmol) in acetonitrile (30 mL) was added with stirring to [VO(acac)$_2$] (1.33 g, 5 mmol) dissolved in acetonitrile (25 mL) and the resultant reaction mixture was heated to reflux on a water bath for 3 h. After cooling to room temperature, a green precipitate of **1** was filtered, washed with acetonitrile and dried in vacuo. Yield 78%. $C_{10}H_9NO_5V$ (274.13): calcd. C 43.80, H 3.31, N 5.11, V 18.59; found C 43.62, H 3.42, N 5.05, V 18.06. IR (KBr): $\tilde{\nu}_{max}$ = 1670 ($\nu_{C=O}$), 1607 ($\nu_{C=N}$), 987 ($\nu_{V=O}$) $cm^{-1}$.

**[VO(fsal-pa)]$_2$ (2) and [VO(fsal-amp)]$_2$ (3):** Complexes **2** and **3** were prepared analogously to **1**, replacing $H_2$fsal-ea for $H_2$fsal-pa and $H_2$fsal-amp, respectively.

**Data for 2:** Yield 76%. $C_{11}H_{11}NO_5V$ (288.15): calcd. C 45.83, H 3.85, N 4.86, V 17.69; found C 45.91, H 3.65, N 4.74, V 17.14. IR (KBr): $\tilde{\nu}_{max}$ = 1673 ($\nu_{C=O}$), 1603 ($\nu_{C=N}$), 985 ($\nu_{V=O}$) $cm^{-1}$.

**Data for 3:** Yield 70%. $C_{12}H_{13}NO_5V$ (302.18): calcd. C 47.68, H 4.34, N 4.64, V 16.87; found C 47.30, H 4.54, N 4.41, V 16.36. IR (KBr): $\tilde{\nu}_{max}$ = 1674 ($\nu_{C=O}$), 1600 ($\nu_{C=N}$), 988 ($\nu_{V=O}$) $cm^{-1}$.

**PS-[VO(fsal-ea)·DMF] (4):** Polymer-anchored ligand PS-$H_2$fsal-ea (2.0 g) was allowed to swell in DMF (30 mL) for 2 h. A solution of [VO(acac)$_2$] (5.30 g, 20 mmol) in DMF (20 mL) was added to the above suspension and the reaction mixture was heated at 90 °C in an oil bath for 15 h while slow mechanical stirring. The blackish green beads of polymer-anchored complex **4** were filtered off, washed with hot DMF followed by hot methanol and dried at 120 °C in an air oven. Found: C 67.08, H 7.74, N 5.04, V 8.5. IR (KBr): $\tilde{\nu}_{max}$ = 1655 ($\nu_{C=O}$), 1607 ($\nu_{C=N}$), 977 ($\nu_{V=O}$) $cm^{-1}$.

**PS-[VO(fsal-pa)·DMF] (5) and PS-[VO(fsal-amp)·DMF] (6):** Complexes **5** and **6** were prepared by following the procedure out lined for **4**.

**Data for 5:** Found: C 68.18, H 7.86, N 4.83, V 7.93. IR (KBr): $\tilde{\nu}_{max}$ = 1659 ($\nu_{C=O}$), 1609 ($\nu_{C=N}$), 993 ($\nu_{V=O}$) $cm^{-1}$.

**Data for 6:** Found: C 64.19, H 7.31, N 4.66, V 7.26. IR (KBr): $\tilde{\nu}_{max}$ = 1675 ($\nu_{C=O}$), 1609 ($\nu_{C=N}$), 964 ($\nu_{V=O}$) $cm^{-1}$.

### Catalytic Activity Studies

**Oxidation of Styrene:** The oxidation of styrene was carried out in a 50 mL reaction flask fitted with a water condenser. All anchored catalysts were allowed to swell in acetonitrile for 2 h prior to their use. In a typical oxidation reaction, styrene (1.04 g, 10 mmol) and aqueous 30% $H_2O_2$ (2.27 g, 20 mmol) were mixed in acetonitrile (10 mL) and the reaction mixture was heated to 80 °C with stirring. The appropriate catalyst (0.040 g) was added to the reaction mixture and stirred for 6 h. The progress of the reaction was monitored by withdrawing small amounts of the reaction mixture at different time intervals and analysing them quantitatively by gas chromatography. The identities of the products were confirmed by GC–MS

 © 2007 Wiley-VCH Verlag GmbH & Co. KGaA, Weinheim 

(Perkin–Elmer, Clarus 500). The effects of various parameters such as temperature, amount of oxidant and catalyst were studied to obtain suitable reaction conditions for the best performance of the catalyst.

**Oxidation of Cumene:** Cumene (1.20 g, 10 mmol), 30% aqueous $H_2O_2$ (2.26 g, 20 mmol) and anchored catalyst (0.060 g), after swelling in acetonitrile as stated above in acetonitrile (10 mL), were heated at 80 °C with stirring and the reaction was monitored as mentioned above. Various parameters such as amount of oxidant and catalyst and temperature of the reaction were considered to see their effect on the reaction products. However, the basic procedure was the same as outlined above.

**Supporting Information** (see also the footnote on the first page of this article): Electronic spectral data (Table S1) and electronic spectra of neat and polymer-anchored oxidovanadium(IV) complexes (Figue S1).

## Acknowledgments

U. K. is thankful to the University Grant Commission (New Delhi, India) for Senior Research Fellowship and M. R. M. thanks the Council of Scientific and Industrial research (New Delhi, India) for financial support of the work. The authors are also thankful to Thermax Limited Pune, India, for generous gift of chloromethylated polystyrene.

[1] a) A. Messerschmidt, R. Wever, *Proc. Natl. Acad. Sci. USA* **1996**, *93*, 392–396; b) S. Macedo-Ribeiro, W. Hemrika, R. Renirie, R. Wever, A. Messerschmidt, *J. Biol. Inorg. Chem.* **1999**, *4*, 209–219.
[2] a) I. Harvey, J. M. Arber, R. R. Eady, B. E. Smith, C. D. Garner, S. S. Hasnain, *Biochem. J.* **1990**, *266*, 929–931.
[3] a) A. N. Antipov, D. Y. Sorokin, N. P. L'Lov, J. G. Kuenen, *Biochem. J.* **2003**, *369*, 185–189; b) A. N. Antipov, N. M. Lyalikova, T. V. Khilniak, N. P. L'Lov, *FEBS Lett.* **1998**, *441*, 257–260.
[4] a) G. J. Colpas, B. J. Hamstra, J. W. Kampf, V. L. Pecoraro, *J. Am. Chem. Soc.* **1996**, *118*, 3469–3478; b) B. J. Hamstra, G. J. Colpas, V. L. Pecoraro, *Inorg. Chem.* **1998**, *37*, 949–955.
[5] a) A. Butler, *Coord. Chem. Rev.* **1999**, *187*, 17–35; b) D. Rehder, *Coord. Chem. Rev.* **1999**, *182*, 297–322.
[6] M. R. Maurya, *Coord. Chem. Rev.* **2003**, *237*, 163–181.
[7] a) V. Conte, F. DiFuria, G. Licini, *Appl. Catal. A* **1997**, *157*, 335–361; b) A. G. J. Ligtenbarg, R. Hage, B. L. Feringa, *Coord. Chem. Rev.* **2003**, *237*, 89–101; c) C. Bolm, *Coord. Chem. Rev.* **2003**, *237*, 245–256.
[8] a) T. S. Smith II, V. L. Pecoraro, *Inorg. Chem.* **2002**, *41*, 6754–6760; b) A. Butler, M. J. Clague, G. E. Meister, *Chem. Rev.* **1994**, *94*, 625–638; c) H. B. ten Brink, A. Tuynman, H. L. Dekker, W. Hemrika, Y. Izumi, T. Oshiro, H. E. Schoemaker, R. Wever, *Inorg. Chem.* **1998**, *37*, 6780–6784; d) M. Andersson, A. Willetts, S. Allenmark, *J. Org. Chem.* **1997**, *62*, 8455–8458; e) V. M. Dembitsky, *Tetrahedron* **2003**, *59*, 4701–4720; f) D. Rehder, G. Santoni, G. M. Licini, C. Schulzke, B. Meier, *Coord. Chem. Rev.* **2003**, *237*, 53–63.
[9] M. R. Maurya, U. Kumar, P. Manikandan, *Dalton Trans.* **2006**, 3561–3575.
[10] a) B. Meunier, *Chem. Rev.* **1992**, *92*, 1411–1456; b) D. C. Sherrington, in *Supported Reagents and Catalyst in Chemistry* (Ed.: B. K. Hodnett, A. P. Keybett, J. H. Clark, K. Smith), Royal Society of Chemistry, Cambridge, **1998**, p. 220.
[11] R. Ando, T. Yagyu, M. Maeda, *Inorg. Chim. Acta* **2004**, *357*, 2237–2244.
[12] A. Syamal, K. S. Kale, *Inorg. Chem.* **1979**, *18*, 992–995.
[13] A. Syamal, K. S. Kale, *Indian J. Chem., Sect. A* **1980**, *19*, 225–228.
[14] A. Syamal, E. F. Carey, L. J. Theriot, *Inorg. Chem.* **1973**, *12*, 245–248.
[15] C. J. Carrano, C. M. Nunn, R. Quan, J. A. Bonadies, V. L. Pecoraro, *Inorg. Chem.* **1990**, *29*, 944–951.
[16] P. Arroyo, S. Gil, A. Munoz, P. Palanca, J. Sanchos, V. Sanz, *J. Mol. Catal. A* **2000**, *160*, 403–408.
[17] P. S. Gahlot, A. Agarwal, V. P. Seth, S. Sanghi, S. K. Gupta, M. Arora, *Spectrochim. Acta, Part A* **2005**, *61*, 1189–1194.
[18] A. Bruckner, H. W. Zanthoff, *Colloids Surf., A* **1999**, *158*, 107–113.
[19] V. Hulea, E. Dumitriu, *Appl. Catal. A* **2004**, *277*, 99–106.
[20] M. R. Maurya, M. Kumar, S. Sikarwar, *React. Funct. Polym.* **2006**, *66*, 808–818.
[21] Z. Fu, D. Yin, Q. Li, L. Zhang, Y. Zhang, *Microporous Mesoporous Mater.* **1999**, *29*, 351–359.
[22] M. R. Maurya, S. Sikarwar, T. Joseph, P. Manikandan, S. B. Halligudi, *React. Funct. Polym.* **2005**, *63*, 71–83.
[23] S. Matsui, T. Fujita, *Catal. Today* **2001**, *71*, 145–152.
[24] S. L. H. Rebelo, M. M. Q. Simoes, M. G. P. M. S. Neves, J. A. S. Cavalerio, *J. Mol. Catal. A* **2003**, *201*, 9–22.
[25] E. N. Panayotova-Björnbom, D. I. Dimitrov, M. P. Popangelova, A. A. Petkov, *J. Catal.* **1980**, *62*, 79–83.
[26] G. R. Verma, W. F. Graydon, *J. Catal.* **1973**, *28*, 236–244.
[27] a) A. K. Agarwal, R. D. Sristava, *J. Catal.* **1976**, *45*, 86–93; b) L. V. G. Krishna, M. S. Rao, R. D. Srivastava, *J. Catal.* **1977**, *49*, 109–111.
[28] a) S. Vetrivel, A. Pandurangan, *J. Mol. Catal. A* **2005**, *227*, 269–278; b) S. Vetrivel, A. Pandurangan, *Catal. Lett.* **2004**, *95*, 167–177.
[29] Y. F. Hsu, C. P. Cheng, *J. Mol. Catal. A* **1998**, *136*, 1–11.
[30] a) Y.-F. He, R.-M. Wang, Y.-Y. Liu, Y. Chang, Y.-P. Wang, C.-G. Xia, J.-S. Suo, *J. Mol. Catal. A* **2000**, *159*, 109–113; b) R.-M. Wang, S.-B. Li, Y.-P. Wang, Y. Chang, Y.-F. He, Z.-Q. Lei, H.-X. Feng, *React. Funct. Polym.* **1999**, *42*, 87–92.
[31] E. Baciocchi, F. d'Acunzo, C. Galli, M. Loele, *J. Chem. Soc., Chem. Commun.* **1995**, 429–430.
[32] M. R. Maurya, S. Khurana, E. Schulzke, D. Rehder, *Eur. J. Inorg. Chem.* **2001**, 779–788.
[33] R. A. Row, M. M. Jones, *Inorg. Synth.* **1957**, *5*, 113 –116.
[34] J. C. Duff, E. J. Bills, *J. Chem. Soc.* **1923**, 1987.
[35] R. L. Dutta, A. Syamal, *Elements of Magnetochemistry*, 2nd ed., Affiliated East-West Press, New Delhi, **1993**, p. 8.
[36] A. Syamal, M. M. Singh, *Indian J. Chem., Sect. A* **1992**, *31*, 110–115.

Received: November 29, 2006
Published Online: April 24, 2007

 © 2007 Wiley-VCH Verlag GmbH & Co. KGaA, Weinheim 

DOI: 10.1002/ejic.200601180

# Lanthanide Complexes with a Calix[8]arene Bearing Phosphinoyl Pendant Arms

**Lada N. Puntus,[a,b] Anne-Sophie Chauvin,[a] Sabi Varbanov,[a,c] and Jean-Claude G. Bünzli*[a]**

**Keywords:** Lanthanides / Calixarenes / Europium / Luminescence

The phosphinoyl-substituted macrocyclic receptor $B_8bL^8$, derived from *p-tert*-butylcalix[8]arene, was synthesized and its structure was studied in solution. According to temperature-dependent $^1H$ and $^{31}P$ NMR spectroscopic data, the calix[8]arene adopts a so-called *in–out* cone conformation. To investigate the influence of the narrow rim substitution, interaction with trivalent lanthanide ions, $Ln^{III}$ (Ln = La, Eu, Tb, Lu), was probed by MS, UV/Vis and NMR spectroscopic titrations. Although both 1:1 (in the presence of triflate) and 2:1 (in the presence of nitrate) $Ln:B_8bL^8$ complexes could be isolated in the solid state, the major species present in methanol is the 1:1 complex, irrespective of the anion. NMR spectroscopic data point to a common conformation for the 1:1 complexes in solution, the lanthanide ions being coordinated by four of the eight phosphinoyl arms, with a coordination sphere completed by methanol molecules or by nitrate ions, as ascertained by IR and MS spectra. The ligand displays a weak absorption at 360 nm that can be assigned to an intraligand charge-transfer (ILCT) state, which is very sensitive to coordination. Photophysical data of the $Eu^{III}$ 2:1 complex point to both metal ion sites providing a very similar chemical environment for the lanthanide ions, with no coordinated water, which is contrary to what is observed for the 1:1 complex. The use of optical electronegativity to predict the energy of the charge-transfer states in the lanthanide systems with inequivalent ligands is discussed and extensive analysis of the vibronic satellites of the $Eu(^5D_0 \rightarrow {}^7F_J)$ transitions ascertains conclusions drawn on the $Eu^{III}$ coordination.
(© Wiley-VCH Verlag GmbH & Co. KGaA, 69451 Weinheim, Germany, 2007)

## Introduction

Calix[*n*]arenes, or [1$_n$]metacyclophanes, present excellent coordination[1] and extraction[2–4] capabilities, in addition to being adequate platforms for the design of catalysts[5] or optical sensors.[6] They also provide suitable frameworks for the construction of more complex noncovalent structures.[7–9] Central to these applications are (1) the availability of calixarenes in various ring sizes, up to $n = 20$,[10] (2) their capacity to assume different conformations that can be tuned by the nature of the substituents and/or by two- or four-point intramolecular bridging,[11] which leads to controlled luminescent properties[12] and (3) their easy functionalization both at the wide and narrow rims, a versatility that opens perspectives in many fields of chemistry. Our interest in lanthanide complexes with calixarenes lies in the development of bimetallic model molecules for the study of energy transfer processes and magnetic interactions,[13] as well as in the design of lanthanide/actinide extraction systems and luminescent probes. With respect to the latter goals, we, among others, have been focusing on *p-tert*-butylcalix[*n*]arenes fitted with dimethylphosphinoylmethylene pendant groups on the narrow rim (Scheme 1) because the latter are known to be good complexation groups for trivalent lanthanide ions, $Ln^{III}$. In addition, similar hosts bearing diphenylphosphinoylmethylene arms have been previously proposed.[14–16] The smaller macrocyclic receptor derived from calix[4]arene, $B_4bL^4$, adopts a flattened cone conformation. It reacts with lanthanide ions to yield both 1:1 and 1:2 (Ln/L) stable complexes with $Ln^{III}$ ions in acetonitrile; the solvent composition, particularly its water content, influences strongly the solvation state of the macrocyclic edifices as well as their luminescent properties.[17] This macrocycle is also quite convenient for the binding of 3d metal ions.[18] When the number of phenolic units is increased to six to yield $B_6bL^6$, the resulting macrocycle exists as a mixture of conformers in dmso with a time-averaged alternate *in–out* conformation at elevated temperature (405 K) of $C_{6v}$ symmetry. Because of the larger conformational flexibility, both 1:1 and 1:2 complexes with $Ln^{III}$ ions are less stable than the corresponding ones with the

[a] École Polytechnique Fédérale, Lausanne, Laboratory of Lanthanide Supramolecular Chemistry, BCH 1401, 1015 Lausanne, Switzerland
E-mail: anne-sophie.chauvin@epfl.ch
jean-claude.bunzli@epfl.ch
[b] Russian Academy of Sciences, Institute of Radio Engineering & Electronics, 125009 Moscow, Russia
E-mail: lada_puntus@mail.ru
[c] Bulgarian Academy of Sciences, Institute of Polymers, 1113 Sofia, Bulgaria
E-mail: varbanov@orgchm.bas.bg
Supporting information for this article is available on the WWW under http://www.eurjic.org or from the author.

 © 2007 Wiley-VCH Verlag GmbH & Co. KGaA, Weinheim 

analogous calix[4]arene, but these complexes still display interesting photophysical properties.[19] Liquid–liquid extraction studies have demonstrated the separation ability of $B_4bL^4$ and $B_6bL^6$ for the lighter actinides, as compared to $Ln^{III}$ ions, and the calix[6]arene receptor revealed to be the best extractant.[20] Owing to the large dimension of their annulus, calix[8]arenes are promising receptors both for medium-sized organic compounds[21] and large metal cations; for instance, they can encapsulate up to two $Ln^{III}$ ions in the same molecular edifice.[13,22] For *p*-substituted calix[8]-arenes, the 1:1 versus 2:1 stoichiometry is simply tuned by the strength of the base used to deprotonate the hydroxy groups.[23,24] However, most of the reported complexes have 2:1 stoichiometry,[25,26] whereas 1:2 molecular ratios are less common.[27] The purpose of this paper is to investigate the influence of the narrow rim substitution of *p*-*tert*-butylcalix[8]arene by phosphinoyl groups on the coordination and photophysical properties of both the octamer toward trivalent lanthanide ions and the resulting complexes. In addition, we probe the effect of the coordination strength of the anion with regard to both the stoichiometry of the complexes and the coordination mode of the macrocycle.

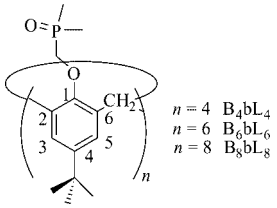


Scheme 1.

## Results and Discussion

### Synthesis and Structural Characterisation of Calixarene $B_8bL^8$ in Solution

The macrocyclic receptor $B_8bL^8$ (Scheme 1) was prepared in 46% yield by a Williamson reaction by refluxing the octasodium derivative of *p*-*tert*-butylcalix[8]arene and chloro(dimethylphosphinoyl)methane in xylene (Scheme 2).

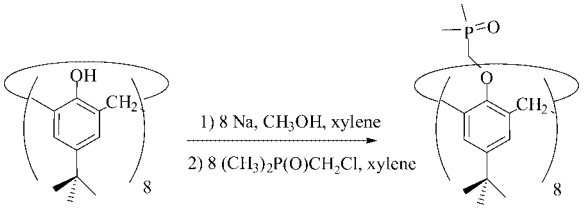


Scheme 2.

The structure of $B_8bL^8$ in a $3.4\times10^{-3}$ M [$D_4$]methanol solution was established by temperature-dependent NMR spectroscopy. At 293 K, the $^{31}P\{^1H\}$ NMR spectrum displays a singlet at $\delta$ = 44.8 ppm, which indicates that the eight phosphorus atoms are equivalent. $^1H$ NMR spectroscopic signals for all protons appear as singlets (Figure 1), except for the $CH_2(P{=}O)$ and $CH_3(P{=}O)$ groups, which generate doublets owing to the coupling with the $^{31}P$ atom.[19,28,29] All $^1H$ and $^{13}C$ NMR spectroscopic data are consistent with a cone conformation,[14,30–32] which suggests a time-averaged molecular structure resulting from fast interconversion between the different conformers. At 213 K, the $^1H$ NMR spectrum is less well-resolved with moderately broadened signals owing to higher solvent viscosity (Figure 1). A double quantum filtered correlation spectroscopic (DQF-COSY) experiment points again to only one conformation for the isomers: the observed correlation peaks can be assigned to (1) $CH_3$ groups bound to the same carbon atom ($\delta$ = 1.36 and 0.82 ppm), (2) aromatic protons belonging to one phenol ring ($\delta$ = 7.36 and 6.56 ppm) and (3) protons from the AB spin system of the eight bridging methylene groups ($\delta$ = 4.3 and 3.9 ppm). Appearance of a correlation peak between the $CH_2$ and $CH_3P{=}O$ groups (see Figure 2) in the rotating frame Overhauser enhancement spectroscopic experiment (ROESY) could be the result of partial inversion, which results from *p*-*tert*-butyl moieties that swing through the annulus. Indeed, two dynamic processes were detected in large calixarenes with substituted phenol groups: macrocyclic ring interconversion and pinched conformer interconversion. The former takes place by way of two different mechanisms: *tert*-butyl-through-the-annulus and oxygen-through-the-annulus pathways,[8,33] The first mechanism, in which the aryl groups swing through the annulus in sequence, always operates in unbridged large calixarenes, as demonstrated for *p*-*tert*-butylcalix[6]arenes.[30,34,35] Alternatively, the presence of sufficiently bulky groups at the narrow rim, as it is the case for $B_8bL^8$, inhibits oxygen-through-the-annulus interconversion so that ring interconversion can only proceed by the *tert*-butyl-through-the-annulus route.

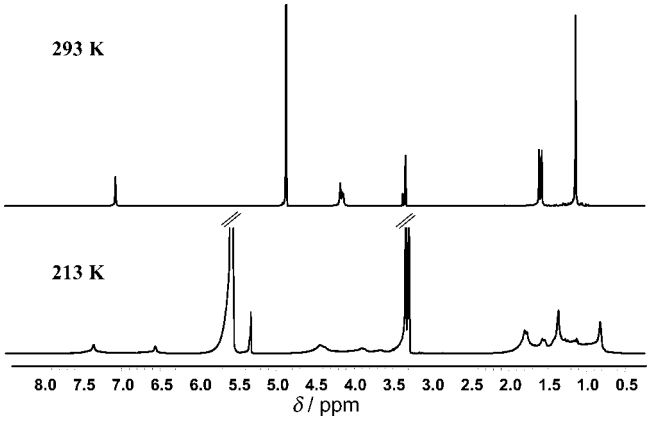


Figure 1. $^1H$ NMR spectra of the $3.4\times10^{-3}$ M solution of $B_8bL^8$ in $CD_3OD$ at (a) 293 and (b) 213 K.

$^1H$ and $^{31}P$ NMR spectroscopic data were obtained over a wide temperature range (193–353 K; Figure S1, Supporting Information). At the lowest temperature, the conformational interconversion processes are not yet completely frozen despite the observation of two distinct resonances in the $^{31}P$ spectrum. For $T \geq 293$ K, sharp, well-resolved reso-

 © 2007 Wiley-VCH Verlag GmbH & Co. KGaA, Weinheim 

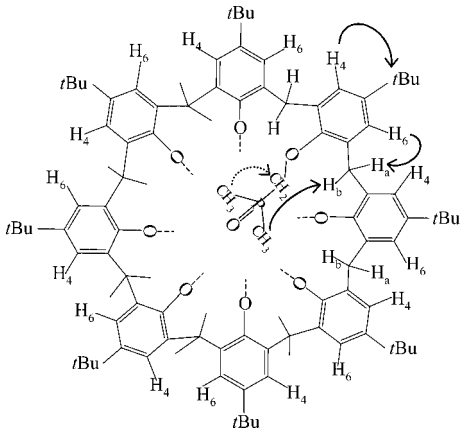

Figure 2. ROESY contacts observed at 213 K for $B_8bL^8$ in $CD_3OD$: plain arrows are for the ligand alone and dotted arrows for the solution containing one equivalent of $Lu(Otf)_3$.

nances are recorded in both the $^1H$ and $^{31}P$ NMR spectra. This reveals that the activation barrier for macrocyclic ring interconversion is low.

### Interaction of $B_8bL^8$ with $Ln^{III}$ in Methanol

To obtain information on the interaction between $B_8bL^8$ and lanthanide ions, a $8.1–8.6 \times 10^{-4}$ M solution of the macrocycle in MeOH was titrated with $Ln(OTf)_3 \cdot xH_2O$ (Ln = La, Eu, Lu; typically $10^{-4}$ M, $x = 10$ for La, 7 for Eu and 9 for Lu) and $Ln(NO_3)_3 \cdot xH_2O$ (Ln = La, Eu; typically $10^{-3}$ M, $x = 4$ for Eu and 3 for Lu) up to a ratio of $R = [Ln^{III}]_{tot}/[B_8bL^8]_{tot} = 4.5$. Titrations were first monitored by electrospray mass spectrometry (ESMS, see Tables S1 and S2, Supporting Information). For $R \leq 1$, both 1:2 $[Eu(B_8bL^8)_2]^{3+}$ ($m/z$ = 1396.40, calcd. 1396.22) and 1:1 $[Eu(B_8bL^8)(CH_3COOH)]^{3+}$ ($m/z$ = 743.32, calcd. 743.45) species are observed. An increase in $R$ leads to the disappearance of the 1:2 species. When $R$ reaches 2, the main species is $[Eu(B_8bL^8)(Otf)]^{2+}$ ($m/z$ = 1159.24, calcd. 1158.95), but $[Eu(B_8bL^8)]^{3+}$ ($m/z$ = 723.20, calcd. 723.44) is also observed. No signal from the free ligand is detected in the latter case, which points to the formation of a stable 1:1 species. Titration of the macrocycle solution with $Eu(NO_3)_3 \cdot 4H_2O$ shows a similar behaviour, except for the stronger coordination of the counterions, as demonstrated by the presence of $[Eu(B_8bL^8)(NO_3)]^{2+}$ ($m/z$ = 1114.97, calcd. 1115.49), $[Eu(B_8bL^8)(NO_3)(H_2O)_2]^{2+}$ ($m/z$ = 1133.44, calcd. 1134.16) and $[Eu(B_8bL^8)(NO_3)(CH_3COOH)]^{2+}$ ($m/z$ = 1145.47, calcd. 1145.52) species for $R = 1$ (Table S2, Supporting Information). Formation of species with stoichiometric ratio $Eu/B_8bL^8$ of 2:1 was not detected in this case, probably owing to its low solubility; a precipitate starts to appear when $R > 1$.

The titrations were repeated with UV/Vis monitoring, starting from concentrations of $1.1 \times 10^{-4}$ M for $B_8bL^8$ and adding lanthanide triflates with concentrations of $\approx 8 \times 10^{-3}$ M. Plots of absorbance versus $R$ evidenced at least two complexed species (Figure S2, Supporting Information) and factor analysis revealed four absorbing species ($B_8bL^8$, 1:2, 1:1, 2:1), which could be satisfactorily fitted to the following model (Table 1):

$Ln^{3+} + B_8bL^8 \rightarrow [Ln(B_8bL^8)]^{3+}$ $\log K_{11}$

$Ln^{3+} + 2\ B_8bL^8 \rightarrow [Ln(B_8bL^8)_2]^{3+}$ $\log K_{12}$

$2\ Ln^{3+} + B_8bL^8 \rightarrow [Ln_2(B_8bL^8)]^{6+}$ $\log K_{21}$

Table 1. Log $K_{ij}$ values ($\pm$ 0.2) extracted from the titration of $B_8bL^8$ with lanthanide triflates in methanol, at 293 K.

| Ln | $\log K_{12}$ | $\log K_{11}$ | $\log K_{21}$ |
|---|---|---|---|
| La | 4.4 | 6.9 | 4.9 |
| Eu | 4.3 | 7.2 | 5.0 |
| Lu | 5.6 | 7.4 | 4.9 |

Because the UV/Vis spectra of the complexes are heavily correlated, these data should be taken as a first estimate. The stability constants obtained are smaller than the ones reported for $B_4bL^4$[17] and $B_6bL^6$[19] as a consequence of the smaller degree of preorganisation of the octamer. The $K_{11}$ values are about two orders of magnitude larger than the $K_{12}$ and $K_{21}$ constants. Calculation of the speciation of $Eu^{III}$ with these data and a total ligand concentration between $10^{-4}$ and $10^{-3}$ M shows that for $R = 1$, the 1:1 species is always largely predominant (> 93%). For all the concentrations at which the titrations have been conducted, and for $R$ in the range 0.5–2.0, the concentration of the bimetallic 2:1 complex remains extremely small.

Finally, the speciation was confirmed by $^1H$ and $^{31}P\{^1H\}$ NMR spectroscopic titration at 293 K. The free ligand, 1:2 and 1:1 species coexist in $3.3 \times 10^{-3}$ M methanolic solutions of $B_8bL^8$ that contain lutetium triflate when $R < 1$ (Figure 3). For $1 < R < 1.6$, the minor 1:2 species disappears whereas the 1:1 species grows until $R > 1.6$. Together with ESMS and spectrophotometric titration data, this can be interpreted as the formation of a thermodynamically stable complex with 1:1 stoichiometry. Coordination through the phosphinoyl groups is established as both the $^1H$ and

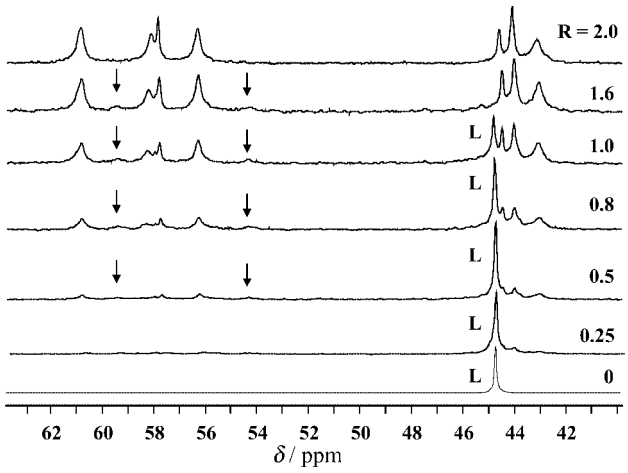


Figure 3. Titration of a $B_8bL^8$ solution ($3.3 \times 10^{-3}$ M) by $Lu(OTf)_3 \cdot 9H_2O$ ($4.5 \times 10^{-2}$ M) in $CD_3OD$ as monitored by $^{31}P\{^1H\}$ NMR spectroscopy at 293 K, $R = [Lu^{III}]_t/[B_8bL^8]_t$; arrows point to the signal of the minor 1:2 species, while L denotes the free ligand signals.

 © 2007 Wiley-VCH Verlag GmbH & Co. KGaA, Weinheim 

$^{31}P\{^1H\}$ NMR signals from the phosphinoyl arms are affected by the complexation. Two $^{31}P$ signals are observed, shifted from 44.6 ppm for the free ligand to 43.7 ppm ($\Delta\delta$ = 0.9 ppm) and 58.5 ppm ($\Delta\delta$ = 13.8 ppm) for the 1:1 lutetium complex. This points to two different chemical environments for the phosphorus atoms in a 1:1 ratio, which suggests that the octamer has four coordinated and four uncoordinated arms. This was further ascertained by temperature-dependent 1D and 2D NMR experiments described in the next section. Taking into account all the results obtained during the titrations, one can conclude that the ESMS, UV/Vis and NMR spectroscopic data are consistent and point to the predominance of the 1:1 species.

### Solution Structure of the 1:1 Complexes with $Lu(OTf)_3$ and $Lu(NO_3)_3$

The $^1H$ NMR spectrum of a $B_8bL^8$ solution $3.3\times10^{-3}$ M in [$D_4$]methanol containing one equivalent of lutetium triflate (Figure 4) displays three typical groups of resonances at 213 K: (1) four signals between 6.6 and 7.6 ppm from the 16 aromatic protons, (2) three pairs of doublets in the range 3.8 to 4.7 ppm from the eight bridging methylene groups and two signals from eight ($CH_2$)P=O groups, and (3) two groups of signals between 0.8 and 1.5 ppm for methylic protons and four doublets from($CH_3$)P=O units in the range 2.1 to 1.6 ppm, which correspond to 24 and 16 protons, respectively. In the DQF-COSY spectrum at the same temperature (Figure S3, Supporting Information) the strongest cross peaks arise from methylene groups. For instance, cross peaks in the aromatic region correspond to protons 3 and 5 (see Scheme 1 for the numbering) for both sets of resonances ($\delta$ = 7.52/7.46 ppm and 6.73/6.56 ppm), which points to two different types of phenol rings. The ratio of their integrated intensities (1:1) and the remarkable difference in the chemical shift ($\Delta$ = 0.85 ppm) fully back the interpretation that four phosphinoyl arms are coordinated. Moreover, the NOE effect evidenced at 293 K between $CH_2P$=O ($\delta$ =4.58 ppm) and $CH_3P$=O ($\delta$ =1.75 ppm) is consistent with a bent conformation of the phosphinoyl arm at this temperature, at which the unbound octamer is conformationally most labile, again pointing to the coordination of the pendant arms.

The methylene resonances give important information on the conformation of the bound calixarene because the $\Delta\delta$ shifts can be used for differentiating between *sin* or *anti* aromatic protons.[30] Assignment of axial and equatorial protons is dependent on DQF-COSY experiments (Figure 5, Table 2). Three types of resonances from the Ar-$CH_2$Ar methylene protons ($H^a$, $H^b$, $H^c$) with intensity ratios 6:4:6 are observed at 213 K in the presence of triflate; two of them appear as pairs of doublets ($H^a$ and $H^c$). The presence of distinct signals for both equatorial and axial protons for every $CH_2$ group points to a cone-like conformation of the corresponding phenolic units.[32] Comparison of the chemical shift differences ($\Delta\delta$ = ≈ 0.6 for $H^a$, ≈ 0.1 ppm for $H^b$ and $H^c$) with those obtained for unbound $B_8bL^8$ ($\delta$ =0.6 ppm) and the anhydrous $[LaB_4bL^4]^{3+}$ complex ($\delta$ =0.15 ppm)[17] leads to the assignment of the signals corresponding to the largest $\Delta\delta$ value to the uncoordinated units of the macrocycle. In favour of this assignment is the fact that unusually small $\Delta\delta$ values are observed when a small guest − in our case the lanthanide ion − enters a calixarene cavity.[15] Upon increasing the temperature to 293 K, methylene bridges give rise to four pairs of resonances ($H^{a'}$, $H^{b'}$, $H^{c'}$, $H^{d'}$) in the ratio 4:4:4:4; two of them ($H^b$, $H^c$) appear as pairs of doublets whereas the other two ($H^a$, $H^d$) feature three components. Finally, two and three signals from $CH_2P$=O in a ratio 4:4 and 4:2:2 were observed at 213 and

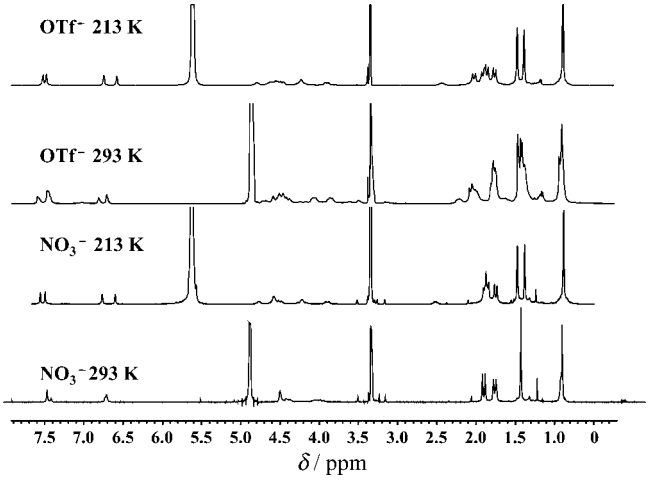


Figure 4. $^1H$ NMR spectra of a solution of $B_8bL^8$ ($3.3\times10^{-3}$ M) with 1 equiv. of $Lu(OTf)_3{\cdot}9H_2O$ or $Lu(NO_3)_3{\cdot}4H_2O$ in $CD_3OD$ at 213 K and 293 K.

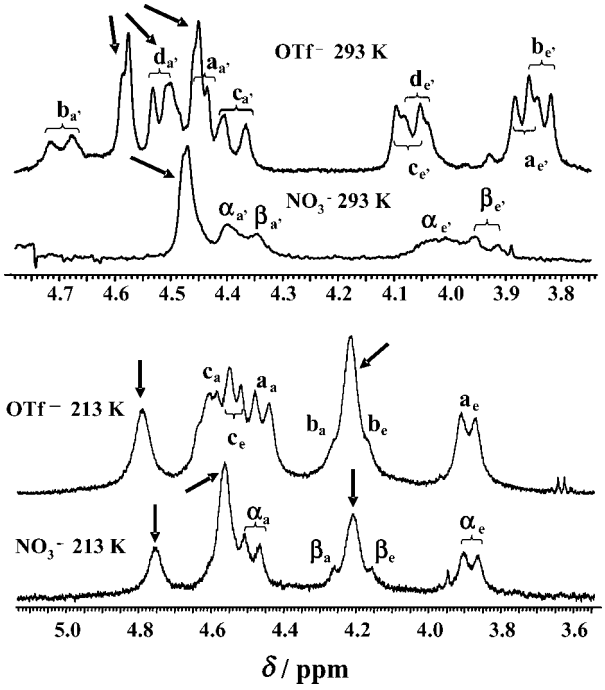


Figure 5. Part of the $^1H$ NMR spectra of a $B_8bL^8$ solution ($3.3\times10^{-3}$ M) with 1 equiv. of $Lu(OTf)_3{\cdot}9H_2O$ or $Lu(NO_3){\cdot}4H_2O$ in $CD_3OD$ at 213 and 293 K. Arrows point to resonances from the $CH_2PO$ methylene groups.

 © 2007 Wiley-VCH Verlag GmbH & Co. KGaA, Weinheim 

Table 2. $^1$H NMR spectroscopic chemical shifts ($\delta$) of the methylene groups of solutions of $B_8bL^8$ in $CD_3OD$ containing 1 equiv. of $[Lu(Otf)_3]$ or $[Lu(NO_3)_3]$.

| T / K | Anion | Proton | $\delta H_{ax}$ / ppm | *h*e / ppm | $\Delta(H_{ax} - H_{eq})$ / ppm | *I* / a.u. | $\delta CH_2(P{=}O)$ / ppm |
|---|---|---|---|---|---|---|---|
| 213 | $Otf^-$ | $H^a$ | 4.46 | 3.88 | 0.58 | 6 | 4.79, 4.22 (4:4) |
| | | $H^b$ | 4.26 | 4.17 | 0.09 | 4 | |
| | | $H^c$ | 4.59 | 4.53 | 0.06 | 6 | |
| 293 | $Otf^-$ | $H^{a'}$ | 4.46 | 3.87 | 0.59 | 4 | 4.58, 4.50, 4.43 (4:2:2) |
| | | $H^{b'}$ | 4.69 | 3.83 | 0.86 | 4 | |
| | | $H^{c'}$ | 4.38 | 4.07 | 0.31 | 4 | |
| | | $H^{d'}$ | 4.52 | 4.06 | 0.46 | 4 | |
| 213 | $NO_3^-$ | Hα | 4.48 | 3.89 | 0.59 | 5 | 4.76, 4.57, 4.21 (2:4:2) |
| | | Hβ | 4.26 | 4.16 | 0.1 | 3 | |
| 293 | $NO_3^-$ | Hα′ | 4.35 | 3.93 | 0.42 | 4 | 4.47 |
| | | Hβ′ | 4.39 | 4.02 | 0.37 | 4 | |

293 K, respectively. These data can be interpreted by a proposed structure (Figure 6a) in which coordination occurs through the central four phosphinoyl pendant arms and possibly implies binding by the phenolic units. Interconversion processes through annulus are then more difficult and the NMR spectrum at room temperature features sharper signals. Alternatively, the coordination sphere may be completed by methanol molecules. Because triflate is very weakly coordinating in methanol,[36] it is reasonable to surmise that this counterion only interacts in the second coordination sphere.

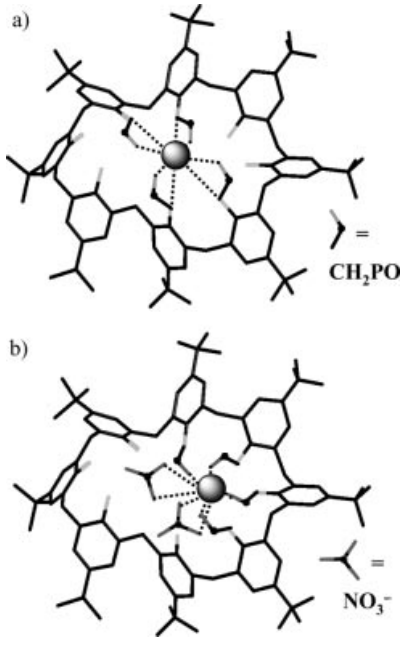


Figure 6. Schematic representation of the possible solution structure of the 1:1 complexes with $B_8bL^8$ compatible with NMR spectroscopic data: (a) central coordination involving phenolic groups in the case of the triflate, (b) side complexation in the case of the nitrate. Note that phosphinoyl arms are only shown when coordinating, for the sake of clarity.

Next we tested the influence of nitrate, which is more strongly coordinating than triflate,[36] by measuring the spectra of 1:1 solutions of $B_8bL^8$ and lutetium nitrate at a concentration of $1.9 \times 10^{-3}$ M. At 213 K, both the 1D (Figure 5) and 2D (Figure S4, Supporting Information) spectra are quite similar to the ones discussed above for lutetium triflate with the exception of the methylene bridge region, which displays only two types of signals instead of three. These signals appear as a pair of doublets (Hα, $\Delta\delta$ = 0.6 ppm) and a singlet ($H_\beta$, $\Delta\delta$ = 0.1 ppm) in a ratio 5:3. By comparing the $\Delta\delta$ values with those obtained for lutetium triflate, this ratio may be explained as arising from the presence of three methylene bridges connecting four units of the octamer with coordinated pendant arms (smaller $\Delta\delta$) and five methylene bridges connecting the other four units with uncoordinated arms (larger $\Delta\delta$). In line with this interpretation is the observation of three resonances in a ratio 4:2:2 for the $CH_2(P{=}O)$ methylene groups; in view of the fluxionality of the calix[8]arene, the uncoordinated pendants experience two different chemical environments.

In contrast, the spectrum recorded at 293 K is remarkably different from the one for the triflate complex: much broader and unresolved signals in the methylene region are observed. The two distinguishable pairs of signals from the methylene groups $H^{\alpha'}$ and $H^{\beta'}$ have average $\Delta\delta \approx 0.4$ ppm, which is in line with faster chemical exchanges on the NMR timescale. Only one averaged resonance is seen for the eight $CH_2P{=}O$ units. Interpretation of these data can be made by reference to a complex with the parent *p-tert*-butylcalix[8]arene $H_8L^8$, $[Eu(H_6L^8)(NO_3)(DMF)_4]$, in which both nitrate and calixarene act as bidentate ligands.[24] In our case, in view of the strong coordinating nature of the pendant arms and of their length and flexibility, one could postulate a "side" coordination as well, but involving one (or two) bidentate nitrate anion(s), as the mono- (85%) and bis(nitrato) (15%) complexes are the predominant species in $Ln(NO_3)_3$ methanol solutions at the concentrations used in this work.[37] Therefore, the above-described data may be interpreted by considering a side coordination of the lutetium ion by four phosphinoyl arms out of the octamer "cavity" (see Figure 6b). The lutetium ion may not be coordinated as deeply in the macrocycle as in the case of the triflate and, as a consequence, methanol molecules may complete the inner coordination sphere or compete with the

 © 2007 Wiley-VCH Verlag GmbH & Co. KGaA, Weinheim 

phosphoryl and nitrate groups. In such a model, the system is more fluxional relative to the triflate complex, which explains the average $\Delta\delta$ values observed at room temperature. Consequently, the choice of the counterion, triflate or nitrate, allows the final structure of the lanthanide complexes to be tuned: four phosphinoyl arms are bound in each case but the coordination geometry and the cation orientation in the calixarene cavity depend on the counterion used.

### Isolation and Characterization of the 1:1 and 2:1 $Ln^{III}$ Complexes

The 1:1 and 2:1 $Ln^{III}$ complexes (Ln = La, Eu, Tb, and Lu) evidenced in solution studies could be isolated from stoichiometric solutions of $B_8bL^8$ ($\approx 3.4 \times 10^{-3}$ M) and lanthanide triflate or nitrate in methanol. For $Eu^{III}$, elemental analyses correspond to formulae $Eu(OTf)_3(B_8bL^8)\cdot 13H_2O$ and $Eu_2(B_8bL^8)(NO_3)_6\cdot H_2O$. Unfortunately, no single crystals of X-ray quality could be obtained, despite numerous trials. The $^1H$ NMR spectra of a methanolic solution of the isolated 1:1 and 2:1 lutetium complexes are similar to the spectra obtained for a solution of $B_8bL^8$ containing one equivalent of lutetium triflate and nitrate, respectively (Figure S5, Supporting Information). The low solubility of these complexes, particularly the lutetium 2:1 species, required heating the solutions and high dilution; as a consequence, the $^1H$ NMR spectra contain traces attributed to the free octamer, which reveals partial decomplexation. High resolution MS (FAB) data for 1:1 (Lu) and 2:1 (Tb) complexes in methanol are shown in Table 3 and Figure S6 (Supporting Information). For the bimetallic complex, only peaks corresponding to a 1:1 species are observed, in line with the corresponding NMR spectroscopic data and pointing again to the low stability of the 2:1 species in solution.

Table 3. Molecular peaks and main fragments observed by MS (FAB) analysis of $Lu(B_8bL^8)(OTf)_3\cdot 13H_2O$ and $Tb_2(B_8bL^8)(NO_3)_6\cdot H_2O$.

| Ln | Mol.Weight | Species | Obsd. *m/z* | Calcd. *m/z* |
|---|---|---|---|---|
| Lu | 2638.84 | $[L + Lu]^{3+}$ | 730.99 | 730.66 |
| | | $[L + 2H]^{2+}$ | 1010.03 | 1009.52 |
| | | $[L + H + Na]^{2+}$ | 1021.02 | 1020.51 |
| | | $[L + H + Na + H_2O]^{2+}$ | 1029.00 | 1029.52 |
| | | $[L + 2Na + 3H_2O + CH_3OH]^{2+}$ | 1073.98 | 1074.53 |
| | | $[L + 2Na + 2H_2O + 2CH_3OH]^{2+}$ | 1080.98 | 1081.54 |
| | | $[L + Lu + OTf]^{2+}$ | 1170.96 | 1170.47 |
| | | $[2\,L + Lu]^{3+}$ | 1403.68 | 1403.00 |
| | | $[L + H]^{+}$ | 2018.06 | 2018.03 |
| | | $[L + Na]^{+}$ | 2041.04 | 2040.01 |
| Tb | 2520.84 | $[L + 6H + 4H_2O + 4CH_3OH]^{6+}$ | 370.45 | 370.54 |
| | | $[L + 6H + 5H_2O + 4CH_3OH]^{6+}$ | 373.29 | 373.54 |
| | | $[L + Tb]^{3+}$ | 725.99 | 725.31 |
| | | $[L + Tb + H_2O]^{3+}$ | 730.33 | 731.32 |
| | | $[L + Tb + 4H_2O + 2CH_3OH]^{3+}$ | 770.97 | 770.68 |
| | | $[L + Tb + 6H_2O + CH_3OH]^{3+}$ | 772.98 | 772.01 |
| | | $[L + 2H + 6H_2O + 3CH_3OH]^{2+}$ | 1110.98 | 1111.60 |
| | | $[L + Tb + NO_3]^{2+}$ | 1119.47 | 1118.97 |
| | | $[2\,L + Tb + 7H_2O + 6CH_3OH]^{3+}$ | 1503.99 | 1503.74 |
| | | $[L + Tb + 2NO_3]^{+}$ | 2300.00 | 2299.94 |

The IR spectra of the 1:1 and 2:1 $Eu^{III}$ complexes (Figure S7, Supporting Information) reveal bathochromic shifts of 25 and 40 $cm^{-1}$, respectively, relative to that of the free ligand, for the ν(P=O) vibration; these shifts confirm the coordination of the macrocycle by the metal ion. A similar redshift (35 $cm^{-1}$) was reported for a 1:2 (Ln/L) lanthanide complex with $B_4bL^4$.[17] Typical vibrations of $CH_2$ groups are observed in the spectral ranges 750 to 760, 935 to 945 and 1290 to 1295 $cm^{-1}$, and they are assigned to out-of-plane C–H twisting, rocking and wagging modes, respectively. Anion vibrations were assigned by comparison with $Eu(OTf)_3\cdot 5H_2O$ and $Eu(NO_3)_3\cdot 6H_2O$. The presence of both coordinated and uncoordinated triflate groups is consequently ascertained for the $Eu^{III}$ 1:1 complex. In the 1100 to 1300 $cm^{-1}$ range, higher frequency $\nu(SO_3)$ and $\nu(CF_3)$ modes of this complex overlap to form a broad structured band that remarkably differs from the corresponding bands for the triflate salt. The presence of a coordinated triflate anion is also confirmed by the appearance of $\nu_s(SO_3)$ and $\nu_{as}(SO_3)$ modes at 1028 and 1238 $cm^{-1}$, respectively.[38] The latter overlaps with the $\nu_s(CF_3)$ mode. Bands at 1280, 1222 and 1164 $cm^{-1}$ are assigned to the $\nu_{as}(SO_3)$, $\nu_s(CF_3)$ and $\nu_{as}(CF_3)$ modes of uncoordinated triflate. In the FIR range, the intense peak at 638 $cm^{-1}$ and the less intense band at 518 $cm^{-1}$ correspond to the $\delta_s(SO_3)$ and $\delta_{as}(SO_3)$ modes. The integral intensity ratio $\delta_s(SO_3)/\delta_{as}(SO_3)$ is 1.6 and 0.9 for the 1:1 complex and triflate salt, respectively. The bands at 570 and 750 $cm^{-1}$ are associated with $\delta_{as}(CF_3)$ and $\delta_s(CF_3)$ but overlap of the latter with $\delta$(CH) vibrations prevents further intensity analysis. The difference in the intensities of the $\delta(SO_3)$ vibrations, as well as the redshift of the $\delta_{as}(SO_3)$ and $\delta_{as}(CF_3)$ bands for the octamer complex in comparison with corresponding bands for europium triflate are compatible with the presence of two uncoordinated triflate anions in the isolated 1:1 complex.

In the IR spectrum of the 2:1 europium nitrato complex, the characteristic nitrate bands appear at 1510 ($\nu_5$), 1280 ($\nu_1$), 1030 ($\nu_2$), 738 and 755 ($\nu_3$) $cm^{-1}$. The splitting of the two strongest absorptions ($\nu_5$ and $\nu_1$) is ≈ 230 $cm^{-1}$, which indicates bidentate coordination by the europium ion with a relatively strong metal–nitrate interaction.[39] All the nitrate groups appear to be coordinated by the lanthanide ion as no band from the free $NO_3^-$ was detected.

Raman spectra of the 1:1 and 2:1 complexes are in line with the above analysis. In addition, the lower effective cross-section of the Raman scattering, as measured by the area of the $\nu$(CH) modes, observed for the 2:1 complex, indicates less changes in polarizability relative to the 1:1 complex. Finally, the appearance of the $\nu$(–O–$CH_2$–) vibration as a doublet with frequencies 1012 and 1028 $cm^{-1}$ in the 1:1 europium complex, relative to a single band at 1012 $cm^{-1}$ for uncoordinated $B_8bL^8$ may be evidence for coordinated ether O atoms.[17]

### Ligand-Centred Photophysical Properties

The absorption spectrum of $B_8bL^8$ in methanol at 293 K (Figure 7) displays a broad band with a maximum at

 © 2007 Wiley-VCH Verlag GmbH & Co. KGaA, Weinheim 

43500 $cm^{-1}$ (230 nm, $\varepsilon$ = 8995 $M^{-1}cm^{-1}$), assigned to a transition mainly involving orbitals located on the phosphinoyl groups, and a less intense and split band at 37170 and 36230 $cm^{-1}$ (276 and 279 nm, $\varepsilon$ = 2910 and 2720 $M^{-1}cm^{-1}$) for transitions mainly located on the phenyl rings. These absorption bands are not affected by the complexation. Finally, a very weak band is observed around 27600 $cm^{-1}$ (360 nm, $\varepsilon$ = 110 $M^{-1}cm^{-1}$), which sustains a large bathochromic shift (≈ 3500 $cm^{-1}$) upon complexation to $Ln^{III}$. Because the energy of this band is independent of the lanthanide ion, it can be assigned to a transition connected with an intraligand charge transfer (ILCT) state. The latter is seen at 27000 $cm^{-1}$ in the excitation spectrum of a powdered sample of $B_8bL^8$ at 293 K, in addition to a band centred at 32800 $cm^{-1}$ and attributed to the $^1\pi\pi^*$ level (Figure S8, Supporting Information). The redshift of the ILCT band in the absorption spectra of solutions containing $B_8bL^8$ and one equivalent of lanthanide salt confirms the complex formation.[40] A similar weak ILCT band was reported at 27030 $cm^{-1}$ in the excitation spectrum of europium benzoate.[41] Moreover, it is known that ILCT energy depends on the position of the carboxylate group in heterocyclic pyridine–carboxylic ligands containing nonbonding electron pairs.[42] According to these data, the large intensity of the ILCT band in complexes with $B_8bL^8$, as well as its strong redshift upon complexation, are typical of a charge transfer from the phenol ring to the oxygen atom of the phosphinoyl groups. Because the ILCT band of the complexes lies at lower energy and is more intense than the corresponding band for the uncoordinated ligand, the transition dipole moment is larger for the complexes.[43]

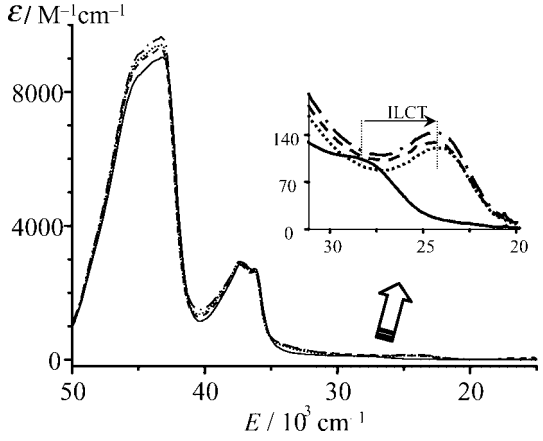


Figure 7. Absorption spectra of $B_8bL^8$ (1.7 × $10^{-4}$ M) in MeOH at 293 K (black curves) with 1 equiv. of $Lu(OTf)_3$ (dot), $Eu(OTf)_3$ (dash) and 2 equiv. of $Eu(OTf)_3$ (dash-dot). The inset zooms on the intraligand charge transfer absorption.

According to emission spectra at 77 K, the $^1\pi\pi^*$ state of a powdered sample of the octameric ligand is located at 32800 $cm^{-1}$. The singlet state energy is not affected by the complexation in the $Lu^{III}$ 1:1 complex but sustains a slight blueshift in the 2:1 complex (+320 $cm^{-1}$). The triplet state emission occurs at 23600 $cm^{-1}$ for $B_8bL^8$ and is only seen for the $Lu^{III}$ complexes, for which it is blueshifted by +400 and +130 $cm^{-1}$ for the 1:1 and 2:1 complexes, respectively. It displays a fine structure with vibronic progressions of ≈ 1470 $cm^{-1}$ (1:1) and 1280 $cm^{-1}$ (2:1) which can be attributed to the vibrational mode of the phenol moieties and nitrate groups, respectively (Figure S9, Supporting Information). The luminescence decay associated with the $^3\pi\pi^*$ state of $B_8bL^8$ is a single exponential function corresponding to a lifetime of 2.61 ms which increases to 3.5–3.6 ms upon complexation. The energy gap $\Delta E(^3\pi\pi^* - {}^1\pi\pi^*)$ amounts to ≈ 8450 and 9150 $cm^{-1}$ (0-phonon transitions) for the investigated 1:1 and 2:1 lutetium complexes, respectively, which is not quite optimum for an efficient ISC.[44] The $^3\pi\pi^*$-to-metal energy transfer efficiency also depends on the energy gap between the feeding triplet state and the accepting $Ln^{III}$ levels. In our case, it appears to be adequate for $Tb^{III}$, with $\Delta E(^3\pi\pi^* - {}^5D_4)$ ≈ 3600–3800 $cm^{-1}$, but somewhat less well-suited for $Eu^{III}$, with $\Delta E(^3\pi\pi^* - {}^5D_0)$ ≈ 6800–7000 $cm^{-1}$.

The excitation spectra of the luminescent lanthanide complexes contain typical broad bands arising from ligand levels, which confirm the energy transfer from coordinated $B_8bL^8$ to $Ln^{III}$, and narrow and characteristic lines from the metal ions. Comparison of the excitation spectra of the 1:1 europium and terbium complexes at 77 K reveals an additional intense broad band centred at 24200 $cm^{-1}$ and expanding to 21400 $cm^{-1}$ in the spectrum of the former, which is assigned to a ligand-to-metal charge transfer (LMCT) band (Figure 8). The strong intensity of this LMCT band is uncommon and could be produced by intensity stealing as the LMCT and ILCT states overlap. A weak band assigned to the LMCT state was also found in the excitation spectrum of the $Eu^{III}$ 2:1 complex with a low-energy edge at 21800 $cm^{-1}$ at 77 K (Figure S10, Supporting Information). The broad band observed in the range 26000 to 28000 $cm^{-1}$ for the 2:1 $Tb^{III}$ complex is assigned to an f–d transition. The optical electronegativity[45] of the ligand in the $Eu^{III}$ 1:1 and 2:1 complexes can be calculated from the energy of the LMCT band and amounts to $\chi_L$ = 2.80 and 2.78, respectively. The slightly smaller $\chi_L$ value for the 2:1 complex is caused by the presence of coordinated nitrate groups. It has indeed been found for mixed-ligand complexes that ligands with high optical electronegativity

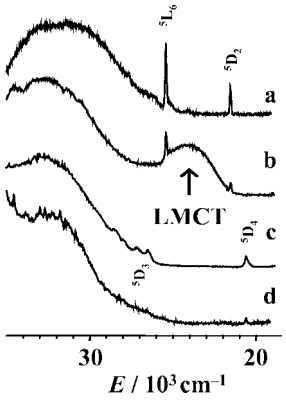


Figure 8. Normalized excitation spectra of the 1:1 powdered complexes with $Eu^{III}$ (a, b) and $Tb^{III}$ (c, d) at 293 K (a, c) and 77 K (b, d). Analysing wavelength set at 612 ($Eu^{III}$) and 545 ($Tb^{III}$) nm, respectively.

 © 2007 Wiley-VCH Verlag GmbH & Co. KGaA, Weinheim 

weaken the metal–ligand interaction of the other ligands with lower $\chi_L$ values.[46,47] Therefore, when nitrate, with high optical electronegativity and low polarizability, is coordinated in the 2:1 $Eu^{III}$ complex, the interaction between the metal ion and the calixarene is weakened, henceforth the smaller intensity of the LMCT band. In absence of nitrate, which is the case for the 1:1 complex, the Eu–$B_8bL^8$ interaction is larger, which leads to a mixing between the ILCT and LMCT states and a concomitant reduction in the efficiency of the excitation of $Eu^{III}$ by the ligand states. Finally, by using the $\chi_L$ values found for $B_8bL^8$, the energy of the LMCT state in the terbium complexes can be estimated to be larger than 51000 $cm^{-1}$.

### Metal-Centred Photophysical Properties in the Solid State

The $^5D_0 \rightarrow {}^7F_J$ transitions of the 1:1 and 2:1 europium complexes recorded at 77 K under broad band excitation display a maximum number of Stark components, which points to low site symmetry (Figure 9; see listing of crystal-field splitting in Table S3, Supporting Information). The integrated intensities of the $^5D_0 \rightarrow {}^7F_J$ transitions relative to $^5D_0 \rightarrow {}^7F_1$, 0.06, 2.28, 0.14 (1:1 complex) and 0.09, 2.55, 0.34 (2:1 complex) for $J$ = 0, 2, 4, respectively, are similar for the two types of complexes.

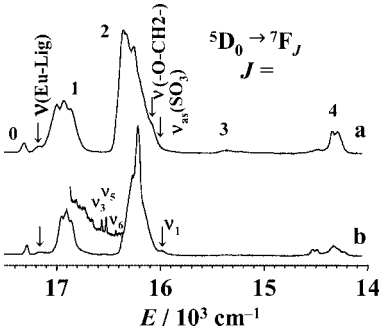


Figure 9. Luminescence spectra of 1:1 (a) and 2:1 (b) europium complexes at 77 K.

Data relevant to the 2:1 complex will first be discussed. The excitation profile of the $^5D_0 \leftarrow {}^7F_0$ transition obtained upon monitoring the $^5D_0 \rightarrow {}^7F_2$ transition (Figure S11, Supporting Information) is symmetric, narrow (full width at half height, fwhh = 7.6 $cm^{-1}$), and occurs at 17254 $cm^{-1}$ at room temperature and at 17242 $cm^{-1}$ at 10 K. This points to a very similar chemical environment for the two $Eu^{III}$ ions, a fact which is further ascertained by the identical emission spectra obtained upon selective laser excitation through the 0–0 band profile (Figure S12, Supporting Information). Moreover, emission from the Eu($^5D_1$) level could also be obtained at 10 K, which is typical of nitrato complexes (Figure S13, Supporting Information). A number of vibronic satellites related to ligand vibrations and associated with the $^5D_0 \rightarrow {}^7F_J$ ($J$ = 0, 1, and 2) transitions are observed in both excitation and emission spectra. At 10 K, we denote the following satellites (see Figure 9): (1) $\nu$(Eu–Lig) with frequencies 195 and 405 $cm^{-1}$ in the range 17400 to 16850 $cm^{-1}$, (2) $\nu_5(NO_3^-)$, $\nu_3(NO_3^-)$ and $\nu_6(NO_3^-)$ around ca. 705, 740 and 820 $cm^{-1}$, respectively, in the range 16420 to 16530 $cm^{-1}$, (3) vibronic repetition of the $^5D_0 \rightarrow {}^7F_1$ transition with frequency 195 $cm^{-1}$ in the range 16800 to 16450 $cm^{-1}$, (4) two stretching vibrations $\nu_1(NO_3^-)$ with frequencies 1280 and 1315 $cm^{-1}$ attributed to nonequivalent nitrates, in the range 15960 to 15930 $cm^{-1}$. In the excitation spectrum, vibronic sidebands appear on the $^5D_2 \leftarrow {}^7F_0$ transition with frequencies 200 (Ln–Lig), 670 ($\delta_{ring}$), 940 (out-of-plane C–H rocking mode), 1020 [$\nu$(–O–$CH_2$–)], 1120 [$\nu$(P=O)] and 1480 $cm^{-1}$ ($\nu_{ring}$). These data confirm the coordination of the P=O groups, which is in line with ES-MS, NMR, and IR data; they also indicate the presence of different types of coordinated nitrate groups. Furthermore, the luminescence decays of the Eu($^5D_0$) and Tb($^5D_4$) levels are single exponential functions (Table 4). They are long enough to ascertain the absence of water molecules in the inner coordination sphere of the lanthanide ion, the latter is protected from such an interaction by the coordination of nitrate ions. The lifetimes vary only slightly with temperature, which points to a small influence of temperature-dependent nonradiative deactivation processes.

Table 4. Lifetimes (ms) of the metal-centred luminescence upon ligand excitation of powdered samples of $Eu^{III}$ and $Tb^{III}$ 1:1 and 2:1 complexes with $B_8bL^8$ in the solid state (ss) and of a $2 \times 10^{-3}$ M solutions (sol) in methanol ($\nu_{exc}$ = 37040 $cm^{-1}$). Standard deviations are given in parentheses.

| T/K | Sample | Eu 1:1 (OTf) | Eu 1:1 ($NO_3$) | Eu 2:1 ($NO_3$) | Tb 1:1 (OTf) | Tb 1:1 ($NO_3$) | Tb 2:1 ($NO_3$) |
|---|---|---|---|---|---|---|---|
| 10 | ss | 1.27(1), 72% 0.39(1), 38% | | 1.62(3) | – | | – |
| 77 | ss | 1.18(4) | | 1.38(2) | 1.35(2) | | 1.93(4) |
| | sol | 1.11(1), 62% 0.5(3), 38% | 1.28(4) | | 1.72(2) | 1.72(2) | |
| 295 | ss | 1.09(2) 53% 0.22(3), 47% | | 1.29(1) | 1.59(1) | | 1.66(3) |
| | sol | 0.93(2), 58% 0.30(2), 42% | 1.10(2) | | 1.52(3) | 1.66(3) | |

Relative to the 2:1 complex, the $^5D_0 \leftarrow {}^7F_0$ transition of the 1:1 species is broader (fwhh ≈ 38 $cm^{-1}$) and weaker. It has a maximum around 17280 $cm^{-1}$ at 293 K and features at least three distinct components separated by about 20 $cm^{-1}$. Such large energy differences point to the presence of differently coordinated europium ions. The analysis could not, however, be pursued further; the very small intensity of the 0–0 transition prevented the selective laser excitation of the various components. Luminescence lifetime data (Table 4) shed more light on the potential $Eu^{III}$ species present in the complex. While data recorded under low resolution reflect one averaged lifetime for both $Eu^{III}$ and $Tb^{III}$, high-resolution conditions used for $Eu^{III}$ led to double exponential functions. The longer lifetime, which contributes 60–70% to the decay, corresponds to an $Eu^{III}$ environment devoid of O–H vibrations, whereas the shorter lifetime corresponds to a metal ion bound to water molecules. Assuming that the extra quenching corresponding to the shorter lifetime

 © 2007 Wiley-VCH Verlag GmbH & Co. KGaA, Weinheim 

only arises from coordinated water molecules, which is reasonable in view of the elemental analysis, an average hydration number $q \approx 2$ can be estimated. As a result, interpretation of both the $^5D_0 \leftarrow ^7F_0$ excitation profile and the lifetime data leads to postulate that two of the three coordination environments have the same hydration number $q \approx 2$, whereas the third environment has $q \approx 0$. This model is feasible in view of the large conformational mobility of the macrocycle and interaction with triflate anions, as shown below. Vibration satellites are also found in the luminescence spectrum of the $Eu^{III}$ 1:1 complex at 10 K: (1) $\nu$(Eu–Lig) with frequencies 107 and 195 $cm^{-1}$ in the range 17160 to 17070 $cm^{-1}$, (2) $\nu_{as}(SO_3)$ and $\nu_s(CF_3)$ vibrations with frequencies 1260 and 1180 $cm^{-1}$, respectively (16000–16090 $cm^{-1}$), (3) a line with frequency 1025 $cm^{-1}$ (16240–16040 $cm^{-1}$) which is a superposition of $\nu_{as}(SO_3)$ and $\nu$(C–O–$CH_2$–) vibrational modes. The appearance of vibronic satellites corresponding to triflate vibrations ascertains coordination to the europium ion. The presence of two lower frequency $\nu$(Eu–Lig) satellites is in line with the biexponential lifetime obtained and confirms the presence of at least two different chemical environments for $Eu^{III}$. Moreover, lines with frequencies 200 (Eu–Lig), 638 ($OTf^-$), 765 (out-of-plane C–H twist) and 1140 $cm^{-1}$ [$\nu$(P=O)] appear in the excitation spectrum at 77 K as vibronic sidebands of the $^5D_2 \leftarrow ^7F_0$ transition. The presence of the second and fourth lines points to the simultaneous coordination of triflate and phosphinoyl arms of the calixarene. The comparatively large intensity of the vibronic sidebands of the $^5D_0 \rightarrow ^7F_2$ electronic transition in both 1:1 and 2:1 complexes is caused by a resonant vibronic effect in which intensity is borrowed from neighbouring electronic transitions.[48] The intensity of the vibronic interaction is slightly higher in the 1:1 complex, which is judged from the integral intensity of the $^5D_0 \rightarrow ^7F_2$ vibronic sidebands normalized to the intensity of the Stark components of this transition. This observation is in agreement with the presence of a LMCT state in the latter complex and with all the previously discussed data regarding the coordination mode of $B_8bL^8$ in 1:1 complexes.

### Metal-Centred Photophysical Properties in Solution

The luminescence decay of an equimolar solution of europium triflate and $B_8bL^8$ in methanol is biexponential with lifetimes similar to those determined for the powdered 1:1 sample (Table 4). In addition, the emission spectra of these two samples are very alike (Figure S14, Supporting Information). This is in line with NMR and MS data and points to a solution structure of the complex similar to the solid state one. In contrast, a single exponential decay with a lifetime slightly shorter than the one for the powdered 2:1 sample is observed for the equimolar solution of europium nitrate and $B_8bL^8$. The emission spectra of this solution and of a powdered 2:1 sample are quite different: (1) the frequency of the $\nu$(Eu–Lig) vibronic satellite is $\approx 10$ $cm^{-1}$ larger in solution, (2) the Stark components of the hypersensitive $^5D_0 \rightarrow ^7F_2$ transition are very different and (3) the relative intensity of the $^5D_0 \rightarrow ^7F_0$ transition is larger in solution. These data could be explained by a transformation of the 1:1 complex into a 2:1 species upon crystallization, as observed with other calix[8]arenes,[22] whereas an inverse 2:1→1:1 transformation occurs upon dissolution.

The absolute quantum yield of the metal-centred luminescence upon ligand excitation for $B_8L^8$ solutions containing one equivalent of $Eu(OTf)_3$ or $Tb(OTf)_3$ in methanol at 293 K is equal to 0.23 and 0.70%, respectively. These low values could be caused by high-energy vibration quenching in addition to a relatively inefficient intersystem crossing process. The quantum yields are somewhat smaller for the solutions containing nitrate, 0.18% (Eu) and 0.53% (Tb). It is worth noting that the powdered 2:1 europium complex has a much higher luminescence intensity than the 1:1 complex.

## Conclusions

The results reported here allow us to discuss the influence of the calixarene size on the complexation properties toward lanthanide ions. The smallest calix[4]arene analogue, $B_4bL^4$, exists in the cone conformation in organic solution and forms stable 1:1 and 1:2 complexes with $Ln^{III}$ ions ($\log\beta_1 \approx 11$ and $\log\beta_2 \approx 20$ in acetonitrile).[17] When the size is increased to yield $B_6bL^6$, the larger flexibility of the macrocyclic host is reflected in an alternate *in–out* conformation, but complexes with the same stoichiometry form, with similar stability ($\log\beta_1 \approx 10$ and $\log\beta_2 \approx 20$ in acetonitrile).[19] With the larger octamer $B_8bL^8$, the major species that forms in methanol (solubility problems prevented the study in acetonitrile) has a 1:1 stoichiometry, whereas the 1:2 species is hardly detected; a minor 2:1 species also forms and can be isolated in the solid state. Observation of the latter species is consistent with the bimetallic complexes usually isolated with calix[8]arenes but only in the presence of a nitrate counterion because of its bidentate chelating mode. However, the strong coordination ability of the phosphinoyl groups toward lanthanide ions tends to equalize the ligand–$Ln^{III}$ interaction in the 1:1 species with the three receptors ($\log K_{11} \approx 7$ in methanol for $B_8bL^8$ compares favourably with $\log\beta_1 \approx 10$ in acetonitrile for the other macrocycles). With respect to the complexes with $B_6bL^6$, the photophysical properties appear to be less interesting, but they were recorded in a more polar solvent, methanol versus acetonitrile, which prevents strict comparison. However, they are better than with the smallest macrocyclic host, $B_4bL^4$, at least as far as $Eu^{III}$ is concerned. In addition, a correlation was observed between the optical electronegativities of the ligands and the luminescence efficiency, in relationship with the energy of the LMCT states in lanthanide complexes with the investigated calix[8]arene. The coordination ability and optical electronegativity of the counterion used can be considered as an instrument for assembling lanthanide complexes with a predetermined structure. This opens perspectives for the molecular design of new luminescent lanthanide systems with inequivalent ligands. With these

 © 2007 Wiley-VCH Verlag GmbH & Co. KGaA, Weinheim 

data at hand, we are now testing the extraction and separation capabilities of the three calixarene receptors towards both lanthanide and actinide cations.[20]

## Experimental Section

**Starting Materials and General Procedures:** All reagents and solvents were of analytical grade and were used without further purification. Chloro(dimethylphosphinoyl)methane was purchased from Hoechst AG (Germany). Stock solutions of lanthanides were made in freshly boiled, doubly distilled water from the corresponding nitrates and triflates, $Ln(NO_3)_3{\cdot}xH_2O$ ($x$ = 3, 4) and $Ln(OTf)_3{\cdot}xH_2O$ (Ln = La, Eu, Tb, Lu; $x$ = 6–10), prepared from their oxides (Rhône–Poulenc, 99.99%) in the usual way.[49] Concentrations of the solutions were determined by complexometric titrations using a standardized $Na_2H_2EDTA$ solution in urotropine buffered medium and with xylenol orange as indicator.[50] Elemental analyses were performed by the Ilse Beetz Laboratory (96301 Kronach, Germany). ESMS spectra were measured with a Finnigan SSQ 710C spectrometer by using a capillary temperature of 200 °C and acceleration potential of 4.5 kV; $10^{-5}$–$10^{-4}$ M solutions of the free ligand or its complexes dissolved in methanol were infused in a mixture of $CH_3CN/H_2O/HCOOH$ (50:50:1) for the ligand, or pure $CH_3OH$ for the complexes. High resolution MS (FAB) spectra were recorded with an FTMS 4.7T BioApex II spectrometer from Bruker by the MS-Service unit of the University of Fribourg (Switzerland).

**5,11,16,23,29,35,41,47-Octa-*tert*-butyl-49,50,51,52,53,54,55,56-octakis(dimethylphosphinoylmethyleneoxy)calix[8]arene ($B_8bL^8$):** A warm solution of chloro(dimethylphosphinoyl)methane (9.24 g, 73.05 mmol) in xylene (20 mL) was added to fine suspension of octasodium derivative of *p*-*tert*-butylcalix[8]arene in refluxing xylene. The latter was prepared by the addition of Na (0.64 g, 27.89 mmol) to a mixture of *p*-*tert*-butylcalix[8]arene (2.26 g, 1.74 mmol), MeOH (70 mL) and xylene (200 mL), followed by distillation of MeOH and part of the xylene. The resulting mixture was heated at reflux and stirred under an atmosphere of nitrogen for 97 h. After cooling to 50–60 °C, the mother liquor was separated by centrifugation, and the precipitate was washed with warm (40–50 °C) xylene (5 × 25 mL) and dichloromethane (150 mL, stirring at room temp. for 2 h). After filtration, the white solid residue (3.73 g) was washed with distilled water (8 × 60 mL), separated by centrifugation and redissolved in MeOH (200 mL). Concentrated HCl (2 mL) was added, the transparent colourless methanol solution was filtered and methanol was evaporated. The residue was washed with water (7 × 80 mL), dried and recrystallised from DMF to give a white solid (1.74 g, 49.5%). $B_8bL^8$ does not melt until 300 °C and is soluble at room temp. in MeOH, EtOH, 2-propanol and chloroform and sparingly soluble at elevated temperatures in DMSO, DMF and acetonitrile; $B_8bL^8$ is insoluble in water, aromatic and aliphatic hydrocarbons (heptane, toluene, xylene), acetone, diethyl ether, THF, acetic acid and diisopropyl ether. It can be recrystallised from DMF, DMSO, and acetonitrile. $^1$H NMR (400 MHz, [D$_6$]DMSO): $\delta$ = 6.98 (s, 16 H, Ar-H), 4.04 (s, 16 H, Ar-$CH_2$-Ar), 3.97 (s, 16 H, $CH_2$P=O), 1.36 [d, $^2J_{HP}$ = 9.2 Hz, 48 H, $(CH_3)_2$PO], 1.04 (s, 72 H, C$(CH_3)_3$]) ppm. $^1$H NMR (400 MHz, $CD_3OD$, 293 K): $\delta$ = 7.07 (s, 16 H, Ar-H), 4.16 (s, 16 H, Ar-$CH_2$-Ar), 4.15 (d, $^2J_{HH}$ = 5.64 Hz, 16 H, $CH_2$P=O), 1.59 [d, $^2J_{HP}$ = 13.32 Hz, 48 H, $(CH_3)_2$P=O], 1.13 (s, 72 H, C$(CH_3)_3$]) ppm. $^{31}$P{$^1$H} NMR (161.9 MHz, [D$_6$]DMSO): $\delta$ = 39.8 ppm. $^{13}$C NMR (100.6 MHz, $CDCl_3$): $\delta$ = 153.2 (d, $^3J_{CP}$ = 11.3 Hz, Ar-*i*), 147.6(s, Ar-*o*), 132.0 (s, Ar-*m*), 126.7 (s, Ar-*p*), 71.5 (d, $J_{CP}$ = 80 Hz, $CH_2$P=O), 34.7(s, tert. C), 31.8 ($CH_3$-*tert*), 29.9 (s, Ar-$CH_2$-Ar), 14.9 (d, $J_{CP}$ = 68.3 Hz, $CH_3$P=O) ppm. IR (KBr disk): $\tilde{\nu}$ = 1171 (P=O) cm$^{-1}$. ESMS: $m/z$ = 1009.98 [$B_8bL^8$ + 2H]$^{2+}$, 2018.35 [$B_8bL^8$ + H]$^{1+}$, 2040.95 [$B_8bL^8$ + Na]$^{1+}$. IR: $\tilde{\nu}$ = 1160 and 1173 (P=O) cm$^{-1}$ (before and after heating for 20 h at 413 K). Raman: $\nu_{ring}$ 1592, 1112 cm$^{-1}$; breathing mode of phenol ring 1008 cm$^{-1}$ for $B_8bL^8{\cdot}5H_2O$. $C_{112}H_{184}O_{24}P_8$ (= $B_8bL^8{\cdot}8H_2O$) (2162.44): calcd. C 62.21, H 8.58, P 11.46; found C 62.34, H 8.99, P 11.42.

**1:1 Complexes:** A methanolic solution (3 mL) of $B_8bL^8$ (0.0215 g, 0.0102 mmol) was heated at 60 °C and a solution of $Ln(OTf)_3{\cdot}xH_2O$ (Ln = La, $x$ = 10; Eu, $x$ = 7; Tb, $x$ = 6; Lu, $x$ = 9; 0.0106 g, 0.0142 mmol for Eu) in MeOH (1.75 mL) was slowly added. A precipitate appeared, and the mixture was stirred for 2 h under an atmosphere of nitrogen at 60 °C. The precipitate was centrifuged, washed repeatedly with MeOH and dried for 48 h at 60 °C and $10^{-2}$ Torr. All compounds are extremely hygroscopic yellow powders. Yields: 62 (La), 58 (Eu), 44 (Tb) and 72% (Lu). $Eu(B_8bL^8)(OTf)_3{\cdot}13H_2O$ (2851.72): calcd. C 48.44, H 6.86, O 21.32, P 8.69, S 3.37; found C 47.43, H 6.26, O 26.15, P 9.02, S 3.51. Formulae of the other complexes were established by $^1$H and $^{31}$P{$^1$H} NMR spectroscopy. HRMS (FAB): $m/z$ = 723.20 [$Eu(B_8bL^8)$]$^{3+}$, 730.99 [$Lu(B_8bL^8)$]$^{3+}$, experimental isotopic distribution patterns matched the calculated ones (Figure S5, Supporting Information). IR: $\tilde{\nu}$ = 1130 (P=O), shift 7, 2, 3 and 9 cm$^{-1}$ for La, Eu, Tb, and Lu, respectively; 635 cm$^{-1}$ ($OTf^-$), shift 1, 2, 1 and 2 for La, Eu, Tb, and Lu, respectively. Raman: $\nu_{ring}$ 1592, 1112 cm$^{-1}$; breathing mode of phenol ring 1012, 1028 cm$^{-1}$ for $Tb(B_8bL^8)$ $(OTf)_3{\cdot}13H_2O$.

**2:1 Complexes:** A MeOH solution (4 mL) of $B_8bL^8$ (0.0226 g; 0.0107 mmol) was heated at 60 °C, and a solution of $Ln(NO_3)_3{\cdot}xH_2O$ (0.0912 g; 0.0222 mmol for Eu; Ln = La, $x$ = 4; Eu, $x$ = 4; Tb, Lu, $x$ = 3) in MeOH (1.4 mL) was added dropwise. A precipitate appeared, and the mixture was stirred for 4 h under an atmosphere of nitrogen at 60 °C. The precipitate was centrifuged, washed with MeOH (2×6 mL) and dried for 48 h at 60 °C and $10^{-2}$ Torr. All the compounds appeared as white hygroscopic powders. Yields: 58 (La), 52 (Eu), 48 (Tb) and 64% (Lu). $Eu_2(B_8bL^8)(NO_3)_6{\cdot}H_2O$ (2712.32): calcd. C 49.60, H 6.32, O 20.62, P 9.13, N 3.10; found C 51.52, H 6.35, O 15.30, P 9.38, N 2.18. Formulae of the other complexes were established by $^1$H and $^{31}$P{$^1$H} NMR experiments. HRMS (FAB): $m/z$ = 723.28 [$Eu(B_8bL^8)$]$^{3+}$, 725.99 [$Tb(B_8bL^8)$]$^{3+}$, experimental isotopic distribution patterns matched the calculated ones. IR: $\tilde{\nu}$ = 1115 (P=O), shift 3, 5 and 10 cm$^{-1}$ for Eu, Tb and Lu, respectively; 735 ($NO_3^-$), shift 3, 5 and 8 cm$^{-1}$ for Eu, Tb and Lu. Raman: $\nu_{ring}$ 1592, 1112 cm$^{-1}$; breathing mode of phenol ring 1036 cm$^{-1}$ for $Lu_2(B_8bL^8)$ $(NO_3)_6{\cdot}H_2O$.

**Analytical and Physicochemical Measurements:** UV/Vis absorption spectra were measured with a Perkin–Elmer Lambda 900 spectrometer with the use of quartz Suprasil® cells of 0.2- and 1-cm path length. Reflectance IR spectra were obtained from powdered samples with a Perkin–Elmer Spectrum One FTIR spectrometer. FIR spectra were recorded with an IFS 13v FTIR spectrometer from Bruker equipped with a pyroelectric DTGS detector. Raman spectra were obtained by means of a Spex 1403 spectrometer with RCA photomultiplier and an argon laser Stabilite 2017 from Spectra-Physics. 1D $^1$H and $^{31}$P{$^1$H} NMR experiments as well as 2D DQF-COSY and ROESY experiments were performed with a Bruker Avance DRX 400 spectrometer. Chemical shifts are given in ppm relative to TMS. All spectra were recorded in $CD_3OD$ (99.9%, Aldrich). Spectrophotometric titrations were performed on a J&M diode-array spectrometer (Tidas series) connected to an external computer in a thermostatted (25.0 ± 0.1 °C) glass-jacketed vessel

 © 2007 Wiley-VCH Verlag GmbH & Co. KGaA, Weinheim 

with quartz cells of 0.100 cm path length. In a typical experiment, $B_8bL^8$ ($10^{-4}$ M; 12 mL) was titrated with solutions of the $Ln^{III}$ salt ($10^{-3}$ M); the titrant (0.1 mL) was added by means of a Socorex® micropipette, and spectra were measured after 5 min to equilibrate the solution. The solvent used (MeOH) was of spectroscopic grade (Fluka AG, Buchs, Switzerland). Factor analysis[51] and mathematical treatment of the spectrophotometric data were performed with the SPECFIT[52,53] program.

Low-resolution luminescence measurements (spectra and lifetimes) were recorded with a Fluorolog FL 3–22 spectrometer from Spex-Jobin–Yvon-Horiba at 293 and 77 K and corrected for the instrumental function. Emission and excitation spectra of solutions were measured in 1-cm path length quartz Suprasil cell. The temperature was kept constant by using a FL-1027 thermostatted cell holder connected to a water bath. Phosphorescence lifetimes ($\tau$, averages of at least three measurements) were measured by using a quartz capillary, monitoring the maxima of the emission spectra, and enforcing a 0.05 ms delay. The decays were analysed with Origin 7.0. Quantum yields of $Eu^{III}$- and $Tb^{III}$-centred luminescence were determined relative to those of the corresponding tris(dipicolinates) in 0.2-cm Quartz Suprasil cells.[54] The refractive indices were 1.333 for solutions in water and 1.3288 for solutions in MeOH, $\lambda_{exc}$ = 279 (ref. $A$ = 0.1938) and 276 (sample, $A$ = 0.1911) nm; a filter (320 nm) was inserted to eliminate Raleigh diffusion and second order spectra. High resolution laser-excited luminescence spectra and lifetimes were measured by using published procedures.[55]

**Supporting Information** (see footnote on the first page of this article): Additional tables of the MS spectrum analysis of $B_8bL^8$ containing different equivalents of $Eu(OTf)_3{\cdot}7H_2O$ or $Eu(NO_3)_3{\cdot}4H_2O$, $^1H$, DQF-COSY and ROESY NMR spectroscopic data of the Lu complexes and their HRMS (FAB) spectra. IR and luminescence data of the europium complexes.

## Acknowledgments

This work is supported by the Swiss Federal Office for Research (COST Action D18, contract C00.0030/506 250). We thank Daniel Baumann for the FIR and Raman spectra and Frédéric Gumy for his help in acquiring the photophysical data.

[1] Z. Asfari, V. Böhmer, J. M. Harrowfield, J. Vicens, *Calixarenes* (Eds.: Z.Asfari, V.Böhmer, J. M.Harrowfield, J.Vicens), Kluwer Academic Publishers, Dordrecht, **2001**.
[2] G. J. Lumetta, R. D. Rogers, A. Gopalan (Eds.) *Calixarenes for Separations*, ACS Symposium Series, American Chemical Society, Washington D. C., **2000**, vol. 757.
[3] F. Sansone, M. Fontanella, A. Casnati, R. Ungaro, V. Böhmer, M. Saadioui, K. Liger, J. F. Dozol, *Tetrahedron* **2006**, *62*, 6749–6753.
[4] F. Arnaud-Neu, J. K. Browne, D. Byrne, D. J. Marrs, M. A. McKervey, P. O'Hagan, M.-J. Schwing-Weill, A. Walker, *Chem. Eur. J.* **1999**, *5*, 175–186.
[5] C. D. Gutsche, *Calixarenes Revisited: Monographs in Supramolecular Chemistry*, (Ed.: J. F.Stoddart), The Royal Society of Chemistry, Cambridge, **1998**.
[6] P. D. Beer, J. Cadman, *Coord. Chem. Rev.* **2000**, *205*, 131–155.
[7] J. L. Atwood, L. J. Barbour, M. J. Hardie, C. L. Raston, *Coord. Chem. Rev.* **2001**, *222*, 3–32.
[8] C. B. Smith, L. J. Barbour, M. Makha, C. L. Raston, A. N. Sobolev, *Chem. Commun.* **2006**, 950–952.
[9] S. E. Matthews, P. Schmitt, V. Felix, M. G. B. Drew, P. D. Beer, *J. Am. Chem. Soc.* **2002**, *124*, 1341–1353.
[10] D. R. Stewart, C. D. Gutsche, *J. Am. Chem. Soc.* **1999**, *121*, 4136–4146.
[11] F. Cunsolo, G. M. L. Consoli, M. Piattelli, P. Neri, *Tetrahedron Lett.* **1996**, *37*, 715–718.
[12] T. Kajiwara, K. Katagiri, M. Hasegawa, A. Ishii, M. Ferbinteanu, S. Takaishi, T. Ito, M. Yamashita, N. Iki, *Inorg. Chem.* **2006**, *45*, 4880–4882.
[13] J.-C. G. Bünzli, F. Besançon, F. Ihringer in *Calixarenes for Separations* (Eds.: G. J. Lumetta, R. D. Rogers, A. Gopalan), American Chemical Society, Washington D. C., **2000**, vol. 757, ch. 14, pp. 179–194, and references therein.
[14] C. B. Dieleman, C. Loeber, D. Matt, A. De Cian, J. Fischer, *J. Chem. Soc., Dalton Trans.* **1995**, 3097–3100.
[15] C. B. Dieleman, D. Matt, P. G. Jones, *J. Organomet. Chem.* **1997**, *546*, 461–473.
[16] M. R. Yaftian, M. Burgard, D. Matt, C. Wieser-Jeunesse, C. B. Dieleman, *J. Incl. Phenom. Mol. Recognit. Chem.* **1997**, *27*, 127–140.
[17] L. Le Saulnier, S. Varbanov, R. Scopelliti, M. Elhabiri, J.-C. G. Bünzli, *J. Chem. Soc., Dalton Trans.* **1999**, 3919–3925.
[18] V. Videva, A.-S. Chauvin, S. Varbanov, C. Baux, R. Scopelliti, M. Mitewa, J.-C. G. Bünzli, *Eur. J. Inorg. Chem.* **2004**, 2173–2179.
[19] F. d. M. Ramirez, S. Varbanov, C. Cécile, G. Muller, N. Fatin-Rouge, R. Scopelliti, J.-C. G. Bünzli, *J. Chem. Soc., Dalton Trans.* **2002**, 4505–4513.
[20] F. d. M.Ramirez, S.Varbanov, J. P.Padilla, J.-C. G.Bünzli, unpublished work, **2006**.
[21] P. Neri, G. M. L. Consoli, F. Cunsolo, C. Geraci, M. Piattelli, *New J. Chem.* **1996**, *20*, 433–446.
[22] J.-C. G. Bünzli, F. Besançon, *Phys. Chem. Chem. Phys.* **2005**, *7*, 2191–2198, and references therein.
[23] J. M. Harrowfield, M. I. Ogden, A. H. White, *Aust. J. Chem.* **1991**, *44*, 1249–1262.
[24] J. M. Harrowfield, M. I. Ogden, W. R. Richmond, A. H. White, *J. Chem. Soc., Dalton Trans.* **1991**, 2153–2160.
[25] J.-C. G. Bünzli, F. Ihringer, *Inorg. Chim. Acta* **1996**, *246*, 195–205.
[26] J.-C. G. Bünzli, F. Ihringer, P. Dumy, C. Sager, R. D. Rogers, *J. Chem. Soc., Dalton Trans.* **1998**, 497–504.
[27] A. Casnati, S. Barboso, H. Rouquette, M. J. Schwing-Weill, F. Arnaud-Neu, J. F. Dozol, R. Ungaro, *J. Am. Chem. Soc.* **2001**, *123*, 12182–12190.
[28] M. M. Mark, C. H. Dungan, M. M. Grutchfield, J. R. van Wazer in *Topics in Phosphorous Chemistry, Compilation of $^{31}P$ NMR Data* (Eds.: M. Grayson, E. J. Griffith), John Wiley & Sons, New York, **1967**, vol. 5, pp. 227–475.
[29] C. Wieser-Jeunesse, D. Matt, M. R. Yaftian, M. Burgard, J. M. Harrowfield, *C. R. Acad. Sci. Paris, Ser. IIc* **1998**, *1*, 479–502.
[30] S. Kanamathareddy, C. D. Gutsche, *J. Org. Chem.* **1994**, *59*, 3871–3879.
[31] C. Jaime, J. de Mendoza, P. Prados, P. M. Nieto, C. Sanchez, *J. Org. Chem.* **1991**, *56*, 3372–3376.
[32] C. D. Gutsche, B. Dhawan, J. A. Levine, K. Hyun No, L. J. Bauer, *Tetrahedron* **1983**, *39*, 409–426.
[33] R. G. Janssen, J. P. M. Vanduynhoven, W. Verboom, G. J. vanhummel, S. Harkema, D. N. Reinhoudt, *J. Am. Chem. Soc.* **1996**, *118*, 3666–3675.
[34] H. Otsuka, K. Araki, T. Sakaki, K. Nakashima, S. Shinkai, *Tetrahedron Lett.* **1993**, *34*, 7275–7278.
[35] J. P. M. van Duynhoven, R. G. Janssen, W. Verboom, S. M. Franken, A. Casnati, A. Pochini, R. Ungaro, J. de Mendoza, P. M. Nieto, P. Prados, D. N. Reinhoudt, *J. Am. Chem. Soc.* **1994**, *116*, 5814–5822.
[36] J.-C. G. Bünzli, A. E. Merbach, R. M. Nielson, *Inorg. Chim. Acta* **1987**, *139*, 151–152.
[37] J.-C. G. Bünzli, A. Milicic-Tang "Solvation and Anion Interaction in Organic Solvents" in *Handbook on the Physics and Chemistry of Rare Earths*, Elsevier, Amsterdam, **1995**, vol. 21. ch.145.

 © 2007 Wiley-VCH Verlag GmbH & Co. KGaA, Weinheim 

[38] P. Di Bernardo, G. R. Choppin, R. Portanova, P. L. Zanonato, *Inorg. Chim. Acta* **1993**, *207*, 85–91.
[39] K. Nakamoto, *Infrared and Raman Spectra of Inorganic and Coordination Compounds Part A: Theory and Applications in Inorganic Chemistry*, Wiley, New York, **1997**.
[40] J.-M. Lehn in *Frontier in Supramolecular Organic Chemistry and Photochemistry* (Eds.: H.-J. Schneider, H. Dürr), VCH, Weinheim, **1991**, pp. 1–28.
[41] V. Tsaryuk, V. Zolin, J. Legendziewicz, *J. Lumin.* **2003**, *102*, 744–750.
[42] V. F. Zolin, L. N. Puntus, V. I. Tsaryuk, V. A. Kudryashova, J. Legendziewicz, P. Gawryszewska, R. Szostak, *J. Alloys Compd.* **2004**, *380*, 279–284.
[43] J. D. Lewis, J. N. Moore, *Dalton Trans.* **2004**, 1376–1385.
[44] F. J. Steemers, W. Verboom, D. N. Reinhoudt, E. B. Vandertol, J. W. Verhoeven, *J. Am. Chem. Soc.* **1995**, *117*, 9408–9414.
[45] C. K. Jorgensen, *Mol. Phys.* **1962**, *5*, 271–277.
[46] V. Tsaryuk, I. Turowska-Tyrk, J. Legendziewicz, V. Zolin, R. Szostak, L. N. Puntus, *J. Alloys Compd.* **2002**, *341*, 323–332.
[47] V. Tsaryuk, J. Legendziewicz, L. N. Puntus, V. Zolin, J. Sokolnicki, *J. Alloys Compd.* **2000**, *300*, 464–470.
[48] V. D. Savchenko, V. I. Tsaryuk, V. F. Zolin, Yu. K. Gusev, *Proc. SPIE-Int. Soc. Opt. Eng.* **1996**, *2706*, 134–141.
[49] J. F. Desreux in *Lanthanide Probes in Life, Chemical and Earth Sciences – Theory and Practice* (Eds.: J.-C. G. Bünzli, G. R. Choppin), Elsevier, Amsterdam, **1989**, ch. 2, pp. 43–64.
[50] G. Schwarzenbach, *Complexometric Titrations*, Chapman & Hall, London, **1957**.
[51] E. R. Malinowski, D. G. Howery, *Factor Analysis in Chemistry*, John Wiley, New York, **1991**.
[52] H. Gampp, M. Maeder, C. J. Meyer, A. D. Zuberbühler, *Talanta* **1985**, *32*, 257–264.
[53] H. Gampp, M. Maeder, C. J. Meyer, A. D. Zuberbühler, *Talanta* **1986**, *33*, 943–951.
[54] A.-S. Chauvin, F. Gumy, D. Imbert, J.-C. G. Bünzli, *Spectrosc. Lett.* **2004**, *37*, 517–532; Erratum: A.-S. Chauvin, F. Gumy, D. Imbert, J.-C. G. Bünzli, *Spectrosc. Lett.* **2007**, *40*, 193.
[55] R. Rodriguez-Cortinas, F. Avecilla, C. Platas-Iglesias, D. Imbert, J.-C. G. Bünzli, A. de Blas, T. Rodriguez-Blas, *Inorg. Chem.* **2002**, *41*, 5336–5349.

Received: December 12, 2006
Published Online: April 16, 2007

 © 2007 Wiley-VCH Verlag GmbH & Co. KGaA, Weinheim 

DOI: 10.1002/ejic.200700002

# Synthesis, Reactivity and DFT Investigation of a Cationic Zirconocene Benzyl Compound with an Appended Phenyl Group

**Jörg Saßmannshausen,*[a] Anna Track,[a] and Tiago A. D. S. Dias[b]**

*Dedicated to M. L. H. Green*

**Keywords:** Density functional calculations / NMR spectroscopy / Polymerisation

The reaction of $[\eta^5\text{-}C_5H_5\text{-}(\eta^5\text{-}C_5H_4CMe_2C_6H_4Me)Zr(CH_2Ph)_2]$ (**1**) with the cation generating agent $B(C_6F_5)_3$ was studied by means of multinuclear NMR and density functional theory (DFT) methods. The clean reaction in $CD_2Cl_2$ at –60 °C yielded the cationic compound $[\eta^5\text{-}C_5H_5\text{-}(\eta^5\text{:}\eta^1\text{-}C_5H_4\text{-}CR_2C_6H_4R)Zr(\eta^2\text{-}CH_2Ph)]$ (R = Me: **2**, R = H: **3**), with a tolyl moiety coordinated to the cationic zirconium centre, in addition to the expected $\eta^2$-coordination of the benzyl moiety. Both coordinations were unambiguously assigned by multinuclear one- and two-dimensional NMR spectroscopy. Detailed DFT calculations of congener **3** at the B3LYP level of theory explain the unusual chemical shift of the coordinated atom of the tolyl moiety. Furthermore, detailed electronic analysis (Bader and NBO analysis) were undertaken to ascertain the type of coordination (agostic versus electrostatic) that the tolyl moiety adopts.
(© Wiley-VCH Verlag GmbH & Co. KGaA, 69451 Weinheim, Germany, 2007)

## Introduction

Group 4 metallocenes are still a point of research interest as they can serve not only as the catalyst in hydrosilylation and hydration reactions, but they are also well known for their ability to polymerise monomers such as ethene, propene and styrene. In the last decades, much effort, both experimentally and theoretically,[1–5] was undertaken to elucidate the role and the nature of the active species in these polymerisation reactions; thus, we have obtained a reasonably good picture of the catalytic process.[6–15] The interaction of the cationic group 4 metallocene, which is accepted as the active species in the catalytic process, with both the neutral catalytic precursor and the anion has been extensively studied.[6,7,9,14] The role of the solvent has been, by comparison, less investigated. Some time ago, we started to develop suitable models for the role of the solvent and showed by low-temperature NMR studies that arenes can coordinate to the cationic metal centre (compound **4**).[16,17] We were also the first to report the formation of a zirconocene *dication*, such as **5**, which is stabilised by intramolecular phenyl coordination (Scheme 1).[18] Recently, we extended this model and used silicon, instead of carbon, as a bridging atom. Here we noticed the formation of two different compounds: the expected formation of zirconocene compound **6**, which is in equilibrium with inner sphere ion pair **7**.[19] Furthermore, we obtained evidence for the formation of dichloromethane adducts in the case of cationic zirconocene *benzyl* compounds **8a**,**b** and explored the electronic properties by DFT calculations.[20]

As mentioned above, group 4 compounds are also used as catalysts for the polymerisation of styrene.[21–23] Recently, Jo et al. demonstrated that in the case of *ansa*-titanocene compounds, secondary insertion of styrene, albeit slower than primary insertion, is actually the process that leads to the formation of polystyrene.[24] One of the identified interim products was a metallocene benzyl compound. With this background, we decided to prepare compound **1** as a precursor to cation **2** to address the following: (1) the possible coordination of the pendant tolyl group, and, if this happens, (2) the nature of the coordination mode of the tolyl group (agostic versus electrostatic). To demonstrate the usability of our model, we firstly report the DFT calculations of **3**, and secondly we discuss the experimentally obtained NMR spectroscopic data of **2** (Scheme 2). Although this might be seen as an unusual way to present the obtained results, we believe that this way not only emphasises the validation of our model systems, but also allows the NMR results to be more easily understood.

[a] TU Graz, Institute for Chemistry and Technology of Organic Materials,
Stremayrgasse 16/I, 8010 Graz, Austria
E-mail: sassmannshausen@tugraz.at
[b] Universidade do Minho, Department of Chemistry, Campus de Gualtar
4710-057 Braga, Portugal
Supporting information for this article is available on the WWW under http://www.eurjic.org or from the author.

 © 2007 Wiley-VCH Verlag GmbH & Co. KGaA, Weinheim 

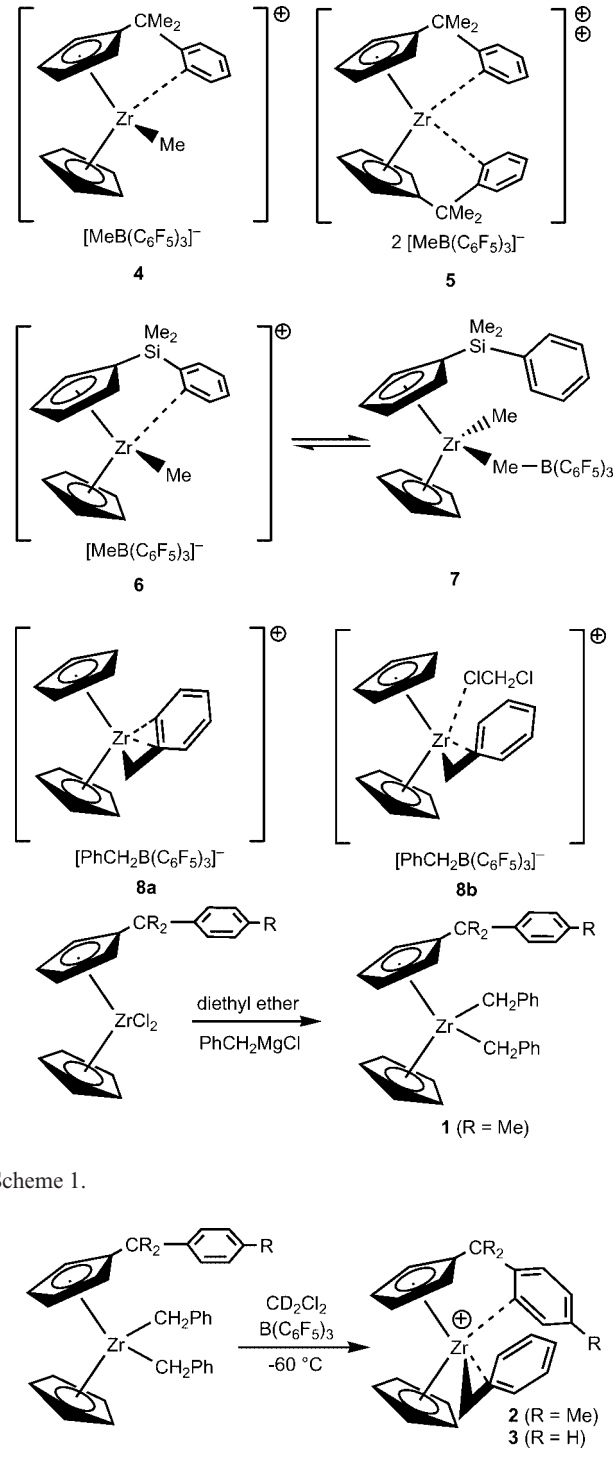


Scheme 1.




Scheme 2.

## Results and Discussion

### DFT Calculations

#### *Structural Investigation*

To save computational time, we substituted the *para* methyl group of the tolyl moiety in **2** with hydrogen, thus converting the tolyl moiety into a phenyl moiety to give **3** (Scheme 2).

We explored the possibility of different coordination modes of both the benzyl and the phenyl moiety to the cationic zirconium centre, and hence, calculated various conformers of **3**. A thorough scan of the potential energy surface revealed that **3a** is the global minimum of all considered coordination modes and that it is in rapid equilibrium with **3b** as confirmed by low-temperature NMR spectroscopy (Figure 1). Significant bond lengths, angles and dihedral angels are summarised in Table 1; the remaining energetically-higher-lying conformers are summarised in Table 2.

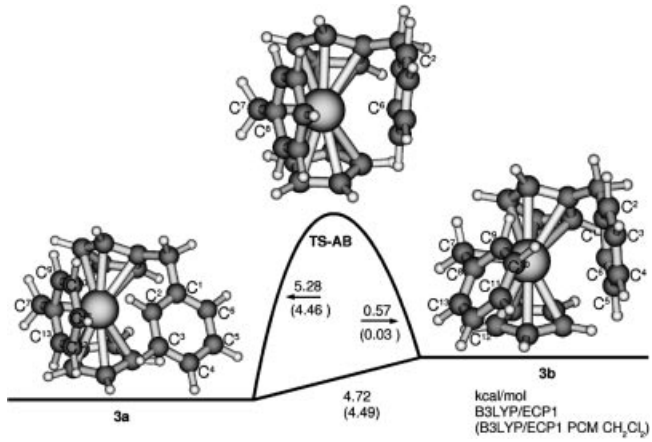


Figure 1. Scan of the potential energy surface of **3**. Values in parenthesis are calculated energies with the PCM solvent model (see text).

Table 1. Significant bond lengths, angles and dihedral angles of **3a** and **3b**.

| | **3a** | **TS-AB** | **3b** |
|---|---|---|---|
| $d$(Zr–C$^7$) | 2.33 Å | 2.32 Å | 2.34 Å |
| $d$(Zr–C$^8$) | 2.71 Å | 2.71 Å | 2.71 Å |
| $d$(Zr–C$^2$) | 2.92 Å | 4.60 Å | |
| $d$(Zr–C$^6$) | – | 3.02 Å | 3.16 Å |
| ∠(Zr–C$^7$–C$^8$) | 87.7° | 88.2° | 87.5° |
| ∠(Zr–C$^7$–C$^8$–C$^9$) | 95.5° | 93.74° | 61.2° |

Here, the benzyl-moiety is bonded in an $\eta^2$ fashion to the zirconium centre and the phenyl moiety is coordinated in the previously described $\eta^1$ mode to the metal.[16,17,25] The Zr–C$^7$–C$^8$–C$^9$ dihedral angle of 95.5° indicates symmetric coordination, with only a small distortion that is probably caused by the coordinated phenyl moiety. As previously reported,[16,19] the hydrogen attached to the coordinated carbon of the phenyl moiety is bent out of the phenyl plane by 9.62°, away from the zirconium metal. A second minimum, **3b**, which is 4.72 kcal/mol higher in energy than **3a**, was obtained by coordination of the second *ortho* carbon of the phenyl moiety to the zirconium centre. Here, the benzyl moiety is slanted significantly (Zr–C$^7$–C$^8$–C$^9$ = 61.2°) towards the metal and adopts an $\eta^3$ coordination to the metal centre. The phenyl moiety, which now points towards the "back" of the metallocene wedge, presumably leaves more space on the "front"; hence, the benzyl moiety

 © 2007 Wiley-VCH Verlag GmbH & Co. KGaA, Weinheim 

Table 2. Energetically higher lying conformers of **3**.

| | 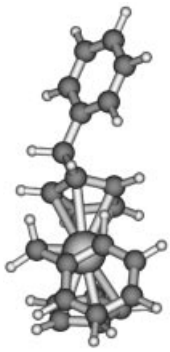 **3c** | 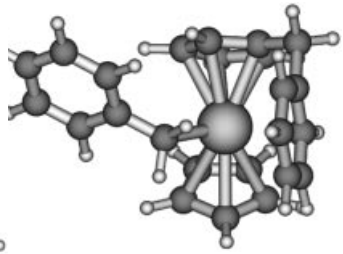 **3d** | 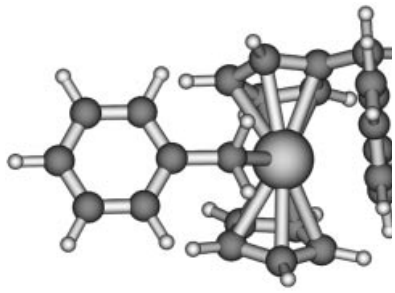 **3e** | 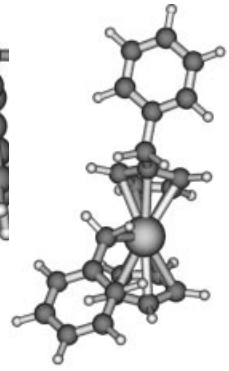 **3f** |
|---|---|---|---|---|
| Energy relative to **3a** [kcal/mol] | 6.65 | 7.18 | 7.38 | |

can adopt a coordination mode more suitable to satisfy the electron-deficient cationic metal centre. A similar coordination of cationic zirconocene benzyl compounds has been observed before.[20] In the absence of coordinating solvents such as dichloromethane, we recently reported the formation of an $\eta^3$-coordinated benzyl moiety to the cationic metallocene centre, compound **8a** ($Zr–C^7–C^8–C^9 = 51.8°$). The addition of one molecule of dichloromethane furnished compound **8b** (cf. Scheme 1). Although in **3b** the electron deficiency of the metal is somehow compensated as a result of the coordination of the phenyl moiety, it is still strong enough to force the benzyl moiety into an $\eta^3$ coordination, albeit the slanting angle is about 10° smaller than that in **8a**. Further exploration of the potential energy surface furnished compounds **3c**–**e**. The last considered structure, **3f**, with no coordination of the benzyl or tolyl moiety, could not be obtained without restricted rotation of the $Zr–CH_2$ bond. In all calculations performed, the benzyl moiety had a strong tendency to move towards the metal centre to yield structures similar to **3c**. To investigate any possible solvent effects, we computed single-point calculations for the optimised energy structures, including the polarisable continuum model (PCM) solvent model implemented in GAUSSIAN03, with dichloromethane as a solvent. In general, the calculated single-point energies are somewhat lower than the solvent-free calculations, and the largest difference was 0.82 kcal/mol (Figure 1, values in parenthesis).

The small energy difference between **3a** and **3b** is important for styrene polymerisation: the incoming monomer (the tolyl group in our model) is attracted by the cationic metal centre and can coordinate to the free coordination site. This coordination can be envisaged for any of the conformers of **3**. However, as the energy barrier of rearrangement between any of the conformers is sufficiently small, the styrene monomer can move into a position so that the C–C double bond adopts a suitable position for insertion to occur.

### *Electronic Structure Investigations*

To ascertain the coordination mode (agostic versus electrostatic) of the phenyl moiety to the zirconium centre, we performed detailed Bader analysis[26] of compounds **3a**,**b**. Scherer and McGrady recently reported a very detailed investigation into the agostic bonding criteria of titanium ethyl compounds and we are using their criteria here to assign the bonding mode of the phenyl group.[27–29] They extended the original definition of agostic bond ("used to discuss the various manifestations of covalent interactions between carbon–hydrogen groups and transition-metal centres in organometallic compounds, in which a hydrogen atom is covalently bonded simultaneously to both a carbon and to a transition-metal atom"[30,31]) to a broader context ("agostic interactions are characterized by the distortion of an organometallic moiety which brings an appended C–H bond into close proximity with the metal centre"[29]), and included heteroatoms such as silicon. Their main criterion for the definition of an agostic bond was the relationship of the electron density distribution $\rho(\boldsymbol{r})$ and the Laplacian of the charge density $\nabla^2\rho(\boldsymbol{r})$ in connection with Bader AIM analysis.[26] To support these so-obtained results, we undertook a detailed NBO analysis to investigate the relevant orbitals that were involved in the coordination of the phenyl moiety.[32]

For **3a**, we found a bonding path and a bond critical point between the zirconium centre and the *ortho* carbon of the phenyl group (BCP1). We did not observe a bonding path or a bond critical point between the zirconium centre and the hydrogen atom bonded to the *ortho* carbon (Figure 2). The electron density at the bond critical point was determined to be $\rho(\boldsymbol{r}) = 0.0171$ and the Laplacian of the charge density $\nabla^2\rho(\boldsymbol{r}) = –0.0136$. For comparison, the bond critical point between the zirconium centre and the $CH_2$ group (BCP2) was $\rho(\boldsymbol{r}) = 0.0812$ and a Laplacian of $\nabla^2\rho(\boldsymbol{r}) = –0.0165$ found. Obviously, as the electron density of BCP1 is lower than the electron density of the BCP2 bond,

 © 2007 Wiley-VCH Verlag GmbH & Co. KGaA, Weinheim 

we concluded that rather than a typical Lewis-type bond between the zirconium centre and the *ortho* carbon of the phenyl moiety, a more polarised bonding mode as we have previously described existed.[16]

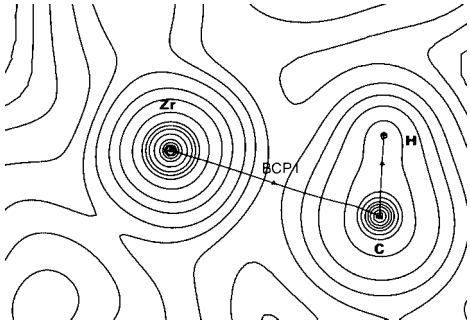


Figure 2. Contour plot of the electron density $\rho(\mathbf{r})$ of **3a**. Plane through zirconium, *ortho* phenyl carbon and hydrogen. Default contour lines used.

NBO analysis revealed electron donation between the CH bonding orbital [$\sigma_{CH} = 0.794(sp^{2.30})_C + 0.607(s)_H$] and the empty Zr orbital of mainly d-character ($LP^*_{Zr} = sd^{3.81}$) with a second-order perturbation energy of 5.12 kcal/mol. For comparison, for the CH bonding orbital in the *para* position of the coordinated carbon, similar values were obtained [$\sigma_{CH} = 0.794(sp^{2.34})_C + 0.608(s)_H$]. Thus, as the second-order perturbation energy for this carbon to zirconium is zero (i.e. no bond), we concluded that although there is a bonding path between the *ortho* carbon and the zirconium centre, the NHO of the two carbons are very similar, which indicates that an electrostatic rather than a covalent bond exists. Coloured plots of the orbitals are available in the Supporting Information (Figures S1–S3).

For **3b**, Bader analysis revealed a bonding path from the zirconium centre to the coordinated *ortho* carbon of the phenyl moiety; however, in this case, a straight line, as in **3a**, was not detected, but a more curved line was found (cf. Figure 3). It appears as if the bonding path first steers towards the bond critical point of the CH bond and just before it reaches this point it turns sharply towards the carbon atom. A similar kind of "conflict catastrophe structure" has been observed before, notably with alkyl titanium chloride cations[33] and for unusual H···π interactions.[34]

The relevant values of the bond critical point (BCP3) were calculated as $\rho(\mathbf{r}) = 0.0114$ and $\nabla^2\rho(\mathbf{r}) = -0.0086$. For comparison, the values of the bond critical point (BCP4) between the zirconium centre and the $CH_2$ group were calculated to be $\rho(\mathbf{r}) = 0.0803$ and $\nabla^2\rho(\mathbf{r}) = -0.0160$, which are similar to BCP2. The values for BCP1 are somewhat higher than the values of BCP3, which indicates a higher electron density between the zirconium centre and the *ortho* carbon of the phenyl moiety in the case of **3a**. NBO analysis of **3b** revealed the expected interaction between the CH bond [$\sigma_{CH} = 0.786(sp^{2.30})_C + 0.618(s)_H$] and the empty orbital ($LP^*_{Zr} = sd^{3.81}$) with a second-order perturbation energy of 3.09 kcal/mol, but furthermore, an interaction between the C–C bond [$\pi_{CC} = 0.675(p)_{C\text{-}ipso} + 0.738(p)_{C\text{-}ortho}$] with an energy of 5.88 kcal/mol (cf. Figures S4–S7). For

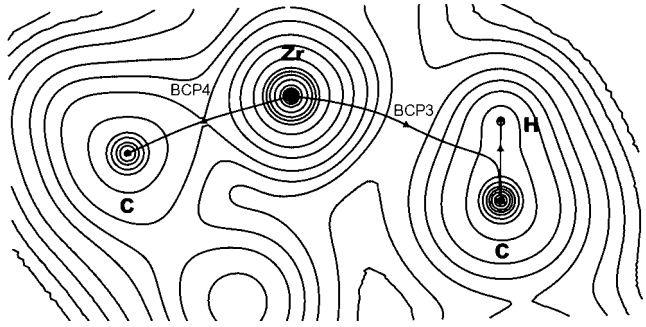


Figure 3. Contour plot of the electron density $\rho(\mathbf{r})$ of **3b**. Plane through zirconium, *ortho*-phenyl carbon and hydrogen. Benzyl $CH_2$ is on the left hand side. Default contour lines used.

comparison, the second C–C bond between the *ipso* and the *ortho* carbon bond [$\pi_{CC} = 0.716(p)_{C\text{-}ipso} + 0.699(p)_{C\text{-}ortho}$] only has an energy of 1.21 kcal/mol. It is tempting to assign this coordination to *agostic coordination*; however, unlike in the cases reported by Scherer and McGrady, we did not find a bonding path between the zirconium centre and the hydrogen atom. It is possible that by replacing the benzyl moiety with a stronger donor this could be shifted towards agostic bonding. Owing to the curvature of the bonding path in **3b**, we concluded that, in this case, a "transition state" somewhere in between a covalent bond and an agostic bond must be present.

### *Chemical Shift Computations*

To verify our computed structures with experimental results, we calculated the chemical shifts of **3a** and **3b**. Because of the low activation barrier between **3a** and **3b** (5.28 kcal/mol), we can assume that both compounds are in equilibrium even at –60 °C. Furthermore, we predict a chemical shift of $\delta_H = 2.64$ ppm for the *ortho* hydrogen of the phenyl moiety. This unusual highfield shift for an aromatic hydrogen can be explained very easily because of the magnetic anisotropy cone of the $\eta^2$-bonded benzyl moiety. This cone points straight to the *ortho* hydrogen of the phenyl moiety, and thus explains the unusual shift for an aromatic hydrogen. Similar observations have been made before.[18] The experimental and calculated shifts are summarised in Table 3.

## Low-Temperature VT-NMR Studies

The reaction between **2** and $B(C_6F_5)_3$ in $CD_2Cl_2$ was monitored by NMR spectroscopy (Figure 4). The spectrum recorded at –60 °C indicates the coordination of both the tolyl and benzyl moieties. The chemical shift of the benzylic $CH_2$ group at $\delta_H = 2.69$ ppm and $\delta_{C\{H\}} = 45.5$ ppm together with the coupling constant $J_{C,H} = 149.0$ Hz clearly indicate an $\eta^2$-coordinated benzyl moiety.[35,36] The chemical shift of the diastereotopic C*Me*$_2$ groups at 1.05 and 1.62 ppm are indicative of coordination of the tolyl moiety. Similar values, albeit with a smaller difference, have been reported before.[18] As predicted, a peak at $\delta_H = 2.33$ ppm

 © 2007 Wiley-VCH Verlag GmbH & Co. KGaA, Weinheim 

Table 3. Chemical shifts for **2** (observed) and **3a**,**b** (calculated).

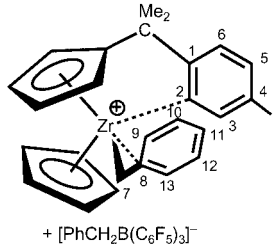


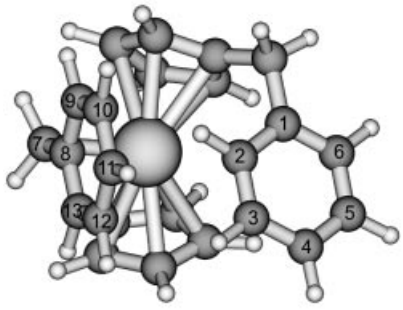

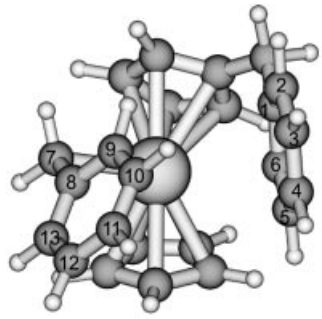

| | **2** | | **3a**[c] | | **3b**[c] | |
|---|---|---|---|---|---|---|
| | $^1$H ($\delta$ [ppm])[a] | $^{13}$C ($\delta$ [ppm])[b] | $^1$H ($\delta$ [ppm]) | $^{12}$C ($\delta$ [ppm]) | $^1$H ($\delta$ [ppm]) | $^{13}$C ($\delta$ [ppm]) |
| Ph$^1$ | | 137.7 | | 140.0 | | 139.4 |
| Ph$^2$ | 2.33 | 98.2 | 2.64 | 103.2 | 7.25 | 128.7 |
| Ph$^3$ | 6.72 | 136.4 | 6.59 | 142.0 | 7.91 | 139.8 |
| Ph$^4$ | – | – | – | 128.5 | – | 131.3 |
| Ph$^5$ | 7.67 | 130.0 | 7.82 | 141.6 | 6.71 | 134.7 |
| Ph$^6$ | 7.13 | 126.5 | 7.04 | 128.3 | 5.46 | 108.8 |
| $CH_2$ | 2.96 | 45.5 | 3.27 | 48.6 | 3.36 | 56.5 |
| | 3.04 | – | 3.39 | – | 2.98 | – |
| Ph$^8$ | – | 123.2 | – | 124.6 | – | 134.7 |
| Ph$^9$ | 6.71 | 128.1 | 7.25 | 140.5 | 5.38 | 104.8 |
| Ph$^{10}$ | 6.91 | 127.9 | 7.65 | 131.4 | 6.02 | 132.7 |
| Ph$^{11}$ | 6.84 | 122.9 | 7.75 | 133.0 | 7.15 | 130.8 |
| Ph$^{12}$ | 6.91 | 127.9 | 7.67 | 131.6 | 7.67 | 136.1 |
| Ph$^{13}$ | 6.71 | 128.1 | 7.16 | 135.7 | 7.37 | 137.4 |
| C*CH$_3$* | 1.05 | 27.5 | – | – | – | – |
| | 1.62 | 26.8 | – | – | – | – |
| *C*CH$_3$ | – | 37.3 | – | – | – | – |
| Ph*CH$_3$* | 2.39 | 20.7 | – | – | – | – |
| Cp | 5.39 | 109.8 | 5.34 | 111.8 | 5.77 | 112.5 |
| Cp′ | 5.22 | 97.7 | 5.26 | 99.9 | 5.94 | 101.8 |
| | 6.18 | 103.6 | 6.26 | 108.6 | 6.10 | 114.5 |
| | 5.79 | 106.4 | 5.88 | 109.1 | 6.18 | 111.3 |
| | 6.66 | 115.8 | 6.58 | 117.9 | 6.71 | 117.6 |

[a] –60 °C, $CD_2Cl_2$, 500 MHz. [b] –60 °C, $CD_2Cl_2$, 125 MHz. [c] B3LYP/IGLOII.

can be assigned to the *ortho* hydrogen of the coordinated tolyl moiety. The predicted equilibrium between **3a** and **3b** could be confirmed by EXSY spectroscopy (Figure 5). The cross peak between $\delta_H$ = 2.33 ppm and $\delta_H \approx$ 7.2 ppm can only be explained by the interconversion between **3a** and **3b**, and fits very well with the predicted values of 2.64 and

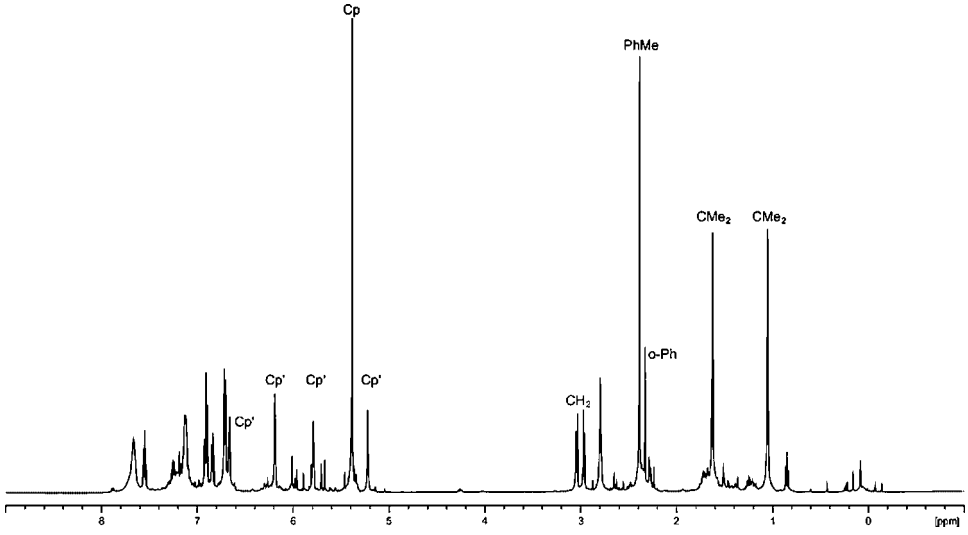


Figure 4. 500 MHz $^1$H NMR spectrum of **2** at –60 °C. Significant peaks of the cation are labelled.

 © 2007 Wiley-VCH Verlag GmbH & Co. KGaA, Weinheim 

7.25 ppm.[37] As expected, this exchange is rapid, even at –60 °C, and thus some broad peaks in the aromatic region of the spectrum can be observed. Lowering the temperature to –90 °C did not resolve the broad peaks, which hampered a detailed kinetic investigation. All calculated and observed chemical shifts are summarised in Table 3.

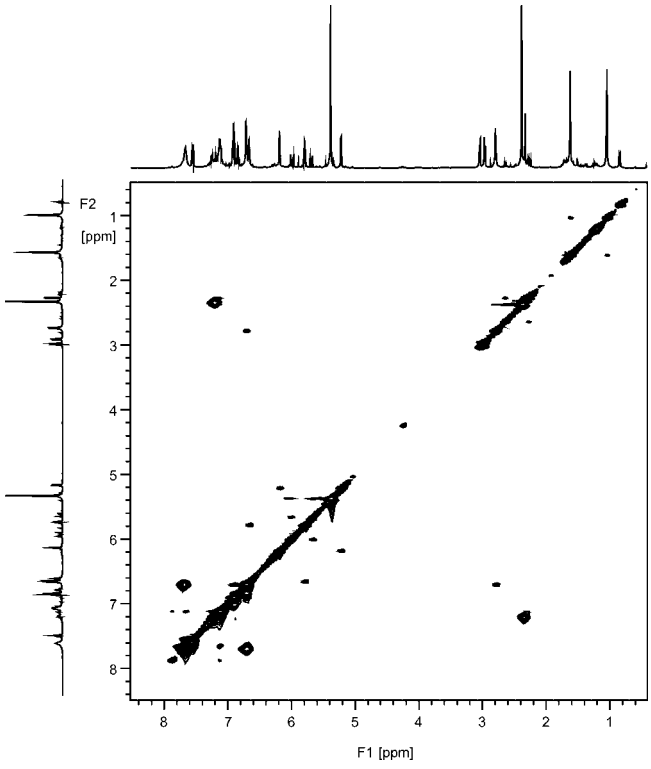


Figure 5. EXSY spectrum of **2** at –60 °C in $CD_2Cl_2$. Strong cross peaks are EXSY, medium ones are NOSY.

## Conclusions

We prepared the benzyl congener [$\eta^5$-$C_5H_5$-($\eta^5$-$C_5H_4CMe_2C_6H_4Me$)Zr($CH_2Ph$)$_2$] (**1**) of the previously reported zirconocene compound [$\eta^5$-$C_5H_5$($\eta^5$-$C_5H_4$-$CMe_2C_6H_4Me$)Zr$Me_2$]. The reaction of **1** with $B(C_6F_5)_3$ in $CD_2Cl_2$ was monitored by low-temperature NMR spectroscopy, and we obtained evidence for the coordination of both the benzyl moiety in the expected and previously reported $\eta^2$-bonding mode and the tolyl moiety. Our experimentally obtained data were predicted correctly from our computational studies. Furthermore, our model system predicted correctly the unusual chemical shift of $\delta_H$ = 2.33 ppm (observed) and $\delta_H$ = 2.64 ppm (calculated) for the *ortho* hydrogen of the coordinated tolyl (phenyl) moiety. Detailed AIM and NBO analysis revealed that although it is tempting to name this coordination "agostic", strictly spoken it is not agostic but rather an electrostatic interaction for **3a**. For **3b**, this coordination mode can be best described as a "transition state" between a covalent bond an agostic bond. These results fit quite well with the reported bonding modes of Ti(Et)$Cl_3$ and dmpeTi(Et)$Cl_3$: only in the case of the dmpe adduct could agostic bonding of the Et moiety be observed. Our model clearly indicates that for styrene polymerisation with *ansa* group 4 metallocenes, the coordination of the phenyl ring from the growing chain does not hamper the coordination of the free monomer: it is possible for the monomer to get caught by the catalyst, rearrange and insert into the polymer chain.

## Experimental Section

**General:** All experiments were carried out under a nitrogen atmosphere by using standard Schlenk techniques. Solvents were dried with sodium (toluene, low in sulfur), sodium/potassium alloy (diethyl ether, light petroleum, b.p. 40–60 °C, pentane), potassium (thf) and calcium hydride (dichloromethane). All chemicals were purchased from Aldrich and used as received. NMR solvents were dried with activated molecular sieves, freeze thawed and stored in Young's Tap sealed ampoules. NMR spectra were recorded with a VARIAN Unity Plus 500 spectrometer and referenced to the residual proton solvent peak for $^1$H. Chemical shifts are quoted in ppm relative to tetramethylsilane. $^{13}$C NMR spectra were referenced with the solvent peak relative to tetramethylsilane and were proton decoupled by using a WALTZ sequence. CH coupling constants were measured with a coupled gHSQC pulse sequence. Low-temperature NMR studies were conducted as previously reported.[19]

**Computational Details:** Density functional theory calculations were carried out by using the GAUSSIAN03[38] program package, running on a Mandrake Linux Dual-Opteron or a Dual-Xeon system, respectively. Geometries were fully optimised without symmetry constraints, which involved the functional combinations according to Becke[39] (hybrid) and Lee, Yang and Parr[40] (denoted B3LYP), with the corresponding pseudopotential basis set for Zr (Stuttgart-Dresden, keyword SDD in Gaussian) and the standard 6-31G* basis set[41] for C, H, Cl and F (denoted as ECP1). The stationary points and transition states were characterised as minima by analytical harmonic frequencies (zero or one imaginary frequency, respectively), which were used without scaling for zero-point and thermal corrections.

Magnetic shieldings $\sigma$ were evaluated for the B3LYP/ECP1 geometries by using a recent implementation of the GIAO (gauge-including atomic orbitals)-DFT method,[42] which involved the same B3LYP level of theory, together with the recommended IGLO II basis[43] on C, H and F. The former approach with this particular combination of functionals and basis sets has proven to be quite effective for chemical shift computations for transition metal complexes.[16] $^1$H and $^{13}$C NMR chemical shifts were calculated relative to benzene, with absolute shieldings for benzene $\sigma$($^1$H) 24.54 and $\sigma$($^{13}$C) 47.83 with the IGLO II basis set. The values for benzene were converted into the TMS scale by using the experimental $\delta$ values of benzene ($\delta$ =7.26 ppm and 128.5 ppm, respectively). Bader analysis was performed using the DZVP all-electron basis set,[44] drawing of the electron charge density plots were performed with the use of an Aim2000 instrument.[45] MOLDEN[46] was used for the chemical representation of the calculated compounds and NBO-View for the representation of the orbitals.[32]

**[$\eta^5$-$C_5H_5$-($\eta^5$-$C_5H_4CMe_2C_6H_4Me$)Zr($CH_2Ph$)$_2$] (1):** Previously prepared [$\eta^5$-$C_5H_5$-($\eta^5$-$C_5H_4CMe_2C_6H_4Me$)Zr$Cl_2$][17] (2.4 g, 5.65 mmol) was added to a rapidly stirred solution of benzylmagnesium chloride in diethyl ether.[20] The colour of the solution changed to orange. The reaction mixture was stirred overnight. The volatiles were removed under reduced pressure, and the orange residue was extracted into pentane. Fractionated crystallisation yielded

 © 2007 Wiley-VCH Verlag GmbH & Co. KGaA, Weinheim 

the desired compound in a moderate yield as orange microcrystals. Yield: 410 mg (13.5%). $^1$H NMR (500 MHz, $CDCl_3$, 20 °C): $\delta$ = 1.51 (s, 6 H, $CCH_3$), 1.82 (s, 4 H, $CH_2$-Ph), 2.24 (2, 3 H, PhC$H_3$), 5.71 (s, 5 H, Cp), 5.76 (apparent t, $J$ = 5 Hz, 2 H, Cp′), 5.87 (apparent t, $J$ = 5 Hz, 2 H, Cp′), 6.76 (t, $J$ = 10 Hz, 2 H, *p*-H-Ph), 7.05 (d, $J$ = 10 Hz, 4 H, *o*-H-Ph), 7.06 (d, $J$ = 10 Hz, 4 H, -$C_4H_4$-Me), 7.09 (t, $J$ = 10 Hz, 4 H, *m*-H-Ph) ppm. $^{12}$C NMR (125 MHz, $CDCl_3$, 20 °C): $\delta$ = 21.1 (-$C_4H_4$-$CH_3$), 30.9 ($CCH_3$), 39.7 ($CCH_3$), 61.4 ($CH_2$-), 111.8 (Cp′), 112.8 (Cp), 120.9 (*p*-C-Ph), 125.7 (*o*-C-Ph), 126.2 (*o*-C-tolyl), 128.2 (*m*-C-Ph), 129.1 (*m*-C-tolyl), 136.0 (*ispo*-C), 138.3 (*ispo*-C), 146.7 (*ispo*-C), 152.5 (*ispo*-C) ppm. $C_{34}H_{36}Zr$ (535.59): calcd. C 76.21, H 6.77; found C 76.10, H 6.65.

**Supporting Information** (see footnote on the first page of this article): Coloured plots of the NBO of **3a**,**b** and tables of the cartesian coordinates of all calculated structures in *x*, *y*, *z* format.

## Acknowledgments

J. S. thanks J. C. Green, M. Bühl and M. Flock for helpful discussions and F. Stelzer for his support. A. T. thanks the Technical University of Graz for a research grant. We want to thank the IT department for computational resources.

[1] M. S. W. Chan, K. Vanka, C. C. Pye, T. Ziegler, *Organometallics* **1999**, *18*, 4624–4636.
[2] K. Vanka, M. S. W. Chan, C. C. Pye, T. Ziegler, *Organometallics* **2000**, *19*, 1841–1849.
[3] K. Vanka, T. Ziegler, *Organometallics* **2001**, *20*, 905–913.
[4] K. Vanka, Z. Xu, M. Seth, T. Ziegler, *Top. Catal.* **2005**, *34*, 143–164.
[5] S.-Y. Yang, T. Ziegler, *Organometallics* **2006**, *25*, 887–900.
[6] M. Bochmann, *J. Chem. Soc., Dalton Trans.* **1996**, 255–270.
[7] M. Bochmann, *Top. Catal.* **1999**, *7*, 9–22.
[8] M. Bochmann, *J. Organomet. Chem.* **2004**, *689*, 3982–3998.
[9] M. Bochmann, G. J. Pindado, S. J. Lancaster, *J. Mol. Catal. A* **1999**, *146*, 179–190.
[10] H.-H. Brintzinger, D. Fischer, R. Mühlhaupt, B. Rieger, R. Waymouth, *Angew. Chem.* **1995**, *107*, 1255–1383.
[11] G. J. P. Britovsek, V. C. Gibson, D. F. Wass, *Angew. Chem. Int. Ed.* **1999**, *38*, 428–447.
[12] E. Y.-X. Chen, T. J. Marks, *Chem. Rev.* **2000**, *100*, 1391–1434.
[13] W. Kaminsky, *J. Polym. Sci., Part A: Polym. Chem.* **2004**, *16*, 3911–3921.
[14] A. Maccioni, *Chem. Rev.* **2005**, *105*, 2039–2073.
[15] G. L. Rempel, J. Huang, *Prog. Polym. Sci.* **1995**, *20*, 459–526.
[16] M. Bühl, J. Saßmannshausen, *J. Chem. Soc., Dalton Trans.* **2001**, 79–84.
[17] L. H. Doerrer, M. L. H. Green, D. Häußinger, J. Saßmannshausen, *J. Chem. Soc., Dalton Trans.* **1999**, 2111–2118.
[18] M. L. H. Green, J. Saßmannshausen, *Chem. Commun.* **1999**, 115–116.
[19] J. Saßmannshausen, J. C. Green, F. Stelzer, J. Baumgartner, *Organometallics* **2006**, *25*, 2796–2805.
[20] J. Saßmannshausen, A. Track, F. Stelzer, *Organometallics* **2006**, *25*, 4427–4432.
[21] N. Ishihara, T. Seimiya, M. Kuramono, M. Uoi, *Polym. Prepr. Jpn.* **1986**, *35*, 240.
[22] C. Schwecke, W. Kaminsky, *J. Polym. Sci., Part A: Polym. Chem.* **2001**, *39*, 2805–2812.
[23] Q. Wang, R. Quyoum, D. J. Gillis, M.-J. Tudoret, D. Jeremic, B. K. Hunter, M. C. Baird, *Organometallics* **1996**, *15*, 693–703.
[24] J. H. Yang, J. Huh, W. H. Jo, *Organometallics* **2006**, *25*, 1144–1150.
[25] M. Bochmann, M. L. H. Green, A. K. Powell, J. Saßmannshausen, M. U. Triller, S. Wocadlo, *J. Chem. Soc., Dalton Trans.* **1999**, 43–49.
[26] R. F. W. Bader, *Atoms in Molecules: A Quantum Theory*, Clarendon Press, Oxford, UK, **1990**.
[27] W. Scherer, W. Hieringer, M. Spiegler, P. Sirsch, G. S. McGrady, A. J. Downs, A. Haarland, B. Pedersen, *Chem. Commun.* **1998**, 2471–2472.
[28] W. Scherer, P. Sirsch, D. Shorokhov, M. Tafipolsky, G. S. McGrady, E. Gullo, *Chem. Eur. J.* **2003**, *9*, 6057–6070.
[29] W. Scherer, G. S. McGrady, *Angew. Chem. Int. Ed.* **2004**, *43*, 1782–1806.
[30] M. Brookhard, M. L. H. Green, *J. Organomet. Chem.* **1983**, *250*, 395–408.
[31] M. Brookhart, M. L. H. Green, L.-L. Wong, *Prog. Inorg. Chem.* **1988**, *36*, 1–124.
[32] E. D. Glendening, J. K. Badenhoop, A. E. Reed, J. E. Carpenter, J. A. Bohmann, C. M. Morales, F. Weinhold in *NBO 5.G.*, Theoretical Chemistry Institute, University of Wisconsin, Madison, WI, **2001**.
[33] P. L. A. Popelier, G. Logothetis, *J. Organomet. Chem.* **1998**, *555*, 101–111.
[34] I. Rozas, I. Alkorta, J. Elguero, *J. Phys. Chem. A.* **1997**, *101*, 9457–9463.
[35] R. F. Jordan, R. E. LaPointe, N. C. Baenzinger, G. D. Hinch, *Organometallics* **1990**, *9*, 1539–1545.
[36] R. F. Jordan, R. E. LaPointe, C. S. Bajgur, S. F. Echols, R. Willet, *J. Am. Chem. Soc.* **1987**, *109*, 4111–4113.
[37] A cross peak between the two methyl groups on the bridging carbon should also be observed. However, the chemical shift difference between the two isomers is probably too small to be observed. For our model compound, we computed a difference around 0.5 ppm.
[38] M. J. Frisch, G. W. Trucks, H. B. Schlegel, G. E. Scuseria, M. A. Robb, J. R. Cheeseman, J. A. Montgomery Jr, T. Vreven, K. N. Kudin, J. C. Burant, J. M. Millam, S. S. Iyengar, J. Tomasi, V. Barone, B. Mennucci, M. Cossi, G. Scalmani, N. Rega, G. A. Petersson, H. Nakatsuji, M. Hada, M. Ehara, K. Toyota, R. Fukuda, J. Hasegawa, M. Ishida, T. Nakajima, Y. Honda, O. Kitao, H. Nakai, M. Klene, X. Li, J. E. Knox, H. P. Hratchian, J. B. Cross, C. Adamo, J. Jaramillo, R. Gomperts, R. E. Stratmann, O. Yazyev, A. J. Austin, R. Cammi, C. Pomelli, J. W. Ochterski, P. Y. Ayala, K. Morokuma, G. A. Voth, P. Salvador, J. J. Dannenberg, V. G. Zakrzewski, S. Dapprich, A. D. Daniels, M. C. Strain, O. Farkas, D. K. Malick, A. D. Rabuck, K. Raghavachari, J. B. Foresman, J. V. Ortiz, Q. Cui, A. G. Baboul, S. Clifford, J. Cioslowski, B. B. Stefanov, G. Liu, A. Liashenko, P. Piskorz, I. Komaromi, R. L. Martin, D. J. Fox, T. Keith, M. A. Al-Laham, C. Y. Peng, A. Nanayakkara, M. Challacombe, P. M. W. Gill, B. Johnson, W. Chen, M. W. Wong, C. Gonzalez, J. A. Pople, *Gaussian 03, Revision C.02*, Gaussian, Inc., Pittsburgh, PA, **2004**.
[39] A. D. Becke, *J. Chem. Phys.* **1993**, *98*, 5648–5652.
[40] C. Lee, W. Yang, R. G. Parr, *Phys. Rev. B* **1988**, *37*, 785–789.
[41] W. J. Hehre, R. Ditchfield, J. A. Pople, *J. Chem. Phys.* **1972**, *56*, 2257–2261.
[42] J. R. Cheeseman, G. W. Trucks, T. A. Keith, M. J. Frisch, *J. Chem. Phys.* **1996**, *104*, 5497–5509.
[43] W. Kutzelnigg, U. Fleischer, M. Schindler in *NMR Basic Principles and Progress Vol. 23*, Springer, Berlin, **1990**, pp. 165–262.
[44] N. Godbout, D. R. Salahub, J. Andzelm, *Can. J. Chem.* **1992**, *70*, 560.
[45] F. Biegler-König, J. Schönbohm, D. Bayles, *J. Comput. Chem.* **2001**, *22*, 545–559.
[46] G. Schaftenaar, J. H. Noordik, *J. Comput. Aided Mol. Des.* **2000**, *14*, 123–134.

Received: January 2, 2007
Published Online: April 18, 2007

 © 2007 Wiley-VCH Verlag GmbH & Co. KGaA, Weinheim 

DOI: 10.1002/ejic.200700095

# A Magnetostructural and Electrochemical Study of $Cu^{II}$ and $Fe^{III}$ Complexes Containing a Tetradentate Aminebis(phenolate) Ligand with a Pendent Tetrahydrofuran Group

**Elham Safaei,[a] Thomas Weyhermüller,[a] Eberhard Bothe,[a] Karl Wieghardt,[a] and Phalguni Chaudhuri*[a]**

**Keywords:** Iron / Copper / Aminebis(phenol) / Electrochemistry / Magnetism

Ligating properties of a tetradentate ligand 2-{bis[(3,5-di-*tert*-butyl-2-hydroxybenzyl)amino]methyl}tetrahydrofuran, $H_2L$, with [O,O,N,O]-donor atoms towards $Cu^{II}$ and $Fe^{III}$ are described. The ligand $H_2L$ yields both mononuclear $LFe^{III}$(acac) (**1**) and dinuclear $[L_2Fe^{III}{}_2(\mu\text{-}OCH_3)\text{-}(\mu\text{-}OH)]$ (**2**), $[L_2Fe^{III}{}_2(\mu\text{-}C_2O_4)]$ (**3**) and $[L_2Cu^{II}{}_2]$ (**4**) complexes, which were characterized by various physical techniques, including X-ray diffraction, Mössbauer, electrochemical and magnetic susceptibility (2–290 K) measurements. That the electrochemical oxidations are ligand-centered, i.e. formation of phenoxyl radicals from the coordinated phenolates, have been shown by voltammetric methods. Complexes **2**–**4** display antiferromagnetic exchange coupling of the neighbouring metal centers. Comparison of the evaluated weak exchange coupling constants ($J$) with the literature values leads to the conclusion that the angle Cu–O–Cu′ is not the only determinant for the nature of the exchange coupling and the capability of the bridging ligands as mediators for spin coupling in case of $Fe^{III}$ follows the order phenoxide ≈ methoxide > hydroxide.
(© Wiley-VCH Verlag GmbH & Co. KGaA, 69451 Weinheim, Germany, 2007)

## Introduction

The amino acid tyrosine and its one-electron oxidized tyrosyl radical are quite common at the active centers of metalloenzymes involved in oxygen-dependent enzymatic radical catalysis.[1] Copper-containing galactose oxidase (GO), iron-containing ribonucleotide reductase (RR) are just two examples among others. This finding has elicited the interest of bioinorganic chemists in using phenol-containing ligands to mimic both structure and function of such metalloenzymes.[2] In this area, we have reported some bioinspired complexes as functional models of metalloenzymes[3] viz. galactose oxidase, catechol oxidase, and amine oxidases. These low-molecular weight complexes exhibit catalytic activity for aerial oxidation of organic substrates like alcohols, amines and catechols.

In continuation of our continuing interest in aminebis(phenol) ligands with O,N,O-donor atoms[4] and with the aim to scrutinize the effect of an additional pendent arm on the ligating property of the resulting tetradentate ligand towards transition metals, we argued for a weak-field donor pendent arm containing an ether group. An obvious choice is a tetrahydrofuran pendent arm. Thus the ligand $H_2L$ was selected for the investigation.

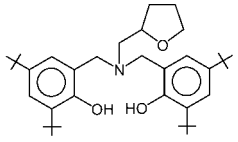


$H_2L$

Such aminebis(phenol) ligands with different pendent arms, such as amines with tetrahydrofuran, have already been used in the field of phosphorus chemistry[5] and for catalytic olefin polymerization involving group IV metal complexes.[6] Scheme 1 shows the complexes prepared with the ligand $H_2L$ together with the labels. We report herein the synthesis, the structural, spectroscopic and magnetic properties of complexes $[LFe^{III}(acac)]$ (**1**), $[L_2Fe^{III}{}_2(\mu\text{-}OCH_3)(\mu\text{-}OH)]$ (**2**), and $[L_2Fe^{III}{}_2(\mu\text{-}C_2O_4)]$ (**3**). The dinuclear $Cu^{II}$ complex $[L_2Cu^{II}{}_2]$ (**4**) will also be described.

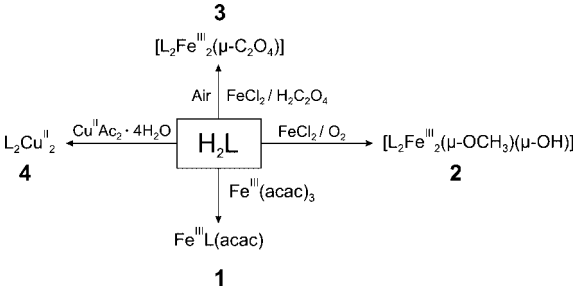


Scheme 1.

[a] Max-Planck-Institute for Bioinorganic Chemistry
Stiftstraße 34–36, 45470 Mülheim an der Ruhr, Germany
E-mail: Chaudh@mpi-muelheim.mpg.de


© 2007 Wiley-VCH Verlag GmbH & Co. KGaA, Weinheim

## Results and Discussion

The ligand 2-{bis[(3,5-di-*tert*-butyl-2-hydroxybenzyl)-amino]methyl}tetrahydrofuran, $H_2L$, was prepared according to a procedure reported in the literature.[6b] The purity of the ligand was checked by liquid chromatography to be 98.7%. The IR, $^1H$ NMR and MS data are in agreement with the literature data (see Experimental Section), no further discussion is necessary here. To gain insight into the metrical parameters of the ligand, we have determined the structure of the ligand by X-ray diffractometry. Figure 1 displays the structure of the ligand $H_2L$ in the solid state. The X-ray analysis of single crystals of $H_2L$, performed at 100 K, reveals moderate hydrogen bonding between the phenolic hydroxy group O(15) and the ether group O(1) of the tetrahydrofuran ring, whereas the second phenolic group O(23) and the amine nitrogen N(7) are hydrogen-bonded [O(15)···O(1) 2.786 Å and O(23)···N(7) 2.731 Å]. The bond lengths and angles for the ligand, listed in Table 1, seem reasonable and do not warrant any special discussion.

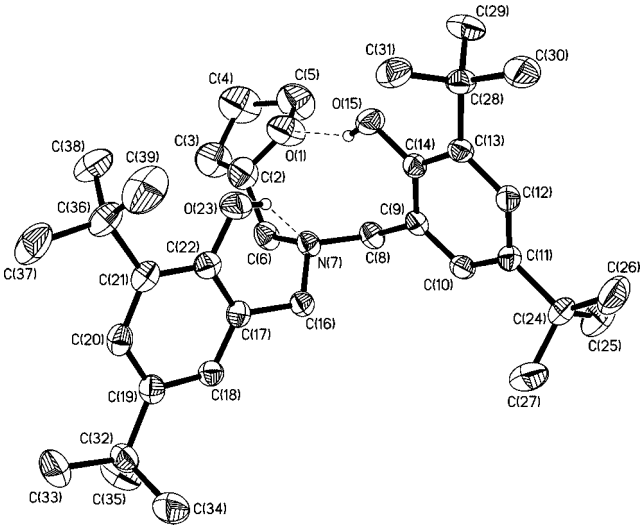


Figure 1. ORTEP representation for the amine bis (phenolato) THF ligand(L) (thermal ellipsoid probability 40%).

Methanolic solutions of $H_2L$ were treated with metal salts, $Et_3N$ and an additional ligand in some cases in suitable ratio and the solutions were heated at reflux to yield the complexes **1**–**4** in good yields. EI mass spectrometry was helpful in detecting the mononuclear nature for **1** and the dinuclear nature for **2**–**4**. The molecular ion peaks at *m*/*z* 690 (47.7%) for **1**, at *m*/*z* 1198 (11%) for **4** and *m*/*z* 1270 (47%) for **3** were observed. The signal at *m*/*z* 1198 (intensity about 12%) for **2** supports the dinuclear nature of **2**.

The ν(OH) stretch for the pure ligand, strong and sharp at 3372 $cm^{-1}$, vanishes after complex formation and is replaced by a very broad signal indicating the coordination of the phenol group to the metal. For **1** the most relevant features occur at 1598 and 1519 $cm^{-1}$ corresponding to the ν(C=O) of the coligand acetylacetonate (acac). A new peak at 1067 $cm^{-1}$ observed for **2** is ascribed to the ν($OCH_3$) group of the bridging methoxide ligand. Complex **3** exhibits strong to moderate vibrations at 1655 $cm^{-1}$ ($\nu_{as}OCO$), 1400 $cm^{-1}$ ($\nu_sOCO$) and 837 $cm^{-1}$ ($\nu_\delta OCO$) as has been observed earlier for similar oxalate-bridged complexes.[7] Selected IR data for complexes **1**–**4** are given in the Experimental Section.

Table 1. Selected bond lengths [Å] and angles [°] for the ligand $H_2L$.

| | |
|---|---|
| O(1)–C(2) | 1.377(4) |
| O(1)–C(5) | 1.458(5) |
| N(7)–C(6) | 1.480(4) |
| N(7)–C(16) | 1.473(2) |
| N(7)–C(8) | 1.480(2) |
| O(23)–C(22) | 1.366(2) |
| O(15)–C(14) | 1.373(2) |
| C(14)–C(13) | 1.403(3) |
| C(13)–C(12) | 1.398(3) |
| C(12)–C(11) | 1.397(3) |
| C(11)–C(10) | 1.382(3) |
| C(10)–C(9) | 1.383(3) |
| C(9)–C(14) | 1.399(3) |
| C(22)–C(21) | 1.406(3) |
| C(21)–C(20) | 1.385(3) |
| C(20)–C(19) | 1.391(3) |
| C(19-C(18) | 1.394(3) |
| C(18)–C(17) | 1.385(3) |
| C(17)–C(22) | 1.402(3) |
| C82)–O(1)–C(5) | 110.2(3) |
| C(16)–N(7)–C(6) | 114.1(2) |
| C(16)–N(7)–C(8) | 109.8(2) |
| C(8)–N(7)–C(6) | 111.9(6) |
| O(23)–C(22)–C(17) | 119.9(2) |
| O(23)–C(22)–C(21) | 119.7(2) |
| O815)–C(14)–C(13) | 118.2(2) |
| O(15)–C(14)–C(9) | 121.0(2) |

### X-ray Diffraction Studies of 1, 2, 3 and 4

Single crystals of deep red [LFe(acac)]·$C_2H_5OC_2H_5$ (**1**) were obtained from an ethereal solution by slow evaporation. As no substantial differences in bond lengths and angles are found for the two crystallographically non-equivalent molecules, only one ORTEP diagram for the structure of compound **1** is displayed in Figure 2. Selected bond lengths and angles are summarized in Table 2. The overall geometry around the iron ion Fe(1) is best described as a distorted octahedron with two *cis* positioned oxygens O(41) and O(45) of the acetylacetonato coligand acac, whereas the doubly deprotonated tripodal ligand $[O\cap N(O)\cap O]^{2-}$ occupies the remaining four coordination sites. All the phenyl rings attached to the phenolate oxygen atoms are found to be planar, indicating that upon coordination the aromaticity of the phenyl rings is retained. The distortion from octahedral geometry is mainly caused by the acute bite angles involving the tetrahydrofuran oxygen O(1). The O(1)–Fe(1)–O(15) and O(23)–Fe(1)–O(45) angles are 166.00(8)° and 167.61(8)°, respectively, while the corresponding O(41)–Fe(1)–N(7) angle at 170.17(9)° also deviates from linearity. All the C–O bond lengths found in complex **1** are unremarkable, average 1.337(5) Å.

 © 2007 Wiley-VCH Verlag GmbH & Co. KGaA, Weinheim 

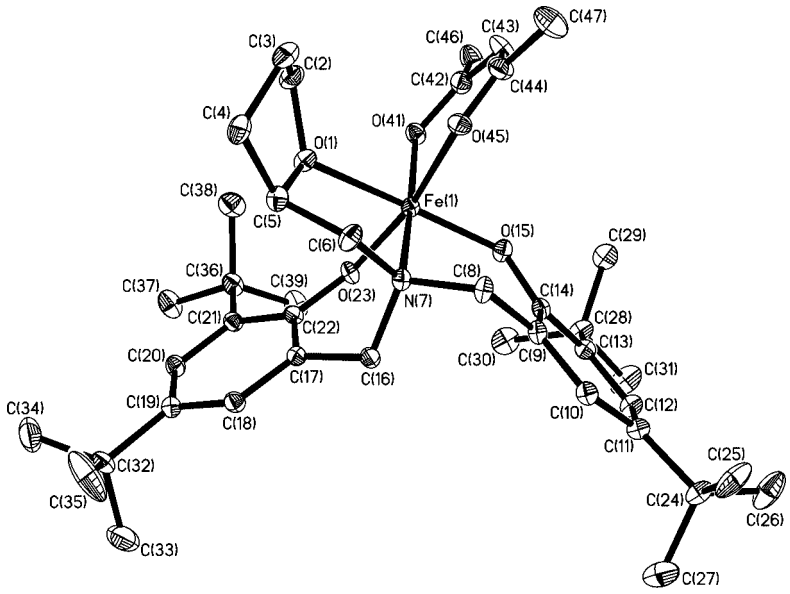


Figure 2. ORTEP diagram and atom labeling scheme for complex **1** (thermal ellipsoid probability 40%).

Table 2. Selected bond lengths [Å] and bond angles [°] for complex **1**·$Et_2O$.

| | | | |
|---|---|---|---|
| Fe(1)–O(15) | 1.883(2) | O(15)–Fe(1)–O(23) | 99.20(9) |
| Fe(1)–O(23) | 1.8891(19) | O(15)–Fe(1)–O(41) | 95.53(8) |
| Fe(1)–O(41) | 1.989(2) | O(23)–Fe(1)–O(41) | 96.29(8) |
| Fe(1)–O(45) | 2.0728(19) | O(15)–Fe(1)–O(45) | 92.45(9) |
| Fe(1)–N(7) | 2.193(2) | O(23)–Fe(1)–O(45) | 167.61(8) |
| Fe(1)–O(1) | 2.223(2) | O(41)–Fe(1)–O(45) | 86.70(8) |
| O(15)–Fe(1)–N(7) | 89.75(8) | O(15)–Fe(1)–O(1) | 166.00(8) |
| O(23)–Fe(1)–N(7) | 90.79(8) | O(23)–Fe(1)–O(1) | 87.66(8) |
| O(41)–Fe(1)–N(7) | 170.37(9) | O(41)–Fe(1)–O(1) | 95.83(8) |
| O(45)–Fe(1)–N(7) | 85.03(8) | O(45)–Fe(1)–O(1) | 80.07(8) |
| N(7)–Fe(1)–O(1) | 77.89(8) | | |
| Fe(2)–O(73) | 1.882(2) | O(73)–Fe(2)–O(65) | 101.18(9) |
| Fe(2)–O(65) | 1.896(2) | O(73)–Fe(2)–O(91) | 95.17(9) |
| Fe(2)–O(95) | 2.083(2) | O(65)–Fe(2)–O(91) | 96.46(8) |
| Fe(2)–N(57) | 2.187(2) | O(73)–Fe(2)–O(95) | 90.07(9) |
| Fe(2)–O(51) | 2.218(2) | O(65)–Fe(2)–O(95) | 168.17(9) |
| Fe(2)–O(91) | 1.988(2) | O(91)–Fe(2)–O(95) | 86.03(9) |
| | | O(73)–Fe(2)–N(57) | 90.40(9) |
| | | O(65)–Fe(2)–N(57) | 89.55(9) |
| | | O(91)–Fe(2)–N(57) | 170.85(9) |
| | | O(95)–Fe(2)–N(57) | 86.71(9) |
| | | O(73)–Fe(2)–O(51) | 165.23(8) |
| | | O(65)–Fe(2)–O(51) | 87.53(8) |
| | | O(91)–Fe(2)–O(51) | 95.67(8) |
| | | O(95)–Fe(2)–O(51) | 80.71(8) |
| | | N(57)–Fe(2)–O(51) | 77.65(8) |
| C(22)–O(23) | 1.341(3) | | |
| C(14)–O(15) | 1.326(3) | | |
| C(64)–O(65) | 1.336(3) | | |
| C(72)–O(73) | 1.343(3) | | |

It is noteworthy that the Fe(1)–O(1) bond length of 2.223(2) Å, involving the THF oxygen atom, is exceedingly long. This probably results in the comparatively short *trans*-positioned Fe(1)–O(15) bond length of 1.883(2) Å, thus indicating stronger Fe–O(phenolate) interactions in comparison to that for Fe–O(THF). The Fe(1)–N(7) distance at 2.193(2) Å falls into the range reported for the structurally characterized mononuclear $Fe^{III}$ complexes.[8] The Fe–O and Fe–N bond lengths are in agreement with those of a high-spin $d^5$ $Fe^{III}$ complex,[9] which corroborates also with the magnetic and Mössbauer measurements.

The structure of complex **2** consists of neutral, well-isolated dinuclear units $[L_2Fe^{III}_2(\mu\text{-}OH)(\mu\text{-}OCH_3)]\cdot C_2H_5\text{-}OC_2H_5$. Selected bond lengths and angles are listed in Table 3. An ORTEP view of the dimeric unit is shown in Figure 3. The two iron(III) atoms are asymmetrically bridged by one methoxy O(81) and one hydroxy O(80) ligands. The iron ion Fe(2) is in distorted octahedral environment, having $FeNO_5$ coordination sphere, whereas five-coordinate Fe(1) is in a square pyramidal $FeNO_4$ environment. The phenolate O(63), the amine N(47) and the bridging O(81) and O(80) form the equatorial plane for the Fe(2) center, whereas the phenolate O(55) and O(41) from the tetrahydrofuran unit are axially *trans*-disposed. As expected for *trans*-influence, the Fe(2)–O(41) distance is long with 2.207(5) Å, while the *trans*-bonded Fe(2) is hydrogen-bonded to the bridging hydroxide O(80). Thus, a distorted square-pyramidal Fe(1) prevails in complex **2**. The $FeNO_4$ coordination sphere is not very common for trivalent iron with O,N-based ligation,[10] octahedral coordination is by far the most commonly observed arrangement for $Fe^{III}$.[11] The bond lengths for the five-coordinate iron center Fe(1) is shorter than those for the six-coordinate Fe(2) center. The asymmetry in the bridging bond lengths is also noteworthy. The angles Fe(1)–O(81)–Fe(2) and Fe(1)–O(80)–Fe(2) at the bridging ligands are 103.3(1)° and 101.5(3)°, respectively and comparable with the reported values for similarly bridged iron(III) complexes.[12] The Fe(1)···Fe(2) separation of 3.116 Å fall in the range reported earlier. The Fe–N and Fe–O bond lengths are consistent with $d^5$ high-spin electron configuration for both $Fe^{III}$ centers with amine nitrogen and phenolate oxygen-donor ligands. The $d^5$ high-spin configuration has also been confirmed both by Mössbauer and magnetic susceptibility measurements.

 © 2007 Wiley-VCH Verlag GmbH & Co. KGaA, Weinheim 

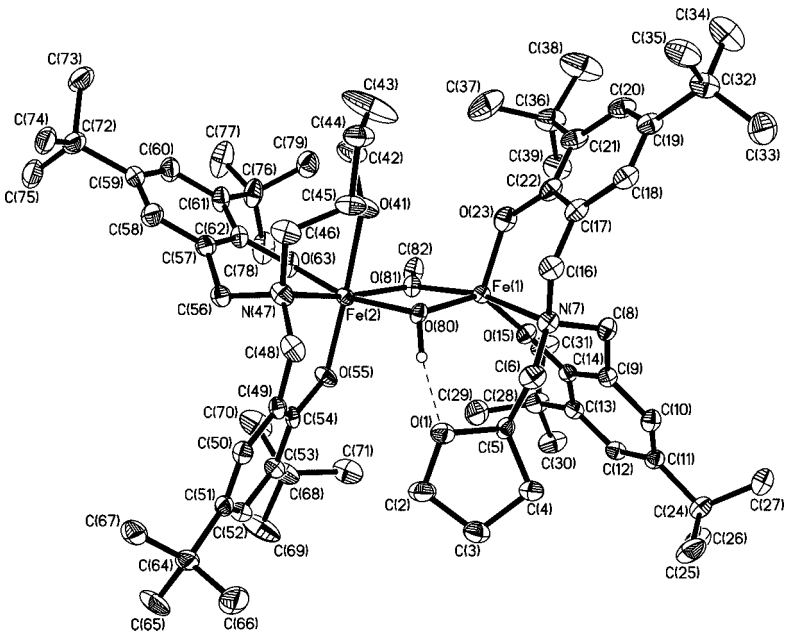


Figure 3. ORTEP diagram and atom labeling scheme for complex **2** (thermal ellipsoid probability 40%).

Table 3. Selected bond lengths [Å] and angles [°] for complex **2**·$Et_2O$.

| | | | |
|---|---|---|---|
| Fe(1)–O(23) | 1.796(2) | O(23)–Fe(1)–O(15) | 108.21(9) |
| Fe(1)–O(15) | 1.9172(19) | O(23)–Fe(1)–O(80) | 113.67(19) |
| Fe(1)–O(80) | 1.946(7) | O(23)–Fe(1)–O(81) | 97.77(9) |
| Fe(1)–O(81) | 1.983(2) | O(15)–Fe(1)–O(81) | 96.65(9) |
| Fe(1)–N(7) | 2.210(2) | O(80)–Fe(1)–O(81) | 78.95(19) |
| Fe(2)–O(55) | 1.887(3) | O(23)–Fe(1)–N(7) | 92.58(8) |
| Fe(2)–O(63) | 1.910(3) | O(15)–Fe(1)–N(7) | 88.55(8) |
| Fe(2)–O(81) | 1.991(2) | O(80)–Fe(1)–N(7) | 87.27(18) |
| Fe(2)–O(80) | 2.075(6) | O(81)–Fe(1)–N(7) | 164.31(9) |
| Fe(2)–N(47) | 2.196(2) | O(63)–Fe(2)–O(80) | 165.8(3) |
| Fe(2)–O(41) | 2.207(5) | O(55)–Fe(2)–O(80) | 92.5(2) |
| O(55)–Fe(2)–O(63) | 101.0(3) | O(81)–Fe(2)–O(80) | 75.8(2) |
| O(55)–Fe(2)–O(81) | 105.64(15) | O(55)–Fe(2)–N(47) | 85.54(13) |
| O(63)–Fe(2)–O(80) | 165.8(3) | O(81)–Fe(2)–N(47) | 163.88(9) |
| O(81)–Fe(2)–O(80) | 75.8(2) | O(55)–Fe(2)–O(41) | 160.3(2) |
| O(63)–Fe(2)–N(47) | 93.04(15) | O(81)–Fe(2)–O(41) | 88.93(17) |
| O(80)–Fe(2)–N(47) | 92.4(2) | N(47)–Fe(2)–O(41) | 77.73(14) |
| O(63)–Fe(2)–O(41) | 90.3(3) | | |
| O(80)–Fe(2)–O(41) | 78.1(3) | | |
| Fe(1)–O(81)–Fe(2) | 103.27(10) | | |

A perspective drawing of complex **3** [$L_2Fe^{III}_2(\mu\text{-}C_2O_4)$] and the atom-labeling Scheme are shown in Figure 4. Crystals of **3** contain two molecules of $CH_2Cl_2$ as solvent molecules of crystallization. Selected bond lengths and angles are given in Table 4. The asymmetric unit contains half of the dimer and consequently the geometries of the two iron centers are identical, with ligation provided by the two oxygen atoms of the bridging oxalate, two phenolate oxygens, one amine nitrogen and one ethereal oxygen belonging to the terminal ligand L resulting in a distorted octahedral arrangement. The two iron centers and the oxalate bridge are coplanar with a maximum deviation of 0.093 Å. As is expected and observed for the structures **1** and **2**, the Fe–O (ether) bond length at 2.178(2) is long and the *trans*-disposed Fe–O (phenolate) length at 1.867(2) Å is significantly short. The Fe–O and Fe–N bond lengths are in conformation with the high-spin $d^5$ electron configuration for the ferric centers in **3**, which corroborates with the Mössbauer and magnetic measurements. The Fe···Fe separation of 5.465 Å is comparable with those reported for other oxalate-bridged differic(III) complexes.[13]

Complex **4**·$C_2H_5OC_2H_5$ adopts a dimeric structure and the molecular structure is shown in Figure 5 along with the atom numbering scheme. Selected bond lengths and angles are listed in Table 5. Each copper atom has a $CuNO_4$ pentacoordinate environment and is bridged by two phenoxide oxygens O(15) and O(63). The $Cu_2O_2$ core is essentially planar, and none of the atoms deviates from the least-square plane by more than 0.38 Å. However, the Cu–O(63) and Cu–O(15) distances are different and the copper centers are separated by 2.766 Å, which is significantly shorter than those reported for phenoxy-bridged dicopper(II) complexes.[14]

The geometrical parameters $\tau$ of 0.31 and 0.29 for Cu(1) and Cu(2), respectively, suggest that the complex has a geometry closer to square-pyramidal ($\tau$ = 0) than to trigonal bipyramidal ($\tau$ = 1).[15] Thus, complex **4** adopts an folded structure with the two square-pyramidal copper centers bridged by the two phenoxide oxygen atoms, O(15) and O(63), with the Cu(1)–O–Cu(2) angles of 87.88(5)° and 88.65(5)°, respectively. The dispositions of the ligands are such that the equatorial tripodal nitrogen atoms N(7) and N(47), are in *syn* positions. Thus, the equatorial plane for each copper center consists of $CuO_3N$ resulting from three phenolate oxygen atoms and the amine nitrogen atom. The oxygen atoms originating from the tetrahydrofuran arms of

 © 2007 Wiley-VCH Verlag GmbH & Co. KGaA, Weinheim 

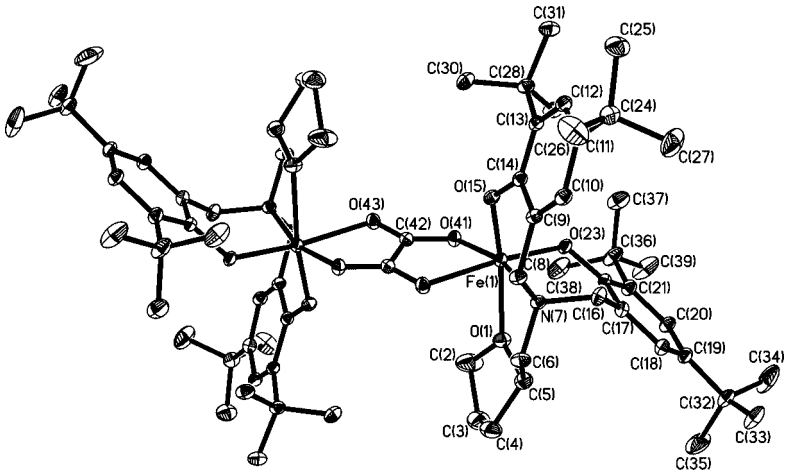


Figure 4. ORTEP diagram and atom labeling scheme for complex **3** (thermal ellipsoid probability 50%).

Table 4. Selected bond lengths [Å] and bond angles [°] for complex **3**·2$CH_2Cl_2$.

| | | | |
|---|---|---|---|
| Fe(1)–O(15) | 1.8665(19) | Fe(1)–O(23) | 1.8728(18) |
| Fe(1)–O(41) | 2.0394(19) | Fe(1)–N(7) | 2.155(2) |
| Fe(1)–O(43) | 2.1747(19) | Fe(1)–O(1) | 2.178(2) |
| O(43)–Fe(1) | 2.1746(19) | N(7)–Fe(1)–O(43) | 89.03(8) |
| O(15)–Fe(1)–O(1) | 164.80(8) | O(23)–Fe(1)–O(1) | 91.14(8) |
| O(41)–Fe(1)–O(1) | 91.19(8) | N(7)–Fe(1)–O(1) | 77.48(8) |
| O(43)–Fe(1)–O(1) | 80.94(8) | O(15)–Fe(1)–O(23) | 100.69(9) |
| O(15)–Fe(1)–O(41) | 96.51(8) | O(23)–Fe(1)–O(41) | 98.11(8) |
| O(15)–Fe(1)–N(7) | 92.36(8) | O(23)–Fe(1)–N(7) | 92.55(8) |
| O(41)–Fe(1)–N(7) | 164.61(8) | O(15)–Fe(1)–O(43) | 87.69(8) |
| O(23)–Fe(1)–O(43) | 171.39(9) | O(41)–Fe(1)–O(43) | 78.82(7) |

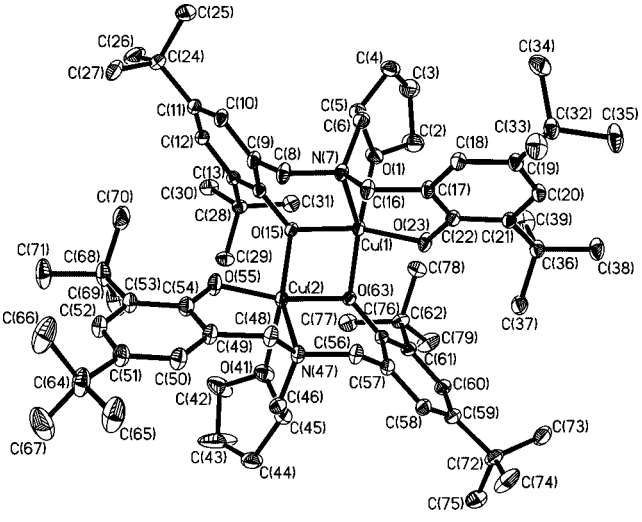


Figure 5. ORTEP diagram and atom labeling scheme for complex **4** (thermal ellipsoid probability 50%).

the aminebis(phenolate) ligand occupy the axial positions with *anti* conformation. As is observed for other structures, Cu–O (ether) bond is appreciably long with 2.334(5) Å and 2.400(4) Å.

Table 5. Selected bond lengths [Å] and angles [°] for complex **4**·$C_2H_5OC_2H_5$.

| | | | |
|---|---|---|---|
| Cu(1)–O(23) | 1.8780(14) | O(15)–Cu(1)–Cu(2) | 47.12(4) |
| Cu(1)–O(15) | 1.9571(13) | O(63)–Cu(1)–Cu(2) | 44.58(4) |
| Cu(1)–O(63) | 2.0156(13) | O(55)–Cu(2)–O(63) | 167.41(6) |
| Cu(1)–N(7) | 2.0482(16) | O(55)–Cu(2)–O(15) | 92.65(6) |
| Cu(1)–O(1) | 2.334(5) | O(63)–Cu(2)–O(15) | 74.81(5) |
| Cu(1)–O(1X) | 2.343(9) | O(55)–Cu(2)–N(47) | 96.94(7) |
| Cu(2)–O(55) | 1.8723(15) | O(63)–Cu(2)–N(47) | 93.63(6) |
| Cu(2)–O(63) | 1.9418(13) | O(15)–Cu(2)–N(47) | 149.94(6) |
| Cu(2)–O(15) | 2.0280(14) | O(55)–Cu(2)–O(41X) | 89.3(3) |
| Cu(2)–N(47) | 2.0543(17) | O(63)–Cu(2)–O(41X) | 99.9(3) |
| Cu(2)–O(41X) | 2.291(11) | O(15)–Cu(2)–O(41X) | 132.3(2) |
| Cu(2)–O(41) | 2.400(4) | N(47)–Cu(2)–O(41X) | 76.4(3) |
| O(23)–Cu(1)–O(15) | 167.37(6) | O(55)–Cu(2)–O(41) | 98.10(9) |
| O(23)–Cu(1)–O(63) | 92.66(6) | O(63)–Cu(2)–O(41) | 90.52(8) |
| O(15)–Cu(1)–O(63) | 74.76(5) | O(15)–Cu(2)–O(41) | 127.24(9) |
| O(23)–Cu(1)–N(7) | 95.90(6) | N(47)–Cu(2)–O(41) | 79.52(9) |
| O(15)–Cu(1)–N(7) | 84.46(6) | Cu(1)–O(15)–Cu(2) | 87.88(5) |
| O(63)–Cu(1)–N(7) | 148.77(6) | Cu(1)–O(63)–Cu(2) | 88.65(5) |
| O(23)–Cu(1)–O(1) | 99.77(11) | Cu(1)···Cu(2) | 2.7658(3) |
| O(15)–Cu(1)–O(1) | 89.37(10) | | |
| O(63)–Cu(1)–O(1) | 129.51(11) | | |
| N(7)–Cu(1)–O(1) | 78.42(11) | | |
| O(23)–Cu(1)–O(1X) | 90.8(2) | | |
| O(15)–Cu(1)–O(1X) | 98.2(2) | | |
| O(63)–Cu(1)–O(1X) | 130.59(18) | | |
| N(7)–Cu(1)–O(1X) | 79.36(19) | | |
| O(23)–Cu(1)–Cu(2) | 122.29(5) | | |

## Mössbauer Isomer Shifts and Quadrupole Splittings

The zero-field Mössbauer spectrum of solid **1** at 80 K is broad and hence the spectrum was recorded in an applied field of 7 T at 4.2 K. This record shows a well-resolved six-line spectrum (Figure 6). A least-square fit of the spectrum yields isomer shift $\delta = 0.54$ mm·s$^{-1}$ and quadrupole splitting $\Delta E_q = 1.55$ mm·s$^{-1}$. The Mössbauer data support the high-spin state of the ferric ion in a distorted octahedral field for complex **1** and are in agreement with the structural data.

Analysis of the zero-field Mössbauer spectra at 80 K for **2** and **3** yields the following parameters: isomer shift $\delta =$ 0.497 mm·s$^{-1}$, quadrupole splitting $\Delta E_q = 1.12$ mm s$^{-1}$ for **2**

 © 2007 Wiley-VCH Verlag GmbH & Co. KGaA, Weinheim 

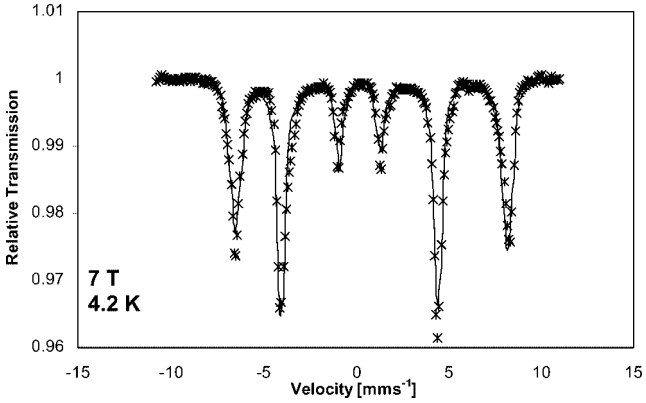


Figure 6. Mössbauer spectrum of **1** (applied field strength 7 T, $T$ = 4.2 K.

and isomer shift $\delta$ = 0.531 mm s$^{-1}$ and quadrupole splitting $\Delta E_q$ = 1.23 mm s$^{-1}$ for **3**. These data indicate the presence of high-spin electronic configuration for the $d^5$ ferric(III) ions present in **2** and **3**.

### Magnetic Susceptibility Measurements

Magnetic susceptibility data for polycrystalline samples of complexes **1**–**4** were collected in the temperature range 2–290 K in an applied magnetic field of 1 T. We start our discussion with the magnetic properties of the mononuclear complex **1**, [LFe$^{III}$(acac]. Complex **1** exhibits above 20 K essentially temperature-independent magnetic moment values $\mu_{eff}$ = 5.90 + 0.01 $\mu_B$, and thus contains clearly a high-spin $d^5$ ion, h.s.Fe$^{III}$.

The magnetic behaviour of **2**, [$Fe_2L_2(\mu\text{-}OCH_3)(\mu\text{-}OH)$] is characteristic of an antiferromagnetically coupled dinuclear complex (Figure 7). At 290 K the $\mu_{eff}$ value of 7.76 $\mu_B$ ($\chi_M \cdot T$ = 7.5295 cm$^3$ K mol$^{-1}$) decreases monotonically with decreasing temperature until it reaches a value of 0.70 $\mu_B$ ($\chi_M \cdot T$ = 0.06127 cm$^3$ K mol$^{-1}$) at 1.9 K; this is a clear indication of exchange coupling between two paramagnetic high-spin Fe$^{III}$ centers ($S_{Fe}$ = $^5/_2$) with a resulting $S_t$ = 0 ground state. We used the Heisenberg–Dirac–van Vleck spin-Hamiltonian in the form $\hat{H} = -2J\hat{S}_1 \cdot \hat{S}_2$ for an isotropic exchange coupling between two spins $S_1$ and $S_2$. The solid line in Figure 7 represents the best fit with the following parameters: $J$ = –5.84 cm$^{-1}$, $g_1 = g_2$ = 2.00 (fixed) and TIP = 140 × 10$^{-6}$ cm$^3$ mol$^{-1}$ emu. The evaluated antiparallel exchange falls in the range observed for comparable diferric complexes containing alkoxo-, phenoxo- and hydroxo-bridges.[12] For comparison purposes, we report here some of our unpublished results on dibridged diferric(III) complexes **A**, **B**, **C**, and **D** comprising of six-coordinate Fe$^{III}_2(\mu\text{-}OH)_2$, 5-coordinated Fe$^{III}_2(\mu\text{-}OH)_2$, six-coordinate Fe$^{III}_2(\mu\text{-}OH)(\mu\text{-}$phenoxo) and six-coordinate Fe$^{III}_2(\mu\text{-}OCH_3)(\mu\text{-}$OAc), respectively.[16] Additionally, we have earlier reported a bis(μ-phenoxo)differic complex (**E**)[4a] containing a five-coordinate and a six-coordinate iron(III) center exhibiting an antiferromagnetic exchange coupling $J$ = –7.4 cm$^{-1}$. Examination of **2** together with complexes **A**–**E** confirms the earlier notion about the exchange coupling ability of the bridging ligands following the trend $OH^- < OC_6H_5^- \approx OCH_3^-$. In addition, the strength of exchange coupling is weaker in five-coordinate Fe$^{III}$ than that in six-coordinate species. The strongest coupling $|J|$ = 14.1 cm$^{-1}$ observed for **D** with the widest bridging angle Fe(1)–O–Fe(2) of about 127°, resulting in an effective overlap between the metal and bridging-atom orbitals, is also in agreement with the existing magneto-structural correlation for the hydroxo-, alkoxo- and phenoxo-bridged diferric complexes.

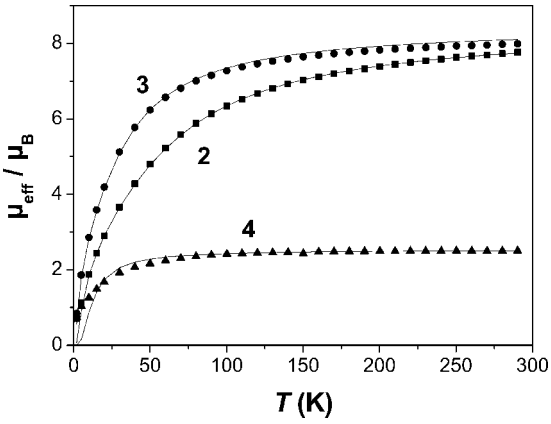


Figure 7. Magnetic measurements for complex **2**, **3** and **4**.

The $\mu_{eff}$ vs. $T$-plot for **3** is also shown in Figure 7 and indicates the nature of coupling operatiang between the two high-spin $d^5$ centers through the oxalate-bridge to be antiferromagnetic. The best parameters evaluated by simulation of the magnetic data are $J$ = –3.1 cm$^{-1}$, $g$ = 2.00. The exchange coupling constant in **3** compares well with those reported previously for oxalato-bridged dinuclear iron(III) complexes[13,17] and emphasizes the remarkable ability of the oxalate-bridge to transmit exchange interactions between paramagnetic centers separated by a distance more than 5 Å. It is noteworthy that structurally characterized oxalato-bridged differic(III) complexes are scarce in the literature.

The effective magnetic moment per molecule, $\mu_{eff}$, for complex **4** (Figure 7) in the temperature range 290–90 K remains nearly constant, 2.50–2.39 $\mu_B$, which is very close to the value of magnetic moment for two uncoupled spins of $S$ = $^1/_2$. Below 90 K, $\mu_{eff}$ starts to decrease with decreasing temperature and reaches a value of $\mu_{eff}$ = 0.74 $\mu_B$ at 1.9 K. The observed temperature dependent magnetic moments for **4** confirms the dimeric nature with an antiferromagnetic exchange coupling of this compound. Simulation of these experimental data results in the following best fit parameters: $J$ = –12.0 cm$^{-1}$, $g$ = 2.05. The exchange coupling is much weaker than those reported for the bis(μ-phenoxide)dicopper(II) core, which in most of the cases is characterized by very strong antiferromagnetic interaction ($|J| \geq$ 100 cm$^{-1}$) with the Cu–O(Ph)–Cu angles ranging from 98.9° to 104.8°;[14] for examples of ferromagnetic coupling the Cu–O(Ph)–Cu angle lies in the range 90.8–96.1° and they are very rare.[14e,14i,14m] The remarkably weak antiferromagnetic interaction in **4** can be accounted for by con-

 © 2007 Wiley-VCH Verlag GmbH & Co. KGaA, Weinheim 

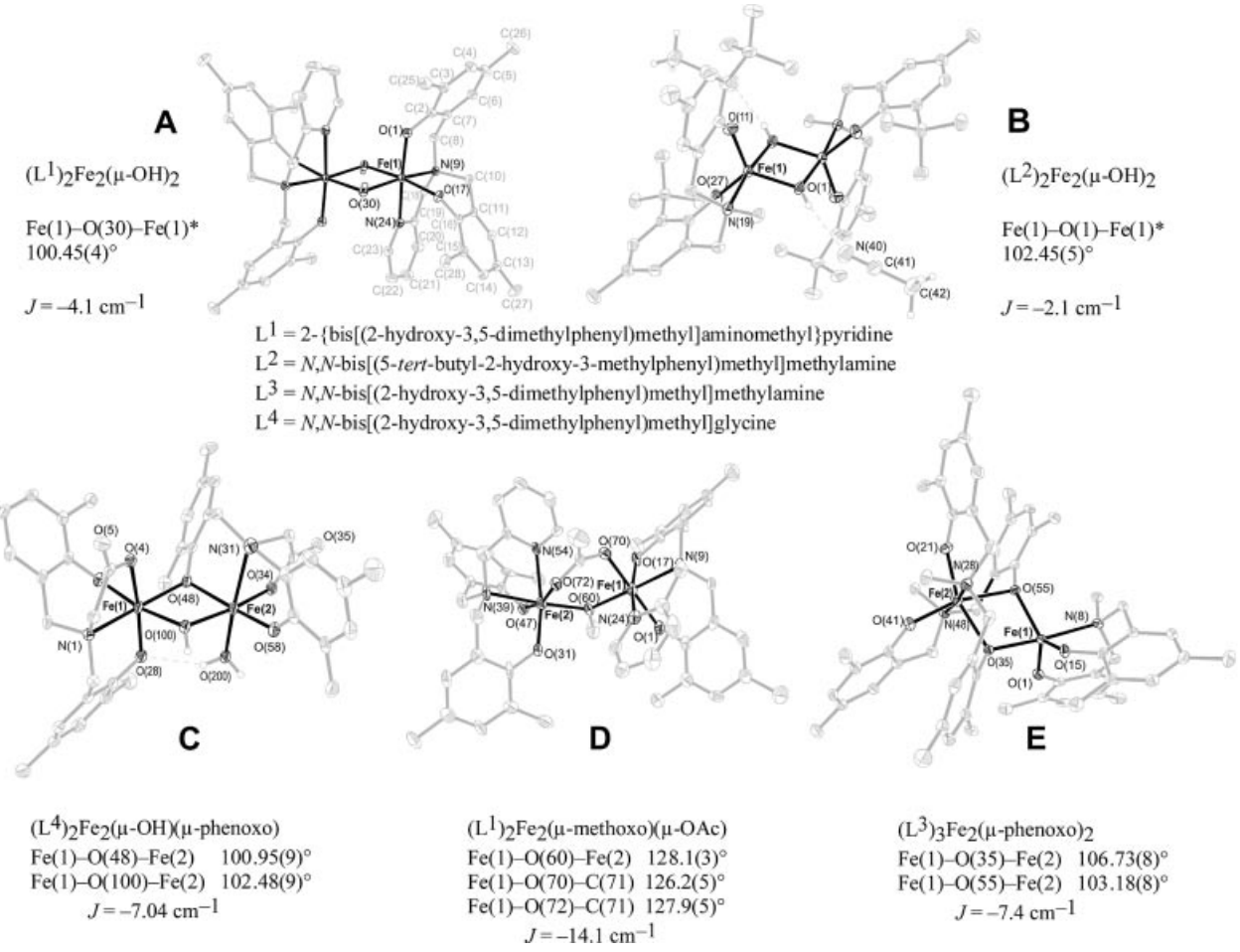


sidering the following major factors controlling the exchange interactions: (i) the equatorial planes of the copper centers, Cu(1)O(15)O(63)N(7)O(23) and Cu(2)O(63)N(47)O(55)O(15) are not planar with a dihedral angle of 81° between the planes, thus reducing the overlap of the magnetic orbitals of the copper centers via the *p*-orbitals of the bridging phenoxide oxygens; (ii) the angles at the bridging oxygen Cu–O(Ph)–Cu of about 88°, the smallest reported so far in the literature, result in considerable ferromagnetic contribution to the overall exchange interactions; (iii) the phenoxo oxygens, O(15) and O(63), adopt distorted pyramidal geometry (340.2° and 342.0°), thus increasing ferromagnetic contributions,[18] and (iv) small Cu···Cu distance of 2.766 Å also favors for decreasing the overall antiferromagnetic interaction by increasing ferromagnetism.[19] Hence, all these combined effects reduce the overall antiferromagnetic interactions drastically. It is remarkable that the Cu–O(Ph)–Cu angle at 88° for **4** with an antiferromagnetic coupling is even smaller than those for the ferromagnetically coupled diphenoxodicopper(II) complexes reported in the literature.[14e,14i,14m] These results suggest for a more intricate rationalization of exchange coupling in such phenoxo-bridged copper(II) complexes.

In this context we would like to point out that the Cu···Cu separation of 2.766 Å is the shortest known for bis(μ-phenoxide)dicopper(II) complexes. A similar bisphenoxo compound, $Cu_2L'_2$, ($H_2L'$ = *N*,*N*-bis(2-hydroxylbenzyl)-*N*,*N*-dimethylethylenediamine) has been reported to exhibit a weak exchange coupling ($J = -10$ cm$^{-1}$);[14h] the two copper centers in $Cu_2L'_2$ are in distorted trigonal-bipyramidal environments with the Cu–O(Ph)–Cu angle at 99.7° and the Cu(1)···Cu(1′) separation of 3.190 Å.

### Electrochemistry and Spectroelectrochemistry

Cyclic- and square-wave voltammograms (CV and SQW) of complexes **1**–**4** have been recorded in $CH_2Cl_2$ solutions containing 0.2 M $[(n\text{Bu})_4\text{N}]PF_6$ as supporting electrolyte. A conventional three electrode arrangement was used, consisting of a glassy carbon working electrode, an $Ag/AgNO_3$ reference electrode and a platinum-wire counter electrode. Ferrocene was added as an internal standard after completion of a set of experiments, and potentials are referenced vs. the ferrocenium/ferrocene couple ($Fc^+$/Fc). Coulometric experiments were performed (at –25 °C) at appropriate fixed potentials to determine the number of electrons/molecule transferred in the redox process under investigation. During coulometry electronic spectra were recorded in order to obtain information about the mechanism of the redox process.

 © 2007 Wiley-VCH Verlag GmbH & Co. KGaA, Weinheim 

The CV and SQW voltammograms (Figure 8) observed with **1**–**4** revealed that each complex can be stepwise two times reversibly oxidized ($E_1^{ox}$ and $E_2^{ox}$ in Table 6). $E_1^{ox}$ and $E_2^{ox}$ are similar for **1**–**4**, which suggests that the oxidation mechanism might be the same for all complexes.

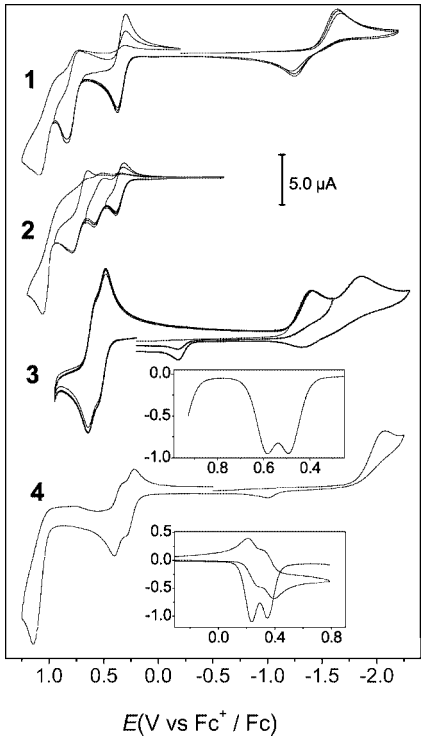


Figure 8. Cyclic and square-wave voltammogramms of complexes **1**–**4** in $CH_2Cl_2$ at room temperature.

Table 6. Electrode potentials (in Volt) for oxidation and reduction of complexes **1**–**4**, measured at ambient temperature in $CH_2Cl_2$ solutions and referenced vs. the $Fc^+/Fc$ couple.

| | $E_4^{ox}$ /V | $E_3^{ox}$ /V | $E_2^{ox}$ /V | $E_1^{ox}$ /V | $E_{red}$ /V |
|---|---|---|---|---|---|
| **1** | | | +0.76[a] | +0.34[a] | –1.4[b] |
| **2** | +1.05[c] | +0.78[a] | +0.55[a] | +0.35[a] | –1.7[c] |
| **3** | | | +0.58[a] | +0.49[a] | –1.4[c]; –1.8[c] |
| **4** | | +1.14[c] | +0.36[a] | +0.25[a] | –2.1[c] |

[a] Reversible reaction, redox potential $E_{1/2}$ is given. [b] Electrochemical quasi-reversible reaction; estimated $E_{1/2}$ is given. [c] Irreversible reaction, peak potential is given.

In a coulometric experiment with the dimeric iron complex **3** it was found that 2 electrons per molecule had passed after completion of electrolysis at +0.8 V. The SQW voltammograms before and after coulometry were identical, indicating that the resulting monocation and dication were stable on the time scale of coulometry (20 min at –25 °C). The electronic spectral changes observed during $2e^-$ oxidation are shown in Figure 9. It is seen that the pattern of the changes is the same for both oxidation steps: a sharp band at 410 nm and a much broader one at 750 nm develop, which are typical for the formation of two phenoxyl radicals. Therefore the two oxidations are ligand centred. The small difference of the two redox potentials (90 mV) suggests that both ligands of the two respective iron-ions get mono-oxidized.

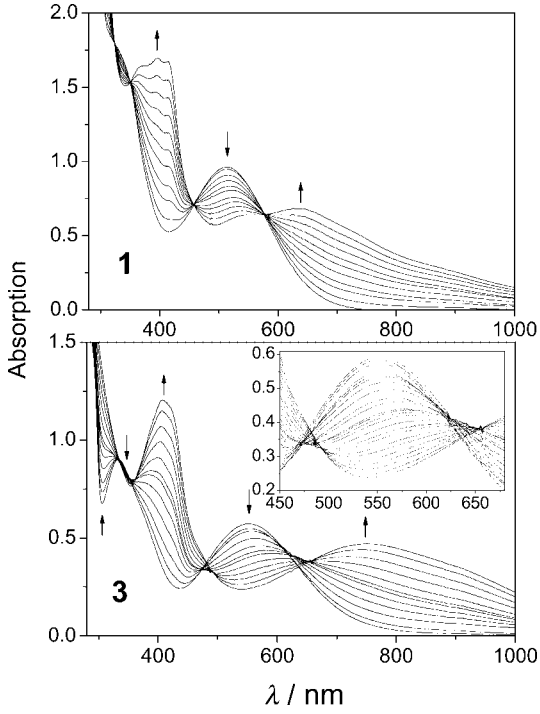


Figure 9. The electronic spectral changes during 1-e-oxidation for **1** and 2-e-oxidation for **3** (coulometry at $T$ = –25 °C).

The CV of the dimeric copper complex **4** exhibits two reversible oxidations with a similar small difference in their redox potentials (110 mV) and also the absolute values of the redox potentials of this copper complex are similar to those of the iron complex **3**. Since furthermore the electronic spectrum of coulometrically generated monocation of **4** has a pronounced and sharp absorption band at 415 nm, we assume the same ligand centred oxidation mechanism for **4** as that for **3**.

The CV of the monomeric iron complex **1** exhibits at room temperature two oxidation waves of reversible appearance, followed by an irreversible oxidation (Figure 8). Already the dication, however, should be quite unstable, since the third oxidation is not observed at low temperatures (–25 °C) and, therefore, most possibly arises from a decomposition product of the dication. The monocation was stable under coulometric conditions and the UV/Vis absorption changes again indicate phenoxyl radical formation: an increase around 400 nm was observed and a new broad range centering around 630 nm (Figure 9).

All oxidized forms of **2** turned out to be unstable under coulometric conditions and, therefore, reliable spectroscopic data of them could not be obtained. However, the similarity of the redox potentials to those of the other complexes speaks again for ligand based oxidations.

At more positive potentials, the cyclic voltammograms of the dimeric complexes **2** and **4** show further oxidation waves, see Table 6. They are most possibly arising from oxidation of further phenolate moieties of the complexes, but there is no direct evidence for this interpretation.

 © 2007 Wiley-VCH Verlag GmbH & Co. KGaA, Weinheim 

In the negative potential range there are reductions discernible in the voltammograms which must be metal-centred. Only the $Fe^{III}/Fe^{II}$ reduction of **1** is chemically reversible and occurs with a low rate of heterogeneous charge transfer, from the electrochemical view the reduction is quasi-reversible. This can be deduced from the high separation of the peaks of reduction and re-oxidation ($\Delta E_p$). The separation is strongly dependent on the scan rate in a way that is typical of quasi-reversible reactions ($\Delta E_p$ = 0.53 V and 0.31 V at scan rates of 0.8 V/s and 0.05 V/s, respectively). The reductions of all other complexes are (chemically) irreversible, even on the time scale of cyclic voltammetry.

## Concluding Remarks

The paper has described diversified ligating properties of a tetradentate ligand with [O,N,O,O] donor atoms. Both mononuclear and dinuclear complexes have been isolated and thoroughly studied. It has been shown that electrochemical oxidations are ligand-centered, i.e. formation of phenoxyl radicals from the coordinated phenolates.

Emphasis has been given in this work to structural and electronic effects arising from the incorporation of a pendent tetrahydrofuran moiety to the aminebis(phenolate) ligand, described earlier by us.[4] As expected the metal–O-(tetrahydrofuran) interactions are weak as judged by the comparatively long M–O(THF) distances. The use of a weak donor atom, THF-O, has made the isolation of an asymmetric diferric(III) complex containing a 5- and a six-coordinate ferric centers viable. A comparison with the hydroxo-, alkoxo- and phenoxo-bridged dinuclear $Fe^{III}$ complexes from our laboratory has allowed us to judge the spin-exchange ability of the mentioned groups as exchange mediators. Moreover, for the diferric series it has been conclusively shown that the Fe–O–Fe angle is a major factor in determining the strength of the exchange interaction.

A bis(μ-phenoxo)dicopper(II) compound **4** with a remarkably weak antiferromagnetic exchange interaction ($J$ = –12 $cm^{-1}$) along with the structural factors contributing to the weak interaction has been described. The copper(II) compound **4** is unique with the most short metal–metal separation of 2.766 Å and the smallest bridging angle Cu–O(Ph)–Cu of about 88° in the literature reported for bis(μ-phenoxo)dicopper(II) systems.

## Experimental Section

**Materials and Physical Measurements:** Reagent or analytical grade materials were obtained from commercial suppliers and used without further purification, except those for electrochemical measurements. Elemental analyses (C,H,N) were performed by the Microanalytical Laboratory Dornis & Kolbe, Mülheim, Germany. Fourier transform infrared spectroscopy on KBr pellets was performed on a Perkin–Elmer 2000 FT IR instrument. Electronic absorption spectra in solution were measured on a Perkin–Elmer Lambda 19 spectrophotometer. Magnetic susceptibilities of *powdered samples* were recorded on a SQUID magnetometer in the temperature range 2–295 K with an applied field of 1 T. Experimental susceptibility data were corrected for the underlying diamagnetism using Pascal's constants and for the TIP contributions.

The Mössbauer spectrometer worked in the conventional constant-acceleration mode with a $^{57}Co/Rh$ source. Isomer shifts are given relative to α-Fe at room temperature (room temp.). Cyclic voltammetric and coulometric measurements were performed on EG&G equipment (potentiostat/galvanostat model 273A). Mass spectra were obtained with either a Finnigan MAT 8200 (electron ionization, EI MS) or a MAT 95 (electrospray ESI MS) instrument; a Bruker DRX 400 instrument was used for NMR spectra. Instrumental conditions for liquid chromatography are as follows: Shimadzu SPD-10 AV, Phenomenex Luna-5 C18, 150 × 4.6 mm column, UV 280 nm, eluent: $CH_3OH/H_2O$ (9:1), room temp., sample size 5 μL, recording speed 0.5 cm $min^{-1}$.

**Synthesis of $H_2L$:** The ligand 2-{bis[(3,5-di-*tert*-butyl-2-hydroxybenzyl)amino]methyl}tetrahydrofuran was prepared as described in the literature.[6b] The purity (98.9%) of the ligand was checked by liquid chromatography; retention time 7.2 min for the eluent methanol with a flow rate of 0.8 mL $min^{-1}$; m.p. 148–149 °C. EI-MS: *m/z* (%) = 537 (32) [$M^+$], 466 (99.7) [$M^+ - C_4H_8O$], 219 (100) [$M^+ - C_{15}H_{23}O$]. $^1H$ NMR ($CDCl_3$): $\delta$ = 8.79 (br. s, 2 H), 7.24 (d, $J$ = 2 Hz, 2 H), 6.86 (d, $J$ = 2 Hz, 2 H), 4.26 (m, 1 H), 4.01 (m, 1 H), 3.88 (m, 1 H), 3.75 (m, 4 H), 2.60 (m, 1 H), 2.51 (m, 1 H), 1.91 (m, 3 H), 1.54 (m, 1 H), 1.40 (s, 18 H), 1.26 (s, 18 H) ppm. IR (KBr): $\tilde{\nu}$ = 3372 (s), 2963 (vs), 2867 (s), 1481 (s), 1443 (m), 1360 (s), 1302 (m), 1241 (s), 1217 (s), 1042 (m), 880 (s) $cm^{-1}$.

**[LFe(acetylacetonate)], [LFe(acac)] (1):** Solid $Fe(acac)_3$ (1 mmol, 0.35 g) was added to a solution of $H_2L$ (1 mmol, 0.54 g) and $Et_3N$ (2.8 mL) in distilled methanol (70 mL). The resulting red-orange solution was refluxed for 0.5 h, whereupon the color changed to dark red. On cooling a dark red solid precipitated. X-ray-quality crystals were grown by recrystallization from a 1:1 mixture of diethyl ether and methanol. Yield 0.47 g (68%). IR (KBr): $\tilde{\nu}$ = 2959, 2902, 1588, 1519, 1474, 1443, 1415, 1379, 1360, 1304, 1271, 1240, 1202, 1169, 1018, 976, 877, 838, 746 $cm^{-1}$. EI-MS: *m/z* (%) = 690 (47.7) [$M^+$], 591 (14) [$M - C_5H_7O_2$], 472 (100) [$M - C_{15}H_{23}O$], 372 (80) [$M - C_5H_7O_2 - C_{15}H_{23}O$]. UV/Vis ($CH_2Cl_2$): $\lambda_{max}$ ($\varepsilon$, $M^{-1}cm^{-1}$) = 329 sh (8224), 517 (4620) nm. $Fe(C_{35}H_{53}NO_3)(C_5H_7O_2)$ (690.87): calcd. C 69.54, H 8.77, N 2.02, Fe 8.08; found C 69.4, H 8.2, N 2.0, Fe 8.1.

**[$L_2Fe_2$(μ-$OCH_3$)(μ-OH)] (2):** Dry $FeCl_2$ (1 mmol, 0.126 g) was added under argon to a thoroughly degassed methanolic solution (70 mL) of $H_2L$ (1 mmol, 0.537 g), $Et_3N$ (2.8 mL) and $PPh_3$ (2 mmol, 0.524 g). The resulting mixture was refluxed for 0.5 h resulting in a pale green solution, which upon exposure to air turned to dark red. The dark red solid was filtered and washed with methanol and air-dried. Yield 0.59 g (55%). X-ray-quality crystals were grown from a 1:1 solvent mixture of ether/methanol. IR (KBr): $\tilde{\nu}$ = 2954, 2902, 2868, 1602, 1471, 1439, 1413, 1361, 1274, 1239, 1203, 1169, 1132, 1067, 914, 874, 841, 809, 749 $cm^{-1}$. ESI-MS (positive mode, diethyl ether solution): *m/z* = 1201.7 (55) [$M^+ - OCH_3$], 591.3 (100) [$FeC_{35}H_{53}NO_3$]. UV/Vis ($CH_2Cl_2$): $\lambda_{max}$ ($\varepsilon$, $M^{-1}cm^{-1}$) = 329 (12540), 465 (7560) nm. $C_{71}H_{110}Fe_2N_2O_8$ (1231.56): calcd. C 70.62, H 8.51, N 2.42, Fe 8.33; found C 69.2, H 9.0, N 2.3, Fe 9.0.

**[$L_2Fe_2$(μ-$C_2O_4$)] (3):** Solid $FeCl_2$ (1 mmol, 0.126 g) was added under argon to a degassed solution in methanol (70 mL) of $H_2L$ (0.537, 1 mmol), $Et_3N$ (5.4 mL) and oxalic acid (0.5 mmol, 0.06 g). The resulting mixture was stirred for 1 h and then exposed to air to yield a violet solution. The solution was filtered to get rid of any solid particles. The mother liquor was evaporated on a rotary evaporator to obtain a violet microcrystalline solid with an yield

 © 2007 Wiley-VCH Verlag GmbH & Co. KGaA, Weinheim 

of 0.51 g (40%). Violet single crystals were grown in a mixture of methanol/dichloromethane (1:1). IR (KBr): $\tilde{\nu}$ = 2952, 2903, 2869, 1655, 1470, 1443, 1438, 1414, 1304, 1268, 1241, 1170, 837, 7.33 $cm^{-1}$. ESI-MS (positive mode, $CH_2Cl_2$ solution): *m/z* = 1271 (68) [$M^+$]. UV/Vis ($CH_2Cl_2$): $\lambda_{max}$ ($\varepsilon$, $M^{-1}cm^{-1}$) = 335 (10340), 554 (6620) nm. $C_{72}H_{106}Fe_2N_2O_{10}$ (1271.3): calcd. C 68.02, H 8.40, N 2.20, Fe 8.78; found C 67.8, H 8.3, N 2.2, Fe 8.7.

**$L_2Cu_2$ (4):** A methanolic solution (75 mL) of $H_2L$ (1 mmol, 0.537 g) containing sodium methoxide (10 mmol, 0.54 g) was treated with solid $Cu(OAc)_2{\cdot}2H_2O$ (1 mmol, 0.199 g) and the resulting mixture was refluxed for 1 h whereupon a dark red solid appeared. The precipitate was collected by filtration, washed with methanol and air-dried; yield 0.74 g (62%). Red-brown single crystals were obtained from a mixture of diethyl ether/methanol (1:1). IR (KBr): $\tilde{\nu}$ = 2952, 2901, 2868, 1606, 1471, 1436, 1415, 1360, 1304, 1298, 1248, 1237, 1204, 1168, 1131, 1071, 1012, 875, 830, 740 $cm^{-1}$. EI-MS: *m/z* (%) = 1198 (1) [$M^+$], 598 (40) [$CuC_{35}H_{53}NO_3$]. UV/Vis ($CH_2Cl_2$): $\lambda_{max}$ ($\varepsilon$, $M^{-1}cm^{-1}$) = 234 sh (8685), 423 (5260), ca. 730 (800) nm. $C_{70}H_{106}Cu_2N_2O_6$ (1198.9): calcd. C 70.13, H 8.91, N 2.34, Cu 10.6; found C 70.1, H 8.9, N 2.2, Cu 10.4.

**X-ray Crystallographic Data Collection and Refinement of the Structures:** Data collection for $H_2L$, **1**–**4**, was carried out on a Bruker-Nonius Kappa CCD diffractometer at 100(2) K by using graphite-monochromated Mo-$K_\alpha$ radiation ($\lambda$ = 0.71073 Å). Final cell constants were obtained from a least-squares fit of all integrated reflections. Intensity data were corrected for Lorentz and polarization effects. The data sets for **1** and **2** were corrected for absorption (SADABS, Bruker-Nonius 2004).[20] The structures were solved by direct method and refined by full-matrix least-squares techniques based on $F^2$ (ShelXTL software package);[21] the neutral atom scattering factors of the program were used. Crystal data and refinement details are listed in Table 7.

Table 7. Crystallographic data for **1**·$C_2H_5OC_2H_5$, **2**·$C_2H_5OC_2H_5$ and **3**·$2CH_2Cl_2$.

| | **1** | **2** | **3** |
|---|---|---|---|
| Empirical formula | $C_{42}H_{65}FeNO_{5.5}$ | $C_{75}H_{120}Fe_2N_2O_9$ | $C_{74}H_{110}Cl_4Fe_2N_2O_{10}$ |
| Formula weight | 727.80 | 1305.43 | 1441.14 |
| Temperature /K | 100(2) | 100(2) | 100(2) |
| Wavelength /Å | 0.71073 | 0.71073 | 0.71073 |
| Crystal system, space group | monoclinic, *Pc*, No. 7 | monoclinic, $P2_1/c$, No. 14 | monoclinic, $P2_1/n$, No. 14 |
| Unit cell dimensions | $a$ = 15.5080(8) Å, $\alpha$ = 90° | $a$ = 15.5175(5) Å, $\alpha$ = 90° | $a$ = 15.2801(5) Å, $\alpha$ = 90° |
| | $b$ = 9.2357(5) Å, $\beta$ = 104.059(5)° | $b$ = 17.7071(6) Å, $\beta$ = 100.105(5)° | $b$ = 17.0204(6) Å, $\beta$ = 103.123(5)° |
| | $c$ = 29.535(2) Å, $\gamma$ = 90° | $c$ = 27.6524(10) Å, $\gamma$ = 90° | $c$ = 15.3018(5) Å, $\gamma$ = 90° |
| Volume /Å$^3$ | 4103.5(4) | 7480.2(4) | 3875.7(2) |
| $Z$, $D_c$ /Mg m$^{-3}$ | 4, 1.178 | 4, 1.159 | 2, 1.235 |
| μ /mm–1 | 0.411 | 0.441 | 0.566 |
| $F$(000) | 1576 | 2832 | 1536 |
| Crystal size /mm | 0.14 × 0.04 × 0.03 | 0.18 × 0.06 × 0.04 | 0.06 × 0.06 × 0.02 |
| Reflections collected/unique | 57159–23295 [$R$(int) = 0.0497] | 96609/17127 [$R$(int) = 0.0491] | 98709/11707 [$R$(int) = 0.0680] |
| Absorption correction | Gaussian | Gaussian | none |
| Refinement method | full-matrix least-squares on $F^2$ | full-matrix least-squares on $F^2$ | full-matrix least-squares fit on $F^2$ |
| Data/restraints/parameters | 23295/21/937 | 17127/670/942 | 11707/30/434 |
| Goodness-of-fit on $F^2$ | 1.072 | 1.047 | 1.236 |
| Final $R$ indices [$I > 2\sigma(I)$] | $R_1$ = 0.0560, $wR_2$ = 0.1120 | $R_1$ = 0.616, $wR_2$ = 0.1435 | $R_1$ = 0.0639, $wR_2$ = 0.1609 |
| $R$ indices (all data) | $R_1$ = 0.0785, $wR_2$ = 0.1215 | $R_1$ = 0.0799, $wR_2$ = 0.1543 | $R_1$ = 0.0728, $wR_2$ = 0.1645 |
| Absolute structure parameter | not reliable | | |
| Largest diff. peak and hole /e·A$^{-3}$ | 0.707 and –0.519 | 0.775 and –0.726 | 0.660 and –0.559 |
| | $H_2L$ | **4**·$C_2H_5OC_2H_5$ | |
| Empirical formula | $C_{35}H_{55}NO_3$ | $C_{74}H_{116}Cu_2N_2O_7$ | |
| Formula weight | 537.80 | 1272.77 | |
| Temperature /K | 100(2) | 100(2) | |
| Wavelength /Å | 0.71073 | 0.71073 | |
| Crystal system, space group | orthorhombic, $P2_12_12_1$, No. 19 | monoclinic, $P2_1/n$, No. 14 | |
| Unit cell dimensions | $a$ = 9.0712(6) Å, $\alpha$ = 90° | $a$ = 18.8386(6) Å, $\alpha$ = 90° | |
| | $b$ = 11.8239(8) Å, $\beta$ = 90° | $b$ = 15.2455(4) Å, $\beta$ = 101.768(4)° | |
| | $c$ = 31.201(2) Å, $\gamma$ = 90° | $c$ = 25.7956(8) Å, $\gamma$ = 90° | |
| Volume /Å$^3$, $Z$ | 3346.5(4), 4 | 7252.9(4), 4 | |
| $D_c$ /Mg m$^{-3}$ | 1.067 | 1.166 | |
| μ /mm$^{-1}$ | 0.066 | 0.637 | |
| $F$(000) | 1184 | 2752 | |
| Crystal size /mm | 0.22 × 0.20 × 0.12 | 0.24 × 0.20 × 0.06 | |
| Reflections collected | 31339 | 138783 | |
| Independent reflections ($R_{int}$) | 6751 (0.0439) | 23088 (0.0563) | |
| Absorption correction | not corrected | none | |
| Refinement method | full-matrix least-squares on $F^2$ | full-matrix least-squares on $F^2$ | |
| Data/restraints/parameters | 6751–14–373 | 23088–161–861 | |
| Goodness-of-fit on $F^2$ | 1.103 | 1.117 | |
| Final $R$ indices [$I > 2\sigma(I)$] | $R_1$ = 0.0543, $wR_2$ = 0.1328 | $R_1$ = 0.0568, $wR_2$ = 0.1263 | |
| $R$ indices (all data) | $R_1$ = 0.0625, $wR_2$ = 0.1383 | $R_1$ = 0.0715, $wR_2$ = 0.1328 | |
| Absolute structure parameter | not reliable | | |
| Largest diff. peak and hole /e·A$^{-3}$ | 0.197 and –0.163 | 1.171 and –1.042 | |

 © 2007 Wiley-VCH Verlag GmbH & Co. KGaA, Weinheim 

CCDC-634567 to -634571 (for **1**, **2**, **3**, **4** and $H_2L$, respectively) contain the supplementary crystallographic data for this paper. These data can be obtained free of charge from The Cambridge Crystallographic Data Centre via www.ccdc.cam.ac.uk/data_request/cif.

## Acknowledgments

E. S. is thankful to the Max-Planck Gesellschaft and Iranian Ministry of Science, Research & Technology for a stipend. Thanks are due to Mrs. H. Schucht, Mrs. R. Wagner and Mr. A. Göbels for skilful technical assistance.

[1] a) J. Stubbe, W. A. van der Donk, *Chem. Rev.* **1998**, *98*, 705; b) R. H. Holm, E. I. Solomon, *Chem. Rev.* **1996**, 96; c) J. W. Whittaker, *Chem. Rev.* **2003**, *103*, 2347; d) J. Stubbe, *Chem. Commun.* **2003**, 2511; e) R. Banerjee, *Chem. Rev.* **2003**, *103*, 2081; f) H. Sigel, A. Sigel (Eds.), *Metal Ions in Biological Systems*, vol. 30, Marcel Dekker, New York, **1994**.

[2] Selected examples: a) J. A. Halfen, B. A. Jazdzewski, S. Mahapatra, L. M. Berreau, E. C. Wilkinson, L. Que Jr, W. B. Tolman, *J. Am. Chem. Soc.* **1997**, *119*, 8217; b) Y. Wang, T. D. P. Stack, *J. Am. Chem. Soc.* **1996**, *118*, 1309; c) D. Zurita, I. Gautier-Luneau, S. Menage, J. L. Pierre, E. Saint-Aman, *J. Biol. Inorg. Chem.* **1997**, *2*, 46; d) E. Bill, J. Müller, T. Weyhermüller, K. Wieghardt, *Inorg. Chem.* **1999**, *38*, 5795; e) Y. Shimazaki, S. Huth, A. Odani, Y. Yamauchi, *Angew. Chem. Int. Ed.* **2000**, *112*, 1666; f) S. Itoh, S. Takayama, R. Arakawa, A. Furuta, M. Kumatsu, A. Ishida, S. Takamuku, S. Fukuzumi, *Inorg. Chem.* **1997**, *36*, 1407; g) C. N. Verani, E. Bothe, D. Burdinski, T. Weyhermüller, U. Flörke, P. Chaudhuri, *Eur. J. Inorg. Chem.* **2001**, 2161.

[3] For example: a) P. Chaudhuri, K. Wieghardt, *Prog. Inorg. Chem.* **2001**, *50*, 151; b) S. Mukherjee, T. Weyhermüller, E. Bothe, K. Wieghardt, P. Chaudhuri, *Dalton Trans.* **2004**, 3842; c) T. K. Paine, T. Weyhermüller, K. Wieghardt, P. Chaudhuri, *Dalton Trans.* **2004**, 2092; d) P. Chaudhuri, K. Wieghardt, T. Weyhermüller, T. K. Paine, S. Mukherjee, C. Mukherjee, *Biol. Chem.* **2005**, *386*, 1023; e) C. Mukherjee, T. Weyhermüller, E. Bothe, P. Chaudhuri, *C. R. Chim.* **2007**, in press.

[4] a) T. Weyhermüller, T. K. Paine, E. Bothe, E. Bill, P. Chaudhuri, *Inorg. Chim. Acta* **2002**, *337*, 344; b) T. K. Paine, E. Rentschler, T. Weyhermüller, P. Chaudhuri, *Eur. J. Inorg. Chem.* **2003**, 3167.

[5] N. V. Timosheva, A. Chandrasekharan, R. O. Day, R. R. Holmes, *Inorg. Chem.* **1998**, *37*, 4945.

[6] a) E. Y. Tshuva, I. Goldberg, M. Kol, *J. Am. Chem. Soc.* **2000**, *122*, 10706; b) S. Groysman, I. Goldberg, M. Kol, E. Genizi, Z. Goldschmidt, *Inorg. Chim. Acta* **2003**, *345*, 137; c) J. Okuda, S. Fokken, T. Kleinhenn, T. P. Spaniol, *Eur. J. Inorg. Chem.* **2000**, 1321; d) E. Y. Tshuva, I. Goldberg, M. Kol, Z. Goldschmidt, *Inorg. Chem.* **2001**, *40*, 4263 and references cited therein.

[7] D. Armentano, G. De Munno, J. Faus, F. Lloret, J. Julve, *Inorg. Chem.* **2001**, *40*, 655.

[8] G. Wilkinson, R. D. Gillard, J. A. McCleverty (Editors), *Comprehensive Coordination Chemistry*, Pergamon Press, Oxford, **1987**.

[9] For example: a) B. S. Synder, G. S. Patterson, A. J. Abrahamson, R. Holm, *J. Am. Chem. Soc.* **1989**, *111*, 5214; b) P. Chaudhuri, M. Winter, P. Fleischhauer, W. Haase, U. Flörke, H.-J. Haupt, *Inorg. Chim. Acta* **1993**, *212*, 241.

[10] E. Bill, C. Krebs, M. Winter, M. Gerdan, A. X. Trautwein, U. Flörke, H.-J. Haupt, P. Chaudhuri, *Chem. Eur. J.* **1997**, *3*, 193.

[11] F. A. Cotton, G. Wilkinson, *Advanced Inorganic Chemistry*, Fifth Ed., Wiley, N. Y., **1988**.

[12] R. Werner, S. Ostrovsky, K. Griesar, W. Haase, *Inorg. Chim. Acta* **2001**, *326*, 78 and references cited therein.

[13] a) S. Rashid, S. S. Turner, P. Day, M. E. Light, M. B. Hursthouse, *Inorg. Chem.* **2000**, *39*, 2426; b) T. Fujino, Y. Hoshino, S. Igarashi, Y. Masuda, Y. Yukawa, *Inorg. Chim. Acta* **2004**, *357*, 11; c) M. Feist, S. Troyanov, E. Kemnitz, *Inorg. Chem.* **1996**, *35*, 3067; d) S. Triki, F. Bérézoksky, J. S. Pala, E. Coronado, C. J. Gómez-Garcia, J. M. Clemente, A. Riou, P. Molinie, *Inorg. Chem.* **2000**, *39*, 3771.

[14] Selected examples: a) B. Chiari, O. Piovesana, T. Tarantelli, P. F. Zanazzi, *Inorg. Chem.* **1988**, *27*, 4149; b) G. S. Speier, S. Tisza, Z. Tyeklár, C. W. Lange, C. G. Pierpont, *Inorg. Chem.* **1994**, *33*, 2041; c) L. K. Thompson, S. K. Mandal, S. S. Tandon, J. N. Bridson, M. K. Park, *Inorg. Chem.* **1996**, *35*, 3117; d) M. M. Whittaker, W. R. Duncan, J. W. Whittaker, *Inorg. Chem.* **1996**, *35*, 382; e) H. L. Shyu, H. H. Wei, G. H. Lee, Y. Wang, *Inorg. Chem.* **1996**, *35*, 5396; f) E. V. Rybak-Akimova, D. H. Busch, P. K. Kahol, N. Pinto, N. W. Alcock, H. J. Clase, *Inorg. Chem.* **1997**, *36*, 510; g) X.-H. Bu, M. Du, Z.-L. Shang, R.-H. Zhang, D.-Z. Liao, M. Shinoya, T. Clifford, *Inorg. Chem.* **2000**, *39*, 4190; h) H. Saimiya, Y. Sunatsuki, M. Kojima, S. Kashino, T. Kambe, M. Hirotsu, H. Akashi, K. Najajima, T. Tokii, *J. Chem. Soc., Dalton Trans.* **2002**, 3737; i) T. Kruse, T. Weyhermüller, K. Wieghardt, *Inorg. Chim. Acta* **2002**, *331*, 81; j) E. Berti, A. Caneschi, C. Daiguebonne, P. Dapporto, M. Formica, V. Fusi, L. Giorgi, A. Guerri, M. Micheloni, P. Paoli, R. Pontelfini, P. Rossi, *Inorg. Chem.* **2003**, *42*, 348; k) M. Thirumavalavan, P. Akilan, M. Kandaswamy, K. Chinnakali, G. S. Kumar, H. K. Fun, *Inorg. Chem.* **2003**, *42*, 3308; l) R. Paschke, S. Liebsch, C. Tschierske, M. A. Oakley, E. Sinn, *Inorg. Chem.* **2003**, *42*, 8230; m) S. Mukhopadhyay, D. Mandal, P. B. Chatterjee, C. Desplanches, J.-P. Sutter, R. J. Butchar, M. Chaudhury, *Inorg. Chem.* **2004**, *43*, 8501.

[15] A. W. Addison, T. N. Rao, J. Reedijk, J. van Rijn, G. Vershoor, *J. Chem. Soc., Dalton Trans.* **1984**, 1349.

[16] P. Chaudhuri, T. Weyhermüller, unpublished results.

[17] M. Julve, O. Kahn, *Inorg. Chim. Acta* **1983**, *76*, L39.

[18] V. H. Crawford, H. W. Richardson, J. R. Wasson, D. J. Hodgson, W. C. Hatfield, *Inorg. Chem.* **1976**, *15*, 2107.

[19] O. Kahn, *Inorg. Chim. Acta* **1982**, *62*, 3.

[20] G. M. Sheldrick, *SADABS Program for area detector absorption correction*, Institute for Inorganic Chemistry, University of Göttingen, Germany, **1996**.

[21] *SHELXTL 6.14 Version*, Bruker AXS, Karlsruhe, Germany.

Received: January 24, 2007
Published Online: April 25, 2007

 © 2007 Wiley-VCH Verlag GmbH & Co. KGaA, Weinheim 

DOI: 10.1002/ejic.200700184

# Synthesis and Functionalization of Germanium Triphenylcorrolate: The First Example of a Partially Brominated Corrole

Sara Nardis,[a] Federica Mandoj,[a] Roberto Paolesse,*[a] Frank R. Fronczek,[b] Kevin M. Smith,[b] Luca Prodi,[c] Marco Montalti,[c] and Gionata Battistini[c]

**Keywords:** Corrole / Bromination / Regioselectivity / Porphyrinoids

Ge complexes of 5,10,15-triphenylcorrole were prepared in refluxing dry DMF using $GeCl_4$ as the source of Ge. Chromatographic separation of the crude reaction mixture afforded the μ-oxo dimer **1** and the methoxy derivative **2a**. The corresponding chloride **2b** can be obtained by treatment of **1** or **2a** with HCl. The reaction of **2a** with $Br_2$ in $CHCl_3$/py afforded the hexabromo derivative **3** as the main product, giving the first indication of the regioselective substitution of pyrroles B and C on the corrole ring. The fully brominated open-chain tetrapyrrole **4** was also characterized as a reaction by-product. Different partially brominated Ge complexes **5** and **6** have been obtained by variation of reaction conditions, while the heptabromo derivative was obtained in a mixture with the corresponding fully brominated Ge corrole. Photophysical characterization of Ge corrolates confirmed the high fluorescence quantum yield of such complexes, and also led to the first observation of phosphorescence emissions from corrole complexes.
(© Wiley-VCH Verlag GmbH & Co. KGaA, 69451 Weinheim, Germany, 2007)

## Introduction

In the last few years corrole has been the object of an increasing number of studies, which have resulted in the exploitation of this macrocycle in different fields, such as catalysis,[1] PDT[2] and chemical sensors.[3] The impetus for this renewed interest is the intriguing behaviour shown by corrole, which makes its chemistry unique in the porphyrinoid scenario. This intriguing character can be related to the molecular structure; since it lacks the C20 *meso* bridge (which confers a corrin-like skeleton) corrole retains an 18 π electron aromatic system, closely resembling porphyrins. It is a trianionic ligand, a feature which, together with a contracted porphyrinoid skeleton, leads to the stabilization of formal high oxidation states[4,5] for coordinated metals, and also to the pronounced non-innocent character of corrole as a ligand.[6] The coordination chemistry of this macrocycle is therefore a challenging arena.

Besides its coordination characteristics, another intriguing aspect of corrole chemistry is the reactivity of the peripheral positions of corrole. The recent definition of different synthetic routes[7] for the preparation of *meso*-arylcorroles from commercially available precursors has allowed the functionalization of β-pyrrolic positions to be studied. This constitutes the first step towards the preparation of more elaborate molecular architectures based on corroles.

The β-functionalization of triphenylcorroles, however, introduces the possible formation of different regioisomers due to the lower symmetry of corrole compared with porphyrin, a further challenging feature that should be taken into account. Many research groups have studied different electrophilic reactions such as nitration, formylation, chlorosulfonation or bromination;[8–13] it is worth mentioning that the first three of these were shown to be regioselective, leading to the isolation of partially substituted corroles. For example, chlorosulfonation and nitration reactions[8] were successfully carried out both on the free base and on the gallium complex of tris-pentafluorophenylcorrole, using chlorosulfonic acid and $NaNO_2$/$CH_3CN$ respectively. The interesting result of these synthetic approaches is that it has been possible to isolate only a few isomers among the several possible regioisomers. In the case of the chlorosulfonation reaction, purification of the 2,17- and the 3,17-sulfonic acid derivatives has been reported, while the $NaNO_2$/$CH_3CN$ reaction afforded the mono-nitro, the 3,17-dinitro and the 2,3,7-trinitro derivative, depending on the amount of the nitrating agent used.

Also, in the case of the formylation[8,9] and carboxylation[13] reactions, mono and bis β-regiosubstituted corroles have been obtained as the major products, even though the novelty of these kinds of reactions is probably better deter-

[a] Dipartimento di Scienze e Tecnologie Chimiche, Università di Roma,
"Tor Vergata" 00133 Rome, Italy
Fax: +39-0672594328
E-mail: roberto.paolesse@uniroma2.it
[b] Department of Chemistry, Louisiana State University, Baton Rouge, LA 70803, USA
[c] Dipartimento di Chimica "G. Ciamician", Latemar Unit, Università di Bologna, Bologna, Italy
Supporting information for this article is available on the WWW under http://www.eurjic.org or from the author.

 © 2007 Wiley-VCH Verlag GmbH & Co. KGaA, Weinheim 

mined by the isolation of inner nitrogen substituted compounds. A general feature of these functionalizations is the regioselectivity; 3 and 17 β-pyrrolic positions of the directly linked A and D pyrroles are the sites of the substitution, in agreement with calculations of electron density at those positions already reported in the literature.[8]

It is interesting to note that in the case of bromination,[10–12] attempts to isolate partially brominated corroles have failed to date. Previous studies have demonstrated that bromination reactions carried out on corroles mainly afford the octabromo products both using the corrole free-base and metal complexes, even in the presence of very small amounts of the brominating agent (either NBS and $Br_2$).

Since brominated corroles have been shown to be useful substrates for palladium(0) mediated cross-coupling reactions,[14] we have been keen to explore the possibility of preparing partially brominated corroles. We have previously reported the bromination of the corrole free base,[10] while other groups studied the same reaction with metal complexes, mainly copper[11] and manganese[12] derivatives. In these studies the major reaction product was always the β-octabromocorrole, in which all pyrrolic positions were substituted. No partially substituted derivatives have been isolated, although mixtures of different isomers were reported when the stoichiometry of the brominating agent was reduced. Yields of reaction carried out with the corrole free base, and either NBS or $Br_2$ as brominating agent, are in general quite low; this is probably due to the instability of the macrocycle, which undergoes decomposition before the substitution takes place if oxidizing reagents are present. For this reason, we decided to investigate the reactivity of germanium derivatives of corroles. We chose this metal complex because it is diamagnetic, thereby allowing an easier characterization of the reaction products, and because corrole stabilizes the coordinated metal in the +4 oxidation state. We suspected that this would allow us to better control the substitution reaction and obtain partially brominated derivatives.

## Results and Discussion

The first phase of our study focused on the preparation of the Ge corrole complex. We have reported the preparation of germanium derivatives in the case of β-alkylcorroles,[15] and, to the best of our knowledge, in the triphenylcorrole series there is only one example of a Ge complex, the Ge($TPF_5PC$)OH reported by Gross.[16] We used the same metalation procedure, reacting triphenylcorrole with $GeCl_4$ in refluxing anhydrous DMF, and observed a prompt colour change of the solution from green to red-violet. The UV/Vis spectrum of the reaction mixture also indicated the formation of the complex, with the disappearance of the free base absorbance bands.

TLC of the crude mixture obtained after vacuum evaporation of the DMF showed the presence of two reaction products. We decided to perform a chromatographic separation of the reaction mixture, despite the possible hydrolysis of the Ge–Cl bond, as observed in the case of previous Ge corrole derivatives. Column chromatography on alumina, using $CH_2Cl_2$ as the eluent, afforded a dichroic green-purple fraction followed by a second purple compound which required a mixture of $CHCl_3$/MeOH (95:5) for elution. The UV/Vis spectra of both fractions were in agreement with the coordination of germanium to the corrole macrocycle, but with a significant blue shift of the absorbance bands of the first fraction with respect to the second. This result, together with a high-field shift of the β-pyrrolic proton resonances in the $^1$H NMR spectrum suggested the formation of a μ-oxo dimer derivative (**1**), which was unambiguously characterized by X-ray crystallography. To the best of our knowledge, this is the first example of such a derivative in the corrole series, other than the iron corrole complexes.[16]

Figure 1 shows one of the two Ge μ-oxo dimers in the asymmetric unit. The Ge atoms have square-pyramidal coordination, lying 0.439 Å (average of four) from the $N_4$ plane. The Ge–N distances are in the range 1.881(9)–1.930(9) Å, with axial Ge–O distances in the range 1.718(11)–1.773(13) Å and Ge–O–Ge angles 147.3(5) and 149.0(4)°. Thus the $N_4$ planes within each dimer are not parallel, forming dihedral angles of 19.4(6) and 19.9(5)°.

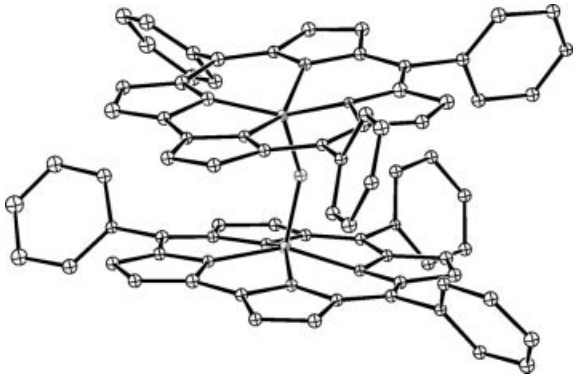

Figure 1. The X-ray structure of **1**.

The characterization of the second fraction indicated the formation of **2a**, in which a methoxy group is present at the axial position. The presence of the methoxy group is due to the well know lability of the Ge–Cl bond toward oxygen ligands and in this case to the solvent mixture used for the elution of the second chromatographic fraction. We also explored the possibility of modifying the nature of the axial ligand, as already observed in the case of β-alkylcorrole complexes,[15] but found not to be possible in the case of $TF_5PC$.[16] Treating a $CHCl_3$ solution of **1** or **2a** with a dilute HCl solution afforded the complex GeTPCCl (**2b**): in the case of **2a** the formation of the chloride complex was monitored by observing the disappearance of the $^1$H NMR signal characteristic of the axial methoxy group which appears at around –1 ppm (Figure 2).

However it should be noted that, in some cases, the isolated complex was contaminated with variable amounts of the corresponding hydroxy derivative, as demonstrated by

 © 2007 Wiley-VCH Verlag GmbH & Co. KGaA, Weinheim 

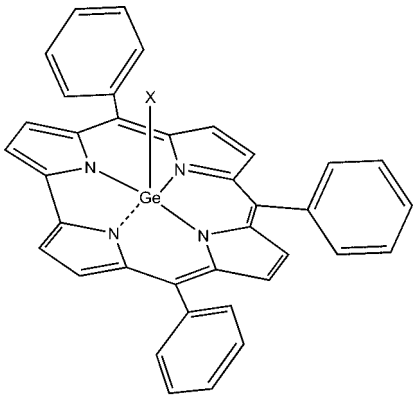


**2a:** X = $OCH_3$
**2b:** X = Cl

Figure 2. Molecular structures of the germanium complexes **2a** and **2b**.

the $^1$H NMR signal for the –OH at –4.4 ppm, thus confirming the easy hydrolysis of the Ge–Cl bond under acidic conditions (Figure 2). The bromination of complex **2a** was carried out according to the previously reported procedure,[11,18] by using liquid bromine in $CHCl_3$/py at room temperature. The reaction was initially carried out with an excess of $Br_2$ in order to drive the reaction to the formation of the fully substituted derivative. This protocol is usually adopted with other metal complexes[11,12] to avoid the potential formation of a mixture of regioisomers. The progress of the reaction was followed by spectrophotometry. A clear red shift of the Soret band was observed, consistent with the presence of halogen atoms in the metal complex structure. However, also with a large excess of $Br_2$, in the case of **2a** TLC of the crude reaction mixture showed a number of products. Work up and purification with a silica plug afforded two main fractions, eluted with $CHCl_3$ and $CHCl_3$/$CH_3OH$ (95:5) respectively. The first fraction contained some residual impurities and was further purified with a silica gel column and $CHCl_3$ as eluent to give an analytically pure product.

The UV/Vis spectrum of this fraction showed the presence of a Soret band, indicating the retention of the corrole macrocycle, but it was interesting to note the presence of a singlet in the β-pyrrolic proton region of the $^1$H NMR, also indicating incomplete peripheral substitution of the complex. The integration ratio corresponded to the presence of two pyrrolic protons, but the presence of a single resonance indicated that substitution had occurred with good regioselectivity. This hypothesis was fully confirmed by the X-ray structure of crystals obtained from $CHCl_3$/$CH_3OH$.

The complex obtained was identified as **3**, possessing six bromine atoms on the peripheral positions. To the best of our knowledge this is the first example of an isolated and characterized partially brominated corrole. The formation of **3**, not only confirms the higher reactivity of the pyrrolic positions on the two directly linked pyrroles A and D, but also gives an indication of the substitution regioselectivity on pyrrole subunits B and C. In this case the reaction leads to the substitution of the protons H8 and H12, closer to the *meso* bridge, with the formation of only one of the three possible regioisomers. This result confirms the behaviour previously observed by Gross and Mahammed in the deuteration of the tris-(pentafluorophenyl)corrole, for which a similar reactivity order, C3 > C2 >> C8 > C7, was reported[19] (Figure 3).

Characterization of the material isolated from the second fraction was more difficult. A Soret-like band was absent from the UV/Vis spectrum, and we observed more resonances than expected in the $^1$H NMR spectrum. In this case, X-ray crystallography was necessary to characterize compound **4**: this derivative is a fully brominated open chain tetrapyrrole (Figure 4).

There are several peculiar features of this compound to be noted. An ethoxy group is added at the former 10-methine bridge of the corrole ring, with the formation of a methane bridge and the consequent interruption of the π conjugation. The ring is opened at the 5-methine bridge and the pyrrole-pyrrole direct link is retained in the tetrapyrrole. The ring opening in this case is different from that observed previously with 10-phenyl-substituted corrole, which afforded the corresponding biliverdin derivatives on reaction with molecular oxygen.[20] As a consequence of the ring opening, a benzoyl group and a pyridinium substituent are present at the terminal α-pyrrolic positions. While the origin of the benzoyl group can be confidently attributed to the oxidation of the methine bridge, the presence of the pyridinium group is more surprising. Furthermore, the positive charge of this group is balanced by the presence of a central divalent ion, which consequently infers a zwitterionic character to the complex. While the identity of the central metal atom is not completely unambiguous, Zn appears most consistent with all available information. Its coordination geometry is square planar, somewhat twisted from planarity by the spiral nature of the ligand. Thus N2 lies 0.62(1) Å and N5 lies –0.43(1) Å out of the plane defined by the metal and the two central N atoms. Zn–N distances vary 1.901(9)–2.016(1) Å.

Further confirmation of the presence of Zn as coordinated metal was given by MALDI mass spectrum, in which a molecular peak at 1360 *m*/*z* was observed. In the FAB spectrum a peak was found at 1299 *m*/*z*, corresponding to the free base derivative after loss of the Zn ion, probably induced by the acidic matrix used in this technique. The source of the coordinated Zn is probably the silica gel used for the chromatographic separation. A similar Zn complex of a fully brominated open chain tetrapyrrole has recently been reported in the literature and was obtained by bromination induced ring-opening of tetraphenylporphyrin.[21]

To explore the possibility of achieving complete bromination of **2a**, the reaction was carried out at reflux for a prolonged time (2 h); in this case we observed significant decomposition of the starting material, with the formation of a mixture of three brominated products. A complete chromatographic separation was difficult to achieve from this mixture, although $^1$H NMR and MALDI-MS charac-

 © 2007 Wiley-VCH Verlag GmbH & Co. KGaA, Weinheim 

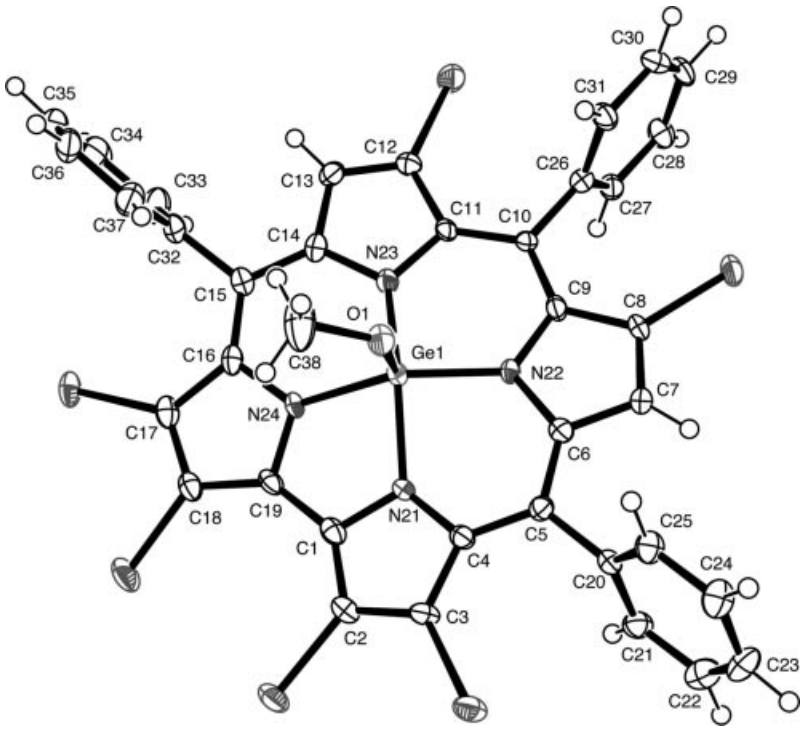


Figure 3. Characterization of **3** by X-ray crystallography.

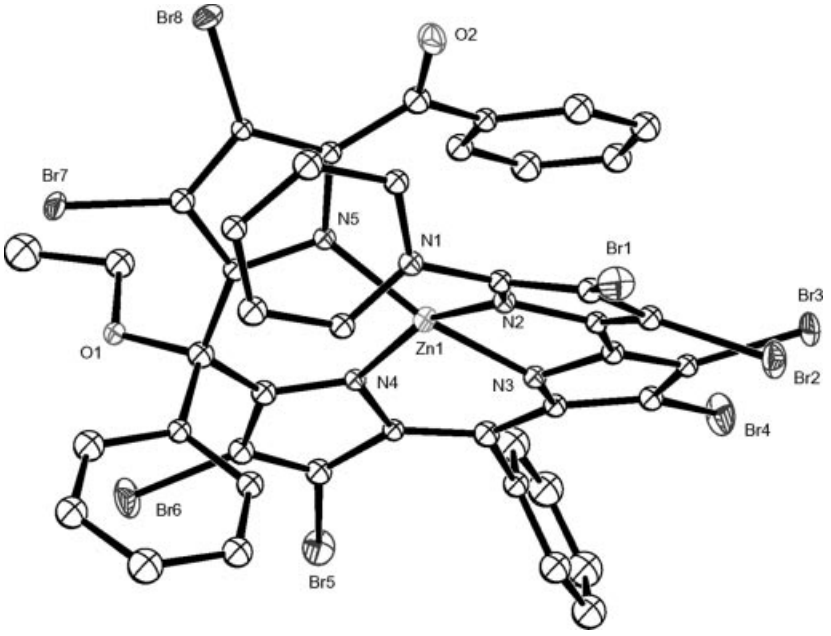


Figure 4. The X-ray structure of **4** (hydrogen atoms omitted).

terization indicated that the main component of the mixture was the heptabromo derivative, with the presence of the fully brominated complex as a minor component. The third component of the mixture, although in a significantly lower amount, was easily identified as **3**, by comparison of the spectroscopic data.

Consequently, these results led us to explore the possibility of obtaining other partially brominated Ge derivatives by reducing the $Br_2$:**2a** ratio. Initially we carried out the reactions reducing the reagent ratio in the range 70:1 to 10:1, obtaining the corresponding pentasubstituted complex as the reaction product. This complex can be reasonably assumed to be **5**, considering that it is the necessary precursor of **3** (Figure 5).

The formation of **5** even with a slight excess of bromine seems to indicate a pronounced reactivity of pyrrole sub-

 © 2007 Wiley-VCH Verlag GmbH & Co. KGaA, Weinheim 

units A and D, which are completely substituted, while the substitution of pyrroles B and C can be modulated by the amount of reagent used.

When we further reduced the amount of $Br_2$ to 1.1 equiv., adding methanol as co-solvent, we observed the formation of a tri-substituted derivative, which can be confidently assumed to be (**6**). Significant decomposition of the starting material was observed in this case, however.

The unprecedented formation of **1** led us to perform a photo-physical characterization of the Ge corrole derivatives, considering that corroles present quantum yield values higher[17] than those of the corresponding porphyrins and that the efficiency of the photophysical process can even be increased by the coordination of small metal ions such as Gallium.[13]

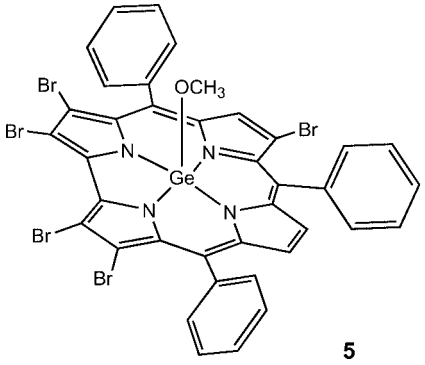


**5**

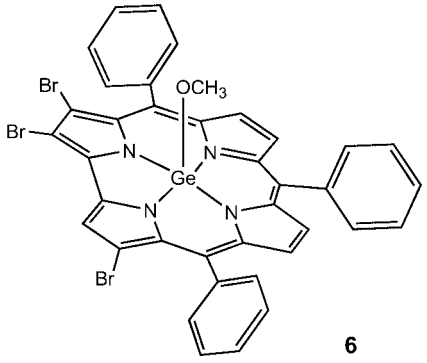


**6**

Figure 5. Molecular structures of **5** and **6**.

The absorption spectra of compounds **1**, **2a** and **3** in dichloromethane are reported in Figure 6, with the most relevant photophysical data reported in Table 1. As expected, because of the already observed validity of the porphyrin four-orbital model for corroles, all three compounds show a Soret band in the 380–440 nm region, and a set of Q bands in the 540–620 nm region. The absorption spectrum of **2a** [that of **2b** is almost identical] is very similar to the one described for Ge(TPF$_5$PC)Cl. This is as expected because the positions of the absorption maxima of corroles are typically unaffected by the nature of the *meso* substituents.[22] For **1**, relevant differences are observed instead: its Soret band, while undergoing an expected almost doubling in intensity, is shifted to a shorter wavelength by 13 nm. On the other hand, the Q bands are much broader and shifted to longer wavelengths. These findings clearly indicate a strong interaction between the two macrocycles in the dimer. It is interesting to note that, at concentrations lower than $10^{-6}$ M, **1** is not stable, since its spectrum slowly changes to become very similar to that of **2a**. As already mentioned, all the bands in **3** are red-shifted compared to **2a**, indicating that the substituents on the β positions are able to affect the photophysical properties of corroles, as already observed for Ga complexes.[23] As far as the fluorescence spectra are concerned, the maximum of the fluorescence band of **2a** (Figure 7) is close to that observed for Ga(TPF$_5$PC)Py (no fluorescence has been previously reported for Ge corroles). In this case, the fluorescence quantum yield, although higher than that of a metallated porphyrin, is lower than that reported for Ga(TPF$_5$PC)Py, probably because of a lower planarity of the macrocycle (Table 2).

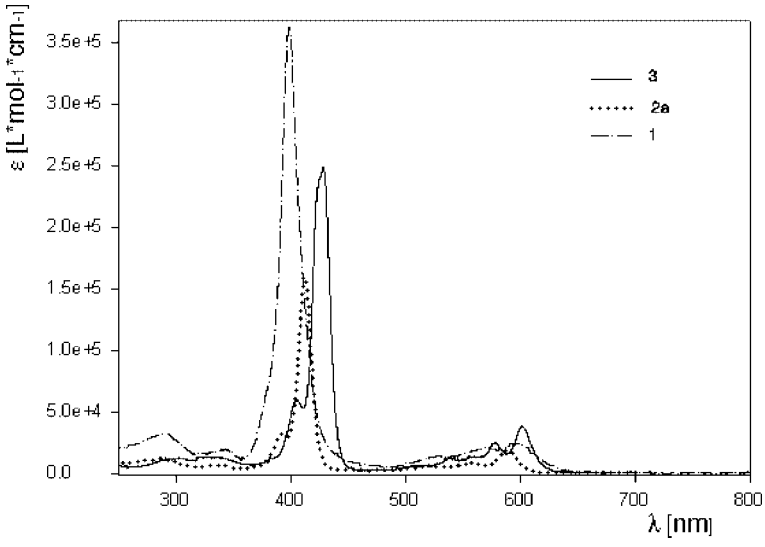


Figure 6. UV/Vis spectra of germanium corrolates.

 © 2007 Wiley-VCH Verlag GmbH & Co. KGaA, Weinheim 

Table 1. Most relevant absorption parameters of **1**, **2a** and **3** in $CH_2Cl_2$ solutions at room temperature and at 77 K.

| Compound | $\lambda_{max}$ [nm] | $\varepsilon_{max}$ [$M^{-1}\,cm^{-1}$] |
|---|---|---|
| **1** | 399 | 363000 |
| | 528 | 13400 |
| | 567 | 21300 |
| | 598 | 24050 |
| **2a** | 412 | 160000 |
| | 5220 | 7600 |
| | 560 | 9650 |
| | 590 | 20600 |
| **3** | 428 | 248000 |
| | 538 | 12050 |
| | 578 | 25100 |
| | 603 | 38000 |

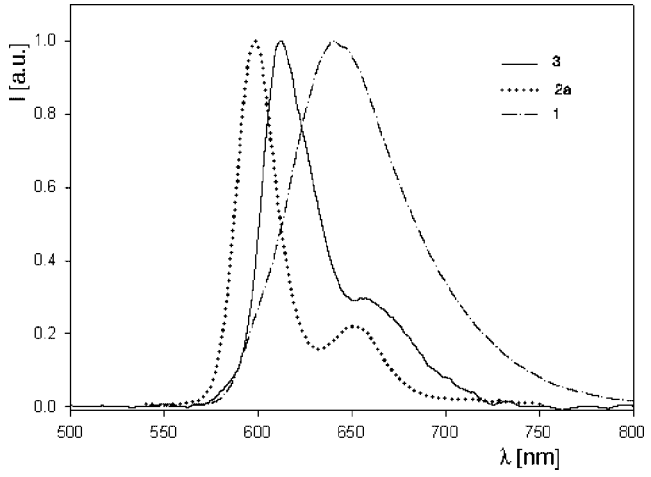


Figure 7. Fluorescence spectra of germanium corrolates.

Table 2. Most relevant luminescence parameters of **1**, **2a** and **3** in $CH_2Cl_2$ solutions at room temperature and at 77 K.

| | Room temperature | | | 77 K | | 77 K | |
|---|---|---|---|---|---|---|---|
| Compd. | $\lambda_{max}$ [nm] | $\Phi$ | $\tau$ [ns] | $\lambda_{max}$ [nm] | $\tau$ [ns] | $\lambda_{max}$ [nm] | $\tau$ [ms] |
| **1** | 660 | 0.033 | < 0.4 | 660 | 2.3 | 818 | 35.2 |
| **2a** | 598 | 0.14 | < 0.4 | 599 | 2.1 | 784 | 28.4 |
| **3** | 614 | 0.005 | < 0.4 | 603 | 3.0 | 806 | 3.2 |

The very short excited state lifetime observed in this case supports this hypothesis, indicating the presence of a very fast ($k_{nr} \geq 2 \times 10^9\ s^{-1}$) non radiative deactivation process. It is interesting to note, however, that the radiative rate constant is also very high ($k_r \geq 2 \times 10^8\ s^{-1}$), especially if compared with other porphyrins and corroles.[22b] This finding is clearly in line with the indication that corroles can be of great interest for their photophysical properties, especially if it is possible to design new systems showing slower non radiative processes. Additionally, for **2a** this latter process is thermally activated as shown by the remarkable increase in the excited state lifetime at 77 K. The brominated compound **3** shows a red shifted fluorescence spectrum in line with its absorption spectrum, with a relatively low quantum yield, most probably due to the heavy atom effect introduced by the presence of bromine atoms. The fluorescence maximum of this compound at 77 K is the only one that shows a blue shift with respect to the maximum observed at room temperature, most probably because its excited state shows a reduced dipole moment compared to the ground state.[22b] The fluorescence spectrum of the dimer **1** is much broader and shifted even more towards longer wavelengths in comparison to the monomer **2a**, again indicating a strong interaction between the two macrocycles. The quantum yield (0.033), although reduced, is still in the same range as those of two very well known metal complexes, ZnTPP and $Ru(bpy)_3^{2+}$. Again, the lifetime is very short, indicating the occurrence of a relatively fast radiative deactivation process also in this case.

Finally, we were able, for the first time, to observe the phosphorescence coming from a corrole complex at 77 K (Figure 8).

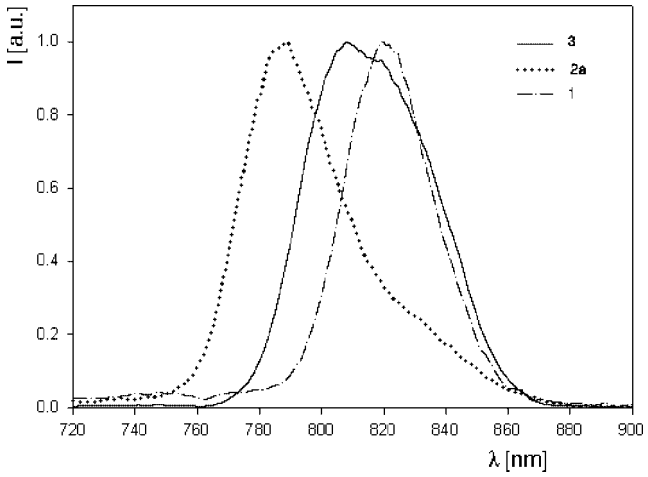


Figure 8. Phosphorescence spectra of germanium corrolates.

All the phosphorescence bands observed were in the 760–840 nm region, following the energetic order observed for the fluorescence bands. It is worth noting that **1** and **2a** showed an excited state lifetime of around 30 ms, while **3** decayed ten times more quickly, indicating a much faster inter-system crossing process, which confirms the presence of the already invoked heavy atom effect in **3**.

## Conclusions

In conclusion, we have detailed here a useful, never previously reported route for the preparation of partially substituted corroles by bromination of the Ge triphenylcorrole complex, together with a further example of the peculiar reactivity of this macrocycle. Photophysical characterization of Ge complexes also led to the first example of phosphorescence emission from corrole derivatives.

## Experimental Section

**Physical Methods:** $^1H$ NMR spectra were recorded with a Bruker AM400 (400 MHz) or Bruker Advance 300 (300 MHz) spectrometer. Chemical shifts are given in ppm relative to tetramethylsilane (TMS). Routine UV/Vis spectra were measured with a Varian Cary

 © 2007 Wiley-VCH Verlag GmbH & Co. KGaA, Weinheim 

50 Spectrophotometer, whereas more precise measurements were performed with a Perkin–Elmer 18 Spectrophotometer equipped with a temperature-controlled cell holder.

**Materials:** Silica gel 60 (70 ± 230 mesh) was used for column chromatography. Reagents and solvents (Aldrich, Merck or Fluka) were of the highest grade available and were used without further purification. $CH_2Cl_2$ used for the spectrophotometric measurements was stored over activated molecular sieves.

**Synthetic Methods:** Triphenylcorrole was prepared as previously reported in the literature.[7b]

**Germanium 5,10,15-Triphenylcorrolates:** In a 100 mL round-bottomed flask equipped with a stirring bar, corrole (0.1 g; 0.2 mmol), was dissolved in anhydrous DMF (20 mL). $GeCl_4$ (96 μL; 0.8 mmol) was added under nitrogen and the mixture was refluxed for about two hours, monitoring the progress of the reaction by UV/Vis spectroscopy. After the absorption peaks of the starting material had disappeared (the color of the solution changed from green to deep purple), the solvent was evaporated and the product purified by chromatography on silica gel, using $CHCl_3$ as the eluent. The first fraction eluted corresponded to the μ-oxo dimer (**1**), while the second fraction, eluted with a mixture of $CHCl_3$/MeOH (95:5), was characterized as the monomeric germanium methoxide (**2a**). GeTPC-Cl was obtained by treatment of fractions (**1**) and (**2a**) with HCl (4 M). Recrystallization from $CH_2Cl_2$/hexane (1:2), afforded GeTPC–Cl (**2b**) in 60% yield (76 mg, 0.12 mmol).

**Spectroscopic Data for 1:** $^1$H NMR (300 MHz, $CDCl_3$): $\delta$ = 8.92 (d, $^1J$ = 4.2 Hz, 4 H, β-pyrrolic), 8.62 (d, $^1J$ = 4.2 Hz, 4 H, β-pyrrolic), 8.55 (d, $^1J$ = 4.8 Hz, 4 H, β-pyrrolic), 8.18 (d, $^1J$ = 4.8 Hz, 4 H, β-pyrrolic), 7.67 (m, 30 H, phenyl) ppm. MS (FAB): *m/z* (%): 1208 (60) [M$^+$]. $C_{74}H_{46}Ge_2N_8O$ (1208.45): calcd. C 73.55, H 3.83, N 9.27; found C 73.42, H 3.61, N 9.55.

**Crystal Data for 1:** Color: dark purple, $C_{74}H_{46}Ge_2N_8O{\cdot}0.5\,CH_2Cl_2$, $M_r$ = 1250.9, triclinic space group *P*-1, $a$ = 14.6167(15), $b$ = 19.802(3), $c$ = 23.156(4) Å, $\alpha$ = 72.715(7), $\beta$ = 85.464(8), $\gamma$ = 68.930(6)°, $V$ = 5968.8(15) Å$^3$, $Z$ = 4, $\rho_{calcd.}$ = 1.440 g cm$^{-3}$, Mo-$K_\alpha$ radiation ($\lambda$ = 0.71073 Å; $\mu$ = 1.11 mm$^{-1}$), $T$ = 110 K, 31760 data by Nonius KappaCCD, $R$ = 0.098 ($F^2 > 2\sigma$), $R_w$ = 0.269 (all $F^2$) for 16529 unique data having $\theta < 23.2°$ and 759 refined parameters. Two Ge oxo dimers were found in the asymmetric unit. Because of the limited crystal quality, it was possible to refine only Ge, Cl and O anisotropically. Further disordered solvent was modeled with partially-populated C positions.

**Spectroscopic Data for 2a:** $^1$H NMR (300 MHz, $CDCl_3$): $\delta$ = 9.40 (d, $^1J$ = 4.2 Hz, 2 H, β-pyrrolic), 9.21 (d, $^1J$ = 4.8 Hz, 2 H, β-pyrrolic), 9.08 (d, $^1J$ = 4.2 Hz, 2 H, β-pyrrolic), 8.91 (d, $^1J$ = 4.8 Hz, 2 H, β-pyrrolic), 8.44 (m, 2 H, phenyl), 8.35 (m, 1 H, phenyl), 8.21 (m, 2 H, phenyl), 8.09 (m, 1 H, phenyl), 7.81 (m, 9 H, phenyl), –0.96 (s, 3 H, O$CH_3$) ppm. MS (FAB): *m/z* (%): 627 (100) [M$^+$]. $C_{38}H_{26}GeN_4O$ (627.26): calcd. C 72.76, H 4.18, N 8.93; found C 72.83, H 4.42, N 8.96.

**Spectroscopic Data for 2b:** $^1$H NMR (300 MHz, $CDCl_3$): $\delta$ = 9.45 (d, $^1J$ = 4.3 Hz, 2 H, β-pyrrolic), 9.24 (d, $^1J$ = 4.9 Hz, 2 H, β-pyrrolic), 9.12 (d, $^1J$ = 4.3 Hz, 2 H, β-pyrrolic), 8.94 (d, $^1J$ = 4.9 Hz, 2 H, β-pyrrolic), 8.42 (m, 2 H, phenyl), 8.34 (m, 1 H, phenyl), 8.24 (m, 2 H, phenyl), 8.11 (m, 1 H, phenyl), 7.81 (m, 9 H, phenyl) ppm. MS (FAB): *m/z* (%): 631 (100) [M$^+$]. $C_{37}H_{23}ClGeN_4$ (631.68): calcd. C 70.35, H 3.67, N 8.87; found C 70.44, H 3.69, N 8.96.

**Bromination of 2 ($Br_2$:2 = 300:1):** In a 250 mL round-bottomed flask equipped with a dropping funnel, complex **2a** (50 mg, 0.08 mmol) was dissolved in $CHCl_3$ (80 mL) and a solution of $Br_2$ (1.2 mL, 24 mmol; d = 3.119) in 30 mL of $CHCl_3$ was added dropwise during 15 min. The resulting mixture was stirred at room temperature for one hour; after this period, pyridine (0.24 mL, 3.02 mmol; d = 0.978) dissolved in $CHCl_3$ (30 mL) was added and the mixture stirred for a further hour. The crude mixture was then washed with an aqueous solution of $Na_2S_2O_5$ (20% w/v). The organic phase was dried with anhydrous $Na_2SO_4$, the solvent was evaporated and the crude mixture purified with silica gel (plug), using $CHCl_3$ as the eluent. A second fraction was eluted with a mixture of $CHCl_3$/MeOH (95:5). The first fraction was further purified by column chromatography on silica gel, using $CHCl_3$ as the eluent. Recrystallization from $CH_2Cl_2$/MeOH (1:2) of both fractions afforded respectively **3** (34%, 30 mg, 0.027 mmol) and **4** (5%, 5.3 mg, 0.004 mmol).

**Spectroscopic Data for 3:** $^1$H NMR (300 MHz, $CDCl_3$): $\delta$ = 9.11 (s, 1 H, β-pyrrolic), 7.99 (m, 5 H, phenyl), 7.78 (m, 10 H, phenyl), –0.78 (s, 3 H, -O$CH_3$) ppm. MS (MALDI): *m/z* (%): 1101.6 (50) [M$^+$]. $C_{38}H_{20}Br_6GeN_4O$ (1100.64): calcd. C 41.47, H 1.83, N 5.09; found C 41.58, H 1.79, N 5.22.

**Crystal Data for 3:** Color: maroon, $C_{38}H_{20}GeBr_6N_4O$, $M_r$ = 1105.2, monoclinic space group $P2_1/n$, $a$ = 13.330(2), $b$ = 17.952(3), $c$ = 15.974(3) Å, $\beta$ = 114.325(6)°, $V$ = 3483.2(10) Å$^3$, $Z$ = 4, $\rho_{calcd.}$ = 2.107 g cm$^{-3}$, Mo-$K_\alpha$ radiation ($\lambda$ = 0.71073 Å; $\mu$ = 7.87 mm$^{-1}$), $T$ = 110 K, 48918 data points by Nonius KappaCCD, $R$ = 0.051 ($F^2 > 2\sigma$), $R_w$ = 0.115 (all $F^2$) for 10534 unique data points having $\theta < 30.5°$ and 460 refined parameters. Residual electron density peaks near C7 and C13 indicated the presence of small amounts of heptabromo and/or octabromo compounds. Refinement of partially populated Br atoms at these positions led to populations of 2.6%.

**Spectroscopic Data for 4:** $^1$H NMR (300 MHz, $CDCl_3$): $\delta$ = 7.78–7.41 (m, 20 H), 3.77 (q, 2 H, -O$CH_2$CH$_3$), 1.25 (t, 3 H, -OCH$_2CH_3$) ppm. UV/Vis ($CH_2Cl_2$): $\lambda_{max}$ ($\varepsilon \times 10^{-3}$) = 440 (9.3), 601 (3.7), 642 nm (2.4). MS (MALDI): *m/z* (%): 1360.2 (20) [M$^+$]. $C_{44}H_{25}Br_8N_5O_2Zn$ (1360.33): calcd. C 38.85, H 1.85, N 5.15; found C 38.90, H 1.83, N 5.24.

**Crystal Data for 4:** Color: dark blue, $C_{44}H_{25}Br_8N_5O_2Zn{\cdot}CHCl_3{\cdot}C_4H_{10}O$, $M_r$ = 1457.1, monoclinic space group $P2_1/a$, $a$ = 15.599(10), $b$ = 13.913(7), $c$ = 24.280(17) Å, $\beta$ = 90.87(2)°, $V$ = 5269(6) Å$^3$, $Z$ = 4, $\rho_{calcd.}$ = 1.837 g cm$^{-3}$, Mo-$K_\alpha$ radiation ($\lambda$ = 0.71073 Å; $\mu$ = 6.65 mm$^{-1}$), $T$ = 110 K, 22209 data points by Nonius KappaCCD, $R$ = 0.072 ($F^2 > 2\sigma$), $R_w$ = 0.154 (all $F^2$) for 7321 unique data having $\theta < 23.5°$ and 352 refined parameters. Because of limited crystal quality and disordered solvent, it was possible to refine only Zn, Br, Cl and O anisotropically. Refinement of the central metal as Ge led to unrealistically high displacement parameters for this atom as well as significantly higher $R$ values.

**Bromination of 2 ($Br_2$:2 = 70:1):** When the bromination is carried out under the reaction conditions described above, with a reduced amount of $Br_2$ (0.3 mL, 5.8 mmol; $d$ = 3.119), the subsequent chromatographic purification afforded **5** in 43% yield (35 mg, 0.034 mmol).

**Spectroscopic Data for 5:** $^1$H NMR (300 MHz, $CDCl_3$): $\delta$ = 9.07 (s, 1 H, β-pyrrolic), 8.91 (d, $^1J$ = 4.98 Hz, 1 H, β-pyrrolic), 8.66 (d, $^1J$ = 4.98 Hz, 1 H, β-pyrrolic), 7.85 (m, 15 H, phenyl), –0.78 (s, 3 H, O$CH_3$) ppm. UV/Vis ($CH_2Cl_2$): $\lambda_{max}$ ($\varepsilon \times 10^{-3}$) = 423 (215), 533 (10.3), 575 (22), 596 nm (33) ppm. MS (FAB): *m/z* (%): 1022 (60) [M$^+$]. $C_{38}H_{21}Br_5GeN_4O$ (1021.74): calcd. C 44.67, H 2.07, N 5.48; found C 44.56, H 1.98, N 5.52.

**Bromination of 2 ($Br_2$:2 = 1.1:1):** When the bromination is carried out under the reaction conditions described above, with **2** (70 mg,

 © 2007 Wiley-VCH Verlag GmbH & Co. KGaA, Weinheim 

0.11 mmol) and 1.1 equiv. of $Br_2$ (6.3 μL, 0.12 mmol; d 3.119), the subsequent chromatographic purification afforded **6** in 49% yield (47 mg, 0.054 mmol).

**Spectroscopic Data for 6:** $^1$H NMR (300 MHz, $CDCl_3$): $\delta$ = 9.38 (s, 1 H, β-pyrrolic), 8.96 (d, $^1J$ = 4.80 Hz, 2 H, β-pyrrolic), 8.81 (d, $^1J$ = 4.80 Hz, 2 H, β-pyrrolic), 8.12 (m, 5 H, phenyl), 7.77 (m, 10 H, phenyl), –0.84 (s, 3 H, O*CH*$_3$) ppm. UV/Vis ($CH_2Cl_2$): $\lambda_{max}$ ($\varepsilon \times 10^{-3}$) = 414 (198), 525 (8.2), 565 (21.5), 589 nm (30.8) ppm. MS (FAB): *m*/*z* (%): 864 (70) [$M^+$]. $C_{38}H_{23}Br_3GeN_4O$ (863.95): calcd. C 52.83, H 2.68, N 6.49; found C 52.71, H 2.73, N 6.34.

CCDC631925 (for **1**), -631926 (for **3**) and -631927 (for **4**) contain the supplementary crystallographic data for this paper. These data can be obtained free of charge from the Crystallographic Data Centre via www.ccdc.cam.ac.uk/data_request/cif.

**Supporting Information** (see footnote on the first page of this article): $^1$H NMR spectra of new compounds are reported.

## Acknowledgments

This work was supported by Ministero dell'Università e della Ricerca–Fondo per gli Investimenti della Ricerca di Base (MIUR-FIRB) (projects RBNE01KZZM and LATEMAR) (see http://www.latemar.polito.it).

[1] a) Z. Gross, N. Galili, L. Simkhovich, I. Saltsman, M. Botoshansky, D. Blaser, I. Goldberg, *Org. Lett.* **1999**, *1*, 599–602; b) L. Simkhovich, Z. Gross, *Tetrahedron Lett.* **2001**, *42*, 8089; c) A. Mahammed, Z. Gross, *J. Am. Chem. Soc.* **2005**, *127*, 2883–2887.
[2] R. J. Luguya, F. R. Fronczek, K. M. Smith, M. G. H. Vicente, *Tetrahedron Lett.* **2005**, *46*, 5365–5368.
[3] J. Radecki, I. Stenka, E. Dolusic, W. Dehaen, *Electrochim. Acta* **2006**, *51*, 2282–2288.
[4] C. Erben, S. Will, K. M. Kadish in *The Porphyrin Handbook*, vol. 2 (Eds.: K. M. Kadish, K. M. Smith, R. Guilard), Academic Press, San Diego, **2000**, pp. 233–300.
[5] E. Vogel, S. Will, A. Shulze-Tilling, L. Neumann, J. Lex, E. Bill, A. X. Trautwein, A. Wieghardt, *Angew. Chem. Int. Ed. Engl.* **1994**, *33*, 731.
[6] F. A. Walker, S. Licoccia, R. Paolesse, *J. Inorg. Biochem.* **2006**, *100*, 810–837.
[7] a) R. Paolesse in *The Porphyrin Handbook*, vol. 2 (Eds.: K. M. Kadish, K. M. Smith, R. Guilard), Academic Press, New York, **2000**, pp. 201–231; b) S. Nardis, D. Monti, R. Paolesse, *Mini-Rev. Org. Chem.* **2005**, *2*, 355–374; c) D. T. Gryko, *Eur. J. Org. Chem.* **2002**, 1735–1743.
[8] I. Saltsman, A. Mahammed, I. Goldberg, E. Tkachenko, M. Botoshansky, Z. Gross, *J. Am. Chem. Soc.* **2002**, *124*, 7411–7420.
[9] R. Paolesse, S. Nardis, M. Venanzi, M. Mastroianni, F. R. Fronczek, M. G. H. Vicente, *Chem. Eur. J.* **2003**, *9*, 1192.
[10] R. Paolesse, S. Nardis, F. Sagone, R. Khoury, *J. Org. Chem.* **2001**, *66*, 550–556.
[11] I. H. Wasbotten, T. Wondimagegn, A. Ghosh, *J. Am. Chem. Soc.* **2002**, *124*, 8104–8116.
[12] G. Golubkov, J. Bendix, H. B. Gray, A. Mahammed, I. Goldberg, A. J. Di Bilio, Z. Gross, *Angew. Chem. Int. Ed.* **2001**, *40*, 2132.
[13] I. Saltsman, I. Goldberg, Z. Gross, *Tetrahedron Lett.* **2003**, *44*, 5669.
[14] A. Scrivanti, V. Beghetto, U. Matteoli, S. Antonaroli, A. Marini, F. Mandoj, R. Paolesse, B. Crociani, *Tetrahedron Lett.* **2004**, *45*, 5861–5864.
[15] R. Paolesse, S. Licoccia, T. Boschi, *Inorg. Chim. Acta* **1990**, *178*, 9.
[16] L. Simkhovich, A. Mahammed, I. Goldberg, Z. Gross, *Chem. Eur. J.* **2001**, *7*, 1041.
[17] T. Ding, E. A. Alemán, D. A. Mordarelle, C. J. Ziegler, *J. Phys. Chem. A* **2005**, *109*, 7411–7417.
[18] a) L. R. Nudy, H. G. Hutchinson, C. Schieber, F. R. Longo, *Tetrahedron* **1984**, *40*, 2359–2363; b) S. G. Di Magno, V. S.-Y. Lin, M. J. Therien, *J. Org. Chem.* **1993**, *58*, 5983–5993.
[19] Z. Gross, A. Mahammed, *J. Porphyrins Phthalocyanines* **2002**, *6*, 553–555.
[20] R. Paolesse, A. Froiio, S. Nardis, M. Mastroianni, M. Russo, D. J. Nurco, K. M. Smith, *J. Porphyrins Phthalocyanines* **2003**, *7*, 585–592.
[21] C. Liu, D.-M. Shen, Q.-Y. Chen, *Chem. Commun.* **2006**, 770.
[22] a) E. Stesene, A. Dey, A. Ghosh, *J. Am. Chem. Soc.* **2003**, *125*, 16300–16309; b) B. Ventura, A. Degli Esposti, B. Koszarna, D. T. Gryko, L. Flamini, *New J. Chem.* **2005**, *29*, 1559–1566.
[23] J. J. Weaver, K. Sorasaenee, M. Sheikh, R. Goldschmidt, E. Tkachenko, Z. Gross, H. B. Gray, *J. Porphyrins Phthalocyanines* **2006**, *10*, 76–86.

Received: January 11, 2007
Published Online: April 17, 2007

 © 2007 Wiley-VCH Verlag GmbH & Co. KGaA, Weinheim 

DOI: 10.1002/ejic.200600987

# Photochemistry of *trans*- and *cis*-[$RuCl_2(dmso)_4$] in Aqueous and Nonaqueous Solutions

**Małgorzata Brindell,[a] Grażyna Stochel,*[a] Valerio Bertolasi,[b] Rita Boaretto,[b] and Silvana Sostero[b]**

**Keywords:** Ruthenium / Photochemistry / Photolabilization / Photoisomerization / Antitumor agents

The photochemical behavior of the *trans*- and *cis*-[$RuCl_2(dmso)_4$] complexes has been investigated in organic coordinating solvents (dmso, $CH_3CN$) and aqueous solutions by means of electronic and $^1H$ NMR spectroscopy as well as chloride-selective electrode measurements. Excitation in the UVA and visible region of the *cis*-[$RuCl_2(dmso)_4$] complex in dmso leads to geometric isomerization with quantum yields $\Phi_{313} = 0.41$ and $\Phi_{365} = 0.49$ to give the photostable *trans* complex, whereas in acetonitrile and aqueous solutions, both isomerization and substitution processes occur. Moreover, in the latter two solvents, the *trans* isomer is photoactive and undergoes substitution reactions. In acetonitrile, for both *trans*- and *cis*-[$RuCl_2(dmso)_4$] isomers, selective photolabilization of the dimethylsulfoxide ligands results in the formation of the *trans*-[$RuCl_2(CH_3CN)_4$] complex. In aqueous solutions, the dmso and $Cl^-$ ligands are gradually substituted by water molecules to give as a final product a mixture of (aqua)ruthenium(II) and (aqua)(chlorido)ruthenium(II) complexes. These species may prove to be useful in the binding of cellular components.
(© Wiley-VCH Verlag GmbH & Co. KGaA, 69451 Weinheim, Germany, 2007)

## Introduction

The *trans* and *cis* isomers of the [$RuCl_2(dmso)_4$] complex exhibit antimetastasizing activity against several experimental tumors such as P388 leukemia, Lewis lung carcinoma, B16 melanoma, and MCa mammary carcinoma.[1–4] However, the side effects associated with the administration of the therapeutically required high doses of the compounds have promoted the search for alternative methods leading to enhanced anticancer activity of these complexes. A new approach involving site-specific photochemical activation of the metal complex in the tumor cells, which minimizes undesired toxic effects on normal cells, has been suggested recently.[5–8] Moreover, our previous results have shown that the cytotoxicity of the *trans* and *cis* isomers of [$RuCl_2(dmso)_4$] complexes against human (SK-Mel 188) and mouse (S91) melanoma cells is significantly increased by irradiation with UVA light.[9] It has been suggested that one of the factors that contribute to the enhanced antiproliferative activity of the two complexes after illumination is phototransformation of the complexes into more active species, which undergo reactions with cellular components.[9] In this respect it is interesting to understand the photochemical behavior of *trans* and *cis* isomers of ruthenium(II) complexes in greater detail. To the best of our knowledge, the photochemistry of the *cis*- and *trans*-[$RuCl_2(dmso)_4$] complexes in aqueous solution has never been investigated, and the only aspect mentioned in the literature concerns the application of light for the synthesis of the *trans* isomer from the *cis* analogue in dmso solution.[10] In this work we have investigated the photochemical behavior of the *trans*- and *cis*-[$RuCl_2(dmso)_4$] complexes upon irradiation with UVA and/or visible light in organic coordinating solvents like dimethylsulfoxide (dmso) and acetonitrile ($CH_3CN$) as well as in aqueous solutions. The results of Alessio et al.[10] are further corroborated by our present studies: the photochemistry is extended into a more synthetically useful area, and the photochemical properties of the [$RuCl_2(dmso)_4$] complexes are discussed in detail.

## Results and Discussion

### Photochemistry of *trans*- and *cis*-[$RuCl_2(dmso)_4$] in dmso

The electronic absorption spectra for the *trans*-[$RuCl_2(dmso)_4$] (**Ia**) and *cis*-[$RuCl_2(dmso)_4$] (**IIa**) complexes dissolved in dmso are presented in Figure 1 (see also Table 1S, Supporting Information).

[a] Faculty of Chemistry, Jagiellonian University, Ingardena 3, 30-060 Krakow, Poland
Fax: +48-12-6340515
E-mail: stochel@chemia.uj.edu.pl
[b] Department of Chemistry, University of Ferrara, Via Borsari 46, 44 100 Ferrara, Italy
Supporting information for this article is available on the WWW under http://www.eurjic.org or from the author.

 © 2007 Wiley-VCH Verlag GmbH & Co. KGaA, Weinheim 

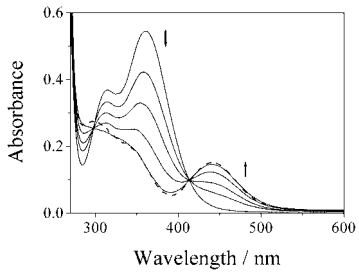


Figure 1. UV/Vis absorption spectra for a 1-mM dmso solution of *cis*-[$RuCl_2(dmso)_4$] irradiated at 365 nm at room temperature for 0, 0.5, 1, 2, and 5 min; the dashed line denotes the spectrum of *trans*-[$RuCl_2(dmso)_4$] in dmso solution.

The *cis* isomer is thermally very stable, whereas the *trans* complex can undergo isomerization to the *cis* analogue [Equation (1)]; however, this process is relatively slow at room temperature ($t_{1/2} \approx 75$ h).[10] Our results have shown that irradiation of a dmso solution of *cis*-[$RuCl_2(dmso)_4$] (**IIa**) with UVA (313 and 365 nm) or visible (400–600 nm) light results in the formation of *trans*-[$RuCl_2(dmso)_4$] (**Ia**). This is in agreement with a previous report by Alessio et al. showing that *trans*-[$RuCl_2(dmso)_4$] can be generated in situ by irradiation of *cis*-[$RuCl_2(dmso)_4$] dissolved in dmso solution with white light.[10]

$$cis\text{-}[RuCl_2(dmso)_3(dmso)] \underset{\Delta}{\overset{h\nu}{\rightleftharpoons}} trans\text{-}[RuCl_2(dmso)_4] \quad (1)$$

The photoisomerization process has been followed by UV/Vis spectroscopic measurements. The absorption band characteristic for the *cis* isomer ($\lambda_{max}$ = 360 nm) decreases in intensity, and a new band characteristic for the *trans* isomer at 441 nm appears upon irradiation (Figure 1). Isosbestic points occurring at 415 and 298 nm confirm simple *cis* to *trans* isomerization. The quantum yields for the photoisomerization reaction have been found to be $0.41 \pm 0.05$ and $0.49 \pm 0.03$ for irradiation at 313 and 365 nm, respectively. The photoisomerization is an efficient process, and the quantum yields are nearly independent of the wavelength of irradiation. This indicates that a good internal conversion of the charge-transfer (CT) manifold to the lowest ligand-field (LF) excited state occurs as observed in early studies of $Ru^{II}$ complexes.[11] No spectral changes have been observed during the irradiation of *trans*-[$RuCl_2(dmso)_4$].

### Photochemistry of *trans*- and *cis*-[$RuCl_2(dmso)_4$] in $CH_3CN$

Given the potential synthetic utility of the photoreaction reported in the Equation (1), we decided to find out whether derivatives of [$RuCl_2(dmso)_4$] could be prepared by photolysis in the presence of almost any coordinating agent L. Our objective here was to see whether sequential substitution of dmso by L is possible until every dmso has been replaced, i.e. whether [$RuCl_2(dmso)_4$] can be converted to [$RuCl_2(CH_3CN)_4$] if L ($CH_3CN$ in this case) resembles dmso in its bonding properties.

The analysis of $^1H$ NMR spectra for the *trans*- and *cis*-[$RuCl_2(dmso)_4$] complexes recorded after their dissolution in $CD_3CN$ indicates that two dmso ligands from the *trans* isomer and one from the *cis* isomer are immediately released and substituted by solvent molecules (Figure 2). These results indicate the formation of [$RuCl_2(dmso)_2(CH_3CN)_2$] from the *trans* isomer and [$RuCl_2(dmso)_3(CH_3CN)$] from the *cis* analogue. The $^1H$ NMR observations are interpreted in terms of the pathways outlined in Scheme 1.

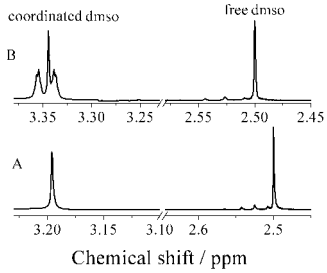


Figure 2. $^1H$ NMR spectra for *trans*-[$RuCl_2(dmso)_4$] (A) and *cis*-[$RuCl_2(dmso)_4$] (B) immediately after dissolution in $CD_3CN$ solution (for the *trans* isomer, the ratio of the integration area of the peak at 3.20 ppm to that at 2.50 ppm is 1:1; for the *cis* isomer, the ratio of the integration area of the peaks at 3.35–3.34 ppm to that at 2.50 ppm is 3:1); $T$ = 20 °C.

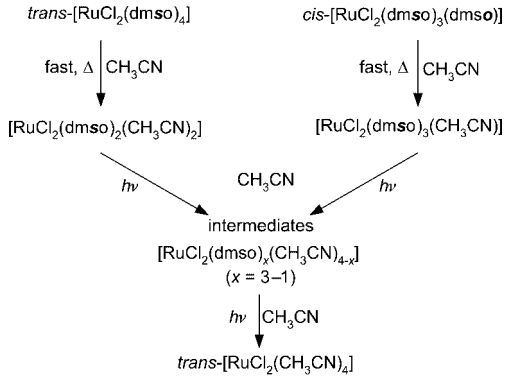


Scheme 1.

The electronic spectra for both complexes in acetonitrile indicated that the complexes are thermally relatively stable and that their further solvolysis process is slow enough not to interfere with our photochemical studies (see Figure 3 for the *trans* isomer).

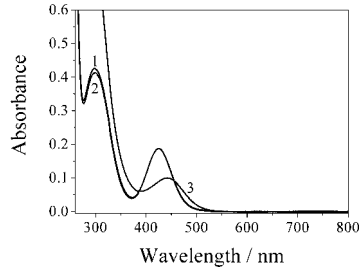


Figure 3. UV/Vis absorption spectra for a 1-mM acetonitrile solution of *trans*-[$RuCl_2(dmso)_4$] recorded immediately after dissolution (1), after 15 min at 20 °C (2), and upon irradiation at $\lambda_{irr} > 400$ nm for 15 min (3); $T$ = 20 °C.

 © 2007 Wiley-VCH Verlag GmbH & Co. KGaA, Weinheim 

Irradiation of the *trans* complex with visible light ($\lambda_{irr} > 400$ nm) results in the gradual dissociation of the remaining coordinated dmso ligands, as revealed in the $^1H$ NMR spectra by the decrease in the intensity of the $CH_3$ resonance at $\delta = 3.20$ ppm originating from the coordinated dmso ligands and the concomitant increase in the intensity of the $CH_3$ resonance at $\delta = 2.50$ ppm ascribed to free dmso in $CD_3CN$ solvent (Figure 4).

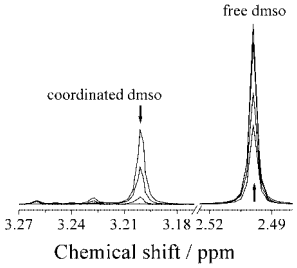


Figure 4. $^1H$ NMR spectra for *trans*-[$RuCl_2(dmso)_4$] ($CD_3CN$ solution) before irradiation (the ratio of the integration area of the peak at 3.20 ppm to that at 2.50 ppm is 1:1) and after being irradiated for 1, 5, and 15 min at $\lambda_{irr} > 400$ nm; $T = 20$ °C.

The photolysis of the *cis* complex proceeds according to the same sequence as that of the *trans* isomer. The possible photolabilization of the $Cl^-$ ligands can be excluded, because $Cl^-$ ions were not detected after photolysis of the complex. Prolonged photolysis of concentrated solutions of the *trans*- or *cis*-[$RuCl_2(dmso)_4$] complexes in $CH_3CN$ led to the formation of the complex *trans*-[$RuCl_2(CH_3CN)_4$]. This was established by elemental analysis, crystallographic data, and by $^1H$ NMR spectra. The resulting *trans* geometry of the complex (see crystallographic data in ref.[17]) was identical to that previously reported for *trans*-[$RuCl_2(CH_3CN)_4$] prepared by classical thermal routes[12–16] or by the photolysis of the [$RuCl_2(\eta^6$-*o*-*n*$Bu_2C_6H_4)]_2$ complex.[17] The new route for the synthesis of *trans*-[$RuCl_2(CH_3CN)_4$] by photosubstitution of dmso ligand with $CH_3CN$ from either the *trans* or *cis* isomer of the [$RuCl_2(dmso)_4$] complex is reported in detail in the Experimental Section.

### Photochemistry of *trans*- and *cis*-[$RuCl_2(dmso)_4$] in $H_2O$

To provide another possible pathway for the photochemical formation of the substitution products, we studied the photochemistry of *trans*- and *cis*-[$RuCl_2(dmso)_4$] in $H_2O$. In water solution, the complexes have been demonstrated[10,18,19] to undergo thermal hydrolysis as shown in Scheme 2.

According to Scheme 2, the two isomers, **Ia** and **IIa**, release two and one dmso ligands, directly after dissolution to afford *trans*,*cis*,*cis*-[$RuCl_2(dmso)_2(H_2O)_2$] (**Ib**) and *cis*,*fac*-[$RuCl_2(dmso)_3(H_2O)$] (**IIb**), respectively. For both complexes, a subsequent slow dissociation of chloride ions occurs. However, this is a very slow process: the half life of the reaction at 37 °C is ca. 1.5 and 1 h for the *trans* and *cis* isomer, respectively.[19] Binding of $H_2O$ to the ruthenium center gives rise to new electronic spectral features for **Ib** and **IIb**. The electronic spectrum of *trans*,*cis*,*cis*-[$RuCl_2(dmso)_2(H_2O)_2$] (**Ib**) (Figure 5A, curve 1), consists of two bands at 432 and 322 nm assigned to LF transitions and one band at 227 nm of CT character.[20,21] Similarly, the electronic spectrum of *cis*,*fac*-[$RuCl_2(dmso)_3(H_2O)$] (**IIb**) is characterized by three bands at 355 nm (LF transition), 310 nm (LF transition), and 255 nm (CT transition)[22] (Figure 5B, curve 1). For both isomers, the molar absorption coefficients for the two lower-energy bands were found to be higher than those for the usual LF transition (Table 1S). This may be due to the mixing of the LF energy levels with those corresponding to the neighboring intense CT band.[22]

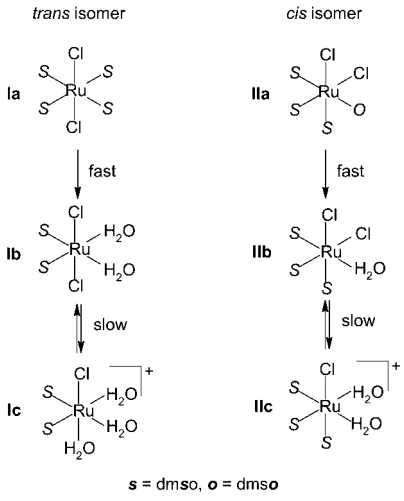


Scheme 2.

The irradiation of a deaerated aqueous solution of the *trans* complex, **Ib**, with visible light induces significant UV/Vis spectral changes as shown in Figure 5A. The absorption maxima at 322 and 432 nm decrease gradually, and a new very weak band at ca. 540 nm and a shoulder at ca. 400 nm appear. Three isosbestic points at 285, 349, and 417 nm are observed upon very short irradiation of **Ib** (up to ca. 1 min, Figure 1S, Supporting Information). Further irradiation leads to the disappearance of these isosbestic points. These results could be interpreted in terms of a subsequent photochemical reaction with conversion of the initial product into new species. Irradiation of a deaerated aqueous solution of the *cis* complex, **IIb**, leads to a regular decrease in the intensity of the band at 355 nm and the concomitant appearance of a shoulder at ca. 420 nm (after 3 min of irradiation, Figure 5B). Further irradiation gives rise to spectral changes similar to those observed for the primary photochemical process of the *trans* analogue. The UV/Vis spectral changes observed for aerated solutions of both isomers, **Ib** and **IIb**, during their irradiation with visible light indicate the initial formation of products similar to those found in the absence of oxygen (Figure 5C and Figure 5D, for **Ib** and **IIb**, respectively).

The prolonged photolysis of both solutions (up to 15 min) results in the appearance of a new relatively intense band at ca. 300 nm, which is not observed for the oxygen-

 © 2007 Wiley-VCH Verlag GmbH & Co. KGaA, Weinheim 

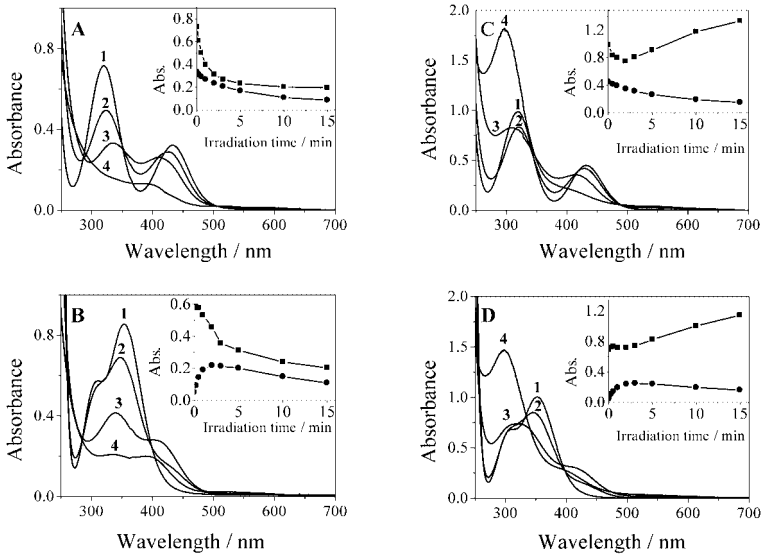


Figure 5. UV/Vis spectral changes during the photolysis ($\lambda_{irr}$ in the range 400–600 nm) of 2-mM aqueous solutions of **Ib** (A) and **IIb** (B) in an argon-saturated solution, and **Ib** (C) and **IIb** (D) in an air-saturated solution at room temperature. Spectra recorded after irradiation times of: 0 (1), 0.5 (2), 3 (3), and 15 min (4); $T$ = 20 °C. Insets: absorbance against irradiation time at 320 (■) and 432 nm (●).

free solution. The same product is also formed, as confirmed by UV/Vis spectra, when previously irradiated deaerated aqueous solutions of complexes **Ib** or **IIb** are purged with oxygen. These findings suggest that, after a long irradiation period in aerated solution, secondary thermal oxidation reactions of the primary photoproducts occur. Photolysis of **Ib** and **IIb** in the presence of $Cl^-$ ions was expected to yield additional information on the reactivity. Irradiation of **Ib** and **IIb** in aqueous solution in the presence of excess of NaCl (0.2 M solution, 100-fold excess over $Ru^{II}$ complexes) yielded the same spectral changes as those described above. The processes occurred with a lower efficiency, however, indicating that the overall mechanism includes a photodissociation of the $Cl^-$ ligands. It is likely that the UV/Vis spectral changes observed for complexes **Ib** and **IIb** occur as a consequence of photosubstitution reactions of the dmso and $Cl^-$ ligands with water molecules. To make sure that substitution of dmso by $H_2O$ occurs, we decided to take advantage of the different chemical shifts in the $^1H$ NMR spectra of the free ligands and of those coordinated to the $Ru^{II}$ center. The $^1H$ NMR spectrum of **Ib** recorded immediately after dissolution of the *trans* complex in $D_2O$ consist of two resonances of equal intensity at 2.73 and 3.36 ppm assigned to the $CH_3$ groups of the free and coordinated dmso ligands, respectively.(Figure 6A and Table 1).

The observation of two resonances is consistent with the mechanism in Scheme 2 showing that dissolution of the *trans*-$[RuCl_2(dmso)_4]$ complex leads to the formation of *trans,cis,cis*-$[RuCl_2(dmso)_2(H_2O)_2]$ (**Ib**) and two free molecules of dmso. Observation of the increase in the intensity of the $CH_3$ resonance at $\delta$ = 2.73 ppm in the $^1H$ NMR spectra (Figure 6A) during photolysis of complex **Ib** is indicative of a gradual dissociation of the dmso ligand. The resulting mixture of products was analyzed by $^1H$ NMR, and it was determined that (99 ± 4)% of the final products is a complex without dmso and the remaining is a complex

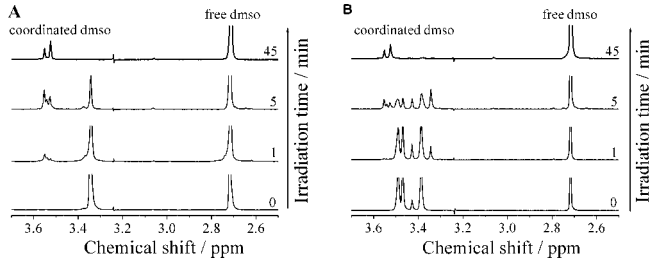


Figure 6. $^1H$ NMR spectra of the complex **Ib** (A) and **IIb** (B) ($D_2O$ solution) at various irradiation times; $\lambda_{irr}$ > 400 nm, $T$ = 20 °C.

Table 1. $^1H$ NMR chemical shifts ($\delta$/ppm) recorded for *trans,cis,cis*-$[RuCl_2(dmso)_2(H_2O)_2]$ (**Ib**) in $D_2O$ solution after irradiation in the range 400–600 nm at $T$ = 20 °C.

| Irradiation time/min | $\delta$/ppm | | | | |
|---|---|---|---|---|---|
| 0 | 2.73[a] | 3.36 | | | |
| 1–15 | 2.73[a] | 3.36 | 3.54 | 3.56 | 3.57 |
| 30–45 | 2.73[a] | – | **3.54** | – | **3.57** |

[a] Resonance assigned to $CH_3$ protons of free dmso.

still containing the dmso ligand (Figure 6A, Figure 7, and Table 1). Upon further investigation, we determined that, during the course of the irradiation, the dmso ligand rather than the $Cl^-$ ligand is labilized first. The analysis of the $^1H$ NMR spectrum indicates the absence of the resonance at $\delta$ = 3.39 ppm attributable to the $CH_3$ group of dmso in *cis,fac*-$[RuCl(dmso)_2(H_2O)_3]^+$ (**Ic**), a possible intermediate complex if $Cl^-$ dissociation is operative in the primary photochemical event.[23] In addition, a comparison of the quantitative data for the release of dmso and $Cl^-$ ligands (Figure 7 and Figure 8, respectively) supports the conclusion that the dmso ligand is more photolabile than the chlorido ligand.

 © 2007 Wiley-VCH Verlag GmbH & Co. KGaA, Weinheim 

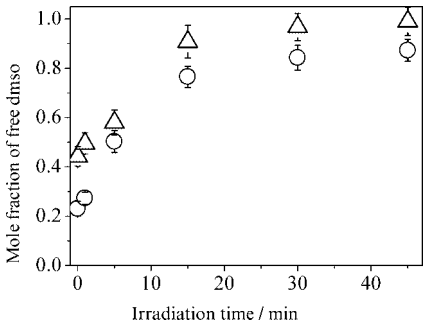


Figure 7. Mole fraction of free dmso molecules [defined as $(n_f)/(n_c + n_f)$, where $n_f$ denotes the number of moles of free dmso and $n_c$ denotes the number of moles of dmso coordinated to ruthenium ion] for **Ib** (Δ) and **IIb** (○) released during irradiation ($\lambda_{irr}$ in the range 400–600 nm; $T$ = 20 °C).

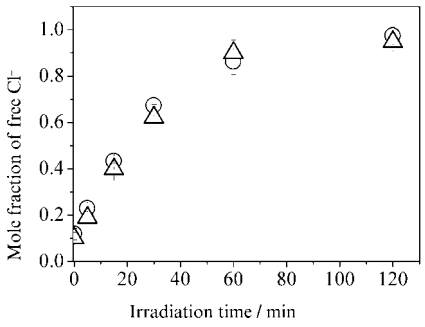


Figure 8. Mole fraction of free chloride ions [defined as $(n_f)/(n_c + n_f)$, where $n_f$ denotes the number of moles of free chloride ions and $n_c$ denotes the number of moles of chloride ions coordinated to ruthenium ion] for **Ib** (Δ) and **IIb** (○) released during irradiation ($\lambda_{irr}$ in the range 400–600 nm; $T$ = 20 °C).

Given the difficulties which can arise in elucidating the mechanism of the photoreactions described above, in order to conclude that Scheme 1 and Scheme 2 are the most likely pathways for the reactions, we felt that some care should be taken in ruling out other possibilities, especially those involving possible intermediates. The $^1$H NMR spectrum of *cis,fac*-[$RuCl_2(dmso)_3(H_2O)$] (**IIb**) presents thee resonances at $\delta$ = 3.40, 3.48, and 3.50 ppm assigned to the $CH_3$ groups of the three coordinated dmso ligands (Table 2).

Table 2. $^1$H NMR chemical shifts ($\delta$/ppm) recorded for *cis,fac*-[$RuCl_2(dmso)_3(H_2O)$] (**IIb**) in $D_2O$ solution after irradiation in the range 400–600 nm at $T$ = 20 °C.

| Irradiation time/min | $\delta$/ppm | | | | | | | | |
|---|---|---|---|---|---|---|---|---|---|
| 0 | 2.73[a] | | 3.40 | 3.44 | 3.48 | 3.50 | | | |
| 1 | 2.73[a] | 3.36 | 3.40 | 3.44 | 3.48 | 3.50 | | | |
| 5 | 2.73[a] | 3.36 | 3.40 | 3.44 | 3.48 | 3.50 | 3.54 | 3.55 | 3.57 |
| 15 | 2.73[a] | 3.36 | – | – | – | – | 3.54 | 3.55 | 3.57 |
| 30–45 | 2.73[a] | – | – | – | – | – | **3.54** | – | **3.57** |

[a] Resonance assigned to $CH_3$ protons of free dmso.

The resonance at $\delta$ = 2.73 ppm is attributed to the $CH_3$ group of the free dmso present in the solution after dissolution of the *cis* isomer (Figure 6B, see also Scheme 2). A very small peak at $\delta$ = 3.44 ppm (the intensity is lower than 10% of the other resonances) is also observed and is attributed to one of the $CH_3$ groups of the dmso ligand in the hydrolyzed form of complex **IIb** (Scheme 2, complex **IIc**). The short irradiation of complex **IIb** leads to the formation of **Ib** as an intermediate. This is confirmed by the appearance in the $^1$H NMR spectrum of the peak at 3.36 ppm, assignable to the $CH_3$ group of the dmso ligand in complex **Ib**. Longer irradiation results in further formation of the intermediate **Ib**, which is photochemically unstable and undergoes secondary photolysis. These processes give rise to changes in the $^1$H NMR spectra leading to (i) gradual disappearance of peaks for the $CH_3$ protons of the dmso ligand of **IIb**; (ii) appearance of a new resonance, the same as that found for the irradiated complex **Ib**. The $^1$H NMR spectrum for the final photoproducts of **IIb** is the same as that observed for complex **Ib** (Figure 6). For both ruthenium(II) complexes, **Ib** and **IIb**, the increase of the peak intensity at $\delta$ = 2.73 ppm assigned to free dmso is a consequence of photolysis, since the increase of the resonance is not observed in thermal hydrolysis. The concentration of dissociated dmso ligands has been estimated by calculation of the area under the $CH_3$ resonance peak at $\delta$ = 2.73 ppm. The relevant measurements indicate an almost complete photodissociation of dmso ligands (Figure 7).

The *trans,cis,cis*-[$RuCl_2(dmso)_2(H_2O)_2$] (**Ib**) and *cis,fac*-[$RuCl_2(dmso)_3(H_2O)$] (**IIb**) complexes have two chlorido ligands in the *trans* and *cis* configuration, respectively. To provide trustworthy estimates of the amount of $Cl^-$ ions which might be present in the photoreaction mixture, we have carried out electrochemical experiments by using the ion-selective chloride electrode. Upon photolysis of complexes **Ib** and **IIb**, one begins to see the formation of $Cl^-$ ions as quantitatively reported in Figure 8. It is important to note that the thermal hydrolysis of the chlorido ligand in both complexes is relatively slow (vide supra). Thus, at the selected temperature (20 °C), the major contribution to the amount of free chloride ions in solution originates from the photodissociation of $Cl^-$ ligands. It appears that the release of chlorido ligands from both isomers takes place with similar yields. Longer irradiation (ca. 2 h) leads to nearly complete chloride dissociation.

The obtained results have shown that LF irradiation of *trans,cis,cis*-[$RuCl_2(dmso)_2(H_2O)_2$] (**Ib**) and *cis,fac*-[$RuCl_2(dmso)_3(H_2O)$] (**IIb**) leads to the photodissociation of dmso and $Cl^-$ ligands, which are substituted by water molecules. The photolysis of the *cis* isomer, **IIb**, generates the *trans* analogue, **Ib**, as an intermediate, which itself is also photoactive, giving the same products as those obtained in the direct photolysis of the *trans* isomer, **Ib** (Scheme 3).

The photolysis of the *trans* and *cis* isomers, **Ib** and **IIb**, results in the formation of the same final products, as confirmed by UV/Vis and $^1$H NMR spectra. On the basis of our findings and literature data,[24–27] these products could be a mixture of (aqua)ruthenium(II) and (aqua)(chlorido) ruthenium(II) complexes (Scheme 3). The photoproducts are very unstable in the presence of oxygen, as demonstrated by UV/Vis spectral changes. The gradual increase in

 © 2007 Wiley-VCH Verlag GmbH & Co. KGaA, Weinheim 

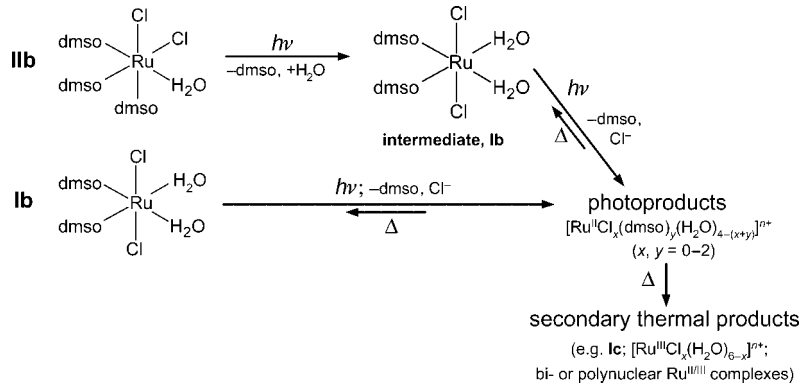


Scheme 3.

the intensity of the maximum at ca. 300 nm observed for aerated solutions, but not observed for deaerated solutions, could be ascribed to a slow thermal oxidation of the (aqua)-ruthenium(II) and (aqua)(chlorido)ruthenium(II) complexes to ruthenium(III) species.[25,27–30] Moreover, the prolonged thermal reaction (over a period of 24 h) at 20 °C results in a darkening of the irradiated solution. This result indicates that polymerization occurs along with hydrolysis, forming bi- or polynuclear species containing chlorido, oxido, or hydroxido bridges.[25,31] In addition to the above products, the $^1$H NMR spectra of photolyzed solutions of complexes **Ib** and **IIb** kept in the dark for 24 h have shown that still minor amounts of **Ib** and **Ic** are present for both isomers. Only in the presence of an excess of chloride ions (ca. 17-fold excess over $Ru^{II}$) are the photoproducts converted back to complex **Ib** (up to 60%) in the prolonged thermal reaction (Scheme 3).

## Conclusions

The various studies that have been conducted point to two main photoreactions of *trans*- and *cis*-$[RuCl_2(dmso)_4]$ complexes. The first is the photoinduced isomerization of the *cis* isomer to the *trans*-$[RuCl_2(dmso)_4]$ complex through the LF excited state. The second reaction appears to involve breakage of the metal–dmso bond, which results in the substitution of dmso with $CH_3CN$ and $H_2O$, when the photoreaction is conducted in acetonitrile and in water, respectively. In aqueous solution, photolysis of *trans*- and *cis*-$[RuCl_2(dmso)_4]$ leads first to the dissociation of the dmso ligand and then, in a secondary photochemical event, dissociation of the $Cl^-$ ligands. The ligand-loss photochemistry of *trans*- and *cis*-$[RuCl_2(dmso)_4]$ results in the formation of products of the type $[RuCl_x(dmso)_y(H_2O)_{4-(x+y)}]^{n+}$ ($x$, $y$ = 0–2). These new species, formed upon irradiation in $H_2O$ solution, have a considerable substitution lability relative to the *cis* and *trans*-$[RuCl_2(dmso)_4]$ complexes. These photoproducts may react quickly and with high efficiency with cellular components through sequential ligand exchange. This judgment is confirmed by our previous results,[9] which demonstrated an enhancement of the antiproliferative activity of the *trans*- and *cis*-$[RuCl_2(dmso)_4]$ complexes upon irradiation. Furthermore, the reaction of both isomers with a short oligonucleotide ($T_2GGT_2$) in aqueous solution is significantly facilitated by irradiation of the reaction mixture with UVA light.[9] These are interesting results, because they suggest that the photolysis of $Ru^{II}$ complexes with photolabile ligands will allow the covalent binding of cellular components.

## Experimental Section

### Materials and Syntheses

The ruthenium complexes, *trans*-$[RuCl_2(dmso)_4]$ (**Ia**) and *cis*-$[RuCl_2(dmso)_4]$ (**IIa**) were synthesized and purified according to published procedures.[10,32] Both elemental analysis {For *trans*-$[RuCl_2(dmso)_4]$ (484.54): calcd. C 19.81, H 4.95, S 26.41; found C 19.72, H 5.01, S 26.83 and for *cis*-$[RuCl_2(dmso)_4]$ (484.54): calcd. C 19.81, H 4.95, S 26.41; found C 19.92, H 5.03, S 27.21.} and electronic spectroscopy have been used for checking their purity (Table 1S, Supporting Information).[10,20–22] All other chemicals used were of analytical grade.

**Synthesis of *trans*-$[RuCl_2(CH_3CN)_4]$:** The complex was synthesized by irradiation of *trans*- or *cis*-$[RuCl_2(dmso)_4]$ (200 mg, 0.41 mmol) dissolved in acetonitrile (20 cm$^3$) with visible light (500-W high-pressure mercury lamp, cut-off: 400 nm) for 1.5 h. The irradiation resulted in the precipitation of a yellow solid, which was collected by filtration, washed with a little acetonitrile, and vacuum-dried at room temperature (98 mg, 71%). $[RuCl_2(CH_3CN)_4]$ (336.19): calcd. C 28.58, H 3.59, N 16.66; found C 28.62, H 3.40, N 16.64. $^1$H NMR (200 MHz, $D_2O$): $\delta$ = 2.60 (s) ppm. X-ray crystallographic analysis was used for the confirmation of the *trans* position of the chlorido ligands in this complex.

**X-ray Structure Determination:** An orange prismatic crystal of compound $[RuCl_2(CH_3CN)_4]$ was mounted on a Nonius Kappa CCD diffractometer with Mo-$K_\alpha$ radiation ($\lambda$ = 0.71073 Å) at room temperature. The cell constants [$a$ = 11.8001(3), $b$ = 8.5722(3), $c$ = 13.1258(4) Å, $\alpha = \beta = \gamma$ = 90°] and the space group *Pbca* were obtained by least-squares refinement of the diffraction data from 7566 reflections with $1° < \theta < 30°$. The obtained crystallographic data perfectly agree with a previous report,[17] showing that the crystals of compound $[RuCl_2(CH_3CN)_4]$ consist of molecules of the complex *trans*-tetrakis(acetonitrile)(dichlorido)ruthenium(II).

**UV/Vis Spectroscopy:** Electronic absorption spectra were recorded in 1-cm quartz cells with a Shimadzu UVPC 2100 or a Hewlett–Packard HP 8463 spectrophotometer.

 © 2007 Wiley-VCH Verlag GmbH & Co. KGaA, Weinheim 

**$^1$H NMR Spectroscopy:** $^1$H NMR spectra were recorded with a BRUKER AC 200 spectrometer operating at 200.13 MHz. The chemical shift values were internally referenced to the dmso resonances ($\delta$ = 2.50 ppm in $CD_3CN$ or 2.73 ppm in $D_2O$).

**Chloride-Selective Electrode Measurements:** A chloride-ion-selective electrode (Carison) was used for the determination of the free chloride ion concentration. Each point in the plot is an average value of at least three independent experiments, and the error corresponds to the standard deviation.

**Photochemical Studies**

Continuous photolysis was carried out in the $\lambda_{irr}$ range from 400 to 600 nm by using a 500-W high-pressure mercury lamp equipped with a 400-nm cut-off filter (Oriel, Stradford – USA). The photolysis of *trans*- and *cis*-[$RuCl_2(dmso)_4$] complexes was carried out in solutions of dmso, $CH_3CN$, and $H_2O$ in 1-cm quartz spectrophotometer cells or in deuterated solvents ($CD_3CN$ and $D_2O$) in NMR tubes at 20 °C. All solutions of ruthenium(II) complexes were freshly prepared before use and deaerated when needed by bubbling argon through them. During irradiation, the solutions were stirred, and the temperature was kept at 20 °C by a refrigerated circulator (JULAB F12-EC). The progress of the photolysis was monitored by UV/Vis and $^1$H NMR spectroscopy, and chloride-selective electrode measurements. For spectroscopic measurements, samples were used as prepared for irradiation (2-mM solutions for UV/Vis and 3.5 mg complex/0.6 mL solvent for $^1$H NMR spectroscopy), whereas for the determination of free chloride ion concentration, the irradiated samples were diluted in 0.1-M $KNO_3$ solution.

For quantum yield determination, a 200-W high-pressure mercury lamp was used as a source of light, and interference filters (VEB Carl Zeiss JENA) were employed for wavelength selection (365 and 313 nm). Ferrioxalate actinometry was used at both wavelengths for light intensity determination.[33] Quantum yields of the photoisomerization of the *cis*-[$RuCl_2(dmso)_4$] into the *trans* analogue was determined from UV/Vis spectral changes upon irradiation of a 5.5-mM dmso solution of the *cis* isomer (the chosen concentration provides a complete absorption of light at both wavelengths).

**Supporting Information** (see footnote on the first page of this article): Electronic spectral data for complexes **Ia**, **IIa**, **Ib**, and **IIb**, and UV/Vis absorption spectra for a 2-mM, argon-saturated aqueous solution of **Ib** upon irradiation at $T$ = 20 °C for various time intervals up to 1 min; ORTEP view of *trans*-[$RuCl_2(dmso)_4$].

## Acknowledgments

We gratefully acknowledge the support from the Polish Ministry of Science and Higher Education (Grant PB-1283/T09/2005/29). The authors thank Prof. Orazio Traverso (University of Ferrara, Italy) for contributing insightful comments.

[1] M. Coluccia, G. Sava, F. Loseto, A. Nassi, A. Boccarelli, D. Giorgano, E. Alessio, G. Mestroni, *Eur. J. Cancer* **1993**, *29A*, 1873–1879.
[2] G. Sava, S. Pacor, S. Zorzet, E. Alessio, G. Mestroni, *Pharmacol. Res.* **1989**, *21*, 617–628.
[3] G. Sava, S. Zorzet, T. Giraldi, G. Mestroni, G. Zassinovich, *Eur. J. Cancer Clin. Oncol.* **1984**, *20*, 841–847.
[4] S. Pacor, E. Luxich, V. Ceschia, G. Sava, E. Alessio, G. Mestroni, *Pharmacol. Res.* **1989**, *21*, 127–128.
[5] K. Szaciłowski, W. Macyk, A. Drzewiecka-Matuszek, M. Brindell, G. Stochel, *Chem. Rev.* **2005**, *105*, 2647–2694.
[6] D. Ossipov, S. Gohil, J. Chattopadhyaya, *J. Am. Chem. Soc.* **2002**, *124*, 13416–13433.
[7] M. Pauly, I. Kayser, M. Schmitz, M. Dicato, A. Del Guerzo, I. Kolber, C. Moucheron, A. Kirsch-De Mesmaeker, *Chem. Commun.* **2002**, 1086–1087.
[8] T. T. Singh, C. Turro, *Inorg. Chem.* **2004**, *43*, 7260–7262.
[9] M. Brindell, E. Kulis, S. C. K. Elmroth, K. Urbanska, G. Stochel, *J. Med. Chem.* **2005**, *23*, 7298–7304.
[10] E. Alessio, G. Mestroni, G. Nardin, W. M. Attia, M. Calligaris, G. Sava, S. Zorzet, *Inorg. Chem.* **1988**, *27*, 4099–4106.
[11] P. P. Zarnegar, C. R. Bock, D. G. Whitten, *J. Am. Chem. Soc.* **1973**, *95*, 4367–4372.
[12] J. D. Gilbert, D. Rose, G. Wilkinson, *J. Chem. Soc. A* **1970**, 2765–2769.
[13] W. E. Newton, J. E. Searles, *Inorg. Chim. Acta* **1973**, *7*, 349–352.
[14] B. F. G. Johnson, J. Lewis, I. E. Ryder, *J. Chem. Soc., Dalton Trans.* **1977**, 719–724.
[15] X. J. Salom-Roig, J.-J. Chambron, C. Goze, V. Heitz, J.-P. Sauvage, *Eur. J. Org. Chem.* **2002**, 3276–3280.
[16] P. Hayoz, A. von Zelewsky, H. Stoeckli-Evans, *J. Am. Chem. Soc.* **1993**, *115*, 5111–5114.
[17] M. Bown, D. C. R. Hockless, *Acta Crystallogr., Sect. C* **1996**, *52*, 1105–1106; M. Brindell, G. Stochel, V. Bertolasi, R. Boaretto, S. Sostero, private communication to the Cambridge Structural Database, deposition number: CCDC-637336, **2007**. These data can be obtained free of charge from The Cambridge Crystallographic Data Centre via www.ccdc.cam.ac.uk/data_request/cif.
[18] S. Cauci, E. Alessio, G. Mestroni, F. Quadrifoglio, *Inorg. Chim. Acta* **1987**, *137*, 19–24.
[19] M. Brindell, S. C. K. Elmroth, G. Stochel, *J. Inorg. Biochem.* **2004**, *98*, 1367–1377.
[20] D. P. Riley, *Inorg. Chim. Acta* **1985**, *99*, 5–11.
[21] T. Bora, M. M. Singh, *Transition Met. Chem.* **1978**, *3*, 27–31.
[22] K. Natarajan, R. K. Poddar, U. Agarwala, *J. Inorg. Nucl. Chem.* **1977**, *39*, 431–435.
[23] Complex *cis,fac*-[$RuCl(dmso)_2(H_2O)_3]^+$ (**Ic**) was prepared by incubation of an aqueous solution of *trans,cis,cis*-[$RuCl_2(dmso)_2(H_2O)_2$] (**Ib**) for ca. 48 h at 37 °C to reach solvolytic equilibrium. The $^1$H NMR spectrum recorded for complex **Ic** prepared in this way consists of two resonances at $\delta$ = 3.36 and 3.39 ppm assigned to the $CH_3$ groups of coordinated dmso ligands and one at $\delta$ = 2.73 ppm attributed to the $CH_3$ group of the free dmso molecule.
[24] T. W. Kallen, J. E. Earley, *Inorg. Chem.* **1971**, *10*, 1149–1151.
[25] M. M. Taqui Khan, G. Ramachandraiah, A. Prakash Rao, *Inorg. Chem.* **1986**, *25*, 655–670.
[26] P. Takahara, C. A. Frederick, S. J. Lippard, *J. Am. Chem. Soc.* **1996**, *118*, 12309–12321.
[27] H. H. Cady, R. E. Connick, *J. Am. Chem. Soc.* **1958**, *80*, 2646–2652.
[28] Z. Harizion, G. Navon, *Inorg. Chem.* **1980**, *19*, 2236–2239.
[29] E. E. Mercer, R. R. Buckley, *Inorg. Chem.* **1965**, *12*, 1692–1695.
[30] R. E. Connick, D. A. Fine, *J. Am. Chem. Soc.* **1960**, *82*, 4187–4191.
[31] P. Wehner, J. C. Hindman, *J. Am. Chem. Soc.* **1950**, *72*, 3911–3918.
[32] I. P. Evans, A. Spencer, G. Wilkinson, *J. Chem. Soc., Dalton Trans.* **1973**, 204–209.
[33] J. G. Calvert, Pitts J. N. Jr in *Photochemistry*, John Wiley & Sons, Inc., New York, **1966**.

Received: October 19, 2006
Published Online: April 17, 2007

 © 2007 Wiley-VCH Verlag GmbH & Co. KGaA, Weinheim

**The EUChemSoc Societies have taken the significant step into the future by merging their traditional journals, to form two leading chemistry journals, the *European Journal of Inorganic Chemistry* and the *European Journal of Organic Chemistry.* Three further EUChemSoc Societies (Austria, Czech Republic and Sweden) are Associates of the two journals.**

**For more on the Société Française de Chimie (SFC) and the development of chemistry over the last 150 years see the editorials on the following pages!**

## COVER PICTURE

**The cover picture shows** the active site of galactose oxidase, as it was crystallized in the middle of the 1990s. Its active form featured an unprecedented copper(II)-tyrosyl (Tyr272•) radical system. Since 1996, several model compounds of this entity have been developed worldwide. They contributed significantly to the enhanced understanding of the spectral properties, structural attributes, and even to the reactivity of the enzyme's active site. Four prototypical complexes are shown; each of them is representative of the main classes of ligands developed (tripodal, salen, TACN, and iminosemiquinone scaffolds). Phenoxyl radicals typically exhibit absorption bands at around 420 and 600−800 nm, as shown in the UV/Vis spectrum. Ten years of this bioinorganic story is discussed in the Microreview by F. Thomas on p. 2379 ff.

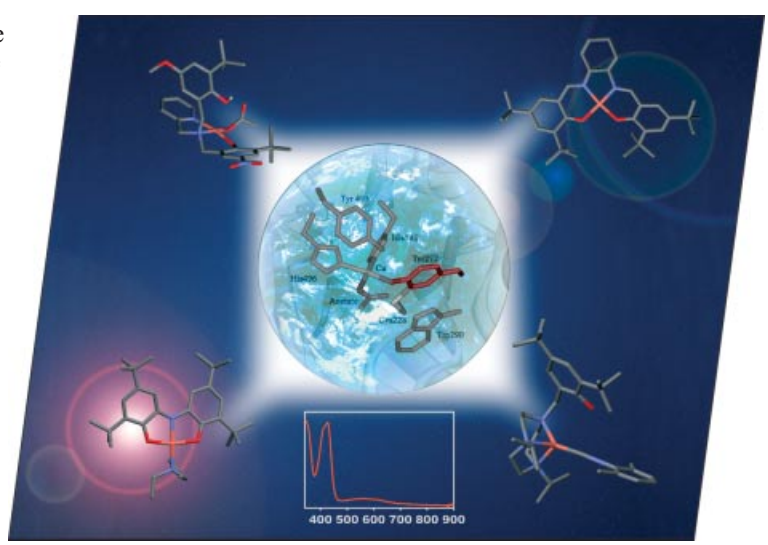


 © 2007 Wiley-VCH Verlag GmbH & Co. KGaA, Weinheim

# Focus on France – The French Chemical Society Is 150 Years Old

Several of the national Chemical Societies of European countries agreed to merge their journals about 10 years ago and create a selected number of thematic European Journals. The 10th anniversary issues of the *European Journal of Inorganic Chemistry* (*EurJIC*) and of the *European Journal of Organic Chemistry* (*EurJOC*), two of the first such journals to see the light of day, will be published later this year. It is therefore not only appropriate, but also incumbent on the European Journals to highlight and contribute to the celebration of the important events of their owner societies. This year is marked by the sesquicentennial anniversary of the *Société Française de Chimie* (SFC, French Chemical Society), one of the oldest in the world. Apparently, only the RSC (UK) has older roots, while the chemical societies of Germany, the United States, and Japan, to name a few, were established later.

The SFC was founded in 1857, though under a different name that has evolved through changes of status and mergers. As a matter of fact, it will soon switch back to its previous name *Société Chimique de France*, or SCF. The purpose of the Society is to gather both natural persons and legal entities from the public or private sector who are involved in the science of chemistry and its applications. It intends to contribute to the development of all aspects of the chemical disciplines, to be the center of information, to provide avenues for the meeting of interested members to diffuse their thoughts and propositions on questions of teaching and research, as well as on industrial, economical, and professional issues, and to represent its members and their disciplines within the society at large. The SFC is currently strong with ca. 4500 active members and has 9 thematic divisions, 13 scientific groups, 15 regional sections, and 15 clubs for younger members. A scientific general meeting is held every two years, and numerous annual meetings are organized by the individual divisions. The Society bestows a number of prestigious awards on French and international chemists and assists young scientists in their entrance into active professional life with an employment clearing house. It publishes, since 1973, a monthly magazine "*L'Actualité Chimique*" for the broad dissemination of knowledge in the chemical sciences and co-publishes, together with other European Societies, the above-mentioned European Journals. Last but not least, it cooperates with other national Chemical Societies through the European Association for Chemical and Molecular Sciences (EuCheMS).

Founded in 1857 as SCF

The SFC has 4500 Active Members

This year's meeting SFC07: "*Chimie du Futur, Futur de la Chimie*", held in Paris between July 16 and 18, 2007, marks the celebration of 150 years of the French Chemical Society. It is impossible to summarize in this short Editorial the impact of the multiple activities that the Society has had in its long and distinguished history. A detailed account of these will appear in a feature article published by "*L'Actualité Chimique*".

SFC07, "*Chimie du Futur, Futur de la Chimie*"

The co-ownership of *EurJIC* and *EurJOC* by the French Chemical Society fulfils one of its goals, to distribute research results. Part of the success of a chemical society (although by no means all of it) can be measured by the success of the research activities of its members. We would like to highlight this particular aspect in this Editorial. The impact of French chemistry research in the past 150 years has been enormous, as is detailed in the article by L. Lestel and I. Tkatchenko (pp. 2368–2371). One may ask the question: where does French chemistry research stand today? It is our proposition that modern French chemistry research is as lively and as vibrant as ever. This conclusion could be simply based on recent individual achievements, as measured, for instance, by recognition with international prizes, or by the number of publications in important international chemical journals. The percentages of papers published in *EurJIC* and *EurJOC* by French chemists are 9 and 12%, respectively, for the year 2006. These figures reflect the importance of French chemistry, in view of the fact that chemists from more than 30 countries publish in *EurJIC* and *EurJOC*. More important, in our opinion, is the active role that France plays in the process of globalization of research. Globalization is not only an economical, a cultural, and a technological phenomenon, but it also affects scientific research. This argument is not restricted to chemistry but applies to all scientific disciplines.

French Chemistry Research is as Lively as Ever

Like in many other European countries, funding of research in France relies in part on national resources (the Ministry of Research, through the newly created and inde-

 © 2007 Wiley-VCH Verlag GmbH & Co. KGaA, Weinheim 

pendently run "*Agence Nationale de la Recherche*", ANR, the "*Centre National de la Recherche Scientifique*", CNRS, and local governmental authorities), but a major portion of research support originates from the European Commission through a multitude of transnational programs. The French Ministry of Foreign Affairs is a leading actor in establishing bilateral scientific cooperation programs (called "Hubert Curien Partnerships", currently extended to almost 50 countries in all continents). Other bilateral programs are sponsored in different forms by the CNRS, including the establishment of virtual thematic research institutes ("*Laboratoire Européen Associé*", LEA; "*Laboratoire International Associé*", LIA) or networks ("*Groupe de Recherche Européen*", GDRE; "*Groupe de Recherche International*", GDRI) that join researchers from France and from other countries on the basis of a common research goal. These cooperation activities are not restricted to other developed countries but also include, and in some cases target specifically, developing ones. The establishment of shared transnational supervision of Ph.D. theses is encouraged and financially supported. Finally, visits of international scientists at all levels are sponsored by a variety of programs offered by Universities (open positions for visiting professors), by the CNRS (post-doctoral and higher-level fellowships), and by the local governmental authorities.

It is likely that globalization of research will continue to expand and that a growing fraction of major advances in science will be achieved through international cooperation. Thus, France and the French scientists seem well equipped to participate in this game by playing a leading role. It is worth underlining that the consolidation of the European Journals can be seen as an expression of this research globalization phenomenon and that chemists (by way of their national chemical societies) have been pioneers, at least at the European level. Within this operation, the French Chemical Society has been proactive since the very beginning of its history. As a matter of fact, the SFC was created by a group of European chemists, only a minority of whom were French. The first two presidents were an Italian (Jacques Arnaudon, from June 30 to the end of 1857) and a Norwegian (Hans Anton Rosing, from January to June 1858). French chemistry has been highly visible since the 19th century, and many European chemists, for instance Justus von Liebig, were attracted to France to pursue their training. In more recent times, besides the above-mentioned important role played in the creation of the new European Journals, the SFC has established, by agreement with its sister societies, binational prizes with Germany, Italy, Spain, Poland, and, since last year, the United Kingdom. These prizes allow extensive scientific exchange through lecture tours of the recipients in the host countries.

**Bilateral Scientific Cooperation Programs**

**Globalization of Research**

To conclude, the SFC is an Old Lady who has found a way to continued youth. Let her live forever!

Rinaldo Poli
Editorial Board Member, *EurJIC*
*Laboratoire de Chimie de Coordination*
*Unité Propre du CNRS*
*Toulouse*

Max Malacria
Chairman of the Editorial Board, *EurJOC*
*Laboratoire de Chimie Organique*
*Université Pierre et Marie Curie*
*Paris*

 © 2007 Wiley-VCH Verlag GmbH & Co. KGaA, Weinheim

# Chemical Pathways: 150 Years of Evolution of Chemistry

**Laurence Lestel[a] and Igor Tkatchenko[b]**

In 1857, a small group of chemists began to meet for informal discussions in Paris, founding the *Société Chimique*. Taking note of its national stature, the society was transformed into the "Société Chimique de France" in 1906. Then, after having merged with the "Société de Chimie Physique", it became the "Société Française de Chimie" in 1984. It celebrates its 150th anniversary this year. The "Société" witnessed the evolution of chemistry and chemists, of their knowledge, and of their goals, as did the other chemical societies created in this era, for example, the Chemical Society of London in 1841, the German Chemical Society in 1867, the Russian Chemical Society in 1868, the American Chemical Society in 1876 or the Chemical Society of Japan in 1878. Can one in a few words seize the impact of these changes?

**Marcellin Berthelot**

**Charles Friedel**

In 1857, organic synthesis was still in its infancy. Berthelot achieved the formation of fats by the combination of glycerol with acids in 1854. In addition his syntheses of organic compounds by means of simple chemical methods, such as those used at that time for inorganic derivatives in the famous "electric egg" apparatus, led to the final fall of the theory of a "vital force" inherent in organic compounds. His book *"Chimie Organique Fondée sur la Synthèse"* (1860) had considerable success and presents Berthelot as the founder of this discipline. At the same time, Perkin deposited his patent "Dyeing fabrics" (1856) in England, describing how to obtain dyes starting from residues of the distillation of coal, and this opened the way for the dye industry. After having deposited 152 patents to cover the development of the industrial process, BASF began the production of indigo in 1897. In these crucial years, the structures that allowed the development of the organic chemical industry fell into place: chemical companies (BASF, Hoechst, Bayer, Ciba, Geigy, British Alizarin, les Usines du Rhône, ...), industrial research laboratories associated to academic research, and new developments in chemistry such as chemical engineering, a term that was introduced in England in 1887 by Davis and rose to greater recognition at MIT, expanded rapidly as a required step for industrial scale-up. After having used "simple" reactions like nitration, reduction or oxidation of organic molecules, chemists started to use reactions specific to organic chemistry, for example, preparation of zinc alkyl iodides by Frankland for hydrocarbon synthesis, the Williamson synthesis for the preparation of ethers, and the use of sodium for the condensation of alkyl or aryl halides by Wurtz and then by Fittig. In 1877, Friedel and Crafts used anhydrous aluminum chloride as catalysts for the condensation of aromatic hydrocarbons and alkyl halides. The Friedel–Crafts reaction was applied to the preparation of perfumes, pharmaceutical products, dyes, and then monomers. It is essential to the chemical industry still today, albeit in more eco-compatible forms. A few years later, the Grignard reaction (1900), which allows the formation of a wide variety of organic compounds by the reaction of magnesium with organic iodides, was acquainted with a singular development, unique in the history of chemistry. Another useful tool was the hydrogenation of olefins by using catalysts as studied by Sabatier and Senderens. Progress in organic chemistry was accompanied by the set-up of its nomenclature during the congress of Geneva in April 1892, after two years of work by the Parisian commission of nomenclature chaired by Friedel.

Then a competition started between nature and artifice, between products resulting from nature and those imitating it or exceeding it. To understand the structure of natural products, the chemist decomposed them into small units, and then tried their synthesis. The apotheosis is the total synthesis of vitamin B12, undertaken by Woodward and his team in Harvard, in collaboration with Eschenmoser of Zürich. More than 100 researchers, including Lehn, took part in it. It was completed in eleven years and was announced in Delhi in 1972.

To fight against the shortage of resources and to improve productivity, the chemist found new synthetic routes (e.g. sodium

[a] Dr. L. Lestel
Conservatoire National des Arts et Métiers C.D.H.T.E.,
5 rue du Vertbois, 75003 Paris, France
E-mail: lestel@cnam.fr
[b] Dr. I. Tkatchenko
CNRS-U. Bourgogne/ICM/SymCat,
9 ave Alain Savary, 21078 Dijon Cedex, France
E-mail: tkatchen@u-bourgogne.fr

 © 2007 Wiley-VCH Verlag GmbH & Co. KGaA, Weinheim 

carbonate by the Solvay process; ammonia through hydrogenation of nitrogen; hydrocarbons and methanol starting from coal). The list is endless. It widened with the isolation of fluorine by Moissan, the discovery of rare gases by Ramsay, and the disclosure of radio elements by the Curie family.

The chemist also created completely new entities, for example, macromolecules. Polymer chemistry took off in the 1920s with Staudinger, who led the scientific community in the synthesis of long chain polymers, the physicochemical properties of which were intriguing for a long time and began to be explained with the soft matter concepts of de Gennes. The understanding of the organization of soft matter thanks to a large variety of weak interactions between molecules, not atoms, led to the design of numerous new man-made materials with improved performances, or "smart" materials mimicking natural ones. This was further extended to the area of liquid crystals, which are essential components of our everyday life. The design of new synthetic strategies and their industrial achievement allowed the development of alternatives to polymeric natural products like silk (Nylon) and rubber (polychloroprene, polybutadiene, polyisoprene, ...). Moreover, new materials appeared with the design of polyesters and polyolefins starting from $C_2-C_6$ building blocks obtained from petroleum cuts. Such developments demonstrate again the continuum existing between basic research and industrial processes: the best example is certainly the discovery of the Ziegler−Natta catalysts, which have heavily contributed to the rise of the petrochemical industry.

**Marie Curie**

**Pierre-Gilles de Gennes**

**Jean Rouxel**

The development in the second half of the 19th century of terrestrial (railways, metallic bridges) and maritime communications (and also armament) triggered the progress of metallurgy. Bessemer, Thomas, Siemens, and Martin designed new processes to obtain steels from cast iron; Hall and Héroult patented the electrolysis of alumina and the arc furnace. A scientific vision of industry is also shown by many contributions from Le Châtelier, professor at College de France then at Sorbonne, both in the fields of metallurgy and cements. Although used in the Neolithic era, ceramics were made in a much more rational manner, leading to a broad diversity of properties and applications. A better understanding of these materials, in which defects are, at the same time, a major disadvantage and a source of original behavior, led to solid-state chemistry, which appeared as a mature discipline at a Bordeaux congress held in 1964. From "hard", "shake and bake" chemistry, it became a tailored, "soft" chemistry, thanks, in particular, to the work of Rouxel and Livage, who approached this new world either with the chemical treatment of preformed materials or the stepwise and controlled synthesis from molecular species in solution. Again, natural structures and synthetic products are intrinsically linked through replication of constructions like the silica architectures of diatoma! A complementary approach relates to microporous materials, sources of "shape-selective" catalysts, membranes, and, even in its latest achievements, traps and reservoirs for molecular species.

The identification of new sources of natural products that have astonishing structures with an impressive number of chiral centers shows the immense diversity of the molecular, macromolecular, and inorganic structures. An Alsatian, Werner, by proposing spatial arrangements of molecular entities around a metal cation to describe coordination complexes, laid the foundations of organization at a supramolecular level. Another Alsatian, Lehn, developed this concept, leading in a rational way to supramolecular chemistry with auto-organization and then self-assembly of increasingly complex entities. Nature, while being based on the multiplicity of ion−ion, ion−molecule, and molecule−molecule interaction modes, exploits this concept with increasing complexity, leading finally to living organisms capable of self-replication. Supramolecular chemistry suggests that if these interactions can be broken in the same way as they are made, a genuine constitutional dynamic chemistry would be in operation, providing original structures capable of auto-repair, another property related to all living things.

Many of these developments would not have taken place if the structure of the organic molecule had not been understood. In 1858, Kekulé proposed to describe organic molecules by their carbonaceous sequence, the carbon atom being tetravalent. The same year, Couper, who worked in the Wurtz laboratory in Paris, presented at the young "Société Chimique de Paris" his ideas on the "forces of attraction" that exist between the various elements of an organic molecule, what we call now bonds between atoms. The Couper formulae were used by Meyer in Germany, then by Boutleroff in France, who proposed the term "chemical structure" in 1864 "to indicate the chemical sequence or the way in which the atoms are connected" in a molecule. In the same year, modern chemical writing was introduced, thanks to Brown who depicted the atoms by their symbols and each connection by a continuous line. In 1874, the tetrahedral image of carbon was proposed by van't Hoff and Le Bel, hence opening the way to the three-dimensional representations of organic molecules. Thus, we can understand why apparently identical molecules are in fact dissymmetrical and deflect light differently. If "only the products born under the influence of Life are dissymmetrical", then "all the molecules prepared in our laboratories are symmetrical", said Pasteur. However, in 1894, Fischer, who studied the stereospecificity of enzymes, deduced from his observations the

 © 2007 Wiley-VCH Verlag GmbH & Co. KGaA, Weinheim 

structural "key−lock" relationship between a sugar and its enzyme. Prelog, Kagan, and many others used all the subtlety of asymmetric synthesis, then of enantioselective catalysis, to obtain man-made optically active compounds.

We have such a clear vision of atoms in our mind that we may have forgotten how strong the opposition was to atoms in France during the 19th century. At that time, atoms were a theoretical concept introduced by Dalton at the beginning of the 19th century, and this concept was adopted by the whole chemistry community during the Karlsruhe meeting in September 1860. In 1877, the Academy of Sciences was the witness of a violent controversy between Berthelot, opposed to, and Wurtz, defender of atomism. Wurtz and his many students employed the "Société Chimique de Paris" and its Bulletin as a mighty place for defending atomism in France, which gradually enabled the conversion of French chemists to this theory. Bohr applied the quantum theory to the planetary model of the atom proposed by Rutherford in 1911. To describe chemical bonding Lewis and Kossel developed, in 1916, the octet relationship, based upon the outer electrons. Hückel in Germany and Mulliken in the United States introduced molecular orbitals; however, Pauling is the true holder of this new approach, by introducing the notion of hybridization of carbon orbitals in a paper issued in 1931, and by publishing his famous book: "The Nature of the Chemical Bond" in 1939. If this era represents the golden age of the covalent bond, then other interactions were already taken into account: from dative bonds, first introduced by Werner, to the generalization of Lewis interactions, to weaker interactions like van der Waals forces present in soft matter. The importance of the hydrogen bond, exemplified by Pimentel's work, strongly contributed to the understanding of interactions occurring in biological systems: let us recall that the DNA structure is controlled by hydrogen bonds, which are also present in supramolecular chemistry. In addition to this diversity of bonding modes, the introduction of new concepts and the improvement of mathematical methods and data-processing led to descriptive and predictive tools for these connections and the resulting properties. Forty years after the foundations were set down by Schrödinger, the work of Hartree and Fock, Kohn and Pople have provided tools like density functional theory (DFT), now unavoidable for the understanding of physical and chemical properties.

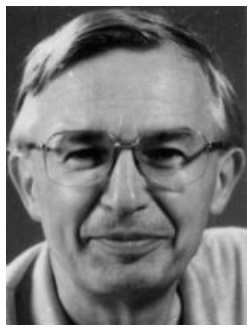

**Jean-Marie Lehn**

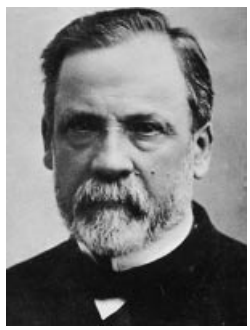

**Louis Pasteur**

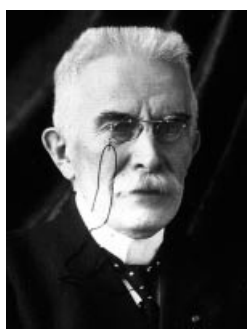

**Henry Le Châtelier**

Parallel to the development of this writing that makes chemistry a science which has its own alphabet, the desire of comprehension of the chemical reactivity was also very strong. Following the seminal works of Carnot, Kelvin, and Clausius, the development of thermodynamics led to the birth of physical chemistry — a junction of chemistry and physics — exemplified by Le Châtelier, Gibbs, Arrhenius, van't Hoff, and Ostwald, who often were chemists as much as they were physicists: Didn't Ostwald develop the ammonia oxidation process? It is worth noting the subtle differences that have appeared since between physical chemistry and chemical physics, if one considers the microscopic and now nanoscopic domains at which new chemical reactivity is being born. Physical chemistry, like analytical sciences, irrigates all the disciplines of chemistry, and the younger generations often neglect its importance; it is, for example, behind the classification of fundamental reactions of organic chemistry established by Ingold!

All these advancements could not have been done without a panoply of analytical tools pushing back the limits of detection and temporal scales of observation for more than two centuries. Centesimal analysis introduced after the works of Lavoisier and Priestley by Gay-Lussac and Thenard, Berzelius, Dumas, Liebig, and Pregl, to quote only the major contributors, was supplemented by isotopic analysis and determination of exact masses by high-resolution mass spectrometry. Separative analysis experienced extraordinary developments following the invention of chromatography by Tswett, a Russian botanist with a predestined name. If we had to wait until 1931 for the work of Kuhn on the separation of carotenes, then the post-war period saw the systematic recourse to this technique and its numerous alternatives, crowned by the Nobel Prize of Sanger in 1958. The pharmaceutical industry even exploits Tswett's technique to obtain optically active molecules from racemates.

Emission and absorption spectroscopy can be applied to an extremely broad frequency range, providing information on the structure and the movement of the chemical objects. This development goes hand in hand with a growing mastery of technology: in 1939, Beckmann introduced the first UV/Vis spectrophotometer, which enabled Woodward to achieve his PhD within one year − the first of the Woodward rules. The advancement of mass spectrometry led to considerable achievements as a spin off of the Manhattan project. In the same way, the rise in the use of increasingly high radio frequencies and intense magnetic fields benefited resonance spectroscopy, leading to the emergence, for example, of 1 GHz NMR spectrometers able to solve the structure of proteins of several tens of thousands of daltons. Lastly, the current data-processing resources has made it possible to systematize the use of Fourier transform with respect to NMR, IR, and EPR spectroscopy, mass spectrometry, and so forth. The discovery of X-rays on the eve of the 20th century has also contributed to the knowledge of the crystalline structure of increasingly complex molecules. In fact, the develop-

 © 2007 Wiley-VCH Verlag GmbH & Co. KGaA, Weinheim 

ment of intense and focused sources (synchrotron radiation), two-dimensional detectors (a consequence of Charpak's work), and powerful computational tools supplements the spectroscopic studies of molecules and macromolecules.

As never satisfied, the chemist also seeks to directly see the object of his studies. The development of magnetic lenses has allowed the visualization of nanometric and sub-nanometric objects by electron microscopy. Scanning electron microscopy is of primary importance for the development of materials and the study of their behavior. A new stage was reached with the work of Rohrer and Binning on scanning tunnelling microscopy (STM) and its derivatives, which allows not only the observation at atomic scale, but also writing on this scale with atoms. The last achievement in microscopy techniques, recently developed by Zewail, takes advantage of laser coherent electron packets generated with femtosecond laser pulses. The combination of spatial and temporal dimensions makes possible the analysis of the dynamic structure of inorganic, organic, and biological materials without damaging the objects by high-resolution electron microscopy.

**Joseph Fourier**

This extraordinary rise in laser technology largely opened the field of the studies including time as the fourth dimension in chemistry. The exploration of the "Femtoland" by Zewail, associated to the modeling of the processes studied, offers extraordinary prospects for the comprehension of chemical reactivity. Other methodologies, with other timescales, also make it possible to access various types of chemical events. Thus, cyclic voltammetry at very high scanning rates contributes to the mechanistic studies of electroactive systems; synchrotron radiation allows time-resolved diffraction experiments, and so forth.

Will we attend the birth of a virtual chemistry? It should be hoped that it does nothing but supplement the pallet of chemistry now extending to constitutional dynamic chemistry. To return to Berthelot, in conclusion, let us recall his remark: "the chemist creates the object of his study". The objects become only more complex and offer a promising future to chemistry and to chemists.

## Acknowledgments

We wish to acknowledge the members of Club d'Histoire de la Chimie and the writers of numerous biographies of former presidents of the "Société Française de Chimie".

 © 2007 Wiley-VCH Verlag GmbH & Co. KGaA, Weinheim 

# CONTENTS

## MICROREVIEW


### Copper-Based Enzymes

**F. Thomas* ..... 2379–2404**

Ten Years of a Biomimetic Approach to the Copper(II) Radical Site of Galactose Oxidase

**Keywords:** Biomimetic chemistry / Copper / Radicals / Bioinorganic chemistry / Enzyme models


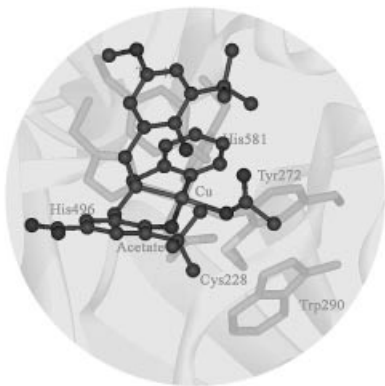


Galactose oxidase is an enzyme whose active site exhibits several unusual features, such as a coordinated tyrosyl radical, post-translationally modified amino acids, and π-stacked residues. The structural attributes, reactivity, electronic properties, self-processing, and many more of its properties have been addressed successfully during the last decade using model complexes.

## SHORT COMMUNICATION


### N-Heterocyclic Germylenes

**F. E. Hahn,* A. V. Zabula, T. Pape, A. Hepp ..... 2405–2408**

Preparation and Molecular Structures of Stable Bis(germylenes) with Pincer Topology

**Keywords:** N-Heterocycles / Germylenes / Pincer ligands


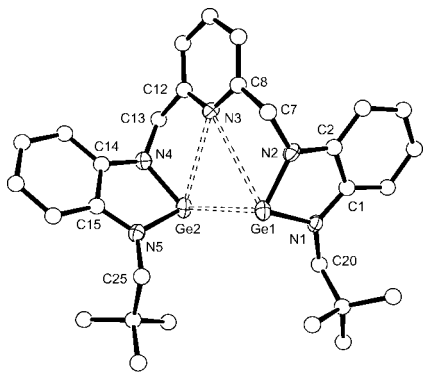


Stable benzannulated bis(germylenes) with pincer topology have been prepared and characterized by X-ray analysis.

## FULL PAPERS


### Single-Molecule Magnetism

**A. K. Boudalis,* Y. Sanakis,* J. M. Clemente-Juan, A. Mari, J.-P. Tuchagues ..... 2409–2415**

A Diferrous Single-Molecule Magnet

**Keywords:** Single-molecule studies / Cluster compounds / Magnetic properties / Iron


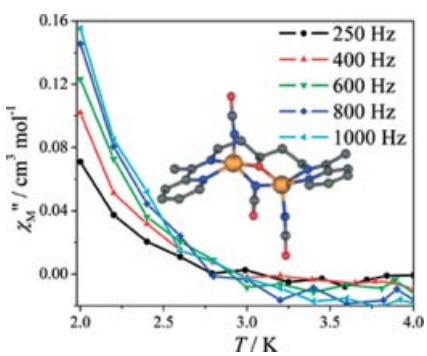


The dissymmetrical diferrous complex $[Fe_2(acpypentO)(NCO)_3]$ displays slowly relaxing magnetization due to ferromagnetic coupling and strong uniaxial anisotropy as evidenced by $^{57}Fe$ Mössbauer spectroscopy and dual-mode X-band EPR spectroscopy.

 © 2007 Wiley-VCH Verlag GmbH & Co. KGaA, Weinheim 

## Porphyrinoid Rotaxanes

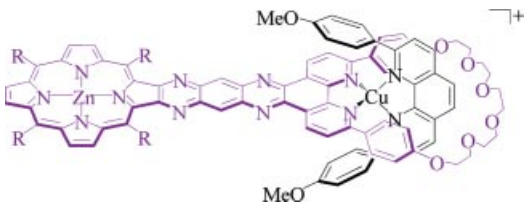


A novel macrocyclic ligand containing a porphyrin moiety was prepared by a stepwise condensation and used in the preparation of a rotaxane-like structure.

**J. Frey, W. Dobbs, V. Heitz,***
**J.-P. Sauvage* ..... 2416–2419**

A 1,10-Phenanthroline-Containing Ring Connected to a Porphyrin by a Rigid Aromatic Spacer and Its Copper-Complexed Pseudorotaxane

**Keywords:** Ligand design / Porphyrinoids / Macrocycles / Template synthesis / Rotaxane

## Molecular Machines

Three pseudo-rotaxanes have been prepared which incorporate the same two-chelate ring and various threaded diimine ligands. Using electrochemical techniques, the pirouetting motions of the axle within the ring have been studied, evidencing that rigidity of the thread-contained chelate and steric hindrance lead to slowly moving molecular machines.

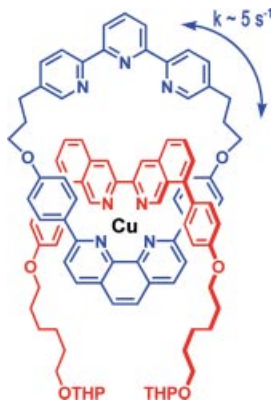


**J.-P. Collin, F. Durola, P. Mobian,**
**J.-P. Sauvage* ..... 2420–2425**

Pirouetting Copper(I)-Assembled Pseudo-Rotaxanes: Strong Influence of the Axle Structure on the Motion Rate

**Keywords:** Pseudo-rotaxanes / Diimine ligands / Copper complexes / Coordination modes / Pirouetting motion

## Iron Porphyrins

$Fe^{II}$ porphyrins, $[Fe(OEPy_4P)(B)_2]^{4+}$, B = Im or Py, were synthesized in three steps from Zn-*β*-octaethylporphyrin and characterized by mass spectrometry, UV/Vis spectroscopy, electrochemistry, and X-ray diffraction (B = Py). They are stable in air, show a highly distorted saddle-shape structure, and bear four positive charges close to the metal.

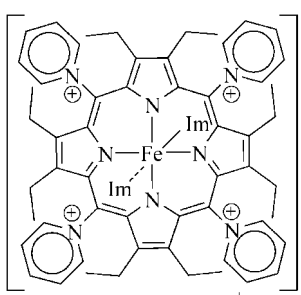


$[Fe(OEPy_4P)(Im)]_4^+$

**M. W. Renner, C. Bochot, A. Héroux,**
**D. Mansuy, P. Battioni* ..... 2426–2433**

Structural, Electrochemical, and Spectroscopic Properties of a Class of Dodecasubstituted Iron Porphyrins Bearing Four Positive Charges Close to the Metal

**Keywords:** Iron / Porphyrins / Ligand design / X-ray diffraction / Voltammetry

## Ti–Hf Chlorometallate Complexes

The heterodimetallic $[TiHfCl_{10}]^{2-}$ ion exists as a discrete species in solution, in equilibrium with a mixture of the corresponding homodimetallic ions, $[Ti_2Cl_{10}]^{2-}$ and $[Hf_2Cl_{10}]^{2-}$. Its partial hydrolysis affords a well-defined oxo-bridged heterodimetallic complex, $[TiHf(\mu\text{-}O)Cl_8]^{2-}$.

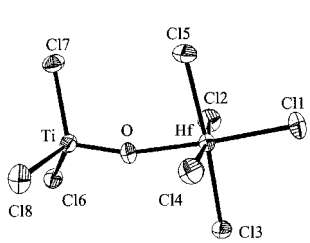


**E. Robé, S. Maria, P. Richard,**
**R. Poli* ..... 2434–2442**

Mixed Titanium–Hafnium Chlorometallate Complexes

**Keywords:** Titanium / Hafnium / Chlorometallate complexes / Mixed-metal complexes

 © 2007 Wiley-VCH Verlag GmbH & Co. KGaA, Weinheim 

# CONTENTS


## NO Analogues

**G. Balázs, J. C. Green,***
**D. M. P. Mingos* ..... 2443–2453**

Electronic Structure of Linearly Coordinated EQ Complexes of the Type [$(N_3N)W(EQ)$] [$N_3N$ = $N(CH_2CH_2NSiMe_3)_3$; E = P, As, Sb, Bi; Q = O, S, Se, Te]: A DFT Study

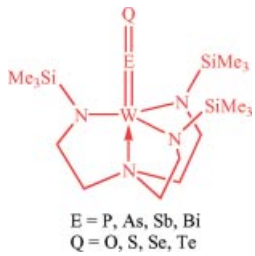


The electronic structure of the terminally coordinated EQ complexes [$(N_3N)W(EQ)$] [$N_3N$ = $N(CH_2CH_2NSiMe_3)_3$; E = P, As, Sb, Bi; Q = O, S, Se, Te] was analysed by DFT methods. The bonding in the W–E–Q unit and the general trends moving from the lighter to the heavier elements are discussed.

**Keywords:** Bonding / Pnicogens / Chalcogens / Tungsten / Density functional calculations

## Vanadium Oxide Catalysts

**M. Engeser, D. Schröder,***
**H. Schwarz ..... 2454–2464**

Dehydration and Dehydrogenation of Alcohols with Mononuclear Cationic Vanadium Oxides in the Gas Phase and Energetics of $VO_nH^{0/+}$ ($n$ = 2, 3)

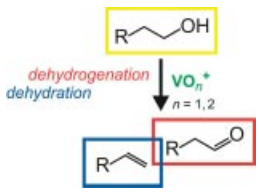


The activation of alkanols by gaseous $VO_n^+$ cations ($n$ = 1, 2) is probed by mass spectrometric experiments, which reveal a competition between dehydrogenation and dehydration to afford the corresponding alkenes and oxidation to carbonyl compounds.

**Keywords:** Alcohol oxidation / Dehydration / Mass spectrometry / Metal alkoxides / Vanadium

## Aqueous-Phase Oxidation

**H. Korpi, P. J. Figiel, E. Lankinen, P. Ryan, M. Leskelä, T. Repo* ..... 2465–2471**

On In Situ Prepared Cu–Phenanthroline Complexes in Aqueous Alkaline Solutions and Their Use in the Catalytic Oxidation of Veratryl Alcohol

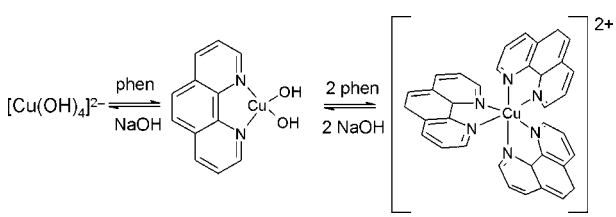


As ligand concentration and pH are interdependent, under optimum reaction conditions, the $OH^-$ concentration needs to be adequate for efficient alcohol oxidation, and the phenanthroline concentration needs to be high enough to preserve the structure of the [Cu(phen)$(OH)_2$] species, whose presence is essential for high catalytic activity.

**Keywords:** Catalysis / Copper / Dioxygen / Active species / Oxidation

## Group 13/15 Heterocycles

**M. Matar, A. Kuczkowski, U. Keßler, S. Schulz,* U. Flörke ..... 2472–2476**

Reactions of $t$Bu$_2$AlH and RE$(SiMe_3)_2$ (R = H, $SiMe_3$) – Synthesis and X-ray Crystal Structures of [$t$Bu$_2$AlP(H)$SiMe_3$]$_2$ and [$t$Bu$_2$AlE$(SiMe_3)_2$]$_2$ (E = Sb, Bi)

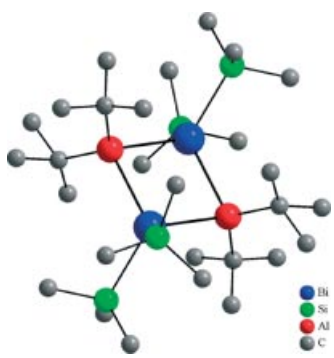


$t$Bu$_2$AlH and E$(SiMe_3)_3$ react with elimination of $Me_3SiH$ and subsequent formation of [$t$Bu$_2$AlE$(SiMe_3)_2$]$_2$ (E = Sb, **1**; Bi, **2**) whereas no reaction was observed with P$(SiMe_3)_3$. In contrast, $t$Bu$_2$AlH also reacts with HP$(SiMe_3)_2$ with $Me_3SiH$ elimination and formation of [$t$Bu$_2$AlP(H)$SiMe_3$]$_2$ (**3**). Complexes **1**–**3** were characterized by various spectroscopic methods, elemental analysis and single-crystal X-ray diffraction.

**Keywords:** Main group elements / Heterocycles / Solid state structures


 © 2007 Wiley-VCH Verlag GmbH & Co. KGaA, Weinheim 

## Catalytic Ethylene Oligomerization

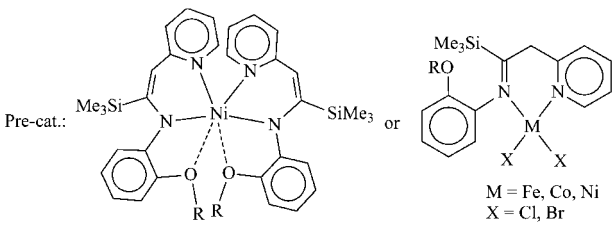


Novel anionic and neutral ligands and their iron, cobalt, and nickel complexes were synthesized and characterized. These complexes showed good catalytic activities for ethylene oligomerization in the presence of appropriate co-catalysts.

**L. Wang, C. Zhang, Z.-X. Wang* ..... 2477–2487**

Synthesis and Characterization of Iron, Cobalt, and Nickel Complexes Bearing Novel *N*,*N*-Chelate Ligands and Their Catalytic Properties in Ethylene Oligomerization

**Keywords:** Iron / Cobalt / Nickel / Catalysis / Ethylene / Oligomerization

## Germanium Chemistry

The first series of phosphane oxide complexes of germanium(IV) halides have been prepared, including *trans*-$[GeF_4(R_3PO)_2]$ (R = Me, Et or Ph), *trans*-$[GeCl_4(Et_3PO)_2]$, *fac*-$[GeCl_3(Me_3PO)_3]_2[GeCl_6]$, and *cis*-$[GeX_2(Me_3PO)_4]X_2$ (X = Cl or Br).

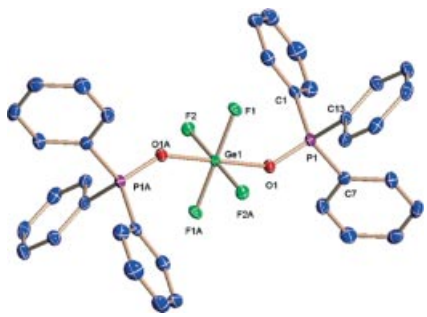


**F. Cheng, M. F. Davis, A. L. Hector, W. Levason,* G. Reid, M. Webster, W. Zhang ..... 2488–2495**

Synthesis, Spectroscopic and Structural Systematics of Complexes of Germanium(IV) Halides ($GeX_4$, X = F, Cl, Br or I) with Phosphane Oxides and Related Oxygen Donor Ligands

**Keywords:** Germanium / Coordination complexes / Phosphane oxides

## Nanocomposite Particles

Colloidal $CdS/SiO_2$ nanocomposite particles were made directly from negatively charged silica particles ($d$ = 150 nm) and positively charged ligand-stabilised CdS particles ($d$ = 3 nm).

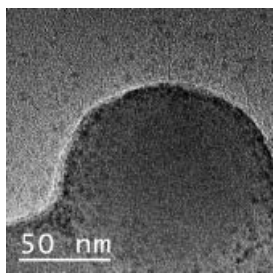


**M. Roskamp, A. K. Schaper, J. H. Wendorff, S. Schlecht* .... 2496–2499**

Colloidal $CdS/SiO_2$ Nanocomposite Particles from Charged Colloids of CdS and Silica

**Keywords:** Colloids / Nanostructures / Semiconductors / CdS / Silica particles

## Arsenomolybdate Polyoxometalates

Two novel heteropolymolybdates have been synthesized and characterized. The complexes resemble a sandwich-type complex and involve the coordination of two transition metals to two $[As^VMo_9O_{33}]^{7-}$ fragments, which derive from the *B*-*β*-Keggin structure.

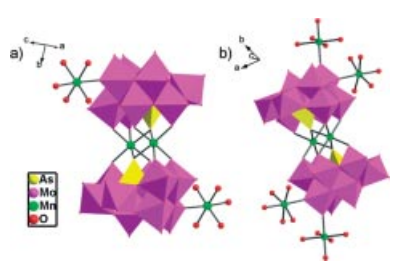


**Y. Yang, L. Xu,* G. Gao, F. Li, Y. Qiu, X. Qu, H. Liu ..... 2500–2505**

Transition-Metal ($Mn^{II}$ and $Co^{II}$) Complexes with the Heteropolymolybdate Fragment $[As^VMo_9O_{33}]^{7-}$: Crystal Structures, Electrochemical and Magnetic Properties

**Keywords:** Polyoxometalates / Molybdenum / Arsenic / Magnetic properties

**If not otherwise indicated in the article, papers in issue 16 were published online on May 15, 2007**

 © 2007 Wiley-VCH Verlag GmbH & Co. KGaA, Weinheim 

# SPOTLIGHTS …

## *Helical Polymers*

Y. Hase, Y. Mitsutsuji, M. Ishikawa, K. Maeda, K. Okoshi, E. Yashima*

**Unexpected Thermally Stable, Cholesteric Liquid-Crystalline Helical Polyisocyanides with Memory of Macromolecular Helicity**

*Chem. Asian J.*
DOI: **10.1002/asia.200700051**

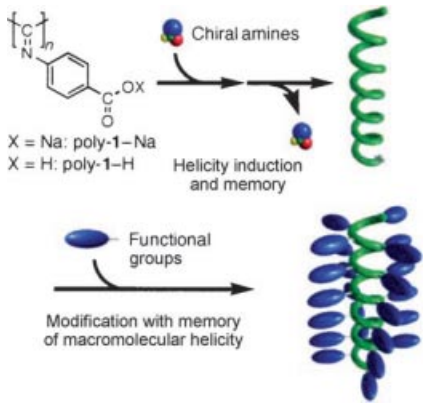


**Remember it well!** The achiral sodium salt of poly(4-carboxyphenyl isocyanide) (poly-**1**–Na) folds into a one-handed helix induced by optically active amines in water, which remains when the amines are completely removed. Further modification of the side groups is possible without loss of memory of macromolecular helicity.

## *Aptamers*

W. Zhao, W. Chiuman, M. A. Brook,* Y. Li*

**Simple and Rapid Colorimetric Biosensors Based on DNA Aptamer and Noncrosslinking Gold Nanoparticle Aggregation**

*ChemBioChem*
DOI: **10.1002/cbic.200700014**

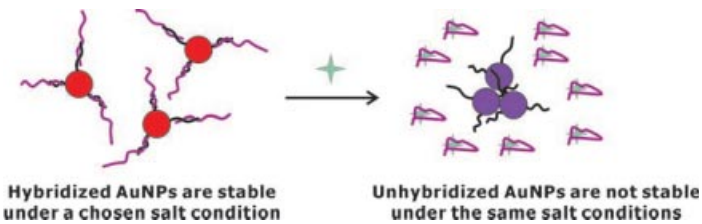


**The color purple**. Upon binding of the target +, negatively charged DNA aptamers (shown in purple) dissociate from a gold nanoparticle surface; this results in nanoparticle aggregation and a color change at a chosen salt concentration.

## *Metallofullerenes*

Y. Ito, W. Fujita, T. Okazaki, T. Sugai, K. Awaga, E. Nishibori, M. Takata, M. Sakata, H. Shinohara*

**Magnetic Properties and Crystal Structure of Solvent-Free Sc@$C_{82}$ Metallofullerene Microcrystals**

*ChemPhysChem*
DOI: **10.1002/cphc.200700097**

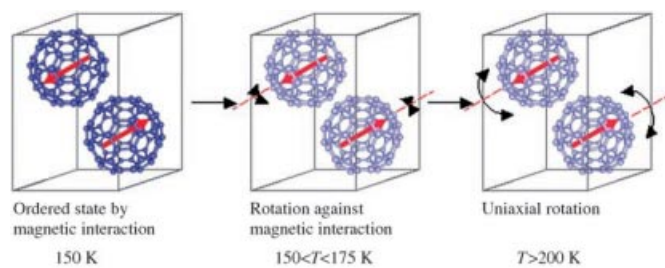


**Abnormal behavior** of the magnetic susceptibility of solvent-free Sc@$C_{82}$ microcrystals is observed between 120 K and 200 K (see figure). The presence of the antiferromagnetic-like interaction exerted among Sc@$C_{82}$ molecules restricts the molecular rotation to uniaxial.

## *Nanosensors*

H. Yao, Y. Zhang, F. Xiao, Z. Xia, J. Rao*

**Quantum Dot/Bioluminescence Resonance Energy Transfer Based Highly Sensitive Detection of Proteases**

*Angew. Chem. Int. Ed.*
DOI: **10.1002/anie.200700280**

**Sensing by BRET**: Quantum dot (QD) nanosensors can detect the activity of matrix metalloproteinases by measuring the bioluminescence resonance energy transfer (BRET) efficiency between the QDs and a bioluminescent fusion protein (see scheme; Luc8 = *Renilla* luciferase; His × 6 = six-histidine tag).

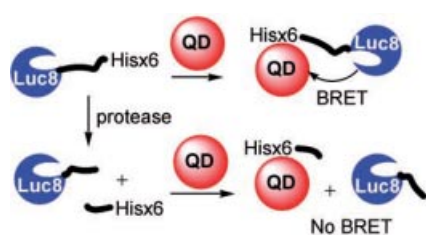


 © 2007 Wiley-VCH Verlag GmbH & Co. KGaA, Weinheim 

# … ON OUR SISTER JOURNALS

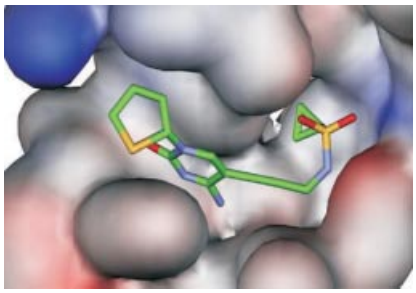

**IspE kinase inhibitors**. The first inhibitors for the kinase IspE, an enzyme of the non-mevalonate pathway, are presented. The nonphosphate based inhibitors avoid binding to the ATP site but instead occupy the substrate site and a small, newly detected hydrophobic subpocket at the active site of IspE. With appropriate filling of this pocket, competitive inhibition constants $K_{ic}$ in the upper nanomolar range are measured.

### *Kinase Inhibitors*

A. K. H. Hirsch, S. Lauw, P. Gersbach, W. B. Schweizer, F. Rohdich, W. Eisenreich,* A. Bacher, F. Diederich*

**Nonphosphate Inhibitors of IspE Protein, a Kinase in the Non-Mevalonate Pathway for Isoprenoid Biosynthesis and a Potential Target for Antimalarial Therapy**

*ChemMedChem*
DOI: **10.1002/cmdc.200700014**

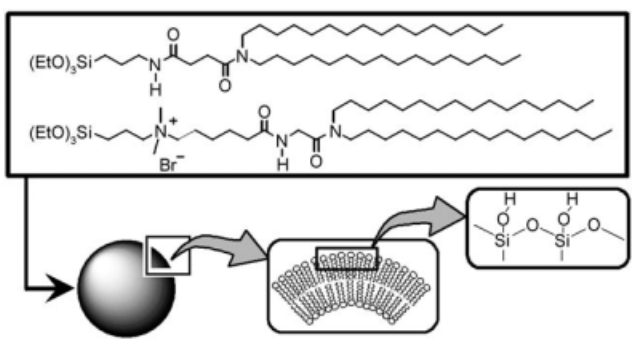

**An organic–inorganic hybrid**, a so-called "cerasome", which has a liposomal bilayer structure and a polysiloxane surface, has been prepared by sol–gel reaction and self-assembly of lipidic organoalkoxysilanes. The formation process and properties of cerasomes are described in detail. It was revealed that cerasomes have high morphological stability compared with conventional liposomes.

### *Sol–Gel Reactions*

K. Katagiri,* M. Hashizume, K. Ariga, T. Terashima, J.-i. Kikuchi*

**Preparation and Characterization of a Novel Organic–Inorganic Nanohybrid "Cerasome" Formed with a Liposomal Membrane and Silicate Surface**

*Chem. Eur. J.*
DOI: **10.1002/chem.200700175**

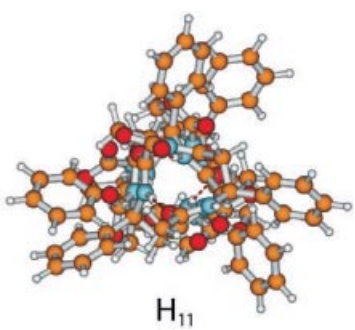


A novel class of foldamers containing (*S*)-β$^3$-homophenylglycine and D-4-carboxyoxazolidin-2-one residues in alternate order is reported. The experimental conformational analysis proved that these oligomers fold into ordered structures and theoretical calculations suggest a helix with 11-membered hydrogen-bonded rings as the preferred secondary structure type.

### *Foldamers*

G. Angelici, G. Luppi, B. Kaptein, Q. B. Broxterman, H.-J. Hofmann, C. Tomasini*

**Synthesis and Secondary Structure of Alternate α,β-Hybrid Peptides Containing Oxazolidin-2-one Moieties**

*Eur. J. Org. Chem.*
DOI: **10.1002/ejoc.200700134**

On these pages, we feature a selection of the excellent work that has recently been published in our sister journals. If you are reading these pages on a computer, click on any of the items to read the full article. Otherwise please see the DOIs for easy online access through Wiley InterScience.

 © 2007 Wiley-VCH Verlag GmbH & Co. KGaA, Weinheim 

DOI: 10.1002/ejic.200601091

# Ten Years of a Biomimetic Approach to the Copper(II) Radical Site of Galactose Oxidase

**Fabrice Thomas*[a]**

**Keywords:** Biomimetic chemistry / Copper / Radicals / Bioinorganic chemistry / Enzyme models

An overview of recent progress in the modeling of the copper(II)-phenoxyl entity of the metalloenzyme Galactose Oxidase (GO) is presented. GO is an enzyme that is extremely engineered by nature: its active site exhibits several unusual features, such as a coordinated tyrosyl radical, post-translationally modified amino acids, and π-stacked residues. Understanding each of these particularities has posed a challenge for chemists, who have consequently developed several biomimetic complexes during the last decade. The properties of representative complexes are described herein, with special emphasis given to copper(II) complexes involving tripodal ligands. All these biomimetic compounds have been developed with the aim of better understanding biologically relevant problems. I show here that the structural attributes, reactivity, electronic properties, self-processing, and many other properties of GO can be addressed successfully using model complexes.

(© Wiley-VCH Verlag GmbH & Co. KGaA, 69451 Weinheim, Germany, 2007)

## Introduction

Various strategies are used by metalloproteins to store and transfer electrons in biochemical processes.[1] In the simplest case, the number of metal ions required for the reaction matches the number of electrons to be transferred. This is illustrated by tyrosinases that catalyze the hydroxylation of phenols, which have an active site that contains two copper ions. An organic cofactor could also complete the metal-driven electron transfer, as in copper amine oxidases that catalyze the oxidative deamination of amines using topaquinone. It has been shown recently that some metalloenzymes are able to generate an organic radical cofactor directly on their own peptidic chain to complete metal-driven electron transfers.[2,3] Galactose oxidase (GO), whose active site includes a tyrosyl radical coordinated to a copper(II) ion, is a prototypical enzyme of this class and is a fascinating example of synergy between a metal and a radical to perform oxidation reactions. The metal-radical array in these systems is much more than an association, and the advantage of maintaining a tyrosyl radical close to the metal ion is that hydrogen abstraction from a C–H bond by radicals is energetically favored over a hydrogen atom transfer to an inorganic metal-based oxidant (the thermodynamic affinity of a tyrosyl radical for a hydrogen atom is high).[4] The tyrosyl radical in GO thus performs the hydrogen atom abstraction while the metal ion is involved in a classical single electron transfer. GO is an enzyme that is extremely engineered by nature: its active site exhibits several unusual features such as post-translationally modified amino acids and π-stacked residues, and understanding each of these particularities poses a challenge for biologists and chemists alike. In studies aimed at understanding this enzyme, biochemists commonly use directed mutagenesis while chemists use a biomimetic approach. The latter consists of synthesizing and characterizing abiotic compounds that exhibit some or all of the enzyme's features. The devel-

[a] Département de Chimie Moléculaire – Chimie Inorganique Redox Biomimétique (CIRE) UMR CNRS 5250, Université Joseph Fourier,
B. P. 53, 38041 Grenoble cedex 9, France
Fax: +33-4-76514836
E-mail: Fabrice.Thomas@ujf-grenoble.fr

*Fabrice Thomas was born in 1973. He did his undergraduate studies in Biochemistry at the University of Grenoble, where he received his Ph.D. degree in Molecular Chemistry in 1999. He then spent one year at the Institute of Physics at the University of Lübeck (Germany) as a postdoctoral fellow supervised by Prof. Trautwein. He worked on the characterization of iron centers in metalloproteins and models by Mössbauer spectroscopy. He is currently assistant professor in the Department of Molecular Chemistry, in the Inorganic Redox Biomimetic Chemistry team (CIRE) at the University of Grenoble. His main research interests are in the areas of inorganic and biomimetic chemistry. More specifically, he works on the metal-radical association in complexes that are bio-inspired by galactose oxidase.*

 © 2007 Wiley-VCH Verlag GmbH & Co. KGaA, Weinheim 

opment of mimics of GO began in 1996, and has contributed significantly to an enhanced understanding of the spectral properties, structural attributes, and even reactivity of its active site. Two reviews concerning the first-generation models of both the active $Cu^{II}$-phenoxyl and inactive $Cu^{II}$-phenolate forms of the GO active site[5,6] appeared in the literature in 2000.

Several complexes involving phenoxyl moieties coordinated to other divalent metal ions, or even trivalent metal ions, have also been synthesized. Many of these have been described by Wieghardt et al., and were reviewed in 2001.[7] These studies gave a lot of insights into the properties of coordinated phenoxyl radicals. More recently, a review focused on the aerobic oxidation of various substrates catalyzed by copper and manganese radical complexes has been published by the same group.[8] In this review I will briefly present the literature prior to 2000 and then focus my attention on more recent $Cu^{II}$-phenoxyl complexes. As a preamble, an overview of the biochemical properties of the GO active site is given. I then describe the properties of representative complexes that have been used as models of GO, with special emphasis on copper(II) complexes involving tripodal ligands, as their rich chemistry has been extensively studied by several groups. Next, I present the biologically relevant problems that have been addressed and solved by biomimetic studies, and finally I describe GO-inspired systems dedicated to the storage of three oxidizing equivalents (i.e. complexes containing either two phenoxyl radicals coordinated to a single copper ion, or a single phenoxyl radical coordinated to two copper ions).

## Galactose Oxidase

The most important aspects of GO chemistry have been recently reviewed, so only a brief presentation of the essential facts will be given here.[9–11] Galactose oxidase is an extracellular type II mononuclear copper protein (68 kDa) of fungal origin. GO catalyses the two-electron oxidation of a wide range of primary alcohols to their corresponding aldehydes with the concomitant reduction of molecular oxygen to hydrogen peroxide. The apparent paradox − a two-electron oxidation performed by a single copper ion − is explained by the involvement of another redox center, namely a tyrosyl radical from the protein, during the catalytic cycle. The physiological role of GO is not clear, although it could be involved in the production of $H_2O_2$ for further use as an co-oxidant for lignin- and cellulose-degrading peroxidases and could also provide an antibiotic defense within the rhizosphere.[10]

### Structure of the Active Site

GO has been crystallized and its X-ray crystal structure was reported about ten years ago (Figure 1).[12,13] Its active site comprises a copper atom in a distorted square-based pyramidal geometry with Tyr495 occupying the axial position. His581, His496, Tyr272, and an exogenous ligand ($H_2O$ or acetate, replacing the substrate) coordinate the copper in equatorial positions. The most striking feature of this complex is the cross-linking of Tyr272 to Cys228 through a thioether bond at the *ortho* position of the OH group, which presumably lowers the tyrosyl/tyrosine redox potential. The indole ring of Trp290 is π-stacked with Tyr272 and is believed to control the access to the active site and shield the Cys-Tyr cofactor from exposure to solvent. The enzyme can exist in three well-defined oxidation levels: the $Cu^{II}$-tyrosyl radical oxidized form, an intermediate $Cu^{II}$-tyrosinate form, and the reduced $Cu^{I}$-tyrosine form. Only the former and latter forms are catalytically active. The $Cu^{II}/Cu^{I}$ redox couple has been estimated to be –0.24 V vs. $Fc^+/Fc$ at pH 7,[14,15] while the tyrosyl/tyrosinate one has been estimated to be 0.01 V vs. $Fc^+/Fc$. The $Cu^{II}$-tyrosyl radical and the fully reduced copper(I) form undergo a rapid bimolecular comproportionation that affords the catalytically inactive $Cu^{II}$-tyrosinate form.[15]

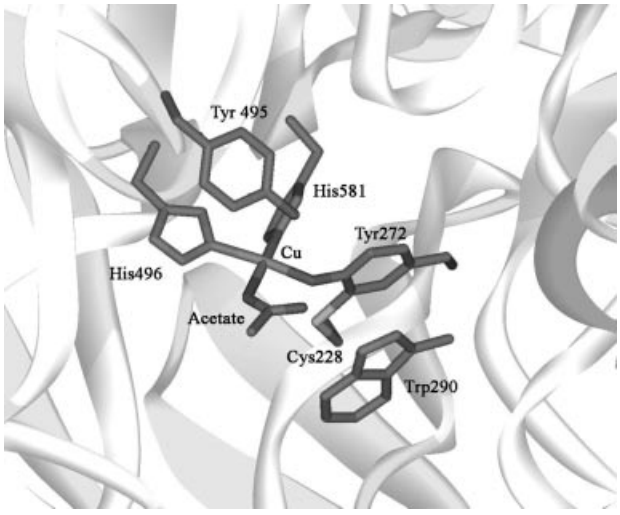


Figure 1. X-ray crystal structure of the active site of GO (adapted from ref.[12]).

The $Cu^{II}$-tyrosinate form possesses spectroscopic signatures that are typical of mononuclear copper(II) complexes, while the reduced form is EPR-silent and colorless. Extensive spectroscopic studies on the active oxidized form have shown that the radical is mainly harbored by the equatorially bound Tyr272 residue. Strong antiferromagnetic exchange coupling between the tyrosyl radical and the paramagnetic copper(II) ion results in a diamagnetic ground state, with a singlet–triplet splitting greater than 200 $cm^{-1}$.[16] A value of 752 $cm^{-1}$ has recently been reported from TD DFT calculations.[17] GO exhibits an unusually intense optical spectrum with absorption bands at around 445 and 800 nm[18] that are assigned to π–π* transitions of the tyrosyl radical.[9–11,17] The enzyme is relatively stable in this form, with a half life ($t_{1/2}$) of 7.2 days for its self-decomposition.[19]

 © 2007 Wiley-VCH Verlag GmbH & Co. KGaA, Weinheim 

**Free Radical Catalysis**

Catalysis by GO proceeds according to a ping-pong turnover reaction.[18,19] In the first half-reaction the alcohol substrate binds to the oxidized $Cu^{II}$-radical active site and reduces both redox centers [tyrosyl radical and copper(II) ion], and the aldehyde product is released. This aldehyde product, which has a low affinity for the complex, is then released into the medium. In the second half-reaction, the $Cu^{I}$-tyrosine site binds $O_2$ and reduces it to $H_2O_2$, thus regenerating the initial $Cu^{II}$-tyrosyl radical state. A proposed catalytic mechanism is shown in path A of Figure 2.[9–11,18–21]

The catalysis is initiated by a weak (almost collisional) association with the substrate. The structure of GO reveals a shallow channel through which substrates bound by Phe194, Phe464, Arg330, and Trp290 reach the catalytic site. Reaction over a wide range of concentrations shows that the enzyme is saturable with a dissociation constant of 71 mM for the formation of the initial complex with D-galactose.[10] This low affinity, which is a consequence of a quite open active site, is consistent with a lack of substrate selectivity. In contrast, the enzyme strictly constrains the orientation of the substrate in its active site, thereby allowing a stereospecific abstraction of the pro-*S* hydrogen by the nearby tyrosyl radical. Modeling galactose coordinated to the copper(II) ion of the native enzyme shows that the pro-α-*S*-hydrogen is located at a hydrogen-bonding distance from Tyr272 (ca. 2.5 Å), while the pro-*R* hydrogen is away from the pro-radical cofactor.[11] The steric constraints that lead to this stereoselectivity are not limited to galactose, as similar selectivity as been demonstrated for any substrate bearing a branched β-C. After binding of the substrate to the copper equatorial position, the first step involves a proton transfer (step 1, Figure 2).[22] Deprotonation of the alcohol is facilitated by copper coordination and a short H-OTyr495 bond (estimated to be around 2.8 Å).[23] This process occurs with a low barrier (nearly isothermic), on a nanosecond timescale, due to the optimized hydrogen-bonding geometry and the close matching of tyrosine $pK_a$ and coordinated alcohol $pK_a$. Two crucial facts result from this first step: the $Cu^{II}$–substrate interaction is strengthened and the C–H bond energy of the deprotonated substrate is lowered by 10 kcal mol$^{-1}$. The second step involves a hydrogen-atom transfer from the alkoxide substrate to the equatorial Tyr272 radical (step 2, Figure 2). This is the major rate-limiting step (at high $O_2$ concentrations) in the whole catalytic pathway, as reflected by the

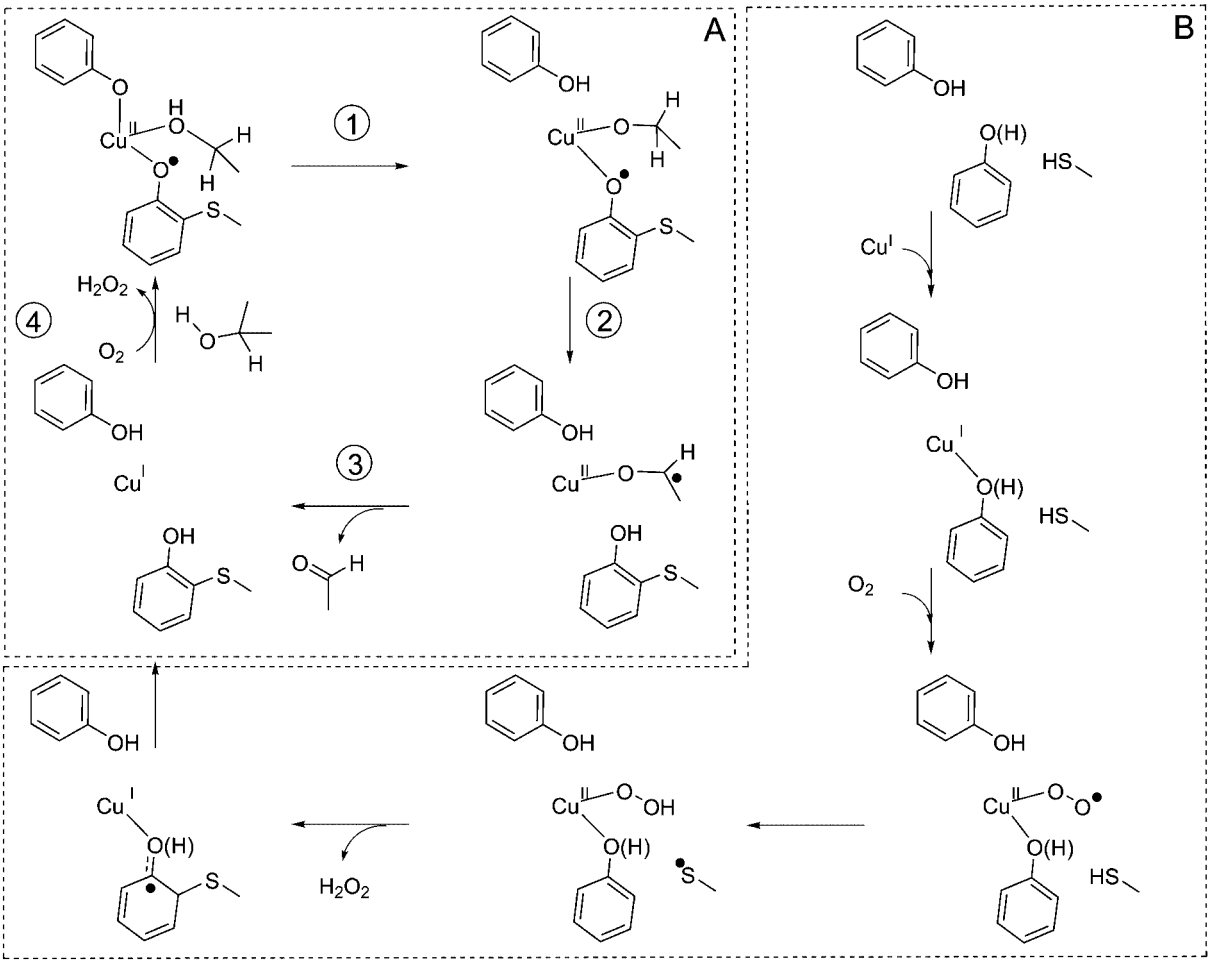


Figure 2. Free radical catalysis by mature GO (A) and self-processing of the pre-form of GO (B) (adapted from ref.[19,30] respectively).

 © 2007 Wiley-VCH Verlag GmbH & Co. KGaA, Weinheim 

large kinetic isotope effect (KIE) of 7.7 for D-galactose (an even larger KIE of 22 has been reported for 1-*O*-methyl-α-D-galactopyranoside)[18] and the fact that GO remains essentially fully oxidized during turnover. The large non classical KIE of 22 as well as a strong temperature dependence of the KIE are clear evidence of the tunneling of a hydrogen atom in the rate-limiting step.

The free activation energy for hydrogen abstraction has been estimated to be 13.6 kcal mol$^{-1}$. An optimized structure for the transition state can be obtained from B3LYP calculations:[23] it has a five-atom cyclic structure in which the O–H bond length is 1.24 Å while the C–H bond length is stretched to 1.36 Å. The hydrogen atom is then transferred perpendicularly to the phenol ring plane, in agreement with a π character of the radical. Mechanism-based inactivation of GO by ultrafast radical probes confirms that a short-lived substrate ketyl radical anion results from the H-abstraction (hydrogen abstraction is rate limiting).[24] The ketyl radical then reduces the metal center (single-electron transfer; step 3, Figure 2) and is released to allow $O_2$ binding (step 4, Figure 2).[9–11,18–21,25]

Quantitative structure–activity relationship correlations using the steady-state rate data for the oxidation of benzyl alcohol derivatives have revealed that the three elementary events, namely proton transfer, single electron transfer, and hydrogen-atom abstraction, are asynchronous components of the whole catalytic process rather than distinct kinetic intermediates.[26,27] The difficult-to-oxidize nitro derivatives as well as pyranosides and physiological substrates exhibit a large substrate KIE associated with a negligible solvent KIE: C–H bond cleavage (hydrogen-atom abstraction) is here fully rate limiting. In contrast, the easier-to-oxidize methoxybenzyl alcohols exhibit a smaller substrate KIE and a non-negligible solvent KIE, thus reflecting a small proton transfer contribution in the transition state and a pronounced single electron transfer character for substrate oxidation.

The re-oxidation step of GO (step 4, Figure 2) is a remarkable example of two-electron chemistry catalyzed by dioxygen, as the ratio of superoxide released does not exceed one for 2000 turnovers. Kinetic data have shown that re-oxygenation of the GO active site occurs with a rate constant of around $8 \times 10^6$ M$^{-1}$ s$^{-1}$ at 277 K.[18] However, the high instability of the oxygenated complex makes this step much less certain than the former, in spite of a main role for the enzyme being formation of hydrogen peroxide.

## Radical Cofactor Formation

GO is a secretory protein, which means that its maturation requires several successive steps: cleavage of a signal sequence that directs translocation, metal binding, and cofactor processing. The structure of a metal-free unprocessed pre-form of the protein has been described recently.[28] Its active site does not contain the Cys-Tyr cross-link, and Cys228 has been found oxidized into a sulfenic acid. This latter modification likely arises from oxidative damage to the protein. Conversion of this pre-form into the catalytically active form appears to be a self-processing event that requires only copper and $O_2$.[29] Copper in both oxidation states induces cross-linking and radical cofactor formation, but with very different time scales [$t_{1/2}$ = 3.9 s at pH 7 with copper(I) and 5.1 h with copper(II)]. The $Cu^I$-dependent biogenesis reaction may thus more closely resemble the physiological process.[30] A mechanism for this reaction, which involves initial copper(I) binding to the pre-form to afford a trigonal copper(I) complex that reacts with $O_2$, has been proposed recently (Figure 2, B). The resulting species is a reactive $Cu^{II}$-$O_2^{\cdot-}$ compound that abstracts a hydrogen atom from Cys228 and releases $H_2O_2$. The thiyl radical then attacks the ε-C ring carbon of Tyr272, and rearomatization occurs by proton and electron transfer to the metal. At this stage, the fully reduced form of the mature GO is obtained. This then readily undergoes two-electron oxidation by $O_2$ to give the catalytically active $Cu^{II}$-tyrosyl radical form of the enzyme and $H_2O_2$.

## Main Classes of Model Compounds for the GO Active Site

The discovery of a $Cu^{II}$-phenoxyl radical entity in the GO active site has stimulated a number of chemists to incorporate this unknown unit in coordination complexes. For phenoxyl radicals to exist as more than a transient intermediate in solution, the *ortho* and *para* positions of the phenol must be blocked by groups that give increased steric protection or resonance stabilization.[31] The phenoxyl radicals are strongly colored − they exhibit characteristic absorption bands in the regions between 400 and 450 nm and above 600 nm that are attributed to π–π* transitions − which makes them easy to detect.[32] During the last decade many efforts have thus been made to incorporate such modified phenols in ligands, leading to the isolation of complexes able to model (functionally or structurally) the GO active site. The main ligand scaffolds developed will be listed below, together with the general properties of the corresponding copper(II) complexes. The following nomenclature will be used: $H_xL^y$ for a ligand $y$ possessing $x$ acido-basic sites and $[Cu(H_xL^y)(X)_z]$ for the copper(II) complex of $H_xL^y$ bearing $z$ coordinated exogenous ligands (X being an anion or solvent molecule). For clarity, the overall charge of the ligands and complexes is omitted. When the oxidation number of the copper ion is not indicated it is +2.

## Salen Ligands

A wide number of copper(II) complexes of salen-type ligands have been described so far, therefore the discussion here will be limited to general considerations and complexes specifically designed to model the GO active site,[33–43] in other words those bearing a sterically bulky substituent at the *ortho* and *para* positions of each phenol to prevent bis(μ-phenolate) dimer formation and to stabilize a phenoxyl radical (Figure 3). The copper(II) ion in these com-

 © 2007 Wiley-VCH Verlag GmbH & Co. KGaA, Weinheim 

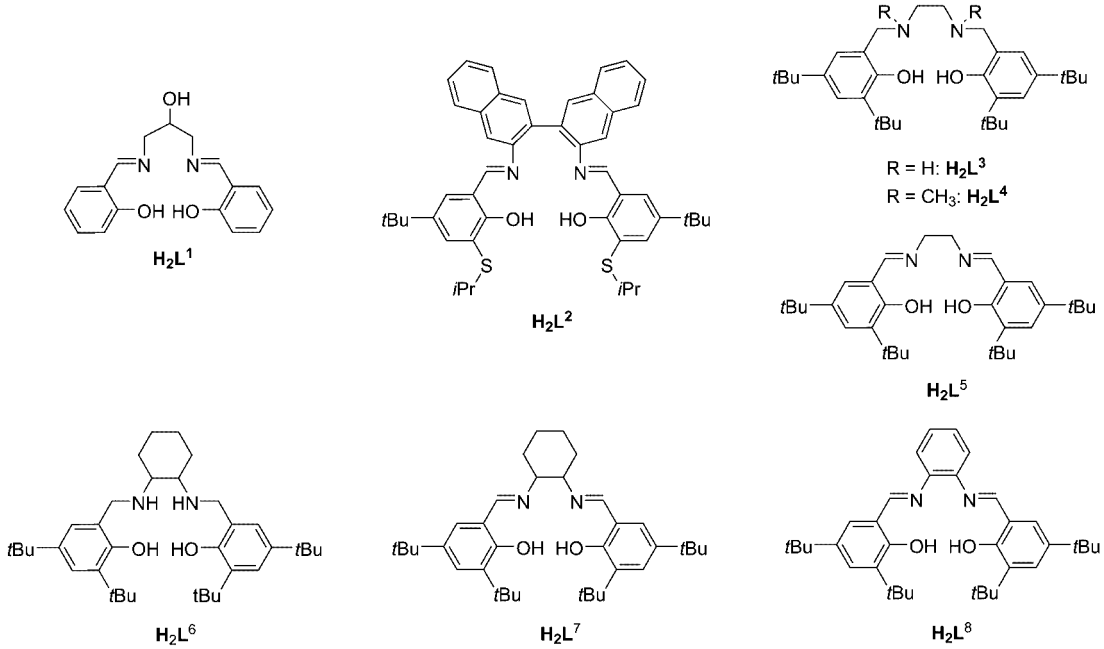


Figure 3. Salen-based ligands: $H_2L^1$ (ref.[33]), $H_2L^2$ (ref.[34,35]), $H_2L^3$ (ref.[36,37]), $H_2L^4$ (ref.[38]), $H_2L^5$ (ref.[37]), $H_2L^6$ (ref.[39,40]), $H_2L^7$ (ref.[37,39,40]), $H_2L^8$ (ref.[37]).

plexes is tetracoordinate in a square planar or tetrahedral geometry, as shown by their X-ray crystal structures and EPR spectroscopy. The flexibility and degree of distortion from square planar towards a tetrahedral geometry can be modulated by the nature of the linker between each salicylidene moiety. The electrochemical behavior of salen complexes is characterized by two oxidation waves at potentials higher than 0.3 V vs. $Fc^+/Fc$ {$[Cu(L^2)]$,[34,35] $[Cu(L^5)]$,[37] $[Cu(L^7)]$,[37,39,40] and $[Cu(L^8)]$[37]}, corresponding to the successive formation of mono- and bis(phenoxyl) radical species (Table 1). The reduced salen complexes {$[Cu(L^{3,4})]$[36–38] and $[Cu(L^6)]$[39,40]} exhibit a similar oxidative behavior, although they are much more easily oxidized. On a spectroscopic point of view, the UV/Vis spectra of the salen complexes is dominated by intense charge-transfer (CT) transitions at around 400 nm ($\varepsilon > 8000\ M^{-1}cm^{-1}$), while the reduced salens exhibit a much less intense phenolate-to-copper CT ($\varepsilon < 2000\ M^{-1}cm^{-1}$). Both exhibit low intensity copper(II) d–d transitions at wavelengths higher than 500 nm. Upon one-electron oxidation, the highest intensity bands of the salen complexes are shifted towards higher wavelengths (Table 1). The UV/Vis spectra of the $Cu^{II}$-phenoxyl complexes of reduced salen complexes are more similar to those of uncoordinated phenoxyl radicals, with classical π–π* transitions at around 400–450 and 600–700 nm (Table 1). Stack et al. have also measured the NIR

ATable 1. Properties of some $Cu^{II}$-phenoxyl radical complexes of salen ligands.

| Complex | $E_{1/2}$[a] | UV/Vis[b] | Solvent | Ref. |
|---|---|---|---|---|
| $[Cu(L^1)]$ | n.d. | 370 (11300), 611 (263) | DMF | [33] |
| $[Cu(L^2)]$ | 0.62 | n.d. | $CH_3CN$ | [34,35] |
| $[Cu(L^3)]$ | 0.11, 0.45 | 410 (1880), 594 (900) | $CH_2Cl_2$/DMSO | [36,37] |
| $[Cu(L^4)]$ | 0.16, 0.32 | 450 (1960), 650 (1370) | $CH_2Cl_2$ | [38] |
| $[Cu(L^5)]$ | 0.31, 0.79 | 306 (4160), 405 (11440), 500 sh (820) | $CH_2Cl_2$ | [37] |
| $[Cu(L^6)]$ | 0.08, 0.21 | n.d. | $CH_2Cl_2$ | [39,40] |
| $[Cu(L^7)]$ | 0.45, 0.65 | 376 (12400), 565 (600) | $CH_2Cl_2$ | [37,39,40] |
| $[Cu(L^8)]$ | 0.65, 0.83 | 402 (17750), 445 (24600) | $CH_2Cl_2$ | [37] |
| Complex[c] | EPR signal[d] | UV/Vis[b] | Solvent | Ref. |
| $[Cu(L^{2\cdot})]$ | silent (77 K) | featureless | $CH_3CN$ | [34,35] |
| $[Cu(L^{3\cdot})]$ | silent (4 K) | 384 (4050), 626 (3310) | $CH_2Cl_2$/DMSO | [36,37] |
| $[Cu(L^{5\cdot})]$ | silent (4 K) | 370 (11760), 552 (7250) | $CH_2Cl_2$ | [37] |
| $[Cu(L^{6\cdot})]$ | silent (77 K) | 413 (3000), 527 (3100), 607 (3400) | $CH_2Cl_2$ | [39,40] |
| $[Cu(L^{6\cdot\cdot})]$ | signal at $g = 2$ | 405 (5800), 418 (5800), 476 sh, 592 (1300) | $CH_2Cl_2$ | [39,40] |
| $[Cu(L^{7\cdot})]$ | silent (4 K) | 345 (11400), 558 (5500), 1750 (2400) | $CH_2Cl_2$ | [37,39,,40] |
| $[Cu(L^{7\cdot\cdot})]$ | $S = 3/2$ | 354 (8170), 380 sh (7510), 443 (10700), 562 br. (2030), 800 br. (2010) | $CH_2Cl_2$ | [37,39,40] |
| $[Cu(L^{8\cdot})]$ | silent (4 K) | 444 (21800), 577 (3530) | $CH_2Cl_2$ | [37] |
| $[Cu(L^{8\cdot\cdot})]$ | $S = 3/2$ | 420 (16600), 446 (18900), 550 sh (4500), 900 br. (4300) | $CH_2Cl_2$ | [37] |

[a] V vs. $Fc^+/Fc$. [b] $\lambda$ [nm] ($\varepsilon$ [$M^{-1}cm^{-1}$]). [c] The properties of the one-electron-oxidized forms of $[Cu(L^1)]$ and $[Cu(L^4)]$ are not reported. [d] X-band. The $Cu^{II}$-phenolate complexes exhibit an $S_{Cu} = ½$ signal.

 © 2007 Wiley-VCH Verlag GmbH & Co. KGaA, Weinheim 

spectra of [Cu($L^{6\cdot}$)] and [Cu($L^{7\cdot}$)] and found intense transitions at 1600 and 1750 nm, respectively, attributed to phenolate-phenoxyl charge transfers.[39,40] All the $Cu^{II}$-monophenoxyl radical complexes were found to be EPR-silent as the result of a magnetic coupling between the coordinated radical and the metal spins.

The first use of salen copper(II) complexes to mimic the reactivity of GO towards alcohol oxidation was reported in 1986 by Katajima et al.[33] Unfortunately, no evidence for a "true" GO-like reactivity, such as phenoxyl radical formation, was shown in the reaction of the copper(II) complex of $H_2L^1$ with alcohols.[33] Stack et al. revisited these kinds of complexes 10 years later. He reported that the copper(II) complex of $H_2L^1$ is able to catalyze the aerobic oxidation of benzyl alcohol into benzaldehyde with high turnovers (1300 at 295 K in 20 h).[34,35] The ligand structure was improved to achieve such reactivity: the phenolate moieties were *ortho*- and *para*-substituted by electron-donating groups to stabilize the phenoxyl radical, and a significant tetrahedral distortion was induced around the copper atom [thus stabilizing the copper(I) ion] by using a binaphthyl linker. They showed experimentally that the active species is the $Cu^{II}$-phenoxyl form of the complex. The substrate adduct was a five-coordinate square-pyramidal $Cu^{II}$-phenoxyl complex (further theoretical studies on its reactivity are presented below). Oxidation of the initial $Cu^{II}$-phenolate complex into the catalytically active $Cu^{II}$-phenoxyl radical species, however, requires addition of a strong oxidant. For this reason we have synthesized the copper(II) complex of the reduced salen ligand $H_2L^3$.[36,37] This complex is much more readily oxidizable, as judged by its redox potential, which is around 0.5 V lower than for Stack's model complex (Table 1). The $Cu^{II}$-phenoxyl complex leads to the oxidation of several unactivated primary alcohols (such as methanol) into aldehydes in the presence of catalytic amounts of base; secondary alcohols are not affected.[36] More recently, copper(II) complexes of reduced salen ligands have also been described by Palaniandavar et al. ($H_2L^4$)[38] as well as Stack et al.[39,40] [Cu($L^6$)], for instance, was shown to model the acceleration of the reaction rate by substrate binding as does GO. Its "true" salen complex derivative [Cu($L^7$)], however, does not exhibit such reactivity. In another approach, we focused our interest on developing planar scaffolds such as $H_2L^5$ and $H_2L^8$ to stabilize copper(II) coordinated bis(phenoxyl) radicals.[37] The $Cu^{II}$-phenoxyl radical complex of [Cu($L^{8\cdot}$)] has been further utilized by other groups[41] for different purposes.[42] A pentadentate reduced salen ligand, which could be oxidized into a $Cu^{II}$-phenoxyl radical species, as shown by its EPR-silence and π–π* transitions at 390 and 408 ($\varepsilon > 1000\ M^{-1}cm^{-1}$) and 600–900 nm ($\varepsilon < 1000\ M^{-1}cm^{-1}$), has also been described by Neves et al.[43]

### Imino-, Thio-, and Semiquinonate Ligands

Wieghardt et al.[44–51] have contributed widely to the development of an extraordinary class of model compounds for GO that involves imino-, thio-, and semiquinonate ligands (Figure 4). These are much more easily oxidizable (the phenolate oxidation potentials are negative vs. $Fc^+/Fc$, which makes them oxidizable by air; Table 2) than other classes of ligands, and are so stable in their radical form that structural characterization could be envisaged. Some of these complexes were also found to be efficient catalysts for the aerobic oxidation of alcohols. Mixing the tridentate ligand $H_2L^9$ with copper(II) in the presence of triethylamine and air affords the EPR-silent dinuclear $Cu^{II}$-phenoxyl complex [Cu($L^{9\cdot}$)]$_2$, which exhibits absorption bands at 408 and 650 nm (Table 2).[44] The mononuclear $Cu^{II}$-phenoxyl complex [Cu($L^{10\cdot}$)($NEt_3$)] was obtained under similar conditions by replacing $H_2L^9$ with $H_3L^{10}$ and structurally characterized.[45] The tridentate ligand is coordinated to a single copper(II) ion and the fourth coordination site is occupied by an $NEt_3$ molecule. This complex is also EPR-silent as a result of an antiferromagnetic coupling between the radical and the metal spin ($J$ estimated at $-137\ cm^{-1}$). Both [Cu($L^{9\cdot}$)]$_2$ and [Cu($L^{10\cdot}$)($NEt_3$)] were found to be very efficient catalysts for the aerobic oxidation of alcohols. Interestingly, treatment of a solution of copper(I) and $H_3L^{10}$ neutralized by $NEt_3$ with pure dry $O_2$ yielded crystals of a copper(II) complex containing a bound superoxide ion, an intermediate suggested in the catalytic pathway of GO. Recently, $H_2L^{11}$, the selenium analogue of $H_2L^9$, has been described.[51] This ligand reacts with copper ions in the pres-

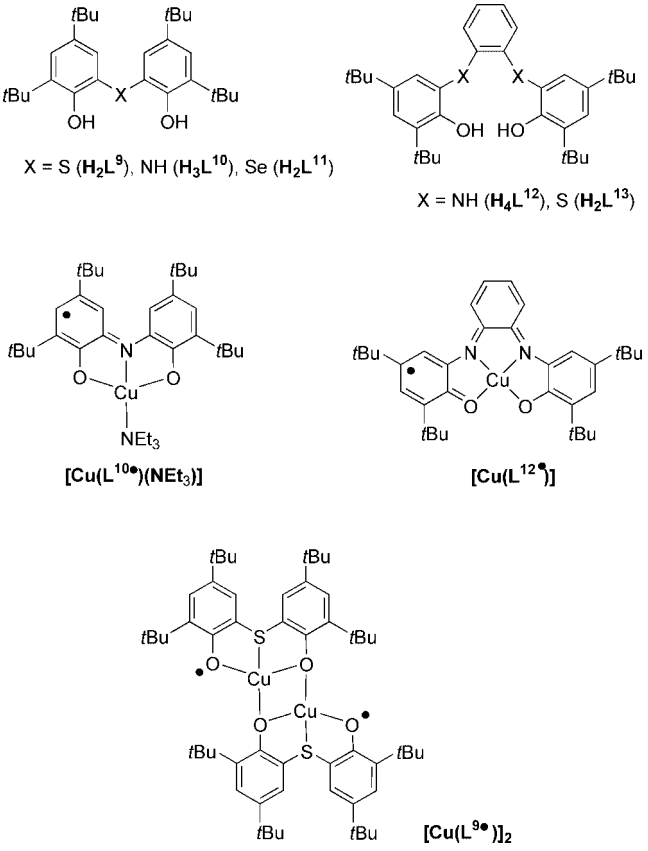


Figure 4. Thioiminosemiquinone ligands and their copper(II) complexes: $H_2L^9$ and [Cu($L^{9\cdot}$)]$_2$ (ref.[44]), $H_3L^{10}$ and [Cu($L^{10\cdot}$)($NEt_3$)] (ref.[45]), $H_2L^{11}$ (ref.[51]), $H_4L^{12}$ and [Cu($L^{12\cdot}$)] (ref.[46]), $H_2L^{13}$ (ref.[48]).

 © 2007 Wiley-VCH Verlag GmbH & Co. KGaA, Weinheim 

Table 2. Properties of some copper(II) complexes of imino- and thiosemiquinone ligands.

| Complex | $E_{1/2}$[a] | EPR signal[b] | UV/Vis[c] | Solvent | Ref. |
|---|---|---|---|---|---|
| $[Cu(L^{9\cdot})]_2$ | –1.26,[d] –0.29[d] | $S = 0$ | 400 sh, 408 (8000), 424 sh, 650 (660) | $CH_2Cl_2$ | [44] |
| $[Cu(L^{10\cdot})(NEt_3)]$ | –1.06,[d] –0.14[d] | $S = 0$ | n.d. | $CH_2Cl_2$ | [45] |
| $[Cu(L^{12\cdot})]$ | –1.42,[d] –0.66,[d] –0.06,[d] 0.41 | $S = 0$ | 320 (5100), 478 (6400), 981 (1200) | $CH_2Cl_2$ | [46] |
| $[Cu(L^{13\cdot})]$ | 0.62 (irr), 0.99 (irr)[e] | unstable | unstable | $CH_2Cl_2$ | [48] |

[a] V vs. $Fc^+$/Fc. [b] X-band. [c] $\lambda$ [nm] ($\varepsilon$ [$M^{-1}\,cm^{-1}$]). [d] Reduction waves. [e] Irreversible processes. The potentials correspond to the $E_p^a$ values obtained from the cyclic voltammetry curve of $[Cu(L^{13})]$.

ence of different amines to give rise to a variety of mono-, di-, and even trinuclear complexes that exhibit distinct reactivities towards alcohol oxidation.

The coordinated tetradentate ligand $H_4L^{12}$ can exist in five oxidation levels (each of which has been fully characterized), two of which are paramagnetic monoradicals and another is a diamagnetic diradical.[46] $[Cu(L^{12\cdot})]$ (and its zinc analog) selectively oxidizes primary alcohols in a stoichiometric fashion under anaerobic conditions to yield the corresponding aldehyde and a protonated form of the two-electron-reduced catalyst. This latter complex can reduce molecular dioxygen into $H_2O_2$, thus regenerating $[Cu(L^{12\cdot})]$. This makes oxidation of alcohols into aldehydes catalytic under aerobic conditions. $H_2L^{13}$, the sulfur analogue of $H_2L^{12}$, has been described along with its copper(II) complexes.[48] Electrochemical experiments showed that the coordinated *o*-thioetherphenolate moieties could be oxidized into phenoxyl radicals. Unfortunately, the oxidized species are very unstable and do not allow further spectroscopic characterization.

## TACN Ligands

The macrocycle 1,4,7-triazacyclononane (TACN) coordinates one metal ion through its three amine groups and can be further derivatized to incorporate one, two, or three additional coordinating groups such as phenols (Figure 5). Many mono- and bis(phenolate) copper(II) complexes have been structurally characterized that show a five-coordinate copper(II) ion in a slightly distorted square-pyramidal geometry. A coordination number of six can be achieved by addition of exogenous bidentate ligands such as $Ph_2acac$.[52] In all of the structures the phenolate donor(s) reside(s) in the equatorial plane (*cis* to each other if two are present), while one amine nitrogen coordinates weakly in the axial position.

Tolman et al. reported one of the first model compounds for the $Cu^{II}$-radical site of GO using this TACN framework, namely the copper(II) complex $[Cu(L^{15})(CH_3CN)]$, in 1996.[53,54]. Its $Cu^{II}$-phenoxyl radical form was found to be relatively stable in $CH_2Cl_2$, as judged in the cyclic voltammograms by the reversible signal at 0.31 V (vs. $Fc^+$/Fc) obtained for the phenoxyl/phenolate redox couple. It is EPR-silent as the result of a magnetic coupling between the radical and the metal. No more phenolate-to-copper CT transitions are observed at 538 nm in the radical complex $[Cu(L^{15\cdot})(CH_3CN)]$. Instead, absorption bands typical for

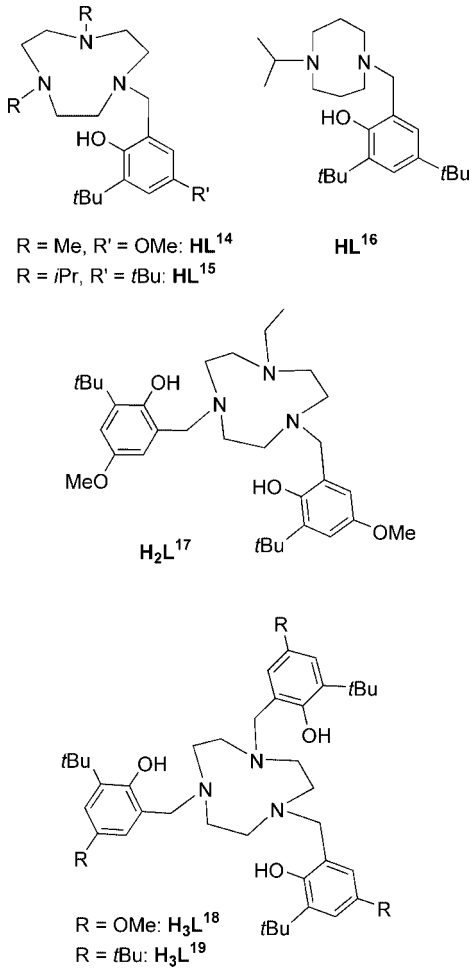


Figure 5. Ligands based on the TACN scaffold: $HL^{14}$ (ref.[52]), $HL^{15}$ (ref.[53,54]), $HL^{16}$ (ref.[55]), $H_2L^{17}$ (ref.[57]), $H_3L^{18,19}$ (ref.[56]).

phenoxyl radicals are observed at 410 and 672 nm (Table 3). The benzyl alkoxide adduct $[Cu(L^{15})(benzyl\ alkoxide)]$ has been crystallized and shows an $O_{phenolato}\cdots H–C_{substrate}$ interaction similar to that proposed for GO during enzyme turnover. More recently, the $Cu^I$-phenolate complexes of $HL^{15}$ and $HL^{16}$ have been isolated with the aim of modeling the reduced form of the GO active site.[55] Their reactivity towards molecular dioxygen will be discussed below.

This TACN scaffold has been developed concomitantly by Wieghardt et al.: the $Cu^{II}$-bis(phenolate) complex $[Cu(L^{17})]$ and its counterpart phenol-phenolate complex $[Cu(HL^{17})]$ could be isolated from the ligand $H_2L^{17}$.[57] The CV curves of $[Cu(L^{17})]$ exhibit two ligand-centered oxi-

 © 2007 Wiley-VCH Verlag GmbH & Co. KGaA, Weinheim 

Table 3. Properties of some $Cu^{II}$-phenoxyl radical complexes of TACN ligands.

| Complex | $E_{1/2}$[a] | UV/Vis[b] | Solvent | Ref. |
|---|---|---|---|---|
| [Cu($L^{14}$)($Ph_2acac$)] | –0.33 | 334 (16700), 358 (16400) | $CH_2Cl_2$ | [52] |
| [Cu($L^{15}$)($CH_3CN$)] | 0.31 | 342 (3600), 538 (1440), 660 sh (600) | $CH_2Cl_2$ | [53,54] |
| [Cu($L^{17}$)] | –0.10, 0.14 | 314 (22000), 458 (1450), 698 (210) | $CH_2Cl_2$ | [57] |
| [Cu($HL^{17}$)] | 0.14 | 312 (7300) | $CH_2Cl_2$ | [57] |
| [Cu($HL^{18}$)] | –0.06, 0.12 | 326 sh, 445 (1500), 680 br. (300) | $CH_3CN$ | [56] |
| [Cu($H_2L^{18}$)] | 0.26 | 321 sh, 565 br. (1200) | $CH_2Cl_2$ | [56] |
| [Cu($HL^{19}$)] | 0.15, 0.38 | 305 sh (11000), 348 sh, 428 (1100), 694 br. (230) | $CH_3CN$ | [56] |
| [Cu($H_2L^{19}$)] | 0.44 | 321 (1700), 707 sh, 822 sh | $CH_2Cl_2$ | [56] |
| Complex | EPR signal[c] | UV/Vis[b] | Solvent | Ref. |
| [Cu($L^{14\cdot}$)($Ph_2acac$)] | $S = 1$ | 304 (24000), 352 (22000), 412 (6100) | $CH_2Cl_2$ | [52] |
| [Cu($L^{15\cdot}$)($CH_3CN$)] | silent (77 K) | 410 (4000), 422 sh (3800), 672 (1000) | $CH_2Cl_2$ | [53,54] |
| [Cu($L^{17\cdot}$)] | silent (77 K) | 309 (18000), 418 (5400), 530 (2300) | $CH_2Cl_2$ | [57] |
| [Cu($HL^{17\cdot}$)] | silent (77 K) | 312 (15000), 413 sh (6800), 431 (8500), 535 (1200) | $CH_2Cl_2$ | [57] |
| [Cu($L^{17\cdot\cdot}$)] | $S = 3/2$ | 319 (24000), 431 (15000), 485 (3500) | $CH_2Cl_2$ | [57] |
| [Cu($HL^{18\cdot}$)] | silent | 300 (14000), 326 sh, 414 (4300), 600 sh | $CH_3CN$ | [56] |
| [Cu($H_2L^{18\cdot}$)] | silent | 300 (21000), 328 sh, 411 (6100), 432 (7600) | $CH_2Cl_2$ | [56] |
| [Cu($HL^{19\cdot}$)] | silent | 387 sh, 402 (2800), 420 sh, 548 br. (1400), | $CH_3CN$ | [56] |
| [Cu($H_2L^{19\cdot}$)] | silent | 309 (10000), 407 (3600), 424 (3500), 645 br. (850) | $CH_2Cl_2$ | [56] |

[a] V vs. $Fc^+/Fc$. [b] $\lambda$ [nm] ($\varepsilon$ [$M^{-1}cm^{-1}$]). [c] X-band. The $Cu^{II}$-phenolate complexes exhibit an $S_{Cu} = ½$ signal.

dation waves, while a single wave is observed for [Cu($HL^{17}$)] (Table 3). The electrochemically generated $Cu^{II}$-phenoxyl complexes [Cu($L^{17\cdot}$)] and [Cu($HL^{17\cdot}$)] are X-band EPR-silent (Table 3), which may be interpreted either by an antiferromagnetic exchange, which yields an $S_t = 0$ ground state, or large ZFS parameters of an $S_t = 1$ ground state.

The phenol-bis(phenolate) copper(II) complexes [Cu($HL^{18,19}$)] and phenolate-bis(phenol) copper(II) complexes [Cu($H_2L^{18,19}$)] have also been isolated from the ligands $H_3L^{18,19}$ (Figure 5).[56] The tris(phenol) form was found not to be stable in solution for prolonged periods. The phenol-bis(phenolate) and phenolate-bis(phenol) forms can interconvert easily by adding one equivalent of base or acid. The X-ray crystal structure of [Cu($HL^{19}$)] shows that one phenol unit is not coordinated to the metal ion. The CV curves of [Cu($HL^{18,19}$)] exhibit two one-electron transfer waves in the –0.06 to 0.38 V range assigned to the successive oxidation of each phenolate moiety. [Cu($H_2L^{18,19}$)], which possess a single phenolate moiety, exhibit a single wave in the 0.26–0.44 V potential range (Table 3). EPR spectroscopy reveals that [Cu($HL^{18,19\cdot}$)] and [Cu($HL^{18,19\cdot}$)], similar to [Cu($L^{17\cdot}$)] and [Cu($HL^{17\cdot}$)], are difficult to detect as they are EPR-silent (Table 3). They exhibit features in their UV/Vis spectra (Table 3) at around 400 nm ($\varepsilon$ values ranging between 2000 and 6000 $M^{-1}cm^{-1}$) and in the 500–800 nm region ($\varepsilon$ values lower than 1300 $M^{-1}cm^{-1}$). The intensity of the 400-nm absorption increases significantly upon protonation and its position is shifted bathochromically. This shows that protonation affects the electronic structure of the $Cu^{II}$-phenoxyl chromophore. The electronic hole of the phenoxyl radical in the [Cu($HL^{18,19\cdot}$)] complexes is thus proposed to be delocalized over both the phenoxyl and the phenolate moieties, whereas the spin of the unpaired electron of the phenoxyl radical is more localized on one aromatic ring in [Cu($H_2L^{18,19\cdot}$)].

## Tripodal Ligands

Several research groups have adapted the well-known tripodal aromatic framework bis(pyridyl)alkylamine connected to a single phenol ($N_3O$ donor set), or mono(pyridyl)alkylamine attached to two phenols ($N_2O_2$ donor set), for GO chemistry (Figure 6).[58–75] The ligand framework has been extensively studied and modulated by modifing (i) the length of the alkyl chain linking the pyridine and the pivotal nitrogen, (ii) the steric bulk provided by the *ortho* substituent of the phenol, (iii) the electronic properties of the *para* substituent of the phenol, and (iv) the basicity of the pyridine donors. A number of monomeric or dimeric complexes have been prepared from different copper(II) salts. The potential of an $N_2O_2$ aliphatic tripodal ligand, where the pyridine has been replaced by a primary amine and one phenol by a hydroxyl, to mimic the GO active site was explored by Hahn et al. in 2001.[76] The copper(II) complex of this ligand was isolated as a dimer that exhibits a phenolate-centered electrochemical activity. Since the coordination chemistry of tripodal aromatic ligands has been widely described during the last decade and now allows the rational design of new complexes, it will be presented in more detail than that of other ligands.

Mononuclear $Cu^{II}$-phenolate complexes of general formula [Cu($L^{N_3O}$)(X)] can be obtained from $N_3O$ ligands in the presence of $NEt_3$ if the following conditions are fulfilled: large steric bulk (*tert*-butyl group) provided by the *ortho* substituent of the phenol[58,59,61] and/or use of a copper(II) salt containing a strong monoanionic donor $X^-$.[71,72] Many of these complexes have been structurally characterized by X-ray crystallography[58–61,64,69,71,72] and show that the copper(II) ion is pentacoordinate, with a solvent or exogenous anion that completes the $N_3O$ donor set of the ligand (Figure 7). The phenolate donor can bind

 © 2007 Wiley-VCH Verlag GmbH & Co. KGaA, Weinheim 

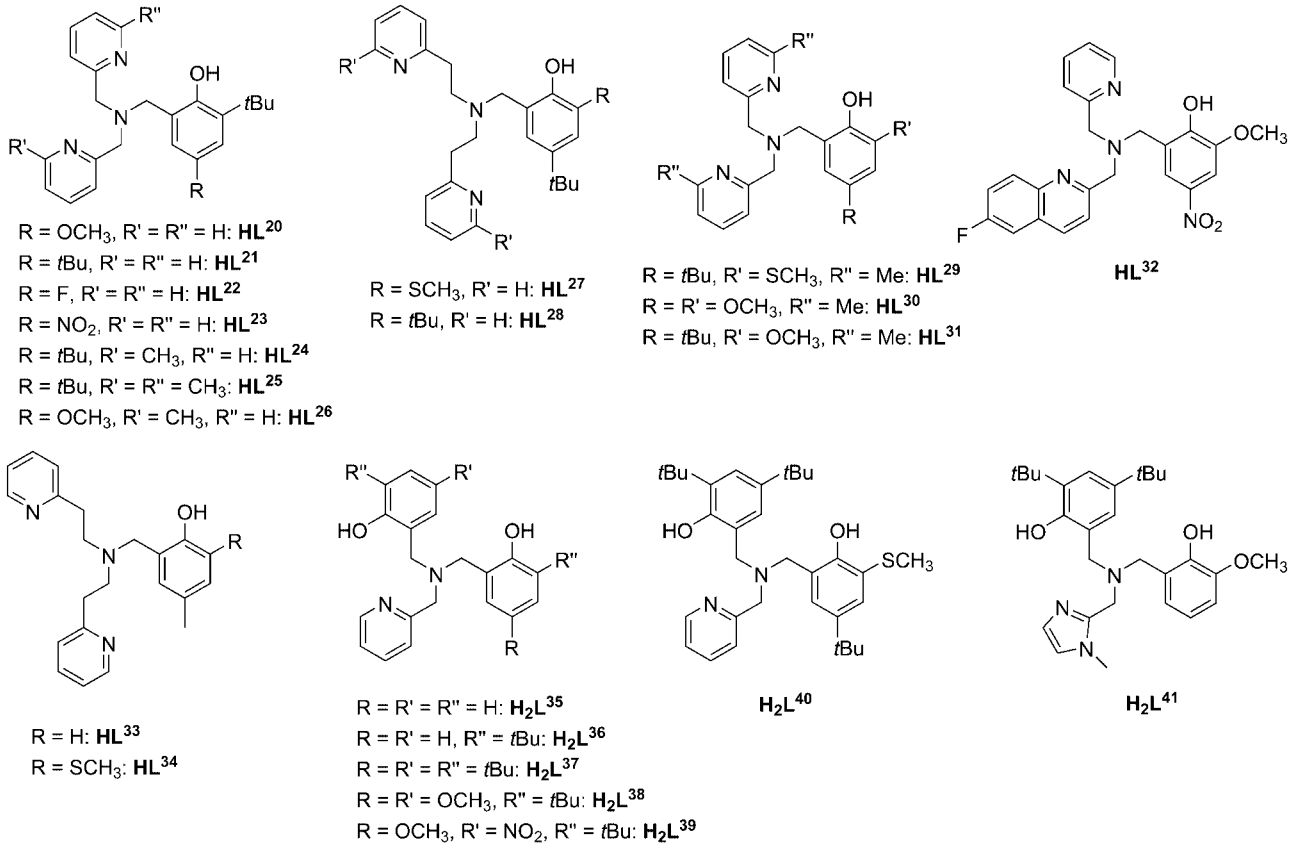


Figure 6. Formulae of some representative tripodal ligands: $HL^{20–23}$ (ref.[58]), $HL^{24,25}$ (ref.[59]), $HL^{26}$ (ref.[60]), $HL^{27,28}$ (ref.[61]), $HL^{29}$ (ref.[62]), $HL^{30,31}$ (ref.[63]), $HL^{32}$ (ref.[64]), $HL^{33,34}$ (ref.[74]), $H_2L^{35}$ (ref.[75]), $H_2L^{36}$ (ref.[65]), $H_2L^{37}$ (ref.[66]), $H_2L^{38}$ (ref.[58]), $H_2L^{39}$ (ref.[58,67]), $H_2L^{40}$ (ref.[68]), $H_2L^{41}$ (ref.[69]).

either in an equatorial[58–61,64,69] or axial[58,71,72] position. The respective influence of the phenolate *para* substituent and alkyl linker arm length on the position of this phenolate have been well documented by Palaniandavar et al. and Fenton et al. (see below). The relative extent of the trigonal-bipyramidal distortion is indicated by the value of $\tau$, which represents the degree of trigonality within the structural continuum between square-planar and trigonal-bipyramidal structures.[70] $\tau$ is usually lower than 0.35 for these complexes, which shows that the geometry around the metal ion is predominantly square pyramidal with a slight distortion towards trigonal bipyramidal.[58–61,64,69,71,72] A sample structure is given in Figure 7. In the $Cu^{II}$-phenolate complexes of $HL^{24,25}$,[59] as well as the $Cu^{II}$-phenol complexes of $HL^{20}$ and $HL^{26}$,[58,60] the $Cu–N_{methylpyridine}$ bond is longer than the $Cu–N_{pyridine}$ one, which is ascribed to steric hindrance around the methylpyridine nitrogen. All these complexes exhibit a phenolate-to-copper CT transition and less intense d–d transitions as a lower energy tail ($\lambda_{max}$ > 600 nm, Table 4) in their UV/Vis spectra. $\lambda_{max}$ of the CT transition is shifted according to the electronic properties of the phenolate substituent (from 565 nm for $[Cu(L^{20})(CH_3CN)]$ to 517 nm for $[Cu(L^{23})(CH_3CN)]$). The EPR spectrum is characterized by a signal that is typical for mononuclear copper(II) species ($S$ = ½; Table 4).

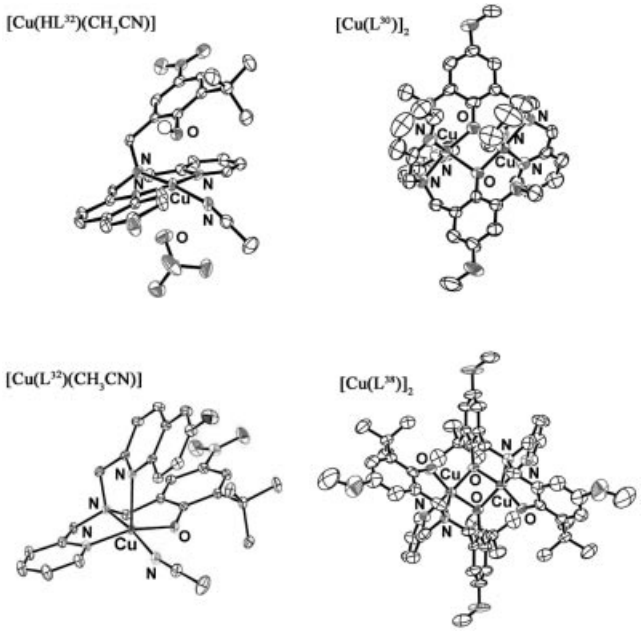


Figure 7. X-ray crystal structures of copper(II) complexes of tripodal ligands $[Cu(HL^{32})(CH_3CN)]$ (ref.[64]), $[Cu(L^{32})(CH_3CN)]$ (ref.[64]), $[Cu(L^{30})]_2$ (ref.[60]), and $[Cu(L^{38})]_2$ (ref.[58]).

 © 2007 Wiley-VCH Verlag GmbH & Co. KGaA, Weinheim 

Table 4. Properties of some $Cu^{II}$-phenoxyl radical complexes of tripodal ligands.

| Complex | $E_{1/2}$[a] | UV/Vis[b] | Solvent | Ref. |
|---|---|---|---|---|
| $[Cu(L^{20})(CH_3CN)]$ | 0.02 | 565 (1040) | $CH_3CN$ | [58] |
| $[Cu(L^{20})(py)]$ | 0.01 | 546 (950) | $CH_3CN$ | [58] |
| $[Cu(HL^{20})(CH_3CN)]$ | >0.8 | 400 br. (320), 590 br. (230) | $CH_3CN$ | [58] |
| $[Cu(L^{21})(CH_3CN)]$ | 0.15 | 553 (935), 950 (180) | $CH_3CN$ | [58] |
| $[Cu(L^{21})(py)]$ | 0.17 | 531 (750), 850 (180) | $CH_3CN$ | [58] |
| $[Cu(HL^{21})(CH_3CN)]$ | >0.8 | 600 (180) | $CH_3CN$ | [58] |
| $[Cu(L^{22})(CH_3CN)]$ | 0.20 | 305 (3400), 535 (920), 930 (130) | $CH_3CN$ | [58] |
| $[Cu(L^{23})(CH_3CN)]$ | 0.70 | 390 (11200), 517 (636) | $CH_3CN$ | [58] |
| $[Cu(L^{24})(Cl)]$ | 0.14 | 519 (1400) | $CH_3CN$ | [59] |
| $[Cu(L^{25})(Cl)]$ | 0.19 | 544 (800) | $CH_3CN$ | [59] |
| $[Cu(L^{26})(CH_3CN)]$ | 0.05 | 564 (870), 660 sh (550) | $CH_3CN$ | [60] |
| $[Cu(L^{27})]_2$ | n.d. | 522 (2990) | $CH_3CN$ | [61] |
| $[Cu(L^{27})(OAc)]$ | 0.05 | 473 (880), 660 (220) | $CH_3CN$ | [61] |
| $[Cu(L^{28})(CH_3CN)]$ | 0.35 | 559 (1090) | $CH_3CN$ | [61] |
| $[Cu(L^{29})]_2$ | n.d. | 520 (2800) | $CH_3CN$ | [62] |
| $[Cu(L^{29})(OAc)]$ | 0.03 | 490 (970), 690 (240) | $CH_3CN$ | [62] |
| $[Cu(L^{30})]_2$ | 0.45 | 471 (440), 875 (165) | $CH_3CN$ | [63] |
| $[Cu(L^{30})(py)]$ | 0.00 | 556 (560), 900 (310) | $CH_3CN$ | [63] |
| $[Cu(L^{31})]_2$ | 0.66 | 466 (230), 870 (150) | $CH_3CN$ | [63] |
| $[Cu(L^{31})(py)]$ | 0.14 | 530 (640), 900 (250) | $CH_3CN$ | [63] |
| $[Cu(L^{36})]_2$ | 0.70 (irr.) | 413 (2550), 480 sh, 650 sh, 764 sh | $CH_2Cl_2$ | [65] |
| $[Cu(L^{36})(CH_3CN)]$ | 0.11, 0.49 (irr.) | 476 (1820) | $CH_3CN$ | [65] |
| $[Cu(HL^{37})(OAc)]$ | 0.20 | 470 (1300) | $CH_3CN/CH_2Cl_2$ | [66] |
| $[Cu(L^{38})]_2$ | –0.14, 0.12 | 302 (16700), 445 (4330), 650 br. (1600) | $CH_2Cl_2$ | [60] |
| $[Cu(L^{38})(py)]$ | –0.16 | 310 (20000), 488 (1400) | $CH_3CN$ | [58] |
| $[Cu(HL^{39})(OAc)]$ | 0.08 | 393 (20000), 500 sh (760), 600 br. (510) | $CH_3CN/CH_2Cl_2$ | [58,67] |
| $[Cu(L^{39})(py)]$ | –0.08 | 305 (6300), 401 (15000), 500 sh (1210), 700 br. (300) | $CH_3CN$ | [58] |
| $[Cu(L^{40})]_2$ | n.d. | 453 (2000), 680 (200) | $CH_3CN$ | [68] |
| $[Cu(L^{40})(py)]$ | 0.10, 0.33[c] | 466 (1360), 710 (100) | $CH_3CN$ | [68] |
| $[Cu(L^{41})(CH_3CN)]$ | –0.07 | 450 (1000) | $CH_3CN$ | [69] |
| **Complex** | **EPR signal[d]** | **UV/Vis[b]** | **Solvent** | **Ref.** |
| $[Cu(L^{20\cdot})(CH_3CN)]$ | $S = 1$ | 426 (5100), 552 (560) | $CH_3CN$ | [58] |
| $[Cu(L^{20\cdot})(py)]$ | $S = 1$ | 406 (8200) | $CH_3CN$ | [58] |
| $[Cu(L^{21\cdot})(CH_3CN)]$ | $S = 1$ | 416 (1900), 650 (500) | $CH_3CN$ | [58] |
| $[Cu(L^{21\cdot})(py)]$ | $S = 1$ | 417 (3500), 660 (800) | $CH_3CN$ | [58] |
| $[Cu(L^{22\cdot})(CH_3CN)]$ | unstable | unstable | $CH_3CN$ | [58] |
| $[Cu(L^{23\cdot})(CH_3CN)]$ | unstable | unstable | $CH_3CN$ | [58] |
| $[Cu(L^{24\cdot})(Cl)]$ | $S = 1$ | 418 (3500), 666 (420) | $CH_3CN$ | [59] |
| $[Cu(L^{25\cdot})(Cl)]$ | $S = 1$ | 406 (2000), 664 (410) | $CH_3CN$ | [59] |
| $[Cu(L^{26\cdot})(CH_3CN)]$ | $S = 1$ | 427 (3070), 580 (225) | $CH_3CN$ | [60] |
| $[Cu(L^{27\cdot})(NO_3)]$ | silent (77 K) | 415 (1790), 867 (550) | $CH_3CN$ | [61] |
| $[Cu(L^{28\cdot})(NO_3)]$ | silent | 411 (2440), 675 (300) | $CH_3CN$ | [61] |
| $[Cu(L^{29\cdot})(CH_3CN)]$ | silent (123 K) | 424 (1920), 870 (920) | $CH_3CN$ | [62] |
| $[Cu(L^{30\cdot})(CH_3CN)]$ | silent (100 K) | 418 (2300), 605 (400)[e] | $CH_3CN$ | [63] |
| $[Cu(L^{30\cdot})(py)]$ | silent (100 K) | 420 (6060), 583 (1370)[f] | $CH_3CN$ | [63] |
| $[Cu(L^{31\cdot})(CH_3CN)]$ | nd | 420 (3200), 620 (350)[e] | $CH_3CN$ | [63] |
| $[Cu(L^{31\cdot})(py)]$ | silent (100 K) | 400 (1125), 687 (300)[f] | $CH_3CN$ | [63] |
| $[Cu(L^{36\cdot})(CH_3CN)]$ | $S = 1/2$ | 439 (16700), 620 (600) | $CH_3CN$ | [65] |
| $[Cu(HL^{37\cdot})(OAc)]$ | unstable | unstable | $CH_3CN/CH_2Cl_2$ | [66] |
| $H_2L^{37} + Cu(ClO_4)_2$[g] | silent | 403 (2000), 654 (400) | $CH_3CN/CH_2Cl_2$ | [66] |
| $[Cu(L^{38\cdot})]_2$ | silent | 416 (3370), 530 (1510), 850 (740)[e] | $CH_2Cl_2$ | [60] |
| $[Cu(L^{38\cdot})(py)]$ | $S = 1$ | 425 (1000)[f] | $CH_3CN$ | [58] |
| $[Cu(L^{38\cdot\cdot})(CH_3CN)]$ | $S = 1/2$ | 426 (3600), 650 (540)[e] | $CH_3CN$ | [58] |
| $[Cu(HL^{39\cdot})(OAc)]$ | silent (100 K) | 410 (19000) | $CH_3CN/CH_2Cl_2$ | [58,67] |
| $[Cu(L^{39\cdot})(py)]$ | $S = 1$ | 390 (15300) | $CH_3CN$ | [58] |
| $[Cu(L^{40\cdot})(py)]$ | silent | 418 (2100), 720 (100) | $CH_3CN$ | [68] |
| $[Cu(L^{41\cdot})]_2$ | $S = 0$ | 478 (4500) | $CH_3CN$ | [69] |

[a] V vs. $Fc^+/Fc$. [b] $\lambda$ [nm] ($\varepsilon$ [$M^{-1}cm^{-1}$]). [c] At –40 °C. [d] X-band. The $Cu^{II}$-phenolate complexes exhibit an $S_{Cu} = ½$ signal except $[Cu(L^{27})]_2$, $[Cu(L^{29–31})]_2$, $[Cu(L^{36})]_2$, $[Cu(L^{38})]_2$ and $[Cu(L^{40})]_2$ (dimeric species). [e] Generated by copper(II) oxidation. [f] Underestimated due to its low stability. [g] Obtained by a disproportionation reaction. No structure reported.

When the complexation reaction is performed with a copper(II) salt that does not contain a strong monoanionic donor and ligands that bear a phenol without steric bulk at its *ortho* position, dimeric species of general formula $[Cu(L^{N_3O})]_2$ are obtained.[61–63,71–75] X-ray structural analysis of $[Cu(L^{30})]_2$ has shown that the two copper ions are

 © 2007 Wiley-VCH Verlag GmbH & Co. KGaA, Weinheim 

square pyramidal but slightly distorted towards trigonal bipyramidal (Figure 7).[60] The copper ions are bridged by the oxygen atoms of two phenolates, one from each ligand, which can occupy either a mixed axial/equatorial[62,71–73] or exclusively equatorial[62,63,73,74] position in the coordination polyhedron of each copper(II) ion. The two copper ions in these structures are separated by 3.1–3.2 Å and exhibit either an $S = 1$ signal or no signal at all in their EPR spectrum, which indicates that the copper(II) spins interact magnetically (Table 4).[61,62,71–74] The CuOCuO core is almost planar when the phenolate coordinates one copper atom in the axial position, while it shows a slight "butterfly" structure when it coordinates exclusively in the equatorial position.

The copper(II) complexes isolated from $N_2O_2$ ligands in the presence of $NEt_3$ are usually dimeric species of general formula $[Cu(L^{N_2O_2})]_2$ irrespective of the bulkiness of the phenolate *o*-substituent.[58,65–67] One example of a mononuclear $[Cu(L^{N_2O_2})(X)]$ structure has been characterized by X-ray diffraction as a biomimetic model of GO,[70] while many others have been obtained by adding coordinating solvents or bases to the $[Cu(L^{N_2O_2})]_2$ dimers.[58,65,75] Even though the chemical formula $[Cu(L^{N_2O_2})]_2$ seems similar to that of $[Cu(L^{N_3O})]_2$, significant differences can be observed between the two. In the $[Cu(L^{N_2O_2})]_2$ dimers, for example, the geometry around the copper(II) ion is more distorted towards trigonal bipyramidal ($\tau = 0.35$ for $[Cu(L^{38})]_2$ shown in Figure 7) and the intermetallic distance is shorter (2.869 Å for $[Cu(L^{38})]_2$). Consequently, the CuOCuO core is not flattened as in $[Cu(L^{N_3O})]_2$ but shows a marked "butterfly" structure (with a dihedral angle of 126° for $[Cu(L^{38})]_2$). The dimers are EPR-silent (Table 4) as a result of a strong antiferromagnetic interaction between the copper(II) ions that we have estimated to be $-189\ cm^{-1}$ for $[Cu(L^{35})]_2$[75] and $-31\ cm^{-1}$ for $[Cu(L^{36})]_2$.[65] The presence of two phenolates per ligand makes the phenolate-to-copper CT transition more intense than in the $[Cu(L^{N_3O})(X)]$ and $[Cu(L^{N_3O})]_2$ complexes (Table 4). We[67] and Fukuzumi et al.[68] have isolated dimeric copper(II) complexes of $N_2O_2$ ligands possessing two differentiated phenolate arms. In $H_2L^{39}$, for example, one phenolate bears an electron -withdrawing nitro group while the other possesses an electron-donating methoxy group. We have shown that the electron-donating methoxyl group compensates more efficiently than the nitro group for the electron deficiency on the bridging oxygen atom. The substitution thus orients the position of the phenolate groups in $[Cu(L^{39})]_2$ according to their electronic properties.[67]

In general, conversion of the dimers $[Cu(L^{N_2O_2})]_2$ and $[Cu(L^{N_3O})]_2$ into monomeric structures can be promoted by addition of exogenous donor ligands (pyridine, acetate) or protons.[58,61–63,65,67,68,73–75] In the case of $[Cu(L^{N_3O})]_2$, oxidation (chemical or electrochemical) has also been shown to induce this dimer-to-monomer conversion.[61–63] Dissociation constants can be obtained from spectrophotometric titration of $[Cu(L^{N_3O})]_2$ in the presence of pyridine or acetate. Steric repulsions caused by the 6-methyl groups of the pyridine nucleus significantly lower (one to two orders of magnitude) the stability of the dimers,[62] while an increase in the length of the alkyl linker arm does not significantly affect the dissociation constant.[73,74] The most striking feature is the influence of the phenol *para* substituent: in the presence of pyridine, the dimer $[Cu(L^{33})]_2$ exhibits a dissociation constant 100 times lower than that of $[Cu(L^{34})]_2$. This fact is consistent with an increased steric bulk at the phenolate *ortho* position caused by the methylthio group in $[Cu(L^{34})]_2$ compared to a hydrogen atom in $[Cu(L^{33})]_2$.[74] The coordination sphere has also been found to influence the solution behavior of the dimers. Thus, $[Cu(L^{38})]_2$ remains dimeric in $CH_3CN$ while no such structures could be detected in the solution of the $Cu^{II}$-phenolate complex of $HL^{20}$, which suggests a greater stability of the $[Cu(L^{N_2O_2})]_2$ dimer than $[Cu(L^{N_3O})]_2$.[58]

Addition of one molar equivalent of proton [relative to the copper(II) concentration] to the $Cu^{II}$-phenolate complexes $[Cu(L^{N_2O_2})]_2$, $[Cu(L^{N_3O})]_2$, and $[Cu(L^{N_3O})(X)]$ results in the formation of the corresponding $Cu^{II}$-phenol complexes $[Cu(HL^{N_2O_2})(X)]$ and $[Cu(HL^{N_3O})(X)]$, as judged by the mononuclear copper(II) signal observed in the final EPR spectrum.[58,63,67,75] The protonation state of these complexes can be confirmed by UV/Vis spectrophotometry as $[Cu(HL^{N_2O_2})(X)]$ and $[Cu(HL^{N_3O})(X)]$ lack the phenolate-to-copper CT transition and only the copper(II) d–d transitions at around 600 nm are observed (Table 4). The copper(II) atom exhibits essentially the same geometry as in the mononuclear $Cu^{II}$-phenolate complexes, in other words square planar slightly distorted towards trigonal bipyramidal (Figure 7). The X-ray crystal structures of the $[Cu(HL^{20–23})(CH_3CN)]$ complexes (ligand with a $N_3O$ donor set) show that the phenol moiety systematically occupies the more labile axial position in the copper coordination sphere, regardless of the substituent.[58] The axial Cu–O distance is usually longer than 2.4 Å in $[Cu(HL^{20–23})(CH_3CN)]$, while it is around 2.2 Å for axially coordinated phenolates. The phenol group thus only coordinates the copper ion weakly. We have recently shown that deprotonation of the complex $[Cu(HL^{32})(CH_3CN)]$, in which the phenol is *axial*, induces an isomerization (Figure 7):[64] the phenolate moiety coordinates in an *equatorial* position in the deprotonated complex $[Cu(L^{32})(CH_3CN)]$. $^{19}F$ NMR spectroscopy allowed us to determine a rate constant of $3000 \pm 100\ s^{-1}$ for the following equilibrium at $T = 226$ K:

$$[Cu(HL^{32})(CH_3CN)]^1 + [Cu(L^{32})(CH_3CN)]^2 \rightleftharpoons [Cu(L^{32})(CH_3CN)]^1 + [Cu(HL^{32})(CH_3CN)]^2$$

where superscripts 1 and 2 represent the two distinct complexes that interconvert.

This rate constant is large, thereby indicating that proton transfer and/or molecular rearrangement is extremely rapid.

In the crystal structures of $[Cu(HL^{37})(OAc)]$[64] and $[Cu(HL^{39})(OAc)]$[65] ($N_2O_2$ ligands) only one phenol is protonated. The ligand in $[Cu(HL^{39})(OAc)]$ possesses two differentiated phenolic arms: since the electron-donating effect of $OCH_3$ relative to $NO_2$ makes deprotonation of the hy-

 © 2007 Wiley-VCH Verlag GmbH & Co. KGaA, Weinheim 

droxyl group more difficult, only that exhibiting the highest $pK_a$ (and thus the lowest oxidation potential) is protonated. This provides evidence for the geometric control of the two different phenolic arms.[67]

The electrochemical behavior of the mononuclear [Cu($L^{20–32}$)(X)] complexes shows an anodic, one-electron redox wave that corresponds to the oxidation of the phenolate moiety to a phenoxyl radical (Figure 8). The oxidation potentials and the chemical stability of the $Cu^{II}$-phenoxyl radical complexes [Cu($L^{20–23\cdot}$)(X)] are strongly correlated to the $\sigma^+_{Hammet}$ of the phenolate *p*-substituent ($E_{1/2}$ ranges between 0.01 and 0.70 V vs. $Fc^+$/Fc, Table 4):[58] The more

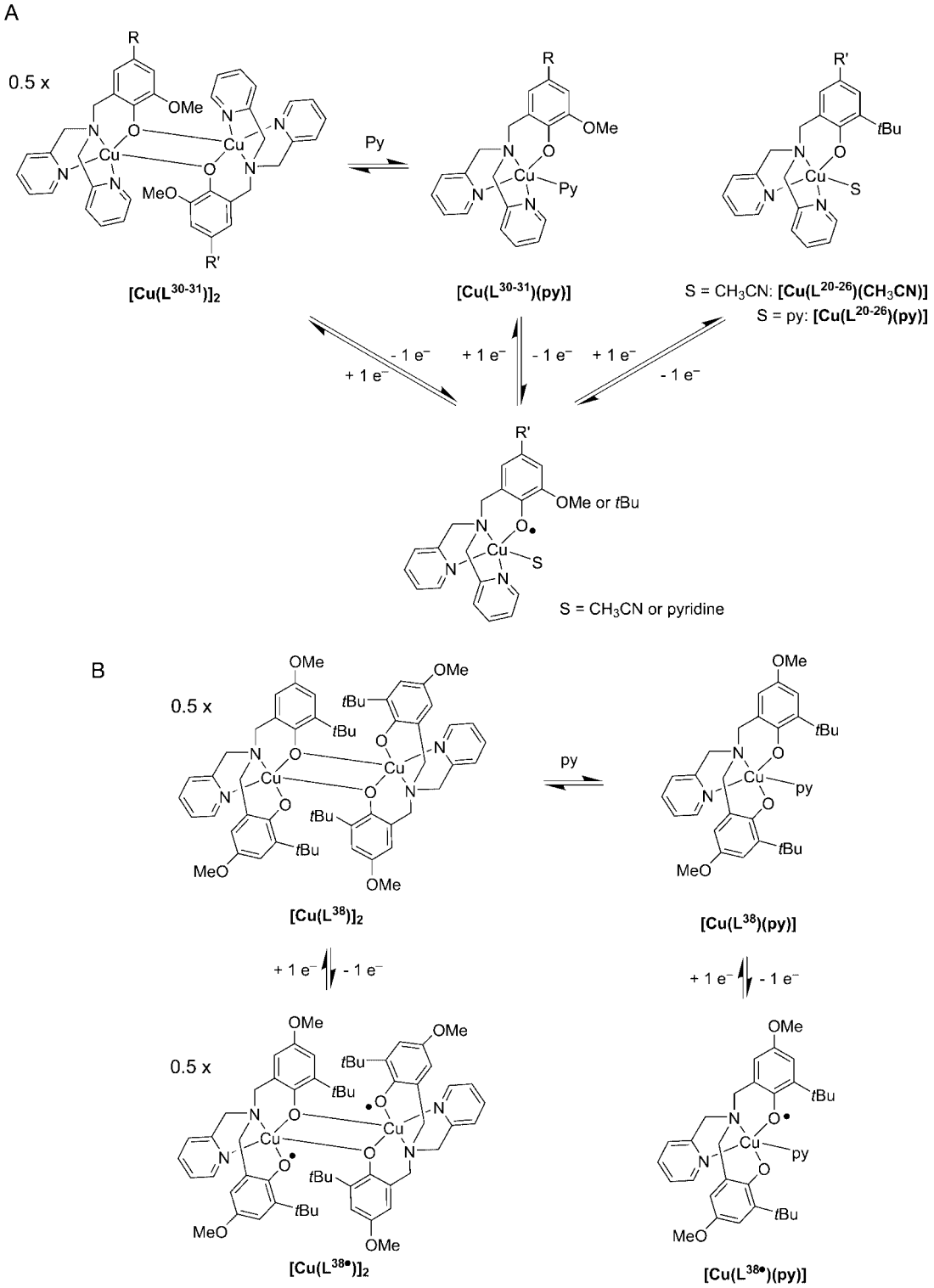


Figure 8. Solution and oxidative chemistry of the copper(II) complexes of $HL^{20–26}$, $HL^{30,31}$, and $H_2L^{38}$.

 © 2007 Wiley-VCH Verlag GmbH & Co. KGaA, Weinheim 

electron-donating substituent affords the more stable radical. In addition, a dependence of the radical stability on the N-donor properties has been observed within the $[Cu(L^{24,25})(Cl)]$ and $[Cu(L^{20,26})(CH_3CN)]$ series.[59,60] Thus the weaker N-donor ability of the 2-methylpyridine group compared to pyridine strongly destabilizes the radical complex. The electrochemically (or chemically) generated radical species are either EPR silent or exhibit an $S = 1$ signal (Table 4), thereby showing that the phenoxyl group remains coordinated to the copper(II) ion.[58–64]

The dinuclear species $[Cu(L^{30,31})]_2$ (Figure 8) exhibit an anodic peak, $E_p^a$, in their CV curves at +0.45 and +0.66 V, respectively, which is associated with a cathodic peak, $E_p^c$, at much lower potential values (+0.03 and +0.12 V respectively). These $E_p^a$ values are much higher than those of the mononuclear complexes $[Cu(L^{30,31})(py)]$ (py = pyridine; Figure 8, Table 4, $E_{1/2}$ = +0.00 and +0.14 respectively) due to the lower electron density on the bridging phenolate oxygen atom. In addition, the $E_p^c$ values for the dimers are close to those obtained for the monomers $[Cu(L^{30,31})(py)]$. We therefore concluded that the dimers are converted into the monomeric form $[Cu(L^{20–31\cdot})(X)]$ upon oxidation (Figure 8).[63]

Few data concerning the oxidation behavior of the phenolate complexes of $N_2O_2$ ligands exist.[58,63,65–69,74] The $Cu^{II}$-phenoxyl complex of $HL^{41}$ has been obtained by treating the ligand with one equivalent of $Cu(ClO_4)_2{\cdot}6H_2O$. A dimeric structure $[Cu(L^{41\cdot})]_2$ with two $Cu^{II}$-phenoxyl radical molecules bridged by phenolato groups has been proposed for this complex.[69] It is EPR-silent as the result of an antiferromagnetic exchange coupling mediated by the phenolato bridges. We have proposed a similar structure for the radical complex $[Cu(L^{38\cdot})]_2$ (Figure 8).[63] The mononuclear $Cu^{II}$-phenoxyl complex $[Cu(L^{38\cdot})(py)]$ (Figure 8) was generated by both chemical oxidation and electrolysis[63] and was found to be much less stable than $[Cu(L^{20\cdot})(py)]$, which possesses a similar phenoxyl moiety.[58] This suggests a lower stability of the radical entity formed with $HL^{N_2O_2}$ ligands compared to $HL^{N_3O}$ ligands in spite of their lower oxidation potentials (the difference of oxidation potentials may be at least partially due to the difference of overall charge of the complex). The radical complex $[Cu(L^{36\cdot})(CH_3CN)]$ has been synthesized by chemical oxidation of $[Cu(L^{36})(CH_3CN)]$ with silver acetate.[65] It was found to be EPR-active, which was interpreted as evidence for a weak ferromagnetic or a dipole–dipole interaction between the copper(II) and the axial phenoxyl radical spins. The electrochemically generated $[Cu(HL^{39\cdot})(OAc)]$ species was found to be relatively stable, in agreement with the reversible redox process observed on the electrolysis timescale.[67] Such behavior suggests that no chemical reaction, for example protonation-deprotonation, is associated with the electron transfer, as expected for the oxidation of a protonated phenol.[77] The radical has thus been proposed to be located on the equatorial nitrophenolate group.[67]

The $Cu^{II}$-phenol complexes $[Cu(HL^{N_3O})(X)]$ exhibit high oxidation potentials (>0.8 V, Table 4) and irreversible cyclic voltammograms,[58,59,63] which can be ascribed to two facts. In uncoordinated phenoxyl radicals, it has been shown that (i) the phenoxonium/phenoxyl redox couple is lower than that for phenoxyl/phenol and (ii) a proton transfer is associated with the electron transfer,[77] which means that the $Cu^{II}$-phenoxyl radical system cannot be generated from $Cu^{II}$-phenol complexes. On the other hand, reversible redox waves are observed within the –0.5 to 0.0 V range for these complexes {for example at $E_{1/2}$ = –0.39 V vs. $Fc^+/Fc$ for $[Cu(HL^{21})(Cl)]$}.[59] These waves are attributed to the $Cu^{II}/Cu^{I}$ redox couple. Their relatively high values suggest that the ligand in these $Cu^{II}$-phenol complexes can efficiently accommodate the copper(I) redox state. In addition, this value is close to that reported for the coordinated phenoxyl/phenolate couple {reversible system at $E_{1/2}$ = +0.02 V vs. $Fc^+/Fc$ for $[Cu(L^{21})(CH_3CN)]$} in the presence of $NEt_3$.[58] For comparison, the $Cu^{II}/Cu^{I}$ redox potential is –0.24 V in GO vs. $Fc^+/Fc$, while the tyrosyl/tyrosinate one has been estimated to be –0.01 V vs. $Fc^+/Fc$ at neutral pH.[12,13] The thermodynamic gap between the $Cu^{II}/Cu^{I}$ and phenoxyl/phenolate redox couples of $[Cu(HL^{21})(Cl)]$ and $[Cu(L^{21})(CH_3CN)]$, respectively, is thus close to that measured for GO (0.25 V).

## Emerging Classes of Model Compounds for the GO Active Site: Peptide Ligands

A general limitation for the use of chemical analogues of metalloenzyme active sites is their low water-solubility and their poor enantioselectivity when catalyzing reactions. Moreover, structural and reactivity studies on metalloproteins have revealed that the properties of their active sites depend on more than the metal coordination sphere. Modeling the second-sphere interaction in order to improve the biological relevance of complexes mimicking the metalloprotein active sites is therefore a new challenge. An emerging approach that accounts for these factors is the use of oligopeptides as ligands. While the copper(II) coordination chemistry of oligopeptides has been extensively studied, much less is known about the incorporation of biologically relevant radicals in such peptides.

The peptidic approach to modeling the active site of GO has been pioneered by Kojima et al.[78] Their approach concerns the use of cyclic tripeptides such as Boc-Gly-e(His-Tyr-OEt) (e is an ethylene bridge) that incorporate both a tyrosine and a histidine ligand for the copper ion. A 2:1 ligand:metal complex is predominantly formed in solution whose structure involves a square-pyramidal monomer complex coordinated to two imidazole nitrogens atoms, two phenolate oxygen atoms, and one external water or solvent molecule. Its electrochemical behavior shows an irreversible ligand-centered oxidation process at +0.91 V vs. $Fc^+/Fc$ attributed to the phenoxyl/phenolate redox couple. This value is much higher than that of GO, which shows that the radical is not stable.

Five years later, two reports by Berkessel[79] and ourselves[80] appeared in the literature, both of which concern the synthesis of peptides designed to stabilize phenoxyl rad-

 © 2007 Wiley-VCH Verlag GmbH & Co. KGaA, Weinheim 

icals generated on their side chains. Berkessel et al. used a strategy based on combinatorial synthesis using peptide chemistry.[79] The general design of the solid-phase-bound decapeptide library is shown in Figure 9. A Pro-Gly sequence is included in order to induce a hairpin that makes the $X_1$–$X_4$ residues orient properly to chelate a copper(II) ion. These four positions ($X_1$–$X_4$) are occupied in a combinatorial manner by histidine, tyrosine, modified cysteine (cross-linked with a di-*tert*-phenol moieties), or a modified TEMPO (stable nitroxide radical). Incubation of the solid-phase-bound library with copper results in a color change, which indicates metal binding. The His-rich sequences gave blue beads, Tyr-rich sequences pale yellow to green complexes, while the presence of the modified TEMPO in the peptide resulted in an orange coloration. The solid-phase-bound peptide libraries were screened for their activity towards benzyl alcohol and 3-methoxybenzyl alcohol oxidation. A pronounced sequence-dependence of the catalytic activity was observed: the most active ligands were those incorporating the modified TEMPO group, which allow up to six turnovers. No deactivation of the catalyst due to oxidative demetalation was observed, and characterization of the (radical) copper complexes is currently in progress.

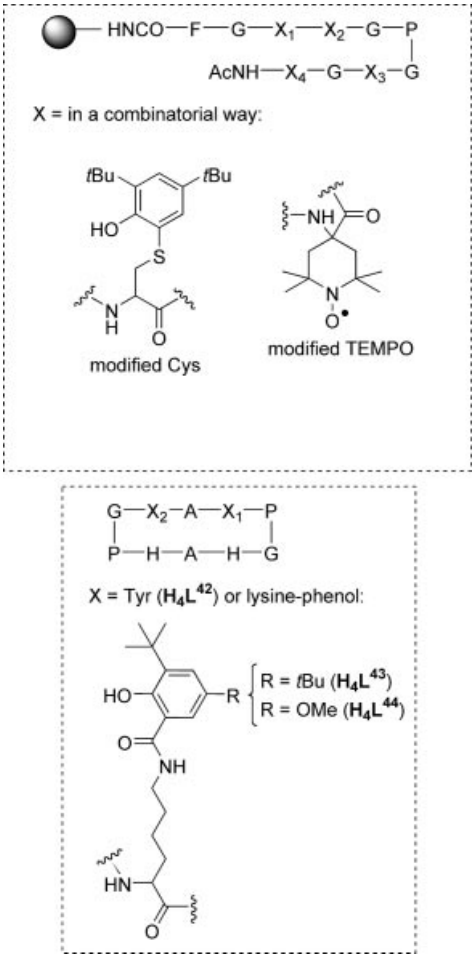


Figure 9. Formulae of peptide ligands. The top structure is adapted from ref.[79] and the bottom one from ref.[80]

In another approach, we have used cyclic decapeptides incorporating two proline-glycine sequences to induce β-turn hairpins.[80] The resulting peptide conformation is constrained into an anti-parallel β sheet and functionalization is achieved above the plane of this motif by two histidines and two amino acids $X_1$ and $X_2$ [$X_1$ and $X_2$ being either tyrosines ($H_4L^{42}$) or a lysine-phenol conjugate ($H_4L^{43,44}$)]. Potentiometric titrations have shown that deprotonation of the phenol moieties requires a pH higher than 12 (the corresponding p$K_a$ values range between 8.96 and 11.34, depending on the amino acid X). At pH 12.2 only the decapeptides incorporating a lysine-phenol conjugate exhibit reversible signals [$E_{1/2}$ = –0.03 V for R = *t*Bu ($L^{43}$) and –0.20 V vs. $Fc^+$/Fc for R = OMe ($L^{44}$)], thereby showing that the stability of the oxidized species is noteworthy. This stability is confirmed by electrochemical oxidation of the peptides, which affords EPR-active species whose spectra are typical of phenoxyl radicals. These compounds are among the first radical-peptides to be generated and persist in solution long enough to be characterized. Evaluation of their coordination chemistry is currently in progress.

### Emerging Classes of Model Compounds for the GO Active Site: Calix[6]arene Ligands

Another platform, namely calix[6]arenes, has been pioneered by Reinaud et al.[81] In these systems, a four- or five-coordinate metal ion is constrained in a mononuclear environment that preserves a binding site buried inside a hydrophobic pocket accessible to small molecules. In order to get model compounds for the GO active site, the calix[6]arene core has been functionalized with one phenol and three *N*-methylimidazole groups. In the copper(II) complex, the metal ion is pentacoordinate and has a square-pyramidal geometry. The phenolate oxygen and one solvent molecule (acetonitrile) bind in equatorial positions, while the three *N*-methylimidazole nitrogens complete the pyramid. The solvent is buried in the conic cavity of the calixarene in a *trans* position relative to the phenolate group, which caps the copper(II) complex. The $Cu^{II}$-phenoxyl radical complex was found to be able to mediate the stoichiometric two-electron oxidation of benzyl alcohol. This reaction is promoted by coordination to the copper and proceeds in an inner-cavity process.

## Modeling the Properties of the GO Active Site

### Influence of the Cys-Tyr Crosslink

In order to better understand the influence of the Cys-Tyr crosslink on the properties of the redox-active Tyr272 residue of the enzyme, Itoh et al. have synthesized a series of 2-methylsulfanylphenols.[74] These compounds exhibit oxidation potentials that are much lower than those of the nonsubstituted parent phenols, with, for example, a drop of 0.35 V on going from the 4-methylphenol to the 4-methyl-2-methylsulfanylphenol. Such behavior is interpreted in

 © 2007 Wiley-VCH Verlag GmbH & Co. KGaA, Weinheim 

terms of the electron-sharing conjugative effect of the methylsulfanyl substituent.

The corresponding phenoxyl radicals have been generated by pulse radiolysis. The 4-methylphenoxyl radical species exhibits two intense absorptions in its UV/Vis spectrum at around 400 nm corresponding to π–π* transitions. The UV/Vis spectrum of the 4-methyl-2-methylsulfanylphenoxyl radical also shows such absorptions at around 400 nm, but exhibits an additional strong absorption band at 850 nm. The origin of this latter absorption has been attributed to an intramolecular charge transfer from the benzene ring to the methylsulfanyl group. It is important to note that this lower-energy feature is quite similar to that of the enzyme in its radical form. It has been proposed that the larger $\varepsilon$ value obtained for GO arises from an interligand charge transfer from the Tyr272 radical to Tyr495.[82] EPR spectroscopy has revealed that a methylsulfanyl substituent induces larger *g*-tensor values for the phenoxyl radical due to the large spin-orbit coupling on the sulfur atom ($g$ = 2.0060 for the 4-methyl-2-methylsulfanylphenoxyl radical; $g$ = 2.0036 for the 2,4,6-trimethylphenoxyl radical).[74] A large amount of spin density thus delocalizes over the sulfur atom of the methylsulfanyl substituent.

Some copper(II) complexes bearing coordinated 2-(alkylsulfanyl)phenoxyl radical derivatives have been synthesized (Figure 10).[34,61,62,83,84] The complex [Cu($L^{45}$)(ppb)], for example, which is obtained by treating one equivalent of 2-hydroxy-5-methyl-3-(methylsulfanyl)benzaldehyde with one equivalent of tris(3-phenylpyrazolyl)borate (ppb) and copper(II), can be oxidized into a radical species. The 2-alkylsulfanylphenol moiety has also been incorporated into Schiff bases ($H_2L^2$)[34] and tripodal ligands ($HL^{27,28}$, $H_2L^{40}$)[61–68] and the corresponding mononuclear $Cu^{II}$-phenoxyl complexes characterized. The UV/Vis spectra of all the non-Schiff base species typically exhibit both the strong absorption bands at around 400 nm and the NIR feature above 800 nm that were observed in the 2-(methylsulfanyl)-phenols. In the Schiff-base series, the anticipated phenoxyl radical absorption feature at 400 nm is obscured by intense ligand absorption bands. All the $Cu^{II}$-phenoxyl species were found to be X-band EPR-silent as a result of a magnetic coupling between the copper(II) and the radical spins.

It has previously been proposed by Stack et al. that salen complexes fail to reproduce the high turnovers of GO because of their inability to form stable copper(I) complexes.[34,35] A pentadentate $NO_2S_2$ ligand ($H_2L^{46}$) that incorporates *ortho*-(alkylsulfanyl)phenol moieties has therefore been prepared.[85] A major difference between this ligand and most of the previous ones is that the sulfanyl groups here are designed to coordinate the copper atom, which is expected to both lower the phenol oxidation potential and increase the redox potential of the $Cu^{II}/Cu^{I}$ couple. Unfortunately, the X-ray crystal structure of its copper(II) complex [Cu($L^{46}$)] shows that the occupied electron-donating sulfur p orbitals are aligned to bond to the copper center rather than π-conjugated with the phenolates, and that the copper(II)–sulfur bonds are long (>2.4 Å). Its high oxidation potentials (+0.47 and +0.62 V vs. $Fc^+/Fc$) confirm

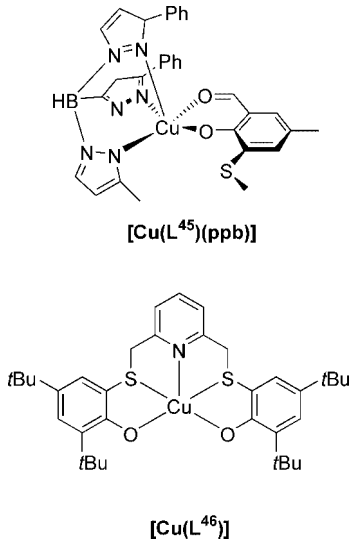


Figure 10. Copper(II) complexes of ligands possessing a 2-(alkylsulfanyl)phenoxyl moiety: [Cu($L^{45}$)(ppb)] (ref.[83]) and [Cu($L^{46}$)] (ref.[85]).

that the sulfur groups behave as electron-withdrawing groups. The reduction wave, which is attributed to the $Cu^{II}/Cu^{I}$ couple, is observed at –1.23 V, close to the value reported for binaphthyl-salen complexes such as [Cu($L^2$)]; all attempts to isolate the copper(I) complex were unsuccessful.

### Modelling the Tyr-Trp π–π Interaction

The X-ray crystal structure of the GO active site has revealed that the redox-active tyrosine is π-stacked with the indole ring of a neighboring tryptophan Trp290 residue. This interaction has been modeled in several ways by Halcrow et al.[86–90] In one approach, they synthesized 3,4-benzo-8,9-(3′-hydroxy-4′-methylsulfanylbenzo)bicyclo-[4.4.1]undeca-3,8-dien-11-one ($HL^{47}$) and its ethylene acetal $HL^{48}$ (Figure 11).[86,87] The ketone adopts a boat/chair conformation while the acetal exhibits a chair/chair conformation with layered benzo rings. The oxidation potential, which is 0.15 V lower for $HL^{48}$ than for $HL^{47}$, may suggest that the π–π interaction contributes to the thermodynamic stability of the oxidized species, although an alternative explanation is that the identity of the bridgehead group (ketone vs. acetal) has an effect on the p-orbital energy. As this suggestion has not yet been quantified, the authors still entertain both possibilities. The cyclic voltammograms also revealed an improved reversibility for $HL^{47}$, which could be attributed to both an intramolecular O–H···S hydrogen bond that would hinder deprotonation of the oxidation product and steric protection afforded by the intramolecular π–π interaction.

In another approach, they have synthesized the ligand $L^{49}$, which contains an oxidizable dimethoxyphenyl substituent.[88–90] In its copper(II) complexes [Cu($L^{49}$)(TpPh)] and [Cu($L^{49}$)(TpCy)] {Tp = tris(3-arylpyrazolyl)hydroborate; TpPh: R = phenyl, TpCy: R = cyclohexyl} the metal ion

 © 2007 Wiley-VCH Verlag GmbH & Co. KGaA, Weinheim 

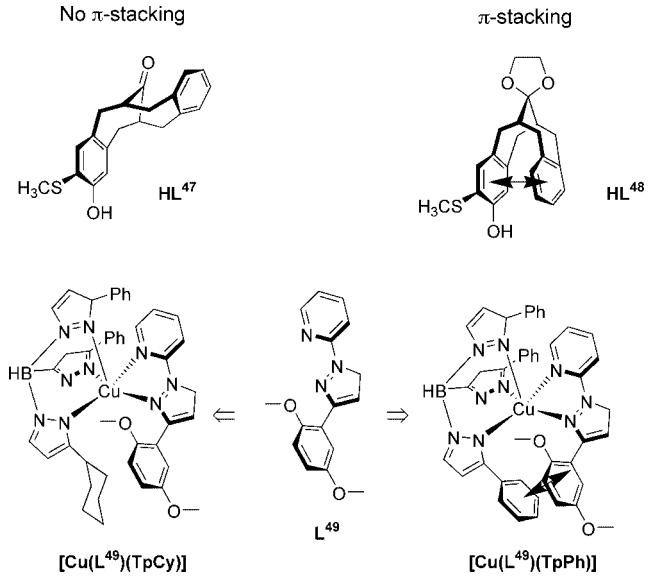


Figure 11. Model compounds for the Tyr-Trp π–π interaction: $HL^{47}$ and $HL^{48}$ (ref.[86,87]), $[Cu(L^{49})(TpCy)]$ and $[Cu(L^{49})(TpPh)]$ (ref.[88–90]).

resides within the same square-pyramidal geometry. Nevertheless, a major difference exists between each complex: The dimethoxyphenyl group in $[Cu(L^{49})(TpPh)]$ takes part in a π–π interaction with a phenyl ring from the TpPh coligand while no such interaction exists within $[Cu(L^{49})(TpCy)]$. The authors have shown that the π–π interaction exhibited by $[Cu(L^{49})(TpPh)]$ is retained following its one-electron oxidation, although deconvolution of the voltammograms led to the conclusion that this interaction has no measurable effect on the kinetic stability of the resultant aryl radical.

Recently, we have suggested a structural role for this interaction:[64] The metal in $[Cu(HL^{32})(CH_3CN)]$ has a square-pyramidal geometry whose apical position is occupied by the phenol moiety. In the deprotonated complex $[Cu(L^{32})(CH_3CN)]$, this phenolate group has shifted to an equatorial position, which means that an isomerization is induced by deprotonation. π–π stacking interactions between the phenolate and quinoline rings that have been detected in the solid state are proposed to contribute, at least partially, to the isomerization and thus the phenolate positioning.

In summary, the Tyr-Trp π–π interaction in GO is supposed to have little or no effect on the chemical reactivity of the tyrosyl radical, except to shield it from external solvent. All these biomimetic studies thus suggest that the role of this interaction in GO is structural rather than electronic – it has been proposed recently that it may be involved in maintaining the cofactor orientation that results in the diamagnetic ground state of GO.[17]

## Understanding the Diamagnetic Ground State of the Oxidized Form of GO

GO is EPR-silent in its copper(II)-tyrosyl radical form as the result of an antiferromagnetic coupling between the radical and the $Cu^{II}$ spins.[16] The relative orientations of the magnetic orbitals of the $Cu^{II}$ ion ($d_{x^2-y^2}$) and of the phenoxyl radical (half-occupied π orbital) are expected to determine the multiplicity of the electronic ground state (Figure 12). Quantification of this orientation can be roughly achieved by measuring the $Cu^{II}$–O–C bond angle ($\alpha$) and the dihedral angle ($\beta$) between the $x,y$ plane at the $Cu^{II}$ ion and the phenyl ring of the radical ligand in the X-ray crystal structures of $Cu^{II}$-phenolate complexes (Figure 12). Wieghardt et al. have been able to tune these angles, and thus the multiplicity of the electronic ground state, in a series of copper(II) complexes of TACN ligands.[52] Increasing the coordination number from five to six does not change $\alpha$ significantly {125.2° in $[Cu(L^{15})(Cl)]$ vs. 129.2° in

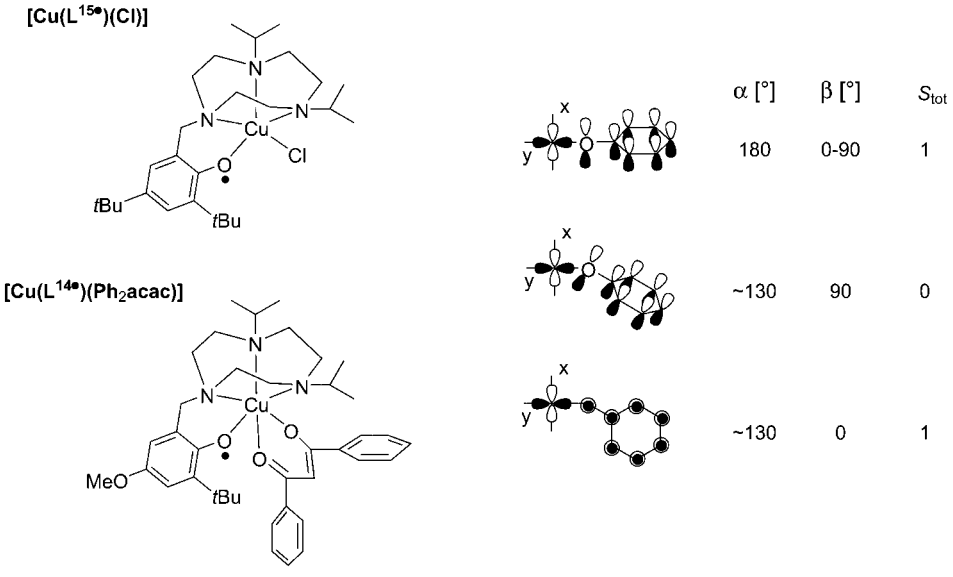


Figure 12. Models for the multiplicity of the ground state of GO (adapted from ref.[52]).

 © 2007 Wiley-VCH Verlag GmbH & Co. KGaA, Weinheim 

[$Cu(L^{14})(Ph_2acac)$]}, whereas $\beta$ decreases by nearly 10° {27.4° in [$Cu(L^{15})(Cl)$] vs. 17.6° in [$Cu(L^{14})(Ph_2acac)$]}. These structural changes induce the inversion of the sign of the magnetic coupling, from antiferromagnetic in [$Cu(L^{15\cdot})(Cl)$] to ferromagnetic in [$Cu(L^{14\cdot})(Ph_2acac)$] ($J = 16 \pm 3$ $cm^{-1}$ for the latter complex). In GO, the bond angles $\alpha$ and $\beta$ are about 129° and 75°, respectively, consistent with an antiferromagnetic coupling, as in [$Cu(L^{15\cdot})(Cl)$].[12,13,52]

### Structural Approaches to the GO Active Site [Axial Copper(II)-Tyrosinate Bond and Coordinated Phenoxyl Radical]

One of the first biomimetic approaches to the GO active site involved modeling the axial copper(II)-tyrosinate bond. Three groups have reported X-ray crystal structures of copper(II) complexes involving unusually axially coordinated phenolates as model compounds for GO.[58,71,72,91–93] The ligands used in these studies possess a tripodal structure with a pendent phenol arm that is substituted at its *para* position by an electron-withdrawing nitro group. In the copper(II) complex [$Cu(L^{50})(Cl)$] (Figure 13), the geometry around the metal center is square pyramidal, with two pyridine nitrogens, one tertiary amine nitrogen, and an exogenous ligand (chloride ion) in the basal plane. The phenolate oxygen binds weakly in the *apical* position, thus making this complex the first that reproduces the axial $Cu^{II}$-phenolate bond of GO.[94] It was initially proposed that the apical coordination of the phenolate is due to the introduction of the nitro substituent *para* to the phenolate group, as in its absence phenolates occupy the equatorial position.[91] The polarity rule, which states that the more electronegative ligand will preferentially occupy the axial position of a tetragonal-based pyramid, was proposed to account for these results in combination with crystal-packing forces. Lately, Fenton et al. have published the X-ray crystal structure of the copper(II) complex of $HL^{51}$ (Figure 13),[71,92] in which the nitrophenolate occupies the *equatorial* position. These contradictory results can be rationalized by considering the size of the chelate rings, since a five/five/six-membered chelate ring sequence is observed in Palaniandavar's complexes whereas a six/six/six-membered chelate ring sequence is observed in Fenton's complex. We have structurally characterized the $Cu^{II}$-phenolate complexes of $HL^{23}$ and $HL^{32}$.[58,64] Both ligands possess similar 2-*tert*-butyl-4-nitrophenol and pyridine moieties but differ in their third chelating arm (a pyridyl group for $HL^{23}$ and a fluoroquinolyl group for $HL^{32}$). The nitrophenolate moiety in [$Cu(L^{23})(Cl)$] is found to coordinate in an axial position while in [$Cu(L^{32})(CH_3CN)$] it occupies the equatorial position. Formation of an axial phenolate oxygen–copper bond thus appears not only related to the electronic properties of the phenolate *para* substituent but also to steric factors arising from the ligand and to the nature of the chelate rings formed.

To duplicate and better understand the anion interactions in the inactive enzyme and the spectral changes ac-

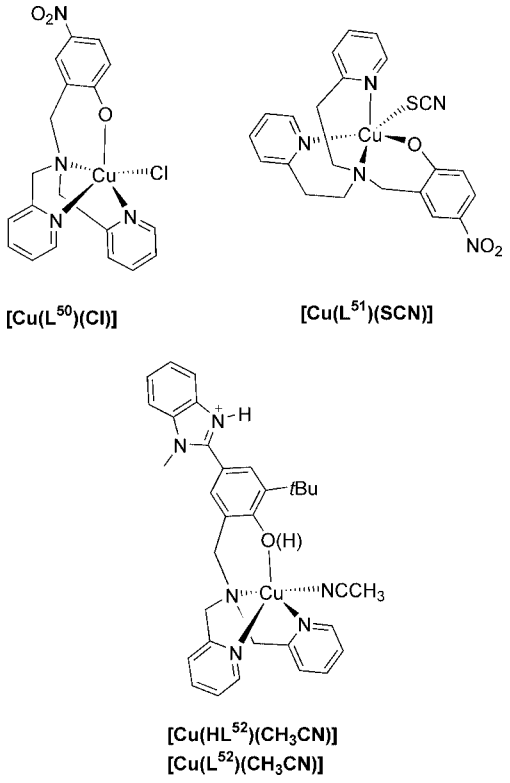


Figure 13. Models for the axial copper-phenolate bond: [$Cu(L^{50})(Cl)$] (ref.[91]), [$Cu(L^{51})(SCN)$] (ref.[92]), [$Cu(HL^{52})(CH_3CN)$] and [$Cu(L^{52})(CH_3CN)$] (ref.[93]).

companying it, )Palaniandavar et al. have determined the crystal structures of a series of [$Cu(L^{50})(X)$] complexes (X = $ClO_4^-$, $SCN^-$, $CH_3CO_2^-$).[72] Replacement of a weakly coordinating ligand X by a strongly coordinating one in the equatorial position has been shown to decrease the electronic interaction between the metal center and the axially coordinated phenolate, and consequently contributes to a lengthening of the axial Cu–O bond [2.186(2), 2.200(3), and 2.268(1) Å for X = $SCN^-$, $XCH_3CO_2^-$ and $Cl^-$, respectively].

With the aim of visualizing the effect of protonation of the axial phenolate on the metal–ligand bonds, we have synthesized the $Cu^{II}$-phenol and $Cu^{II}$-phenolate complexes of $HL^{23}$.[58] The phenolate complex [$Cu(L^{23})(Cl)$] exhibits a geometry that is roughly similar to that of [$Cu(L^{50})(Cl)$] described by Palaniandavar et al.[94] We also reported the X-ray crystal structures of the phenol complex [$Cu(HL^{23})(CH_3CN)$], but as the exogenous ligand is different in the phenolate and phenol structures (an acetonitrile molecule in the former and a chloride ion in the latter) it was difficult to estimate the influence of the protonation of the axial phenolate on the equatorial bonds. We therefore synthesized the copper(II) complex of $HL^{52}$, which bears an electron-withdrawing *N*-methylbenzimidazolium instead of a nitro substituent.[93] The phenolate and phenol complexes could be crystallized with the same exogenous ligand (acetonitrile molecule). From the X-ray structure analysis, it appears clear that deprotonation of the axial phenol forces the metal to move out of the basal plane towards the oxygen atom (as a consequence of a stronger axial bond),

 © 2007 Wiley-VCH Verlag GmbH & Co. KGaA, Weinheim 

and that both Cu–$N_{pyridine}$ bond lengths increase, thereby reflecting the weakening of the equatorial bonds (Figure 14). Interestingly, the phenolate compound [Cu($L^{52}$)($CH_3CN$)] exhibits the shortest axial Cu–$O_{phenolate}$ distance in the whole series of complexes [2.133(4) Å].

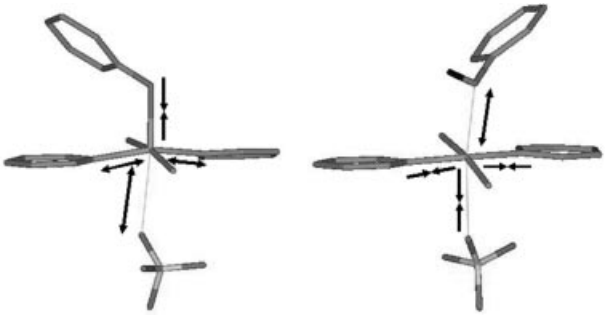

Figure 14. Effect of the protonation of the phenolate moiety on the bond lengths around the copper atom (reproduced from ref.[93]).

Several X-ray crystal structures of transition metal complexes of ligands possessing iminosemiquinonate moieties have been reported.[45,95] The first X-ray crystal structure of coordinated phenoxyl radical was reported in 1996 by Wieghardt et al.[96] for a phenoxylchromium complex. The crystal structure of a copper(II)-coordinated phenoxyl radical was obtained in 2001.[97,98] The complex [Cu($L^{53}$)$_2$] has been structurally characterized (Figure 15) and chemically oxidized to [Cu($L^{53\cdot}$)($L^{53}$)]. The two ligands in [Cu($L^{53\cdot}$)($L^{53}$)] are structurally inequivalent (Figure 15): one ($L^{53}$) exhibits C–C, C–O, and C–N bond lengths that are similar to those of [Cu($L^{53}$)$_2$], whereas in the second ($L^{53\cdot}$) the phenol C–O distance is significantly shorter and the two adjacent C–C bonds and the Cu–O bond are longer than those in [Cu($L^{53}$)$_2$]. The C–O distance of 1.264(5) Å reported for $L^{53\cdot}$ emphasizes the C=O character of this bond [it is 1.322(5) Å in $L^{53}$]. The other metal–ligand bonds in [Cu($L^{53\cdot}$)($L^{53}$)] are significantly shorter than in [Cu($L^{53}$)$_2$]. All these C–O and C–C bond lengths are in agreement with the electronic structure depicted in Figure 15, where the unpaired electron of the phenoxyl group is delocalized over both *ortho* positions.

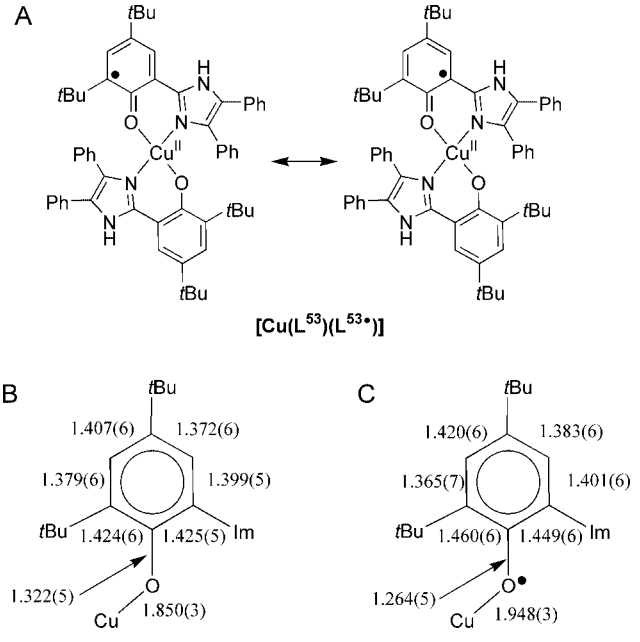


Figure 15. Formula of [Cu($L^{53}$)($L^{53\cdot}$)] and its resonance structures (A) and bond lengths of the phenolate moiety (B) and phenoxyl radical moiety (C) coordinated to the copper(II) ion of [Cu($L^{53}$)($L^{53\cdot}$)] (adapted from ref.[97]).

## Reactivity of Copper(I) Complexes Towards $O_2$

The catalytic reaction for GO occurs via a ping-pong mechanism.[9–11] The first half-reaction involves binding and oxidation of the alcohol substrate by the $Cu^{II}$-tyrosyl radical form to yield aldehyde and the reduced copper(I) state. In the second half-reaction dioxygen is bound and reduced, releasing $H_2O_2$ and the $Cu^{II}$-tyrosyl radical form of the enzyme. The first step has been studied extensively, while very little is known about the dioxygen reactivation step. It has been speculated that $O_2$ binds to the three-coordinate copper(I) site to form a $Cu^{II}$-superoxide species, which evolves into a $Cu^{II}$-hydroperoxide-tyrosyl radical intermediate. A proton transfer from the axial tyrosine leads to the release of $H_2O_2$ and regeneration of the initial $Cu^{II}$-tyrosyl radical form of the enzyme. With the goal of obtaining insights into the dioxygen reactivation step, Tolman et al. have characterized $Cu^{I}$-phenolate complexes and studied their reactivity towards $O_2$ by low-temperature stopped-flow experiments.[55] They have shown that the copper(I) phenolate complex [$Cu^{I}$($L^{15}$)] has a four-coordi-

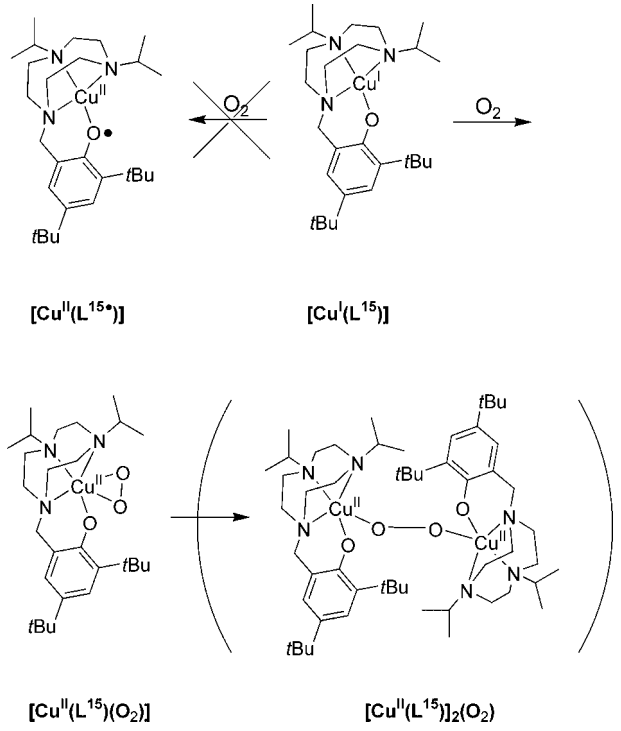


Figure 16. Reactivity of TACN complexes with $O_2$ (ref.[55]).

 © 2007 Wiley-VCH Verlag GmbH & Co. KGaA, Weinheim 

nate geometry (Figure 16) while $[Cu^{I}(L^{16})]$ adopts a planar three-coordinate geometry. The average metal–ligand bond lengths are 2.13 Å in $[Cu^{I}(L^{15})]$ and 2.05 Å in $[Cu^{I}(L^{16})]$. The former fits much better with the value of 1.99 Å determined from EXAFS measurements in the enzyme, thereby suggesting that a coordination number of about three is more appropriate for the enzyme. $[Cu^{I}(L^{16})]$ was found to be too reactive with $O_2$ even at cryogenic temperatures, thus precluding a detailed investigation. Mixing $[Cu^{I}(L^{15})]$ with excess $O_2$ produced dark-green solutions, while sub-stoichiometric amounts of $O_2$ afforded a green solution that reacted rapidly to form an intensely purple species.

This was interpreted in terms of the following reaction sequence (see also Figure 16).

$[Cu^{I}(L^{15})] + O_2 \rightleftharpoons [Cu^{II}(L^{15})(O_2)]$ "green species"

$[Cu^{II}(L^{15})(O_2)] + [Cu^{I}(L^{15})] \rightarrow [Cu^{II}(L^{15})]_2(O_2)$ "purple species"

$2 \times [Cu^{II}(L^{15})(O_2)] \rightarrow [Cu^{II}(L^{15})]_2(O_2) + O_2$ "purple species"

$[Cu^{II}(L^{15})]_2(O_2) \rightarrow$ decomposition

The dark-green species $[Cu^{II}(L^{15})(O_2)]$ exhibits $\lambda_{max}$ values at 416 ($\varepsilon$ = 4600) and 654 nm (1800 $M^{-1}cm^{-1}$), which are slightly different than those of the corresponding and fully characterized $Cu^{II}$-phenoxyl radical species $[Cu^{II}(L^{15\cdot})(CH_3CN)]$ [$\lambda_{max}$ = 410 ($\varepsilon$ = 4000) and 672 nm (1000 $M^{-1}cm^{-1}$); Table 3].[54] The Raman spectrum of $[Cu^{II}(L^{15})(O_2)]$ is characterized by a peak at 1120 $cm^{-1}$, for the $^{16}O_2$ sample, which shifts to 1058 $cm^{-1}$ when $^{18}O_2$ is used. Based on comparison with literature data, this could be attributed to the ν(O–O) mode of a superoxidocopper(II) complex (Figure 16). With mixed isotopically labeled gas an additional sharp peak was observed at 1093 $cm^{-1}$, without splitting, which suggests a symmetric ($\eta^2$) binding of the superoxide ligand (Figure 16). The ν(Cu–$O_2$) mode was observed at 422 and 450 $cm^{-1}$, while additional features not sensitive to $^{18}O_2$ substitution, corresponding to a phenolate mode, are observed at approximately 1300 $cm^{-1}$ and in the region 1500–1700 $cm^{-1}$. This species is EPR-silent as the result of a magnetic coupling between the copper(II) and the superoxide ligand.

The purple species $[Cu^{II}(L^{15})]_2(O_2)$, which exhibits multiple broad bands that are sensitive to $^{18}O$-isotope substitution in the regions 500–550 and 700–850 $cm^{-1}$, could be described as a peroxidodicopper complex (Figure 16). The unusual broadening of these signals is attributed to the existence of multiple conformational isomers that differ with respect to the metal ion geometry and/or the relative ligand donor disposition (Figure 15).

The peroxido species $[Cu^{II}(L^{15})]_2(O_2)$ prevails at all temperatures while the superoxido one $[Cu^{II}(L^{15})(O_2)]$ cannot be observed unless $[Cu^{I}(L^{15})]$ is present in excess. In contrast, in most previously described systems the peroxido compound is the stable species in the presence of excess $O_2$ while the superoxido complex is no more than an intermediate. Such a difference may result from the presence of a phenolate (and its electronic effect) or steric bulk provided by the *i*Pr and *t*Bu substituents in $HL^{15}$. The light-green decomposition products are probably multinuclear copper(II)-containing species, although their exact nature is unknown.

We have studied the reactivity of copper(I) complexes of tripodal ligands that are precursors of stable phenoxyl radicals with $O_2$.[63] The copper(I) complexes were generated in situ and oxygenation was performed at 233 K. We have shown in the case of the copper(I) complex of the $N_3O$ ligands $HL^{20}$ and $HL^{30}$ that $O_2$ does not oxidize the phenol into a phenoxyl radical. Instead, a $Cu^{II}$-phenolate complex is obtained. In contrast, reaction of $O_2$ with the copper(I) complex of the $N_2O_2$ ligand $H_2L^{38}$ affords products whose spectral properties are quite different to those of isolated $Cu^{II}$-phenolate and $Cu^{II}$-phenoxyl species. A highly reactive transient species is then formed and decomposes in solution, although its nature remains unclear.

### Radical Cofactor Formation: Reactivity of Tripodal Ligands Towards $Cu^{2+}$

It has recently been shown that formation of the radical cofactor of GO can be achieved by treating copper and $O_2$ with the pre-form of GO.[29,30] With the aim of better understanding the way in which copper(II) might be involved in GO activation, we have studied the reactivity of several tripodal ligands at various copper(II) [added as its $Cu(ClO_4)_2{\cdot}6H_2O$ salt], base, and dioxygen concentrations in $CH_3CN$.[63] Addition of 0–1 molar equivalents of $Cu^{2+}$ to the phenolate complex $[Cu(L^{20})(CH_3CN)]$ (ligand possessing a $N_3O$ donor set) or 1–2 molar equivalents of $Cu^{2+}$ to the ligand $HL^{20}$ in the presence of $NEt_3$ results in dramatic color changes. No more changes were observed beyond two molar equivalents of added copper(II). UV/Vis, EPR, and electrochemical characterizations indicated that the reaction product was the $Cu^{II}$-phenoxyl radical complex $[Cu(L^{20\cdot})(CH_3CN)]$, which is quantitatively formed by chemical oxidation of $[Cu(L^{20})(CH_3CN)]$ by excess solvated $Cu^{2+}$ according to:

$$[Cu(L^{20})(CH_3CN)] + Cu^{2+} \rightarrow [Cu(L^{20\cdot})(CH_3CN)] + Cu^{+}$$

A reverse titration, in other words addition of $HL^{20}$ to $Cu^{2+}$ in the presence of $NEt_3$, showed that half an equivalent of $[Cu(L^{20\cdot})(CH_3CN)]$ is formed at a $HL^{20}/Cu^{2+}$ ratio of 0.5, the remaining copper being in the $Cu^{+}$ redox state. At one molar equivalent of added ligand, $[Cu(L^{20})(CH_3CN)]$ is formed quantitatively in a comproportionation reaction.

$$\mathbf{[Cu(L^{20\cdot})(CH_3CN)]} + Cu^{+} + \mathbf{HL^{20}} \xrightarrow{NEt_3} \mathbf{2\,[Cu(L^{20})(CH_3CN)]}$$

Addition of one molar equivalent of $Cu^{2+}$ to the phenol complex $[Cu(HL^{20})(CH_3CN)]$ ($N_3O$ ligand) or two molar equivalents of $Cu^{2+}$ to $HL^{20}$ without base results in the formation of less than 8% of $[Cu(L^{20\cdot})(CH_3CN)]$. This low

 © 2007 Wiley-VCH Verlag GmbH & Co. KGaA, Weinheim 

yield for the $Cu^{2+}$-promoted oxidation reaction is consistent with an oxidation potential that is much higher for a phenol than for a phenolate group. Similar results were obtained when $HL^{20}$ was replaced by $HL^{30}$ (and also $[Cu(L^{20})(CH_3CN)]$ by $[Cu(L^{30})]_2$), thus showing that the nuclearity of the $Cu^{II}$-phenolate complex does not significantly influence the $Cu^{2+}$-promoted oxidation reaction.

A completely different behavior was observed upon treating $HL^{37}$ and $HL^{38}$ (ligand possessing a $N_2O_2$ donor set) with $Cu^{2+}$: as soon as copper is added a $Cu^{II}$-phenoxyl radical complex is formed in a disproportionation reaction.[63,66] The radical species $[Cu(L^{38\cdot})]_2$ is formed quantitatively in the presence of $NEt_3$ at two molar equivalent of added $Cu^{2+}$.[63] This species can also be formed in the absence of base, although it decomposes much faster. Addition of $Cu^{2+}$ to $[Cu(L^{38\cdot})]_2$ results in the formation of a $Cu^{II}$ bis(phenoxyl) species whose structure is proposed to be the monomeric complex $[Cu(L^{38\cdot\cdot})(CH_3CN)]$.

These results show that a change in the donor set of the ligand can direct the reaction from comproportionation towards disproportionation.

Ligands with $N_2O_2$ donor set:

$$2\ Cu^{II}\text{-}O \rightleftharpoons Cu^{II}\text{-}O^{\bullet} + \text{copper(I)}$$

Ligands with $N_3O$ donor set:

$$2\ Cu^{II}\text{-}O \rightleftharpoons Cu^{II}\text{-}O^{\bullet} + \text{copper(I)}$$

A phenoxyl radical can thus be spontaneously formed by adding small amounts of $Cu^{2+}$ to ligands possessing the same donor set as this enzyme.

### Metamorphosing a GO's Reactivity by Using a Ligand Possessing a Five-Atom Donor Set

A ligand built on a triiminocyclohexane scaffold ($H_2L^{54}$; Figure 17) has been described by Walton et al.[99] The X-ray crystal structure of its copper(II) complex $[Cu(L^{54})]$ shows a pentacoordinate metal ion that resides in a square-pyramidal geometry as in GO. Unlike GO, however, which has a four-atom donor set with the fifth position vacant for substrate binding, no position seems to be available for substrate binding (and subsequent catalytic activity) in $[Cu(L^{54})]$ as the ligand already provides the five-atom donor set. Nevertheless, $[Cu(L^{54})]$ has been found to be active for the oxidation of benzyl alcohol (the substrate being added in its deprotonated alkoxide form) with molecular dioxygen as co-oxidant.[99] This result can be explained by considering the formation of an octahedral six-coordinate copper(II) complex in which the alcoholate is bound to the metal (see Figure 17).

### Reactivity Studies

Several $Cu^{II}$-radical complexes have been found to be active towards oxidation of various substrates; we present here the reactivity of selected complexes belonging to each class. Theoretical approaches to catalytic mechanisms will be presented in the next chapter.

In 1996 Tolman et al. described $[Cu(L^{15})(CH_3CN)]$ as one of the first model complexes for the GO active site.[53] Bulk electrolysis of $[Cu(L^{15})(CH_3CN)]$ at a potential slightly higher than $E_{1/2}$ corresponding to the phenoxyl/phenolate redox couple affords a relatively stable $Cu^{II}$-phenoxyl radical complex. The electrochemical behavior of $[Cu(L^{15})$(benzyl alkoxide)] is characterized by a total loss of reversibility of the redox wave corresponding to the phenoxyl/phenolate couple ($E_p^a$ = –0.01 V vs. $Fc^+$/Fc), as expected for an electrocatalytic process. In addition, bulk electrolysis of $[Cu(L^{15})$(benzyl alcoholate)] affords benzaldehyde in 46% yield, thus showing that the catalyst is only active as its $Cu^{II}$-phenoxyl radical form and that it exhibits a reactivity similar to that of GO towards the oxidation of alcohols.

The mononuclear $Cu^{II}$-diphenolate complex $[Cu(L^{11})]$ described by Wieghardt et al. catalyzes the aerobic oxidation of benzyl alcohol into benzaldehyde with a turnover number of 95 (24 h in the presence of catalytic amounts of base).[51] The proposed mechanism is similar to that reported for GO, in other words the active species is a $Cu^{II}$-phenoxyl radical species. In the presence of copper(I) and $H_2L^{11}$, primary amines with a least one α-H atom undergo an oxidative deamination reaction to yield Schiff base condensation products (17 turnovers in 24 h with benzylamine as substrate). The copper(II) complexes of $H_2L^{11}$ are thus interesting examples of functional models for both GO and copper amine oxidase.

The copper(II) complex $[Cu(L^{12\cdot})]$ {and its zinc analog $[Zn(L^{12\cdot})]$} selectively oxidizes primary alcohols (methanol, ethanol, benzyl alcohol) stoichiometrically under anaerobic conditions in the presence of two equivalents of $NEt_3$ to yield the corresponding aldehyde, two equivalents of $HNEt_3^+$, and a protonated form of the two-electron-reduced catalyst (Figure 17, A).[46] No reaction was observed when using secondary alcohols such as 2-propanol or diphenylcarbinol, or when replacing $[Cu(L^{12\cdot})]$ with $[Cu(L^{12})]$. The mechanism involves reversible binding of an alkoxide ligand to $[Cu(L^{12\cdot})]$ to afford a five-coordinate, square-based-pyramidal complex where the axially bound phenolate is *cis* to the phenoxyl moiety (Figure 17, A). Irreversible oxidation of the substrate into a coordinated ketyl radical anion is the rate-determining step, with a remarkable KIE ($k_H/k_D$) of 54 for the reaction of methanol with $[Cu(L^{12\cdot})]$. The resulting intermediate is proposed to undergo a rapid intramolecular one-electron transfer, with the formation of aldehyde that dissociates. The ultimate electron acceptor is the *o*-diiminoquinone moiety of the doubly protonated ligand. The two-electron-reduced catalyst then reacts with molecular dioxygen to yield $H_2O_2$ in the presence of protons, thus regenerating $[Cu(L^{12\cdot})]$. A copper(II)-coordinated superoxide intermediate is proposed (Figure 17, A). Up to 5000 turnovers in 50 h are achieved for aerobic oxidation of methanol (turnover frequency of 0.03 $s^{-1}$). In contrast, the zinc analog is less efficient, with 170 turnovers achieved

 © 2007 Wiley-VCH Verlag GmbH & Co. KGaA, Weinheim 

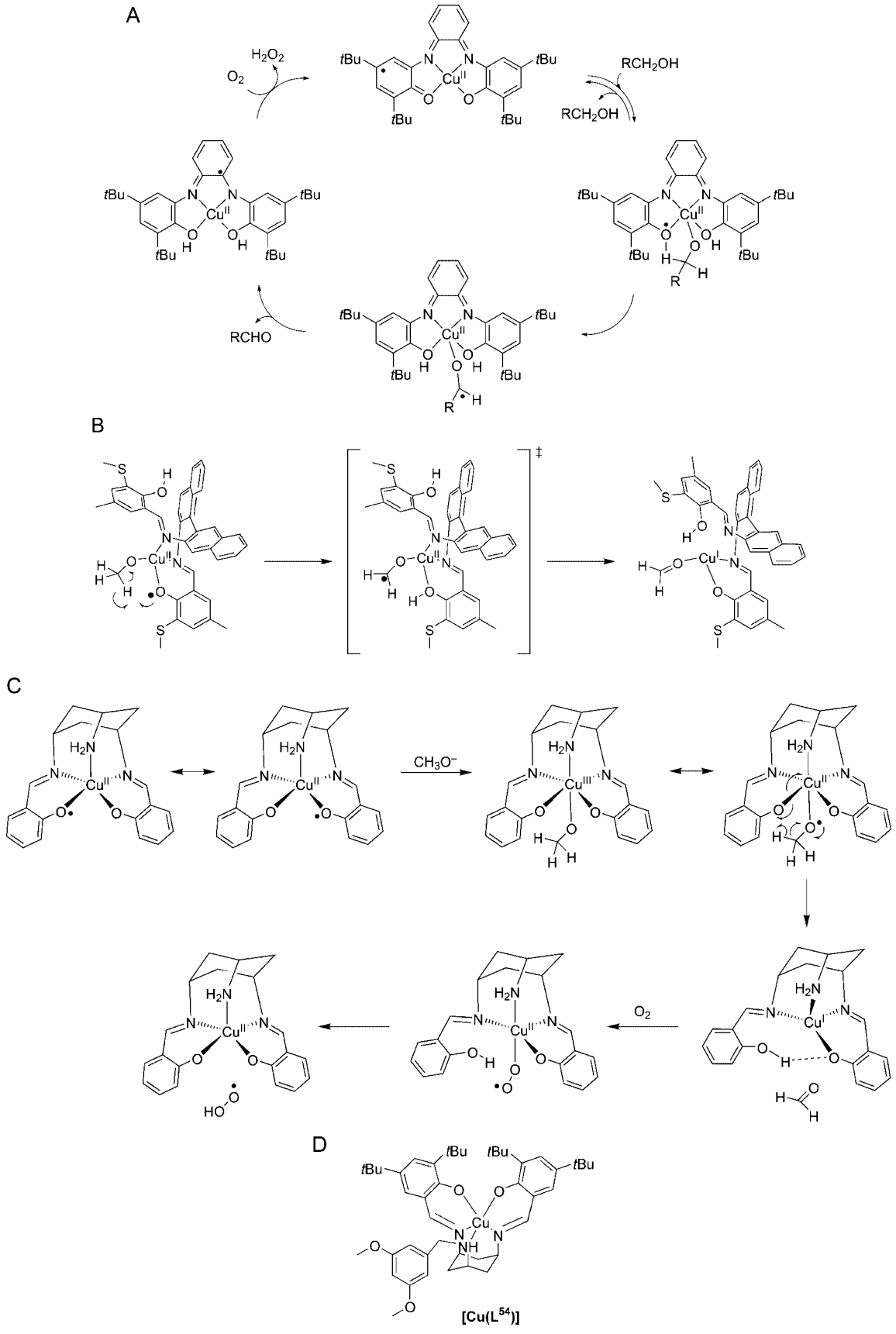


Figure 17. Proposed mechanisms for the catalytic oxidation of alcohols by [Cu($L^{12\cdot}$)] (A), and simplified models of [Cu($L^{2}$)] (B) and [Cu($L^{54}$)] (C) [adapted from ref.[46] (A), ref.[102,103] (B) and ref.[104] (C)]. The formula of [Cu($L^{54}$)] is also shown (D).

 © 2007 Wiley-VCH Verlag GmbH & Co. KGaA, Weinheim 

in 24 h (turnover frequency of 0.002 $s^{-1}$), which is attributed to a slower rate constant for hydrogen abstraction.

Itoh et al. have shown that [Cu($L^{27\cdot}$)($NO_3$)] oxidizes benzyl alcohol stoichiometrically to benzaldehyde following pseudo-first-order kinetics.[100] The $Cu^{I}$-phenol complex of $HL^{27}$ was recovered almost quantitatively at the end of reaction. In addition, a KIE of 8 was reported when $\alpha_D$-benzyl alcohol was used, which shows that hydrogen abstraction is the rate-determining step in the reaction. [Cu($L^{27\cdot}$)($NO_3$)] could thus be considered as a functional model of GO that stores two oxidative equivalents, one at the radical and the other at the copper(II) ion. It also stoichiometrically oxidizes phenols into phenoxyl radicals and 1,4-cyclohexadiene into benzene without a redox reaction at the metal center.[101] Phenol substrates are oxidized much faster than 1,4-cyclohexadiene in spite of the larger bond dissociation energy of the former. In addition, the steric effects of the phenol substituents are significant, with the reactivity order being 2,4,6-tri-*tert*-butylphenol < 2,6-di-*tert*-butylphenol < 2,4-di-*tert*-butylphenol. This strongly suggests that hydrogen atom abstraction from the phenol substrates is significantly enhanced by the coordinative interaction of the OH group to the metal ion center of the complex.

Yamauchi et al.[69] and ourselves[58,67] have reported that $Cu^{II}$-radical complexes of tripodal ligands possessing an $N_2O_2$ donor oxidize unactivated alcohols catalytically in the presence of small amounts of base. Using [Cu($HL^{39\cdot}$)(OAc)] as catalyst, 80 turnovers were achieved in one day for the oxidation of ethanol and 300 for the oxidation of benzyl alcohol, although the secondary alcohol cyclohexanol was not oxidized.[67] This catalyst thus reproduces the chemoselectivity of GO. A KIE was observed for the oxidation of benzyl alcohol, thereby suggesting that the rate-determining step is hydrogen abstraction. Hydrogen peroxide could not be detected, presumably due to its fast decomposition in the basic medium used, although its presence could be detected upon treating $H_2L^{39}$ with CuCl.

Stack et al. have studied the reactivity of [Cu($L^6$)] and [Cu($L^7$)] with benzyl alcohol and 9,10-dihydroanthracene as substrates.[40] Regardless of the substrate or complex, the same overall stoichiometry of the reaction was observed: two equivalents of complex oxidize one equivalent of substrate, in other words the complex is effectively only a one-electron oxidant. More surprisingly, the reaction of benzyl alcohol with [Cu($L^6$)] proceeds 10 times faster than with [Cu($L^7$)] despite the fact that the former is a significantly weaker oxidant ($\Delta E$ = 0.37 V). These differences in rate constants have been interpreted as being due to mechanistic differences between the two reactions: The rate-determining step is a simple bimolecular reaction between [Cu($L^7$)] and benzyl alcohol, while an associative mechanism involving a substrate-binding equilibrium prevails for the reaction of [Cu($L^6$)] with $PhCH_2OH$. The opposite behavior was observed with 9,10-dihydroanthracene as substrate − the simple bimolecular reaction is observed between [Cu($L^6$)] and 9,10-dihydroanthracene and the substrate-binding equilibrium preceding a unimolecular reaction in the reaction of [Cu($L^7$)] with 9,10-dihydroanthracene. Reactions that include a substrate-binding equilibrium are faster than those occurring in simple bimolecular reactions due to the lowering of the entropic cost of the rate-determining steps induced by the substrate-binding equilibrium. The fact that saturation behavior could be observed for the reaction of [Cu($L^7$)] with 9,10-dihydroanthracene indicates that the substrate-binding interaction is not associated with the presence of a polar hydroxyl group but may arise from either π–π stacking interactions or cation–π interactions (a high concentration of substrate may also change the solvent properties and thereby affect the reaction rates). 9,10-Dihydroanthracene reacts 25–300 times faster than benzyl alcohol, as expected for the lower bond dissociation energy of the former substrate. Large kinetic isotope effects were observed for all the substrates ($k_H/k_D > 5$) with a remarkable value of 19 for the reaction of [Cu($L^7$)] with benzyl alcohol. These results show that the rate-determining step in the reaction is the homolytic cleavage of the C–H bond and that deprotonation of the alcoholic substrate probably does not occur prior to hydrogen atom abstraction. Results concerning the rate of reaction with 9,10-dihydroanthracene also indicate that the hydrogen atom abstraction abilities of the two $Cu^{II}$-phenoxyl species are comparable. The products of this hydrogen abstraction step are a highly reactive radical and the protonated form of the copper(II) complexes ([Cu($HL^6$)] or [Cu($HL^7$)]). The activation energies, and thus the rates for atom transfer reactions, were found to be correlated to the strength of the O(phenolate)–H bonds being formed in [Cu($HL^6$)] and [Cu($HL^7$)].

Complex [Cu($L^{6\cdot}$)] thus models the acceleration of the reaction rate upon substrate binding found in GO, although in the enzyme the acceleration is amplified by several orders of magnitude, presumably due to the formation of an extended hydrogen-bond network between the substrate and GO and deprotonation of the substrate by Tyr495 prior to hydrogen atom abstraction, which lowers the bond dissociation energy of its α-C–H bond.

### Theoretical Approaches to Catalytic Mechanisms

Theoretical approaches to the oxidation of methoxide by [Cu($L^{2\cdot}$)][102,103] and [Cu($L^{54\cdot}$)][104] (in their $Cu^{II}$-phenoxyl radical form) have been undertaken. Ab initio molecular dynamics studies on [Cu($L^{2\cdot}$)] have shown that the methoxide adduct is a five-coordinate distorted pyramidal phenoxylcopper(II) complex.[102,103] The methoxide binds in the equatorial plane with a short Cu–O bond (1.93 Å), whereas the phenoxyl becomes an axial ligand with a much longer Cu–O bond (2.54 Å). This optimized structure is in good agreement with the EXAFS data. The unpaired electron switches from the axial to the equatorial position upon protonation of one phenolate (Figure 17, B). The $p_z$ orbital hosting the unpaired electron in this structure is found to be orthogonal to the $d_{x^2-y^2}$ orbital of the copper.[103] In the transition state, the structural rearrangements are concentrated on the substrate, which moves towards the equatorial

 © 2007 Wiley-VCH Verlag GmbH & Co. KGaA, Weinheim 

oxygen. The unpaired electron that was previously located on the phenoxyl oxygen (and sulfur atom) mainly moves to the substrate, which may explain why this system only converts aromatic but not aliphatic alcohols. The electron transfer from the ketyl species to the copper ion then occurs spontaneously upon relaxation, thereby suggesting that hydrogen atom abstraction and electron transfer take place quasi-simultaneously, unlike in GO. A copper(I) compound is obtained as the product of the hydrogen atom abstraction step. Substantial geometric rearrangements are observed upon going from the transition state to this compound: one of the imine nitrogen moves away from the copper in such a way that the whole aromatic system (naphthyl and phenol) lies essentially in the same plane. The $Cu^{I}$ ion in the resulting complex is tightly bound to one imine nitrogen and the aldehyde substrate, with one phenol oxygen being weakly bound as a third ligand. This suggests that release of the substrate is difficult and that molecular oxygen may bind when the aldehyde is still present.

DFT studies on [Cu($L^{54\cdot}$)] have revealed that substrate binding, as a sixth ligand, drives an intramolecular electron transfer that reduces the phenoxyl radical back to phenolate (Figure 17, C).[104] The substrate adduct is therefore formally an octahedral $Cu^{III}$-phenolate species, unlike in GO. This dramatic difference can be explained in terms of a proton transfer that occurs only in GO. Thus, after binding, the substrate transfers its alcohol proton to the axial tyrosinate Tyr495 residue that consequently coordinates only very weakly to afford an almost square-planar copper center (see part A of Figure 2, path 1). In [Cu($L^{54\cdot}$)], proton transfer leading to decoordination of a phenolate ring is prevented by the rigidity of the ligand framework and substrate binding generates an octahedral copper center instead. The substrate adduct of [Cu($L^{54\cdot}$)] also exhibits a large spin density on the methoxide oxygen, which indicates that it should be best formulated as lying between the $Cu^{III}$-OMe and $Cu^{II}$-$OMe^{\cdot}$ limits. In the hydrogen-transfer transition state, the SOMO is shifted to the carbon and rotated so that it points towards the phenolate oxygen. The barrier is 11.9 kcal mol$^{-1}$ above that of GO (estimated with $CH_3OH$ as substrate), which suggests a reduced activity of [Cu($L^{54\cdot}$)] relative to the enzyme and is consistent with a low turnover rate. A weakly bound $Cu^{I}$-aldehyde complex is obtained following the hydrogen atom and electron transfer, then the aldehyde is released and the metallic center is re-oxidized by molecular dioxygen into [Cu($L^{54\cdot}$)].

## Bio-Inspired Systems

### From Coordinated Mono- to Bis(phenoxyl) Radicals

Copper(II)-coordinated bis(phenoxyl) radicals have been described by Wieghardt et al. and ourselves with two types of ligands (TACN and salen).[37,56,57] This choice of ligand was dictated by the geometry of the copper(II) complexes: both phenolate moieties occupy the equatorial positions in the square-pyramidal copper(II)-TACN complex, while a square-planar (slightly distorted towards tetrahedral) environment is observed around the copper(II) ion in salen complexes [phenolate axial ligation consequently does not occur in any of these complexes, unlike copper(II) complexes of tripodal ligands].

The modular macrocycle TACN was used by Wieghardt et al.[56,57] The ligands $H_3L^{18,19}$ (Figure 5)[56] exhibit two one-electron transfer waves assigned to the successive oxidation of each phenolate moiety in their CV curve. The electrochemically generated $Cu^{II}$-phenoxyl complexes [Cu($HL^{18,19\cdot}$)] and [Cu($HL^{18,19\cdot}$)] could be obtained, but it was not possible to obtain the diradical form of [Cu($HL^{18,19\cdot}$)] even by performing controlled potential electrolysis at 243 K. The diradical complex [Cu($L^{17\cdot\cdot}$)] (Figure 18) could be obtained from the ligand $H_2L^{17}$.[57] It exhibits signals in the broad field range at effective $g$ factors close to 5 and 3 in its EPR spectrum. This spectrum has been interpreted by considering a ferromagnetic coupling of $Cu^{II}$ and each of the radicals that dominates the weaker antiferromagnetic radical–radical interaction. Simulation yielded a large $D$ value of 0.4 cm$^{-1}$, in agreement with a strong dipolar interaction between the $Cu^{II}$ and coordinated phenoxyl radicals. This situation thus contrasts sharply with that of the $Cu^{II}$-bis(iminosemiquinonate) diradical complex [Cu($L^{12\cdot\cdot}$)], which exhibits an $S$ = 1/2 ground state.[46]

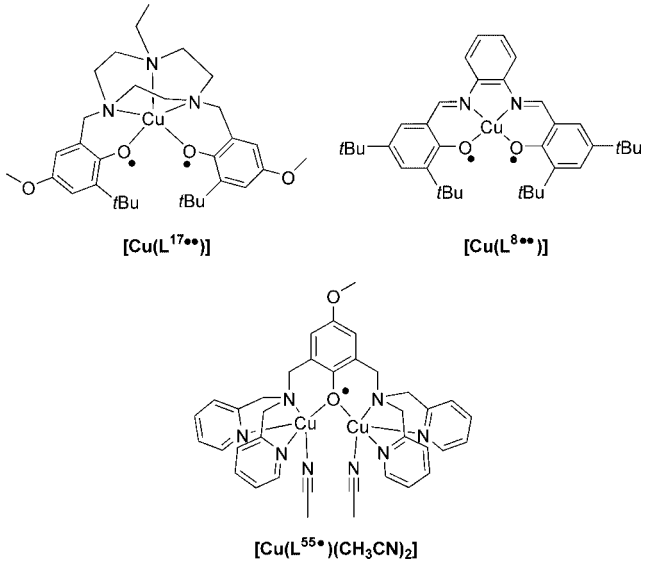


Figure 18. Bio-inspired system formally storing three oxidizing equivalents: [Cu($L^{17\cdot\cdot}$)] (ref.[57]), [Cu($L^{8\cdot\cdot}$)] (ref.[37]), [Cu($L^{55\cdot}$)-$(CH_3CN)_2$] (ref.[73]).

In another approach we have used salen-type ligands to study the respective influence of the hybridization of the nitrogens and flexibility of the linker between these two atoms on the properties of the electrogenerated $Cu^{II}$-phenoxyl and $Cu^{II}$-bis(phenoxyl) radical complexes (Figure 18).[37] The copper(II) complexes used are those of $H_2L^3$, $H_2L^5$, and $H_2L^{7,8}$ (Figure 3). While [Cu($L^7$)] and [Cu($L^8$)] incorporate a rigid linker, [Cu($L^3$)] and [Cu($L^5$)] contain a flexible one. The geometry around the metal ion is planar for [Cu($L^5$)] and [Cu($L^8$)] while it is slightly distorted towards tetrahedral for [Cu($L^3$)] and [Cu($L^7$)].

 © 2007 Wiley-VCH Verlag GmbH & Co. KGaA, Weinheim 

The electrochemically generated monoradical species [Cu(L$^{3\cdot}$)], [Cu(L$^{5\cdot}$)], and [Cu(L$^{7,8\cdot}$)] are relatively stable and X-band EPR-silent at 4–100 K, similar to other Cu$^{II}$-phenoxyl salen complexes,[34,35,39,43] thereby indicating that the phenoxyl moiety remains coordinated to the copper atom. The two-electron-oxidized species exhibit X-band EPR spectra that depend strongly on the ligand structure. The EPR spectra of [Cu(L$^{7\cdot\cdot}$)] and [Cu(L$^{8\cdot\cdot}$)] at 4 K exhibit signals that are distributed over the entire spectral width, similar to the Cu$^{II}$-bis(phenoxyl) radical complex [Cu(L$^{17\cdot\cdot}$)] described by Wieghardt et al.[57] A similar electronic structure is thus proposed, in other words a dominant ferromagnetic coupling between the Cu$^{II}$ and each of the radicals that yields large $D$ values. The EPR spectra of [Cu(L$^{3\cdot\cdot}$)] and [Cu(L$^{5\cdot\cdot}$)] are completely different as they are the superposition of two spectra, one typical of an organic radical (narrow signal at $g$ = 2.005) and the other corresponding to a mononuclear copper(II) complex. The ethyl linker is thus too flexible to maintain both phenoxyl moieties coordinated to the metal ion. The rigid linkers prevent decomplexation, regardless of whether the geometry around the metal center is planar {[Cu(L$^{8\cdot\cdot}$)]} or distorted towards tetrahedral {[Cu(L$^{7\cdot\cdot}$)]}.

### A Bridging Phenoxyl Radical in Dicopper(II) Complexes

In order to get a μ-phenoxyldicopper(II) system, a building block comprising at least one μ-phenolatedicopper(II) entity has to be oxidized. As discussed above, tripodal ligands show a marked tendency to assemble as dimers (of formula [Cu(L$^{N_3O}$)]$_2$ and [Cu(L$^{N_2O_2}$)]$_2$) that possess such a core when the steric bulk at the *o*-position of the phenolate is small to moderate (Figure 7). Unfortunately, we have shown that oxidation of [Cu(L$^{30,31}$)]$_2$ affords the corresponding mononuclear [Cu(L$^{30,31\cdot}$)(CH$_3$CN)] species,[63] while oxidation of [Cu(L$^{38,41}$)]$_2$ takes place at the nonbridging phenolate group to afford dimeric structures [Cu(L$^{38,41\cdot}$)]$_2$ with two Cu$^{II}$-phenoxyl radical molecules bridged by phenolato groups.[58,69] We have therefore synthesized the dicopper(II) complexes of the dinucleating ligand HL$^{55}$.[73] Two complexes were isolated, whose structures depend on the amount of NEt$_3$ added during the synthesis. [Cu(L$^{55}$)(CH$_3$CN)$_2$] was obtained in the presence of a single equivalent. This complex contains two copper(II) atoms with square-pyramidal geometries that are coordinated to one μ-phenolate oxygen and three nitrogens from the ligand, and one nitrogen from an exogenous acetonitrile molecule. The metal centers are separated by 4.059(5) Å and interact magnetically, as shown by the spin triplet resonance in the EPR spectrum of this complex. [Cu(L$^{55}$)(μ-OH)] was isolated when two molar equivalents of NEt$_3$ were used. Its structure differs from that of [Cu(L$^{55}$)(CH$_3$CN)$_2$] in several points: the geometry around the copper atom is trigonal bipyramidal, the exogenous acetonitrile ligands are replaced by a single μ-OH molecule, and the intermetallic distance is much shorter [2.980(9) Å]. Consequently, the interaction between the copper(II) atoms in [Cu(L$^{55}$)(μ-OH)] is strongly antiferromagnetic, as opposed to the ferromagnetic interaction observed in [Cu(L$^{55}$)(CH$_3$CN)$_2$]. These two complexes are oxidized to the μ-phenoxyl radical species [Cu(L$^{55\cdot}$)(μ-OH)] and [Cu(L$^{55\cdot}$)(CH$_3$CN)$_2$] over the same potential range (0.36–0.45 V). The former was found to be much less stable than the latter (the half-lives are <20 s and 22.3 min, respectively, at 298 K), thus showing that the reactivity is finely tuned by the nature of the coordinating ligand. The EPR spectrum of the most stable complex [Cu(L$^{55\cdot}$)(CH$_3$CN)$_2$] at 4 K exhibits a $\Delta M_S = \pm 3$ transition at $g$ = 8 that is the signature of an $S$ = 3/2 system. Its temperature dependence shows that it corresponds to the ground state. The $D$ value (–0.056 cm$^{-1}$) is close to that reported for an excited $S$ = 3/2 spin state in a triangular tricopper(II) system, but much higher than those reported for triradicals and lower than those reported for copper(II)-coordinated bis(phenoxyl) radicals. Since tyrosyl radicals are ubiquitous in metalloenzymes, such species could be biologically relevant. In addition, Karlin et al. have recently proposed the involvement of such species in a ligand cross-linking reaction promoted by a hydroperoxidodicopper(II) complex.[105]

## Conclusions

The biomimetic approach to the GO active site developed concomitantly by a number of research groups has led to the synthesis and characterization of a wide range of Cu$^{II}$-phenoxyl complexes. Enormous progress has thus been made from an entity that was unknown in coordination chemistry ten years ago. Many features of the GO active site have been reproduced successfully, providing valuable information on its spectroscopic signature, structure, and even reactivity. Replication of its oxidative chemistry has been achieved, although this reactivity is limited compared to that of the enzyme. Recent results in this field concerning bio-inspired complexes of aminyl radical ligands[106,107] or theoretical calculations[108] suggest that a catalytic efficiency approaching that of the enzyme is conceivable. This bio-inorganic story concerning coordinated radicals is thus far from finished, and the number of articles concerning radical metalloenzymes, specifically new copper(II)-radical metalloenzymes,[109–111] and metal-radical complexes will increase further in the near future.

## Acknowledgments

I am grateful to Prof. J.-L. Pierre for his interest in this work and fruitful discussions.

[1] J. L. Pierre, *Chem. Soc. Rev.* **2000**, *29*, 251–257.
[2] J. A. Stubbe, W. Van Der Donk, *Chem. Rev.* **1998**, *98*, 705–762.
[3] M. S. Rodgers, D. M. Dooley, *Curr. Opin. Chem. Biol.* **2003**, *7*, 189–196.
[4] M. Fontecave, J. L. Pierre, *Bull. Soc. Chim. Fr.* **1996**, *133*, 653–660.
[5] B. A. Jazdzewski, W. B. Tolman, *Coord. Chem. Rev.* **2000**, *200–202*, 633–685.

 © 2007 Wiley-VCH Verlag GmbH & Co. KGaA, Weinheim 

[6] S. Itoh, M. Taki, S. Fukuzumi, *Coord. Chem. Rev.* **2000**, *198*, 3–20.
[7] P. Chaudhuri, K. Wieghardt, *Prog. Inorg. Chem.* **2001**, *50*, 151–216.
[8] P. Chaudhuri, K. Wieghardt, T. Weyhermüller, T. K. Paine, S. Mukherjee, C. Mukherjee, *Biol. Chem.* **2005**, *386*, 1023–1033.
[9] C. D. Borman, C. G. Saysell, A. Sokolowski, M. B. Twitchett, C. Wright, A. G. Sykes, *Coord. Chem. Rev.* **1999**, *190–192*, 771–779.
[10] M. J. McPherson, M. R. Parsons, R. K. Spooner, C. M. Wilmot, *Handbook of Metalloproteins*, John Wiley and Sons, Chichester, **2001**, 1272–1283.
[11] J. W. Whittaker, *Chem. Rev.* **2003**, *103*, 2347–2363.
[12] N. Ito, S. E. V. Philips, C. Stevens, Z. B. Ogel, M. J. McPherson, J. N. Keen, K. D. S. Yadav, P. F. Knowles, *Nature* **1991**, *350*, 87–90.
[13] N. Ito, S. E. V. Philips, K. D. S. Yadav, P. F. Knowles, *J. Mol. Biol.* **1994**, *238*, 794–814.
[14] In order to facilitate comparison between the systems, all electrochemical potentials are given relative to the $Fc^+/Fc$ reference. When potentials have been reported relative to other standards, corrections are applied according to the following references: N. G. Connelly, W. E. Geiger, *Chem. Rev.* **1996**, *96*, 877–910; V. V. Pavlishchuk, A. W. Addison, *Inorg. Chim. Acta* **2000**, *298*, 97–102. Differences in solvent, electrolyte, and ionic strength may, however, complicate the comparison.
[15] C. Wright, A. G. Sykes, *J. Inorg. Biochem.* **2001**, *85*, 237–243.
[16] M. M. Whittaker, C. A. Ekberg, J. Peterson, M. S. Sendova, E. P. Day, J. W. Whittaker, *J. Mol. Catal. B* **2000**, *8*, 3–15.
[17] D. Rokhsana, D. M. Dooley, R. K. Szilagyi, *J. Am. Chem. Soc.* **2006**, ASAP.
[18] M. M. Whittaker, J. W. Whittaker, *J. Biol. Chem.* **1988**, *263*, 6074–6080.
[19] M. M. Whittaker, D. P. Ballou, J. W. Whittaker, *Biochemistry* **1998**, *37*, 8426–8436.
[20] B. P. Branchaud, M. P. Montague-Smith, D. J. Kosman, F. R. McLaren, *J. Am. Chem. Soc.* **1993**, *115*, 798–800.
[21] R. M. Wachter, B. P. Branchaud, *Biochim. Biophys. Acta* **1998**, *1384*, 43–54.
[22] M. M. Whittaker, J. W. Whittaker, *Biophys. J.* **1993**, *64*, 762–772.
[23] F. Himo, L. A. Eriksson, F. Maseras, P. E. M. Siegbahn, *J. Am. Chem. Soc.* **2000**, *122*, 8031–8036.
[24] B. E. Turner, B. P. Branchaud, *Bioorg. Med. Chem. Lett.* **1999**, *9*, 3341–3346.
[25] R. M. Wachter, B. P. Branchaud, *Biochim. Biophys. Acta* **1998**, *1384*, 43–54.
[26] M. M. Whittaker, J. W. Whittaker, *Biochemistry* **2001**, *40*, 7140–7148.
[27] S. G. Minasian, M. M. Whittaker, J. W. Whittaker, *Biochemistry* **2004**, *43*, 13683–13693.
[28] S. J. Firbank, M. S. Rogers, C. M. Wilmot, D. M. Dooley, M. A. Halcrow, P. F. Knowles, M. J. McPherson, S. E. V. Phillips, *Proc. Natl. Acad. Sci. USA* **2001**, *98*, 12932–12937.
[29] M. S. Rogers, A. J. Baron, M. J. McPherson, P. F. Knowles, D. M. Dooley, *J. Am. Chem. Soc.* **2000**, *122*, 990–991.
[30] M. M. Whittaker, J. W. Whittaker, *J. Biol. Chem.* **2003**, *278*, 22090–22101.
[31] E. R. Altwicker, *Chem. Rev.* **1967**, *67*, 475–531.
[32] J. G. Radziszewski, M. Gil, A. Gorski, J. Spanget-Larsen, J. Waluk, B. J. Mroz, *J. Chem. Phys.* **2001**, *115*, 9733–9738.
[33] N. Katajima, K. Whang, Y. Moro-Oka, A. Uchida, Y. Sasada, *J. Chem. Soc., Chem. Commun.* **1986**, 1504–1505.
[34] Y. Wang, T. D. P. Stack, *J. Am. Chem. Soc.* **1996**, *118*, 13097–13098.
[35] Y. Wang, J. L. Dubois, B. Hedman, K. O. Hodgson, T. D. P. Stack, *Science* **1998**, *279*, 537–540.
[36] E. Saint-Aman, S. Ménage, J.-L. Pierre, E. Defrancq, G. Gellon, *New J. Chem.* **1998**, *22*, 393–394.
[37] F. Thomas, O. Jarjayes, C. Duboc, C. Philouze, E. Saint-Aman, J.-L. Pierre, *Dalton Trans.* **2004**, 2662–2669.
[38] M. Vaidyanathan, M. Palaniandavar, R. S. Gopalan, *Ind. J. Chem.* **2003**, *42A*, 2210–2222.
[39] R. C. Pratt, T. D. P. Stack, *J. Am. Chem. Soc.* **2003**, *125*, 8716–8717.
[40] R. C. Pratt, T. D. P. Stack, *Inorg. Chem.* **2005**, *44*, 2367–2375.
[41] I. Sylvestre, J. Wolowska, C. A. Kilner, E. J. L. McInnes, M. A. Halcrow, *Dalton Trans.* **2005**, 3241–3249.
[42] Y. Pellegrin, A. Quaranta, P. Dorlet, M.-F. Charlot, W. Leibl, A. Aukauloo, *Chem. Eur. J.* **2005**, *11*, 3698–3710.
[43] A. dos Anjos, A. J. Bortoluzzi, R. E. H. M. B. Osorio, R. A. Peralta, G. R. Friedermann, A. S. Mangrich, A. Neves, *Inorg. Chem. Commun.* **2005**, *8*, 249–253.
[44] P. Chaudhuri, M. Hess, U. Flörke, K. Wieghardt, *Angew. Chem.* **1998**, *110*, 2340–2343; *Angew. Chem. Int. Ed.* **1998**, *37*, 2217–2220.
[45] P. Chaudhuri, M. Hess, T. Weyhermüller, K. Wieghardt, *Angew. Chem.* **1999**, *111*, 1165–1168; *Angew. Chem. Int. Ed.* **1999**, *38*, 1095–1098.
[46] P. Chaudhuri, M. Hess, J. Müller, K. Hildenbrandt, E. Bill, T. Weyhermüller, K. Wieghardt, *J. Am. Chem. Soc.* **1999**, *121*, 9599–9610.
[47] P. Chaudhuri, C. N. Nazari, E. Bill, E. Bothe, T. Weyhermüller, K. Wieghardt, *J. Am. Chem. Soc.* **2001**, *123*, 2213–2223.
[48] T. Kruse, T. Weyhermüller, K. Wieghardt, *Inorg. Chim. Acta* **2002**, *331*, 81–89.
[49] S. Mukherjee, E. Rentschler, T. Weyhermüller, K. Wieghardt, P. Chaudhuri, *Chem. Commun.* **2003**, 1828–1829.
[50] K. S. Min, T. Weyhermüller, E. Bothe, K. Wieghardt, *Inorg. Chem.* **2004**, *43*, 2922–2931.
[51] T. K. Paine, T. Weyhermüller, K. Wieghardt, P. Chaudhuri, *Dalton Trans.* **2004**, 2092–2101.
[52] J. Müller, T. Weyhermüller, E. Bill, P. Hildebrandt, L. Ould-Moussa, T. Glaser, K. Wieghardt, *Angew. Chem.* **1998**, *110*, 637–640; *Angew. Chem. Int. Ed.* **1998**, *37*, 616–619.
[53] J. A. Halfen, V. G. Young Jr, W. B. Tolman, *Angew. Chem.* **1998**, *108*, 1832–1835; *Angew. Chem. Int. Ed. Engl.* **1996**, *35*, 1687–1690.
[54] J. A. Halfen, B. A. Jazdzewski, S. Mahapatra, L. M. Berreau, E. C. Wilkinson, L. Que Jr, W. B. Tolman, *J. Am. Chem. Soc.* **1997**, *119*, 8217–8227.
[55] B. A. Jazdzewski, A. M. Reynolds, P. L. Holland, V. G. Young Jr, S. Kaderli, A. D. Zuberbühler, W. B. Tolman, *J. Biol. Inorg. Chem.* **2003**, *8*, 381–393.
[56] A. Sokolowski, H. Leutbecher, T. Weyhermüller, R. Schnepf, E. Bothe, E. Bill, P. Hildebrandt, K. Wieghardt, *J. Biol. Inorg. Chem.* **1997**, *2*, 444–453.
[57] E. Bill, J. Müller, T. Weyhermüller, K. Wieghardt, *Inorg. Chem.* **1999**, *38*, 5795–5802.
[58] A. Philibert, F. Thomas, C. Philouze, S. Hamman, E. Saint-Aman, J. L. Pierre, *Chem. Eur. J.* **2003**, *9*, 3803–3812.
[59] Y. Shimazaki, S. Huth, S. Hirota, O. Yamauchi, *Bull. Chem. Soc. Jpn.* **2000**, *73*, 1187–1195.
[60] F. Michel, F. Thomas, C. Philouze, S. Hamman, E. Saint-Aman, J. L. Pierre, unpublished results.
[61] S. Itoh, M. Taki, H. Kumei, S. Takayama, S. Nagatomo, T. Kitagawa, N. Sakurada, R. Arakawa, S. Fukuzumi, *Inorg. Chem.* **2000**, *39*, 3708–3711.
[62] M. Taki, H. Hattori, T. Osako, S. Nagatomo, M. Shiro, T. Kitagawa, S. Itoh, *Inorg. Chim. Acta* **2004**, *357*, 3369–3381.
[63] F. Michel, F. Thomas, S. Hamman, E. Saint-Aman, C. Bucher, J. L. Pierre, *Chem. Eur. J.* **2004**, *10*, 4115–4125.
[64] F. Michel, S. Hamman, F. Thomas, C. Philouze, I. Gautier-Luneau, J. L. Pierre, *Chem. Commun.* **2006**, 4122–4124.
[65] D. Zurita, I. Gautier-Luneau, S. Ménage, J. L. Pierre, E. Saint-Aman, *J. Biol. Inorg. Chem.* **1997**, *2*, 46–55.
[66] Y. Shimazaki, S. Huth, A. Odani, O. Yamauchi, *Angew. Chem.* **2000**, *112*, 1732–1735; *Angew. Chem. Int. Ed.* **2000**, *39*, 1666–1669.


 © 2007 Wiley-VCH Verlag GmbH & Co. KGaA, Weinheim 

[67] F. Thomas, G. Gellon, I. Gautier-Luneau, E. Saint-Aman, J. L. Pierre, *Angew. Chem.* **2002**, *114*, 3173–3176; *Angew. Chem. Int. Ed.* **2002**, *41*, 3047–3050.
[68] M. Taki, H. Kumei, S. Nagatomo, T. Kitagawa, S. Itoh, S. Fukuzumi, *Inorg. Chim. Acta* **2000**, *300–302*, 622–632.
[69] Y. Shimazaki, S. Huth, S. Hirota, O. Yamauchi, *Inorg. Chim. Acta* **2002**, *331*, 168–177.
[70] The value of $\tau$ is zero for a perfect square pyramid and unity for a trigonal bipyramid. See: A. W. Addison, T. N. Rao, J. Reedijk, J. van Rijn, G. C. Verschoor, *J. Chem. Soc., Dalton Trans.* **1984**, 1349–1356.
[71] H. Adams, N. A. Bailey, I. K. Campbell, D. E. Fenton, Q.-Y. He, *J. Chem. Soc., Dalton Trans.* **1996**, 2233–2237.
[72] M. Vaidyanathan, R. Viswanathan, M. Palaniandavar, T. Balasubramanian, P. Prabhaharan, T. P. Muthiah, *Inorg. Chem.* **1998**, *37*, 6418–6427.
[73] F. Michel, S. Torelli, F. Thomas, C. Duboc, C. Philouze, C. Belle, S. Hamman, E. Saint-Aman, J. L. Pierre, *Angew. Chem.* **2005**, *117*, 442–445; *Angew. Chem. Int. Ed.* **2005**, *44*, 438–441.
[74] S. Itoh, S. Takayama, R. Arakawa, A. Furuta, M. Komatsu, A. Ishida, S. Takamuku, S. Fukuzumi, *Inorg. Chem.* **1997**, *36*, 1407–1416.
[75] D. Zurita, C. Scheer, J. L. Pierre, E. Saint-Aman, *J. Chem. Soc., Dalton Trans.* **1996**, 4331–4336.
[76] C. Ochs, F. E. Hahn, R. Fröhlich, *Eur. J. Inorg. Chem.* **2001**, 2427–2436.
[77] A. J. Bard, L. R. Faulkner, *Electrochemical Methods, Fundamentals and Applications*, Wiley, New York, **1980**.
[78] K. Yamato, T. Inada, M. Doe, A. Ichimura, T. Takui, Y. Kojima, T. Kikunaga, N. Yanagihara, T. Onaka, S. Yano, *Bull. Chem. Soc. Jpn.* **2000**, *73*, 903–912.
[79] A. Berkessel, M. Doucet, S. Bulat, K. Glaubitz, *Biol. Chem.* **2005**, *386*, 1035–1041.
[80] M. A. Hossain, F. Thomas, S. Hamman, E. Saint-Aman, D. Boturyn, P. Dumy, J.-L. Pierre, *J. Pept. Sci.* **2006**, *12*, 612–619.
[81] O. Sénèque, M. Campion, B. Douziech, M. Giorgi, Y. Le Mest, O. Reinaud, *Dalton Trans.* **2003**, 4216–4218.
[82] M. L. McGlashen, D. D. Eads, T. Spiro, J. W. Whittaker, *J. Phys. Chem.* **1995**, *99*, 4918–4922.
[83] M. A. Halcrow, L. M. L. Chia, X. Liu, E. J. L. McInnes, L. J. Yellowlees, F. E. Mabbs, J. E. Davies, *Chem. Commun.* **1998**, 2465–2466.
[84] M. A. Halcrow, L. M. L. Chia, X. Liu, E. J. L. McInnes, L. J. Yellowlees, F. E. Mabbs, I. J. Scowen, M. McPartlin, J. E. Davies, *J. Chem. Soc., Dalton Trans.* **1999**, 1753–1762.
[85] R. C. Pratt, L. M. Mirica, T. D. P. Stack, *Inorg. Chem.* **2004**, *43*, 8030–8039.
[86] X. Liu, E. J. L. McInnes, C. A. Kilner, M. Thornton-Pett, M. A. Halcrow, *Polyhedron* **2001**, *20*, 2889–2900.
[87] X. Liu, S. A. Barrett, C. A. Kilner, M. Thornton-Pett, M. A. Halcrow, *Tetrahedron* **2002**, *58*, 603–611.
[88] M. A. Halcrow, E. J. L. McInnes, F. E. Mabbs, I. J. Scowen, M. McPartlin, H. R. Powell, J. E. Davies, *J. Chem. Soc., Dalton Trans.* **1997**, 4025–4035.
[89] M. A. Halcrow, N. L. Cromhout, P. R. Raithby, *Polyhedron* **1997**, *16*, 4257–4264.
[90] X. Liu, L. M. L. Chia, C. A. Kilner, L. J. Yellowlees, M. Thornton-Pett, S. Trofimenko, M. A. Halcrow, *Chem. Commun.* **2000**, 1947–1948.
[91] R. Uma, R. Viswanathan, M. Palaniandavar, M. Lakshminarayanan, *J. Chem. Soc., Dalton Trans.* **1994**, 1219–1226.
[92] H. Adams, N. A. Bailey, C. O. Rodriguez de Barbarin, D. E. Fenton, Q.-Y. He, *J. Chem. Soc., Dalton Trans.* **1995**, 2323–2331.
[93] F. Michel, F. Thomas, S. Hamman, C. Philouze, E. Saint-Aman, J.-L. Pierre, *Eur. J. Inorg. Chem.* **2006**, 3684–3696.
[94] K. D. Karlin, B. I. Cohen, J. C. Hayes, A. Farooq, J. Zubieta, *Inorg. Chem.* **1987**, *26*, 147–153.
[95] For recent articles see: S. Mukherjee, E. Rentschler, T. Weyhermüller, K. Wieghardt, P. Chaudhuri, *Chem. Commun.* **2003**, 1828–1829; K. Sik Min, T. Weyhermüller, K. Wieghardt, *Dalton Trans.* **2003**, 1126–1132; S. Mukherjee, T. Weyhermüller, K. Wieghardt, P. Chaudhuri, *Dalton Trans.* **2003**, 3483–3485; P. Ghosh, E. Bill, T. Weyhermüller, K. Wieghardt, *J. Am. Chem. Soc.* **2003**, *125*, 3967–3979; K. Sik Min, T. Weyhermüller, K. Wieghardt, *Dalton Trans.* **2004**, 178–186; S. Mukherjee, T. Weyhermüller, E. Bothe, K. Wieghardt, P. Chaudhuri, *Dalton Trans.* **2004**, 3842–3853; K. S. Min, T. Weyhermüller, E. Bothe, K. Wieghardt, *Inorg. Chem.* **2004**, *43*, 2922–2931; K. Chlopek, E. Bill, T. Weyhermüller, F. Neese, K. Wieghardt, *Inorg. Chem.* **2005**, *44*, 3636–3656; C. Mukherjee, T. Weyhermüller, K. Wieghardt, P. Chaudhuri, *Dalton Trans.* **2006**, 2169–2171; K. Chlopek, E. Bothe, F. Neese, T. Weyhermüller, K. Wieghardt, *Inorg. Chem.* **2006**, *45*, 6298–6307.
[96] A. Sokolowski, E. Bothe, E. Bill, T. Weyhermüller, K. Wieghardt, *Chem. Commun.* **1996**, 1671–1672.
[97] L. Benisvy, A. J. Blake, D. Collison, E. S. Davies, C. D. Garner, E. J. L. McInnes, J. McMaster, G. Whittaker, C. Wilson, *Chem. Commun.* **2001**, 1824–1825.
[98] L. Benisvy, A. J. Blake, D. Collison, E. S. Davies, C. D. Garner, E. J. L. McInnes, J. McMaster, G. Whittaker, C. Wilson, *Dalton Trans.* **2003**, 1975–1985.
[99] A. K. Nairn, S. J. Archibald, R. Bhalla, B. C. Gilbert, E. J. MacLean, S. J. Teat, P. H. Walton, *Dalton Trans.* **2006**, *1*, 172–176.
[100] S. Itoh, M. Taki, S. Takayama, S. Nagatomo, T. Kitagawa, N. Sakurada, R. Arakawa, S. Fukuzumi, *Angew. Chem.* **1999**, *111*, 2944–2946; *Angew. Chem. Int. Ed.* **1999**, *38*, 2774–2776.
[101] M. Taki, H. Kumei, S. Itoh, S. Fukuzumi, *J. Inorg. Biochem.* **2000**, *78*, 1–5.
[102] U. Rothlisberger, P. Carloni, *Int. J. Quant. Chem.* **1999**, *73*, 209–218.
[103] U. Rothlisberger, P. Carloni, K. Doclo, M. Parrinello, *J. Biol. Inorg. Chem.* **2000**, *5*, 236–250.
[104] E. Zueva, P. H. Walton, J. E. McGrady, *Dalton Trans.* **2006**, *1*, 159–167.
[105] L. Li, N. Sarjeant, K. D. Karlin, *Inorg. Chem.* **2006**, *45*, 7160–7172.
[106] T. Büttner, J. Geier, G. Frison, J. Harmer, C. Calle, A. Schweiger, H. Schönberg, H. Grützmacher, *Science* **2005**, *307*, 235–238.
[107] H. Grützmacher, personal communication.
[108] L. Guidoni, K. Spiegel, M. Zumstein, U. Röthlisberger, *Angew. Chem.* **2004**, *116*, 3348–3351; *Angew. Chem. Int. Ed.* **2004**, *43*, 3286–3289.
[109] M. M. Whittaker, P. J. Kersten, N. Nakamura, J. Sandres-Loehr, E. S. Schweizer, J. W. Whittaker, *J. Biol. Chem.* **1996**, *271*, 681–687.
[110] M. M. Whittaker, P. J. Kersten, D. Cullen, J. W. Whittaker, *J. Biol. Chem.* **1999**, *274*, 36226–36232.
[111] M. M. Whittaker, J. W. Whittaker, *Arch. Biochem. Biophys.* **2006**, *452*, 108–118.

Received: November 21, 2006
Published Online: April 13, 2007

 © 2007 Wiley-VCH Verlag GmbH & Co. KGaA, Weinheim 

DOI: 10.1002/ejic.200700295

# Preparation and Molecular Structures of Stable Bis(germylenes) with Pincer Topology

F. Ekkehardt Hahn,*[a] Alexander V. Zabula,[a] Tania Pape,[a] and Alexander Hepp[a]

**Keywords:** N-Heterocycles / Germylenes / Pincer ligands

Benzannulated N-heterocyclic bis(germylenes) with pincer ligand topology have been prepared by the reaction of *N*,*N*′,*N*′′,*N*′′′-tetralithiated tetraamines with $GeCl_2$·1,4-dioxane or by the transamination reaction between a tetraamine and $Ge[N(SiMe_3)_2]_2$. X-ray diffraction studies have shown, that the bis(germylenes) exist as monomers in the solid state. Significant intramolecular Ge···Ge and Ge···N interactions have been observed for the lutidine-bridged bis(germylene). (© Wiley-VCH Verlag GmbH & Co. KGaA, 69451 Weinheim, Germany, 2007)

## Introduction

Polydentate N-heterocyclic carbene (NHC) ligands[1] containing two imidazolin-2-ylidene[2] or benzimidazolin-2-ylidene[3] donor groups, which are capable of forming chelate complexes including tridentate derivatives with pincer topology,[4] are known. In addition, some tris(imidazolin-2-ylidenes)[5] and complexes with cyclic tetrakis(benzimidazolin-2-ylidene)[6] and [11]ane-$P_2C^{NHC}$ ligands[7] have been described. Much less is known about polydentate silylenes, germylenes and stannylenes which can act as chelate ligands, although the monodentate derivatives have been prepared.[8–10]

Previously we described the preparation and coordination chemistry of germanium analogues of benzannulated N-heterocyclic bis(carbenes) in which two benzimidazolin-2-germylene moieties are linked together with an aryl or an alkyl group.[11] It has been demonstrated that these bis(germylenes) can act as bidentate chelate ligands. Continuing our investigations in this field, we report now on the preparation of the N-heterocyclic benzannulated bis(germylenes) with pincer topology which are potentially tridentate ligands.

## Results and Discussion

The N-heterocyclic bis(germylenes) were obtained from the tetraamines **2a** and **2b** which were prepared by reduction of the carbonyl groups in the corresponding tetraamides **1a** and **1b** (Scheme 1). The tetraamides are obtained by acylation of *N*-(*ortho*-aminophenyl)amides with benzene- (**1a**) or lutidine-2,6-bis(carboxylic chlorides) (**1b**) in the presence of $Et_3N$. The bridging unit present in the tetraamides determined which reducing agent had to be used in the subsequent reaction. Reduction of the carbonyl groups in the phenylene-bridged tetraamide **1a** was achieved with $AlH_3$ in THF at ambient temperature. The four carbonyl groups in tetraamide **1b** were reduced in good yield (81%) by an excess of freshly prepared $BH_3$ in THF.

The bis(germylene) **3** was obtained by lithiation of the corresponding tetraamine **2a** at –78 °C in THF followed by the reaction of the generated organolithium compound with $GeCl_2$·1,4-dioxane (Scheme 2). An analogous reaction sequence gave also the bis(germylene) **4**, but the product was quite impure and the overall yield was finally less than 30% after multiple recrystallization steps. The yield of bis(germylene) **4** could be impoved significantly to 60–65% by reaction of the tetraamine **2b** with $Ge[N(SiMe_3)_2]_2$ in boiling THF.

Bis(germylene) **3** was crystallized from hexane. The structure analysis shows monomeric units of the bis(germylene) which exhibit no significant inter- or intramolecular interactions (Figure 1). Bond lengths and angles in **3** are similar to those reported for a monodentate benzannulated germylene[9e] and other related bis(germylenes).[11] The nitrogen atoms are planarized as was observed for the analogous benzannulated N-heteroclic carbenes.[12] The shortest distance between two germanium atoms is the intermolecular separation between Ge1 and Ge2 [4.226(5) Å] which is too long to be regarded as an interaction. The lack of Ge···Ge interactions in **3** is possibly caused by the sterically demanding *N*-substituents. We have observed such Ge···Ge interactions in bis(germylenes) with sterically less demanding *N*-substituents.[11]

The molecular structure of bis(germylene) **4** containing a lutidine bridge between the germylene units is depicted in Figure 2. Its conformation is distincly different to that of **3**. While no significant intermolecular interactions were noticed, short intramolecular Ge···Ge and Ge···N contacts

[a] Institut für Anorganische und Analytische Chemie der Westfälischen Wilhelms-Universität Münster,
Corrensstrasse 36, 48149 Münster, Germany
Fax: +49-251-83-33108
E-mail: fehahn@uni-muenster.de

 © 2007 Wiley-VCH Verlag GmbH & Co. KGaA, Weinheim InterScience 

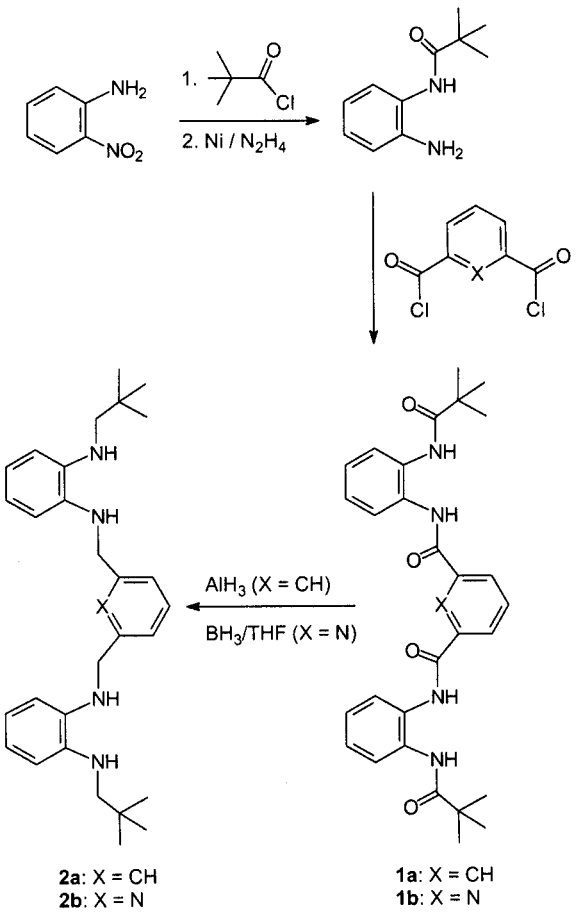


Scheme 1. Preparation of compounds **1a**, **1b** and **2a**, **2b**.

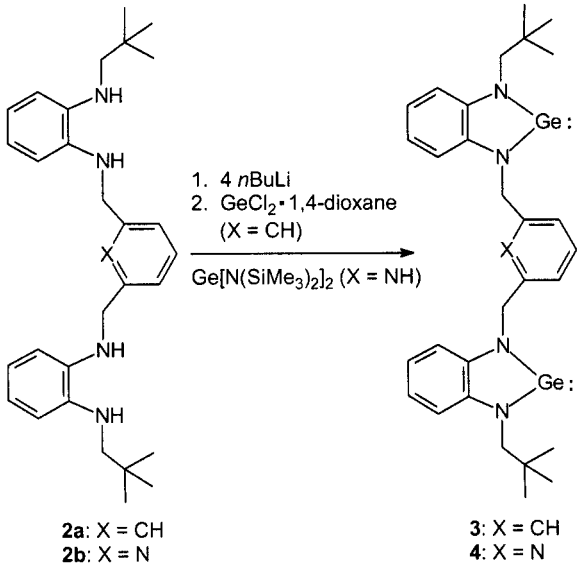


Scheme 2. Preparation of bis(germylenes) **3** and **4**.

were found in the molecular structure of **4**. The Ge1···Ge2 separation is 3.041(5) Å which is significantly shorter than twice the van der Waals radius of the germanium atom.[13] It is also shorter than the Ge···Ge separation which we found for alkyl-bridged bis(germylenes) [3.577(2) Å].[11] The

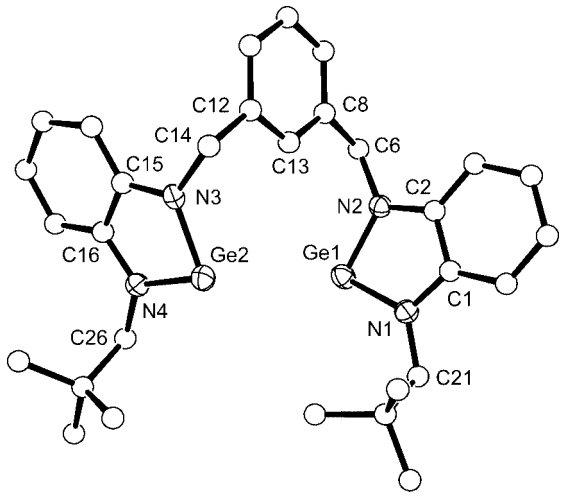


Figure 1. Molecular structure of **3**. Selected bond lengths [Å] and angles [°]: Ge1–N1 1.861(2), Ge1–N2 1.852(2), Ge2–N3 1.851(2), Ge2–N4 1.859(2), N1–C1 1.396(3), N1–C21 1.469(4), N2–C2 1.384(3), N2–C7 1.462(3), N3–C15 1.381(3), N3–C14 1.460(3), N4–C16 1.395(3), N4–C26 1.469(3), C1–C2 1.415(4), C15–C16 1.408(4); N1–Ge1–N2 85.05(10), N3–Ge2–N4 85.05(10), Ge1–N1–C1 114.0(2), Ge1–N2–C2 114.5(2), Ge2–N3–C15 114.2(2), Ge2–N4–C16 114.0(2).

geometry of the $N_2Ge1\cdots Ge2N_2$ moiety is similar to the distorted *trans*-bent arrangement found for E=E double bonds of heavier homologues of alkenes. The intramolecular distances Ge1···N3 [3.386(7) Å] and Ge2···N3 [3.154(7) Å] are again shorter than those found in bimolecular aggregates of bis(germylene) with intermolecular Ge···N separations of about 3.53 Å.[11]

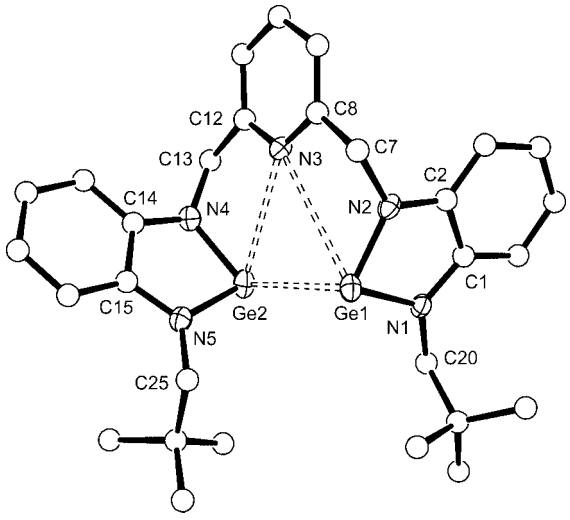


Figure 2. Molecular structure of **4**. Selected bond lengths [Å] and angles [°]: Ge1–N1 1.862(3), Ge1–N2 1.847(3), Ge2–N4 1.845(3), Ge2–N5 1.862(3), N1–C1 1.386(5), N1–C20 1.462(5), N2–C2 1.372(5), N2–C7 1.455(5), N4–C14 1.377(5), N4–C13 1.456(5), N5–C15 1.385(5), N5–C25 1.462(5), C1–C2 1.422(5), C14–C15 1.425(5); N1–Ge1–N2 84.88(13), N4–Ge2–N5 85.01(14), Ge1–N1–C1 114.1(2), Ge1–N2–C2 114.9(2), Ge2–N4–C14 115.0(2), Ge2–N5–C15 113.9(3); Ge2···Ge1 3.041(5), Ge1···N3 3.386(7), Ge2···N3 3.154(7).

 © 2007 Wiley-VCH Verlag GmbH & Co. KGaA, Weinheim 

## Conclusions

We have prepared the bis(germylenes) **3** and **4** containing two N-heterocyclic germylene (NHGe) units bridged by a 1,3-phenylene- or 1,3-pyridinediylbis(methylene) group, respectively. These compounds are germanium analogues of N-heterocyclic pincer-type bis(carbene) ligands. Their use in the complex formation with transition metal ions and the properties of such pincer complexes are currently investigated.

## Experimental Section

**Starting Materials, Reaction Conditions and Instrumentation:** All manipulation were carried out under argon using Schlenk or glovebox techniques. Toluene and *n*-hexane were dried with sodium/benzophenone and were freshly distilled prior to use. [$D_8$]Toluene was dried with Na/K alloy. The preparation of the tetraamide **1a** and the tetraamine **2a** have been described.[11] Compounds **1a** and **1b** were obtained by similar methods. However, **2b** was prepared in analogy to **2a** by using $BH_3$ instead of $AlH_3$ as a reducing agent. $Ge[N(SiMe_3)_2]_2$ was prepared as described in the literature.[14] $^1H$ and $^{13}C$ NMR spectra were recorded with a Bruker AC-200 spectrometer.

**Tetraamide 1b:** Yield 75%, white solid. $^1H$ NMR (200 MHz, [$D_6$]-DMSO): $\delta$ = 10.91 [s, 2 H, N*H*–C(O)–$C_5H_3N$], 9.07 [s, 2 H, N*H*–C(O)–$C(CH_3)_3$], 8.45–8.34 (m, 3 H, Ar–H $C_5H_3N$), 7.73–7.68 (m, 2 H, Ar–H $C_6H_4$), 7.52–7.47 (m, 2 H, Ar–H $C_6H_4$), 7.31–7.26 (m, 4 H, Ar–H $C_6H_4$), 1.01 [s, 18 H, $C(CH_3)_3$] ppm. $^{13}C$ NMR (50.3 MHz, [$D_6$]DMSO): $\delta$ = 176.9 [*C*(O)–$C_5H_3N$], 161.4 ($C_\alpha$-$C_5H_3N$), 148.2 [*C*(O)–$C(CH_3)_3$], 140.5 ($C_\gamma$-$C_5H_3N$), 131.4, 130.6 (Ar–$C_{ipso}$ $C_6H_4$), 126.2 ($C_\beta$-$C_5H_3N$), 125.7, 125.5, 125.1, 125.0 (Ar–$C_{meta}$ and Ar–$C_{ortho}$ $C_6H_4$), 38.7 [*C*$(CH_3)_3$], 26.9 [C(*C*$H_3)_3$] ppm. MS (MALDI): *m*/*z* (%) = 516 $[M + H]^+$, 538 $[M + Na]^+$.

**Tetraamine 2b:** A 1 M solution of $BH_3$ in THF (40 mmol, 40 mL) was added to the solid tetraamide **1b** (500 mg, 0.97 mmol) at 0 °C. The mixture was stirred at room temperature for 3 h, than heated under reflux for 4 h. Excess $BH_3$ was hydrolyzed with $CH_3OH$ at 0 °C. The resulting boron compound was transformed into the tetraamine by hydrolysis in a THF/$H_2O$ mixture with NaOH. **2b** was extracted from the reaction mixture 3 times with $CH_2Cl_2$ (20 mL each). The combined organic phases were dried with $Na_2SO_4$. Removal of the solvent gave an oil, which was dissolved in hexane and filtered. Evaporation of the hexane gave **2b** as a colorless or yellowish air-sensitive oil. Yield 360 mg (81%). $^1H$ NMR (200 MHz, $CDCl_3$): $\delta$ = 7.52 (t, 1 H, $H_\gamma$-$C_5H_3N$), 7.11 (d, 2 H, $H_\beta$-$C_5H_3N$), 6.75–6.52 (m, 8 H, Ar–H $C_6H_4$), 4.37 (s, 4 H, NC*H*$_2$–$C_5H_3N$), 3.81 (s br, 4 H, NH), 2.79 [s, 4 H, NC*H*$_2$–$C(CH_3)_3$], 0.96 [s, 18 H, $C(CH_3)_3$] ppm. $^{13}C$ NMR (50.3 MHz, $CDCl_3$): $\delta$ = 158.2 ($C_\alpha$-$C_5H_3N$), 138.0, 137.2, 137.0 [Ar–$C_{ipso}$ for $(NH)_2C_6H_4$ and $C_\gamma$-$C_5H_3N$], 119.7 ($C_\beta$-$C_5H_3N$), 119.4, 118.9 [Ar–$C_{meta}$ for $(NH)_2$-$C_6H_4$], 112.1, 111.8 [Ar–$C_{ortho}$ for $(NH)_2C_6H_4$], 56.1 (N*C*$H_2$–$C_5H_3N$), 49.7 [N*C*$H_2$–$C(CH_3)_3$], 31.4 [*C*$(CH_3)_3$], 27.8 [C(*C*$H_3)_3$] ppm. MS (EI, 70 eV): *m*/*z* (%) = 459 (100) $[M]^+$.

**Bis(germylenes) 3 and 4:** The bis(germylenes) were prepared from $GeCl_2$·1,4-dioxane or $Ge[N(SiMe_3)_2]_2$ as described by us for related derivatives.[11] Crystals for the X-ray analyses were grown by slow diffusion of hexane into a saturated solution of **4** in toluene or directly from an *n*-hexane solution of **3**.

**Selected Spectroscopic Data for 3:** Yield 80%. $^1H$ NMR (200 MHz, [$D_8$]toluene): $\delta$ = 7.14–7.00 (m, 12 H, Ar–H), 4.82 (s, 4 H, NC*H*$_2$–$C_6H_4$), 3.85 [s, 4 H, NC*H*$_2$–$C(CH_3)_3$], 0.86 [s, 18 H, $C(CH_3)_3$] ppm. $^{13}C$ NMR (50.3 MHz, [$D_8$]toluene): $\delta$ = 144.2, 142.2 (Ar–$C_{ipso}$ $GeN_2$–$C_6H_4$), 140.6 (Ar–$C_{ipso}$ $NCH_2$–*C*$_6H_4$), 129.2, 128.3, 127.3 ($NCH_2$–*C*$_6H_4$), 118.7, 118.1 (Ar–$C_{meta}$ $GeN_2$–$C_6H_4$),110.5, 110.3 (Ar–$C_{ortho}$ $GeN_2$–$C_6H_4$), 56.8 (N*C*$H_2$–$C_6H_4$), 50.5 [N*C*$H_2$–$C(CH_3)_3$], 33.0 [*C*$(CH_3)_3$], 28.6 [C(*C*$H_3)_3$] ppm. MS (EI, 70 eV): *m*/*z* (%) = 600 (68) $[M]^+$, 543 (91) $[M - t\text{Bu}]^+$.

**Selected Spectroscopic Data for 4:** Yield 240 mg (64%). $^1H$ NMR (200 MHz, [$D_8$]toluene): $\delta$ = 7.02–6.59 (m, 11 H, Ar–H), 5.18 (s, 4 H, NC*H*$_2$–$C_5H_3N$), 3.77 [s, 4 H, NC*H*$_2$–$C(CH_3)_3$], 0.90 [s, 18 H, $C(CH_3)_3$] ppm. $^{13}C$ NMR (50.3 MHz, [$D_8$]toluene): $\delta$ = 159.3 ($C_\alpha$-$C_5H_3N$), 144.0, 142.1 (Ar–$C_{ipso}$ $C_6H_4$), 137.2 ($C_\gamma$-$C_5H_3N$), 119.8 ($C_\beta$-$C_5H_3N$), 118.6, 118.1 (Ar–$C_{meta}$ $C_6H_4$), 110.4, 110.3 (Ar–$C_{ortho}$ $C_6H_4$), 56.8 (N*C*$H_2$–$C_5H_3N$), 51.9 [N*C*$H_2$–$C(CH_3)_3$], 33.0 [*C*$(CH_3)_3$], 28.6 [C(*C*$H_3)_3$] ppm. MS (EI, 70 eV): *m*/*z* (%) = 601 (46) $[M]^+$, 544 (100) $[M - t\text{Bu}]^+$.

**X-ray Diffraction Studies:** Diffraction data for **3** and **4** were collected with a Bruker AXS APEX CCD diffractometer equipped with a rotation anode at 153(2) K using graphite-monochromated Mo-$K_\alpha$ radiation ($\lambda$ = 0.71073 Å). Diffraction data were collected over the full sphere and were corrected for absorption. The data reduction was performed with the Bruker SMART[15] program package. The structures were solved with the SHELXS-97[16] package using the heavy-atom method and were refined with SHELXL-97[17] against $|F^2|$ using first isotropic and then anisotropic thermal parameters for all non-hydrogen atoms. Hydrogen atoms were added to the structure models in calculated positions. CCDC-641062 (**3**) and -641063 (**4**) contain the supplementary crystallographic data for this paper. These data can be obtained free of charge from The Cambridge Crystallographic Data Centre via www.ccdc.cam.ac.uk./data/request/cif.

**Crystal Data for Bis(germylene) 3:** $C_{30}H_{38}Ge_2N_4$, $M$ = 599.82, triclinic, $P\bar{1}$, $Z$ = 2, $a$ = 9.4855(12), $b$ = 9.8055(12), $c$ = 15.744(2) Å, $\alpha$ = 85.590(3), $\beta$ = 89.526(2), $\gamma$ = 77.424(2)°, $V$ = 1427.7(3) Å$^3$, 14127 measured reflections, 6544 unique reflections ($R_{int}$ = 0.0371), $R$ = 0.0414, $wR$ = 0.0905 for 4947 contributing reflections [$I \geq 2\sigma(I)$], refinement against $|F^2|$ with anisotropic thermal parameters for all non-hydrogen atoms and hydrogen atoms in calculated positions.

**Crystal Data for Bis(germylene) 4:** $C_{29}H_{37}Ge_2N_5$, $M$ = 600.82, triclinic, $P\bar{1}$, $Z$ = 2, $a$ = 9.690(2), $b$ = 9.807(2), $c$ = 14.792(3) Å, $\alpha$ = 91.743(4), $\beta$ = 96.699(4), $\gamma$ = 96.715(4)°, $V$ = 1385.1(4) Å$^3$, 11194 measured reflections, 4890 unique reflections ($R_{int}$ = 0.0392), $R$ = 0.0449, $wR$ = 0.1143 for 3839 contributing reflections [$I \geq 2\sigma(I)$], refinement against $|F^2|$ with anisotropic thermal parameters for all non-hydrogen atoms and hydrogen atoms in calculated positions.

## Acknowledgments

The authors thank the Deutsche Forschungsgemeinschaft and the Fonds der Chemischen Industrie for financial support. A. V. Z. thanks the NRW Graduate School of Chemistry, Münster for a predoctoral grant.

[1] a) Recent short review on NHC ligands: F. E. Hahn, *Angew. Chem.* **2006**, *118*, 1374–1378; *Angew. Chem. Int. Ed.* **2006**, *45*, 1348–1352; b) W. A. Herrmann, *Angew. Chem.* **2002**, *114*, 1342–1363; *Angew. Chem. Int. Ed.* **2002**, *41*, 1290–1309; c) B. Bourissou, O. Guerret, F. P. Gabbaï, G. Bertrand, *Chem. Rev.* **2000**, *100*, 39–91.

[2] a) W. A. Herrmann, M. Elison, J. Fischer, C. Köcher, G. R. J. Artus, *Angew. Chem.* **1995**, *107*, 2602–2605; *Angew. Chem. Int.*

 © 2007 Wiley-VCH Verlag GmbH & Co. KGaA, Weinheim 

*Ed. Engl.* **1995**, *34*, 2371–2374; b) K. Öfele, W. A. Herrmann, D. Mihailios, M. Elison, E. Herdtweck, T. Priermeier, P. Kiprof, *J. Organomet. Chem.* **1995**, *498*, 1–14; c) R. E. Douthwaite, D. Haüssinger, M. L. H. Green, P. J. Silcock, P. D. Gomes, A. M. Martins, A. A. Danopoulos, *Organometallics* **1999**, *18*, 4584–4590; d) J. Schwarz, V. P. W. Böhm, M. J. Gardiner, M. Grosche, W. A. Herrmann, W. Hieringer, G. Raudaschl-Sieber, *Chem. Eur. J.* **2000**, *6*, 1773–1780; e) M. V. Baker, B. W. Skelton, A. H. White, C. C. Williams, *J. Chem. Soc., Dalton Trans.* **2001**, 111–120; f) M. Muehlhofer, T. Strassner, W. A. Herrmann, *Angew. Chem.* **2002**, *114*, 1817–1819; *Angew. Chem. Int. Ed.* **2002**, *41*, 1745–1747; g) M. Albrecht, R. H. Crabtree, J. Mata, E. Peris, *Chem. Commun.* **2002**, 32–33; h) L. G. Bonnet, R. E. Douthwaite, R. Hodgson, *Organometallics* **2003**, *22*, 4384–4386; i) J. A. Mata, A. R. Chianese, J. R. Miecznikowski, M. Poyatos, E. Peris, J. W. Faller, R. H. Crabtree, *Organometallics* **2004**, *23*, 1253–1263.

[3] a) F. E. Hahn, M. Foth, *J. Organomet. Chem.* **1999**, *585*, 241–245; b) F. E. Hahn, L. Wittenbecher, D. Le Van, W. Fröhlich, *Angew. Chem.* **2000**, *112*, 551–554; *Angew. Chem. Int. Ed.* **2000**, *39*, 541–544; c) F. E. Hahn, T. von Fehren, T. Lügger, *Inorg. Chim. Acta* **2005**, *358*, 4137–4144; d) D. M. Khamarov, A. J. Boydston, C. W. Bielawski, *Angew. Chem.* **2006**, *118*, 6332–6335; *Angew. Chem. Int. Ed.* **2006**, *45*, 6186–6189.

[4] a) Review: D. Pugh, A. A. Danopoulos, *Coord. Chem. Rev.* **2007**, *251*, 610–641; b) F. E. Hahn, M. C. Jahnke, T. Pape, *Organometallics* **2006**, *25*, 5927–5936; c) F. E. Hahn, M. C. Jahnke, T. Pape, *Organometallics* **2007**, *26*, 150–154.

[5] a) U. Kernbach, M. Ramm, P. Luger, W. P. Fehlhammer, *Angew. Chem.* **1996**, *108*, 333–335; *Angew. Chem. Int. Ed. Engl.* **1996**, *35*, 310–312; b) review: X. Hu, K. Meyer, *J. Organomet. Chem.* **2005**, *690*, 5474–5484.

[6] F. E. Hahn, V. Langenhahn, T. Lügger, T. Pape, D. Le Van, *Angew. Chem.* **2005**, *117*, 3825–3829; *Angew. Chem. Int. Ed.* **2005**, *44*, 3759–3763.

[7] O. Kaufhold, A. Stasch, P. G. Edwards, F. E. Hahn, *Chem. Commun.*, DOI: 10.1039/b617033a.

[8] a) B. Gehrhus, M. F. Lappert, J. Heinicke, R. Boese, D. Bläser, *J. Chem. Soc., Chem. Commun.* **1995**, 1931–1932; b) B. Gehrhus, P. B. Hitchcock, M. F. Lappert, J. Heinicke, R. Boese, D. Bläser, *J. Organomet. Chem.* **1996**, *521*, 211–220; c) B. Gehrhus, P. B. Hitchcock, M. F. Lappert, *J. Chem. Soc., Dalton Trans.* **2000**, 3094–3099; d) B. Gehrhus, P. B. Hitchcock, M. F. Lappert, *Z. Anorg. Allg. Chem.* **2005**, *631*, 1383–1386; e) B. Gehrhus, M. F. Lappert, *J. Organomet. Chem.* **2001**, *617–618*, 209–223; f) M. Haaf, T. A. Schmedake, R. West, *Acc. Chem. Res.* **2000**, *33*, 704–714; g) N. J. Hill, R. West, *J. Organomet. Chem.* **2004**, *689*, 4165–4183.

[9] a) J. Pfeiffer, W. Maringgele, M. Noltemeyer, A. Meller, *Chem. Ber.* **1989**, *122*, 245–252; b) W. A. Herrmann, M. Denk, J. Behm, W. Scherer, F.-R. Klingan, H. Bock, B. Solouki, M. Wagner, *Angew. Chem.* **1992**, *104*, 1489–1492; *Angew. Chem. Int. Ed. Engl.* **1992**, *31*, 1485–1488; c) J. Heinicke, A. Oprea, M. K. Kindermann, T. Karpati, L. Nyulászi, T. Veszprémi, *Chem. Eur. J.* **1998**, *4*, 541–545; d) P. Bazinet, G. P. A. Yap, D. S. Richeson, *J. Am. Chem. Soc.* **2001**, *123*, 11162–11167; e) O. Kühl, P. Lönnecke, J. Heinicke, *Polyhedron* **2001**, *20*, 2215–2222.

[10] a) H. Braunschweig, B. Gehrhus, P. B. Hitchcock, M. F. Lappert, *Z. Anorg. Allg. Chem.* **1995**, *621*, 1922–1928; b) F. E. Hahn, L. Wittenbecher, M. Kühn, T. Lügger, R. Fröhlich, *J. Organomet. Chem.* **2001**, *617–618*, 629–634.

[11] A. V. Zabula, F. E. Hahn, T. Pape, A. Hepp, *Organometallics* **2007**, *26*, 1972–1980.

[12] a) F. E. Hahn, L. Wittenbecher, R. Boese, D. Bläser, *Chem. Eur. J.* **1999**, *5*, 1931–1935; b) F. E. Hahn, L. Wittenbecher, D. Le Van, R. Fröhlich, *Angew. Chem.* **2000**, *112*, 551–554; *Angew. Chem. Int. Ed.* **2000**, *39*, 1541–1544.

[13] L. A. Leites, A. V. Zabula, S. S. Bukalov, A. A. Korlyukov, P. S. Koroteev, O. S. Maslennikova, M. P. Egorov, O. M. Nefedov, *J. Mol. Struct.* **2005**, *750*, 116–122.

[14] D. H. Harris, M. F. Lappert, *J. Chem. Soc., Chem. Commun.* **1974**, 895–896.

[15] SMART: Bruker AXS, **2000**.

[16] SHELXS-97: G. M. Sheldrick, *Acta Crystallogr., Sect. A* **1990**, *46*, 467.

[17] SHELXL-97: G. M. Sheldrick, University of Göttingen, **1997**.

Received: March 15, 2007
Published Online: May 3, 2007

 © 2007 Wiley-VCH Verlag GmbH & Co. KGaA, Weinheim 

DOI: 10.1002/ejic.200700203

# A Diferrous Single-Molecule Magnet

**Athanassios K. Boudalis,*[a] Yiannis Sanakis,*[a] Juan Modesto Clemente-Juan,[b] Alain Mari,[c] and Jean-Pierre Tuchagues[c]**

**Keywords:** Single-molecule studies / Cluster compounds / Magnetic properties / Iron

The diferrous complex $[Fe_2(acpypentO)(NCO)_3]$ (**1**), (acpypentO$^-$ = the anion of 1,5-bis[2-pyridyl(1-ethylimino)]-pentane-3-ol) was studied by spectroscopic (dual-mode X-band EPR and $^{57}$Fe-Mössbauer) and magnetic (AC magnetic susceptibility) techniques. Complex **1** (A. K. Boudalis et al., *Inorg. Chem.* **2004**, *43*, 1574) was previously shown to exhibit an intramolecular ferromagnetic coupling with important single-ion anisotropies with marked differences in the single-ion electronic parameters of the two iron sites. In this contribution, additional studies are carried out to probe its dynamic magnetic properties. Mössbauer spectra recorded at liquid helium temperatures indicate slow paramagnetic relaxation and a ground state of the system characterized by a non-Kramers doublet with an Ising-type anisotropy, a condition which favours single-molecule magnet (SMM) behaviour. A frequency-dependent out-of-phase signal observed below 3 K in AC susceptibility measurements is in line with such a picture. The out-of-phase signal, however, is relatively weak in comparison with the in-phase signal. Dual mode X-band EPR spectroscopy revealed characteristic signals, the analysis of which suggests inhomogeneities in the system. For some molecules, the splitting $\Delta_0$ of the non-Kramers ground doublet is vanishingly small, which gives rise to out-of-phase signals in AC susceptibility measurements and magnetically split Mössbauer spectra in the absence of external magnetic fields. Other molecules, however, are characterized by a non-negligible $\Delta_0$, which gives rise to the dual mode X-band EPR signals. For these molecules the magnetic relaxation is fast.
(© Wiley-VCH Verlag GmbH & Co. KGaA, 69451 Weinheim, Germany, 2007)

## Introduction

Molecule-based magnetic materials have been a field of intense scientific research during the past decades. A reason for their increasing interest both to chemists and physicists is that molecular objects like complexes (0D) or chains (1D), which otherwise are best described by quantum mechanics, display phenomena like slow magnetic relaxation, usually seen in classical magnetic materials. These classical phenomena are observed alongside purely quantum phenomena like quantum tunnelling of the magnetization (QTM) thus bridging the classical (macroscopic) and the quantum (microscopic) worlds. In this field, single-molecule magnets (SMMs) and single-chain magnets (SCMs) are classes of molecules that have generated much excitement because they exhibit both slow magnetic relaxation and Arrhenius kinetics due to strong uniaxial anisotropy, without experiencing 3D magnetic ordering.

Since the first observation of the SMM phenomenon for the dodecanuclear manganese cluster $[Mn_{12}O_{12}(O_2CMe)_{16}(H_2O)_4]$, many other clusters have been shown to exhibit the same phenomenon, with nuclearities reaching 84, as observed in the giant $\{Mn_{84}\}$[1] torus reported by Christou et al. The maximum ground spin-state ever attained is 83/2 reported for a $\{Mn_{19}\}$ complex by Powell et al.[2] However, smaller molecules have been reported to exhibit slow relaxation of their magnetization, like mononuclear $Co^{II}$[3,4] and $Ln^{III}$ (Ln = Tb, Dy) complexes[5] or dinuclear $Fe^{III}$,[6] $Mn^{III}$,[7] $Tb^{III}$–$Cu^{II}$[8] and $Fe^{III}$–$Dy^{III}$[9] clusters. These species are particularly interesting as their small size allows us to study their electronic properties with exact methods, and fewer approximations. It is thus possible to correlate their observable behaviour with more fundamental parameters and to subsequently gain insight into the behaviour of larger systems. Moreover, they allow us to envisage applications concerning memory recording at the smallest scale.[10]

Dinuclear complexes comprising high-spin ferrous ions have been synthesized and studied as synthetic models for the active sites of metalloenzymes.[11] In a number of cases, ferromagnetic interactions have been observed that result in magnetic ground states.[12] Moreover, electron paramagnetic resonance (EPR) and Mössbauer spectroscopy indicate that the ground state is characterized by a non-Kramers doublet with an Ising-type magnetic anisotropy. This special feature, in combination with the relatively large spin, is one of the requirements for a molecule to exhibit single-molecule magnetic behaviour.

[a] Institute of Materials Science, NCSR "Demokritos", 15310 Aghia Paraskevi Attikis, Greece
[b] Instituto de Ciencia Molecular, Fundación General de la Universidad de Valencia y Universidad de Valencia, Polígono de la Coma, s/n, 46980 Paterna, Spain
[c] Laboratoire de Chimie de Coordination du CNRS, UPR 8241, 205 route de Narbonne, 31077 Toulouse Cedex 04, France
Supporting information for this article is available on the WWW under http://www.eurjic.org or from the author.

 © 2007 Wiley-VCH Verlag GmbH & Co. KGaA, Weinheim 

Recently, we reported the synthesis and physical characterization of a series of polynuclear $Fe^{II}$ complexes including the dinuclear species $[Fe_2(acpypentO)(NCO)_3]$ (**1**),[13] where $acpypentO^-$ is the anion of 1,5-bis[2-pyridyl(1-ethylimino)]pentane-3-ol (Figure 1). This complex was found to contain two pentacoordinate $Fe^{II}$ ions bridged by one alkoxido oxygen belonging to the ligand, and one end-on cyanato anion. Analysis of the thermal variation of the $\chi_M T$ product of **1** indicated that the two $S = 2$ spins are ferromagnetically coupled with $J = 3\ cm^{-1}$. In addition, the analysis of the magnetic susceptibility measurements indicated the critical involvement of zero-field splitting interactions. Under appropriate conditions, these interactions might eventually lead to an important anisotropy of the ground state. Indeed, the two $Fe^{II}$ ions showed important differences in their axial and rhombic single-ion anisotropies with $D_1 = 1.6\ cm^{-1}$, $E_1 = -0.35\ cm^{-1}$ ($\lambda_1 = 0.22\ cm^{-1}$) and $D_2 = -12.2\ cm^{-1}$, $E_2 = 1.1\ cm^{-1}$ ($\lambda_2 = 0.09\ cm^{-1}$).

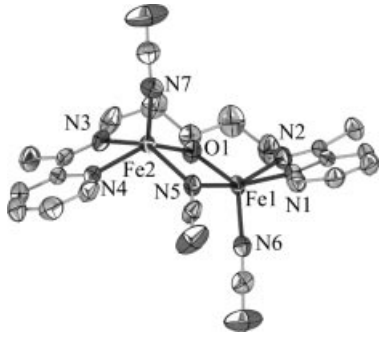


Figure 1. Molecular structure of complex **1**.

With these in mind, we considered it worthy to examine the properties of the ground state of this system in more detail and to monitor its dynamic magnetic properties at low temperatures. Taking into account the ferrous nature and the high reactivity of this dinuclear complex with dioxygen, we considered Mössbauer and X-band EPR ($\perp$ and $\parallel$ modes) spectroscopy to be the most appropriate techniques for elucidating the properties of its ground state.

### Mössbauer Spectroscopy

The Mössbauer spectra at temperatures above liquid nitrogen consist of two quadrupole-split doublets attributed to the two different irons sites of the molecule. At 78 K, the two ferrous sites are characterized by $\delta_1 = 1.01\ mm\,s^{-1}$, $\Delta E_{Q1} = 2.27\ mm\,s^{-1}$ and $\delta_2 = 1.01\ mm\,s^{-1}$, $\Delta E_{Q2} = 3.38\ mm\,s^{-1}$.[13] The temperature dependence of the isomer shifts above 78 K is attributed to the second-order Doppler effect whereas the dependence of the quadrupole splitting values is typical for high-spin ferrous ions.

In the present work, we study spectra recorded at temperatures below 78 K. Representative spectra are shown in Figure 2. In the temperature range 10–78 K, there is no significant variation of the doublets: the two sites exhibit almost temperature-independent isomer shifts and quadrupole splittings. For temperatures below 10 K, the spectra exhibit line-broadening and a spectrum with magnetic features is observed at 4.2 K. These spectra look slightly different from those recorded previously[13] *essentially* because of a remarkable sensitivity related to a strong dependence of the relaxation times on temperature below 7 K.

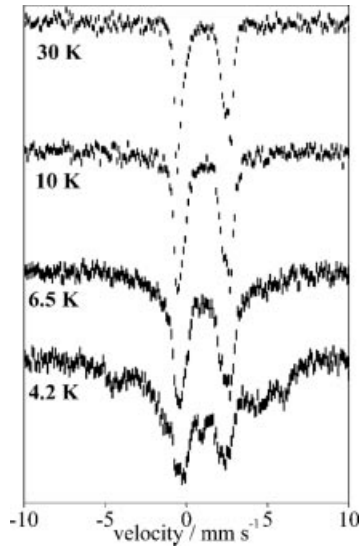


Figure 2. Zero-field Mössbauer spectra from a powdered sample of **1** at liquid helium temperatures.

From DC magnetic susceptibility measurements, no evidence for long-range effects were observed, which suggests that the magnetically split spectrum at 4.2 K is due to slow paramagnetic relaxation. The Mössbauer spectra are in line with the magnetic susceptibility measurements, which indicate ferromagnetic coupling between the ferrous ions. In the case of antiferromagnetic coupling, the ground state would be diamagnetic ($S_T = 0$) and quadrupole-split doublets would be observed in zero-field at liquid helium temperatures. The magnetic ground state of **1** is further supported by spectra recorded in the presence of applied magnetic fields.

Figure 3 shows the Mössbauer spectra of a powdered sample of **1** in the presence of external magnetic fields up to 5.0 T applied perpendicularly to the γ-rays. Clearly, the magnetically perturbed spectra are incompatible with an $S_T = 0$ ground state.[12d] Useful information may be derived by considering the dependence of the spectra on the strength of the applied magnetic field. This can be visualized by following the shift of the absorption peak at ca. $-4.5\ mm\,s^{-1}$ in the zero-field spectrum. This peak does not shift further to more negative velocities under a 0.55 T field, but its intensity increases. For higher magnetic fields, this peak shifts *inwards*, which indicates that the external magnetic field opposes the intrinsic one. This indicates that the internal magnetic field has reached saturation for a relatively small external magnetic field (vide infra). This overall behaviour implies a number of properties regarding the nature of the electronic ground state of the system as commented next.

The $^{57}Fe$ Mössbauer spectra of high-spin ferrous compounds usually exhibit fast spin relaxation even at liquid helium temperatures and in such a case quadrupole-split

 © 2007 Wiley-VCH Verlag GmbH & Co. KGaA, Weinheim 

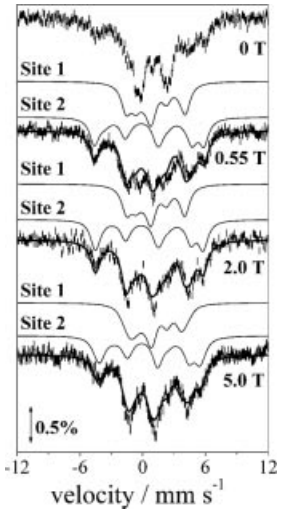


Figure 3. Mössbauer spectra of a powdered sample of **1** at 4.2 K in the absence and in the presence of external magnetic fields applied perpendicular to the γ-rays. Continuous lines are theoretical simulations obtained by assuming two different ferrous sites as described in the text. The contribution of each site is shown separately.

doublets are observed. However, slow paramagnetic relaxation effects were observed in the spectra of a number of high-spin ferrous compounds.[14] The magnetic spectra resulting from paramagnetic relaxation are related with non-Kramers doublets exhibiting a significant Ising-type anisotropy. The magnetically split spectra at zero external magnetic field are due to mixing between the electronic and nuclear spin states.[15] On the contrary, the Mössbauer spectra associated with singlets from such systems consist of quadrupole-split doublets.[16] The non-Kramers character of the ground state with an Ising-type anisotropy is further supported by simulations of the Mössbauer spectra described in a subsequent section.

### Dynamic Magnetic Properties

The Mössbauer spectroscopic results presented above indicate that the ground state of complex **1** is characterized by a uniaxial doublet. This, in combination with the nominally high spin of the system, encouraged us to investigate the possibility of slow magnetic relaxation phenomena in **1**, using AC magnetic susceptibility (Figure 4). Indeed, the out-of-phase data clearly show a frequency-dependent signal below ca. 3 K, which indicates the occurrence of slow relaxation phenomena. The maximum of the signal was not observed down to 2 K, which was the lower limit of our SQUID facility. This hampered us from carrying out a quantitative analysis of the relaxation phenomena, but it was clear evidence for the onset of slow magnetic relaxation. Rough estimations may be obtained by considering the following.[17,18h] From the temperature dependence of the zero-field spectra, we may assume that at 4.2 K the spin relaxation time $\tau \approx 10^{-7}$–$10^{-8}$ s, the characteristic time of the Mössbauer spectroscopy.[17d] From the AC susceptibility data we may estimate that at 2 K, $\tau \approx 10^{-3}$ s. Assuming an Arrhenius dependence of $\tau$ ($\tau = \tau_0 e^{\Delta E/kT}$), we estimate $\tau_0 \approx 10^{-11}$–$10^{-13}$ s and $\Delta E < 40$ K (28 cm$^{-1}$). Under a zero applied static field, and for a 250 Hz oscillating field, the $\chi_M'T$ product at 2 K was 9.72 cm$^3$ mol$^{-1}$ K, which is close to the expected value on the basis of the analysis of the DC susceptibility data.[13] Upon raising the static magnetic field, there is a decrease in the $\chi_M'T$ product that is due to the increased splitting of the Zeeman states. This is similar to the sudden drop of the $\chi_M T$ product at low temperatures, as evidenced in the DC data.[13]

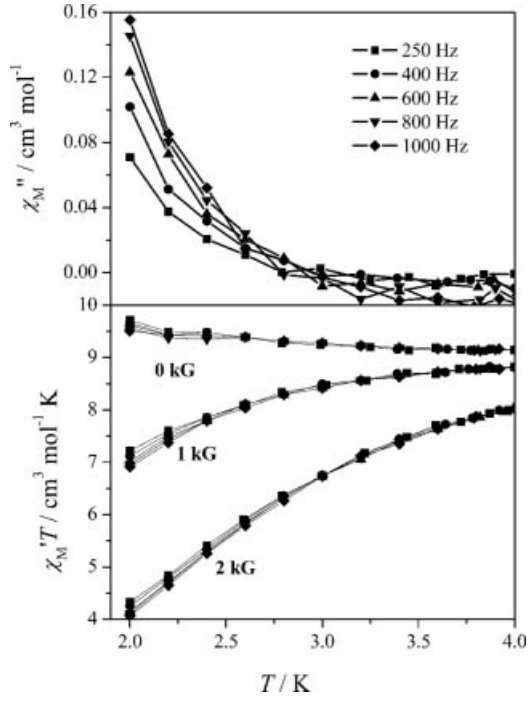


Figure 4. Out-of-phase, $\chi_M''$ vs. $T$, AC magnetic susceptibility data for complex **1** (top) under a zero static magnetic field and with oscillating frequencies of 250, 400, 600, 800 and 1000 Hz. The effect of the static magnetic field on the in-phase signals is depicted in the $\chi_M'T$ vs. $T$ curves (bottom), for fields of 1 and 2 kG.

The imaginary component of the ac susceptibility signal is rather small (≈3.5% of the real part). This is not unprecedented as many molecules exhibiting SMM behaviour have a similarly weak $\chi''/\chi'$ ratio.[18] A possible origin for this behaviour might be the existence of heterogeneities concerning the relaxation properties of the molecules. Namely, a fraction of the molecules is characterized by slow relaxation whereas another fraction is relaxing fast, as further commented below.

The pertinent spin Hamiltonian that describes the magnetic properties of **1** is depicted in Equation (1).[19]

$$\hat{H}_1 = -2J\hat{\mathbf{S}}_1 \cdot \hat{\mathbf{S}}_2 + \sum_{i=1}^{2}\left[D_i\left(\hat{S}_{z,i}^2 - 2\right) + E_i\left(\hat{S}_{x,i}^2 - \hat{S}_{y,i}^2\right) + \beta\hat{\mathbf{S}}_i\mathbf{g}_i\mathbf{H}\right] \quad (1)$$

In the case of axial symmetry ($E = 0$), the ground state of the system is characterized by a non-Kramers doublet with an Ising-type anisotropy. In this case, slow relaxation

 © 2007 Wiley-VCH Verlag GmbH & Co. KGaA, Weinheim 

might be favoured. If, however, rhombic distortions ($E \neq 0$) are present, the degeneracy of the non-Kramers doublet splits by an amount $\Delta_0$[20] and in this case, fast relaxation may occur through quantum tunnelling effects.[21] The existence of molecules for which $\Delta_0$ is nonzero can be monitored by dual-mode X-band EPR spectroscopy (vide infra).

### Dual-Mode EPR Studies

For an isolated non-Kramers doublet, intradoublet transition is expected provided that the transition probability $P \neq 0$. Because $P \approx \Delta_0^2$, no signals are observed in the case of $\Delta_0 \approx 0$, whereas signals are observed for $0 < \Delta_0 < h\nu$ ($h\nu \approx 0.3\ cm^{-1}$ at X-band). In Figure 5, we show X-band EPR spectra of a powdered sample of **1** recorded at 4.2 K. Strong signals are observed in the low-field region in both the parallel and perpendicular modes. No signals attributable to half-integer spin systems are observed (i.e. a "$g \approx 4.3$" signal at ≈1500 G), which indicates that the samples are not oxidized. The signals exhibit saturation effects at 4.2 K and decrease as the temperature increases. The latter indicates that the signals arise from the ground state.

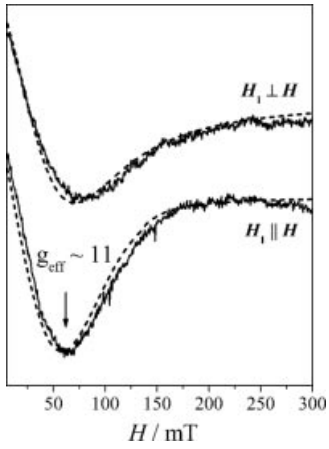


Figure 5. Dual-mode X-band EPR spectra for a powdered sample of **1** at 4.2 K under nonsaturating conditions. Dashed lines are theoretical simulations obtained as described in the text. EPR conditions: Microwave power: 0.13 mW, modulation amplitude: 1.0 mT, microwave frequency: 9.60 (perpendicular mode), 9.36 GHz (parallel mode).

The line-shape of the EPR signals is consistent with an integer spin system[22] as expected for **1**. The EPR properties of diferrous complexes have been extensively studied by Hendrich et al.[11,23] The dashed lines superimposed above the experimental spectra are simulated spectra considering an effective $S = 4$ spin Hamiltonian [Equation (2)].[24]

$$\hat{H}_2 = D\left(\hat{S}_z^2 - 20/3\right) + E\left(\hat{S}_x^2 - \hat{S}_y^2\right) + \beta\hat{\mathbf{S}}\mathbf{g}\mathbf{H} \quad (2)$$

Satisfactory simulations were obtained with different sets of parameters [from Equation (1)] that is, there is not a unique set of parameters for simulating the spectra. However, these different sets result in a unique description regarding the magnetic properties of the doublet giving rise to the signal.[24] The signal arises from transitions within a non-Kramers doublet with uniaxial magnetic properties which is split by an amount $\Delta_0 \approx 0.3\ cm^{-1}$ at zero field.[23a,20] To account properly for the line shape of the EPR spectra, a Gaussian distribution of $\Delta_0$ with an apparent width $\sigma\Delta_0 = 0.06\ cm^{-1}$ must be incorporated. The $\Delta_0$ distribution is due to a distribution of parameters such as *D*, *E* and *J*. Alternatively, solid-state effects may effectively lead to line broadening. As a conclusion, the results from dual mode X-band EPR spectroscopy indicate that the system contains molecules for which $\Delta_0$ is nonnegligible.

### Simulations of the Mössbauer spectra

It was noticed that the analysis of Mössbauer spectra from diferrous complexes is not trivial when the zero-field splitting terms and the exchange coupling constant are of comparable magnitude[12a,12d,25] because the number of parameters involved is large. Therefore, a unique set of parameters cannot be obtained unambiguously. A complete analysis of the spectra was not pursued; however, we checked whether the behaviour of the magnetically perturbed Mössbauer spectra is consistent with the results from X-band EPR spectroscopy discussed above. The EPR spectra were analyzed within the framework of Hamiltonian in Equation (2) and it was found that the ground non-Kramers doublet of the system is characterized by a distributed $\Delta_0$, centred at $0.3\ cm^{-1}$.

For the magnetically perturbed Mössbauer spectra we assumed two sites at a 1:1 ratio and we used the effective spin Hamiltonian $\hat{H}_3$ for $S = 4$ (strong exchange limit) [Equation (3)]:

$$\hat{H}_3 = \hat{H}_2 + \sum_{i=1,2}\left[\hat{\mathbf{S}}\tilde{\mathbf{A}}_i\hat{\mathbf{I}}_i - g_n\beta_n\hat{\mathbf{I}}_i\mathbf{H} + \hat{H}_{Q,i}\right] \quad (3)$$

with [Equation (4)]:

$$\hat{H}_{Qi} = \frac{eQV_{\zeta\zeta}}{12}\left[3\hat{I}_{\zeta i}^2 - \frac{15}{4} + \eta_i\left(\hat{I}_{\xi i}^2 - \hat{I}_{\eta i}^2\right)\right] \quad (4)$$

where ($\xi$, $\eta$, $\zeta$) designates the principal axis system of the electric field gradient (EFG) tensor and where $\eta_i = (V_{\xi\xi i} - V_{\eta\eta i})/V_{\zeta\zeta i}$ is the asymmetry parameter. Equation (3) is written in the coupled representation.

For the isomer shift and quadrupole splittings we used the values obtained from the zero-field spectra recorded at 78 K ($\delta_1 = 1.01\ mm\,s^{-1}$, $\Delta E_{Q1} = 2.27\ mm\,s^{-1}$ and $\delta_2 = 1.01\ mm\,s^{-1}$, $\Delta E_{Q2} = 3.38\ mm\,s^{-1}$). For the parameters involved in the electronic part of Hamiltonian $\hat{H}_2$ we used the values from the analysis of the EPR spectra.[24] The

 © 2007 Wiley-VCH Verlag GmbH & Co. KGaA, Weinheim 

splittings observed in the magnetically perturbed spectra reflect a total magnetic field acting on the $^{57}$Fe nucleus, $\mathbf{H} = \mathbf{H}_{appl} + \mathbf{H}_{int}$ where the internal field is given by Equation (5).

$$\mathbf{H}_{int} = -\frac{\langle \hat{\mathbf{S}}_i \rangle \tilde{\mathbf{A}}_i}{g_n \beta_n} \quad (5)$$

For the given zero-field splitting values $D$, $E/D$, the easy axis of magnetization is $y$ for the ground non-Kramers doublet, and the magnetically perturbed Mössbauer spectra at liquid helium temperature are sensitive only on $\langle \hat{S}_{yi} \rangle$. Therefore, as far as the hyperfine tensor of the ferrous ions is concerned, only the $A_{yi}$ components may be estimated. The spectra recorded at different magnetic fields can be reasonably reproduced with a common set of parameters (Figure 3) with $A_{y1}$ = –6.2 MHz and $A_{y2}$ = –10.2 MHz. With this model, the characteristic feature at –4.5 mm s$^{-1}$ observed in the low-field spectra belongs to the spectrum from site 2.

It is inferred that the magnetically perturbed spectra are consistent with the dual-mode X-band EPR results. For non-Kramers systems, saturation of the internal magnetic field, $\mathbf{H}_{int}$, requires the application of an external magnetic field, $\mathbf{H}_{ext}$, the value of which depends on $\Delta_0$ (Figure 6). For $\Delta_0 = 0$, a very small magnetic field suffices to saturate $H_{int}$. In that case, a characteristic magnetic Mössbauer spectrum is observed. In the present case, a magnetic spectrum is already observed in the absence of external magnetic fields. We assume that this spectrum arises from a fraction of molecules for which $\Delta_0$ is vanishingly small. Application of a moderate magnetic field (0.55 T) induces an intensity increase in the ca. –4.5 mm s$^{-1}$ peak. We suggest that this increase arises from molecules that require an external magnetic field to induce saturation of $\mathbf{H}_{int}$ and therefore for these molecules $\Delta_0 \neq 0$.

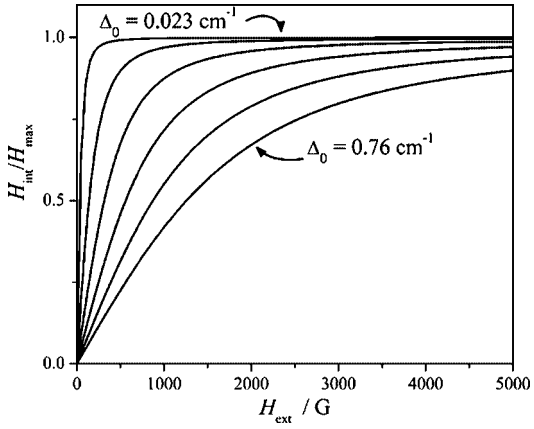


Figure 6. Dependence of the $H_{int}/H_{sat}$ ratio on the externally applied magnetic field along the easy axis ($H_{ext}$) for a non-Kramers doublet with various $\Delta_0$ values (0.023, 0.090, 0.200, 0.352, 0.540 and 0.760 cm$^{-1}$).

## Discussion and Conclusions

In the present work we study the dynamic magnetic behaviour of differous compound **1** by applying AC susceptibility measurements and dual mode X-band EPR and Mössbauer spectroscopic techniques. The incentive for this study stems from the bulk DC magnetic measurements which revealed ferromagnetic interactions between the two ferrous ions leading to a ground state with a relatively large nominal spin.[13] AC susceptibility measurements presented herein indicate slow relaxation effects at liquid helium temperatures.

The combined results from the present studies offer an explanation for the relaxation behaviour of **1**. We suggest that the molecules are characterized by inhomogeneities which eventually affect the splitting of the non-Kramers ground doublet. For a fraction of molecules, $\Delta_0$ is negligible (ideally 0), which gives rise to the magnetically split Mössbauer spectrum at zero-field. Because the quantum tunnelling rate is proportional to $\Delta_0$, these molecules are expected to have slow relaxation properties and cause an out-of-phase AC signal. On the contrary, a fraction of the molecules appears to be characterized by significant $\Delta_0$ as deduced by the dual mode X-band EPR measurements. For these molecules, quantum tunnelling is expected to be favoured, which results in fast relaxation. We should stress that as a result of the molecular nature of **1**, these inhomogeneities must be at the molecular level, that is, not discernible by X-ray crystallography.

In assessing the origin of the slow magnetic relaxation in **1**, one might readily argue that the relatively high effective spin of the ground state in combination with a high uniaxial magnetic anisotropy established by spectroscopic techniques leads to an SMM behaviour. However, we explored the possibility that slow relaxation might stem from an SCM behaviour due to weak intermolecular interactions.[26] The packing diagram of **1** (Figure S1) revealed weak π–π interactions between pyridyl rings of the ligand in adjacent molecules (2 – $x$, 1 – $y$, 1 – $z$), but not the presence of 1D chains.[27] This finding excludes to possibly attribute the observed slow relaxation to single-chain magnetism; thus, the slow relaxation must be related to superparamagnetism. From this point of view, **1** can be viewed as a rare example of an iron(II) single-molecule magnet, with the only other examples being three {$Fe_4$} cubanes prepared by Oshio et al.[28] and the enneanuclear complex [$Fe_9(O_2CMe)_8\{(py)_2CO_2\}_4(N_3)_2$].[29] Further originality of this compound stems from the fact that the two $Fe^{II}$ centres have different ligand field symmetries.

In the literature, several examples of diferrous complexes exhibiting ferromagnetic interactions yielding a magnetic ground state exist. To the best of our knowledge, **1** is the first for which the spin dynamics has been monitored directly by AC susceptibility and slow relaxation was observed. It would be interesting to explore the possibility of slow magnetic relaxation in other similar diferrous complexes as well. A majority of these complexes, apart from DC susceptibility measurements, were studied by spectro-

 © 2007 Wiley-VCH Verlag GmbH & Co. KGaA, Weinheim 

scopic techniques, which give additional information regarding the nature of the ground state. We showed here that Mössbauer spectroscopy is a useful technique, which can probe whether the ground state satisfies the conditions for slow relaxation. We suggest that observation of a magnetically split spectrum in the absence of applied magnetic field (not arising from long-range magnetic ordering) indicates that these complexes may be suitable SMM candidates. On the contrary, quadrupole-split doublets are related either to singlets, fast relaxation ($<10^{-7}$ s), or non-Kramers doublets with relatively large zero-field splitting, $\Delta_0$. For the cases found in the literature, quadrupole-split doublets have been observed at liquid helium temperatures: these complexes are thus unlikely candidates for slow magnetic relaxation.

The above discussion may be extended to ferrous complexes of higher nuclearity. We have recently observed single-molecule magnet behaviour for enneanuclear ferrous compounds.[29] In these cases, magnetically split Mössbauer spectra are observed in the absence of an applied magnetic field as a result of slow paramagnetic relaxation in the temperature range 4.2–10 K. At present, we are not aware of relevant studies for the cubanes reported by Oshio et al.[28]

In the present work we report the first example of a diferrous single-molecule magnet and a rare example of ferrous SMM. In addition, we probe the relaxation mechanism through various techniques and show that owing to molecular-level inhomogeneities, slow relaxation requirements are fulfilled for a fraction of the molecules only. This realization is particularly important for molecular species, which are generally considered as "monodisperse". Although it is reasonable to assume that this situation may occur in other SMMs as well, its verification in the present system was possible mainly due to the probing of its ground state and relaxation mechanism through techniques like AC susceptibility and Mössbauer and dual-mode X-band EPR spectroscopy.

## Experimental Section

Complex **1** was synthesized as described previously.[13] Mössbauer measurements were recorded with a constant-acceleration conventional spectrometer with a 50 mCi source of $^{57}$Co (Rh matrix). The absorber was a powdered sample enclosed in a 20-mm diameter cylindrical plastic sample holder, the size of which was determined to optimize the absorption. To avoid oxidation of the sample, the sample holder was sealed with Araldite and stored in liquid nitrogen. Variable-temperature spectra were obtained in the 4.2–300 K range, by using Oxford cryostats, operating at 4.2–300 K. One cryostat was equipped with a superconducting magnet that allowed application of external magnetic fields up to 5.0 T perpendicular to the $\gamma$-rays. Isomer shift values ($\delta$) are relative to iron foil at 293 K. The magnetically perturbed spectra were analyzed with the WMOSS software package (WEB Research, Edina, MN). Variable-temperature (2.0–5.0 K) AC magnetic susceptibility data were collected from a powdered microcrystalline sample with a Quantum Design MPMS SQUID susceptometer. The sample was moulded into a pellet inside the glove box to avoid orientation in the magnetic field. Data were corrected with the standard procedure for the contribution of the sample holder and diamagnetism of the sample. X-band EPR measurements were carried out with a Bruker ER-200D spectrometer equipped with a Bruker Dual Mode cavity, an Anritsu frequency counter, an NMR Gaussmeter and an Oxford ESR-9 cryostat. EPR tubes were flame-sealed under vacuum to avoid air-oxidation of the sample. ***Caution:*** *Molten quartz generates large amounts of harmful UV radiation, thus proper eye-protection should be worn.* Simulations of the spectra were carried out with SpinCount software kindly provided to us by Prof. M. Hendrich, Dept. of Chemistry, Carnegie Mellon University, Pittsburgh, PA, USA.

**Supporting Information** (see footnote on the first page of this article): Packing diagram of **1**, which shows the intermolecular $\pi$–$\pi$ interactions.


[1] A. J. Tasiopoulos, A. Vinslava, W. Wernsdorfer, K. A. Abboud, G. Christou, *Angew. Chem. Int. Ed.* **2004**, *43*, 2117–2121.
[2] A. M. Ako, I. J. Hewitt, V. Mereacre, R. Clérac, W. Wernsdorfer, C. E. Anson, A. K. Powell, *Angew. Chem. Int. Ed.* **2006**, *45*, 4926–4929.
[3] S. Karasawa, G. Zhou, H. Morikawa, N. Koga, *J. Am. Chem. Soc.* **2003**, *125*, 13676–13677.
[4] S. Kanegawa, S. Karasawa, M. Nakano, N. Koga, *Chem. Commun.* **2004**, 1750–1751.
[5] N. Ishikawa, M. Sugita, T. Ishikawa, S. Koshihara, Y. Kaizu, *J. Am. Chem. Soc.* **2003**, *125*, 8694–8695.
[6] R. Schenker, M. L. Leuenberger, G. Chaboussant, H. U. Güdel, D. Loss, *Chem. Phys. Lett.* **2002**, *358*, 413–418.
[7] a) H. Miyasaka, R. Clérac, W. Wernsdorfer, L. Lecren, C. Bonhomme, K.-I. Sugiura, M. Yamashita, *Angew. Chem. Int. Ed.* **2004**, *43*, 2801–2805; b) Z. Lü, M. Yuan, F. Pan, S. Gao, D. Zhang, D. Zhu, *Inorg. Chem.* **2006**, *45*, 3538–3548; c) C. Kachi-Tarajima, H. Miyasaka, K. Sugiura, R. Clérac, H. Nojiri, *Inorg. Chem.* **2006**, *45*, 4381–4390; d) C.-H. Ge, A.-L. Cui, Z.-H. Ni, Y.-B. Jiang, L.-F. Zhang, J. Ribas, H. Z. Kou, *Inorg. Chem.* **2006**, *45*, 4883–4885.
[8] J.-P. Costes, F. Dahan, W. Wernsdorfer, *Inorg. Chem.* **2006**, *45*, 5–7.
[9] M. Ferbinteanu, T. Kajiwara, K.-Y. Choi, H. Nojiri, A. Nakamoto, N. Kojima, F. Cimpoesu, Y. Fujimara, S. Takaishi, M. Yamashita, *J. Am. Chem. Soc.* **2006**, *128*, 9008–9009.
[10] M. Cavallini, J. Gomez-Segura, D. Ruiz-Molina, M. Massi, C. Albonetti, C. Rovira, J. Veciana, F. Biscarini, *Angew. Chem. Int. Ed.* **2005**, *44*, 888–892.
[11] E. Tshuva, S. Lippard, *Chem. Rev.* **2004**, *104*, 987–1012.
[12] a) A. S. Borovik, M. P. Hendrich, T. R. Holman, E. Münck, V. Papaefthymiou, L. Que Jr, *J. Am. Chem. Soc.* **1990**, *112*, 6031–6038; b) A. Stassinopoulos, G. Schulte, G. C. Papaefthymiou, J. P. Caradonna, *J. Am. Chem. Soc.* **1991**, *113*, 8686–8697; c) Y. Zang, H. G. Jang, Y.-M. Chiou, M. P. Hendrich, L. Que Jr, *Inorg. Chim. Acta* **1993**, *213*, 41–48; d) A. Stubna, A. D.-H. Jo, M. Costas, W. W. Brenessel, H. Andres, E. L. Bominaar, E. Münck, L. Que Jr, *Inorg. Chem.* **2004**, *43*, 3067–3079.
[13] A. K. Boudalis, J. M. Clemente-Juan, F. Dahan, J.-P. Tuchagues, *Inorg. Chem.* **2004**, *43*, 1574–1586.
[14] a) H. N. Ok, *Phys. Rev.* **1969**, *185*, 472–476; b) V. Petrouleas, A. Simopoulos, A. Kostikas, *Phys. Rev. B* **1975**, *12*, 4675–4681; c) D. C. Price, C. E. Johnson, I. Maartense, *J. Phys. C: Solid State Phys.* **1977**, *10*, 4843–4853; d) C. Nicolini, W. M. Reiff, *Inorg. Chem.* **1980**, *19*, 2676–2679; e) K. K. P. Srivastava, *J. Phys. C: Solid State Phys.* **1983**, *16*, L53–L55; f) F. F. Charron, W. M. Reiff, *Inorg. Chem.* **1986**, *25*, 2786–2790; g) B. D. Howes, D. Creagh, D. C. Price, *J. Phys. C: Solid State Phys.* **1988**, *21*, 2439–2451; h) P. Garge, R. Chikate, S. Padhye, J.-M. Savariault, P. de Loth, J.-P. Tuchagues, *Inorg. Chem.* **1990**, *29*, 3315–3320; i) M. A. Martinez-Lorente, F. Dahan, Y. Sanakis, V. Petrouleas, A. Bousseksou, J.-P. Tuchagues, *Inorg. Chem.* **1995**, *34*, 5346–5357; j) W. M. Reiff, A. M. LePointe, E. H. Witten, *J. Am. Chem. Soc.* **2004**, *126*, 10206–10207; k) K. L. Taft, A.


 © 2007 Wiley-VCH Verlag GmbH & Co. KGaA, Weinheim 

Caneschi, L. E. Pence, C. D. Delfs, G. C. Papaefthymiou, S. J. Lippard, *J. Am. Chem. Soc.* **1993**, *115*, 11753–11766.
[15] K. K. Surerus, M. P. Hendrich, P. D. Christie, D. Rottgardt, W. H. Orme-johnson, E. Münck, *J. Am. Chem. Soc.* **1992**, *114*, 8579–8590.
[16] a) J. Chappert, G. Jehanno, F. Varret, *J. Phys. Paris* **1977**, *38*, 411–418; b) Y. Sanakis, P. P. Power, A. Stubna, E. Münck, *Inorg. Chem.* **2002**, *41*, 2690–2696.
[17] a) A.-L. Barra, P. Debrunner, D. Gatteschi, C. E. Shulz, R. Sessoli, *Europhys. Lett.* **1996**, *35*, 133; b) A. Caneschi, L. Cianchi, F. Del Gallo, D. Gatteschi, P. Moretti, F. Pieralli, G. Spina, *J. Phys.: Condens. Matter* **1999**, *11*, 3395–3403; c) L. Cianchi, F. Del Giallo, G. Spina, W. M. Reiff, A. Caneschi, *Phys. Rev. B* **2002**, *65*, 064415; d) P. Gütlich, R. Link, A. Trautwein in *Mössbauer Spectroscopy and Transition Metal Chemistry*, Springer, Berlin, Heidelberg, New York, **1978**.
[18] a) C. Dendrinou-Samara, M. Alexiou, C. M. Zaleski, J. W. Kampf, M. L. Kirk, D. P. Kessissoglou, V. L. Pecoraro, *Angew. Chem. Int. Ed.* **2003**, *42*, 3763–3766; b) S. Wang, J.-L. Zuo, H.-C. Zhou, H. J. Choi, Y. Ke, J. R. Long, X.-Z. You, *Angew. Chem. Int. Ed.* **2004**, *43*, 5940–5943; c) H. J. Choi, J. J. Sokol, J. R. Long, *Inorg. Chem.* **2004**, *43*, 1606–1608; d) M. Murugesu, J. Raftery, W. Wernsdorfer, G. Christou, E. K. Brechin, *Inorg. Chem.* **2004**, *43*, 4203–4209; e) P. King, W. Wernsdorfer, K. A. Abboud, G. Christou, *Inorg. Chem.* **2004**, *43*, 7315–7323; f) E. M. Rumberger, S. J. Shah, C. C. Beedle, L. N. Zakharov, A. L. Rheingold, D. N. Hendrickson, *Inorg. Chem.* **2005**, *44*, 2742–2752; g) Y. Li, W. Wernsdorfer, R. Clérac, I. J. Hewitt, C. E. Anson, A. K. Powell, *Inorg. Chem.* **2006**, *45*, 2376–2378; h) J. van Slageren, P. Rosa, A. Caneschi, R. Sessoli, H. Casellas, Y. V. Rakitin, L. Cianchi, F. Del Giallo, G. Spina, A. Bino, A.-L. Barra, T. Guidi, S. Carretta, R. Caciuffo, *Phys. Rev. B* **2006**, *73*, 014422.
[19] a) R. C. Reem, E. I. Solomon, *J. Am. Chem. Soc.* **1987**, *109*, 1216–1226; b) A. Bencini A, D. Gatteschi, *EPR of Spin Coupled Systems*, Springer, New York, **1991**.
[20] In the strong exchange limit where we may assume that the ground state is characterized by $S = 4$, $\Delta_0 \approx (35/16)|D|(E/D)^4$ for $D < 0$. In the case of weak ferromagnetic coupling between two equivalent ferrous sites, $\Delta_0 \approx \Delta\iota^2/16|J|$ with $\Delta\iota = 3|D_i|(E_i/D_i)^2$ ($i = 1,2$).[18a]
[21] F. Hartmann-Boutron, *J. Phys. I* **1995**, *5*, 1281–1300.
[22] M. P. Hendrich, P. G. Debrunner, *Biophys. J.* **1989**, *56*, 489–506.
[23] a) M. P. Hendrich, L. L. Pearce, L. Que Jr, N. D. Chasteen, E. P. Day, *J. Am. Chem. Soc.* **1991**, *113*, 3039–3044; b) M. P. Hendrich, E. Münck, B. G. Fox, J. D. Lipscomb, *J. Am. Chem. Soc.* **1990**, *112*, 5861–5865; c) H. G. Jang, M. P. Hendrich, L. Que Jr, *Inorg. Chem.* **1993**, *32*, 911–918; d) M. P. Hendrich, E. D. Day, C.-P. Wang, B. S. Synder, R. H. Holm, E. Münck, *Inorg. Chem.* **1994**, *33*, 2848–2856.
[24] Although Equation (1) is more appropriate in the present case, Equation (2) suffices to describe the X-band EPR spectra from the ground-state non-Kramer's doublet of **1**. The simulations shown in Figure 5 were obtained with $D = +2.97\ cm^{-1}$, $E/D = 0.21$, $\sigma_{E/D} = 0.0241$, $g = 2.0$ and an intrinsic linewidth of 2.4 mT.
[25] B. G. Fox, M. P. Hendrich, K. K. Surereus, K. K. Andersson, W. A. Froland, J. D. Lipscomb, E. Münck, *J. Am. Chem. Soc.* **1993**, *115*, 3688–3701.
[26] N. Chakov, W. Wernsdorfer, K. A. Abboud, G. Christou, *Inorg. Chem.* **2004**, *43*, 5919–5930.
[27] In the original paper it was inadvertently noted that **1** forms pairs of 1D chains through π–π interactions in the crystal lattice. This was not detrimental to the discussion of its magnetic properties to that particular direction, but for the purposes of the present work a more careful structural analysis was carried out. This revealed that **1** actually forms pairs of molecules through π–π stacking.
[28] a) H. Oshio, N. Hoshino, T. Ito, *J. Am. Chem. Soc.* **2000**, *122*, 12602–12603; b) H. Oshio, N. Hoshino, T. Ito, M. Nakano, *J. Am. Chem. Soc.* **2004**, *126*, 8805–8812.
[29] A. K. Boudalis, B. Donnadieu, V. Nastopoulos, J. M. Clemente-Juan, A. Mari, Y. Sanakis, J.-P. Tuchagues, S. P. Perlepes, *Angew. Chem. Int. Ed.* **2004**, *43*, 2266–2270, and manuscript in preparation.

Received: February 13, 2007
Published Online: April 12, 2007

 © 2007 Wiley-VCH Verlag GmbH & Co. KGaA, Weinheim 

DOI: 10.1002/ejic.200700177

# A 1,10-Phenanthroline-Containing Ring Connected to a Porphyrin by a Rigid Aromatic Spacer and Its Copper-Complexed Pseudorotaxane

**Julien Frey,[a] William Dobbs,[a] Valérie Heitz,*[a] and Jean-Pierre Sauvage*[a]**

**Keywords:** Ligand design / Porphyrinoids / Macrocycles / Template synthesis / Rotaxane

A condensation reaction involving a free base tetraarylporphyrin-2,3-dione, a macrocyclic compound containing a 1,10-phenanthroline-5,6-dione and a 1,2,4,5-tetraminobenzene as a linker affords the corresponding conjugate in good yield. The porphyrin ring and the phenanthroline fragment of the other ring are connected in such a way that mutual rotation between these two groups is prohibited. Metallation of the porphyrinic site affords the corresponding zinc complex. By reacting this zinc porphyrin with copper(I), followed by the addition of the bidentate chelate 2,9-bis(*p*-anisyl)-1,10-phenanthroline, the threading reaction leading to the corresponding pseudorotaxane takes place quantitatively.
(© Wiley-VCH Verlag GmbH & Co. KGaA, 69451 Weinheim, Germany, 2007)

Porphyrins have been incorporated in rotaxanes and catenanes as electro- and photoactive components, mostly in relation to models of the photosynthetic reaction centre, to host–guest chemistry or to dynamic systems able to undergo large amplitude motions.[1] Our group has been particularly interested in energy and electron transfer studies within such rotaxanes or catenanes.[2] The porphyrin nucleus can be used as a stopper (for rotaxanes), either attached to or part of the ring.[3] Till now, limited geometrical control could be achieved as the mutual orientation between the porphyrin and the ring was not controlled, especially when the porphyrin fragment was appended to the cyclic component(s) of the rotaxane or the catenane. To have strict geometrical control over the system, it is necessary to connect the porphyrin and the ring by a rigid spacer, for which free rotation is not allowed. In the present report, we would like to describe the synthesis of such a conjugate consisting of a 30-membered ring built from 2,9-diaryl-1,10-phenanthroline and a free-base porphyrin or a zinc-complexed porphyrin. The spacer between these two components is a rigid aromatic nucleus. In addition, to demonstrate that the rigidly held porphyrin-macrocycle conjugates prepared can be used as components of interlocking structure, we have assembled a pseudorotaxane using the copper(I)-based strategy already applied in other related reactions.[2,3] The threaded species obtained by mixing the Zn-containing porphyrin-ring conjugate, copper(I) and a coordinating fragment of the 1,10-phenanthroline family, is indeed obtained in quantitative yield.

[a] Laboratoire de Chimie Organo-Minérale, LC 3 UMR 7177 du CNRS, Institut de Chimie, Université Louis Pasteur, 4 rue Blaise Pascal, 67070 Strasbourg Cedex, France
E-mail: heitz@chimie.u-strasbg.fr
sauvage@chimie.u-strasbg.fr

The synthetic strategy relies on porphyrin α-dione **1** similar to that used by Crossley and coworkers for making di- and multiporphyrins as well as electrodeficient porphyrins with quinoxaline groups at their periphery.[4] The other important fragment, namely the macrocycle containing phenanthroline dione **2**, was prepared in our group in the frame of another project dealing with multirotaxanes.[5] Phenanthroline–porphyrin conjugates with back-to-back connection were described recently by other groups but in these examples, the 1,10-phenanthroline part was not contained within the macrocycle.[6]

Starting diones **1** and **2**, as well as the condensation reaction leading to porphyrin conjugates **4** and **5**, are represented in Figure 1.

The synthesis of porphyrin α-dione **1** proceeds from the copper(II) complex of *meso*-tetra(3′,5′-di-*tert*-butylphenyl)-porphyrin, which was first reacted with $LiNO_3$ in AcOH/$Ac_2O$ to afford the corresponding β-nitro copper(II) porphyrin in high yield (90%) as described by Callot.[7] Then, adapted from Burn's methodology,[8] this porphyrin was demetallated with $H_2SO_4$ and the $NO_2$ function was reduced to an $NH_2$ group by $SnCl_2$ and HCl in $CH_2Cl_2$. The subsequent oxidation reaction leading to **1** was carried out by using Dess–Martin periodinane. The analytical and spectroscopic properties of the compound obtained are similar to those of the literature.[8] Compound **1** was obtained from the starting copper(II) porphyrin in four steps (nitration, demetallation, reduction and oxidation) with an overall yield of approximately 40%.

The coupling reaction between **1** and **2**[5] was performed by a stepwise condensation using 1,2,4,5-benzenetetramine.[6] Porphyrin α-dione **1** and benzenetetramine tetrahydrochloride **3** (1.2 equiv.) were dissolved in freshly distilled pyridine, and the reaction mixture was kept in the

 © 2007 Wiley-VCH Verlag GmbH & Co. KGaA, Weinheim 

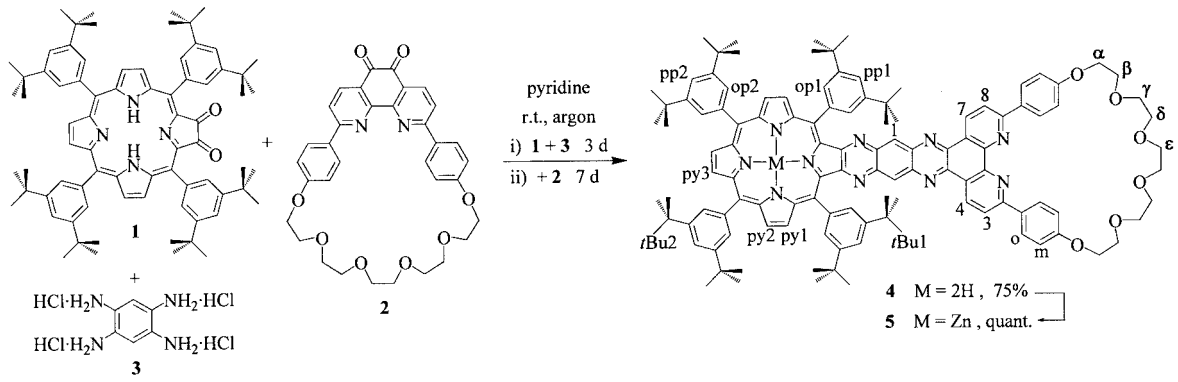


Figure 1. Stepwise condensation of the two diones with the bridging spacer.

dark. After gentle stirring at room temperature under an atmosphere of argon for 3 d, macrocycle **2** (1.5 equiv.) was added, and the reaction was prolonged under the same reaction conditions for an additional week. After workup and chromatographic purification (silica gel, $CH_2Cl_2$ with increasing amounts of $CH_3OH$ – up to 0.3% – as eluent), **4** was obtained as a violet solid in 75% yield. It was fully characterised by $^1H$ NMR spectroscopy and high resolution (HR) ESMS.

Metallation of the porphyrinic site of **4** was selectively carried out by the addition of $Zn(OAc)_2$ (5 equiv., dissolved in $CH_3OH$) to a solution of **4** in $CH_2Cl_2$ heated at reflux.[6] Further treatment with an EDTA solution to remove $Zn^{II}$ from the phenanthroline chelate allowed **5** to be obtained quantitatively from **4**.

The $^1H$ NMR spectra are in accordance with the structures of the compounds (Figure 2). As expected from the formation of the bridge at the back of the phenanthroline, protons 1 and 4,7 are strongly shifted upfield. Owing to the $C_{2v}$ symmetry of the molecule, protons *t*Bu1 differ from protons *t*Bu2, which gives rise to two sets of signals. For the same reason, proton py3 is assigned to a characteristic singlet at $\delta$ = 8.76 ppm.

Compounds **4** and **5** are well adapted to the synthesis of more elaborate catenanes and rotaxanes. As an example, pseudorotaxane **7**·$PF_6$ was prepared quantitatively from the various corresponding organic fragments, **5** and **6**, in the presence of copper(I), acting as a gathering and threading centre. As represented in Figure 3, **6** is a 2,9-disubstituted 1,10-phenanthroline that is able to form very stable four-coordinate complexes with copper(I) once associated to another bidentate chelate of the 1,10-phenanthroline family. As expected, the reaction proceeded very cleanly: stoichiometric amounts of **5** and $[Cu(CH_3CN)_4](PF_6)$ were first mixed in dichloromethane to afford the desired copper(I) complex. Subsequently, a stoichiometric quantity of **6** was added, which led to desired pseudorotaxane **7** quantitatively after workup. Compound **7**·$PF_6$ is a deep purple solid, which was characterised by $^1H$ NMR (COSY-ROESY) and electronic spectroscopy and HRESMS.

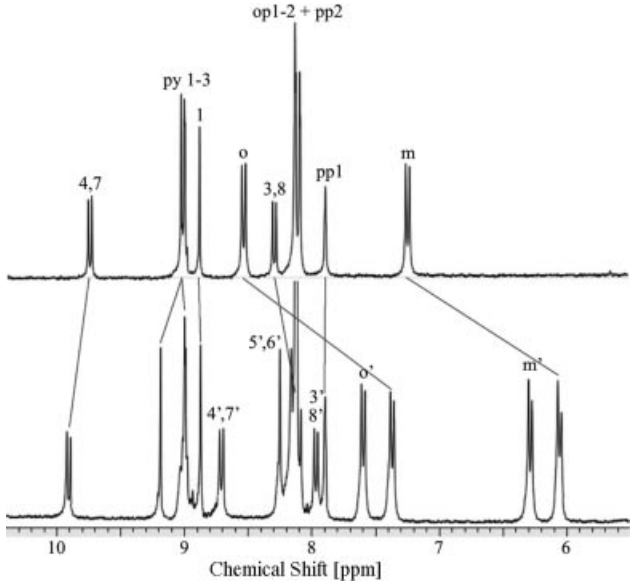


Figure 2. $^1H$ NMR spectra (aromatic region) of compounds **5** and **7**·$PF_6$ in $CD_2Cl_2$.

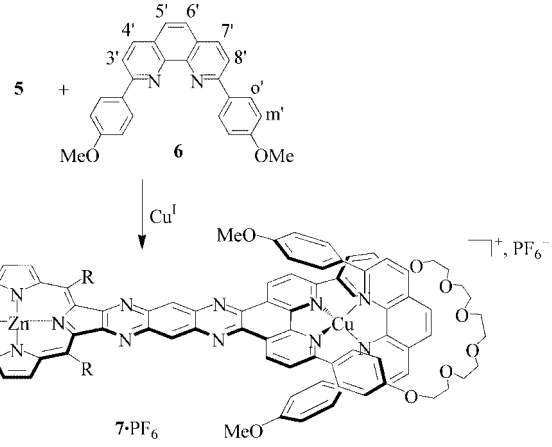


Figure 3. The threading reaction affording pseudorotaxane **7**.

To estimate the electronic coupling between the various aromatic fragments of **5** and **7** (the 1,10-phenanthroline chelate and the zinc-containing porphyrin), electronic absorption and emission measurements were performed. The absorption and emission spectra of the two compounds are represented in Figure 4.

 © 2007 Wiley-VCH Verlag GmbH & Co. KGaA, Weinheim 

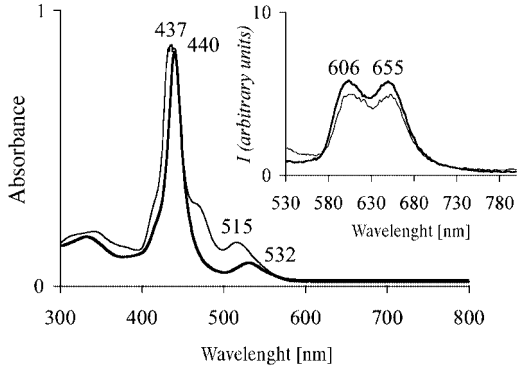


Figure 4. Normalised absorption and emission spectra (inset) of an optically matched solution of **5** (thin) and **7**·$PF_6$ (bold) (excitation at 438 nm) at 298 K in dichloromethane.

Interestingly, the Soret band for the two porphyrin-containing compounds is bathochromically shifted relative to that of the classical tetraaryl porphyrins.[9] Whereas a normal Soret band is typically observed around 420 nm for Zn porphyrins of this series, the present compounds show a Soret band in the range 435–440 nm. In addition, significant broadening is observed, which is a clear indication that the aromatic system is perturbed by the presence of the tetraazaanthracene nucleus at the periphery of the porphyrin, as already observed by Flamigni and coworkers.[10] The observed broadening is likely to be due to the loss of symmetry of the porphyrin aromatic system by introducing a tetraazaanthracene fragment at its rim. A contribution of a hypothetical 1,10-phenanthroline-porphyrin electronic coupling cannot be excluded.

Whereas the absorption spectra of **5** and **7** are significantly different from that of a normal zinc(II) tetraarylporphyrin, their emission spectra have emission maxima at similar values (**5** and **7**; $\lambda$ = 606, 655 nm). The tetraazaanthracene phenanthroline aromatic fragment at the back of the porphyrin has therefore little influence on the energy level of the lowest excited state of the porphyrin ring. This is quite surprising considering that in related tetraazaanthracene-substituted porphyrins studied by Flamigni and coworkers,[10] the excited state was stabilised by 0.2 eV. Nevertheless, in **5** and **7**, the emission intensity decreases dramatically and the quantum yield of the emission relative to that of zinc(II) 5,10,15,20-tetrakis(3,5-di-*tert*-butylphenyl)porphyrin is only 0.3%. Further photophysical studies will be performed to understand these results.

In conclusion, a new conjugate consisting of a porphyrin and a coordinating ring was prepared in a few steps from sophisticated organic fragments, with a relatively good overall yield. The zinc-complexed porphyrinic system was further utilised to prepare a novel pseudorotaxane by taking advantage of the template effect of copper(I). The conjugate itself, either containing a free base or a zinc porphyrin, is rigid, which allows strict control over the geometry of the system and over that of the pseudorotaxane prepared. The same will hold true for future, more complex rotaxanes and catenanes containing **4** and **5**.

## Experimental Section

**General:** Nuclear Magnetic Resonance (NMR) spectra were acquired with a Bruker AM300 spectrometer operating at 300.17 MHz. The spectra were referenced internally to residual proton-solvent reference. High resolution electrospray mass spectra (HRESMS) were recorded with a VG BOIQ triple quadrupole spectrometer by the Service de Spectrométrie de Masse (ISIS, Strasbourg). All anhydrous solvents were prepared by distillation under an atmosphere of argon with the use of the appropriate drying agents. All commercial chemicals were at the best commercially available grade and used without further purification. Thin layer chromatography was carried out with precoated polymeric sheets of silica gel (Macheray-Nagel, POLYGRAM, SIL G/$UV_{254}$) and preparative column chromatography was carried out by using silica gel (Merck Kiesegel, silica gel 60, 0.063–0.200 mm).

**Compound 4:** Avoiding light exposure, porphyrin tetraone **1** (50 mg, $4.58 \times 10^{-5}$ mol) and benzene tetramine tetrahydrochloride **3** (15.7 mg, $5.53 \times 10^{-5}$ mol, 1.2 equiv.) were dissolved in freshly distilled pyridine (25 mL), and the mixture was stirred at room temperature under an atmosphere of argon. After 2 d, macrocyclic dione **2** (41 mg, $6.87 \times 10^{-5}$ mol, 1.5 equiv.) was added under a stream of argon, and the solution was reacted for another week under the same conditions. After removal of the solvent, the product was extracted with $CH_2Cl_2$ (50 mL) and water (50 mL). The organic layers were separated, washed with water ($2 \times 50$ mL) and the solvents evaporated to dryness. The crude product (154 mg) was subjected to column chromatography (110 g of silica, prepared in $CH_2Cl_2$, gradient elution from $CH_2Cl_2$/MeOH 0 to 0.3%) to give compound **4** as a purple solid (60 mg, 75%). $^1$H NMR (300 MHz, $CD_2Cl_2$, COSY-ROESY, 25 °C): $\delta$ = 9.75 (d, $^3J_{H,H}$ = 8.4 Hz, 2 H, $H_{4,7}$), 9.10 (d, $^3J_{H,H}$ = 4.9 Hz, 2 H, $H_{py1}$), 9.03 (d, $^3J_{H,H}$ = 4.9 Hz, 2 H, $H_{py2}$), 8.95 (s, 2 H, $H_{py3}$), 8.76 (s, 2 H, $H_1$), 8.56 (m, $^3J_{H,H}$ = 8.8 Hz, 4 H, $H_o$), 8.31 (d, $^3J_{H,H}$ = 8.5 Hz, 2 H, $H_{3,8}$), 8.12–8.05 (m, 10 H, $H_{op1}$, $H_{op2}$, $H_{pp2}$), 7.86 (t, $^4J_{H,H}$ = 1.8 Hz, 2 H, $H_{pp1}$), 7.28 (m, $^3J_{H,H}$ = 8.9 Hz, 4 H, $H_m$), 4.39 (t, $^3J_{H,H}$ = 5.9 Hz, 4 H, $H_\alpha$), 3.88 (t, $^3J_{H,H}$ = 5.9 Hz, 4 H, $H_\beta$), 3.76–3.64 (m, 12 H, $H_\gamma$, $H_\delta$, $H_\varepsilon$), 1.57 (s, 36 H, $H_{tBu2}$), 1.54 (s, 36 H, $H_{tBu1}$), –2.35 (br. s, 2 H, $H_{NH}$) ppm. UV/Vis ($CH_2Cl_2$): $\lambda$ (log$\varepsilon$) = 434 (5.54) nm. HRESMS: calcd. for $C_{166}H_{127}N_{10}O_6$ and for 1/2[$C_{166}H_{127}N_{10}O_6$]$_2$ [**4** + H]$^+$ and [**4** + H]$_2^{2+}$ 1756.9967; found 1757.0025.

**Compound 5:** A solution of $Zn(OAc)_2$ (34 mg, $1.55 \times 10^{-4}$ mol, ca. 5 equiv.) in MeOH (7 mL) was added to a boiling solution of compound **4** (50 mg, $2.85 \times 10^{-5}$ mol) in $CH_2Cl_2$ (25 mL), and the mixture was heated at reflux for 6 h. After removal of the solvents, the product was extracted with $CH_2Cl_2$ (50 mL) and water ($2 \times 50$ mL). The organic layers were separated, and the volume of the solution was reduced to approximately 30 mL. A solution of [EDTA]$Na_4$ (0.1 M, pH ca. 4–5, 10 mL) was added, and the mixture was stirred for 24 h. The organic layers were then extracted with $CH_2Cl_2$ (80 mL), separated, washed with saturated $Na_2CO_3$ (50 mL), brine (50 mL) and water (100 mL) and the solvents evaporated to dryness to give quantitatively compound **5** (51 mg). $^1$H NMR (300 MHz, $CD_2Cl_2$, COSY-ROESY, 25 °C): $\delta$ = 9.69 (d, $^3J_{H,H}$ = 8.4 Hz, 2 H, $H_{4,7}$), 8.98 (s, 2 H, $H_{py3}$), 8.97–8.94 (2d, $^3J_{H,H}$ = 4.8 Hz, 4 H, $H_{py1}$, $H_{py2}$), 8.85 (s, 2 H, $H_1$), 8.48 (m, $^3J_{H,H}$ = 8.8 Hz, 4 H, $H_o$), 8.24 (d, $^3J_{H,H}$ = 8.5 Hz, 2 H, $H_{3,8}$), 8.11–8.04 (m, 10 H, $H_{op1}$, $H_{op2}$, $H_{pp2}$), 7.85 (t, $^4J_{H,H}$ = 1.8 Hz, 2 H, $H_{pp1}$), 7.18 (m, $^3J_{H,H}$ = 8.8 Hz, 4 H, $H_m$), 4.26 (t, $^3J_{H,H}$ = 5.9 Hz, 4 H, $H_\alpha$), 3.73 (t, $^3J_{H,H}$ = 5.9 Hz, 4 H, $H_\beta$), 3.62–3.51 (m, 12 H, $H_\gamma$, $H_\delta$, $H_\varepsilon$), 1.57 (s, 36 H, $H_{tBu2}$), 1.55 (s, 36 H, $H_{tBu1}$) ppm. UV/Vis ($CH_2Cl_2$): $\lambda$ (log$\varepsilon$) = 437 (5.47), 515 (4.66) nm. HRESMS: calcd. for $C_{116}H_{124}N_{10}O_6Zn$ [**5** – e]$^+$

 © 2007 Wiley-VCH Verlag GmbH & Co. KGaA, Weinheim 

1818.9017; found 1818.8987 and calcd. for $C_{116}H_{125}N_{10}O_6Zn$ [**5** + H]$^+$ 1819.9095; found 1819.9013.

**Compound 7·PF$_6$:** A solution of $[Cu(MeCN)_4](PF_6)$ (3.6 mg, $9.34 \times 10^{-6}$ mol) in MeCN (5 mL) was added by cannula to a degassed solution of **4** (17.0 mg, $9.34 \times 10^{-6}$ mol) in $CH_2Cl_2$ (5 mL), and the mixture was stirred under an atmosphere of argon for 30 min. A degassed solution of dianisyl phenanthroline **6** (3.67 mg, $9.34 \times 10^{-6}$ mol) in $CH_2Cl_2$ (5 mL) was then also added by cannula. After stirring for 2 h, the solution was extracted with $CH_2Cl_2$ (50 mL) and water (50 mL); the organic layers were separated, dried with $MgSO_4$ and evaporated to give pure rotaxane **7** as its $PF_6$ salt (22 mg, 97%). $^1$H NMR (300 MHz, $CD_2Cl_2$, COSY-ROESY, 25 °C): $\delta$ = 9.88 (d, $^3J_{H,H}$ = 8.4 Hz, 2 H, $H_{4,7}$), 9.16 (s, 2 H, $H_{py3}$), 8.97–8.98 (2d, $^3J_{H,H}$ = 4.6 Hz, 4 H, $H_{py1}$, $H_{py2}$), 8.86 (s, 2 H, $H_1$), 8.68 (d, $^3J_{H,H}$ = 8.4 Hz, 2 H, $H_{4',7'}$), 8.22 (s, 2 H, $H_{5',6'}$), 8.13 (t, $^4J_{H,H}$ = 1.8 Hz, 2 H, $H_{pp2}$), 8.13 (t, $^4J_{H,H}$ = 1.7 Hz, 2 H, $H_{pp1}$), 8.06 (m, 10 H, $H_{3,8}$, $H_{op1}$, $H_{op2}$), 7.94 (d, $^3J_{H,H}$ = 8.4 Hz, 2 H, $H_{3',8'}$), 7.87 (t, $^4J_{H,H}$ = 1.7 Hz, 2 H, $H_{pp1}$), 7.57 (m, $^3J_{H,H}$ = 8.6 Hz, 4 H, $H_{o'}$), 7.35 (m, $^3J_{H,H}$ = 8.6 Hz, 4 H, $H_o$), 6.27 (m, $^3J_{H,H}$ = 8.6 Hz, 4 H, $H_{m'}$), 6.04 (m, $^3J_{H,H}$ = 8.6 Hz, 4 H, $H_m$), 3.85 (s, 4 H, $H_\varepsilon$), 3.79–3.55 (3m, 16 H, $H_\delta$, $H_\gamma$, $H_\beta$, $H_\alpha$), 3.26 (s, 6 H, $H_{OMe}$), 1.60 (s, 36 H, $H_{tBu2}$), 1.55 (s, 36 H, $H_{tBu1}$) ppm. UV/Vis ($CH_2Cl_2$): $\lambda$ (log$\varepsilon$) = 440 (5.55), 532 (4.55) nm. HRESMS: calcd. for $C_{142}H_{144}N_{12}O_8CuZn$ 2274.9843; found 2274.9647.

## Acknowledgments

We thank the Ministry of Education for a fellowship to J. F. We are also grateful to Professor H. Callot for helpful discussions.

[1] a) J.-C. Chambron, V. Heitz, J.-P. Sauvage, "Non Covalent Multiporphyrin Assemblies" in *Handbook of Porphyrins* **1999**, vol. 6, pp. 1–42; b) N. Solladié, J.-C. Chambron, J.-P. Sauvage, *J. Am. Chem. Soc.* **1999**, *121*, 3684–3692; c) M.-J. Blanco, J.-C. Chambron, V. Heitz, J.-P. Sauvage, *Org. Lett.* **2000**, *2*, 3051–3054; d) N. Watanabe, N. Kihara, Y. Furusho, T. Takata, Y. Araki, O. Ito, *Angew. Chem. Int. Ed.* **2003**, *42*, 682–683; e) K. Li, P. Bracher, D. M. Guldi, M. A. Herranz, L. Echegoyen, D. I. Schuster, *J. Am. Chem. Soc.* **2004**, *126*, 9156–9157; f) K. Li, D. I. Schuster, D. M. Guldi, M. A. Herranz, L. Echegoyen, *J. Am. Chem. Soc.* **2004**, *126*, 3388–3389; g) D. I. Schuster, K. Li, D. M. Guldi, J. Ramey, *Org. Lett.* **2004**, *6*, 1919–1922; h) M. J. Gunter, T. P. Jeynes, P. Turner, *Eur. J. Org. Chem.* **2004**, 193–208 and references cited therein.

[2] a) J.-C. Chambron, A. Harriman, V. Heitz, J.-P. Sauvage, *J. Am. Chem. Soc.* **1993**, *115*, 6109–6114; b) A. Harriman, V. Heitz, J.-C. Chambron, J.-P. Sauvage, *Coord. Chem. Rev.* **1994**, *132*, 229–234; c) J.-C. Chambron, J.-P. Collin, J.-O. Dalbavie, C. O. Dietrich-Buchecker, V. Heitz, F. Odobel, N. Solladié, J.-P. Sauvage, *Coord. Chem. Rev.* **1998**, *178–180*, 1299–1312; d) L. Flamigni, N. Armaroli, F. Barigelletti, J.-C. Chambron, J.-P. Sauvage, N. Solladié, *New J. Chem.* **1999**, *23*, 115–1158; e) M.-J. Blanco, M. Consuelo Jiménez, J.-C. Chambron, V. Heitz, M. Linke, J.-P. Sauvage, *Chem. Soc. Rev.* **1999**, *28*, 293–305.

[3] a) M. Linke, J.-C. Chambron, V. Heitz, J.-P. Sauvage, *J. Am. Chem. Soc.* **1997**, *119*, 11329–11330; b) M. Linke, J.-C. Chambron, V. Heitz, J.-P. Sauvage, V. Semetey, *Chem. Commun.* **1998**, 2469–2470; c) D. B. Amabilino, J.-P. Sauvage, *New J. Chem.* **1998**, *22*, 395–409; d) M. Andersson, M. Linke, J.-C. Chambron, J. Davidsson, V. Heitz, J.-P. Sauvage, *J. Am. Chem. Soc.* **2000**, *122*, 3526–3527; e) M. Linke, N. Fujita, J.-C. Chambron, V. Heitz, J.-P. Sauvage, *New J. Chem.* **2001**, *25*, 790–796; f) L. Flamigni, A. M. Talarico, J.-C. Chambron, V. Heitz, M. Linke, N. Fujita, J.-P. Sauvage, *Chem. Eur. J.* **2004**, *10*, 2689–2699.

[4] a) M. J. Crossley, L. G. King, *J. Chem. Soc., Chem. Commun.* **1984**, 920–922; b) M. M. Catalano, M. J. Crossley, M. M. Harding, L. G. King, *J. Chem. Soc., Chem. Commun.* **1984**, 1535–1536; c) M. J. Crossley, P. Thordarson, *Angew. Chem. Int. Ed.* **2002**, *41*, 1709–1712; d) Z. Ou, K. M. Kadish, E. Wenbo, J. Shao, P. J. Sintic, K. Ohkubo, S. Fukuzumi, M. J. Crossley, *Inorg. Chem.* **2004**, *43*, 2078–2086.

[5] a) J. Frey, T. Kraus, V. Heitz, J.-P. Sauvage, *Chem. Commun.* **2005**, 5310–5312; b) T. Kraus, M. Buděšinsky, J. Cvačka, J.-P. Sauvage, *Angew. Chem. Int. Ed.* **2006**, *45*, 258–261.

[6] For a related reaction, see: a) M. J. Crossley, P. L. Burn, S. J. Langford, J. K. Prashar, *J. Chem. Soc., Chem. Commun.* **1995**, 1921–1923; b) T. Vannelli, T. B. Karpishin, *Inorg. Chem.* **1999**, *38*, 2246–2247.

[7] S. Richeter, C. Jeandon, J.-P. Gisselbrecht, R. Ruppert, H. Callot, *Inorg. Chem.* **2004**, *43*, 251–263.

[8] V. Promarak, P. L. Burn, *J. Chem. Soc., Perkin Trans. 1* **2001**, 14–20.

[9] M. Gouterman, *The Porphyrins* (Ed.: D. Dolphin), Academic Press, New York, **1978**, vol 3, pp. 1–12.

[10] L. Flamigni, G. Marconi, M. R. Johnston, *Chem. Phys. Phys. Chem.* **2001**, *3*, 4488–4494.

Received: February 6, 2007
Published Online: April 16, 2007

 © 2007 Wiley-VCH Verlag GmbH & Co. KGaA, Weinheim 

DOI: 10.1002/ejic.200700215

# Pirouetting Copper(I)-Assembled Pseudo-Rotaxanes: Strong Influence of the Axle Structure on the Motion Rate

**Jean-Paul Collin,[a] Fabien Durola,[a] Pierre Mobian,[a] and Jean-Pierre Sauvage*[a]**

**Keywords:** Pseudo-rotaxanes / Diimine ligands / Copper complexes / Coordination modes / Pirouetting motion

Based on the gathering and threading effect of copper(I), three different pseudo-rotaxanes have been prepared and characterised in solution. They consist of the same two-chelate ring and various coordinating fragments threaded through the ring. The ring-incorporated chelates are a 2,2′,6′,6′′-terpyridine (terpy) unit and a 2,9-diphenyl-1,10-phenanthroline (dpp) motif. The threaded chelates are a 2,9-bis(*p*-anisyl)-1,10-phenanthroline (dap), a 6,6′-bis(*p*-anisyl)-2,2′-bipyridine (dabipy) or a 8,8′-diphenyl-3,3′-biisoquinoline (dpbiiq) derivative. Using electrochemical techniques, the pirouetting motions of the axle within the ring through which it is threaded have been investigated. In dichloromethane/acetonitrile, a strong dependence of the motion rate on the structure of the threaded chelate has been observed, evidencing that rigidity of the thread-contained chelate and steric hindrance lead to slow moving molecular machines. Pirouetting is the main dynamic process observed but unthreading of the string-like organic component represents another minor electrochemically induced reaction.

(© Wiley-VCH Verlag GmbH & Co. KGaA, 69451 Weinheim, Germany, 2007)

## Introduction

The field of synthetic molecular machines and motors is receiving much attention,[1] either in relation to catenanes and rotaxanes[2] or based on non-interlocking molecules.[3] In this former family of compounds, transition metal-containing systems have been much investigated.[4] As far as interlocking molecular assemblies are concerned, transition metals play an equally important role. Our group has proposed several types of dynamic systems, the mobile components of the machine being set in motion either by an electrochemical signal,[5] a photochemical stimulus[6] or a chemical reaction.[7] Copper-containing pirouetting rotaxanes represent an interesting subclass of such dynamic systems. They can be regarded as simple models of future rotary motors, whose elaboration seems today to be highly complex when interlocking compounds are used.[8] They can also be of interest by themselves as bistable species whose states display very different geometrical properties.

In this article we would like to report on the synthesis and the dynamic properties of three copper-complexed pseudo-rotaxanes whose motions are triggered by a redox process ($Cu^{II}/Cu^{I}$). By comparing the electrochemical behaviour of these three compounds, important information on the influence of the structural parameters on the motion rate could be obtained. As far as we are aware, limited studies have been carried out on the controlled dynamic properties of pseudo-rotaxanes. The first one is particularly significant since it triggered the interest of the scientific community for interlocking compounds-based molecular machines.[9] Later on, our group has made and investigated a shuttle-like pseudo-rotaxane[10] and its corresponding rotaxane.[11] Although shuttling of the pseudo-rotaxane was clearly evidenced, we could also identify another process, the unthreading reaction, which interfered with the ring translation motion. Obviously, the rates of both processes must be related since some of the rearrangement steps for these distinct reactions are identical.

## Results and Discussions

The pirouetting rearrangement described herein is sketched in Scheme 1. The three threaded species have been prepared according to the classical procedure from our group, based on coordination of two bidentate chelates on a copper(I) centre.[12] Obviously, the cyclic nature of **4** prevents formation of tetrahedral copper(I) complexes consisting of two such dpp-containing ligands. This simple principle has important consequences since the coordination reaction will necessarily lead to the formation of a threaded species provided the correct copper(I)-two-bidentate ligand stoichiometry is respected.[13] The copper(I)-induced gathering and threading reaction is represented in Figure 1 along with the chemical formulae of the various precursors and the products.

Compound **4** is a 33-membered ring that has been used in several studies carried out in our group on controlled dynamic catenanes and rotaxanes. The presence of the terpy

[a] Laboratoire de Chimie Organo-Minerale, UMR 7177 du CNRS
Institut de Chimie, Université Louis Pasteur,
1 rue Blaise Pascal, 67000 Strasbourg Cedex, France
Fax: +33-390-241-368
E-mail: sauvage@chimie.u-strasbg.fr

 InterScience © 2007 Wiley-VCH Verlag GmbH & Co. KGaA, Weinheim 

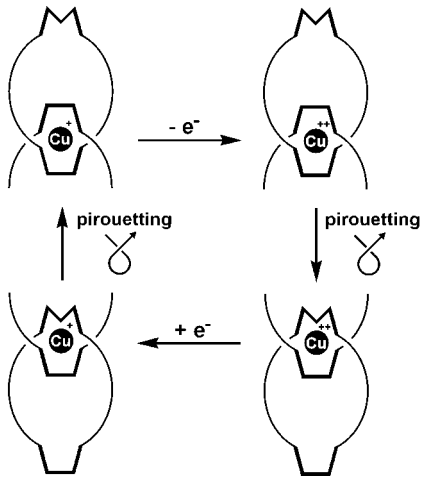


Scheme 1. Pirouetting principle of copper complexed pseudo-rotaxanes. The U-shaped symbols represent bidentate chelates (dpp for the ring-comprised chelate and dap, dabipy or dpbiiq for the chelates belonging to the thread). The M-shaped symbol designates the tridentate terpy coordinating motif.

site in its structure does not interfere with the threading reaction since copper(I) interacts preferably with bidentate chelates such as dpp. This behaviour has been unambiguously demonstrated by $^1$H-NMR analysis of the concerned pseudo-rotaxanes. The three string-like fragments contain markedly different chelates. **5** incorporates a dpp unit. It is thus a highly rigid block due to the presence of the 1,10-phenanthroline core. At the same time it is rather bulky due to the two phenyl groups close to the coordination site of the ligand. **6** is equally sterically hindering but the pyridine nuclei of the 2,2′-bipy fragment can easily rotate with respect to one another about the $C^2$–$C^{2'}$ bond. Finally, the dpbiiq fragment of **7** is such that steric hindrance around the complexing site of the ligand is limited, due to the large separation between the two lateral phenyl rings borne by the 3,3′-biisoquinoline nucleus. In addition, free rotation about the $C^3$–$C^{3'}$ bond allows this ligand to rearrange easily. Ligand **7** could be obtained in high yield via a two-step procedure as depicted in Figure 2. The first step concerns the formation of diphenol compound **9** from 8,8′-dianisyl-3,3′-biisoquinoline (**8**) using a classical ether deprotection method. The resulting diphenol **9** was then converted into the target ligand **7** following a classical Williamson methodology ($Cs_2CO_3$, DMF, 55 °C) by reaction with 2 equiv. of commercially available 2-(6-bromohexyloxy)-tetrahydro-2*H*-pyran.

Three complexes $\mathbf{1}_4^+$, $\mathbf{2}_4^+$ and $\mathbf{3}_4^+$ were synthesized as shown in Figure 1. The synthesis of these copper complexes were performed using a methodology usually employed in our group. In a typical procedure, the macrocycle **4** was dissolved in a degassed solution of dichloromethane and

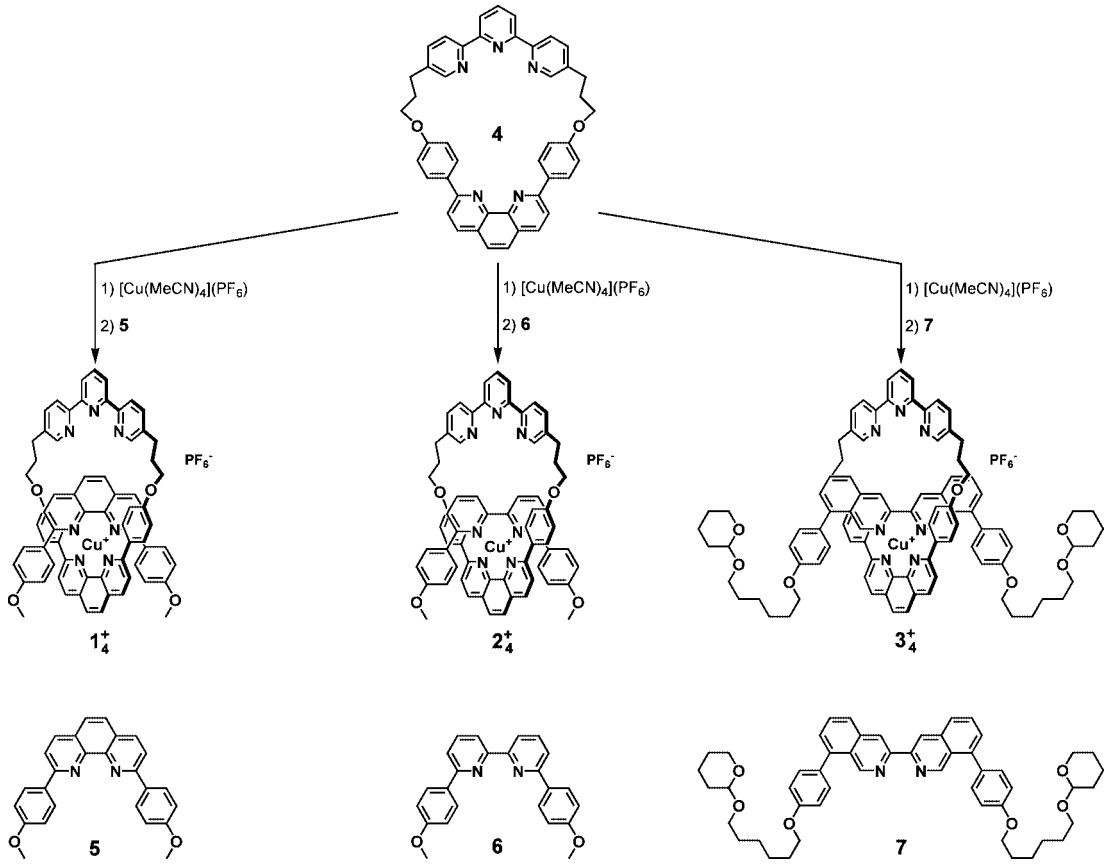


Figure 1. Copper(I)-directed synthesis of the three pseudo-rotaxanes $\mathbf{1}_4^+$, $\mathbf{2}_4^+$ and $\mathbf{3}_4^+$ described in this article. The subscript 4 refers to the coordination number of the copper centre. In the copper(I) complexes of the graphic, the coordination number is equal to 4 since the metal is coordinated to a dpp fragment and another bidentate chelate belonging to the thread.

 © 2007 Wiley-VCH Verlag GmbH & Co. KGaA, Weinheim 

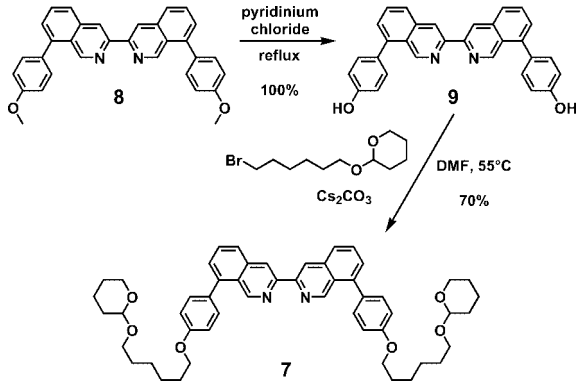


Figure 2. Preparation of ligand **7** from 8,8′-bis(*p*-anisyl)-3,3′-biisoquinoline (**8**). The demethylation reaction is quantitative. Compound **7** can be obtained in good yield from **9** after chromatographic separation.

acetonitrile (1:1). Upon addition of the copper salt (1 equiv.), the solution turned immediately to dark orange. The reaction mixture was stirred for 20 min and the diimine ligand (respectively **5**, **6** and **7**) was then added. A dark red solution was instantaneously obtained. This color, which is characteristic of copper(I) complexes of aromatic diimine ligands, indicates that the complexation process occurred efficiently. After, the solution was stirred for two hours under argon at room temperature, and the solvents were evaporated. The complexation process occurred quasi-quantitavely as evidence by $^1$H-NMR spectroscopy. Due to their instability on chromatographic supports, complexes $\mathbf{1}_4^+$, $\mathbf{2}_4^+$ or $\mathbf{3}_4^+$ were not further purified and were directly submitted to the electrochemical measurements.

## Electrochemically-Driven Molecular Motions

The cyclic voltammograms of Scheme 2 have been obtained by scanning first from –0.4 V to +1.0 V, with a silver wire as a pseudo-reference electrode, the return scan being carried out immediately after the potential of +1.0 V was reached. The oxidation potential for the reaction

4-coordinate $Cu^I$ complex – $e^- \rightarrow$ 4-coordinate $Cu^{II}$ complex

is thus easily read from the cyclic voltammograms. Their values at a scan rate of 800 mV/s are indicated on the Scheme 2.

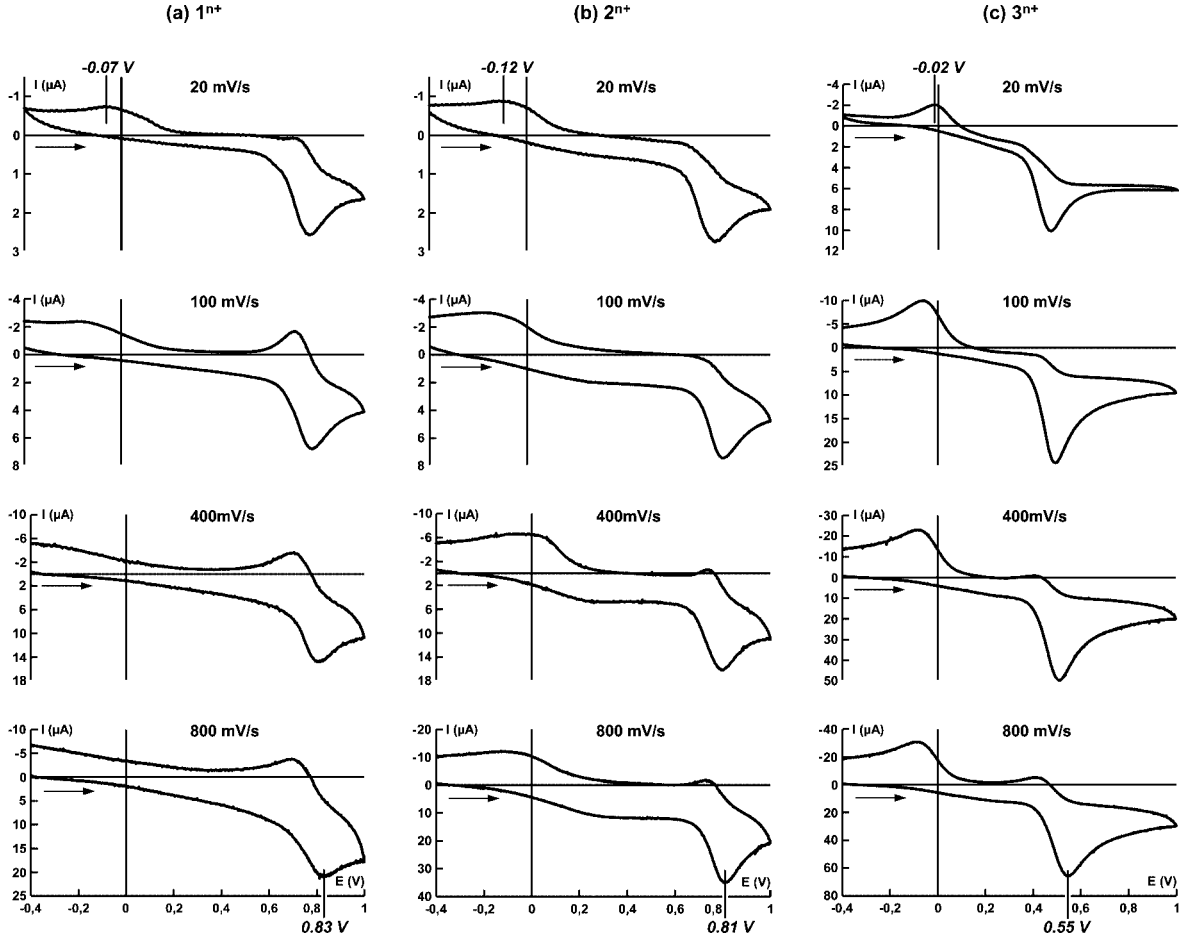


Scheme 2. Cyclic voltammograms of complexes $\mathbf{1}_4^+$, $\mathbf{2}_4^+$ and $\mathbf{3}_4^+$ recorded with a Pt working electrode in $CH_2Cl_2/CH_3CN$ (1:9) with 0.1 M $Bu_4NBF_4$ at four different scan rates (20, 100, 400 and 800 mV/s). The electrochemical responses of the four-coordinate copper(II) complexes are found around +0.7 V (for $\mathbf{1}^{2+}$ and $\mathbf{2}^{2+}$) or around +0.5 V (for $\mathbf{3}^{2+}$), whereas reduction of five-coordinate copper(II) complexes $\mathbf{1}_5^{2+}$, $\mathbf{2}_5^{2+}$ and $\mathbf{3}_5^{2+}$ occurs around –0.1 V.

 © 2007 Wiley-VCH Verlag GmbH & Co. KGaA, Weinheim 

At a high scan rate, the return wave corresponding to the following process

4-coordinate $Cu^{II}$ complex + $e^- \rightarrow$ 4-coordinate $Cu^{I}$ complex

is easily observed, which allows to determine $E_{1/2}$ and $\Delta Ep$ for the three studied complexes:

$\mathbf{1}_4^{2+}/\mathbf{1}_4^{+}$: $E_{1/2}$ = +0.76 V

$\mathbf{2}_4^{2+}/\mathbf{2}_4^{+}$: $E_{1/2}$ = +0.77 V

$\mathbf{3}_4^{2+}/\mathbf{3}_4^{+}$: $E_{1/2}$ = +0.49 V

$\Delta Ep$ varies between 80 mV and 120 mV within the series of three complexes. At a lower scan rate, rearrangement of the thermodynamically unstable four-coordinate copper(II) takes place, at least in part, before this complex is reduced back to its monovalent corresponding state. This is clearly seen by the presence of a peak between –0.2 V and 0 V.

From the $E_{1/2}$ values of the four-coordinate complexes, it is clear that the four-coordinate copper(I) state is more stabilised in $\mathbf{1}_4^{+}$ and $\mathbf{2}_4^{+}$ than in complex $\mathbf{3}_4^{+}$. This can easily be understood by considering the steric arrangements of the compounds. Whereas $\mathbf{1}_4^{+}$ and $\mathbf{2}_4^{+}$ contain a highly shielding set of ligands (both chelates of each complex bear phenyl rings attached on the *ortho* positions to the N atoms), the thread of $\mathbf{3}_4^{+}$ is less encumbering.

As far as the five-coordinate copper(I) or copper(II) states are concerned, important information can be obtained at low scan rate. By analogy with the oxidation potentials of the four-coordinate copper(I) complexe, the reduction potentials of the corresponding five-coordinate copper(II) complexes can easily be estimated from the cyclic voltammograms. They are also indicated on Scheme 2, for a scan rate of 20 mV/s. It is noteworthy that the reduction potentials ($Cu^{II}/Cu^{I}$) for the three studied complexes are almost identical ($E_{red} \approx$ –0.07 V). This observation tends to indicate that, as expected, the five-coordinate state is less sensitive to steric hindrance than the tetrahedral or pseudo-tetrahedral geometry.

The chemical reversibility of the redox processes depends much on the nature of the complex and on the scan rate. As already observed with pirouetting rotaxanes,[5] as the scan rate is increased, the reversibility of the four-coordinate copper(I) complex oxidation reaction increases. By scanning at a lower and lower rate, rearrangement of the system becomes more and more noticeable, as evidenced by the increase of the wave corresponding to the reduction of the five-coordinate copper(II) complex. In parallel, the reduction wave for the four-coordinate complex decreases. Generally speaking, if this latter one is intense, this implies that the compound has no time to rearrange substantially. By contrast, if the reduction wave around +0.42 V (for $\mathbf{3}_4^{2+}$) is small, the complex undergoes a complete rearrangement to a large proportion.

If the scan rate is sufficently slow (< 20 mV/s), the three complexes have time to rearrange as shown by the absence of any reduction wave at +0.4 V to +0.8 V. On the other hand, the presence of a reduction wave at a slightly negative potential may indicate that a certain proportion of the four-coordinate copper(II) complex underwent a pirouetting motion, which does not exclude that a certain amount led to unthreading and dissociation.

By comparing $\mathbf{1}^{n+}$ and $\mathbf{2}^{n+}$, especially at 100 mV/s, it is obvious that $\mathbf{1}_4^{2+}$ is much less mobile than $\mathbf{2}_4^{2+}$. This is confirmed at 400 mV/s since at this scan rate, $\mathbf{1}_4^{2+}$ does not seem to rearrange significantly whereas the major part of $\mathbf{2}_4^{2+}$ is converted into the rearranged complex $\mathbf{2}_5^{2+}$. The difference between $\mathbf{1}^{n+}$ and $\mathbf{2}^{n+}$ holds to the presence of a 1,10-phenanthroline (phen) unit in the thread of the former complex and 2,2′-bipyridine (bipy) chelate for the latter complex. The comparison between their electrochemical properties allows to estimate the effect of having a rigid block (phen) vs. a potentially flexible chelate (bipy) with rotation around the C–C bond connecting the two pyridine nuclei. It should be noticed that both threads (in $\mathbf{1}^{n+}$ and $\mathbf{2}^{n+}$) are equally sterically hindering since they contain the same number of phenyl rings at identical positions.

Very spectacular is the effect of the biisoquinoline ligand, as demonstrated by the electrochemical behaviour of $\mathbf{3}^{n+}$. Even at 800 mV/s reversibility is almost completely lost, with the appearance of a relatively intense wave at ≈ –0.1 V corresponding to the reduction process of the rearranged complex $\mathbf{3}_5^{2+}$. This observation is directly related to the non sterically hindering nature of **7** which facilitates ligand exchange in the coordination sphere of the metal. The presence of two elongating groups attached on the phenolic oxygen atoms of **7** may also increase the chemical reversibility of the pirouetting process, inhibiting at least in part the unthreading reaction.

A rough estimation of the rate constant for the rearrangement of the four-coordinate copper(II) complex can be obtained from electrochemical measurements and, in particular, from Scheme 2:

$\mathbf{1}_4^{2+} \rightarrow \mathbf{1}_5^{2+}$, $k \approx 0.1\ s^{-1}$

$\mathbf{2}_4^{2+} \rightarrow \mathbf{2}_5^{2+}$, $k \approx 1\ s^{-1}$

$\mathbf{3}_4^{2+} \rightarrow \mathbf{3}_5^{2+}$, $k \approx 5\ s^{-1}$

Concerning the pirouetting motion, pseudo-rotaxane $\mathbf{3}^{n+}$, incorporating a dpbiiq fragment in its thread, is about 50 times more efficient than pseudo-rotaxane $\mathbf{1}^{n+}$, which threaded ligand (dap) is more rigid and more sterically hindering.

As far as the rearrangement of the five-coordinate copper(I) complexes is concerned, the reaction was shown to be too fast for the presently used electrochemical techniques. This is in good agreement with previous studies.[5]

## Conclusion

Three copper(I)-assembled pseudo-rotaxanes were synthesized. These molecular machine precursors contain the same two-chelate ring and three different diimine ligands threaded through the macrocycle. The rearrangement of these complexes from the four-coordinate $Cu^{II}$ to the five-coordinate $Cu^{II}$ species has been investigated by cyclic voltammetry. The electrochemical responses clearly show a great difference of dynamic behaviour between these three

 © 2007 Wiley-VCH Verlag GmbH & Co. KGaA, Weinheim 

prepared pseudo-rotaxanes. An estimation of the rate of ligand exchange was possible. These results highlight that the flexibility of the threaded chelate and low steric hindrance of its coordination site give rise to fast-moving molecular machines.

## Experimental Section

The following chemicals were obtained commercially and were used without further purification: 2-(6-bromohexyloxy)-tetrahydro-2*H*-pyran (Aldrich), cesium carbonate (Aldrich).

Dry solvents were obtained with suitable dessicants: *N*,*N*-dimethylformamide was distilled from anhydrous aluminum oxide, dichloromethane from calcium hydride. Fluka aluminum oxide (no. 17994) was used for alumina columns and filtrations.

$^1$H NMR spectra were recorded with a Bruker AVANCE 300 (300 MHz, $^1$H) spectrometer using deuterated solvents. The spectra were collected at 25 °C and the chemical shifts were referenced to residual solvent protons as internal standards. $^1$H: [D$_6$]DMSO δ = 2.50 ppm, $CD_2Cl_2$ δ = 5.32 ppm, $CD_3CN$ δ = 1.93 ppm. Mass spectra were obtained with a VG ZAB-HF spectrometer (FAB) and a VG-BIOQ triple quadrupole in positive or negative mode (ES-MS).

Electrochemical measurements were performed with a three-electrode system consisting of a platinum working electrode, a platinum wire counter electrode, and a silver wire as a pseudo-reference electrode. All measurements were carried out at room temperature under Ar, in degassed spectroscopic grade solvents, using 0.1 M $n$Bu$_4$NBF$_4$ solutions in $CH_2Cl_2$/$CH_3CN$ (1:9) as supporting electrolyte. An EG&G Princeton Applied Research model 273A potentiostat connected to a computer was used (software from Electrochemistry Research).

**8,8′-Dihydroxyphenyl-3,3′-biisoquinoline (9):** 8,8′-Dianisyl-3,3′-biisoquinoline (**8**) (1.00 g, 2.13 mmol) and pyridinium chloride (about 10 equiv., 2.5 g) are mixed into a little flask and heated to reflux in an adapted microwave oven for 10 min. Twice, the same quantity of pyridinium chloride is added and the mixture heated to reflux again for 10 min. The mixture is dissolved in distilled water (1 L) and then neutralised with sodium hydroxide to give a suspension of a pale yellow precipitate. After filtration, the given compound is quantitatively obtained without further purification (pale yellow solid, 94 mg, 100%). M.p. > 300 °C. $^1$H NMR ([D$_6$]-DMSO, 300 MHz): $\delta$ = 9.35 (s, 2 H), 9.09 (s, 2 H), 8.15 (d, $J$ = 8.2 Hz, 2 H), 7.94 (t, $J$ = 7.7 Hz, 2 H), 7.65 (d, $J$ = 7.0 Hz, 2 H), 7.45 (d, $J$ = 8.4 Hz, 4 H), 7.00 (d, $J$ = 8.4 Hz, 4 H) ppm. ES-MS: $m/z$ = 441.1559 (calculated 441.1598 for $C_{30}H_{20}N_2O_2 + H^+$).

**Ligand 7:** 2-(6-Bromohexyloxy)-tetrahydro-2*H*-pyran (180 mg, 0.68 mmol), cesium carbonate (150 mg, 0.45 mmol) and 8,8′-dihydroxyphenyl-3,3′-biisoquinoline **9** (50 mg, 0.11 mmol) were mixed in dry DMF (10 mL) and stirred under Ar at 55 °C overnight. The solvent was removed and the residue was taken up with $CH_2Cl_2$/$H_2O$. The organic phase was separated and the aqueous phase extracted twice with dichloromethane. The combined organic phases were washed first with brine, then with distilled water. The solvent was removed and the residue purified by chromatography over aluminium oxide by using dichloromethane/pentane (1:4) as the eluent to give the title compound (white solid, 60 mg, 65%). $^1$H NMR ($CD_2Cl_2$, 300 MHz): $\delta$ = 9.47 (s, 2 H), 8.98 (s, 2 H), 8.00 (d, $J$ = 8.4 Hz, 2 H), 7.78 (dd, $J$ = 8.1, 8.4 Hz, 2 H), 7.55 (d, $J$ = 8.1 Hz, 2 H), 7.54 (d, $J$ = 8.7 Hz, 4 H), 7.12 (d, $J$ = 8.7 Hz, 4 H), 4.60 (t, $J$ = 3.7 Hz, 2 H), 4.12 (t, $J$ = 6.6 Hz, 4 H), 3.92–3.74 (m, 4 H), 3.54–3.40 (m, 4 H), 1.93–1.42 (m, 28 H) ppm. ES-MS: $m/z$ = 809.4720 (calculated 809.4530 for $C_{52}H_{60}N_2O_6 + H^+$).

**Cu$^I$ Complexes $1_4^+$, $2_4^+$ and $3_4^+$:** In a typical procedure, $Cu(CH_3CN)_4PF_6$ was added to a stirred and degassed solution of macrocycle **4** dissolved in $CH_2Cl_2$/$CH_3CN$ (50:50). A deep orange coloration appeared instantly. After 30 min at room temperature, the diimine ligand (respectively **5**, **6** or **7**) was added as a solid to the solution, which immediately turned dark red. After the solution was stirred for two hours under argon at room temperature, the solvents were removed under high vacuum. A dark red solid was obtained quasi-quantitavely (NMR control). Due to its instability on alumina and on silica gel, complexes were not further purified and were directly submitted to the electrochemical measurements.

**$1_4^+$:** $^1$H NMR ($CD_2Cl_2$, 300 MHz): $\delta$ = 8.76 (d, $J$ = 7.2 Hz, 2 H), 8.68 (br., 2 H), 8.49 (d, $J$ = 8.4 Hz, 2 H), 8.45 (d, $J$ = 8.7 Hz, 2 H), 8.41 (br., 2 H), 8.10 (t, $J$ = 7.2 Hz, 1 H), 8.04 (s, 2 H), 7.99 (s, 2 H), 7.89 (d, $J$ = 8.4 Hz, 2 H), 7.85 (d, $J$ = 8.7 Hz, 2 H), 7.75 (br., 2 H), 7.48 (d, $J$ = 8.7 Hz, 4 H), 7.40–7.34 (m, 4 H), 6.11–6.00 (m, 8 H), 3.49 (s, 6 H), 3.25 (br., 4 H), 2.95 (br., 4 H), 2.14 (br., 4 H) ppm. ES-MS: $m/z$ = 1132.3584 (calculated 1132.3606 for $C_{71}H_{55}CuN_7O_4^+$).

**$2_4^+$:** $^1$H NMR ($CD_2Cl_2$, 300 MHz): $\delta$ = 8.84 (d, $J$ = 7.8 Hz, 2 H), 8.75 (br. s, 2 H), 8.51 (d, $J$ = 7.8 Hz, 2 H), 8.40 (d, $J$ = 8.4 Hz, 2 H), 8.05 (t, $J$ = 7.5 Hz, 1 H), 7.92 (s, 2 H), 7.84 (d, $J$ = 8.4 Hz, 4 H), 7.74–7.67 (m, 4 H), 7.57 (d, $J$ = 8.7 Hz, 4 H), 7.35 (d, $J$ = 6.9 Hz, 2 H), 7.21 (d, $J$ = 8.7 Hz, 4 H), 6.36 (d, $J$ = 8.7 Hz, 4 H), 5.95 (d, $J$ = 8.7 Hz, 4 H), 3.69 (br., 4 H), 3.35 (s, 6 H), 3.06 (br., 4 H), 2.29 (br., 4 H) ppm. ES-MS: $m/z$ = 1108.3585 (calculated 1108.3606 for $C_{69}H_{55}CuN_7O_4^+$).

**$3_4^+$:** $^1$H NMR ($CD_3CN$, 300 MHz): $\delta$ = 9.03 (s, 2 H), 8.71 (br. s, 2 H), 8.59 (d, $J$ = 8.4 Hz, 2 H), 8.55 (s, 2 H), 8.50 (d, $J$ = 7.8 Hz, 2 H), 8.32 (s, 2 H), 8.12 (t, $J$ = 7.8 Hz, 1 H), 8.04 (d, $J$ = 8.4 Hz, 2 H), 8.01 (s, 2 H), 7.80–7.74 (m, 6 H), 7.56–7.53 (m, 6 H), 7.15 (d, $J$ = 8.7 Hz, 4 H), 6.86 (d, $J$ = 8.4 Hz, 4 H), 6.14 (d, $J$ = 8.7 Hz, 4 H), 4.48 (t, $J$ = 4.5 Hz, 2 H), 3.94–3.90 (m, 4 H), 3.74–3.60 (m, 4 H), 3.35 (br., 8 H), 2.90 (br., 4 H), 2.03 (br., 4 H), 1.70–1.38 (m, 28 H) ppm. ES-MS: $m/z$ = 1548.6520 (calculated 1548.6533 for $C_{97}H_{95}CuN_7O_8^+$).

## Acknowledgments

Funding from the following institutions is gratefully acknowledged: the Centre National de la Recherche Scientifique (CNRS) and the Région Alsace (fellowship to F. D.), the European Commission (MOLDYNLOGIC) and the European Communities (BIOMACH NMP-2002-3.4.1.1-3, contract 505487-1; financial support and fellowship to P. M.).

[1] Special Issue: *Acc. Chem. Res.* **2001**, *34*, 341; J.-P. Sauvage, *Structure and Bonding: Molecular Machines and Motors*, Springer: Berlin, Heidelberg, **2001**, *99*; V. Balzani, M. Venturi, A. Credi, *Molecular Devices and Machines*, Wiley-VCH, Weinhein, **2003**; E. R. Kay, D. A. Leigh, F. Zerbetto, *Angew. Chem. Int. Ed.* **2007**, *46*, 72.

[2] R. A. Bissell, E. Córdova, A. E. Kaifer, J. F. Stoddart, *Nature* **1994**, *369*, 133; J.-P. Sauvage and C. O. Dietrich-Buchecker, *Molecular Catenanes, Rotaxanes and Knots*, Wiley-VCH, Weinheim, **1999**; C. P. Collier, G. Mattersteig, E. W. Wong, Y. Luo, K. Beverly, J. Sampaio, F. M. Raymo, J. F. Stoddart, J. R. Heath, *Science* **2000**, *289*, 1172; A. N. Shipway, I. Willner, *Acc. Chem. Res.* **2001**, *34*, 421; A. Harada, *Acc. Chem. Res.* **2001**, *34*, 456; D. A. Leigh, J. K. Y. Wong, F. Dehez, F. Zerbetto, *Na-*

 © 2007 Wiley-VCH Verlag GmbH & Co. KGaA, Weinheim 

*ture* **2003**, *424*, 174; B. Korybut-Daszkiewicz, A. Wieçkowska, R. Bilewicz, S. Domagata, K. Wozniak, *Angew. Chem. Int. Ed.* **2004**, *43*, 1668; J. D. Badjic, V. Balzani, A. Credi, S. Silvi, J. F. Stoddart, *Science* **2004**, *303*, 1845; K. Kinbara, T. Aida, *Chem. Rev.* **2005**, *105*, 1377; J. Berná, D. A. Leigh, M. Lubomska, S. M. Mendoza, E. M. Pérez, P. Rudolf, G. Teobaldi, F. Zerbetto, *Nat. Mater.* **2005**, *4*, 704; V. Balzani, M. Clemente-Leon, A. Credi, B. Ferrer, M. Venturi, A. H. Flood, J. F. Stoddart, *PNAS* **2006**, *103*, 1178.

[3] L. Zeeikovich, J. Libman, A. Shanzer, *Nature* **1995**, *374*, 790; T. R. Kelly, H. de Silva, R. A. Silva, *Nature* **1999**, *401*, 150; L. Fabbrizzi, F. Foti, S. Patroni, P. Pallavicini, A. Taglietti, *Angew. Chem. Int. Ed.* **2004**, *43*, 5073; A. Koçer, M. Walko, W. Meijberg, B. L. Feringa, *Science* **2005**, *309*, 755; J. Vicario, N. Katsonis, B. Serrano Ramon, C. W. M. Bastiaansen, D. J. Broer, B. L. Feringa, *Nature* **2006**, *440*, 163.

[4] S. Bonnet, J.-P. Collin, M. Koizumi, P. Mobian, J.-P. Sauvage, *Adv. Mater.* **2006**, *18*, 1239; B. Champin, P. Mobian, J.-P. Sauvage, *Chem. Soc. Rev.* **2007**, *36*, 358.

[5] A. Livoreil, C. O. Dietrich-Buchecker, J.-P. Sauvage, *J. Am. Chem. Soc.* **1994**, *116*, 9399; L. Raehm, J.-M. Kern, J.-P. Sauvage, *Chem. Eur. J.* **1999**, *5*, 3310; M. C. Jiménez, C. Dietrich-Buchecker, J.-P. Sauvage, *Angew. Chem. Int. Ed.* **2000**, *39*, 3284; I. Poleschak, J.-M. Kern, J.-P. Sauvage, *Chem. Commun.* **2004**, 474; U. Létinois-Halbes, D. Hanss, J. M. Beierle, J.-P. Collin, J.-P. Sauvage, *Org. Lett.* **2005**, *7*, 5753.

[6] N. Armaroli, V. Balzani, J.-P. Collin, P. Gaviña, J.-P. Sauvage, B. Ventura, *J. Am. Chem. Soc.* **1999**, *121*, 4397; J.-P. Collin, A.-C. Laemmel, J.-P. Sauvage, *New J. Chem.* **2001**, *25*, 22; P. Mobian, J.-M. Kern, J.-P. Sauvage, *Angew. Chem. Int. Ed.* **2004**, *43*, 2392; S. Bonnet, J.-P. Collin, J.-P. Sauvage, *Inorg. Chem.* **2006**, *45*, 4024.

[7] M. C. Jiménez, C. Dietrich-Buchecker, J.-P. Sauvage, *Angew. Chem. Int. Ed.* **2000**, *39*, 3284–3287; J.-P. Collin, C. O. Dietrich-Buchecker, P. Gaviña, M. C. Jiménez-Molero, J.-P. Sauvage, *Acc. Chem. Res.* **2001**, *34*, 477.

[8] D. A. Leigh, J. K. Y. Wong, F. Dehez, F. Zerbetto, *Nature* **2003**, *424*, 177; J. V. Hernandez, E. R. Kay, D. A. Leigh, *Science* **2004**, *306*, 1532.

[9] R. Ballardini, V. Balzani, M. T. Gandolfi, L. Prodi, M. Venturi, D. Philp, H. G. Ricketts, J. F. Stoddart, *Angew. Chem. Int. Ed. Engl.* **1993**, *32*, 1301.

[10] J.-P. Collin, P. Gaviña, J.-P. Sauvage, *Chem. Commun.* **1996**, 2005.

[11] J.-P. Collin, P. Gaviña, J.-P. Sauvage, *New J. Chem.* **1997**, *21*, 525; N. Armaroli, V. Balzani, J.-P. Collin, P. Gaviña, J.-P. Sauvage, B. Ventura, *J. Am. Chem. Soc.* **1999**, *121*, 4397.

[12] C. O. Dietrich-Buchecker, J.-P. Sauvage, J.-P. Kintzinger, *Tetrahedron Lett.* **1983**, *24*, 5098; C. O. Dietrich-Buchecker, J.-P. Sauvage, *Chem. Rev.* **1987**, *87*, 795.

[13] J.-C. Chambron, C. O. Dietrich-Buchecker, J.-F. Nierengarten, J.-P. Sauvage, *J. Chem. Soc., Chem. Commun.* **1993**, 801; J.-C. Chambron, C. O. Dietrich-Buchecker, J.-F. Nierengarten, J.-P. Sauvage, *Pure Appl. Chem.* **1994**, *66*, 1543.

Received: February 16, 2007
Published Online: April 26, 2007

 © 2007 Wiley-VCH Verlag GmbH & Co. KGaA, Weinheim 

DOI: 10.1002/ejic.200601181

# Structural, Electrochemical, and Spectroscopic Properties of a Class of Dodecasubstituted Iron Porphyrins Bearing Four Positive Charges Close to the Metal

**Mark W. Renner,[a] Constance Bochot,[b] Annie Héroux,[c] Daniel Mansuy,[b] and Pierrette Battioni*[b]**

**Keywords:** Iron / Porphyrins / Ligand design / X-ray diffraction / Voltammetry

The first iron complexes of the tetracationic 2,3,7,8,12,13,17,18-octaethyl-5,10,15,20-tetra-*N*-pyridiniumylporphyrin, (OEPy$_4$P)$^{4+}$, in which four pyridine molecules are attached to the *meso*-carbon atoms through their nitrogen atoms, were synthesized in three steps starting from Zn(OEP) (Zn-β-octaethylporphyrin) with an overall yield of ca. 30 %. The X-ray structure of [Fe$^{II}$(OEPy$_4$P)(pyridine)$_2$](CF$_3$SO$_3$)$_3$(Br) established that the molecule adopts a severely distorted nonplanar saddle conformation. $^1$H NMR spectroscopy showed that the [Fe$^{II}$(OEPy$_4$P)(B)$_2$]$^{4+}$ ligated complexes, B = pyridine (Py) or imidazole (Im), are low-spin, Fe$^{II}$, $S$ = 0. These complexes exhibit redox potentials for the Fe$^{III}$/Fe$^{II}$ couple that range between 0.62 and 0.38 V (vs. Ag/AgCl) and are shifted by as much as +0.7 V relative to those of the corresponding planar iron complexes of OEP and of the nonplanar complexes of OETPP. Such highly positive redox potentials explain the stability of these iron(II) porphyrins in air. As previously found for dodecasubstituted iron porphyrins bearing electron-withdrawing groups, the UV/Vis spectra of the [Fe$^{II}$(OEPy$_4$P)(B)$_2$]$^{4+}$ complexes exhibit Soret and visible bands which are redshifted by ca. 40 nm relative to those of Fe(OEP)(Py)$_2$. These metallo-OEPy$_4$P$^{4+}$complexes offer promising synthetic avenues to novel classes of highly charged porphyrins and multiporphyrin arrays, which are soluble in aqueous and polar organic solvents.

(© Wiley-VCH Verlag GmbH & Co. KGaA, 69451 Weinheim, Germany, 2007)

## Introduction

Many porphyrin cofactors that are present in living systems, such as photosynthetic reaction centers, light harvesting antenna complexes, and heme proteins, exhibit nonplanar macrocycles.[1] Such macrocycle distortions are believed to influence the biological functions of these cofactors. In vivo, the scaffolding, hydrogen bonding, macrocycle saturation, and axial ligation modulate the porphyrin conformations. In model porphyrins, specific macrocycle configurations have been generated by introduction of bulky and multiple peripheral substituents. By varying the macrocycle modes and degrees of distortion, as well as the nature of the metal, the chemical and physical properties of the tetrapyrroles can thus be fine-tuned. Indeed, such nonplanar distortions have been shown to alter the redox, magnetic, electronic, ligand binding, and excited-state properties of metalloporphyrins.[1,2]

In some cytochromes, the heme iron is coordinated by two axial histidine residues whose relative orientation with respect to each other can alter both their spectroscopic and redox properties.[1,3] In model studies of bis-ligated iron porphyrins, the relative and absolute orientation of the axial ligands have also been shown to modulate the electronic structure, and the magnetic and redox properties of the hemes.[3] In the numerous crystal structures of bis-ligated iron porphyrins reported so far, the relative orientations of the axial ligands are preferentially perpendicular in Fe$^{III}$ and parallel in Fe$^{II}$ porphyrins.[3,4] However, structures of iron(II) porphyrins with perpendicular axial pyridine or imidazole orientations have been reported in which this orientation was controlled by steric interactions imposed by the porphyrin and its substituents.[3,4] As well, crystallographic studies of highly saddled metalloporphyrins have further shown that the combination of macrocycle distortion and peripheral substituents forms trenches which tend to orient the axial ligands perpendicular to each other.[5]

Many dodecasubstituted porphyrins have been synthesized, most of which exhibit nonplanar, highly distorted structures.[1,2] Iron and manganese porphyrins bearing up to twelve electron-withdrawing substituents are especially interesting because of their significantly altered redox potentials and their catalytic properties.[1,6–9] Dodecasubstituted metalloporphyrins bearing multiple charges should be

[a] Condensed Matter Physics and Materials Science Department, Brookhaven National Laboratory,
Building 555, Upton, NY 11973-5000, USA
[b] UMR 8601, Laboratoire de Chimie et Biochimie Pharmacologiques et Toxicologiques, Université Paris 5
45 rue des Saints-Pères, 75270 Paris Cedex 06, France
[c] Biology Department, Brookhaven National Laboratory
Upton, NY 11973-5000, USA

Supporting information for this article is available on the WWW under http://www.eurjic.org or from the author.

 © 2007 Wiley-VCH Verlag GmbH & Co. KGaA, Weinheim 

of particular interest because of their solubility in water and their possible interactions with various biological targets such as proteins and nucleic acids. Water-soluble metalloporphyrins exhibit interesting properties as photosensitizers for photodynamic therapy of cancer,[10] and as antimalarial,[11] antibacterial,[12] anti-HIV,[13,14] and antiprion[15] agents. Moreover, cationic metalloporphyrins have been explored for the treatment of pathologies in which the superoxide radical and its progeny are suspected of playing important roles.[16–19] *N*-methylpyridiniumyl-*meso*-substituted metalloporphyrins have been used very often for this purpose. This is indeed the case for the first reported dodecasubstituted tetracationic metalloporphyrins that were derived from β-octabromo-*meso*-tetra(*N*-methylpyridiniumyl)porphyrin.[16]

Recently, a polycationic porphyrin bearing 20 positive charges was obtained by nucleophilic substitution of the F substituents of *meso*-tetra(pentafluorophenyl)porphyrin ($H_2$TFPP) with 4-dimethylaminopyridine in the presence of trimethysilyl triflate.[20] Moreover, a tetracationic $Zn^{II}$ dodecasubstituted porphyrin, $Zn(OEPy_4P)^{4+}$ ($OEPy_4P$: β-octaethyl-*meso*-tetra-(pyridiniumyl-1)porphyrinato) (Scheme 1), bearing four pyridinium groups bound at the *meso* position through their nitrogen atom, was reported.[21] It was the first representative of a new class of dodecasubstituted, nonplanar metalloporphyrins bearing four positive charges less than 5 Å from the metal center. Even more recently, the corresponding free-base porphyrin $H_2OEPy_4P^{4+}$, and its Mn complexes, were synthesized.[22] The latter are new biomimetic hydroxylation catalysts that exhibit good solubility in both polar aprotic solvents and water.[22]

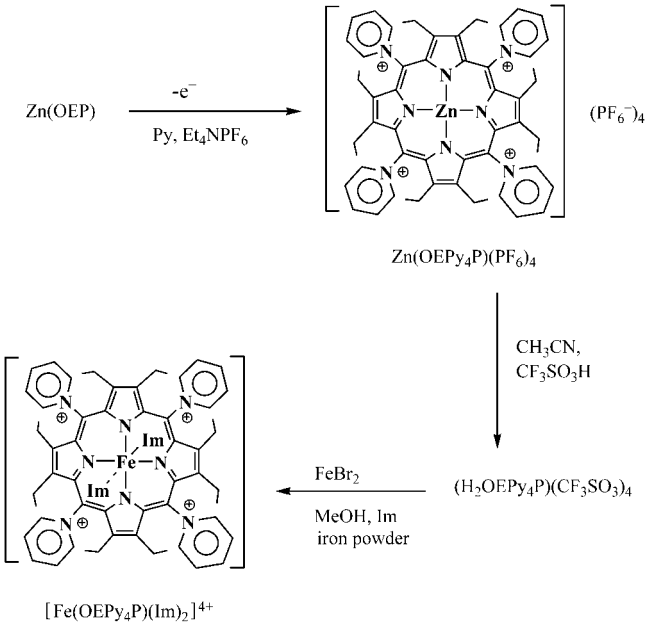


Scheme 1. Synthesis of $[Fe(OEPy_4P)(Im)_2]^{4+}$ in three steps from Zn(OEP).

We report here the synthesis and the spectral and electrochemical properties of iron complexes of $H_2OEPy_4P^{4+}$, and the first X-ray structure of a bis(pyridine)$Fe^{II}$ complex of this novel class of tetracationic dodecasubstituted porphyrins. These metallo-$OEPy_4P^{4+}$ complexes offer promising synthetic avenues to additional novel classes of highly charged porphyrins and multiporphyrin arrays that are soluble in aqueous and polar organic solvents.[23]

## Results and Discussion

### Synthesis of $[Fe(OEPy_4P)(Im)_2]^{4+}$

The iron complex of $OEPy_4P$ was prepared in three steps starting from Zn(OEP) (OEP: β-octaethylporphyrinato) (Scheme 1). The first step that led to $[Zn(OEPy_4P)](PF_6)_4$ was done according to published procedures[21] (Scheme 1). Demetallation of this Zn complex involved its treatment with excess $CF_3SO_3H$,[24,25] which led to the $CF_3SO_3^-$ salt of $[H_2OEPy_4P]^{4+}$ in a 80% yield.[22] The last step, the insertion of iron, was done under an atmosphere of argon by using 2.5 equiv. of $FeBr_2$ in the presence of imidazole (Im) and iron powder. The resulting complex was found to be a diamagnetic $Fe^{II}$ complex of $OEPy_4P$ including two axial imidazole ligands as shown by $^1$H NMR spectroscopy. Its $^1$H NMR spectrum exhibits all the signals expected for the pyridinium (in the 8.5–10.5 ppm region) and ethyl (in the 0.5–2.6 ppm region) substituents of the porphyrin ring, and for the imidazole ligands (signals at $\delta$ = 3.05, 3.83, and 5.20 ppm) (see Experimental Section). Integration of these signals is consistent with two imidazole ligands per porphyrin. In the presence of excess imidazole, the signals of the free and bound imidazole coexist in the $^1$H NMR spectra, which indicates that the exchange between free and bound imidazole is slow on the NMR time scale. Temperature-dependent $^1$H NMR spectroscopic studies performed in $CD_3OD$ in the presence of either 5 or 50 equiv. of imidazole, between 300 and 200 K, did not show significant changes in the shape of the peaks, and only showed small variations in the chemical shifts.

A high resolution mass spectrometry (HRMS) analysis of the $[Fe(OEPy_4P)(Im)_2]^{4+}$ complex, with the use of nanoelectrospray ionization and Fourier transform mass spectrometry (nano-ESI-FTMS), showed a molecular ion at $m/z$ = 1496.2405, which corresponds to $[Fe(OEPy_4P)(CF_3SO_3)_4]^+$ (monoisotopic $m/z$ calculated for $C_{60}H_{60}N_8S_4O_{12}F_{12}Fe$ = 1496.2368; isotopic distribution of the peaks cluster identical to that calculated for the above formula). This molecular ion should derive from the $[Fe(OEPy_4P)(Im)_2](CF_3SO_3)_4$ complex having lost its two axial ligands under the MS conditions, as usually found for such Fe(porphyrin)$(Im)_2$ complexes. A smaller peak at $m/z$ = 1426.1999, which corresponds to $[Fe(OEPy_4P)(CF_3SO_3)_3(Br)]^+$ (theoretical monoisotopic $m/z$ = 1426.2033; isotopic distribution in agreement with the formula $C_{59}H_{60}N_8S_3O_9F_9BrFe$), was also observed. This peak should come from the $[Fe(OEPy_4P)(Im)_2](CF_3SO_3)_3(Br)$ complex, which was present in the analyzed sample as a result of the exchange of a $CF_3SO_3^-$ counterion of $[Fe(OEPy_4P)(Im)_2](CF_3SO_3)_4$ by $Br^-$ coming from $FeBr_2$ in the metallation step. The presence of such a $[Fe(OEPy_4P)(Im)_2]^{4+}$

 © 2007 Wiley-VCH Verlag GmbH & Co. KGaA, Weinheim 

complex associated with three $CF_3SO_3^-$ counterions and one $Br^-$ counterion is in agreement with the X-ray study performed on the complex obtained by replacement of the Im ligands with pyridine. This X-ray study definitely established a $[Fe(OEPy_4P)(Py)_2](CF_3SO_3)_3(Br)$ structure for the latter complex (see below). Obviously, the nature of the counterions of these $[Fe(OEPy_4P)(B)_2]^{4+}$ complexes, with B = Im or Py, should greatly depend on the synthesis protocol and on the medium in which they are studied. Therefore, these complexes will simply be called $[Fe(OEPy_4P)(B)_2]^{4+}$ in the following sections.

The UV/Vis spectra of $[Fe(OEPy_4P)(B)_2]^{4+}$, with B = Im or Py, exhibit Soret and visible bands that are all redshifted ca. 40 nm relative to $Fe^{II}(OEP)(Py)_2$ (Table 1). These UV/Vis spectra are similar to those of the previously reported low-spin bispyridine dodecasubstituted $Fe^{II}$ porphyrins bearing electron-withdrawing groups [see $Fe(F_{20}DPP)(Py)_2$ in Table 1, $F_{20}DPP$: β-octaphenyl-*meso*-tetrapentafluorophenylporphyrinato], whereas they clearly differ from the spectra of $[Fe^{III}(porphyrin)(Py)_2]^+$ and $Fe^{II}(porphyrin)$ complexes (Table 1). The redshifted optical spectra of $[Fe(OEPy_4P)(B)_2]^{4+}$ are likely due to the presence of the four electron-withdrawing pyridinium substituents and to the distorted structure of the porphyrin macrocycle (see below), relative to that of $Fe^{II}(OEP)(Py)_2$ which is planar.[4] In distorted porphyrins, the highest occupied molecular orbital (HOMO) is destabilized more than the lowest unoccupied orbital (LUMO), which results in a decrease in the HOMO to LUMO energy gap and a redshift in the absorption bands.[26–28]

Table 1. UV/Vis characteristics of the $[Fe(OEPy_4P)(B)_2]^{4+}$ complexes and related iron porphyrins.[a]

| Compound | Solvent | $\lambda_{max}$ [nm, Soret] |
|---|---|---|
| $Fe(F_{20}DPP)$[37] | benzonitrile | 327, 432, 534, 586 |
| $Fe(F_{20}DPP)(Py)_2$[37] | pyridine | 351, 447, 551, 588 |
| $[Fe(Br_8TFPP)(Py)_2]^+$[33] | $CH_2Cl_2$ | 454, 556, 588 |
| $[Fe(OEP)(Py)_2]Cl$[38] | pyridine | 396, 510, 529, 625 |
| Fe(OEP)[39] | $CH_2Cl_2$ | 405, 531, 556 |
| $Fe(OEP)(Py)_2$[40] | pyridine | 408, 517, 546 |
| $[Fe(OEPy_4P)(Py)_2]^{4+}$[a] | MeCN, Py | 366, 439, 458, 556, 588 |
| $[Fe(OEPy_4P)(Im)_2]^{4+}$[a] | MeCN, Im | 366, 458, 568, 601 |

[a] This work, spectra in MeCN containing 5% Py or 100 μM Im.

### Electrochemical Properties of $[Fe(OEPy_4P)(B)_2]^{4+}$

The redox chemistry of these iron complexes was studied by cyclic voltammetry (Figure 1 and Table 2). The $E_{1/2}$ values for $[Fe(OEPy_4P)(Im)_2]^{4+}$ and $[Fe(OEPy_4P)(Py)_2]^{4+}$ are +0.38 and +0.62 V respectively, vs. Ag/AgCl in MeCN. The $E_{1/2}$ peak potential separations for these complexes are 100 and 60 mV, respectively. The $Fe^{III/II}$ couple is obviously sensitive to the axial ligands and shifts − 240 mV upon replacement of the pyridine groups with imidazole moieties. For bis-ligated $Fe^{III}$ porphyrins, the $Fe^{III/II}$ $E_{1/2}$ potential undergoes a negative shift as the pKa of the axial ligands increases.[6] The electron-withdrawing *meso*-pyridinium substituents on the porphyrin shift the $Fe^{III/II}$ couple anodically, which stabilizes the iron(II) oxidation state. The redox potentials of iron porphyrins with a varying number of electron-withdrawing substituents have been reported, and the $Fe^{III/II}$ redox couple undergoes a positive shift with an increasing number of electron-withdrawing groups.[6,29] Comparison of the $E_{1/2}$ of $Fe(OETPP)(B)_2$ (OETPP: β-octaethyl-*meso*-tetraphenylporphyrinato) and $[Fe(OEPy_4P)(B)_2]^{4+}$ shows a large positive shift in the metal redox potentials upon replacing the *meso*-phenyl with *meso*-pyridinium groups (+730 mV and +870 mV for B = Im and Py, respectively, Table 2). Because these compounds have similar nonplanar conformations (see below), electronic, rather than structural, factors seem to cause this large positive shift.

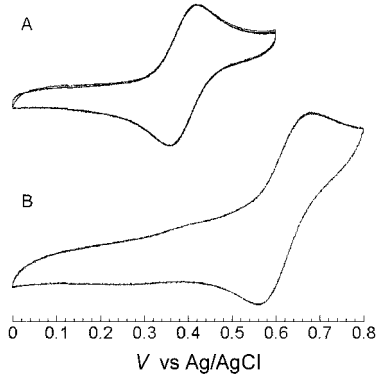


Figure 1. Cyclic voltammograms of $[Fe(OEPy_4P)(Im)_2]^{4+}$ (A) and $[Fe(OEPy_4P)(Py)_2]^{4+}$ (B) in MeCN containing 0.1 M TBAP. Scan rate: 100 mV $s^{-1}$.

Table 2. Electrochemical data for the $[Fe(OEPy_4P)(B)_2]^{4+}$ complexes and related iron porphyrins.

| Compound | $Fe^{III}/Fe^{II}$ [V] | Conditions[a] |
|---|---|---|
| $[Fe(OEP)(Py)_2]^+$[41] | –0.02 | PrCN, TBAP, SCE |
| $[Fe(OEP)(1\text{-}MeIm)_2]^+$[41] | –0.39 | $CH_2Cl_2$, TBAP, SCE |
| $[Fe(F_{20}DPP)(Py)_2]^+$[41] | +0.53 | Pyr, TBAP, SCE |
| $[Fe(Br_8TFPP)(Py)_2]^+$[33] | +0.82 | $CH_2Cl_2$, TBAP, Ag/AgCl |
| $[Fe(OETPP)(Im)_2]^+$[b] | –0.31 | PrCN, TBAP, SCE |
| $[Fe(OETPP)(Py)_2]^+$[b] | –0.21 | PrCN, TBAP, SCE |
| $[Fe(OEPy_4P)(Py)_2]^{4+}$[c] | +0.62 | MeCN, TBAP, Ag/AgCl |
| $[Fe(OEPy_4P)(Im)_2]^{4+}$[c] | +0.38 | MeCN, TBAP, Ag/AgCl |

[a] Redox potentials were measured in the indicated solvent containing 0.1 M TBAP (tetrabutylammonium perchlorate). Values are in V relative either to the saturated calomel electrode (SCE) or to the Ag/AgCl electrode. [b] M. W. Renner and J. Fajer, unpublished results. [c] This work.

Two electronic structures are theoretically possible for $S = 0$ $Fe(porphyrin)(L)_2$ complexes, a low-spin d6 $Fe^{II}$ porphyrin structure and a structure involving a low-spin d5 $Fe^{III}$ ion antiferromagnetically coupled to a porphyrin radical. However, presently, there is no indication in favor of the latter structure for all the $S = 0$ $Fe(porphyrin)(L)_2$ complexes published so far in the literature. An electronic structure resulting from an intramolecular electron transfer from $Fe^{II}$ to the porphyrin should be favored by the presence of porphyrin electron withdrawing substituents. However,

 © 2007 Wiley-VCH Verlag GmbH & Co. KGaA, Weinheim 

Mössbauer data of the β-octanitrated Fe[TDCP$(NO_2)_8$P]-$(EtOH)_2$ complex, which exhibits the highest redox potential described so far for a Fe(porphyrin)$(L)_2$ complex (1030 mV vs. SCE[30]), clearly showed that it is a $Fe^{II}$ complex.[30] Moreover, metal(porphyrin radical) complexes usually exhibit a characteristic porphyrin radical absorption in the 700–1000 nm region; for instance $Zn^{II}$[TDCP$(NO_2)_7$-P]$^{\cdot-}$ and $Ni^{II}$[TDCP$(NO_2)_7$P]$^{\cdot-}$ complexes show bands at 900 and 770 nm, respectively.[31] However, the UV/Vis spectra of [Fe$(OEPy_4P)(Im)_2]^{4+}$ and [Fe$(OEPy_4P)(Py)_2]^{4+}$ failed to show any band in the 700–1000 nm region. Finally, the $^1$H NMR spectra of [Fe$(OEPy_4P)(B)_2]^{4+}$ complexes exhibit peaks, whose shapes and chemical shifts are highly similar to those of Zn[$(OEPy_4P)]^{4+}$ and $H_2$[$(OEPy_4P)]^{4+}$ in which the porphyrin ligand does not involve any radical species. All these data are in favor of the low-spin d6 $Fe^{II}$ porphyrin electronic structure, as the one proposed for all the previously described $S = 0$ Fe(porphyrin)$(L)_2$ complexes.[4]

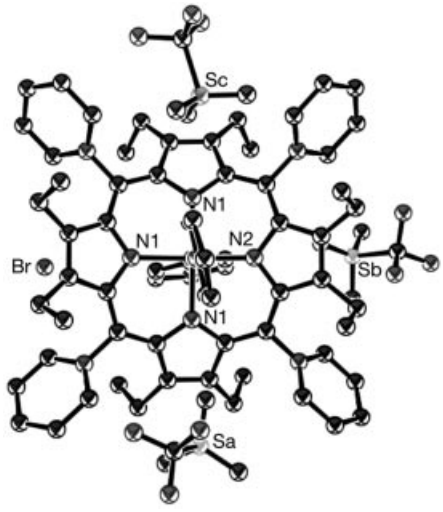


Figure 2. ORTEP diagram of **1** with the anions included. The thermal ellipsoids are drawn at the 30% probability level.

## Structural Studies

Owing to the small crystal size ($0.6 \times 0.4 \times 0.1$ mm) and quality, the X-ray diffraction experiments were performed with the use of high intensity X-rays from the National Synchrotron Light Source at Brookhaven National Laboratory beamline X26C. The molecular structure of [Fe(OE-$Py_4P)(Py)_2](CF_3SO_3)_3(Br)$ (**1**) and the atom numbering scheme are displayed in Figures 2 and 3. Selected bond lengths and angles are listed in Table 3. [Fe$(OEPy_4P)$-$(Py)_2]^{4+}$ crystallizes with four anions, three $CF_3SO_3^-$, and one $Br^-$, which are located between adjacent *meso*-pyridinium groups and above the pyrrole rings (Figure 2). One of the original $CF_3SO_3^-$ ions of the free base must therefore have been replaced by a $Br^-$ during the metal insertion reaction with $FeBr_2$. The molecular structure of **1** exhibits a $S_4$ saddle-shape distortion with an absolute displacement of 1.22 Å for the pyrrole $C_\beta$ atoms relative to the 24-atom plane; an edge-on view of **1** is shown in Figure 3. The displacements of the porphyrin atoms from the 24-atom core, the axial ligand plane orientations, and a "clothesline" representation of the macrocycle distortions are shown in Figure 4.

The trenches formed by the nonplanar porphyrin conformation and the β-ethyl groups align the axial pyridines perpendicular to each other and along the $N_p$–Fe–$N_p$ axes. The dihedral angle between the axial pyridine and the closest $N_p$–Fe–$N_{ax}$ plane (ϕ) are 11.2 and 13.3° for pyridine N9 and N10, respectively. The pyridines are effectively orthogonal to each other with a dihedral angle between the two axial pyridine planes of 87°. A comparison of the structural parameters of **1** and other related bispyridine iron porphyrins are listed in Table 4. As with other bispyridine iron(II) porphyrins,[4] the iron atom resides in the $4N_p$ plane, displaced 0.01 Å toward the axial pyridine N10. The axial pyridines are approximately perpendicular to the macrocycle plane with dihedral angles of 81.1° and 89.3° for pyridine N9 and N10, respectively. Pyridine N9 is tilted ca. 9° relative to the $4N_p$ plane which could be a result of hydrogen bonding between the pyridine C–H and the oxygen atom of a nearby $CF_3SO_3^-$ anion; the C59···O distance is 3.33 Å.

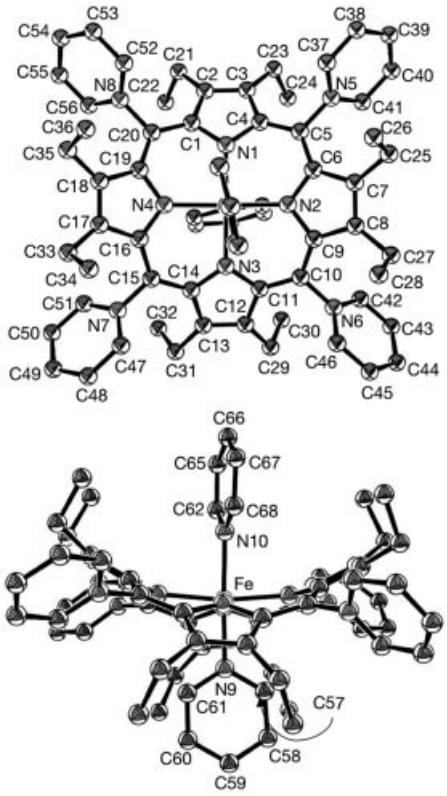


Figure 3. Molecular structure and numbering scheme for **1**, thermal ellipsoids drawn at the 30% probability level; the hydrogen atoms and the counterions are removed for clarity.

Typically, for bis-ligated low-spin iron(II) porphyrins[4] the equatorial Fe–$N_p$ distances are ca. 2.00 Å. The average equatorial Fe–$N_p$ distance in complex **1** [1.953(3) Å] is slightly shorter than in the dodecasubstituted complexes [$Fe^{III}$(OETPP)$(Py)_2]ClO_4$ at 80 K [1.957(3) Å] and $Fe^{II}$-

 © 2007 Wiley-VCH Verlag GmbH & Co. KGaA, Weinheim 

Table 3. Selected bond lengths and bond angles for [$Fe^{II}$(OE-$Py_4P$)$(Py)_2$]$(CF_3SO_3)_3$(Br) (**1**).

| Bond | Distance [Å] | Bond | Distance [Å] |
|---|---|---|---|
| Fe–N1 | 1.955(3) | Fe–N4 | 1.958(3) |
| Fe–N2 | 1.949(3) | Fe–N5 | 2.028(3) |
| Fe–N3 | 1.951(3) | Fe–N6 | 2.027(3) |
| N1–C1 | 1.382(4) | N2–C6 | 1.380(4) |
| N1–C4 | 1.372(4) | N2–C9 | 1.375(4) |
| C1–C2 | 1.453(5) | C6–C7 | 1.455(5) |
| C2–C3 | 1.366(5) | C7–C8 | 1.359(5) |
| C3–C4 | 1.459(5) | C8–C9 | 1.457(5) |
| C4–C5 | 1.392(5) | C9–C10 | 1.389(5) |
| C5–C6 | 1.390(5) | C10–C11 | 1.393(5) |
| C5–N5 | 1.463(5) | C20–N8 | 1.463(4) |
| Angle | Value [°] | Angle | Value [°] |
| N1–Fe–N2 | 89.79(12) | N1–C4–C5 | 119.1(3) |
| N2–Fe–N3 | 91.46(12) | N1–C1–C20 | 118.7(3) |
| N3–Fe–N4 | 90.29(12) | C1–N1–C4 | 105.2(3) |
| N1–Fe–N4 | 89.99(12) | C2–N1–C20 | 130.6(3) |
| N1–Fe–N3 | 169.98(13) | C1–C2–C3 | 106.4(3) |
| N2–Fe–N4 | 171.11(13) | C2–C3–C4 | 106.3(3) |
| N1–Fe–N9 | 85.99(12) | C3–C4–C5 | 130.3(3) |
| N1–Fe–N10 | 97.20(12) | C4–C5–C6 | 126.6(3) |
| N1–C1–C2 | 110.4(3) | C4–C5–N6 | 115.9(3) |
| N1–C4–C3 | 110.6(3) | C1–C20–N8 | 115.7(3) |

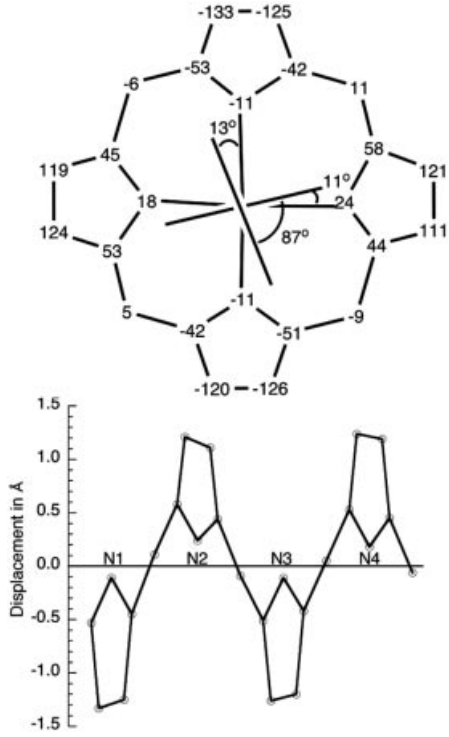


Figure 4. Top: Displacements of the 24-atom core in units of 0.01 Å and the orientation of the axial pyridine ligand planes of **1**. Bottom: Linear display of the out-of-plane displacements of the core atoms of **1** from the average plane of the 24 atoms (the horizontal axis is not to scale).

$(Br_8TFPP)(Py)_2$ ($Br_8TFPP$: β-octabromo-*meso*-tetrapentafluorophenylporphyrinato) [1.963(7) Å].[32,33] The increased distortion in **1** relative to $Fe^{II}(Br_8TFPP)(Py)_2$, (see below), could account for the decreased Fe–$N_p$ distance. In planar porphyrins, the Fe–$N_{ax}$ bond lengths are longer in $Fe^{II}$ than in $Fe^{III}$ porphyrins[4] and this trend is maintained in **1** [2.028(3) Å] when compared to $[Fe^{III}(OETPP)(Py)_2]ClO_4$ [1.993(3) Å].[32] As a result of the limited structural data available for highly saddled bis-ligated low-spin $Fe^{II}$ and $Fe^{III}$ porphyrins, no meaningful conclusions can be made regarding any relationship between the Fe–$N_p$ or Fe–$N_{ax}$ distances and the oxidation state of the metal.

A normal-coordinate structural decomposition (NSD)[34] analysis of the macrocycle distortions in **1** and several related iron porphyrins are listed in Table 5. The results from the analysis indicate that the predominant distortion in **1** is *sad* with a small *ruf* contribution. Recently, Scheidt et al. reported a correlation between the Fe–$N_p$ distance and the absolute *meso*-carbon displacement in ruffled $Fe^{II}$ and $Fe^{III}$ porphyrins.[35] This correlation does not appear to hold for porphyrins with a saddled conformation within the limited data available.

In saddled porphyrins there is a significant increase in the $C_m$–$C_\alpha$–$C_\beta$ angle and a decrease in the N–$C_\alpha$–$C_\beta$ and N–$C_\alpha$–$C_m$ angles relative to planar porphyrins. This trend holds for **1** and, in addition, there is a ca. 3° increase in the

Table 4. Average bond lengths [Å] and angles [°] for **1** and related complexes.

| Complex | Fe–$N_p$ | Fe–$N_{Ax}$ | $C_\beta$[c] | $C_m$[d] | ϕ[e] | Relative orientation[f] |
|---|---|---|---|---|---|---|
| $Fe^{II}(Br_8TFPP)(Py)_2$[33] | 1.963(7) | 2.012(7) | 0.97 | 0.11 | 0.7, 21.7 | 67.8 |
| $Fe^{II}[T(C_3F_7)P](Py)_2$[a][42] | 1.958(6) | 2.002(6) | 0.24 | 0.62 | 41.3, 46.0 | 87.5 |
| **1**[b] | 1.953(3) | 2.028(3) | 1.22 | 0.08 | 11.2, 13.3 | 87 |
| $[Fe^{III}(OETPP)(Py)_2]ClO_4$[32] | 1.957(3) | 1.993(3) | 1.21 | 0.05 | 6.3, 11.6 | 85.1 |
| Complex | $C_\alpha$-N–$C_\alpha$ | Fe–N–$C_\alpha$ | N–$C_\alpha$-$C_m$ | $C_m$–$C_\alpha$-$C_\beta$ | $C_\alpha$–$C_m$–$C_\alpha$ | |
| **1**[b] *sad* | 105.5 | 125.0 | 118.9 | 130.4 | 126.7 | |
| $Fe^{II}(Br_8TFPP)(Py)_2$[33] *sad* | 106.1 | 125.9 | 122.5 | 128.1 | 123.9 | |
| $Fe^{II}$ $[T(C_3F_7)P](Py)_2$[a][42] *ruf* | 105.4 | 127.3 | 122.4 | 128.6 | 125.5 | |
| $Fe^{II}(TPP)(Py)_2$[4] planar | 105.1 | 127.2 | 125.9 | 123.4 | 123.4 | |
| $[Fe^{III}(OETPP)(Py)_2]ClO_4$[32] *sad* | 106.6 | 123.7 | 121.8 | 128.4 | 121.8 | |

[a] $T(C_3F_7)P$ is the dianion of *meso*-tetraheptafluoropropylporphyrin. [b] This work. [c] $C_\beta$ = Average absolute value of the displacement of the pyrrole β carbons from the 24-atom mean plane. [d] $C_m$ = Average absolute value of the displacement of the methine carbons from the 24-atom mean plane. [e] ϕ = Dihedral angle between the plane defined by the closest $N_p$–Fe–$N_{pyr}$ and the pyridine plane. [f] Relative orientation: dihedral angle between two axial ligands.

 © 2007 Wiley-VCH Verlag GmbH & Co. KGaA, Weinheim 

Table 5. Out-of-plane displacements (in Å) for the crystal structures of distorted Fe porphyrin complexes from normal-coordinate structural decomposition.[34]

| Porphyrin | Total distortion | | $B_{2u}$ | $B_{1u}$ | $A_{2u}$ | $E_{g(x)}$ | $E_{g(y)}$ | $A_{1u}$ |
|---|---|---|---|---|---|---|---|---|
| | $d_{obsd.}$ | $d_{calcd.}$ | $d_{sad}$ | $d_{ruf}$ | $d_{dom}$ | $d_{wav(x)}$ | $d_{wav(y)}$ | $d_{pro}$ |
| Fe(OETPP)Cl[43,44] | 3.537 | 3.520 | 3.478 | 0.527 | 0.090 | 0.020 | 0.032 | 0.010 |
| [Fe(OETPP)(Py)$_2$]ClO$_4$[32] | 3.682 | 3.666 | 3.657 | 0.147 | 0.190 | 0.070 | 0.031 | 0.002 |
| Fe(Br$_8$TFPP)Cl[33] | 3.322 | 3.304 | 3.272 | 0.408 | 0.022 | 0.163 | 0.112 | 0.009 |
| Fe(Br$_8$TFPP)(Py)$_2$[33] | 3.005 | 3.000 | 2.981 | 0.313 | 0.046 | 0.099 | 0.029 | 0.017 |
| **1**[a] | 3.752 | 3.743 | 3.731 | 0.237 | 0.150 | 0.075 | 0.067 | 0.005 |

[a] This work.

$C_\alpha$–$C_m$–$C_\alpha$ angle (Table 4).[4] Another consequence of the increased saddle distortion in **1** is a decrease in the dihedral angle of the *meso*-pyridinum rings relative to the 4$N_p$ plane, 47.3°. However, the average $C_m$–*meso*–$N_{py}$ distance [1.462(4) Å] does not suggest any significant increased π–π overlap. Similar observations were noted in highly saddled OETPP porphyrins, again without any indication of increased porphyrin–phenyl π overlap.[1,36]

## Conclusions

A procedure was developed for the synthesis of iron complexes of [$H_2$OEPy$_4$P](CF$_3$SO$_3$)$_4$, in three steps starting from Zn(OEP) with an overall yield of ca. 30%. The molecular structure of [Fe(OEPy$_4$P)(Py)$_2$](CF$_3$SO$_3$)$_3$(Br) was determined by X-ray crystallography. The molecule was shown to adopt a severely nonplanar distorted saddle conformation, and the nonplanar macrocycle and its substituents form cavities that orient the axial ligands orthogonally to each other and along the Np–Fe–Np axes. [Fe(OEPy$_4$P)(B)$_2$]$^{4+}$, B = Py or Im, are the first iron complexes of a dodecasubstituted porphyrin bearing four positive charges close to the metal (<5 Å). The $Fe^{III}/Fe^{II}$ redox potentials of +0.62 (B = Py) and +0.38 V (B = Im) (relative to Ag/AgCl) are shifted by as much as ca. +0.7 V when compared to the redox potentials of the corresponding planar complexes of OEP and of the nonplanar, saddle-shaped, complexes of OETPP. These highly positive redox potentials values, that are comparable to those previously reported for dodecasubstituted iron porphyrins bearing electron-withdrawing groups, such as Fe(Br$_8$TFPP)(Py)$_2$ or Fe(F$_{20}$DPP)(Py)$_2$,[33,37] explain the stability of these $Fe^{II}$ porphyrins in air. As previously reported for other iron dodecasubstituted porphyrins bearing electron-withdrawing groups,[29,33,37] the UV/Vis absorption spectra of the [Fe(OEPy$_4$P)(B)$_2$]$^{4+}$ complexes exhibit Soret and visible bands greatly redshifted relative to Fe(OEP)(Py)$_2$. Potential applications in biomedicine, catalysis, and material sciences of these novel iron porphyrins that offer the advantage of being stable in air and also soluble in polar organic solvents as well as in water are currently being pursued.

## Experimental Section

**Materials and Methods:** Methanol (MeOH), diethyl ether ($Et_2O$) and Celite 545 were purchased from SDS and used without further purification. Trifluoromethanesulfonic acid, Zn(β-octaethylporphyrin = OEP), dichloromethane ($CH_2Cl_2$), [$D_2$]dichloromethane ($CD_2Cl_2$), pyridine (Py), [$D_5$]pyridine, imidazole (Im), tetraethylammonium hexafluorophosphate ($Et_4NPF_6$), acetonitrile (MeCN), and Sephadex LH20 were purchased from Aldrich. Tetrabutylammonium perchlorate ($Bu_4NClO_4$) was obtained from Alfa, pyridine (Py) (extra dry, water <50 ppm) from Acros, and anhydrous $FeBr_2$ and iron powder from Alfa-Ventron.

At BNL, UV/Vis absorption spectra were recorded with a Cary 500 spectrophotometer. Cyclic voltammetry was carried out with a Voltalab 80 electrochemical analyzer. A three-electrode system was used and consisted of a glassy carbon working electrode (GCE, 3.0 mm diameter, BAS), a Pt wire counter electrode, and a Ag/AgCl reference electrode. The solvent was MeCN with 0.1 M $Bu_4NClO_4$ as the supporting electrolyte and they were purified by standard techniques. $^1$H NMR spectra were recorded with a Bruker DRX-400 spectrophotometer operating at 400.132 MHz $^1$H frequency. The NMR spectra were referenced to the residual $CD_2Cl_2$ solvent peak ($\delta$ =5.32 ppm). The DQF-COSY data were recorded at 296 K and processed by using the Xwinnmr software package.

At Paris 5, UV/Vis absorption spectra were recorded with a SAFAS mc2 spectrophotometer operating at room temperature and $^1$H NMR spectra were recorded at 300 K with a Bruker WR250 spectrometer. Electrochemical experiments were carried out with an EGG-PAR model 173 potentiostat, or with a Tacussel PJT 120–1 potentiostat controlled by a PC computer by a Tacussel IMT-1 interface.

HRMS analyses were carried out at Ecole Polytechnique, Palaiseau, France with a 7-T APEX III FT-ICR mass spectrometer (Bruker Daltonik, Bremen, Germany) equipped with a 7 Tesla actively shielded superconducting magnet and an infinity cell. Nanoelectrospray was used as the ionization source, and nanoelectrospray needles were purchased from Proxeon (Odense, Denmark) and filled with 2 μL of a solution of complex (20 pmol L$^{-1}$ in 50% MeOH/water/0.2% formic acid). Mass spectra were acquired from *m*/*z* 500 to 3000 with 256k data points. MS analysis were performed at "Laboratoire de spectrométrie de masse bio-organique" ECPM, Strasbourg, France with a MicroTof apparatus (Bruker, Wissembourg France) (electrospray).

**[Fe(OEPy$_4$P)(Im)$_2$]$^{4+}$:** The preparation of Zn(OEPy$_4$P)(PF$_6$)$_4$ from Zn(OEP) was performed as described previously.[21] This complex was demetallated by treatment with $CF_3SO_3H$.[22] Iron was inserted into the free base porphyrin as follows: $H_2$OEPy$_4$P(CF$_3$SO$_3$)$_4$ (100 mg, 0.069 mmol) was dissolved in MeOH (3 mL) in the presence of imidazole (5 equiv.). The solution was deoxygenated, anhydrous $FeBr_2$ (36.6 mg, 2.5 equiv.) and Fe powder were added, and the solution was heated at reflux under an argon atmosphere for 18 h. Iron powder was added to reduce the ferric impurities present in $FeBr_2$. After cooling to room temperature, the solution was passed through a short celite column (to remove iron salts). After

 © 2007 Wiley-VCH Verlag GmbH & Co. KGaA, Weinheim 

evaporation of the solvent, the resulting product was washed with $Et_2O$ (300 mL). Yield: 50 mg (48% assuming a $[Fe(OEPy_4P)(Im)_2]^{4+}$ structure with 4 $CF_3SO_3^-$ counterions as suggested by HRMS). $^1H$ NMR (250 MHz, $CD_3OD$, of $[Fe^{II}(OEPy_4P)(Im)_2]^{4+}$ in the presence of 5 equiv. of Im, 300 K): $\delta$ = 10.45 (d, $J$ = 6 Hz, 8 H, *o*-H of $Py^+$), 9.21 (t, $J$ = 7.5 Hz, 4 H, *p*-H of $Py^+$), 8.65 (dd, $J$ = 6.8 Hz, 8 H, *m*-H of $Py^+$), 8.18–7.29 (free Im), 5.20 (2 H, bound Im), 3.83 (2 H, bound Im), 3.06 (2 H, bound Im), 2.58 (m, 8 H, $CH_2$ of $CH_2CH_3$), 1.15 (m, 8 H, $CH_2$ of $CH_2CH_3$), 0.41 (m, 24 H, $CH_3$) ppm. UV/Vis ($CH_3CN$ containing 100 μM Im, under Ar): $\lambda$ ($\varepsilon$, $M^{-1}cm^{-1}$) = 366 (70530), 458 (88280), 568 (23250), 601(24170) nm. MS (electrospray, TOF): $m/z$ = 1347.4 $[Fe(OEPy_4P)(CF_3SO_3)_3]^+$, 1279.3 $[Fe(OEPy_4P)(CF_3SO_3)_2(Br)]^+$, 599.3 $[Fe(OEPy_4P)(CF_3SO_3)_2]^{2+}$, 349.9 $[Fe(OEPy_4P)(CF_3SO_3)]^{3+}$, 326.8 $[Fe(OEPy_4P)(Br)]^{3+}$, 225.7 $[Fe(OEPy_4P)]^{4+}$.

**$[Fe(OEPy_4P)(Py)_2]^{4+}$:** A dichloromethane solution of the above $[Fe^{II}(OEPy_4P)(Im)_2]^{4+}$ complex was treated with an excess of pyridine (5% vol). The NMR sample was prepared directly in the NMR tube by adding an excess of [$D_5$]pyridine to a $CD_2Cl_2$ solution of the $[Fe^{II}(OEPy_4P)(Im)_2]^{4+}$ complex. $^1H$ NMR [400 MHz, $CD_2Cl_2$ containing 5% (vol) of $C_5D_5N$, 296 K]: $\delta$ = 10.46 (d, $J$ = 6 Hz, 8 H, *o*-H of $Py^+$), 8.99 (t, $J$ = 7.5 Hz, 4 H, *p*-H of $Py^+$), 8.45 (t, $J$ = 6.8 Hz, *m*-H of $Py^+$), 2.48 (m, 16 H, $CH_2$ of $CH_2CH_3$), 0.22 (t, $J$ = 7.1 Hz, 24 H, $CH_3$). The peaks assignments were made from the DQF-COSY spectrum. UV/Vis ($CH_3CN$): $\lambda$ = 366, 439, 458, 556, 588 nm.

**Crystallography:** Selected crystallographic experimental data are presented in Table 6. Crystals of $[Fe(OEPy_4P)(Py)_2](CF_3SO_3)_3(Br)$ were grown by vapor diffusion of pentane into a solution of the complex in $CH_2Cl_2$. A crystalline sample was placed in Paratone-N, the single crystal was suspended in a nylon loop and transferred to the liquid nitrogen cold stream of the diffractometer. Crystallographic data were collected at beamline X26C of the National Synchrotron Light Source at Brookhaven National Laboratory. 360° of data were collected by the rotation method on an ADSC Quantum 4 area detector and processed with Denzo/Scalepack. Lattice parameters for the synchrotron data were determined separately for each recorded image and are mean values derived from the reproducibility of the determinations. The structures were solved by direct methods and refined against $F^2$ by using SHELXL-97 in the SHELXTL version 5 package. Hydrogens were included in idealized positions by using a riding model. CCDC-630557 contains the supplementary crystallographic data for this paper. These data can be obtained free of charge from The Cambridge Crystallographic Data Centre via www.ccdc.cam.ac.uk/data_request/cif.

Table 6. Crystallographic details for $[Fe(OEPy_4P)(Py)_2](CF_3SO_3)_3(Br)$ (**1**).

| | |
|---|---|
| Empirical formula | $C_{69}H_{70}BrF_9FeN_{10}O_9S_3$ |
| Formula mass [g mol$^{-1}$] | 1586.28 |
| Space group | $P2_1/c$ |
| $T$ [K] | 103(2) |
| $a$ [Å] | 14.261(3) |
| $b$ [Å] | 26.501(5) |
| $c$ [Å] | 21.202(4) |
| $\alpha$ [°] | 90.00 |
| $\beta$ [°] | 107.52(3) |
| $\gamma$ [°] | 90.00 |
| $V$ [Å$^3$] | 7641(3) |
| $Z$ | 4 |
| $\lambda$ [Å] | 0.8950 |
| $D_{calcd.}$ [g cm$^{-3}$] | 1.435 |
| $\mu$ [mm$^{-1}$] | 0.890 |
| $R_1$ [$F_o > 4\sigma(F_o)$] | 0.0686 |
| $wR_2$ (all data) | 0.2021 |

**Supporting Information** (see footnote on the first page of this article): $^1H$ NMR spectrum of the $[Fe(OEPy_4P)(Im)_2]^{4+}$ complex and a figure illustrating the hydrogen bond between the pyridine C59···H and a triflate anion oxygen atom.

## Acknowledgments

The work at Brookhaven was supported by the Offices of Biological and Environmental Research and of Basic Energy Sciences of the US Department of Energy under Contract No. DE-AC02-98CH10886, and by the National Center for Research Resources of the National Institutes of Health. Financial support for C. B., D. M., and P. B. came from CNRS and University Paris 5. The authors thank Drs. A. Giraudeau, A. Brisach-Wittmayer (UMR 7512, Strasbourg, France) and L. Ruhlmann (Université Paris-Sud, Orsay, France) for their crucial help in the synthesis of Zn(OEPy$_4$P)(PF$_6$)$_4$ and for a gift of this complex at the beginning of this work. We also thank Dr. J. Fajer for important discussions and help during this work, and Dr. Chamot-Rooke (Laboratoire des Mécanismes Réactionnels, Palaiseau, France) for HRMS measurements.

[1] M. O. Senge, "Highly Substituted Porphyrins" in *The Porphyrin Handbook* (Eds.: K. M. Kadish K. M. Smith, R. Guilard), Academic Press, New York, **2000**, vol. 1, ch. 6, p. 239.
[2] M. O. Senge, *Chem. Commun.* **2006**, 243–256.
[3] F. A. Walker, *Chem. Rev.* **2004**, *104*, 589–615.
[4] W. R. Scheidt, "Systematics of the Stereochemistry of Porphyrins and Metalloporphyrins" in *The Porphyrin Handbook* (Eds.: K. M. Kadish, K. M. Smith, R. Guilard), Academic Press, New York, **2000**, vol. 3, ch. 16, p. 49.
[5] M. W. Renner, K. M. Barkigia, J. Fajer, *Inorg. Chim. Acta* **1997**, *263*, 181–187.
[6] K. M. Kadish, E. Van Caemelbecke, G. Royal, "Electrochemistry of Metalloporphyrins in Nonaqueous Media" in *The Porphyrin Handbook* (Eds.: K. M. Kadish, K. M. Smith, R. Guilard), Academic Press, New York, **2000**, vol. 8, ch. 55, p. 1.
[7] B. Meunier, A. Robert, G. Pratviel, J. Bernardou, "Metalloporphyrins in Catalytic Oxidations and Oxidative DNA Cleavage" in *The Porphyrin Handbook* (Eds.: K. M. Kadish, K. M. Smith, R. Guilard), Academic Press, New York, **2000**, vol.4, ch. 31, p. 119.
[8] D. Dolphin, T. G. Traylor, L. Y. Xie, *Acc. Chem. Res.* **1997**, *30*, 251–259.
[9] D. Mansuy, *Coord. Chem. Rev.* **1993**, *125*, 129–142.
[10] E. D. Sternberg, D. Dolphin, C. Brückner, *Tetrahedron* **1998**, *54*, 4151–4202.
[11] Z. Ziegler, L. Pasierb, K. A. Cole, D. W. Wright, *J. Inorg. Biochem.* **2003**, *96*, 478–486.
[12] J. P. C. Tomé, M. G. P. M. S. Neves, A. C. Tomé, J. A. S. Cavaleiro, M. Soncin, M. Magaraggia, S. Ferro, G. Jori, *J. Med. Chem.* **2004**, *47*, 6649–6652.
[13] A. V. Vzorov, D. W. Dixon, J. S. Trommel, L. G. Marzilli, R. W. Compans, *Antimicrob. Agents Chemother.* **2002**, 3917–3925.
[14] R. W.-Y. Sun, W.-Y. Yu, H. Sun, C.-M. Che, *ChemBioChem* **2004**, *5*, 1293–1298.
[15] W. S. Caughey, L. D. Raymond, M. Horiuchi, B. Caughey, *Proc. Natl. Acad. Sci. USA* **1998**, *95*, 12117–12122.
[16] I. Batinic-Haberle, I. Spasojevic, P. Hambright, L. Benov, A. L. Crumbliss, I. Fridovich, *Inorg. Chem.* **1999**, *38*, 4011–4022.
[17] T. P. Misko, M. K. Highkin, A. M. Veenhuinzen, P. T. Manning, M. K. Stern, M. G. Currie, D. Salvemini, *J. Biol. Chem.* **1998**, *273*, 15646–15653.
[18] J. Lee, J. A. Hunt, J. T. Groves, *J. Am. Chem. Soc.* **1998**, *120*, 6053–6061.

 © 2007 Wiley-VCH Verlag GmbH & Co. KGaA, Weinheim 

[19] I. Batinic-Haberle, S. I. Liochev, I. Spasojevic, I. Fridovich, *Arch. Biochem. Biophys.* **1997**, *343*, 225–233.
[20] R. Weiss, F. Pühlhofer, N. Jux, K. Merz, *Angew. Chem. Int. Ed.* **2002**, *41*, 3815–3817.
[21] A. Giraudeau, S. Lobstein, L. Ruhlmann, D. Melamed, K. M. Barkigia, J. Fajer, *J. Porphyrins Phthalocyanines* **2001**, *5*, 793–797.
[22] C. Bochot, J.-F. Bartoli, Y. Frapart, P. M. Dansette, D. Mansuy, P. Battioni, *J. Mol. Catal., A* **2007**, *263*, 200–205.
[23] L. Ruhlmann, S. Lobstein, M. Gross, A. Giraudeau, *J. Org. Chem.* **1999**, *64*, 1352–1355.
[24] K. Ozette, P. Battioni, P. Leduc, J.-F. Bartoli, D. Mansuy, *Inorg. Chim. Acta* **1998**, *272*, 4–6.
[25] J.-F. Bartoli, V. Mouries-Mansuy, K. Le Barch-Ozette, M. Palacio, P. Battioni, D. Mansuy, *Chem. Commun.* **2000**, 827–828.
[26] K. M. Barkigia, L. Chantranupong, K. M. Smith, J. Fajer, *J. Am. Chem. Soc.* **1988**, *110*, 7566–7567.
[27] M. O. Senge, R. W. Renner, W. W. Kalisch, J. Fajer, *J. Chem. Soc., Dalton Trans.* **2000**, 381–385.
[28] P. Ochsenbein, K. Ayougou, D. Mandon, J. Fischer, R. Weiss, R. N. Austin, K. Jayaraj, A. Gold, J. Terner, J. Fajer, *Angew. Chem. Int. Ed. Engl.* **1994**, *33*, 348–350.
[29] J.-F. Bartoli, K. Le Barch, M. Palacio, P. Battioni, D. Mansuy, *Chem. Commun.* **2001**, 1718–1719.
[30] K. M. Barkigia, M. Palacio, Y. Sun, M. Nogues, M. W. Renner, F. Varret, P. Battioni, D. Mansuy, J. Fajer, *Inorg. Chem.* **2002**, *41*, 5647–5649.
[31] K. Ozette, P. Leduc, M. Palacio, J.-F. Bartoli, K. M. Barkigia, J. Fajer, P. Battioni, D. Mansuy, *J. Am. Chem. Soc.* **1997**, *119*, 6442–6443.
[32] M. Nakamura, *Coord. Chem. Rev.* **2006**, *250*, 2271–2294.
[33] M. W. Grinstaff, M. G. Hill, E. R. Birnbaum, W. P. Schaefer, J. A. Labinger, H. Gray, *Inorg. Chem.* **1995**, *34*, 4896–4902.
[34] L. Sun, W. Jentzen, J. A. Shelnutt, *The Coordinate Structural Decomposition Engine*, http://jasheln.unm.edu.
[35] C. Hu, B. C. Noll, C. E. Schulz, W. R. Scheidt, *Inorg. Chem.* **2005**, *44*, 4346–4358.
[36] K. M. Barkigia, M. D. Berber, J. Fajer, C. J. Medforth, M. W. Renner, K. M. Smith, *J. Am. Chem. Soc.* **1990**, *112*, 8851–8857.
[37] K. M. Kadish, E. Van Caemelbecke, F. D'Souza, M. Lin, D. J. Nurco, C. J. Medforth, T. P. Forsyth, B. Krattinger, K. M. Smith, S. Fukuzumi, I. Nakanishi, J. A. Shelnutt, *Inorg. Chem.* **1999**, *38*, 2188–2198.
[38] V. P. Shedbalkar, L. B. Dugad, S. Mazumdar, S. Mitra, *Inorg. Chim. Acta* **1988**, *148*, 17–20.
[39] L. Edwards, D. H. Dolphin, M. Gouterman, *J. Mol. Spectrosc.* **1970**, *35*, 90–109.
[40] R. Bonnett, M. J. Dimsdale, *J. Chem. Soc., Perkin Trans. 1* **1972**, 2540–2548.
[41] K. M. Kadish, E. Van Caemelbecke, G. Royal, "Electrochemistry of Metalloporphyrins in Nonaqueous Media: Data Bases of Redox Potentials Media" in *The Porphyrin Handbook* (Eds.: K. M. Kadish, K. M. Smith, R. Guilard), Academic Press, New York, **2000**, vol. 9, ch. 59, p. 1.
[42] K. T. Moore, J. T. Fletcher, M. J. Therien, *J. Am. Chem. Soc.* **1999**, *121*, 5196–5209.
[43] R.-J. Cheng, P.-Y. Chen, P.-R. Gau, C.-C. Chen, S.-M. Peng, *J. Am. Chem. Soc.* **1997**, *119*, 2563–2569.
[44] V. Schünemann, M. Gerdan, A. X. Trautwein, N. Haoudi, D. Mandon, J. Fischer, R. Weiss, A. Tabard, R. Guilard, *Angew. Chem. Int. Ed.* **1999**, *38*, 3181–3183.

Received: December 12, 2006
Published Online: May 4, 2007

 © 2007 Wiley-VCH Verlag GmbH & Co. KGaA, Weinheim 

DOI: 10.1002/ejic.200700056

# Mixed Titanium–Hafnium Chloridometallate Complexes

**Emmanuel Robé,[a] Sébastien Maria,[a] Philippe Richard,[a] and Rinaldo Poli*[b]**

**Keywords:** Titanium / Hafnium / Chloridometallate complexes / Mixed-metal complexes

The addition of either $NEt_3BzCl$ or $[Ph_3PNPPh_3]Cl$ (1 equiv. chloride per metal) to a 1:1 mixture of $HfCl_4$ and $TiCl_3$ in $SOCl_2$ results in Ti oxidation and leads to the corresponding salts of the $[TiHfCl_{10}]^{2-}$ ion. A solution IR investigation in the ν(M–Cl) region indicates that this ion is in equilibrium with the homodimetallic $[Ti_2Cl_{10}]^{2-}$ and $[Hf_2Cl_{10}]^{2-}$ ions. An X-ray study of the $NEt_3Bz^+$ salt reveals an edge-sharing bioctahedral dianion sitting on a crystallographic inversion centre. The crystal is a solid solution of different species with compositional disorder at the metal site, each metal position having the occupancy $Ti_{0.685}Hf_{0.315}$. The M–M and M–Cl distances have intermediate values between those of the homodimetallic analogues. The results of DFT calculations rationalize the structural, energetic and M–Cl bonding differences. An electrochemical investigation, in comparison with that of $[Ti_2Cl_{10}]^{2-}$ and the parallel IR studies, provides further information on the solution equilibria. Adventitious hydrolysis during the crystallization of the $[Ph_3PNPPh_3]^+$ salt affords crystals of $[Ph_3PNPPh_3]_2[Cl_3Ti(\mu\text{-}O)HfCl_5]$, whose dianion contains a tetrahedral $Ti^{IV}$ centre and an octahedral $Hf^{IV}$ centre bridged by an oxygen atom. A bond-length analysis allows the description of this dianion as containing the hitherto unknown $[Ti(O)Cl_3]^-$ complex, which acts as an oxygen-based donor ligand to $[HfCl_5]^-$.
(© Wiley-VCH Verlag GmbH & Co. KGaA, 69451 Weinheim, Germany, 2007)

## Introduction

Titanium chlorides are of fundamental importance in Ziegler–Natta polymerization. The first catalyst for this process was prepared by mixing $TiCl_4$ and $AlEt_3$ or $Et_2AlCl$.[1–3] Other metal halides have been extensively investigated, and the literature abounds with reviews and patents on this subject, but the characterization of heterogeneous Ziegler–Natta catalysts at the atomic level is still actively pursued.[4–15] Among several improvements over the original catalyst, the use of mixed-metal systems, for instance Ti–V systems, are worth of particular mention.[16–18] Recently, mixed hafnium–titanium based catalysts have been explored as substitutes for the high-temperature polyethylene process.[19–21] To the best of our knowledge, the role played by the Hf metal has not yet been elucidated. Far from answering questions related to the structure and mechanism of the heterogeneous catalyst active sites, simple model compounds may nevertheless provide at least a basis to address the nature of the resting state of a surface active site, and the effect that a second (additive) metal may have on the ground-state properties of the first (catalytically active) one.

Only a limited number of well-defined compounds that contain both titanium and hafnium in the same molecule can be found in the literature. The only examples that we have been able to find are restricted to $(NMe_2)_2Ti(\mu\text{-}NMe_2)_2HfCl_4$,[22] $Cp_2Ti(\mu\text{-}CH_2)_2HfCp_2$,[23,24] $Cl_4Ti(\mu\text{-}C_{12}H_6N_2O_2)HfCl_4$ and $Cp_2Ti(\mu\text{-}C_{12}H_6N_2O_2)HfCl_4$ ($C_{12}H_6N_2O_2$ = 1,10-phenanthroline-5,6-dione, $\kappa^2$-*N*,*N*-coordinated to $HfCl_2$ and $\kappa^2$-*O*,*O*-coordinated to $TiCl_4$ or $Cp_2Ti$)[25] and two octametallic oxo- and methacrylato-bridged compounds, $Ti_4Hf_4O_6(OPr)_4(O_2CCMe{=}CH_2)_{16}$ and $Ti_2Zr_5HfO_6(O_2CCMe{=}CH_2)_{20}$,[26] the latter ones being apparently the only structurally characterized examples. Since the preparation of Ziegler–Natta catalysts is generally performed from simple, commercially available chloride compounds, it is of interest to explore mixed-metal systems where chlorides are the only available supporting ligands. In catalyst preparation, intimate mixtures or solid solutions of the metal halides are generally treated in situ with the organoaluminium activating agent, which therefore introduces alkylated active sites on the surface of the mixed-metal halide material.

In general, simple molecular chloridometallate complexes can be viewed as stabilized chunks of solid-state structures. For instance, the solid-state $HfCl_4$ structure displays hexagonal packing of chloride ions; the $Hf^{4+}$ ions occupy 1/4 of the octahedral sites, which results in bioctahedral moieties that are arranged pairwise and share an edge or a triangular face.[27,28] The well-defined dinuclear

[a] Institut de Chimie Moléculaire de l'Université de Bourgogne, UMR-CNRS-5260, Faculté des Sciences "Mirande", Université de Bourgogne
9 Avenue Alain Savary, 21078 Dijon cedex, France
Fax: +33-561553003
E-mail: poli@lcc-toulouse.fr
[b] Laboratoire de Chimie de Coordination, UPR CNRS 8241 liée par convention à l'Université Paul Sabatier et à l'Institut National Polytechnique de Toulouse
205 Route de Narbonne, 31077 Toulouse cedex, France

 © 2007 Wiley-VCH Verlag GmbH & Co. KGaA, Weinheim 

$[Hf_2Cl_{10}]^{2-}$ and $[Hf_2Cl_9]^-$ complexes, described a few years ago by Calderazzo and co-workers,[29,30] may be considered to be derived from the solid-state structure of $HfCl_4$ by chopping off "$Hf_2Cl_8$" pieces and stabilizing them by addition of controlled amounts of additional chloride ions to the resulting unsaturations, whereas the addition of excess $Cl^-$ leads to the mononuclear octahedral $[HfCl_6]^{2-}$ complex[31] (Scheme 1). $Ti^{IV}$ edge-sharing and face-sharing bioctahedral analogues ($[Ti_2Cl_{10}]^{2-}$ and $[Ti_2Cl_9]^-$) also exist,[32] and we have recently reported spectroscopic evidence for the existence of $[Ti_2Cl_{11}]^{3-}$.[33] On the other hand, the neutral system is a molecular, mononuclear four-coordinate complex, $TiCl_4$, rather than an extended solid. A face-sharing bioctahedral complex, $[Ti_2Cl_9]^{3-}$, is also known for $Ti^{III}$.[34,35] This is related to the solid-state structure of the catalytically relevant violet $TiCl_3$, whereas hafnium analogues are not known. We set out to prepare and characterize mixed-metal (Ti,Hf) chloridometallate complexes by addition of chloride ions to a mixture of Ti and Hf chlorides in the appropriate stoichiometry and report here the results of these investigations.

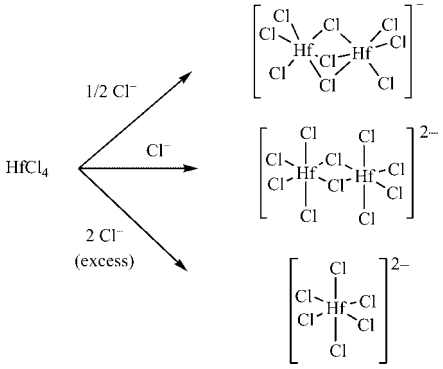


Scheme 1.

## Results and Discussion

### Synthetic Work

Before attempting to prepare mixed-metal complexes, we optimized the conditions for the preparation of single-metal species. Our strategy is described in Scheme 1, using the chloride salts $NEt_3Bz^+Cl^-$ and $[Ph_3PNPPh_3]^+Cl^-$ (the latter one will be abbreviated as $PPN^+Cl^-$). The addition of these salts to commercially available $HfCl_4$ suspended in $CH_2Cl_2$, however, did not result in any apparent interaction. Since this is in apparent contradiction with the literature (a decachloridodihafnate salt of the $Ph_3C^+$ cation has been obtained by addition of $Ph_3CX$ to $HfCl_4$)[29] and since commercial $HfCl_4$ is typically contaminated by partially hydrolyzed oxo impurities, the reaction was then conducted in $SOCl_2$ in order to reconvert in situ any impurities to $HfCl_4$. Under these conditions the reaction takes place smoothly [Equation (1), ($Cat^+ = NEt_3Bz^+$, $PPN^+$)], leading to the isolation of white, analytically pure $[NEt_3Bz]_2[Hf_2Cl_{10}]$ and $[PPN]_2[Hf_2Cl_{10}]$ in excellent yields. We have also successfully used an alternative two-step procedure, consisting of the regeneration of pure $HfCl_4$ from the commercial source by treatment with $SOCl_2$ followed by reaction with $Cat^+Cl^-$ in $CH_2Cl_2$. However, the direct reaction in $SOCl_2$ is a more practical procedure. After isolation, the compounds are readily soluble in dichloridomethane (the PPN salt has a significantly higher solubility). Analogous titanium complexes have been obtained and reported recently by us from the reaction of the same chloride salts with $TiCl_3$ in $SOCl_2$ [Equation (2)],[33] where the oxidation of the titanium centre occurs by intervention of the solvent as a source of chlorine atoms. Since $TiCl_3$ is more convenient to handle than $TiCl_4$ as starting compound, we have used the same strategy to access mixed-metal systems in this work. When the same reaction shown in Equation (1) and Equation (2) was carried out with a 1:1 mixture of $TiCl_3$ and $HfCl_4$, products corresponding to the expected mixed-metal $TiHfCl_{10}^{2-}$ stoichiometry were obtained in excellent yields [Equation (3), ($Cat^+ = NEt_3Bz^+$, $PPN^+$)]. The isolated compounds are yellow, which is the expected colour for $Ti^{IV}$ (the $[Ti_2Cl_{10}]^{2-}$ salts are also yellow).

$$2\ HfCl_4 + 2\ Cat^+Cl^- \rightarrow Cat_2[Hf_2Cl_{10}] \quad (1)$$

$$2\ TiCl_3 + 2\ Cat^+Cl^- + 2\ \{Cl\} \rightarrow Cat_2[Ti_2Cl_{10}] \quad (2)$$

$$TiCl_3 + HfCl_4 + 2\ Cat^+Cl^- + 2\ \{Cl\} \rightarrow Cat_2[TiHfCl_{10}] \quad (3)$$

The major issue at this point is to find evidence for the existence of the mixed-metal species, as opposed to a 1:1 mixture of the homoleptic dimers, and to measure or at least estimate the position of the corresponding equilibrium [Equation (4)]. Both the homometallic and the heterodimetallic complexes are devoid of simple spectroscopic probes such as nuclei with a spin of 1/2 that would be suitable for an NMR investigation or with unpaired electrons for an EPR investigation, allowing them to be easily distinguished. The use of $^{47}Ti$, $^{49}Ti$, $^{177}Hf$ and $^{179}Hf$ NMR spectroscopy is unsatisfactory for compounds in which the metal centre has lower than cubic symmetry.[36,37]

$$[Ti_2Cl_{10}]^{2-} + [Hf_2Cl_{10}]^{2-} \rightleftarrows 2\ [TiHfCl_{10}]^{2-} \quad (4)$$

### Infrared Characterization

Useful information was obtained from far-IR spectroscopy, which is sensitive to M–Cl modes, with samples in $CH_2Cl_2$ solutions in polyethylene cells. The effectiveness of this technique was previously shown for the homoleptic chloridotitanate species, in that the existence and solution-stability of the previously unknown $[Ti_2Cl_{11}]^{3-}$ ion could be unambiguously demonstrated.[33] Only the more soluble $PPN^+$ series of compounds gave sufficiently intense bands, and the results are shown in Figure 1. Note that the most distinct band of the $PPN^+$ cation at ca. 465 $cm^{-1}$ (as measured for a PPNCl solution, Figure 1c) is seen in all spectra. A less distinct $PPN^+$ band at 393 $cm^{-1}$ is also found in all other spectra, but at much higher relative intensity. How-

 © 2007 Wiley-VCH Verlag GmbH & Co. KGaA, Weinheim 

ever, our previous studies on the $[Ti_2Cl_{10}]^{2-}$ species have shown that adventitious hydrolytic impurities also generate a band at this frequency.[33] The relative intensity of this band varies as a function of the care with which the solutions are handled and increases when undried dichloromethane is used as solvent. All reported spectra were recorded in carefully dried solvent and all glassware and transfer syringes were silylated by rinsing with a 10% v/v chloroform solution of $Me_3SiCl$. However, we have been unable to completely eliminate this band. Given the extreme moisture-sensitivity of the $Ti^{IV}$–Cl bonds, it is possible that some hydrolysis occurred during the isolation procedure (washing and transfer into the storage ampoules). An analogous band is observed here also for the hafnium sample. This may also be a hydrolytic impurity coincidentally absorbing at the same frequency, or a real band for this complex. Anyhow, we will disregard this particular band in our conclusions.

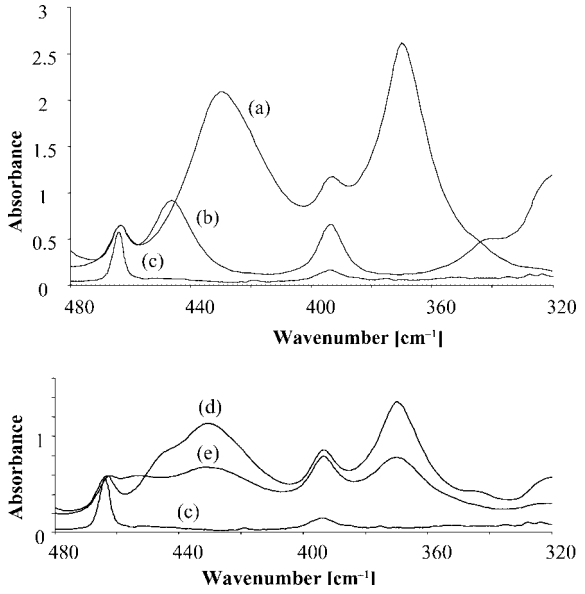


Figure 1. Far-IR spectra of PPN salts in $CH_2Cl_2$. All spectra are recorded at the same $PPN^+$ cation concentration ($10^{-2}$ M). (a) $[PPN]_2[Ti_2Cl_{10}]$; (b) $[PPN]_2[Hf_2Cl_{10}]$; (c) [PPN]Cl; (d) electronic average of $[PPN]_2[Ti_2Cl_{10}]$ and $[PPN]_2[Hf_2Cl_{10}]$; (e) 1:1 mixture of $[PPN]_2[Ti_2Cl_{10}]$ and $[PPN]_2[Hf_2Cl_{10}]$.

$[Ti_2Cl_{10}]^{2-}$ displays two major bands at ca. 370 and 430 $cm^{-1}$ (Figure 1a) of much stronger intensity than the band of the hafnium analogue at ca. 450 $cm^{-1}$ (Figure 1b). The spectrum of a solution of the mixed-metal complex, at the same molar concentration of the $PPN^+$ cation, is shown in Figure 1e. This spectrum is identical with that obtained by mixing equimolar amounts of $Ti_2Cl_{10}^{2-}$ and $Hf_2Cl_{10}^{2-}$. This observation establishes the notion that the equilibrium shown in Equation (4) is very rapid. This spectrum shows the same maxima that are individually observed in the spectra of the two homoleptic species, and any new bands are absent. However, the overall intensity is distinctly *lower* relative to the electronic average of the spectra of the two homoleptic species (Figure 1d). The height of the peak of the $PPN^+$ cation at 465 $cm^{-1}$ serves as an internal consistency check, showing the reliability of the difference between spectra (d) and (e). Since the intensity of the $[Hf_2Cl_{10}]^{2-}$ bands are so much lower than those of the corresponding titanium species, a mixed-metal analogue is likely to have intermediate intensity. Thus, the presence of some amount of the mixed-metal species is consistent with the decrease in intensity in going from the 1:1 mixture of $[Ti_2Cl_{10}]^{2-}$ and $[Hf_2Cl_{10}]^{2-}$ (Figure 1d) to the equilibrium mixture (Figure 1e). In other words, this decrease constitutes experimental evidence for the presence of mixed-metal species at equilibrium.

## Structural Characterization

Single crystals have been obtained from the mixed-metal solution of the $NEt_3Bz^+$ salt and have been investigated by X-ray diffraction (Figure 2). Unfortunately, the compound crystallizes in a centrosymmetric space group with one half of the dianion in the asymmetric unit. Consequently, the two metal sites in the bioctahedral geometry are symmetry-disordered. Furthermore, a free occupancy refinement for the metal site as $x$Ti + $(1 - x)$Hf gives $x = 0.685$. Therefore, the compound has excess titanium relative to the 1:1 stoichiometry. It is a solid solution containing 37% $[Ti_2Cl_{10}]^{2-}$, while the remaining 63% could be either pure $[TiHfCl_{10}]^{2-}$, or a 1:1 mixture of the $Ti_2$ and $Hf_2$ salts, or anything between these two extremes. The presence of excess titanium indicates a lower solubility for the lighter $Ti_2$ salt, which is then expected to shift the equilibrium of Equation (4) toward the left during the crystallization process. However, the geometrical features and the distances and angles, in comparison with those of the $[Ti_2Cl_{10}]^{2-}$ and $[Hf_2Cl_{10}]^{2-}$ anions (Table 1), are as expected and confirm the mixed-metal nature of the dianion. While the bond angles are approximately identical for the three dianions, the M–M/M′ and M–Cl bond lengths steadily increase in the order $Ti_2$ < $Ti_{1.37}Hf_{0.63}$ < $Hf_2$, as expected from the increase in the metal radius.

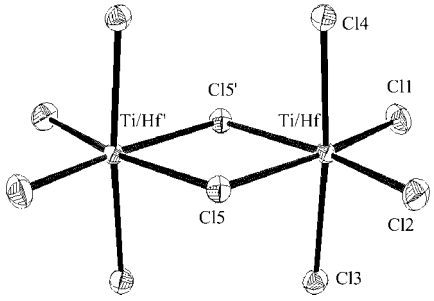


Figure 2. ORTEP view of the mixed-metal $[Ti_{1.37}Hf_{0.63}Cl_{10}]^{2-}$ anion.

 © 2007 Wiley-VCH Verlag GmbH & Co. KGaA, Weinheim 

Table 1. Selected bond lengths [Å] and angles [°] for the dianion in compound $[NEt_3Bz]_2[Ti_{1.37}Hf_{0.63}Cl_{10}]\cdot 2CH_2Cl_2$, and comparison with the analogous $Ti_2$ and $Hf_2$ anions.

| | M = M′ = Ti [a] | MM′ = $Ti_{1.37}Hf_{0.63}$ | M = M′ = Hf [b] |
|---|---|---|---|
| M–M′ | 3.855(3) | 3.8886(4) | 4.020(15) |
| M–$Cl_{br}$ | 2.494(13) | 2.5549(6)<br>2.5040(6) | 2.585(25) |
| M–$Cl_{ax}$ | 2.296(5) | 2.3320(6)<br>2.3408(6) | 2.406(13) |
| M–$Cl_{eq}$ | 2.258(11) | 2.2929(7)<br>2.3028(6) | 2.377(10) |
| $Cl_{br}$–M–$Cl_{br}$ | 78.78(8) | 79.54(2) | 78.1(1) |
| $Cl_{br}$–M–$Cl_{ax}$ | 87.9(8) | 86.85(2)<br>87.87(2)<br>87.62(2)<br>88.71(2) | 88.04(1) |
| $Cl_{br}$–M–$Cl_{eq}$(*cis*) | 90(2) | 91.54(2)<br>88.91(2) | 90.4(4) |
| $Cl_{br}$–M–$Cl_{eq}$(*trans*) | 169(2) | 171.07(2)<br>168.43(2) | 168.48(19) |
| $Cl_{ax}$–M–$Cl_{eq}$ | 91.7(10) | 92.61(2)<br>92.47(2)<br>90.95(2)<br>91.40(2) | 91.48(1) |
| $Cl_{ax}$–M–Cl′$_{ax}$ | 174.2(2) | 173.95(2) | 174.6(1) |
| $Cl_{eq}$–M–Cl′$_{eq}$ | 100.33(9) | 100.02(3) | 101.1(3) |
| M–$Cl_{br}$–M′ | 101.21(9) | 100.46(2) | 101.85(1) |

[a] Averages of chemically equivalent values in the structure of the $PCl_4^+$ salt.[32] [b] Averages of chemically equivalent values in the structure of the $Ph_3C^+$ salt.[29]

## DFT Studies

DFT calculations have been carried out on complexes $[Ti_2Cl_{10}]^{2-}$, $[TiHfCl_{10}]^{2-}$ and $[Hf_2Cl_{10}]^{2-}$ by using two different functionals (B3LYP and B3PW91) and the LANL2DZ basis set. These combinations usually give good-quality results for geometries and energies of transition-metal compounds. The calculations included a frequency analysis, and the zero-point energy, thermal and entropy corrections to give the free energies at room temperature. According to these calculations, the mixed complex is favoured relative to the mixture of the two homometallic dinuclear species by 2.04 (B3LYP) and 1.99 (B3PW91) kcal mole$^{-1}$, corresponding to $K \approx 30$ for the above equilibrium. More precisely, the equilibrium would consist of 13% of each of the homometallic species and 74% of the dimetallic species for a Ti/Hf ratio of 1:1. This result is in qualitative agreement with the IR results. The optimized distances (Table 2) tend to be slightly long (cf. Table 1); the B3PW91 results are closer to the experimental observations. Interestingly, whereas the M–Cl distances in the TiHf compound are, as expected, shorter for Ti than for Hf when bonded to $Cl_{ax}$ and to $Cl_{eq}$, there is very little difference in the M–$Cl_{br}$ distances involving the two different metals. This is rationalized in the next paragraph.

Table 2. Calculated bond lengths [Å] and angles [°] for $[MM'Cl_{10}]^{2-}$ (M, M′ = Ti, Hf).

| | M = M' = Ti | | M = Ti; M' = Hf | | M = M' = Hf | |
|---|---|---|---|---|---|---|
| | B3LYP | B3PW91 | B3LYP | B3PW91 | B3LYP | B3PW91 |
| M–M' | 4.098 | 4.037 | 4.175 | 4.120 | 4.243 | 4.192 |
| M–$Cl_{br}$ | 2.613 | 2.585 | 2.664 | 2.632 | 2.687 | 2.664 |
| M'–$Cl_{br}$ | | | 2.646 | 2.632 | | |
| M–$Cl_{ax}$ | 2.317 | 2.303 | 2.303 | 2.290 | 2.456 | 2.442 |
| M'–$Cl_{ax}$ | | | 2.467 | 2.453 | | |
| M–$Cl_{eq}$ | 2.305 | 2.291 | 2.291 | 2.278 | 2.440 | 2.427 |
| M'–$Cl_{eq}$ | | | 2.453 | 2.440 | | |
| $Cl_{br}$–M–$Cl_{br}$ | 76.74 | 77.30 | 76.00 | 76.94 | 75.72 | 76.25 |
| $Cl_{br}$–M'–$Cl_{br}$ | | | 76.61 | 76.95 | | |
| $Cl_{br}$–M–$Cl_{ax}$ | 87.51 | 87.40 | 86.26 | 86.25 | 88.34 | 88.22 |
| $Cl_{br}$–M'–$Cl_{ax}$ | | | 89.49 | 89.20 | | |
| $Cl_{br}$–M–$Cl_{eq}$(*cis*) | 91.60 | 91.33 | 91.97 | 91.53 | 92.34 | 92.14 |
| $Cl_{br}$–M'–$Cl_{eq}$(*cis*) | | | 92.06 | 91.85 | | |
| $Cl_{br}$–M–$Cl_{eq}$(*trans*) | 168.35 | 168.63 | 167.97 | 168.47 | 168.06 | 168.39 |
| $Cl_{br}$–M'–$Cl_{eq}$(*trans*) | | | 168.67 | 168.80 | | |
| $Cl_{ax}$–M–$Cl_{eq}$ | 92.04 | 92.14 | 93.04 | 93.08 | 91.36 | 91.46 |
| $Cl_{ax}$–M'–$Cl_{eq}$ | | | 90.42 | 90.66 | | |
| $Cl_{ax}$–M–Cl'$_{ax}$ | 171.65 | 173.35 | 170.51 | 170.42 | 175.79 | 175.47 |
| $Cl_{ax}$–M'–Cl'$_{ax}$ | | | 178.63 | 177.96 | | |
| $Cl_{eq}$–M–Cl'$_{eq}$ | 100.05 | 100.05 | 100.07 | 100.00 | 99.60 | 99.48 |
| $Cl_{eq}$–M'–Cl'$_{eq}$ | | | 99.28 | 90.34 | | |
| M–$Cl_{br}$–M' | 103.25 | 102.70 | 103.70 | 103.05 | 104.28 | 103.75 |

A charge analysis (Table 3) was carried out on the B3PW91 results both at the Mulliken and at the NBO (Natural Bond Orbital) level. The latter is believed to be more descriptive for highly ionic and for weak interactions,[38] while the Mulliken analysis tends to overemphasize bond covalency. At both levels, it is clear that the Ti–Cl interactions are less polarized than the Hf–Cl interactions, as expected. The greatest difference is in the calculated charge for the bridging Cl atoms. For the TiHf compound, the calculated charges for the $Cl_{ax}$ and $Cl_{eq}$ atoms attached to each metal are rather close to the values of the same type of atoms in the corresponding monometallic species. The calculated charges on the $Cl_{br}$ atoms, on the other hand, are intermediate between those of the $Ti_2$ and $Hf_2$ compounds. The result is that the Ti–$Cl_{br}$ bond becomes more polarized (and consequently longer) in the mixed-metal complex rela-

Table 3. Mulliken and NBO charge analysis (B3PW91) for $[MM'Cl_{10}]^{2-}$ (M, M′ = Ti, Hf).

| | M = M′ = Ti | | M = Ti; M′ = Hf | | M = M′ = Hf | |
|---|---|---|---|---|---|---|
| | Mulliken | NBO | Mulliken | NBO | Mulliken | NBO |
| M | 0.2349 | 0.2032 | 0.2848 | 0.2187 | | |
| M′ | | | 0.5404 | 1.0804 | 0.5906 | 1.0877 |
| $Cl_{br}$ | –0. 1769 | –0. 2530 | –0.2354 | –0.3346 | –0.2829 | –0.3838 |
| $Cl_{ax}$(M) | –0. 2390 | –0. 2321 | –0.2212 | –0.2112 | | |
| $Cl_{ax}$(M′) | | | –0.3343 | –0.4448 | –0. 3216 | –0. 4316 |
| $Cl_{eq}$(M) | –0.2900 | –0. 24301 | –0.2797 | –0.2236 | | |
| $Cl_{eq}$(M′) | | | –0.3421 | –0.4354 | –0. 3323 | –0. 4204 |

 © 2007 Wiley-VCH Verlag GmbH & Co. KGaA, Weinheim 

tive to the $Ti_2$ complex, whereas the Hf–$Cl_{br}$ bond becomes less polarized (and consequently shorter) in the mixed-metal complex relative to the $Hf_2$ complex. Conversely, the other Ti–Cl bonds become less polarized, and the Hf–Cl more polarized, in the mixed-metal system. This charge shift introduces a permanent dipole in the dianion (Scheme 2). The variation of the Ti–Cl bond polarity may affect the performance of the catalytic site for the ethylene polymerization process.

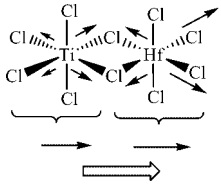


Scheme 2.

### Electrochemical Investigation

A dichloromethane solution of the $[NBzEt_3]_2[TiHfCl_{10}]$ salt was investigated by cyclic voltammetry, in comparison with the analogous study reported recently for $[Ti_2Cl_{10}]^{2-}$.[33] The results are shown in Figure 3. The mixed-metal dianion exhibits a broad irreversible peak with a maximum cathode current at ca. –0.9 V vs. ferrocene, whereas the $[Ti_2Cl_{10}]^{2-}$ dianion shows two overlapping waves (a peak at ca. –1.06 V with a shoulder at ca. –0.7 V). As expected, the $[Hf_2Cl_{10}]^{2-}$ species does not exhibit any reduction process in this potential range (an irreversible reduction takes place only below –2 V).

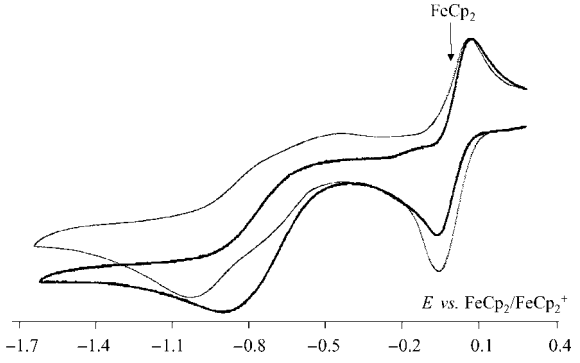


Figure 3. Cyclic voltammograms of $[NBzEt_3]_2[Ti_2Cl_{10}]$ (thinner line) and $[NBzEt_3]_2[TiHfCl_{10}]$ (thicker line). Solvent: $CH_2Cl_2$.

The two processes of the $[Ti_2Cl_{10}]^{2-}$ solution were shown to be related to the existence of the ligand redistribution equilibrium between the dianionic complex and complexes $[Ti_2Cl_9]^-$ and $[Ti_2Cl_{11}]^{3-}$ [Equation (5)]. Although the equilibrium is shifted to the left hand side in solution (as shown by IR spectroscopy), the easier reduction of the $[Ti_2Cl_9]^-$ ion (which is responsible for the shoulder at –0.7 V), coupled to the fast ligand redistribution process, shifts the equilibrium to the right in the diffusion layer. Thus, the peak with maximum cathode current at ca. –1.06 V is due to the reduction of the $[Ti_2Cl_{11}]^{3-}$ species. It is logical that the reduction of the latter species is placed at a more negative potential, since the positive charge density on the Ti centres is lower. The shape and position of the reduction wave for the mixed-metal dianion shows that it may correspond to a species whose charge density is similar to that of $[Ti_2Cl_9]^-$, whereas there is definitely no activity in the characteristic region of $[Ti_2Cl_{11}]^{3-}$. It is therefore rather logical to formulate the hypothesis of a similar chloride redistribution equilibrium for the mixed-metal dianion. However, because of the greater Lewis acidity of $Hf^{IV}$ relative to $Ti^{IV}$, the former metal centre will preferentially form the chloride-richer species while $Ti^{IV}$ will preferentially form the chloride-poorer species, as shown in Equation (6). Obviously, other species such as $[TiHfCl_9]^-$ may also be present in solution, given the complexity of the coupled equilibria, and contribute to the shape of the observed reduction wave.

$$2\,[Ti_2Cl_{10}]^{2-} \rightleftarrows [Ti_2Cl_9]^- + [Ti_2Cl_{11}]^{3-} \quad (5)$$

$$2\,[TiHfCl_{10}]^{2-} \rightleftarrows [Ti_2Cl_9]^- + [Hf_2Cl_{11}]^{3-} \quad (6)$$

### Structure of a Partial Hydrolysis Product

With the objective of obtaining a nondisordered solid-state structure of the mixed-metal dianion, we attempted to grow crystals of the $PPN^+$ salt. The crystals that slowly formed, however, turned out to be $[PPN]_2[Cl_3Ti(\mu\text{-}O)HfCl_5]$. The structure of the oxo-bridged dianion is shown in Figure 4. The two metal centres are bridged by a single oxygen atom and possess different coordination geometries, tetrahedral with three terminal Cl atoms and the bridging O atom for titanium, octahedral with five terminal Cl atoms and the bridging O atom for hafnium. Therefore, the two metal centres are not disordered in this structure. The formation of this compound can be explained by a partial hydrolysis of the decachlorido mixed-metal dianion, as shown in Equation (7). The possibility that it is obtained directly from a $HfOCl_2$ impurity in $HfCl_4$ is unlikely, since the synthesis was conducted in $SOCl_2$ as solvent (see Experimental Section). Unfortunately, we did not obtain a sufficient amount of this product to carry out an analytical and spectroscopic characterization. Its formation, however, validates the notion that well-defined mixed-metal titanium-hafnium complexes may be formed with this strategy. Given the high oxophilicity of both $Ti^{IV}$ and $Hf^{IV}$ chlorides, it is quite possible that Ziegler–Natta catalyst precursors contain oxo-bridged dimetallic units in the bulk or on the surface, for which this complex may represent a suitable structural model. Even though partial alkylation of the catalyst occurs in the presence of the aluminium alkyl activator, the metal–chloride bonds are expected to be alkylated preferentially, and oxo ligands may be present in the active form of the catalyst.

$$[TiHfCl_{10}]^{2-} + H_2O \rightarrow [TiHf(O)Cl_8]^{2-} + 2\,HCl \quad (7)$$

 © 2007 Wiley-VCH Verlag GmbH & Co. KGaA, Weinheim 

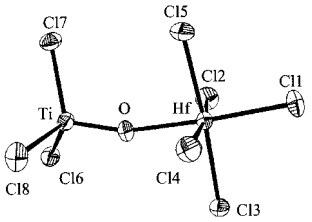


Figure 4. ORTEP view of the $[Cl_3Ti(\mu\text{-}O)HfCl_5]^{2-}$ ion.

Relevant bond lengths and angles for the $[Cl_3Ti(\mu\text{-}O)HfCl_5]^{2-}$ ion are collected in Table 4. The most interesting feature is the marked asymmetry of the oxo bridge, the Ti–O distance [1.655(4) Å] being much shorter than the Hf–O distance [2.142(3) Å]. The former is typical for terminal $Ti^{IV}O$ bond lengths, of which 25 were found in the Cambridge Structural Database (CSD), with an average value of 1.65(5) Å. There are also 7 structures in the CSD containing a Ti=O···M moiety (M = any metal). After discarding one of them (KATPUQ01), whose extremely long (> 2.1 Å) Ti=O bond length suggests a possible crystallographic problem, the remaining six bonds give an average length of 1.69(3) Å. On the other hand, the Hf–O distance is much longer than that in terminal Hf=O moieties [only one example, $(C_5Me_4Et)Hf(O)(py)$,[39] with a distance of 1.826(9) Å, has apparently been reported] and even longer than the distance of typical covalent single Hf–O bonds. For these bonds, an average of 1.97(4) Å is calculated from 148 distances found in the CSD (after excluding the values for π-delocalized donors such as carboxylates and acetylacetonates, which are significantly longer). An example where an oxygen atom bridges two metal atoms is $Cp_2(Me)Hf\text{–}O\text{–}Hf(Me)Cp_2$, with Hf–O distances of 1.941(3) Å.[40] The Hf–O distance in our ion is much closer to that of dative bonds established by neutral donors, as for instance in complex $[Hf(DMSO)_8]^{4+}$ [(2.160(12) Å].[41] Therefore, the $[Cl_3Ti(\mu\text{-}O)HfCl_5]^{2-}$ ion is best interpreted as resulting from the coordination of the hypothetical $[Ti(=O)Cl_3]^-$ anion, via a lone pair of the oxo ligand, to a $[HfCl_5]^-$ anion. Interestingly, $[TiOCl_3]^-$ does not appear to exist as an isolated species, whereas its chloride adducts $[TiOCl_4]^{2-}$ and $[TiOCl_5]^{3-}$ have been reported,[31,42–45] the former being structurally characterized as the $NEt_4^+$ salt (Ti–O: 1.79 Å).[46] A substructure search in the CSD for the four-coordinate $Cl_3TiO$ moiety only reveals neutral compounds where the oxygen atom is further bonded to an alkyl, aryl or silyl group.

The Ti–Cl distances in the $[Cl_3Ti(\mu\text{-}O)HfCl_5]^{2-}$ ion average 2.232(5) Å; they are significantly longer than the average of all Ti–Cl distances in four-coordinate $Cl_3TiX$ structures from the CSD [2.18(3) Å over 150 distances]. This is certainly related to the negative charge in this complex (formally –1 on the Ti atom), while all the literature examples are neutral complexes. The average Ti–Cl distance in the above-mentioned $[TiOCl_4]^{2-}$ ion is even longer, 2.33 Å.[46] The Hf–Cl distance *trans* to the Hf–O bond (2.4074(13) Å] is significantly shorter than the other four Hf–Cl distances, which average 2.442(9) Å. The latter compare very well with the average of all Hf–Cl distances found in all six-coordinate $Cl_5HfX$ structures from the CSD [2.44(2) Å over 55 distances]. This is not surprising, since all CSD complexes are also anionic (monoanions with X = thf or the dinuclear $Hf_2Cl_{10}^{2-}$, or dianions of $HfCl_6^{2-}$). As expected, the distance is shorter [average of 2.302(9) Å] in the cationic complex $[(\eta^6\text{-}C_6Me_6)HfCl_3]^+$,[30] which is also formally six-coordinate from the electronic point of view. The shorter Hf–Cl1 distance in $[Cl_3Ti(\mu\text{-}O)HfCl_5]^{2-}$ indicates that the oxygen donor $[TiOCl_3]^-$ "ligand" exerts a weaker *trans* influence relative to the chloride ion.

Table 4. Selected bond lengths [Å] and angles [°] for compound $[PPN]_2[Cl_3Ti(\mu\text{-}O)HfCl_5]$.

| | | | |
|---|---|---|---|
| Ti–O | 1.655(4) | Hf–Cl4 | 2.4307(13) |
| Hf–O | 2.142(3) | Hf–Cl5 | 2.4408(14) |
| Hf–Cl1 | 2.4074(13) | Ti–Cl6 | 2.2297(15) |
| Hf–Cl2 | 2.4520(13) | Ti–Cl7 | 2.2383(16) |
| Hf–Cl3 | 2.4437(12) | Ti–Cl8 | 2.2285(16) |
| Ti–O–Hf | 163.0(2) | O–Hf–Cl5 | 85.94(10) |
| O–Ti–Cl6 | 107.21(13) | Cl1–Hf–Cl2 | 93.94(5) |
| O–Ti–Cl7 | 110.51(13) | Cl1–Hf–Cl3 | 93.02(5) |
| O–Ti–Cl8 | 108.94(13) | Cl1–Hf–Cl4 | 93.45(5) |
| Cl6–Ti–Cl7 | 108.01(6) | Cl1–Hf–Cl5 | 90.81(5) |
| Cl6–Ti–Cl8 | 110.22(6) | Cl2–Hf–Cl3 | 90.16(5) |
| Cl7–Ti–Cl8 | 111.84(7) | Cl2–Hf–Cl4 | 172.60(5) |
| O–Hf–Cl1 | 176.75(10) | Cl2–Hf–Cl5 | 91.04(5) |
| O–Hf–Cl2 | 85.90(10) | Cl3–Hf–Cl4 | 89.80(5) |
| O–Hf–Cl3 | 90.23(10) | Cl3–Hf–Cl5 | 175.90(5) |
| O–Hf–Cl4 | 86.70(10) | Cl4–Hf–Cl5 | 88.50(5) |

## Conclusions

This work has explored the existence and relative stability of mixed-metal Ti–Hf chloridometallate complexes, focusing on the edge-sharing bioctahedral system, $[MM'Cl_{10}]^{2-}$ (M, M′ = Ti, Hf). We have provided evidence (by a combination of low-energy IR, X-ray crystallography, DFT calculations and cyclic voltammetry) that the mixed-metal system $[TiHfCl_{10}]^{2-}$ does exist and that it is thermodynamically more stable by a small amount than the equivalent 1:1 mixture of the homodinuclear complexes, $[Ti_2Cl_{10}]^{2-}$ and $[Hf_2Cl_{10}]^{2-}$. The comparison with the previously reported electrochemical behaviour of $[Ti_2Cl_{10}]^{2-}$ suggests a stronger preference for the $Ti_2$ complex to lose one $Cl^-$ ligand, yielding $[Ti_2Cl_9]^-$, and a corresponding stronger preference for the $Hf_2$ complex to add one more $Cl^-$ ligand, yielding $[Hf_2Cl_{11}]^{3-}$. A partial hydrolysis product obtained from the above mixture is an unprecedented mixed Ti–Hf chloridometallate ion, $[Cl_3Ti(\mu\text{-}O)HfCl_5]^{2-}$, the structure of which is best interpreted as an octahedral $[HfCl_5X]^{2-}$ complex where X is the previously unknown tetrahedral $[Cl_3Ti(O)]^-$ ion. The oxygen atom that bridges the two metals is doubly bonded to the Ti centre and donates a lone pair to the Hf centre.

## Experimental Section

**General Procedures:** All preparations and manipulations were carried out with Schlenk techniques under an oxygen-free argon atmo-

 © 2007 Wiley-VCH Verlag GmbH & Co. KGaA, Weinheim 

sphere. All glassware was oven-dried at 120 °C. For particular applications (see Results and Discussion) it was silylated by being washed with a $CHCl_3$ solution of $Me_3SiCl$ (10% v/v). Solvents were dried by standard procedures and distilled under dinitrogen prior to use.

**Materials:** $CH_2Cl_2$ was purified by reflux and distillation over $P_4O_{10}$ under argon. Pentane was purified by reflux over sodium benzophenone ketyl and distilled under argon. $TiCl_3$, $HfCl_4$ and the chloride salts triethylbenzylammonium chloride, $[NEt_3Bz]Cl$, and bis(triphenylphosphanyl)iminium chloride, [PPN]Cl, were purchased from Aldrich and used as received. Complexes $[NEt_3Bz]_2[Ti_2Cl_{10}]$ and $[PPN]_2[Ti_2Cl_{10}]$ were prepared as recently described.[33]

**Instrumentation:** The infrared spectra were recorded with a Bruker Vector 22 instrument equipped with a Globar (MIR) source. The solution spectra in the far-IR (480–300 $cm^{-1}$) region were obtained from $CH_2Cl_2$ solutions in polyethylene cells (0.5 mm path length). Cyclic voltammograms were recorded with an EG&G 362 potentiostat connected to a Macintosh computer through MacLab hardware/software. The electrochemical cell was fitted with an Ag/AgCl reference electrode, a platinum disk working electrode and a platinum wire counterelectrode. $[Bu_4N]PF_6$ (ca. 0.1 M) was used as supporting electrolyte in thf. All potentials are reported relative to the ferrocene standard, which was added to each solution and measured at the end of the experiments. Elemental analyses were carried out with a Fisons EA 1108 instrument by the analytical services of LSEO.

**Preparation of $[NEt_3Bz]_2[Hf_2Cl_{10}]$:** A Schlenk tube was charged with $HfCl_4$ (1.161 g, 3.62 mmol) and $[NEt_3Bz]Cl$ (0.826 g, 3.62 mmol). Thionyl chloride (10 mL) was added by syringe under magnetic stirring and the apparatus was connected to an oil bubbler. *Warning: The reaction between $SOCl_2$ and water (potentially present as a contaminant in the starting salts) produces toxic $SO_2$ and HCl; therefore, the reaction must be carried out under a well-ventilated fume hood.* A white suspension was observed. The reaction mixture was heated to 65 °C for 1 h in an oil bath and then cooled to room temperature. After stirring for 1 h at room temperature, pentane (20 mL) was added, causing the precipitation of the product as a white powder. After being filtered, the solid was washed with pentane and dried under vacuum overnight. Yield: 1.858 g (94%). $C_{26}H_{44}Cl_{10}Hf_2N_2$ (1096.14): calcd. C 28.5, H 4.0, N 2.6; found C 27.8, H 4.2, N 2.7.

**Preparation of $[PPN]_2[Hf_2Cl_{10}]$:** By following a procedure identical to that described above for $[NEt_3Bz]_2[Hf_2Cl_{10}]$, $[PPN]_2[Hf_2Cl_{10}]$ (3.292 g, 92%) was obtained starting from $HfCl_4$ (1.994 g, 6.23 mmol) and PPNCl (3.570 g, 6.23 mmol). $C_{72}H_{60}Cl_{10}Hf_2N_2P_4$ (1788.66): calcd. C 48.4, H 3.4, N 1.6; found C 48.1, H 3.4, N 1.8.

**Preparation of $[NEt_3Bz]_2[TiHfCl_{10}]$:** A Schlenk tube was charged with $HfCl_4$ (1.688 g, 5.27 mmol), $TiCl_3$ (0.809 g, 5.25 mmol) and $[NEt_3Bz]Cl$ (2.392 g, 10.50 mmol). Thionyl chloride (50 mL) was

Table 5. Crystal data and structure refinement for both compounds.

| Compound | $[NEt_3Bz]_2[Ti_{1.37}Hf_{0.63}Cl_{10}]\cdot 2CH_2Cl_2$ | $[PPN]_2[Cl_3Ti(\mu\text{-}O)HfCl_5]$ |
|---|---|---|
| Formula | $C_{28}H_{48}Cl_{14}Hf_{0.63}N_2Ti_{1.37}$ | $C_{72}H_{60}Cl_8HfN_2OP_4Ti$ |
| $M_r$ | 1087.01 | 1603.09 |
| $T$ [K] | 110(2) | 110(2) |
| Crystal system | triclinic | monoclinic |
| Space group | $P\bar{1}$ | $P2_1/c$ |
| $a$ [Å] | 7.6739(2) | 25.7548(5) |
| $b$ [Å] | 10.9860(2) | 12.8363(2) |
| $c$ [Å] | 14.2333(4) | 21.1674(3) |
| $\alpha$ [°] | 108.938(1) | 90.0 |
| $\beta$ [°] | 97.971(1) | 78.562(1) |
| $\gamma$ [°] | 104.494(1) | 90.0 |
| $V$ [Å]$^3$ | 1066.72(5) | 6858.9(2) |
| Z | 1 | 4 |
| $F(000)$ | 543.5 | 3216 |
| $D_{calc}$ [g cm$^{-3}$] | 1.692 | 1.552 |
| Diffractometer | Nonius KappaCSD | Nonius KappaCSD |
| Scan type | &πηι; rot. and $\psi$ scans | &πηι; rot. and $\psi$ scans |
| $\lambda$ [Å] | 0.71073 | 0.71073 |
| $\mu$ [mm$^{-1}$] | 2.69 | 2.08 |
| Crystal size [mm$^3$] | $0.45\times0.20\times0.05$ | $0.37\times0.25\times0.15$ |
| $\sin(\theta)/\lambda$ max [Å$^{-1}$] | 0.65 | 0.65 |
| Index ranges | $h$:–9; 9 | $h$:–33; 32 |
| | $k$:–14; 13 | $k$:–16; 13 |
| | $l$:–18; 18 | $l$:–27; 27 |
| RC = Refl. Collected | 8402 | 38133 |
| IRC = independent RC | 4787 [$R$(int) = 0.032] | 15599 [$R$(int) = 0.058] |
| IRCGT = IRC and [$I>2\sigma(I)$] | 4253 | 10420 |
| Refinement method | Full-matrix L.S. on $F^2$ | Full-matrix L.S. on $F^2$ |
| Data/restraints/param. | 4787/0/210 | 15599/0/802 |
| $R$ for IRCGT | $R_1$[a] = 0.033, $wR_2$[b] = 0.081 | $R_1$[a] = 0.051, $wR_2$[b] = 0.112 |
| $R$ for IRC | $R_1$[a] = 0.039, $wR_2$[b] = 0.084 | $R_1$[a] = 0.095, $wR_2$[b] = 0.126 |
| Goodness-of-fit[c] | 1.042 | 1.033 |
| $\Delta\rho$, max, min [e Å$^{-3}$] | 0.764 and –1.122 | 2.22 and –1.26 |

[a] $R_1 = \Sigma\,(||F_o| - |F_c||)/\Sigma|F_o|$. [b] $wR_2 = [\Sigma w(F_o^2 - F_c^2)^2/\Sigma\,[w(F_o^2)^2]^{1/2}$ where $w = 1/[\sigma^2(F_o^2 + (0.046P)^2 + 0.37P]$ for $[NEt_3Bz]_2[Ti_{1.37}Hf_{0.63}Cl_{10}]$ and $w = 1/[\sigma^2(F_o^2 + (0.060P)^2 + 0.86P]$for $[PPN]_2[Cl_3Ti(\mu\text{-}O)HfCl_5]$ where $P = (\mathrm{Max}(F_o^2,0) + 2*F_c^2)/3$. [c] Goodness of fit = $[\Sigma w(F_o^2 - F_c^2)^2/(N_o - N_v)]^{1/2}$.

 © 2007 Wiley-VCH Verlag GmbH & Co. KGaA, Weinheim 

added by syringe under magnetic stirring, and the apparatus was connected to an oil bubbler. A dark purple suspension was observed. The reaction mixture was refluxed for 1 h in an oil bath. The dark-purple suspension transformed gradually into a yellow solution. It was then cooled to room temperature and stirred for two hours. Thionyl chloride was partially removed under vacuum until a precipitate began to form. Pentane (20 mL) was then added to complete the precipitation of the product as a yellow powder. After being filtered, the solid was washed with pentane and dried under vacuum for two hours. Yield: 4.587 g (94%) $C_{26}H_{44}Cl_{10}HfN_2Ti$ (965.52): calcd. C 32.3, H 4.6, N 2.9; found C 32.1, H 4.6, N 2.9.

**Preparation of $[PPN]_2[TiHfCl_{10}]$:** By following a procedure identical to that described above for $[NEt_3Bz]_2[TiHfCl_{10}]$, $[PPN]_2[TiHfCl_{10}]$ (2.463 g, 94%) was obtained starting from $HfCl_4$ (0.506 g, 1.58 mmol), $TiCl_3$ (0.244 g, 1.58 mmol) and PPNCl (1.816 g, 3.16 mmol). $C_{72}H_{60}Cl_{10}HfN_2P_4Ti$ (1658.03): calcd. C 52.2, H 3.6, N 1.7; found C 53.0, H 3.6, N 2.0.

**X-ray Diffraction Studies:** Intensity data for both compounds were collected with a Nonius Kappa CSD at 110 K. The structures were solved by a Patterson search program and refined with full-matrix least-squares methods based on $F^2$ (SHELXL-97)[47] with the aid of the WINGX program.[48] All non-hydrogen atoms were refined with anisotropic thermal parameters. Hydrogen atoms were included in their calculated positions and refined with a riding model. The $[Ti_xHf_{2-x}Cl_{10}]^{2-}$ dimetallic complex is located on a centre of inversion; as a consequence, the two metal atoms are disordered and occupy the same crystallographic position. Furthermore, the two metal atoms are not in a 1:1 ratio, the occupation factors converged to $m_1 = 0.685$ for the Ti atom and $m_2 = 1 - m_1$ for the Hf atom. A first attempt to refine independently both metallic positions lead to a nonrealistic result; therefore, the two positions and the anisotropic displacement parameters where constrained to be identical for both metallic centres. The molecules were drawn with ORTEP32.[49] Crystal data and refinement parameters are shown in Table 5.

CCDC-633154 and CCDC-633155 contain the supplementary crystallographic data for this paper. These data can be obtained free of charge from The Cambridge Crystallographic Data Centre via www.ccdc.cam.ac.uk/data_request/cif.

**Computational Details:** Calculations were carried out with the Gaussian 03 package[50] at the DFT level by means of either the B3LYP[51–53] or the B3PW91[54,55] functional and the LANL2DZ basis set.[56] All geometries were fully optimized without symmetry restrictions and were characterized as local minima of the potential energy surface (PES) by inspection of the sign of the second derivatives obtained from frequency calculations. The Gibbs free energies were obtained after correction for the ZPVE, PV and TS terms under the ideal gas approximation. The temperature used was 298.15 K.

## Acknowledgments

We are grateful to the CNRS for support of this work.

[1] K. Ziegler, E. Holzkamp, H. Breil, H. Martin, *Angew. Chem.* **1955**, *67*, 541–547.
[2] K. Ziegler, *Nobel lecture*, http://nobelprize.org/nobel_prizes/chemistry/laureates/1963/ziegler-lecture.html, **1963**.
[3] G. Natta, *Nobel lecture*, http://nobelprize.org/nobel_prizes/chemistry/laureates/1963/natta-lecture.html, **1963**.
[4] P. Corradini, G. Guerra, L. Cavallo, *Acc. Chem. Res.* **2004**, *37*, 231–241.
[5] M. Chang, X. Liu, P. J. Nelson, G. R. Munzing, T. A. Gegan, Y. V. Kissin, *J. Catal.* **2006**, *239*, 347–353.
[6] N. Cui, Y. Ke, H. Li, Z. Zhang, C. Guo, Z. Lv, Y. Hu, *J. Appl. Polym. Sci.* **2006**, *99*, 1399–1404.
[7] Q. Wang, N. Murayama, B. Liu, M. Terano, *Macromol. Chem. Phys.* **2005**, *206*, 961–966.
[8] M. Seth, T. Ziegler, *Macromolecules* **2004**, *37*, 9191–9200.
[9] B. Liu, T. Nitta, H. Nakatani, M. Terano, *Macromol. Symp.* **2004**, *213*, 7–18.
[10] G. Kwag, J.-G. Lee, C. Bae, S. N. Lee, *Polymer* **2003**, *44*, 6555–6558.
[11] B. Liu, T. Nitta, H. Nakatani, M. Terano, *Macromol. Chem. Phys.* **2003**, *204*, 395–402.
[12] B. Liu, T. Nitta, H. Nakatani, M. Terano, *Macromol. Chem. Phys.* **2002**, *203*, 2412–2421.
[13] M. Seth, P. M. Margl, T. Ziegler, *Macromolecules* **2002**, *35*, 7815–7829.
[14] H. Weiss, M. Boero, M. Parrinello, *Macromol. Symp.* **2001**, *173*, 137–147.
[15] V. P. Oleshko, P. A. Crozier, R. D. Cantrell, A. D. Westwood, *Macromol. Rapid Commun.* **2001**, *22*, 34–40.
[16] I. Jaber, S. J. Brown, *Patent Appl. 99–304060* [assigned to Nova Chemicals (International) S. A., Switzerland], **2000**.
[17] A. Greco, G. Perego, M. Cesari, S. Cesca, *J. Appl. Polym. Sci.* **1979**, *23*, 1319–1332.
[18] F. Calderazzo, G. Pampaloni, F. Masi, A. Moalli, R. Invernizzi, *Patent Appl. 89–202199* (assigned to Enichem Anic S. p. A., Italy), **1990**, 9 pp.
[19] F. Masi, S. Malquori, L. Barazzoni, C. Ferrero, A. Moalli, F. Menconi, R. Invernizzi, N. Zandona, A. Altonmare, F. Ciardelli, *Makromol. Chem. Suppl.* **1989**, *15*, 147–165.
[20] T. Tanaka, E. Tanaka, *WO1980JP00006* (Assigned to Mitsubishi Chem. Ind.), **1980**.
[21] F. Menconi, G. Conti, A. Zanellato, A. Moalli, *US6723809* (assigned to Polimeri Europa SRL), **2004**.
[22] S. R. Wade, M. G. H. Wallbridge, G. R. Willey, *J. Chem. Soc., Dalton Trans.* **1982**, 271–274.
[23] B. J. J. Van De Heisteeg, G. Schat, O. S. Akkerman, F. Bickelhaupt, *Organometallics* **1985**, *4*, 1141–1142.
[24] B. J. J. Van De Heisteeg, G. Schat, O. S. Akkerman, F. Bickelhaupt, *J. Organomet. Chem.* **1986**, *308*, 1–10.
[25] F. Calderazzo, F. Marchetti, G. Pampaloni, V. Passarelli, *J. Chem. Soc., Dalton Trans.* **1999**, 4389–4396.
[26] S. Gross, G. Kickelbick, M. Puchberger, U. Schubert, *Monatsh. Chem.* **2003**, *134*, 1053–1063.
[27] R. Niewa, H. Jacobs, *Z. Kristallogr.* **1995**, *210*, 687.
[28] L. B. Serezhkina, V. N. Serezhkin, R. L. Davidovich, *Russ. J. Coord. Chem.* **2000**, *26*, 18–22.
[29] F. Calderazzo, P. Pallavicini, G. Pampaloni, P. F. Zanazzi, *J. Chem. Soc., Dalton Trans.* **1990**, 2743–2746.
[30] F. Calderazzo, I. Ferri, G. Pampaloni, S. Troyanov, *J. Organomet. Chem.* **1996**, *518*, 189–196.
[31] J. E. D. Davies, D. A. Long, *J. Chem. Soc. A* **1968**, 2560–2564.
[32] T. J. Kistenmacher, G. D. Stucky, *Inorg. Chem.* **1971**, *10*, 122–132.
[33] E. Robé, J.-C. Daran, S. Vincendeau, R. Poli, *Eur. J. Inorg. Chem.* **2004**, 4108–4114.
[34] P. C. Crouch, G. W. A. Fowles, R. A. Walton, *J. Chem. Soc. A* **1969**, 972–976.
[35] B. Briat, O. Kahn, I. Morgensternbadarau, J. C. Rivoal, *Inorg. Chem.* **1981**, *20*, 4193–4200.
[36] N. Hao, B. Sayer, G. Denes, D. Bickley, C. Detellier, M. Mcglinchey, *J. Magn. Reson.* **1982**, *50*, 50–63.
[37] R. T. Carlin, R. A. Osteryoung, J. S. Wilkes, J. Rovang, *Inorg. Chem.* **1990**, *29*, 3003–3009.
[38] A. E. Reed, L. A. Curtiss, F. Weinhold, *Chem. Rev.* **1988**, *88*, 899–926.

 © 2007 Wiley-VCH Verlag GmbH & Co. KGaA, Weinheim 

[39] W. A. Howard, G. Parkin, *J. Organomet. Chem.* **1994**, *472*, C1–C4.
[40] F. R. Fronczek, E. C. Baker, P. R. Sharp, K. N. Raymond, H. G. Alt, M. D. Rausch, *Inorg. Chem.* **1976**, *15*, 2284–2289.
[41] C. Hagfeldt, V. Kessler, I. Persson, *Dalton Trans.* **2004**, 2142–2151.
[42] A. Feltz, *Z. Anorg. Allg. Chem.* **1965**, *334*, 242–249.
[43] A. Feltz, *Z. Chem.* **1967**, *7*, 158.
[44] H. Linga, Z. Stojek, R. A. Osteryoung, *J. Am. Chem. Soc.* **1981**, *103*, 3754–3760.
[45] I. W. Sun, E. H. Ward, C. L. Hussey, *Inorg. Chem.* **1987**, *26*, 4309–4311.
[46] W. Haase, H. Hoppe, *Acta Crystallogr., Sect. B* **1968**, *24*, 282–283.
[47] G. M. Sheldrick, *SHELXL97. Program for Crystal Structure Refinement*, University of Göttingen, Göttingen, Germany, **1997**.
[48] L. J. Farrugia, *J. Appl. Crystallogr.* **1999**, *32*, 837–838.
[49] L. J. Farrugia, *J. Appl. Crystallogr.* **1997**, *32*, 565.
[50] M. J. Frisch, G. W. Trucks, H. B. Schlegel, G. E. Scuseria, M. A. Robb, J. R. Cheeseman, J. Montgomery, J. A., T. Vreven, K. N. Kudin, J. C. Burant, J. M. Millam, S. S. Iyengar, J. Tomasi, V. Barone, B. Mennucci, M. Cossi, G. Scalmani, N. Rega, G. A. Petersson, H. Nakatsuji, M. Hada, M. Ehara, K. Toyota, R. Fukuda, J. Hasegawa, M. Ishida, T. Nakajima, Y. Honda, O. Kitao, H. Nakai, M. Klene, X. Li, J. E. Knox, H. P. Hratchian, J. B. Cross, C. Adamo, J. Jaramillo, R. Gomperts, R. E. Stratmann, O. Yazyev, A. J. Austin, R. Cammi, C. Pomelli, J. W. Ochterski, P. Y. Ayala, K. Morokuma, G. A. Voth, P. Salvador, J. J. Dannenberg, V. G. Zakrzewski, S. Dapprich, A. D. Daniels, M. C. Strain, O. Farkas, D. K. Malick, A. D. Rabuck, K. Raghavachari, J. B. Foresman, J. V. Ortiz, Q. Cui, A. G. Baboul, S. Clifford, J. Cioslowski, B. B. Stefanov, G. Liu, A. Liashenko, P. Piskorz, I. Komaromi, R. L. Martin, D. J. Fox, T. Keith, M. A. Al-Laham, C. Y. Peng, A. Nanayakkara, M. Challacombe, P. M. W. Gill, B. Johnson, W. Chen, M. W. Wong, C. Gonzalez, J. A. Pople, *Gaussian 03, Revision C.02*, Gaussian, Inc., Wallingford CT, **2004**.
[51] A. D. Becke, *J. Chem. Phys.* **1993**, *98*, 5648–5652.
[52] C. T. Lee, W. T. Yang, R. G. Parr, *Phys. Rev. B* **1988**, *37*, 785–789.
[53] P. Stephens, F. Devlin, C. Chabalowski, M. Frisch, *J. Phys. Chem.* **1994**, *98*, 11623–11627.
[54] J. P. Perdew, *Phys. Rev. B: Condens. Matter* **1986**, *33*, 8822–8824.
[55] K. Burke, J. P. Perdew, Y. Wang, *Electronic Density Functional Theory: Recent Progress and New Directions* (Eds.: J. F. Dobson, G. Vignale, M. P. Das), Plenum Press, New York, **1998**.
[56] P. J. Hay, W. R. Wadt, *J. Chem. Phys.* **1985**, *82*, 270–283.

Received: January 17, 2007
Published Online: April 25, 2007

 © 2007 Wiley-VCH Verlag GmbH & Co. KGaA, Weinheim 

DOI: 10.1002/ejic.200700040

# Electronic Structure of Linearly Coordinated EQ Complexes of the Type [$(N_3N)W(EQ)$] [$N_3N = N(CH_2CH_2NSiMe_3)_3$; E = P, As, Sb, Bi; Q = O, S, Se, Te]: A DFT Study

**Gábor Balázs,[a] Jennifer C. Green,*[a] and D. Michael P. Mingos*[b]**

**Keywords:** Bonding / Pnicogens / Chalcogens / Tungsten / Density functional calculations

Density functional theory (DFT) calculations were carried out on the terminal EQ complexes [$(N_3N)W(EQ)$] {$N_3N = N(CH_2CH_2NSiMe_3)_3$; E = P, As, Sb, Bi; Q = O, S, Se Te} to clarify the bonding situation within the linear $N_{ax}$–W–E–Q core. This unusual structural motif gives rise to a bonding arrangement in which the π-electron density is delocalised over the three atoms of the W–E–Q unit. Fragment calculations and natural bond order (NBO) data indicated that the σ-bonding component of the $N_{ax}$–W–E–Q unit comprises two occupied σ orbitals, while the π component of bonding comprises two sets of degenerate π orbitals. In general, the π orbitals of the $N_{ax}$–W–E–Q core are higher in energy compared to the σ orbitals. The phosphorus monoxide (EQ = PO) complexes provide an exception to this rule, with the 1π orbitals of the W–P–O core lower in energy than the σ orbitals. Generally, as the atomic number of either the pnicogen (E) or chalcogen (Q) atom increases the extent of σ-orbital delocalisation decreases, whereas the π-orbital delocalisation increases. Fractional bond orders and Wiberg bond indices were used to establish whether localisation of the π-electron density gives rise to a W–E or an E–Q double or triple bond. Both methods indicate a W–E as well as an E–Q double bond. The ionic nature of the complexes were analysed by inspection of the Hirschfeld charge distribution which shows only a moderate ionic character. Exceptions are the pnicogen monoxide complexes, which are more ionic.
(© Wiley-VCH Verlag GmbH & Co. KGaA, 69451 Weinheim, Germany, 2007)

## Introduction

Transition metal complexes of nitrogen monoxide (NO) underwent significant research in the early 1970s as a result of the wide range of bonding motifs that can be adopted by this versatile ligand. NO represented the fore-runner of a wider range of the pnicogen–chalcogen (E–Q) moieties bonding to a variety of transition metal fragments.[1] The coordination chemistries of the heavier EQ analogues (E = P, As, Sb, Bi; Q = O, S, Se, Te) remain relatively poorly studied. This is partly due to the unavailability of the free EQ ligands as well as to their poor coordinating abilities.[2] The majority of transition metal complexes bearing heavier EQ ligands contain PQ (Q = O, S, Se and Te) ligands that are coordinated to three metal centres in a $\mu_3$ fashion. Selected examples include [$\{Ni(C_5iPr_4H)\}_2W(CO)_4(\mu_3\text{-}PO)_2$],[3] [$\{Ru(CO)\}_3(\mu_3\text{-}PO)]^-[iPr_2NH_2]^+$[4] [$\{W(CO)_2Cp\}_3(\mu_3\text{-}PS)$],[5] [$\{Co(C_5tBu_2H_3)\}_3(\mu_3\text{-}PQ)_2$] (Q = O, S, Se),[6] [$\{Co(C_5tBu_2H_3)\}_3(\mu_3\text{-}PQ)(\mu_3\text{-}P)$] (Q = Se,[5] Te[6]), [$\{Ni(C_5iPr_4H)\}_2W(CO)_4(\mu_3\text{-}PS)_2$][7] and [$\{FeCp(CO)_2\}\{Fe_2(CO)_3Cp_2\}(\mu_3\text{-}PS)_2$].[8] The synthesis of such PQ-containing complexes is typically achieved by oxidation of the corresponding phosphido complex with the chalcogen (e.g. S, Se, Te) or a suitable chalcogen source (e.g. dimethyldioxirane, ethylene sulfide). Hydrolysis of a $\mu_3$-$P(NiPr_2)$ functional group has also been effective in preparation of the more polar PO complex [$\{Ru(CO)\}_3(\mu_3\text{-}PO)]^-[iPr_2NH_2]^+$.[4]

Synthesis of the terminal pnictido complexes [$(ArRN)_3Mo{\equiv}P$] [Ar = 3,5-$Me_2C_6H_3$, R = $C(CD_3)_2Me$][9] and [$(N_3N)W{\equiv}E$] [$N_3N{=}N(CH_2CH_2NSiMe_3)_3$; E = P,[10] As[11,12] and Sb[13]] presented clear opportunities for the preparation of transition metal complexes containing an $\eta^1$-coordinated EQ ligands. Indeed, Cummins et al. reported the isolation and characterisation of the PO [$(ArRN)_3Mo(PO)$][14] and PS [$(ArRN)_3Mo(PS)$][9,15] complexes, which were prepared by oxidation of the corresponding phosphido complex [$(ArRN)_3Mo{\equiv}P$] with dimethyldioxirane and sulfur, respectively. More recently, Scheer et al. reported preparation of the $\eta^1$-coordinated PS and AsS complexes [$(N_3N)W(ES)$] (E = P and As)[16] by oxidation of the terminal phosphido and arsenido complexes [$(N_3N)W{\equiv}E$] (E = P and As) with cyclohexene sulfide.

The bonding in the $\eta^1$-coordinated PS complexes was investigated by Frenking and Wagener who performed calculations on a series of model complexes of the type [$(NH_2)_3M(PS)$] and [$NH_3(NH_2)_3M(PS)$] (M = Mo, W). They proposed two Lewis formulae, one based on an NBO partitioning Scheme (**I**) and a second one based on Wiberg

[a] Inorganic Chemistry Laboratory, Oxford University, South Parks Road, Oxford, OX1 3QR, United Kingdom
[b] St. Edmund Hall, Oxford University, Queen's Lane, Oxford OX1 4AR, UK
E-mail: jennifer.green@chem.ox.ac.uk
Supporting information for this article is available on the WWW under http://www.eurjic.org or from the author.

 © 2007 Wiley-VCH Verlag GmbH & Co. KGaA, Weinheim 

bond indices (**II**). Both resonance canonical forms represented as Lewis structures are depicted in Scheme 1.[18] The dissociation of an amido ligand from the metal atom in **II** makes that Lewis structure less likely. The electron count of complexes of the type $[NH_3(NH_2)_3M(EQ)]$ depend on whether the amido nitrogen atoms are one- or three-electron donors. Since the $a_2$ combination of the lone-pair orbitals of the three amido ligands does not have a symmetry match among the tungsten orbitals (the three amido nitrogen atoms effectively donate seven electrons altogether), it follows that complexes of the type $[NH_3(NH_2)_3M(EQ)]$ obey the 18-electron rule, and the complexes of the type $[(NH_2)_3M(PS)]$ are 16-electron species.

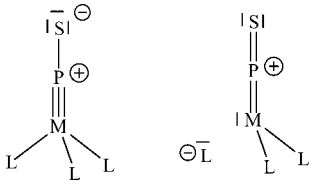


Scheme 1. Proposed Lewis structures of $[L_nM(PS)]$ complexes.[17]

Recently, we reported the results of calculations on $[(N_3N)W(ES)]$ $[N_3N=N(CH_2CH_2NSiMe_3)_3$; E = P, As and Sb].[16] Inclusion of the $Me_3Si$ substituents on the imido nitrogen atoms was important for achieving good agreement of our calculated geometries with structural parameters obtained from X-ray crystallographic analyses of these complexes. We assume this is due to the strong electron-donating properties of these substituents. Most significantly, our study demonstrated that π bonding in the W–E–Q unit can best be described as two three-centre four-electron bonds (3c-4e).[16] To further our understanding of the structural and electronic properties of $\eta^1$-coordinated EQ complexes, we have extended our analysis to the complete series of $[(N_3N)W(EQ)]$ complexes (E = P, As, Sb, Bi; Q = O, S, Se and Te). In this paper we analyse the structural trends and use several theoretical tools to gain insight into the important bonding features for the heavier EQ ligands.

## Results and Discussion

### Geometries and Binding Energies

Calculated geometries for complexes **1**–**4** were pseudo-$C_3$-symmetric with the $N_{ax}$–W–E–Q core aligned with the $C_3$ axis. Given the isostructural nature of these complexes, the optimised geometry of $[(N_3N)W(PO)]$ (**1a**) is depicted in Figure 1 as representative of this series. Selected bond lengths and angles for the calculated structures are provided in Table 1. Our benchmarks for the optimised structures are the complexes **1b** and **2b**, whose crystal structures were reported recently.[16] The calculated geometrical parameters for **1b** (P–S 1.94 Å; W–P 2.15 Å) and **2b** (As–S 2.05 Å; W–As 2.25 Å) compare excellently with the reported experimental values [E–S 1.9410(16) Å and 2.048(2) Å; W–E 2.1579(10) Å and 2.2557(8) Å for **1b** and **2b**, respectively].[16] The $N_{ax}$–W distances in **1b** (2.22 Å) and **2b** (2.21 Å) also agree favourably with the reported experimental values for these complexes [**1b** 2.217(3) Å; **2b** 2.214(6) Å].[16] Earlier calculations on the pnictido complexes $[(N_3N)W{\equiv}E]$ (E = P, As, Sb and Bi)[12,13] provided $N_{ax}$–W distances that were longer than those measured in single-crystal X-ray analysis of these complexes.

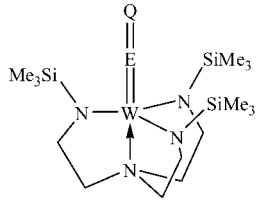


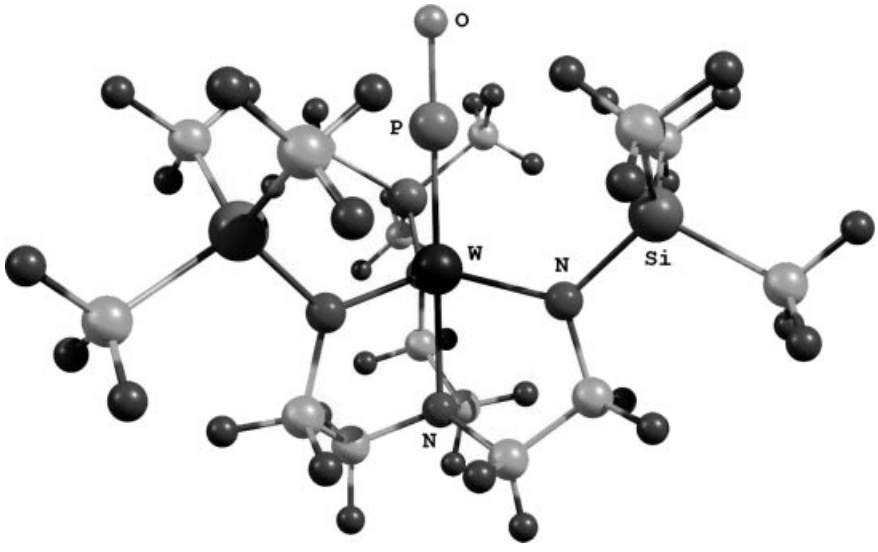


Figure 1. Calculated geometry of $[(N_3N)W(PO)]$ (**1a**).

 © 2007 Wiley-VCH Verlag GmbH & Co. KGaA, Weinheim 

Table 1. Calculated bond lengths [Å] and W–E and E–Q bond dissociation energies (BDE). The experimental bond lengths for **1b** and **2b** are given in parentheses.

| | E | Q | E–Q | W–E | $N_{ax}$–W | $N_{eq}$–W (av.) | W–E BDE [kJ/mol] | E–Q BDE [kJ/mol] |
|---|---|---|---|---|---|---|---|---|
| **1a** | P | O | 1.48 | 2.13 | 2.21 | 1.995 | –414.6 | –557.6 |
| **1b** | | S | 1.94 (1.940) | 2.15 (2.158) | 2.22 (2.217) | 1.98 (1.99) | –400.9 | –348.8 |
| **1c** | | Se | 2.08 | 2.15 | 2.23 | 1.98 | –399.6 | –286.6 |
| **1d** | | Te | 2.30 | 2.16 | 2.23 | 1.98 | –401.0 | –211.9 |
| **2a** | As | O | 1.64 | 2.24 | 2.20 | 1.99 | –340.9 | –438.5 |
| **2b** | | S | 2.05 (2.048) | 2.25 (2.256) | 2.21 (2.214) | 1.98 (1.99) | –338.9 | –301.6 |
| **2c** | | Se | 2.18 | 2.25 | 2.22 | 1.98 | –339.4 | –255.3 |
| **2d** | | Te | 2.39 | 2.26 | 2.22 | 1.98 | –340.2 | –196.5 |
| **3a** | Sb | O | 1.84 | 2.44 | 2.19 | 1.99 | –259.1 | –382.9 |
| **3b** | | S | 2.25 | 2.45 | 2.20 | 1.98 | –262.4 | –280.6 |
| **3c** | | Se | 2.36 | 2.46 | 2.20 | 1.98 | –258.9 | –244.3 |
| **3d** | | Te | 2.58 | 2.46 | 2.21 | 1.98 | –261.3 | –189.5 |
| **4a** | Bi | O | 1.94 | 2.53 | 2.19 | 1.99 | –203.7 | –326.1 |
| **4b** | | S | 2.34 | 2.53 | 2.19 | 1.99 | –206.8 | –248.4 |
| **4c** | | Se | 2.46 | 2.54 | 2.19 | 1.99 | –205.4 | –218.7 |
| **4d** | | Te | 2.662 | 2.54 | 2.19 | 1.99 | –207.6 | –172.6 |

The experimental $N_{ax}$–W distances in pnictido complexes [$(N_3N)W{\equiv}E$] [2.34(1) Å, 2.336(6) Å and 2.33(1) Å for E = P,[10] As[12] and Sb,[13] respectively] are longer than in the complexes **1**–**4**, showing the stronger *trans* influence of an E ligand compared to an EQ ligand. Although the variation of the $N_{ax}$–W distance with the nature of the EQ ligand is small a trend can clearly be observed. In general, the $N_{ax}$–W distance decreases as the atomic number of E increases, indicating that EQ ligands of the heavier pnicogens exhibit a weaker *trans* influence than their lighter analogues (Figure 2). In contrast, as the atomic number of Q increases the $N_{ax}$–W distance increases, indicating that EQ ligands of the heavier chalcogens exhibit a stronger *trans* influence.

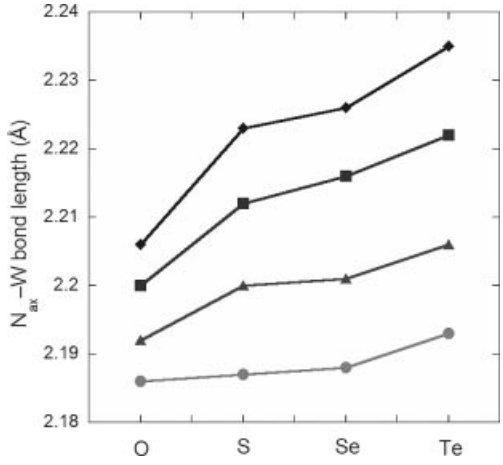


Figure 2. Variation of the $N_{ax}$–W distances [Å] with Q in complexes [$(N_3N)W(EQ)$] (**1**–**4**). Legend: P = ♦, As = ■, Sb = ▲ and Bi = ●.

The major differences in the structure upon moving from the lighter to the heavier congeners is observed in the W–E and E–Q distances. As expected, as the atomic number of E or Q increases, the E–Q and the W–E bond lengths also increase. The shortest E–Q distance is predicted for **1a** (1.48 Å) and the longest distance for **4d** (2.66 Å). The W–E distance increases only slightly for a particular E, as Q becomes heavier (Figure 3). This trend is observed when E = P, As and Sb, whereas for the BiQ complexes the W–Bi distance remains constant on going from Q = O to Te.

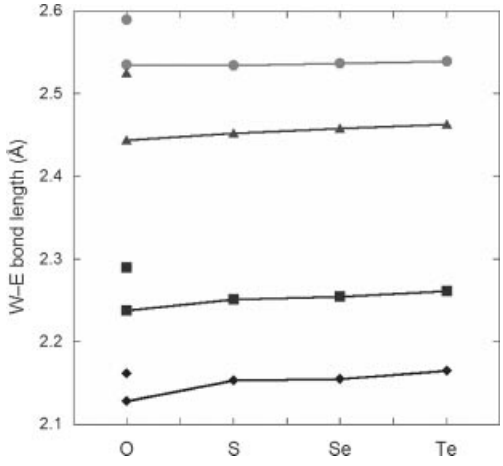


Figure 3. Variation of the W–E distances in complexes [$(N_3N)$-W(EQ)] (**1**–**4**). Legend: P = ♦, As = ■, Sb = ▲ and Bi = ●. The detached points correspond to the experimental W–E distances in the corresponding [$(N_3N)W{\equiv}E$] complexes for E = P, As and Sb and with the calculated distance for E = Bi.

Comparison of the W–E distances in the complexes **1**–**4** with the experimental W–E distances in the pnictido complexes [$(N_3N)W{\equiv}E$] (E = P, As, and Sb) [2.162(4) Å,[10] 2.2903(11) Å[12] and 2.5255(17) Å[13] for E = P, As and Sb, respectively] shows that, upon oxidation of the [$(N_3N)$-$W{\equiv}E$] complexes, the W–E distance became shorter, a phenomenon which is more accentuated for the heavier homologues of E (Figure 3). The exception is the phosphorus monotelluride complex **1d** in which the predicted W–P dis-

 © 2007 Wiley-VCH Verlag GmbH & Co. KGaA, Weinheim 

tance is slightly longer than the W–P distance in the corresponding phosphido complex. A similar shortening is observed for the experimental Mo–P distance in [$(ArRN)_3$-Mo(PQ)] (Q = O,[14] S[15]) where the Mo–P distances are 0.04 Å and 0.09 Å shorter than in the parent pnictido complex [$(ArRN)_3Mo{\equiv}P$].[9] The W–E distances in complexes **2**–**4** are comparable to the sum of the triple-bond covalent radii[19] of the corresponding elements, whereas in complexes **1** the W–E distances are slightly longer.

In order to gain insight into the strength of the E–Q bonding and stability of the complexes, the E–Q bond dissociation energies were calculated (Table 1). This shows that complexes **1**–**4** are stable with respect to the dissociation into the pnictido complexes and chalcogen. Furthermore, the E–Q bond dissociation energies present the expected periodic variation; an approximately linear decrease for a given pnicogen (E) upon going from Q = S to Te (Figure 4). The pnicogen monoxide complexes (**a**) exhibit a larger BDE than would be anticipated upon linear extrapolation of the BDE plots for complexes **b**–**d**. The stability of the complexes is also supported by the high HOMO–LUMO gap.

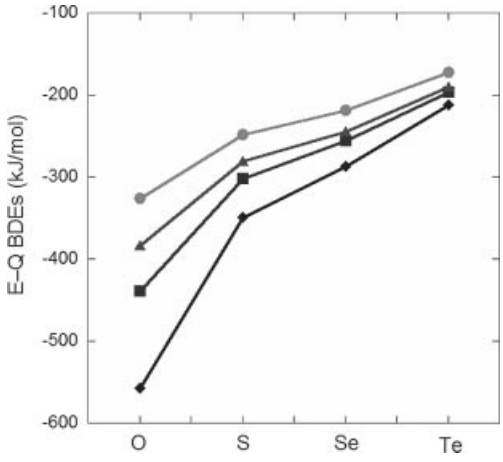


Figure 4. Variation of the E–Q bond dissociation energies [kJ/mol] in complexes [$(N_3N)W(EQ)$] (**1**–**4**). Legend: P = ♦, As = ■, Sb = ▲ and Bi = ●.

The E–Q BDEs also demonstrate a dependence on the atomic number of the pnicogen (E) for a given chalcogen (Q). For example, complexes **a** (Q = O), show a decrease in the BDE going from **1a** to **4a**.

To enable the comparison of the strength of the W–E bonding in the complexes **1**–**4** with the parent pnictido [$(N_3N)W{\equiv}E$] complexes, the W–E BDEs were calculated. Similarly to the E–Q BDEs, the W–E BDEs decrease as the atomic number of E increases for a particular Q, but are not influenced by the nature of Q (Table 1). The comparison of the W–E BDEs in complexes **1**–**4** (Table 1) and the pnictido complexes [$(N_3N)W{\equiv}E$] (481.9 kJ/mol, 429.0 kJ/mol, 333.4 kJ/mol and 293.3 kJ/mol for E = P, As, Sb and Bi, respectively)[13] shows that the strength of the W–E bonding is ca. 80–100 kJ/mol weaker in the complexes **1**–**4** than in the parent pnictido complexes. This shows that upon oxidation of the pnictido complexes the W–E triple bond is weakened thermodynamically.

## Bonding Analysis

The bonding arrangement in complexes **1**–**4** was further probed using fragment calculations and Natural Bond Orbital (NBO) analyses. Complexes **1**–**4** were separated into two fragments either by cleavage of the E–Q bond, to provide ($N_3N$)WE and Q fragments, or by cleavage of the W–E bond to provide ($N_3N$)W and EQ fragments. Contributions to the bonding in the [$(N_3N)W(EQ)$] complex can then be understood in terms of linear combinations of the fragment MOs. The bonding in the complex [($N_3N$)W-

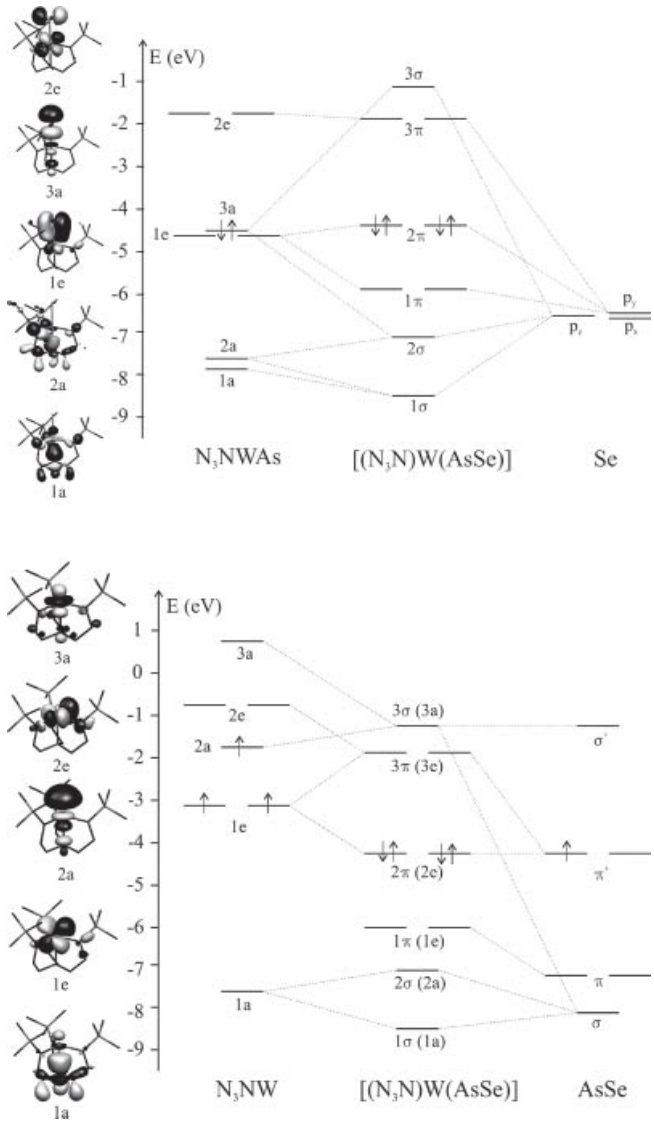


Figure 5. Molecular orbital interaction scheme for [$(N_3N)W(AsSe)$] (**2c**). The ($N_3N$)W and ($N_3N$)WAs fragment levels are labelled in $C_3$ symmetry and those of **2c** with σ and π symmetry with respect to the NWAs axis (the labels in parentheses are in $C_3$ symmetry). The relevant molecular orbitals of the ($N_3N$)W and ($N_3N$)WAs fragments are given on the left-hand side of the diagram.

 © 2007 Wiley-VCH Verlag GmbH & Co. KGaA, Weinheim 

(AsS)] (**2b**) was described elsewhere.[16] Here we describe the bonding in the complex [(N3N)W(AsSe)] (**2c**) as a representative example of this series of structures in order to give a basis for discussion of the trends in the bonding upon moving from the lighter EQ congeners to the heavier ones.

The molecular orbital interaction scheme for the complex **2c** is depicted in Figure 5. The (N3N)W and (N3N)WAs fragment levels are labelled in $C_3$ symmetry and those of the complex with σ and π symmetry (the labels in the $C_3$ symmetry are given in parentheses) with respect to the NWAs axis. The relevant molecular orbitals of the (N3N)W and (N3N)WAs fragments are given on the left-hand side of the diagram.

The results of a fragment analysis, in which the complex **2c** was separated into an Se and an (N3N)WAs fragment, shows that the $p_z$ orbital of Se mixes with the 1a orbitals of the (N3N)WAs fragment, containing contributions from $N_{ax}$ ($p_z$), As ($p_z$) and W ($d_{z^2}$ and s) to form two occupied molecular orbitals of σ symmetry (1σ and 2σ, Figures 5 and 6). 1σ is an all-in-phase combination, whereas 2σ is As–Se bonding, but has minimal W contribution and thus is W–As and W–$N_{ax}$ nonbonding. The $p_x$ and $p_y$ orbitals of the Se interact with the two degenerate π orbitals of the WAs unit (1e) to give two occupied sets of π orbitals (1π and 2π) from which the 1π set is bonding over all three atoms (W, As and Se) but with only a minor contribution from W. The 2π set is antibonding with respect to the AsSe and bonding with respect to the WAs unit (Figure 6).

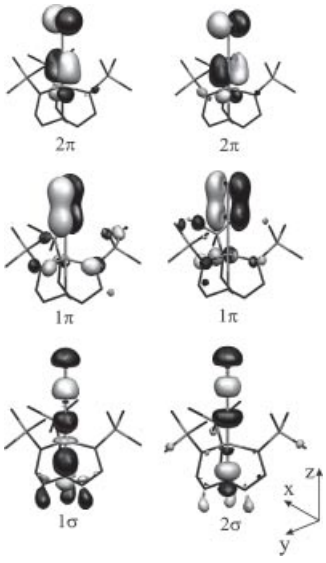


Figure 6. Isosurfaces of 2π (2e), 1π (1e) and 1σ (1a) and 2σ (2a) MO of [(N3N)W(AsSe)] (**2c**).

An analysis of the interaction of the AsSe fragment with the (N3N)W fragment shows that the π orbitals of the AsSe fragment increase slightly in energy due to the increasing charge, but do not mix significantly with the orbitals of the (N3N)W fragment, remaining localised as As–Se π bonds (forming 1π in the complex; Figures 5 and 6). In contrast, the π* orbitals of the AsSe fragment interact with the orbitals 1e of the (N3N)W fragment, containing mainly the tungsten $d_{yz}$ and $d_{xz}$ orbitals, respectively, to give a W–As π-bonding interaction (2π). The out-of-phase combination is unoccupied and forms the LUMO (3π). The 2π MO encapsulates back-donation of the tungsten atom to the AsSe ligand. Overall, the WAsSe π system is best described by two three-centre four-electron (3c-4e) bonds. This orbital interaction scheme describes qualitatively the bonding in complexes **1**–**4**.

## General Trends

Although the bonding in complexes **1**–**4** is similar, significant changes appear in the σ bonding going from the lighter to the heavier homologues. In the pnicogen monoxide complexes (**1a**–**4a**) the contribution of atomic orbitals of E to 1σ decreases as its atomic number increases (Figure 7). However, the most distinct changes were observed for the pnicogen monotelluride complexes **1d**–**4d** (Figure 8). In the PTe complex (**1d**) the 1σ is an extended bonding MO over the $N_{ax}$–W–E–Q core. In contrast to that the 1σ in the bismuth monotelluride complex (**4d**) is a localised $N_{ax}$–W bonding molecular orbital, having a strong 1a contribution

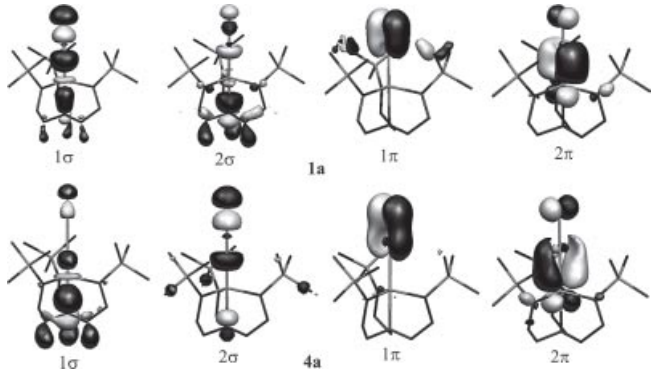


Figure 7. Isosurfaces of the 1σ, 2σ, 1π and 2π MOs of the phosphorus monoxide and bismuth monoxide complexes **1a** and **4a**, respectively. From the degenerated 1π and 2π sets only one orbital is represented.

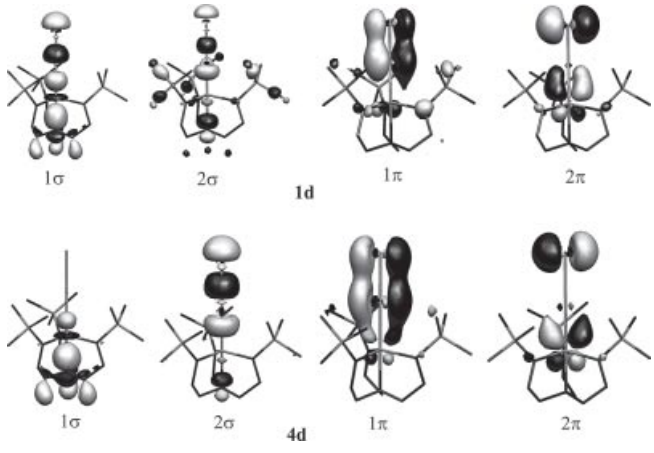


Figure 8. Isosurfaces of the 1σ, 2σ, 1π and 2π MOs of the phosphorus monotelluride complexes **1d** and **4d**, respectively. From the degenerate 1π and 2π sets only one orbital is represented.

 © 2007 Wiley-VCH Verlag GmbH & Co. KGaA, Weinheim 

(88.2%) of the $N_3NW$ fragment. The bonding in the arsenic and antimony montelluride complexes (**2d** and **3d**, respectively) constitute a transition between the two extremes (**1d** and **4d**). In **2d** and **3d** there is a mixing of the ETe (E = As, Sb) fragment σ orbital with $(N_3N)W$ fragment orbitals containing Si and C p-orbital contributions. A comparative energy level diagram is given in Figure 9. For 2σ the opposite trend than for 1σ was observed, but the changes are not so accentuated. Generally, as the atomic number of E increases, its contribution to 2σ increases. Also, the contribution of the EQ fragment σ orbital to 2σ increases as the atomic number of either E or Q increases. This leads to a localised E–Q bonding MO.

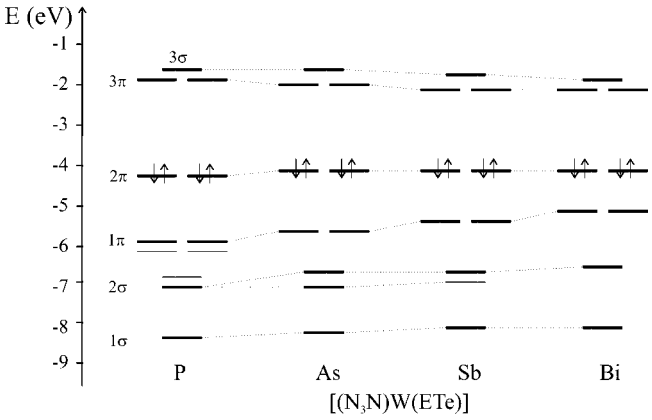


Figure 9. Comparative MO energy level diagram for the pnictido monotelluride complexes $[(N_3N)W(ETe)]$ (**1d**–**4d**). The energy levels marked with thin lines ("ghost" levels) represent combinations of the ETe fragment σ or π orbitals with energetically close-lying orbitals of the $(N_3N)W$ fragment localised on the $N_3N$ ligand. The contribution of the ETe fragment orbitals to the "ghost" levels is relatively small, except for E = As.

The nature of the 1σ MO can explain the relative strength of the *trans* influence of the EQ ligands. The complexes with an extended 1σ MO over the $N_{ax}$–W–E–Q core, such as the phosphorus monotelluride complex (**1d**) have a stronger *trans* influence than the complexes with 1σ localised on $N_{ax}$–W (Figures 2 and 8). However, the *trans* influence of the EQ ligands in complexes **1**–**4** (Figure 2) can easily be rationalised in terms of the interaction of the $(N_3N)W$ and EQ fragments σ-type orbitals. The stronger the interaction of the EQ σ orbital with the 1a orbital of the $(N_3N)W$ fragment (Figure 5) the weaker the $N_{ax}$–W orbital interaction. Since the energy of the 1a orbital of the relaxed $(N_3N)W$ fragment does not change, the *trans* influence will be determined by the relative energy of the EQ fragment σ orbitals. For example, in the case of the PQ complexes (**1**) the energy difference between the σ orbital of the PQ fragments varies strongly between the PO and PTe ($\Delta E$ = 1.793 eV), leading to a variation in the mixing with the $(N_3N)W$ fragment 1a orbital. This variation affects strongly the $N_{ax}$–W distances and hence leads to a variation in the *trans* influence of the different PQ ligands. In contrast, in the BiQ complexes (**4**) the σ orbitals of the BiQ fragments lie energetically close to each other (overall variation in energy $\Delta E$ = 0.616 eV) and therefore the variation in the *trans* influence of the BiQ ligands is much lower.

The analysis of the π bonding in the pnicogen monoxide complexes **1a**–**4a** (Figure 10) shows that the relative energy of the 1π set increases considerably as the atomic number of E increases, whereas the 2π set increases and the 3π set decreases only slightly in energy. The more pronounced increase in the energy of the 1π set going from E = P to As (**1a** to **2a**) is not unexpected if we consider that it contains a higher contribution of the EO fragment π orbitals (69.2, 73.8, 86.8 and 86.7% for E = P, As, Sb and Bi, respectively), as well as a high energy difference of the PO and EO (E = As, Sb and Bi) fragments π orbitals. The consequence of the low energy of the PO fragment π orbital is that in the phosphorus monoxide complex (**1a**) the 1π set is lower in energy than 2σ. A similar orbital energy ordering as for **1a** was reported by Carty et al. for the model complex $[(H_2N)_3Mo(PO)]$.[20] In the EQ complexes **b**, **c** and **d** a similar increase in energy of 1π and 2π set and a decrease in energy of 3π set occurs upon increasing the atomic number of E.

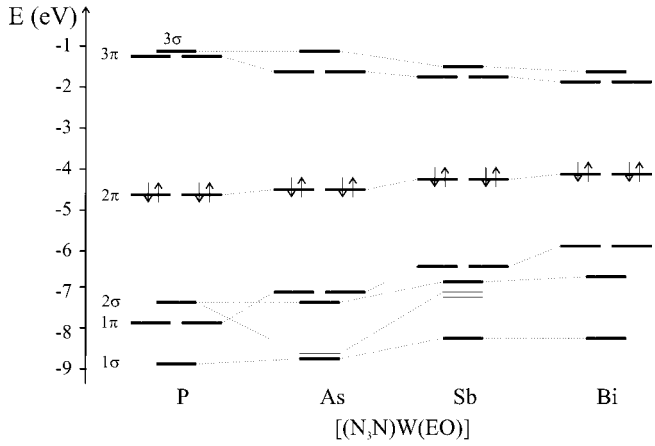


Figure 10. Comparative MO energy level diagram for the pnicogen monoxide complexes $[(N_3N)W(EO)]$ (**1a**–**4a**). The energy levels marked with thin lines ("ghost" levels) represent combination of the EO fragment σ orbitals with energetically close-lying orbitals of the $(N_3N)W$ fragment localised on the $N_3N$ ligand. The contribution of the EO fragment orbitals to the "ghost" levels is relatively small.

Apart from the changes in the energy of the 1π set upon increasing the atomic number of E or Q, changes in the extent of its delocalisation are also apparent. The delocalisation is more accentuated for the heavier congeners (Figures 7 and 8). As the atomic number of the pnicogen E increases, the contribution of the $(N_3N)W$ fragment (1e orbital of the fragment) to the 1π set also increases. Since the 1π set is an in-phase combination over all three atoms (W, E and Q), that leads to a stronger delocalisation of 1π. It is noteworthy, that in phosphorus monotelluride complex **1d** the π set of the PTe fragment mixes not only with the 1e set of the $N_3NW$ fragment to give the 1π set, but also mixes slightly with other orbitals of the $N_3NW$ fragment (containing mainly C, H and Si contributions). That mixing decreases as E becomes heavier so that in the arsenic monotel-

 © 2007 Wiley-VCH Verlag GmbH & Co. KGaA, Weinheim 

luride complex **2d** only the 1π set contains considerable AsTe π contribution. Changes appears also in the 2π set, which represents the back-bonding of tungsten to the EQ ligand moving from the lighter to the heavier congeners. As the atomic number of E increases, its contribution to the 2π set decreases. That has the effect that 2π becomes permanently weaker bonding (Figure 8). The nature of Q has a similar effect to the nature of E on the 1π and 2π set MOs. Overall, the changes in the π bonding in the complexes **1**–**4** are similar to those in the σ-bonding mainfold; however, they progress in opposite directions.

Based on the fragment calculations we have determined the overall W–E fractional bond order by considering the $(N_3N)$WE fragment 1e orbitals as W–E bonding, the 2e as W–E antibonding and the 3a orbital as bonding and considering the fragment occupation in the molecule. Similarly, the E–Q fractional bond order can be calculated by considering the occupation of the π, π*, σ and σ* orbitals of the EQ fragment in the complex. Furthermore, by considering the occupations of the fragment σ-type orbitals or π-type orbitals the fractional bond order can be split into a σ- and a π-contribution term. The W–E and E–Q fractional bond orders as well as its σ and π components are summarised in Table 2.

Table 2. Fractional W–E and E–Q bond orders in complexes $[(N_3N)W(EQ)]$ (**1**–**4**).

| | E | W–E | E–Q | W–E | | E–Q | |
|---|---|---|---|---|---|---|---|
| | | | | σ | π | σ | π |
| | | | | Q = O | | | |
| **1a** | P | 2.12 | 2.07 | 0.35 | 1.77 | 0.88 | 1.19 |
| **2a** | As | 2.09 | 1.97 | 0.34 | 1.75 | 0.92 | 1.05 |
| **3a** | Sb | 2.12 | 2.13 | 0.34 | 1.79 | 0.82 | 1.31 |
| **4a** | Bi | 2.14 | 2.18 | 0.35 | 1.79 | 0.87 | 1.31 |
| | | | | Q = S | | | |
| **1b** | P | 2.22 | 2.03 | 0.50 | 1.73 | 0.86 | 1.17 |
| **2b** | As | 2.24 | 1.83 | 0.49 | 1.75 | 0.84 | 0.99 |
| **3b** | Sb | 2.20 | 2.12 | 0.46 | 1.74 | 0.83 | 1.29 |
| **4b** | Bi | 2.23 | 2.10 | 0.47 | 1.76 | 0.88 | 1.22 |
| | | | | Q = Se | | | |
| **1c** | P | 2.24 | 1.98 | 0.52 | 1.72 | 0.87 | 1.11 |
| **2c** | As | 2.26 | 1.82 | 0.50 | 1.76 | 0.84 | 0.98 |
| **3c** | Sb | 2.23 | 2.09 | 0.48 | 1.75 | 0.84 | 1.25 |
| **4c** | Bi | 2.26 | 2.08 | 0.50 | 1.76 | 0.89 | 1.19 |
| | | | | Q = Te | | | |
| **1d** | P | 2.32 | 1.92 | 0.59 | 1.73 | 0.81 | 1.11 |
| **2d** | As | 2.33 | 1.73 | 0.58 | 1.75 | 0.74 | 0.97 |
| **3d** | Sb | 2.28 | 2.05 | 0.55 | 1.73 | 0.84 | 1.21 |
| **4d** | Bi | 2.30 | 2.06 | 0.56 | 1.74 | 0.88 | 1.18 |

From Table 2 it may be seen, that the W–E fractional bond orders are lower for the pnicogen monoxide complexes (**1a**–**4a**) than for the complexes of the **b**, **c** or **d** series. For a particular Q the W–E fractional bond order can be considered to be constant within the standard errors. However, as the atomic number of Q increases, for a particular E the fractional bond order increases slightly (Figure 11). The E–Q fractional bond orders do not vary strongly between the complexes **1**–**4**. They increase slightly for a particular Q on going from P to Bi, this being in accordance with the decrease of the tungsten back-donation to the EQ ligand. For a particular E the E–Q fractional bond order decreases on going from O to Te (Figure 12). It is noteworthy that the As–Q fractional bond orders are generally lower, for which the low oxidation ability of As is responsible.

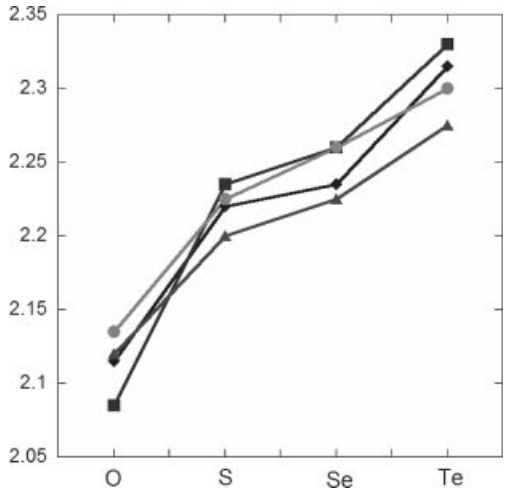


Figure 11. Variation of the W–E fractional bond orders with Q in complexes $[(N_3N)W(EQ)]$ (**1**–**4**). Legend: P = ♦, As = ■, Sb = ▲ and Bi = ●.

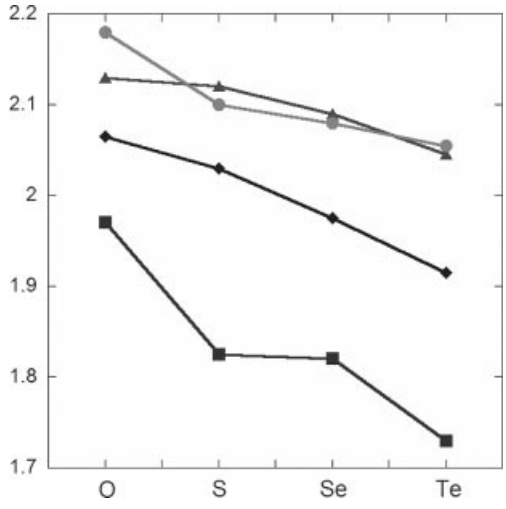


Figure 12. Variation of the E–Q fractional bond orders in complexes $[(N_3N)W(EQ)]$ (**1**–**4**). Legend: P = ♦, As = ■, Sb = ▲ and Bi = ●.

To determine whether the σ and π components of the W–E bond order go in opposite directions, and to obtain insight into the strengths of the σ- and π-bonding ratio, the fractional bond orders were split into their σ and π components (Table 2). The inspection of the σ contributions to the bond orders reveals that the σ part is responsible for the low W–E bond order in the phosphorus monoxide complexes **1a**–**4a**. This increases slightly for a particular E by going from O to Te (Figure 13), while for a particular Q (Q = S, Se and Te) it decreases slightly as the atomic number of E increases. In the pnictido monoxide complexes

 © 2007 Wiley-VCH Verlag GmbH & Co. KGaA, Weinheim 

the σ component of the W–E fractional bond order stays approximately constant as the atomic number of E increases.

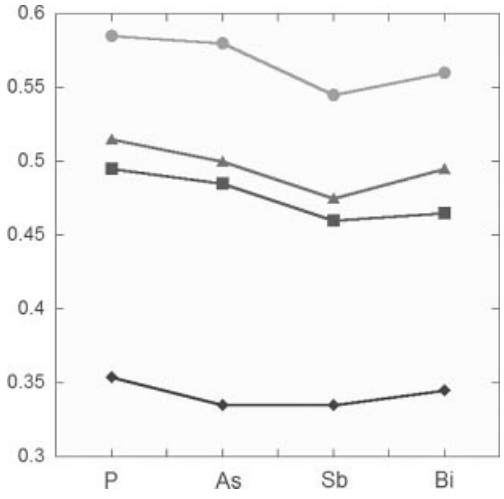


Figure 13. Variation of the σ component of the W–E fractional bond order with E in complexes [$(N_3N)W(EQ)$] (**1**–**4**). Legend: O = ♦, S = ■, Se = ▲ and Te = ●.

The π components of the W–E fractional bond order are not affected by the nature of Q for a particular E and stay essentially constant. Instead, for a particular Q the W–E fractional bond order increases slightly moving from P to Bi. The σ component of the E–Q, as judged by the fractional bond order, is not influenced by either the nature of E or Q, remaining constant. In contrast, the π component of the E–Q bond shows a decrease for a particular E as the atomic number of Q increases and an increase for a particular Q as the atomic number of E increases (Figure 14). The π component of the As–Q fractional bond orders are lower compared with the other complexes, confirming the lower oxidising ability of the arsenic.

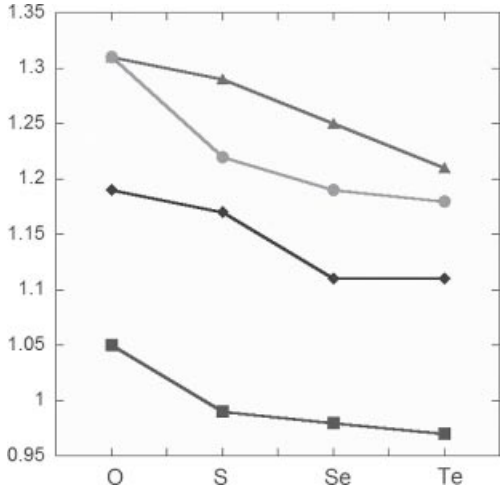


Figure 14. Variation of the π component of the E–Q fractional bond order with Q in complexes [$(N_3N)W(EQ)$] (**1**–**4**). Legend: P = ♦, As = ■, Sb = ▲ and Bi = ●.

The relative small variation of the fractional bond orders does not indicate that the bond strength stays constant. The strength of the bonding or antibonding of the molecular orbitals is not explicitly incorporated in this model and as shown in Table 1 the bond strengths decrease with atomic number.

The relative composition of the σ and π components to the fractional bond order was also investigated. The W–E and the E–Q bonds show a very different σ and π composition. Whereas in the W–E bond σ/π ratio (ca. 1:5 for the EQ complexes and 1:3.6 for the complexes of the series **b**, **c** and **d**) is relatively low, the σ/π ratio of the E–Q bond is much higher (1:1.4).

To enable the comparison of the results obtained with the literature data, we have calculated the Wiberg bond indices (WBI)[21] for the W–E and E–Q bonds of the complexes **1**–**4** (Table 3). Generally, the WBI either of the W–E and E–Q bonds are lower than the corresponding fractional bond orders, but that is compensated by adding a W–Q bond index of which the magnitude varies between 0.3 and 0.4. Similar WBIs were reported for [$NH_3(NH_2)_3W(PS)$] (W–P 1.89 and P–S 1.59). For the W–E triple bond in the pnictido complexes [$(N_3N)W{\equiv}E$] (2.38, 2.35, 2.28 and 2.27 for E = P, As, Sb and Bi, respectively)[13] and [$(MeO)_3W{\equiv}E$] (2.56, 2.55, 2.54 and 2.54 for E = P, As, Sb and Bi, respectively) higher WBI were reported.[22]

Table 3. Wiberg bond indices for the W–E and E–Q bonds in complexes [$(N_3N)W(EQ)$] (**1**–**4**).

| | E | W–E | E–Q | W–Q |
|---|---|---|---|---|
| | | Q = O | | |
| **1a** | P | 1.83 | 1.34 | 0.30 |
| **2a** | As | 1.80 | 1.30 | 0.30 |
| **3a** | Sb | 1.70 | 1.20 | 0.28 |
| **4a** | Bi | 1.61 | 1.17 | 0.30 |
| | | Q = S | | |
| **1b** | P | 1.79 | 1.54 | 0.41 |
| **2b** | As | 1.79 | 1.49 | 0.39 |
| **3b** | Sb | 1.70 | 1.43 | 0.35 |
| **4b** | Bi | 1.62 | 1.39 | 0.35 |
| | | Q = Se | | |
| **1c** | P | 1.81 | 1.52 | 0.43 |
| **2c** | As | 1.79 | 1.48 | 0.41 |
| **3c** | Sb | 1.67 | 1.44 | 0.37 |
| **4c** | Bi | 1.59 | 1.41 | 0.37 |
| | | Q = Te | | |
| **1d** | P | 1.81 | 1.44 | 0.43 |
| **2d** | As | 1.79 | 1.43 | 0.41 |
| **3d** | Sb | 1.73 | 1.42 | 0.38 |
| **4d** | Bi | 1.64 | 1.42 | 0.38 |

In general, the W–E WBI decreases as the atomic number of E increases for a particular Q. The W–E WBI is not influenced by the nature of Q for a particular E and remains constant in the series. Also, the E–Q WIB decreases as the atomic number of E increases for a particular Q, but for the series **b**, **c** and **d** it is lower in magnitude then the decrease of the W–E WBI. For a particular E by moving from S to Te only a slight decrease of the E–Q WIB is observed. The WBI for the pnicogen monoxide complexes (**a**) are ca. 0.2 lower than for the other EQ complexes (**b**, **c**

 © 2007 Wiley-VCH Verlag GmbH & Co. KGaA, Weinheim 

and **d**). This is probably due to the higher ionicity of the pnicogen monoxide complexes.

To evaluate the ionic character of the complexes **1**–**4** we have analysed the Hirshfeld charge distribution (Table 4).[23,24] This shows that the equatorial nitrogen atoms of the amido ($N_3N$) ligands are negatively charged (–0.23), whereas the axial nitrogen atom is almost neutral (varies between 0 to –0.01) and both are not influenced by the nature of the EQ ligand. The positive charge on the tungsten atom is only slightly influenced by the nature of the EQ ligand (it varies between 0.33 and 0.40). As the atomic number of Q increases for a particular E the charge on the tungsten atom increases but it decreases as the atomic number of E increases for a particular Q (Figure 15). The charges on the pnicogen atom (E) vary between 0 and 0.34 for the PTe and BiO complexes, respectively (**1d** and **4a**, respectively), indicating a relatively strong variation (Table 4). Similarly, the negative charge on the chalcogen atoms also varies relatively strongly between the two extremes –0.12 and –0.44 for **1d** and **4a**, respectively. Generally, for a particular E the charges on either E and Q decrease as Q become heavier, while for a particular Q the charges on either E and Q increase as E becomes heavier (Figure 16). The Hirshfeld charge analysis shows that the complexes **b**–**d** are only moderately charged, while the pnicogen monoxide complexes (**a**) are more polar.

Table 4. Selected Hirshfeld charges in complexes [($N_3N$)W(EQ)] (**1**–**4**).

| | E | W | E | Q |
|---|---|---|---|---|
| | | Q = O | | |
| **1a** | P | 0.36 | 0.17 | –0.31 |
| **2a** | As | 0.36 | 0.21 | –0.35 |
| **3a** | Sb | 0.33 | 0.32 | –0.42 |
| **4a** | Bi | 0.33 | 0.34 | –0.44 |
| | | Q = S | | |
| **1b** | P | 0.38 | 0.05 | –0.18 |
| **2b** | As | 0.38 | 0.10 | –0.22 |
| **3b** | Sb | 0.35 | 0.22 | –0.30 |
| **4b** | Bi | 0.34 | 0.25 | –0.32 |
| | | Q = Se | | |
| **1c** | P | 0.39 | 0.03 | –0.15 |
| **2c** | As | 0.39 | 0.08 | –0.20 |
| **3c** | Sb | 0.35 | 0.19 | –0.27 |
| **4c** | Bi | 0.34 | 0.22 | –0.30 |
| | | Q = Te | | |
| **1d** | P | 0.40 | 0.00 | –0.12 |
| **2d** | As | 0.39 | 0.04 | –0.16 |
| **3d** | Sb | 0.36 | 0.15 | –0.22 |
| **4d** | Bi | 0.35 | 0.18 | –0.25 |

One might expect that the decrease of the W–E bond strength (BDEs in Table 1) would be accompanied by an increase of the W–E distance. However, in the complexes **1**–**4** the W–E distances are shorter (except for **1d**) than in the pnictido complexes [($N_3N$)W≡E], although the W–E BDEs are lower. This can be explained by the different hybridisation of the pnicogens in the two types of complexes. In the complexes **1**–**4** the pnicogen atom in the σ bonding is almost sp-hybridised ($sp^{0.5–0.7}$), while in the pnictido complexes it is $sp^{3.30}$- (E = P) to $sp^{6.06}$-hybridised (E = Bi).[13]

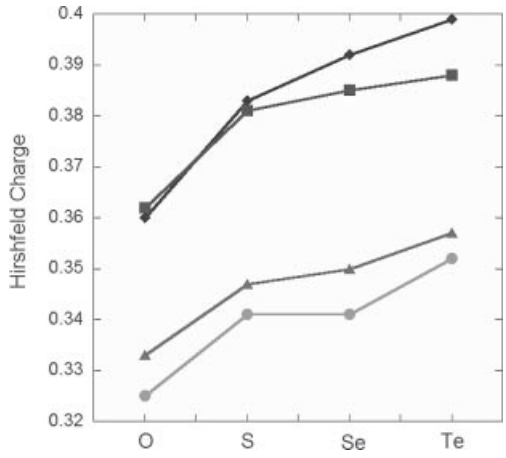


Figure 15. Variation of the Hirshfeld charges on tungsten in complexes [($N_3N$)W(EQ)] (**1**–**4**). Legend: P = ♦, As = ■, Sb = ▲ and Bi = ●.

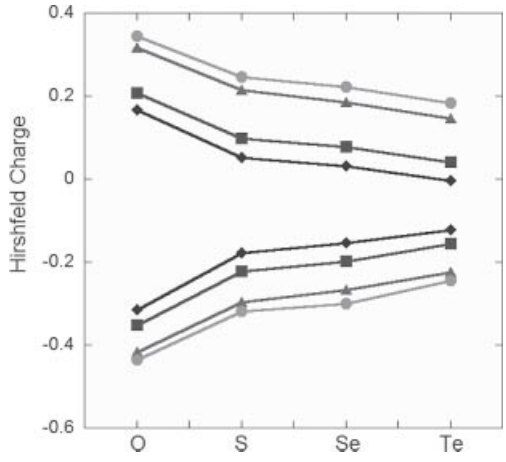


Figure 16. Variation of the Hirshfeld charges on E (positive) and Q (negative) in complexes [($N_3N$)W(EQ)] (**1**–**4**). Legend: P = ♦, As = ■, Sb = ▲ and Bi = ●.

Since the s orbitals are more compact compared with the more diffuse p orbitals it is not unexpected that the effective radius of the pnicogen decreases with increase of the s contribution to the hybrid orbital through which the W–E σ bonding is realised. This decrease of the effective radius of E due to hybridisation is responsible for the shorter W–E bond in complexes **1**–**4** than in the corresponding pnictido [($N_3N$)W≡E] complexes. Since the s-orbital contraction is more accentuated for the heavy elements, the shortening of the W–E bond will be more pronounced for the heavier congeners of E. This is consistent with the results of our calculations. It has to be noted that for the π bonding the pnicogen atoms use almost pure p orbitals in complexes **1**–**4** and [($N_3N$)W≡E].

Conclusions about the hybridisation of the pnicogen atom in the phosphido complex [($N_3N$)W≡P] was made based on $^{31}P$ NMR spectroscopy. The phosphido complex [($N_3N$)W≡P] shows an unusual $^{31}P$ chemical shift ($\delta$ = 1080.0 ppm) and a small tungsten-phosphorus coupling constant ($^1J_{W-P}$ = 138 Hz).[10] The small tungsten-phospho-

 © 2007 Wiley-VCH Verlag GmbH & Co. KGaA, Weinheim 

rus coupling in the phosphido complex [($N_3N$)W≡P] was attributed to the low s-orbital contribution to the W–P σ bonding[25] while the chemical shift was attributed to the paramagnetic shilding perpendicular to the W≡P triple bond.[26] In contrast to that, the phosphorus monosulfide complex **1b** presents a large phosphorus-tungsten coupling ($^1J_{W\text{-}P}$ = 771.5 Hz),[16] indicating a considerably higher amount of s-orbital contribution to the W–P σ bonding. We have calculated the $^{31}$P chemical shift ($\delta$ = 356.8 ppm) and tungsten-phosphorus coupling ($^1J_{W\text{-}P}$ = 753.9 Hz) for **1b** which compare well with the experimental data ($\delta$ = 342.3 ppm, $^1J_{W\text{-}P}$ = 771.5 Hz). The NMR data and its predictibilty by computational procedures provides good evidence for the inferred cause of this unusual anti-correlation between bond strength and bond length.

Throughout chemistry there is a general correlation between bond length and bond strength, i.e. shorter bonds are stronger than longer bonds. However, there are exceptions. There are known examples where the bond lengths do not correlate with the bond strengths or force constants. For example in the $H_nNF_{3-n}$ or $Me_nNF_{3-n}$ series the N–F force constants increase with increasing bond length.[27] Also, for some polyfluorinated hydrocarbons an increase of the C–C dissociation energy with the bond length and increasing fluorine substitution was observed.[28] Distances were analysed computationally by Kaupp et al. with respect to their bond length/bond strength abnormality.[29] It was found that the Sn–Sn bond dissociation energy decreases clearly with increasing fluorine substitution but the Sn–Sn distance remains constant. Also, no correlation between the bond lengths and force constants was observed. This abnormality was attributed to "hybridisation-deficiency"[30] caused by "hybridisation defects" (reduced mixing and non-uniformity of the s and p orbitals due to their different radial distributions).[31] This work provides evidence that similar effects, i.e. hybridisation defects, cause the shortening of the W–E bond in complexes **1**–**4** compared to the pnictido complexes [($N_3N$)W≡E].

## Conclusions

In this paper we have shown, that the linear arrangement of the $N_{ax}$–W–E–Q framework in complexes of the type [($N_3N$)W(EQ)] renders a bonding situation with a π-delocalised electron system which is best described as two three-centred four-electron bonds. The σ-electron systems becomes more localised as the atomic number of either E or Q increases. In contrast to the σ-electron system the π bonding becomes more delocalised as the atomic number of either E and Q increases. The strength of the *trans* influence of the EQ ligands in the complexes **1**–**4** is determined by the relative energy of the EQ fragment σ orbitals.

The shorter W–E distances in complexes **1**–**4** than in the pnictido complexes [($N_3N$)W≡E] (E = P, As, Sb and Bi) have been attributed to the different hybridisation, i.e. considerable increase of s contribution to the σ MOs of the pnicogen atoms in complexes **1**–**4** compared to the pnictido [($N_3N$)W≡E] complexes. Complexes **1**–**4** are moderately charged, except for the phosphorus monoxide complexes (**a**) which exhibit a more significant ionic character.

The W–E and E–Q bond dissociation energies of complexes **1**–**4** are relatively high, and show the expected periodic variations. The BDEs indicate that even the heavier congeners should be stable enough to be isolated. Both fragment calculations and WIB give very similar bond orders and trends herein. Overall, the bonding in the W–E–Q unit is best pictorially represented by two double bonds (Scheme 2).

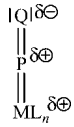


Scheme 2. Proposed Lewis structure for the complexes [($N_3N$)-W(EQ)].

## Computational Methods

DFT calculations were carried out using the Amsterdam Density Functional program (ADF) versions 2004.01 and 2005.01.[32–35] Scalar relativistic corrections were included via the Zero Order Regular Approximation (ZORA) method.[36–40] The generalized gradient approximation was employed, using the local density approximation of Vosko, Wilk, and Nusair[41] together with the nonlocal exchange correction by Becke[42,43] and nonlocal correlation corrections by Perdew.[44] The Slater-type orbital (STO) basis sets were of triple-ζ quality augmented with a single polarization function and two diffuse functions (ADF basis TZP++). The cores of the atoms were frozen up to 1s for C and N, 2p for P, S and Si, 3p for As and Se, 4p for Sb and Te, 5p for Bi and 4d for W. Optimisations were performed without symmetry restraints. Fragment calculations were performed to enable analysis of the orbital interactions to the W–E and E–Q bonds. In these calculations the complex is divided into two fragments, whose molecular and electronic structures are calculated in a single-point optimisation with a restricted singlet spin state. The geometry of the fragment is preserved from the optimised structure of the full complex. The molecular orbitals (MOs) of the complex are formed through linear combination of the MOs of the two fragments. The bond dissociation energies (BDEs) were calculated as the difference between the energy of the complex and the energy of the fragments in their ground state [Q triplet, ($N_3N$)WE singlet, EQ doublet and ($N_3N$)W quartet]. For the BDEs the SCF energies were used without correction. The $^{31}$P NMR chemical shift and P–W coupling constant for **1b** were calculated on the optimised geometry using the corresponding program modules as implemented in ADF.[45–49] The geometry of **1b** was optimised with the TZ2P basis sets for all atoms, with no core electrons and using a tight convergence criterion as well as an integration grid of 6. The relativistic effects were incorporated via the ZORA method. NBO analyses were performed with the Gaussian03 program[50] using the BP86[42–44] functional and the 6-31G* basis sets[51–59] with one diffuse function added, for C, H, N, Si, P, S, As and Se. The Dunning–Hunzinaga[60] type basis set with Stuttgart–Dresden SDD[61,62] core potentials was applied for Sb, Te, W and Bi.

**Supporting Information** (see footnote on the first page of this article): Tables of the fragment analyses and cartesian coordinates for all optimised structures. Figures in colour are also included.

 © 2007 Wiley-VCH Verlag GmbH & Co. KGaA, Weinheim 

## Acknowledgments

G. B. thanks the von Humboldt Foundation for a Feodor Lynen fellowship. The Oxford Supercomputing Centre is acknowledged for the computing facilities.

[1] J. E. Huheey, E. A. Kreiter, R. L. Kreiter, *Inorganic Chemistry: Principles of Structure and Reactivity*, 4th ed., Addison-Wesley, New York, **1993**.
[2] A. Holleman, E. Wiberg, *Lehrbuch der Anorganischen Chemie*, de Gruyter, Berlin, **1995**.
[3] O. J. Scherer, J. Braun, P. Walther, G. Heckmann, G. Wolmershaeuser, *Angew. Chem.* **1991**, *103*, 861.
[4] J. F. Corrigan, S. Doherty, N. J. Taylor, A. J. Carty, *J. Am. Chem. Soc.* **1994**, *116*, 9799.
[5] J. E. Davies, M. J. Mays, E. J. Pook, P. R. Raithby, P. K. Tompkin, *Chem. Commun.* **1997**, 1997.
[6] O. J. Scherer, S. Weigel, G. Wolmershauser, *Heteroat. Chem.* **1999**, *10*, 622.
[7] O. J. Scherer, C. Vondung, G. Wolmershauser, *Angew. Chem. Int. Ed. Engl.* **1997**, *36*, 1303.
[8] I.-P. Lorenz, W. Pohl, K. Polborn, *Chem. Ber.* **1996**, *129*, 11.
[9] C. E. Laplaza, W. M. Davis, C. C. Cummins, *Angew. Chem. Int. Ed. Engl.* **1995**, *34*, 2042.
[10] N. C. Zanetti, R. R. Schrock, W. M. Davis, *Angew. Chem. Int. Ed. Engl.* **1995**, *34*, 2044.
[11] N. C. Moesch-Zanetti, R. R. Schrock, W. M. Davis, K. Wanninger, S. W. Seidel, M. B. O'Donoghue, *J. Am. Chem. Soc.* **1997**, *119*, 11037.
[12] M. Scheer, J. Müller, M. Häser, *Angew. Chem. Int. Ed. Engl.* **1996**, *35*, 2492.
[13] G. Balázs, M. Sierka, M. Scheer, *Angew. Chem. Int. Ed.* **2005**, *44*, 4920.
[14] M. J. A. Johnson, A. L. Odom, C. C. Cummins, *Chem. Commun.* **1997**, 1523.
[15] C. C. Cummins, *Chem. Commun.* **1998**, 1777.
[16] G. Balázs, J. C. Green, M. Scheer, *Chem. Eur. J.* **2006**, *12*, 8603.
[17] T. Wagener, G. Frenking, *Inorg. Chem.* **1998**, *37*, 6402.
[18] T. Wagener, G. Frenking, *Inorg. Chem.* **1998**, *37*, 1805.
[19] P. Pyykkö, S. Riedel, M. Patzschke, *Chem. Eur. J.* **2005**, *11*, 3511.
[20] A. Bérces, O. Koentjoro, B. T. Sterenberg, J. H. Yamamoto, J. Tse, A. J. Carty, *Organometallics* **2000**, *19*, 4336.
[21] K. B. Wiberg, *Tetrahedron* **1968**, *24*, 1083.
[22] K. K. Pandey, G. Frenking, *Eur. J. Inorg. Chem.* **2004**, 4388.
[23] K. B. Wiberg, P. R. Rablen, *J. Comput. Chem.* **1993**, *14*, 1504.
[24] F. L. Hirshfeld, *Theor. Chim. Acta* **1977**, *44*, 129.
[25] J. A. Johnson-Carr, N. C. Zanetti, R. R. Schrock, M. D. Hopkins, *J. Am. Chem. Soc.* **1996**, *118*, 11305.
[26] G. Wu, D. Rovnyak, M. J. A. Johnson, N. C. Zanetti, D. G. Musaev, K. Morokuma, R. R. Schrock, R. G. Griffin, C. C. Cummins, *J. Am. Chem. Soc.* **1996**, *118*, 10654.
[27] D. Christen, O. D. Gupta, J. Kadel, R. L. Kirchmeier, H. G. Mack, H. Oberhammer, J. M. Shreeve, *J. Am. Chem. Soc.* **1991**, *113*, 9131.
[28] B. E. Smart, in *Molecular Structures and Energetics*, vol. 3 (Eds.: J. F. Liebmann, A. Greenberg), Verlag Chemie, Weinheim, **1968**, p. 141.
[29] M. Kaupp, B. Metz, H. Stoll, *Angew. Chem. Int. Ed.* **2000**, *39*, 4607.
[30] W. Kutzelnigg, *Angew. Chem.* **1984**, *96*, 262.
[31] M. Kaupp, P. v. R. Schleyer, *J. Am. Chem. Soc.* **1993**, *115*, 1061.
[32] G. Te Velde, F. M. Bickelhaupt, E. J. Baerends, C. Fonseca Guerra, S. J. A. Van Gisbergen, J. G. Snijders, T. Ziegler, *J. Comput. Chem.* **2001**, *22*, 931.
[33] C. Fonseca Guerra, J. G. Snijder, G. Te Velde, E. J. Baerends, *Theor. Chem. Acc.* **1998**, *99*, 391.
[34] In ADF2004.01, SCM, Theoretical Chemistry, Vrije Universiteit, Amsterdam, The Netherlands, http://www.scm.com.
[35] In ADF2002.02, SCM, Theoretical Chemistry, Vrije Universiteit, Amsterdam, The Netherlands, http://www.scm.com.
[36] E. van Lenthe, A. Ehlers, E. J. Baerends, *J. Chem. Phys.* **1999**, *110*, 8943.
[37] E. van Lenthe, R. van Leeuwen, E. J. Baerends, J. G. Snijders, *Int. J. Quantum Chem.* **1996**, *57*, 281.
[38] E. van Lenthe, E. J. Baerends, J. G. Snijders, *J. Chem. Phys.* **1996**, *105*, 6505.
[39] E. van Lenthe, E. J. Baerends, J. G. Snijders, *J. Chem. Phys.* **1994**, *101*, 9783.
[40] E. van Lenthe, E. J. Baerends, J. G. Snijders, *J. Chem. Phys.* **1993**, *99*, 4597.
[41] S. H. Vosko, L. Wilk, M. Nusair, *Can. J. Phys.* **1980**, *58*, 1200.
[42] A. D. Becke, *J. Chem. Phys.* **1988**, *88*, 1053.
[43] A. D. Becke, *Phys. Rev. A* **1988**, *38*, 3098.
[44] J. P. Perdew, *Phys. Rev. B* **1986**, *33*, 8800.
[45] J. Autschbach, T. Ziegler, *J. Chem. Phys.* **2000**, *113*, 936.
[46] J. Autschbach, T. Ziegler, *J. Chem. Phys.* **2000**, *113*, 9410.
[47] G. Schreckenbach, T. Ziegler, *J. Phys. Chem.* **1995**, *99*, 606.
[48] G. Schreckenbach, T. Ziegler, *Int. J. Quantum Chem.* **1997**, *61*, 899.
[49] S. K. Wolff, T. Ziegler, *J. Chem. Phys.* **1998**, *109*, 895.
[50] M. J. Frisch, G. W. Trucks, H. B. Schlegel, G. E. Scuseria, M. A. Robb, J. R. Cheeseman, J. A. Montgomery, T. Vreven, K. N. Kudin, J. C. Burant, J. M. Millam, S. S. Iyengar, J. Tomasi, V. Barone, B. Mennucci, M. Cossi, G. Scalmani, N. Rega, G. A. Petersson, H. Nakatsuji, M. Hada, M. Ehara, K. Toyota, R. Fukuda, J. Hasegawa, M. Ishida, T. Nakajima, Y. Honda, O. Kitao, H. Nakai, M. Klene, X. Li, J. E. Knox, H. P. Hratchian, J. B. Cross, V. Bakken, C. Adamo, J. Jaramillo, R. Gomperts, R. E. Stratmann, O. Yazyev, A. J. Austin, R. Cammi, C. Pomelli, J. W. Ochterski, P. Y. Ayala, K. Morokuma, G. A. Voth, P. Salvador, J. J. Dannenberg, V. G. Zakrzewski, S. Dapprich, A. D. Daniels, M. C. Strain, O. Farkas, D. K. Malick, A. D. Rabuck, K. Raghavachari, J. B. Foresman, J. V. Ortiz, Q. Cui, A. G. Baboul, S. Clifford, J. Cioslowski, B. B. Stefanov, G. Liu, A. Liashenko, P. Piskorz, I. Komaromi, R. L. Martin, D. J. Fox, T. Keith, M. A. Al-Laham, C. Y. Peng, A. Nanayakkara, M. Challacombe, P. M. W. Gill, B. Johnson, W. Chen, M. W. Wong, C. Gonzalez, J. A. Pople, *Gaussian03*, Gaussian Inc., Wallingford CT, **2004**.
[51] R. Ditchfield, W. J. Hehre, J. A. Pople, *J. Chem. Phys.* **1971**, *54*, 724.
[52] W. J. Hehre, R. Ditchfield, J. A. Pople, *J. Chem. Phys.* **1972**, *56*, 2257.
[53] P. C. Hariharan, J. A. Pople, *Theor. Chim. Acta* **1973**, *28*, 213.
[54] P. C. Hariharan, J. A. Pople, *Mol. Phys.* **1974**, *27*, 209.
[55] M. M. Francl, W. J. Pietro, W. J. Hehre, J. S. Binkley, D. J. DeFrees, J. A. Pople, M. S. Gordon, *J. Chem. Phys.* **1982**, *77*, 3654.
[56] R. C. J. Binning, L. A. Curtiss, *J. Comput. Chem.* **1990**, *11*, 1206.
[57] J.-P. Blaudeau, M. P. McGrath, L. A. Curtiss, L. Radom, *J. Chem. Phys.* **1997**, *107*, 5016.
[58] V. A. Rassolov, J. A. Pople, M. A. Ratner, T. L. Windus, *J. Chem. Phys.* **1998**, *109*, 1223.
[59] V. A. Rassolov, M. A. Ratner, J. A. Pople, P. C. Redfern, L. A. Curtiss, *J. Comput. Chem.* **2001**, *22*, 976.
[60] T. H. Dunning, P. J. Hay, in *Modern Theoretical Chemistry*, vol. 3 (Ed.: H. F. Schaefer), Plenum, New York, **1976**, p. 1.
[61] M. Dolg, U. Wedig, H. Stoll, H. Preuss, *J. Chem. Phys.* **1987**, *86*, 866.
[62] A. Bergner, M. Dolg, W. Kuechle, H. Stoll, H. Preuss, *Mol. Phys.* **1993**, *80*, 1431.

Received: January 12, 2007
Published Online: April 30, 2007

 © 2007 Wiley-VCH Verlag GmbH & Co. KGaA, Weinheim 

DOI: 10.1002/ejic.200700062

# Dehydration and Dehydrogenation of Alcohols with Mononuclear Cationic Vanadium Oxides in the Gas Phase and Energetics of $VO_nH^{0/+}$ ($n$ = 2, 3)

**Marianne Engeser,[a] Detlef Schröder,*[b] and Helmut Schwarz[c]**

*Dedicated to Professor Peter Hofmann on the occasion of his 60th birthday*

**Keywords:** Alcohol oxidation / Dehydration / Mass spectrometry / Metal alkoxides / Vanadium

The ion/molecule reactions of selected alcohols with the vanadium oxide cations $VO^+$ and $VO_2^+$ are studied by Fourier-transform ion-cyclotron resonance (FT-ICR) mass spectrometry. Dehydrogenation is the dominating reaction pathway for methanol and allyl alcohols. With larger or less unsaturated alcohols, dehydration and carbocation formations prevail. While the valence in $VO^+$ remains unchanged during alcohol dehydrogenation, $VO_2^+$ is reduced to $V^{III}$. Thermochemical data for $VO_2H^{0/+}$, $VO_3H$ and $VO_3H_2^+$ are derived by means of ICR bracketing. The experimental results are further complemented by ab initio calculations using density functional theory.
(© Wiley-VCH Verlag GmbH & Co. KGaA, 69451 Weinheim, Germany, 2007)

## Introduction

Part of the large interest in transition-metal oxides is due to their key role in heterogeneous catalysis,[1] particularly in oxidation reactions. For example, vanadium oxide compounds are used as heterogeneous catalysts[2] for the oxidation of $SO_2$ in the production of sulfuric acid and for selective hydrocarbon oxidation, i.e. the production of maleic anhydride directly from butane. The mechanisms of such complicated hydrocarbon activations are still not fully understood and widely debated.[1] Among others, alcohols and alkoxides have been proposed as intermediates in alkane oxidation catalyzed by metal-oxide compounds.[1–3] Further, the oxidation of alcohols itself is important for industrial processes, e.g. the production of formaldehyde from methanol.[1,4] For larger molecules containing alcoholic OH groups, acidic properties of an oxide catalyst may induce dehydration instead of dehydrogenation.[1,2] Hence, a selective oxidation catalyst is characterized by handling the delicate interplay between oxidizing and acidic properties. The roles of formal oxidation states and of functional groups that form the active sites of a catalyst are of particular interest in this respect.

Gas-phase experiments represent a powerful means for conducting model studies of complicated reactions,[5,6] ranging even to models for heterogeneous catalysis,[7] because they facilitate an understanding of mechanistic details at a molecular level. It has to be stated though that the extreme simplification also entails that a direct extrapolation of the findings to applied catalysis may be impossible.[8] The gas-phase behavior of vanadium alkoxides have been studied for methanol[9,10] and larger homologues.[11] As far as detailed studies are concerned, only methanol dehydrogenation by vanadium cations has been previously addressed.[12–14] Here, we present an experimental investigation of the gas-phase ion/molecule reactions of the mononuclear vanadium-oxide cations $VO^+$ and $VO_2^+$ with a variety of alcohols. The results have some implications for the ion thermochemistry of the vanadium-oxide hydroxides $VO_2H$ and $VO_3H$, which has not been reported so far.

[a] Kekulé-Institut für Organische Chemie und Biochemie der Universität Bonn,
Gerhard-Domagk-Strasse 1, 53121 Bonn, Germany
[b] Institute of Organic Chemistry and Biochemistry,
Flemingovo nám. 2, 16610 Prague, Czech Republic
[c] Institut für Chemie der Technischen Universität Berlin,
Strasse des 17. Juni 135, 10623 Berlin, Germany

## Results

### Ion/Molecule Reactions of $VO^+$ with Selected Alcohols

In the comparatively sluggish reaction of $VO^+$ with methanol, the major process corresponds to dehydrogenation, which has been shown to proceed via a selective 1,2-elimination.[13] In contrast, dehydrogenation is an only minor pathway in the reaction of $VO^+$ with ethanol (Table 1). The longer carbon chain enables a new reaction pathway (alkene formation) which is also reflected in an enhanced overall reaction efficiency ($\phi$ = 35%).[15] Use of the labeled reactant [2,2,2-$D_3$]ethanol leads to an exclusive loss of $C_2H_2D_2$. Thus, ethene formation takes place via a selective 1,2-elimination. The cationic product $[VO_2H_2]^+$ may be both the water complex $VO(H_2O)^+$ or the more

 © 2007 Wiley-VCH Verlag GmbH & Co. KGaA, Weinheim 

Table 1. Experimental second-order rate constants ($k$), reaction efficiencies ($\phi$)[15] and primary neutral products[a] for the ion/molecule reactions of $VO^+$ with alcohols.

| | $CH_3OH$[b] | $C_2H_5OH$ | $n$-$C_3H_7OH$ | $iso$-$C_3H_7OH$ | $n$-$C_4H_9OH$ | $sec$-$C_4H_9OH$ | $CH_2CHCH_2OH$ | $CH_3CHCHCH_2OH$ | $CH_2CHCHOHCH_3$ | $CH_2CHCH_2CH_2OH$ |
|---|---|---|---|---|---|---|---|---|---|---|
| $k$[c] | 1.2 | 6.7 | 7.3 | 6.4 | 9.1 | 8.6 | 9.6 | 7.0 | 8.2 | 5.3 |
| $\phi$ [%] | 6 | 35 | 40 | 35 | 50 | 50 | 50 | 40 | 45 | 30 |
| $H_2$ | 95 | 20 | 5 | 4 | [d] | [d] | 32 | 1 | 3 | 2 |
| 2 $H_2$ | | | 3 | 2 | 1 | 2 | | 1 | 1 | 2 |
| $CH_4$ | 5 | | 1 | 1 | | | | | | 1 |
| $CH_4$, $H_2$ | | | | | 8 | 4 | | | | |
| $H_2O$ | | 2 | 1 | 3 | | | 6 | 13 | 20 | 15 |
| $H_2$, $H_2O$ | | | | | 22 | 10 | | 3 | 5 | 4 |
| $C_2H_4$ | | 77 | | | | 1 | 5 | 6 | 9 | 10 |
| $C_2H_6$ | | | | | 10 | 40 | | | | |
| $C_3H_4$ | | | | | | | 7 | | | |
| $C_3H_6$ | | | 75 | 77 | 1 | | | | | 17 |
| $C_4H_6$ | | | | | | | | 30 | 32 | 22 |
| $C_4H_8$ | | | | | 52 | 38 | | | | |
| $CH_2O$ | | | | | | | 5 | | | 8 |
| $VO_2H$ | | | 15 | 13 | 6 | 5 | 28 | 45 | 30 | 19 |
| $C_3H_5$ | | | | | | | 17 | | | |

[a] Intensities are normalized to a sum of 100%. For all systems, fragmentation channels with abundances ≤ 1% are neglected. [b] Taken from ref.[13] [c] Given in $10^{-10}$ $cm^3$ $molecule^{-1}$ $s^{-1}$; the absolute error is assumed to be ± 30%. [d] This ion is formed in a quick and efficient secondary reaction, which may contribute to the primary branching ratio with max. 2%.

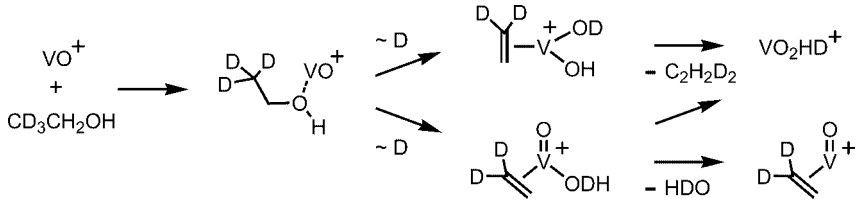


Scheme 1.

stable dihydroxide $V(OH)_2^+$.[16,17] In competition with ethene loss, water is expelled in a much smaller amount, and as far as site-selectivity is concerned, investigation of [2,2,2-$D_3$]ethanol demonstrates high selectivity (Scheme 1). Both reaction pathways result in a dehydration of ethanol to ethene, even though the bisligated complex $VO(C_2H_4)(H_2O)^+$ does not necessarily need to serve as a common intermediate in both cases.[18]

Most of the fragmentation pathways in the ion/molecule reaction of $VO^+$ with propanol (Table 1) resemble the ethanol case, i.e. elimination of propene concomitant with formation of $VO_2H_2^+$ represents the most abundant reaction channel and dehydrogenation takes place in even lower amounts. The latter yields the ion $[VC_3H_6O_2]^+$, which has been previously characterized as the allyl complex $(C_3H_5)$-$VO(OH)^+$.[19] Further, formation of the carbocation $C_3H_7^+$ appears as a new pathway which is not observed for the smaller alcohols (Scheme 2). The nature of the neutral species $[VO_2H]$ lost in this process cannot be probed in our type of experiments. Nevertheless, it is reasonable to interpret it as a vanadium-oxide hydroxide O=V–OH, because combined elimination of VO and HO· is endothermic ($\Delta_r H$ = 415 kJ/mol for 2-propanol) and hence for this channel impossible in ion/molecule reactions with thermalized reactants. The overall oxidation state of vanadium therefore does not change during this reaction which can be viewed as a transfer of a hydroxide anion from the alcohol to the metal cation. Even though the hydroxy group is situated at different positions in the two propanol isomers, the spectra of 1- and 2-propanol are indistinguishable (Table 1). Starting from 1-propanol, a direct hydroxide transfer would lead to an energetically demanding primary carbocation. On the other hand, an additional hydrogen rearrangement in the positively polarized hydrocarbon ligand yields the more stable secondary carbocation which is formed directly in the 2-propanol case and can thus account for the experimental observations.

Similar to propanol, the reactions of $VO^+$ with isomeric butanols predominantly result in the formation of $VO_2H_2^+$ concomitant with loss of butene. In addition, hydroxide abstraction, yielding $C_4H_9^+$ is also observed. No significant differences between the two butanol isomers are observed, again indicating the formation of a secondary carbocation in both cases. As a new reaction channel, a combined elimination of $H_2O$ and $H_2$ takes place, which leads to $[VC_4H_6O]^+$. Tentatively, this product ion is assigned to the complex $VO(C_4H_6)^+$ with 1,3-butadiene as a bidentate ligand.[19] In addition, some C=C bond cleaving channels are observed, which do not take place for the smaller alcohols. Among these, the formation of $[VC_2H_4O_2]^+$ via loss of ethane or $C_2H_4$ + $H_2$ is especially noteworthy because it is strongly enhanced for *sec*-butyl alcohol compared to 1-butanol. The pronounced difference demonstrates that the position of the hydroxy group is crucial for this kind of C–C bond cleavage and that OH abstraction should not be involved.

 © 2007 Wiley-VCH Verlag GmbH & Co. KGaA, Weinheim 

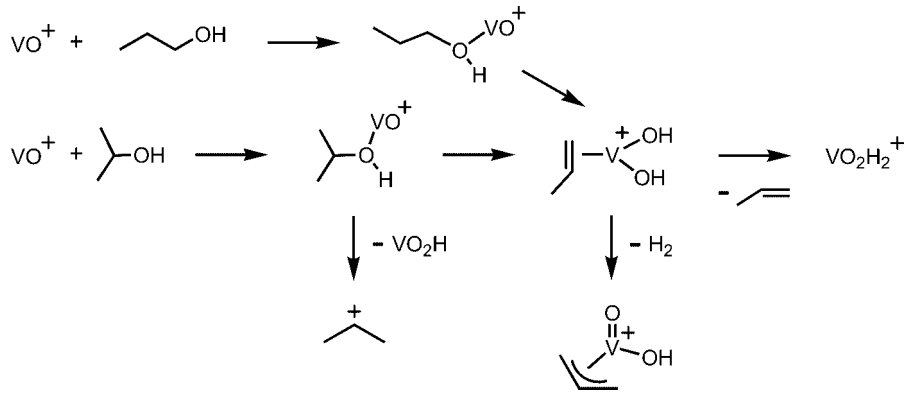


Scheme 2.

Allyl alcohol is also dehydrated by $VO^+$, but dehydrogenation and OH-transfer give rise to the dominating reaction channels. In analogy to the methanol case, the cationic dehydrogenation product is tentatively assigned to the acrolein complex $VO(CH_2CHCHO)^+$. Further, losses of ethene and $[CH_2O]$ are detected in small amounts, the latter may be formaldehyde or, less probable, a consecutive expulsion of CO after dehydrogenation. Interestingly, OH-abstraction does not only lead to the allyl cation $C_3H_5^+$ and neutral $VO_2H$, but also to the alternative couple of products with the opposite charge distribution $VO_2H^+ + C_3H_5^{\cdot}$: note that this the only case in the present investigation in which the cationic species $VO_2H^+$ was observed (see below).

Finally, the reactions of $VO^+$ with isomeric butenoles result in the main fragmentation channels expected according to the preceding results: Dehydration leads to both $VO(C_4H_6)^+$ and $VO_2H_2^+$, whereas hydroxide transfer results in $C_4H_7^+$. Note that $VO_2H^+$ is not observed reflecting the lower ionization energy of $C_4H_7^{\cdot}$ compared to $C_3H_5^{\cdot}$ (7.9 eV vs. 8.18 eV).[20] Further, small amounts of ethene loss are detected which may correspond to the expulsion of $[C_2H_6]$ as observed for the butanols. With regard to the three butenol isomers studied here, the differences between the two allylic alcohols are mostly confined to relatively small variations of abundances, whereas two additional products are observed for $CH_2CHCH_2CH_2OH$; these correspond to the eliminations of propene and $[CH_2O]$, respectively. The latter processes resemble the expulsions of ethene as well as $[CH_2O]$ from allyl alcohol/$VO^+$ (see above).

In summary, the main pathway in the reactions of $VO^+$ with alcohols is dehydration. Both alkenes and water may be expelled as neutral products, but alkene loss is far more favored. Dehydrogenation to aldehyde or ketone complexes is also possible, but can only compete efficiently if alkene formation cannot take place (methanol) or if the substrate already is too unsaturated (allyl alcohol). As a third important reaction pathway, hydroxide abstraction by $VO^+$ is observed. The $C_4$-alcohols further undergo cracking processes in which C–C bonds are cleaved. In any case, the metal's oxidation state ($V^{III}$) remains unchanged in the products formed.

### Ion/Molecule Reactions of $VO_2^+$ with Selected Alcohols

When reacted with bare $VO_2^+$, methanol is converted to formaldehyde with $VO(CH_2O)^+$ and $VO_2H_2^+$ as the corresponding ionic products.[13] In contrast to the $VO^+$ case, the reaction can be termed as an oxidative dehydrogenation, i.e. water is formed instead of $H_2$, while the metal is reduced from $V^V$ to $V^{III}$. In the reaction of $VO_2^+$ with ethanol (Table 2), oxidative dehydrogenation is expressed in the losses of $H_2O$ and $[C_2H_4O]$. The latter is tentatively assigned to acetaldehyde. Yet, the enhancement in reaction rate ($\phi$ = 50% as compared to $\phi$ = 10% for the $VO_2^+$/$CH_3OH$ system) is attributed to ethene formation representing the by far most abundant reaction channel. This scenario resembles very much the behavior of $VO^+$ described above. The product ion $VO_3H_2^+$ may be interpreted as doubly protonated vanadate $VO_3^-$. In solution, condensation to polyvanadates takes place upon acidification of vanadate solutions.[21] In the gas phase, however, any oligomerization is strictly prevented by the real Coulomb charge of the ions. Therefore, stable protonated monomeric species such as $VO_3H_2^+$ are feasible as well. A reaction pathway unique to the ethanol/$VO_2^+$ system leads to $[VCH_3O_2]^+$ via methyl loss. Whereas expulsion of $CH_3^{\cdot}$ has also been reported for the reaction of $FeO^+$ with ethanol,[22] a similar process has not been observed so far in any ion/molecule reaction of vanadium oxides with alcohols or hydrocarbons.[19] Formation of an open-shell fragment results in a reduction of $V^V$ in $VO_2^+$ to $V^{IV}$ in the product ion. A reasonable structure is $OV(OH)(CH_2O)^+$ formed by methyl loss from the putative ethoxy intermediate $OVOH(OC_2H_5)^+$ (Scheme 3). However, the reaction with [2,2,2-$D_3$]ethanol demonstrates that partial H/D exchange precedes all reaction pathways depicted in Scheme 3. As a possible candidate for an intermediate in the H/D equilibration one may consider the structure $VO(OH)_2(C_2H_4)^+$ with two identical hydroxy and methylene groups.

The ion/molecule reactions of $VO_2^+$ with 1- and 2-propanol do not show any significant differences. Similar to dehydration of ethanol by $VO^+$, formation of $VO_3H_2^+$ concomitant with elimination of propene is a prominent reaction

 © 2007 Wiley-VCH Verlag GmbH & Co. KGaA, Weinheim 

Table 2. Experimental second-order rate constants ($k$), reaction efficiencies ($\phi$),[15] and primary neutral products[a] for the ion/molecule reactions of $VO_2^+$ with alcohols.

| | $CH_3OH$[b] | $C_2H_5OH$ | *n*-$C_3H_7OH$ | *iso*-$C_3H_7OH$ | *n*-$C_4H_9OH$ | *sec*-$C_4H_9OH$ | $CH_2CHCH_2OH$ | $CH_3CHCHCH_2OH$ | $CH_2CHCHOHCH_3$ | $CH_2CHCH_2CH_2OH$ |
|---|---|---|---|---|---|---|---|---|---|---|
| $k$[c] | 2.0 | 9.0 | 10.5 | 9.4 | 7.6 | 8.4 | 6.9 | 7.9 | 9.6 | 7.8 |
| $\phi$ [%] | 10 | 50 | 60 | 55 | 45 | 50 | 40 | 45 | 55 | 45 |
| $CH_3$ | | 3 | | | | | | | | |
| $H_2O$ | 28 | 5 | | 1 | 1 | | | | | |
| $H_2$, $H_2O$ | | | 4 | 3 | 1 | 5 | | | | |
| $CH_2O$ | 72 | | | | | | 5 | | | |
| $C_2H_6$ | | | | | | 10 | | | | |
| $C_2H_4$ | | 76 | | | | | | | | |
| $C_3H_4$ | | | | | | | 10 | | | |
| $C_3H_6$ | | | 38 | 37 | | | | | | 5 |
| $C_3H_8$ | | | | | 8 | | | | | |
| $C_2H_4O$ | | 10 | | | | | | 1 | 3 | |
| $[C_2H_6O]$ | | | | | 8 | 7 | | | | |
| $C_4H_6$ | | | | | | | | 4 | 7 | 1 |
| $C_3H_4O$ | | | | | | | 10 | | | |
| $C_4H_8$ | | | | | 20 | 18 | | | | |
| $C_3H_6O$ | | | 4 | 2 | | 4 | | | | |
| $C_4H_8O$ | | | | | 7 | 10 | | | | |
| $[C_2H_6O_2]$ | | 4 | | | | | | | | |
| $[C_4H_{10}O_2]$ | | | | | 5 | 4 | | | | |
| $VO_3H$ | | | 54 | 53 | 39 | 33 | 75 | 93 | 85 | 90 |
| $[VC_2H_5O_2]$ | | | | | | | | | 3 | |

[a] Intensities are normalized to a sum of 100%. For all systems, fragmentation channels with abundances $\leq$ 2% not listed. Note that the nature of the lost neutral molecule is not known, and that the mass difference may correspond to two (or more) smaller molecules. [b] Taken from ref.[13] [c] Given in $10^{-10}$ $cm^3$ $molecule^{-1}$ $s^{-1}$; the absolute error is assumed to be $\pm$ 30%.

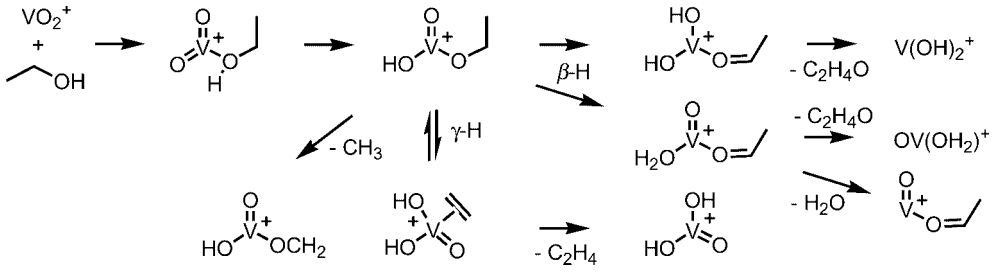


Scheme 3.

pathway. The major route is associated with hydroxide abstraction to afford neutral $VO_3H$. The facile formation of a carbenium ion may also account for the lack of differentiation between 1- and 2-propanol.

In the reactions with isomeric butanols, butene formation and hydroxide abstraction represent the main reaction pathways. However, they are not as favored as in the propanol cases. In addition, a manifold of minor and almost negligible reaction channels is observed as well, which we do not pursue in any further detail.[23] Further, several types of C–C bond cleavages take place, some of which exhibit significant differences between *n*-butyl and *sec*-butyl alcohol. For example, *sec*-butyl alcohol/$VO_2^+$ shows loss of $C_2H_6$, whereas $C_3H_8$ is expelled in the case of 1-butanol. Thus, the position of the OH group has a significant effect on the cracking processes both in the reactions of $VO^+$ and $VO_2^+$.

The spectra of ion/molecule reactions of $VO_2^+$ with unsaturated alcohols are comparatively simple (Table 2). With allyl alcohol, the formations of $C_3H_5^+$ as the major and $VO^+$, $VO_2H_2^+$, $VO_3H_2^+$ as minor primary products are observed in analogy to the results described above. The reaction of $VO_2^+$ with butenol isomers finally reveals a pronounced preference for carbocation formation; only traces of other reaction channels are observed.

In summary, the two most favored pathways in the alcohol/$VO_2^+$ systems, alkene expulsion and carbocation formation, both include C–O bond cleavage of the alcohol. Hydroxide transfer takes place if the resulting carbenium ion is sufficiently stabilized. Labeling experiments suggest that the two pathways are connected by tautomerism between alkene and hydroxide complexes before dissociation. With unsaturated alcohols, hydroxide abstraction is observed almost exclusively in accordance with the enhanced stability of allyl cations.

### Secondary Ion/Molecule Reactions in the Alcohol/$VO^+$ and Alcohol/$VO_2^+$ Systems

Cascades of the subsequent ion/molecule reactions of $VO_n^+$ cations with methanol have previously been studied in detail.[13] The key reactions steps comprise condensation reactions of the type [V]OH + $CH_3OH$ → [V]$OCH_3$ + $H_2O$, where [V] stands for a bare or ligated, neutral or charged vanadium core. A similar behavior is observed for other

 © 2007 Wiley-VCH Verlag GmbH & Co. KGaA, Weinheim 

alcohols ROH as well, for which ions of the formula $V(OH)(OR)^+$ and $V(OR)_2^+$ are formed from $VO_2H_2^+$ and the respective alcohol. On the other hand, isomeric complexes $VO(ROH)^+$ may be present too. They stem from other intermediates and are formed via ligand exchange according to $VO(L)^+ + ROH \rightarrow VO(ROH)^+ + L$ (L = $CH_3CHO$, for example), even though they should be significantly less stable than the alkoxide isomers.[13] Further, the presence of complexes of the type $OVOH(R)^+$ as a third class of isomers is quite reasonable for larger alcohols which form more stable carbenium ions.[19] $VO_3H_4^+$ is another common product observed at longer reaction times with alcohols larger than methanol. This ion is produced via alcohol dehydration/alkene loss from the precursor ion $VO_2H_2^+$. Similarly, $VO_4H_4^+$ is formed from $VO_3H_2^+$; condensation leads to $VO(OH)(OR)^+$ and $VO(OR)_2^+$ in this case. If a carbocation is generated in the first step, it readily reacts with alcohol molecules in acid-base type reactions, yielding protonated alcohols and a typical series of organic cations derived there from. In addition to these more general observations, the reaction of $VO^+$ with the isomeric butanols shows a peculiarity in that the expected alkoxide product $[VC_4H_{10}O_2]^+$ is less abundant than the dehydrogenated ion $[VC_4H_8O_2]^+$. The latter may be assigned to a mixture of a butadiene complex $V(OH)_2(C_4H_6)^+$ and an unsaturated alkoxide $HOVC_4H_7^+$ formed via remote functionalization,[24] because a similar product is not observed for smaller alcohols.

Finally, the reactivity of the product $VO_2H^+$, generated from allyl alcohol/$VO^+$, was explored with regard to possible thermochemical implications. In the reaction of $VO_2H^+$ with allyl alcohol, mostly $C_3H_5^+$ concomitant with neutral $[VO_3H_2]$ are formed via a second hydroxide abstraction. Additional minor products correspond to $VO_2H_2^+$, $VO_3H_3^+$, $[C_3H_5O]^+$, and $[VC_3H_7O_3]^+$. The hydrogen-atom abstraction to yield a hydroxy-substituted allyl cation will again be addressed in the thermochemical section further below (Table 3).

### Fragmentation of VO(alcohol)$^+$ Complexes in a Sector-Field Instrument

To gain further insight into the reaction mechanisms, an alternative instrumental technique has been used to study some of the postulated intermediates. To this end, the complexes $VO(alcohol)^+$ were attempted to be generated by chemical ionization of a mixture of $(C_5H_5)V(CO)_3$ and the respective alcohol with $N_2O$ as reagent gas. The cations emerging from the CI source were then analyzed in a four-sector instrument by recording metastable ion spectra. By this technique, the charged fragments formed via unimolecular dissociations in the field-free region of the mass spectrometer are detected.

In the presence of methanol, a signal at *m*/*z* 99, as expected for $VO(CH_3OH)^+$, can be generated under CI conditions. The MI spectrum of the mass-selected ion shows $H_2$-loss as the main fragmentation channel (Table 3) with $VO^+$ and $VO_2^+$ as additional ionic fragments. All pathways are in accordance with previous findings[9] and the results obtained in ion/molecule reaction of $VO^+$ with methanol (see above). The exclusive loss of HD from $CD_3OH/VO^+$ confirms once more the operation of a selective 1,2-elimination. Similarly, selecting the ion at *m*/*z* 113 observed in the presence of ethanol leads to the observation of the same ions as in the respective ICR ion/molecule reaction. However, the relative abundances of the fragmentation channels differ significantly: dehydrogenation is now much more pronounced than dehydration, which can in part be associated with the conservation of angular momentum which leads to a preference for the losses of light fragments in the metastable ion spectra.[25,26] Further, the loss of 28 u shifts to 32 u when perdeuterated [$D_6$]ethanol is used, thus corroborating the formation of $VO_2H_2^+$ and neutral ethene. Elimination of $H_2$ remains the main fragmentation channel also for the two isomeric propanol complexes; minor losses of water or propene are observed as well. A difference between the two propanol isomers occurs with respect to the abundance of

Table 3. MI mass spectra of selected $VO(alcohol)^+$ or isomeric complexes.[a]

| | | $CH_3OH$[b] | $CD_3OH$[b] | $CH_3CH_2OH$ | $CD_3CD_2OD$ | *n*-$C_3H_7OH$ | *iso*-$C_3H_7OH$ | $CH_2CHCH_2OH$ |
|---|---|---|---|---|---|---|---|---|
| $[M^+ - 1]$ | H | | | | | 2 | | 5 |
| $[M^+ - 2]$ | $H_2$ | 100 | | 100 | | 100 | 100 | 100 |
| $[M^+ - 3]$ | HD | | 100 | | | | | |
| | $H_2 + H$ | | | | | 4 | | |
| $[M^+ - 4]$ | $D_2$ | | 15 | | 100 | | | |
| $[M^+ - 16]$ | $CH_4$ | 50 | | | | | | |
| $[M^+ - 18]$ | $H_2O$ | | | 15 | | 20 | 20 | 55 |
| $[M^+ - 19]$ | $CD_3H$ | | 30 | | | | | |
| | $[H_3O]$ | | | | | 15 | 4 | 3 |
| $[M^+ - 20]$ | $D_2O$ | | | | 15 | | | |
| $[M^+ - 28]$ | $C_2H_4$, CO | | | 85 | | 25 | | 5 |
| $[M^+ - 32]$ | $CH_3OH$, $C_2D_4$ | 25 | | | 70 | | | |
| $[M^+ - 35]$ | $CD_3OH$ | | 25 | | | | | |
| $[M^+ - 40]$ | $C_3H_4$ | | | | | | | 5 |
| $[M^+ - 42]$ | $C_3H_6$ | | | | | 15 | 65 | |
| $[M^+ - 52]$ | $CD_3CD_2OD$ | | | [b] | 15 | | | |

[a] Intensities are normalized to the base peak (100); errors are assumed to be < 10%. [b] The overall abundances in the methanol and ethanol systems were rather low such that signals with $I < 15$ could not be detected.

 © 2007 Wiley-VCH Verlag GmbH & Co. KGaA, Weinheim 

propene expulsion, which is significantly enhanced for 2-propanol. Interestingly, the formation of $C_3H_7^+$ via loss of neutral $VO_2H$, as observed in the corresponding ion/molecule reactions, is not observed in the MI-spectra. In addition, two other fragment ions corresponding to losses 19 u and 28 u, respectively, are observed. Whereas the latter is assigned to $C_2H_4$ because it is only detected for 1-propanol, but not for 2-propanol,[27] with regard to the former we cannot strictly exclude an isobaric interference in the MI experiments. Finally, the MI spectra obtained for the $VO^+$ complex of allyl alcohol display dehydrogenation as the most abundant process, but also significant amounts of water are lost. Instead of the loss of $CH_2O$ observed in the ICR measurements, cleavage of atomic $H^{\cdot}$ is found. In conclusion, the sector experiments are consistent with the other data obtained, but at least for this particular system their information content remains somewhat limited due to the relatively weak signal abundances, caused by the lack of a suitable precursor for high yields of reasonably clean $VO^+$ ions.

## Discussion

### Ion/Molecule Reactions of $VO^+$ and $VO_2^+$ with Alcohols

Comparison of the observed reactions of $VO^+$ with those of $VO_2^+$ reveals similarities as well as some differences. Intuitively, similarities are expected for the reaction channels in which the cations act like Lewis acids, i.e. hydroxide abstraction and dehydration, whereas differences should appear in oxidation reactions like dehydrogenation, because $V^V$ compounds ($VO_2^+$) are stronger oxidizing agents than $V^{III}$-species ($VO^+$). The reaction efficiencies do not differ significantly. In contrast to the reactions of $VO^+$ and $VO_2^+$ with alkanes,[19] the reactivity towards alcohols is not enhanced significantly by the second oxygen atom in $VO_2^+$. This behavior is in agreement with a Lewis-acid type interaction of the metal with the OH-group dominating the reactions of the two cations with alcohols larger than methanol, whereas the C–H bond activation necessary for alkane dehydrogenation is affected by the oxidation state of the metal.

The most important reaction channel in the methanol/$VO^+$ system is the formation of a formaldehyde complex by elimination of $H_2$. In the respective reaction with $VO_2^+$, two complementary fragmentation channels involve oxidation of methanol to $CH_2O$, i.e. loss of water and loss of $CH_2O$. As already stated above, oxidative dehydrogenation instead of pure dehydrogenation occurs with $VO_2^+$ instead of $VO^+$. In the $VO^+$ system, formaldehyde is not expelled, most probably because the hypothetical cationic product $HVOH^+$ is not as stable as the observed complex $VO(CH_2O)^+$. In contrast, $V(OH)_2^+$ is a likely product when the system contains an additional oxygen atom. A similar reasoning applies for the ethanol case simply by replacing an α-H atom by a methyl group. Still, oxidative dehydrogenation is less favored than dehydration to ethene for both vanadium-oxide cations. The discrimination of $H_2$-loss is even stronger with larger alcohols. From propanol on, the possible generation of stabilized secondary carbocations enables hydroxide abstraction from the substrate. The latter is more pronounced than dehydration only with $VO_2^+$, but not with $VO^+$, indicating that the proton affinity of $VO_2H$ is lower than the one of $VO_3H$. Similarly, in the reactions with allyl alcohol, carbocation formation is significantly more pronounced with $VO_2^+$ than with $VO^+$. Further, the reverse charge distribution is only observed with $VO^+$, but not with $VO_2^+$. Therefore, the ionization energy of $VO_3H$ must be significantly larger than $IE(C_3H_5^{\cdot})$ and thus $IE(VO_2H)$, in accordance with the more general observation of increasing ionization energies of vanadium-oxide species with increasing oxygen content.[28]

### Comparison with Ion/Molecule Reactions of Other Cationic Transition-Metal Oxides

The reactions of $FeO^+$ with alcohols may be chosen for comparison with a typical late transition-metal oxide.[22,29] As compared to the behavior of $FeO^+$, the selectivity of $VO^+$ is markedly enhanced. Thus, losses of radicals are not observed at all for the latter, and a cleavage of propanol C–C bonds does not occur either in the ion/molecule reactions of $VO^+$. Further, carbocation formation does not occur for primary alcohols and $FeO^+$, whereas rearrangement to the more stable secondary carbocation obviously takes place in the alcohol/$VO^+$ systems. The main products in the reactions of $FeO^+$ with alcohols have been divided into three categories: α-oxidation, alkene loss, and carbocation formation. The same classification can be applied for the $VO^+$ reactions as well, but the channels follow rather different reaction mechanisms. For example, α-oxidation with $FeO^+$ leads to loss of $H_2O$, whereas $H_2$ is formed in the $VO^+$ reaction. This behavior reflects the significantly larger oxophilicity of the early transition metal vanadium in comparison to the late transition metal iron.[8] With respect to alcohol dehydrogenation, $FeO^+$ resembles more the vanadium dioxide $VO_2^+$ rather than the monoxide $VO^+$, as has already been predicted from similar M–O bond dissociation energies in $FeO^+$ and $VO_2^+$.[8]

In addition, the ion/molecule reactions of $MoO^+$ with alcohols have been reported.[30] Not surprisingly, the similarities to $VO^+$ are much more pronounced here. Thus, the strong M–O bond is never cleaved for both $VO^+$ and $MoO^+$. Nevertheless, some deviations still are detectable. For example, a selective α-oxidation of methanol occurs for both metal oxides. However, $H_2$ is lost as a neutral molecule in the case of $VO^+$, whereas $CH_2O$ is expelled with $MoO^+$. Similarly, dehydration of ethanol to ethene takes place with both metal oxides, but water instead of ethene is lost with $MoO^+$. Finally, $MoO^+$ does not show any cracking products with butanols, again in contrast to the reactions of $VO^+$. In summary, $VO^+$ only effectively dehydrogenates alcohols if dehydration cannot compete, whereas dehydro-

 © 2007 Wiley-VCH Verlag GmbH & Co. KGaA, Weinheim 

genation is always a good choice for $MoO^+$. Further, loss of oxygen-containing neutral molecules like aldehydes or water takes place with $MoO^+$, but is almost prohibited for $VO^+$.

### Comparison of ICR and Sector-Field Results

According to the elemental composition, the same ions are sampled in the ICR- and MI-spectra described above. Nevertheless, quite large deviations in relative intensities are observed which cannot be explained only by mass discrimination effects known to enhance losses of small neutral molecules in sector instruments[31] and effects of angular momentum.[25,26] As another likely reason for the differences we therefore propose different ion internal energies in both experiments. In general, unimolecular fragmentation channels of metastable ions generated under CI conditions are less energy-demanding than fragmentations of the corresponding encounter complexes formed in ion/molecule reactions under single-collision conditions.[32] In the alcohol/$VO^+$ systems discussed here, the main difference concerns the enhanced amount of dehydrogenation instead of dehydration as observed in the MI spectra. According to DFT calculations of *n*-propanol/$VO^+$, dehydrogenation indeed is the lowest exit channel.[19] The strong preference for the energetically slightly more demanding dehydration of propanol in the ICR experiments might be due to spin restrictions,[33] such an argumentation has been proposed for the related system propane/$VO_2^+$.[19] However, spin restrictions cannot explain the similar results observed for ethanol, because both dehydrogenation and dehydration occur only on one (triplet) spin state in this case. Nevertheless, dehydrogenation again is preferred in the MI spectra, whereas dehydration to $VO_2H_2^+$ prevails under ICR conditions. As an alternative, rearrangements taking place during the formation and stabilization of the ions by collisions in the CI source should be taken into account. In our case, isomerization from an alcohol complex $VO(ROH)^+$ to the more stable alkoxide $V(OH)(OR)^+$ is likely to happen and should even be catalyzed by collisions with alcohol molecules.[17,34] Some indications for the presence of an alkoxide structure can be found in the CA spectra which show signals at *m*/*z* 68 ($VOH^+$) and *m*/*z* 84 ($VO_2H^+$) in addition to the one at *m*/*z* 67 ($VO^+$). Formation of these ions in high-energy collisions is more likely from $V(OH)(OR)^+$ isomers than from $VO(ROH)^+$. In conclusion, the observed MI spectra might stem from a mixture of two non-interconverting isomers. With the assumption that the ICR branching ratios roughly represent the fragmentations of the alcohol complexes $VO(ROH)^+$, the differences to the MI spectra can be ascribed to the alkoxides $V(OH)(OR)^+$. Thus, the alcohol complex mostly yields alkene formation, whereas $H_2$-loss is preferred for the alkoxide. The different reactivities can be understood as follows. In the alcohol complex, the C–OH bond is weakened to some extent due to coordination to the Lewis-acidic metal oxide cation. It is even broken completely for allyl alcohol resulting in a complex $(C_3H_5)V(O)(OH)^+$. Dehydration of the alcohol to an alkene is then easily accomplished by transfer of a hydrogen atom from the hydrocarbon backbone to the vanadyl oxygen which may proceed directly via a six-membered transition structure (Scheme 4). In contrast, the isomeric alkoxide could undergo a $\beta$-H elimination to initiate hydrogen elimination leading to aldehyde or ketone complexes, respectively. For example, formaldehyde expulsion is observed upon dissociation of gaseous $OV(OCH_3)_3^+$ and several of its fragment ions.[9] Thus, the assumption of a mixture of isomers can explain the observed results reasonably well (Table 4).

Table 4. Heats of formation (in kJ mol$^{-1}$)[a] of species used in the data analysis.

| | $\Delta_fH$ | | $\Delta_fH$ |
|---|---|---|---|
| H | 218.0[b] | $OH^-$ | 138.9[k] |
| O | 249.2 ± 0.1[c] | $C_2H_5^+$ | 902 ± 4[k] |
| OH | 39.3 ± 0.2[d] | $C_2H_5OH$ | –234.8 ± 0.2[k] |
| $V^+$ | 1162 ± 8[c] | $C_2H_5OH_2^+$ | 507[k] |
| VO | 134 ± 12[e] | $C_3H_5^{\cdot}$ | 161[k] |
| $VO^+$ | 832 ± 12[f] | $C_3H_5OH$ | –123.6 ± 1.5[k] |
| $VOH^+$ | 768 ± 15[g] | *sec*-$C_3H_7^+$ | 801 ± 4[b] |
| $VO_2$ | –201 ± 55[h] | *iso*-$C_3H_7OH$ | –272.5 ± 0.4[k] |
| $VO_2^+$ | 716 ± 16[i] | $CH_2CHCHOH$ | 15.4[l] |
| $V(OH)_2^+$ | 372 ± 40[j] | $CH_3CCH$ | 185.4 ± 0.9[b] |

[a] Values for gaseous species at 298 K. [b] Ref.[20] [c] Ref.[49] [d] Ref.[50] [e] Derived using *IE*(VO) = 7.2386 eV.[51] [f] Derived using $D_0(V^+–O)$ = 5.99 ± 0.1 eV.[52] [g] Derived using $D_0(V^+–OH)$ = 4.50 ± 0.15 eV.[52] [h] Derived using *IE*($VO_2$) = 9.5 ± 0.4 eV.[42] [i] Ref.[13] [j] Estimated using $\Delta_fH(V(OH)_2^+) = \Delta_fH(V^+) + 2\,\Delta_fH(OH) - 2\,D_0(V^+–OH)$. [k] Ref.[53] [l] Ref.[54]

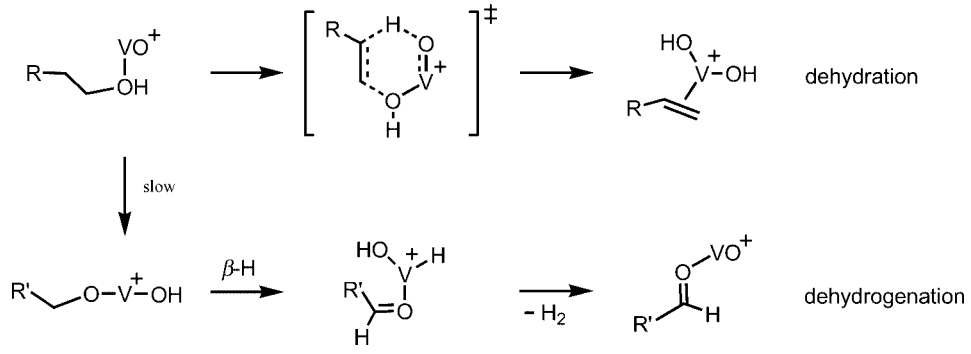


Scheme 4.

 © 2007 Wiley-VCH Verlag GmbH & Co. KGaA, Weinheim 

### Thermochemical Implications

For several of the molecules mentioned above, no thermochemical data have been reported so far, i.e. the hydroxide-oxides $VO_2H^{0/+}$, $VO_3H$ and $VO_3H_2^+$. Accordingly, we summarize the thermochemical information which can be derived from the ICR experiments in which endothermic reactions cannot take place ("bracketing approach").

Neutral $VO_2H$ cannot be observed directly by mass spectrometric means. Nevertheless, its formation can be deduced from carbocation observation in the reactions of $VO^+$ with alcohols. As already mentioned above, the alternative of generating two neutral molecules (VO + OH$^{\cdot}$) can be excluded due to its endothermicity. Therefore, carbocation formation can be used to derive upper limits for the enthalpy of formation $\Delta_fH(VO_2H)$. The lowest upper boundary $\Delta_fH(VO_2H) \leq -242 \pm 16$ kJ mol$^{-1}$ results from the reaction $VO^+$ + 2-propanol → *sec*-$C_3H_7^+$ + $VO_2H$. An estimate of a lower limit may be calculated from the non-occurrence of a similar process in the ethanol case: $\Delta_fH(VO_2H) \geq -305 \pm 16$ kJ/mol. The corresponding cation $VO_2H^+$ is formed from $VO^+$ and allyl alcohol: $VO^+$ + $C_2H_3CH_2OH$ → $C_3H_5^{\cdot}$ + $VO_2H^+$, thus yielding $\Delta_fH(VO_2H^+) \leq 547 \pm 20$ kJ mol$^{-1}$. For a lower boundary, the subsequent reactions of $VO_2H^+$ with allyl alcohol are examined. However, the heat of formation of at least one product is not known for all reaction pathways. In the H-atom abstraction $VO_2H^+$ + $C_2H_3CH_2OH$ → $VO_2H_2^+$ + $[C_3H_5O]$, the formation of the radical $CH_2CHC^{\cdot}HOH$ may be assumed. Combined with an estimate for the enthalpy of formation $\Delta_fH(V(OH)_2^+)$ (Table 4), this leads to a lower bound of $\Delta_fH(VO_2H^+) \geq 511 \pm 40$ kJ mol$^{-1}$. A comparison of the two bracketed values gives an estimate for the ionization energy $IE(VO_2H) = 8.3 \pm 0.2$ eV. This ionization energy can also be deduced directly. In the allyl alcohol/$VO^+$ system, the product channels $C_3H_5^+$ + $VO_2H$ and $VO_2H^+$ + $C_3H_5^{\cdot}$ are observed in a ratio of about 2:1, thus indicating $IE(VO_2H) \approx IE(C_3H_5^{\cdot}) = 8.18$ eV.[20] This result is further confirmed by the formation of $C_4H_7^+$ from but-3-en-2-ol/$VO^+$, whereas $VO_2H^+$ is not formed at all in this case, thus $IE(VO_2H) > IE(C_4H_7^{\cdot}) = 7.49$ eV.[20] On the other hand, hydroxide abstraction is not observed in the reaction of $VO^+$ with phenol,[35] which might be interpreted as an indication for $IE(VO_2H) < IE(C_6H_5^{\cdot}) = 8.32$ eV.[20]

In addition, DFT calculations on neutral and cationic $V(O)(OH)^{0/+}$ have been performed (Table 5). Previous benchmark calculations[9,36,37] have shown that the chosen level is convenient for a sufficiently accurate comparison with experimental results on mononuclear vanadium-oxide compounds, even though further calculations at highest ab initio levels are still desirable. The results obtained for the fragments fully confirm geometries and energetics reported previously.[19,36–40] The geometry of cationic $V(O)(OH)^+$ in the energetically most favorable doublet spin state ($^2A''$) meets the expectations: The V–O bond length ($d_{VO}$ = 1.55 Å) is typical for cationic vanadyl units and the V–OH bond length fits to previous calculations of related compounds.[12] Compared to the cation, the V–O bonds in neutral V(O)(OH) with a triplet ground state ($^3A''$) are elongated. The calculated adiabatic ionization energy $IE_{calc}(V(O)(OH)) = 8.22$ eV is in perfect agreement with the experimental value $IE_{exp}(V(O)(OH)) = 8.18$ eV derived above. Comparison of the experimental and calculated bond energies (Table 6) further shows that the theoretical level is sufficiently high because the deviations are in acceptable ranges.

Table 5. Total energies $E_{tot}$ (in Hartree) and selected geometric parameters[a] of neutral and cationic V(O)(OH) and some fragments calculated with B3LYP/TZVP.

| | | $E_{tot}$ | $d_{VO}$[b] | $d_{OH}$ | $a_{OVO}$ | $a_{VOH}$ |
|---|---|---|---|---|---|---|
| V(O)(OH) | $^3A''$ | –1095.151804 | 1.61; 1.85 | 0.96 | 153.7 | 157.1 |
| | $^1A'$ | –1095.115031 | 1.60; 1.84 | 0.96 | 147.7 | 151.2 |
| | $^5A''$ | –1095.073974 | 1.79; 1.90 | 0.96 | 170.0 | 170.0 |
| $V(O)(OH)^+$ | $^2A''$ | –1094.849715 | 1.55; 1.74 | 0.97 | 120.7 | 141.8 |
| | $^4A'$ | –1094.772115 | 1.72; 1.80 | 0.97 | 153.0 | 165.3 |
| $VO_2$ | $^2A_1$ | –1094.523949 | 1.62 | | 115.0 | |
| $VO_2^+$ | $^1A_1$ | –1094.195535 | 1.56 | | 105.9 | |
| VO | $^4\Sigma^-$ | –1019.237027 | 1.59 | | | |
| $VO^+$ | $^3\Sigma^-$ | –1018.964283 | 1.55 | | | |
| VOH | $^5A'$ | –1019.818921 | 1.85 | 0.96 | | 129.2 |
| | $^1A'$ | –1019.759570 | 1.72 | 0.96 | | 179.9 |
| | $^3A'$ | –1019.740494 | 1.77 | 0.96 | | 140.1 |
| $VOH^+$ | $^4A''$ | –1019.580107 | 1.73 | 0.97 | | 155.5 |
| OH | $^2\Pi$ | –75.757786 | | 0.98 | | |
| O | $^3P$ | –75.095258 | | | | |
| H | $^2S$ | –0.502154 | | | | |

[a] Bond lengths *d* [Å] and bond angles *a* [°]. [b] The first value given corresponds to the vanadyl V=O bond, the second to the V–O single bond.

Table 6. Comparison of some selected calculated and experimental bond dissociation energies for $VO_2H_n^{0/+}$ (*n* = 0–2) in kJ mol$^{-1}$.

| X–Y | $D(X–Y)_{calc}$ | $D(X–Y)_{exp}$ |
|---|---|---|
| $OV^+$–O | 357 | $365 \pm 20$[a] |
| OV–O | 503 | $585 \pm 60$[a] |
| $OV^+$–OH | 335 | $340 \pm 40$[b] |
| OV–OH | 412 | $450 \pm 40$[b] |
| $OVO^+$–H | 399 | $405 \pm 40$[b] |
| OVO–H | 330 | $290 \pm 40$[b] |

[a] Derived from the data in Table 4. [b] This work.

In conclusion, the bond dissociation energy $D(OVO–H) = 290 \pm 40$ kJ mol$^{-1}$ in neutral $VO_2H$ reflects a weak O–H bond, whereas the OV–OH bond is rather strong ($D(OV–OH) = 450 \pm 40$ kJ mol$^{-1}$). Ionization of V(O)(OH) to $V(O)(OH)^+$ requires $IE_{exp}(OVOH) = 8.18$ eV and leads to a decrease in V–OH bond strength $D(OV^+–OH) = 340 \pm 40$ kJ mol$^{-1}$, whereas the strength of the VO–H bond rises to $D(OVO^+–H) = 405 \pm 40$ kJ mol$^{-1}$, which is significantly more than $D(VO^+–H) = 282 \pm 15$ kJ mol$^{-1}$ in $VOH^+$.

Very similar to the $VO_2H$ case, reasonable boundaries for the enthalpy of formation of neutral $VO_3H$ can be obtained from its formation in the reaction of $VO_2^+$ with 2-propanol ($\Delta_fH(VO_3H) \leq -358 \pm 16$ kJ mol$^{-1}$) and its non-occurrence in the reaction with ethanol ($\Delta_fH(VO_3H) \geq -421 \pm 16$ kJ mol$^{-1}$). For the corresponding protonated species $VO_3H_2^+$, the upper limit $\Delta_fH(VO_3H_2^+) \leq 407 \pm 17$ kJ mol$^{-1}$ is based on the reaction $VO_2^+$ +

 © 2007 Wiley-VCH Verlag GmbH & Co. KGaA, Weinheim 

$C_2H_3CH_2OH \rightarrow VO_3H_2^+$ + propyne. As stated above, formation of protonated alcohols is one of the major subsequent products in the alcohol/$VO_2^+$ systems. Thus, the reaction $VO_3H_2^+ + C_2H_5OH \rightarrow VO_3H + C_2H_5OH_2^+$ may be used to derive $\Delta_fH(VO_3H_2^+) \geq 350 \pm 50$ kJ mol$^{-1}$. Note that this limit might be too high because the intermediate $VO_3H_2^+$ has not been thermalized.

In the reactions of $VO_2^+$ with alcohols, formation of both product channels $VO_3H_2^+$ + alkene and $VO_3H$ + alkyl$^+$ takes place. The relative carbocation abundance $I_{rel}$ correlates with the proton affinity of the hydrocarbon involved (Figure 1). This is an indication for the presence of a tautomer equilibrium before dissociation, i.e. $[C_mH_n^+ \cdot VO_3H]$ and $[C_mH_{n-1} \cdot VO_3H_2^+]$. The former complex can arise by direct hydroxide transfer from the alcohol to $VO_2^+$. The existence of the latter has already been proposed in the discussion (Scheme 3) due to partial H/D exchange observed during the reaction. A similar mechanistic scenario has been described earlier for the reactions of $FeO^+$ with alcohols.[22] According to Figure 1, the proton affinity $PA(VO_3H)$ lies between $PA(C_2H_4)$ = 680 kJ mol$^{-1}$ and $PA(C_4H_6)$ = 783 kJ mol$^{-1}$, because for ethanol the equilibrium is shifted completely on the side of $VO_3H_2^+$ and mostly to the carbocation side for the isomeric butenols. $I_{rel}$ = 0.5 is expected for a proton affinity slightly lower than the one of propene, thus leading to $PA(VO_3H) = 730 \pm 10$ kJ mol$^{-1}$. Note that $I_{rel} = I(C_3H_5^+)/(I(VO_3H_2^+) + I(C_3H_5^+)) = 0.88$ for the reaction of allyl alcohol with $VO_2^+$ suggests that the hydroxide abstraction is not followed by a rearrangement of allene to the thermochemically more stable propyne,[20] because the amount of $VO_3H_2^+$ is significantly lower than in the butanol systems even though the proton affinities of propyne and *trans*-butene are similar. Combination of $\Delta_fH(VO_3H) = -390 \pm 50$ kJ mol$^{-1}$ and $PA(VO_3H) = 730 \pm 10$ kJ mol$^{-1}$ leads to $\Delta_fH(VO_3H_2^+) = 410 \pm 60$ kJ mol$^{-1}$, which compares reasonably well with the lower boundary derived above.

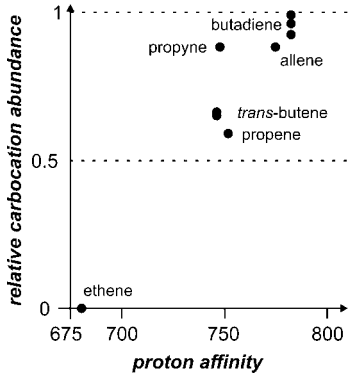


Figure 1. Relative carbocation abundance $I_{rel} = I(\text{carbocation})/[I(\text{carbocation}) + I(VO_3H_2^+)]$ vs. proton affinities[20] (in kJ mol$^{-1}$) of the produced alkenes in the reactions of $VO_2^+$ with alcohols.

The different branching ratios for the reactions of $VO_2^+$ and $VO^+$ with alcohols cannot be explained by the stability of the carbocations formed because they are the same in both cases. But one may assume that the difference in selectivity might be due to an enhanced exothermicity of the charge recombination reaction $VO_2^+ + OH^- \rightarrow VO_3H$ compared to the similar formation of $VO_2H$ from $VO^+$ which could also lower the corresponding transition structure. However, the formation of neutral $VO_3H$ from $VO_2^+ + OH^-$ ($\Delta_rH$ = –1245 kJ mol$^{-1}$) is not favored compared to $VO^+ + OH^- \rightarrow VO_2H$ ($\Delta_rH$ = –1246 kJ mol$^{-1}$) according to the data derived here. Thus, the different bond dissociation energies simply reflect the different ionization energies of VO and $VO_2$.

## Conclusions

Due to the Lewis-acidic character of vanadium-oxide cations, dehydration prevails in their ion/molecule reactions with most alcohols investigated. Oxidation of the alcohol can only compete efficiently for methanol and allyl alcohol, for which dehydration is unfavorable. The monoxide $VO^+$ mediates dehydrogenation without changing the metal's oxidation state ($V^{III}$). The reaction with $VO_2^+$ ($V^V$) leads to the very same product ions. The metal therefore is reduced and water instead of hydrogen is formed. Thus, $VO_2^+$ induces an oxidative dehydrogenation of alcohols. During the major pathways of larger alcohols with $VO_2^+$, a pre-equilibrium between alkene and hydroxide complexes is proposed as the relative amount of carbocation vs. alkene formation clearly reflects the respective proton affinities. In contrast to the fragmentation behavior of the alcohol complexes $VO(ROH)^+$, the metastable ion spectra of the isomeric alkoxides $V(OH)(OR)^+$ reveal a preference for dehydrogenation even for alcohols larger than methanol.

## Experimental Section and Computational Details

Ion/molecule reactions were examined with a Spectrospin CMS 47X FT-ICR mass spectrometer equipped with an external ion source as described elsewhere.[32,41] In brief, $V^+$ is generated by laser ablation of a vanadium target using a Nd:YAG laser operating at 1064 nm. A series of potentials and ion lenses is used to transfer the ions into the ICR cell, which is positioned in the bore of a 7.05 T superconducting magnet. Mass-selected $^{51}V^+$ is then converted to $VO^+$ or $VO_2^+$ by reaction with pulsed-in $O_2$ or $N_2O$, respectively.[17,42] During the gas pulses, the ions undergo several hundreds of collisions such that the product ions are assumed to be thermalized.[43] The reactivity of the mass-selected ion of interest was studied by introducing neutral reactants via leak valves at stationary pressures in the order of $10^{-8}$ mbar. The experimental second-order rate constants are evaluated assuming the pseudo first-order kinetic approximation after calibration of the measured pressures and acknowledgement of the ion gauge sensitivities;[44] the error of the absolute rate constants is assumed to be ± 30%, while the error for the relative rate constants is only 10%.

Additional experiments were performed with a modified VG ZAB/HF/AMD 604 four-sector mass spectrometer of BEBE configuration (B stands for magnetic and E for electric sector) which has been described in detail previously.[45] Briefly, cations were generated by chemical ionization (CI) of mixture of $(C_5H_5)V(CO)_4$ and the respective alcohol using $N_2O$ as reagent gas. After acceleration to a kinetic energy of 8 keV, the ions were mass-selected and subjected to metastable ion (MI) and collisional activation (CA) stud-

 © 2007 Wiley-VCH Verlag GmbH & Co. KGaA, Weinheim 

ies. MI spectra of B(1)/E(1) mass-selected ions were recorded by detection of the charged fragments formed unimolecularly in the field-free region between E(1) and B(2) by scanning the latter sector. CA spectra were recorded in the same manner using helium (80% transmission) as a stationary collision gas. As the CA spectra were all dominated by the MI signals, only the MI spectra are discussed here. Nevertheless, the CA spectra confirm that the selected ion really is a vanadium-oxide species as indicated by the presence of signals for $V^+$, $VO^+$, $VOH^+$, $VO_2^+$, $VO_2H^+$ or $VO_2H_2^+$. The error of the reported abundances amounts up to 10% due to low yields in the gas-phase synthesis of the desired complexes.

All unlabeled reagents and $(C_5H_5)V(CO)_4$ were used as purchased and introduced by conventional vacuum techniques. The labeled alcohols were synthesized following well-known laboratory procedures.[27]

All calculations employed the hybrid density-functional theory (DFT) B3LYP method[46] implemented in the Gaussian 98 program package[47] in combination with Ahlrichs' valence triple-ζ basis sets with polarization functions on all atoms[48] which yielded good results in a previous benchmark study of vanadium alkoxides.[9] Vibrational frequencies were computed for all stationary points obtained in order to confirm that each optimized geometry corresponds to a local minimum. All energies given below refer to 0 K and include zero-point energy correction.

## Acknowledgments

Financial support by the Deutsche Forschungsgemeinschaft (SFB 546) and the Fonds der Chemischen Industrie is appreciated. Further, we thank the Konrad-Zuse-Zentrum, Berlin, for generous allocation of computer time.

[1] *Selective Oxidation by Heterogeneous Catalysis* (Eds.: G. Centi, F. Cavani, F. Trifiró), Kluwer Academic/Plenum Publishers, New York, **2001**.
[2] *Appl. Catal. A* **1997**, *175*; the entire volume deals with this topic.
[3] Y. Zhang-Lin, M. Forissier, R. P. Sneeden, J. C. Védrine, J. C. Volta, *J. Catal.* **1994**, *145*, 267–275.
[4] B. M. Weckhuysen, D. E. Keller, *Catal. Today* **2003**, *78*, 25–46.
[5] D. Schröder, H. Schwarz, *Angew. Chem.* **1995**, *107*, 2126–2150; *Angew. Chem. Int. Ed. Engl.* **1995**, *34*, 1973–1995.
[6] D. K. Bohme, H. Schwarz, *Angew. Chem.* **2005**, *117*, 2388–2406; *Angew. Chem. Int. Ed.* **2005**, *44*, 2336–2354; and references cited therein.
[7] K. Koszinowski, D. Schröder, H. Schwarz, *Angew. Chem.* **2004**, *116*, 124–127; *Angew. Chem. Int. Ed.* **2004**, *43*, 121–124.
[8] D. Schröder, H. Schwarz, S. Shaik, *Struct. Bond.* **2000**, *97*, 91–123.
[9] a) D. Schröder, J. Loos, M. Engeser, H. Schwarz, H.-C. Jankowiak, R. Berger, R. Thissen, O. Dutuit, J. Döbler, J. Sauer, *Inorg. Chem.* **2004**, *43*, 1976–1985; b) D. Schröder, M. Engeser, H. Schwarz, E. C. E. Rosenthal, J. Doebler, J. Sauer, *Inorg. Chem.* **2006**, *45*, 6235–6245.
[10] D. Schröder, M. Engeser, M. Brönstrup, C. Daniel, J. Spandl, H. Hartl, *Int. J. Mass Spectrom.* **2003**, *228*, 743–757.
[11] M. Kaczorowska, D. Schröder, H. Schwarz, *Eur. J. Inorg. Chem.* **2005**, 2919–2923.
[12] a) Y. Cao, X. Zhao, B. Xin, S. Xiong, Z. Tang, *J. Mol. Struct. (Theochem)* **2004**, *683*, 141–146; b) D. R. Justes, N. A. Moore, A. W. Castleman Jr, *J. Phys. Chem. B* **2004**, *108*, 3855–3862.
[13] M. Engeser, D. Schröder, H. Schwarz, *Chem. Eur. J.* **2005**, *11*, 5975–5987.
[14] S. Feyel, L. Scharfenberg, C. Daniel, H. Hartl, D. Schröder, H. Schwarz, *J. Phys. Chem. A*; DOI: 10.1021/jp067454o.
[15] Efficiency relative to the gas-kinetic collision rate calculated according to: T. Su, *J. Chem. Phys.* **1988**, *89*, 5355–5356.
[16] J. R. Sambrano, J. Andrés, L. Gracia, V. S. Safont, A. Beltrán, *Chem. Phys. Lett.* **2004**, *384*, 56–62.
[17] G. K. Koyanagi, D. K. Bohme, I. Kretzschmar, D. Schröder, H. Schwarz, *J. Phys. Chem. A* **2001**, *105*, 4259–4271.
[18] See also: C. Trage, M. Diefenbach, D. Schröder, H. Schwarz, *Chem. Eur. J.* **2006**, *12*, 2454–2464.
[19] M. Engeser, M. Schlangen, D. Schröder, H. Schwarz, T. Yumura, K. Yoshizawa, *Organometallics* **2003**, *22*, 3933–3943.
[20] NIST Standard Reference Database: http://webbook.nist.gov/chemistry.
[21] *Lehrbuch der Anorganischen Chemie*, A. F. Hollemann, E. Wiberg, N. Wiberg, 91–100th ed., de Gruyter, Berlin, **1985**, p. 1073.
[22] D. Schröder, R. Wesendrup, C. A. Schalley, W. Zummack, H. Schwarz, *Helv. Chim. Acta* **1996**, *79*, 123–132.
[23] For the sake of simplicity, reaction products with relative abundances below 2% are not listed in Table 2. Therefore, the sum of all entries is lower than 100% in some cases.
[24] J. Loos, D. Schröder, W. Zummack, H. Schwarz, *Int. J. Mass Spectrom.* **2002**, *217*, 169–177, and references therein.
[25] P. A. M. van Koppen, M. T. Bowers, E. R. Fisher, P. B. Armentrout, *J. Am. Chem. Soc.* **1994**, *116*, 3780–3791.
[26] See also: B. Leyh, E. Gridelet, R. Locht, J. C. Lorquet, *Int. J. Mass Spectrom.* **2006**, *249*, 330–339.
[27] See also:a) C. Trage, W. Zummack, D. Schröder, H. Schwarz, *Angew. Chem.* **2001**, *113*, 2780–2782; *Angew. Chem. Int. Ed.* **2001**, *40*, 2708–2710; b) C. Trage, D. Schröder, H. Schwarz, *Organometallics* **2003**, *22*, 693–707.
[28] R. C. Bell, K. A. Zemski, A. W. Castleman Jr, *J. Cluster Sci.* **1999**, *10*, 509–524.
[29] K. Yoshizawa, Y. Kagawa, *J. Phys. Chem. A* **2000**, *104*, 9347–9355.
[30] E. F. Fialko, A. V. Kikhtenko, V. B. Goncharov, *Organometallics* **1998**, *17*, 25–31.
[31] B. A. Rumpf, C. E. Allison, P. J. Derrick, *Org. Mass Spectrom.* **1986**, *21*, 295–299.
[32] K. Eller, W. Zummack, H. Schwarz, *J. Am. Chem. Soc.* **1990**, *112*, 621–627.
[33] H. Schwarz, *Int. J. Mass Spectrom.* **2004**, *237*, 75–105.
[34] L. Gracia, J. R. Sambrano, V. S. Safont, A. Beltrán, *Organometallics* **2004**, *23*, 730–739.
[35] M. Engeser, Dissertation, Logos, Berlin, **2004**.
[36] D. Schröder, M. Engeser, H. Schwarz, J. N. Harvey, *ChemPhysChem* **2002**, *3*, 584–591.
[37] M. Pykavy, C. van Wüllen, *J. Phys. Chem. A* **2003**, *107*, 5566–5572.
[38] L. B. Knight Jr, R. Babb, M. Ray, T. J. Banisaukas III, L. Russon, R. S. Dailey, R. Davidson, *J. Chem. Phys.* **1996**, *105*, 10237–10250.
[39] M. Calatayud, B. Silvi, J. Andrés, A. Beltrán, *Chem. Phys. Lett.* **2001**, *333*, 493–503.
[40] S. F. Vyboishchikov, J. Sauer, *J. Phys. Chem. A* **2001**, *105*, 8588–8598.
[41] K. Eller, H. Schwarz, *Int. J. Mass Spectrom. Ion Processes* **1989**, *93*, 243–257.
[42] J. N. Harvey, M. Diefenbach, D. Schröder, H. Schwarz, *Int. J. Mass Spectrom.* **1999**, *182/183*, 85–97.
[43] D. Schröder, H. Schwarz, D. E. Clemmer, Y.-M. Chen, P. B. Armentrout, V. I. Baranov, D. K. Böhme, *Int. J. Mass Spectrom. Ion Processes* **1997**, *161*, 175–191.
[44] J. E. Bartmess, R. M. Georgiadis, Vacuum **1983**, *33*, 149–153.
[45] C. A. Schalley, D. Schröder, H. Schwarz, *Int. J. Mass Spectrom. Ion Processes* **1996**, *153*, 173–199.
[46] a) C. Lee, W. Yang, R. G. Parr, *Phys. Rev. B* **1988**, *37*, 785–789; b) B. Miehlich, A. Savin, H. Stoll, H. Preuss, *Chem. Phys. Lett.* **1989**, *157*, 200–206; c) A. D. Becke, *J. Chem. Phys.* **1993**, *98*, 5648–5652.
[47] M. J. Frisch, G. W. Trucks, H. B. Schlegel, G. E. Scuseria, M. A. Robb, J. R. Cheeseman, V. G. Zakrzewski, J. A. Mont-

 © 2007 Wiley-VCH Verlag GmbH & Co. KGaA, Weinheim 

gomery, R. E. Stratmann, J. C. Burant, S. Dapprich, J. M. Millam, A. D. Daniels, K. N. Kudin, M. C. Strain, O. Farkas, J. Tomasi, V. Barone, M. Cossi, R. Cammi, B. Mennucci, C. Pomelli, C. Adamo, S. Clifford, J. Ochterski, G. A. Petersson, P. Y. Ayala, Q. Cui, K. Morokuma, D. K. Malick, A. D. Rabuck, K. Raghavachari, J. B. Foresman, J. Cioslowski, J. V. Ortiz, B. B. Stefanov, G. Liu, A. Liashenko, P. Piskorz, I. Komaromi, R. Gomperts, R. L. Martin, D. J. Fox, T. Keith, M. A. Al-Laham, C. Y. Peng, A. Nanayakkara, C. Gonzalez, M. Challacombe, P. M. W. Gill, B. G. Johnson, W. Chen, M. W. Wong, J. L. Andres, M. Head-Gordon, E. S. Replogle, J. A. Pople, *Gaussian 98* (Revision A.7), Gaussian, Inc., Pittsburgh, PA, **1998**.

[48] A. Schäfer, C. Huber, R. Ahlrichs, *J. Chem. Phys.* **1994**, *100*, 5829–5835.

[49] M. W. Chase Jr, *J. Phys. Chem. Ref. Data* **1998**, *9*, 1–1951.

[50] J. Berkowitz, G. B. Ellison, D. Gutman, *J. Phys. Chem.* **1994**, *98*, 2744–2765.

[51] J. Harrington, J. C. Weisshaar, *J. Chem. Phys.* **1992**, *97*, 2809–2812.

[52] D. E. Clemmer, N. Aristov, P. B. Armentrout, *J. Phys. Chem.* **1993**, *97*, 544–552.

[53] S. G. Lias, J. E. Bartmess, J. F. Liebman, J. L. Holmes, R. D. Levin, W. G. Mallard, *J. Phys. Chem. Ref. Data* **1988**, *17*, Suppl. 1.

[54] X. Zhong, J. W. Bozzelli, *Int. J. Chem. Kinet.* **1997**, *29*, 893–913.

Received: January 18, 2007
Published Online: April 26, 2007

 © 2007 Wiley-VCH Verlag GmbH & Co. KGaA, Weinheim 

DOI: 10.1002/ejic.200600908

# On In Situ Prepared Cu–Phenanthroline Complexes in Aqueous Alkaline Solutions and Their Use in the Catalytic Oxidation of Veratryl Alcohol

**Heikki Korpi,[a] Paweł J. Figiel,[a] Elina Lankinen,[a] Paul Ryan,[a] Markku Leskelä,[a] and Timo Repo*[a]**

**Keywords:** Catalysis / Copper / Dioxygen / Active species / Oxidation

The in situ prepared complex based on copper(II) sulfate and 1,10-phenanthroline (phen) and its performance in the catalytic oxidation of veratryl alcohol (3,4-dimethoxybenzyl alcohol) to veratraldehyde with $O_2$ in alkaline aqueous solutions have been studied. In aqueous solution, the structure of Cu–phen complexes varies with reaction conditions; by changing either the copper-to-ligand molar ratio or the pH, the amount of coordinated 1,10-phenanthroline and hydroxido ligands in the coordination sphere of copper can be altered in a controlled manner. The highest activities are achieved in the pH range 12.6–13.3, which correlates with the presence of the [Cu(phen)$(OH)_2$] species according to complex distribution curves. According to the UV/Vis and EPR studies, the oxidation reaction is initiated by the reduction of [Cu(phen)$(OH)_2$] to $Cu^I$ species by veratryl alcohol, which can be seen as a disappearance of the $Cu^{2+}$ EPR signal and as a shift of the UV/Vis absorbance maximum from about 690 nm to the 410 and 525 nm regions. When molecular oxygen is added, the $Cu^I$ species is readily oxidised back to $Cu^{II}$ species, and the catalytic formation of aldehyde is initiated. On the basis of these observations, a mechanism for the catalytic oxidation is proposed.
(© Wiley-VCH Verlag GmbH & Co. KGaA, 69451 Weinheim, Germany, 2007)

## Introduction

Selective oxidation of alcohols to the corresponding aldehydes, ketones and acids finds its importance in the pharmaceutical industry as well as in the large-scale chemical industry. For further development of these applications towards more sustainable processes, the use of aqueous solutions and molecular oxygen as a cheap, easily available and environmentally friendly oxidant would be highly beneficial.[1]

(Diimine)copper complexes with different polypyridyl ligands like 2,2′-bipyridine (bipy) and 1,10-phenanthroline (phen) have been studied as catalysts in the oxidation of primary alcohols since the 1970s.[2,3] Because of their potency to activate molecular oxygen, various applications have been developed including (diimine)copper-catalysed DNA scission,[4] oxidation reactions[2,3] and pulp bleaching.[5,6] Lately, highly active catalysts combining Cu–diimine complexes and TEMPO,[7] $DEADH_2$ (= diethylhydrazine dicarboxylate) or $DBADH_2$ (= di-*tert*-butylhydrazine dicarboxylate)[8] as co-activators have been reported for the oxidation of primary and secondary alcohols to corresponding aldehydes and ketones by air. In addition to the diimine-based catalysts, efficient copper phenoxyl radical catalysts have recently been introduced for the oxidation of alcohols.[9,10]

We recently reported that various in situ prepared (diimine)copper complexes catalyse selective oxidation of veratryl alcohol in aqueous solutions.[6,11] However, the alkaline reaction conditions needed for high catalytic activity together with the presence of paramagnetic Cu species reduce the choice of the analytical methods that can be used to elucidate the solution structures of the complexes and their catalytic reactions. By combining UV/Vis measurements with EPR spectroscopy, complementary pH and GC monitoring of the reaction, consistent information about the catalyst structure and the oxidation reaction were gathered. As a result of these measurements, we report herein the studies of the structure of an in situ prepared (phenanthroline)copper(II) complex under alkaline conditions and its use in the catalytic oxidation reaction.

## Results and Discussion

### The Nature of In Situ Prepared $Cu^{II}$ Complexes

UV/Vis spectroscopy is a method that is widely used to investigate qualitative as well as quantitative changes in the coordination sphere of transition-metal complexes, and extensive studies on $Cu^{II}$ species in aqueous media have been reported. In fact, the first visible spectra of (diimine)copper complexes were reported already in the 1950s[12] followed by numerous studies elucidating the structures of these complexes and their spectroscopic properties.[13a] Because of the available data and simple sample preparation, we

[a] Laboratory of Inorganic Chemistry, Department of Chemistry, P. O. Box 55, 00014 University of Helsinki, Finland
Fax: +358-9-191-50198
E-mail: timo.repo@helsinki.fi

 © 2007 Wiley-VCH Verlag GmbH & Co. KGaA, Weinheim 

Table 1. Main UV/Vis absorbances of selected Cu–phen complexes at a copper concentration of 0.01 M.

| Molar ratio M/L | $[OH^-]$ /M | $\lambda_{max}$ /nm | $\varepsilon_{max}$ /$M^{-1}cm^{-1}$ | Main species |
|---|---|---|---|---|
| $CuSO_4$ | – | 800 | 12 | $[Cu(H_2O)_6]^{2+}$ |
| 1:1 | – | 710 | 12 | $[Cu(phen)]^{2+}$, $Cu(phen)SO_4$ precipitates |
| 1:2 | – | 720, ≈920 | 57 | $[Cu(phen)_2]^{2+}$ |
| 1:4 | – | 680 | 46 | $[Cu(phen)_3]^{2+}$ |
| 1:1 | 0.05 | 660 | 45 | $[Cu(phen)(OH)]_2^{2+}$ |
| 1:2 | 0.01–0.05 | 690, ≈920 | 55 | $[Cu(phen)_{2-3}]^{2+}$, $[Cu(phen)(OH)_2]$ |
| 1:2 | 0.1–0.5 | 690 | 44 | $[Cu(phen)(OH)_2]$ |
| 1:2 | 0.5–2.0 | 620–600 | 40–38 | $[Cu(OH)_4]^{2-}$ |
| 1:4 | 0.05 | 690, ≈920 | 56 | $[Cu(phen)_{2-3}]^{2+}$, $[Cu(phen)(OH)_2]$ |

found UV/Vis spectroscopy to be a useful method to investigate these efficient in situ prepared Cu–phenanthroline catalysts under alkaline conditions.

When reaction conditions are varied, the formation of different Cu–phen complexes in aqueous solutions is fast and reversible. In pure aqueous solution, copper(II) sulfate forms a light blue (aqua)copper complex, $[Cu(H_2O)_6]^{2+}$ (Figure 1, species A), which has a wide absorbance maximum at the 800-nm region (Table 1). When one equivalent of the phenanthroline ligand is added, the absorbance is shifted to 710 nm and light blue $Cu(phen)SO_4$ precipitates. Addition of a second equivalent of the ligand dissolves this precipitate and forms a $[Cu(phen)_2]^{2+}$ complex in which either a sulfate anion or water molecules complete the coordination sphere of copper. This solution has its main peak in the 720-nm region, while another peak/shoulder is observed at 920 nm (Figure 1, species B). When more than two equivalents of phenanthroline are added, a tris(chelated) $[Cu(phen)_3]^{2+}$ complex (Figure 1, species C) becomes the major species in neutral solution, the absorbance maximum is shifted to 680 nm and the shoulder at 920 nm assigned to the $[Cu(phen)_2]^{2+}$ complex disappears.

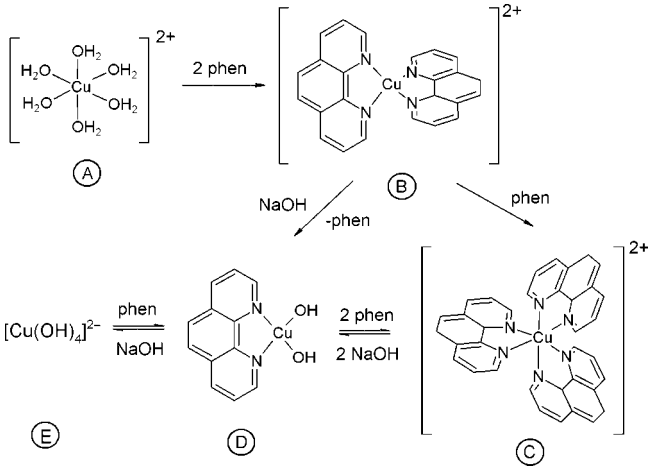


Figure 1. Formation of the catalytically active species D. The amount of coordinated phenanthroline and hydroxido ligands (marked as phen and NaOH) can be controlled by varying the concentration.

The $Cu(phen)SO_4$ precipitate can also be dissolved with an addition of sodium hydroxide (0.05 M), which leads to the formation of a dark blue solution with an absorbance maximum at around 660 nm. According to the distribution plots, the $[Cu(phen)(OH)]_2^{2+}$ dimer is the major component in this solution (Figure 2A). Similar spectra have previously been measured for isolated dihydroxido-bridged Cu–phen complexes.[14] Apparently, in alkaline conditions, the system studied becomes dynamic, and as a result, the $\lambda$ values are rather a sum of different species than those for one independent complex in the solution.

Addition of 0.05 M NaOH to the $[Cu(phen)_2]^{2+}$ solution leads readily to the formation of the $[Cu(phen)(OH)_2]$ complex, and the main absorbance maximum is shifted to a wavelength of 690 nm (Figure 2B and Figure 1, species D). Similarly, when $OH^-$ is added to a $[Cu(phen)_3]^{2+}$ solution, the absorbance maximum is again shifted to 690 nm (Figure 1, species D), indicating the replacement of two phenanthroline ligands by hydroxido ligands and formation of the $[Cu(phen)(OH)_2]$ species. Increasing the $OH^-$ concentration above 0.5 M shifts the absorbance maximum towards shorter wavelengths as the coordinated phenanthroline ligand is replaced by hydroxido ligands (Figure 1, species E, Figure 2). On the basis of the above results, it is obvious that, by varying hydroxide ion and ligand concentrations, the amount of coordinated phenanthroline and hydroxido ligands can be controlled. These observations are comparable with the studies of Garribba et al., in which they demonstrated by UV/Vis and EPR spectroscopic measurements how the structure of the (2,2′-bipyridine)copper complex changes in alkaline solutions.[13a]

Our previous oxidation studies have revealed that the catalytic activity of these in situ prepared copper complexes is significantly dependent on the applied pH and the ligand concentration.[6,11] The stability constant of a complex determines the optimum copper-to-ligand molar ratio at a chosen $OH^-$ concentration, and thus strongly coordinating phenanthroline has maximum activity at the copper/ligand molar ratio 1:5 at high pH (>12.6; 0.05 M NaOH). Under these optimised reaction conditions, the $[Cu(phen)(OH)_2]$ complex is the predominant species (the absorbance maximum of the solution is at about 690 nm) and seems to be responsible for the catalytic activity (Figure 2C). When the copper/ligand molar ratio 1:2 is employed, $OH^-$ concentrations above 0.05 M shift the absorbance maximum towards shorter wavelengths as a result of complex decomposition and $Cu(OH)_4^{2-}$ formation (Figure 2B). However, when the optimised copper/ligand molar ratio is applied, the absorption maximum at 690 nm remains until the $OH^-$ concentration exceeds 0.5 M. While the high pH is a prerequisite for

 © 2007 Wiley-VCH Verlag GmbH & Co. KGaA, Weinheim 

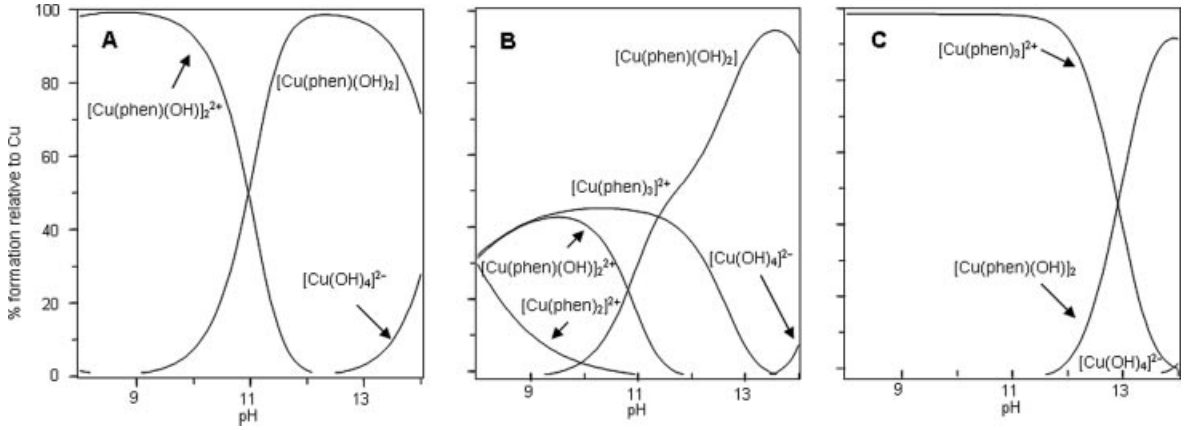


Figure 2. Complex distribution curves for (phenanthroline)copper complexes in alkaline water solutions. Calculated for [Cu] = 0.01 M, ionic strength = 0.1 M, Cu/phen = 1:1 (A), 1:2 (B) and 1:4 (C). See the Experimental Section for details.

the efficiency of the oxidation reaction, the role of the ligand excess is, according to these results, to protect the [Cu(phen)(OH)$_2$] complex from the destructive coordination of a hydroxide ion.

### Isolated [Cu(phen)$_2$]$^{2+}$ Complex

When the authentic catalyst solution is allowed to stand in an open vessel, the Cu(phen)$_2$CO$_3$·7H$_2$O complex crystallises out as a result of the slow evaporation of water. X-ray crystallographic analysis of the crystals revealed that the coordination polyhedron of the copper atom has a square pyramidal geometry as reported previously by van Eldik et al. (cell parameters are given in the Experimental Section).[15] In the complex, the OH$^-$ ligand is replaced by a carbonate anion as a consequence of $CO_2$ dissolution during the crystallisation procedure (Figure 3).

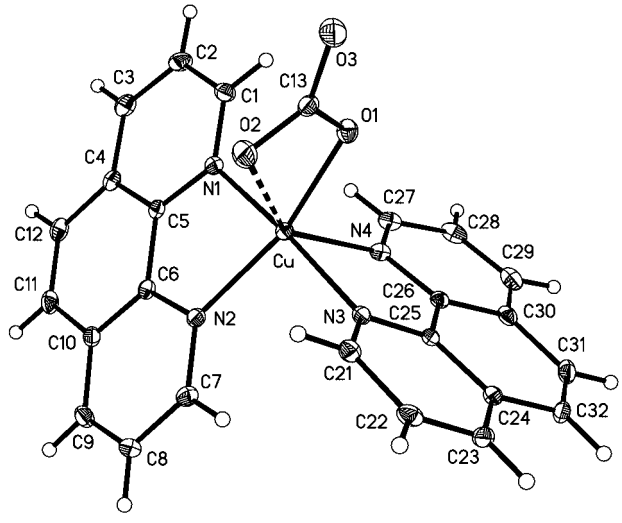


Figure 3. Solid-state structure of Cu(phen)$_2$CO$_3$ which crystallised out from the authentic catalyst solution kept in an open vessel.

The isolated Cu(phen)$_2$CO$_3$ complex behaves quite similarly to the in situ prepared catalyst upon variation of the reaction conditions. When the Cu(phen)$_2$CO$_3$ complex is dissolved in water, an absorbance maximum appears in the visible spectrum at 680 nm, while addition of excess ligand (total M/L molar ratio 1:4) to the solution removes the carbonate anion from the coordination sphere of copper, and the $\lambda_{max}$ of [Cu(phen)$_3$]$^{2+}$ appears. In alkaline solution (0.05 M), the absorbance maximum of the isolated complex is shifted to 690 nm, which indicates the formation of the [Cu(phen)(OH)$_2$] complex. In highly basic conditions, the absorbance maximum is shifted to shorter wavelengths as the phenanthroline ligand is replaced by a hydroxide ion. Analogously, in oxidation experiments at pH 12.6, the addition of free ligand to the Cu(phen)$_2$CO$_3$ solution enhanced the catalytic activity.[16]

### Reaction Monitoring by pH and GC Analysis

The oxidation of veratryl alcohol with Cu–phen catalyst was monitored with parallel pH and GC analysis in order to determine any possible correlations between aldehyde formation and the consumption of hydroxide ions. In these reactions, an initial pH of 11.6 (0.005 M NaOH) was applied, as even modern pH electrodes seem to be too inaccurate for such a study at pH values higher than 12. During the first 20 min of the reaction the pH decreases rapidly. This decrease is mainly related to the initiation of the catalytic reaction. In general, veratryl alcohol oxidation and OH$^-$ consumption proceed parallel to one another (Figure 4); the actual molar ratio of these two species is around 10. After 2 h, the pH is reduced to around 10 and the oxidation decelerates. The reaction rate can be increased again by the addition of NaOH (marked in Figure 4). The high aldehyde/OH$^-$ ratio indicates that, after initiation, the catalytic oxidation reaction itself does not consume OH$^-$ ions. A possible reason for the minor OH$^-$ consumption during the reaction is the formation of a hydroperoxyl radical, which consumes base when forming the superoxide radical anion.[17] Another reason for the decrease in pH is the formation of traces of veratric acid as detected by GC–MS.

 © 2007 Wiley-VCH Verlag GmbH & Co. KGaA, Weinheim 

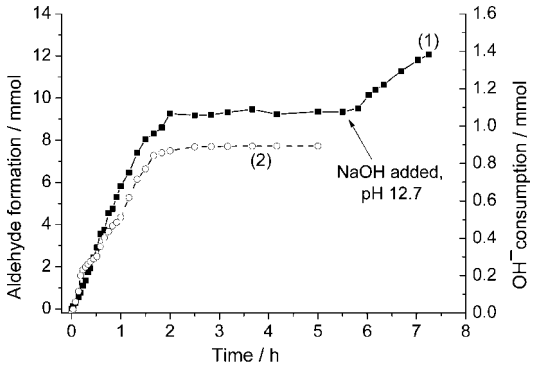


Figure 4. Rate of oxidation and total $OH^-$ consumption in the Cu–phen-catalysed reaction: (1) formation of veratraldehyde and (2) consumption of $OH^-$ ions. Reaction conditions: 80 °C, 10 bar $O_2$, initial pH 11.6, Cu/veratryl alcohol molar ratio 1:500.

### Visible Spectrum of $Cu^I$–phen

A copper(I) complex prepared from $Cu_2O$ and phenanthroline gives a dark red solution in alkaline aqueous media under an argon atmosphere. In solution, the bis(phenanthroline)copper(I) should possess nearly regular $D_{2d}$ symmetry.[18,19] As a result of the presence of the low-energy π* orbitals of the phenanthroline ligand, the complex exhibits strong metal-to-ligand charge-transfer absorption bands in the visible spectrum (Figure 5). The absorption involves the transfer of an electron from the d shell of the copper centre to π* orbitals of the coordinated ligand. Solutions of the $Cu^I$–phen complex can be stored under argon, but are oxidised to $[Cu(phen)(OH)_2]$ by oxygen after a few minutes as the absorbances maxima at 405 and 535 nm disappear and that at 690 nm strengthens. This process is assisted by hydrogen peroxide formation; when a solution of the bis(phenanthroline)copper(I) complex was exposed to air, small amounts (≈2 mg $L^{-1}$) of $H_2O_2$ were detected.[20] In conclusion, changes in the oxidation state of copper can be determined in the visible region as $Cu^I$ and $Cu^{II}$ species have characteristic absorbances at different wavelengths.

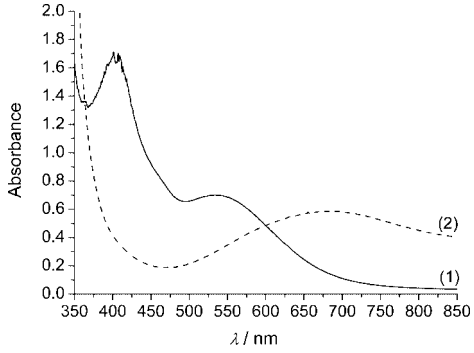


Figure 5. UV/Vis spectrum of $[Cu(phen)_2]^+$ oxidation by $O_2$: (1) the spectrum of the complex under an argon atmosphere, (2) the spectrum after $O_2$ bubbling. The $Cu^I$ sample was diluted for the measurement. Conditions: 25 °C, [NaOH] 0.05 M, [Cu] 0.01 M.

### Reaction Monitoring by UV/Vis Spectroscopy

UV/Vis spectroscopy turned out to be highly useful for monitoring the reaction. The addition of veratryl alcohol to an alkaline catalyst solution results in the formation of small absorption bands in the 410 and 525 nm regions, which indicates the presence of the $Cu^I$ species. The reduction of $Cu^{II}$ is seen more clearly when the reaction is carried out under an argon atmosphere (Figure 6, spectra 1–3); the absorbance maximum at 690 nm decreases while absorbances at 410 nm and 525 nm increase. Upon addition of oxygen, the characteristic absorbance maximum of the $Cu^{II}$ species increases again (spectra 4–5).

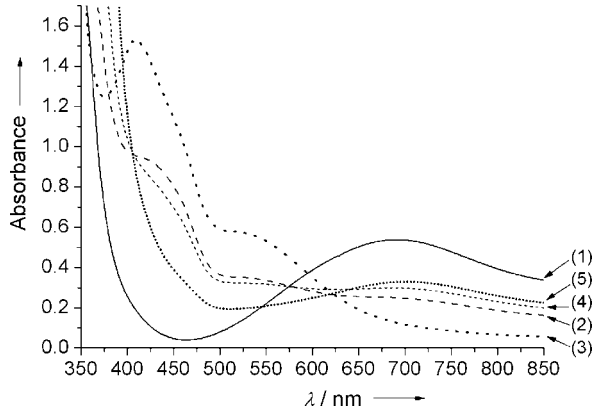


Figure 6. A UV/Vis spectrum of $Cu^{II}$ reduction to $Cu^I$ by alcohol under argon and reoxidation after oxygen addition. (1) $Cu^{II}$–phen complex under argon, (2) veratryl alcohol added, (3) 60 h under argon, (4) 1 h after $O_2$ addition, 18% aldehyde (5) 23 h, 93% aldehyde. Reaction conditions: 80 °C, 1 bar $O_2$, pH 12.6, [Cu] 0.01 M, Cu/veratryl alcohol molar ratio 1:20. The $Cu^I$ samples were diluted for the measurement.

A small percentage of aldehyde (4%) can be detected when a 10 mol-% loading of Cu vs. alcohol is used under an argon atmosphere. In these conditions, the Cu/aldehyde ratio is 2.5, which indicates that two electrons are involved in veratryl alcohol oxidation. However, significant aldehyde formation only begins after the addition of oxygen. If $Cu^I$–phen (prepared from $Cu_2O$ and phen) is used in the reaction in place of $Cu^{II}$–phen, no aldehyde is formed under an argon atmosphere. This shows that the alcohol is able to reduce copper(II) under anaerobic conditions, and the catalytic cycle begins when oxygen is added. If the reaction solution is degassed and set under an argon atmosphere again, the colour changes to dark brown, and the absorbances of $Cu^I$ strengthen again.

Formation of the $Cu^I$ species has also been observed in the oxidation of benzyl alcohol with $[Cu(bipy)_2]^{2+}$ catalyst, but it was concluded that in acetonitrile solution the $Cu^I$ species inhibits the oxidation while the actual catalysis proceeds via $Cu^{III}$ intermediates.[2f] However, under the applied reaction conditions here, the reduction of $Cu^{II}$ to $Cu^I$ is a prerequisite for the formation of aldehyde, and during the reaction both $Cu^I$ and $Cu^{II}$ complexes are present. In this respect, the redox behaviour of the Cu species resembles that observed by Tretyakov et al. for the oxidation of propanol.[3]

 © 2007 Wiley-VCH Verlag GmbH & Co. KGaA, Weinheim 

### EPR Studies

The EPR spectrum of the in situ prepared $Cu^{II}$–phen complex in alkaline medium at room temperature is shown in Figure 7a. The typical four-line Cu hyperfine split signal (without sfhs from N atoms) with $g_{\|} = 2.33$, $g_{\perp} = 2.06$ and hfs constant $A_{\|} = 75$ G is in good agreement with previous reports for $Cu^{II}$–diamine tetragonal complexes with ground state $d_{x^2-y^2}$.[13]

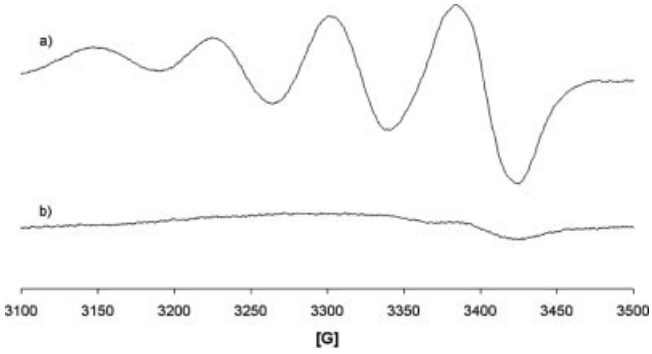


Figure 7. X-band EPR spectrum of the reduction of $Cu^{II}$ to $Cu^{I}$ by alcohol under nitrogen, (a) $Cu^{II}$–phen complex under nitrogen, (b) excess veratryl alcohol added. Reaction conditions: room temp., pH 12.6, [Cu] = 0.01 M, Cu/veratryl alcohol molar ratio ca. 1:200.

The addition of an excess of veratryl alcohol (alcohol/[Cu]: c.a. 200) to the $Cu^{II}$–phen complex solution in the absence of oxygen (nitrogen atmosphere) results in the disappearance of the $Cu^{II}$ signal (Figure 7b). This suggests that alcohol can reduce the $Cu^{II}$–phen complex to an EPR-silent $Cu^{I}$ ($d^{10}$) species. An identical solution of the $Cu^{II}$–phen complex in alkaline medium containing an excess of veratryl alcohol exposed to air under the same conditions exhibits no reduction of $Cu^{II}$ to $Cu^{I}$. These EPR spectroscopic observations confirm the previous UV/Vis spectroscopic interpretations (see previous section).

### Catalytically Active Species

The correlation between the catalytic activity and absorbance of the in situ prepared complex in alkaline aqueous solution indicates that high pH and the presence of the $[Cu(phen)(OH)_2]$ complex are essential for catalytic activity. As demonstrated above, in the presence of hydroxide ions and veratryl alcohol, the $[Cu^{II}(phen)(OH)_2]$ species is reduced by veratryl alcohol to $[Cu^{I}(phen)(OH)]$ [Equation (1)]. Consequently, in the absence of oxygen, the formation a small percentage of aldehyde is observed at low copper/alcohol ratios (1:10). In neutral or acidic solutions, neither catalyst reduction nor aldehyde formation was observed.

The $Cu^{I}$–phen complex formed is oxidised to $Cu^{II}$–phen species by oxygen as shown in Figure 5. In this process, hydrogen peroxide is formed even in the absence of veratryl alcohol [Equation (2)]. As shown in Figure 1 and Figure 2, the coordination sphere of the $Cu^{II}$ complex is balanced by a dynamic self-assembly process under alkaline conditions, and the formation of initial species, $Cu^{II}(phen)(OH)_2$ is feasible [Equation (3)].

$$2[Cu^{(II)}(phen)(OH)_2] + RCH_2OH \longrightarrow 2[Cu^{(I)}(phen)(OH)] + RCHO + 2H_2O \quad (1)$$

$$2[Cu^{(I)}(phen)(OH)] + O_2 + 2H_2O \longrightarrow 2[Cu^{(II)}(phen)(OH)] + H_2O_2 + 2OH^- \quad (2)$$

$$2[Cu^{(II)}(phen)(OH)] + 2\ OH^- \longrightarrow 2[Cu^{(I)}(phen)(OH)_2] \quad (3)$$

$$\text{overall: } RCH_2OH + O_2 \longrightarrow RCHO + H_2O_2 \quad (4)$$

On the basis of these results, a proposed mechanism for the Cu–phen-catalysed oxidation reaction is summarised in Figure 8. Unfortunately, direct spectroscopic evidence for the short-lived intermediates in the catalytic cycle is not available. Therefore, it can not be excluded that, under alkaline conditions, an alcohol molecule could also coordinate to the $[Cu^{I}(phen)(OH)]$ complex to form a $Cu^{I}$–alkoxide complex, which converts alcohol to aldehyde via a copper(II) alkoxide peroxo species. Also in this pathway hydrogen peroxide is released, but $Cu^{I}$ works as the actual catalyst. The formation of hydrogen peroxide with the catalyst but in the presence of alcohol has also been shown earlier.[21] However, all of the experimental observations, such as the reduction of $Cu^{II}$ by alcohol, the minor $OH^-$ consumption during the catalytic cycle, the oxidation of $Cu^{I}$ by oxygen and the formation of hydrogen peroxide even in the absence of alcohol can be reasonably explained by the proposed mechanism in Figure 8. After all, the proposed catalytic cycle has similarities with a ping-pong mechanism proposed previously for galactose oxidase.[22]

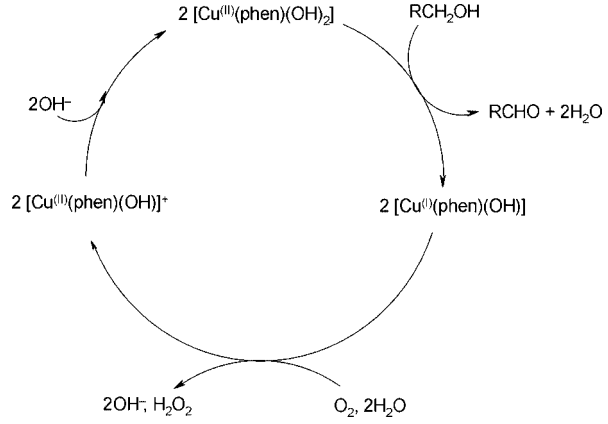


Figure 8. The proposed catalytic cycle for the oxidation of veratryl alcohol in alkaline media with the in situ prepared Cu–phen catalyst by using dioxygen as the end-oxidant.

## Conclusions

In alkaline aqueous solution, in situ addition of copper sulfate to phenanthroline leads to the formation of various complexes by a self-assembly process depending on the $OH^-$ concentration and phenanthroline-to-copper molar ratio. The dynamic changes in the coordination sphere of the

 © 2007 Wiley-VCH Verlag GmbH & Co. KGaA, Weinheim 

catalyst upon variation of the reaction conditions were identified by UV/Vis spectroscopy and verified with the complex distribution curves. As the ligand concentration and pH are interdependent, under optimum reaction conditions the $OH^-$ concentration needs to be adequate for efficient alcohol oxidation, and the phenanthroline concentration should be high enough to preserve the structure of the $[Cu(phen)(OH)_2]$ species, whose presence is essential for high catalytic activity.

Under alkaline conditions and in the presence of veratryl alcohol, $[Cu^{II}(phen)(OH)_2]$ is reduced to the $[Cu^{I}(phen)(OH)]$ species. When oxygen is added, the $Cu^{I}$ species is readily oxidised back to the $Cu^{II}$ species, and the catalytic formation of aldehyde is initiated. The catalytic reaction was further studied by combining pH and gas chromatographic monitoring with UV/Vis and EPR spectroscopy. On the basis of these results, a catalytic cycle for the oxidation of veratryl alcohol was proposed.

## Experimental Section

Commercially available copper sulfate, 1,10-phenanthroline and veratryl alcohol (3,4-dimethoxybenzyl alcohol, 96%) were used without further purification. Deionised water and oxygen (AGA 99.5) were used for the reactions.

### pH and Oxidation Monitoring

For the pH and gas chromatographic reaction monitoring, veratryl alcohol (4.0 mL, 27.5 mmol) and catalyst in a molar ratio of 1:500 (0.055 mmol) to veratryl alcohol were mixed in NaOH solution (200 mL). A copper/phenanthroline molar ratio of 1:2 was used. A 400-mL glass vessel with a magnetic stirring bar was fitted inside a 1-L steel autoclave, and the desired oxygen pressure (10 bar) and temperature (80 °C) were set. Samples were taken from the reactor and cooled to room temperature. The pH was measured, and a sample was prepared for GC analysis by a method described earlier (extraction with ethyl acetate) and analysed with GC/FID Agilent 6890N using an HP-5 30 m × 320 μm × 0.25 μm capillary column.[11] After extraction, the aldehyde was the only product. However, if alcohol conversions were remarkably high, also a small amount of veratric acid (< 1%) was detected by HPLC analysis.

### UV/Vis Spectroscopy

UV/Vis spectroscopic measurements were carried out with a HP 8453 spectrophotometer, and the data was analysed with UV/Vis ChemStation software. To see the changes in the visible region of the UV/Vis spectra, high catalyst concentrations (0.01 M) were used. For a usual reaction $CuSO_4$ (0.160 g, 1.0 mmol), 1,10-phenanthroline (0.3965 g, 2.0 mmol) and veratryl alcohol (2.9 mL, 20 mmol) were mixed in $H_2O$ (100 mL). In the oxidation reactions monitored with UV/Vis spectroscopy, the oxygen atmosphere was maintained by using a balloon of oxygen. For the $Cu^{I}$ species, the samples were diluted to 0.001–0.0015-M solutions (of copper) with degassed solvent. Complex distribution charts (Figure 2) were calculated by using the HySS program.[23] Stability constants for the relevant species were obtained from the NIST Standard Reference Database 46.[24]

### EPR Spectroscopy

For an EPR experiment, a solution of Cu–phenanthroline complex (0.01 M) in NaOH (0.05 M) was prepared from $CuSO_4$ (0.016 g, 0.1 mmol) and 1,10-phenanthroline (0.0396 g, 0.2 mmol) in $H_2O$ (10 mL). To observe the decay of the $Cu^{II}$ signal, veratryl alcohol (2.9 mL, 20 mmol) was mixed with the Cu–phenanthroline complex. Samples were degassed with flow of nitrogen gas (30 min) and contained in quartz capillary tubes.

X-band EPR spectra were measured with a Bruker ESP 300E spectrophotometer equipped with the Bruker NMR gaussmeter ER035 M and the Hewlett–Packard microwave frequency counter with 100-kHz field modulation and a microwave power of 20 mW at room temperature. The data obtained was analysed with Bruker WinEPR software.

### Isolated $Cu(phen)_2CO_3·7H_2O$

Crystallisation of the Cu–phen complex was achieved by dissolving $CuSO_4$ (0.10 g, 0.63 mmol) and 1,10-phenanthroline (0.25 g, 1.26 mmol) in NaOH solution (0.05 M). Slow evaporation of water in room temperature yielded blue crystals of $Cu(phen)_2CO_3·7H_2O$. Crystal data for $C_{25}H_{30}CuN_4O_{10}$: $M_r$ = 610.07, space group $P2_1/c$, $a$ = 9.87930(10), $b$ = 26.2067(3), $c$ = 10.49350(10) Å, $\beta$ = 105.8390(10)°, $V$ = 2613.66(5) Å$^3$, $Z$ = 4, $D_c$ = 1.550 g cm$^{-3}$, $\mu$(Mo-$K_\alpha$) = 0.901 mm$^{-1}$, $T$ = 120(2) K, 5984 reflections measured, $F^2$ refinement, $R_1$ = 0.0555, $wR_2$ = 0.0856, 4647 independent observed absorption-corrected reflections, 363 parameters.

## Acknowledgments

The financial support from the University of Helsinki, the National Technology Agency of Finland (Tekes), the Academy of Finland (project no. 204408), M-real Oyj, UPM-Kymmene Oyj, Stora Enso Oyj, Andritz Oy and Kemira Oyj are gratefully acknowledged. We also thank Prof. Ahlgren (University of Joensuu) and Mika Polamo (University of Helsinki) for the X-ray measurement, and Mrs. J. Kędzierska (University of Wrocław, Poland) for help in EPR measurements.

[1] P. T. Anastas, J. C. Warner, *Green Chemistry*, Oxford University Press, Oxford, **1998**.
[2] a) C. Jallabert, H. Riviere, *Tetrahedron Lett.* **1977**, *18*, 1215–1218; b) C. Jallabert, C. Lapinte, H. Riviere, *J. Mol. Catal.* **1980**, *7*, 127–136; c) M. Munakata, S. Nishibayashi, H. Sakamoto, *J. Chem. Soc., Chem. Commun.* **1980**, 219–220; d) P. Capdevielle, D. Sparfel, J. Baranne-Lafont, N. Cuong, M. J. Maumy, *J. Chem. Res. Synop.* **1993**, 10–11; e) I. Skibida, A. Sakharov, *Catal. Today* **1996**, *27*, 187–193; f) X. Liu, A. Qiu, D. Sawyer, *J. Am. Chem. Soc.* **1993**, *115*, 3239–3243.
[3] a) V. P. Tretyakov, E. S. Rudakov, V. V. Chudaev, G. P. Zimtseva, *React. Kinet. Catal. Lett.* **1982**, *21*, 391–396; b) V. P. Tretyakov, V. V. Chudaev, E. S. Rudakov, E. S. Anufrienko, V. F. Poluboyarov, N. V. Ryabtseva, *Ukr. Khim. Zh. (Russ. Ed.)* **1985**, *51*, 10–13; c) V. P. Tretyakov, V. V. Chudaev, G. P. Zimtseva, *Ukr. Khim. Zh. (Russ. Ed.)* **1985**, *51*, 942–946.
[4] a) D. S. Sigman, A. Mazumder, D. M. Perrin, *Chem. Rev.* **1993**, *93*, 2295–2316; b) C. Chi-hong, L. Milne, R. Landgraf, D. M. Perrin, D. S. Sigman, *ChemBioChem* **2001**, *2*, 735–740; c) D. R. McMllin, K. M. McNett, *Chem. Rev.* **1998**, *98*, 1201–1219; d) C. X. Zhang, H.-C. Liang, K. J. Humphreys, K. D. Karlin, *Catalysis by Metal Complexes, Vol. 26* (Ed.: L. Simandi), Kluwer Academic Publishers, Dordrecht, **2003**, pp. 111–121.
[5] a) E. Germer, *Proceedings of the Fifth European Workshop on Lignocellulosics and Pulp*, University of Aveiro, Portugal, August 30 – September 2, **1998**, 33–38; b) E. Germer, *Proceedings of the International Pulp Bleaching Conference*, Halifax, Canada, June 27-30, **2000**, 55–56; c) E. Germer, *Tappi J.* **1995**, *78*, 121–124.
[6] H. Korpi, P. Lahtinen, V. Sippola, O. Krause, M. Leskelä, T. Repo, *Appl. Catal.* **2004**, *268*, 199–206.

 © 2007 Wiley-VCH Verlag GmbH & Co. KGaA, Weinheim 

[7] a) P. Gamez, I. W. C. E. Arends, J. Reedijk, R. A. Sheldon, *Chem. Commun.* **2003**, 2414–2415; b) P. Gamez, I. W. C. E. Arends, R. A. Sheldon, J. Reedijk, *Adv. Synth. Catal.* **2004**, *346*, 805–811; c) G. Ragagnin, B. Betzemeier, S. Quici, P. Knochel, *Tetrahedron* **2002**, *58*, 3985–3991.
[8] a) I. E. Marko, P. R. Giles, M. Tsukazaki, S. M. Brown, C. J. Urch, *Science* **1996**, *274*, 2044–2046; b) I. E. Marko, P. R. Giles, M. Tsukazaki, I. Chelle-Regnaut, A. Gautier, S. M. Brown, C. J. Urch, *J. Org. Chem.* **1999**, *64*, 2433–2439; c) I. E. Marko, A. Gautier, R. Dumeunier, K. Doda, F. Philippart, S. M. Brown, C. J. Urch, *Angew. Chem. Int. Ed.* **2004**, *43*, 1588–1591.
[9] a) T. K. Paine, T. Weyhermueller, K. Wieghardt, P. Chaudhuri, *Dalton Trans.* **2004**, 2092–2101; b) P. Chaudhuri, M. Hess, U. Flörke, K. Wieghardt, *Angew. Chem. Int. Ed. Engl.* **1998**, *37*, 2217–2220; c) P. Chaudhuri, M. Hess, J. Mueller, K. Hildenbrand, E. Bill, T. Weyhermueller, K. Wieghardt, *J. Am. Chem. Soc.* **1999**, *121*, 9599–9610; d) P. Chaudhuri, M. Hess, T. Weyhermueller, K. Wieghardt, *Angew. Chem. Int. Ed.* **1999**, *38*, 1095–1098; P. Lahtinen, E. Lankinen, M. Leskelä, T. Repo, *Appl. Catal. A General* **2005**, *95*, 177–184.
[10] a) S. Itoh, M. Taki, S. Takayama, S. Nagatomo, T. Kitagawa, N. Sakurada, R. Arakawa, S. Fukuzumi, *Angew. Chem. Int. Ed.* **1999**, *38*, 2774; b) Y. Wang, J. L. DuBois, B. Hedman, K. O. Hodgson, T. D. P. Stack, *Science* **1998**, *279*, 537–540; c) F. Thomas, G. Gellon, I. Gautier-Luneau, E. Saint-Aman, J.-L. Pierre, *Angew. Chem. Int. Ed.* **2002**, *41*, 3047–3050.
[11] P. Lahtinen, H. Korpi, E. Haavisto, M. Leskelä, T. Repo, *J. Comb. Chem.* **2004**, *6*, 967–973.
[12] a) G. H. Faye, *Can. J. Chem.* **1966**, *44*, 2165–2171; b) W. Brackman, C. J. Gaasbeek, *J. Inorg. Nucl. Chem.* **1965**, *27*, 1793–1804; c) C. K. Jorgensen, *Acta Chem. Scand.* **1955**, *9*, 1362–1377; d) B. R. James, M. Parris, R. J. P. Williams, *J. Chem. Soc.* **1961**, 4630–4637.
[13] a) E. Garribba, G. Micera, D. Sanna, L. Strinna-Erre, *Inorg. Chim. Acta* **2000**, *299*, 253–261; b) M. A. Zoroddu, S. Zanetti, R. Pogni, R. Basosi, *J. Inorg. Biochem.* **1996**, *63*, 291; c) M. Chikira, Y. Tomizawa, D. Fukita, T. Sugizaki, N. Sugawara, T. Yamazaki, A. Sasano, H. Shindo, M. Palaniadavar, W. E. Antholine, *J. Inorg. Biochem.* **2002**, *89*, 163.
[14] C. M. Harris, E. Sinn, W. R. Walker, P. R. Woolliams, *Aust. J. Chem.* **1968**, *21*, 631–640.
[15] Z.-W. Mao, F. Heinemann, G. Liehr, R. van Eldik, *J. Chem. Soc., Dalton Trans.* **2001**, 3652–3662.
[16] A 3-h oxidation experiment at pH 12.6, 10 bar $O_2$, 80 °C, a copper/veratryl alcohol molar ratio of 1:500 and a total ratio of Cu/phen 1:5 yielded 81% conversion, while the conversion of the reaction catalysed by the isolated complex was 49%.
[17] W. Zhu, W. T. Ford, *J. Mol. Catal.* **1993**, *78*, 367–378.
[18] A. K. Ichinaga, J. R. Kirchhoff, D. R. McMillin, C. O. Dietrich-Buchecker, P. A. Marnot, J.-P. Sauvage, *Inorg. Chem.* **1987**, *26*, 4290–4292.
[19] D. R. McMillin, K. M. McNett, *Chem. Rev.* **1998**, *98*, 1201–1219.
[20] The amount of $H_2O_2$ in the oxidation of $Cu^I$–phen complex in alkaline solution was estimated semiquantitatively by Ozonelabs™ Quantofix® Peroxide Strips. Hydrogen peroxide formation was also measured by adding phenylglyoxylic acid, a reagent that rapidly reacts with hydrogen peroxide to form benzoic acid, to the reaction solution: V. O. Sippola, A. O. I. Krause, *Catal. Today* **2005**, *100*, 237–242.
[21] A. Sobkowiak, A. Qiu, X. Liu, A. Liobet, D. T. Sawyer, *J. Am. Chem. Soc.* **1993**, *115*, 609–614.
[22] a) J. W. Whittaker, *Chem. Rev.* **2003**, *103*, 2347–2364; b) S. Itoh, M. Taki, S. Fukuzumi, *Coord. Chem. Rev.* **2000**, *198*, 3–20.
[23] L. Alderighi, P. Gans, A. Ienco, D. Peters, A. Sabatini, A. Vacca, *Coord. Chem. Rev.* **1999**, *184*, 311–318.
[24] http://www.nist.gov/srd/nist46.htm.

Received: September 26, 2006
Published Online: April 26, 2007

 © 2007 Wiley-VCH Verlag GmbH & Co. KGaA, Weinheim 

DOI: 10.1002/ejic.200601027

# Reactions of $t$Bu$_2$AlH and RE(SiMe$_3$)$_2$ (R = H, SiMe$_3$) – Synthesis and X-ray Crystal Structures of [$t$Bu$_2$AlP(H)SiMe$_3$]$_2$ and [$t$Bu$_2$AlE(SiMe$_3$)$_2$]$_2$ (E = Sb, Bi)

**Madhat Matar,[a] Andreas Kuczkowski,[a] Ulrich Keßler,[a] Stephan Schulz,*[a] and Ulrich Flörke[a]**

**Keywords:** Main group elements / Heterocycles / Solid state structures

Dehydrosilylation reactions between $t$Bu$_2$AlH and E(SiMe$_3$)$_3$ yielded the four-membered heterocycles [$t$Bu$_2$AlE(SiMe$_3$)$_2$]$_2$ (E = Sb, **1**; Bi, **2**), whereas no reaction was observed with P(SiMe$_3$)$_3$. In contrast, the reaction of $t$Bu$_2$AlH with HP(SiMe$_3$)$_2$ also proceeds with elimination of Me$_3$SiH and subsequent formation of [$t$Bu$_2$AlP(H)SiMe$_3$]$_2$ (**3**). Complexes **1**–**3** were characterized by multinuclear NMR ($^1$H, $^{13}$C{$^1$H}, $^{31}$P{$^1$H}) and mass spectroscopy, elemental analysis, and single-crystal X-ray diffraction.

(© Wiley-VCH Verlag GmbH & Co. KGaA, 69451 Weinheim, Germany, 2007)

## Introduction

Heterocyclic group 13/15 compounds of the type [R$_2$MER′$_2$]$_x$ have been studied for many years. In particular, amino-, phosphanyl- and arsinoalanes, -gallanes and -indanes [R$_2$MER′$_2$]$_x$ (M = Al, Ga, In; E = N, P, As) have been synthesized in large numbers by standard synthetic procedures such as alkane, hydrogen, and salt elimination reactions and structurally characterized.[1] Unfortunately, these reaction types almost completely failed to synthesize analogous group 13 stibides and bismuthides [R$_2$MER′$_2$]$_x$ (M = Al, Ga, In; E = Sb, Bi).[2] Therefore, alternative synthetic pathways had to be developed. The dehalosilylation reaction, which was introduced by Wells et al. for the synthesis of arsinogallanes in 1986,[3] was found to be suitable for the preparation of stibinogallanes and -indanes,[4] whereas the corresponding stibinoalanes,[5] as well as bismuthinoalanes[6] and -gallanes,[7] were synthesized by the dehydrosilylation reaction. This particular reaction sequence, which was introduced by Nöth et al. for the synthesis of phosphanylboranes [H$_2$BPR$_2$]$_3$,[8] is generally applicable for the synthesis of the desired group 13/15 heterocycles [R$_2$MER′$_2$]$_x$ (M = Al, Ga; E = P, As, Sb, Bi), as the reaction can be performed under kinetically controlled reaction conditions at low reaction temperatures,[9] which were found to be essential for the synthesis of group 13/Bi heterocycles such as [Me$_2$GaBi(SiMe$_3$)$_2$]$_3$ and [Me$_2$InBi(SiMe$_3$)$_2$]$_3$.[10] Mechanistic studies on the reactions of Et$_2$PSiMe$_3$ with HAlCl$_2$ and H$_2$AlCl clearly demonstrated that the dehydrosilylation reaction is favored over the dehalosilylation reaction.[11] In addition, the reaction of Me$_2$AlH with HP(SiMe$_3$)$_2$ also proceeds preferably with dehydrosilylation rather than H$_2$ elimination, even though subsequent transphosphanation reactions resulted in the formation of several Me$_2$AlP(SiMe$_3$)$_2$-containing species such as the trimeric phosphanylalane [(Me$_2$Al)$_3$(P(H)SiMe$_3$)$_2$P(SiMe$_3$)$_2$], which could be isolated[12] and structurally characterized.[13] In remarkable contrast to these findings, $i$Bu$_2$AlH preferably reacts with HP(SiMe$_3$)$_2$ with H$_2$ elimination and subsequent formation of [$i$Bu$_2$AlP(SiMe$_3$)$_2$]$_2$.[14] An analogous reaction sequence was observed for the reaction of $i$Bu$_2$AlH with Ph$_3$SiPH$_2$, also yielding the H$_2$ elimination product [$i$Bu$_2$AlP(H)SiPh$_3$]$_2$.[15] Obviously, the reaction mode is strongly influenced by the organic substituents bound to the Al atom.

Because of our general interest in group 13/15 chemistry of the heavier group 15 elements (Sb, Bi), we investigated reactions of $t$Bu$_2$AlH with E(SiMe$_3$)$_3$ (E = P, Sb, Bi) and HP(SiMe$_3$)$_2$ and report herein on the synthesis and single-crystal X-ray analyses of [$t$Bu$_2$AlE(SiMe$_3$)$_2$]$_2$ (E = Sb, **1**; Bi, **2**) and [$t$Bu$_2$AlP(H)SiMe$_3$]$_2$ (**3**), respectively.

## Results and Discussion

Equimolar amounts of $t$Bu$_2$AlH and E(SiMe$_3$)$_3$ (E = Sb, Bi) react at ambient temperature with elimination of Me$_3$SiH and subsequent formation of [$t$Bu$_2$AlE(SiMe$_3$)$_2$]$_2$ (E = Sb, **1**; Bi, **2**). In contrast, no reaction was observed with P(SiMe$_3$)$_3$, even at 180 °C.[16] Complex **2** was formed in only 25% yield because of decomposition reactions with subsequent formation of Bi$_2$(SiMe$_3$)$_4$, which has been previously shown to be the typical decomposition product of [Me$_2$MBi(SiMe$_3$)$_2$]$_3$ (M = Al,[6] Ga,[7] In[10]). To the best of our knowledge, **2** represents only the second structurally characterized heterocyclic bismuthinoalane to date [Equation (1)].

[a] Department Chemie, Universität Paderborn,
Warburger Straße 100, 33098 Paderborn, Germany
Fax: +49-5251-603423
E-mail: stephan.schulz@upb.de

 InterScience © 2007 Wiley-VCH Verlag GmbH & Co. KGaA, Weinheim 

$$2\ t\mathrm{Bu_2AlH} + 2\ \mathrm{E(SiMe_3)_3} \xrightarrow[-\ 2\ \mathrm{Me_3SiH}]{} [t\mathrm{Bu_2AlE(SiMe_3)_2}]_2 \quad \mathrm{E = Sb\ \mathbf{1},\ Bi\ \mathbf{2}} \qquad (1)$$

Complexes **1** and **2** were characterized in detail by multinuclear NMR spectroscopy. $^1$H and $^{13}$C{$^1$H} NMR spectra of both compounds each show two sets of resonances due to the organic substituents (*t*Bu, $SiMe_3$). Mass spectra of **1** and **2** do not show the molecular ion peaks. The peak with the highest mass observed in both spectra corresponds to the monomeric unit ($M^+/2$).

Single crystals of **1** and **2** suitable for X-ray structure determination were obtained from solutions in toluene at –40 °C (Figures 1 and 2).

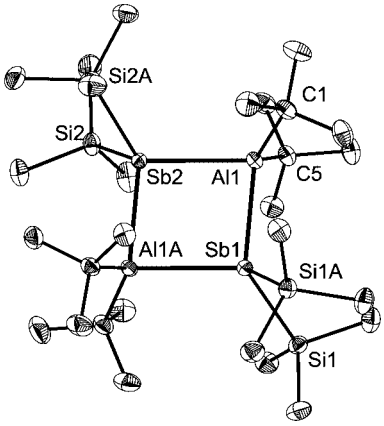


Figure 1. ORTEP plot (50% probability level; H omitted for clarity) showing the solid-state structure and atom-numbering scheme for **1**. Selected bond lengths [Å] and angles [°]: Al1–Sb1 2.786(1), Al1–Sb2 2.781(1), Sb1–Si1 2.587(1), Sb1–Si1A 2.587(1), Al1–C1 2.004(2), Al1–C5 2.005(2); Al1–Sb1–Al1A 94.1(1), Al1–Sb2–Al1A 94.3(1), Sb1–Al1–Sb2 85.8(1), C1–Al1–C5 117.5(1), Si1–Sb1–Si1A2 96.7(1), Si2–Sb2–Si2A2 96.2(1).

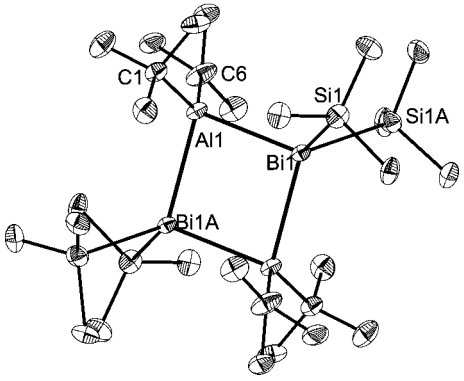


Figure 2. ORTEP plot (50% probability level; H omitted for clarity) showing the solid-state structure and atom-numbering scheme for **2**. Selected bond lengths [Å] and angles [°]: Al1–Bi1 2.840(2), Al1–Bi1A 2.840(2), Bi1–Si1 2.660(2), Bi1–Si1A 2.660(2), Al1–C1 2.008(7), Al1–C6 1.999(8); Al1–Bi1–Al1A 94.1(1), Al1–Bi2–Al1A 95.9(1), Bi1–Al1–Bi1A 84.1(1), C1–Al1–C6 118.9(3), Si1–Bi1–Si1A2 95.6(1).

Complexes **1** and **2** crystallize in the monoclinic space group *C*2/*c* (no. 15) **1** and *C*2/*m* (no. 12) **2** and adopt planar four-membered rings. The ring atoms reside in distorted tetrahedral environments, as is typical for this type of compound. The Al–Sb bond length (av. 2.784 Å **1**) is elongated compared to that of other heterocyclic stibinoalanes $[R_2AlSb(SiMe_3)_2]_x$ (av. values: R = Me, 2.719;[5b] Et, 2.726;[5a] *i*Bu, 2.744 Å[5a]) and base-stabilized monomeric derivatives dmap–$AlR_2Sb(SiMe_3)_2$ [R = Me, 2.691(1); Et, 2.680(1) Å],[17] most likely because of increased repulsive interactions between the sterically demanding organic substituents. Analogous trends are observed for the average Al–Bi bond length in **2** [2.840(2) Å], which is also longer than the average Al–Bi bond length observed in $[Me_2AlBi(SiMe_3)_2]_3$ (2.774 Å)[6] and dmap–$AlR_2Bi(SiMe_3)_2$ [R = Me, 2.755(2); Et, 2.750(2) Å],[18] the only structurally characterized organometallic Al–Bi compounds to date. The endocyclic Al–E–Al bond angles (94.2°, **1**; 95.9°, **2**) are bigger than the Al–E–Al bond angles (85.8°, **1**; 84.1°, **2**), as is typical for this type of heterocycle. The presence of bulky *t*Bu substituents leads to elongated Al–C bond lengths (av. 2.005 Å, **1**) compared to other four-membered Al–Sb heterocycles $[R_2AlSb(SiMe_3)_2]_2$ [R = Et, 1.971 Å, 117.3(1)°; *i*Bu, 1.983 Å, 121.3(1)°], as was previously reported for heterocyclic phosphanylalanes $[R_2AlP(SiMe_3)_2]_2$ (R = Me,[19] Et,[20] *i*Bu[12]). Surprisingly, the C–Al–C bond angle in **1** [117.5(1)°] is smaller than that observed for $[i\mathrm{Bu_2AlSb(SiMe_3)_2}]_2$ [121.3(1)°] and almost identical to that of $[Et_2AlSb(SiMe_3)_2]_2$ [117.3(1)°] despite the increased steric demand of the *t*Bu groups. The Al–C bond length (av. 2.004 Å) and C–Al–C bond angle in **2** [118.9(3)°] are comparable to those in **1**. The Sb–Si and Bi–Si bond lengths (av. 2.587 Å, **1**; 2.660 Å, **2**) are within the expected ranges; the average Si–Sb–Si bond angle in **1** (96.5°) is slightly bigger than the Si–Bi–Si bond angle of **2** (95.6°).

To our surprise, no reaction occurred when $t\mathrm{Bu_2AlH}$ and $P(SiMe_3)_3$ were heated up to 180 °C.[16] In contrast, $i\mathrm{Bu_2AlH}$ was reported to react slowly with $P(SiMe_3)_3$ at ambient temperature with formation of $[i\mathrm{Bu_2AlP(SiMe_3)_2}]_2$.[14,21] This finding prompted our interest in the reaction of $t\mathrm{Bu_2AlH}$ and $HP(SiMe_3)_2$, yielding $[t\mathrm{Bu_2AlP(H)SiMe_3}]_2$ **3** in high yield. $^{31}$P NMR spectroscopic studies gave no sign of any transphosphanation reaction involving species such as $PH_3$ and $Me_3SiPH_2$ as was reported for the reaction of $Me_2AlH$ and $HP(SiMe_3)_2$[12] [Equation (2)].

$$2\ t\mathrm{Bu_2AlH} + 2\ \mathrm{HP(SiMe_3)_2} \xrightarrow[-\ 2\ \mathrm{Me_3SiH}]{} [t\mathrm{Bu_2AlP(H)SiMe_3}]_2\ \ \mathbf{3} \qquad (2)$$

Complex **3** was characterized in detail by multinuclear NMR spectroscopy ($^1$H, $^{13}$C{$^1$H}, $^{31}$P{$^1$H}). The NMR spectra clearly proved the presence of a mixture of the *cis* and *trans* isomers of the four-membered ring in solution. The integration of the three resonances of the *t*Bu groups in the $^1$H NMR spectrum revealed the formation of a 1:1 mixture of the *trans* (one signal) and *cis* isomer (two signals). The $^{31}$P spectrum of **3** shows two multiplets of the AA′XX′ spin system (AA′ parts) and the $^{31}$P{$^1$H} spectrum shows two singlets of almost equal intensity at –229.6 and –232.8 ppm, respectively, for the *cis* and the *trans* iso-

 © 2007 Wiley-VCH Verlag GmbH & Co. KGaA, Weinheim 

mer. The $^{31}P\{^{1}H\}$ spectra of the mother liquor and the recrystallized product show the same relative intensities of both isomers (Figure 3).

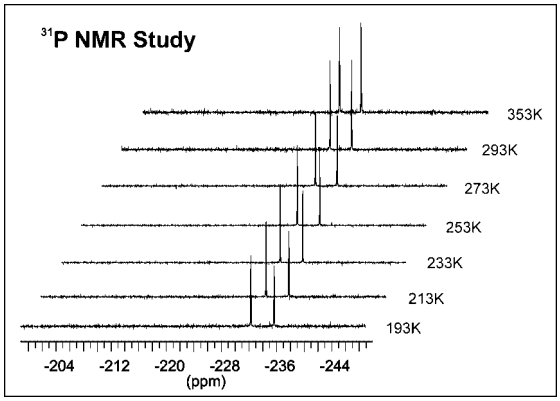


Figure 3. Temperature-dependent $^{31}P\{^{1}H\}$ NMR study of **3** in $[D_8]$toluene.

The formation of *cis* and *trans* isomers has been described previously for four-membered $M_2P_2$ heterocycles of the type $[R_2MP(H)R']_2$ such as $[Et_2InP(H)Si(iPr)_3]_2$,[22] $[Et_2GaP(H)SiMe_2(CMe_2iPr)]_2$,[23] and $[tBu_2InP(H)SiMe_3]_2$.[24] Surprisingly, a temperature-dependent $^{31}P\{^{1}H\}$ NMR study in $[D_8]$toluene of recrystallized **3** clearly revealed that there is no dynamic equilibrium between both isomers in solution in the temperature range from –80 to +80 °C. The relative concentrations of both isomers do not change and no coalescence was observed. A powder X-ray diffraction study proved the crystalline material to be exclusively the *trans* isomer (Figure 4). According to this result, cocrystallization of the *trans* and the *cis* isomer can be excluded.[25]

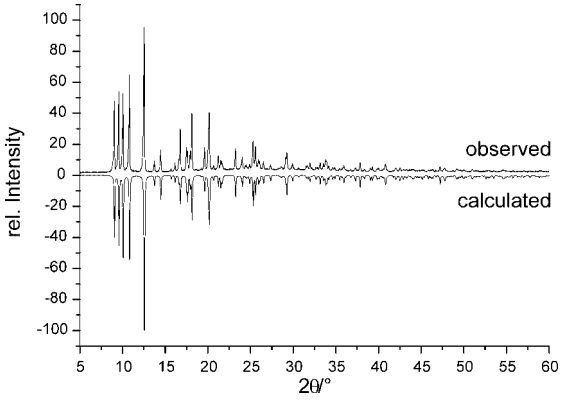


Figure 4. Experimental and calculated powder X-ray diffraction pattern of **3**.

The mass spectrum of **3** does not show the molecular ion peak but $M^+/2$ as was observed for **1** and **2**. An additional signal at *m*/*z* 363 ($[tBuAl_2P_2(SiMe_3)H]^+$) at very high intensity indicates the stability of the central four-membered $Al_2P_2$ ring under these specific conditions.

Single crystals of **3** suitable for X-ray structure determination were obtained from a solution in *n*-hexane at –40 °C. Figure 5 shows the solid-state structure of **3**.

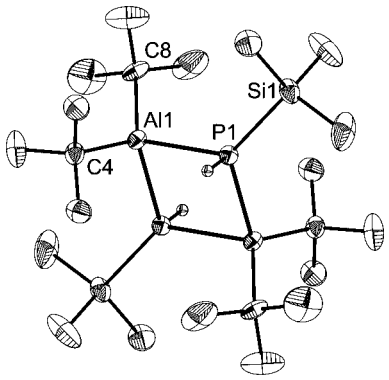


Figure 5. ORTEP plot (50% probability level; H omitted for clarity) showing the solid-state structure and atom-numbering scheme for **3**. Selected bond lengths [Å] and angles [°]: Al1–P1 2.465(1), Al1–P1A 2.459(1), P1–Si1 2.255(1), Al1–C4 1.998(2), Al1–C8 1.994(2); Al1–P1–Al1A 94.4(1), P1–Al1–P1A 85.6(1), C4–Al1–C8 121.0(2), Si1–P1–Al1 129.9(1), Si1–P1–Al1A 127.3(1).

Complex **3** crystallizes in the triclinic space group $P\bar{1}$ (no. 2) and adopts a planar four-membered heterocyclic structure. To the best of our knowledge, **3** represents the first structurally characterized dimeric phosphanylalane containing primary phosphido ($[RPH]^-$) bridges.[26] Comparable phosphanylgallanes $[R_2GaPHR']_2$ were shown to form either planar ($[Cl_2GaP(H)Si(tBu)_3]_2$,[27] $[tBu_2GaP(H)tBu]_2$,[28] $[tBu_2GaP(H)Cp]_2$[29]) or butterfly-type ring structures ($[Me_2GaP(H)Si(tBu)_3]_2$[27]). The formation of a four-membered ring is caused by the steric demand of the *t*Bu substituents, as can be seen when comparing **3** with sterically less hindered phosphanylalanes $[(Me_2Al)_3(P(H)SiMe_3)_2P(SiMe_3)_2]$[13] and $[Me_2AlP(H)Si(iPr)_3]_2$,[30] which form six-membered rings in the solid state. The Al–P bond length in **3** (av. 2.462 Å) is comparable to those reported for $[Me_2AlP(SiMe_3)_2]_2$ (2.457 Å), $[Et_2AlP(SiMe_3)_2]_2$ (2.458 Å), and $[iBu_2AlP(SiMe_3)_2]_2$ (2.476 Å). The central ring atoms reside in distorted tetrahedral environments with the $SiMe_3$ groups and H atoms bound to the P atoms showing a *transoid* orientation. The endocyclic Al–P–Al bond angle of 94.4(1)° is bigger than the P–Al–P angle of 85.6(1)°, as was expected. Both bond angles significantly deviate from those of $[R_2AlP(SiMe_3)_2]_2$ [Al–P–Al: R = Me, 90.6(1); Et, 90.2(1); *i*Bu, 91.0(1); P–Al–P: R = Me, 89.4(1); Et, 89.8(1); *i*Bu, 89.0(1)°]. The average Al–C bond length as observed for **3** (1.996 Å) is elongated and the C–Al–C bond angle [121.0(2)°] is bigger than in $[R_2AlP(SiMe_3)_2]_2$ [R = Me, 1.959 Å, 113.4(2)°; Et, 1.972 Å, 114.2(2)°; *i*Bu, 1.977 Å, 117.1(2)°], in accordance with the higher steric demand of the *t*Bu groups, whereas the P–Si bond lengths [2.255(1) Å] are almost identical.

## Experimental Section

**General:** All manipulations were performed in a glovebox under $N_2$ or by standard Schlenk techniques. $tBu_2AlH$,[31] $HP(SiMe_3)_2$,[32] $P(SiMe_3)_3$,[33] $Sb(SiMe_3)_3$,[33] and $Bi(SiMe_3)_3$[33] were prepared according to literature methods. $^{1}H$, $^{13}C\{^{1}H\}$, and $^{31}P\{^{1}H\}$ spectra were recorded with a Bruker Avance 500 spectrometer and are ref-

 © 2007 Wiley-VCH Verlag GmbH & Co. KGaA, Weinheim 

erenced to internal $C_6D_5H$ ($^1H$ $\delta$ = 7.154, $^{13}C$ $\delta$ = 128.0 ppm) and external $H_3PO_4$, respectively. Melting points were measured in sealed capillaries and are not corrected. Mass spectra (EI) were recorded with a Finnigan MAT 8230 spectrometer. Melting points were measured in sealed capillaries and were not corrected. Elemental analyses were performed at the Elementaranalyse Labor of the University of Paderborn. The results obtained for **1** and **2** deviate from the calculated values because of their expressed sensitivity toward air and moisture.

**Synthesis of [*t*Bu$_2$AlE(SiMe$_3$)$_2$]$_2$:** Equimolar amounts of *t*Bu$_2$AlH (0.14 g, 1 mmol) and E(SiMe$_3$)$_3$ (E = Sb, 0.34 g; Bi, 0.43 g) were combined at ambient temperature and stirred until gas evolution had stopped. The resulting solids were dissolved in toluene (10 mL) and stored at –40 °C. Colorless crystals of **1** and **2** were formed within 24 h. Yields are given for isolated compounds after recrystallization.

**[*t*Bu$_2$AlSb(SiMe$_3$)$_2$]$_2$ (1):** Yield 0.37 g, 0.45 mmol, 90%. *M* = 818.68 g/mol; m.p. 220 °C (dec.). Found: C 40.2, H 8.6; $C_{28}H_{72}Al_2Sb_2Si_4$ requires C 41.1, H 8.9. $^1H$ NMR (500 MHz, $C_6D_5H$, 25 °C): $\delta$ = 0.59 (18 H, s, *Me*$_3$Si), 1.29 (18 H, s, *Me*$_3$CAl) ppm. $^{13}C\{^1H\}$ NMR (125 MHz, $C_6D_5H$, 25 °C): $\delta$ = 6.0 [s, *Me*$_3$Si], 31.4 [s, *Me*$_3$CAl] ppm. EI-MS (70 eV, 70 °C): *m*/*z* (%) = 534 (5) [Sb$_2$(SiMe$_3$)$_4$]$^+$, 498 (5) [M/2 + H]$^+$, 408 (55) [M/2]$^+$, 351 (75) [M/2 – (*t*Bu)]$^+$, 295 (60) [M/2 – 2*t*Bu]$^+$, 221 (60) [M/2 – 2*t*Bu – SiMe$_3$]$^+$, 73 (100) [SiMe$_3$]$^+$, 58 (80) [*t*BuH]$^+$, 43 (65) [*t*BuH – Me]$^+$.

**[*t*Bu$_2$AlBi(SiMe$_3$)$_2$]$_2$ (2):** Yield 0.13 g, 0.13 mmol, 25%. *M* = 993.14 g/mol; m.p. 165 °C (dec.). Found: C 32.8, H 6.9; $C_{28}H_{72}Al_2Bi_2Si_4$ requires C 33.9, H 7.3. $^1H$ NMR (500 MHz, $C_6D_5H$, 25 °C): $\delta$ = 0.82 (18 H, s, *Me*$_3$Si), 1.30 (18 H, s, *Me*$_3$CAl) ppm. $^{13}C\{^1H\}$ NMR (125 MHz, $C_6D_5H$, 25 °C): $\delta$ = 7.1 (s, *Me*$_3$Si), 31.1 (s, *Me*$_3$CAl) ppm. EI-MS (70 eV, 70 °C): *m*/*z* (%) = 498 (5) [M/2 + H]$^+$, 423 (15) [M/2 – SiMe$_3$]$^+$, 366 (25) [M/2 – SiMe$_3$ – (*t*Bu)]$^+$, 146 (65) [Si$_2$Me$_6$]$^+$, 73 (100) [SiMe$_3$]$^+$, 58 (45) [*t*BuH]$^+$, 43 (70) [*t*BuH – Me]$^+$.

**Synthesis of [*t*Bu$_2$AlP(H)SiMe$_3$]$_2$ (3):** *t*Bu$_2$AlH (1 mmol, 0.14 g) was added to HP(SiMe$_3$)$_2$ (1 mmol, 0.17 g) at ambient temperature. Immediately, a gas evolution was observed and after a few minutes the mixture solidified. The colorless solid was dissolved in *n*-hexane (10 mL) and stored at –40 °C. Colorless crystals of **3** were formed within 48 h. The yield is given for the isolated compound after recrystallization. Yield 0.21 g, 0.43 mmol, 86%. *M* = 492.75 g/mol; m.p. 98–100 °C. Found: C 53.4, H 11.3; $C_{22}H_{56}Al_2Si_2P_2$ requires C 53.6, H 11.5. $^1H$ NMR (500 MHz, $C_6D_5H$, 25 °C): $\delta$ = 0.26–0.28 (18 H, *Me*$_3$Si), 1.22 (9 H, s, *Me*$_3$CAl, *cis* isomer), 1.23 (18 H, s, *Me*$_3$CAl, *trans* isomer), 1.26 (9 H, s, *Me*$_3$CAl, *cis* isomer) ppm. $^{13}C\{^1H\}$ NMR (125 MHz, $C_6D_5H$, 25 °C): $\delta$ = 3.1 [dt, $^2J$(C-P) = 4.2, $^4J$(C-P) = 2.0 Hz, *Me*$_3$Si], 30.9 (s, *Me*$_3$CAl), 31.3 (s, *Me*$_3$CAl), 31.8 (s, *Me*$_3$CAl) ppm. $^{31}P\{^1H\}$ NMR (200 MHz, $C_6D_5H$, 25 °C): $\delta$ = –229.6 [dd, $^1J$(P-H) = 167.6, $^2J$(P-P) = 67.7 Hz, *cis* isomer], –232.8 [dd, $^1J$(P-H) = 171.3, $^2J$(P-P) = 71.4 Hz, *trans* isomer] ppm. EI-MS (70 eV, 70 °C): *m*/*z* (%) = 363 (90) [*t*BuAl$_2$P$_2$(SiMe$_3$)H]$^+$, 246 (50) [M/2]$^+$, 147 (80) [Si$_2$Me$_6$]$^+$, 73 (75) [SiMe$_3$]$^+$, 58 (60) [*t*BuH]$^+$, 43 (100) [*t*BuH – Me]$^+$.

**X-ray Structure Solution and Refinement:** Crystallographic data of **1**–**3** are summarized in Table 1. Figures 1, 2 and 5 show ORTEP diagrams of the solid-state structures of **1**–**3**. Data were collected with a Bruker SMART APEX CCD diffractometer[34] using Mo-$K_\alpha$ radiation ($\lambda$ = 0.71073 Å) at *T* = 120(2) K, and data reduction and absorption corrections were done with SAINT[34] and SADABS.[34] The structures were solved by direct and Fourier methods (SHELXTL),[34] and refined by full-matrix least-squares on $F^2$. All non-hydrogen atoms in **1**–**3** were refined anisotropically and hydrogen atoms were located from $\Delta F$ maps and refined at idealized positions with a riding model (SHELXTL). The Si–C distances of the disordered SiMe$_3$ group in **2** have been restrained with the SADI command of SHELX.

CCDC-626081 (for **1**), -626082 (for **2**), and -626083 (for **3**) contain the supplementary crystallographic data for this paper. These data can be obtained free of charge from the Cambridge Crystallographic Data Centre via www.ccdc.cam.ac.uk/data_request/cif.

Table 1. Crystallographic data for [*t*Bu$_2$AlSb(SiMe$_3$)$_2$]$_2$ (**1**), [*t*Bu$_2$AlBi(SiMe$_3$)$_2$]$_2$ (**2**) and [*t*Bu$_2$AlP(H)SiMe$_3$]$_2$ (**3**).

| | [*t*Bu$_2$AlSb(SiMe$_3$)$_2$]$_2$ (**1**) | [*t*Bu$_2$AlBi(SiMe$_3$)$_2$]$_2$ (**2**) | [*t*Bu$_2$AlP(H)SiMe$_3$]$_2$ (**3**) |
|---|---|---|---|
| Molecular formula | $C_{28}H_{72}Al_2Sb_2Si_4$ | $C_{28}H_{72}Al_2Bi_2Si_4$ | $C_{22}H_{56}Al_2P_2Si_2$ |
| Formula mass | 818.68 | 993.14 | 492.75 |
| Crystal system | monoclinic | monoclinic | triclinic |
| Space group | *C*2/*c* (no. 15) | *C*2/*m* (no. 12) | $P\bar{1}$ (no. 2) |
| *a* [Å] | 19.6350(8) | 18.3305(12) | 8.4864(9) |
| *b* [Å] | 13.2645(5) | 13.3815(9) | 10.4671(11) |
| *c* [Å] | 18.2399(7) | 9.9129(6) | 10.7269(11) |
| $\alpha$ [°] | | | 63.790(2) |
| $\beta$ [°] | 117.121(1) | 117.869(1) | 80.170(2) |
| $\gamma$ [°] | | | 73.546(2) |
| *V* [Å$^3$] | 4228.2(3) | 2149.5(2) | 818.7(2) |
| *Z* | 4 | 2 | 1 |
| $\mu$ [mm$^{-1}$] | 1.448 | 8.343 | 0.267 |
| $D_{calcd.}$ [g/cm$^3$] | 1.286 | 1.534 | 0.999 |
| Crystal dimensions [mm] | 0.22 × 0.20 × 0.13 | 0.22 × 0.08 × 0.07 | 0.41 × 0.38 × 0.32 |
| Measured reflections | 18182 | 9501 | 7070 |
| Unique reflections | 5018 | 2652 | 3709 |
| $R_{merg}$ | 0.0199 | 0.0466 | 0.0574 |
| No. of parameters refined/restraints | 164/0 | 138/21 | 131/0 |
| $R_1$[a]; $wR_2$[b] | 0.0207, 0.0524 | 0.0303, 0.0659 | 0.0418, 0.1368 |
| Gof[c] | 1.043 | 1.040 | 1.118 |
| Final max, min $\Delta\rho$ [e/Å$^3$] | 0.768, –0.273 | 1.577, –1.073 | 0.349, –0.349 |

[a] $R_1 = \Sigma(||F_o| - |F_c||)/\Sigma|F_o|$ [for $I > 2\sigma(I)$]. [b] $wR_2 = \{\Sigma[w(F_o^2 - F_c^2)^2]/\Sigma[w(F_o^2)^2]\}^{1/2}$. [c] Goodness of fit = $\{\Sigma[w(|F_o^2| - |F_c^2|)^2]/(N_{obs} - N_{param})\}^{1/2}$.

 © 2007 Wiley-VCH Verlag GmbH & Co. KGaA, Weinheim 

## Acknowledgments

This work was financially supported by the Deutsche Forschungsgemeinschaft (DFG), Fonds der Chemischen Industrie, and the Bundesministerium für Bildung, Wissenschaft, Forschung und Technologie (BMBF).

[1] a) C.-C. Chang, M. S. Ameerunisha, *Coord. Chem. Rev.* **1999**, *189*, 199; b) C. J. Carmalt, *Coord. Chem. Rev.* **2001**, *223*, 217; c) R. L. Wells, *Coord. Chem. Rev.* **1992**, *112*, 273; d) A. H. Cowley, R. A. Jones, *Angew. Chem. Int. Ed. Engl.* **1989**, *28*, 1208.

[2] $[Me_2MSb(tBu)_2]_3$ (M = Ga, In) were prepared in rather low yields by salt elimination reaction. (A. H. Cowley, R. A. Jones, C. M. Nunn, D. L. Westmoreland, *Chem. Mater.* **1990**, *2*, 221) In addition, $(Cp^*Al)_3Sb_2$ was prepared by reaction of $[Cp^*Al]_4$ and $[tBuSb]_4$. (S. Schulz, T. Schoop, H. W. Roesky, L. Häming, A. Steiner, R. Herbst-Irmer, *Angew. Chem. Int. Ed. Engl.* **1995**, *34*, 919).

[3] C. G. Pitt, A. P. Purdy, K. T. Higa, R. L. Wells, *Organometallics* **1986**, *5*, 1266; for a review article see: R. L. Wells, *Coord. Chem. Rev.* **1992**, *112*, 273.

[4] a) A. H. Cowley, R. A. Jones, K. B. Kidd, C. M. Nunn, D. L. Westmoreland, *J. Organomet. Chem.* **1988**, *341*, C1; b) A. R. Barron, A. H. Cowley, R. A. Jones, C. M. Nunn, D. L. Westmoreland, *Polyhedron* **1988**, *7*, 77; c) R. A. Baldwin, E. E. Foos, R. L. Wells, P. S. White, A. L. Rheingold, G. P. A. Yap, *Organometallics* **1996**, *15*, 5035; d) R. L. Wells, E. E. Foos, P. S. White, A. L. Rheingold, L. M. Liable-Sands, *Organometallics* **1997**, *16*, 4771; e) S. Schulz, M. Nieger, *J. Organomet. Chem.* **1998**, *570*, 275; f) E. E. Foos, R. L. Wells, A. L. Rheingold, *J. Cluster Sci.* **1999**, *10*, 121; g) E. E. Foos, R. J. Jouet, R. L. Wells, A. L. Rheingold, L. M. Liable-Sands, *J. Organomet. Chem.* **1999**, *582*, 45; h) E. E. Foos, R. J. Jouet, R. L. Wells, P. S. White, *J. Organomet. Chem.* **2000**, *598*, 182.

[5] a) S. Schulz, M. Nieger, *Organometallics* **1998**, *17*, 3398; b) S. Schulz, M. Nieger, *Organometallics* **1999**, *18*, 315; c) S. Schulz, A. Kuczkowski, M. Nieger, *Organometallics* **2000**, *19*, 699.

[6] S. Schulz, M. Nieger, *Angew. Chem. Int. Ed.* **1999**, *38*, 967.

[7] F. Thomas, S. Schulz, M. Nieger, *Organometallics* **2002**, *21*, 2793.

[8] a) H. Nöth, W. Schrägle, *Z. Naturforsch., B: Chem. Sci.* **1961**, *16*, 473; b) H. Nöth, W. Schrägle, *Chem. Ber.* **1965**, *98*, 473; c) G. L. Wood, D. Dou, C. K. Narula, E. N. Duesler, R. T. Paine, H. Nöth, *Chem. Ber.* **1990**, *123*, 1455.

[9] Reactions of $Me_2AlH$ with $P(SiMe_3)_3$ and $As(SiMe_3)_3$ also resulted in the formation of the corresponding heterocycles $[Me_2AlP(SiMe_3)_2]_2$ and $[Me_2AlAs(SiMe_3)_2]_2$. See the following and refs. cited therein: F. Thomas, S. Schulz, M. Nieger, *Z. Anorg. Allg. Chem.* **2002**, *628*, 235.

[10] F. Thomas, S. Schulz, M. Nieger, *Angew. Chem. Int. Ed.* **2003**, *42*, 5641.

[11] G. Fritz, R. Emül, *Z. Anorg. Allg. Chem.* **1975**, *416*, 19.

[12] L. K. Krannich, C. L. Watkins, S. J. Schauer, *Organometallics* **1995**, *14*, 3094.

[13] A. Schaller, H.-D. Hausen, J. Weidlein, *Z. Anorg. Allg. Chem.* **2000**, *626*, 616.

[14] L. K. Krannich, C. L. Watkins, S. J. Schauer, C. H. Lake, *Organometallics* **1996**, *15*, 3980. The authors also reported on the formation of a compound with the composition $iBu_2AlP(SiMe_3)_2 \cdot iBu_2AlP(H)SiMe_3$ in about 15% yield, which unfortunately could not be isolated. However, the formation of this compound indicated that $Me_3SiH$ elimination occurs to some extent.

[15] A. H. Cowley, R. A. Jones, M. A. Mardones, J. L. Atwood, S. G. Bott, *Angew. Chem. Int. Ed. Engl.* **1990**, *29*, 1409.

[16] Above 180 °C only decomposition reactions were observed.

[17] S. Schulz, M. Nieger, *Organometallics* **2000**, *19*, 2640.

[18] S. Schulz, F. Thomas, A. Kuczkowski, H. Hupfer, M. Nieger, *Organometallics* **2000**, *19*, 5758.

[19] F. Hey-Hawkins, M. F. Lappert, J. L. Atwood, S. G. Bott, *J. Chem. Soc., Dalton Trans.* **1991**, 939.

[20] S. M. Stuczynski, R. L. Opila, P. Marsh, J. G. Brennan, M. L. Steigerwald, *Chem. Mater.* **1991**, *3*, 379.

[21] The reaction of $iBu_2AlH$ and $P(SiMe_3)_3$ in refluxing hexane gave $[iBu_2AlP(SiMe_3)_2]_2$ in high yield within 6 h (ref.[13]).

[22] C. v. Hänisch, B. Rolli, *Z. Anorg. Allg. Chem.* **2002**, *628*, 2255.

[23] C. v. Hänisch, B. Rolli, *Phosphorus, Sulfur Silicon Relat. Elem.* **2004**, *179*, 749.

[24] T. J. Trentler, S. C. Goel, K. M. Hickman, A. M. Viano, M. Y. Chiang, A. M. Beatty, P. C. Gibbons, W. E. Buhro, *J. Am. Chem. Soc.* **1997**, *119*, 2172.

[25] Cell parameters (Å [°]) as obtained by powder X-ray diffraction (273.2 K): $a$ = 10.6138(15), $b$ = 10.9145(15), $c$ = 8.5549(13); $a$ = 100.194(9) (=79.806), $b$ = 107.237(7) (=72.763), $c$ = 63.639(8), $V$ = 846.9(3) Å$^3$.

[26] The formulation of $[tBu_2AlP(H)tBu]_2$ as a dimer is based on NMR spectroscopy studies.[27]

[27] M. Westerhausen, T. Rotter, C. Pfaller, A. N. Kneifel, A. Schulz, *Inorg. Chim. Acta* **2005**, *358*, 4253.

[28] a) D. L. Atwood, A. H. Cowley, P. R. Harris, R. A. Jones, S. U. Koschmieder, C. M. Nunn, *J. Organomet. Chem.* **1993**, *449*, 61; b) K. Kirschbaum, D. M. Giolando, *Acta Crystallogr., Sect. C* **1994**, *50*, 1244.

[29] D. E. Heaton, R. A. Jones, K. B. Kidd, A. H. Cowley, C. M. Nunn, *Polyhedron* **1988**, *7*, 1901.

[30] M. Driess, S. Kuntz, C. Monsé, K. Merz, *Chem. Eur. J.* **2000**, *6*, 4343.

[31] W. Uhl, *Z. Anorg. Allg. Chem.* **1989**, *570*, 37.

[32] G. Becker, M. Rössler, W. Uhl, *Z. Anorg. Allg. Chem.* **1981**, *473*, 7.

[33] W. A. Hermann, G. Brauer, *Synthetic Methods of Organometallic and Inorganic Chemistry*, vol. 3, *Phosphorus, Arsenic, Antimony and Bismuth*, Thieme, Stuttgart, **1996**.

[34] Bruker, *SMART (Version 5.62), SAINT (Version 6.02), SHELXTL (Version 6.10) and SADABS (Version 2.03)*, Bruker AXS Inc., Madison, WI, USA, **2002**.

Received: November 1, 2006
Published Online: May 4, 2007

 © 2007 Wiley-VCH Verlag GmbH & Co. KGaA, Weinheim 

DOI: 10.1002/ejic.200700020

# Synthesis and Characterization of Iron, Cobalt, and Nickel Complexes Bearing Novel *N*,*N*-Chelate Ligands and Their Catalytic Properties in Ethylene Oligomerization

**Li Wang,[a] Cheng Zhang,[a] and Zhong-Xia Wang*[a]**

**Keywords:** Iron / Cobalt / Nickel / Catalysis / Ethylene / Oligomerization

Treatment of *o*-$ROC_6H_4NC$ (R = $PhCH_2$, *i*Pr) with [Li{2-$CH(SiMe_3)C_5H_4N$}] afforded dimeric lithium complexes [Li{N(*o*-$ROC_6H_4$)$C(SiMe_3)CH(2$-$C_5H_4N)$}]$_2$ (**3**, R = $PhCH_2$; **4**, R = *i*Pr). Reaction of the lithium complexes with 1 equiv. of (dme)$NiCl_2$ gave nickel complexes [Ni{N(*o*-$ROC_6H_4$)-$C(SiMe_3)CH(2$-$C_5H_4N)$}$_2$] (**5**, R = $PhCH_2$; **6**, R = *i*Pr). The stoichiometric reaction of complexes **3** and **4** with $Et_3NH^+Cl^-$ formed 2-{*o*-$ROC_6H_4NHC(SiMe_3)CH$}$C_5H_4N$ (**7**, R = $PhCH_2$; **8**, R = *i*Pr) in quantitative yields. Reaction of **7** or **8** with metal halides, including (dme)$NiCl_2$, $NiBr_2$, $FeCl_2{\cdot}4H_2O$, and $CoCl_2$ yielded complexes [$MX_2${(*o*-$ROC_6H_4$)$N{=}C(SiMe_3)CH_2$(2-$C_5H_4N$)}] (**9**, R = $PhCH_2$, M = Ni, X = Cl; **10**, R = *i*Pr, M = Ni, X = Cl; **11**, R = $PhCH_2$, M = Ni, X = Br; **12**, R = *i*Pr, M = Ni, X = Br; **13**, R = $PhCH_2$, M = Fe, X = Cl; **14**, R = *i*Pr, M = Fe, X = Cl; **15**, R = $PhCH_2$, M = Co, X = Cl; **16**, R = *i*Pr, M = Co, X = Cl). For comparasion, nickel and cobalt complexes [$MX_2${(*o*-$MeC_6H_4$)$N{=}C(SiMe_3)CH_2$(2-$C_5H_4N$)}] (M = Ni, X = Br, **18**; M = Co, X = Cl, **19**) were similarly synthesized through reaction of 2-{*o*-$MeC_6H_4NHC(SiMe_3)CH$}$C_5H_4N$ (**17**) with $NiBr_2$ and $CoCl_2$, respectively. These compounds were characterized by NMR (for **3**, **4**, **7**, **8**, and **17**) and IR (for **5**–**19**) spectroscopy, elemental analyses and HRMS (for **5**, **6**, and **9**–**19**). The molecular structures of complexes **3**, **6**, **12**, and **14** were characterized by single-crystal X-ray diffraction techniques. The catalytic behavior in ethylene oligomerization of complexes **5**, **6**, **9**–**16**, **18**, and **19** was investigated. Under optimal conditions, the complexes showed good catalytic activities upon activation with appropriate aluminum co-catalysts ($8.72\times10^2$ to $18.2\times10^2$ kg/mol h atm for the nickel complexes upon activation with $Et_2AlCl$ and $4.3\times10^2$ to $8.1\times10^2$ kg/mol h atm for the iron and cobalt complexes upon activation with MMAO).
(© Wiley-VCH Verlag GmbH & Co. KGaA, 69451 Weinheim, Germany, 2007)

## Introduction

Late-transition-metal complexes with *N*,*N*-chelate ligands have attracted considerable attention due to their catalytic actions, especially for developing non-metallocene catalysts for the polymerization of ethylene and α-olefins.[1] Following the pioneering studies of Keim and Fink,[1d,2] Brookhart and co-workers reported on the discovery of the α-diimine complexes of $Ni^{II}$ and $Pd^{II}$ catalysts for the polymerization of ethylene and α-olefins.[3] Subsequently, the number of academic publications and patents for polyolefins and oligomers obtained with late-transition-metal complexes increased remarkably.[1,4] A large number of structural variations of diimines have also been reported to adjust the steric and electronic properties of the *N*,*N*-chelate ligands.[1,5] These include β-diimines and analogues whose complexes of $Ni^{II}$ and $Pd^{II}$, however, usually exhibit lower catalytic activities than the α-diimine complexes.[1a,6] A further modification is to append a donor sidearm, constructing tridentate chelating ligands such as *N*,*N*,*O*,[7] *N*,*N*,*P*,[8] and *N*,*N*,*N* ligands.[9] A representative example are bis(imino)pyridine ligands whose iron complexes showed exceptionally high activities for ethylene polymerization when activated with MAO.[10]

Furthermore, late-transition-metal complexes could act as better candidates for ethylene oligomerization because of their facile β-H elimination.[11] Many neutral and cationic late-transition-metal complexes with chelate ligands have been successfully applied in the field of olefin oligomerization.[12,13] The Shell Higher Olefin Process (SHOP) is an excellent example. However, the demand for linear α-olefins in the $C_4$–$C_{10}$ range is growing fast. Much effort is still devoted to the development of highly selective ethylene oligomerization catalysts, and identifying and fine-tuning the parameters that influence the activity and selectivity of suitable catalysts continues to represent a challenge.[13] Our current efforts focus on the synthesis of new functional ligands and their corresponding late-transition-metal complexes as well as the catalytic behavior for ethylene oligomerization. Herein, we report on the synthesis and characterization of new ligands and their lithium and late-transition-metal complexes, while their catalytic behavior for ethylene oligomerization was also investigated and discussed.

[a] Department of Chemistry, University of Science and Technology of China,
Hefei, Anhui 230026, P. R. China

 © 2007 Wiley-VCH Verlag GmbH & Co. KGaA, Weinheim 

## Results and Discussion

### Synthesis and Characterization

Compounds **1** and **2** were prepared according to a literature method.[14] Syntheses of **3**–**16** are summarized in Scheme 1. Reaction of *o*-$ROC_6H_4NC$ (R = $PhCH_2$, *i*Pr) with [Li{2-$CH(SiMe_3)C_5H_4N$}] afforded dimeric lithium complexes [Li{$N(o\text{-}ROC_6H_4)C(SiMe_3)CH(2\text{-}C_5H_4N)$}]$_2$ (**3**, R = $PhCH_2$; **4**, R = *i*Pr) as yellow, air-sensitive solids. In the reaction, a 1,2-$SiMe_3$ migration from the α- to the β-carbon atom took place. This type of reaction between an isocyanide and (trimethylsilyl)methyllithium has been reported.[15] Reaction of **3** and **4** with 1 equiv. of (dme)$NiCl_2$ gave nickel complexes [Ni{$N(o\text{-}ROC_6H_4)C(SiMe_3)CH(2\text{-}C_5H_4N)$}$_2$] (**5**, R = $PhCH_2$; **6**, R = *i*Pr). Attempts to synthesize [NiCl{$N(o\text{-}ROC_6H_4)C(SiMe_3)CH(2\text{-}C_5H_4N)$}] by reaction of **3** or **4** with various amounts of (dme)$NiCl_2$ were unsuccessful. Complexes **3** and **4** were treated with 1 equiv. of $Et_3NH^+Cl^-$ to afford 2-{*o*-$ROC_6H_4NHC(SiMe_3)CH$}$C_5H_4N$ (**7**, R = $PhCH_2$; **8**, R = *i*Pr) as a pale yellow solid (**7**) or a yellowish oil (**8**), each existing in an enamine form. Reaction of **7** or **8** with metal halides, including (dme)$NiCl_2$, $NiBr_2$, $FeCl_2{\cdot}4H_2O$ and $CoCl_2$, yielded [$MX_2${$(o\text{-}ROC_6H_4)N{=}C(SiMe_3)CH_2(2\text{-}C_5H_4N)$}] (**9**, R = $PhCH_2$, M = Ni, X = Cl; **10**, R = *i*Pr, M = Ni, X = Cl; **11**, R = $PhCH_2$, M = Ni, X = Br; **12**, R = *i*Pr, M = Ni, X = Br; **13**, R = $PhCH_2$, M = Fe, X = Cl; **14**, R = *i*Pr, M = Fe, X = Cl; **15**, R = $PhCH_2$, M = Co, X = Cl; **16**, R = *i*Pr, M = Co, X = Cl). Compound **17** was prepared with a similar procedure as for **7** and **8** (Scheme 2). Thus, reaction of *o*-$MeC_6H_4NC$ with [Li{2-$CH(SiMe_3)C_5H_4N$}] in $Et_2O$ gave the lithium complex [Li{$N(o\text{-}MeC_6H_4)C(SiMe_3)CH(2\text{-}C_5H_4N)$}], which was hydrolyzed directly by treatment with 1 equiv. of water to afford neutral enamine **17**. Complexes **18** and **19** were synthesized through reaction of **17** with $NiBr_2$ or $CoCl_2$ in thf, just as for complexes **9**–**16**.

Complexes **3** and **4** were fully characterized by $^1H$ and $^{13}C$ NMR spectroscopy and elemental analyses. The data are consistent with their respective structure. Complexes **5** and **6** are paramagnetic and were characterized by IR spectroscopy, elemental analyses, and high-resolution mass spectrometry. Compounds **7** and **8** were characterized by $^1H$, $^{13}C$ NMR, and IR spectroscopy and elemental analyses. The $^1H$ NMR spectra of **7** and **8** exhibit NH proton signals at δ = 11.77 and 11.58 ppm, respectively, and ethenyl proton signals at δ = 5.69 and 5.59 ppm, respectively. Their $^{13}C$ NMR spectra also show the existence of the C–C double bonds. These data prove the enamine forms of **7** and **8**. The similar compound **17** also exists in an enamine form, being a mixture of (*Z*) and (*E*) isomers. It was characterized by $^1H$ NMR and IR spectroscopy and high-resolution mass spectrometry. Complexes **9**–**16**, **18**, and **19** are crystalline solids or powders and paramagnetic; the complexes are yellow (**9**, **13**, and **14**), purple (**10** and **18**), red (**11** and **12**), or blue (**15**, **16**, and **19**). They gave satisfactory elemental analyses and high-resolution mass spectra. The IR spectra show C=N double-bond absorptions, proving

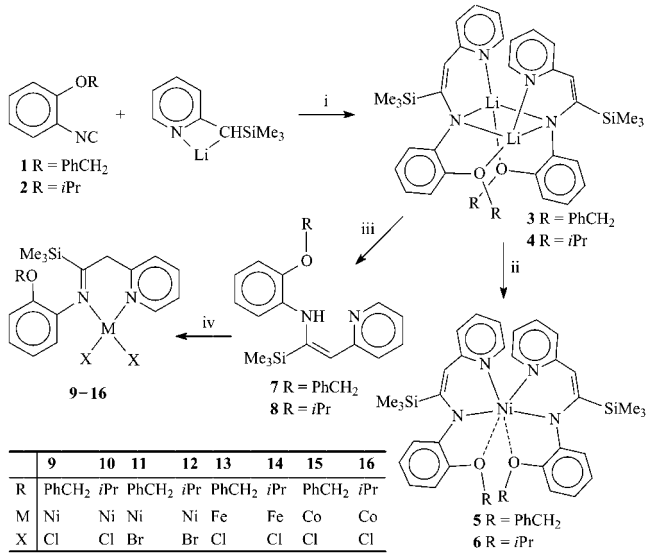


| | 9 | 10 | 11 | 12 | 13 | 14 | 15 | 16 |
|---|---|---|---|---|---|---|---|---|
| R | $PhCH_2$ | *i*Pr | $PhCH_2$ | *i*Pr | $PhCH_2$ | *i*Pr | $PhCH_2$ | *i*Pr |
| M | Ni | Ni | Ni | Ni | Fe | Fe | Co | Co |
| X | Cl | Cl | Br | Br | Cl | Cl | Cl | Cl |

Scheme 1. Synthesis of compounds **3**–**16**. Reagents and conditions: i: $Et_2O$, –30 °C to room temperature, 15 h; ii: (dme)$NiCl_2$, thf, –80 °C to room temperature, 15 h; iii: $Et_3NH^+Cl^-$, toluene, 0 °C to room temperature, 20 h; iv: $L^1MX_2$ [$L^1MX_2$ = (dme)$NiCl_2$, $NiBr_2$, $FeCl_2{\cdot}4H_2O$, $CoCl_2$], thf, 0 °C to room temperature, 15 h.

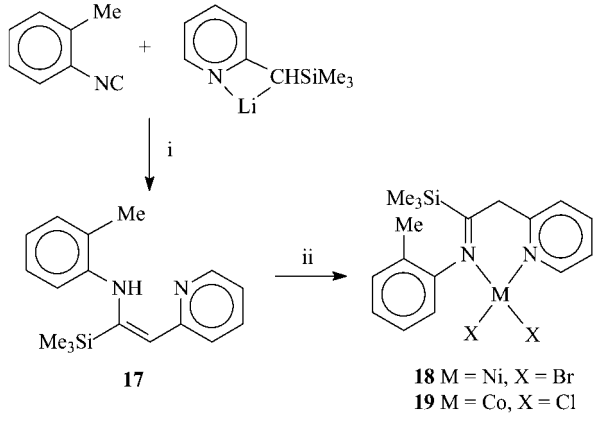


Scheme 2. Synthesis of compounds **17**–**19**. Reagents and conditions: i: $Et_2O$, –30 °C to room temperature, 15 h, and then $H_2O$, thf, 0 °C to room temperature, 10 min.; ii: $NiBr_2$ or $CoCl_2$, thf, 0 °C to room temperature, 15 h.

the coordinated ligands as imine forms in the complexes. This is also consistent with the single-crystal X-ray diffraction results of complexes **12** and **14**.

Complexes **3**, **6**, **12**, and **14** were further characterized by single-crystal X-ray diffraction techniques. The structure of complex **3** is presented in Figure 1 along with selected bond lengths and bond angles. The structure shows that complex **3** is dimeric in the solid state, in which two lithium atoms are bridged by two enamine nitrogen atoms, forming a 1,3-$Li_2N_2$ four-membered ring. With the 1,3-$Li_2N_2$ ring as the base, the $NC_3NLi$ and $NC_2OLi$ rings form the flaps of an "open-box"-like structural framework, in which each four-coordinate lithium atom has a distorted tetrahedral geometry. The Li–N distances from 1.967(8) to 2.108(8) Å are in the normal range. For example, the Li–N distances in

 © 2007 Wiley-VCH Verlag GmbH & Co. KGaA, Weinheim 

$[Li\{N(SiMe_3)C(R^2)C(R^1)(C_5H_4N\text{-}2)\}]_2$ ($R^1$ = H, $R^2$ = *t*Bu; $R^1$ = $SiMe_3$, $R^2$ = Ph) vary from 1.968(6) to 2.032(6) Å, and in $[Li\{N(SiMe_3)C(Ph)\}_2CH]_2$ from 1.952(10) to 2.095(2) Å.[16]

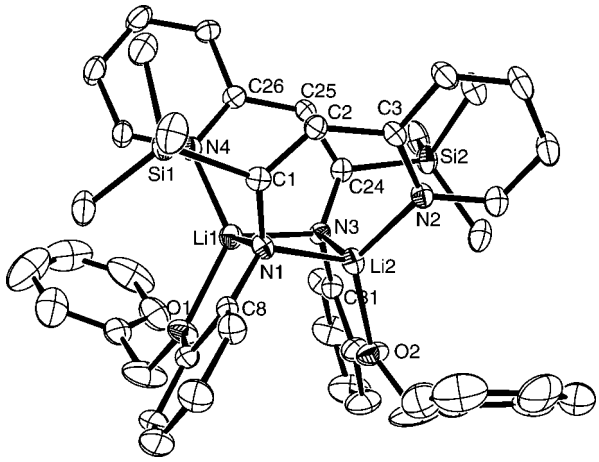


Figure 1. ORTEP drawing of complex **3** with 30% probability thermal ellipsoids. Selected bond lengths [Å] and bond angles [°]: Li(1)–N(1) 2.108(8), Li(1)–N(3) 1.990(8), Li(1)–N(4) 1.967(8), Li(1)–O(1) 2.055(8), Li(2)–N(1) 2.016(8), Li(2)–N(2) 1.982(8), Li(2)–N(3) 2.072(8), Li(2)–O(2) 2.037(8), Li(1)–Li(2) 2.495(10), N(1)–C(1) 1.403(5), C(1)–C(2) 1.363(5), N(3)–C(24) 1.394(5), C(24)–C(25) 1.363(5); N(1)–Li(1)–N(3) 103.8(3), N(1)–Li(1)–N(4) 119.0(4), N(3)–Li(1)–N(4) 98.9(4), N(3)–Li(1)–O(1) 121.7(4), N(4)–Li(1)–O(1) 130.7(4), N(1)–Li(1)–O(1) 79.8(3), N(1)–Li(2)–N(2) 98.4(3), N(1)–Li(2)–N(3) 104.2(3), N(2)–Li(2)–N(3) 119.3(4), N(1)–Li(2)–O(2) 122.2(4), N(2)–Li(2)–O(2) 129.2(4), N(3)–Li(2)–O(2) 81.3(3), Li(1)–N(1)–Li(2) 74.4(3), Li(1)–N(3)–Li(2) 75.8(3).

The molecular structure of complex **6** is depicted in Figure 2 along with selected bond lengths and bond angles. In the structure, a noteworthy feature is the distances between the Ni atom and the oxygen atoms. The Ni···O distances (2.574 and 2.586 Å, respectively) are longer than the sum of the covalent radii, however, much shorter than the sum of the van der Waals radii.[17] Hence, interactions between the Ni atom and the O atoms should be present. In this case, the coordination geometry of the Ni atom can be regarded as a distorted octahedron. The N1,N4,O1,N2 atoms are approximately coplanar, the torsion angle of N1–N4–O1–N2 being 0.7°, while the Ni atom is out of the plane.

The molecular structure of complex **12** is depicted in Figure 3 along with selected bond lengths and bond angles. The crystalline complex **12** is monomeric and the Ni center is in a distorted tetrahedral environment. The Ni···O distance of 3.781 Å shows no interactions between the atoms. The six-membered metallacycle exhibits a boat conformation. This is very similar to that of $[CH_2\{C(Me)=NAr\}_2]NiBr_2$ (Ar = 2,6-*i*$Pr_2C_6H_3$).[6a] The C5,N1,N2,C7 atoms are approximately coplanar, the torsion angle being 1.5°. The distance of Ni1–N1 [1.986(3) Å] is slightly shorter than that of Ni1–N2 [1.993(3) Å], and both are close to those found in $[2\text{-}\{Ph_2P=N(2',6'\text{-}Me_2C_6H_3)\}\text{-}6\text{-}Me_3SiC_5H_3N]NiBr_2$ [1.996(8) Å] and $[2\text{-}(Ph_3P=NCH_2)\text{-}6\text{-}MeC_5H_3N]NiBr_2$ [1.983(3) Å],[18] and slightly shorter than those of

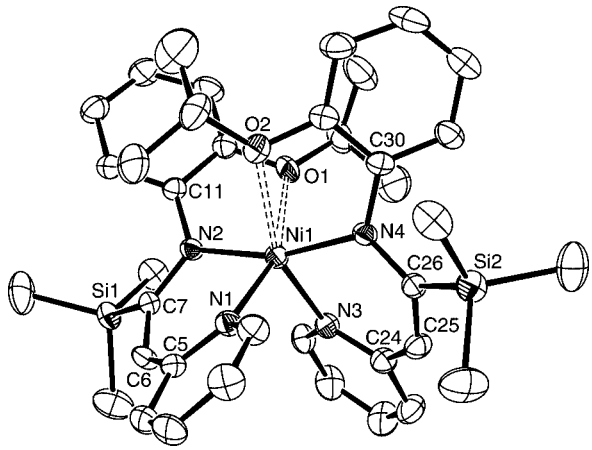


Figure 2. ORTEP drawing of complex **6** with 30% probability thermal ellipsoids. Selected bond lengths [Å] and bond angles [°]: Ni(1)–N(1) 2.045(3), Ni(1)–N(2) 1.968(3), Ni(1)–N(3) 2.043(4), Ni(1)–N(4) 1.976(3), Ni(1)···O(1) 2.574, Ni(1)···O(2) 2.586, C(6)–C(7) 1.377(6), C(25)–C(26) 1.371(6), N(2)–C(7) 1.377(5), N(4)–C(26) 1.373(5); N(1)–Ni(1)–N(2) 90.42(14), N(1)–Ni(1)–N(3) 100.11(14), N(1)–Ni(1)–N(4) 100.42(14), N(2)–Ni(1)–N(3) 100.77(14), N(2)–Ni(1)–N(4) 163.29(13), N(3)–Ni(1)–N(4) 89.88(14), O(1)–Ni(1)–N(1) 158.89, O(2)–Ni(1)–N(3) 158.58.

$[CH_2\{C(Me)=NAr\}_2]NiBr_2$ [2.010(5) and 2.022(5) Å, respectively].[6a] The Ni1–Br1 distance [2.3599(7) Å] is longer than that of Ni1–Br2 [2.3419(7) Å], and both are normal for four-coordinate $Ni^{II}$ complexes.[19] The N2–C7 distance of 1.288(4) Å agrees with that of a C=N double bond, indicating that the enamine tautomerizes to an imine after coordination to $Ni^{II}$. The N1–Ni1–N2 bond angle of 91.76(12)° is close to that of $[CH_2\{C(Me)=NAr\}_2]NiBr_2$ [93.7(2)°].[6a] However, the Br1–Ni1–Br2 bond angle of 124.78(3)° is wider than that of $[CH_2\{C(Me)=NAr\}_2]NiBr_2$ [118.54(5)°].[6a]

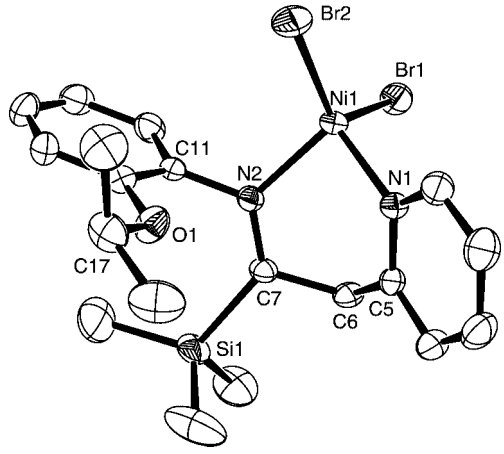


Figure 3. ORTEP drawing of complex **12** with 30% probability thermal ellipsoids. Selected bond lengths [Å] and bond angles [°]: Ni(1)–N(1) 1.986(3), Ni(1)–N(2) 1.993(3), Ni(1)–Br(1) 2.3599(7), Ni(1)–Br(2) 2.3419(7), Ni(1)···O(1) 3.781, C(5)–C(6) 1.501(6), C(6)–C(7) 1.527(5), N(2)–C(7) 1.288(4); N(1)–Ni(1)–N(2) 91.76(12), N(1)–Ni(1)–Br(1) 109.96(9), N(1)–Ni(1)–Br(2) 106.84(9), N(2)–Ni(1)–Br(1) 104.81(9), N(2)–Ni(1)–Br(2) 113.73(9), Br(1)–Ni(1)–Br(2) 124.78(3).

 © 2007 Wiley-VCH Verlag GmbH & Co. KGaA, Weinheim 

The structure of complex **14** is presented in Figure 4 along with selected bond lengths and bond angles. The crystalline **14** is monomeric and has a skeletal structure similar to that of **12**, including tetrahedral metal coordination geometry and the boat conformation of the six-membered metallacycle. The Fe1–N1 distance of 2.103(2) Å is slightly shorter than that of Fe1–N2 [2.115(2) Å], and both are within the normal range for this class of four-coordinate iron complexes. The Fe1–Cl1 distance of 2.2405(11) Å is longer than that of Fe1–Cl2 [2.2264(10) Å]. They are close to those in [2-{$Ph_2P$=N(2′,6′-$R'_2C_6H_3$)}-6-$RC_5H_3N$]$FeCl_2$ (R = Ph, $SiMe_3$; R′ = Me, *i*Pr) [2.2451(11)–2.2754(15) Å].[18] The Fe···O distance of 3.812 Å is beyond the distance of bonding interaction. The N2–C7 distance of 1.287(3) Å is almost the same as that of complex **12**, showing the ligand also to exist in an imine form.

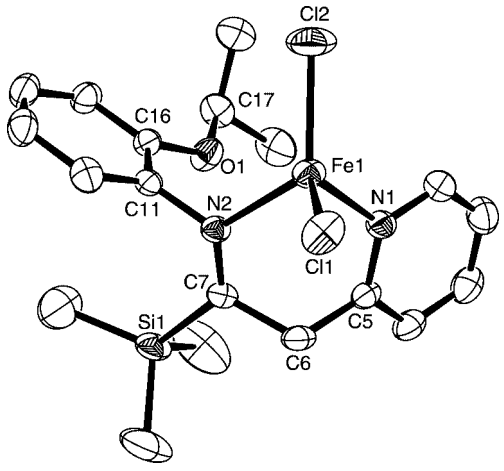


Figure 4. ORTEP drawing of complex **14** with 30% probability thermal ellipsoids. Selected bond lengths [Å] and bond angles [°]: Fe(1)–N(1) 2.103(2), Fe(1)–N(2) 2.115(2), Fe(1)–Cl(1) 2.2405(11), Fe(1)–Cl(2) 2.2264(10), Fe(1)···O(1) 3.812, N(2)–C(7) 1.287(3); N(1)–Fe(1)–N(2) 86.08(9), N(1)–Fe(1)–Cl(1) 112.84(7), N(1)–Fe(1)–Cl(2) 108.80(7), N(2)–Fe(1)–Cl(1) 108.49(7), N(2)–Fe(1)–Cl(2) 113.78(7), Cl(1)–Fe(1)–Cl(2) 121.39(4).

### Catalytic Properties of Complexes 5, 6, 9–16, 18, and 19 for Ethylene Oligomerization

It has been reported that bis(chelate)nickel complexes can catalyze vinylic polymerization of norbornene, polymerization or oligomerization of ethylene or α-olefins in the presence of appropriate organoaluminum co-catalysts. Some showed high catalytic activity and good selectivity.[5f,20] We determined the catalytic activity for ethylene polymerization or oligomerization of complexes **5** and **6** upon activation with MAO or MMAO and the results are listed in Table 1. All catalytic reactions shown in Table 1 were carried out at 20 °C and 1 atm ethylene pressure for 0.5 h. When MMAO was used as the co-catalyst, the Al/Ni ratio of 800:1 revealed very low catalytic activity for complexes **5** and **6**. Complex **5** exhibited the highest catalytic activity upon activation with 1000 equiv. of MMAO, while complex **6** reached its best activity in the presence of 1500 equiv. of MMAO (Entries 2 and 6 in Table 1). When MAO was used as the co-catalyst, the Al/Ni ratio of 800:1 gave the best catalytic activities for both complexes **5** and **6** (Entries 1 and 4 in Table 1). Higher or lower Al/Ni ratios resulted in a decline of the catalytic activities. The catalytic reactions predominantly formed dimers of ethylene in the presence of either MAO or MMAO, and the content of α-olefin is from 24.9 to 77.8%.

It was reported that in the catalytic reaction of bis(chelate)nickel complexes the active species was in situ generated by treatment of the nickel complexes with the organoaluminum compound under ethylene.[20c–20e,21] In our catalytic systems, the bis(chelate)nickel complexes **5** and **6** may go through a similar reaction in the presence of MAO and ethylene as shown in Figure 5. Thus, active species **I** was generated by reaction of **5** or **6** with MAO and ethylene. The active intermediate may be stabilized by a weak coordination of the RO group to the nickel center. Subsequently, the ethylene molecule coordinates to the nickel center to carry out the further reactions.

The nickel complexes **9**–**12** can catalyze ethylene dimerization and trimerization in the presence of MAO, MMAO, or $Et_2AlCl$. However, using $Et_2AlCl$ as the co-catalyst revealed higher activity. Therefore, a systematic investigation of the catalytic behavior of complexes **9**–**12** was performed using $Et_2AlCl$ as the co-catalyst (Table 2). In each case the polymerization reaction gave a mixture of $C_4$ and $C_6$ species. At 20 °C and 1 atm ethylene pressure for 0.5 h, the Al/Ni molar ratio of 200:1 afforded the highest catalytic activity for complexes **9**–**12** (**9**, $1.2\times10^3$; **10**, $1.21\times10^3$; **11**, $1.82\times10^3$; and **12**, $1.25\times10^3$ kg/mol h, respectively, Entries 2, 5, 8, and 17 in Table 2). Longer reaction times resulted in decline of both turnover frequency and the proportion of $C_4$ components (Entries 15 and 18 in Table 2). The decrease of the activity can be attributed to the deactivation of the active species during a longer reaction period. In the reaction catalyzed by **9**/$Et_2AlCl$, augmentation of the Al/Ni ratio resulted in enhancement of the proportion of

Table 1. Ethylene oligomerization with complexes **5** and **6**.[a]

| Entry | Complex | Co-catalyst | Al/M | Activity[b] | $C_4$ [%][c] | α-$C_4$[c] | $C_6$ [%][c] | α-$C_6$[c] |
|---|---|---|---|---|---|---|---|---|
| 1 | **5** | MAO | 800 | 78 | >99 | 24.9 | | |
| 2 | **5** | MMAO | 1000 | 395 | >99 | 77.8 | | |
| 3 | **5** | MMAO | 1500 | 177 | >99 | 65.7 | | |
| 4 | **6** | MAO | 800 | 71 | 97.4 | 51.5 | 2.6 | 35.7 |
| 5 | **6** | MMAO | 1000 | 52 | >99 | 67.8 | | |
| 6 | **6** | MMAO | 1500 | 224 | >99 | 58.6 | | |

[a] Conditions: 5 μmol of pre-catalyst, 30 mL of toluene, 1 atm ethylene, 0.5 h. [b] kg/mol h. [c] Weight percent determined by GC analysis.

 © 2007 Wiley-VCH Verlag GmbH & Co. KGaA, Weinheim 

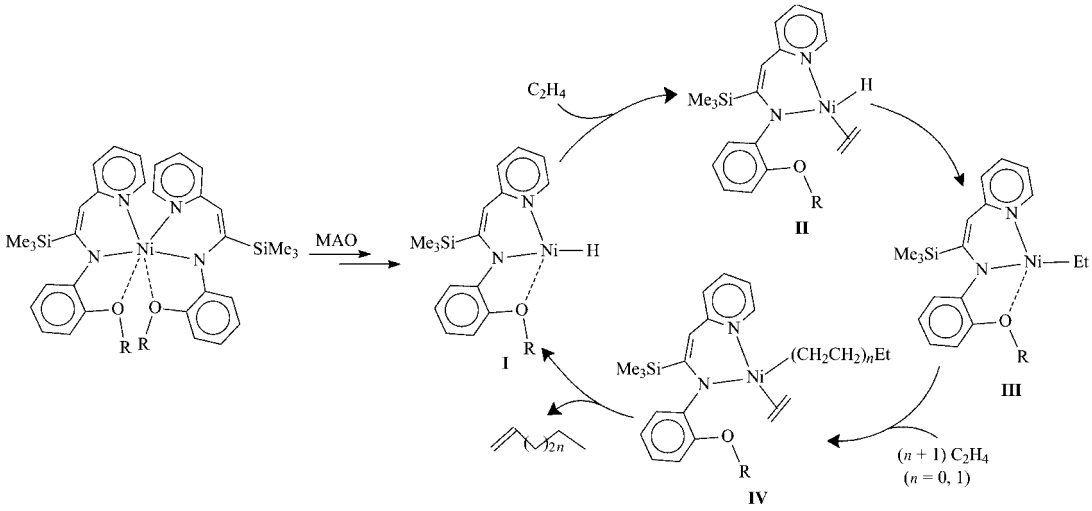


Figure 5. Possible mechanism for ethylene oligomerization catalyzed by **5** and **6**/MAO.

Table 2. Ethylene oligomerization with complexes **9**–**12**.[a]

| Entry | Complex | Al/Ni | *P* [atm] | Time [h] | *T* [°C] | Activity[b] | $C_4$ [%][c] | $C_6$ [%][c] |
|---|---|---|---|---|---|---|---|---|
| 1 | **9** | 50 | 1 | 0.5 | 20 | 5.4 | 76.2 | 23.8 |
| 2 | **9** | 200 | 1 | 0.5 | 20 | 12 | 76.4 | 23.6 |
| 3 | **9** | 400 | 1 | 0.5 | 20 | 2.45 | 97.2 | 2.8 |
| 4 | **9** | 600 | 1 | 0.5 | 20 | 2.21 | 95.0 | 5.0 |
| 5 | **10** | 200 | 1 | 0.5 | 20 | 12.1 | 60.2 | 39.8 |
| 6 | **11** | 50 | 1 | 0.5 | 20 | 7.78 | 83.8 | 16.2 |
| 7 | **11** | 100 | 1 | 0.5 | 20 | 8.47 | 86.3 | 13.7 |
| 8 | **11** | 200 | 1 | 0.5 | 20 | 18.2 | 72.3 | 27.7 |
| 9 | **11** | 300 | 1 | 0.5 | 20 | 4.83 | 89.4 | 10.6 |
| 10 | **11** | 400 | 1 | 0.5 | 20 | 4.3 | 91.4 | 8.6 |
| 11 | **11** | 500 | 1 | 0.5 | 20 | 2.72 | 82.0 | 18.0 |
| 12 | **11** | 200 | 1 | 0.5 | 0 | 5.65 | 88.2 | 11.8 |
| 13 | **11** | 200 | 1 | 0.5 | 40 | 4.27 | 59.0 | 41.0 |
| 14 | **11** | 200 | 1 | 0.5 | 60 | 3.28 | 6.7 | 93.3 |
| 15 | **11** | 200 | 1 | 1 | 20 | 12.8 | 46.2 | 53.8 |
| 16 | **11** | 200 | 10 | 0.5 | 20 | 92 | 78.0 | 22.0 |
| 17 | **12** | 200 | 1 | 0.5 | 20 | 12.5 | 66.2 | 33.8 |
| 18 | **12** | 200 | 1 | 1 | 20 | 8.72 | 59.8 | 40.2 |
| 19 | **12** | 200 | 10 | 0.5 | 20 | 8.63 | 75.8 | 24.2 |

[a] Conditions: 5 μmol of pre-catalyst, $Et_2AlCl$ as co-catalyst, 30 mL of toluene (120 mL of toluene when determined under 10 atm ethylene). [b] $10^2$ kg/mol h. [c] Weight percent determined by GC analysis.

$C_4$ component in the products. While in the reaction catalyzed by the **11**/$Et_2AlCl$ system, the Al/Ni ratio of 400:1 gave the highest proportion of $C_4$ component. A change in the reaction temperature also dramatically affected the distribution of the polymerization products. We tested the catalytic reaction of the **11**/$Et_2AlCl$ system with a 200:1 Al/Ni ratio under 1 atm ethylene pressure at 0 °C, 20 °C, 40 °C, and 60 °C, respectively, and found that the proportion of $C_6$ component increased as the reaction temperature increased (Entries 8 and 12–14 in Table 2). In addition, it was also noted that an increase in ethylene pressure did not enhance the catalytic activity of the catalysts in terms of unit pressure (Entries 16 and 19 in Table 2).

It has been reported that (β-diimine)nickel and (8-quinolylimine)nickel catalysts (Scheme 3) showed very low catalytic activity for ethylene polymerization compared with (α-diimine)nickel complexes and the difference was attributed to the chelate ring size.[6] In our catalytic systems each of the complexes **9**–**12** exhibited good catalytic activity under the optimal conditions. Single-crystal X-ray diffraction results show that complex **12** has a similar skeletal structure and bond lengths and angles to that of the (β-diimine)nickel complex $[CH_2\{C(Me)=NAr\}_2]NiBr_2$ (Ar = 2,6-$i$Pr$_2$C$_6$H$_3$).[6a] Therefore, the relatively high catalytic activity of **9**–**12** is most likely the result of the existence of the *o*-

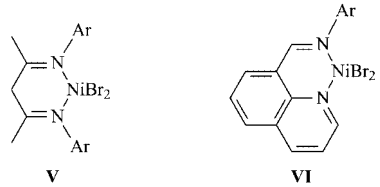


Scheme 3.

 © 2007 Wiley-VCH Verlag GmbH & Co. KGaA, Weinheim 

OR substituent on the phenylene ring of the ligands. The oxygen atom of the OR group may stabilize the active intermediate through coordination to the metal center during the reaction (see below).

The nature of aluminum co-catalysts greatly affected the catalytic activities of the pre-catalysts and the distribution of the products. The cobalt and iron complexes **13**–**16** were inactive for ethylene oligomerization when $Et_2AlCl$ was used as the co-catalyst. However, these cobalt and iron complexes exhibited catalytic activities for ethylene oligomerization in the presence of MMAO or MAO (Table 3). When MMAO was used as the co-catalyst, the complexes revealed high catalytic activity (up to $8.01 \times 10^2$ kg/mol h, Entry 12 in Table 3) and the polymerization products were almost solely $C_4$ species in most cases. When MAO was used as the co-catalyst, complexes **13** and **14** showed very low catalytic activity, while **15** and **16** exhibited moderate activity (up to 24.6 kg/mol h, Entry 14 in Table 3) and the major polymerization products were $C_6$ species. We also examined the effect of Al/M ratio for complexes **13** and **15**, respectively. When MMAO was used as co-catalyst, the catalytic activity increased with the enhancement of Al/M molar ratio until 1500:1 for complex **13** and 2000:1 for complex **15** (Entries 4 and 11 in Table 3). When MAO was used as co-catalyst, the Al/Co ratio of 800:1 resulted in the highest catalytic activity for complex **15** (Entry 14 in Table 3), higher or lower Al/Co ratios leading to decrease of the catalytic activity.

Table 3. Ethylene oligomerization with complexes **13**–**16**.[a]

| Entry | Complex | Co-catalyst | Al/M | Activity[b] | $C_4$ [%][c] | $C_6$ [%][c] |
|---|---|---|---|---|---|---|
| 1 | **13** | MMAO | 500 | 121 | 98.4 | 1.6 |
| 2 | **13** | MMAO | 800 | 195 | 98.7 | 1.3 |
| 3 | **13** | MMAO | 1000 | 233 | 98.9 | 1.1 |
| 4 | **13** | MMAO | 1500 | 550 | 92.8 | 7.2 |
| 5 | **13** | MMAO | 2000 | 518 | 99.3 | 0.7 |
| 6 | **14** | MMAO | 1500 | 430 | 99.4 | 0.6 |
| 7 | **15** | MMAO | 500 | 174 | 96.0 | 4.0 |
| 8 | **15** | MMAO | 800 | 340 | 99.3 | 0.7 |
| 9 | **15** | MMAO | 1000 | 426 | 99.4 | 0.6 |
| 10 | **15** | MMAO | 1500 | 470 | 99.5 | 0.5 |
| 11 | **15** | MMAO | 2000 | 623 | 99.8 | 0.2 |
| 12 | **16** | MMAO | 2000 | 801 | 99.6 | 0.4 |
| 13 | **15** | MAO | 500 | 8.5 | 3.0 | 97.0 |
| 14 | **15** | MAO | 800 | 24.6 | 19.8 | 80.2 |
| 15 | **15** | MAO | 1000 | 12.8 | 10.5 | 89.5 |
| 16 | **15** | MAO | 1200 | 6 | 4.9 | 95.1 |
| 17 | **16** | MAO | 800 | 11 | 21.0 | 79.0 |

[a] Conditions: 5 μmol of pre-catalyst, 30 mL of toluene, 1 atm ethylene, 20 °C, 0.5 h. [b] kg/mol h. [c] Weight percent determined by GC analysis.

It is very rare to see that iron and cobalt complexes with a six-membered *N*,*N*-chelate ring exhibit high catalytic activity for ethylene polymerization or oligomerization. Good activity shown by complexes **13**–**16** upon activation with MMAO is also attributed to the existence of *o*-OR substituents on the phenylene ring of the ligands.

The proportion of terminal olefins in the dimers or trimers was also determined for the reactions catalyzed by complexes **9**–**16** under representative reaction conditions (Table 4). At 20 °C and 1 atm ethylene pressure for 0.5 h, the reactions catalyzed by the **9**–**12**/$Et_2AlCl$ (1:200) systems gave relatively low α-butene and α-hexene proportions. When activated with MMAO, each of the complexes **13**–**16** led to relatively high α-butene proportions, from 84.5 to 90.7%.

In order to understand the role of *o*-OR substituents on the phenylene ring of the ligands in complexes **9**–**16**, we investigated the catalytic behavior of complex **18** whose ligand does not contain an extra donor group on the phenylene ring. The results are shown in Table 5. Compared with complexes **11** and **12** under the same polymerization conditions, complex **18** exhibited lower catalytic activity. Hence, we think that the existence of *o*-RO substituents on the phenylene ring in the nickel complexes may stabilize the active intermediate through a weak coordination of the oxygen atom to the metal center, which leads to the rise in their catalytic activities (Scheme 4). Although the stabilizing action of the aluminum activator to the active intermediate is usually important, the intramolecular coordination may provide extra stabilization in our catalytic systems. Bianchini and co-workers also observed that complex **IX** exhibits higher catalytic activity than complex **X** in ethylene oligomerization upon activation with MAO and they thought that the sulfur atom of the former may play an active role (Scheme 5).[22] In addition, the activity of complex **19** is also lower than that of complexes **15** or **16** whether MAO or MMAO was used as the co-catalyst. This is possibly due to the existence of the same stabilization in the **15** or **16**/activator system.

Table 4. Oligomer composition catalyzed by pre-catalysts **9**–**16**[a].

| Entry | Complex | Co-catalyst | Al/Ni | *T* [°C] | Activity[b] | $C_4$ [%][c] | α-$C_4$ [%][c] | $C_6$ [%][c] | α-$C_6$ [%][c] |
|---|---|---|---|---|---|---|---|---|---|
| 1 | **9** | $Et_2AlCl$ | 200 | 20 | 10.8 | 79.8 | 26.4 | 20.2 | 32.4 |
| 2 | **10** | $Et_2AlCl$ | 200 | 20 | 11.2 | 66.0 | 18.6 | 34 | 29.5 |
| 3 | **11** | $Et_2AlCl$ | 200 | 20 | 17.1 | 78.0 | 29.7 | 22.0 | 44.3 |
| 4 | **11** | $Et_2AlCl$ | 200 | 0 | 5.77 | 85.6 | 36.6 | 14.4 | 38.2 |
| 5 | **12** | $Et_2AlCl$ | 200 | 20 | 11.5 | 69.4 | 32.0 | 30.6 | 26.4 |
| 6 | **13** | MMAO | 1500 | 20 | 5.75 | 97.7 | 90.7 | 2.3 | 28 |
| 7 | **14** | MMAO | 1500 | 20 | 4.14 | >99 | 86.4 | | |
| 8 | **15** | MMAO | 2000 | 20 | 6.72 | >99 | 84.5 | | |
| 9 | **16** | MMAO | 2000 | 20 | 8.28 | >99 | 90.0 | | |

[a] Conditions: 5 μmol of pre-catalyst, 30 mL of toluene, 1 atm ethylene, 0.5 h. [b] $10^2$ kg/mol h. [c] Weight percent determined by GC analysis.

 © 2007 Wiley-VCH Verlag GmbH & Co. KGaA, Weinheim 

Table 5. Ethylene oligomerization with complexes **18** and **19**.[a]

| Entry | Complex | Co-catalyst | Al/M | Activity[b] | $C_4$ [%][c] | α-$C_4$ [%][c] | $C_6$ [%][c] | α-$C_6$ [%][c] |
|---|---|---|---|---|---|---|---|---|
| 1 | **18** | $Et_2AlCl$ | 100 | 126 | 43.8 | 11.6 | 56.2 | 23.7 |
| 2 | **18** | $Et_2AlCl$ | 200 | 159 | 98.2 | 58.5 | 1.8 | 14.5 |
| 3 | **18** | $Et_2AlCl$ | 500 | 220 | 45.5 | 29.5 | 54.5 | 12.3 |
| 4 | **19** | MMAO | 800 | 142 | 98.4 | 65.7 | 1.6 | 56.4 |
| 5 | **19** | MMAO | 2000 | 129 | >99 | 98 | | |
| 6 | **19** | MAO | 800 | 4 | 81.6 | | 18.4 | |
| 7 | **19** | MAO | 2000 | 1.2 | 37.8 | | 62.2 | |

[a] Conditions: 5 μmol of pre-catalyst, 30 mL of toluene, 1 atm ethylene, 0.5 h. [b] kg/mol h. [c] Weight percent determined by GC analysis.

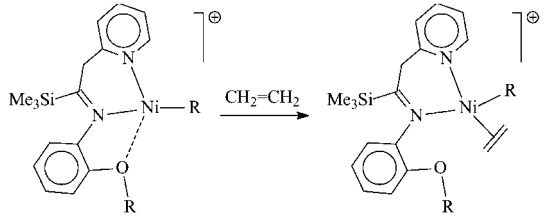


Scheme 4. Possible active intermediates of **9**–**12**/$Et_2AlCl$ systems.

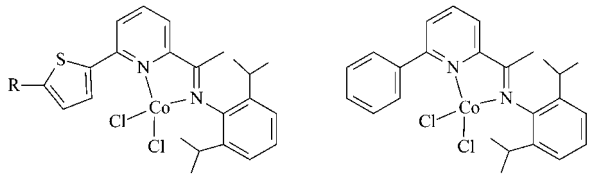


Scheme 5.

## Conclusions

We have synthesized novel anionic and neutral *N*,*N*-chelate ligands and their iron, cobalt, and nickel complexes. Single-crystal X-ray diffraction revealed that in bis(chelate)-nickel complex **6** there are relatively weak bonding interactions between the O atoms and the Ni atoms. Investigation of catalytic behavior for ethylene oligomerization showed that complexes **5** and **6** could catalyze ethylene oligomerization with good activity in the presence of MAO or MMAO, giving mainly $C_4$ species. The nickel complexes with neutral ligands exhibited high catalytic activity upon activation with $Et_2AlCl$. This relatively high activity compared with previously reported (β-diimine)nickel complexes and analogues is attributed to the stabilizing action of the *o*-OR group on the phenylene ring of the ligands to the active species through coordination of the oxygen atom to the metal center. The iron and cobalt complexes bearing neutral ligands also exhibited good catalytic activity upon activation with MMAO. However, when MAO was used as the co-catalyst, the iron and cobalt complexes showed relatively low activities.

## Experimental Section

**General Procedure:** All air-sensitive manipulations were performed under $N_2$ using standard Schlenk and vacuum-line techniques. Solvents were distilled under $N_2$ from sodium/benzophenone (toluene, *n*-hexane, thf, and $Et_2O$) or $CaH_2$ ($CH_2Cl_2$) and degassed prior to use. NMR spectra were recorded with a Bruker av300 spectrometer at ambient temperature. The chemical shifts of $^1H$ and $^{13}C$ NMR spectra are referenced to internal solvent resonances. IR spectra were recorded with a Bruker VECTOR-22 spectrometer. HRMS data were determined with an Agilent6890/Micromass GCT-MS spectrometer. Elemental analyses were performed by the Analytical Center of the University of Science and Technology of China. The magnetic moments of the paramagnetic complexes were determined by the Evans NMR method.[23] Gas chromatographic analyses were performed with a Carlo Erba Strumentazione gas chromatograph equipped with a flame-ionization detector and a 30 m (0.25 mm i.d., 0.25-μm film thickness) DM-1 silica capillary column or with an HP5890 gas chromatograph equipped with a flame-ionization detector and a 30 m (0.25 mm i.d., 0.25-μm film thickness) CAT-7221 silica capillary column. High-purity ethylene was purchased from Beijing Yanshan Petrochemical Co. and used as received. Methylaluminoxane (MAO, 1.46 M in toluene) and modified methylaluminoxane (MMAO, 1.93 M in heptane) were purchased from Akzo Nobel Corp. $Et_2AlCl$ was purchased from Fluka as a 1.90 M solution in hexane.

### Preparations

***o*-PhCH$_2$OC$_6$H$_4$NC (1):** Compound **1** was prepared according to a literature method.[12] $^1H$ NMR ($CDCl_3$): $\delta$ = 5.20 (s, 2 H, $CH_2$), 6.91–7.01 (m, 2 H, Ph, $C_6H_4$), 7.26–7.49 (m, 7 H, Ph, $C_6H_4$) ppm. IR (KBr): $\tilde{\nu}$ = 3072 (w), 3034 (w), 2947 (w), 2936 (w), 2876 (w), 2127 (vs), 1593 (s), 1492 (vs), 1469 (m), 1454 (s), 1382 (m), 1301 (m), 1287 (vs), 1251 (vs), 1162 (m), 1109 (s), 1080 (w), 1040 (w), 1001 (s), 932 (w), 917 (m), 857 (m), 760 (m), 744 (vs), 695 (s), 617 (w) $cm^{-1}$.

***o*-*i*PrOC$_6$H$_4$NC (2):** Compound **2** was prepared according to the same method as for **1** as a colorless oil, b.p. 100 °C/2 Torr. $^1H$ NMR ($CDCl_3$): $\delta$ = 1.33 (d, $J$ = 6.1 Hz, 6 H, *i*Pr), 4.55 (sept, $J$ = 6 Hz, 1 H, CH), 6.80–6.91 (m, 2 H, $C_6H_4$), 7.21–7.27 (m, 2 H, $C_6H_4$) ppm. IR (liquid film): $\tilde{\nu}$ = 3076 (w), 2981 (s), 2935 (m), 2125 (vs), 1596 (s), 1492 (vs), 1455 (m), 1386 (m), 1376 (m), 1286 (s), 1260 (s), 1176 (w), 1162 (m), 1139 (m), 1117 (s), 1043 (m), 952 (s), 867 (w), 752 (s) $cm^{-1}$.

**[LiN(*o*-PhCH$_2$OC$_6$H$_4$){C(SiMe$_3$)CHC$_5$H$_4$N-2}]$_2$ (3):** To a stirred solution of [Li(TMEDA){2-CH(SiMe$_3$)C$_5$H$_4$N}] (3.84 g, 13.38 mmol) in diethyl ether (20 mL) was added compound **1** (2.80 g, 13.40 mmol) at –30 °C. The resultant solution was warmed to room temperature and stirred overnight. The mixture was filtered and the precipitate was washed with diethyl ether (2 × 5 mL). The solid was dried in vacuo to give a yellow powder of **3** (4.21 g, 82.7%), m.p. 181–182 °C. $^1H$ NMR ($C_6D_6$): $\delta$ = 0.48 (s, 9 H, $SiMe_3$), 4.42 (d, $J$ = 11.7 Hz, 1 H, $CH_2$), 4.58 (d, $J$ = 11.4 Hz, 1 H, $CH_2$), 5.62 (s, 1 H, CH), 6.48–6.53 (m, 1 H, Ar), 6.57 (d, $J$ = 8.4 Hz, 1 H, Ar), 6.66 (d, $J$ = 7.8 Hz, 1 H, Ar), 6.92–7.22 (m, 6 H,

 © 2007 Wiley-VCH Verlag GmbH & Co. KGaA, Weinheim 

Ar), 7.42 (d, $J$ = 7.8 Hz, 1 H, Ar), 7.98–8.01 (m, 1 H, Ar) ppm. $^{13}$C NMR ($C_6D_6$): $\delta$ = 2.60, 70.17, 110.49, 110.88, 114.93, 119.02, 121.95, 122.38, 125.24, 128.22, 128.57, 128.81, 135.52, 136.35, 147.24, 148.87, 151.64, 157.50, 168.08 ppm. $C_{23}H_{25}LiN_2OSi$ (380.484): calcd. C 72.60, H 6.62, N 7.36; found C 71.92, H 6.62, N 7.30.

**[LiN(*o*-*i*PrOC$_6$H$_4$){C(SiMe$_3$)CHC$_5$H$_4$N-2}]$_2$ (4):** Complex **4** was prepared according to the same method as for **3**. To a solution of [Li(TMEDA){2-CH(SiMe$_3$)C$_5$H$_4$N}] (3.55 g, 12.37 mmol) in diethyl ether (20 mL) was added compound **2** (2.00 g, 12.42 mmol) at –30 °C. The mixture was warmed to room temperature and stirred overnight. The resultant precipitate was washed with diethyl ether and dried in vacuo to afford a yellow powder of **4** (3.85 g, 93.5%), m.p. 242–243 °C. $^1$H NMR ($C_6D_6$): $\delta$ = 0.46 (s, 9 H, SiMe$_3$), 0.97 (d, $J$ = 6 Hz, 3 H, *i*Pr), 1.35 (d, $J$ = 6 Hz, 3 H, *i*Pr), 4.36 (heptet, $J$ = 6 Hz, 1 H, *i*Pr), 5.81 (s, 1 H, CH), 6.68–6.75 (m, 2 H, Ar), 6.84 (d, $J$ = 8.4 Hz, 1 H, Ar), 7.01–7.06 (m, 1 H, Ar), 7.14–7.17 (m, 2 H, Ar), 7.21–7.27 (m, 1 H, Ar), 8.40 (dd, $J$ = 1.2, 5.1 Hz, 1 H, Ar) ppm. $^{13}$C NMR ($C_6D_6$): $\delta$ = 2.40, 20.43, 22.01, 70.29, 110.85, 110.93, 115.39, 119.21, 121.71, 123.20, 125.70, 135.86, 147.17, 149.42, 150.43, 157.97, 169.99 ppm. $C_{19}H_{25}LiN_2OSi$ (332.441): calcd. C 68.64, H 7.58, N 8.43; found C 68.21, H 7.57, N 8.26.

**Ni[N(*o*-PhCH$_2$OC$_6$H$_4$){C(SiMe$_3$)CHC$_5$H$_4$N-2}]$_2$ (5):** To a stirred suspension of (dme)NiCl$_2$ (0.15 g, 0.684 mmol) in thf (5 mL) was added compound **3** (0.26 g, 0.684 mmol) at about –80 °C. The resultant mixture was warmed to room temperature and stirred overnight. Volatiles were removed in vacuo and the residue was extracted with Et$_2$O. The diethyl ether solution was filtered and the filtrate concentrated in vacuo to form dark red-brown crystals of **5** (0.25 g, 91%), m.p. 169–170 °C. IR (KBr): $\tilde{\nu}$ = 3088 (vw), 3053 (w), 3024 (w), 2951 (w), 2894 (vw), 1600 (m), 1572 (w), 1557 (w), 1501 (m), 1481 (s), 1469 (vs), 1453 (m), 1418 (m), 1384 (vs), 1314 (w), 1277 (m), 1260 (m), 1246 (m), 1208 (m), 1189 (m), 1153 (m), 1113 (w), 1102 (vw), 1022 (w), 1004 (w), 847 (m), 783 (w), 751 (w), 732 (m), 693 (w) cm$^{-1}$. $C_{46}H_{50}N_4NiO_2Si_2$ (805.779): calcd. C 68.57, H 6.25, N 6.95; found C 68.77, H 6.43, N 6.90. HRMS (EI): calcd. for $C_{46}H_{50}N_4NiO_2Si_2$ [M]$^+$ 804.2826; found 804.2820. $\mu_{eff}$ = 3.77 BM.

**Ni[N(*o*-*i*PrOC$_6$H$_4$){C(SiMe$_3$)CHC$_5$H$_4$N-2}]$_2$ (6):** Complex **6** was prepared according to a procedure similar to that of **5**. Reaction of (dme)NiCl$_2$ (0.195 g, 0.886 mmol) with **4** (0.30 g, 0.904 mmol) in thf gave, after workup, dark red-brown crystals of **6** (0.295 g, 92%), m.p. 180–182 °C. IR (KBr): $\tilde{\nu}$ = 3052 (vw), 2974 (w), 2948 (w), 2894 (w), 1599 (m), 1572 (w), 1558 (w), 1503 (m), 1480, 1469 (vs), 1420 (s), 1369 (vs), 1309 (w), 1289 (s), 1265 (s), 1244 (m), 1207 (m), 1154 (m), 1138 (m), 1117 (m), 1048 (w), 1005 (w), 948 (w), 846 (s), 786 (s), 740 (s), 684 (vw), 621 (vw) cm$^{-1}$. $C_{38}H_{50}N_4NiO_2Si_2$ (709.694): calcd. C 64.31, H 7.10, N 7.89; found C 64.39, H 7.03, N 8.01. HRMS (EI): calcd. for $C_{38}H_{50}N_4NiO_2Si_2$ [M]$^+$ 708.2826; found 708.2823. $\mu_{eff}$ = 3.70 BM.

***o*-PhCH$_2$OC$_6$H$_4$NHC(SiMe$_3$)CHC$_5$H$_4$N-2 (7):** To a stirred solution of **3** (1.488 g, 3.92 mmol) in toluene (20 mL) was added Et$_3$NH$^+$Cl$^-$ (0.54 g, 3.93 mmol) at 0 °C. The resultant mixture was warmed to room temperature and stirred for 20 h. The solution was filtered and volatiles were removed from the filtrate in vacuo to afford **7** as a yellowish oil (1.464 g, 100%). The oil was dissolved in hexane and cooled to –30 °C to form a pale yellow precipitate. The precipitate was filtered at –30 °C and then dried in vacuo to afford a pale yellow solid, m.p. 81–83 °C. $^1$H NMR ($CDCl_3$): $\delta$ = 0.20 (s, 9 H, SiMe$_3$), 5.17 (s, 2 H, CH$_2$), 5.69 (s, 1 H, CH), 6.84–6.95 (m, 4 H, Ar), 7.02 (d, $J$ = 8.1 Hz, 1 H, Ar), 7.10 (d, $J$ = 7.5 Hz, 1 H, Ar), 7.29–7.37 (m, 3 H, Ar), 7.48–7.55 (m, 3 H, Ar), 8.23–8.25 (m, 1 H, Ar), 11.77 (s, 1 H, NH) ppm. $^{13}$C NMR ($CDCl_3$): $\delta$ = 1.01, 70.29, 109.88, 112.66, 118.26, 120.78, 122.16, 122.32, 122.65, 127.22, 127.72, 128.53, 134.31, 135.63, 137.55, 147.37, 150.62, 152.84, 159.30 ppm. IR (liquid film): $\tilde{\nu}$ = 3064 (w), 3036 (w), 2953 (w), 2897 (vw), 1590 (s), 1577 (vs), 1540 (vs), 1507 (m), 1463 (m), 1450 (m), 1411 (w), 1360 (m), 1301 (w), 1259 (s), 1217 (s), 1158 (w), 1109 (w), 1046, 1024 (w), 911 (vw), 847 (s), 804 (m), 738 (s), 694 (m) cm$^{-1}$. $C_{23}H_{26}N_2OSi$ (374.551): calcd. C 73.76, H 7.00, N 7.48; found C 73.46, H 7.10, N 7.40.

***o*-*i*PrOC$_6$H$_4$NHC(SiMe$_3$)CHC$_5$H$_4$N-2 (8):** Compound **8** was prepared according to a procedure similar to that of **7**. Treatment of **4** (1.412 g, 4.25 mmol) with Et$_3$NH$^+$Cl$^-$ (0.60 g, 4.36 mmol) in toluene afforded, after workup, compound **8** (1.386 g, 100%) as a yellowish oil. $^1$H NMR ($CDCl_3$): $\delta$ = 0.13 (s, 9 H, SiMe$_3$), 1.31 (d, $J$ = 6 Hz, 6 H, *i*Pr), 4.47 (sept, $J$ = 6 Hz, 1 H, *i*Pr), 5.59 (s, 1 H, CH), 6.74–6.85 (m, 4 H, Ar), 6.92–6.98 (m, 2 H, Ar), 7.40–7.46 (m, 1 H, Ar), 8.32–8.34 (m, 1 H, Ar), 11.58 (s, 1, NH) ppm. $^{13}$C NMR ($CDCl_3$): $\delta$ = 1.04, 22.39, 71.36, 109.77, 115.16, 118.19, 120.66, 121.50, 122.22, 122.26, 135.33, 135.58, 147.19, 149.33, 152.39, 159.22 ppm. IR (liquid film): $\tilde{\nu}$ = 3065 (w), 3007 (w), 2975 (m), 2904 (w), 1590 (vs), 1578 (vs), 1540 (vs), 1505 (m), 1463 (m), 1411 (w), 1361 (m), 1301 (w), 1258 (vs), 1218 (s), 1160 (w), 1150 (w), 1118 (m), 1044 (vw), 956 (vw), 912 (vw), 848 (s), 802 (m), 739 (m), 687 (w) cm$^{-1}$. $C_{19}H_{26}N_2OSi$ (326.508): calcd. C 69.89, H 8.03, N 8.58; found C 69.72, H 8.13, N 8.46.

**[NiCl$_2${N(*o*-PhCH$_2$OC$_6$H$_4$)=C(SiMe$_3$)CH$_2$C$_5$H$_4$N-2}] (9):** To a stirred suspension of (dme)NiCl$_2$ (0.35 g, 1.59 mmol) in thf (5 mL) was added **7** (0.60 g, 1.60 mmol) in thf (10 mL) at 0 °C. The mixture was warmed to room temperature and stirred overnight. Volatiles were removed in vacuo and the yellow solids were washed with Et$_2$O (2 × 2 mL). The solid was dissolved in $CH_2Cl_2$ and filtered through Celite. Toluene (10 mL) was added to the filtrate. Concentration of the solution in vacuo gave yellow-green crystals of complex **9** (0.59 g, 74.2%), m.p. 192–194 °C. IR (KBr): $\tilde{\nu}$ = 3057 (s), 3036 (m), 2951 (m), 2897 (vw), 2875 (m), 1603 (s), 1590 (m), 1579 (m), 1488 (vs), 1452 (s), 1442 (s), 1397 (w), 1377 (w), 1347 (w), 1320 (m), 1288 (m), 1267 (m), 1254 (s), 1235 (s), 1207 (m), 1195 (m), 1161 (m), 1115 (m), 1063 (m), 1045 (m), 1018 (s), 897 (w), 871 (s), 846 (vs), 791 (w), 758 (vs), 736 (s), 725 (s), 692 (m), 651 (w), 634 (w) cm$^{-1}$. $C_{23}H_{26}Cl_2N_2NiOSi$ (504.15): calcd. C 54.80, H 5.20, N5.56; found C 55.01, H 5.27, N 5.45. HRMS (EI): calcd. for $C_{23}H_{26}ClN_2NiOSi$ [M – Cl]$^+$ 467.0856; found 467.1482. $\mu_{eff}$ = 3.82 BM.

**[NiCl$_2${N(*o*-*i*PrOC$_6$H$_4$)=C(SiMe$_3$)CH$_2$C$_5$H$_4$N-2}] (10):** Complex **10** was prepared according to a procedure similar to that for **9**. Treatment of (dme)NiCl$_2$ (0.27 g, 1.23 mmol) with **8** (0.40 g, 1.23 mmol) in thf formed, after similar workup, purple crystals of **10** (0.42 g, 75.1%), m.p. 182–184 °C. IR (KBr): $\tilde{\nu}$ = 3104 (vw), 3068 (w), 3029 (w), 2977 (m), 2931 (w), 2896 (w), 1605 (m), 1592 (s), 1569 (w), 1485 (vs), 1446 (s), 1417 (w), 1372 (w), 1358 (w), 1283 (vw), 1250 (s), 1203 (w), 1176 (w), 1159 (w), 1139 (w), 1120 (w), 1095 (m), 1067 (w), 1030 (w), 955 (w), 933 (w), 924 (w), 853 (vs), 803 (w), 765 (vs), 700 (w), 680 (vw) cm$^{-1}$. $C_{19}H_{26}Cl_2N_2NiOSi$ (456.107): calcd. C 50.03, H 5.75, N 6.14; found C 49.93, H 5.74, N 6.14. HRMS (EI): calcd. for $C_{19}H_{26}ClN_2NiOSi$ [M – Cl]$^+$ 419.0856; found 419.0849. $\mu_{eff}$ = 3.88 BM.

**[NiBr$_2${N(*o*-PhCH$_2$OC$_6$H$_4$)=C(SiMe$_3$)CH$_2$C$_5$H$_4$N-2}] (11):** To a stirred suspension of NiBr$_2$ (0.14 g, 0.64 mmol) in thf (5 mL) was added **7** (0.25 g 0.67 mmol) in thf (10 mL) at 0 °C. The resultant mixture was warmed to room temperature and stirred overnight. The color of the solution changed from straw-yellow to red. Volatiles were removed in vacuo and the red solid residue was dissolved in $CH_2Cl_2$. After filtration through Celite, the solvent was removed

 © 2007 Wiley-VCH Verlag GmbH & Co. KGaA, Weinheim 

from the filtrate and the solid was washed with diethyl ether (2 × 2 mL) to give red crystalline **11** (0.302 g, 77.4%), m.p. 189–191 °C. IR (KBr): ṽ = 3056 (m), 2953 (m), 2860 (m), 1604 (m), 1593 (m), 1574 (w), 1486 (s), 1444 (s), 1407 (w), 1372 (w), 1348 (w), 1315 (w), 1285 (w), 1253 (s), 1239 (m), 1205 (w), 1161 (w), 1112 (m), 1067 (w), 1040 (w), 1020 (m), 942 (vw), 921 (vw), 904 (vw), 851 (vs), 801 (w), 766 (s), 735 (s), 695 (m), 655 (vw), 632 (w), 613 (vw) cm$^{-1}$. $C_{23}H_{26}Br_2N_2NiOSi$ (593.052): calcd. C 46.58, H 4.42, N 4.72; found C 46.66, H 4.39, N 4.70. HRMS (EI): calcd. for $C_{23}H_{26}Br_2N_2NiOSi$ $[M]^+$ 589.9535; found 589.9540. $\mu_{eff}$ = 3.86 BM.

**[NiBr$_2${N(*o*-*i*PrOC$_6$H$_4$)=C(SiMe$_3$)CH$_2$C$_5$H$_4$N-2}] (12):** Complex **12** was prepared according to the same route as for **11**. Thus, reaction of $NiBr_2$ (0.15 g, 0.68 mmol) with **8** (0.23 g, 0.70 mmol) in thf gave, after similar workup, complex **12** (0.30 g, 78.9%) as red crystals, m.p. 209–211 °C. IR (KBr): ṽ = 3103 (w), 3070 (w), 3028 (w), 2974 (m), 2934 (w), 2903 (w), 1595 (s), 1569 (vw), 1488 (vs), 1445 (s), 1422 (w), 1384 (m), 1375 (m), 1351 (w), 1301 (m), 1280 (m), 1252 (vs), 1207 (w), 1174 (w), 1158 (w), 1141 (w), 1118 (s), 1071 (vw), 1039 (w), 1031 (w), 956 (m), 846 (vs), 772 (s), 758 (s), 705 (vw), 677 (vw), 643 (w) cm$^{-1}$. $C_{19}H_{26}Br_2N_2NiOSi$ (545.01): calcd. C 41.87, H 4.81, N 5.14; found C 41.97, H 4.80, N 5.16. HRMS (EI): calcd. for $C_{19}H_{26}Br_2N_2NiOSi$ $[M]^+$ 541.9535; found 541.9536. $\mu_{eff}$ = 4.20 BM.

**[FeCl$_2${N(*o*-PhCH$_2$OC$_6$H$_4$)=C(SiMe$_3$)CH$_2$C$_5$H$_4$N-2}] (13):** Complex **13** was prepared according to a procedure similar to that for **11**. Treatment of $FeCl_2{\cdot}4H_2O$ (0.188 g, 0.945 mmol) with **7** (0.358 g, 0.957 mmol) in thf afforded, after similar workup, a yellow crystalline complex (0.3 g, 63%) as yellow crystals, m.p.189–191 °C. IR (KBr): ṽ = 3065 (m), 3030 (m), 2956 (m), 1593 (s), 1569 (w), 1491 (s), 1484 (m), 1445 (s), 1381 (w), 1344 (w), 1280 (w), 1253 (vs), 1203 (w), 1162 (w), 1115 (m), 1063 (w), 1022 (m), 850 (vs), 809 (w), 773 (s), 761 (vs), 730 (m), 692 (m), 675 (w), 639 (w), 615 (w) cm$^{-1}$. $C_{23}H_{26}Cl_2FeN_2OSi$ (501.301): calcd. C 55.11, H 5.23, N 5.59; found C 54.89, H 5.10, N 5.54. HRMS (EI): calcd. for $C_{23}H_{26}Cl_2FeN_2OSi$ $[M]^+$ 500.0541; found 500.0550. $\mu_{eff}$ = 7.00 BM.

**[FeCl$_2${N(*o*-*i*PrOC$_6$H$_4$)=C(SiMe$_3$)CH$_2$C$_5$H$_4$N-2}] (14):** Complex **14** was prepared according to a procedure similar to that for **11**. Treatment of $FeCl_2{\cdot}4H_2O$ (0.191 g, 0.96 mmol) with **8** (0.302 g, 0.926 mmol) in thf formed, after similar workup, yellow crystalline complex **14** (0.296 g, 71.4%) as yellow crystals, m.p.178–180 °C. IR (KBr): ṽ = 3102 (m), 3067 (m), 3027 (m), 2979 (s), 2899 (m), 1604 (m), 1585 (m), 1568 (w), 1484 (vs), 1444 (s), 1382 (w), 1374 (w), 1348 (w), 1279 (w), 1249 (s), 1201 (w), 1157 (w), 1141 (w), 1118 (m), 1063 (w), 1037 (w), 1022 (w), 953 (w), 934 (w), 854 (vs), 772 (s), 730 (m), 696 (w), 676 (vw), 640 (w), 607 (w) cm$^{-1}$. $C_{19}H_{26}Cl_2FeN_2OSi$ (453.259): calcd. C 50.35, H 5.78, N 6.18; found C 50.29, H 5.70, N 6.08. HRMS (EI): calcd. for $C_{19}H_{26}Cl_2FeN_2OSi$ $[M]^+$ 452.0541; found 452.0527. $\mu_{eff}$ = 6.93 BM.

**[CoCl$_2${N(*o*-PhCH$_2$OC$_6$H$_4$)=C(SiMe$_3$)CH$_2$C$_5$H$_4$N-2}] (15):** To a solution of $CoCl_2$ (0.067 g, 0.515 mmol) in thf (5 mL) was added **7** (0.196 g, 0.524 mmol) in thf (10 mL) at 0 °C while stirring. The mixture was warmed to room temperature and stirred overnight. The color of the solution changed to blue. Volatiles were removed in vacuo and the residue was washed with diethyl ether (2 × 2 mL). The solid was dissolved in $CH_2Cl_2$ and then filtered. Toluene was added to the solution and then concentrated to afford **15** (0.16 g, 60.8%) as blue crystals, m.p. 196–198 °C. IR (KBr): ṽ = 3072 (w), 3028 (m), 2953 (m), 2897 (w), 1596 (s), 1568 (w), 1492 (s), 1446 (s), 1381 (w), 1347 (w), 1279 (w), 1254 (vs), 1205 (w), 1163 (w), 1116 (w), 1067 (vw), 1039 (w), 1026 (m), 933 (vw), 850 (vs), 774 (s), 763 (vs), 730 (w), 692 (w), 643 (vw) cm$^{-1}$. $C_{23}H_{26}Cl_2CoN_2OSi$ (504.39): calcd. C 54.77, H 5.20, N 5.55; found C 54.99, H 5.28, N 5.65. HRMS (EI): calcd. for $C_{23}H_{26}Cl_2CoN_2OSi$ $[M]^+$ 503.0523; found 503.0515. $\mu_{eff}$ = 6.46 BM.

**[CoCl$_2${N(*o*-*i*PrOC$_6$H$_4$)=C(SiMe$_3$)CH$_2$C$_5$H$_4$N-2}] (16):** Complex **16** was prepared according to a procedure similar to that for **15**. Treatment of $CoCl_2$ (0.208 g, 1.6 mmol) with **8** (0.532 g, 1.63 mmol) in thf afforded, after workup, complex **16** (0.72 g, 99%) as blue crystals, m.p. 199–201 °C. IR (KBr): ṽ = 3072 (w), 3027 (m), 2978 (m), 2941 (w), 2897 (w), 1605 (m), 1592 (s), 1572 (w), 1488 (vs), 1445 (s), 1379 (m), 1346 (w), 1300 (w), 1280 (w), 1250 (vs), 1207 (w), 1175 (w), 1158 (w), 1142 (w), 1118 (s), 1067 (vw), 1039 (w), 1028 (w), 956 (m), 937 (w), 845 (vs), 774 (s), 760 (vs), 736 (w), 651 (w), 643 (w) cm$^{-1}$. $C_{19}H_{26}Cl_2CoN_2OSi$ (456.347): calcd. C 50.01, H 5.74, N 6.14; found C 49.99, H 5.58, N 6.13. HRMS (EI): calcd. for $C_{19}H_{26}Cl_2CoN_2OSi$ $[M]^+$ 455.0523; found 455.0523. $\mu_{eff}$ = 6.54 BM.

***o*-MeC$_6$H$_4$NHC(SiMe$_3$)CHC$_5$H$_4$N-2 (17):** To a solution of [Li(TMEDA)][2-CH(SiMe$_3$)C$_5$H$_4$N] (1.07 g, 3.73 mmol) in diethyl ether (15 mL) was added 2-methylphenyl isocyanide (0.44 g 3.76 mmol) at –30 °C. The resultant mixture was warmed to room temperature and stirred overnight to give a dark red solution. Volatiles were removed in vacuo and thf (10 mL) was added. To the solution $H_2O$ (0.068 g) was added at 0 °C and the mixture stirred for 10 min to give a greenish-yellow solution. The solvent was removed in vacuo and *n*-hexane was added. The mixture was filtered and the solvent was removed from the filtrate in vacuo. The residue was distilled under reduced pressure to give a pale yellow oil (0.80 g, 76%) as a mixture of (*Z*) and (*E*) isomers [(*Z*)/(*E*) = 1:3.4], b.p. 130 °C/0.1 Torr. $^1$H NMR ($C_6D_6$, 300 MHz): (*E*) isomer: $\delta$ = 0.24 (s, 9 H, $SiMe_3$), 2.51 (s, 3 H, Me), 5.75 (s, 1 H, =CH), 6.55 (d, $J$ = 9.9 Hz, 1 H, $C_6H_4$), 6.99–7.33 (m, 5 H, $C_6H_4$, $C_5H_4N$), 7.62–7.68 (m, 1 H, $C_5H_4N$), 8.49–8.51 (m, 1 H, $C_5H_4N$), 11.76 (s, 1 H, NH) ppm. (*Z*) isomer: $\delta$ = 0.34 (s, 9 H, $SiMe_3$), 2.16 (s, 3 H, Me), 5.52 (d, $J$ = 10.2 Hz, 1 H, =CH) ppm, aromatic ring region overlaps that of (*E*) isomer. IR (liquid film): ṽ = 3006 (w), 2953 (m), 2897 (w), 1643 (m), 1622 (s), 1584 (vs), 1539 (s), 1496 (m), 1469 (s), 1410 (m), 1352 (s), 1303 (m), 1250 (s), 1217 (s), 1149 (s), 1110 (w), 1076 (w), 1045 (w), 993 (w), 934 (vw), 912 (w), 848 (vs), 801 (m), 758 (s), 729 (m) cm$^{-1}$. HRMS (EI): calcd. for $C_{17}H_{22}N_2Si$ $[M]^+$ 282.1552; found 282.1546.

**[NiBr$_2${N(*o*-MeC$_6$H$_4$)=C(SiMe$_3$)CH$_2$C$_5$H$_4$N-2}] (18):** To a suspension of $NiBr_2$ (0.195 g, 0.89 mmol) in thf (5 mL) was added a solution of **17** (0.25 g 0.89 mmol) in thf (10 mL) at 0 °C. The resultant mixture was warmed to room temperature and stirred overnight. Volatiles were removed in vacuo and the residual solid was dissolved in $CH_2Cl_2$ and filtered. The solvent was removed in vacuo from the filtrate and the residue washed with thf (3 × 2 mL) to afford purple-red crystals of **18** (0.27 g, 61%), m.p. 274–276 °C. IR (KBr): ṽ = 3102 (w), 3047 (w), 2956 (w), 2917 (w), 1599 (s), 1567 (w), 1482 (s), 1443 (s), 1411 (m), 1359 (w), 1286 (w), 1254 (s), 1191 (w), 1113 (m), 1070 (w), 1041 (w), 1029 (w), 849 (vs), 796 (w), 766 (vs), 718 (w), 703 (w) cm$^{-1}$. $C_{17}H_{22}Br_2N_2NiSi$ (500.957): calcd. C 40.76, H 4.43, N 5.59; found C 40.87, H 4.49, N 5.78. HRMS (EI): calcd. for $C_{17}H_{22}Br_2N_2NiSi$ $[M]^+$ 497.9272; found 497.9263. $\mu_{eff}$ = 3.95 BM.

**[CoCl$_2${N(*o*-MeC$_6$H$_4$)=C(SiMe$_3$)CH$_2$C$_5$H$_4$N-2}] (19):** To a suspension of $CoCl_2$ (0.092 g, 0.71 mmol) in thf (5 mL) was added a solution of **17** (0.2 g 0.71 mmol) in thf (10 mL) at 0 °C. The resultant mixture was warmed to room temperature and stirred overnight. Volatiles were removed in vacuo and the residue was dissolved in $CH_2Cl_2$ and filtered. The solvent was removed in vacuo from the filtrate and the residue washed with thf (2 mL × 3) to give a blue

 © 2007 Wiley-VCH Verlag GmbH & Co. KGaA, Weinheim 

Table 6. Details of the X-ray structure determinations of compounds **3**, **6**, **12**, and **14**.

| | **3** | **6** | **12** | **14** |
|---|---|---|---|---|
| Empirical formula | $C_{46}H_{50}Li_2N_4O_2Si_2$ | $C_{38}H_{50}N_4NiO_2Si_2$ | $C_{19}H_{26}Br_2N_2NiOSi$ | $C_{19}H_{26}Cl_2FeN_2OSi$ |
| Formula mass | 760.96 | 709.71 | 545.04 | 453.26 |
| Crystal system | monoclinic | monoclinic | monoclinic | monoclinic |
| Space group | $P2_1/c$ | $P2_1/n$ | $P2(1)/c$ | $P2(1)/c$ |
| $a$ [Å] | 11.1979(19) | 19.736(3) | 9.1529(9) | 9.1215(12) |
| $b$ [Å] | 23.748(4) | 11.1103(15) | 10.9906(11) | 10.8936(16) |
| $c$ [Å] | 17.346(3) | 19.857(3) | 23.504(2) | 23.224(3) |
| $\beta$ [°] | 107.884(3) | 116.108(2) | 95.151(2) | 94.339(2) |
| $V$ [Å$^3$] | 4389.9(13) | 3909.8(9) | 2354.9(4) | 2301.1(5) |
| $Z$ | 4 | 4 | 4 | 4 |
| $D_{calcd.}$ [g/cm$^3$] | 1.151 | 1.206 | 1.537 | 1.308 |
| $F(000)$ | 1616 | 1512 | 1096 | 944 |
| $\mu$ [mm$^{-1}$] | 0.121 | 0.594 | 4.278 | 0.950 |
| $\theta$ range for data collection [°] | 1.50 to 25.00 | 1.94 to 26.39 | 1.74 to 26.46 | 2.07 to 26.40 |
| No. of reflections collected | 18479 | 21552 | 12793 | 12689 |
| No. of independent reflections ($R_{int}$) | 7713 ($R_{int}$ = 0.0942) | 7978 ($R_{int}$ = 0.0771) | 4847 ($R_{int}$ = 0.0336) | 4711 ($R_{int}$ = 0.0355) |
| No. of data/restraints/parameters | 7713/0/511 | 7978/0/434 | 4847/6/240 | 4711/6/240 |
| Goodness of fit on $F^2$ | 0.995 | 0.988 | 0.997 | 1.004 |
| Final $R$ indices[a] [$I > 2\sigma(I)$] | $R1$ = 0.0673; $wR_2$ = 0.1324 | $R_1$ = 0.0542; $wR_2$ = 0.1290 | $R_1$ = 0.0377; $wR_2$ = 0.0758 | $R_1$ = 0.0409; $wR_2$ = 0.0876 |
| $R$ indices (all data) | $R_1$ = 0.1926; $wR_2$ = 0.1842 | $R_1$ = 0.1481; $wR_2$ = 0.1688 | $R_1$ = 0.0764; $wR_2$ = 0.0896 | $R_1$ = 0.0787; $wR_2$ = 0.1038 |
| Largest difference peak/hole [e Å$^{-3}$] | 0.356/–0.423 | 1.056/–0.389 | 0.811/–0.690 | 0.338/–0.251 |

[a] $\Sigma||F_o| - |F_c||/\Sigma|F_o|$; $wR_2 = [\Sigma w(F_o^2 - F_c^2/\Sigma w(F_o^4)]^{1/2}$.

powder of **19** (0.19 g, 65%), m.p. 255–260 °C. IR (KBr): $\tilde{\nu}$ = 3100 (w), 3071 (w), 3026 (w), 2979 (w), 2952 (w), 1604 (m), 1587 (s), 1477 (m), 1442 (s), 1346 (w), 1255 (m), 1157 (w), 1112 (w), 1061 (w), 1027 (w), 849 (vs), 796 (w), 774 (s), 762 (s), 719 (w) cm$^{-1}$. $C_{17}H_{22}Cl_2CoN_2Si$ (412.294): calcd. C 49.52, H 5.38, N 6.79; found C 49.23, H 5.48, N 6.75. HRMS (EI): calcd. for $C_{17}H_{22}Cl_2CoN_2Si$ $[M]^+$ 411.0261; found 411.0266. $\mu_{eff}$ = 6.48 BM.

**Crystal Structure Determination:** Crystals were mounted in Lindemann capillaries under $N_2$. Diffraction data were collected with a Siemens CCD area-detector at 294(2) K with graphite-monochromated Mo-$K_\alpha$ radiation ($\lambda$ = 0.71073 Å). A semi-empirical absorption correction was applied to the data. The structures were solved by direct methods using SHELXS-97[24] and refined against $F^2$ by full-matrix least squares using SHELXL-97.[25] Crystal data and experimental details of the structure determinations are listed in Table 6. CCDC-632191 to -632194 contain the supplementary crystallographic data for this paper. These data can be obtained free of charge from The Cambridge Crystallographic Data Centre via www.ccdc.cam.ac.uk/data_request/cif.

**Catalytic Oligomerization of Ethylene:** The oligomerization with 1 atm ethylene was carried out in a Schlenk tube. In a dried Schlenk tube was placed the pre-catalyst (5 μmol) and then the Schlenk tube was back-filled three times with $N_2$ and twice with ethylene. Toluene (30 mL) was added to the Schlenk tube and then the appropriate co-catalyst solution was added through a syringe. The reaction mixture was vigorously stirred at the given temperature under 1 atm ethylene. After the desired period of time (30 min or 60 min), the reaction was terminated by cooling the system to about –10 °C and then adding 10% HCl solution (30 mL). About 1 mL of the organic layer was dried with anhydrous $Na_2SO_4$ in a sealed Schlenk tube at about –10 °C for gas chromatographic analysis. To the remaining solution was added ethanol (100 mL), no polymer was observed. The oligomerization with 10 atm ethylene was carried out in a stainless steel autoclave (0.25 L capacity) equipped with gas ballast through a solenoid valve for continuous feeding of ethylene at constant pressure. Toluene (120 mL) containing the pre-catalyst was transferred into the fully dried reactor under $N_2$. The required amount of co-catalyst was injected into the reactor through a syringe. As the desired temperature was reached, the reactor was pressurized to 10 atm. After stirring for 30 min, the reactor was cooled to about –10 °C and depressurized. The contents were transferred into a cooled flask and then 10% HCl solution (30 mL) was added. The mixture was worked up and analyzed using the same procedure as described above for the 1 atm reaction.

## Acknowledgments

We thank the National Natural Science Foundation of China (Grant No. 20272056) for support. We are also grateful to Professor W.-H. Sun of the Institute of Chemistry, The Chinese Academy of Sciences, for his kind help in determining the catalytic ethylene oligomerization activities of the complexes and Professors H.-B. Song and H.-G. Wang of Nankai University for single-crystal X-ray structure determinations.

[1] a) S. D. Ittel, L. K. Johnson, M. Brookhart, *Chem. Rev.* **2000**, *100*, 1169–1204; b) V. C. Gibson, S. K. Spitzmesser, *Chem. Rev.* **2003**, *103*, 283–316; c) G. J. P. Britovsek, V. C. Gibson, D. F. Wass, *Angew. Chem. Int. Ed.* **1999**, *38*, 428–447; d) S. Mecking, *Angew. Chem. Int. Ed.* **2001**, *40*, 534–540; e) S. Park, Y. Ham, S. K. Kim, J. Lee, H. K. Kim, Y. Do, *J. Organomet. Chem.* **2004**, *689*, 4263–4276; f) B. Rieger, L. S. Baugh, S. Kacker, S. Striegler (Eds.), *Late Transition Metal Polymerization Catalysts*, Wiley-VCH, Weinheim, **2003**.

[2] a) W. Keim, R. Appel, A. Storeck, C. Krüger, R. Goddard, *Angew. Chem. Int. Ed. Engl.* **1981**, *20*, 116–117; b) W. Keim, *Angew. Chem. Int. Ed. Engl.* **1990**, *29*, 235–244; c) G. Wilke, *Angew. Chem. Int. Ed. Engl.* **1988**, *27*, 185–206.

[3] a) L. K. Johnson, C. M. Killian, M. Brookhart, *J. Am. Chem. Soc.* **1995**, *117*, 6414–6415; b) L. K. Johnson, S. Mecking, M. Brookhart, *J. Am. Chem. Soc.* **1996**, *118*, 267–268.

 © 2007 Wiley-VCH Verlag GmbH & Co. KGaA, Weinheim 

[4] W.-H. Sun, D. Zhang, S. Zhang, S. Jie, J. Hou, *Kinet. Catal.* **2006**, *47*, 278–283, and references therein.
[5] a) M. Sauthier, F. Leca, R. F. de Souza, K. Bernardo-Gusmão, L. F. T. Queiroz, L. Toupet, R. Réau, *New J. Chem.* **2002**, *26*, 630–635; b) S. Al-Benna, M. J. Sarsfield, M. Thornton-Pett, D. L. Ormsby, P. J. Maddox, P. Brès, M. Bochmann, *J. Chem. Soc., Dalton Trans.* **2000**, 4247–4257; c) K. V. Axenov, M. Leskelä, T. Repo, *J. Catal.* **2006**, *238*, 196–205; d) S. Plentz-Meneghetti, P. J. Lutz, J. Kress, *Organometallics* **1999**, *18*, 2734–2737; e) J. Zhang, X. Wang, G.-X. Jin, *Coord. Chem. Rev.* **2006**, *250*, 95–109; f) E. Nelkenbaum, M. Kapon, M. S. Eisen, *Organometallics* **2005**, *24*, 2645–2659.
[6] a) J. Feldman, S. J. Mclain, A. Parthasarathy, W. J. Marshall, J. C. Calabrese, S. D. Arthur, *Organometallics* **1997**, *16*, 1514–1516; b) J. Zhang, Z. Ke, F. Bao, J. Long, H. Gao, F. Zhu, Q. Wu, *J. Mol. Catal. A* **2006**, *249*, 31–39; c) G. J. P. Britovsek, S. P. D. Baugh, O. Hoarau, V. C. Gibson, D. F. Wass, A. J. P. White, D. J. Williams, *Inorg. Chim. Acta* **2003**, *345*, 279–291.
[7] a) X. Tang, W.-H. Sun, T. Gao, J. Hou, J. Chen, W. Chen, *J. Organomet. Chem.* **2005**, *690*, 1570–1580; b) W.-H. Sun, X. Tang, T. Gao, B. Wu, W. Zhang, H. Ma, *Organometallics* **2004**, *23*, 5037–5047.
[8] J. Hou, W.-H. Sun, S. Zhang, H. Ma, Y. Deng, X. Lu, *Organometallics* **2006**, *25*, 236–244.
[9] a) W.-H. Sun, S. Jie, S. Zhang, W. Zhang, Y. Song, H. Ma, J. Chen, K. Wedeking, R. Fröhlich, *Organometallics* **2006**, *25*, 666–677; b) A. R. Karam, E. L. Catarí, F. López-Linares, G. Agrifoglio, C. L. Albano, A. Díaz-Barrios, T. E. Lehmann, S. V. Pekerar, L. A. Albornoz, R. Atencio, T. González, H. B. Ortega, P. Joskowics, *Appl. Catal., A* **2005**, *280*, 165–173; c) M. J. Overett, R. Meijboom, J. R. Moss, *Dalton Trans.* **2005**, 551–555; d) K. P. Tellmann, V. C. Gibson, A. J. P. White, D. J. Williams, *Organometallics* **2005**, *24*, 280–286; e) R. Schmidt, M. B. Welch, R. D. Knudsen, S. Gottfriedc, H. G. Alt, *J. Mol. Catal. A* **2004**, *222*, 17–25; f) B. L. Small, M. J. Carney, D. M. Holman, C. E. O'Rourke, J. A. Halfen, *Macromolecules* **2004**, *37*, 4375–4386; g) N. Ajellal, M. C. A. Kuhn, A. D. G. Boff, M. Hörner, C. M. Thomas, J.-F. Carpentier, O. L. Casagrande Jr, *Organometallics* **2006**, *25*, 1213–1216.
[10] a) G. J. P. Britovsek, V. C. Gibson, B. S. Kimberley, P. J. Maddox, S. J. McTavish, G. A. Solan, A. J. P. White, D. J. Williams, *Chem. Commun.* **1998**, 849–850; b) B. L. Small, M. Brookhart, A. M. A. Bennett, *J. Am. Chem. Soc.* **1998**, *120*, 4049–4050.
[11] W. Zhao, Y. Qian, J. Huang, J. Duan, *J. Organomet. Chem.* **2004**, *689*, 2614–2623, and references therein.
[12] a) Z. Weng, S. Teo, L. L. Koh, T. S. A. Hor, *Angew. Chem. Int. Ed.* **2005**, *44*, 7560–7564; b) Y. Chen, G. Wu, G. C. Bazan, *Angew. Chem. Int. Ed.* **2005**, *44*, 1108–1112; c) D. S. McGuinness, V. C. Gibson, J. W. Steed, *Organometallics* **2004**, *23*, 6288–6292; d) F. Speiser, P. Braunstein, L. Saussine, *Organometallics* **2004**, *23*, 2633–2640; e) F. Speiser, P. Braunstein, L. Saussine, *Organometallics* **2004**, *23*, 2625–2632; f) Y. Chen, R. Chen, C. Qian, X. Dong, J. Sun, *Organometallics* **2003**, *22*, 4312–4321; g) D. Sirbu, G. Consiglio, S. Gischig, *J. Organomet. Chem.* **2006**, *691*, 1143–1150; h) I. Kim, C. H. Kwak, J. S. Kim, C.-S. Ha, *App. Catal., A* **2005**, *287*, 98–107.
[13] F. Speiser, P. Braunstein, L. Saussine, *Acc. Chem. Res.* **2005**, *38*, 784–793.
[14] R. Obrecht, R. Herrmann, I. Ugi, *Synthesis* **1985**, 400–402.
[15] W.-P. Leung, H. Cheng, D.-S. Liu, Q.-G. Wang, T. C. W. Mak, *Organometallics* **2000**, *19*, 3001–3007.
[16] a) B.-J. Deelman, M. F. Lappert, H.-K. Lee, T. C. W. Mak, W.-P. Leung, P.-R. Wei, *Organometallics* **1997**, *16*, 1247–1252; b) P. B. Hitchcock, M. F. Lappert, D.-S. Liu, *J. Chem. Soc., Chem. Commun.* **1994**, 1699–1700.
[17] N. L. Allinger, X. Zhou, J. Bergsma, *J. Mol. Struct., Theochem.* **1994**, *312*, 69–83.
[18] L. P. Spencer, R. Altwer, P. Wei, L. Gelmini, J. Gauld, D. W. Stephan, *Organometallics* **2003**, *22*, 3841–3854.
[19] a) Z. Guan, W. J. Marshall, *Organometallics* **2002**, *21*, 3580–3586; b) D. P. Gates, S. A. Svejda, E. Oñate, C. M. Killian, L. K. Johnson, P. S. White, M. Brookhart, *Macromolecules* **2000**, *33*, 2320–2334.
[20] a) H.-Y. Wang, J. Zhang, X. Meng, G.-X. Jin, *J. Organomet. Chem.* **2006**, *691*, 1275–1281; b) F. Bao, R. Ma, X. Lü, G. Gui, Q. Wu, *Appl. Organomet. Chem.* **2006**, *20*, 32–38; c) S. Wu, S. Lu, *J. Mol. Catal. A: Chem.* **2003**, *198*, 29–38; d) I. Kim, C. H. Kwak, J. S. Kim, C.-S. Ha, *Appl. Catal., A* **2005**, *287*, 98–107; e) C. Carlini, M. Isola, V. Liuzzo, A. M. R. Galletti, G. Sbrana, *Appl. Catal., A* **2002**, *231*, 307–320; f) Y.-Z. Zhu, J.-Y. Liu, Y.-S. Li, Y.-J. Tong, *J. Organomet. Chem.* **2004**, *689*, 1295–1303.
[21] C. Carlini, M. Marchionna, A. M. R. Galletti, G. Sbrana, *Appl. Catal., A* **2001**, *206*, 1–12.
[22] C. Bianchini, G. Mantovani, A. Meli, F. Migliacci, *Organometallics* **2003**, *22*, 2545–2547.
[23] D. F. Evans, *J. Chem. Soc.* **1959**, 2003–2005.
[24] G. M. Sheldrick, *Acta Crystallogr., Sect. A* **1990**, *46*, 467–473.
[25] G. M. Sheldrick, *SHELXL97, Program for the refinement of crystal structures*, University of Göttingen, Göttingen, Germany, **1997**.

Received: January 7, 2007
Published Online: May 4, 2007

 © 2007 Wiley-VCH Verlag GmbH & Co. KGaA, Weinheim 

DOI: 10.1002/ejic.200700233

# Synthesis, Spectroscopic and Structural Systematics of Complexes of Germanium(IV) Halides ($GeX_4$, X = F, Cl, Br or I) with Phosphane Oxides and Related Oxygen Donor Ligands

**Fei Cheng,[a] Martin F. Davis,[a] Andrew L. Hector,[a] William Levason,*[a] Gillian Reid,[a] Michael Webster,[a] and Wenjian Zhang[a]**

**Keywords:** Germanium / Coordination complexes / Phosphane oxides

The first series of phosphane oxide complexes of germanium(IV) halides have been prepared, including *trans*-$[GeF_4(R_3PO)_2]$ (R = Me, Et or Ph), *trans*-$[GeCl_4(Et_3PO)_2]$, *fac*-$[GeCl_3(Me_3PO)_3]_2[GeCl_6]$ and *cis*-$[GeX_2(Me_3PO)_4]X_2$ (X = Cl or Br) and characterised by IR and multinuclear NMR ($^1H$, $^{19}F\{^1H\}$ and $^{31}P\{^1H\}$) spectroscopy. Crystal structures of all the above (except *trans*-$[GeCl_4(Et_3PO)_2]$) are described. Remarkably, under mild conditions $Me_3PO$ displaces halide ligands from $GeX_4$ (X = Cl, Br) to form the cationic species above. $Ph_3AsO$ forms *trans*-$[GeF_4(Ph_3AsO)_2]$, but reaction of $Ph_3AsO$ or $Me_3AsO$ with $GeCl_4$ leads to the corresponding $R_3AsCl_2$. The complexes $[GeF_4(MeCN)_2]$, $[GeF_4(thf)_2]$ and $[GeF_4(MeOCH_2CH_2OMe)]$ are also described and the relative Lewis acidities of $GeX_4$ established.
(© Wiley-VCH Verlag GmbH & Co. KGaA, 69451 Weinheim, Germany, 2007)

## Introduction

Germanium is a technologically important element, particularly in the electronics field, and of growing interest in optics and ceramics,[1,2] and new applications often require new Ge-containing precursor compounds. Whilst organogermanium chemistry[3] has been studied in great detail, the coordination chemistry remains little explored.[4] This is in marked contrast to the heavier analogue, tin, whose coordination chemistry is among the most extensive of the p-block metals and metalloids. Studies in the 1960–1970s established that germanium(IV) halides exhibited modest Lewis acidity, although markedly less than that of the $Sn^{IV}$ analogues.[5] A few more examples have been reported in the intervening years, including structurally characterised $[GeCl_3(Me_3[9]aneN_3)]^+$ and $[GeBr_3(1,3,5\text{-trimethyl-1,3,5-triazacyclohexane})]^+$,[6] $[GeCl_4(2,2'\text{-bipy})]$,[7] $[GeCl_4(Me_2NCH_2CH_2NMe_2)]$,[8] and $[GeCl_4(AsMe_3)_2]$,[9] but data on series of complexes (to reveal trends), solution speciation studies, or even determination of the boundaries of complex formation are lacking. Only two examples with O-donor ligands have been fully characterised, $[GeF_4(Et_2O)_2]$,[10] and $[GeCl_4(dmso)_2]$.[11] We report here studies of the four tetrahalides as Lewis acids towards some neutral oxygen donor ligands.

## Results and Discussion

The germanium(IV) halides and their complexes are all moisture sensitive to varying degrees and all syntheses were carried out using rigorously anhydrous conditions. $GeF_4$ is a gas (sub. 236 K) and although it can be used directly in the syntheses, a solid precursor would be more convenient to handle. One possibility is $[GeF_4(Et_2O)_2]$[10] but this sublimes and dissociates at near ambient temperatures; the adduct $[GeF_4(MeCN)_2]$[12] is a more convenient precursor. The $[GeF_4(MeCN)_2]$ is made by bubbling $GeF_4$ into excess MeCN at room temperature, whereupon it separates as a white solid, which can be kept indefinitely in a glove box or Schlenk, although it vapourises slowly in a dynamic vacuum. The IR spectrum shows three ν(CN) at 2333, 2295 and 2252 $cm^{-1}$ and broad overlapping features assignable as ν(GeF) at 688, 657 and 639 $cm^{-1}$, suggesting a mixture of *cis* and *trans* isomers. In $CD_2Cl_2$ solution at ambient temperatures both the $^1H$ and $^{19}F\{^1H\}$ NMR spectra are single lines, but at 180 K the $^{19}F\{^1H\}$ NMR spectrum shows a singlet at –108.2 and two rather broad triplets, $\delta$ = –101.2 and –134.2 ($^2J_{FF} \approx 55$ Hz), attributable to *trans* and *cis* isomers respectively in approximate ratio 1:10, showing the complex is dynamic in solution down to quite low temperatures.

### Phosphane Oxides

The reactions of $[GeF_4(MeCN)_2]$ with $R_3PO$ (R = Me, Et or Ph) in 1:2 molar ratio in dry $CH_2Cl_2$ afford white powders $[GeF_4(R_3PO)_2]$. Colourless crystals of $[GeF_4(R_3PO)_2]$ (R = Me or Et) were grown from MeCN solution, and crystals of $[GeF_4(Ph_3PO)_2]$ serendipitously from the reaction mixture of $[GeF_4(MeCN)_2]$ and $Ph_3P$ in $CH_2Cl_2$[13] and crystal structure determinations showed all

[a] School of Chemistry, University of Southampton, Southampton SO17 1BJ, UK

 © 2007 Wiley-VCH Verlag GmbH & Co. KGaA, Weinheim 

to be the *trans* isomers. The P–O distances are significantly lengthened from those in the parent phosphane oxide 1.489(6) Å ($Me_3PO$),[14] 1.483(2) Å ($Ph_3PO$).[15] The *trans*-[$GeF_4(Me_3PO)_2$] (Figure 1, Table 1) is isostructural with the tin(IV) analogue,[16] and the *d*(P–O) 1.528(5) Å is very similar to that in *trans*-[$SnF_4(Me_3PO)_2$] [1.532(3) Å]. The *d*(Ge–F) 1.772(4) and 1.776(4) Å are longer than in the diethyl ether adduct [$GeF_4(Et_2O)_2$][10] [1.754(2), 1.747(2) Å] and considerably longer than in crystalline $GeF_4$ [1.661(1) Å].[17] In the ether adduct the *d*(Ge–O) is 1.975(2) Å consistent with the much weaker binding of the ether to the germanium. Similar bond length patterns are seen in the other phosphane oxide structures (Tables 2 and 3, Figures 2 and 3). The trialkylphosphane oxide complexes are easily soluble in chlorocarbons and MeCN, that of $Ph_3PO$ poorly soluble, and in marked contrast to the analogues with the heavier halides, are relatively air-stable in the solid state and do not hydrolyse rapidly even in solution. The $^{19}F\{^1H\}$ NMR spectrum of [$GeF_4(Me_3PO)_2$] in $CH_2Cl_2$ shows a singlet at $\delta$ = –109.9 ppm due to the *trans* isomer and much weaker triplets at $\delta$ = –107.6 and –121.6 ppm ($^2J_{FF}$ = 58 Hz) of the *cis* isomer, with the latter making up ca. 5% of the sample. The $^{31}P\{^1H\}$ NMR spectrum confirms the assignment with resonances at $\delta$ = 65.8 (*trans*) and $\delta$ = 65.1 ppm (*cis*). In the presence of added $Me_3PO$ no other complexes were formed, showing that in contrast to the case with the heavier halides (below), the phosphane oxide cannot displace fluoride from the $Ge^{IV}$ centre. The IR spectrum of [$GeF_4(Me_3PO)_2$] shows a very strong, broad band at 1087 $cm^{-1}$, assigned as ν(PO) (compare 1166 $cm^{-1}$ in $Me_3PO$) and ν(Ge–F) at 626 and 612 $cm^{-1}$. The presence of two ν(Ge–F) stretches of similar intensity is a solid state effect (theory for a *trans* isomer is one – $e_u$), since in $CH_2Cl_2$ solution a single band at 629 $cm^{-1}$ is present. The [$GeF_4(Et_3PO)_2$] is very similar (Experimental Section) although the *cis* isomer is rather more abundant (≈10% in $CH_2Cl_2$ solution). The [$GeF_4(Ph_3PO)_2$] shows approximately equal amounts of *cis* and *trans* isomers present in both the $^{19}F\{^1H\}$ and $^{31}P\{^1H\}$ NMR spectra at 253 K ($CDCl_3$ solution), but at 295 K only the resonances of the *trans* isomer are evident. The chemical shift in the room temperature $^{19}F\{^1H\}$ spectrum is not a weighted average of the low temperature values, but corresponds to that of the *trans* isomer, indicating that the *cis* isomer is undergoing some dynamic process at ambient temperatures, but that *cis*-*trans* exchange is slow. The reaction of $Et_3PO$ and $GeCl_4$ in $CH_2Cl_2$ gave a white solid [$GeCl_4(Et_3PO)_2$]. Although this has not been characterised by an X-ray structure, the spectroscopic properties ν(PO) = 1087 $cm^{-1}$, ν(Ge–Cl) = 321 $cm^{-1}$ and $\delta(^{31}P\{^1H\})$ = 60.1 ($Et_3PO$: $\delta$ = 52.1 ppm) are consistent with its formulation as the *trans* isomer (cf. the fluoride described above).

Table 1. Selected bond lengths [Å] and angles [°] for [$GeF_4(Me_3PO)_2$].[a]

| | | | |
|---|---|---|---|
| Ge1–F1 | 1.772(4) | Ge1–F2 | 1.776(4) |
| Ge1–O1 | 1.898(5) | P1–O1 | 1.528(5) |
| F1–Ge1–F2 | 90.7(2) | F1–Ge1–O1 | 90.6(2) |
| F1–Ge1–F2a | 89.3(2) | F2–Ge1–O1 | 89.1(2) |
| Ge1–O1–P1 | 130.4(3) | O1–P1–C | 108.2(3)–112.3(3) |

[a] Symmetry operation, a: –*x*, –*y*, 1 – *z*.

Table 2. Selected bond lengths [Å] and angles [°] for [$GeF_4(Et_3PO)_2$]·1/3$CH_2Cl_2$.

| | | | |
|---|---|---|---|
| Ge1–F1 | 1.770(2) | Ge1–F2 | 1.769(2) |
| Ge1–O1 | 1.904(2) | P1–O1 | 1.526(2) |
| P1–C | 1.783(2)–1.800(2) | | |
| F1–Ge1–F2 | 90.24(8) | F1–Ge1–O1 | 89.72(7) |
| F2–Ge1–O1 | 91.17(7) | Ge1–O1–P1 | 133.8(1) |
| O1–P1–C | 105.4(1)–113.8(1) | | |

Table 3. Selected bond lengths [Å] and angles [°] for [$GeF_4(Ph_3PO)_2$]·2$CH_2Cl_2$.

| | | | |
|---|---|---|---|
| Ge1–F1 | 1.774(1) | Ge1–F2 | 1.772(1) |
| Ge1–O1 | 1.925(2) | P1–O1 | 1.522(2) |
| F1–Ge–F2 | 89.53(6) | F1–Ge1–O1 | 91.76(6) |
| F2–Ge1–O1 | 90.82(6) | Ge1–O1–P1 | 142.5(1) |
| O1–P1–C | 107.4(1)–113.5(1) | | |

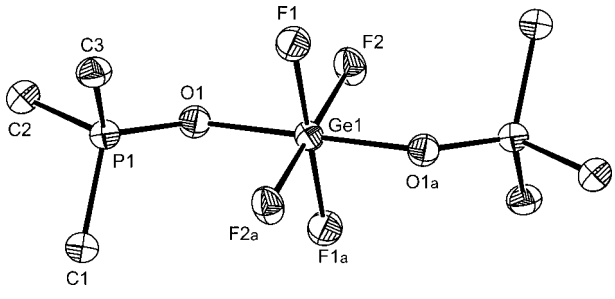


Figure 1. View of the molecule of [$GeF_4(Me_3PO)_2$] with the atom numbering scheme adopted. Ellipsoids are drawn at the 50% probability level and H atoms are omitted for clarity. Symmetry operation, a: –*x*, –*y*, 1 – *z*.

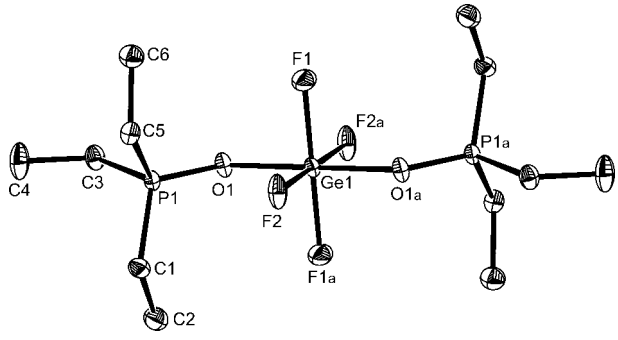


Figure 2. View of the molecule of [$GeF_4(Et_3PO)_2$] with the atom numbering scheme adopted. Ellipsoids are drawn at the 50% probability level and H atoms are omitted for clarity. Symmetry operation, a: 1 – *x*, 1 – *y*, –*z*.

In marked contrast to the stable fluoride adduct, the phosphane oxide complexes of $GeCl_4$ and $GeBr_4$ with $Me_3PO$ are moisture sensitive and very labile in solution. The reaction of $Me_3PO$ and $GeCl_4$ in a 2:1 molar ratio in rigorously anhydrous $CH_2Cl_2$ resulted in a white powder with an analytical composition corresponding to $GeCl_4(Me_3PO)_2$. Crystals grown from an $CH_2Cl_2$ solution of this material were found to be *fac*-[$GeCl_3(Me_3PO)_3]_2$-

 © 2007 Wiley-VCH Verlag GmbH & Co. KGaA, Weinheim 

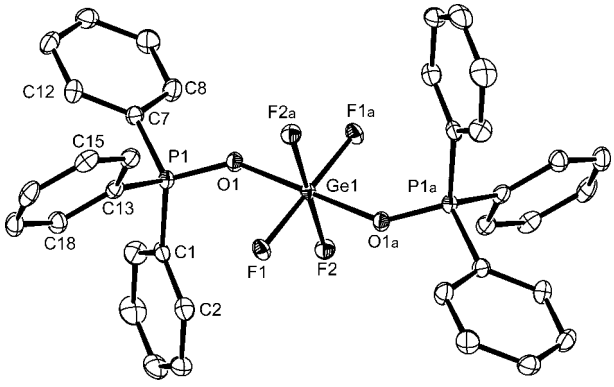


Figure 3. View of the molecule of $[GeF_4(Ph_3PO)_2]$ with the atom numbering scheme adopted. Ellipsoids are drawn at the 50% probability level and H atoms are omitted for clarity. Symmetry operation, a: $1 - x$, $1 - y$, $1 - z$.

$[GeCl_6]$, (which has the same 1:2 Ge:$Me_3PO$ stoichiometry). The structure (Figure 4, Table 4) shows an octahedral cation with a *facial* arrangement of ligands $d$(Ge–O) = 1.891(3) Å, not significantly different from that in the fluoride complex above, and with $d$(Ge–Cl) = 2.260(1) Å. The $[GeCl_6]^{2-}$ anion is very close to a regular octahedron with $d$(Ge–Cl) = 2.289(1) Å, which compares with the values in $[Ph_4P]_2[GeCl_6]$ of 2.283–2.298 Å.[19] The Nujol mull IR spectrum of the bulk powder and of the crystals were the same and showed two ν(PO) absorptions at 1122(m) and 1065 (s, br) $cm^{-1}$, and ν(Ge–Cl) at 344 (m), 308 (m), 293 (s) $cm^{-1}$. The 293 $cm^{-1}$ band is assigned as the $t_{1u}$ mode of $[GeCl_6]^{2-}$,[20] and the higher frequency Ge–Cl modes are the $a_1$ and e expected for the *fac* ($C_{3v}$) cation. The material has an essentially identical IR spectrum to the compound formulated as $[GeCl_4(Me_3PO)_2]$ in an early report[21] and it is clear from the results above that this complex should be reformulated. In anhydrous $CH_2Cl_2$ solution at ambient temperatures the complex exhibits a broad singlet in the $^{31}P\{^1H\}$ NMR spectrum at $\delta$ ca. 41. On cooling the solution the resonance broadens, then sharpens on further cooling, and at 180 K the major resonance is now at $\delta$ = 63.7 ppm with much weaker features at $\delta$ = 67.4, 66.5 and 65.7 ppm. The behaviour suggests a rapidly exchanging system, extensively dissociated at room temperature and which has several species present at low temperatures (no "free" $Me_3PO$, $\delta$ = 38 ppm, was observed at low temperature). In the presence of added $Me_3PO$ the solution shows a broad resonance consistent with fast exchange at $T > 220$ K, but at 180 K several resonances are resolved in addition to that of uncoordinated $Me_3PO$, notably the species with $\delta$ = 63.7 ppm is absent and the three higher frequency resonances are now dominant. Under different experimental conditions a second complex, identified as *cis*-$[GeCl_2(Me_3PO)_4]Cl_2$ was produced, also as colourless crystals. The structure (Figure 5, Table 5) shows a distorted octahedral cation with rather shorter $d$(Ge–Cl) [2.228(2) Å] than in the $[GeCl_3(Me_3PO)_3]^+$ [2.260(1) Å] and the $d(Ge–O)_{trans\text{-}O}$ [1.886(4) Å] is significantly longer than $d(Ge–O)_{trans\text{-}Cl}$ [1.857(4) Å]. In solution the variable temperature $^{31}P\{^1H\}$ NMR spectra are qualitatively similar to those described above for $[GeCl_3(Me_3PO)_3]^+$, except that at 180 K some "free" $Me_3PO$ is present. Whilst a definitive assignment of the low temperature spectra of the two $GeCl_4/Me_3PO$ systems is not possible, a plausible interpretation consistent with the ratios of $GeCl_4$:$Me_3PO$ present, and the effect of added $Me_3PO$, is that the resonances at $\delta$ = 67.4 and 66.5 ppm (which are always of equal intensity) correspond to the di-cation *cis*-$[GeCl_2(Me_3PO)_4]^{2+}$, the resonance at $\delta$ = 65.7 ppm is of the *fac*-$[GeCl_3(Me_3PO)_3]^+$ and the major feature at $\delta$ = 63.7 ppm is a $[GeCl_4(Me_3PO)_2]$ complex (since this resonance largely disappears when a large excess of $Me_3PO$ is present). Repeated attempts to isolate adducts of $GeCl_4$ with $Ph_3PO$ were unsuccessful, no solids separated from solutions of the constituents in anhydrous $CH_2Cl_2$, and removal of all volatiles from the reaction mixtures in vacuo resulted in loss of the $GeCl_4$. Attempts to isolate complexes with the diphosphane dioxides $Ph_2P(O)CH_2P(O)Ph_2$ or *o*-$C_6H_4[P(O)Ph_2]_2$ also failed. All of these form complexes with $SnCl_4$,[16,18] and although $GeCl_4$ is clearly a weaker Lewis acid, it is possible that steric factors disfavour complexes with these bulky ligands on the small $Ge^{IV}$ centre.

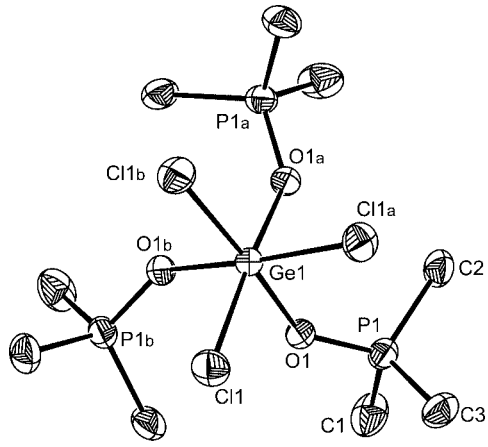


Figure 4. View of the cation in $[GeCl_3(Me_3PO)_3]_2$ $[GeCl_6]$ with the atom numbering scheme adopted. Ellipsoids are drawn at the 50% probability level and H atoms are omitted for clarity. Symmetry operation, a: $1 - y$, $1 + x - y$, $z$; b = $-x + y$, $1 - x$, $z$.

Table 4. Selected bond lengths [Å] and angles [°] for $[GeCl_3(Me_3PO)_3]_2[GeCl_6]$.[a]

| | | | |
|---|---|---|---|
| Ge1–Cl1 | 2.260(1) | Ge1–O1 | 1.891(3) |
| Ge2–Cl2 | 2.289(1) | P1–O1 | 1.530(3) |
| O1–Ge1–O1a | 85.6(1) | O1–Ge1–Cl1a | 93.3(1) |
| O1–Ge1–Cl1 | 88.1(1) | Cl1–Ge1–Cl1a | 92.89(5) |
| O1–P1–C | 107.4(2)–113.6(2) | Ge1–O1–P1 | 140.8(2) |
| Cl2–Ge2–Cl2c | 89.97(4) | | |

[a] Symmetry operations, a: $1 - y$, $1 + x - y$, $z$; c: $-y$, $x - y$, $z$.

The $GeBr_4/R_3PO$ systems in $CH_2Cl_2$ or MeCN are more extensively dissociated and it is harder to obtain a pure complex. However, as described in the Experimental Section, colourless crystals were obtained which proved to be *cis*-$[GeBr_2(Me_3PO)_4]Br_2$ (Table 6, Figure 6). The structure

 © 2007 Wiley-VCH Verlag GmbH & Co. KGaA, Weinheim 

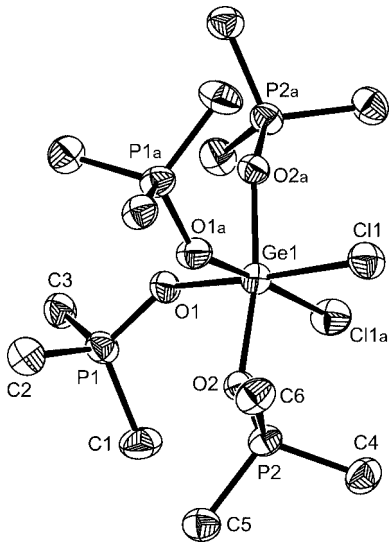


Figure 5. View of the cation in $[GeCl_2(Me_3PO)_4]Cl_2$ with the atom numbering scheme adopted. Ellipsoids are drawn at the 50% probability level and H atoms are omitted for clarity. Symmetry operation, a: $1 - x$, $y$, $1/2 - z$.

Table 5. Selected bond lengths [Å] and angles [°] for $[GeCl_2(Me_3PO)_4]Cl_2$.[a]

| | | | |
|---|---|---|---|
| Ge1–Cl1 | 2.228(2) | P1–O1 | 1.530(4) |
| Ge1–O1 | 1.857(4) | P2–O2 | 1.538(4) |
| Ge1–O2 | 1.886(4) | | |
| O1–Ge1–O1a | 91.0(3) | O1–Ge1–O2 | 88.0(2) |
| O1–Ge1–O2a | 85.2(2) | O2–Ge1–O2a | 170.3(2) |
| O1–Ge1–Cl1 | 176.3(1) | O1a–Ge1–Cl1 | 89.8(2) |
| O2–Ge1–Cl1 | 95.7(1) | O2–Ge1–Cl1a | 91.2(1) |
| Cl1–Ge1–Cl1a | 89.6(1) | Ge1–O1–P1 | 141.6(2) |
| O1–P1–C | 107.1(3)–114.1(3) | Ge1–O2–P2 | 137.1(3) |
| O2–P2–C | 108.1(3)–113.7(3) | | |

[a] Symmetry operation, a: $1 - x$, $y$, $1/2 - z$.

is analogous to that of the chloride, with a corresponding pattern of bond lengths. In $CH_2Cl_2$ solution the complex exhibits a very broad $^{31}P\{^1H\}$ NMR resonance at $\delta$ ca. 42 ppm, which on cooling to < 220 K resolves into a major peak at 65.5 ppm, and very minor features at 67.6 and 68.7 ppm in addition to some "free" $Me_3PO$. Addition of excess $Me_3PO$ to the solution results in a broad signal, typical of an exchanging system, down to very low temperatures, and even at 180 K the features $\delta$ ca. 65–69 ppm are broad, showing that the low temperature limiting spectrum cannot be reached before the solvent freezes. Based upon the spectroscopic data it can be concluded that solution lability increases in these systems with halide F << Cl < Br. Comparison of the four crystal structures containing $Me_3PO$ (Table 1, 4, 5 and 6) shows only small differences in $d$(Ge–O), although only for the two $[GeX_2(Me_3PO)_4]^{2+}$ ions are the Ge environments the same. It is possible that the effects of increasing formal charge on the Ge along the series $[GeF_4(Me_3PO)_2]$, $[GeCl_3(Me_3PO)_3]^+$, $[GeCl_2(Me_3PO)_4]^{2+}$ obscures any differences due to stronger Lewis acidity in the fluoride. Certainly charge seems to have a marked effect on $d$(Ge–Cl) along the series $[GeCl_6]^{2-}$ [2.289(1) Å], $[GeCl_3(Me_3PO)_3]^+$ [2.260(1) Å], $[GeCl_2(Me_3PO)_4]^{2+}$ [2.228(2) Å].

Table 6. Selected bond lengths [Å] and angles [°] for $[GeBr_2(Me_3PO)_4]Br_2$.[a]

| | | | |
|---|---|---|---|
| Ge1–Br1 | 2.399(1) | P1–O1 | 1.547(6) |
| Ge1–O1 | 1.901(5) | P2–O2 | 1.528(6) |
| Ge1–O2 | 1.859(6) | | |
| O2–Ge1–O2a | 90.5(4) | O2a–Ge1–O1 | 87.5(3) |
| O2–Ge1–O1 | 85.6(3) | O1–Ge1–O1a | 170.2(4) |
| O1–Ge1–Br1 | 97.1(2) | O2–Ge1–Br1 | 90.4(2) |
| O1a–Ge1–Br1 | 89.9(2) | Br1–Ge1–Br1a | 89.12(7) |
| Ge1–O1–P1 | 137.8(4) | Ge1–O2–P2 | 143.7(4) |
| O1–P1–C | 107.8(4)–113.7(4) | O2–P2–C | 107.8(4)–114.2(4) |

[a] Symmetry operation, a: $1 - x$, $y$, $1/2 - z$.

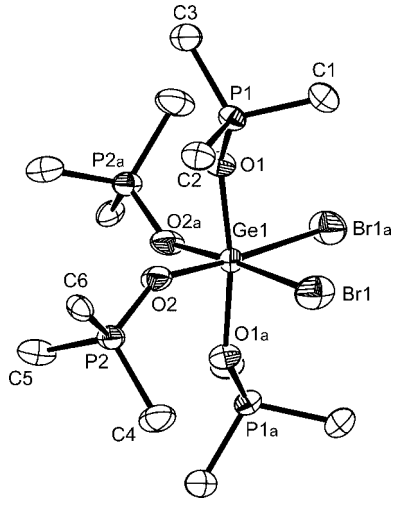


Figure 6. View of the cation in $[GeBr_2(Me_3PO)_4]Br_2$ with the atom numbering scheme adopted. Ellipsoids are drawn at the 50% probability level and H atoms are omitted for clarity. Symmetry operation, a: $1 - x$, $y$, $1/2 - z$.

The reactions of $GeI_4$ with $Me_3PO$ in $CH_2Cl_2$ gave red solutions, but crystals obtained from these were found by crystal structure determinations to be $GeI_4$ and $[Me_3POH][I_3]$, and we have been unable to isolate any phosphane oxide adducts.

The ability of $Me_3PO$ to displace chloride or bromide from the germanium centre was entirely unexpected; in the extensively studied systems $SnX_4$–$R_3PO$ (X = Cl, Br or I; R = Me, Ph etc)[21,22] all the complexes are of type $[SnX_4(R_3PO)_2]$ (usually a mixture of *cis*/*trans* isomers) and complexes with higher $R_3PO/SnX_4$ ratios do not form.

### Arsane Oxides

The reaction of $[GeF_4(MeCN)_2]$ with $Ph_3AsO$ in $CH_2Cl_2$ gave white $[GeF_4(Ph_3AsO)_2]$ which exhibited a strong broad $\nu$(AsO) at 868 $cm^{-1}$ and $\nu$(Ge–F) at 608 $cm^{-1}$. In solution the $^{19}F\{^1H\}$ NMR spectrum in $CH_2Cl_2$ contains a singlet at $\delta$ = –98.2, and two triplets at –94.4 and –112.9 ($^2J_{FF}$ = 60 Hz), consistent with a mixture of *cis* and *trans* isomers.

 © 2007 Wiley-VCH Verlag GmbH & Co. KGaA, Weinheim 

However, the products isolated from stirring $R_3AsO$ (R = Me or Ph) with $GeCl_4$ in MeCN or $CH_2Cl_2$ solution were colourless crystalline solids which showed no evidence for ν(AsO) vibrations in their IR spectra. The crystals were identified by comparison of their unit cells with literature data,[23,24] as the dichlorotriorganoarsenic(V), $R_3AsCl_2$, and this was confirmed by comparison of their IR spectra with literature data.[25,26] In a similar way, $GeBr_4$ and $Me_3AsO$ gave $Me_3AsBr_2$. The conversion of $R_3AsO$ to $R_3AsCl_2$ has been reported to be achieved by a number of reagents including MeCOCl,[27] $COCl_2$,[28] $PCl_3$ and $AsCl_3$,[29] and with aqueous HCl,[30] but for $GeCl_4$ to behave in this way under such mild conditions was unexpected, and again contrasts with $SnCl_4$ which readily forms $[SnCl_4(R_3AsO)_2]$ adducts.[31]

The ether adducts $[GeF_4(thf)_2]$ and $[GeF_4(MeOCH_2CH_2OMe)]$, both reported some years ago[12,32] but with few details, were reexamined. Both are moisture sensitive white solids, with unexceptional spectroscopic properties (see Experimental section). The $[GeF_4(thf)_2]$ is a mixture of *cis* and *trans* isomers in solution in $CH_2Cl_2$ at low temperatures, but on warming the solution to > ca. 243 K the triplets in the $^{19}F\{^1H\}$ NMR spectrum due to the *cis* isomer collapse and then disappear, whilst the singlet due to the *trans* form is unchanged. This behaviour is similar to that of $[GeF_4(Ph_3PO)_2]$ (q.v.) and similarly rationalised.

## Conclusions

A series of neutral O-donor complexes of $GeX_4$ have been prepared and characterised structurally and spectroscopically. The data support the expected trend that Lewis acidity decreases $GeF_4 > GeCl_4 > GeBr_4 >> GeI_4$, and are consistent with lower acceptor power for Ge compared with Sn. We note that the overall trends will reflect both the strength of the donor-acceptor interaction and also the reorganisation energy ("floppiness") consumed in deforming the tetrahedral $GeX_4$ into a four-coordinate fragment of the octahedron produced on bonding the Lewis base.[33] Completely unexpected was the displacement of halide by $Me_3PO$ in $GeX_4$ (X = Cl or Br) to form mono- or di-cations; whilst the cationic species are probably stabilised in the solid state by the lattice, the displacement of $X^-$ by the weakly bound phosphane oxide in solution is surprising. The stronger Ge–F bond presumably prevents this happening in the fluorides under similar conditions. Also surprising was the conversion of $R_3AsO$ into $R_3AsX_2$ by $GeX_4$ (X = Cl or Br) under mild conditions, again the strength of the Ge–F bond would account for the different reaction (simple adduct formation) observed with $GeF_4$.

## Experimental Section

All reactions were conducted using Schlenk, vacuum line and glove-box techniques and under a dry dinitrogen atmosphere. The germanium(IV) halides $GeF_4$, $GeBr_4$ and $GeI_4$ were obtained from Aldrich and used as received. $GeCl_4$ (Aldrich) was distilled from a mixture of $CaCl_2/Na_2CO_3$, which removes traces of water and HCl. MeCN and $CH_2Cl_2$ were dried by distillation from $CaH_2$, THF and $MeOCH_2CH_2OMe$ distilled from Na-benzophenone ketyl. $Me_3PO$ and $Et_3PO$ were freshly sublimed in vacuo. $Ph_3PO$ and $Ph_3AsO$ were heated in vacuo. IR spectra were recorded as Nujol mulls with a Perkin–Elmer PE 983G spectrometer, $^1H$ NMR spectra in $CDCl_3$, $CD_2Cl_2$ or $CD_3CN$ solutions with a Bruker AV300, $^{31}P\{^1H\}$ and $^{19}F\{^1H\}$ NMR spectra with a Bruker DPX400 and referenced to 85% $H_3PO_4$ and $CFCl_3$, respectively. Microanalytical measurements on new complexes were performed by the microanalytical service at Strathclyde University.

**$[GeF_4(MeCN)_2]$:** Prepared as described.[12] $^1H$ NMR (300 MHz, $CDCl_3$, 293 K): $\delta$ = 1.99 (s) ppm. $^{19}F\{^1H\}$ NMR ($CDCl_3$, 180 K): $\delta$ = –101.2 (t, $^2J_{FF} \approx 55$ Hz), –108.2 (s), –134.2 (t) ppm. IR (Nujol): $\tilde{\nu}$ = 2333, 2295, 2252 [ν(CN)], 688 (s), 657 (vs), 639 (s) [ν(Ge–F)] $cm^{-1}$.

**$[GeF_4(Me_3PO)_2]$:** Freshly sublimed $Me_3PO$ (0.046 g, 0.50 mmol) was added to a solution of $[GeF_4(MeCN)_2]$ (0.058 g, 0.25 mmol) in $CH_2Cl_2$ (20 mL) at room temperature with stirring. A white precipitate formed gradually in the reaction mixture. After stirring for 10 min, the $^{19}F\{^1H\}$ NMR spectrum showed one major singlet at $\delta$ = –109.9 ppm and two minor triplets at –107.6 and –121.6 ppm. The solvent was removed in vacuo, and the white residue was dissolved in $CH_3CN$. Colourless air-stable crystals were obtained by vapour diffusion of diethyl ether into the solution. Yield 0.07 g, 85%. $C_6H_{18}F_4GeO_2P_2$ (332.7): calcd. C 21.7, H 5.5; found C 22.0, H 5.5. $^1H$ NMR (300 MHz, $CDCl_3$, 293 K): $\delta$ = 1.76 (*d*, $^2J_{HP}$ = 13.5 Hz) ppm. $^{31}P\{^1H\}$ NMR ($CDCl_3$, 293 K): $\delta$ = 65.8 (s, major), 65.1 (s, minor) ppm. $^{19}F\{^1H\}$ NMR ($CDCl_3$, 293 K): $\delta$ = –107.6 (t, $^2J_{FF}$ = 58 Hz), –109.9 (s), –121.6 (t) ppm. IR (Nujol): $\tilde{\nu}$ = 1087 (vs, br) [ν(P=O)], 626 (s), 612 (s) [ν(Ge–F)] $cm^{-1}$.

**$[GeF_4(Et_3PO)_2]$:** $Et_3PO$ (0.067 g, 0.50 mmol) was added to a solution of $[GeF_4(MeCN)_2]$ (0.058 g, 0.25 mmol) in $CH_2Cl_2$ (20 mL) at room temperature to give a clear solution. The $^{19}F\{^1H\}$ NMR spectrum showed one major singlet at –110.2 and two minor triplets at –107.8 and –121.8 ppm. The solvent and volatiles were evaporated, and the white residue was washed with diethyl ether (10 mL) and dried. Yield 0.93 g, 90%. Colourless crystals were obtained from $CH_2Cl_2$ solution by slow evaporation of solvent under $N_2$. $C_{12}H_{30}F_4GeO_2P_2$ (416.9): calcd. C 34.4, H 7.2; found C 34.8, H 7.1. $^1H$ NMR (300 MHz, $CDCl_3$, 295 K): $\delta$ = 1.1 (m, 3 H), 2.05 (m, 2 H) ppm. $^{19}F\{^1H\}$ NMR ($CDCl_3$): $\delta$ = –107.8 (t, $^2J_{FF}$ = 59 Hz), –110.1 (s), –122.1 (t) ppm. $^{31}P\{^1H\}$ NMR ($CDCl_3$): $\delta$ = 76.4 (s, major), 76.1 (s, minor) ppm. IR (Nujol): $\tilde{\nu}$ = 1092 (vs, br) [ν(P=O)], 614 (s) [ν(Ge–F)] $cm^{-1}$.

**$[GeF_4(Ph_3PO)_2]$:** $Ph_3PO$ (0.146 g, 0.50 mmol) was added to a solution of $[GeF_4(MeCN)_2]$ (0.058 g, 0.25 mmol) in MeCN (20 mL) at room temperature, which led to the gradual formation of a white precipitate. After stirring for 10 min, the solvent was removed in vacuo, and the white residue was washed with small amount of $CH_2Cl_2$ and dried in vacuo. Yield 0.090 g, 90%. $C_{36}H_{30}F_4GeO_2P_2$ (705.2): calcd. C 61.3, H 4.3; found C 60.7, H 4.2. $^{19}F\{^1H\}$ NMR ($CDCl_3$, 253 K): $\delta$ = –100.9 (t, $^2J_{FF}$ = 64 Hz), –105.3 (s), –120.6 (t) ppm. $^{31}P\{^1H\}$ NMR ($CDCl_3$, 253 K): $\delta$ = 40.8, 40.2 ppm. IR (Nujol): $\tilde{\nu}$ = 1133, 1078 [ν(P=O)], 636 (s) [ν(Ge–F)] $cm^{-1}$.

**$[GeCl_3(Me_3PO)_3]_2[GeCl_6]$:** Trimethylphosphane oxide (0.09 g, 1.0 mmol) was added to a solution of $GeCl_4$ (0.11 g, 0.5 mmol) in $CH_2Cl_2$ (20 mL) at room temperature, and stirred overnight. The solution, now containing some precipitate, was taken to dryness in vacuo to leave the white solid. Yield 0.15 g, 90%. Colourless crystals separated from the solution in $CH_2Cl_2$ kept at –20 °C for a few days. $C_{18}H_{54}Cl_{12}Ge_3O_6P_6$ (1195.7): calcd. C 18.1, H 4.6; found C

 © 2007 Wiley-VCH Verlag GmbH & Co. KGaA, Weinheim 

18.6, H 4.7. $^1$H NMR (300 MHz, $CDCl_3$, 295 K): $\delta$ = 1.45 (d, $^2J_{HP}$ = 13.5 Hz) ppm. $^{31}P\{^1H\}$ NMR ($CDCl_3$, 298 K): $\delta$ = 45.0 (br) ppm. IR (Nujol): $\tilde{\nu}$ = 1065 [$\nu$(P=O)], 344, 308, 295 [$\nu$(Ge–Cl)] cm$^{-1}$.

**[$GeCl_2(Me_3PO)_4$]$Cl_2$:** Trimethylphosphane oxide (0.18 g, 2.0 mmol) was added to a solution of $GeCl_4$ (0.11 g, 0.5 mmol) in MeCN (20 mL) at room temperature, and stirred overnight. The solution was filtered and concentrated to ca. 5 mL. Colourless crystals separated from the solution kept at –20 °C for a few days. Yield 0.23 g, 80%. $C_{12}H_{36}Cl_4GeO_4P_4$ (582.7): calcd. C 24.7, H 6.2; found C 24.6, H 6.6. $^1$H NMR (300 MHz, $CDCl_3$, 295 K): $\delta$ = 1.40 (d, $^2J_{HP}$ = 13.5 Hz) ppm. $^{31}P\{^1H\}$ NMR ($CDCl_3$, 295 K): $\delta$ = 40.1 (br) ppm. IR (Nujol): $\tilde{\nu}$ = 1138 (sh), 1053 (s, br) [$\nu$(P=O)], 352 (m), 300 (w) [$\nu$(Ge–Cl)] cm$^{-1}$.

**[$GeBr_2(Me_3PO)_4$]$Br_2$:** Trimethylphosphane oxide (0.09 g, 1.0 mmol) was added to a solution of $GeBr_4$ (0.19 g, 0.5 mmol) in $CH_2Cl_2$ (20 mL) at room temperature that lead to the immediate formation of a white solid. After stirring for several minutes, the solvent was removed in vacuo. The solid residue was dissolved in MeCN (20 mL), filtered, and concentrated. Colourless crystals separated from the solution kept at –20 °C for a few days. Yield 0.16 g, 55%. $C_{12}H_{36}Br_4GeO_4P_4$ (760.5): calcd. C 19.0, H 4.8; found C 19.2, H 4.7. $^1$H NMR (300 MHz, $CDCl_3$, 295 K): $\delta$ = 1.40 (d, $^2J_{HP}$ = 13.5 Hz) ppm. $^{31}P\{^1H\}$ NMR ($CDCl_3$, 295 K): $\delta$ = 41.8 (v.br) ppm. See text for low temperature data. IR (Nujol): $\tilde{\nu}$ = 1131 (sh), 1101 (sh), 1051 (s, br) [$\nu$(P=O)], 245 (m) [$\nu$(Ge–Br)] cm$^{-1}$.

**[$GeCl_4(Et_3PO)_2$]:** Freshly sublimed $Et_3PO$ (0.13 g, 1.0 mmol) was added to a solution of $GeCl_4$ (0.11 g, 0.5 mmol) in $CH_2Cl_2$ (20 mL) at room temperature. The reaction mixture was stirred overnight giving a clear solution. The solvent and all volatiles were removed in vacuo, leaving the product as solid. Yield 0.22 g, 90%. $C_{12}H_{30}Cl_4GeO_2P_2$ (481.96): calcd. C 30.0, H 6.3; found C 29.8, H 6.1. $^{31}P\{^1H\}$ NMR ($CH_2Cl_2$, 295 K): $\delta$ = 60.1 (s) ppm. IR (Nujol): $\tilde{\nu}$ = 1087 (br) [$\nu$(P=O)], 321 (m, br) [$\nu$(Ge–Cl)] cm$^{-1}$.

**[$GeF_4(Ph_3AsO)_2$]:** $Ph_3AsO$ (0.16 g, 0.5 mmol) was added to a solution of [$GeF_4(MeCN)_2$] (0.058 g, 0.25 mmol) in $CH_2Cl_2$ (20 mL) at room temperature with stirring. A white precipitate formed gradually in the reaction mixture. After continued stirring overnight, the solution was filtered. The white solid residue was washed with $CH_2Cl_2$ (10 mL) and dried in vacuo. Yield 0.22 g, 90%. $C_{36}H_{30}As_2F_4GeO_2{\cdot}CH_2Cl_2$ (878.0): calcd. C 50.6, H 3.7; found C 50.1, H 3.3. $^{19}F\{^1H\}$ NMR ($CD_2Cl_2$, 298 K): $\delta$ = –94.4 (t, $^2J_{FF}$ = 60 Hz), –98.2 (s), –112.9 (t) ppm. IR (Nujol): $\tilde{\nu}$ = 868 (s) [$\nu$(As=O)], 608 (s) [$\nu$(Ge–F)] cm$^{-1}$.

**[$GeF_4(MeOCH_2CH_2OMe)$]:**[12,32] [$GeF_4(MeCN)_2$] (0.550 g, 2.38 mmol) was dissolved in $CH_2Cl_2$ (10 mL) and stirred while $MeOCH_2CH_2OMe$ (0.215 g, 2.39 mmol) was added dropwise. The solution was stirred for 3 h before half the solvent was removed in vacuo. Hexane (15 mL) was added and stirring continued for a further 30 min. The solid was filtered and dried briefly in vacuo. Yield 0.25 g, 44%. $^1$H NMR (300 MHz, $CDCl_3$, 243 K): $\delta$ = 4.22 (s, $CH_2$), 4.00 (s, Me) ppm. $^{19}F\{^1H\}$ NMR ($CH_2Cl_2$, 223 K): $\delta$ = –131.0 (t, $^2J_{FF}$ = 81 Hz), –151.1 (t) ppm. IR (Nujol): $\tilde{\nu}$ = 671 (s), 639 (s) [$\nu$(Ge–F)] cm$^{-1}$.

**[$GeF_4(thf)_2$]:**[32] [$GeF_4(MeCN)_2$] (0.62 g, 2.67 mmol) was stirred in thf (20 mL) for 3 h. The solvent was then removed in vacuo to leave a white solid. Yield 0.75 g, 96%. $^1$H NMR (300 MHz, $CDCl_3$, 298 K): $\delta$ = 2.13 (s), 4.45 (s) ppm. $^{19}F\{^1H\}$ NMR ($CH_2Cl_2$, 243 K): $\delta$ = –166.7 (s), –166.2 (t, $^2J_{FF}$ = 72 Hz), –178.8 (t) ppm. IR (Nujol): $\tilde{\nu}$ = 1017 (s, br), 852 (s, br) [$\nu$(COC)], 650 (vbr) [$\nu$(Ge–F)] cm$^{-1}$.

**X-ray Crystallography:** Details of the crystallographic data collection and refinement parameters are given in Table 7 and Table 8. Colourless, air-stable crystals of [$GeF_4(Me_3PO)_2$] were obtained by diffusion of diethyl ether vapour into a MeCN solution; [$GeF_4(Et_3PO)_2$]·1/3$CH_2Cl_2$ crystals were obtained from a $CH_2Cl_2$ solution by slow evaporation of the solvent under $N_2$; [$GeF_4(Ph_3PO)_2$]·2$CH_2Cl_2$ crystals were obtained from $CH_2Cl_2$; crystals of [$GeCl_3(Me_3PO)_3$]$_2$[$GeCl_6$] separated from the $CH_2Cl_2$ reactant solution kept at –20 °C for a few days; [$GeCl_2(Me_3PO)_4$]$Cl_2$ and [$GeBr_2(Me_3PO)_4$]$Br_2$ crystals separated from a MeCN solution kept at –20 °C for a few days. Data collections used a Bruker-Nonius Kappa CCD diffractometer fitted with Mo-$K_\alpha$ radiation ($\lambda$ = 0.71073 Å) and either a graphite monochromator or confocal mirrors, with the crystals held at 120 K in a nitrogen gas stream. Struc-

Table 7. Crystallographic parameters.[a]

| Compound | [$GeF_4(Me_3PO)_2$] | [$GeF_4(Et_3PO)_2$]·1/3$CH_2Cl_2$ | [$GeF_4(Ph_3PO)_2$]·2$CH_2Cl_2$ |
|---|---|---|---|
| Formula | $C_6H_{18}F_4GeO_2P_2$ | $C_{12.33}H_{30.67}Cl_{0.67}F_4GeO_2P_2$ | $C_{38}H_{34}Cl_4F_4GeO_2P_2$ |
| $M$ | 332.73 | 445.20 | 874.98 |
| Crystal system | monoclinic | trigonal | monoclinic |
| Space group | $P2_1/n$ (no. 14) | $R\bar{3}$ (no. 148) | $P2_1/n$ (no. 14) |
| $a$ [Å] | 6.300(4) | 25.711(4) | 8.840(2) |
| $b$ [Å] | 9.536(5) | 25.711(4) | 14.769(3) |
| $c$ [Å] | 10.368(4) | 7.3385(10) | 14.174(3) |
| $\alpha$ [°] | 90 | 90 | 90 |
| $\beta$ [°] | 96.33(3) | 90 | 94.824(10) |
| $\gamma$ [°] | 90 | 120 | 90 |
| $V$ [Å$^3$] | 619.0(5) | 4201.1(11) | 1844.0(6) |
| $Z$ | 2 | 9 | 2 |
| $\mu$(Mo-$K_\alpha$) [mm$^{-1}$] | 2.763 | 1.946 | 1.263 |
| Total no. reflections | 6778 | 9949 | 16281 |
| $R_{int}$ | 0.062 | 0.046 | 0.048 |
| Unique reflections | 1206 | 2134 | 4227 |
| No. of parameters | 74 | 103 | 232 |
| $R_1$ [$I_o > 2\sigma(I_o)$] | 0.059 | 0.035 | 0.036 |
| $R_1$ [all data] | 0.072 | 0.046 | 0.051 |
| $wR_2$ [$I_o > 2\sigma(I_o)$] | 0.161 | 0.087 | 0.074 |
| $wR_2$ [all data] | 0.169 | 0.092 | 0.080 |

[a] Common items: $T$ = 120 K; wavelength (Mo-$K_\alpha$) = 0.71073 Å; $\theta$(max) = 27.5°; $R_1 = \Sigma||F_o| - |F_c||/\Sigma|F_o|$; $wR_2 = [\Sigma w(F_o^2 - F_c^2)^2/\Sigma wF_o^4]^{1/2}$.

 © 2007 Wiley-VCH Verlag GmbH & Co. KGaA, Weinheim 

Table 8. Crystallographic parameters.

| Compound | $[GeCl_3(Me_3PO)_3]_2[GeCl_6]$ | $[GeCl_2(Me_3PO)_4]Cl_2$ | $[GeBr_2(Me_3PO)_4]Br_2$ |
|---|---|---|---|
| Formula | $C_{18}H_{54}Cl_{12}Ge_3O_6P_6$ | $C_{12}H_{36}Cl_4GeO_4P_4$ | $C_{12}H_{36}Br_4GeO_4P_4$ |
| $M$ | 1195.60 | 582.68 | 760.52 |
| Crystal system | trigonal | monoclinic | monoclinic |
| Space group | $P\bar{3}$ (no. 147) | $C2/c$ (no. 15) | $C2/c$ (no. 15) |
| $a$ [Å] | 13.448(2) | 17.0680(18) | 17.296(3) |
| $b$ [Å] | 13.448(2) | 11.634(2) | 11.6929(16) |
| $c$ [Å] | 7.4233(10) | 13.226(2) | 13.907(3) |
| $\alpha$ [°] | 90 | 90 | 90 |
| $\beta$ [°] | 90 | 92.227(9) | 92.612(10) |
| $\gamma$ [°] | 120 | 90 | 90 |
| $V$ [Å$^3$] | 1162.5(3) | 2624.2(7) | 2809.7(8) |
| $Z$ | 1 | 4 | 4 |
| $\mu$(Mo-$K_\alpha$) [mm$^{-1}$] | 2.853 | 1.833 | 7.020 |
| Total no. reflections | 34223 | 16460 | 14426 |
| $R_{int}$ | 0.069 | 0.214[a] | 0.086 |
| Unique reflections | 1775 | 3027 | 3238 |
| No. of parameters | 72 | 120 | 120 |
| $R_1$ [$I_o > 2\sigma(I_o)$] | 0.043 | 0.068 | 0.073 |
| $R_1$[all data] | 0.062 | 0.173 | 0.125 |
| $wR_2$ [$I_o > 2\sigma(I_o)$] | 0.103 | 0.128 | 0.126 |
| $wR_2$ [all data] | 0.112 | 0.164 | 0.148 |

[a] Very weak data [50% of reflections with $I > 2\sigma(I)$].

ture solution and refinement were straightforward,[34–36] with H atoms introduced into the models in calculated positions. Selected bond lengths and angles are given in Tables 1, 2, 3, 4, 5, and 6.

CCDC-637438 (for F/Me), -637439 (for F/Et), -637440 (for F/Ph), -637441 (for Cl/Me), -637442 (for Cl/Me), -637443 (for Br/Me) contain the supplementary crystallographic data for this paper (the groups in parentheses indicate the species in the compounds). These data can be obtained free of charge from The Cambridge Crystallographic Data Centre via www.ccdc.cam.ac.uk/data_request/cif.

## Acknowledgments

We thank UK Research Councils (RCUK) (EP/C006763/1) and Engineering and Physical Sciences Research Council (EPSRC) (GR/T09613/01) for support and for access to the chemical database service at Daresbury. A. L. H. thanks the Royal Society for Support.

[1] M. P. Shemkunas, W. T. Petuskey, A. V. G. Chizmeshya, K. Leinenweber, G. H. Wolf, *J. Mater. Res.* **2004**, *19*, 1392–1399.
[2] a) A. M. Marygaryan, *Photodetectors and Fiber Optics*, **2001**, 369–458. Academic Press, San Diego, USA; b) C. Jing, X. Zhao, H. Tao, X. Wang, A. Liu, *J. Mater. Chem.* **2003**, *13*, 3066–3071.
[3] Z. Rappoport, *The Chemistry of Organic Germanium, Tin and Lead Compounds* (2 vols.), **2002**, Wiley, NY.
[4] J. Parr, in *Comprehensive Coordination Chemistry II* (Eds.: J. A. McCleverty, T. J. Meyer), **2003**, *3*, 545–608, Elsevier, Oxford.
[5] F. Glockling, *The Chemistry of Germanium*, **1969**, Academic Press, NY.
[6] G. R. Willey, T. J. Woodman, U. Somasundaram, D. R. Aris, W. Errington, *J. Chem. Soc., Dalton Trans.* **1998**, 2573–2576.
[7] G. R. Willey, U. Somasunderam, D. R. Aris, W. Errington, *Inorg. Chim. Acta* **2001**, *315*, 191–195.
[8] J. Ejfler, S. Szafert, H. Jiao, P. Sobota, *New J. Chem.* **2002**, *26*, 803–805.
[9] S. M. Godfrey, I. Mushtaq, R. G. Pritchard, *J. Chem. Soc., Dalton Trans.* **1999**, 1319–1323.
[10] N. W. Mitzel, U. Losehand, K. Vojinovic, *Inorg. Chem.* **2001**, *40*, 5302–5303.
[11] A. V. Yatsenko, S. V. Medvedev, L. A. Aslanov, *Koord. Khim.* **1991**, *17*, 1338–1341.
[12] E. L. Muetterties, *J. Am. Chem. Soc.* **1960**, *82*, 1082–1087.
[13] M. F. Davis, unpublished work, **2006**.
[14] L. M. Engelhardt, C. L. Raston, C. R. Whitaker, A. H. White, *Aust. J. Chem.* **1986**, *39*, 2151–2154.
[15] A. L. Speck, *Acta Crystallogr., Sect. C* **1987**, *43*, 1233–1235.
[16] M. F. Davis, W. Levason, G. Reid, M. Webster, *Polyhedron* **2006**, *25*, 930–936.
[17] J. Kohler, A. Simon, R. Hoppe, *J. Less-Common Met.* **1988**, *137*, 333–341.
[18] A. R. J. Genge, W. Levason, G. Reid, *Inorg. Chim. Acta* **1999**, *288*, 142–149.
[19] H. Gruber, U. Mueller, *Z. Krystallogr.* **1997**, *212*, 497–498.
[20] I. R. Beattie, G. P. McQuillan, L. Rule, M. Webster, *J. Chem. Soc.* **1963**, 1514–1518.
[21] S. H. Hunter, V. M. Langford, G. A. Rodley, C. J. Wilkins, *J. Chem. Soc. A* **1968**, 305–308.
[22] a) D. Tudela, J. D. Tornero, A. Monge, A. J. Sanchez-Herencia, *Inorg. Chem.* **1993**, *32*, 3928–3930; b) A. I. Tursina, L. A. Aslanov, S. V. Medvedev, A. V. Yatsenko, *Koord. Khim.* **1987**, *11*, 417–424; c) A. I. Tursina, A. V. Yatsenko, S. V. Medvedev, V. V. Chermyshev, L. A. Aslanov, *Zh. Strukt. Khim.* **1986**, *27*, 157–159 and references cited therein.
[23] M. B. Hursthouse, I. A. Steer, *J. Organomet. Chem.* **1971**, *27*, C11–C12.
[24] B. Neumuller, S. Chitsaz, K. Dehnicke, *Z. Naturforsch., Teil B* **1999**, *54*, 1611–1614.
[25] M. H. O'Brien, G. O. Doak, G. G. Long, *Inorg. Chim. Acta* **1967**, *1*, 34–40.
[26] L. Verdonck, G. P. Van der Kelen, *Spectrochim. Acta Sect. A* **1977**, *33*, 601–605.
[27] G. M. Usacheva, G. K. Khami, *Izv. Akad. Nauk. SSSR, Ser. Khim.* **1970**, 1432–1434.
[28] R. Appel, D. Rebhan, *Chem. Ber.* **1969**, *102*, 3955–3957.
[29] V. S. Gamayurova, V. K. Gordeev, B. D. Chernokal'skii, *Zh. Obsch. Khim.* **1979**, *49*, 2780–2781.
[30] B. E. Abalonin, Yu. F. Galitov, Z. M. Izmailova, *Zh. Obsch. Khim.* **1977**, *47*, 624–625.

 © 2007 Wiley-VCH Verlag GmbH & Co. KGaA, Weinheim 

[31] J. P. Clark, V. M. Langford, C. J. Wilkins, *J. Chem. Soc. A* **1967**, 792–796.
[32] R. C. Aggarwal, M. Onyszchuk, *Proc. Chem. Soc.* **1962**, 20.
[33] H. Fleischer, *Eur. J. Inorg. Chem.* **2001**, 393–404.
[34] G. M. Sheldrick, SHELXS-97, *Program for crystal structure solution*, University of Göttingen, Germany, **1997**.
[35] G. M. Sheldrick, SHELXL-97, *Program for crystal structure refinement*, University of Göttingen, Germany, **1997**.
[36] G. M. Sheldrick, SADABS, *Bruker-Nonius area detector scaling and absorption correction* (V2.10), University of Göttingen, Germany, **2003**.

Received: February 21, 2007
Published Online: May 8, 2007

 © 2007 Wiley-VCH Verlag GmbH & Co. KGaA, Weinheim 

DOI: 10.1002/ejic.200601154

# Colloidal $CdS/SiO_2$ Nanocomposite Particles from Charged Colloids of CdS and Silica

**Meike Roskamp,[a] Andreas K. Schaper,[b] Joachim H. Wendorff,[b,c] and Sabine Schlecht*[a]**

**Keywords:** Colloids / Nanostructures / Semiconductors / CdS / Silica particles

Colloidal $CdS/SiO_2$ nanocomposite particles were prepared from soluble negatively charged silica particles ($d$ = 150 nm) and positively charged ligand-stabilised CdS particles ($d$ = 3 nm). The positively charged ligand shell of the CdS particles is constituted of thiocholine [TC, trimethyl(2-sulfanylethyl)azanium chloride]. As a quaternary nitrogen atom carries the charge in this ligand, the positive charge on the particles is basically independent of the pH value of the solution. A neutral pH value was chosen for the deposition of the CdS particles on the larger silica particles which already contain a significant negative charge under these conditions. The obtained nanocomposite particles were characterised by optical spectroscopy, gel electrophoresis and electron microscopy.

(© Wiley-VCH Verlag GmbH & Co. KGaA, 69451 Weinheim, Germany, 2007)

## Introduction

The preparation and investigation of nanocomposite systems are very generally motivated by the idea of a superior combination of different property profiles brought to the nanocomposite by its individual components. Different types of systems can be considered nanocomposites in this context: small nanoparticles that are embedded in a macroscopic polymeric or oxidic matrix,[1–5] loose assemblies of nanoparticles and silica spheres[6] or isolated spherical structures consisting of chemically different components such as silica-coated quantum dots[7,8] or silica spheres decorated with smaller nanoparticles. With this last type of composite structure, a desired combination of properties such as photoluminescence and solubility in water[7] or magnetism combined with optical emission[9] can be realised. When water solubility together with either magnetic or optical properties is required, silica particles are frequently the component of choice as they are optically inactive and are soluble in water up to a much bigger particle size than most other nanoparticles.[10] Consequently, nanocomposites containing silica particles in combination with particles of II/VI compound semiconductors,[11] of noble metals[12] or of other oxides[13] were described. Ideally, the nanocomposite will exhibit the properties of the smaller particles in the quantum size regime such as blueshifted photoluminescence, plasmon bands or superparamagnetism together with the convenience in handling that the larger silica particles can provide. Regarding the attachment of the semiconductor particles or metal particles on silica, several modes of connectivity were described in the literature. The two most prominent methods to attach smaller functional particles on silica are the coordinative binding of salts or other precursors with subsequent formation of the desired particles on the silica surface[14] and the deposition of preformed small particles on the surface of the silica. The latter concept has the advantage that monodisperse functionalized particles can be used whereas the formation of small particles directly on the surface of the silica support yields quite polydisperse and aggregated products[11a,14,15] because no protecting agent surrounds the primary grains at the moment of their formation. When preformed monodisperse quantum dots such as CdS particles are deposited on a silica support, this can either be done on functionalised silica with a modified surface covered by, for example, thiol groups[3,4] or by the use of appropriately functionalized small particles that are deposited on pure silica spheres. As silica spheres are negatively charged at neutral pH, the application of polycationic polymers as mediators for an attachment of neutral particles proved successful.[16] As an additional variant of such nanocomposites, embedded small functional particles that are covered by an additional silica layer on the original silica sphere were introduced recently.[17] The direct addition of oppositely charged particles as it is applied for the production of ordered superstructures of polymer spheres or semiconductor particles[18] is much less common for the deposition of particles in nanocomposite synthesis. Here, we present the preparation of $CdS/SiO_2$ nanocomposite structures with monodisperse CdS particles and without the need of additional reagents.

[a] Institut für Chemie und Biochemie, Freie Universität Berlin, Fabeckstrasse 34–36, 14195 Berlin, Germany
Fax: +49-30-83853310
E-mail: schlecht@chemie.fu-berlin.de
[b] Wissenschaftliches Zentrum für Materialwissenschaften, Philipps-Universität Marburg, Hans-Meerwein-Strasse, 35032 Marburg, Germany
[c] Fachbereich Chemie der Philipps-Universität Marburg, Hans-Meerwein-Strasse, 35032 Marburg, Germany

 © 2007 Wiley-VCH Verlag GmbH & Co. KGaA, Weinheim 

## Results and Discussion

Colloidal nanoparticles of cadmium sulfide CdS capped with a thiocholin (TC) shell were prepared from cadmium chloride, hexamethyldisilathiane $(Me_3Si)_2S$ and freshly prepared thiocholine in an experimental procedure similar to the one described by Barglik-Chory et al.[19] (Scheme 1).

Instead of a mixture of water and ethanol, ultrapure water was used as a reaction medium and the reaction time was shortened to 15 min. This protocol yielded colloidal CdS particles with a mean diameter of 2.9 nm after dialysis at a pH value of 7. The stability of the resulting colloid was significantly improved by the use of ultrapure water and by previous extensive rinsing of all glassware with ultrapure water. Whereas colloids in glassware without prior treatment precipitated within a few days, those in rinsed glassware could be stored at 4 °C for at least three months without precipitation. However, even with this precaution taken, strongly diluted colloid solutions precipitated within 24 h because the equilibrium of the cooordinated thiocholin ligand and its uncoordinated form is shifted away from a stabilising coordination. The resulting precipitation was found to be irreversible.

The stable colloids of thiocholine-capped CdS particles were characterized by UV/Vis spectroscopy and by transmission electron microscopy (TEM). The UV/Vis absorption spectrum of the colloidal particles in aqueous solution (Figure 1) shows an absorption maximum at $\lambda_{max}$ = 369 nm. This value indicates a mean diameter of the particles of 2.8–3.0 nm.[20] This particle size was confirmed by TEM images of the stabilized particles (Figure 2). An overview of the CdS particles (Figure 2a) shows that they are not agglomerated but evenly distributed on the TEM grid. A high resolution TEM image (Figure 2b) shows individual particles of 3 nm size. For some particles, the lattice planes of CdS are also visible.

To give evidence for a charged ligand shell on the particles in solution, the CdS particles were subjected to gel electrophoresis. To compare the charge and the mobility of the thiocholine-capped particles with similar charged colloids, we ran solutions of colloidal particles with ligand shells of 11-mercaptoundecanoic acid (MUDA), reduced glutathione (GSH) and dimethylaminoethanethiol (DMAET) as well as negatively charged particles of $SiO_2$ in parallel. The results are depicted in Figure 3. As expected, the silica particles and the CdS particles with ligand

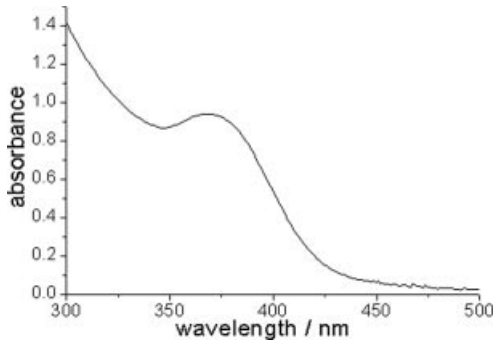


Figure 1. UV/Vis absorption spectrum of thiocholine-capped nanoparticles of CdS ($\lambda_{max}$ = 369 nm).

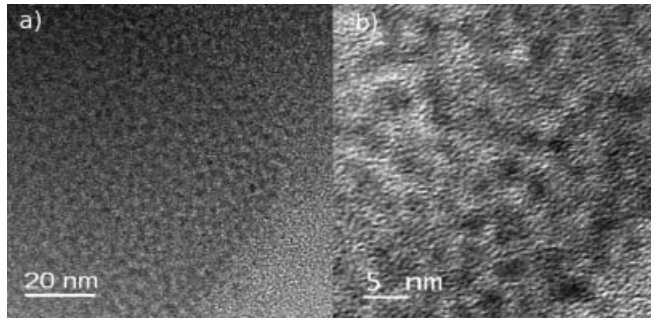


Figure 2. (a) Overview TEM image of thiocholine-capped CdS nanoparticles ($d$ = 3 nm); (b) high resolution TEM image of the particles.

shells of MUDA and GSH were found to move towards the anode in the gel. In contrast, the particles covered by ammonium-functionalized ligands such as DMAET or TC moved towards the cathode. This shows that the TC colloid is sufficiently stable at pH 7 and that it can be used as a

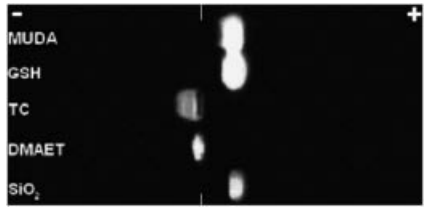


Figure 3. Agarose gel of colloidal nanoparticles of CdS with capping shells of mercaptoundecanoic acid (MUDA), glutathione (GSH), thiocholine (TC) and dimethylaminoethanethiol (DMAET) as well as of silica particles.

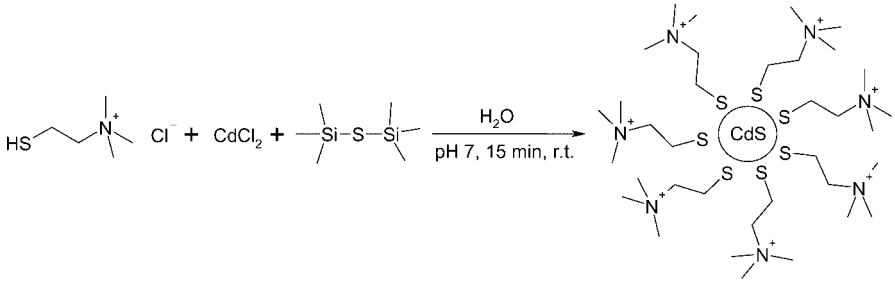


Scheme 1. Preparation of colloidal nanoparticles of CdS with a thiocholine shell.

 © 2007 Wiley-VCH Verlag GmbH & Co. KGaA, Weinheim 

carrier of a permanent positive charge on the shell in nanocomposite synthesis.

Starting from these stable, positively charged particles of CdS and soluble negatively charged particles of silica, we prepared colloidal nanocomposites of $SiO_2$/CdS where the smaller CdS particles are deposited on the surface of the anionic silica particles at neutral pH value. As the negative charge is situated directly on the particle surface, not on a ligand covering the silica particles, no ligand exchange of oppositely charged ligands of the two types of particles can occur. The silica particles used for the formation of $SiO_2$/CdS composite particles have a diameter of 150 nm which is much larger than the diameter of only 3 nm of the CdS particles with the thiocholine shell. Thus, no regular packing of spheres as in ordered superstructures of particles of similar size, but a coverage of the bigger particles with a large number of small ones is to be expected. An investigation of the nanocomposite particles by UV/Vis spectroscopy, by TEM and by gel electrophoresis confirmed this picture. In the TEM images (Figure 4) of the nanocomposite particles it can be seen that the surface of the big silica spheres is covered by a large number of darker CdS particles of a few nanometres size. This confirms a significant interaction between the oppositely charged particles making the formation of a stable nanocomposite possible.

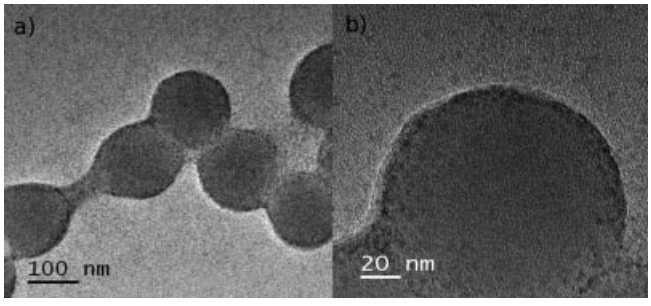


Figure 4. (a) TEM overview image of $SiO_2$/CdS nanocomposite particles; (b) TEM image of a single $SiO_2$/CdS nanocomposite particle, which shows the small CdS particles on the surface of the silica sphere.

It was shown by gel electrophoresis that the degree of coverage of the silica spheres with CdS particles is determined by electroneutrality. In contrast to the pure silica particles, which moved towards the anode (Figure 3), and the thiocholine-capped particles of CdS, which moved towards the cathode (Figures 3 and 5), the nanocomposite particles acted as neutral species (Figure 5). For comparison, anionic CdS particles with shells of MUDA and GSH were run in the gel.

Additional evidence for the formation of nanocomposite particles of $SiO_2$/CdS with a relatively close coverage of the silica surface comes from UV/Vis absorption spectroscopy on aqueous solutions of the particles. The absorption band of the TC-capped CdS particles (Figure 6) is shifted after the deposition from an absorption maximum of $\lambda_{max}$ = 369 nm to a value of $\lambda_{max}$ = 400 nm and it is significantly broadened. Both effects are expected for a closer contact of

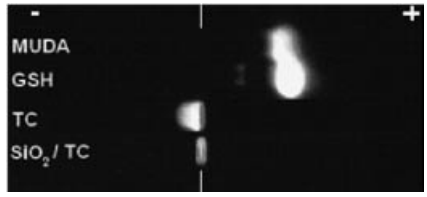


Figure 5. Agarose gel of pure CdS nanoparticles with capping shells of 11-mercaptoundecanoic acid (MUDA), glutathione (GSH) and thiocholine (TC) as well as of $SiO_2$/TC nanocomposite particles.

CdS particles on the surface of the silica particles. The shift of the absorption band towards lower energy can be attributed to dipolar interaction between the CdS particles as well as between the CdS particles and the silica. Changes in the electronic structure of the CdS due to their close contacts with each other are known to lead to a broadening of the absorption band.[21]

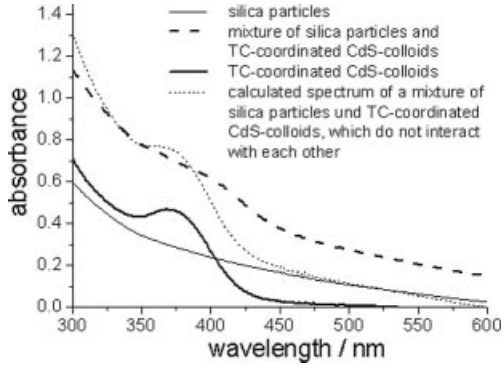


Figure 6. UV/Vis absorption spectra of aqueous solutions of nanoparticles of TC-capped CdS, $SiO_2$ and the $SiO_2$/CdS nanocomposite.

## Summary and Conclusions

The addition of thiocholine-capped CdS nanoparticles to a colloidal solution of larger silica particles at pH 7 leads to a deposition of the cationic CdS particles on the negatively charged surface of the silica until neutrality of the composite particles is reached. The optical properties of the CdS particles are altered by the deposition, and the absorption maximum is shifter to longer wavelengths. The $SiO_2$/CdS particles can be handled as a colloidal solution under neutral aqueous conditions. Thus, it was shown that the direct deposition of positively charged nanoparticles of CdS with a thiocholine shell on anionic silica particles as a support is well feasible and leads to a soluble nanocomposite material with the mechanical properties of the larger silica spheres but with the optical characteristics of small quantum confined systems.

## Experimental Section

**General:** For the syntheses and for rinsing all glassware, ultrapure water taken from a purifier of the type Seralpur Pro 90 CN was used. Cadmium chloride $CdCl_2 \cdot 2.5H_2O$ and hexamethyldisilathiane $(Me_3Si)_2S$ (HMDST) were purchased from Acros. Glutathione

 © 2007 Wiley-VCH Verlag GmbH & Co. KGaA, Weinheim 

(GSH), *N*,*N*-dimethylaminoethanethiol·HCl (DMAET·HCl), tetramethylammonium hydroxide solution (TMAH, 25 wt.% in methanol) and an aqueous suspension of silica particles (d = 150 nm) were purchased from Fluka. 11-Mercaptoundecanoic acid (MUDA) and *S*-acetylthiocholine chloride (S–Ac–TC) were obtained from Sigma–Aldrich. All chemicals were used as received.

**Preparation of Thiocholine-capped CdS Particles:** In an argon-flooded Schlenk flask, S–Ac–TC (0.188 g, 0.95 mmol, 5 equiv.) was dissolved in ethanol (10 mL). After the addition of concentrated hydrochloric acid (20 mL), the reaction mixture was stirred for 3 h at 80 °C. The solvent was then removed under vacuum at 70 °C, and the residue was dissolved in pure water (40 mL). Subsequently, $CdCl_2·2.5H_2O$ (43 mg, 0.19 mmol) was added and as much TMAH as was needed to reach a pH value of 7.0 was also added. Fast addition of HMDST (36 μL, 0.19 mmol) resulted in a yellowish solution. After 15 min, the reaction solution was transferred to dialysis tubing and dialysed against pure water (3 × 600 mL). The resulting slightly cloudy solution was filtered through a 0.2 μm filter to give a clear yellowish solution that was stable at 4 °C for several weeks. $^1H$ NMR (300 MHz, $D_2O$, 25 °C): $\delta$ = 2.92 (m, 2 H, $CH_2$), 3.12 (s, 9 H, $CH_3$), 3.52 (m, 2 H, $CH_2$) ppm.

**Preparation of Glutathione-capped CdS Particles:** A sample of GSH (0.544 g, 1.80 mmol, 3 equiv.) and $CdCl_2·2.5H_2O$ (0.135 g, 0.59 mmol) was dissolved in pure water (30 mL) in an argon-flooded Schlenk flask and stirred at room temperature for 5 min. TMAH (1.4 mL, 3.4 mmol) and pure water (53 mL) were then added. After an additional 10 min of stirring, HMDST (124 μL, 0.59 mmol) was quickly added. After 15 min, the reaction solution was transferred to dialysis tubing and dialysed against pure water (4 × 300 mL). The resulting slightly cloudy solution was filtered through a 0.2 μm filter to give a clear yellowish solution that was stable at 4 °C for several weeks.

**Preparation of MUDA-capped CdS Particles:** A sample of MUDA (0.500 g, 2.30 mmol, 1.9 equiv.) and $CdCl_2·2.5H_2O$ (0.285 g, 0.59 mmol) was suspended in pure water (60 mL) in an argon-flooded Schlenk flask. After the addition of TMAH (2.5 mL, 5.9 mmol) and 10 min of stirring, MUDA completely dissolved and HMDST (263 μL, 1.24 mmol) was quickly added. After 15 min, the reaction solution was transferred to a dialysis tube and dialysed against pure water (4 × 400 mL). The resulting slightly cloudy solution was filtered through a 0.2 μm filter to give a clear yellowish solution that was stable at 4 °C for several weeks.

**Preparation of DMAET-capped CdS Particles:** A sample of DMAET·HCl (0.533 g, 3.77 mmol, 6 equiv.) and $CdCl_2·2.5H_2O$ (0.143 g, 0.62 mmol) was dissolved in pure water (38 mL) in an argon-flooded Schlenk flask and stirred at room temperature for 5 min. TMAH (0.9 mL, 2.1 mmol) was then added. After an additional 10 min of stirring, HMDST (132 μL, 0.62 mmol) was quickly added. After 30 min, the reaction solution was transferred to dialysis tubing and dialysed against pure water (4 × 300 mL). The resulting slightly cloudy solution was filtered through a 0.2 μm filter to give a clear yellowish solution that was stable at 4 °C for several weeks.

**Preparation of $SiO_2$/CdS Nanocomposite Particles:** An aqueous suspension of silica particles (10 μL) and a concentrated aqueous solution of thiocholin-capped CdS colloids (250 μL) were added one after the other to pure water (1 mL). This procedure ensures an excess of CdS colloids in the mixture. The resulting suspension was diluted and dropped on a grid without further purification.

**Transmission Electron Microscopy:** TEM images were taken with a JEOL JEM 3010 electron microscope operated at an accelerating voltage of 300 kV. All samples were deposited on a carbon foil covering a copper grid. The colloids were diluted by a factor of ca. 30 before they were transferred to the grid.


[1] L. Sorensen, G. F. Strouse, A. E. Stiegman, *Adv. Mater.* **2006**, *18*, 1965–1967.
[2] C. Tura, N. Coombs, Ö. Dag, *Chem. Mater.* **2005**, *17*, 573–579.
[3] W. Xu, Y. Liao, D. L. Akins, *J. Phys. Chem. B* **2002**, *106*, 11127–11131.
[4] F. Gao, Q. Lu, D. Zhao, *Chem. Phys. Lett.* **2002**, *360*, 585–591.
[5] V. I. Boev, A. Soloviev, C. J. R. Silva, M. J. M. Gomes, *Solid State Sci.* **2006**, *8*, 50–58.
[6] S. Chang, L. Liu, S. A. Asher, *J. Am. Chem. Soc.* **1994**, *116*, 6739–6744.
[7] a) M. Darbandi, R. Thomann, T. Nann, *Chem. Mater.* **2005**, *17*, 5720–5725; b) N. Hebalkar, S. Kharrazi, A. Ethiraj, J. Urban, R. Fink, S. K. Kulkarni, *J. Colloid Interface Sci.* **2004**, *278*, 107–114; c) M. Bruchez, M. Moronne, P. Gin, S. Weiss, A. P. Alivisatos, *Science* **1998**, *281*, 2013–2016.
[8] D. K. Yi, S. T. Selvan, S. S. Lee, G. C. Papaefthymiou, D. Kundaliya, J. Y. Ying, *J. Am. Chem. Soc.* **2005**, *127*, 4990–4991.
[9] a) D. Ortega, J. S. Garitaonandia, C. Barrera-Solano, M. Ramírez-del-Solar, E. Blanco, M. Domínguez, *J. Non-Cryst. Solids* **2006**, *352*, 2801–2810; b) D. Caruntu, B. L. Cushing, G. Caruntu, C. J. O'Connor, *Chem. Mater.* **2005**, *17*, 3398–3402.
[10] a) W. Li, T. Fu, S. He, *Mater. Sci. Eng. A* **2006**, *441*, 239–244; b) M. Kobayashi, F. Juillerat, P. Galletto, P. Bowen, M. Borkovec, *Langmuir* **2005**, *21*, 5761–5769.
[11] a) O. C. Monteiro, A. C. C. Esteves, T. Trindade, *Chem. Mater.* **2002**, *14*, 2900–2904; b) A. S. Ethiraj, N. Hebalkar, S. R. Sainkar, J. Urban, S. K. Kulkarni, *Surf. Eng.* **2004**, *20*, 367–372; c) J. Kim, J. E. Lee, J. Lee, Y. Jang, S.-W. Kim, K. An, J. H. Yu, T. Hyeon, *Angew. Chem. Int. Ed.* **2006**, *45*, 4789–4793.
[12] K. Kim, H. S. Kim, H. K. Park, *Langmuir* **2006**, *22*, 8083–8088.
[13] K. Cheng, Y. P. He, Y. M. Miao, B. S. Zou, Y. G. Wang, T. H. Wang, X. T. Zhang, Z. L. Du, *J. Phys. Chem. B* **2006**, *110*, 7259–7264.
[14] I. Pastoriza-Santos, D. Gomez, J. Pérez-Juste, L. M. Liz-Marzán, P. Mulvaney, *Phys. Chem. Chem. Phys.* **2004**, *6*, 5056–5060.
[15] N. A. Dhas, A. Gedanken, *Appl. Phys. Lett.* **1998**, *72*, 2514–2516.
[16] a) F. Caruso, *Adv. Mater.* **2001**, *13*, 11–22; b) F. Caruso, *Top. Curr. Chem.* **2003**, *227*, 145–168.
[17] C. Graf, S. Dembski, A. Hofmann, E. Rühl, *Langmuir* **2006**, *22*, 5604–5610.
[18] a) E. V. Shevchenko, D. V. Talapin, N. A. Kotov, S. O'Brian, C. B. Murray, *Nature* **2006**, *439*, 55–59; b) J. Kolny, A. Kornowski, H. Weller, *Nano Lett.* **2002**, *2*, 361–364; c) M. E. Leunissen, C. G. Christova, A.-P. Hynninen, C. P. Royall, A. I. Campbell, A. Imhof, M. Dijkstra, R. van Roij, A. van Blaaderen, *Nature* **2005**, *437*, 235–240; d) A. M. Kalsin, M. Fialkowski, M. Paszewski, S. K. Smoukov, K. J. M. Bishop, B. A. Grzybowski, *Science* **2006**, *312*, 420–424.
[19] C. Barglik-Chory, D. Buchold, M. Schmitt, W. Kiefer, C. Heske, C. Kumpf, O. Fuchs, L. Weinhardt, A. Stahl, E. Umbach, M. Lentze, J. Geurts, G. Müller, *Chem. Phys. Lett.* **2003**, *379*, 443–451.
[20] a) K. Murakoshi, H. Hosokawa, M. Saitoh, Y. Wada, T. Sakata, H. Mori, M. Satoh, S. Yanagida, *J. Chem. Soc., Faraday Trans.* **1998**, *94*, 579–586; b) H. Döllefeld, K. Hoppe, J. Kolny, K. Schilling, H. Weller, A. Eychmüller, *Phys. Chem. Chem. Phys.* **2002**, *4*, 4747–4753.
[21] H. Döllefeld, H. Weller, A. Eychmüller, *Nano Lett.* **2001**, *1*, 267–269.


Received: December 7, 2006
Published Online: May 9, 2007

 © 2007 Wiley-VCH Verlag GmbH & Co. KGaA, Weinheim 

DOI: 10.1002/ejic.200600519

# Transition-Metal ($Mn^{II}$ and $Co^{II}$) Complexes with the Heteropolymolybdate Fragment $[As^{V}Mo_9O_{33}]^{7-}$: Crystal Structures, Electrochemical and Magnetic Properties

**Yanyan Yang,[a] Lin Xu,*[a] Guanggang Gao,[a] Fengyan Li,[a] Yunfeng Qiu,[a] Xiaoshu Qu,[a] and Hong Liu[a]**

**Keywords:** Polyoxometalates / Molybdenum / Arsenic / Magnetic properties

Two novel heteropolymolybdates, $[(CH_3)_4N]_{8n}[M(H_2O)_5]_{2n}(H_3O)_{2n}[\{M(H_2O)_5\}_2(MAs^{V}Mo_9O_{33})_2]_n[M(H_2O)_4(MAs^{V}Mo_9O_{33})_2]_n{\cdot}20nH_2O$ (M = $Mn^{2+}$, **1**; M = $Co^{2+}$, **2**), constructed from the new fragment $(As^{V}Mo_9O_{33})^{7-}$ and a transition metal have been synthesized in aqueous solution and characterized by elemental analysis, IR spectroscopy, thermal gravimetric analysis, and single-crystal X-ray diffraction. Structurally the title complexes resemble a sandwich-type complex because they involve the coordination of two transition metals to two $[As^{V}Mo_9O_{33}]^{7-}$ fragments, which derive from the well-known *B*-β-Keggin structure. Compounds **1** and **2** exhibit a one-dimensional chain-like framework $[M(H_2O)_4(MAs^{V}Mo_9O_{33})_2]^{8n-}$ with isolated $\{[M(H_2O)_5]_2(MAs^{V}Mo_9O_{33})_2\}^{6-}$ units residing among the chains. The magnetic properties of the two complexes were investigated to indicate typical antiferromagnetic interactions through the $Mn^{II}$–O–$Mn^{II}$ bridge unit for complex **1** and the $Co^{II}$–O–$Co^{II}$ bridge unit for complex **2**.

(© Wiley-VCH Verlag GmbH & Co. KGaA, 69451 Weinheim, Germany, 2007)

## Introduction

Polyoxometalates (POMs), a well-known class of metal oxygen clusters with a large variety of compositions and structures, together with their physicochemical properties, are of considerable interest because of their potential application in areas of catalysis, materials science, medicine, and so forth.[1–7] In virtue of a great family of POM building blocks, significant effort has gone into creating rational assemblies to obtain new compounds with desired functional properties. In the class of polyoxometalates, the sandwich-type complexes consisting of polyoxometalates and a transition-metal ion are an important subfamily because of their structural and magnetic diversity.[8–12] Recently, the sandwich-type complexes based on the lacunary heteropolytungstates have been synthesized and structurally characterized in increasing numbers.[13–15] In addition, among the sandwich-type complexes, a large number of magnetic clusters with various nuclearities and original topologies were formed by using the lacunary heteropolytungstates as the main ligand units. In contrast with the above situation, a true heteropolymolybdate analogue of a sandwich-type cluster has not been reported so far, and only a heteropolymolybdate formulated as $[Cu_2(SiMo_9O_{33})_2]^{12-}$, whose structure resembles a sandwich-type POM cluster, has been isolated and structurally characterized since 1981.[16] Why has only one example of a heteropolymolybdate with this structure appeared in the past 25 years? This is mainly because the lacunary heteropolymolybdate behaves with structural lability in aqueous solution, so that the isolation of a stable sandwich-type complex of lacunary heteropolymolybdate is considerably difficult. Müller and co-workers reported the existence of an $\{As^{III}Mo_9O_{33}\}$ fragment in the complexes $K_7[(AsOH)_3(MoO_3)_3(AsMo_9O_{33})]{\cdot}15H_2O$, $K_{10}[(AsOH)_6(MoO_3)_2(O_2Mo{-}O{-}MoO_2)_2(AsMo_9O_{33})_2]{\cdot}12H_2O$, and $(HNMe_3)_8[H_6As_{10}Mo_{24}O_{90}]{\cdot}9H_2O$,[17,18] but the $\{As^{III}Mo_9O_{33}\}$ fragment can rapidly rearrange into a Keggin-type cluster of $\{As^{V}Mo_{12}O_{40}\}$, suggesting that it is very difficult to obtain complexes consisting of the $\{As^{V}Mo_9O_{33}\}$ fragment from aqueous solution. Hence, the successful synthesis of a heteropolymolybdate-based sandwich complex remains a challenge. In particular, the complexes consisting of both heteropolymolybdates and a transition metal may produce unexpected magnetic properties, providing a great opportunity to explore heteropolymolybdate-based magnetic materials.

In our work, we try to find the rational reaction condition to obtain stable sandwich-type complexes consisting of heteropolymolybdates and a transition metal. Herein we report the syntheses, crystal structures, and magnetic properties of two new complexes consisting of arsenomolybdates and transition metals, $[(CH_3)_4N]_{8n}[M(H_2O)_5]_{2n}(H_3O)_{2n}$-

[a] Key Laboratory of Polyoxometalates Science of Ministry of Education,
College of Chemistry, Northeast Normal University,
Changchun 130024, P.R. China
E-mail: linxu@nenu.edu.cn

Supporting information for this article is available on the WWW under http://www.eurjic.org or from the author.

 © 2007 Wiley-VCH Verlag GmbH & Co. KGaA, Weinheim 

$[\{M(H_2O)_5\}_2(MAs^{V}Mo_9O_{33})_2]_n[M(H_2O)_4(MAs^{V}Mo_9O_{33})_2]_n\cdot 20nH_2O$, in which two crystallographically independent $[\{M(H_2O)_5\}_2(MAs^{V}Mo_9O_{33})_2]^{6-}$ (**1a**) and $[M(H_2O)_4(MAs^{V}Mo_9O_{33})_2]^{8n-}$ (**1b**) units coexist in their crystal structure. Notably, the complexes structurally resemble a sandwich-type complex because they involve the coordination of two transition metals to two $[As^{V}Mo_9O_{33}]^{7-}$ fragments, and the $[As^{V}Mo_9O_{33}]^{7-}$ fragment in **1** and **2** is not an ordinary trivacant α-Keggin ion but a special derivative of the well-known *B*-β-Keggin structure. To the best of our knowledge, they represent the first example of structurally characterized complexes containing both a $\{As^{V}Mo_9O_{33}\}$ fragment and a transition metal, although the component of the unit is isostructural with the reported $[Cu_2(SiMo_9O_{33})_2]^{12-}$ anion. The physicochemical properties of the two complexes were also characterized by thermal gravimetric analysis, cyclic voltammograms, and magnetic susceptibility measurement.

## Results and Discussion

In contrast to heteropolytungstates, heteropolymolybdate anions generally show more structural lability in aqueous solution, so it is very difficult to isolate a sandwich-type complex containing lacunary heteropolymolybdate species. The reaction of $Mn^{2+}$ ions with α-$As^{V}Mo_{12}O_{40}^{3-}$ in the ratio 16:1 (pH adjusted to 4.2) produced the unexpected $[(CH_3)_4N]_{8n}[M(H_2O)_5]_{2n}(H_3O)_{2n}[\{M(H_2O)_5\}_2(MAs^{V}Mo_9O_{33})_2]_n[M(H_2O)_4(MAs^{V}Mo_9O_{33})_2]_n\cdot 20nH_2O$ (M = $Mn^{2+}$, **1**; M = $Co^{2+}$, **2**), in which the $[As^{V}Mo_9O_{33}]^{7-}$ fragment derives from the well-known (*B*-β-$XMo_9O_{33}$) structure, and whose structure resembles that of the sandwich-type complex. Syntheses of **1** and **2** were conveniently carried out in aqueous solution, and the key factor for the successful synthesis was a rational choice of the solution pH and a suitable countercation. A solution pH of 4.2 is appropriate for both the generation of a $[As^{V}Mo_9O_{33}]^{7-}$ fragment and the formation of complexes **1** and **2**. However, some larger countercations, such as $[Bu_4N]^+$, $[Et_4N]^+$, and $Cs^+$, could quickly cause the precipitation of all the cluster anions in the solution, making it impossible to obtain a stable single crystal.

Single-crystal X-ray diffraction analysis revealed that complex **1** consists of six kinds of subunits: $[\{Mn(H_2O)_5\}_2(MnAs^{V}Mo_9O_{33})_2]^{6-}$ fragment (**1a**), one-dimension chain built of $[Mn(H_2O)_4(MnAs^{V}Mo_9O_{33})_2]^{8n-}$ fragment (**1b**), $[(CH_3)_4N]^+$ cation, $Mn^{2+}$ cation, coordinated water molecules, and isolated water molecules. The bond-valence sum calculation for complex **1** suggests that all Mo atoms are in the +6 oxidation state with an average value of 5.947, all As atoms are in the +5 oxidation state with an average value of 4.881, and all O atoms are in the –2 oxidation state with an average value of 1.964.[19] As complex **1** was isolated from acidic aqueous solution, two protons were attached to isolated water molecules to compensate for charge balance. The thermal gravimetric (TG) curve indicated the existence of 22 crystalline water molecules in complex **1**. In complex **1**, a novel building block $[\{Mn(H_2O)_5\}_2(MnAs^{V}Mo_9O_{33})_2]^{6-}$ (**1a**), whose structure is shown in Figure 1a, displays $C_{2h}$ symmetry with a $C_2$ axis through two $Mn^{II}$ centers. The building block is composed of two unusual $[As^{V}Mo_9O_{33}]^{7-}$ (**1c**) moieties linked with a $\{Mn_2O_{10}\}$ group. As shown in Scheme 1, the unusual $\{XMo_9O_{33}\}$ unit in **1c** derives from the well-known (*B*-β-$XMo_9O_{33}$) structure by moving one $MoO_6$ octahedron from the *B*-β-$XMo_9O_{33}$ unit to the other side itself, and the $MoO_6$ octahedron covers what would otherwise be a hole (as compared with the Keggin structure) between the two $Mo_3O_{13}$ units.[20] The $MoO_6$ octahedron has two terminal oxygen atoms, and this structural feature is similar to the first reported example of $(NH_4)_{12}[Cu_2Si_2Mo_{18}O_{66}]\cdot 14H_2O$. Also, the geometric topology of the $Mn_2O_{10}$ group is similar to that of the $\{Cu_2O_{10}\}$ group in $(NH_4)_{12}[Cu_2Si_2Mo_{18}O_{66}]\cdot 14H_2O$. One notable feature of **1a** is that one terminal oxygen atom from the $MoO_6$ octahedron of two terminal oxygen atoms acts as a ligand, together with five ligand water molecules, to bond with a $Mn^{2+}$ ion, resulting in the formation of a six-coordinate mononuclear $Mn^{II}$ complex.

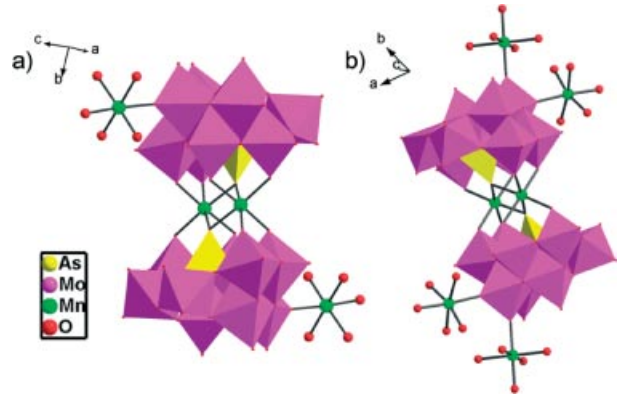


Figure 1. Combined polyhedral/ball-and-stick representation of the $[\{Mn(H_2O)_5\}_2(MnAs^{V}Mo_9O_{33})_2]^{6-}$ fragment (**1a**) and a part of the one-dimensional chain-like $[Mn(H_2O)_4(MnAs^{V}Mo_9O_{33})_2]^{8n-}$ fragment (**1b**). The color code: $MoO_6$ (purple), $AsO_4$ (yellow), Mn (green), O (red).

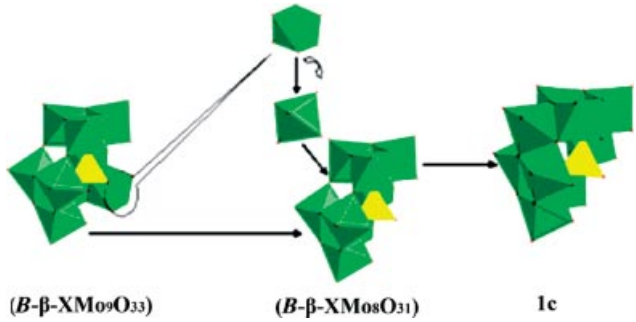


Scheme 1. The unusual $\{XMo_9O_{33}\}$ unit in **1c** derives from the well-known (*B*-β-$XMo_9O_{33}$) structure.

The other interesting feature of **1** is its novel one-dimensional chain structure, which consists of the **1b** unit linked by an octahedral $\{MnO_2(H_2O)_4\}$ group (see Figure 2). A

 © 2007 Wiley-VCH Verlag GmbH & Co. KGaA, Weinheim 

mirror plane through the chain and mononuclear $Mn^{II}$ ions can be found if the slight deviations from two Mn–O bonds are omitted. As shown in Figure 2, the linkage between the **1b** unit and $\{MnO_2(H_2O)_4\}$ group depends entirely on a ligand oxygen atom coming from the end of a **1b** unit. It is noteworthy that the ligand oxygen atom is one of two terminal oxygen atoms from a $MoO_6$ octahedron of **1b**, and the other terminal oxygen atom from the $MoO_6$ octahedron becomes a ligand of the mononuclear $Mn^{II}$ complex attached to the $[As^{V}Mo_9O_{33}]^{7-}$ moiety. In the mononuclear $Mn^{II}$ complex acting as chain linker, Mn–O bond lengths related with water ligands appear to differ little [2.236(10) Å, 2.311(9) Å], while two Mn–O bond lengths related with the terminal oxygen atoms from two different $MoO_6$ octahedra are obviously shorter [2.130(6) Å]. It was well known that the electron delocalization generally occurs in the reduced heteropolymolybdate (heteropoly blue).[20–22] If this type of one-dimensional chain can be reduced reversibly, the additional electrons on the reduced heteropolymolybdate group will behave as electron delocalization, so that an indirect magnetic exchange interaction may happen between the magnetic groups and the reduced heteropolymolybdate groups. Thus, the development of such a magnetic chain is of considerable significance for exploring new molecular magnets. A further investigation on the heteropoly blue of **1** and its magnetic and electrochemical properties is in progress in our research group. The packing diagrams of **1** along the *a* axis are shown in Figure 2, in which those free anions of **1a** were alternately located between the parallel one-dimensional chains. In addition, all the $[(CH_3)_4N]^+$ cations, the $Mn^{2+}$ cation and crystallized water molecules freely fill in the space of the crystal structure. Multipoint hydrogen bonds also exist between the surface oxygen atoms of the $[AsMo_9O_{33}]^{7-}$ fragment and the water molecules to stabilize the solid-state framework of **1**. The crystal structure of **2** is mostly similar to that of **1**, though the replacement of $Mn^{II}$ by $Co^{II}$ causes some differences in bond lengths. The two Co–O bond lengths related with the terminal oxygen atoms from two different $MoO_6$ octahedra are obviously shorter (2.046 Å) than the Mn–O bond lengths [2.130(6) Å]. The Co–O bond lengths related with water ligands are 2.074(13), 2.106(12), 2.074(13), and 2.106(12) Å.

The building blocks of **1a** and **1b** are composed of two $[As^{V}Mo_9O_{33}]^{7-}$ fragments derived from the well-known (*B*-β-$AsMo_9O_{33}$) structure. In polyoxoanion chemistry, this $[As^{V}Mo_9O_{33}]^{7-}$ fragment had not been observed until our work. By the same synthesis method, we have recently obtained another manganese-substituted arsenomolybdate containing the same fragment, which will be reported elsewhere. We should note that complexes **1** and **2** were synthesized from the starting material of $[\alpha\text{-}As^{V}Mo_{12}O_{40}]^{3-}$, but the resulting product was a derivative of the *B*-β-$AsMo_9O_{33}$ unit. Therefore, the mechanism of the formation of **1** and **2** must involve a loss of molybdenum atoms, rotational isomerization (α-Keggin → *B*-β-$AsMo_9O_{33}$), and metal insertion. It is not clear if **1** and **2** are formed by initial loss of molybdenum atom or first by rotational isomerization.[23]

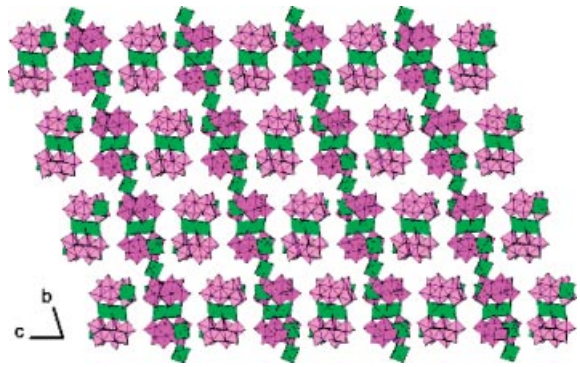


Figure 2. Polyhedral representation of plane in complexes **1** and **2**, viewed along the *a* axis. The cations and water molecules are omitted for clarity. The color code: $MoO_6$ (purple), $MnO_6$ (green).

To investigate the solution stability of complex **1**, we carried out a control measurement for the cyclic voltammograms and UV/Vis spectra in the solid state and in aqueous solutions. First, the redox peaks and shape of the cyclic voltammogram in solid state [using the carbon paste electrode (CPE)] is clearly different from those of the voltammogram in aqueous solution (1 M $H_2SO_4$). Second, in the UV/Vis spectra, the absorption peak positions for the solid state of complex **1** (using the diffuse reflectance electronic spectra) are also different from those for the aqueous solution of complex **1**. Thus, considering these experimental results, we infer that the one-dimensional chain-like framework of complex **1** may have been disintegrated into some fragments once it was dissolved in aqueous solution, indicating its instability in aqueous solution. However, the aqueous solution of **1** can retain stability with a pH value of 0–4; this is confirmed by the fact that the UV/Vis spectra of the solution with a pH value of 0–4 did not change when monitored for 12 h at room temperature, showing that the resulting fragments are stable in aqueous solution.

The electrochemical behavior of complex **1** was investigated using complex **1**-modified carbon paste electrode (CPE) as the working electrode to measure cyclic voltammograms both in the solid state (see Figure 3, a) and aqueous solutions (see Figure 3, b). There are only two anodic peaks in solution: $E_{pa}$ of 284.5 and 467.9 mV. In contrast, by using the **1**-modified CPE, three reversible redox peaks appeared in the potential range from +600 to –130 mV and the peak potentials $E_{1/2} = (E_{pa} + E_{pc})/2$ are 400 (I), 262.5 (II), and –39 (III) mV (scan rate: 100 mV $s^{-1}$). The redox peaks I–I′ and II–II′ should be ascribed to two consecutive two-electron processes, and redox peak III–III′ should be ascribed to a one-electron process.

The thermal gravimetric (TG) curve of complex **1** exhibits two steps of weight loss in the temperature range 30–700 °C (see Figure 4, a). The first weight loss of 5.06% in the temperature range 30–191 °C corresponds to the release of 22 crystalline water molecules. The second stage, which occurs from 291 to 461 °C, is attributed to the loss of 8 organic molecules and 24 coordinated water molecules; the observed weight loss (12.89%) is in agreement with the calculated value (13.01%). The thermal gravimetric (TG) curve

 © 2007 Wiley-VCH Verlag GmbH & Co. KGaA, Weinheim 

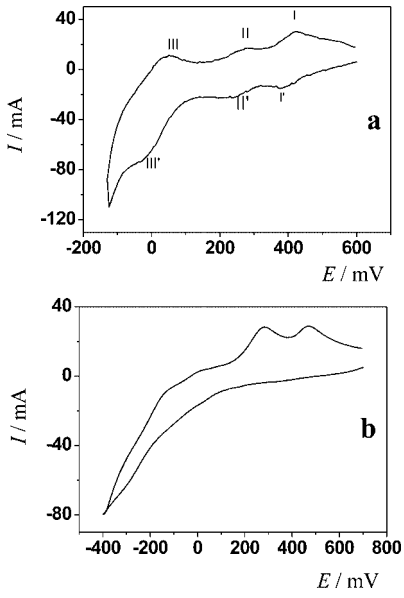


Figure 3. (a) Cyclic voltammogram of the carbon paste electrode (CPE) in 1 M $H_2SO_4$ aqueous solution for **1**. (b) Cyclic voltammogram of **1** in $H_2SO_4$ solution (pH = 2). Cyclic voltammograms were obtained with a CHI 660 electrochemical workstation at room temperature. A platinum wire was used as counter electrode and an Ag/AgCl (KCl 3 mol $L^{-1}$) was used as reference electrode. A chemically bulk-modified CPE or glassy carbon was used as working electrode. Potentials are quoted against a saturated calomel electrode (SCE).

of compound **2** (see Figure 4, b) is similar to that of **1**. The first weight loss of 4.97% in the temperature range 20–194 °C is attributed to the loss of crystalline water and the second weight loss of 12.79% in temperature range 300–465 °C is in agreement with the calculated value (13.84%).

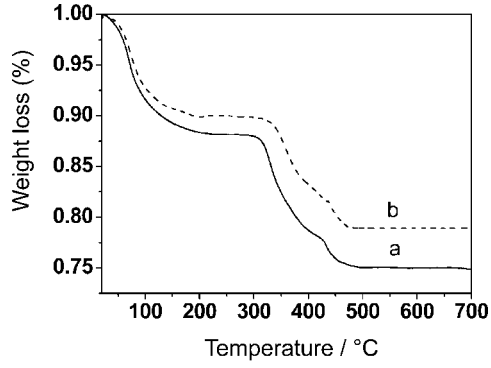


Figure 4. TGA curves of compound **1** (a) and **2** (b).

The magnetic behaviors of the two sandwich-type complexes in the temperature range 2–300 K are shown as plots of the product $\chi_m T$ versus $T$ in Figures S12a and S12b for **1** and **2**, respectively. Because of the coexistence of dimeric and different monomeric magnetic entities in the two compounds, the exact theoretical treatment fitting the experimental data becomes practically difficult, if not impossible. The $\chi_m T$ value of complex **1** at 300 K is about 32.38 $cm^3 K mol^{-1}$ (16.09 μB); this value is slightly smaller than that expected (17.74 μB) for the isolated nine $Mn^{II}$ ion ($S$ = 45/2; $g$ = 2.00). The $1/\chi_m$ versus $T$ plot in Figure S8 for **1** displays Curie–Weiss paramagnetic behavior from 10 to 300 K. The best linear fit of $\chi_m^{-1}(T)$ data above 40 K yields $C$ = 45.1 emu $mol^{-1}$ and $\theta$ = –1.10 K. The experimental data can approximately be fitted to a modified Heisenberg–Dirac–Van-Vleck $\mathbf{S}_A = \mathbf{S}_B$ = 5/2 spin-coupled model assuming $\mathbf{H} = -2J\mathbf{S}_A\mathbf{S}_B$ (see Supporting Information).[24] The best fit gives magnetic coupling constant $J$ = –0.43 $cm^{-1}$ assuming $g$ = 2.00, $C$ = 82.1 emu $mol^{-1}$, and $\theta$ = –1.76 K, with agreement factor $R$ {defined as $\sum_i[(\chi_m T)_{obs}(i) - (\chi_m T)_{calc}(i)]^2/\sum_i[(\chi_m T)_{obs}(i)]^2$} being $7.0 \times 10^{-5}$. The small negative $J$ and $\theta$ values suggest the occurrence of a weak antiferromagnetic $Mn^{II}$–$Mn^{II}$ interaction in **1**, being in good agreement with the result of linear fitting based on Curie–Weiss equation.

The $\chi_m T$ value of complex **2** at 300 K is about 27.59 $cm^3 K mol^{-1}$ (14.85 μB), which is higher than that expected (11.60 μB) for the isolated nine $Co^{II}$ ion ($S$ = 45/2; $g$ = 2.00). The experimental magnetic data for complex **2** can approximately be fitted to a modified Heisenberg spin Hamiltonian $\mathbf{H} = -2J\mathbf{S}_A\mathbf{S}_B$ (see electronic supporting information).[25] The best fit gives magnetic coupling constant $J$ = –0.64 $cm^{-1}$, $g$ = 2.24, $C$ = 21.61 emu $mol^{-1}$, and $\theta$ = –1.31 K, with agreement factor $R$ {defined as $\sum_i[(\chi_m T)_{obs}(i) - (\chi_m T)_{calc}(i)]^2/\sum_i[(\chi_m T)_{obs}(i)]^2$} being $8.2 \times 10^{-4}$ (see Figure S12). As shown in Figure S12b, the plot of $\chi_m T$ versus $T$ for **2** shows an obvious decrease from 300 to 20 K, followed by a quick drop to 2 K, being indicative of a typical antiferromagnetic $Co^{II}$–$Co^{II}$ interaction. The bridge linkage of $Co^{II}$–O–$Co^{II}$ in the $Co_2O_{10}$ group may be responsible for the behavior of antiferromagnetic interactions in **2**. In the same way, a best linear fit of $\chi_m^{-1}(T)$ data above 20 K gives $C$ = 20.6 emu $mol^{-1}$ and $\theta$ = –0.49 K, which is in agreement with the result from the plot of $\chi_m T$ versus $T$. However, a good least-squares fit for **2** cannot be achieved because of the possible deviation of the theoretical model.

## Conclusions

Two unusual heteropolymolybdates, $[(CH_3)_4N]_{8n}[M(H_2O)_5]_{2n}(H_3O)_{2n}[\{M(H_2O)_5\}_2(MAs^{V}Mo_9O_{33})_2]_n[M(H_2O)_4(MAs^{V}Mo_9O_{33})_2]_n \cdot 20nH_2O$ (M = $Mn^{2+}$, **1**; M = $Co^{2+}$, **2**), were synthesized by reaction of $MnSO_4$ ($CoSO_4$) with α-$H_3As^{V}Mo_{12}O_{40} \cdot 30H_2O$ in aqueous acidic medium (pH 4.2), isolated as a mixed tetramethyl ammonium salt and characterized by single-crystal X-ray diffraction. This work shows a promising perspective to develop the class of complexes consisting of arsenomolybdates and transition metals. The two typical compounds of this class with M = $Mn^{II}$ and $Co^{II}$ establish a new series of heteropolymolybdate complexes based on an $[As^{V}Mo_9O_{33}]^{7-}$ fragment. The magnetic properties of the two complexes were investigated to indicate typical antiferromagnetic interaction through the $Mn^{II}$–O–$Mn^{II}$ bridge unit for complex **1** and the $Co^{II}$–O–$Co^{II}$ bridge unit for complex **2**.

 © 2007 Wiley-VCH Verlag GmbH & Co. KGaA, Weinheim 

## Experimental Section

**General Methods and Materials:** As, Mn, Co, and Mo were determined by a Leaman inductively coupled plasma (ICP) spectrometer. IR spectra were obtained with an Alpha Centaurt FTIR spectrometer with KBr pellets in the 400–4000 $cm^{-1}$ region. The UV/Vis spectra were recorded with a 756 CRT UV/Vis spectrophotometer with $2\times10^{-6}$ M solutions of the relevant polyanion. Matched 1.000 cm optical path quartz cuvettes were used. The TG analyses were performed on a Perkin–Elmer TGA7 instrument in flowing $N_2$ with a heating rate of 10 °C $min^{-1}$. Cyclic voltammograms were obtained with a CHI 660 electrochemical workstation at room temperature. A platinum wire was used as counter electrode and a Ag/AgCl was used as reference electrode. A chemically bulk-modified CPE was used as working electrode. The glassy carbon samples had a diameter of 3 mm. Potentials are quoted against a saturated calomel electrode (SCE). All experiments were performed at room temperature. The polyanion precursor α-$H_3As^VMo_{12}O_{40}\cdot30H_2O$ was prepared according to the literature method.[26] The purity of α-$H_3As^VMo_{12}O_{40}\cdot30H_2O$ was checked by cyclic voltammogram. All reagents and solvents for the syntheses were purchased from commercial sources and used as received.

**Synthesis of $[(CH_3)_4N]_{8n}[Mn(H_2O)_5]_{2n}(H_3O)_{2n}[\{Mn(H_2O)_5\}_2(MnAs^VMo_9O_{33})_2]_n[Mn(H_2O)_4(MnAs^VMo_9O_{33})_2]_n\cdot20nH_2O$ (1):** α-$H_3As^VMo_{12}O_{40}\cdot30H_2O$ (1.78 g, 1 mmol) was dissolved in $H_2O$ (40 mL), and $MnSO_4$ (8 mL of 1 mol $L^{-1}$ solution) was added. The solution was heated to 60 °C on the water bath. The pH of the solution was adjusted to 4.2 by addition of the saturated $NaHCO_3$ solution, and then the color of the solution changed from yellow to orange. After 2 h, the solution was cooled to room temperature, and $(CH_3)_4NBr$ (4 mL of 1 mol $L^{-1}$ solution) was added into the stirred solution. After about 48 h, the yellow block crystals deposited from the filtrate by evaporation at room temperature. The crystals exposed in air quickly lost luster because of the volatilization of crystallized water molecules. Elemental analysis (%): calcd. (found) for **1**: Mn 6.35 (6.40), As 3.85 (3.92), Mo 44.37 (45.20). IR (KBr disk) for **1**: $\tilde{\nu}$ = 3419, 2359, 1635, 1483, 946, 860, 787, 703, 508 $cm^{-1}$.

**Synthesis of $[(CH_3)_4N]_{8n}[Co(H_2O)_5]_{2n}(H_3O)_{2n}[\{Co(H_2O)_5\}_2(CoAs^VMo_9O_{33})_2]_n[Co(H_2O)_4(CoAs^VMo_9O_{33})_2]_n\cdot20nH_2O$ (2):** The preparation of **2** was similar to that of **1**, except that $CoSO_4$ (8 mL of 1 mol $L^{-1}$ solution) was added. Elemental analysis (%): calcd. (found) for **2**: Co 6.78 (6.89), As 3.83 (3.89), Mo 44.17 (44.39). IR (KBr disk) for **2**: $\tilde{\nu}$ = 3419, 2360, 1616, 1483, 946, 861, 702, 508 $cm^{-1}$.

**X-ray Crystallography:** Crystal data for $[(CH_3)_4N]_{8n}[Mn(H_2O)_5]_{2n}(H_3O)_{2n}[\{Mn(H_2O)_5\}_2(MnAs^VMo_9O_{33})_2]_n[Mn(H_2O)_4(MnAs^VMo_9O_{33})_2]_n\cdot20nH_2O$ (**1**): triclinic, $P\bar{1}$ (no. 2), $a$ = 14.2108(10) Å, $b$ = 18.8804(13) Å, $c$ = 22.5052(16) Å, $\alpha$ = 71.6940(10)°, $\beta$ = 83.8250(10)°, $\gamma$ = 71.5560(10)°, $V$ = 5438.0(7) $Å^3$, $\rho_{calcd}$ = 2.338 g $cm^{-3}$, 21517 independent reflections with $I > 2\sigma(I)$, $1.68 < \theta < 26.05$, 1195 parameters, final $R$ factors $R_1$ = 0.0646 and $wR_2$ = 0.1203. Crystal data for $[(CH_3)_4N]_{8n}[Co(H_2O)_5]_{2n}(H_3O)_{2n}[\{Co(H_2O)_5\}_2(CoAs^VMo_9O_{33})_2]_n[Co(H_2O)_4(CoAs^VMo_9O_{33})_2]_n\cdot20nH_2O$ (**2**): triclinic, $P\bar{1}$ (no. 2), $a$ = 14.102(2) Å, $b$ = 18.880(3) Å, $c$ = 22.783(3) Å, $\alpha$ = 71.074(3)°, $\beta$ = 83.106(3)°, $\gamma$ = 70.615(2)°, $V$ = 5412.3(14) $Å^3$, $\rho_{calcd}$ = 2.331 g $cm^{-3}$, 21504 independent reflections with $I > 2\sigma(I)$, $1.81 < \theta < 26.10$, 1168 parameters, final $R$ factors $R_1$ = 0.0664 and $wR_2$ = 0.1311. The X-ray crystallographic data were collected at 183 K for **1** and **2** on a Bruker SMART CCD single-crystal diffractometer using Mo-$K_\alpha$ radiation (0.71073 Å). Direct methods were used to solve the structure and to locate the heavy atoms (SHELX97). Both compounds exhibit some disorder in the range of counterions and water molecules, as is often the case with polyoxometalates. Some of the oxygen atoms are disordered, which indicates that the quality of **1** is rather poor. Although we have repeated the experiment a few times, the suitable single crystal data cannot be obtained yet. This is most likely due to the result of the low-quality single crystals (thin plates). Nevertheless, the identity of fragment **2** was clearly established (Table 1).

Table 1. Crystal data and structure refinement for compounds **1** and **2**.

| | **1** | **2** |
|---|---|---|
| Empirial formula | $C_{32}H_{190}As_4Mn_9Mo_{36}N_8O_{178}$ | $C_{32}H_{190}As_4Co_9Mo_{36}N_8O_{178}$ |
| Formula mass | 7783.77 | 7819.72 |
| Space group | $P\bar{1}$ | $P\bar{1}$ |
| $a$ [Å] | 14.2108(10) | 14.102(2) |
| $b$ [Å] | 18.8804(13) | 18.880(3) |
| $c$ [Å] | 22.5052(16) | 22.783(3) |
| $\alpha$ [°] | 71.6940(10) | 71.074(3) |
| $\beta$ [°] | 83.8250(10) | 83.106(3) |
| $\gamma$ [°] | 71.5560(16) | 70.615(2) |
| $V$ [$Å^3$] | 5438.0(7) | 5412.3(14) |
| $Z$ | 1 | 1 |
| $T$ [K] | 183(2) | 183(2) |
| Wavelength [Å] | 0.71073 | 0.71073 |
| $D_{calcd.}$ [M g $m^{-3}$] | 2.338 | 2.331 |
| $T_{min}$, $T_{max}$ | 0.328, 0.382 | 0.532, 0.805 |
| Final $R_1$[a], $wR_2$[b] [$I > 2\sigma(I)$] | 0.0646, 0.1203 | 0.0664, 0.1311 |
| Final $R_1$[a], $wR_2$[b] [all data] | 0.0815, 0.1272 | 0.1334, 0.1594 |

[a] $R_1 = \Sigma||F_o| - |F_c||/\Sigma|F_o|$. [b] $wR_2 = \{\Sigma[w(F_o^2 - F_c^2)^2]/\Sigma[w(F_o^2)^2]\}^{0.5}$.

CCDC-269468 (for **1**) and -269311 (for **2**) contain the supplementary crystallographic data for this paper. These data can be obtained free of charge from The Cambridge Crystallographic Data Centre via www.ccdc.cam.ac.uk/data_request/cif.

**Electrochemical Experiments:** The compositions of the various media used for UV/Vis spectroscopy were as follows: for pH 0, $H_2SO_4$; for pH 1–3, 0.2 M $Na_2SO_4$ + $H_2SO_4$; for pH 4 and 5, 0.4 M $CH_3COONa$ + $CH_3COOH$. The test was realized on $2\times10^{-6}$ M solutions of compound **1**. The solutions were deaerated thoroughly for at least 30 min with pure argon and kept under a positive pressure of this gas during the experiments.

**Preparation of Compound 1-Modified Carbon Paste Electrode (CPE):** Compound **1**-modified CPE was fabricated as follows: 0.5 g graphite powder and 0.05 g compound **1** were mixed, and ground together by an agate mortar and pestle to achieve an even, dry mixture; 0.50 mL paraffin oil was added to the mixture and stirred with a glass rod; then the mixture was packed into a glass tube with the diameter of 3 mm, and the surface was pressed tightly onto weighing paper with a copper rod through the back. Electrical contact was established with a copper rod through the back of the electrode.

**Stability Studies:** For identifying the solution stability of complex **1**, the UV/Vis spectrum of the solution was monitored as a function of pH over a period of at least 12 h at room temperature. The spectra reproducible with respect to shape, absorbance, and wavelength location over this period of time were considered to indicate complete stability.

**Supporting Information** (see also the footnote on the first page of this article): Several ball-and-stick representations, IR spectra, magnetic data and selected bond lengths angles for **1** and **2**.

 © 2007 Wiley-VCH Verlag GmbH & Co. KGaA, Weinheim 

## Acknowledgments

The authors are thankful for the financial support from the National Natural Science Foundation of China (Grant numbers 20371010; 20671017) and the Specialized Research Fund for the Doctoral Program of Higher Education.

[1] a) M. T. Pope, A. Müller, *Angew. Chem. Int. Ed. Engl.* **1991**, *30*, 34–48; b) M. T. Pope, A. Müller (Eds.), *Polyoxometalates: from Platonic Solids to Anti Retroviral Activity*, Kluwer, Dordrecht, **1994**.
[2] a) C. L. Hill, C. M. Prosser-McCartha, *Coord. Chem. Rev.* **1995**, *143*, 407–455; b) C. L. Hill (Ed.), *Chemical Reviews, Polyoxometalates*, American Chemical Society, Washington, DC, **1998**.
[3] M. T. Pope, A. Müller (Eds.), *Polyoxometalate Chemistry: From Topology via Self-Assembly to Applications*, Kluwer, Dordrecht, The Netherlands, **2001**.
[4] T. Yamase, M. T. Pope (Eds.), *Polyoxometalate Chemistry for Nano-Composite Design*, Kluwer, Dordrecht, The Netherlands, **2002**.
[5] M. T. Pope, *Compr. Coord. Chem.* **2003**, *4*, 635–677.
[6] T. Liu, E. Diemann, H. Li, A. Dress, A. Müller, *Nature* **2003**, *426*, 59–62.
[7] T. Liu, *J. Am. Chem. Soc.* **2003**, *125*, 312–313.
[8] K. C. Kim, M. T. Pope, *J. Am. Chem. Soc.* **1999**, *121*, 8512–8517.
[9] X. Zhang, Q. Chen, D. C. Duncan, R. J. Lachicotte, C. L. Hill, *Inorg. Chem.* **1997**, *36*, 4381–4386.
[10] X. Zhang, T. M. Anderson, Q. Chen, C. L. Hill, *Inorg. Chem.* **2001**, *40*, 418–424.
[11] L. H. Bi, U. Kortz, B. Keita, L. Nadjo, H. Borrmann, *Inorg. Chem.* **2004**, *43*, 8367–8372.
[12] P. Mialane, J. Marrot, A. Mallard, G. Herve, *Inorg. Chim. Acta* **2002**, *238*, 81–86.
[13] a) I. M. Mbomekalle, B. Keita, L. Nadjo, K. I. Hardcastle, C. L. Hill, T. M. Anderson, *Dalton Trans.* **2004**, 4094–4095; b) L. H. Bi, M. Reicke, U. Kortz, B. Keita, L. Nadjo, R. J. Clark, *Inorg. Chem.* **2004**, *43*, 3915–3920; c) X. K. Fang, T. M. Anderson, W. A. Neiwert, C. L. Hill, *Inorg. Chem.* **2003**, *42*, 8600–8602; d) M. D. Ritorto, T. M. Anderson, W. A. Neiwert, C. L. Hill, *Inorg. Chem.* **2004**, *43*, 44–49.
[14] a) E. M. Limanski, D. Drewes, E. Droste, R. Böhner, B. Krebs, *J. Mol. Struct.* **2003**, *656*, 17–25; b) A. J. Gaunt, I. May, R. Copping, A. I. Bhatt, D. Collison, O. D. Fox, K. T. Holman, M. T. Pope, *Dalton Trans.* **2003**, 3009–3014; c) I. M. Mbomekalle, B. Keita, L. Nadjo, P. Berthet, W. A. Neiwert, C. L. Hill, M. D. Ritorto, T. M. Anderson, *Dalton Trans.* **2003**, 2646–2650.
[15] a) E. M. Limanski, M. Piepenbrink, E. Droste, K. Burgemeister, B. Krebs, *J. Cluster Sci.* **2002**, *13*, 369–379; b) L. Ruhlmann, J. Canny, R. Contant, R. Thouvenot, *Inorg. Chem.* **2002**, *41*, 3811–3819; c) T. M. Anderson, X. Zhang, K. I. Hardcastle, C. L. Hill, *Inorg. Chem.* **2002**, *41*, 2477–2488; d) A. C. Stowe, S. Nellutla, N. S. Dalal, U. Kortz, *Eur. J. Inorg. Chem.* **2004**, 3792–3797.
[16] H. F. Fukushima, A. Kobayashi, Y. Sasaki, *Acta Crystallogr., Sect. B: Struct. Sci.* **1981**, *37*, 1613–1615.
[17] A. Müller, E. Krickemeyer, S. Dillinger, J. Meyer, H. Bögge, A. Stammler, *Angew. Chem. Int. Ed. Engl.* **1996**, *35*, 171–173.
[18] A. Müller, E. Krickemeyer, M. Penk, V. Wittneben, J. Döring, *Angew. Chem. Int. Ed. Engl.* **1990**, *29*, 88–90.
[19] I. D. Brown, D. Altermatt, *Acta Crystallogr., Sect. B: Struct. Sci.* **1985**, *41*, 244–246.
[20] M. T. Pope, *Heteropoly and Isopoly Oxometalates*, Springer-Verlag, Berlin, **1983**, p. 101.
[21] R. A. Prados, M. T. Pope, *Inorg. Chem.* **1976**, *15*, 2547–2553.
[22] C. Sanchez, J. Livage, J. P. Launay, M. Fournier, *J. Am. Chem. Soc.* **1983**, *105*, 6817–6823.
[23] a) P. Mialane, A. Dolbecq, J. Marrot, E. Rivière, F. Sécheresse, *Eur. J. Inorg. Chem.* **2005**, 1771–1778; b) B. S. Bassil, S. Nellutla, U. Kortz, A. C. Stowe, J. van Tol, N. S. Dalal, B. Keita, L. Nadjo, *Inorg. Chem.* **2005**, *44*, 2659–2665.
[24] O. Kahn, *Molecular Magnetism*, VCH Verlagsgesellschaft, Weinheim, **1993**, p. 114.
[25] S. Q. Bai, E. Q. Gao, Z. He, C. J. Fang, C. H. Yan, *New J. Chem.* **2005**, *29*, 935.
[26] C. Sanchez, J. Livage, J. P. Launay, M. Fournier, Y. Jeannin, *J. Am. Chem. Soc*. **1982**, *104*, 3194–3202.

Received: June 3, 2006
Revised Version Received: February 21, 2007
Published Online: May 9, 2007

 © 2007 Wiley-VCH Verlag GmbH & Co. KGaA, Weinheim 

EurJIC
European Journal of Inorganic Chemistry

## FRONT COVER PICTURE

**The front cover picture shows** a bioinspired model for the active site of [NiFe] hydrogenases. Interactions between the metal centers in combination with the structural features at the active site allow these complexes to serve as suitable catalysts for $H_2$ electroproduction. Details are discussed in the article by V. Artero, M. Fontecave et al. on p. 2613 ff.

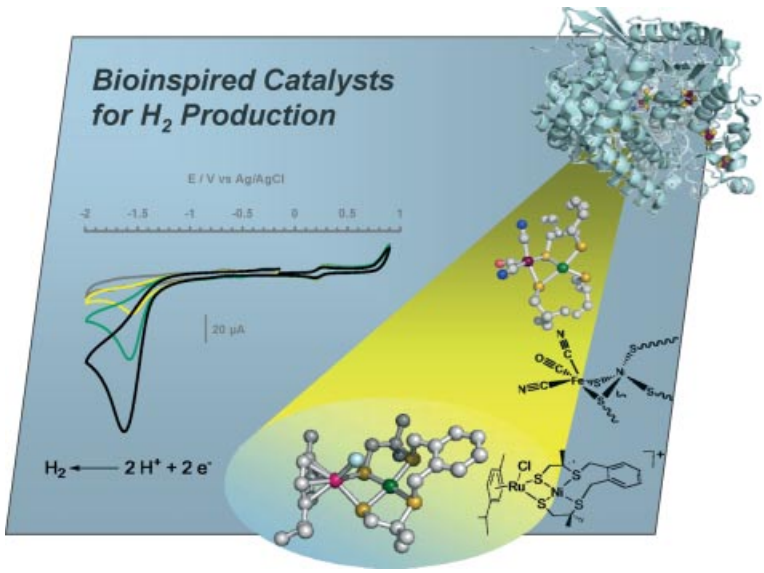


## BACK COVER PICTURE

**The back cover picture shows** the $Ln_4H_8$ core structure of the tetranuclear rare earth metal octahydride complexes $[(C_5Me_4SiMe_3)_4Ln_4H_8(THF)_n]$ (Ln = Sc, Y, Gd, Dy, Ho, Er, Tm, Lu; $n$ = 0, 1, or 2). These hydride clusters exhibit extremely high and unique reactivity towards a variety of unsaturated substrates, which leads to the formation of a new family of polynuclear compounds. Details are discussed in the Microreview by Z. Hou et al. on p. 2535 ff.

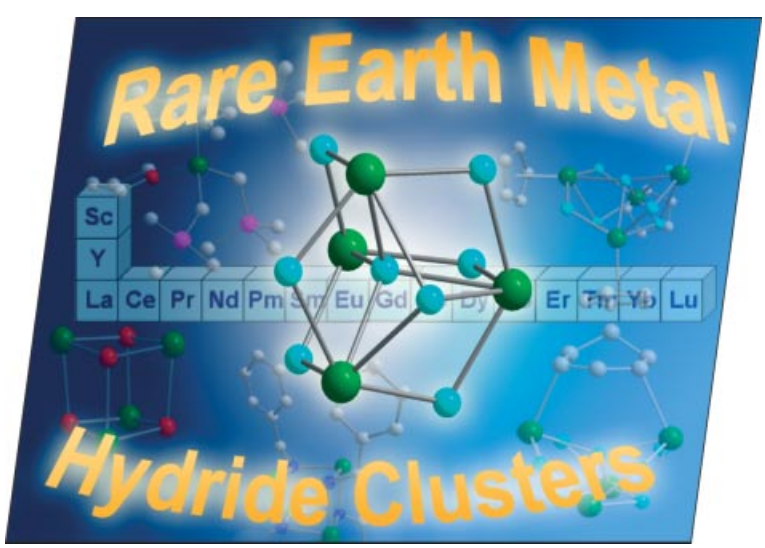


 © 2007 Wiley-VCH Verlag GmbH & Co. KGaA, Weinheim 

EurJIC
European Journal of Inorganic Chemistry

## FRONT COVER PICTURE

**The front cover picture shows** a bioinspired model for the active site of [NiFe] hydrogenases. Interactions between the metal centers in combination with the structural features at the active site allow these complexes to serve as suitable catalysts for $H_2$ electroproduction. Details are discussed in the article by V. Artero, M. Fontecave et al. on p. 2613 ff.

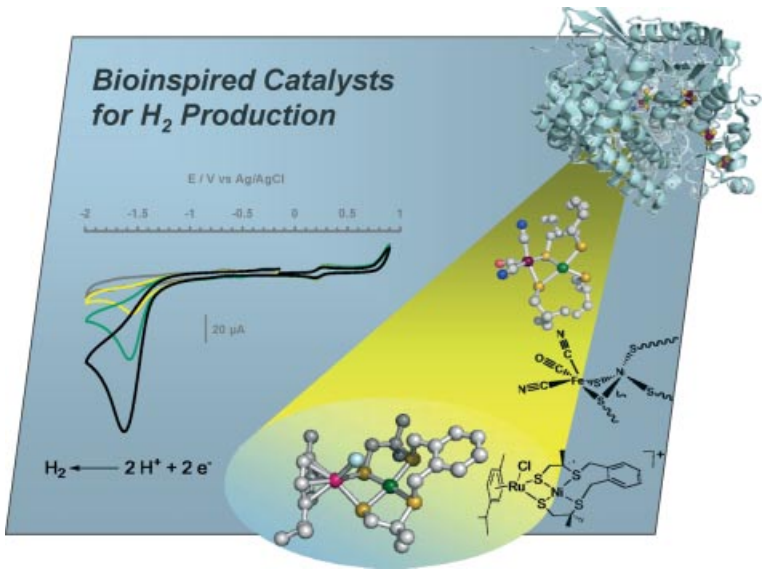


## BACK COVER PICTURE

**The back cover picture shows** the $Ln_4H_8$ core structure of the tetranuclear rare earth metal octahydride complexes $[(C_5Me_4SiMe_3)_4Ln_4H_8(THF)_n]$ (Ln = Sc, Y, Gd, Dy, Ho, Er, Tm, Lu; $n$ = 0, 1, or 2). These hydride clusters exhibit extremely high and unique reactivity towards a variety of unsaturated substrates, which leads to the formation of a new family of polynuclear compounds. Details are discussed in the Microreview by Z. Hou et al. on p. 2535 ff.

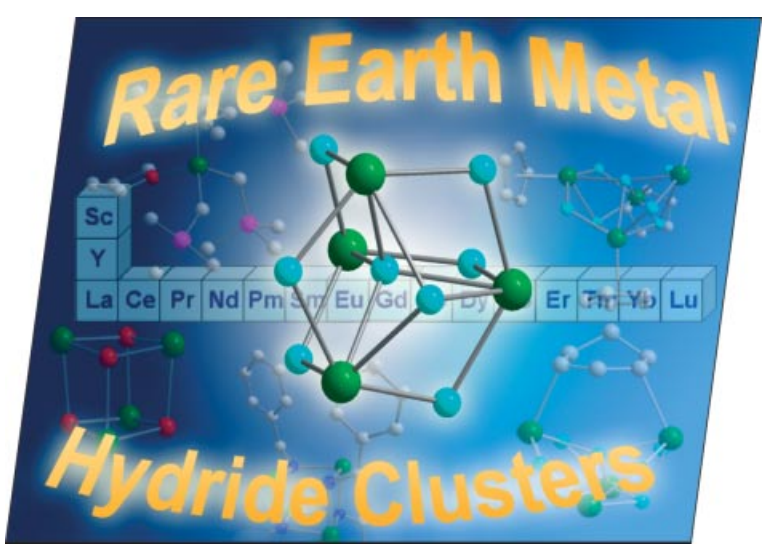


 © 2007 Wiley-VCH Verlag GmbH & Co. KGaA, Weinheim

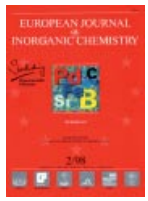

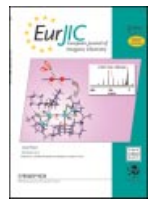

Karen Hindson

## The Changing Face of Chemistry Society Publishing

The start of the European Journal of Inorganic Chemistry ten years ago added another major player to the field of Inorganic Chemistry society journals. The move was unprecedented: attempts at European cooperation in the earliest stages of chemistry publishing had not got off the ground. By the second half of the 20th century three major single society publishing hubs had emerged, besides many other societies that published their own national general chemistry journal, often with commercial publishers. The time was ripe for change. European chemists began to work for a paradigm shift.

Upon the initiative of Jean-Marie Lehn, Peter Gölitz, the GDCh, and Wiley-VCH (the publishing partner of the GDCh), the publication of one journal (*Chemistry – A European Journal*) coowned by a union of societies was started in 1995. Understandably the vision of two journals with a strong base in Inorganic and Organic Chemistry to replace the many national journals took longer (see the view of Jan Reedijk who was active from the start), as the societies had to secure an equitable partnership. Heindirk tom Dieck of the German Chemical Society and Eva Wille of Wiley-VCH worked ceaselessly, travelling across Europe to meet with society officials to discuss terms of the amalgamation. First two (see the first cover at), then six, nine, ten and finally thirteen European chemical societies now profit from the development. Originally the editors of the individual journals acted as a panel of Editors-in-Chief for the new journals, till the growing number of submissions led to the formation of an editorial board and one editor employed by Wiley-VCH, similar to the structure of the other European Journals. The changeover was exactly in the middle of the ten years!

Not only was the union of societies growing. The growing trust in each other and their publisher Wiley-VCH led the French society to give up their journal *Journal de Chimie Physique et de Physico-Chimie Biologique* to make way for a co-owned, high-quality platform for the union's members whose research lies on the border of physics, chemistry and biophysics. Scientists working in interdisciplinary research in chemistry and biology could not be left out – *ChemPhysChem* and *ChemBioChem* were born in 2000. The growing family of journals prompted the societies to formalize their union as the Editorial Union of Chemical Societies (EUChemSoc) in 2002. Again the closer ties led the Italian society to offer two journals to the family, *Il Farmaco – An International Journal of Medicinal Chemistry and Pharmaceutical Chemistry* as springboard for *ChemMedChem* (2006) and *Annali di Chimica* as basis for the imminent journal *ChemSusChem* (2008).

In line with the development in Europe, chemical societies in Asia have banded together to form the Asian Chemical Editorial Society (ACES). Thus in 2007 with the emergence of multisociety publishing groupings, the number of society publishing hubs has grown and smaller societies also share in the advantages. Finally, Wiley-VCH is part of John Wiley & Sons, who in this February – in *their* bicentennial year – merged with Blackwell Publishing to form Wiley-Blackwell, now the world's leading society publisher. The strengthened global outlook of the company ensures that the European Journals family will combine the European touch with an international appeal. May not only EurJIC, but also the sister journals and the societies in EUChemSoc, go from strength to strength.

Karen Hindson
Editor, EurJIC

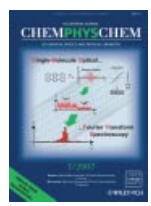

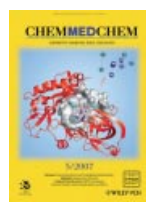

 © 2007 Wiley-VCH Verlag GmbH & Co. KGaA, Weinheim

**The EUChemSoc Societies have taken the significant step into the future by merging their traditional journals, to form two leading chemistry journals, the *European Journal of Inorganic Chemistry* and the *European Journal of Organic Chemistry.* Three further EUChemSoc Societies (Austria, Czech Republic and Sweden) are Associates of the two journals.**

## GREETING

An anniversary is a time both to look forward and to look back. Ten years ago, the seminal bilateral cooperation between the Gesellschaft Deutscher Chemiker and the Koninklijke Nederlandse Chemische Vereniging that enabled the publication of "Chemische Berichte/Recueil" and "Liebigs Annalen/Recueil" was successfully expanded by agreements with the chemical societies of France (Société Française de Chimie), Italy (Società Chimica Italiana), and Belgium (Koninklijke Vlaamse Chemische Vereniging and the Société Royale de Chimie) to bring together their journals to create two truly European journals, the European Journal of Inorganic Chemistry (*EurJIC*) and the European Journal of Organic Chemistry (*EurJOC*). The first issue of these journals appeared on January 1, 1998. The journals of the chemical societies of Spain (Real Sociedad Española de Química), Portugal (Sociedade Portuguesa de Química), and Greece (Association of Greek Chemists) were also amalgamated in 1998.

The integration of nine individual national journals into two high-quality European journals has undoubtedly created an important sense of union within the European community of chemists. Some guiding principles have been quality and flexibility, with the aim of fewer but better journals dealing with inorganic and organic chemistry. In 2002, the Magyar Tudományos Akadémia / Magyar Kémikusok by Egyesülete (Hungary) joined the consortium by merging the journal ACH – Models in Chemistry, and in 2003, Svenska Kemistsamfundet (Sweden), Gesellschaft Österreichischer Chemiker (Austria), and Česká Společnost Chemická (Czech Republic) also joined the consortium as Associate Members. Actually, the Editorial Union of Chemical Societies (EuChemSoc) is an organization of 14 European institutions.

As president of the EuChemSoc partnership for *EurJIC* and *EurJOC*, I note with great satisfaction that the initiative of merging nine national journals to create *EurJIC* and *EurJOC* has been a very important development. Furthermore, the journals are attracting a growing number of authors from outside Europe, and the continued success of these specialized journals has led to the decision to increase the frequency of publication from 24 to 36 issues for both journals. With the on-going vigorous support of our societies, authors, reviewers, and readers I am confident that the stature of *EurJIC* and *EurJOC* will grow as rapidly as it has over the last ten years. A sustained emphasis on the publication of papers reporting high-quality work, especially at the cutting-edge of the disciplines, should help to ensure that the journals will continue their successful development.

Luis A. Oro
President of the EuChemSoc
Partnership for *EurJIC* and *EurJOC*

 © 2007 Wiley-VCH Verlag GmbH & Co. KGaA, Weinheim 

# The Jubilee Issue

This issue marks the 10th Anniversary of the *European Journal of Inorganic Chemistry (EurJIC)* and represents a major landmark in the still young history of this journal. *EurJIC* was launched as a new journal in 1998 as a result of the merging of eight historical chemical journals owned by eight national chemical societies. The editor of the first issue was Heinrich Nöth. The number of chemical societies that own the journal, however, has been steadily growing, reflecting the increasing integration of European research. Nowadays *EurJIC* provides a European and international forum respected worldwide for Short Communications, Full Papers, and Microreviews, covering all topics of modern inorganic chemistry. As stated in the 1999 editorial of *EurJIC*, "the objective to reach the level of the top three Inorganic Chemistry journals on a worldwide scale within 3−5 years" has indeed been achieved beyond expectations. In fact, *EurJIC* is the fastest growing inorganic chemistry journal with a current impact factor of 2.514.

H. Nöth

**Fastest Growing Inorganic Chemistry Journal**

In order to pay tribute to the successful story of *EurJIC*, a journal which is truly European in spirit and fully international in appeal, the idea of publishing a special issue of the journal seemed timely to the Editorial Board. It has been a great honour for us to serve as Guest Editors for this celebratory 10th Anniversary issue of *EurJIC*, and it has been a great challenge to fulfil our duty. Beyond doubt, *EurJIC* is a cornerstone in the vital area of inorganic chemistry, and, to reflect its internationality, we decided to invite some leading scientists from all over the world with expertise in a wide range of research areas. The response to this invitation was indeed enthusiastic and has resulted in the present collection of 45 excellent articles coming from 11 European countries as well as from China, Israel, Japan, and the USA. The quality of the articles received, all of which have undergone a top-level independent evaluation process that is proper of *EurJIC*, is very high, making this issue a truly outstanding one and, we hope, a memorable snapshot of the hot topics in inorganic chemistry at the beginning of the 21st century.

**European in Spirit and International in Appeal**

The selection of the cover picture was also a difficult task as many of the articles received were worth highlighting on the cover. Accordingly, we decided, for the first time in *EurJIC* history, to highlight two contributions on the front and the back cover. Those we have chosen are the papers received from the Fontecave and Hou groups, two of the most valuable articles in this celebratory issue.

I. Bertini

Of the contributions received, there are six Microreviews, including a sound contribution on metalloproteoma by Ivano Bertini who served with proverbial energy and competence as Chairman of the Editorial Board of *EurJIC* from 1999 to 2006. Moreover, this issue includes the usual mix of Microreviews, Full Papers, and Short Communications, 45 articles in all, reflecting the full spectrum of modern inorganic chemistry from main group to bioinorganic, organometallic/catalysis, coordination, supramolecular, and material/solid-state chemistry, and, in some cases, the content of the articles clearly crosses these boundaries. It has to be mentioned that five of the articles received are from members of the Journal's Boards, including articles from Jan Reedijk, the present Chairman of the Editorial Board, and Rinaldo Poli, a member of the Editorial Board, as well as from Hansjörg Grützmacher, Lechosław Latos-Grażyński, and Carlos Romão, current Members of the International Advisory Board.

**The Full Spectrum of Modern Inorganic Chemistry**

It is not by chance that the Anniversary issue of *EurJIC* will be distributed at the 9th FIGIPAS Meeting in Inorganic Chemistry that takes place in Vienna this July, as both of these events represent sound milestones in the efforts of European Inorganic Chemists to achieve not only strong European ties but worldwide integration as well.

**9th FIGIPAS Meeting in Inorganic Chemistry**

In closing, we would like to mention that it has been a pleasure for us to collaborate and interact with the Editor, Karen Hindson, and her staff in the preparation of this Celebratory *EurJIC* issue. Heartfelt thanks to our authors, referees, and readers, and Happy Anniversary to *EurJIC*.

Guest Editor
Maurizio Perruzzini
ICCOM CNR
Florence

Guest Editor
Karl Kirchner
Vienna University of Technology

 © 2007 Wiley-VCH Verlag GmbH & Co. KGaA, Weinheim 

# Celebrating Ten Years

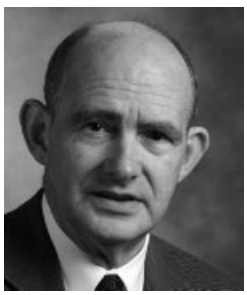

Ten years ago in an editorial I wrote "*In 1997 a new journal structure for the chemical literature in Europe will begin to evolve*". The occasion was the appearance of the first issue of the joint journal *Chemische Berichte/Recueil*, the prelude to the *European Journal of Inorganic Chemistry* (*EurJIC*) that came into being in 1998 with the participation of six European Chemical Societies. Another group of societies was waiting in the wings to amalgamate their journals, the criterion for entry, a year later. More recently, others joined as Associate Members, without merging journals, to bring the total number of societies that are now involved to 13 from 12 different countries (see Table 1).

Table 1. The European Chemical Societies that co-own *EurJIC*.

| Country | Society | Founded |
|---|---|---|
| Austria | Gesellschaft Österreichischer Chemiker (GÖCh) | 1897 |
| Belgium | La Société Royale de Chimie (SRC) | 1887 |
| Belgium | Koninklijke Vlaamse Chemische Vereniging (KVCV) | 1939 |
| Czech Republic | Česká Společnost Chemická (ČSCh) | 1866 |
| France | Société Française de Chimie (SFC) | 1857 |
| Germany | Gesellschaft Deutscher Chemiker (GDCh) | 1867 |
| Greece | Association of Greek Chemists (AGC) | 1924 |
| Hungary | Magyar Kémikusok Egyesülete (MKE) | 1907 |
| | Magyar Tudományos Akadémia (MTA) | 1825 |
| Italy | Società Chimica Italiana (SCI) | 1909 |
| The Netherlands | Koninklijke Nederlandse Chemische Vereniging (KNCV) | 1903 |
| Portugal | Sociedade Portuguesa de Química (SPQ) | 1911 |
| Spain | Real Sociedad Española de Química (RSEQ) | 1903 |
| Sweden | Svenska Kemistsamfundet | 1883 |

**13 Societies from 12 Countries**

On this 10th Anniversary of the merger journal *EurJIC*, a number of people will still remember that the discussions on the foundation of joint European Journals in the field of chemistry had started gaining momentum in the 1980s. The process was long and time-consuming, even more so because many chemical societies were not ready to give up their own specialized journals at the same time. Furthermore, not all interested societies owned a journal. The regular changing of boards and chairs of the several societies, as was required by their by-laws, also did not help to speed up the process. In Europe, the Royal Society had, and still has, its own publishing house, and understandably, wanted to keep that successful institution.

In addition, some commercial publishers in the 1970s and 1980s had launched a number of new journals, with titles containing the words "European Journal of .....". Already in the early 1990s, to protect some titles, the names *European Journal of Organic Chemistry* (*EurJOC*) and *European Journal of Inorganic Chemistry* were deposited for possible future use. The key societies from five countries were almost ready to begin the new journals in 1993, but at that stage only the new general chemistry journal, *Chemistry – A European Journal*, was realized. That journal, which several societies co-own, was eventually launched in 1995.

**A Growing Family of European Journals**

At a crucial meeting in 1996, the German and Dutch chemical societies made the historic decision to merge their journals *Chemische Berichte* and *Recueil des Travaux Chimiques des Pays-Bas* (J. Royal Neth. Chem. Soc.), initially under the name of *Chemische Berichte / Recueil*. This process appeared to be a good catalyst, as in 1997 the six chemical societies indeed decided to merge their organic/inorganic chemistry journals to form two new journals with the names that had been deposited earlier: *EurJIC* and *EurJOC*. The first issues of the two journals appeared on January 1, 1998.

**First Issue in January 1998**

The national chemical societies must be congratulated on implementing their modern concept for European publishing, which today still remains open for further European Chemical Societies to benefit.

Of course the authorship and readership of the journal is not restricted to these countries and societies but is open to the international community – as we say "*EurJIC* is made in Europe for the world". We can, in fact, see the international interest, for instance, by the percentage of downloads of published papers distributed over the globe (see Figure 1). A high-quality journal, nowadays, is by definition international. The ACS and RSC journals have always been open to non-member chemists; likewise, *EurJIC* (and the family of European Journals) has always welcomed scientists from non-partner countries (see Figure 2). It is indeed a pleasure to see that we enjoy an increasing interest from

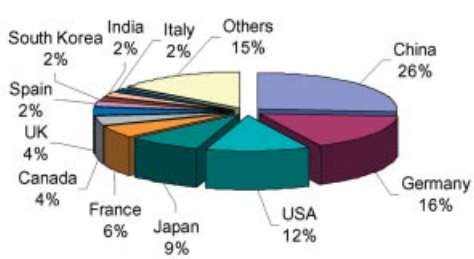


**Figure 1.** International interest in *EurJIC* as reflected by the percentage of downloads from each country.

 © 2007 Wiley-VCH Verlag GmbH & Co. KGaA, Weinheim 

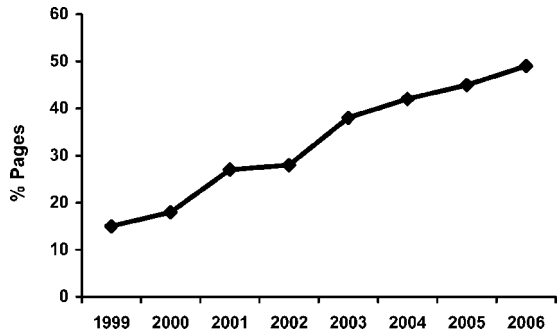


**Figure 2.** The percentage of published papers by scentists from non-partner countries.

top scientists outside Europe. The dominance of any one country as a result of the merger of national journals has been reduced, and the authorship has become international.

After 10 volumes it is legitimate to ask: How has the journal evolved over these years? Since the inauguration of the journal, the success of *EurJIC* can be seen in terms of the increase in the number of submissions (see Figure 3) and the number of pages published (see Figure 4). More importantly, the rejection rate, which can serve as an indicator of high quality, has also increased substantially (see Figure 5). The ISI impact factor has also risen and is currently stable at a value of 2.5. In 1998, *EurJIC* started with 12 issues per year. This number rose to 24 in the year 2003, and, to enable quick access to the latest developments in inorganic chemistry, *EurJIC* publishes 36 issues per year from 2007.

36 Issues per Year from 2007

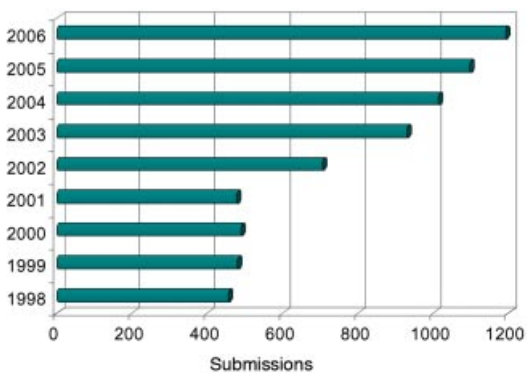


**Figure 3.** Number of submissions to *EurJIC* per year from 1998 to 2006.

The first new cover, with a changing cover picture for each issue, appeared in 2002. The authors of high-quality contributions were invited to submit proposals for the cover picture. As this concept was well received, we have continued with this tradition.

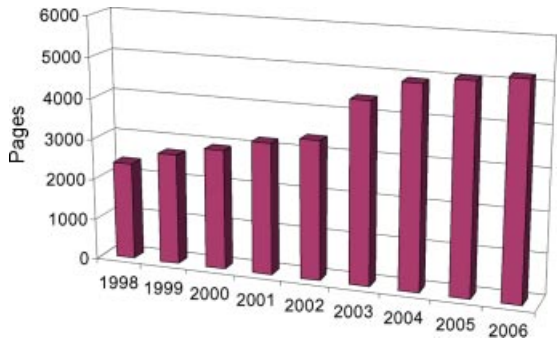


**Figure 4.** Page development of *EurJIC* from 1998 to 2006.

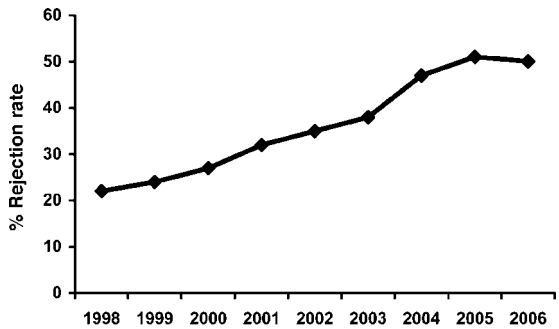


**Figure 5.** Rejection rates from 1998 to 2006.

A new layout to assist browsing with a colored table of contents, text as well as graphic, and a "Key Topic" rang in the 10th year.

As we live in an ever-changing and rapidly growing technological world, *EurJIC* realizes the importance of not only keeping up-to-date, but of being at the forefront. Although our readers have had access to e-mailing Alerts for some time, RSS feeds are now available (an RSS feed provides updates of the content of web pages to a computer, or even to a mobile phone). Also *EurJIC* is a member of CrossRef, which is a service that links reference citations to the online content of those references.

In 1997 I already wrote: "The word *European* is not meant to be exclusive". The present jubilee issue shows that the chemistry world has fully accepted the *European Journal of Inorganic Chemistry* as a high-ranking inorganic chemistry journal by the wide range of contributions from all over the world. Now we can congratulate the authors, reviewers, readers, editors, societies, and publisher on a mature journal, which has found its position in the international community. I wish *EurJIC* a successful continuation.

Made in Europe for the World

Jan Reedijk
Chairman of the Editorial Board, *EurJIC*

 © 2007 Wiley-VCH Verlag GmbH & Co. KGaA, Weinheim 

# CONTENTS

## MICROREVIEWS


### Rare Earth Metal Polyhydrides

**Z. Hou,* M. Nishiura, T. Shima ..... 2535–2545**

Synthesis and Reactions of Polynuclear Polyhydrido Rare Earth Metal Complexes Containing "$(C_5Me_4SiMe_3)LnH_2$" Units: A New Frontier in Rare Earth Metal Hydride Chemistry

**Keywords:** are earths / Hydride ligands / Cyclopentadienyl ligands / Cluster compounds / Hydrogenation

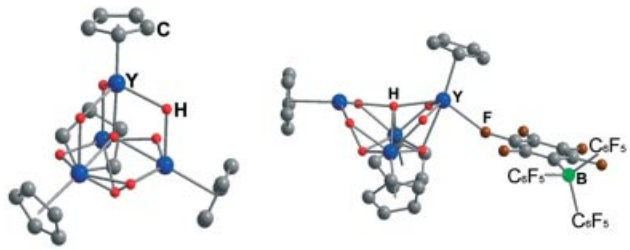


The synthesis, structures, and novel reactions of a series of neutral (left) and cationic (right) polyhydrido rare earth metal complexes are reviewed.

### Metalloproteomes

**I. Bertini*, A. Rosato ..... 2546–2555**

From Genes to Metalloproteins: A Bioinformatic Approach

**Keywords:** Iron / Zinc / Copper / Heme proteins / Metalloproteins / Bioinformatics

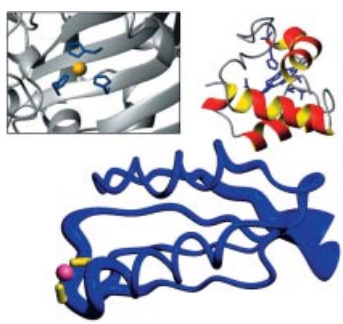

A significant fraction of the proteins that organisms produce and exploit to sustain cellular life require metal ions for their biological function (metalloproteins). Because the experimental characterization of metal requirements at the whole genome level is still not routinely feasible, catalogues of metalloproteins can only be compiled through bioinformatic methods. This review discusses the results of the application of bioinformatics to the identification of various metalloprotein types in selected organisms whose complete genome sequence is available. An overview of the usage of different essential metal ions across domains of life is provided.

### Diimino/Enediamido Complexes

**C. Mealli,* A. Ienco, A. D. Phillips, A. Galindo* ..... 2556–2568**

A Critical Review of Electronic Effects in Enediamido and α-Diimino Complexes of the Group 4 Metals

**Keywords:** N ligands / Group 4 metals / Metallacycles / Density functional calculations / Electronic structure

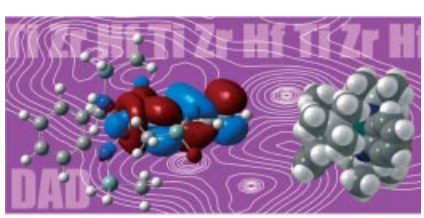


The stereochemical features of the group 4 metal complexes with *noninnocent* α-diimino chelates such as 1,4-diaza-1,3-butadiene (DAD) are systematically reviewed from an electronic point of view with the help of density functional calculations. The Quantum Theory of Atoms in Molecules (QTAIM) approach is also used to interpret the dichotomy of planar/bent metallacycles which is observed in very similar homoleptic $[M(DAD)_2]$ complexes.

### Metalloenzymes

**A. S. Pereira, P. Tavares, F. Folgosa, R. M. Almeida, I. Moura,* J. J. G. Moura ..... 2569–2581**

Superoxide Reductases

**Keywords:** Bioinorganic chemistry / Non-heme iron centres / Superoxide / Structure-activity relationships

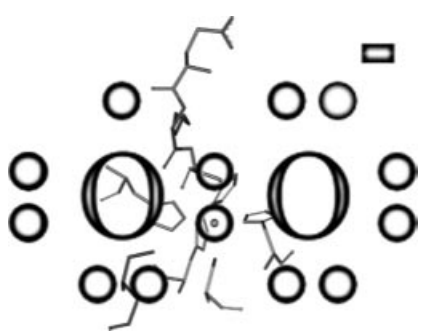

This review aims to describe the structural characteristics of superoxide reductases and the mechanistic aspects of biological superoxide anion reduction. The geometry of the active site, the possible electron donors in vivo and the current hypothesis for the catalytic mechanism are discussed. Some phylogenetic considerations are presented.


 © 2007 Wiley-VCH Verlag GmbH & Co. KGaA, Weinheim 

**Pd-Catalysed Copolymerisation**

Co- and terpolymerisations of carbon monoxide and alkenes are usually catalysed by palladium complexes, and the recent introduction of phosphane-sulfonate ligands has allowed this reactivity to be extended to non-alternating CO/ethene copolymerisation. After a general overview of the topic, selected recent advances in this field are described.

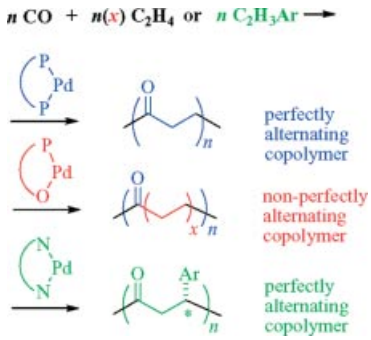


**E. J. García Suárez, C. Godard, A. Ruiz, C. Claver* ..... 2582–2593**

Alternating and Non-Alternating Pd-Catalysed Co- and Terpolymerisation of Carbon Monoxide and Alkenes

**Keywords:** Polymerisation / Polyketones / Palladium / Carbon monoxide / Alkenes

**Metallocarbaporphyrinoids**

This microreview presents the general characteristics of paramagnetic metallocarbaporphyrinoids with a focus on NMR studies. NMR spectroscopy of paramagnetic molecules is a powerful probe of several intriguing aspects of their molecular and electronic structures, structural rearrangements, and reactivity, including oxidation and oxygenation.

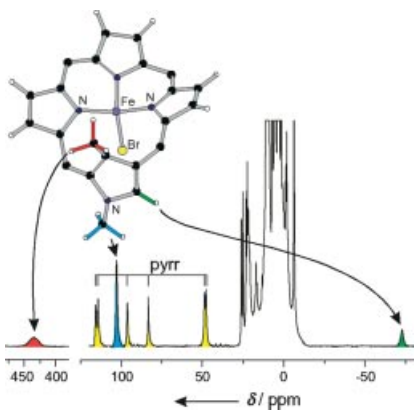


**E. Pacholska-Dudziak, L. Latos-Grażyński* ..... 2594–2608**

NMR Studies of Paramagnetic Metallocarbaporphyrinoids

**Keywords:** Carbaporphyrinoids / Porphyrinoids / NMR spectroscopy / Organometallic chemistry

# SHORT COMMUNICATION

**Sol-Gel Films**

Silica films on glass substrates with homogeneously dispersed platinum, gold or silver nanoparticles were prepared by sol-gel processing of triethoxysilyl-substituted complexes, followed by hydrogen treatment of the films at elevated temperatures.

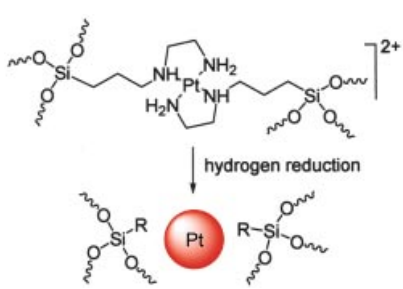


**M. Malenovska, S. Martinez, M.-A. Neouze, U. Schubert* ..... 2609–2611**

Growth of Metal Nanoparticles in a Sol-Gel Silica Thin Film

**Keywords:** Thin films / Nanostructures / Inorganic-organic hybrid materials / Nanocomposites

 © 2007 Wiley-VCH Verlag GmbH & Co. KGaA, Weinheim 

# CONTENTS

## FULL PAPERS

### Hydrogenase Models

**Y. Oudart, V. Artero,* J. Pécaut, C. Lebrun, M. Fontecave ..... 2613–2626**

Dinuclear Nickel–Ruthenium Complexes as Functional Bio-Inspired Models of [NiFe] Hydrogenases

**Keywords:** Nickel / Ruthenium / Hydrogen / Electrocatalysis / Biomimetic chemistry / Hydrogenases

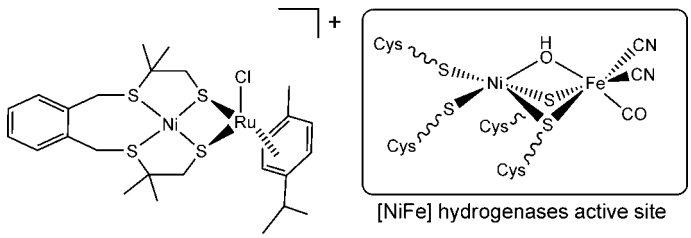


New dinuclear nickel-ruthenium catalysts for $H_2$ production that mimic the active site of [NiFe] hydrogenases are described. The activity of these new complexes is explained by the existence of a cooperative effect between the metal centers and is further related to their electronic properties.

### Biological Charge Transport

**T. E. de Jongh, M. Hoffmann, O. Einsle, D. Cavazzini, G.-L. Rossi, M. Ubbink, G. W. Canters* ..... 2627–2634**

Inter- and Intramolecular Electron Transfer in Modified Azurin Dimers

**Keywords:** Metalloproteins / Protein structures / Copper protein / Electronic coupling / Hydrophobic patch

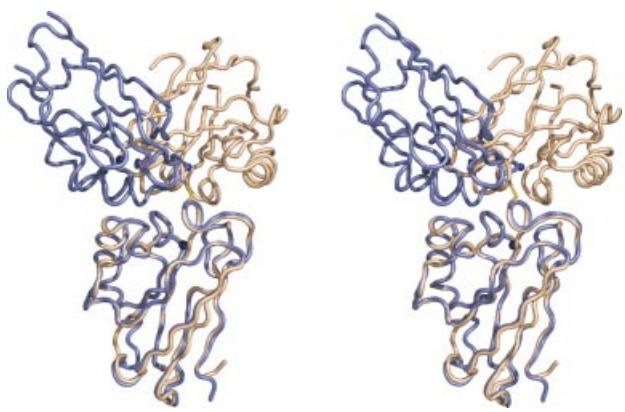

Crystal packing (stereo view) of wild-type azurin (beige) and the disulfide linked dimer of N42C/M64E azurin (blue). The packing has a profound effect on the electron exchange.

### Ligand Versatility

**M. Viciano-Chumillas, S. Tanase, G. Aromí, J. M. M. Smits, R. de Gelder, X. Solans, E. Bouwman, J. Reedijk* ..... 2635–2640**

Coordination Versatility of 5(3)-(2-Hydroxyphenyl)-3(5)-methylpyrazole: Synthesis, Crystal Structure and Properties of $Co^{III}$, $Ni^{II}$ and $Cu^{II}$ Complexes

**Keywords:** Cobalt / Nickel / Copper / Pyrazoles / Phenols / Crystal structures

The stabilization of a highly asymmetric dinuclear cobalt(III) complex containing four different coordination modes of the 5(3)-(2-hydroxyphenyl)-3(5)-methylpyrazole ligand and the synthesis and characterization of two mononuclear complexes of $Ni^{II}$ and $Cu^{II}$ are discussed in detail.

### Vitamin $B_{12}$ Derivatives

**B. Spingler, S. Mundwiler, P. Ruiz-Sánchez, D. R. van Staveren, R. Alberto* ..... 2641–2647**

Structures of the b- and d-Acid Derivatives of Vitamin $B_{12}$ and Their Complexes with $[M(CO)_3]^+$ (M = $^{99m}$Tc, Re)

**Keywords:** Vitamins / X-ray diffraction / Rhenium / Technetium / Labelling

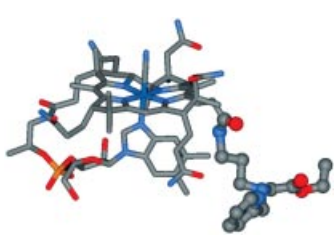

Vitamin $B_{12}$ has been conjugated to tridentate chelators at the b- and d-positions on the corrin periphery. X-ray structure analyses confirmed the corresponding assignments from NMR spectroscopy.

 © 2007 Wiley-VCH Verlag GmbH & Co. KGaA, Weinheim 

## Dithiobenzoquinone Complexes

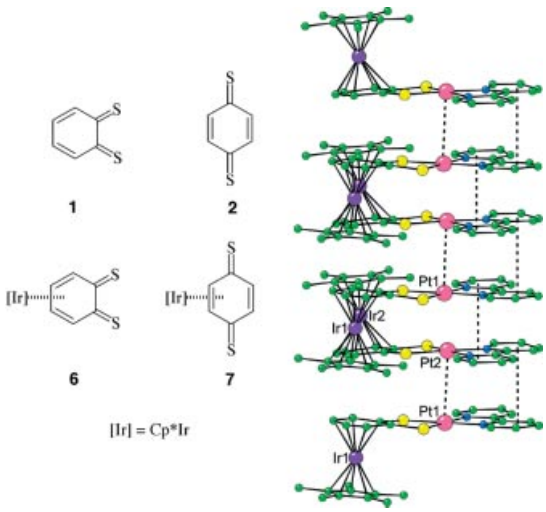


Overcoming a long-standing challenge, the *o*- and *p*-dithiobenzoquinone iridium complexes **6** and **7** were synthesized for the first time, and the X-ray molecular structure of [Cp*Ir-*p*-($\eta^4$-$C_6H_4S_2$)] (**7**) is reported. The organometallic linker **6** reacts with "Pt(bpy)" subunits to give the complex [Pt(bpy){Cp*Ir-*o*-($\eta^4$-$C_6H_4S_2$)}][OTf]$_2$ (**10**), which forms a supramolecular chain through π−π/Pt···Pt interactions.

**J. Moussa, M. N. Rager, K. Boubekeur, H. Amouri* ..... 2648−2653**

*ortho*- and *para*-Thioquinonoid π-Complexes: First Synthesis, Reactivity, and Crystal Structure Determination

**Keywords:** Reactive intermediates / Coordination modes / Sulfur / Thioquinones / Iridium

## Coordination Polymorphism

Either a very bulky monodenate phosphane ligand (cone angle about 250°) or a tetradentate $\kappa^1$:$\eta^6$ ligand. These are the coordination modes of the highly rigid tris(5*H*-dibenzo[*a*,*d*]cyclohepten-5-yl)phosphane (trop$_3$P) in $d^{10}$ [$Ag^I$, $Au^I$] and $d^8$ [$Rh^I$, $Ir^I$, $Pd^{II}$] valence configured metal complexes.

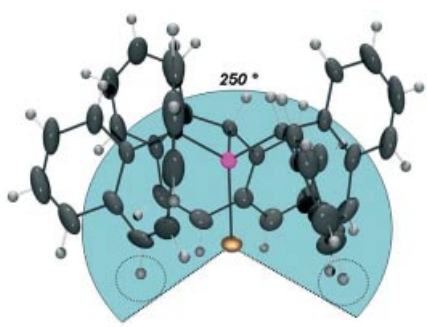


**U. Fischbach, H. Rüegger, H. Grützmacher* ..... 2654−2667**

Tris(dibenzo[*a*,*d*]cycloheptenyl)phosphane: A Bulky Monodentate or Tetrapodal Ligand

**Keywords:** Alkene ligands / Gold / Iridium / Palladium / Phosphane ligands / Rhodium / Silver / Tetradentate ligands / Solid-state NMR spectroscopy

## Coordination Polymers

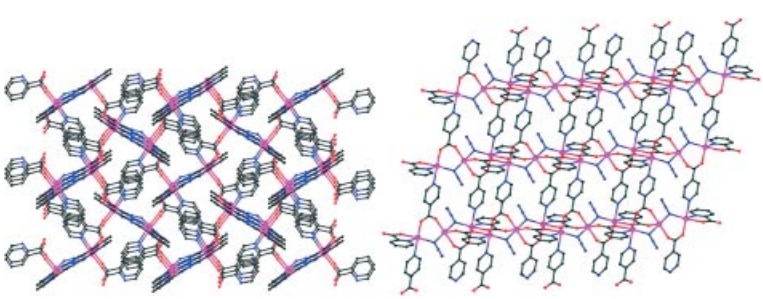

Two $Mn^{II}$ coordination polymers, $[Mn_2(bpt)(pa)_2(N_3)]_n$ [**1**; Hpa = picolinic acid, Hbpt = 3,5-bis(2-pyridyl)-4*H*-1,2,4-triazole] and $[Mn_3(ina)_2(pa)_2(N_3)_2]_n$ (**2**; Hina = isonicotinic acid), containing in situ generated bpt and pa ligands have been synthesized under solvothermal conditions. They exhibit spin-canting magnetism and topological ferrimagnetism with an AF-AF-F sequence, respectively.

**L. Cheng, W.-X. Zhang, B.-H. Ye,* J.-B. Lin, X.-M. Chen* ..... 2668−2676**

Spin Canting and Topological Ferrimagnetism in Two Manganese(II) Coordination Polymers Generated by In Situ Solvothermal Ligand Reactions

**Keywords:** Solvothermal ligand reaction / Coordination polymers / Spin canting / Topological ferrimagnetism

 © 2007 Wiley-VCH Verlag GmbH & Co. KGaA, Weinheim 

# CONTENTS

## Titanium Chemistry

**T. E. Hanna, E. Lobkovsky, P. J. Chirik* ..... 2677–2685**

N–H Group Transfer and Oxidative Addition Chemistry Promoted by Isolable Bis(cyclopentadienyl)titanium Sandwich Complexes

**Keywords:** Titanium / Oxidative addition / Cyclopentadienyl / Group transfer / Nitrogen

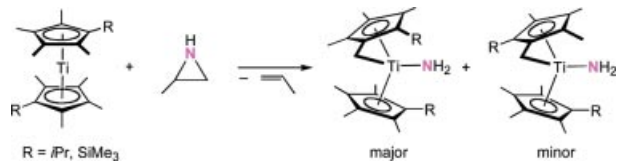


Addition of propylenimine to isolable titanocene complexes has resulted in [NH] group transfer which is followed by rapid cyclometalation. This reactivity contrasts [O] atom transfer where isolable titanocene oxides were obtained.

## Phosphane Complexes

**A. M. Kirillov, P. Smoleński, M. F. C. Guedes da Silva, A. J. L. Pombeiro* ..... 2686–2692**

The First Copper Complexes Bearing the 1,3,5-Triaza-7-phosphaadamantane (PTA) Ligand

**Keywords:** Copper / N,P ligands / Structure elucidation / Phosphane ligands

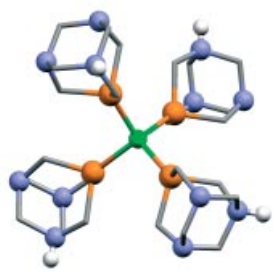

The water-soluble $Cu^{I}$ compounds $[Cu(PTAH)_4](NO_3)_5$ and $[Cu(PTA)_4](NO_3)$ were easily prepared and fully characterized, providing the first examples of Cu complexes bearing PTA or any derived ligand with a cagelike PTA core.

## Alkyne Oligomerization

**T. B. Wen, W. Y. Hung, H. H.-Y. Sung, Z. Zhou, I. D. Williams, G. Jia* ..... 2693–2701**

Coupling Reactions of an Allenylcarbene Complex with Alkynes and Styrene

**Keywords:** Osmium / Fulvenes / Carbenes / Alkynes / Alkenes

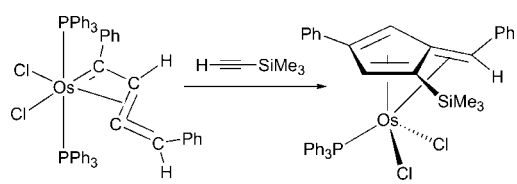


The allenylcarbene complex $[OsCl_2\{=CPh(\eta^2\text{-}CH=C=CHPh)\}(PPh_3)_2]$ undergoes coupling reactions with alkynes to produce fulvene complexes. A similar coupling reaction also occurs between this complex and styrene.

## CO/Ethene Copolymerization

**C. Bianchini,* A. Meli, W. Oberhauser,* C. Claver, E. J. Garcia Suarez ..... 2702–2710**

Unraveling the *o*-Methoxy Effect in the CO/Ethene Copolymerization Reaction by Diphosphanepalladium(II) Catalysis

**Keywords:** Polyketones / Palladium / Diphosphane ligands / Catalysis / Copolymerization / Kinetics

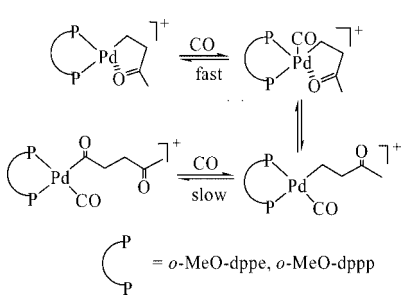


*o*-MeO substituents on the phosphorus aryl rings of chelating diphosphane ligands increase the activity of $Pd^{II}$ catalysts for the alternating CO/ethene copolymerization in either protic or aprotic solvents. In particular, the presence of *o*-MeO substituents affects the kinetics of the copolymerization process that becomes independent of the CO pressure. In situ high-pressure NMR experiments have provided valuable information on relevant steps of the copolymerization process.

 © 2007 Wiley-VCH Verlag GmbH & Co. KGaA, Weinheim 

## Iridabenzenes

A new synthesis of iridabenzene species is described. Surprisingly, the coupling of the iridacyclopentadienes **1** and **1-H** with propene is highly dependent on the nature of the substituents in the starting metallacycle.

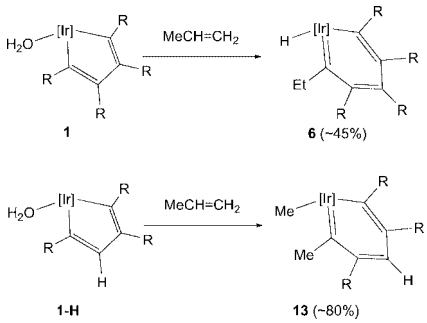


**M. Paneque,* M. L. Poveda,* N. Rendón, E. Álvarez, E. Carmona ..... 2711–2720**

The Synthesis of Iridabenzenes by the Coupling of Iridacyclopentadienes and Olefins

**Keywords:** Metallacycles / Olefins / Insertion / Isomerisation / Alkylidenes

## Supramolecular Cages

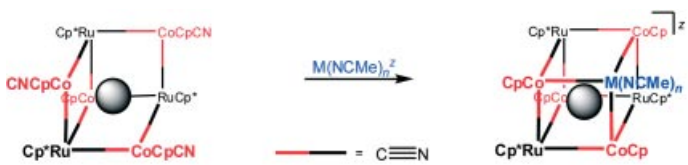


The coordination chemistry of the unusual metallo-ligand $Cs\subset[CpCo(CN)_3]_4[Cp^*Ru]_3$ ($Cs\subset Co_4Ru_3$) is described with attention to the behavior of the ligand itself, its binding to Lewis-acidic metal cations, and its ability to stabilize catalytically relevant $Ru-PPh_3$ fragments.

**J. L. Boyer, H. Yao, M. L. Kuhlman, T. B. Rauchfuss,* S. Wilson ... 2721–2728**

Cyanometalate Cages with Exchangeable Terminal Ligands

**Keywords:** Cyanide / Ruthenium / Hydrogen bonds / Cage compounds / Heterometallic complexes

## Metal–Fullerene Complexes

$\eta^1$-Allyl and $\eta^3$-allyl, ethyl, and hydrido ruthenium complexes of pentamethyl[60]-fullerene, $Ru(\eta^5\text{-}C_{60}Me_5)R(CO)_2$ (R = $\eta^1$-allyl, Et, H) and $Ru(\eta^5\text{-}C_{60}Me_5)(\eta^3\text{-allyl})(CO)$, were prepared. Conversion of the $\eta^1$-allyl complex to the $\eta^3$-allyl complex and catalytic performance of the hydrido complex in the isomerization of 1-decene to internal decenes are described.

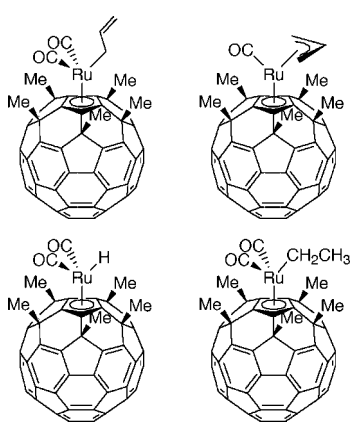


**Y. Matsuo, T. Uematsu, E. Nakamura* ..... 2729–2733**

Synthesis and Catalytic Activity of $\eta^1$-Allyl and $\eta^3$-Allyl, Ethyl, and Hydrido Complexes of Ruthenium–Pentamethyl[60]-fullerene

**Keywords:** Ruthenium / Fullerenes / Allyl complexes / Hydrido complexes / Isomerization

## Coordination Chemistry

Large bathochromic shifts in emission energy at 77 K can be achieved by adding a conjugated styryl group to the ppy ligand of the $[Ir(C^{\wedge}N\text{-ppy})_2(acac)]$ complex and by introducing either a strong electron-donating (dialkylamino, $\lambda_{em}$ = 651 nm) or -withdrawing (nitro, $\lambda_{em}$ = 647 nm) group.

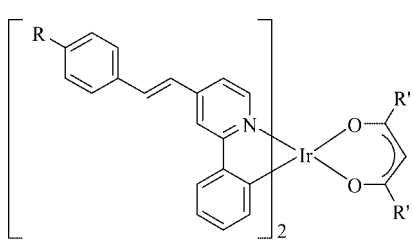


R' = $CH_3$; R = OMe, $NEt_2$, H, $NO_2$
R' = *t*Bu; R = OMe, $NEt_2$

**M. Lepeltier, T. K.-M. Lee, K. K.-W. Lo,* L. Toupet, H. Le Bozec, V. Guerchais* ..... 2734–2747**

Synthesis and Photophysical Properties of Bis-Cyclometallated Iridium(III)–Styryl Complexes and Their Saturated Analogues

**Keywords:** Iridium / Luminescence / Biscyclometallated complexes

 © 2007 Wiley-VCH Verlag GmbH & Co. KGaA, Weinheim 

# CONTENTS


## [Fe-only]-Hydrogenase Models

**J. Windhager, M. Rudolph,* S. Bräutigam, H. Görls, W. Weigand* ..... 2748–2760**

Reactions of 1,2,4-Trithiolane, 1,2,5-Trithiepane, 1,2,5-Trithiocane and 1,2,6-Trithionane with Nonacarbonyldiiron: Structural Determination and Electrochemical Investigation

**Keywords:** Iron / Cluster compounds / S ligands / Hydrogenase / Electrocatalysis / Dihydrogen

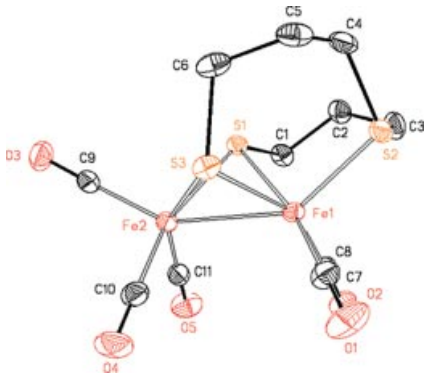


The syntheses of novel [Fe-only]-hydrogenase models starting from 1,2,4-trithiolane, 1,2,5-trithiepane, 1,2,5-trithiocane and 1,2,6-trithionane are described. The products were characterised by spectroscopic methods and X-ray structure analyses. The electrochemical behaviour of one representative complex is described in detail.

## Nickel Cluster Chemistry

**C. Papatriantafyllopoulou, G. Aromi, A. J. Tasiopoulos, V. Nastopoulos, C. P. Raptopoulou, S. J. Teat,* A. Escuer,* S. P. Perlepes* ..... 2761–2774**

Use of the Sulfato Ligand in 3d-Metal Cluster Chemistry: A Family of Hexanuclear Nickel(II) Complexes with 2-Pyridyl-Substituted Oxime Ligands

**Keywords:** Nickel(II) clusters / Magnetic properties / Sulfato complexes / Oxime complexes

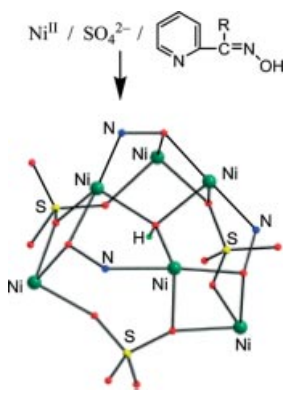


The shown general reaction scheme (R = Me, Ph) gives a family of hexanuclear nickel(II) clusters containing the $[Ni_3(\mu_3\text{-}OH)(\mu_3\text{-}SO_4)_3(\mu_3\text{-}ONR')_3]^{2+}$ core. The complexes exhibit an overall antiferromagnetic behavior, with a simple 2-*J* model adequately describing the thermal variation of the molar magnetic susceptibility.

## Coordination Polymers

**M. Scheer,* L. J. Gregoriades, M. Zabel, M. Sierka, L. Zhang, H. Eckert* ..... 2775–2782**

Conformational Analysis of One-Dimensional Coordination Polymers Based on $[Cp_2Cr_2(CO)_4(\mu,\eta^2\text{-}P_2)]$ by Solid-State Multinuclear NMR Spectroscopy and Density Functional Calculations

**Keywords:** Chromium / Copper / Halides / Density functional calculations / NMR spectroscopy / Phosphorus

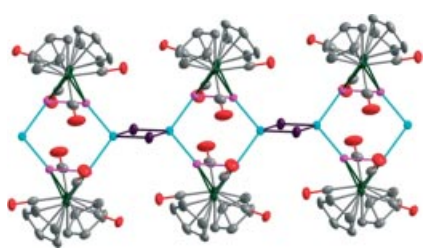

The complex $[Cp_2Cr_2(CO)_4(\mu,\eta^2\text{-}P_2)]$ reacts with copper(I) halides to yield new 1D coordination polymers (iodide derivative shown). Solid-state multinuclear NMR spectroscopy demonstrates the extreme sensitivity of the chemical shift to apparently minor structural variations, and density functional calculations corroborate the conclusions deduced from the experimental evidence.

## Fluorescent (Arene)Ru$^{II}$ Complexes

**F. Zobi, B. B. Mood, P. A. Wood, F. P. A. Fabbiani, S. Parsons, P. J. Sadler* ..... 2783–2796**

Tagging (Arene)ruthenium(II) Anticancer Complexes with Fluorescent Labels

**Keywords:** Anticancer agents / Organometallic compounds / Fluorescence / Ruthenium / Hydrolysis

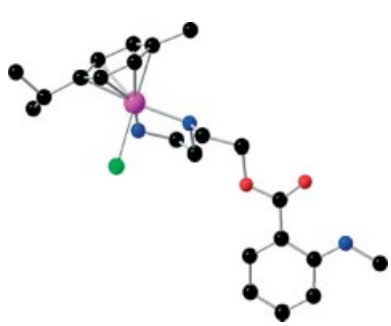

Fluorescent (arene)ruthenium(II) complexes, obtained from the reaction of the $[(p\text{-cymene})RuCl_2]_2$ dimer with isatoic acid based ligands, were structurally characterized and their solution and fluorescence properties investigated. When the fluorogenic reporter is tagged onto the complex through an ester bond, the resulting compound is a substrate for cytosolic esterases. Compounds bearing an ester bond may be models for esterase-activated Ru-based prodrug delivery systems.


 © 2007 Wiley-VCH Verlag GmbH & Co. KGaA, Weinheim 

## Doped Silica Films

A surfactant–hafnium alkoxide complex was used as a template in a sol–gel dip-coating process to produce hafnium oxide doped silica films with ratios between 1:60 and 1:6. The influence of subsequent heat treatment was studied by GISAXS and TEM. The surface and in-depth molecular composition of the films was studied by XPS.

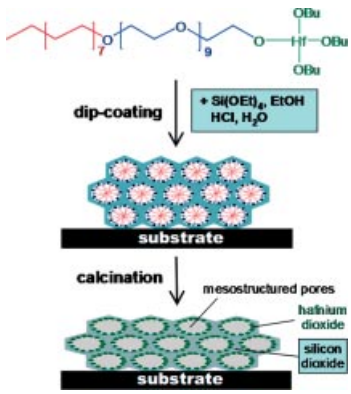


**R. Supplit, N. Hüsing,* S. Gross, S. Bernstorff, M. Puchberger ... 2797–2802**

Hafnium Oxide Doped Mesostructured Silica Films

**Keywords:** Mesostructured films / Ligand-assisted templating / Self-assembly / Surfactants

## Water-Soluble Ru Complexes

Water-soluble ruthenium(II) complexes have been synthesized and characterised. The crystal structure of [RuCp-(mTPPMS)($PPh_3$)(PTA)]·$2H_2O$, which is the first half-sandwich ruthenium complex to contain three different phosphanes, has been determined. The binding properties of the complexes obtained and of the ligand mTPPMS towards DNA have been studied using the mobility shift assay.

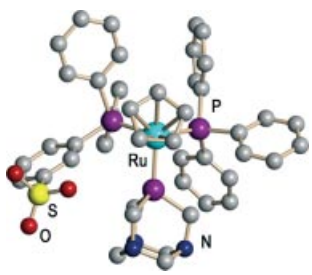


**A. Romerosa,* M. Saoud, T. Campos-Malpartida, C. Lidrissi, M. Serrano-Ruiz, M. Peruzzini, J. A. Garrido, F. García-Maroto ..... 2803–2812**

DNA Interactions Mediated by Cyclopentadienidoruthenium(II) Complexes Containing Water-Soluble Phosphanes

**Keywords:** Ruthenium / Cyclopentadienyl ligands / Phosphanes / DNA / Bioinorganic chemistry

## Hydride Protonation

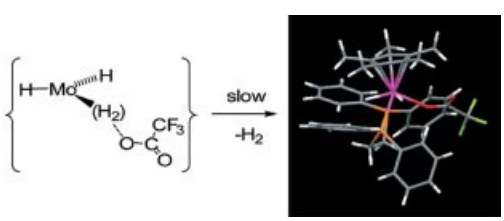


The outcome of proton transfer from $CF_3COOH$ to [Cp*Mo(dppe)$H_3$] is highly solvent-dependent: either formation of separated [Cp*Mo(dppe)$H_4$]$^+$ and trifluoroacetate ions or $H_2$ evolution with formation of the new [Cp*Mo(dppe)$H_2$-($O_2CCF_3$)] complex is observed.

**P. A. Dub, M. Baya, J. Houghton, N. V. Belkova, J.-C. Daran, R. Poli,* L. M. Epstein, E. S. Shubina* ..... 2813–2826**

Solvent Control in the Protonation of [Cp*Mo(dppe)$H_3$] by $CF_3COOH$

**Keywords:** Molybdenum / Hydrido ligand / Trifluoroacetato ligand / Proton transfer / Dihydrogen bonding

## Functionalized Molybdenocenes

[$Mo(CO)_2(NCCH_3)_2$(Cp′)][$BF_4$] (Cp′ = Cp, Ind) react with spiro[2.4]hepta-4,6-diene and spiro[4.4]nona-1,3-diene to give $\eta^4$-compounds or products of a ring-opening reaction. The *ansa* compound [Mo($\eta^5$-$C_5H_4CH_2$-$\eta^1$-$CH_2$)(CO)(Ind)][$BF_4$] was found to be a suitable precursor for the synthesis of ring-functionalized molybdenocenes.

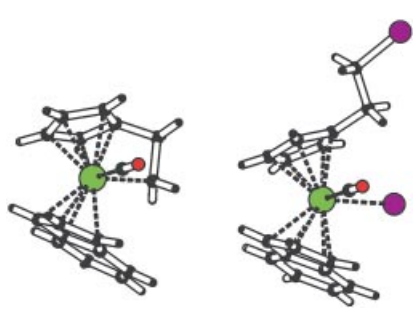

**J. Honzíček, F. A. Almeida Paz, C. C. Romão* ..... 2827–2838**

Synthesis, Characterization and Stability of Spirodiene Complexes of Molybdenum(II): New Route to *ansa*-Molybdenocene and Ring-Functionalized Molybdenocene Compounds

**Keywords:** Metallocenes / Molybdenum / Spiro compounds / Functionalized cyclopentadienes / X-ray diffraction

 © 2007 Wiley-VCH Verlag GmbH & Co. KGaA, Weinheim 

# CONTENTS


## C−F Bond Activation

**R. D. Rieth, W. W. Brennessel, W. D. Jones* ..... 2839−2847**

Activation of Aromatic, Aliphatic, and Olefinic Carbon−Fluorine Bonds Using $Cp^*_2HfH_2$

**Keywords:** Metallocenes / Hydrides / Reduction / Fluorocarbons

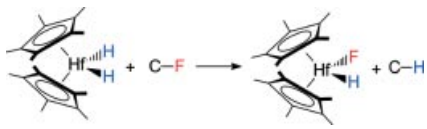


The hafnium metallocene complex $Cp^*_2HfH_2$ has been shown to react with a variety of carbon−fluorine bonds in aromatic, vinylic, and aliphatic organic substrates. The mechanism(s) of reaction are discussed and compared with the zirconium analog.

## Catalyst-Loading Effects

**A. Caballero, M. M. Díaz-Requejo, S. Trofimenko, T. R. Belderraín,* P. J. Pérez* ..... 2848−2852**

The Effect of Catalyst Loading in Copper-Catalyzed Cyclohexane Functionalization by Carbene Insertion

**Keywords:** Copper / C−H activation / Homogeneous catalysis / Carbenes / N ligands

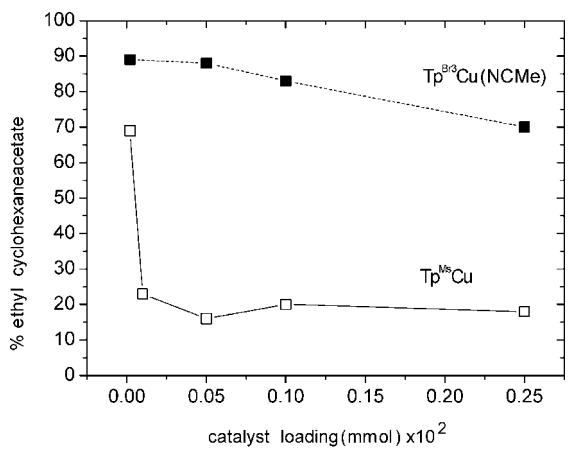


A study of the insertion of the :$CHCO_2Et$ group into the C−H bonds of cyclohexane in the presence of a Tp*x*Cu complex as catalyst has demonstrated an anomalous effect of the catalyst loading, namely that the use of low concentrations of catalyst produces an increase in the yield of the C−H activation product.

## Luminescent Lanthanides

**M. Gagliardo, F. Rizzo, M. Lutz, A. L. Spek, G. P. M. van Klink, A. E. Merbach, L. De Cola, G. van Koten* ..... 2853−2861**

A PCP-Pincer $Ru^{II}$−Terpyridine Building Block as a Potential "Antenna Unit" for Intramolecular Sensitization

**Keywords:** Ruthenium / Lanthanides / Pincer ligands / Luminescence

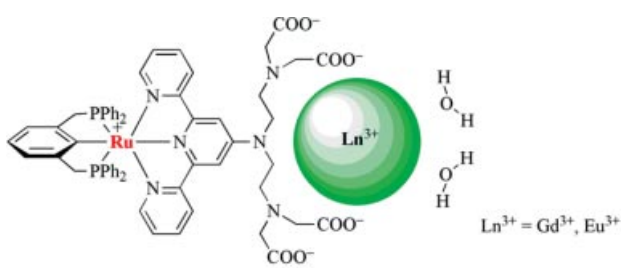


Through application of the "complex as ligand" approach, the heterodinuclear complexes $[Ru(PCP)(tpy\text{-}DTTA)Ln(H_2O)_2]$ were prepared by coordination of $Gd^{III}$ and $Eu^{III}$ ions to the chromophoric moiety of $[Ru(PCP)(tpy\text{-}DTTANa_4)]Cl$. Weak d→f energy transfer occurs in the complex $[Ru(PCP)(tpy\text{-}DTTA)Eu(H_2O)_2]$, which results in sensitized luminescence from the $Eu^{III}$ ion.

## Ruthenium−NHC Chelates

**I. Özdemir,* S. Demir, B. Çetinkaya, L. Toupet, R. Castarlenas, C. Fischmeister, P. H. Dixneuf* ..... 2862−2869**

Chelating $\eta^6$-Arene-$\eta^1$-carbene Ligands in Ruthenium Complexes

**Keywords:** Ruthenium−arene / NHCs / Imidazolinylidene / Metathesis / ROMP / Polymerization

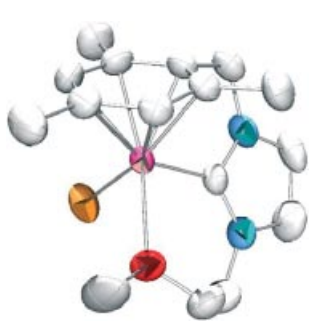

A series of ruthenium complexes bearing di- or tridentate ligands incorporating an N-heterocyclic carbene (NHC) is reported. X-ray structures are provided, and the catalytic activity for the ring opening metathesis polymerization (ROMP) of norbornene is investigated.


 © 2007 Wiley-VCH Verlag GmbH & Co. KGaA, Weinheim 

## Antitumour Agents

The first water-soluble ruthenium(II) complex with mixed thiosemicarbazone/PTA ligands has been prepared and characterised by X-ray crystallography and spectroscopic methods. The complex shows pH-dependent antiproliferative activity in vitro in micromolar concentrations.

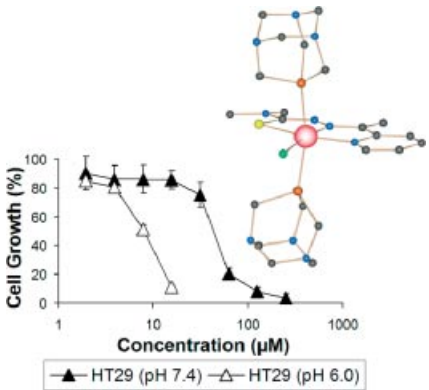


**S. Grguric-Sipka, C. R. Kowol, S.-M. Valiahdi, R. Eichinger, M. A. Jakupec, A. Roller, S. Shova, V. B. Arion,* B. K. Keppler* .... 2870–2878**

Ruthenium(II) Complexes of Thiosemicarbazones: The First Water-Soluble Complex with pH-Dependent Antiproliferative Activity

**Keywords:** Antitumour agents / Ruthenium / N,S ligands / X-ray diffraction

## Aqueous Alkyne Semihydrogenation

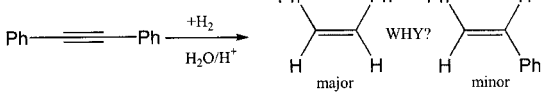


Density functional theory was applied to describe the reaction mechanism of the stereoselective hydrogenation of phenyl-substituted alkynes with the water-soluble ruthenium complex [{$RuCl_2$(*m*tppms)$_2$}$_2$] in acidic aqueous solution.

**G. Kovács, G. Ujaque, A. Lledós,* F. Joó* ..... 2879–2889**

The Role of Water in the Stereoselective Hydrogenation of 1,2-Diphenylacetylene Catalyzed by the Water-Soluble [{$RuCl_2$-(*m*tppms)$_2$}$_2$]

**Keywords:** Alkynes / Biphasic catalysis / Density functional calculations / Hydrogenation / Reaction mechanisms

## Dendritic Phthalocyanine Complexes

The first generation of a phosphorus-containing dendrimer possessing a metal-free phthalocyanine as its core is used to complex cobalt, and then the synthesis of the dendrimer is pursued up to the eighth generation. The progressive influence of the branches upon the core is studied by UV/Vis spectroscopy.

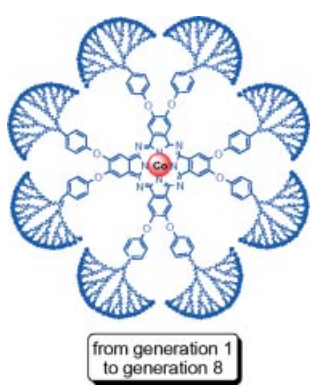


**J. Leclaire, R. Dagiral, A. Pla-Quintana, A.-M. Caminade,* J.-P. Majoral* ..... 2890–2896**

Metallated Phthalocyanines as the Core of Dendrimers – Synthesis and Spectroscopic Studies

**Keywords:** Dendrimers / Phthalocyanine / Phosphorus / UV/Vis spectroscopy / Cobalt

## Early–Late Dimetallic Complexes

Tris(phosphinoamide)zirconium complexes, $(PPh_2NR)_3ZrCl$ [R = *t*Bu (**1a**), *i*Pr (**1b**)], are synthesized by the reaction of 3 equiv. of Li($PPh_2NR$) with $ZrCl_4$. Treatment of CuCl or $Mo(CO)_3(CH_3CN)_3$ with **1a**,**b** afforded the novel heterodimetallic complexes $ClCu(Ph_2PNR)_3ZrCl$ [R = *t*Bu (**2a**), *i*Pr (**2b**)] and $(CO)_3Mo(Ph_2PNiPr)_3$-ZrCl (**3**).

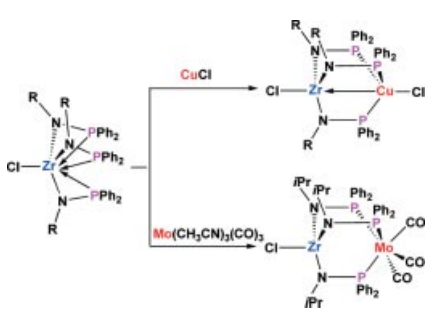


**T. Sue, Y. Sunada, H. Nagashima* ..... 2897–2908**

Zirconium(IV) Tris(phosphinoamide) Complexes as a Tripodal-Type Metalloligand: A Route to Zr–M (M = Cu, Mo, Pt) Heterodimetallic Complexes

**Keywords:** Phosphinoamide / Heterodimetallic / Tripodal ligands

 © 2007 Wiley-VCH Verlag GmbH & Co. KGaA, Weinheim 

# CONTENTS

## Transfer Hydrogenation

**A. Del Zotto,* C. Greco, W. Baratta, K. Siega, P. Rigo ..... 2909–2916**

Transfer Hydrogenation Reactions Catalyzed by Free or Silica-Immobilized $[RuCl_2(ampy)\{RN(CH_2PPh_2)_2\}]$ Complexes

**Keywords:** Ruthenium / Transfer hydrogenation / Heterogeneous catalysis / Silica / Ketones

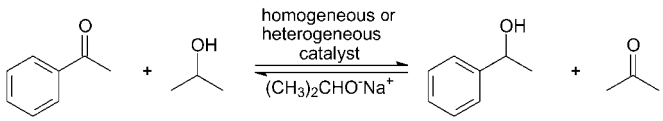


Ruthenium(II) complexes bearing ampy and diphosphane ligands with a C–N–C backbone show very high activity in the homogeneous transfer hydrogenation of ketones. When the catalysts are immobilized on silica supports, the activity is still good but a decrease in the catalytic efficiency is generally observed on recycling.

## LDH Polymerization Catalysts

**M. Vasconcellos-Dias, C. D. Nunes,* P. D. Vaz, P. Ferreira, M. J. Calhorda* ..... 2917–2925**

Pyridine Carboxylate Complexes of $Mo^{II}$ as Active Catalysts in Homogeneous and Heterogeneous Polymerization

**Keywords:** Molybdenum / Lamellar materials / Polymerization / Heptacoordination / Catalysis

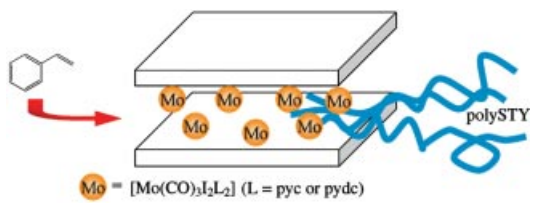


Hydrotalcite–molybdenum hybrid materials: New lamellar materials intercalated with molybdenum(II) organometallic complexes were prepared by a stepwise procedure with pyridine carboxylate derivatives as ligands. Their activity as catalysts in olefin polymerization was determined and compared with that of analogous homogeneous systems.

## Liquid Metals

**E. Vergara, S. Miranda, F. Mohr, E. Cerrada, E. R. T. Tiekink, P. Romero, A. Mendía,* M. Laguna* ..... 2926–2933**

Gold(I) and Palladium(II) Thiolato Complexes Containing Water-Soluble Phosphane Ligands

**Keywords:** Phosphane ligands / Palladium / Gold / Thiolato complexes

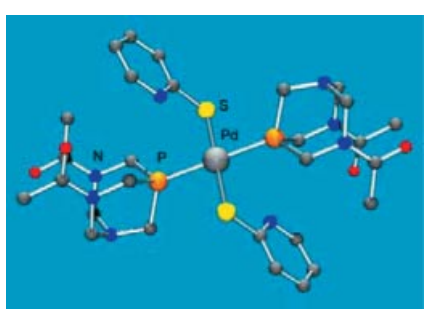


Water-soluble gold(I) and palladium(II) complexes containing different thiolates and the phosphane ligands 1,3,5-triaza-7-phosphaadamantane (PTA) and 3,7-diacetyl-1,3,7-triaza-5-phosphabicyclo[3.3.1]-nonane (DAPTA) are described and were characterised by spectroscopic techniques and X-ray crystallography.

## Unimolecular Photoinitiators

**E. P. Kündig,* L.-H. Xu, M. Kondratenko, A. F. Cunningham Jr.,* M. Kunz ..... 2934–2943**

Photoinitiation of Acrylate Polymerization with (Arene)chromium Complexes

**Keywords:** Acrylate polymerization / Photoinitiators / Arene complexes / Chromium / Radiation curing

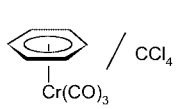


**1**

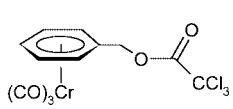


**17a**

It is known that the couple **1**/$CCl_4$ can induce photoinitiated polymerization (radiation curing) of acrylates. A new investigation into the mechanism of this process shows that photolytic CO/acrylate exchange leads to a complex in which the arene–metal bond is labilized. This then creates a highly reactive metal center that initiates $CCl_3$ radical formation. The proximity of the $COCCl_3$ group makes **17a** a much more active catalyst than **1**/$CCl_4$.

 © 2007 Wiley-VCH Verlag GmbH & Co. KGaA, Weinheim 

## Metallosupramolecular Chemistry

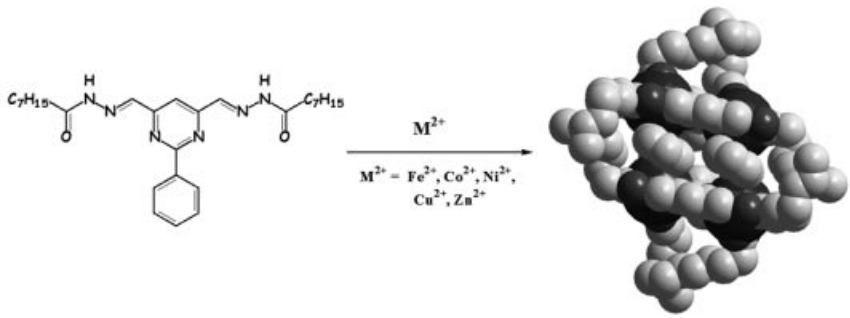


Acylhydrazones formed from 2-phenylpyrimidine-4,6-dicarbaldehyde generate [2×2] grids with a variety of transition metals. The acyl groups provide lateral functionality in these structures.

**X.-Y. Cao, J. Harrowfield, J. Nitschke, J. Ramírez, A.-M. Stadler, N. Kyritsakas-Gruber, A. Madalan, K. Rissanen, L. Russo, G. Vaughan, J.-M. Lehn* ..... 2944–2965**

Generation of [2×2] Grid Metallosupramolecular Architectures from Preformed Ditopic Bis(acylhydrazone) Ligands and through Component Self-Assembly

**Keywords:** Grids / Ditopic acylhydrazones / Component assembly / Crystal structures

## Cytochrome P450 Models

Density functional calculations on the mechanism of toluene hydroxylation leading to benzyl alcohol and *p*-cresol products are performed. In an enzyme-mimicked environment with all hydrogen atoms of toluene replaced by deuterium atoms the two processes are competitive.

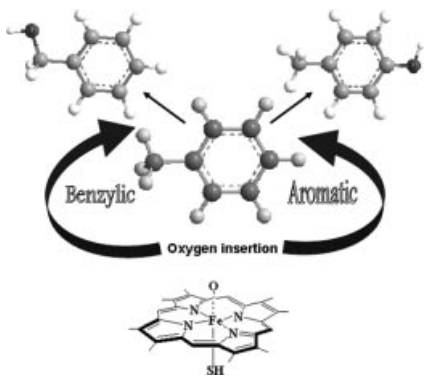


**C. Hazan, D. Kumar, S. P. de Visser,* S. Shaik* ..... 2966–2974**

A Density Functional Study of the Factors That Influence the Regioselectivity of Toluene Hydroxylation by Cytochrome P450 Enzymes

**Keywords:** Density functional calculations / Enzyme catalysis / Enzyme models / Isotope effects / Metalloenzymes

## Silsesquioxanes

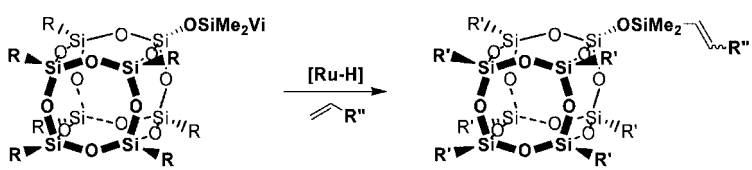


R = *i*Bu (**1**), $ViMe_2SiO$ (**2**)

R' = *i*Bu (**3**–**8**), $OSiMe_2CH{=}CHR"$ (**10**–**15**)

Highly effective synthesis of β-functionalized vinylspherosilicates **1** and **2** by Ru(H)(Cl)(CO)$(PCy_3)_2$-catalyzed silylative coupling with α olefins is reported.

**J. Waehner, B. Marciniec,* P. Pawluć ..... 2975–2980**

Functionalization of Vinylspherosilicates by Ruthenium-Catalyzed Silylative Coupling Reactions

**Keywords:** Spherosilicate / Silsesquioxane / Cross-coupling / Ruthenium / Hydrides

**If not otherwise indicated in the article, papers in issue 17 were published online on May 29, 2007**

 © 2007 Wiley-VCH Verlag GmbH & Co. KGaA, Weinheim 

# SPOTLIGHTS …

## *Multicomponent Reactions*

S. Hübner, H. Jiao, D. Michalik, H. Neumann, S. Klaus, D. Strübing, A. Spannenberg, M. Beller*

**In Situ Generation of Chiral *N*-Dienyl Lactams in a Multicomponent Reaction: An Efficient and Highly Selective Way to Asymmetric Amidocyclohexenes**

*Chem. Asian J.*
DOI: **10.1002/asia.200600428**

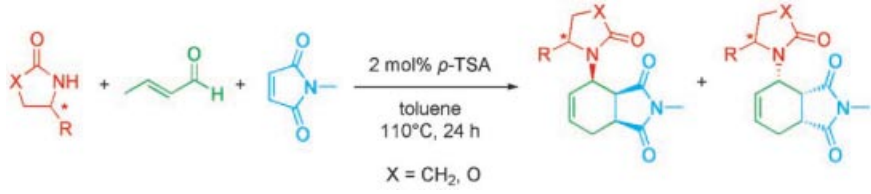


**Three Amigos**: The employment of chiral amides in combination with aldehydes and dienophiles in our novel multicomponent procedure allows the simple and efficient synthesis of amido-functionalized cyclohexene derivatives (see scheme; *p*-TSA = *para*-toluenesulfonic acid). The multicomponent methodology circumvents the circuitous preparation of chiral *N*-dienyl lactams as they are generated in situ.

## *Polyketide Synthases*

S. Grüschow, T. J. Buchholz, W. Seufert, J. S. Dordick, D. H. Sherman*

**Substrate Profile Analysis and ACP-Mediated Acyl Transfer in *Streptomyces coelicolor* Type III Polyketide Synthases**

*ChemBioChem*
DOI: **10.1002/cbic.200700026**

**Protein partners**. We report the biochemical characterization of two type III polyketide synthases (PKS) from *Streptomyces coelicolor*. Remarkably, germicidin synthase (Gcs)/SCO7221 was able to utilize both acyl-CoA and acyl-ACP as starter units for the production of pyrone containing compounds.

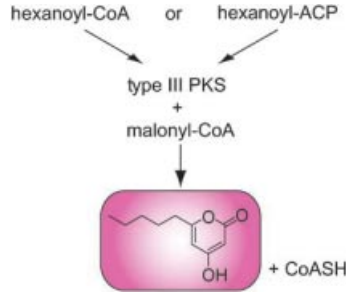


## *Electron Transfer*

A. Van Vooren, V. Lemaur, A. Ye, D. Beljonne, J. Cornil*

**Impact of Bridging Units on the Dynamics of Photoinduced Charge Generation and Charge Recombination in Donor–Acceptor Dyads**

*ChemPhysChem*
DOI: **10.1002/cphc.200700130**

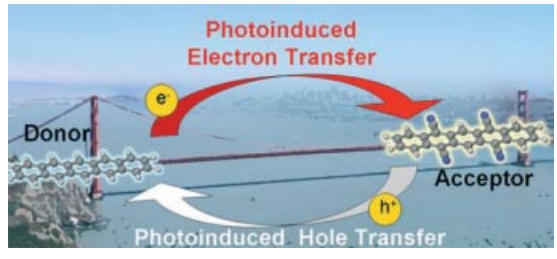


**Donor–bridge–acceptor architectures:** The authors estimate, at a full quantum-chemical level, the various molecular parameters governing charge-transfer rates in model organic structures containing a donor and an acceptor unit connected by a bridging unit (see picture). The nature, size, and conformation of the bridging unit have been systematically varied.

## *Cheminformatics*

R. van Deursen, J.-L. Reymond

**Chemical Space Travel**

*ChemMedChem*
DOI: **10.1002/cmdc.200700021**

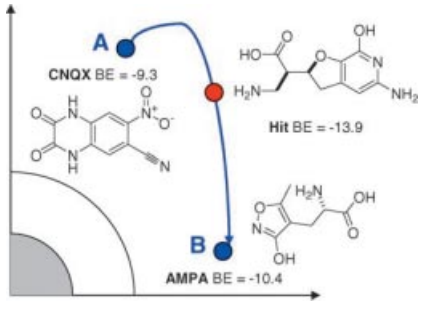


**Space the final frontier!** Modern medicine depends on the discovery of new drugs however, detailed knowledge of all possible organic molecules is not available. To travel in this so-called chemical space and discover new compounds, we wrote a spaceship program combining a point mutation generator with a selection module for target similarity. Thus, allowing travel from a starting molecule A to a target molecule B through a continuum of structural mutations.

 © 2007 Wiley-VCH Verlag GmbH & Co. KGaA, Weinheim 

# … ON OUR SISTER JOURNALS

**An unprecedented hydride adduct** was formed upon the addition of formate to a dicationic palladium cluster $[Pd_3(dppm)_3(\mu_3\text{-}CO)]^{2+}$ (dppm = bis(diphenylphosphinomethane). This is just one of the routes that can be used to form this product (see scheme). The palladium–hydride cluster has been fully characterised by both spectroscopic and electroanalytical methods.

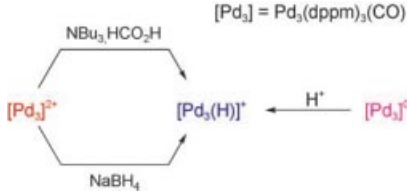


### *Cluster Compounds*

C. Cugnet, D. Lucas,* E. Collange, B. Hanquet, A. Vallat, Y. Mugnier, A. Soldera, P. D. Harvey*

**Generation, Characterization, and Electrochemical Behavior of the Palladium–Hydride Cluster $[Pd_3(dppm)_3(\mu_3\text{-}CO)(\mu_3\text{-}H)]^+$ (dppm = Bis(diphenylphosphinomethane)**

*Chem. Eur. J.*
DOI: **10.1002/chem.200700069**

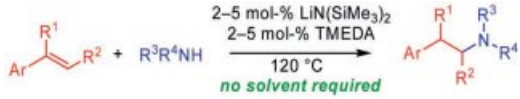


$LiN(SiMe_3)_2$/TMEDA is an efficient catalyst for the anti-Markovnikov addition of primary and secondary amines to vinylarenes. Reactions proceed readily at 120 °C in the absence of solvent. The mechanism of the lithium-catalyzed hydroamination and the influence of TMEDA was studied with DFT methods.

### *Hydroamination*

P. Horrillo-Martínez, K. C. Hultzsch,* A. Gil, V. Branchadell

**Base-Catalyzed Anti-Markovnikov Hydroamination of Vinylarenes – Scope, Limitations and Computational Studies**

*Eur. J. Org. Chem.*
DOI: **10.1002/ejoc.200700147**

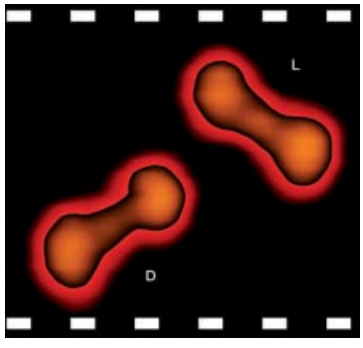


**Lights, camera, action!** The general mechanism of biomolecular recognition introduced by Pauling more than 50 years ago has now been brought to the movie screen (see still frame; D: D-Phe-D-Phe, L: L-Phe-L-Phe). With STM movies, the chiral-recognition process of individual adsorbed di-phenylalanine molecules is followed to illustrate the dynamic induced-fit mechanism at the single-molecule level.

### *Molecular Recognition*

M. Lingenfelder,* G. Tomba, G. Costantini, L. Colombi Ciacchi, A. De Vita, K. Kern

**Tracking the Chiral Recognition of Adsorbed Dipeptides at the Single-Molecule Level**

*Angew. Chem. Int. Ed.*
DOI: **10.1002/anie.200700194**

On these pages, we feature a selection of the excellent work that has recently been published in our sister journals. If you are reading these pages on a computer, click on any of the items to read the full article. Otherwise please see the DOIs for easy online access through Wiley InterScience.

 © 2007 Wiley-VCH Verlag GmbH & Co. KGaA, Weinheim 

DOI: 10.1002/ejic.200700085

# Synthesis and Reactions of Polynuclear Polyhydrido Rare Earth Metal Complexes Containing "$(C_5Me_4SiMe_3)LnH_2$" Units: A New Frontier in Rare Earth Metal Hydride Chemistry

**Zhaomin Hou,*[a] Masayoshi Nishiura,[a] and Takanori Shima[a]**

**Keywords:** Rare earths / Hydride ligands / Cyclopentadienyl ligands / Cluster compounds / Hydrogenation

A series of tetranuclear octahydrido rare earth metal complexes of general formula $[(C_5Me_4SiMe_3)Ln(\mu\text{-}H)_2]_4(THF)_n$ (Ln = Sc, Y, Gd, Dy, Ho, Er, Tm, Lu; $n$ = 0, 1, or 2) that contain $C_5Me_4SiMe_3$ as an ancillary ligand have been prepared and structurally characterized. These hydride clusters are soluble in common organic solvents such as THF, toluene, and hexane, and maintain their tetranuclear framework in solution. Such polynuclear polyhydrido complexes exhibit extremely high and unique reactivity toward a variety of unsaturated substrates including CO, $CO_2$, and nitriles. The reaction of these neutral polyhydrides with one equivalent of $[Ph_3C][B(C_6F_5)_4]$ affords the corresponding cationic hydride clusters $[(C_5Me_4SiMe_3)_4Ln_4H_7(THF)_n][B(C_6F_5)_4]$, which can act as catalysts for the syndiospecific polymerization of styrene and regio- and stereospecific *cis*-1,4-polymerization of 1,3-cyclohexadiene.
(© Wiley-VCH Verlag GmbH & Co. KGaA, 69451 Weinheim, Germany, 2007)

## 1. Introduction

Metal hydrides are fundamental components in a wide range of stoichiometric and catalytic reactions, and their importance in modern inorganic and organic chemistry cannot be overemphasized.[1,2] A large number of monohydride complexes of the rare earth (group 3 and lanthanide) metals of the general type "$L_2MH$" or "(L)(L′)MH", which are supported by two anionic ancillary ligands per metal, have been synthesized and studied[2] since the first rare earth metallocene hydride complex was reported in the early 1980s.[3] In contrast, dihydrido rare earth metal complexes of the type "$LMH_2$", which bear one anionic ancillary ligand per metal, have been much less extensively investigated even though such complexes are of great interest both structurally and chemically. A major factor that has hampered the investigation of rare earth metal dihydride or polyhydride complexes is the difficulty in isolating structurally well defined complexes. Early attempts to prepare a dihydrido rare earth metal complex by reaction of dialkyl complexes such as $[(C_5Me_5)Lu(CH_2CMe_3)_2(THF)]$[4] or $[(C_5Me_4SiMe_3)Y(CH_2SiMe_3)_2(THF)]$[5] with $H_2$ did not afford a structurally characterized hydride species. The first structurally characterized dihydrido rare earth metal species was isolated as the $Sm^{III}$/K heteropolymetallic form $[\{(C_5Me_5)Sm(\mu\text{-}H)_2\}_6\{KH(THF)_2\}_3]$, which formally consists of six "$(C_5Me_5)SmH_2$" units and three "$KH(THF)_2$" units.[6a] This complex was serendipitously obtained by the reaction (σ-bond metathesis and subsequent oxidation) of the $Sm^{II}$ alkyl complex $[\{(C_5Me_5)SmCH(SiMe_3)_2[(C_5Me_5)K(THF)_2]\}_n]$[6] with an excess of $PhSiH_3$. Very recently, a series of salt-free polynuclear polyhydrido rare earth metal complexes that contain "$(C_5Me_4SiMe_3)LnH_2$" units has been synthesized from the $C_5Me_4SiMe_3$-ligated dialkyl complexes $[(C_5Me_4SiMe_3)Ln(CH_2SiMe_3)_2(THF)]$ (Ln = Sc, Y, Gd, Dy, Ho, Er, Tm, Lu). It has been found that these polyhydrido rare earth metal complexes show a unique reactivity that differs from that of conventional monohydride complexes. This article summarizes recent studies on this new class of rare earth metal hydride complexes.

## 2. Synthesis and Structures of Tetranuclear Octahydrido Rare Earth Metal Complexes

Hydrogenolysis of the $C_5Me_4SiMe_3$-ligated bis(trimethylsilylmethyl)scandium complex $[(C_5Me_4SiMe_3)Sc(CH_2SiMe_3)_2(THF)]$ with $H_2$ in toluene at room temperature gives the THF-free tetranuclear octahydride complex $[\{(C_5Me_4SiMe_3)Sc(\mu\text{-}H)_2\}_4]$ (**1**) (Scheme 1).[7] This complex can be viewed as being the result of a self-assembly of four "$(C_5Me_4SiMe_3)ScH_2$" units in a tetrahedron through "intermolecular" Sc–H interactions. There are a total of eight hydride ligands in the molecule, one of which is body-centered in a $\mu_4$-H–$Sc_4$ fashion, one is face-capped in a $\mu_3$-

[a] Organometallic Chemistry Laboratory, RIKEN (The Institute of Physical and Chemical Research), and PRESTO, Japan Science and Technology Agency (JST),
Hirosawa 2-1, Wako, Saitama 351-0198, Japan
Fax: +81-48-462-4665
E-mail: houz@riken.jp

 © 2007 Wiley-VCH Verlag GmbH & Co. KGaA, Weinheim 

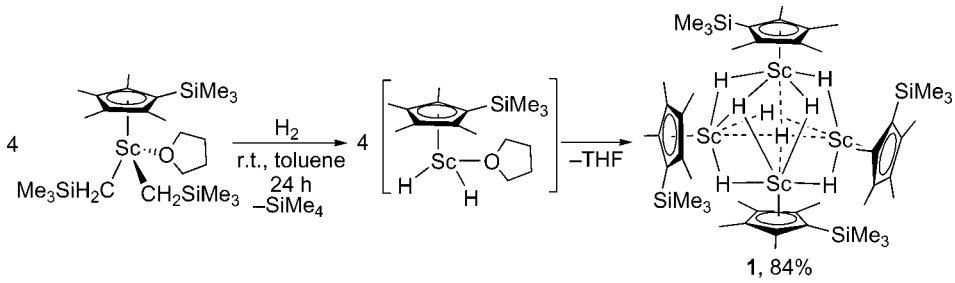


Scheme 1. Synthesis of a tetranuclear octahydrido scandium complex.

$H–Sc_3$ form, and six are edge-bridged in a $\mu_2$-H–$Sc_2$ style. The THF ligand bonded originally to the scandium metal center of the alkyl precursor is squeezed out in the hydride complex due to the formation of "intermolecular" Sc–H bonds.

Hydrogenolysis of the bis(trimethylsilylmethyl) complexes of larger rare earth metals such as Y, Er, and Tm in toluene affords the corresponding tetranuclear octahydride complexes $[\{(C_5Me_4SiMe_3)Ln(\mu\text{-}H)_2\}_4(THF)]$ (**2**: Ln = Y;[8] **3**: Ln = Er;[9] **4**: Ln = Tm[9]) where one of the four metal centers in these complexes bears an additional THF ligand (Scheme 2). The overall structure of the mono(THF)-containing polyhydride complexes **2**–**4** is almost the same as that of the THF-free Sc complex **1**. In the case of the analogous complexes of larger metals such as Gd (**5**),[9] Dy (**6**),[9] and Ho (**7**),[9] an agostic interaction between the metal center and a methyl group of an adjacent $C_5Me_4SiMe_3$ ligand is also observed, probably due to the greater steric unsaturation of these larger metal centers (Scheme 2).[9,10] These results show that the fine structures of the tetranuclear octahydride complexes are, to some extent, dependent on the ionic radius of the metal centers.

In the case of lutetium, the reaction of the bisalkyl complex $[(C_5Me_4SiMe_3)Lu(CH_2SiMe_3)_2(THF)]$ with $H_2$ did not give a single hydride complex.[11] However, hydrogenolysis of the hydride-bridged dimeric mixed alkyl/hydride complex $[\{(C_5Me_4SiMe_3)Lu(CH_2SiMe_3)(\mu\text{-}H)(THF)\}_2]$ (**8**), which was prepared by reaction of $[(C_5Me_4SiMe_3)Lu(CH_2SiMe_3)_2$-(THF)] with one equivalent of $PhSiH_3$, affords the tetranuclear mono(THF)-coordinated lutetium octahydride complex $[\{(C_5Me_4SiMe_3)Lu(\mu\text{-}H)_2\}_4(THF)]$ (**9**) in THF (Scheme 3).[12] The structure of **9** is identical with those of the analogous mono(THF)-containing complexes **2**–**4**. When the reaction of the alkyl/hydride complex **8** with $H_2$

*Zhaomin Hou was born in Shandong Province, China, in 1961. He received his B.Sc. from the China University of Petroleum (Shandong, China) in 1982, and his M.Sc. and Ph.D. from Kyushu University (Fukuoka, Japan) in 1986 and 1989, respectively. He joined RIKEN (The Institute of Physical and Chemical Research) in 1989, where he is now Chief Scientist and Director of the Organometallic Chemistry Laboratory. The current research activity in his group includes development of new catalysts for regio- and stereospecific olefin polymerization/copolymerization, new catalysts for efficient organic synthesis, and rare earth metal complexes with novel structures and reactivities, as well as synthesis of new functional materials. He is a recipient of the Japan Society of Coordination Chemistry Award for Young Scientists (1996), the Rare Earth Society of Japan Award for Young Scientists (1997), the Progress Award in Synthetic Organic Chemistry, Japan (2000), the JSPS Prize (2007), the Chemical Society of Japan Award for Creative Work for 2007, and the Mitsui Chemicals Catalysis Science Award (2007).*

*Masayoshi Nishiura was born in Hokkaido, Japan in 1971. He did his graduate studies at Chiba University under the supervision of Professor Tsuneo Imamoto, and received his Ph.D. in 2000 from the same University. He moved to RIKEN as a special postdoctoral researcher in 2000 and was promoted to Research Scientist at RIKEN in 2003. His research focuses on development of organometallic catalysts for organic synthesis and olefin polymerization.*

*Takanori Shima was born in Osaka, Japan, in 1972. He obtained his Ph.D. degree in 2001 from Tokyo Institute of Technology on the study of multinuclear polyhydrido complexes, under the supervision of Prof. Hiroharu Suzuki. He undertook postdoctoral research in the group of Prof. John A. Gladysz in the Institute für Organische Chemie of Friedrich-Alexander Universität (Erlangen, Germany) as an Alexander von Humboldt fellow in 2002. He joined RIKEN in 2004. His research interests include the synthesis and development of new rare earth metal polyhydrido complexes.*

 © 2007 Wiley-VCH Verlag GmbH & Co. KGaA, Weinheim 

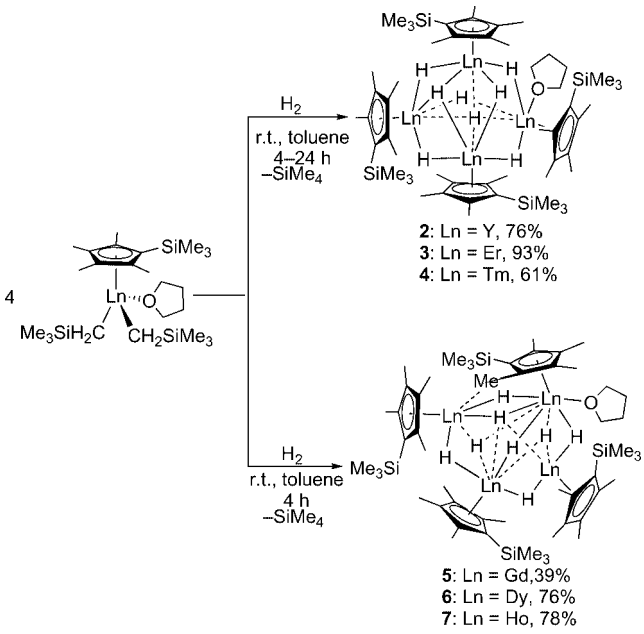


Scheme 2. Synthesis of mono(THF)-coordinated tetranuclear octahydrido rare earth metal complexes.

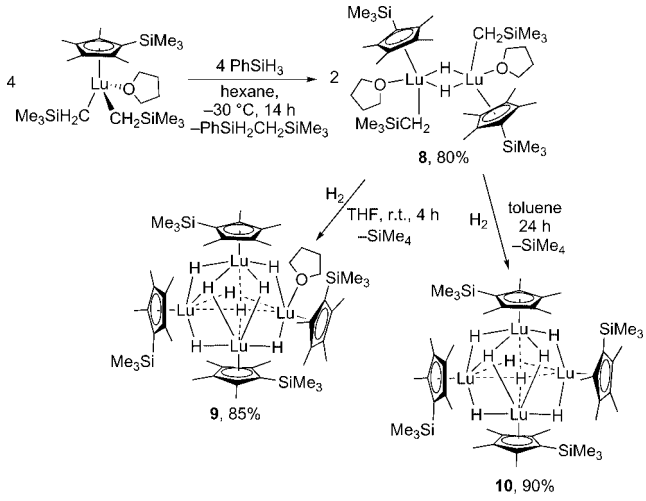


Scheme 3. Synthesis of THF-free and mono(THF)-coordinated lutetium polyhydride complexes.

was carried out in toluene, the corresponding THF-free tetranuclear lutetium octahydride complex **10** was obtained (Scheme 3).[12]

The octahydride complexes **1**–**7**, **9**, and **10** are all soluble in common organic solvents such as THF, toluene, and hexane, and their tetranuclear frameworks are maintained in solution. In the case of yttrium, recrystallization of the mono(THF) complex **2** from THF gives the structurally characterizable bis(THF)-coordinated complex **11** (Scheme 4);[9,12,13] formation of an analogous bis(THF)

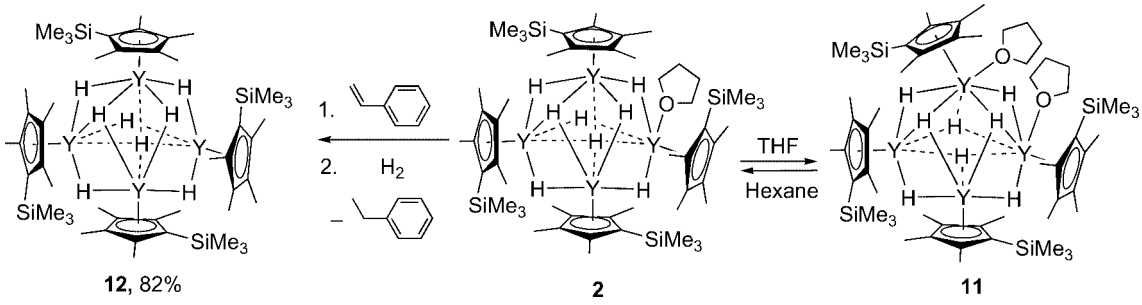


Scheme 4. Formation of yttrium polyhydride complexes with and without THF ligands.

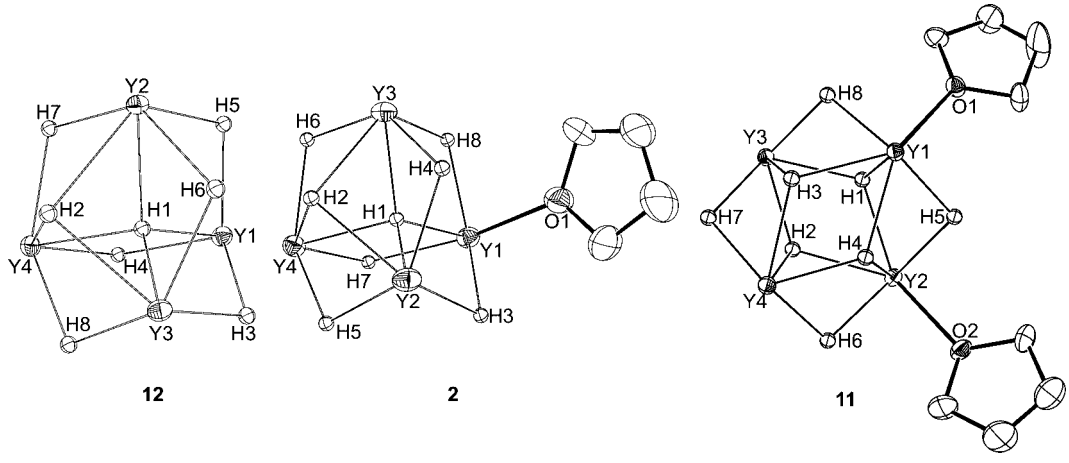


Figure 1. ORTEP drawings of the $Y_4H_8$ core structures of **12** (left, THF-free), **2** (middle, with one THF ligand), and **11** (right, with two THF ligands).

 © 2007 Wiley-VCH Verlag GmbH & Co. KGaA, Weinheim 

complex was not observed under the same conditions for the smaller Sc and Lu complexes **1**, **9**, and **10**. The bis(THF)-coordinated yttrium polyhydride **11** also adopts a tetrahedral metal skeleton, but it has four $\mu_3$-H and four $\mu_2$-H ligands whereas the mono(THF) analogue **2** possesses one $\mu_4$-H, one $\mu_3$-H, and six $\mu_2$-H ligands (Figure 1). Recrystallization of the bis(THF) complex **11** from hexane regenerates the mono(THF) complex **2**, while treatment of the mono(THF) yttrium complex **2** with styrene followed by hydrogenolysis of the resultant product in benzene yields the corresponding THF-free octahydride complex **12** (Schemes 4 and 5).[8,14] ORTEP drawings of the $Y_4H_8$ core structures of **2**, **11**, and **12** are shown in Figure 1.

## 3. Reaction of Rare Earth Metal Polyhydrides with Unsaturated C–C Bonds

Reaction of the mono(THF)-coordinated tetranuclear yttrium octahydride complex **2** with styrene yields a product formed by insertion of a single molecule of styrene − the benzylic allyl heptahydride complex **13** − in which the allyl part is bonded to one Y atom in an $\eta^3$-fashion and the phenyl part is bonded to another Y atom in an $\eta^2$-form (Scheme 5).[8] No further reaction was observed even when an excess of styrene was present. Hydrogenolysis of the benzylic allyl complex **13** with $H_2$ (1 atm) in benzene affords ethylbenzene and the THF-free yttrium octahydride complex $[\{(C_5Me_4SiMe_3)Y(\mu\text{-}H)_2\}_4]$ (**12**).[14] Under 1 atm of $H_2$, styrene can be catalytically hydrogenated into ethylbenzene by **2** or **12**.

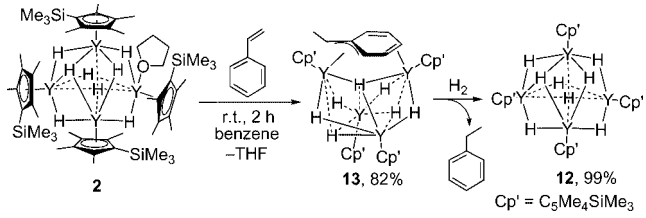


Scheme 5. Formation of a tetranuclear yttrium benzylic allyl heptahydride complex and its reaction with $H_2$.

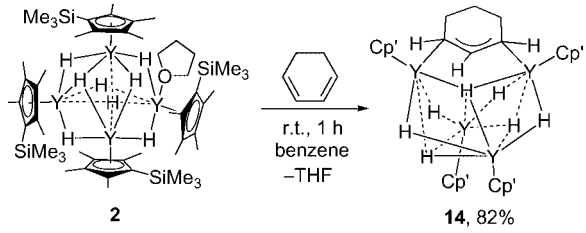


Scheme 6. Reaction of an yttrium polyhydride complex with 1,3-cyclohexadiene. Cp′ = $C_5Me_4SiMe_3$.

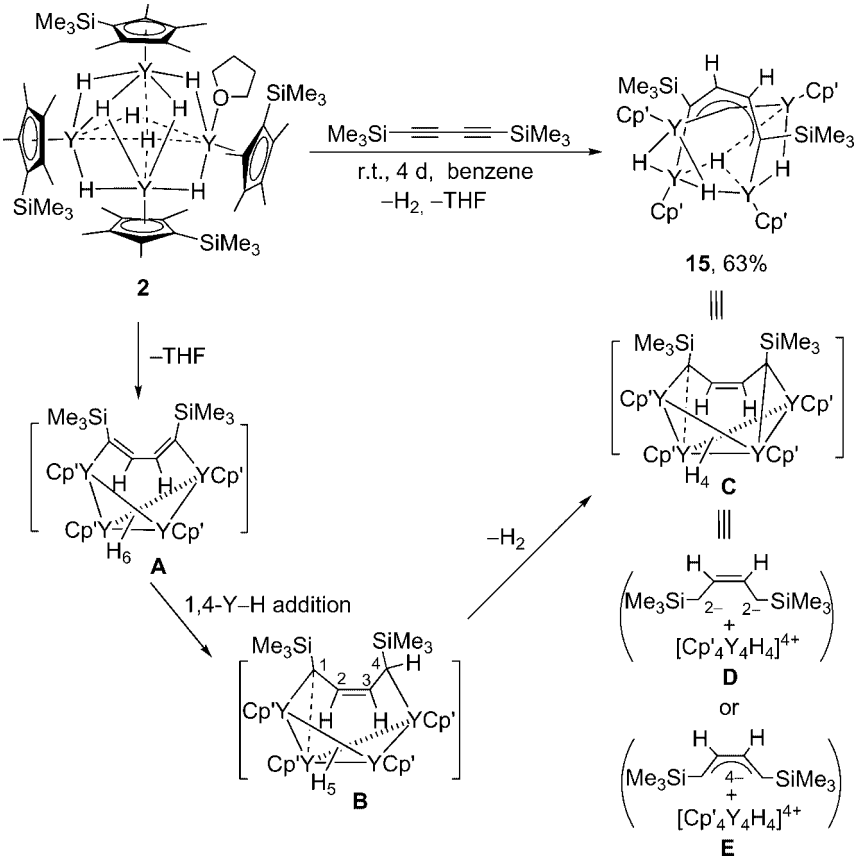


Scheme 7. Reaction of an yttrium polyhydride complex with 1,4-bis(trimethylsilyl)-1,3-butadiyne. Cp′ = $C_5Me_4SiMe_3$.

 © 2007 Wiley-VCH Verlag GmbH & Co. KGaA, Weinheim 

The reaction of **2** with 1,3-cyclohexadiene (CHD) yields the 1,4-addition product **14** in which the resulting allyl unit interacts with two Y atoms through the two "terminal" carbon atoms, each of which bonds to one metal center in an $\eta^1$-fashion (Scheme 6).[9] As in the case of styrene, the use of an excess amount of CHD does not lead to further reaction.

The reaction of **2** with 1,4-bis(trimethylsilyl)-1,3-butadiyne affords the tetranuclear yttrium tetrahydride complex **15**, which formally consists of a $[(C_5Me_4SiMe_3)YH]_4^{4+}$ unit and a butene-tetraanion species (Scheme 7).[8] This butene-tetraanion moiety is bonded to two yttrium atoms in a $\pi,\eta^4$-"inverse-sandwich" fashion and to the other two yttrium atoms in a $\sigma_1,\mu_1$-terminal form at the two terminal carbon atoms. The formation of **15** can be explained as follows. Addition of two Y–H units of **2** to the two C≡C units of 1,4-bis(trimethylsilyl)-1,3-butadiyne in a "2,1" fashion yields the 1,3-butadien-1,4-diyl (or butadiene-dianion)/hexahydride species **A** (Scheme 7). Subsequent 1,4-Y–H addition to the 1,3-butadiene unit in **A** could give the 2-buten-1,1′4-triyl/pentahydride species **B**. Deprotonation at the C4 position of the butene species by a Y–H unit in **B** should afford the 2-buten-1,1′,4,4′-tetrayl/tetrahydride species **C**. This species can be regarded as a resonance structure (a localized form) of **15** (cf. alo **D** and **E**).

## 4. Reaction of Rare Earth Metal Polyhydrides with Unsaturated C–O Bonds

Reaction of the lutetium octahydride complex **9** with γ-butyrolactone gives the tetranuclear mixed alkoxido/dihydrido complex **16** (Scheme 8).[8] γ-Butyrolactone is a stable, non-polymerizable cyclic ester. In this reaction, three molecules of γ-butyrolactone are completely reductively ring-opened by six of the eight hydride ligands in **9** to give the linear diolate species "-O(CH$_2$)$_4$O-", thus demonstrating the unusually high reactivity of this rare earth metal polyhydride complex. Further reaction between **16** and γ-butyrolactone was not observed, even when an excess amount of γ-butyrolactone was present. However, both **9** and **16** show high activity for the ring-opening polymerization of ε-caprolactone.

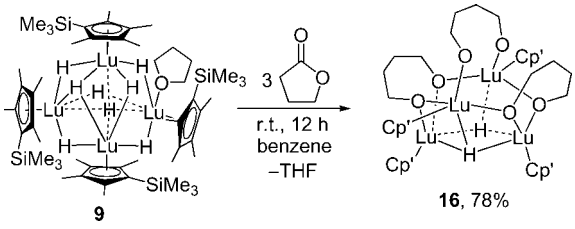


Scheme 8. Reaction of a lutetium polyhydride complex with γ-butyrolactone. Cp′ = $C_5Me_4SiMe_3$.

The reaction of **2** with CO in toluene at –10 °C occurs rapidly to give the hexahydrido/oxymethylene yttrium complex **17** (Scheme 9).[15] When **17** is stirred at –10 °C in the presence of CO for a few minutes and then at room temperature in the absence of CO for 1 h, the dioxo/tetrahydrido complex $[(C_5Me_4SiMe_3Y)_4(\mu_3\text{-}O)_2(\mu\text{-}H)_4(THF)]$ (**20**) is obtained with simultaneous release of ethylene. Complex **20** can also be isolated directly from the reaction of **2** with CO without isolating **17**. $^1$H NMR monitoring of the reaction of **17** with CO in [D$_8$]THF at low temperatures revealed the formation of an enolate intermediate such as $[(C_5Me_4SiMe_3Y)_4(OCH{=}CH_2)(\mu\text{-}O)(\mu\text{-}H)_5(THF)]$ (**19**). Further reaction of the yttrium tetrahydrido/dioxo complex **20** with CO gives the corresponding tetraoxo complex **21** and ethylene.

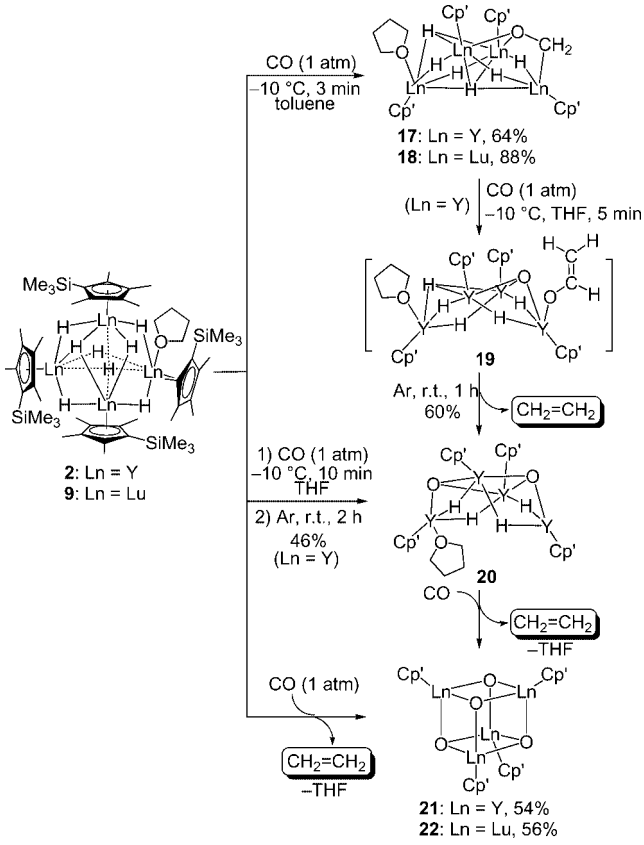


Scheme 9. Selective formation of ethylene by deoxygenative C–C coupling of carbon monoxide. Cp′ = $C_5Me_4SiMe_3$.

Reaction of the lutetium octahydride complex **9** with CO (1 atm) affords the analogous lutetium hexahydrido/oxymethylene complex **18** and the tetraoxo lutetium cubane complex **22** with release of ethylene (Scheme 9); formation of a tetrahydrido/dioxo Lu complex intermediate analogous to **20** was not observed. The solid-state structure of **22** is shown in Figure 2.

Although the reactions of CO with various transition metal hydrides, including lanthanide and actinide metallocene hydrides, have been reported,[16] the selective formation of ethylene by reduction of CO is unprecedented. These results demonstrate again the unique reactivity of polyhydrido rare earth metal complexes.

A possible reaction mechanism for the formation of ethylene is shown in Scheme 10. Addition of two Y–H bonds in **2** across the C–O triple bond of one molecule of CO could give the oxymethylene complex **17**. Subsequent inser-

 © 2007 Wiley-VCH Verlag GmbH & Co. KGaA, Weinheim 

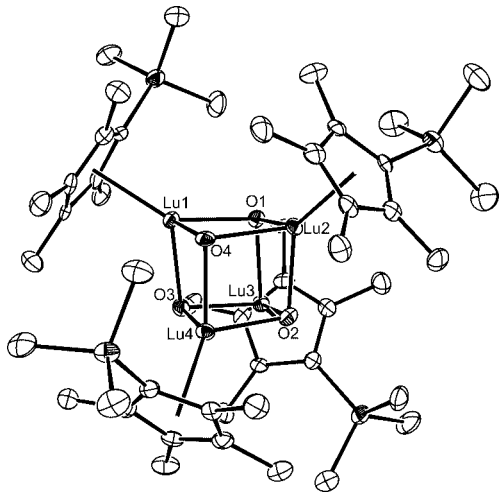


Figure 2. ORTEP drawing of **22**.

tion of another molecule of CO into the Y–$CH_2$ bond in **17** would afford an α-oxyacetyl species such as **F** (or its carbenoid isomer). Y–H bond addition across the acyl C–O double bond in **F** could yield the oxametallacyclopropane species **G**, which would produce the enolate species **19** by rupture of a C–O and the C–Y bond. Addition of another Y–H bond across the C–C double bond of the enolate unit might give the β-oxyethylene species **H**, which, after cleavage of the C–Y and the C–O bond, yields the dioxo complex **20** with release of ethylene. Formation of the tetraoxo complex **21** and ethylene from the reaction of **20** with CO could follow an analogous process, although intermediate species analogous to the oxymethylene **17** or an enolate species **19** have not been observed.

Reaction of the octahydride complex **2** with $CO_2$ also takes place very rapidly, although a characterizable product could not be isolated from this reaction. However, the structurally characterizable bis(methylene diolate) complex **23** was obtained in high yield from the reaction of the butene-tetraanion/tetrahydrido complex **15** with $CO_2$, (Scheme 11).[17] In this reaction, the two C–O double bonds of $CO_2$ are completely reduced to C–O single bonds. This reaction takes place only at the hydride sites and the butene-tetraanion unit remains unchanged. Although a large number of studies on the hydrogenation of $CO_2$ with both homogeneous and heterogeneous systems have been reported, the observation of formation of a methylene diolate species remains rare.[18] The present formation of the methylene diolate species is in sharp contrast with what was observed previously in the case of other transition metal polyhydride complexes such as $[\{(C_5H_5)Ti(\mu\text{-}H)\}_2(C_{10}H_8)]$,[19] $[(C_5H_5)_2Zr(H)(\mu\text{-}H)(\mu\text{-}N\textit{t}Bu)Ir(C_5Me_5)]$,[20] $[H_2Ru(dmpe)_2]$,[21] and $[H_4Mo(dmpe)_2]$,[22] [dmpe = 1,2-bis(dimethylphosphanyl)ethane] which yield either bis(formate),[18,21] mixed hydride/formate,[19,20] or mixed hydride/carbonate complexes[21] upon reaction with $CO_2$. Further insertion of $CO_2$ into the metal-diolate bonds in **23** could also take place to give the mono- and dicarbonate complexes **24** and **25** in a stepwise manner, with possible release of formaldehyde (HCHO; Scheme 11).

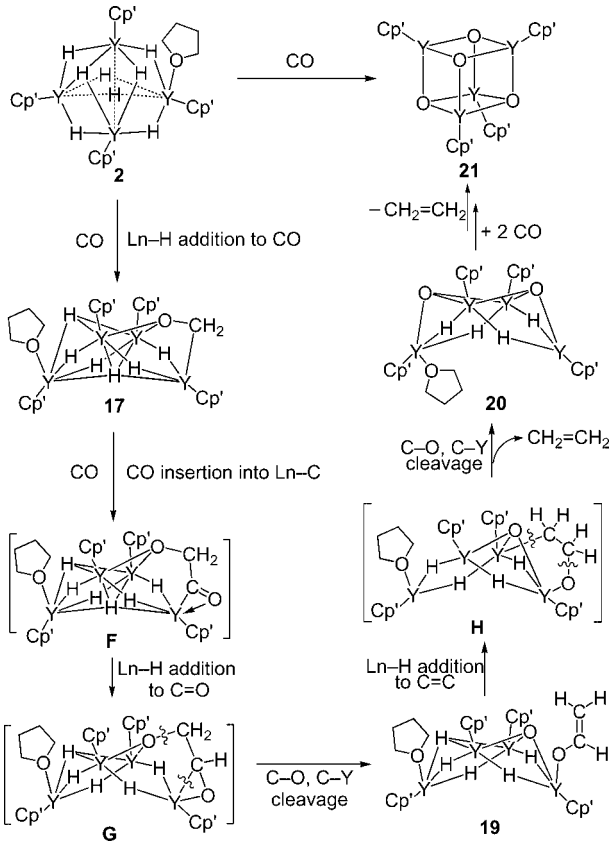


Scheme 10. A possible mechanism for the reaction of an yttrium polyhydride complex with carbon monoxide. Cp′ = $C_5Me_4SiMe_3$.

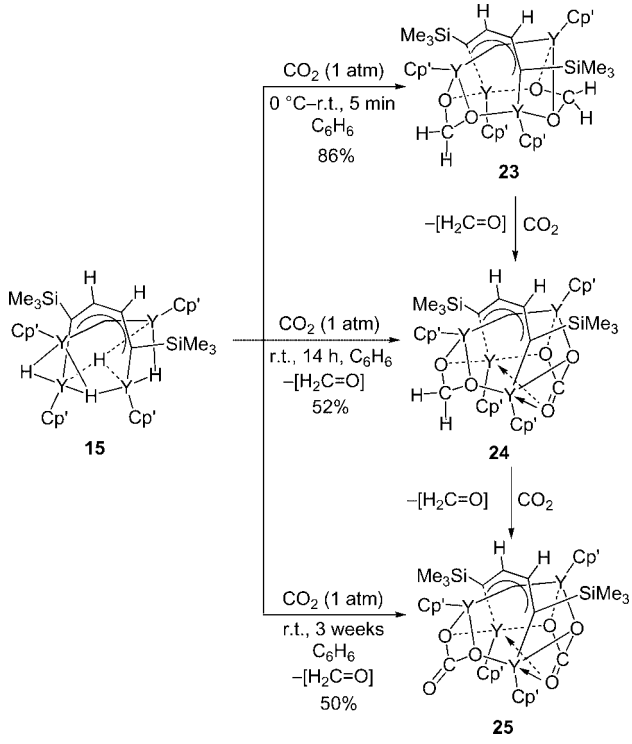


Scheme 11. Reduction of $CO_2$ into methylene diolate species and subsequent $CO_2$ insertion reactions. Cp′ = $C_5Me_4SiMe_3$.

 © 2007 Wiley-VCH Verlag GmbH & Co. KGaA, Weinheim 

To see how complex **15** would behave toward an isocyanate, which is a commonly accepted model for $CO_2$ with respect to reaction patterns,[23] the reactions of **15** with aryl isocyanates have been studied.[17] When **15** was allowed to react with two equivalents of phenyl isocyanate or 1-naphthyl isocyanate, the dioxo complex **26** was formed together with the corresponding aromatic imine compounds, probably via the bis(methylene olate/amido) intermediate **I** (Scheme 12). Exposure of the di-$\mu_3$-oxo complex **26** to an atmosphere of $CO_2$ at room temperature led to immediate formation of the dicarbonate complex **25** (Scheme 12). Although formation of metal oxo complexes, such as $[\{Cp_2ZrCl\}_2(\mu\text{-}O)]$,[24] $[\{Cp_2Zr(\mu\text{-}O)\}_3]$,[25] and $[\{(C_5H_4SiMe_3)_3U\}_2(\mu\text{-}O)]$,[26] has been observed in various $CO_2$ reduction reactions, the insertion of $CO_2$ into such a metal oxo species has not been reported previously. The present reaction of **26** with $CO_2$ may provide, at a molecular level, a nice piece of evidence for interactions of $CO_2$ with metal oxides.[27]

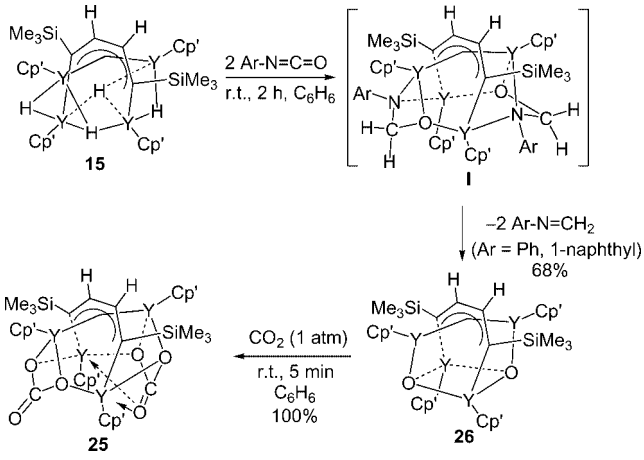


Scheme 12. Formation of a $\mu_3$-oxo yttrium complex and its reaction with $CO_2$. Cp′ = $C_5Me_4SiMe_3$.

Polyhydride complexes such as **2**, **6**, and **9** can also act as single-component catalysts for the ring-opening homopolymerization of cyclohexene oxide (CHO) and the alternating copolymerization of CHO and $CO_2$. The homopolymerization of CHO in bulk takes place much more rapidly than in solution and affords the corresponding polyethers [$M_n = (60\text{–}80) \times 10^3$ and $M_w/M_n \approx 2$] in high yields in most cases. The copolymerization of CHO and $CO_2$ at 70–110 °C under 12 atm of $CO_2$ yields the corresponding polycarbonates [$M_n = (20\text{–}40) \times 10^3$, $M_w/M_n = 4\text{–}5$; carbonate linkages = 95–99%] with a TOF of up to 2000 g polymer/(mol Ln h)$^{-1}$ (Scheme 13).[28] The first step in the copolymerization could be the formation of a methylene diolate species by insertion of one molecule of $CO_2$ into two Ln–H bonds.

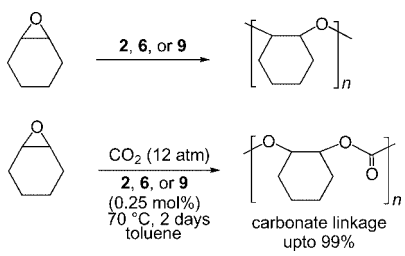


Scheme 13. Homopolymerization of cyclohexene oxide (CHO) and copolymerization of CHO with $CO_2$.

## 5. Reaction of Rare Earth Metal Polyhydrides with Nitriles

The reaction of the yttrium or lutetium octahydride complex (**2**, **9**) with four equivalents of benzonitrile or acetonitrile affords the corresponding tetranuclear cubane-like imido complexes $[\{(C_5Me_4SiMe_3)Ln(\mu_3\text{-}NCH_2Ph)\}_4]$ (Ln = Y (**27**), Lu (**28**)] or $[\{(C_5Me_4SiMe_3)Y(\mu_3\text{-}NCH_2Ph)\}_4]$ (**29**), respectively (Scheme 14).[8] The solid-state structure of the yttrium complex **27** is shown in Figure 3. In these reactions, the C–N triple bond of a nitrile compound is completely reduced to a C–N single bond by double Ln–H addition. This is in sharp contrast to the previously reported reactions of rare earth metallocene hydride complexes[29] or zirconocene dihydride complexes[30] with nitriles, which yielded only single-insertion products such as $[\{(C_5H_5)_2Y(\mu\text{-}N{=}CH\textit{t}Bu)\}_2]$ or $[(C_5Me_5)_2Zr(H)(N{=}CHR)]$ (R = $C_6H_4Me$-*p*). The reaction of polyhydrido rare earth metal complexes with nitriles may offer a convenient salt-free route to the corresponding rare earth metal imido complexes, a class of compounds that are of considerable current interest but still remain very limited in number.[31]

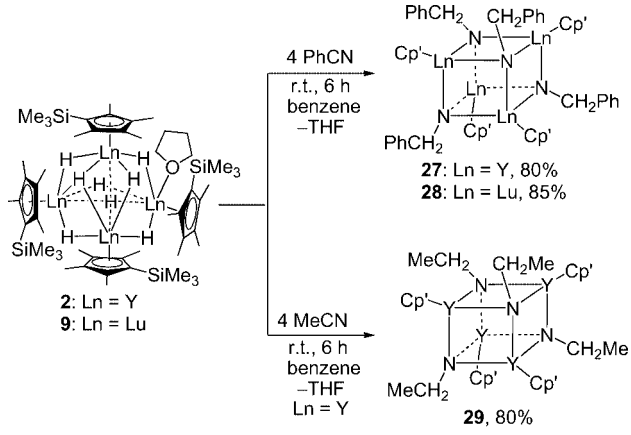


Scheme 14. Formation of cubane-type imido complexes by reduction of nitriles. Cp′ = $C_5Me_4SiMe_3$.

Further reactions of the rare earth metal imido complexes with nitriles can also take place. The reaction of the benzylimidolutetium complex $[\{(C_5Me_4SiMe_3)Lu(\mu_3\text{-}NCH_2Ph)\}_4]$ (**28**) with four equivalents of benzonitrile at room temperature, for instance, gives the benzamidinate-dianion complex **30** (Scheme 15).[32] An X-ray analysis showed that **30** possesses a dimeric structure in which the two Lu atoms are bridged by the ketimido nitrogen atom and the amido nitrogen atom is bonded terminally to one Lu atom. The formation of **30** apparently proceeds by nucleophilic addition of the imido unit in **28** to the CN group of benzonitrile, which demonstrates that a rare earth metal imido bond, even in a bridging form, is very reactive. This

 © 2007 Wiley-VCH Verlag GmbH & Co. KGaA, Weinheim 

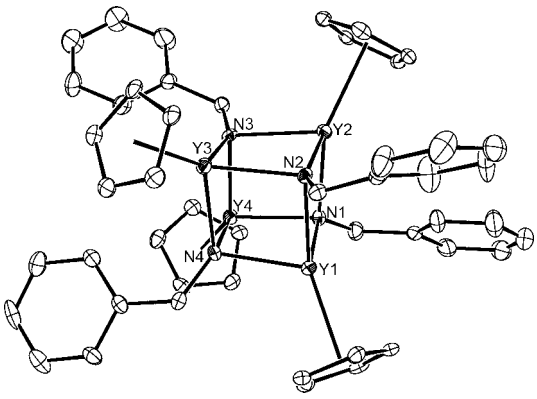


Figure 3. ORTEP drawing of **27**. The $Me_3Si$ and Me groups in $C_5Me_4SiMe_3$ have been omitted for clarity.

contrasts with what was observed previously for transition metal imido bridging bonds, which are usually robust and unreactive.[33]

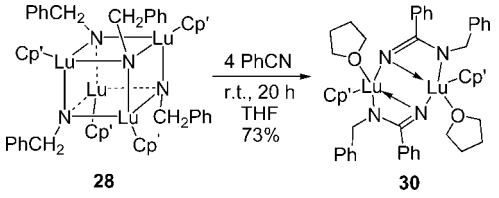


Scheme 15. Nucleophilic addition of an imido complex to benzonitrile. Cp′ = $C_5Me_4SiMe_3$.

In sharp contrast to the above-mentioned nucleophilic addition reaction of the benzylimido complex **28**, the reaction of the ethylimido complex [{$(C_5Me_4SiMe_3)Y(\mu_3$-$NCH_2CH_3)$}$_4$] (**29**) with benzonitrile gives the mixed benzaldimido/ethylimido complex **31** rather than an insertion product (Scheme 16). An X-ray analysis established that **31** adopts a tetranuclear crown-like core structure in which the four Y atoms are unsymmetrically bridged by four $\mu_2$-benzaldimido and two $\mu_3$-ethylimido ligands. Four molecules of benzonitrile are hydrogenated in this reaction to give four benzaldimido species (PhCH=N$^-$) by abstraction of four methylene hydrogen atoms from two of the four ethylimido units ($CH_3CH_2N^{2-}$) in **29** with the release of two molecules of acetonitrile ($CH_3CN$); the other two ethylimido units remain unchanged (Scheme 16). This formation of an aldimido species through hydrogen transfer from an alkyl imido species to a nitrile compound is, as far as we are aware, unprecedented.

The reaction of 10 equivalents of benzonitrile with the benzylimido complexes **27** or **28** gives the benzonitrile tetramerization products **32** or **33**, respectively (Scheme 17). The reaction of the benzamidinate-dianion complex **30** with three equivalents of benzonitrile also affords **33** in high yield. These results suggest that **30** should be an intermediate in the formation of **33** from **28**. The reaction of the polyhydride complex **2** with 14 equivalents of benzonitrile also affords **32**. A possible reaction mechanism for the formation of the benzonitrile tetramerization product **32** or **33** is shown in Scheme 18. The coordination of one molecule of benzonitrile to each metal atom in **30** should yield **M**. Hydrogen transfer from a methylene group to a coordinated PhCN in **M** (path *a*) should then afford **N**. Nucleophilic addition of the newly formed benzaldimido unit to the aldimine group (path *b*) could yield **O**, which gives **P** upon coordination of one molecule of PhCN. Migration of the

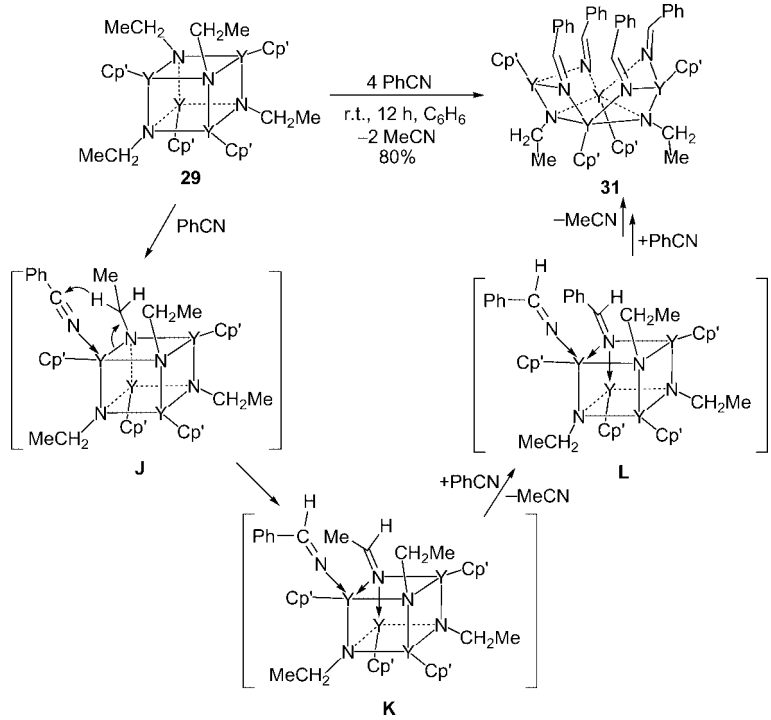


Scheme 16. Unique hydrogen transfer from ethyl imido species to benzonitrile. Cp′ = $C_5Me_4SiMe_3$.

 © 2007 Wiley-VCH Verlag GmbH & Co. KGaA, Weinheim 

methine hydrogen to the PhCN unit in **P** (path *c*), followed by addition of the resulting aldimido unit to the aldimine group in the resultant **Q** (path *d*), should give **33**.

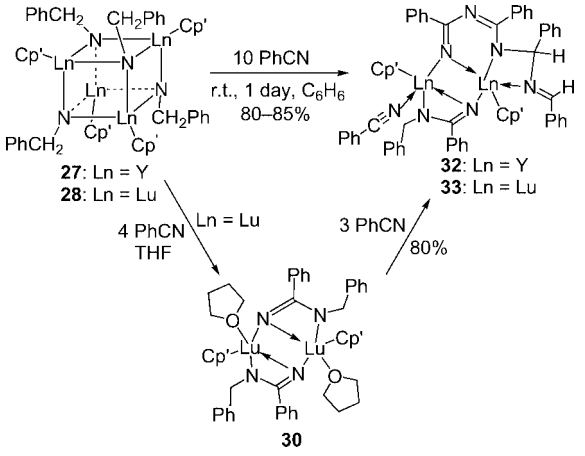


Scheme 17. Tetramerization of benzonitrile. Cp′ = $C_5Me_4SiMe_3$.

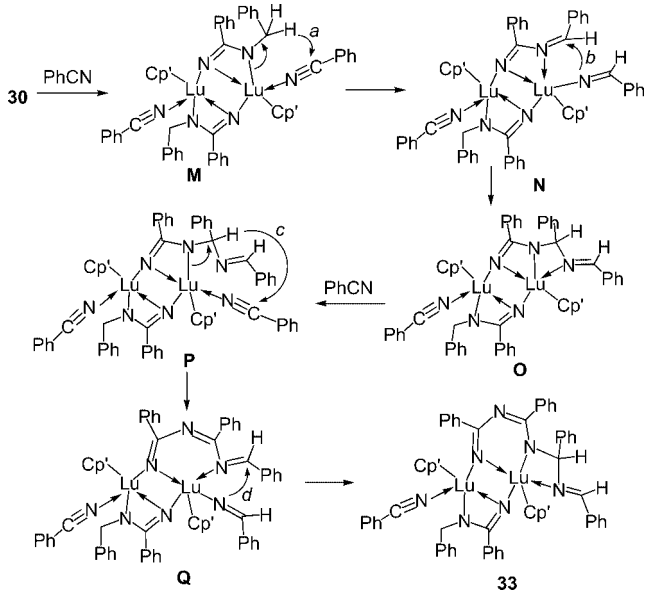


Scheme 18. Possible mechanism for the formation of **33**. Cp′ = $C_5Me_4SiMe_3$.

When an excess amount of benzonitrile was added to a toluene solution of **32** or **33**, the benzonitrile-cyclotrimerization product, namely triphenyl triazine $(PhCN)_3$, is formed selectively (Scheme 19).[32] The recovery of **32** or **33** from these reactions confirms that these benzonitrile-tetramerized complexes are true catalysts. The polyhydride complexes **2** and **9**, the imido complexes **27** and **28**, and the benzamidinate-dianion complex **30** are also active for the catalytic trimerization of benzonitrile. A possible mechanism for the catalytic cyclotrimerization of benzonitrile by **32** or **33** is shown in Scheme 20. The coordination of one molecule of benzonitrile to a metal center in **32** (or **33**) could give **R**, and methine hydrogen transfer (step *e*) to coordinated benzonitrile would afford **S**. Subsequent intramolecular nucleophilic addition of the ketimido unit to the newly formed imine moiety (step *f*) could give **T**, and aromatization of the resultant six-membered ring in **T** (step *g*, Ln–N bond cleavage and C=N bond formation and step *h*, C–N bond cleavage and Ln–N bond formation) should release the triazine and generate **U**. Insertion of benzonitrile into **U** would then give **V**, which resembles intermediate **N** in Scheme 18 and could regenerate **32** (or **33**) as described above. Thus, the combination of C–N bond formation, hydrogen transfer, and C–N bond cleavage steps constitutes a unique catalytic cycle for the cyclotrimerization of benzonitrile.[34]

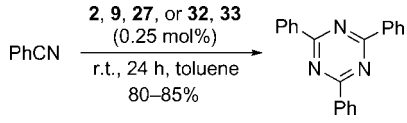


Scheme 19. Catalytic cyclotrimerization of benzonitrile. Cp′ = $C_5Me_4SiMe_3$.

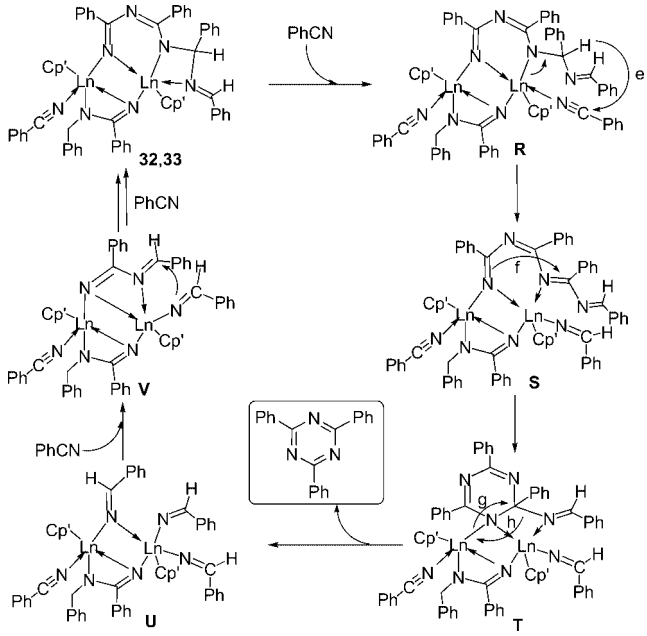


Scheme 20. A possible mechanism for the catalytic cyclotrimerization of benzonitrile. Cp′ = $C_5Me_4SiMe_3$.

## 6. Cationic Rare Earth Metal Polyhydride Complexes

In contrast to cationic rare earth metal alkyl complexes, which have received much interest as novel polymerization catalysts,[35,36] cationic hydrido rare earth metal complexes remain almost unexplored. It has recently been found that tetranuclear rare earth metal octahydride complexes such as **1**–**7** and **9**–**12** are suitable precursors for the preparation of cationic hydrido rare earth metal species.[9] For example, the reactions of the yttrium octahydride complexes **2**, **11**, and **12** with one equivalent of $[Ph_3C][B(C_6F_5)_4]$ afford the corresponding cationic heptahydride complexes **35**, **36**, and **34**, respectively, in high yields (Scheme 21). An direct bonding interaction between the $[(C_5Me_4SiMe_3)_4Y_4H_7]^+$ cation and

 © 2007 Wiley-VCH Verlag GmbH & Co. KGaA, Weinheim 

the $[B(C_6F_5)_4]^-$ anion via a Y–F bond is observed in the THF-free complex **34**, while complexes **35** and **36** are solvent (THF)-separated ion pairs. The X-ray structures of **34** and **36** are shown in Figures 4 and 5, respectively. These complexes are the first examples of well-defined cationic hydrido rare earth metal complexes.

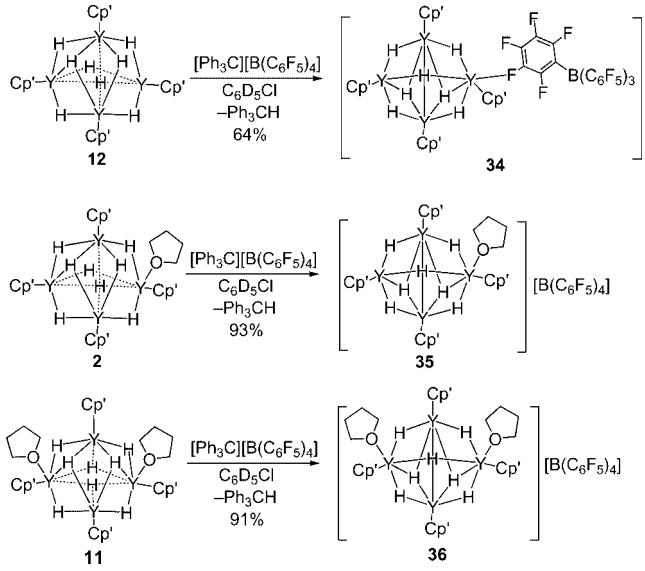


Scheme 21. Synthesis of cationic yttrium polyhydride complexes. Cp′ = $C_5Me_4SiMe_3$.

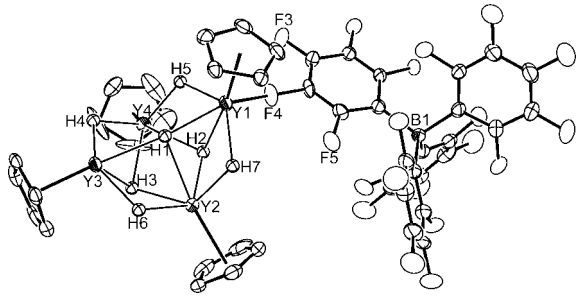


Figure 4. ORTEP drawing of **34**. The $Me_3Si$ and Me groups in $C_5Me_4SiMe_3$ have been omitted for clarity.

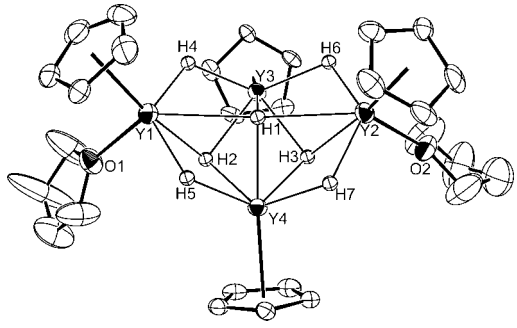


Figure 5. ORTEP drawing of **36**. The $Me_3Si$ and Me groups in $C_5Me_4SiMe_3$ and the $[B(C_6F_5)_4]$ ion have been omitted for clarity.

In contrast to the neutral hydride cluster **2**, which yields a single Y–H addition product **13** or **14** on reaction with styrene or 1,3-cyclohexadiene (CHD), respectively, as described above, the THF-free or mono(THF)-coordinated cationic hydride clusters such as **34** or **35** (either isolated or generated in situ) are active catalysts for the syndiospecific polymerization of styrene and the regio- and stereoselective *cis*-1,4-polymerization of CHD (Scheme 22).[9] The bis(THF)-coordinated cationic complex **36**, however, is not catalytically activity under the same conditions, probably due to the occupation of the active metal centers by two strongly coordinative THF ligands.

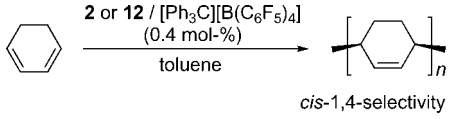


Scheme 22. *cis*-1,4-Selective polymerization of 1,3-cyclohexadiene by cationic yttrium polyhydride complexes.

## 7. Conclusion and Perspective

Hydrogenolysis of the bisalkyl complexes $[(C_5Me_4SiMe_3)Ln(CH_2SiMe_3)_2(THF)]$ leads to the formation of a series of structurally characterizable polyhydrido polynuclear rare earth metal complexes. These polyhydride complexes show a unique reactivity towards various substrates, such as hydrogenation of the C–N triple bond of a nitrile compound into a C–N single bond, reduction of carbon dioxide into a methylene diolate species, and deoxygenative C–C coupling of CO into ethylene. These reactions are in sharp contrast with what has been observed for the analogous monohydrido metallocene complexes. A new class of polynuclear rare earth metal complexes, such as cubane-type imido and oxo complexes, has also been derived from the polyhydride complexes. Abstraction of a hydride ligand from the neutral hydride clusters leads to the formation of structurally characterizable cationic polyhydrido rare earth metal complexes.

It should also be noted, however, that the synthesis and reactivity studies of polyhydrido rare earth metal complexes is still in its infancy, and well defined polyhydrido rare earth metal complexes reported in the literature are limited essentially to those bearing a $C_5Me_4SiMe_3$ ligand. As the expertise in this field increases and more complexes with new ligand systems are prepared,[37] the diverse chemistry of polyhydrido rare earth metal complexes will certainly be further extended. An exciting and prosperous future in this area can therefore be expected.

[1] Selected reviews on d-block transition metal hydride complexes: a) G. S. McGrady, G. Guilera, *Chem. Soc. Rev.* **2003**, *32*, 383–392; b) H. Suzuki, *Eur. J. Inorg. Chem.* **2002**, 1009–1023; c) F. Maseras, A. Lledós, E. Clot, O. Eisenstein, *Chem. Rev.* **2000**, *100*, 601–636; d) S. Sabo-Etienne, B. Chaudret, *Chem. Rev.* **1998**, *98*, 2077–2092; e) R. Bau, M. H. Drabnis, *Inorg. Chim. Acta* **1997**, *259*, 27–50; f) Z. Lin, M. B. Hall, *Coord. Chem. Rev.* **1994**, *135/136*, 845–879; g) R. H. Crabtree, in *Comprehensive Coordination Chemistry* (Eds.: G. Wilkinson, R. D. Gillard, J. A. McCleverty), Pergamon, Oxford, **1987**, vol. 2, p. 689; h) G. G. Hlatky, R. H. Crabtree, *Coord. Chem. Rev.*

 © 2007 Wiley-VCH Verlag GmbH & Co. KGaA, Weinheim 

**1985**, *65*, 1–48; i) L. M. Venanzi, *Coord. Chem. Rev.* **1982**, *43*, 251–274.
[2] Selected reviews on rare earth metal hydride complexes: a) Z. Hou, *Bull. Chem. Soc. Jpn.* **2003**, *76*, 2253–2266; b) J. Okuda, *Dalton Trans.* **2003**, 2367–2378; c) S. Arndt, J. Okuda, *Chem. Rev.* **2002**, *102*, 1953–1976; d) G. A. Molander, J. A. C. Romero, *Chem. Rev.* **2002**, *102*, 2161–2186; e) Z. Hou, Y. Wakatsuki, *Coord. Chem. Rev.* **2002**, *231*, 1–22; f) Z. Hou, Y. Wakatsuki, in *Science of Synthesis* (Eds.: T. Imamoto, R. Noyori), Thieme, Stuttgart, **2002**, vol. 2, p. 849–942; g) A. J. Hoskin, D. W. Stephan, *Coord. Chem. Rev.* **2002**, *233–234*, 107–129; h) M. Ephritikhine, *Chem. Rev.* **1997**, *97*, 2193–2242; i) H. Schumann, J. A. Meese-Marktscheffel, L. Esser, *Chem. Rev.* **1995**, *95*, 865–986; j) F. T. Edelmann, in *Comprehensive Organometallic Chemistry II* (Eds.: E. W. Abel, F. G. A. Stone, G. Wilkinson, M. F. Lappert), Pergamon, Oxford, **1995**, vol. 4, p. 11–212; k) C. J. Schaverien, *Adv. Organomet. Chem.* **1994**, *36*, 283–362.
[3] W. J. Evans, J. H. Meadows, A. L. Wayda, W. E. Hunter, J. L. Atwood, *J. Am. Chem. Soc.* **1982**, *104*, 2008–2014.
[4] H. van der Heijden, P. Pasman, E. J. M. de Boer, C. J. Schaverien, *Organometallics* **1989**, *8*, 1459–1467.
[5] K. C. Hultzsch, T. P. Spaniol, J. Okuda, *Angew. Chem. Int. Ed.* **1999**, *38*, 227–230.
[6] a) Z. Hou, Y. Zhang, O. Tardif, Y. Wakatsuki, *J. Am. Chem. Soc.* **2001**, *123*, 9216–9217; b) Z. Hou, Y. Zhang, M. Nishiura, Y. Wakatsuki, *Organometallics* **2003**, *22*, 129–135.
[7] M. Nishiura, J. Baldamus, T. Shima, Z. Hou, manuscript in preparation.
[8] D. Cui, O. Tardif, Z. Hou, *J. Am. Chem. Soc.* **2004**, *126*, 1312–1313.
[9] X. Li, J. Baldamus, M. Nishiura, O. Tardif, Z. Hou, *Angew. Chem. Int. Ed.* **2006**, *45*, 8184–8188.
[10] R. D. Shannon, *Acta Crystallogr., Sect. A* **1976**, *32*, 751–767.
[11] A mixture of trinuclear and tetranuclear polyhydride complexes was obtained (M. Nishiura, J. Baldamus, T. Shima, Z. Hou, unpublished results).
[12] O. Tardif, M. Nishiura, Z. Hou, *Organometallics* **2003**, *22*, 1171–1173.
[13] K. C. Hultzsch, P. Voth, T. P. Spaniol, J. Okuda, *Z. Anorg. Allg. Chem.* **2003**, *629*, 1272–1276.
[14] Y. Luo, J. Baldamus, O. Tardif, Z. Hou, *Organometallics* **2005**, *24*, 4362–4366.
[15] T. Shima, Z. Hou, *J. Am. Chem. Soc.* **2006**, *128*, 8124–8125.
[16] For examples, see: a) T. Matsuo, H. Kawaguchi, *J. Am. Chem. Soc.* **2005**, *127*, 17198–17199; b) W. J. Evans, J. W. Grate, R. J. Doedens, *J. Am. Chem. Soc.* **1985**, *107*, 1671–1679; c) K. G. Moloy, T. J. Marks, *J. Am. Chem. Soc.* **1984**, *106*, 7051–7064; d) S. Gambarotta, C. Floriani, A. Chiesi-Villa, C. Guastini, *J. Am. Chem. Soc.* **1983**, *105*, 1690–1691; e) D. A. Katahira, K. G. Moloy, T. J. Marks, *Organometallics* **1982**, *1*, 1723–1726; f) P. J. Fagan, K. G. Moloy, T. J. Marks, *J. Am. Chem. Soc.* **1981**, *103*, 6959–6962; g) P. T. Wolczanski, R. S. Threlkel, J. E. Bercaw, *J. Am. Chem. Soc.* **1979**, *101*, 218–220; h) J. M. Manriquez, D. R. McAlister, R. D. Sanner, J. E. Bercaw, *J. Am. Chem. Soc.* **1978**, *100*, 2716–2724.
[17] O. Tardif, D. Hashizume, Z. Hou, *J. Am. Chem. Soc.* **2004**, *126*, 8080–8081.
[18] a) N. E. Schlörer, S. Berger, *Organometallics* **2001**, *20*, 1703–1704; b) N. E. Schlörer, E. J. Cabrita, S. Berger, *Angew. Chem. Int. Ed.* **2002**, *41*, 107–109; c) J. C. Berthet, M. Ephritikhine, *New J. Chem.* **1992**, *16*, 767–768; d) A. Cutler, M. Raja, A. Todaro, *Inorg. Chem.* **1987**, *26*, 2877–2881.
[19] J. Ni, Y. Qiu, T. M. Cox, C. A. Jones, C. Berry, L. Melon, S. Bott, *Organometallics* **1996**, *15*, 4669–4671.
[20] T. A. Hanna, A. M. Baranger, R. G. Bergman, *J. Am. Chem. Soc.* **1995**, *117*, 11363–11364.
[21] M. K. Whittlesey, R. N. Perutz, M. H. Moore, *Organometallics* **1996**, *15*, 5166–5169.
[22] L. K. Fong, J. R. Fox, N. J. Cooper, *Organometallics* **1987**, *6*, 223–231.
[23] P. Braunstein, D. Nobel, *Chem. Rev.* **1989**, *89*, 1927–1945.
[24] a) N. E. Schlörer, E. J. Cabrita, S. Berger, *Angew. Chem. Int. Ed.* **2002**, *41*, 107–109; b) N. E. Schlörer, S. Berger, *Organometallics* **2001**, *20*, 1703–1704; c) A. Cutler, M. Raja, A. Todaro, *Inorg. Chem.* **1987**, *26*, 2877–2881; d) S. Gambarotta, S. Strologo, C. Floriani, A. Chiesi-Villa, C. Guastini, *J. Am. Chem. Soc.* **1985**, *107*, 6278–6282; e) G. Fachinetti, C. Floriani, A. Roselli, S. Pucci, *J. Chem. Soc., Chem. Commun.* **1978**, 269–270.
[25] G. Fachinetti, C. Floriani, A. Chiesi-Villa, C. Guastini, *J. Am. Chem. Soc.* **1979**, *101*, 1767–1775.
[26] J. C. Berthet, M. Ephritikhine, *New J. Chem.* **1992**, *16*, 767–768.
[27] a) I. A. Fisher, A. T. Bell, *J. Catal.* **1997**, *172*, 222–237; b) J. C. J. Bart, R. P. A. Sneeden, *Catal. Today* **1987**, *2*, 1–124; c) J. B. Peri, *J. Phys. Chem.* **1966**, *70*, 3168–3179; d) N. D. Parkyns, *J. Chem. Soc. A* **1969**, 410–417; e) L. Fan, K. Fujimoto, *J. Catal.* **1997**, *172*, 238–242.
[28] D. Cui, M. Nishiura, Z. Hou, *Macromolecules* **2005**, *38*, 4089–4095.
[29] W. J. Evans, J. H. Meadows, W. E. Hunter, J. L. Atwood, *J. Am. Chem. Soc.* **1984**, *106*, 1291–1300.
[30] J. E. Bercaw, D. L. Davies, P. T. Wolczanski, *Organometallics* **1986**, *5*, 443–450.
[31] a) H.-S. Chan, H.-W. Li, Z. Xie, *Chem. Commun.* **2002**, 652–653; b) J. C. Gordon, G. R. Giesbrecht, D. L. Clark, P. J. Hay, D. W. Keogh, R. Poli, B. L. Scott, J. G. Watkin, *Organometallics* **2002**, *21*, 4726–4734; c) G. R. Giesbrecht, J. C. Gordon, *Dalton Trans.* **2004**, 2387–2393.
[32] D. Cui, M. Nishiura, Z. Hou, *Angew. Chem. Int. Ed.* **2005**, *44*, 959–962.
[33] a) J. R. Fulton, T. A. Hanna, R. G. Bergman, *Organometallics* **2000**, *19*, 602–614; b) D. A. Dobbs, R. G. Bergman, *Organometallics* **1994**, *13*, 4594–4605; c) S. Takemoto, T. Kobayashi, H. Matsuzaka, *J. Am. Chem. Soc.* **2004**, *126*, 10802–10803; d) J.-S. Song, S.-H. Han, S. T. Nguyen, G. L. Geoffroy, *Organometallics* **1990**, *9*, 2386–2395.
[34] Although benzonitrile cyclotrimerization is known, the mechanistic aspects of this process are not well understood. For examples, see: a) J. H. Forsberg, V. T. Spaziano, T. M. Balasubramanian, G. K. Liu, S. A. Kinsley, C. A. Duckworth, J. J. Poteruca, P. S. Brown, J. L. Miller, *J. Org. Chem.* **1987**, *52*, 1017–1021; b) F. Xu, J. H. Sun, H. B. Yan, Q. Shen, *Synth. Commun.* **2000**, *30*, 1017–1022.
[35] Selected reviews on cationic rare earth metal alkyl complexes: a) P. M. Zeimentz, S. Arndt, B. R. Elvidge, J. Okuda, *Chem. Rev.* **2006**, *106*, 2404–2433; b) Z. Hou, Y. Luo, X. Li, *J. Organomet. Chem.* **2006**, *691*, 3114–3121; c) S. Arndt, J. Okuda, *Adv. Synth. Catal.* **2005**, *347*, 339–354; d) J. Gromada, J. F. Carpentier, A. Mortreux, *Coord. Chem. Rev.* **2004**, *248*, 397–410; e) W. E. Piers, D. J. H. Emslie, *Coord. Chem. Rev.* **2002**, *233–234*, 131–135; f) Z. Hou, Y. Wakatsuki, *Coord. Chem. Rev.* **2002**, *231*, 1–22.
[36] a) Y. Luo, J. Baldamus, Z. Hou, *J. Am. Chem. Soc.* **2004**, *126*, 13910–13911; b) X. Li, Z. Hou, *Macromolecules* **2005**, *38*, 6767–6769; c) X. Li, J. Baldamus, Z. Hou, *Angew. Chem. Int. Ed.* **2005**, *44*, 962–964; d) L. Zhang, Y. Luo, Z. Hou, *J. Am. Chem. Soc.* **2005**, *127*, 14562–14563; e) L. Zhang, T. Suzuki, Y. Luo, M. Nishiura, Z. Hou, *Angew. Chem. Int. Ed.* **2007**, *46*, 1909–1913.
[37] We recently found that the use of $C_5Me_5$ instead of $C_5Me_4SiMe_3$ as an ancillary ligand led to formation of the corresponding octahedral dodecahydride complexes (M. Nishiura, K. Mori, T. Mashiko, Z. Hou, unpublished results).

Received: January 23, 2007
Published Online: April 17, 2007

 © 2007 Wiley-VCH Verlag GmbH & Co. KGaA, Weinheim 

DOI: 10.1002/ejic.200700186

# From Genes to Metalloproteins: A Bioinformatic Approach

Ivano Bertini*[a] and Antonio Rosato[a]

**Keywords:** Iron / Zinc / Copper / Heme proteins / Metalloproteins / Bioinformatics

Genome sequencing projects have provided researchers with detailed information on every gene present in a large variety of organisms. Each of these genes is responsible for producing one or more proteins (depending on processes such as alternative splicing and post-translational modification) that constitute the machineries needed to sustain cellular life. The ensemble of proteins that an organism is capable of producing is called the proteome. A significant share of each organism's proteome requires metal ions or metal-containing cofactors to carry out its physiological function (metalloproteome). Experimental methods for the characterization of the metalloproteome of even simple prokaryotic organisms are still not routinely available, therefore significant insights can currently be only obtained using bioinformatic approaches. Herein we review the results obtained from the bioinformatic analyses of a variety of organisms, including humans, in which the distribution of iron-, copper-, and zinc-binding proteins across the kingdoms of life were investigated. It was found that among the metals, zinc is required by the largest number of proteins in most organisms (on average, 10 % of the proteome in eukaryota is predicted to be zinc-binding), whereas copper is the least common. In addition, the majority of non-heme iron-binding proteins have homologs in each taxonomic domain (archaea, bacteria, eukaryota), whereas zinc- and copper-binding proteins are substantially differentiated in eukaryota with respect to prokaryotic organisms.
(© Wiley-VCH Verlag GmbH & Co. KGaA, 69451 Weinheim, Germany, 2007)

## Introduction

The term bioinorganic chemistry (or biological inorganic chemistry or inorganic biochemistry) refers to the discipline in which the interactions between inorganic ions or complexes and molecules of biological interest are studied.[1] This is a vast field of science whose importance stems from the fact that life originated and developed on the Earth's crust, an eminently inorganic environment. A core part of bioinorganic chemistry is focused on the study of metalloproteins, which are defined as those proteins that bind tightly (with an association constant greater than $10^8$ $M^{-1}$) to one or more metal ions or metal-containing cofactors,

[a] Magnetic Resonance Center (CERM) and Department of Chemistry – University of Florence,
via L. Sacconi 6, 50019 Sesto Fiorentino, Italy
Fax: +39-055-457-4271
E-mail: ivanobertini@cerm.unifi.it

*Ivano Bertini (http://www.cerm.unifi.it/bertini.html) received his doctorate in chemistry from the University of Florence in 1964 and became full professor of Chemistry in 1975 at the same University. He is the Director of the Magnetic Resonance Center (CERM http://www.cerm.unifi.it/) of the University of Florence. His main research interests are NMR spectroscopy, the expression and preparation of metalloproteins, their structural characterization, and the investigation of their interactions with emphasis on understanding cellular processes at the molecular level. He has authored over 600 papers and many books. He received the Chugaev Diploma of the Kurnakov Institute of the Academy of Science, USSR, in 1981, the Golden Medal of the Magnetic Resonance Group of the Italian Chemical Society in 1991, the Prize Accademia dei Lincei, Italy in 1993, the Bijvoet Medal, Utrecht, NL, in 1998, the Sapio NMR Prize, Italy, in 1999, the Cannizzaro Medal of the Italian Chemical Society and the Basolo medal in 2006. Amongst the special lectures: A. D. Little Lecturer at MIT, Cambridge, MS, USA, in 1997, E. L. Mütterties Lecturer at Berkeley, CA, USA, in 1997, and FECS lecturer, Athens, Greece, in 2002. He has received three honorary doctorates and is a member of the Accademia Nazionale dei Lincei and of the Academia Europaea.*

*Antonio Rosato (http://www.cerm.unifi.it/rosato/) obtained his doctorate from the University of Florence (Italy) in 1998. He is now Associate Professor of Chemistry at the same University. His research interests focus on the theory and practice of NMR spectroscopy applied to paramagnetic systems, metal-mediated protein–protein interactions, and on the application and development of bioinformatic tools to browse gene banks and genome sequences, with a particular interest in metalloproteins. He has co-authored more than 60 articles in peer-reviewed journals.*

 © 2007 Wiley-VCH Verlag GmbH & Co. KGaA, Weinheim 

and of metal–protein adducts, which are defined as adducts formed by metal ions or metal-containing cofactors with proteins (with an association constant lower than $10^8$ $M^{-1}$). The metal may play a physiologically relevant role in both metalloproteins and metal–protein adducts. For simplicity, from here on we will collectively refer to "true" metalloproteins and metal–protein adducts as metalloproteins. From a more biologically oriented point of view, metalloproteins can be defined as those proteins requiring one or more metal ions or metal-containing cofactors to carry out their biological function. The two definitions overlap to a large extent. Note that the metal may be required not only because it is the center of catalysis, as in many metalloenzymes, but also for structural reasons (i.e. to stabilize the metalloprotein's fold) or regulatory ones (e.g. as in calmodulin).

In the early years of bioinorganic chemistry, the quantification of the interactions of metal ions with living organisms focused mainly on determining the quantity of metal present in a healthy organism per kilogram of weight (in the case of higher organisms such as mammals or plants) or per cell (in the case of unicellular organisms). These investigations provided valuable information on the importance of metal ions for the correct functioning of cells as well as on several diseases caused by defects in the metabolism of metal ions and metal-containing cofactors. The success of genome sequencing initiatives, however, has added a new dimension to bioinorganic chemistry, namely the quantification of *how many proteins are metalloproteins*. This aspect deals with identifying how many and which metabolic pathways require or involve metal ions in addition to establishing how much of a metal is needed to support the life of an organism. These two facets are highly complementary and are both essential in order for bioinorganic chemistry to fully contribute to the Life Sciences.

Genome sequencing projects have provided the amino acid sequences of proteins encoded in the genome (besides the possible effects of alternative splicing or of post-translational modifications, which contribute to effectively expanding the proteome) of an ever increasing number of organisms. The large majority of these proteins lack any experimental functional information, as functional characterization of proteins at the whole proteome level is still not routinely possible. To cope with this limitation, bioinformatic tools have been extensively exploited to predict functional features from the analysis of amino acid sequences.[2–5] In addition, projects in structural biology and structural genomics (the structural characterization of all proteins in a proteome) have prompted the development of several bioinformatic approaches to predict function from structure.[6–9] The functional information obtained either experimentally or through bioinformatics is generally summarized in an annotation, which is associated with the various individual proteins in any sequenced genome. The annotation of gene products is still, however, a far from trivial process. Predicting function from sequence, even when structural information is available,[10–12] often remains an elusive endeavor that is further complicated by difficulties in the exact identification of the coding sequence, especially in higher organisms.[13,14]

The concepts outlined in the preceding paragraph also apply to metalloproteins,[15] although these systems are even more challenging because metal-binding ability is not easily detected from standard sequence analysis. On the other hand, the presence of a motif suitable for protein binding to metal ion(s) can be exploited for more reliable identification and classification (including functional inferences) of these proteins.[15–18] Genome-wide identification and classification of metalloproteins is also difficult experimentally, although some systematic efforts in this direction have been described.[19–21] Since 2004, specific bioinformatic approaches have been developed, refined, and applied at the whole genome level to identify the fraction of an organism's proteome that (putatively) requires metal ions for its function, in other words to identify all metalloproteins encoded by an organism's genome.[18,22–24] The ensemble of the metalloproteins of an organism is hereafter called the *metalloproteome*. Herein we review the results of these efforts and provide an overview of the use of different essential metal ions by organisms in the three domains of life, including humans.

## On the Reasons Why Identifying Metal-Binding Sites is Difficult

Metal ions can bind to metalloproteins at a variety of different sites. However, the specificity of a metal-binding site for a metal may be poor as the same site can often bind different metal ions with similar affinities (the physiologically relevant metal ion may sometimes actually not be the tightest binder), a phenomenon that has allowed researchers to obtain structural details of metal-binding sites through a combination of spectroscopic tools and metal replacement.[25,26] This can also be true for polymetallic cofactors such as iron-sulfur clusters.[27] When preference for a given metal ion indeed occurs at a binding site, it can be tuned through site-directed mutagenesis, typically by substituting one or two protein residues.[28]

Even when 3D data are available from X-ray crystallography, the identification of the presence of a metal-binding site or the identification of the metal bound at a site is often far from trivial.[29,30] There have been several examinations of the whole protein data bank (PDB) in order to identify, classify, and attempt to devise general rules for confirming the presence of metal-binding sites.[31–34] However, these efforts have not provided guidelines that can be applied safely and systematically, even with structural data in hand. When the protein structure is solved in its apo form, a further obstacle to the prediction of the presence of a metal-binding site may arise because of structural rearrangements between the apo and holo forms of the protein, especially, but not exclusively, those involving the side chain atoms of the amino acidic metal ligands.[35]

 © 2007 Wiley-VCH Verlag GmbH & Co. KGaA, Weinheim 

X-ray fluorescence analysis is a suitable strategy to experimentally identify the nature of an unknown metal ion bound to a protein.[36] Another suitable approach is the study of X-ray anomalous diffraction.[37] NMR analysis can also be informative.[38] The exact details of metal coordination can often be obtained upon substitution of the metal with a paramagnetic metal ion through the application of purposefully designed NMR experiments[39,40] and/or of advanced computational approaches.[41] Alternatively, NMR-active diamagnetic metals, such as Ag, Cd, or Hg, can be exploited to directly detect proton–metal correlations in heteronuclear two-dimensional experiments.[42–45]

Another possible approach to the identification of metalloproteins is high-throughput screening.[19–21] These methods, which are based on XAS or colorimetry, can identify unprecedented metalloproteins and provide hints about the identity of the bound metal. They do not, however, provide detailed information on the nature, identity, and location of amino acidic ligands within the protein sequence.

## Sequence-Based Bioinformatic Identification of Metalloproteins

Because of the difficulties mentioned in the preceding section, it is important to develop methods that can predict metal-binding capabilities and metal-binding sites based only on the experimental information directly obtainable from genome sequencing, namely the amino acid sequence of the proteins. In other words, the scientific community working in bioinorganic chemistry would benefit from bioinformatic tools that can identify metalloproteins within proteomes.

Bioinformatic resources designed for bioinorganic chemists are relatively limited with respect to the plethora of resources available to the general biologists' community.[15] In particular, no web servers are currently available for the prediction of metal-binding capabilities based on protein sequence. On the other hand, a few algorithms suitable for the identification of metalloproteins in proteomes have been published; these are addressed below.

Before discussing the methods available for the prediction of metal-binding properties based on sequence, it is useful to briefly describe the application to metalloproteins of protein structure modeling based on homology (so-called homology modeling or comparative modeling).[46,47] Homology modeling has been applied to metalloproteins with success in a number of instances, yielding interesting insights into the determinants of structure and function of the systems investigated.[16,48–58] If one is uncertain about the metal-binding properties of a given protein, homology modeling is a potential method for building a 3D structural model that may subsequently be inspected for the presence of putative metal-binding sites. This approach, however, presents various potential pitfalls, some of which are linked to the intrinsic shortcomings of the homology modeling approach, such as the difficulty in correctly modeling the conformation of amino acid side-chains and loop regions,[46] where metal-binding sites are often located. However, it has been suggested that, especially in systems binding metal-containing cofactors of a relatively large size, such as iron-sulfur clusters or iron porphyrins, modeling of a metalloprotein structure in its apo form can lead to significant distortions of even the global protein fold with respect to the structure of the holo protein.[16,48] Such distortions would prevent reliable use of the modeled structure for the identification of binding sites.

The simplest approach to assigning metal-binding capabilities to a protein is to look for the presence of a known metal-binding pattern (MBP). MBPs can be automatically extracted from the PDB and can be described in detail using the COMe formalism.[17] Simpler formalisms essentially report the identity of ligands, the spacing between them, and, sometimes, the presence of other conserved residues within or near the MBP. The simplest representation of an MBP is in the format $AX_nBX_mC$..., where A, B, and C are the metal-binding amino acids and $n$, $m$,... are the number of amino acid residues in between two subsequent ligands. A non-specialized database of functional patterns is PROSITE.[59] However, simply looking for the occurrence of an MBP within a sequence can be misleading[18] and may lead to the assignment of an excessively high number of metalloproteins. A simple example is given by the case of proteins that bind metals with pairs of cysteines, which in many systems are involved in the formation of disulfide bridges rather than in metal binding. Based on the presence of cysteine pairs (with a given spacing), these proteins would be erroneously assigned as metalloproteins (note that in fact they may be able to bind metals in vitro in their reduced state). A more refined, less error-prone approach takes into account the presence of local sequence similarity around the MBP[18] with respect to a known metalloprotein. The presence of local sequence similarity is indicative of local structural similarity, which implies similar conformation for the amino acidic ligands of the MBP and thus formation of the metal-binding site.[18] The main weakness of this approach lies in the detection of metalloproteins containing an MBP site where the spacing between ligands is very large. As an example, consider a case where two ligands are close to one another, say within five amino acids, a third one is 30 amino acids away, and a fourth one is another 30 amino acids away; these types of situations are relatively easy to overlook. To enhance sensitivity and reliability, the analysis of MBPs can be successfully complemented by analyzing the occurrence of protein domains known to be metal-binding taken from domain libraries such as Pfam[60] or SCOP.[61] In the case of human zinc-binding proteins, it has been shown that these two approaches independently provide metal-binding predictions that are in good agreement with one another, and at the same time their combination enhances coverage in terms of zinc-binding proteins detected.[22] The combined use of MBPs and protein domains for metalloprotein identification is also useful in the reduction of the number of false positives (i.e. of non-metalloproteins that are erroneously

 © 2007 Wiley-VCH Verlag GmbH & Co. KGaA, Weinheim 

assigned as metalloproteins).[23,24] The use of only metal-binding protein domains does not provide the same benefits.

Alternatively, machine learning methods have shown better performance than an approach based on the simple detection of the occurrence of an MBP within a sequence.[62] These methods can provide indications at the level of an individual cysteine or histidine residue and predict whether it is bound to a metal or not. Metalloproteins are identified as proteins containing one or more metal-bound cysteines or histidines.[62] Although this approach may be promising, especially because it may identify unprecedented MBPs, significant improvement is still needed, especially as other amino acids (aspartic acid, glutamic acid, tyrosine, etc.) must be taken into account as possible ligands.

It must be remembered that the performance of any predictive method depends not only on the quality and ingenuity of the underlying algorithm(s) but also on the quality and amount of experimental data available to perfect the computational approach. Figure 1 shows the number of predictions for zinc-binding proteins based on the approach described by Andreini et al.,[18] which is based solely on structural information available from the PDB, as a function of the number of structures of zinc proteins available. It can clearly be seen that a dramatic increase in the number of predicted human zinc proteins occurs after a "critical mass" of available structures is reached. However, the subsequent growth of the number of structures of zinc proteins in the PDB that occurred after the mid-90s yielded only a relatively small additional increase in the number of predicted zinc-binding proteins (a 10-fold increase in structures corresponds to slightly less than a twofold increase in predicted sequences). This is presumably a consequence of the relatively low structural diversity additionally contained in the newest structures.

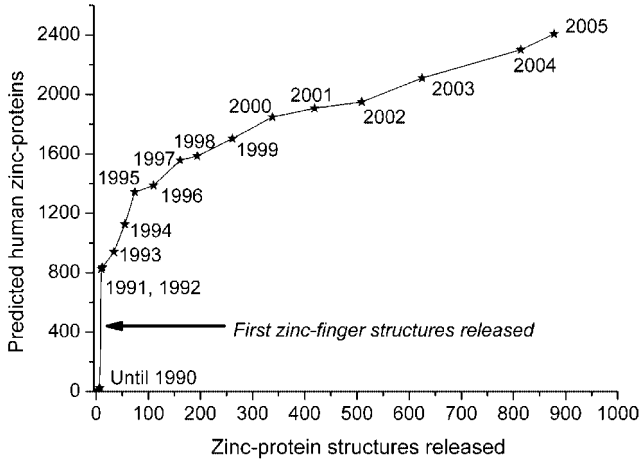


Figure 1. Number of human zinc proteins predicted as a function of the number of experimental zinc protein structures available from the PDB. The abscissa of each point corresponds to the number of structures availble at the end of the indicated year.

## The Metalloproteomes

### The Zinc Metalloproteome

Zinc-binding proteins are found in essentially all organisms[24] and are quite abundant in eukaryotic organisms such as humans.[22] Zinc-binding patterns most commonly include four (70% of instances in the PDB) or three (23% of instances in the PDB) protein ligands (not distinguishing between mono- and bidentate carboxylate ligands). In zinc-binding patterns with three protein ligands, the metal ion often completes its first coordination sphere by binding a water or buffer molecule. The most common amino acidic ligands for zinc are cysteine and histidine: 68% of the patterns contain at least one cysteine while 65% contain at least one histidine. Figure 2 shows a distribution of the various types of zinc-binding patterns grouped on the basis of the number, identity, and order in sequence of protein ligands, in predicted human zinc-binding proteins.[22]

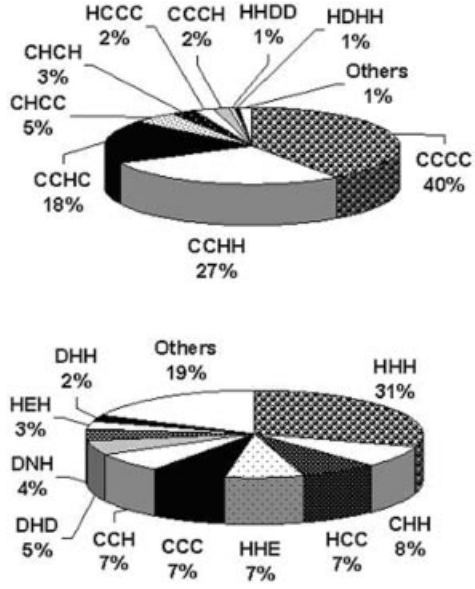


Figure 2. Distribution of four- and three-ligand MBP types detected in putative human zinc proteins. MBPs are grouped based on their amino acid composition and on the order of the protein ligands in the sequence. For example, the MBPs $HX_3HX_5C$ and $HX_8HX_4C$ are grouped together as HHC; all MBPs containing four cysteines are grouped together as CCCC.

Human zinc enzymes are present in all enzyme classes, with hydrolases being the most common zinc-dependent enzymes.[22] Indeed, it is well known that a zinc-activated water molecule is responsible for nucleophilic attack on the substrate in these systems.[63,64] However, the largest percentage of all human zinc-binding proteins for which a function can be proposed (>40%) are transcription factors. These consist mainly of zinc fingers; note, however, that zinc fingers do not interact only with DNA, but can also mediate interactions with RNA or proteins.[65] As the human zinc proteome makes up approximately 10% of the entire proteome, it follows from the above figures that 4%

 © 2007 Wiley-VCH Verlag GmbH & Co. KGaA, Weinheim 

of the human proteome is involved in zinc-dependent regulation of gene expression. Of course, to have a full picture of the importance of gene regulation in humans, one should add to this figure all the proteins involved in regulation that do not depend on zinc.

Some types of zinc-binding patterns are specifically associated with a given function, such as the CCHH type (C = cysteine, H = histidine), which is characteristic for transcription factors and contributes crucially to the stabilization of their 3D structure, whereas others can be associated with very different functional groups spanning different enzyme classes.[22] Even when contained in enzymes, the zinc ion is not necessarily the center of catalysis, but, as in the case of transcription factors, it may act as a contributor to the stability of the structure of the protein. Zinc-binding sites are thus useful modules that can be exploited not only for catalysis but also for structural purposes, for example to drive/stabilize the fold of a protein.

As mentioned, zinc-binding proteins are present in organisms from all domains of life (archaea, bacteria, eukaryotes), although they constitute a significantly diverse proportion of their proteomes.[24] General trends can be readily identified that point to archaeal and bacterial proteomes having a similar content of zinc proteins (5% to 6%), while the zinc proteomes of eukaryotic organisms constitute a much more important fraction of the whole proteome (around 9%). The incidence of eukaryotic zinc proteomes is higher due mainly to increased needs for regulation of gene expression, cell compartmentalization, and cell differentiation in multicellular organisms. Indeed, eukaryotic zinc-binding proteins involved in regulation of expression contribute nearly all the additional zinc proteins with respect to simpler organisms. Eukaryotes have recruited new zinc-binding proteins that are not needed, and indeed are not encoded, by archaea and bacteria specifically for the above purpose. As a result, the majority of the eukaryotic zinc proteome is unique to eukaryotes, in other words the majority of eukaryotic zinc proteins do not have homologs in archaeal or bacterial proteomes (Figure 3).

The role of zinc in the latter organisms is mainly as the catalytic center of hydrolytic enzymes, while very little use is made of zinc in regulatory proteins.[24] An interesting example is that of a metal-binding helix-turn-helix domain present in some bacterial and archaeal metal-sensing repressors where transcription is regulated as a function of intracellular metal concentration, such as that in the zinc-sensing SmtB protein from *Synechococcus* PCC 7942.[66,67] Intriguingly, an analysis of the zinc-proteome size of archaeal and bacterial organisms based on their range of growth temperature (i.e. by dividing them into hyperthermophilic, thermophilic, mesophilic, or psychrophilic organisms) suggests that the proteome of organisms living at higher temperatures is enriched in putative zinc-binding proteins. The zinc proteome of the 11 hyperthermophilic organisms studied in a previous paper[24] constitutes 7.0% ± 1.1% of the entire proteome, compared to 6.0% ± 1.0% of five thermophilic organisms, 5.3% ± 1.0% of 34 mesophilic organisms, and 4.5% ± 0.2% of two psychrophilic organisms. This effect may be due to an increased use of zinc for structural stability by organisms living at higher temperatures.

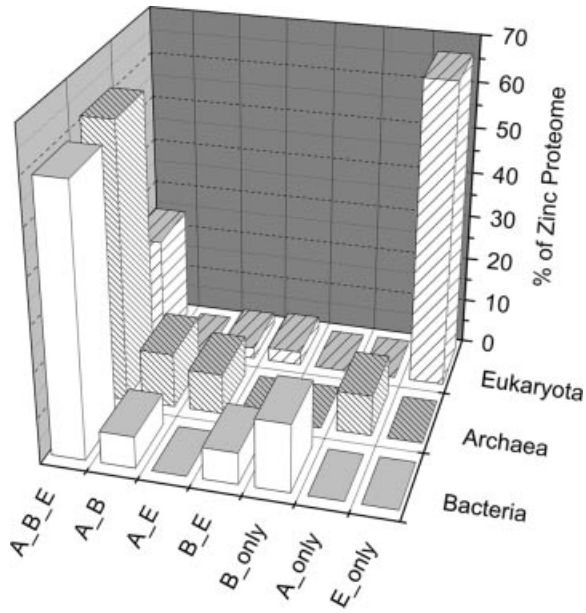


Figure 3. Fraction (with respect to the entire zinc-proteome) of predicted zinc-binding proteins in each domain of life having homologues in all three, two, or only one domain of life (A: archaea; B: bacteria; E: eukaryota). As an example, 60% of archaeal zinc-binding proteins have bacterial and eukaryotic homologues.

## The Non-Heme-Iron Metalloproteome

In biological systems, iron can be incorporated into metalloproteins in a variety of cofactors, usually in the oxidation states +3 or +2 (other oxidation states may be generated during the catalytic cycle of iron enzymes). The simplest iron-binding protein is probably rubredoxin, a small electron-transfer protein that binds a single iron ion through the side-chain sulfur atoms of four cysteines. Due to its simplicity and ease of preparation and purification, the three-dimensional structure of rubredoxin has been studied in great detail.[68–71] However, iron-binding proteins are normally much more complicated than rubredoxin, as discussed below. The chemical complexity of most iron-containing cofactors (as well as, at least in the case of heme, their poor solubility), together with the need to control the extremely versatile reactivity of this metal to prevent undesired reactions, have resulted in the evolution of complex molecular machineries dedicated to the uptake/assembly and intracellular distribution of the cofactors.[72–76]

Many proteins bind iron in polymetallic clusters composed of iron and sulfide ions that can have various stoichiometries (e.g., $Fe_2S_2$, $Fe_3S_4$, $Fe_4S_4$).[77] These proteins are therefore called iron-sulfur proteins (or ferredoxins) and typically employ the side chains of cysteines or cysteines together with histidines to bind the iron-sulfur complex, although some exceptions exist. Clearly, the properties of these systems depend crucially on the bound cluster, but

 © 2007 Wiley-VCH Verlag GmbH & Co. KGaA, Weinheim 

also on the protein environment surrounding it.[78–80] A variety of heterometallic clusters containing iron together with other metals can also be formed and bound by proteins.[81] Finally, in very many metalloproteins iron is contained at the center of a variously substituted porphyrin (heme). The porphyrin provides four nitrogen ligands to the metal ion while the fifth coordination position is filled by a protein ligand and the sixth is filled by either a protein ligand or water, or remains vacant. The most common of these heme-containing systems are called cytochromes and are distinguished by the type of heme bound, which, in turn, is determined by the chemical nature of the substituents of the porphyrin. In some cytochrome variants, called *c*-type cytochromes, the heme substituents react with the protein to form covalent bonds between the polypeptide chain and the cofactor. Proteome-level analyses of the occurrence of heme-containing proteins cannot be carried out by exploiting MBPs as these involve only one or two protein ligands. In addition, the extensive hydrophobic interactions between the porphyrin moiety and the protein chain provide a significant contribution in driving binding, which must be taken into account. For these reasons, the heme proteome must be analyzed using approaches based on fold recognition together with the analysis of the occurrence of known protein sequence motifs, as done recently for mitochondrial-type mono-heme cytochromes *c*.[82] For proteins containing *b*-type heme, initial analyses based on the known folds (e.g., the globin fold or the peroxidase fold) indicate that their percentage in eukaryotic proteomes is in the range 0.3–1.0% (unpublished data from our laboratory). The corresponding figures for bacteria and archaea are also quite variable but have a clear tendency toward being smaller than for eukaryotes (in the range 0.0–0.5%).

The methods described in the section on "Sequence-based bioinformatic identification of metalloproteins" exploiting known MBPs can be successfully applied to the analysis of proteins binding non-heme iron.[23] Of the various types of MBPs relevant to this section, the most common ones contain only cysteine residues. This is presumably due to the fact that cysteine-only MBPs are involved in binding iron-sulfur clusters by most ferredoxins. Approximately half of all MBPs that bind non-heme iron are formed by various combinations of histidine, glutamic acid, and aspartic acid residues, without cysteines.

At variance with what is observed for zinc-binding proteins, in the case of non-heme iron-proteins there is no expansion of the fraction of the proteome that is metal-binding in eukaryotes with respect to simpler organisms. For some organisms, such as yeast, a contraction is actually observed.[23] Non-heme iron proteins constitute, on average, 7.1% ± 2.1% of archaeal proteomes, 3.9% ± 1.6% of bacterial proteomes, and only 1.1% ± 0.4% of eukaryotic proteomes (Figure 4).

Because eukaryotic proteomes are somewhat larger than those of simpler organisms, possibly with the exception of yeast, the above numbers mainly indicate that the non-heme

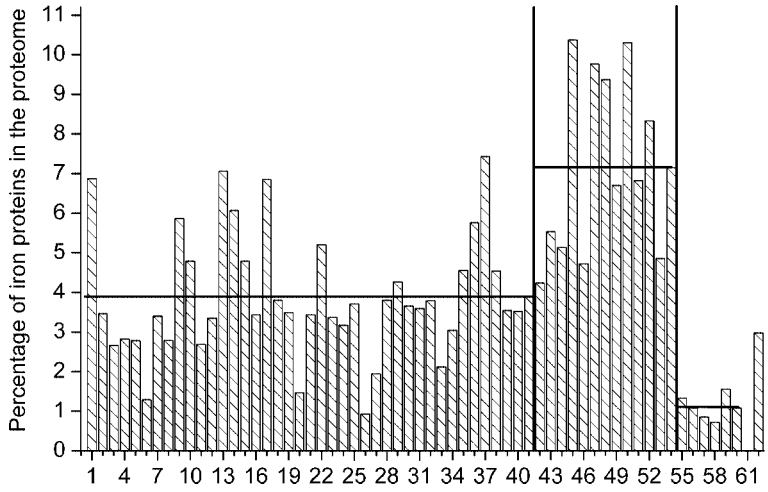


Figure 4. Percentage of iron-binding proteins identified in each proteome analyzed. The average values for all bacterial, archaeal, and eukaryotic organisms are also shown. Vertical lines separate the three domains and horizontal lines show the average values within each domain. The horizontal axis reports the data for, from left to right: 1. *Aquifex aeolicus*, 2. *Bacillus subtilis*, 3. *Bacteroides thetaiotaomicron*, 4. *Bdellovibrio bacteriovorus*, 5. *Bifidobacterium longum*, 6. *Borrelia burgdorferi*, 7. *Caulobacter crescentus*, 8. *Chlamydia trachomatis*, 9. *Chlorobium tepidum*, 10. *Clostridium acetobutylicum*, 11. *Coxiella burnetii*, 12. *Deinococcus radiodurans*, 13. *Desulfotalea psychrophila*, 14. *Desulfovibrio vulgaris*, 15. *Escherichia coli*, 16. *Fusobacterium nucleatum*, 17. *Geobacter sulfurreducens*, 18. *Haemophilus influenzae*, 19. *Helicobacter pylori*, 20. *Mesoplasma florum*, 21. *Mesorhizobium loti*, 22. *Methylococcus capsulatus*, 23. *Neisseria meningitides*, 24. *Nitrosomonas europaea*, 25. *Nostoc sp*, 26. Onion yellows, 27. *Rhodopirellula baltica*, 28. *Prochlorococcus marinus*, 29. *Pseudomonas aeruginosa*, 30. *Ralstonia solanacearum*, 31. *Rickettsia prowazekii*, 32. *Shewanella oneidensis*, 33. *Streptococcus pyogenes*, 34. *Streptomyces coelicolor*, 35. *Synechocystis sp*, 36. *Thermoanaerobacter tengcongensis*, 37. *Thermotoga maritime*, 38. *Thermus thermophilus*, 39. *Vibrio parahaemolyticus*, 40. *Xanthomonas campestris*, 41. All bacteria, 42. *Aeropyrum pernix*, 43. *Pyrobaculum aerophilum*, 44. *Sulfolobus tokodaii*, 45. *Archaeoglobus fulgidus*, 46. *Halobacterium sp*, 47. *Methanocaldococcus jannaschii*, 48. *Methanopyrus kandleri*, 49. *Methanosarcina acetivorans*, 50. *Methanothermobacter thermautotrophicus*, 51. *Thermoplasma acidophilum*, 52. *Pyrococcus abyssi*, 53. *Nanoarchaeum equitans*, 54. All archaea, 55. *Saccharomyces cerevisiae*, 56. *Drosophila melanogaster*, 57. *Caenorhabditis elegans*, 58. *Homo sapiens*, 59. *Arabidopsis thaliana*, 60. All eukaryota, 61. Empty, 62. All organisms.

 © 2007 Wiley-VCH Verlag GmbH & Co. KGaA, Weinheim 

iron proteome does not expand with the increase of proteome size that accompanies the increase in complexity of higher eukaryotic organisms. Indeed, in absolute terms, the number of non-heme iron proteins predicted in eukaryotes and in the bacteria with the largest proteomes span the same range. Figure 5 shows that the majority of non-heme iron proteins have homologues in all domains of life and that only about 10% of the non-heme iron proteome is specific to an individual domain. Taken together, these data point to non-heme iron being a cofactor of a set of metalloproteins that carry out an ensemble of basic functions which have changed very little with evolution. It can thus be concluded that the protein repertoire that sustains the increased complexity of eukaryotic organisms, and which is unique to these organisms, comprises very few predicted non-heme iron proteins.

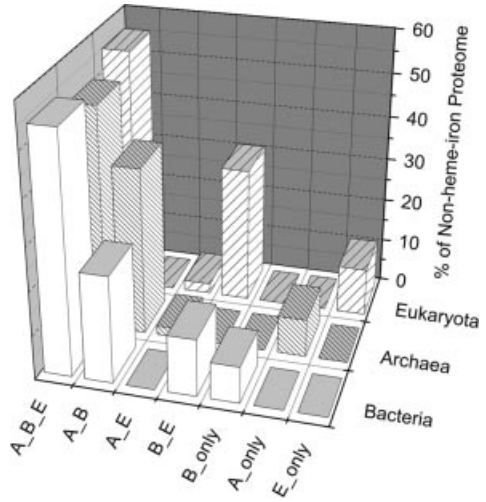


Figure 5. Fraction (with respect to the entire non-heme iron-proteome) of predicted iron-binding proteins in each domain of life having homologues in all three, two or only one domain of Life (A: Archaea; B: Bacteria; E: Eukaryota).

Overall, the non-heme iron proteome of organisms appears to be evolutionarily more ancient than the zinc proteome, with variations in its composition driven much more by loss of genes due to changes in environmental conditions that made some functions unnecessary than by recruitment of new iron proteins to cope with new functional needs (e.g. due to the evolution of multicellular organisms).[23]

### The Copper Proteome

Copper is the least pervasive of all the metallic cofactors described in this review. Nevertheless, copper plays a crucial role in a number of fundamental biological processes such as aerobic respiration (in the enzyme cytochrome *c* oxidase). Copper is a redox-active metal that can shuttle between the +2 and +1 states. It is potentially toxic to the cell, as it can lead to the formation of reactive oxygen species (ROS), in particular hydroxyl radicals, through a Fenton reaction. Consequently, nature has evolved complex pathways to control the intracellular concentration and distribution of copper,[83–85] parts of which have been structurally characterized.[86] Recent structural studies of proteins involved in the above pathways in eukaryotic systems are available, for example of proteins involved in copper delivery to cytochrome *c* oxidase[87] or in copper delivery to the trans-Golgi network.[88,89]

Copper ions are most commonly bound by cysteine and histidine side-chains, followed by methionine, and, to a lesser extent, glutamic and aspartic acid. Copper-binding proteins are typically predicted (by applying essentially the same approach as for non-heme iron proteins) to account for less than 1% of an organism's proteome (unpublished data from our laboratory). In particular, eukaryotic proteomes contain between 0.2% and 0.5% of copper proteins, with an average of 0.3%. These figures correspond to eukaryotic organisms encoding a few tens up to around one hundred copper-binding proteins. Among eukaryotes, the plant *Arabidopsis thaliana* seems to be richer in copper enzymes (as well as in non-heme iron proteins, see preceding section) than the average. The copper proteome of archaea and bacteria is composed mainly of proteins that have homologs either in all domains of life or at least in the two prokaryotic domains (unpublished data from our laboratory, Figure 6). Eukaryotes instead contain a significant share of eukaryote-specific copper proteins. These proteins are mainly copper-dependent oxidoreductases, whose number could be higher with respect to what is found in less complex organisms because of the compartmentalization of the eukaryotic cell. In agreement with this, a parallel increase, albeit less important in numerical terms, of copper-ion transporters is also observed.

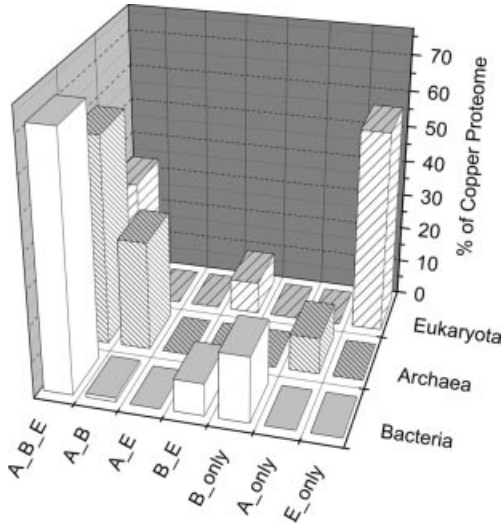


Figure 6. Fraction (with respect to the entire copper proteome) of predicted copper-binding proteins in each domain of life having homologues in all three, two, or only one domain of life (A: archaea; B: Bacteria; E: Eukaryota).

With the exception of hemocyanins, which have a role in dioxygen transport, the vast majority of copper enzymes can be assigned as catalyzing redox reactions. The second most common role for copper proteins is in metal-ion transport (e.g. these proteins are devoted to shuttling copper ions

 © 2007 Wiley-VCH Verlag GmbH & Co. KGaA, Weinheim 

within the cell, or to the uptake or excretion of copper). Copper transport is generally coupled to ATP hydrolysis.

Because of the extensively discussed (potential) toxicity of copper ions, systems devoted to controlling copper trafficking with the cells are present in a very large majority of all organisms that encode copper-dependent proteins. Some of these mechanisms have been so successful that they have significant similarities across a wide variety of prokaryotic as well as eukaryotic organisms. These include, for example, the chaperone/metalloATPase system for copper removal from the cytosol[53] or the Sco proteins, which are devoted to the assembly of cytochrome *c* oxidase and possibly of other copper-dependent oxidases.[90,91]

## Concluding Remarks

As mentioned for iron and copper, the uptake, transport, release, and incorporation of metal cofactors in proteins may require a specialized machinery whose malfunction may even lead to illness.[92] This could be expected for particularly large or chemically complex metal-containing cofactors such as heme or iron-sulfur clusters, but also holds for individual metal ions. As an example, the covalent attachment of heme to *c*-type cytochromes requires up to eight different proteins in bacteria (so called cytochrome *c* maturation genes, *c*cm*ABCDEFGH*).[93] Of the proteins encoded by these genes, one (ccmE) is devoted to transporting the insoluble heme cofactor, which is bound to ccmE through a very unusual heme–protein covalent bond, in the bacterial periplasm.[94] The structure of ccmE, however, has only been solved only in the apo form.[74,95] As regards individual metal ions, the most intensely studied soluble transporters (called metallochaperones) are probably those that handle copper,[96–99] although metallochaperones are also known for other metal ions such as nickel[100] or arsenic.[101]

The presence of delivery systems for metal ions serves two purposes, namely to prevent metals from binding to adventitious sites on proteins different from the intended targets and to incorporate the appropriate metal ion at each site regardless of the affinity of other metals for the same site. This second aspect is particularly relevant because of the need to overcome the intrinsic trend in the variation of stability of the metal complexes along the *d* series (the so-called Irving–Williams series) in order to incorporate the metal needed for the biochemical function of the system and not the most thermodynamically favored metal at each site. In other words, metallochaperones allow the incorporation of metal ions into metalloproteins to take place under kinetic rather than thermodynamic control, thereby ensuring proper maturation and thus functioning of metalloenzymes and metalloproteins in general. From the chemical point of view, this unfortunately poses some problems, because predictions cannot rely on thermodynamic properties to define which metal is bound at which site, even if the presence of a metal-binding site is known. In addition, experimental procedures for protein purification may lead to exchange of the biologically relevant metal ion with other ions contained in the buffers that bind to the protein more tightly (e.g. metallophosphatases).[102,103] On the other hand, nature can exploit this property to incorporate different metals in a protein, depending on their availability.[104]

In summary, there are now methods available that allow the prediction of an organism's metalloprotein content with some confidence. A systematic application of these methods shows significant differences in the use of metals by archaeal, bacterial, and eukaryotic organisms, the latter of which have significantly expanded their zinc proteome over evolutionary time to cope with the increased need for regulatory proteins arising from increased cell complexity and cellular differentiation. On the other hand, non-heme iron-binding proteins have not evolved significantly from simpler to more complex organisms; in fact, their number has actually diminished, with the exception of *Arabidopsis thaliana*, in eukaryotes, possibly reflecting reduced iron bioavailability. Finally, copper proteins are relatively uncommon in all organisms across the three domains of life and their number and distribution does not show significant trends. It should be kept in mind, however, that at the level of the individual protein metal binding is also dependent on the action of suitable metal-delivery pathways, which may always leave some uncertainty regarding the correctness of predictions but also of experimental data when the metalloprotein has been expressed heterologously or manipulated in some ways.


[1] I. Bertini, A. Sigel, H. Sigel, *Handbook on Metalloproteins*, 1st ed., Marcel Dekker, New York, **2001**.
[2] E. Marcotte, M. Pellegrini, M. Thompson, T. Yeates, D. Eisenberg, *Nature* **1999**, *402*, 83–86.
[3] M. Y. Galperin, E. V. Koonin, *Nat. Biotechnol.* **2000**, *18*, 609–613.
[4] R. L. Tatusov, E. V. Koonin, D. J. Lipman, *Science* **1997**, *278*, 631–637.
[5] A. Valencia, *Curr. Opin. Struct. Biol.* **2005**, *15*, 267–274.
[6] J. M. Thornton, A. E. Todd, D. Milburn, N. Borkakoti, C. A. Orengo, *Nat. Struct. Biol.* **2000**, *7* (suppl.), 991–994.
[7] J. Moult, E. Melamud, *Curr. Opin. Struct. Biol.* **2000**, *10*, 384–389.
[8] J. C. Whisstock, A. M. Lesk, *Q. Rev. Biophys.* **2003**, *36*, 307–340.
[9] R. L. Marsden, J. A. Ranea, A. Sillero, O. Redfern, C. Yeats, M. Maibaum, D. Lee, S. Addou, G. A. Reeves, T. J. Dallman, C. A. Orengo, *Philos. Trans. R. Soc., B* **2006**, 425–440.
[10] J. D. Watson, R. A. Laskowski, J. M. Thornton, *Curr. Opin. Struct. Biol.* **2005**, *15*, 275–284.
[11] R. A. Laskowski, J. D. Watson, J. M. Thornton, *J. Struct. Funct. Genomics* **2003**, *4*, 167–177.
[12] D. Pal, D. Eisenberg, *Structure* **2005**, *13*, 121–130.
[13] M. R. Brent, *Genome Res.* **2005**, *15*, 1777–1786.
[14] A. J. Windsor, T. Mitchell-Olds, *Curr. Opin. Biotechnol.* **2006**, *17*, 161–167.
[15] I. Bertini, A. Rosato, *Proc. Natl. Acad. Sci. USA* **2003**, *100*, 3601–3604.
[16] I. Bertini, C. Luchinat, A. Provenzani, A. Rosato, P. R. Vasos, *Proteins Struct. Funct. Genet.* **2002**, *46*, 110–127.
[17] K. Degtyarenko, S. Contrino, *BMC Struct. Biol.* **2004**, *4*, 3.
[18] C. Andreini, I. Bertini, A. Rosato, *Bioinformatics* **2004**, *20*, 1373–1380.


 © 2007 Wiley-VCH Verlag GmbH & Co. KGaA, Weinheim 

[19] R. A. Scott, J. E. Shokes, N. J. Cosper, F. E. Jenney, M. W. W. Adams, *J. Synchrotron Rad.* **2005**, *12*, 19–22.
[20] M. Hogbom, U. B. Ericsson, R. Lam, H. M. Bakali, E. Kuznetsova, P. Nordlund, D. B. Zamble, *Mol. Cell Proteomics.* **2005**, *4*, 827–834.
[21] W. Shi, C. Zhan, A. Ignatov, B. A. Manjasetty, N. Marinkovic, M. Sullivan, R. Huang, M. R. Chance, *Structure (Cambridge, MA, U. S.)* **2005**, *13*, 1473–1486.
[22] C. Andreini, L. Banci, I. Bertini, A. Rosato, *J. Proteome Res.* **2006**, *5*, 196–201.
[23] C. Andreini, L. Banci, I. Bertini, S. Elmi, A. Rosato, *Proteins* **2007**, *67*, 317–324.
[24] C. Andreini, L. Banci, I. Bertini, A. Rosato, *J. Proteome Res.* **2006**, *5*, 3173–3178.
[25] L. Banci, M. Piccioli, *Cobalt(II) and Nickel(II) Substituted Proteins* (Eds.: D. M. Grant, R. K. Harris), *Encyclopedia of Magnetic Resonance*, *Encycl. of Nuclear Magn. Reson.*, **1996**, p. 1365.
[26] L. Banci, I. Bertini, E. Gallori, C. Luchinat, F. Paoletti, M. Polsinelli, M. S. Viezzoli, *J. Inorg. Biochem.* **1987**, *30*, 77–85.
[27] S. Benini, S. Ciurli, C. Luchinat, *Inorg. Chem.* **1995**, *34*, 417–420.
[28] I. Bertini, I. Gelis, N. Katsaros, C. Luchinat, A. Provenzani, *Biochemistry* **2003**, *42*, 8011–8021.
[29] P. Muller, S. Kopke, G. M. Sheldrick, *Acta Crystallogr., Sect. D* **2003**, *59*, 32–37.
[30] J. W. Schymkowitz, F. Rousseau, I. C. Martins, J. Ferkinghoff-Borg, F. Stricher, L. Serrano, *Proc. Natl. Acad. Sci. U. S. A* **2005**, *102*, 10147–10152.
[31] E. Pidcock, G. R. Moore, *J. Biol. Inorg. Chem.* **2001**, *6*, 479–489.
[32] M. M. Yamashita, L. Wesson, G. Eisenman, D. Eisenberg, *Proc. Natl. Acad. Sci. USA* **1990**, *87*, 5648–5652.
[33] M. M. Harding, *Acta Crystallogr., Sect. D.* **2006**, *62*, 678–682.
[34] M. M. Harding, *Acta Crystallogr., Sect. D.* **2004**, *60*, 849–859.
[35] M. Babor, H. M. Greenblatt, M. Edelman, V. Sobolev, *Proteins* **2005**, *59*, 221–230.
[36] C. Zhan, E. V. Fedorov, W. Shi, U. A. Ramagopal, R. Thirumuruhan, B. A. Manjasetty, S. C. Almo, A. Fiser, M. R. Chance, A. A. Fedorov, *Acta Crystallogr., Sect. F: Struct. Biol. Cryst. Commun.* **2005**, *61*, 959–963.
[37] J. T. Bolin, A. E. Ronco, T. V. Morgan, L. E. Mortenson, N. H. Xuong, *Proc. Natl. Acad. Sci. USA* **1993**, *90*, 1078–1082.
[38] G. J. Kornhaber, D. Snyder, H. N. Moseley, G. T. Montelione, *J. Biomol. NMR* **2006**, *34*, 259–269.
[39] I. Bertini, C. Luchinat, M. Piccioli, *Methods Enzymol.* **2001**, *339*, 314–340.
[40] I. Bertini, Y.-M. Lee, C. Luchinat, M. Piccioli, L. Poggi, *ChemBioChem* **2001**, *2*, 550–558.
[41] D. F. Hansen, J. J. Led, *Proc. Natl. Acad. Sci. USA* **2006**, *103*, 1738–1743.
[42] L. M. Utschig, J. W. Bryson, T. V. O'Halloran, *Science* **1995**, *268*, 380–385.
[43] L. M. Utschig, J. G. Wright, G. Dieckmann, V. L. Pecoraro, T. V. O'Halloran, *Inorg. Chem.* **1995**, *34*, 2497–2498.
[44] K. Zangger, G. Oz, J. D. Otvos, I. M. Armitage, *Protein Sci.* **1999**, *8*, 2630–2638.
[45] S. S. Narula, D. R. Winge, I. M. Armitage, *Biochemistry* **1993**, *32*, 6773–6787.
[46] M. A. Marti-Renom, A. C. Stuart, A. Fiser, R. Sanchez, F. Melo, A. Sali, *Annu. Rev. Biophys. Biomol. Struct.* **2000**, *29*, 291–325.
[47] A. Sali, T. L. Blundell, *J. Mol. Biol.* **1993**, *234*, 779–815.
[48] L. Banci, I. Bertini, A. Rosato, G. Varani, *J. Biol. Inorg. Chem.* **1999**, *4*, 824–837.
[49] L. Banci, I. Bertini, S. Ciurli, A. Dikiy, J. Dittmer, A. Rosato, G. Sciara, A. R. Thompsett, *ChemBioChem* **2002**, *3*, 299–310.
[50] I. Bartalesi, I. Bertini, P. Hajieva, A. Rosato, P. R. Vasos, *Biochemistry* **2002**, *41*, 5112–5119.
[51] C. Andreini, L. Banci, I. Bertini, C. Luchinat, A. Rosato, *J. Proteome Res.* **2004**, *3*, 21–31.
[52] C. Andreini, L. Banci, I. Bertini, S. Elmi, A. Rosato, *J. Proteome Res.* **2005**, *4*, 881–888.
[53] F. Arnesano, L. Banci, I. Bertini, S. Ciofi-Baffoni, E. Molteni, D. L. Huffman, T. V. O'Halloran, *Genome Res.* **2002**, *12*, 255–271.
[54] F. Musiani, B. Zambelli, M. Stola, S. Ciurli, *J. Inorg. Biochem.* **2004**, *98*, 803–813.
[55] S. Ciurli, F. Musiani, *Photosynth. Res.* **2005**, *85*, 115–131.
[56] B. Zambelli, M. Stola, F. Musiani, K. De Vriendt, B. Samyn, B. Devreese, J. Van Beeumen, P. Turano, A. Dikiy, D. A. Bryant, S. Ciurli, *J. Biol. Chem.* **2005**, *280*, 4684–4695.
[57] S. C. Tosatto, G. M. Giacometti, G. Valle, P. Costantini, *Biochem. Biophys. Res. Commun.* **2006**, *339*, 277–283.
[58] J. S. Oakhill, B. J. Sutton, A. R. Gorringe, R. W. Evans, *Protein Eng. Des. Sel.* **2005**, *18*, 221–228.
[59] N. Hulo, A. Bairoch, V. Bulliard, L. Cerutti, E. De Castro, P. S. Langendijk-Genevaux, M. Pagni, C. J. Sigrist, *Nucleic Acids Res.* **2006**, *34*, D227–D230.
[60] R. D. Finn, J. Mistry, B. Schuster-Bockler, S. Griffiths-Jones, V. Hollich, T. Lassmann, S. Moxon, M. Marshall, A. Khanna, R. Durbin, S. R. Eddy, E. L. Sonnhammer, A. Bateman, *Nucleic Acids Res.* **2006**, *34*, D247–D251.
[61] A. Andreeva, D. Howorth, S. E. Brenner, T. J. Hubbard, C. Chothia, A. G. Murzin, *Nucleic Acids Res.* **2004**, *32*, D226–D229.
[62] A. Passerini, M. Punta, A. Ceroni, B. Rost, P. Frasconi, *Proteins* **2006**, *65*, 305–316.
[63] J. E. Coleman, *Curr. Opin. Chem. Biol.* **1998**, *2*, 222–234.
[64] I. Bertini, C. Luchinat, M. S. Viezzoli, "Metal substitution as a tool for the investigation of zinc proteins" in *Zinc Enzymes* (Eds.: I. Bertini, C. Luchinat, W. Maret, M. Zeppezauer), Birkhäuser, Basel, **1986**, pp. 27–47.
[65] J. M. Matthews, M. Sunde, *IUBMB Life* **2002**, *54*, 351–355.
[66] J. L. Erbe, K. B. Taylor, L. M. Hall, *Nucleic Acids Res.* **1995**, *23*, 2472–2478.
[67] W. J. Cook, S. R. Kar, K. B. Taylor, L. M. Hall, *J. Mol. Biol.* **1998**, *275*, 337–346.
[68] B. F. Volkman, S. J. Wilkens, A. L. Lee, B. Xia, W. M. Westler, R. Berger, J. L. Markley, *J. Am. Chem. Soc.* **1999**, *121*, 4677–4683.
[69] R. Bau, D. C. Rees, D. M. Kurtz, Jr., R. A. Scott, H. S. Huang, M. W. W. Adams, M. K. Eidsness, *J. Biol. Inorg. Chem.* **1998**, *3*, 484–493.
[70] I. Bertini, D. M. Kurtz, Jr., M. K. Eidsness, G. Liu, C. Luchinat, A. Rosato, R. A. Scott, *J. Biol. Inorg. Chem.* **1998**, *3*, 401–410.
[71] Z. Dauter, K. S. Wilson, L. C. Sieker, J.-M. Moulis, J. Meyer, *Proc. Natl. Acad. Sci. USA* **1996**, *93*, 8836–8840.
[72] L. Thony-Meyer, *Biochemistry* **2003**, *42*, 13099–13105.
[73] L. Thony-Meyer, *Biochem. Soc. Trans.* **2002**, *30*, 633–638.
[74] F. Arnesano, L. Banci, P. D. Barker, I. Bertini, A. Rosato, X. C. Su, M. S. Viezzoli, *Biochemistry* **2002**, *41*, 13587–13594.
[75] R. Lill, R. Dutkiewicz, H. P. Elsasser, A. Hausmann, D. J. Netz, A. J. Pierik, O. Stehling, E. Urzica, U. Muhlenhoff, *Biochim. Biophys. Acta* **2006**, *1763*, 652–667.
[76] S. S. Mansy, J. A. Cowan, *Acc. Chem. Res.* **2004**, *37*, 719–725.
[77] H. Beinert, R. H. Holm, E. Münck, *Science* **1997**, *277*, 653–659.
[78] C. Luchinat, F. Capozzi, D. Bentrop, *Iron-Sulfur Proteins* (Eds.: I. Bertini, A. Sigel, H. Sigel), *Handbook on Metalloproteins*, Marcel Dekker, New York, **2001**.
[79] I. Bertini, C. Luchinat, A. Rosato, *NMR Spectra of Iron-Sulfur Proteins* (Eds.: A. G. Sykes, R. Cammack), *Advances in Inorganic Chemistry*, Academic Press, San Diego, **1999**, p. 251.
[80] I. Bertini, S. Ciurli, C. Luchinat, *Struct. Bonding (Berlin)* **1995**, *83*, 1–54.
[81] L. Banci, I. Bertini, C. Luchinat, P. Turano, *Special Cofactors and Metal Clusters* (Eds.: I. Bertini, B. H. Gray, J. S. Valentine,

 © 2007 Wiley-VCH Verlag GmbH & Co. KGaA, Weinheim 

E. I. Stiefel), *Biological Inorganic Chemistry: Structure & Reactivity*, University Science Books, Sausalito (CA), **2006**, p. 43.
[82] I. Bertini, G. Cavallaro, A. Rosato, *Chem. Rev.* **2006**, *106*, 90–115.
[83] L. A. Finney, T. V. O'Halloran, *Science* **2003**, *300*, 931–936.
[84] M. D. Harrison, C. E. Jones, C. T. Dameron, *J. Biol. Inorg. Chem.* **1999**, *4*, 145–153.
[85] T. V. O'Halloran, V. C. Culotta, *J. Biol. Chem.* **2000**, *275*, 25057–25060.
[86] L. Banci, A. Rosato, *Acc. Chem. Res.* **2003**, *36*, 215–221.
[87] L. Banci, I. Bertini, S. Ciofi-Baffoni, I. Leontari, M. Martinelli, P. Palumaa, R. Sillard, S. Wang, *Proc. Natl. Acad. Sci. U. S. A* **2007**, *104*, 15–20.
[88] L. Banci, I. Bertini, F. Cantini, N. DellaMalva, T. Herrmann, A. Rosato, K. Wuthrich, *J. Biol. Chem.* **2006**, *281*, 29141–29147.
[89] L. Banci, I. Bertini, F. Cantini, I. C. Felli, L. Gonnelli, N. Hadjiliadis, R. Pierattelli, A. Rosato, P. Voulgaris, *Nat. Chem. Biol.* **2006**, *2*, 367–368.
[90] F. Arnesano, L. Banci, I. Bertini, M. Martinelli, *J. Proteome Res.* **2005**, *4*, 63–70.
[91] L. Banci, I. Bertini, G. Cavallaro, A. Rosato, *J. Proteome Res.* **2007**, *6*, 1568–1579.
[92] D. Strausak, J. F. Mercer, H. D. Hermann, W. Stremmel, G. Multhaup, *Brain Res. Bull.* **2001**, *55*, 175–185.
[93] L. Thony-Meyer, *Microbiol. Mol. Biol. Rev.* **1997**, *61*, 337–376.
[94] H. Schulz, H. Hennecke, L. Thony-Meyer, *Science* **1998**, *281*, 1197–1200.
[95] E. Enggist, L. Thony-Meyer, P. Guntert, K. Pervushin, *Structure* **2002**, *10*, 1551–1557.
[96] A. L. Lamb, A. K. Wernimont, R. A. Pufahl, V. C. Culotta, T. V. O'Halloran, A. C. Rosenzweig, *Nat. Struct. Biol.* **1999**, *6*, 724–729.
[97] A. L. Lamb, A. S. Torres, T. V. O'Halloran, A. C. Rosenzweig, *Nat. Struct. Biol.* **2001**, *8*, 751–755.
[98] I. Anastassopoulou, L. Banci, I. Bertini, F. Cantini, E. Katsari, A. Rosato, *Biochemistry* **2004**, *43*, 13046–13053.
[99] E. Balatri, L. Banci, I. Bertini, F. Cantini, S. Ciofi-Baffoni, *Structure* **2003**, *11*, 1431–1443.
[100] H. Remaut, N. Safarov, S. Ciurli, J. J. Van Beeumen, *J. Biol. Chem.* **2001**, *276*, 49365–49370.
[101] Y. F. Lin, A. R. Walmsley, B. P. Rosen, *Proc. Natl. Acad. Sci. USA* **2006**, *103*, 15617–15622.
[102] D. Namgaladze, H. W. Hofer, V. Ullrich, *J. Biol. Chem.* **2002**, *277*, 5962–5969.
[103] M. R. Swingle, R. E. Honkanen, E. M. Ciszak, *J. Biol. Chem.* **2004**, *279*, 33992–33999.
[104] M. Schmidt, B. Meier, F. Parak, *J. Biol. Inorg. Chem.* **1996**, *1*, 532–541.

Received: February 8, 2007
Published Online: May 16, 2007

 © 2007 Wiley-VCH Verlag GmbH & Co. KGaA, Weinheim 

DOI: 10.1002/ejic.200700076

# A Critical Review of Electronic Effects in Enediamido and α-Diimino Complexes of the Group 4 Metals

Carlo Mealli,*[a] Andrea Ienco,[a] Andrew D. Phillips,[a] and Agustín Galindo*[b]

**Keywords:** N ligands / Group 4 metals / Metallacycles / Density functional calculations / Electronic structure

The α-diimino chelating ligand 1,4-diaza-1,3-butadiene, or its dianionic enediamido form (generically defined as DAD), forms a variety of complexes with group 4 transition metals either with or without other co-ligands. The known species are either pseudo-octahedral [$L_4M(DAD)$] or tetracoordinate [$L_2M(DAD)$] with a lower degree of metal saturation in the latter case. Additionally, there are a number of known $CpML_n$ species and homoleptic complexes with the formula [$M(DAD)_3$] or [$M(DAD)_2$]. The M-DAD metallacycle is generally either planar or folded at the N···N vector, the latter arrangement being observed when the number of co-ligands is reduced and hence there is insufficient saturation at the metal. The conformation also depends on the relative electron population of DAD, which is a *noninnocent* ligand and exists as a continuum between the neutral and dianionic resonance forms. Herein some theoretical concepts, that have previously been developed to describe the bonding capabilities of DAD toward different triads of transition metals, are extended to complexes of the group 4 metals. New electronic aspects of the [$M(DAD)_3$] complexes are described together with a completely new analysis of the [$M(DAD)_2$] complexes. These exhibit the planar/bent conformational dichotomy, which may have an electronic and/or steric origin as it is affected by the type of substituent at the nitrogen atoms. A reasonable justification of the observed conformational preferences is found from a combination of density functional and QTAIM analyses. The latter clearly demonstrates that a peculiar intramolecular hydrogen bonding can contribute to the stabilization of planar-type structures.

(© Wiley-VCH Verlag GmbH & Co. KGaA, 69451 Weinheim, Germany, 2007)

## 1. Introduction

This article analyzes the bonding capabilities of ligands based on the 1,4-diaza-1,3-butadiene or *o*-diiminobenzene skeleton (generally abbreviated as DAD) towards a transition metal of group 4. The electron population in these molecules varies depending on the nature of the coordinated metal atom.[1] Thus, the chelate is considered a neutral α-diimino species when bound to late transition metals as occurs, for example, in the nickel(II) and palladium(II) complexes, which are capable of converting ethylene into high molecular weight polymers with low polydispersity.[2] More commonly, the ligand behaves as an enediamido dianion with early transition metals. The corresponding complexes have been proposed as a more versatile alternative to metallocene catalysts for polymerization reactions.[3]

With a few exceptions, the coordination of DAD in the enediamido form is characterized by a nonplanar arrangement of the five-membered metallacycle (an N–N folded envelope). We have already dedicated a number of theoretical studies to interpreting the general bonding capabilities of these ligands with metal atoms of groups 5,[4] 6,[5] and 8.[6] Herein, the dichotomy between the diimino and enediamido forms (see Scheme 1), which is a classic example of *noninnocent* behavior,[7] is discussed on the basis of the electronic and structural characteristics of the $ML_n$ metal fragment (M = Ti, Zr, Hf).

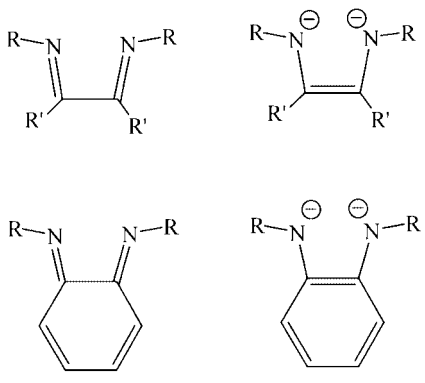


Scheme 1. Diimino vs. enediamido resonance forms in ligands derived from the 1,4-diaza-1,3-butadiene or *o*-diiminobenzene skeletons (DAD).

[a] ICCOM, CNR,
Via Madonna del piano, 50019 Sesto Fiorentino, Firenze, Italy
E-mail: mealli@iccom.cnr.it
[b] Departamento de Química Inorgánica, Universidad de Sevilla, Aptdo. 553, 41701 Sevilla, Spain
E-mail: galindo@us.es
Supporting information for this article is available on the WWW under http://www.eurjic.org or from the author.

 © 2007 Wiley-VCH Verlag GmbH & Co. KGaA, Weinheim 

A search of the Cambridge Crystallographic Database[8] for mononuclear[9,10] complexes of a group 4 metal with at least one DAD ligand yields examples that exhibit both resonance forms depending on the nature of the supporting $ML_n$ fragment, which are of the type $MX_2$, CpMX, $Cp_2M$, $MX_2L_2$, and $MX_4$ (L = two-electron-donor ligand, X = halide, Cp = cyclopentadienido anion). The set of ancillary ligands may occasionally include other DAD chelates, and homoleptic complexes of formulae $[M(DAD)_2]$ or $[M(DAD)_3]$ are observed in some cases. A few transition metals exhibit examples of both types,[11] although interconversion between the species has only been found to occur in the case of group 4 metals. This unique behavior requires a reasonable interpretation of the electronic structure and ligand-metal bonding as the mentioned dichotomy of the M(DAD) metallacycle (folded or planar) applies to homoleptic complexes as well.

In reviewing the general electronic features of all the group 4 complexes, we focus on the homoleptic species in particular. Given the interest raised by some of the examined species, new ad hoc quantum-chemical calculations have been performed and are presented here for the first time. For this reason, Supporting Information is also available.

## 2. General Considerations Regarding the Structural and Electronic Aspects of the α-Diimino and Enediamido Forms

The electronic aspects of the 1,4-diaza-1,3-butadiene ligand have been discussed previously in terms of a qualitative assessment of the relevant molecular orbitals [MOs; the various combinations of atomic orbitals (AOs) are represented in Scheme 2].[12] These include two filled nitrogen σ lone pairs (in-phase $\sigma_{ip}$ and out-of-phase $\sigma_{op}$ combinations) and four π levels. Only two of the latter are filled ($\pi_1$, $\pi_2$) when DAD has the α-diimino form, whereas $\pi_3$* is also populated (ligand's HOMO) when DAD behaves as an enediamido dianion.

*Carlo Mealli received his doctoral degree in chemistry from the Università di Firenze in 1969. After postdoctoral work with Prof. E. C. Lingafelter at the University of Washington (Seattle), he joined the CNR Institute of Florence directed by Prof. L. Sacconi, where he reached the position of Research Director in 1991. As visiting scientist, he has worked in famous laboratories around the world, including that of the Nobel Laureate Prof. R. Hoffmann (Cornell University). His research interests currently involve the relationship between 3D structures and chemical aspects (including reactivity) of transition metal complexes through computational analysis. For the latter, he has developed, together with D. M. Proserpio and A. Ienco the worldwide used package CACAO. He is the author of more than 200 publications in the field of inorganic/organometallic chemistry.*

*Andrea Ienco was born in Florence, Italy. He received his chemistry degree from the Università di Firenze in 1993. He then worked in Roald Hoffmann's group at Cornell University. He presently has a research position in Florence at the Istituto di Chimica dei Composti Organometallici of the CNR. His main scientific interest is the application of computational methods in organometallic and transition metal systems.*

*Agustín Galindo was born in 1960 in Seville, Spain, where he received both his graduate and doctoral (1986, under the direction of Prof. Ernesto Carmona) degrees. After postdoctoral work with Prof. René Mathieu and Prof. Jean-Pierre Majoral (Toulouse), he returned to the Universidad de Sevilla, where he reached the position of Lecturer (1989) and finally that of Professor of Inorganic Chemistry (2001). His research interests are related to transition metal chemistry and the application of coordination/organometallic complexes in homogeneous catalysis (recently extended to nonconventional media).*

*Andrew D. Phillips completed his B.Sc at the University of Toronto, before proceeding to Dalhousie University, Halifax, where he completed his Ph.D. with Dr. Neil Burford in low-coordinate phosphorus-nitrogen chemistry. Continuing his passion for the synthesis of main-group complexes, a two-year postdoctoral study was completed with Dr. Philip P. Power at U.C. Davis, with whom he is a co-author of over 22 publications. His interest in organometallics and computational chemistry was aroused by research performed at the CNR in Firenze with Drs. Maurizio Peruzzini and Carlo Mealli. At present he is partaking in an independent research project funded by the European Commission's Marie Curie Fellowship program at the Ecole Polytechnique Fédérale de Lasuanne, in collaboration with Dr. Paul J. Dyson. His primary interests include the development of catalytic processes using complexes with sterically demanding ligands.*

 © 2007 Wiley-VCH Verlag GmbH & Co. KGaA, Weinheim 

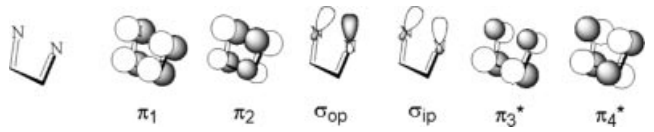


Scheme 2. Relevant MOs of the 1,4-diaza-1,3-butadiene ligand.

The complexes reported in the Cambridge Crystallographic Database can be separated into two distinct groups in which the M(DAD) metallacycle is either planar or bent depending on the value of the torsion angle M–N–N–C. If the latter is less than 170° the system is considered bent. We have previously addressed the electronic factors which determine the structural arrangement of enediamido ligands in complexes such as $[TiCl_2(DAD)]$ and $[W(NR)Cl_2(DAD)]$.[13] In particular, we pointed out that a dianionic character is acquired on bending (oxidized metal center) and the ligand becomes the donor of three rather than two electron pairs. At variance with other interpretations, which attribute the extra donation to the localized C=C π bond in the dianionic DAD,[14] we proposed that the electron pair involved is a filled combination of the nitrogen pπ orbitals that are acting as σ donors.[15] The present study confirms this point of view and discusses other factors that govern the electron distribution and shape of the metallacycle.

As mentioned above, a planar metallacycle implies an extended π-type delocalization of the metal's electrons over the entire skeleton of the chelate. Thus, one electron pair available at the $d^4$ metal is involved in back-donation to DAD without necessarily implying a complete electron transfer from the metal to DAD (oxidative addition). In contrast, a dianionic enediamido formulation of the ligand seems more appropriate when the ring is folded. A key factor for discriminating between the neutral or dianionic forms of the chelate is the population of the $\pi^*_3$ MO (see Scheme 2). Since this is a combination of both C=C π-bonding and C–N π*-antibonding character, a larger electron transfer from the metal atom (up to the point of oxidative addition) is manifested by the elongation of the C–N bonds and shortening of the intermediate C=C bond. This point has been extensively discussed by Wieghardt in several papers devoted to complexes of the late transition metals with *o*-diiminobenzene (alternatively behaving as *o*-diiminobenzosemiquinonato) and other related ligands.[16] This author concluded that the discrimination between the diimino or enediamido forms cannot be based solely on the geometric parameters, especially when the crystallographic data are not of the highest quality.

Finally, the recent discovery of planar metallacycles in $[Zr\{(Me_3SiN)_2C_6H_4\}_2]$[17] has shown that the bent/planar dichotomy is also present in homoleptic $[M(DAD)_2]$ complexes. This point requires special consideration and has been treated by a combination of MO calculations and electron density analysis.

## 3. $[M(DAD)_3]$ Complexes

Our examination of the electron-richer complexes, in which the group 4 metal is hexacoordinate, starts with the homoleptic $[M(DAD)_3]$ species. These will be later correlated with the general pseudo-octahedral complexes. Table 1 summarizes the known $[M(DAD)_3]$ complexes along with their CCDC refcode.[8] All the M(DAD) metallacycles are planar.

Table 1. Structurally characterized homoleptic $[M(DAD)_3]$ complexes.

| Composition (M, DAD) | CCDC refcode |
|---|---|
| Ti, *i*PrNC(H)C(Ph)N*i*Pr | WIMROZ[18] |
| Zr, *p*-TolNC(Ph)C(Ph)N-*p*-Tol | YOBYAP[19] |
| Hf, *p*-TolNC(Ph)C(Ph)N-*p*-Tol | YOBYET[19] |

A density functional analysis of an equivalent group 5 metal complex, namely the redox species $[M(iPrNC(H)=C(H)NiPr)_3]^{0,+1}$ (M = Nb, Ta), is available.[20] Based on the MO architecture, it has been suggested that conversion between the two redox complexes is ligand-based. We have examined analogous group 4 complexes and have optimized the model $[Ti\{MeNC(H)=C(H)NMe\}_3]$ (**1**; Figure 1).

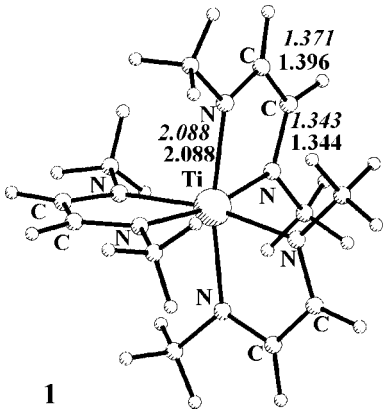


Figure 1. Optimized structure of the model $[Ti\{MeNC(H)=C(H)NMe\}_3]$ (**1**). The experimental geometric parameters of WIMROZ are given in italics.

The structure has essential $D_3$ symmetry and the agreement with the experimental parameters of $[Ti\{iPrNC(H)=C(H)NiPr\}_3]$ (WIMROZ) is satisfactory since the metallacycles are planar and only the C=C double bond is slightly overestimated (by about 0.02 Å).

The MO picture is similar to that proposed for the analogous group 5 system. Amongst the important MOs of the DAD ligands (see Scheme 2) we can highlight the in-phase ($\sigma_{ip}$) and out-of-phase ($\sigma_{op}$) combinations of the nitrogen lone pairs, which donate a total of 12 electrons to the metal. Other interactions involve the π-orbitals of the ligands, some symmetry combinations ($D_3$ point group) of which are shown on the right-hand side of Scheme 3. Of these, the combinations of $\pi_1$ and $\pi_2$ orbitals (see Scheme 2) are all populated but are only partially involved in metal interactions (see below). The most critical relationships concern the $\pi_3$* orbitals, which determine the *noninnocent* character of the ligands. Given the pseudo-octahedral geometry of the complex, the classical metal "$t_{2g}$" levels (presented as the $a_1$ and e levels on the left-hand side of Scheme 3) are

 © 2007 Wiley-VCH Verlag GmbH & Co. KGaA, Weinheim 

close in energy to the $\pi_3$* combinations of the ligands ($a_2$ and e), hence a strong interaction occurs between the two degenerate e sets. The combined 1e MO (the degenerate HOMO depicted in Figure 2) is stabilized due to its bonding character.

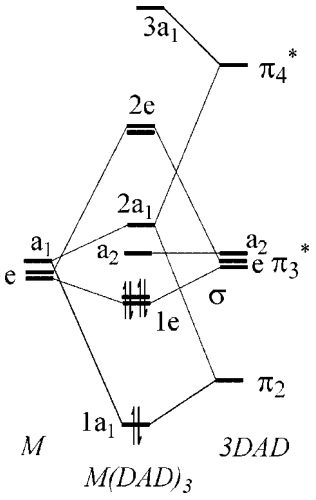


Scheme 3. Simplified MO diagram for [M(DAD)$_3$] complexes.

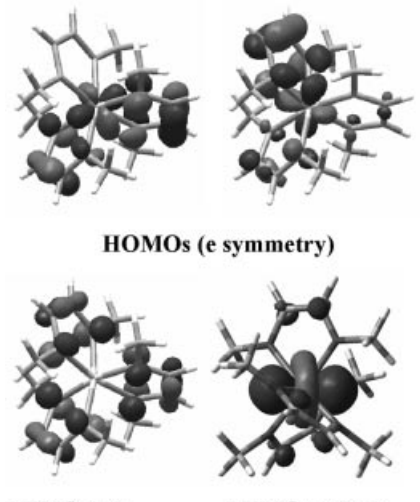


Figure 2. Important frontier MOs associated with model complex **1**.

Given the small energy gap between the interacting levels, it is difficult to discriminate the actual amount of metal- or ligand-based character associated with the four frontier electrons in the 1e level. However, even if a complete metal-to-ligand charge transfer has occurred (oxidative addition), only a maximum of two out of the three ligands could be considered completely dianionic. This is inconsistent with the equivalence of all the ligands constrained by the threefold symmetry. Also, in view of the planarity of the metallacycles, it seems reasonable that the metal is synergetically engaged in back-donation of four electrons into the three DAD ligands.

The two lowest and unpopulated levels (LUMOs in Figure 2) are a combination of pure $\pi_3$* ligand-based orbitals ($a_2$) and a metal "$t_{2g}$" orbital with some M–L antibonding character ($2a_1$). As shown in Scheme 3, the $2a_1$ level arises from a weak dative interaction between a combination of lower and filled C=N $\pi_2$ bonding levels. There is also a stabilizing effect connected with the higher $3a_1$ level (based on a $\pi_4$* combination), which justifies why there is no nitrogen contribution in $2a_1$ (see Scheme 2). In any case, the participation of the DAD $\pi_2$ MOs in metal donation allows the $d^4$ metal center to reach a formal 18 electron count. Curiously, it should be noted that the electron richer $d^5$ complex also has 18 electrons since experimental and computational studies for the neutral [Ta(*i*Pr$_2$-DAD)$_3$] complex confirm that the SOMO has exclusively ligand-based character.[20] This is consistent with the EPR spectra. Moreover, a significantly larger energy gain is computed for singly populating $a_2$ instead of $a_1$, while the C–C bond and C–N distances are comparatively shorter and longer, respectively, in the neutral species than in the monocation.[20] In spite of the ligand-based redox chemistry, it might be improper to formulate a prevailing dianionic character of the ligands as this would imply intra-ligand repulsion. Although the additional electron in [Ta(*i*Pr$_2$-DAD)$_3$] is assigned to the ligand, there is no evidence of Ta–N bond elongation. This in an indirect confirmation that the electrons in 1e are mainly metallic in character.

The other two known structures of homoleptic [M(DAD)$_3$] complexes, namely [M{[*p*-TolNC(Ph)]$_2$}$_3$] (YOBYAP and YOBYET for M = Zr and Hf, respectively),[19] are remarkable for having one metallacycle that is different from the other two. In YOBYET,[19] for instance, the two Hf–N distances for one chelate are significantly shorter than the other four (average values of 2.150(12) vs. 2.216(15) Å] and the C–C distance in the unique metallacycle is correspondingly shorter [1.34(2) vs. 1.405(19) Å]. Since this effect is common to two structures, it cannot be attributed to the poor quality of the crystal data. In principle, a break of the threefold symmetry could be due to an electronic effect of the Jahn–Teller type, since there four electrons are available for three metal–ligand π interactions and the HOMO–LUMO gap is relatively small (see Scheme 3). A DFT optimization of the simple model [Zr{MeNC(H)=C(H)NMe}$_3$], which is similar to the Ti species **1**, shows no electronic bias toward a broken threefold symmetry. A careful examination of the intramolecular contacts in the Zr and Hf structures indicates that the bulky phenyl and tolyl substituents at any core atom of DAD determine the steric hindrance. Rather than a symmetrical weakening of all the M–N distances, the system allows one ligand to be more strongly bound than the other two. A Walsh diagram, constructed at the Extended Hückel Molecular Orbital (EHMO) level,[21] for the simultaneous lengthening of two out of three metal–ligand interactions (the ideal $D_3$ symmetry of the complete model is lowered to $C_2$) shows that this distortion produces a large energy gain of about 30 kcal mol$^{-1}$. Evidently, some four-electron repulsions between the H atoms of the aromatic rings are progressively relieved. Remarkably, the energy minimum found at this low computational level almost corresponds to the

 © 2007 Wiley-VCH Verlag GmbH & Co. KGaA, Weinheim 

experimental structure. Further metal–ligand weakening steeply raises the energy.

## 4. Pseudo-Octahedral Complexes with $ML_4$ Fragments

In order to gain further insight on the electronic peculiarities of the homoleptic $[M(DAD)_3]$ species, it is useful to draw a comparison with pseudo-octahedral DAD complexes supported by an $ML_4$ fragment (L = two-electron-donor ligand or a halide X). Table 2 lists the structurally characterized examples. In particular, the complexes $[ZrCl_4\{RNC(Ph)=C(Ph)NR\}]$ (**2**; YOBXUI,[19] R = *p*-MeO-$C_6H_4$), $[TiCl_2(thf)_2\{CyNC(H)=C(H)NCy\}]$ (**3**; PEBCOQ[22]), and $[ZrCl_2(tmeda)\{o\text{-}(Me_3SiN)_2C_6H_4\}]$ (**4**; GUHYEN,[23] tmeda = $Me_2NCH_2CH_2NMe_2$) have been examined. Complex **4** uniquely features a somewhat folded metallacycle.

Table 2. Structurally characterized pseudo-octahedral complexes with $ML_4$ fragments.

| Ancillary fragment | Composition | CCDC refcode |
|---|---|---|
| $ML_4$ | [Zr(DAD)(macrocycle)] | NOVNUH[24] |
| | | POCKAT[25] |
| | | POCKUN[25] |
| $ML_2X_2$ | $[TiCl_2(DAD)(thf)_2]$ | PEBQOC[22] |
| | $[ZrCl_2(DAD)(tmeda)]$, *bent* | GUHYEN[23] |
| | [Zr(guanidinate)$_2$(DAD)] | PUXTEH[26] |
| $M(NR)X_2L$ | $[TiCl_2(DAD)(NAr)(py)]$ | VEBYIK[27] |
| $MX_4$ | $[ZrCl_4(DAD)]$ | YOBXUI[19] |

First of all, we satisfactorily optimized models of complexes **2** and **3** with the unsubstituted DAD ligand (see Figure 3). The Ti–N distances and Cl–Ti–Cl angle are underestimated and overestimated with respect to the experimental structure of PEBCOQ[22] by about 0.04 Å and 13°, respectively, in **3**. This is most likely due to important C–H···Cl intramolecular interactions involving the cyclohexyl substituents that are present in the experimental complex but neglected in the calculations.

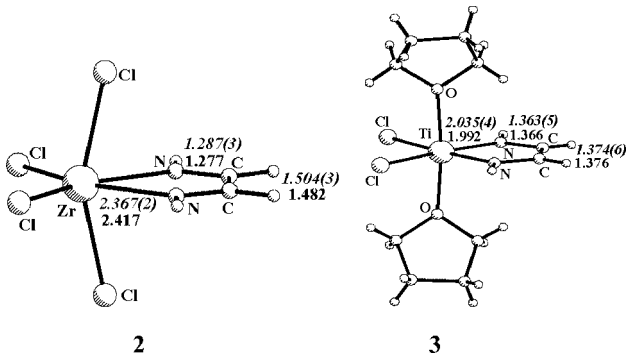


**2** **3**

Figure 3. Optimized structures of the model complexes **2** and **3**.

Given the common pseudo-octahedral geometry of complexes **1**, **2**, and **3** and the variety of formal oxidation states (0, IV, and II, respectively), the metallacycle(s) must have a different electronic nature even though they are all planar. For instance, four Cl co-ligands in **2** ($d^0$ configuration) exclude both the enediamido character of DAD and the metal back-donation. Such a limiting situation is well expressed by the longer C–C (1.482 Å) and shorter C–N (av. 1.278 Å) distances, which suggest that the α-diimino ligand ideally features a single C–C bond and two double C=N bonds. The lack of back-donation should also be reflected by long Zr–N bonds in **2**, which are not directly comparable with the Ti–N distances of 1.992 and 2.088 Å in **3** and **1**, respectively. The latter significant difference is probably due to full engagement of the unique electron pair in **3** ($d^2$ configuration) in back-donation to one DAD ligand, whereas the two electron pairs ($d^4$ configuration) in **1** are shared by three DAD ligands.

The diagram for the interaction between the metal fragment and DAD (see Scheme 4) is general for complexes containing four π-donor co-ligands (e.g., halides) and is essentially similar to that proposed by us previously to interpret the features of octahedral *o*-phenylendiamido complexes of group 6 metals.[5] Taking into account these latter

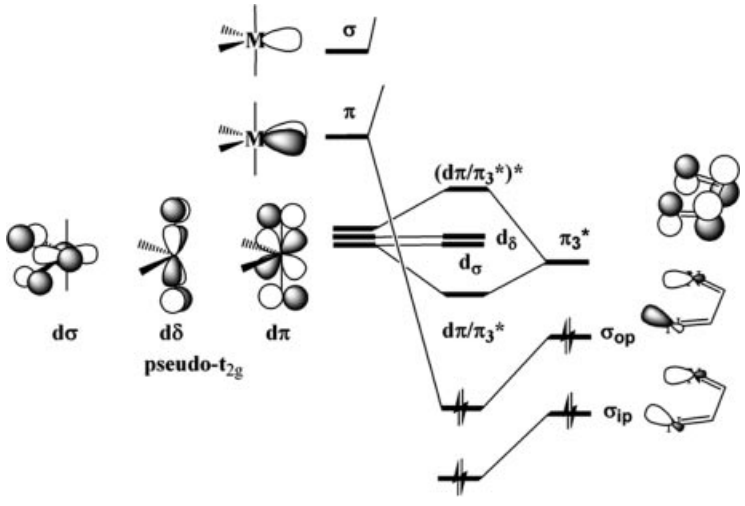


Scheme 4. Simplified MO diagram for $[L_4M(DAD)]$ complexes.

 © 2007 Wiley-VCH Verlag GmbH & Co. KGaA, Weinheim 

complexes, the population of the four highest frontier MOs in this scheme can vary between 0 and 6 electrons.

Donations of the ligand $\sigma_{op}$ and $\sigma_{ip}$ lone-pair combinations into the appropriate σ and dπ hybrid orbitals of the metal are the most effective and general. In **3**, there is a π-type interaction (see the bonding HOMO dπ/$\pi_3$* in Figure 4), while the two remaining "$t_{2g}$" orbitals (dσ and dδ) are apparently unsaturated. This is not completely true, since electron density is provided by the filled pπ orbitals of the halide co-ligands. This point is highlighted by the drawings of the $ML_4$ frontier orbitals on the left-hand side of Scheme 4.

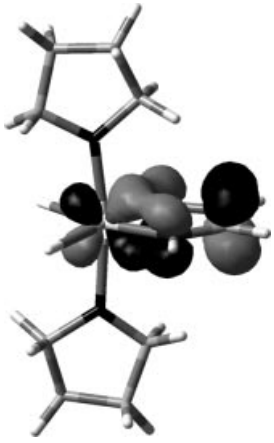

Figure 4. 3D isosurfaces corresponding to the computed HOMO of complex **3**.

Switching the Cl and thf ligands between the equatorial and axial positions in **3** should reduce the saturation of the dσ level because of the weaker π donor capabilities of thf. Conversely, dδ is less affected because it continues to receive the electron density donated from the low-lying $\pi_2$ orbital of DAD (see Scheme 2), which complements to the better donation from the Cl ligands. These trends were verified by optimizing three possible isomers, namely *trans*-thf,*cis*-chloride, *trans*-chloride,*cis*-thf and *trans*-chloride/thf,*cis*-chloride/thf. The latter two species are significantly less stable than the observed structure by +14.3 and +13.3 kcal mol$^{-1}$, respectively (see Supporting Information). A similar problem is found for the formally $d^2$ complex [$ZrCl_2$(tmeda){*o*-($Me_3SiN)_2C_6H_4$}][28] (**4**), which uniquely features a folded Zr(DAD) metallacycle (42° rotation about the N···N vector). In this case, the most stable conformer with the two chloride ligands in the equatorial plane is prevented from forming by the presence of the ethylenediamine chelate, which has no π-donor capabilities. Optimization of the simplest model [$ZrCl_2$(eda)(DAD)] (eda = $H_2NCH_2CH_2NH_2$) did not reproduce any bending of the metallacycle (see Supporting Information). A better result is obtained for the model **4a** with $SiH_3$ substituents at the nitrogen atoms of DAD, since this ligand exhibits a limited folding of 20°. The other geometric parameters are also in better agreement with the experimental ones (see Figure 5, a). The HOMO of the species in question (Figure 5, b) clearly shows that the $\pi_3$* level of DAD exerts a σ-type interaction with one lobe of a d orbital rather than the classic dπ/$\pi_3$* one. This was also our original interpretation of the chelate's bending in highly electron-deficient species such as [$TiCl_2$(DAD)],[13] for which a dianionic character of the chelate must be assumed.

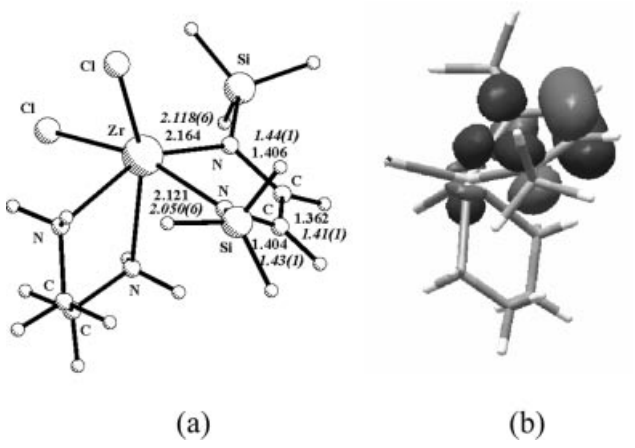


Figure 5. (a) Optimized structure of the model [$ZrCl_2$($H_3$Si-DAD)(eda)] (**4a**). (b) 3D isosurfaces corresponding to the computed HOMO of **4a**.

Folding of the metallacycle is as large as 54° in the optimized structure of an isomer of **4a** with two axial Cl ligands and the equatorial eda chelating, although the total energy is only 1.0 kcal mol$^{-1}$ higher. In this case, the larger unsaturation of the metal dσ orbital may again be partially compensated by an interaction with the nitrogen pπ lobes of the $\pi_3$* level as σ donors.

In summary, the examined pseudo-octahedral complexes have four frontier levels that are relatively close in energy (see Schemes 3 and 4) and can host up to four electrons (or five in the group 5 derivative). In the homoleptic systems, all the $t_2$-based orbitals ($a_1$ + e) are sufficiently saturated by electron donation from suitable combinations of the three DAD ligands. In halide complexes, the electron deficiency at the metal is compensated by the π-donor capabilities of the co-ligands. However, if the co-ligands do not have sufficient donor power or are not properly arranged, insufficient destabilization of a $t_{2g}$ orbital may cause a second-order Jahn–Teller effect. This is likely the cause for the bending of the metallacycle and the shift of the electrons toward DAD, with a consequent improvement of its donor capabilities.

## 5. Compounds Containing the Fragments $CpML_n$ and $Cp_2M$

Cyclopentadienido rings can also stabilize an M(DAD) metallacycle. A complex of the type [CpLM(DAD)] can be considered pseudo-octahedral, similarly to the species examined in the previous sections. In some cases, however, the number of co-ligands is higher. In fact, metal fragments of the type $CpML_2$, $CpML_3$ (L = two-electron donor or halide), and $Cp_2M$ can also support DAD coordination. Table 3 summarizes all the species containing at least one

 © 2007 Wiley-VCH Verlag GmbH & Co. KGaA, Weinheim 

Cp ligand that have been characterized by X-ray diffraction methods. The DAD ligand is generally folded in the latter, with a few exceptions, and hence is dianionic and the oxidation state of the group 4 metal is +4 ($d^0$ configuration). As underlined before, DAD behaves as the equivalent of a six-electron donor by exploiting a filled combination of the N pπ orbitals for the third σ-type donation.

Table 3. Structurally characterized mononuclear complexes formed by the fragments $CpML_n$ or $Cp_2M$ and one DAD ligand.

| Fragment $CpML_n$ type | Simplified formula[a] | CCDC refcode |
|---|---|---|
| $d^0$-CpMX | [Cp′Ti(DAD)Cl] | KISZOB[30] |
| | | WEVVUO[31] |
| | | WEVWAV[31] |
| | | YADBEL[32] |
| | | YADBIP[32] |
| | [CpTi(DAD)($NR_2$)] | WORGIT[33] |
| | | YAJCIV[34] |
| | [Cp′Zr(DAD)($NR_2$)] | NETZAN[35] |
| | | NETZER[35] |
| | [Cp*Ti(DAD)(CN)] | FAFMIJ[36] |
| CpMR | [Cp*Ti(DAD)($CH_3$)] | ICEGUS[37] |
| | [CpTi(DAD)($CH_2Ph$)] | QULSAR[38] |
| $CpML_2$ | [Cp′Zr(DAD)(allyl)] | POWVEC[39] |
| | [CpZr(DAD)(acetylacetoneiminato)] | QULRIY[38] |
| | [Cp*Hf(DAD)Cl(L)] (L = imino group) | YADYEH[40] |
| | [Cp′Zr(DAD)($NR_2$)($NHR_2$)] | WOJLAI[29] |
| $CpML_2X$ | [Cp′Zr(DAD)Cl($NHR_2$)$_2$] | WOJLEM[29] |
| CpM | [Cp*Ti(DAD)]$^+$[MeB($C_6F_5$)$_3$]$^-$ | TEGTAB[41] |
| $Cp_2M$ type | | |
| $Cp_2M$ | [$Cp_2$Ti(DAD)] | FUQCID[42] |
| | | JOFCIQ[43] |
| | [Cp′$_2$Zr(DAD)] | FATBAD[44] |
| | | HISWIP[45] |
| | | JOYXIE[46] |
| | | SINCAT[47] |
| | | VIZWEG[48] |
| | | VIZWIK[48] |
| | | BAMQUC[49] |
| | [$Cp_2$Hf(DAD)] | QULRUK[38] |

[a] Cp* = $C_5Me_5^-$, Cp = $C_5H_5^-$, Cp′ = substituted cyclopentadienido ligand.

Two of the complexes in Table 3 are exceptional in that they contain a planar M(DAD) metallacycle. Their simplified formulae are [Cp′Zr($NR_2$)($NHR_2$)(DAD)] and [Cp′ZrCl($NHR_2$)$_2$(DAD)] (see Figure 6) and refer to the species WOJLAI and WOJLEM,[29] respectively. The supporting metal fragments in the latter are electron rich because of the large number of co-ligands. In fact, both complexes can be assigned 18 electrons by assuming a formally uncharged DAD ligand ($d^2$ metal configuration). The fragments $CpML_2$ (in WOJLAI) and $CpML_3$ (in WOJLEM) can be considered isoelectronic by assuming that the amido ligand is able to donate as many as two electron pairs to the metal.

Also, it cannot be excluded that the planar coordination of DAD is not directly correlated with an uncharged α-diimino character but is a consequence of a geometric constraint in this case. In fact, the Cp′ and DAD units in both complexes are linked to each other by a $Si(CH_3)_2$ bridge between one N atom and one Cp′ carbon atom. Such a connectivity can reduce the flexibility of DAD and therefore its capability for bending. Moreover, the octacoordinate complex (the geometry can be roughly described as a capped four-legged piano stool, see Figure 6) is highly hindered and the metal may not be able to receive an extra lone pair on the side opposite to the Cp′ ring. Interestingly, the complex [CpHfL(Cl)(DAD)] (refcode YADYEH[40]), which is also of the type [$CpML_2$(DAD)], adopts a four-legged, uncapped piano-stool coordination and shows an evident, although not large, folding of the metallacycle (about 20°). The DAD ligand is also not isolated in this case but is directly connected to other co-ligands.

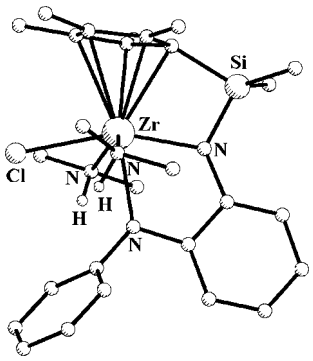


Figure 6. Experimental structure of [Cp′Zr(DAD)Cl($NHR_2$)$_2$] (refcode WOJLEM).

The relation between the rigidity and electronic structure of these complexes might deserve an ad hoc theoretical study. In general, the concept of isolobality is helpful for drawing useful relations between the Cp derivatives in question and other [$L_n$M(DAD)] complexes. MO diagrams similar to those in Schemes 3 and 4 can also be constructed for the $Cp_2M$ and $CpL_nM$ complexes of DAD. The easiest parallelism applies to the orbital interactions in the [$L_4$M(DAD)] and [CpMCl(DAD)] models, and these qualitative arguments can also be extended to more complex systems. Some of the points concerning the electronic structures of selected Cp metal complexes of DAD have been addressed by some of us in a previous theoretical paper.[50] Here, we simply note that DFT calculations with a QTAIM analysis[51] fully confirmed that, upon bending of DAD, the donation of a third electron pair to the metal occurs through the nitrogen pπ orbitals and not through the C=C π bond of the dianionic enediamido ligand, as often stressed by other authors.[14]

## 6. Electron-Deficient [$X_2$M(DAD)] Complexes and Related Homoleptic [M(DAD)$_2$] Species

The DAD ligand, together with only two co-ligands, is found to stabilize pseudo-tetrahedral coordination at a group 4 metal. The upper part of Table 4 lists the known structures of type [$L_2$M(DAD)], where the metallacycle is invariably folded. For this reason DAD is considered dianionic. In turn, the metal has a $d^0$ configuration and the

 © 2007 Wiley-VCH Verlag GmbH & Co. KGaA, Weinheim 

Table 4. Structurally characterized mononuclear complexes of the types $[MX_2(DAD)]$ and $[M(DAD)_2]$.

| Fragment $ML_2$ typ | Simplified formula | CCDC refcode |
|---|---|---|
| $ML_2$ | $[Ti(DAD)(OAr)_2]$ | FOMZAI[53] |
| | | FOMZIQ[53] |
| | | HOZGAE[54] |
| | | HOZGAE01[55] |
| | $[Zr(DAD)(OAr)_2]$ | FOMZEM[56] |
| | | FOMZEM10[56] |
| | $[Ti(DAD)(BH_4)Cl]$ | JUWSID[57] |
| | $[Ti(DAD)(BH_4)_2]$ | JUWSOJ[57] |
| | $[Ti(DAD)(BH_4)_2]$ | JUWSUP[57] |
| | $[Ti(DAD)Cl_2]$ | ZUJSEC[58] |
| Homoleptic | | |
| $M(DAD)_2$ | $[Ti\{(o\text{-}MeC_6H_4)NC(Me)C(Me)N(o\text{-}MeC_6H_4)\}_2]$ | WEZXAA[59] |
| | $[Zr\{(iPr_3SiN)_2C_6H_4\}_2]$ | ZUJSAY[58] |
| | $[Zr\{(Me_3SiN)_2C_6H_4\}_2]$ | FIFQER[17] |

system can, in principle, be related to classical tetrahedral complexes of the main group elements. On the other hand, the ability of a bent DAD to donate three electron pairs confirms that the d orbitals play a role, although they obviously cannot be saturated by a single DAD ligand. Thus, the two co-ligands (e.g. halides, phenoxides, and $BH_4^-$; see Table 4) also act as π donors. The electronic structure of $[X_2M(DAD)]$ species has previously been investigated by us from a theoretical viewpoint[13] and will therefore not be addressed in detail here. $[L_2M(DAD)]$ complexes have also been analyzed theoretically as the end-products of the intramolecular coupling of two $\eta^2$-iminoacyl ligands in bis(aryloxide) complexes of zirconium.[52] We therefore focus on the homoleptic species $[M(DAD)_2]$ (see the lower part of Table 4), which raise the most intriguing questions because of the recently ascertained dichotomy of planar or bent metallacycles.

We start with a qualitative MO Scheme for a $[M(DAD)_2]$ model with two planar perpendicularly oriented metallacycles (see Scheme 5).

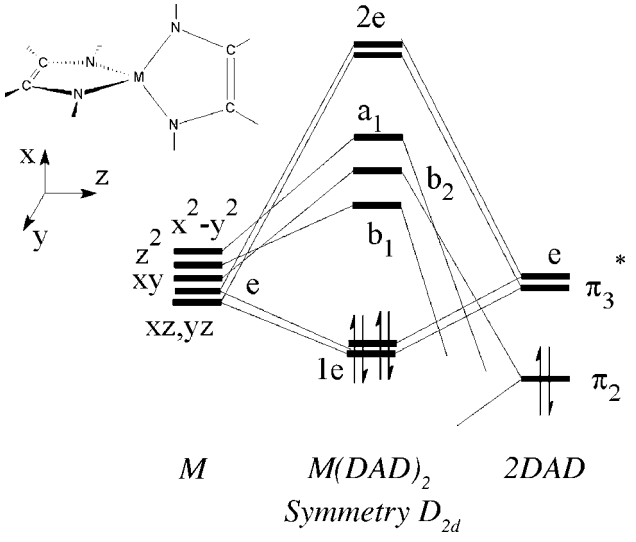


Scheme 5. Simplified MO diagram for $D_{2d}$-symmetric $[M(DAD)_2]$ complexes.

Four low-lying σ bonding MOs, which correspond to the donation from nitrogen lone pairs into s and p metal orbitals, are not shown. It is evident from the frontier region of the diagram that a degenerate bonding set (1e) is formed between the metal *xz* and *yz* orbitals and suitable $\pi_3$* orbitals of the two ligands. The three remaining d orbitals are destabilized from other low-lying and filled ligand orbitals, which means that the HOMO–LUMO gap is sufficiently large (>1 eV). In particular, the *xy* orbital interacts with a combination of the $\pi_2$ ligand levels (see Scheme 2), while $x^2$–$y^2$ and $z^2$ are pushed higher by suitable combinations of the nitrogen σ lone pairs, which are already used for donation into high lying s and p metal orbitals. If the saturation of $x^2$–$y^2$ and $z^2$ is insufficient, folding of the two metallacycles may be induced by a second-order Jahn–Teller effect similar to that mentioned above for some pseudo-octahedral species.

The first two complexes of the type $[M(DAD)_2]$ to be characterized, namely $[Ti\{(o\text{-}MeC_6H_4)N(CMe)\}_2]$ (**5**; WEZXAA[59]) and $[Zr\{(iPr_3SiN)_2C_6H_4\}_2]$ (**6**; ZUJSAY[58]) are bent metallacycles, while in the more recently characterized species $[Zr\{(Me_3SiN)_2C_6H_4\}_2]$ (**7**; FIFQER[17]) the two rings are perfectly planar and orthogonal. It is noteworthy that the two non-isostructural zirconium complexes **6** and **7** have the same $C_6H_4$ backbone and differ only in the nature of the silyl substituents at the N atoms. The subtle electronic factors that affect the dichotomy have therefore been examined by different computational techniques.

The simplest models $[M\{MeNC(H)=C(H)NMe\}_2]$ (M = Ti **5a**, Zr **6a**) with $C_2$ symmetry were optimized first at the DFT level. The absolute minima invariably contain bent metallacycles, as indicated in Figure 7.

The pseudo-tetrahedral geometry observed in the X-ray structures of **5** and **6** is satisfactorily reproduced, as is the amount of twisting of each metallacycle (about 50° about the N···N vector). The shorter C–C distance in **6a** (by 0.05 Å) is most likely a consequence of the replacement of the more delocalized $C_6H_4$ backbone with the CH=CH grouping in the DAD ligand.

 © 2007 Wiley-VCH Verlag GmbH & Co. KGaA, Weinheim 

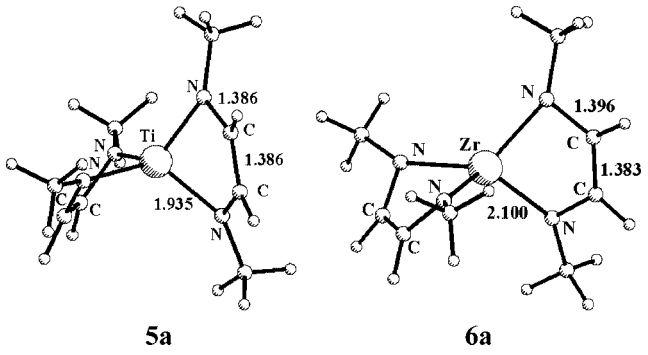


Figure 7. Optimized structures of the homoleptic model complexes [M(Me-DAD)$_2$] (M = Ti **5a**, Zr **6a**) with bent metallacycles.

With respect to the MOs in Scheme 5, the lowering of the symmetry from $D_{2d}$ to $C_2$ mixes the character of the barely saturated $x^2$–$y^2$ and $z^2$ orbitals into the highest two filled MOs (the previous 1e HOMOs). As pointed out in our original work on [TiCl$_2$(DAD)][13] and here for some [L$_4$M(DAD)] species, bending transforms most of the dπ–pπ bonding character of the frontier orbitals into a σ-type interaction between the nitrogen pπ lobes and single lobes of the $x^2$–$y^2$ and $z^2$ orbitals. This aspect is highlighted by the HOMO and HOMO–1 for complex **5a** (see Figure 8).

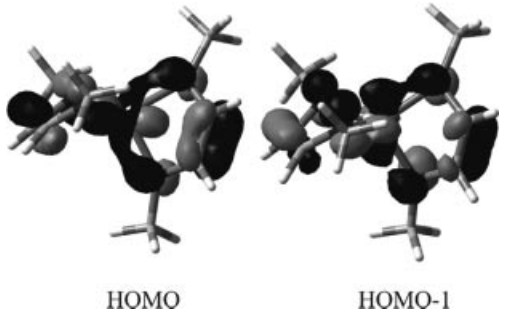


Figure 8. 3D isosurfaces corresponding to the computed HOMO and HOMO–1 of **5a**.

The optimized model complexes **5b** and **6b** with planar metallacycles ($D_{2d}$ symmetry) are associated with two high imaginary frequencies, which clearly indicates the preference of the two ligands to fold. The total energy is higher than that at the absolute $C_2$ minimum by as much as 20 kcal mol$^{-1}$. The energy difference between the planar and bent forms is reduced to the order of only 1–3 kcal mol$^{-1}$, when the calculations are repeated with DAD ligands having a C$_6$H$_4$ backbone. This is most likely due to a significant delocalization of the electron density toward the aromatic ring and away from the nitrogen atoms. This reduces the possibility of the latter jointly becoming the donors of a third electron pair when the metallacycle is bent. Under these circumstances, it is possible for DAD to maintain the enediamido character associated with the planar conformation, which means that the dichotomy of the two geometries and the existence of two isomers is plausible. Since the zirconium complexes **6** and **7** have different ring geometries and differ only in having *i*Pr$_3$Si or Me$_3$Si substituents, respectively, the relative effects of the latter on the stability of each isomer must be rationalized.

One CH$_3$ group of each silyl substituent in the experimental structure of **7** hangs over the metal atom with two relatively close H atoms and one C–H vector pointing away. Although the shortest Zr···H separation is as long as 3.04 Å, such an arrangement is reminiscent of the Zr–η$^3$-CH$_2$ agostic interactions that have been classified by some of us recently,[60] and this is also the classical bonding mode between a metal center and a free alkane.[61] Thus, the metal center in **7** seems to be involved in four simultaneous interactions of the latter type with four different CH$_3$ groups, which are pairwise aligned roughly along the two main perpendicular directions.

To verify whether the agostic interactions really exist, various models of **7** have been investigated (see Figure 9).

First of all two $D_{2d}$ structures (**7a** and **7b** in Figure 9) were optimized with MeH$_2$Si substituents in place of the Me$_3$Si ones. These model complexes have imposed planar metallacycles but differ in the orientation of the unique methyl groups, which can either lie close to or away from the metal center. The shortest Zr···H distances in **7a** are much longer than the experimental ones (3.45 vs. 3.043 Å) and the computed N–Si–C angle is less closed [107.5° vs. 103.5(1)°], which suggests that the agostic interactions, if real, are not reproduced by the calculations. Further information was expected from model **7b** which, due to its stereochemistry, cannot feature any agostic interaction. This conformer, which is not even a minimum on the PES (imaginary frequencies are present), is energetically disfavored with respect to **7a** by 22 kcal mol$^{-1}$. This difference is not a proof of the agostic interactions in **7a** but has a clear steric origin. In fact, the significantly open N–Si–C angles (120.7°) best highlight the short contacts between the C$_6$H$_4$ backbone and the coplanar methyl groups, and hence their repulsive effects.

Finally, the most complete model of complex **7**, with actual Me$_3$Si substituents, was optimized in both $D_{2d}$ and $C_2$ symmetries (**7c** and **7d**, respectively, in Figure 9). The results with these complexes show that the molecule can exist in the gas phase with either planar or bent metallacycles since both models are real minima on the PES. Importantly, the folding of the ligand in **7d** still causes a stabilization of only 2 kcal mol$^{-1}$, which is one order of magnitude smaller than that found for species without the aryl backbone. For this reason, it is not totally surprising that isomer **7c** is found in the solid state. Furthermore, the small energy difference is in agreement with the fluxional behavior observed in several [X$_2$M(DAD)] complexes,[38,47,58,59] as shown schematically in Scheme 6.

With regard to the critical geometrical parameters of the Me$_3$Si displacement in **7c**, the agreement with those of the experimental structure is good but not excellent. In any case, the trends with respect to **7a** indicate shorter Zr···H contact distances (3.30 Å) and more acute N–Si–C angles (105.5°). Again, the closeness of one methyl group to the metal atom seems due to the steric repulsions between the C$_6$H$_4$ ring and the other methyl groups rather than to an actual agostic interaction.

 © 2007 Wiley-VCH Verlag GmbH & Co. KGaA, Weinheim 

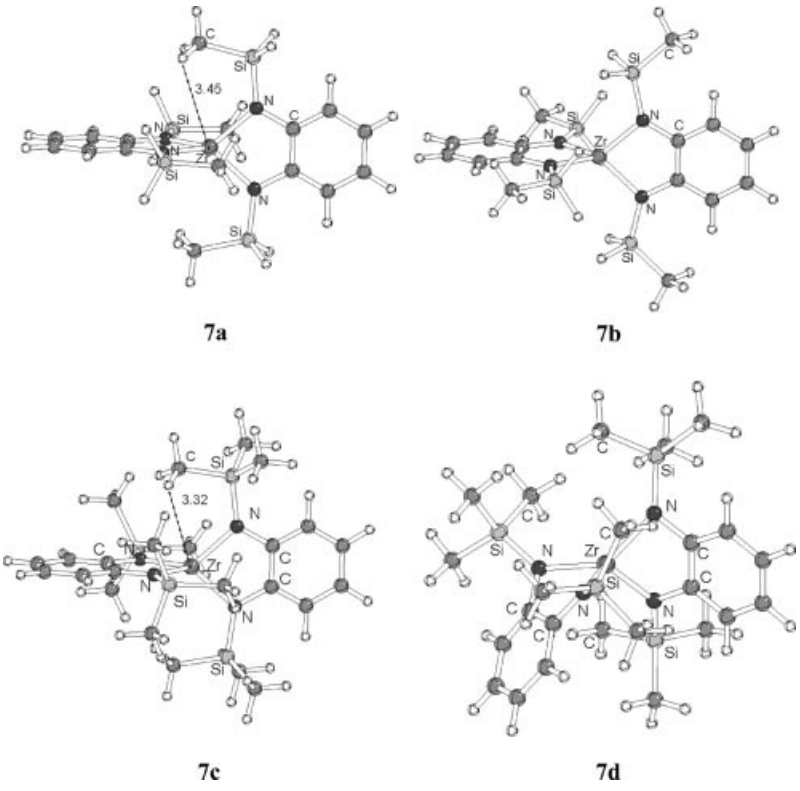


Figure 9. Optimized $D_{2d}$ structures of $[Zr\{(MeH_2SiN)_2C_6H_4\}_2]$ with 180°-reoriented $MeH_2Si$ substituents (models **7a** and **7b**). Structures **7c** and **7d** are $D_{2d}$- (planar metallacycles) and $C_2$-symmetric (bent metallacycles) models of complex **7** with $Me_3Si$ substituents. The dotted lines in **7a** and **7c** highlight one of the equivalent shortest Zr···H contacts.

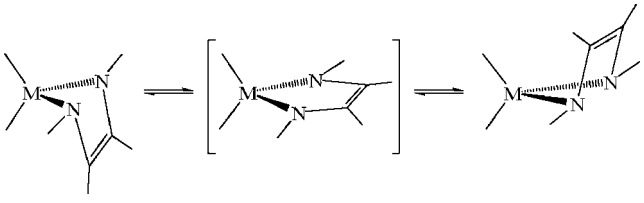

Scheme 6. Dynamic equilibrium between the conformers of folded DAD complexes.

## 7. QTAIM Analysis of the Homoleptic [Zr(DAD)$_2$] Species

In order to find a reasonable answer to the nature of the interaction, which in complex **7** pushes four methyl groups toward the inner coordination sphere of the metal, a QTAIM[51] analysis was carried out for model **7c** as other QTAIM studies have been able to clearly highlight Ti···H and Zr···H interactions in systems where they really exist.[62]

The structures in Figure 10 (see part A) show all the expected bond critical points (bcp's) for the normal interatomic interactions, none of which appears in the region of possible Zr···H interactions. Furthermore, the Laplacian map indicates a localized depletion in these regions, which means that no confirmation of the agostic bonds is found. A similar study by Coppens et al., also using the QTAIM method, was also unable to detect any agostic interactions in the open zirconocene complex $[Zr(2,4\text{-}C_7H_{11})\{(i\text{Pr})NCHPhCH_2\text{-}CMe{=}CHCMe{=}CH_2\}]$.[63]

Remarkably, another type of attractive interaction can be seen from Figure 10 (A), namely eight bcp's appear between the N atoms and the methyl H atoms, which were initially supposed to participate in agostic interactions with the metal. These bcp's essentially correspond to weak C–H···N hydrogen bonds, although it remains questionable whether these can be the driving force for the $Me_3Si$ group to lean toward the metal. The computed N···H separations of 3.12 Å (av.) are somewhat longer than the experimental average value of 3.05 Å, which also means that the electron density at the bcp's is rather small (0.005 e Å$^{-3}$). In any case, the cumulative strength of as many as eight interactions of this type could be stabilizing. Incidentally, an equivalent situation (not shown) is found for the structure of $[Zr\{(Me_3SiN)_2C_6H_{10}\}_2]$,[64] which differs from **7** in having a cyclohexyl backbone instead of an aryl one (in other words the carbon atoms of the metallacycle are fully saturated). The DFT calculations for this molecule indicate that there is only one conformer with two quasi-planar and perpendicular metallacycles.

Rather different results are obtained from the QTAIM analysis of the $C_2$ isomer **7d** with bent metallacycles (Figure 10, B). Recall that the latter conformation is observed in complex **6** (ZUJSAY) with $i\text{Pr}_3Si$ substituents in place of the $Me_3Si$ ones. Only two of the eight C–H···N bcp's remain in isomer **7d**, and their densities are at least 20% lower than those in **7c**.

In conclusion, the larger number of stabilizing N···H interactions in **7a** seem to justify the reduced energy difference

 © 2007 Wiley-VCH Verlag GmbH & Co. KGaA, Weinheim 

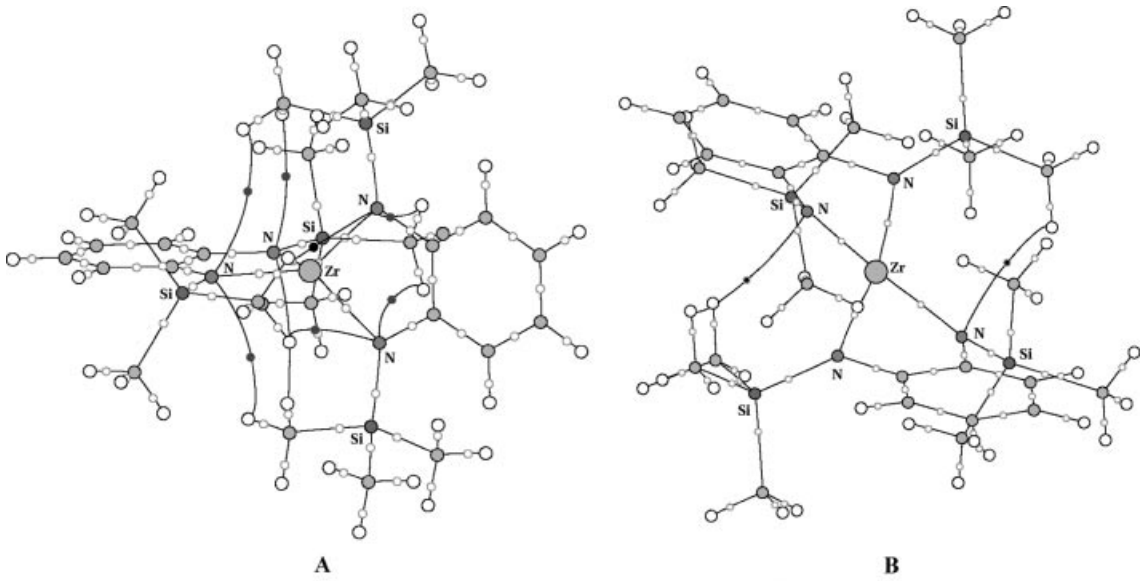


Figure 10. Molecular graphs of the $D_{2d}$- and $C_2$-symmetric models **7c** and **7d** (A and B, respectively). All calculated bcp's are shown except for ring and cage critical points. The black bcp's represent curves associated with the N···H interactions.

between the isomers and the isolation of this complex in the solid state. Recall that when the metallacycles are folded, the N pπ orbitals of the DAD ligands (lone pair combinations) give rise to σ-type interactions with the metal center. In this case, the feature is contrasted by the hydrogen bonding, which, by restricting the added donor capabilities of the combined nitrogen atoms, can partially favor the planar conformation.

In any case, the planar metallacycles observed in complex **7** must be considered rather exceptional and are only possible when at least three main factors occur simultaneously. These are: i) the peculiar conformation of the $Me_3Si$-substituted DAD ligands, which places one $CH_3$ group over the Zr–N bonds; ii) the role played by the eight N···H interactions; iii) the incorporation of the aromatic backbone in DAD. In fact, when [Zr($Me_3$Si-DAD)$_2$] models are optimized with the simplest enediamido skeleton in place of the *o*-phenylenediamido one, the bent conformation is stabilized by as much as –19.3 kcal mol$^{-1}$. In this case, a QTAIM analysis reveals no bcp's associated with any N···H interaction.

## 8. Relationship Between [M(DAD)$_3$] and [M(DAD)$_2$] Complexes

The existence of both the 1:2 and 1:3 homoleptic species also raises the interesting problem of their interconvertibility. The energies of all the species that appear in Equation (1) are available, which means that it should be possible to gain some useful hints regarding their interconversion.

$$[Ti(Me\text{-}DAD)_2] + Me\text{-}DAD \rightleftharpoons [Ti(Me\text{-}DAD)_3] \quad (1)$$

The thermochemical values calculated for the gas phase indicate that the enthalpy of reaction and the Gibbs free energy (at 298 K) are –27.0 and –13.2 kcal mol$^{-1}$, respectively, which means that the reaction is exothermic, as would be expected in view of the better metal saturation in the [Ti(Me-DAD)$_3$] species. This result is compatible with some experimental findings. For example, tom Dieck and co-workers have reported that the addition of *i*Pr-DAD to [Ti(*i*Pr-DAD)$_2$] yields the complex [Ti(*i*Pr-DAD)$_3$],[65] and Scholz and co-workers have described that the reduction of [$TiCl_4$(thf)$_2$] in the presence of magnesium gives [Ti(DAD)$_2$] in the presence of two equivalents of DAD or [Ti(DAD)$_3$] with an excess of ligand.[59] As for the reverse reaction, the expulsion of one ligand from [M(DAD)$_3$] introduces significant metal unsaturation, which the system generally compensates for by ligand folding. In this regard, the nature of the substituents attached to the nitrogen centers can play a decisive role, as described previously. Two recent contributions with metals other than those of group 4 have demonstrated the decisive influence of the substituents. Thus, substitution of the *t*Bu groups with $C_6F_5$ ones in a diazabutadiene ligand induces a variation in the oxidation state of europium,[66] and the selection of alkyl or aryl substituents in α-diimino ligands coordinated to iron affects the spin state of the metal, which is correlated with a specific catalytic activity.[67]

## 9. Conclusions

We have extensively reviewed the known complexes formed by a metal of the group 4 and at least one α-diimino ligand. The latter, due to its *noninnocent* character, can also be described as a dianionic enediamido species. We have focused our attention on the electronic aspects of the metal–DAD bonding and on geometric effects, which are triggered depending on the ligand's electronic and steric properties and the number of co-ligands as well as the oxidation state of the metal. In particular, the frontier MOs are strongly affected by the folding of the metallacycles, which permits a greater electron donation ability from the ligand. In general, com-

 © 2007 Wiley-VCH Verlag GmbH & Co. KGaA, Weinheim 

plexes with a higher coordination number (pseudo-octahedral), including the homoleptic $[M(DAD)_3]$ class, feature planar metallacycles, which contrasts with the folding of the metallacycles observed in $[L_2M(DAD)]$, CpLn, and $[M(DAD)_2]$ complexes, where the metal is less saturated (higher oxidation state). Notable exceptions have been highlighted. The various cases have been analyzed in terms of DFT calculations and qualitative MO arguments. When the findings are ambiguous (where the DFT response does not allow for discerning the structural preferences) the QTAIM method has been adopted to extract useful information about the distribution of the electron density within the models. In particular, we have found that for a given stereochemistry, unpredicted C–H···N hydrogen bonding can contribute to the stability for specific types of planar metallacycles. Finally, we have analyzed the energetics behind the interconversion between $[M(DAD)_2]$ and $[M(DAD)_3]$ complexes, which has been found to be exclusive to group 4 metals.

**Supporting Information** (see also the footnote on the first page of this article): Seven tables (labeled S1–S7) with selected structural data (bond lengths and angles), relative energies, and optimized stuctures for calculated and experimental complexes. Five tables with optimized coordinates for compounds **7a**–**d**. Additional information regarding the QTAIM analyses is also provided.

## Acknowledgments

Financial support from the Secretaría de Estado de Educación y Universidades (sabbatical stay at ICCOM, A. G.) and the Ministerio de Educación y Ciencia (CTQ2004-00084) is gratefully acknowledged. The quantum-chemical calculations were carried out with the High Performance Systems of the Centro di Calcolo Interuniversitario CINECA (CNR-CINECA agreement) and the facilities of SIC (University of Seville).

[1] a) G. van Koten, K. Vrieze, *Adv. Organomet. Chem.* **1982**, *21*, 151; b) K. Vrieze, *J. Organomet. Chem.* **1986**, *300*, 307.
[2] See, for example: L. K. Johnson, C. M. Killian, M. Brookhart, *J. Am. Chem. Soc.* **1995**, *117*, 6414.
[3] For selected examples see: a) D. F. Wass, G. J. P. Britovsek, V. C. Gibson, *Angew. Chem. Int. Ed.* **1999**, *38*, 428; b) J. D. Scollard, D. H. McConville, J. J. Vittal, N. C. Payne, *J. Mol. Catal. A* **1998**, *128*, 201; c) S. T. Rettig, J. D. Scollard, D. H. McConville, *Organometallics* **1997**, *16*, 1810; d) J. J. Vittal, J. D. Scollard, D. H. McConville, *Organometallics* **1997**, *16*, 4415; e) J. J. Vittal, J. D. Scollard, D. H. McConville, N. C. Payne, *Macromolecules* **1996**, *29*, 5241; f) A. McCamley, S. Tinkler, R. J. Deeth, D. J. Duncalf, *Chem. Commun.* **1996**, 2623; g) A. D. Horton, J. de With, *Chem. Commun.* **1996**, 1375.
[4] a) A. Galindo, M. Gómez, D. del Río, F. Sánchez, *Eur. J. Inorg. Chem.* **2002**, 1326; b) D. del Río, A. Galindo, *J. Organomet. Chem.* **2002**, *655*, 16.
[5] A. Galindo, A. Mealli, C. Ienco, *Comments Inorg. Chem.* **2002**, *23*, 401.
[6] A. Anillo, S. Garcia-Granda, R. Obeso-Rosete, A. Galindo, A. Ienco, C. Mealli, *Inorg. Chim. Acta* **2003**, *350*, 557.
[7] See, for example: M. D. Ward, J. A. McCleverty, *J. Chem. Soc., Dalton Trans.* **2002**, 275 and references cited therein.
[8] *Cambridge Structural Database System*, Cambridge Crystallographic Data Centre, 12 Union Road, Cambridge, CB2 1EZ, UK.
[9] For studies of binuclear complexes with a bridging diazabutadiene ligand see: a) A. Galindo, *C. R. Chimie* **2005**, *8*, 1353; b) A. Anillo, M. R. Díaz, S. García-Granda, R. Obeso-Rosete, A. Galindo, A. Ienco, C. Mealli, *Organometallics* **2004**, *23*, 471.
[10] Selected examples of structurally characterized binuclear complexes containing one or more DAD ligands can be found at the following refcodes: GUHYIR, GUHYAJ, GUHXUC, KIMNOJ, QULROE, UBUZEW, and XOFPIR.
[11] See, for example, Co complexes in: M. M. Khusniyarov, K. Harms, O. Burghays, J. Sundermeyer, *Eur. J. Inorg. Chem.* **2006**, 2985.
[12] C. Mealli, A. Ienco, A. Anillo, S. Garcia-Granda, R. Obeso-Rosete, *Inorg. Chem.* **1997**, *36*, 3724.
[13] A. Galindo, A. Ienco, C. Mealli, *New J. Chem.* **2000**, *24*, 73.
[14] See, for example: A. Nakamura, K. Mashima, *J. Organomet. Chem.* **2001**, *621*, 224.
[15] An interaction between a C=C bond and uranium metal (through a 5f orbital) has recently been proposed as being responsible for the folded conformation in a dithiolene ligand: L. Belkhiri, T. Arliguie, P. Thuéry, M. Fourmigué, A. Boucekkine, M. Ephritikhine, *Organometallics* **2006**, *25*, 2782.
[16] a) E. Bill, E. Bothe, P. Chaudhuri, K. Chlopek, D. Herebian, S. Kokatam, K. Ray, T. Weyhermüller, F. Neese, K. Wieghardt, *Chem. Eur. J.* **2005**, *11*, 204; b) D. Herebian, E. Bothe, F. Neese, T. Weyhermüller, K. Wieghardt, *J. Am. Chem. Soc.* **2003**, *125*, 9116; c) V. Bachler, G. Olbrich, F. Neese, K. Wieghardt, *Inorg. Chem.* **2002**, *41*, 4179.
[17] A. F. Heyduk, K. J. Blackmore, N. A. Ketterer, J. W. Ziller, *Inorg. Chem.* **2005**, *44*, 468.
[18] K.-H. Thiele, B. Richter, B. Neumuller, *Z. Anorg. Allg. Chem.* **1994**, *620*, 1627.
[19] B. Richter, J. Scholz, B. Neumuller, R. Weimann, H. Schumann, *Z. Anorg. Allg. Chem.* **1995**, *621*, 365.
[20] P. J. Daff, M. Etienne, B. Donnadieu, S. Z. Knottenbelt, J. E. McGrady, *J. Am. Chem. Soc.* **2002**, *124*, 3818.
[21] a) R. Hoffmann, W. N. Lipscomb, *J. Chem. Phys.* **1962**, *36*, 2872; b) R. Hoffmann, W. N. Lipscomb, *J. Chem. Phys.* **1962**, *37*, 3489; c) C. Mealli, A. Ienco, D. M. Proserpio, *Book of Abstracts of the XXXIII ICCC*, Florence, Italy, **1998**, p. 510; d) C. Mealli, D. Proserpio, *J. Chem. Educ.* **1990**, *67*, 399.
[22] T. Spaniel, H. Gorls, J. Scholz, *Angew. Chem. Int. Ed.* **1998**, *37*, 1862.
[23] S. Danièle, P. B. Hitchcock, M. F. Lappert, P. G. Merle, *J. Chem. Soc., Dalton Trans.* **2001**, 13.
[24] L. Giannini, A. Caselli, E. Solari, C. Floriani, A. Chiesi-Villa, C. Rizzoli, N. Re, A. Sgamellotti, *J. Am. Chem. Soc.* **1997**, *119*, 9709.
[25] M. J. Scott, S. J. Lippard, *Organometallics* **1997**, *16*, 5857.
[26] T.-G. Ong, D. Wood, G. P. A. Yap, D. S. Richeson, *Organometallics* **2002**, *21*, 1.
[27] J. M. McInnes, A. J. Blake, P. Mountford, *J. Chem. Soc., Dalton Trans.* **1998**, 3623.
[28] S. Danièle, P. B. Hitchcock, M. F. Lappert, P. G. Merle, *J. Chem. Soc., Dalton Trans.* **2001**, 13.
[29] P. Doufou, K. A. Abboud, J. M. Boncella, *J. Organomet. Chem.* **2000**, *603*, 213.
[30] J. Scholz, A. Dietrich, H. Schumann, K.-H. Thiele, *Chem. Ber.* **1991**, *124*, 1035.
[31] G. A. Hadi, J. Wunderle, K.-H. Thiele, R. Froehlich, *Z. Kristallogr.* **1994**, *209*, 372.
[32] E. Herdtweck, V. Tabernero, T. Cuenca, *Eur. J. Inorg. Chem.* **2004**, 3154.
[33] R. Tomaszewski, K.-C. Lam, A. L. Reinghold, R. D. Ernst, *Organometallics* **1999**, *18*, 4174.
[34] T. E. Waldman, A. M. Wilson, A. L. Rheingold, R. D. Ernst, E. Melendez, *Organometallics* **1992**, *11*, 3201.
[35] L. Kloppenburg, J. L. Petersen, *Organometallics* **1997**, *16*, 3548.
[36] G. Greidanus-Strom, C. A. G. Carter, J. M. Stryker, *Organometallics* **2002**, *21*, 1011.
[37] F. Amor, P. Gomez-Sal, P. Okuda, J. Royo, *Organometallics* **2000**, *19*, 5168.

 © 2007 Wiley-VCH Verlag GmbH & Co. KGaA, Weinheim 

[38] J. Scholz, G. A. Hadi, K.-H. Thiele, H. Gorls, R. Weimann, H. Sieler, J. Schumann, *J. Organomet. Chem.* **2001**, *626*, 243.
[39] G. J. Pindado, M. Bochmann, M. Thornton-Pett, *J. Chem. Soc., Dalton Trans.* **1998**, 393.
[40] J. E. Bol, B. Hessen, J. H. Teuben, W. J. J. Smeets, A. L. Spek, *Organometallics* **1992**, *11*, 1981.
[41] V. Tabernero, M. C. Maestre, G. Jiménez, T. Cuenca, C. Ramírez de Arellano, *Organometallics* **2006**, *25*, 1723.
[42] A. Spannenberg, T. Rosenthal, U. Zippel, *Z. Kristallogr.* **2000**, *215*, 365.
[43] A. Tillack, P. Arndt, A. Spannenberg, R. Kempe, T. Zippel, U. Rosenthal, *Z. Anorg. Allg. Chem.* **1998**, *624*, 2038.
[44] J. R. Bocarsly, C. Floriani, A. Chiesi-Villa, C. Guastini, *Organometallics* **1986**, *5*, 2380.
[45] T. Zippel, P. Arndt, A. Ohff, A. Spannenberg, R. Kempe, U. Rosenthal, *Organometallics* **1998**, *17*, 4429.
[46] F. J. Petersen, J. L. Berg, *Tetrahedron* **1992**, *48*, 4749.
[47] J. Scholz, M. Dlikan, D. Strohl, A. Dietrich, H. Schumann, K.-H. Thiele, *Chem. Ber.* **1990**, *123*, 2279.
[48] F. J. Petersen, J. L. Berg, *Organometallics* **1991**, *10*, 1599.
[49] T. V. V. Ramakrishna, S. Lushnikova, *Organometallics* **2002**, *21*, 5685.
[50] A. Galindo, D. del Río, C. Mealli, A. Ienco, C. Bo, *J. Organomet. Chem.* **2004**, *689*, 2847.
[51] R. F. W. Bader, *Atoms in Molecules: A Quantum Theory*, Oxford University Press, Oxford, **1990**.
[52] a) F. de Angelis, A. Sgamelloti, N. Re, A. Fantacci, *Organometallics* **2005**, *24*, 1867; b) J. H. Hardesty, T. A. Albright, S. Kahla, *Organometallics* **2000**, *19*, 4159.
[53] a) L. R. Chamberlain, L. D. Durfee, P. E. Fanwick, L. M. Kobriger, S. L. Latesky, A. K. McMullen, B. D. Steffey, I. P. Rothwell, K. Folting, J. C. Huffman, *J. Am. Chem. Soc.* **1987**, *109*, 6068; b) L. R. Chamberlain, I. P. Rothwell, J. C. Huffman, *J. Chem. Soc., Chem. Commun.* **1986**, 1203.
[54] M. G. Thorn, P. E. Fanwick, I. P. Rothwell, *Organometallics* **1999**, *18*, 4442.
[55] R. E. Marsh, *Acta Crystallogr., Sect. B* **2005**, *61*, 359.
[56] S. L. Latesky, A. K. McMullen, G. P. Niccolai, I. P. Rothwell, J. C. Huffman, *Organometallics* **1985**, *4*, 1896.
[57] W. A. Herrmann, M. Denk, W. Scherer, F.-R. Klingan, *J. Organomet. Chem.* **1993**, *444*, C21.
[58] K. Aoyagi, P. K. Gantzel, K. Kalai, T. D. Tilley, *Organometallics* **1996**, *15*, 923.
[59] R. Goddard, C. Kruger, G. A. Hadi, K.-H. Thiele, J. Scholz, *Z. Naturforsch., Teil B* **1994**, *49*, 519.
[60] W. Baratta, C. Mealli, E. Herdtweck, A. Ienco, S. A. Mason, P. Rigo, *J. Am. Chem. Soc.* **2004**, *126*, 5549–5562.
[61] a) G. S. Hill, R. J. Puddephatt, *Organometallics* **1998**, *17*, 1478; b) J. Song, M. B. Hall, *Organometallics* **1993**, *12*, 3118; c) N. Koga, K. Morokuma, *J. Am. Chem. Soc.* **1993**, *115*, 6883; d) P. Margl, T. Ziegler, P. E. Blöchl, *J. Am. Chem. Soc.* **1995**, *117*, 12625; e) H. Heiberg, L. Hohansson, O. Gropen, O. B. Ryan, O. Swang, M. Tilset, *J. Am. Chem. Soc.* **2000**, *122*, 10831; f) K. E. Janak, D. G. Churchill, G. Parkin, *Chem. Commun.* **2003**, 22; g) J. C. Green, J. N. Harvey, R. Poli, *J. Chem. Soc., Dalton Trans.* **2002**, 1861.
[62] a) P. L. A. Popelier, G. Logotheties, *J. Organomet. Chem.* **1998**, *555*, 101; b) I. Vidal, S. Melchor, I. Alkorta, J. Elguero, M. R. Sundberg, J. A. Dobado, *Organometallics* **2006**, *25*, 5638; c) W. Scherer, W. Hieringer, M. Spiegler, P. Sirsch, G. S. McGrady, A. J. Downs, A. Haaland, B. Pedersen, *Chem. Commun.* **1998**, 2471.
[63] P. Coppens, B. Iversen, F. K. Larsen, *Coord. Chem. Rev.* **2005**, *249*, 179.
[64] a) J.-F. Li, L.-H. Weng, S.-P. Huang, H.-B. Tong, D.-S. Liu, *Acta Crystallogr., Sect. E* **2002**, *58*, m510; b) N. A. H. Male, M. Thornton-Pett, M. Bochmann, *J. Chem. Soc., Dalton Trans.* **1997**, 2487.
[65] H. tom Dieck, H. J. Rieger, G. Fendesak, *Inorg. Chim. Acta* **1990**, *177*, 191.
[66] J. A. Moore, A. H. Cowley, J. C. Gordon, *Organometallics* **2006**, *25*, 5207.
[67] M. P. Shaver, L. E. N. Allan, H. S. Rzepa, V. C. Gibson, *Angew. Chem. Int. Ed.* **2006**, *45*, 1241.

Received: January 22, 2007
Published Online: April 23, 2007

 © 2007 Wiley-VCH Verlag GmbH & Co. KGaA, Weinheim 

DOI: 10.1002/ejic.200700008

# Superoxide Reductases

**Alice S. Pereira,[a] Pedro Tavares,[a] Filipe Folgosa,[a] Rui M. Almeida,[a] Isabel Moura,*[a] and José J. G. Moura[a]**

**Keywords:** Bioinorganic chemistry / Nonheme iron centres / Superoxide / Structure-activity relationships

Reactive oxygen species (ROS), when in excess, are among the most deleterious species an organism can deal with. The physiological effects of ROS include amino acid chain cleavage, DNA degradation and lipid oxidation, among others. They can be formed in the cytoplasm in a variety of ways, including autooxidation reactions (FMN- and FAD-containing enzymes) and Fenton reactions as a result of the cytoplasmatic pool of iron ions. The superoxide anion ($O_2^{\cdot-}$), despite its short half-life in solution, is particularly pernicious as it can form other reactive ROS (such as the strong oxidant peroxynitrite) or oxidize and/or reduce cellular components. For strict anaerobic or microaerophilic bacteria it is of particular importance to be able to dispose of ROS in a controlled manner, especially if these organisms are temporarily exposed to air. This review aims to describe the structural characteristics of superoxide reductases (SORs) and mechanistic aspects of biological superoxide anion reduction. SORs can be considered the main class of enzymes behind the oxygen detoxification pathway of anaerobic and microaerophilic bacteria. The geometry of the active site (three classes have been described), the possible electron donors in vivo and the current hypothesis for the catalytic mechanism will be discussed. Some phylogenetic considerations are presented, regarding the primary structure of SORs currently available in genome databases.

(© Wiley-VCH Verlag GmbH & Co. KGaA, 69451 Weinheim, Germany, 2007)

## Introduction

Reactive oxygen species have been implicated in different metabolic pathways. ROS can be divided into radical (superoxide, hydroxyl, peroxyl, alkoxyl and hydroperoxyl) and nonradical (hydrogen peroxide, ozone, singlet oxygen, peroxynitrite and hypochlorous acid) entities. At higher concentrations they present problems to the normal cellular functions by, for example, oxidizing lipids, reducing sugars and amino acids or causing a large number of purine and pyrimidine modifications.[1–3] Reactions with proteins can lead to protein cleavage, cross-linkage or the loss of structural and/or catalytic function. Cellular protein degradation systems may, or may not, recognize these abnormal proteins. When not recognized, abnormal proteins will accumulate and, over time, will cause harmful effects in the cells or organisms. Although it is usual to think of ROS species as byproducts of cell metabolism, at physiological levels ROS can serve other purposes, for example, being involved in cell signalling and other important functions. At this level, ROS can be valuable or even required for a particular physiological reaction. More than 30 years ago, it was shown that the superoxide anion stimulated the formation of cGMP.[4] Interestingly, a recent study unveiled one beneficial role of ROS.[5] According to the authors, ROS are implicated in otoconia (small calcium carbonate crystals present in the inner ears of mammals) formation and could be required for interactions between otoconial components. As a result, ROS seem crucial to the mechanism by which vertebrates are able to sense gravity and maintain balance. For all the above reasons, understanding enzymes that can control ROS concentration is extremely important.

One significant ROS is the superoxide anion ($O_2^{\cdot-}$). The superoxide anion is generated by a one-electron reduction of molecular oxygen.[6–12] Some of the known sources of superoxide are: (1) Electron leakage, which can promote the reduction of $O_2$ to $O_2^{\cdot-}$. For example, it is known that several components of the mitochondrial electron transport chain (*b*-type cytochromes, coenzyme Q) can leak electrons. Also, in fatty acid desaturation, electron donors of the desaturase enzyme (flavoproteins and cytochrome $b_5$) can produce $O_2^{\cdot-}$. (2) Heme-containing proteins, namely hemoglobin and myoglobin, will produce $O_2^{\cdot-}$ by conversion of the oxy form into the met form of the protein. (3) Uncoupling of P450 oxidase activity with concomitant production of $H_2O_2/O_2^{\cdot-}$. (4) Enzymatic production of $O_2^{\cdot-}$ by xanthine oxidase, peroxidases and other oxidases. (5) The so-called autooxidation reactions where several molecules (reduced forms of FMN and FAD, adrenalin, thiol-containing mole-

[a] Requimte, Centro de Química Fina e Biotecnologia, Faculdade de Ciências e Tecnologia, Universidade Nova de Lisboa, Quinta da Torre, 2829-516 Caparica, Portugal
Fax: +351-21-2948550
E-mail: isa@dq.fct.unl.pt

Supporting information for this article is available on the WWW under http://www.eurjic.org or from the author.

 © 2007 Wiley-VCH Verlag GmbH & Co. KGaA, Weinheim 

cules and others) can slowly reduce $O_2$ to $O_2^{\cdot-}$, most probably in the presence of catalytic amounts of metal ions. (6) Fenton reactions where the products (ferric ions, hydroxyl radical) can react with hydrogen peroxide to produce $O_2^{\cdot-}$. (7) Iron(II) oxidation by ferritin produces $H_2O_2$ as a secondary product. (8) Intentional production of $O_2^{\cdot-}$, for example in the plasma membrane of macrophages by an enzymatic complex (containing FAD and *b*-type cytochrome) that uses NADPH as the reducing agent.

How long-lived is the superoxide anion after its generation? In aqueous solutions, the superoxide anion readily dismutates into hydrogen peroxide and molecular oxygen. This is a pH-dependent phenomenon, which probably occurs by protonation of at least one superoxide anion. It was calculated that, at pH 7.0, the dismutation reaction has an approximate rate constant of $5 \times 10^5$ M$^{-1}$ s$^{-1}$, which means that superoxide will only subsist for a few microseconds. Nevertheless, during that time superoxide can react with some cellular components to give rise to other potentially toxic species. Chemically, the superoxide anion can act as an oxidizing or a reducing agent. At low levels, the superoxide anion will not react with proteins unless there are accessible thiol groups. In such a case, the thiol groups are oxidized, and thiol-rich or-containing enzymes can be targeted and their functionalities modified. The superoxide anion can also be involved in enzyme reduction such as cytochrome *c* or ferritins. One of the most striking examples of superoxide damage is the oxidation of the [4Fe-4S] cluster of aconitase, a Krebs' cycle enzyme, with concomitant inactivation of the enzyme and release of reactive iron.[13] Other small molecules can also react with superoxide. For instance, NO reacts with superoxide to give rise to peroxynitrite, which is recognized as a potent oxidizing agent. These reactions have deleterious effects and will sequester the superoxide anion from solution and prevent the dismutation reaction.[14,15] For a complete panorama on superoxide, and ROS in general, the reader is advised to consult the excellent book on the matter by Halliwell and Gutteridge.[16]

To avoid the pernicious effects described above and, in a controlled manner, to dispose of intracellular superoxide anions, organisms possess one (or in rare cases, both) of two different enzymatic systems: superoxide dismutases and superoxide reductases. Under optimal conditions these enzymes will sequester the superoxide anion prior to dismutation or its reaction with other cellular components.[17]

In this review we aim to provide a concise, yet all-embracing, focused review on superoxide reductases. Hopefully, we will be able to communicate to the reader the his-

*Alice S. Pereira (front row, 2nd from left) received her Ph.D. from Universidade Nova de Lisboa in 1995 and worked on the purification and characterization of iron–sulfur proteins from sulfate-reducing bacteria and was a Postdoctoral Fellow at U.S.F (1995) and at Emory University (1995–1997). From October 1997 to March 2000 she was part of the Centro de Química Física e Biotecnologia in the Department of Chemistry of the Universidade Nova de Lisboa as a Postdoctoral Fellow. She has been a faculty member in the Department of Chemistry of the Universidade Nova de Lisboa since 2000. Her research is focused on the study of metalloenzymes involved in iron metabolism and oxygen activation.*

*Pedro Tavares (front row, left) received his Ph.D. from Universidade Nova de Lisboa in 1994. In 1995, he joined the Physics Department of Emory University as a postdoctoral research fellow. Since 1999, he has been a faculty member in the Department of Chemistry of the Universidade Nova de Lisboa. His current research interests are centred on the study of catalytic mechanisms of iron-containing enzymes implicated in detoxification mechanisms and oxygen activation.*

*Filipe Folgosa (back row, left) was born in Lisbon, Portugal. He received a Bachelor of Science degree in Biochemistry from Universidade de Lisboa in 2004 and joined the Department of Chemistry at Faculdade de Ciências e Tecnologia – Universidade Nova de Lisboa as a PhD student. He works with Professor Pedro Tavares and his scientific interests are focused on non-heme iron proteins, such as superoxide reductases, using fast kinetics techniques to study them.*

*Rui M. Almeida (back row, right) was born in Lagos, Portugal. He received a Bachelor of Science degree in Biochemistry from Universidade de Lisboa in 2004, and the following year he joined the Department of Chemistry at Faculdade de Ciências e Tecnologia – Universidade Nova de Lisboa as a PhD student. He works in Professor José Moura's group and studies the interactions of superoxide reductases with its physiological partners through the use of NMR spectroscopy and in silico molecular docking studies.*

*Isabel Moura (front row, 2nd from right) received her Ph.D. from Universidade Nova de Lisboa, in Biochemistry, in 1981. She has served as a Professor of Chemistry in the Department of Chemistry, Faculdade de Ciências e Tecnologia, Universidade Nova de Lisboa (FCT-UNL) since 1999. From 1979 to 1981 she was a researcher at the Fresh Water Biological Institute, University of Minnesota, USA. During the period of 1984–2000 she acted as an Adjunct Professor at the University of Georgia, Athens, GA, USA, and in 2003 she was the President of the Chemistry Department at FCT-UNL. Research topics are focused in the field of bioinorganic chemistry, mainly related to the characterization of enzymes of the S- and N-biocycles. Structure–function relationships and the role of metal ions in biology are also areas of interest. She has authored circa 280 publications.*

*José J. G. Moura (front row, right) received his Ph.D. from Universidade Nova de Lisboa, in Bioiniorganic Chemistry, in 1979. Since 1994 he has acted as a Professor of Chemistry in the Department of Chemistry, Faculdade de Ciências e Tecnologia, Universidade Nova de Lisboa (FCT-UNL). Other duties include being a Research Specialist at the Fresh Water Biological Institute, University of Minnesota, USA from 1979 to 1981, an Adjunct Professor at the University of Georgia, Athens, GA, USA from 1984 to 2000, a member of the Research Panels in NATO, INTAS, COST and EC Councils from 1991 to 1994, the President of the Chemistry Department (FCT-UNL) from 1997 to 2000, the President of the Scientific Council (FCT-UNL) from 2003 to 2006 and the Director of FCT-UNL Library in 1996. Research topics are focused in the field of bioinorganic chemistry; the role of metal ions in biology, bioelectrochemistry and protein–protein interactions are areas of interest, and he has circa 320 publications.*

 © 2007 Wiley-VCH Verlag GmbH & Co. KGaA, Weinheim 

Table 1. Numbering of functionally important residues in different SOR enzymes.

| Organism | Glutamate | Lysine | Histidines | Isoleucine | Cysteine |
|---|---|---|---|---|---|
| *D. vulgaris Hildenborough* | 47 | 48 | 49, 69, 75, 119 | 77 | 116 |
| *D. baarsii* | 47 | 48 | 49, 69, 75, 119 | 77 | 116 |
| *D. desulfuricans* ATCC 27774 | 46 | 47 | 48, 68, 74, 118 | 76 | 115 |
| *T. pallidum* | 48 | 49 | 50, 70, 76, 122 | 78 | 119 |
| *T. maritima* | 15 | 16 | 17, 45, 51, 118 | 53 | 115 |
| *P. furiosus* | 14 | 15 | 16, 41, 47, 114 | 49 | 111 |

torical aspects of this interesting class of enzymes and at the same time provide the information needed to build an up-to-date knowledge in this research area.

The reader should note that throughout this article we will refer to SORs by the initial, "historical" names given to the enzymes before their enzymatic activity was characterized; hence, desulfoferrodoxin (Dfx) refers to class I SORs and neelaredoxin (Nlr) to class II SORs. Class III SORs have no official historical name, although they are frequently also called neelaredoxins owing to the UV/Vis spectrum similarities to class II SORs. These enzymes were also once called rubredoxin oxidoreductases (Rbo), when it was discovered that rubredoxin (Rd) could provide electrons to SORs, although this terminology is scarcely used anymore, except to denominate their coding gene (see below).

Furthermore, the reader is advised that in this review residue numbering is always quoted with regard to the numbering established in the work being cited. For the convenience of the readers, Table 1 and Appendix I (in Supporting Information) contain the number of homologous residues in different protein sequences

## Desulfoferrodoxin – Class I SOR

In 1990, the purification and characterization of a protein containing a new type of nonheme iron from crude extracts of the sulfate and nitrate reducer *Desulfovibrio (D.) desulfuricans* ATCC 27774 as well as from extracts of *D. vulgaris* Hildenborough was reported.[18] Currently, five Dfx proteins were isolated and characterized from *D. desulfuricans* ATCC 27774, *D. vulgaris* Hildenborough, *D. baarsii*, *Archaeoglobus (A.) fulgidus* and *Methanobacterium (M.) thermoautotrophicum* (Table 2).

The protein from *D. desulfuricans* ATCC 27774 was subjected to extensive biochemical and spectroscopic characterization. This dimeric protein ($2 \times 14$ kDa) contained two iron atoms per monomer, and the as-isolated form showed a visible spectrum dominated by maxima at 495, 368 and 279 nm, thus exhibiting a pink colour. The EPR spectrum of this form showed a set of resonances ($g$ = 7.7, 5.7, 4.1 and 1.8) characteristic of a high-spin ferric ion ($S$ = 5/2) with an E/D value of 0.08. Mössbauer spectroscopy clearly indicated the presence of two high-spin iron centres, one being ferric and the other ferrous. All these spectroscopic data pointed to the fact that this protein contained one iron centre (centre I) of the $FeS_4$ type, closely resembling the one found in desulforedoxin (Dx) from *D. gigas*,[19–22] and a second ferrous centre (centre II). Owing to the unusual combination of iron centres, the protein was denominated desulfoferrodoxin. Although initially purified in a semireduced state, named pink form, it was also possible to isolate the fully oxidized state of the protein.[23] In this form, named gray form according to its colour, the UV/Vis spectrum shows additional bands at 335 and 635 nm, the EPR spectrum has additional resonances at $g$ = 4.3 and 9.6 and the Mössbauer spectral component attributed to centre II is characteristic of a high-spin ferric ion with E/D of approximately 1/3. Potentiometric redox titrations of Dfx showed that centre II has a rather high midpoint redox potential (ca. +240 mV at pH 7.6) that is in agreement with the fact that the protein could be aerobically isolated in the semireduced state.

The primary structure of Dfx determined by automated Edman degradation and mass spectrometry of the composing peptides confirmed not only the expected homology with Dx but also revealed a high homology to another iron-containing protein from *D. gigas* named neelaredoxin, which possesses one iron centre similar to centre II of Dfx, but no centre I (described in detail in the next section).[24] In conjunction with Mössbauer and Resonance Raman spectroscopic data, the sequence data indicated that centre

Table 2. List of SOR enzymes isolated and characterized.

| Source | Type | Number of Iron Centres | Origin | PDB | Reference |
|---|---|---|---|---|---|
| *A. fulgidus* | Nlr (Class II) | 1 | Native/Recombinant | – | [58] |
| *A. fulgidus* | Dfx (Class I) | 2 | Recombinant | – | [86] |
| *D. baarsii* | Dfx (Class I) | 2 | Recombinant | 1VZG, 1VZH, 1VZI | [34,47] |
| *D. desulfuricans* ATCC 27774 | Dfx (Class I) | 2 | Native | 1DFX | [18,29] |
| *D. gigas* | Nlr (Class II) | 1 | Native/Recombinant | – | [37,95] |
| *D. vulgaris Hildenborough* | Dfx (Class I) | 2 | Native/Recombinant | – | [18,72] |
| *M. thermautotrophicus* | Dfx (Class I) | 2 | Recombinant | – | [31] |
| *P. furiosus* | Nlr (Class II) | 1 | Native/Recombinant | 1DO6, 1DQI, 1DQK | [39,54] |
| *T. maritima* | Nlr (Class II) | 1 | Recombinant | 2AMU | [96] |
| *T. pallidum* | Class III | 1 | Recombinant | 1Y07 | [46,47,50] |

 © 2007 Wiley-VCH Verlag GmbH & Co. KGaA, Weinheim 

II should have only one cysteinyl S ligand in an octahedral coordination of nitrogen and/or oxygen ligands. Sequence comparison also revealed that Dfx from *D. desulfuricans* ATCC 27774 was highly homologous with the product of the *D. vulgaris* Hildenborough *rbo* gene that encodes for Dfx,[25] whereas the N-terminal sequence of the *D. vulgaris* Hildenborough Dfx was identical to the deduced amino acid sequence. It was also found that a single transcript contained both *rub* and *rbo* genes (enconding for rubredoxin and Dfx, respectively), pointing to the fact that Rd could be a redox partner of Dfx. The origin of the Dfx coding gene, *rbo*, was also questioned.[26] It was shown that in *D. vulgaris* the *rbo* gene is expressed as a 14 kDa protein whereas in *D. gigas* the *dsr* gene coding for Dx and the gene coding for Nlr are expressed independently. Thus, Dx is not formed by post-translational modification of Dfx, but most probably the *rbo* gene originated from a gene-fusion event between the genes coding for the Dx and Nlr proteins. So, the Dfx monomer can be described as a 14 kDa polypeptide chain with an approximately 4 kDa N-terminus similar to Dx and a C-terminal region of ca. 10 kDa homologous to Nlr. In fact, two constructs were engineered where either the N-terminal or the C-terminal region was cloned and expressed separately in *Escherichia (E.) coli*.[27] The N-terminal variant consisted of a DNA fragment encoding the first 39 amino acids from *D. vulgaris* Hildenborough Dfx (DfxN), sharing approximately 50% sequence identity with *D. gigas* Dx. The C-terminal domain consisted of a DNA fragment encoding the last 92 amino acids of *D. vulgaris* Hildenborough Dfx (DfxC). Both recombinant fragments were able to bind iron. Biochemical and spectroscopic characterization showed that DfxN and DfxC exhibited properties similar to Dx and Nlr, respectively.

The first crystallographic structure of a superoxide reductase was obtained for *D. desulfuricans* ATCC 27774 Dfx.[28,29] The structure was solved by MAD phasing, using the iron centres present in the protein as anomalous scatterers, up to 1.9 Å resolution (see Figures 1 and 2). The crystallographic model showed the expected two domains: spherical domain I is notably similar to that of Dx (rms deviation of 0.59 Å for the backbone atoms), and the larger domain II harbours an iron site with square-pyramidal coordination to four histidine equatorial ligands and one cysteine axial ligand. The coordination geometry is such that three histidine ligands (His48, His68 and His74) coordinate to the iron ion through their N2 atom, with the exception of His118, which bonds through Nδ1. Cys115 binds in the axial position. A possible sixth ligand was not found, and an axial position is easily accessible to the solvent, which is thus available for substrate binding. Another important feature is that several β-sheets extend from monomer to monomer, which supports the existence of a functional dimer. Domain I and II are linked by a region of polypeptide chain (residues 34–39), which creates an elongated cavity with an approximate volume of 430 $Å^3$. A calcium ion was also found at the dimer interface coordinated by eight oxygen atoms (Ser87, Thr89 from both monomers and two water molecules). The dimeric nature of *D. desulfuricans*

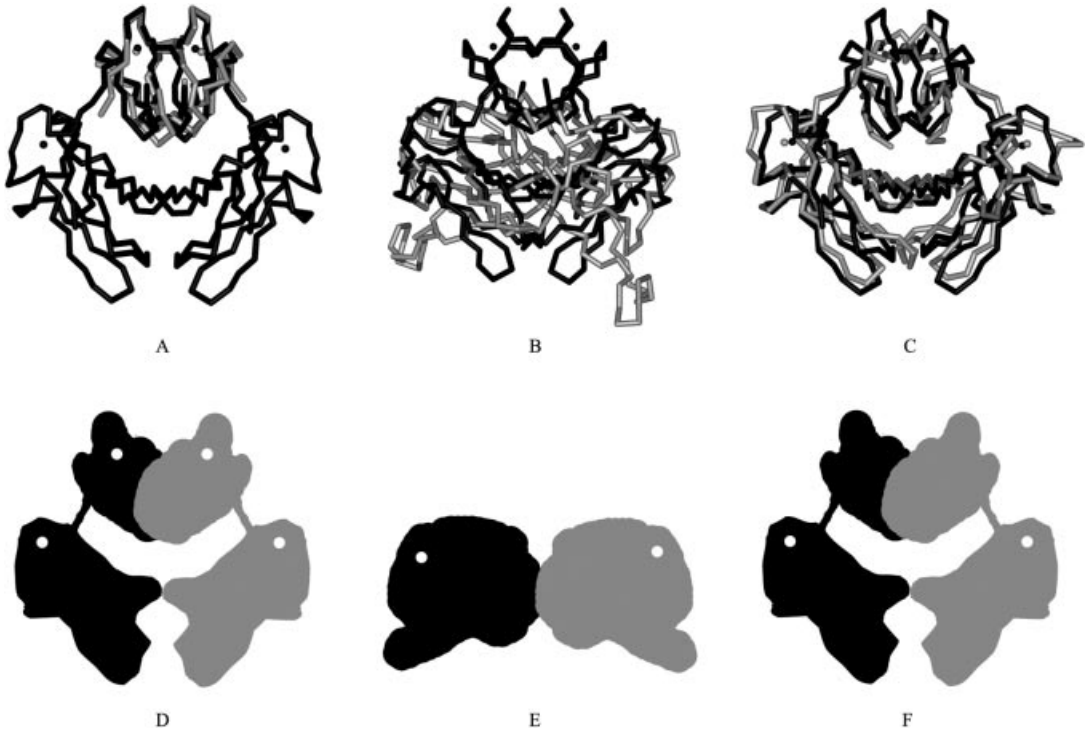


Figure 1. Structural fit of SOR- and SOR-related proteins structures compared to *D. desulfuricans* ATCC 27774 Dfx (represented in black). In grey: (A) *D. gigas* Dx; (B) *P. furiosus* Nlr; and (C) *T. pallidum* SOR. Schematic representation of the three SOR classes: (A) class I, Dfx dimer; (B) class II, Nlr dimer and (C) class III SOR dimer. Alignments were performed by using Chemera 3.0 (http://www.cqfb.fct.unl.pt/bioin/chemera/Chemera/Intro.html).

 © 2007 Wiley-VCH Verlag GmbH & Co. KGaA, Weinheim 

ATCC 27774 Dfx was also probed in equilibrium unfolding experiments.[30] By using the concentration dependence of aromatic residue emission, the dissociation constant of Dfx was determined to be ca. 1 μM. With the use of guanidine hydrochloride as a denaturating agent and with short incubation times, it was possible to observe one reversible transition (without loss of secondary structure) independent of the Dfx concentration. Only at longer incubation times was complete irreversible unfolding, with iron centre dissociation, observed. On the basis of these studies, a model was proposed where the equilibrium unfolding involves a monomeric intermediate with a native-like secondary structure. Such a finding is in agreement with the observation that mass spectroscopy and gel filtration results of *D. desulfuricans* ATCC 27774 protein are not consistent with a dimeric form.[18,24] However, in the case of the recombinant Dfx of *M. thermoautotrophicum*, more than two oligomeric species exist, with the smallest stable form being the dimeric one.[31]

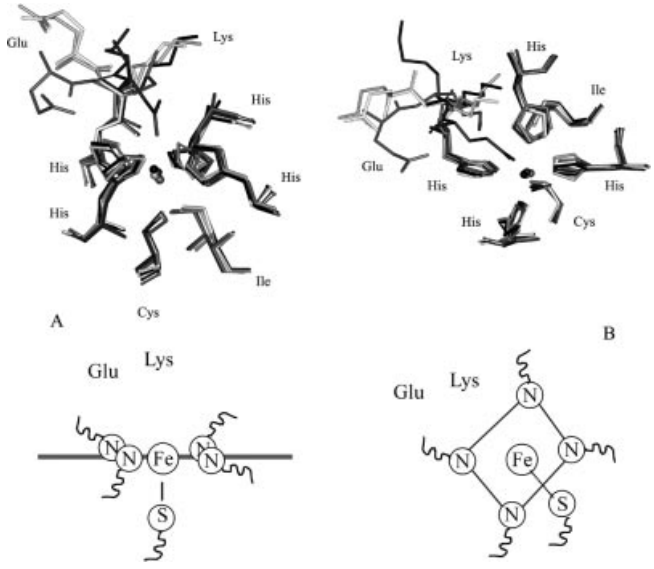


Figure 2. SOR active site showing the iron ligands and other functionally important/conserved residues. Overlapping of five different structures (aligned on the basis of the iron atom) obtained for *D. desulfuricans* ATCC 27774 (white), *T. pallidum* (light grey), *T. maritima* (grey), *P. furiosus* (dark grey), and *D. baarsii* (black). Cartoons below each set of structures intent to explain the view angle: (A) histidine ligands plane oriented transversal to the plane of the paper; (B) histidine ligands plane coincident with plane of the paper.

The accessibility of centre II towards external molecules was also evident by the characterization of a stable cyano-bridged dinuclear iron cluster.[32–34] This adduct is formed upon oxidation of ferrous centre II with potassium ferricyanide to afford the mixed-valence cyano-bridged [$Fe^{III}$–NC–$Fe^{II}(CN)_5$] complex. As proven by spectroscopic and crystallographic studies, this cyano-bridged diiron complex adopts a bent geometry. In the case of the enzyme of *D. baarsii*, the determined crystallographic structure of the complex shows both electrostatic and steric complementarities between the active site and the ferricyanide anion.

Two different types of studies showed the possibility of structural changes in centre II. In one particular work, the redox-induced structural changes were monitored by using FTIR coupled to electrochemical techniques.[35] The use of both the wild type and mutant proteins led to the proposal that centre II can bind a sixth ligand, namely a glutamate, in its ferric state [supporting the different coordination states observed in the crystallographic structure of *Pyrococcus (P.) furiosus* enzyme, see below]. The same study ruled out any relevant role, other than electrostatic interaction with substrate molecules, of a nearby lysine residue. In a different type of study, with the use of variable temperature UV/Vis, MCD, CD and EPR spectroscopy, it was shown that major electronic–vibrational changes in both centres result from the conversion of the all-ferric, grey form, to the semireduced, pink form.[36] It is suggested that an extended environmental reorganization of the region between centre I and centre II controls the electron transfer. Nonetheless, up to the moment this review was written, no direct proof of such a transfer existed, and its viability is always hindered by the large iron-to-iron distance (ca. 22 Å).

## Neelaredoxin – Class II SOR

In 1994, Chen and coworkers reported the isolation, from extracts of *D. gigas*, of an iron-containing blue protein that was named neelaredoxin.[37] Since then, this protein was also purified from other organisms, including *P. furiosus*, and extensive spectroscopic studies were performed.[38] The crystallographic structures were also determined for the oxidized and reduced states (at resolutions of 1.7 and 2.0 Å, respectively).[39] The primary structures of *D. gigas* and *P. furiosus* Nlrs have ca. 50% identity, and both are highly homologous to the C-terminal domain of Dfx proteins. As expected, the observed spectroscopic properties are similar to those obtained for Dfx centre II. In practice, one can consider Nlr to be a short Dfx, only containing the equivalent of the Dfx domain II (see Figure 1).

*P. furiosus* Nlr is a homotetrameric protein with a subunit molecular mass of about 14 kDa. Each subunit contains one mononuclear iron centre that is similar to the Dfx centre II. The 3D structure of the protein in the reduced state [Protein Data Bank (PDB) entry 1DQK] shows that the ferrous iron centre is coordinated to the imidazole nitrogen atoms from four histidine ligands that occupy the equatorial positions and a cysteine ligand that occupies the axial position. This square-pyramidal coordination leaves a sixth position that is vacant or occupied by a solvent molecule. However, in two subunits of the oxidized Nlr structure (ferric state) a carboxylate group from a nearby glutamate becomes the sixth ligand (see Figure 2). This finding implies that the glutamate residue might have an important role in catalysis. A possible explanation is that the glutamate residue regulates the accessibility of the substrate to the active site. The vacant sixth position in the reduced state would allow substrate binding to centre II with concomitant substrate reduction and release. However, in the ferric state the coordinated glutamate would either slow down or even pre-

 © 2007 Wiley-VCH Verlag GmbH & Co. KGaA, Weinheim 

vent substrate binding and enzymatic catalysis. Although this is an important finding, one should be aware that this is the only structure available that shows fully occupied coordination of the iron centre and that some mutant studies challenged the proposed gating mechanism (see below). The presence of a glutamate residue as the sixth ligand was shown to be pH-dependent. Despite Resonance Raman spectra not showing it clearly, UV/Vis spectroscopic data present significant changes, which strongly suggest that at higher pH levels or in the E14A mutant protein the glutamate can be substituted for a hydroxide functionality or by Lys15.[40]

Also important is that a potential Rd binding site is found in the vicinity of the solvent-exposed residues that are close to the iron centre. The proposed site contains iron ligands (Glu14, His47 and His114) in addition to adjacent residues (Trp11, Ile39, Pro40, Pro42, Thr44 and Ile113). Binding at this site will result in an iron-to-iron distance of approximately 8 Å.

Possible electron-transfer pathways were identified in a Resonance Raman study of the *P. furiosus* enzyme.[40] In this work, an analogy was made with type 1 copper proteins and an almost-conserved Tyr-Cys-X-X-His motif in class I and II SORs. This hypothesis is especially attractive to class I enzymes where the Tyr residue lays between domains I and II, in a direct path between iron centres. However, the *P. furiosus* structural data shows that the proposed Tyr residue is not responsible for mediating the electron transfer from Rd to Nlr because in this case the residue is located at a subunit interface of the homotetramer and buried inside the protein.

It is noteworthy to mention that in class I and III enzymes [*D. baarsii* and *Treponema (T.) pallidum*, respectively], a high-spin ferric hydroxide species in the active site was identified at basic pH values.[41] This hydroxide species is postulated to occur at the end of the catalytic process and in a pH-dependent equilibrium with the glutamate-coordinated species. Small molecules such as cyanide or nitric oxide can also bind to the Nlr active site. Nitric oxide was used as a substrate analogue to probe the structural and electronic environment of the active site.[42] It was shown that NO binds reversibly to the ferrous centre. The NO adduct is hexacoordinate, with NO binding in a bent mode *trans* to the cysteinyl S ligand, which gives rise to an EPR signal that is characteristic of a near-axial ($S$ = 3/2) spin system ($E/D$ = 0.06). Such a system was rationalized to result from the antiferromagnetic coupling between a high-spin ferric iron ($S$ = 5/2) and a $NO^-$ ion ($S$ = 1). The addition of $CN^-$ to class I and II enzymes in the oxidized form results in the conversion of the native high-spin ferric state ($S$ = 5/2) into a heterogeneous low-spin ferric state ($S$ = 1/2).[43] Combined spectroscopic data (Resonance Raman, FTIR and ENDOR) showed that the bound cyanide adopts three distinct conformations and that this heterogeneity is observed at room temperature. Also, the heterogeneity is not present in ferrous class II enzyme adducts, where a homogeneous near-linear conformation is observed. The use of mutant proteins with the replacement of either glutamate or lysine residues (present in the vicinity of the substrate binding site) by alanine did not reveal any significant spectroscopic difference. Thus, the mutated residues do not interact with the bound cyanide and therefore most probably do not play a role in the orientation and/or protonation of ferric reaction intermediates.

It is also curious to note that it was possible to express the *P. furiosus* enzyme in plant cells, in which case the survival at high temperatures is enhanced.[44] Such experiments are useful to demonstrate that the Nlr gene can produce functional recombinant proteins in plants, altering the eukaryotic metabolism.

## Class III SOR

Class I and II enzymes were found in anaerobic bacteria (or, at the most, microaerotolerant). Interestingly, a third class of SOR was found in a microaerophilic obligate pathogen of humans. *T. pallidum* is the agent responsible for venereal syphilis and during infection disseminates hematogenously to invade several tissue types. Throughout this process the bacteria must tolerate significant oxidative stress.[45] An analysis of *T. pallidum* genome does not show the presence of enzymes typically needed to deal with ROS, such as superoxide dismutases, catalases or peroxidases. However, it is possible to find a gene highly homologous to Dfx, the expression of which was shown through reverse transcriptase–polymerase chain reaction.[46,47] Gene sequence analysis showed that the gene product should be a ca. 14 kDa protein containing two domains homologous to Dfx domain I and II. In this case, domain I lacked three of the four cysteine residues responsible for centre I iron binding. The gene was cloned and expressed in *E. coli*, and the gene product was subjected to biochemical and spectroscopic characterization. The protein was found to be a homodimer containing a sole iron site per monomer. This iron site had almost equal visible, EPR and Mössbauer spectra to those of Dfx centre II, and exhibited a midpoint redox potential of approximately +210 mV (pH 7.8).

Enzymatic studies revealed that the protein was able to catalyze superoxide reduction to hydrogen peroxide and that the rubredoxin of the same organism is capable of functioning as an electron donor in this catalytic reaction.[46–48]

The crystal structure of *T. pallidum* SOR was recently obtained (Figures 1 and 2).[49,50] The enzyme shows a structure similar to Dfx, with two domains. As expected, the N-terminal domain does not contain an iron centre, but it is able to maintain the β-barrel topology in an overall arrangement that is very similar to the one found in Dfx. It is noted that the absence of cysteine residues does cause a decrease in the cohesion of the domain and that in the region corresponding to the one where centre I is present in Dfx some disorder is observed. The C-terminal region contains a pentacoordinate iron atom with four histidine and one cysteine residues in a square-pyramidal geometry. This iron centre is highly exposed to the solvent. The axial posi-

 © 2007 Wiley-VCH Verlag GmbH & Co. KGaA, Weinheim 

tion *trans* to the cysteine residue is vacant, with a water molecule located at approximately 4.3 Å from the iron centre. However, in one of the molecules present in the asymmetric unit it was found that the same water molecule was located closer to the iron atom (2.6 Å), similar to what was found in the *P. furiosus* enzyme for the reduced iron centre. In contrast to what was found for Dfx, calcium does not seem to be essential for dimerization.

## Discovery of New Enzymatic Activity – Superoxide Anion Reduction

The function of these proteins was partially unveiled in 1996 when Touati and coworkers reported that Dfx from sulfate-reducing bacterium *D. baarsii* could suppress all deleterious effects caused by superoxide dismutase (SOD) deficiency in *E. coli*.[51] The authors were trying to isolate the superoxide dismutase gene from *D. baarsii* when they noticed that a DNA fragment containing two open reading frames with homologous sequences to the *rbo* and *rub* genes of *D. vulgaris* Hildenborough functionally complemented an *E. coli* mutant deficient in cytoplasmic SODs. The experiments proved that the *E. coli* mutant regains the ability to grow on minimal medium (without the addition of branched amino acids), and that its growth on gluconate and succinate as the sole carbon sources was no longer impaired. It was also observed that iron–sulfur cluster containing enzymes were protected from inactivation and that oxygen-dependent spontaneous mutagenesis returned to values closed to those observed in the wild type strain. It was possible to ascertain that Dfx centre II was in fact the responsible agent for this effect as neither Rd nor Dx, when expressed independently, were able to significantly raise the aerobic survival of the *E. coli* mutant. In contrast, expression of Dfx would allow complete avoidance of superoxide stress. Subsequently, Liochev and Fridovich proposed that Dfx would be involved in a "direct" or "indirect" mechanism of $O_2^{\cdot-}$ scavenging,[52] but without exhibiting significant SOD activity. Similar to the previous study, these authors were able to confirm that overexpression of Dfx complemented the SOD defects, preventing inactivation of iron–sulfur-containing fumarases.

Additional evidence that Dfx was involved in an oxygen defense mechanism was reported by Voordouw and Voordouw.[53] In this work, the *rbo* gene was deleted from the *D. vulgaris* Hildenborough genome and the resultant mutant was able to grow normally under anaerobic conditions, but it clearly became more sensitive to oxygen inactivation (with 100-fold drop in CFU by exposure to air for 24 hours, when compared to the wild type strain).

The definitive identification of the enzymatic activity of Nlr and Dfx was reported in 1999.[54,55] In an attempt to purify a putative superoxide dismutase from cell-free extracts of *P. furiosus*, Adams and coworkers isolated, for the first time, the above-described *P. furiosus* Nlr. This protein exhibited high activity in the standard SOD assay (values comparable to bovine SOD). In this assay, a constant flux of $O_2^{\cdot-}$ was produced by using a mixture of xanthine and xanthine oxidase under aerobic conditions. This mixture also contained horse heart cytochrome *c*, which could be directly reduced by $O_2^{\cdot-}$, and the reduction rate of cytochrome *c* would thus be representative of $O_2^{\cdot-}$ production (ca. 14 μM $min^{-1}$).[56,57] The addition of SOD to the reaction mixture would decrease the cytochrome *c* reduction rate as a result of the competition towards $O_2^{\cdot-}$. Excess SOD would completely avoid cytochrome *c* reduction. Replacement of SOD by *P. furiosus* Nlr would have a similar effect, except that for excess amounts of enzyme cytochrome *c* oxidation was observed. Such a fact can only be explained if Nlr can use cytochrome *c* as an electron donor for a redox reaction that involves $O_2^{\cdot-}$ as the substrate. It was then proposed that this reaction would be the direct reduction of $O_2^{\cdot-}$ to peroxide:

$$O_2^{\cdot-} + 2H^+ + D_{red} \rightarrow H_2O_2 + D_{ox}$$

where $D_{red}$ and $D_{ox}$ represent the reduced and oxidized forms of an electron donor. The activity was designated by cytochrome *c* superoxide oxidoreductase or SOR activity. Additionally, it was observed that Rd from the same organism was able to replace cytochrome *c* as the electron donor. This distinct catalytic reaction was further confirmed by testing the SOD activity of Nlr in assays with different superoxide detection methods where no Nlr electron donor was present (pyrogallol, epinephrine or nitroblue tetrazolium oxidation and acetylated cytochrome *c* reduction). In this case, SOR activity was reduced by at least 95% relative to that of SOD. Subsequent works confirmed that Dfx, as well as other Nlr proteins, possessed SOR activity,[46,58,59] that Rd is the putative physiologic electron donor in this reaction[48,57,60] and that the electron transfer between Rd and SOR was in fact the rate-limiting step of the overall reaction in the case of *D. vulgaris* Hildenborough, as shown in an in vitro study by Kurtz and coworkers.[17] These studies definitively pointed to the fact that SOR enzymes are deeply involved in oxygen detoxification systems of either strict anaerobic, microaerotolerant or microaerophilic bacteria. Other work with *D. vulgaris* Hildenborough mutant strains also showed that SOR plays a key role in oxygen defense when this organism is subjected to fully aerobic conditions and for superoxide anions generated in the cytoplasm.[61,62] For microaerophilic conditions, SOD seems to be important for protection of periplasmic components.[63] It was also found that overproduction of Dfx might interfere with the reducing pathway that keeps SoxR in its active form.[64] SoxR is a [2Fe-2S]-containing transcription factor that is oxidized as a response to oxidative stress and that activates global response to oxidative stress.[65–67] However, Wildschut and coworkers reported that rubredoxin:oxygen oxidoreductase (ROO) is also an important component of this system as it can enhance the survival of *D. vulgaris* Hildenborough by itself under microaerophilic conditions.[68]

It was also pointed out that SOR is engineered to perform one reaction (superoxide reduction) whereas SOD can perform both superoxide reduction and oxidation, effec-

 © 2007 Wiley-VCH Verlag GmbH & Co. KGaA, Weinheim 

tively becoming a superoxide dismutase.[69] Interestingly, it was also proposed that *A. fulgidus* Nlr can be a bifunctional enzyme, and the possibility of ferric Nlr being reduced by the superoxide anion was put forward.[70]

Recently, it was reported that *D. baarsii* Dfx cyano-bridged [$Fe^{III}$–NC–$Fe^{II}(CN)_5$] complex could react with the superoxide anion.[71] In this case, the authors proposed that superoxide suffers a one-electron reduction with concomitant oxidation of an organic substrate to form alkyl peroxide and a water molecule, and that this catalysis was carried out by the ferrocyanide moiety of the complex.

## The Catalytic Mechanism of Superoxide Anion Reduction

How do SORs reduce $O_2^{\cdot-}$? To address this question several researchers tried to identify catalytic intermediates of the reduction process. Several studies based on pulse radiolysis were able to identify different intermediates[70,72–77] and some characterization was done with the aid of UV/Vis, EPR, Resonance Raman and Mössbauer spectroscopy.[41,75,78–81] In these studies, relevant mutants were used, in particular point mutations in glutamate (*D. baarsii* E47A) and lysine (*D. baarsii* K48I) residues located at the active site. While the emergent picture is still not complete (with some discrepancies in the number and nature of the intermediates that depend on the source of the enzyme under study), it is reasonable to describe the catalysis in the following way. The active enzyme (Figure 3, form a) is in the ferrous, pentacoordinate state, which is in redox equilibrium (pH dependent) with the hexacoordinate resting ferric state. As described previously, the active iron centre can have either a hydroxide (Figure 3, form f) or a glutamate (Figure 3, form h) as the sixth ligand. This coordination is pH dependent, with the hydroxide ligand being favoured at higher pH values ($pK_a \approx 9.0$). Catalysis proceeds with substrate binding to the ferrous site. The superoxide anion might be attracted, owing to electrostatic interaction, by a lysine residue (*D. vulgaris* Hildenborough K48 homologue). The first intermediate formed seems to be a ferric–peroxo species that forms with a rate constant $k_1 = 10^9\ M^{-1}\,s^{-1}$ and a characteristic maximum at 600 nm (Figure 3, form b). A

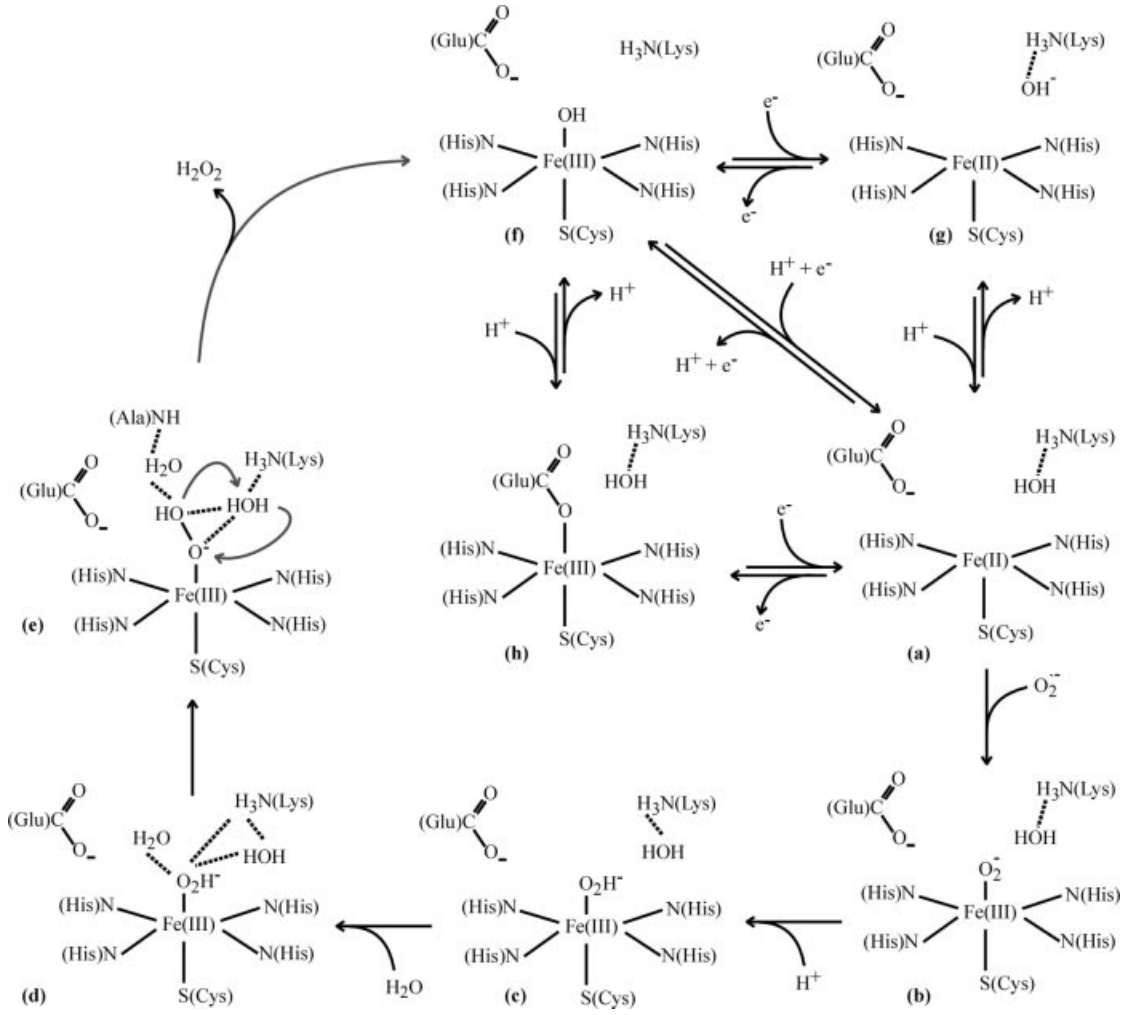


Figure 3. Catalytic scheme of superoxide anion reduction. The following enzyme forms were considered: (a) ferrous active state; (b) ferric peroxo intermediate; (c) ferric hydroperoxo intermediate; (d) an extra water molecule is recruited; (e) rearrangement leading to protonation; (f) ferric hydroxyl-bound resting state and (h) ferric carboxylate-bound resting state.

 © 2007 Wiley-VCH Verlag GmbH & Co. KGaA, Weinheim 

probable analogue of this intermediate can be obtained by reacting a mutant protein (*D. vulgaris* Hildenborough E47A homologue) with excess $H_2O_2$. The absence of the glutamate residue does not affect the natural substrate binding, but does stabilize a ferric–peroxo species. This species was characterized by Resonance Raman and Mössbauer spectroscopy and is best described as a high-spin $Fe^{3+}$-$\eta^2$-peroxo derivative. Although some authors claim that in the *D. vulgaris* Hildenborough and *A. fulgidus* enzymes this first intermediate undergoes direct protonation to yield the final products,[75] there is enough evidence (collected for *D. baarsii* and *T. pallidum* SORs) that a second intermediate is formed (Figure 3, form c).[73,74,76] The second intermediate has a characteristic peak at 625 nm and, contrary to the first intermediate, the rate constant for its formation is proportional to the proton concentration of the solvent ($k_2 = k_1 \cdot [H^+]$), which indicates that the protonation process occurs directly from the solvent.[76] As a result of this fact, proton transfer seems to be the rate-limiting step, and thus it is fair to assume that this second intermediate is a ferric hydroperoxo species. Subsequently, protonation of the second intermediate leads to $H_2O_2$ release. It was proposed that the proton donor could be a water molecule that is hydrogen-bonded to a nearby lysine residue, which would result in a high-spin ferric hydroxide species. Lysine interaction can lower the apparent p$K_a$ of water molecules, which makes it a suitable proton donor to the ferric hydroperoxo intermediate. Experimental evidence supports this conclusion. In the crystallographic structure of *T. pallidum*, it was possible to model a H-bonding network through water molecules that interact with the conserved lysine residue,[50] and, in *D. baarsii*, Resonance Raman studies showed the formation, at basic pH, of a ferric hydroxide species. At more acidic pH values, the conserved glutamate residue replaces the hydroxide moiety. Very recently, a study by Katona et al. was published[82] in which an elegant methodology combining Resonance Raman spectroscopy and kinetic crystallography was used to study *D. baarsii* SOR crystals soaked with $H_2O_2$. This study revealed that in a E114A mutant (known to stabilize ferric peroxide complexes) the superoxide anion binds in a side-on mode ($\eta^1$) and is subsequently reduced by the iron atom. The authors further proposed that upon protonation and coordination to two water molecules, which were recruited and activated by nearby lysine and alanine residues, a second protonation step yields hydrogen peroxide which is then released, leaving the iron centre coordinated to a hydroxy group. This work clearly identifies the role of the water molecules that are present in the active site, whose action avoids the formation of an oxo–ferryl species by enabling the protonation of the proximal oxygen atom (Figure 3, forms d and e).

Computational studies were conducted in an effort to explain this $O_2^{\cdot-}$ reduction mechanism.[83] In this work the use of DFT and ZINDO/S-CI results support the existence of a peroxo or hydroperoxo intermediate and point to the importance of the protonation of this intermediate in the production of $H_2O_2$, in contrast to possible cleavage of the O–O bond found in heme enzymes.

For purposes of clarity, we did not include in the above discussion the oxidation state of Dfx centre I. The electrons necessary for $O_2^{\cdot-}$ reduction can be donated by Rd either directly to the active site or through centre I, and under physiological conditions it might be possible that this donation will prevent the formation of the glutamate-coordinated species because reduction can occur rapidly after $H_2O_2$ release, as observed in pulse radiolysis experiments where excess reductant was used.[77] One curious observation is that in a *D. vulgaris* Hildenborough Dfx mutant where one cysteine residue, which was responsible for the iron binding in the Dx-like centre I, was replaced by a serine residue, the resulting protein lacked centre I but possessed a normal centre II and its catalytic properties were almost identical to those of the wild type protein.[84] Thus, this *D. vulgaris* Hildenborough Dfx variant functions in a similar manner to class III SOR. Electron transfer studies, in the absence or presence of substrate, between Rd and the different classes of SOR showed that there is a trend in the specificity for the electron donor and acceptor from the same organism.[48,57] One interesting result was that in *D. gigas*, Dx was able to transfer electrons to SOR more efficiently (with an apparent three times greater rate constant) than Rd. Clearly more studies need to be performed to unveil the role of centre I in catalysis as well as to understand the interaction between redox partners.

In *P. furiosus*, it was possible to reconstitute, in vitro, the reduction pathway.[85] In this case it was shown that Rd is reduced by NAD(P)H by an NAD(P)H rubredoxin oxidoreductase (NROR) and that the reconstitution of the full

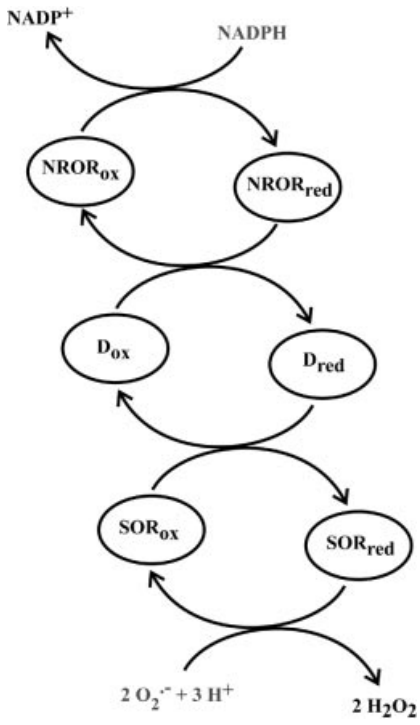


Figure 4. Proposed electron-transfer pathway in superoxide anion reduction. NROR–NADPH: rubredoxin oxidoreductase; D–Rd or Dx; SOR–Dfx, Nlr or class III SOR.

 © 2007 Wiley-VCH Verlag GmbH & Co. KGaA, Weinheim 

pathway allowed the reduction of the superoxide anion to hydrogen peroxide by using NAD(P)H as the electron donor (Figure 4).

## Phylogenetic Considerations

Searching the microbial genomic databases yields a total of 50 SOR analogues, with approximately 12% of the sequenced genomes containing at least one gene coding for this enzyme. A comparison of all 50 amino acid sequences can be found in Appendix I and the phylogenetic relationships among SOR enzymes are displayed in Figure 5. From the 50 different sequences, it was possible to identify 23 Dfx, 20 Nlr and 6 class III enzymes. One sequence (*Geobacter sp.* FRC-32) showed a high homology to the C-terminal part of Dfx proteins but completely lacked the N-terminal part, and so it can be described as a short Nlr protein (please note that for this case the genome is not completely sequenced). Comparison of all sequences reveals that only seven amino acids are completely conserved. These are the five ligands of the active site (four histidine and one cysteine residues), one proline and one isoleucine, both located near the active site and, so far, with no direct implication on the catalytic mechanism. Both the lysine and glutamate residues were judged necessary for catalysis and are highly conserved. In one instance the lysine residue

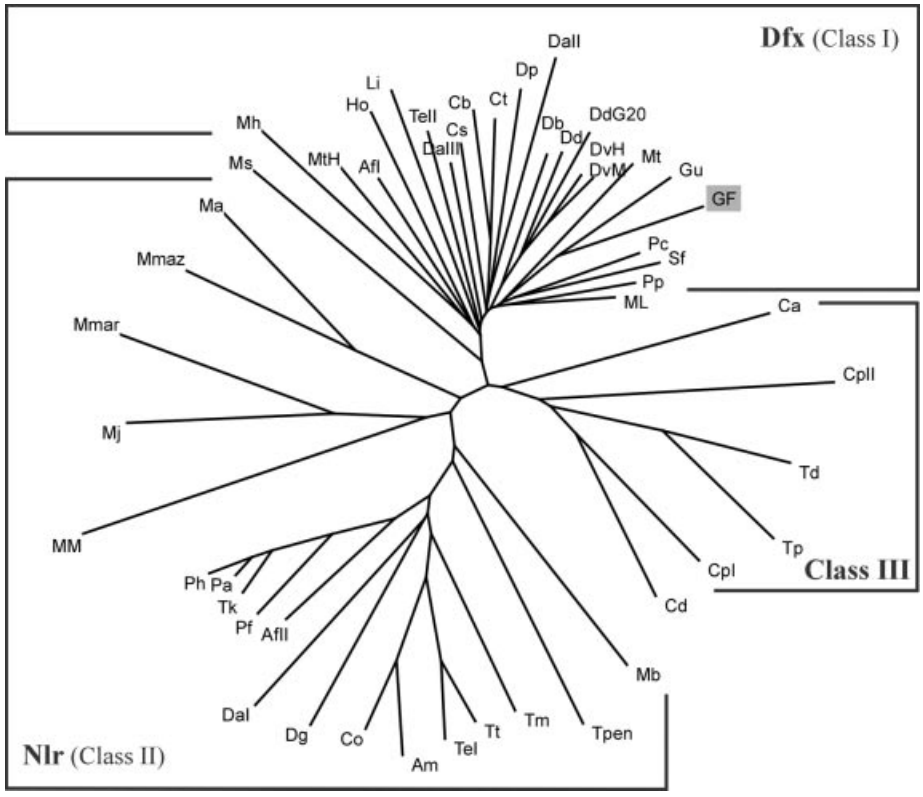


Figure 5. Phylogenetic relationship among SOR enzymes considering the three classes described in the text. Sequences were obtained in the integrated microbial genomes, DOE Joint Genome Institute (http://img.jgi.doe.gov/cgi-bin/pub/main.cgi), The Institute for Genomic Research (http://www.tigr.org/), RCSB PDB database (http://www.rcsb.org/pdb/home/home.do) or through the NCBI website (http://www.ncbi.nlm.nih.gov/). Sequence alignment and tree construction were performed with ClustalX[94] and the tree displayed with TreeView (http://taxonomy.zoology.gla.ac.uk/rod/treeview.html). The grey box denotes the special case of class I SORs, *Geobacter sp.* FRC-32. The following abbreviations were used: **AfI**, *Archaeoglobus fulgidus* DSM4304; **AfII**, *Archaeoglobus fulgidus*; **Am**, *Alkaliphilus metalliredigens* QYMF; **Ca**, *Clostridium acetobutylicum* ATCC 824; **Cb**, *Clostridium beijerinckii* NCIMB 8052; **Cd**, *Clostridium difficile* 630; **Co**, *Clostridium sp.* OhILAs; **CpI**, *Clostridium phytofermentans* ISDg; **CpII**, *Clostridium phytofermentans* ISDg; **Cs**, *Caldicellulosiruptor saccharolyticus* DSM 8903; **Ct**, *Clostridium tetani* E88; **DaI**, *Desulfuromonas acetoxidans* DSM 684; **DaII**, *Desulfuromonas acetoxidans* DSM 684; **DaIII**, *Desulfuromonas acetoxidans* DSM 684; **Db**, *Desulfovibrio baarsii*; **Dd**, *Desulfovibrio desulfuricans* ATCC 27774; *Desulfovibrio desulfuricans* G20; **Dg**, *Desulfovibrio gigas*; **Dp**, *Desulfotalea psychrophila* LSv54; **DdG20**, *Desulfovibrio desulfuricans* G20; **DvH**, *Desulfovibrio vulgaris subsp. vulgaris* str. Hildenborough; **DvM**, *Desulfovibrio vulgaris* Myazaki; **GF**, *Geobacter sp.* FRC-32; **Gu**, *Geobacter uraniumreducens* Rf4; **Ho**, *Halothermothrix orenii* H 168; **Li**, *Lawsonia intracellularis*; **Ma**, *Methanosarcina acetivorans* C2A; **Mb**, *Methanococcoides burtonii* DSM 6242; **Mh**, *Methanospirillum hungatei* JF-1; **Mj**, *Methanocaldococcus jannaschii* DSM 2661; **ML**, delta proteobacterium MLMS-1; **MM**, *Magnetococcus sp.* MC-1; **Mmar**, *Methanococcus maripaludis* strain S2; **Mmaz**, *Methanosarcina mazei* strain Goe1; **Ms**, *Methanosphaera stadtmanae* DSM 3091; **Mt**, *Moorella thermoacetica* ATCC 39073; **MtH**, *Methanobacterium thermoautotrophicum* delta H; **Pa**, *Pyrococcus abyssi* GE5; **Pc**, *Pelobacter carbinolicus* DSM 2380; **Pf**, *Pyrococcus furiosus* DSM 3638; **Ph**, *Pyrococcus horikoshii shinkaj* OT3; **Pp**, *Pelobacter propionicus* DSM 2379; **Sf**, *Syntrophobacter fumaroxidans* MPOB; **Td**, *Treponema denticola* ATCC 35405; **TeI**, *Thermoanaerobacter ethanolicus* ATCC 33223; **TeII**, *Thermoanaerobacter ethanolicus* ATCC 33223; **Tk**, *Thermococcus kodakaraensis* KOD1; **Tm**, *Thermotoga maritima* MSB8; **Tp**, *Treponema pallidum subsp. pallidum* str. Nichols; **Tpen**, *Thermofilum pendens* Hrk 5; **Tt**, *Thermoanaerobacter tengcongensis* MB4;.

 © 2007 Wiley-VCH Verlag GmbH & Co. KGaA, Weinheim 

seemed to be replaced by an arginine residue whereas glutamate can be either located one residue further away from the active site (primary sequence wise) or be replaced by an aspartate residue (in one case). They are, however, highly conserved as one would expect from the mechanistic studies referred above. It is noteworthy that some organisms contain more than one gene coding for different SOR enzymes, such as the case of *Clostridium phytofermentans* where two different class III putative SOR enzymes exist and *Desulfuromonas acetoxidans* with three putative SOR coding genes. In the case of *A. fulgidus*, *Desulfuromonas acetoxidans* and *Thermoanaerobacter ethanolicus* it is even possible to find genes coding for both Dfx and Nlr enzymes. In the case of *A. fulgidus*, both gene products were already isolated.[70,86]

Another striking feature is that genes coding for Dx, one of the possible redox partners of SOR enzymes, could be found in *D. gigas*, where it was originally identified, but also in *Methanosarcina mazei* and *Methanospirillum hungatei*. Whereas the first two organisms contain genes coding for Nlr enzymes, the last one only seems to contain a gene for the Dfx enzyme.

Another striking example is the one found for *P. horikoshii*, where it was not possible to find any Rd or Dx coding gene. In this case, it will be necessary to consider a different electron donor.

## Outlook

SORs are now structurally well-characterized proteins, with a considerable amount of biochemical, spectroscopic and crystallographic data on all three classes of enzymes. The mechanism of superoxide anion reduction is, however, still under evaluation. It is not yet completely understood why some enzymes of the same class will have two reaction intermediates (peroxo and hydroperoxo species) whereas others (of different classes) seem to have a single intermediate that undergoes direct protonation with concomitant $H_2O_2$ release.

The importance of Dfx centre I in catalysis is also elusive. Is this centre the primary recipient of electrons, delivering them to the active site in a regulated manner? This is apparently not the case because in Dfx mutants, where centre I was destroyed, activity remained similar to that of the wild type proteins.[84]Also, class III enzymes show a similar overall quaternary structure and are able to function without centre I. Nevertheless, almost half the genes found are ascribed to Dfx-type enzymes, which means that evolution decided to maintain centre I regardless of its apparent lack of function. It was suggested that centre I might have a catalytic role such as reducing molecular oxygen to superoxide that, consequently, could be further reduced in Dfx centre II.[84] While this is certainly an attractive proposal because organisms could in a single enzyme cope with oxygen and superoxide tolerance, no proof of such a catalysis exists.

Could the role of centre I be related to the nature of the physiologic electron donor? Up until now, both Rd and Dx were identified as possible electron donors. Dx was thought to be present only in *D. gigas* and was shown to be able to conduct superoxide-mediated electron transfer to *D. gigas* Nlr and *T. pallidum* SOR. It was now found that a putative Dx gene exists in *Methanospirillum hungatei* that also contains a putative Dfx coding gene. Therefore, it would be interesting to know if Dx could also act as an electron donor for Dfx enzymes.

Finally, the reader should be aware that during the past years some authors have addressed the biological function of superoxide reductase[87–92] as well as the use of biomimetic models to understand the catalytic mechanism.[93]

**Supporting Information** (see footnote on the first page of this article)**:** Sequence alignment of all SOR and putative SOR proteins found done with ClustalX.[94] Figure was prepared using the ESPript program.[97]

## Acknowledgments

F. F. and R. M. A would like to acknowledge Fundação para a Ciência e Tecnologia for the PhD grants SFRH/BD/18905/2004 and SFRH/BD/25342/2005, respectively. A. S. P would like to acknowledge Fundação para a Ciência e Tecnologia (POCI/QUI/57475/2004).

[1] K. Keyer, A. S. Gort, J. A. Imlay, *J. Bacteriol.* **1995**, *177*, 6782–6790.
[2] B. Halliwell, J. M. Gutteridge, C. E. Cross, *J. Lab. Clin. Med.* **1992**, *119*, 598–620.
[3] J. M. Gutteridge, B. Halliwell, *Baillieres Clin. Haematol.* **1989**, *2*, 195–256.
[4] C. K. Mittal, F. Murad, *Proc. Natl. Acad. Sci. USA* **1977**, *74*, 4360–4364.
[5] P. J. Kiss, J. Knisz, Y. Zhang, J. Baltrusaitis, C. D. Sigmund, R. Thalmann, R. J. Smith, E. Verpy, B. Banfi, *Curr. Biol.* **2006**, *16*, 208–213.
[6] I. Fridovich, *Annu. Rev. Biochem.* **1995**, *64*, 97–112.
[7] H. de Groot, A. Littauer, *Free Radical Biol. Med.* **1989**, *6*, 541–551.
[8] J. Carlsson, G. Nyberg, J. Wrethen, *Appl. Environ. Microbiol.* **1978**, *36*, 223–229.
[9] J. Membrillo-Hernandez, N. Ioannidis, R. K. Poole, *FEBS Lett.* **1996**, *382*, 141–144.
[10] J. F. Turrens, *Biosci. Rep.* **1997**, *17*, 3–8.
[11] J. A. Imlay, *J. Biol. Chem.* **1995**, *270*, 19767–19777.
[12] A. R. Goeptar, H. Scheerens, N. P. Vermeulen, *Crit. Rev. Toxicol.* **1995**, *25*, 25–65.
[13] P. R. Gardner, *Biosci. Rep.* **1997**, *17*, 33–42.
[14] S. I. Liochev, I. Fridovich, *Iubmb Life* **1999**, *48*, 157–161.
[15] F. Auchere, F. Rusnak, *J. Biol. Inorg. Chem.* **2002**, *7*, 664–667.
[16] J. M. Gutteridge, B. Halliwell, *Free Radicals in Biology and Medicine*, 4th ed., Oxford University Press, **2007**.
[17] J. P. Emerson, E. D. Coulter, R. S. Phillips, D. M. Kurtz, *J. Biol. Chem.* **2003**, *278*, 39662–39668.
[18] I. Moura, P. Tavares, J. J. G. Moura, N. Ravi, B. H. Huynh, M. Y. Liu, J. Legall, *J. Biol. Chem.* **1990**, *265*, 21596–21602.
[19] C. Czaja, R. Litwiller, A. J. Tomlinson, S. Naylor, P. Tavares, J. Legall, J. J. G. Moura, I. Moura, F. Rusnak, *J. Biol. Chem.* **1995**, *270*, 20273–20277.
[20] B. J. Goodfellow, F. Rusnak, I. Moura, T. Domke, J. J. Moura, *Protein Sci.* **1998**, *7*, 928–937.
[21] M. Archer, R. Huber, P. Tavares, I. Moura, J. J. Moura, M. A. Carrondo, L. C. Sieker, J. LeGall, M. J. Romao, *J. Mol. Biol.* **1995**, *251*, 690–702.

 © 2007 Wiley-VCH Verlag GmbH & Co. KGaA, Weinheim 

[22] I. Moura, M. Bruschi, J. Le Gall, J. J. Moura, A. V. Xavier, *Biochem. Biophys. Res. Commun.* **1977**, *75*, 1037–1044.
[23] P. Tavares, N. Ravi, J. J. G. Moura, J. Legall, Y. H. Huang, B. R. Crouse, M. K. Johnson, B. H. Huynh, I. Moura, *J. Biol. Chem.* **1994**, *269*, 10504–10510.
[24] B. Devreese, P. Tavares, J. Lampreia, N. VanDamme, J. LeGall, J. J. G. Moura, J. VanBeeumen, I. Moura, *FEBS Lett.* **1996**, *385*, 138–142.
[25] M. J. Brumlik, G. Voordouw, *J. Bacteriol.* **1989**, *171*, 4996–5004.
[26] M. J. Brumlik, G. Leroy, M. Bruschi, G. Voordouw, *J. Bacteriol.* **1990**, *172*, 7289–7292.
[27] C. Ascenso, F. Rusnak, I. Cabrito, M. J. Lima, S. Naylor, I. Moura, J. J. G. Moura, *J. Biol. Inorg. Chem.* **2000**, *5*, 720–729.
[28] A. V. Coelho, P. M. Matias, M. A. Carrondo, P. Tavares, J. J. G. Moura, I. Moura, V. Fulop, J. Hajdu, J. LeGall, *Protein Sci.* **1996**, *5*, 1189–1191.
[29] A. V. Coelho, P. Matias, V. Fulop, A. Thompson, A. Gonzalez, M. A. Carrondo, *J. Biol. Inorg. Chem.* **1997**, *2*, 680–689.
[30] D. Apiyo, K. Jones, J. Guidry, P. Wittung-Stafshede, *Biochemistry* **2001**, *40*, 4940–4948.
[31] Y. K. Chae, *Mol. Cells* **2002**, *13*, 259–263.
[32] M. D. Clay, J. P. Emerson, E. D. Coulter, D. M. Kurtz, M. K. Johnson, *J. Biol. Inorg. Chem.* **2003**, *8*, 671–682.
[33] F. Auchere, P. Raleiras, L. Benson, S. Y. Venyaminov, P. Tavares, J. J. G. Moura, I. Moura, F. Rusnak, *Inorg. Chem.* **2003**, *42*, 938–940.
[34] V. Adam, A. Royant, V. Niviere, F. P. Molina-Heredia, D. Bourgeois, *Structure* **2004**, *12*, 1729–1740.
[35] C. Berthomieu, F. Dupeyrat, M. Fontecave, A. Vermeglio, V. Niviere, *Biochemistry* **2002**, *41*, 10360–10368.
[36] N. H. Andersen, S. E. Harnung, I. Trabjerg, I. Moura, J. J. G. Moura, J. Ulstrup, *Dalton Trans.* **2003**, 3328–3338.
[37] L. A. Chen, P. Sharma, J. Legall, A. M. Mariano, M. Teixeira, A. V. Xavier, *Eur. J. Biochem.* **1994**, *226*, 613–618.
[38] M. D. Clay, F. E. Jenney, P. L. Hagedoorn, G. N. George, M. W. W. Adams, M. K. Johnson, *J. Am. Chem. Soc.* **2002**, *124*, 788–805.
[39] A. P. Yeh, Y. L. Hu, F. E. Jenney, M. W. W. Adams, D. C. Rees, *Biochemistry* **2000**, *39*, 2499–2508.
[40] M. D. Clay, F. E. Jenney, H. J. Noh, P. L. Hagedoorn, M. W. W. Adams, M. K. Johnson, *Biochemistry* **2002**, *41*, 9833–9841.
[41] C. Mathe, V. Niviere, T. A. Mattioli, *J. Am. Chem. Soc.* **2005**, *127*, 16436–16441.
[42] M. D. Clay, C. A. Cosper, F. E. Jenney, M. W. W. Adams, M. K. Johnson, *Proc. Natl. Acad. Sci. USA* **2003**, *100*, 3796–3801.
[43] M. D. Clay, T. C. Yang, F. E. Jenney, I. Y. Kung, C. A. Cosper, R. Krishnan, D. M. Kurtz, M. W. W. Adams, B. M. Hoffman, M. K. Johnson, *Biochemistry* **2006**, *45*, 427–438.
[44] Y. J. Im, M. K. Ji, A. M. Lee, W. F. Boss, A. M. Grunden, *FEBS Lett.* **2005**, *579*, 5521–5526.
[45] K. R. Hazlett, D. L. Cox, R. A. Sikkink, F. Auch′ere, F. Rusnak, J. D. Radolf, *Methods Enzymol.* **2002**, *353*, 140–156.
[46] T. Jovanovic, C. Ascenso, K. R. O. Hazlett, R. Sikkink, C. Krebs, R. Litwiller, L. M. Benson, I. Moura, J. J. G. Moura, J. D. Radolf, B. H. Huynh, S. Naylor, F. Rusnak, *J. Biol. Chem.* **2000**, *275*, 28439–28448.
[47] M. Lombard, D. Touati, M. Fontecave, V. Niviere, *J. Biol. Chem.* **2000**, *275*, 27021–27026.
[48] F. Auchere, R. Sikkink, C. Cordas, P. Raleiras, P. Tavares, I. Moura, J. J. G. Moura, *J. Biol. Inorg. Chem.* **2004**, *9*, 839–849.
[49] T. Santos-Silva, J. Trincao, A. L. Carvalho, C. Bonifacio, F. Auchere, I. Moura, J. J. G. Moura, M. J. Romao, *Acta Crystallogr., Sect. F: Struct. Biology. Cryst. Commun.* **2005**, *61*, 967–970.
[50] T. Santos-Silva, J. Trincao, A. L. Carvalho, C. Bonifacio, F. Auchere, P. Raleiras, I. Moura, J. J. G. Moura, M. J. Romao, *J. Biol. Inorg. Chem.* **2006**, *11*, 548–558.
[51] M. J. Pianzzola, M. Soubes, D. Touati, *J. Bacteriol.* **1996**, *178*, 6736–6742.
[52] S. I. Liochev, I. Fridovich, *J. Biol. Chem.* **1997**, *272*, 25573–25575.
[53] J. K. Voordouw, G. Voordouw, *Appl. Environ. Microbiol.* **1998**, *64*, 2882–2887.
[54] F. E. Jenney, M. F. J. M. Verhagen, X. Y. Cui, M. W. W. Adams, *Science* **1999**, *286*, 306–309.
[55] F. E. Jenney, M. F. J. M. Verhagen, M. W. W. Adams, *J. Inorg. Biochem.* **1999**, *74*, 181–181.
[56] J. M. McCord, I. Fridovich, *J. Biol. Chem.* **1969**, *244*, 6049–6055.
[57] F. Auchere, S. R. Pauleta, P. Tavares, I. Moura, J. J. G. Moura, *J. Biol. Inorg. Chem.* **2006**, *11*, 433–444.
[58] I. A. Abreu, L. M. Saraiva, J. Carita, H. Huber, K. O. Stetter, D. Cabelli, M. Teixeira, *Mol. Microbiol.* **2000**, *38*, 322–334.
[59] M. Lombard, M. Fontecave, D. Touati, V. Niviere, *J. Biol. Chem.* **2000**, *275*, 115–121.
[60] J. V. Rodrigues, I. A. Abreu, L. M. Saraiva, M. Teixeira, *Biochem. Biophys. Res. Commun.* **2005**, *329*, 1300–1305.
[61] M. Fournier, Y. Zhang, J. D. Wildschut, A. Dolla, J. K. Voordouw, D. C. Schriemer, G. Voordouw, *J. Bacteriol.* **2003**, *185*, 71–79.
[62] H. L. Lumppio, N. V. Shenvi, A. O. Summers, G. Voordouw, D. M. Kurtz, *J. Bacteriol.* **2001**, *183*, 101–108.
[63] M. N. Davydova, R. Z. Sabirova, *Anaerobe* **2003**, *9*, 39–41.
[64] P. Gaudu, S. Dubrac, D. Touati, *J. Bacteriol.* **2000**, *182*, 1761–1763.
[65] H. Ding, E. Hidalgo, B. Demple, *J. Biol. Chem.* **1996**, *271*, 33173–33175.
[66] P. Gaudu, B. Weiss, *Proc. Natl. Acad. Sci. USA* **1996**, *93*, 10094–10098.
[67] E. Hidalgo, H. Ding, B. Demple, *Cell* **1997**, *88*, 121–129.
[68] J. D. Wildschut, R. M. Lang, J. K. Voordouw, G. Voordouw, *J. Bacteriol.* **2006**, *188*, 6253–6260.
[69] S. I. Liochev, I. Fridovich, *J. Biol. Chem.* **2000**, *275*, 38482–38485.
[70] I. A. Abreu, L. M. Saraiva, C. M. Soares, M. Teixeira, D. E. Cabelli, *J. Biol. Chem.* **2001**, *276*, 38995–39001.
[71] F. P. Molina-Heredia, C. Houee-Levin, C. Berthomieu, D. Touati, E. Tremey, V. Favaudon, V. Adam, V. Niviere, *Proc. Natl. Acad. Sci. USA* **2006**, *103*, 14750–14755.
[72] E. D. Coulter, J. P. Emerson, D. M. Kurtz, D. E. Cabelli, *J. Am. Chem. Soc.* **2000**, *122*, 11555–11556.
[73] V. Niviere, M. Lombard, M. Fontecave, C. Houee-Levin, *FEBS Lett.* **2001**, *497*, 171–173.
[74] M. Lombard, C. Houee-Levin, D. Touati, M. Fontecave, V. Niviere, *Biochemistry* **2001**, *40*, 5032–5040.
[75] J. P. Emerson, E. D. Coulter, D. E. Cabelli, R. S. Phillips, D. M. Kurtz, *Biochemistry* **2002**, *41*, 4348–4357.
[76] V. Niviere, M. Asso, C. O. Weill, M. Lombard, B. Guigliarelli, V. Favaudon, C. Houee-Levin, *Biochemistry* **2004**, *43*, 808–818.
[77] J. V. Rodrigues, I. A. Abreu, D. Cabelli, M. Teixeira, *Biochemistry* **2006**, *45*, 9266–9278.
[78] C. Mathe, T. A. Mattioli, O. Horner, M. Lombard, J. M. Latour, M. Fontecave, V. Niviere, *J. Am. Chem. Soc.* **2002**, *124*, 4966–4967.
[79] O. Horner, J. M. Mouesca, J. L. Oddou, C. Jeandey, V. Niviere, T. A. Mattioli, C. Mathe, M. Fontecave, P. Maldivi, P. Bonville, J. A. Halfen, J. M. Latour, *Biochemistry* **2004**, *43*, 8815–8825.
[80] C. Mathe, V. Niviere, C. Houee-Levin, T. A. Mattioli, *Biophys. Chem.* **2006**, *119*, 38–48.
[81] P. Raleiras in "Superoxide Reductases, Structural and Functional Aspects", PhD thesis, Universidade Nova de Lisboa, Lisboa, **2005**.
[82] G. Katona, P. Carpentier, V. Niviere, P. Amara, V. Adam, J. Ohana, N. Tsanov, D. Bourgeois, *Science* **2007**, *316*, 449–453.
[83] R. Silaghi-Dumitrescu, L. Silaghi-Dumitrescu, E. D. Coulter, D. M. Kurtz, *Inorg. Chem.* **2003**, *42*, 446–456.

 © 2007 Wiley-VCH Verlag GmbH & Co. KGaA, Weinheim 

[84] J. P. Emerson, D. E. Cabelli, D. M. Kurtz, *Proc. Natl. Acad. Sci. USA* **2003**, *100*, 3802–3807.
[85] A. A. Grunden, F. E. Jenney, K. S. Ma, M. Y. Ji, M. V. Weinberg, M. W. W. Adams, *Appl. Environ. Microbiol.* **2005**, *71*, 1522–1530.
[86] J. V. Rodrigues, L. M. Saraiva, I. A. Abreu, M. Teixeira, D. E. Cabelli, *J. Biol. Inorg. Chem.* **2007**, *12*, 248–256.
[87] J. A. Imlay, *J. Biol. Inorg. Chem.* **2002**, *7*, 659–663.
[88] D. M. Kurtz, *Acc. Chem. Res.* **2004**, *37*, 902–908.
[89] M. W. W. Adams, F. E. Jenney, M. D. Clay, M. K. Johnson, *J. Biol. Inorg. Chem.* **2002**, *7*, 647–652.
[90] D. M. Kurtz, *J. Inorg. Biochem.* **2006**, *100*, 679–693.
[91] D. M. Kurtz, E. D. Coulter, *J. Biol. Inorg. Chem.* **2002**, *7*, 653–658.
[92] V. Niviere, M. Fontecave, *J. Biol. Inorg. Chem.* **2004**, *9*, 119–123.
[93] L. M. Brines, J. A. Kovacs, *Eur. J. Inorg. Chem.* **2006**, 29–38.
[94] J. D. Thompson, T. J. Gibson, F. Plewniak, F. Jeanmougin, D. G. Higgins, *Nucleic Acids Res.* **1997**, *25*, 4876–4882.
[95] G. Silva, S. Oliveira, C. M. Gomes, I. Pacheco, M. Y. Liu, A. V. Xavier, M. Teixeira, J. LeGall, C. Rodrigues-Pousada, *Eur. J. Biochem.* **1999**, *259*, 235–243.
[96] R. G. Zhang, Y. Kim, T. Skarina, S. Beasley, R. Laskowski, C. Arrowsmith, A. Edwards, A. Joachimiak, A. Savchenko, *J. Biol. Chem.* **2002**, *277*, 19183–19190.
[97] P. Gouet, E. Courcelle, D. I. Stuart, F. Metoz, *Bioinformatics* **1999**, *15*, 305–308.

Received: January 3, 2007
Published Online: May 23, 2007

 © 2007 Wiley-VCH Verlag GmbH & Co. KGaA, Weinheim 

DOI: 10.1002/ejic.200700024

# Alternating and Non-Alternating Pd-Catalysed Co- and Terpolymerisation of Carbon Monoxide and Alkenes

**Eduardo J. García Suárez,[a] Cyril Godard,[a] Aurora Ruiz,[a] and Carmen Claver*[a]**

**Keywords:** Polymerisation / Polyketones / Palladium / Carbon monoxide / Alkenes

The co- and terpolymerisation of carbon monoxide and alkenes are usually catalysed by palladium complexes, and the properties of the produced polyketones can be finely tuned by an appropriate choice of catalyst and olefinic monomer. After a general overview of the topic, selected recent advances in this field are described. The use of palladium systems containing modified diphosphane and/or new phosphorus-based ligands, and the results obtained using a series of modular N and S ligands, including chiral ligands, in CO/styrene co- and terpolymerisations are reported. The use of new P-O ligands in non-alternating CO/ethene copolymerisation is also described.
(© Wiley-VCH Verlag GmbH & Co. KGaA, 69451 Weinheim, Germany, 2007)

## Introduction

The industrial interest in polyketones obtained by the catalytic copolymerisation of carbon monoxide with one or more alkene monomers has increased relentlessly over the last few decades. These materials represent a class of low-cost thermoplastics whose synthesis, properties and applications are still the object of intense fundamental and applied research. At least two of these CO/olefins polymers are produced industrially, namely Carilon® by Shell[1] and Ketonex® by BP.[2]

Polyketones provide a unique web of chemical and physical properties, which include photo- and biodegradability, good chemical resistance to acids, bases and solvents, impermeability to hydrocarbons and strong rigidity and impact strength.[3,4] These properties can be both modified and improved by changing the number or nature of the comonomers and tuning the structure of the metal catalyst. The diversity of their properties makes polyketones superior to polyolefins, polyamides and polyacetals.[5]

With this review, we wish to present a concise overview of relevant advances in Pd-catalysed CO/olefin co- and ter-

[a] Departament de Química Física i Inorgànica, Universitat Rovira i Virgili,
Campus Sescelades, Marcel.li Domingo s/n, 43007 Tarragona, Spain

*Cyril Godard (left) was born in Saint-Rémy, France, in 1974. He was awarded a Ph.D. from the University of York in 2004 (with Prof. R. N. Perutz and Dr. S. B. Duckett). After postdoctoral work on mechanistic studies using Para-Hydrogen Induced Polarisation techniques, he joined the Universtat Rovira i Virgili in Tarragona where he is currently a Juan de la Cierva research fellow and is working on nanocatalysis. His research interests lie in the areas of organometallic chemistry, enantioselective processes and mechanisms in metal-catalysed catalysis.*

*Carmen Claver (second from left) is Professor of Inorganic Chemistry at the University Rovira i Virgili (URV) in Tarragona, Spain, a position she has held since 1991. She received her PhD in 1978 from the University of Zaragoza, Spain, working in the field of organometallic chemistry and homogeneous catalysis. Her research is aimed at the development of advanced transition metal catalysis and covers the synthesis of ligands and complexes and the characterisation of intermediates, focusing mainly on their application in enantioselective catalysis and polymerisation processes. She has co-authored scientific contributions in this field and has participated in the edition and publication of several books. She has received several scientific awards, and was recognised in 2003 as a Distinguished Researcher by the Catalan Government.*

*Eduardo J. García Suárez (second from right) was born in 1973 in Gijón, Spain. He completed his undergraduate studies in 2002 at the Universidad de Oviedo. In 2003, he was awarded a Marie Curie training fellowship at the Istituto di Chimica dei Composti Organometallici in Florence, Italy. He is currently working towards his PhD under the supervision of Prof. Carmen Claver and Dr. Claudio Bianchini at the Universitat Rovira i Virgili in Tarragona, Spain.*

*Aurora Ruiz (right) completed her undergraduate studies in chemistry at the Universitat de Barcelona (UB) and was awarded a PhD from the same university in 1983. She is now Professor of Inorganic Chemistry at the Faculty of Chemistry of the Universitat Rovira i Virgili (URV) in Tarragona. Her current research field is homogeneous catalysis covering aspects of synthesis, characterisation of chiral organometallic complexes and their application in asymmetric catalysis.*

 © 2007 Wiley-VCH Verlag GmbH & Co. KGaA, Weinheim 

polymerisation. As the first developments have already been reviewed,[6] particular focus will be given to recent advances in this field, including contributions from our research group.

### Perfectly Alternating CO/Ethene Copolymerisation

The simplest polyketone is the CO/ethene copolymer (Scheme 1).

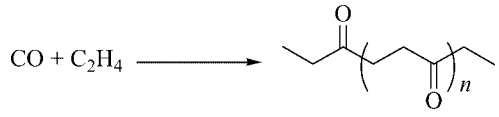

Scheme 1. Polyketone formation by alternating CO/ethene copolymerisation.

Perfectly alternating CO/ethene copolymerisation is efficiently carried out in methanol at moderate temperatures (about 80 °C) in the presence of a catalyst system that contains a $Pd^{II}$ salt with a weakly coordinating counterion and a chelating diphosphane as essential components (Figure 1).[6]

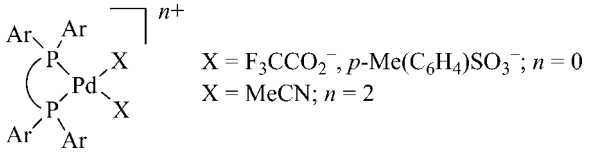


Figure 1. Usual pre-catalysts for perfectly alternating CO/ethene copolymerisation.

1,3-Bis(diphenylphosphanyl)propane (dppp) was the ligand that opened the way to the efficient synthesis of polyketones.[7] Pressures between 30 and 60 bar of CO/ethene are usually employed. When all the CO has been consumed, the catalyst promotes the dimerisation of ethene into butenes. Polyketones with different combinations of end groups such as diketone, keto-ester and diester groups can be obtained.

The optimal reaction conditions in methanol require the presence of both a strong oxidant ($E^0 \geq 0$) and a protic acid ($pK_a \leq 4$) whose conjugate base must have a low binding affinity to $Pd^{II}$. 1,4-Benzoquinone (BQ) and *p*-toluenesulfonic acid (TsOH) are two examples that fulfil these requirements and are the stabilising compounds for the most productive catalytic systems. Productivities as high as 11000 g CP (g Pd h)$^{-1}$ (CP = copolymer) can be obtained under these experimental conditions.[6]

The role of the 1,4-benzoquinone is to oxidise the $Pd^0$ or $Pd^I$ species that are formed in the catalytic process to $Pd^{II}$, and the main role of the protic acid is to prevent the deactivation of the palladium(II) catalyst into inactive (P-P)$Pd^0$ by protonating the latter species to reform the catalytically active species [(P-P)PdH]$^+$.

### Ligand Systems Used in CO/Ethene Copolymerisation

One of the advantages of catalytic systems bearing phosphorus-based ligands is the structural diversity and the ease of modification of this type of ligand. Drent et al.[6a,7b] were the first to investigate the influence of the structure of the diphosphane ligand on the activity of the $Pd^{II}$ catalyst. This study found a strong dependence of the catalytic activity on the chain length of the carbon backbone between the two phosphorus atoms, with dppp giving the highest productivity.

Since the discovery of the efficiency of the Pd-dppp catalyst by Shell Research in 1984, various dppp-like ligands have been designed and successfully employed to catalyse CO/ethene copolymerisation in combination with $Pd^{II}$ salts. Most ligand variations have involved substitutions in both phenyl groups and/or the carbon backbone, and a considerable increase in the productivity (ca. 50%) was obtained when alkyl groups were introduced in both the 1- and 3-positions of the dppp backbone to yield *meso*-2,4-bis(diphenylphosphanyl)pentane (bdpp). Both electronic and steric factors have been suggested to explain the remarkable activity of these catalysts, and it was proposed that the increased activity of Pd(*meso*-bdpp) could be due to the more facile re-oxidation of the one-electron-reduced species by both 1,4-benzoquinone or $H^+$, which would result in a larger number of active Pd centres in the catalytic mixture.

In terms of productivity and catalyst stability, the introduction of *ortho*-methoxy groups at each phenyl unit of the dppp ligand has also been shown to have a beneficial influence (Figure 2).[8]

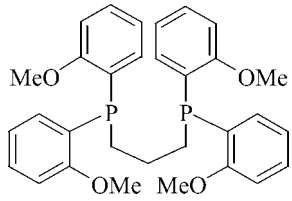


Figure 2. *o*-MeO-dppp used in CO/ethene copolymerisation.

A water-soluble version of *o*-MeO-dppp containing *m*-sodium sulfonatophenyl groups has also been used, which shows that the *ortho*-methoxy moiety can exert both a steric and an electronic influence on the palladium centre.[8b]

Modifications of the ligand backbone of dppe-based ligands have also been investigated and it was found that the backbone rigidity and the overall steric crowding at the Pd centre play a crucial role in determining the catalytic activity.[9] Thus, $Pd^{II}$ catalysts bearing the *cyclo*-tetraphos ligand (Figure 3) are 10-times more efficient than those with dppe.

The beneficial effect of the ligand rigidity for copolymerisation reactions has also been confirmed using bis-phospholyl-substituted carbon backbones.[10]

Experimental evidence has also shown that four-membered ring systems with isopropyl-substituted phenyl rings can also exhibit high catalytic activity (Figure 4).[11]

Phosphorus-metallocene based ligands have also been tested recently for the copolymerisation of CO/ethene.[12] Relatively low molecular weight copolymers were obtained and both the catalytic activity and the chemoselectivity of the copolymerisation reaction were shown to depend on the

 © 2007 Wiley-VCH Verlag GmbH & Co. KGaA, Weinheim 

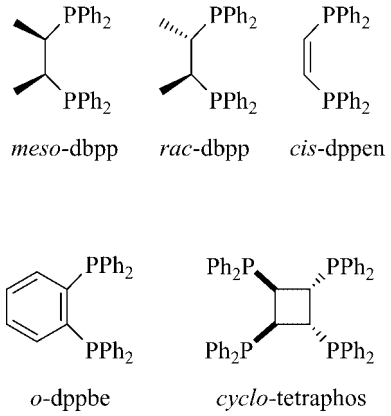


Figure 3. Rigid diphosphane ligands forming five-membered metallacycles.

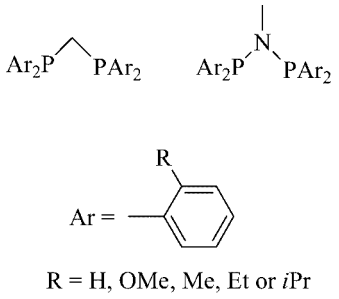


Figure 4. Ligands that form four-membered metallacycles.

sandwiched metal centre, the substituents on the cyclopentadienido ring and on the substituents bonded to the phosphorus donor atoms.

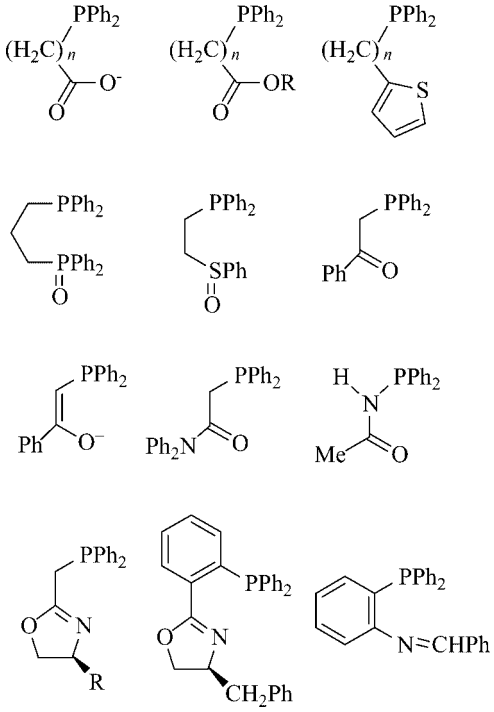


Figure 5. Hemilabile P-O, P-N and P-S ligands.

Another class of ligands used for CO/ethene copolymerisation corresponds to hemilabile phosphane ligands containing oxygen, nitrogen or sulfur donor atoms,[13] although their catalytic activity is lower than that of dinitrogen and diphosphane ligands. Some of the P-O, P-N and P-S ligands that have been studied with the aim of forming efficient catalysts for CO/ethene copolymerisation are presented in Figure 5.

Sterically rigid dinitrogen ligands such as bipyridine (bipy), phenanthroline (phen) and their alkyl-substituted derivatives form efficient catalysts for alternating CO/ethene copolymerisation under both homogeneous and heterogeneous conditions.[14]

## CO/Styrene Copolymerisation

Unlike aliphatic olefins, the copolymerisation of styrene and its derivatives with CO requires the use of $Pd^{II}$ catalysts with chelating dinitrogen ligands[3,6a,15,16] – the use of Pd catalysts bearing diphosphane ligands gives only low molecular weight oligomers.[6a,16c,16f,17] It is commonly agreed that termination by β-H elimination is favoured over propagation of the polymer due to the higher electron density on the palladium centre in phosphane-modified catalysts,[6,16–18] and it has also been suggested that the (diphosphane)Pd–styryl intermediates formed in the initial steps of the CO/styrene copolymerisation are so strongly stabilised by π-benzylic coordination that this inhibits CO insertion. Termination by β-H elimination thus becomes favoured and oligoketones are formed instead of polyketones.[17]

Copolymers of the general formula $[CH(Ar)CH_2CO]_n$ show regio- and stereoisomerism due to the presence of truly stereogenic centres in the polymer backbone.[19] Depending on the regioselectivity of the monomer insertion, either primary (1,2-mode) or secondary (2,1-mode), into the polymer chain, three different arrangements are possible during the polymerisation: tail-to-tail, head-to-tail and head-to-head. With dinitrogen ligands styrene insertion into the Pd–acyl bond takes place exclusively in a 2,1-fashion and leads only to head-to-tail units. However, a mechanistic study using a phosphane-phosphite ligand showed that 1,2-insertion of styrene can occur and that in this case β-H elimination occurs from the 2,1-complex rather than the 1,2-complex.[17c]

Syndiotactic and isotactic alternating copolymers present very low and high optical activities, respectively, and control of the regio- and enantioselectivities of styrene insertion, ultimately leading to stereoregular polyketones, can be achieved by a suitable choice of bidentate ligands.

Copolymerisation catalysts usually contain achiral ligands that lead to the formation of products of head-to-tail regioselectivity and syndiotactic stereoselectivity. The stereoselectivity is a result of chain control, with the enantioface of the incoming styrene being directed by the stereogenic centre of the last incorporated styrene unit, taking into account that styrene inserts exclusively in a 2,1-mode.[16b,16d]

 © 2007 Wiley-VCH Verlag GmbH & Co. KGaA, Weinheim 

Typical catalysts used for perfectly alternating copolymerisation of CO and styrene for the production of syndiotactic copolymers contain a $Pd^{II}$ salt and a chelating dinitrogen ligand such as bipy or phen. This reaction requires the presence of a Brønsted acid (e.g. TsOH) and a large excess of a strong oxidant such as BQ with respect to Pd. The production of copolymer is strongly decreased in the absence of oxidant, although the molecular weight of the copolymer is inversely proportional to the concentration of BQ.[3,6,15,16] The solvent of choice is usually methanol, although a striking effect has been observed on the stability of the catalytic systems with 2,2,2-trifluoroethanol (TFE) as solvent.[20] This effect was attributed to the higher stability of Pd-acyl intermediates in TFE than in methanol. For instance, the lower nucleophilicity of TFE could inhibit the chain end by alcoholysis. The palladium(II) complex $[Pd(bipy)_2][PF_6]_2$ has been found to still be active in TFE after 48 h of reaction and to yield high molecular weight copolymers with a productivity of 360 g CP (g Pd h)$^{-1}$, and high yields and high molecular weight copolymers are obtained even in the absence of oxidant.[21]

The influence of various counterions has also been investigated, with the result that the catalytic activity decreases in the order B[3,5-$(CF_3)_2C_6H_3]_4$ (BArF) > $SbF_6/PF_6$> $BF_4$ > OTf >> $BPh_4$ (OTf = triflate). The strength of the interionic interactions has been shown to have a negative effect on the productivity of the catalysts.[22]

The production of syndiotactic copolymers of 4-methylstyrene and CO has been achieved at 0 °C at 1 atm of CO with the Pd complex **1** (Figure 6), which was also used as a precursor in studies of the first steps of the polymer chain-growth, as catalyst.

It has been demonstrated that when a catalyst bearing ligands that contain one or several stereogenic centres is used, the enantioface discrimination is directed by the ligand and not the chain end control. Brookhart and coworkers, for example, have reported the first enantioselective copolymerisation of CO and styrene using a Pd(bisoxazoline) system (complex **2**, Figure 6). The reaction was performed under 1 atm of CO at room temperature with 4-*tert*-butylstyrene as both solvent and substrate and yielded copolymers with both a highly isotactic microstructure and high optical activity as a result of enantiomorphic site control.[23] The orientation of the incoming styrene was shown to be strongly controlled by the presence of substituents in the 4-positions of the oxazoline ring. However, the use of palladium systems bearing oxazolinyl-pyridine ligands (complex **3**, Figure 6) leads to the production of mainly syndiotactic copolymers, which indicates that chain control predominates.

The production of chiral alternating CO/styrene copolymers has also been reported, although with a lower stereoregularity, with a pyridine-imine system (complex **4**, Figure 6),[24] and Carfagna et al. have reported the production of highly isotactic optically active copolymers of CO and styrene or 4-methylstyrene with a bisoxazoline catalytic system (complex **5**, Figure 6). They obtained only low yields, however, and attributed this to the weak coordinating properties of this ligand which result in a destabilisation of the catalyst under these reaction conditions.[25] Productivities as high as 21 g CP (g Pd h)$^{-1}$ for average molecular weight copolymers have been obtained at room temperature under a constant CO pressure of 1 bar with palladium complexes bearing chiral diketimines or dialdimines.[26]

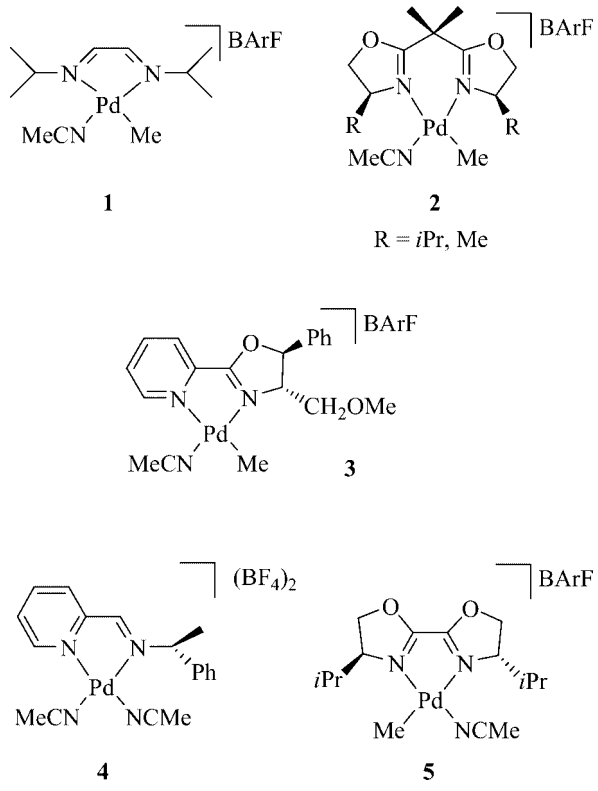


Figure 6. Some systems used in Pd-catalysed CO/styrene copolymerisation.

Brookhart et al., in a particularly inventive strategy, have achieved the production of stereoblock polyketones by exchanging ligands during the catalytic reaction. Thus, an isotactic segment is produced in a first step using the bisoxazoline system **2** (Figure 6), then addition of bipyridine to the reaction medium results in the elongation of the copolymer in a syndiotactic way.[27]

## CO/Olefins Terpolymerisation

Despite the fact that the two polyketones that have been commercialised are terpolymers of CO/ethene/propene,[1,2] terpolymerisation reactions have been much less studied than copolymerisations. Similarly to the copolymerisation catalysts, the terpolymerisation of CO with aliphatic olefins is usually performed using complexes bearing phosphorus-based ligands,[28] and the only reported example of terpolymerisation of CO with two vinylarenes is promoted by Pd(phen) complexes.[13h,29] The terpolymerisation of CO with one aliphatic and one aromatic olefin is somewhat more versatile and various types of ligand systems have been successfully used, such as P-P,[30] P-OP,[31] P-N[13h,32] and N-N[15,16d,22,30,33–35] (Figure 7).

 © 2007 Wiley-VCH Verlag GmbH & Co. KGaA, Weinheim 

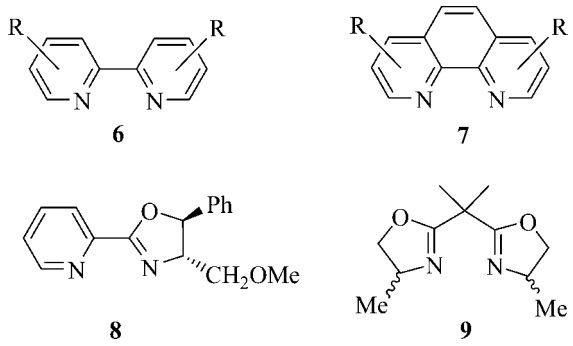


Figure 7. N-N ligands used for the Pd-catalysed terpolymerisation of CO with one aliphatic and one aromatic olefin.

The propagation step of this reaction is based on alternating migratory insertion of CO into a Pd–alkyl bond and of one of the olefins into a Pd–acyl bond. Depending on the characteristics of both the olefins and the catalyst, the resulting terpolymers can have a distinct composition and thus distinct properties.

The dinitrogen systems used for this reaction are essentially derived from planar bipy and phen systems (**6** and **7** in Figure 7), although Brookhart and Consiglio have reported that the use of chiral ligands (**8** and **9**, Figure 7) in this reaction produces optically active terpolymers.

### Mechanism

The first detailed mechanistic study of the Pd-catalysed perfectly alternating CO/ethene copolymerisation was reported by Drent et al. in 1991, and since then a large number of studies from both an experimental and theoretical viewpoint have been reported and have contributed to a better understanding of each step of the catalytic reaction. These studies have also helped to identify, and obtain information about, the active species and resting states in the reaction. Most of these studies have been reviewed before therefore only a brief description of the catalytic cycle will be given here.[6,3,36]

As shown in Scheme 2, two competing cycles that are connected by cross terminating steps and whose prevalence depends on the reaction conditions participate in the production of polyketones. One cycle initiates with a Pd–H species and is favoured by traces of water in the solvent (methanol) via the Water Gas Shift reaction.[37] Rapid insertion of ethene gives an alkyl species that reacts reversibly with CO to yield an acyl complex, which then irreversibly inserts a second ethene molecule. The propagation thus occurs through alternating CO and ethene insertions. Keto esters and diketones can be produced from this cycle, depending on the termination path: the methanolysis of an acyl species yields a keto ester whereas protonolysis of an alkyl complex yields a diketone. The second cycle initiates with a Pd-methoxy species that reacts with CO to form a methoxycarbonyl-Pd complex. Keto esters are also produced during this cycle, together with copolymers with a diester structure that are produced by methanolysis of a acyl-Pd. The palladium hydride species is the most probable initiator in the presence of organic oxidants, and methanolysis is therefore the main termination mechanism. Kinetic studies have shown that ethene insertion is the rate-limiting step of the reaction.[6]

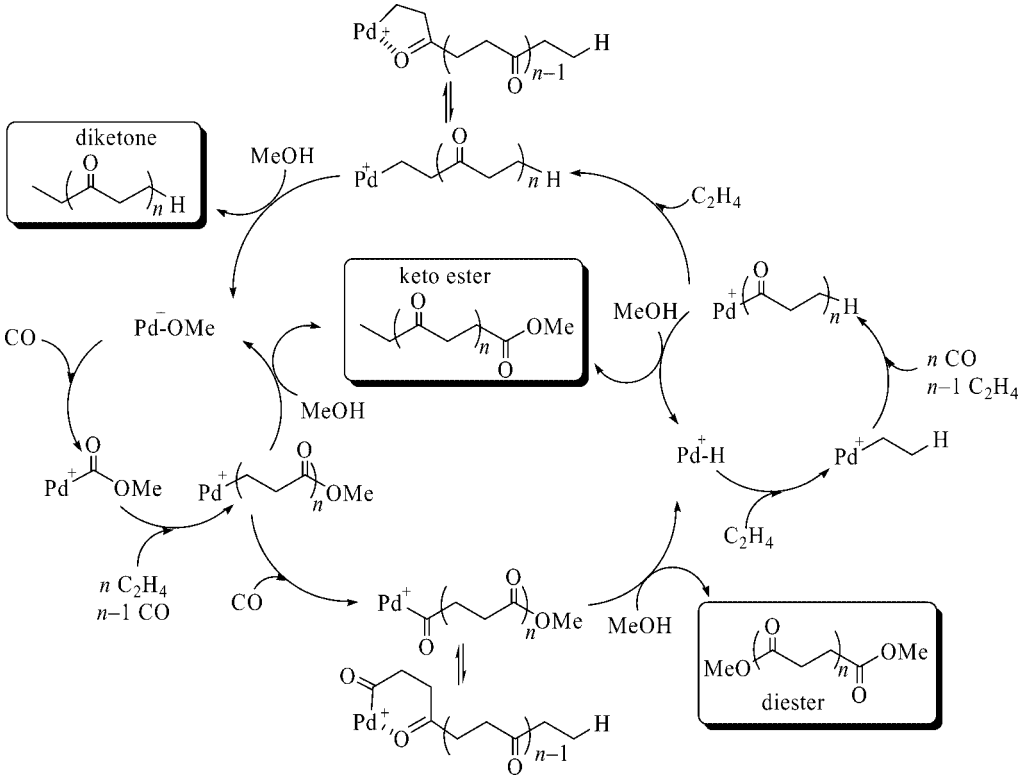


Scheme 2. Proposed mechanism for CO/ethene copolymerisation by diphosphanepalladium catalysts.

 © 2007 Wiley-VCH Verlag GmbH & Co. KGaA, Weinheim 

Two competing chain-transfer mechanisms have been proposed for the alternating copolymerisation of CO and ethene. One involves termination by an unexpected isomerisation into the enolate followed by protonation with methanol and subsequent initiation by insertion of CO into the methoxypalladium species, and the second one involves termination by methanolysis of the acylpalladium species and subsequent initiation by insertion of ethene into the palladium–hydride bond.[38]

The main features of the catalytic cycle for CO/styrene copolymerisation are similar to those of CO/ethene copolymerisation. The propagation step, in particular, is identical, with alternating insertions of CO into Pd–alkyl bonds and of styrene into Pd–acyl bonds. However, the initiation and termination steps are distinct and depend on the nature of the olefinic substrate.[6] The termination pathway that prevails in methanol involves fast β-hydrogen elimination from alkyl species and thus yields a Pd–H complex at the end of the cycle.

We will now focus on selected recent advances in this field. We describe the use of palladium systems containing modified diphosphane and/or new phosphorus ligands, and the results obtained using a series of modular N and S ligands, including chiral ligands, in CO/styrene co- and terpolymerisation. The use of new P-O ligands in non-alternating CO/ethene copolymerisation is also described.

## Ligand Tuning: Modified Diphosphane and Related P-P Ligands

As mentioned in the introduction, $Pd^{II}$ catalysts based on diphosphane ligands have been shown to be the most suitable catalyst systems for the alternating copolymerisation of carbon monoxide and ethene.[6a] Many attempts have been carried out to improve this catalytic system by modifying the diphosphane moiety.[8b] The introduction of methoxy groups in the *ortho* positions in the phenyl rings attached to the phosphorus atoms, for example, has been shown to have a beneficial effect on the copolymerisation in terms of productivity and average molecular weight of the resulting polyketones.[39,40]

Two new chelating diphosphanes ligands have been synthesised and tested in the alternating copolymerisation reaction of carbon monoxide and ethene (Figure 8).[41] The aim of this study was to compare the diphosphane ligand **10** with the neutral and less rigid $C_3$-bridged diphosphane ligand **11** in the copolymerisation reaction. Ligand **10** is the first example of a diphosphonium ligand for the copolymerisation of carbon monoxide and ethene. The square-planar complexes [$PdCl_2$(P-P)] and [$Pd(OAc)_2$(P-P)] (P-P = **10**, **11**) were used as catalyst precursors for the CO/ethene copolymerisation reaction and showed high activity and remarkable control of the molecular weight of the alternating polyketone products.

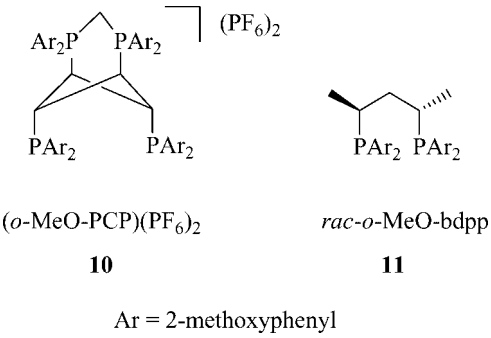


Figure 8. New chelating ligands used in CO/ethene copolymerisation.

[$PdX_2$(P-P)] (P-P = **10**, **11**) complexes (X = Cl or OAc) were then used to generate very active Pd species in water/AcOH mixtures or in MeOH in the presence of *p*-TsOH. The dichloride complexes were tested in mixtures of water and AcOH under standard experimental conditions (40 bar, CO:ethene = 1:1, 85 °C). Perfectly alternating polyketones were obtained in all cases, with only ketone end-groups.

The mechanism of CO/ethene copolymerisation catalysed by [$PdCl_2$(P-P)] complexes in acidic aqueous media is well known, and the chain transfer and propagation steps have been studied in some detail.[6,42] It is usually accepted that neutral $Pd^{II}$–H complexes are generated from the dichloride precursors by the a Water Gas Shift (WGS) reaction.[43]

[$Pd(OAc)_2$(P-P)] complexes were found to be good precursors for the copolymerisation reaction in MeOH in the presence of 2 and 20 equivalents of *p*-TsOH. The acid was used both as a scavenger of the acetate ion and as oxidising agent to form $Pd^{II}$ species from $Pd^0$.[6,42] With both catalyst precursors, the copolymer product contained keto and ester end-groups in a 1:1 ratio. Both catalysts gave polymers with larger $M_n$ (number-average molecular weights) values than the polymers obtained in water/AcOH. It was therefore concluded that the chain-transfer step is slower in MeOH than in water/AcOH. In contrast with the trend usually observed for CO/ethene copolymerisation in MeOH catalysed by $Pd^{II}$–diphosphane complexes,[6,40b] an inverse dependence of the productivity on the acid concentration was found for the reactions catalysed by [$Pd(OAc)_2$(**11**)].

The polyketones obtained with the diphosphonium-diphosphane catalysts showed $M_n$ values up to five times lower than those obtained with the less rigid $C_3$ diphosphane catalysts. These results can be explained by a faster chain-transfer due to the electronic and steric properties of the diphosphonium-diphosphane ligand.

In order to gain an understanding on the beneficial effect of the *ortho*-methoxy group on the alternating copolymerisation of carbon monoxide and ethene,[42,44] neutral and dicationic palladium(II) complexes bearing *o*-MeO-dppe, *o*-MeO-dppp and their analogous precursors with dppe and dppp were synthesised. The catalytic activities were compared in various reaction media (MeOH, $CH_2Cl_2$, TFE, toluene and $H_2O$/AcOH). In addition, in situ and in operando HP-NMR experiments were performed in order to provide

 © 2007 Wiley-VCH Verlag GmbH & Co. KGaA, Weinheim 

valuable information on catalysis resting states and intermediates. Independently of the reaction media, higher catalyst productivities and polyketone molecular weights were achieved using the modified ligands, except in TFE, in which both productivities and molecular weights were lower. This unexpected behaviour in TFE was suggested to be due to the formation of an effective web of hydrogen-bonding interactions between solvent molecules and the *o*-methoxy oxygen atoms of either *o*-MeO-dppp or *o*-MeO-dppe. A slower diffusion of the monomers would take place as a result of the increased congestion at the metal centre, thus lowering the propagation rate. Although this hypothesis was not supported by experimental evidence, such interactions have previously been reported for related palladium systems.[45] The differences observed in productivity between modified and unmodified ligands for the different reaction media can be attributed to both steric and electronic factors related to the *o*-methoxy groups, which would induce a lower tendency to form inactive bis-chelates and dimers, reduced phosphane oxidation,[46] an increased basicity of the metal centre,[40b] and a reduced stability of catalyst resting states such as β-keto alkyl chelates.[42]

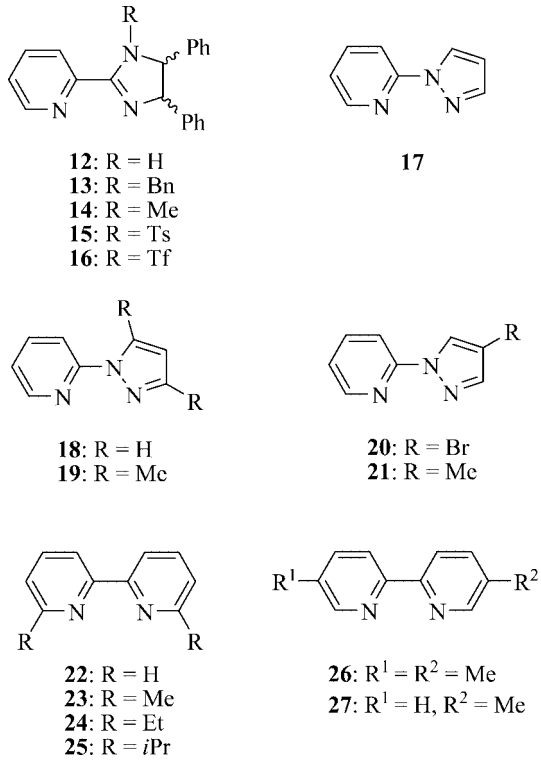


Figure 9. N-N′ ligands used in our group for CO/TBS copolymerisation.

### Modular N-N′ Ligands for the Copolymerisation of CO and Styrene

As discussed above, the Pd-catalysed copolymerisation of CO and vinyl arenes has been reported to be more efficient with nitrogen donor ligands than with phosphorus-based ligands.[3,6a,15,16] In contrast with CO/ethene copolymerisation, a stereogenic centre is created in each -(COCHRCH$_2$)- unit, therefore the use of a chiral ligand is of interest. The alternating CO/4-*tert*-butylstyrene (TBS) copolymerisation reaction has been investigated in our research group using various systems containing chelating asymmetric dinitrogen ligands (Figure 9).

When modular imidazolyl-pyridine ligands **12**–**16** were used, the stereochemistry of the corresponding palladium complexes [PdMe(NCMe)(N-N′)][BArF] was found to be influenced by the electronic properties of the R substituents of the imidazole moieties.[47,48] Indeed, in the case of ligands **12**–**14** the imidazole unit was always found to be *cis* to the methyl group bonded to Pd whereas in the case of ligands **15** and **16**, which contain electron-withdrawing substituents, a mixture of *cis* and *trans* isomers was obtained. This correlation between the relative stability of the *cis* and *trans* isomers of these cationic complexes and the nature of the R substituents was also confirmed by density functional theory calculations.[48] In terms of catalysis, productivities between about 2 and 30 g CP (g Pd h)$^{-1}$ were achieved, with molecular weights of between 17000 and about 80000 under mild conditions ($P_{CO}$ = 1 bar, room temp., TBS/Pd = 620). The nature of the substituents was found to influence both the productivity of the catalyst and the stereoregularity of the polymer but had no effect on the molecular weight of the polyketones. The catalysts bearing the less basic imidazole moieties **15** and **16** were found to be the most active, probably because they favour the coordination of the styrene substrate. They were also shown to favour the production of *u* diads, giving highly syndiotactic copolymers. The microstructure of the polyketones obtained with the (*R*,*S*)-4′,5′-imidazolines was found to depend on the electronic properties of the ligands, whereas only syndiotactic polyketones were obtained when the (*R*,*R*) diastereoisomers were used. This result indicates that chain-end control is more effective than enantiosite control. A comparison of the structures of the complexes containing (*R*,*R*)- and (*R*,*S*)-4′,5′ imidazoline moieties showed that the presence of the (*R*,*R*) diastereoisomers leads to a lower degree of distortion that stabilises the complexes during catalysis, although no direct trend with the productivity of the catalyst could be determined.

When the imidazole moiety was replaced by a pyrazole unit (ligand **17**), the productivity of the catalyst and the molecular weight of the polyketone produced were both found to be moderate under the same conditions (ca. 20 g CP (g Pd h)$^{-1}$ and 30000, respectively).[49]

In the case of pyrimidine-pyrazole ligands, the coordination to the palladium centre to give [PdMe(NCMe)-(N-N′)]$^+$ complexes was found to be directed by the steric bulk of the pyrazole moiety.[49,50] Indeed, when ligand **18** was used, the pyrazole moiety was found to be in a *cis* position to the PdMe group. However, when methyl substituents were introduced in positions 3 and 5 of the pyrazole unit (ligand **19**), the pyrimidine moiety was found to be *cis* to the methyl group. The corresponding polyketones were obtained in high yield with a molecular weight of up to 82000

 © 2007 Wiley-VCH Verlag GmbH & Co. KGaA, Weinheim 

and polydispersities ranging between 1.3 and 1.7, which are close to the best values reported for planar $C_s$-symmetric dinitrogen ligands with styrene derivatives. The high yield is due to the stability of the active species when the reaction is carried out in TFE. Similarly, the enhanced growth of the polymeric chain, as a result of competition between the propagation and the termination steps, is due to the greatly enhanced stability of the acyl- and/or alkylpalladium intermediate in TFE with respect to $CH_2Cl_2$ or chlorobenzene, which causes a remarkable increase in the catalyst lifetime. Optimisation of the amount of trifluoroethanol required for the copolymerisation reaction was performed with bipyridyl ligands and was shown to have a direct effect on the productivity of the catalyst.[51] This effect is shown in Figure 10 using $[Pd(bipy)_2][BArF]_2$ as catalyst precursor.

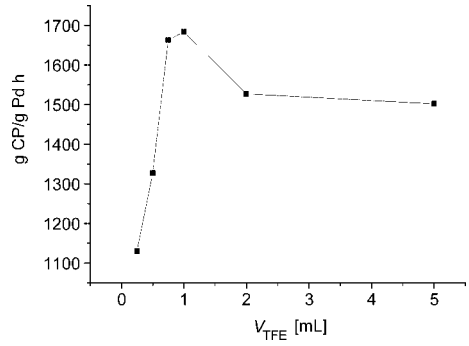


Figure 10. Optimisation of the amount of trifluoroethanol required for CO/TBS copolymerisation ($T$ = 60 °C, $V_{TBS}$ = 10 mL, nPd = $5.1 \times 10^{-4}$ mmol; nBQ = $5.1 \times 10^{-3}$ mmol).

The cationic palladium systems [PdMe(NCMe)(N-N′)][BArF] containing imidazolyl-pyridine ligands *cis*-**12**, *cis*-**13**, *cis*- and *trans*-**15** and pyrazolyl-pyridines **18**, **20** and **21** have also been used for the terpolymerisation of CO/TBS/ethene.[50,52] It was found that the choice of the olefin preferentially inserted into the terpolymer is strictly related to the nature of the nitrogen ligand present in the catalyst and not only to the kind of ligand. Thus, a slight modification in the chelating N ligands coordinated to palladium terpolymerisation catalysts leads to unexpected results in the composition of the terpolymers. For example, the catalysts containing imidazolyl-pyridines **12**, **13** and **15** readily insert ethylene, even at low pressures, and terpolymers with a perfectly controlled composition are obtained if the ethylene/styrene ratio is varied. However, complexes with ligands **18**, **20** and **21** show less versatility towards ethylene pressure and give terpolymers with similar amounts of both olefins. Differences are also encountered in activity/stability: while catalysts bearing ligands *trans*-**15**, **18** and **21** are highly active, those with ligands **12**, **13** and *cis*-**15** decompose quickly. Upon comparing the planar ligands **18** and **21** with the bulkier chiral ones **12**, **13** and **15**, it seems that the chiral imidazolyl-pyridines interfere more with the coordination/insertion of the olefin, which is the rate-determining step of the reaction. This would explain why the systems containing planar ligands **18** and **21** are more active than the system containing *trans*-**15**. The similarity between ligands *cis*-**15** and *trans*-**15**, which only differ in the configuration of one asymmetric carbon atom, and their disparate productivities show that it is more probable that a steric rather than an electronic, effect is responsible for these results. In fact, X-ray analysis of the complex $[Pd(Cl)_2$(*trans*-**15**)] shows that this ligand presents a unique distortion in the imidazoline plane, which may account for the high reactivity observed with this ligand. Comparison with the CO/TBS results shows that the size of the polymer chain is lower when the chain contains ethylene, which favours β-H elimination. Circular dichroism (CD) analysis of the terpolymer obtained with the enantiomerically pure ligand **15** shows that it is optically active. Since this ligand is not able to induce chirality in the CO/TBS copolymerisation (syndiotactic copolymers were obtained), it is clear that the presence of ethylene in the growing polymer chain decreases the probability of chain-end control exerted by the last inserted styrene unit and makes enantiomorphic site control possible.

The effect of the counterion on the copolymerisation reaction has also been studied.[51] Comparison between the known $[Pd(bipy)_2][PF_6]_2$ system and its BArF analogue showed that the use of the latter system increases the catalyst activity considerably. Important differences were also observed in the X-ray structures of the two complexes. However, the introduction of substituents in the 6-position of the dipyridyl ligands **23**–**25** was found to completely inhibit the catalytic reaction when $[Pd(bipy^R)_2][BArF]_2$ complexes were used as catalyst precursors. Catalyst precursors with mixed ligands such as $[Pd(bipy^R)(bipy)][BArF]_2$ gave copolymers of higher molecular weight than with $[Pd(bipy)_2][BArF]_2$, although the catalyst activity was greatly reduced. However, the introduction of one or two methyl substituents in the 5-position of the pyridyl rings (ligands **26** and **27**) was found to have a positive effect on the productivity of the catalysts, although no effect was observed on the molecular weight and tacticity of the polymers produced.

### Modular S-S Ligands in CO/Styrene Copolymerisation

Sulfur-containing ligands have rarely been used in copolymerisation reactions although bis(alkyl)thioether systems have been shown to be active in the copolymerisation of CO/styrene, even though a loss of stereocontrol occurred.[6a,53] We have reported the synthesis and use of thioether ligands in various catalytic processes and we therefore thought that these ligands could provide interesting results in the Pd-catalysed copolymerisation of CO and 4-*tert*-butylstyrene. In 2002, we reported the use of the thioether ligands **28**–**30** for this reaction (Figure 11).[54]

The palladium complexes [PdMe(NCMe)(**28**–**30**)][BArF] were synthesised and used as catalyst precursors. The catalytic results obtained were similar to those reported using chiral P-OP, N-N, and P-N ligands in terms of activity and molecular weights.[23,55,56] However, it should be noted that these results were obtained under mild conditions (1 atm

 © 2007 Wiley-VCH Verlag GmbH & Co. KGaA, Weinheim 

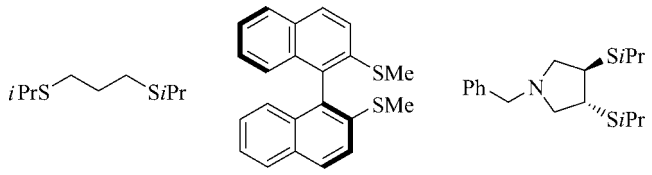


28 29 30

Figure 11. Thioether ligands used in copolymerisation reactions.

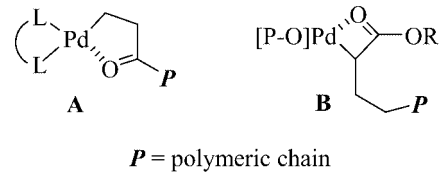


A B

*P* = polymeric chain

Figure 12. Chelates formed during the copolymerisation reaction.

CO and room temperature). Nevertheless, the activities and molecular weights of the polymers obtained were much lower than those achieved with planar N–N ligands such as bipyridine. The rather high polydispersity values and the non-linear relationship between time and molecular weights indicated that these systems are not living.[16d] Although the productivity of the catalyst bearing ligand **28** was found to increase when the CO pressure was increased from 1 to 5 atm, these systems were found to decompose with time under these reaction conditions and long reaction times resulted in a decrease of the catalyst productivities. These systems were, however, stabilised by large excesses of olefinic substrates under 1 atm of CO. Furthermore, although it was suggested that the atactic nature of the copolymers produced using thioether ligands is due to the flexibility of the donor atom structure,[6a] the system bearing ligand **30** yielded polymers with prevailing isotacticity, which therefore indicates that control of the stereoregularity can be achieved using this type of ligand.

### P-O Ligands in Non-Alternating CO/Ethene Copolymerisation

In previous sections we have dealt with the palladium-catalysed perfectly alternating copolymerisation of ethene and carbon monoxide and its mechanism. It is well known that the double insertion of carbon monoxide in this reaction does not occur for thermodynamic reasons, whereas the double insertion of ethene is kinetically disfavoured. The formation of a stable five-membered cationic palladium metallacycle (see **A**, Figure 12) by an electrostatic interaction between the oxygen of the carbonyl and the cationic palladium centre, known as "back-biting", kinetically favours the insertion of carbon monoxide over ethene insertion.[17b,57] In over two decades of research in the area of late transition metal catalysed polymerisation of carbon monoxide and ethene, no extra insertions of ethene or carbon monoxide have ever been reported; even high ethene/carbon monoxide ratios produce exclusively error-free polyketone until all the carbon monoxide has been consumed.[7b,58] Nevertheless, the double insertion of ethene should be possible, as the same cationic palladium species that is used for the copolymerisation is known to efficiently dimerise ethene into butenes.[59]

The development of novel late transition metal catalysts for the synthesis of new copolymers containing a non-polar backbone and a controlled amount of a polar monomer is of considerable interest to both academia and industry.[59] However, the design of metal catalysts for such copolymerisation reactions is not a trivial task and, despite the many attempts that have been made in this area so far, only a very few new materials have been obtained.[60] The production of non-perfectly alternating carbon monoxide and ethene copolymers is one of the main aims in polyketone research in order to obtain new materials with desirable properties and which can be further functionalised.

In 2002, Drent et al. reported the first example of a palladium-catalysed non-perfectly alternating copolymerisation of carbon monoxide and ethene. The Pd-containing catalyst precursors bearing alkoxy-arylphosphane ligands containing sulfonic acid groups were formed in situ by mixing palladium acetate and the ligand in a near stoichiometric ratio. Double, triple and quadruple insertions of ethene into the growing polyketone chain were observed. The production of extra insertions of ethene was attributed to the destabilisation of the neutral chelate (**B**; Figure 12) to the extent that ethene effectively competes with carbon monoxide for the next insertion.[61]

More recently, Rieger et al. have reported the first examples of neutral $Pd^{II}$ complexes bearing sulfonated phosphane ligands (Scheme 3). Higher activities as well as higher insertion of extra amounts of ethene (up to 30%) into the copolymer chain were achieved[62] when compared to the previously reported in situ copolymerisation reactions.[61]

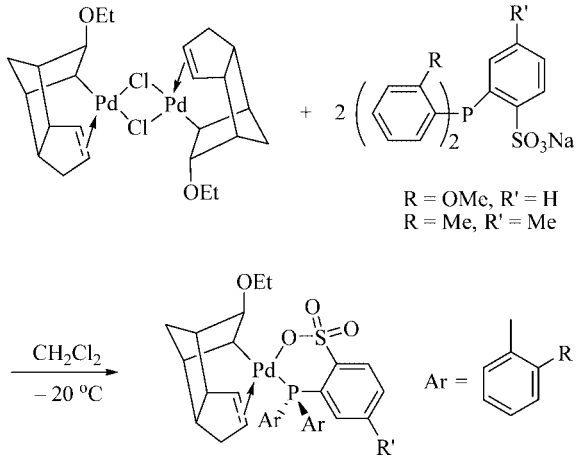


Scheme 3. $Pd^{II}$ complexes bearing sulfonated phosphane ligands.

 © 2007 Wiley-VCH Verlag GmbH & Co. KGaA, Weinheim 

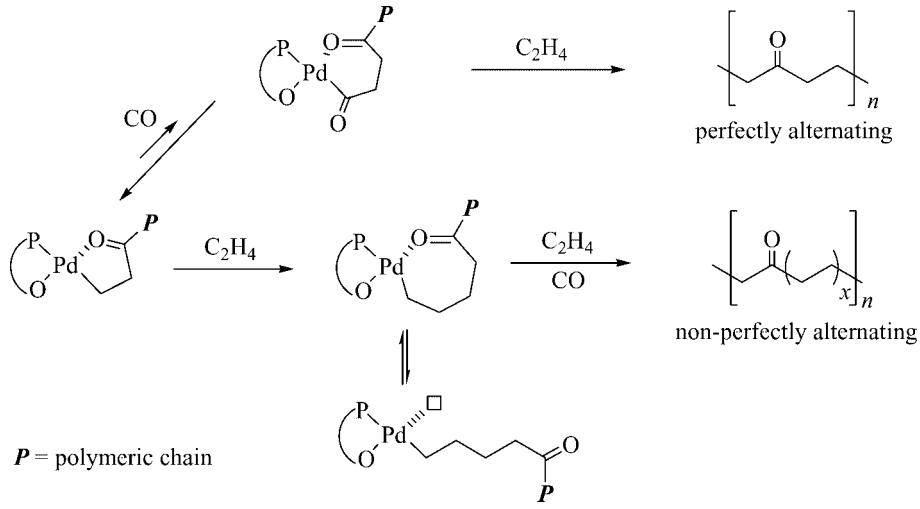


Scheme 4. Mechanism for non-perfectly alternating CO/ethene copolymerisation (□ = vacant site).

The mechanism of the perfectly alternating copolymerisation of carbon monoxide and ethene by $Pd^{II}$ catalysts based on diphosphane ligands has been extensively studied and is now well known.[6] However, only a few studies on the mechanism of the non-alternating copolymerisation of carbon monoxide and ethene have been published.[61–63] Rieger et al. have proposed that this new polymerisation proceeds via two intertwined pathways (Scheme 4), where the same active species may switch between the production of alternating and non-alternating blocks in the same polymer chain.[62] Multiple ethene insertions are suggested to be facilitated by a stereoelectronic destabilisation of the neutral chelate to an extent that enables ethene to effectively compete with carbon monoxide for the next insertion, as previously proposed by Drent et al.[61]

Based on this report, it was assumed that the neutral nature of the CO-inserted 6-membered chelate could lead to a decarbonylation reaction yielding the five-membered ring complex that could then react with ethene to form a seven-membered chelate, which is proposed to open more easily and therefore facilitates the incorporation of further ethylene units. Furthermore, increasing the pressure of ethene and employing high CO/ethene gas blend ratios (1:20) statistically provides a higher probability of ethene insertion over carbon monoxide insertion.

Ziegler and co-workers have reported work based on Drent's ligands that explains the formation of a non-perfectly alternating copolymer based on the decarbonylation of the acylpalladium complexes formed during the catalytic process.[63] This is possible if the acylpalladium complex with sulfonated phosphane ligands does not form a Pd–O chelate bond between the metal and a carbonyl group on the polyketone chain, thus favouring the decarbonylation.

## Conclusions

Although co- and terpolymerisation of carbon monoxide and olefins has been the subject of numerous investigations, the demand from industry for new types of material makes this area still challenging and offers new possibilities.

The modification of diphosphane ligands by introducing methoxy groups yields more efficient systems, although the presence of TFE decreases the productivity of the catalysts. Chiral N-N′ and S-S ligands can be used in CO/styrene copolymerisation systems to control the stereochemistry of the catalysts and the stereoregularity of the resulting copolymers. Finally, non-alternating CO/ethene copolymerisation, which can provide new materials with interesting properties, is now possible with Pd/P-O systems. Research in this area is still at a very early stage, however, and therefore represents a new challenge in the field of CO/ethene copolymerisation.

## Acknowledgments

The authors are grateful to all the co-workers who participated in the polymerisation studies and especially to Amaia Bastero, whose contribution was essential to the studies mentioned in this review. We also wish to thank the Spanish Ministerio de Educación y Ciencia (CTQ2004-04412/BQU, Consolider Ingenio 2010 CSD2006-0003 and a Juan de la Cierva fellowship to C. Godard), the Generalitat de Catalunya (2005SGR007777 and Distinction for Research Promotion, 2003 C. C.) and the European Commission (EC) (HPRN-CT-2002-00196) for financial support.

[1] Shell, *Carilon® Thermoplastic Polymers*, information sheet, **1994**.
[2] *European Plastics News*, October, **1995**, p. 57.
[3] A. Sommazzi, F. Garbassi, *Prog. Polym. Sci.* **1997**, *22*, 1547–1605.
[4] a) B. J. Lommerts, E. A. Klop, J. J. Aerts, *Polym. Sci. Polym. Phys. B* **1993**, *31*, 1319–1330; b) M. A. Del Nobile, G. Mensitieri, L. Nicolais, A. Sommazzi, F. J. Garbassi, *Appl. Polym. Sci.* **1993**, *50*, 1261–1268; c) M. D. E. Forbes, *Macromolecules* **1994**, *27*, 1020–1026; d) S. De Vito, F. Ciardelli, G. Ruggeri, O. Chiantore, A. Moro, *Polym. Int.* **1998**, *45*, 353–365.
[5] a) B. J. Lommerts, Eur. Pat. 456306, **1991**; b) C. E. Ash, *Int. J. Polym. Mater.* **1995**, *30*, 1–13.

 © 2007 Wiley-VCH Verlag GmbH & Co. KGaA, Weinheim 

[6] a) E. Drent, P. H. M. Budzelaar, *Chem. Rev.* **1996**, *96*, 663–681; b) C. Bianchini, A. Meli, *Coord. Chem. Rev.* **2002**, *225*, 35–66.

[7] a) E. Drent, Eur. Pat. Appl. 121965A2, **1984**; b) E. Drent, J. A. M. van Broekhoven, M. J. Doyle, *J. Organomet. Chem.* **1991**, *417*, 235–251.

[8] a) J. A. M. Van Broekhoven, R. L. Wife, United States Pat. 4,843,144, **1989**; b) G. Verspui, F. Schanssema, R. A. Sheldon, *Angew. Chem. Int. Ed.* **2000**, *39*, 804–806.

[9] C. Bianchini, H. M. Lee, A. Meli, W. Oberhauser, F. Vizza, P. Brüggeller, R. Haid, C. Langes, *Chem. Commun.* **2000**, 777–778.

[10] S. Doherty, G. R. Eastham, R. P. Tooze, D. W. Scanlan, M. R. J. Elsegood, W. Clegg, *Organometallics* **1999**, *18*, 3558–3560.

[11] S. J. Dossett, A. Gillon, A. G. Orpen, J. S. Fleming, P. G. Pringle, D. F. Wass, M. D. Jones, *Chem. Commun.* **2001**, 699–700.

[12] a) O. V. Gusev, A. M. Kal'sin, M. G. Peterleitner, P. V. Petrovskii, K. A. Lyssenko, N. G. Akhmedov, C. Bianchini, A. Meli, W. Oberhauser, *Organometallics* **2002**, *21*, 3637–3649; b) C. Bianchini, A. Meli, W. Oberhauser, P. W. N. M. van Leeuwen, A. M. Zuideveld, Z. Freixa, P. C. J. Kamer, A. L. Spek, O. V. Gusev, A. M. Kal'sin, *Organometallics* **2003**, *22*, 2409–2421; c) C. Bianchini, A. Meli, W. Oberhauser, S. Parisel, E. Passaglia, F. Ciardelli, O. V. Gusev, A. M. Kal'sin, N. V. Vologdin, *Organometallics* **2005**, *24*, 1018–1030; d) O. G. Gusev, A. M. Kalsin, P. V. Petrovskii, K. A. Lyssenko, Y. F. Oprunenko, C. Bianchini, A. Meli, W. Oberhauser, *Organometallics* **2003**, *22*, 913–915.

[13] a) P. Braunstein, C. Frison, X. Morise, *Angew. Chem. Int. Ed.* **2000**, *39*, 2867–2870; b) P. Braunstein, M. D. Fryzuk, M. Le Dall, F. Naud, S. Rettig, F. Speiser, *J. Chem. Soc., Dalton Trans.* **2000**, 1067–1074; c) P. Braunstein, J. Durand, M. Knorr, C. Strohmann, *Chem. Commun.* **2001**, 211–212; d) J. Andrieu, P. Braunstein, F. Naud, R. D. Adams, *J. Organomet. Chem.* **2000**, *601*, 43–50; e) K. R. Reddy, C.-L. Chen, Y.-H. Hung Liu, S.-M. Peng, J.-T. Chen, S.-T. Liu, *Organometallics* **1999**, *18*, 2574–2576; f) M. Sperrle, A. Aeby, G. Consiglio, A. Pfaltz, *Helv. Chim. Acta* **1996**, *79*, 1387–1392; g) A. Aeby, A. Gsponner, G. Consiglio, *J. Am. Chem. Soc.* **1998**, *120*, 11000–11001; h) A. Aeby, G. Consiglio, *J. Chem. Soc., Dalton Trans.* **1999**, 655–656; i) G. J. P. Britovsek, W. Keim, S. Mecking, D. Sainz, T. Wagner, *J. Chem. Soc., Chem. Commun.* **1993**, 1632–1633.

[14] a) A. Sommazzi, F. Garbassi, G. Mestroni, B. Milani, US Pat. 5310871, **1994**; b) A. Sommazzi, F. Garbassi, G. Mestroni, B. Dilani, L. Vicentini, It. Pat. MIA002368, **1995**; c) A. Sommazzi, S. Margherita, G. Lugli, F. Garbassi, F. Calderazzo, D. B. Dell' Amico, US Pat. 5314856, **1994**; d) A. Sommazzi, S. Margherita, G. Lugli, F. Garbassi, F. Calderazzo, D. B. Dell' Amico, US Pat. 5324701, **1994**; e) Z. Jiang, A. Sen, *Macromolecules* **1994**, *27*, 7215–7216; f) K. Nozaki, *J. Polym. Sci., Part A: Polym. Chem.* **2004**, *42*, 215–221; g) K. Nakano, N. Kosaka, T. Hiyama, K. Nozaki, *Dalton Trans.* **2003**, 4039–4050; h) J. Durand, B. Milani, *Coord. Chem. Rev.* **2006**, *250*, 542–560.

[15] A. Sen, Z. Jiang, *Macromolecules* **1993**, *26*, 911–915.

[16] a) E. Drent, *Eur. Pat. Appl.* 229408, **1986**; b) P. Corradini, C. De Rosa, A. Panunzi, G. Petrucci, P. Pino, *Chimia* **1990**, *44*, 52–54; c) M. Barsaccchi, G. Consiglio, L. Medici, G. Petrucci, U. W. Suter, *Angew. Chem. Int. Ed. Engl.* **1991**, *30*, 989–991; d) M. Brookhart, F. C. Rix, J. M. DeSimone, J. C. Barborak, *J. Am. Chem. Soc.* **1992**, *114*, 5894–5895; e) C. Pisano, A. Mezzetti, G. Consiglio, *Organometallics* **1992**, *11*, 20–22; f) M. Barsaccchi, A. Batistini, G. Consiglio, U. W. Suter, *Macromolecules* **1992**, *25*, 3604–3606; g) B. Milani, E. Alessio, G. Mestroni, A. Sommazzi, F. Garbassi, E. Zangrando, N. Bresciani-Pahor, L. Randaccio, *J. Chem. Soc., Dalton Trans.* **1994**, 1903–1911; h) B. Milani, G. Mestroni, A. Sommazzi, F. Garbassi, *It. Pat.* MIA000337, **1995**; i) Y. Feng, J. Sun, Y. Zhu, W. Chen, *J. Polym. Sci., Part A: Polym. Chem.* **1997**, *35*, 1283–1291; j) Y. Feng, J. Sun, F. Yao, Y. Yu, *J. Appl. Polym. Sci.* **1997**, *68*, 855–857.

[17] a) K. Nozaki, N. Sato, H. Takaya, *J. Am. Chem. Soc.* **1995**, *117*, 9911–9912; b) K. Nozaki, N. Sato, Y. Tonomura, M. Yasutoni, H. Takaya, T. Hiyama, T. Matsubara, N. Koga, *J. Am. Chem. Soc.* **1997**, *119*, 12779–12795; c) K. Nozaki, H. Komaki, Y. Kawashima, T. Hiyama, T. Matsubara, *J. Am. Chem. Soc.* **2001**, *123*, 534–544.

[18] B. Milani, F. Baronetto, E. Zangrando, *J. Chem. Soc., Dalton Trans.* **2000**, 3055–3057.

[19] S. Bruckner, C. De Rosa, P. Corradini, W. Porzio, A. Musco, *Macromolecules* **1996**, *29*, 1535–1539.

[20] B. Milani, A. Anzilutti, L. Vicentini, A. Sessanta Santi, E. Zangrando, S. Geremia, G. Mestroni, *Organometallics* **1997**, *16*, 5064–5075.

[21] B. Milani, G. Corso, G. Mestroni, C. Carfagna, M. Formica, R. Seraglia, *Organometallics* **2000**, *19*, 3435–3441.

[22] A. Macchioni, G. Bellachioma, G. Cardaci, M. Travaglia, C. Zuccaccia, B. Milani, G. Corso, E. Zangrando, G. Mestroni, C. Carfagna, M. Formica, *Organometallics* **1999**, *18*, 3061–3069.

[23] M. Brookhart, M. I. Wagner, G. G. A. Balavoine, H. A. Haddou, *J. Am. Chem. Soc.* **1994**, *116*, 3641–3642.

[24] Z. Jang, S. E. Adams, A. Sen, *Macromolecules* **1994**, *27*, 2694–2700.

[25] S. Bartolini, C. Carfagna, A. Musco, *Macromol. Rapid Commun.* **1995**, *16*, 9–14.

[26] M. T. Reetz, G. Haderlein, K. Angermund, *J. Am. Chem. Soc.* **2000**, *122*, 996–997.

[27] M. Brookhart, M. I. Wagner, *J. Am. Chem. Soc.* **1996**, *118*, 7219–7220.

[28] a) B. Sesto, S. Bronco, E. L. Gindro, G. Consiglio, *Macromol. Chem. Phys.* **2001**, *202*, 2059–2064; b) C. Bianchini, H. M. Lee, A. Meli, S. Moneti, V. Patinec, G. Petrucci, F. Vizza, *Macromolecules* **1999**, *32*, 3859–3866; c) E. Lindner, M. Schmidt, J. Wald, J. A. Queisser, M. Geprägs, P. Wegner, C. Nachtigal, *J. Organomet. Chem.* **2000**, *602*, 173–187; d) B. Milani, L. Vincentini, A. Sommazzi, F. Garbassi, E. Chiarparin, E. Zangrando, G. Mestroni, *J. Chem. Soc., Dalton Trans.* **1996**, 3139–3144.

[29] B. Milani, A. Scarel, J. Durand, G. Mestroni, R. Seraglia, C. Carfagna, B. Binotti, *Macromolecules* **2003**, *36*, 6295–6297.

[30] S. Kacker, J. A. Sissano, D. N. Schulz, *J. Polym. Sci., Part A: Polym. Chem.* **2000**, *38*, 752–757.

[31] a) K. Nozaki, Y. Kawashima, K. Nakamoto, T. Hiyama, *Macromolecules* **1999**, *32*, 5168–5170; b) Y. Kawashima, K. Nozaki, T. Hiyama, *Inorg. Chim. Acta* **2003**, *350*, 577–582.

[32] A. Aeby, G. Consiglio, *Helv. Chim. Acta* **1998**, *81*, 35–39.

[33] A. Aeby, A. Gsponer, M. Sperrle, G. Consiglio, *J. Organomet. Chem.* **2000**, *603*, 122–127.

[34] B. T. Muellers, J.-W. Park, M. S. Brookhart, M. M. Green, *Macromolecules* **2001**, *34*, 572–581.

[35] a) B. Milani, A. Mistaro, G. Mestroni, *ISHC12*, Stockholm, **2000**, Abstract p.216; b) J. Durand, A. Scarel, B. Milani, R. Seraglia, S. Gladiali, C. Carfagna, B. Binotti, *Helv. Chim. Acta* **2006**, *89*, 1752–1771.

[36] A. Sen, *Acc. Chem. Res.* **1993**, *26*, 303–310.

[37] A. Vavasori, L. Toniolo, *J. Mol. Catal. A* **1996**, *110*, 13–23.

[38] M. A. Zuideveld, P. C. J. Kamer, P. W. N. M. van Leeuwen, P. A. A. Klusener, H. A. Stil, C. F. Roobeek, *J. Am. Chem. Soc.* **1998**, *120*, 7977–7978.

[39] a) J. Schwarz, E. Herdtweck, W. A. Herrmann, M. G. Gardiner, *Organometallics* **2000**, *19*, 3154–3160; b) C. Bianchini, H. M. Lee, A. Meli, W. Oberhauser, M. Peruzzini, F. Vizza, *Organometallics* **2002**, *21*, 16–33; c) C. Bianchini, A. Meli, G. Müller, W. Oberhauser, E. Passaglia, *Organometallics* **2002**, *21*, 4965–4977; d) C. Bianchini, A. Meli, W. Oberhauser, A. M. Segarra, C. Claver, E. J. Garcia Suarez, *J. Mol. Catal. A: Chem.* **2006**, *265*, 291–304.

[40] a) R. van der Drift, E. Bouwman, E. Drent, H. Koojiman, A. L. Spek, A. B. van Oort, W. P. Mul, *Organometallics* **2002**,

 © 2007 Wiley-VCH Verlag GmbH & Co. KGaA, Weinheim 

*21*, 3401–3407; b) K. R. Dunbar, J.-S. Sun, A. Quillevere, *Inorg. Chem.* **1994**, *33*, 3598–3601.
[41] a) A. Vavasori, L. Toniolo, G. Cabinato, *J. Mol. Catal. A: Chem.* **2004**, *215*, 63–72; b) A. Vavasori, L. Toniolo, G. Cabinato, F. Visentin, *J. Mol. Catal. A* **2003**, *205*, 295–303.
[42] C. Bianchini, A. Meli, W. Oberhauser, *Dalton Trans.* **2003**, 2627–2635.
[43] a) V. N. Zudin, V. D. Chinakov, V. M. Nekipelow, V. A. Likholobov, Y. I. Yermakov, *J. Organomet. Chem.* **1985**, *289*, 425–430; b) V. N. Zudin, G. N. Ll'inich, V. A. Likholobow, Y. I. Yermakov, *J. Chem. Soc., Chem. Commun.* **1984**, 545–546.
[44] a) R. van der Drift, E. Bouwman, E. Drent, H. Koojiman, A. L. Spek, A. B. van Oort, W. P. Mul, *Organometallics* **2002**, *21*, 3401–3407.
[45] J. Vicente, A. Arcas, *Coord. Chem. Rev.* **2005**, *249*, 1135–1154.
[46] I. M. Angulo, E. Bouwman, M. Lutz, W. P. Mul, A. L. Spek, *Inorg. Chem.* **2001**, *40*, 2073–2082.
[47] A. Bastero, C. Claver, A. Ruiz, S. Castillón, *Eur. J. Inorg. Chem.* **2001**, 3009–3011.
[48] A. Bastero, C. Claver, A. Ruiz, S. Castillón, E. Daura, C. Bo, E. Zangrando, *Chem. Eur. J.* **2004**, *10*, 3747–3760.
[49] A. Bastero, A. Ruiz, J. A. Reina, C. Claver, A. M. Guerrero, F. A. Jalón, B. R. Manzano, *J. Organomet. Chem.* **2001**, *619*, 287–292.
[50] A. F. Bella, A. Ruiz, C. Claver, F. Sepúlveda, F. A. Jalón, B. R. Manzano, **2006**, manuscript to be submitted to *J. Organomet. Chem.*.
[51] S. Stoccoro, G. Alesso, M. Agostina Cinellu, G. Minghetti, A. Zucca, A. Bastero, C. Claver, M. Manassero, *J. Organomet. Chem.* **2002**, *664*, 77–84.
[52] A. Bastero, A. Ruiz, C. Claver, A. F. Bella, B. Milani, B. Moreno-Lara, F. A. Jalón, B. R. Manzano, *Adv. Synth. Catal.* **2005**, *347*, 839–846.
[53] J. A. Van Doorn, E. Drent, *Eur. Pat. Appl.* 345847, **1989**.
[54] A. Bastero, C. Claver, A. Ruiz, *Catal. Lett.* **2002**, *82*, 1–2; A. Bastero, C. Claver, A. Ruiz, *Catal. Lett.* **2002**, *82*, 85–88.
[55] K. Nozaki, T. Hiyama, *J. Organomet. Chem.* **1999**, *576*, 248–253.
[56] J. C. Yuan, S. J. Lu, *J. Polym. Sci., Part A: Polym. Chem.* **2000**, *38*, 2919–2924.
[57] a) F. C. Rix, M. Brookhart, *J. Am. Chem. Soc.* **1995**, *117*, 1137–1138; b) F. C. Rix, M. Brookhart, P. S. White, *J. Am. Chem. Soc.* **1996**, *118*, 4746–4764; c) P. Margl, T. Ziegler, *J. Am. Chem. Soc.* **1996**, *118*, 7337–7344.
[58] E. Drent, *Pure Appl. Chem.* **1990**, *62*, 661–669.
[59] a) G. J. P. Britowsek, V. C. Gibson, D. F. Wass, *Angew. Chem. Int. Ed.* **1999**, *38*, 428–447; b) L. S. Boffa, B. M. Novak, *Chem. Rev.* **2000**, *100*, 1479–1494; c) S. D. Ittel, L. K. Johnson, M. Brookhart, *Chem. Rev.* **2000**, *100*, 1169–1204.
[60] a) M. M. Brubaker, D. D. Coffman, H. H. Hoehn, *J. Am. Chem. Soc.* **1952**, *74*, 1509–1515; b) D. V. Deubel, T. Ziegler, *Organometallics* **2002**, *21*, 1603–1611; c) A. Michalak, T. Ziegler, *Organometallics* **2001**, *20*, 1521–1532; d) A. Michalak, T. Ziegler, *J. Am. Chem. Soc.* **2001**, *123*, 12266–12278; e) C. S. Shultz, J. M. DeSimone, M. Brookhart, *Organometallics* **2002**, *20*, 16–18; f) K. Tanaka, M. Furo, E. Ihara, H. Yasuda, *J. Polym. Sci., Part A: Polym. Chem.* **2001**, *39*, 1382–1390; g) G. Desurmont, T. Tokimitsu, H. Yasuda, *Macromolecules* **2000**, *33*, 7679–7681.
[61] E. Drent, R. van Dijk, R. van Ginkel, B. van Oort, R. I. Pugh, *Chem. Commun.* **2002**, 964–965.
[62] A. K. Hearley, R. J. Nowack, B. Rieger, *Organometallics* **2005**, *24*, 2755–2763.
[63] A. Haras, A. Michalak, B. Rieger, T. Ziegler, *Organometallics* **2006**, *25*, 946–953.

Received: January 8, 2007
Published Online: April 16, 2007

 © 2007 Wiley-VCH Verlag GmbH & Co. KGaA, Weinheim 

DOI: 10.1002/ejic.200700078

# NMR Studies of Paramagnetic Metallocarbaporphyrinoids

**Ewa Pacholska-Dudziak[a] and Lechosław Latos-Grażyński*[a]**

**Keywords:** Carbaporphyrinoids / Porphyrinoids / NMR spectroscopy / Organometallic chemistry

Carbaporphyrinoids provide a suitable macrocyclic platform for organometallic investigations that provide unique opportunities for modifying a macrocyclic structure. Alteration of a coordination core is a route of choice for stabilizing unusual metal ion oxidation states and coordination geometries. This microreview presents the general characteristic of paramagnetic metallocarbaporphyrinoids, with a focus on NMR studies. NMR spectroscopy of paramagnetic molecules can be considered as a powerful probe of several intriguing aspects of the molecular and electronic structures, structural rearrangements, and reactivity, including oxidation and oxygenation, of this fascinating class of compounds. The chosen examples address paramagnetic organometallic nickel(II) and nickel(III) complexes of *N*-confused porphyrins, the reactions of nickel(II) dimethylated *N*-confused porphyrins with organometallic reagents, the stabilization of rare organocopper(II) species, the investigation of weak intramolecular metal–arene interactions, and the conformational flexibility of nickel(II) benziporphyrin and vacataporphyrin. Particular emphasis is placed on NMR studies as an efficient way of detecting intermediate species formed in the course of oxidation and oxygenation of iron(*n*) carbaporphyrinoids.
(© Wiley-VCH Verlag GmbH & Co. KGaA, 69451 Weinheim, Germany, 2007)

## Introduction

$^1$H NMR spectroscopy has been extensively applied to paramagnetic molecules including a variety of paramagnetic metalloproteins. The fundamental theoretical description of the electron–nucleus interaction, as reflected by the NMR parameters, illustrated by appropriate examples of applications has been presented in several monographic works.[1–10] In particular, the amount of NMR information provided by the contact shift and dipolar shift, and their temperature dependency, have been addressed. Relaxation phenomena related to the presence of unpaired electrons have also been a topic of some interest. Amongst others, the following subjects have been investigated: spin density delocalization correlated to the electronic structure, structural and electronic equilibria, the dynamics of intramolecular rearrangements, stereochemistry, solvation, and the structure of the second coordination sphere.

$^1$H NMR spectroscopy has been found to be a particularly useful method for detecting and characterizing iron complexes of porphyrins,[7] *N*-substituted porphyrins,[11–15] heteroporphyrins,[16–19] and hemoproteins in different coor-

[a] Department of Chemistry, University of Wrocław,
14 F. Joliot-Curie St., Wrocław 50 383, Poland

*Ewa Dudziak (née Pacholska) was born in Wrocław, Poland, in 1969. She completed her PhD in 2000 under the supervision of Prof. Latos-Grażyński at the University of Wrocław, where she also obtained her BSc in 1993. She was a postdoctoral researcher in Dijon with Prof. Roger Guilard at the University of Burgundy, France. She is now working in Prof. Latos-Grażyński's group at the University of Wrocław on complexes of core-modified porphyrins with a flexible skeleton involved in organometallic coordination.*

*Professor Latos-Grażyński (the corresponding member of the Polish Academy of Sciences) is the Polish representative on the Editorial Board of this journal. Prof. Latos-Grażyński's involvement in porphyrin chemistry stems from his interest in the NMR of paramagnetic systems. Thus, much of his research has been devoted to the electronic structure and reactivity of paramagnetic metalloporphyrins, especially hemes. He has investigated model systems for heme enzymes, heme degradation, the activation of dioxygen by metalloporphyrins, the reactivity of metalloporphyrin π-radicals, and the properties of unusually oxidized systems, for example organocopper(II) species. The attention of Prof. Latos-Grażyński and his group is currently focused on the synthesis of novel porphyrinoids that have at least one of the regular pyrroles replaced by a carbo- or heterocyclic moiety. The organometallic species that can be made from carbaporphyrinoids are of special interest.*

 © 2007 Wiley-VCH Verlag GmbH & Co. KGaA, Weinheim 

dination/oxidation states.[8,20] These studies have yielded an insight into the mechanisms of spin-density transfer in paramagnetic metalloporphyrins. In particular, it has been found that this technique is extremely sensitive toward fine structural effects such as substitution, electronic asymmetry, axial ligation (steric hindrance and basicity), or puckering of an equatorial macrocycle. Exchange and rotation of the molecular fragments have also been a subject of interest, and the intermediate iron porphyrin species that act in dioxygen activation or oxygen-atom transfer have been "trapped" by NMR spectroscopy.[21–23] Recently, octaethylporphyrin degradation (coupled oxidation) has been explored in order to establish the reactivity of iron complexes in various stages of heme degradation.[24–35] For instance, the paramagnetic shift patterns for the model iron octaethylbiliverdin-related radical complexes present several useful probes for detecting analogous species in hemoproteins by $^1$H NMR spectroscopy.[35]

Recent progress in the $^1$H NMR spectroscopic characterization of paramagnetic hemoproteins is related to the search for suitable spectroscopic models that involve the synthesis of fine-tuned iron porphyrins. These models mimic the spectroscopic properties encountered in hemoproteins for a given electronic state.[7] The application of two-dimensional techniques initially afforded an unambiguous assignment of resonances related to the active hemoprotein site and eventually yielded three-dimensional hemoprotein structures in solution.[8,20]

In light of the format of a microreview, here we intend to present an overview centered on our most recent efforts in the field of paramagnetic metallocarbaporphyrinoids, with a focus on the application of $^1$H NMR spectroscopy to this unique class of compounds. Thus, variations of the porphyrin core involving the introduction of a hydrocarbon unit in place of one of pyrrolic nitrogens have led to a new class of macrocycles − carbaporphyrinoids (Scheme 1) − that have interesting properties both in terms of their aromatic character and their potential ability to bind metal ions.[36,37]

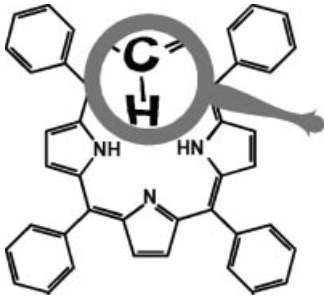


Scheme 1. A carbaporphyrinoid.

Such a replacement preserves three regular pyrrole moieties while the ($C_n$NNN) core determines the monocarbaporphyrinoid structure.[38–45] The internal carbon atom(s) belong(s) to the carbo- or heterocycles that replace(s) the original pyrrole ring of the porphyrin. In general, carbaporphyrinoids provide a unique molecular platform that is suitable for exploring organometallic chemistry in a peculiar macrocyclic environment and forcing an unusual coordination geometry and/or oxidation state of the metal ions.[39–41,44,45] Systematic, comprehensive summaries of the current state-of-the-art in carbaporphyrinoid chemistry are contained in several review articles.[38–46]

## Carbaporphyrinoids

The synthesis of 2-aza-21-carba-5,10,15,20-tetraarylporphyrin ("inverted porphyrin", "*N*-confused porphyrin", "mutant porphyrin", "carbaporphyrin") was seminal for the field of cabaporphyrinoids.[36,37] An inverted porphyrin is a constitutional isomer of a porphyrin which preserves its general structural framework.[46,47] The synthesis of this molecule prompted intense synthetic work to generate a whole class of carbaporphyrinoids.[36–40,43–45,48–50]

Here, we have gathered together the representative structures of two tautomers of this *N*-confused porphyrin, namely (CP*H*)H$_2$ and (*H*CP*H*)H,[36,37] and the alkylated *N*-confused porphyrins (*R*CP*H*)H, (CP*R*)H$_2$ and (*R*CP*R*$_1$)-H,[44,51–55] *m*-benziporphyrin (*m*BP*H*)H,[56] *m*-benziporphodimethene (*m*BDM*H*)H,[57] *p*-benziporphyrin (*p*BP*H*$_2$)H,[57] vacataporphyrin (VP*H*$_2$)H,[58] and *N*-confused pyriporphyrin (*N*PyP*H*)H (3-aza-*m*-benziporphyrin)[59] that have been used in our laboratory to synthesize paramagnetic compounds for subsequent NMR investigation (Scheme 2).

We will use the symbol CP to denote the trianion obtained from the inverted porphyrin by abstraction of all pyrrolic NH protons and the *C*-bound H(21) hydrogen. The groups attached to the N(2) atom are indicated by a prefix in italics and the group attached to C(21) as a suffix in italics. A similar method is used to form acronyms for other carbaporphynoids, as shown above.

## Paramagnetic Organometallic Nickel(II) *N*-Confused Porphyrin Derivatives

Methylation of a diamagnetic nickel(II) complex of [(*H*CP)Ni$^{II}$] with methyl iodide yields stable organonickel-(II) complexes (Scheme 3), namely diamagnetic [(CP*Me*)-Ni$^{II}$] and the two paramagnetic species [(*H*CP*Me*)Ni$^{II}$X] (X = Cl, I) and [(*Me*CP*Me*)Ni$^{II}$I].[52]

The mechanism of this methylation involves oxidative addition of the methyl cation to the carbaporphyrin C(21), which is activated due to Ni–C coordination. The concerted reversible addition of HX converts diamagnetic [(CP*Me*)-Ni$^{II}$] into paramagnetic [(*H*CP*Me*)Ni$^{II}$X]. The axial coordination step is accompanied by protonation of the peripheral nitrogen. The $^1$H and $^2$H NMR spectra of paramagnetic [(*H*CP*Me*)Ni$^{II}$X] and [(*Me*CP*Me*)Ni$^{II}$I] were analyzed by considering their $C_1$ symmetry (Figure 1). There are seven distinct pyrrole C-H positions for [(*H*CP*Me*)Ni$^{II}$X], an NH(2) position analogous to the CH(2) of the regular porphyrin, and four inequivalent *meso*-aryl rings. The resonances were assigned by making use of selective deuteration and 2D COSY experiments. Thus, the characteristic pattern of six downfield-shifted pyrrole resonances accompanied by

 © 2007 Wiley-VCH Verlag GmbH & Co. KGaA, Weinheim 

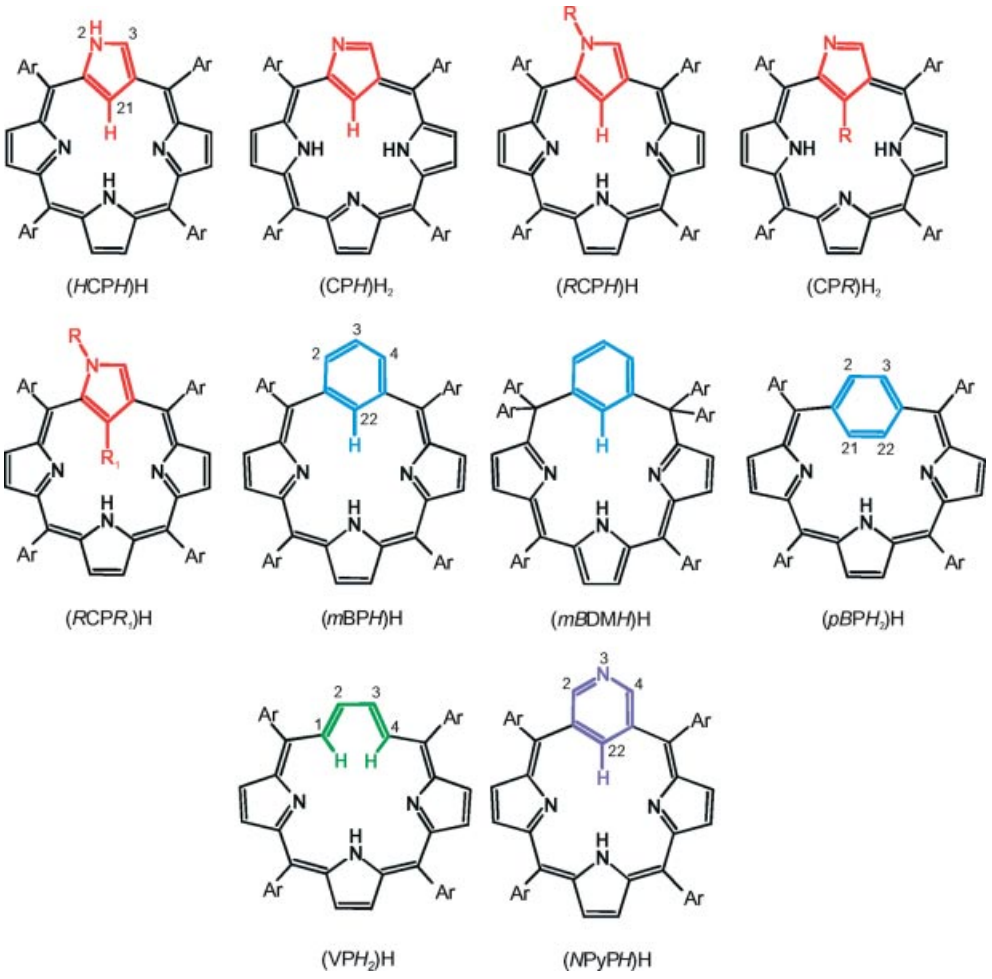


Scheme 2. Carbaporphyrinoids applied as ligands of paramagnetic complexes (partial numbering included).

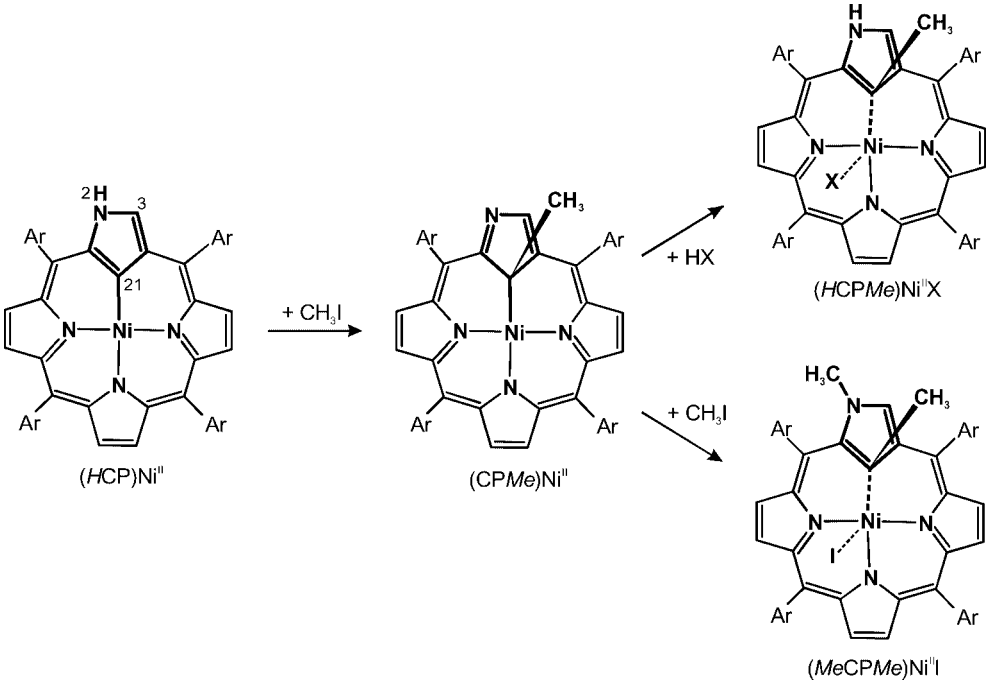


Scheme 3. Methylation of [(*H*CP)Ni$^{II}$] (X = Cl, I).

 © 2007 Wiley-VCH Verlag GmbH & Co. KGaA, Weinheim 

upfield-shifted H(3) and NH(2) resonances is diagnostic of *C*-methylation. The most characteristic feature, namely the broad downfield resonance (linewidth: 1320 Hz) at $\delta$ = 109.7 ppm, was assigned to the 21-Me group.

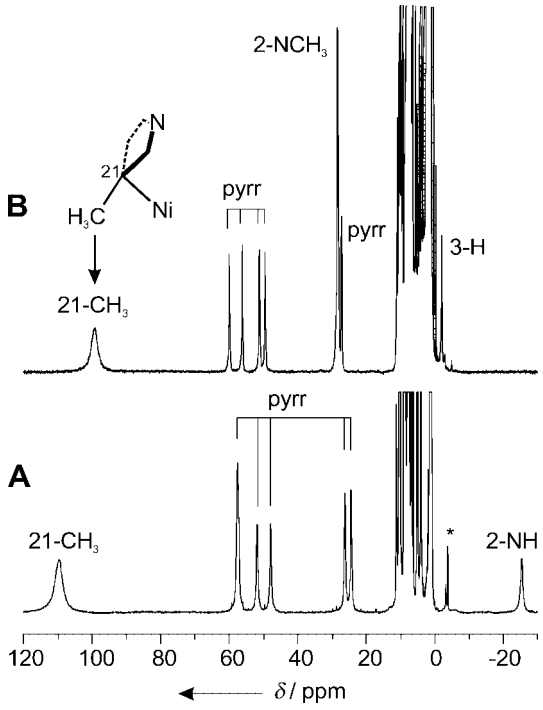


Figure 1. $^1$H NMR spectra ($CDCl_3$, 293 K) of paramagnetic mono- and dimethylated nickel(II) carbaporphyrins [(*H*CP*Me*)Ni$^{II}$Cl] (A) and [(*Me*CP*Me*)Ni$^{II}$I] (B). The peak labels follow systematic numbering of the porphyrin ring or denote proton groups; pyrr: regular pyrrole ring protons. Reproduced, with permission, from ref.[52] Copyright 1996 American Chemical Society.

As in the case of methylation, the reaction of [(*H*CP)-Ni$^{II}$] with haloalkanes in the presence of proton scavengers yielded the C(21)-alkylated complexes [(CP*CH$_2$R*)Ni$^{II}$]. Protonation of the external nitrogen of the inverted pyrrole during HX addition (X = Cl, I) combines with coordination of the apical ligand and leads to paramagnetic nickel(II) complexes. A very strong differentiation of the isotropic shift for the diastereotopic methylene protons was observed in the $^1$H NMR spectra of the protonated paramagnetic species [(*H*CP*CH$_2$*R)Ni$^{II}$X].[54]

The downfield shift of the pyrrolic and *C*-methyl resonances of [(*Me*CP*Me*)Ni$^{II}$X] indicates a σ-delocalization of the spin density. This is consistent with the ground state of Ni$^{II}$, which has two unpaired electrons in the σ-symmetry orbitals $(d_{x^2-y^2})^1(d_{z^2})^1$. The large differences in β-H contact shifts result from the π-spin density delocalized into the porphyrin framework, which originates from the peculiar spin-density transfer within the inverted pyrrole ring. The isotropic shift of the inverted *C*-methylated pyrrole ring is of significance with respect to the nature of the Ni–inverted pyrrole interaction in this paramagnetic organonickel(II) complex. The considerable downfield C(21)-$CH_3$ shift can be accounted for by direct σ-delocalization over three single bonds in the Ni–C(21)–$C_{(methyl)}$–H fragment. The tilt of the inverted *C*-methylated ring changes the geometry of the spin-density delocalization path as compared to regular pyrrole rings. The unpaired spin density is localized on the molecular orbital dominated by the $p_z$ component, which can transfer the σ-spin density but simultaneously contributes to π-orbitals of the inverted pyrrole ring. Such an overlap within the inverted ring will permit direct transfer of the unpaired spin density of the C(21) $p_z$ into the π system without any π M–L bonding.

## Organometallic Ni$^{III}$ Complexes

The one-electron oxidation of [(*H*CP)Ni$^{II}$] and [(*Me*CP)-Ni$^{II}$] results in the formation of extremely rare organonickel(III) derivatives.[60] The EPR spectral patterns of the one-electron-oxidized species depend on the axial ligand introduced by the oxidant or by metathesis. In each case the spin-Hamiltonian parameters [$g_{av} > 2.1$ (77 K) or $g_{iso} > 2.1$ (298 K)] reveal a metal-centered oxidation rather than formation of a radical cation ($g_{iso} \approx 2.002$). The localization of the one-electron oxidation on the nickel ion was supported by analysis of the observed $^{61}$Ni hyperfine splitting. $^2$H NMR spectroscopy was used as an independent probe to determine the electronic structure of the nickel(III). Such an approach can be complementary to the EPR studies and allows a direct observation of the spin-density delocalization on the macrocycle.

In light of the EPR results two representative species, namely [($D_7$-*H*CP)Ni$^{III}$Br] and [($D_7$-*H*CP)Ni$^{III}$($NO_3$)] were selected for $^2$H NMR investigation [($D_7$-*H*CP)H has all β-positions substituted with deuterium]. The well-resolved EPR spectra of this complex suggest that its $^1$H NMR resonances could be beyond detection due to the relatively long electron spin-lattice relaxation time $T_{1e}$.[9] Line widths for deuterium resonances are theoretically predicted to be 42 times smaller than the corresponding proton resonances due to the different electron-nuclear dipolar relaxation.[61] This narrowing has been observed experimentally for many paramagnetic species and renders $^2$H NMR spectroscopy particularly useful in detecting those paramagnetically broadened resonances that are visible in the $^1$H NMR spectrum.

In the case of [($D_7$-*H*CP)Ni$^{III}$Br], all resonance peaks assigned to the pyrrole deuterons are located within the region $\delta$ = 2–8 ppm that is consistent with the $(d_{z^2})^1$ formulation of the electronic ground state (Figure 2, trace A). No spin density is present in the β-pyrrole positions since there is no overlap of the metal out-of-plane orbital with the ligand orbital. On the contrary, all but one pyrrole resonances of [($D_7$-*H*CP)Ni$^{III}$($NO_3$)] are shifted downfield and are widely spread, covering the $\delta$ = 0–50 ppm region (Figure 2, trace B). This downfield shift of the pyrrole resonances is indicative of σ-delocalization of the spin density and requires a considerable $d_{x^2-y^2}$ metal orbital contribution to the SOMO, as determined previously by EPR spectroscopy.

 © 2007 Wiley-VCH Verlag GmbH & Co. KGaA, Weinheim 

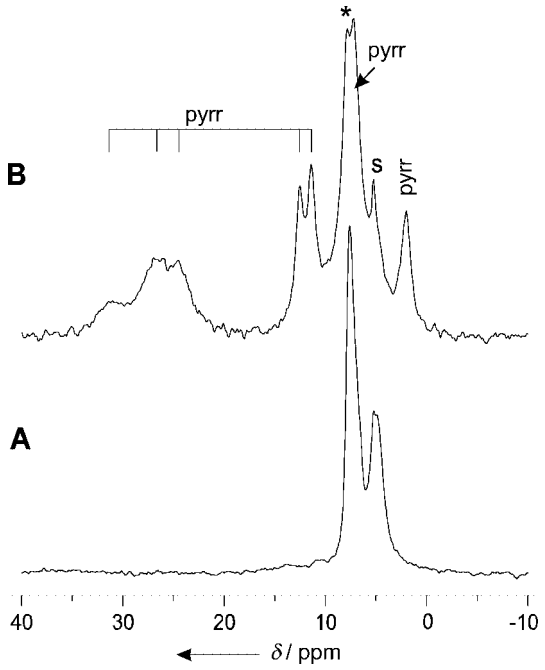


Figure 2. $^2$H NMR spectra (298 K in $CH_2Cl_2$) of [($D_7$-*H*CP)-$Ni^{III}$Br] (A) and [($D_7$-*H*CP)$Ni^{III}(NO_3)$] (B); s: solvent. Reproduced, with permission, from ref.[60] Copyright 1997 American Chemical Society.

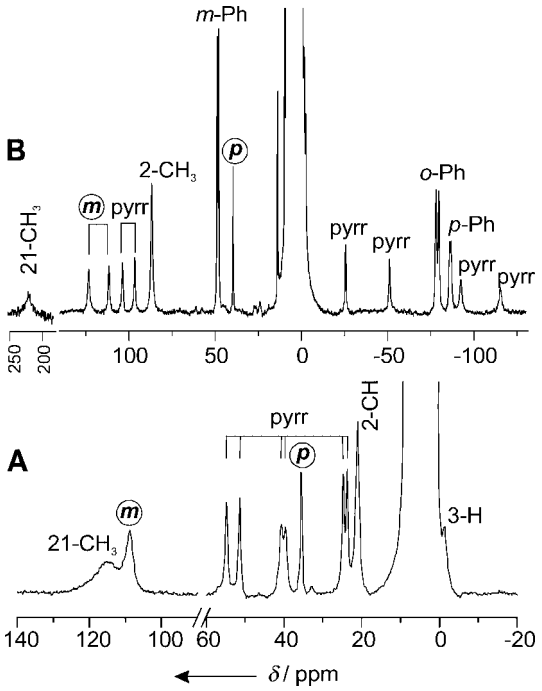


Figure 3. $^1$H NMR spectra of [(*Me*CP*Me*)$Ni^{II}$Ph] (A; 293 K, $C_7D_8$) and [(*Me*CP*Me*)$Ni^{II}$Ph]$^-$ (B; $C_7D_8$, 253 K) formed by treating [(*Me*CP*Me*)$Ni^{II}$Cl] with phenyllithium in toluene at 203 K. The peaks of the Ni-coordinated phenyl group are marked by circles. Reproduced, with permission, from ref.[62] Copyright 2000 American Chemical Society.

## Reactions of [(*Me*CP*Me*)$Ni^{II}$Cl] with Organometallic Reagents

Addition of phenylmagnesium iodide to a toluene solution of the nickel(II) chloride complex of dimethylated inverted porphyrin [(*Me*CP*Me*)$Ni^{II}$Cl] at 203 K results in the formation of a rare paramagnetic σ-phenylnickel(II) species [(*Me*CP*Me*)$Ni^{II}$Ph], which contains both equatorial and apical $Ni^{II}$–C bonds.[62] The coordination of the σ-phenyl group was determined by the unique pattern of three σ-phenyl resonances (*ortho*: $\delta$ = 361.3 ppm; *meta*: $\delta$ = 103.2 ppm; *para*: $\delta$ = 34.8 ppm at 273 K) in the $^1$H and $^2$H NMR spectra (Figure 3).

Predictably, the first step in the titration with phenyllithium results in the formation of [(*Me*CP*Me*)$Ni^{II}$Ph] and the subsequent one-electron reduction with excess PhLi yields [(*Me*CP*Me*)$Ni^{II}$Ph]$^-$, which can also be generated by an independent route, namely by reduction of [(*Me*CP*Me*)-$Ni^{II}$Ph] with lithium triethylborohydride or tetrabutylammonium borohydride. The spectroscopic data (Figure 3, trace B) indicate that [(*Me*CP*Me*)$Ni^{II}$Ph] undergoes a one-electron reduction without a substantial disruption of the molecular geometry. The presence of two paramagnetic centers in [(*Me*CP*Me*)$Ni^{II}$Ph]$^-$, namely the high-spin nickel(II) and the carbaporphyrin radical anion, produces a remarkable variation in the spectral pattern, such as upfield and downfield positions of the pyrrole resonances and a sign alternation of the *meso*-phenyl resonances.

A single species was detected in the $^1$H NMR titration of [(*Me*CP*Me*)$Ni^{II}$Cl] with *n*-butyllithium. The formation of the one- or two-electron-reduced species {[(*Me*CP*Me*)-$Ni^{II}$Bu]$^-$ or [(*Me*CP*Me*)$Ni^{II}$Bu]$^{2-}$, respectively} can be considered to account for the peculiar spectroscopic properties [pyrrole: $\delta$ = 17.33, 15.45, –5.79, –7.74, –14.62, –58.14 ppm; $CH_3$(21): $\delta$ = 3 ppm at 203 K]. The temperature dependencies of the hyperfine shifts demonstrate the pronounced anti-Curie behavior, which was interpreted in terms of a temperature-dependent spin equilibrium.

## Organocopper(II) *N*-Confused Porphyrin and Its Methylated Derivatives

The inverted porphyrin and its methylated derivatives stabilize the rare organocopper(II) complexes [(*H*CP)$Cu^{II}$], [(*Me*CP)$Cu^{II}$], [(*H*CP*H*)$Cu^{II}$X], [(*Me*CP*H*)$Cu^{II}$X] (X = $Cl^-$, $CF_3CO_2^-$), and [(*Me*CP*Me*)$Cu^{II}$Cl].[63] The EPR spectra of these complexes reveal typical features that are diagnostic of the copper(II) electronic structure.[63] In particular, the superhyperfine coupling pattern indicates the presence of three nitrogen donors in the first coordination sphere.[63,64] Addition of an acid (HX) to [(*H*CP)$Cu^{II}$] and [(*Me*CP)$Cu^{II}$] yields [(*H*CP*H*)$Cu^{II}$X] and [(*Me*CP*H*)$Cu^{II}$X], respectively. The mechanism of this reaction includes protonation of the inner C(21) accompanied by an axial coordination of the anion. The $^2$H NMR investigations (Figure 4) carried out for the pyrrole deuterated derivatives [($D_7$-CP)$Cu^{II}$] and [($D_7$-*Me*CP*Me*)$Cu^{II}$Cl] and the methyl deuterated complex

 © 2007 Wiley-VCH Verlag GmbH & Co. KGaA, Weinheim 

[($CH_3$CP$CD_3$)$Cu^{II}$Cl] independently confirmed the copper(II) electronic structure, which has a considerable $d_{x^2-y^2}$ metal orbital contribution to the SOMO.

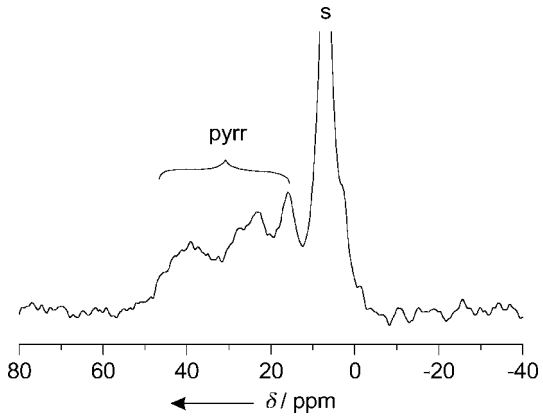


Figure 4. $^2$H NMR spectrum of [($D_7$-*H*CP)$Cu^{II}$] (333 K, toluene); s: solvent. Reproduced, with permission, from ref.[63] Copyright 2000 American Chemical Society.

## Nickel(II) Complexes of Benziporphyrins – A Study of Weak Intramolecular Metal–Arene Interactions

Owing to the nonplanar coordination geometry of the metal ion the nickel complexes [(*m*BP*H*)$Ni^{II}$Cl] and [(*p*BP$H_2$)$Ni^{II}$Cl] are all paramagnetic, with $S = 1$.[65] The $^1$H NMR spectra shown in Figure 5 correspond to effective $C_s$ symmetry of the molecules. The observed pattern of chemical shifts is typical for high-spin $Ni^{II}$ complexes of porphyrins and porphyrin analogues, with most of the β-H pyrrole resonances in the downfield region ($\delta$ = 10–60 ppm) and the *meso*-aryl peaks in the range $\delta$ = 0–10 ppm.[39] A similar spectroscopic pattern has been observed for [(*m*BP*OAc*)$Ni^{II}$Cl].[66] Almost complete assignment of these signals was achieved from the 2D COSY spectrum.

The shifts of the *m*-phenylene protons of [(*m*BP*H*)$Ni^{II}$Cl] are of special interest. The signals for H(2,4) and H(3) show evident sign alteration ($\delta$ = 22.5 and –40.8 ppm at 298 K, respectively). The broadened signal, which is shifted to $\delta$ = 386 ppm in the spectrum of [(*m*BP*H*)$Ni^{II}$Cl] (298 K), is assigned to the inner H(22). This is easily verified by acidifying a solution of ([*m*BP)$Ni^{II}$] with DCl rather than HCl. The resulting species, [(*m*BP*D*)$Ni^{II}$Cl], is selectively deuterated at position 22 and no low-field signal is observed. The above assignment also relied on the significant broadening of the H(22) signal relative to H(2,4), which is caused by the proximity of the paramagnetic $Ni^{II}$ center. This argument was reinforced by a quantitative analysis of relaxation times, which yielded approximate distances between the nickel ion and certain protons in the molecule (Figure 6).[2,5,65] The $^1$H NMR spectrum of [(*p*BP$H_2$)$Ni^{II}$Cl] appears to be similar to the preceding spectrum of [(*m*BP*H*)-$Ni^{II}$Cl] except that the *p*-phenylene resonances H(2,3) and H(21,22) are located at $\delta$ = –10.5 and 0.0 ppm, respectively (298 K), rather than in the far downfield region.

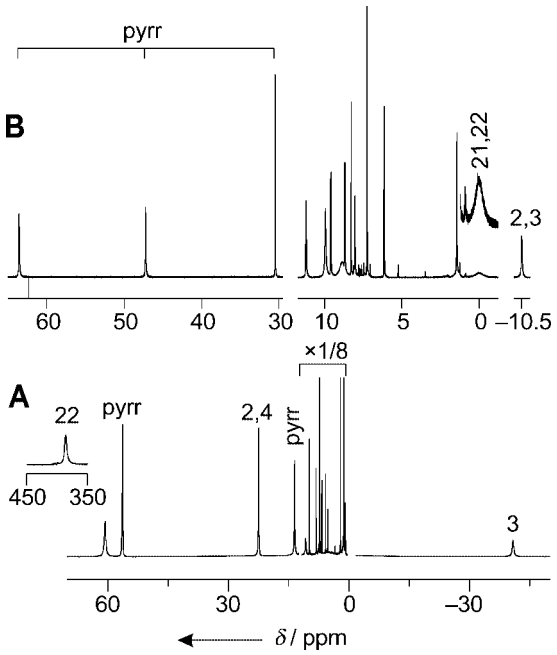


Figure 5. $^1$H NMR spectra ($CDCl_3$, 298 K) of [(*m*BP*H*)$Ni^{II}$Cl] (A) and [(*p*BP$H_2$)$Ni^{II}$Cl] (B). Reproduced, with permission, from ref.[65] Copyright 2004 American Chemical Society.

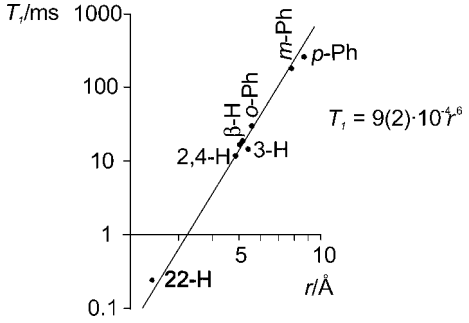


Figure 6. Relaxation plots for [(*m*BP*H*)$Ni^{II}$Cl]. The dependence between $T_1$ ($CDCl_3$, 298 K) and *r* (crystal structure averages) is linear in bilogarithmic axes.[65] Reproduced, with permission, from ref.[65] Copyright 2004 American Chemical Society.

X-ray studies performed on [(*m*BP*H*)$Ni^{II}$Cl] show that the arene fragment approaches the metal ion at a distance much shorter than the sum of the van der Waals radii, which corresponds to the formation of a weak agostic bond. Consequently, an agostic mechanism of spin-density transfer was proposed to explain the enormous H(22) shift as a result of electron donation from the CH bond to the metal. To account for the shifts of protons H(2,4) and H(3) it is necessary to assume π delocalization into the arene ring, which may result either from direct interaction with the metal center or from σ-π polarization.

## Conformational Flexibility of Nickel(II) Benziporphyrins

The linewidths of certain signals for [(*m*BP*H*)$Ni^{II}$Cl] and [(*p*BP$H_2$)$Ni^{II}$Cl] exhibit an unusual temperature depen-

 © 2007 Wiley-VCH Verlag GmbH & Co. KGaA, Weinheim 

dence that is characteristic of a dynamic process.[67] This was interpreted in terms of an equilibrium wherein one of the forms is present at a very small concentration and cannot be observed directly. The two exchanging forms are only present at comparable concentrations, and therefore yield separate signals in the slow exchange limit, for the nickel(II) benziporphodimethene complex [(*m*BDM*H*)-Ni$^{II}$Cl]. A mechanism involving motion of the phenylene moiety was proposed to account for the observed exchange process (Scheme 4).

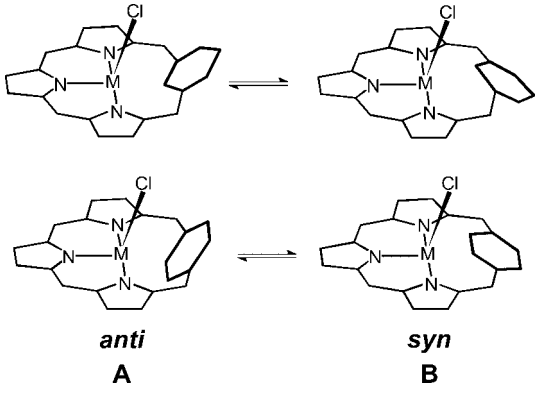


Scheme 4. Conformational equilibria in [(*m*BDM*H*)Ni$^{II}$Cl].

The temperature-dependence of the linewidths in the $^1$H NMR spectrum of [(*m*BP*H*)Ni$^{II}$Cl] is shown in Figure 7 for the *m*-phenylene H(2,4) signal. The logarithm of $\nu_{1/2}$ is plotted against $T^{-1}$ as this has often been found to yield a linear plot for a paramagnetic species in the absence of chemical exchange.[68,69]

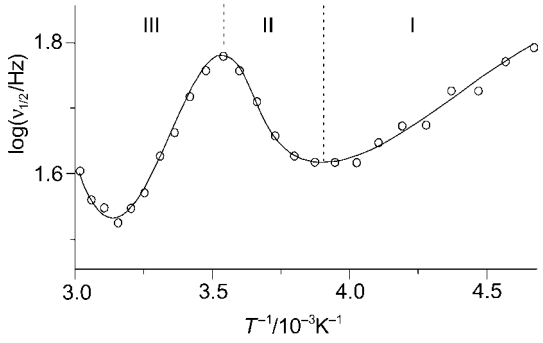


Figure 7. Temperature dependence of the linewidths in the $^1$H NMR spectrum for H(2,4) of [(*m*BP*H*)Ni$^{II}$Cl] ($CDCl_3$, 213–333 K). The continuous line is for illustrative purposes only. Reproduced, with permission, from ref.[67] Copyright 2004 American Chemical Society.

The temperature profile (regions I–III) corresponds to an exchange process between two paramagnetic species A and B, one of which is significantly less populated ($P_A >> P_B$) and thus impossible to observe directly.[5,61,68] The dynamic process is slow in region I and the observed dependence may therefore be attributed solely to paramagnetic broadening and extrapolated into regions II and III.[68] The analysis concentrated on region II, which corresponds to the slow-exchange limit between A and B. The pre-exchange lifetime for A ($\tau_A$) was obtained experimentally by determining line widths, $\nu_{1/2,A,i}$, over a wide temperature range, and an Eyring plot of the [(*m*BP*H*)Ni$^{II}$Cl] data for region II collected in deuterated chloroform yielded the activation parameters. The values $\Delta H^{\ddagger}$ = 63 kJ mol$^{-1}$ and $\Delta S^{\ddagger}$ = 20 J/mol K yield a $\Delta G^{\ddagger}$ of 57 kJ mol$^{-1}$ (298 K). These values are in the range found for various dynamic processes observed in porphyrins, including rotation of *meso*-aryl substituents and macrocycle inversion.[70–72]

Benziporphyrin macrocycles are generally more flexible than regular porphyrins, as can be judged from the puckered structures observed in the solid state for free bases and their complexes.[56,57,65,66] This is a result of the loss (or decrease) of macrocyclic aromaticity combined with the steric constraints generated by the introduction of a phenylene ring into the macrocyclic structure. Conformational dynamics involves puckering of the benziporphyrin macrocycle, rotation of *meso*-aryl rings, or both. The preferred conformation of the macrocycle in the metal complexes [(*m*BP*H*)-Ni$^{II}$Cl] and [(*p*BP$H_2$)Ni$^{II}$Cl] has the phenylene ring tilted away from the metal center with the inner CH bonds and the axial MX bond in an *anti* orientation (Scheme 4), as confirmed by their respective X-ray structures.[57,65] However, it is possible that minute amounts of *syn* conformers may be present in solution and rapidly equilibrate with the respective *anti* forms. Actually the DFT modeling, carried out for benziporphyrin complexes of zinc(II) and cadmium(II), indicates that the postulated *syn* conformers are thermally accessible.

## Two Coordination Modes of Vacataporphyrin

5,10,15,20-Tetraaryl-21-vacataporphyrin (butadieneporphyrin, annulene-porphyrin hybrid),[58] which contains a vacant space instead of a heteroatomic bridge, forms paramagnetic nickel(II) complexes where a metal ion is bound in the macrocyclic cavity by three pyrrolic nitrogens.[73] Coordination imposes a steric constraint on the geometry of the ligand and leads to two directly detectable stereoisomers with the butadiene fragment oriented towards [(VP$H_2$)-Ni$^{II}$Cl-*i*] or away from [(VP$H_2$)Ni$^{II}$Cl-*o*] the macrocyclic center (Scheme 5).

The specific assignment of two sets of resonances to [(VP$H_2$)Ni$^{II}$Cl-*o*] and [(VP$H_2$)Ni$^{II}$Cl-*i*] (Figure 8) was based on the notion that the butadiene fragment in the folded conformation of [(VP$H_2$)Ni$^{II}$Cl-*i*] blocks the coordination of the second axial ligand, which contrasts with the behavior of [(VP$H_2$)Ni$^{II}$Cl-*o*].

The H(2,3) signals of [(VP$H_2$)Ni$^{II}$Cl-*o*] or [(VP$H_2$)-Ni$^{II}$Cl-*i*] have chemical shifts that are typical for the β-H pyrrolic positions of nickel(II) 21-heteroporphyrins in spite of the vacancy.[39] The extremely broad H(1,4) signal of [(VPH$_2$)Ni$^{II}$Cl-*o*] was detected by $^2$H NMR spectroscopy at $\delta$ = –3.5 ppm (298 K).

A plot of $\log \nu_{1/2}$ against $T^{-1}$ yields a straight line for [(VP$H_2$)Ni$^{II}$Cl-*i*], which suggests the absence of any chemical exchange.[18,19,39,52,67–69,74] On the other hand, the line widths of certain signals of [(VP$H_2$)Ni$^{II}$Cl-*o*] exhibit an un-

 © 2007 Wiley-VCH Verlag GmbH & Co. KGaA, Weinheim 

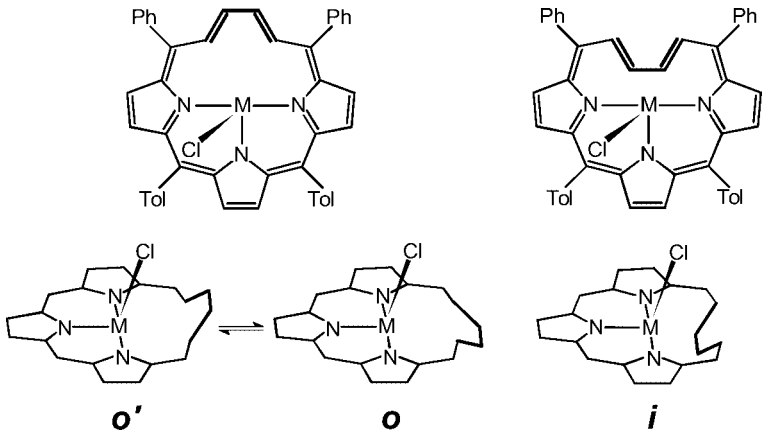


Scheme 5. Stereoisomers of [(VP$H_2$)Ni$^{II}$Cl]. Reproduced, with permission, from ref.[73] Copyright 2005 American Chemical Society.

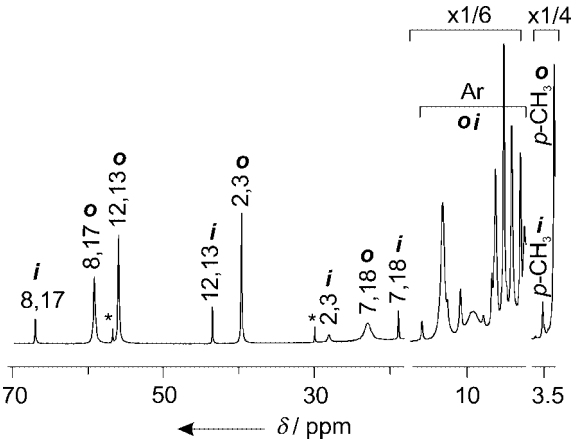


Figure 8. $^1$H NMR spectra of [(VP$H_2$)Ni$^{II}$Cl] ($CDCl_3$, 298 K). The resonances of the different stereoisomers are marked. Reproduced, with permission, from ref.[73] Copyright 2005 American Chemical Society.

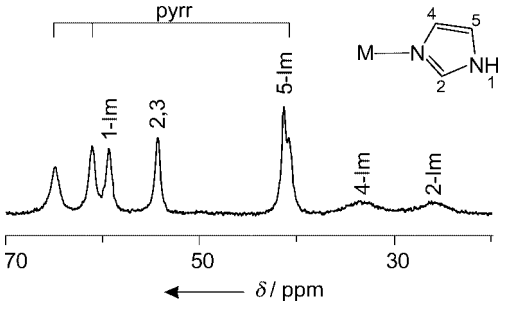


Figure 9. $^1$H NMR ($CDCl_3$, 298 K) spectra of [(VP$H_2$)Ni$^{II}$Cl] in the presence of imidazole. The molar ratio (VP$H_2$)Ni$^{II}$Cl/imidazole is 1:2.5. Reproduced, with permission, from ref.[73] Copyright 2005 American Chemical Society.

usual temperature dependence that is characteristic of a dynamic process.[67–69] This behavior can be interpreted in terms of a conformational equilibrium in which one of the forms is present at a very low concentration.[5,61,68] The conformational equilibrium presented in Scheme 5 may contribute to this mechanism providing that the concentration of [(VP$H_2$)Ni$^{II}$Cl-*o*] is much greater than that of [(VP$H_2$)Ni$^{II}$Cl-*o′*] and that the process is in the slow-exchange limit. Thus, two co-existing stereoisomers reveal a different conformational flexibility in the same solution.

The markedly different spectra of [(VP$H_2$)Ni$^{II}$Cl-*i*] in [$D_4$]MeOH or [$D_3$]acetonitrile as compared to chlorinated solvents are attributed to an axial coordination of two solvent molecules and formation of a single species, namely [(VP$H_2$)Ni$^{II}$($CD_3OD$)$_2$]$^+$ or [(VP$H_2$)Ni$^{II}$($CD_3CN$)$_2$]$^+$. Similarly, the addition of two equivalents of imidazole converts [(VP$H_2$)Ni$^{II}$Cl-*o*] and [(VP$H_2$)Ni$^{II}$Cl-*i*] into [(VP$H_2$)-Ni$^{II}$(Im)$_2$]$^+$ (Figure 9). All resonances of the coordinated imidazole are clearly discernible and have been assigned by line width analysis and selective deuteration. Their positions are similar to those determined for other imidazole adducts of nickel(II) heteroporphyrins.[75]

## Iron(II) Complexes of Benziporphyrins

The molecular structure of [(*m*BP*H*)Fe$^{II}$Br] resembles that of [(*m*BP*H*)Ni$^{II}$Cl].[65,76] The distances between iron and the pyrrolic nitrogens are in the range for high-spin Fe$^{II}$ porphyrin complexes and the tripyrrolic fragment arranges in a dome-shaped geometry. The distances from iron to the inner C atom [C(22)] and inner hydrogen [H(22)] are 2.579(4) and 2.439(36) Å, respectively. Nevertheless, these values are small compared to the van der Waals contact and suggest the formation of a weak agostic bond.

The β-pyrrolic signals in the $^1$H NMR spectrum of [(*m*BP*H*)Fe$^{II}$Br] (Figure 10) are located at $\delta$ = 49.4, 21.1, and 6.5 ppm at 298 K, as shown by $^2$H NMR spectroscopy for [($D_6$-*m*BP*H*)Fe$^{II}$Br].[76] These values are close to those reported for the high-spin nickel(II) complexes [(*m*BP*OAc*)-Ni$^{II}$Cl] and [(*m*BP*H*)Ni$^{II}$Cl].[65,66] The hydrogens on the *m*-phenylene ring were identified at $\delta$ = 440 [H(22)], 65.8 [H(2,4)], and –33.2 [H(3)] ppm (298 K). An agostic mechanism of spin-density transfer, as described previously for [(*m*BP*H*)Ni$^{II}$Cl], explains the shifts of [(*m*BP*H*)Fe$^{II}$Br] as resulting from electron donation from the C–H bond to the metal.

 © 2007 Wiley-VCH Verlag GmbH & Co. KGaA, Weinheim 

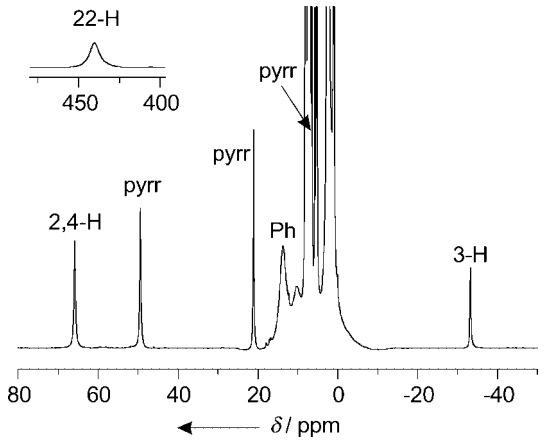


Figure 10. $^1$H NMR spectrum of [(*m*BP*H*)Fe$^{II}$Br] ($^1$H NMR, $CD_2Cl_2$, 298 K). The inset shows the downfield region containing the 22-H resonance. Reproduced, with permission, from ref.[76] Copyright 2004 American Chemical Society.

## High-Spin Iron Complexes of *N*-Confused Pyriporphyrin

Insertion of iron(II) into *N*-confused pyriporphyrin, which is the simplest homologue of *N*-confused 5,10,15,20-tetraarylporphyrin, yields the high-spin iron(II) complex [(*N*PyP*H*)Fe$^{II}$Br] and the diiron species [(Br$_2$LFe$^{II}$-*N*PyP*H*)Fe$^{II}$Br] (L = coordinating solvent) where the second iron(II) coordinates to the perimeter nitrogen atom (Scheme 6).[77]

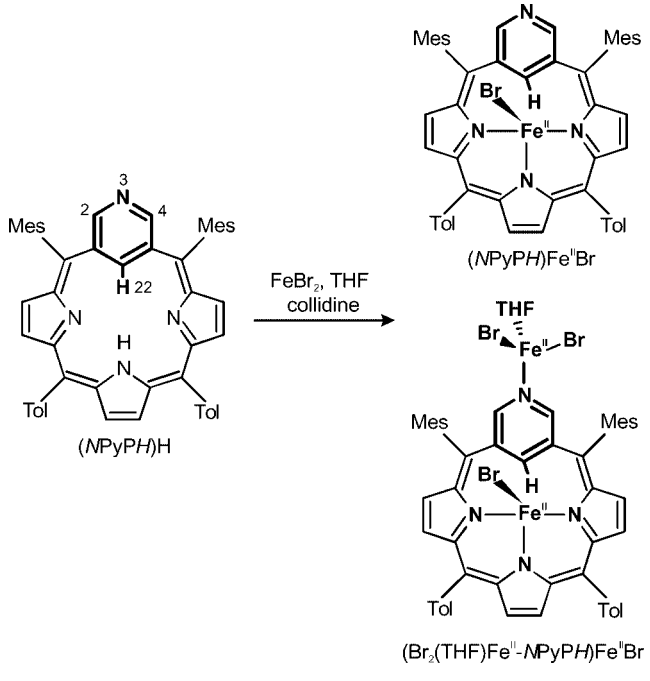


Scheme 6. Synthesis of iron(II) *N*-confused pyriporphyrin complexes. Reproduced, with permission, from ref.[77] Copyright 2006 American Chemical Society.

The characteristic patterns of the pyrrole and pyridine resonances in the $^1$H NMR spectra were found to be diagnostic of the ground electronic state of iron and the donor properties of C(22)–H and N(3) centers (Figure 11). The downfield H(22) resonances, which are found for iron(II) *N*-confused pyriporphyrin in a very unusual spectroscopic window ($\delta$ = 350–800 ppm) for a range of axial ligands, can be considered as a diagnostic sign of an agostic Fe$^{II}$–{C(22)-H} interaction.[76]

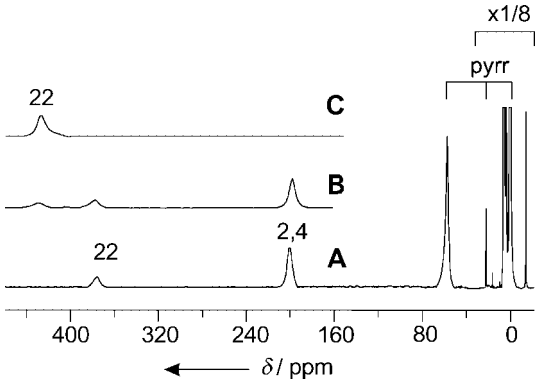


Figure 11. (A) $^1$H NMR spectrum of [(Br$_2$LFe$^{II}$-*N*PyP*H*)Fe$^{II}$Br]; (B) conversion of [(Br$_2$LFe$^{II}$-*N*PyP)Fe$^{II}$Br] into [(*N*PyP)Fe$^{II}$Br] during titration with Br$_2$; (C) [(*N*PyP)Fe$^{II}$Br]. All spectra were recorded in $CD_2Cl_2$ at 298 K; L = thf. Reproduced, with permission, from ref.[77] Copyright 2006 American Chemical Society.

To probe the ability of the perimeter nitrogen to bind iron(II) a systematic titration of [(*N*PyP*H*)Fe$^{II}$Cl] in [D$_3$]-acetonitrile or [D$_8$]THF was carried out. Smooth changes of the chemical shifts of the pyridine moiety directly engaged in coordination were observed during the course of the titration of [(*N*PyP*H*)Fe$^{II}$Cl] with Fe$^{II}$Cl$_2$, which was explained by an equilibrium involving a diiron species.

The spectroscopic pattern of [(Br$_2$LFe$^{II}$-*N*PyP*H*)Fe$^{II}$Br] in non-coordinating solvents resembles that of the monoiron species [(*N*PyP*H*)Fe$^{II}$Br], although the H(2,4) resonance is remarkably shifted to $\delta$ = 201 ppm (298 K; Figure 11). [(Br$_2$LFe$^{II}$-*N*PyP)Fe$^{II}$Br] can be easily converted into [(*N*PyP)Fe$^{II}$Br] by addition of competing ligands (pyridine) or by an external iron(II)-directed oxidation, which promotes dissociation. In spite of the enormous line widths the far downfield shifted resonances provide an analytically valuable pattern that is unique for the *N*-confused diiron species. The downfield position of the H(2,4) resonance for [(Br$_2$LFe$^{II}$-*N*PyP)Fe$^{II}$Br] is consistent with coordination to the high-spin iron(II) assuming that the spin-delocalization pathways are identical to that determined for nickel(II) thiaporphyrin.[78]

Addition of Br$_2$ to a solution of [(*N*PyP*H*)Fe$^{II}$Br] in the absence of dioxygen results in a one-electron oxidation that yields the high-spin iron(III) *N*-confused pyriporpyrin [(*N*PyP*H*)Fe$^{III}$Br]$^+$ (Scheme 7). The high-spin complex preserves the side-on interaction between the inverted pyridine ring and iron(III) as in [(*N*PyP*H*)Fe$^{II}$Br]. The characteristic set of three pyrrole resonances at $\delta$ = 122.4, 79.6 and 70.4 ppm ([D$_2$]dichloromethane, 298 K) can be readily assigned to [(*N*PyP)Fe$^{III}$Br]$^+$. The reaction of [(*N*PyP*H*)-Fe$^{II}$Br] with dioxygen results in the formation of five-coordinate [(*N*PyPO)Fe$^{III}$Br] [(*N*PyPO*H*)H = 3-aza-22-hydroxy-*m*-benziporphyrin; Scheme 7].

 © 2007 Wiley-VCH Verlag GmbH & Co. KGaA, Weinheim 

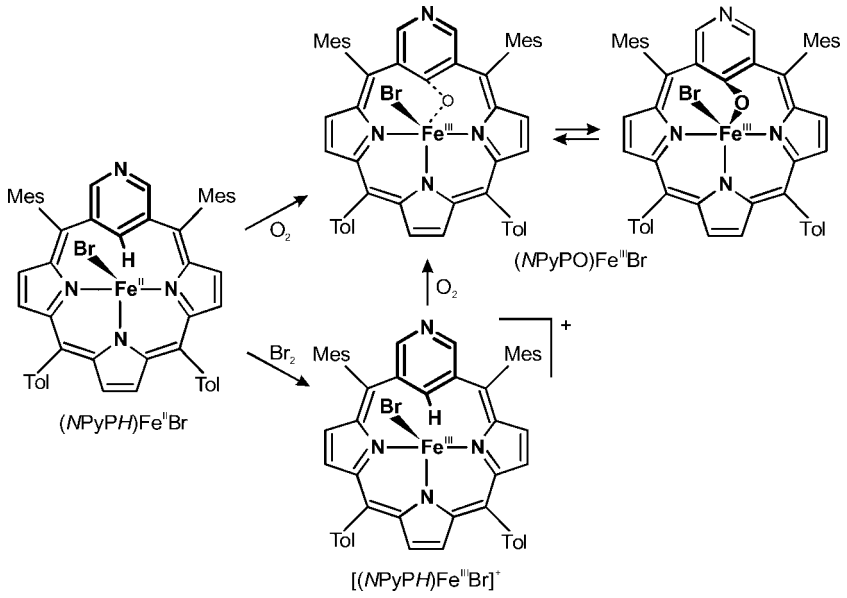


Scheme 7. Oxidation and oxygenation of [(*N*PyPH)Fe$^{II}$Br]. Reproduced, with permission, from ref.[77] Copyright 2006 American Chemical Society.

## Low-Spin Organoiron(III) *N*-Confused Pyriporphyrin

The one-electron oxidation of [(*N*PyPH)Fe$^{II}$Br] with dioxygen in pyridine, which is accompanied by deprotonation of a C(22)H fragment and formation of an Fe–C(22) bond, produces the low-spin, six-coordinate iron(III) complex [(*N*PyP)Fe$^{III}$(py)$_2$]$^+$ (Scheme 8), as confirmed by a combination of $^1$H NMR, EPR and structural data.[79]

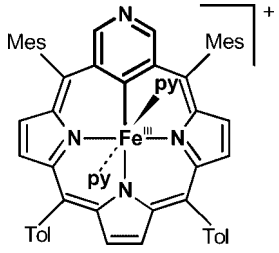


Scheme 8. [(*N*PyP)Fe$^{III}$(py)$_2$]$^+$.

The cationic complex involves a six-coordinate iron atom bound to the *N*-confused pyriporphyrin through its three pyrrolic nitrogens and the trigonal pyridyl C(22) atom. The porphyrin is strongly ruffled, defining two deep grooves along the $C_{meso}$–$C_{meso}$ axes that are at right angles to each other. The $^1$H NMR spectrum of [(PyP)Fe$^{III}$(D$_5$-py)$_2$]$^+$ is clearly distinct from that of any known low-spin iron(III) porphyrin [β-H: $\delta$ = 21.3, 16.2, and 4.1 ppm ($CD_2Cl_2$, 298 K)]. In fact, only the recently described low-spin iron(III) complex of the "true" pyriporphyrin reveals a similar $^1$H NMR spectrum.[80] Still, the spectroscopic pattern of the pyrrole and *meso*-aryl resonances is consistent with the features assigned to the less common $(d_{xz}d_{yz})^4(d_{xy})^1$ low-spin ground electronic state.[7,81–83] This unique spectroscopic feature can be related to the extensive ruffling of the macrocycle,[82,84–86] equatorial C-coordination, and/or axial pyridine coordination.[7] A conformational rearrangement process was detected which involves two structures differentiated by macrocyclic ruffling.

## Remarkable Paramagnetically Shifted $^1$H and $^2$H NMR Spectra of Iron(II) 2-Aza-21-carbaporphyrin

An uncommon type of metal ion–inverted pyrrole ring interaction detected in the solid-state structure of iron(II) 2-aza-21-carbaporphyrin [(*H*CP*H*)Fe$^{II}$Br] has raised the question of its impact on the $^1$H NMR spectroscopic features.[87,88] [(*H*CP*H*)Fe$^{II}$Br] has a conformation where the iron is side-on with respect to the inverted pyrrole plane[87] and the inverted pyrrole ring is sharply bent from the porphyrin plane. The Fe···C(21) distance (2.361 Å) is longer than a regular Fe–C bond but shorter than the sum of the van der Waals radii.

The solid-state geometry of the Fe$^{II}$···{C(21)–H(21)} fragment in [(*H*CP*H*)Fe$^{II}$Br] is within the range of an agostic interaction [Fe···H(21) = 1.971 Å].[87] The $^1$H NMR spectrum of [(*H*CP*H*)Fe$^{II}$Br] is substantially similar to the spectra of high-spin iron(II) core-modified porphyrins.[14,16,89] Five pyrrole resonances of [(*H*CP*H*)Fe$^{II}$Br] are spread over the low-field region from $\delta$ = 30 to 50 ppm, and two other β-H resonances occur at $\delta$ = 8.4 and 0.78 ppm. The resonance at $\delta$ = –8.0 ppm (293 K) was assigned to the N(2)H hydrogen. The most characteristic $^1$H NMR ($^2$H NMR) feature of [(*H*CP*H*)Fe$^{II}$Br], namely the downfield shifted resonance at $\delta$ = 812 ppm (linewidth of 6200 Hz at 293 K in [D$_2$]dichloromethane), was unambiguously assigned to the internal H(21) hydrogen.[88] The $^2$H NMR spectrum of [(D$_7$-*H*CP*D*)Fe$^{II}$Br], which stretches over a window of almost 900 ppm, shows the remarkably large paramagnetic shift of C(21)D, as the $^2$H NMR spectrum

 © 2007 Wiley-VCH Verlag GmbH & Co. KGaA, Weinheim 

combines simultaneously all pyrrole resonances, including the C(21)D one (Figure 12). Variable-temperature NMR measurements for the C(21)H resonance of [(*H*CP*H*)Fe$^{II}$Br] revealed remarkable changes of the chemical shifts, which fall in a window of 1244 ppm at 208 K. Addition of 2-methylimidazole to a [$D_2$]dichloromethane solution of [(*H*CP*H*)Fe$^{II}$Br] results in the formation of the high-spin five-coordinate species [(*H*CP*H*)Fe$^{II}$(2-MeIm)]$^+$, which was identified by the unique chemical shift of the C(21)H resonance ($\delta$ = 1090 ppm). To the best of our knowledge these are the largest chemical shifts reported thus far for iron porphyrins or iron porphyrin derivatives[7,90,91] and are even larger than the extreme chemical shifts determined for paramagnetic compounds, including σ-aryl complexes of nickel(II) heteroporphyrins (e.g. *ortho*-H: $\delta$ = 568 ppm at 203 K).[6,39,78,92] Extreme contact shifts have been reported for the β-$CH_2$ hydrogens of cysteines that ligate iron in oxidized ruberodoxin ($\delta$ = 300–900 ppm, 303 K)[93] and copper(II) in azurin ($\delta$ = 800, 850 ppm at 278 K).[94]

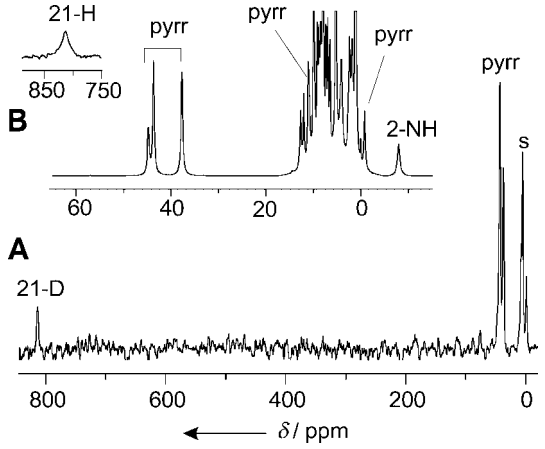


Figure 12. (A) $^2$H NMR spectrum of [($D_7$-*H*CP*D*)Fe$^{II}$Br] ($CH_2Cl_2$, 298 K). (B) $^1$H NMR spectrum of [(*H*CP*H*)Fe$^{II}$Br] ($CD_2Cl_2$, 298 K); s: solvent. The inset in (B) shows the H(21) resonance. Reproduced, with permission, from ref.[88] Copyright 2003 American Chemical Society.

The $^1$H NMR spectra of iron(II) 2-aza-21-carbaporphyrins display the spread of regular β-H resonances, which is markedly larger than for their more symmetrical counterparts.[11,89,95] The paramagnetic shifts of [(*H*CP*H*)Fe$^{II}$Br] can be explained by a model that is typically applied to high-spin iron(II) porphyrins and iron(II) *N*-substituted porphyrins. In the case of a high-spin iron(II) center [$(d_{xy})^2(d_{xz}d_{yz})^2(d_{z^2})^1(d_{x^2-y^2})^1$] both σ and π routes of spin density delocalization can operate. The contact shift predominates for the regular pyrrole resonances, which determines their downfield positions.[7,14,16] The typical delocalization pathways involve delocalization through a σ-framework by way of σ-donation to the half occupied $d_{x^2-y^2}$ iron(II) orbital.[14] Actually, the variation of the β-H positions in the $^1$H NMR spectrum may be accounted for by specific π-delocalization mechanisms that have been discussed in detail for iron(III) porphyrins.[96,97] One pyrrole 3-H and the 2-NH resonance are evidently different from the other six and show upfield shifts. Thus, the side-on location of the iron(II) with respect to the pyrrole ring primarily affects spin transfer to the modified pyrrole ring. An analogous effect has been observed for paramagnetic nickel(II) 2-aza-21-carbaporphyrin and metalloheteroporphyrins.[39,52] Significantly, the peculiar metal ion–inverted pyrrole ring interaction detected in the solid-state structure of [(*H*CP*H*)Fe$^{II}$Br] is clearly reflected by an unprecedented isotropic shift of the H(21) atom that is involved in an agostic interaction [Fe$^{II}$–C(21)H] in solution.

## Oxidation and Oxygenation of Iron(II) 2-Aza-21-carbaporphyrin

Dioxygen reacts cleanly with iron(II) 2-aza-21-carbaporphyrin to form the corresponding five-coordinate intermediate-spin iron(III) complexes and, eventually, the 2-aza-21-carbaporphyrin gains an oxo functionality.[98] Generally speaking insertion of an oxygen atom into an M–C bond (a carbon atom built into the aromatic moiety) is quite rare,[99–109] and no direct evidence for the formation of intermediates in the oxygenation process has been found.

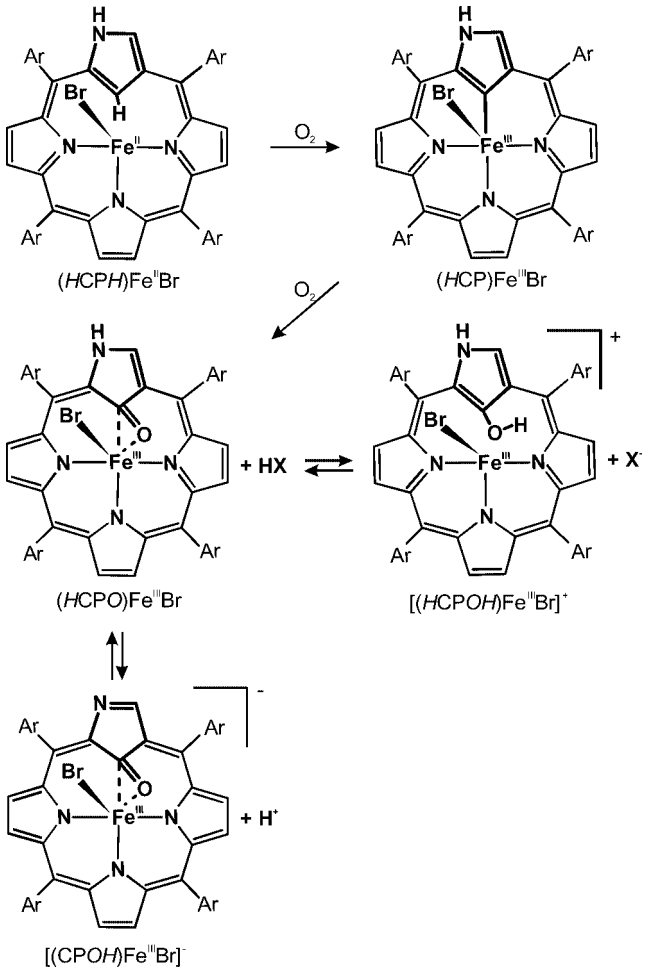


Scheme 9. Reaction of [(*H*CP*H*)Fe$^{II}$Br] with dioxygen. Reproduced, with permission, from ref.[98] Copyright 2004 American Chemical Society.

 © 2007 Wiley-VCH Verlag GmbH & Co. KGaA, Weinheim 

The oxidation and oxygenation of [(*H*CP*H*)$Fe^{II}$Br] have been followed by $^1$H and $^2$H NMR spectroscopy.[98] Thus, addition of dioxygen to [(*H*CP*H*)$Fe^{II}$Br] in dichloromethane yields a series of iron(III) complexes in consecutive reactions (Scheme 9).

One-electron oxidation with dioxygen, which is accompanied by deprotonation of a C(21)H fragment and formation of an Fe–C(21) bond, produces the intermediate-spin, five-coordinate iron(III) complex [(*H*CP)$Fe^{III}$Br] (Scheme 10). Insertion of an oxygen atom into the preformed $Fe^{III}$–C(21) bond in the subsequent step yields [(*H*CP*O*)$Fe^{III}$Br]. Protonation at the oxygen atom then affords [(*H*CP*OH*)$Fe^{III}Br]^+$. The considered mechanism of [(*H*CP)$Fe^{III}$Br] oxygenation involves the insertion of dioxygen into the Fe–C bond. The O–O bond of the transient species cleaves rapidly and 2-aza-carbaporphyrin acquires an oxo functionality [C(21)O] in the coordination core.

Addition of $I_2$ or $Br_2$ to a solution of [(*H*CP*H*)$Fe^{II}$Br] in the absence of dioxygen results in a one-electron oxidation that yields [(*H*CP*H*)$Fe^{III}Br]^+$. This iron(III) compound has also been obtained by titration of [(*H*CP)$Fe^{III}$Br] with acids due to protonation at C(21). Addition of $Br_2$ to a solution containing [(*H*CP)$Fe^{III}$Br] or [(*H*CP*H*)$Fe^{III}Br]^+$ results in bromination at C(21) to yield [(*H*CP*Br*)$Fe^{III}Br]^+$, in agreement with the typical reactivity of inverted porphyrins.[51,110] Subsequent reaction with water results finally in formation of the C=O fragment in [(*H*CP*O*)$Fe^{III}$Br]. This complex contains a ligand which is a 2-aza-21-carbaporphyrin derivative with the oxygen atom located on the inner carbon, in other words *N*-confused porphyrin *C*-oxide. Such a ligand was first detected in the dimeric product of [{(CP*H*)$Fe^{II}$}$_2$] oxygenation, although in a different tautomeric form,[111] and in the oxidation of [(*H*CPH)$Ni^{II}$] with $OsO_4$.[112]

Selected spectra that emphasize the utility of $^1$H NMR spectroscopy for observing oxidation/oxygenation transformations of [(*H*CP*H*)$Fe^{II}$Br] are presented in Figure 13. The characteristic patterns of pyrrole and N(2)H resonances are diagnostic of the ground electronic state of iron and the donor character of C(21).

The average chemical shift of the perimeter resonances ($\delta_{av}$) at 298 K was considered here as a suitable parameter for characterizing the ground electronic/spin state of iron(*n*) inverted porphyrins. Thus, the value of $\delta_{av}$ for six regular pyrroles was examined for [(*H*CP*H*)$Fe^{II}$Br], [(*H*CP*H*)-$Fe^{III}Br]^+$, and [(*H*CP*Br*)$Fe^{III}Br]^+$, where a side-on location of the metal ion with respect to the *N*-confused pyrrole ring has been determined. The values of $\delta_{av}$ for [(*H*CP*O*)-$Fe^{III}$Br], [(*H*CP*OH*)$Fe^{III}Br]^+$, [(*H*CP*H*)$Fe^{III}Br]^+$, and [(*H*CP*Br*)$Fe^{III}Br]^+$ approach those found for high-spin iron(III) tetraarylporphyrins,[7] iron(III) β-substituted tetraarylporphyrin,[96] and iron(III) *N*-methyltetraarylporphyrin ($\delta_{av}$ for regular pyrrole rings),[13] and the average chemical shift of [(*H*CP*H*)$Fe^{II}$Br] is consistent with that found for high-spin iron(II) tetraarylporphyrins, iron(II) *N*-methyltetraarylporphyrin, and iron(II) 21-thiatetraarylporphyrin.[7,14,89] Finally, the upfield β-H positions seen for [(*H*CP)$Fe^{III}$Br] and [(*H*CP)$Fe^{III}$(1-MeIm)]$_2^+$ are clearly consistent with intermediate- and low-spin states, respectively, considering the asymmetric iron(III) porphyrins as reference molecules.[7,11,95,113,114]

The isotropic shift pattern for the β-H pyrrole of [(*H*CP)-$Fe^{III}$Br] and [(*H*CP)$Fe^{III}$(1-MeIm)]$_2^+$ reflects the extensive spin delocalization into the π molecular orbitals of the in-

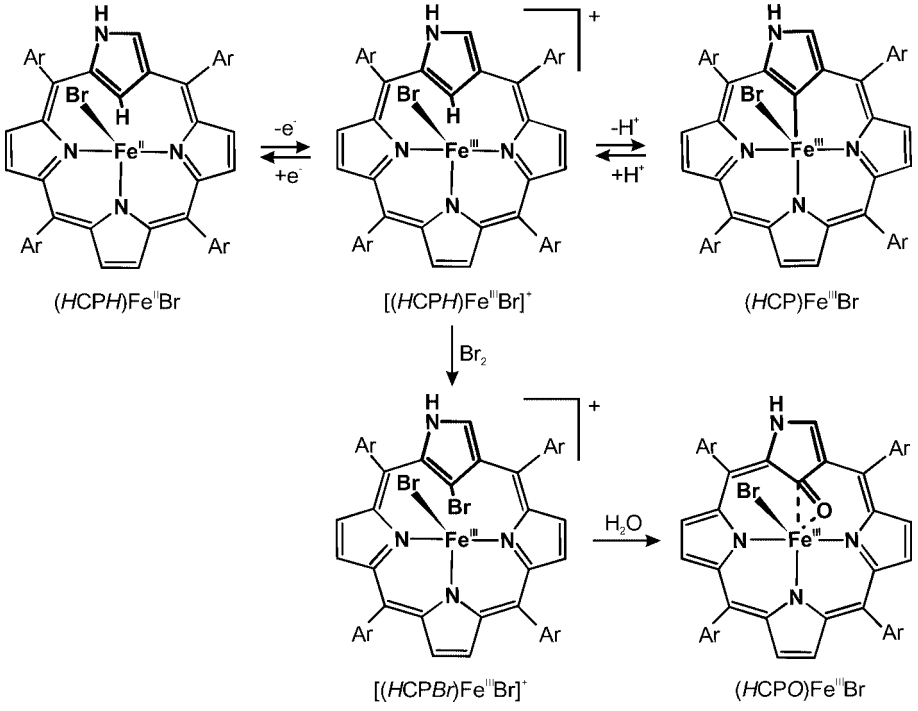


Scheme 10. Oxidation of [(*H*CP*H*)$Fe^{II}$Br]. Reproduced, with permission, from ref.[98] Copyright 2004 American Chemical Society.

 © 2007 Wiley-VCH Verlag GmbH & Co. KGaA, Weinheim 

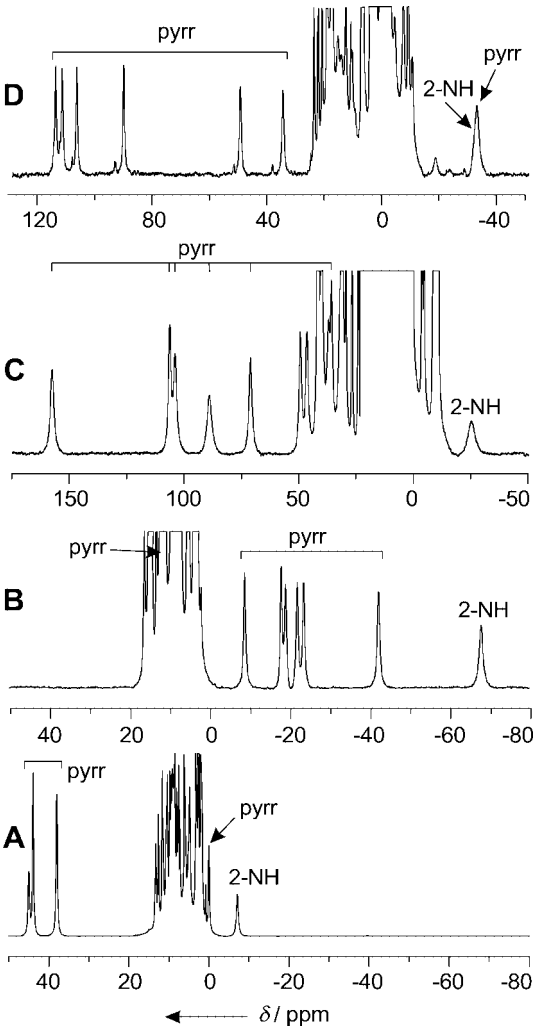


Figure 13. Oxidation and oxygenation of iron inverted porphyrins as followed by $^1$H NMR spectroscopy ($CD_2Cl_2$, 298 K): (A) [(*H*CP*H*)Fe$^{II}$Br]; (B) [(*H*CP)Fe$^{III}$Br]; (C) ([*H*CP*O*)Fe$^{III}$Br]; (D) [(*H*CP*H*)Fe$^{III}$Br]$^+$. Reproduced, with permission, from ref.[98] Copyright 2004, American Chemical Society.

verted porphyrin. The dominance of the π-spin transfer mechanism has been taken as direct evidence that $d_{x^2-y^2}$ is not populated in [(*H*CP)Fe$^{III}$Br] and [(*H*CP)Fe$^{III}$-(1-MeIm)]$_2^+$. Thus, the ground state can be related to the following models of the electronic configuration: intermediate-spin $(d_{xy})^2(d_{xz})^1(d_{yz})^1(d_{z^2})^1(d_{x^2-y^2})^0$ for [(*H*CP)Fe$^{III}$Br] and low-spin $(d_{xy})^2(d_{xz}d_{yz})^3(d_{z^2})^0(d_{x^2-y^2})^0$ for [(*H*CP)Fe$^{III}$-(1-MeIm)]$_2^+$. The β-H shifts of [(*H*CP)Fe$^{III}$Br] are larger as there are two π-symmetry unpaired electrons in the $S$ = 3/2 state in comparison to one π electron in [(*H*CP)Fe$^{III}$-(1-MeIm)]$_2^+$ ($S$ = 1/2).[113]

An extension of these investigations to *N*- and *C*-methylated iron porphyrins allowed the similarities of iron(*n*) *N*-confused and *C*- and *N*-methylated *N*-confused porphyrin complexes for a given oxidation/spin state to be established.[115] There are considerable similarities in the $^1$H NMR properties within each of these pairs. The analytically useful hyperfine shift patterns determined previously for iron(II) and iron(III) *N*-confused porphyrin provided useful and potentially unique probes for detecting the analogous species by $^1$H NMR spectroscopy. This spectroscopic means of identification has gained an additional advantage, namely the characteristic large downfield C-*Me* contact shift provides a well-defined signal in a unique window ($\delta$ = 420–520 ppm) for iron(III) *C*-methylated *N*-confused porphyrins, which contrasts with the relatively small values for iron(II) *C*-methylated derivatives ($\delta$ = 50–80 ppm). The most characteristic $^1$H NMR features of [(*H*CP*Me*)-Fe$^{III}$Br]$^+$ and [(*Me*CP*Me*)Fe$^{III}$Br]$^+$, namely the broad resonances at $\delta$ = 498 or 432 ppm, can be assigned to the internal C-*Me* groups. The directions and magnitudes of these shifts resemble those reported for the N-*Me* group of the [(*Me*TPP)Fe$^{III}$Cl]$^+$ complex.[13]

Dioxygen reacts cleanly with the carbaporphyrin complex [(*Me*CP*H*)Fe$^{II}$Br] to form the corresponding five-coordinate intermediate-spin iron(III) complex [(*Me*CP)Fe$^{III}$Br] although, contrary to 2-aza-21-carbaporphyrin, the *N*-methylated derivative does not acquire an oxo functionality. Similarly, the C-*Me* group, which is positioned near the center of the carbaporphyrin, presents a serious steric barrier that plays an essential role in governing the reactivity of this iron *C*-methylated *N*-confused porphyrin. For instance, [(*Me*CP*Me*)Fe$^{II}$Br] undergoes only one-electron oxidation. Further investigations of the iron carbaporphyrinoid complexes are expected to afford a unique insight into the reactivity of a metal–C bond as specifically tuned carbaporphyrins can be expected to influence feasible pathways of oxygenation processes.

## Conclusions

In a sense, in this microreview we have intended to remind the community of inorganic chemists that NMR of paramagnetic molecules can be considered as a powerful spectroscopic probe of intriguing aspects of molecular and electronic structures, structural rearrangements, and reactivity. The chosen examples address the chemistry of a new class of carbaporphyrinoid complexes that has recently been explored in our laboratory. As presented, the entrapment of metal ions in the coordination core of carbaporphyrinoids creates a very efficient protection of the metal–C bond and allows the stabilization of extremely rare or virtually unknown oxidation/electronic states of metal ions in an organometallic environment, such as copper(II),[63,116,117] silver(III),[118,119] iron(III),[98] or paramagnetic nickel(II).[44,52] Extensive studies on the NMR of paramagnetic metallocarbaporphyrinoids (reviewed above) have established a general relationship between the isotropic shift pattern of these porphyrin-like macrocycles and their electronic and molecular structures. In particular, we have found that the restraints introduced by incorporating the carbocyclic moiety into an appropriately sized carbaporphyrinoid allow the creation of a geometry that affords metal–carbocyclic ring distances that can be classified as intermediate between a regular chemical bond and a van der Waals interaction.[57,65,67,76] The proximity of a dia-

 © 2007 Wiley-VCH Verlag GmbH & Co. KGaA, Weinheim 

magnetic metal ion and an arene gives rise to observable $^{1}$H-M and $^{13}$C-M scalar couplings in the NMR spectra (M = NMR-active metal ion). Such couplings are usually classified as "through-space" or "nonbonding" because their magnitude cannot be rationalized in terms of the network of regular bonds in the molecule.[57,65,120] The metal–arene interactions of nickel(II), iron(II), and iron(III) have been probed in complementary investigations using their paramagnetically shifted $^{1}$H NMR spectra.[52,65,76,88,98] NMR spectroscopy provides a uniquely useful probe for studying this type of interaction. Apart from purely structural considerations, the understanding of such a "borderline" M···C–H interaction is fundamental for the exploration of transient states that might be active in organometallic catalysis.

## Acknowledgments

Financial support from the Ministry of Science and Higher Education (grant no. 3 T09A 162 28) is gratefully acknowledged.

[1] *NMR of Paramagnetic Molecules. Principles and Applications* (Eds.: G. N. La Mar, W. DeWitt Horrocks Jr, R. H. Holm), Academic Press, New York, **1973**.
[2] G. N. La Mar, F. A. Walker, *NMR of Paramagnetic Porphyrins*, in *The Porphyrins* (Ed.: D. Dolphin), Academic Press, New York, **1979**, p. 57.
[3] F. A. Walker, U. Simonis, N*MR of Paramagnetic Molecules*, in *Biological Magnetic Resonance* (Eds.: L. J. Berliner, S. Reuben), Plenum Press, New York, **1993**, p. 133.
[4] *NMR of Paramagnetic Molecules* (Eds.: L. J. Berliner, J. Reuben), Plenum Press, New York, **1993**.
[5] I. Bertini, C. Luchinat, *Coord. Chem. Rev.* **1996**, *150*, 1.
[6] F. A. Walker, *Advances in Single- and Multidimensional NMR Spectroscopy of Paramagnetic Metal Complexes*, in *Spectroscopic Methods in Bioinorganic Chemistry; ACS Symposium Books* (Eds.: E. I. Solomon, K. Hodgson), American Chemical Society, Washington, D. C., **1998**, p. 30.
[7] F. A. Walker, *Proton NMR and EPR Spectroscopy of Paramagnetic Metalloporphyrins*, in *The Porphyrin Handbook* (Eds.: K. M. Kadish, K. M. Smith, R. Guilard), Academic Press, San Diego, CA, **2000**, p. 81.
[8] G. N. La Mar, J. D. Satterlee, J. S. De Ropp, *Nuclear Magnetic Resonance of Hemoproteins*, in *The Porphyrin Handbook* (Eds.: K. M. Kadish, K. M. Smith, R. Guilard), Academic Press, San Diego, CA, **2000**, p. 185.
[9] I. Bertini, C. Luchinat, G. Parigi, *Solution NMR of Paramagnetic Molecules, Application to Metallobiomolecules and Models*, vol. 2, *Current Methods in Inorganic Chemistry*, Elsevier, Amsterdam, **2001**.
[10] F. A. Walker, *Inorg. Chem.* **2003**, *42*, 4526.
[11] A. L. Balch, C. R. Cornman, L. Latos-Grażyński, M. M. Olmstead, *J. Am. Chem. Soc.* **1990**, *112*, 7552.
[12] A. L. Balch, C. R. Cornman, L. Latos-Grażyński, M. W. Renner, *J. Am. Chem. Soc.* **1992**, *114*, 2230.
[13] A. L. Balch, G. N. La Mar, L. Latos-Grażyński, M. W. Renner, *Inorg. Chem.* **1985**, *24*, 2432.
[14] A. L. Balch, Y.-W. Chan, G. N. La Mar, L. Latos-Grażyński, M. W. Renner, *Inorg. Chem.* **1985**, *24*, 1437.
[15] A. Wysłouch, L. Latos-Grażyński, M. Grzeszczuk, K. Drabent, T. Bartczak, *J. Chem. Soc., Chem. Commun.* **1988**, 1377.
[16] M. Pawlicki, L. Latos-Grażyński, *Inorg. Chem.* **2002**, *41*, 5866.
[17] M. Pawlicki, L. Latos-Grażyński, *Inorg. Chem.* **2004**, *43*, 5564.
[18] P. J. Chmielewski, L. Latos-Grażyński, M. M. Olmstead, A. L. Balch, *Chem. Eur. J.* **1997**, *3*, 268.
[19] P. J. Chmielewski, L. Latos-Grażyński, *Inorg. Chem.* **1998**, *37*, 4179.
[20] L. Banci, I. Bertini, C. Luchinat, P. Turano, *Solution Structures of Hemoproteins*, in *The Porphyrin Handbook* (Eds.: K. M. Kadish, K. M. Smith, R. Guilard), Academic Press, San Diego, CA, **2000**, p. 323.
[21] A. L. Balch, Y.-W. Chan, R.-J. Cheng, G. N. La Mar, L. Latos-Grażyński, M. W. Renner, *J. Am. Chem. Soc.* **1984**, *106*, 7779.
[22] A. L. Balch, L. Latos-Grażyński, M. W. Renner, *J. Am. Chem. Soc.* **1985**, *107*, 2983.
[23] K. Rachlewicz, L. Latos-Grażyński, E. Vogel, *Inorg. Chem.* **2000**, *39*, 3247.
[24] A. L. Balch, L. Latos-Grażyński, B. C. Noll, M. M. Olmstead, N. Safari, *J. Am. Chem. Soc.* **1993**, *115*, 9056.
[25] A. L. Balch, L. Latos-Grażyński, B. C. Noll, M. M. Olmstead, L. Szterenberg, E. P. Zovinka, *J. Am. Chem. Soc.* **1993**, *115*, 11846.
[26] A. L. Balch, L. Latos-Grażyński, T. N. St. Claire, *Inorg. Chem.* **1995**, *34*, 1395.
[27] A. L. Balch, R. Koerner, L. Latos-Grażyński, B. C. Noll, *J. Am. Chem. Soc.* **1996**, *118*, 2760.
[28] A. L. Balch, R. Koerner, L. Latos-Grażyński, J. E. Lewis, T. N. St. Claire, E. P. Zovinka, *Inorg. Chem.* **1997**, *36*, 3892.
[29] R. Koerner, L. Latos-Grażyński, A. L. Balch, *J. Am. Chem. Soc.* **1998**, *120*, 9246.
[30] H. Kalish, L. Latos-Grażyński, A. L. Balch, *J. Am. Chem. Soc.* **2000**, *122*, 12478.
[31] H. Kalish, J. E. Camp, M. Stępień, L. Latos-Grażyński, A. L. Balch, *J. Am. Chem. Soc.* **2001**, *123*, 11719.
[32] H. Kalish, J. E. Camp, M. Stępień, L. Latos-Grażyński, M. M. Olmstead, A. L. Balch, *Inorg. Chem.* **2002**, *41*, 989.
[33] L. Szterenberg, L. Latos-Grażyński, J. Wojaczyński, *ChemPhysChem.* **2003**, *4*, 691.
[34] H. Kalish, H. M. Lee, M. M. Olmstead, L. Latos-Grażyński, S. P. Rath, A. L. Balch, *J. Am. Chem. Soc.* **2003**, *125*, 4674.
[35] K. T. Nguyen, S. P. Rath, L. Latos-Grażyński, M. M. Olmstead, A. L. Balch, *J. Am. Chem. Soc.* **2004**, *126*, 6210.
[36] P. J. Chmielewski, L. Latos-Grażyński, K. Rachlewicz, T. Głowiak, *Angew. Chem. Int. Ed. Engl.* **1994**, *33*, 779.
[37] H. Furuta, T. Asano, T. Ogawa, *J. Am. Chem. Soc.* **1994**, *116*, 767.
[38] T. D. Lash, *Synlett* **1999**, 279.
[39] L. Latos-Grażyński, *Core Modified Heteroanalogues of Porphyrins and Metalloporphyrins*, in *The Porphyrin Handbook* (Eds.: K. M. Kadish, K. M. Smith, R. Guilard), Academic Press, New York, **2000**, p. 361.
[40] H. Furuta, H. Maeda, A. Osuka, *Chem. Commun.* **2002**, 1795.
[41] J. D. Harvey, C. J. Ziegler, *Coord. Chem. Rev.* **2003**, *247*, 1.
[42] A. Ghosh, *Angew. Chem. Int. Ed.* **2004**, *43*, 1918.
[43] A. Srinivasan, H. Furuta, *Acc. Chem. Res.* **2005**, *38*, 10.
[44] P. J. Chmielewski, L. Latos-Grażyński, *Coord. Chem. Rev.* **2005**, *249*, 2510.
[45] M. Stępień, L. Latos-Grażyński, *Acc. Chem. Res.* **2005**, *38*, 88.
[46] F.-P. Monforts, M. Glasenapp-Breiling, D. Kusch, *Porphyrins and Related Compounds*, in *Hetarenes*, Thieme, Stuttgart, New York, **1998**, p. 577.
[47] J. L. Sessler, A. Gebauer, E. Vogel, *Porphyrin Isomers*, in *The Porphyrin Handbook* (Eds.: K. M. Kadish, K. M. Smith, R. Guilard), Academic Press, San Diego, CA, **2000**, p. 1.
[48] K. Berlin, E. Breitmaier, *Angew. Chem. Int. Ed. Engl.* **1994**, *33*, 1246.
[49] T. D. Lash, *Angew. Chem. Int. Ed. Engl.* **1995**, *34*, 2533.
[50] T. D. Lash, *Syntheses of Novel Porphyrinoid Chromophores*, in *The Porphyrin Handbook* (Eds.: K. M. Kadish, K. M. Smith, R. Guilard), Academic Press, San Diego, CA, **2000**, p. 125.
[51] P. J. Chmielewski, L. Latos-Grażyński, *J. Chem. Soc., Perkin Trans. 2* **1995**, 503.
[52] P. J. Chmielewski, L. Latos-Grażyński, T. Głowiak, *J. Am. Chem. Soc.* **1996**, *118*, 5690.
[53] I. Schmidt, P. J. Chmielewski, *Tetrahedron Lett.* **2001**, *42*, 6389.

 © 2007 Wiley-VCH Verlag GmbH & Co. KGaA, Weinheim 

[54] I. Schmidt, P. J. Chmielewski, *Inorg. Chem.* **2003**, *42*, 5579.
[55] I. Schmidt, P. J. Chmielewski, Z. Ciunik, *J. Org. Chem.* **2002**, *67*, 8917.
[56] M. Stępień, L. Latos-Grażyński, *Chem. Eur. J.* **2001**, *7*, 5113.
[57] M. Stępień, L. Latos-Grażyński, *J. Am. Chem. Soc.* **2002**, *124*, 3838.
[58] E. Pacholska, L. Latos-Grażyński, Z. Ciunik, *Chem. Eur. J.* **2002**, *8*, 5403.
[59] R. Myśliborski, L. Latos-Grażyński, *Eur. J. Org. Chem.* **2005**, 5039.
[60] P. J. Chmielewski, L. Latos-Grażyński, *Inorg. Chem.* **1997**, *36*, 840.
[61] T. J. Swift, *The Paramagnetic Linewidth*, in *NMR of Paramagnetic Molecules. Principles and Applications* (Eds.: G. N. La Mar, W. D. Holm Jr, R. H. Horrocks), Academic Press, New York, **1973**, p. 53.
[62] P. J. Chmielewski, L. Latos-Grażyński, *Inorg. Chem.* **2000**, *39*, 5639.
[63] P. J. Chmielewski, L. Latos-Grażyński, I. Schmidt, *Inorg. Chem.* **2000**, *39*, 5475.
[64] G. Mitrikas, C. Calle, A. Schweiger, *Angew. Chem. Int. Ed.* **2005**, *44*, 3301.
[65] M. Stępień, L. Latos-Grażyński, L. Szterenberg, J. Panek, Z. Latajka, *J. Am. Chem. Soc.* **2004**, *126*, 4566.
[66] M. Stępień, L. Latos-Grażyński, *Inorg. Chem.* **2003**, *42*, 6183.
[67] M. Stępień, L. Latos-Grażyński, L. Szterenberg, *Inorg. Chem.* **2004**, *43*, 6654.
[68] J. D. Satterlee, G. N. La Mar, T. J. Bold, *J. Am. Chem. Soc.* **1977**, *99*, 1088.
[69] G. N. La Mar, E. O. Sherman, *J. Am. Chem. Soc.* **1970**, *92*, 2691.
[70] K. M. Barkigia, M. D. Berber, C. J. Medforth, M. W. Renner, K. M. Smith, *J. Am. Chem. Soc.* **1990**, *112*, 8851.
[71] C. J. Medforth, *NMR Spectroscopy of Diamagnetic Porphyrins*, in *The Porphyrin Handbook* (Eds.: K. M. Kadish, K. M. Smith, R. Guilard), Academic Press, San Diego, CA, **2000**, p. 1.
[72] C. J. Medforth, M. D. Berber, K. M. Smith, J. A. Shelnutt, *Tetrahedron Lett.* **1990**, *31*, 3719.
[73] E. Pacholska-Dudziak, J. Skonieczny, M. Pawlicki, L. Latos-Grażyński, L. Szterenberg, *Inorg. Chem.* **2005**, *44*, 8794.
[74] J. Lisowski, L. Latos-Grażyński, L. Szterenberg, *Inorg. Chem.* **1992**, *31*, 1933.
[75] L. Latos-Grażyński, E. Pacholska, P. J. Chmielewski, M. M. Olmstead, A. L. Balch, *Inorg. Chem.* **1996**, *35*, 566.
[76] C.-H. Hung, F.-C. Chang, C.-Y. Lin, K. Rachlewicz, M. Stępień, L. Latos-Grażyński, G.-H. Lee, S.-M. Peng, *Inorg. Chem.* **2004**, *43*, 4118.
[77] R. Myśliborski, K. Rachlewicz, L. Latos-Grażyński, *Inorg. Chem.* **2006**, *45*, 7828.
[78] P. J. Chmielewski, L. Latos-Grażyński, *Inorg. Chem.* **1992**, *31*, 5231.
[79] R. Myśliborski, K. Rachlewicz, L. Latos-Grażyński, *J. Porphyrins Phthalocyanines* **2007**, in press.
[80] R. Myśliborski, L. Latos-Grażyński, L. Szterenberg, *Eur. J. Org. Chem.* **2006**, 3064.
[81] G. Simonneaux, F. Hindre, M. Le Plouzennec, *Inorg. Chem.* **1989**, *28*, 823.
[82] S. Wołowiec, L. Latos-Grażyński, M. Mazzanti, J.-C. Marchon, *Inorg. Chem.* **1997**, *36*, 5761.
[83] S. Wołowiec, L. Latos-Grażyński, D. Toronto, J.-C. Marchon, *Inorg. Chem.* **1998**, *37*, 724.
[84] M. Nakamura, T. Ikeue, H. Fujii, T. Yoshimura, *J. Am. Chem. Soc.* **1997**, *119*, 6284.
[85] T. Ikeue, Y. Ohgo, T. Saitoh, T. Yamaguchi, M. Nakamura, *Inorg. Chem.* **2001**, *40*, 3423.
[86] H. Ogura, L. Yatsunyk, C. J. Medforth, K. M. Smith, K. M. Barkigia, M. W. Renner, D. Melamed, F. A. Walker, *J. Am. Chem. Soc.* **2001**, *123*, 6564.
[87] W.-C. Chen, C.-H. Hung, *Inorg. Chem.* **2001**, *40*, 5070.
[88] K. Rachlewicz, S.-L. Wang, C.-H. Peng, C.-H. Hung, L. Latos-Grażyński, *Inorg. Chem.* **2003**, *42*, 7348.
[89] L. Latos-Grażyński, J. Lisowski, M. M. Olmstead, A. L. Balch, *Inorg. Chem.* **1989**, *28*, 1183.
[90] Z. Li, H. M. Goff, *Inorg. Chem.* **1992**, *31*, 1548.
[91] L. Latos-Grażyński, J. Wojaczyński, R. Koerner, J. J. Johnson, A. L. Balch, *Inorg. Chem.* **2001**, *40*, 4971.
[92] C. Luchinat, S. Steuernagel, P. Turano, *Inorg. Chem.* **1990**, *29*, 4351.
[93] B. Xia, W. M. Westler, H. Cheng, J. Meyer, J.-M. Moulis, J. L. Markley, *J. Am. Chem. Soc.* **1995**, *117*, 5347.
[94] I. Bertini, C. O. Fernández, B. G. Karlsson, J. Leckner, C. Luchinat, B. G. Malmström, A. M. Nersissian, R. Pierattelli, E. Ship, J. S. Valentine, A. J. Vila, *J. Am. Chem. Soc.* **2000**, *122*, 3701.
[95] A. L. Balch, R.-J. Cheng, G. N. La Mar, L. Latos-Grażyński, *Inorg. Chem.* **1985**, *24*, 2651.
[96] J. Wojaczyński, L. Latos-Grażyński, W. Hrycyk, E. Pacholska, K. Rachlewicz, L. Szterenberg, *Inorg. Chem.* **1996**, *35*, 6861.
[97] R.-J. Cheng, P.-Y. Chen, T. Lovell, T. Liu, L. Noodleman, D. A. Case, *J. Am. Chem. Soc.* **2003**, *125*, 6774.
[98] K. Rachlewicz, S.-L. Wang, J.-L. Ko, C.-H. Hung, L. Latos-Grażyński, *J. Am. Chem. Soc.* **2004**, *126*, 4420.
[99] B. A. Grigor, A. Neilson, *J. Organomet. Chem.* **1977**, *129*, C17.
[100] K. Kamaraj, D. Bandyopadhyay, *J. Am. Chem. Soc.* **1997**, *119*, 8099.
[101] P. Wadhwani, M. Mukherjee, D. Bandyopadhyay, *J. Am. Chem. Soc.* **2001**, *123*, 12430.
[102] A. D. Ryabov, *Synthesis* **1985**, 233.
[103] A. K. Mahapatra, D. Bandyopadhyay, P. Bandyopadhyay, A. Chakravorty, *Inorg. Chem.* **1986**, *25*, 2214.
[104] C. Sinha, D. Bandyopadhyay, A. Chakravorty, *Inorg. Chem.* **1988**, *27*, 1173.
[105] S. Chattopadhyay, C. Sinha, P. Basu, A. Chakravorty, *Organometallics* **1991**, *10*, 1135.
[106] A. Marsella, S. Agapakis, F. Pinna, G. Strukul, *Organometallics* **1992**, *11*, 3578.
[107] J.-M. Valk, J. Boersma, G. van Koten, *Organometallics* **1996**, *15*, 4366.
[108] R. D. Arasasingham, A. L. Balch, R. H. Hart, L. Latos-Grażyński, *J. Am. Chem. Soc.* **1990**, *112*, 7566.
[109] A. L. Balch, R. H. Hart, L. Latos-Grażyński, *Inorg. Chem.* **1990**, *29*, 3253.
[110] H. Furuta, T. Ishizuka, A. Osuka, T. Ogawa, *J. Am. Chem. Soc.* **1999**, *121*, 2945.
[111] C.-H. Hung, W.-C. Chen, G.-H. Lee, S.-M. Peng, *Chem. Commun.* **2002**, 1516.
[112] Z. Xiao, B. O. Patrick, D. Dolphin, *Inorg. Chem.* **2003**, *42*, 8125.
[113] J.-P. Simonato, J. Pécaut, L. Le Pape, J.-L. Oddou, C. Jeandey, M. Shang, W. R. Scheidt, J. Wojaczyński, S. Wołowiec, L. Latos-Grażyński, J.-C. Marchon, *Inorg. Chem.* **2000**, *39*, 3978.
[114] K. Rachlewicz, L. Latos-Grażyński, E. Vogel, Z. Ciunik, L. Jerzykiewicz, *Inorg. Chem.* **2002**, *41*, 1979.
[115] K. Rachlewicz, D. Gorzelańczyk, L. Latos-Grażyński, *Inorg. Chem.* **2006**, *45*, 9742.
[116] H. Furuta, T. Ishizuka, A. Osuka, Y. Uwatoko, Y. Ishikawa, *Angew. Chem. Int. Ed.* **2001**, *40*, 2323.
[117] H. Maeda, Y. Ishikawa, T. Matsuda, A. Osuka, H. Furuta, *J. Am. Chem. Soc.* **2003**, *125*, 11822.
[118] H. Furuta, T. Ogawa, Y. Uwatoko, K. Araki, *Inorg. Chem.* **1999**, *38*, 2676.
[119] M. Pawlicki, L. Latos-Grażyński, *Chem. Eur. J.* **2003**, *9*, 4650.
[120] J. Hilton, L. H. Sutcliffe, *Prog. NMR Spectrosc.* **1975**, *10*, 27.

Received: January 22, 2007
Published Online: April 24, 2007

 © 2007 Wiley-VCH Verlag GmbH & Co. KGaA, Weinheim 

DOI: 10.1002/ejic.200601254

# Growth of Metal Nanoparticles in a Sol-Gel Silica Thin Film

**Miroslava Malenovska,[a] Sandra Martinez,[a][‡] Marie-Alexandra Neouze,[a] and Ulrich Schubert*[a]**

**Keywords:** Thin films / Nanostructures / Inorganic-organic hybrid materials / Nanocomposites

Silica films on glass substrates with homogeneously dispersed platinum, gold or silver nanoparticles were prepared by sol-gel processing mixtures of tetraethoxysilane and {3-[(2-aminoethyl)amino]propyl}triethoxysilane complexes of the corresponding metal ions, followed by dip-coating and hydrogen treatment of the films at elevated temperatures.
(© Wiley-VCH Verlag GmbH & Co. KGaA, 69451 Weinheim, Germany, 2007)

## Introduction

Numerous work has been published on the synthesis of metal oxide or metal nanoparticles[1] in polymeric,[2] inorganic,[3] or hybrid organic-inorganic matrices.[4] Independent of the type of matrix material, the principles of introducing the nanoparticles are rather similar. Thus, the matrix can be formed around pre-formed (stabilized) nanoparticles, the particles can be generated in the pre-formed matrix, or matrix and nanoparticles can be synthesized concomitantly. All methods, when properly controlled, can lead to homogeneously dispersed materials.

We have previously developed a sol-gel method by which nanometer-sized metal oxide or metal particles with narrow size distributions are generated within a silica matrix.[5–7] The nanoparticles prepared by this method are not agglomerated and are homogeneously distributed in the $SiO_2$ matrix, even in materials with high metal loading. The high metal dispersion in the nanocomposites was achieved by tethering metal ions to the matrix generated during sol-gel processing. To this end, trialkoxysilyl-substituted metal complexes of the type $[(RO)_3Si(CH_2)_nA]_nMX_m$, formed in situ by reaction of a metal salt ($MX_m$) with alkoxysilanes $(RO)_3Si(CH_2)_nA$ (A = a coordinating group), were used as precursors for sol-gel processing. Metal coordination is retained during gel formation, and the metal complexes are tethered to the gel network through the $(CH_2)_nSiO_{3/2}$ groups. The metal loading can be adjusted by using $Si(OR)_4$ as a co-precursor. The resulting gels with the idealized composition $[O_{3/2}Si(CH_2)_nA]_nMX_m{\cdot}xSiO_2$ had the typical color of the corresponding metal complexes. When the metal complex containing gels were subsequently heated in air, all organic moieties were oxidized and/or pyrolyzed, i.e. carbon-free materials were obtained, and nanosized metal oxide particles [i.e., the nanocomposites $MO_y{\cdot}(x+n)SiO_2$] were formed in the silica matrix. In the final step, the oxide particles were reduced by hydrogen, resulting in metal/silica nanocomposites, $M{\cdot}(x+n)SiO_2$. Since the nanoparticles are formed during the *oxidation* step, the reaction conditions during this step, including the nature of the organic groups (counterion, tethering groups) being burnt, determine the size of the obtained metal oxide nanoparticles.[7] The particle size is not changed significantly during the subsequent reduction step.

This procedure results in nanocomposite *powders*, due to the removal of the organic groups. Although we have previously shown that the synthesis of metal/silica nanocomposite powders by the coordination/oxidation/reduction protocol can also be applied to the coating of porous silica pellets with Pt nanoparticle-containing gels,[6] this synthesis protocol is not suitable to prepare coherent nanoparticle-containing *films*. Such sol-gel films are interesting for a variety of applications.

It was recently shown for aerogels that metal nanoparticles are also formed by direct reduction of tethered metal complexes without prior removal of the organic groups.[8] Since removal of the organic groups is detrimental to good film properties, this modification of the synthesis protocol may also allow to obtain metal nanoparticle containing films. However, this is not at all a straightforward modification of the existing procedure, because the *metal* particles will not be formed by reduction of existing metal oxide particles, but instead by nucleation and growth during the reduction step. Since nucleation and growth of the nanoparticles occurs under completely different conditions, one cannot assume that the modified approach necessarily also results in nearly monodisperse, highly dispersed metal particles as were obtained by the described coordination/oxidation/reduction route.

[a] Institute of Materials Chemistry, Vienna University of Technology,
Getreidemarkt 9/165, 1060 Vienna, Austria
E-mail: Ulrich.Schubert@tuwien.ac.at
[‡] Current address: Department of Materials Science, Technische Universität Darmstadt, Petersenstr. 23, 64287 Darmstadt, Germany

 © 2007 Wiley-VCH Verlag GmbH & Co. KGaA, Weinheim 

We now show that metal particle containing sol-gel films can be prepared by exposing the films to hydrogen at elevated temperatures without prior calcination. Gold/silver alloy particles with diameters of 2.5–7 nm in a silica film were already obtained by UV irradiation of sol-gel films.[9] The work reported in this contribution has proof-of-concept character, without optimization of the reaction conditions, the metal particle sizes or the properties of the silica matrix.

## Results and Discussion

The metal nanoparticle containing sol-gel films were synthesized in three successive steps. In the first step (Scheme 1 for $Pt^{2+}$), metal complexes substituted by {3-[(2-aminoethyl)amino]propyl}triethoxysilane (AEAPTS), a trialkoxysilyl-substituted derivative of ethylenediamine, were prepared in situ. In the second step (Scheme 1), a sol was formed by hydrolytic polycondensation of the (AEAPTS) metal complex and $Si(OEt)_4$. This sol was dip-coated on glass slides resulting in thin, transparent films of the metal complex containing inorganic-organic hybrid material. In the final step, the metal ions in the sol-gel film were reduced by exposure to hydrogen at elevated temperatures, resulting in the formation of metal nanoparticles.

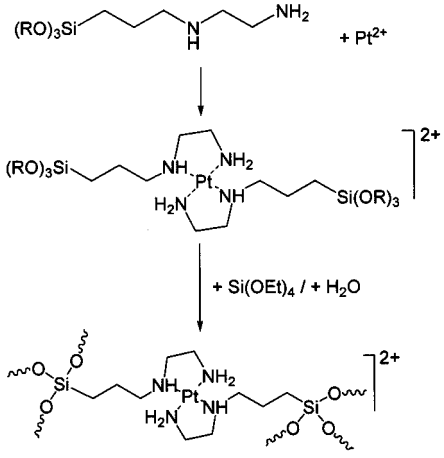


Scheme 1.

The advantage of this approach is that films can be prepared by standard coating technologies. The presence of the organic groups not only renders possible an atomic dispersion of the metal component during film formation, but also allows, in principle, to adjust the properties of the coating sol in the same way as for other well-known applications of alkoxysilane mixtures.

The reduction of the metal was followed by X-ray diffraction (Figure 1), which confirms the "postsynthesis reduction" in the last synthesis step, i.e. after formation of the silica film. Only a broad bump corresponding to amorphous silica was observed before the films were exposed to hydrogen and after the films were heated in hydrogen up to 200 °C. Only when the reduction temperature was increased to 400 °C, did reflections of elemental Pt emerge additionally. An average diameter of 6.8 nm was calculated by Scherrer's equation from the half-height widths of the reflections. When the reduction temperature was raised to 500 °C, the reflections became sharper, as expected, and the average particle diameter increased to 22 nm.

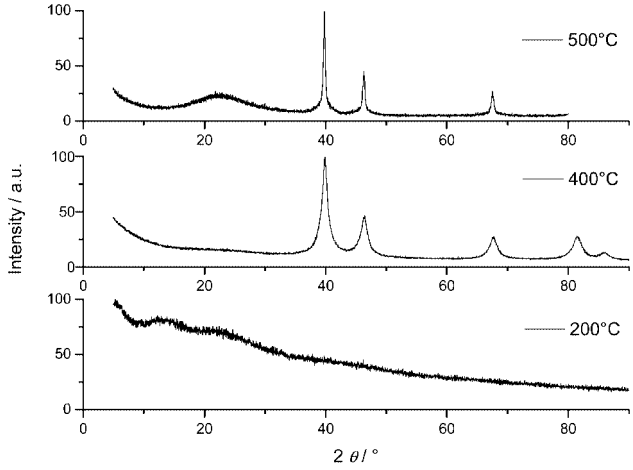


Figure 1. Temperature-dependent XRD on the reduction of platinum in the sol-gel films. The films were kept at each temperature in hydrogen for 2 h before the diffractogram was taken.

Silica films containing gold or silver nanoparticles were similarly prepared. The diffraction patterns (Figure 2) showed both the broad bump for amorphous silica and the characteristic reflections of the reduced gold or silver particles. An average diameter of 7.9 nm was calculated for the Au particles by Scherrer's equation, and of 13.1 nm for the silver particles.

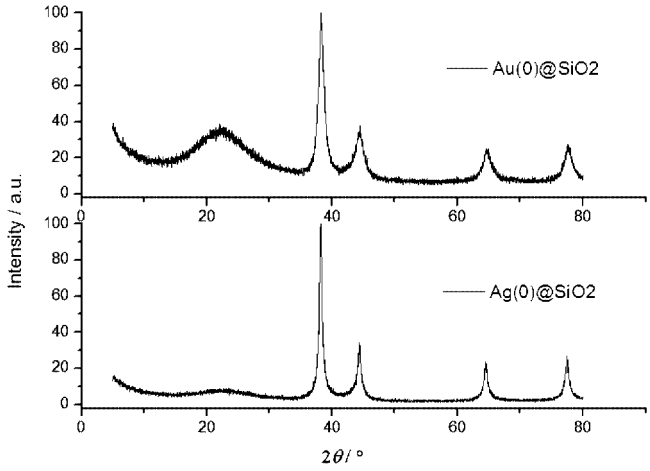


Figure 2. XRD of silica films containing gold or silver nanoparticles after reduction at 500 °C.

As a consequence of the tethering of the metal complexes, the metal ions are perfectly dispersed in the film before being reduced. During reduction of the metal ions, growth of the resulting metal particles is limited by the sur-

 © 2007 Wiley-VCH Verlag GmbH & Co. KGaA, Weinheim 

rounding silica matrix. This leads to a homogeneous dispersion of the metal nanoparticles. Figure 3 shows the TEM of the silica film with platinum nanoparticles in the range 10–100 nm (average ca. 30 nm). The metal particle size is of course also dependent on the reduction temperature, and larger average particle sizes were consequently obtained when the temperature was increased.

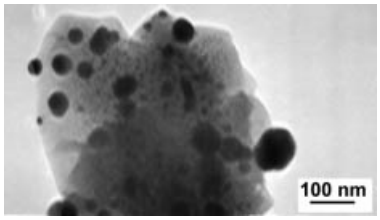


Figure 3. TEM of $Pt^0$ nanoparticles dispersed in the silica film after reduction at 500 °C.

A key issue in this work was also the film properties. Even after hydrogen treatment at 500 °C for 2 h, the film remained transparent. Adhesion of the film after reduction was as good as before, and the films were crack-free.

## Conclusions

The present work shows the feasibility of preparing silica *films* with dispersed noble metal nanoparticles by sol-gel processing. Reduction is performed after coating, i.e. in the deposited sol-gel film, in which the metal cations are chelated by the amino groups and thus linked to the silica network. Contrary to synthesis protocols for carbon-free nanocomposite *powders*, the organic tethers and the counterions of the employed metal salts were not oxidatively removed prior to reduction. This had a beneficial influence on the quality of the final coating.

The metal nanoparticles obtained are highly dispersed in the silica film. However, the obtained metal particles have a much broader particle size distribution than those prepared by the coordination/oxidation/reduction protocol. This may be due to different nucleation and growths mechanisms in the reduction step and/or the influence of the substrate. This will be subject to further work.

The possibility to generate metal nanoparticles without completely destroying the organic groups of the gel opens the possibility of optimizing the properties of the coatings, e.g. adhesion to substrates or compliance of the films, by using organically substituted trialkoxysilanes $R'Si(OR)_3$ as co-reactants.

The goal of the work reported here was a proof of principle. We have neither optimized the reduction conditions nor the film or particle properties. Future work also needs to address the fate of the organic groups during hydrogen reduction at elevated temperatures and their influence on the particle growth and the film properties.

## Experimental Section

**General:** {3-[(2-aminoethyl)amino]propyl}triethoxysilane (AEAPTS) and ethanol were distilled before use and kept under inert gas. Ethanol was kept over molecular sieves under an inert gas.

**Preparation of the Coating Solutions:** An amount of 0.1 mmol of $AgNO_3$, $HAuCl_4$, or $Pt(acac)_2$ (acac = acetylacetonate), was dissolved in 10 mL of freshly distilled, dried ethanol. An amount of AEAPTS was added to the solution of the metal salt which corresponded to a metal/AEAPTS molar ratio of 1:2, 1:3, and 1:4 for silver, gold and platinum, respectively. The mixture was stirred at room temperature until the color of the solution did not change any more, which indicated the formation of the metal complexes $[Ag(AEAPTS)_2]^+$, $[Au(AEAPTS)_2]^{3+}$, or $[Pt(AEAPTS)_2]^{2+}$.[5,7] An amount of 0.2 mmol of tetraethoxysilane (TEOS) was added to the metal complex solution and sol-gel reactions were started by addition of 40 mL of 0.2 N aqueous $NH_4OH$. The resulting colloidal suspensions, which had the typical color of the corresponding metal complexes, were heated to 70 °C for 72 h.

**Dip-Coating:** Glass sides were cleaned by treatment with a concentrated sodium hydroxide solution followed by successive rinsing with ethanol and deionised water and then coated by dip-coating with a withdrawal speed of 24 $cm\,min^{-1}$.

**Metal Reduction:** The coated glass plates were put in an oven flushed with hydrogen. The temperature was then raised to 500 °C at 10 $°C \cdot min^{-1}$ and kept at this temperature under hydrogen for 2 h.

**Characterization:** The obtained films were characterized by transmission electron microscopy (TEM) with a JEOL 200CX. X-ray analyses were carried out with a Philips X'Pert diffractometer using Cu-$K_\alpha$ radiation. For both investigations, the films were scraped off from the glass slides.

## Acknowledgments

This work was supported by the European Commission in the framework of the Integrated Project NAPOLYDE (contract no. NMP2-CT-2005-515846).

[1] M.-I. Baraton (Ed.), *Synthesis Functionalization and Surface Treatment of Nanoparticles*, American Scientific Publishers, Stevenson Ranch, **2003**.
[2] Recent examples: S. Ding, Y. Xing, M. Radosz, Y. Shen, *Macromolecules* **2006**, *39*, 6399–6405; B. J. Kim, J. Bang, C. J. Hawker, E. J. Kramer, *Macromolecules* **2006**, *39*, 4108–4114; F. Mirkhalaf, J. Paprotny, D. J. Schiffrin, *J. Am. Chem. Soc.* **2006**, *128*, 7400–7401; A.-S. Duwez, P. Guillet, C. Colard, J.-F. Gohy, C.-A. Fustin, *Macromolecules* **2006**, *39*, 2729–2731.
[3] Recent examples: I. U. Arachchige, S. L. Brock, *J. Am. Chem. Soc.* **2006**, *128*, 7964–7971; L. Qu, L. Dai, E. Osawa, *J. Am. Chem. Soc.* **2006**, *128*, 5523–5532.
[4] Recent examples: S. Pan, Z. Wang, L. J. Rothberg, *J. Phys. Chem. B* **2006**, *110*, 17383–17387; S. E. Hunyadi, C. J. Murphy, *J. Phys. Chem. B* **2006**, *110*, 7226–7231.
[5] B. Breitscheidel, J. Zieder, U. Schubert, *Chem. Mater.* **1991**, *3*, 559–566.
[6] U. Schubert, S. Amberg-Schwab, B. Breitscheidel, *Chem. Mater.* **1989**, *1*, 576–578; G. Trimmel, U. Schubert, *J. Non-Cryst. Solids* **2001**, *296*, 188–200; G. Trimmel, C. Lembacher, G. Kickelbick, U. Schubert, *New J. Chem.* **2002**, *26*, 759–765.
[7] C. Lembacher, U. Schubert, *New J. Chem.* **1998**, *22*, 721–724.
[8] S. Martinez, M. Moreno-Manas, A. Vallribera, U. Schubert, A. Roig, E. Molins, *New J. Chem.* **2006**, *30*, 1093–1097.
[9] S. Pal, G. De, *Chem. Mater.* **2005**, *17*, 6161–6166.

Received: December 28, 2006
Published Online: May 14, 2007

 © 2007 Wiley-VCH Verlag GmbH & Co. KGaA, Weinheim 

DOI: 10.1002/ejic.200700067

# Dinuclear Nickel–Ruthenium Complexes as Functional Bio-Inspired Models of [NiFe] Hydrogenases

**Yohan Oudart,[a] Vincent Artero,*[a] Jacques Pécaut,[b] Colette Lebrun,[b] and Marc Fontecave[a]**

**Keywords:** Nickel / Ruthenium / Hydrogen / Electrocatalysis / Biomimetic chemistry / Hydrogenases

Three new dinuclear nickel ruthenium complexes, namely $[Ni(xbsms)Ru(p\text{-cymene})Cl]^+$, $[Ni(emi)Ru(CO)_2Cl_2]^{2-}$ and $[Ni(emi)Ru(p\text{-cymene})Cl]^-$ [$H_2$xbsms = 1,2-bis(4-mercapto-3,3-dimethyl-2-thiabutyl)benzene, $H_2$emi = *N*,*N*′-ethylenebis(2-mercaptoisobutyramide], have been synthesized and fully characterized as models of the active site of [NiFe] hydrogenases. The three-dimensional structure of $[Ni(xbsms)Ru(p\text{-cymene})Cl]^+$ reveals a nickel center in a square-planar dithioether-dithiolate environment that is connected to a ruthenium moiety via a $Ni(\mu\text{-}SR)_2Ru$ bridge. These complexes catalyze hydrogen evolution by electroreduction of the weakly acidic $Et_3NH^+$ ions in dimethylformamide and are therefore among the first bio-inspired functional models of [NiFe] hydrogenases. The catalytic activity of these new complexes is explained by the existence of a cooperative effect between the metal centers and is further related to their electronic properties.

(© Wiley-VCH Verlag GmbH & Co. KGaA, 69451 Weinheim, Germany, 2007)

## Introduction

Hydrogenase enzymes catalyze the reversible formation/oxidation of dihydrogen and can be divided into two main classes, depending on their metal content.[1] In addition to classical Fe/S clusters, Fe-only hydrogenases display a hexanuclear active site (H-cluster) constituted by a [4Fe-4S] cluster bound through a cysteine-derived sulfur bridge to the $[Fe_2(\mu_2\eta^4\text{-}SRS)(CO)_3(CN)_2L]$ sub-site (R is proposed to be -$CH_2NHCH_2$-, L = $H_2O$, $H_2$ or $H^-$; Figure 1). By contrast, [NiFe] hydrogenases contain a dinuclear nickel-iron active center.[2] In the reduced active state the nickel ion is only coordinated by four cysteinate residues, two of which also bridge an organometallic {Fe(CO)$(CN)_2$} moiety (Figure 1). The [NiFe] hydrogenase from *Allochromatium vinosum* displays a Nernstian catalytic behavior for hydrogen oxidation when immobilized on a pyrolytic graphite "edge" electrode.[8] As unique molecular catalysts for $H_2/H^+$ interconversion, hydrogenases are thus competitive with platinum metal, which has prompted the synthesis, pioneered by Darensbourg et al., of a great variety of biomimetic complexes[9–11] with the aim of both better understanding the catalytic mechanism of native [NiFe] hydrogenases at the molecular level and developing new electrocatalysts to be used in fuel-cells for hydrogen uptake or in electrolytic/photosynthetic cells for hydrogen production. The most accurate of these structural mimics are $[(bdt)Ni(\mu_2\text{-}"S_3")Fe(CO)(PMe_3)_2]$ [$H_2$"$S_3$" = bis(2-mercaptophenyl)sulfide; $H_2$bdt = 1,2-benzenedithiol],[12] $[Ni(xbsms)Fe(CO)_2I_2]$ [$H_2$xbsms = 1,2-bis(4-mercapto-3,3-dimethyl-2-thiabutyl)-benzene],[13] and $[(dedtc)Ni(pdt)Fe(CO)_2(CN)_2]^-$ (dedtc$^-$ = diethyldithiocarbamato anion; $H_2$pdt = propanedithiol),[14] all of which have a nickel ion in an $S_4$ environment and CO ligands bound to iron (Figure 2). However, no catalytic activity has been reported so far for dinuclear nickel-iron complexes, and hydrogen evolution activity has only been demonstrated with trinuclear biomimetic complexes: $[(bdt)\{Ni(PMe_3)\}_2(bdt)_2Fe(CO)]$[15] stoichiometrically reduces $HBF_4$ to $H_2$ and $[Ni(L)Fe_2(CO)_6]$ [L = *S*,*S*′-bis(2-mercapto-5-methylphenyl)-1,4-dithiabutane] electrocatalyzes the reduction of $CF_3COOH$ to $H_2$ at –1.64 V vs. Fc/$Fc^+$ in $CH_2Cl_2$.[16] In a bio-inspired approach, we recently

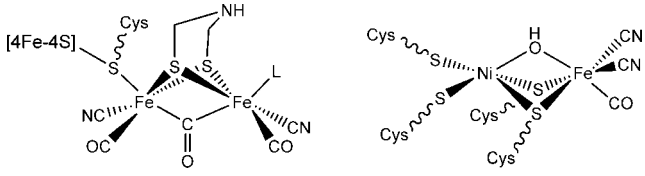


Figure 1. Structure of the active sites of iron-only hydrogenases in the oxidized state (left, L = $H_2O$, $H_2$ or $H^-$)[3,4] and [NiFe] hydrogenases in the Ni-B inactive ready state[5,6] (right, the bridging hydroxido ligand is not present in the reduced active states[7]).

[a] Laboratoire de Chimie et Biologie des Métaux; Université Joseph Fourier, CNRS UMR 5249, CEA, DSV/iRTSV/LCBM, Bâtiment K',
17 Rue des Martyrs, 38054 Grenoble Cedex 9, France
[b] Laboratoire de Reconnaissance Ionique et Chimie de Coordination, LCIB (UMR-E 3 CEA-UJF) DRFMC,
17 Rue des Martyrs, 38054 Grenoble Cedex 9, France

Supporting information for this article is available on the WWW under http://www.eurjic.org or from the author.

 © 2007 Wiley-VCH Verlag GmbH & Co. KGaA, Weinheim 

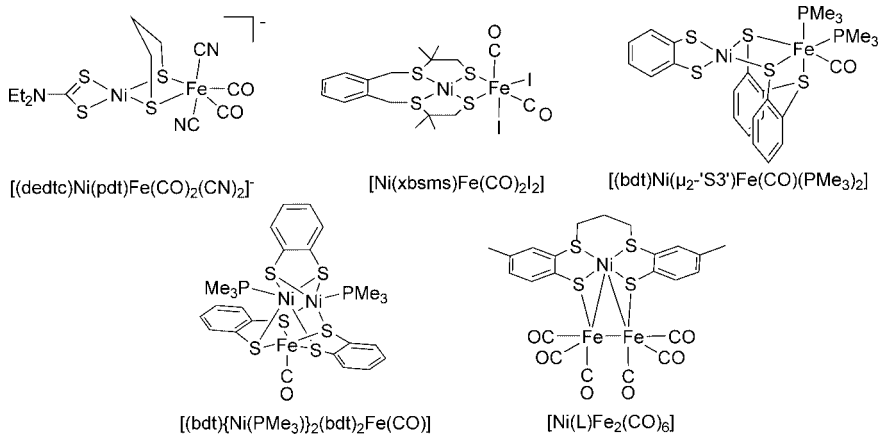


Figure 2. Selected structural models for [NiFe] hydrogenases from the literature (references are given in the text).

reported the catalytic activity of a dinuclear nickel-ruthenium complex in which an electron-rich organometallic moiety is introduced as a surrogate for the {Fe(CO)(CN)$_2$} fragment.[17] In order to shed light on the structure-function relationships in this class of catalysts, and to gain more insight into the reaction mechanism, we have prepared three new compounds that vary in both the tetradentate ligand around the nickel ion and the organometallic ligand set of the ruthenium center. Their catalytic activity for $Et_3NH^+$ reduction in dimethylformamide is investigated, and further comparison with the activity of structurally related mononuclear complexes of nickel and ruthenium provides evidence for a synergic effect between the metal centers in these dinuclear catalysts.

## Results

### Syntheses

Treatment of [Ni(xbsms)][18] with half an equivalent of [RuCl$_2$(*p*-cymene)$_2$]$_2$ in $CH_2Cl_2$ under argon afforded [Ni(xbsms)Ru(*p*-cymene)Cl]Cl (**1**Cl, Figure 3) in high yield, chromatographic purification of which yielded an analytically pure compound. Subsequent treatment with one equivalent of $AgBF_4$ in $CH_2Cl_2$ yielded **1**$BF_4$. This synthesis is very similar to that used previously for the preparation of [Ni(xbsms)Ru(CO)$_2$Cl$_2$] (**2**).[17]

Similarly, treatment of (NEt$_4$)$_2$[Ni(emi)] [H$_2$emi = *N*,*N*′-ethylenebis(2-mercaptoisobutyramide)][19] with half an equivalent of [RuCl$_2$(*p*-cymene)$_2$]$_2$ in $CH_2Cl_2$ under argon afforded (NEt$_4$)[Ni(emi)Ru(*p*-cymene)Cl] [(NEt$_4$)**3**, Figure 3]. (NEt$_4$)**3** can be purified by precipitation upon addition of pentane to a tetrahydrofuran solution even though samples proved to be systematically contaminated with $Et_4NCl$ salt. The compound (NEt$_4$)$_2$[Ni(emi)Ru(CO)$_2$Cl$_2$] [(NEt$_4$)$_2$**4**, Figure 3] was obtained from the stoichiometric reaction of (NEt$_4$)$_2$[Ni(emi)] with [Ru(CO)$_2$Cl$_2$]$_n$ although it proved difficult to purify, the major impurities being $Et_4NCl$ and (NEt$_4$)[Ni(emi)Ru(CO)$_3$Cl]. The latter arises from the reaction of (NEt$_4$)$_2$[Ni(emi)] with [Ru(CO)$_3$Cl$_2$], which often contaminates samples of [Ru(CO)$_2$Cl$_2$].

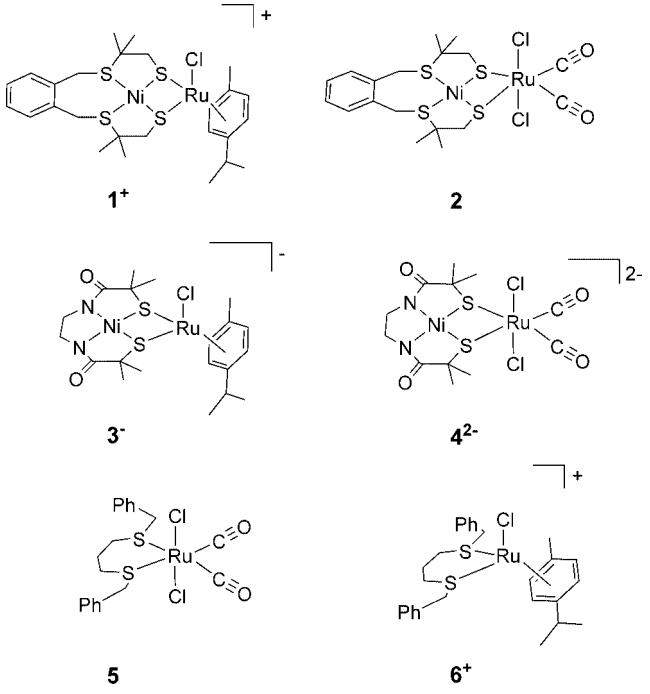


Figure 3. Molecular structures of the dinuclear nickel-ruthenium and mononuclear ruthenium complexes.

Two mononuclear ruthenium compounds, namely [("$C_3S_2$")Ru(CO)$_2$Cl$_2$] (**5**, Figure 3) and [("$C_3S_2$")RuCl(*p*-cymene)$_2$]Cl (**6**Cl, Figure 3) were also prepared by reaction of [Ru(CO)$_2$Cl$_2$]$_n$ and [RuCl$_2$(*p*-cymene)$_2$]$_2$ with 1,7-diphenyl-2,6-dithiaheptane ("$C_3S_2$"),[20] a bidentate ligand bearing two dithioether functions, in order to compare the dinuclear catalysts with mononuclear compounds having the same coordination sphere. Both complexes were purified by silica gel column chromatography to afford analytically pure powders.

### *Structures of [Ni(xbsms)Ru(p-cymene)Cl]$BF_4$ and [("$C_3S_2$")Ru(p-cymene)Cl]$BF_4$*

The structure of the dinuclear cation **1**$^+$ in **1**$BF_4$ (Figure 4) is very similar to that of **2**,[17] with the *p*-cymene ligand replacing both the CO ligands and one chloride. Com-

 © 2007 Wiley-VCH Verlag GmbH & Co. KGaA, Weinheim 

plex $\mathbf{1}^+$ is furthermore structurally related to $[Ni(S_2N_2)Ru(arene)Cl]^+$ {arene = *p*-cymene or $C_6Me_6$; $S_2N_2^{2-}$ = $[S(CH_2)_2NMe(CH_2)]_2^{2-}$}, which was recently described by Rauchfuss et al.[21] The nickel atom is in a square-planar environment formed by the four sulfur atoms and the sulfur atoms of the thiolate groups are involved in two bridges with the ruthenium atom. Due to steric interactions with the axial methyl groups of the {Ni(xbsms)} fragment, the ruthenium moiety is located *trans* to the axial methyl groups and therefore *cis* to the aromatic cycle of the xbsms ligand.[22] A chloride ligand bound to ruthenium is directed towards, but does not interact with, the nickel atom [$d$(Cl···Ni) = 3.20 Å]. The ruthenium is in an octahedral environment and the nickel–ruthenium distance (3.29 Å) is longer than that in complex **2**, although both Ni–S [2.1692(15) and 2.1858(14) Å] and Ru–S [2.4020(14) and 2.4210(14) Å] bonds are only 0.02 Å shorter. This could be the consequence of a less-pronounced bending of the $Ni(\mu\text{-}S)_2Ru$ core (hinge angle 129.8° as compared to 124.1° in **2**). Significant distortion in the equatorial plane of the ruthenium octahedra arises from the acute S1–Ru–S4 angle [71.10(5)°] due to bridging constraints.

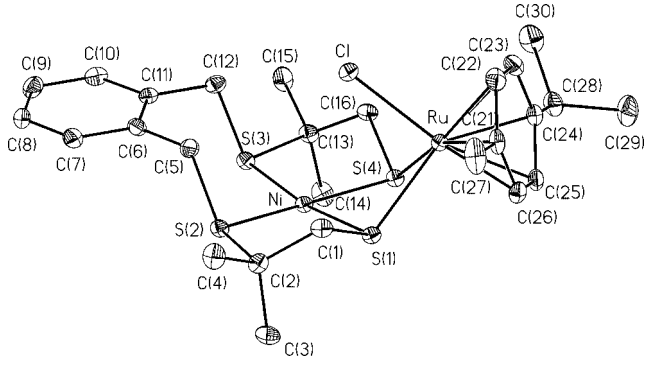


Figure 4. Structure of the cation $\mathbf{1}^+$ in $\mathbf{1}BF_4$ (30% probability thermal ellipsoids).

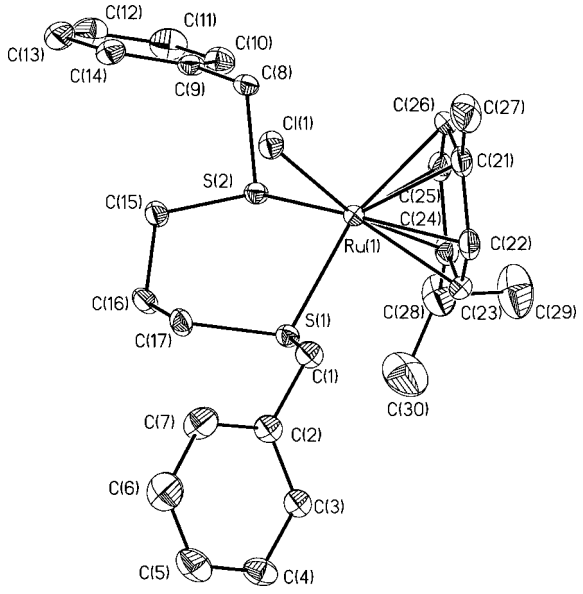


Figure 5. Structure of the cation $\mathbf{6}^+$ in $\mathbf{6}Cl{\cdot}2CH_2Cl_2$ (30% probability thermal ellipsoids).

The structure of complex $\mathbf{6}^+$ is shown in Figure 5. The ruthenium atom is in a pseudo-octahedral environment formed by the aromatic ligand, two thioether groups, and a chloride anion. The sulfur–ruthenium bonds [2.3737(11) and 2.3825(10) Å] are only slightly shorter than the ruthenium-thiolate bonds in $\mathbf{1}^+$, which means that $\mathbf{6}^+$ can thus be considered as a good comparative model for the ruthenium coordination sphere in $\mathbf{1}^+$.

## Spectroscopic Characterization

### *Infrared Spectroscopy*

The infrared spectra of **2**, $\mathbf{4}^{2-}$, and **5**, which have the same ruthenium moiety, display two $\nu_{CO}$ bands of equal intensity, in agreement with a *cis* arrangement of the carbonyl ligands at the ruthenium center ($A_1$ and $B_1$ stretching modes in $C_{2v}$ symmetry). Extraction of the force constants $k_{CO}$ (Figure 14) was done using the secular equations in the $C_{2v}$ symmetry group.[23] As the C≡O force constant is directly related to the intensity of the metal-to-ligand π-backbonding, we were able to order all three compounds with regard to the electron richness of the ruthenium center and thus the electronic properties of their ligands. As expected, the dithioether ligand in complex **5** is less electron-donating than [Ni(xbsms)], which coordinates to ruthenium through its thiolate groups in complex **2**. $[Ni(emi)]^{2-}$ is the most electron-donating ligand in this series, probably due to its negative charge.

### *NMR Spectroscopy*

The $^1H$ and $^{13}C$ NMR spectra of $\mathbf{1}^+$ indicate a $C_s$ symmetry with heterotopic faces for the xbsms ligand. As 2D NMR correlation experiments correlate with crystallographic distances, the solid-state molecular structure is probably retained in solution, as previously reported for **2**.[17] The observation of two doublets ($^3J$ = 5.7 and 6 Hz) for the aromatic protons of the *p*-cymene moiety in $\mathbf{1}^+$ and $\mathbf{3}^-$ indicates a free rotation around the ruthenium-arene bond. The $^1H$ NMR spectra of $(NEt_4)\mathbf{3}$ and $(NEt_4)_2\mathbf{4}$ display two singlets for the methyl and methylene groups of the $emi^{2-}$ ligand, with chemical shifts different from the corresponding ones in the parent $[Ni(emi)]^{2-}$ complex. This suggests a symmetrical coupling of the nickel and ruthenium moieties. One singlet is masked by the signals of the $Et_4N^+$ cation but is clearly seen in the 2D $^1H$-$^{13}C$ spectra. Integration measurements are nevertheless in good agreement with the proposed charges of the complexes. A comparison of the chemical shifts for the aromatic protons in the organometallic moieties of $\mathbf{1}^+$, $\mathbf{3}^-$, and $\mathbf{6}^+$ establishes the same order as established above for the different ligands of ruthenium regarding their electron-donating properties.

### *Electrochemistry*

The cyclic voltammograms recorded at a scan rate of 100 mV s$^{-1}$ for complexes **5** and $\mathbf{6}^+$ in dimethylformamide

 © 2007 Wiley-VCH Verlag GmbH & Co. KGaA, Weinheim 

display one irreversible reduction wave at –1.29 V and –0.97 V vs. Ag/AgCl, respectively (see Supporting Information). Coulometry during bulk electrolysis experiments revealed that these waves represent a one-electron process and can thus be assigned to the reduction of $Ru^{II}$ to $Ru^{I}$. Complex **5** is more difficult to reduce than $\mathbf{6}^{+}$ and thus the metal in the $\{Ru(CO)_2Cl_2\}$ moiety is more electron-rich than in $\{Ru(p\text{-cymene})Cl\}^{+}$.

The cyclic voltammogram of **1**Cl (Figure 6, trace a) in dimethylformamide shows a reversible electron-transfer process at +0.60 V vs. Ag/AgCl. This process has not yet been definitely assigned but we have evidence that the oxidation concerns the whole $\{Ni(\mu\text{-}S)_2Ru\}$ moiety. In addition, as in $[Ru(p\text{-cymene})Cl_2]_2$, the ruthenium center in **1**Cl displays a chemically irreversible one-electron reduction peak at –0.82 V with the corresponding anodic peak at –0.15 V. These features are consistent with an ECE mechanism (E = electron-transfer step; C = chemical step) involving the irreversible loss of a chloride ligand to yield a coordinatively unsaturated $Ru^{I}$ species. Such a mechanism, although bielectronic, has previously been observed for *trans*(Cl)-$[Ru(bipy)(CO)_2Cl_2]$.[24] Furthermore, an irreversible one-electron process is observed at –1.42 V. This can be tentatively assigned to a nickel-centered reduction by comparison with the cyclic voltammogram of [Ni(xbsms)], which shows an irreversible cathodic peak at –1.45 V vs. Ag/AgCl in dimethylformamide (see trace a in Figure 9).

The cyclic voltammograms of $(NEt_4)$**3** (Figure 7, trace a) and $(NEt_4)_2$**4** (Figure 8, trace a) display a reversible wave at 0.24 V and 0.39 V vs. Ag/AgCl, respectively. The cyclic

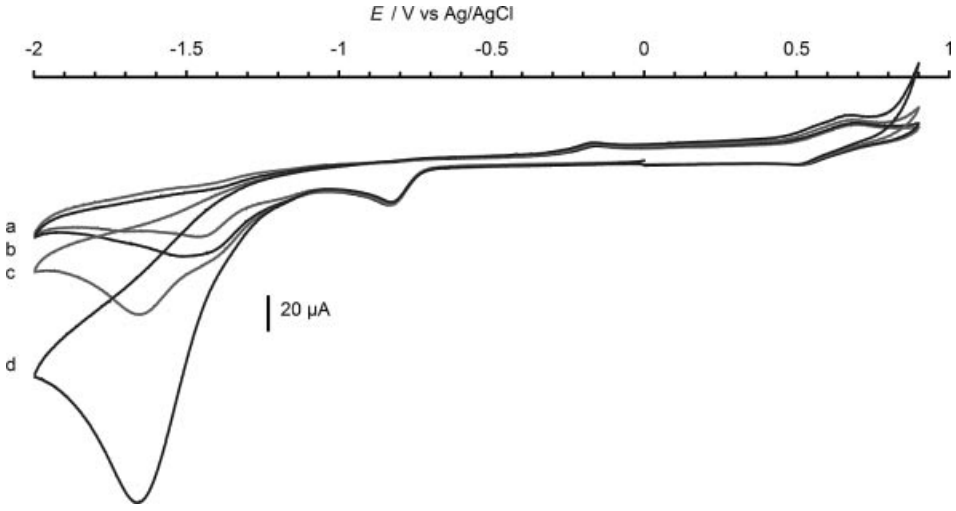


Figure 6. Cyclic voltammograms of **1**Cl (1.0 mM) in the presence of various amounts of $Et_3NHCl$ recorded in a dimethylformamide solution of $n Bu_4NBF_4$ (0.1 M) on a glassy carbon electrode at 100 mV $s^{-1}$: a) 0 equiv.; b) 1.5 equiv.; c) 3.0 equiv.; d) 10 equiv.

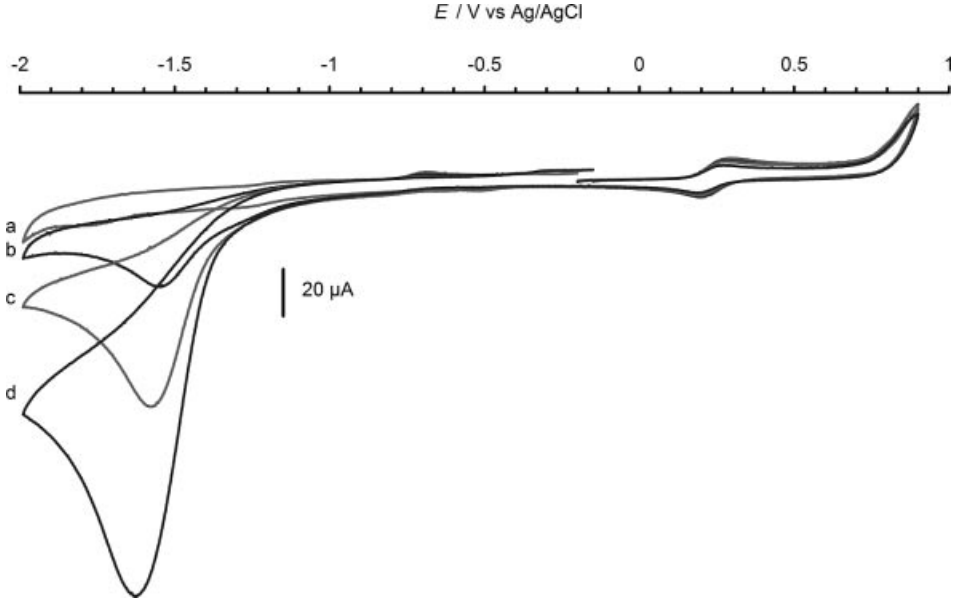


Figure 7. Cyclic voltammograms of $(NEt_4)$**3** (1.0 mM) in the presence of various amounts of $Et_3NHCl$ recorded in a dimethylformamide solution of $n Bu_4NBF_4$ (0.1 M) on a glassy carbon electrode at 100 mV $s^{-1}$: a) 0 equiv.; b) 1.5 equiv.; c) 3.0 equiv.; d) 10 equiv.

 © 2007 Wiley-VCH Verlag GmbH & Co. KGaA, Weinheim 

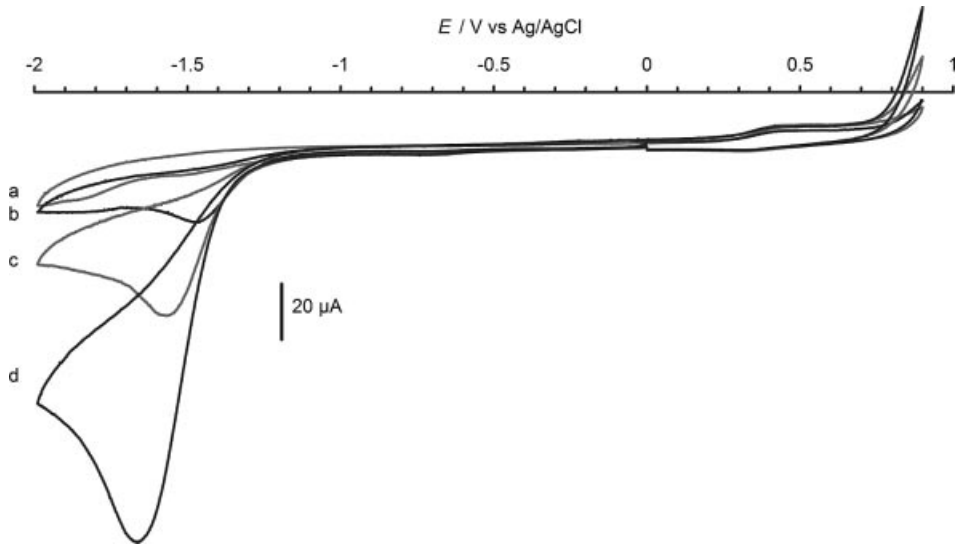


Figure 8. Cyclic voltammograms of $(NEt_4)_2$**4** (1.0 mM) in the presence of various amounts of $Et_3NHCl$ recorded in a dimethylformamide solution of $nBu_4NBF_4$ (0.1 M) on a glassy carbon electrode at 100 mV $s^{-1}$: a) 0 equiv.; b) 1.5 equiv.; c) 3.0 equiv.; d) 10 equiv.

voltammogram of $(NEt_4)$**3** exhibits two cathodic irreversible and flattened waves at –1.30 and –1.85 V vs. Ag/AgCl, which were shown to be monoelectronic by coulometric experiments. An irreversible anodic peak is seen at –0.66 V vs. Ag/AgCl on the reverse scan. As for **1**Cl, an ECE mechanism involving loss of a chloride ligand from the ruthenium center can be proposed. $(NEt_4)_2$**4** is also monoelectronically and irreversibly reduced at –1.54 V vs. Ag/AgCl, although no anodic peak can be observed in the reverse scan.

## Proton Reduction Electrocatalysis

### *Cyclic Voltammetry*

Addition of increasing amounts of $Et_3NHCl$ to dimethylformamide solutions of **1**Cl (Figure 6), $(NEt_4)$**3** (Figure 7), or $(NEt_4)_2$**4** (Figure 8) leads to the appearance of an electrocatalytic wave corresponding to hydrogen evolution, which increases in height and shifts to lower potentials. The peak potentials of the electrocatalytic waves as a function of the number of equivalents of acid added, which range from –1.46 to –1.57 V vs. Ag/AgCl, are listed in Table 1. The appearance of this electrocatalytic wave is the only observed modification of the cyclic voltammogram upon addition of acid, which suggests that these complexes are not prone to protonation in the $Ni^{II}$-$Ru^{II}$ state. In the cases of **1**Cl and $(NEt_4)$**3**, the electrocatalytic wave is a new cathodic process that occurs after an irreversible reduction step. A similar behavior has already been observed for **2**.[17] As far as $(NEt_4)_2$**4** is concerned, the electrocatalytic wave develops on the irreversible cathodic process observed at –1.54 V vs. Ag/AgCl in the absence of acid.

The nickel precursor [Ni(xbsms)] also catalyzes the hydrogen evolution reaction from $Et_3NHCl$ at –1.45 V vs. Ag/AgCl in dimethylformamide (Figure 9). The electrocatalytic behavior in this case consists of the appearance of a new wave at –1.35 V vs. Ag/AgCl upon addition of one equivalent of $Et_3NH^+$. This wave increases in height and shifts to lower potential upon further addition of acid.

$(NEt_4)_2$[Ni(emi)] is not stable in the presence of $Et_3NHCl$ in dimethylformamide, as revealed by the formation of a black precipitate. We suspect that a disproportionation reaction takes place after protonation of $[Ni^{II}(emi)]^{2-}$ to produce a $Ni^{III}$ species together with elemental nickel. The resulting mixture catalyzes $Et_3NHCl$ electroreduction, poss-

Table 1. Electrocatalytic properties of **1**Cl, **2**, $(NEt_4)$**3**, $(NEt_4)_2$**4**, [Ni(xbsms)], and $(NEt_4)_2$[Ni(emi)]. Electrocatalytic peak potentials ($E_{her}$, V) were determined by cyclic voltammetry at 100 m V $s^{-1}$ in a dimethylformamide solution of $nBu_4NBF_4$ (0.1 M) on a glassy carbon electrode. TOF and total TON were determined by bulk electrolysis experiments at –1.60 V of a dimethylformamide solution (6 mL) of $nBu_4NBF_4$ (0.1 M) and $Et_3NHCl$ (0.5 mmol) at a mercury pool (1.23 $cm^2$) in the presence of millimolar concentrations of catalyst. All potentials are quoted with respect to Ag/AgCl.

| | **1**Cl | **2** | $(Et_4N)$**3** | $(Et_4N)_2$**4** | [Ni(xbsms)] | $(Et_4N)_2$[Ni(emi)] |
|---|---|---|---|---|---|---|
| $E_{her}$ with 1.5 equiv. of $Et_3NHCl$ | –1.57 | –1.59 | –1.55 | –1.46 | –1.45 | – |
| $E_{her}$ with 3 equiv. of $Et_3NHCl$ | –1.65 | –1.66 | –1.60 | –1.57 | –1.46 | – |
| $E_{her}$ with 10 equiv. of $Et_3NHCl$ | –1.66 | –1.78 | –1.64 | –1.67 | –1.52 | – |
| Total TON after 4.5 h | 28.9 | 12.4 | 26.5 | 6.8 | 6.4 | 5.5 |
| TOF [$h^{-1}$] | 6.4 | 2.75 | 5.9 | 1.5 | 1.4 | 1.2 |
| TON during the first hour of electrolysis (= TOF) | 5.4 | 3.5 | 7.75 | 2.3 | 2 | 1.2 |

 © 2007 Wiley-VCH Verlag GmbH & Co. KGaA, Weinheim 

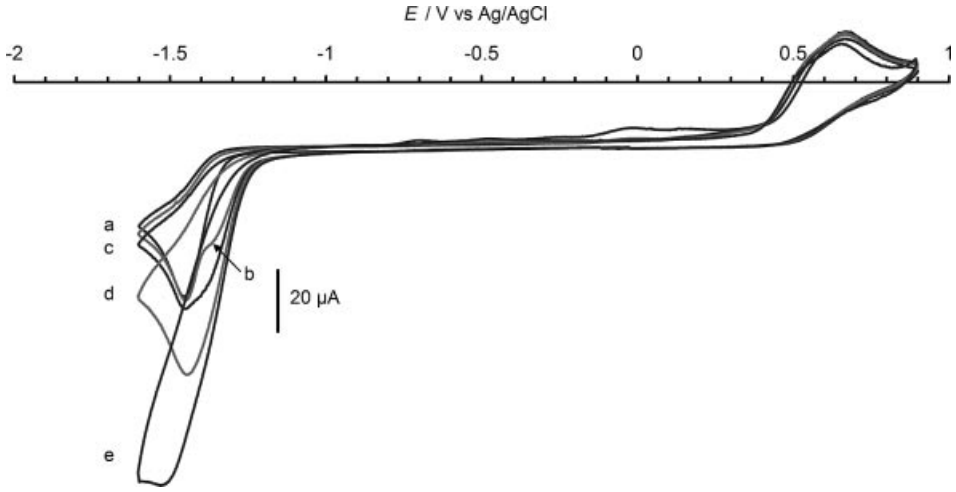


Figure 9. Cyclic voltammograms of [Ni(xbsms)] (1.0 mM) in the presence of various amounts of $Et_3NHCl$ recorded in a dimethylformamide solution of $nBu_4NBF_4$ (0.1 M) on a glassy carbon electrode at 100 mV $s^{-1}$: a) 0 equiv.; b) 1.0 equiv.; c) 1.5 equiv.; d) 3.0 equiv.; e) 10 equiv.

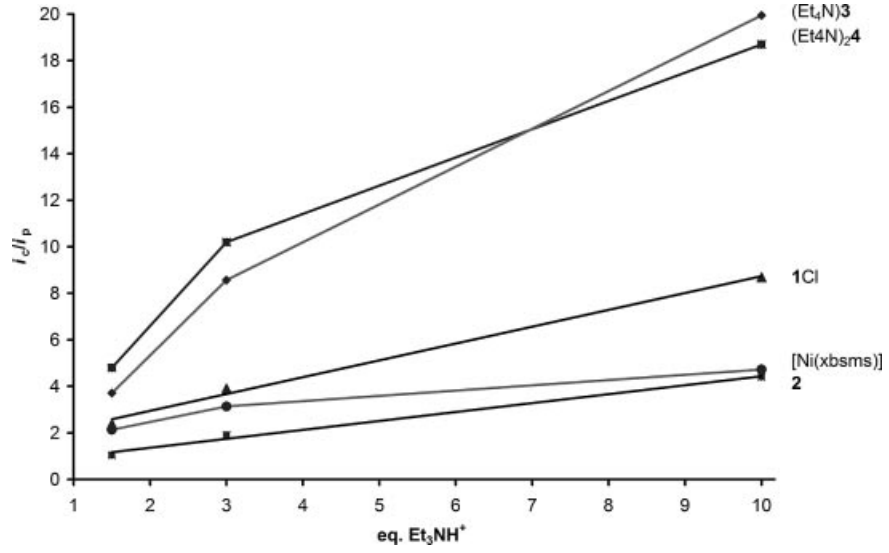


Figure 10. Evolution of the $i_c/i_p$ ratio between the catalytic peak current and the current of a monoelectronic wave as a function of the number of equivalents of acid added for **1**Cl, **2**, $(NEt_4)$**3**, $(NEt_4)_2$**4**, and [Ni(xbsms)].

ibly due to heterogeneous catalysis by elemental nickel, as shown by the appearance of an electrocatalytic wave with peak maxima below –1.7 V vs. Ag/AgCl in the cyclic voltammograms (see Supporting Information).

In contrast, the mononuclear ruthenium complex **6**Cl does not exhibit electrocatalytic activities. As far as complex **5** is concerned, some electrocatalytical activity is observed at potentials below –1.8 V vs. Ag/AgCl. Thus, for millimolar solutions of **5** in the presence of 10 equivalents of $Et_3NHCl$, the reduction current between –1.8 and –2.0 V vs. Ag/AgCl is higher than that observed by direct reduction at the electrode in the absence of catalyst (see Supporting Information).

Figure 10 shows the evolution of the $i_c/i_p$ ratio, where $i_c$ is the catalytic peak current and $i_p$ the peak current of a monoelectronic wave, as a function of the number of equivalents of acid added. It is clear that the {Ni(emi)}-based catalysts have much higher catalytic peak intensities than the {Ni(xbsms)}-based catalysts. This reveals that the {Ni(emi)} moiety enhances the catalytic rate. It also appears that the evolution of the catalytic peak current for **1**Cl and **2** is proportional to the number of equivalents of added acid, which could indicate that the rate-determining step is a protonation.

### *Modeling Cyclic Voltammograms*

In order to characterize the mechanisms for hydrogen production, we modeled the cyclic voltammograms for the electroreduction of $Et_3NH^+$ catalyzed by **2** and $(NEt_4)_2$**4** in dimethylformamide using the DigiElch software.[25–30] Proton reduction yields dihydrogen following two general pathways depending on whether the H–H bond is formed in a homolytic or a heterolytic step.[31] The general mechanistic schemes are given in Scheme 1. Both pathways include pro-

 © 2007 Wiley-VCH Verlag GmbH & Co. KGaA, Weinheim 

tonation of the metal center to give a metal hydride complex. In the homolytic mechanism, $H_2$ evolution results from a reductive elimination reaction from two metal hydride moieties, whereas in the heterolytic pathway the metal hydride species is subjected to proton attack, which results in hydrogen production. We were unable to model the experimental cyclic voltammograms, namely to reproduce high $i_c/i_p$ ratios, using the homolytic hydrogen formation mechanism. This could be due to the fact that the rate of a step which is second-order with regard to the catalyst is necessarily slow and thus makes the homolytic pathway less kinetically favorable than the heterolytic one. In the following we will therefore only consider the heterolytic pathway.

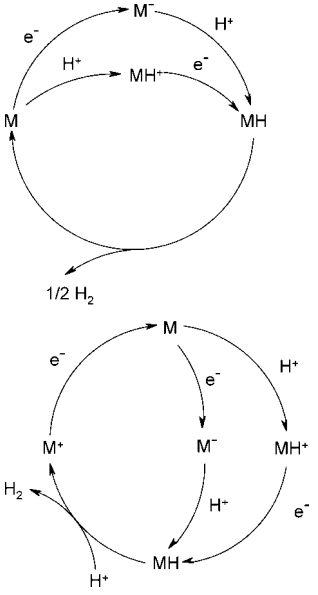


Scheme 1. Homolytic (top) and heterolytic (bottom) pathways for proton reduction catalyzed by a coordination compound.

The relative order of the two one-electron transfer and two protonation steps in the mechanism can be immediately determined by a simple examination of the voltammograms. In the cases of **1**Cl, **2**, and $(NEt_4)$**3**, the electrocatalytic wave develops at potentials more negative than the reduction potential of the catalyst; this implies that the hydride moiety formed by protonation after reduction of the catalyst needs to be activated by further reduction. The ECEC mechanism used for simulation of the electrocatalytic behavior of **2** is shown in Scheme 2. By contrast, the development of an electrocatalytic wave on a reduction wave of the catalyst, as

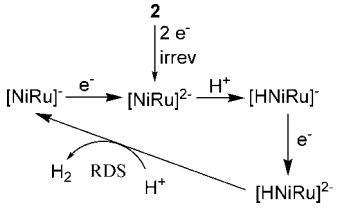


Scheme 2. Catalytic ECEC mechanism used for modeling the electrocatalytic behavior of **2** (RDS indicates the rate-determining step).

in the case of $(NEt_4)_2$**4**, suggests that the two one-reduction steps occur before the two protonation steps. Scheme 3 shows the suggested ECCE mechanism for this complex.

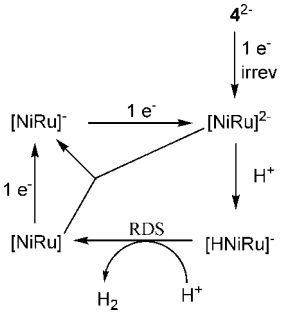


Scheme 3. Catalytic ECCE mechanism used for modeling the electrocatalytic behavior of $(NEt_4)_2$**4** (RDS indicates the rate-determining step).

The charge-transfer parameters ($E^0$, $a$, $k_s$) and diffusion coefficients describing the redox properties of the catalysts were determined from voltammograms obtained in the absence of acid and then used as such for simulation in the presence of acid. Heterogeneous charge-transfer processes are relatively slow, with rate constants $k_s$ ranging from $10^{-3}$ to $10^{-2}$ cm s$^{-1}$. Total and fast chemical reactions were introduced into the model to account for the irreversibility of the electrochemical processes.

By including the catalytic steps shown in Schemes 2 and 3 we succeeded in modeling the experimental cyclic voltammograms (Figures 11 and 12) and were able to reproduce the experimental data recorded at variable scan rates in the presence of a 1/1.5-, 3-, and 10-fold molar excess of $Et_3NHCl$ with one set of thermodynamic and kinetic constants for each compound. We chose the height, position, and shape of the catalytic wave as relevant criteria for the evaluation of the simulations. As can be seen in Figures 11 and 12, the major difference between simulated and experimental values concerns the reverse scan. In the case of $(NEt_4)_2$**4**, a disproportionation reaction was introduced to better reproduce the reverse scan of the electrocatalytic wave. Its equilibrium constant was calculated from the standard potentials of the corresponding redox couples and the scan rate was set as being diffusion-controlled.

The second protonation step was found to be the rate-determining step in both cases since the value of its rate constant [$10^3$ mol$^{-1}$ L s$^{-1}$ for **2** and $10^4$ mol$^{-1}$ L s$^{-1}$ for $(NEt_4)_2$**4**] determines the height of the electrocatalytic wave.

### *Bulk Electrolysis Experiments*

As for **2**, hydrogen evolution was detected and quantified by gas chromatography and volumetry during bulk electrolysis experiments of $Et_3NHCl$ on a mercury pool at –1.60 V vs. Ag/AgCl in dimethylformamide with **1**Cl, $(NEt_4)$**3**, $(NEt_4)_2$**4**, and [Ni(xbsms)] as electrocatalysts. As an example, Figure 13 shows the evolution of the charge passed during the bulk electrolysis of 0.5 mmol of $Et_3NHCl$ in the presence of 5 μmol of **1**Cl. The correlation between the charge and volume of evolved hydrogen is shown in the

 © 2007 Wiley-VCH Verlag GmbH & Co. KGaA, Weinheim 

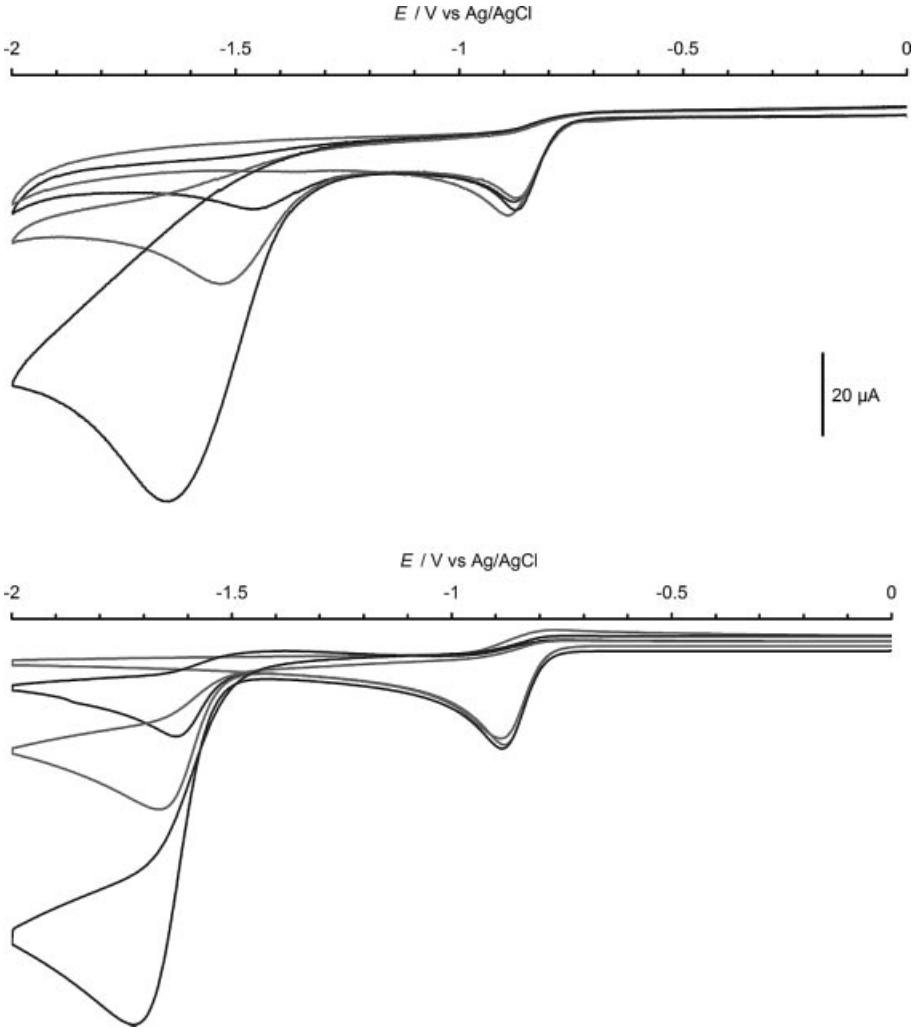


Figure 11. Experimental (top) and simulated (bottom) cyclic voltammograms of **2** (1.0 mM) recorded in a dimethylformamide solution of $n$Bu$_4$NBF$_4$ (0.1 mM) at a glassy carbon electrode in the presence of Et$_3$NHCl (1.0, 3.0, and 10 equiv.). Scan rate: 100 mV s$^{-1}$.

inset. The faradaic yield reaches 98%. Et$_3$NHCl is quantitatively converted to $H_2$ (50 turnovers) in 4 h [maximum turnover frequency ($TOF_{max}$) of 22 h$^{-1}$]. Addition of a further 0.5 mmol of Et$_3$NHCl allowed a second electrolytic run, with comparable yield and slightly lower rate, thereby indicating the chemical stability of the catalyst.

Table 1 summarizes the catalytic parameters of the various compounds, including complex **2**, determined under the same conditions and in the same electrolysis cell with a mercury pool of smaller but reproducible area. All of the dinuclear complexes catalyze Et$_3$NHCl reduction faster than their corresponding nickel precursor and all except (NEt$_4$)$_2$**4** are more active than [Ni(xbsms)]. The {Ru(*p*-cymene)Cl}$^+$ derivatives **1**Cl and (NEt$_4$)**3** are clearly the most efficient catalysts during bulk electrolysis experiments. Complexes **5** and **6**Cl are totally inactive under these conditions at –1.6 V vs. Ag/AgCl.

Finally, in order to compare the catalysts in terms of their chemical stability during cycling, we recorded cyclic voltammograms and/or steady-state rotating-disk-electrode voltammograms for the oxidative process before and after catalysis. Whereas the anodic wave disappears completely after 15 turnovers for catalysts **1**Cl and **2**, complexes (NEt$_4$)**3** and (NEt$_4$)$_2$**4** are quite stable under the catalytic conditions since the oxidative process appears quite unaffected after 29 and 27 turnovers, respectively (see Supporting Information).

## Discussion

The rational synthesis of heterodinuclear complexes that model the active sites of [NiFe] hydrogenases is a promising but challenging approach to the design of new catalysts for $H_2$ production or activation.[31] As far as nickel thiolate complexes are concerned, the main difficulty resides in the control of the nuclearity of the synthetic compound. The use of chelating ligands serves to avoid the formation of homometallic nickel clusters and a careful design of the precursor for the second metal site is required to avoid the formation of heterometallic oligomers. In particular, this implies that only a few labile ligands can be present on this

 © 2007 Wiley-VCH Verlag GmbH & Co. KGaA, Weinheim 

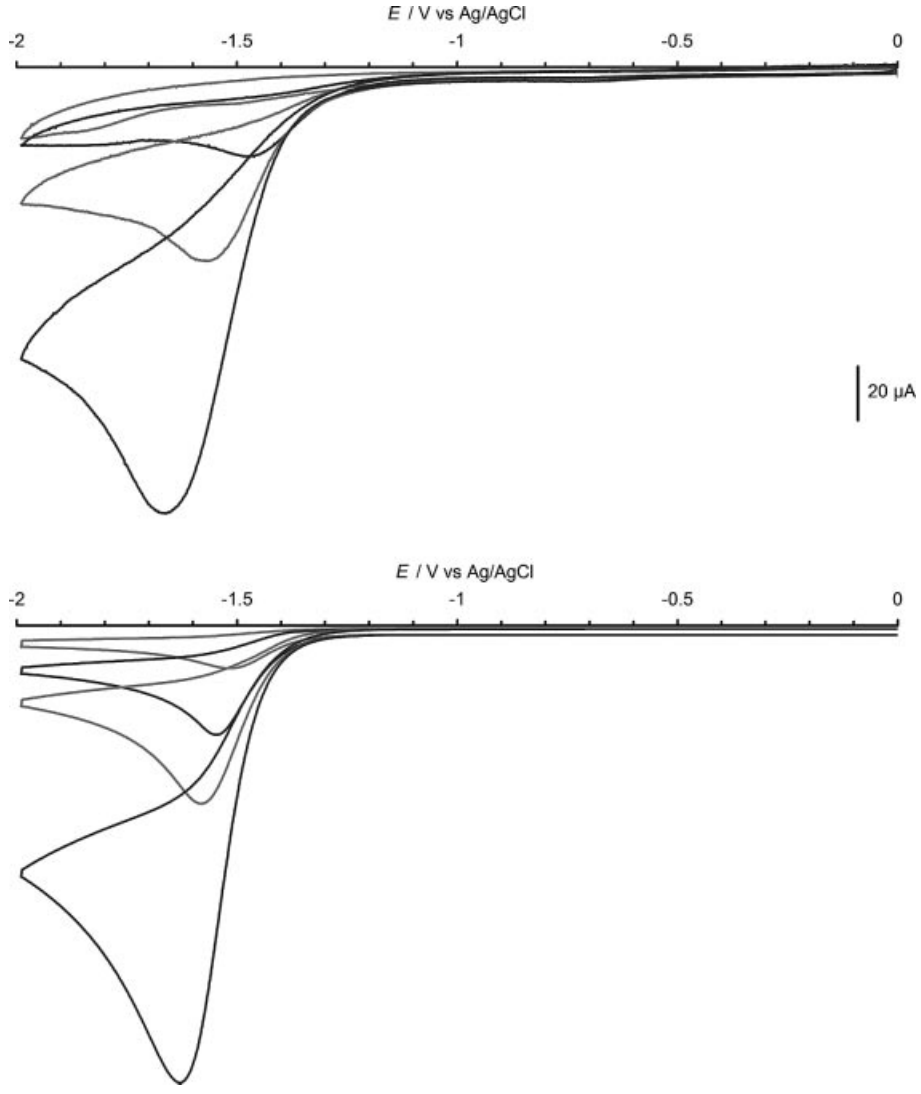


Figure 12. Experimental (top) and simulated (bottom) cyclic voltammograms of $(NEt_4)_2$**4** (1.0 mM) recorded in a dimethylformamide solution of $n$Bu$_4$NBF$_4$ (0.1 M) at a glassy carbon electrode in the presence of Et$_3$NHCl (1.5, 3.0, and 10 equiv.)). Scan rate: 100 mV s$^{-1}$.

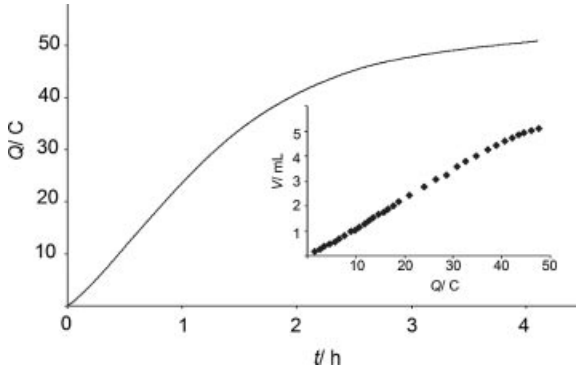


Figure 13. Coulometry for bulk electrolysis at –1.60 V vs. Ag/AgCl of a dimethylformamide solution (10 mL) of Et$_3$NHCl (0.05 M) and $n$Bu$_4$NBF$_4$ (0.1 M) at a mercury pool (approx. 3 cm$^2$) in the presence of **1**Cl (0.5 mM). The volume of hydrogen evolved as a function of charge is represented in the inset.

precursor. However, as a consequence, most of the reported models display a coordinatively saturated coordination sphere around the iron center with consequent low reactivity. Exceptions for nickel-iron assemblies are found for [Ni(xbsms)Fe(CO)$_2$I$_2$],[13] which contains labile iodide ligands, and [Ni(S{(CH$_2$)$_2$NMe(CH$_2$)$_2$S}$_2$)FeCp]$^+$,[32] which displays a vacant coordination site at the iron center. Unfortunately, no reactivity study regarding proton reduction or hydrogen oxidation has been reported either for these two complexes or for the other dinuclear nickel-iron complexes described to date. This may be due to some inherent instability of these complexes upon redox switching during catalysis. We thus decided to substitute iron for the heavier metal ruthenium with the aim of isolating species stable enough for the observation of electrochemical catalysis of hydrogen production. This approach initially allowed the preparation of **2** and we report here the synthesis and characterization of three novel nickel-ruthenium heterodinu-

 © 2007 Wiley-VCH Verlag GmbH & Co. KGaA, Weinheim 

clear complexes carrying labile chloride ligands at the ruthenium metal center. In each case, the desired complex is the sole product of the reaction and separation from the salts is the sole purification step required. All four complexes contain the $\{Ni(\mu\text{-}SR)_2Ru\}$ fragment with bidentate coordination of the nickel complex to the ruthenium center. The hinge angles in **2** and $\mathbf{1}^+$ are in the range usually found in naturally occurring hydrogenases,[32] and the nickel–ruthenium distances are similar to the longer Ni–Fe distances observed in enzymes by X-ray crystallography: most of the nickel–iron distances determined for hydrogenases lie between 2.53 and 2.97 Å, which indicates some direct electronic interaction between the two metal centers, although, as an exception, a Ni–Fe distance of 3.23 Å was observed for the [NiFe] hydrogenase from *Desulfovibrio desulfuricans*.[33] However, computational modeling predicts large variations of this bond length in the active site depending on the redox state of the enzyme.[34]

### *Activation Potential*

All three new nickel-ruthenium compounds synthesized exhibit electrocatalytic activity for hydrogen production with overvoltages (also called activation potential: the difference between the electrocatalytic potential and the equilibrium potential of the $H^+/H_2$ couple under the same conditions) of 0.8–1.0 V, as estimated from the tabulated value of –1.31 V vs. $Fc/Fc^+$ for the $Et_3NH^+/H_2$ couple in dimethylformamide.[35] There is no net benefit in substituting either arene for CO ligands on ruthenium or $emi^{2-}$ for $xbsms^{2-}$ around the nickel ion as regards overvoltage.

For comparison, a variety of square-planar nickel complexes are known to catalyze proton electroreduction, most of which have an $N_4$ coordination sphere with mixed amino, imino, or pyridine ligands assembled in a macrocycle.[36–39] Except for $[Ni(L_{N4})]^+$ $\{L_{N4}^- = 2,6\text{-}HN[(CH_2)_3N{=}C(CH_3)]_2\text{-}C_5H_3N^-\}$, which is active at –1.1 V vs. SCE in acidic (pH 2) aqueous solution,[38] all of these catalysts are active at –1.5 to –1.6 V vs. SCE towards relatively weak acids or in neutral aqueous solutions. Two functional bio-inspired catalysts, namely $[(bdt)\{Ni(PMe_3)\}_2Fe(CO)(bdt)_2]$,[15] which stoichiometrically reduces $HBF_4$ into $H_2$, and $[Ni(L)\text{-}Fe_2(CO)_6]$ $[L = (CH_3C_6H_3S_2)_2(CH_2)_3]$, which electrocatalyzes the reduction of $CF_3COOH$ into $H_2$ at –1.64 V vs. $Fc/Fc^+$ in $CH_2Cl_2$, were described recently.[16] All these complexes catalyze proton electroreduction with an activation potential of 0.8 to 1.2 V. Very recently, DuBois et al. have described a series of nickel bis(diphosphane) complexes that are very competitive, as regards electrocatalytic potential, as electrocatalysts for both proton reduction and hydrogen oxidation.[40,41] However, the unique catalytic properties of these new catalysts are due to the presence of pendant basic sites and are not directly related to the nature of the coordination sphere around nickel [amino residues located on the ligands play the role of proton relays and greatly enhance the activity relative to classical noncatalytic nickel bis(diphosphane) complexes].

### *Catalytic Rate and Stability*

As seen in Figure 10, both $(NEt_4)$**3** and $(NEt_4)_2$**4** show high catalytic peak current enhancement relative to **1**Cl and **2**. Even though no direct analytical relationship between the catalytic peak current measured by cyclic voltammetry and turnover frequency exists, a comparison of the cyclic voltammograms recorded under the same conditions shows that the catalytic rate is greatly enhanced by the introduction of the $emi^{2-}$ anion as a ligand in place of $xbsms^{2-}$.

The same considerations based on $i_c/i_p$ values lead to the conclusion that the presence of an arene ligand rather than carbonyl ligands on the ruthenium center improves the efficiency of the catalyst. This is further confirmed by bulk electrolysis experiments: thus, when substituting $\{(p\text{-cymene})RuCl\}^+$ for $\{Ru(CO)_2Cl_2\}$ the rate of hydrogen production in both the {Ni(emi)} and {Ni(xbsms)} series is improved (Table 1).

Catalysis always takes place on or after an irreversible wave so that the isolated and structurally characterized dinuclear species are likely to be pre-catalysts rather than active catalysts. The exact nature of the chemical reaction following reduction is unknown. Loss of chloride ligand from the ruthenium center is likely, although radical reactions involving hydrogen atoms in the β-position with regards to the nickel center, as identified in mononuclear nickel thiolate complexes,[42] cannot be ruled out. Furthermore, no evidence for any breakdown of the dinuclear species could be obtained, and we could demonstrate that $\mathbf{3}^-$ and $\mathbf{4}^{2-}$ do not decompose during catalysis.

### *Cooperativity Between Metal Centers*

The electrocatalytic properties of dinuclear complexes for hydrogen production clearly denote the existence of a cooperative effect between nickel and ruthenium. Thus, while $(NEt_4)_2$[Ni(emi)] and **5** or $\mathbf{6}^+$ display no or only weak catalytic activity (e.g. at potentials below –1.8 V vs. Ag/AgCl and with low turnover frequencies) the dinuclear catalysts $(NEt_4)$**3** and $(NEt_4)_2$**4** readily catalyze $Et_3NHCl$ reduction near –1.6 V vs. Ag/AgCl, and hydrogen evolution during bulk electrolysis experiments at –1.6 V vs. Ag/AgCl is five times faster in the presence of $(NEt_4)$**3** than in the presence of $(NEt_4)_2$[Ni(emi)]. As for the [Ni(xbsms)] derivatives, coupling with ruthenium moieties results in an enhancement of the rate of hydrogen evolution by a factor of two (complex **2**) or five (complex **1**Cl). However, this is at the expense of the electrocatalytic potential, which is about 200 mV more negative than the electrocatalytic potential of [Ni(xbsms)] under the same conditions. Such a cooperative effect has been suggested to account for the higher activity of $[Ni_2(bis\text{-}cyclam)]^{4+}$ compared to $[Ni(cyclam)]^{2+}$ for proton reduction[37] and for the high activity in photoelectrochemical production of hydrogen catalyzed by bis(metallocene)s such as [1.1]ferrocenophane.[43]

Figure 14 shows the inverse correlation between the electrocatalytic potential and the C≡O force constant as a probe of the electron density on the metal centers for the three CO-containing compounds in this study. The nickel-iron hydrogenase from *D. gigas* nicely fits in this correlation

 © 2007 Wiley-VCH Verlag GmbH & Co. KGaA, Weinheim 

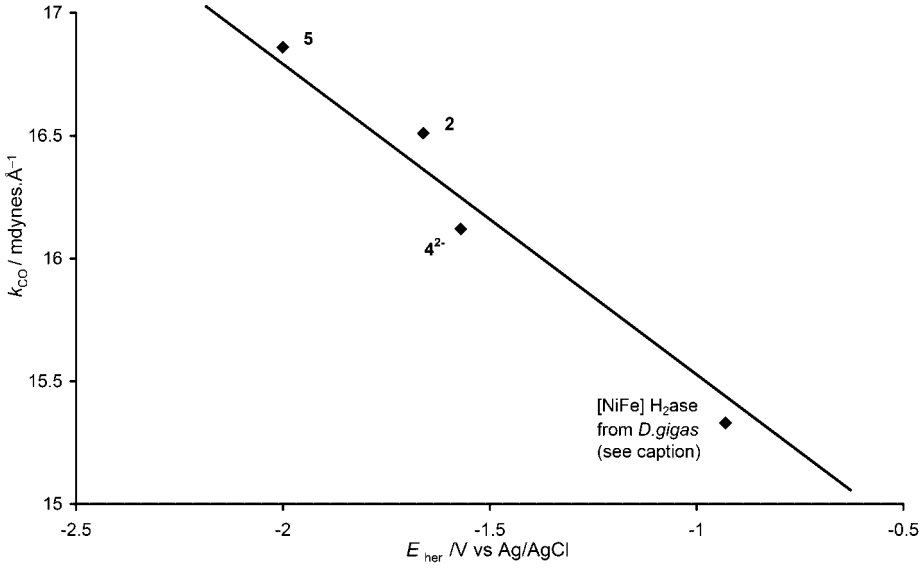


Figure 14. Correlation between the C≡O force constant ($k_{CO}$) and the electrocatalytic potential ($E_{her}$) for compounds **2**, $(NEt_4)_2$**4**, and **5**. Data have been extrapolated for [NiFe] hydrogenase from *D. gigas* in dimethylformamide solution using the measured $\nu_{CO}$ frequency for native enzyme in water and the experimental potential for reduction of $Et_3NHCl$ on a platinum electrode in dimethylformamide.[35]

when extrapolating the redox potential measured in water to dimethylformamide solution. We can conclude from this correlation that the more electron-rich the metal center the better the catalyst as far as overvoltage is concerned. This implies that the rate-determining step has a nucleophilic nature and may involve a protonation. This is further supported, in the case of **1**Cl and **2**, by the relative linearity of the $i_c/i_p$ ratio as a function of the number of equivalents of added acid and by modeling studies of the cyclic voltammograms of **2** and $(NEt_4)_2$**4**.

Modeling of the voltammograms was possible with classical catalytic mechanisms involving metal hydride species[44] resulting from the interaction of protons with the reduced dinuclear complexes. Two distinct mechanisms have been identified: $\mathbf{1}^+$, **2**, and $\mathbf{3}^-$ catalyze proton reduction by an ECEC mechanism similar to that (Scheme 3) proposed for proton electroreduction catalyzed by a rhodium porphyrin[45] and the $\{BF_2\}$-bridged cobaloxime $[Co(dmgBF_2)_2L_2]$ (L = $H_2O$, $CH_3CN$, dmf).[46] In contrast, $\mathbf{4}^{2-}$-catalyzed hydrogen evolution proceeds by an ECCE pathway similar to the catalytic mechanism for hydrogen evolution determined for iron porphyrin[47] or cobaloxime complexes.[48] The rate-determining step was found to be protonation of the hydride intermediate in both cases, as previously reported for iron porphyrin[47] or cobaloxime complexes.[48]

## Conclusions

We have synthesized a series of novel bio-inspired dinuclear nickel-ruthenium complexes that are efficient catalysts for proton reduction under quite neutral conditions in dimethylformamide and have found evidence for a cooperative effect between the metal centers which enhances the catalytic rate, whereas high electron density at the metal centers favors low overvoltages. The catalysts are more stable when no hydrogen atom is present in the β-position with regard to the nickel center. These general trends may help in the synthesis of new catalysts with a lower overvoltage and higher stability.

## Experimental Section

**Materials:** All reactions were carried out under argon using standard Schlenk techniques. Solvents were distilled under argon. NMR solvents were deoxygenated by three freeze-pump-thaw cycles and stored over molecular sieves. Commercial dimethylformamide and acetonitrile for electrochemistry were degassed by bubbling nitrogen through them. $(NEt_4)_2$[Ni(emi)],[19] [Ru(*p*-cymene)$Cl_2]_2$,[49,50] $[Ru(CO)_2Cl_2]_n$,[51,52] [Ni(xbsms)],[18] and 1,7-diphenyl-2,6-dithiaheptane ("$C_3S_2$")[20] were prepared according to reported procedures. The supporting electrolyte ($n$Bu$_4$N)$BF_4$ was prepared from ($n$Bu$_4$N)$HSO_4$ (Aldrich) and $NaBF_4$ (Aldrich) and dried overnight at 80 °C under vacuum. Triethylammonium chloride (Acros) was used as received.

**Methods and Instrumentation:** $^1$H NMR spectra were recorded at room temperature in 5-mm tubes with a Bruker AC300 spectrometer equipped with a QNP probehead. $^1$H NMR signals were assigned by NOE difference experiments performed using standard pulse sequences. IR spectra were recorded with a Bruker Vector 22 spectrophotometer (400–4000 cm$^{-1}$, Class 3A laser). The spectra were recorded in solution, using a KBr cell. UV/Vis spectra were recorded with a Carry Bio1 (Varian) spectrophotometer in quartz Schlenk cells. ESI mass spectra were recorded with a Finnigan LCQ thermoquest ion-trap. Elemental analyses were performed by the Service Central d'Analyse of the CNRS (Vernaison, France). All electrochemical measurements were carried out under nitrogen in a thermostatted cell at 20 °C. A standard three-electrode configuration was used consisting of a glassy carbon (3 mm in diameter) or platinum (2 mm in diameter) disk as the working electrode, an auxiliary platinum wire and an Ag/AgCl/aqueous $AgCl_{sat}$ + KCl

 © 2007 Wiley-VCH Verlag GmbH & Co. KGaA, Weinheim 

3 M (named Ag/AgCl through this text) reference electrode closed by a Vycor frit and dipped directly into the solution. In order to take into account the liquid junction potential between aqueous and non-aqueous solution, this electrode was calibrated with the internal reference system $Fc^+/Fc$, which was found at 0.46 V vs. Ag/AgCl in $CH_3CN$ (0.53 V in dimethylformamide). The $Fc^+/Fc$ couple ($E^0$ = 0.400 V vs. SHE)[53] can be used to quote potentials relative to an SHE, when needed.

Cyclic voltammograms were recorded with a EG&G PAR 273A instrument. Solution concentrations were approx. 1 mM for the catalyst and 0.1 M for the supporting electrolyte ($n$-$Bu_4N$)$BF_4$. Electrodes were polished with an MD-Nap polishing pad with 1-μm monocrystalline diamond DP suspension and DP lubricant blue (Struers). Additions of $Et_3NHCl$ were made by syringe as a 50 mM solution in dimethylformamide.

Bulk electrolysis experiments and coulometry were carried out on an EG&G PAR 273A instrument in dimethylformamide, using a mercury pool cathode. The platinum-grid + carbon-foam counter electrode was placed in a separate compartment connected by a glass-frit and filled with a 0.1 M solution of ($n$$Bu_4N$)$BF_4$ in degassed dimethylformamide. A made-to-measure electrolysis cell with a cylindrical reservoir was used. The mercury pool surface was therefore identical from one experiment to another. The mercury surface was measured as 1.23 $cm^2$. The electrolysis cell constant was determined to be $2.34 \times 10^{-4}$ $s^{-1}$ by performing bulk electrolysis of methylviologen hexafluorophosphate.[54]

The following procedure was followed for catalytic acid reduction bulk electrolysis: A degassed dimethylformamide solution (6–10 mL) containing 0.1 M ($n$$Bu_4N$)$BF_4$ was first electrolyzed at –1.60 V vs. Ag/AgCl until the current reached 1% of its initial value. The catalyst was then added and electrolysis was also performed at –1.60 V vs. Ag/AgCl until the current reached 1% of its initial value. $Et_3NHCl$ was then added and electrolysis was still performed at –1.60 V vs. Ag/AgCl. The faradaic yield was estimated from a periodic volumetric measurement of the amount of evolved gas. Hydrogen was tested for purity using a Delsi Nermag DN200 GC chromatograph equipped with a 3 m Porapack column and a thermal conductivity detector (TCD). Except when using $(Et_4N)_2$[Ni(emi)] as the catalyst, the electrolytic solutions remained clear after catalysis. We checked that neither the mercury pool nor the graphite electrode exhibit catalytic activity when washed after electrochemical experiments and replaced under the same conditions in the absence of catalyst. We can thus rule out the formation of any heterogeneous catalysis (coating or amalgam).

Cyclic voltammograms were simulated using the DigiElch software.[25–30] A first simulation and best-fitting was performed for **2** and $(NEt_4)_2$**4** in dimethylformamide in the absence of added acid. Parameters were refined until voltammograms recorded at 20, 50, and 100 mV $s^{-1}$ could be simulated using the same set of values. The resulting parameters were kept unchanged for simulation of voltammograms recorded in the presence of acid. The model was then modified to include the catalytic steps and the new parameters refined until one set of values provided correct simulation of the voltammograms recorded in the presence of various amounts of added acid (1, 1.5, 3, and 10 equiv.) at different scan rates (20, 50, and 100 mV $s^{-1}$).

**Crystal Structure Analysis:** Crystallographic data are summarized in Table 2. Data collection was performed at 298 K with a Bruker SMART diffractometer with a CCD area detector, with graphite-monochromated Mo-$K_\alpha$ radiation ($\lambda$ = 0.71073 Å). Empirical absorption correction (Sadabs) was performed. Molecular structures were solved by direct methods and refined on $F^2$ by full-matrix least-squares techniques with the SHELXTL package,[55] with anisotropic thermal parameters. All non-hydrogen atoms were refined anisotropically; hydrogen atoms were generally found and refined isotropically. The hydrogen atoms of the methyl and isopropyl groups of the $p$-cymene ligands and the solvent molecules were placed in ideal positions and refined as riding atoms with individual isotopic displacement parameters.

Table 2. Crystallographic data for **6**Cl·2$CHCl_3$ and **1**$BF_4$.

| | **6**Cl·2$CH_2Cl_2$ | **1**$BF_4$ |
|---|---|---|
| Formula | $C_{29}H_{38}Cl_6RuS_2$ | $C_{26}H_{38}BClF_4NiRuS_4$ |
| Molecular mass | 764.53 | 760.84 |
| Color | orange | red |
| Crystal size [$mm^3$] | $0.50 \times 0.20 \times 0.20$ | $0.30 \times 0.10 \times 0.05$ |
| Crystal system | triclinic | monoclinic |
| Space group | $P\bar{1}$ | $P2_1/n$ |
| $a$ [Å] | 13.900 (6) | 13.823(4) |
| $b$ [Å] | 14.225(6) | 11.843(3) |
| $c$ [Å] | 17.531(7) | 18.598(5) |
| $\alpha$ [°] | 96.280(8) | 90 |
| $\beta$ [°] | 92.949(7) | 97.029(6) |
| $\gamma$ [°] | 98.191(8) | 90 |
| $V$ [$Å^3$] | 3402(2) | 3021.7(14) |
| $Z$ | 4 | 4 |
| $\rho_{calcd}$ [mg $m^{-3}$] | 1.492 | 1.672 |
| $\mu$ [$cm^{-1}$] | 10.73 | 15.29 |
| Reflections measured | 21319 | 8075 |
| Unique reflections ($R_{int}$) | 15538 ($R$int = 0.0127) | 4189 ($R$int = 0.0251) |
| Refined parameters | 913 | 514 |
| Observed reflections [$I > 2\sigma(I)$] | 13084 | 3596 |
| $R$ indices (all data) | $R_1$[a] = 0.0581, $wR_2$[b] = 0.1001 | $R_1$ = 0. 0592, $wR_2$ = 0.1471 |
| Goodness of fit ($S$) | 1.12 | 1.03 |
| $\Delta\rho$ (max/min) [e $Å^{-3}$] | 1.081/–1.077 | 1.993/–1.711 |

[a] $R_1 = \Sigma||F_o| - |F_c||/\Sigma|F_o|$. [b] $wR_2 = \{\Sigma[w(F_o^2 - F_c^2)^2]/\Sigma[w(F_o^2)^2]\}^{1/2}$, $w = 1/[\sigma^2(F_o^2) + (aP)^2 + bP]$ where $P = [2F_c^2 + \max.(F_o^2, 0)]/3$ (see CIF file for values of $a$ and $b$).

 © 2007 Wiley-VCH Verlag GmbH & Co. KGaA, Weinheim 

Crystals of **1**$BF_4$ were grown from a filtered solution of equimolar amounts of **1**Cl and $AgBF_4$ in chloroform with added pentane at 4 °C. The asymmetric unit contains one $\mathbf{1}^+$ cation and one $BF_4^-$ anion disordered over two positions around the boron atom.

Crystals of **6**Cl·2$CH_2Cl_2$ suitable for X-ray diffraction were grown from a dichloromethane/pentane solution of **6**Cl at 4 °C. The asymmetric unit contains two $\mathbf{6}^+$ cations, two chloride anions, and four molecules of $CH_2Cl_2$, one of which is disordered over two positions.

CCDC-281929 (for **1**BF4) and -631503 (for **6**Cl·2$CHCl_3$) contain the supplementary crystallographic data for this paper. These data can be obtained free of charge from the Cambridge Crystallographic Data Center via ww.ccdc.cam.ac.uk/datarequest/cif.

**[Ni(xbsms)Ru(*p*-cymene)Cl]Cl (1Cl):** [Ru(*p*-cymene)$Cl_2$]$_2$ (101 mg, 0.160 mmol) and [Ni(xbsms)] (128 mg, 0.318 mmol) were dissolved in dichloromethane (5 mL). After 30 min stirring at room temperature, the mixture was evaporated to dryness. The product was passed through a silica gel column using an acetonitrile/methanol (10:1, v/v) mixture as eluent. The first fraction was dried under vacuum to yield pure **1**Cl·0.5$CH_2Cl_2$·2.5$H_2O$ as a red powder (158 mg, 74%). $^1$H NMR (300 MHz, $CD_3OD$): $\delta$ = 7.28 (s, 4 H, Ar), 5.73 (d, $J$ = 5.7 Hz, 2 H, Ru-Ar), 5.54 (d, $J$ = 5.7 Hz, 2 H, Ru-Ar), 5.33 (d, $J_{A,B}$ = 12 Hz, 2 H, ArC$H_{ax}$$H_{eq}$S), 3.87 (d, $J_{A,B}$ = 12 Hz, 2 H, ArC$H_{eq}$$H_{ax}$S), 3.02 [d, $J_{A,B}$ = 12 Hz, 2 H, $(CH_3)_2$CC$H_{eq}$$H_{ax}$], 2.51 [sept, $J$ = 6.9 Hz, 1 H, $(CH_3)_2$C$H$Ar], 2.50 [d, $J_{A,B}$ = 12 Hz, 2 H, $(CH_3)_2$CC$H_{eq}$$H_{ax}$], 2.12 (s, 3 H, Ru-ArC$H_3$), 1.72 (s, 6 H, $Me_{ax}$),1.45 (s, 6 H, $Me_{eq}$), 1.21 [d, $J$ = 6.9 Hz, 6 H, $(CH_3)_2$CHAr] ppm. ESI-MS: *m*/*z* (%) 675 (100) [M]. $C_{26.5}H_{44}Cl_3NiO_{2.5}RuS_4$ (797.02): calcd. C 39.93, H 5.56, Cl 13.83, Ni 7.36, Ru 12.68, S 16.09; found C 40.19, H 5.34, Cl 12.56, Ni 7.32, Ru 11.66, S 13.21. UV/Vis: $\lambda_{max}$ ($\varepsilon$) = 453 nm (706 $M^{-1}cm^{-1}$), 337.

**(NEt$_4$)[Ni(emi)Ru(*p*-cymene)Cl] [(NEt$_4$)3]:** [Ru(*p*-cymene)$Cl_2$]$_2$ (37.5 mg, 0.118 mmol) and $[NEt_4]_2$[Ni(emi)] (69 mg, 0.119 mmol) were dissolved in dichloromethane (5 mL). After 30 min stirring at room temperature, the mixture was evaporated to dryness. The product was extracted twice with tetrahydrofuran then pentane was added to the combined filtrates. Crystallization of this solution occurred at 4 °C. The resultant small red crystals were separated by filtration with a 71% yield (60 mg). $^1$H NMR (300 MHz, $CD_3OD$): $\delta$ = 5.49 (d, $J$ = 6 Hz, 2 H, Ru-Ar), 5.44 (d, $J$ = 6 Hz, 2 H, Ru-Ar), 3.35 [m, 8 H, N(C$H_2$$CH_3$)$_4^+$], 2.78 [sept, $J$ = 7.2 Hz, 1 H, $(CH_3)_2$C$H$Ar], 2.11 (s, 3 H, Ru-ArC$H_3$), 1.57 (s, 4 H, NC$H_2$), 1.3 [m, 24 H, $(CH_3)_2$CS and N($CH_2$C$H_3$)$_4^+$], 1.12 [d, $J$ = 7.2 Hz, 6 H, $(CH_3)_2$CHAr] ppm. $^{13}$C NMR (76 MHz, $CD_3OD$): $\delta$ = 85.98, 82.53 (Ar), 52.78, 52.74, 52.69 [N($CH_2$$CH_3$)$_4^+$], 32.16 or 30.57 [$(CH_3)_2$CS], 28.60 (N$CH_2$), 21.73 [$(CH_3)_2$CHAr], 17.56 [$(CH_3)_2$CHAr], 7.05 [N($CH_2$$CH_3$)$_4^+$] ppm. UV/Vis: $\lambda_{max}$ ($\varepsilon$) = 523 nm (198 $M^{-1}cm^{-1}$), 430 (263), 353, 240.

**(NEt$_4$)$_2$[Ni(emi)Ru(CO)$_2$Cl$_2$] [(NEt$_4$)$_2$4]:** [Ru(CO)$_2$Cl$_2$]$_n$ (12.4 mg, 0.054 mmol) and $[NEt_4]_2$[Ni(emi)] (30 mg, 0.052 mmol) were dissolved in dichloromethane (5 mL). After 5 min stirring at room temperature, the mixture was evaporated to dryness to give a red solid. $^1$H NMR (300 MHz, $CD_3OD$): $\delta$ = 3.47 [m, 16 H, N(C$H_2$$CH_3$)$_4^+$], 3.16 (s, 4 H, NC$H_2$), 1.62 [m, 12 H, $(CH_3)_2$CS], 1.38 [m, 24 H, N($CH_2$C$H_3$)$_4^+$] ppm. IR: ($CH_2Cl_2$): $\nu_{CO}$ = 2037 (s), 1958 (s) $cm^{-1}$. UV/Vis: $\lambda_{max}$ ($\varepsilon$) = 517 nm (185 $M^{-1}cm^{-1}$), 390–410.

**[("$C_3S_2$")Ru(CO)$_2$Cl$_2$] (5):** [Ru(CO)$_2$Cl$_2$]$_n$ (219 mg, 0.961 mmol) and 1,7-diphenyl-2,6-dithiaheptane ("$C_3S_2$"; 274 mg, 0.951 mmol) were dissolved in methanol (5 mL). After stirring for 1 h at room temperature, the mixture was filtered and the filtrate evaporated to dryness. The product was passed through a silica gel column using dichloromethane as eluent. The first pale-yellow fraction was dried under vacuum to yield [("$C_3S_2$")Ru(CO)$_2$Cl$_2$]·0.5$CH_2Cl_2$·0.9$CH_3CN$ as a red powder (132 mg, 26.7%). $^1$H NMR (300 MHz, $CDCl_3$): $\delta$ = 7.37 (m, 10 H, Ar), 4.23 (s, 4 H, PhC$H_2$S), 2.83 (m, 4 H, $CH_2$C$H_2$S), 2.13 (m, 2 H, C$H_2$$CH_2$S) ppm. $^{13}$C NMR (76 MHz, $CDCl_3$): $\delta$ = 191.93 (CO), 130.42, 130.00, 129.72, 129.54, 129.39 (Ar), 41.77 (Ph$CH_2$S), 28.49 ($CH_2$$CH_2$S), 24.19 ($CH_2$$CH_2$S) ppm. IR ($CH_2Cl_2$): $\nu_{CO}$ = 2074 (s), 2007 (s) $cm^{-1}$. $C_{21.3}H_{23.2}Cl_{2.5}N_{0.9}O_2RuS_2$ (577.66): calcd. C 44.28, H 4.04, Cl 15.34, Ru 17.49, S 11.10; found C 43.83, H 4.13, Cl 13.77, Ru 17.66, S 11.44. UV/Vis: $\lambda_{max}$ ($\varepsilon$) = 381 nm (295 $M^{-1}cm^{-1}$).

**[("$C_3S_2$")Ru(*p*-cymene)Cl]Cl (6Cl):** [Ru(*p*-cymene)$Cl_2$]$_2$ (166 mg, 0.524 mmol) and "$C_3S_2$" (151 mg, 0.524 mmol) were dissolved in dichloromethane (5 mL). After 30 min stirring at room temperature, the mixture was evaporated to dryness. The product was then passed through a silica gel column using methanol as eluent. The first red fraction was dried under vacuum to yield [("$C_3S_2$")Ru(*p*-cymene)Cl]Cl·2$CH_2Cl_2$ (187 mg, 48%) as a red powder. $^1$H NMR (300 MHz, $CD_3OD$): $\delta$ = 7.47 (m, 10 H, Ar), 5.87 (d, $J$ = 6 Hz, 2 H, Ru-Ar), 5.71 (d, $J$ = 6 Hz, 2 H, Ru-Ar), 4.32 (dd, $J_{A,B}$ = 12.9 Hz, $\nu_A$ = 5.36, $\nu_B$ = 5.29, 4 H, PhC$H_2$S), 2.8 (m, 4 H, SC$H_2$$CH_2$), 2.77 [sept, 1 H, $(CH_3)_2$C$H$Ar], 2.32 (m, 2 H, $SCH_2$C$H_2$), 2.26 (s, 3 H, Ru-Ar$CH_3$), 1.35 [d, $J$ = 7.2 Hz, 6 H, $(CH_3)_2$CHAr] ppm. $^{13}$C NMR (76 MHz, $CD_3OD$): $\delta$ = 134.77, 130.64, 129.72, 129.43, 129.20 (Ar), 88.29, 87.86 (Ru-Ar), 47–50 ($PhCH_2$S), 31.55, 30.39, 30.24, 29.70 [$(CH_3)_2$CHAr, S$CH_2$$CH_2$, $SCH_2$$CH_2$], 22.06 [$(CH_3)_2$CHAr], 17.86 (Ru-Ar$CH_3$) ppm. ESI-MS: *m*/*z* (%) 596 (100) [M]$^+$. $C_{29}H_{38}Cl_6RuS_2$ (764.53): calcd. C 45.56, H 5.01, Cl 27.82, Ru 13.22, S 8.39; found C 42.25, H 4.41, Cl 24.56, Ru 11.37, S 7.86. UV/Vis: $\lambda_{max}$ ($\varepsilon$) = 351 nm (886 $M^{-1}cm^{-1}$), 429.

**Supporting Information** (see also the footnote on the first page of this article): Cyclic voltammograms of **5**, **6**Cl, and $Et_3NHCl$ in dimethylformamide solution; cyclic voltammograms of $(Et_4N)_2$[Ni(emi)] in the presence of various amounts of $Et_3NHCl$ in dimethylformamide solution; cyclic voltammograms and steady-state rotating-disk-electrode voltammograms recorded for (NEt$_4$)**3** and (NEt$_4$)**4** before and after catalysis and parameters used to simulate cyclic voltammograms using the mechanisms described in Schemes 2 and 3 using DigiElch 2.0.

**Note Added in Proof** (May 2, 2007): During correction of the proofs, the synthesis and full characterization of the bridging hydride derivative of a dinuclear complex [(L)Ni(μ-H)Ru($C_6Me_6$)]$^+$ was reported by Ogo et al.[56] This species was obtained from the hydrogen reduction of a nickel-ruthenium compound very similar to $\mathbf{1}^+$ and $\mathbf{3}^-$. As this reaction corresponds to the addition of two electrons and one proton to the $Ni^{II}$-$Ru^{II}$ state, this new compound is a stable analogue of the reactive intermediates proposed here in the catalytic mechanisms for hydrogen electro-production.

## Acknowledgments

The authors thank Dr. Nicolas Duraffourg for performing two-dimensional NMR experiments and the Life Science Division of the CEA for financial support within the Biohydrogen program.

[1] D. J. Evans, C. J. Pickett, *Chem. Soc. Rev.* **2003**, *32*, 268–275.
[2] A. Volbeda, J. C. Fontecilla-Camps, *Dalton Trans.* **2003**, 4030–4038.
[3] Y. Nicolet, C. Piras, P. Legrand, C. E. Hatchikian, J. C. Fontecilla-Camps, *Structure Fold. Des.* **1999**, *7*, 13–23.

 © 2007 Wiley-VCH Verlag GmbH & Co. KGaA, Weinheim 

[4] J. W. Peters, W. N. Lanzilotta, B. J. Lemon, L. C. Seefeldt, *Science* **1998**, *282*, 1853–1858.
[5] A. Volbeda, M. H. Charon, C. Piras, E. C. Hatchikian, M. Frey, J. C. Fontecilla-Camps, *Nature* **1995**, *373*, 580–587.
[6] A. Volbeda, E. Garcin, C. Piras, A. L. de Lacey, V. M. Fernandez, E. C. Hatchikian, M. Frey, J. C. Fontecilla-Camps, *J. Am. Chem. Soc.* **1996**, *118*, 12989–12996.
[7] Y. Higuchi, H. Ogata, K. Miki, N. Yasuoka, T. Yagi, *Structure* **1999**, *7*, 549–556.
[8] A. K. Jones, E. Sillery, S. P. J. Albracht, F. A. Armstrong, *Chem. Commun.* **2002**, 866–867.
[9] M. Y. Darensbourg, E. J. Lyon, J. J. Smee, *Coord. Chem. Rev.* **2000**, *206*, 533–561.
[10] E. Bouwman, J. Reedijk, *Coord. Chem. Rev.* **2005**, *249*, 1555–1581.
[11] A. C. Marr, D. J. E. Spencer, M. Schroder, *Coord. Chem. Rev.* **2001**, *219*, 1055–1074.
[12] D. Sellmann, F. Geipel, F. Lauderbach, F. W. Heinemann, *Angew. Chem. Int. Ed.* **2002**, *41*, 632–634.
[13] J. A. W. Verhagen, M. Lutz, A. L. Spek, E. Bouwman, *Eur. J. Inorg. Chem.* **2003**, 3968–3974.
[14] Z. L. Li, Y. Ohki, K. Tatsumi, *J. Am. Chem. Soc.* **2005**, *127*, 8950–8951.
[15] D. Sellmann, F. Lauderbach, F. Geipel, F. W. Heinemann, M. Moll, *Angew. Chem. Int. Ed.* **2004**, *43*, 3141–3144.
[16] A. Perra, E. S. Davies, J. R. Hyde, Q. Wang, J. McMaster, M. Schröder, *Chem. Commun.* **2006**, 1103–1105.
[17] Y. Oudart, V. Artero, J. Pecaut, M. Fontecave, *Inorg. Chem.* **2006**, *45*, 4334–4336.
[18] J. A. W. Verhagen, D. D. Ellis, M. Lutz, A. L. Spek, E. Bouwman, *J. Chem. Soc., Dalton Trans.* **2002**, 1275–1280.
[19] H. J. Kruger, G. Peng, R. H. Holm, *Inorg. Chem.* **1991**, *30*, 734–742.
[20] W. Autenrieth, K. Wolff, *Ber. Dtsch. Chem. Ges.* **1899**, *32*, 1373.
[21] M. A. Reynolds, T. B. Rauchfuss, S. R. Wilson, *Organometallics* **2003**, *22*, 1619–1625.
[22] M. V. Rampersad, S. P. Jeffery, M. L. Golden, J. Lee, J. H. Reibenspies, D. J. Darensbourg, M. Y. Darensbourg, *J. Am. Chem. Soc.* **2005**, *127*, 17323–17334.
[23] F. A. Cotton, C. A. Kraihanzel, *Inorg. Chem.* **1963**, *2*, 533–540.
[24] S. Chardon-Noblat, A. Deronzier, R. Ziessel, D. Zsoldos, *Inorg. Chem.* **1997**, *36*, 5384–5389.
[25] M. Rudolph, *J. Electroanal. Chem.* **2003**, *543*, 23–39.
[26] M. Rudolph, *J. Electroanal. Chem.* **2003**, *558*, 171–176.
[27] M. Rudolph, *J. Electroanal. Chem.* **2004**, *571*, 289–307.
[28] M. Rudolph, *J. Comput. Chem.* **2005**, *26*, 619–632.
[29] M. Rudolph, *J. Comput. Chem.* **2005**, *26*, 633–641.
[30] M. Rudolph, *J. Comput. Chem.* **2005**, *26*, 1193–1204.
[31] V. Artero, M. Fontecave, *Coord. Chem. Rev.* **2005**, *249*, 1518–1535.
[32] W. F. Zhu, A. C. Marr, Q. Wang, F. Neese, D. J. E. Spencer, A. J. Blake, P. A. Cooke, C. Wilson, M. Schröder, *Proc. Natl. Acad. Sci. USA* **2005**, *102*, 18280–18285.
[33] M. Rousset, Y. Montet, B. Guigliarelli, N. Forget, M. Asso, P. Bertrand, J. C. Fontecilla-Camps, E. C. Hatchikian, *Proc. Natl. Acad. Sci. USA* **1998**, *95*, 11625–11630.
[34] M. C. Smith, J. E. Barclay, S. P. Cramer, S. C. Davies, W. W. Gu, D. L. Hughes, S. Longhurst, D. J. Evans, *J. Chem. Soc., Dalton Trans.* **2002**, 3410–3410.
[35] G. A. N. Felton, R. S. Glass, D. L. Lichtenberger, D. H. Evans, *Inorg. Chem.* **2006**, *45*, 9181–9184.
[36] M. Beley, J. P. Collin, R. Ruppert, J. P. Sauvage, *J. Am. Chem. Soc.* **1986**, *108*, 7461–7467.
[37] J. P. Collin, A. Jouaiti, J. P. Sauvage, *Inorg. Chem.* **1988**, *27*, 1986–1990.
[38] L. L. Efros, H. H. Thorp, G. W. Brudvig, R. H. Crabtree, *Inorg. Chem.* **1992**, *31*, 1722–1724.
[39] B. Fisher, R. Eisenberg, *J. Am. Chem. Soc.* **1980**, *102*, 7361–7363.
[40] C. J. Curtis, A. Miedaner, R. Ciancanelli, W. W. Ellis, B. C. Noll, M. R. DuBois, D. L. DuBois, *Inorg. Chem.* **2003**, *42*, 216–227.
[41] A. D. Wilson, R. H. Newell, M. J. McNevin, J. T. Muckerman, M. R. DuBois, D. L. DuBois, *J. Am. Chem. Soc.* **2006**, *128*, 358–366.
[42] T. Yamamura, S. Sakurai, H. Arai, H. Miyamae, *J. Chem. Soc., Chem. Commun.* **1993**, 1656–1658.
[43] U. T. Mueller-Westerhoff, A. Nazzal, *J. Am. Chem. Soc.* **1984**, *106*, 5381–5382.
[44] We were unfortunately unable to characterize or isolate a hydride intermediate. Reaction of the dinuclear compounds with hydride donors such as formiate, methoxide, or tetrahydroborate anions leads to intractable mixtures.
[45] V. Grass, D. Lexa, J. M. Saveant, *J. Am. Chem. Soc.* **1997**, *119*, 7526–7532.
[46] C. Baffert, V. Artero, M. Fontecave, *Inorg. Chem.* **2007**, *46*, 1817–1824.
[47] I. Bhugun, D. Lexa, J. M. Saveant, *J. Am. Chem. Soc.* **1996**, *118*, 3982–3983.
[48] M. Razavet, V. Artero, M. Fontecave, *Inorg. Chem.* **2005**, *44*, 4786–4795.
[49] M. A. Bennett, T. N. Huang, T. W. Matheson, A. K. Smith, *Inorg. Synth.* **1982**, *21*, 74–78.
[50] M. A. Bennett, A. K. Smith, *J. Chem. Soc., Dalton Trans.* **1974**, 233–241.
[51] M. J. Cleare, W. P. Griffith, *J. Chem. Soc. A* **1969**, 372.
[52] S. C. Grocott, S. B. Wild, *Inorg. Chem.* **1982**, *21*, 3535–3540.
[53] H. M. Koepp, H. Wedt, H. Strehlow, *Z. Elektrochem.* **1960**, *64*, 483.
[54] D. Plechter, *A First Course in Electrode Processes*, The Electrochemical Consultancy, Huant, UK, **1991**.
[55] G. M. Sheldrick, *SHELXTL 6.10*, 5th ed., University of Göttingen, Germany, **1994**.
[56] S. Ogo, R. Kabe, K. Uehara, B. Kure, T. Nishimura, S. C. Menon, R. Harada, S. Fukuzumi, Y. Higuchi, T. Ohhara, T. Tamada, R. Kuroki, *Science* **2007**, *316*, 585.

Received: January 19, 2007
Published Online: May 14, 2007

 © 2007 Wiley-VCH Verlag GmbH & Co. KGaA, Weinheim 

DOI: 10.1002/ejic.200601234

# Inter- and Intramolecular Electron Transfer in Modified Azurin Dimers

Thyra E. de Jongh,[a] Maren Hoffmann,[b] Oliver Einsle,[b] Davide Cavazzini,[c] Gian-Luigi Rossi,[c] Marcellus Ubbink,[a] and Gerard W. Canters*[a]

**Keywords:** Metalloproteins / Protein structures / Copper protein / Electronic coupling / Hydrophobic patch

A dimer of N42C azurin (*P. aeruginosa*), formed by intermolecular disulfide bond formation between the introduced surface-exposed cysteine residues, was previously shown to exhibit low rates of intramolecular electron self-exchange. The work presented here aims to render the construct sensitive to pH by the introduction of an additional surface mutation (M64E). The structural and mechanistic effects of ionisable residues in the hydrophobic patch were analysed as a function of pH. A crystal structure of the dimer at pH = 3.1, solved to 2.3 Å resolution, displays an orientation distinct from other known azurin complexes. The dimer exhibits slow intramolecular self-exchange at pH* = 4.5 ($k_{ese}^{intra} \approx 25\ s^{-1}$), in line with the Cu–Cu distance of 20.5 Å observed in the crystal structure of the dimer. The intermolecular electron self-exchange rate constant amounts to $k_{inter} = (1.8 \pm 0.1) \times 10^4\ M^{-1}s^{-1}$. Thus, at protein concentrations less than 1 mM, the intramolecular process dominates the electron self-exchange. A change from low to high pH results in a slowing down of the electron-exchange processes. A partitioning between intra- and intermolecular exchange proved impossible at low pH due to the limited precision of the experimental data.
(© Wiley-VCH Verlag GmbH & Co. KGaA, 69451 Weinheim, Germany, 2007)

## Introduction

Abbreviations: 1,5-dip: 1,5-bis(imidazol-1-yl)pentane; 1,6-dih: 1,6-bis(imidazol-1-yl)hexane; wt: wild type; Azu: azurin; BMME: bis(maleimidomethyl) ether.

Among the physico-chemical processes that constitute the basis of life, the formation of protein–protein complexes occupies a prominent place. An example of this kind is provided by the metabolic processes in the living cell. They are mediated by protein–protein complexes that promote interprotein electron transfer (ET). These complexes have a transient nature. Their lifetimes reflect the rate at which metabolic processes take place in the cell and generally lie within the range of from 1 to 1000 ms. It is precisely their fleeting existence which makes these transient complexes difficult to study by conventional means such as crystallography. Two main alternative routes of research have been explored in the recent past. One technique relies on the use of NMR which is a form of spectroscopy that is eminently suited for the study of dynamic processes and short-lived structures.[1–4] The other is to freeze the complexes by covalently linking them as soon as they have formed in the hope that the covalently linked complex preserves the active conformation. The cross-linked complex can then be studied in detail.

Previous research has focused on complexes in which two monomers of the electron-transfer protein azurin (Azu) have been linked.[5,6] The rationale for studying these complexes is twofold. First, the covalent linking of the partners in an encounter complex may lead to a configuration that is different from the active configuration, i.e. the configuration that leads to protein–protein ET. For this reason it is important to study how the linking may affect the structure of the complex and how small changes in the contact surface may influence the details of this structure. Secondly, it is of interest to know how the structure of the complex and thereby the ET process may be modified by applying changes in the surface of the contact area. This may be relevant for the technological implementation of proteins in electronic devices such as sensors, actuating elements and fuel cells etc.

Azurin from *Pseudomonas aeruginosa* is a so-called blue copper protein of 14 kDa, in which a single Cu ion is immobilized in the protein structure through bonds to two histidines, a cysteine and a methionine. The backbone carbonyl oxygen atom of a glycine completes the coordination shell through a weak coordinate bond. The electron self-exchange (ese) rate of the protein is high ($1 \times 10^6\ M^{-1}s^{-1}$, at room temperature) and insensitive to pH.[7] The crystal

[a] Leiden Institute of Chemistry, Leiden University, Gorlaeus Laboratories,
P. O. Box 9502, 2300 RA Leiden, The Netherlands
Fax: +31-71-527-4349
E-mail: canters@chem.leidenuniv.nl
URL: http://www.chem.leidenuniv.nl/metprot
[b] Institut für Mikrobiologie und Genetik, Georg-August-Universität Göttingen
Justus-von-Liebig-Weg 11, 37077 Göttingen, Germany
[c] Department of Biochemistry and Molecular Biology, University of Parma
V.le G. P. Usberti 23/A., 43100 Parma, Italy
Supporting information for this article is available on the WWW under http://www.eurjic.org or from the author.

 © 2007 Wiley-VCH Verlag GmbH & Co. KGaA, Weinheim 

structure of Azu provides a clue as to why the ese rate is so high.[8] The Azu molecules pack with their so-called hydrophobic patches positioning the His117 ligands of the Cu atoms in the monomers directly opposite each other.[8] This configuration optimises the electronic coupling between the Cu centres in the two monomers. The coupling is further enhanced by the presence of two water molecules that form an H-bonded pathway between the $N^{\varepsilon}$ atoms of the two histidines.[8,9]

Confirmation that this is a favoured orientation for two Azu molecules in an ET-active complex came from studies of complexes in which two Azu molecules were covalently linked. By introducing a cysteine at position 42 (Asn42Cys mutation) and incubating the mutated protein with bis(maleimidomethyl) ether (BMME), a covalently linked dimer of Azu was obtained in which the hydrophobic patches face each other.[5] A high intramolecular ese rate was observed ($>10^4\ s^{-1}$) while the intermolecular rate (i.e. between two different dimers) was too slow to be measurable.[5] The latter observation confirmed that the packing of the Azu moieties in the dimer blocks the hydrophobic patch, thereby rendering intermolecular ET virtually impossible. Leaving out the BMME linker and connecting the two Azu molecules directly by the Cys42–Cys42 disulfide bridge resulted in a complex in which the two Azu molecules had rotated around the Cys42 –Cys42 link, apparently to relieve a slight steric hindrance. As a result intra-ese stopped. Inter-ese was only slightly slower than observed for wild-type (wt) Azu.[5,6]

Earlier evidence for the involvement of the hydrophobic patch in the ese reaction of (monomeric) azurin had been obtained from studies of azurin variants in which charges had been introduced in the hydrophobic patch. The Met44-Lys mutation, for instance, was found to diminish the ese rate by two orders of magnitude in the pH range in which the Lys side chain is protonated and therefore charged, while the ese rate returns to its wt value at high pH, at which the Lys side chain becomes deprotonated and therefore uncharged.[10–12] Likewise, the Met64Glu mutation caused a slowing down of the ese reaction at high pH where the Glu side chain becomes charged.[13]

The present study deals with Azu dimers that are linked directly through a Cys–Cys link at position 42. In addition, a charge was introduced in the hydrophobic patch by the mutation M64E. The effect of pH on the inter- and intra-dimer electron self-exchange was studied. The expectation was that the inter-dimer ese rate would be affected by pH while, by analogy with earlier results on the Cys42–Cys42-coupled dimer, the intra-protein rate would be too slow to be measurable and independent of pH. Contrary to this expectation, the latter rate appeared to be clearly non-zero. Also, the structure of the complex as determined by X-ray diffraction shows that the two Azu moieties are in an orientation that differs from both the BMME- and the disulfide-linked dimers of the N42C Azu variant. NMR spectroscopic studies substantiate the absence of significant structural variations in time, as well as the absence of significant perturbations of the interface between the two monomers. The observed rates can be rationalised with the help of current models of ET on the basis of the observed structure of the complex. The results show that our present understanding of the parameters that determine the structure of an association complex is insufficient to predict structural variations on the basis of simple intuitive arguments.

## Results

Electron self-exchange rates were determined by monitoring the resolved NMR signal of the $H^{\gamma 2}$ methyl group of Val31. In oxidised wt Azu, this signal occurs at $\delta$ = –0.77 ppm at room temperature and pH = 8.5, while it occurs at $\delta$ = –0.69 ppm in reduced Azu. In a partly reduced/partly oxidised solution of Azu, two signals can therefore be observed at –0.77 and –0.69 ppm, which coalesce in the case when there is fast electron self-exchange between reduced and oxidized Azu, while only broadening of the individual signals is seen when the ese is slow. By analysing the shape of the Val31 γ2-methyl signal the ese rate can be extracted. Repeating the measurements at a series of different pH values gives the pH dependence of the ese rate.

For wt Azu, the position of the Val31 signal is pH-dependent.[12] At low pH the signal occurs at $\delta$ = –0.670 and –0.720 ppm for reduced and oxidised Azu, respectively, while at high pH these positions are $\delta$ = –0.690 and –0.770 ppm, respectively. At intermediate pH values the peaks of both the high- and the low-pH forms can be seen simultaneously, their relative intensities varying with pH. This is illustrated in Figure 1A. Apparently, the protein is involved in a protonation/deprotonation equilibrium with slow exchange kinetics. It is known that the residue involved is His35.[11,12,14] The pH dependence of the Val31 signals, with different $pK_a$ values for the oxidised and reduced forms (Figure 1B), complicates the analysis of the electron self-exchange data considerably. Therefore, His35 was eliminated by replacing it with phenylalanine. This is one of a series of His35 mutations which are known only to marginally affect the structure of the Azu and its ET kinetics.[11,15] It was checked that the H35F mutation eliminated the pH dependence of the Val31 resonances (Figure 1A).

For the next experiments, Azu was prepared in which the following mutations had been applied: His35Phe, Asn42Cys and Met64Glu. Subsequently, dimers were constructed in which the Azu moieties were connected through the C42–C42 S–S bridge. In solutions of partly reduced/oxidised dimers broadening but no coalescence of the Val31 γ2-methyl signals was observed when compared with signals from the fully reduced or oxidised solutions (Figure 2). Qualitatively it can be concluded that the exchange is in the slow regime.

To distinguish the contributions to the line broadening that derive from inter-dimer and intra-dimer electron self-exchange, the Val31 γ2-methyl signals were measured as a function of total concentration of the dimer. One would expect the *intra*-dimer contribution to be constant and the *inter*-dimer contribution to diminish at lower concentrations. The signals measured at pH* = 4.5 and 295 K (Fig-

 © 2007 Wiley-VCH Verlag GmbH & Co. KGaA, Weinheim 

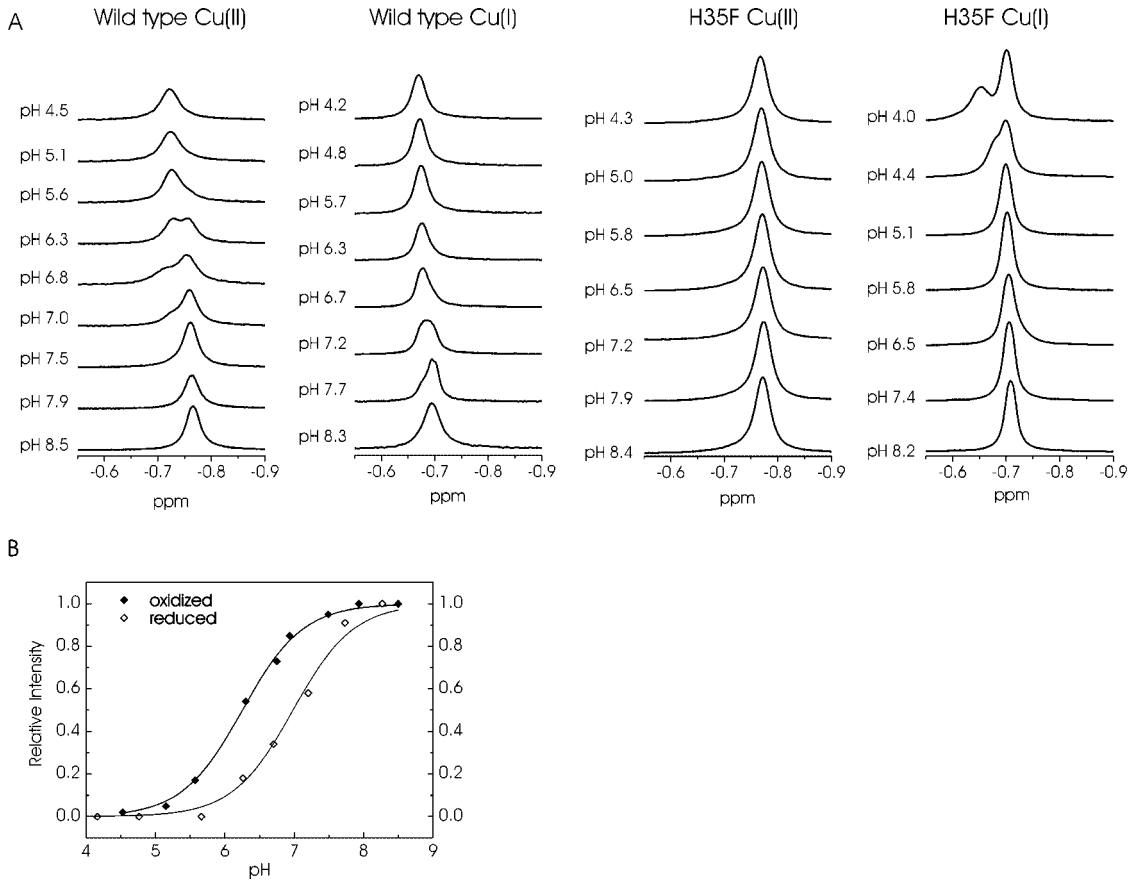


Figure 1. A. Upfield region of the $^1$H NMR spectrum of oxidised and reduced wt azurin (left) and His35Phe azurin (right) showing the Val31 $^1H^{\gamma 2}$ resonance at various pH values. The extra peak developing in the spectrum of reduced H35F azurin towards low pH is due to the start of denaturation. B. Normalised integrated intensity of the high-pH resonance of $Cu^{II}$ (filled diamonds) and $Cu^{I}$ (open diamonds) wt azurin vs. pH. Solid lines represent fits to the Henderson–Hasselbalch equation from which $pK_{a,ox}$ and $pK_{a,red}$ were determined at 6.3 and 7.0, respectively.

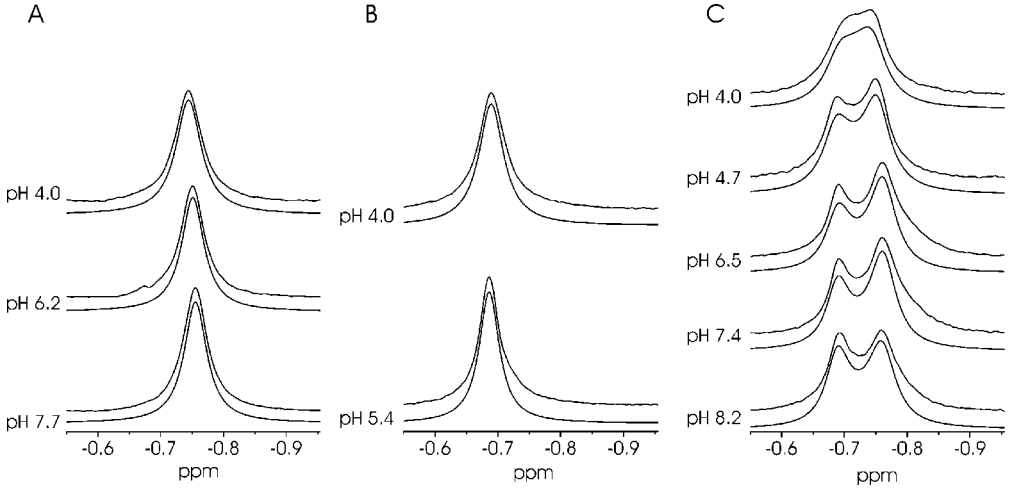


Figure 2. Val31 γ2-methyl resonance in the $^1$H NMR spectrum of H35F/N42C/M64E disulfide azurin at (A) 100%, (B) 0% and (C) 50–60% oxidation (1 mM of dimer protein in 25 mM potassium phosphate, $T$ = 295 K). The upper traces represent the experimental data, while the simulated spectra generated using the MEX software program are shown in the lower traces. The experimental spectra have been corrected for the presence of a small (≈ 5%) amount of redox-inactive azurin with a resonance at δ ≈ –0.69 ppm.

ure 3A) were simulated with the MEX/MEXICO software.[16] The input parameters consisted of the line widths and positions of the signals measured at the highest and lowest dilution for the 100% *ox* and 100% *red* solutions. The inter- and intramolecular electron self-exchange rates were varied until the best fit with experiment was obtained.

 © 2007 Wiley-VCH Verlag GmbH & Co. KGaA, Weinheim 

The fits are reproduced in Figure 3A and the observed rates as a function of dimer concentration are shown in Figure 3B. The intra-dimer contribution is constant, as expected, and corresponds to an intra-dimer ese rate of $k_{intra}$ = 25 $s^{-1}$. The inter-dimer contribution is proportional to the concentration. The slope yields the second-order rate constant which amounts to $k_{inter} = (1.8 \pm 0.1) \times 10^4$ $M^{-1} s^{-1}$.

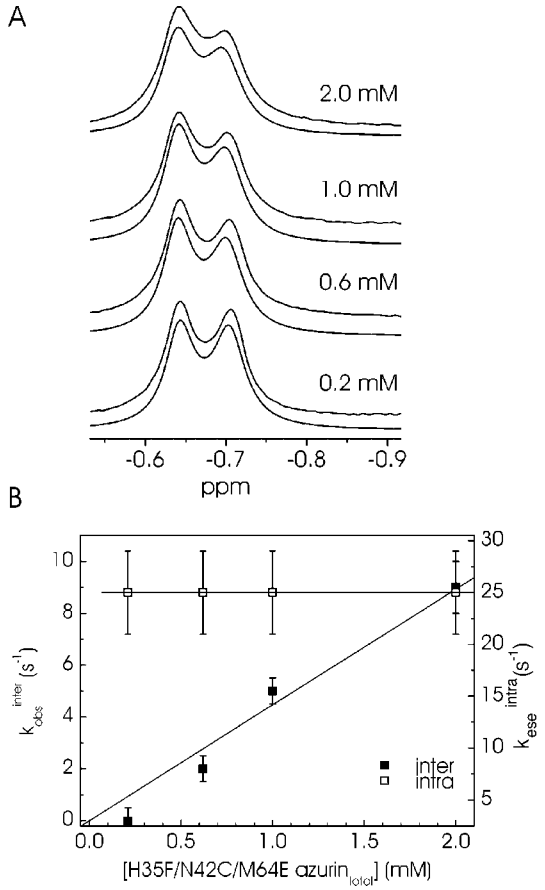


Figure 3. A. Upfield region of the $^1$H NMR spectrum of H35F/N42C/M64E disulfide azurin at (50 ± 3) % oxidation at several dilutions. The upper traces show the experimental data, the MEX-simulated spectra are shown in the lower traces ($T$ = 295 K, 25 mM potassium phosphate, pH* = 4.5). B. $k_{obs}^{inter}$ (filled squares) and $k_{ese}^{intra}$ (open squares) values for H35F/N42C/M64E disulfide azurin that correspond to the simulated traces shown in panel A vs. the protein dimer concentration. The lines indicate least-squares linear fits.

The next question to be addressed deals with the pH dependence of the line broadening. It is clear from Figure 2C that the broadening becomes less at high pH, indicating that the electron self-exchange processes slow down in a similar way to that observed for the monomeric species in solution.[13] Simulation with the MEX software shows that the combined contributions from the intra- and inter-electron self-exchange processes decrease by a factor of 3 when going from pH = 4.0 to 8.2. The partitioning between these two processes was not possible. This was because of insufficient precision of the data resulting from the difficulty in keeping the degree of oxidation/reduction of the solution precisely fixed during the pH titration.

To aid in the interpretation of the data, the structure of the N42C/M64E azurin S–S dimer at pH = 3.1 was determined to 2.3 Å resolution by X-ray diffraction. The results are presented in Table 1. Crystals obtained at high pH did not diffract well enough for structure analysis. The structure of the dimer is shown in Figure 4B. For comparison the packing of the monomers in the crystal of wt Azu is shown in Figure 4A.[8] In Figure 4C the C42–C42-connected dimer of Azu is depicted in which no other than the N42C mutation had been applied.[5] It is clear that in Figure 4C the two halves of the dimer have rotated around the Cys–Cys link when compared with Figure 4A. Remarkably, the structure in Figure 4B is intermediate.

Table 1. Data collection and refinement statistics.

| | |
|---|---|
| Space group | $P2_12_12$ |
| Unit cell | $a$ = 68.57 Å |
| | $b$ = 116.98 Å |
| | $c$ = 30.29 Å |
| Molecules in asymmetric unit[a] | 2 |
| Resolution limits | 60.0–2.3 Å |
| Independent reflections | 10369 |
| Completeness (last shell) | 95.1% (95.6%) |
| $R_{merge}$ (last shell) | 0.095 (0.060) |
| $I/\sigma(I)$ (last shell) | 8.3 (2.4) |
| $R_{cryst}$ ($R_{free}$) | 0.208 (0.281) |
| r.m.s.d. bonds | 0.034 |
| r.m.s.d. angles | 2.843 |

[a] Molecules seen as monomeric azurin subunits.

Comparison of each of the subunits of the N42C/M64E azurin dimer with the structure of reduced wt azurin at pH = 5.5 (PDB access code 1E5Y) shows that they are largely unaffected by the introduction of the mutations. The overall backbone atom root-mean-square difference between the wt structure and each of the monomers in the N42C/M64E dimers amounts to 0.6 Å, excluding the N- and C-terminal residues. The regions directly around the sites of the mutation are relatively unperturbed. The two subunits share a contact surface, with the contacts between the two surfaces consisting mainly of weak hydrophobic interactions in a manner that is clearly distinct from the classical hydrophobic packing in crystals of wt azurin.[8] In the dimer interface, two water molecules can be found that form several hydrogen bonds with the protein (Figure 5). A hydrogen-bonding network across the interface is formed which stabilises the conformation of the dimer by forming hydrogen bonds between each of the water molecules to Glu64 $O^{\varepsilon}$ or the backbone oxygen atoms of Cys42 on both protein chains. The shortest Cu–Cu distance observed is the intramolecular distance of 20.5 Å. All Cu–Cu distances between dimers in adjacent asymmetric units within the crystal exceed 25 Å. These intermolecular interactions can therefore be considered irrelevant for the electron self-exchange analysis.

To probe the dynamic aspects of the dimer structure, HSQC NMR spectra were obtained for the $^{15}$N-labelled dimer and compared with those of the $^{15}$N-labelled monomer. The spectra were measured at a number of pH values (Supporting Information: Figure S2). The dimer spectra are al-

 © 2007 Wiley-VCH Verlag GmbH & Co. KGaA, Weinheim 

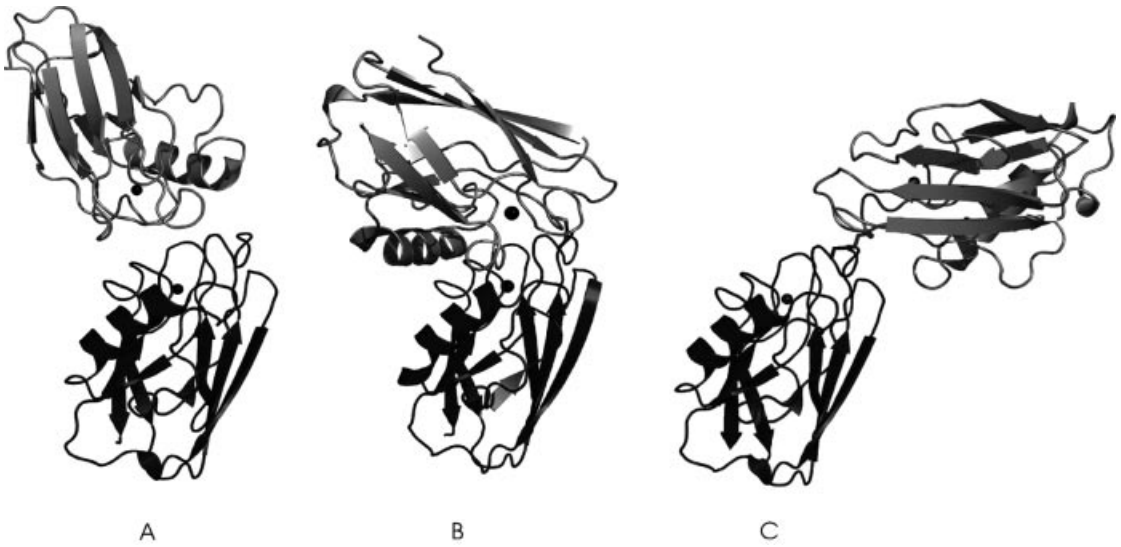


Figure 4. A. Packing of two molecules of reduced wt azurin from *Pseudomonas aeruginosa* in the crystal structure of the protein at pH = 5.5; data from pdb entry 1E5Y. B. Structure of the Cys42–Cys42-linked dimer of azurin carrying in each monomer the mutations Asn42Cys and Met64Glu. The Cu centres are oxidised; pH = 3.1; data from pdb entry 2OJ1. C. Structure of the Cys42–Cys42-linked dimer of azurin carrying in each monomer the mutations Asn42Cys. The Cu centres are oxidised; pH = 8.5; data from pdb entry 1JVO.

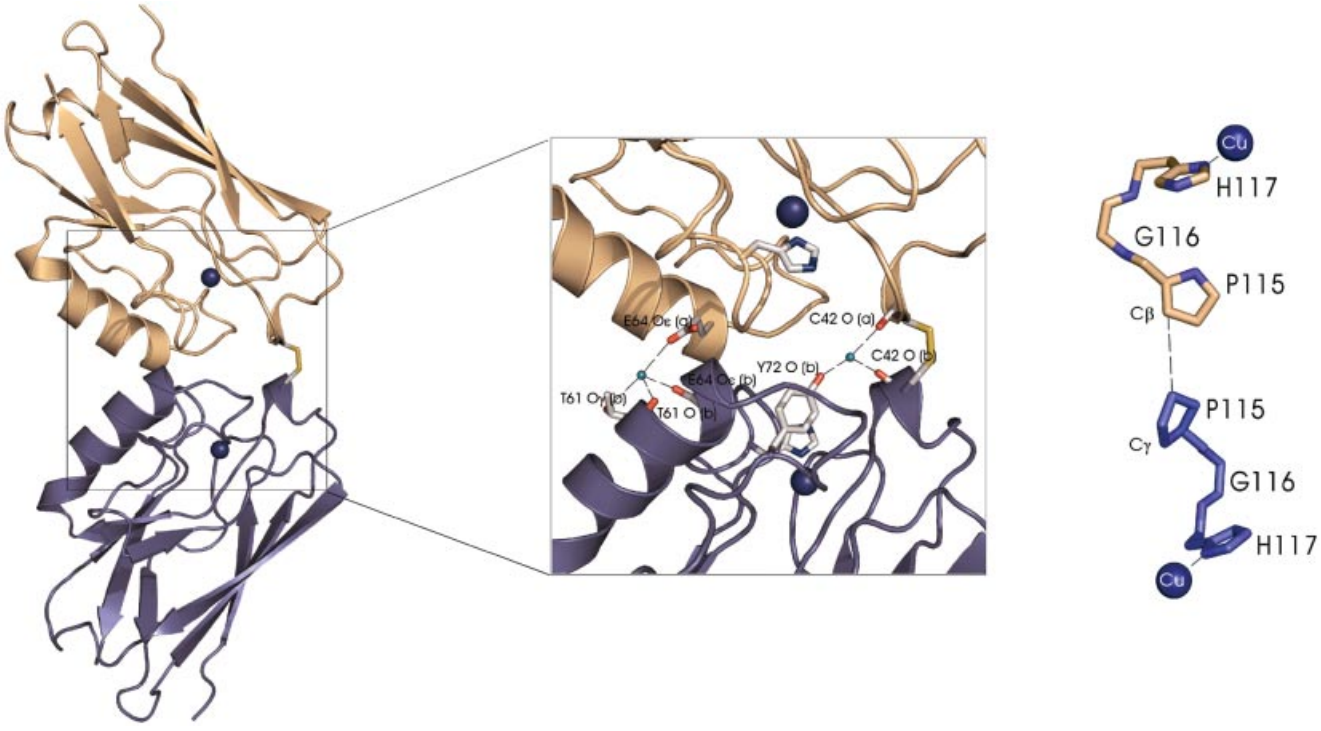


Figure 5. Left: Crystal structure of the N42C/M64E azurin disulfide-bridged dimer at pH = 3.1. The copper centres are depicted as dark-blue spheres. Close-up: Interface of the dimer showing the ordered water molecules (small light-blue spheres). All residues involved in hydrogen bonding with these water molecules are shown (sticks) and labelled. The hydrogen bonds are shown as dashed lines. The letters within parentheses indicate the individual protein chains (a and b). Also shown are the Cu ligands H117 (sticks). Right: Tunnelling pathway between the copper centres of the N42C/M64E disulfide-bridged dimer of azurin as calculated with the programme HARLEM.[22] The through-space jump between Pro115(A) C-β and Pro115(B) C-γ is indicated by a dashed line.

most identical to those of the monomer except for a few residues in the hydrophobic patch, viz. C42, V43 and M44. When increasing the pH from 4.4 to 8.4 the cross peaks corresponding to these residues move to slightly different positions (Figure S2). The transition occurs at a somewhat lower pH for the dimer. There is no evidence for strong interactions between the subunits since, overall, no severe perturbations of the resonance patterns can be observed.

 © 2007 Wiley-VCH Verlag GmbH & Co. KGaA, Weinheim 

## Discussion

The aim of the work presented here was to construct a protein complex with pH-dependent structural and ET properties. To this end, a covalently cross-linked homodimer of the blue copper protein azurin was created by intermolecular disulfide bond formation between engineered surface-exposed cysteines. The pH dependence was introduced by substitution of the interfacial M64 by an ionisable Glu residue. Analysis of the ET rate as a function of pH required additional replacement of the protonatable H35 residue by Phe. It was shown that over the entire pH range studied, the complex exhibited slow electron self-exchange. Although no unambiguous distinction could be made between the inter- and intramolecular contributions to the ese process from the pH-dependent data, the concentration dependence of the observed ese rate identifies intramolecular exchange as the dominant process (see Figure 3).

Despite the presence of several ionisable groups in the interface, the electron self-exchange behaviour of the complex shows only moderate pH dependence. The low exchange rates observed for the H35F/N42C/M64E dimer ($1.8 \times 10^4$ M$^{-1}$ s$^{-1}$) contrast with what is observed for the N42C azurin dimer for which a roughly ten times higher $k_{ese}^{inter}$ was determined ($2.8 \times 10^5$ M$^{-1}$ s$^{-1}$). It is tempting to relate this difference to the clear difference between the crystallographically determined structures of the two complexes. Whereas the N42C dimer adopts a rather "open" dimer conformation [interfaces are $a = (1.8 \times 10^2)$ Å$^2$] with an intramolecular Cu–Cu distance >25 Å, the N42C/M64E dimer at pH = 3.1 forms a much more closed conformation [interfaces are $a = (7.0 \times 10^2)$ Å$^2$] in which the straight intramolecular Cu–Cu distance is only 20.5 Å. Although this distance is still rather large, it is within the limits that allow for intramolecular e.s.e., albeit with low rates. The alternative explanation that in the H35F/N42C/M64E dimer the Glu64 unit in the interface is deprotonated and therefore intermolecular association is slowed down, is less likely since at the employed pH* of 4.5 the ese rate of the monomer is not yet affected by deprotonation of Glu64.[13]

According to Dutton et al., the rate of ET, $k_{ET}$, between two redox centres separated by a homogeneous medium is given by Equation (1),[17,18] in which $\rho$ denotes the packing density, $d$ the distance separating the donor and acceptor sites, $\lambda$ the reorganization energy and $\Delta G^0$ the standard free energy of the reaction (energies are in eV).

$$\log k_{ET} = 13.0 - (1.2 - 0.8\rho)(d - 3.6) - (\Delta G^0 + \lambda)^2/\lambda \quad (1)$$

For the N42C azurin dimer, these parameters are $\lambda$ = 0.7 eV, $\rho$ = 0.75 and $\Delta G^0$ = 0 eV (e.s.e.).[5] Based on these parameters and a Cu–Cu distance of 20.5 Å, a value of $k_{ese}^{intra} \approx 1.4 \times 10^2$ s$^{-1}$ can be predicted, in reasonable agreement with the experimentally determined rate.

Alternatively, ET can be viewed as proceeding along defined tunnelling pathways (TPs).[19–22] In the crystal structure of the N42C/M64E dimer a path can be identified that involves residues H117, G116 and P115 on both chains and a large through-space jump of 4.0 Å between the C-β and C-γ atoms of Pro115 on either chain, respectively (Figure 5). The coupling efficiency of this pathway is extremely low ($\Pi_\varepsilon < 10^{-8}$) and is, in fact, too low for ET to occur at a discernible rate. The pathway algorithm, however, calculates couplings in static structures with fixed distances between atoms. In reality, protein motions may temporarily shorten through-space distances, increasing the coupling strength. Also, although in the crystal structure no ordered water molecules were observed within hydrogen-bonding distances of the P115 residues, in solution solvent molecules may temporarily contribute to the electronic coupling and enhance the electron self-exchange.

## Conclusions

Chemical shift perturbation analysis of the dimer indicates that the dimer interface is not strongly perturbed by the covalent linking of the monomers throughout the investigated pH range. Also, contrary to expectation, the neutralisation of the Glu64 side chain has little effect on the conformation of the dimer. The crystal structure of the dimer at low pH shows, again contrary to expectation, that the two Azu moieties in the dimer move less far apart (through a rotation around the Cys42–Cys42 link) than in the dimer without the M64E mutation.

The observed ese rates are in accordance with the structural features. The intermolecular rate is lower than in the C42–C42 dimer without the M64E mutation, in agreement with the smaller surface accessible area in the hydrophobic patch. The intramolecular ese rate on the other hand is larger, in line with the smaller Cu–Cu distance.

The phenomenological model of Dutton et al. gives a value for the ese rate that is in accordance with observation whereas the pathway model of Beratan, Betts and Onuchic predicts a rate that is orders of magnitude too small because there is a gap in the pathway that has to be bridged. It means that the structure may have dynamic features, by which the gap is closed some of the time; although, on a millisecond time scale, the NMR spectroscopic data provide no indication for time-dependent features of the dimer structure within the investigated pH range. Alternatively, water molecules may bridge the gap as seen in several other dimer-like structures of Azu. No water molecules could be observed in the structure suggesting that there are no ordered water molecules in the interface. However, this does not necessarily mean that in the course of time they cannot provide effective electronic coupling.

The overall conclusion is that the ET rates and the structural data produce a consistent picture of the Azu (N42C/M64E) dimer that is clearly different from simple intuition. Why the N42C/M64E Azu dimer behaves counter-intuitively remains open to further experimentation.

## Experimental Section

**Mutagenesis:** The secondary mutation M64E was introduced into the N42C azurin gene by splice overlap extension (SOE) site-directed mutagenesis for which two partially complementary oligo-

 © 2007 Wiley-VCH Verlag GmbH & Co. KGaA, Weinheim 

nucleotides were designed. The forward primer (i.e. extending in the coding direction) 5′-*GGGCGTGCTCAC*CGACGGC**GA**-GGCTTCCG encodes for the replacement of methionine-64 by a glutamate. The reverse primer 5′-*GTGACCACGCCC*-TGCATGTC**T**GC**A**GCGGTGCT includes two silent mutations that encode a *Pst*I restriction site for screening purposes. The section in *italics* shows the complimentary regions in the two primers, the mutation sites are shown in bold. As a template, the N42C azu containing plasmid pIA02, derived from pUC18, was used.[6] The presence of the N42C/M64E azurin gene in the newly created plasmid pTJ01 was confirmed by sequence analysis and the obtained plasmid was then used as a template for the one-step synthesis of the H35F/N42C/M64E azurin gene in a procedure based on the Stratagene's ExSite® PCR-Based Site-Directed Mutagenesis Kit. Two fully complementary 32 base-pair-long oligonucleotides encoding the His35Phe mutation were used as primers: (forward primer) 5′-CCGTCAACCTGTCC**TTC**CCCGG*G*AACC-TGCCG. The mutated codon for the H35F substitution is indicated in bold and an additional silent mutation that was introduced for screening by *Xma*I digestion is in *italics.* Sequence analysis confirmed the presence of all desired mutations in the resultant pTJ02 plasmid. The H35F/N42C/M64E azurin gene was subcloned into a pET28a vector for cytoplasmic expression by removal of the signal sequence. Gene amplification was performed using primers for *N*-terminal signal peptide removal (5′-GGTCAGCG*CCATGG*CCGAGTGC TCGGTGG (*Nco*I site is in *italics*) and addition of a *C*-terminal *Bam*HI/*Bst*YI recognition site (in *italics*) (5′-CCGA*GGATCC*GCATCACTTCAGGG). Insertion into a pET28a vector was accomplished by digestion of the gene fragment using the restriction enzymes *Bst*YI and *Nco*I. The vector was digested by the enzymes *Bam*HI and *Nco*I, after which the gene and vector fragments were ligated resulting in the plasmid named pTJ13.

**Protein Expression and Purification:** Wild-type and H35F azurin were expressed and produced as described previously.[11,23] Non-isotopically labelled N42C/M64E azurin and H35F/N42C/M64E azurin were produced in the periplasmic space of *E. coli* JM109 cells transformed with plasmids pTJ01 or pTJ02, respectively. Cells were cultured on an LB medium at 37 °C/250 rpm to an $OD_{600}$ of 0.6 before induction by addition of 100 μM IPTG. Cells were harvested by centrifugation typically about 5 h after induction. Both mutants were isolated and purified from the medium as described for N42C azurin with yields of 10–15 mg/L.[6] Up to 50% of the purified azurin was found to contain zinc in the metal-binding site and was thus redox-inactive. Uniformly $^{15}$N-labelled H35F/N42C/M64E azurin was produced in the cytoplasm of BL21 *E. coli* cells transformed with pTJ13 and grown on isotopically labelled OD2-N medium (Silantes GmbH) supplemented with 50 μM kanamycin at 30 °C/200 rpm. Once an $OD_{600}$ of 0.5 was obtained, the temperature was lowered to 25 °C followed by induction with 1 mM IPTG after 30 min. Due to lower growth rates, cells grown on the OD2-N medium were not harvested until 15 h after induction. The cytoplasmically produced protein was released from the cells by resuspension in 20 mM MES, 100 mM NaCl, pH = 6.5 and disruption of the cells in a French Press cell in the presence of phenylmethylsulfonyl fluoride (PMSF) (1 mM) and DNase I (50 mg mL$^{-1}$). After centrifugation, the protein was isolated from the resultant supernatant following a protocol similar to that used for periplasmically expressed azurin. The protein was initially purified in the apo form and reconstituted with copper before further purification on a DEAE ion exchange column.

**Cross Linking:** Disulfide-linked dimers of N42C/M64E and H35F/N42C/M64E holo-azurin were spontaneously formed upon addition of a slight molar excess of $Cu(NO_3)_2$ and an approximately five-fold excess of $K_3Fe(CN)_6$. Excess $Cu(NO_3)_2$ and $K_3Fe(CN)_6$ were subsequently removed by repeated rounds of dilution and concentration using a Centricon concentration device (Molecular weight cut-off: 10 kDa). Analysis of the protein sample by SDS-PAGE under non-reducing conditions showed near complete dimerization.

**NMR Sample Preparation:** Fully reduced samples were obtained by incubation with 2 mM ascorbate at room temp. until the sample had turned completely colourless. Ascorbate was then removed from the sample by washing with deaerated 25 mM potassium phosphate ($KP_i$) at pH = 7.0. All NMR samples of unlabelled protein were prepared in 25 mM $KP_i$ at pH* = 7.0 (* uncorrected for deuterium isotope effect), 99.9% $D_2O$ and concentrated to 1–2 mM of protein. For experiments in which the protein concentration had to be varied, the sample was stepwise diluted with 25 mM $KP_i$ at pH* = 7.0 until dilution by a factor of 10 was reached. The pH of the samples was adjusted to the desired value by addition of small amounts of NaOD or DCl. Partially oxidised samples were attained by mixing of fully oxidised and fully reduced protein in the required ratios. The degree of oxidation of the samples was determined by measuring the absorbance at 628 nm relative to a fully oxidised sample of the same concentration. UV/Vis spectra were recorded with a Perkin–Elmer lambda 800 spectrophotometer using a special sample holder for NMR tubes equipped with fibre-optic light guides (Hellma). A sample of fully reduced, monomeric $^{15}$N-H35F/N42C/M64E azurin was prepared in 25 mM $KP_i$ at pH = 5.7, 5 mM dithiotreitol (DTT) supplemented with 6% $D_2O$ and concentrated to 2 mM. The pH of the sample was adjusted by addition of small amounts of NaOH or HCl. After recording the NMR spectra, DTT was removed by repeated rounds of concentration and dilution with 25 mM $KP_i$. Dimerisation of the protein was accomplished by addition of a catalytic amount of $Cu(NO_3)_2$ and an approximately ten-fold molar excess of $K_3Fe(CN)_6$. Once fully dimerised, as confirmed by SDS-PAGE analysis, the protein was transferred to a solution containing 25 mM $KP_i$ at pH = 4.3. Selective reduction to $Cu^I$ azurin without disruption of the intermolecular disulfide bond was performed by addition of 2 mM ascorbate. Titration to the desired pH was achieved by addition of small amounts of either NaOH or HCl.

**NMR Spectroscopy:** All $^1$H NMR experiments were performed at 295 K with a Bruker Avance DMX 600 MHz spectrometer. Spectra were calibrated against an internal reference of 200 μM 3-(trimethylsilyl)propionate-$d_4$ (TSP). As the chemical shift of TSP ($\delta$) is sensitive to pH ($pK_a$ = 5.0), its reference position was corrected for pH according to Equation (2).[24]

$$\delta = 0.003 - 0.019 \times (1 + 10^{(5.0-pH)})^{-1} \quad (2)$$

In addition to the Val31 $^1$H signal of the oxidised protein, the spectra of the fully oxidised samples indicated the presence of a small amount (≈ 5%) of an additional species for which a low-intensity resonance was observed at δ ≈ –0.69 ppm at all pH values. This feature is commonly encountered in samples of azurin and can be attributed to the presence of a small amount of redox-inactive azurin. This resonance was subtracted from the experimental spectra shown in Figure 2. Multi-dimensional NMR experiments were performed at 302 K. Data sets were processed in the AZARA program suite (available at http://www.bio.cam.ac.uk) and analysed with ANSIG for WINDOWS 1.0.[25,26] Backbone assignments were obtained through standard sequential assignment procedures using the [$^{15}$N,$^1$H] HSQC, NOESY-HSQC and TOCSY-HSQC spectra on the basis of assignments available for wild-type azurin.[27]

 © 2007 Wiley-VCH Verlag GmbH & Co. KGaA, Weinheim 

**Electron Self-Exchange Rate Determination:** The ese rates were determined by simulation of the line shape of the Val31 methyl $^1$H NMR resonance using the MEX/MEXICO program suite developed by Bain and Duns.[16] All possible intermolecular and intramolecular exchange processes were taken into account (see Supporting Information). The chemical shifts and linewidths of the fully oxidised and fully reduced protein were given as input parameters whilst both the inter- and intramolecular ese rates were manually iterated until simulations were obtained that resembled the experimental traces best, as judged by visual inspection.

**Crystallisation and Structure Solution:** The disulfide-linked dimer of N42C/M64E azurin was crystallised by sitting drop vapour diffusion using a reservoir solution containing 30% (w/v) polyethylene glycol 4000 and 0.1 M sodium citrate buffer at pH = 3.1. The protein was concentrated to 8 mg mL$^{-1}$ and mixed in a 1:1 ratio with the reservoir solution. Rod-shaped crystals grew within 2 d. Due to the high content of PEG 4000, the mother liquor turned out to be sufficiently cryoprotective for direct flash-cooling of the crystals in liquid nitrogen without formation of ice. Data were collected with a Rigaku MicroMax 007 rotating-anode X-ray generator with a mar345dtb image plate detector. For structure solution, the model of the native azurin from *P. aeruginosa* was used with the program MOLREP. Two monomers were found in the asymmetric unit, clearly connected through a disulfide bridge between residues 42. The N42C and M64E mutations were modelled with O,[28] and refinement was carried out with REFMAC5.[29] The coordinates and structure factors have been deposited in the Protein Data Bank under accession code 2OJ1. Figures 4 and 5 were generated using PyMOL 0.98.[30]

**Solvent Accessibility and Interface Areas:** The solvent-accessible surface area (ASA) was calculated using the program NACCESS 2.1.1 with a probe radius of 1.4 Å. The interface area was defined as the sum of the ASAs of the individual proteins minus the ASA of the complex. The interface in disulfide-bridged dimers of N42C azurin was defined as the average of the two dimers in the asymmetric unit of the structure deposited in the protein data bank with accession code 1JVO.[6]

**Supporting Information** (see footnote on the first page of this article): This material contains, first, a description of the model used as a basis for the lineshape simulations. The simulations were used to determine the electron self-exchange rates for the azurin dimer. Second, it contains the 2D-NMR data as a function of pH obtained on the H35F/N42C/M64E azurin monomers and the H35F/N42C/M64E azurin dimers.

[1] P. B. Crowley, M. Ubbink, *Acc. Chem. Res.* **2003**, *36*, 723–730.
[2] M. Prudêncio, M. Ubbink, *J. Mol. Recognit.* **2004**, *17*, 524–539.
[3] M. Ubbink, *Photosynth. Res.* **2004**, *81*, 277–287.
[4] A. N. Volkov, J. A. R. Worrall, E. Holtzmann, M. Ubbink, *Proc. Natl. Acad. Sci. USA* **2006**, *103*, 18945–18950.
[5] I. M. C. van Amsterdam, M. Ubbink, O. Einsle, A. Messerschmidt, A. Merli, D. Cavazzini, G. L. Rossi, G. W. Canters, *Nat. Struct. Biol.* **2002**, *9*, 48–52.
[6] I. M. C. van Amsterdam, M. Ubbink, L. J. C. Jeuken, M. P. Verbeet, O. Einsle, A. Messerschmidt, G. W. Canters, *Chem. Eur. J.* **2001**, *7*, 2398–2406.
[7] C. M. Groeneveld, G. W. Canters, *Eur. J. Biochem.* **1985**, *153*, 559–564.
[8] H. Nar, A. Messerschmidt, R. Huber, M. van de Kamp, G. W. Canters, *J. Mol. Biol.* **1991**, *221*, 765–772.
[9] K. V. Mikkelsen, L. K. Skov, H. Nar, O. Farver, *Proc. Natl. Acad. Sci. USA* **1993**, *90*, 5443–5445.
[10] M. van de Kamp, G. W. Canters, C. R. Andrew, J. Sanders-Loehr, C. J. Bender, J. Peisach, *Eur. J. Biochem.* **1993**, *218*, 229–238.
[11] M. van de Kamp, M. C. Silvestrini, M. Brunori, J. van Beeumen, F. C. Hali, G. W. Canters, *Eur. J. Biochem.* **1990**, *194*, 109–118.
[12] M. van de Kamp, Thesis, Leiden University, **1993**.
[13] G. van Pouderoyen, S. Mazumdar, N. I. Hunt, H. A. O. Hill, G. W. Canters, *Eur. J. Biochem.* **1994**, *222*, 583–588.
[14] M. C. Silvestrini, M. Brunori, M. T. Wilson, V. M. Darleyusmar, *J. Inorg. Biochem.* **1981**, *14*, 327–338.
[15] H. Nar, A. Messerschmidt, R. Huber, M. van de Kamp, G. W. Canters, *J. Mol. Biol.* **1991**, *218*, 427–447.
[16] A. D. Bain, G. J. Duns, *Can. J. Chem.* **1996**, *74*, 819–824.
[17] C. C. Moser, C. C. Page, X. Chen, P. L. Dutton, *J. Biol. Inorg. Chem.* **1997**, *2*, 393–398.
[18] C. C. Moser, J. M. Keske, K. Warncke, R. S. Farid, P. L. Dutton, *Nature* **1992**, *355*, 796–802.
[19] D. N. Beratan, J. N. Onuchic, J. N. Winkler, H. B. Gray, *Science* **1992**, *258*, 1740–1741.
[20] D. N. Beratan, J. N. Onuchic, J. J. Hopfield, *J. Chem. Phys.* **1987**, *86*, 4488–4498.
[21] D. N. Beratan, J. N. Betts, J. N. Onuchic, *Science* **1991**, *252*, 1285–1288.
[22] I. V. Kurnikov, D. N. Beratan, *J. Chem. Phys.* **1996**, *105*, 9561.
[23] M. van de Kamp, F. C. Hali, N. Rosato, A. F. Agro, G. W. Canters, *Biochim. Biophys. Acta* **1990**, *1019*, 283–292.
[24] D. S. Wishart, C. G. Bigam, J. Yao, F. Abildgaard, H. J. Dyson, E. Oldfield, J. L. Markley, B. D. Sykes, *J. Biomol. NMR* **1995**, *6*, 135–140.
[25] M. Helgstrand, P. Kraulis, P. Allard, T. Hard, *J. Biomol. NMR* **2000**, *18*, 329–336.
[26] P. J. Kraulis, *J. Magn. Reson.* **1989**, *84*, 627–633.
[27] M. van de Kamp, G. W. Canters, S. S. Wijmenga, A. Lommen, C. W. Hilbers, H. Nar, A. Messerschmidt, R. Huber, *Biochemistry* **1992**, *31*, 10194–10207.
[28] T. A. Jones, J. Y. Zou, S. W. Cowan, M. Kjeldgaard, *Acta Crystallogr., Sect. A* **1991**, *47*, 110–119.
[29] S. Bailey, *Acta Crystallogr., Sect. D* **1994**, *50*, 760–763.
[30] W. L. DeLano, *The PyMOL Molecular Graphics System*, San Carlos, CA, USA **2002**, http://www.pymol.org

Received: December 22, 2006
Published Online: May 8, 2007

 © 2007 Wiley-VCH Verlag GmbH & Co. KGaA, Weinheim 

DOI: 10.1002/ejic.200700313

# Coordination Versatility of 5(3)-(2-Hydroxyphenyl)-3(5)-methylpyrazole: Synthesis, Crystal Structure and Properties of $Co^{III}$, $Ni^{II}$ and $Cu^{II}$ Complexes

**Marta Viciano-Chumillas,[a] Stefania Tanase,[a] Guillem Aromí,[b] Jan M. M. Smits,[c] René de Gelder,[c] Xavier Solans,[d] Elisabeth Bouwman,[a] and Jan Reedijk*[a]**

**Keywords:** Cobalt / Nickel / Copper / Pyrazoles / Phenols / Crystal structures

New complexes with 5(3)-(2-hydroxyphenyl)-3(5)-methylpyrazole ($H_2$phpz), $[Co_2(H_2phpz)(Hphpz)_2(phpz)_2]\cdot 3CH_3CN$ (**1**), $[Ni(Hphpz)_2]$ (**2**) and $[Cu(Hphpz)_2]$ (**3**), were synthesized and structurally characterized. The ligand coordinates in the form of 3-(2-hydroxyphenyl)-5-methylpyrazole in all cases, except for one ligand in the $Co^{III}$ complex, where it coordinates in the 5-(2-hydroxyphenyl)-3-methylpyrazole mode. Crystallographic analysis revealed that **1** contains two chemically and crystallographically distinct cobalt(III) ions triply bridged by one phenoxide and two pyrazolate groups, giving rise to a $[Co_2(N\text{-}N)_2O]$ core with a Co···Co distance of 3.154 Å. Additionally, the $H_2$phpz ligand shows four different coordination modes with the metal ions, demonstrating its versatility. The dinuclear unit of **1** is stabilized by strong intramolecular N–H···O hydrogen-bonding interactions involving the phenol oxygen atom of the $H_2$phpz ligand and the N–H functionality of the pyrazole ring. The crystal structure of the isomorphous complexes **2** and **3** reveals the presence of centrosymmetric mononuclear units with the $MN_2O_2$ [M = $Ni^{II}$ (**2**), $Cu^{II}$ (**3**)] chromophore displaying a slightly distorted square-planar geometry. The mononuclear structures of **2** and **3** are further stabilized by intramolecular hydrogen bonds established between the acid N–H group as donor and the phenoxide group of the $H_2$phpz ligand as acceptor. Spectroscopic studies, ESI-MS and cyclic voltammetry were performed, supporting the crystallographic analysis.
(© Wiley-VCH Verlag GmbH & Co. KGaA, 69451 Weinheim, Germany, 2007)

## Introduction

Pyrazole-based ligands have received a great deal of attention over the last decades because of their interesting coordination chemistry, unusual structural features, and remarkable physical and chemical properties.[1,2] The incorporation of pyrazole groups in the design of new ligands allows the study of their structural properties to serve specific stereochemical requirements for a particular metal-binding site. In addition to its remarkable capacity to coordinate to a variety of metal ions, the pyrazole entity also has the ability to bring two metal centres into close proximity and provide an intramolecular pathway for spin-exchange interactions.[3] Although a significant number of coordination compounds containing pyrazole ligands have been obtained to date, the design and synthesis of novel pyrazole-containing complexes by employing more versatile ligands or by varying the nature of the reactants and synthetic conditions are still under investigation. We have recently reported that the ligand 5(3)-(2-hydroxyphenyl)-3(5)-methylpyrazole ($H_2$phpz) exhibits a variety of coordination abilities and tends to form large metal cluster aggregates.[4,5] The amount of base or the type of solvent are paramount in controlling the different coordination modes, thereby providing a rich versatility to the ligand.

In the present study we extended our investigations to the coordination of this ligand with cobalt, nickel and copper ions, and we report the synthesis, characterization and crystal structure of a quite unusual dinuclear cobalt(III) complex, $[Co_2(H_2phpz)(Hphpz)_2(phpz)_2]\cdot 3CH_3CN$ (**1**), triply bridged by one phenoxide and two pyrazolate groups, as well as two new isomorphous mononuclear complexes $[Ni(Hphpz)_2]$ (**2**) and $[Cu(Hphpz)_2]$ (**3**), and a dopant of $Cu^{II}$ in **2**. To the best of our knowledge, **1** is the first example of a dinuclear cobalt(III) complex bridged by both pyrazolate and phenoxide groups. A remarkable feature of this compound is the observed binding versatility of the $H_2$phpz ligand, which is coordinated in four different modes to the two cobalt(III) ions (Scheme 1).

[a] Gorlaeus Laboratories, Leiden Institute of Chemistry, Leiden University,
P. O. Box 9502, 2300 RA Leiden, The Netherlands
Fax: +31-71-527-4671
E-mail: reedijk@chem.leidenuniv.nl
[b] Departament de Química Inorgànica, Grup d'Interaccions Magnètiques, Universitat de Barcelona,
Diagonal 647, 08028, Barcelona, Spain
[c] Molecular Materials, Institute for Molecules and Materials, Radboud University Nijmegen,
Toernooiveld 1, 6525 ED Nijmegen, The Netherlands
[d] Departament de Cristallografia i Mineralogia, Universitat de Barcelona,
Martí i Franquès s/n, 08028, Barcelona, Spain
Supporting information for this article is available on the WWW under http://www.eurjic.org or from the author.

 © 2007 Wiley-VCH Verlag GmbH & Co. KGaA, Weinheim 

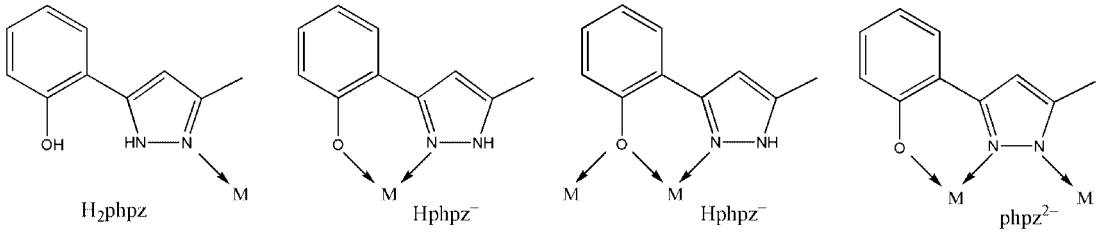


Scheme 1. Four different coordination modes of the 5(3)-(2-hydroxyphenyl)-3(5)-methylpyrazole ligand in complex **1**.

## Results and Discussion

### Synthesis and Spectroscopic Properties

The reaction of 5(3)-(2-hydroxyphenyl)-3(5)-methylpyrazole ($H_2$phpz) with $Co(ClO_4)_2·6H_2O$ in the ratio 2:1 in the presence of 2 equiv. triethylamine yielded the diamagnetic cobalt(III) complex $[Co_2(H_2phpz)(Hphpz)_2(phpz)_2]·3CH_3CN$ (**1**) as a purple solid. After filtration, slow evaporation of the solution afforded dark-brown crystals suitable for X-ray crystallography. The presence of base as well as the aerobic conditions are responsible for the oxidation of cobalt(II) to cobalt(III). The infrared spectrum of **1** suggests the coordination of the ligand to the cobalt(III) ion, as indicated by the shift of the $\nu_{C-O}$ stretching vibration from 1636 $cm^{-1}$ in the free ligand to 1596 $cm^{-1}$ in the complex and the $\nu_{C=N}$ stretching vibration from 1576 $cm^{-1}$ in the free ligand to 1558 $cm^{-1}$ in the complex. The peak observed at 3425 $cm^{-1}$ can be assigned to the phenol hydrogen atom of the $H_2$phpz ligand that remains neutral by coordination to cobalt(III). The band due to $\nu_{N-H}$ stretching vibration is observed at 3280 $cm^{-1}$ and is less broad than that of the free ligand because of the coordination of the ligands in the complex.[6] The ligand field spectrum of **1** in the solid state exhibits a broad absorption band at 576 nm that is characteristic of octahedral cobalt(III) complexes. The band at 335 nm can be assigned based on its intensity to a $p_\pi \rightarrow d_\sigma^*$ transition, whilst the band at 271 nm arises from a $\pi$-$\pi^*$ ligand transition.[7]

The reaction of $Ni(ClO_4)_2·6H_2O$, $H_2$phpz and $Bu_4NOH$ in a 1:1:2 ratio in methanol yielded a green compound that upon dissolution in dichloromethane followed by slow diffusion of diethyl ether afforded complex **2** as dark-green crystals. The infrared spectrum of **2** displays a strong band assignable to the $\nu_{N-H}$ stretching vibration at 3299 $cm^{-1}$. Several sharp weak bands observed in the range 2900–3150 $cm^{-1}$ are likely to be caused by the $\nu_{C-H}$ stretches of the methyl group. As the free $H_2$phpz ligand displays the $\nu_{C-O}$ stretching vibration at 1636 $cm^{-1}$, the shift of this band to 1600 $cm^{-1}$ in complex **2** suggests the coordination of the phenol oxygen atom. The ligand field spectrum of **2** displays two broad bands at 490 and 622 nm assigned to d-d transitions for the low-spin $Ni^{II}$ compound; the absorption band at 622 nm is assigned to a $d_{x^2-y^2} \rightarrow d_{zy}$ transition, whilst the absorption band at 490 nm is attributed to the $d_{z^2} \rightarrow d_{zy}$ transition.[8] The absorptions observed in the range 420 to 270 nm are likely to be caused by the metal-to-ligand and inter- or intra-ligand charge-transfer transitions. The solid compound turned out to be diamagnetic as expected for square-planar $Ni^{II}$, thereby allowing the study of a solid solution (dopant) of the isomorphous $Cu^{II}$ compound.

Complex **3** was obtained by reaction of $Cu(ClO_4)_2·6H_2O$ and $H_2$phpz in a 1:1 ratio and in the presence of 2 equiv. sodium methoxide as base. The reaction of $H_2$phpz with $Ni(OAc)_2$ and $Cu(OAc)_2$ in acetonitrile and in the absence of base afforded **2** and **3**, respectively, as polycrystalline samples with yields up to 76% for **2** and 72% for **3**. The infrared spectrum of complex **3** is very similar to that of complex **2**, and it exhibits the bands expected for the monoanionic Hphpz$^-$ ligand. Notably, the stretching vibrations $\nu_{C-O}$ at 1599 $cm^{-1}$ and $\nu_{C=N}$ at 1548 $cm^{-1}$ are observed at lower energies compared with the IR spectrum of the pure ligand. The ligand field spectrum shows a broad asymmetric band at 660 nm attributed to d-d transitions of copper(II) complexes with square-planar geometry; the absorption bands in the range 455–350 nm are a result of Cu–O and Cu–N charge-transfer transitions.

### Description of the Crystal Structures

A single-crystal X-ray analysis of **1** revealed the identity of the product as $[Co_2(H_2phpz)(Hphpz)_2(phpz)_2]·3CH_3CN$. Selected bond lengths and angles for **1** are given in Table 1.

Table 1. Selected bond lengths [Å] and angles [°] for the complex $[Co_2(H_2phpz)(Hphpz)_2(phpz)_2]·3CH_3CN$ (**1**).

| Bond lengths | | | |
|---|---|---|---|
| Co1–O21 | 1.865(4) | Co2–N11 | 1.929(5) |
| Co1–N12 | 1.875(5) | Co2–O41 | 1.879(4) |
| Co1–N31 | 1.925(6) | Co2–N32 | 1.875(6) |
| Co1–O81 | 1.919(4) | Co2–O61 | 1.916(4) |
| Co1–N72 | 1.914(5) | Co2–N52 | 1.893(5) |
| Co1–N91 | 1.969(6) | Co2–O81 | 2.002(4) |
| Co1···Co2 | 3.154 | | |
| **Bond angles** | | | |
| Co1–O81–Co2 | 107.1(2) | N91–Co1–O81 | 88.0(2) |
| N31–Co1–O21 | 92.5(2) | N72–Co1–N91 | 90.4(2) |
| O21–Co1–N91 | 88.0(2) | O21–Co1–N12 | 91.6(2) |
| O21–Co1–N72 | 88.4(2) | O21–Co1–O81 | 179.31(18) |
| O81–Co1–N12 | 88.0(2) | O81–Co1–N72 | 92.0(2) |
| N32–Co2–N11 | 88.8(2) | N32–Co2–O81 | 84.8(2) |
| N11–Co2–O81 | 84.9(2) | N52–Co2–N32 | 92.0(2) |
| N52–Co2–O61 | 89.9(2) | N52–Co2–O81 | 91.0(2) |
| N52–Co2–O41 | 90.7(2) | O41–Co2–N11 | 93.6(2) |
| O41–Co2–N32 | 90.3(2) | O61–Co2–N11 | 89.5(2) |
| O61–Co2–O41 | 87.76(17) | O81–Co2–O61 | 97.07(17) |

 © 2007 Wiley-VCH Verlag GmbH & Co. KGaA, Weinheim 

As shown in Figure 1, the molecular structure of **1** consists of a highly asymmetric dinuclear unit with two cobalt(III) ions bridged by two pyrazolate groups and one phenoxide group with a Co···Co separation of 3.154 Å. This distance is slightly longer than those observed for other triply bridged dinuclear cobalt(III) complexes.[9] Most remarkably, the $H_2$phpz ligand shows four different coordination modes in the molecular structure of **1**: (i) quite unusual, the $H_2$phpz ligand remains neutral and is N-monodentate bound to Co2, with the ligand present in the 5-(2-hydroxyphenyl)-3-methylpyrazole mode; (ii) a uninegative Hphpz$^-$ ligand is NO-chelating to Co1; (iii) a second uninegative Hphpz$^-$ molecule acts as a NO-bidentate chelating ligand, and it links the two cobalt(III) ions through a phenoxido bridge; and (iv) two ligand molecules are doubly deprotonated, and these phpz$^{2-}$ ligands coordinate in a $N_2O$-tridentate manner to link the two cobalt(III) ions by a double pyrazolato bridge. In the last three modes the ligand is present in the 3-(2-hydroxyphenyl)-5-methylpyrazole conformation. As a result, both cobalt(III) ions have a distorted octahedral geometry and are in quite different coordination environments. The Co1 ion has a $CoN_4O_2$ donor set in a *trans* octahedral geometry, whilst the Co2 ion has a $CoN_3O_3$ donor set in a *mer* octahedral geometry. The cobalt(III) to oxygen and cobalt(III) to nitrogen bond lengths are in the ranges of 1.865–2.002 Å and 1.875–1.969 Å, respectively, as expected for low-spin cobalt(III) complexes.[10] The largest deviation from the octahedral geometry is observed for the *trans* angle which is O81–Co2–O41 174.90(17)°. The Co–O–Co angle is 107.09°, and it is slightly smaller than the angle normally observed for phenoxido-bridged dinuclear cobalt(III) complexes.[11,12] The least-squares plane of the aromatic ring of the $N_2O$-tridentate phpz$^{2-}$ ligand and the plane defined by Co1, Co2 and O81 have a dihedral angle of 38.11°. The bending angle of the bridging pyrazole least-squares planes to the Co1–N12–N11–Co2 and Co1–N31–N32–Co2 coordination planes is 5.36° and 5.64°, respectively. The dihedral angle between the planes of the two bridging pyrazole rings is 79.91°, whilst the dihedral angle between the $CoN_{pz}N_{pz}Co$ planes is 75.98°.

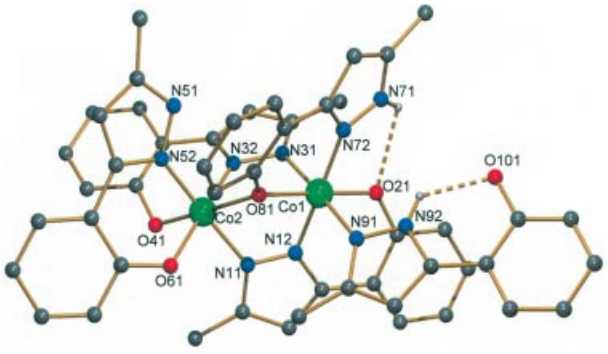


Figure 1. Pluton projection of the neutral complex $[Co_2(H_2phpz)(Hphpz)_2(phpz)_2]\cdot 3CH_3CN$ (**1**) showing the intramolecular hydrogen-bonding interactions. Hydrogen atoms that are not involved in hydrogen bonds and the acetonitrile molecules have been omitted for clarity.

The ligands adopt conformations that vary from nearly planar to considerably twisted with the dihedral angle between the phenyl and pyrazole ring planes ranging from 1.34° to 23.37°. These conformations are determined by the presence of strong intramolecular and intermolecular hydrogen bonds involving the O(phenol)–H and N(pz)–H moieties, as well as acetonitrile lattice molecules. The strongest intramolecular hydrogen bond involves the N–H group of the N-monodentate ligand bound to Co1 (N92–H92···O101 2.624 Å); the distance N71–H71···O21 of 2.756 Å would also suggest hydrogen bonding, but the angle of 107.9° is rather small. In addition, the O–H group of O101 participates in an intermolecular donor hydrogen-bonding interaction with a lattice acetonitrile molecule (O101–H101···N3 2.800 Å). The other two acetonitrile lattice molecules are at longer hydrogen-bond lengths (from N51 and N71). The acetonitrile molecules are kept rather weakly bound in the lattice, as is also seen from the elemental analyses (C, H and N), and some acetonitrile molecules might be replaced by atmospheric water. Table 2 gives some details of the hydrogen-bonding patterns.

Table 2. Hydrogen-bond details (distances [Å] and angles [°]) for $[Co_2(H_2phpz)(Hphpz)_2(phpz)_2]\cdot 3CH_3CN$ (**1**).

| Donor–H···Acceptor | D–H | H···A | D···A | D–H···A |
|---|---|---|---|---|
| N71–H71···O21 | 0.87 | 2.36 | 2.756(8) | 107.9 |
| N92–H92···O101 | 0.87 | 2.03 | 2.624(8) | 124.6 |
| O101–H101···N3 | 0.83 | 2.01 | 2.800(9) | 159.8 |
| N51–H51···N6 | 0.87 | 2.17 | 2.996(9) | 157.9 |
| N71–H71···N9 | 0.87 | 2.49 | 3.271(12) | 149.8 |

Complexes **2** and **3** are isostructural, and they crystallize in the space group $P2_1/n$. In both cases, the asymmetric unit contains half of a centrosymmetric mononuclear unit. The metal ion has a *trans*-$MN_2O_2$ environment formed by two Hphpz$^-$ ligand molecules that bind in a NO-bidentate chelating manner in the 3-(2-hydroxyphenyl)-5-methylpyrazole mode. The molecular structure of **2** is shown in Figure 2. The structure of **3** is presented in the electronic supporting information. The coordination geometry of the $NiN_2O_2$ chromophore is slightly distorted square-planar [N1–Ni–O1 91.90°, O1–Ni–N1a 88.10(8)°]. The Ni–N [1.862(2) Å] and Ni–O1 [1.868(2) Å] bond lengths agree well with the values expected for a low-spin $Ni^{II}$ ion in a square-planar environment.[13] The dihedral angle between the phenyl and pyrazole ring planes within the ligand is 4.62°. Examination of the crystallographic data (Supporting Information) reveals that the $Cu^{II}$ coordination environment of complex **3** is somewhat more distorted than that of the $Ni^{II}$ ion in **2**. As shown in Figure 2, there are two strong intramolecular hydrogen bonds with the acid N–H group as donor and the phenoxide group as acceptor [N2···O1a 2.612(3) Å, N2–H2···O1a 111°]. The crystal lattice is further stabilized by very weak π-π interactions involving the pyrazole rings; the shortest distance between the pyrazole planes is 3.919 Å. The closest Ni···Ni separation is 5.735 Å. Details for the $Cu^{II}$ compound are given in the electronic supporting information.

 © 2007 Wiley-VCH Verlag GmbH & Co. KGaA, Weinheim 

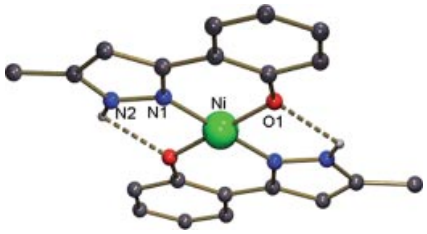


Figure 2. Pluton projection of the molecular structure of [Ni(Hphpz)$_2$] (**2**) showing the intramolecular hydrogen-bonding interactions. Hydrogen atoms that are not involved in hydrogen bonds have been omitted for clarity.

### EPR and Magnetic Susceptibility

Complexes **1** and **2** display no EPR signal, neither in the solid state nor in $CH_2Cl_2$ solution, at room temperature or at 77 K. These results strongly indicate that **1** and **2** are diamagnetic ($S = 0$), as expected for low-spin $d^6$ octahedral $Co^{III}$ complexes and low-spin $d^8$ square-planar $Ni^{II}$ complexes.

The polycrystalline powder EPR spectrum of **3** recorded at room temperature and 77 K shows a broad spectrum ($g = 2.06$), and no resolved hyperfine splitting was observed (Figure 3). When $Cu^{II}$ ions were separated by dilution as a 2% dopant in the diamagnetic host lattice of **2**, both hyperfine and superhyperfine splitting were observed (Figure 3). The superhyperfine structure is observed in the perpendicular region of the spectrum, arising from the interaction of the $Cu^{II}$ unpaired electron with the two nitrogen donor atoms of two ligand molecules that results in a five line splitting ($A_N = 10$ G). The magnitude of $g_\parallel$ and $A_\parallel$ (2.25 and 200 G, respectively) and the five superhyperfine lines indicate that the $Cu^{II}$ ion has an axial coordination geometry with two nitrogen donors in the equatorial plane,[14] in agreement with the X-ray crystal structure. The spectrum shows an unusual transition in the perpendicular region. This transition is caused by overshoot features which result in overlap of the perpendicular and the parallel transitions.[15]

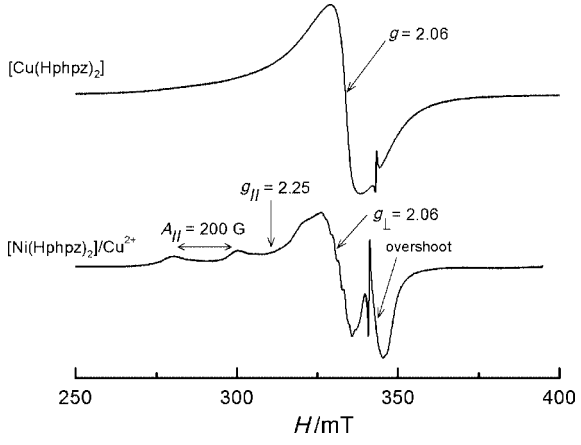


Figure 3. EPR spectra recorded at room temperature of [Cu(Hphpz)$_2$] (top) and [Ni(Hphpz)$_2$]/$Cu^{2+}$ (bottom), with the radical DPPH marker at $g = 2.00$.

The temperature-dependent magnetic susceptibility of **3** in the range 2–300 K shows paramagnetic behaviour which results from the absence of effective exchange magnetic interactions between the mononuclear units. At 300 K, the $\chi_M T$ value is equal to 0.35 $cm^3 K mol^{-1}$ which is close to the theoretical value of 0.375 $cm^3 K mol^{-1}$ expected for a single noncoupled $Cu^{II}$ centre ($S = 1/2$). The Ni compound was found to be diamagnetic.

### Solution Chemistry

The positive-ion mass spectrum of **1** in methanol solution exhibits prominent signals at $m/z = 983$ and 810 that can be assigned to the molecular ion $\{[Co_2(H_2phpz)(Hphpz)_2(phpz)_2] + H\}^+$ and the fragment $\{[Co_2(Hphpz)_2(phpz)_2] + H\}^+$. These results suggest that complex **1** retains its dinuclear structure in solution. Therefore, the redox behaviour of **1** was studied in acetonitrile solution within the potential range –1.8 to 1.5 V vs. a Ag/AgCl electrode at ambient temperature (300 K). The cyclic voltammogram of complex **1** shows one irreversible wave at +1.2 V that could be assigned to the oxidation of the ligand on the electrode surface. No cathodic peak was observed, in agreement with the high stability of the dinuclear cobalt(III) core in solution.

The NMR spectroscopic analysis of **1** shows a complicated spectrum due to the low symmetry of the complex. The peaks could not be assigned because of the splitting of multiple peaks in the aromatic region of the complex as compared with the five peaks of the free ligand. Nevertheless, the integration of the aromatic peaks is in agreement with the different coordination modes of the ligand in the complex.

The study of the electrochemical behaviour of the $Ni^{II}$ and $Cu^{II}$ complexes was carried out in $CH_2Cl_2$ solution in the range +1.2 to –1 V. For both **2** and **3**, a quasireversible ligand oxidation at 0.9 V was observed in the positive range. No other redox processes were observed for **2**. For **3**, the additional anodic process observed at 0.62 V can be assigned to a quasireversible one-electron oxidation of $Cu^{II}$ to $Cu^{III}$, and no cathodic process was observed. This result is not surprising given the preference of $Cu^{I}$ for nonplanar coordination geometry and the anionic nature of the ligand.

## Conclusions

In this study, the synthesis, crystal structure and spectroscopic characterization of an unusual dinuclear cobalt(III) complex and two new mononuclear $Ni^{II}$ and $Cu^{II}$ complexes have been presented. The reaction of the ligand 5(3)-(2-hydroxyphenyl)-3(5)-methylpyrazole with cobalt provided access to a new dinuclear complex, in which the versatility of the ligand showing four different coordination modes is beautifully illustrated. This dinuclear cobalt complex is unique, as it is triply bridged by two pyrazolate moieties and one phenoxide moiety with a Co···Co distance of 3.154 Å. This compound is stabilized through N–H···O in-

 © 2007 Wiley-VCH Verlag GmbH & Co. KGaA, Weinheim 

tramolecular hydrogen interactions. Also, N–H···N intermolecular hydrogen interactions are present with acetonitrile lattice molecules. ESI-MS and cyclic voltammetry studies showed that the dinuclear complex is highly stable in solution. Additionally, the reaction of the ligand with $Ni^{II}$ and $Cu^{II}$ ions readily afforded mononuclear species of type $[M(Hphpz)_2]$, in which the ligand appears to be strong enough to generate the low-spin $Ni^{II}$ cation. The EPR spectrum of the $Cu^{II}$ dopant in this lattice confirmed the geometry and chromophore. Further work aimed at the synthesis of higher nuclearity species is in progress.

## Experimental Section

**General Remarks, Analysis and Spectroscopy:** Starting materials were purchased from Aldrich, and all manipulations were performed using materials as received. The $H_2$phpz ligand was synthesized according to the reported procedure.[16] Elemental analyses (C, H and N) were performed with a Perkin–Elmer 2400 series II analyser. Infrared spectra (4000–300 $cm^{-1}$) were recorded with a Perkin–Elmer Paragon 1000 FTIR spectrometer equipped with a Golden Gate ATR device, using the reflectance technique. Ligand field spectra were obtained with a Perkin–Elmer Lambda 900 spectrophotometer using the diffuse reflectance technique, with MgO as a reference. The electrochemical measurements were performed with an Autolab PGstat10 potentiostat controlled by GPES4 software. A three-electrode system was used, consisting of a platinum working electrode, a platinum auxiliary electrode and a Ag/AgCl reference electrode. The experiments were carried out at room temp. under argon with tetrabutylammonium hexafluorophosphate as supporting electrolyte. All potentials are reported relative to Ag/AgCl. Electrospray mass spectra in acetonitrile/water (80:20) were recorded with a Thermo Finnigan AQA apparatus. X-band powder EPR spectra were obtained with a JEOL RE2x electron-spin resonance spectrometer using DPPH ($g$ = 2.0036) as a standard. Magnetic susceptibility measurements (2–300 K) were carried out at 0.1 T using a Quantum Design MPMS-5 5 T SQUID magnetometer.

**Synthesis of $[Co_2(H_2phpz)(Hphpz)_2(phpz)_2]\cdot 3CH_3CN$ (1):** A solution of 5(3)-(2-hydroxyphenyl)-3(5)-methylpyrazole (61 mg, 0.35 mmol) and triethylamine (67 mg, 0.66 mmol) in acetonitrile (7 mL) was slowly added to a solution of $Co(ClO_4)_2\cdot 6H_2O$ (66 mg, 0.18 mmol) in acetonitrile (2 mL). The resulting purple solution was stirred for 5 min to give a purple precipitate. The purple solid was collected by filtration, washed with acetonitrile and ether and dried in air. Yield: 26.03 mg (34%). Crystals suitable for X-ray diffraction were obtained by slow evaporation of the filtrate. $C_{56}H_{53}Co_2N_{13}O_5$ (1105.97): calcd. C 60.82, H 4.83, N 16.46; found C 58.13, H 5.00, N 15.08. Loss of some lattice acetonitrile molecules may result in lower C, H and N analyses as the acetonitrile molecules are weakly held in the lattice; replacement of one acetonitrile molecule by three molecules of water would generate a more accurate C,H,N analysis [complex·$2CH_3CN\cdot 3H_2O$, $C_{54}H_{56}Co_2N_{12}O_8$ (1118.98): calcd. C 57.96, H 5.04, N 15.02]. IR: $\tilde{\nu}$ = 3425 (w), 3280 (w), 1596 (m), 1558 (s), 1463 (s), 1456 (s), 1299 (m), 1229 (s), 1188 (w), 1116 (m), 1038 (w), 986 (s), 850 (s), 772 (m), 752 (m), 744 (m), 641 (m), 602 (m), 584 (s), 436 (m), 418 (s) $cm^{-1}$. UV/Vis: $\lambda_{max}$ = 576, 335, 271 nm.

**Synthesis of $[Ni(Hphpz)_2]$ (2):** The ligand $H_2$phpz (161 mg, 0.92 mmol) and 1 M methanol solution of $Bu_4NOH$ (2 mL, 2 mmol) were dissolved in methanol (10 mL). To this solution was added a solution of $Ni(ClO_4)_2\cdot 6H_2O$ (367 mg, 1 mmol) in methanol (10 mL), and the mixture was then stirred. A green microcrystalline precipitate formed immediately. After a few minutes, the solid (230 mg) was collected by filtration and dissolved in $CH_2Cl_2$ (20 mL). The dark-green solution was layered with $Et_2O$ in various sealed tubes. After a few days, large dark-green crystals suitable for X-ray crystallography were collected. Yield: 27.53 mg (15%). $C_{20}H_{18}NiN_4O_2$ (405.09): calcd. C 53.16, H 4.19, N 11.95 (The calculated values given here are for the complex **2**·$0.75CH_2Cl_2$. The presence of $CH_2Cl_2$ is not unexpected as the complex was crystallized from this solvent); found C 53.87, H 4.36, N 12.42. IR: $\tilde{\nu}$ = 3299 (s), 1600 (s), 1553 (s), 1471 (s), 1412 (s), 1314 (s), 1249 (s), 1197 (m), 1121 (m), 1039 (m), 1117 (m), 864 (s), 788 (s), 738 (m), 668 (m), 645 (m), 587 (s), 475 (m), 384 (s) $cm^{-1}$. UV/Vis: $\lambda_{max}$ =

Table 3. Crystal data and structure refinements for $[Co_2(H_2phpz)(Hphpz)_2(phpz)_2]\cdot 3CH_3CN$ (**1**), $[Ni(Hphpz)_2]$ (**2**) and $[Cu(Hphpz)_2]$ (**3**).

| Formula | $C_{56}H_{53}Co_2N_{13}O_5$ (**1**) | $C_{20}H_{18}NiN_4O_2$ (**2**) | $C_{20}H_{18}CuN_4O_2$ (**3**) |
|---|---|---|---|
| Formula mass [g mol$^{-1}$] | 1105.97 | 405.09 | 409.93 |
| Crystal system | monoclinic | monoclinic | monoclinic |
| Space group | $P2_1/c$ | $P2_1/n$ | $P2_1/n$ |
| $a$ [Å] | 10.6796(14) | 12.637(8) | 12.5018(13) |
| $b$ [Å] | 26.103(3) | 5.735(3) | 5.6636(6) |
| $c$ [Å] | 18.3933(12) | 12.736(4) | 12.785(4) |
| $\beta$ [°] | 92.492(8) | 110.64(2) | 110.420(11) |
| $V$ [Å$^3$] | 5122.6(10) | 863.8(8) | 848.4(3) |
| $Z$ | 4 | 2 | 2 |
| $D_{calcd.}$ [g cm$^{-3}$] | 1.434 | 1.557 | 1.605 |
| Crystal size [mm] | $0.22\times0.12\times0.04$ | $0.11\times0.13\times0.18$ | $0.38\times0.07\times0.04$ |
| Crystal shape and colour | dark-brown, regular platelets | green needles | dark brown-red needles |
| Number of collected reflections (unique) | 76586 (9012) | 6786 (2121) | 9188 (1494) |
| Number of observed reflections [$I_o > 2\sigma(I_o)$] | 6636 | 1883 | 1089 |
| Internal $R$ factor | 0.0953 | 0.058 | 0.052 |
| Number of parameters | 694 | 124 | 125 |
| Goodness-of-fit $S$ on $F^2$ | 1.247 | 1.11 | 1.08 |
| $\mu$ [mm$^{-1}$] | 0.712 | 1.147 | 1.312 |
| $R_1$[a] [$I > 2\sigma(I)$] | 0.0861 | 0.0547 | 0.0458 |
| $wR_2$[b] (all data) | 0.1780 | 0.1495 | 0.0870 |
| $T$ [K] | 208 | 293 | 208 |

[a] $R_1 = \Sigma||F_o| - |F_c||/\Sigma|F_o|$. [b] $wR_2 = \{\Sigma[w(F_o^2 - F_c^2)^2]/\Sigma w(F_o^2)^2\}^{1/2}$.

 © 2007 Wiley-VCH Verlag GmbH & Co. KGaA, Weinheim 

622, 490, 415, 360, 268 nm. The reaction of 2 equiv. $H_2$phpz with 1 equiv. $Ni(OAc)_2$ in acetonitrile and in the absence of base afforded **2** as a polycrystalline sample with a yield of 76%. The $Cu^{II}$-doped $Ni^{II}$ compound was prepared using this method but using a Ni/Cu ratio of 100:2.

**Synthesis of [Cu(Hphpz)$_2$] (3):** A solution of $H_2$phpz (35 mg, 0.20 mmol) and sodium methoxide (22 mg, 0.40 mmol) in methanol (5 mL) was slowly added to a solution of $Cu(ClO_4)_2 \cdot 6H_2O$ (76 mg, 0.20 mmol) in methanol (2 mL). The resulting green solution was stirred for 5 min to give a green precipitate. The solid was removed by filtration, and slow evaporation of the filtrate gave large dark-brown-red needles suitable for X-ray crystallography. Yield: 23.78 mg (58%). $C_{20}H_{18}CuN_4O_2$ (409.93): calcd. C 58.60, H 4.43, N 13.67; found C 58.43, H 4.30, N 13.76. IR: $\tilde{\nu}$ = 3311 (s), 1599 (m), 1548 (s), 1464 (s), 1316 (s), 1247 (m), 1196 (w), 1121 (m), 1065 (m), 1039 (w), 1018 (m), 857 (s), 791 (m), 739 (m), 668 (m), 641 (m), 618 (m), 593 (s), 575 (s), 470 (m), 371 (s) $cm^{-1}$. UV/Vis: $\lambda_{max}$ = 660, 455, 380, 350, 263 nm. The reaction of 2 equiv. $H_2$phpz with 1 equiv. $Cu(OAc)_2$ in acetonitrile and in the absence of base afforded **3** as a polycrystalline sample with a yield of 72%.

**X-ray Crystallographic Study:** Intensity data for single crystals were collected using Mo-$K_\alpha$ radiation ($\lambda$ = 0.71073 Å) with a Nonius KappaCCD diffractometer. Crystal and refinement data are shown in Table 3 for **1**, **2** and **3**. The intensity data were corrected for Lorentz and polarization effects, and for absorption (multiscan absorption correction[17]). The structures were solved by Patterson methods.[18] The programs EvalCCD, DIRDIF96 and SHELXL-97 were used for data reduction, structure solution, refinement and evaluation.[19–22] All non-hydrogen atoms were refined with anisotropic displacement parameters. All hydrogen atoms were placed at calculated positions and were refined riding on the parent atoms. Geometric calculations and molecular graphics were performed with the PLATON package.[23]

CCDC-628568, -639396 and -641268 contain the supplementary crystallographic data for this paper. These data can be obtained free of charge from The Cambridge Crystallographic Data Centre via www.ccdc.cam.ac.uk/data_request/cif.

**Supporting Information** (see also the footnote on the first page of this article): Table S1 summarizes the selected bond lengths [Å] and angles [°] for the complexes [Ni(Hphpz)$_2$] (**2**) and [Cu(Hphpz)$_2$] (**3**), and Figure S1 shows the crystal structure of [Cu(Hphpz)$_2$] (**3**).

## Acknowledgments

This work was financially supported by the Netherlands Economy, Ecology, Technology (EET) programme, the EC-RTN "QuEMolNa" (No. MRTN-CT-2003-504880) and the ECNetwork of Excellence "MAGMANet" (No. 515767-2). S. T. acknowledges the Netherlands Organization for Scientific Research (NWO) for a Veni grant. We would like to acknowledge Prof. L. J. de Jongh for useful discussions.

[1] R. Mukherjee, *Coord. Chem. Rev.* **2000**, *203*, 151–218.
[2] E. C. Constable, P. J. Steel, *Coord. Chem. Rev.* **1989**, *93*, 205–223.
[3] S. Tanase, I. A. Koval, E. Bouwman, R. de Gelder, J. Reedijk, *Inorg. Chem.* **2005**, *44*, 7860–7865.
[4] S. Tanase, G. Aromi, E. Bouwman, H. Kooijman, A. L. Spek, J. Reedijk, *Chem. Commun.* **2005**, 3147–3149.
[5] S. Tanase, E. Bouwman, G. J. Long, A. M. Shahin, A. M. Mills, A. L. Spek, J. Reedijk, *Eur. J. Inorg. Chem.* **2004**, 4572–4578.
[6] K. Nakamoto, *Infrared and Raman Spectra of Inorganic and Coordination Compounds*, John Wiley & Sons, New York, **1997**.
[7] A. B. P. Lever, *Inorganic Electronic Spectroscopy*, Elsevier, Amsterdam, **1997**.
[8] R. Dingle, *Inorg. Chem.* **1971**, *10*, 1141–1144.
[9] R. Dreos, G. Tauzher, D. H. Trendafilova, G. Nardin, L. Randaccio, *Inorg. Chem.* **1996**, *35*, 2715–2716.
[10] S. Chattopadhyay, G. Bocelli, A. Musatti, A. Ghosh, *Inorg. Chem. Commun.* **2006**, *9*, 1053–1057.
[11] V. D. Campbell, E. J. Parsons, W. T. Pennington, *Inorg. Chem.* **1993**, *32*, 1773–1778.
[12] J. S. Seo, R. C. Hynes, D. Williams, J. Chin, N. D. Sung, *J. Am. Chem. Soc.* **1998**, *120*, 9943–9944.
[13] L. Benisvy, R. Kannappan, Y. F. Song, S. Milikisyants, M. Huber, U. Mutikainen, P. Turpeinen, P. Gamez, L. Bernasconi, E. J. Baerends, F. Hartl, J. Reedijk, *Eur. J. Inorg. Chem.* **2007**, 637–642.
[14] B. J. Hathaway in *Comprehensive Coordination Chemistry* (Eds.: G. Wilkinson, R. D. Gillard, J. A. McCleverty), Pergamon Press, UK, **1987**.
[15] F. E. Mabbs, D. Collison, *Electronic Paramagnetic Resonance of d Transition Metal Compounds*, Elsevier, Amsterdam, **1992**.
[16] A. W. Addison, P. J. Burke, *J. Heterocycl. Chem.* **1981**, *18*, 803–805.
[17] G. M. Sheldrick, *Program for Emperical Absorption Correction*, University of Göttingen, Germany, **1996**.
[18] P. T. Beurskens, G. Beurskens, M. Strumpel, C. E. Nordman in *Patterson and Pattersons* (Eds.: J. P. Glusker, B. K. Patterson, M. Rossi), Clarendon Press, Oxford, **1987**.
[19] P. T. Beurskens, G. Beurskens, W. P. Bosman, R. de Gelder, S. García-Granda, R. O. Gould, R. Israël, J. M. M. Smits, C. Smykalla, *The DIRDIF96, A computer program system for the crystal structure determination by Patterson methods and direct methods applied to difference structure factors*, Crystallography Laboratory, University of Nijmegen, Nijmegen, The Netherlands, **1996**.
[20] G. M. Sheldrick, *SHELXL-97, Program for the refinement of crystal structures*, University of Göttingen, Germany, **1997**.
[21] A. J. M. Duisenberg, *Reflections on Area Detectors*, Ph. D. Thesis, Utrecht University, **1998**.
[22] *COLLECT, data collection software*, Nonius B. V., **1999**.
[23] A. L. Spek, *PLATON, A Multipurpose Crystallographic Tool*, Utrecht University, The Netherlands, **2003**.

Received: March 21, 2007
Published Online: May 16, 2007

 © 2007 Wiley-VCH Verlag GmbH & Co. KGaA, Weinheim 

DOI: 10.1002/ejic.200601195

# Structures of the b- and d-Acid Derivatives of Vitamin $B_{12}$ and Their Complexes with $[M(CO)_3]^+$ (M = $^{99m}$Tc, Re)

**Bernhard Spingler,[a] Stefan Mundwiler,[a] Pilar Ruiz-Sánchez,[a] Dave R. van Staveren,[a] and Roger Alberto*[a]**

**Keywords:** Vitamins / X-ray diffraction / Rhenium / Technetium / Labelling

The acid hydrolysis of natural vitamin $B_{12}$ yields several products in which the acetamide or propionamide side chains on the corrin framework are converted into the corresponding acids. These acids can be derivatised with further functionalities. We have separated in particular the b- and the d-acid derivatives **1** and **2**, respectively, since functionalisation at these positions of the corrin ring generally keeps the affinity for vitamin $B_{12}$ transport proteins intact. Although the authenticity of **1** and **2** seemed evident from $^1$H NMR investigations, it has not been supported by X-ray structure analysis. The coupling of ethyl *N*-(3-aminopropyl)-*N*-(pyridin-2-ylmethyl)glycinate (**3**) to the carboxylate groups in **1** and **2** by peptide synthetic methods gave the vitamin $B_{12}$ derivatives **4** and **5**, respectively. The structures of **4** and **5** could be characterised by X-ray analysis, which unambiguously confirmed the presence of the b- and d-acid in **1** and **2**, respectively. The reaction of **4** and **5** with the complex $[Re(OH_2)_3(CO)_3]^+$ in water gave the corresponding vitamin $B_{12}$ derivatives **8** and **9**, and the aqueous reaction of **4** and **5** with the complex $[^{99m}Tc(OH_2)_3(CO)_3]^+$ afforded the $^{99m}$Tc homologues **10** and **11**, respectively.

(© Wiley-VCH Verlag GmbH & Co. KGaA, 69451 Weinheim, Germany, 2007)

## Introduction

Cyanocobalamin or vitamin $B_{12}$ (abbreviated as $B_{12}$ in the following) is, like most of the vitamins, not synthesised by mammals but by a few bacteria only. However, essentially all higher organisms are $B_{12}$ dependent, and the human body in particular has developed a highly complex system for the uptake and biochemical conversion of $B_{12}$ into the two coenzymes methyl- and adenosylcobalamin. Excellent and comprehensive reviews appeared recently covering all aspects of $B_{12}$ chemistry, biochemistry and physiology.[1–3] $B_{12}$ has been proposed as a Trojan horse for cyto- or radiotoxic compounds, since it is essential for the human body. Vitamin-mediated drug uptake by rapidly growing and dividing aggressive tumours having a high density of transcobalamin receptors seems to be an attractive strategy.[4] Covalent conjugation of bioactive molecules to the $B_{12}$ molecule can be performed at several functional sites. The 5′-OH group of the α-ribofuranoside in the backloop would be such a versatile site according to structure–activity relationships. However, little functionalisation has been reported, because of the complexity of site-specific derivatisation.[5] Furthermore, the b- and d-acid sites are attractive positions for conjugation of functionalities or metal complexes. It could be shown by Hogenkamp et al. that covalent binding of a spacer with DTPA and subsequent labelling with $^{111}$In led to a good uptake in the tumour cells, but the uptake was also high in the kidneys.[6,7] We have chosen the b- and d-acids for derivatisation. Although it is known that the affinity of such derivatives for transcobalamin proteins decreases, it is still strong enough for binding and transportation.[8–10] In our previous work, we attached histidine derivatives at the b- or d-acids of $B_{12}$.[11,12] Preliminary studies with $^{99m}$Tc-labelled $B_{12}$ derivatives led to very promising results in vitro and in vivo. Biologically active molecules have also been introduced by direct coordination to the $Co^{III}$ atom in $B_{12}$ or through the cyano group bound to it. Grissom et al. coupled fluorescing molecules by a Co–C bond to $B_{12}$ and used this derivative for lymphatic mapping.[13,14] We bound several rhenium, technetium and platinum complexes to the cyano group and could confirm the authenticity of the products by X-ray structure analysis.[15,16]

The preferred site for derivatisation are the three propionamide and the two acetamide groups bound to the periphery of the corrin ring, which is, like the backloop, bound to three propionamide and two acetamide groups. Scheme 1 gives an overview of the structure of $B_{12}$ and the relative positions of the respective groups.

Characterisation of $B_{12}$ derivatives is mainly performed with NMR spectroscopy. NMR-restrained molecular mechanics/molecular dynamics methods have successfully been used to structurally characterise $B_{12}$ derivatives.[17] Nevertheless, X-ray structure analysis would be preferable, but

[a] Institute of Inorganic Chemistry, University of Zürich, Winterthurerstrasse 190, 8057 Zürich, Switzerland
E-mail: ariel@aci.unizh.ch

Supporting information for this article is available on the WWW under http://www.eurjic.org or from the author.

 © 2007 Wiley-VCH Verlag GmbH & Co. KGaA, Weinheim 

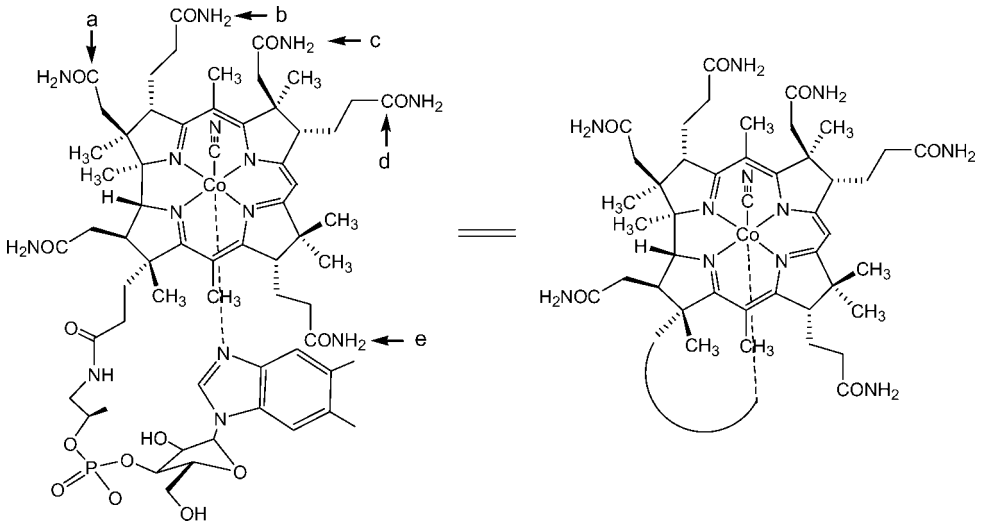


Scheme 1. Assignment of the side chains on the periphery of the corrin ring in $B_{12}$.

some $B_{12}$ derivatives are very difficult to crystallise. Milestones in $B_{12}$ structure analysis were certainly the elucidation of the structure of native $B_{12}$ by Hodgkin et al.,[18] and those of methylcobalamin and finally adenosylcobalamin (coenzyme $B_{12}$).[19,20] X-ray crystallography of $B_{12}$ and its derivatives has recently been reviewed extensively.[21–23] These reviews reveal the surprising fact that no X-ray analysis of a $B_{12}$ derivative in which one of the amide side chains has been functionalised is available. To the best of our knowledge, the only available X-ray structure of the product of a derivatisation at the corrin ring is that of one in which the C10-H has been replaced by a chlorine atom.[24] We present in this study the synthesis and the first X-ray structures of $B_{12}$ molecules that were derivatised at either the b- or the d-acid with a ligand for binding to transition metals. In a second step, these $B_{12}$ derivatives were labelled with the *fac*-$[M(CO)_3]^+$ (M = Re, $^{99m}$Tc) moiety.

## Results and Discussion

### Syntheses

Mild acid hydrolysis of the amide side chains in $B_{12}$ yields a mixture of monocarboxylic b-, d- and e-acids. These can be separated and obtained in pure form by sequential ion-exchange chromatography and RP-HPLC methods.[8,25–27] With a slightly modified method (see Experimental Section) we obtained 280 mg (15%) of the b-acid **1** and 132 mg (7%) of the d-acid **2**, starting with 1.9 g of vitamin $B_{12}$ (Scheme 2). These yields are consistent with the literature. However, we isolated only 94 mg (5%) of the e-acid.

The determination of the exact structures of the products of hydrolysis turned out to be difficult. Initially, the main product, compound **1**, was thought to be the e-acid because

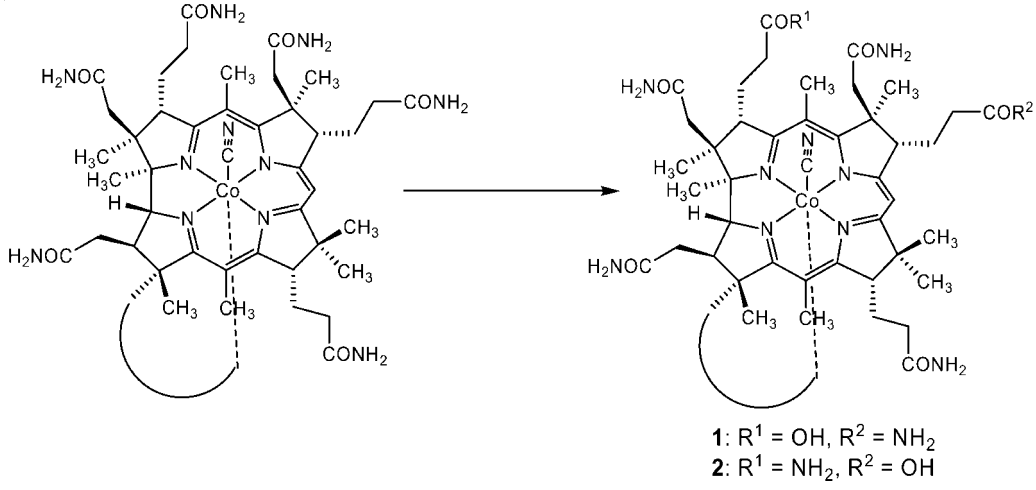


Scheme 2. Mild hydrolysis of $B_{12}$ yields the b- and d-acids **1** and **2**.[8,25–27]

 © 2007 Wiley-VCH Verlag GmbH & Co. KGaA, Weinheim 

of its ability to hydrolyse the backloop and from the results of X-ray and neutron diffraction studies.[26,28] Subsequent neutron diffraction studies indicated that it could be the b-acid, an assumption that was later confirmed by sophisticated multi-dimensional NMR measurements.[29–32] The similar diffraction power of the OH and $NH_2$ groups was the problem in X-ray analysis. Cobalamin crystals were rarely obtained in the quality required for an unambiguous differentiation between these two groups. An X-ray structure analysis of respective derivatives such as esters or alkylamides would solve this problem (see later). However, initially all attempts failed, because the conjugated groups prevented crystallisation or were disordered.[23,33]

Since we are interested in the introduction of coordinating ligands rather than simple organic groups, we selected the tridentate chelate *N*-(pyridin-2-ylmethyl)glycine. This basic ligand structure is known to form strong complexes with the *fac*-$[M(CO)_3]^+$ moiety that are stable in vivo.[34] To enable the conjugation of the basic ligand framework to the biomolecule, an alkyl chain with a terminal functionality was introduced to the secondary amine by adaptation of known synthetic pathways.[35] In this case, the 3-aminopropyl chain bound to the secondary amine group in the basic ligand structure gave compound **3**, which then comprised the tridentate chelate (after de-esterification) and an additional primary amine for coupling with the b- and d-carboxylic acids (Scheme 3).

The reaction of **1** and **2** in the presence of ligand **3** and coupling reagents gave the corresponding derivatives **4** (b-acid) and **5** (d-acid), respectively, after HPLC purification, in about 30% yield. In order to obtain the free tridentate ligand, the ester functionality can be removed from the ligand by alkaline hydrolysis. It turned out, however, that the hydrolysis in advance was not required, since coordination to the *fac*-$[M(CO)_3]^+$ moiety catalysed this reaction and led to immediate hydrolysis during the coordination process.

X-ray-quality crystals could be grown by very slow vapour diffusion of either acetone or acetonitrile into an aqueous solution of **4** or **5**, respectively. The crystals of **4** were of exceptional quality for $B_{12}$ crystals, which is shown by the $R_1$ value of 5.9% for the strong reflections. Furthermore, more than 92% of all reflections with a resolution better than 0.75 Å had an intensity higher than 2 sigma. On the other hand, the diffraction of the crystals of **5** was not strong enough on our Mo home source; therefore, we collected synchrotron data on the F1 beamline at HASYLAB/DESY to a resolution of 0.99 Å. Both structures crystallised in the "typical" $B_{12}$ space group $P2_12_12_1$. In the literature, the family of $B_{12}$ crystal structures with the $P2_12_12_1$ space group is subdivided into four clusters on the basis of the ratio of the cell axes *b*/*a* and *c*/*a*.[21] Introduction of the rather large unit of **3** into the $B_{12}$ framework apparently did not distort the normal $B_{12}$ crystal packing. The corresponding ratios for the crystal structures of **4** and **5** are 1.40 and 1.39 for *b*/*a* and 1.61 and 1.61 for *c*/*a*, respectively. These values place **4** and **5** clearly into cluster II. Furthermore, an overlay of the two structures reveals an almost identical conformation of all substituted as well as unsubstituted amide side chains (Figure 1). The ORTEP plots of **4** and **5** are shown in Figure 2 and Figure 3, respectively. It should be noted that both ligand structures include the ethyl ester as the pendent since the coupling was performed directly with compound **3**. This was confirmed by the mass spectra of both compounds. Because of the disorder in the structure of **5**, we were only able to localise the terminal $CH_3$ group in **4** but not that in **5**; hence, it does not appear in the line drawings or the ORTEP drawings.

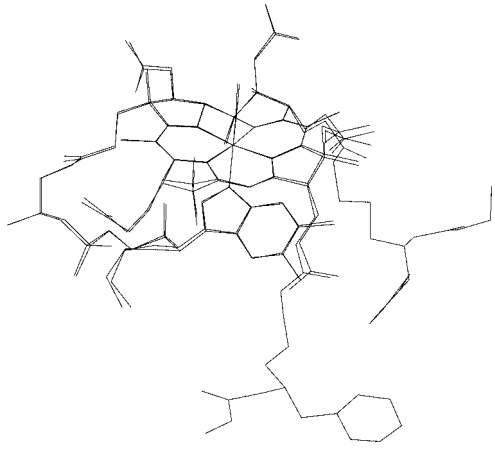

Figure 1. Overlay of the X-ray structures of **4** and **5**.

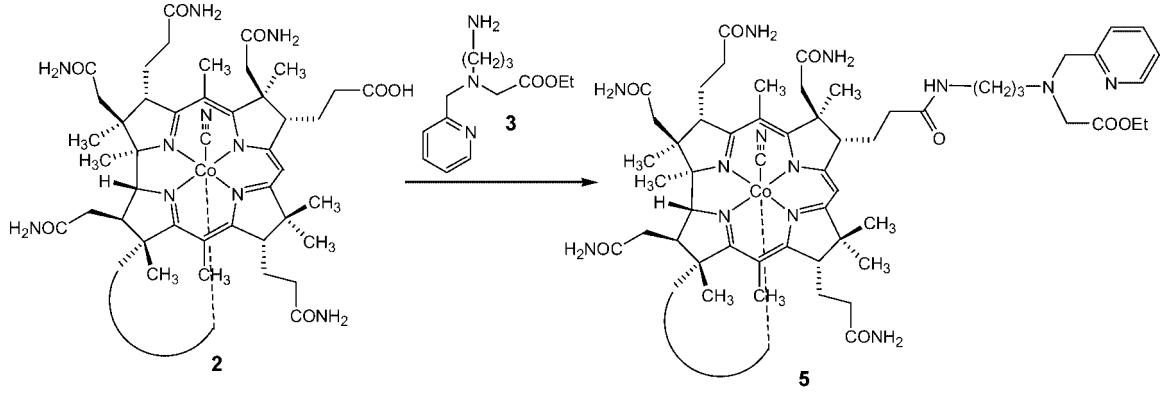


Scheme 3. Derivatisation of $B_{12}$ d-acid **2** with ligand **3** to yield compound **5**.

 © 2007 Wiley-VCH Verlag GmbH & Co. KGaA, Weinheim 

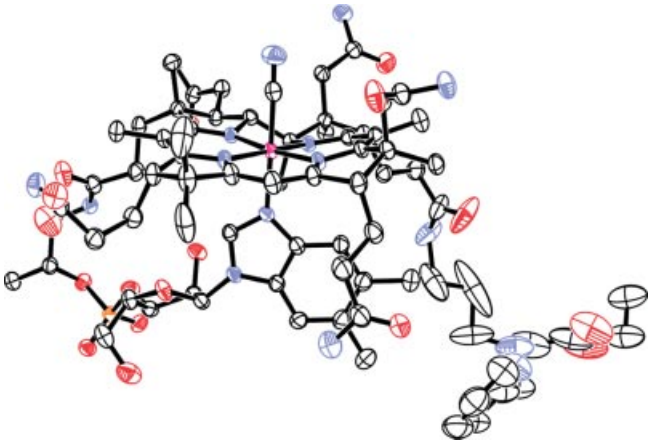

Figure 2. ORTEP plot of **4**. Hydrogen atoms and some water molecules were omitted for clarity.

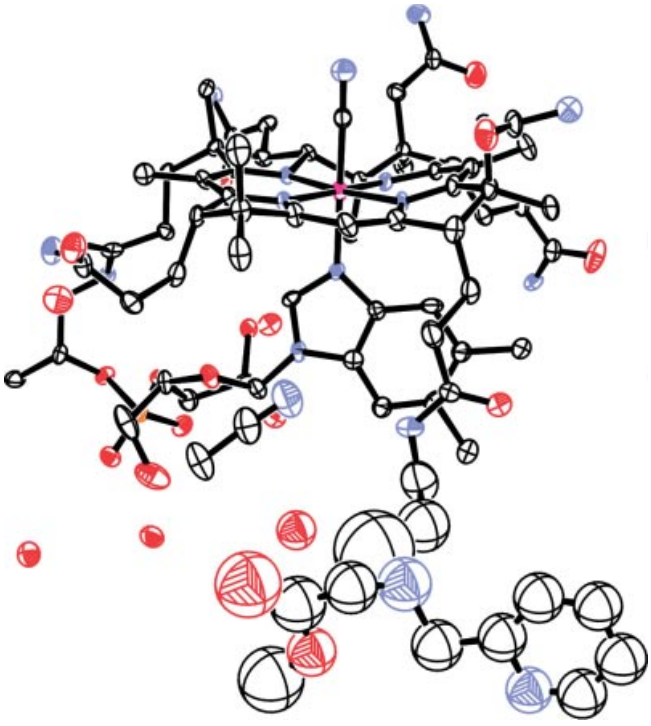

Figure 3. ORTEP plot of **5**. Hydrogen atoms and some water molecules were omitted for clarity.

The nitrogen atom of the pyridine group in **4** is hydrogen-bonded to a five-membered cluster of water molecules with extensive contact between three $B_{12}$ molecules. The nitrogen atom of the pyridine group in **5** has two hydrogen bonds with symmetry-generated neighbouring molecules in a Y-shaped alignment of three water molecules (Table 1).

### Complexation with $[Re(OH_2)_3(CO)_3]^+$ and Labelling with $[^{99m}Tc(OH_2)_3(CO)_3]^+$

In compounds **4** and **5**, the carboxylate group is still protected by an ester functionality. Mild alkaline hydrolysis of the ethyl ester over an extended period would convert the ester into the acid and render all three coordination sites available; however, decomposition products were observed during this process, presumably as a result of c-lactam formation. The formation of the c-lactam of $B_{12}$ in alkaline media is a known reaction.[36,37] During the reaction of **4** and **5** with $[Re(OH_2)_3(CO)_3]^+$ in water, we observed that ester cleavage was catalysed by the presence of the metal complex, probably after initial coordination to one or two of the nitrogen donors. A similar observation was made with histidine complexes, in which an ester function was also converted quantitatively to the carboxylate during coordination.[12] After the reaction was completed, we found a mixture of two complexes, one of which was the desired product **8** (for the b-derivative). The highest yield for a single product, however, was obtained by an indirect pathway. The formation of the complex **6** from **3** and $[Re(OH_2)_3(CO)_3]^+$ is quantitative. Complex **6** was then coupled to acid **1** and afforded complex **8** directly in very good yield without byproducts (Scheme 4). The second strategy, as described before, refers to the prelabelling of biomolecules with $^{99m}Tc$. Since yields are usually far from quantitative, prelabelling is not the method of choice for technetium. We had observed previously that ester bonds are much more efficiently cleaved in the presence of technetium than in the presence of rhenium. This observation was confirmed by treating $[^{99m}Tc(OH_2)_3(CO)_3]^+$ with **4** or **5** at moderate temperature. We observed the exclusive formation of the desired products **10** and **11** without any byproducts, even though byproducts had been observed in the corresponding reactions with $[Re(OH_2)_3(CO)_3]^+$. Comparison of the retention times of **10** and **11** with **8** and **9** confirmed the identity of the corresponding homologues. These technetium complexes are stable in human serum albumin for at least 24 h without reoxidation to $[^{99m}TcO_4]^-$. Compounds **10** and **11** therefore represent excellent radiotracers for uptake studies in cancer cells or microbial infections.

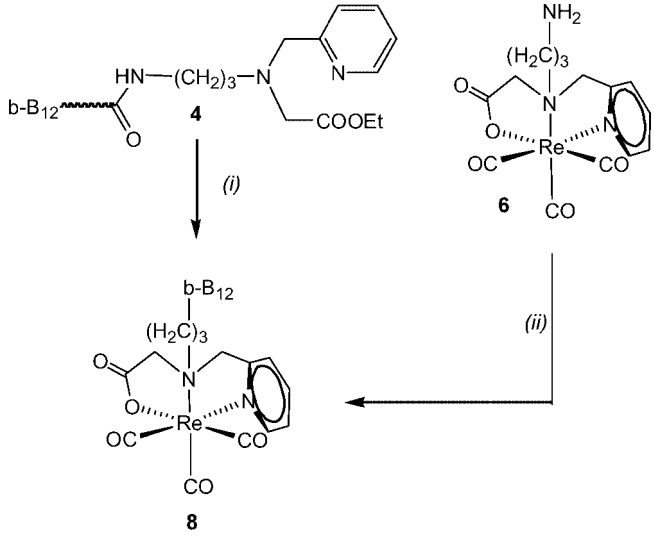


Scheme 4. Reaction pathways to **8**, (*i*) direct reaction of **4** with $[Re(OH_2)_3(CO)_3]^+$ to give **8** (postlabelling) or (*ii*) conjugation of preformed **6** to **1** (prelabelling).

 © 2007 Wiley-VCH Verlag GmbH & Co. KGaA, Weinheim 

## Conclusions

We have synthesised two $B_{12}$ derivatives that comprise tridentate chelators attached to the corrin periphery. For the first time, an X-ray structure analysis of a $B_{12}$ compound with corrin side-chain derivatisation could be elucidated confirming the assignments of earlier NMR investigations. The derivatives are coordinated to $[Re(OH_2)_3(CO)_3]^+$ and to $[^{99m}Tc(OH_2)_3(CO)_3]^+$, thus representing useful radiolabelled $B_{12}$ compounds for in vitro and in vivo studies.

## Experimental Section

**General Remarks:** Reagent grade chemicals were obtained from Merck, Dietikon (CH), Aldrich, Fluka or Buchs (CH) and were used without further purification. HPLC analyses were performed with a Merck-Hitachi L-7000 system equipped with a EG&G Berthold LB 508 radiometric detector, using Waters XTerra RP8 columns (5-μm particle size, $1 \times 100$ mm) and a flow rate of 1 mL min$^{-1}$. Chromatograms were recorded at 250 and 360 nm. Sodium acetate buffer A1 was prepared by mixing acetic acid (2.9 mL) and sodium hydroxide (4.55 mL, 2 M) in water (900 mL) and methanol (100 mL). Tris buffer A2 was prepared by dissolving 2-amino-2-(hydroxymethyl)propane-1,3-diol (605 mg) in water, adding HCl (2 M) to reach a pH of 8.2, adjusting the volume to 1000 mL and adding acetonitrile (10 mL). Eluent B was always methanol. Preparative HPLC separations were performed with a Varian Prostar system equipped with two Prostar 215 pumps and a Prostar 320 UV/Vis detector using Waters XTerra Prep RP8 columns (5-μm particle size, $3 \times 100$ mm and $30 \times 100$ mm). Flow rates were 4 mL min$^{-1}$ for the $3 \times 100$-mm column and 30 mL min$^{-1}$ for the $30 \times 100$-mm column. UV/Vis spectra were recorded with a Varian Cary 50 spectrometer, IR spectra were recorded with a Bio-Rad FTS-45 spectrometer in KBr. ESI-MS were recorded with a Merck Hitachi M-8000 spectrometer. The values of the $^{187}Re$ isotope are reported for Re compounds. NMR spectra were recorded with a Bruker DRX 500 MHz spectrometer.

Cobalamin derivatives were desalted by applying an aqueous solution of the compound to a Chromafix RP18ce cartridge and then thoroughly rinsing with water. The desalted product was then eluted with methanol, the solvent was removed, and the resulting product was dried in high vacuum.

The ethyl ester of *N*-(3-aminopropyl)-*N*-(pyridin-2-ylmethyl)glycinate, compound **3**, was prepared as described for its pentyl analogue.[35] Cyclisation of the compound was observed under basic conditions; therefore, the Boc-protected precursor was stored and deprotected with TFA just prior to further functionalisation. [Re({*N*-(3-aminopropyl)*N*-pyridin-2-ylmethylamino}acetato)$(CO)_3$] (**6**) was prepared by treating the fully deprotected [*N*-(3-aminopropyl)-*N*-pyridin-2-ylmethylamino]acetic acid with $(Et_4N)_2[Re(Br)_3(CO)_3]$ in water (see below). The syntheses of the b- and d-acids **1** and **2** of $B_{12}$ were performed according to the literature but with some slight modifications in the purification process as described below.[8]

**X-ray Crystallography:** Suitable crystals were covered with Paratone N oil, the mother liquor was removed, and the crystals were finally mounted with the help of the magnetic loops. Single-crystal diffraction data for **4** were collected with a Stoe IPDS diffractometer at 183(2) K by using graphite-monochromated Mo radiation (0.71073 Å). Data were corrected for Lorentz and polarisation effects as well as for absorption. Single-crystal diffraction data of **5** were collected at the F1 beamline at HASYLAB/DESY with a Huber Kappa diffractometer at 100(2) K, by using $\lambda = 0.7500$ Å radiation and a MarCCD 165 detector. Integration of intensities was performed with the XDS program.[38] A series of 190 frames with a 1.0-degree phi rotation and an exposure time of 90 s was collected. The XDS program compensated for the beam intensity loss between two refills. Both structures were solved with direct methods by using SIR97[39] and refined by full-matrix least-squares methods on $F^2$ with SHELXL-97.[40] Appropriate restraints had to be used to constrain the geometry of the highly flexible ligand part in **5**. The terminal carbon atom of the ethyl ester in **5** could not be localised in the electron density map. ORTEP plots were generated by the ORTEP32 software and are drawn at 30% probability. The crystal data and refinement parameters of **4** and **5** are summarised in Table 1. CCDC-630989 and CCDC-630990 contain the supple-

Table 1. Crystal and structure refinement data for **4** and **5**.

| Compound No. | **4** | **5** |
|---|---|---|
| X-ray source | sealed Mo tube | F1 beamline at HASYLAB/DESY |
| Detector | Stoe IPDS | MarCCD 165 |
| Wavelength [Å] | 0.71073 | 0.7500 |
| Formula[a] | $C_{79}H_{132}CoN_{16}O_{27}P$ | $C_{77}H_{122}CoN_{17}O_{24}P$ |
| $M_r$ | 1827.91 | 1759.82 |
| Crystal system | orthorhombic | orthorhombic |
| Space group | $P2_12_12_1$ | $P2_12_12_1$ |
| $a$ [Å] | 15.9566(6) | 15.9200(15) |
| $b$ [Å] | 22.3021(8) | 22.1900(18) |
| $c$ [Å] | 25.6917(12) | 25.680(3) |
| $V$ [Å$^3$] | 9142.8(6) | 9071.8(15) |
| $Z$ | 4 | 4 |
| $D_c$ [g cm$^{-3}$] | 1.328 | 1.288 |
| Goodness-of-fit on $F^2$ | 1.046 | 1.138 |
| $R$[b,c] | 0.0594 | 0.0824 |
| $wR_2$[b,d] | 0.1600 | 0.1979 |
| Flack parameter | 0.009(9) | –0.06(3) |
| Max., min. peaks [e·Å$^{-3}$] | 1.034, –0.815 | 0.698, –0.852 |

[a] Formulas are different since various amounts of solvent molecules were found in the structures. [b] Observation criterion: $I > 2\sigma(I)$. [c] $R = \Sigma||F_o| - |F_c||/\Sigma|F_o|$. [d] $wR_2 = \{\Sigma[w(F_o^2 - F_c^2)^2]/\Sigma[w(F_o^2)^2]\}^{1/2}$.

 © 2007 Wiley-VCH Verlag GmbH & Co. KGaA, Weinheim 

mentary crystallographic data for this paper. They can be obtained free of charge from The Cambridge Crystallographic Data Centre via www.ccdc.cam.ac.uk/data_request/cif.

**Synthesis of Vitamin $B_{12}$ b- and d-Acids 1 and 2:** Vitamin $B_{12}$ (1.88 g, 1.39 mmol) was hydrolysed in HCl (0.1 M, 190 mL) as described in literature.[8] The purification was modified in the following way. After desalting the crude reaction mixture by phenol extractions, three fractions were isolated on a Dowex column. The first fraction contained exclusively **2**, the second one a mixture of **1** and **2**, and the third one contained **2** and the e-acid. The second fraction (mixture of **1** and **2**) was separated by preparative HPLC (column: Waters XTerra Prep RP8, 5 μm, 30 × 100 mm; buffer A1; gradient: 0.5%min$^{-1}$ starting from 100% A1). The mixture of **2** and the e-acid was separated on the same system but using the buffer A2. Compound **1** was isolated in a yield of 280.6 mg (14.9%), compound **2** in a yield of 131.5 mg (7.0%), and the e-acid was obtained in a yield of 94.26 mg (5.0%). Assignment of the isomers was carried out by comparison with the HPLC retention order given in literature.

**Synthesis of 4:** A solution of freshly prepared **3** (361 μmol) in water (1 mL) was added to **1** (65.0 mg, 48.1 μmol). EDC (46.1 mg, 240 μmol) was added, and the pH was adjusted to 5.5 with NaOH (0.1 M). After the mixture was stirred at room temperature for 15 h, HPLC analysis exhibited about 50% of product **4**. More EDC (46.1 mg, 240 μmol) was added, but even extended stirring at room temperature did not lead to a significant amount of formation of more **4**. The solvent was removed in vacuo, and the residue was purified by preparative HPLC (buffer A1, gradient: 0.5%min$^{-1}$ starting from 100% A1). The main fraction was collected, the solvent was removed in vacuo, and the product was desalted to give **4** in a yield of 25.8 mg (16.2 μmol, 33.3%). $R_t$ = 13.1 min (gradient A1/B). $^1$H NMR (500 MHz, $CD_3OD$, 300 K): $\delta$ = 8.43 (d, $J$ = 4.9 Hz, 1 H, L12), 7.77 (t, $J$ = 7.7 Hz, 1 H, L10), 7.58 (d, $J$ = 7.8 Hz, 1 H, L9), 7.28 (t, $J$ = 6.9 Hz, 1 H, L11), 7.25 (s, 1 H, B7), 7.12 (s, 1 H, B2), 6.56 (s, 1 H, B4), 6.27 (d, $J$ = 3.0 Hz, 1 H, R1), 6.04 (s, 1 H, C10) ppm. $^{13}$C NMR (125.8 MHz, $CD_3OD$, 293 K): $\delta$ = 181.65, 180.20, 177.67, 176.73, 175.65, 175.58, 175.43, 174.72, 174.48, 174.34, 173.19, 167.22, 166.98, 160.49, 160.44, 149.67, 143.55, 138.86, 138.34, 135.72, 133.88, 131.56, 125.07, 124.04, 117.92, 112.65, 108.77, 105.21, 95.76, 88.05, 86.50, 83.74 (d, $J_{C,P}$ = 5.6 Hz), 76.40, 75.55, 73.69 (d, $J_{C,P}$ = 6.1 Hz), 71.66, 70.80, 70.56, 62.74, 61.79, 60.85, 60.45, 57.75, 56.97, 55.91, 55.67, 55.13, 53.31, 52.64, 50–49 (1 C below solvent), 46.91, 43.99, 43.16, 40.22, 38.88, 37.06, 35.43, 33.58, 33.09, 33.06, 32.42, 29.74, 28.01, 27.96, 27.52, 21.07, 20.61, 20.43, 20.26 (d, $J_{C,P}$ = 3.8 Hz), 20.02, 17.67, 17.16, 16.51, 16.21, 14.71 ppm. ESI-MS: $m/z$ = 806.5 $[M + H + Na]^{2+}$, 795.6 $[M + 2 H]^{2+}$. UV/Vis (methanol): $\lambda$ ($\varepsilon$, L mol$^{-1}$ cm$^{-1}$) = 278.0 (8500), 361.1 (26500), 549.1 (8000) nm. A full $^1$H NMR spectrum is shown in the Supporting Information. The ester can be hydrolysed to the acid. Because of self-catalysed cleavage processes (see above) this compound has to be labelled immediately. Labelling can be performed directly with **4** without the need for prior deesterification. $R_t$ = 10.8 min.

**Synthesis of 5:** The procedure is similar to the preparation of **4**. Compound **2** (9.3 mg, 6.9 μmol) was treated with **3** (7 μmol) and EDC (6.6 mg, 34 μmol) as described for the synthesis of **4**. After HPLC purification, the product **5** was isolated in a yield of 3.6 mg (33%). $R_t$ = 15.5 min (gradient A1/B). $^1$H NMR (500 MHz, $CD_3OD$, 300 K): $\delta$ = 8.41 (d, $J$ = 4.9 Hz, 1 H, L12), 7.79 (t, $J$ = 7.7 Hz, 1 H, L10), 7.56 (d, $J$ = 7.8 Hz, 1 H, L9), 7.30 (t, $J$ = 5.6 Hz, 1 H, L11), 7.25 (s, 1 H, B7), 7.12 (s, 1 H, B2), 6.56 (s, 1 H, B4), 6.27 (d, $J$ = 3.0 Hz, 1 H, R1), 6.05 (s, 1 H, C10) ppm. $^{13}$C NMR (125.8 MHz, $CD_3OD$, 293 K): $\delta$ = 181.72, 180.27, 177.77, 177.64, 177.50, 175.86, 175.69, 175.47, 174.72, 174.36, 173.84, 173.05, 167.25, 167.05, 160.65, 149.63, 143.58, 138.90, 138.43, 135.60, 134.00, 131.59, 125.10, 124.06, 118.02, 112.62, 108.82, 105.24, 95.76, 88.11, 86.56, 83.84 (d, $J_{C,P}$ = 5.6 Hz), 76.49, 75.65, 73.77 (d, $J_{C,P}$ = 6.1 Hz), 70.85, 62.84, 61.75, 60.86, 60.51, 57.79, 57.02, 55.73, 55.15, 53.10, 52.62, 46.95, 44.02, 43.19, 40.25, 38.59, 36.37, 35.45, 33.78, 33.63, 33.13, 32.52, 32.45, 29.79, 28.21, 27.78, 27.57, 21.09, 20.60, 20.51, 20.33 (d, $J_{C,P}$ = 3.8 Hz), 20.09, 17.65, 17.24, 16.53, 16.25, 14.77 ppm. $^{31}$P NMR (300 MHz, $CD_3OD$, 300 K): $\delta$ = 1.373 ppm. ESI-MS: $m/z$ = 1612 $[M + Na]^+$, 1590 $[M + H]^+$, 806 $[M + H + Na]^{2+}$, 795.1 $[M + 2 H]^{2+}$. UV/Vis (methanol): $\lambda$ ($\varepsilon$, L mol$^{-1}$ cm$^{-1}$) = 279.0 (13400), 361.1 (23300), 549.1 (7200) nm. Free acid $R_t$ = 10.6 min (A1/B). Full $^1$H and $^{13}$C NMR spectra are shown in the Supporting Information.

**Synthesis of 6:** Complex $[NEt_4]_2[ReBr_3(CO)_3]$ (75 mg, 0.09 mmol) was dissolved in water (10 mL), and a solution of fully deprotected **3** (36 mg, 0.13 mmol) in methanol was added. The solution was heated to 70–80 °C for 2 h. The proceeding of the reaction was monitored by HPLC: the peak with $R_t$ = 6.2 min ($[Re(OH_2)_3(CO)_3]^+$) disappeared, and a new peak (product **6**) with $R_t$ = 15.1 min appeared. After 2 h, the conversion was complete. When the reaction mixture was cooled, a white powder precipitated from solution. This precipitate was filtered, washed with small amounts of cold water and dried in vacuo. Yield: 32 mg (72%); the rest remained in the filtrate. It is important to apply temperatures above 70 °C in order to ensure ester hydrolysis during complexation. $^1$H NMR (300 MHz, $CD_3OD$, 300 K): $\delta$ = 8.83 (d, $J$ = 5.7 Hz, 1 H), 8.11 (t, $J$ = 7.8 Hz, 1 H), 7.74 (d, $J$ = 8.1 Hz, 1 H), 7.56 (t, 1 H, $J$ = 6.9 Hz), 4.78 (d, 1 H, $J$ = 15.6 Hz), 4.55 (d, 1 H, $J$ = 15.9 Hz), 3.90 (d, 1 H, $J$ = 17.1 Hz), 3.70 (m, 2 H), 3.53 (d, $J$ = 16.8 Hz, 1 H), 3.04 (t, $J$ = 7.5 Hz, 2 H), 2.18 (m, 2 H) ppm. ESI-MS: $m/z$ = 493.80 $[M + H]^+$. $C_{12}H_{18}F_3N_3O_7Re$ (6·TFA): calcd. C 25.76, H 3.24, N 7.51; found C 25.23, H 3.21, N 7.33.

**Synthesis of 8:** Two synthetic procedures are possible. The direct reaction of **4** with $[Re(OH_2)_3(CO)_3]^+$ in water gives compound **8** in good yield. Alternatively, the complex **6** can be preformed by the reaction of fully deprotected **3** and $[Re(OH_2)_3(CO)_3]^+$ followed by coupling to **1** as described in the following part. Compound **1** (26.7 mg, 19.8 μmol), complex **6** (29.2 mg, 60 μmol), EDC (11.5 mg, 60 μmol) and *N*-hydroxysuccinimide (6.9 mg, 60 μmol) were dissolved in a mixture of water (5 mL) and DMSO (0.5 mL), and the pH was adjusted to 5.5. After 5 h at room temperature, HPLC analysis exhibited about 33% of product **8**. More EDC and *N*-hydroxysuccinimide were added and the stirring was continued for 3 d with addition of EDC and *N*-hydroxysuccinimide in 24-h intervals. The water was removed in vacuo, and the product was precipitated by adding diethyl ether. The oily suspension was centrifuged and decanted. Washing with diethyl ether was repeated twice (5 mL each time) until a fine precipitate formed. The crude product was dried at high vacuum, purified by preparative HPLC (A1, gradient 1%min$^{-1}$ starting from 100% A1) and desalted to give **8** in a yield of 9.1 mg (23%). $R_t$ = 14.2 min (gradient A1/B). IR (KBr): $\tilde{\nu}$ = 2927, 2134, 2024, 1913, 1897, 1662 cm$^{-1}$. $^1$H NMR (500 MHz, $CD_3OD$, 300 K): $\delta$ = 8.1 (d, $J$ = 4.5 Hz, 1 H, L12), 8.10 (t, $J$ = 8 Hz, 1 H, L10), 7.73 (m, 1 H, L9), 7.54 (m, 1 H, L11), 7.26 (s, 1 H, B7), 7.14 (s, 1 H, B2), 6.59 (m, 1 H, B4), 6.27 (s, 1 H, R1), 6.05 (s, 1 H, C10) ppm. $^{13}$C NMR (125.8 MHz, $CD_3OD$, 300 K): $\delta$ = 198.39, 198.24, 197.46, 183.33, 181.75, 180.28, 177.72, 177.68, 176.77, 175.74, 175.69, 175.46 (2 C), 174.90, 174.76, 174.36, 167.27 (2 C), 160.90, 153.72, 143.63, 141.85, 138.39, 135.77, 133.97, 131.63, 127.20, 125.19, 117.99, 112.65, 105.25, 102.57, 95.74, 88.13, 86.59, 83.83 (d, $J_{C,P}$ = 4.5 Hz), 76.52, 75.74, 73.72 (d, $J_{C,P}$ =

 © 2007 Wiley-VCH Verlag GmbH & Co. KGaA, Weinheim 

5.4 Hz), 70.89, 69.44, 68.87, 62.90, 62.04, 60.55, 55.27, 55.77, 49–50 (1C below solvent), 46.93, 44.35, 43.04, 40.29, 38.01, 36.44, 35.51 (2 C), 33.66, 33.11 (2 C), 32.45 (2 C), 29.74, 27.60, 26.46, 21.13, 20.64, 20.47, 20.31 (d, $J_{C,P}$ = 3.2 Hz), 20.09, 17.65, 17.25, 16.69, 16.24 ppm. ESI-MS: $m/z$ = 1831.7 $[M + H]^+$, 916.1 $[M + H]^{2+}$. UV/Vis (methanol): $\lambda$ = 278.0, 361.1, 519.9, 551.1 nm. A full $^1$H NMR spectrum is shown in the Supporting Information.

**Synthesis of 9:** Compound **9** was prepared following one of the procedures described for **8**. Full $^1$H and $^{13}$C NMR spectra are shown in the Supporting Information.

**Labelling of 3 and 4 with $[^{99m}Tc(OH_2)_3(CO)_3]^+$ (10 and 11):** Solutions of the precursor $[^{99m}Tc(OH_2)_3(CO)_3]^+$ were prepared from $[^{99m}TcO_4]^-$ as described in the literature or by using the Isolink® kits as commercially available from Mallinckrodt Med. B.V. Petten NL.[41] Labelling of **4** and **5** was performed in a 10-mL glass vial with a rubber stopper which was flushed with $N_2$ for 10 min. In this vial, a solution of the respective $B_{12}$ derivative (20 μL, 0.001 M in water), MES buffer pH 6.2 (20 μL or 40 μL, final conc. 0.1 M) and a $[^{99m}Tc(OH_2)_3(CO)_3]^+$ solution (160 or 1940 μL) were mixed, and the reaction mixture was kept at 75 °C for 1–2 h. The final $B_{12}$ concentration was $10^{-4}$ to $10^{-5}$ M. HPLC analysis with γ-detection was performed to verify full conversion of the $^{99m}$Tc precursor. Under these conditions, the ester protecting groups of the chelators were cleaved to enable tridentate complexation. Comparison with the retention times of the corresponding rhenium complexes confirmed the authenticity of the labelled compounds. $R_t$ (**8**) = 15.1 min, $R_t$ (**9**) = 17.9 min. The delay is a result of the two separate detectors. Both compounds labelled with $^{99m}$Tc were stable in human serum albumin for at least 24 h at 37 °C.

**Supporting Information** (see footnote on the first page of this article): $^1$H NMR spectra for compounds **4**, **8**, **5** and **9** and $^{13}$C NMR spectra for compounds **5** and **9**.

## Acknowledgments

We thank Dr. C. Paulmann for support during our stay at the F1 beamline at HASYLAB/DESY. This project was financially supported by Solidago AG Bern, Switzerland.

[1] G. J. Russel-Jones, D. H. Alpers, *Chemistry and Biochemistry of Vitamin $B_{12}$*, John Wiley & Sons, New York, **1999**, pp. 411–441.
[2] B. Kräutler, D. Arigoni, B. T. Golding (Eds.), *Vitamin $B_{12}$ and $B_{12}$-Proteins*, Wiley-VCH, Weinheim, **1998**.
[3] K. L. Brown, *Chem. Rev.* **2005**, *105*, 2075–2149.
[4] G. Russell-Jones, K. McTavish, J. McEwan, J. Rice, D. Nowotnik, *J. Inorg. Biochem.* **2004**, *98*, 1625–1633.
[5] R. A. Horton, J. D. Bagnato, C. B. Grissom, *J. Org. Chem.* **2003**, *68*, 7108–7111.
[6] D. A. Collins, H. P. C. Hogenkamp, *J. Nucl. Med.* **1997**, *38*, 717–723.
[7] D. A. Collins, H. P. C. Hogenkamp, M. W. Gebhard, *Mayo Clin. Proc.* **1999**, *74*, 687–691.
[8] P. M. Pathare, D. S. Wilbur, S. Heusser, E. V. Quadros, P. McLoughlin, A. C. Morgan, *Bioconjugate Chem.* **1996**, *7*, 217–232.
[9] P. M. Pathare, D. S. Wilbur, D. K. Hamlin, S. Heusser, E. V. Quadros, P. McLoughlin, A. C. Morgan, *Bioconjugate Chem.* **1997**, *8*, 161–172.
[10] D. S. Wilbur, P. M. Pathare, D. K. Hamlin, S. P. Rothenberg, E. V. Quadros, *Bioconjugate Chem.* **1999**, *10*, 912–920.
[11] D. R. van Staveren, R. Waibel, S. Mundwiler, P. A. Schubiger, R. Alberto, *J. Organomet. Chem.* **2004**, *689*, 4803–4810.
[12] D. R. van Staveren, S. Mundwiler, U. Hoffmanns, J. K. Pak, B. Spingler, N. Metzler-Nolte, R. Alberto, *Org. Biomol. Chem.* **2004**, *2*, 2593–2603.
[13] S. N. Fedosov, C. B. Grissom, N. U. Fedosova, S. K. Moestrup, E. Nexo, T. E. Petersen, *FEBS Lett.* **2006**, *273*, 4742–4753.
[14] J. M. McGreevy, M. J. Cannon, C. B. Grissom, *J. Surg. Res.* **2003**, *111*, 38–44.
[15] S. Kunze, F. Zobi, P. Kurz, B. Spingler, R. Alberto, *Angew. Chem. Int. Ed.* **2004**, *43*, 5025–5029.
[16] S. Mundwiler, B. Spingler, P. Kurz, S. Kunze, R. Alberto, *Chem. Eur. J.* **2005**, *11*, 4089–4095.
[17] C. B. Perry, K. L. Brown, X. Zou, H. A. Marques, *J. Mol. Struct.* **2005**, *737*, 245–258.
[18] D. C. Hodgkin, J. G. White, K. N. Trueblood, R. A. Sparks, J. Lindsey, *Proc. R. Soc. London, Ser. A* **1962**, *266*, 494–517.
[19] P. G. Lenhert, D. C. Hodgkin, *Nature* **1961**, *192*, 937–938.
[20] M. Rossi, J. P. Glusker, L. Randaccio, M. F. Summers, P. J. Toscano, L. G. Marzilli, *J. Am. Chem. Soc.* **1985**, *107*, 1729–1738.
[21] L. Randaccio, S. Geremia, G. Nardin, J. Wuerges, *Coord. Chem. Rev.* **2006**, *250*, 1332–1350.
[22] K. Gruber, G. Jogl, G. Klintschar, C. Kratky, "High Resolution Crystal Structures of Cobalamins" in *Vitamin $B_{12}$ and $B_{12}$-Proteins* (Eds.: B. Kräutler, D. Arigoni, B. T. Golding), Wiley-VCH, Weinheim, **1998**, pp. 335–349.
[23] C. B. Perry, H. M. Marques, *S. Afr. J. Sci.* **2004**, *100*, 368–380.
[24] K. L. Brown, S. F. Cheng, X. Zou, J. D. Zubkowski, E. J. Valente, L. Knapton, H. M. Marques, *Inorg. Chem.* **1997**, *36*, 3666–3675.
[25] J. B. Armitage, J. R. Cannon, A. W. Johnson, L. F. J. Parker, E. L. Smith, W. H. Stafford, A. R. Todd, *J. Chem. Soc.* **1953**, 3849–3864.
[26] K. Bernhauer, F. Wagner, H. Beisbarth, P. Rietz, H. Vogelmann, *Biochem. Z.* **1966**, *344*, 289–309.
[27] H. M. Marques, D. C. Scooby, M. Victor, K. L. Brown, *Inorg. Chim. Acta* **1989**, *162*, 151–155.
[28] C. K. Nockolds, S. Ramasesh, D. C. Hodgkin, T. N. M. Waters, J. M. Waters, F. M. Moore, B. T. M. Willis, *Nature* **1967**, *214*, 129–130.
[29] C. E. Nockolds, S. Ramaseshan, *Proc. Indian Acad. Sci. (Chem. Sci.)* **1984**, *93*, 197–218.
[30] F. H. Moore, B. H. Oconnor, B. T. M. Willis, D. C. Hodgkin, *Proc. Indian Acad. Sci. (Chem. Sci.)* **1984**, *93*, 235–260.
[31] J. M. Waters, T. N. M. Waters, *Proc. Indian Acad. Sci. (Chem. Sci.)* **1984**, *93*, 219–234.
[32] T. G. Pagano, L. G. Marzilli, *Biochemistry* **1989**, *28*, 7213–7223.
[33] D. C. Hodgkin, *Proc. Indian Acad. Sci. (Chem. Sci.)* **1984**, *93*, 195–196.
[34] R. Alberto, R. Schibli, R. Waibel, U. Abram, A. P. Schubiger, *Coord. Chem. Rev.* **1999**, *192*, 901–919.
[35] A. Stichelberger, R. Waibel, C. Dumas, P. A. Schubiger, R. Schibli, *Nucl. Med. Biol.* **2003**, *30*, 465–470.
[36] M. Binder, J. F. Kolhouse, K. C. Vanhorne, R. H. Allen, *Anal. Biochem.* **1982**, *125*, 253–258.
[37] R. Bonnett, J. R. Cannon, V. M. Clark, A. W. Johnson, L. F. J. Parker, E. L. Smith, A. Todd, *J. Chem. Soc.* **1957**, 1158–1168.
[38] W. Kabsch, *J. Appl. Crystallogr.* **1993**, *26*, 795–800.
[39] A. Altomare, M. C. Burla, M. Camalli, G. L. Cascarano, C. Giacovazzo, A. Guagliardi, A. G. G. Moliterni, G. Polidori, R. Spagna, *J. Appl. Crystallogr.* **1999**, *32*, 115–119.
[40] G. M. Sheldrick, *SHELXL97–2: Program for the Refinement of Crystal Structures*, University of Göttingen, Germany, **1997**.
[41] R. Alberto, K. Ortner, N. Wheatley, R. Schibli, A. P. Schubiger, *J. Am. Chem. Soc.* **2001**, *123*, 3135–3136.

Received: December 16, 2006
Published Online: May 8, 2007

 © 2007 Wiley-VCH Verlag GmbH & Co. KGaA, Weinheim 

DOI: 10.1002/ejic.200600956

# *ortho*- and *para*-Thioquinonoid π-Complexes: First Synthesis, Reactivity, and Crystal Structure Determination

**Jamal Moussa,[a] Marie Noelle Rager,[b] Kamal Boubekeur,[a] and Hani Amouri*[a]**

**Keywords:** Reactive intermediates / Coordination modes / Sulfur / Thioquinones / Iridium

Overcoming a long-standing challenge, the *o*- and *p*-dithiobenzoquinone iridium complexes [Cp*Ir-*o*-($\eta^4$-$C_6H_4S_2$)] (**6**) and [Cp*Ir-*p*-($\eta^4$-$C_6H_4S_2$)] (**7**) were rationally synthesized and fully characterized for the first time including the X-ray molecular structure of [Cp*Ir-*p*-($\eta^4$-$C_6H_4S_2$)] (**7**). Our strategic approach involves the preparation of the halogenated 1,2- and 1,4-dichloro arene π complexes [Cp*Ir-*o*-($\eta^6$-$C_6H_4Cl_2$)][$BF_4$]$_2$ (**4**) and [Cp*Ir-*p*-($\eta^6$-$C_6H_4Cl_2$)][$BF_4$]$_2$ (**5**), which are the key molecules for **6** and **7**. Subsequent treatment of **4** and **5** with NaSH and halogen displacement provides the target thioquinonoid π complexes **6** and **7** in 88 % and 95 % yields respectively. Further, the coordination chemistry of the *o*-dithiobenzoquinone iridium complex [Cp*Ir-*o*-($\eta^4$-$C_6H_4S_2$)] (**6**) was studied by treating **6** with [(bpy)$PtCl_2$] in the presence of AgOTf, which provided the novel platinum complex [Pt(bpy){Cp*Ir-*o*-($\eta^4$-$C_6H_4S_2$)}][OTf]$_2$ (**10**) in 91 % yield. The X-ray molecular structure of **10** is reported and shows as outstanding features the formation of 1D supramolecular assembly, which results from π–π ($d$ = 3.484 Å; $d$ = 3.669 Å) and Pt···Pt ($d$ = 3.574 Å) interactions between individual subunits.

(© Wiley-VCH Verlag GmbH & Co. KGaA, 69451 Weinheim, Germany, 2007)

## Introduction

Although the chemistry of *o*- and *p*-benzoquinone is well documented,[1] very little is known about the related *o*- and *p*-dithiobenzoquinone (**1**, **2**) (Figure 1). Unlike benzoquinones, the sulfur analogues are highly reactive owing to their instability, making their handling and isolation in pure form a difficult task. Thus examples of isolated thioquinones are scarce and in fact *p*-dithiobenzoquinone (**2**) has been generated and characterized spectroscopically only at low temperature (10 K) in an argon matrix because it is extremely reactive and was observed to decompose in an unknown manner on moderate warming of the matrix.[2] Recently Oda and co-workers reported the synthesis of 2,6-di-*tert*-butyl-1-thio-1,4-benzoquinone, where the presence of two *tert*-butyl groups at the 2- and 6-positions offers steric protection and increases the stability of the mono-thiobenzoquinone.[3] More recently, Cava and co-workers reported the synthesis of dithioanthraquinone analogue in 16% yield by several steps: first annelation of thiophene rings to benzoquinone produced the anthraquinone analogue, and subsequent treatment with Lawesson's reagent and/or Davy reagent methyl for 18 h produced the mono- and dithio-anthraquinone analogues.[4] However, none of the previous attempts allowed the isolation of *p*-dithiobenzoquinone (**2**).

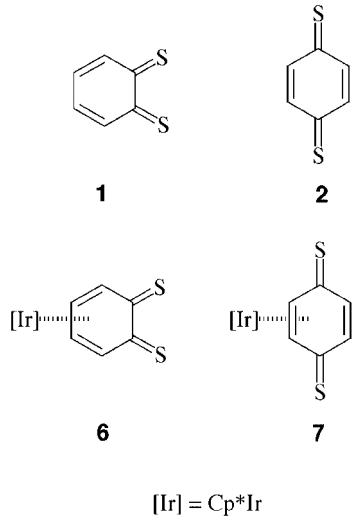


Figure 1. *o*- and *p*-dithiobenzoquiones complexes.

The isomeric *o*-dithiobenzoquinone (**1**) has proven to be even more elusive. Three attempts to generate this compound have been recorded. (i) The matrix-isolated product from pyrolysis of 1,3-benzodithiol-2-one showed an ultraviolet spectrum suggestive of the transient benzodithiete rather than that expected of *o*-dithiobenzoquinone (**1**).[5] (ii) The photolysis of the same starting material 1,3-benzodi-

[a] Laboratoire de Chimie Inorganique et Matériaux Moléculaires, UMR CNRS 7071, Université Pierre et Marie Curie, 4, place Jussieu, case 42, 75252 Paris Cedex 05, France
Fax: +33-1-44273841
E-mail: amouri@ccr.jussieu.fr
[b] NMR Services of Ecole Nationale Supérieure de Chimie de Paris, 11 rue Pierre et Marie Curie, 75231 Paris Cedex 05, France

Supporting information for this article is available on the WWW under http://www.eurjic.org or from the author.

 © 2007 Wiley-VCH Verlag GmbH & Co. KGaA, Weinheim 

thiol-2-one also did not afford **1** as an isolable product but its transient generation was proven by trapping it with dimethyl acetylenedicarboxylate to give dimethyl 1,4-benzodithiin-2,3-dicarboxylate in moderate yield.[6] (iii) Finally, Perkin and Green's diaminodithioquinone approach did not yield the monomeric elusive dithione (**1**) either; instead a polymeric species featuring disulfide bonds was proposed.[7] All these procedures illustrate the difficulty in isolating and stabilizing *o*- and *p*-dithiobenzoquinones (**1**, **2**).

In contrast, here we report a rational synthetic procedure to isolate and fully characterize the first stable $\eta^4$-dithio-*o*- and -*p*-benzoquinone complexes (**6**, **7**) (Figure 1). The parent compounds were obtained as iridium complexes [Cp*Ir-*o*-($\eta^4$-$C_6H_4S_2$)] (**6**) and [Cp*Ir-*p*-($\eta^4$-$C_6H_4S_2$)] (**7**) and were fully characterized including the first X-ray molecular structure of the dithio-*p*-benzoquinone as a metal complex **7**.

In a previous work we reported the first example of metal-stabilized *o*-quinone methide, and showed that the Cp*Ir can stabilize this highly reactive intermediate through $\eta^4$-coordination to the internal diene moiety of the simple quinone methide.[8] Pursuing our research in this area, that is, stabilization of reactive intermediates,[9] we discovered that Cp*Ir can also stabilize the elusive *o*- and *p*-dithiobenzoquinone intermediates; a previous communication on the stabilization of **2** has recently been published.[10] Our synthetic approach is completely different to that reported for the quinone methide. It involves the synthesis of halogenated 1,2- and 1,4-dichloroarene π complexes [Cp*Ir-*o*-($\eta^6$-$C_6H_4Cl_2$)][$BF_4$]$_2$ (**4**) and [Cp*Ir-*p*-($\eta^6$-$C_6H_4Cl_2$)][$BF_4$]$_2$ (**5**), which are the key molecules for **6** and **7**. Subsequent substitution of the chlorides by ($HS^-$) provided the title compounds [Cp*Ir-*o*-($\eta^4$-$C_6H_4S_2$)] (**6**) and [Cp*Ir-*p*-($\eta^4$-$C_6H_4S_2$)] (**7**) in high yields (Figure 1).

## Results and Discussion

### Synthesis and Characterization of the Halogenated Arene π Complexes 4, 5 and Their Related *o*- and *p*-$\eta^4$-Dithiobenzoquinones 6, 7

We recently discovered that the π complexing ability of the $Cp^*Ir^{2+}$ moiety is dramatically enhanced towards electron-poor halogenated arenes when the reaction is conducted in $BF_3{\cdot}2H_2O$ solution. These experimental conditions allow a smooth and efficient complexation of highly electron-deficient aromatics. Thus treatment of an excess of *o*- and/or *p*-dichlorobenzene with the solvated iridium complex [Cp*Ir(acetone)$_3$][OTf]$_2$ (**3**) in $BF_3{\cdot}2H_2O$ solution gave the iridium complexes [Cp*Ir-*o*-($\eta^6$-$C_6H_4Cl_2$)][$BF_4$]$_2$ (**4**) and [Cp*Ir-*p*-($\eta^6$-$C_6H_4Cl_2$)][$BF_4$]$_2$ (**5**) quantitatively as white microcrystalline complexes (Scheme 1). These air- and moisture-sensitive compounds were completely characterized. The $^1$H NMR spectra recorded for **4** and **5** in $CD_3NO_2$ were similar, for instance, to the *ortho* complex **4**, which showed the presence of two doublets of doublets at $\delta$ = 7.52 and 7.83 ppm attributed to the aromatic protons and another singlet at $\delta$ = 2.35 ppm attributed to the methyl protons of Cp*Ir. In a similar fashion the *para* isomer **5** gave a singlet at $\delta$ = 7.82 ppm assigned to the ring protons and at $\delta$ = 2.48 ppm attributed to the methyl protons of Cp*Ir. The $^{19}$F NMR spectra of both complexes showed a singlet at –152.7 ppm for **4** and at –153.6 ppm for **5** designated to the free $BF_4$ anion.[11] Further, the infrared spectra also showed a large band at 1083 cm$^{-1}$ attributed to $BF_4$ anions. The $^{13}$C NMR spectrum is in agreement with the proposed formula (see Experimental Section). As mentioned before, compounds **4** and **5** were very air- and moisture-sensitive and hence were kept under argon at low temperature because of the lability of the C–Cl bond of the coordinated arenes.

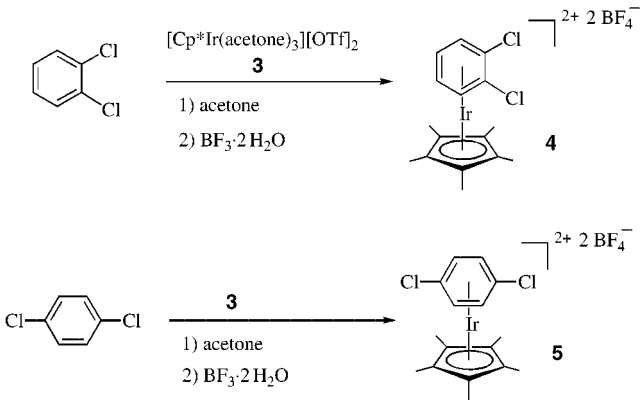


Scheme 1.

We then treated the white powder complexes **4** and **5** with an excess of dried NaSH in $CH_3CN$ for 20 min. Reaction workup provided the neutral *o*- and *p*-$\eta^4$-dithiobenzoquinone complexes [Cp*Ir-*o*-($\eta^4$-$C_6H_4S_2$)] (**6**) and [Cp*Ir-*p*-($\eta^4$-$C_6H_4S_2$)] (**7**). Compounds **6** and **7** were obtained as red and orange microcrystalline materials, analytically pure and stable under argon. For instance, the infrared spectrum of **6** recorded in KBr discs displayed a sharp band at 1085 cm$^{-1}$, while that of **7** gave a band at 1096 cm$^{-1}$, which we attribute to C=S vibration. This thiocarbonyl stretching frequency is lower than that of the free monothio-1,4-benzoquinone (1141 cm$^{-1}$).[3] Such a trend has been observed for the C=O vibration in the related free and metallated 1,4-benzoquinone.[12] It is worth mentioning that infrared data for *o*- and *p*-dithiobenzoquinone complexes have not been reported before. All attempts to obtain crystals of *o*-dithiobenzoquinone metal complex **6** for an X-ray study were not successful, however we were able to obtain crystals of the *p*-isomer [Cp*Ir-*p*-($\eta^4$-$C_6H_4S_2$)] (**7**) and the structure was determined (vide infra).

The structure of the *p*-dithiobenzoquinone [Cp*Ir-*p*-($\eta^4$-$C_6H_4S_2$)] (**7**) was confirmed by a single-crystal X-ray diffraction study (Scheme 2). Crystals of **7** were grown by vapor diffusion of diethyl ether into a solution of the complex in $CH_2Cl_2$. Complex **7** crystallizes in the monoclinic unit cell with space group $P2_1/m$ with $Z$ = 2. The asymmetric unit consists of three half complexes (I, II, and III), which are totally generated by crystallographic mirror planes and one molecule of $CH_2Cl_2$ with 25% occupation.

 © 2007 Wiley-VCH Verlag GmbH & Co. KGaA, Weinheim 

Molecules I and II show π–π interactions between (a) the $\eta^5$-Cp*Ir moiety of molecule I and the $\eta^4$-(S–$C_6H_4$–S) unit of another thioquinone metal complex (II) with $d$ = 3.565(4) Å and $\alpha$ = 21.30(12)° and (b) the $\eta^5$-Cp*Ir moiety of molecule II and the $\eta^4$-(S–$C_6H_4$–S) unit of another thioquinone metal complex (I) with $d$ = 3.631(3) Å and $\alpha$ = 17.69(15)°, providing a one-dimensional supramolecular chain (Figure 2, a).

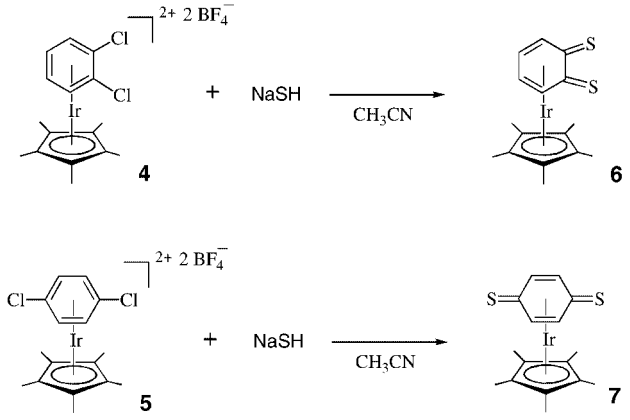


Scheme 2. X-ray molecular structures of *p*-dithiobenzoquinone [Cp*Ir-*p*-($\eta^4$-$C_6H_4S_2$)] (**7**) and [Pt(bpy){Cp*Ir-*o*-($\eta^4$-$C_6H_4S_2$)}]-[OTf]$_2$ (**10**).

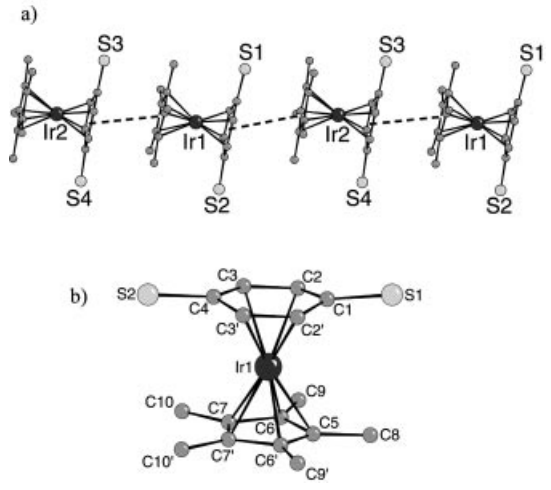


Figure 2. X-ray molecular structure of *p*-dithiobenzoquinone complex [Cp*Ir-*p*-($\eta^4$-$C_6H_4S_2$)] (**7**). (a) 1D supramolecular chain formed through π–π contacts between molecules I and II. (b) Selected bond lengths [Å] and angles [°] for **7** molecule I: Ir1···C1 2.353(8), Ir1···C2 2.210(6), Ir1···C3 2.219(5), Ir1···C4 2.346(7), C1···S1 1.726(10), C4···S2 1.713(9), C2–C1–C2′ 114.2(9), C3–C4–C3′ 115.0(8).

The distance between the closest sulfur atoms of two independent molecules II and III is 4.23 Å, suggesting the absence of an interatomic contact (sum of van der Waals radii of sulfur is 3.7 Å).[13] A view of complex **7** with selected bond lengths and angles is shown in Figure 2b. The structure of **7** clearly shows the Cp*Ir moiety is coordinated to only four diene carbons of the π-thioquinone ligand. For instance the average values of the Ir–C distances are 2.367, 2.358 Å longer than those of the diene subunit (average bond lengths of 2.206, 2.214 Å) in molecules I, II and III. Further, the $\eta^4$-thioquinone ligand acquires a boat-like conformation with the thioquinoid carbons bent out of the diene plane by $\theta$ = 8.22(0.7)° and $\theta$ = 8.21(0.4)° in molecule I, while in molecule II the two dihedral angles are $\theta$ = 8.49(0.6)°, $\theta$ = 7.69(0.3)°, and $\theta$ = 12.94 (0.8) and $\theta$ = 10.04(1.1) in molecule III. These angle values are smaller than those reported for the analogous iridium benzoquinone complex ($\theta$ = 16°).[12a] The C–S bond lengths for the three independent molecules (I, II, III) are 1.719, 1.705, and 1.710 Å, which on average is 1.711 Å and characteristic of a partial double bond character (vide infra). This bond length is shorter than the simple C–S bond of 1.796 Å reported for 1,4-benzenedithiol[14] and 1.766 Å for 4,4′-biphenyldithiol,[15] but comparable to C=S bond lengths of 1.674–1.702 Å reported for several thiourea compounds.[16] To the best of our knowledge this is the first X-ray structure of the parent thioquinone complex reported in the literature.

Protonation of a suspension of either [Cp*Ir-*o*-($\eta^4$-$C_6H_4S_2$)] (**6**) or [Cp*Ir-*p*-($\eta^4$-$C_6H_4S_2$)] (**7**) in $CH_3CN$ by $HBF_4{\cdot}Et_2O$ provided a rapid color change, giving rise to a red solution for **6** and yellow solution for **7**. Reaction work-up allowed the isolation of the related dithiophenol complexes [Cp*Ir-*o*-($\eta^6$-HS–$C_6H_4$–SH)][$BF_4$]$_2$ (**8**) or [Cp*Ir-*p*-($\eta^6$-HS–$C_6H_4$–SH)][$BF_4$]$_2$ (**9**) in 95% and 93% yields respectively as red and pale yellow microcrystalline solids (Scheme 3).

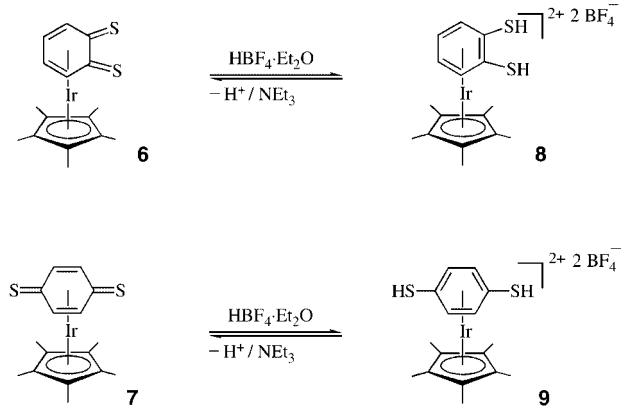


Scheme 3.

Compound **9** was characterized by spectroscopic data ($^1$H, IR). For instance the $^1$H NMR of **9** recorded in $CD_3CN$ showed the presence of a singlet at $\delta$ = 1.98 ppm attributed to the methyl protons of $\eta^5$-Cp*Ir and another singlet at $\delta$ = 7.15 ppm assigned to the aromatic protons that integrate to four protons. In a similar way complex **8** showed one singlet at $\delta$ = 2.10 ppm and two doublet of doublets at $\delta$ = 6.83 and 7.70 ppm, respectively. Upon treatment of the NMR tube sample of **9** in $CD_3CN$ with $NEt_3$, the starting material [Cp*Ir-*p*-($\eta^4$-$C_6H_4S_2$)] (**7**) was recovered. A similar behavior was also observed to the *o*-dithiophenol complex **8**.

 © 2007 Wiley-VCH Verlag GmbH & Co. KGaA, Weinheim 

In a previous work[10] we investigated, by an ab initio computational approach employing the hybrid density functional B3LYP method, the role of the metal in stabilizing the elusive intermediate *p*-dithiobenzoquinone in **7**. Computational analyses using density functional theory confirm a net transfer of about 0.8 units of electron density to the π* ligand LUMO. This additional electron density is largely localized around the thiocarbonyl bonds, resulting in a reduction in C=S bond order as well as the anticipated decrease in C=C bond order. This provides further confirmation of the versatility of the "Cp*Ir" metal fragment in stabilizing reactive π systems. Having these thioquinoid complexes in hand for the first time, we investigated the reactivity of the *o*-thioquinoid metal complex [Cp*Ir-*o*-($\eta^4$-$C_6H_4S_2$)] (**6**) towards electrophilic platinum adduct "(bpy)-$Pt(OTf)_2$".

When the *o*-dithiobenzoquinone metal complex [Cp*Ir-*o*-($\eta^4$-$C_6H_4S_2$)] (**6**) was treated with [(bpy)$PtCl_2$] in $CH_3CN$ in the presence AgOTf, a new compound was obtained, which was fully characterized as [Pt(bpy){Cp*Ir-*o*-($\eta^4$-$C_6H_4S_2$)}][OTf]$_2$ (**10**) (see Experimental Section); further, the X-ray molecular structure of **10** was determined. The $^1$H NMR of **10** recorded in $CD_3CN$ shows the presence of two doublets of doublets at $\delta$ = 6.68 ppm and at $\delta$ = 7.07 ppm attributed to the metallated *o*-thioquinone and a singlet at $\delta$ = 1.98 ppm assigned to the Cp*Ir moiety. Further, we note the presence of four multiplets assigned to the "(bpy)Pt" fragment. Red crystals of **10** were obtained from nitromethane/ether solution. Complex **10** crystallizes in the monoclinic unit cell, space group $P2_1/c$. A view of the cationic part of the complex and selected bond lengths and angles are shown in Figure 3. The structure of **10** shows indeed that the *o*-thioquinone iridium complex chelates the "(bpy)Pt" fragment through the two sulfur centers such that the coordination geometry around the Pt becomes square planar. Because of this coordination mode, the aromatic ring of the *o*-thioquinone is planar and symmetrically bound ($\eta^6$-) to the Cp*Ir moiety.

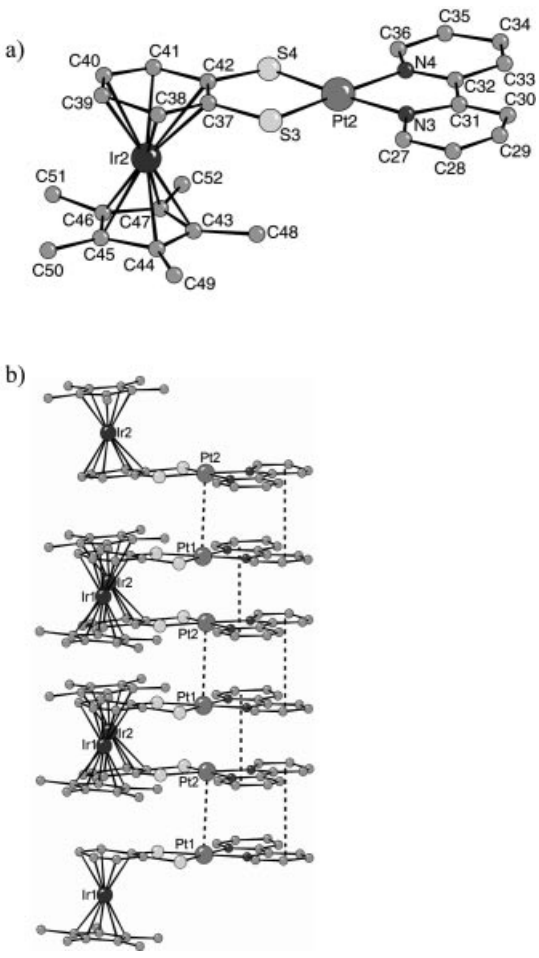


Figure 3. (a) View of the cationic part of complex **10**. Selected bond lengths [Å] and angles [°] for **10**: Ir2···C37 2.382(5), Ir2···C38 2.350(1), Ir2···C39 2.290(3), Ir2···C40 2.215(7), Ir2···C41 2.252(5), Ir2···C42 2.341(5), C42···S4 1.748(5), C37···S3 1.709(0), Pt2···S4 2.283(2), Pt2···S3 2.301(8), Pt2···N4 2.093(7), Pt2···N3 2.098(1), S4–Pt2–S3 89.51(1), S4–Pt2–N4 96.07(2), S3–Pt2–N3 94.99(2), N4–Pt2–N3 79.40(1). (b) 1D supramolecular chain formed through π–π and Pt···Pt contacts between individual molecules.

Further examination of the crystal packing of **10** reveals important information such as: the molecules are stacked in a head-to-tail orientation with several π–π interactions between adjacent bipyridyl ligands with $d$ = 3.484 Å and $d$ = 3.669 Å and also show the presence of a Pt1···Pt2 interaction at $d$ = 3.574 Å. These Pt···Pt/π–π interactions occur in an alternate fashion among the individual molecules of [Pt(bpy){Cp*Ir-*o*-($\eta^4$-$C_6H_4S_2$)}]$^{2+}$, describing a 1D supramolecular chain. In this supramolecular assembly each square planar Pt(bpy) subunit is rotated by 38.54° relative to the adjacent molecule. Other platinum(II) polypyridyl complexes have shown similar extended linear chain packing.[17] Our results, in which we describe the structure of a *o*-thioquinone metal complex for the first time and also its coordination chemistry, are unprecedented.

## Concluding Remarks

In this paper we have reported the first synthesis and full characterization of *o*- and *p*-thiobenzoquinone metal complexes [Cp*Ir-*o*-($\eta^4$-$C_6H_4S_2$)] (**6**) and [Cp*Ir-*p*-($\eta^4$-$C_6H_4S_2$)] (**7**). The key molecules to their synthesis are the halogenated arene π complexes [Cp*Ir-*o*-($\eta^6$-$C_6H_4Cl_2$)][$BF_4$]$_2$ (**4**) and [Cp*Ir-*p*-($\eta^6$-$C_6H_4Cl_2$)][$BF_4$]$_2$ (**5**), which we prepared following a novel synthetic procedure. The structure of **7** was also reported and shows the "Cp*Ir" moiety is coordinated in a $\eta^4$-fashion to the *p*-thiobenzoquinone. This illustrates the role of the "Cp*Ir" fragment in stabilizing such reactive intermediates. The *o*-thiobenzoquinone iridium complex can be used as an *organometallic linker* and chelates the electrophilic "(bpy)$Pt(OTf)_2$" adduct, which provides a 1D supramolecular assembly [Pt(bpy){Cp*Ir-*o*-($\eta^4$-$C_6H_4S_2$)}][OTf]$_2$ (**10**). Our future objectives are directed towards the use of these first thioquinoid complexes **6** and **7** as *organometallic linkers* in a similar way to the related benzoquinone metal complex[18] in order to construct novel supramolecular coordination polymers exhibiting short Pt···Pt contacts and also to study their photoluminescence properties.

 © 2007 Wiley-VCH Verlag GmbH & Co. KGaA, Weinheim 

## Experimental Section

All experimental manipulations were carried out under argon using Schlenk tube techniques. The $^1H$, $^{13}C$, and $^{19}F$ NMR spectra were recorded in $CD_2Cl_2$, $CD_3CN$, and $CD_3NO_2$ using a Bruker Avance 400 NMR spectrometer at 400.13, 100.61, and 376.45 MHz, respectively. Infrared spectra were recorded from KBr discs on a Bio-Rad FTIR spectrometer FTS 165.

**Synthesis of [Cp*Ir-*o*-($\eta^6$-$C_6H_4Cl_2$)][$BF_4$]$_2$ (4):** A solution of $AgCF_3SO_3$ (260 mg, 1.0 mmol) in acetone (10 mL) was added to [Cp*Ir(μ-Cl)Cl]$_2$ (200 mg, 0.25 mmol) in acetone (5 mL) to rapidly give a white precipitate of AgCl. The reaction mixture was stirred for 15 min then the resulting yellow solution of [Cp*Ir(acetone)$_3$][OTf]$_2$ (**3**) was filtered under argon into a dry Schlenk tube containing 1,2-dichlorobenzene (0.6 mL, 5.0 mmol) and the solvent was removed under vacuum. $BF_3{\cdot}2H_2O$ (1 mL) was added to the yellow residue, which immediately decolorized. The mixture was stirred for 30 min at room temperature, then diethyl ether (60 mL) was added. Complex **4** precipitated out as a white microcrystalline air-sensitive powder that was filtered and washed several times with diethyl ether (20 mL) and dried under vacuum (300 mg, 0.47 mmol). Yield: 94%. This complex is highly air- and moisture-sensitive and hence accurate elemental analysis could not be obtained. $C_{16}H_{19}B_2Cl_2F_8Ir$ (648 g mol$^{-1}$): calcd. C 29.65, H 2.96; found C 28.40, H 2.87. $^1H$ NMR (400 MHz, $CD_3NO_2$): $\delta$ = 2.35 (s, 15 H, Cp*), 7.52 (dd, 2 H, aromatic, $^3J_{H,H}$ = 4.7, $^4J_{H,H}$ = 2.7 Hz), 7.83 (dd, 2 H, aromatic, $^3J_{H,H}$ = 4.7, $^4J_{H,H}$ = 2.7 Hz) ppm. $^{13}C\{^1H\}$ NMR (100 MHz, $CD_3NO_2$): $\delta$ = 9.4 (s, –$CH_3$, Cp*), 109.3 (s, C=C, Cp*), 99.1 (s, C–H, aromatic), 100.3 (s, C–H, aromatic), 117.3 (s, C–Cl, aromatic) ppm. $^{19}F$ NMR (376 MHz, $CD_3NO_2$): $\delta$ = –152.7 (s, $BF_4$) ppm. IR (KBr disk): $\tilde{\nu}$(B–F) = 1083 cm$^{-1}$.

**Synthesis of [Cp*Ir-*p*-($\eta^6$-$C_6H_4Cl_2$)][$BF_4$]$_2$ (5):** This complex was prepared in a similar way to that of [Cp*Ir-*o*-($\eta^6$-$C_6H_4Cl_2$)][$BF_4$]$_2$ (**4**), using $AgCF_3SO_3$ (520 mg, 2 mmol), [Cp*Ir(μ-Cl)Cl]$_2$ (400 mg, 0.5 mmol) and $BF_3{\cdot}2H_2O$ (1 mL). Yield: 80% (515 mg, 0.8 mmol). This complex is highly air- and moisture-sensitive and hence accurate elemental analysis could not be obtained. $C_{16}H_{19}B_2Cl_2F_8Ir$ (648 g mol$^{-1}$): calcd. C 29.65, H 2.96; found C 27.39, H 2.96. $^1H$ NMR (400 MHz, $CD_3NO_2$): $\delta$ = 2.48 (s, 15 H, Cp*), 7.82 (s, 4 H, aromatic) ppm. $^{13}C\{^1H\}$ NMR (100 MHz, $CD_3NO_2$): $\delta$ = 8.3 (s, –$CH_3$, Cp*), 108.5 (s, C=C, Cp*), 99.4 (s, C–H, aromatic), 114.9 (s, C–Cl, aromatic) ppm. $^{19}F$ NMR (376 MHz, $CD_3NO_2$): $\delta$ = –153.6 (s, $BF_4$) ppm. IR (KBr disk): $\tilde{\nu}$(B–F) = 1083 cm$^{-1}$.

**Synthesis of [Cp*Ir-*o*-($\eta^4$-$C_6H_4S_2$)] (6):** A solution of **3** (340 mg, 0.52 mmol) in $CH_3CN$ (10 mL) was added to a suspension of dried HSNa (360 mg, 6.0 mmol) in $CH_3CN$ (5 mL) and the mixture was stirred for 20 min at room temperature, then the solvent was removed by evaporation under vacuum. The residue was extracted by $CH_2Cl_2$ (20 mL) and filtered through Celite. After filtration through Celite, $CH_2Cl_2$ was evaporated under vacuum. Complex **6** was obtained as an orange microcrystalline powder (238 mg, 0.49 mmol). Yield: 88%. M.p. 185 °C (dec.) $C_{16}H_{19}IrS_2{\cdot}3H_2O$ (522 g mol$^{-1}$): calcd. C 36.73, H 4.30, S 12.39; found C 36.84, H 4.83, S 12.29. $^1H$ NMR (300 MHz, $CD_2Cl_2$): $\delta$ = 1.87 (s, 15 H, Cp*), 5.90 (dd, 2 H, diene, $^3J_{H,H}$ = 7.37, $^4J_{H,H}$ = 1.77 Hz), 6.44 (dd, 2 H, diene, $^3J_{H,H}$ = 7.37, $^4J_{H,H}$ = 1.77 Hz) ppm. IR (KBr disk): $\tilde{\nu}$(C=S) = 1085 cm$^{-1}$.

**Synthesis of [Cp*Ir-*p*-($\eta^4$-$C_6H_4S_2$)] (7):** This complex was prepared in a similar way to that of Cp*Ir-*o*-($\eta^4$-$C_6H_4S_2$)] (**6**), using HSNa (360 mg, 6.0 mmol) and **3** (340 mg, 0.52 mmol). Complex **7** was obtained as an orange microcrystalline powder (238 mg, 0.49 mmol). Yield: 95%. M.p. 160 °C (dec.) $C_{16}H_{19}IrS_2{\cdot}H_2O$ (486 g mol$^{-1}$): calcd. C 39.57, H 4.36, S 13.20; found C 38.96, H 4.32, S 13.24. $^1H$ NMR (400 MHz, $CD_2Cl_2$): $\delta$ = 1.91 (s, 15 H, Cp*), 5.96 (s, 4 H, aromatic) ppm. $^{13}C\{^1H\}$ NMR (100 MHz, $CD_2Cl_2$): $\delta$ = 7.1 (s, –$CH_3$, Cp*), 96.25 (s, C=C, Cp*), 91.8 (s, C–H, aromatic), 148.1 (s, C=S, aromatic) ppm. IR (KBr disk): $\tilde{\nu}$(C=S) = 1096 cm$^{-1}$.

**Synthesis of [Cp*Ir-*o*-($\eta^6$-HS–$C_6H_4$-SH)][$BF_4$]$_2$ (8):** $HBF_4{\cdot}Et_2O$ (1 mL) was added to a solution of [Cp*Ir-*o*-($\eta^4$-$C_6H_4S_2$)] (50 mg, 0.1 mmol) in $CH_3CN$ (3 mL), causing the purple solution to rapidly turn red. The reaction was left to proceed for 10 min. Addition of $Et_2O$ (50 mL) provided a red oil-like substance (61 mg, 0.095 mmol). Yield: 95%. This compound is unstable, hence elemental analysis could not be performed. $^1H$ NMR (300 MHz, $CD_3CN$): $\delta$ = 2.10 (s, 15 H, Cp*), 6.83 (dd, 2 H, diene, $^3J_{H,H}$ = 7.37, $^4J_{H,H}$ = 1.77 Hz), 7.70 (dd, 2 H, diene, $^3J_{H,H}$ = 7.37, $^4J_{H,H}$ = 1.77 Hz) ppm. IR (KBr disk): $\tilde{\nu}$(B–F) = 1083 (s, br) cm$^{-1}$.

**Synthesis of [Cp*Ir-*p*-($\eta^6$-HS–$C_6H_4$-SH)][$BF_4$]$_2$ (9):** This compound was prepared in a similar way to that of **8**. Complex **9** was obtained as a yellow microcrystalline substance. Yield: 93%. This compound is unstable, hence elemental analysis could not be performed. $^1H$ NMR (300 MHz, $CD_3CN$): $\delta$ = 1.98 (s, 15 H, Cp*), 7.15 (s, 4 H, diene) ppm. IR (KBr disk): $\tilde{\nu}$(B–F) = 1083 (s, br) cm$^{-1}$.

**Synthesis of [Pt(bpy){Cp*Ir-*o*-($\eta^4$-$C_6H_4S_2$)}][OTf]$_2$ (10):** A solution of AgOTf (52 mg, 0.20 mmol) in $CH_3CN$ (10 mL) was added to a suspension of [(bpy)$PtCl_2$][19] (42 mg, 0.10 mmol) in $CH_3CN$ (10 mL) and the mixture was stirred for 4 h at room temperature and then filtered through Celite. [Cp*Ir-*o*-($\eta^4$-$C_6H_4S_2$)] (53 mg, 0.11 mmol) in $CH_3CN$ (10 mL) was added to the pale yellow filtrate solution (60 mL); after one hour at room temperature, the solvent was removed under vacuum and the orange powder obtained was washed twice with acetone (5 mL) and $CH_2Cl_2$ (5 mL). Complex **10** was obtained as an orange microcrystalline powder (101 mg, 0.09 mmol). Yield: 91%. $C_{28}H_{27}F_6IrN_2O_6PtS_4{\cdot}CH_2Cl_2$ (1200.95 g mol$^{-1}$): calcd. C 28.98, H 2.43, N 2.33, S 10.67; found C 28.96, H 2.33, N 2.45, S 11.32. $^1H$ NMR (300 MHz, $CD_3CN$): $\delta$ = 1.98 (s, 15 H, Cp*), 6.68 (dd, 2 H, aromatic, $^3J_{H,H}$ = 4.63, $^4J_{H,H}$ = 2.41 Hz), 7.07 (dd, 2 H, aromatic, $^3J_{H,H}$ = 4.63, $^4J_{H,H}$ = 2.41 Hz), 7.74 (ddd, 2 H, bpy, $^3J_{H,H}$ = 7.42 Hz, $^3J_{H,H}$ = 5.65, $^4J_{H,H}$ = 1.69 Hz), 8.34 (m, 2 H, bpy), 8.39 (m, 2 H, bpy), 8.84 (dd, bpy, 2 H, $^3J_{H,H}$ = 5.73, $^4J_{H,H}$ = 1.53, $^5J_{H,H}$ = 0.69 Hz) ppm. IR (KBr disk): $\tilde{\nu}$($CF_3SO_3^-$) = 1031; 1260 cm$^{-1}$.

**X-ray Molecular Structures of 7 and 10:** Suitable crystals of [Cp*Ir-*p*-($\eta^4$-$C_6H_4S_2$)] (**7**) or [Pt(bpy){Cp*Ir-*o*-($\eta^4$-$C_6H_4S_2$)}][OTf]$_2$ (**10**) were obtained using slow diffusion techniques from $CH_2Cl_2$/diethyl ether solution for **7** and from $CH_3NO_2$/diethyl ether for **10**. The selected crystal of the very moisture-sensitive **7** or **10** was rapidly selected, mounted onto a glass fiber, and transferred in a cold nitrogen gas stream. Orange crystals of **7**: $C_{48}H_{57}Ir_3S_6{\cdot}1/2CH_2Cl_2$, monoclinic, $P2_1/m$, $a$ = 14.5450(5), $b$ = 9.2730(11), $c$ = 20.6380(3) Å, $\beta$ = 94.271(4)°, $V$ = 2775.8(5) Å$^3$, $Z$ = 2, $T$ = 250(2) K, $\mu$ = 7.476 mm$^{-1}$, 33263 reflections measured, 8342 independent ($R_{int}$ = 0.0413), 6364 observed [$I \geq 2\sigma(I)$], 321 parameters, final $R$ indices $R_1$ [$I \geq 2\sigma(I)$] = 0.0335 and $wR_2$ (all data) = 0.0956, gof on $F^2$ = 1.027, max./min. residual electron density = 1.31/–1.34 e Å$^{-3}$. Red crystals (**10**): $(C_{26}H_{27}IrN_2PtS_2)_2(CF_3O_3S)_4{\cdot}CH_3NO_2$, monoclinic, $P2_1/c$, $a$ = 8.793(3), $b$ = 34.296(9), $c$ = 25.208(6) Å, $\beta$ = 91.621(9)°, $V$ = 7599(4) Å$^3$, $Z$ = 4, $T$ = 200(2) K, $\mu$ = 7.471 mm$^{-1}$, 65719 reflections measured, 22256 independent ($R_{int}$ = 0.0615), 9023 observed [$I > 2\sigma(I)$], 848 parameters, final $R$ indices $R_1$ [$I > 2\sigma(I)$] = 0.0832 and $wR_2$ (all data) = 0.1928, gof on $F^2$ = 1.033, max./min. residual electron density = 3.33/–3.29 e Å$^{-3}$. Intensity data were collected with a Bruker-Nonius Kappa-CCD with graphite-mono-

 © 2007 Wiley-VCH Verlag GmbH & Co. KGaA, Weinheim 

chromated Mo-$K_\alpha$ radiation. Unit-cell parameters determination, data collection strategy and integration were carried out with the Nonius EVAL-14 suite of programs.[20] The structures were solved by direct methods using the SHELXS-86 program[21] and refined anisotropically by full-matrix least-squares methods using the SHELXL-97 software package.[22]

CCDC-293581 (for **7**) and -620737 (for **10**) contain the supplementary crystallographic data for this paper. These data can be obtained free of charge from the Cambridge Crystallographic Data Centre via www.ccdc.cam.ac.uk/data_request/cif.

**Supporting Information** (see also the footnote on the first page of this article): $^1$H NMR spectra of complexes **4**, **5**, **8**, and **9** are included in the supplementary material.

## Acknowledgments

Supported by the Centre National de la Recherche Scientifique (CNRS) and the Université Pierre et Marie Curie is gratefully acknowledged. H. A. would like also to thank the Ministère de la Recherche et de la Technologie for a PhD grant to J. M., without which this research could not have been accomplished.

[1] S. Patai, Z. Rappoport, *The Chemistry of the Quinonoid Compounds*, 2nd ed., Wiley, New York, **1988**.
[2] H. Bock, S. Mohmand, T. Hirabayashi, G. Maier, H. P. Reisenauer, *Chem. Ber.* **1983**, *116*, 273–281.
[3] R. Suzuki, K. Matsumoto, H. Kurata, M. Oda, *Chem. Commun.* **2000**, 1357–1358.
[4] Y. A. Jackson, D. Rajagopal, J. Bendolph, M. Guillory, M. V. Lakshmikantham, J. Yang, M. P. Cava, *Org. Lett.* **2003**, *5*, 1883–1885.
[5] M. Breitenstein, R. Schulz, A. Schweig, *J. Org. Chem.* **1982**, *47*, 1979–1980.
[6] P. de Mayo, A. C. Weedon, G. S. K. Wong, *J. Org. Chem.* **1979**, *44*, 1977–1981.
[7] M. V. Laksshmikantham, M. S. Raasch, M. P. Cava, S. G. Bott, J. L. Atwood, *J. Org. Chem.* **1987**, *52*, 1874–1877.
[8] H. Amouri, J. Le Bras, *Acc. Chem. Res.* **2002**, *35*, 501–510 and references cited therein.
[9] a) W. H. Hersh, R. G. Bergman, *J. Am. Chem. Soc.* **1981**, *103*, 6992–6994; b) A. Vigalok, D. Milstein, *J. Am. Chem. Soc.* **1997**, *119*, 7873–7874; c) D. B. Grotjahn, G. A. Bikzhanova, L. S. B. Collins, T. Concolino, K.-C. Lam, A. L. Rheingold, *J. Am. Chem. Soc.* **2000**, *122*, 5222–5223; d) Q. Zheng, J. A. Gladysz, *J. Am. Chem. Soc.* **2005**, *127*, 10508–10509.
[10] J. Moussa, D. A. Lev, K. Boubekeur, M. N. Rager, H. Amouri, *Angew. Chem.* **2006**, *118*, 3938–3942; *Angew. Chem. Int. Ed.* **2006**, *45*, 3854–3858.
[11] a) E. F. Mooney, *An Introduction to $^{19}$F NMR Spectroscopy*, Heyden & Son, Universities Press, Belfast, **1970**, chapter 6, p. 63; b) H. Amouri, M. N. Rager, F. Cagnol, J. Vaissermann, *Angew. Chem.* **2001**, *113*, 3748–3750; *Angew. Chem. Int. Ed.* **2001**, *40*, 3636–3638; c) H. Amouri, L. Mimassi, M. N. Rager, B. E. Mann, C. Guyard-Duhayon, L. Raehm, *Angew. Chem.* **2005**, *117*, 4619–4622; *Angew. Chem. Int. Ed.* **2005**, *44*, 4543–4546.
[12] a) J. Le Bras, H. Amouri, J. Vaissermann, *Organometallics* **1998**, *17*, 1116–1121; b) J. Moussa, C. Guyard-Duhayon, P. Herson, H. Amouri, M. N. Rager, A. Jutand, *Organometallics* **2004**, *23*, 6231–6238.
[13] a) A. Bondi, *J. Phys. Chem.* **1964**, *68*, 441–451; b) S.-Y. Kwon, J.-H. Cho, H.-I. Lee, U. Lee, D.-Y. Noh, *Inorg. Chem. Commun.* **2005**, *8*, 510–512.
[14] T. Ohashi, E. Kobayashi, T. Jinbo, J. Furukawa, *J. Polym. Sci., Part A: Polym. Chem.* **1997**, *35*, 1621–1625.
[15] M. Ratajczak-Sitarz, A. Katrusiak, Z. Kaluski, J. Garbarczyk, *Acta Crystallogr., Sect. C: Cryst. Struct. Commun.* **1987**, *43*, 2389–2391.
[16] T. K. Venkatachalam, E. Sudbeck, F. M. Uckun, *J. Mol. Struct.* **2005**, *751*, 41–54.
[17] a) V. W. W. Yam, K. M. C. Wong, N. Zhu, *J. Am. Chem. Soc.* **2002**, *124*, 6506–6507; b) T. J. Wadas, Q. M. Wang, Y. J. Kim, C. Flaschenreim, T. N. Blanton, R. Eisenberg, *J. Am. Chem. Soc.* **2004**, *126*, 16841–16849.
[18] J. Moussa, K. Boubekeur, H. Amouri, *Eur. J. Inorg. Chem.* **2005**, 3808–3810.
[19] T. J. Egan, K. R. Koch, P. L. Swan, C. Clarkson, D. A. Van Schalkwyk, P. J. Smith, *J. Med. Chem.* **2004**, *47*, 2926–2934.
[20] A. J. M. Duisenberg, L. M. J. Kroon-Batenburg, A. M. M. Schreurs, *J. Appl. Crystallogr.* **2003**, *36*, 220.
[21] G. M. Sheldrick, *SHELXS-86*, University of Göttingen, **1986**.
[22] G. M. Sheldrick, *SHELXL-97*, University of Göttingen, Germany, **1997**.

Received: October 11, 2006
Published Online: January 4, 2007

 © 2007 Wiley-VCH Verlag GmbH & Co. KGaA, Weinheim 

DOI: 10.1002/ejic.200601008

# Tris(dibenzo[*a*,*d*]cycloheptenyl)phosphane: A Bulky Monodentate or Tetrapodal Ligand

**Urs Fischbach,[a] Heinz Rüegger,[a] and Hansjörg Grützmacher*[a]**

**Keywords:** Alkene ligands / Gold / Iridium / Palladium / Phosphane ligands / Rhodium / Silver / Tetradentate ligands / Solid-state NMR spectroscopy

The tetradendate phosphane tris(5*H*-dibenzo[*a*,*d*]cyclohepten-5-yl)phosphane ($trop_3P$, **1**) was synthesized from tris(trimethylsilyl)phosphane and 5-chloro-5*H*-dibenzo[*a*,*d*]cycloheptene. Sulfurization of **1** with elemental sulfur led to $trop_3P$=S. Complexes of **1** with $Ag^I$, $Au^I$, $Rh^I$, $Ir^I$, and $Pd^{II}$ were prepared. The structures of $trop_3P$ (**1**), $trop_3P$=S (**2**), [AgCl($trop_3P$)] (**3**), [Au($trop_3P$)(MeCN)]$PF_6$ (**5**), [RhCl($trop_3P$)] (**6**) and [Pd($trop_3P$)($H_2O$)]$(OTf)_2$ (**9**) were determined by X-ray diffraction studies. In the coinage metal complexes, **1** serves as monodentate extremely bulky $\kappa^1$-phosphane ligand (cone angle ca. 250°). In the $Rh^I$, $Ir^I$, and $Pd^{II}$ complexes, **1** acts as tetradendate ligand. CP MAS NMR spectroscopy shows that the span of the chemical shift tensor increases in **7**, **6**, and **9** in this order ($\Omega$ = 310 ppm, 410 ppm, 465 ppm) and contains two strongly deshielded components, which are responsible for the unusual high frequency isotropic shift of the $^{31}P$ resonances. This property correlates inversely with the metal to olefin backbonding (M→C=$C_{trop}$) and $\delta(^{31}P)$ decreases with increasing M→C=$C_{trop}$ in the order **9** ($\delta$ = 260 ppm) > **7** ($\delta$ = 196 ppm) > **6** ($\delta$ = 135 ppm) > **3** ($\delta$ = –30.9 ppm).
(© Wiley-VCH Verlag GmbH & Co. KGaA, 69451 Weinheim, Germany, 2007)

## Introduction

Both phosphanes and alkenes look back on a history of more than one and a half centuries as ligands in metal coordination chemistry.[1] Metal complexes with these ligands have undergone constant development ever since their discovery. The combination of both types of binding sites in one molecule generates bi- or polydentate ligands and was achieved in the group of Nyholm in the mid-sixties with the synthesis of the first chelating phosphane–alkene ligands.[2] The most prominent feature of these chelating ligands is their hemilabile character: while the phosphane moiety usually binds quite strongly to a metal center, the olefin is less tightly attached and thus often prone to dissociation. Many different potentially chelating phosphane–olefin ligands have been prepared in the past forty years. Scheme 1 shows selected examples.

Acyclic alkenylphosphanes are the most obvious type of chelating phosphane–alkene ligands and mono, di- and trialkenylphosphanes (**I**, **II** and **III**) have been synthesized and characterized some decades ago.[3] Their coordination behaviour towards $Mo^0$,[4] $W^0$,[5] $Pd^{II}$,[6] $Pt^{II}$[7] and $Rh^I$[8] was investigated. Depending on the size of the resulting chelate ring, alkenylphosphanes act either as monodentate phosphanes or as multidentate chelating ligands, specifically with short chains ($n < 2$) the alkenyl group remains uncoordinated. Chemical transformations of the alkenyl group (hydrogenation, nucleophilic attack) were observed. Dialkenylphosphanes **II** often bind with one alkenyl group only to the metal center, i.e. they do not serve as tripodal ligands in the electronic ground state structures of the complexes. A large number of *ortho*-alkenylphenylphosphanes (**IV**, **V**) have been prepared[9] and $V^0$,[10] $Cr^0$, $Mo^0$ and $W^0$,[11] $Mn^I$ and $Re^I$,[12] $Fe^0$ and $Ru^0$,[13] $Rh^I$,[14] $Pd^{II}$,[15] and $Pt^{II}$,[16] $Cu^I$ and $Ag^I$[17] complexes were prepared and structurally characterized. Bidentate coordination of the ligands **IV** was established in all complexes. The ligands were prone to addition and isomerization reactions, e.g. hydrogenation or migration of the double bond.

Difurylphosphanes **VI** were applied in the cobalt-catalyzed homologation of methanol and conversions of up to 70% and ethanol selectivities of up to 50% were achieved.[18] The mixed anhydrides of diphenylphosphinous acid and acrylic acids **VII** may coordinate via the acrylic double bond (observed with $Rh^I$[19]) or via the oxygen atom of the carbonyl group (observed with $Ru^{II}$[20]). Binding of the double bond in $Rh^I$ complexes is weak and degradation occurred.[21] A ligand of type **VII** was found to be active in the $Rh^I$-catalyzed hydrogenation of acrylic acids.[22] The bidentate phosphane–alkene ligand **VIII** obtained from the condensation of chlorodiphenylphosphane with diallylamine was reported recently. The ligand coordinates to $W^0$, $Ru^{II}$, $Rh^I$, $Pd^{II}$ and $Pt^{II}$ and both, $\kappa^1$:$\eta^2$- and $\kappa^1$-coordination, were observed.[23]

For $Rh^I$ complexes with type **I**, **III**, **IV** and **V** ligands, trigonal bipyramidal (TBP) structures were observed.[24]

[a] Department of Chemistry and Applied Biosciences, ETH Zürich,
Wolfgang-Pauli-Strasse 10, 8093 Zürich, Switzerland
Fax: +41-44-633-1031
E-mail: gruetzmacher@inorg.chem.ethz.ch

 © 2007 Wiley-VCH Verlag GmbH & Co. KGaA, Weinheim 

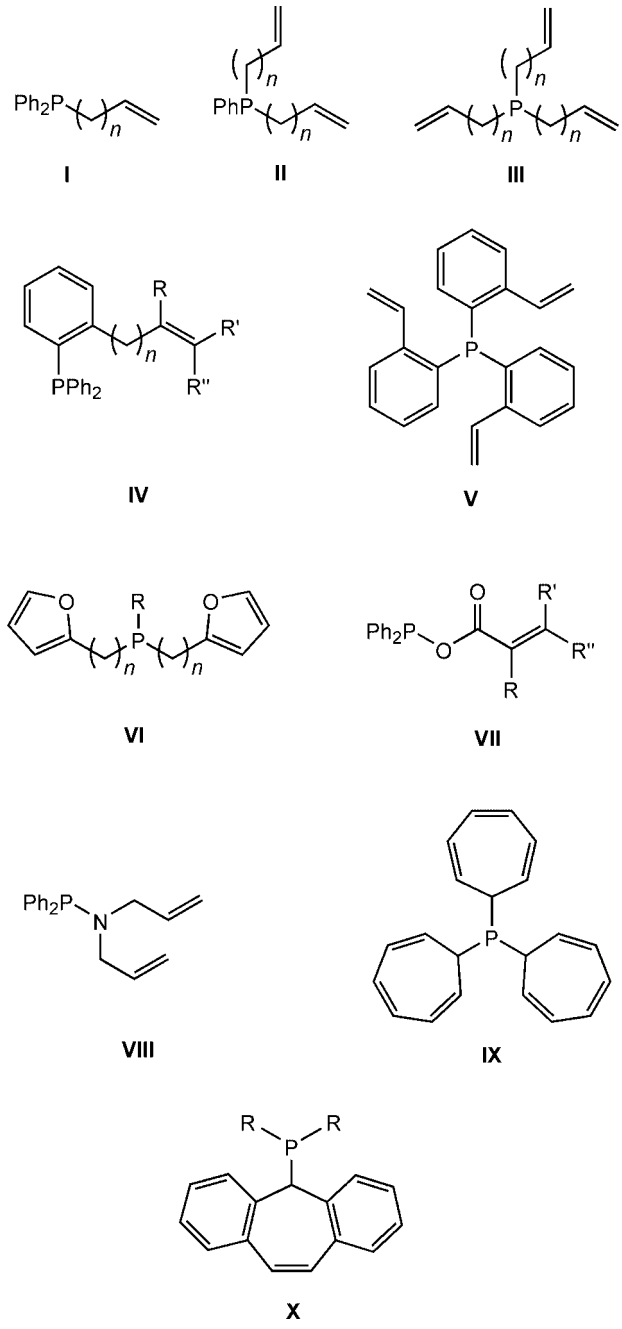


Scheme 1. Mono-, di- and triolefin phosphanes.

This form should be especially favoured by tetradentate tris(alkenyl)phosphanes like **III** and **V**. While X-ray diffraction studies show that $Rh^{I}$ complexes have the P-donor in the axial and the three C=C donors in the equatorial plane, NMR spectroscopic studies revealed that the latter are fluxional on the NMR time scale and likely dissociate.[25]

The phosphane $cht_3P$ **IX** (cht = cycloheptatrienyl) was synthesized by Herberhold and co-workers in 1994.[26] Due to the boat conformation of the seven-membered cht rings, this phosphane is preorganized for binding to a transition metal center by the P-donor and the opposite C=C bonds and stabilization of TBP structures can be expected. However, rotation around the P–C bonds, facile inversion of the boat conformation of the cht ring, and additional coordination of metals through the C=C bonds adjacent to the P-atom make the ligand fluxional and complicate its coordination chemistry. Indeed a variety of coordination modes are observed in complexes which do not show a special preference for TBP structures, such as $V^{0}$[27] ($\kappa^1$), $Cr^0$, $Mo^0$, $W^0$,[28] $Mn^{I}$,[29] $Fe^0$ and $Ru^{0}$[30] complexes ($\kappa^1$-, $\kappa^1$:$\eta^2$- and $\kappa^1$:$\eta^4$-coordination). With $Rh^{I}$ and $Ir^{I}$ the expected trigonal bipyramidal complexes were isolated and these are quite stable, indeed, and it needed other polydentate ligands to displace $cht_3P$ **IX**.[31] A bidentate coordination mode is observed for **IX** in fluxional $Pd^{II}$ and $Pt^{II}$ dichloride complexes,[32] but the abstraction of one chloride leads to cationic $[MX(cht_3P)]^+$ complexes with TBP structures.[33] In complexes with $Cu^{I}$ and $Ag^{I}$, ligand **IX** binds via the P-atom and small but detectable interactions with the opposite C=C bonds of the cht rings were discussed on the basis of solid-state structure data (distances of the metal center to the centroids of the coordinated C=C double bonds in the range of 2.6–3.0 Å were observed[34,35]).

In parallel to the work of Herberhold et al., we started about 10 years ago the investigation of (5*H*-dibenzo[*a*,*d*]cyclohepten-5-yl)phosphanes **X** as ligands, which we named tropp (from dibenzo**trop**ylidenyl**p**hosphane). The trivial name dibenzotropylidenyl (= trop) will be used throughout this paper instead of 5*H*-dibenzo[*a*,*d*]cyclohepten-5-yl.[36] The annelated benzo groups make these compounds especially rigid with the phosphanyl substituent in 5-position residing in the energetically preferred *endo*-conformation. A concave binding site results, which is perfectly pre-organized for transition metal binding. A large number of structurally different ligands based on the trop platform[37] and a variety of complexes with $Rh^{I}$ and $Ir^{I}$,[38] $Pd^{II}$, $Pd^0$, $Pt^{II}$, $Pt^0$,[37a–37c,37g] $Cu^{I}$, $Ag^{I}$ and $Au^{I}$[39] as metal centers were prepared. Noteworthy is the ability of the tropp-type ligands to stabilize complexes with transition metal centers in formally low oxidation states, that is the first stable paramagnetic $Rh^0$ and $Ir^0$ complexes could be isolated.[40]

In the continuation of our work, we report here the synthesis of the ligand tris(5*H*-dibenzo[*a*,*d*]cyclohepten-5-yl)-phosphane ($trop_3P$, **1**) and the synthesis of various transition metal complexes. The coinage metals only exert weak (if any) interactions with the olefinic double bonds, while with $Rh^{I}$, $Ir^{I}$ and $Pd^{II}$ trigonal bipyramidal complexes are obtained in which the $C{=}C_{trop}$ groups are tightly bound and $trop_3P$ acts as tetrapodal ligand.

## Results and Discussion

### Synthesis and Structural Characterization of $trop_3P$ (1)

The phosphane $trop_3P$ was obtained by treating tris(trimethylsilyl)phosphane with 3.5 equiv. of tropCl. The product precipitated from the solution as its hydrochloride salt after the addition of methanol to the reaction mixture and was easily isolated. Further work-up under standard conditions led to the final product (Scheme 2). $Trop_3P$ can be stored without special precautions on air for at least two

 © 2007 Wiley-VCH Verlag GmbH & Co. KGaA, Weinheim 

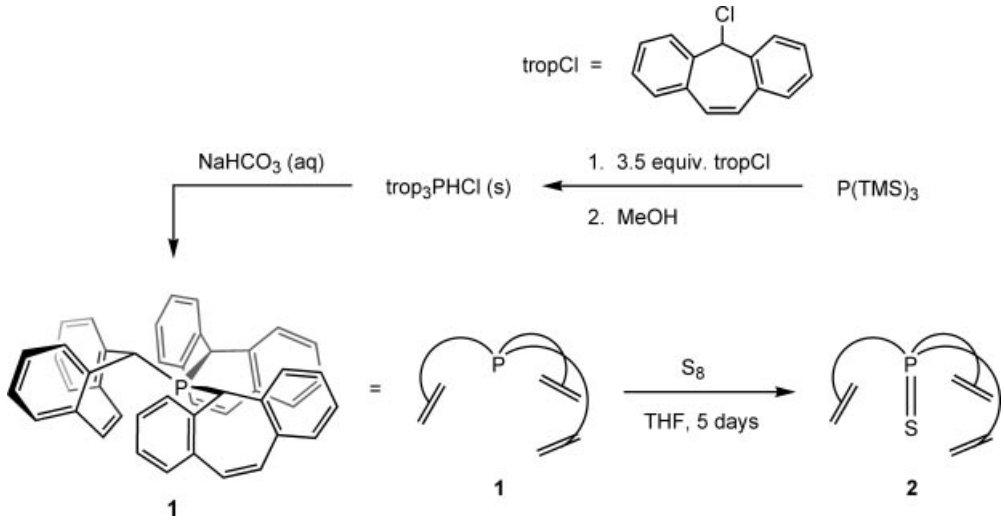


Scheme 2. Synthesis of $trop_3P$ (**1**) and $trop_3P{=}S$ (**2**).

years and in substance is not oxygenated by 1 atm of $O_2$ at room temperature. The structure of **1** was determined by X-ray diffraction. Figure 1 and Figure 2 show the molecule from two different angles; selected bond lengths and angles are given in the Figure caption, pertinent crystal data are given in Table 4. The threefold symmetry axis of the cubic unit cell coincides with the $C_3$ molcular symmetry axis. There are no mirror planes in the crystal due to the slight twist of the trop moieties and the space group is chiral ($P\bar{4}3n$), that is the crystals exist in two enantiomorphic forms. The prominent structural feature of **1** is the *endo-endo-endo* conformation of the $trop_2P$ substituents at each individual seven-membered ring, which all have a boat conformation. NMR spectra indicate that this highly symmetric structure is also present in solution. Hence, **1** is a highly pre-organized rigid ligand for tetradentate binding in TBP structures with a typical sum of bond angles at the P-atom, $\Sigma°(P) = 295.5°$.

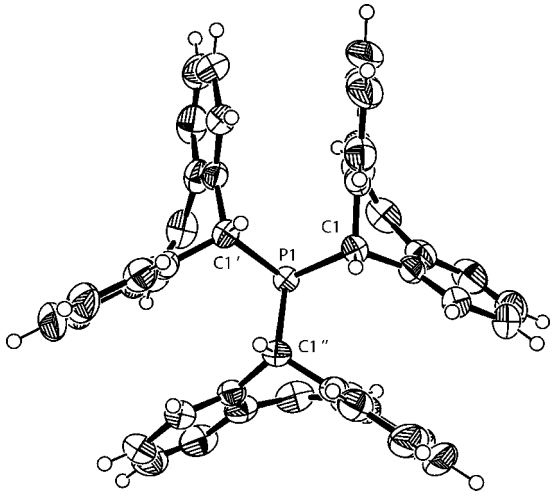


Figure 1. ORTEP plot of $trop_3P$ (**1**) (thermal ellipsoids at 50% probability). View along the threefold symmetry axis of both the molecule and the crystal. Sum of bond angles at P1: 295.5°.

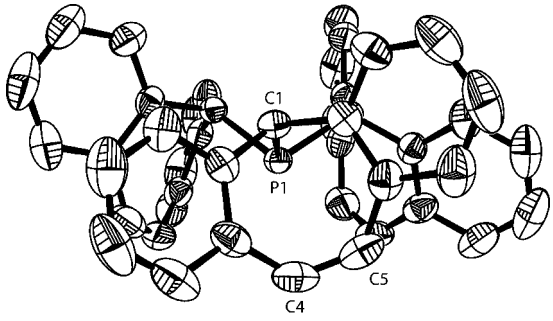


Figure 2. ORTEP plot of $trop_3P$ (**1**) (thermal ellipsoids at 50% probability, hydrogen atoms omitted for clarity). View perpendicular to the threefold symmetry axis. Selected bond lengths [Å] and angles [°]: P1–C1: 1.9015(22); C4–C5: 1.330(4); C1–P1–C1′: 98.50(9). Torsion angles [°]: C1′–P1–C1–C7: 45.14(21); C31–P1–C1–C2: 89.98(20).

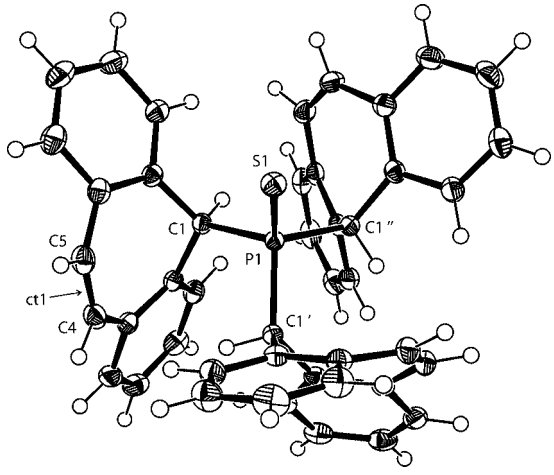


Figure 3. ORTEP plot of $trop_3P{=}S$ (**2**) (thermal ellipsoids at 50% probability, solvent molecules omitted for clarity). Selected bond lenghts [Å] and angles [°]: P1–S1: 1.9409(9); P1–C1: 1.9181(14); mean C=C (double bond): 1.333(2); S1–P1–C1: 112.42(5); C1–P1–C1′: 106.37(5). Sum of bond angles of the three carbon substituents at P1: 319°. Torsion angle $\varphi$(S1–P1–C1–ct1): 73.2°.

 © 2007 Wiley-VCH Verlag GmbH & Co. KGaA, Weinheim 

In order to test whether the phosphorus atom can be involved in a chemical reaction, **1** was treated with $S_8$ (Scheme 2). After stirring in THF at 60 °C for about five days, $trop_3P{=}S$ (**2**) precipitated and could be isolated (higher reaction temperatures led to decomposition). A plot of the structure obtained by X-ray diffraction is shown in Figure 3 (selected bond lengths and angles are given in the Figure caption, pertinent crystal data are given in Table 4). In contrast to **1**, the trop substituents in **2** are considerably more twisted. This is indicated by the torsion angle $\varphi$ = X–P1–C1–ct1 = 73.2° in **2** vs. $\varphi$ = 23.0° in **1** where X stands for the phosphorus lone pair or a substituent and ct for the centroid of the $C{=}C_{trop}$ unit (ideally $C_{3v}$ with $\varphi$ = 0°, that is the $C{=}C_{trop}$ group is orthogonal to the P–X vector). As expected, the sum of the C–P–C angles at the phosphorus atom increases to 319° upon sulfurization. Noteworthy is the slight lengthening of the P–C bonds in **2** [1.918(1) Å] with respect to **1** [1.902(2) Å] while usually a shortening is observed upon increasing the formal oxidation state at the phosphorus center to $P^V$.

### Metal Complexes of $trop_3P$

The coordination chemistry of $trop_3P$ (**1**) was investigated through the synthesis of complexes containing the $d^{10}$ noble metal ions, $Ag^I$ and $Au^I$, and the $d^8$ valence electron configured metal ions, $Rh^I$, $Ir^I$ and $Pd^{II}$. The first two metal ions are expected to bind weakly, the latter strongly to the $C{=}C_{trop}$ units. The coordination to the $C{=}C_{trop}$ bonds can be evaluated by NMR spectroscopic data and inspection of the molecular structures. Low-frequency $^{13}C$ NMR resonances for the significantly shielded $C{=}C_{trop}$ carbon nuclei and torsion angles $\varphi$ close to 0° are expected when the olefinic units are tightly bound.

### Silver and Gold

Despite its low solubility, AgCl is dissolved completely when stirred in a $CH_2Cl_2$ solution of phosphane **1** at room temperature. After about 20 h [AgCl($trop_3P$)] (**3**) is quantitatively obtained (Scheme 3). The silver salts AgOTf and

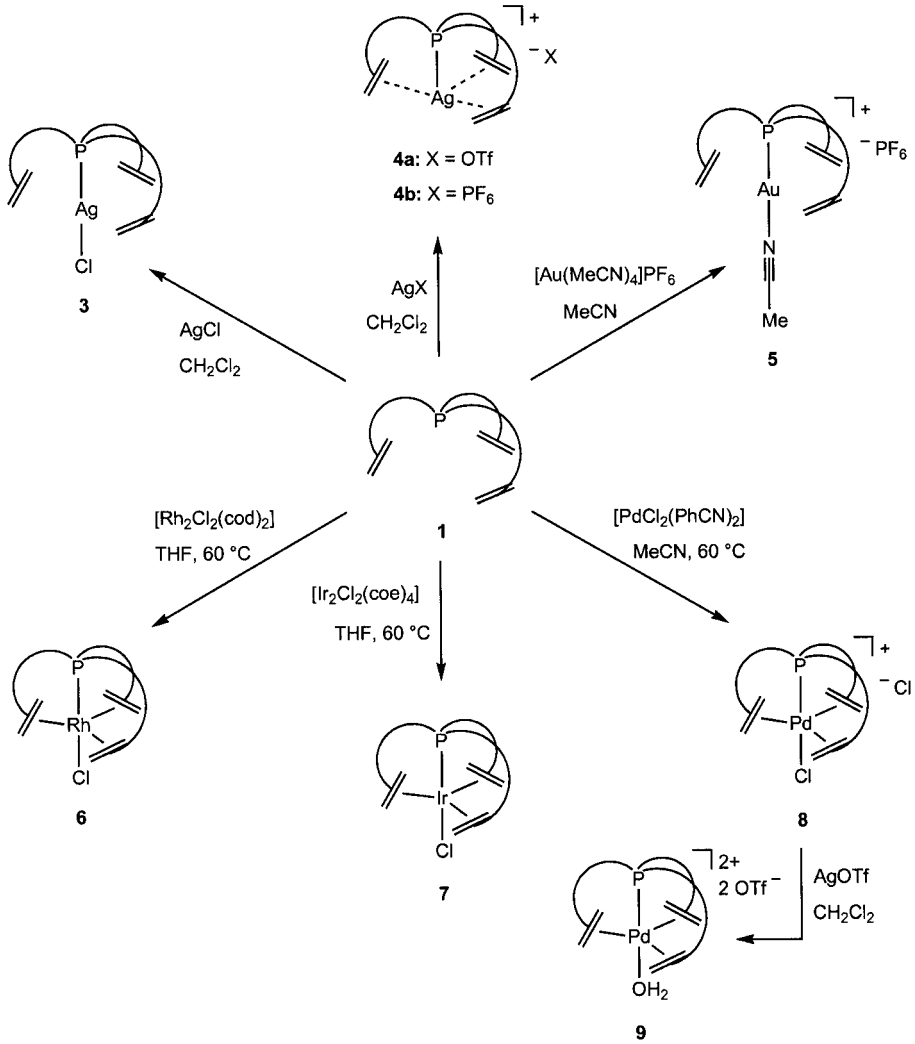


Scheme 3. Synthesis of $trop_3P$ transition metal complexes.

 © 2007 Wiley-VCH Verlag GmbH & Co. KGaA, Weinheim 

$[Ag(MeCN)_4]PF_6$ reacted rapidly with **1** to give the complexes $[Ag(trop_3P)]OTf$ (**4a**) and $[Ag(trop_3P)]PF_6$ (**4b**), respectively. Crystals of the compounds **3**, **4a** and **4b** were grown and investigated by X-ray diffraction. We were unable to refine the data sets of compounds **4a**, **4b** likely because of severe disorder of the $OTf^-$ and $PF_6^-$ anions. The structure of **3** was solved and a plot of the structure is shown in Figure 4 (see the Figure caption for selected bond lengths and angles and Table 4 for pertinent crystal data). As expected, P1 and Cl1 coordinate to the Ag center in an almost linear fashion (P1–Ag1–Cl1: 173.1°). The structural data give no indications for coordination of the $C{=}C_{trop}$ bonds. The mean distance between the Ag atom and the double bond centroids, ct, is approximately 3.2 Å, the $C{=}C_{trop}$ bonds are not elongated in **3** [$C{=}C_{trop}$ 1.328(1) Å] with respect to the free phosphane **1** [$C{=}C_{trop}$ 1.330(4) Å], and the torsion angle $\varphi$ (Ag1–P1–C1–ct1) = 27(7)° remains large.

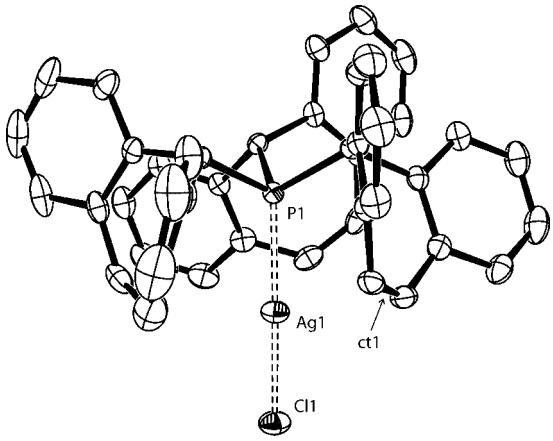


Figure 4. ORTEP plot of $[AgCl(trop_3P)]$ (**3**) (thermal ellipsoids at 30% probability, hydrogen atoms and solvent molecules omitted for clarity, only one of two independent molecules shown). Selected bond lenghts [Å] and angles [°]: Ag1–P1: 2.3677(21); Ag1–Cl1: 2.3528(23); mean Ag1–ct: 3.16(12); mean C=C (double bond): 1.328(12); P1–Ag1–Cl1: 173.10(3). Sum of bond angles of the three carbon substituents at P1: 305°. Mean torsion angle $\varphi$(Ag1–P1–C1–ct1): 27(7)°.

These conclusions are supported by NMR spectroscopy. The element silver consists of two NMR-active isotopes, $^{107}Ag$ (51.84%) and $^{109}Ag$ (48.16%) with $I$ = 1/2. Due to weak coordination and rapid exchange processes, $^{31}P$ NMR spectra of silver phosphane complexes often display a single broad resonance signal at room temperature, which sometimes can be resolved at low temperatures. The silver complex **3** is persistent even at room temperature and the two couplings $^1J(^{107}Ag,^{31}P)$ and $^1J(^{109}Ag,^{31}P)$ are clearly resolved in the $^{31}P$ NMR spectrum (Figure 5).

A $^1H,^{109}Ag$ HMQC spectrum was measured in order to search for indications of Ag–($CH{=}CH_{trop}$) interactions (Figure 6). The sizeable Ag–H coupling of 9.0 Hz to the benzylic protons (easily observed in the standard $^1H$ NMR spectrum) gives rise to strong cross peaks in the two-dimensional spectrum. None of the other protons couple strongly enough to generate cross peaks that are detectable above

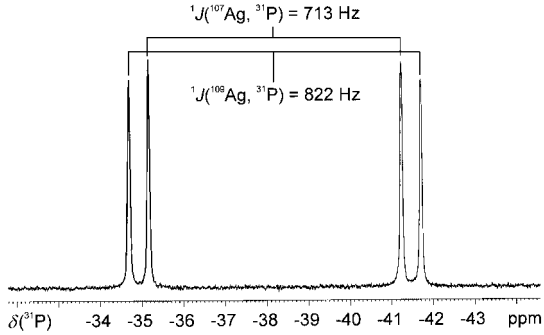


Figure 5. $^{31}P$ NMR spectrum of $[Ag(trop_3P)]OTf$ (**4a**) at room temperature. Coupling to the two almost equally abundant silver isotopes $^{107}Ag$ and $^{109}Ag$ is clearly resolved.

the noise level. In a second experiment, the Ag–H coupling constants were measured by means of a $^{31}P$, $^1H$ HMQC spectrum (Figure 7). Additional nuclei besides $^{31}P$ and $^1H$ in the spin system will cause a doubling of the resonances in the 2D spectrum. Furthermore, a diagonal displacement of the cross peaks will be observed, which corresponds to the coupling with the additional nuclei. This is clearly visible for the benzylic hydrogen atoms, which do couple with the $^{107}Ag$ and $^{109}Ag$ nuclei and give eight diagonally displaced cross peaks. Note that from this spectrum individual $^3J(^{109}Ag,^1H)$ and $^3J(^{107}Ag,^1H)$ coupling constants can be obtained as a consequence of the resolution in the $^{31}P$ domain. Furthermore, the signs of $^3J_{Ag,H}$ and $^1J_{Ag,P}$ are the same. For the olefinic protons, only four cross peaks can be

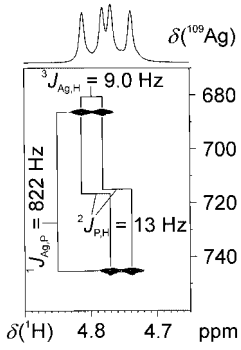


Figure 6. Section of the $^1H,^{109}Ag$ HMQC spectrum of **4a**. Cross peaks with the benzylic protons.

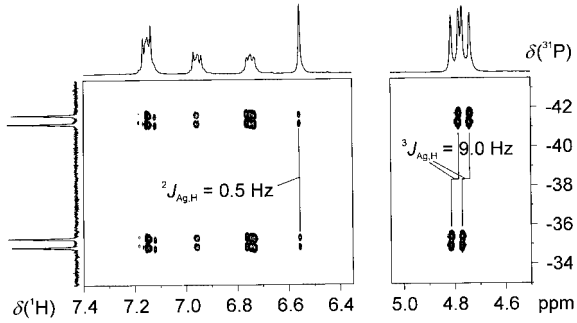


Figure 7. Section of the $^1H,^{31}P$ HMQC spectrum of **4a**. Ag–H couplings are visible for the benzylic and for the olefinic protons.

 © 2007 Wiley-VCH Verlag GmbH & Co. KGaA, Weinheim 

recorded, but there is in fact a tiny shift of –0.5 Hz in the $^1$H NMR dimension. To the best of our knowledge this is the second coupling constant between a silver nucleus and an olefinic proton that could be measured.[39] Its small magnitude indicates a very weak and likely dynamic interaction between the C=$C_{trop}$ double bonds and the Ag atom. We note that although the unlike signs of $^2J$(Ag,$H_{olefinic}$) and $^3J$(Ag,$H_{benzylic}$) are in agreement with such an explanation, we cannot exclude a coupling mechanism involving just the olefinic proton and extended lone pairs on silver, similar to the ones often encountered in fluorine chemistry. In any case, our data give no indications of metal-to-olefin, Ag→C=$C_{trop}$, π-back-donation and if there were a silver–olefin interaction, this would consists in an olefin to metal, C=$C_{trop}$→Ag, σ-donation within the Dewar–Chatt–Duncanson terminology. This view is fully supported by inspection of the $^{13}$C NMR spectroscopic data of the C=$C_{trop}$ carbon nuclei (see Table 2 and the discussion below).

We were especially interested in the synthesis of a monophosphane gold complex, possibly with an additional labile ligand. Therefore we reacted $trop_3P$ (**1**) with [$Au^I(MeCN)_4$]-$PF_6$, which was obtained by electrolysis of a gold wire in an acetonitrile solution containing the $PF_6^-$ anion.[41,42] Upon mixing a suspension of **1** in MeCN with a MeCN solution of [$Au^I(MeCN)_4$]$PF_6$, immediate dissolution of **1** was observed. The product [Au($trop_3P$)(MeCN)]$PF_6$ (**5**) was subsequently precipitated by adding toluene (Scheme 3). The structure of **5** is displayed in Figure 8 (see the Figure caption for selected bond lengths and angles and Table 4 for pertinent crystal data obtained by X-ray diffraction). The gold center is coordinated by the phosphorus atom of the $trop_3P$ ligand and a nitrogen atom of the MeCN ligand in a linear coordination sphere (P1–Au1–N1 176.3°). The

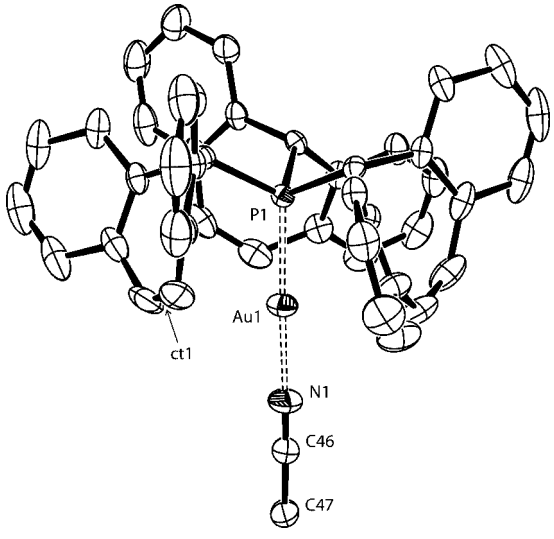


Figure 8. ORTEP plot of [Au($trop_3P$)(MeCN)]$PF_6$ (**5**) (thermal ellipsoids at 30% probability, hydrogen atoms and counteranion omitted for clarity). Selected bond lenghts [Å] and angles [°]: Au1–P1: 2.2343(9); Au1–N1: 2.043(4); mean Au1–ct: 3.14(6); mean C=C (double bond): 1.33(3); P1–Au1–N1: 176.30(13); Au1–N1–C46: 175.5(5). Sum of bond angles of the three carbon substituents at P1: 309°. Mean torsion angle φ(Au1–P1–C1–ct1): 24(7)°.

Au1–P1 and the Au1–N1 distances are in good accordance with reported bond lengths.[43] The long distances between the gold atom and surrounding C=$C_{trop}$ groups (average 3.139 Å) and the twist of the C=$C_{trop}$ units (average φ = 24.4°) exclude any significant interaction. This is also corroborated by the $^{13}$C NMR shifts of the C=$C_{trop}$ units, which again show high frequency shifts upon coordination (see Table 2 below).

Thus, in $d^{10}$ valence electron configured silver and gold complexes, **1** behaves as extremely bulky monodentate phosphane ligand (cone angle approx. 250°)[44] and the resulting complexes are kinetically inert.

### Rhodium, Iridium, and Palladium

When [$Rh_2(\mu\text{-}Cl)_2(cod)_2$] was treated with **1** in THF at 60 °C, quantitative conversion to the desired product [RhCl($trop_3P$)] (**6**) was observed after 30 h (Scheme 3). Complex **6** precipitated directly from the reaction solution and was isolated as yellow powder by simple filtration. Concentrations higher than 0.03 M should be avoided, because partial decomposition of the ligand with formation of bi(dibenzo[*a*,*d*]cyclohepten-5-yl), $trop_2$, was observed. The structure of **6** was determined by X-ray diffraction. Figure 9 shows a plot, selected bond lengths and angles are listed in the Figure caption, and in Table 4 pertinent crystal data are given. Complex **6** has an almost perfect trigonal bipyramidal structure with the P- and Cl-atoms in the apical and the three C=$C_{trop}$ units in the equatorial positions; the P1–Rh1–Cl1 angle is 179° and the ct–Rh–ct angles vary between 119.2° and 121.4°. Clearly, the C=$C_{trop}$ double bonds are coordinated: The averaged Rh–ct distances are short (2.15 Å), the C=C bonds are elongated to 1.40 Å, and the torsion angles φ are smaller than 10°. This leads to an almost perfect parallel stacking of the benzo rings of neighbouring trop groups at distances of about 3.2 Å. The structural data of **6** very closely match the ones reported for the complex [RhCl($cht_3P$)] by Herberhold et al.,[45] only the Rh–C distances are marginally shorter by about 1%. Table 1 gives a compilation of selected structure parameters for both compounds.

The iridium complex [IrCl($trop_3P$)] (**7**) was prepared in about 70% yield when **1** was treated with [$Ir_2(\mu\text{-}Cl_2)(coe)_4$] for 3 d at 60 °C in THF. The reaction is somewhat more sluggish than in the case of the synthesis of **6** but after removal of impurities, **7** is obtained as bright white powder (Scheme 3). Crystals of **7** showed merohedral twinning and we were unable to refine the structure satisfactorily. However, the gross structural features were determined and show that **7** has as expected, a structure analogous to the rhodium complex **6**.

[$PdCl_2(PhCN)_2$] reacted with **1** in $CH_2Cl_2$ at room temperature to form an $\eta^2$ complex, likely [$PdCl_2$-($trop_3P$)(PhCN)] with only one double bond of one trop substituent coordinated, while the phosphorus center and the other two C=$C_{trop}$ bonds remain uncoordinated, which is indicated by the rather low-frequency $^{31}$P NMR reso-

 © 2007 Wiley-VCH Verlag GmbH & Co. KGaA, Weinheim 

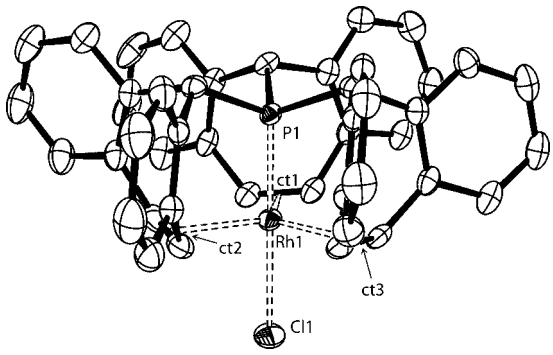


Figure 9. ORTEP plot of [RhCl(trop$_3$P)] (**6**) (thermal ellipsoids at 50% probability, hydrogen atoms and solvent molecules omitted for clarity). Selected bond lenghts [Å] and angles [°]: Rh1–P1: 2.1413(8); Rh1–Cl1: 2.4601(8); mean Rh1–ct: 2.150(9); mean C=C (double bond): 1.401(7); P1–Rh1–Cl1: 179.06(3). Sum of bond angles of the three carbon substituents at P1: 320°. Mean torsion angle $\varphi$(Rh1–P1–C1–ct1): 7.1(4)°.

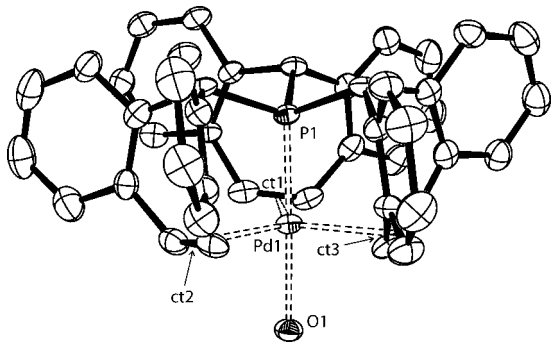


Figure 10. ORTEP plot of [Pd(trop$_3$P)(H$_2$O)](OTf)$_2$ (**9**) (thermal ellipsoids at 50% probability, hydrogen atoms, counter anions and solvent molecules omitted for clarity, only one of two independent molecules shown). Selected bond lenghts [Å] and angles [°]: Pd1–P1: 2.1736(14); Pd1–O1: 2.142(4); mean Rh1–ct: 2.28(5); mean C=C (double bond): 1.383(20); P1–Pd1–O1: 177.21(11). Sum of bond angles of the three carbon substituents at P1: 322°. Mean torsion angle $\varphi$(Rh1–P1–C1–ct1): 9.5(8)°.

Table 1. Comparison of structural parameters.

| Bond/Angle | [RhCl(trop$_3$P)] (**6**) | [RhCl(cht$_3$P)][a] |
|---|---|---|
| Rh–P | 2.1413(8)[b]Å | 2.153(1) Å |
| Rh–Cl | 2.4601(8) Å | 2.460(1) Å |
| Rh=C | 2.265(3) Å | 2.283(2) Å |
| | 2.244(3) Å | 2.282(2) Å |
| | 2.274(3) Å | 2.279(2) Å |
| | 2.248(3) Å | 2.280(2) Å |
| | 2.280(3) Å | 2.295(2) Å |
| | 2.254(3) Å | 2.287(2) Å |
| P–Rh–Cl | 179.06(3)° | 178.9(1)° |

[a] Data from ref.[45]. [b] Standard deviation.

nance at $\delta$ = –48.1 ppm. Performing the reaction in THF or acetonitrile as solvent and heating the reaction mixture to 60 °C for 24 h caused vanishing of the initial yellow color and a red solid started to precipitate. This compound showed a $^{31}$P NMR shift at $\delta$ = 263.8 ppm and was identified as [Pd(trop$_3$P)Cl]Cl (**8**) (Scheme 3). Exchange of the chlorides by triflate anions using AgOTf was a straightforward reaction and gave an intense ruby red solution ($\lambda_{max}$ = 497 nm). From this solution, very dark crystals of the composition [Pd(trop$_3$P)(H$_2$O)](OTf)$_2$ (**9**) were obtained which were subjected to a X-ray diffraction study. The dication [Pd(trop$_3$P)(H$_2$O)]$^{2+}$ has a TBP structure with the P-atom of the trop$_3$P ligand and an oxygen atom of a water molecule in the axial positions (Figure 10, see the Figure caption for selected bond lengths and angles and Table 4 for pertinent crystal data). The three C=C$_{trop}$ units are bound in the equatorial positions at about 2.3 Å. This distance is significantly longer (ca. 0.13 Å) than the one in the Rh$^{I}$ complex **6**. The less pronounced Pd→C=C$_{trop}$ π-backbonding also leads to shorter C=C$_{trop}$ bonds (average 1.383 Å) when compared to the Rh$^{I}$ complex **6**. The averaged torsion angle $\varphi$ is again smaller than 10°. The Pd1–O1 bond length [2.142(4) Å] is very similar to Pd–O distances found in structures of tetracoordinate planar Pd$^{II}$ aqua complexes, while **9** seems to be the first structurally characterized pentacoordinate Pd$^{II}$ aqua complex.

## NMR Spectroscopy

Selected $^{31}$P, $^{1}$H, and $^{13}$C solution NMR spectroscopic data of trop$_3$P (**1**), [AgCl(trop$_3$P)] (**3**), [Au(trop$_3$P)(MeCN)]-PF$_6$ (**5**), [RhCl(trop$_3$P)] (**6**), [IrCl(trop$_3$P)] (**7**), and [Pd-(trop$_3$P)(H$_2$O)](OTf)$_2$ (**9**) are listed in entries 1–6 in Table 2.

For comparison we also list the corresponding data for analogous cht$_3$P complexes (entries 7–12). The proton and $^{13}$C NMR spectroscopic data are remarkably similar in both series. The proton in β-position (denoted as H$_{benz}$) is little influenced by metal coordination to the P-atom as long as the complex remains neutral (especially in the rhodium and iridium complexes, **6** and **7**, respectively). Metal charge has an influence, that is an increasingly positive charge of the complex shifts the H$_{benz}$ resonance to higher frequencies (by 1.63 ppm in the dication **9**, by 0.76 ppm in the mono-cation **5**). Metal to C=C$_{trop}$ π-backbonding, M→C=C$_{trop}$, is reflected in the chemical shifts of the $^{13}$C$_{olef}$ and $^{13}$C$_{benz}$ and to a certain extent in the $^{1}$H$_{olef}$ nuclei. Increasing π-backbonding causes a low-frequency shift (shielding) of the $^{13}$C$_{olef}$ resonances of the C=C$_{trop}$ units. The data clearly show that M→C=C$_{trop}$ backbonding in the silver and gold complexes is negligible as already stated above, the coordination shifts $\Delta\delta$ = ($\delta_{complex}$ – $\delta_{free\ ligand}$) are even positive (+7 and +5 ppm for **3** and **5**, respectively) while negative $\Delta\delta$ are expected when π-backdonation is significant. This is the case in the Pd$^{II}$ complex **9** ($\Delta\delta$ = –15.4), Rh$^{I}$ complex **6** ($\Delta\delta$ = –45.6), and Ir$^{I}$ complex **7** ($\Delta\delta$ = –59.4) and backbonding increases in this order. The increasing slight shift to lower frequency of the $^{13}$C$_{benz}$ resonance in the same order is a consequence of the increasing bending of the central seven-membered ring upon shortening of the metal C=C$_{trop}$ distances. This effect causes a slight decrease of the sum of the two P–C$_{benz}$–C and the C–C$_{benz}$–C angle (336.0° in the free phosphane **1**; 334° in **9**, and 331° in **6**). The $^{1}$H$_{olef}$ resonances are also increasingly shifted to low frequency (by 0.3 ppm in **6**, 0.9 ppm in **7**) upon increasing the metal to olefin backbonding, but this effect is counterbalanced by the formal charge at the metal center and in

 © 2007 Wiley-VCH Verlag GmbH & Co. KGaA, Weinheim 

Table 2. Comparison of NMR spectroscopic data[a] for $trop_3P$ and $cht_3P$ complexes.

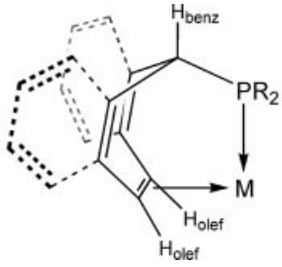


| Compound | Solvent | $^{31}P$ NMR [ppm] | $^{1}H$ NMR [ppm] | | $^{13}C$ NMR [ppm] | |
|---|---|---|---|---|---|---|
| | | | $H_{olef}$ | $H_{benz}$ | $C_{olef}$ | $C_{benz}$ |
| $trop_3P$ (**1**) | $CDCl_3$ | –22.4 | 6.30 | 4.16 | 125.0 | 55.6 |
| $[AgCl(trop_3P)]$ (**3**) | $CD_2Cl_2$ | –27.7 | 6.54 | 4.46 | 132.0 | 54.4 |
| $[Au(trop_3P)(MeCN)]PF_6$ (**5**) | $CD_3CN$ | 0.7 | 6.48 | 4.92 | 130.3 | 54.2 |
| $[RhCl(trop_3P)]$ (**6**) | $CD_2Cl_2$ | 191.7 | 5.93 | 3.97 | 79.4 | 48.4 |
| $[IrCl(trop_3P)]$ (**7**) | $CD_2Cl_2$ | 134.1 | 5.40 | 4.15 | 65.6 | 44.8 |
| $[Pd(trop_3P)(H_2O)](OTf)_2$ (**9**) | $CD_2Cl_2$ | 270.6 | 7.40 | 5.79 | 109.6 | 51.9 |
| $cht_3P$[b] | $CDCl_3$ | –12.8 | 6.53 | 2.32 | 130.9 | 36.1 |
| $[AgCl(cht_3P)]$[b] | $CDCl_3$ | –13.8 | 6.62 | 2.92 | 132.0 | 36.0 |
| $[RhCl(cht_3P)]$[c] | $CDCl_3$ | 325.3 | 5.45 | 1.94 | 80.9 | 35.9 |
| $[IrCl(cht_3P)]$[c] | $CDCl_3$ | 265.2 | 4.81 | 1.95 | 65.4 | 31.1 |
| $[PdCl(cht_3P)]PF_6$[c] | $(CD_3)_2CO$ | 435.9 | 7.13 | 3.77 | 110.6 | 43.9 |
| $[PtCl(cht_3P)]PF_6$[c] | $(CD_3)_2CO$ | 353.1 | 6.37 | 3.60 | 92.7 | 36.5 |

[a] Table includes only chemical shift data; multiplicities and coupling constants are omitted for simplicity. [b] Data from ref.[35]. [c] Data from ref.[33].

the $Pd^{II}$ complex **9** $H_{olef}$ is even deshielded by 1.1 ppm. The same trends are observed in the $cht_3P$ complexes (see entries 7–12).

A remarkable feature of the $M(trop_3P)$ and $M(cht_3P)$ complexes with $M{\rightarrow}C{=}C_{trop}$ backbonding are the unusual high frequency shifts of the $^{31}P$ resonances. Especially in the $Pd^{II}$ complexes, the $^{31}P$ coordination chemical shifts are almost 300 ppm for **9** and approx. 450 ppm for $[Pd(cht_3P)Cl]^+$, which shows likely the least shielded $^{31}P$ nucleus for a seemingly "ordinary" phosphane complex.[34] Interestingly, this unusual shift to high frequencies becomes smaller when the $M{\rightarrow}C{=}C_{trop}$ backbonding increases, that is in the order Pd > Rh > Ir the $^{31}P$ resonance frequencies decrease. On the contrary, for the $d^{10}$-metal complexes, especially for the silver complexes, small coordination shifts of the $^{31}P$ resonance are observed.

In order to gain some insight into these unusual $^{31}P$ NMR shifts, we recorded CP MAS spectra of **1**, **3**, **6**, **7**, and **9**. The top of Figure 11 shows the spectra obtained for **1** and **3** at a spinning frequency of 8 and 7 kHz, respectively. On the bottom of Figure 11, the spectra on static powder samples are displayed. A single sharp resonance with very small side bands is observed for $trop_3P$ (**1**). The spectrum obtained with a non-rotating sample is indicative for an axial chemical shift tensor in complete accordance with the high symmetry determined in the X-ray diffraction study. The anisotropy of the chemical shift tensor, expressed in its span $\Omega$, is about 19 ppm, which is within the expected range for free phosphanes. The $^{31}P$ CP MAS spectrum of $[AgCl(trop_3P)]$ (**3**) at 7 kHz shows a sharp doublet, that is the one bond coupling to silver is resolved under these conditions, but not to the individual $^{109}Ag$ and $^{107}Ag$ isotopes (cf. Figure 5). A non-spinning probe showed a typical rhombic signal of moderate band width with $\Omega \approx 24$ ppm close to the one of the free phosphane **1**.

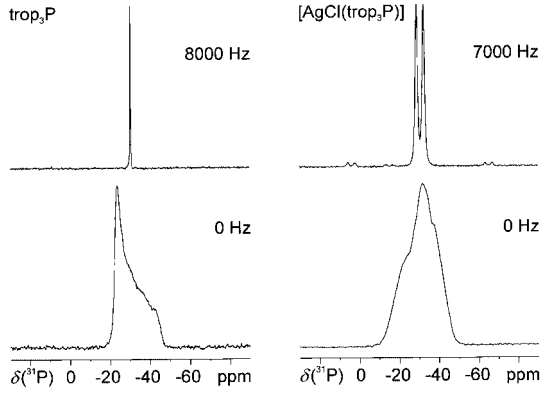


Figure 11. 202 MHz $^{31}P\{^1H\}$ CP MAS spectra of $trop_3P$ (**1**) and $[AgCl(trop_3P)]$ (**3**) at 8/7 kHz and 0 Hz spinning frequency, respectively.

Figure 12 shows the experimental spectra of $[RhCl(trop_3P)]$ (**6**), $[IrCl(trop_3P)]$ (**7**) and $[Pd(trop_3P)(H_2O)]^{2+}$ (**9**). At 3 kHz rotation frequency of the samples, the spectra observed for **6** and **7** are not significantly different from the axial type (skew $\kappa > 0.9$), but a rhombic spectrum is seen for **9** ($\kappa = 0.87$). In all cases two components of the chemical shift tensor, $\delta_{11}$ and $\delta_{22}$, were recorded at frequencies typical of weak shielding while the remaining, $\delta_{33}$, was observed at negative values rather similar for all investigated compounds **1**–**9**. The largest anisotropy $\Omega \approx 460$ ppm is obtained for the $Pd^{II}$ complex **9**. Clearly, the components $\delta_{11}$ and $\delta_{22}$ are responsible for the isotropic high-frequency shift

 © 2007 Wiley-VCH Verlag GmbH & Co. KGaA, Weinheim 

Table 3. Compilation of solid state NMR spectroscopic data (ppm) for $trop_3P$ complexes.

| Compound | $\delta_{iso}$ | $\delta_{11}$ | $\delta_{22}$ | $\delta_{33}$ | $\delta_{iso}$, calcd. | $\Omega$ |
|---|---|---|---|---|---|---|
| $trop_3P$[a] | –30.3 | –24.0(5) | –24.0(5) | –43.0(5) | –30 | 19(1) |
| [AgCl($trop_3P$)] (**3**) | –30.9 | [b] | [b] | [b] | | |
| [RhCl($trop_3P$)] (**6**)[c] | 196 | 330(5) | 330(5) | –70(5) | 197 | 400(10) |
| [IrCl($trop_3P$)] (**7**)[c] | 135 | 245(5) | 245(5) | –85(5) | 135 | 330(10) |
| [Pd($trop_3P$)($H_2O$)]($OTf)_2$ (**9**)[c] | 260 | 425(5) | 395(5) | –40(5) | 260 | 465(10) |

[a] Values determined by line shape analysis at 0 Hz spinning frequency. [b] The contributions of the anisotropies of scalar coupling, dipolar coupling and chemical shift can not be separated satisfactorily. [c] Values determined by analysis of the experimental MAS spectrum and then fitting a simulation.

recorded in solution. Simulation of the spectra led to the chemical shift tensor elements listed in Table 3. The axial spectra of **6** and **7** allow to conclude that the $\delta_{33}$ element is aligned with the M–P vector and $\delta_{11}$ and $\delta_{22}$ are consequently orthogonal to M–P and parallel to the equatorial coordination plane with the metal C=$C_{trop}$ arrangement.[46] As Table 3 shows, the deshielding of $\delta_{11}$ and $\delta_{22}$ decreases in the order **9** < **6** < **7** as the M→C=$C_{trop}$ backbonding increases.

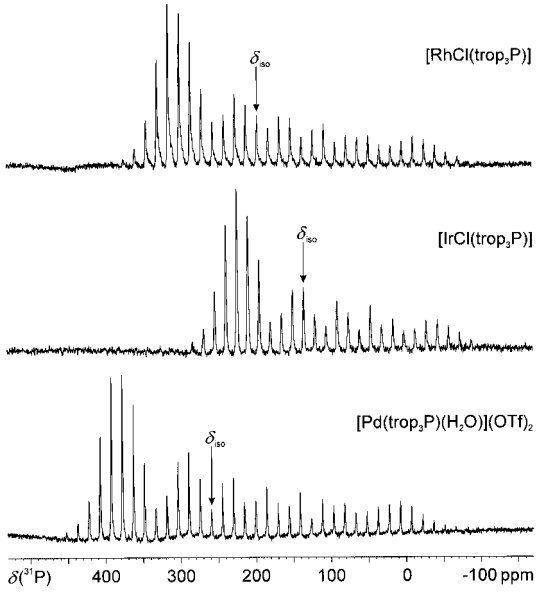


Figure 12. 202 MHz $^{31}P\{^1H\}$ CP MAS spectra of [RhCl($trop_3P$)] (**6**) (top), [IrCl($trop_3P$)] (**7**) (middle) and [Pd($trop_3P$)($H_2O$)]($OTf)_2$ (**9**) (bottom) at 3 kHz rotation frequency.

## Conclusions

The new phosphane $trop_3P$ was synthesized in an unexpected simple manner from $P(SiMe_3)_3$ and 5-chlorodibenzo[*a*,*d*]cycloheptene, tropCl. The structure of $trop_3P$ is very rigid and the phosphorus atom is deeply embedded in a concave pocket formed by the three trop substituents. This makes the phosphane infinitely stable against oxidation on air and long reaction times are needed for converting $trop_3P$ into the corresponding thiophosphorane, $trop_3P$=S, or to bind transition metals into the pocket. In complexes with $d^{10}$ valence electron configured metal complexes, $trop_3P$ behaves as an extremely bulky monodenate ligand with a cone angle of approx. 250°. Consequently, complexes of $Ag^I$ and $Au^I$ are kinetically stabilized and the isolation of a rare stable cationic monophosphane acetonitrile complex [Au($trop_3P$)(MeCN)]$^+$ (**5**) was achieved.[47] Although questionless a silver–olefin interaction exists in compounds like $[Ag(C_2H_4)_3]^+$ $Al[OC(CF_3)_3]_4^-$,[48] our data do not support the idea that any significant interaction (in the sense of a chemical bond formed by orbital overlap) exists in linearly coordinated $ML_2$ complexes where M = $Ag^+$ or $Au^+$, which have additional olefinic moieties in close proximity. In complexes with $d^8$ valence electron configured transition metals, $trop_3P$ serves as tetradentate ligand and trigonal pyramidal [M($trop_3P$)] fragments were observed[49] with M = $Rh^I$, $Ir^I$, and $Pd^{II}$ to which a fifth ligand X = $Cl^-$, $H_2O$ binds in the remaining axial position. Structural and NMR spectroscopic data suggest that π-backbonding from filled d-orbitals at the transition metal center to the π* orbitals of the coordinated C=C double bonds increases as expected in the order $Pd^{II}$ < $Rh^I$ < $Ir^I$. Remarkably, the $^{31}P$ NMR shifts react most sensitively to this effect and a decrease in M→C=$C_{trop}$ backbonding causes a strong deshielding, that is shifts to higher frequencies. $^{31}P$ CP MAS NMR spectroscopy allowed the chemical shift tensor to be determined and shows that the unusual deshielding of the $^{31}P$ nuclei in the [MX($trop_3P$)] complexes is caused by large positive $\delta_{11}$ and $\delta_{22}$ components, which are in plane with the three coordinated C=$C_{trop}$ units and the metal center M = $Pd^{II}$, $Rh^I$, $Ir^I$. The third component, $\delta_{33}$, is aligned with the M–P bond and has similar negative values for all complexes. Under the assumption that the $^{31}P$ NMR shift is dominated by the paramagnetic shift term, excitations into unoccupied orbitals are likely responsible for this phenomenon. We suggest that these relevant unoccupied orbitals are those which correspond to an antibonding interaction between a filled d-orbital at the metal center and the π*-orbital of the C=$C_{trop}$ bond. A strong M→C=$C_{trop}$ backbonding will stabilize the bonding d(M)–π*(C=C) interaction at low energies but lift the antibonding d(M)–π*(C=C) interaction to high energies. Inversely, a weak M→C=$C_{trop}$ backbonding will create an energetically low lying antibonding d(M)–π*(C=C) interaction and excitations into this orbital are made responsible for the exceptional coordination shifts leading to unusally high-frequency-shifted $^{31}P$ resonances in the $Pd^{II}$ complexes {$\delta(^{31}P)$ = 270.6 ppm in [Pd($trop_3P$)($H_2O$)]$^{2+}$}; [$\delta(^{31}P)$ = 435.9 ppm in [Pd($cht_3P$)(Cl)]$^+$]. For

 © 2007 Wiley-VCH Verlag GmbH & Co. KGaA, Weinheim 

a detailed explanation of this phenomenon, an in-depth quantum chemical analysis is needed, which however was beyond the scope of this study.

## Experimental Section

**General Procedures:** All manipulations of air- or moisture-sensitive compounds were performed on a standard vacuum line in flame-dried flasks under an atmosphere of argon. Solvents were distilled under argon from Na (toluene), Na/benzophenone (THF, diethyl ether), Na/benzophenone/tetraglyme (*n*-hexane), $CaH_2$ ($CH_2Cl_2$, chloroform, acetonitrile), $P_2O_5$ (acetonitrile). Air-sensitive compounds were stored and weighed in gloveboxes. Basic chemicals were ordered from commercial suppliers and used as received. The following organic compounds and metal precursors were prepared according to literature methods: tropCl,[50] $(TMS)_3P$,[51] $[Ir_2(COE)_4(\mu\text{-}Cl)_2]$.[52] IR spectra were recorded on a Perkin–Elmer Spectrum 2000 FT-IR-Raman spectrometer with the ATR technique. Mass spectra of organic compounds were recorded on a Finnigan MAT SSQ 7000 mass spectrometer using electron ionization. Melting points were determined with a Büchi melting point apparatus and are not corrected. UV/Vis spectra were recorded on a UV/Vis/NIR lambda 19 spectrometer in 5-mm quartz cuvettes (200–1000 nm). Solution NMR spectra were recorded on Bruker Avance 400, 300, 250 and 200 spectrometers. Chemical shifts ($\delta$) are measured and referenced according to IUPAC[53] and expressed in ppm. $^{31}P$ CP MAS solid state NMR spectra were acquired at room temperature on a Bruker Avance instrument operating at a $^1H$ Larmor frequency of 500 MHz. Conventional cross-polarization and magic-angle-spinning techniques were implemented by using 4-mm rotors with which rotational frequencies of at least 11 kHz were achieved. The strength of the magnetic field was adjusted such that the $^{13}C$ carboxylate resonance of α-glycine appeared at $\delta$ = 176.0 ppm. In consequence referencing of all isotopes could be achieved as for the solution NMR using the unified $\Xi$ scale.[53] Chemical shifts are expressed relative to $H_3PO_4$. CP MAS spectra were simulated by using the SIMPSON program package.[54]

**Preparation of Tris(5*H*-dibenzo[*a*,*d*]cycloheptен-5-yl)phosphane (1):** TropCl (13.4 g, 59 mmol) was placed under argon in a 500-mL round-bottom Schlenk flask. It was dissolved in 250 mL freshly distilled, dry THF. $P(SiMe_3)_3$ (4.5 mL, 3.9 g, 16 mmol) was added dropwise to this solution. The resulting mixture was stirred at room temperature for several days and the reaction was monitored by $^{31}P$ NMR spectroscopy. The first substitution leading to $trop(SiMe_3)_2P$ [$\delta(^{31}P)$ = –148.2 ppm] is quite fast, the second step to $trop_2(SiMe_3)P$ [$\delta(^{31}P)$ = –70.3 ppm] and third step to **1** proceed more slowly. When the $^{31}P$ NMR spectrum showed almost complete conversion to $trop_3P$ **1** (after 4 to 6 d), MeOH (2.5 mL, 2.0 g, 62 mmol) was added and stirring was continued for another 12 h. During this time a white precipitate formed in the reaction mixture ($trop_3P{\cdot}HCl$) [$\delta(^{31}P)$ = –45.5 ($^1J_{P,H}$ = 480 Hz) ppm]. This precipitate was collected by filtration and washed with THF. The product was obtained by suspending ($trop_3P{\cdot}HCl$) in a concentrated $NaHCO_3$ solution and extracting the resulting mixture twice with $CH_2Cl_2$. The combined organic phases were dried with $Na_2SO_4$ and concentrated to dryness. The product was dried in high vacuum giving a fine white powder of high purity. If necessary, **1** can be further purified by recrystallization from toluene. Yield: 7.54 g (80%). M.p. 247 °C. $C_{45}H_{33}P$ (604.72): calcd. C 89.38, H 5.50, P 5.12; found C 89.12, H 5.66. IR (ATR): $\tilde{\nu}$ = 3013 (w, $\nu_{CH}$), 1592 (w), 1488 (m), 1453 (m), 1432 (m), 1329 (m), 1287 (m), 796 (s), 781 (s), 728 (s), 633 (s) $cm^{-1}$. MS (EI): *m*/*z* 603 ($M^+$), 191 ($C_{15}H_{11}^+$). $^1H$ NMR (300 MHz, $CDCl_3$, 25 °C): $\delta$ = 4.16 (d, $^2J_{P,H}$ = 1.8 Hz, 3 H, $H_{benz}$), 6.30 (s, 6 H, $H_{olef}$), 6.44–6.51 (m, 6 H, $H_{aryl}$), 6.81–6.87 (m, 6 H, $H_{aryl}$), 6.97–7.06 (m, 12 H, $H_{aryl}$) ppm. $^{13}C\{^1H\}$ NMR (75.5 MHz, $CDCl_3$, 25 °C): $\delta$ = 55.6 (d, $^1J_{P,C}$ = 36.3 Hz, 3 C, $C_{benz}$), 125.0 (d, $J_{P,C}$ = 0.7 Hz, 6 C, $C_{olef}$), 128.3 (s, 6 C, $C_{aryl}$), 128.6 (s, 6 C, $C_{aryl}$), 128.6 (d, $J_{P,C}$ = 3.1 Hz, 6 C, $C_{aryl}$), 131.6 (d, $J_{P,C}$ = 5.7 Hz, 6 C, $C_{aryl}$), 135.4 (d, $J_{P,C}$ = 3.5 Hz, 6 C, $C_{aryl}$), 139.3 (d, $J_{P,C}$ = 9.0 Hz, 6 C, $C_{aryl}$) ppm. $^{31}P\{^1H\}$ NMR (121.5 MHz, $CDCl_3$, 25 °C): $\delta$ = –22.7 (s) ppm.

**Preparation of Tris(5*H*-dibenzo[*a*,*d*]cycloheptен-5-yl)phosphane Sulfide (2):** In a Schlenk flask, $trop_3P$ (240 mg, 0.40 mmol) and $S_8$ (14 mg, 0.44 mmol) were suspended in THF (20 mL). This mixture was heated to 60 °C and stirred for several days. Conversion was about 20% after 17 h and about 40% after 40 h. After five days, a white precipitate had formed, which was collected by filtration and washed with THF. The filtrate still contained about 50% starting material. The collected product was dried in high vacuum to give a microcrystalline white solid. Yield: 35 mg (14%). M.p. 212 °C. $C_{45}H_{33}PS$ (636.78): calcd. C 84.88, H 5.22, P 4.86; found C 84.43, H 4.91. IR (ATR): $\tilde{\nu}$ = 3017 (w, $\nu_{CH}$), 2972 (w, $\nu_{CH}$), 2852 (w, $\nu_{CH}$), 1494 (m), 1456 (m), 1432 (m), 1160 (m), 1065 (m), 803 (s), 779 (s), 769 (s), 726 (s), 687 (s), 615 (m). $^1H$ NMR (300 MHz, $CD_2Cl_2$, 25 °C): $\delta$ = 5.39 (d, $^2J_{P,H}$ = 16 Hz, 3 H, $H_{benz}$), 6.34 (br. s, 6 H, $H_{olef}$), 7.10–7.25 (m, 12 H, $H_{aryl}$), 7.25–7.40 (m, 6 H, $H_{aryl}$), 7.40–7.50 (m, 12 H, $H_{aryl}$) ppm. $^{13}C\{^1H\}$ NMR (75.5 MHz, $CD_2Cl_2$, 25 °C): $\delta$ = 59.5 (d, $^1J_{P,C}$ = 23.5 Hz, 3 C, $C_{benz}$), 127.3 (s, 6 C, $C_{olef}$), 128.8 (s, 6 C, $C_{aryl}$), 129.9 (s, 6 C, $C_{aryl}$), 131.7 (d, $J_{P,C}$ = 6.5 Hz, 6 C, $C_{aryl}$), 133.2 (s, 6 C, $C_{aryl}$), 135.8 (s, 6 C, $C_{aryl,quat}$), 136.0 (s, 6 C, $C_{aryl,quat}$) ppm. $^{31}P\{^1H\}$ NMR (121.5 MHz, $CD_2Cl_2$, 25 °C): $\delta$ = 79.5 (s) ppm.

**Preparation of Chloro[tris(5*H*-dibenzo[*a*,*d*]cycloheptен-5-yl)phosphane]silver(I) (3):** Aqueous solutions of $AgNO_3$ (2.0 g, 12 mmol) and $NH_4Cl$ (1.0 g, 19 mmol) were aggregated to precipitate AgCl. This precipitate was collected by filtration, washed with water, ethanol and diethyl ether and dried on air. $trop_3P$ **1** (158 mg, 0.26 mmol) and an excess of the freshly precipitated AgCl (123 mg, 0.86 mmol) were combined in $CH_2Cl_2$ (20 mL). This mixture was stirred for 16 h. The remaining AgCl was removed by filtration and washed with $CH_2Cl_2$. The filtrate was concentrated to dryness. Then the product was washed with small amounts of pentane and dried in high vacuum. The product was obtained as a bright white microcrystalline solid. Yield: 135 mg (69%). M.p. 251–260 °C (decomposition). $C_{45}H_{33}AgClP$ (748.04): calcd. C 72.25, H 4.45, P 4.14; found C 71.98, H 4.58. IR (ATR): $\tilde{\nu}$ = 3017 (w, $\nu_{CH}$), 1594 (w), 1486 (m), 1455 (m), 1434 (m), 1334 (m), 1296 (m), 798 (s), 785 (s), 729 (s), 637 (s) $cm^{-1}$. $^1H$ NMR (300 MHz, $CD_2Cl_2$, 25 °C): $\delta$ = 4.46 (dd, $^2J_{P,H}$ = 12 Hz, $^3J_{Ag,H}$ = 7.8 Hz, 3 H, $H_{benz}$), 6.54 (s, 6 H, $H_{olef}$), 6.56 (d br, $^3J_{H,H}$ = 7.2 Hz, 6 H, $H_{aryl}$), 7.01 (dd, $^3J_{H,H}$ = 7.2 Hz, $^4J_{H,H}$ = 1.8 Hz, 6 H, $H_{aryl}$), 7.16 (ddd, $^3J_{H,H}$ = 7.2 Hz, 7.2 Hz; $^4J_{H,H}$ = 1.8 Hz, 6 H, $H_{aryl}$), 7.20 (dd br, $^3J_{H,H}$ = 7.2 Hz, 7.2 Hz; 6 H, $H_{aryl}$) ppm. $^{13}C\{^1H\}$ NMR (75.5 MHz, $CD_2Cl_2$, 25 °C): $\delta$ = 54.4 (dd, $^1J_{P,C}$ = 5.7 Hz, $^2J_{Ag,C}$ = 1.5 Hz, 3 C, $C_{benz}$), 126.7 (d, $J_{P,C}$ = 1.7 Hz, 6 C, $C_{aryl}$), 129.2 (s, 6 C, $C_{aryl}$), 129.4 (d, $^3J_{P,C}$ = 4.6 Hz, 6 C, $C_{aryl}$), 129.5 (d, $J_{P,C}$ = 1.7 Hz, 6 C, $C_{aryl}$), 132.0 (dd, $^4J_{P,C}$ = 5.3 Hz, $^1J_{Ag,C}$ = 2.0 Hz, 6 C, $C_{olef}$), 135.0 (d, $J_{P,C}$ = 4.6 Hz, 6 C, $C_{aryl,quat}$), 136.0 (d, $J_{P,C}$ = 3.3 Hz, 6 C, $C_{aryl,quat}$) ppm. $^{31}P\{^1H\}$ NMR (121.5 MHz, $CD_2Cl_2$, 25 °C): $\delta$ = –27.7 (d, $^1J_{107Ag,P}$ = 669 Hz, $^1J_{109Ag,P}$ = 771 Hz) ppm.

**Preparation of [Tris(5*H*-dibenzo[*a*,*d*]cycloheptен-5-yl)phosphane]silver(I) Trifluoromethanesulfonate (4a):** In a Schlenk flask, $trop_3P$ **1** (480 mg, 0.79 mmol) was dissolved in THF. AgOTf (204 mg,

 © 2007 Wiley-VCH Verlag GmbH & Co. KGaA, Weinheim 

0.79 mmol) was added to this solution and the resulting mixture was stirred for three days. Any precipitates were removed by filtration through celite. The filtrate was concentrated to about one third of its volume and left at –20 °C for crystallization. The precipitated product was collected by filtration and dried in high vacuum. The product was an off-white powder. Yield: 360 mg (53%). M.p. 223–228 °C (decomposition). Due to the light sensitivity of the compound, we were not able to obtain reliable elemental analytical data. IR (ATR): $\tilde{\nu}$ = 3362(br., $\nu_{H2O}$), 3020 (w, $\nu_{CH}$), 1594 (w), 1489 (m), 1455 (m), 1434 (m), 1330 (m), 1265 (s), 1234 (s), 1156 (s), 1027 (s), 802 (s), 788 (s), 763 (s) 732 (s), 635 (s) cm$^{-1}$. $^1$H NMR (300 MHz, $CD_3CN$, 25 °C): $\delta$ = 4.78 (dd, $^2J_{P,H}$ = 13 Hz, $^3J_{Ag,H}$ = 9.0 Hz, 3 H, $H_{benz}$), 6.56 (s, 6 H, $H_{olef}$), 6.71–6.78 (m, 6 H, $H_{aryl}$), 6.92–6.99 (m, 6 H, $H_{aryl}$), 7.10–7.19 (m, 12 H, $H_{aryl}$) ppm. $^{13}$C{$^1$H} NMR (75.5 MHz, $CD_3CN$, 25 °C): $\delta$ = 52.9 (dd, $^1J_{P,C}$ = 5.6 Hz, $^2J_{Ag,C}$ = 3.6 Hz, 3 C, $C_{benz}$), 126.6 (d, $^5J_{P,C}$ = 1.5 Hz, 6 C, $C_g$), 129.2 (d, $^4J_{P,C}$ = 1.7 Hz, 6 C, $C_h$), 129.6 (d, $^3J_{P,C}$ = 4.6 Hz, 6 C, $C_e$),129.9 (s, 6 C, $C_f$), 131.2 (dd, $^4J_{P,C}$ = 6.0 Hz, $^1J_{Ag,C}$ = 1.7 Hz, 6 C, $C_{olef}$), 134.1 (d, $^3J_{P,C}$ = 4.5 Hz, 6 C, $C_c$), 135.6 (d, $^2J_{P,C}$ = 2.7 Hz, 6 C, $C_b$) ppm. $^{19}$F{$^1$H} NMR (188.3 MHz, $CD_3CN$, 25 °C): $\delta$ = –79.2 (s) ppm. $^{31}$P{$^1$H} NMR (121.5 MHz, $CD_3CN$, 25 °C): $\delta$ = –38.3 (d, $^1J_{107Ag,P}$ = 713 Hz, $^1J_{109Ag,P}$ = 822 Hz) ppm. $^{109}$Ag{$^1$H} NMR (13.4 MHz, $CD_3CN$, 25 °C): $\delta$ = 717 (d, $^1J_{Ag,P}$ = 822 Hz) ppm.

**Preparation of [Tris(5*H*-dibenzo[*a*,*d*]cyclohepten-5-yl)phosphane]silver(I) Hexafluorophosphate (4b):** A solution of trop$_3$P **1** (195 mg, 0.33 mmol) in THF was added dropwise to a solution of [Ag(MeCN)$_2$]$PF_6$ (110 mg, 0.33 mmol) in THF. The reaction mixture was left overnight under strict exclusion of light for crystallization. The precipitated product was collected by filtration and dissolved in acetonitrile. Impurities were removed by filtration and the filtrate was concentrated to dryness. Recrystallization from THF and drying in high vacuum yielded the product as a slightly off-white microcrystalline powder. Yield: 131 mg (47%). M.p. 198–202 °C (decomposition). Due to the light sensitivity of the compound, we were not able to obtain reliable elemental analytical data. IR (ATR): $\tilde{\nu}$ = 3057 (w, $\nu_{CH}$), 1595 (w), 1490 (w), 1455 (w), 1434 (w), 1330 (w), 1295 (w), 834 (s), 803 (s), 788 (m), 765 (m), 734 (m), 637 (m) cm$^{-1}$. $^1$H NMR (300.1 MHz, $CD_3CN$, 25 °C): $\delta$ = 4.76 (dd, $^2J_{P,H}$ = 12.9 Hz, $^3J_{Ag,H}$ = 9.0 Hz, 3 H, $H_{benz}$), 6.55 (s, 6 H, $H_{olef}$), 6.71–6.78 (m, 6 H, $H_{aryl}$), 6.92–6.99 (m, 6 H, $H_{aryl}$), 7.12–7.21 (m, 12 H, $H_{aryl}$) ppm. $^{19}$F{$^1$H} NMR (188.3 MHz, $CD_3CN$, 25 °C): $\delta$ = –72.8 (d, $^1J_{P,F}$ = 706 Hz) ppm. $^{31}$P{$^1$H} NMR (121.5 MHz, $CD_3CN$, 25 °C): $\delta$ = –37.9 (d, $^1J_{107Ag,P}$ = 715 Hz, $^1J_{109Ag,P}$ = 825 Hz, trop$_3$*P*), –144.5 (hept, $^1J_{P,F}$ = 706 Hz, *P*$F_6$) ppm.

**Preparation of (Acetonitrile)[tris(5*H*-dibenzo[*a*,*d*]cyclohepten-5-yl)-phosphane]gold(I) Hexafluorophosphate (5):** Due to the strong oxidizing potential of Au$^I$ this synthesis was carried out under inert conditions. The precursor complex [Au(MeCN)$_4$]$PF_6$ was synthesized using a slightly modified published procedure.[41] [Au(MeCN)$_4$]$^+$ is generated by oxidation of a gold wire in an electrolysis apparatus. The anode consisted of a coiled gold wire, whereas for the cathode a coiled silver wire was used. The three compartments were separated by two anion-selective membranes. [Ag(MeCN)$_2$]$PF_6$ (1.67 g, 4.99 mmol) and $Me_4NPF_6$ (1.29 g, 5.9 mmol) were dissolved in acetonitrile (50 mL) and transferred into the cathodic compartment. The bridge compartment was filled with $Me_4NPF_6$ (1.33 g, 6.1 mmol) dissolved in acetonitrile (30 mL). To neat acetonitrile (50 mL) in the anodic compartment, 0.5 mL of a solution of $Et_4NI$ ($6\cdot10^{-4}$ M, $3\cdot10^{-4}$ mmol) were added (the resulting solution was $6\cdot10^{-6}$ M in $Et_4NI$). The iodide catalytically activated the surface of the gold wire. After the electrolysis the product solution in the anodic compartment was separated by cannula filtration from colloidal Au$^0$ precipitates and used immediately afterwards. Separately, trop$_3$P **1** (0.19 g, 0.31 mmol) was suspended in freshly distilled acetonitrile (50 mL). Then the decanted solution of [Au(MeCN)$_4$]$PF_6$ in acetonitrile was added dropwise until the reaction mixture became clear (about 15 mL). Toluene was added until some precipitate started to form. Leaving the mixture at room temperature overnight gave cubic shaped crystals suitable for X-ray diffraction (50 mg, 16%). Further product was obtained by concentration of the solution and was collected by filtration. The slightly yellow micro-crystalline powder was washed with toluene and dried in high vacuum. Yield: 236 mg (76%). M.p. 208–212 °C (decomposition). IR (ATR): $\tilde{\nu}$ = 3021 (w, $\nu_{CH}$), 1491 (m), 1455 (m), 1433 (m), 1334 (m), 1301 (m), 834 (s), 797 (s), 763 (s), 734 (s), 641 (m) cm$^{-1}$. $^1$H NMR (300 MHz, $CD_3CN$, 25 °C): $\delta$ = 4.92 (d, $^2J_{P,H}$ = 15 Hz, 3 H, $H_{benz}$), 6.48 (s, 6 H, $H_{olef}$), 6.67–6.73 (m, 6 H, $H_{aryl}$), 7.02–7.07 (m, 6 H, $H_{aryl}$), 7.18–7.30 (m, 12 H, $H_{aryl}$) ppm. $^{13}$C{$^1$H} NMR (75.5 MHz, $CD_3CN$, 25 °C): $\delta$ = 54.2 (d, $^1J_{P,C}$ = 25 Hz, 3 C, $C_{benz}$), 127.3 (d, $J_{P,C}$ = 2.0 Hz, 6 C, $C_{aryl}$), 129.3 (d, $J_{P,C}$ = 2.1 Hz, 6 C, $C_{aryl}$), 129.5 (s, 6 C, $C_{aryl}$), 130.3 (d, $^4J_{P,C}$ = 6.4 Hz, 6 C, $C_{olef}$), 131.7 (d, $J_{P,C}$ = 2.2 Hz, 6 C, $C_{aryl}$), 134.5 (s, 6 C, $C_{aryl,quat}$), 135.1 (d, $J_{P,C}$ = 4.5 Hz, 6 C, $C_{aryl,quat}$) ppm. $^{19}$F{$^1$H} NMR (188.3 MHz, $CD_3CN$, 25 °C): $\delta$ = –72.8 (d, $^1J_{P,F}$ = 706 Hz, P$F_6$) ppm. $^{31}$P{$^1$H} NMR (121.5 MHz, $CD_3CN$, 25 °C): $\delta$ = 0.7 (s, trop$_3$*P*), –144.5 (hept, $^1J_{P,F}$ = 706 Hz, *P*$F_6$) ppm.

**Preparation of (Chloro)[tris(5*H*-dibenzo[*a*,*d*]cyclohepten-5-yl)phosphane]rhodium(I) (6):** In a Schlenk flask [Rh$_2$(μ-Cl)$_2$(COD)$_2$] (201 mg, 0.41 mmol) and trop$_3$P **1** (493 mg, 0.82 mmol) were suspended in THF (12 mL). This orange suspension was stirred at 60 °C. Upon heating, all solids dissolved. After 30 h of stirring at 60 °C, a pale yellow precipitate had formed and the $^{31}$P NMR spectrum showed almost complete conversion. The mixture was left at –20 °C overnight in order to complete crystallization. The precipitate was collected by filtration, washed with THF (5 mL), and dried in high vacuum. The product was a light yellow powder. Yield: 424 mg (70%). M.p. 320 °C (starting decomposition). $C_{45}H_{33}ClPRh$ (743.08): calcd. C 72.74, H 4.48, P 4.17; found C 72.64, H 4.74. IR (ATR): $\tilde{\nu}$ = 3017 (w, $\nu_{CH}$), 1937 (w), 1599 (w), 1574 (w), 1483 (m), 1451 (m), 1417 (m), 1325 (w), 1286 (m), 743 (s), 731 (s), 643 (m) cm$^{-1}$. MS (EI): *m*/*z* 742 ($M^+$), 191 ($C_{15}H_{11}^+$). $^1$H NMR (300 MHz, $CD_2Cl_2$, 25 °C): $\delta$ = 3.97 (d, $^2J_{P,H}$ = 13 Hz, 3 H, $H_{benz}$), 5.93 (s, 6 H, $H_{olef}$), 6.50 (d, $^3J_{H,H}$ = 7.2 Hz, 6 H, $H_{aryl}$), 6.77 (dd, $^3J_{H,H}$ = 7.2 Hz, 7.2 Hz; 6 H, $H_{aryl}$), 6.86 (dd, $^3J_{H,H}$ = 7.2 Hz, 7.2 Hz; 6 H, $H_{aryl}$), 7.02 (d, $^3J_{H,H}$ = 7.2 Hz, 6 H, $H_{aryl}$) ppm. $^{13}$C{$^1$H} NMR (75.5 MHz, $CD_2Cl_2$, 25 °C): $\delta$ = 48.4 (d, $^1J_{P,C}$ = 21.7 Hz, 3 C, $C_{benz}$), 79.4 (d, $^2J_{P,C}$ = 6.3 Hz, 6 C, $C_{olef}$), 126.7 (s, 6 C, $C_{aryl}$), 127.1 (d, $J_{P,C}$ = 7.2 Hz, 6 C, $C_{aryl}$), 127.5 (s, 6 C, $C_{aryl}$), 130.5 (s, 6 C, $C_{aryl}$), 133.7 (d, $J_{P,C}$ = 5.1 Hz, 6 C, $C_{aryl}$), 135.6 (s, 6 C, $C_{aryl}$) ppm. $^{31}$P{$^1$H} NMR (121.5 MHz, $CD_2Cl_2$, 25 °C): $\delta$ = 191.7 (d, $^1J_{Rh,P}$ = 147.5 Hz) ppm.

**Preparation of (Chloro)[tris(5*H*-dibenzo[*a*,*d*]cyclohepten-5-yl)phosphane]iridium(I) (7):** Because [Ir$_2$(μ-Cl)$_2$(coe)$_4$] is very air- and moisture-sensitive, the reaction was carried out under strictly inert conditions. In a Schlenk flask [Ir$_2$(μ-Cl)$_2$(coe)$_4$] (232 mg, 0.26 mmol) and **1** (314 mg, 0.52 mmol) were suspended in THF (18 mL). This orange suspension was stirred at 60 °C. Upon heating, all the solids dissolved and the color darkened. After 70 h of stirring at 60 °C the solution was dark brown and the $^{31}$P NMR spectrum showed about 70% conversion to the product. The reaction mixture was filtered over Celite and the filtrate was concentrated. Leaving the sample at –20 °C overnight allowed to crystallize the product in form of fine white needles. These were collected by filtration. To remove residual iridium metal, the product was dissolved in $CH_2Cl_2$ and filtered over a short silica gel column

 © 2007 Wiley-VCH Verlag GmbH & Co. KGaA, Weinheim 

($R_f$ = 0.3). The product was precipitated with *n*-hexane and dried in high vacuum to give a white microcrystalline powder. Yield: 115 mg (53%). M.p. 340 °C (starting slight decomposition). $C_{45}H_{33}ClIrP$ (832.39): calcd. C 64.93, H 4.00, P 3.72; found C 64.72, H 4.03. IR (ATR): $\tilde{\nu}$ = 3014 (w, $\nu_{CH}$), 1600 (w), 1575 (w), 1483 (m), 1403 (w), 1286 (m), 746 (s), 732 (s), 644 (m) $cm^{-1}$. MS (EI): *m*/*z* 832 ($M^+$), 191 ($C_{15}H_{11}^+$). $^1H$ NMR (300 MHz, $CD_2Cl_2$, 25 °C): $\delta$ = 4.15 (d, $^2J_{P,H}$ = 13 Hz, 3 H, $H_{benz}$), 5.40 (s, 6 H, $H_{olef}$), 6.46 (d, $^3J_{H,H}$ = 6.9 Hz, 6 H, $H_{aryl}$), 6.70–6.84 (m, 12 H, $H_{aryl}$), 7.02 (d, $^3J_{H,H}$ = 6.9 Hz, 6 H, $H_{aryl}$) ppm. $^{13}C\{^1H\}$ NMR (75.5 MHz, $CD_2Cl_2$, 25 °C): $\delta$ = 44.8 (d, $^1J_{P,C}$ = 21.7 Hz, 3 C, $C_{benz}$), 65.6 (s, 6 C, $C_{olef}$), 126.4 (s, 6 C, $C_{aryl}$), 127.6 (d, $J_{P,C}$ = 7.5 Hz, 6 C, $C_{aryl}$), 127.8 (d, $J_{P,C}$ = 1.2 Hz, 6 C, $C_{aryl}$), 131.7 (d, $J_{P,C}$ = 1.6 Hz, 6 C, $C_{aryl}$), 133.4 (d, $J_{P,C}$ = 5.1 Hz, 6 C, $C_{aryl}$), 135.7 (s, 6 C, $C_{aryl}$) ppm. $^{31}P\{^1H\}$ NMR (121.5 MHz, $CD_2Cl_2$, 25 °C): $\delta$ = 134.1 (s) ppm.

**Preparation of (Aqua)[tris(5*H*-dibenzo[*a*,*d*]cyclohepten-5-yl)phosphane]palladium(II) Trifluoromethanesulfonate (9):** In a Schlenk flask, $[PdCl_2(MeCN)_2]$ (166 mg, 0.43 mmol) and **1** (262 mg, 0.43 mmol) were suspended in acetonitrile (12 mL). This orange suspension was stirred at 60 °C. Upon heating, the suspension became red. After 24 h of stirring at 60 °C a dark red precipitate had formed and the $^{31}P$ NMR spectrum showed complete conversion. The mixture was left at –20 °C overnight in order to complete crystallization. The precipitate was collected by filtration and dried in high vacuum. The filtrate was evaporated to dryness and the residue dissolved in THF. A further crop of product was precipitated with *n*-hexane, collected by filtration, and subsequently dried in high vacuum for 24 h. $^{31}P$ NMR spectroscopy showed that this material consisted in majority of $[PdCl(trop_3P)]Cl$ [$\delta(^{31}P)$ = 263.8 ppm] and some $[Pd(trop_3P)(MeCN)]Cl_2$ [$\delta(^{31}P)$ = 256.1 ppm]. Subsequently, this product mixture (134 mg, 0.17 mmol) was dissolved in $CH_2Cl_2$ (15 mL) and AgOTf (133 mg, 0.52 mmol) was added. The resulting suspension was stirred for 16 h. The color changed from dark red to dark ruby red. The suspension was filtered through Celite, concentrated, and the product was precipitated with *n*-hexane. After washing with pentane, the dark ruby powder was dried in high vacuum. Yield: 162 mg (92%). M.p. 166–171 °C (decomposition). $C_{47}H_{35}F_6O_7PPdS_2$ (1027.29): calcd. C 54.95, H 3.43, P 3.02; found C 54.71, H 3.65. IR (ATR): $\tilde{\nu}$ = 3048 (w, $\nu_{CH}$), 1599 (w), 1507 (w), 1457 (m), 1431 (w), 1221 (s), 1159 (s), 1025 (s) 747 (s), 632 (s) $cm^{-1}$. UV ($CH_2Cl_2$): $\lambda_{max}$ = 497 nm. $^1H$ NMR (300 MHz, $CD_2Cl_2$, 25 °C): $\delta$ = 5.79 (d, $^2J_{P,H}$ = 11 Hz, 3 H, $H_{benz}$), 6.96–7.03 (m, 6 H, $H_{aryl}$), 7.05–7.13 (m, 12 H, $H_{aryl}$), 7.16–7.22 (m, 6 H, $H_{aryl}$), 7.40 (s, 6 H, $H_{olef}$) ppm. $^{13}C\{^1H\}$ NMR (75.5 MHz, $CD_2Cl_2$, 25 °C): $\delta$ = 51.9 (d, $^1J_{P,C}$ = 16.0 Hz, 3 C, $C_{benz}$), 109.6 (s, 6 C, $C_{olef}$), 128.5 (d, $J_{P,C}$ = 1.4 Hz, 6 C, $C_{aryl}$), 128.7 (d, $J_{P,C}$ = 8.6 Hz, 6 C, $C_{aryl}$), 129.4 (d, $J_{P,C}$ = 5.1 Hz, 6 C, $C_{aryl}$), 129.6 (d, $J_{P,C}$ = 1.5 Hz, 6 C, $C_{aryl}$), 131.3 (s, 6 C, $C_{aryl}$), 135.6 (d, $J_{P,C}$ = 1.1 Hz, 6 C, $C_{aryl}$) ppm. $^{19}F$ NMR (188.3 MHz, $CD_2Cl_2$, 25 °C): $\delta$ = –78.1 (br. s, 3 F), –77.9 (s, 3 F) ppm. $^{31}P\{^1H\}$ NMR (121.5 MHz, $CD_2Cl_2$, 25 °C): $\delta$ = 270.6 (s) ppm.

**X-ray Crystallography:** Crystals of **1** were grown from a THF solution that was layered with hexane. Crystals of **2** were obtained by slow cooling of a saturated toluene solution. Crystals of **3** grew from a reaction mixture of **4a** and $nBu_4NCl$ in acetonitrile. Crystals of **5** were obtained by layering an acetonitrile solution of the compound with toluene. Crystals of **6** and **9** were grown by slow evaporation of THF and $CH_2Cl_2$ solutions, respectively. Data collection for the X-ray structure determinations were performed on Bruker SMART 1 K and SMART APEX platforms with graphite-monochromated Mo-$K_\alpha$ radiation ($\lambda$ = 0.71073 Å). The reflex intensities were measured by CCD area detectors. The collected frames were processed with the proprietary software SAINT[55] and an absorption correction was applied (SADABS[56]). Solution and refinement of the structures was performed with SHELXS-97[57] and SHELXL-97[58] respectively. All non-hydrogen atoms were refined with anisotropic displacement parameters. Hydrogen atoms were placed in their idealized positions and allowed to ride on the respective carbon atoms. Associated crystallographic data and other experimental details are summarized in Table 4.

Table 4. Crystal data and refinement for compounds **1**, **2**, **3**, **5**, **6** and **9**.

| | **1** | **2** × ca. 0.5 $C_6H_5CH_3$ | 2 **3**·3$CH_3CN$ | **5** | **6**·2THF | 2 **9**·3$CH_2Cl_2$ |
|---|---|---|---|---|---|---|
| Empirical formula | $C_{45}H_{33}P$ | $C_{48.13}H_{33}PS$ | $C_{96}H_{75}Ag_2Cl_2N_3P_2$ | $C_{47}H_{36}AuF_6NP_2$ | $C_{53}H_{49}ClO_2PRh$ | $C_{97}H_{76}Cl_6F_{12}O_{14}P_2Pd_2S_4$ |
| Formula mass | 604.68 | 674.34 | 1619.17 | 987.67 | 887.25 | 2309.26 |
| Crystal system | cubic | trigonal | monoclinic | orthorhombic | monclinic | triclinic |
| Space group | $P\bar{4}3n$ | $P\bar{3}$ | $P2_1/c$ | *Pbca* | $P2_1/n$ | $P\bar{1}$ |
| *a* [Å] | 18.8014(6) | 12.9046(3) | 20.08(2) | 16.8961(9) | 11.9029(6) | 15.4752(13) |
| *b* [Å] | 18.8014(6) | 12.9046(3) | 12.045(14) | 20.4423(11) | 23.5360(12) | 16.7033(14) |
| *c* [Å] | 18.8014(6) | 11.9912(4) | 32.24(4) | 23.0917(13) | 15.8534(8) | 21.8310(18) |
| $\alpha$ [°] | 90 | 90 | 90 | 90 | 90 | 71.5240(10) |
| $\beta$ [°] | 90 | 90 | 106.32(2) | 90 | 111.7970(10) | 70.0620(10) |
| $\gamma$ [°] | 90 | 120 | 90 | 90 | 90 | 65.0040(10) |
| *V* [Å$^3$] | 6646.2(4) | 1729.35(8) | 7485(15) | 7975.8(8) | 4123.7(4) | 4708.0(7) |
| *Z* | 8 | 2 | 4 | 8 | 4 | 2 |
| *F*(000) | 2544 | 706 | 3320 | 3904 | 1840 | 2332 |
| Crystal size [mm] | 0.58 × 0.45 × 0.40 | 0.30 × 0.28 × 0.23 | 0.56 × 0.29 × 0.25 | 0.61 × 0.52 × 0.50 | 0.30 × 0.28 × 0.03 | 0.38 × 0.33 × 0.12 |
| $\rho_{calcd.}$ [g cm$^{-3}$] | 1.209 | 1.295 | 1.437 | 1.645 | 1.429 | 1.629 |
| $\mu$ [cm$^{-1}$] | 0.114 | 0.175 | 0.690 | 3.833 | 0.561 | 0.763 |
| *T* [K] | 298 | 200 | 298 | 298 | 200 | 200 |
| Rflns. collected | 40979 | 15090 | 51917 | 69728 | 29373 | 23022 |
| Unique rflns. | 2283 | 2693 | 13039 | 8160 | 7028 | 16360 |
| Flack parameter | 0.10(19) | – | – | – | – | – |
| GOF on $F^2$ | 1.234 | 1.048 | 1.045 | 1.023 | 1.101 | 1.018 |
| $R_1$, $wR_2$ [$I > 2\sigma(I)$] | 0.0545, 0.1577 | 0.0414, 0.1066 | 0.0315, 0.0795 | 0.0321, 0.0799 | 0.0374, 0.0863 | 0.0561, 0.1429 |
| $R_1$, $wR_2$ (all data) | 0.0579, 0.1626 | 0.0499, 0.1126 | 0.0504, 0.0909 | 0.0469, 0.0890 | 0.0466, 0.0902 | 0.0958, 0.1675 |

 © 2007 Wiley-VCH Verlag GmbH & Co. KGaA, Weinheim 

CCDC-622887 (for **1**), -622888 (for **2**), -622883 (for **3**), -622884 (for **5**), -622886 (for **6**) and -622885 (for **9**) contain the supplementary crystallographic data for this paper. These data can be obtained free of charge from The Cambridge Crystallographic Data Centre via www.ccdc.cam.ac.uk/data_request/cif.

## Acknowledgments

The financial support of the ETHZ (Eidgenössische Technische Hochschule Zürich) and the SNF (Schweizerischer Nationalfonds) is gratefully acknowledged.

[1] a) W. C. Zeise, *Ann. Phys. Chem.* **1831**, *21*, 497–541; b) A. Cahours, A. W. Hofmann, *Ann. Chem. Pharm.* **1857**, *104*, 1–39.
[2] a) M. A. Bennett, R. S. Nyholm, J. Lewis, H. W. Kouwenhoven, *J. Chem. Soc.* **1964**, 4570–4577; b) L. V. Interrante, M. A. Bennett, R. S. Nyholm, *Inorg. Chem.* **1966**, *5*, 2212–2217.
[3] a) P. W. Clark, J. L. S. Curtis, P. E. Garrou, G. E. Hartwell, *Can. J. Chem.* **1974**, *52*, 1714–1720; b) I. H. Wang, P. H. Wermer, C. B. Dobson, G. R. Dobson, *Inorg. Chim. Acta* **1991**, *183*, 31–38.
[4] P. E. Garrou, G. E. Hartwell, *J. Organomet. Chem.* **1973**, *55*, 331–341.
[5] a) P. H. Wermer, C. B. Dobson, G. R. Dobson, *J. Organomet. Chem.* **1986**, *311*, C47–C50; b) S. L. Zhang, I. H. Wang, P. H. Wermer, C. B. Dobson, G. R. Dobson, *Inorg. Chem.* **1992**, *31*, 3482–3488; c) H. H. Awad, G. R. Dobson, R. Vaneldik, *J. Chem. Soc., Chem. Commun.* **1987**, 1839–1841.
[6] a) R. N. Haszeldine, R. J. Lunt, R. V. Parish, *J. Chem. Soc. A* **1971**, 3705–3711; b) P. E. Garrou, G. E. Hartwell, *J. Organomet. Chem.* **1974**, *71*, 443–452.
[7] a) M. B. Hursthouse, K. M. A. Malik, F. A. Hart, D. W. Owen, *Polyhedron* **1996**, *15*, 23–26; b) W. Hewertson, I. C. Taylor, *J. Chem. Soc. D* **1970**, 428–429; c) S. Tsutsuminai, N. Komine, M. Hirano, S. Komiya, *Organometallics* **2004**, *23*, 44–53.
[8] a) G. E. Hartwell, P. W. Clark, *J. Chem. Soc. D* **1970**, 1115; b) P. W. Clark, G. E. Hartwell, *Inorg. Chem.* **1970**, *9*, 1948–1951; c) P. W. Clark, G. E. Hartwell, *J. Organomet. Chem.* **1975**, *97*, 117–129.
[9] a) M. A. Bennett, R. S. Nyholm, J. D. Saxby, *J. Organomet. Chem.* **1967**, *10*, 301–306; b) D. I. Hall, R. S. Nyholm, *J. Chem. Soc. A* **1971**, 1491–1493.
[10] L. V. Interrante, G. V. Nelson, *J. Organomet. Chem.* **1970**, *25*, 153–160.
[11] a) M. A. Bennett, L. V. Interrante, R. S. Nyholm, *Z. Naturforsch., B: Chem. Sci.* **1965**, *20*, 633–634; b) H. Luth, M. R. Truter, A. Robson, *J. Chem. Soc. A* **1969**, 28–41; c) I. H. Wang, G. R. Dobson, *J. Organomet. Chem.* **1988**, *356*, 77–84.
[12] L. V. Interrante, G. V. Nelson, *Inorg. Chem.* **1968**, *7*, 2059–2063.
[13] M. A. Bennett, G. B. Robertson, I. B. Tomkins, P. O. Whimp, *J. Chem. Soc. D* **1971**, 341–342.
[14] a) M. A. Bennett, E. J. Hann, *J. Organomet. Chem.* **1971**, *29*, C15–C16; b) P. R. Brookes, *J. Organomet. Chem.* **1972**, *42*, 459–469; c) P. R. Brookes, *J. Organomet. Chem.* **1972**, *43*, 415–423; d) D. I. Hall, R. Nyholm, *J. Chem. Soc., Dalton Trans.* **1972**, 804–808.
[15] M. A. Bennett, W. R. Kneen, R. S. Nyholm, *Inorg. Chem.* **1968**, *7*, 556–560.
[16] a) M. A. Bennett, R. Bramley, I. B. Tomkins, *J. Chem. Soc., Dalton Trans.* **1973**, 166–168; b) M. A. Bennett, H. K. Chee, J. C. Jeffery, G. B. Robertson, *Inorg. Chem.* **1979**, *18*, 1071–1076; c) M. A. Bennett, W. R. Kneen, R. S. Nyholm, *J. Organomet. Chem.* **1971**, *26*, 293–303.
[17] M. A. Bennett, W. R. Kneen, R. S. Nyholm, *Inorg. Chem.* **1968**, *7*, 552–556.
[18] a) E. Lindner, H. Rauleder, C. Scheytt, H. A. Mayer, W. Hiller, R. Fawzi, P. Wegner, *Z. Naturforsch., B: Chem. Sci.* **1984**, *39*, 632–642; b) E. Lindner, C. Scheytt, *Z. Naturforsch., B: Chem. Sci.* **1986**, *41*, 10–17; c) E. Lindner, C. Scheytt, P. Wegner, *J. Organomet. Chem.* **1986**, *308*, 311–323.
[19] a) A. F. Borowski, A. Iraqi, D. C. Cupertino, D. J. Irvine, D. J. Cole-Hamilton, M. H. Harmon, M. B. Hursthouse, *J. Chem. Soc., Dalton Trans.* **1990**, 29–34; b) D. J. Irvine, C. Glidewell, D. J. Cole-Hamilton, J. C. Barnes, A. Howie, *J. Chem. Soc., Dalton Trans.* **1991**, 1765–1772; c) D. C. Cupertino, M. M. Harding, D. J. Cole-Hamilton, *J. Organomet. Chem.* **1985**, *294*, C29–C32; d) D. C. Cupertino, D. J. Cole-Hamilton, *J. Chem. Soc., Dalton Trans.* **1987**, 443–449.
[20] D. J. Irvine, S. A. Preston, D. J. Cole-Hamilton, J. C. Barnes, *J. Chem. Soc., Dalton Trans.* **1991**, 2413–2418.
[21] a) D. J. Irvine, A. F. Borowski, D. J. Cole-Hamilton, *J. Chem. Soc., Dalton Trans.* **1990**, 3549–3550; b) D. J. Irvine, D. J. Cole-Hamilton, J. Barnes, P. K. Hodgson, *Polyhedron* **1989**, *8*, 1575–1577.
[22] a) S. A. Preston, D. C. Cupertino, P. Palma-Ramirez, D. J. Cole-Hamilton, *J. Chem. Soc., Chem. Commun.* **1986**, 977–978; b) A. Iraqi, N. R. FairFax, S. A. Preston, D. C. Cupertino, D. J. Irvine, D. J. Cole-Hamilton, *J. Chem. Soc., Dalton Trans.* **1991**, 1929–1935.
[23] a) A. M. Z. Slawin, H. L. Milton, J. Wheatley, J. D. Woollins, *Polyhedron* **2004**, *23*, 3125–3132; b) A. M. Z. Slawin, J. Wheatley, J. D. Woollins, *Eur. J. Inorg. Chem.* **2005**, 713–720.
[24] a) P. W. Clark, G. E. Hartwell, *J. Organomet. Chem.* **1975**, *102*, 387–396; b) P. W. Clark, G. E. Hartwell, *J. Organomet. Chem.* **1975**, *96*, 451–459; c) M. A. Bennett, E. J. Hann, R. N. Johnson, *J. Organomet. Chem.* **1977**, *124*, 189–211; d) P. E. Garrou, J. L. S. Curtis, G. E. Hartwell, *Inorg. Chem.* **1976**, *15*, 3094–3097; e) R. R. Ryan, R. Schaeffer, P. Clark, G. Hartwell, *Inorg. Chem.* **1975**, *14*, 3039–3042.
[25] a) M. O. Visscher, J. C. Huffman, W. E. Streib, *Inorg. Chem.* **1974**, *13*, 792–797; b) D. I. Hall, R. S. Nyholm, *J. Chem. Soc. D* **1970**, 488–489; c) C. Nave, M. R. Truter, *J. Chem. Soc. D* **1971**, 1253–1254; d) C. Nave, M. R. Truter, *J. Chem. Soc., Dalton Trans.* **1973**, 2202–2204; e) P. W. Clark, A. J. Jones, *J. Organomet. Chem.* **1976**, *122*, C41–C48.
[26] M. Herberhold, K. Bauer, W. Milius, *Z. Anorg. Allg. Chem.* **1994**, *620*, 2108–2113.
[27] M. Herberhold, T. Schmalz, W. Milius, B. Wrackmeyer, *Inorg. Chim. Acta* **2002**, *334*, 10–16.
[28] a) M. Herberhold, K. Bauer, W. Milius, *J. Organomet. Chem.* **1997**, *546*, 267–275; b) M. Herberhold, K. Bauer, W. Milius, *Z. Naturforsch. B: Chem. Sci.* **1999**, *54*, 63–72.
[29] a) M. Herberhold, A. Pfeifer, W. Milius, *Z. Anorg. Allg. Chem.* **2002**, *628*, 2919–2929; b) M. Herberhold, W. Milius, A. Pfeifer, *Z. Naturforsch. B: Chem. Sci.* **2003**, *58*, 1–10; c) M. Herberhold, W. Milius, A. Pfeifer, *Z. Naturforsch. B: Chem. Sci.* **2003**, *58*, 11–15.
[30] M. Herberhold, K. Bauer, W. Milius, *J. Organomet. Chem.* **1998**, *563*, 227–233.
[31] a) M. Herberhold, W. Milius, S. Eibl, *Z. Anorg. Allg. Chem.* **1999**, *625*, 341–346; b) M. Herberhold, S. Eibl, W. Milius, B. Wrackmeyer, *Z. Anorg. Allg. Chem.* **2000**, *626*, 552–555; c) M. Herberhold, S. Eibl, W. Milius, *J. Organomet. Chem.* **2001**, *621*, 166–172.
[32] a) M. Herberhold, T. Schmalz, W. Milius, B. Wrackmeyer, *Z. Anorg. Allg. Chem.* **2002**, *628*, 437–445; b) M. Herberhold, T. Schmalz, W. Milius, B. Wrackmeyer, *J. Organomet. Chem.* **2002**, *641*, 173–184; c) M. Herberhold, T. Schmalz, W. Milius, B. Wrackmeyer, *Z. Naturforsch. B: Chem. Sci.* **2002**, *57*, 53–60; d) M. Herberhold, T. Schmalz, W. Milius, B. Wrackmeyer, *Z. Anorg. Allg. Chem.* **2002**, *628*, 979–986; e) M. Herberhold, T. Schmalz, W. Milius, B. Wrackmeyer, *Inorg. Chim. Acta* **2003**, *352*, 51–60.
[33] M. Herberhold, T. Schmalz, W. Milius, B. Wrackmeyer, *Z. Naturforsch. B: Chem. Sci.* **2002**, *57*, 255–258.

 © 2007 Wiley-VCH Verlag GmbH & Co. KGaA, Weinheim 

[34] a) M. Herberhold, N. Akkus, W. Milius, *Z. Naturforsch. B: Chem. Sci.* **2003**, *58*, 528–532; b) M. Herberhold, W. Milius, N. Akkus, *Z. Anorg. Allg. Chem.* **2006**, *632*, 97–100.
[35] M. Herberhold, N. Akkus, W. Milius, *Z. Anorg. Allg. Chem.* **2003**, *629*, 2458–2464.
[36] J. Thomaier, Diss. Albert-Ludwigs-Universität (79104 Freiburg, Germany), **1996**.
[37] a) S. Deblon, Diss. ETH Nr. 13920 (Zürich), **2000**; b) P. Maire, Diss. ETH Nr. 14396 (Zürich), **2001**; c) C. Böhler, Diss. ETH Nr. 14420 (Zürich), **2002**; d) C. Laporte, C. Böhler, H. Schönberg, H. Grützmacher, *J. Organomet. Chem.* **2002**, *641*, 227–234; e) C. Laporte, F. Breher, J. Geier, J. Harmer, A. Schweiger, H. Grützmacher, *Angew. Chem.* **2004**, *116*, 2621–2624; *Angew. Chem. Int. Ed.* **2004**, *43*, 2567–2570; f) C. Laporte, T. Büttner, H. Rüegger, J. Geier, H. Schönberg, H. Grützmacher, *Inorg. Chim. Acta* **2004**, *357*, 1931–1947; g) C. Laporte, Diss. ETH Nr. 15137 (Zürich), **2003**; h) P. Maire, S. Deblon, F. Breher, J. Geier, C. Böhler, H. Rüegger, H. Schönberg, H. Grützmacher, *Chem. Eur. J.* **2004**, *10*, 4198–4205.
[38] a) H. Schönberg, S. Boulmaaz, M. Wörle, L. Liesum, A. Schweiger, H. Grützmacher, *Angew. Chem.* **1998**, *110*, 1492–1494; *Angew. Chem. Int. Ed.* **1998**, *37*, 1423–1426; b) S. Boulmaaz, M. Mlakar, S. Loss, H. Schönberg, S. Deblon, M. Wörle, R. Nesper, H. Grützmacher, *Chem. Commun.* **1998**, 2623–2624.
[39] J. Thomaier, S. Boulmaaz, H. Schönberg, H. Rüegger, A. Currao, H. Grützmacher, H. Hillebrecht, H. Pritzkow, *New J. Chem.* **1998**, *22*, 947–958.
[40] a) S. Deblon, L. Liesum, J. Harmer, H. Schönberg, A. Schweiger, H. Grützmacher, *Chem. Eur. J.* **2002**, *8*, 601–611; b) M. Mlakar, S. Boulmaaz, H. Schönberg, H. Grützmacher, *Electroanalysis* **2003**, *15*, 1043–1053; c) S. Deblon, H. Rüegger, H. Schönberg, S. Loss, V. Gramlich, H. Grützmacher, *New J. Chem.* **2001**, *25*, 83–92.
[41] R. Kissner, P. Latal, G. Geier, *J. Chem. Soc., Chem. Commun.* **1993**, 136–137.
[42] a) R. Kissner, *J. Electroanal. Chem.* **1995**, *385*, 71–75; b) R. Kissner, G. Welti, G. Geier, *J. Chem. Soc., Dalton Trans.* **1997**, 1773–1777.
[43] A. G. Orpen, L. Brammer, F. H. Allen, O. Kennard, D. G. Watson, R. Taylor, *J. Chem. Soc., Dalton Trans.* **1989**, S1–S83.
[44] A somewhat larger cone angle (265°) was reported for the triarylphosphane(2,6-*i*Pr-$C_6H_3$)$_3$P: R. T. Boeré, Y. K. Zhang, *J. Organomet. Chem.* **2005**, *690*, 2651–2657.
[45] M. Herberhold, K. Bauer, W. Milius, *J. Organomet. Chem.* **1995**, *502*, C1–C4.
[46] a) E. Lindner, R. Fawzi, H. A. Mayer, K. Eichele, K. Pohmer, *Inorg. Chem.* **1991**, *30*, 1102–1107; b) M. D. Lumsden, K. Eichele, R. E. Wasylishen, T. S. Cameron, J. F. Britten, *J. Am. Chem. Soc.* **1994**, *116*, 11129–11136.
[47] For a recent second example of a [Au($PR_3$)(MeCN)]$^+$ complex, see: Q. S. Li, C. Q. Wan, R. Y. Zou, F. B. Xu, H. B. Song, X. J. Wan, Z. Z. Zhang, *Inorg. Chem.* **2006**, *45*, 1888–1890.
[48] I. Krossing, A. Reisinger, *Angew. Chem.* **2003**, *115*, 5903–5906; *Angew. Chem. Int. Ed.* **2003**, *42*, 5725–5728.
[49] D. Ostendorf, C. Landis, H. Grützmacher, *Angew. Chem.* **2006**, *118*, 5293–5297; *Angew. Chem. Int. Ed.* **2006**, *45*, 5169–5173.
[50] G. Berti, *J. Org. Chem.* **1957**, *22*, 230–230.
[51] H. H. Karsch, *Phosphorus, Arsenic, Antimony and Bismuth*, vol. 3, Thieme, Stuttgart, **1996**.
[52] J. L. Herdé, C. V. Senoff, *Inorg. Nucl. Chem. Lett.* **1971**, *7*, 1029–1031.
[53] R. K. Harris, E. D. Becker, S. M. C. De Menezes, R. Goodfellow, P. Granger, *Pure Appl. Chem.* **2001**, *73*, 1795–1818.
[54] M. Bak, J. T. Rasmussen, N. C. Nielsen, *J. Magn. Reson.* **2000**, *147*, 296–330.
[55] *SAINT, Reference manual*, Siemens Energy and Automation, Madison, WI, **1994–1996**.
[56] G. M. Sheldrick, *SADABS, Empirical Absorption Correction Program*, University of Göttingen, Germany, **1997**.
[57] G. M. Sheldrick, *SHELXS-97, Program for Crystal Structure Solution*, University of Göttingen, Germany, **1997**.
[58] G. M. Sheldrick, *SHELXL-97, Program for Crystal Structure Refinement*, University of Göttingen, Germany, **1997**.

Received: October 25, 2006
Published Online: January 25, 2007

 © 2007 Wiley-VCH Verlag GmbH & Co. KGaA, Weinheim 

DOI: 10.1002/ejic.200601014

# Spin Canting and Topological Ferrimagnetism in Two Manganese(II) Coordination Polymers Generated by In Situ Solvothermal Ligand Reactions

Lin Cheng,[a] Wei-Xiong Zhang,[a] Bao-Hui Ye,*[a] Jian-Bin Lin,[a] and Xiao-Ming Chen*[a]

**Keywords:** Solvothermal ligand reaction / Coordination polymers / Spin canting / Topological ferrimagnetism

Two manganese(II) coordination polymers, $[Mn_2(bpt)(pa)_2(N_3)]_n$ [**1**; Hpa = picolinic acid, Hbpt = 3,5-bis(2-pyridyl)-4*H*-1,2,4-triazole] and $[Mn_3(ina)_2(pa)_2(N_3)_2]_n$ (**2**; Hina = isonicotinic acid), have been synthesized by solvothermal treatment, in which the ligands bpt and pa were generated in situ by cyclocondensation and hydrolysis of 2-pyridylamidrazone, respectively. In **1**, each binuclear subunit $[Mn_2(bpt)(N_3)]$ bridged by bpt and $N_3^-$ ligands is interlinked to four adjacent subunits via four tridentate pa ligands into a diamondoid 3D network, which shows spin-canting magnetism arising from the lack of inversion centers between the interacting spin centers. In **2**, the $Mn^{II}$ ions are alternately connected by double $\mu_{1,3}$-carboxylate/$\mu_{1,1}$-azide and double $\mu_{1,1}$-carboxylate bridges into a 1D magnetic chain, which exhibits a topological ferrimagnetic behavior in an antiferromagnetic-antiferromagnetic-ferromagnetic sequence. These chains are further interlinked via ina ligands into a 2D network.

(© Wiley-VCH Verlag GmbH & Co. KGaA, 69451 Weinheim, Germany, 2007)

## Introduction

Recent years have witnessed an explosion of interest in molecular-based magnetic materials, since such materials can help in understanding magneto-structural correlations and some fundamental phenomena of magnetism, and may have potential applications.[1–4] A basic design route for this kind of magnetic materials is to appropriately organize the paramagnetic ions into ordered polynuclear architectures by use of bridging ligands that can efficiently transmit magnetic superexchange. In addition to the nature of the metal centers, the bulk magnetic properties mainly depend on the bridging modes and bridging geometries of the bridging ligands. This fact provides an opportunity to produce new molecule-based magnetic materials by crystal engineering, although so far the pursuit of designing polynuclear complexes and extended networks with predictable magnetic properties is still a challenge, because the structural factors governing the exchange coupling between paramagnetic centers are complex and elusive. Azide was widely used to connect metal ions, and the correlation between the structure and magnetic properties of the end-on (EO), or $\mu_{1,1}$-azide, and end-to-end (EE), or $\mu_{1,3}$-azide, coordination modes was observed, generally giving ferro- (F) and antiferromagnetic (AF) interactions, respectively. The interactions also depend highly on the M–N–M angle;[5,6] however, these angles are mutable and difficult to predict and control in the uniquely azide-bridged complexes. Therefore, the introduction of a second bridging ligand to control the exchange angle between the metal ions may provide a feasible approach to the construction of bulk magnetic materials. Furthermore, multidentate ligands containing a carboxylate and a pyridyl group, such as nicotinate (na), isonicotinate (ina), and picolinate (pa), have been frequently used in the preparation of magnetic materials, because the various coordination modes adopted by the carboxylate group can transmit the magnetic coupling in different degrees, and the coordination of the pyridyl and carboxylate groups in these ligands may result in extended frameworks.[7] Unfortunately, the examples of higher dimensional (2D and 3D) molecule-based magnetic materials in which bridging azide and carboxylate groups coexist are relatively rare so far.[8]

Meanwhile, the hydro(solvo)thermal technique has been successfully applied to synthesize inorganic materials,[9] inorganic–organic hybrid materials, and coordination polymers.[10] It facilitates not only the assembly and crystallization of functional metal coordination polymers that can not be directly assembled from the organic ligands and metal ions,[10] but also some important in situ ligand reactions,[11–13] leading to the formation of in situ generated mixed-ligand coordination polymers that can not be easily obtained otherwise.[13f]

During our study of the reaction mechanisms of different organonitriles with hydrazine hydrate,[14] two new mixed-ligand polymeric manganese(II) complexes, $[Mn_2(bpt)(pa)_2(N_3)]_n$ [**1**; Hpa = picolinic acid, Hbpt = 3,5-bis(2-pyridyl)-4*H*-1,2,4-triazole] and $[Mn_3(ina)_2(pa)_2(N_3)_2]_n$ (**2**; Hina =

[a] MOE Key Laboratory of Bioinorganic and Synthetic Chemistry, School of Chemistry and Chemical Engineering, Sun Yat-Sen University,
Guangzhou 510275, China
Fax: +86-20-8411-2245
E-mail: cesybh@mail.sysu.edu.cn
cxm@mail.sysu.edu.cn

Supporting information for this article is available on the WWW under http://www.eurjic.org or from the author.

 © 2007 Wiley-VCH Verlag GmbH & Co. KGaA, Weinheim 

isonicotinic acid), containing azide and carboxylate bridges, have been synthesized and characterized by single-crystal X-ray diffraction and low-temperature magnetic studies.

## Results and Discussion

### Synthesis

Compound **1** was synthesized under solvothermal conditions with 2-pyridylamidrazone and azide anion in the presence of $Mn^{II}$ salt, in which both bpt and pa ligands were generated in situ (Scheme 1). Interestingly, bpt was obtained by the cyclocondensation reaction of 2-pyridylamidrazone in the presence of $Mn^{II}$ ion.[14] Meanwhile, the hydrolysis reaction was also observed. It is not surprising to observe the hydrolysis reaction of 2-pyridylamidrazone to pa at high temperature and pressure, since amidrazone groups can be hydrolyzed to carboxylate groups under common reaction conditions.[15] Presumably, $Mn^{II}$ ions promote the hydrolysis of 2-pyridylamidrazone.[16] When $Mn(ina)_2$ salt was used in place of $MnC_2O_4{\cdot}3H_2O$, **2** was produced, and only the hydrolysis but not the cyclocondensation reaction was observed. This fact may be attributed to the different $Mn^{II}$ sources, as the structure of the 3D $Mn(ina)_2{\cdot}0.5EtOH{\cdot}0.5H_2O$ is more stable than that of the 1D $MnC_2O_4{\cdot}3H_2O$.[17,18] Obviously, it is more difficult to release $Mn^{II}$ ions, which can facilitate cyclocondensation reactions, from the more stable $Mn^{II}$ salt.

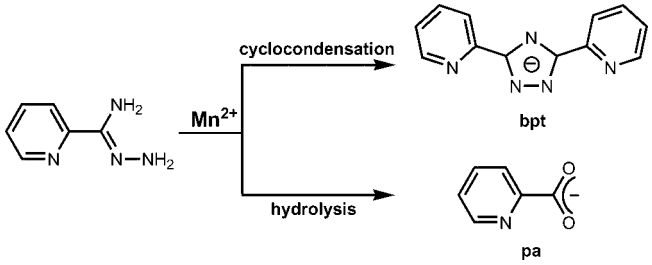


Scheme 1. The in situ solvothermal ligand reaction of 2-pyridylamidrazone in the presence of $Mn^{II}$.

### Description of the Crystal Structures

#### *[Mn$_2$(bpt)(pa)$_2$(N$_3$)]$_n$ (1)*

Compound **1** crystallizes in the acentric *Fdd*2 space group. Each bpt ligand binds to two $Mn^{II}$ ions [Mn1–N1 2.301(4) and Mn1–N2 2.222(4) Å] in a *cis* bis(chelate) mode. A pair of $Mn^{II}$ ions are additionally bridged by an azide ligand in the EE mode [Mn1–N5 2.198(4) Å] and further coordinated by four pa ligands derived from the hydrolysis of 2-pyridylamidrazone to furnish a dinuclear secondary building unit (SBU) (Figure 1a). The intradimer distance Mn1···Mn1A is 4.665 Å, much shorter than that in the dinuclear $Mn^{II}$ complexes double bridged by EE azide (5.166–5.485 Å).[5c,19] Furthermore, each SBU connects four adjacent SBUs via the μ-carboxylate bridges of four pa ligands into a 3D coordination polymer (Figure 1b), in which each pa acts as a tridentate ligand and each carboxylate group bridges two SBUs in a *syn-anti* coordination mode (Mn···Mn 6.080 Å). From the topological point of view, each SBU can be considered as a four-connecting node, which is connected by four bridging pa ligands as two-connecting linkers. Consequently, the 3D network can be regarded as a diamondoid structure, as shown in Figure 1c.

#### *[Mn$_3$(ina)$_2$(pa)$_2$(N$_3$)$_2$]$_n$ (2)*

Compound **2** is a 2D coordination polymer constructed by trinuclear SBUs with the bridging ligands ina, pa, and $N_3^-$. There are two crystallographically independent $Mn^{II}$ ions in each SBU (Figure 2a), in which Mn1 is located at a crystallographic inversion center and displays a slightly distorted octahedral geometry, being surrounded by four oxygen atoms [Mn1–O4 2.125(2) and Mn1–O2A 2.207(1) Å] from two pa and two ina ligands as well as by two nitrogen atoms [Mn1–N3 2.227(2) Å] from two $N_3^-$. On the other hand, the Mn2 atom adopts an $N_3O_3$ geometry, being coordinated by a chelating pa ligand [Mn2–N1 2.257(2), Mn2–O1 2.216(2) Å], one bridging oxygen atom from another pa, and a nitrogen atom of one EO azide [Mn2–N3 2.134(2) Å] ligand, as well as one oxygen and one nitrogen atom from two ina ligands [Mn2–N2d 2.357(2), Mn2–O3 2.168(1) Å]. The coordination modes of ina, pa, and azide in **2** are depicted in Figure 3. The Mn1 and Mn2 atoms are bridged by two *syn-syn* μ-1,3-carboxylate groups of the ina and pa ligands as well as by an EO azide ligand. Furthermore, the SBUs are interlinked to each other via two single oxygen bridges to form a chain. The Mn1···Mn2 distance is 3.569 Å, being markedly shorter than that of a mixed-ligand $Mn^{II}$ complex featuring a *syn-syn* carboxylate and an EO azide (3.861 Å) ligand.[8c] The Mn1–N3–Mn2 angle [109.86(8)°] is significantly larger than the crossover angle between AF and F interactions on the EO coordination mode of azide[5a] and the experimental observations (100.5–104.1°),[5c,19] but much smaller than that reported in $[Mn_3(N_3)_2(na)_4(H_2O)_2]$ (118.6°).[8c] The Mn2···Mn2A distance is 3.512 Å, comparable with those in carboxylate-bridged trinuclear $Mn^{II}$ complexes,[20] and the Mn2–O1–Mn2A angle is 105.56(6)°. The adjacent chains are further linked by tridentate ina ligands (Figure 3a) into a 2D network. The interchain Mn···Mn distances across the ina ligands are 9.073 and 9.527 Å.

### Magnetic Properties

#### *Magnetic Properties of 1*

The magnetic susceptibility of powder **1** was investigated in the temperature range 2–300 K at an applied field of 500 G, and the plots of $\chi_M$ and $\chi_M T$ vs. $T$ are shown in Figure 4. When the sample is cooled from 300 K, the $\chi_M$ per $Mn^{II}$ exhibits a smooth increase to a rounded maximum of 0.038 emu mol$^{-1}$ at ca. 25 K, then decreases slightly to 0.037 emu mol$^{-1}$ at 7.8 K, and thereafter increases rapidly to 0.110 emu mol$^{-1}$ at 2 K. Meanwhile, the $\chi_M T$ per $Mn^{II}$

 © 2007 Wiley-VCH Verlag GmbH & Co. KGaA, Weinheim 

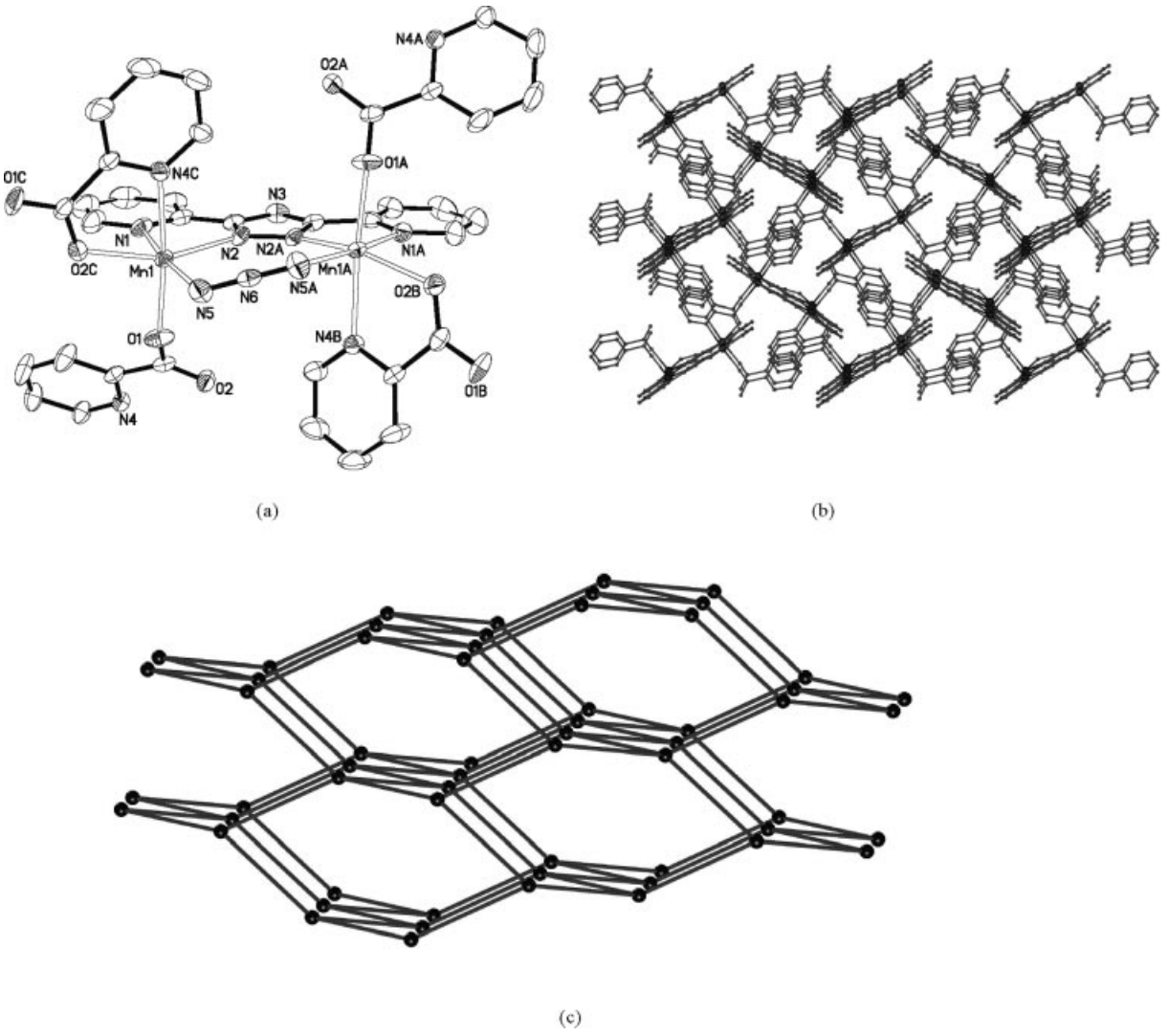


Figure 1. Views of the dinuclear SBU (a) (symmetry codes, A: $-x$, $1-y$, $z$; B: $-1/4-x$, $1/4+y$, $-1/4+z$; C: $1/4+x$, $3/4-y$, $-1/4+z$), the 3D structure (b), and the topology (each ball represents a $Mn_2$ SBU) (c) of **1**.

displays a sharp decrease upon cooling to a minimum of 0.27 emu K mol$^{-1}$ at 7.2 K, and then a slight increase to a maximum of 0.51 emu K mol$^{-1}$ at 5.7 K, finally decreasing again upon further cooling to 2 K.

The $\chi_M T$ value per $Mn^{II}$ of ca. 3.82 emu K mol$^{-1}$ at 300 K is slightly lower than the calculated value of 4.38 emu K mol$^{-1}$ for magnetically isolated high-spin $Mn^{II}$ ions ($S = 5/2$, $g = 2.0$). The temperature dependence of magnetic susceptibility above 100 K obeys the Curie–Weiss law $\chi_M = C/(T - \theta)$ with a Weiss constant $\theta = -70.0(6)$ K and a Curie constant $C = 4.73(1)$ cm$^3$ mol$^{-1}$ K, indicating a dominant AF interaction between the metal centers (Figure 4, inset). Therefore, we can assume an AF coupling between the dimetallic centers via the EE-azide and *cis*-bpt bridges, probably together with a weak AF coupling between the dimeric SBUs in the 3D structure via the *syn-anti* carboxylate bridge. These are in agreement with the observation of AF interactions for $Mn^{II}$ complexes connected via EE-azide, *cis*-bpt,[21] or *syn-anti* carboxylate bridges.[22] The magnetic exchange between the $Mn^{II}$ ions follows two pathways: intradimeric via EE-azide and *cis*-bpt, as well as interdimeric via *syn-anti* carboxylate bridges. The intradimeric interaction ($J$) can be expressed as: $\hat{H}_{ex} = -2J\hat{S}_1\hat{S}_2$. The susceptibility per $Mn_2$ ($\chi'_{dimer}$) can be given as shown in Equation (1).[23]

$$\chi'_{dimer} = \frac{2N\beta^2 g^2}{kT}\left[\frac{55e^{30x} + 30e^{20x} + 14e^{12x} + 5e^{6x} + e^{2x}}{11e^{30x} + 9e^{20x} + 7e^{12x} + 5e^{6x} + 3e^{2x} + 1}\right] \quad (1)$$

Taking into consideration the possibility of the interactions between the dinuclear SBUs in the crystal lattice, a correction for the molecular field is made [Equation (2)].

$$\chi_M = \frac{\chi'_{dimer}}{1 - 2zJ'\chi'_{dimer}/N\beta^2 g^2} \quad (2)$$

Where $N$ is the Avogadro number, $\beta$ is the Bohr magneton, $k$ is the Boltzmann constant, $x = J/kT$, $J$ is the intra-

 © 2007 Wiley-VCH Verlag GmbH & Co. KGaA, Weinheim 

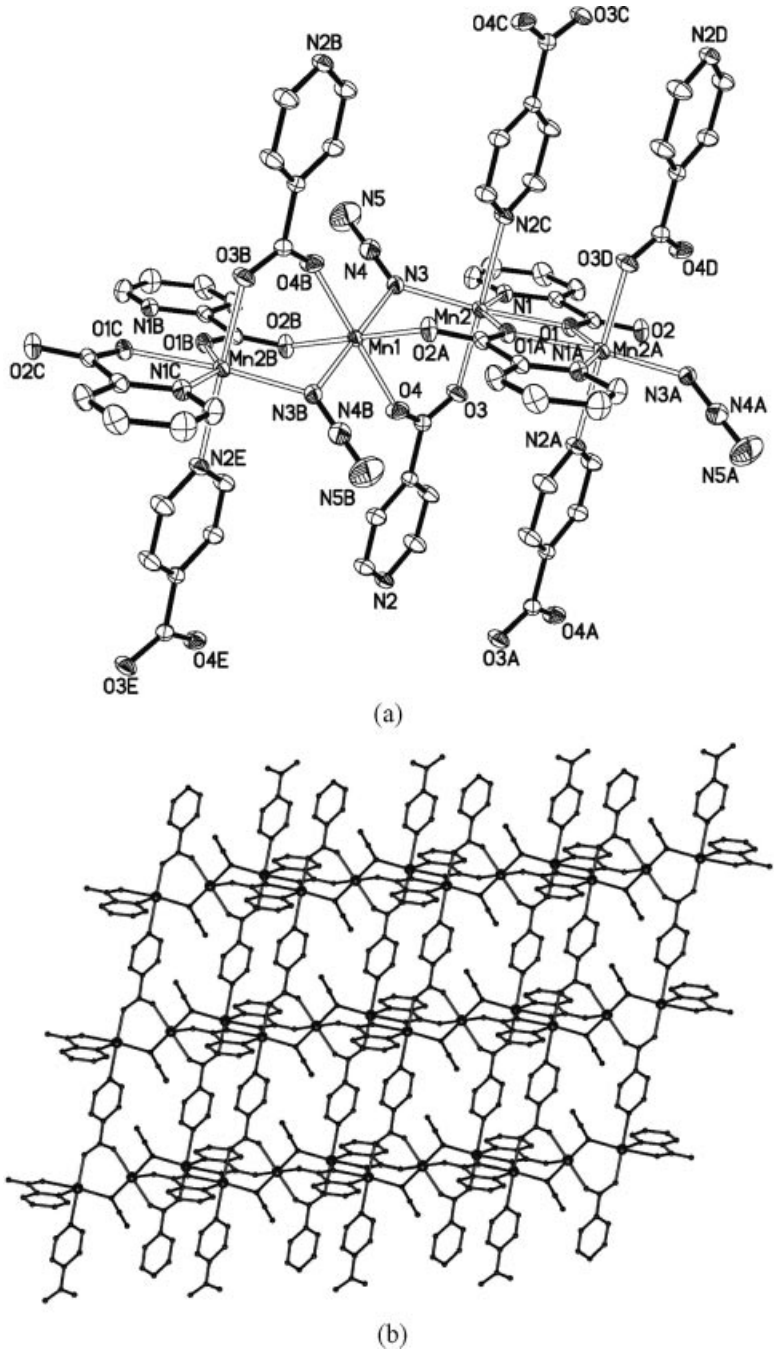


Figure 2. Views of the SBU (a) (symmetry codes, A: $-x, -y, -z$; B: $1-x, -y, -z$; C: $1+x, y, z$; D: $x, 1+y, z$; E: $-x, -1-y, -z$; F: $1-x, -1-y, -z$) and the 2D structure viewed along the $c$ axis (b) in **2**.

dimer coupling constant, $J'$ is the interdimer exchange interaction, and $z$ is the number of nearest neighbors of the dimer. The best fitting of the experimental magnetic data above 40 K to Equation 2 gives the following parameters: $g = 2.04(1)$, $J = -3.71(2)\ cm^{-1}$, $zJ' = -1.35(3)\ cm^{-1}$ and $R = 6.95\times10^{-7}$, where $R = \Sigma[(\chi_M T)_{obs} - (\chi_M T)_{calcd}]^2/\Sigma[(\chi_M T)_{obs}]^2$. The results are in good agreement with those reported for 2D $Mn^{II}$ complexes containing EE azide bridging networks [19,24] and confirm that the interactions mediated via the EE-azide and *cis*-bpt, and *syn-anti* carboxylate bridges are all AF interactions. However, it should be noted that the fitted values for $J$ and $zJ'$ are only qualitatively valid, because their comparability in magnitude does not meet the requirement of the molecular field approximation that $zJ'$ should be much smaller than $J$.[24]

The magnetic properties of **1** in the low-temperature region are more complicated: the susceptibility exhibits first an increase, then a decrease, and finally a rapid increase. Though the intradimer and interdimer AF interactions tend to align the $Mn^{II}$ spins in a compensated way to give a zero

 © 2007 Wiley-VCH Verlag GmbH & Co. KGaA, Weinheim 

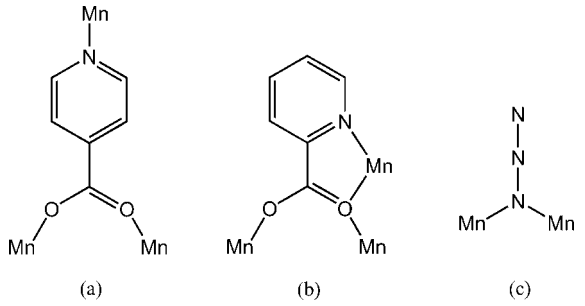


Figure 3. Coordination modes of ina (a), pa (b), and azide (c) in **2**.

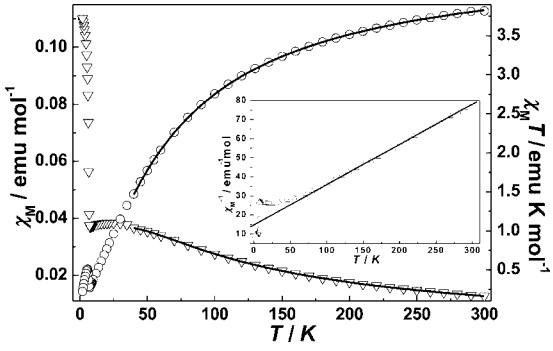


Figure 4. Temperature dependence of $\chi_M$ (▽) and $\chi_M T$ (○) for **1**. The dots are experimental values and the solid lines represent the best fits. Inset: temperature dependence of $\chi_M^{-1}$ (Δ) for **1**; the solid line represents the best fit of the Curie–Weiss law $\chi_M = C/(T - \theta)$.

residual moment, the low-temperature magnetic behavior of **1**, in which both $\chi_M$ and $\chi_M T$ increase sharply, suggests the existence of uncompensated residual spin moments and the occurrence of long-range weak F ordering.[25] The weak ferromagnetism may come from spin canting: the antiferromagnetically coupled local spins are not perfectly antiparallel but canted to each other, resulting in uncompensated residual spins.[19,24] The correlation between the residual spins may lead to long-range ordering. In **1**, the $\chi_M T$ values increase rapidly upon cooling below 7 K, indicating an F-like correlation. To further observe the magnetic transition at low temperature, FC (field-cooled) and ZFC (zero-field-cooled) magnetization measurements were carried out at 100 G below 30 K. As depicted in Figure 5a, compound **1** displays weak spontaneous magnetization that can be attributed to the onset of long-range ordering of the canted spins. The divergence of the ZFC and FC data below $T_c$ = 6.5 K indicates irreversibility arising from the formation of an ordered magnetic state. To confirm this phenomenon, FC magnetizations at different fields were applied, as the magnetic behavior of a weak ferromagnetism arising from spin canting is rather field-dependent. As expected, the field dependence of the FC magnetization was really observed (Figure 5b). The increase in the $\chi_M$ and $\chi_M T$ values become imperceptible at higher fields at the measured temperature, and these curves show no rise anymore at a magnetic field of 20 kG or above, indicating that the weak 3D AF interaction is overcome by the external field to result in an ordered F phase.

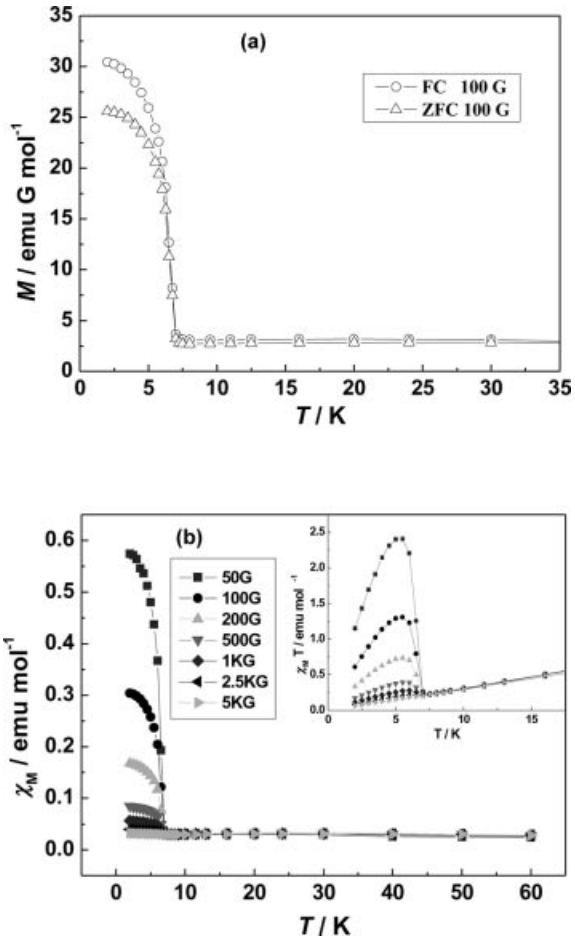


Figure 5. FC and ZFC magnetization plots at 100 G (a) and FC magnetizations in the forms of $\chi_M$ and $\chi_M T$ (inset) vs. $T$ plots at different fields (b) for **1**.

Further experimental evidence for the spin-canted weak ferromagnetism in **1** comes from field-dependent isothermal magnetization measurements at 2 K (Figure 6). In the high-field region ($H > 15$ kG), the magnetization increases linearly with the field, and the magnetization value (0.364 N$\beta$) at the highest field (70 kG) is far below the saturation value (5 N$\beta$) expected for $Mn^{II}$ species ($S$ = 5/2). This behavior is consistent with weak ferromagnetism due to spin canting.[25] A hysteresis loop was observed at 2 K with a remnant magnetization ($M_r$) of 0.005 N$\beta$ and a coercive field ($H_c$) of 820 G (Figure 6, inset), confirming the weak F ordering at low temperature.

It is well-known that spin canting may arise from single-ion magnetic anisotropy and/or antisymmetric exchange (Dzyaloshinsky–Moriya interaction).[26,27] Considering the isotropic character of the $Mn^{II}$ ion, it has been often suggested that the Dzyaloshinsky–Moriya interaction is the main source of spin canting in $Mn^{II}$ compounds,[27,28] which is consistent with the acentric *Fdd2* space group of **1**. This may suggest that spin canting has a significant contribution from acentric symmetry between the interacting spin centers.

 © 2007 Wiley-VCH Verlag GmbH & Co. KGaA, Weinheim 

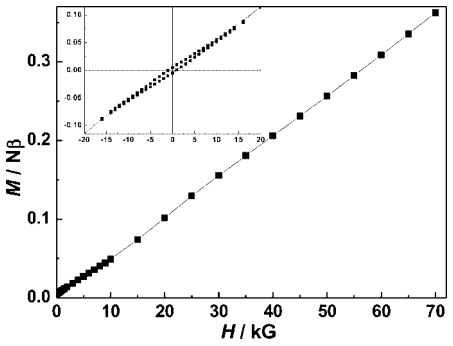


Figure 6. Field dependence of magnetization of **1** at 2 K. Inset: The hysteresis loop at 2 K.

### *Magnetic Properties of 2*

The $\chi_M T$ vs. $T$ plot for compound **2** is shown in Figure 7. The $\chi_M T$ value (4.01 emu K mol$^{-1}$) per $Mn^{II}$ at 300 K is somewhat lower than that expected for a high-spin $Mn^{II}$ ion (4.38 emu K mol$^{-1}$). The magnetic susceptibility above 50 K obeys the Curie–Weiss law with a Weiss constant, $\theta$ = –45.1(3) K, and a Curie constant, $C$ = 4.63(1) cm$^3$ mol$^{-1}$ K, indicating the presence of a dominant AF interaction (Figure 7, inset). On cooling, $\chi_M T$ falls to 1.67 emu K mol$^{-1}$ at 14 K and then rises at lower temperatures to reach a maximum value of 3.49 emu K mol$^{-1}$ at 2 K. This behavior is the typical of ferrimagnetism.

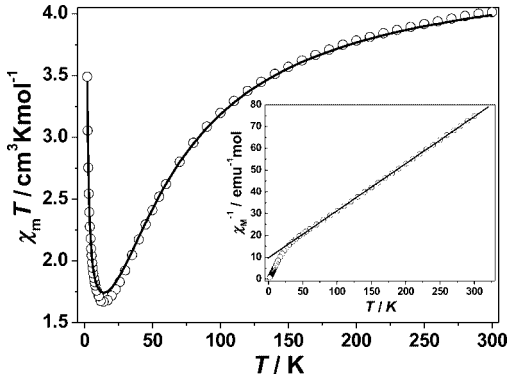


Figure 7. Plot of $\chi_M T$ vs. $T$ for **2**; the solid line represents the best fit of the data according to the theoretical model. Inset: temperature dependence of $\chi_M^{-1}$ for **2**; the solid line represents the best fit of the Curie–Weiss law $\chi_M = C/(T - \theta)$.

The ferrimagnetic behavior of **2** can be suggested to arise from intrachain magnetic interactions due to the fact that the $Mn^{II}$ chains are well separated by the ina bridges, in agreement with the absence of peaks in the real parts, $\chi'$, above 2 K in the curves of ac susceptibility (Figure S1). There are two kinds of magnetic exchange pathways in compound **2** with a $J_1J_1J_2$ repeating sequence according to the chain topology: one consists of two *syn-syn* $\mu_2$-1,3-carboxylate bridges and an EO azide bridge; the other consists of two $\mu_{1,1}$-O bridges from two $\mu_3$-carboxylate groups (Figure 8a). Due to noncompensation in spin moments within such a chain, the magnetic exchange through the former kind of bridges should be AF and that through the latter must be F. The exchanges alternate according to an AF-AF-F repeating sequence to produce the spin topology that corresponds to a (5, 5/2) ferromagnetic chain (Figure 8b). The field-dependent magnetization curve at 2 K indicates that the saturation magnetization per $Mn^{II}$ atom, achieved at 70 kG, is ca. 1.73 N$\beta$ (Figure 9). This value is consistent with an $S$ = 5/2 spin state per $[Mn_3(ina)_2(pa)_2(N_3)_2]$ basic unit, indicating that the $Mn^{II}$ chain is a typical (5, 5/2) topological ferrimagnetic chain with alternating AF-AF-F interaction.[25,29–31]

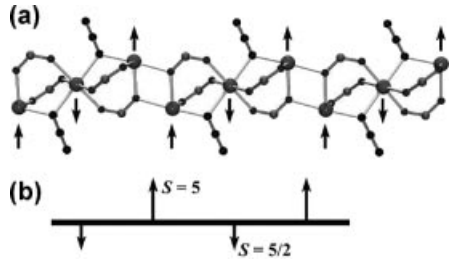


Figure 8. Bridging chain (a) and spin topology of the (5, 5/2) ferrimagnetic chain (b) in **2**.

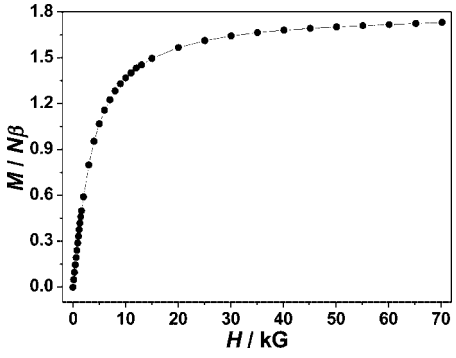


Figure 9. The field-dependent magnetization curve of **2** at 2 K.

To evaluate the exchanges, a nonlinear least-squares fitting of the theoretical expression proposed by Escuer et al.[31a,31b] to the experimental data has been performed by varying $g$, $J_1$, $J_2$ and minimizing the residual $R = [\Sigma(\chi_{obs}T - \chi_{calc}T)^2/\Sigma(\chi_{obs}T)^2]$. The best fit to the data above 2 K is achieved with $g$ = 2.02(1), $J_1$ = –6.21(8) cm$^{-1}$, $J_2$ = 0.22(1) cm$^{-1}$, $R = 1.10 \times 10^{-4}$. The $J_1$ value is associated with the AF exchange through the mixed carboxylate/azide (EO) bridges, in agreement with the previous observations in $Mn^{II}$ complexes,[8c,32] whereas the double $\mu_{1,1}$-O bridges mediate a ferromagnetic ($J_2$) interaction, which may arise from accidental orthogonality between magnetic orbitals around the metal ions.[29,33] Relative to the 3D complex of trinuclear SBUs $[Mn_3(4\text{-aba})_6]_n$ ($J_1$ = –4.5 cm$^{-1}$, $J_2$ = 0.38 cm$^{-1}$),[29] the AF is slightly stronger, while the F is slightly weaker, which may be attributed to the fact that $\mu_{1,1}$-azide bridges transmit stronger AF interactions with a large Mn1–N3–Mn2 angle [109.86(8)°], while $\mu_{1,1}$-O bridges transmit a weaker F exchange as the Mn2–O1–Mn2A angle [105.56(6)°] is larger than that in $[Mn_3(4\text{-aba})_6]_n$ (97.10°).

 © 2007 Wiley-VCH Verlag GmbH & Co. KGaA, Weinheim 

## Conclusions

Two manganese(II) coordination polymers, $[Mn_2(bpt)(pa)_2(N_3)]_n$ (**1**) and $[Mn_3(ina)_2(pa)_2(N_3)_2]_n$ (**2**), have been synthesized under solvothermal conditions. The bpt and pa ligands were generated in situ by cyclocondensation and hydrolysis of 2-pyridylamidrazone, respectively. Magnetic studies show that **1**, featuring a diamondoid network, exhibits spin-canting magnetism due to the lack of inversion centers between the interacting spin centers, while **2** shows a topological ferrimagnetic behavior in an AF-AF-F sequence, in which the magnetic exchanges through the mixed $\mu_{1,3}$-carboxylate/$\mu_{1,1}$-azide bridges and the double $\mu_{1,1}$-carboxylate bridges are AF and F, respectively.

## Experimental Section

**General Remarks:** The reagents and solvents employed were commercially available and used as received without further purification. The C, H, and N microanalyses were carried out with a Vario EL elemental analyzer. The FTIR spectra were recorded from KBr pellets in the range 400–4000 $cm^{-1}$ with a Bruker TENSOR 27 FTIR spectrometer. Magnetic susceptibility data of powder samples were collected in the temperature range 2–300 K with the use of a Quantum Design MPMS XL-7 SQUID magnetometer. The diamagnetic corrections were estimated from the Pascal's constants. 2-Pyridylamidrazone,[34] $MnC_2O_4{\cdot}3H_2O$,[17] and $Mn(ina)_2{\cdot}0.5EtOH{\cdot}0.5H_2O$[18] were synthesized according to the published procedures, and their identities were confirmed with NMR spectra or elemental analysis.

**Synthesis of $[Mn_2(bpt)(pa)_2(N_3)]_n$ (1):** A mixture of 2-pyridylamidrazone (0.272 g, 2 mmol), $MnC_2O_4{\cdot}3H_2O$ (0.197 g, 1 mmol), $NaN_3$ (0.130 g, 2 mmol), and 95% $C_2H_5OH$ (4 mL) was heated in a 15-mL Teflon-lined autoclave at 120 °C for 3 d, followed by slow cooling (5 °C $h^{-1}$) to room temperature. After the mixture was filtered and washed with 95% ethanol, yellow block crystals were collected and dried in air (0.247 g, yield ca. 80% based on Mn). $C_{24}H_{16}Mn_2N_{10}O_4$ (618.34): C 46.62, H 2.61, N 22.65; found C 46.62, H 2.65, N 22.66. FTIR: $\tilde{\nu}$ = 3852 (w), 3745 (w), 3387 (vs), 3077 (w), 2061 (s), 1575 (s), 1463 (m), 1389 (vs), 1145 (m), 1092 (m), 1043 (m), 848 (w), 806 (w), 759 (m), 700 (m), 637 (m), 528 (m) $cm^{-1}$.

**Synthesis of $[Mn_3(ina)_2(pa)_2(N_3)_2]_n$ (2):** The reaction was carried out by a method similar to that for **1**, using $Mn(ina)_2{\cdot}0.5EtOH{\cdot}0.5H_2O$ (0.331 g, 1 mmol) instead of $MnC_2O_4{\cdot}3H_2O$. After the mixture was filtered and washed with 95% ethanol, yellow block crystals were collected and dried in air (0.181 g, yield ca. 74% based on Mn). $C_{24}H_{16}Mn_3N_{10}O_8$ (737.28): C 39.10, H 2.19, N 19.00; found C 39.07, H 2.21, N 18.86. FTIR: $\tilde{\nu}$ = 3745 (w), 3393 (m), 3348 (m), 3068 (w), 2979 (w), 2622 (w), 2001 (s), 1620 (s), 1550 (vs), 1475 (m), 1395 (s), 1336 (m), 1292 (m), 1171 (w), 1092 (w), 1050 (m), 1010 (m), 850 (m), 770 (m), 698 (vs), 648 (w), 603 (w), 556 (w), 451 (m) $cm^{-1}$.

**X-ray Crystallographic Study:** Diffraction intensities for the compounds were collected at 293(2) K with a Bruker Apex CCD area-detector diffractometer (Mo-$K_\alpha$, $\lambda$ = 0.71073 Å). Absorption corrections were applied by using the multiscan program SADABS.[35] The structures were solved with direct methods and refined with the full-matrix least-squares technique using the SHELXTL program package.[36] Anisotropic thermal parameters were applied to all the non-hydrogen atoms. The organic hydrogen atoms were generated geometrically (C–H: 0.96 Å). The absolute structure of **1** has been determined with a Flack parameter of 0.01(3).[37] Crystal data as well as details of data collection and refinement for the com-

Table 1. Crystallographic data and structure refinement for **1** and **2**.

| Complex | **1** | **2** |
|---|---|---|
| Molecular formula | $C_{24}H_{16}Mn_2N_{10}O_4$ | $C_{24}H_{16}Mn_3N_{10}O_8$ |
| Formula weight | 618.34 | 737.28 |
| Crystal system | orthorhombic | triclinic |
| Space group | *Fdd*2 | $P\bar{1}$ |
| *a*/Å | 19.549(3) | 8.8369(6) |
| *b*/Å | 27.242(4) | 9.5269(6) |
| *c*/Å | 9.6170(13) | 9.9558(7) |
| *α*/° | 90 | 105.425(1) |
| *β*/° | 90 | 107.066(1) |
| *γ*/° | 90 | 106.808(1) |
| *V*/Å$^3$ | 5121.6(12) | 708.42(8) |
| *Z* | 8 | 1 |
| $\rho_{calcd.}$/g $cm^{-3}$ | 1.604 | 1.728 |
| $\mu$/$mm^{-1}$ | 1.039 | 1.384 |
| Reflections collected | 4666 | 5749 |
| Independent reflections | 2584 | 2926 |
| Data/restraints/parameters | 2216/0/182 | 2683/0/205 |
| *R* indices $[I > 2\sigma(I)]$[a], *wR2*[b] (all data) | 0.0558, 0.1042 | 0.0280, 0.0777 |
| $(\Delta\rho_{max}/\Delta\rho_{min})$/e Å$^{-3}$ | 0.54/–0.36 | 0.39/–0.22 |

[a] $R_1 = \Sigma||F_o| - |F_c||/\Sigma|F_o|$. [b] $wR_2 = [\Sigma w(F_o^2 - F_c^2)^2/\Sigma w(F_o^2)^2]^{1/2}$.

Table 2. Selected bond lengths [Å] and bond angles [°] of **1** and **2**.[a]

| | | | |
|---|---|---|---|
| **1** | | | |
| Mn1–O1 | 2.114(3) | Mn1–N1 | 2.301(4) |
| Mn1–N2 | 2.222(4) | Mn1–N5 | 2.198(4) |
| Mn1–O2C | 2.166(4) | Mn1–N4C | 2.283(4) |
| O1–Mn1–N1 | 87.7(1) | O1–Mn1–N2 | 96.1(1) |
| O1–Mn1–N5 | 92.3(2) | O1–Mn1–O2C | 99.4(1) |
| O1–Mn1–N4C | 173.2(1) | N1–Mn1–N2 | 73.3(1) |
| N1–Mn1–N5 | 172.1(2) | N1–Mn1–N4C | 94.5(11) |
| N2–Mn1–N4C | 90.8(1) | N2–Mn1–N5 | 98.8(1) |
| O2C–Mn1–N2 | 158.7(1) | O2C–Mn1–N1 | 92.7(1) |
| O2C–Mn1–N5 | 95.1(2) | O2C–Mn1–N4C | 74.1(1) |
| N4C–Mn1–N5 | 86.3(2) | Mn1–N5–N6 | 119.0(3) |
| **2** | | | |
| Mn1–O2A | 2.207(1) | Mn1–O4 | 2.125(2) |
| Mn1–N3 | 2.227(2) | Mn2–O1 | 2.216(2) |
| Mn2–N3 | 2.133(2) | Mn2–N1 | 2.257(2) |
| Mn2–O3 | 2.168(2) | Mn2–N2D | 2.357(2) |
| O4–Mn1–N3 | 89.30(7) | O2C–Mn1–O4 | 91.74(7) |
| O2A–Mn1–O4 | 88.26(7) | O2C–Mn1–N3 | 84.77(6) |
| O4–Mn1–N3B | 90.70(7) | O4B–Mn1–N3 | 90.70(7) |
| O2A–Mn1–N3 | 95.23(6) | O2C–Mn1–N3B | 95.23(6) |
| O2C–Mn1–O4B | 88.26(7) | O2A–Mn1–N3B | 84.77(6) |
| O2A–Mn1–O4B | 91.74(7) | O1–Mn2–O3 | 93.46(6) |
| O4B–Mn1–N3B | 89.30(7) | O1–Mn2–N3 | 171.85(7) |
| O1–Mn2–N1 | 72.86(6) | O1–Mn2–O1A | 74.44(5) |
| O1–Mn2–N2D | 87.44(6) | O3–Mn2–N3 | 93.31(7) |
| O3–Mn2–N1 | 89.86(7) | O1A–Mn2–O3 | 94.71(6) |
| O3–Mn2–N2D | 177.78(6) | N1–Mn2–N2D | 88.46(7) |
| N1–Mn2–N3 | 111.69(7) | N2D–Mn2–N3 | 85.95(7) |
| O1A–Mn2–N1 | 147.18(7) | O1A–Mn2–N2D | 87.49(6) |
| O1A–Mn2–N3 | 100.48(6) | Mn1–N3–N4 | 121.30(18) |
| Mn2–O1–Mn2A | 105.56(6) | Mn1–N3–Mn2 | 109.86(8) |

[a] Symmetry codes for **1**: C: 1/4 + *x*, 3/4 – *y*, –1/4 + *z*. For **2**: A: –*x*, –*y*, –*z*; B: 1 – *x*, –*y*, –*z*; D: *x*, 1 + *y*, *z*.

 © 2007 Wiley-VCH Verlag GmbH & Co. KGaA, Weinheim 

plexes are summarized in Table 1. Selected bond lengths and bond angles are listed in Table 2.

CCDC 624799–624800 contain the supplementary crystallographic data for this paper. These data can be obtained free of charge via www.ccdc.cam.ac.uk/conts/retrieving.html (or from the Cambridge Crystallographic Data Centre, 12 Union Road, Cambridge CB21EZ, UK; Fax: +44-1223-336-033).

**Supporting Information** (see footnote on the first page of this article): Temperature dependence of the real $\chi'$ and imaginary $\chi''$ parts of the ac susceptibility ($H_{dc}$ = 0 Oe, $H_{ac}$ = 3 Oe) for **1**.

## Acknowledgments

This work was supported by the National Natural Science Foundation of China (No. 20531070) and the Science and Technology Department of Guangdong Province (No. 04205405).

[1] O. Kahn, *Molecular Magnetism*, VCH, Weinheim, Germany, **1993**.

[2] a) O. Kahn, *Acc. Chem. Res.* **2000**, *33*, 647–657; b) J. S. Miller, J. L. Manson, *Acc. Chem. Res.* **2001**, *34*, 563–570; c) M. Sakamoto, K. Manseki, H. Ökawa, *Coord. Chem. Rev.* **2001**, *219–221*, 379–414; d) C. Benelli, D. Gatteschi, *Chem. Rev.* **2002**, *102*, 2369–2388; e) I. Ciofini, C. A. Daul, *Coord. Chem. Rev.* **2003**, *238–239*, 187–209.

[3] a) A. L. Barra, A. Caneschi, A. Cornia, F. Fabrizi de Biani, D. Gatteschi, C. Sangregorio, R. Sessoli, L. Sorace, *J. Am. Chem. Soc.* **1999**, *121*, 5302–5310; b) D. Gatteschi, R. Sessoli, *Angew. Chem. Int. Ed.* **2003**, *42*, 268–297; c) R. H. Laye, E. J. L. McInnes, *Eur. J. Inorg. Chem.* **2004**, 2811–2818; d) E. K. Brechin, *Chem. Commun.* **2005**, 5141–5153; e) N. T. Madhu, J.-K. Tang, I. J. Hewitt, R. Clerac, W. Wernsdorfer, J. van Slageren, C. E. Anson, A. K. Powell, *Polyhedron* **2005**, *24*, 2864–2869.

[4] a) Y.-Z. Zheng, M.-L. Tong, W.-X. Zhang, X.-M. Chen, *Angew. Chem. Int. Ed.* **2006**, *45*, 6310–6314; b) Y.-Z. Zheng, M.-L. Tong, W.-X. Zhang, X.-M. Chen, *Chem. Commun.* **2006**, 165–167; c) X.-N. Cheng, W.-X. Zhang, Y.-Z. Zheng, X.-M. Chen, *Chem. Commun.* **2006**, 3603–3605; d) M.-H. Zeng, B. Wang, X.-Y. Wang, W.-X. Zhang, X.-M. Chen, S. Gao, *Inorg. Chem.* **2006**, *45*, 7069–7076; e) M.-H. Zeng, W.-X. Zhang, X.-Z. Sun, X.-M. Chen, *Angew. Chem. Int. Ed.* **2005**, *44*, 3079–3082; f) S. Xiang, X.-T. Wu, J.-J. Zhang, R.-B. Fu, S.-M. Hu, X.-D. Zhang, *J. Am. Chem. Soc.* **2005**, *127*, 16352–16353.

[5] a) E. Ruiz, J. Cano, S. Alvarez, P. Alemany, *J. Am. Chem. Soc.* **1998**, *120*, 11122–11129; b) M. A. M. Abu-Youssef, A. Escuer, D. Gatteschi, M. A. S. Goher, F. A. Mautner, R. Vicente, *Inorg. Chem.* **1999**, *38*, 5716–5723; c) J. L. Manson, A. M. Arif, J. S. Miller, *Chem. Commun.* **1999**, 1479–1480; d) S.-B. Wang, G.-M. Yang, D.-Z. Liao, L.-C. Li, *Inorg. Chem.* **2004**, *43*, 852–854; e) C.-M. Liu, S. Gao, D.-Q. Zhang, Y.-H. Huang, R.-G. Xiong, Z.-L. Liu, F.-C. Jiang, D.-B. Zhu, *Angew. Chem. Int. Ed.* **2004**, *43*, 990–994; f) J. Cano, Y. Journaux, M. A. S. Goher, M. A. M. Abu-Youssef, F. A. Mautner, G. J. Reiß, A. Escuer, R. Vicente, *New J. Chem.* **2005**, *29*, 306–314; g) Y.-Z. Zhang, H.-Y. Wei, F. Pan, Z.-M. Wang, Z.-D. Chen, S. Gao, *Angew. Chem. Int. Ed.* **2005**, *44*, 5841–5846; h) T. Liu, Y.-J. Zhang, Z.-M. Wang, S. Gao, *Inorg. Chem.* **2006**, *45*, 2782–2784; i) X.-Y. Wang, L. Wang, Z.-M. Wang, S. Gao, *J. Am. Chem. Soc.* **2006**, *128*, 674–675; j) C.-H. Ge, A.-L. Cui, Z.-H. Ni, Y.-B. Jiang, L.-F. Zhang, J. Ribas, H.-Z. Kou, *Inorg. Chem.* **2006**, *45*, 4883–4885.

[6] a) S. S. Tandon, L. K. Thompson, M. E. Manuel, J. N. Bridson, *Inorg. Chem.* **1994**, *33*, 5555–5570; b) L. K. Thompson, S. S. Tandon, M. E. Manuel, *Inorg. Chem.* **1995**, *34*, 2356–2366.

[7] a) Y.-H. Liu, H.-L. Tsai, Y.-L. Lu, Y.-S. Wen, J.-C. Wang, K.-L. Lu, *Inorg. Chem.* **2001**, *40*, 6426–6431; b) R.-G. Xiong, Y.-R. Xie, C.-M. Che, *J. Chem. Soc., Dalton Trans.* **2001**, 777–779.

[8] a) M. A. S. Goher, M. A. M. Abu-Youssef, F. A. Mautner, A. Popitsch, *Polyhedron* **1992**, *11*, 2137–2141; b) A. Escuer, R. Vicente, F. A. Mautner, M. A. S. Goher, *Inorg. Chem.* **1997**, *36*, 1233–1236; c) H.-J. Chen, Z.-W. Mao, S. Gao, X.-M. Chen, *Chem. Commun.* **2001**, 2320–2321; d) F.-C. Liu, Y.-F. Zeng, J.-R. Li, X.-H. Bu, H.-J. Zhang, J. Ribas, *Inorg. Chem.* **2005**, *44*, 7298–7300; e) F.-C. Liu, Y.-F. Zeng, J. Jiao, X.-H. Bu, J. Ribas, S.-R. Batten, *Inorg. Chem.* **2006**, *45*, 2776–2778; f) F.-C. Liu, Y.-F. Zeng, J. Jiao, J.-R. Li, X.-H. Bu, J. Ribas, S.-R. Batten, *Inorg. Chem.* **2006**, *45*, 6129–6131; g) Y.-F. Zeng, F.-C. Liu, J.-P. Zhao, S. Cai, X.-H. Bu, J. Ribas, *Chem. Commun.* **2006**, 2227–2229; h) Z. He, Z.-M. Wang, S. Gao, C.-H. Yan, *Inorg. Chem.* **2006**, *45*, 6694–6705.

[9] a) S.-H. Feng, R.-R. Xu, *Acc. Chem. Res.* **2001**, *34*, 239–247; b) C. S. Cundy, P. A. Cox, *Chem. Rev.* **2003**, *103*, 663–702.

[10] a) O. R. Evans, W.-B. Lin, *Acc. Chem. Res.* **2002**, *35*, 511–522; b) J.-Y. Lu, *Coord. Chem. Rev.* **2003**, *246*, 327–347.

[11] a) X.-M. Zhang, *Coord. Chem. Rev.* **2005**, *249*, 1201–1219; b) X.-M. Chen, M.-L. Tong, *Acc. Chem. Res.* **2007**, *40*, 162–170.

[12] a) R.-G. Xiong, X. Xue, H. Zhao, X.-Z. You, B. F. Abrahams, Z.-L. Xue, *Angew. Chem. Int. Ed.* **2002**, *41*, 3800–3803; b) C.-M. Liu, S. Gao, H.-Z. Kou, *Chem. Commun.* **2001**, 1670–1671; c) R.-H. Wang, M.-C. Hong, J.-H. Luo, R. Cao, J.-B. Weng, *Chem. Commun.* **2003**, 1018–1019.

[13] a) X.-M. Zhang, M.-L. Tong, X.-M. Chen, *Angew. Chem. Int. Ed.* **2002**, *41*, 1029–1031; b) J. Tao, Y. Zhang, M.-L. Tong, X.-M. Chen, T. Yuen, C.-L. Lin, X.-Y. Huang, J. Li, *Chem. Commun.* **2002**, *13*, 1342–1343; c) J.-P. Zhang, S.-L. Zheng, X.-C. Huang, X.-M. Chen, *Angew. Chem. Int. Ed.* **2004**, *43*, 206–209; d) J.-P. Zhang, Y.-Y. Lin, X.-C. Huang, X.-M. Chen, *J. Am. Chem. Soc.* **2005**, *127*, 5495–5506; e) Y.-Z. Zheng, M.-L. Tong, X.-M. Chen, *New J. Chem.* **2004**, *28*, 1412–1415; f) Y.-T. Wang, M.-L. Tong, H.-H. Fan, H.-Z. Wang, X.-M. Chen, *Dalton Trans.* **2005**, 424–426.

[14] L. Cheng, W.-X. Zhang, B.-H. Ye, J.-B. Lin, X.-M. Chen, *Inorg. Chem.* **2007**, *46*, 1135–1143.

[15] A. S. Shawali, A. Osman, H. H. Hassaneen, *Indian J. Chem.* **1972**, *10*, 965–967.

[16] X.-Y. Wang, L. Gan, S.-W. Zhang, S. Gao, *Inorg. Chem.* **2004**, *43*, 4615–4625.

[17] W.-Y. Wu, Y. Song, Y.-Z. Li, X.-Z. You, *Inorg. Chem. Commun.* **2005**, *8*, 732–736.

[18] Q. Wei, M. Nieuwenhuyzen, S. L. James, *Microporous Mesoporous Mater.* **2004**, *73*, 97–100.

[19] E.-Q. Gao, Y.-F. Yue, S.-Q. Bai, Z. He, S.-W. Zhang, C.-H. Yan, *Chem. Mater.* **2004**, *16*, 1590–1596.

[20] a) R. L. Rardin, P. Poganiuch, A. Bino, D. P. Goldberg, W. B. Tolman, S. Liu, S. J. Lippard, *J. Am. Chem. Soc.* **1992**, *114*, 5240–5249; b) V. Tangoulis, D. A. Malamatari, K. Soulti, V. Stergiou, C. P. Raptopoulou, A. Terzis, T. A. Kabanos, D. P. Kessissoglou, *Inorg. Chem.* **1996**, *35*, 4974–4983; c) G. Fernández, M. Corbella, J. Mahía, M. A. Maestro, *Eur. J. Inorg. Chem.* **2002**, 2502–2510.

[21] R. P. Paul, J. M. W. L. Birker, J. G. Haasnoot, G. C. Verschoor, J. Reedijk, *Inorg. Chem.* **1985**, *24*, 4128–4133.

[22] a) X.-M. Chen, Y.-X. Tong, Z.-T. Xu, T. C. W. Mak, *J. Chem. Soc., Dalton Trans.* **1995**, 4001–4004; b) H. Iikura, T. Nagata, *Inorg. Chem.* **1998**, *37*, 4702–4711; c) W. Zhao, Y. Song, T. Okamura, J. Fan, W.-Y. Sun, N. Ueyama, *Inorg. Chem.* **2005**, *44*, 3330–3336.

[23] a) M. E. Fisher, *Am. J. Phys.* **1964**, *32*, 343–346; b) C. J. O'Connor, *Prog. Inorg. Chem.* **1982**, *29*, 203–283.

[24] E.-Q. Gao, A.-L. Cheng, Y.-X. Xu, M.-Y. He, C.-H. Yan, *Inorg. Chem.* **2005**, *44*, 8822–8835.

[25] E.-Q. Gao, Y.-F. Yue, S.-Q. Bai, Z. He, C.-H. Yan, *J. Am. Chem. Soc.* **2004**, *126*, 1419–1429.

[26] a) I. E. Dzyaloshinsky, *Phys. Chem. Solids* **1958**, *4*, 241–255; b) T. Moriya, *Phys. Rev.* **1960**, *120*, 91–98.

 © 2007 Wiley-VCH Verlag GmbH & Co. KGaA, Weinheim 

[27] a) R. L. Carlin, *Magnetochemistry*, Springer-Verlag, Berlin, **1986**, pp. 148–154; b) S. R. Batten, P. Jensen, C. J. Kepert, M. Kurmoo, B. Moubaraki, K. S. Murray, D. J. Price, *J. Chem. Soc., Dalton Trans.* **1999**, 2987–2997; c) S. G. Carling, P. Day, D. Visser, R. K. Kremer, *J. Solid State Chem.* **1993**, *106*, 111–119.
[28] S. Han, J. L. Manson, J. Kim, J. S. Miller, *Inorg. Chem.* **2000**, *39*, 4182–4185.
[29] R.-H. Wang, E.-Q. Gao, M.-C. Hong, S. Gao, J.-H. Luo, Z.-Z. Lin, L. Han, R. Cao, *Inorg. Chem.* **2003**, *42*, 5486–5488.
[30] A. K. Ghosh, D. Ghoshal, E. Zangrando, J. Ribas, N. R. Chaudhuri, *Inorg. Chem.* **2005**, *44*, 1786–1793.
[31] a) M. A. M. Abu-Youssef, M. Drillon, A. Escuer, M. A. S. Goher, F. A. Mautner, R. Vicente, *Inorg. Chem.* **2000**, *39*, 5022–5027; b) A. Escuer, F. A. Mautner, M. A. S. Goher, M. A. M. Abu-Youssef, R. Vicente, *Chem. Commun.* **2005**, 605–606; c) M. A. M. Abu-Youssef, A. Escuer, A. S. G. Mohamed, F. A. Mautner, G. J. Reiß, R. Vicente, *Angew. Chem. Int. Ed.* **2000**, *39*, 1624–1626.
[32] L.-Y. Wang, Z.-L. Liu, C.-X. Zhang, Z.-Q. Liu, D.-Z. Liao, Z.-H. Jiang, S.-P. Yan, *Sci. China, Ser. B* **2003**, *46*, 533–537.
[33] W. E. Hatfield in *Magneto-Structural Correlations in Exchange Coupled Systems* (Eds.: R. D. Willet, D. Gatteschi, O. Kahn), Reidel, Dordrecht, **1984**, p. 555.
[34] F. H. Case, *J. Org. Chem.* **1965**, *30*, 931–933.
[35] G. M. Sheldrick, *SADABS 2.05*, University of Göttingen, **2002**.
[36] *SHELXTL 6.10*, Bruker Analytical Instrumentation, Madison, Wisconsin, USA, **2000**.
[37] H. D. Flack, *Acta Crystallogr., Sect. A* **1983**, *39*, 876–881.

Received: October 27, 2006
Published Online: April 23, 2007

 © 2007 Wiley-VCH Verlag GmbH & Co. KGaA, Weinheim 

DOI: 10.1002/ejic.200601134

# N–H Group Transfer and Oxidative Addition Chemistry Promoted by Isolable Bis(cyclopentadienyl)titanium Sandwich Complexes

**Tamara E. Hanna,[a] Emil Lobkovsky,[a] and Paul J. Chirik*[a]**

**Keywords:** Titanium / Oxidative addition / Cyclopentadienyl / Group transfer / Nitrogen

Addition of propylenimine (2-methylaziridine) to the bis(cyclopentadienyl)titanium sandwich complexes, $(\eta^5\text{-}C_5Me_4R)_2$-Ti (R = *i*Pr, $SiMe_3$), resulted in rapid [NH] group transfer followed by C–H activation of a cyclopentadienyl methyl group to yield the corresponding cyclometalated titanocene amido compounds. Exposure of these molecules to 4 atm of $H_2$ at 55 °C resulted in hydrogenolysis of the metal–carbon bond to form the titanium amido hydride compounds, $(\eta^5\text{-}C_5Me_4R)_2$-$Ti(NH_2)H$. Deuteriolysis with DCl gas confirmed exclusive cyclometalation from the positions adjacent to the isopropyl and trimethylsilyl substituent. Oxidative addition of the N–H bonds of amines has also been observed. Addition of $NH_3$ to either $(\eta^5\text{-}C_5Me_4SiMe_3)_2Ti$ or $(\eta^5\text{-}C_5Me_4iPr)_2Ti$ yielded the corresponding titanocene amido hydrides along with the titanocene(III) amides, $(\eta^5\text{-}C_5Me_4R)_2TiNH_2$, arising from formal deprotonation by unreacted sandwich from the putative titanocene ammonia complex.

(© Wiley-VCH Verlag GmbH & Co. KGaA, 69451 Weinheim, Germany, 2007)

## Introduction

The synthesis of isolable, thermally stable bis(cyclopentadienyl)titanium sandwich complexes by introduction of sterically demanding ring substituents has offered the rare opportunity to explore the fundamental coordination chemistry of a well-defined divalent titanium center.[1,2] Our laboratory has discovered that several complexes of the general formula, $(\eta^5\text{-}C_5Me_4R)_2Ti$ (R = *i*Pr, *t*Bu, $SiMe_3$, $SiMe_2Ph$) coordinate dinitrogen upon cooling in solution (Figure 1).[3] Both the maximum temperature of dinitrogen coordination[3] and the number of $N_2$ ligands[4] are sensitive to the nature of the ring substituents, where smaller, electron-withdrawing groups increase the azophilicity of the titanium. Unusual examples of titanocene monocarbonyl complexes have also been prepared by careful addition of CO to the

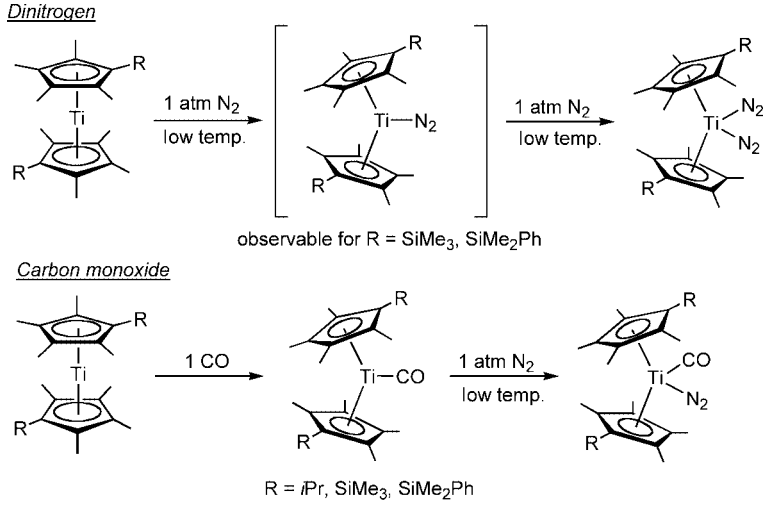


Figure 1. Unusual examples of mono(dinitrogen), bis(dinitrogen), monocarbonyl and mixed carbonyl-dinitrogen complexes of bis(cyclopentadienyl) titanium sandwich compounds.

[a] Department of Chemistry and Chemical Biology, Baker Laboratory, Cornell University,
Ithaca, New York 14853, USA

Supporting information for this article is available on the WWW under http://www.eurjic.org or from the author.

 © 2007 Wiley-VCH Verlag GmbH & Co. KGaA, Weinheim 

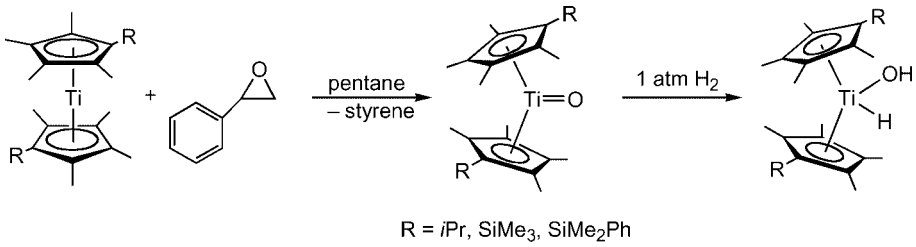


Figure 2. Synthesis and hydrogenation of bis(cyclopentadienyl)titanium oxo complexes.

corresponding sandwich (Figure 1).[4] At low temperature, these molecules coordinate $N_2$ to yield mixed carbonyl-dinitrogen compounds.[4]

Subsequent studies have focused on the oxidation of the isolable bis(cyclopentadienyl)titanium sandwiches with the goal of generating titanium ligand multiple bonds that do not require stabilization by coordination of additional base. Our initial studies have focused on the preparation of monomeric, base-free titanocene oxo complexes. Treatment of $(\eta^5\text{-}C_5Me_4R)_2Ti$ [R = *i*Pr (**1**), $SiMe_3$ (**2**), $SiMe_2Ph$ (**3**)] with styrene oxide induced oxygen atom abstraction affording the desired terminal oxo complexes, $(\eta^5\text{-}C_5Me_4R)_2Ti{=}O$, and free olefin (Figure 2).[5] While the isopropyl-substituted variant **1=O** is only stable in [$D_6$]benzene for hours at 23 °C, the silylated compounds **2=O** and **3=O** were isolated in the solid state and in the case of **3=O** characterized by X-ray diffraction. The relative thermal stability of these compounds contrasts $(\eta^5\text{-}C_5Me_5)_2Ti{=}O$, which requires the presence of a Lewis base such as 4-phenylpyridine for observation and isolation.[6,7]

Exposure of each of the monomeric, base-free titanocene oxo complexes to $H_2$ results in rapid hydrogenation of the Ti=O bond to furnish the corresponding hydroxy hydride derivatives, $(\eta^5\text{-}C_5Me_4R)_2Ti(OH)H$. This behavior highlights the benefits of the base-free species as addition of dihydrogen to $(\eta^5\text{-}C_5Me_5)_2Ti(O)L$ (L = pyridine) yields a mixture of products from which $(\eta^5\text{-}C_5Me_5)_2Ti(OH)_2$ and $(\eta^5\text{-}C_5Me_5)_2Ti(OH)H$ were identified.[8] The pressure dependence on the rate of hydrogenation of **2=O** established a first order dependence on $H_2$.[5] This rate law, in combination with the measurement of a normal, primary kinetic isotope effect of 2.7(3) at 23 °C, supports a 1,2-addition pathway for hydrogenation of the Ti=O bond. Similar results were obtained for hydrosilylation of **2=O** to yield the corresponding hydrido titanocene siloxide. In contrast, C–H bonds of saturated and unsaturated hydrocarbons have proven unreactive, most likely a result of the strong Ti=O π-bond.

Inspired by these observations, the synthesis of the corresponding "parent imido" complexes, $(\eta^5\text{-}C_5Me_4R)_2Ti{=}NH$, was targeted. Many isolable titanium imides have been reported and their chemistry extensively studied,[9] especially with respect to C–H activation.[10] Most of these compounds contain sterically demanding nitrogen substituents (e.g. *t*Bu, aryl, $SiMe_3$), which impart stability. Parent imido derivatives, $L_nTi{=}NH$, are by comparison relatively rare[11] despite their potential intermediacy in the preparation of titanium nitride thin films.[12] In this contribution, we describe our efforts to prepare parent titanocene imido derivatives by [NH] group transfer and also explore N–H oxidative addition of amines. The stability of the transient parent imides is also compared with isolable titanocene oxo compounds.

## Results and Discussion

Our synthetic approach for the preparation of $(\eta^5\text{-}C_5Me_4R)_2Ti{=}NH$ compounds was inspired by the [O]-atom transfer chemistry used to prepare the corresponding oxo derivatives. Treatment of a [$D_6$]benzene solution of **1** with a stoichiometric quantity of propylenimine yielded one equivalent of propylene and an initial equimolar mixture of two new $C_1$-symmetric titanium products, inconsistent with formation of the desired imido compound.

Over the course of one week at 23 °C, the mixture of diastereomers (vide infra) converts to a single thermodynamic product. The major isomer exhibits two doublets centered at $\delta$ = 1.78 and 2.90 ppm, indicating cyclometalation of one of the cyclopentadienyl methyl groups. Similar resonances centered at $\delta$ = 1.94 and 2.82 ppm are observed for the minor thermodynamic isomer. In addition, both compounds exhibit N–H resonances that integrate to two protons, consistent with formation of two diastereomers of the cyclometalated amide complex **1-CM-NH$_2$** [Equation (1)].

A similar outcome was observed with the silylated titanium sandwich, **2**. Addition of one equivalent of propylenimine again resulted in rapid evolution of one equivalent of propylene and formation of two $C_1$-symmetric titanocene compounds. In this case, a 3:1 mixture of diastereomers of the cyclometalated titanium amide complex **2-CM-NH$_2$** was formed [Equation (1)]. No change in the ratio of the mixture of isomers was observed after standing for one week at 23 °C. Thermolysis at 65 °C over the course of days resulted in gradual decomposition.

The assignment of the stereochemistry of the observed diastereomers of **1-CM-NH$_2$** and **2-CM-NH$_2$** was accomplished by a combination of two-dimensional (NOESY, HSQC, HMBC) NMR experiments. Complete details are reported in the Supporting Information. Observation of cyclometalated titanocene amide complexes following addition of propylenimine suggests that the desired parent imido compounds, $(\eta^5\text{-}C_5Me_4R)_2Ti{=}NH$, are formed transiently but undergo rapid 1,2-addition of a C–H bond from

 © 2007 Wiley-VCH Verlag GmbH & Co. KGaA, Weinheim 

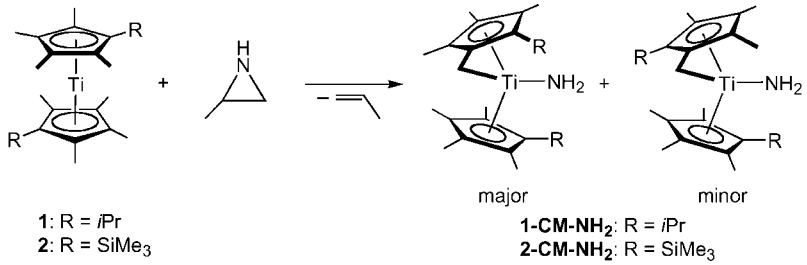


(1)

the diastereotopic cyclopentadienyl methyl groups adjacent to the isopropyl or trimethylsilyl substituent. The conversion of the kinetic mixture of diastereomers of **1-CM-NH$_2$** to a sole thermodynamic isomer demonstrates that the C–H activation reaction is reversible. In the case of **2-CM-NH$_2$** where the ratio of diastereomers remains constant, we are unable to distinguish between the kinetic and thermodynamic preferences for methyl group cyclometalation.

To determine whether bis(cyclopentadienyl)titanium imido complexes bearing larger nitrogen substituents would exhibit improved thermal stability, ($\eta^5$-$C_5Me_4SiMe_3$)$_2$-Ti=NSiMe$_3$ (**2=NSiMe$_3$**) was prepared by addition of $Me_3SiN_3$ to **2** [Equation (2)]. As was observed with [$\eta^5$-$C_5H_3$-1,3-($SiMe_3$)$_2$]$_2$Ti=NSiMe$_3$,[13] the [D$_6$]benzene $^1$H and $^{13}$C NMR spectra of **2=NSiMe$_3$** exhibit the number of resonances expected for a $C_2$-symmetric imide complex. It should be noted that in the solid state, [$\eta^5$-$C_5H_3$-1,3-($SiMe_3$)$_2$]$_2$Ti=NSiMe$_3$ contains a near linear Ti=N–Si linkage.[13]

Allowing [D$_6$]benzene solutions of **2=NSiMe$_3$** to stand at 23 °C for days resulted in cyclometalation of the cyclopentadienyl methyl groups both adjacent and distal to the [SiMe$_3$] substituent. All four diastereomers were detected by NMR spectroscopy, but only two formed in appreciable quantities. The major isomer was identified as one of the diastereomers arising from distal methyl group cyclometalation while the other is one of the diastereomers from adjacent methyl group C–H activation. The two minor diastereomers account for less than 10% of the mixture. Because the presence of four isomeric $C_1$-symmetric titanocene compounds produces complex NMR spectra with considerable peak overlap, the stereochemistry of each diastereomer could not be reliably assigned.

Confirmation of the regiochemistry of cyclometalation was provided by treating the mixture of products with DCl. Analysis of the resulting isotopomers of **2-Cl$_2$** established deuterium incorporation into both methyl positions. Importantly, no deuterium incorporation into the [SiMe$_3$] substituents was observed, confirming that these positions do not undergo C–H activation.

The reactivity of **1-CM-NH$_2$** and **2-CM-NH$_2$** was also explored. Exposure of the kinetic mixture of diastereomers of **1-CM-NH$_2$** to 4 atm of $H_2$ resulted in slow hydrogenation to give the hydrido titanocene amido complex ($\eta^5$-$C_5Me_4iPr$)$_2$Ti($NH_2$)H [**1-(NH$_2$)H**] upon heating to 55 °C for three days. Performing the experiment with $D_2$ gas yielded the deuterated isotopologue with the isotopic labels incorporated into the appropriate cyclopentadienyl methyl groups and the titanium-hydride (deuteride). Incorporation of the isotopic label was also observed in the N–H position, consistent with reversible 1,2-addition and elimination sequences. Similar hydrogenation chemistry was observed with **2-CM-NH$_2$** to yield ($\eta^5$-$C_5Me_4SiMe_3$)$_2$Ti($NH_2$)H [**2-(NH$_2$)H**] (Figure 3).

Intramolecular hydrogen exchange was explored with **2-(NH$_2$)H** by EXSY NMR spectroscopy. No crosspeaks indicative of exchange were observed up to temperatures of 90 °C with mixing times of 700 ms. Intermolecular exchange was probed by addition of four atmospheres of $D_2$ gas to a [D$_6$]benzene solution of **2-(NH$_2$)H** and no isotopic incorporation was observed over the course of days at 23 °C. The failure to observe isotopic exchange at ambient temperature demonstrates that the barrier for 1,2-elimination of $H_2$ is higher for **2-(NH$_2$)H** than **2-(OH)H**.[5]

The isolation of the thermally stable bis(cyclopentadienyl)titanium amido hydrides **1-(NH$_2$)H** and **2-(NH$_2$)H** suggested that these compounds could also be prepared by N–H oxidative addition of ammonia.[14,15] Addition of one equivalent of $NH_3$ gas to a [D$_6$]benzene solution of **1** yielded only small amounts (about 10%) of the desired amido hydride **1-(NH$_2$)H** (Figure 4). The major product

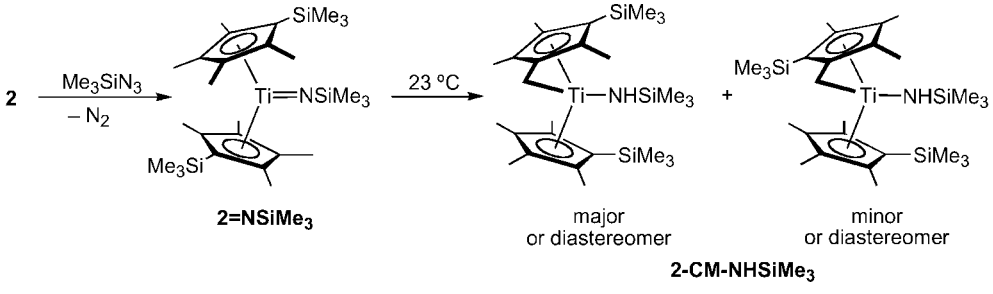


(2)

 © 2007 Wiley-VCH Verlag GmbH & Co. KGaA, Weinheim 

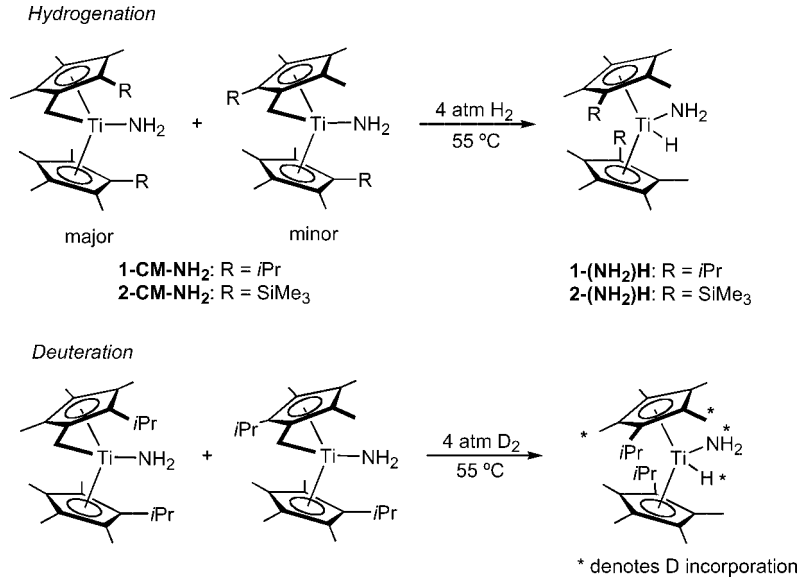


Figure 3. Hydrogenation and deuteration of bis(cyclopentadienyl)titanium cyclometalated amide complexes.

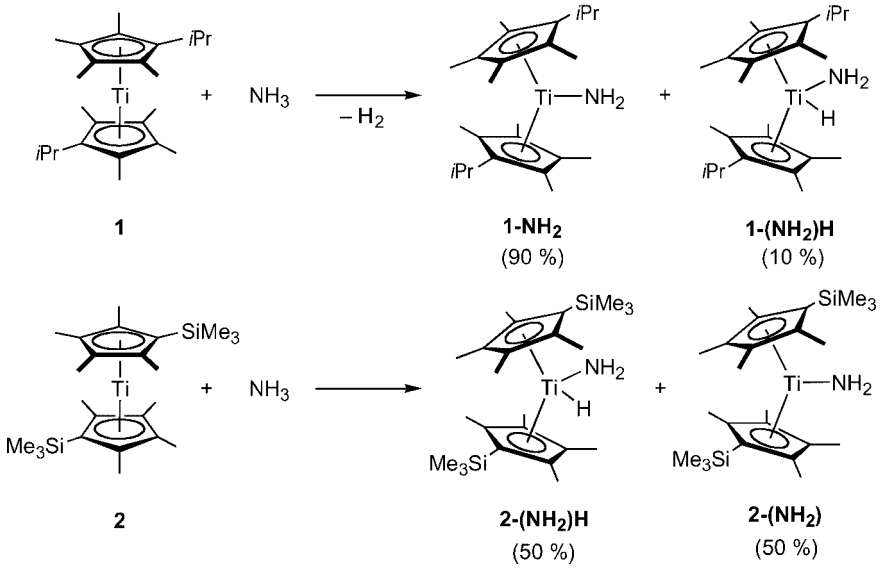


Figure 4. Ammonia addition to **1** and **2**.

was identified as the paramagnetic titanium(III) amido complex, $(\eta^5\text{-}C_5Me_4iPr)_2Ti(NH_2)$ (**1-NH$_2$**).[16]

For the silylated sandwich **2**, ammonia addition yielded approximately 50% of **2-(NH$_2$)H** along with an NMR-silent titanium compound, assigned as **2-NH$_2$**. This mixture was formed reproducibly and was unchanged when either an excess or stoichiometric quantity of $NH_3$ was added. The identity of **2-NH$_2$** was established by treatment with PhSSPh to yield diamagnetic $(\eta^5\text{-}C_5Me_4SiMe_3)_2Ti(NH_2)$-(SPh) [**2-(NH$_2$)(SPh)**].

Several additional experiments were performed to elucidate the origin of **1-NH$_2$**. Inverting the order of addition whereby **1** was added to a saturated [$D_6$]benzene solution of ammonia increased the amount of **1-(NH$_2$)H** formed. Treatment of **1** with a slightly larger amine, $MeNH_2$, produced only the oxidative addition product, $(\eta^5\text{-}C_5Me_4iPr)_2$-Ti(NHMe)H [**1-(NHMe)H**] (Figure 5). No reaction was observed upon addition of $tBuNH_2$, $PhNH_2$ or $Me_2NH$.

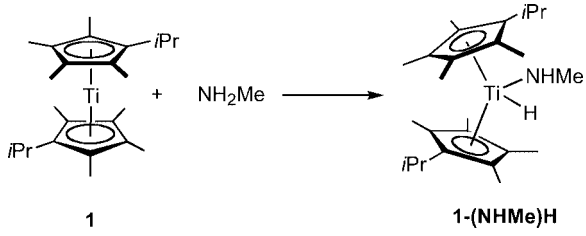


Figure 5. Methylamine addition to **1**.

Based on the experimental data, a mechanism for the formation of **1-NH$_2$** was proposed and is presented in Figure 6. Addition of ammonia to the sandwich forms the transient ammonia complex **1-NH$_3$**, which in the presence

 © 2007 Wiley-VCH Verlag GmbH & Co. KGaA, Weinheim 

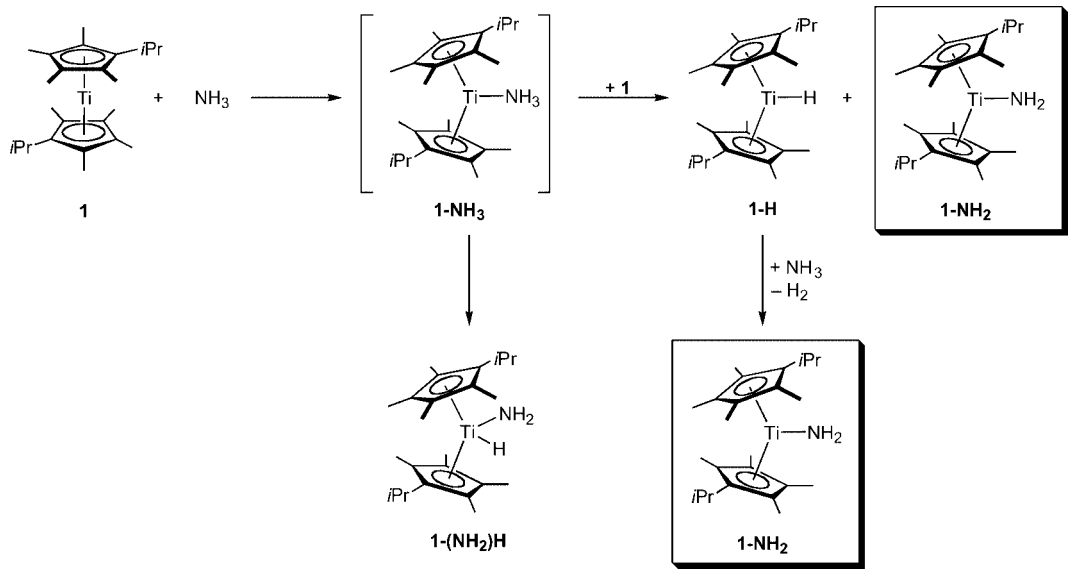


Figure 6. Proposed mechanism for the formation of **1-NH$_2$** from $NH_3$ addition to **1**.

of unreacted **1** undergoes formal deprotonation to yield **1-NH$_2$** and the titanium(III) hydride **1-H**. Increased amounts of the N–H oxidative addition product **1-(NH$_2$)H** from the inverse addition experiment support this initial pathway. Furthermore, the observation of sole N–H oxidative addition chemistry upon $MeNH_2$ addition to **1** is also consistent with this proposal, as bimolecular reactions are less likely with a more hindered amine. Addition of ammonia to **1-H** liberates dihydrogen (experimentally observed) and yields additional **1-NH$_2$** (Figure 6). The feasibility of this reaction has been confirmed experimentally by treatment of isolated **1-H** (vide infra) with ammonia.[16]

The proposed intermediacy of **1-H** during formation of **1-NH$_2$** prompted exploration of the hydrogenation chemistry of **1**. Addition of four atmospheres of $H_2$ to **1** forms a bright orange [$D_6$]benzene solution signaling formation of diamagnetic **1-H$_2$**. The $^1$H NMR spectrum of **1-H$_2$** suggests a dynamic process involving the cyclopentadienyl methyl groups in solution as these resonances are broadened while those for the isopropyl substituents remain sharp. Monitoring the addition of $D_2$ gas to **1** by $^2$H NMR spectroscopy revealed rapid incorporation of the isotopic label into both methyl positions of **1-D$_2$** (Figure 7), consistent with reversible cyclometalation on the NMR time scale. Much like ($\eta^5$-$C_5Me_5)_2TiH_2$,[17] removal of the dihydrogen atmosphere from **1-H$_2$** resulted in rapid conversion to the titanium(III) monohydride **1-H**, demonstrating that the introduction of the isopropyl substituent into the cyclopentadienyl rings offers little increased stability for the corresponding titanocene dihydride.

The reactivity of the titanium sandwich **1** with heterocycles was also explored. Our laboratory has previously demonstrated that the $\eta^9$,$\eta^5$-bis(indenyl)zirconium sandwich complex, [$\eta^9$-$C_9H_5$-1,3-$(SiMe_3)_2$][$\eta^5$-$C_9H_5$-1,3-$(SiMe_3)_2$]Zr, promotes the C–H activation of 4-(dimethylamino)pyridine

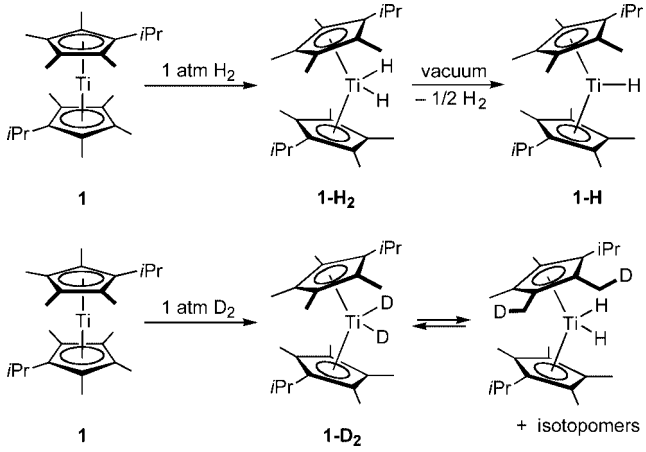


Figure 7. Addition of dihydrogen and dideuterium to **1**.

(DMAP) to yield the corresponding zirconium aryl hydride compound.[18] We were curious if the less reducing first row transition metal was sufficiently potent to promote C–H activation or if a stable titanium(II) ligand complex would form. If the later scenario was favored, the spin state ($S$ = 0 or 1) of the resulting bent titanocene derivative was of interest. With the exception of dicarbonyl and dinitrogen derivatives, bis(cyclopentadienyl)titanium(II) ligand complexes are relatively rare. Examples include ($\eta^5$-$C_5R_5)_2$Ti(bipy) (R = H, Me; bipy = bipyridine),[19] ($\eta^5$-$C_5H_5)_2$Ti(pyrrole)$_2$,[20] ($\eta^5$-$C_5H_5)_2$Ti$(PMe_3)_2$[21] and ($\eta^5$-$C_5H_5)_2$Ti$(PF_3)_2$.[22] As expected for coordinatively saturated complexes, all of these compounds, with the exception of ($\eta^5$-$C_5Me_5)_2$Ti(bipy), are diamagnetic.

Stirring a diethyl ether solution of **1** with a stoichiometric quantity of DMAP followed by recrystallization at –35 °C furnished red rods identified as the paramagnetic DMAP complex **1-DMAP** [Equation (3)]. A solid state magnetic

 © 2007 Wiley-VCH Verlag GmbH & Co. KGaA, Weinheim 

moment of 2.7 $\mu_B$ was determined by magnetic susceptibility balance at 23 °C and is consistent with the spin only value for two unpaired electrons. A slightly lower value of 2.3 $\mu_B$ was measured by Evans method in [$D_6$]benzene solution but is also consistent with an $S = 1$ titanium(II) center.

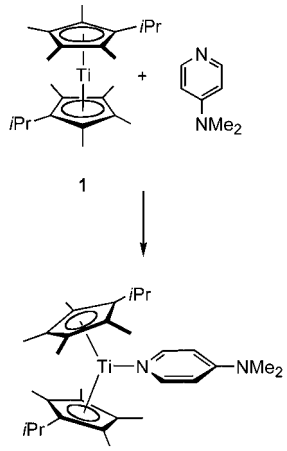


(3)

The solid-state structure of **1-DMAP** was determined by X-ray diffraction and a representation is presented in Figure 8. The overall molecular geometry is typical for a group 4 bent metallocene derivative with an idealized $C_2$ axis of molecular symmetry defined by the Ti(1)–N(1) bond. The plane of the DMAP ring lies in the titanocene wedge and is nearly coplanar with the dimethylamino group. The metrical parameters for the coordinated heterocycle are similar to free DMAP,[23] indicating little reduction by the titanium center. Attempts to induce C–H activation by thermolysis of **1-DMAP** have been unsuccessful. Warming [$D_6$]benzene solutions of the compound to 95 °C for 3 d produced no observable change by $^1$H NMR spectroscopy.

### Comparison of Ti=E Species to Promote 1,2-Addition Chemistry

Our laboratory has synthesized a family of substituted bis(cyclopentadienyl)titanium oxo,[5] imido, and transient alkylidene compounds.[13] The propensity of each class of Ti=E (E = O, NR, $CR_2$) linkage to promote the C–H activation of the cyclopentadienyl methyl groups provides insights into the relative stability of each type of titanium element (or group) multiple bond. Within the series of imides, the nitrogen substituent influences the rate of 1,2-addition as the more sterically protected [Ti=N$SiMe_3$] and [Ti=N*Ar*] (*Ar* = substituted aryl) linkages are isolable[13] while [Ti=NH] species have yet to be observed directly.

The identity of the titanium–ligand multiple bond also dictates the rate of C–H activation by 1,2-addition. Whereas the transient alkylidene, [[$\eta^5$-$C_5H_3$-1,3-($SiMe_3$)$_2$]$_2$-Ti=CH($SiMe_3$)], has proven too reactive to observe, similar imide complexes have been isolated and shown to promote C–H activation.[13] In contrast, the titanocene oxo derivatives are reluctant to activate C–H bonds. These differences are most likely a result of the strength of the Ti=E π-bond, where the Ti=O fragment is expected to be the strongest and Ti=$CR_2$ the weakest. Simply comparing O–H and C–H bond strengths of small molecules such as water and $Ph_2CH_2$ and assuming the overall entropy change in the 1,2-addition reaction is approximately –30 eu, the Ti=O π bond strength can be estimated as approximately 30 kcal/mol stronger than that for Ti=$CR_2$. Using the N–H bond strength of ammonia in a similar approximation places the Ti=NH π bond strength only 10 kcal/mol weaker than the oxo and accounts for the stability of certain variants of these compounds but also the ability to undergo intramolecular 1,2-addition of C–H bonds.

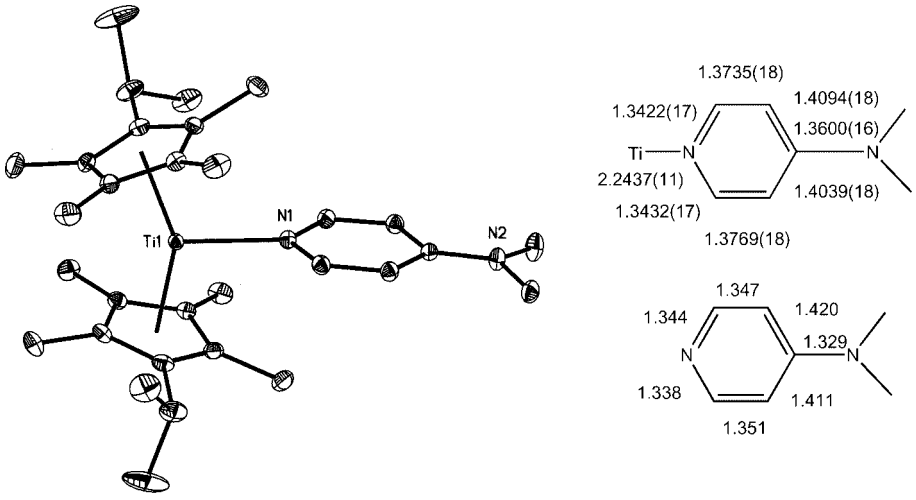


Figure 8. Molecular structure of **1-DMAP** at 30% probability ellipsoids. Hydrogen atoms omitted for clarity.

 © 2007 Wiley-VCH Verlag GmbH & Co. KGaA, Weinheim 

## Concluding Remarks

Treatment of isolable bis(cyclopentadienyl)titanium sandwich complexes with propylenimine resulted in [NH] group transfer followed by rapid C–H activation of a cyclopentadienyl methyl group to yield cyclometalated titanocene amido compounds. These observations suggest that the relative strength of the Ti=E π bond (E = O > NR > $CR_2$) determines the propensity of the titanium compound to participate in 1,2-addition of C–H bonds. Exposure of the resulting cyclometalated titanocene amido compounds to dihydrogen at 55 °C yielded the corresponding amido hydride complexes. For the silylated derivative, ($\eta^5$-$C_5Me_4SiMe_3$)$_2$Ti($NH_2$)H, this compound was also prepared by oxidative addition of an N–H bond of ammonia along with ($\eta^5$-$C_5Me_4SiMe_3$)$_2$Ti$NH_2$. Similar chemistry was observed with the more open titanocene sandwich, ($\eta^5$-$C_5Me_4$*i*Pr)$_2$Ti, as significant quantities of the titanium(III) amide complex, ($\eta^5$-$C_5Me_4$*i*Pr)$_2$Ti$NH_2$, were obtained upon addition of $NH_3$. Subsequent experiments changing the order of addition and the size of the amine support a pathway involving deprotonation from coordinated ammonia by free bis(cyclopentadienyl)titanium sandwich.

## Experimental Section

**General Considerations:** All air- and moisture-sensitive manipulations were carried out using standard high vacuum line, Schlenk or cannula techniques or in an M. Braun inert atmosphere drybox containing purified nitrogen. The Braun drybox was equipped with a cold well designed for freezing samples in liquid nitrogen. Solvents for air- and moisture-sensitive manipulations were dried and deoxygenated using literature procedures.[24] Toluene, benzene, pentane and heptane were further dried by distillation from "titanocene".[25] Deuterated solvents for NMR spectroscopy were distilled from sodium metal under an atmosphere of argon and stored over 4-Å molecular sieves. Argon and hydrogen gas were purchased from Airgas Incorporated and passed through a column containing manganese oxide on vermiculite and 4-Å molecular sieves before admission to the high vacuum line. DMAP was recrystallized from pentane and dried under vacuum. Propylenimine was initially dried with 4-Å molecular sieves and distilled immediately before use. The compounds ($\eta^5$-$C_5Me_4$*i*Pr)$_2$Ti($N_2$)$_2$ [**1-($N_2$)$_2$**],[3] ($\eta^5$-$C_5Me_4SiMe_3$)$_2$-Ti (**2**)[2] and ($\eta^5$-$C_5Me_4SiMe_2Ph$)$_2$Ti($N_2$) [**3-($N_2$)**][4] were prepared according to literature procedures.

$^1$H NMR spectra were recorded on a Varian Inova 400 Spectrometer operating at 399.860 MHz. All chemical shifts are reported relative to $SiMe_4$ using $^1$H (residual) chemical shifts of the solvent as a secondary standard. $^2$H and $^{13}$C NMR spectra were recorded on a Varian Inova 500 Spectrometer operating at 76.848 and 125.716 MHz, respectively. $^2$H and $^{13}$C chemical shifts are reported relative to $SiMe_4$ using chemical shifts of the solvent as a secondary standard.

Single crystals suitable for X-ray diffraction were coated with polyisobutylene oil in a drybox, transferred to a nylon loop and then quickly transferred to the goniometer head of a Bruker X8 APEX2 diffractometer equipped with a molybdenum X-ray tube ($\lambda$ = 0.71073 Å). Preliminary data revealed the crystal system. A hemisphere routine was used for data collection and determination of lattice constants. The space group was identified and the data were processed using the Bruker SAINT+ program and corrected for absorption using SADABS. The structures were solved by direct methods (SHELXS) completed by subsequent Fourier synthesis and refined by full-matrix least-squares procedures. CCDC-628974 (for **1-DMAP**) contains supplementary crystallographic data. These data can be obtained free of charge from The Cambridge Crystallographic Data Centre via www.ccdc.cam.ac.uk/data_request/cif.

Elemental analyses were performed at Robertson Microlit Laboratories, Inc., in Madison, NJ.

**Preparation of ($\eta^5$-$C_5Me_4$iPr)($\eta^5$-$C_5Me_3$-$\eta^1$-2-$CH_2$-$CHMe_2$)Ti-$NH_2$ (1-CM-$NH_2$):** A J. Young NMR tube was charged with 0.033 g (0.077 mmol) of **1-($N_2$)$_2$** and approximately 0.5 mL of [$D_6$]-benzene were added. On the high vacuum line, the tube was degassed at liquid nitrogen temperature and 45 Torr of propylenimine (0.077 mmol) were added with a 31.6 mL calibrated gas bulb. The tube was shaken and thawed, resulting in an immediate colour change from dark red to bright red. The solvent was removed to yield **1-CM-$NH_2$** as a red oil. $^1$H NMR ([$D_6$]benzene, major thermodynamic isomer): $\delta$ = 1.18 (d, *J* = 6 Hz, 3 H, $C_5Me_3$-$\eta^1$-2-$CH_2$-CH*$Me_2$*), 1.22 (d, *J* = 6 Hz, 3 H, $C_5Me_3$-$\eta^1$-2-$CH_2$-CH*$Me_2$*), 1.22 (d, *J* = 6 Hz, 6 H, $C_5Me_4$CH*$Me_2$*), 1.46 (s, 3 H, $C_5$*$Me_3$*-$\eta^1$-2-$CH_2$-$CHMe_2$), 1.66 (s, 3 H, $C_5$*$Me_3$*-$\eta^1$-2-$CH_2$-$CHMe_2$), 1.67 (s, 3 H, $C_5$*$Me_4$*$CHMe_2$), 1.74 (s, 3 H, $C_5$*$Me_4$*$CHMe_2$), 1.78 (d, *J* = 3 Hz, 1 H, $C_5Me_3$-$\eta^1$-2-C*$H_2$*-$CHMe_2$), 1.82 (s, 3 H, $C_5$*$Me_4$*$CHMe_2$), 1.91 (s, 3 H, $C_5$*$Me_3$*-$\eta^1$-2-$CH_2$-$CHMe_2$), 2.04 (s, 3 H, $C_5$*$Me_4$*$CHMe_2$), 2.50 (m, 1 H, $C_5Me_3$-$\eta^1$-2-$CH_2$-C*H*$Me_2$), 2.66 (m, 1 H, $C_5Me_4$C*H*$Me_2$), 2.90 (d, *J* = 3 Hz, 1 H, $C_5Me_3$-$\eta^1$-2-C*$H_2$*-$CHMe_2$), 4.90 (br. s, 2 H, N*$H_2$*) ppm. $^1$H NMR ([$D_6$]benzene, minor thermodynamic isomer): $\delta$ = 1.12 (d, *J* = 6 Hz, 3 H, $C_5Me_3$-$\eta^1$-2-$CH_2$-CH*$Me_2$*), 1.13 (d, *J* = 6 Hz, 3 H, $C_5Me_3$-$\eta^1$-2-$CH_2$-CH*$Me_2$*), 1.24 (d, *J* = 6 Hz, 6 H, $C_5Me_4$CH*$Me_2$*), 1.63 (s, 3 H, $C_5$*$Me_3$*-$\eta^1$-2-$CH_2$-$CHMe_2$), 1.73 (s, 3 H, $C_5$*$Me_3$*-$\eta^1$-2-$CH_2$-$CHMe_2$), 1.75 (s, 3 H, $C_5$*$Me_4$*$CHMe_2$), 1.78 (s, 3 H, $C_5$*$Me_3$*-$\eta^1$-2-$CH_2$-$CHMe_2$), 1.80 (s, 3 H, $C_5$*$Me_4$*$CHMe_2$), 1.85 (s, 3 H, $C_5$*$Me_4$*$CHMe_2$), 1.94 (d, *J* = 3 Hz, 1 H, $C_5Me_3$-$\eta^1$-2-C*$H_2$*-$CHMe_2$), 2.10 (s, 3 H, $C_5$*$Me_4$*$CHMe_2$), 2.55 (m, 1 H, $C_5Me_3$-$\eta^1$-2-$CH_2$-C*H*$Me_2$), 2.67 (m, 1 H, $C_5Me_4$C*H*$Me_2$), 2.82 (d, *J* = 3 Hz, 1 H, $C_5Me_3$-$\eta^1$-2-C*$H_2$*-$CHMe_2$), 4.85 (br. s, 2 H, N*$H_2$*) ppm. $^{13}$C NMR ([$D_6$]benzene): $\delta$ = 11.16, 11.21, 11.69, 11.84, 11.96, 12.06, 12.09, 12.14, 12.18, 12.26, 12.88, 13.64, 13.90 (Me), 21.01, 22.22, 23.14, 23.22, 23.26, 23.43, 26.33, 27.31, 27.37, 27.55, 27.87, 30.48 (*C*$HMe_2$/CH*$Me_2$*), 69.56, 70.05 (*C*$H_2$), 110.67, 111.25, 114.84, 115.18, 116.07, 117.42, 117.90, 117.98, 118.17, 118.42, 118.91, 119.04, 120.78, 121.24, 122.32, 123.35, 123.55, 128.45, 132.21, 137.51 (Cp) ppm. IR (KBr): $\tilde{\nu}$ = 3369, 3439 ($NH_2$) $cm^{-1}$.

**Preparation of ($\eta^5$-$C_5Me_4SiMe_3$)($\eta^5$-$C_5Me_3$-$\eta^1$-2-$CH_2$-$SiMe_3$)Ti-$NH_2$ (2-CM-$NH_2$):** This compound was prepared using a similar procedure to that described for **1-CM-$NH_2$** with 0.027 g (0.0621 mmol) of **2**, 37 Torr (0.0621 mmol, 31.6 mL gas volume) of propylenimine and approximately 0.5 mL [$D_6$]benzene resulting in a colour change from dark red to bright red. The solvent was removed to yield a red oil. $^1$H NMR ([$D_6$]benzene, major isomer): $\delta$ = 0.30 (s, 9 H, $C_5Me_3$-$\eta^1$-2-$CH_2$-Si*$Me_3$*), 0.33 (s, 9 H, $C_5Me_4$-Si*$Me_3$*), 1.42 (s, 3 H, $C_5$*$Me_3$*-$\eta^1$-2-$CH_2$-$SiMe_3$), 1.61 (s, 3 H, $C_5$*$Me_4$*-$SiMe_3$), 1.64 (s, 3 H, $C_5$*$Me_4$*$SiMe_3$), 1.67 (s, 3 H, $C_5$*$Me_3$*-$\eta^1$-2-$CH_2$-$SiMe_3$), 1.88 (s, 3 H, $C_5$*$Me_4$*$SiMe_3$), 1.92 (s, 3 H, $C_5$*$Me_4$*$SiMe_3$), 1.98 (d, *J* = 2 Hz, 1 H, $C_5Me_3$-$\eta^1$-2-C*$H_2$*-$SiMe_3$), 2.16 (s, 3 H, $C_5$*$Me_3$*-$\eta^1$-2-$CH_2$-$CHMe_2$), 2.84 (d, *J* = 3 Hz, 1 H, $C_5Me_3$-$\eta^1$-2-C*$H_2$*-$SiMe_3$), 5.40 (br. s, 2 H, N*$H_2$*) ppm. $^1$H NMR ([$D_6$]benzene, minor isomer): $\delta$ = 0.30 (s, 9 H, $C_5Me_3$-$\eta^1$-2-$CH_2$-Si*$Me_3$*), 0.31 (s, 9 H, $C_5Me_4$-Si*$Me_3$*), 1.56 (s, 3 H, $C_5$*$Me_3$*-$\eta^1$-2-$CH_2$-$SiMe_3$), 1.71 (s, 3 H, $C_5$*$Me_4$*-$SiMe_3$), 1.75 (s, 3 H, $C_5$*$Me_3$*-$\eta^1$-2-$CH_2$-$SiMe_3$), 1.87 (d, *J* = 2 Hz, 1

 © 2007 Wiley-VCH Verlag GmbH & Co. KGaA, Weinheim 

H, $C_5Me_3$-η$^1$-2-C$H_2$-SiMe$_3$), 1.87 (s, 3 H, $C_5Me_4$SiMe$_3$), 1.90 (s, 3 H, $C_5Me_4$SiMe$_3$), 1.94 (s, 3 H, $C_5Me_3$-η$^1$-2-CH$_2$-SiMe$_3$), 2.06 (s, 3 H, $C_5Me_4$SiMe$_3$), 2.81 (d, $J$ = 3 Hz, 1 H, $C_5Me_3$-η$^1$-2-C$H_2$-SiMe$_3$), 4.79 (br. s, 2 H, N$H_2$) ppm. $^{13}$C NMR ([D$_6$]benzene): $\delta$ = 2.05, 2.49, 3.18 (Si$Me_3$), 10.94, 11.08, 11.18, 11.39, 11.57, 12.40, 12.52, 12.73, 14.25, 14.56, 14.78, 14.96, 15.06, 15.35 (Me), 69.89, 70.04 ($CH_2$), 107.11, 109.03, 114.57, 117.27, 118.50, 120.31, 120.66, 123.37, 123.93, 124.33, 125.17, 125.42, 127.62, 128.24, 128.63, 128.96, 130.29, 130.77, 131.25, 135.26 (Cp) ppm. IR (KBr): $\tilde{\nu}$ = 3377, 3453 (NH$_2$) cm$^{-1}$.

**Preparation of (η$^5$-C$_5$Me$_4$iPr)$_2$Ti(NH$_2$)(H) [1-(NH$_2$)(H)]:** A J. Young NMR tube was charged with 0.033 g (0.077 mmol) of **1-CM-NH$_2$** and approximately 0.5 mL of [D$_6$]benzene were added. On the high vacuum line, the tube was degassed at –196 °C and 1 atm of $H_2$ was added. The tube was then heated to 55 °C for three days resulting in a colour change to orange. The solvent was removed in vacuo to yield 0.029 g (96.7%) of **1-(NH$_2$)(H)** as an orange solid. $^1$H NMR ([D$_6$]benzene): $\delta$ = 1.32 (d, $J$ = 3 Hz, 6 H, $C_5Me_4CH$$Me_2$), 1.34 (d, $J$ = 3 Hz, 6 H, $C_5Me_4CH$$Me_2$), 1.78 (s, 6 H, $C_5$$Me_4$CHMe$_2$), 1.89 (s, 6 H, $C_5$$Me_4$CHMe$_2$), 1.91 (s, 6 H, $C_5$$Me_4$CHMe$_2$), 1.92 (s, 6 H, $C_5$$Me_4$CHMe$_2$), 2.13 (s, 1 H, Ti-$H$), 2.88 (m, 2 H, $C_5Me_4C$$H$Me$_2$), 5.88 (br. s, 2 H, N$H_2$) ppm. $^{13}$C NMR ([D$_6$]benzene): $\delta$ = 11.36, 12.05, 12.38, 12.58 (Me), 23.15, 23.31, 28.29 ($C$HMe$_2$/CH$Me_2$), 113.24, 114.21, 114.28, 115.34, 126.71 (Cp) ppm. IR (KBr): $\tilde{\nu}$ = 1644 (Ti–H), 3361, 3435 (NH$_2$) cm$^{-1}$.

**Preparation of (η$^5$-C$_5$Me$_4$SiMe$_3$)$_2$Ti(NH$_2$)(H) [2-(NH$_2$)(H)]:** This molecule was prepared in an identical manner to **1-(NH$_2$)(H)** with 0.027 g (0.0621 mmol) of **2-CM-NH$_2$**, approximately 0.5 mL of [D$_6$]benzene and one atmosphere of dihydrogen to afford **2-(NH$_2$)-(H)** as an orange solid after 3 d of heating. $C_{24}H_{45}NSi_2Ti$ (451.63): calcd. C 63.82, H 10.04, N 3.10; found C 63.72, H 9.88, N 3.24. $^1$H NMR ([D$_6$]benzene): $\delta$ = 0.42 (s, 18 H, $C_5Me_4Si$$Me_3$), 1.71 (s, 6 H, $C_5$$Me_4$SiMe$_3$), 1.73 (s, 6 H, $C_5$$Me_4$SiMe$_3$), 1.83 (s, 6 H, $C_5$$Me_4$-SiMe$_3$), 1.94 (s, 6 H, $C_5$$Me_4$SiMe$_3$), 2.08 (s, 1 H, Ti-$H$), 5.96 (br. s, 2 H, N$H_2$) ppm. $^{13}$C NMR ([D$_6$]benzene): $\delta$ = 2.56 (SiMe$_3$), 10.94, 11.58, 14.35, 14.82 (Me), 110.07, 117.04, 118.65, 119.59, 125.43 (Cp) ppm. IR (KBr): $\tilde{\nu}$ = 1610 (Ti–H), 3373, 3444 (NH$_2$) cm$^{-1}$.

**Preparation of (η$^5$-C$_5$Me$_4$iPr)$_2$Ti(NHMe)(H) [1-(NHMe)(H)]:** A J. Young NMR tube was charged with 0.036 g (0.0836 mmol) of **1-(N$_2$)$_2$** and approximately 0.5 mL of [D$_6$]benzene were added. On the high vacuum line, the tube was degassed at –196 °C and methylamine was admitted with a 31.6 mL gas bulb (0.0836 mmol, 49 Torr). Upon thawing, a colour change from red to bright red was observed. The solvent was removed in vacuo to yield 0.032 g (94.1%) of **1-(NHMe)(H)** as a red solid. $C_{25}H_{43}NTi$ (405.46): calcd. C 74.05, H 10.69, N 3.45; found C 73.86, H 10.86, N 3.79. $^1$H NMR ([D$_6$]benzene): $\delta$ = 1.32 (d, $J$ = 8 Hz, 12 H, $C_5Me_4CH$$Me_2$), 1.81 (s, 6 H, $C_5$$Me_4$CHMe$_2$), 1.96 (s, 18 H, $C_5$$Me_4$CHMe$_2$), 2.13 (s, 1 H, Ti-$H$), 2.86 (m, 2 H, $C_5Me_4C$$H$Me$_2$), 3.19 (d, $J$ = 8 Hz, 3 H, NH$Me$), 6.71 (br. s, 1 H, N$H$Me) ppm. $^{13}$C NMR ([D$_6$]benzene): $\delta$ = 11.90, 12.61, 12.79, 13.37 (Me), 23.08, 23.21, 27.82 ($C$HMe$_2$/CH$Me_2$), 43.71 (NH$Me$), 113.52, 114.24, 115.78, 116.67, 125.52 (Cp) ppm. IR (KBr): $\tilde{\nu}$ = 1626 (Ti–H), 3381, 3414 (N–H) cm$^{-1}$.

**Preparation of (η$^5$-C$_5$Me$_4$SiMe$_3$)$_2$Ti=NSiMe$_3$ (2=NSiMe$_3$):** A 20 mL scintillation vial was charged with 0.052 g (0.1196 mmol) of **2** and approximately 5 mL pentane were added. Azidotrimethylsilane (16.1 μL, 0.1196 mmol) was added by syringe and the solution was stirred for 10 min. An immediate colour change from red to bright red was observed, signaling formation of **2=NSiMe$_3$**. The solvent was removed in vacuo to yield a red oil which was then dissolved in benzene and lyophilized to yield 0.042 g (67.7%) of **2=NSiMe$_3$** as a red solid. $C_{27}H_{51}NSi_3Ti$ (521.80): calcd. C 62.14, H 9.85, N 2.68; found C 61.77, H 9.87, N 2.28. $^1$H NMR ([D$_6$]-benzene): $\delta$ = 0.17 (s, 18 H, $C_5Me_4Si$$Me_3$), 0.37 (s, 9 H, NSi$Me_3$), 1.80 (s, 12 H, $C_5$$Me_4$SiMe$_3$), 2.52 (s, 12 H, $C_5$$Me_4$SiMe$_3$) ppm. $^{13}$C NMR ([D$_6$]benzene): $\delta$ = 1.95 (SiMe$_3$), 6.08 (NSi$Me_3$), 12.36, 17.66 (Me), 121.06, 125.28, 137.13 (Cp) ppm.

**Preparation of (η$^5$-C$_5$Me$_4$SiMe$_3$)(η$^5$-C$_5$Me$_3$-η$^1$-3-CH$_2$-SiMe$_3$)Ti-NHSiMe$_3$ and (η$^5$-C$_5$Me$_4$SiMe$_3$)(η$^5$-C$_5$Me$_3$-η$^1$-2-CH$_2$-SiMe$_3$)Ti-NHSiMe$_3$ (2-CM-NHSiMe$_3$):** A J. Young NMR tube was charged with 0.030 g (0.057 mmol) of **2=NSiMe$_3$** and approximately 0.5 mL of [D$_6$]benzene were added. The solution was heated to 45 °C over the course of one week, resulting in a colour change from red to dark red/brown. The solvent was removed in vacuo to yield a dark oil. $^1$H NMR ([D$_6$]benzene, major isomer): $\delta$ = 0.22 (s, 9 H, NHSi$Me_3$), 0.31 (s, 9 H, $C_5Me_4Si$$Me_3$), 0.34 (s, 9 H, $C_5Me_3$-η$^1$-3-CH$_2$-Si$Me_3$), 1.30 (s, 3 H, $C_5Me_3$-η$^1$-3-CH$_2$-SiMe$_3$), 1.58 (s, 3 H, $C_5$$Me_4$SiMe$_3$), 1.66 (s, 3 H, $C_5$$Me_4$SiMe$_3$), 1.93 (s, 3 H, $C_5Me_3$-η$^1$-3-CH$_2$-SiMe$_3$), 1.97 (s, 3 H, $C_5Me_3$-η$^1$-3-CH$_2$-CHMe$_2$), 1.99 (d, $J$ = 5 Hz, 1 H, $C_5Me_3$-η$^1$-3-C$H_2$-SiMe$_3$), 2.10 (s, 3 H, $C_5$$Me_4$SiMe$_3$), 2.33 (s, 3 H, $C_5$$Me_4$SiMe$_3$), 2.56 (d, $J$ = 5 Hz, 1 H, $C_5Me_3$-η$^1$-3-C$H_2$-SiMe$_3$), 3.70 (br. s, 1 H, N$H$SiMe$_3$) ppm. $^1$H NMR ([D$_6$]benzene, minor isomer): $\delta$ = 0.19 (s, 9 H, NHSi$Me_3$), 0.22 (s, 9 H, $C_5Me_3$-η$^1$-2-CH$_2$-Si$Me_3$), 0.31 (s, 9 H, $C_5Me_4Si$$Me_3$), 1.65 (s, 3 H, $C_5$$Me_4$SiMe$_3$), 1.85 (s, 3 H, $C_5$$Me_4$SiMe$_3$), 1.87 (d, $J$ = 5 Hz, 1 H, $C_5Me_3$-η$^1$-2-C$H_2$-SiMe$_3$), 1.88 (s, 3 H, $C_5Me_3$-η$^1$-2-CH$_2$-SiMe$_3$), 1.90 (s, 3 H, $C_5Me_3$-η$^1$-2-CH$_2$-SiMe$_3$), 1.95 (s, 3 H, $C_5Me_3$-η$^1$-2-CH$_2$-CHMe$_2$), 1.95 (s, 3 H, $C_5$$Me_4$SiMe$_3$), 2.11 (s, 3 H, $C_5$$Me_4$-SiMe$_3$), 2.82 (d, $J$ = 5 Hz, 1 H, $C_5Me_3$-η$^1$-2-C$H_2$-SiMe$_3$), 3.10 (br. s, 1 H, N$H$SiMe$_3$) ppm. $^{13}$C NMR ([D$_6$]benzene): $\delta$ = 2.17, 2.47, 2.92, 3.49, 6.45, 6.84 (Si$Me_3$), 11.72, 12.35, 12.42, 12.73, 12.91, 13.05, 14.53, 15.29, 15.43, 16.91, 17.33, 18.02, 18.33 (Me), 71.05, 74.93 ($CH_2$), 104.68, 108.42, 117.71, 118.88, 119.44, 120.83, 122.89, 123.67, 124.46, 127.24, 129.14, 129.19, 130.72, 130.68, 131.61, 131.82, 132.54, 136.16, 139.68, 140.57 (Cp) ppm.

**Generation of (η$^5$-C$_5$Me$_4$iPr)$_2$TiH$_2$ (1-H$_2$):** A J. Young NMR tube was charged with 0.016 g (0.037 mmol) of **1-(N$_2$)$_2$** and approximately 0.5 mL [D$_8$]toluene were added. On the high vacuum line, the tube was cooled to –196 °C, degassed and one atmosphere of dihydrogen was added. Upon thawing, the colour changed from red to bright orange. Cooling the solution to –75 °C under an atmosphere of dihydrogen revealed formation of **1-H$_2$**. $^1$H NMR ([D$_8$]toluene, –75 °C): $\delta$ = 1.32 (d, $J$ = 7 Hz, 12 H, $C_5Me_4CH$$Me_2$), 1.52 (s, 12 H, $C_5$$Me_4$CHMe$_2$), 2.08 (s, 12 H, $C_5$$Me_4$CHMe$_2$), 3.25 (s, 2 H, Ti-$H$), 3.41 (m, 2 H, $C_5Me_4C$$H$Me$_2$) ppm. $^{13}$C NMR ([D$_8$]-toluene, –75 °C): $\delta$ = 11.73, 14.25 (Me), 24.10, 30.47 ($C$HMe$_2$/CH$Me_2$), 118.00, 119.42, 134.69 (Cp) ppm.

**Preparation of (η$^5$-C$_5$Me$_4$iPr)$_2$Ti(DMAP) (1-DMAP):** A 20 mL scintillation vial was charged with 0.102 g (0.237 mmol) of **1-(N$_2$)$_2$**, 0.029 g (0.237 mmol) of 4-(dimethylamino)pyridine (DMAP) and approximately 5 mL diethyl ether. The reaction was stirred for one hour at ambient temperature and the solvent was removed in vacuo, yielding a red/brown solid. The compound was washed with pentane and recrystallized from diethyl ether at –35 °C to yield 0.084 g (71.2%) of **1-DMAP** as red rods. $C_{31}H_{48}N_2Ti$ (496.56): calcd. C 74.98, H 9.74, N 5.64; found C 74.93, H 9.23, N 5.17. $^1$H NMR ([D$_6$]benzene): $\delta$ = 3.74 ($\Delta\nu_{1/2}$ = 129 Hz). $\mu_{eff}$ = 2.7 $\mu_B$ (solid state), 2.3 $\mu_B$ (Evans) ppm.

**Observation of (η$^5$-C$_5$Me$_4$SiMe$_3$)$_2$Ti(NH$_2$)(SPh) [2-(NH$_2$)(SPh)]:** A J. Young NMR tube was charged with 0.018 g (0.040 mmol) of **2-NH$_2$**, 0.005 g (0.040 mmol) of $Ph_2S_2$ and approximately 0.5 mL [D$_6$]benzene. The tube was placed in a 45 °C oil bath for approximately 18 h, leading to a colour change from orange to bright red.

 © 2007 Wiley-VCH Verlag GmbH & Co. KGaA, Weinheim 

$^1$H NMR ([D$_6$]benzene): $\delta$ = 0.33 (s, 18 H, $C_5Me_4Si\mathit{Me}_3$), 1.67 (s, 6 H, $C_5\mathit{Me}_4SiMe_3$), 1.79 (s, 6 H, $C_5\mathit{Me}_4SiMe_3$), 1.98 (s, 6 H, $C_5\mathit{Me}_4SiMe_3$), 2.04 (s, 6 H, $C_5\mathit{Me}_4SiMe_3$), 6.86 (m, 1 H, Ph), 7.10 (t, 2 H, Ph), 7.50 (d, $J$ = 7 Hz, 2 H, Ph), 7.75 (br. s, 2 H, $NH_2$) ppm. $^{13}$C NMR ([D$_6$]benzene): $\delta$ = 2.60 ($SiMe_3$), 11.58, 13.01, 15.03, 15.91 (Me), 120.29, 122.05, 126.26, 127.31, 128.62, 129.80, 131.96, 133.87, 148.16 (Cp/Ph) ppm. IR (KBr): $\tilde{\nu}$ = 3368, 3452 (N–H) cm$^{-1}$.

**Supporting Information** (see also the footnote on the first page of this article): Selected $^1$H NMR spectra, isomer assignments, and checkcif results.

## Acknowledgments

We thank the National Science Foundation and the Director, the Office of Basic Energy Sciences and Chemical Sciences Division of the US Department of Energy (DE-FG02-05ER15659) for financial support. P. J. C. is a Cottrell Scholar sponsored by the Research Corporation, a David and Lucile Packard Fellow in science and engineering and a Camille Dreyfus Teacher-Scholar.

[1] P. B. Hitchcock, F. Kerton, G. A. Lawless, *J. Am. Chem. Soc.* **1998**, *120*, 10264–10265.
[2] a) L. Lukesová, M. Horácek, P. Stepnicka, K. Fejfarová, R. Gyepes, I. Cisorová, J. Kubista, K. Mach, *J. Organomet. Chem.* **2002**, *663*, 134–144; b) M. Horácek, V. Kupfer, U. Thewalt, P. Stepnicka, M. Polasek, K. Mach, *Organometallics* **1999**, *18*, 3572–3578.
[3] T. E. Hanna, E. Lobkovsky, P. J. Chirik, *J. Am. Chem. Soc.* **2004**, *126*, 14688–14689.
[4] T. E. Hanna, E. Lobkovsky, P. J. Chirik, *J. Am. Chem. Soc.* **2006**, *128*, 6018–6019.
[5] T. E. Hanna, E. Lobkovsky, P. J. Chirik, *Inorg. Chem.*, DOI: 10.1021/ic070205+.
[6] F. Bottomley, G. O. Egharevba, I. J. B. Lin, P. S. White, *Organometallics* **1985**, *4*, 550–553.
[7] M. R. Smith, P. T. Matsunaga, R. A. Andersen, *J. Am. Chem. Soc.* **1993**, *115*, 7049–7050.
[8] Z. K. Sweeney, J. L. Polse, R. G. Bergman, R. A. Andersen, *Organometallics* **1999**, *18*, 5502–5510.
[9] N. Hazari, P. Mountford, *Acc. Chem. Res.* **2005**, *38*, 839–849.
[10] a) C. C. Cummins, C. P. Schaller, G. D. Van Duyne, P. T. Wolczanski, A. W. E. Chan, R. Hoffmann, *J. Am. Chem. Soc.* **1991**, *113*, 2985–2994; b) J. L. Bennett, P. T. Wolczanski, *J. Am. Chem. Soc.* **1997**, *119*, 10696–10719; c) H. M. Hoyt, F. E. Michael, R. G. Bergman, *J. Am. Chem. Soc.* **2004**, *126*, 1018–1019.
[11] P. J. McKarns, G. P. A. Yap, A. L. Rheingold, C. H. Winter, *Inorg. Chem.* **1996**, *35*, 5968–5969.
[12] J. B. Everhart, B. S. Ault, *Inorg. Chem.* **1995**, *34*, 4379–4384.
[13] T. E. Hanna, I. Keresztes, E. Lobkovsky, W. H. Bernskoetter, P. J. Chirik, *Organometallics* **2004**, *23*, 3448–3458.
[14] G. L. Hillhouse, J. E. Bercaw, *J. Am. Chem. Soc.* **1984**, *106*, 5472–5478.
[15] a) J. Zhao, A. S. Goldman, J. F. Hartwig, *Science* **2005**, *307*, 1080–1082; b) T. Braun, *Angew. Chem. Int. Ed.* **2005**, *44*, 5012–5014; c) Y. Nakajima, H. Kameo, H. Suzuki, *Angew. Chem. Int. Ed.* **2006**, *45*, 950–952; d) A. L. Casalnuovo, J. C. Calabrese, D. Milstein, *Inorg. Chem.* **1987**, *26*, 971–973.
[16] Examples of bis(cyclopentadienyl)titanium(III)amide compounds prepared by interaction of ammonia with the corresponding methyl complex: a) C. D. Sofield, M. D. Walter, R. A. Andersen, *Acta Crystallogr., Sect. C* **2004**, *60*, m465–m466; b) E. Brady, W. W. Lukens Jr, J. R. Telford, G. Mitchell, *Acta Crystallogr., Sect. C* **1995**, *51*, 558–560.
[17] a) J. E. Bercaw, R. H. Marvich, L. G. Bell, H. H. Brintzinger, *J. Am. Chem. Soc.* **1972**, *94*, 1219–1238; b) J. E. Bercaw, *J. Am. Chem. Soc.* **1974**, *96*, 5087–5095.
[18] C. A. Bradley, E. Lobkovsky, P. J. Chirik, *J. Am. Chem. Soc.* **2003**, *125*, 8110–8111.
[19] R. Gyepes, P. T. Witte, M. Horacek, I. Cisarova, K. Mach, *J. Organomet. Chem.* **1998**, *551*, 207–213.
[20] R. V. Bynum, W. E. Hunter, R. D. Rogers, J. L. Atwood, *Inorg. Chem.* **1980**, *19*, 2368–2374.
[21] L. B. Kool, M. D. Rausch, H. G. Alt, M. Herberhold, U. Thewalt, B. Wolf, *Angew. Chem. Int. Ed. Engl.* **1985**, *24*, 394–401.
[22] B. H. Edwards, R. D. Rogers, D. J. Sikora, J. L. Atwood, M. D. Rausch, *J. Am. Chem. Soc.* **1983**, *105*, 416–426.
[23] U. Ohms, H. Guth, *Z. Kristallographie* **1983**, *162*, 174–175.
[24] A. B. Pangborn, M. A. Giardello, R. H. Grubbs, R. K. Rosen, F. J. Timmers, *Organometallics* **1996**, *15*, 1518–1520.
[25] R. H. Marvich, H. H. Brintzinger, *J. Am. Chem. Soc.* **1971**, *93*, 2046–2048.

Received: November 29, 2006
Published Online: March 16, 2007

 © 2007 Wiley-VCH Verlag GmbH & Co. KGaA, Weinheim 

DOI: 10.1002/ejic.200601152

# The First Copper Complexes Bearing the 1,3,5-Triaza-7-phosphaadamantane (PTA) Ligand

**Alexander M. Kirillov,[a] Piotr Smoleński,[a] M. Fátima C. Guedes da Silva,[a] and Armando J. L. Pombeiro*[a]**

**Keywords:** Copper / N,P ligands / Structure elucidation / Phosphane ligands

The $Cu^{I}$ compound $[Cu(PTAH)_4](NO_3)_5$ (**1**) {PTAH = *N*-protonated form of 1,3,5-triaza-7-phosphaadamantane (PTA)} was easily prepared by reacting hydrated $Cu(NO_3)_2$ and PTA in aqueous acidic solution at room temperature. Further treatment of **1** with sodium hydroxide in water led to an unprotonated PTA derivative $[Cu(PTA)_4](NO_3)$ (**2**). Both compounds are water-soluble and air-stable, and were characterized by IR, $^{1}H$-, $^{13}C\{^{1}H\}$-, $^{31}P\{^{1}H\}$- and $^{63}Cu$ NMR spectroscopy, FAB-MS(+), elemental and single-crystal X-ray diffraction structural analyses. They exhibit a nearly regular tetrahedral coordination environment about each copper centre filled by the phosphorus atoms of the four PTAH/PTA moieties, which show distinct and unusual geometrical arrangements if viewed along the P–Cu bonds. The $^{31}P\{^{1}H\}$- and $^{63}Cu$ NMR spectra of **2** in $D_2O$ solution show spin coupling between the $^{31}P$ and $^{63}Cu$ nuclei at room temperature. These compounds represent the first examples of Cu complexes bearing PTA or any derived ligand with a cagelike PTA core and expand the restricted family of aqua-soluble copper phosphane complexes.
(© Wiley-VCH Verlag GmbH & Co. KGaA, 69451 Weinheim, Germany, 2007)

## Introduction

The coordination chemistry of the aqua-soluble phosphane 1,3,5-triaza-7-phosphaadamantane (PTA) and derived species has received increased attention in recent years.[1] This is mainly due to the good solubility of transition-metal PTA complexes in water, thus making possible their efficient application in aqueous phase catalysis,[2] as water-soluble antitumor agents[1,3] and as photoluminescent materials.[1,4] In particular, one of us has reported that Rh and Ru complexes with PTA or its *N*-alkylated derivatives are catalysts for the hydrogenation, hydroformylation and isomerization of alkenes.[5]

However, although a large variety of copper phosphane complexes has been reported,[6] known water-soluble examples remain rather scarce and include compounds with, for example, tris(*m*-sulfonatophenyl)phosphane,[7a] tris(hydroxymethyl)phosphane,[7b] tris(*m*-tolyl)phosphane[7c] and tris(*p*-fluorophenyl)phosphane[7c] [the aqua solubility of the last two examples should arise from the other ligands such as dihydrobis(3-nitro-1,2,4-triazol-1-yl)borate]. Moreover, the Cu–PTA chemistry is virtually unknown;[1] only one study reported the formation of $[Cu_nS_m(PTA)]^-$ ($n$ = 1, 2, 4 and 5; $m$ = 2–4) species in the gas phase under the Fourier transform ion cyclotron resonance (FTICR) mass spectrometry conditions,[8] whereas there are no examples of *isolated* copper complexes with PTA or its derivatives. In contrast, more than 100 complexes with a cagelike PTA core and with other transition metals have already been synthesized[1,3–5,9] and structurally characterized.[6]

By extending PTA coordination chemistry to our recent studies on the synthesis of water-soluble Cu complexes with other ligands (which catalyze the mild functionalization of alkanes),[10] we now report the easy synthesis of the new aqua-soluble $Cu^{I}$–PTA compounds $[Cu(PTAH)_4](NO_3)_5$ (**1**) and $[Cu(PTA)_4](NO_3)$ (**2**). They constitute, as far as we are aware of, the first isolated examples of copper complexes bearing PTA or any derived ligand with a cagelike PTA core. They were characterized by IR, $^{1}H$-, $^{13}C\{^{1}H\}$-, $^{31}P\{^{1}H\}$- and $^{63}Cu$ NMR spectroscopy, FAB-MS(+), elemental and single-crystal X-ray diffraction structural analyses.

## Results and Discussion

### Synthesis and Spectroscopic Characterization

Addition of an excess of PTA to an acidic aqueous solution of $Cu^{II}$ nitrate provided the formation, at room temperature and in air, of the cationic $Cu^{I}$ complex $[Cu(PTAH)_4](NO_3)_5$ (**1**) by a redox process resulting in the reduction of $Cu^{II}$ to $Cu^{I}$ and partial oxidation of PTA to the corresponding phosphane oxide (Scheme 1, **a**), which was identified by $^{31}P\{^{1}H\}$ NMR spectroscopic data of the reaction mixture and by the unit-cell parameters of isolated single crystals measured by X-ray diffraction which are in

[a] Centro de Química Estrutural, Complexo I, Instituto Superior Técnico,
Av. Rovisco Pais, 1049-001 Lisbon, Portugal
Fax: +351-21-846-4455
E-mail: pombeiro@ist.utl.pt

 © 2007 Wiley-VCH Verlag GmbH & Co. KGaA, Weinheim 

agreement with those already reported.[11] This correlates with the previously described[12] ability of PTA to act as a reductant and to stabilize low-oxidation metal states, thus leading to the synthesis of, for example, $Pt^0$, $Pd^0$, $Ni^0$ and $Ru^{II}$ PTA complexes starting from the corresponding metal(II/III) chlorides.[5a,12] Compound **1** was further precipitated by addition of EtOH to the reaction mixture, and it was isolated as a white microcrystalline solid in 92% yield, based on $Cu^{II}$ nitrate. Further treatment of **1** with 4 equiv. sodium hydroxide in water at room temperature (Scheme 1, **b**) led to the formation of the unprotonated derivative $[Cu(PTA)_4](NO_3)$ (**2**), which was isolated, upon recrystallization from MeOH, in 57% yield as a white microcrystalline solid. Compound **2** was also obtained directly (83% yield) from $Cu^{II}$ nitrate upon reaction with an excess of PTA in refluxing EtOH (Scheme 1, **c**). Moreover, protonation of **2** led to **1**, thus showing the reversibility of their interconversion. Both compounds **1** and **2** are air-stable solids, which are soluble and stable in water ($S_{25\,°C} \approx 6$ and 64 mg mL$^{-1}$, respectively) and in DMSO solutions.

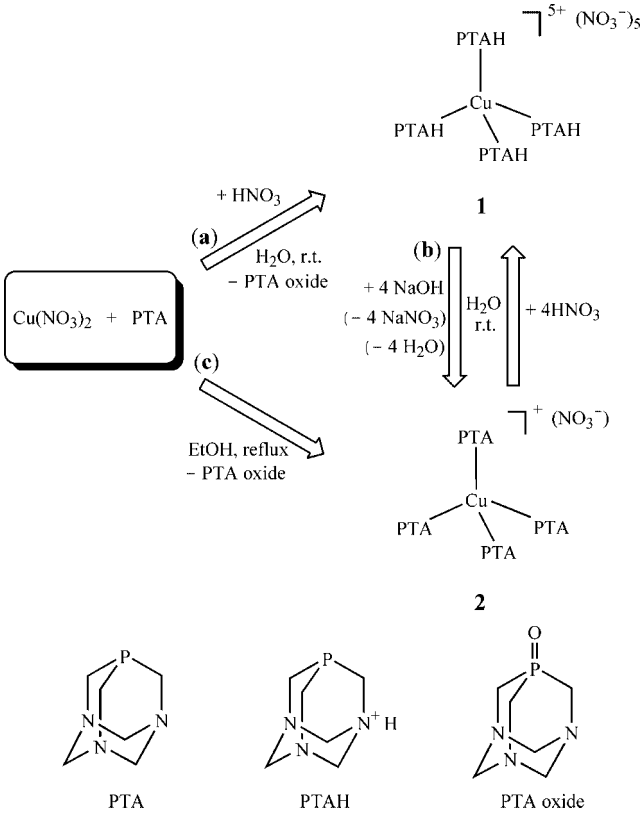


Scheme 1.

The IR spectra of **1** and **2** (KBr pellet) show a set of vibrations typical of coordinated PTAH/PTA, as well as broad and strong bands (1382 and 1363 cm$^{-1}$, respectively) due to the nitrate ions. The complex molecular ion with four unprotonated PTA ligands, $[Cu(PTA)_4]^+$, is clearly observed at $m/z$ = 691 with the expected isotopic pattern in the FAB-MS(+) spectra of both compounds **1** and **2**, whereas the heaviest detected fragment ($m/z$ = 816) $[Cu(PTA)_4 + 2Cu – 3H]^+$ results from coupling of the molecular ion with two copper ions. Other typical peaks correspond to the stepwise fragmentations by loss of one to four PTA ligands, followed in **1** by the recombination of obtained species with $Cu^+$.

The $^1$H NMR spectra of both compounds, recorded in $D_2O$ solution, show two types of methylene protons. Hence, the PC$H_2$N protons occur as a doublet at $\delta$ = 4.2 ppm ($^2J_{P–H}$ = 4.8 Hz) and as a broad singlet at $\delta$ = 4.1 ppm in **1** and **2**, respectively, while the AB spin system due to the NC$H_{ax}$N and NC$H_{eq}$N protons[13] is centred at $\delta \approx 4.8$ ppm ($^2J_{AB}$ = 7.0 Hz) (for **1**) and 4.6 ppm ($^2J_{AB}$ = 13.5 Hz) (for **2**). Their $^{13}$C{$^1$H} NMR spectra are similar, presenting two broad singlets at $\delta$ ca. 74 and 53 ppm, assigned to the N$CH_2$N and P$CH_2$N carbon nuclei, respectively. The $^{31}$P{$^1$H} NMR spectrum of **1**, in $D_2O$, exhibits a broad singlet at $\delta$ = –82.5 ppm (Figure 1, **a**) which, on addition of an excess of free PTA or PTAH, shifts upfield (see parts **a** and **c**, respectively, in Figure 1) without observing a distinct resonance of the free phosphane ligand, which is consistent with fast exchange of coordinated and free phosphane ligands.

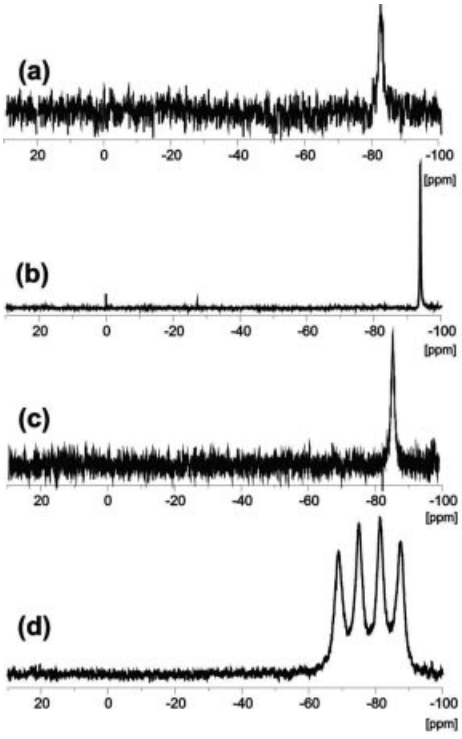


Figure 1. $^{31}$P{$^1$H} NMR spectra of **1** in $D_2O$ solution: (a) standard spectrum; (b, c) with an excess of added PTA (b) or PTAH (c); (d) at pH = 8.0 (after addition of NaOH, with formation of **2**).

The $^{31}$P{$^1$H} NMR spectrum of **2** displays a 1:1:1:1 quartet at $\delta$ = –78.2 ppm ($^1J_{P–Cu}$ = 761 Hz) (Figure 1, **d**) which, in contrast to **1**, does not show appreciable change upon addition of an excess of free PTA; the spectrum is maintained with the appearance of the singlet of free PTA at $\delta$ = –95.0 ppm. This indicates that the mentioned fast phosphane exchange is not detected in the case of **2**, and

 © 2007 Wiley-VCH Verlag GmbH & Co. KGaA, Weinheim 

the $^{31}P$–$^{63}Cu$ spin coupling ($^{63}Cu$ and $^{65}Cu$, $I = 3/2$) is observed. In agreement, the $^{63}Cu$ NMR spectrum of **2** (Figure 2) shows a 1:4:6:4:1 quintet, with the same $^{1}J_{P–Cu}$ at $\delta$ = 181.5 ppm (relative to $[Cu(MeCN)_4][PF_6]$), although no $^{63}Cu$ resonance was detected in the case of **1**, even upon long acquisition time.

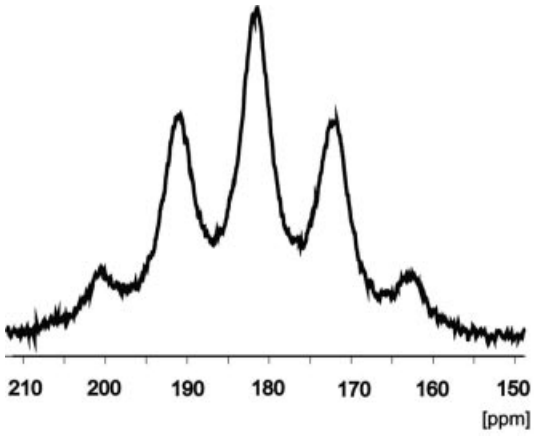


Figure 2. $^{63}Cu$ NMR spectrum of **2** in $D_2O$ (or **1** after addition of NaOH).

Hence in our systems, protonation of PTA appears to have a marked effect on the rate of that dynamic process in solution and/or on the quadrupolar relaxation of the Cu nuclei in the $^{63}Cu$ NMR spectroscopy.[14] The significance of distortion from the regular tetrahedral geometry in the solid state[14–16] cannot be ascribed in our case, namely in view of the fluxional behaviour in solution. The effect of the phosphane Tolman cone angle also cannot be recognized in our study since PTA and PTAH are expected to have similar values of the cone angle (103° for PTA[1,17] is a relatively small value in comparison with those of common organophosphane ligands). This differs from other systems for which the type of $^{31}P\{^{1}H\}$ NMR spectrum was associated with the Tolman angle. For example, as for complex **1** (in spite of its small PTAH cone angle), a broad singlet was observed in the $^{31}P\{^{1}H\}$ NMR spectrum (without reporting any $^{63}Cu$ NMR signal) of $[Cu(PPh_3)_4][BF_4]$[15] bearing a phosphane ligand with a cone angle higher than 136°. However, for $[CuL_4][PF_6]$ (L = $PMe_3$, $PMe_2Ph$, $PPh_2H$, $PPhH_2$)[15] and $[Cu\{P(CH_2OH)_3\}_3\{P(CH_2OH)_2(CH_2O^-)\}]$,[7b] which also have a distorted geometry of the metal centres but bear phosphane ligands with the Tolman cone angle lower than 136° (as in complex **1**), the characteristic quartet due to the coupling with copper (as in complex **2** but not in **1**) was detected. The chemical shift ($\delta$ = 181.5 ppm) observed in the $^{63}Cu$ NMR spectrum of **2** is comparable to those reported for other tetrahedral $Cu^{I}$ complexes, for example, $[Cu(PMePh_2)_4][BF_4]$ ($\delta$ = 192 ppm),[15] while $^{1}J_{P–Cu}$ (761 Hz) is also close to the values of 796 and 785 Hz found for $[Cu(PMe_3)_4][PF_6]$ and $[Cu(PMe_2Ph)_4][PF_6]$, respectively, although at different chemical shifts (i.e., $\delta$ = 287 and 265 ppm, respectively).[15]

Interestingly, upon changing the pH of the aqueous solution of **1** to a slightly basic value (i.e., pH ≈ 8 after addition of NaOH), one observes in the $^{31}P\{^{1}H\}$ NMR spectrum the conversion of the singlet (Figure 1, **a**) to the 1:1:1:1 quartet of **2** (Figure 1, **d**), in agreement with the deprotonation of **1** to afford **2** (Scheme 1, **b**). A corresponding feature is revealed by the $^{63}Cu$ NMR spectrum (Figure 2) which shows the appearance of the 1:4:6:4:1 quintet of **2**. The conversion of **1** into **2** can also be monitored by $^{1}H$ NMR spectroscopy which displays an upfield shift of the $NCH_2N$ protons.

Elemental analyses agree with the proposed formulations of **1** and **2** which are authenticated by single-crystal X-ray diffraction studies, as discussed now.

## X-ray Crystal Structures

The asymmetric unit of **1** consists of the $[Cu(PTAH)_4]^{5+}$ cation bearing a +5 charge (due to the protonated character of all the phosphane ligands), which is balanced by five nitrate ions. A thermal ellipsoid plot of the cationic part of **1** is depicted in part (**a**) of Figure 3. The nearly tetrahedral coordination environment about the copper centre is filled by four phosphorus atoms with the corresponding P–Cu–P

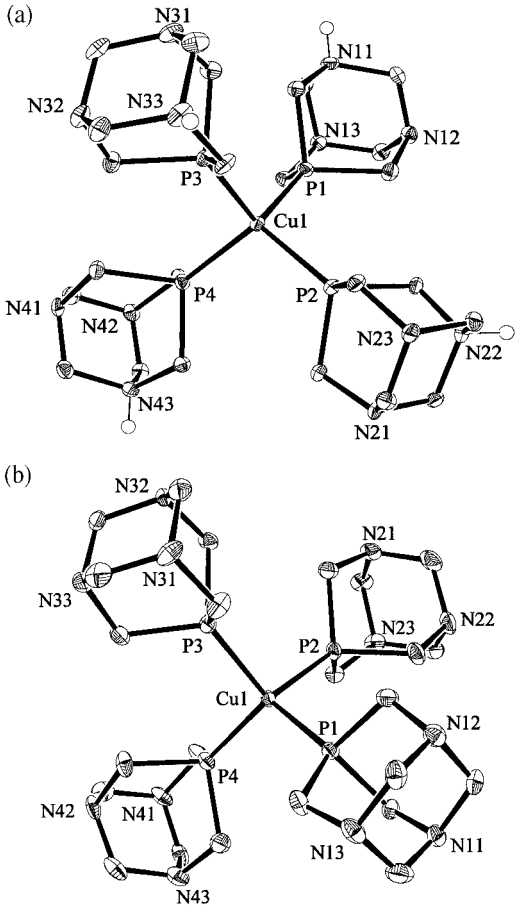


Figure 3. Thermal ellipsoid plots of the cationic parts of **1** (**a**) and **2** (**b**) with a partial labelling scheme. The methylene hydrogen atoms are omitted for clarity. Displacement ellipsoids are drawn at the 50% probability level. Hydrogen atoms are represented by circles of arbitrary radii.

 © 2007 Wiley-VCH Verlag GmbH & Co. KGaA, Weinheim 

angles ranging from 108.14(3) to 111.21(3)° [the average value of 109.46(3)° is very close to that of a regular tetrahedron], with an average P···P separation of ca. 3.752 Å. The Cu–P bonds display almost equal, within 3σ, distances [i.e., 2.298(1) Å, average value] (Table 1) which correlate with those reported for other $Cu^{I}$ complexes bearing four monodentate phosphane ligands, for example, $[Cu\{P(CH_2OH)_3\}_3\{P(CH_2OH)_2(CH_2O^-)\}]$,[7b] $[Cu(PMe_3)_4]X$ {X = Cl,[18] Br,[18] I,[18] $[CuCl_2]^-$[19] or $[CuMe_2]^-$[20]} and $[Cu\{PH_2(mes)\}_4][PF_6]$ (mes = mesityl).[21] In **1**, all the 1,3,5-triaza-7-phosphaadamantane ligands possess a similar geometry and are protonated at one of the nitrogen atoms (i.e., N11, N22, N33 and N43) of each PTAH moiety (Figure 3, **a**), thus resulting in a slight elongation of the (H)N–C bonds [1.519(4) Å, average value] relative to other N–C distances [1.463(4) Å, average value] concerning the unprotonated nitrogen atoms (Table 1). Similar features of the (H)N–C bond elongation were reported for other transition-metal complexes with PTAH ligands.[22] Each NH proton of **1** is further involved in two hydrogen-bonding contacts with nitrate ions, with N···O distances ranging from 2.795(3) to 3.103(3) Å [2.940(3) Å, average value] and N–H···O angles from 122(2) to 177(2)° [142(3)°, average value] (Figure 4). In general, most of the bonding parameters do not significantly differ from the expected values found for related tetrahedral-type transition-metal PTAH/PTA complexes, for example, $[M(PTAH)]Cl_4$ (M = Pt, Pd, Ni),[22a] $[Pt(PTA)_2(PTAH)_2][BF_4]$,[12] $[Pt(PTA)_3(PTAH)]Cl$,[12] $[Au(PTA)(PTAH)_3][PF_6]_4$[22b] and $[Au(PTA)_4]X$ (X = Cl,[22b,23] $PF_6$[22b]).

Table 1. Selected bond lengths [Å] and angles [°] for compounds **1** and **2**.

| | **1** | **2** |
|---|---|---|
| Cu1–P1 | 2.2971(7) | 2.2870(15) |
| Cu1–P2 | 2.2917(8) | 2.2806(16) |
| Cu1–P3 | 2.2958(9) | 2.2863(15) |
| Cu1–P4 | 2.3083(8) | 2.2832(15) |
| P–C | 1.856(3)[a] | 1.851(6)[a] |
| (H)N–C | 1.519(4)[a] | – |
| N–C | 1.463(4)[b] | 1.470(7)[c] |
| P1–Cu1–P2 | 111.21(3) | 105.90(6) |
| P1–Cu1–P3 | 109.46(3) | 107.38(5) |
| P1–Cu1–P4 | 108.63(3) | 113.57(6) |
| P2–Cu1–P3 | 110.24(3) | 109.57(6) |
| P2–Cu1–P4 | 109.08(3) | 111.10(6) |
| P3–Cu1–P4 | 108.14(3) | 109.18(6) |

[a] Average distance calculated from 12 bonds. [b] Average distance calculated from 24 bonds. [c] Average distance calculated from 36 bonds.

The crystal structure of **2** bears the $[Cu(PTA)_4]^+$ cation (Figure 3, **b**) with all the phosphane ligands being unprotonated and one nitrate anion balancing the overall charge. The tetrahedral environment around the copper atom is slightly more distorted than that of **1**, exhibiting higher deviations from the idealized geometry, with the minimal and maximal P–Cu–P angles of 105.90(6) and 113.57(6)°, respectively (Table 1). Although the structure of **2**, with mostly similar bonding parameters, resembles that of **1** and

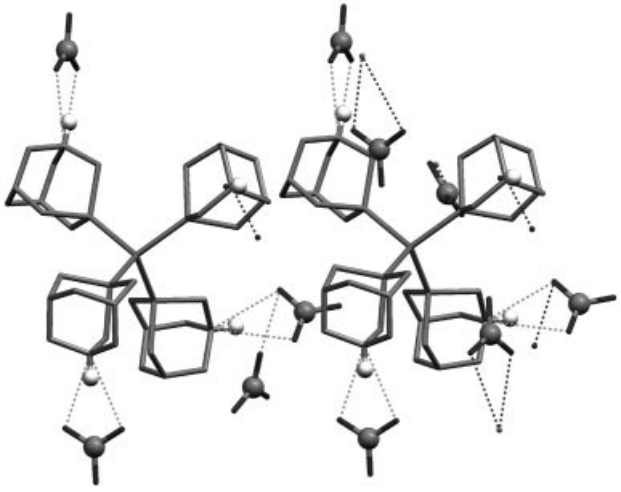

Figure 4. Fragment of the crystal packing diagram of **1** showing the N–H···O hydrogen bonds (dashed lines). NH hydrogen atoms and nitrate nitrogen atoms are shown as white and grey balls, respectively. The methylene hydrogen atoms are omitted for clarity.

therefore is not discussed in detail, it is noteworthy to mention the different geometric arrangements of the phosphane ligands in these compounds (Figure 3).

Hence, in **1** all the PTAH ligands show nearly equivalent arrangements if viewed along the P–Cu bond (Figure 5, **a**), where the three nitrogen atoms of each PTAH ligand are oriented similarly in relation to the other phosphane ligands forming coplanar P∩N,P sets. In contrast, in compound **2** the PTA ligands are not geometrically equivalent and are arranged in different ways (see parts **b** and **c** in Figure 5) from that in **1** (Figure 5, **a**). Thus, two of the phosphane ligands in **2**, that is, P1 and P4, if viewed down the P–Cu bond are ca. 45° (Figure 5, **b**) and 15° (Figure 5, **c**) rotated, respectively, relative to the orientation of PTAH ligands in **1** (Figure 5, **a**), whereas the other two phosphane ligands (i.e., P2 and P3) are less rotated (ca. 5–8°) approaching the arrangement depicted in part **a** of Figure 5. The analysis of previously reported X-ray crystal structures[6] of a dozen compounds with the $[M(L)_4]$ (L = PTA, PTAH or *N*-methyl-1,3,5-triaza-7-phosphaadamantane) unit reveals that the most common phosphane arrangement is that depicted in part **b** of Figure 5 (i.e., observed in 11 compounds, 3 of them also having 1 phosphane moiety arranged as in

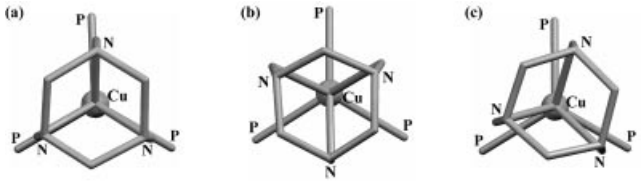


Figure 5. Ball-and-stick partial representation of the X-ray crystal structures of **1** (a) and **2** (b, c) down the P3–Cu1 (a), P1–Cu1 (b) and P4–Cu1 (c) bonds, showing the perspective arrangement of one PTAH/PTA ligand (to which belong the three represented nitrogen atoms) relative to the copper centre and the other phosphane ligands (only the Cu–P bonds are shown). Hydrogen atoms are omitted for clarity.

 © 2007 Wiley-VCH Verlag GmbH & Co. KGaA, Weinheim 

Figure 5, **c**). Only one compound, $[Au(PTA)(PTAH)_3][PF_6]_4$,[22b] possesses a phosphane arrangement similar to **1** (Figure 5, **a**), whereas there are no examples (apart from **2**) of compounds exhibiting the combination of three types of geometries close to those depicted in parts **a**–**c** of Figure 5.

## Conclusions

We have found a simple route to new $Cu^I$ complexes with 1,3,5-triaza-7-phosphaadamantane ligands based on a redox reaction of a $Cu^{II}$ salt with free PTA in aqueous solution at room temperature, thus showing that the reducing ability of PTA[12] can be also extended to copper(II) centres.

Protonation of ligated PTA promotes the ligand exchange and has a drastic effect on both the $^{31}P\{^1H\}$- and $^{63}Cu$ NMR spectra, with loss of the detection of $^1J_{P-Cu}$ coupling. The recognition of this NMR dependence on the solution pH is of significance towards the NMR characterization of further $Cu^I$–PTA complexes. The lack of a NMR resonance in spectra of samples obtained in acidic medium could have been a difficulty encountered by others, preventing the characterization and report of Cu complexes with such phosphane ligands, prior to the current study.

The enhanced lability of the PTA ligand upon protonation can be of synthetic value and deserves to be further explored for the preparation of derived complexes.

The obtained $Cu^I$ compounds **1** and **2** show, in the solid state, unusual relative orientations of the PTA (or PTAH) ligands.

The study also shows that it is possible to conveniently prepare Cu complexes bearing PTA (or its protonated form) ligands, allowing the expansion of the still limited group of water-soluble copper phosphane complexes, which encourages the search for their possible applications in aqueous media.

The extension of the work towards the synthesis of Cu compounds with *N*-alkylated PTA derivatives as well as the catalytic activity tests of Cu–PTA species in aqueous medium are currently in progress and will be reported elsewhere.

## Experimental Section

**General Materials and Experimental Procedures:** All chemicals were obtained from commercial sources and used as received. 1,3,5-Triaza-7-phosphaadamantane (PTA) was prepared by a published method.[24] C, H and N elemental analyses were carried out by the Microanalytical Service of the Instituto Superior Técnico. Melting points were determined with a Kofler Table. The FAB-MS(+) spectra were obtained with a Trio 2000 instrument by bombarding 3-nitrobenzyl alcohol (*m*-NBA) matrices of the samples with 8 keV (ca. $1.18 \times 10^{15}$ J) Xe atoms. Mass calibration for data system acquisition was achieved using CsI. Infrared spectra (4000–400 $cm^{-1}$) were recorded with a BIO-RAD FTS 3000MX instrument in KBr pellets. $^1H$-, $^{13}C\{^1H\}$-, $^{31}P\{^1H\}$- and $^{63}Cu$ NMR spectra were measured with a Varian UNITY 300 spectrometer at ambient temp. The $^{31}P$ and $^{63}Cu$ chemical shifts are relative to an external 85% $H_3PO_4$ aqueous solution and an $[D_3]MeCN$ solution of $[Cu(MeCN)_4][PF_6]$,[14] respectively.

**$[Cu(PTAH)_4](NO_3)_5$ (1):** To an aqueous solution (10.0 mL) of $Cu(NO_3)_2 \cdot 2.5H_2O$ (232 mg, 1.00 mmol) were added concentrated $HNO_3$ (65% in $H_2O$, 277 μL, 4.00 mmol) and an excess of an aqueous solution (5.00 mL) of PTA (786 mg, 5.00 mmol) with continuous stirring at room temp. The resulting white suspension was stirred for 1 h, followed by the addition of EtOH (15.0 mL) to provide further precipitation of the product. This was filtered off, washed with EtOH ($3 \times 10$ mL) and dried in vacuo to afford complex **1** as a white microcrystalline solid. Yield: 92% (926 mg), based on copper nitrate. Complex **1** is slightly soluble in $H_2O$ ($S_{25\,°C} \approx 6\ mg\,mL^{-1}$) and $Me_2CO$, is soluble in DMSO and is insoluble in EtOH, MeOH, $C_6H_6$, $CHCl_3$, $CH_2Cl_2$ and MeCN. M.p. ca. 215 °C. $C_{24}H_{52}CuN_{17}O_{15}P_4$ (1006.2): calcd. C 28.65, H 5.21, N 23.66; found C 28.64, H 5.59, N 23.35. FAB-MS(+) (*m*-NBA): *m*/*z* = 816 $[Cu(PTA)_4 + 2Cu - 3H]^+$, 691 $[Cu(PTA)_4]^+$, 659 $[Cu(PTA)_3 + 2Cu - 3H]^+$, 597 $[Cu(PTA)_3 + Cu]^+$, 534 $[Cu(PTA)_3]^+$, 502 $[Cu(PTA)_2 + 2Cu - 3H]^+$, 440 $[Cu(PTA)_2 + Cu]^+$, 377 $[Cu(PTA)_2]^+$, 220 $[Cu(PTA)]^+$, 63 $[Cu]^+$. IR (KBr): $\tilde{\nu}$ = 2984 (br. s) ν(NH + CH), 1382 (br. vs) $\nu(NO_3)$, 1120 (m), 1131 (s), 988 (s), 955 (s), 854 (m), 813 (m), 774 (s), 708 (w), 648 (w), 611 (w), 560 (s), 482 (w) and 449 (m) (PTA bands) $cm^{-1}$. $^1H$ NMR (300 MHz, $D_2O$, $Me_4Si$): $\delta$ = 4.74 $H^A$ and 4.87 $H^B$ ($^2J_{AB}$ = 7.0 Hz, 24 H, $NCH^AH^BN^+$ and $NCH^AH^BN$), 4.18 (br. d, $^2J_{P-H}$ = 4.8 Hz, 24 H, $PCH_2N$) ppm. $^1H$ NMR (300 MHz, $[D_6]$dmso, $Me_4Si$): $\delta$ = 4.79 (br. s, 24 H, $NCH_2N$), 4.11 (br. s, 24 H, $PCH_2N$) ppm. $^{13}C\{^1H\}$ NMR (75.4 MHz, $D_2O$, $Me_4Si$): $\delta$ = 73.8 (br. s, $NCH_2N$), 53.1 (br. s, $PCH_2N$) ppm. $^{31}P\{^1H\}$ NMR (121.4 MHz, $D_2O$, 85% $H_3PO_4$): $\delta$ = –82.5 (br. s) ppm. $^{31}P\{^1H\}$ NMR (121.4 MHz, $[D_6]$dmso, 85% $H_3PO_4$): $\delta$ = –82.6 (br. s) ppm. X-ray-quality single crystals were grown by slow evaporation, in air at room temp., of the reaction filtrate or $H_2O$ solution of **1**.

**$[Cu(PTA)_4](NO_3)\cdot 2H_2O$ ($2\cdot 2H_2O$). Method 1:** An aqueous cloudy solution (20 mL) of **1** (211 mg, 0.210 mmol) was neutralized by an aqueous 0.168 M NaOH solution (5.0 mL, 0.840 mmol) for 10 min, followed by evaporation of the obtained clear colourless solution in vacuo. The resulting white solid was treated with hot MeOH (ca. 40 mL) to produce a cloudy solution, which was filtered off. The obtained colourless filtrate was left in a fridge at ca. 5 °C for 2 d to afford compound $\mathbf{2}\cdot 2H_2O$ as a white crystalline solid, which was isolated by filtration. Yield: 57% (95 mg), based on **1**. Complex **2** is soluble in $H_2O$ ($S_{25\,°C} \approx 64\ mg\,mL^{-1}$), DMSO, MeOH and EtOH, is sparingly soluble in THF and $Me_2CO$ and is insoluble in nonpolar solvents. M.p. ca. 245 °C. $C_{24}H_{52}CuN_{13}O_5P_4$ (790.20): calcd. C 36.48, H 6.63, N 23.04; found C 36.55, H 6.80, N 22.42. FAB-MS(+) (*m*-NBA): *m*/*z* = 816 $[Cu(PTA)_4 + 2Cu - 3H]^+$, 691 $[Cu(PTA)_4]^+$, 534 $[Cu(PTA)_3]^+$, 377 $[Cu(PTA)_2]^+$, 220 $[Cu(PTA)]^+$. IR (KBr): $\tilde{\nu}$ = 3400 (br. s) and 3233 (br. s) $\nu(H_2O)$, 2902 (br. s) ν(CH), 1363 (br. s) $\nu(NO_3)$, 1243 (m), 1105 (m), 1014 (s), 974 (s), 807 (m) (PTA bands) $cm^{-1}$. $^1H$ NMR (300 MHz, $D_2O$, $Me_4Si$): $\delta$ = 4.61 $H^A$ and 4.58 $H^B$ ($^2J_{AB}$ = 13.5 Hz, 24 H, $NCH^AH^BN^+$ and $NCH^AH^BN$), 4.14 (br. s, 24 H, $PCH_2N$) ppm. $^{13}C\{^1H\}$ NMR (75.4 MHz, $D_2O$, $Me_4Si$): $\delta$ = 73.8 (br. s, $NCH_2N$), 53.1 (br. s, $PCH_2N$) ppm. $^{31}P\{^1H\}$ NMR (121.4 MHz, $D_2O$, 85% $H_3PO_4$): $\delta$ = –78.2 (br. q, $^1J_{^{63}Cu-^{31}P}$ = 761 Hz) ppm. $^{63}Cu$ NMR (79.5 MHz, $D_2O$, $[Cu(MeCN)_4][PF_6]$): $\delta$ = 181.5 (br. quint, $^1J_{^{63}Cu-^{31}P}$ = 761 Hz) ppm. X-ray-quality crystals of $\mathbf{2}\cdot 2MeOH$ were grown by slow evaporation of the filtrate (left after isolation of **2**) in conical tubes in air for several days.

**Method 2:** To the blue ethanol solution (30.0 mL) of $Cu(NO_3)_2 \cdot 2.5H_2O$ (79 mg, 0.34 mmol) was added an excess of solid PTA (321 mg, 2.04 mmol). The obtained mixture was refluxed for 1 h under dinitrogen, leading to a pale-green suspension. The solid was filtered off, washed with cold EtOH ($2 \times 30$ mL) and $CHCl_3$

 © 2007 Wiley-VCH Verlag GmbH & Co. KGaA, Weinheim 

(2 × 15 mL) (to remove the excess phosphane and the formed phosphane oxide) and dried in vacuo to afford complex **2** as a white powder. Yield: 83% (209 mg), based on copper nitrate.

**Refinement Details for the X-ray Crystal Structure Analysis of 1 and 2:** Intensity data were collected using a Bruker AXS-KAPPA APEX II diffractometer with graphite-monochromated Mo-$K_\alpha$ radiation. Data were collected at 150 K using omega scans of 0.5° per frame, and a full sphere of data was obtained. Cell parameters were retrieved using Bruker SMART software and refined using Bruker SAINT on all the observed reflections. Absorption corrections were applied using SADABS. Structures were solved by direct methods by using the SHELXS-97 package[25] and refined with SHELXL-97[26] with the WinGX graphical user interface.[27] All hydrogen atoms were inserted in calculated positions. Least square refinement with anisotropic thermal motion parameters for all the non-hydrogen atoms (except for C2 in a methanol molecule in **2** which was refined isotropically) and isotropic for the remaining atoms gave $R_1$ = 0.0357 (for **1**) and 0.0569 (for **2**). In **2**, the maximum and minimum peaks in the final difference electron density map are 1.704 and –0.933 e Å$^{-3}$, respectively, close to one of the methanol molecules of crystallization (C2–O2) possibly indicating a disorder which, however, could not be modulated. The selected bonding parameters for **1** and **2** are given in Table 1, and the crystallographic data is summarized in Table 2.

Table 2. Crystal data and structure refinement details for **1** and **2**.

| | **1** | **2**·2MeOH |
|---|---|---|
| Empirical formula | $C_{24}H_{52}CuN_{17}O_{15}P_4$ | $C_{26}H_{56}CuN_{13}O_5P_4$ |
| Formula weight | 1006.25 | 818.26 |
| Temperature [K] | 150(2) | 150(2) |
| $\lambda$ [Å] | 0.71073 | 0.71073 |
| Crystal system | monoclinic | monoclinic |
| Space group | *Cc* | $P2_1/c$ |
| *a* [Å] | 14.1077(14) | 12.3982(19) |
| *b* [Å] | 13.9568(13) | 12.4093(19) |
| *c* [Å] | 20.206(2) | 23.181(3) |
| $\alpha$ [°] | 90 | 90 |
| $\beta$ [°] | 92.508(4) | 95.474(4) |
| $\gamma$ [°] | 90 | 90 |
| *V* [Å$^3$] | 3974.6(7) | 3550.1(9) |
| *Z* | 4 | 4 |
| $\rho_{calcd.}$ [mg m$^{-3}$] | 1.682 | 1.531 |
| $\mu$(Mo-$K_\alpha$) [mm$^{-1}$] | 0.800 | 0.853 |
| No. of collected reflections | 15992 | 23796 |
| No. of unique reflections | 8817 | 5899 |
| $R_{int}$ | 0.0369 | 0.1193 |
| Final $R_1$,[a] $wR_2$[b] [$I \geq 2\sigma$] | 0.0357, 0.0706 | 0.0569, 0.1241 |
| GOF on $F^2$ | 1.001 | 0.973 |

[a] $R_1 = \Sigma||F_o| - |F_c||/\Sigma|F_o|$. [b] $wR_2 = \{\Sigma[w(F_o^2 - F_c^2)^2]/\Sigma[w(F_o^2)^2]\}^{1/2}$.

CCDC-629755 (for **1**) and -629756 (for **2**) contain the supplementary crystallographic data for this paper. These data can be obtained free of charge from The Cambridge Crystallographic Data Centre via www.ccdc.cam.ac.uk/data_request/cif.

## Acknowledgments

This work has been partially supported by the Fundação para a Ciência e a Tecnologia (FCT), Portugal, grants BPD/28729/06 and BPD/20869/04, and FCT/POCI 2010 programme (the latter founded by FEDER) as well as by the Human Resources and Mobility Marie Curie Research Training Network (AQUACHEM project, CMTN-CT-2003-503864).

[1] For recent review, see: A. D. Phillips, L. Gonsalvi, A. Romerosa, F. Vizza, M. Peruzzini, *Coord. Chem. Rev.* **2004**, *248*, 955, and references therein.

[2] a) F. Joó, *Aqueous Organometallic Catalysis*, Kluwer Academic Publishers, Dordrecht, **2001**; b) B. Cornils, W. A. Herrmann (Eds.), *Aqueous Phase Organometallic Catalysis*, Wiley-VCH, Weinheim, **1998**; c) I. T. Horvath, F. Joó (Eds.), *Aqueous Organometallic Chemistry and Catalysis*, NATO ASI Series 3/5, Kluwer Academic Publishers, Dordrecht, **1995**.

[3] a) C. Scolaro, T. J. Geldbach, S. Rochat, A. Dorcier, C. Gossens, A. Bergamo, M. Cocchietto, I. Tavernelli, G. Sava, U. Rothlisberger, P. J. Dyson, *Organometallics* **2006**, *25*, 756; b) C. Scolaro, A. Bergamo, L. Brescacin, R. Delfino, M. Cocchietto, G. Laurenczy, T. J. Geldbach, G. Sava, P. J. Dyson, *J. Med. Chem.* **2005**, *48*, 4161; c) B. Serli, E. Zangrando, T. Gianferrara, C. Scolaro, P. J. Dyson, A. Bergamo, E. Alessio, *Eur. J. Inorg. Chem.* **2005**, 3423.

[4] a) F. Mohr, S. Sanz, E. R. T. Tiekink, M. Laguna, *Organometallics* **2006**, *25*, 3084; b) F. Mohr, E. Cerrada, M. Laguna, *Organometallics* **2006**, *25*, 644.

[5] a) P. Smoleński, F. P. Pruchnik, Z. Ciunik, T. Lis, *Inorg. Chem.* **2003**, *42*, 3318; b) F. P. Pruchnik, P. Smoleński, *Appl. Organomet. Chem.* **1999**, *13*, 829; c) F. P. Pruchnik, P. Smoleński, K. Wajda-Hermanowicz, *J. Organomet. Chem.* **1998**, *570*, 63; d) F. P. Pruchnik, P. Smoleński, E. Gałdecka, Z. Gałdecki, *New J. Chem.* **1998**, *22*, 1395; e) F. P. Pruchnik, P. Smoleński, E. Gałdecka, Z. Gałdecki, *Inorg. Chim. Acta* **1999**, *293*, 110; f) F. P. Pruchnik, P. Smoleński, I. Raksa, *Pol. J. Chem.* **1995**, *69*, 5.

[6] For example, see the Cambridge Structural Database (CSD); F. H. Allen, *Acta Crystallogr., Sect. B* **2002**, *58*, 380.

[7] a) F. Tisato, F. Refoso, G. Bandoli, G. Pilloni, B. Corain, *Inorg. Chem.* **2001**, *40*, 1394; b) D. S. Bharathi, M. A. Sridhar, J. S. Prasad, A. G. Samuelson, *Inorg. Chem. Commun.* **2001**, *4*, 490; c) C. Marzano, M. Pellei, S. Alidori, A. Brossa, G. G. Lobbia, F. Tisato, C. Santini, *J. Inorg. Biochem.* **2006**, *100*, 299.

[8] K. Fisher, I. Dance, G. Willett, *Polyhedron* **1997**, *16*, 2731.

[9] For recent examples, see: a) A. D. Phillips, S. Bolano, S. S. Bosquain, J. C. Daran, R. Malacea, M. Peruzzini, R. Poli, L. Gonsalvi, *Organometallics* **2006**, *25*, 2189; b) F. Mohr, L. R. Falvello, M. Laguna, *Eur. J. Inorg. Chem.* **2006**, 3152; c) B. J. Frost, C. M. Bautista, R. C. Huang, J. Shearer, *Inorg. Chem.* **2006**, *45*, 3481; d) A. Romerosa, T. Campos-Malpartida, C. Lidrissi, M. Saoud, M. Serrano-Ruiz, M. Peruzzini, J. A. Garrido-Cardenas, F. Garcia-Maroto, *Inorg. Chem.* **2006**, *45*, 1289; e) B. J. Frost, S. B. Miller, K. O. Rove, D. M. Pearson, J. D. Korinek, J. L. Harkreader, C. A. Mebi, J. Shearer, *Inorg. Chim. Acta* **2006**, *359*, 283; f) C. Lidrissi, A. Romerosa, M. Saoud, M. Serrano-Ruiz, L. Gonsalvi, M. Peruzzini, *Angew. Chem. Int. Ed.* **2005**, *44*, 2568; g) R. Mejia-Rodriguez, D. Chong, J. H. Reibenspies, M. P. Soriaga, M. Y. Darensbourg, *J. Am. Chem. Soc.* **2004**, *126*, 12004.

[10] a) Y. Y. Karabach, A. M. Kirillov, M. F. C. Guedes da Silva, M. N. Kopylovich, A. J. L. Pombeiro, *Cryst. Growth Des.* **2006**, *6*, 2200; b) A. M. Kirillov, M. N. Kopylovich, M. V. Kirillova, E. Y. Karabach, M. Haukka, M. F. C. Guedes da Silva, A. J. L. Pombeiro, *Adv. Synth. Catal.* **2006**, *348*, 159; c) A. M. Kirillov, M. N. Kopylovich, M. V. Kirillova, M. Haukka, M. F. C. Guedes da Silva, A. J. L. Pombeiro, *Angew. Chem. Int. Ed.* **2005**, *44*, 4345.

[11] a) K. H. Jogun, J. J. Stezowski, E. Fluck, J. Weidlein, *Phosphorus Sulfur* **1978**, *4*, 199; b) R. E. Marsh, M. Kapon, S. Hu, F. H. Herbstein, *Acta Crystallogr., Sect. B* **2002**, *58*, 62.

[12] D. J. Darensbourg, J. B. Robertson, D. L. Larkins, J. H. Reibenspies, *Inorg. Chem.* **1999**, *38*, 2473.

[13] R. Schibli, K. V. Katti, W. A. Volkert, C. L. Barnes, *Inorg. Chem.* **1998**, *37*, 5306.

[14] I. Szymanska, *Pol. J. Chem.* **2006**, *80*, 1095.

 © 2007 Wiley-VCH Verlag GmbH & Co. KGaA, Weinheim 

[15] J. R. Black, W. Levason, M. D. Spicer, M. Webster, *J. Chem. Soc., Dalton Trans.* **1993**, 3129.
[16] C. A. Tolman, *Chem. Rev.* **1977**, *77*, 313.
[17] C. A. McAuliffe, in *Comprehensive Coordination Chemistry* (Eds.: G. Wilkinson, R. D. Gillard, J. A. McCleverty), Pergamon Press, New York, **1987**, vol. 2, chapter 14, pp. 1016–1017.
[18] G. A. Bowmaker, P. C. Healy, L. M. Engelhardt, J. D. Kildea, B. W. Skelton, A. H. White, *Aust. J. Chem.* **1990**, *43*, 1697.
[19] K.-M. Chi, J. Farkas, M. J. Hampden-Smith, T. T. Kodas, E. N. Duesler, *J. Chem. Soc., Dalton Trans.* **1992**, 3111.
[20] D. F. Dempsey, G. S. Girolami, *Organometallics* **1988**, *7*, 1208.
[21] I. V. Kourkine, S. V. Maslennikov, R. Ditchfield, D. S. Glueck, G. P. A. Yap, L. M. Liable-Sands, A. L. Rheingold, *Inorg. Chem.* **1996**, *35*, 6708.
[22] a) D. J. Darensbourg, T. J. Decuir, N. W. Stafford, J. B. Robertson, J. D. Draper, J. H. Reibenspies, A. Katho, F. Joó, *Inorg. Chem.* **1997**, *36*, 4218; b) J. M. Forward, Z. Assefa, R. J. Staples, J. P. Fackler Jr, *Inorg. Chem.* **1996**, *35*, 16.
[23] J. M. Forward, D. Bohmann, J. P. Fackler Jr, *Z. Kristallogr.* **1996**, *211*, 485.
[24] a) D. J. Daigle, A. B. Pepperman Jr, S. L. Vail, *J. Heterocycl. Chem.* **1974**, *11*, 407; b) D. J. Daigle, *Inorg. Synth.* **1998**, *32*, 40.
[25] G. M. Sheldrick, *Acta Crystallogr., Sect. A* **1990**, *46*, 467.
[26] G. M. Sheldrick, *SHELXL-97*, University of Göttingen, Germany, **1997**.
[27] L. J. Farrugia, *J. Appl. Crystallogr.* **1999**, *32*, 837.

Received: December 6, 2006
Published Online: March 16, 2007

 © 2007 Wiley-VCH Verlag GmbH & Co. KGaA, Weinheim 

DOI: 10.1002/ejic.200601251

# Coupling Reactions of an Allenylcarbene Complex with Alkynes and Styrene

**Ting Bin Wen,[a] Wai Yiu Hung,[a] Herman H.-Y. Sung,[a] Zhongyuan Zhou,[b] Ian D. Williams,[a] and Guochen Jia*[a]**

**Keywords:** Osmium / Fulvenes / Carbenes / Alkynes / Alkenes

The allenylcarbene complex $[OsCl_2\{=CPh(\eta^2\text{-}CH=C=CHPh)\}(PPh_3)_2]$ undergoes coupling reactions with $HC\equiv CSiMe_3$ and $PhC\equiv CC\equiv CPh$ to produce the fulvene complexes $[OsCl_2\{\eta^6\text{-}C_5H_2(Ph)(SiMe_3)(=CHPh)\}(PPh_3)]$ and $[OsCl_2\{\eta^6\text{-}C_5H(Ph)_2(C\equiv CPh)(=CHPh)\}(PPh_3)]$, respectively. A similar coupling reaction also occurs between $[OsCl_2\{=CPh(\eta^2\text{-}CH=C=CHPh)\}(PPh_3)_2]$ and styrene.

(© Wiley-VCH Verlag GmbH & Co. KGaA, 69451 Weinheim, Germany, 2007)

## Introduction

The [2+2+2] cyclotrimerization of alkynes to give six-membered aromatic rings is one of the most common reactions promoted by transition metal complexes and has been utilized in the synthesis of many useful natural products and novel organic materials.[1–3] In sharp contrast, examples of metal-mediated [2+2+1] cyclotrimerization of alkynes to give thermodynamically less stable isomeric fulvene derivatives are limited to only a few scattered reports.

The stoichiometric formation of fulvene metal complexes from formal [2+2+1] cyclotrimerizations of alkynes has been reported for the reaction of rhodium,[4] iridium,[5] and palladium[6] complexes with alkynes. Reported catalytic cyclotrimerization reactions of alkynes to give fulvenes include the titanium aryloxide/LiC≡C*t*Bu-catalyzed cyclotrimerization of *tert*-butylacetylene[7] and the $[(\eta^3\text{-}C_3H_5)PdCl]_2$/dppf-catalyzed cyclotrimerization of aliphatic alkynes.[8] Fulvene or fulvenyl intermediates may also be involved in the reactions of terminal alkynes with transition metal complexes to give complexes with ligands derived from the oligomerization of alkynes.[9–15]

There are several possible pathways that can lead to the formation of fulvenes from the [2+2+1] cyclotrimerization of alkynes; these are illustrated in Scheme 1. Fulvenes may be formed via a metallacyclopentadiene route, which involves oxidative coupling of two molecules of alkynes at the metal to give a metallacyclopentadiene intermediate, isomerization of another molecule of alkyne to a vinylidene ligand, and reductive cyclization to a fulvene product by coupling of the vinylidene ligand and the metallacyclopentadiene ring (Scheme 1, path a). Reactions of preformed iridiacyclopentadiene compounds with terminal alkynes have been shown to produce fulvene complexes.[5] In the reaction involving a base (Scheme 1, path b), for example the titanium aryloxide/LiC≡C*t*Bu-catalyzed cyclotrimerization of *tert*-butylacetylene, a metallacyclopentadiene-acetylide intermediate has been proposed. This intermediate undergoes reductive coupling followed by an insertion to give the fulvenyl complex, which reacts with alkyne to give fulvene and regenerate the metallacyclopentadiene-acetylide intermediate.[7] In principle, fulvenes could also be formed via metallacyclobutene intermediates (Scheme 1, path c). This reaction has been proposed for the formation of a fulvene complex from the reaction of $[RhCl(COD)]_2$ (COD = cycloocta-1,5-diene) with HC≡C*t*Bu in the presence of $AgPF_6$.[4] In this regard, it would be interesting to demonstrate that preformed metallacyclobutene complexes could react with alkynes to give fulvene complexes.

We have recently reported the synthesis of the $\eta^2$-allenylcarbene complex $[OsCl_2\{=CPh(\eta^2\text{-}CH=C=CHPh)\}(PPh_3)_2]$ (**1**),[16,17] which can be regarded as an isomer of an osmacyclobutene, from the reaction of PhC≡CH with the vinylidene complex $[OsCl_2(=C=CHPh)(PPh_3)_2]$ or $[OsCl_2(PPh_3)_3]$. In this work, we will describe its coupling reactions with alkynes. Its reaction with styrene has also been investigated for comparison.

## Results and Discussion

### Coupling Reaction of $[OsCl_2\{=CPh(\eta^2\text{-}CH=C=CHPh)\}(PPh_3)_2]$ (1) with Alkynes

Treatment of **1** with $HC\equiv CSiMe_3$ in dichloromethane produced the $\eta^6$-fulvene complex $[OsCl_2\{\eta^6\text{-}C_5H_2(Ph)(SiMe_3)(=CHPh)\}(PPh_3)]$ (**2**), which was isolated as a green solid in 81% yield (Scheme 2). The NMR spectroscopic

[a] Department of Chemistry, The Hong Kong University of Science and Technology,
Clear Water Bay, Kowloon, Hong Kong
Fax: +852-2358-1594
E-mail: chjiag@ust.hk
[b] Department of Applied Biology & Chemical Technology, The Hong Kong Polytechnic University,
Hung Hom, Kowloon, Hong Kong

 © 2007 Wiley-VCH Verlag GmbH & Co. KGaA, Weinheim 

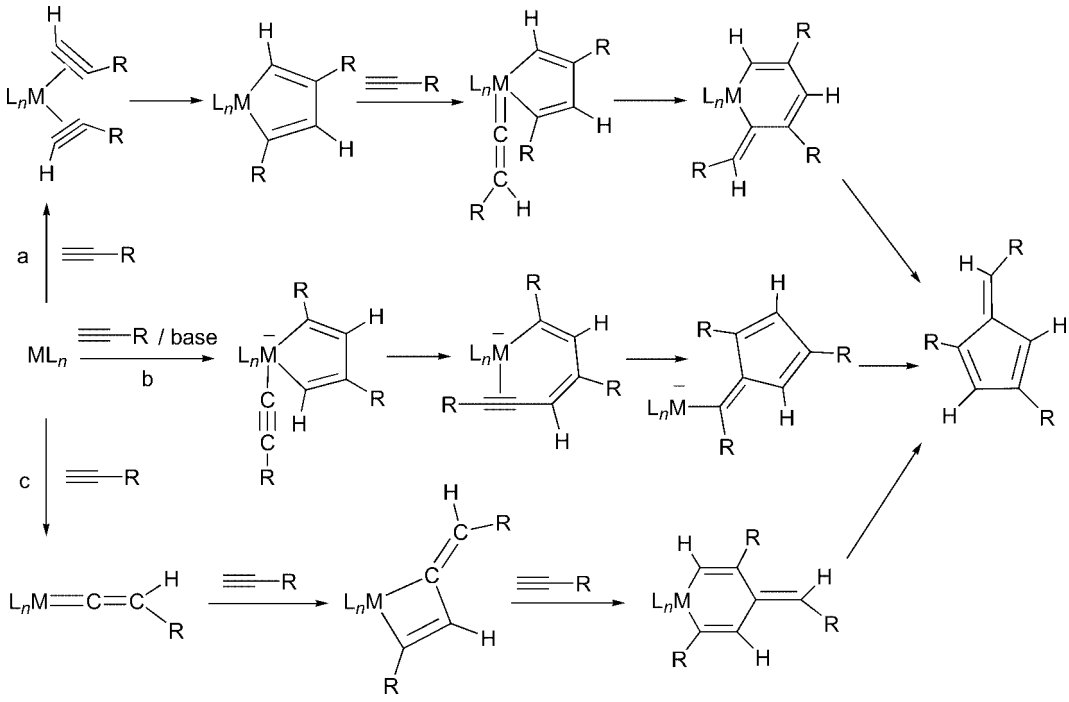

Scheme 1.

data (in $CD_2Cl_2$) of the isolated solid suggest the presence of two isomers (**2a** and **2b**) in a ratio of 4.5:1 in solution (Scheme 2).

The structure of **2a** was determined by X-ray diffraction analysis of a single crystal grown from a $CH_2Cl_2$ solution of **2** layered with hexane. Selected bond lengths and angles are shown in Table 1. The structure shown in Figure 1 clearly reveals that coupling of $HC{\equiv}CSiMe_3$ with the allenylcarbene ligand has occurred to give the $\eta^6$-4,6-diphenyl-2-(trimethylsilyl)fulvene complex **2**.

The interaction of osmium and the exocyclic double bond in complex **2a** is indicated by the inclination of the C(1)–C(6) bond toward osmium, with an angle of 26.9° from the fulvene ring plane. The displacement of C(6) from the fulvene ring plane is 0.625 Å. However, this interaction is weak, as reflected by the rather long Os–C(6) separation [2.632(4) Å] and the relatively short exocyclic double bond [the C(1)–C(6) distance being 1.380(5) Å]. Three extreme canonical forms (see Scheme 3), namely an $\eta^6$-triene (**2**), an $\eta^5$-cyclopentadienido-σ-alkyl ("tucked-in", **2′**), and a zwit-

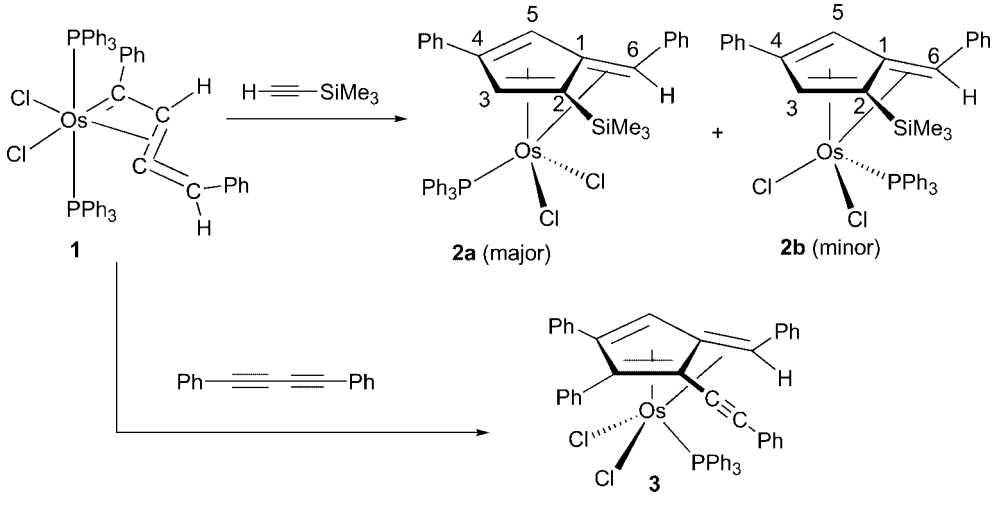

Scheme 2.

 © 2007 Wiley-VCH Verlag GmbH & Co. KGaA, Weinheim 

Table 1. Selected bond lengths [Å] and angles [°] for [$OsCl_2$\{$\eta^6$-$C_5H_2$(Ph)($SiMe_3$)(=CHPh=\}($PPh_3$)] (**2a**).

| | | | |
|---|---|---|---|
| Os(1)–C(1) | 2.143(3) | Os(1)–C(2) | 2.182(4) |
| Os(1)–C(3) | 2.183(4) | Os(1)–C(4) | 2.288(3) |
| Os(1)–C(5) | 2.184(4) | Os(1)–C(6) | 2.632(4) |
| Os(1)–Cl(1) | 2.3920(9) | Os(1)–Cl(2) | 2.3952(9) |
| Os(1)–P(1) | 2.3547(9) | C(1)–C(2) | 1.480(5) |
| C(2)–C(3) | 1.421(5) | C(3)–C(4) | 1.429(5) |
| C(4)–C(5) | 1.417(5) | C(1)–C(5) | 1.461(5) |
| C(1)–C(6) | 1.380(5) | C(2)–Si(1) | 1.882(4) |
| C(4)–C(11) | 1.481(5) | C(6)–C(21) | 1.449(5) |
| C(1)–Os(1)–P(1) | 156.95(10) | C(4)–Os(1)–P(1) | 95.76(9) |
| C(2)–Os(1)–P(1) | 123.38(10) | C(5)–Os(1)–P(1) | 127.21(10) |
| C(3)–Os(1)–P(1) | 93.60(10) | C(6)–Os(1)–P(1) | 170.78(9) |
| C(1)–Os(1)–Cl(1) | 110.50(10) | C(4)–Os(1)–Cl(1) | 155.96(10) |
| C(2)–Os(1)–Cl(1) | 96.06(10) | C(5)–Os(1)–Cl(1) | 148.68(10) |
| C(3)–Os(1)–Cl(1) | 118.77(10) | C(6)–Os(1)–Cl(1) | 87.50(10) |
| C(1)–Os(1)–Cl(2) | 109.88(10) | C(4)–Os(1)–Cl(2) | 115.23(10) |
| C(2)–Os(1)–Cl(2) | 148.99(10) | C(5)–Os(1)–Cl(2) | 94.71(11) |
| C(3)–Os(1)–Cl(2) | 152.39(10) | C(6)–Os(1)–Cl(2) | 88.80(10) |
| P(1)–Os(1)–Cl(1) | 83.99(3) | P(1)–Os(1)–Cl(2) | 87.55(3) |
| Cl(1)–Os(1)–Cl(2) | 88.80(3) | C(1)–Os(1)–C(2) | 40.00(13) |
| C(5)–C(1)–C(2) | 107.9(3) | C(3)–C(2)–C(1) | 104.3(3) |
| C(2)–C(3)–C(4) | 112.6(3) | C(5)–C(4)–C(3) | 106.4(3) |
| C(4)–C(5)–C(1) | 108.7(3) | C(6)–C(1)–Os(1) | 94.2(2) |
| C(6)–C(1)–C(2) | 119.6(3) | C(6)–C(1)–C(5) | 122.8(4) |
| C(1)–C(6)–C(21) | 129.8(4) | | |

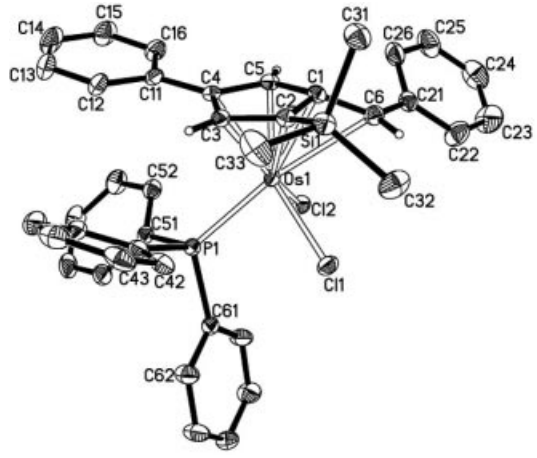


Figure 1. Molecular structure of [$OsCl_2$\{$\eta^6$-$C_5H_2$(Ph)($SiMe_3$)-(=CHPh)\}($PPh_3$)] (**2a**).

terionic form (**2"**), can be considered for the fulvene complex.[18] The structural data of **2a** suggest that the fulvene ligand in **2a** can be regarded as being bound to the osmium in an $\eta^6$-triene fashion. As shown in Table 2, the Os–C(exocyclic) bond lengths in the structurally characterized osmium fulvene complexes [($\eta^5$-$C_5Me_5$)Os\{$\eta^6$-$C_5Me_4$-(=$CPh_2$)\}]($PF_6$),[19] [($\eta^5$-$C_5Me_5$)Os\{$\eta^6$-$C_5Me_4$(=$CH_2$)\}]-($BPh_4$),[20] and [($\eta^5$-$C_5Me_5$)Os\{$\eta^6$-$C_5Me_4$(=$CHC_6F_5$)\}]-($PF_6$)[21] are significantly shorter and the exocyclic C–C bond lengths significantly longer than those in complex **2a**, which is indicative of a "tucked-in" bonding type in these complexes. As expected, the inclination angles in these complexes are also significantly larger (35.6–41.8°) than that in **2a** (26.9°).

The $^{31}P\{^1H\}$ NMR spectrum of **2** in $C_6D_6$ at room temperature displays two singlets at $\delta$ = –0.3 (major) and –7.8 ppm (minor), thereby indicating the presence of two isomers in solution. In the $^1H$ NMR spectrum, the major isomer displays a singlet at $\delta$ = 6.51 ppm and two doublets at $\delta$ = 5.00 and 7.83 ppm for the three fulvene protons. The splitting of the signals at $\delta$ = 5.00 and 7.83 ppm is due to coupling with the $^{31}P$ nuclei, as suggested by $^1H\{^{31}P\}$ NMR experiments. The $^1H$ NMR spectrum of the minor isomer exhibits three singlets in the $^1H$ NMR spectrum at $\delta$ = 5.49, 6.31, and 6.80 ppm for the fulvene protons. Fulvene complexes such as [$Re(C_6F_5)$\{($\eta^6$-$C_5Me_4$(=$CH_2$)\}$(CO)_2$][18a,18b] and [$RuCl_2$(py)\{($\eta^6$-$C_5Me_4$(=$CPh_2$)\}][22] also exist as two isomers in solution. This isomerism has been attributed to the presence of conformational isomers due to restricted rotation about the metal-fulvene bond. A similar isomerism can be proposed for **2**. Scheme 4 shows three possible conformers of **2**. On the basis of steric reasons, one would expect the stability of these three conformers to be in the order **2a** > **2b** > **2c**.

The two isomers observed in solution by NMR spectroscopy can be attributed to **2a** and **2b**. The major isomer can be assigned to the conformer revealed by the X-ray structure (**2a**), in which the exocyclic double bond is *trans* to $PPh_3$. In agreement with the structure, the $^1H$ NMR spectrum shows two signals at $\delta$ = 7.83 ($J_{P,H}$ = 5.8 Hz) and 5.00 ppm ($J_{P,H}$ = 4.0 Hz) assignable to C(6)H and C(5)H, respectively, and a singlet at $\delta$ = 6.51 ppm assignable to C(3)H. The minor isomer observed in solution may correspond to conformer **2b** in which the exocyclic double bond is *cis* to $PPh_3$. The three fulvene signals at $\delta$ = 5.49, 6.31, and 6.80 ppm observed for the minor isomer can be assigned to C(5)H, C(3)H, and C(6)H, respectively.

Scheme 5 shows a plausible mechanism for the formation of **2** from the coupling reaction. Complex **1** could rearrange

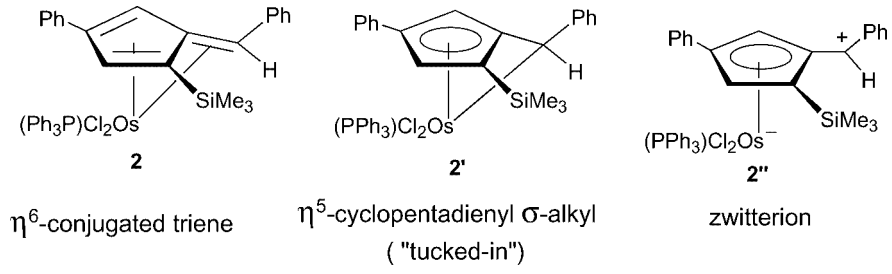


Scheme 3.

 © 2007 Wiley-VCH Verlag GmbH & Co. KGaA, Weinheim 

Table 2. Principal structural parameters of selected osmium fulvene complexes.

| Compound | Os–C(1) [Å] | Os–C(6) [Å] | C(1)–C(6) [Å] | Inclination angle [°] | Ref. |
|---|---|---|---|---|---|
| 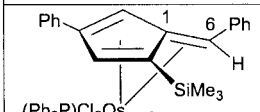 2 | 2.143(3) | 2.632(4) | 1.380(5) | 26.9 | this work |
| 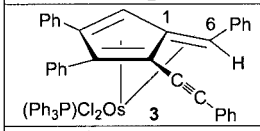 3 | 2.097(4) | 2.392(4) | 1.424(6) | 38.2 | this work |
| 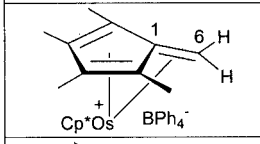 | 2.069(4) | 2.224(5) | 1.426(7) | 41.8 | [20] |
| 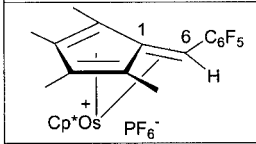 | 2.086(5) | 2.401(6) | 1.428(8) | 35.6 | [21] |
| 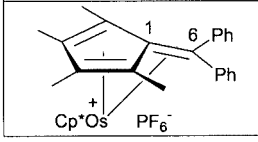 | 2.088(7) | 2.387(9) | 1.459(12) | 38.4 | [19] |

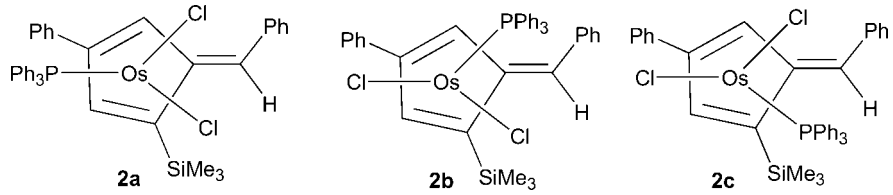


Scheme 4.

to metallacyclobutene **A**, which undergoes cycloaddition with $HC{\equiv}CSiMe_3$ to give the metallacyclohexadiene intermediate **B** or **B1**. Complex **B** or **B1** could then undergo reductive elimination, followed by coordination of the fulvene to osmium and loss of one $PPh_3$ ligand to give **2**. A similar mechanism has been proposed previously.[4,9]

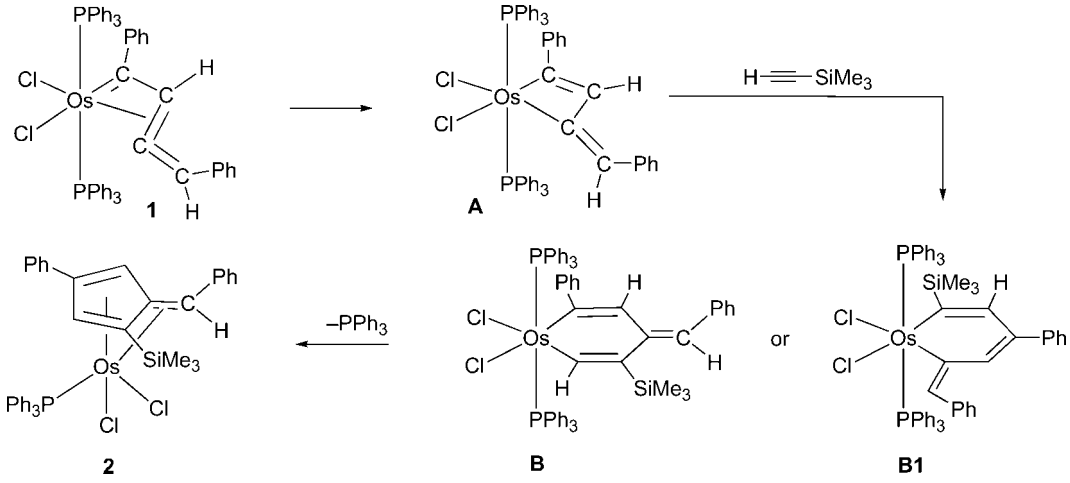


Scheme 5.

 © 2007 Wiley-VCH Verlag GmbH & Co. KGaA, Weinheim 

The reaction of **1** with PhC≡C–C≡CPh produced the analogous fulvene complex **3** (Scheme 1), although the reaction is slow in dichloromethane at room temperature. When a mixture of **1** and PhC≡C–C≡CPh in benzene was refluxed for 1 h, a brown solution containing **3** along with small amounts of unreacted **1** and an unidentified species with a $^{31}P$ chemical shift of $\delta$ = –16.0 ppm was produced. Complex **3** was isolated in 43% yield from the reaction mixture. Attempts to isolate and identify the unknown species with a $^{31}P$ chemical shift of $\delta$ = –16.0 ppm failed. The structure of **3** was also confirmed by a single-crystal X-ray diffraction study. A view of the molecular structure is shown in Figure 2 and selected bond lengths and angles are listed in Table 3.

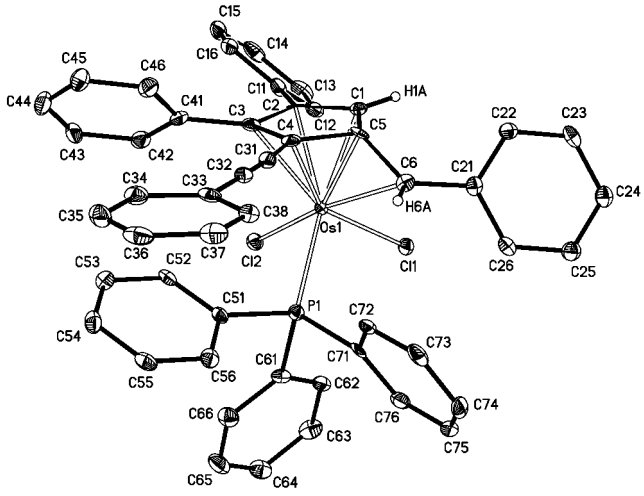


Figure 2. Molecular structure of $[OsCl_2\{\eta^6\text{-}C_5H(C{\equiv}CPh)(Ph)_2(=CHPh)\}(PPh_3)]$ (**3**).

Like complex **2**, the fulvene ligand in **3** is also $\eta^6$-coordinated to osmium. However, the interaction between the exocyclic double bond and the osmium center is stronger for **3**. Thus, the Os–C(6) bond length is 2.392(4) Å and the exocyclic C–C double bond [C(5)–C(6)] bond length is 1.424(6) Å. For comparison, the Os–C(exocyclic) bond length is 2.632(4) Å and the exocyclic C–C bond length is 1.380(5) Å in complex **2a**. The inclination angle of **3** (38.2°) is also significantly larger than that of **2a** (26.9°). The structural features associated with the Os($\eta^6$-fulvene) moiety in **3** are similar to those of the previously reported osmium fulvene complexes $[(\eta^5\text{-}C_5Me_5)Os\{\eta^6\text{-}C_5Me_4(=CPh_2)\}](PF_6)$,[19] $[(\eta^5\text{-}C_5Me_5)Os\{\eta^6\text{-}C_5Me_4(=CH_2)\}](BPh_4)$,[20] and $[(\eta^5\text{-}C_5Me_5)Os\{\eta^6\text{-}C_5Me_4(=CHC_6F_5)\}](PF_6)$[21] (see Table 2).

Consistent with the solid-state structure, the $^1H$ NMR spectrum displays two signals at $\delta$ = 6.00 and 6.62 ppm assignable to the ring proton and the exocyclic =CH proton, respectively. The $^{31}P\{^1H\}$ NMR spectrum shows a singlet at $\delta$ = –8.0 ppm (in $CD_2Cl_2$). It is interesting to note that two isomers are observed for **2** in solution but only one isomer is observed for **3**. Complex **3** can, in principle, also exhibit conformational isomerism in solution, and the exact reason why only one conformer is observed for **3** is not clear. The possibility that the fulvene ring is rotating very rapidly in **3** was excluded as additional $^{31}P$ signals were not observed for a $CD_2Cl_2$ solution of **3** at low temperature (220 K). Since in situ $^{31}P$ NMR spectroscopy showed a minor $^{31}P$ signal along with that of **3** (see above), we tentatively assume that another conformer of **3** may also be produced in the reaction, although we were not able to isolate or identify it. We note that two isomers have been observed for $[RuCl_2(py)\{(\eta^6\text{-}C_5Me_4(=CPh_2)\}]$ whereas only one isomer was observed for the closely related complex $[RuCl_2(dmso)\{(\eta^6\text{-}C_5Me_4(=CPh_2)\}]$.[22]

Table 3. Selected bond lengths [Å] and angles [°] for $[OsCl_2\{\eta^6\text{-}C_5H(C{\equiv}CPh)(Ph)_2(=CHPh)\}(PPh_3)]\cdot 3C_6D_6$ (**3**·$3C_6D_6$).

| | | | |
|---|---|---|---|
| Os(1)–C(1) | 2.199(4) | Os(1)–C(2) | 2.276(4) |
| Os(1)–C(3) | 2.287(4) | Os(1)–C(4) | 2.188(4) |
| Os(1)–C(5) | 2.097(4) | Os(1)–C(6) | 2.392(4) |
| Os(1)–Cl(1) | 2.3898(11) | Os(1)–Cl(2) | 2.3840(11) |
| Os(1)–P(1) | 2.3686(12) | C(1)–C(2) | 1.398(6) |
| C(2)–C(3) | 1.462(6) | C(3)–C(4) | 1.437(6) |
| C(4)–C(5) | 1.453(6) | C(1)–C(5) | 1.445(6) |
| C(5)–C(6) | 1.424(6) | C(2)–C(11) | 1.483(6) |
| C(6)–C(21) | 1.461(6) | C(3)–C(41) | 1.486(6) |
| C(4)–C(31) | 1.442(6) | C(31)–C(32) | 1.190(6) |
| C(32)–C(33) | 1.444(6) | | |
| C(1)–Os(1)–P(1) | 159.92(11) | C(4)–Os(1)–P(1) | 102.79(12) |
| C(2)–Os(1)–P(1) | 152.66(11) | C(5)–Os(1)–P(1) | 120.96(12) |
| C(3)–Os(1)–P(1) | 117.11(11) | C(6)–Os(1)–P(1) | 95.15(11) |
| C(1)–Os(1)–Cl(1) | 91.24(11) | C(4)–Os(1)–Cl(1) | 146.74(12) |
| C(2)–Os(1)–Cl(1) | 110.52(11) | C(5)–Os(1)–Cl(1) | 107.24(12) |
| C(3)–Os(1)–Cl(1) | 147.87(11) | C(6)–Os(1)–Cl(1) | 85.47(11) |
| C(1)–Os(1)–Cl(2) | 116.47(11) | C(4)–Os(1)–Cl(2) | 124.62(12) |
| C(2)–Os(1)–Cl(2) | 86.85(11) | C(5)–Os(1)–Cl(2) | 150.61(12) |
| C(3)–Os(1)–Cl(2) | 90.49(11) | C(6)–Os(1)–Cl(2) | 170.55(11) |
| P(1)–Os(1)–Cl(1) | 94.06(4) | P(1)–Os(1)–Cl(2) | 83.30(4) |
| Cl(1)–Os(1)–Cl(2) | 85.34(4) | C(5)–Os(1)–C(4) | 39.58(16) |
| C(2)–C(1)–C(5) | 109.5(4) | C(1)–C(2)–C(3) | 108.6(4) |
| C(4)–C(3)–C(2) | 106.8(4) | C(3)–C(4)–C(5) | 108.6(4) |
| C(1)–C(5)–C(4) | 106.5(4) | C(6)–C(5)–Os(1) | 83.3(3) |
| C(6)–C(5)–C(1) | 121.6(4) | C(6)–C(5)–C(4) | 117.6(4) |
| C(5)–C(6)–C(21) | 125.3(4) | C(4)–C(31)–C(32) | 176.2(5) |
| C(31)–C(32)–C(33) | 176.8(5) | C(3)–C(4)–C(31) | 126.3(4) |
| C(31)–C(4)–C(5) | 125.2(4) | | |

It is interesting to note that complexes **2a** and **3** adopt different conformations in the solid state. This difference could be related to the relative bulkiness of $SiMe_3$, Ph, and C≡CPh. One might expect that the steric effects of these groups are in the order $SiMe_3$ > Ph > C≡CPh, therefore the bulky $PPh_3$ ligand tends to be in a position close to C≡CPh rather than Ph in **3**, but close to Ph rather than $SiMe_3$ in **2a**.

We also studied the reaction of **1** with $SiMe_3C{\equiv}C–C{\equiv}CSiMe_3$. However, the reaction produced many unidentified phosphorus-containing species which proved difficult to separate and identify.

### Coupling Reaction of $[OsCl_2\{=CPh(\eta^2\text{-}CH=C=CHPh)\}(PPh_3)_2]$ (1) with Styrene

The easy formation of fulvene complexes from the reaction of $[OsCl_2\{=CPh(\eta^2\text{-}CH=C=CHPh)\}(PPh_3)_2]$ (**1**) with alkynes promoted us to investigate the reaction of **1** with

 © 2007 Wiley-VCH Verlag GmbH & Co. KGaA, Weinheim 

styrene. Treatment of complex **1** with an excess of styrene in wet $CH_2Cl_2$ leads to the formation of the bimetallic complex $[(PPh_3)_2ClOs(\mu\text{-}Cl)_3Os(H_2O)(PPh_3)_2]$ (**4**) as the only phosphorus-containing product (Scheme 6).

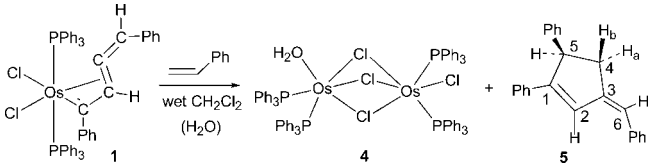


Scheme 6.

Complex **4** was isolated as a light-brown solid in 75% yield and was characterized by elemental analysis, NMR spectroscopy, and mass spectrometry. The $^{31}P\{^1H\}$ NMR spectrum of **4** in $C_6D_6$ displays four sets of doublets of equal intensity at $\delta$ = –6.5, –7.8 ($J_{P,P}$ = 11.4 Hz), –16.4, and –17.4 ppm ($J_{P,P}$ = 16.7 Hz), thereby indicating the presence of four inequivalent phosphorus nuclei. This pattern is closely analogous to that of the dinuclear complex $[(PPh_3)_2ClOs(\mu\text{-}Cl)_3Os\{=C=CH[C(OH)Ph_2]\}(PPh_3)_2]$[23] and suggests the formation of a bimetallic complex of the type $[(PPh_3)_2ClOs(\mu\text{-}Cl)_3Os(L)(PPh_3)_2]$.

Definite proof of the structure came from a single-crystal X-ray structure analysis. Crystals suitable for X-ray diffraction were grown from a $CH_2Cl_2$ solution of **4** layered with hexane. Selected bond lengths and angles are given in Table 4 and a view of the molecular geometry of **4** is shown in Figure 3. The structure of **4** is similar to that of $[(PPh_3)_2ClOs(\mu\text{-}Cl)_3Os\{=C=CH[C(OH)Ph_2]\}(PPh_3)_2]$,[23] with replacement of the vinylidene ligand in the latter complex by an aqua ligand, and deserves no further comments.

Table 4. Selected bond lengths [Å] and angles [°] for $[(PPh_3)_2ClOs(\mu\text{-}Cl)_3Os(H_2O)(PPh_3)_2]\cdot CH_2Cl_2$ (**4**·$CH_2Cl_2$).

| | | | |
|---|---|---|---|
| Os(1)–P(1) | 2.337(3) | Os(2)–P(3) | 2.278(3) |
| Os(1)–P(2) | 2.335(3) | Os(2)–P(4) | 2.287(3) |
| Os(1)–Cl(1) | 2.439(2) | Os(2)–Cl(1) | 2.392(3) |
| Os(1)–Cl(2) | 2.463(3) | Os(2)–Cl(2) | 2.523(3) |
| Os(1)–Cl(3) | 2.403(3) | Os(2)–Cl(3) | 2.540(2) |
| Os(1)–O(1) | 2.294(9) | Os(2)–Cl(4) | 2.401(3) |
| P(2)–Os(1)–P(1) | 99.51(10) | P(3)–Os(2)–P(4) | 98.21(10) |
| P(1)–Os(1)–Cl(1) | 168.96(10) | Cl(1)–Os(2)–Cl(4) | 161.17(8) |
| P(2)–Os(1)–Cl(2) | 168.35(9) | P(3)–Os(2)–Cl(2) | 170.58(9) |
| O(1)–Os(1)–Cl(3) | 165.29(18) | P(4)–Os(2)–Cl(3) | 164.24(9) |
| P(1)–Os(1)–Cl(3) | 93.65(10) | P(3)–Os(2)–Cl(1) | 93.34(9) |
| P(2)–Os(1)–Cl(3) | 100.64(10) | P(4)–Os(2)–Cl(1) | 94.19(10) |
| P(2)–Os(1)–Cl(1) | 90.13(9) | P(3)–Os(2)–Cl(4) | 96.76(10) |
| Cl(3)–Os(1)–Cl(1) | 79.18(9) | P(4)–Os(2)–Cl(4) | 100.03(10) |
| P(1)–Os(1)–Cl(2) | 91.70(9) | P(4)–Os(2)–Cl(2) | 87.51(9) |
| Cl(3)–Os(1)–Cl(2) | 81.66(9) | Cl(1)–Os(2)–Cl(2) | 79.03(8) |
| Cl(1)–Os(1)–Cl(2) | 79.03(8) | Cl(4)–Os(2)–Cl(2) | 89.56(10) |
| O(1)–Os(1)–P(1) | 92.64(17) | P(3)–Os(2)–Cl(3) | 95.59(9) |
| O(1)–Os(1)–P(2) | 91.41(19) | Cl(1)–Os(2)–Cl(3) | 77.40(8) |
| O(1)–Os(1)–Cl(1) | 92.49(17) | Cl(4)–Os(2)–Cl(3) | 85.80(9) |
| O(1)–Os(1)–Cl(2) | 84.88(19) | Cl(2)–Os(2)–Cl(3) | 77.85(8) |
| Os(2)–Cl(1)–Os(1) | 87.48(8) | Os(1)–Cl(2)–Os(2) | 84.10(8) |
| Os(1)–Cl(3)–Os(2) | 84.97(8) | | |

Obviously, the hydrocarbon ligand of **1** has been eliminated from the metal center in the reaction. The $^1H$ NMR spectrum of the reaction mixture shows the formation of several organic products, among which compound **5** is the most dominant (ca. 78%). A sample of compound **5** could be isolated as an oil by column chromatography on silica gel using hexane as the eluent, and its structure was readily deduced from spectroscopic data. Thus, the FAB mass spectrum shows an ion peak at *m*/*z* 308.1, indicating that it is composed of a molecule of styrene and the original allenylcarbene unit of **1**. The $^1H$ NMR spectrum ($C_6D_6$) shows two multiplets at $\delta$ = 2.98 and 3.29 ppm, which could be assigned to the two diastereotopic C$H_2$ ring protons C(4)$H_a$ and C(4)$H_b$, respectively (see Scheme 6 for labelling). The $^1H$ and $^1H$-$^1H$ COSY NMR spectra clearly indicate that the $CH_2$ group is adjacent to a CH group, which has its $^1H$ NMR signal at $\delta$ = 4.16 ppm and is assignable to the signal of C(5)H. The presence of the stereogenic center at C5 is responsible for the different environments around C(4)$H_a$ and C(4)$H_b$. The coupling constant between C(4)$H_a$ and C(4)$H_b$ is 17.3 Hz, while the coupling constants between C(5)H and C(4)Hs are 3.7 and 8.3 Hz for C(4)$H_a$ and C(4)$H_b$, respectively, consistent with the assignment that the latter is formally *trans* to C(5)H. In the $^1H$ NMR spectrum, the signal of the C(2)H ring proton appears at $\delta$ = 6.32 ppm and the signal of the exocyclic C*H*Ph proton [C(6)H] appears as a triplet at $\delta$ = 7.51 ppm due to coupling with the protons of the $CH_2$ group.

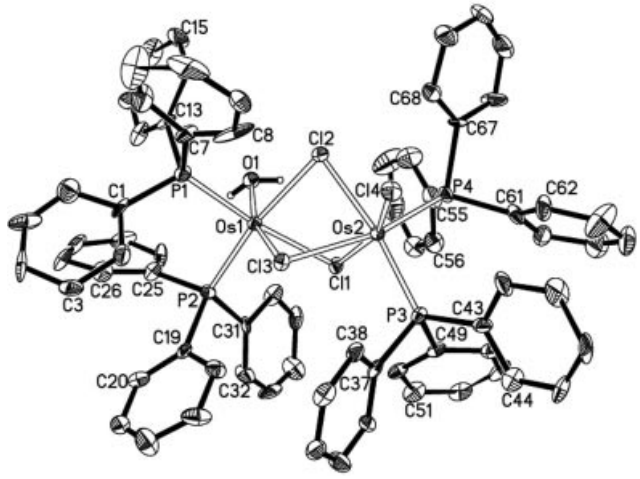


Figure 3. Molecular structure of $[(PPh_3)_2ClOs(\mu\text{-}Cl)_3Os(H_2O)(PPh_3)_2]$ (**4**).

Scheme 7 shows a plausible mechanism for the formation of **4** and **5** from the reaction of **1** with styrene. Complex **1** can rearrange to metallacyclobutene **A**, which can undergo cycloaddition with styrene to give the metallacyclic intermediate **C** or **C1**. Subsequent reductive elimination of **C** or **C1** would give **5** and the transient $OsCl_2(PPh_3)_2$ fragment, which reacts with water in solution to give **4**. Although we have no direct evidence for intermediates **C** and **C1**, they are closely related to intermediates **B** and **B1**.

The allenylcarbene complex **1** was originally derived from the coupling of two molecules of phenylacetylene. Thus, the net transformation involving formation of **1** and the coupling of **1** with styrene represenst a rare example of a [2+2+1] co-cyclotrimerization of alkynes and alkenes.

 © 2007 Wiley-VCH Verlag GmbH & Co. KGaA, Weinheim 

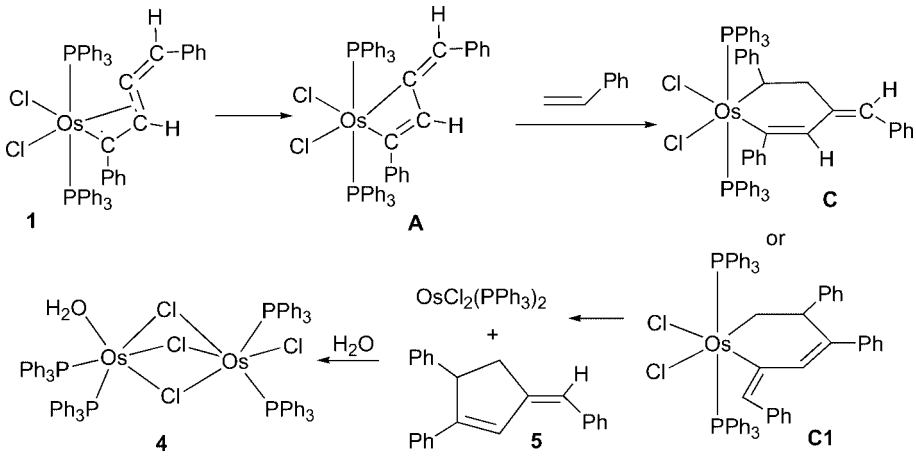


Scheme 7.

While many examples of [2+2+2] co-cyclotrimerization of alkynes and alkenes to give cyclohexadienes are known,[24] the related [2+2+1] co-cyclotrimerization of alkynes and alkenes, to the best of our knowledge, is still unknown.

In summary, we have demonstrated that the allenylcarbene complex $[OsCl_2\{=CPh(\eta^2\text{-}CH=C=CHPh)\}(PPh_3)_2]$ (**1**), which is originally derived from the coupling of two molecules of phenylacetylene at osmium, can undergo coupling reactions with alkynes to give fulvene complexes. The reactions reported here support a previously proposed mechanism that [2+2+1] cyclotrimerization of alkynes could occur via metallacyclobutene intermediates. We have also shown that complex **1** can undergo a similar coupling reaction with styrene. This result is interesting as it represents a rare example of metal-mediated [2+2+1] co-cyclotrimerization of alkynes and alkenes.

## Experimental Section

All manipulations were carried out under nitrogen using standard Schlenk techniques unless otherwise stated. Solvents were distilled under nitrogen from sodium benzophenone (hexane, diethyl ether, thf), sodium (benzene), or calcium hydride ($CH_2Cl_2$). $[Os\{=CPh(\eta^2\text{-}CH=C=CHPh)\}(PPh_3)_2]$[16] was prepared according to the literature method. All other reagents were used as received from Aldrich Chemical Co. USA.

Microanalyses were performed by M-H-W Laboratories (Phoenix, AZ). $^1H$, $^{13}C\{^1H\}$, and $^{31}P\{^1H\}$ NMR spectra were recorded with a JEOL EX-400 spectrometer (400 MHz) or a Bruker ARX-300 spectrometer (300 MHz). $^1H$ and $^{13}C$ NMR shifts are quoted relative to TMS, and $^{31}P$ chemical shifts relative to 85% $H_3PO_4$. Mass spectra were recorded with a Finnigan TSQ7000 spectrometer.

**$[OsCl_2\{\eta^6\text{-}C_5H_2(Ph)(SiMe_3)(=CHPh)\}(PPh_3)]$ (2):** $HC{\equiv}CSiMe_3$ (0.43 mL, 3.0 mmol) was added to a solution of $[OsCl_2(=CPh\text{-}CH=C=CPh)(PPh_3)_2]$ (0.50 g, 0.50 mmol) in $CH_2Cl_2$ (50 mL) and the reaction mixture was stirred at room temperature for 72 h to give a brown solution. The volume of the mixture was reduced to about 1 mL, then diethyl ether (20 mL) was added slowly with stirring and the mixture was filtered to remove a small amount of dark brown precipitate. The filtrate was evacuated to dryness under vacuum and the residue was extracted with 1 mL of benzene to give a brown solution. Addition of hexane (30 mL) to the benzene extract produced a green precipitate, which was collected by filtration, washed with hexane (2 × 30 mL), and dried under vacuum overnight. The $^{31}P\{^1H\}$ and $^1H$ NMR spectra indicate the presence of two isomers in a ratio of about 1:4.5. Yield: 0.34 g (81%). FAB-MS (NBA): *m/z* 826 [$M^+$]. $C_{39}H_{37}Cl_2OsP_2Si$: calcd. C 56.72, H 4.52; found C 56.68, H 4.61.

**2a** ($PPh_3$ is *trans* to the exocyclic double bond): $^1H$ NMR (300.13 MHz, $CD_2Cl_2$, see Scheme 1 for labels): $\delta$ = 0.45 (s, 9 H, $SiMe_3$), 5.00 [d, $J_{P,H}$ = 4.0 Hz, 1 H, C(5)-H], 6.51 [s, 1 H, C(3)-H], 7.06–7.65 (m, $C_6H_5$, $PPh_3$, mixed with those of **2b**), 7.83 [d, $J_{P,H}$ = 5.8 Hz, 1 H, C(6)-H] ppm. $^{13}C\{^1H\}$ NMR (100.4 MHz, $CD_2Cl_2$): $\delta$ = 0.5 (s, $SiMe_3$), 73.3 (s, C-3), 82.00 (s, C-5), 83.4 (d, $J_{P,C}$ = 2.6 Hz, C-2), 98.1 (s, C-1), 108.1 (s, C-4), 108.5 (d, $J_{P,C}$ = 16.4 Hz, C-6), 127.6–135.9 (m, $C_6H_5$, $PPh_3$, mixed with those of **2b**) ppm. $^{31}P\{^1H\}$ NMR (121.5 MHz, $C_6D_6$): $\delta$ = –0.3 (s) ppm.

**2b** ($PPh_3$ is *cis* to the exocyclic double bond): $^1H$ NMR (300.13 MHz, $CD_2Cl_2$): $\delta$ = 0.50 (s, 9 H, $SiMe_3$), 5.49 [s, 1 H, C(5)-H], 6.31 [s, 1 H, C(3)-H], 6.80 [s, 1 H, C(6)-H], 7.06–7.65 (m, $C_6H_5$, $PPh_3$, mixed with those of **2a**) ppm. $^{13}C\{^1H\}$ NMR (100.4 MHz, $CD_2Cl_2$): $\delta$ = –0.1 (s, $SiMe_3$), 79.2 (s, C-5), 82.6 (s, C-6), 94.5 (s, C-4), 97.5 (s, C-1), 100.4 (d, $J_{P,C}$ = 10.3 Hz, C-2), 111.5 (d, $J_{P,C}$ = 8.9 Hz, C-3), 127.9–137.1 (m, $C_6H_5$, $PPh_3$, mixed with those of **2a**) ppm. $^{31}P\{^1H\}$ NMR (121.5 MHz, $C_6D_6$): $\delta$ = –7.8 (s) ppm.

**$[OsCl_2\{\eta^6\text{-}C_5H(C{\equiv}CPh)(Ph)_2(=CHPh)\}(PPh_3)]$ (3):** A mixture of $[Os\{=CPh(\eta^2\text{-}CH=C=CHPh)Cl_2(PPh_3)_2]$ (0.20 g, 0.20 mmol) and $PhC{\equiv}C\text{–}C{\equiv}CPh$ (0.20 g, 0.99 mmol) in benzene (15 mL) was refluxed for 1 h. Unreacted $[OsCl_2\{=CPh(CH=C=CPh)(PPh_3)_2]$ was then removed by filtration and residue was washed with benzene (2 × 5 mL). The solvent was removed from the brown filtrate under vacuum and the residue dissolved in $CH_2Cl_2$ (2 mL). Addition of diethyl ether (8 mL) to the residue gave a greenish brown precipitate, which was collected by filtration, washed with diethyl ether (3 × 2 mL), and dried under vacuum. The residue was recrystallized from benzene to give a red precipitate, which was collected by filtration, washed with benzene (2 mL) and diethyl ether (2 × 3 mL), and dried under vacuum. Yield: 80 mg (43%). $C_{50}H_{37}Cl_2OsP{\cdot}0.25CH_2Cl_2$: calcd. C 63.45, H 3.97; found C 63.70, H 4.20. $^1H$ NMR (300.13 MHz, $CD_2Cl_2$): $\delta$ = 6.00 (d, $J_{P,H}$ = 2.1 Hz, 1 H, =CH), 6.62 (d, $J_{P,H}$ = 5.1 Hz, 1 H, =C*H*Ph), 6.30–7.74 (m, 35 H, $C_6H_5$, $PPh_3$) ppm. $^{31}P\{^1H\}$ NMR (121.5 MHz, $CD_2Cl_2$): $\delta$ = –8.0 (s) ppm.

**$[(PPh_3)_2ClOs(\mu\text{-}Cl)_3Os(H_2O)(PPh_3)_2]$ (4) and 5:** Styrene (0.18 mL, 1.6 mmol) was added to a solution of $[OsCl_2\{=CPh\text{-}$

 © 2007 Wiley-VCH Verlag GmbH & Co. KGaA, Weinheim 

Table 5. Crystallographic details for complexes **2a**, **3**, and **4**.

| | **2a** | **3**·3$C_6D_6$ | **4**·$CH_2Cl_2$ |
|---|---|---|---|
| Empirical formula | $C_{39}H_{37}Cl_2OsPSi$ | $C_{50}H_{37}Cl_2OsP·3C_6D_6$ | $C_{72}H_{62}Cl_4OOs_2P_4·CH_2Cl_2$ |
| Formula weight | 825.85 | 1164.19 | 1674.22 |
| Temperature [K] | 293(2) | 100(2) | 293(2) |
| Radiation (Mo-$K_\alpha$) [Å] | 0.71073 | 0.71073 | 0.71073 |
| Crystal system | tetragonal | triclinic | triclinic |
| Space group | $P4_2/n$ | $P\bar{1}$ | $P\bar{1}$ (no. 2) |
| $a$ [Å] | 26.474(3) | 12.6406(9) | 14.162(5) |
| $b$ [Å] | 26.474(3) | 14.4993(10) | 14.612(5) |
| $c$ [Å] | 9.9105(15) | 14.6828(10) | 20.423(7) |
| $\alpha$ [°] | 90 | 86.7760(10) | 77.944(8) |
| $\beta$ [°] | 90 | 89.6520(10) | 76.462(9) |
| $V$ [Å$^3$] | 6945.8(15) | 2622(3) | 3870(2) |
| $Z$ | 8 | 2 | 2 |
| $d_{calcd}$, [g cm$^{-3}$] | 1.579 | 1.475 | 1.437 |
| Absorption coefficient [mm$^{-1}$] | 3.933 | 2.607 | 3.608 |
| $F$(000) | 3280 | 1176 | 1648 |
| Crystal size [mm] | 0.35 × 0.30 × 0.30 | 0.20 × 0.15 × 0.05 | 0.12 × 0.04 × 0.04 |
| $\theta$ range [°] | 2.18 to 27.55 | 1.39 to 25.00 | 1.54 to 25.00 |
| Reflections collected | 45630 | 25255 | 18978 |
| Independent reflections | 7989 ($R_{int}$ = 0.0488) | 9174($R_{int}$ = 0.0499) | 12237 ($R_{int}$ = 0.0937) |
| Data / restraints / parameters | 7989 / 0 / 409 | 9174 / 0 / 649 | 12237 / 62 / 780 |
| Goodness-of-fit on $F^2$ | 0.930 | 0.992 | 0.943 |
| Final $R$ [$I > 2\sigma(I)$] | $R_1$ = 0.0287<br>$wR_2$ = 0.0631 | $R_1$ = 0.0379<br>$wR_2$ = 0.0654 | $R_1$ = 0.0770<br>$wR_2$ = 0.1186 |
| Largest diff. peak and hole [e Å$^{-3}$] | 1.177 and –0.747 | 1.137 and –1.506 | 1.542 and –1.062 |

(CH=C=CPh)($PPh_3$)$_2$] (0.32 g, 0.32 mmol) in $CH_2Cl_2$ (20 mL) and the reaction mixture was stirred at room temperature for 24 h to give a light-brown solution. The volume of the reaction solution was reduced to about 1 mL and hexane (30 mL) was then added slowly with stirring to produce a light-brown precipitate. The mixture was further stirred for 10 min and then filtered. The solid was collected by filtration, washed with diethyl ether (2 × 15 mL) and hexane (15 mL), and dried under vacuum to give **4**. Yield: 0.19 g (75%). $C_{72}H_{62}Cl_4P_4Os_2$: calcd. C 54.41, H 3.93; found C 54.52, H 4.12. FAB-MS (NBA): $m/z$ 1570.8 [M – $H_2O$]$^+$. $^1$H NMR (300.13 MHz, $C_6D_6$): $\delta$ = 7.00–7.16 (m, 22 H), 7.26–7.35 (m, 26 H), 7.80–8.03 (m, 12 H), ($PPh_3$) ppm. $^{31}$P{$^1$H} NMR (121.5 MHz, $C_6D_6$): $\delta$ = –6.5 (d), –7.8 (d), ($J_{P,P}$ = 11.4 Hz), –16.4 (d), –17.4 (d) ($J_{P,P}$ = 16.7 Hz) ppm. The filtrate and the washing solution obtained above were collected together and the solvent was pumped off. The residue was extracted with 1 mL of benzene and loaded onto a silica gel column. The column was eluted with hexane to give the organic compound **5** along with a small amount of other unidentified organic species as a yellow solution, which was evaporated to dryness on a rotary evaporator and dried under vacuum to give a yellow oil. FAB-MS (NBA): $m/z$ 308.1 [M$^+$]. $^1$H NMR (300.13 MHz, $C_6D_6$, see Scheme 6 for labels): $\delta$ = 2.98 [m, $^2J_{C(4)\text{-}H_a,C(4)\text{-}H_b}$ = 17.3, $^3J_{C(4)\text{-}H_a,C(5)\text{-}H}$ = 3.7, $^4J_{C(4)\text{-}H_a,C(6)\text{-}H} \approx$ 1.8, $^4J_{C(4)\text{-}H_a,C(2)\text{-}H} \approx$ 0.9 Hz, 1 H, C(4)-$H_a$], 3.29 [m, $^2J_{C(4)\text{-}H_a,C(4)\text{-}H_b}$ = 17.3, $^3J_{C(4)\text{-}H,C(5)\text{-}H}$ = 8.3, $^4J_{C(4)\text{-}H_b,C(6)\text{-}H} \approx$ 2.0, $^4J_{C(4)\text{-}H_b,C(2)\text{-}H} \approx$ 0.9 Hz, 1 H, C(4)-$H_b$], 4.16 [ddd, $^3J_{C(4)\text{-}H_b,C(5)\text{-}H}$ = 8.3, $^3J_{C(4)\text{-}H_a,C(5)\text{-}H}$ = 3.7, $^4J_{C(2)\text{-}H,C(5)\text{-}H}$ = 2.5 Hz, 1 H, C(5)-H], 6.32 [br. s, $W_{1/2}$ = 4.5 Hz, 1 H, C(2)-H], 7.51 [br. t, $^4J_{C(4)\text{-}H,\ C(6)\text{-}H}$ = 1.8 Hz, 1 H, C(6)-H], 6.77–7.77 (m, 15 H, Ph) ppm.

**Crystallographic Details for 2a, 3, and 4:** Crystals of **2** and **4** suitable for X-ray diffraction were grown from $CH_2Cl_2$ solutions of **2** and **4** layered with hexane, and crystals of **3** were grown from a $CH_2Cl_2$ solution layered with benzene. Data collections were performed with a Bruker AXS diffractometer equipped with a SMART APEX CCD area detector. Intensity data were collected using graphite-monochromated Mo-$K_\alpha$ radiation ($\lambda$ = 0.71073 Å) at room temperature for **2** and **4**, and at 100 K for **3**. Data reduction and absorption correction were performed using SAINT v.6.26 and SADABS v.2.03, respectively. Structure solution and refinement were performed using the SHELXTL v.6.10 software package. All three structures were solved by direct methods, expanded by difference Fourier syntheses, and refined by full-matrix least-squares on $F^2$. Non-hydrogen atoms were refined anisotropically, except for the $CH_2Cl_2$ solvent in **4**. This was found to be severely disordered and its atoms were given split occupancies and refined isotropically using C–Cl bond length restraints. Some phenyl rings of the $PPh_3$ ligands in **4** also exhibited extensive disorder and were refined with ideal C–C distances and planarity restraints. All hydrogen atoms were placed in geometrical positions and with riding parameters. Further crystallographic details are given in Table 5.

CCDC-631969 (for **2a**), -631970 (for **3**), and -631971 (for **4**) contain the supplementary crystallographic data for this paper. These data can be obtained free of charge from The Cambridge Crystallographic Data Centre via www.ccdc.cam.ac.uk/data_request/cif.

## Acknowledgments

This work was supported by the Hong Kong Research Grant Council (project no. 601804) and the National Natural Science Foundation of China through the Outstanding Young Investigator Award Fund (project no. 20429201).

[1] a) S. Kotha, E. Brahmachary, K. Lahiri, *Eur. J. Org. Chem.* **2005**, 4741–4767; b) S. Saito, Y. Yamamoto, *Chem. Rev.* **2000**, *100*, 2901–2915; c) M. Lautens, W. Klute, W. Tam, *Chem. Rev.* **1996**, *96*, 49–92; d) H. W. Frühauf, *Chem. Rev.* **1997**, *97*, 523–596.

[2] For examples of recent work on the catalytic cyclotrimerization of alkynes, see: a) V. Cadierno, S. E. García-Garrido, J. Gimeno, *J. Am. Chem. Soc.* **2006**, *128*, 15094–15095; b) M. Kakeya, T. Fujihara, T. Kasaya, A. Nagasawa, *Organometallics* **2006**, *25*, 4131–4137; c) Y. Yamamoto, T. Hashimoto, K. Hat-

 © 2007 Wiley-VCH Verlag GmbH & Co. KGaA, Weinheim 

tori, M. Kikuchi, H. Nishiyama, *Org. Lett.* **2006**, *8*, 3565–3568; d) N. Saino, F. Amemiya, E. Tanabe, K. Kase, S. Okamoto, *Org. Lett.* **2006**, *8*, 1439–1442; e) K. Tanaka, G. Nishida, M. Ogino, M. Hirano, K. Noguchi, *Org. Lett.* **2005**, *7*, 3119–3121; f) Y. Yamamoto, J. I. Ishii, H. Nishiyama, K. Itoh, *J. Am. Chem. Soc.* **2005**, *127*, 9625–9631; g) L. V. R. Boñaga, H. C. Zhang, A. F. Moretto, H. Ye, D. A. Gauthier, J. Li, G. C. Leo, B. E. Maryanoff, *J. Am. Chem. Soc.* **2005**, *127*, 3473–3485; h) E. Rüba, R. Schmid, K. Kirchner, M. J. Calhorda, *J. Organomet. Chem.* **2003**, *682*, 204–211; i) K. Kirchner, M. J. Calhorda, R. Schmid, L. F. Veiros, *J. Am. Chem. Soc.* **2003**, *125*, 11721–11729.

[3] For examples of the formation of benzene complexes, see: a) Y. Yamamoto, T. Arakawa, R. Ogawa, K. Itoh, *J. Am. Chem. Soc.* **2003**, *125*, 12143–12160; b) C. Bianchini, K. G. Caulton, T. J. Johnson, A. Meli, M. Peruzzini, F. Vizza, *Organometallics* **1995**, *14*, 933–943; c) C. Bianchini, K. G. Caulton, C. Chardon, M. L. Doublet, O. Eisenstein, S. A. Jackson, T. J. Johnson, A. Meli, M. Peruzzini, W. E. Streib, A. Vacca, F. Vizza, *Organometallics* **1994**, *13*, 2010–2023; d) C. Bianchini, M. Graziani, J. Kaspar, A. Meli, F. Vizza, *Organometallics* **1994**, *13*, 1165–1173; e) C. Bianchini, P. Frediani, M. Graziani, J. Kaspar, A. Meli, M. Peruzzini, F. Vizza, *Organometallics* **1993**, *12*, 2886–2887.

[4] G. Moran, M. Green, A. G. Orpen, *J. Organomet. Chem.* **1983**, *250*, C15–C20.

[5] a) J. M. O'Connor, K. Hübner, R. Merwin, P. K. Gantzel, B. S. Fong, *J. Am. Chem. Soc.* **1997**, *119*, 3631–3632; b) J. M. O'Connor, A. Closson, K. Hübner, R. Merwin, P. Gantzel, D. M. Roddick, *Organometallics* **2001**, *20*, 3710–3717.

[6] H. J. Kim, N. S. Choi, S. W. Lee, *J. Organomet. Chem.* **2000**, *616*, 67–73.

[7] E. S. Johnson, G. J. Balaich, P. E. Fanwick, I. P. Rothwell, *J. Am. Chem. Soc.* **1997**, *119*, 11086–11087.

[8] U. Radhakrishnan, V. Gevorgyan, Y. Yamamoto, *Tetrahedron Lett.* **2000**, *41*, 1971–1974.

[9] W. S. Han, S. W. Lee, *Organometallics* **2005**, *24*, 997–1003.

[10] A. D. Burrows, M. Green, J. C. Jeffery, J. M. Lynam, M. F. Mahon, *Angew. Chem. Int. Ed.* **1999**, *38*, 3043–3045.

[11] H. Komatsu, Y. Suzuki, H. Yamazaki, *Chem. Lett.* **2001**, 998–999.

[12] J. Moreto, K. Maruya, P. M. Bailey, P. M. Maitlis, *J. Chem. Soc., Dalton Trans.* **1982**, 1341–1347.

[13] K. W. Chiu, C. G. Howard, H. S. Rzepa, R. N. Sheppard, G. Wilkinson, A. M. R. Galas, M. B. Hursthouse, *Polyhedron* **1982**, *1*, 441–451.

[14] T. B. Wen, Z. Y. Zhou, G. Jia, *Angew. Chem. Int. Ed.* **2006**, *45*, 5842–5846.

[15] E. Becker, K. Mereiter, M. Puchberger, R. Schmid, K. Kirchner, A. Doppiu, A. Salzer, *Organometallics* **2003**, *22*, 3164–3170.

[16] T. B. Wen, W. Y. Hung, H. H. Y. Sung, I. D. Williams, G. Jia, *J. Am. Chem. Soc.* **2005**, *127*, 2856–2857.

[17] Allenylcarbene complexes are still rare. For examples of other reported allenylcarbene complexes, see: a) E. Rüba, K. Mereiter, R. Schmid, V. N. Sapunov, K. Kirchner, H. Schottenberger, M. J. Calhorda, L. F. Veiros, *Chem. Eur. J.* **2002**, *8*, 3948–3961; b) E. Rüba, K. Mereiter, R. Schmid, K. Kirchner, H. Schottenberger, *J. Organomet. Chem.* **2001**, *637–639*, 70–74; c) R. Schmid, K. Kirchner, *Eur. J. Inorg. Chem.* **2004**, 2609–2626.

[18] a) A. H. Klahn, B. Oelckers, F. Godoy, M. T. Garland, A. Vega, R. N. Perutz, C. L. Higgitt, *J. Chem. Soc., Dalton Trans.* **1998**, 3079–3086; b) A. H. Klahn, M. H. Moore, R. N. Perutz, *J. Chem. Soc., Chem. Commun.* **1992**, 1699–1701; c) F. G. N. Cloke, J. P. Day, J. C. Green, C. P. Moreley, A. C. Swain, *J. Chem. Soc., Dalton Trans.* **1991**, 789–804.

[19] U. Turpeinen, A. Z. Kreindlin, P. V. Petrovskii, M. I. Rybinskaya, *J. Organomet. Chem.* **1992**, *441*, 109–116.

[20] M. I. Rybinskaya, A. Z. Kreindlin, Y. T. Struchkov, A. I. Yanovsky, *J. Organomet. Chem.* **1989**, *359*, 233–243.

[21] A. Z. Kreindlin, K. Y. Suponitsky, F. M. Dolgushin, Z. A. Starikova, M. I. Rybinskaya, *Russ. Chem. Bull. Int. Ed.* **2001**, *50*, 1616–1619.

[22] L. Fan, C. Wei, F. I. Aigbirhio, M. L. Turner, O. V. Gusev, L. N. Morozova, D. R. T. Knowles, P. M. Maitlis, *Organometallics* **1996**, *15*, 98–104.

[23] T. B. Wen, Z. Y. Zhou, M. F. Lo, I. D. Williams, G. Jia, *Organometallics* **2003**, *22*, 5217–5225.

[24] See, for example: a) V. Gandon, N. Agenet, K. P. C. Vollhardt, M. Malacria, C. Aubert, *J. Am. Chem. Soc.* **2006**, *128*, 8509–8520; b) M. J. Eichberg, R. L. Dorta, D. B. Grotjahn, K. Lamottke, M. Schmidt, K. P. C. Vollhardt, *J. Am. Chem. Soc.* **2001**, *123*, 9324–9337 and references cited therein.

Received: December 28, 2006
Published Online: April 23, 2007

 © 2007 Wiley-VCH Verlag GmbH & Co. KGaA, Weinheim 

DOI: 10.1002/ejic.200601255

# Unraveling the *o*-Methoxy Effect in the CO/Ethene Copolymerization Reaction by Diphosphanepalladium(II) Catalysis

**Claudio Bianchini,*[a] Andrea Meli,[a] Werner Oberhauser,*[a] Carmen Claver,[b] and Eduardo J. Garcia Suarez[b]**

**Keywords:** Polyketones / Palladium / Diphosphane ligands / Catalysis / Copolymerization / Kinetics

Relevant steps in the CO/ethene copolymerization reaction, namely the migratory insertion of $[Pd(Me)(CO)(P\text{-}P)]BAr'_4$ and the carbonylation of the β-keto chelates $[Pd(CH_2CH_2C(O)Me)(P\text{-}P)]BAr'_4$ have been studied by in situ high-pressure NMR spectroscopy in $CH_2Cl_2$; P-P = 1,2-bis[bis(2-methoxyphenyl)phosphanyl]ethane or 1,3-bis[bis(2-methoxyphenyl)phosphanyl]propane. This study, backed by batch catalytic reactions in the same solvent, has contributed to rationalizing the higher catalytic activity of $Pd^{II}$ catalysts modified with *o*-methoxy-substituted diphosphane ligands as compared to analogous $Pd^{II}$ catalysts with 1,2-bis(diphenylphosphanyl)ethane (dppe) and 1,3-bis(diphenylphosphanyl)propane (dppp) ligands. It was found that *o*-MeO substituents on the phosphorus aryl rings ease the opening of the β-chelate ring by CO and affect the kinetics of the overall CO/ethene copolymerization. Indeed, unlike the catalysts with the dppe and dppp ligands, the rate of carbonylation of the *o*-MeO-modified β-keto chelates is limited by the Pd(alkyl)(CO) migratory insertion, which makes the overall copolymerization process independent of the CO pressure.
(© Wiley-VCH Verlag GmbH & Co. KGaA, 69451 Weinheim, Germany, 2007)

## Introduction

Perfectly alternating polyketones are high-performance thermoplastics obtainable by copolymerization of carbon monoxide and alkenes, generally ethene, in the presence of $Pd^{II}$ catalysts modified with chelating diphosphanes (Scheme 1).[1] The copolymerization reactions are commonly performed in protic solvents (alcohols, preferentially methanol), yet aprotic solvents such as $CH_2Cl_2$ are used in reactions catalyzed by $Pd^{II}$ alkyl precursors as well as in model mechanistic studies.[2]

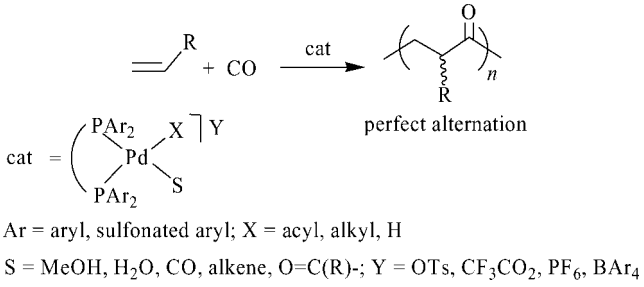


Scheme 1. Copolymerization reaction with $Pd^{II}(P\text{-}P)$ complexes.

The introduction of one *o*-methoxy substituent on each phosphorus aryl ring of the ligand greatly enhances the productivity as compared to reactions promoted by catalysts with unsubstituted diphosphanes.[2d,3]

Both steric and electronic factors have been invoked to account for the positive effect of the *o*-methoxy groups on the catalyst activity, yet no clear-cut explanation has been put forward so far. Indeed, most of the previous hypotheses are based on indirect observations such as the decreased formation of catalytically inactive bis-chelates or binuclear species;[4] the reduced tendency towards phosphane oxidation;[5a] the increased basicity of the metal center;[5b] and the reduced stability of catalyst resting states.[5c]

Intrigued by the possibility of elucidating the *ortho-methoxy effect*, we decided to look at two well-known reactions occurring during the propagation step of the alternating $CO/C_2H_4$ copolymerization: (i) the migratory insertion of $[Pd(Me)(CO)(P\text{-}P)]^+$ complexes and (ii) the carbonylation of the β-keto chelates $[Pd(CH_2CH_2C(O)Me)(P\text{-}P)]^+$ (Scheme 2).[5b,5c]

To this purpose, complexes stabilized by the two couples of ligands shown in Scheme 3 were employed as model compounds.[5b,5c]

In situ high-pressure NMR (HPNMR) and IR techniques have been employed to determine kinetic and thermodynamic parameters, while batch catalytic reactions under different experimental conditions have provided information on the dependence of the reaction rate on CO and ethene pressures. Incorporation of the results obtained

[a] Istituto di Chimica dei Composti Organometallici (ICCOM-CNR), Area di Ricerca CNR di Firenze,
Via Madonna del Piano 10, 50019 Sesto Fiorentino, Italy
Fax: +39-0555225203
E-mail: claudio.bianchini@iccom.cnr.it
werner.oberhauser@iccom.cnr.it
[b] Dept. De Quìmica Fìsica i Inorganica, Facultat de Quìmica, Universitat Rovira i Virgili,
c/Marcel.li Domingo s/n, 43007 Tarragona, Spain

 © 2007 Wiley-VCH Verlag GmbH & Co. KGaA, Weinheim 

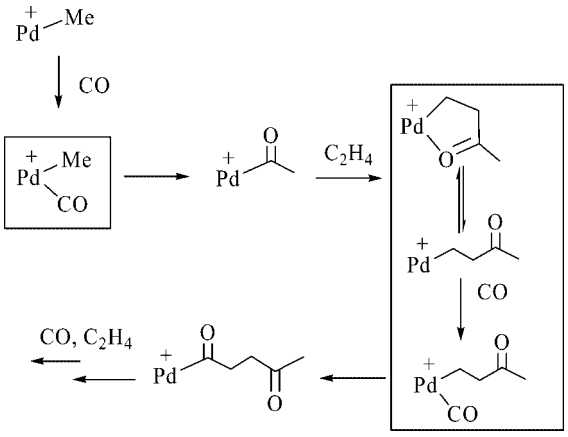


Scheme 2.

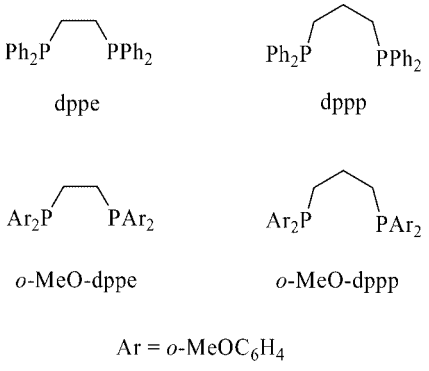


Scheme 3.

unambiguously show that the *o*-methoxy groups can interact with the metal center, leading to a mechanism where the opening of the β-keto chelates and the overall copolymerization rate as well are zero-order with respect to the CO pressure.

## Results and Discussion

### Generation of the β-Keto Chelates [Pd($CH_2CH_2C(O)Me$)(P-P)]$BAr'_4$

The synthetic procedure for the β-keto chelate complexes [Pd($CH_2CH_2C(O)Me$)(P-P)]$BAr'_4$ (P-P = *o*-MeO-dppe, **3c**; *o*-MeO-dppp, **4c**; Ar′ = 3,5-$(CF_3)_2$-$C_6H_3$) is illustrated in Scheme 4.

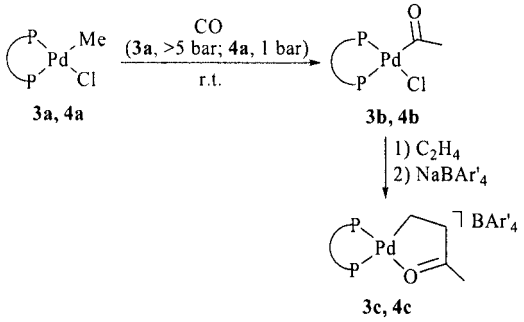


Scheme 4. In situ synthesis of the $Pd^{II}$ β-keto chelates **3c** and **4c**.

The chlorido-methyl precursors [PdCl(Me)(P-P)] (P-P = *o*-MeO-dppe, **3a**; *o*-MeO-dppp, **4a**) were conveniently prepared by the plain reaction of PdCl(Me)(COD) (COD = cycloocta-1,5-diene) with the appropriate diphosphane and isolated as off-white crystalline solids in 78 and 67% yield, respectively.[2d] Unambiguous characterization of **3a** and **4a** in solution was achieved by variable-temperature $^1H$ and $^{31}P\{^1H\}$ NMR spectroscopy in $CD_2Cl_2$. Complexes **3a** and **4a** exhibit fluxional behavior on the NMR time-scale due to the exchange of equatorial and axial aryl groups. The $^1H$ NMR spectrum at 21 °C of either complex displayed one set of resonances for the aryl hydrogen atoms ($\delta$ = 6.87–7.91 and 6.87–7.58 ppm, respectively) and two singlets for the methoxy groups ($\delta$ = 3.59/3.60 and 3.66/3.76 ppm, respectively), which is consistent with the presence of two couples of equivalent aryl groups in the *o*-MeO-ligands. Decreasing the temperature led to a progressive broadening of all resonances. At –70 °C, the $^1H$ NMR spectra of **3a** and **4a** showed four singlets for the methoxy groups at $\delta$ = 3.42, 3.44, 3.75, and 3.76 ppm and $\delta$ = 3.56, 3.67, 3.69, and 3.72 ppm, respectively. This pattern can be safely attributed to the formation of equatorially and axially oriented methoxy groups as illustrated in the sketch reported in Scheme 5.[2d,6]

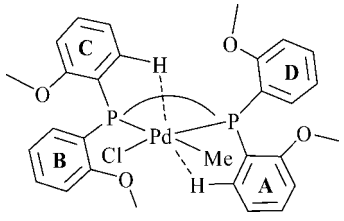


Scheme 5. Low temperature conformation of **3a** and **4a**.

The $^1H$ NMR spectra at –70 °C showed also a significant downfield shift of the resonances of two aryl hydrogen atoms ($\delta$ = 8.45/8.61 and 8.55/8.74 ppm, respectively), which, on the basis of $^1H$-$^{31}P$ COSY experiments, can be assigned to the *o*-H atoms of the axial aryl rings **A** and **C** interacting with the metal center. Analogous fluxional behavior has been previously reported for the X-ray authenticated complexes $PdCl_2$(P-P) (P-P = *o*-MeO-dppe, *o*-MeO-dppp).[2d] Further spectroscopic evidence in support of the conformation proposed in Scheme 5 was provided by a $^1H$ ROESY experiment at –70 °C of **3a**, indicating two significant correlations between the hydrogen atoms of the Pd methyl group and the *o*-H atoms of the aryl rings **A** and **C**.

A single-crystal X-ray analysis of **3a**·$CHCl_3$ has confirmed the structure proposed in solution. Suitable crystals were obtained by slow diffusion of toluene into a $CHCl_3$ solution of **3a**. An ORTEP drawing of **3a**·$CHCl_3$ is shown in Figure 1, while selected distances and angles are reported in Table 1.

The crystal structure shows a square-planar palladium center coordinated by *cis* phosphorus atoms. The Pd–P bond lengths of 2.221(2) Å (*trans* to chloride) and 2.343(2) Å (*trans* to methyl) are in line with the greater *trans*-influence of the methyl group as compared to chlo-

 © 2007 Wiley-VCH Verlag GmbH & Co. KGaA, Weinheim 

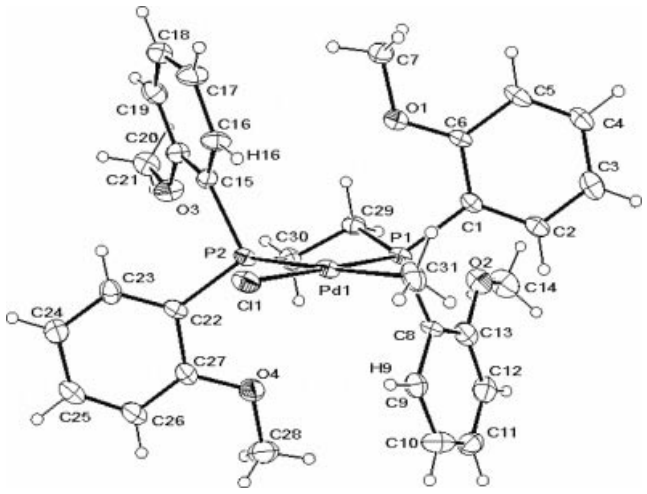


Figure 1. ORTEP plot of **3a**·$CHCl_3$. The solvent molecule was omitted for clarity. Thermal ellipsoids are shown at the 30% probability level.

Table 1. Selected bond lengths and bond angles for **3a·CHCl$_3$**.

| Bond lengths [Å] and bond angles [°] | |
|---|---|
| Pd(1)–P(1) | 2.221(2) |
| Pd(1)–P(2) | 2.343(2) |
| Pd(1)–Cl(1) | 2.389(2) |
| Pd(1)–C(31) | 2.095(8) |
| P(1)–Pd(1)–P(2) | 86.27(9) |
| C(31)–Pd(1)–Cl(1) | 89.30(20) |
| **Intramolecular distances [Å]** | |
| Pd(1)–O(1) | 3.573(6) |
| Pd(1)–O(2) | 5.181(6) |
| Pd(1)–O(3) | 5.271(7) |
| Pd(1)–O(4) | 3.870(6) |
| Pd(1)–H(9) | 2.809 |
| Pd(1)–H(16) | 2.855 |

ride. The four *o*-methoxy oxygen atoms are disposed around the palladium center in such a way that two of them, O(1) and O(4), point to the metal center occupying a pseudo-apical position (Pd···O distances of 3.573(6) and 3.870(6) Å], while the other two, O(2) and O(3), are close to pseudo-equatorial positions (Pd···O distances of 5.181(6) and 5.271(7) Å]. All of these Pd···O distances are too large for an effective electrostatic interaction between palladium and the *o*-methoxy groups. In contrast, the *o*-H atoms H(9) and H(16) show short intramolecular Pd···H distances of 2.809 and 2.855 Å, respectively, which are comparable to those found in the crystal structure of $PdCl_2$(*o*-MeO-dppe).[2d]

Pressurizing a $CH_2Cl_2$ solution of **3a** with >5 bar CO in a 10-mm-OD HPNMR tube at room temperature led to the immediate formation of the acetyl complex PdCl(COMe)(*o*-MeO-dppe) (**3b**). In contrast, the formation of the complex PdCl(COMe)(*o*-MeO-dppp) (**4b**) from **4a** required no pressurization as it was quantitatively obtained by bubbling CO into a $CH_2Cl_2$ solution of the methyl complex at room temperature (Scheme 4). Once formed, the acetyl complexes were stable in solution even in the absence of CO.

Ethene bubbling into $CH_2Cl_2$ solutions of the acyl complexes **3b** and **4b** for 2 min, followed by the addition of stoichiometric $NaBAr'_4$, gave the β-keto chelates **3c** and **4c** (Scheme 4). Compounds **3b**, **3c**, **4b**, and **4c** have been unambiguously characterized by variable-temperature $^{31}P\{^1H\}$ and $^1H$ NMR spectroscopy. Selected NMR spectroscopic data are reported in Table 2 and Table 3, respectively.

Like the chlorido-methyl precursors **3a** and **4a**, the β-keto chelates **3c** and **4c** exhibit fluxional behavior in $CD_2Cl_2$ solution at room temperature, due to the exchange of equatorial and axial aryl groups. At –70 °C both compounds adopt the conformation shown in Scheme 6.

The $^1H$ NMR spectra of **3c** and **4c** at –70 °C showed a multiplet at $\delta$ = 8.48 and 8.28 ppm, respectively, which, on the basis of $^1H$-$^{31}P$ COSY experiments, was assigned to the

Table 2. $^{31}P\{^1H\}$ NMR chemical shifts in ppm, multiplicities in parentheses, and PP coupling constants (Hz) in square brackets for the palladium complexes $[Pd(X)(Y)(P\text{-}P)]^{0/+}$ in $CD_2Cl_2$ solutions at temperatures (°C) given in curly brackets.

| P-P | X = COMe<br>Y = Cl | X, Y = $(CH_2)_2$COMe | X = $(CH_2)_2$COMe<br>Y = CO | X = $CO(CH_2)_2$COMe<br>Y = CO |
|---|---|---|---|---|
| *o*-MeO-dppe | 37.50 (d) [48.7]<br>27.80 (d) {22} | 58.00 (d) [26.0]<br>26.77 (d) {–50} | 57.55 (d) [29.5]<br>25.80 (d) {–50} | 36.02 (d) [49.6]<br>16.74 (d) {–30} |
| *o*-MeO-dppp | 15.40 (d) [75.9]<br>–3.20 (d) {22} | 33.90 (d) [57.6]<br>–12.00 (br. s) {–90} | 21.30 (d) [67.1]<br>–30.50 (br. s) {–90} | 8.86 (d) [86.9]<br>–29.16 (d) {–30} |

Table 3. $^1H$ NMR chemical shifts in ppm, multiplicities in parentheses, for the palladium complexes $[Pd(X)(Y)(P\text{-}P)]^{0/+}$ in $CD_2Cl_2$ solutions at temperatures (°C) given in curly brackets.

| P-P | X = COMe<br>Y = Cl | X, Y = $(CH_2)_2$COMe | X = $(CH_2)_2$COMe<br>Y = CO | X = $CO(CH_2)_2$COMe<br>Y = CO |
|---|---|---|---|---|
| *o*-MeO-dppe | 1.79 (s)<br>CO*Me* {22} | 0.82 (br. m) Pd$CH_2$<br>2.40 (s) CO*Me*<br>3.13 (m) $CH_2$COMe {–50} | 0.30 (br. m) Pd$CH_2$<br>2.10 (s) CO*Me*<br>2.65 (m) $CH_2$COMe {–50} | 1.88 (s) CO*Me*<br>3.10 (m) $CH_2$COMe<br>2.25 (m) PdCO$CH_2$ {–30} |
| *o*-MeO-dppp | 1.73 (s)<br>CO*Me* {22} | 0.84 (br. m) Pd$CH_2$<br>2.17 (s) CO*Me*<br>2.89 (m) $CH_2$COMe {–90} | 0.37 (br. m) Pd$CH_2$<br>1.51 (s) CO*Me*<br>2.42 (m) $CH_2$COMe {–90} | 1.92 (s) CO*Me*<br>2.52 (m) $CH_2$COMe<br>2.08 (m) PdCO$CH_2$ {–30} |

 © 2007 Wiley-VCH Verlag GmbH & Co. KGaA, Weinheim 

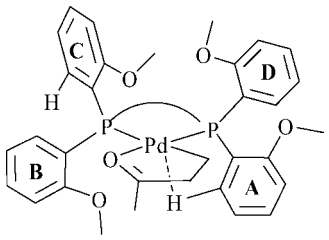


Scheme 6. Low temperature conformation of **3c** and **4c**.

*o*-H atom of ring **A**. At the same temperature, a $^1$H-ROESY experiment of **3c** revealed the existence of significant correlations between the Pd-$CH_2$ unit and the *o*-H atoms of the aryl rings **A** and **D** and between the *o*-methoxy hydrogen atoms from the equatorial aryl ring **B** and the hydrogen atoms of the COMe unit. The stereochemical position of the aryl ring **C** could not be unambiguously determined, yet, due to the lack of the downfield-shifted multiplet of the *o*-H atom of ring **C** in the $^1$H NMR spectrum, it is likely that ring **C** is turned around in such a way that the corresponding *o*-methoxy group points towards the metal center.

The β-keto chelates **3c** and **4c** and the corresponding derivatives with dppe (**1c**) and dppp (**2c**) were also characterized by in-situ IR spectroscopy in $CH_2Cl_2$ at room temperature (Table 4). The spectra were scarcely informative except for showing a blue shift of ca. 6 $cm^{-1}$ of the C=O stretching band for the *o*-methoxy-susbstituted complexes, which is consistent with the higher σ-donor ability of *o*-MeO-dppe and *o*-MeO-dppp as compared to dppe and dppp.

Table 4. Selected IR absorption bands in $CH_2Cl_2$ of selected complexes.

| | [Pd($CH_2CH_2C$(O)Me)-(P-P)]BAr′$_4$ ν(C=O) [$cm^{-1}$] | [Pd(CO)(COMe)-(P-P)]BAr′$_4$ ν(CO)/ν(C=O) [$cm^{-1}$] |
|---|---|---|
| *o*-MeO-dppe | 1636 | 2122/1696 |
| dppe | 1629 | 2130/1693 |
| *o*-MeO-dppp | 1636 | 2122/1700 |
| dppp | 1630 | 2129/1694 |

## Generation and Migratory Insertion Barriers of [PdMe(CO)(P-P)]BAr′$_4$

The carbonyl-methyl complexes [PdMe(CO)(P-P)]BAr′$_4$ (P-P = *o*-MeO-dppe, **3d**; *o*-MeO-dppp, **4d**) were selectively generated in situ by bubbling CO into a HPNMR tube containing a $CD_2Cl_2$ solution of the corresponding chloridomethyl complex at –120 °C.

The kinetics of conversion of the carbonyl-methyl complexes to the (acetyl)carbonyl products [Pd(CO)(COMe)-(P-P)]BAr′$_4$ (P-P = *o*-MeO-dppe, **3e**; *o*-MeO-dppp, **4e**) (Scheme 7) were conveniently followed by variable-temperature $^{31}P\{^1H\}$ NMR spectroscopy in $CD_2Cl_2$. $^{31}P\{^1H\}$ and $^1$H NMR spectroscopic data for **3d**–**4e** are given in Table 5 and Table 6, respectively.

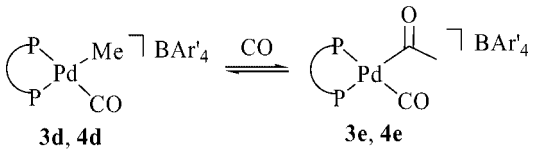


Scheme 7. Migratory insertion of **3d** and **4d**.

Table 5. $^{31}P\{^1H\}$ NMR chemical shifts in ppm, multiplicities in parentheses, and PP coupling constants (Hz) in square brackets for the palladium complexes [Pd(X)(Y)(P-P)]BAr′$_4$ in $CD_2Cl_2$ solutions at temperatures (°C) given in curly brackets.

| P-P | X = Me,Y = CO | X = COMe, Y = CO |
|---|---|---|
| *o*-MeO-dppe | 57.59 (d) [31.0] | 35.75 (d) [48.7] |
| | 24.34 (d) {–50} | 16.55 (d) {–40} |
| *o*-MeO-dppp | 22.40 (d) [62.8] | 8.00 (d) [88.7] |
| | –29.9 (br. s) {–90} | –28.5 (d) {–40} |

Table 6. $^1$H NMR chemical shifts in ppm and multiplicities in parentheses for the palladium complexes [Pd(X)(Y)(P-P)]BAr′$_4$ in $CD_2Cl_2$ solutions at temperatures (°C) given in curly brackets.

| P-P | X = Me, Y = CO | X = COMe, Y = CO |
|---|---|---|
| *o*-MeO-dppe | 0.43 (m) {–50} | 1.65 (s) {–40} |
| *o*-MeO-dppp | 0.08 (m) {–90} | 1.88 (s) {–40} |

Consistent with the greater σ-donor ability of *o*-MeO-dppe and *o*-MeO-dppp vs. dppe and dppp, the IR spectra of the (acetyl)carbonyl complexes **3e** and **4e** in $CH_2Cl_2$ (Table 4) showed a blue shift of the COMe absorption band (3–6 $cm^{-1}$) and a red shift of the CO absorption band (7–8 $cm^{-1}$) as compared to the analogue derivatives [Pd(CO)-(COMe)(P-P)]BAr′$_4$ with dppe (**1e**) and dppp (**2e**).[2b,2c]

The study of the migratory insertion of the methyl(carbonyl) complexes was carried out at different CO pressures (5–20 bar), showing the reaction rate to be independent of the CO concentration. According to first-order kinetics, the free energy of activation for the migration insertion process was calculated applying the equation: $\Delta G^{\ddagger} = RT(\ln kT/h -$

Table 7. Experimental activation barriers and temperatures for the migratory insertions of (alkyl)carbonyl complexes and for the carbonylation of β-chelates.

| P-P | [Pd(Me)(CO)(P-P)]$^+$ | | | [Pd($CH_2CH_2C$(O)Me)(P-P)]$^+$ | | | [Pd($CH_2CH_2C$(O)Me)(CO)(P-P)]$^+$ | | |
|---|---|---|---|---|---|---|---|---|---|
| | $T$ [°C] | $t_{1/2}$ [min] | $\Delta G^{\ddagger}$ [kcal/mol] | $T$ [°C] | $t_{1/2}$ [min] | $p$(CO) [bar] | $T$ [°C] | $t_{1/2}$ [min] | $\Delta G^{\ddagger}$ [kcal/mol] |
| *o*-MeO-dppe | –40 | 52 | 17.4(1) | –60 | 25 | 20 | –40 | 100 | 17.7(1) |
| dppe[2b] | –40 | 12 | 16.9(1) | –20 | 15 | 20 | | | |
| *o*-MeO-dppp | –80 | 105 | 14.6(1) | –90 | 6 | 20 | –60 | 10 | 15.2(1) |
| dppp[2c] | –60 | 10 | 15.2(1) | –70 | 84 | 20 | | | |

 © 2007 Wiley-VCH Verlag GmbH & Co. KGaA, Weinheim 

$\ln k_r$) with $k_r = \ln 2/t_{1/2}$ ($T$ = temperature during the conversion; $t_{1/2}$ = half-life time in seconds).[2b,2c] The values of the activation energies for the migratory insertion in **3d** and **4d** are given in Table 7 that also reports data previously reported for the dppe and dppp analogues [PdMe(CO)(P-P)]-$BAr'_4$ (P-P = dppe, **1d**; dppp, **2d**).[2b,2c]

The results obtained showed the migratory insertion of PdMe(CO) to be a low-energy process for all complexes; in addition it was lower for the dppp complexes than for the dppe ones and, in particular, for the *o*-MeO-dppp complex **4d**, which is known to generate the most active catalysts in several reaction media.[2d]

### Carbonylation Reactions of the β-Keto Chelates

The reactions of the β-keto chelates **3c** and **4c** with 20 bar CO in $CD_2Cl_2$ were studied in situ by $^1H$ and $^{31}P\{^1H\}$ HPNMR spectroscopy at low temperature. HPNMR tubes containing $CD_2Cl_2$ solutions of these complexes under nitrogen were cooled to ca. –120 °C, pressurized with 20 bar CO, and then inserted into the NMR probe-head pre-cooled to –90 °C. The conversion of the β-keto chelates into the (acyl)carbonyl complexes [Pd(CO)-$(COCH_2CH_2C(O)Me)$(P-P)]$BAr'_4$ (P-P = *o*-MeO-dppe, **3g**; *o*-MeO-dppp, **4g**) was found to involve (alkyl)carbonyl intermediates of the formula [Pd(CO)$(CH_2CH_2C(O)Me)$-(P-P)]$BAr'_4$ (P-P = *o*-MeO-dppe, **3f**; *o*-MeO-dppp, **4f**) (Scheme 8). Selected $^{31}P\{^1H\}$ and $^1H$ NMR spectroscopic data of the final products and intermediates are reported in Table 2 and Table 3, respectively, while sequences of $^{31}P\{^1H\}$ NMR spectra acquired during the carbonylation of either **3c** or **4c** with 20 bar CO are reported in Figure 2 and Figure 3, respectively.

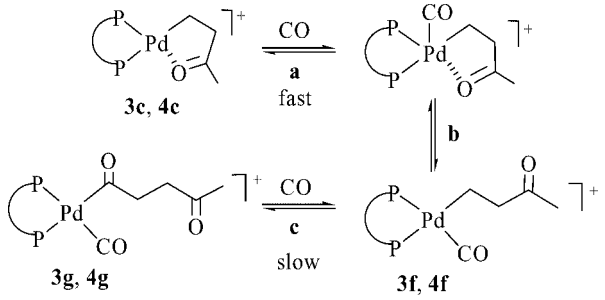


Scheme 8. Carbonylation of **3c** and **4c**.

Compound **3c** started to convert into the (alkyl)carbonyl complex **3f** at –60 °C with a $t_{1/2}$ value of 25 min (Figure 2, trace b). Increasing the temperature to –40° led to the quantitative formation of **3f** already after recording the first $^{31}P\{^1H\}$ NMR spectrum (trace c). At this temperature, **3f** slowly converted into the (acyl)carbonyl complex **3g** (trace d), which was the only phosphorus-containing species at room temperature (trace e).

In an analogous experiment, **4c** was found to convert already at –90 °C into the (alkyl)carbonyl complex **4f** (Figure 3, trace b), which, in turn, started to transform into the final (acyl)carbonyl product **4g** at –80 °C. Because of the slow conversion rate at this temperature, the migratory insertion of **4f** was more conveniently evaluated at –60 °C (trace d).

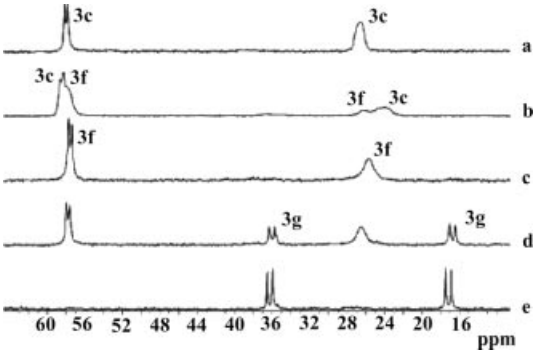


Figure 2. Variable-temperature $^{31}P\{^1H\}$ NMR study (sapphire tube, $CD_2Cl_2$, 81.01 MHz) of the carbonylation reaction of **3c**: (a) under nitrogen at –90 °C; (b) under CO (20 bar) after 40 min at –60 °C; (c) after 5 min at –40 °C; (d) after 80 min at –40 °C; (e) at room temperature.

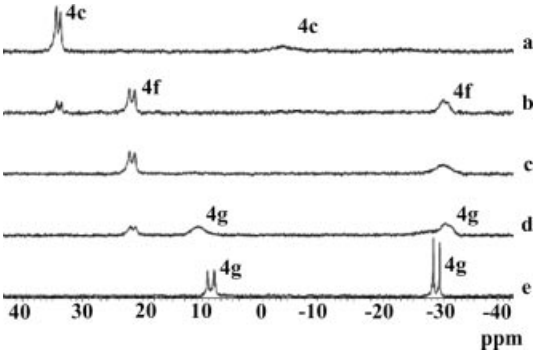


Figure 3. Variable-temperature $^{31}P\{^1H\}$ NMR study (sapphire tube, $CD_2Cl_2$, 81.01 MHz) of the carbonylation reaction of **4c**: (a) under nitrogen at –90 °C; (b) under CO (20 bar) after 30 min at –90 °C; (c) after 30 min at –80 °C; (d) after 10 min at –60 °C; (e) at room temperature.

To the best of our knowledge, (alkyl)carbonyl compounds such as **3f** and **4f** have never been intercepted along the carbonylation of diphosphane-modified palladium alkyl complexes. Like all the other new products obtained in situ, the characterization of the (alkyl)carbonyl complexes was achieved by NMR spectroscopy as well as by comparison with the spectra of similar or related complexes (i.e., γ-keto acyl chelates)[7] described in the literature (Table 2 and Table 3). Experimental evidence supporting the (alkyl)carbonyl structure of **3f** and **4f** was provided by the $^{31}P$ chemical shifts and the $^2J_{PP}$ coupling constants that were practically identical to those of the carbonyl-methyl complexes **3d** and **4d**. Moreover, the $^1H$ NMR shifts of the $PdCH_2CH_2C(O)Me$ units were significantly upfield shifted with respect to the values observed for the β-keto chelates (**3c** vs. **3f**: C(O)Me, $\delta$ = 2.40 vs. 2.10 ppm; $PdCH_2$, $\delta$ = 0.82 vs. 0.30 ppm; **4c** vs. **4f**: C(O)Me, $\delta$ = 2.17 vs. 1.51 ppm;

 © 2007 Wiley-VCH Verlag GmbH & Co. KGaA, Weinheim 

$PdCH_2$, $\delta$ = 0.84 vs. 0.37 ppm). In particular, the high-field shift of the C(O)Me singlets agrees well with the de-coordination of the carbonyl-oxygen atom from the metal center.[7g]

Temperatures and $t_{1/2}$ values for the conversion of the β-chelates **3c** and **4c** into the corresponding (alkyl)carbonyl product and the activation energies of the migratory insertions of the latter compounds are reported in Table 7. The opening of the β-chelate ring by CO is apparently easier for the *o*-MeO-susbstituted complexes than for the $PPh_2$-ones, which might well account for the greater catalytic activity of the former complexes in batch reactions.[2d,3–5]

In the light of the kinetic and thermodynamic data relative to the opening of the β-chelate ring by CO and to the alkyl migration to CO (Table 7), one may safely conclude that the latter process (step **c** of Scheme 8) limits the overall rate of the transformation of **3c** and **4c** into the (acyl)carbonyl products **3g** and **4g**, which is a relevant step in the propagation mechanism of the CO/ethene copolymerization by $Pd^{II}$-diphosphane catalysis.[1] Accordingly, since the Pd(CO)alkyl migratory insertion is independent of the CO pressure (vide infra), the overall copolymerization process would be independent of the CO pressure, at least under a gas pressure of 20 bar. This result dramatically differs from the previously reported studies of CO/ethene copolymerization by the $PPh_2$-precursors **1c** and **2c** where the actual copolymerization rate depends on both CO and $C_2H_4$ pressure[8] and the opening of the β-chelates by CO is the rate-limiting step in the propagation step involving CO insertion (Table 7).[2b,2c]

### Catalytic CO/Ethene Copolymerization Reactions

In an attempt to determine the dependence of the copolymerization rate on CO and ethene pressures under actual catalytic conditions, several batch reactions were carried out using either the *o*-MeO-modified chlorido-methyl complex **4a** or the analogous dppp derivative **2a** in $CH_2Cl_2$ at 50 °C.[2d] The results of this study are summarized in Table 8 which also reports data obtained in MeOH with the known catalyst $[Pd(H_2O)_2(o\text{-MeO-dppp})](OTs)_2$ (**4h**).[2d] In excellent accord with the present kinetic study, the catalytic activity of **4a** did not vary with the CO pressure in the range from 5 to 30 bar (entries 1, 2, 4), whereas an increase in activity occurred on increasing the $C_2H_4$ pressure (entry 3 vs. 2). In contrast, the productivity of the dppp precursor **2a** showed a clear dependence on the CO pressure (entries 5–6), which is in agreement with a previous kinetic study by Toniolo and Chaudhary for reactions carried out in MeOH.[8] The latter solvent was therefore used in reactions catalyzed by the *o*-MeO-dppp precursor **4h** (entries 7–9) which showed no dependence on the CO pressure above 10 bar, thus confirming and generalizing the results of the present kinetic study in $CH_2Cl_2$. Noteworthy, a zero-order dependence on the CO pressure has also been reported for the CO/ethene/propene terpolymerization catalyzed by the water-soluble system Pd acetate/sulfonated *o*-MeO-dppp.[3d]

Table 8. Ethene/CO copolymerization reactions catalyzed by diphosphanepalladium precursors in different solvents.

| Entry[a] | Precursor | P(CO) [bar] | $P(C_2H_4)$ [bar] | Productivity[b] |
|---|---|---|---|---|
| 1 | PdCl(Me)(*o*-MeO-dppp) | 5 | 20 | 5.0 |
| 2 | PdCl(Me)(*o*-MeO-dppp) | 20 | 20 | 5.1 |
| 3 | PdCl(Me)(*o*-MeO-dppp) | 20 | 40 | 7.4 |
| 4 | PdCl(Me)(*o*-MeO-dppp) | 30 | 20 | 4.9 |
| 5 | PdCl(Me)(dppp) | 5 | 20 | 0.6 |
| 6 | PdCl(Me)(dppp) | 20 | 20 | 2.8 |
| 7[c] | $[Pd(H_2O)_2(o\text{-MeO-dppp})](OTs)_2$ | 10 | 20 | 17.0 |
| 8[c] | $[Pd(H_2O)_2(o\text{-MeO-dppp})](OTs)_2$ | 15 | 20 | 16.8 |
| 9[c] | $[Pd(H_2O)_2(o\text{-MeO-dppp})](OTs)_2$ | 20 | 20 | 18.1 |

[a] Reaction conditions: precursor (0.010 mmol), $CH_2Cl_2$ (75 mL), $NaBAr'_4$ (1.5 equiv.), BQ (80 equiv.), 20 min, 50 °C, 1200 rpm. [b] Productivity: kilograms of alt-E-CO (g Pd × h)$^{-1}$. [c] Reaction conditions: precursor (0.0024 mmol), MeOH (100 mL), 1 h, 85 °C, 1200 rpm.

## Conclusions

The present study confirms that *o*-MeO substituents on the P-aryl rings of chelating diphosphanes exert a beneficial effect on the activity of $Pd^{II}$ catalysts for the alternating CO/ethene copolymerization. Electronic effects, related to the ability of the methoxy oxygen atoms to interact with the metal center, seem to play a major role in driving the catalytic activity. Indeed, even though no direct evidence for the coordination of the *o*-MeO group to palladium has been observed in the course of either migratory insertion or carbonylation reactions, NMR spectroscopy has shown the aryl rings to adopt a conformation which favors the interaction between the *o*-MeO oxygen atoms and the metal center.

High-pressure NMR studies supported by batch catalytic reactions have unambiguously shown that the presence of *o*-MeO substituents on the P-aryl rings affects the kinetics of the CO/ethene copolymerization by $Pd^{II}$-chelating diphosphane catalysis. Unlike analogous catalysts without *o*-methoxy-substituted ligands, the rate of carbonylation of the β-keto chelates is limited by the Pd(alkyl)(CO) migratory insertion, which makes the overall copolymerization process independent of the CO pressure, at least in the range of the partial CO pressures investigated (5–30 bar).

## Experimental Section

**General Procedures:** All reactions and manipulations were carried out under nitrogen using Schlenk-type techniques. The solvents were generally distilled from dehydrating reagents and were deoxygenated before use. The reagents were used as purchased from Aldrich or Fluka, unless stated otherwise. PdCl(Me)(COD)[9] (COD = cycloocta-1,5-diene), $[Pd(CH_2CH_2C(O)Me)(dppe)]BAr'_4$ (**1c**),[2b] $[Pd(CH_2CH_2C(O)Me)(dppp)]BAr'_4$ (**2c**),[2c] [Pd(CO)(C(O)Me)-(dppe)]$BAr'_4$ (**1e**),[2b] [Pd(CO)(C(O)Me)(dppp)]$BAr'_4$ (**2e**),[2c] and $NaBAr'_4$[10] were prepared according to literature methods. All the isolated solid samples were collected on sintered-glass frits and washed with appropriate solvents before being dried under a stream of nitrogen. Copolymerization reactions were performed with a 250-mL stainless steel autoclave, constructed at the ICCOM-CNR

 © 2007 Wiley-VCH Verlag GmbH & Co. KGaA, Weinheim 

(Florence, Italy), equipped with a magnetic drive stirrer and a Parr 4842 temperature and pressure controller. The autoclave was connected to a gas reservoir to maintain a constant pressure during the catalytic reactions. GC/MS analyses of the solutions were performed on a Shimadzu QP2100S apparatus equipped with a SPB-1 Supelco fused silica capillary column (30 m, 0.25 mm i.d., 0.25 μm film thickness). Deuterated solvents for routine NMR measurements were dried with molecular sieves. $^{1}H$, $^{13}C\{^{1}H\}$, $^{31}P\{^{1}H\}$ NMR spectra were obtained with either a Bruker ACP 200 (200.13, 50.32 and 81.01 MHz, respectively) or a Bruker Avance DRX-400 spectrometer (400.13, 100.62 and 161.98 MHz), respectively. Chemical shifts are reported in ppm ($\delta$) relative to TMS, referenced to the chemical shifts of residual solvent resonances ($^{1}H$ and $^{13}C$ NMR) or 85% $H_3PO_4$ ($^{31}P$ NMR). $^{1}H$-$^{31}P$ COSY spectra and $^{1}H$ ROESY were recorded with a Bruker Avance DRX-400 spectrometer. High-pressure NMR experiments were carried out on the Bruker ACP 200 using a 10-mm sapphire NMR tube, which was purchased from Saphikon (Milford, NH), while the titanium high-pressure charging head was constructed at the ISSECC-CNR (Florence, Italy).[11] Elemental analyses were performed using a Carlo Erba Model 1106 elemental analyzer. Infrared spectra were recorded on a FT-IR Spectrum GX instrument (Perkin–Elmer).

***S*ynthesis of the Methyl-chlorido Complexes PdCl(Me)(P-P):**[2d] A solid sample of PdCl(Me)(COD) (0.20 mmol, 52.99 mg) was added to a stirred solution of the appropriate diphosphane ligand (0.20 mmol) in $CH_2Cl_2$ (20 mL) at room temperature. After 1 h, the resulting colorless solution was concentrated to ca. 5 mL under reduced pressure. Addition of *n*-pentane/diethyl ether (1:1, v/v; 20 mL) led to the precipitation of [PdCl(Me)(P-P)] (P-P = *o*-MeO-dppe, **3a**; *o*-MeO-dppp, **4a**) as an off-white solid, which was filtered off, washed with *n*-pentane, and dried under a stream of nitrogen.

**3a:** Yield 78%, 105.31 mg. $C_{31}H_{35}ClO_4P_2Pd$ (675.11): calcd. C 55.13, H 5.22; found C 55.09, H 5.24. $^{31}P\{^{1}H\}$ NMR (81.1 MHz, $CDCl_3$, 21 °C): $\delta$ = 61.09 (d, $^{2}J_{P,P}$ = 22.0 Hz, $P_A$), 39.07 (d, $P_M$) ppm. $^{1}H$ NMR (200.13 MHz, $CDCl_3$, 21 °C): $\delta$ = 0.40 (dd, $^{3}J_{H,PM}$ = 8.0 Hz, $^{3}J_{H,PA}$ = 3.2 Hz, 3 H, PdMe), 2.19–2.93 (m, 4 H, $PCH_2$), 3.59 (s, 6 H, OMe), 3.60 (s, 6 H, OMe), 6.87–7.91 (m, 16 H, Ar) ppm. $^{31}P\{^{1}H\}$ NMR (161.98 MHz, $CD_2Cl_2$, –70 °C): $\delta$ = 60.70 (d, $^{2}J_{P,P}$ = 23.2 Hz, $P_A$), 38.32 (d, $P_M$) ppm. $^{1}H$ NMR (400.16 MHz, $CD_2Cl_2$, –70 °C): $\delta$ = 0.40 (dd, $^{3}J_{H,PM}$ = 8.0 Hz, $^{3}J_{H,PA}$ = 3.0 Hz, 3 H, PdMe), 2.08 (m, 1 H, PCH*H*), 2.38 (m, 1 H, P′CH*H*), 2.91 (dt, $^{2}J_{H,P}$ = 56.0 Hz, $^{3}J_{H,H}$ = 13.6 Hz, 1 H, PC*H*H), 3.08 (dt, $^{2}J_{H,P}$ = 56.0 Hz, $^{3}J_{H,H}$ = 13.6 Hz, 1 H, P′C*H*H), 3.42 (s, 3 H, OMe), 3.44 (s, 3 H, OMe), 3.76 (s, 6 H, OMe), 6.72–7.73 (m, 14 H, Ar), 8.45 (dd, $^{2}J_{H,P}$ = 15.9 Hz, $^{3}J_{H,H}$ = 7.3 Hz, 1 H, *o*-H-$Ar_{ax.}$(A), 8.61 (dd, $^{2}J_{H,P}$ = 15.1 Hz, $^{3}J_{H,H}$ = 7.5 Hz, 1 H, *o*-H-$Ar_{ax.}$(C)) ppm.

**4a:** Yield 67%, 91.92 mg. $C_{32}H_{37}ClO_4P_2Pd$ (689.11): calcd. C 55.75, H 5.41; found C 55.74, H 5.43. $^{31}P\{^{1}H\}$ NMR (81.01 MHz, $CDCl_3$, 21 °C): $\delta$ = 30.80 (d, $^{2}J_{P,P}$ = 52.5 Hz, $P_A$), –0.56 (d, $P_M$) ppm. $^{1}H$ NMR (200.13 MHz, $CDCl_3$, 21 °C): $\delta$ = 0.32 (dd, $^{3}J_{H,PM}$ = 7.9 Hz, $^{3}J_{H,PA}$ = 3.5 Hz, PdMe), 1.92 (m, 2 H, $CH_2$), 2.43 (m, 2 H, $PCH_2$), 2.57 (m, 2 H, $PCH_2$), 3.66 (s, 6 H, OMe), 3.75 (s, 3 H, OMe), 3.76 (s, 3 H, OMe), 6.87–7.58 (m, 16 H, Ar) ppm. $^{31}P\{^{1}H\}$ NMR (161.98 MHz, $CD_2Cl_2$, –70 °C): $\delta$ = 30.88 (d, $^{2}J_{P,P}$ = 51.4 Hz, $P_A$), –2.42 (d, $P_M$) ppm. $^{1}H$ NMR (400.16 MHz, $CD_2Cl_2$, –70 °C): $\delta$ = –0.89 (dd, $^{3}J_{H,PM}$ = 7.7 Hz, $^{3}J_{HPA}$ = 3.2 Hz, PdMe), 1.70 (m, 1 H, CH*H*)), 1.92 (m, 1 H, C*H*H), 2.20 (m, 1 H, PCH*H*), 2.30 (m, 1 H, P′CH*H*), 2.48 (m, 1 H, PC*H*H), 2.79 (m, 1 H, P′C*H*H), 3.56 (s, 3 H, OMe), 3.67 (s, 3 H, OMe), 3.69 (s, 3 H, OMe), 3.72 (s, 3 H, OMe), 6.67–7.71 (m, 14 H, Ar), 8.55 (dd, $^{2}J_{H,P}$ = 16.4 Hz, $^{3}J_{H,H}$ = 7.3 Hz, 1 H, *o*-H-$Ar_{ax.}$(A)), 8.74 (dd, $^{2}J_{H,P}$ = 14.7 Hz, $^{3}J_{H,H}$ = 7.1 Hz, 1 H, *o*-H-$Ar_{ax.}$(C)) ppm.

**In Situ Synthesis of the (Acetyl)Chloride Complexes PdCl(COMe)-(P-P):** In a typical experiment, a solid sample of the methyl-chlorido complex PdCl(Me)(P-P) (0.03 mmol) was dissolved in a Schlenk tube containing $CD_2Cl_2$ (2 mL) under nitrogen at room temperature. The resulting solution was first transferred into a 10-mm sapphire tube and then pressurized to >5 bar of CO at room temperature. Irrespective of the diphosphane the quantitative formation of the corresponding (acetyl)chloride complex PdCl(CO-Me)(P-P) (P-P = *o*-MeO-dppe, **3b**; *o*-MeO-dppp, **4b**) occurred at room temperature. The most relevant $^{31}P\{^{1}H\}$ and $^{1}H$ NMR chemical shifts and coupling constants for **3b** and **4b** are reported in Tables 2 and 3, respectively. The excess CO was released and nitrogen was gently bubbled through the solution previously cooled to –30 °C for 2 min to eliminate any trace of CO. Both complexes were found to be stable also in the absence of CO. Unlike **3b**, **4b** was generated even by bubbling CO through **4a** solutions for 5 min at room temperature. A procedure analogous to that described above was applied to prepare $CH_2Cl_2$ solutions of **3b** and **4b** for the IR characterization: ν(C=O) 1669 (**3b**), 1674 (**4b**) $cm^{-1}$.

**In Situ Synthesis of the β-Keto Chelates [Pd($CH_2CH_2C$(O)Me)-(P-P)]$BAr'_4$:** In a typical experiment, a solution of PdCl(COMe)-(P-P) (0.03 mmol) in $CD_2Cl_2$ (2 mL) was prepared as above in a Schlenk tube at –30 °C under nitrogen. Ethene was bubbled through the solution maintained at –30 °C for 2 min and then a solid sample of $NaBAr'_4$ (0.03 mmol) was added to the solution to scavenge the chloride ligand from Pd. The resulting solution was transferred into a 10-mm sapphire tube. $^{31}P\{^{1}H\}$ and $^{1}H$ NMR spectra were acquired in the temperature range from 20 to –90 °C. Irrespective of the diphosphane ligand, the $^{31}P\{^{1}H\}$ and $^{1}H$ NMR spectra of this sample showed the quantitative conversion of the (acyl)chloride complex into the corresponding β-chelate complex [Pd($CH_2CH_2C$(O)Me)(P-P)]$BAr'_4$ (P-P = *o*-MeO-dppe, **3c**; *o*-MeO-dppp, **4c**). IR spectra of **3c** and **4c** were acquired from $CH_2Cl_2$ solutions of these compounds prepared by applying the same synthetic protocol as described above, using $CH_2Cl_2$ instead of $CD_2Cl_2$. The IR values of the CO stretching frequencies are reported in Table 4.

**3c:** $^{31}P\{^{1}H\}$ NMR (161.98 MHz, $CD_2Cl_2$, –70 °C): $\delta$ = 57.36 (d, $^{2}J_{P,P}$ = 26.9 Hz, $P_A$), 25.43 (br., $P_M$) ppm. $^{1}H$ NMR (400.13 MHz, $CD_2Cl_2$, –70 °C): $\delta$ = 0.82 (m, 1 H, PdCH*H*), 1.21 (m, 1 H, PdC*H*H), 2.05 (m, 2 H, $PCH_2$), 2.42 (m, 3 H, COMe), 2.58 (m, 2 H, P′$CH_2$), 2.80 (m, 1 H, COCH*H*), 3.08 (m, 4 H, COC*H*H + OMe), 3.51 (s, 3 H, OMe), 3.80 (s, 3 H, OMe), 3.83 (s, 3 H, OMe), 6.72–7.82 (m, 27 H, Ar), 8.48 [dd, $^{2}J_{H,P}$ = 17.0 Hz, $^{3}J_{H,H}$ = 7.3 Hz, 1 H, *o*-H-$Ar_{ax.}$(A)] ppm.

**4c:** $^{31}P\{^{1}H\}$ NMR (161.98 MHz, $CD_2Cl_2$, –70 °C): $\delta$ = 33.51 (d, $^{2}J_{PP}$ = 57.9 Hz, $P_A$), –12.4 (br., $P_M$) ppm. $^{1}H$ NMR (400.13 MHz, $CD_2Cl_2$, –70 °C): $\delta$ = 0.95 (m, 2 H, $PdCH_2$), 2.21 (s, 3 H, COMe), 2.31 (m, 3 H, PC*H*H + C$H_2$), 2.51 (m, 2 H, PCH*H* + P′CH*H*), 2.92 (m, 3 H, $COCH_2$ + P′C*H*H), 3.59 (s, 3 H, OMe), 3.70 (s, 3 H, OMe), 3.83 (s, 3 H, OMe), 3.86 (s, 3 H, OMe), 6.62–7.83 (m, 27 H, Ar), 8.28 [dd, $^{2}J_{H,P}$ = 17.0 Hz, $^{3}J_{H,H}$ = 7.1 Hz, 1 H, *o*-H-$Ar_{ax.}$(A)] ppm.

**In Situ Generation and Migratory Insertion Barriers of [PdMe(CO)-(P-P)]$BAr'_4$. HPNMR Experiments:** In a typical experiment, the methyl-chlorido complex [PdCl(Me)(P-P)] (0.03 mmol) was dissolved in deoxygenated $CD_2Cl_2$ (2 mL) and the resulting solution was then transferred into a 10-mm sapphire tube, which was cooled to –120 °C by means of an ethanol/liquid nitrogen bath. CO was bubbled through this solution for 2 min at this temperature, fol-

 © 2007 Wiley-VCH Verlag GmbH & Co. KGaA, Weinheim 

lowed by the addition of $NaBAr'_4$ (0.03 mmol). The CO pressure was adjusted to the desired value (5–20 bar). The solution was shaken for 2 min at –120 °C, followed by the introduction of the sapphire tube into the probe-head previously cooled to –90 °C. Irrespective of the diphosphane ligand, the $^{31}P\{^1H\}$ and $^1H$ NMR spectra showed the quantitative conversion of the starting methyl-chlorido complex into the corresponding carbonyl-methyl complexes [PdMe(CO)(P-P)]$BAr'_4$ (P-P = *o*-MeO-dppe, **3d**; *o*-MeO-dppp, **4d**) (selected $^{31}P\{^1H\}$ and $^1H$ NMR spectroscopic data of the carbonyl-methyl complexes are reported in Tables 5 and 6, respectively). Afterwards the probe temperature was gradually increased and $^{31}P\{^1H\}$ and $^1H$ NMR spectra were recorded at each intermediate temperature. Increasing the temperature converted each carbonyl-methyl complex into the corresponding (acetyl)carbonyl derivative [Pd(COMe)(CO)(P-P)]$BAr'_4$ (P-P = *o*-MeO-dppe, **3e**; *o*-MeO-dppp, **4e**) (selected $^{31}P\{^1H\}$ and $^1H$ NMR spectroscopic data of the (acetyl)carbonyl complexes are reported in Tables 5 and 6, respectively). At the conversion temperature, the decrease in concentration of the carbonyl-methyl complex was followed by $^{31}P\{^1H\}$ NMR spectroscopy. Spectra were taken at intervals of 5–10 min, depending on conditions. The reaction was followed for 2–3 half-lives. IR spectra of **3e** and **4e** were acquired from $CH_2Cl_2$ solutions of these compounds prepared by applying the same synthetic protocol as described above, using $CH_2Cl_2$ instead of $CD_2Cl_2$. The IR values of the CO stretching frequencies are reported in Table 4.

**Carbonylation of the β-Keto Chelates [Pd($CH_2CH_2C(O)Me$)(P-P)]$BAr'_4$. HPNMR Experiments:** $CD_2Cl_2$ (2 mL) solutions of the β-keto chelates [Pd($CH_2CH_2C(O)Me$)(P-P)]$BAr'_4$ (P-P = *o*-MeO-dppe, **3c**; *o*-MeO-dppp, **4c**) (0.03 mmol) were synthesized in situ in a Schlenk tube at –30 °C, as described above. Nitrogen was bubbled through the solution to eliminate any trace of ethene. The solutions were transferred into a 10-mm sapphire tube at room temperature. Then the sapphire tube was introduced in a pre-cooled NMR probe (–90 °C) and $^{31}P\{^1H\}$ and $^1H$ NMR spectra were acquired at this temperature. The sapphire tube was then removed from the probe and immersed in an ethanol/liquid nitrogen thermostat bath (ca. –120 °C) before to be charged with CO (5–20 bar). Afterwards the sapphire tube was introduced again into the NMR probe head at –90 °C. $^{31}P\{^1H\}$ and $^1H$ NMR spectra showed that the β-chelate complexes were still present. Afterwards the probe temperature was gradually increased and $^{31}P\{^1H\}$ and $^1H$ NMR spectra were recorded at each intermediate temperature. Increasing the temperature caused the conversion of the β-chelate complex into the corresponding (acyl)carbonyl derivative [Pd(CO)($COCH_2CH_2C(O)Me$)(P-P)]$BAr'_4$ (P-P = *o*-MeO-dppe, **3g**; *o*-MeO-dppp, **4g**) via the (alkyl)carbonyl complexes [Pd(CO)($CH_2CH_2C(O)Me$)(P-P)]$BAr'_4$ (P-P = *o*-MeO-dppe, **3f**; *o*-MeO-dppp, **4f**). Selected high-pressure $^{31}P\{^1H\}$ NMR spectra of the carbonylation of either **3c** or **4c** under 20 bar of CO are shown in Figures 2 and 3, respectively. Selected $^{31}P\{^1H\}$ and $^1H$ NMR spectroscopic data of the complexes **3f**, **4f**, **3g**, and **4g** are reported in Tables 2 and 3, respectively. At the conversion temperature the decrease in concentration of the β-keto chelates was followed by $^{31}P\{^1H\}$ NMR spectroscopy. Spectra were taken at intervals of 5–10 min, depending on conditions. The reaction was followed for 2–3 half-lives.

**[Pd($CH_2CH_2C(O)Me$)(P-P)]$BAr'_4$/[Pd($COCH_2CH_2C(O)Me$)(CO)(P-P)]$BAr'_4$ Equilibria:** Solutions of the (acyl)carbonyl complexes **3g** and **4g**, prepared as reported above in HPNMR tubes, were immersed in a thermostat bath at –20 °C. CO was released and then couples of vacuum-nitrogen cycles were applied. $^{31}P\{^1H\}$ and $^1H$ NMR spectra of these samples acquired at –20 °C allowed us to follow the transformation of the (acyl)carbonyl complexes into the corresponding β-chelates **3c** and **4c**.

**Catalytic Copolymerization Reactions in $CH_2Cl_2$:** $CH_2Cl_2$ (75 mL), saturated with CO at room temperature, was introduced by suction into an autoclave (250 mL), previously evacuated by a vacuum pump, containing the catalyst precursor (0.010 mmol) and $NaBAr'_4$ (0.012 mmol). The autoclave was charged with the required pressures of CO and $C_2H_4$ at room temperature and then heated. As soon as the temperature reached 50 °C, stirring (1200 rpm) was started and the catalytic reaction was conducted under constant pressure. After 20 min, the autoclave was cooled by means of an ice-water bath and the unreacted gases were released. The insoluble copolymer was filtered off, washed with $CH_2Cl_2$, and dried under vacuum at 60 °C to constant weight.

**Catalytic Copolymerization Reactions in MeOH:** Typically, MeOH (100 mL), was introduced by suction into an autoclave (250 mL), previously evacuated by a vacuum pump, containing the catalyst precursor (0.0024 mmol) and 1,4-benzoquinone (BQ, 0.192 mmol). The autoclave was charged with the desired pressure of CO and $C_2H_4$ at room temperature and then heated. As soon as the temperature reached 85 °C, stirring (1200 rpm) was started and the catalytic reaction was conducted under constant pressure for 1 h. Afterwards the autoclave was cooled by means of an ice-water bath and the unreacted gases were released. The insoluble copolymer was filtered off, washed with MeOH, and dried under vacuum at 60 °C to constant weight.

**Crystal Structure Determination of 3a·$CHCl_3$:** Several crystallization attempts with different solvents were performed and only the diffusion of toluene into a $CHCl_3$ solution of **3a** gave a single crystal, although of poor quality. Crystal data and structure refinement details for **3a·$CHCl_3$** are reported in Table 9.

Table 9. Crystal data and structure refinement details for **3a·$CHCl_3$**.

| Empirical formula | $C_{32}H_{36}Cl_4O_4P_2Pd$ |
|---|---|
| Molecular mass [g mol$^{-1}$] | 794.75 |
| Crystal color, shape | white, plate |
| Crystal size [mm] | $0.20 \times 0.10 \times 0.05$ |
| Temperature [K] | 223 |
| Crystal system | monoclinic |
| Space group | $P2_1/c$ |
| *a* [Å] | 9.294(6) |
| *b* [Å] | 23.054(10) |
| *c* [Å] | 22.295(11) |
| $\beta$ [°] | 94.75(5) |
| *V* [Å$^3$] | 4761(4) |
| *Z* | 4 |
| Density (calculated) [g cm$^{-3}$] | 1.109 |
| *F*(000) | 1616 |
| $\theta$ range [°] | 3.98–23.27 |
| Radiation wavelength [Å] | Mo-$K_\alpha$/0.71073 |
| Absorption coefficient [mm$^{-1}$] | 0.707 |
| Reflections collected | 18877 |
| Independent reflections | 6802 |
| Data/restraints/parameters | 5200/0/390 |
| Gof on $F^2$ | 1.111 |
| *R*1, *wR*2 [$I > 2\sigma(I)$] | 0.1038, 0.2801 |
| *R*1, *wR*2 (all data) | 0.1190, 0.2970 |
| Largest diff. peak/hole [e Å$^{-3}$] | 1.915/–2.054 |

X-ray diffraction intensity data were collected at 223 K with an Oxford Diffraction CCD diffractometer with graphite-monochromated Mo-$K_\alpha$ radiation ($\lambda$ = 0.71073 Å) using ω-scans. Cell refinement, data reduction, and empirical absorption correction were

 © 2007 Wiley-VCH Verlag GmbH & Co. KGaA, Weinheim 

carried out with the Oxford diffraction software and SADABS.[12a] All structure determination calculations were performed with the WINGX package[12b] with SIR-97,[12c] SHELXL-97,[12d] and ORTEP-3 programs.[12e] Final refinements based on $F^2$ were carried out with anisotropic thermal parameters for all non-hydrogen atoms, which were included using a riding model with isotropic $U$ values depending on the $U_{eq}$ of the adjacent carbon atoms.

CCDC-632065 contains the supplementary crystallographic data for this paper. These data can be obtained free of charge from The Cambridge Crystallographic Data Centre via www.ccdc.cam.ac.uk/data_request/cif.

## Acknowledgments

Thanks are due to the European Commission for financing the following projects: PALLADIUM (RTN contract no. HPRN-CT-2002-00196), IDECAT (NoE contract no. NMP3-CT-2005-011730), and NANOHYBRID (STREP contract no. NMP3-CT-2005-516972).

[1] a) E. Drent, P. H. M. Budzelaar, *Chem. Rev.* **1996**, *96*, 663–681; b) C. Bianchini, A. Meli, *Coord. Chem. Rev.* **2002**, *225*, 35–66.

[2] a) J. Schwarz, E. Herdtweck, W. A. Herrmann, M. G. Gardiner, *Organometallics* **2000**, *19*, 3154–3160; b) C. Bianchini, H. M. Lee, A. Meli, W. Oberhauser, M. Peruzzini, F. Vizza, *Organometallics* **2002**, *21*, 16–33; c) C. Bianchini, A. Meli, G. Müller, W. Oberhauser, E. Passaglia, *Organometallics* **2002**, *21*, 4965–4977; d) C. Bianchini, A. Meli, W. Oberhauser, A. M. Segarra, C. Claver, E. J. Garcia Suarez, *J. Mol. Catal. A: Chemical* **2006**, in press; e) M. A. Zuideveld, P. C. J. Kamer, P. W. N. M. van Leeuwen, P. A. A. Klusener, H. A. Stil, C. F. Roobeek, *J. Am. Chem. Soc.* **1998**, *120*, 7977–7978.

[3] a) G. Vespui, F. Schanssema, A. R. Sheldon, *Angew. Chem. Int. Ed.* **2000**, *39*, 804–806; b) E. Drent, W. P. Mul, A. A. Smaardijk, "Polyketones" in *Encyclopedia of Polymer Science and Technology*, 3rd ed., Wiley-Interscience, New York, **2002**; c) W. P. Mul, E. Drent, P. Jansens, A. H. Kramer, N. H. W. Sonnemans, *J. Am. Chem. Soc.* **2001**, *123*, 5350–5351; d) W. P. Mul, H. Dirkzwager, A. A. Broekhuis, H. J. Heeres, A. J. van der Linden, A. Guy Orpen, *Inorg. Chim. Acta* **2002**, *327*, 147–159, and refs therein.

[4] I. M. Angulo, E. Bouwman, R. van Gorkum, S. M. Lok, M. Lutz, A. L. Spek, *J. Mol. Catal. A* **2003**, *202*, 97–106.

[5] a) I. M. Angulo, E. Bouwman, M. Lutz, W. P. Mul, A. L. Spek, *Inorg. Chem.* **2001**, *40*, 2073–2082; b) K. R. Dunbar, J.-S. Sun, A. Quillevèrè, *Inorg. Chem.* **1994**, *33*, 3598–3601; c) C. Bianchini, A. Meli, W. Oberhauser, *Dalton Trans.* **2003**, 2627–2635.

[6] I. M. Angulo, E. Bouwman, S. M. Lok, M. Lutz, W. P. Mul, A. L. Spek, *Eur. J. Inorg. Chem.* **2001**, 1465–1473.

[7] a) P. Braunstein, J. Durand, M. Knorr, C. Strohmann, *Chem. Commun.* **2001**, 211–212; b) W. P. Mul, H. Oosterbeek, G. A. Beitel, G. J. Kramer, E. Drent, *Angew. Chem. Int. Ed.* **2000**, *39*, 1848–1851; c) J. Liu, B. T. Heaton, J. A. Iggo, R. Whyman, J. F. Bickley, A. Steiner, *Chem. Eur. J.* **2006**, *12*, 4417–4430; d) P. Braunstein, C. Frison, X. Morise, *Angew. Chem. Int. Ed.* **2000**, *39*, 2867–2870; e) J. Liu, B. T. Heaton, J. A. Iggo, R. Whyman, *Angew. Chem. Int. Ed.* **2004**, *43*, 90–94; f) K. Nozaki, N. Sato, Y. Tonomura, M. Yasutomi, H. Takaya, T. Hiyama, T. Matsubara, N. Koga, *J. Am. Chem. Soc.* **1997**, *119*, 12779–12795; g) F. C. Rix, M. Brookhart, P. S. White, *J. Am. Chem. Soc.* **1996**, *118*, 4746–4764.

[8] L. Toniolo, S. M. Kulkarni, D. Fatutto, R. V. Chaudhari, *Ind. Eng. Chem. Res.* **2001**, *40*, 2037–2045.

[9] R. E. Rülke, J. M. Ernsting, A. L. Spek, C. J. Elsevier, P. W. N. M. van Leeuwen, K. Vrieze, *Inorg. Chem.* **1993**, *32*, 5769–5778.

[10] M. Brookhart, B. Grant, A. F. Volpe, *Organometallics* **1992**, *11*, 3920–3922.

[11] C. Bianchini, A. Meli, A. Traversi, Ital. Pat. FI A,000,025, **1997**.

[12] a) G. M. Sheldrick, *SADABS*, Program for empirical absorption corrections, University of Göttingen, Göttingen, Germany, **1986**; b) L. J. Farrugia, *J. Appl. Crystallogr.* **1999**, *32*, 837–838; c) A. Altomare, M. C. Burla, M. Cavalli, G. L. Cascarano, C. Giacovazzo, A. Gagliardi, G. G. Moliterni, G. Polidori, R. Spagna, *J. Appl. Crystallogr.* **1999**, *32*, 115–119; d) G. M. Sheldrick, *SHELX-97*, University of Göttingen, Germany, **1997**; e) M. N. Burnett, C. K. Johnson, *ORTEP-3*, Report ORNL-6895, Oak Ridge National Laboratory, Oak Ridge, TN, **1996**.

Received: December 29, 2006
Published Online: April 18, 2007

 © 2007 Wiley-VCH Verlag GmbH & Co. KGaA, Weinheim 

DOI: 10.1002/ejic.200601257

# The Synthesis of Iridabenzenes by the Coupling of Iridacyclopentadienes and Olefins

**Margarita Paneque,*[a] Manuel L. Poveda,*[a] Nuria Rendón,[a] Eleuterio Álvarez,[a] and Ernesto Carmona[a]**

**Keywords:** Metallacycles / Olefins / Insertion / Isomerisation / Alkylidenes

The iridacyclopentadiene [(Tp$^{Me2}$)Ir{C$^1$(R)=C(R)C(R)=C$^4$(R)}(H$_2$O)(*Ir–C$^4$*)] (**1**; R = CO$_2$Me) reacts with propene at 60 °C to give the iridabenzene [(Tp$^{Me2}$)Ir{C$^1$(Et)C(R)C(R)C(R)C$^5$(R)}(H)(*Ir–C$^5$*)] (**6**), which also contains a hydride ligand, as the main product, accompanied by complexes **7** and **8** derived from the insertion of propene into the Ir–C bonds of **1**. In contrast, the closely related metallacycle [(Tp$^{Me2}$)Ir{C$^1$(R)=C(H)C(R)=C$^4$(R)}(H$_2$O)(*Ir–C$^4$*)] (**1-H**) gives the iridabenzene [(Tp$^{Me2}$)Ir{C$^1$(Me)C(R)C(H)C(R)C$^5$(R)}(Me)(*Ir–C$^5$*)] (**13**), which contains an iridium-bonded methyl group, upon treatment with propene at 20 °C. The proposed mechanism for the formation of metallabenzenes **6** and **13** postulates Ir–propene → Ir=CHEt or Ir–propene → Ir=CMe$_2$ isomerisations, followed by insertion of the alkylidene ligand into an Ir–C(R) bond (regioselective for **1-H**) and α-H or α-Me elimination from the resulting alkyliridium moiety. At 25 °C, neat acetonitrile induces stereoselective hydride migration onto both the Ir=C bonds of **6** to give a kinetic mixture (6:1 ratio) of the isomeric adducts [(Tp$^{Me2}$)Ir{C$^1$H(Et)C(R)=C(R)C(R)=C$^5$(R)}(MeCN)(*Ir–C$^5$*)] (**9**) and [(Tp$^{Me2}$)Ir{C$^1$H(R)C(R)=C(R)C(R)=C$^5$(Et)}(MeCN)(*Ir–C$^5$*)] (**10**), with the latter being the thermodynamically preferred product. In contrast, complex **13** is stable in acetonitrile up to 100 °C, where it mainly experiences ring fragmentation to give the iridacyclopentadiene **1-H** as its MeCN adduct. All new compounds have been fully characterised by microanalysis and spectroscopy. Additionally, the solid-state structures of **5**, **6** and **13** have been determined by X-ray crystallography.
(© Wiley-VCH Verlag GmbH & Co. KGaA, 69451 Weinheim, Germany, 2007)

## Introduction

We have recently reported on the reaction of the iridacyclopentadiene [(Tp$^{Me2}$)Ir{C$^1$(R)=C(R)C(R)=C$^4$(R)}(H$_2$O)(*Ir–C$^4$*)] [**1**; Tp$^{Me2}$ = hydrotris(3,5-dimethylpyrazolyl)borate, R = CO$_2$Me] with ethylene (Scheme 1).[1] The first species formed is the iridacycloheptadiene **2** as the result of the insertion of C$_2$H$_4$ into one of the two identical Ir–C bonds. This species rearranges readily at room temperature to the hydride-alkenyl derivative **3** by extrusion of H$_2$O and β-H elimination, whereas upon heating at 40–60 °C the alkyl-allyl complex **4** is obtained by means of a stereoselective hydride migration. In a parallel study we have observed that (Scheme 1) the iridacyclopentadiene [(Tp$^{Me2}$)Ir{C$^1$(R)=C(H)C(R)=C$^4$(R)}(H$_2$O)(*Ir–C$^4$*)] (**1-H**) gives rise to related species (**3-H** and **4-H**, respectively) under similar conditions, thereby implying that ethylene inserts regioselectively into the Ir–C bond close to the C–H functionality. In this paper we describe the different and unusual chemistry observed when **1** and **1-H** are treated with propene and 1-butene. Part of the findings reported herein have been briefly communicated.[2]

[a] Instituto de Investigaciones Químicas and Departamento de Química Inorgánica, Consejo Superior de Investigaciones Científicas (CSIC) and Universidad de Sevilla,
Avda. Américo Vespucio 49, Isla de la Cartuja, 41092 Sevilla, Spain
E-mail: paneque@iiq.csic.es

## Results and Discussion

### Reaction of Complex 1 with Propene

Bubbling propene through a solution of complex **1** in CH$_2$Cl$_2$ at room temperature leads to partial conversion to the metallacycloheptadiene **5**, as deduced from the NMR spectra of the reaction mixture [Equation (1)], in a spectroscopic yield of about 50%. The yield does not improve upon extending the reaction time. Complex **5** is closely related to species **2**, which forms in the reaction of **1** with ethylene, and is probably formed by the same mechanism, namely temporary displacement of the water ligand by a molecule of propene followed by insertion of the olefin into one of the equivalent Ir–C bonds and subsequent coordination of H$_2$O.[1] Interestingly, this insertion process is highly selective as only one of the four possible stereoisomers is observed.

Complex **5** can be isolated as a pale-yellow, microcrystalline solid by column chromatography on silica gel. The most characteristic $^1$H NMR signals of this compound are those corresponding to the two diastereotopic protons of the methylene group bonded to the metal, which appear at $\delta$ = 3.46 and 2.84 ppm (doublet of doublets and triplet, respectively), while the corresponding carbon atom resonates at $\delta$ = 6.5 ppm ($^1J_{C,H}$ = 126 Hz) in the $^{13}$C{$^1$H} NMR spectrum. The MeCH group of the metallacycle gives rise

 © 2007 Wiley-VCH Verlag GmbH & Co. KGaA, Weinheim InterScience 

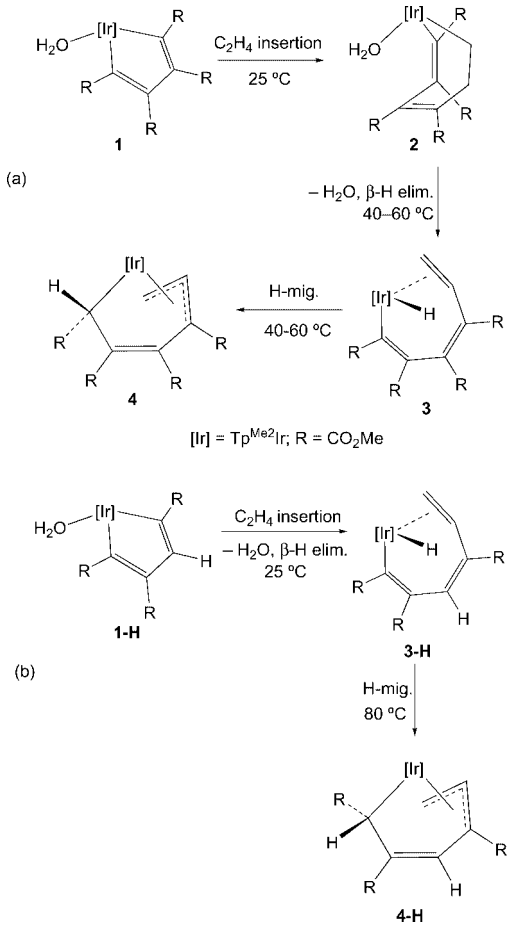


Scheme 1. Reaction of complexes **1** (a) and **1-H** (b) with $C_2H_4$.

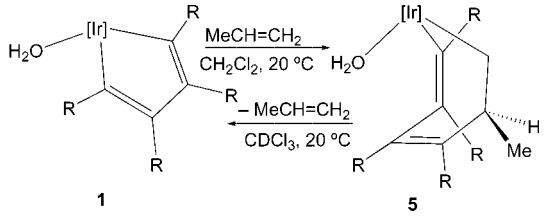


(1)

to $^1$H NMR resonances at $\delta$ = 3.22 (m, CH) and 1.25 ppm (d, *Me*CH) and to $^{13}$C{$^1$H} NMR signals at $\delta$ = 38.5 (*C*HMe) and 19.4 ppm (CH*Me*). The configuration of the CHMe group was derived from an X-ray study, the results of which are shown in Figure 1. The corresponding crystallographic data are collected in the Experimental Section, while selected bond lengths and angles for complex **5** are shown in Table 1. As expected, the Ir–C(sp$^3$) bond (2.08 Å) is somewhat longer than the Ir–C(sp$^2$) one (2.02 Å).[3] It should also be noted that, of the three Ir–N bonds, that *trans* to water is appreciably shorter (2.03 Å) than the other two (2.16 Å av.),[1] which are *trans* to the two different Ir–C σ bonds and the Ir–C(sp$^3$) and the Ir–C(sp$^2$) bonds (Ir–C16 and Ir–C28, respectively).

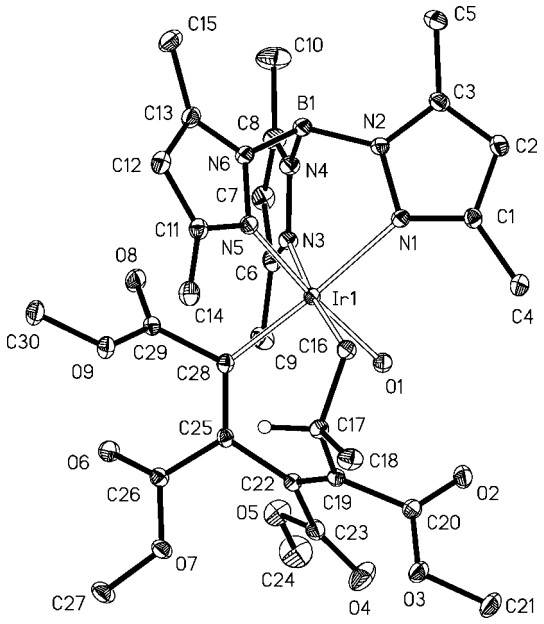


Figure 1. X-ray structure of complex **5**.

Table 1. Selected bond lengths [Å] and angles [°] for **5**.

| | | | |
|---|---|---|---|
| Ir(1)–N(1) | 2.160(2) | C(16)–C(17) | 1.549(3) |
| Ir(1)–N(3) | 2.166(2) | C(17)–C(19) | 1.516(3) |
| Ir(1)–N(5) | 2.029(2) | C(19)–C(22) | 1.346(3) |
| Ir(1)–C(16) | 2.079(2) | C(22)–C(25) | 1.479(3) |
| Ir(1)–C(28) | 2.017(2) | C(25)–C(28) | 1.366(3) |
| Ir(1)–O(1) | 2.122(2) | | |
| C(28)–Ir(1)–N(5) | 91.0(8) | C(16)–Ir(1)–N(1) | 90.4(8) |
| C(28)–Ir(1)–C(16) | 94.1(8) | O(1)–Ir(1)–N(1) | 88.4(6) |
| N(5)–Ir(1)–C(16) | 92.8(8) | C(28)–Ir(1)–N(3) | 90.1(7) |
| C(28)–Ir(1)–O(1) | 92.9(7) | N(5)–Ir(1)–N(3) | 91.2(7) |
| N(5)–Ir(1)–O(1) | 174.6(6) | C(16)–Ir(1)–N(3) | 174.1(7) |
| C(16)–Ir(1)–O(1) | 90.7(8) | O(1)–Ir(1)–N(3) | 85.0(6) |
| C(28)–Ir(1)–N(1) | 175.3(7) | N(1)–Ir(1)–N(3) | 85.4(7) |
| N(5)–Ir(1)–N(1) | 87.4(7) | | |

Interestingly, the rearrangement of **1** to **5** shown in Equation (1) does not proceed when thf is used as the reaction solvent, possibly because thf coordination prevents binding of the alkene. We have also found that propene insertion is reversible, at least in $CDCl_3$ and $C_6D_6$. Thus, upon standing at room temperature for several hours, solutions of **5** in these deuterated solvents revert to **1** and free propene. This occurs even in the presence of added propene, although in these cases the back reaction is naturally slower. In contrast, solutions of **5** in hexane/diethyl ether mixtures remain unchanged for at least 48 h.

Different results are observed when compound **1** is treated with propene in $CH_2Cl_2$ at 60 °C; this reaction gives the mixture of compounds **6**–**8** shown in Equation (2). Complexes **6** and **7** were isolated as green and dark-yellow microcrystalline solids, respectively, by column chromatography on silica gel, although characterisation of **8** required its direct preparation from **7** (see below). The analytical and spectroscopic data for **6**–**8** support its proposed formulation, which for **6** was confirmed by an X-ray structure determination.

 © 2007 Wiley-VCH Verlag GmbH & Co. KGaA, Weinheim 

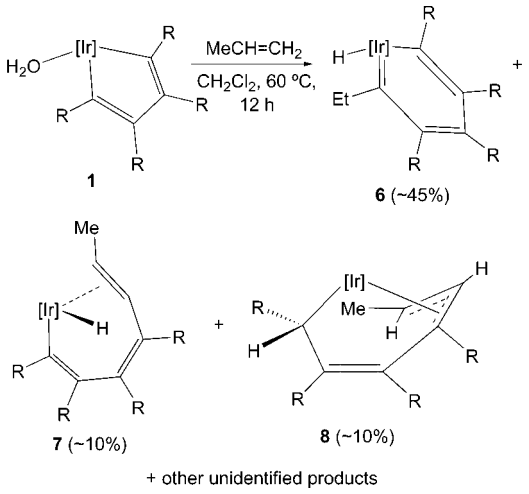


(2)

Compound **6**, which is the major product of Equation (2), has an iridabenzene structure. Its formation from **1** and propene, that is, by coupling of an alkene with a metallacyclopentadiene, constitutes a novel synthetic procedure for this kind of aromatic metallacycle.[4] Its hydride ligand resonates at $\delta$ = –21.41 ppm in the $^1$H NMR spectrum, while the low field resonances at $\delta$ = 274.2 and 202.1 ppm found in the $^{13}C\{^1H\}$NMR spectrum are due to the Ir–*C*(Et) and Ir–*C*($CO_2$Me) carbon nuclei, respectively. Both these values suggest a partial double-bond character of the Ir–C bonds,[4] with a higher carbene character for the carbon atom bonded to the stronger electron-donating alkyl group. In other words, the electronic structure of **6** may be thought of as being intermediate between those of **I** and **II** below, with a larger contribution of the former.

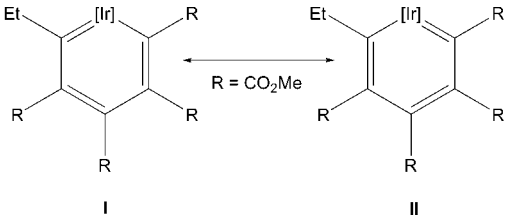


This assumption was reinforced by the solid-state structural data obtained by X-ray crystallography[2] (Figure 2 and Table 2). Even though the two Ir–C bond lengths are similar, the Ir–C(Et) bond [1.922(4) Å] is shorter than the Ir–C($CO_2$Me) bond [1.979(4) Å]. The iridium atom in **6** deviates appreciably from the mean plane defined by the five ring-carbon atoms (0.57 Å), this deviation being intermediate between values found in the iridabenzene [($Tp^{Me2}$)-Ir{$C^1$(R)C(R)C(R)C(R)$C^5$(R)}(OCOR)(*Ir*–$C^5$)], which contains bulkier substituents (0.74 Å),[4f] and in the less congested species [($Tp^{Me2}$)Ir{$C^1$(H)C(Me)C(Me)C(H)$C^5$-(Me)}(H)(*Ir*–$C^5$)][3] (0.50 Å).

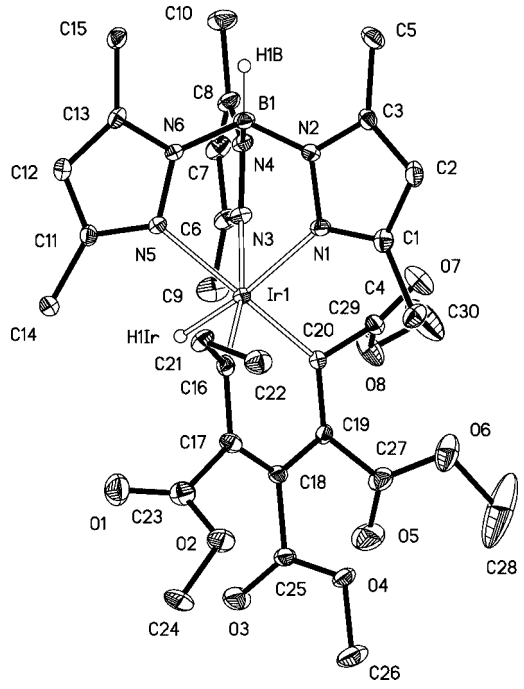


Figure 2. X-ray structure of complex **6**.

Table 2. Selected bond lengths [Å] and angles [°] for **6**.

| | | | |
|---|---|---|---|
| Ir(1)–N(1) | 2.150(3) | Ir(1)–H(1Ir) | 1.608 |
| Ir(1)–N(3) | 2.150(3) | C(16)–C(17) | 1.426(6) |
| Ir(1)–N(5) | 2.144(3) | C(17)–C(18) | 1.386(6) |
| Ir(1)–C(16) | 1.922(4) | C(18)–C(19) | 1.434(6) |
| Ir(1)–C(20) | 1.979(4) | C(19)–C(20) | 1.372(5) |
| C(16)–Ir(1)–C(20) | 90.5(2) | N(5)–Ir(1)–N(3) | 80.4(1) |
| C(16)–Ir(1)–N(5) | 92.1(2) | N(1)–Ir(1)–N(3) | 87.4(1) |
| C(20)–Ir(1)–N(5) | 176.4(2) | C(16)–Ir(1)–H(1Ir) | 89.1 |
| C(16)–Ir(1)–N(1) | 98.5(2) | C(20)–Ir(1)–H(1Ir) | 90.4 |
| C(20)–Ir(1)–N(1) | 93.2(2) | N(5)–Ir(1)–H(1Ir) | 87.2 |
| N(5)–Ir(1)–N(1) | 88.8(1) | N(1)–Ir(1)–H(1Ir) | 171.5 |
| C(16)–Ir(1)–N(3) | 170.4(2) | N(3)–Ir(1)–H(1Ir) | 84.5 |
| C(20)–Ir(1)–N(3) | 96.7(2) | | |

A plausible mechanism for the formation of complex **6** is shown in Scheme 2. Coordination of the olefin after displacement of the molecule of $H_2O$ gives intermediate **A**, which is proposed to undergo alkene isomerisation into a propylidene (to give **B**) and then a stereoselective migratory carbene insertion into one of the Ir–C bonds of the metallacycle. The resulting species **C** converts into the observed iridabenzene by means of an α-hydride elimination. An alkene-to-alkylidene rearrangement is an uncommon process, although there is literature precedent.[5] The migratory insertion of alkylidenes into M–C bonds[6] and the α-hydride elimination are well-known elementary steps.[7] Other mechanistic (also highly speculative) pathways for the formation of **6** can, however, also be envisaged.[8]

The hydride ligand of complex **7** gives rise to a high-field resonance at $\delta$ = –16.93 ppm in the $^1$H NMR spectrum, while the π-coordinated alkene terminus exhibits resonances at $\delta$ = 6.01 (d), 4.34 (m) and 1.15 ppm (d) for the C*H*=CHMe, CH=C*H*Me and CH=CH*Me* protons, respectively. The *trans* disposition of the olefinic protons was de-

 © 2007 Wiley-VCH Verlag GmbH & Co. KGaA, Weinheim 

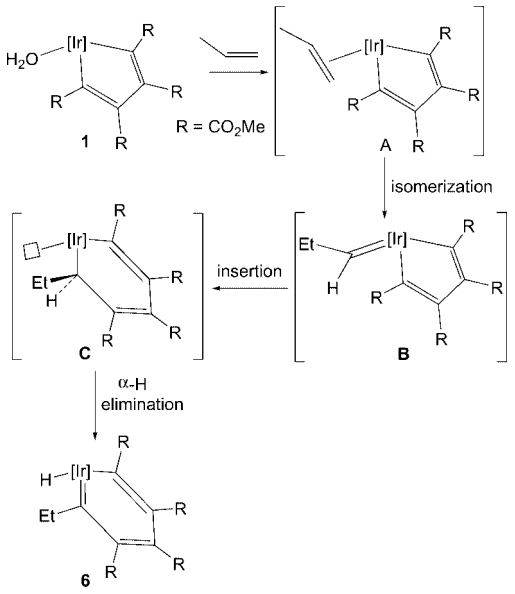


Scheme 2. Proposed mechanism for the formation of **6**.

duced from their $^3J_{H,H}$ coupling constant (11 Hz). The $^{13}C$ NMR spectroscopic data as well as two-dimensional experiments are also in agreement with the structure proposed. In particular, the NOESY spectrum confirmed the *trans* configuration of the coordinated olefin and also its coordination to the metal through the face displayed in Equation (2). The hydride-alkenyl **7** is related to **3** (see Introduction) and it is important to highlight that only the represented stereoisomer is observed. It probably forms from intermediate **D** by a β-H elimination process (Scheme 3), while, in turn, **D** forms from **A** by an olefin insertion reaction that has a stereoselectivity different to that leading to **5** (note that the configuration of the CHMe group of this complex cannot yield a vinyl compound by β-H elimination).

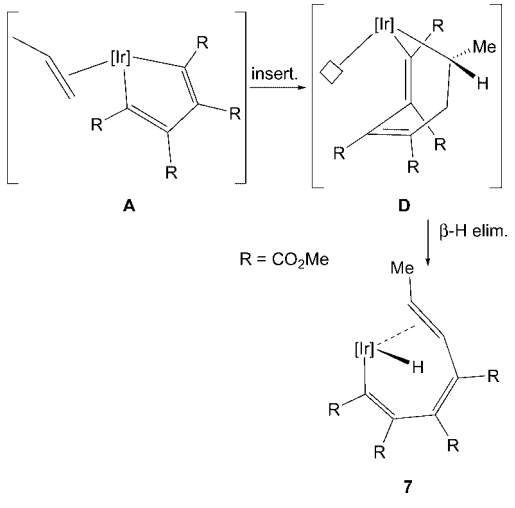


Scheme 3. Proposed mechanism for the formation of **7**.

Compound **3** is stable in solution for only a short period of time at room temperature as it transforms slowly into the allyl derivative **4**.[1] In contrast, **7** is stable under these conditions, although, upon heating, it also gives rise to an allyl species (**8**) due to the stereospecific transfer of the hydride to the α-carbon atom of the alkenyl ligand of **7** [Equation (3)]. Compound **8** exhibits $^1H$ NMR resonances due to the π-coordinated allyl moiety at $\delta$ = 7.11 (d, CH), 3.61 (m, C*H*Me) and 1.47 ppm (d, CH*Me*), while the carbon nuclei of this fragment produce $^{13}C$ NMR resonances at $\delta$ = 93.7 (CH), 38.5 (*C*HMe) and 68.2 ppm ($C_q$), with these values being similar to those found for the related species **3**.[1] It is interesting to note that **8** contains a catenated $\eta^1$-allyl-$\eta^3$-allyl ligand which, in principle, can isomerize by concomitant change of the hapticity of the two allyl moieties. However, as for **4**,[1] only the species with the $CO_2Me$ group on the $sp^3$ carbon bonded to the metal is observed.

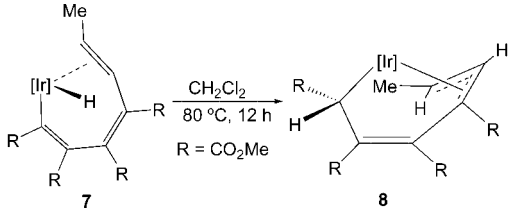


(3)

### Reaction of the Iridabenzene 6 with MeCN

As represented in Scheme 4, iridabenzene **6** reacts with neat MeCN at 20 °C to give a 6:1 kinetic mixture of the isomeric metallacyclohexadienes[4c,4h,9] **9** and **10**, which are the products of the stereospecific migration of the hydride ligand onto the two different Ir–C bonds followed by coordination of MeCN. Both complexes can be cleanly separated by chromatography and have been fully characterised by spectroscopic methods. The aliphatic carbon bonded to iridium in complex **9** resonates at $\delta$ = 4.8 ppm in the $^{13}C\{^1H\}$ NMR while the corresponding nucleus of **10** appears at $\delta$ = 4.6 ppm. The latter species is the thermodynamic product of the reaction, as **9** transforms cleanly and almost quantitatively into **10** in $C_6D_6$ at 90 °C ($t_{1/2}$ = 4 h). Interestingly, the kinetic ratio of **9** to **10** in neat MeCN was found to vary with temperature (5 at 30 °C, 4.2 at 40 °C, 2.8 at 60 °C and 2.1 at 80 °C) and a graphic representation of ln[**9**]/[**10**] vs. $1/T$ gives a straight line (Figure 3) from which the values of $\Delta\Delta H^{\neq}$ = 3.75 kcal mol$^{-1}$ and $\Delta\Delta S^{\neq}$ = 5 cal mol$^{-1}$ K$^{-1}$ can be computed (the latter favours the formation of **10** at high temperatures).

The proposed mechanism[9] for the formation of these adducts is also shown in Scheme 4 and implies the competitive transformation of complex **6** into the unsaturated intermediates **C** and **E**, which are then trapped by MeCN. As commented above, complex **9** transforms into the thermodynamically more stable isomer **10** when heated at 90 °C in $C_6D_6$. In principle, this reaction could be the result of a direct 1,5-suprafacial shift of the hydrogen atom between the two Cα positions.[9] However, several indications appear to be more in agreement with a mechanism in which iridabenzene **6** is a true intermediate of this rearrangement,

 © 2007 Wiley-VCH Verlag GmbH & Co. KGaA, Weinheim 

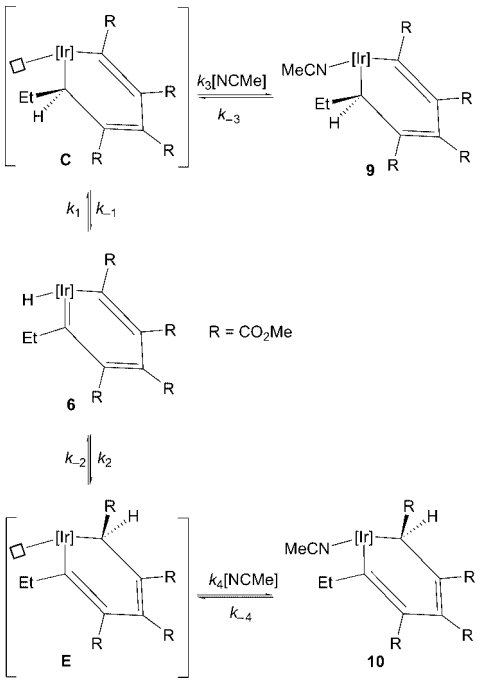


Scheme 4. Proposed mechanism for the formation of complexes **9** and **10**.

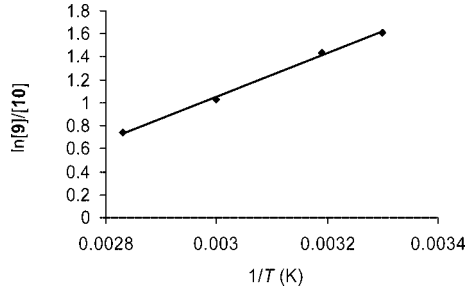


Figure 3. Variation of ln [**9**]/[**10**] with 1/*T*.

which means that, as shown in Scheme 4, all reaction steps are reversible. Thus, under the above conditions ($C_6D_6$, 90 °C) it is observed that: (i) NMR monitoring of the **9** → **10** rearrangement reveals the formation of observable concentrations of iridabenzene **6**, which is not detected when the reaction is effected in the presence of around 10 equivalents of MeCN or [$D_3$]MeCN; (ii) the rate of disappearance of **9** does not vary in the presence of 10 equivalents of MeCN (or [$D_3$]MeCN); (iii) in the presence of [$D_3$]-MeCN (10 equiv.), **10** contains [$D_3$]MeCN almost exclusively at 50% conversion whereas **9** is only partially deuterated (50%); (iv) **10** exchanges MeCN for [$D_3$]MeCN (10 equiv. [$D_3$]MeCN), although the exchange rate is appreciably slower than the transformation of **9** into **10** (around 50% incorporation after 16 h). All these observations are in agreement with the transformation of **9** into **10** proceeding via iridabenzene **6** (Scheme 4), with the rate-determining step being the dissociation of the acetonitrile ligand of **9** ($k_{-3}$).

### Reaction of Complex 1 with 1-Butene

To complete our study of the reactivity of **1** towards olefins, its reaction with 1-butene was also investigated. As expected, the results are similar to those previously discussed for propene, with a mixture of compounds **11** and **12** [Equation (4)] being obtained at 80 °C. Column chromatography of the crude reaction mixture allowed isolation of **11**, and even though the allyl species **12** could not be isolated as a pure solid we were able to characterise it by NMR spectroscopy. Spectroscopic data for these two compounds can be found in the Experimental Section and do not warrant further discussion.

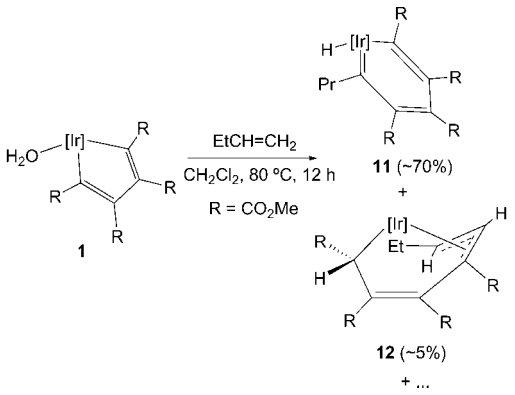


(4)

### Reaction of Complex 1-H with Propene

An unexpected redistribution reaction occurs when propene is bubbled through a solution of complex **1-H** in $CH_2Cl_2$ (25 or 60 °C). Equation (5) shows the nature of the resulting product (iridabenzene **13**), which, quite surprisingly, has a metal-bound methyl group instead of a hydride ligand. This methyl group must proceed from the olefin. Additionally, it is important to note that the coupling process that gives rise to the metallacycle is highly selective, since only the iridabenzene that bears the hydrogen substituent in the *para* position is obtained. Compound **13** was fully characterised by NMR spectroscopy and also by X-ray diffraction studies. Once more, the resonance due to the carbon atom bonded to iridium which supports the Me group, Ir–*C*(Me), appears at lower field than the related Ir–*C*($CO_2$Me) ($\delta$ = 272.7 and 217.6 ppm, respectively). Another characteristic $^{13}C\{^1H\}$ NMR signal is that of the methyl group bonded to iridium, which appears at high field ($\delta$ = –17.6 ppm). The $^1H$ NMR spectrum shows two singlets at $\delta$ = 1.98 and 0.91 ppm for the Me group in the α-position of the metallacycle and for the Me group bonded to iridium, respectively, while the CH of the iridabenzene ring resonates at $\delta$ = 9.15 ppm.

 © 2007 Wiley-VCH Verlag GmbH & Co. KGaA, Weinheim 

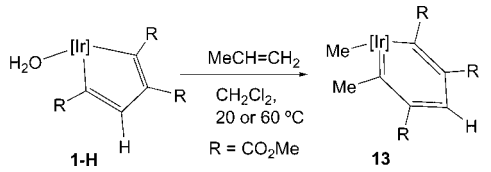


(5)

Figure 4 shows an ORTEP view of the molecule of **13**[2] while Table 3 contains selected bond lengths and angles. The Ir atom in this iridacycle deviates by 0.70 Å from the plane defined by the five carbon atoms of the metallacycle. The two Ir–C(ring) distances are different, showing once more the unsymmetrical electronic delocalisation: the Ir–C(Me) bond [1.936(2) Å] is slightly shorter than the Ir–C($CO_2$Me) [1.957(2) Å].

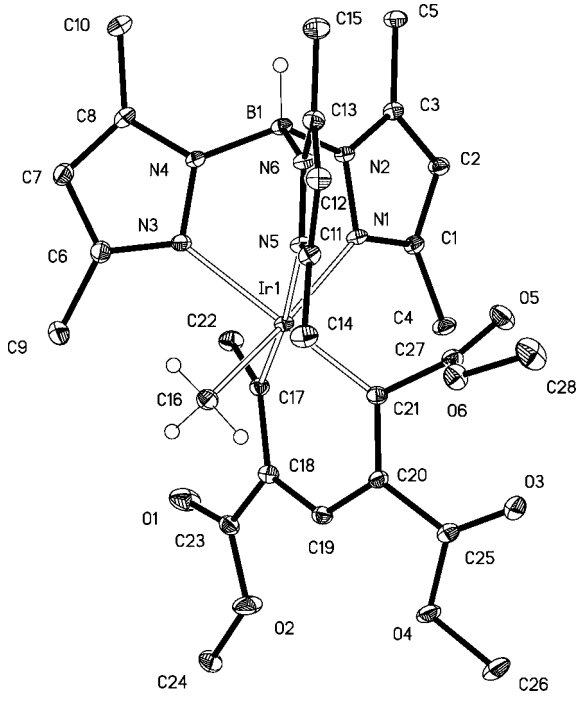


Figure 4. ORTEP view of complex **13**.

Table 3. Selected bond lengths [Å] and angles [°] for **13**.

| | | | |
|---|---|---|---|
| Ir(1)–N(1) | 2.152(2) | Ir(1)–C(21) | 1.957(2) |
| Ir(1)–N(3) | 2.156(2) | C(17)–C(18) | 1.428(3) |
| Ir(1)–N(5) | 2.194(2) | C(18)–C(19) | 1.392(3) |
| Ir(1)–C(16) | 2.095(2) | C(19)–C(20) | 1.415(3) |
| Ir(1)–C(17) | 1.936(2) | C(20)–C(21) | 1.396(3) |
| C(17)–Ir(1)–C(21) | 90.9(9) | C(16)–Ir(1)–N(3) | 88.6(8) |
| C(17)–Ir(1)–C(16) | 90.6(1) | N(1)–Ir(1)–N(3) | 87.5(7) |
| C(21)–Ir(1)–C(16) | 90.0(9) | C(17)–Ir(1)–N(5) | 174.5(8) |
| C(17)–Ir(1)–N(1) | 92.2(8) | C(21)–Ir(1)–N(5) | 94.7(8) |
| C(21)–Ir(1)–N(1) | 93.8(8) | C(16)–Ir(1)–N(5) | 89.0(9) |
| C(16)–Ir(1)–N(1) | 175.2(8) | N(1)–Ir(1)–N(5) | 87.8(7) |
| C(17)–Ir(1)–N(3) | 92.1(8) | N(3)–Ir(1)–N(5) | 82.4(7) |
| C(21)–Ir(1)–N(3) | 176.8(8) | | |

Scheme 5 shows a possible mechanism for the formation of **13**. Once again, it is proposed that an alkylidene, **G**, resulting from the isomerisation of the propene ligand in **F** is a key intermediate, although for reasons that are difficult to explain a dimethylcarbene unit, $=CMe_2$, appears to be favoured over the linear propylidene, =C(H)Et. This isomerisation would be followed by a regioselective migration of the alkenyl carbon atom adjacent to the CH group onto the alkylidene, to give **H**, and finally by an α-Me elimination. This last process, namely the α-elimination of alkyl or aryl groups, is unusual, although some examples are known.[10] Clearly other mechanistic possibilities can be envisaged for the formation of complex **13** but, once again, they include highly speculative assumptions.[8]

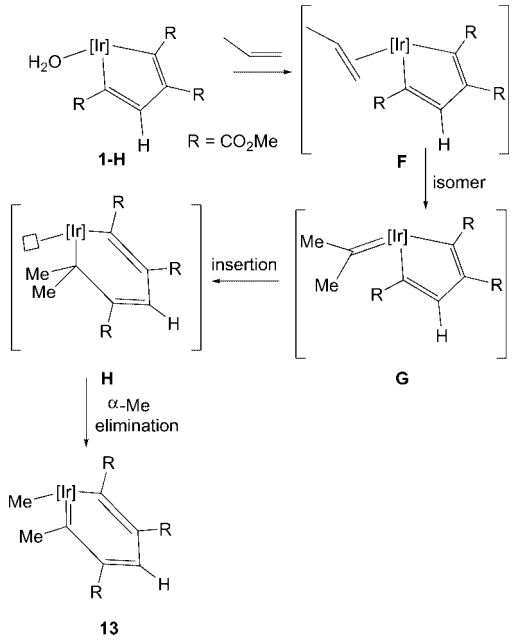


Scheme 5. Proposed mechanism for the formation of **13**.

## Reaction of the Iridabenzene 13 with MeCN

Preliminary studies on the reactivity of the iridabenzene **13** reveal interesting differences with respect to the behaviour observed for **6**. Thus, **13** does not react with neat acetonitrile at 20 °C, and at 100 °C it mainly reverts to iridacycle **1-H**, which was isolated in the form of the known MeCN adduct **1-H·MeCN** [Equation (6)], a complex that has already been reported as resulting from the reaction of **1-H** with MeCN.[1] This clearly demonstrates that, despite requiring C–C bond formation and cleavage, the reaction of **1-H** with propene is a reversible process. Furthermore, Equation (6) represents an unusual fragmentation of a metallabenzene species.

Compound **1-H·MeCN** is not the only compound formed in the reaction of **13** and MeCN at 100 °C (approx. 80% spectroscopic yield) as the $^1$H NMR spectrum of the crude product mixture shows the presence of a second species − the new compound **14** (approx. 10% spectroscopic yield, separated by column chromatography) − for which the structure shown in Equation (6) can be tentatively suggested on the basis of NMR spectroscopic studies. It is pro-

 © 2007 Wiley-VCH Verlag GmbH & Co. KGaA, Weinheim 

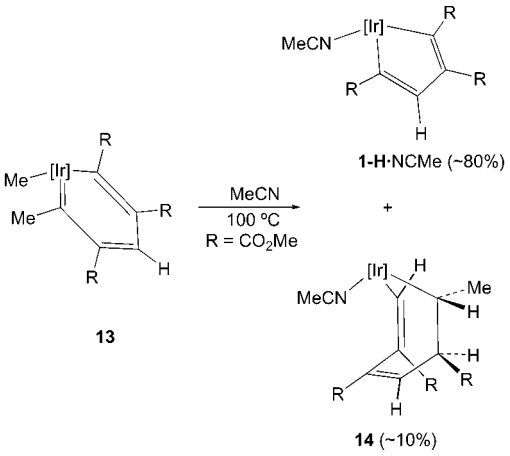


(6)

posed that the three carbon atoms of the original molecule of propene become incorporated into the metallacycle skeleton of **14**, although the complexity of the structure and the absence of mechanistic information advise against a discussion of possible reaction routes, which at this stage would be highly speculative.

### Reaction of Complex 1-H with 1-Butene

Finally, reaction of **1** with $EtCH{=}CH_2$ at 60 °C takes place with formation of a complex reaction mixture from which only complex **15** (approx. 5% spectroscopic yield, separated by column chromatography) has been unequivocally identified [Equation (7)]. The major product (approx. 20% spectroscopic yield) is an isolable compound following chromatographic procedures but an unambiguous formulation cannot be proposed with the available data. It seems clear, however, that it is structurally related to other compounds that are generated in very small amounts during the reactions of **1** and **1-H** with propene and 1-butene.

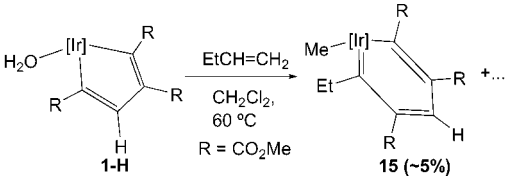


(7)

## Conclusions

Iridabenzene complexes that also contain metal-bound hydride or methyl groups have been obtained by a new synthetic method that consists of the coupling of iridacyclopentadienes with olefins in a process that is proposed to occur by an olefin-to-alkylidene isomerisation in the metal coordination sphere. Interestingly, the reaction outcome depends strongly on the substitution pattern of the five-membered metallacycle and the nature of the olefin (propene being very efficient as a metallabenzene generator while ethylene gives only products derived from the insertion of the olefin into the Ir–C bonds). The reactivity of these iridabenzenes with acetonitrile has been studied and it has been found that the hydride ligand migrates easily and reversibly onto the Ir–C bonds of the metallacycle. Finally, a very unusual thermal fragmentation of a metallabenzene has also been observed.

## Experimental Section

**General Procedures:** Microanalyses were performed by the Microanalytical Service of the Instituto de Investigaciones Químicas (Sevilla). Infrared spectra were obtained with Perkin–Elmer 577 and 684 spectrometers. NMR spectra were recorded with Bruker DRX-500, DRX-400 and DPX-300 spectrometers. Spectra are referenced to external $SiMe_4$ ($\delta$ = 0 ppm) using the residual protio solvent peaks ($^1$H NMR experiments) or the characteristic resonances of the solvent nuclei ($^{13}$C NMR experiments) as internal standards. Spectral assignments were made by means of routine one- and two-dimensional NMR experiments where appropriate. Manipulations were performed either in air or under oxygen-free dinitrogen, following conventional Schlenk techniques. The complexes [($Tp^{Me2}$)-Ir{$C^1$(R)=C(R)C(R)=$C^4$(R)}($H_2O$)(*Ir–C*$^4$)] (**1**) and [($Tp^{Me2}$)-Ir{$C^1$(R)=C(H)C(R)=$C^4$(R)}($H_2O$)(*Ir–C*$^4$)] (**1-H**) were obtained by published procedures.[1]

**Complex 5:** $MeCH{=}CH_2$ was bubbled through a solution of **1** in $CH_2Cl_2$ (0.2 g, 0.25 mmol; 7 mL) for 7 min. The resulting mixture was stirred under propene in a sealed vessel at room temperature for 12 h, and the solvent was then removed under reduced pressure. The $^1$H NMR spectrum of the residue showed it to consist of a mixture of **1** and **5** in a 1:1 ratio. Complex **1** was isolated by column chromatography on silica gel, with a mixture of hexane and $Et_2O$ (1:1) as eluent, in 32% yield. An analytically pure sample was obtained by crystallisation from a mixture of hexane and $Et_2O$ (1:1) at –20 °C (pale-yellow crystals). $R_f$ = 0.18 [silica gel, hexane/$Et_2O$ (1:5)]. IR (Nujol): $\nu$(OH) = 3381 cm$^{-1}$ (br). $^1$H NMR ($CDCl_3$, 25 °C): $\delta$ = 5.77, 5.71, 5.66 (s, 1 H each, 3 $CH_{pz}$), 3.95, 3.65, 3.58, 3.05 (s, 3 H each, 4 $CO_2$Me), 3.46, 2.84 (dd+t, $^2J_{H,H}$ = 12.4, $^3J_{H,H}$ = 3.7 Hz, 1 H each, $IrCH_2$), 3.22 (m, 1 H, C*H*Me), 2.37, 2.36, 2.36, 2.31, 2.16, 2.13 (s, 3 H each, 6 $Me_{pz}$), 1.25 (d, $^3J_{H,H}$ = 6.8 Hz, 3 H, CH*Me*) ppm; the coordinated molecule of $H_2O$ could not be located. $^{13}$C{$^1$H} NMR ($CDCl_3$, 25 °C): $\delta$ = 178.2, 175.8, 169.9, 164.9 (*C*$O_2$Me), 164.0 ($C^1$), 153.6, 151.2, 149.9, 144.2, 143.6, 142.3 ($C_{qpz}$), 145.6 ($C^4$), 132.1, 129.2 ($C^3$, $C^4$), 108.4, 107.8, 106.5 ($CH_{pz}$), 52.8, 52.0, 51.2, 50.4 ($CO_2$*Me*), 38.5 ($^1J_{C,H}$ = 133 Hz, *C*HMe), 19.4 (CH*Me*), 14.8, 14.2, 13.4, 12.9, 12.6, 12.4 ($Me_{pz}$), 6.5 ($^1J_{C,H}$ = 126 Hz, $CH_2$) ppm. $C_{30}H_{42}BIrN_6O_9{\cdot}0.5Et_2O$ (870.03): calcd. C 44.2, H 5.4, N 9.6; found C 44.4, H 5.4, N 9.2.

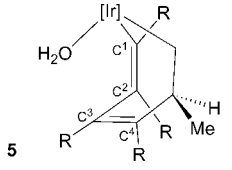


**Complexes 6–8:** Compound **1** was dissolved in $CH_2Cl_2$ (0.5 g, 0.63 mmol; 12 mL), then $MeCH{=}CH_2$ was bubbled through the solution for 7 min and the stirring was continued under propene, in a closed vessel, for 12 h at 60 °C. After this period the solvent

 © 2007 Wiley-VCH Verlag GmbH & Co. KGaA, Weinheim 

was removed under reduced pressure and the formation of a mixture of complexes **6** (approx. 45%), **7** (approx. 10%) and **8** (approx. 10%), along with other by-products, was ascertained by $^1$H NMR spectroscopy. Complexes **6**–**8** were separated by column chromatography (silica gel) with hexane/$Et_2O$ (1:1) as eluent. Complex **6** (34% yield) was purified by crystallisation from a mixture of pentane and $CH_2Cl_2$ (1:1) at –20 °C (dark-green crystals). Complex **7** (10% yield) was obtained analytically pure by crystallisation from a mixture of hexane and $CH_2Cl_2$ (1:1) at –20 °C (dark-yellow solid). Complex **8** could not be obtained as a pure solid by this method, but it could be alternatively and satisfactorily obtained as follows: Compound **7** was dissolved in $CH_2Cl_2$ (0.020 g, 0.02 mmol; 2 mL) and the solution stirred at 80 °C for 12 h. After this period of time the solvent was removed under vacuum and $^1$H NMR monitoring of the crude reaction showed quantitative transformation of **7** into **8**. This compound could be purified by crystallisation from a mixture of hexane and $CH_2Cl_2$ (1:1) at –20 °C (yellow solid).

**6:** $R_f$ = 0.47 [silica gel, hexane/$Et_2O$ (1:3)]. IR (Nujol): ν(Ir–H) = 2162 cm$^{-1}$. $^1$H NMR ($CDCl_3$, 25 °C): $\delta$ = 5.80, 5.72, 5.69 (s, 1 H each, 3 $CH_{pz}$), 3.85, 3.80, 3.70, 3.18 (s, 3 H each, 4 $CO_2Me$), 3.13, 2.38 (dq, $^2J_{H,H}$ = 15.8, $^3J_{H,H}$ = 7.7 Hz, 1 H each, $CH_3CH_2$), 2.47, 2.42, 2.37, 2.06, 2.03, 1.17 (s, 3 H each, 6 $Me_{pz}$), 0.74 (t, 3 H, $CH_3CH_2$), –21.41 (s, 1 H, Ir-H) ppm; the signal at $\delta$ = 2.38 ppm is obscured by the resonances of the $Me_{pz}$ and was detected in the COSY spectrum. $^{13}$C{$^1$H} NMR ($CDCl_3$, 25 °C): $\delta$ = 274.2 ($C^1$), 202.1 ($C^5$), 179.0, 170.8, 168.2, 167.0 ($CO_2$Me), 154.0, 152.0, 150.3, 146.1, 145.4, 143.2 ($C_{qpz}$), 151.7 ($C^3$), 140.1 ($C^2$), 131.1 ($C^4$), 106.6, 106.5, 105.3 ($CH_{pz}$), 52.9, 52.7, 52.6, 51.2 ($CO_2Me$), 51.3 ($^1J_{C,H}$ = 130 Hz, $CH_3CH_2$), 16.3, 16.2, 13.9, 13.0, 12.9 (1:1:1:2:1, $Me_{pz}$), 11.4 ($CH_3CH_2$) ppm. $C_{30}H_{40}BIrN_6O_8$ (815.03): calcd. C 44.2, H 4.9, N 10.3; found C 43.9, H 4.8, N 10.0.

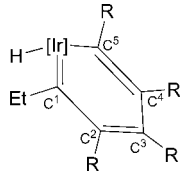

**6**

**7:** $R_f$ = 0.39 [silica gel, hexane/$Et_2O$ (1:8)]. IR (Nujol): ν(Ir–H) = 2194 cm$^{-1}$. $^1$H NMR ($CDCl_3$, 25 °C): $\delta$ = 6.01 (d, $^3J_{B,A}$ = 11 Hz, 1 H, $H_B$), 5.92, 5.76, 5.62 (s, 1 H each, 3 $CH_{pz}$), 4.34 (m, 1 H, $H_A$), 3.83, 3.75, 3.52, 3.06 (s, 3 H each, 4 $CO_2Me$), 2.43, 2.30, 2.29, 2.28, 2.26, 2.18 (s, 3 H each, 6 $Me_{pz}$), 1.15 (d, $^3J_{H,H}$ = 6.0 Hz, 3 H, $CH_AMe$), –16.93 (s, 1 H, Ir-H) ppm. $^{13}$C{$^1$H} NMR ($CDCl_3$, 25 °C): $\delta$ = 174.6, 169.5, 167.6, 166.9 ($CO_2$Me), 152.4, 152.3, 150.5, 144.8, 143.5, 143.5 ($C_{qpz}$), 138.3, 133.8, 128.8, 126.7 ($CCO_2$Me), 108.5, 107.9, 106.1 ($CH_{pz}$), 61.1 ($CH_B$), 56.4 ($CH_A$), 52.5, 52.3, 51.8, 50.7 ($CO_2Me$), 17.8 ($CH_AMe$), 16.5, 16.5, 15.9, 12.9, 12.9, 12.7 ($Me_{pz}$) ppm. $C_{30}H_{40}BIrN_6O_8$·1.25$CH_2Cl_2$ (921.28): calcd. C 40.7, H 4.6, N 9.1; found C 40.7, H 4.8, N 8.6.

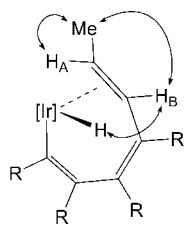

**7**

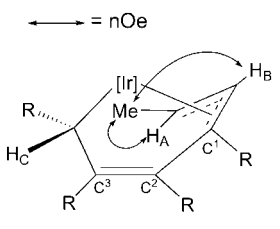

**8**

**8:** $^1$H NMR ($CDCl_3$, 25 °C): $\delta$ = 7.11 (d, $^3J_{B,A}$ = 10.3 Hz, 1 H, $H_B$), 5.86, 5.80, 5.59 (s, 1 H each, 3 $CH_{pz}$), 5.06 (s, 1 H, $H_C$), 3.72, 3.64, 3.45, 3.35 (br) (s, 3 H each, 4 $CO_2$Me), 3.61 (m, 1 H, $H_A$), 2.70, 2.41, 2.36, 2.28, 2.24, 2.17 (s, 3 H each, 6 $Me_{pz}$), 1.47 (d, $^3J_{H,H}$ = 5.7 Hz, 3 H, $CH_AMe$) ppm. $^{13}$C{$^1$H} NMR ($CDCl_3$, 25 °C): $\delta$ = 175.0, 166.8 (2:2, $CO_2$Me), 152.5, 151.8, 144.5, 143.4 (1:2:1:2, $C_{qpz}$), 130.9, 128.8 ($C^2$, $C^3$), 110.6, 108.7, 107.2 ($CH_{pz}$), 93.7 ($^1J_{C,H}$ = 161 Hz, $CH_B$), 68.2 ($C^1$), 52.2, 51.9, 51.6, 50.9 ($CO_2Me$), 38.5 ($CH_A$), 19.2 ($CH_AMe$), 17.8, 15.7, 13.6, 13.5, 13.1, 12.8 ($Me_{pz}$), 9.9 ($^1J_{C,H}$ = 134 Hz, $CH_C$) ppm. $C_{30}H_{40}BIrN_6O_8$ (815.03): calcd. C 44.2, H 4.9, N 10.3; found C 44.5, H 4.9, N 10.1.

**Complex 9:** Compound **6** was dissolved in MeCN (0.01 g, 0.01 mmol; 2 mL) and the mixture was stirred at room temperature for 12 h. After this period of time the solvent was removed under reduced pressure and the formation of a mixture of **9** and **10** in a 6:1 ratio was ascertained by $^1$H NMR spectroscopy. Compound **9** (dark-yellow crystals) could be separated by column chromatography on silica gel with diethyl ether as eluent. $R_f$ = 0.57 [silica gel, $Et_2O$]. IR (Nujol): ν(CN) = 2303 cm$^{-1}$. $^1$H NMR ($CDCl_3$, 25 °C): $\delta$ = 5.70, 5.69, 5.65 (s, 1 H each, 3 $CH_{pz}$), 4.21 (t, $^3J_{H,H}$ = 6.6 Hz, 1 H, $C^1H$), 3.74, 3.71, 3.59, 3.09 (s, 3 H each, 4 $CO_2$Me), 2.52 (s, 3 H, MeCN), 2.47, 2.38, 2.33, 2.29, 2.23, 2.12 (s, 3 H each, 6 $Me_{pz}$), 1.06 (m, 2 H, $CH_3CH_2$), 0.16 (t, $^3J_{H,H}$ = 7.3 Hz, 3 H, $CH_3CH_2$) ppm. $^{13}$C{$^1$H} NMR ($CDCl_3$, 25 °C): $\delta$ = 176.0, 171.0, 170.5, 167.3 ($CO_2$Me), 167.8 ($C^5$), 153.6, 150.1, 149.9, 143.2, 143.2, 142.7 ($C_{qpz}$), 142.3, 134.1 ($C^2$, $C^3$), 131.0 ($C^4$), 116.3 (Me*C*N), 108.0, 107.5, 106.2 ($CH_{pz}$), 51.9, 51.8, 51.6, 50.2 ($CO_2Me$), 31.5 ($^1J_{C,H}$ = 128 Hz, $CH_3CH_2$), 16.6, 14.3, 14.3, 13.3, 12.7, 12.5 ($Me_{pz}$), 13.7 ($CH_3CH_2$), 4.8 ($^1J_{C,H}$ = 123 Hz, $C^1$), 3.6 (*Me*CN) ppm. $C_{32}H_{43}BIrN_7O_8$ (856.03): calcd. C 44.9, H 5.0, N 11.4; found C 44.8, H 5.0, N 11.3.

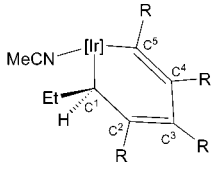

**9**

**Complex 10:** Compound **9** or a mixture of **9** and **10** (obtained as described above) was heated in cyclohexane with a drop of MeCN at 90 °C for 48 h and the solvent was then removed under reduced pressure. $^1$H NMR analysis of the dark-yellow residue showed almost quantitative formation of **10**. IR (Nujol): ν(CN) = 2243 cm$^{-1}$. $^1$H NMR ($CDCl_3$, 25 °C): $\delta$ = 5.73, 5.65 (s, 2:1, 3 $CH_{pz}$), 5.58 (s, 1 H, $C^1H$), 3.73, 3.67, 3.66, 2.97 (s, 3 H each, 4 $CO_2$Me), 2.54 (s, 3 H, MeCN), 2.40, 2.38, 2.36, 2.35, 2.10, 2.08 (s, 3 H each, 6 $Me_{pz}$), 2.29, 2.18 (m, 1 H each, $CH_3CH_2$), 0.66 (t, $^3J_{H,H}$ = 7.3 Hz, 3 H, $CH_3CH_2$) ppm. $^{13}$C{$^1$H} NMR ($CDCl_3$, 25 °C): $\delta$ = 183.5, 171.5, 169.7, 169.3 ($CO_2$Me), 165.5 ($C^5$), 153.3, 149.9, 149.3, 143.5, 143.3, 142.6 ($C_{qpz}$), 144.1, 127.4 ($C^2$, $C^3$), 129.9 ($C^4$), 116.9 (Me*C*N), 107.5, 107.1, 106.7 ($CH_{pz}$), 51.9, 51.8, 51.3, 50.3 ($CO_2Me$), 36.4 ($^1J_{C,H}$ = 125 Hz, $CH_3CH_2$), 15.6, 14.8, 14.1, 13.8, 13.2, 12.6 ($Me_{pz}$), 14.0 ($CH_3CH_2$), 4.6 ($^1J_{C,H}$ = 123 Hz, $C^1$), 3.6 (*Me*CN) ppm. $C_{32}H_{43}BIrN_7O_8$ (856.03): calcd. C 44.9, H 5.0, N 11.4; found C 44.8, H 4.9, N 11.4.

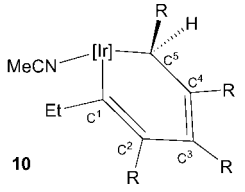

**10**

**Complexes 11 and 12:** Compound **1** was dissolved in $CH_2Cl_2$ (0.2 g, 0.25 mmol; 7 mL), and EtCH=$CH_2$ was bubbled through the solu-

 © 2007 Wiley-VCH Verlag GmbH & Co. KGaA, Weinheim 

tion for 5 min. The resulting solution was stirred under 1-butene in a closed vessel for 12 h at 80 °C. After this period of time the solvent was removed under vacuum and the formation of a mixture of complexes **11** (approx. 70%) and **12** (approx. 5%), along with other by-products, was ascertained by $^1$H NMR spectroscopy. Complexes **11** and **12** were separated by column chromatography (silica gel) with hexane/$Et_2O$ (1:1) as eluent. Complex **11** (38% yield) could be purified by crystallisation from a mixture of pentane and $CH_2Cl_2$ (1:1) at –20 °C (pale brown crystals). Complex **12** could not be separated by column chromatography and was characterised by NMR spectroscopy of the crude mixture.

**11:** $R_f$ = 0.38 [silica gel, hexane/$Et_2O$ (1:3)]. IR (Nujol): ν(Ir–H) = 2157 cm$^{-1}$. $^1$H NMR ($CDCl_3$, 25 °C): $\delta$ = 5.79, 5.72, 5.68 (s, 1 H each, 3 $CH_{pz}$), 3.84, 3.80, 3.69, 3.17 (s, 3 H each, 4 $CO_2Me$), 3.04, 2.34 (dt + m, $^2J_{H,H}$ = 13.5, $^3J_{H,H}$ = 5 Hz, $CH_3CH_2CH_2$, 1 H each), 2.48, 2.42, 2.37, 2.06, 2.03, 1.16 (s, 3 H each, 6 $Me_{pz}$), 1.33, 1.12 (m, m, 1 H each, $CH_3CH_2CH_2$), 0.61 (t, $^3J_{H,H}$ = 7.3 Hz, 3 H, $CH_3CH_2CH_2$), –21.41 (s, 1 H, Ir-H) ppm. $^{13}$C{$^1$H} NMR ($CDCl_3$, 25 °C): $\delta$ = 272.8 ($C^1$), 201.5 ($C^5$), 178.8, 170.5, 168.0, 166.8 ($CO_2Me$), 153.8, 151.7, 150.0, 145.8, 145.1, 143.0 ($C_{qpz}$), 151.1 ($C^3$), 140.3 ($C^2$), 130.8 ($C^4$), 106.3, 106.3, 105.0 ($CH_{pz}$), 60.6 ($CH_3CH_2CH_2$), 52.6, 52.4, 52.3, 50.9 ($CO_2Me$), 20.5 ($CH_3CH_2CH_2$), 16.0, 16.0, 13.6, 12.8, 12.7, 12.7 ($Me_{pz}$), 15.0 ($CH_3CH_2CH_2$) ppm. $C_{31}H_{42}BIrN_6O_8$ (829.74): calcd. C 44.9, H 5.1, N 10.1; found C 44.5, H 5.2, N 9.8.

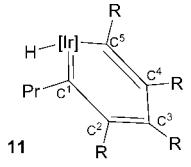

11

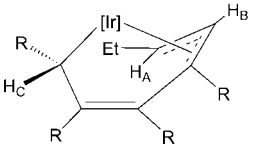

12

**12:** $R_f$ = 0.30 [silica gel, hexane/$Et_2O$ (1:3)]. $^1$H NMR ($CDCl_3$, 25 °C): $\delta$ = 7.05 (d, $^3J_{B,A}$ = 10.0 Hz, 1 H, $H_B$), 5.86, 5.79, 5.59 (s, 1 H each, 3 $CH_{pz}$), 5.09 (s, 1 H, $H_C$), 3.74, 3.72, 3.45, 2.69 (s, 3 H each, 4 $CO_2Me$), 3.58 (this signal is obscured by the $CO_2Me$ resonances and was detected by a COSY spectrum, 1 H, $H_A$), 2.40, 2.35, 2.27, 2.25, 2.18, 1.41 (s, 3 H each, 6 $Me_{pz}$), 1.90, 1.54 (signals detected by a COSY spectrum, 1 H each, $CH_2CH_3$), 1.27 (t, $^3J_{H,H}$ = 7.2 Hz, 3 H, $CH_2CH_3$) ppm. $^{13}$C{$^1$H} NMR ($CDCl_3$, 25 °C): $\delta$ = 92.8 ($^1J_{C,H}$ = 162 Hz, $CH_B$), 46.9 ($^1J_{C,H}$ = 166 Hz, $CH_A$), 26.9 ($^1J_{C,H}$ = 126 Hz, $CH_2CH_3$), 9.4 ($^1J_{C,H}$ = 135 Hz, $CH_C$) ppm.

**Complex 13:** MeCH=$CH_2$ was bubbled through a solution of **1-H** in $CH_2Cl_2$ (0.32 g, 0.44 mmol; 10 mL) for 5 min. The resulting mixture was stirred under propene at room temperature for 15 h, and after this period of time the solution had turned from dark yellow to green. The solvent was removed under reduced pressure and formation of compound **13** in 80% spectroscopic yield was determined by $^1$H NMR spectroscopy. Complex **13** could be purified by column chromatography on silica gel with a mixture of hexane and $Et_2O$ (2:1) as eluent (54% yield). It could be crystallised from a mixture of hexane and $Et_2O$ (2:1) at –20 °C as thin, dark-green needles. $^1$H NMR ($CDCl_3$, 25 °C): $\delta$ = 9.15 (s, 1 H, $C^3$H), 5.84, 5.80, 5.65 (s, 1 H each, 3 $CH_{pz}$), 3.87, 3.79, 3.25 (s, 3 H each, 3 $CO_2Me$), 2.43, 2.41, 2.19, 2.07, 0.99 (s, 2:1:1:1:1, 6 $Me_{pz}$), 1.98 (s, 3 H, $C^1$Me), 0.91 (s, 3 H, IrMe) ppm. $^{13}$C{$^1$H} NMR ($CDCl_3$, 25 °C): $\delta$ = 272.7 ($C^1$), 217.6 ($C^5$), 179.9, 166.0, 165.4 ($CO_2Me$), 154.5, 151.8, 148.8, 144.6, 144.5, 142.5 ($C_{qpz}$), 153.7 ($^1J_{C,H}$ = 158 Hz, $C^3$), 139.5 ($C^2$), 132.0 ($C^4$), 108.1, 107.9, 105.5 ($CH_{pz}$), 52.1, 51.9, 50.7 ($CO_2Me$), 44.9 ($^1J_{C,H}$ = 128 Hz, $C^1Me$), 15.4, 14.9, 13.1, 13.0, 12.9, 12.6 ($Me_{pz}$), –17.6 ($^1J_{C,H}$ = 130 Hz, IrMe) ppm. $C_{28}H_{38}BIrN_6O_6\cdot Et_2O$ (831.03): calcd. C 46.2, H 5.8, N 10.1; found C 46.0, H 5.6, N 10.3.

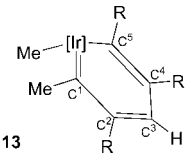

13

**Complex 14:** Two or three drops of MeCN were added to a solution of compound **13** in cyclohexane (0.03 g, 0.04 mmol; 2 mL) and the mixture was stirred at 100 °C for 15 h. After this period of time the solvent was removed under reduced pressure and the $^1$H NMR spectrum of the crude reaction mixture showed the presence of complex **14** in 12% spectroscopic yield. It could be isolated by column chromatography on silica gel, with a mixture of hexane and $Et_2O$ (1:3) as eluent, in 7% yield (dark yellow crystals). $^1$H NMR ($CDCl_3$, 25 °C): $\delta$ = 10.76 (s, 1 H, $H_D$), 6.87 (d, $^3J_{H,H}$ = 7.1 Hz, 1 H, $H_C$), 5.76, 5.71, 5.69 (s, 1 H each, 3 $CH_{pz}$), 3.72, 3.65, 3.63 (s, 3 H each, 3 $CO_2Me$), 3.46 (m, 1 H, $H_B$), 3.39 (m, 1 H, $H_A$), 2.38, 2.36, 2.32, 2.14, 2.09 (s, 1:1:2:1:1, 6 $Me_{pz}$), 0.40 (d, $^3J_{H,H}$ = 7.1 Hz, 3 H, $CH_AMe$), 2.29 (s, 3 H, MeCN) ppm. In $C_6D_6$ $H_C$ resonates at $\delta$ = 7.47 ppm (d, $^3J_{C,B}$ = 8.1 Hz) while $H_B$ appears at $\delta$ = 3.99 ppm (dd, $^3J_{B,A}$ = 11.6 Hz) and $H_A$ at $\delta$ = 3.80 ppm (dq, $^3J_{A,Me}$ = 7.3 Hz). The NOESY connections shown above were obtained in this solvent. $^{13}$C{$^1$H} NMR ($CDCl_3$, 25 °C): $\delta$ = 176.8, 170.4, 166.4 ($CO_2Me$), 163.1 ($^1J_{C,H}$ = 139 Hz, $CH_D$), 151.5, 150.3, 150.2, 143.8, 143.4, 143.0 ($C_{qpz}$), 137.1 ($^1J_{C,H}$ = 161 Hz, $CH_C$), 134.1, 128.9 ($C_qCO_2Me$), 116.8 (Me$CN$), 108.2, 108.0, 106.8 ($CH_{pz}$), 55.5 ($^1J_{C,H}$ = 136 Hz, $CH_B$), 51.5, 51.0, 50.9 ($CO_2Me$), 21.6 ($CH_AMe$), 15.8, 14.0, 13.4, 12.7, 12.4 (1:1:1:2:1, $Me_{pz}$), 9.1 ($^1J_{C,H}$ = 128 Hz, $CH_A$), 3.5 ($Me$CN) ppm. $C_{30}H_{41}BIrN_7O_6$ (798.03): calcd. C 45.1, H 5.2, N 12.3; found C 44.6, H 5.8, N 12.2.

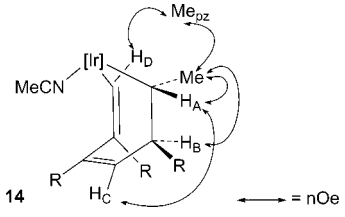

14

**Complex 15:** EtCH=$CH_2$ was bubbled through a solution of **1-H** in $CH_2Cl_2$ (0.4 g, 0.54 mmol; 12 mL) for 5 min. The resulting mixture was stirred under 1-butene at 60 °C for 15 h, and after this period of time the solvent was removed under reduced pressure. The $^1$H NMR spectrum of the crude reaction mixture showed the formation of compound **15** (6%) along with other by-products. It was separated by column chromatography on silica gel, with a mixture of hexane and $Et_2O$ (5:1) as eluent, in 5% yield (dark-green crystals). $R_f$ = 0.23 [silica gel, hexane/$Et_2O$ (1:1)]. $^1$H NMR ($CDCl_3$, 25 °C): $\delta$ = 8.95 (s, 1 H, $C^3$H), 5.82, 5.76, 5.65 (s, 1 H each, 3 $CH_{pz}$), 3.87, 3.78, 3.25 (s, 3 H each, 3 $CO_2Me$), 2.95, 2.15 (m, 1 H each, $CH_2CH_3$), 2.44, 2.43, 2.39, 2.17, 2.13, 1.09 (s, 3 H each, 6 $Me_{pz}$), 0.90 (s, 3 H, IrMe), 0.81 (t, $^3J_{H,H}$ = 7.3 Hz, 3 H, $CH_2CH_3$) ppm. $^{13}$C{$^1$H} NMR ($CDCl_3$, 25 °C): $\delta$ = 283.4 ($C^1$), 210.7 ($C^5$), 179.2, 166.5, 165.5 ($CO_2Me$), 154.2, 151.7, 149.4, 144.8, 144.3, 142.4 ($C_{qpz}$), 152.8 ($^1J_{C,H}$ = 159 Hz, $C^3$), 139.9 ($C^2$), 131.0 ($C^4$), 108.1, 107.9, 105.3 ($CH_{pz}$), 52.1, 52.0, 50.8 ($CO_2Me$), 50.8 ($CH_2CH_3$), 15.1, 13.7, 13.0, 12.8, 12.6 (2:1:2:1:1, $Me_{pz}$, $CH_2CH_3$), –18.4 ($^1J_{C,H}$ = 128 Hz, IrMe) ppm. $C_{29}H_{40}BIrN_6O_6\cdot Et_2O$ (845.03): calcd. C 46.9, H 5.9, N 9.9; found C 46.6, H 5.9, N 9.8.

 © 2007 Wiley-VCH Verlag GmbH & Co. KGaA, Weinheim 

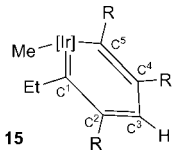


15

**X-ray Crystallography:** The X-ray structures of complexes **6** and **13** were reported in a preliminary communication.[2] Data for compound **5** were collected with a Bruker-Nonius X8APEX-II CCD diffractometer by using ω and ϕ scans with a scan width of 0.3° (in the range $5.60° < 2\theta < 61.16°$) and a 20-s exposure time with a crystal-to-detector distance of 37.5 mm. The data were reduced (SAINT)[11] and corrected for Lorentz polarisation effects and absorption by a multiscan method with SADABS.[12] The structure was solved by direct methods (SIR-2002)[13] and refined against all $F^2$ data by full-matrix least-squares techniques (SHELXTL-6.12).[14] All the non-hydrogen atoms were refined with anisotropic displacement parameters. The hydrogen atoms were included in calculated positions and refined as riding on their respective carbon atoms with isotropic displacement parameters. $C_{35}H_{54}BIrN_6O_9$ [$C_{30}H_{54}BIrN_6O_9{\cdot}C_5H_{12}$], $M_r$ = 905.85, yellow prism crystal ($0.24 \times 0.22 \times 0.19$ mm) from pentane/diethyl ether; triclinic, space group $P\bar{1}$ (no. 2), $a$ = 10.7973(3), $b$ = 11.2238(3), $c$ = 16.5423(4) Å, $\alpha$ = 102.7200(10)°, $\beta$ = 90.3650(10)°, $\gamma$ = 101.6970(10)°, $V$ = 1912.16(9) Å$^3$, $Z$ = 2, $\rho_{calcd.}$ = 1.573 g cm$^{-3}$, $\lambda$(Mo-$K_\alpha$) = 0.71073 Å, $F$(000) = 920, $\mu$ = 3.551 mm$^{-1}$, $T$ = 100(2) K. 39188 Measured reflections, of which 11594 were unique ($R_{int}$ = 0.0257); 469 refined parameters, final $R_1$ = 0.0226 for reflections with $I > 2\sigma(I)$, $wR_2$ = 0.0619 (all data), GOF = 1.095.

CCDC-631538 (for **5**) contains the supplementary crystallographic data for this paper. These data can be obtained free of charge from The Cambridge Crystallographic Data Centre via www.ccdc.cam.ac.uk/data_request/cif.

## Acknowledgments

Financial support from the Spanish Ministerio de Educación y Ciencia (MEC) (projects CTQ2004-00409/BQU, FEDER support) and from the Junta de Andalucía is gratefully acknowledged. N. R. thanks the MEC and the CSIC for research grants.

[1] M. Paneque, C. M. Posadas, M. L. Poveda, N. Rendón, E. Álvarez, K. Mereiter, *Chem. Eur. J.*, in press.
[2] E. Álvarez, M. Paneque, M. L. Poveda, N. Rendón, *Angew. Chem. Int. Ed.* **2006**, *45*, 474.
[3] K. Ilg, M. Paneque, M. L. Poveda, N. Rendón, L. L. Santos, E. Carmona, K. Mereiter, *Organometallics* **2006**, *25*, 2230.
[4] a) J. R. Bleeke, *Chem. Rev.* **2001**, *101*, 1205; b) C. W. Landford, M. M. Haley, *Angew. Chem. Int. Ed.* **2006**, *45*, 3914; c) C. S. Chin, H. Lee, *Chem. Eur. J.* **2004**, *10*, 4518; d) H. Xia, G. He, H. Zhang, T. B. Wen, H. H. Y. Sung, I. D. Williams, G. Jia, *J. Am. Chem. Soc.* **2004**, *126*, 6862; e) P. Barrio, M. A. Esteruelas, E. Oñate, *J. Am. Chem. Soc.* **2004**, *126*, 1946; f) M. Paneque, C. M. Posadas, M. L. Poveda, N. Rendón, V. Salazar, E. Oñate, K. Mereiter, *J. Am. Chem. Soc.* **2003**, *125*, 9898; g) V. Jacob, T. J. R. Weakley, M. M. Haley, *Angew. Chem. Int. Ed.* **2002**, *41*, 3470; h) G. R. Clark, P. M. Johns, W. R. Roper, L. J. Wright, *Organometallics* **2006**, *25*, 1771, and ref.[3] For recent theoretical work on this type of compound, see: i) M. A. Iron, A. C. B. Lucassen, H. Cohen, M. E. van der Boom, J. M. L. Martin, *J. Am. Chem. Soc.* **2004**, *126*, 11699; j) M. A. Iron, J. M. L. Martin, M. E. van der Boom, *J. Am. Chem. Soc.* **2003**, *125*, 13020.
[5] a) L. Giannini, G. Guillemot, E. Solari, C. Floriani, N. Re, A. Chiesi-Villa, C. Rizzoli, *J. Am. Chem. Soc.* **1999**, *121*, 2797; b) J. S. Freundlich, R. R. Schrock, W. M. Davis, *J. Am. Chem. Soc.* **1996**, *118*, 3643; c) M. Paneque, M. L. Poveda, L. L. Santos, E. Carmona, A. Lledós, G. Ujaque, K. Mereiter, *Angew. Chem. Int. Ed.* **2004**, *43*, 3708; d) G. Parkin, E. Bunel, B. J. Burger, M. S. Trimmer, A. van Asselt, J. E. Bercaw, *J. Mol. Catal.* **1987**, *41*, 21; e) O. V. Ozerov, L. A. Watson, M. Pink, K. G. Caulton, *J. Am. Chem. Soc.* **2003**, *125*, 9604; f) O. V. Ozerov, L. A. Watson, M. Pink, K. G. Caulton, *J. Am. Chem. Soc.* **2004**, *126*, 6363; g) V. F. Kuznetsov, K. Abdur-Rashid, A. J. Lough, D. G. Gusev, *J. Am. Chem. Soc.* **2006**, *128*, 14388.
[6] a) F. M. Alías, P. J. Daff, M. Paneque, M. L. Poveda, E. Carmona, P. J. Pérez, V. Salazar, Y. Alvarado, R. Atencio, R. Sánchez-Delgado, *Chem. Eur. J.* **2002**, *8*, 5132; b) F. M. Alías, M. L. Poveda, M. Sellin, E. Carmona, *J. Am. Chem. Soc.* **1998**, *120*, 5816.
[7] a) E. Carmona, M. Paneque, M. L. Poveda, *Dalton Trans.* **2003**, 4022; b) E. Clot, J. Chen, D.-H. Lee, S. Y. Sung, L. N. Appelhans, J. W. Faller, R. H. Crabtree, O. Eisenstein, *J. Am. Chem. Soc.* **2004**, *126*, 8795; c) R. R. Schrock, S. W. Seidel, N. C. Mösch-Zanetti, K.-Y. Shih, M. B. O'Donoghue, W. M. Reiff, *J. Am. Chem. Soc.* **1997**, *119*, 11876.
[8] As suggested by a referee of our preliminary communication,[2] intermediate **C** may be reached by a sequence of olefin insertion and H transposition via the metal centre. However, it is difficult to understand in this case why the involved hydride intermediate does not transform into an allyl species as described in Scheme 1 and ref.[1] The same reasoning applies to intermediate **H** in Scheme 5.
[9] For a related system, see: R. P. Hughes, H. A. Trujillo, J. W. Egan Jr., A. L. Rheingold, *J. Am. Chem. Soc.* **2000**, *122*, 2261.
[10] a) K. Ferré, G. Poignant, L. Toupet, V. Guerchais, *J. Organomet. Chem.* **2001**, *629*, 19; b) M. Albrecht, G. van Koten, *Angew. Chem. Int. Ed.* **2001**, *40*, 3750; c) B. Rybtchinski, D. Milstein, *Angew. Chem. Int. Ed.* **1999**, *38*, 870.
[11] *SAINT 6.02*, BRUKER-AXS, Inc., Madison, WI 53711-5373, USA, **1997–1999**.
[12] *SADABS*, G. Sheldrick, Bruker AXS, Inc., Madison, Wisconsin, USA, **1999**.
[13] *SIR2002*: M. C. Burla, M. Camalli, B. Carrozzini, G. L. Cascarano, C. Giacovazzo, G. Polidori, R. Spagna, *J. Appl. Crystallogr.* **2003**, *36*, 1103.
[14] *SHELXTL 6.14*, Bruker AXS, Inc., Madison, Wisconsin, USA, **2000–2003**.

Received: December 29, 2006
Published Online: April 30, 2007

 © 2007 Wiley-VCH Verlag GmbH & Co. KGaA, Weinheim 

DOI: 10.1002/ejic.200700001

# Cyanometalate Cages with Exchangeable Terminal Ligands

**Julie L. Boyer,[a] Haijun Yao,[a] Matthew L. Kuhlman,[a] Thomas B. Rauchfuss,*[a] and Scott Wilson[a]**

**Keywords:** Cyanide / Ruthenium / Hydrogen bonds / Cage compounds / Heterometallic complexes

The coordination chemistry of the unusual metallo-ligand $Cs\subset[CpCo(CN)_3]_4[Cp^*Ru]_3$ ($Cs\subset Co_4Ru_3$) is described with attention to the behavior of the ligand itself, its binding to Lewis-acidic metal cations, and its ability to stabilize catalytically relevant Ru–$PPh_3$ fragments. A series of tests demonstrate that the "rim" $[CpCo(CN)_3]^-$ groups in $Cs\subset Co_4Ru_3$ are exchangeable. Upon treatment with $[(MeC_5H_4)Co(CN)_3]^-$ (Co′) $Cs\subset Co_4Ru_3$ undergoes vertex exchange to give $Cs\subset Co_{4-x}Co'_xRu_3$. Similarly the cage is degraded by CO. Most convincing, $Cs\subset Co_4Ru_3$ reacts with $PhNH_3OTf$ to precipitate the polymer $PhNH_3CpCo(CN)_3$ and form the molecular box $[Cs\subset Co_4Ru_4]^+$. Treatment of $Cs\subset Co_4Ru_3$ with $[M(NCMe)_x]PF_6$ (M = Cu, Ag) gave the Lewis acidic cages $\{Cs\subset[CpCo(CN)_3]_4[Cp^*Ru]_3M(NCMe)\}PF_6$, which reacted with tertiary phosphane ligands to give adducts $[Cs\subset Co_4Ru_3M(PPh_3)]PF_6$. Lewis acidic octahedral vertices were installed using Fe, Ni, and Ru reagents. The boxes $[Cs\subset Co_4Ru_3M(NCMe)_3]^{2+}$ (M = Ni, Fe) formed readily from the reaction $Cs\subset Co_4Ru_3$ with $[Ni(NCMe)_6](BF_4)_2$ and $[Fe(NCMe)_6](PF_6)_2$. Displacement of the MeCN ligands gives $[Cs\subset Co_4Ru_3Ni(9\text{-ane-}S3)](BF_4)_2$. A series of boxes were prepared by the reaction of $Cs\subset Co_4Ru_3$ and $RuCl_2(PPh_3)_3$, $RuHCl(PPh_3)_3$, and $[(C_6H_6)Ru(NCMe)_3](PF_6)_2$. The derivative of the hydride, $[Cs\subset Co_4Ru_3Ru(NCMe)(PPh_3)_2](PF_6)_2$, was characterized crystallographically.

(© Wiley-VCH Verlag GmbH & Co. KGaA, 69451 Weinheim, Germany, 2007)

## Introduction

The centuries old field of metal cyanide chemistry[1] has experienced a renaissance due the zeolitic,[2,3] magnetic,[4] and electronic properties[5] of cyanometalate materials. Parallel to these application-driven studies, we have focused on synthetic methodologies leading to discrete molecular architectures that can be characterized in solution. In recent years we have developed families of molecular cyanometalate ensembles that are synthesized analogously to Prussian Blue (PB), except that our molecular building blocks are tricyanometalates.[6] Half of the coordination sphere of these tricyanometalates is occupied by a strongly coordinating, non-displaceable co-ligand such as $C_5H_5^-$. The face-capping co-ligand inhibits the formation of polymers, by minimizing cross-linking, but still allows the formation of three-dimensional structures, which resemble subunits of PB.[7,8]

Our first attempt at molecular cyanometalate cages afforded the cationic cage $[CpCo(CN)_3]_4[Cp^*Rh]_4^{4+}$.[7] Replacing the dicationic tritopic Lewis acid with a monocationic analog results in charge-neutral ionophilic molecular cages.[9] Specifically, the reaction $[CpCo(CN)_3]^-$, $[Cp^*Ru(NCMe)_3]^+$, and CsOTf at the ratio of 4:4:1 produces the molecular box $\{Cs\subset[CpCo(CN)_3]_4[Cp^*Ru]_4\}^+$ ($Cs\subset Co_4Ru_4^+$).[10] By changing the ratio of the reactants to 4:3:1, one obtains instead the violet-colored "defect" box $Cs\subset[CpCo(CN)_3]_4[Cp^*Ru]_3$ ($Cs\subset Co_4Ru_3$).[10] Aside from its novel structure, an exciting aspect of $Cs\subset Co_4Ru_3$ is its potential as a well-defined building block for the assembly of novel molecular cages via $Cs\subset Co_4Ru_3 + ML_n^z \rightarrow Cs\subset Co_4Ru_3ML_n^z$, a box-completion process. Proof-of-concept was provided by the finding that $Cs\subset Co_4Ru_3$ reacts with one equiv. of $[Cp^*M(NCMe)_3](PF_6)_n$ to give the completed box $Cs\subset Co_4Ru_3M^z$ (M = Cp*Ru, Cp*Rh, $z$ = 1, 2) in high yield.[10]

All previously synthesized cyanometalate boxes and defect boxes possessed non-displaceable ligands such as Cp and Cp*. Isolable cyanometalate cages with *displaceable* ligands L, e.g. $Cs\subset[CpCo(CN)_3]_4[Cp^*Ru]_3ML_n^z$ (L = MeCN, $n$ = 1, 3), represent intriguing targets, which would enable the generation of ensembles of greater complexity and enhanced reactivity. For example, one could envision a modular approach to the preparation of "boxes-of-boxes." Few cyanometalates of nuclearity >8 have been well-characterized *in solution*.[11] We previously described the "double boxes" $\{[Cs\subset Co_4Ru_3]_2M\}^z$, and we anticipate that still higher nuclearity cages can be achieved. The construction of such oligo-cages will require boxes with one or more vertices that contain labile terminal ligands. This paper outlines our initial efforts toward this goal (Scheme 1).

[a] Department of Chemistry, University of Illinois at Urbana-Champaign,
Urbana, IL 61801, USA
E-mail: rauchfuz@uiuc.edu

 © 2007 Wiley-VCH Verlag GmbH & Co. KGaA, Weinheim 

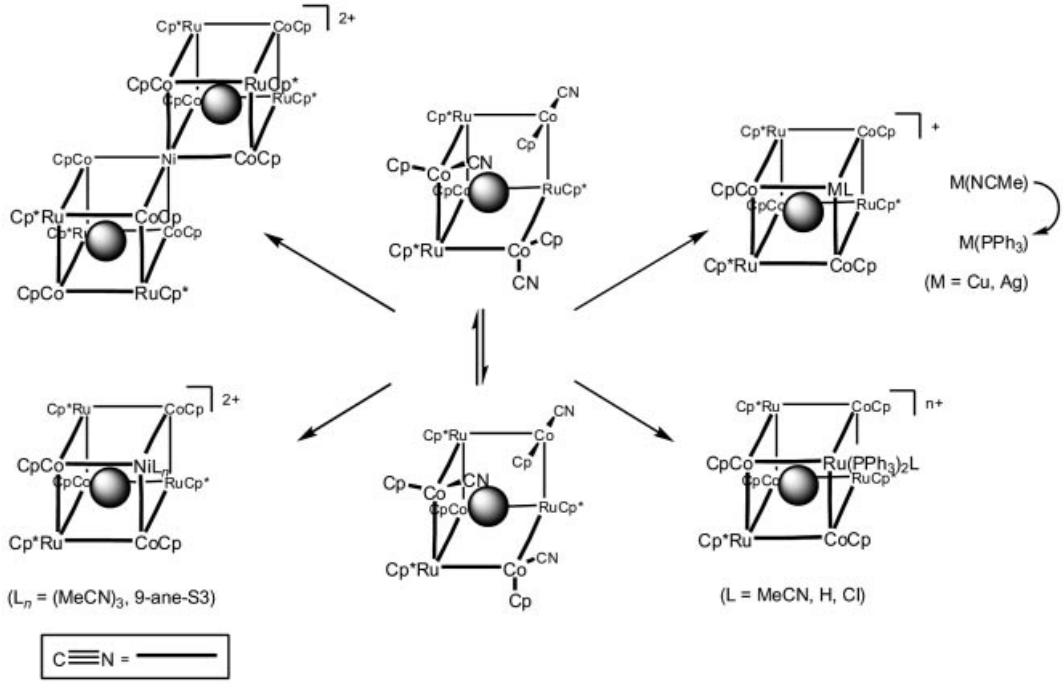


Scheme 1. Box-completion reactions of $Cs\subset Co_4Ru_3$ described in this report.

## Results and Discussion

### Solution Properties of the $Cs\subset Co_4Ru_3$ Metallo-Ligand

Prior to examining the complexation properties of $Cs\subset Co_4Ru_3$, we conducted experiments aimed at elucidating the solution behavior of this "defect box." Four isomers are possible, depending on the relative stereochemistry of the three $CpCo(CN)_3$ units situated on the "rim" (Scheme 2). Two $C_s$ isomers are observed by $^1H$ NMR spectroscopy.[10] The interconversion of these two $C_s$ isomers is hypothesized to occur through the scission of one Ru–N bond, rotation of the unidentate $[CpCo(CN)_3]^-$ subunit, and reformation of the Ru–N bond to a different cyano group of the same $[CpCo(CN)_3]^-$ subunit (Scheme 2).

The stereochemical nonrigidity of the rim $[CpCo(CN)_3]^-$ groups is indicated by the effect of solvent on the *endo*$_2$*exo*$_1$/*endo*$_1$*exo*$_2$ isomer ratio. In THF solution, the ratio is 3:1, whereas addition of 10% MeCN shifts this ratio to 9:1 (Figure 1). The presence of MeCN favors the $C_s$ isomer with two *endo* $CN_t$ ligands (see Scheme 2). Furthermore, small amount of MeCN cause the chemical shifts of the Cp signals to shift downfield, possibly due an apparent interaction of the Cp protons with the triple bond of the MeCN. The interaction between the MeCN protons and the cyanide linkers of the cage framework was previously indicated with the solid-state structure of $Cs\subset Co_4Ru_3$.[2]

Labeling studies provided further evidence that the $Cs\subset Co_4Ru_3$ cage undergoes partial disassembly in solution. Two Ru–N bonds must break to dissociate a "rim" $CpCo(CN)_3^-$ subunit. As monitored by ESI-MS, $Cs\subset Co_4Ru_3$ was shown to exchange with $K[(MeC_5H_4)Co(CN)_3]$ (Co′) to give $Cs\subset Co_{4-x}Co'_xRu_3$ over the course of days. Altering the amount of Co′ from one to four equiv. did not increase the rate vertex exchange, suggesting that vertex exchange is dissociative, being dependent only on $[Cs\subset Co_4Ru_3]$. In a similar experiment, we found that the

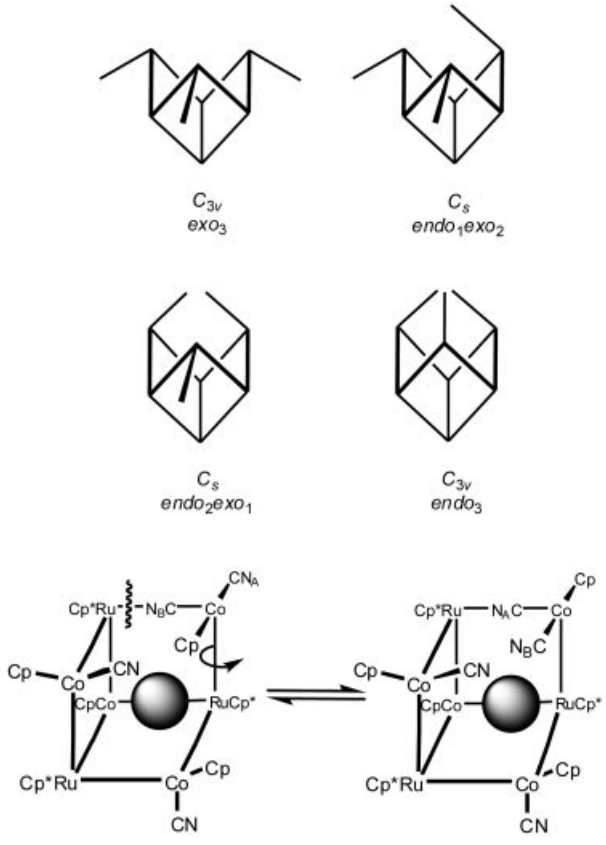


Scheme 2. Schematic depiction of isomers for the $M_7$ defect cages (top), and pathway that interconverts the two $C_s$ isomers (bottom).

 © 2007 Wiley-VCH Verlag GmbH & Co. KGaA, Weinheim 

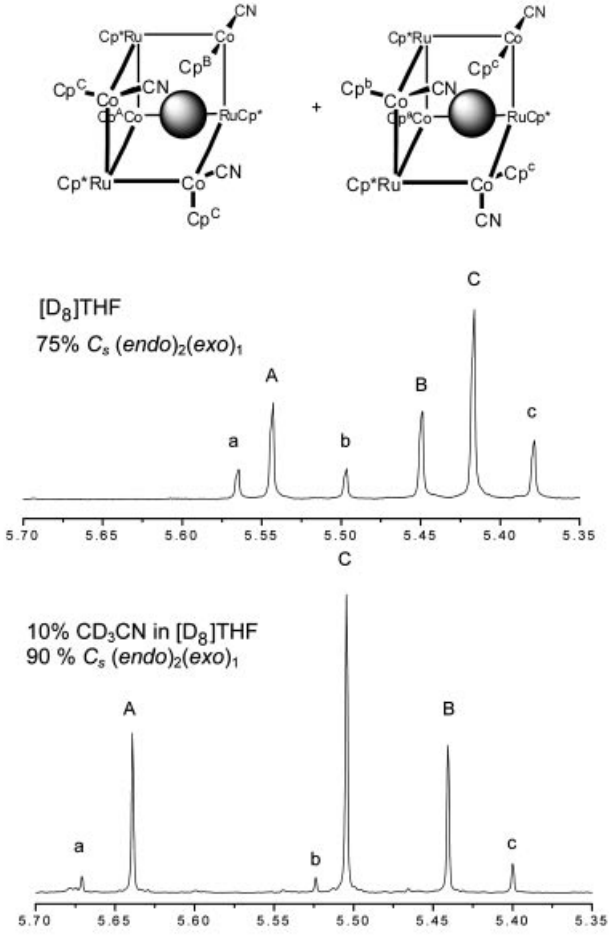


Figure 1. Schematic of the two detected isomers of $Cs\subset Co_4Ru_3$ (top), $^1H$ NMR spectra of $Cs\subset Co_4Ru_3$ in various solvents (bottom).

defect box $[CpCo(CN)_3]_4[Cp^*Rh]_3^{2+}$ ($Co_4Rh_3^{2+}$) underwent rapid exchange with Co′ to give $Co_{4-x}Co'_xRh_3^{2+}$ in under 5 h.

Treatment of a solution of $Cs\subset Co_4Ru_3$ with CO resulted in rapid degradation as indicated by the appearance of a $\nu_{CO}$ band at 1943 $cm^{-1}$. ESI-MS of the reaction mixture featured peaks corresponding to $\{[CpCo(CN)_3]_2[Cp^*Ru(CO)]_3\}^+$. We propose $\{[CpCo(CN)_3]_2[Cp^*Ru(CO)]_3\}^+$ is a trigonal-bipyramidal cage, other examples of which are known in cyanometalate chemistry.[12]

Further evidence for the mobility of the $CpCo(CN)_3^-$ vertices in $Cs\subset Co_4Ru_3$ came from vertex extraction reactions involving ammonium ions. Thus treatment of this cage with $PhNH_3OTf$ afforded the coordination polymer $PhNH_3CpCo(CN)_3$ [Equation (1)].

$$4\ Cs\subset Co_4Ru_3 + 4\ PhNH_3^+ \rightarrow 4\ PhNH_3CpCo(CN)_3 + 3\ [Cs\subset Co_4Ru_4]^+ + Cs^+ \quad (1)$$

This polymeric species was independently synthesized by treating an MeCN solution of $PPN[CpCo(CN)_3]$ with $PhNH_3OTf$ ($PPN^+ = Ph_3PNPPh_3^+$). The yellow solid was soluble only in polar solvents, i.e. those expected to compete for hydrogen bonds. The polymer adopts a "folded tape" motif, constructed from strong hydrogen bonds connecting the acidic protons and the basic cyanide ligands (Figure 2). The ammonium cyanide distances (*N*···*N*C–Co) range from 2.747 to 2.999 Å indicating strong hydrogen bonds.[13]

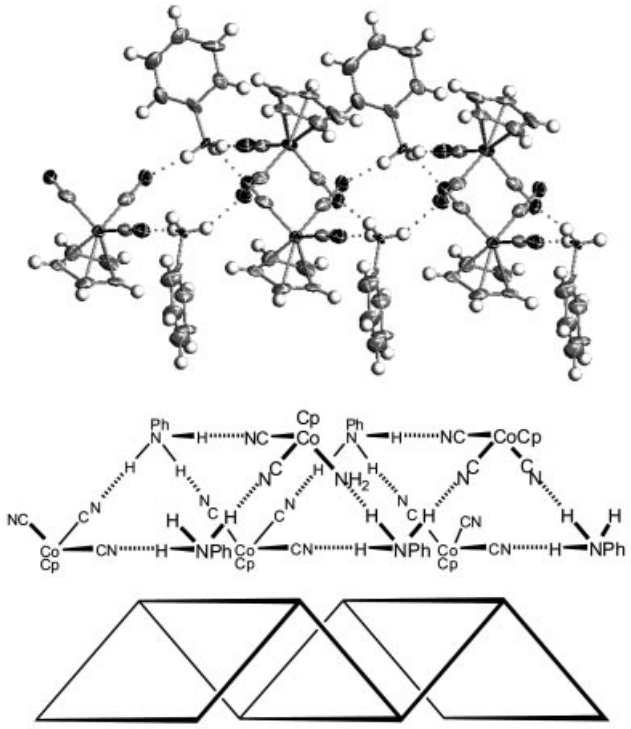

Figure 2. Structure of the hydrogen-bonded polymer $PhNH_3CpCo(CN)_3$ (top). Schematic illustrating the bonding in the tape polymer (bottom).

Although the defect box $Cs\subset Co_4Ru_3$ does undergo partial disassembly in solution, it displayed greater stability than the analogous $Co_4Rh_3^{2+}$, which lacks a centrally "gluing" $Cs^+$ center. The $Co_4Rh_3^{2+} + [Cp^*Ru(NCMe)_3]^+$ reaction afforded a mixture of $Co_4Rh_4^{4+}$, $Co_4Rh_3Ru^{3+}$, and $Co_4Rh_2Ru_2^{2+}$. These products, especially $Co_4Rh_4^{4+}$, indicate that the starting $Co_4Rh_3^{2+}$ disassembles followed by reassembly of $[Cp^*Rh(NCMe)_3]^{2+}$, $[Cp^*Ru(NCMe)_3]^+$, and $[CpCo(CN)_3]^-$ in a nearly statistical manner. Slightly different products are obtained when the $Co_4Rh_3^{2+} + [Cp^*Ru(NCMe)_3]^+$ reaction was conducted in the presence of $Cs^+$. Again, the main products are $Co_4Rh_4^{4+}$ and $Co_4Rh_3Ru^{3+}$, but we also obtained small amounts of $Cs\subset Co_4Rh_2Ru_2^{3+}$ and $Cs\subset Co_4Rh_3Ru^{4+}$. These latter two species are unprecedented examples of cationic receptors binding $Cs^+$. In contrast to the behavior of the Cs-free cages, $Cs\subset Co_4Ru_3$ remained intact upon complexation to $[Cp^*Rh(NCMe)_3]^{2+}$ to produce $Cs\subset Co_4Ru_3Rh^{2+}$ quantitatively.

### Boxes with Lewis-Acidic Tetrahedral Vertices: Copper(I) and Silver(I)

Treatment of a MeCN solution of $[Cu(NCMe)_4]PF_6$ with a THF solution of $Cs\subset Co_4Ru_3$ at 0 °C gave red

 © 2007 Wiley-VCH Verlag GmbH & Co. KGaA, Weinheim 

$\{Cs\subset[CpCo(CN)_3]_4[Cp^*Ru]_3Cu(NCMe)\}PF_6$ ($[Cs\subset Co_4Ru_3Cu(NCMe)]PF_6$). The $^1H$ NMR spectrum confirmed the $C_{3v}$ symmetry with two Cp resonances in a 3:1 ratio and single resonance for Cp*. The IR spectrum of $[Cs\subset Co_4Ru_3Cu(NCMe)]PF_6$ featured a single broad $\nu_{CN}$ band at 2144 $cm^{-1}$, which is higher in energy vs. $\nu_{CN}$ for the terminal cyanides of $Cs\subset Co_4Ru_3$ (2129 $cm^{-1}$). The ESI-MS of the product solution supported the formulation. The red-colored silver derivative $[Cs\subset Co_4Ru_3Ag(NCMe)]^+$ was prepared analogously from $AgPF_6$ and $Cs\subset Co_4Ru_3$.

The MeCN ligands in $[Cs\subset Co_4Ru_3M(NCMe)]^+$ (M = Ag, Cu) exchange readily. Treatment of these cages with $PPh_3$ yielded the expected adducts $[Cs\subset Co_4Ru_3MPPh_3]PF_6$, which were characterized spectroscopically. We attempted to generate higher nuclearity cyanometalates by exploiting the Lewis acidities of $[Cs\subset Co_4Ru_3M(NCMe)]^+$ by their condensation with (18-crown-6 K)$_3[Co(CN)_6]$ or $Et_4NCN$. Such reactions only regenerated $Cs\subset Co_4Ru_3$, suggesting that the metallo-ligand $Cs\subset Co_4Ru_3$ is only weakly bound to the coinage metal.

### Boxes with Lewis-Acidic Octahedral Vertices: Nickel

Condensation of $Cs\subset Co_4Ru_3$ with $[Ni(NCMe)_6](BF_4)_2$ gave the trimetallic cage $\{Cs[CpCo(CN)_3]_4[Cp^*Ru]_3Ni(NCMe)_3\}^{2+}$ ($[Cs\subset Co_4Ru_3Ni(NCMe)_3]^{2+}$). To prevent the generation of the $\{\{Cs[CpCo(CN)_3]_4[Cp^*Ru]_3\}_2Ni\}^{2+}$ byproduct, the $Cs\subset Co_4Ru_3$ cage was added as an MeCN slurry to a concentrated solution of $[Ni(NCMe)_6](BF_4)_2$. The $^1H$ NMR spectrum of the red product indicated $C_{3v}$ symmetry. The signals, especially those of the "rim" CpCo centers, are broadened due to their adjacency to the paramagnetic octahedral $Ni^{II}$ center. The IR spectrum of $[Cs\subset Co_4Ru_3Ni(NCMe)_3](BF_4)_2$ featured a single broad $\nu_{CN}$ band at 2170 $cm^{-1}$; absent was the $\nu_{CNt}$ band at 2129 $cm^{-1}$ for $Cs\subset Co_4Ru_3$. The ESI-MS of the product solution supported the formation of $[Cs\subset Co_4Ru_3Ni(NCMe)_3]^{2+}$ ($m/z$ = 855); signals corresponding to $\{(Cs\subset Co_4Ru_3)_2Ni\}^{2+}$ were not detected. The metalation route enjoys some generality: a slurry of $Cs\subset Co_4Ru_3$ was found to react with $[Fe(NCMe)_6](PF_6)_2$ to afford $[Cs\subset Co_4Ru_3Fe(NCMe)_3](PF_6)_2$, which was identified by ESI-MS.

The MeCN ligands of $[Cs\subset Co_4Ru_3Ni(NCMe)_3]^{2+}$ exchange with a variety of Lewis bases. Qualitative tests using ESI-MS showed that 9-ane-S3 formed adducts (9-ane-S3 is 1,4,7-trithiacyclononane). Preparative-scale reaction gave the red crystalline species $[Cs\subset Co_4Ru_3Ni(9\text{-ane-}S3)](BF_4)_2$, which was characterized crystallographically (see below).

Attempts were made to generate higher nuclearity cages by exploiting the Lewis acidity of $[Cs\subset Co_4Ru_3Ni(NCMe)_3]^{2+}$. Treatment of these cages, however, with $K[(C_5R_5)M(CN)_3]$ [$(C_5R_5)$M = Cp*Rh, CpCo] or $Et_4NCN$ generated the double box $\{(Cs\subset Co_4Ru_3)_2Ni\}^{2+}$, as indicated by ESI-MS analysis. Apparently, scission of the Ni–N(cage) bonds is facile. A sample $\{[Cs\subset Co_4Ru_3]_2Ni\}(BF_4)_2$ was generated independently by treatment of $Cs\subset Co_4Ru_3$ with 0.5 equiv. of $[Ni(NCMe)_6](BF_4)_2$ and characterized by $^1H$ NMR and IR spectroscopy, as well as ESI-MS.

### Boxes Completed with Lewis-Acidic Octahedral Vertices: Ruthenium

The metallo-ligand $Cs\subset Co_4Ru_3$ was shown to bind a variety of ruthenium $PPh_3$ complexes. Thus, $RuCl_2(PPh_3)_3$ and $RuHCl(PPh_3)_3$ afforded the corresponding eight-vertex cages (Scheme 1). The $^1H$ NMR spectra of $[Cs\subset Co_4Ru_3Ru(PPh_3)_2Cl]Cl$ and $[Cs\subset Co_4Ru_3Ru(PPh_3)_2H]Cl$ are consistent with $C_s$ symmetry (Figure 3). Treatment of $[Cs\subset Co_4Ru_3Ru(PPh_3)_2H]Cl$ with an MeCN solution of $AgPF_6$ gave $[Cs\subset Co_4Ru_3Ru(PPh_3)_2(NCMe)](PF_6)_2$, concomitant with formation of Ag. This MeCN-containing product was characterized by proton NMR spectroscopy and X-ray crystallography.

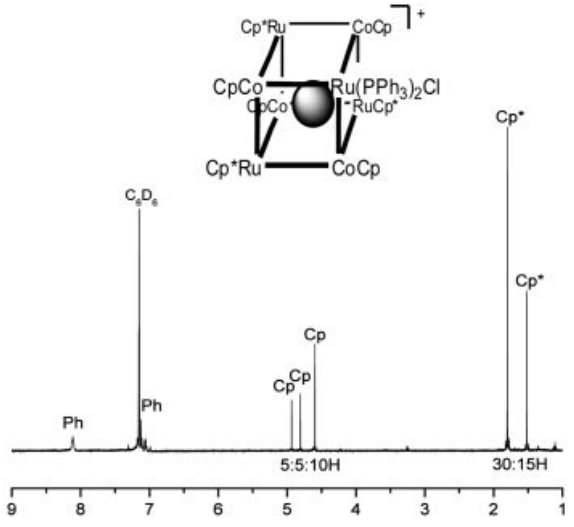


Figure 3. $^1H$ NMR spectrum of $\{Cs\subset[CpCo(CN)_3]_4[Cp^*Ru]_3[Ru(PPh_3)_2Cl]\}Cl$ in $C_6D_6$ solution.

A cage containing one $Ru(C_6H_6)^{2+}$ vertex was prepared from the reaction of $Cs\subset Co_4Ru_3$ and $[(C_6H_6)Ru(NCMe)_3](PF_6)_2$. Photolysis of $[Cs\subset Co_4Ru_3Ru(C_6H_6)](PF_6)_2$ was anticipated to afford the corresponding $[Ru(NCMe)_3]$ derivative, which would be promising building block. Unfortunately, photolysis of $[Cs\subset Co_4Ru_3Ru(C_6H_6)](PF_6)_2$ was a slow process. Only 30% conversion to $[Cs\subset Co_4Ru_3Ru(NCMe)_3](PF_6)_2$ was observed after four days.[14]

### X-ray Crystallographic Results on New Molecular Boxes

Single crystal X-ray structure of $[Cs\subset Co_4Ru_3Ni(9\text{-ane-}S_3)](BF_4)_2$ confirmed the structure of the completed box. The $Cs\subset Co_4Ru_3$ subunit remains intact and binds the Ni(9-ane-S3) subunit in a tridentate fashion forming the trimetallic cube framework, analogous to previously reported completed boxes (Figure 4).[15] In the case of $[Cs\subset Co_4Ru_3Ru(PPh_3)_2(NCMe)](PF_6)_2$, the dicationic cage consists of a $Co_4Ru_4(\mu\text{-}CN)_{12}$ cube with a $Ru(PPh_3)_2(NCMe)^{2+}$ vertex and three Cp*Ru vertices. The cyanide linkages in both the

 © 2007 Wiley-VCH Verlag GmbH & Co. KGaA, Weinheim 

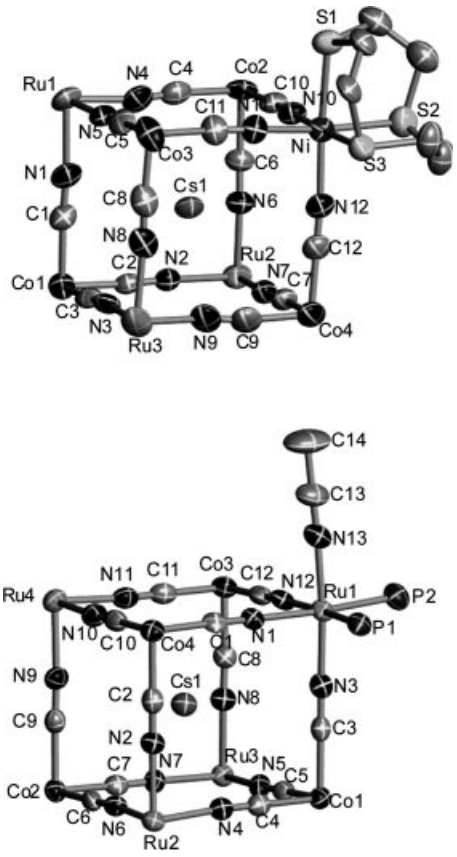


Figure 4. Molecular structures from left to right: {Cs⊂[CpCo(CN)$_3$]$_4$[Cp*Ru]$_3$Ni(9-ane-S3)}(BF$_4$)$_2$ and {Cs⊂[CpCo(CN)$_3$]$_4$[Cp*Ru]$_3$[Ru(NCMe)(PPh$_3$)$_2$]}(PF$_6$)$_2$. Cp and Cp* rings, phenyl groups, and counterions were omitted for clarity. Thermal ellipsoids are set at the 50% level.

Table 1. Selected bond lengths [Å] and angles [°] for [Cs⊂Co$_4$Ru$_3$Ni(9-ane-S$_3$)](BF$_4$)$_2$.

| | | | |
|---|---|---|---|
| Ni–N(10) | 2.0035 | N(10)–Ni–N(11) | 93.97 |
| Ni–N(11) | 2.0786 | N(10)–Ni–N(12) | 93.68 |
| Ni–N(12) | 2.0005 | N(11)–Ni–N(12) | 92.33 |
| Ru(2)–N(2) | 2.0963 | N(2)–Ru(2)–N(6) | 88.10 |
| Ru(2)–N(6) | 2.0698 | N(2)–Ru(2)–N(7) | 85.53 |
| Ru(2)–N(7) | 2.0409 | N(6)–Ru(2)–N(7) | 83.34 |
| Co(2)–C(4) | 1.8224 | C(4)–Co(2)–C(6) | 88.27 |
| Co(2)–C(6) | 1.8830 | C(4)–Co(2)–C(10) | 92.99 |
| Co(2)–C(10) | 1.9023 | C(6)–Co(2)–C(10) | 87.48 |

Table 2. Selected bond lengths [Å] and angles [°] for {Cs⊂[CpCo(CN)$_3$]$_4$[Cp*Ru]$_3$[Ru(NCMe)(PPh$_3$)$_2$]}(PF$_6$)$_2$.

| | | | |
|---|---|---|---|
| Ru(2)–N(2) | 2.0920 | N(2)–Ru(2)–N(4) | 85.72 |
| Ru(2)–N(4) | 2.0954 | N(2)–Ru(2)–N(6) | 85.81 |
| Ru(2)–N(6) | 2.0829 | N(4)–Ru(2)–N(6) | 87.81 |
| Co(1)–C(3) | 1.8644 | C(3)–Co(1)–C(4) | 91.23 |
| Co(1)–C(4) | 1.8833 | C(3)–Co(1)–C(5) | 92.62 |
| Co(1)–C(5) | 1.8739 | C(4)–Co(1)–C(5) | 89.96 |
| Ru(1)–N(1) | 2.0841 | N(1)–Ru(1)–N(3) | 88.49 |
| Ru(1)–N(3) | 2.0423 | N(1)–Ru(1)–N(12) | 86.94 |
| Ru(1)–N(12) | 2.0781 | N(3)–Ru(1)–N(12) | 87.22 |
| Ru(1)–N(13) | 2.0841 | | |
| Ru(1)–P(1) | 2.3403 | | |
| Ru(1)–P(2) | 2.3475 | | |

[Cs⊂Co$_4$Ru$_3$Ni(9-ane-S$_3$)](BF$_4$)$_2$ and [Cs⊂Co$_4$Ru$_3$Ru(PPh$_3$)$_2$(NCMe)](PF$_6$)$_2$ cages are ordered, as indicated by characteristically short Co-C distances. The cage frameworks conform well to the geometry of a cube with ca. 90° N–M–N and C–M–C angles (Table 1 and Table 2).

## Conclusions

The cage Cs⊂Co$_4$Ru$_3$ is a versatile metallo-ligand, despite its stereochemical complications. Neither of the two isomers of this cage are poised to serve as a tridentate ligand: reorientation of the terminal cyanide ligands is required. Metalation of Cs⊂Co$_4$Ru$_3$ is complete upon addition of the electrophile. The isomerization of the terminal cyanides would appear to require the scission of at least one intra-cage Ru–NC–Co linkage, which allows it to exchange sites with the terminal cyanide ligand. Various chemical tests – cage degradation with CO and PhNH$_3^+$, as well as quasi-degenerate exchange reactions – show that vertex exchange occurs, however, more slowly than complexation.

The metallo-ligand Cs⊂Co$_4$Ru$_3$ exhibits exceptional affinity for binding to diverse metal centers. This work substantially extends this range to include a range of metal centers that bear reactive ligands. We show that these site-differentiated cages can undergo selective substitution reactions without disruption of the M$_8$(μ-CN)$_{12}$ framework. It appears that this first generation of reactive cages are insufficiently robust, so further work is merited on the design of new cyanometalate cage-ligands. The Cs⊂Co$_4$Ru$_3$ ligand functions as a facially capping tridentate ligand akin to tris(pyrazolyl)borate (Tp) and triazacyclononane (TACN). Complexes of the type Tp$_2$M$^z$ and (TACN)$_2$M$^z$ are common, whereas the half-sandwich complexes are rarer.[16]

## Experimental Section

Reactions and manipulations were performed under nitrogen, using standard Schlenk-line techniques. Solvents were dried and deoxygenated prior to use K(MeC$_5$H$_4$)Co(CN)$_3$,[17] [Cu(NCMe)$_4$]PF$_6$,[18] [Ni(NCMe)$_6$](BF$_4$)$_2$,[19] [Fe(NCMe)$_6$](PF$_6$)$_2$,[20] Ru(PPh$_3$)$_3$Cl$_2$,[21] [(C$_6$H$_6$)Ru(NCMe)$_3$](PF$_6$)$_2$[22] and {Cs⊂[CpCo(CN)$_3$]$_4$[Cp*Ru]$_3$}[10] were prepared according to literature methods. Elemental analyses were conducted by the School of Chemical Sciences Microanalytical Laboratory. $^1$H and $^{31}$P NMR spectra were acquired with Varian Unity 400 and 500. Electrospray ionization-mass spectra (ESI-MS) and MS-MS measurements were acquired with a Micromass Quattro QHQ quadrupole-hexapole-quadrupole instrument. Infrared spectra were obtained with a Mattson Galaxy Series FT-IR 3000 on pressed KBr pellets.

**Crystallography:** Crystals were mounted to a thin glass fiber using oil (Paratone-N, Exxon). Data were filtered to remove statistical outliers. The integration software (SAINT) was used to test for crystal decay as a bilinear function of X-ray exposure time and sine ($\theta$). Data were collected with a Siemens Platform/CCD automated diffractometer. Crystal and refinement details are given in supplementary material. The structures were solved using SHELXTL by direct methods; correct atomic positions were deduced from an E map or by an unweighted difference Fourier synthesis. H atom $U$ values were assigned as 1.2 times the $U_{eq}$ values of adjacent C

 © 2007 Wiley-VCH Verlag GmbH & Co. KGaA, Weinheim 

atoms. Non-H atoms were refined with anisotropic thermal coefficients. Successful convergence of the full-matrix least-squares refinement of $F^2$ was indicated by the maximum shift/error for the last cycle.

CCDC-632474 for {Cs⊂[CpCo(CN)$_3$]$_4$[Cp*Ru]$_3$Ni(9-ane-S3)}-(BF$_4$)$_2$, -632475 for PhNH$_3$CpCo(CN)$_3$, and -632476 for {Cs⊂[CpCo(CN)$_3$]$_4$[Cp*Ru]$_3$Ru(NCMe)(PPh$_3$)$_2$}(PF$_6$)$_2$) contain the supplementary crystallographic data for this paper. These data can be obtained free of charge from the Cambridge Crystallographic Data Centre at www.ccdc.cam.ac.uk/data_request/cif.

**$^1$H NMR Properties of Cs⊂Co$_4$Ru$_3$:** *THF (Cp signals only)*: $\delta$ = 5.43 [s, 10 H, Cp, for (*endo*)$_2$(*exo*)$_1$], 5.45 [s, 5 H, Cp, for (*endo*)$_2$-(*exo*)$_1$], 5.59 [s, 5 H, Cp, for (*endo*)$_2$(*exo*)$_1$], 5.38 [s, 10 H, Cp, for (*endo*)$_1$(*exo*)$_2$], 5.50 [s, 5 H, Cp, for (*endo*)$_1$(*exo*)$_2$], 5.62 [s, 5 H, Cp, for (*endo*)$_1$(*exo*)$_2$] ppm. *THF/MeCN, 9:1 (Cp signals only)*: $\delta$ = 5.51 [s, 10 H, Cp, for (*endo*)$_2$(*exo*)$_1$], 5.44 [s, 5 H, Cp, for (*endo*)$_2$(*exo*)$_1$], 5.64 [s, 5 H, Cp, for (*endo*)$_2$(*exo*)$_1$], 5.40 [s, 10 H, Cp, for (*endo*)$_1$-(*exo*)$_2$], 5.53 [s, 5 H, Cp, for (*endo*)$_1$(*exo*)$_2$], 5.67 [s, 5 H, Cp, for (*endo*)$_1$(*exo*)$_2$] ppm.

**Vertex Exchange in Cs⊂Co$_4$Ru$_3$:** A mixture of K[MeC$_5$H$_4$Co-(CN)$_3$] (20.5 mg, 0.08 mmol) and Cs⊂[CpCo(CN)$_3$]$_4$[Cp*Ru]$_3$ (33 mg, 0.02 mmol) was stirred in MeCN (5 mL) and THF (5 mL) for 5 h. A 0.1-mL sample of reaction mixture was diluted with 3 mL MeCN/THF (1:1) and analyzed by ESI-MS over the course of 96 h.

43 h: *m*/*z* (%) = 1678 (100) [{Cs[CpCo(CN)$_3$]$_2$[MeC$_5$H$_4$Co(CN)$_3$]$_2$-[Cp*Ru]$_3$}$^+$].

67 h: *m*/*z* (%) = 1678 (74) [{Cs[CpCo(CN)$_3$]$_2$[MeC$_5$H$_4$Co(CN)$_3$]$_2$-[Cp*Ru]$_3$}$^+$], 1692 (100) [{Cs[CpCo(CN)$_3$][MeC$_5$H$_4$Co(CN)$_3$]$_3$-[Cp*Ru]$_3$}$^+$] and 1706 (28) [{Cs[MeC$_5$H$_4$Co(CN)$_3$]$_4$[Cp*Ru]$_3$}$^+$].

96 h: *m*/*z* (%) = 1678 (56) [{Cs[CpCo(CN)$_3$]$_2$[MeC$_5$H$_4$Co(CN)$_3$]$_2$-[Cp*Ru]$_3$}$^+$], 1692 (100) [{Cs[CpCo(CN)$_3$][MeC$_5$H$_4$Co(CN)$_3$]$_3$-[Cp*Ru]$_3$}$^+$] and 1706 (52) [{Cs[MeC$_5$H$_4$Co(CN)$_3$]$_4$[Cp*Ru]$_3$}$^+$].

**Vertex Exchange in Co$_4$Rh$_3^{2+}$:** A mixture of PPN[MeC$_5$H$_4$Co-(CN)$_3$] (59.8 mg, 0.08 mmol) and {[CpCo(CN)$_3$]$_4$[Cp*Rh]$_3$}(PF$_6$)$_2$ (35.9 mg, 0.02 mmol) was stirred in MeCN (10 mL ) for 5 h. A 0.1-mL sample of the reaction mixture was diluted with 3 mL MeCN and analyzed by ESI-MS.

5 h: *m*/*z* (%) = 761 [{[CpCo(CN)$_3$]$_4$[Cp*Rh]$_3$}$^{2+}$], 768 [{[CpCo-(CN)$_3$]$_3$[MeC$_5$H$_4$Co(CN)$_3$][Cp*Rh]$_3$}$^{2+}$], 775 [{[CpCo(CN)$_3$]$_2$-[MeC$_5$H$_4$Co(CN)$_3$]$_2$[Cp*Rh]$_3$}$^{2+}$], 782 [{[CpCo(CN)$_3$][MeC$_5$H$_4$Co-(CN)$_3$]$_3$[Cp*Rh]$_3$}$^{2+}$], 789 [{[MeC$_5$H$_4$Co(CN)$_3$]$_4$[Cp*Rh]$_3$}$^{2+}$].

**Degradation of Cs⊂Co$_4$Ru$_3$ with CO:** A solution of Cs⊂[CpCo(CN)$_3$]$_4$[Cp*Ru]$_3$ (50.3 mg, 0.031 mmol) in $CH_2Cl_2$ (20 mL) was purged with CO for 7 h. The solvent was then removed in vacuo and the red residue was extracted into MeCN and $CH_2Cl_2$ and analyzed by mass spectrometry and IR spectroscopy, respectively ESI-MS: (*m*/*z*) = 1198 [{[CpCo(CN)$_3$]$_2$[Cp*RuCO]$_3$}$^+$]. IR ($CH_2Cl_2$): $\tilde{\nu}$ = 1947 ($\nu_{CO}$), 2165 ($\nu_{CN}$), 2126 cm$^{-1}$.

**Degradation with PhNH$_3^+$. Generation of PhNH$_3$CpCo(CN)$_3$:** A THF stock solution of PhNH$_3$OTf (1 mL, 0.004 M) was added to 7.4 mg (0.004 mmol) of Cs⊂[CpCo(CN)$_3$]$_4$[Cp*Ru]$_3$. After 7 d, a yellow-colored precipitate, PhNH$_3$[CpCo(CN)$_3$], formed. This species was independently prepared by addition of a solution of PhNH$_3$OTf (97.2 mg, 0.4 mmol) in MeCN (50 mL) to a solution of PPN[CpCo(CN)$_3$] (294.7 mg, 0.4 mmol) in MeCN (20 mL) to afford yellow microcrystals. Yield: 0.0761 g (64%). IR (KBr): $\tilde{\nu}$ = 2129 ($\nu_{CN}$) cm$^{-1}$, 2603 ($\nu_{NH}$) cm$^{-1}$. C$_{14}$H$_{13}$CoN$_4$ (296.05): calcd. C 56.75, H 4.43, N 18.92; found C 56.38, H 4.36, N 18.53. The salt was insoluble in acetone, $CH_2Cl_2$, THF, MeCN but dissolved in EtOH and DMSO. Single crystals were grown by vapor diffusion of Et$_2$O into an EtOH solution.

**{Cs⊂[CpCo(CN)$_3$]$_4$[Cp*Ru]$_3$[Cu(NCMe)]}PF$_6$, [Cs⊂Co$_4$Ru$_3$Cu-(NCMe)]PF$_6$:** A solution of Cs⊂[CpCo(CN)$_3$]$_4$[Cp*Ru]$_3$ (413 mg, 0.25 mmol) in THF (30 mL) was added dropwise to a stirred solution of [Cu(MeCN)$_4$]PF$_6$ (93 mg, 0.25 mmol) in MeCN (15 mL) at 0 °C over 1 h. The resulting dark red solution was stirred for 5 h, and the solvent was removed under vacuum. Yield: 394 mg (83%). $^1$H NMR (CD$_3$CN): $\delta$ = 1.68 (s, 45 H, Cp*), 5.53 (s, 15 H, Cp), 5.60 (s, 5 H, Cp) ppm. ESI-MS: *m*/*z* = 1714 [M$^+$ – MeCN]. IR (KBr): $\tilde{\nu}$ = 2144 ($\nu_{CN}$) cm$^{-1}$. C$_{64}$H$_{68}$Co$_4$CsCuF$_6$N$_{13}$PRu$_3$ (1898.94): calcd. C 40.46, H 3.61, N 9.59; found C 40.93, H 3.75, N 10.07.

**{Cs⊂[CpCo(CN)$_3$]$_4$[Cp*Ru]$_3$Cu(PPh$_3$)}PF$_6$, [CsCo$_4$Ru$_3$Cu(PPh$_3$)]-PF$_6$:** An MeCN stock solution of PPh$_3$ (1 mL, 0.0012 M) was added dropwise to a stirred solution of [Cs⊂Co$_4$Ru$_3$Cu(NCMe)]PF$_6$ (2.2 mg, 0.0012 mmol) in MeCN (5 mL). $^1$H NMR (CD$_3$CN): $\delta$ = 1.68 (s, 45 H), 5.51 (s, 15 H), 5.61 (s, 5 H), 7.55 (m, 15 H) ppm. $^{31}$P NMR (CD$_3$CN): $\delta$ = 21.89 ppm. ESI-MS: *m*/*z* = 1977 [{Cs[CpCo(CN)$_3$]$_4$[Cp*Ru]$_3$[CuPPh$_3$]}$^+$].

**{Cs⊂[CpCo(CN)$_3$]$_4$[Cp*Ru]$_3$Ag(NCMe)}PF$_6$, [Cs⊂Co$_4$Ru$_3$Ag-(NCMe)]PF$_6$:** A solution of AgPF$_6$ (33.4 mg, 0.13 mmol) in MeCN (10 mL) was added dropwise to a slurry of Cs⊂Co$_4$Ru$_3$ (218 mg, 0.13 mmol) in MeCN (15 mL) at 0 °C. The deep red solution was warmed to room temperature. After stirring for 1 h, the solvent was evaporated. Yield: 87% (220 mg). $^1$H NMR (CD$_3$CN): $\delta$ = 1.68 (s, 45 H, Cp*), 1.96 (s, 3 H, MeCN), 5.54 (s, 15 H, Cp), 5.62 (s, 5 H, Cp) ppm. ESI-MS: *m*/*z* = 1758 [{Cs[CpCo(CN)$_3$]$_4$-[Cp*Ru]$_3$Ag}$^+$]. IR (KBr): $\tilde{\nu}$ = 2141 ($\nu_{CN}$) cm$^{-1}$. C$_{64}$H$_{68}$AgCo$_4$CsN$_{13}$F$_6$PRu$_3$ (1943.26): calcd. C 39.52, H 3.53, N 9.37; found C 39.13, H 3.55, N 9.60.

**{Cs⊂[CpCo(CN)$_3$]$_4$[Cp*Ru]$_3$Ag(PPh$_3$)}PF$_6$, [Cs⊂Co$_4$Ru$_3$Ag(PPh$_3$)]-PF$_6$:** A solution of PPh$_3$ (12.8 mg, 0.05 mmol) in MeCN (10 mL) was added dropwise to a stirred solution of [Cs⊂Co$_4$Ru$_3$-Ag(NCMe)]PF$_6$ (95.2 mg, 0.05 mmol) in MeCN (20 mL). The solvent was removed under vacuum. $^1$H NMR (CD$_3$CN): $\delta$ = 1.68 (s, 45 H, Cp*), 5.51 (s, 15 H, Cp), 5.62 (s, 5 H, Cp), 7.54–7.53 (m, 15 H, Ph) ppm. $^{31}$P NMR (CD$_3$CN): $\delta$ = 10.7 [d, $^1J$(P, $^{107}$Ag) = 577 Hz], 10.70 [d, $^1J$(P, $^{109}$Ag) = 651.9 Hz] ppm. ESI-MS: *m*/*z* = 2021 [{Cs[CpCo(CN)$_3$]$_4$[Cp*Ru]$_3$AgPPh$_3$}$^+$].

**{Cs⊂[CpCo(CN)$_3$]$_4$[Cp*Ru]$_3$Ni(NCMe)$_3$}(BF$_4$)$_2$, [Cs⊂Co$_4$Ru$_3$Ni-(NCMe)$_3$](BF$_4$)$_2$:** A slurry of Cs⊂Co$_4$Ru$_3$ (224 mg, 0.14 mmol) in MeCN (90 mL) was added dropwise to a solution of [Ni(NCMe)$_6$]-(BF$_4$)$_2$ (65.2 mg, 0.14 mmol) in MeCN (10 mL) at 0 °C. The deep red solution was warmed to room temperature. After stirring for 1 h, the solvent was removed in vacuo. Yield: 227 mg (85%). $^1$H NMR (CD$_3$CN): $\delta$ = 1.70 (s, 45 H, Cp*), 1.96 (s, 9 H, MeCN), 4.99 (br. s, 15 H, Cp), 5.63 (s, 5 H, Cp) ppm. IR (KBr): $\tilde{\nu}$ = 2170 ($\nu_{CN}$) cm$^{-1}$. ESI-MS: *m*/*z* = 855 [{Cs[CpCo(CN)$_3$]$_4$-[Cp*Ru]$_3$Ni}$^{2+}$], 1796 [{Cs[CpCo(CN)$_3$]$_4$[Cp*Ru]$_3$Ni}BF$_4^+$]. C$_{68}$H$_{74}$B$_2$Co$_4$CsF$_8$N$_{15}$NiRu$_3$ (2005.16): calcd. C 40.69, H 3.72, N 10.48; found C 41.05, H 3.96, N 10.77.

**[{Cs⊂[CpCo(CN)$_3$]$_4$[Cp*Ru]$_3$}$_2$Ni](BF$_4$)$_2$:** A solution of Cs⊂Co$_4$Ru$_3$ (197.1 mg, 0.12 mmol) in $CH_2Cl_2$/MeCN (40 mL, 1:1) was treated with a solution of [Ni(NCMe)$_6$](BF$_4$)$_2$ (28.6 mg, 0.06 mmol) in MeCN (10 mL). The solvent was removed in vacuo. Yield: 169 mg (80%). $^1$H NMR (CD$_3$CN): $\delta$ = 1.68 (s, 90 H, Cp*), 5.09 (br. s, 30 H, Cp), 5.62 (s, 10 H, Cp) ppm. ESI-MS: *m*/*z* = 1680 [[{Cs[CpCo(CN)$_3$]$_4$[Cp*Ru]$_3$}$_2$Ni]$^{2+}$]. C$_{124}$H$_{130}$B$_2$Co$_{88}$Cs$_2$N$_{24}$NiRu$_6$ (3531.48): calcd. C 42.14, H 3.71, N, 9.52; found C 42.56, H 3.74, N 9.80.

**{Cs⊂[CpCo(CN)$_3$]$_4$[Cp*Ru]$_3$Fe(NCMe)$_3$}(PF$_6$)$_2$:** A slurry of Cs⊂Co$_4$Ru$_3$ (168.5 mg, 0.1 mmol) in MeCN (70 mL) was added

 © 2007 Wiley-VCH Verlag GmbH & Co. KGaA, Weinheim 

dropwise to a stirred solution of $[Fe(NCMe)_6](PF_6)_2$ (60.5 mg, 0.1 mmol) in MeCN (8 mL) at 0 °C. The deep red solution was warmed to room temperature. After a further 1 h, the solvent was removed in vacuo. Yield: 170 mg (80%). IR (KBr): $\tilde{\nu}$ = 2153 ($\nu_{CN}$) $cm^{-1}$. ESI-MS: *m*/*z* = 854 [{Cs[CpCo(CN)$_3$]$_4$[Cp*Ru]$_3$Fe}$^{2+}$]. $C_{68}H_{74}Co_4CsF_{12}FeN_{15}P_2Ru_3$ (2118.26): calcd. C 38.52, H, 3.52, N, 9.92; found C 39.03, H 3.56, N 9.81.

**{Cs⊂[CpCo(CN)$_3$]$_4$[Cp*Ru]$_3$Ni(9-ane-S3)}(BF$_4$)$_2$, [CsCo$_4$Ru$_3$Ni(9-ane-S3)](BF$_4$)$_2$:** A solution of 9-ane-S3 (7.3 mg, 0.04 mmol) in MeCN (10 mL) was added to a solution of $[Cs{\subset}Co_4Ru_3Ni(NCMe)_3](BF_4)_2$ (81.5 mg, 0.04 mmol) in of MeCN (10 mL). The red solution was stirred for 1 h, and the solvent was removed in vacuo. ESI-MS: *m*/*z* = 945 [{Cs[CpCo(CN)$_3$]$_4$[Cp*Ru]$_3$Ni(9-ane-S3)}$^{2+}$]. Single crystals were grown by vapor diffusion of $Et_2O$ into a $CH_2Cl_2$/acetone solution of $[Cs{\subset}Co_4Ru_3Ni(9\text{-ane-S3})](BF_4)_2$.

**{Cs⊂[CpCo(CN)$_3$]$_4$[Cp*Ru]$_3$RuCl(PPh$_3$)$_2$}Cl:** A solution of $Cs{\subset}Co_4Ru_3$ (440 mg, 0.266 mmol) in THF (40 mL) was added dropwise to a stirred solution of $RuCl_2(PPh_3)_3$ (256 mg, 0.266 mmol) in THF (40 mL) at 0 °C over the course of 1 h. After stirring the resulting dark red solution for 16 h, the solvent was removed under vacuum. The residue was extracted with $Et_2O$ (60 mL), and this extract was concentrated under vacuum. Addition of hexane gave a dark red solid. Yield: 390 mg (63%). $^1$H NMR ([D$_8$]THF): $\delta$ = 1.69 (s, 15 H, Cp*), 1.73 (s, 30 H, Cp*), 4.83 (s, 5 H, Cp), 4.96 (s, 10 H, Cp), 5.54 (s, 5 H, Cp), 7.08 (m, 12 H, Ph), 7.45 (m, 6 H, Ph), 7.73 (m, 12 H, Ph) ppm. ESI-MS: *m*/*z* = 2312 [M$^+$, (Cs⊂{[CpCo(CN)$_3$]$_4$[Cp*Ru]$_3$RuCl(PPh$_3$)$_2$}$)^+$]. $C_{98}H_{95}Cl_2Co_4CsN_{12}P_2Ru_4$ (2345.56): calcd. C 50.16, H 4.08, N 7.16; found C 50.33, H 3.21, N 7.27.

**{Cs⊂[CpCo(CN)$_3$]$_4$[Cp*Ru]$_3$RuH(PPh$_3$)$_2$}Cl:** A solution of $Cs{\subset}Co_4Ru_3$ (330 mg, 0.2 mmol) in THF (30 mL) was added dropwise to a stirred solution of $RuHCl(PPh_3)_3$ (185 mg, 0.2 mmol) in THF (30 mL) at 0 °C over the course of 1 h. After stirring the dark red solution for 16 h, it was concentrated under vacuum to ca. 10 mL. Addition of 50 mL of hexane gave a dark red precipitate, which was washed with hexane, dried under vacuum to give a dark red solid. Yield: 348 mg (75%). $^1$H NMR ($CD_3CN$): $\delta$ = –15.24 (t, $J_{Ru\text{-}H}$ = 27 Hz, 1 H, Ru-H), 1.68 (s, 15 H, Cp*), 1.73 (s, 30 H, Cp*), 4.83 (s, 10 H, Cp), 5.01 (s, 5 H, Cp), 5.60 (s, 5 H, Cp), 7.20 (m, $J_{H\text{-}H}$ = 7 Hz, 12 H, Ph), 7.27 (m, $J_{H\text{-}H}$ = 7 Hz, 6 H, Ph), 7.52 (m, $J_{H\text{-}H}$ = 7 Hz, 12 H, Ph) ppm. ESI-MS: *m*/*z* = 2278 [M$^+$, (Cs⊂{[CpCo(CN)$_3$]$_4$[Cp*Ru]$_3$RuH(PPh$_3$)$_2$}$)^+$]. $C_{98}H_{96}ClCo_4CsN_{12}P_2Ru_4$ (2311.12): calcd. C 50.91, H, 4.18, N, 7.27; found C 51.03, H 4.23, N 8.62.

**{Cs⊂[CpCo(CN)$_3$]$_4$[Cp*Ru]$_3$Ru(NCMe)(PPh$_3$)$_2$}(PF$_6$)$_2$:** A mixture of {Cs⊂[CpCo(CN)$_3$]$_4$[Cp*Ru]$_3$RuH(PPh$_3$)$_2$}Cl (46 mg, 0.02 mmol) and $AgPF_6$ (5 mg, 0.0.02 mmol) in THF (5 mL) was stirred overnight. After the solvent was removed under vacuum, the residue was extracted with MeCN (5 mL), which was concentrated to ca. 1 mL. Dilution of this extract with $Et_2O$ (5 mL ) gave a red-colored solid. The product was crystallized by dissolution in MeCN followed by the slow addition of $Et_2O$. Crystals were grown by liquid diffusion of diethyl ether into acetonitrile solution. ESI-MS: *m*/*z* = 1139 [M$^+$, {Cs⊂[CpCo(CN)$_3$]$_4$[Cp*Ru]$_3$Ru(NCMe)(PPh$_3$)$_2$}$^{2+}$].

**{Cs⊂[CpCo(CN)$_3$]$_4$[Cp*Ru]$_3$Ru(C$_6$H$_6$)}(PF$_6$)$_2$:** A solution of $Cs{\subset}Co_4Ru_3$ (330 mg, 0.2 mmol) in THF (15 mL) was added dropwise to a solution of $[(C_6H_6)Ru(NCMe)_3](PF_6)_2$ (119 mg, 0.2 mmol) in MeCN (25 mL) at 0 °C over 1 h. After stirring for 16 h, the resulting dark red solution was evaporated. Yield: 340 mg (80%). $^1$H NMR ($CD_3CN$): $\delta$ = 1.66 (s, 45 H, Cp*), 5.58 (s, 5 H, Cp), 5.73 (s, 15 H, Cp), 6.17 (s, 6 H, $C_6H_6$) ppm. ESI-MS: *m*/*z* = 915 [M$^{2+}$, {Cs⊂[CpCo(CN)$_3$]$_4$[Cp*Ru]$_3$Ru(C$_6$H$_6$)}$^{2+}$]. $C_{98}H_{96}ClCo_4CsN_{12}P_2Ru_4{\cdot}CH_3CN{\cdot}Et_2O$: calcd. C 39.78, H 3.79, N 8.15; found C 40.42, H 3.64, N 8.36. A solution of {Cs⊂[CpCo(CN)$_3$]$_4$[Cp*Ru]$_3$Ru(C$_6$H$_6$)}(PF$_6$)$_2$ (9 mg) in $CD_3CN$ (0.7 mL) in a NMR tube was subjected to photolysis using a mercury lamp. After 96 h, the ESI-MS and NMR spectra of the reaction mixture showed a 30% conversion to {Cs⊂[CpCo(CN)$_3$]$_4$[Cp*Ru]$_3$Ru(NCCD$_3$)$_3$}(PF$_6$)$_2$.

## Acknowledgments

This research was supported by the US Department of Energy (DEFG02-90ER 14146).

[1] a) K. R. Dunbar, R. A. Heintz, *Prog. Inorg. Chem.* **1997**, *45*, 283; b) A. G. Sharpe, *The Chemistry of Cyano Complexes of the Transition Metals*, Academic Press, London, **1976**.
[2] M. L. Kuhlman, T. B. Rauchfuss, *J. Am. Chem. Soc.* **2003**, *125*, 10084.
[3] a) G. M. J. Boxhoorn, J. G. F. Coolegem, R. A. van Santen, *J. Chem. Soc., Chem. Commun.* **1985**, 1305; b) T. Iwamoto, S.-i. Nishikiori, T. Kitazawa, H. Yuge, *J. Chem. Soc., Dalton Trans.* **1997**, 4127; c) S. C. N. Hsu, M. Ramesh, J. H. Espenson, T. B. Rauchfuss, *Angew. Chem. Int. Ed.* **2003**, *42*, 2663; d) S. S. Kaye, J. R. Long, *J. Am. Chem. Soc.* **2005**, *127*, 6506; e) K. K. Klausmeyer, S. R. Wilson, T. B. Rauchfuss, *J. Am. Chem. Soc.* **1999**, *121*, 2705.
[4] a) L. M. C. Beltran, J. R. Long, *Acc. Chem. Res.* **2005**, *38*, 325; b) D. Li, S. Parkin, G. Wang, G. T. Yee, R. Clérac, W. Wernsdorfer, S. M. Holmes, *J. Am. Chem. Soc.* **2006**, *128*, 4214; c) E. J. Schelter, A. V. Prosvirin, W. M. Reiff, K. R. Dunbar, *Angew. Chem. Int. Ed.* **2004**, *43*, 4912.
[5] a) C. A. Bignozzi, J. R. Schoonover, F. Scandola, *Prog. Inorg. Chem.* **1997**, *44*, 1; b) H. Vahrenkamp, A. Geiss, G. N. Richardson, *J. Chem. Soc., Dalton Trans.* **1997**, 3643.
[6] S. M. Contakes, K. K. Klausmeyer, T. B. Rauchfuss, *Inorg. Synth.* **2004**, *34*, 166.
[7] K. K. Klausmeyer, T. B. Rauchfuss, S. R. Wilson, *Angew. Chem. Int. Ed. Engl.* **1998**, *37*, 1694.
[8] J. L. Heinrich, P. A. Berseth, J. R. Long, *Chem. Commun.* **1998**, 1231.
[9] J. L. Boyer, M. L. Kuhlman, T. B. Rauchfuss, *Acc. Chem. Res.* in press, **2007**.
[10] S. M. Contakes, M. L. Kuhlman, M. Ramesh, S. R. Wilson, T. B. Rauchfuss, *Proc. Natl. Acad. Sci. USA* **2002**, *99*, 4889.
[11] a) P. A. Berseth, J. J. Sokol, M. P. Shores, J. L. Heinrich, J. R. Long, *J. Am. Chem. Soc.* **2000**, *122*, 9655; b) J. J. Sokol, M. P. Shores, J. R. Long, *Angew. Chem. Int. Ed.* **2001**, *40*, 236; c) J. J. Sokol, M. P. Shores, J. R. Long, *Inorg. Chem.* **2002**, *41*, 3052; d) J. Y. Yang, M. P. Shores, J. J. Sokol, J. R. Long, *Inorg. Chem.* **2003**, *42*, 1403; e) S. Wang, J.-L. Zuo, H.-C. Zhou, H. J. Choi, Y. Ke, J. R. Long, X.-Z. You, *Angew. Chem. Int. Ed.* **2004**, *43*, 5940.
[12] a) C. P. Berlinguette, D. Vaughn, C. Cañada-Vilalta, J. R. Galán-Mascarós, K. R. Dunbar, *Angew. Chem. Int. Ed.* **2003**, *42*, 1523; b) J. A. Smith, J. R. Galán-Mascarós, R. Clérac, J. S. Sun, X. Ouyang, K. R. Dunbar, *Polyhedron* **2001**, *20*, 1727; c) Z.-G. Gu, Q.-F. Yang, W. Liu, Y. Song, Y.-Z. Li, J.-L. Zuo, X.-Z. You, *Inorg. Chem.* **2006**, *45*, 8895; d) C.-F. Wang, J.-L. Zuo, B. M. Bartlett, Y. Song, J. R. Long, X.-Z. You, *J. Am. Chem. Soc.* **2006**, *128*, 7162; e) V. Jacob, G. Huttner, E. Kaifer, P. Kircher, P. Rutsch, *Eur. J. Inorg. Chem.* **2001**, 2783; f) A. Marvilliers, Y. Pei, J. C. Boquera, E. Rivière, J.-P. Audière, T. Mallah, *Chem. Commun.* **1999**, 1951; g) K. Van Langenberg, S. R. Batten, K. J. Berry, D. C. R. Hockless, B. Moubaraki, K. S. Murray, *Inorg. Chem.* **1997**, *36*, 5006; h) K. E. Vostrikova, D. Luneau, W. Wernsdorfer, P. Rey, M. Verdaguer, *J. Am. Chem. Soc.* **2000**, *122*, 718.

 © 2007 Wiley-VCH Verlag GmbH & Co. KGaA, Weinheim 

[13] a) J. W. Steed, J. L. Atwood, *Supramolecular Chemistry*, John Wiley & Sons, Inc., New York, **2000**; b) A. Ebina, S. Nishikiori, T. Iwamoto, *J. Chem. Soc., Chem. Commun.* **1994**, 233; c) A. Bencini, A. Bianchi, E. Garcia-España, M. Giusti, S. Mangani, M. Micheloni, P. Orioli, P. Paoletti, *Inorg. Chem.* **1987**, *26*, 3902; d) P. C. Crawford, A. L. Gillon, J. Green, A. G. Orpen, T. J. Podesta, S. V. Pritchard, *CrystEngComm* **2004**, *6*, 419; e) S. Ferlay, V. Bulach, O. Félix, M. W. Hosseini, J.-M. Planeix, N. Kyritsakas, *CrystEngComm* **2002**, *4*, 447.
[14] J. L. Schrenk, A. M. McNair, F. B. McCormick, K. R. Mann, *Inorg. Chem.* **1986**, *25*, 3501.
[15] M. L. Kuhlman, T. B. Rauchfuss, *Inorg. Chem.* **2004**, *43*, 430.
[16] a) K. Uehara, S. Hikichi, M. Akita, *J. Chem. Soc., Dalton Trans.* **2002**, 3529; b) S. Hikichi, Y. Sasakura, M. Yoshizawa, Y. Ohzu, Y. Moro-oka, M. Akita, *Bull. Chem. Soc. Jpn.* **2002**, *75*, 1255.
[17] J. L. Boyer, M. Ramesh, H. Yao, T. B. Rauchfuss, S. R. Wilson, *J. Am. Chem. Soc.* **2007**, *129*, 1931.
[18] G. J. Kubas, *Inorg. Synth.* **1990**, *28*, 68.
[19] R. A. Heintz, J. A. Smith, P. S. Szalay, A. Weisgerber, K. R. Dunbar, *Inorg. Synth.* **2002**, *33*, 75.
[20] W. W. Brennessel, N. R. Brooks, M. P. Mehn, L. Que Jr, V. G. Young Jr, *Acta Crystallogr., Sect. E* **2001**, *57*, m545.
[21] T. A. Stephenson, G. Wilkinson, *J. Inorg. Nucl. Chem.* **1966**, *28*, 945.
[22] a) M. Stebler-Röthlisberger, A. Ludi, *Polyhedron* **1986**, *5*, 1217; b) M. A. Bennett, A. K. Smith, *J. Chem. Soc., Dalton Trans.* **1974**, 233.

Received: January 1, 2007
Published Online: March 27, 2007

 © 2007 Wiley-VCH Verlag GmbH & Co. KGaA, Weinheim 

DOI: 10.1002/ejic.200700013

# Synthesis and Catalytic Activity of $\eta^1$-Allyl and $\eta^3$-Allyl, Ethyl, and Hydrido Complexes of Ruthenium–Pentamethyl[60]fullerene

**Yutaka Matsuo,[a] Takashi Uematsu,[b] and Eiichi Nakamura*[a,b]**

**Keywords:** Ruthenium / Fullerenes / Allyl complexes / Hydrido complexes / Isomerization

$\eta^1$-Allyl and $\eta^3$-allyl, ethyl, and hydrido ruthenium complexes of pentamethyl[60]fullerene, $Ru(\eta^5\text{-}C_{60}Me_5)R(CO)_2$ (R = $\eta^1$-allyl, Et, H) and $Ru(\eta^5\text{-}C_{60}Me_5)(\eta^3\text{-allyl})(CO)$ were synthesized by the reaction of a chlorido complex $Ru(\eta^5\text{-}C_{60}Me_5)Cl(CO)_2$ with an allyl and an ethyl Grignard reagent or lithium aluminum hydride. Conversion of the $\eta^1$-allyl complex to the corresponding $\eta^3$-allyl complex and the catalytic performance of the hydrido and the chlorido complexes in the isomerization reaction of 1-decene to internal decenes are described.
(© Wiley-VCH Verlag GmbH & Co. KGaA, 69451 Weinheim, Germany, 2007)

## Introduction

Cooperative effects of fullerene conjugated systems and transition metal atoms have attracted the interest of inorganic and organometallic chemists[1] because of the possible dπ-conjugative synergy that may create new properties unavailable from individual systems.[2] We have employed pentaorgano[60]fullerenes[3] as $\eta^5$-fullerene ligands and synthesized various metal–fullerene complexes involving Re,[4] Fe,[5] Ru,[6] Rh,[7] Ir,[8] Ni,[9] Pd,[9] and Pt[9] atoms. Among them, many ruthenium(II) complexes are particularly interesting because of stable facial coordination of the pentaorgano[60]fullerene ligands to the $d^6$ metal center with the octahedral geometry.[6a] Indeed, ruthenium complex $Ru(\eta^5\text{-}C_{60}Me_5)Cl(CO)_2$ was obtained in high yield on a large scale and was used as a useful starting material for the study of the organometallic chemistry of the metal–fullerene complexes.[6a] As an extension of our work in this area, we have investigated further derivatization of the ruthenium complex and obtained various ruthenium–pentamethyl[60]fullerene complexes. Herein we report the synthesis and catalytic activity of $\eta^1$- and $\eta^3$-allyl, ethyl, and hydrido ruthenium complexes of pentamethyl[60]fullerene (Scheme 1).

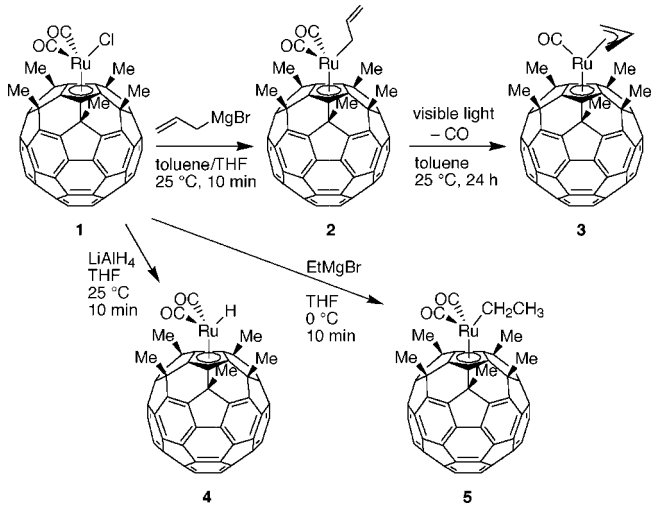


Scheme 1. Syntheses of allyl, ethyl, and hydrido complexes.

## Results and Discussion

### Synthesis of $\eta^1$- and $\eta^3$-Allyl Ruthenium Complexes of Pentamethyl[60]fullerene

Treatment of a solution of $Ru(\eta^5\text{-}C_{60}Me_5)Cl(CO)_2$ (**1**)[6a] in toluene with a solution of allylmagnesium bromide in thf at 25 °C led to a ligand exchange reaction to afford $\eta^1$-allyl complex **2**, $Ru(\eta^5\text{-}C_{60}Me_5)(\eta^1\text{-allyl})(CO)_2$, in quantitative yield (Scheme 1). Product **2** was purified by neutral alumina chromatography to remove magnesium salts. Decomposition of **2** through loss of the ruthenium metal was observed upon silica gel column chromatography, which resulted in the formation of an oxidized compound of pentamethyl[60]fullerene, $C_{60}Me_5O_2OH$.[10] This product was identified by MS (APCI–) (*m*/*z* = 844 $[M]^-$). Compound **2** was isolated as an orange powder and was stable in air as a solid for over one month. Characterization of **2** was performed by $^1H$ and $^{13}C$ NMR, IR, and UV/Vis spectroscopic measurements, and combustion analysis. In the $^1H$ NMR spectrum, a set of three signals due to the olefinic protons was observed in lower field at $\delta$ = 4.86, 5.14, and 6.51 ppm, which indicates that the complex is a σ-allyl complex. The IR spectrum exhibited asymmetric and symmetric stretch-

[a] Nakamura Functional Carbon Cluster Project, ERATO, Japan Science and Technology Agency
Hongo, Bunkyo-ku, Tokyo 113-0033, Japan
Fax: +81-3-5800-6889
E-mail: nakamura@chem.s.u-tokyo.ac.jp
[b] Department of Chemistry, University of Tokyo
Hongo, Bunkyo-ku, Tokyo 113-0033, Japan

 © 2007 Wiley-VCH Verlag GmbH & Co. KGaA, Weinheim 

ing vibrations of the carbonyl groups at 2016 and 1960 $cm^{-1}$, which suggests two carbonyl ligands remain on the ruthenium center.

We next investigated conversion of $\eta^1$-allyl complex **2** into an $\eta^3$-allyl complex through decarbonylation. Compound **2** did not react at all in $C_6D_6$ at 25 °C for 24 h. However, when the $C_6D_6$ solution of **2** was irradiated by visible light with 60 W incandescent light at 25 °C for 14 h, $\eta^3$-allyl compound **3**, Ru($\eta^5$-$C_{60}Me_5$)($\eta^3$-allyl)(CO), formed. According to the ligand field theory, such as light-induced decarbonylation process involves electron transition to antibonding orbital of the metal–carbonyl bond. The effect of the strongly light-absorbing fullerene part is therefore apparent. The progress of the reaction was monitored by analysis of the $^1H$ NMR spectra (Figure 1). After three hours of irradiation, the $\eta^1$- and $\eta^3$-allyl complexes were observed in a 1:1 ratio. Irradiation for 14 h completed this conversion. On heating the reaction mixture to 110 °C in $C_6D_6$ for 24 h in a sealed tube, instead of the light irradiation, $\eta^3$-allyl compound **3** slowly formed (only with ca. 10% conversion). It is known that an $\eta^5$-cyclopentadienyl-$\eta^3$-allyl metal complex exists in two isomeric forms: *exo* and *endo* isomers (Figure 2).[11] In contrast, the present reaction produced only an *exo* isomer (see below). If a pathway of *endo–exo* interconversion exists (which may involve pseudorotation of the $\eta^3$-allyl group about the allyl–metal bond axis or an equilibrium that goes through an $\eta^1$-allyl intermediate), the experimental observation would suggest that the *exo* isomer is thermodynamically much more stable than the *endo* isomer. It must then be the steric bulk of the pentamethyl[60]fullerene ligand that is responsible for the *exo* preference. Such a tendency, though less pronounced, in the stability of the *exo* isomer has also been observed in usual $\eta^5$-cyclopentadienyl-$\eta^3$-allyl ruthenium systems.[12]

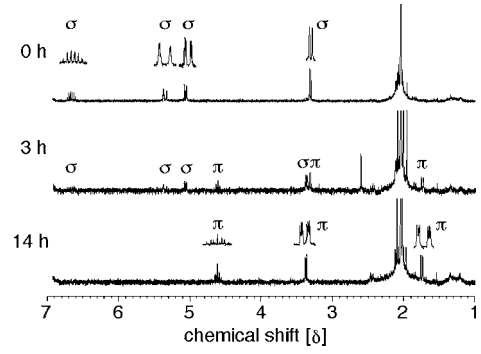


Figure 1. Conversion of **2** to **3** as monitored with $^1H$ NMR spectroscopic measurements.

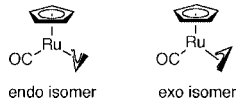


Figure 2. The *endo* and *exo* isomers of $\eta^5$-Cp-$\eta^3$-allyl ruthenium carbonyl complex.

$\eta^3$-Allyl complex **3** was isolated in 49% yield by preparative HPLC. Side products were the oxidized pentamethyl[60]fullerene and unidentified insoluble products. Identification of the *exo* form of **3** was achieved by $^1H$ and $^{13}C$ NMR, IR, and UV/Vis spectroscopic measurements, and combustion analysis as well as an X-ray crystallographic study (Figure 3). The $^1H$ NMR spectrum displayed a signal pattern typical for an $\eta^3$-allyl group. Signals due to the *syn* and *anti* protons on the terminal carbon atoms and one proton on the center carbon atom were observed at $\delta$ = 3.38, 1.75, and 4.61, respectively. The IR spectrum showed one strong CO absorption at 1943 $cm^{-1}$. The X-ray analysis clearly showed the *exo* form of the $\eta^3$-allyl ligand. As shown in the top view, the carbonyl ligand are located in the space among two methyl groups of the pentamethyl-[60]fullerene ligand and the $\eta^3$-allyl ligand. The side view indicates roughly parallel coordination of the $\eta^3$-allyl ligand to the $\eta^5$-cyclopentadienyl part of the pentamethyl[60]-fullerene moiety. The angle between a least-squares plane consisting of the three carbon atoms of the $\eta^3$-allyl and that of the five carbon atoms of the $\eta^5$-cyclopentadienyl part is 11.24(2)°. Although some ruthenium $\eta^3$-allyl complexes have been used in catalysis,[13] complex **3** was too stable to show catalytic activity.

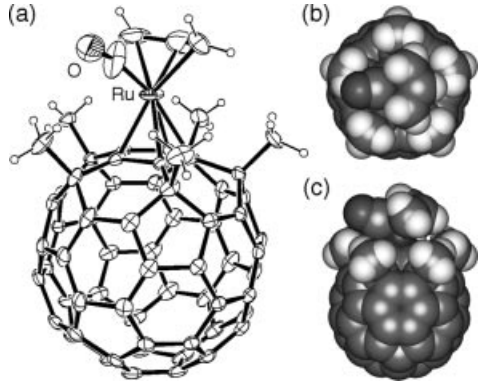


Figure 3. X-ray crystal structure of **3**·$CS_2$. Solvent molecules are omitted for clarity. (a) ORTEP drawing with 30% probability level ellipsoids. (b) CPK model, top view. (c) CPK model, side view.

### Synthesis of Hydrido Ruthenium Complexes of Pentamethyl[60]fullerene

Synthesis of hydrido complex **4**, Ru($\eta^5$-$C_{60}Me_5$)$H(CO)_2$, was performed next. We used three hydrogenation reagents: lithium aluminum hydride (LAH), diisobutylaluminum hydride (DIBAL), and sodium borohydride ($NaBH_4$). Target compound **4** was obtained in 76% isolated yield by the reaction of chlorido complex **1** with LAH in thf at 25 °C (Scheme 1). Treatment of **1** with DIBAL in thf afforded **4** in 42% yield. The reaction of **1** with $NaBH_4$ did not yield the desired hydrido complex but gave several unidentified complexes. This may be due to hydroboration taking place on the fullerene moiety of **1**. Characterization of **4** was performed by $^1H$, $^{13}C$ NMR, IR, and UV/Vis spectroscopic measurements and combustion analysis. In the $^1H$ NMR spectrum, a proton signal characteristic of the hydride group was observed at $\delta$ = –10.07 ppm. The IR spectrum exhibited asymmetric and symmetric vibration absorptions

 © 2007 Wiley-VCH Verlag GmbH & Co. KGaA, Weinheim 

Table 1. Isomerization of 1-decene to internal alkenes catalyzed by ruthenium–pentamethyl[60]fullerene complexes.

| Entry | Catalyst | 1-Decene [equiv.] | Temp. [°]C | Time [h] | Conversion [%] | Yield [%] 2-Decene (*E*/*Z*) | Other internal alkenes |
|---|---|---|---|---|---|---|---|
| 1 | **4** | 10000 | 140 | 6 | 95 | 49 (2.0) | 46 |
| 2 | **4** | 2600 | 100 | 16 | 24 | 14 (1.8) | 10 |
| 3 | **4** | 2600 | 60 | 16 | 0 | – | – |
| 4 | **3** | 2600 | 100 | 16 | 0 | – | – |
| 5 | **1** | 2600 | 140 | 18 | 96 | 56 (1.8) | 40 |
| 6 | **1** | 2600 | 100 | 16 | 12 | ND | ND |

at 2062 and 2024 $cm^{-1}$ that are due to the two carbonyl ligands.

We then examined the catalytic activity of the pentamethyl[60]fullerene ruthenium complexes in alkene isomerization reactions from terminal alkenes to internal alkenes. Many active catalysts using transition metal complexes, such as Fe, Pd, Rh, Pt, Ni, Ir, Ru, Cr, Ti, and Zr complexes, have been used in isomerization reactions of alkenes.[14] In general, two reaction pathways have been considered. One is a metal hydride addition/elimination mechanism (Scheme 2a), and the other is a π-allyl metal hydride mechanism (Scheme 2b). Motivated by the former reaction mechanism, we used hydrido complex **4** in the isomerization reaction of 1-octene. Complex **4** was found to be catalytically active at high temperature. The reaction with the use of 0.01 mol-% of **4** for 6 h at 140 °C took place with 95% conversion to give 49% of 2-decene in an *E*/*Z* ratio of 2.0 and 46% of other internal alkenes (Table 1, Entry 1). When the reaction was heated to 100 °C with 0.083 mol-% of **4** for 18 h, only 24% conversion with a similar product distribution (Table 1, Entry 2) was observed, whereas the reaction heated at 25 or 60 °C did not afford any isomerization products at all (Table 1, Entry 3).

In this reaction, high temperature was essential, which could be due to the high activation energy for decarbonylation of catalyst precursor **4** to the catalytically active monocarbonyl complex. We therefore attempted this alkene isomerization reaction at 25 °C with visible light irradiation which was effective for the conversion of **2** into **3**, but the isomerized products were not obtained. This may then be due to decomposition of the intermediates by further loss of the carbonyl ligand.

Allyl complex **3** did not show any catalytic activity in the alkene isomerization reaction even at 100 °C, whereas chlorido complex **1** gave the isomerized products in 96% conversion at 140 °C, and in 12% conversion at 100 °C. The latter result can be attributed to the formation of **4** from **1** in the presence of alkenes or to a catalytic cycle involving the π-allyl metal hydride (Scheme 2b).

Although ruthenium alkyl complexes having no β-hydrogen such as Ru($\eta^5$-$C_{60}Me_5$)Me$(CO)_2$ and Ru($\eta^5$-$C_{60}Me_5$)-$(CH_2SiMe_3)(CO)_2$[6a] have been synthesized, syntheses of ruthenium alkyl complexes having β-hydrogen atoms are still scarce.[15] In the present fullerene complex series, we could synthesize a stable ruthenium ethyl complex Ru($\eta^5$-$C_{60}Me_5$)Et$(CO)_2$ (**5**) by the reaction of **1** with ethylmagnesium bromide in thf at 0 °C in 48% yield. This complex was perfectly stable and did not show any tendency of β-hydride

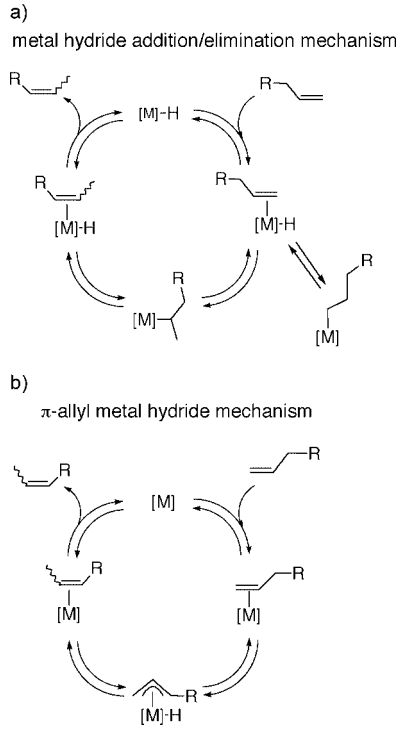


Scheme 2. Two possible mechanisms for transition-metal-catalyzed alkene isomerization.

elimination under light irradiation and under heating. We considered that the elimination reaction was inhibited because of either conformational or electronic effects of the $\eta^5$-$C_{60}Me_5$ moiety. One may recall the strong stabilization effect of this fullerene ligand in $\eta^3$-allylnickel chemistry.[9a]

## Conclusion

We have synthesized $\eta^1$-allyl and $\eta^3$-allyl, ethyl, and hydrido ruthenium complexes of pentamethyl[60]fullerene and showed that the hydrido complex catalyzes the 1-decene isomerization reaction. The present set of experiments suggests new opportunities for the exploration of reactivities of the ruthenium–carbon and –hydrogen bonds, especially under excitation of the fullerene ligand by light irradiation.

## Experimental Section

**General Procedure:** All manipulations involving air- and moisture-sensitive compounds were carried out under an atmosphere of argon by using standard Schlenk techniques. Toluene and thf were

 © 2007 Wiley-VCH Verlag GmbH & Co. KGaA, Weinheim 

distilled from Na/K alloy and thoroughly degassed by trap-to-trap distillation before use. Ru($\eta^5$-$C_{60}Me_5$)Cl(CO)$_2$ was prepared according to the literature.[6a] Solutions of *t*BuOK in thf and allylmagnesium bromide in thf were purchased from Sigma–Aldrich Co. and used as received. Other commercial reagents were used without purification. HPLC analyses were performed with a Shimadzu LC-10A system equipped with a SPD-M10A diode array detector and a Cosmosil-Buckyprep column (4.6 × 250 mm, Nacalai Tesque Co.). Preparative HPLC separations were performed by the use of a preparative scale Buckyprep column (20 mm × 250 mm). The $^1$H and $^{13}$C NMR spectra were recorded with a JEOL EX 400 spectrometer. The $^1$H NMR spectra are reported in parts per million from internal tetramethylsilane and in the $^{13}$C NMR spectra from 77.0 ppm ($CDCl_3$) or from 128.0 ppm ($C_6D_6$). Other spectra were recorded with the use of the following instruments: IR, ReactIR 1000; UV/Vis, JASCO V-570; mass spectra, Waters ZQ2000. Elemental analyses were performed at organic elemental analysis laboratory in the Department of Chemistry, University of Tokyo.

**Ru($\eta^5$-$C_{60}Me_5$)($\eta^1$-allyl)(CO)$_2$ (2):** A solution of allylmagnesium bromide (0.090 mmol) in thf (0.090 mL) was added to a solution of **1** (30 mg, 0.030 mmol) in toluene (6 mL) under an atmosphere of argon at room temperature. After stirring for 10 min, a small amount of ethanol was added to the resulting brown solution. The solution was passed through a pad of neutral alumina, and the red-colored filtrate was dried under vacuum to obtain **2** (30 mg, 99% yield) as an orange powder. M.p. 215–220 °C (dec.). $^1$H NMR (400 MHz, $CDCl_3$, 25 °C): $\delta$ = 6.51 (ddt, $^3J_{H-H}$ = 16.6 (*trans*), 9.8 (*cis*), 8.4 Hz, 1 H, Ru-$CH_2$-C*H*), 5.14 (dd, $^3J_{H-H}$ = 16.6 Hz (*trans*), $^2J_{H-H}$ = 1.9 Hz (*gem*), 1 H, Ru-$CH_2$-CH=C$H_2$), 4.86 (dd, $^3J_{H-H}$ = 9.8 Hz (*cis*), $^2J_{H-H}$ = 1.9 Hz (*gem*), 1 H, Ru-$CH_2$-CH=C$H_2$), 3.32 (d, $^3J_{H-H}$ = 8.4, 2 H, Ru-C$H_2$), 2.41 (s, 15 H, $C_{60}Me_5$) ppm. $^{13}$C NMR (100 MHz, $CDCl_3$, 25 °C): $\delta$ = 29.79 (1 C, Ru-*C*$H_2$CH=$CH_2$), 30.43 (5 C, $C_{60}Me_5$), 51.11 [5 C, $C_{60}(sp^3)$], 108.48 (1 C, Ru-$CH_2$CH=*C*$H_2$), 111.82 [5 C, $C_{60}$(Cp)], 143.56 (10 C, $C_{60}$), 143.85 (10 C, $C_{60}$), 146.78 (1 C, Ru-$CH_2$*C*H=$CH_2$), 147.64 (5 C, $C_{60}$), 148.02 (10 C, $C_{60}$), 148.40 (5 C, $C_{60}$), 152.56 (10 C, $C_{60}$), 201.50 (2 C, CO) ppm. UV/Vis (toluene/2-propanol, 7:3): $\lambda$ = 287, 355 (sh), 395 nm. IR (diamond probe): $\tilde{\nu}$1960 (s) (CO), 2016 (s). MS (APCI–): *m*/*z* = 993 [M]$^-$, 952 [M – allyl]$^-$. HPLC (toluene/2-propanol, 7:3; flow rate: 1 mL min$^{-1}$): $t_R$ = 8.2 min. $C_{70}H_{20}O_2Ru$ (994.00): calcd. C 84.58, H 2.03; found C 84.38, H 2.00.

**Ru($\eta^5$-$C_{60}Me_5$)($\eta^3$-allyl)(CO) (3):** Compound **2** (30 mg, 0.030 mmol) was dissolved in toluene (12 mL) under an atmosphere of argon. This solution was stirred vigorously and irradiated with 60 W incandescent light at room temperature. After 24 h, the resulting red-colored solution was purified by preparative HPLC (toluene/2-propanol, 7:3; flow rate: 20 mL min$^{-1}$). The fractions containing **3** were collected, and the solvents were evaporated to dryness to obtain **3** (14 mg, 49% yield) as orange microcrystals. M.p. 240–245 °C (dec.). $^1$H NMR (400 MHz, $C_6D_6$, 25 °C): $\delta$ = 4.61 (m, 1 H, $H_{center}$), 3.38 (dt, $^3J_{H(center)-H(syn)}$ = 6.8 Hz, 2 H, $H_{syn}$), 2.05 (s, 15 H, $C_{60}Me_5$), 1.75 (dt, $^3J_{H(center)-H(anti)}$ = 11.2 Hz, 2 H, $H_{anti}$) ppm. $^{13}$C NMR (100 MHz; $CDCl_3/CS_2$, 1:1; 25 °C): $\delta$ = 30.45 (5 C, $C_{60}Me_5$), 33.69 (2 C, $C_3H_5$), 50.73 [5 C, $C_{60}(sp^3)$], 69.61 (1 C, $C_3H_5$), 106.77 [5 C, $C_{60}$(Cp)], 143.28 (10 C, $C_{60}$), 143.77 (10 C, $C_{60}$), 146.65 (5 C, $C_{60}$), 147.73 (10 C, $C_{60}$), 148.14 (5 C, $C_{60}$), 153.05 (10 C, $C_{60}$), 192.50 (1 C, CO) ppm. UV/Vis (toluene/2-propanol, 7:3): $\lambda$ = 291, 348 (sh), 394 nm. IR(diamond probe): $\tilde{\nu}$1943 (s) (CO). MS (APCI–): *m*/*z* = 965 [M]$^-$. HPLC (toluene/2-propanol, 7:3; flow rate: 1 mL min$^{-1}$): $t_R$ = 7.39 min. $C_{69}H_{20}ORu$ (965.99): calcd. C 85.79, H 2.09; found C 84.68, H 2.01.

**Synthesis of Ru($\eta^5$-$C_{60}Me_5$)H(CO)$_2$ (4):** To a solution of **1** (10 mg, 0.050 mmol) in thf (1.7 mL) was added powdered $LiAlH_4$ (0.38 mg, 0.050 mmol) at 25 °C. After stirring for 10 min, the color of the solution changed from red to brown. After the reaction was quenched with a small amount of ethanol, the solution was evaporated to dryness. The residue was dissolved in toluene (10 mL), and the supernatant was separated from the insoluble salts by filtration. The filtrate was evaporated to dryness and dried under vacuum for 5 h to obtain the title compound (7.2 mg, 0.38 mmol, 76% yield). M.p. 180–190 °C (dec.). $^1$H NMR (400 MHz; $CDCl_3/CS_2$, 1:1; 25 °C): $\delta$ = –10.07 (s, 1 H, Ru-*H*), 2.30 (s, 15 H, $C_{60}Me_5$) ppm. $^{13}$C NMR (100 MHz; $CDCl_3/CS_2$, 1:1; 25 °C): $\delta$ = 32.16 (5 C, $C_{60}Me_5$), 49.88 [5 C, $C_{60}(sp^3)$], 110.70 [5 C, $C_{60}$(Cp)], 143.41 (10 C, $C_{60}$), 143.82 (10 C, $C_{60}$), 146.55 (5 C, $C_{60}$), 147.63 (10 C, $C_{60}$), 148.19 (5 C, $C_{60}$), 152.34 (10 C, $C_{60}$), 199.73 (2 C, CO) ppm. UV/Vis (toluene/2-propanol, 7:3): $\lambda$ = 287, 349 (sh), 396 nm. IR (diamond probe): $\tilde{\nu}$ 1962 (s) (CO), 2024 (s). MS (APCI–): *m*/*z* = 954 [M]$^-$. HPLC (toluene/2-propanol, 7:3; flow rate: 1 mL min$^{-1}$): $t_R$ = 8.02 min. $C_{67}H_{16}O_2Ru$ (953.93): calcd. C 84.36, H 1.69; found C 84.01, H 1.41.

**Ru($\eta^5$-$C_{60}Me_5$)Et(CO)$_2$ (5):** A solution of EtMgBr (0.075 mmol) in thf (0.083 mL) was added to a solution of **1** (50 mg, 0.050 mmol) in toluene (16 mL)under an atmosphere of argon at 0 °C. After stirring for 10 min, the resulting brown suspension was quenched with a small amount of ethanol and passed through a pad of silica gel. This eluent was purified by HPLC (toluene/2-propanol, 7:3; flow rate: 20 mL min$^{-1}$). The fractions containing the title compound were collected, and the solvents were evaporated to dryness. The solid was then dissolved again in a small amount of $CS_2$, and this solution was dried under vacuum to obtain the title compound (23 mg, 0.025 mmol, 48% yield). M.p. 210–215 °C (dec.). $^1$H NMR (400 MHz; $CDCl_3/CS_2$, 1:1; 25 °C): $\delta$ = 2.63 (q, $^3J_{H-H}$ = 7.6 Hz, 2 H, Ru-C$H_2$CH$_3$), 2.40 (s, 15 H, $C_{60}Me_5$), 1.75 (t, $^3J_{H-H}$ = 7.6 Hz, 3 H, Ru-$CH_2$C$H_3$) ppm. $^{13}$C NMR (100 MHz; $CDCl_3/CS_2$, 1:1; 25 °C): $\delta$ = –8.31 (1 C, Ru-*C*$H_2$CH$_3$), 23.19 (1 C, Ru-$CH_2$*C*H$_3$), 30.07 (5 C, $C_{60}Me_5$), 50.79 [5 C, $C_{60}(sp^3)$], 111.68 [5 C, $C_{60}$(Cp)], 143.36 (10 C, $C_{60}$), 143.62 (10 C, $C_{60}$), 146.46 (5 C, $C_{60}$), 147.63 (10 C, $C_{60}$), 148.12 (5 C, $C_{60}$), 152.34 (10 C, $C_{60}$), 201.88 (2 C, CO) ppm. UV/Vis (toluene/2-propanol, 7:3): $\lambda$ = 285, 355 (sh), 395 nm. IR(diamond probe): $\tilde{\nu}$ 2008 (s) (CO), 1950 (s). MS (APCI–): *m*/*z* = 981 [M]$^-$. HPLC (toluene/2-propanol, 7:3; flow rate: 1 mL min$^{-1}$): $t_R$ = 7.67 min. $C_{69}H_{20}O_2Ru$ (981.99): calcd. C 84.40, H 2.05; found C 84.11, H 1.80.

**NMR-Monitoring of Conversion from 2 to 3:** Compound **2** was placed in an NMR tube connected to a vacuum system and $C_6D_6$ (0.6 mL) was transferred into it by trap-to-trap distillation. The NMR tube was sealed by flame and subjected to the reaction conditions: light irradiation with 60 W incandescent light or heating at 110 °C. Conversion of **3** into **2** was monitored by $^1$H NMR spectroscopy.

**Isomerization of 1-Decene**: Compound **4** and 10000 equiv. of 1-decene were placed in a Schlenk tube and heated at 140 °C. After stirring at this temperature for 6 h, the solution was passed through a cotton plug and subjected to the $^1$H NMR and GC measurements to estimate the product distributions. In the $^1$H NMR spectrum, terminal and internal olefin protons were observed at $\delta$ = 4.9 ppm and $\delta$ = 5.4 ppm, respectively.

**X-ray Crystallographic Analysis:** Single crystals of **3** suitable for X-ray diffraction studies were grown and subjected to data collection. The data sets were collected with a MacScience DIP2030 Imaging Plate diffractometer by using Mo-$K_\alpha$ (graphite monochromated, $\lambda$ = 0.71069 Å) radiation. The structure of **3** was solved by direct methods (SIR97).[16] The positional and thermal parameters of non-hydrogen atoms were refined anisotropically on $F^2$ by the full-

 © 2007 Wiley-VCH Verlag GmbH & Co. KGaA, Weinheim 

matrix least-squares method by using SHELXL-97.[17] Hydrogen atoms were placed at calculated positions and refined with riding mode on their corresponding carbon atoms. In the subsequent refinement, the function $\Sigma\omega(F_o^2 - F_c^2)^2$ was minimized, where $|F_o|$ and $|F_c|$ are the observed and calculated structure factor amplitudes, respectively. The agreement indices are defined as $R_1 = \Sigma(||F_o| - |F_c||)/\Sigma|F_o|$ and $wR_2 = [\Sigma\omega (F_o^2 - F_c^2)^2/\Sigma (\omega F_o^4)]^{1/2}$. CCDC-632009 contains the supplementary crystallographic information for **3**. This data can be obtained free of charge from The Cambridge Crystallographic Data Centre via www.ccdc.cam.ac.uk/data_request/cif.


[1] a) A. H. H. Stephens, M. L. H. Green, *Adv. Inorg. Chem.* **1997**, *44*, 1–43; b) A. L. Balch, M. M. Olmstead, *Chem. Rev.* **1998**, *98*, 2123–2165.

[2] D. M. Guldi, N. Martin (Eds.), *Fullerenes: From Synthesis to Optoelectronic Properties*, Kluwer Academic Publishers, Dordrecht, **2002**.

[3] a) M. Sawamura, H. Iikura, E. Nakamura, *J. Am. Chem. Soc.* **1996**, *118*, 12850–12851; b) H. Iikura, S. Mori, M. Sawamura, E. Nakamura, *J. Org. Chem.* **1997**, *62*, 7912–7913; c) M. Sawamura, H. Iikura, T. Ohama, U. E. Hackler, E. Nakamura, *J. Organomet. Chem.* **2000**, *599*, 32–36; d) M. Sawamura, M. Toganoh, Y. Kuninobu, S. Kato, E. Nakamura, *Chem. Lett.* **2000**, 270–271; e) E. Nakamura, H. Isobe, *Acc. Chem. Res.* **2003**, *36*, 807–815; f) R. Hamasaki, Y. Matsuo, E. Nakamura, *Chem. Lett.* **2004**, *33*, 328–329; g) Y.-W. Zhong, Y. Matsuo, E. Nakamura, *Org. Lett.* **2006**, *7*, 1463–1466; h) Y. Matsuo, A. Muramatsu, K. Tahara, M. Koide, E. Nakamura, *Org. Synth.* **2006**, *83*, 80–87.

[4] M. Toganoh, Y. Matsuo, E. Nakamura, *Angew. Chem. Int. Ed.* **2003**, *42*, 3530–3532.

[5] a) M. Sawamura, Y. Kuninobu, M. Toganoh, Y. Matsuo, M. Yamanaka, E. Nakamura, *J. Am. Chem. Soc.* **2002**, *124*, 9354–9355; b) E. Nakamura, *Pure Appl. Chem.* **2003**, *75*, 427–434; c) M. Toganoh, Y. Matsuo, E. Nakamura, *J. Am. Chem. Soc.* **2003**, *125*, 13974–13975; d) E. Nakamura, *J. Organomet. Chem.* **2004**, *689*, 4630–4635; e) R. H. Herber, I. Nowik, Y. Matsuo, M. Toganoh, Y. Kuninobu, E. Nakamura, *Inorg. Chem.* **2005**, *44*, 5629–5635; f) Y. Matsuo, H. Isobe, T. Tanaka, Y. Murata, M. Murata, K. Komatsu, E. Nakamura, *J. Am. Chem. Soc.* **2005**, *127*, 17148–17148; g) Y. Matsuo, K. Tahara, E. Nakamura, *J. Am. Chem. Soc.* **2006**, *128*, 7154–7155; h) D. M. Guldi, G. M. A. Rahman, R. Marczak, Y. Matsuo, M. Yamanaka, E. Nakamura, *J. Am. Chem. Soc.* **2006**, *128*, 9420–9427; i) Y. Matsuo, A. Muramatsu, Y. Kamikawa, T. Kato, E. Nakamura, *J. Am. Chem. Soc.* **2006**, *128*, 9586–9587.

[6] a) Y. Matsuo, E. Nakamura, *Organometallics* **2003**, *22*, 2554–2563; b) Y. Matsuo, Y. Kuninobu, S. Ito, E. Nakamura, *Chem. Lett.* **2004**, *33*, 68–69; c) Y. Matsuo, E. Nakamura, *J. Am. Chem. Soc.* **2005**, *127*, 8457–8466; d) Y. Matsuo, Y. Mitani, Y.-W. Zhong, E. Nakamura, *Organometallics* **2006**, *25*, 2826–2832.

[7] a) M. Sawamura, Y. Kuninobu, E. Nakamura, *J. Am. Chem. Soc.* **2000**, *122*, 12407–12408; b) M. Toganoh, Y. Matsuo, E. Nakamura, *J. Organomet. Chem.* **2003**, *683*, 295–300; c) Y. Matsuo, E. Nakamura, *Inorg. Chim. Acta* **2006**, *359*, 1979–1982.

[8] a) Y. Matsuo, A. Iwashita, E. Nakamura, *Organometallics* **2005**, *24*, 89–95; b) Y. Matsuo, A. Iwashita, E. Nakamura, *Chem. Lett.* **2006**, *35*, 858–859.

[9] a) Y. Kuninobu, Y. Matsuo, M. Toganoh, M. Sawamura, E. Nakamura, *Organometallics* **2004**, *23*, 3259–3266; b) Y. Matsuo, K. Tahara, M. Sawamura, E. Nakamura, *J. Am. Chem. Soc.* **2004**, *126*, 8725–8734.

[10] a) H. Al-Matar, P. B. Hitchcock, A. G. Avent, R. Taylor, *Chem. Commun.* **2000**, 1071–1072; b) H. Al-Matar, A. K. Abdul-Sada, A. G. Avent, P. W. Fowler, P. B. Hitchcock, K. M. Rogers, R. Taylor, *J. Chem. Soc., Perkin Trans. 2* **2002**, 53–58; c) R. Taylor, *C. R. Chimie* **2006**, *9*, 982–1000.

[11] a) J. W. Faller, *Adv. Organomet. Chem.* **1977**, *16*, 211–239; b) D. H. Gibson, W. L. Hsu, A. L. Steinmetz, *J. Organomet. Chem.* **1981**, *208*, 89–102.

[12] a) J. W. Faller, B. V. Johnson, T. P. Dryja, *J. Organomet. Chem.* **1974**, *65*, 395–400; b) E. W. Abel, S. Moorhouse, *J. Chem. Soc., Dalton Trans.* **1973**, 1706–1711.

[13] a) J.-L. Renaud, B. Demerseman, M. D. Mbaye, C. Bruneau, *Curr. Org. Chem.* **2006**, *10*, 115–133; b) T. Kondo, T. Mitsudo, *Curr. Org. Chem.* **2002**, *6*, 1163–1179; c) V. Cadierno, P. Crochet, S. E. Garcia-Garrido, J. Gimeno, *Curr. Org. Chem.* **2006**, *10*, 165–183.

[14] a) Fe: P. W. Jolly, F. G. A. Stone, K. Mackenzie, *J. Chem. Soc.* **1965**, 6416–6420; b) Pd: P. Golbern, F. Scheinmann, *J. Chem. Soc., Perkin Trans. 1* **1973**, 2870–2875; c) Rh: E. J. Corey, J. W. Suggs, *J. Org. Chem.* **1973**, *38*, 3224; d) Ni: C. F. Lochow, R. G. Miller, *J. Org. Chem.* **1976**, *41*, 3020–3022; e) Ir: D. Baudry, M. Ephritikhine, H. Felkin, *J. Chem. Soc., Chem. Commun.* **1978**, 694–695; f) Ru: H. Suzuki, Y. Koyama, Y. Moro-oka, T. Ikawa, *Tetrahedron Lett.* **1979**, 1415–1418; g) Cr: M. Sodeoka, H. Yamada, M. Shibasaki, *J. Am. Chem. Soc.* **1990**, *112*, 4906–4911; h) Pt: H. C. Clark, H. Kurosawa, *Inorg. Chem.* **1973**, *12*, 357–362; i) Ti, Zr: A. Ohff, V. V. Burlakov, U. Rosenthal, *J. Mol. Cat. A: Chem.* **1996**, *105*, 103–110.

[15] a) W.-K. Wong, K. W. Chiu, J. A. Statler, G. Wilkinson, M. Motevalli, M. B. Hursthouse, *Polyhedron* **1984**, *3*, 1255–1265; b) K. P. Finch, J. R. Moss, M. L. Niven, *Inorg. Chim. Acta* **1989**, *166*, 181–188; c) S. I. Black, A. C. Skapski, G. B. Young, *J. Chem. Soc., Chem. Commun.* **1989**, 911–913; d) S. J. Archer, K. P. Finch, H. B. Friedrich, J. R. Moss, A. M. Crouch, *Inorg. Chim. Acta* **1991**, *182*, 145–152; e) F. R. Lemke, D. J. Szalda, R. M. Bullock, *J. Am. Chem. Soc.* **1991**, *113*, 8466–8477; f) J. L. Hubbard, A. Morneau, R. M. Burns, O. W. Nadeau, *J. Am. Chem. Soc.* **1991**, *113*, 9180–9184; g) A. Takahashi, Y. Mizobe, H. Matsuzaka, S. Dev, M. Hidai, *J. Organomet. Chem.* **1993**, *456*, 243–253; h) A. Takahashi, Y. Mizobe, T. Tanase, M. Hidai, *J. Organomet. Chem.* **1995**, *496*, 109–115; i) M. J. Burn, M. G. Fickers, F. J. Hollander, R. G. Bergman, *Organometallics* **1995**, *14*, 137–150; j) M. A. Gafoor, A. T. Hutton, J. R. Moss, *J. Organomet. Chem.* **1996**, *510*, 233–241; k) S. Fabre, P. Kalck, G. Lavigne, *Angew. Chem. Int. Ed. Engl.* **1997**, *36*, 1092–1095; l) T. Funaioli, C. Cavazza, F. Marchetti, G. Fachinetti, *Inorg. Chem.* **1999**, *38*, 3361–3368; m) H. B. Friedrich, R. A. Howie, M. O. Onari, *Acta Crystallogr., Sect. E.* **2003**, *59*, m145–m147; n) M. Lail, C. M. Bell, D. Conner, T. R. Cundari, T. B. Gunnoe, J. L. Petersen, *Organometallics* **2004**, *23*, 5007–5020.

[16] A. Altomare, M. C. Burla, M. Camalli, G. L. Cascarano, C. Giacovazzo, A. Guagliardi, A. G. G. Moliterni, G. Polidori, R. Spagna, *J. Appl. Crystallogr.* **1999**, *32*, 115–119.

[17] G. M. Sheldrick, *Programs for Crystal Structure Analysis (Release 97–2)*, Göttingen, Germany, **1998**.


Received: January 5, 2007
Published Online: April 12, 2007

 © 2007 Wiley-VCH Verlag GmbH & Co. KGaA, Weinheim 

DOI: 10.1002/ejic.200700042

# Synthesis and Photophysical Properties of Bis-Cyclometallated Iridium(III)–Styryl Complexes and Their Saturated Analogues

**Marc Lepeltier,[a] Terence Kwok-Ming Lee,[b] Kenneth Kam-Wing Lo,*[b] Loic Toupet,[c] Hubert Le Bozec,[a] and Véronique Guerchais*[a]**

**Keywords:** Iridium / Luminescence / Bis-cyclometallated complexes

This manuscript reports the synthesis and photophysical investigation of a series of $Ir^{III}$ complexes $Ir(C^{\wedge}N)_2(O^{\wedge}O)$ which are functionalized in the *para* position of the pyridine ring by styryl groups substituted with electron-donor and -acceptor end groups. The saturated derivative $Ir(C^{\wedge}N$-ppy-4-$CH_2CH_2C_6H_4OMe)_2(O^{\wedge}O$-acac) (**4a**-$H_2$) was formed from $[Ir(C^{\wedge}N$-ppy-4-$CH{=}CHC_6H_4OMe)_2]_2(\mu\text{-}Cl)_2$ (**3a**) at 140 °C, whereas at 80 °C the parent unsaturated complexes $Ir(C^{\wedge}N$-ppy-4-$CH{=}CHC_6H_4R)_2(O^{\wedge}O)$ [$O^{\wedge}O$ = acac, R = OMe (**4a**), $NEt_2$ (**4b**), H (**4c**), $NO_2$ (**4d**); $O^{\wedge}O$ = dpm, R = OMe (**5a**), $NEt_2$ (**5b**)] were isolated. The saturated complex **4a**-$H_2$ exhibits intense green emission with a 36 % quantum yield at 298 K. The styryl complexes **4a**–**4d**, **5a** and **5b** are very weakly emissive at 298 K, but show intense red luminescence in alcohol glass at 77 K. The amino- and nitro-substituted complexes **4b** and **4d** give low-energy emission ($\lambda_{em}$ = 651 and 647 nm, respectively). The emissive states of these complexes are believed to possess predominant triplet intra-ligand charge-transfer ($^3$ILCT) and metal-to-ligand charge-transfer ($^3$MLCT) character, respectively.
(© Wiley-VCH Verlag GmbH & Co. KGaA, 69451 Weinheim, Germany, 2007)

## Introduction

There is a growing interest in the study and design of luminescent heavy-transition-metal complexes for their potential applications in optoelectronic devices such as light-emitting diodes (OLEDs) and luminescent probes for biomolecules.[1–3] Iridium complexes, homoleptic and heteroleptic, featuring cyclometallated phenylpyridine (ppy) ligands and relative derivatives have been extensively studied in recent years. The emission is believed to arise from a strong mixing between the MLCT and LC excited states. The colour of the emission depends highly on the choice of the cyclometallating ligand, and efforts are focused on the design and synthesis of new ligands for optimization of the luminescence properties.[4,5] In this context, we have started a research program on the luminescence properties of functionalized styryl Ir complexes in order to study the influence of the ligand modification on the photophysical properties of the resulting complexes. The synthesis of tris-chelate iridium(III) complexes is, in fact, very versatile; this requires drastic conditions and depends on the nature of the cyclometallating ligands used.[6] In a recent attempt to prepare tris-cyclometallated iridium(III)–styryl complexes *fac*-$Ir(C^{\wedge}N$-ppy-4-$CH{=}CHC_6H_4R)_3$ [R = OMe (**2a**), $NEt_2$ (**2b**)] by the classical route, that is, from the corresponding bis-cyclometallated chloro-bridged dimers **3a**,**3b** and 4-(donor-substituted-styryl)-2-phenylpyridines **1a**,**1b** in refluxing glycerol, we observed the unexpected formation of the fully saturated complexes **2**-$H_2$.[7a] To overcome this problem, an alternative smooth procedure was developed by direct functionalization of the tris-chelate-methyl complex *fac*-$Ir(C^{\wedge}N$-ppy-4-$Me)_3$. However, this very attractive "chemistry-on-the-complex" procedure was restricted to only donor-substituted styryl derivatives and did not allow the introduction of acceptor end groups.

We showed that extension of the ligand π-conjugation induces a strong redshift of the emission band of more than 100 nm relative to the unsubstituted complex $Ir(C^{\wedge}N$-ppy$)_3$ (in 77 K glass, **2a**-$H_2$ and **2a** emit at 496 and 616 nm, respectively). Moreover, the presence of a donor-acceptor D–A interaction by introducing a diethylamino group instead of a methoxy group leads to an additional redshift of 35 nm ($\lambda_{em}$ = 651 nm for **2b** in 77 K glass). In order to rationalize the electronic effects of the styryl end group, we have directed our studies towards the corresponding neutral heteroleptic bis-cyclometallated complexes $Ir(C^{\wedge}N$-ppy-4-$CH{=}CHC_6H_4R)_2(O^{\wedge}O)$ containing different end groups from strong donors to strong acceptors (R = $NEt_2$, OMe, H, $NO_2$). Bis-cyclometallated species, where the third ligand $O^{\wedge}O$ is an anionic acetylacetonate (acac) or dipyvaloylme-

[a] Sciences Chimiques de Rennes, UMR 6626 CNRS – Université de Rennes 1,
Campus de Beaulieu, 35042 Rennes Cedex, France
E-mail: veronique.guerchais@univ-rennes1.fr
[b] Department of Biology and Chemistry, City University of Hong Kong,
Tat Chee Avenue, Kowloon, Hong Kong, P. R. China
E-mail: bhkenlo@cityu.edu.hk
[c] Groupe Matière Condensée, UMR 6626 CNRS – Université de Rennes 1,
Campus de Beaulieu, 35042 Rennes Cedex, France
Supporting information for this article is available on the WWW under http://www.eurjic.org or from the author.

 © 2007 Wiley-VCH Verlag GmbH & Co. KGaA, Weinheim 

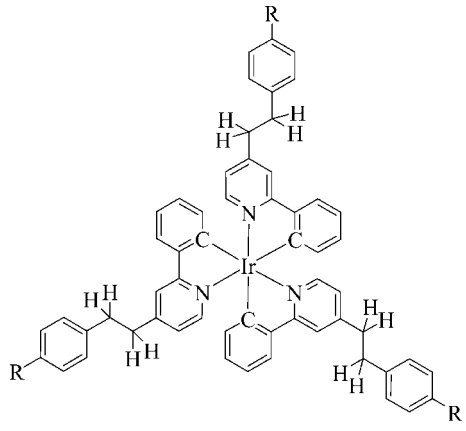

**2a**-$H_2$: R = OMe, **2b**-$H_2$: R = $NEt_2$

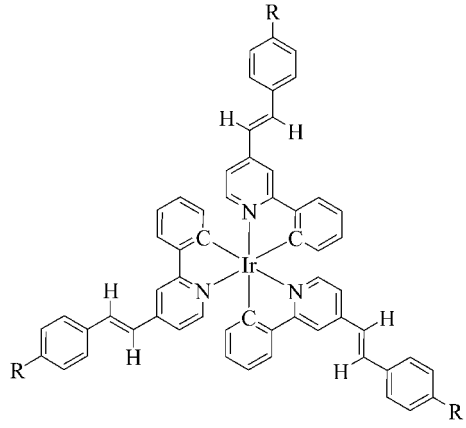

**2a**: R = OMe, **2b**: R = $NEt_2$

thane (dpm) ligand, are easily accessible whatever the nature of R. The photophysical properties of these neutral Ir(*C*^*N*-ppy)$_2$(*O*^*O*) derivatives have been shown to be very similar to those of the corresponding tris-cyclometallated species.[4] The hydrogenation reaction of the styryl C=C double bond observed during the course of the synthesis of tris-cyclometallated complexes is inhibited in this case, simply by lowering the reaction temperature.

We report here the synthesis and spectroscopic characterization of a new family of bis-cyclometallated iridium–styryl complexes and the saturated complex Ir(*C*^*N*-ppy-4-$CH_2CH_2C_6H_4OMe)_2$(*O*^*O*-acac) (**4a**-$H_2$); the effects of the styryl substituent R on their photophysical properties will be discussed. The synthesis and X-ray crystal structures of the free ligands will also be described.

## Results and Discussion

### Synthesis of the Ligands

The donor-substituted phenylpyridine derivatives, the methoxy-, diethylamino- and non-substituted 4-styryl-2-phenylpyridine derivatives (ppy-4-CH=$CHC_6H_4$R) [R = OMe (**1a**), $NEt_2$ (**1b**), H (**1c**)], were obtained from 4-picoline in a two-step procedure. The first step was the phenylation at the α position, upon addition of PhLi followed by oxidation with $MnO_2$.[8] Then deprotonation of the methyl group with *t*BuOK and condensation with the appropriate aldehyde *p*-R-$C_6H_4$-CHO (R = OMe, $NEt_2$, H) afforded, by in situ dehydration, the expected unsaturated derivatives **1** (Scheme 1). Compounds **1a**–**1c** were purified by crystallization from a mixture of toluene/pentane and were isolated in 86, 96 and 34% yield, respectively, from ppy-4-Me (4-methyl-2-phenylpyridine). In all cases, the *E* configuration of the C=C double bond was confirmed by the presence of an AB system with a characteristic $^3J_{H–H}$ coupling of 16 Hz. We did not observe any photoisomerization process $E \rightarrow Z$ in acidic medium or under sunlight (vide infra).

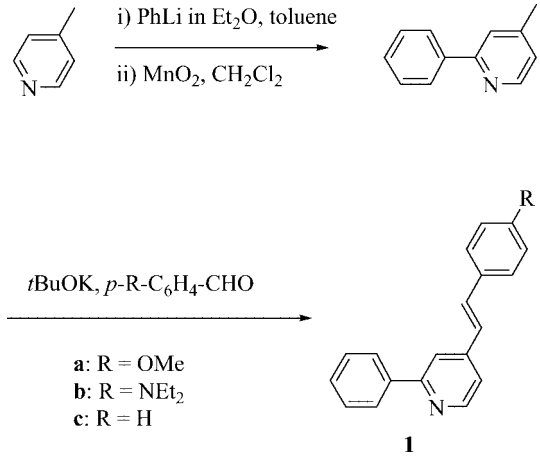


Scheme 1.

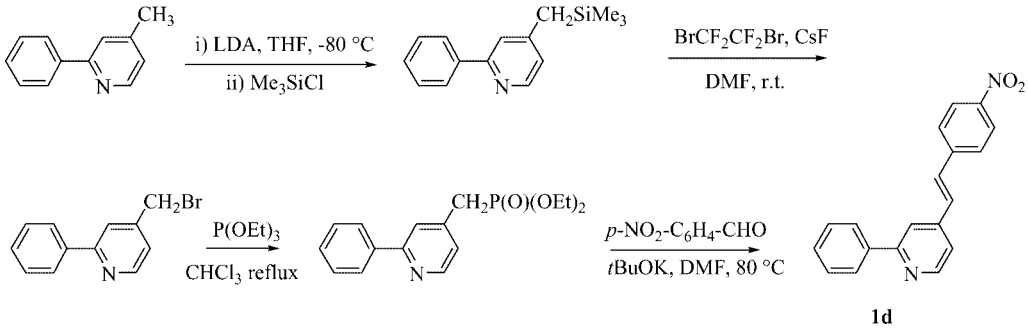


Scheme 2.

 © 2007 Wiley-VCH Verlag GmbH & Co. KGaA, Weinheim 

The described procedure cannot be applied to benzaldehyde featuring an electron-withdrawing group.[9] The nitro derivative **1d** was prepared by a different procedure (Scheme 2). This synthesis involved a Wadsworth–Emmons reaction between the (diethylphosphoryl)methyl-2-phenylpyridine and *p*-nitrobenzaldehyde. The phosphonate derivative was prepared in a two-step procedure, following the method described for 2,2′-bipyridines.[10–12] The first step was the deprotonation of the methyl precursor ppy-4-Me and subsequent addition of TMSCl to give 4-(trimethylsilylmethyl)-2-phenylpyridine; the latter was then converted into the 4-(bromomethyl)-2-phenylpyridine, and eventually the phosphonate derivative was formed by means of an Arbuzov reaction. Compound **1d** was isolated in an overall yield of 33%. The *E* configuration was ascertained by the presence of the AB system which appears at $\delta$ = 7.42 ($^3J$ = 16 Hz) and 7.28 ppm.

### X-ray Crystal Studies of 1a, 1b and 1d

The styryl derivatives **1a**, **1b** and **1d** were characterized by X-ray diffraction studies (Figures 1, 2 and 3, respectively). Crystals were obtained by slow diffusion of pentane in toluene solutions of **1a**, **1b** and **1d**. Selected distances and angles are listed in Table 1. Derivatives **1a**, **1b** and **1d** crystallized as dimers. The two molecules are almost identical, except in the case of **1b** for which the conformation about the C12–C9 bond is different; *s-cis* and *s-trans* isomers (C12–C13 and C9–C10) are observed. In all compounds, the *E* configuration of the C=C double bond of the styryl group is confirmed; the C12–C13 bond length in **1a** and **1d** is characteristic of a double bond and compares well with that of the bipyridine analogues.[9] In contrast, the C12–C13 distance in **1b** is significantly shorter, probably because of the crystal packing. In the *s-trans* isomer, the

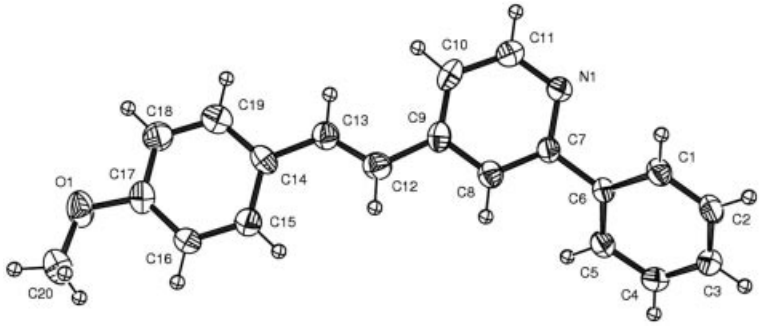


Figure 1. ORTEP drawing of **1a**.

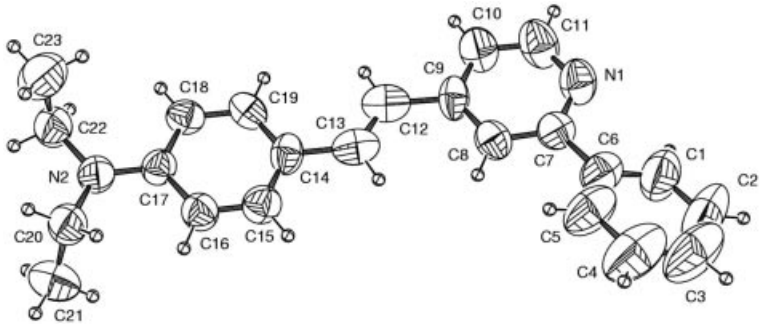


Figure 2. ORTEP drawing of **1b**. Only the *s-cis* isomer is shown for clarity.

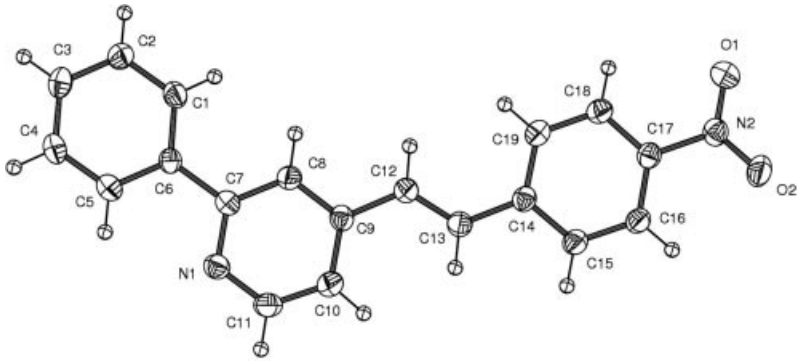


Figure 3. ORTEP drawing of **1d**.

 © 2007 Wiley-VCH Verlag GmbH & Co. KGaA, Weinheim 

phenyl group is tilted relative to the adjacent pyridine ring (dihedral angle N1–C7–C6–C1 –25.35°), whereas the planarity is better for the *s-cis* isomer (dihedral angle 3.63°). The styryl group is almost coplanar with the nitrogen ring in the former isomer, whereas the deviation is about 20° in the latter isomer.

Table 1. Selected bond lengths [Å] and angles [°] for **1a**, **1b** and **1d**.

| Compound | **1a** | **1b** (*s-trans*) | **1b** (*s-cis*) | **1d** |
|---|---|---|---|---|
| C12–C13 | 1.328(7) | 1.260(5) | 1.285(5) | 1.340(3) |
| C13–C14 | 1.453(6) | 1.522(6) | 1.468(6) | 1.463(3) |
| C9–C12 | 1.497(6) | 1.509(6) | 1.505(6) | 1.474(3) |
| N1–C7 | 1.353(6) | 1.338(5) | 1.329(5) | 1.350(3) |
| C6–C7 | 1.489(6) | 1.451(6) | 1.474(6) | 1.492(3) |
| C7–C8 | 1.389(6) | 1.390(5) | 1.374(5) | 1.397(3) |
| C12–C13–C14 | 127.9(5) | 128.6(5) | 128.4(5) | 126.6(2) |
| C9–C12–C13 | 123.6(4) | 125.6(5) | 126.1(5) | 125.0(2) |
| N1–C7–C6 | 116.0(4) | 115.9(5) | 116.8(5) | 116.2(2) |
| C7–C6–C1 | 119.3(4) | 120.8(6) | 121.3(6) | 121.9(2) |
| C11–N1–C7 | 115.5(4) | 117.3(4) | 117.5(4) | 116.8(2) |

## Synthesis of the Metal Complexes

The precursor dimers $[Ir(C^{\wedge}N\text{-ppy-4-CH=CHC}_6H_4R)_2]_2(\mu\text{-Cl})_2$ [R = OMe (**3a**), $NEt_2$ (**3b**), H (**3c**), $NO_2$ (**3d**)] were prepared following classical procedures starting from $IrCl_3{\cdot}nH_2O$ (140 °C).[13,14] For comparison, we also prepared the methyl complex $[Ir(C^{\wedge}N\text{-ppy-4-Me})_2]_2(\mu\text{-Cl})_2$ (**3e**).[15] Compounds **3a**–**3d** were isolated as orange powders and **3e** as a yellow powder. They are sparingly soluble in $CH_2Cl_2$. The $NO_2$-derivative **3d** is too insoluble in $CD_2Cl_2$ to be characterized by $^1H$ NMR spectroscopy, but dissolution in DMSO gives rise to the formation of the DMSO adduct $[Ir(C^{\wedge}N\text{-ppy-4-CH=CHC}_6H_4NO_2)_2(DMSO)(Cl)]$ (**3d**-DMSO). Such solvation by strong coordinating solvents ($H_2O$, $CH_3CN$, DMF) has been already reported; the reaction products were not isolated because of re-formation of the corresponding chloro-bridged dimer.[16] The $^1H$ NMR spectrum of the DMSO adduct **3d**-DMSO shows two different sets of signals for the magnetically nonequivalent C^N ligands. For instance, two pyridine signals ($py^6$) are observed at low field at $\delta$ = 9.82 and 9.50 ppm. The $^1H$ NMR spectra of crude **3a**–**3c** show the presence of only one set of signals which is attributed to the racemic mixture ($\Delta\Delta/\Lambda\Lambda$) as indicated by a characteristic low-field doublet at $\delta$ = 9.15 ppm (**3a**) for the pyridine proton in the 6-position. The *E* ($^3J_{H-H}$ = 16 Hz) configuration of the double bond of the styryl group of **3** was maintained during the synthesis. Exposure of the $CD_2Cl_2$ solutions of **3a**–**3c** to sunlight for a few hours, however, resulted in the appearance of new aromatic signals. Several doublets from $\delta$ = 9.28 ppm to $\delta$ = 9.04 ppm were then observed for the proton $H^6$ of the pyridine ring of **3a**. We assume that *trans*/*cis* isomerization of the C=C double bond occurs under these conditions (vide infra).

Dimers were then converted upon cleavage of the chloro bridges with bidentate ligands, such as 1,3-diketonates, into mononuclear complexes. We used acetylacetone (acacH) and dipivaloylmethane (dpmH). Treatment of **3a** with acacH and $Na_2CO_3$ in 2-ethoxyethanol at 140 °C led to the formation of the bis-cyclometallated complex **4a**-$H_2$, in which the C=C double bonds of the styryl groups were hydrogenated (Scheme 3). Moreover, the free hydrogenated ligand $HC^{\wedge}N\text{-}H_2$ **1a**-$H_2$ was also isolated. Compound **4a**-$H_2$ was obtained as a yellow powder, and its structure was confirmed by $^1H$- and $^{13}C$ NMR spectroscopy and elemental analysis. The methylene protons appear as multiplets at

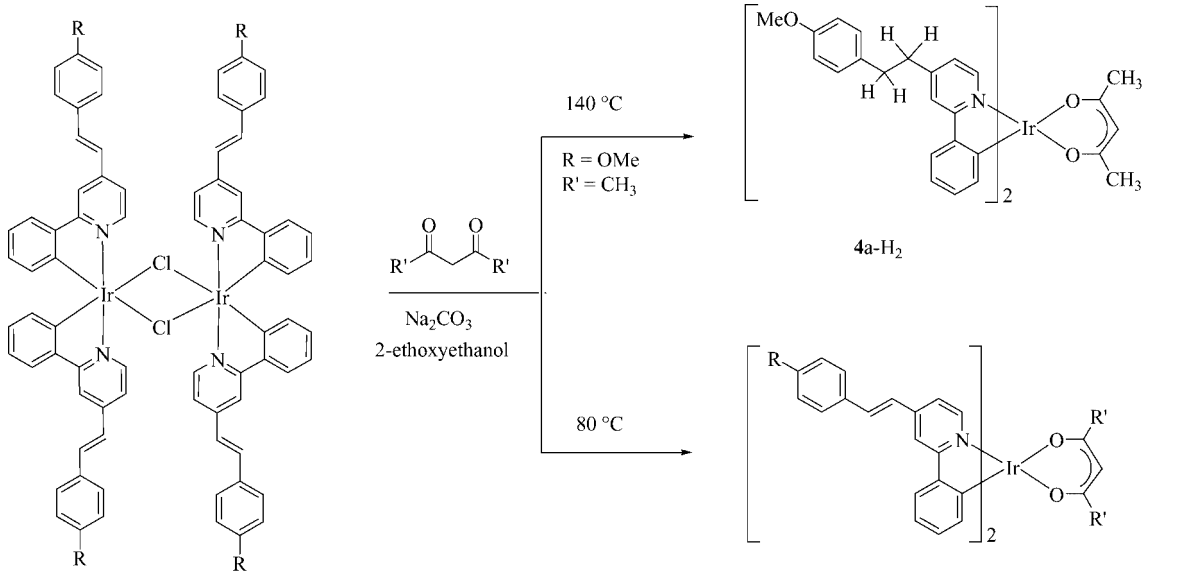


Scheme 3. Synthesis of the bis-cyclometallated complexes: influence of the reaction temperature.

 © 2007 Wiley-VCH Verlag GmbH & Co. KGaA, Weinheim 

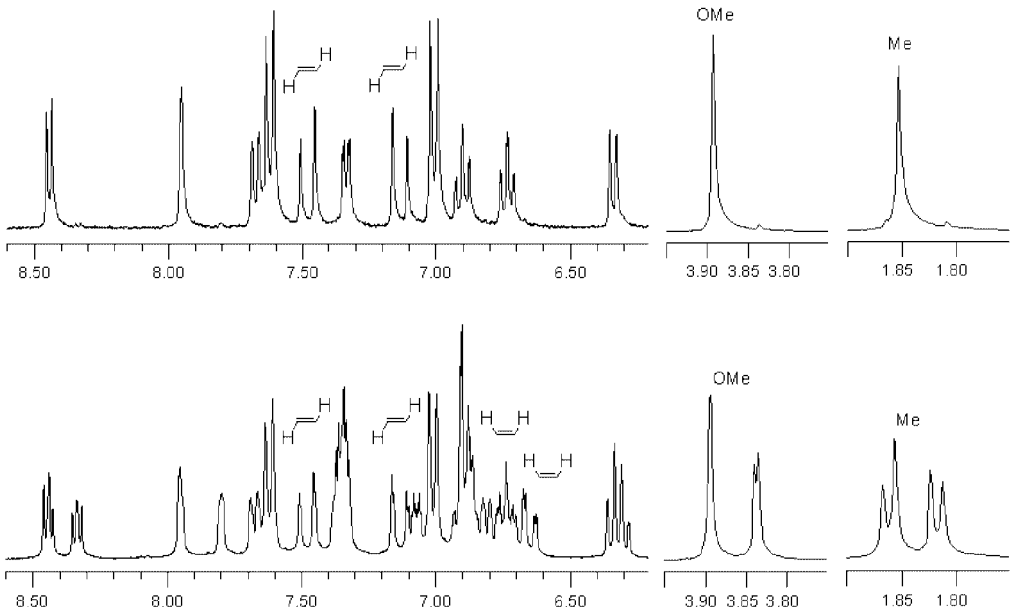


Figure 4. NMR spectra (δ values given in ppm) of **4a**: before (top) and after (bottom) exposure for one hour in the sunlight.

$\delta$ = 3.14 ppm ($\delta$ = $^{13}$C 37.5 ppm) and 3.07 ppm ($\delta$ = $^{13}$C 35.7 ppm). Such a hydrogenation reaction could be mediated by Ir species which are known to catalyse hydrogen transfer reductions.[17] This feature was also observed in the attempted synthesis of the parent tris-cyclometallated styryl species **2**. Since the saturated derivative Ir(*C*^*N*-ppy-$CH_2CH_2C_6H_4OMe)_3$ was formed, an alternative synthesis involving functionalization after complexation was developed.[7a] It is likely that the drastic conditions used for the synthesis of Ir complexes, the presence of an alcohol (hydrogen donor) and a base all favour this process. It is noteworthy that the dimers **3** were not hydrogenated since no base was present in the reaction medium.

Concerning the bis-cyclometallated mononuclear species (the oxygenated derivatives **4** and **5**), side hydrogenation reactions could be avoided by performing the syntheses at lower temperature, namely 80 °C instead of 140 °C. Selective formation of the styryl complexes Ir(*C*^*N*-ppy-4-$CH=CHC_6H_4R)_2$(*O*^*O*) [O^O = acac, R = OMe (**4a**), $NEt_2$ (**4b**), H (**4c**), $NO_2$ (**4d**); O^O = dpm, R = OMe (**5a**), $NEt_2$ (**5b**)] can occur at this reaction temperature (Scheme 3). Compounds were isolated in excellent yield (ca. 90%) as red-brown powders. Similarly, the saturated complex Ir(*C*^*N*-ppy-4-Me)$_2$(*O*^*O*-acac) (**4e**) was isolated as a yellow compound. The cleavage of the dimers occurred with retention of the configuration, that is, the resulting products **4a**–**4d**, **5a** and **5b** have $C_2$ symmetry.

We note that the aromatic regions of the $^1$H NMR spectra of **4** and **5** are similar to those of dimers **3**; the aromatic signals appear in the same order. For example, the lowest field signal ($\delta \approx$ 8.30 ppm) is assigned to the proton in the α position of the nitrogen atom of the pyridine ring as a characteristic signature, in contrast to that of the tris-chelate species, which is due to the pyridine proton H$^3$. Upon exposure of $CH_2Cl_2$ solutions to sunlight, the complexes

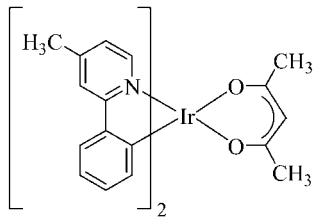


**4e**

**4a**–**4c**, **5a** and **5b**, like the dimer precursors, undergo partial isomerization of the C=C double bond leading to the formation of three isomers (*E*/*E*, *E*/*Z*, *Z*/*Z*). For instance, the $^1$H NMR spectra display two sets of signals for vinylic protons of the *cis*-alkenyl group of the *E*/*Z* and *Z*/*Z* isomers of **4a**; one signal is located at $\delta$ = 6.65 ppm ($^3J_{H-H}$ = 12 Hz, the second doublet is masked), and the second set is found at $\delta$ = 7.49 and 7.14 ppm, as the result of the splitting of the former AB system of the *E*/*E* isomer (Figure 4). It is noteworthy that the $NO_2$ derivative **4d** was not prone to isomerization under such conditions; no change was observed by $^1$H NMR spectroscopy.

## Absorption and Emission Properties of the Ligands and Complexes

The photophysical data of the free ligands **1a**–**1d** in $CH_2Cl_2$ solutions at 298 K are presented in Table 2. Compounds **1a**, **1c** and **1d** display an intense absorption band between 290–390 nm that is assigned to a ligand-centred ($^1$LC) ($\pi \rightarrow \pi^*$) transition (Figure 5). The strong absorption bands of compounds **1c** and **1d** are comparable to those of their non-phenylated counterparts, namely styrylpyridine and (*p*-nitrostyryl)pyridine [292 nm (31300 $M^{-1}cm^{-1}$) and

 © 2007 Wiley-VCH Verlag GmbH & Co. KGaA, Weinheim 

Table 2. Absorption and emission spectroscopic data of ppy-4-CH=CHC$_6$H$_4$R (**1**) in $CH_2Cl_2$ at 298 K.

| | R | $\lambda_{max}$/nm ($\varepsilon$/M$^{-1}$cm$^{-1}$) | $\lambda_{em}$/nm | $\Phi$[a] |
|---|---|---|---|---|
| **1a** | OMe | 264 (16000), 309 sh (23000), 310 sh (23000), 327 (29000) | 404 | 0.008 |
| **1b** | $NEt_2$ | 251 (27000), 277 sh (18000), 335 (9400), 382 (17000) | 487 | 0.078 |
| **1c** | H | 262 (24000), 312 (33000), 328 sh (20000) | 364 | – |
| **1d** | $NO_2$ | 257 (25000), 335 (33000) | – | – |

[a] Emission quantum yields were determined using quinine sulfate as the standard.

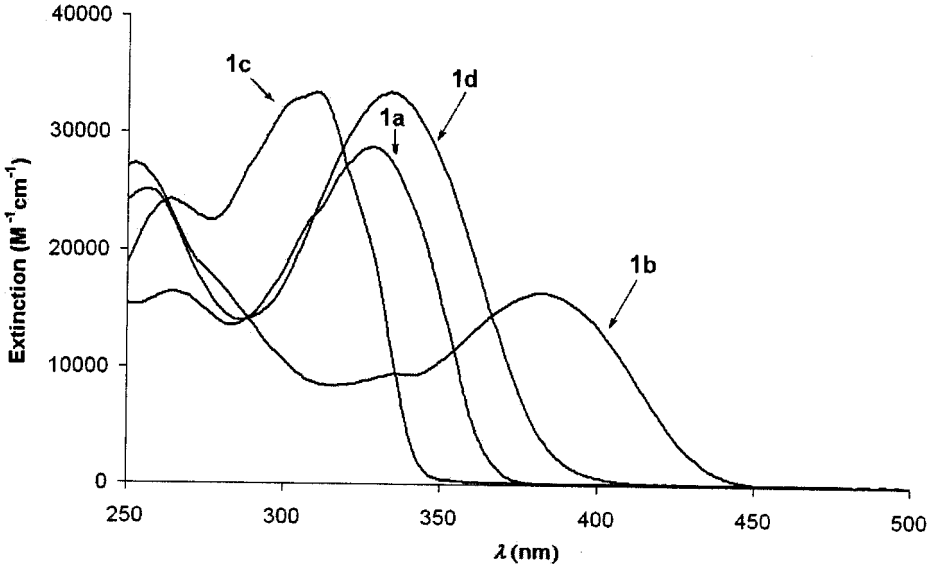


Figure 5. Absorption spectra of ppy-4-CH=CHC$_6$H$_4$R **1a**–**d** in $CH_2Cl_2$ solutions at 298 K.

332 nm (30875 M$^{-1}$cm$^{-1}$) in $CH_3CN$, respectively].[18] Interestingly, the absorption spectrum of the amino-styryl ligand **1b** shows a strong band at 382 nm (17000 M$^{-1}$cm$^{-1}$) which can be assigned to an intra-ligand charge-transfer ($^1$ILCT) transition from the electron-donating amino group to the electron-accepting pyridine ring via the π-linker styryl group. This intense and structureless band is typical for "push-pull" molecules and compares well with that found for the related bipyridine derivative bpy-4-styryl-$NEt_2$, for which absorption maximum occurs at 394 nm in $CH_3CN$.[19]

Compounds **1a**–**1c** are fluorescent upon photoexcitation. The emission colour of the compounds in $CH_2Cl_2$ at 298 K ranges from blue to green (Figure 6), depending on the identity of the substituent R. The emission energy decreases in the order **1c** (364 nm) > **1a** (404 nm) > **1b** (487 nm),

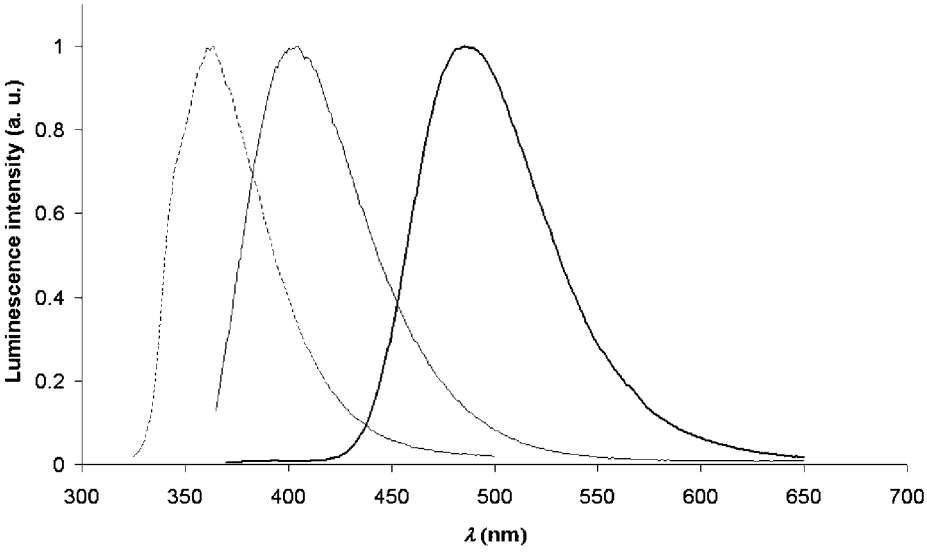


Figure 6. Normalized emission spectra of ppy-4-CH=CHC$_6$H$_4$R **1a** (−), **1b** (−) and **1c** (---) in $CH_2Cl_2$ solutions at 298 K.

 © 2007 Wiley-VCH Verlag GmbH & Co. KGaA, Weinheim 

which is consistent with the electron-donating ability of the substituent R. Compound **1d** is non-emissive. The observation of a positive solvatochromic shift on the emission band of **1b** in solvents ranging from toluene to DMSO, is in agreement with a charge-transfer emissive state (Table 3, Figure 7). The emission quantum yields for **1a** and **1b** are comparable to those reported for the bpy-styryl-4-R derivatives (R = $NBu_2$, 3.6%;[19] R = OOct, 1%).[9]

Table 3. Absorption and emission wavelengths of **1b** in various solvents at 298 K.

| Solvent | $\lambda_{abs}$/nm | $\lambda_{em}$/nm |
|---|---|---|
| Toluene | 383 | 457 |
| Acetone | 384 | 495 |
| $CH_2Cl_2$ | 382 | 488 |
| Ethanol | 386 | 510 |
| DMSO | 395 | 517 |

The absorption spectra of the dimers **3a**–**3d** show intense bands between 250–350 nm (Table 4), which are assigned to $^1$LC ($\pi\rightarrow\pi^*$) transitions of the cyclometallated ligands. The characteristic $^1$ILCT absorption band of **3b** occurs at 431 nm. The redshift of 48 nm compared to the absorption band of the free ligand is ascribed to the increased electron-accepting properties of the pyridine ring after its coordination to the iridium(III) centre. A similar shift was observed for related $[M(bpy\text{-}4\text{-}CH{=}CHC_6H_4R)_3]^{2+}$ complexes.[20] Moderately intense bands are present in the lower energy region (450–550 nm). The absorption bands of **3c** at 467 nm and **3d** at 500 nm are tentatively assigned to an admixture of $^1$MLCT/$^3$MLCT transitions. The nitro group of **3d** significantly shifts the MLCT absorption band to lower energy (500 nm), compared with that of the styryl derivative **3c** (467 nm). The shift is attributed to the strong electron-accepting properties of the nitro substituent, which substantially lower the LUMO of the complex.[7b] The MLCT transition of **3b** is not clearly resolved and is probably embedded in the intense and broad ILCT band.

The absorption spectra of the bis-cyclometallated acac (**4a**–**4d**) and dpm (**5a** and **5b**) complexes closely resemble those of the corresponding dimers. The absorption features originate mainly from the $Ir(C^{\wedge}N)_2$ moieties (Figure 8,

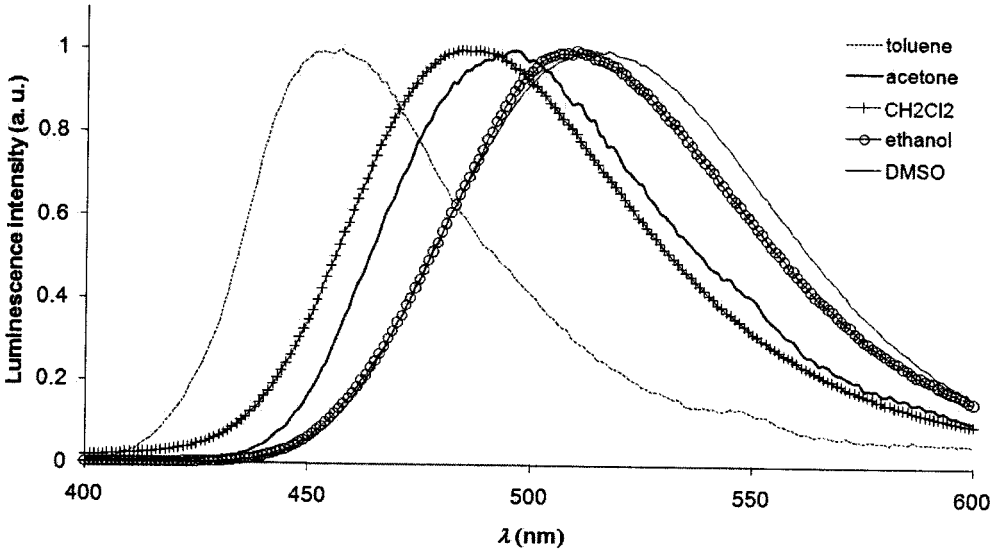


Figure 7. Emission spectra of ppy-4-CH=$CHC_6H_4NEt_2$ (**1b**) in different solvents in fluid solutions at 298 K.

Table 4. Photophysical data for the styryl-containing complexes.

| | R | $\lambda_{abs}$/nm ($\varepsilon$/M$^{-1}$ cm$^{-1}$)[a] | $\lambda_{em}$/nm[b] | $\tau_o$/μs[b] |
|---|---|---|---|---|
| $[Ir(C^{\wedge}N\text{-ppy-4-CH}{=}CHC_6H_4R)_2]_2(\mu\text{-Cl})_2$ (**3a**–**3d**) | | | | |
| **3a** | OMe | 256, 303, 328, 374, 407 sh, 455 | 611 (max.), 674, 744 sh | 5.0 |
| **3b** | $NEt_2$ | 261, 293, 404 sh, 431, 473 sh | 651 (max.), 713, 796 sh | 20.4 |
| **3c** | H | 271, 311, 371, 411 sh, 467 | 605 (max.), 664, 729 sh | 2.9 |
| **3d** | $NO_2$ | 262, 331, 392 sh, 432 sh, 500, 552 sh | 639, 660 (max.), 727 sh | 1.0 |
| $Ir(C^{\wedge}N\text{-ppy-4-CH}{=}CHC_6H_4R)_2(O^{\wedge}O)$ (**4a**–**4d**, **5a**, **5b**) | | | | |
| **4a** | OMe | 270 (62000), 330 (45000), 373 (39000), 415 sh (21000), 475 (5300) | 613 (max.), 673, 740 sh | 4.6 |
| **5a** | OMe | 266 (62000), 327 (48000), 377 (39000), 418 sh (21000), 476 (7200) | 616 (max.), 676, 759 sh | 2.9 |
| **4b** | $NEt_2$ | 265 (40000), 410 (23000), 433 (26000), 480 sh (5500) | 651 (max.), 715 | 12.1 |
| **5b** | $NEt_2$ | 263 (35000), 412 (38000), 438 (42000), 482 sh (8500) | 651 (max.), 717 | 9.1 |
| **4c** | H | 268 (44000), 306 (45000), 370 (25000), 410 sh (12000), 468 (4700) | 609 (max.), 667, 734 sh | 2.2 |
| **4d** | $NO_2$ | 263 (38000), 282 (36000), 332 (48000), 400 (33000), 442 sh (18000), 518 (5200) | 647 (max.), 705, 788 sh | 1.0 |

[a] In $CH_2Cl_2$ at 298 K (the extinction coefficients for complexes **3a**–**3d** could not be determined with accuracy because of the low solubility of the complexes). [b] In $CH_2Cl_2$/EtOH/MeOH (1:4:1, v/v/v) at 77 K.

 © 2007 Wiley-VCH Verlag GmbH & Co. KGaA, Weinheim 

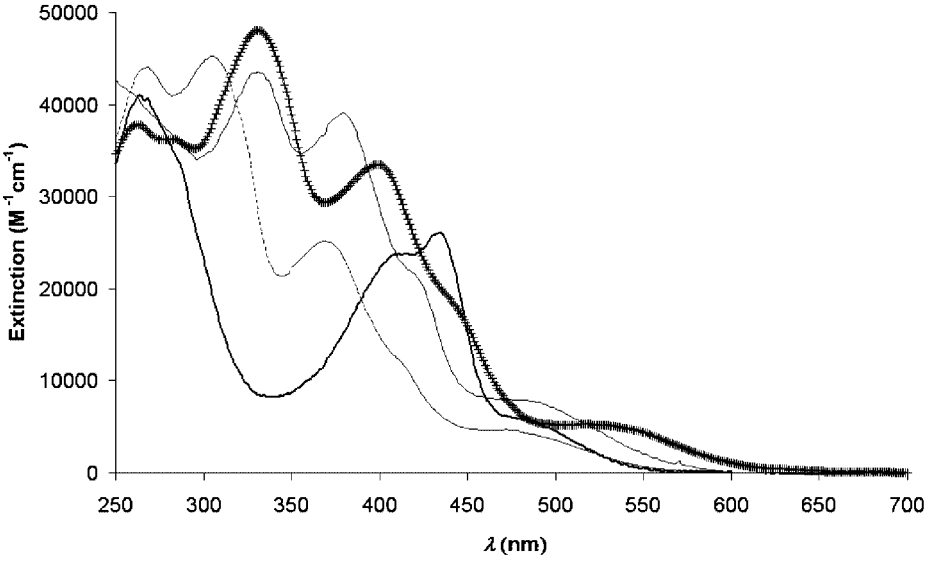


Figure 8. Absorption spectra of **4a** (−), **4b** (−), **4c** (---) and **4d** (+++) in 2-Me-THF solutions at 298 K.

Table 4). For example, the ligand-centred bands of **4a** (373 nm) and **4b** (433 nm) are comparable to that of their respective dimeric precursors **3a** and **3b**. The dpm complexes **5a** and **5b** display similar absorption features. Analogous findings were observed for the related complexes Ir($C^{\wedge}N$)$_2$($O^{\wedge}O$).[4a,4b]

The saturated complex **4a**-$H_2$ exhibits a strong LC absorption band at 337 nm (Table 5, Figure 9). Since no ILCT band is present, the $^1$MLCT and mixed $^1$MLCT/$^3$MLCT transitions are observed at 403, 460 and 485 nm, respectively, with tailings extended to 500 nm. The singlet and triplet MLCT bands for Ir($C^{\wedge}N$-ppy)$_2$($O^{\wedge}O$-acac) were

Table 5. Photophysical data for the alkyl-substituted complexes **3e**, **4e** and **4a**-$H_2$.

| | $\lambda_{abs}$/nm ($\varepsilon$/M$^{-1}$ cm$^{-1}$)[a] | $T$/K | $\lambda_{em}$/nm | $\Phi$ | $\tau_o$/μs |
|---|---|---|---|---|---|
| **3e** | 262 (62000), 330 (12000), 400 (6300), 450 (3700), 480 (950) | 298[a] | 507 (max), 534 sh, 590 sh | 0.0039[c] | 0.7 |
| | | 77[b] | 494 (max), 531, 572 sh | – | 4.4 |
| **4e** | 261 (37000), 336 (9200), 400 sh (4100), 450 sh (2600), 483 sh (900) | 298[a] | 511, 544 sh | 0.51[d] | 1.4 |
| | | 77[b] | 497 (max), 534, 577 sh | – | 4.7 |
| **4a**-$H_2$ | 265 (40000), 337 (11000), 403 sh (4900), 460 sh (3000), 485 sh (1500) | 298[a] | 516, 549 sh | 0.36[d] | 1.3 |
| | | 77[b] | 496 (max), 531, 579 sh | – | 3.8 |

[a] $CH_2Cl_2$. [b] $CH_2Cl_2$/EtOH/MeOH (1:4:1, v/v/v). [c] $[Ru(bpy)_3]^{2+}$ was used as the standard. [d] Quinine sulfate was used as the standard.

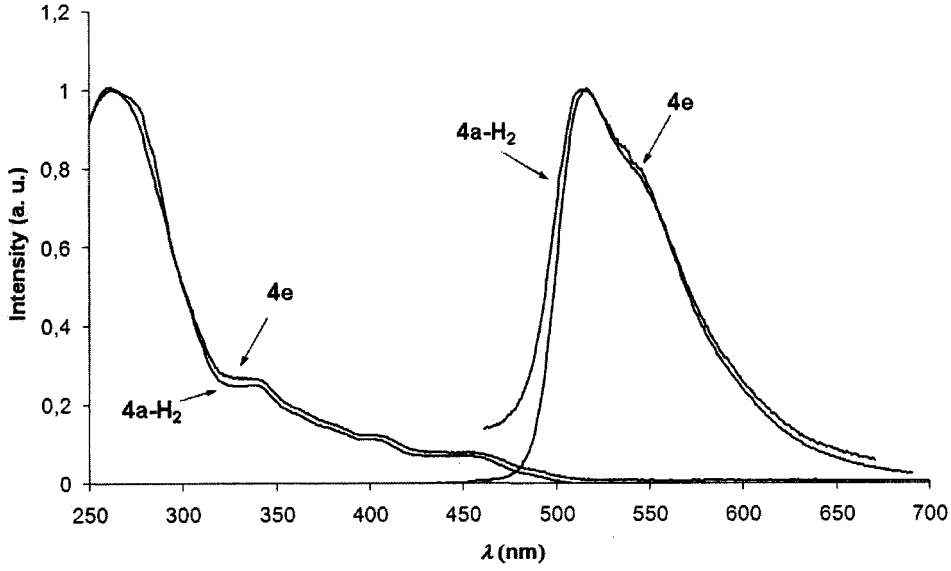


Figure 9. Absorption and emission spectra of **4e** and **4a**-$H_2$ in $CH_2Cl_2$ solutions at 298 K.

 © 2007 Wiley-VCH Verlag GmbH & Co. KGaA, Weinheim 

found at 412, 460 and 490 nm, respectively. Thus, addition of the alkyl group $CH_2CH_2C_6H_4OMe$ to the ppy ligand causes no significant changes.[4a]

Upon excitation, complex **4a**-$H_2$ in $CH_2Cl_2$ solution at 298 K shows strong green emission (Figure 9, Table 5). The emission properties of this complex are very similar to those of the dimethyl complexes $Ir(dmppy)_3$[15] and $Ir(dmppy)_2(acac)$[21] [Hdmppy = 4-methyl-2-(4-methylphenyl)pyridine]. The presence of a methyl or an alkyl group such as $CH_2CH_2$-$C_6H_4OMe$ in the *para* position of the pyridine ring brings no significant effects to the photophysical properties of these types of complexes. The emission of **4a**-$H_2$ is assigned to a state of an admixture of $^3$MLCT and $^3$LC character.[4a,22]

The emission data for complexes **3a**–**3d**, **4a**–**4d**, **5a** and **5b** are summarized in Table 4. All the styryl complexes show very weak emission in fluid solutions at room temperature (Figure 10).[7] In alcohol glass at 77 K, they become strongly emissive. The emission bands of the complexes show rich vibronic structures with progressional spacings of ca. 1400 $cm^{-1}$, typical of C=C aromatic stretching. The emission behaviour of the complexes depends strongly on the cyclometallating ligands, whereas the ancillary ligands acac and dpm O^O or the chloro bridge play a minor role. For these reasons, only the emission properties of the acac complexes **4a**–**4d** are discussed.

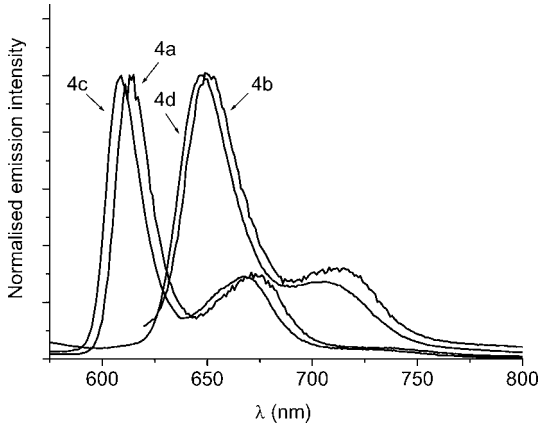


Figure 10. Emission spectra of complexes **4a**–**4d** in $CH_2Cl_2$/EtOH/MeOH (1:4:1, v/v/v) at 77 K.

At 77 K, complexes **4a**–**4d** emit in the red region from 609 to 788 nm with a lifetime in the microsecond timescale. As expected, increasing the π-conjugation of the C^N ligand induces a bathochromic shift of the emission band; for example, the emission of $Ir(C^N\text{-ppy})_2(O^O\text{-acac})$ shifts from 516 to 548 nm when benzoquinoline is used as the C^N ligand.[4a,4b] In this work, a shift from green to red emission is observed after the addition of a styryl group to the ppy ligand. The emission energy difference is significant [$Ir(C^N\text{-ppy})_2(O^O\text{-acac})$ in 77 K glass, $\lambda_{em}$ = 492 nm; for **4c**, $\lambda_{em}$ = 609 nm]. This is also in line with the data observed for the saturated complex **4a**-$H_2$; breaking the conjugation of the styryl group gives rise to green emission. Substitution of the hydrogen atom in **4c** by a methoxy end group has no marked effects on the emission maximum. In both cases, the emission is believed to arise from an admixture of $^3$MLCT and $^3$IL states. In contrast, substitution by an amino group induces a redshift to 651 nm in **4b**. It is likely that the presence of an amino group results in $^3$ILCT character in the emissive states of **4b** and **5b**. The nitro-derivative **4d** also gives low-energy emission ($\lambda_{em}$ = 647 nm). Owing to the strong electron-accepting properties of the nitro substituent, the emissive state of complex **4d** should possess predominantly $^3$MLCT character, resulting from the stabilization of the π*-acceptor orbitals of the C^N ligand.[7]

## Conclusions

A new family of bis-cyclometallated iridium(III)–styryl complexes were prepared. Reduction of the C=C double bond can be avoided by performing the synthesis under mild reaction conditions. Low-temperature glass of all the styryl complexes **4a**–**4d**, **5a** and **5b** gives intense red emission upon photoexcitation. Compared with the unmodified $[Ir(C^N\text{-ppy})_2(O^O)]$ complexes, large bathochromic shifts in emission energy were achieved by adding a conjugated styryl group to the ppy ligand and by introducing a strong electron-withdrawing nitro group. Incorporation of a diethylamino substituent into the cyclometallating ligand leads to a switch of emissive-state character from $^3$MLCT to $^3$ILCT, resulting in increased emission lifetimes. We anticipate that these luminescent iridium(III) complexes can act as interesting building blocks for luminescent macromolecular architectures.

## Experimental Section

All manipulations were performed using Schlenk techniques under argon. All solvents were dried and purified by standard procedures. All starting materials were used as received. NMR spectra were recorded with Bruker DPX-200, AV 300 or AV 500 MHz spectrometers. $^1$H and $^{13}$C chemical shifts are given versus $SiMe_4$ and were determined by reference to residual $^1$H and $^{13}$C solvent signals. $^{31}$P chemical shifts are given versus ext. $H_3PO_4$ (85%). Attribution of carbon atoms was based on HMBC, HMQC and COSY experiments. UV/Vis absorption spectra were recorded using a UVIKON 9413 spectrophotometer, and emission spectra were measured with a PTI C 60 fluorescence spectrophotometer. High resolution mass spectra (HRMS) were performed using a MS/MS ZABSpec TOF at the CRMPO (Centre de Mesures Physiques de l'Ouest) in Rennes. Elemental analyses were performed by the Service central d'analyse du CNRS at Vernaison. Cyclic voltammograms were recorded using a PAR model 273 Autolab. The working electrode was polished Pt, the counter electrode was a Pt wire, and a saturated calomel electrode (SCE) was used as the reference electrode. The $Cp_2Fe/Cp_2Fe^+$ redox couple was used as a secondary internal reference.

Luminescence quantum yields were measured by the optically dilute method[23] using an aerated aqueous solution of $[Ru(bpy)_3]Cl_2$ ($\Phi_{em}$ = 0.028) or quinine sulfate in 1 N $H_2SO_4$ as the standard solutions.[24] Low-temperature (77 K) glass photophysical measurements were performed with the sample loaded in a quartz tube inside a quartz-walled Dewar flask filled with liquid nitrogen. The

 © 2007 Wiley-VCH Verlag GmbH & Co. KGaA, Weinheim 

excitation source for emission lifetime measurements was the 355 nm output (third harmonic) of a Quanta-Ray Q-switched GCR-150–10 pulsed Nd-YAG laser. Luminescence decay signals from a Hamamatsu R928 photomultiplier tube were converted to potential changes by a 50 Ω load resistor and then recorded with a Tektronix Model TDS 620A digital oscilloscope.

**Synthesis of 4-Methyl-2-phenylpyridine:** To a solution of 4-methylpyridine (5 g, 53.8 mmol) in toluene (70 mL) was added a freshly prepared solution of PhLi in $Et_2O$ (70 mL) [from PhBr (22.6 mL, 215 mmol) and Li metal (2.98 g, 430 mmol)]. After 24 h of stirring, the solution was hydrolysed with water (150 mL), and the compound was extracted with $CH_2Cl_2$ (3 × 200 mL). The organic phase was dried with $MgSO_4$, and $MnO_2$ (56 g, 645 mmol) was added. The solution was stirred for 3 h, filtered and the solvent was evaporated. Chromatography on silica gel using heptane/ethyl acetate (90:10) gave ppy-4-Me as orange crystals. Yield 4.57 g (50%). $^1$H NMR (200 MHz, $CDCl_3$): $\delta$ = 8.55 (d, $^3J$ = 4.8 Hz, 1 H, py$^6$), 7.98 (m, 2 H, Ph *ortho*), 7.55 (d, $^4J$ = 1 Hz, 1 H, py$^3$), 7.43 (m, 3 H, Ph *meta* and *para*), 7.05 (dd, $^3J$ = 4.8 Hz, $^4J$ = 1 Hz, 1 H, py$^5$), 2.41 (s, 3 H, $CH_3$) ppm. $^{13}$C{$^1$H} NMR (75 MHz, $CDCl_3$): $\delta$ = 157.2 (C$^4$-py), 149.4 (C$^6$-py), 147.7 (C$^2$-py), 139.5 (Ph *ipso*), 128.8 (Ph *para*), 128.7 (Ph *meta*), 126.9 (Ph *ortho*), 123.1 (C$^5$-py), 121.1 (C$^3$-py), 21.1 ($CH_3$) ppm. HRMS: calcd. for $C_{12}H_{11}N$ [M]$^+$ 169.0892; found 169.0885.

**Synthesis of Pyridines 1a–1c:** 4-Methyl-2-phenylpyridine (0.5 g, 2.96 mmol), the appropriate aldehyde [4-methoxybenzaldehyde, 4-(diethylamino)benzaldehyde or benzaldehyde (3.5 mmol)] and *t*BuOK (0.4 g, 3.5 mmol) were dissolved in DMF (20 mL). The reaction mixture was refluxed for 3 h, and then $CH_2Cl_2$ (150 mL) was added. The organic phase was washed with water and an aqueous solution of 1 M KOH, and dried with $MgSO_4$. The product was crystallized from a toluene/pentane mixture.

**4-(4-Methoxystyryl)-2-phenylpyridine (1a):** White powder. Yield 0.73 g (86%). $^1$H NMR (500 MHz, $CDCl_3$): $\delta$ = 8.66 (d, $^3J$ = 5 Hz, 1 H, py$^6$), 8.07 (m, 2 H, Ph *ortho*), 7.77 (s, 1 H, py$^3$), 7.53 (m, 4 H, $C_6H_4$ and Ph *meta*), 7.47 (m, 1 H, Ph *para*), 7.31 (m, 2 H, =CH and py$^5$), 6.96 (m, 3 H, =CH and $C_6H_4$), 3.85 (s, 3 H, $OCH_3$) ppm. $^{13}$C{$^1$H} NMR (125 MHz, $CDCl_3$): $\delta$ = 160.2 (C$^1$-$C_6H_4$), 158.0 (C$^2$-py), 150.0 (C$^6$-py), 145.8 (C$^4$-py), 139.6 (Ph *ipso*), 132.6 (=CH), 129.0 (Ph *para*, C$^4$-$C_6H_4$), 128.8 (Ph *meta*), 128.5 (C$^3$-$C_6H_4$), 127.0 (Ph *ortho*), 124.0 (=CH), 119.0 (C$^5$-py), 117.9 (C$^3$-py), 114.3 (C$^2$-$C_6H_4$), 55.4 ($OCH_3$) ppm. HRMS: calcd. for $C_{20}H_{17}NO$ [M]$^+$ 287.1310; found 287.1307. $C_{20}H_{17}NO$ (287.36): calcd. C 83.60, H 5.96, N 4.87, O 5.57; found C 83.22, H 5.85, N 4.87, O 5.76.

**4-[*p*-(Diethylamino)styryl]-2-phenylpyridine (1b):** Yellow powder. Yield 0.93 g (96%). $^1$H NMR (500 MHz, $CD_2Cl_2$): $\delta$ = 8.64 (d, $^3J$ = 5.1 Hz, 1 H, py$^6$), 8.09 (m, 2 H, Ph *ortho*), 7.78 (s, 1 H, py$^3$), 7.54 (m, 2 H, Ph *meta*), 7.48 (m, 3 H, $C_6H_4$ and Ph *para*), 7.33 (d, $^3J$ = 16.2 Hz, 1 H, =CH), 7.30 (d, $^3J$ = 5.1 Hz, 1 H, py$^5$), 6.89 (d, $^3J$ = 16.2 Hz, 1 H, =CH), 6.71 (d, $^3J$ = 8.8 Hz, 2 H, $C_6H_4$), 3.42 (q, $^3J$ = 7.1 Hz, 4 H, $CH_2$), 1.23 (t, $^3J$ = 7.1 Hz, 6 H, $CH_3$) ppm. $^{13}$C{$^1$H} NMR (125 MHz, $CD_2Cl_2$): $\delta$ = 157.5 (C$^2$-py), 149.8 (C$^6$-py), 148.3 (C$^1$-$C_6H_4$), 146.5 (C$^4$-py), 139.8 (Ph *ipso*), 133.4 (=CH), 128.8 (Ph *para*), 128.7 (Ph *meta*, C$^3$-$C_6H_4$), 126.9 (Ph *ortho*), 123.2 (C$^4$-$C_6H_4$), 120.5 (=CH), 118.7 (C$^5$-py), 117.3 (C$^3$-py), 111.5 (C$^2$-$C_6H_4$), 44.4 ($CH_2$), 12.7 ($CH_3$) ppm. HRMS: calcd. for $C_{23}H_{23}N_2$ [M]$^+$ 328.1940; found 328.1941. $C_{23}H_{24}N_2$ (328.46): calcd. C 84.11, H 7.37, N 8.53; found C 84.10, H 7.49, N 8.56.

**2-Phenyl-4-styrylpyridine (1c):** White powder. Yield 0.26 g (34%). $^1$H NMR (300 MHz, $CDCl_3$): $\delta$ = 8.69 (d, $^3J$ = 5 Hz, 1 H, py$^6$), 8.07 (m, 2 H, Ph *ortho*), 7.81 (s, 1 H, py$^3$), 7.60 (m, 2 H, Ph* *ortho*), 7.53 (m, 3 H, Ph *para* and *meta*), 7.49 (m, 3 H, Ph* *para* and *meta*), 7.39 (m, 1 H, =CH), 7.35 (m, 1 H, py$^5$), 7.12 (d, $^3J$ = 16 Hz, 1 H, =CH) ppm. $^{13}$C{$^1$H} NMR (75 MHz, $CDCl_3$): $\delta$ = 158.1 (C$^2$-py), 150.0 (C$^6$-py), 145.4 (C$^4$-py), 139.5 (Ph *ipso*), 136.2 (Ph* *ipso*), 133.1 (=CH), 129.0 (Ph/Ph* *para*), 128.9 (Ph/Ph* *meta*), 128.8 (Ph/Ph* *para* and *meta*), 127.1 (Ph* *ortho*), 127.0 (Ph *ortho*), 126.3 (=CH), 119.2 (C$^5$-py), 118.1 (C$^3$-py) ppm. HRMS: calcd. for $C_{19}H_{15}N$ [M]$^+$ 257.1205; found 257.1214. $C_{19}H_{15}N$ (257.34): calcd. C 88.68, H 5.88, N 5.44; found C 88.86, H 5.98, N 5.29.

**Synthesis of 2-Phenyl-4-[(trimethylsilyl)methyl]pyridine:** Lithium diisopropylamine, freshly prepared from diisopropylamine (6.9 mL, 47 mmol) and *n*BuLi (1.6 M in hexane, 29.6 mL, 47.3 mmol), in THF (50 mL) at –80 °C was added to a solution of 4-methyl-2-phenylpyridine (2.05 g, 12.3 mmol) in THF (15 mL) at –80 °C. The reaction mixture was stirred at –80 °C for 0.5 h and then at –10 °C for an additional 0.5 h. At –80 °C, TMSCl (1.53 mL, 17.8 mmol) was added. The reaction was quenched after 2 min of stirring by the addition of absolute ethanol (20 mL), followed by a saturated aqueous solution of $NaHCO_3$ (20 mL). Ethyl acetate (100 mL) was added, and the organic phase was washed with water (100 mL) and a saturated aqueous solution of NaCl (100 mL). The organic phase was dried with $MgSO_4$, and the solvent was evaporated to give an orange oil. Yield 2.78 g (98%). $^1$H NMR (200 MHz, [D$_6$]acetone): $\delta$ = 8.47 (d, $^3J$ = 5 Hz, 1 H, py$^6$), 8.12 (m, 2 H, Ph *ortho*), 7.62 (s, 1 H, py$^3$), 7.47 (m, 3 H, Ph *meta* and *para*), 7.01 (d, $^3J$ = 5 Hz, 1 H, py$^5$), 2.29 (s, 2 H, $CH_2$), 0.07 (s, 9 H, $SiMe_3$) ppm. $^{13}$C{$^1$H} NMR (75 MHz, [D$_6$]acetone): $\delta$ = 156.4 (C$^2$-py), 150.9 (C$^4$-py), 149.2 (C$^6$-py), 139.7 (Ph *ipso*), 128.7 (Ph *para*), 128.5 (Ph *meta*), 126.7 (Ph *ortho*), 122.2 (py), 119.7 (py), 26.7 ($CH_2$), –2.7 ($SiMe_3$) ppm. HRMS: calcd. for $C_{15}H_{19}NSi$ [M]$^+$ 241.1313; found 241.1287.

**Synthesis of 4-(Bromomethyl)-2-phenylpyridine:** 2-Phenyl-4-[(trimethylsilyl)methyl]pyridine (0.66 g, 2.73 mmol) was dissolved in DMF (15 mL), and 1,2-dibromotetrafluoroethane (2.84 g, 10.9 mmol) and cesium fluoride (1.66 g, 10.9 mmol) were added. The reaction mixture was stirred at room temp. for 2 h. Ethyl acetate (50 mL) was added, and the organic phase was washed with water (3 × 50 mL). The organic phase was dried with $MgSO_4$, and the solvent was evaporated. The product was purified by column chromatography over silica [heptane/ethyl acetate (80:20)] to give a brown oil. Yield 0.55 g (81%). $^1$H NMR (200 MHz, $CDCl_3$): $\delta$ = 8.68 (d, $^3J$ = 5 Hz, 1 H, py$^6$), 8.02 (m, 2 H, Ph *ortho*), 7.74 (s, 1 H, py$^3$), 7.50 (m, 3 H, Ph *meta* and *para*), 7.25 (d, $^3J$ = 5 Hz, 1 H, py$^5$), 4.45 (s, 2 H, $CH_2$) ppm. $^{13}$C{$^1$H} NMR (50 MHz, $CDCl_3$): $\delta$ = 158.5 (C$^2$-py), 150.6 (C$^6$-py), 147.3 (Ph *ipso*), 139.3 (C$^4$-py), 129.7 (Ph *para*), 129.3 (Ph *ortho*), 127.4 (Ph *meta*), 122.4 (C$^3$-py), 120.8 (C$^5$-py), 31.4 ($CH_2$) ppm.

**Synthesis of 4-[(Diethoxyphosphoryl)methyl]-2-phenylpyridine:** To a solution of 4-(bromomethyl)-2-phenylpyridine (1.85 g, 7.46 mmol) in $CHCl_3$ (10 mL) was added triethylphosphite (10.2 mL, 9.89 g, 59.6 mmol). The reaction mixture was refluxed for 3 h. The solvent was evaporated, and the residue was washed with pentane and then dried under vacuum to give a black oil. Yield 1 g (45%). $^1$H NMR (200 MHz, $CDCl_3$): $\delta$ = 8.66 (d, $^3J_{H-H}$ = 5 Hz, 1 H, py$^6$), 8.01 (m, 2 H, Ph *ortho*), 7.76 (s, 1 H, py$^3$), 7.47 (m, 3 H, Ph *meta* and *para*), 7.21 (m, 1 H, py$^5$), 4.09 (dq, $^3J_{H-P}$ = $^3J_{H-H}$ = 7 Hz, 4 H, Et), 3.21 (d, $^2J_{H-P}$ = 22 Hz, 2 H, $CH_2P$), 1.29 (t, $^3J_{H-H}$ = 7 Hz, 6 H, Et) ppm. $^{13}$C{$^1$H} NMR (75 MHz, $CDCl_3$): $\delta$ = 157.6 (C$^6$-py), 149.7 (d, $^4J_{C-P}$ = 2.6 Hz, C$^2$-py), 141.9 (d, $^2J_{C-P}$ = 8.5 Hz, C$^4$-py), 139.1 (Ph *ipso*), 129.1 (Ph *para*), 128.7 (Ph *meta*), 127.0 (Ph *ortho*), 123.4 (d, $^3J_{C-P}$ = 6 Hz, C$^3$-py), 121.9 (d, $^3J_{C-P}$ = 6.3 Hz, C$^5$-py), 62.4 (d, $^1J_{C-P}$ = 6.8 Hz, $CH_2$), 33.7 (d, $^2J_{C-P}$ = 137.3 Hz, OEt), 16.4 (d, $^3J_{C-P}$ = 6 Hz, OEt) ppm. $^{31}$P{$^1$H} NMR (81 MHz, $CDCl_3$): $\delta$ = 25.7 [P(O)(OEt)$_2$] ppm.

 © 2007 Wiley-VCH Verlag GmbH & Co. KGaA, Weinheim 

**Synthesis of 4-(4-Nitrostyryl)-2-phenylpyridine (1d):** To a solution of 4-[(diethoxyphosphoryl)methyl]-2-phenylpyridine (0.71 g, 2.33 mmol) and *p*-nitrobenzaldehyde (0.52 g, 3.45 mmol) in THF (20 mL) was added *t*BuOK (0.65 g, 5.8 mmol). The reaction mixture was stirred for 2 h and then hydrolysed with water (20 mL). THF was removed under reduced pressure, and the residue was extracted with $CH_2Cl_2$ (3 × 50 mL). The organic phase was dried with $MgSO_4$. The solvent was evaporated, and chromatography on silica gel with heptane/ethyl acetate (80:20) afforded **1d** as a yellow powder. Yield 0.640 g (91%). $^1$H NMR (500 MHz, $CDCl_3$): $\delta$ = 8.74 (d, $^3J$ = 5 Hz, 1 H, py$^6$), 8.29 (d, $^3J$ = 8.7 Hz, 2 H, $C_6H_4$), 8.06 (m, 2 H, Ph *ortho*), 7.84 (s, 1 H, py$^3$), 7.73 (d, $^3J$ = 8.7 Hz, 2 H, $C_6H_4$), 7.53 (m, 2 H, Ph *meta*), 7.48 (m, 1 H, Ph *para*), 7.42 (d, $^3J$ = 16 Hz, 1 H, =CH), 7.39 (dd, $^3J$ = 5 Hz, $^4J$ = 1 Hz, 1 H, py$^5$), 7.28 (d, 1 H, =CH) ppm. $^{13}$C{$^1$H} NMR (125 MHz, $CDCl_3$): $\delta$ = 158.4 (C$^2$-py), 150.3 (C$^6$-py), 147.5 (C$^1$-$C_6H_4$), 144.2 (C$^4$-py), 142.6 (C$^4$-$C_6H_4$), 139.2 (Ph *ipso*), 130.8 (=CH), 130.6 (=CH), 129.3 (Ph *para*), 128.9 (Ph *meta*), 127.5 (C$^3$-$C_6H_4$), 127.0 (Ph *ortho*), 124.3 (C$^2$-$C_6H_4$), 119.4 (C$^5$-py), 118.3 (C$^3$-py) ppm. HRMS: calcd. for $C_{19}H_{14}N_2O_2$ [M]$^+$ 302.1055; found 302.1059. $C_{19}H_{14}N_2O_2$ (302.33): calcd. C 75.48, H 4.67, N 9.27; found C 75.03, H 4.62, N 9.07.

**Syntheses of Chloro-Bridged Dimers [Ir(*C*^*N*-ppy-4-CH=CHC$_6$H$_4$R)$_2$]$_2$(μ-Cl)$_2$ (3):** A Schlenk flask was charged with $IrCl_3 \cdot 3H_2O$ (0.289 g, 0.82 mmol), the appropriate ligand H*C*^*N* (3.5 equiv.) and a mixture of 2-ethoxyethanol/water, (75:25, 10 mL). The mixture was refluxed for 24 h. The precipitate was then washed with water, ethanol and acetone.

**[Ir(*C*^*N*-ppy-4-CH=CHC$_6$H$_4$OMe)$_2$]$_2$(μ-Cl)$_2$ (3a):** Yield 0.62 g (95%). $^1$H NMR (500 MHz, $CD_2Cl_2$): $\delta$ = 9.15 (d, $^3J$ = 5.9 Hz, 4 H, py$^6$), 7.94 (s, 4 H, py$^3$), 7.62 (d, $^3J$ = 7.5 Hz, 8 H, $C_6H_4$), 7.39 (m, 8 H, =CH and Ph), 7.12 (d, $^3J$ = 16 Hz, 4 H, =CH), 6.93 (d, 4 H, py$^5$), 6.82 (m, 12 H, $C_6H_4$ and Ph), 6.32 (t, $^3J$ = 6.8 Hz, 4 H, Ph), 6.02 (d, $^3J$ = 8.0 Hz, 4 H, Ph), 3.85 (s, 12 H, $OCH_3$) ppm. HRMS: calcd. for $C_{80}H_{62}Cl_2{}^{193}Ir_2N_4O_4$ [M – Cl]$^+$ 1565.3876; found 1565.3893.

**[Ir(*C*^*N*-ppy-4-CH=CHC$_6$H$_4$NEt$_2$)$_2$]$_2$(μ-Cl)$_2$ (3b):** Yield 0.68 g (94%). $^1$H NMR (500 MHz, $CDCl_3$): $\delta$ = 9.10 (d, $^3J$ = 6 Hz, 4 H, py$^6$), 7.88 (s, 4 H, py$^3$), 7.58 (d, 4 H, py$^5$), 7.44 (d, $^3J$ = 8.6 Hz, 8 H, $C_6H_4$), 7.38 (d, $^3J$ = 16 Hz, 4 H, =CH), 7.02 (d, $^3J$ = 16 Hz, 4 H, =CH), 6.86 (d, 4 H, Ph), 6.77 (t, $^3J$ = 7.0 Hz, 4 H, Ph), 6.68 (d, $^3J$ = 8.6 Hz, 8 H, $C_6H_4$), 6.60 (t, 4 H, Ph), 6.14 (d, $^3J$ = 7.0 Hz, 4 H, Ph), 3.48 (q, $^3J$ = 6.8 Hz, 16 H, $CH_2$), 1.27 (t, $^3J$ = 6.8 Hz, 24 H, $CH_3$) ppm. HRMS: calcd. for $C_{92}H_{92}Cl^{193}Ir_2N_8$ [M – Cl]$^+$ 1729.6396; found 1729.6435.

**[Ir(*C*^*N*-ppy-4-CH=CHC$_6$H$_5$)$_2$]$_2$(μ-Cl)$_2$ (3c):** Yield 0.54 g (89%). $^1$H NMR (500 MHz, $CD_2Cl_2$): $\delta$ = 9.25 (d, $^3J$ = 6 Hz, 4 H, py$^6$), 8.06 (s, 4 H, py$^3$), 7.71 (d, $^3J$ = 7.5 Hz, 4 H, Ph), 7.54 (m, 12 H, =CH and Ph *ortho*), 7.36 (m, $^3J$ = 16 Hz, 16 H, =CH and Ph *meta* and Ph *para*), 7.02 (d, $^3J$ = 6 Hz, 4 H, py$^5$), 6.90 (t, $^3J$ = 7.5 Hz, 4 H, Ph), 6.69 (t, $^3J$ = 6.8 Hz, 4 H, Ph), 6.09 (d, $^3J$ = 8.0 Hz, 4 H, Ph) ppm. HRMS: calcd. for $C_{76}H_{56}Cl_2{}^{193}Ir_2N_4$ [M]$^+$ 1480.3130; found 1480.3135.

**[Ir(*C*^*N*-ppy-4-CH=CHC$_6$H$_4$NO$_2$)$_2$]$_2$(μ-Cl)$_2$ (3d):** Cleavage with DMSO to form [Ir(*C*^*N*-ppy-4-CH=CHC$_6$H$_4$NO$_2$)(DMSO)(Cl)] (**3d**-DMSO). Quantitative spectroscopic yield. $^1$H NMR (300 MHz, [D$_6$]DMSO): $\delta$ = 9.82 (d, $^3J$ = 6.2 Hz, 1 H, py$^6$), 9.50 (d, $^3J$ = 6.2 Hz, 1 H, py$^6$), 8.54 (s, 1 H, py$^3$), 8.44 (s, 1 H, py$^3$), 8.35 (d, $^3J$ = 7.8 Hz, 2 H, $C_6H_4$), 8.08–7.68 (m, 12 H, $C_6H_4$, =CH, py$^5$, Ph$^3$), 6.95 (t, $^3J$ = 7.2 Hz, 1 H, Ph), 6.89 (t, $^3J$ = 7.4 Hz, 1 H, Ph), 6.78 (t, $^3J$ = 7.6 Hz, 1 H, Ph), 6.74 (t, $^3J$ = 7.2 Hz, 1 H, Ph), 6.34 (d, $^3J$ = 7.7 Hz, 1 H, Ph$^6$), 5.79 (d, $^3J$ = 7.6 Hz, 1 H, Ph$^6$) ppm.

**[Ir(*C*^*N*(ppy-4-Me)$_2$]$_2$(μ-Cl)$_2$ (3e):** Yield 0.45 g (96%). $^1$H NMR (300 MHz, $CD_2Cl_2$): $\delta$ = 9.10 (d, $^3J$ = 6 Hz, 4 H, py$^6$), 7.79 (br. s, 4 H, py$^3$), 7.57 (dd, $^3J$ = 7.8 Hz, $^4J$ = 1.3 Hz, 4 H, Ph$^3$), 6.83 (td, $^3J$ = 7.4 Hz, $^4J$ = 1.2 Hz, 4 H, Ph$^4$), 6.68 (dd, $^3J$ = 6 Hz, $^4J$ = 1.2 Hz, 4 H, py$^5$), 6.62 (td, $^3J$ = 7.6 Hz, $^4J$ = 1.4 Hz, 4 H, Ph$^5$), 5.93 (td, $^3J$ = 7.8 Hz, $^4J$ = 1.1 Hz, 4 H, Ph$^6$), 2.70 (s, 12 H, $CH_3$) ppm. HRMS: calcd. for $C_{48}H_{38}Cl_2{}^{193}Ir_2N_4$ [M – Cl]$^+$ 1092.2200; found 1093.2206.

**Syntheses of Bis-Cyclometallated Complexes Ir(*C*^*N*)$_2$(*O*^*O*) 4 and 5:** In a Schlenk tube, to a 2-ethoxyethanol solution (10 mL) were added the chloro-bridged iridium dimer (0.057 mmol), 1,3-diketone (acetylacetone or dipyvaloylmethane) (0.14 mmol) and $Na_2CO_3$ (60 mg, 0.57 mmol). The reaction mixture was heated for 15 h. When the reaction mixture was heated at 140 °C, the hydrogenated compounds **4a**-$H_2$ and **1a**-$H_2$ were isolated, whereas at 80 °C the pure styryl derivatives **4**,**5** were obtained. After addition of water (20 mL), the precipitate was filtered and washed with water and diethyl ether. The products were then isolated as powders after crystallization from a mixture of $CH_2Cl_2$/$Et_2O$.

**Ir(*C*^*N*-ppy-4-CH$_2$CH$_2$C$_6$H$_4$OMe)$_2$(acac) (4a-H$_2$):** Yellow powder. Yield 0.045 g (46%). $^1$H NMR (300 MHz, $CD_2Cl_2$): $\delta$ = 8.36 (d, $^3J$ = 5.7 Hz, 2 H, py$^6$), 7.70 (s, 2 H, py$^3$), 7.56 (d, $^3J$ = 7.5 Hz, 2 H, Ph$^3$), 7.19 (d, $^3J$ = 8.2 Hz, 4 H, $C_6H_4$), 7.01 (d, $^3J$ = 6.0 Hz, 2 H, py$^5$), 6.88 (m, 6 H, $C_6H_4$ and Ph$^4$), 6.73 (t, $^3J$ = 7.5 Hz, 2 H, Ph$^5$), 6.24 (d, $^3J$ = 7.5 Hz, 2 H, Ph$^6$), 5.31 (s, 1 H, CH), 3.82 (s, 6 H, $OCH_3$), 3.14 (m, 4 H, $CH_2$), 3.07 (m, 4 H, $CH_2$), 1.83 (s, 6 H, $CH_3$) ppm. $^{13}$C{$^1$H} NMR (75 MHz, $CD_2Cl_2$): $\delta$ = 184.5 (CO), 167.6 (C$^2$-py), 158.2 (C$^1$-$C_6H_4$), 152.3 (C$^4$-py), 147.6 (C$^6$-py), 147.4 (C$^1$-Ph), 145.3 (C$^2$-Ph), 133.1 (C$^6$-Ph), 132.6 (C$^4$-$C_6H_4$), 129.4 (C$^3$-$C_6H_4$), 128.5 (C$^5$-Ph), 123.5 (C$^3$-Ph), 122.3 (C$^5$-py), 120.6 (C$^4$-Ph), 118.6 (C$^3$-py), 113.9 (C$^2$-$C_6H_4$), 100.2 (CH), 55.2 ($OCH_3$), 37.5 ($CH_2$), 35.7 ($CH_2$), 28.3 ($CH_3$) ppm. HRMS: calcd. for $C_{45}H_{43}{}^{193}IrN_2O_4Na$ [M + Na]$^+$ 891.2750; found 891.2770. $C_{45}H_{43}IrN_2O_4 \cdot 0.5H_2O$ (888.08): calcd. C 61.62, H 5.06, N 3.19; found C 61.59, H 4.85, N 3.13.

**ppy-4-CH$_2$CH$_2$C$_6$H$_4$OMe (1a-H$_2$):** Evaporation of the diethyl ether solution gave a yellow oil identified as **1a**-$H_2$. $^1$H NMR (300 MHz, $CD_2Cl_2$): $\delta$ = 8.57 (d, $^3J$ = 4.9 Hz, 1 H, py$^6$), 8.02 (m, 2 H, Ph *ortho*), 7.57 (s, 1 H, py$^3$), 7.47 (m, 3 H, Ph *para* and *meta*), 7.15 (d, $^3J$ = 8.5 Hz, 2 H, $C_6H_4$), 7.09 (d, $^3J$ = 4.9 Hz, 1 H, py$^5$), 6.87 (d, $^3J$ = 8.5 Hz, 2 H, $C_6H_4$), 3.81 (s, 3 H, $OCH_3$), 2.98 (m, 4 H, $CH_2$) ppm. HRMS: calcd. for $C_{19}H_{19}NO$ [M]$^+$ 289.1467; found 289.1455.

**Ir(*C*^*N*-ppy-4-CH=CHC$_6$H$_4$OMe)$_2$(acac) (4a):** Red powder. Yield 0.092 g (93%). $^1$H NMR (300 MHz, $CD_2Cl_2$): $\delta$ = 8.45 (d, $^3J$ = 6.0 Hz, 2 H, py$^6$), 7.96 (d, $^4J$ = 1.7 Hz, 2 H, py$^3$), 7.68 (dd, $^3J$ = 7.7 Hz, $^4J$ = 1.1 Hz, 2 H, Ph$^3$), 7.63 (d, $^3J$ = 8.7 Hz, 4 H, $C_6H_4$), 7.49 (d, $^3J$ = 16.3 Hz, 2 H, =CH), 7.34 (dd, $^3J$ = 6 Hz, $^4J$ = 1.7 Hz, 2 H, py$^5$), 7.14 (d, $^3J$ = 16.3 Hz, 2 H, =CH), 7.01 (d, $^3J$ = 8.7 Hz, 4 H, $C_6H_4$), 6.91 (td, $^3J$ = 7.7 Hz, $^4J$ = 1.1 Hz, 2 H, Ph$^4$), 6.74 (td, $^3J$ = 7.7 Hz, $^4J$ = 1.1 Hz, 2 H, Ph$^5$), 6.35 (dd, $^3J$ = 7.7 Hz, $^4J$ = 1.1 Hz, 2 H, Ph$^6$), 5.34 (s, 1 H, CH), 3.90 (s, 6 H, $OCH_3$), 1.86 (s, 6 H, $CH_3$) ppm. $^{13}$C{$^1$H} NMR (75 MHz, $CD_2Cl_2$): $\delta$ = 184.7 (CO), 167.9 (C$^2$-py), 160.6 (C$^1$-$C_6H_4$), 147.8 (C$^6$-py), 147.5 (C$^1$-Ph), 146.3 (C$^4$-py), 145.2 (C$^2$-Ph), 134.1 (=CH), 133.3 (C$^6$-Ph), 128.7 (C$^4$-$C_6H_4$, C$^3$-$C_6H_4$, C$^5$-Ph), 123.6 (C$^3$-Ph), 122.8 (=CH), 120.7 (C$^4$-Ph), 118.5 (C$^5$-py), 115.4 (C$^3$-py), 114.3 (C$^2$-$C_6H_4$), 100.3 (CH), 55.4 ($OCH_3$), 28.3 ($CH_3$) ppm. HRMS: calcd. for $C_{45}H_{39}{}^{193}IrN_2O_4$ [M]$^+$ 864.2539; found 864.2528. In $CD_2Cl_2$ solution, partial isomerization of the C=C double bond occurs, and the $^1$H NMR spectrum exhibits three isomers (*E*/*E*, *E*/*Z*, *Z*/*Z*); some signals are clearly resolved. $^1$H NMR (300 MHz, $CD_2Cl_2$): $\delta$ = 8.45 (d, $^3J$ = 6.0 Hz, py$^6$, *E*/*E*), 8.43 (d, py$^6$, *E*/*Z*), 8.34 (d, py$^6$, *E*/*Z*), 8.33 (d,

 © 2007 Wiley-VCH Verlag GmbH & Co. KGaA, Weinheim 

py[6], *Z*/*Z*), 7.96 (s, py[3], *E*/*E* and *E*/*Z*), 7.80 (d, py[3], *E*/*Z* and *Z*/*Z*), 7.49 (d, $^3J$ = 16.3 Hz, =CH, *E*/*E* and *E*/*Z*), 7.34 (m, py[5], *E*/*E* and *E*/*Z*), 7.14 (d, $^3J$ = 16.2 Hz, 2 H, =CH, *E*/*E*), 7.13 (d, $^3J$ = 16.2 Hz, =CH, *E*/*Z*), 7.07 (m, py[5], *E*/*Z*), 6.89 (m, =CH, *E*/*Z* and *Z*/*Z*), 6.65 (d, $^3J$ = 12.2 Hz, =CH, *E*/*Z* and *Z*/*Z*), 5.34 (s, 1 H, CH-acac), 3.90 (s, 6 H, $OCH_3$, *E*/*E* and *E*/*Z*), 3.84 (s, 6 H, $OCH_3$, *E*/*Z* and *Z*/*Z*), 1.87 (s, 3 H, $CH_3$, *E*/*Z*), 1.86 (s, 3 H, $CH_3$, *E*/*Z* and *E*/*E*), 1.82 (s, 6 H, $CH_3$, *Z*/*Z*) ppm.

**Ir(*C*^*N*-ppy-4-CH=CHC$_6$H$_4$OMe)$_2$(dpm) (5a):** Red powder. Yield 0.1 g (93%). $^1$H NMR (300 MHz, $CD_2Cl_2$): $\delta$ = 8.35 (d, $^3J$ = 6.1 Hz, 2 H, py[6]), 7.94 (d, $^4J$ = 1.7 Hz, 2 H, py[3]), 7.69 (d, $^3J$ = 7.4 Hz, 2 H, Ph[3]), 7.61 (d, $^3J$ = 8.8 Hz, 4 H, $C_6H_4$), 7.47 (d, $^3J$ = 16 Hz, 2 H, =CH), 7.27 (dd, $^3J$ = 6.1 Hz, $^4J$ = 1.7 Hz, 2 H, py[5]), 7.12 (d, $^3J$ = 16 Hz, 2 H, =CH), 7.00 (d, $^3J$ = 8.8 Hz, 4 H, $C_6H_4$), 6.89 (td, $^3J$ = 7.4 Hz, $^4J$ = 1.0 Hz, 2 H, Ph[4]), 6.72 (td, $^3J$ = 7.4 Hz, $^4J$ = 1 Hz, 2 H, Ph[5]), 6.41 (dd, $^3J$ = 7.4 Hz, $^4J$ = 1 Hz, 2 H, Ph[6]), 5.60 (s, 1 H, CH-dpm), 3.89 (s, 6 H, $OCH_3$), 0.98 (s, 18 H, *t*Bu) ppm. $^{13}C\{^1H\}$ NMR (75 MHz, $CD_2Cl_2$): $\delta$ = 194.5 (CO), 168.2 (C[2]-py), 160.5 (C[1]-$C_6H_4$), 149.2 (C[1]-Ph), 147.9 (C[6]-py), 145.9 (C[4]-py), 145.1 (C[2]-Ph), 133.8 (=CH), 133.5 (C[6]-Ph), 128.8 (C[4]-$C_6H_4$), 128.6 (C[3]-$C_6H_4$), 128.4 (C[5]-Ph), 123.4 (C[3]-Ph), 123.0 (=CH), 120.2 (C[4]-Ph), 118.1 (C[5]-py), 115.0 (C[3]-py), 114.3 (C[2]-$C_6H_4$), 90.1 (CH), 55.3 ($OCH_3$), 41.0 (*t*Bu), 27.9 ($CH_3$) ppm. HRMS: calcd. for $C_{51}H_{51}{}^{193}IrN_2O_4$ $[M]^+$ 948.3478; found 948.3474. $C_{51}H_{51}IrN_2O_4{\cdot}2H_2O$ (968.23): calcd. C 62.24, H 5.63, N 2.85; found C 62.30, H 5.39, N 2.99.

**Ir(*C*^*N*-ppy-4-CH=CHC$_6$H$_4$NEt$_2$)$_2$(acac) (4b):** Orange powder. Yield 0.1 g (93%). $^1$H NMR (500 MHz, $CD_2Cl_2$): $\delta$ = 8.40 (d, $^3J$ = 6 Hz, 2 H, py[6]), 7.92 (s, 2 H, py[3]), 7.67 (d, $^3J$ = 7.5 Hz, 2 H, Ph[3]), 7.53 (d, $^3J$ = 8.6 Hz, 4 H, $C_6H_4$), 7.44 (d, $^3J$ = 16 Hz, 2 H, =CH), 7.31 (d, $^3J$ = 6 Hz, 2 H, py[5]), 7.01 (d, $^3J$ = 16 Hz, 2 H, =CH), 6.90 (t, $^3J$ = 7.5 Hz, 2 H, Ph[4]), 6.74 (m, 6 H, Ph[5], $C_6H_4$), 6.36 (d, $^3J$ = 7.5 Hz, 2 H, Ph[6]), 5.33 (s, 1 H, CH), 3.47 (q, $^3J$ = 6.8 Hz, 8 H, $CH_2$), 1.86 (s, 6 H, $CH_3$), 1.25 (t, $^3J$ = 6.8 Hz, 12 H, $NEt_2$) ppm. $^{13}C\{^1H\}$ NMR (125 MHz, $CD_2Cl_2$): $\delta$ = 184.5 (CO), 167.7 (C[2]-py), 151.0 (C[2]-Ph), 148.6 (C[1]-$C_6H_4$), 147.6 (C[6]-py), 147.4 (C[1]-Ph), 146.9 (C[4]-py), 134.9 (=CH), 133.5 (C[6]-Ph), 128.9 (C[3]-$C_6H_4$), 128.5 (C[5]-Ph), 123.4 (C[3]-Ph), 122.9 (C[4]-$C_6H_4$), 120.6 (C[4]-Ph), 119.3 (=CH), 118.1 (C[5]-py), 114.9 (C[3]-py), 111.4 (C[2]-$C_6H_4$), 100.3 (CH), 44.4 ($CH_2$), 28.3 ($CH_3$), 12.4 ($NEt_2$) ppm. HRMS: calcd. for $C_{51}H_{53}{}^{193}IrN_4O_2$ $[M]^+$ 946.3802; found 946.3814. $C_{51}H_{53}{}^{193}IrN_4O_2{\cdot}H_2O$ (964.24): calcd. C 63.52, H 5.75, N 5.81; found C 63.74, H 5.30, N 6.17.

**Ir(*C*^*N*-ppy-4-CH=CHC$_6$H$_4$NEt$_2$)$_2$(dpm) (5b):** Red powder. Yield 0.096 g (82%). $^1$H NMR (300 MHz, $CD_2Cl_2$): $\delta$ = 8.27 (d, $^3J$ = 6 Hz, 2 H, py[6]), 7.90 (s, 2 H, py[3]), 7.67 (d, $^3J$ = 7.5 Hz, 2 H, Ph[3]), 7.51 (d, $^3J$ = 8.5 Hz, 4 H, $C_6H_4$), 7.42 (d, $^3J$ = 16 Hz, 2 H, =CH), 7.23 (d, $^3J$ = 6 Hz, 2 H, py[5]), 6.98 (d, $^3J$ = 16 Hz, 2 H, =CH), 6.89 (t, $^3J$ = 7.3 Hz, 2 H, Ph[4]), 6.74 (d, $^3J$ = 8.5 Hz, 4 H, $C_6H_4$), 6.69 (t, $^3J$ = 7.3 Hz, 2 H, Ph[5]), 6.42 (d, $^3J$ = 7.3 Hz, 2 H, Ph[6]), 5.60 (s, 1 H, CH), 3.48 (q, $^3J$ = 7 Hz, 8 H, $CH_2$), 1.19 (t, $^3J$ = 7 Hz, 12 H, $CH_3$), 0.98 (s, 18 H, *t*Bu) ppm. $^{13}C\{^1H\}$ NMR (75 MHz, $CD_2Cl_2$): $\delta$ = 194.4 (CO), 167.9 (C[2]-py), 149.1 (C[1]-Ph), 148.6 (C[1]-$C_6H_4$), 147.7 (C[6]-py), 146.5 (C[4]-py), 145.3 (C[2]-Ph), 134.6 (=CH), 133.5 (C[6]-Ph), 128.8 (C[3]-$C_6H_4$), 128.2 (C[5]-Ph), 123.3 (C[3]-Ph), 122.9 (C[4]-$C_6H_4$), 120.1 (C[4]-Ph), 119.5 (=CH), 117.1 (C[5]-py), 114.6 (C[3]-py), 111.4 (C[2]-$C_6H_4$), 90.0 (CH), 44.4 ($CH_2$), 41.0 (*t*Bu), 27.9 ($CH_3$), 12.4 ($NEt_2$) ppm. HRMS: calcd. for $C_{57}H_{65}{}^{193}IrN_2O_4$ $[M]^+$ 1030.4742; found 1030.4736.

**Ir(*C*^*N*-ppy-4-CH=CHC$_6$H$_5$)$_2$(acac) (4c):** Red powder. Yield 0.082 g (90%). $^1$H NMR (300 MHz, $CD_2Cl_2$): $\delta$ = 8.48 (d, $^3J$ = 6 Hz, 2 H, py[6]), 7.99 (s, 2 H, py[3]), 7.68 (m, 6 H, Ph *ortho* and Ph[3]), 7.53 (d, $^3J$ = 16.4 Hz, 2 H, =CH), 7.45 (m, 6 H, Ph *meta* and *para*), 7.37 (dd, $^3J$ = 6 Hz, $^4J$ = 1.7 Hz, 2 H, py[5]), 7.28 (d, $^3J$ = 16.4 Hz, 2 H, =CH), 6.91 (t, $^3J$ = 7.6 Hz, 2 H, Ph[4]), 6.74 (t, $^3J$ = 7.6 Hz, 2 H, Ph[5]), 6.35 (d, $^3J$ = 7.6 Hz, 2 H, Ph[6]), 5.34 (s, 1 H, CH), 1.86 (s, 6 H, $CH_3$) ppm. $^{13}C\{^1H\}$ NMR (75 MHz, $CD_2Cl_2$): $\delta$ = 184.8 (CO), 168.1, 147.9, 147.5, 145.9, 145.1, 136.0, 134.5, 133.3, 133.1, 129.1 (Ph), 128.8 (Ph), 127.3 (Ph), 125.2 (Ph), 123.7, 120.8, 118.8 (py), 115.7 (py), 100.4 (CH), 28.3 ($CH_3$) ppm. HRMS: calcd. for $C_{43}H_{35}{}^{193}IrN_2O_2$ $[M + H]^+$ 804.23280; found 804.2326. $C_{43}H_{35}IrN_2O_2{\cdot}2H_2O$ (840.01): calcd. C 61.48, H 4.68, N 3.33; found C 61.59, H 4.46, N 3.33.

Table 6. Crystallographic data and refinement for **1a**, **1b** and **1d**.

| Compound | **1a** | **1b** | **1d** |
|---|---|---|---|
| Empirical formula | $C_{20}H_{17}NO$ | $C_{23}H_{24}N_2$ | $C_{20}H_{14}N_2O_2$ |
| Formula mass | 287.34 | 656.88 | 314.33 |
| Crystal system | monoclinic | monoclinic | monoclinic |
| Space group | $P2_1$ | $P2_1/n$ | $P2_1$ |
| *a*/Å | 6.0688(2) | 9.9420(10) | 5.8871(2) |
| *b*/Å | 7.5638(3) | 11.888(2) | 16.4674(6) |
| *c*/Å | 32.5570(10) | 33.025(6) | 7.4517(3) |
| $\beta$/° | 94.183(2) | 92.96(5) | 94.816(3) |
| *V*/Å$^3$ | 1490.49(9) | 4936.1(1) | 719.86(5) |
| *Z* | 2 | 4 | 2 |
| $D_{calcd.}$/g cm$^{-3}$ | 1.281 | 1.119 | 1.450 |
| *F*(000) | 608 | 2196 | 328 |
| $\lambda$(Mo-$K_\alpha$)/Å | 0.71069 | 0.71073 | 0.71069 |
| $\theta$ range/° | 2.76–27.38 | 2.48–27.50 | 2.47–27.47 |
| Data collected (*h*,*k*,*l*) | 0/7, 0/9, ±42 | ±9, ±10, ±30 | 0/7, 0/21, ±9 |
| No. of reflections collected | 3557 | 11257 | 1712 |
| No. of unique reflections | 3557 | 11257 | 1712 |
| No. of observed reflections [$I > 2\sigma(I)$] | 2898 | 9931 | 1602 |
| No. of parameters | 397 | 596 | 209 |
| Goodness-of-fit on $F^2$ | 1.039 | 1.023 | 1.069 |
| R (all data) | 0.0949, 0.2091 | 0.0697, 0.1565 | 0.0451, 0.1143 |
| Final *R*, $R_w$ | 0.0743, 0.1887 | 0.044, 0.112 | 0.0417, 0.1114 |
| $\Delta\rho_{max.,min.}$/e Å$^{-3}$ | 0.840, –0.259 | 2.4, –1.126 | 0.268, –0.255 |

 © 2007 Wiley-VCH Verlag GmbH & Co. KGaA, Weinheim 

**Ir($C^{\wedge}N$-ppy-4-CH=CHC$_6$H$_4$NO$_2$)$_2$(acac) (4d):** Red powder. Yield 0.092 g (90%). $^1$H NMR (300 MHz, $CD_2Cl_2$): $\delta$ = 8.54 (d, $^3J$ = 6 Hz, 2 H, py$^6$), 8.32 (d, $^3J$ = 8.7 Hz, 4 H, $C_6H_4$), 8.03 (s, 2 H, py$^3$), 7.83 (d, $^3J$ = 8.7 Hz, 4 H, $C_6H_4$), 7.71 (d, $^3J$ = 7.3 Hz, 2 H, Ph$^3$), 7.57 (d, $^3J$ = 16 Hz, 2 H, =CH), 7.43 (d, $^3J$ = 16 Hz, 2 H, =CH), 7.40 (m, 2 H, py$^5$), 6.93 (t, $^3J$ = 6.5 Hz, 2 H, Ph$^4$), 6.72 (t, $^3J$ = 6.5 Hz, 2 H, Ph$^5$), 6.41 (d, $^3J$ = 6.5 Hz, 2 H, Ph$^6$), 5.35 (s, 1 H, CH), 1.87 (s, 6 H, $CH_3$) ppm. HRMS: calcd. for $C_{43}H_{34}{}^{193}IrN_4O_6$ [M + H]$^+$ 895.2108; found 895.2118.

**Ir($C^{\wedge}N$-ppy-4-Me)$_2$(acac) (4e):** Yellow powder. Yield 0.07 g (98%). $^1$H NMR (300 MHz, $CD_2Cl_2$): $\delta$ = 8.36 (d, $^3J$ = 5.9 Hz, 2 H, py$^6$), 7.74 (br. s, 2 H, py$^3$), 7.59 (dd, $^3J$ = 7.5 Hz, $^4J$ = 1.1 Hz, 2 H, Ph$^3$), 7.07 (dd, $^3J$ = 5.9 Hz, $^4J$ = 1.2 Hz, 2 H, py$^5$), 6.87 (td, $^3J$ = 7.5 Hz, $^4J$ = 0.9 Hz, 2 H, Ph$^4$), 6.71 (td, $^3J$ = 7.5 Hz, $^4J$ = 1.1 Hz, 2 H, Ph$^5$), 6.27 (dd, $^3J$ = 7.5 Hz, $^4J$ = 0.9 Hz, 2 H, Ph$^6$), 5.30 (s, 1 H, CH), 2.64 (s, 6 H, $CH_3$), 1.83 (s, 6 H, $CH_3$) ppm. $^{13}$C{$^1$H} NMR (75 MHz, $CD_2Cl_2$): $\delta$ = 184.6 (CO), 167.6 (C$^2$-py), 149.0 (C$^4$-py), 147.5 (C$^1$-Ph, C$^6$-py), 145.3 (C$^2$-Ph), 133.2 (C$^6$-Ph), 128.5 (C$^5$-Ph), 123.5 (C$^3$-Ph), 122.9 (C$^5$-py), 120.6 (C$^4$-Ph), 119.3 (C$^3$-py), 100.2 (CH), 28.3 ($CH_3$), 21.1 ($CH_3$) ppm. HRMS: calcd. for $C_{29}H_{27}{}^{193}IrN_2O_2$ [M]$^+$ 628.1703; found 628.1727.

**X-ray Crystallography:** Single crystals for X-ray diffraction studies were grown by slow diffusion of pentane in a toluene solution of complexes **1a**, **1b** and **1d** at 20 °C. The samples **1a** and **1d** were studied with an NONIUS Kappa CCD and **1b** with a Bruker AXS X8-APEX II with graphite-monochromatized Mo-$K_\alpha$ radiation. The data collection and refinement parameters are presented in Table 6. The structures were solved with SIR-97[25] which reveals the non-hydrogen atoms of the molecules. The whole structures were refined by full-matrix least-square techniques on $F^2$, with hydrogen atoms refined using the Riding mode. Structures were solved by Patterson or direct methods. The structures were completed by subsequent difference Fourier techniques and refined by full-matrix least-squares on $F^2$ (SHELXL-97) with initial isotropic parameters.[26a] Atomic scattering factors from International Tables for X-ray Crystallography. ORTEP views were realized with PLATON.[26b]

CCDC-272375 (for **1a**), -257689 (for **1b**) and -275435 (for **1d**) contain the supplementary crystallographic data for this paper. These data can be obtained free of charge from The Cambridge Crystallographic Data Centre via www.ccdc.cam.ac.uk/data_request/cif.

**Supporting Information** (see also the footnote on the first page of this article): Absorption and emission spectra of **3a** and **3d**. Comparison of the absorption and emission spectra of the acac **4a** and dpm adduct **5a**.

## Acknowledgments

We acknowledge the award of a grant by the Centre National de la Recherche Scientifique (CNRS)/Research Grants Council (RGC) (F-HK02/04T) under the PROCORE, France–Hong Kong Joint Research Scheme. M. L. thanks the Région Bretagne for a grant. Muriel Escadeillas is gratefully acknowledged for her help. We thank Prof. Vivian W. W. Yam of The University of Hong Kong for access to equipment for photophysical measurements.

[1] a) M. A. Baldo, S. Lamansky, P. E. Burrows, M. E. Thompson, S. R. Forrest, *Appl. Phys. Lett.* **1999**, *75*, 4; b) M. A. Baldo, D. F. O'Brien, Y. You, A. Shoustikov, S. Sibley, M. E. Thompson, S. R. Forrest, *Nature* **1998**, *395*, 151.

[2] a) C. Adachi, M. A. Baldo, M. E. Thompson, S. R. Forrest, *Appl. Phys. Lett.* **2001**, *90*, 5048; b) C. Adachi, M. A. Baldo, S. R. Forrest, S. Lamansky, M. E. Thompson, R. C. Kwong, *Appl. Phys. Lett.* **2001**, *78*, 1622; c) F.-C. Chen, Y. Yang, M. E. Thompson, J. Kido, *Appl. Phys. Lett.* **2002**, *80*, 2308; d) S. Lamansky, P. I. Djurovich, F. Abdel-Razzaq, S. Garon, D. L. Murphy, M. E. Thompson, *J. Appl. Phys.* **2002**, *92*, 1570; e) J. Jiang, C. Jiang, W. Yang, H. Zhen, F. Huang, Y. Cao, *Macromolecules* **2005**, *38*, 4072; f) J.-P. Duan, P.-P. Sun, C.-H. Cheng, *Adv. Mater.* **2003**, *15*, 224; g) D. K. Rayabarapu, B. M. J. S. Paulose, J.-P. Duan, C.-H. Cheng, *Adv. Mater.* **2005**, *17*, 349; h) C. Jiang, W. Yang, J. Peng, S. Xia, Y. Cao, *Adv. Mater.* **2004**, *16*, 537; i) C.-H. Yang, C.-C. Tai, I.-W. Sun, *J. Mater. Chem.* **2004**, *14*, 947; j) Y.-J. Su, H.-L. Huang, C.-L. Li, C.-H. Chien, Y.-T. Tao, P.-T. Chou, S. Datta, R.-S. Liu, *Adv. Mater.* **2003**, *15*, 884; k) Y.-H. Niu, B. Chen, S. Liu, H. Yip, J. Bardecker, A. K.-Y. Jen, J. Kavitha, Y. Chi, C.-F. Shu, Y.-H. Tseng, C.-H. Chien, *Appl. Phys. Lett.* **2004**, *85*, 1619; l) N. R. Evans, L. S. Devi, C. S. K. Mak, S. E. Watkins, S. I. Pascu, A. Köhler, R. H. Friend, C. K. Williams, A. B. Holmes, *J. Am. Chem. Soc.* **2006**, *128*, 6647.

[3] a) K. K.-W. Lo, C.-K. Chung, T. K.-M. Lee, L.-K. Lui, K. H.-K. Tsang, N. Zhu, *Inorg. Chem.* **2003**, *42*, 6886; b) K. K.-W. Lo, C.-K. Chung, N. Zhu, *Chem. Eur. J.* **2003**, *9*, 475; c) K. K.-W. Lo, J. S.-W. Chan, L.-H. Lui, C. K. Chung, *Organometallics* **2004**, *23*, 3108; d) K. K.-W. Lo, C.-K. Li, J. S.-Y. Lau, *Organometallics* **2005**, *24*, 4594; e) K. K.-W. Lo, C.-K. Chung, N. Zhu, *Chem. Eur. J.* **2006**, *12*, 1500.

[4] a) S. Lamansky, P. Djurovich, D. Murphy, F. Abdel-Razzaq, R. Kwong, I. Tsyba, M. Bortz, B. Mui, R. Bau, M. E. Thompson, *Inorg. Chem.* **2001**, *40*, 1704; b) S. Lamansky, P. Djurovich, D. Murphy, F. Abdel-Razzaq, H. E. Lee, C. Adachi, P. E. Burrows, S. R. Forrest, M. E. Thompson, *J. Am. Chem. Soc.* **2001**, *123*, 4304; c) T. Tsuzuki, N. Shirasawa, T. Suzuki, S. Tokito, *Adv. Mater.* **2003**, *15*, 1455; d) A. Tsuboyama, H. Iwawaki, M. Furugori, T. Mukaide, J. Kamatani, S. Igawa, T. Moriyama, S. Miura, T. Takiguchi, S. Okada, M. Hoshino, K. Ueno, *J. Am. Chem. Soc.* **2003**, *125*, 12971; e) J. Li, P. I. Djurovich, B. D. Alleyne, I. Tsyba, N. N. Ho, R. Bau, M. E. Thompson, *Polyhedron* **2004**, *23*, 419; f) W.-S. Huang, J. T. Lin, C.-H. Chien, Y. T. Tao, S.-S. Sun, Y.-S. Wen, *Chem. Mater.* **2004**, *16*, 2480; g) M. C. DeRosa, D. J. Hodgson, G. D. Enright, B. Dawson, C. E. B. Evans, R. J. Crutchley, *J. Am. Chem. Soc.* **2004**, *126*, 7619; h) I. R. Laskar, T.-M. Chen, *Chem. Mater.* **2004**, *16*, 111; i) J. Li, P. I. Djurovich, B. D. Alleyne, M. Yousufuddin, N. N. Ho, J. C. Thomas, J. C. Peters, R. Bau, M. E. Thompson, *Inorg. Chem.* **2005**, *44*, 1713; j) Y.-T. Huang, T.-H. Chuang, Y.-L. Shu, Y.-C. Kuo, P.-L. Wu, C.-H. Yang, I.-W. Sun, *Organometallics* **2005**, *24*, 6230; k) Y. You, S. Y. Park, *J. Am. Chem. Soc.* **2005**, *127*, 12438; l) T.-H. Kwon, H. S. Cho, M. K. Kim, J.-W. Kim, J.-J. Kim, K. H. Lee, S. J. Park, I.-S. Shin, H. Kim, D. M. Shin, Y. K. Chung, J.-I. Hong, *Organometallics* **2005**, *24*, 1578; m) J. Ding, J. Gao, Q. Fu, Y. Cheng, D. Ma, L. Wang, *Synth. Met.* **2005**, *155*, 539; n) F.-M. Hwang, H.-Y. Chen, C.-S. Liu, Y. Chi, C.-F. Shu, F.-L. Wu, P.-T. Chou, S.-M. Peng, G.-H. Lee, *Inorg. Chem.* **2005**, *44*, 1344; o) H. C. Li, P.-T. Chou, Y.-H. Hu, Y.-M. Cheng, R.-S. Liu, *Organometallics* **2005**, *24*, 1329; p) K. R. J. Thomas, M. Velusamy, J. T. Lin, C.-H. Chien, Y.-T. Tao, Y. S. Wen, Y.-H. Hu, P.-T. Chou, *Inorg. Chem.* **2005**, *44*, 5677.

[5] a) P. Coppo, E. A. Plummer, L. De Cola, *Chem. Commun.* **2004**, 1774; b) C. S. K. Mak, A. Hayer, S. I. Pascu, S. E. Watkins, A. B. Holmes, A. Köhler, R. H. Friend, *Chem. Commun.* **2005**, 4708; c) R. Gao, D. G. Ho, B. Hernandez, M. Selke, D. Murphy, P. I. Djurovich, M. E. Thompson, *J. Am. Chem. Soc.* **2002**, *124*, 14828; d) C.-H. Yang, S.-W. Li, Y. Chi, Y.-M. Cheng, Y.-S. Yeh, P.-T. Chou, G.-H. Lee, C.-H. Wang, C.-F. Shu, *Inorg. Chem.* **2005**, *44*, 7770; e) Y. H. Song, S.-J. Yeh, C.-T. Chen, Y. Chi, C.-S. Liu, J.-K. Yu, Y.-H. Hu, P.-T. Chou, S.-M. Peng, G.-H. Lee, *Adv. Funct. Mater.* **2004**, *14*, 1221.

[6] a) K. A. King, P. J. Spellane, R. J. Watts, *J. Am. Chem. Soc.* **1985**, *107*, 1431; b) K. Dedian, P. I. Djurovich, F. O. Garces, G. Carlson, R. J. Watts, *Inorg. Chem.* **1991**, *30*, 1687; c) M. G.

 © 2007 Wiley-VCH Verlag GmbH & Co. KGaA, Weinheim 

Colombo, T. C. Brunold, T. Riedener, H. U. Güdel, M. Förtsch, H.-B. Bügi, *Inorg. Chem.* **1994**, *33*, 545; d) A. B. Tamayo, B. D. Alleyne, P. I. Djurovich, S. Lamansky, I. Tsyba, N. N. Ho, R. Bau, M. E. Thompson, *J. Am. Chem. Soc.* **2003**, *125*, 7377; e) V. V. Grushin, N. Herron, D. D. LeCloux, W. J. Marshall, V. A. Petrov, Y. Wang, *Chem. Commun.* **2001**, 1494; f) S. Huo, J. C. Deaton, M. Rajeswaran, W. C. Lenhart, *Inorg. Chem.* **2006**, *45*, 3155.

[7] a) M. Lepeltier, H. Le Bozec, V. Guerchais, T. K.-M. Lee, K. K.-W. Lo, *Organometallics* **2005**, *24*, 6069; b) B. Yin, F. Niemeyer, J. A. G. Williams, J. Jiang, A. Boucekkine, L. Toupet, H. Le Bozec, V. Guerchais, *Inorg. Chem.* **2006**, *45*, 8584.

[8] C. O. Dietrich-Buchecker, P. A. Marnot, J. P. Sauvage, *Tetrahedron Lett.* **1982**, *23*, 5291.

[9] O. Maury, J.-P. Guégan, T. Renouard, A. Hilton, P. Dupau, N. Sandon, L. Toupet, H. Le Bozec, *New J. Chem.* **2001**, *25*, 1553.

[10] C. L. Fraser, N. R. Anastasi, J. J. S. Lamba, *J. Org. Chem.* **1997**, *62*, 9314.

[11] S. G. Yan, J. T. Hupp, *J. Phys. Chem.* **1996**, *100*, 6867.

[12] L. Viau, O. Maury, H. Le Bozec, *Tetrahedron Lett.* **2004**, *45*, 125.

[13] M. Nonoyama, *Bull. Chem. Soc. Jpn.* **1974**, *47*, 767.

[14] S. Sprouse, K. A. King, P. J. Spellane, R. J. Watts, *J. Am. Chem. Soc.* **1984**, *106*, 6647.

[15] C.-H. Yang, F.-K. Fang, C.-H. Chen, I.-W. Sun, *Chem. Commun.* **2004**, 2232.

[16] B. Schmid, F. O. Garces, R. J. Watts, *Inorg. Chem.* **1994**, *33*, 9.

[17] a) M. Albrecht, R. H. Crabtree, J. Mata, E. Peris, *Chem. Commun.* **2002**, 32; b) M. Albrecht, J. R. Miecznikowski, A. Samuel, J. W. Faller, R. H. Crabtree, *Organometallics* **2002**, *21*, 3596.

[18] V. W.-W. Yam, V. C.-Y. Lau, L.-X. Wu, *J. Chem. Soc., Dalton Trans.* **1998**, 1461.

[19] R. Ziessel, A. Juris, M. Venturi, *Inorg. Chem.* **1998**, *37*, 5061.

[20] O. Maury, L. Viau, K. Sénéchall, B. Corre, J.-P. Guégan, T. Renouard, I. Ledoux, J. Zyss, H. Le Bozec, *Chem. Eur. J.* **2004**, *10*, 4454.

[21] S. Jung, Y. Kang, H.-S. Kim, Y.-H. Kim, C.-L. Lee, J.-J. Kim, S.-K. Lee, S.-K. Kwon, *Eur. J. Inorg. Chem.* **2004**, 3415.

[22] P. J. Hay, *J. Phys. Chem. A* **2002**, *106*, 1634.

[23] J. N. Demas, G. A. Crosby, *J. Phys. Chem.* **1971**, *75*, 991.

[24] K. Nakamaru, *Bull. Chem. Soc. Jpn.* **1982**, *55*, 2697.

[25] *Sir97*: a new tool for crystal structure determination and refinement: A. Altomare, M. C. Burla, M. Camalli, G. Cascarano, C. Giacovazzo, A. Guagliardi, A. G. G. Moliterni, G. Polidori, R. Spagna, *J. Appl. Crystallogr.* **1998**, *31*, 74.

[26] a) G. M. Sheldrick, *SHELX97–2 Program for Crystal Structure Refinement*, Göttingen, Germany, **1997**. A. J. C. Wilson (Ed.), *International Tables for X-ray Crystallography*, vol. C, Kluwer Academic Publishers, Dordrecht, **1992**; b) A. L. Spek, *PLATON A Multipurpose Crystallographic Tool*, Utrecht University, Utrecht, The Netherlands, **1998**.

Received: January 12, 2007
Published Online: May 10, 2007

 © 2007 Wiley-VCH Verlag GmbH & Co. KGaA, Weinheim 

DOI: 10.1002/ejic.200700049

# Reactions of 1,2,4-Trithiolane, 1,2,5-Trithiepane, 1,2,5-Trithiocane and 1,2,6-Trithionane with Nonacarbonyldiiron: Structural Determination and Electrochemical Investigation

**Jochen Windhager,[a] Manfred Rudolph,*[a] Silvio Bräutigam,[a] Helmar Görls,[a] and Wolfgang Weigand*[a]**

*Dedicated to Prof. Wolfgang Beck on the occasion of his 75th birthday*

**Keywords:** Iron / Cluster compounds / S ligands / Hydrogenase / Electrocatalysis / Dihydrogen

The reactions of 1,2,4-trithiolane (**1**), 1,2,5-trithiepane (**6**), 1,2,5-trithiocane (**12**) and 1,2,6-trithionane (**10**) with nonacarbonyldiiron (**2**) have been investigated. A novel diiron model complex, which can serve as a model complex of the active site of [Fe-only]-hydrogenase, was formed from the reaction with **1**. In contrast, the reaction of **6** with **2** afforded the trinuclear iron cluster **7**. Interestingly, the diiron compound **11** was obtained with 1,2,6-trithionane (**10**), which can be attributed to the more flexible dithiolato ligand **10**. Furthermore, the reaction with 1,2,5-trithiocane (**12**) yielded the trinuclear cluster **13**. X-ray structure analyses were performed on compounds **3**, **7**, **10**, **11** and **13**. The reactions of the reduced iron species **3** with pivalic acid (HP) were studied electrochemically. The most significant features of the experimental cyclic voltammograms (CVs) could be reproduced by digital simulation on the basis of a reaction scheme that includes both the coordination of HP as well as the catalytic generation of hydrogen.
(© Wiley-VCH Verlag GmbH & Co. KGaA, 69451 Weinheim, Germany, 2007)

## Introduction

The recent generation of thiosulfine **A** and the first dithiirane **B** by flash vacuum pyrolysis (FVP) of 1,2,4-trithiolane (**1**), in argon matrices at 10 K, was monitored by both IR and UV/Vis spectroscopy (Scheme 1).[1] In 1993, Nakayama and Ishii et al. reported the first synthesis of stable dithiirane.[2] We have shown that platinum(0) complexes, for instance $Pt(\eta^2\text{-}C_2H_4)(Ph_3P)_2$, react with 1,2,4-trithiolane (**1**) by insertion along the S–S bond. When two equivalents of the platinum(0) complex were used, dithiolatoplatinum(II) **C** was obtained (Scheme 2). This complex decomposed to give the –platinum complex **E** and the methylenedithiolato complex **D**.[3]

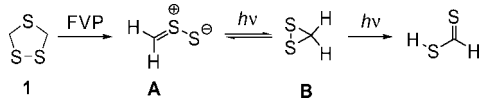


Scheme 1. Flash vacuum pyrolysis (FVP) of 1,2,4-trithiolane **1**.

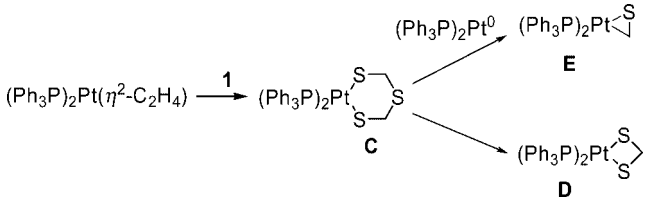


Scheme 2. Treatment of 2 equiv. $Pt(\eta^2\text{-}C_2H_4)(Ph_3P)_2$ with 1,2,4-trithiolane (**1**) to give a 1:1 mixture of methylenedithiolato complex **D** and thioformaldehyde complex **E**.

The oxidative addition of low-valent metal complexes to cyclic disulfides has received significant attention in recent years.[4] As an extension of previous work, reaction of **1** with nonacarbonyldiiron (**2**) was conducted to investigate whether **2** would insert into the S–S bond with the formation of a novel type of dithiolato-bridged diiron complex, which can serve as a model for the active site of [Fe-only]-hydrogenases. Since the first X-ray structure determination of [Fe-only]-hydrogenase was reported,[5] several research groups have prepared simple dinuclear iron complexes that have structural, spectroscopic and functional properties similar to those of the active site of [Fe-only]-hydrogenase.[6] Moreover, the two iron atoms in the active site are bridged by a three-atom-linked dithiolato ligand $SCH_2XCH_2S$;

[a] Institut für Anorganische und Analytische Chemie, Friedrich-Schiller Universität Jena,
August-Bebel-Strasse 2, 07743 Jena, Germany
Fax: +49-3641-948102
E-mail: c8wewo@uni-jena.de
Supporting information for this article is available on the WWW under http://www.eurjic.org or from the author.

 © 2007 Wiley-VCH Verlag GmbH & Co. KGaA, Weinheim 

however, the nature of the X group remains unclear. Nevertheless, it has been postulated that X is an NH unit that is hydrogen bonded to a nearby cysteine-SH unit.[5a]

In order to elucidate the influence of the X group on the hydrogenase activity, we set out to prepare model complexes with X = S by reaction of **1** with **2**. We also tested the reactivity of 1,2,5-trithiepane (**6**), 1,2,5-trithiocane (**13**) and 1,2,6-trithionane (**10**) towards **2** to determine the role of the length of the dithiolate linker in the model complexes (Scheme 3). Very recently, Darensbourg and Hall et al. performed theoretical calculations to determine the influence of the nature of X and the lengthening of the dithiolato bridge on the conformational structure of the model complexes.[7]

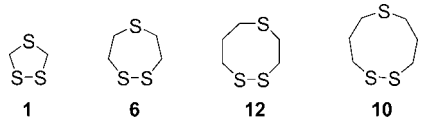


Scheme 3. The sulfur heterocycles **1**, **6**, **10** and **12**.

## Results and Discussion

### Reaction of $Fe_2(CO)_9$ (2) with 1,2,4-Trithiolane (1)

Treatment of 3 equiv. $Fe_2(CO)_9$ (**2**) with 1 equiv. 1,2,4-trithiolane (**1**) in thf for 15 min at 65 °C afforded a mixture of three compounds **3**–**5**, which were separated and isolated by using column chromatography (Scheme 4).

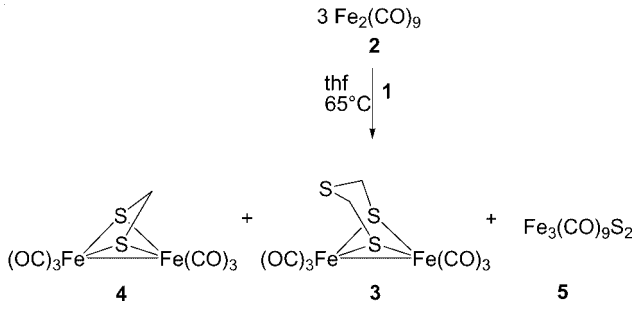


Scheme 4. Reaction of 3 equiv. $Fe_2(CO)_9$ (**2**) with 1 equiv. 1,2,4-trithiolane (**1**).

The $^1$H NMR spectra of **3** and **4** shows one singlet each at $\delta$ = 3.21 and 4.61 ppm, respectively. On the basis of the $^1$H and $^{13}$C NMR spectroscopic data, compound **4** was identified as the known methylenedithiolato-bridged compound.[8] The crystal data of product **5** confirms the presence of a trinuclear complex $Fe_3S_2(CO)_9$.[9] MS analysis shows the stepwise fragmentation of six CO groups and the molecular peak at *m*/*z* = 404 for product **3**, which suggests the presence of a diiron hexacarbonyl complex fragment coordinated to the sulfurdithiolato ligand (SDT). Single-crystal X-ray analysis reveals the proposed structure of **3** (Figure 1); the iron coordination geometry in **3** is rather similar to that in its oxadithiolate (ODT) analogue $Fe_2(\mu\text{-}SCH_2OCH_2S\text{-}\mu)(CO)_6$.[6i] The Fe–Fe bond length in **3** is 2.5120(5) Å, a value very similar to those in the propanedithiolate (PDT) analogue [2.5103(11) Å][6a–6d] and in the ODT analogue [2.5113(13) Å],[6i,6l] but slightly longer (0.02 Å) than that in the azadithiolato (ADT) complex [2.4924(7) Å].[6e–6g] The Fe–Fe bond in **3** is slightly shorter than those reported for the oxidised state diiron subsite (2.62 and 2.60 Å) and that in the reduced state diiron subsite of the enzyme structure (2.55 Å).[5a] Similar to the ODT complex, the bridgehead sulfur atom is disordered (50%).

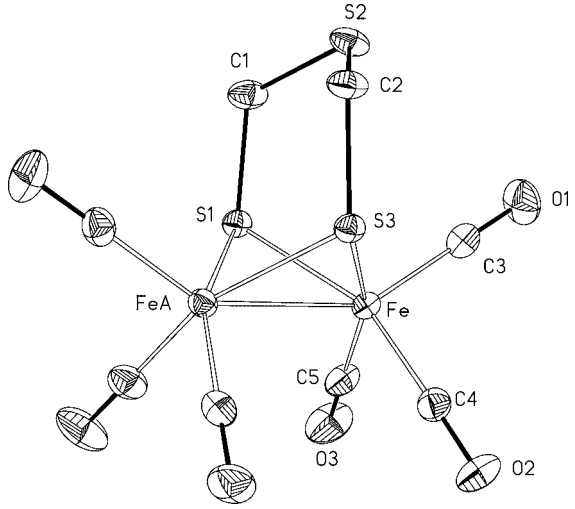


Figure 1. Structure of $Fe_2(SDT)(CO)_6$ (**3**) with thermal ellipsoids set at the 50% probability level (hydrogen atoms are omitted for clarity). Selected distances [Å] and angles [°]: Fe–FeA 2.5120(5), Fe–C3 1.800(9), Fe–C4 1.794(5), Fe–C5 1.800(8), Fe–S1 2.2514(5), Fe–S3 2.2557(7); Fe–S1–FeA 67.672(19), Fe–S3–FeA 67.82(2).

### Reaction of $Fe_2(CO)_9$ (2) with 1,2,5-Trithiepane (6)

By analogy with 1,2,4-trithiolane (**1**), the reaction of 1,2,5-trithiepane (**6**) with **2** was carried out in thf for 15 min at 65 °C. The crude mixture was separated by using column chromatography. Products **7** and **8** were isolated as analytically pure orange and green solids, respectively. For compound **8**, the $^1$H NMR analysis reveals one singlet at $\delta$ = 2.34 ppm. Oxidation of **8** with excess dimethyldioxirane (DMD) quantitatively afforded complex **9**, which was subsequently analysed by X-ray diffraction analysis (Scheme 5). Compounds **8** and **9** have been mentioned previously in the literature.[10]

$^1$H-$^1$H COSY and $^1$H-$^{13}$C HSQC spectra of **7** reveal four groups of $^1$H resonances in a 1:1:1:1 ratio as well as two $^{13}$C signals at $\delta$ = 39.68 and 45.59 ppm. DEI-MS shows the $[M]^+$ ion at *m*/*z* = 572, with the stepwise fragmentation of nine CO groups. On the basis of spectroscopic data, it is suggested that **7** consists of more than two $Fe(CO)_3$ moieties, a result that is further confirmed by the X-ray structure analysis as a trinuclear cluster. The isostructural ruthenium cluster was synthesised by the reaction of $Ru_3(CO)_{12}$ and 1,4,7-trithiacyclononane (9S3) in thf.[11] Alternatively, when the complex $Ru_3(CO)_7(\mu\text{-}CO)_2(1,1,1\text{-}\eta^3\text{-}9S3)$ is heated at reflux for 16 h, an analogous ruthenium cluster is obtained.[12]

 © 2007 Wiley-VCH Verlag GmbH & Co. KGaA, Weinheim 

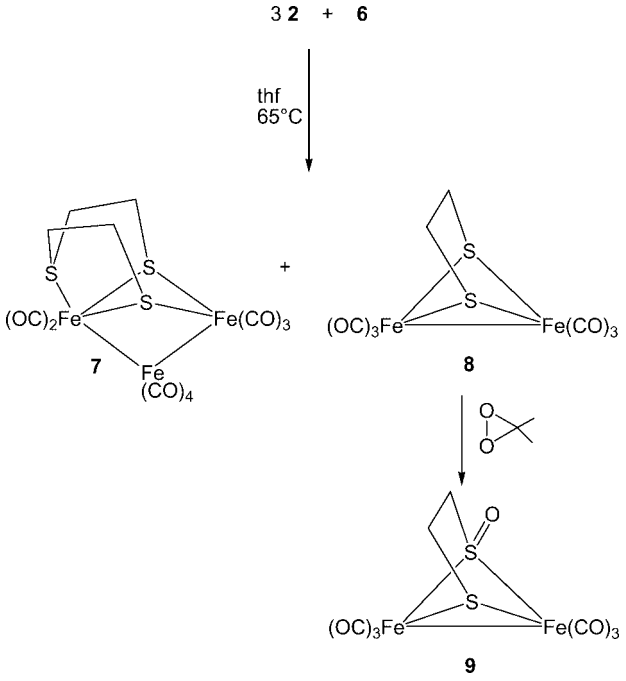


Scheme 5. Reaction of 1,2,5-trithiepane (**6**) with **2**.

As shown in Figure 2, all iron atoms display a distorted octahedral coordination geometry. The Fe1 and Fe2 centres are $\mu^2$-bridged by the bis(thiolatoethylene sulfide) ligand (BTES). Because of the two additional methylene groups in the BTES ligand relative to that in **3**, the thioether S atom coordinates to Fe1. A similar motif was also observed in the complex $[(ON)Ni(\mu\text{-BTES})Fe(NO)_2]$.[13]

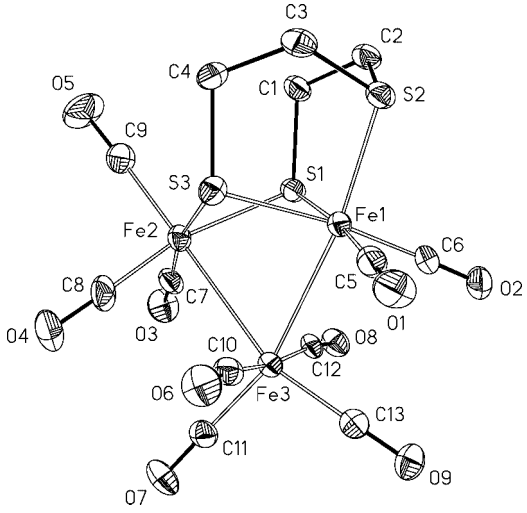


Figure 2. Structure of $Fe_3(\mu\text{-BTES})(CO)_9$ (**7**) with thermal ellipsoids set at the 50% probability level (hydrogen atoms are omitted for clarity). Selected distances [Å] and angles [°]: Fe1–Fe3 2.7355(13), Fe2–Fe3 2.7622(14), Fe1–S1 2.314(2), Fe1–S3 2.302(2), Fe2–S1 2.317(2), Fe2–S3 2.318(2), Fe2–S2 2.250(2); Fe1–S1–Fe2 81.92(6), Fe1–S3–Fe2 82.18(7).

The Fe–S bond lengths for the bridging sulfur atoms in **7** are 2.312 Å (mean), but the Fe1–S2 bond is remarkably shorter [2.250(2) Å]. The Fe1–S1/S3–Fe2 angles of 81.92(6)° and 82.18(7)° differ significantly from the corresponding angles in **3**, 67.82(2)° and 67.67(2)°, respectively. Accordingly, the Fe1···Fe2 distance in **7** (3.036 Å) is significantly longer than that in **3** [2.5120(5) Å]. As a consequence, a $Fe(CO)_4$ fragment inserts into the Fe1 and Fe2 bond, leading to cluster species **7**, a cluster with a total electron count of 50, which is classified as hypho according to the Wade–Mingos rules.

### Reactions of $Fe_2(CO)_9$ (2) with 1,2,6-Trithionane (10)

1,2,6-Trithionane (**10**) was conveniently obtained by a reported procedure.[14] Colourless needles that were suitable for X-ray diffraction analysis were obtained by recrystallising **10** from hexane at –25 °C. The nine-membered ring shows a nonplanar structure (Figure 3) with a for C3–S3–S4–C4 torsion angle of 60.62(15)°. The S3–S4 bond is 1.993(3) Å and is slightly shorter than the corresponding bond in $\alpha\text{-}S_8$ (2.05 Å).[15]

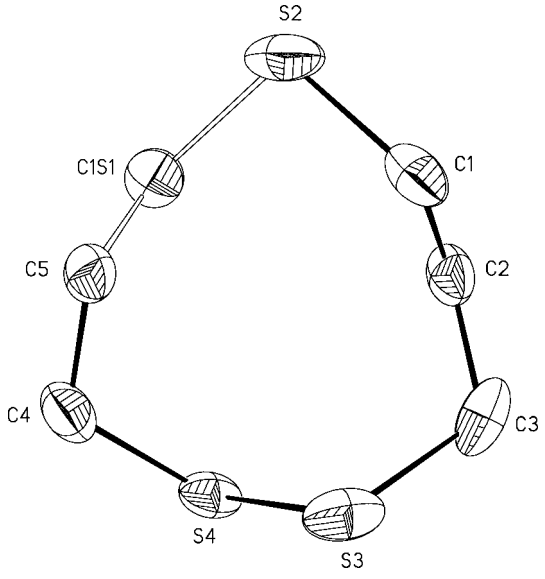


Figure 3. Structure of 1,2,6-trithionane (**10**) with thermal ellipsoids set at the 50% probability level (hydrogen atoms are omitted for clarity). Selected distances [Å] and angles [°]: S3–S4 1.993(3); C3–S3–S4–C4 60.62(15)°.

When **10** was treated with 3 equiv. **2** in thf at 65 °C, a red-brown solution was obtained. After 15 min, the reaction was complete, and compound **11** was isolated after workup as a brown solid by column chromatography (Scheme 6).

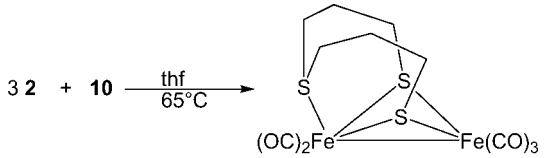


Scheme 6. Reaction of 1,2,6-trithionane (**10**) with **2**.

$^1H$-$^1H$ COSY and $^1H$-$^{13}C$ HSQC analysis of **11** allowed the assignment of the $^{13}C$ resonances at $\delta$ = 18.90 and 27.01 ppm to the C5 and C2 atoms, respectively; the reso-

 © 2007 Wiley-VCH Verlag GmbH & Co. KGaA, Weinheim 

nances at 28.41 and 28.47 ppm are assigned to the C1 and C6 atoms and those at 36.72 and 37.56 ppm to the C3 and C4 atoms, respectively. The latter 4 carbon atoms are directly connected to the thiolato groups and thioether group, respectively. All signals in the $^1$H NMR spectrum are assigned to the 12 diastereotopic protons. DEI-MS reveals the $[M]^+$ ion at $m/z$ = 432 and a stepwise fragmentation of five CO groups. These results indicate the formation of a diiron complex with both $Fe(CO)_2$ and $Fe(CO)_3$ moieties.

This structural motif was confirmed by X-ray diffraction (Figure 4). Red-brown crystals of **11** were obtained from hexane at –25 °C. The crystals were stable in air for weeks at room temperature, but decomposed in solution under argon above 0 °C within one day to form an insoluble brown solid. Complex **11** displays two five-coordinate iron centres with square-pyramidal geometry and an Fe–Fe bond length of 2.5016(5) Å, which is slightly shorter than that in **3**. Complex **11** may be compared with $[Fe_2\{MeSCH_2C(Me)(CH_2S)_2\}(CO)_5]$, showing a similar Fe–Fe distance [2.5086(9) Å].[16]

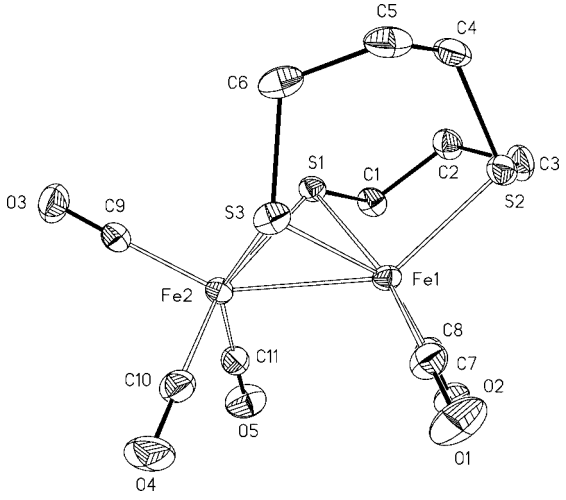


Figure 4. Structure of $Fe_2(\mu$-BTPS$)(CO)_5$ (**11**) with thermal ellipsoids set at the 50% probability level (hydrogen atoms are omitted for clarity). Selected distances [Å] and angles [°]: Fe1–Fe2 2.5016(5), Fe1–S1 2.2568(7), Fe1–S3 2.2448(8), Fe2–S1 2.2481(7), Fe2–S3 2.3040(8), Fe1–S2 2.2449(7); Fe1–S1–Fe2 67.46(2), Fe1–S3–Fe2 66.71(2).

The thiolato sulfur atoms S1 and S3 are $\mu^2$-coordinated to Fe1 and Fe2. In addition, the thioether atom (S2) is connected to Fe1. The angles Fe1–S1–Fe2 [67.46(2)°] and Fe1–S3–Fe2 [66.71(2)°] compare well to those in **3** [67.82(2)° and 67.67(2)°], but in contrast to **3**, **11** does not contain a mirror plane. The presence of the extra methylene groups in **11** relative to **7** reduces steric strain and thus provides the BTPS ligand with more flexibility, which enables the coordination of the thioether S2 atom to Fe1 with the formation of a Fe–Fe bond. With the exception of the Fe2–S3 bond length [2.3040(8) Å], the remaining Fe–S distances are quite similar [2.2448(8), 2.2449(7), 2.2481(7), 2.2568(7) Å].

### Reactions of $Fe_2(CO)_9$ (2) with 1,2,5-Trithiocane (12)

In order to elucidate the influence of the size of the dithiolato thioethers on the structure of the iron complexes, we also treated **12** with **2** at 65 °C in thf. After workup, compounds **8** and **13** were isolated by column chromatography (Scheme 7). Additionally, two green side-fractions were obtained, but unfortunately, we have not been able to characterise them yet. The fraction containing **13** was dissolved in chloroform. After diffusion of pentane into the concentrated solution, red-brown crystals were afforded after 2 d at 0 °C.

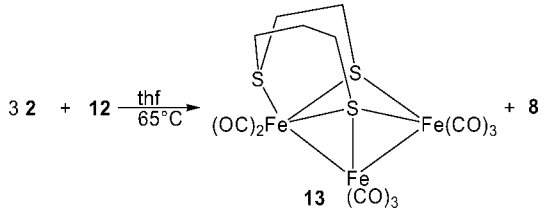


Scheme 7. Reaction of 1,2,5-trithiocane (**12**) with **2**.

The $^1$H-$^1$H COSY spectrum of **13** shows ten groups of resonance signals, which were assigned to the ten diastereotopic protons. According to the $^1$H-$^1$H COSY and $^1$H-$^{13}$C HSQC spectra of **13**, the $^{13}$C resonances at $\delta$ = 34.54 and 34.75 ppm are attributed to the carbon atoms of the ethylene group [C1 and C2] and the signals at 25.41, 31.71 and 36.92 ppm to the C4, C5 and C3 atoms, respectively. DEI-MS reveals the $[M]^+$ ion at $m/z$ = 558 and a stepwise fragmentation of eight CO groups.

As shown in Figure 5, complex **13** has a distorted "non-closed" square-pyramidal $Fe_3S_2$ core with Fe1–Fe2, Fe2–Fe3 and Fe2–S3 distances of 2.7352(9), 2.6888(9) and 2.1173(12) Å, respectively. As in the molecular structure of **7**, all iron atoms have a distorted octahedral coordination geometry. The geometry of Fe1–S1–Fe3–S3 is almost square planar, with a mean deviation from planarity of 0.0941 Å. The Fe1–S1–Fe3 angle of 93.65(4)° and Fe1–S3–Fe3 angle of 100.56(4)° are significantly larger than the corresponding angles in **7** [81.92(6)° and 82.18(7)°]. As a result, the Fe1···Fe3 distance is considerably longer (3.376 Å) than the corresponding distance in **7**. The 3-(2-thiolatoethylthio)-propane-1-thiolato ligand is coordinated to the Fe1 and Fe3 atoms, but the S3 atom is $\mu^3$-coordinated to the three iron atoms as a result of the almost planar geometry of the Fe1–S1–Fe3–S3 moiety, which is remarkably different from that observed in **7**. Therefore, instead of an $Fe(CO)_4$ unit as in **7**, an $Fe(CO)_3$ complex fragment coordinates in **13**, which leads to an arachno cluster. In contrast to compound **7**, the Fe–S distances are quite different from each other. The Fe1–S1 [2.3255(12) Å] and Fe3–S1 [2.3042(12) Å] bonds are significantly longer than the Fe1–S3 [2.2040(12) Å] and Fe3–S3 [2.1854(12) Å] bonds, which can be attributed to the larger strain caused by the ethylenethiolato group than that caused by the propylenethiolato group.

 © 2007 Wiley-VCH Verlag GmbH & Co. KGaA, Weinheim 

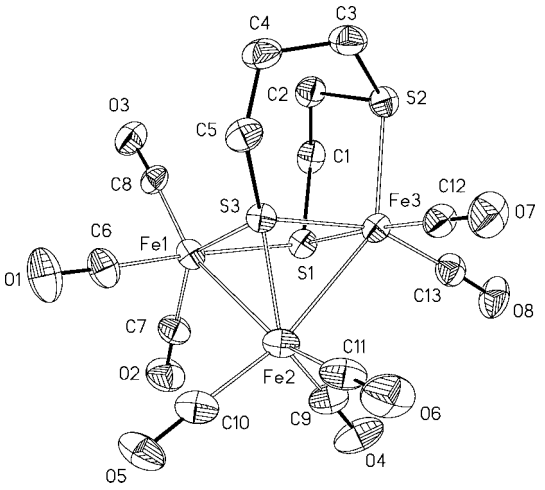


Figure 5. Structure of $Fe_3(S(CH_2)_2S(CH_2)_3S)(CO)_8$ (**13**) with thermal ellipsoids set at the 50% probability level (hydrogen atoms are omitted for clarity). Selected distances [Å] and angles [°]: Fe1–Fe2 2.7352(9), Fe2–Fe3 2.6888(9), Fe1–S1 2.3255(12), Fe1–S3 2.2040(12), Fe3–S1 2.3042(12), Fe3–S3 2.1854(12), Fe2–S3 2.1173(12), Fe3–S2 2.2545(13); Fe1–S1–Fe3 93.65(4), Fe1–S3–Fe3 100.56(4).

## Electrochemical Investigations

The electrochemical behaviour of **3** was studied in the aprotic solvent acetonitrile by varying the concentration of pivalic acid (denoted as HP). This Brønsted acid is electrochemically inactive in the required potential range so that site effects originating from the steady-state concentration of electrochemically produced radicals can be excluded. Moreover, the use of pivalic acid in anhydrous acetonitrile leads to the favourable situation in which catalytic hydrogen generation does not occur in the potential range where the two-electron reduction of the iron species proceeds. Unlike the processes reported, for instance, by Best, Pickett et al.[17] or those for the system denoted as **1-P** by Darensbourg et al.[18c] and Rauchfuss et al.[18a,18b] in which the overall current is dominated by the catalytic reactions as soon as acid is present, the interaction between reduced iron species and pivalic acid that occurs prior to the catalytic cycle can be studied independently in a well-separated potential range. A similar situation was observed for the model system 1 of the above-mentioned articles by Darensbourg and Rauchfuss et al.[18]

### Electrochemistry of 3 in the Absence of Pivalic Acid

The solid lines in Figure 6 show the cyclic voltammetric reduction of **3** in acetonitrile measured by varying the scan rate from 5 to 200 V $s^{-1}$. The open-circle traces show theoretical CVs simulated on the basis of the following reaction scheme (**3** is denoted as Fe–Fe).

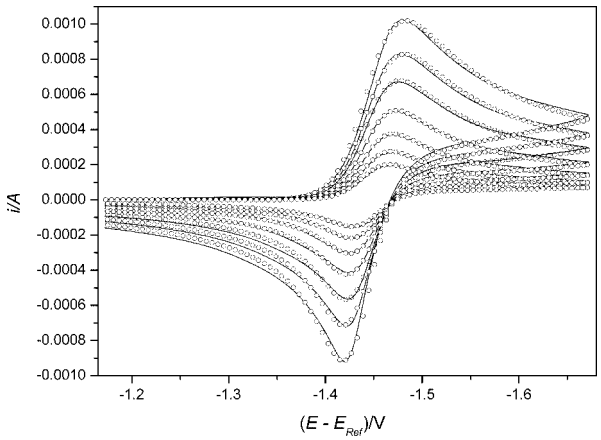


Figure 6. Experimental (solid lines) and simulated (open circles) CVs for the reduction of 2.46 mM **3** in acetonitrile with scan rates of 5, 10, 20, 40, 80, 125 and 200 V $s^{-1}$. The simulated curves refer to the mechanism postulated in (R1)–(R3).

The reduction proceeds in a stepwise manner with two one-electron steps; the second step occurs at more positive potentials than the first and is so fast that only a lower limit can be estimated for $k_s^0$ in (R2).

$$\mathrm{Fe{-}Fe} + e \leftrightarrow {}^{-}\mathrm{Fe{-}Fe} \quad \left(U_1^0 = -1.505\ \mathrm{V};\ k_1^0 \approx 0.65\ \mathrm{cm/s}\right) \quad \text{(R1)}$$

$${}^{-}\mathrm{Fe{-}Fe} + e \leftrightarrow {}^{-}\mathrm{Fe{-}Fe}^{-} \quad \left(U_2^0 = -1.39\ \mathrm{V};\ k_2^0 > 1\ \mathrm{cm/s}\right) \quad \text{(R2)}$$

$${}^{-}\mathrm{Fe{-}Fe}^{-} \rightarrow Q \quad \left(k_{f3} \approx 1\ \mathrm{s}^{-1};\ k_{b3} \ll k_{f3}\right) \quad \text{(R3)}$$

The fact that the electron transfer results in a cleavage of the iron–iron bond is not considered in the above reaction scheme[21] because this information cannot unambiguously be extracted from the experimental CVs. There are only some indirect indications that a bond cleavage in (R1) could account for the higher energy and the slower rate constant associated with this reaction. It would also explain why the reoxidation of the reduced iron species does not proceed in a fully reversible manner. By convoluting the experimental CVs with $t^{-1/2}$ (a procedure called "semi-integration" in the electrochemical literature[21]) as shown in Figure S1[22] (see Supporting Information), it is revealed that the electrons consumed in the forward scan are almost completely regained in the backward scan, but about 3% of the iron species is reoxidised at a slightly more positive potential. This is an indication of the existence of an unknown decomposition product postulated in (R3). However, the effect was too small to examine the reoxidation process via the unknown product.

### Electrochemistry of 3 in the Presence of Pivalic Acid

Figure 7 presents the CVs of **3** in acetonitrile (solid line) at different concentrations of pivalic acid. By looking at the semi-integrated curves shown in Figure S2[22], it is revealed that the overall number of electrons consumed in the forward scan up to about –1.55 V is independent of HP concentration. Consequently, the reduced iron species are not yet able to produce hydrogen from pivalic acid by homogeneous electron transfer in the potential range in which the

 © 2007 Wiley-VCH Verlag GmbH & Co. KGaA, Weinheim 

(heterogeneous) two-electron reduction proceeds. Moreover, the electrons consumed in the reduction process are completely regained in the backward scan irrespective of the HP concentration [except for a small difference that corresponds roughly to the amount assigned to the unknown product *Q* in reaction (R3)], but the overall reoxidation occurs in four processes (indicated by P2–P5 in Figure 7) if the acid is present.

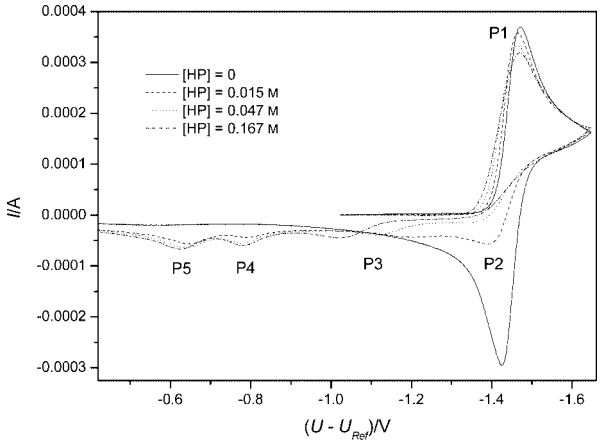


Figure 7. Cyclic voltammograms of 2.46 mM **3** in the absence and presence of pivalic acid. The scan rate is $v = 20\ V\,s^{-1}$.

Further reduction is observed when the potential scan is extended to negative potentials beyond –1.6 V, as can be seen in Figure 8a,b. The additional reduction process P6 at about –2.2 V is not observed in the absence of pivalic acid, and the current of this peak grows with increasing HP concentration. The most likely explanation for this observation is the catalytic reduction of pivalic acid to hydrogen, mediated by the iron complex. The importance of understanding the electrochemistry of the processes leading to the catalytic formation of hydrogen is revealed when **3** is considered as a model complex for the active site of [Fe-only]-hydrogenase.

Figure 7 makes it clear that the peaks associated with processes P2–P5 exhibit very different potential shifts as a function of the HP concentration. While P4 is rather independent of the HP concentration, a tenfold increase in [HP] results in a shift in P5 to more positive potentials by about 59/2 mV. The strongest dependence is observed for P3, where the potential shift is about three Nernst factors. The last observation could be explained by assuming that the charge-transfer reaction in P3 occurs in the form of a preceding chemical reaction caused by the dissociation of three HP molecules. Indeed, the current curve referring to [HP] = 0.015 M in Figure 7 shows the plateau shape expected for a preceding chemical reaction, but as the HP concentration increases, the curve becomes increasingly peak-shaped. It is therefore more likely that P3 represents a ladder scheme or that the equilibrium concentration of the species that is reoxidised is not negligibly small at higher HP concentrations.

In this paper we have mostly focussed on the reactions leading to P1, P2 and P3 in Figure 7 and to P6 in Figure 8. On looking at Figure 9, it can be seen that P1–P3 can be reproduced very well by adding the reactions to (R1)–(R2).

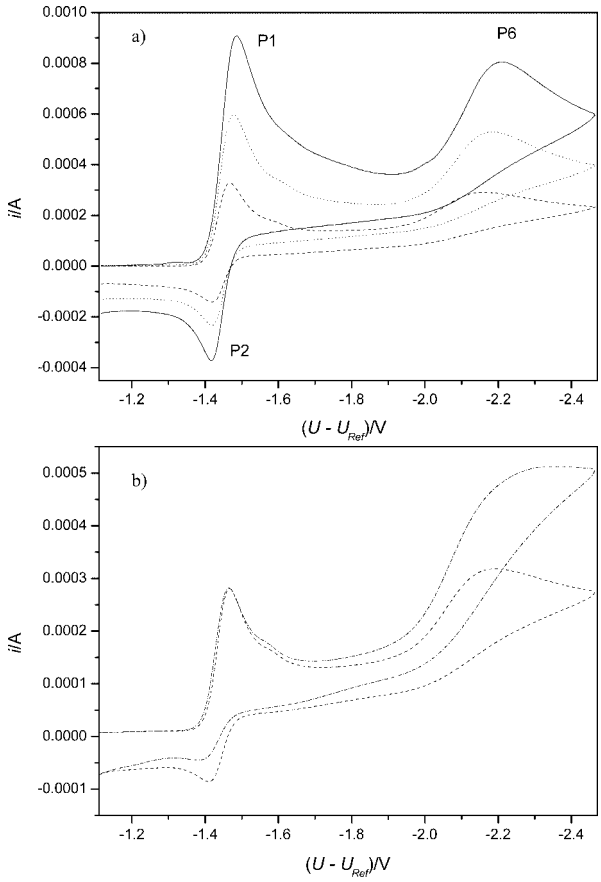


Figure 8. Cyclic voltammograms of **3** in the presence of pivalic acid. (a) 2.2 mM **3** and 10 mM HP, scan rate 20 $V\,s^{-1}$ (dashed line), 77 $V\,s^{-1}$ (dotted line) and 200 $V\,s^{-1}$ (solid line). (b) 2.0 mM **3** and 10 mM (dashed line) or 20 mM (dotted and dashed line) HP, scan rate 20 $V\,s^{-1}$.

It is important to emphasise that parameter couplings prevent the determination of some parameters in the above reaction scheme. This means that virtually the same standard deviation is obtained with different parameter combinations. Despite this uncertainty, the signature of the above reaction scheme is that it may serve as a basis for interpreting (at least qualitatively) the pathway leading to the catalytic generation of hydrogen shown in the CVs in Figure 8.

The reaction of the reduced iron species **3** in the presence of pivalic acid starts with the formation of 1:1 and 1:2 complexes. In the case of the monoanion, only the 1:1 complex needs to be considered because the equilibrium for reaction (R8) seems to lie far to the left. Actually, electrochemical methods such as cyclic voltammetry are not able to distinguish whether undissociated HP molecules are hydrogen-bonded in (R4)–(R7) and (R10) or if a proton transfer occurs as formulated here for (R4).

However, the fact that the ratio of the peak currents associated with P1 and P2 exhibits virtually no scan-rate dependence even when using only a relatively small excess of pivalic acid (see Figure 9a) can be explained only if the complex formation in (R4)–(R6) proceeds as an irreversible process where the effect of the dissociation reaction remains

 © 2007 Wiley-VCH Verlag GmbH & Co. KGaA, Weinheim 

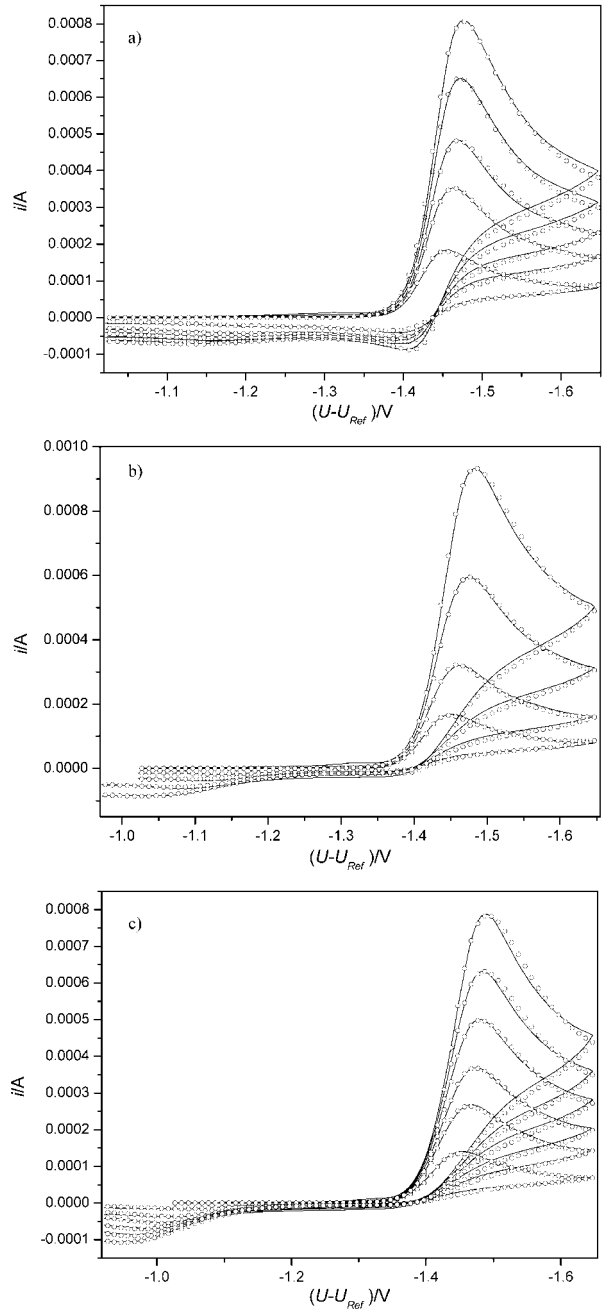


Figure 9. Experimental (solid lines) and simulated (open circles) CVs for the reduction of 2.46 mM **3** in the presence of pivalic acid. (a) [HP] = 0.015 mol L$^{-1}$; $v$ = 5, 20, 40, 77, 125 V s$^{-1}$. (b) [HP] = 0.047 mol L$^{-1}$; $v$ = 5, 20, 77, 200 V s$^{-1}$. (c) [HP] = 0.167 mol L$^{-1}$; $v$ = 5, 20, 40, 77, 125, 200 V s$^{-1}$. The simulated curves refer to the mechanism postulated in (R4)–(R11), with $n$ = 3 in (R7).

$$^{-}Fe-Fe + HP \rightarrow {}^{-}Fe-Fe(HP) \quad (K_4 >> 1; k_{f4} \approx 10^5\,M^{-1}s^{-1}) \quad (R4)$$

$$Fe-Fe + HP \rightarrow Fe-Fe(HP) \quad (K_5; k_{f5} \approx 10^5\,M^{-1}s^{-1}) \quad (R5)$$

$$^{-}Fe-Fe^{-}(HP) + HP \rightarrow {}^{-}Fe-Fe^{-}(HP)_2 \quad (K_5K_6 >> 1; k_{f6} >> k_{b5}) \quad (R6)$$

$$^{-}Fe-Fe^{-}(HP)_2 + nHP \leftrightarrow {}^{-}Fe-Fe^{-}(HP)_2[HP]_n \quad (K_7 \approx 55; k_{f7} \approx 3\times10^6\,M^{-1}s^{-1}) \quad (R7)$$

$$^{-}Fe-Fe(HP) + e \leftrightarrow {}^{-}Fe-Fe^{-}(HP) \quad (U_8^0 \approx -1.6\,V; k_8^0 \approx 0.3\,s^{-1}) \quad (R8)$$

$$^{-}Fe-Fe(HP)_2 + e \leftrightarrow {}^{-}Fe-Fe^{-}(HP)_2 \quad (U_9^0 \approx -1.09\,V; k_9^0 \approx 0.3\,s^{-1}) \quad (R9)$$

$$^{-}Fe-Fe(HP) + HP \leftarrow {}^{-}Fe-Fe(HP)_2 \quad (K_{10} << 1; k_{b10} >> 1) \quad (R10)$$

$$^{-}Fe-Fe^{-}(HP)_2[HP]_n \rightarrow Q^{*} \quad (k_{f11} \approx 4; k_{b11} << k_{f11}) \quad (R11)$$

$$^{-}Fe-Fe + HP \rightarrow Fe-Fe(H) + P^{-} \quad (R12)$$

negligibly small. The latter effect may rather be expected for the formation of a protonated species where the opposite charge of the ions counteracts the dissociation reaction. On the other hand, HP is a very weak acid in acetonitrile and is not dissociated. The p$K_a$ value of acetic acid (which is rather a stronger acid) in anhydrous acetonitrile is only 22.3.[23] However, one should keep in mind that the basicity of the anions of **3** could be increased in the same way that the acidity of pivalic acid is decreased under anhydrous conditions. Nevertheless, it is unlikely that more protons are coordinated than that required to compensate for the negative charge of the reduced iron species, and it remains even questionable whether the dianion of **3** is a strong enough base for the deprotonation of two molecules of pivalic acid. For this reason, we prefer a neutral formulation Fe–Fe(HP), where (HP) in parenthesis represents either a strongly hydrogen-bonded HP molecule or a proton. This type of $H^+$/HP-bonding must be clearly distinguished from the weak and labile bonding of HP molecules postulated in (R7), for which square brackets are used.

Unfortunately, the number $n$ of HP molecules coordinated in this step [R(7)] could not unambiguously be determined. The numbers reported in (R7) refer to $n$ = 1. The problem is that the effect of reaction (R7) is mostly visible in P3, but the average height of the plateau current can be satisfactorily well reproduced with the values $1 \leq n \leq 3$. Thus, for instance, a standard deviation of $s$ = 0.013 was obtained by fitting the experimental data based on reactions (R1), (R2) and (R4)–(R11) with $n$ = 1, while a minimum of $s$ = 0.012 was found for $n$ = 3. This finding is not very significant. However, inspection of all simulated and experimental curves in the potential range associated with P3 reveals that the correct shift for the (half) peak potential of the plateau current as a function of HP concentration is attained only for $n$ = 3, which is in agreement with the potential shift of about three Nernst factors mentioned above. It should be emphasised that we were not able to simulate the experimental data when only (R7) was used with $n$ = 3 and (R5) and (R6) were omitted. We assumed a strong irreversible coordination in the first step and a weaker and labile coordination in the follow-up reaction.

The weak hydrogen bonding of three additional HP molecules could occur, for instance, at the sulfur centres of the molecule provided that the species postulated in (R7) is really a di- or at least a monoanion. Arguments supporting such an assumption can be found in the literature. For example, hydrogen bonding of three undissociated acid molecules at a radical monoanion was postulated in the reduction pathway of 3,5-di-*tert*-butyl-1,2-benzoquinone in the presence of 2,2,2-trifluoroethanol.[24]

Finally it should be mentioned that reaction (R11) plays a similar role to that of process P3 in the absence of pivalic acid. A somewhat larger rate constant was used for (R11), which is in agreement with the results from semi-integration shown in Figures S1 and S2[22].

We will now deal with the most critical question arising from the above reaction scheme: where do the additional processes P4 and P5 in Figure 7 come from? The most

 © 2007 Wiley-VCH Verlag GmbH & Co. KGaA, Weinheim 

straightforward explanation is that $n$ in (R7) really equals 3 and that the three peaks represent the reoxidation processes associated with $n = 1$, 2 and 3 for the corresponding species not yet consumed in the dissociative pathway. Of course, this situation cannot be simulated on the basis of the above reaction scheme that takes only the gross reaction but not the successive complex formation steps into account. The description of more detailed investigations that focus particularly on these processes is beyond the scope of this paper. These findings will be published separately; a detailed knowledge of these processes does not seem to be necessary for the understanding of the pathway that leads to the catalytic current (P6) in Figure 8.

As a first step, this process was analysed by determining the number of electrons additionally consumed in the presence of pivalic acid in the potential range between –1.6 and –2.5 V. The latter was accomplished by semi-integrating the experimental CVs measured with a small excess of pivalic acid. Figure S3 (Supporting Information) shows the number of electrons, $z$, determined in this way as a function of the scan rate. It can be concluded that two additional electrons are consumed in this potential range in the limiting case $v \rightarrow \infty$, where the contributions of the catalytic reactions become negligibly small.

A more detailed analysis reveals that a catalytic process is still not detectable when only one more electron is transferred to the doubly reduced iron species (at least when working with a small excess of pivalic acid).

P6 is governed equally by heterogeneous and homogeneous charge-transfer reactions when as little as a fivefold excess and scan rates between 20 and 200 $V s^{-1}$ are used. Moreover, the formulation of feasible follow-up reactions is simplified by the fact that $^{-}$Fe–Fe$^{-}$(HP)$_2$ is the dominating species in the postulated reaction scheme. Hence, only two further reduction steps of this species were taken into consideration. On looking at Figure 8, it can be seen that the curve remains peak-shaped and no reoxidation process is visible in the potential range associated with P6, independent of the scan rate. Thus, at least the first reduction step (apparently not yet involved in a catalytic process) must be slow and fully irreversible. This could be explained by assuming that further reduction of the HP complexes proceeds as a concerted proton and electron transfer (CPET) reaction in which electron transfer from the electrode to the complex occurs simultaneously with proton transfer from a hydrogen-bonded HP molecule within the complex. CPET reactions have also been invoked for the electrochemical reduction of superoxide,[25] the oxidation of an amino phenol[26] and the oxidation of 1,4-hydrobenzoquinone-2,5-dicarboxylate.[27] Arguments supporting the CPET designation, rather than the possible two-step pathways, have been fully developed for each case.

Because of the perfect coupling between the heterogeneous rate constants and the standard potential for an irreversible charge-transfer process, the heterogeneous rate constants were set to more or less arbitrary values and the standard potential was then adjusted together with the charge-transfer coefficient to simulate the shape of the current curve, at least qualitatively. The following values were used: $U^0_{15} = -1.475$ V, $k^0_{15} = 10^{-3}$ cm $s^{-1}$, $\alpha_{15} \approx 0.25$; $U^0_{16} = -1.77$ V, $k^0_{16} = 1.2 \times 10^{-3}$ cm $s^{-1}$, $\alpha_{16} \approx 0.35$.

The assumption that the catalytic cycle is obtained by a reaction of type (R15), which forms a product that can then be directly re-reduced according to the pathway (R1), (R2), (R5), (R6), (R13) and (R14), is not in agreement with the experimental results.

$$^{-}Fe - Fe^{-}(HP)_2 + e \rightarrow {}^{-}H - Fe - Fe^{-}(HP) + P^{-} \quad (R13)$$

$$^{-}H - Fe - Fe^{-}(HP) + e \rightarrow {}^{-}H - Fe - Fe - H^{-} + P^{-} \quad (R14)$$

$$^{-}H - Fe - Fe - H^{-} + 2HP \rightarrow Fe - Fe + H_2 + 2P^{-} \quad (R15)$$

The assumption mentioned above inevitably leads to the situation in which the current curve does not remain peak-shaped for each scan rate. It becomes increasingly plateau-shaped, as expected for a first-order catalytic mechanism when the scan rate is reduced. Therefore, the shape of the peak for P6 in Figure 8 cannot result from a second-order catalytic reaction in which the depletion of HP accounts for the decay in the catalytic current after a maximum value is reached. A reasonable agreement between simulation and experiment could be obtained only by assuming that the species produced in the first catalytic step [R(16)] does not only undergo a catalytic regeneration reaction according to reactions R(17) or R(18), but also a deactivation reaction in the form of a slow irreversible charge-transfer step [R(19)] that results in the formation of a species that does not participate in the catalytic cycle. It is very possible that this species, simply denoted as $^{-}$H–Fe–Fe$^{-}$, is stabilised by hydrogen-bonded HP molecules or through follow-up reactions.

$$^{-}H - Fe - Fe - H^{-} + HP \xrightarrow{k_{f18}} {}^{-}H - Fe - Fe + H_2 + P^{-} \quad (R16)$$

$$^{-}H - Fe - Fe + HP \xrightarrow{k_{f19}} {}^{-}H - Fe - Fe(HP)$$

$$\xrightarrow{e} {}^{-}H - Fe - Fe^{-}(HP) \quad (R17)$$

$$^{-}H - Fe - Fe + 2HP \rightarrow {}^{-}Fe - Fe(HP)_2 + H \quad (R18)$$

$$^{-}H - Fe - Fe + e \rightarrow {}^{-}H - Fe - Fe^{-} \quad (R19)$$

This leads to the following situation: if the HP concentration is low, the current for the process P6 is governed by reactions (R16) and (R17), while the catalytic cycle [going from (R17) or (R18) back to (R13) or (R10), respectively] has a relatively small effect. The forward scan of the experimental CVs shown in Figure 8 can be reproduced very well for this limiting case by using $k_{f18} \approx 5 \times 10^6$ $M^{-1} s^{-1}$, $k_{f19} \leq 10^4$ $M^{-1} s^{-1}$ and the following charge transfer parameters for (R17) and (R19): $U^0 = -1.82$ V, $k^0 = 10^{-3}$ cm $s^{-1}$, $\alpha \approx 0.5$. However, because of the irreversibility of the reduction steps postulated in the catalytic cycle, the height of the curve for P2 is much smaller than that in the experimental CVs. Very good agreement for both scan segments can be attained if the product on the right-hand side of the last equation [R(19)] is reoxidised in two steps to **3**. As $^{-}$H–Fe–Fe$^{-}$ is formally a triply reduced iron species, a follow-up

 © 2007 Wiley-VCH Verlag GmbH & Co. KGaA, Weinheim 

reaction (maybe with the release of hydrogen) has to occur before, after or in a concerted way with the charge transfer. The standard potential(s) and the heterogeneous rate constant(s) for the two reoxidation steps are not critical as long as this pathway remains much faster (in the potential range associated with P2) than the return of the species into the catalytic cycle by reactions (R13) and (R14). The CVs simulated for this limiting case (under the same experimental conditions as those for Figure 8a) are shown in Figure 10.

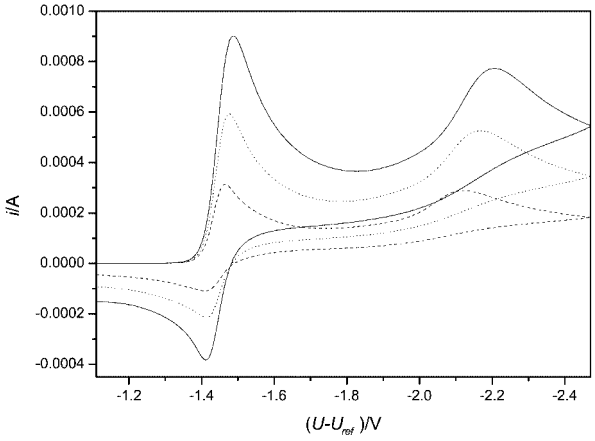


Figure 10. CVs simulated on the basis of (R13), (R14), (R17), (R18) and (R20) by using the same experimental conditions as those given for Figure 8 (a) and the kinetic parameters mentioned in the text.

By increasing the HP concentration, reactions (R17) or (R18) should be favoured, at the expense of reaction (R19). Consequently, the current for the process P6 should grow, while that for P2 becomes smaller. This exact result is observed in the experimental CVs shown in Figure 8 b. This effect and the fact that the height of the peak for P6 not only increases but also broadens when the HP concentration is doubled could be reproduced well in the simulated CVs shown in Figure 11.

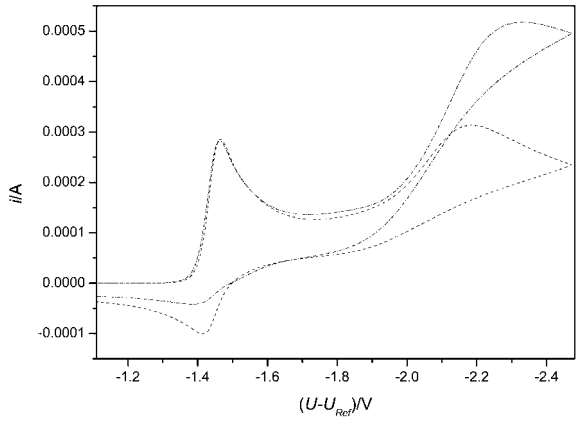


Figure 11. CVs simulated on the basis of (R13), (R14), (R17), (R18) and (R20) by using the same experimental conditions as those given for Figure 8b. Note, however, that different values for $k_{f18}$ and $k_{f19}$ were used in both curves to reproduce the most characteristic features of the experimental CVs.

However, the characteristic changes in the experimental CVs mentioned above could not be attained by repeating the simulations with twice the HP concentration with the same kinetic parameters as those for Figure 10. When the HP concentration is doubled, a simulated CV that matches the experimental CV was obtained with the parameters $k_{f18} \approx 10^5\ M^{-1}\,s^{-1}$ and $k_{f19} \approx 8 \times 10^6\ M^{-1}\,s^{-1}$ and by shifting the $U^0_{15}$ value in a positive direction by about 0.1 V (a similar effect can also be achieved by analogously shifting the $U^0_{21}$ value instead of varying $k_{f19}$).

In principle, this result is not surprising because only products derived from the 1:2 complex were considered to participate in the catalytic cycle. This means that the rate constants optimised in this way describe the overall effect of all HP complexes that can be activated in the catalytic cycle by reduction steps that are analogous to reactions (R13) and (R14). In the best case, such an approach applies to one particular HP concentration. Other more subtle effects may also play a role. For instance, the conditional standard potential for CPET reactions such as (R13) and (R14) is not independent of the HP concentration if the anions on both sides of the reaction are stabilised in different ways by hydrogen bonding to HP molecules. The results obtained on the basis of the simplified reaction scheme in this paper are therefore a promising first step worth pursuing in further studies.

## Conclusions

The present study shows that the heterocyclic compounds **1**, **6**, **10** and **13** react with $Fe_2(CO)_9$ (**2**) by insertion along the S–S bond to provide novel model complexes for [Fe-only]-hydrogenase. The structures of the resulting products are dependent on the ring size of the heterocycles: the reaction with 1,2,4-trithiolane (**1**) yields the diiron complex **3** that adopts a structure quite similar to $Fe_2(PDT)(CO)_6$, $Fe_2(ADT)(CO)_6$ and $Fe_2(ODT)(CO)_6$.[6a–6g,6i,6l] The seven- and eight-membered heterocycles **6** and **13** lead to the three-iron clusters **7** and **13** with intramolecular coordination of the thioether moiety. Furthermore, we have demonstrated that the nine-membered ring compound **10** delivers a diiron complex containing the coordinating thioether. The structures can be attributed to the different flexibilities of the heterocycles **1**, **6**, **10** and **13**.

The electrochemical reduction of **3** proceeds through two reversible, one-electron steps. The second step is faster and has a more positive standard potential than the first. The chemical reversibility of these processes is lost after a weak Brønsted acid is added. In the case of pivalic acid, the experimental CVs can be explained by assuming that either two undissociated HP molecules are strongly coordinated to the dianion by hydrogen bonds or a neutral species is formed by proton transfer. Additionally, up to three HP molecules may be weakly coordinated by hydrogen bonds, but no catalytic hydrogen generation is observed in the potential range in which the two-electron reduction occurs.

 © 2007 Wiley-VCH Verlag GmbH & Co. KGaA, Weinheim 

Hydride species (usually considered as the catalytically active species in the literature) are generated in two further one-electron reduction steps. However, unlike most of the systems reported in the literature,[28] the hydrides of **3** are produced in slow and irreversible charge-transfer processes, which result in a well-separated current peak at a distinctly more negative potential. The latter may be attributed to the particularly low acidity of pivalic acid in acetonitrile under anhydrous conditions. The shape of this peak and the scan rate dependence of its height are not in agreement with the postulation of a catalytic cycle in which the direct regeneration of the electrocatalytically active species is the rate-determining step. The experimental curves could be reproduced sufficiently well by assuming that a deactivation reaction in the form of an irreversible charge-transfer reaction proceeds simultaneously with the regeneration of the electrocatalytically active species.

## Experimental Section

**General:** The $^1H$ and $^{13}C\{^1H\}$ NMR spectra were recorded with a Bruker DRX 200 or DRX 400 spectrometer by using the solvent as a standard. 2D NMR spectra were recorded with the DRX 400 spectrometer. The mass spectra were recorded with a FINNIGAN MAT SSQ 710 instrument. The IR spectra (KBr pellet technique) were recorded with a Thermoelectron Nicolet AVATAR 30070 DTGS or with a Biorad FTF 25 apparatus (ATR cuvettes for neat samples). 1,2,4-Trithiolane (**1**),[29] 1,2,5-trithiepane (**6**), 1,2,6-trithionane (**10**) and 1,2,5-trithiocane (**13**)[14] were prepared according to literature protocols. Elemental analyses were performed with a LECO CHNS-932 apparatus. Solvents and $Fe_2(CO)_9$ (**2**) were purchased from Sigma–Aldrich. Tetrahydrofuran (thf) was dried with sodium/benzophenone before use. Reported yields refer to the amount of purified products. For column chromatography Merck Silica gel 60 (0.015–0.040 mm) was used. Merck TLC aluminium sheets silica gel 60 $F_{254}$ were used for TLC.

**$Fe_2(SDT)(CO)_6$ (3):** Nonacarbonyldiiron (**2**) (2 g, 5.5 mmol) and 1,2,4-trithiolane (**1**) (227 mg, 1.83 mmol) were dissolved in thf (20 mL) and stirred at 65 °C for 15 min under argon. The colour of the light orange solution became deep red, and a brown solid (inorganic iron sulfides) precipitated. The reaction mixture was cooled to room temperature, and the solvent was removed under reduced pressure. The crude product was purified by column chromatography by using hexane as eluent. The orange fraction ($R_f$ = 0.5) was collected, and the solvent was removed. The product was obtained as a red-orange solid. Crystals suitable for X-ray diffraction analysis were obtained by slow evaporation of a concentrated pentane solution of **3** into hexane at 0 °C. Product **3** was also crystallised from a solution of hexane at –25 °C. Yield 279 mg (37.8%). $C_8H_4Fe_2O_6S_3$ (404): calcd. C 23.78, H 0.99, S 23.81; found C 23.81, H 1.26, S 23.48. $^1H$ NMR (200 MHz, $CDCl_3$, 25 °C): $\delta$ = 3.21 (s, 4 H, C$H_2$) ppm. $^{13}C\{^1H\}$ NMR (100 MHz, $CDCl_3$): $\delta$ = 27.7 (*C*$H_2$), 206.79 (*C*O) ppm. FTIR (KBr): $\tilde{\nu}$ = 2075 (s), 2027 (s), 1999 (vs, $\nu$CO, terminal) $cm^{-1}$. MS (DEI = 70 eV): *m*/*z* (%) = 404 (16) [$M^+$], 376 (100) [$M^+$ – 28; CO], 348 (70) [$M^+$ – 56; 2 CO], 320 (46) [$M^+$ – 84; 3 CO], 292 (17) [$M^+$ – 112; 4 CO], 264 (42) [$M^+$ – 140; 5 CO], 236 (58) [$M^+$ – 168; 6 CO], 208 (58) [264 – 56; Fe], 176 (26) [208 – 32; S], 144 (68) [176 – 32; S], 122 (12) [144 – 32; S], 78 (8) [$CH_2S_2$], 56 (26), 45 (12) [CHS].

**$Fe_3(BTES)(CO)_9$ (7):** Nonacarbonyldiiron (**2**) (1.49 g, 4.08 mmol) and 1,2,5-trithiepane (**6**) (207 mg, 1.36 mmol) in thf (15 mL) were stirred at 65 °C for 15 min under argon. The colour of the light orange solution became deep green, and a brown solid (mixture of inorganic iron sulfides) precipitated. The reaction mixture was cooled to room temperature, and the solvent removed under reduced pressure. The crude brown product was purified by column chromatography with diethyl ether as eluent. The dark green fraction ($R_f$ = 0.5) was collected, and the solvent removed. The product was obtained as a dark green solid. Crystals suitable for X-ray diffraction analysis were obtained by slow evaporation of a concentrated ether solution of **7** into hexane at 0 °C. Yield 327 mg (41.4%). $C_{13}H_8Fe_3O_9S_3$ (571.93): calcd. C 27.30, H 1.41, S 16.82; found C 27.26, H 1.65, S 16.65. $^1H$ NMR (400 MHz, $CDCl_3$, 25 °C): $\delta$ = 1.69 (ddd, $^2J_{AB}$ = 13.4, $^3J_{AC}$ = 19.6, $^3J_{AD}$ = 5.2 Hz, 2 H, $H_BH_ACSCH_AH_B$), 2.34 (ddd, $^2J_{CD}$ = 13.7, $^3J_{CA}$ = 19.6, $^3J_{CB}$ = 6.9 Hz, 2 H, $SCH_CH_D$), 3.13 (dd, $^2J_{AB}$ = 13.4, $^3J_{BC}$ = 6.9 Hz, 2 H, $H_BH_ACSCH_AH_B$), 3.27 (dd, $^2J_{CD}$ = 13.7, $^3J_{DA}$ = 5.2 Hz, 2 H, $SCH_CH_D$) ppm. $^{13}C\{^1H\}$ NMR (100 MHz, $CDCl_3$): $\delta$ = 39.7 ($CH_2SCH_2$), 45.6 ($SCH_2CH_2$), 202.5, 208.6, 211.1, 211.8, 213.7 (*C*O) ppm. FTIR (KBr): $\tilde{\nu}$ = 2073 (s), 2033 (vs), 1958 (vs, $\nu$CO, terminal) $cm^{-1}$. FTIR (ATR cuvette): $\tilde{\nu}$ = 2071 (s), 2034 (m), 2021 (m), 2001 (s), 1974 (s), 1968 (s), 1953 (s), 1939 (s, $\nu$CO, terminal) $cm^{-1}$. MS (DEI = 70 eV): *m*/*z* (%) = 572 (2) [$M^+$], 544 (1) [$M^+$ – 28; CO], 516 (3) [$M^+$ – 56; 2 CO], 488 (2) [$M^+$ – 84; 3 CO], 460 (2) [$M^+$ – 112; 4CO], 432 (2) [$M^+$ – 140; 5CO], 404 (5) [$M^+$ – 168; 6 CO], 376 (12) [$M^+$ – 196; 7 CO], 348 (12) [$M^+$ – 224; 8 CO], 316 (10) [$M^+$ – 252; 9 CO].

**$Fe_2(BTPS)(CO)_5$ (11):** Nonacarbonyldiiron (**2**) (1.01 g, 2.77 mmol) and 1,2,6-trithionane (**10**) (166 mg, 0.92 mmol) in thf (15 mL) were stirred for 15 min at 65 °C under argon. The colour of the light orange solution became red-brown, and a brown solid (inorganic iron sulfides) precipitated. The reaction mixture was cooled to room temperature, and the solvent removed under reduced pressure. The crude brown product was purified by column chromatography with diethyl ether as eluent. The red-brown fraction ($R_f$ = 0.6) was collected, and the solvent removed. Product **11** was a brown solid, which was crystallised from a solution of hexane at –25 °C. Yield 56 mg (14.1%). $C_{11}H_{12}Fe_2O_5S_3$ (432.09): calcd. C 30.58, H 2.80, S 22.26; found C 31.03, H 3.15, S 22.02. $^1H$ NMR (400 MHz, $CDCl_3$, 25 °C): $\delta$ = 1.32 [m, 1 H, $H_BH_AC(6)SCH_AH_B$], 2.12 [ddd, $^2J$ = 15.5, $^3J$ = 10.1, $^3J$ = 4.5 Hz, 1 H, $H_BH_AC(6)SCH_AH_B$], 2.23 [t, $^2J$ = 11.8 Hz, 1 H, $CH_2C(5)H_CH_DCH_2$], 2.33–2.40 [m, 2 H, $CH_2C(5)H_CH_DCH_2$ and $SC(4)H_EH_F$], 2.44 [ddd, $^2J$ = 12.3, $^3J$ = 7.9, $^3J$ = 3.7 Hz, 2 H, $H_BH_AC(1)SCH_AH_B$], 2.76–2.87 [m, 3 H, $CH_2C(2)H_CH_DCH_2$ and $SC(3)H_EH_F$], 2.96 [ddd, $^2J$ = 11.8, $^3J$ = 7.4, $^3J$ = 3.7 Hz, 1 H, $SC(3)H_EH_F$], 3.19 [ddd, $^2J$ = 14.3, $^3J$ = 5.6, $^3J$ = 2.8 Hz, 1 H, $H_BH_AC(4)SCH_AH_B$] ppm. $^{13}C\{^1H\}$ NMR (100 MHz, $CDCl_3$): $\delta$ = 18.9 [*C*(5)], 27.0 [*C*(2)], 28.41, 28.47 [*C*(1), *C*(6)], 36.7 [*C*(3)], 37.6 [*C*(4)], 209.7, 211.9, 213.9 (*C*O) ppm. FTIR (ATR cuvette): $\tilde{\nu}$ = 2040 (s), 1952 (vs), 1906 (vs, $\nu$CO, terminal) $cm^{-1}$. MS (DEI = 70 eV): *m*/*z* (%) = 432 (10) [$M^+$], 404 (18) [$M^+$ – 28; CO], 376 (28) [$M^+$ – 56; 2 CO], 348 (46) [$M^+$ – 84; 3 CO], 320 (52) [$M^+$ – 112; 4 CO], 292 (97) [$M^+$ – 140; 5 CO].

**$Fe_3(S(CH_2)_2S(CH_2)_3S)(CO)_8$ (13):** Nonacarbonyldiiron (**2**) (1.315 g, 3.6 mmol) and 1,2,5-trithiocane (**12**) (200 mg, 1.2 mmol) in thf (20 mL) were stirred for 15 min at 65 °C under argon. The colour of the light orange solution became red-brown, and a brown solid (inorganic iron sulfides) precipitated. The reaction mixture was cooled to room temperature, and the solvent was removed under reduced pressure. The crude red-brown product was purified by column chromatography using diethyl ether as eluent. The main orange fraction ($R_f$ = 0.9) was identified as complex **8** (yield:

 © 2007 Wiley-VCH Verlag GmbH & Co. KGaA, Weinheim 

154 mg, 34.5%), and the yield of the nonidentified green fractions was 57 mg. The red-brown fraction ($R_f$ = 0.13) was collected, the solvent was removed and compound **13** was obtained as a red-brown solid. Crystals suitable for X-ray diffraction analysis were obtained by slow evaporation of pentane into a concentrated solution of **13** in chloroform at 0 °C. Yield 46 mg (6.8%). $^1$H NMR (400 MHz, $CDCl_3$, 25 °C): $\delta$ = 1.64 [m, 1 H, $H_BH_AC(2)SCH_AH_B$], 2.48 [m, $^2J$ = 15.5, $^3J$ = 10.1, $^3J$ = 4.5 Hz, 1 H, $H_BH_AC(2)$-$SCH_AH_B$], 2.83–2.95 [m, 2 H, $CH_2C(4)H_CH_DCH_2$ and $H_BH_AC(3)$-$SCH_AH_B$], 3.10 [m, 1 H, $SC(5)H_EH_F$], 3.24 [m, 1 H, $H_BH_AC(4)$-$SCH_AH_B$], 3.44 [m, 1 H, $SC(5)H_EH_F$], 3.59 [m, 1 H, $SC(1)H_CH_D$], 3.68 [m, 1 H, $H_BH_AC(3)SCH_AH_B$], 3.88 [m, 1 H, $SC(1)H_CH_D$] ppm. $^{13}C\{^1H\}$ NMR (100 MHz, $CDCl_3$): $\delta$ = 25.4 [C(4)], 31.7 [C(3)], 34.5 [C(2)], 34.7 [C(3)], 36.9 [C(5)], 214.8 (*C*O) ppm. FTIR (ATR cuvette): $\tilde{\nu}$ = 2053 (s), 1982 (vs), 1962 (vs), 1938 (vs), 1920 (vs, $\nu$CO, terminal) cm$^{-1}$. MS (DEI = 70 eV): *m*/*z* (%) = 558 (2) [M$^+$], 530 (9) [M$^+$ – 28; CO], 502 (15) [M$^+$ – 56; 2 CO], 474 (5) [M$^+$ – 84; 3 CO], 446 (15) [M$^+$ – 112; 4 CO], 418 (48) [M$^+$ – 140; 5 CO].

**Electrochemistry – Instrumentation and Procedures:** Cyclic voltammetric measurements were conducted using a three-electrode technique with a home-built computer-controlled device based on a PCI 6110-E data acquisition board (National Instruments). The measurements were performed in acetonitrile (containing 0.25 M tetra-*n*-butylammonium perchlorate) under a blanket of solvent-saturated argon. The ohmic resistance, which had to be compensated for, was determined by measuring the impedance of the system at potentials where the faradaic current was negligibly small. Background correction was accomplished by subtracting the CVs of the blank electrolyte (containing the same concentration of supporting electrolyte) from the experimental CVs. The reference electrode was an Ag|AgCl electrode in acetonitrile containing 0.25 M tetra-*n*-butylammonium chloride. As recommended by IUPAC,[19] all data reported in this paper were referenced to the ferrocenium/ferrocene couple; the measurements were taken at the end of the experiments. The working electrode was a hanging mercury drop (*m* = 2.79 mg) produced by a CGME instrument (Bioanalytical Systems, Inc., West Lafayette, USA).

Theoretical CVs were simulated by using the DigiElch simulation package (www.DigiElch.de). The simulation algorithm used in this program has been described previously.[20]

Unless otherwise stated, all charge-transfer coefficients were assumed to be 0.5, and the diffusion coefficients of all iron species postulated in the reaction schemes were set to $(1.02 \pm 0.03) \times 10^{-5}$ cm$^2$ s$^{-1}$. This is the value determined for **3**. The diffusion coefficient of pivalic acid was estimated to be $2.5 \times 10^{-5}$ cm$^2$ s$^{-1}$.

In a typical series of experiments, about 0.002 mol L$^{-1}$ of the complex was employed for the measurements consisting of seven scan rates ranging from 5 to 200 V s$^{-1}$ and six different HP concentrations ranging from 0.01 to 0.2 mol L$^{-1}$. All experimental curves were then used for finding a suitable mechanism by making use of DigiElch's nonlinear regression procedure. The standard deviation between simulated and experimental CVs was normalised with respect to the maximum peak current found in the experimental CV. Hence, an overall standard deviation of $s$ = 0.01 means that the average difference between the simulated and experimental CVs is 1% of the (average) peak current.

**Crystal Structure Determination:** The intensity data for the compounds were collected with a Nonius KappaCCD diffractometer, using graphite-monochromated Mo-$K_\alpha$ radiation. Data were corrected for Lorentz and polarisation effects, but not for absorption effects.[30,31] The structures were solved by direct methods (SHELXS[32]) and refined by full-matrix least-squares techniques against $F_o^2$ (SHELXL-97[33]). For compound **10**, the hydrogen atoms were located by difference Fourier synthesis and refined isotropically. For other compounds, the hydrogen atoms were included at calculated positions with fixed thermal parameters. All non-hydrogen atoms were refined anisotropically.[32] The XP software (SIEMENS Analytical X-ray Instruments, Inc.) was used for structure representations.

**Crystal Data for 3:** $C_8H_4Fe_2O_6S_3$, $M_r$ = 403.99 g mol$^{-1}$, red-brown prism, size 0.03 × 0.03 × 0.02 mm, monoclinic, space group $P2_1/m$, $a$ = 6.8211(3), $b$ = 13.3393(7), $c$ = 7.8888(3) Å, $\beta$ = 107.898(3)°, $V$ = 683.05(5) Å$^3$, $T$ = –90 °C, $Z$ = 2, $\rho_{calcd.}$ = 1.964 g cm$^{-3}$, $\mu$(Mo-$K_\alpha$) = 25.96 cm$^{-1}$, $F$(000) = 400, 4305 reflections in $h$(–8/7), $k$(–17/16), $l$(–9/10), measured in the range 2.71° ≤ $\Theta$ ≤ 27.46°, completeness $\Theta_{max}$ = 99.8%, 1630 independent reflections, $R_{int}$ = 0.033, 1389 reflections with $F_o > 4\sigma(F_o)$, 83 parameters, 0 restraints, $R1_{obs}$ = 0.025, $wR_{2obs}$ = 0.060, $R1_{all}$ = 0.034, $wR_{2all}$ = 0.063, GOF = 1.029, largest difference peak and hole: 0.352/–0.541 e Å$^{-3}$.

**Crystal Data for 7:** $C_{13}H_8Fe_3O_9S_3$, $M_r$ = 571.92 g mol$^{-1}$, black prism, size 0.03 × 0.03 × 0.01 mm, orthorhombic, space group $P2_12_12_1$, $a$ = 8.5561(3), $b$ = 13.8497(7), $c$ = 16.5594(6) Å, $V$ = 1962.28(14) Å$^3$, $T$ = –90 °C, $Z$ = 4, $\rho_{calcd.}$ = 1.936 g cm$^{-3}$, $\mu$(Mo-$K_\alpha$) = 25.51 cm$^{-1}$, $F$(000) = 1136, 13746 reflections in $h$(–11/10), $k$(–16/17), $l$(–21/21), measured in the range 1.92° ≤ $\Theta$ ≤ 27.48°, completeness $\Theta_{max}$ = 99.8%, 4485 independent reflections, $R_{int}$ = 0.123, 3575 reflections with $F_o > 4\sigma(F_o)$, 253 parameters, 0 restraints, $R1_{obs}$ = 0.063, $wR_{2obs}$ = 0.150, $R1_{all}$ = 0.085, $wR_{2all}$ = 0.164, GOF = 1.049, Flack-parameter –0.01(3), largest difference peak and hole: 1.417/–1.033 e Å$^{-3}$.

**Crystal Data for 10:** $C_6H_{10}S_3$, $M_r$ = 178.32 g mol$^{-1}$, colourless prism, size 0.10 × 0.10 × 0.06 mm, monoclinic, space group $P2_1/c$, $a$ = 9.4696(6), $b$ = 12.4325(9), $c$ = 7.8849(3) Å, $\beta$ = 113.932(3)°, $V$ = 848.49(9) Å$^3$, $T$ = –90 °C, $Z$ = 4, $\rho_{calcd.}$ = 1.396 g cm$^{-3}$, $\mu$(Mo-$K_\alpha$) = 7.88 cm$^{-1}$, $F$(000) = 376, 5708 reflections in $h$(–12/11), $k$(–14/16), $l$(–9/10), measured in the range 2.35° ≤ $\Theta$ ≤ 27.49°, completeness $\Theta_{max}$ = 99.1%, 1937 independent reflections, $R_{int}$ = 0.045, 1346 reflections with $F_o > 4\sigma(F_o)$, 91 parameters, 0 restraints, $R1_{obs}$ = 0.041, $wR_{2obs}$ = 0.097, $R1_{all}$ = 0.072, $wR_{2all}$ = 0.112, GOF = 1.040, largest difference peak and hole: 0.272/–0.374 e Å$^{-3}$.

**Crystal Data for 11:** $C_{11}H_{12}Fe_2O_5S_3$, $M_r$ = 432.09 g mol$^{-1}$, red-brown prism, size 0.06 × 0.06 × 0.05 mm, monoclinic, space group $P2_1/c$, $a$ = 10.2933(5), $b$ = 9.3713(4), $c$ = 16.2889(6) Å, $\beta$ = 90.898(3)°, $V$ = 1571.06(12) Å$^3$, $T$ = –90 °C, $Z$ = 4, $\rho_{calcd.}$ = 1.827 g cm$^{-3}$, $\mu$(Mo-$K_\alpha$) = 22.59 cm$^{-1}$, $F$(000) = 872, 10241 reflections in $h$(–13/12), $k$(–12/10), $l$(–20/20), measured in the range 1.98° ≤ $\Theta$ ≤ 27.48°, completeness $\Theta_{max}$ = 99.2%, 3567 independent reflections, $R_{int}$ = 0.047, 2681 reflections with $F_o > 4\sigma(F_o)$, 190 parameters, 0 restraints, $R1_{obs}$ = 0.033, $wR_{2obs}$ = 0.069, $R1_{all}$ = 0.0560, $wR_{2all}$ = 0.078, GOF = 0.967, largest difference peak and hole: 0.361/–0.445 e Å$^{-3}$.

**Crystal Data for 13:** $C_{13}H_{10}Fe_3O_8S_3$, $M_r$ = 557.94 g mol$^{-1}$, red-brown prism, size 0.05 × 0.05 × 0.05 mm, monoclinic, space group $P2_1/c$, $a$ = 13.8117(6), $b$ = 9.5857(4), $c$ = 14.9198(7) Å, $\beta$ = 100.243(4)°, $V$ = 1943.82(15) Å$^3$, $T$ = –90 °C, $Z$ = 4, $\rho_{calcd.}$ = 1.907 g cm$^{-3}$, $\mu$(Mo-$K_\alpha$) = 25.68 cm$^{-1}$, $F$(000) = 1112, 12736 reflections in $h$(–16/17), $k$(–11/12), $l$(–19/17), measured in the range 3.07° ≤ $\Theta$ ≤ 27.49°, completeness $\Theta_{max}$ = 99.1%, 4422 independent reflections, $R_{int}$ = 0.052, 3214 reflections with $F_o > 4\sigma(F_o)$, 244 parameters, 0 restraints, $R1_{obs}$ = 0.046, $wR_{2obs}$ = 0.101, $R1_{all}$ = 0.076, $wR_{2all}$ = 0.112, GOF = 1.021, largest difference peak and hole: 1.084/–0.638 e Å$^{-3}$.

 © 2007 Wiley-VCH Verlag GmbH & Co. KGaA, Weinheim 

CCDC-630342 (for **3**), -630343 (for **7**), -630344 (for **10**), -631279 (for **11**) and -631280 (for **13**) contain the supplementary crystallographic data for this paper. These data can be obtained free of charge from The Cambridge Crystallographic Data Centre via www.ccdc.cam.ac.uk/data_request/cif.

**Supporting Information** (see footnote on the first page of this article)(see also the footnote on the first page of this article): Two figures with semi-integral curves of experimental cyclic voltammograms[22] and a figure showing the overall number of electrons consumed at –2.5 V.

## Acknowledgments

Financial support for this work was provided by the Freistaat Thüringen (Landesgraduiertenstipendium to J. W.). We are grateful to Prof. K. Ruhlandt-Senge for valuable discussions.

[1] G. Mloston, J. Romanski, H. P. Reisenauer, G. Maier, *Angew. Chem.* **2001**, *113*, 401–404; *Angew. Chem. Int. Ed.* **2001**, *40*, 393–396.

[2] a) A. Ishii, T. Akazawa, M.-X. Ding, T. Honjo, J. Nakayama, M. Hoshino, M. Shiro, *J. Am. Chem. Soc.* **1993**, *115*, 4914–4915; b) A. Ishii, T. Akazawa, T. Maruta, J. Nakayama, M. Hoshino, M. Shiro, *Angew. Chem. Int. Ed. Engl.* **1994**, *33*, 777–779.

[3] W. Weigand, S. Bräutigam, G. Mloston, *Coord. Chem. Rev.* **2003**, *245*, 167–175 and ref. cited therein.

[4] a) S. M. Aucott, H. L. Milton, S. D. Robertson, A. M. Z. Slawin, G. B. Walker, J. D. Woollins, *Chem. Eur. J.* **2004**, *10*, 1666–1676; b) S. M. Aucott, P. Kilian, S. D. Robertson, A. M. Z. Slawin, J. D. Woollins, *Chem. Eur. J.* **2006**, *12*, 895–902; c) S. M. Aucott, P. Kilian, H. L. Milton, S. D. Robertson, A. M. Z. Slawin, J. D. Woollins, *Inorg. Chem.* **2005**, *44*, 2710–2718; d) A. Ishii, M. Saito, M. Murata, J. Nakayama, *Eur. J. Org. Chem.* **2002**, 979–982; e) A. Ishii, T. Kawai, M. Noji, J. Nakayama, *Tetrahedron* **2005**, *61*, 6693–6699; f) A. Ishii, M. Murata, H. Oshida, K. Matsumoto, J. Nakayama, *Eur. J. Inorg. Chem.* **2003**, 3716–3721.

[5] a) Y. Nicolet, A. L. de Lacey, X. Vernède, V. M. Fernandez, E. C. Hatchikian, J. C. Fontecilla-Camps, *J. Am. Chem. Soc.* **2001**, *123*, 1596–1601; b) Y. Nicolet, B. J. Lemon, J. C. Fontecilla-Camps, J. W. Peters, *Trends Biochem. Sci.* **2000**, *25*, 138–143; c) Y. Nicolet, C. Piras, P. Legrand, C. E. Hatchikian, J. C. Fontecilla-Camps, *Structure* **1999**, *7*, 13–23.

[6] a) X. Zhao, I. P. Georgakaki, M. L. Miller, J. C. Yarbrough, M. Y. Darensbourg, *J. Am. Chem. Soc.* **2001**, *123*, 9710–9711; b) F. Gloaguen, J. D. Lawrence, M. Schmidt, S. R. Wilson, T. B. Rauchfuss, *J. Am. Chem. Soc.* **2001**, *123*, 12518–12527; c) E. J. Lyon, I. P. Georgakaki, J. H. Reibenspies, M. Y. Darensbourg, *J. Am. Chem. Soc.* **2001**, *123*, 3268–3278; d) M. Razavet, S. C. Davies, D. L. Hughes, J. E. Barclay, D. J. Evans, S. A. Fairhurst, X. Liu, C. J. Pickett, *Dalton Trans.* **2003**, 586–595; e) J. D. Lawrence, H. Li, T. B. Rauchfuss, M. Benard, M.-M. Rohmer, *Angew. Chem. Int. Ed.* **2001**, *40*, 1768–1771; f) H. Li, T. B. Rauchfuss, *J. Am. Chem. Soc.* **2002**, *124*, 726–727; g) S. Ott, M. Kritikos, B. Åkermark, L. Sun, *Angew. Chem. Int. Ed.* **2003**, *42*, 3285–3288; h) C. Tard, X. Liu, S. K. Ibrahim, M. Bruschi, L. De Gioia, S. C. Davies, X. Yang, L.-S. Wang, G. Sawers, C. J. Pickett, *Nature* **2005**, *433*, 610–613; i) L.-C. Song, Z.-Y. Yang, H.-Z. Bian, Q.-M. Hu, *Organometallics* **2004**, *23*, 3082–3084; j) D. Seyferth, R. S. Henderson, L.-C. Song, *Organometallics* **1982**, *1*, 125–133; k) D. Seyferth, R. S. Henderson, L.-C. Song, *J. Organomet. Chem.* **1980**, *192*, C1; l) L.-C. Song, Z.-Y. Yang, H.-Z. Bian, Y. Liu, H.-T. Wang, X.-F. Liu, Q.-M. Hu, *Organometallics* **2005**, *24*, 6126–6135; m) M. Y. Darensbourg, E. J. Lyon, J. J. Smee, *Coord. Chem. Rev.* **2000**, *206–207*, 533–561; n) R. C. Linck, T. B. Rauchfuss in *Bioorganometallics* (Ed.: D. Jaouen), Wiley-VCH, Weinheim, **2006**, 403–435; o) X. Zhang, C. Y. Chiang, M. L. Miller, M. V. Rampersad, M. Y. Darensbourg, *J. Am. Chem. Soc.* **2003**, *125*, 518–524; p) J. D. Lawrence, H. Li, T. B. Rauchfuss, *Chem. Commun.* **2001**, 1482–1483; q) L. C. Song, J. Gao, H. T. Wang, Y. J. Hua, H. T. Fan, X. G. Zhang, Q. M. Hu, *Organometallics* **2006**, *25*, 5724–5729.

[7] J. W. Tye, M. Y. Darensbourg, M. B. Hall, *Inorg. Chem.* **2006**, *45*, 1552–1559.

[8] A. Shaver, P. J. Fitzpatrick, K. Steliou, J. S. Butler, *J. Am. Chem. Soc.* **1979**, *101*, 1313–1315.

[9] R. Seidel, B. Schnautz, G. Henkel, *Angew. Chem. Int. Ed. Engl.* **1996**, *35*, 1710–1712.

[10] a) J. Messelhäuser, K. U. Gutensohn, I.-P. Lorenz, W. Hiller, *J. Organomet. Chem.* **1987**, *321*, 377–388; b) J. Messelhäuser, K. Haug, I.-P. Lorenz, W. Hiller, *Z. Naturforsch., B: Chem. Sci.* **1985**, *40*, 1064.

[11] S. Rossi, K. Kallinen, J. Pursiainen, T. T. Pakkanen, T. A. Pakkanen, *J. Organomet. Chem.* **1992**, *440*, 367–387.

[12] R. D. Adams, J. H. Yamamoto, *Organometallics* **1995**, *14*, 3704–3711.

[13] W.-F. Liaw, C.-Y. Chiang, G.-H. Lee, S. M. Peng, C.-H. Lai, M. Y. Darensbourg, *Inorg. Chem.* **2000**, *39*, 480–484.

[14] M. H. Goodrow, W. K. Musker, *Synthesis* **1981**, 457–459.

[15] A. F. Holleman, N. Wiberg, *Lehrbuch der Anorganischen Chemie*, Walter de Gruyter Verlag, Berlin, **1995**.

[16] M. Razavet, S. C. Davies, D. L. Hughes, C. J. Pickett, *Chem. Commun.* **2001**, 847–848.

[17] S. J. Borg, Th. Behrsing, S. P. Best, M. Razavet, X. Liu, C. J. Pickett, *J. Am. Chem. Soc.* **2004**, *126*, 16988–16999.

[18] a) F. Gloaguen, J. D. Lawrence, T. B. Rauchfuss, *J. Am. Chem. Soc.* **2001**, *123*, 9476–9477; b) F. Gloaguen, J. D. Lawrence, T. B. Rauchfuss, M. Bénard, M.-M. Rohmer, *Inorg. Chem.* **2002**, *41*, 6573–6582; c) D. Chong, I. P. Georgakaki, R. Meía-Rodríguez, J. Sanabria-Chinchilla, M. P. Soriaga, M. Y. Darensbourg, *Dalton Trans.* **2003**, 4158–4163.

[19] G. Gritzner, J. Kuta, *Pure Appl. Chem.* **1982**, *54*, 1527–1532.

[20] M. Rudolph, *J. Comput. Chem.* **2005**, *26*, 1193–1204, and literature cited therein.

[21] C. Greco, G. Zampella, L. Bertini, M. Bruschi, P. Fantucci, L. de Gioia, *Inorg. Chem.* **2007**, *46*, 108–116.

[22] A. J. Bard, L. R. Faulkner, *Electrochemical Methods, Fundamentals and Applications*, 2nd ed., John Wiley & Sons, New York, **2001**, pp. 247–252.

[23] G. A. N. Felton, R. S. Glass, D. L. Lichtenberger, D. H. Evans, *Inorg. Chem.* **2006**, *45*, 9181–9184.

[24] N. A. Macìas-Ruvalcaba, N. Okumura, D. H. Evans, *J. Phys. Chem. B* **2006**, *110*, 22043–22047.

[25] a) C. Costentin, D. H. Evans, M. Robert, J.-M. Savéant, P. S. Singh, *J. Am. Chem. Soc.* **2005**, *127*, 12490–12491; b) P. S. Singh, D. H. Evans, *J. Phys. Chem. B* **2006**, *110*, 637–644.

[26] C. Costentin, M. Robert, J.-M. Savéant, *J. Am. Chem. Soc.* **2006**, *128*, 4552–4553.

[27] C. Costentin, M. Robert, J.-M. Savéant, *J. Am. Chem. Soc.* **2006**, *128*, 8726–8727.

[28] a) J. F. Capon, F. Gloaguen, Ph. Schollhammer, J. Talarmin, *Coord. Chem. Rev.* **2005**, *249*, 1664–1676 and literature cited therein; b) X. Liu, S. K. Ibrahim, C. Tard, C. J. Pickett, *Coord. Chem. Rev.* **2005**, *249*, 1641–1652; c) D. J. Evans, C. J. Pickett, *Chem. Soc. Rev.* **2003**, *32*, 268–275.

[29] F. Asinger, M. Thiel, G. Lipfert, *Justus Liebigs Ann. Chem.* **1959**, *627*, 195.

[30] *COLLECT*, Data Collection Software, Nonius B. V., Netherlands, **1998**.

[31] Z. Otwinowski, W. Minor, "Processing of X-ray Diffraction Data Collected in Oscillation Mode" in *Methods in Enzymology*, Vol. 276, *Macromolecular Crystallography*, Part A

 © 2007 Wiley-VCH Verlag GmbH & Co. KGaA, Weinheim 

(Eds. C. W. Carter, R. M. Sweet), Academic Press, New York, **1997**, pp. 307–326.
[32] G. M. Sheldrick, *Acta Crystallogr., Sect. A: Found. Crystallogr.* **1990**, *46*, 467–473.
[33] G. M. Sheldrick, *SHELXL-97 (Release 97–2)*, University of Göttingen, Germany, **1997**.

Received: January 15, 2007
Published Online: April 24, 2007

 © 2007 Wiley-VCH Verlag GmbH & Co. KGaA, Weinheim 

DOI: 10.1002/ejic.200700063

# Use of the Sulfato Ligand in 3d-Metal Cluster Chemistry: A Family of Hexanuclear Nickel(II) Complexes with 2-Pyridyl-Substituted Oxime Ligands

**Constantina Papatriantafyllopoulou,[a] Guillem Aromi,[b] Anastasios J. Tasiopoulos,[c] Vassilios Nastopoulos,[a] Catherine P. Raptopoulou,[d] Simon J. Teat,*[e] Albert Escuer,*[b] and Spyros P. Perlepes*[a]**

**Keywords:** Nickel(II) clusters / Magnetic properties / Sulfato complexes / Oxime complexes

The initial use of 2-pyridyl-substituted oximes [(py)C(R)-NOH; R = Me, Ph]/sulfate blend in nickel(II) chemistry has yielded a family of hexanuclear clusters. The syntheses, structures and magnetic properties are reported of $[Ni_6(SO_4)_4(OH)\{(py)C(Me)NO\}_3\{(py)C(Me)NOH\}_3(MeOH)_2(H_2O)]$ (**1**), $[Ni_6(SO_4)_4(OH)\{(py)C(ph)NO\}_3\{(py)C(ph)NOH\}_3(MeOH)_3]$ (**2**) and $[Ni_6(SO_4)_4(OH)\{(py)C(ph)NO\}_3\{(py)C(ph)NOH\}_3(H_2O)_3]$ (**3**), where (py)C(Me)NOH is methyl 2-pyridyl ketone oxime and (py)C(ph)NOH is phenyl 2-pyridyl ketone oxime. The hexanuclear molecules present in the three complexes have similar structures which contain the $[Ni_6(\mu_3\text{-}OH)(\mu_3\text{-}SO_4)_3(\mu_3\text{-}ONR)_3]^{2+}$ core. The core consists of six $Ni^{II}$ ions arranged as two parallel equilateral triangular subunits, one small (Ni···Ni ca. 3.3 Å) and the other larger (Ni···Ni ca. 6.0 Å). Characteristic IR bands are discussed in terms of the known structures of **1**–**3**. The magnetic properties of **1** and **2** have been studied by variable-temperature dc magnetic susceptibility techniques which indicate antiferromagnetic interactions. A simple 2-*J* model was found to be adequate to describe the similar thermal variation of the molar magnetic susceptibilities of **1** and **2**.

(© Wiley-VCH Verlag GmbH & Co. KGaA, 69451 Weinheim, Germany, 2007)

## Introduction

There continues to be a great interest in the synthesis and physicochemical study of polynuclear metal complexes (clusters) containing paramagnetic metal ions. Among the reasons for this is the search for various nuclearity oxido-bridged metal clusters to model $M_x$ sites in biomolecules.[1] In addition, 3d-metal clusters often display interesting and sometimes novel magnetic properties, including high ground state spin values, currently up to $S = 83/2$,[2] and single-molecule magnetism (SMM) behavior.[3] Crucial to such efforts and others is the continuing development of new synthetic procedures to polynuclear species. However, there is no obvious and guaranteed route to such species.[4] The lack of control has led to the neologism "self-assembly" being introduced.

[a] Department of Chemistry, University of Patras, 26504 Patras, Greece
E-mail: perlepes@patreas.upatras.gr
[b] Departament de Quimica Inorganica, Universitat de Barcelona, Diagonal 647, 08028 Barcelona, Spain
E-mail: albert.escuer@qi.ub.es
[c] Department of Chemistry, University of Cyprus, 1678 Nicosia, Cyprus
[d] Institute of Materials Science, NCSR "Demokritos", 15310 Aghia Paraskevi Attikis, Greece
[e] Advanced Light Source, Lawrence Berkeley National Laboratory, 1 Cyclotron Road, Mail stop 2-400, Berkeley, CA 94720, USA
E-mail: SJTeat@lbl.gov

In recent years several groups have been introducing an element of design into the assembly process by choosing rigid ligands with predictable and controllable binding modes.[5–7] Other researchers use a complementary approach named "serendipitous assembly",[8] where the variables in the reaction system are modified following certain rationales to influence the product found, rather than to control or design the target molecule. Since it is clear that inorganic chemists cannot simply trust to luck in preparing metal clusters, there has to be considerable forethought in the ligands, metals and conditions used for any significant progress to be made.[9]

With the points mentioned above in mind, and in the context of "serendipitous assembly",[8] our group[10] and others[11] have been exploring "ligand blend" reactions involving the monoanions $(py)C(R)NO^-$ of various 2-pyridyl-substituted oximes[12] [Figure 1; R can be a non-donor group or a group containing an extra donor site, i.e. a second 2-pyridyl group in the particular case of di-2-pyridyl ketone oximate $(py)_2CNO^-$] *and* carboxylates, *with* or *without* additional inorganic monoanions ($Cl^-$, $Br^-$, $NO_3^-$, $N_3^-$, $SCN^-$), with the belief that they might foster formation of transition-metal clusters. The immense structural diversity displayed by the complexes reported stems in part from the ability of $(py)C(R)NO^-$ to exhibit many distinct bridging coordination modes. Employment of additional inorganic monoanions with a good coordination capacity gives an ex-

 © 2007 Wiley-VCH Verlag GmbH & Co. KGaA, Weinheim InterScience 

traordinary structural versatility in the *ternary* ligand systems. Thus, the (py)C(R)NO$^-$/R′CO$_2^-$ (R = H, Me, Ph, py; R′ = H, Me, Et, Ph) "blends", without or with additional inorganic anions (Cl$^-$, Br$^-$, NO$_3^-$, N$_3^-$, SCN$^-$) have led to a variety of Cr, Mn, Fe, Co, Ni and Cu clusters[10–12] with nuclearities ranging from 3 to 12 and with interesting magnetic properties, including SMM behavior.[10h,10n]

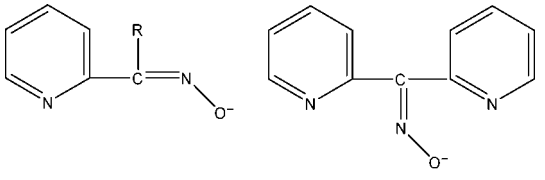


Figure 1. The structural formulae and abbreviations of the ligands discussed in the text.

Very recently we decided to begin a program which can be considered as a modification of the above *binary* ligand system approach. We have been exploring the use of the sulfato ligand, $SO_4^{2-}$, instead of the carboxylato ligand, R′CO$_2^-$. The great coordinative flexibility and versatility of the (py)C(R)NO$^-$ ligands, as well as the $\mu_2$, $\mu_3$, $\mu_4$, $\mu_5$ or $\mu_6$ potential of $SO_4^{2-}$ (Figure 2),[13] prompted as to combine the 2-pyridyl oximates with the sulfate ligand to aim for new types of clusters. Our belief was that the simultaneous employment of the two ligand types in 3d-metal chemistry would give structural flexibility in the (py)C(R)NO$^-$/$SO_4^{2-}$ "blends". The possible advantages of using $SO_4^{2-}$ instead of R′CO$_2^-$ include (i) the possibility of triggering aggregation of preformed smaller cationic species[14] containing *only* (py)C(R)NO$^-$ into new, higher-nuclearity products, and (ii) the possible diversion of known reaction systems developed using *mono*anionic carboxylates to new species as a result of the higher charge and higher denticity/bridging capability of sulfates.

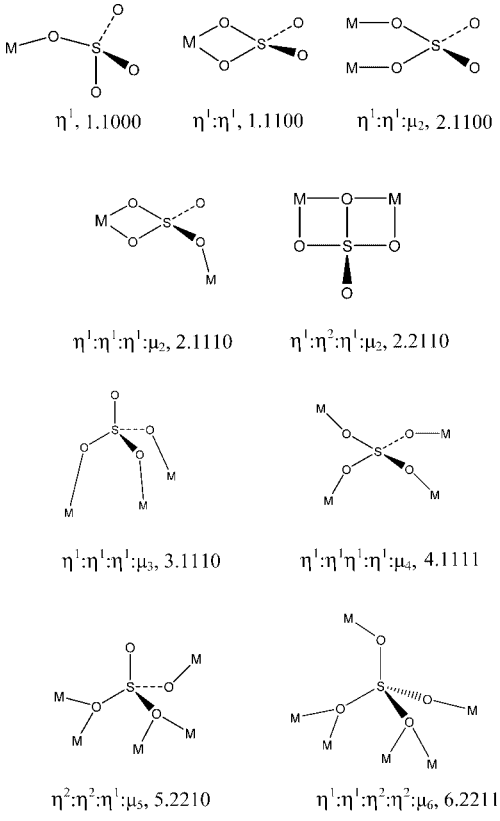


Figure 2. The up to now crystallographically established coordination modes of the sulfato ligand, and the η/μ and Harris[21] notations which describe these modes. The novel $\eta^1$:$\eta^2$:$\mu_3$ (3.2100) ligation mode that appears in the clusters described here is not included (see Figure 4).

The sulfate ion is currently a ligand of intense interest.[13,15] Somewhat to our surprise, the sulfato ligand has not been used in transition-metal cluster chemistry. On the other hand, there is currently a renewed interest in the coordination chemistry of oximes.[16] 2-Pyridyl-substituted oximes are a subclass of oxime ligands, currently very popular in several aspects of coordination chemistry.[12,16c,17]

We herein report the first use of $SO_4^{2-}$ in 3d-metal/2-pyridyloximate chemistry. We describe synthetic procedures to a family of novel hexanuclear Ni$^{II}$/$SO_4^{2-}$/(py)C(R)NO$^-$ (R = Me, Ph) complexes, which have been characterized by single-crystal X-ray crystallography and IR spectroscopy; the magnetic properties of two representative complexes are also described and analyzed. With one exception,[18] the prepared compounds are the first Ni$^{II}$/$SO_4^{2-}$ clusters that appear in the literature. Moreover, they allow the initial assessment of ligation tendencies of the $SO_4^{2-}$ ion in the coordination chemistry of 2-pyridyl-substituted oximes.

## Results and Discussion

### Synthesis and IR Characterization

The original aim of this synthetic program was to explore the versatile bridging potential of the binary (py)C(R)NO$^-$/$SO_4^{2-}$ system for the assembly of Ni$^{II}$ ions into clusters with novel structures and magnetic properties. Our general synthetic approach for the isolation of heteroleptic Ni$^{II}$ clusters was to treat an excess of the metal sulfate with (py)C(R)NOH (R = Me, Ph) and a base in MeOH. The addition of base is necessary for the deprotonation of the organic ligand. Note that reactions in the absence of base lead to complexes [Ni(SO$_4$){(py)C(Me)NOH}(H$_2$O)$_3$], [Ni(SO$_4$)-{(py)C(Me)NOH}$_2$(H$_2$O)], [Ni$_2$(SO$_4$)$_2${(py)C(ph)NOH}$_4$] and [Ni{(py)C(ph)NOH}$_3$](SO$_4$)[19] that contain the neutral ligands.

Treatment of NiSO$_4$·6H$_2$O with one equivalent of (py)C(Me)NOH and one equivalent of NaOMe in MeOH gave a green solution from which the hexanuclear cluster [Ni$_6$(SO$_4$)$_4$(OH){(py)C(Me)NO}$_3${(py)C(Me)NOH}$_3$(MeOH)$_2$(H$_2$O)] (**1**) was obtained in 65% yield. The methoxide ions act as proton acceptors to facilitate formation of OH$^-$ and (py)C(Me)NO$^-$ ligands. Reactions with small variations in the Ni$^{II}$/(py)C(Me)NOH ratio gave the same Ni$_6$ compound **1**. As expected, the nature of the base is not crucial for the identity of the product; we were able to isolate

 © 2007 Wiley-VCH Verlag GmbH & Co. KGaA, Weinheim 

**1** by using a plethora of bases such as $NEt_3$, $NMe_4OH$, $NEt_4OH$, $LiOH·H_2O$ etc. (see Method B in the Experimental Section). Because cluster **1** has a $Ni^{II}$/organic ligand ratio of 1:1, we wondered whether the hexanuclear complex could be prepared by the reaction of $[Ni(SO_4)\{(py)C(Me)NOH\}(H_2O)_3]$ with the appropriate amount of the base. The conversion of the mononuclear to the hexanuclear complex can be accomplished easily by treatment of the former with the stoichiometric amount of $LiOH·H_2O$ in MeOH at 35–40 °C.

We initially came across complexes $[Ni_6(SO_4)_4(OH)\{(py)C(ph)NO\}_3\{(py)C(ph)NOH\}_3(MeOH)_3]$ (**2**) and $[Ni_6(SO_4)_4(OH)\{(py)C(ph)NO\}_3\{(py)C(ph)NOH\}_3(H_2O)_3]$ (**3**) when we tried to prepare the $(py)C(ph)NO^-$/(py)C(ph)NOH analog of complex **1**. The 1:1:1 $NiSO_4·6H_2O$/(py)C(ph)NOH/NaOMe reaction mixture in MeOH gave an orange solution, which upon layering with $Et_2O$ yielded crystals that were obviously a mixture of two products. Microscopic examination showed both greenish-yellow prisms and yellow plates to be present in a visual ratio of roughly 1:1. Their not-too-dissimilar solubility prevented chemical separation; however, the differences in color and crystal shape allowed easy manual separation of the two materials. The prismatic and plate-like crystals were crystallographically identified as complexes **2**·3.2 MeOH·1.5 $H_2O$ and **3**·3 $H_2O$, respectively.

With the identities of **2** and **3** established, convenient syntheses of pure materials were sought under alternative reaction conditions. This was not possible for **2**. Thus, the manual separation of the prismatic crystals from their above-described mixture with **3** remains the only source of complex **2** to date for further measurements. Complex **3** has $H_2O$ molecules as the only solvate ligands; thus attempts to obtain pure **3** were made by adding $H_2O$ in the reaction mixture. Working with an 8:2 (v/v) MeOH/$H_2O$ solvent mixture, we were lucky enough to isolate the yellow plates of **3** as the only product. It is likely that factors such as

Table 1. Selected interatomic distances [Å] and angles [°] for $[Ni_6(SO_4)_4(OH)\{(py)C(Me)NO\}_3\{(py)C(Me)NOH\}_3(MeOH)_2(H_2O)]$·2.53 MeOH·1.60 $H_2O$ (**1**·2.53 MeOH·1.60 $H_2O$).

| | | | |
|---|---|---|---|
| Ni(1)···Ni(2) | 3.304(4) | Ni(3)–N(6) | 2.047(4) |
| Ni(1)···Ni(3) | 3.293(4) | Ni(4)–O(1) | 2.058(3) |
| Ni(2)···Ni(3) | 3.304(4) | Ni(4)–O(12) | 2.028(3) |
| Ni(4)···Ni(5) | 5.970(4) | Ni(4)–O(17) | 2.078(3) |
| Ni(4)···Ni(6) | 5.947(4) | Ni(4)–OW(24) | 2.084(3) |
| Ni(5)···Ni(6) | 6.004(4) | Ni(4)–N(7) | 2.063(4) |
| Ni(1)–O(2) | 2.061(3) | Ni(4)–N(8) | 2.057(4) |
| Ni(1)–O(7) | 2.059(3) | Ni(5)–O(3) | 2.057(3) |
| Ni(1)–O(14) | 2.157(3) | Ni(5)–O(18) | 2.034(3) |
| Ni(1)–O(23) | 2.008(3) | Ni(5)–O(21) | 2.078(3) |
| Ni(1)–N(1) | 2.046(4) | Ni(5)–OM(25) | 2.105(4) |
| Ni(1)–N(2) | 2.045(4) | Ni(5)–N(9) | 2.049(5) |
| Ni(2)–O(3) | 2.069(3) | Ni(5)–N(10) | 2.056(4) |
| Ni(2)–O(9) | 2.063(3) | Ni(6)–O(2) | 2.053(3) |
| Ni(2)–O(21) | 2.128(3) | Ni(6)–O(14) | 2.068(3) |
| Ni(2)–O(23) | 2.009(4) | Ni(6)–O(22) | 2.033(3) |
| Ni(2)–N(3) | 2.055(4) | Ni(6)–OM(26) | 2.086(4) |
| Ni(2)–N(4) | 2.047(4) | Ni(6)–N(11) | 2.060(4) |
| Ni(3)–O(1) | 2.074(3) | Ni(6)–N(12) | 2.061(4) |
| Ni(3)–O(8) | 2.060(3) | S(3)–O(15) | 1.464(3) |
| Ni(3)–O(17) | 2.112(3) | S(3)–O(16) | 1.454(3) |
| Ni(3)–O(23) | 2.007(3) | S(3)–O(17) | 1.496(3) |
| Ni(3)–N(5) | 2.056(4) | S(3)–O(18) | 1.463(3) |
| O(2)–Ni(1)–N(2) | 175.6(1) | N(7)–Ni(4)–N(8) | 78.2(2) |
| O(7)–Ni(1)–O(14) | 166.5(1) | O(3)–Ni(5)–OM(25) | 173.0(2) |
| O(14)–Ni(1)–N(1) | 90.9(1) | O(18)–Ni(5)–O(21) | 90.4(1) |
| O(23)–Ni(1)–N(1) | 168.4(2) | O(18)–Ni(5)–N(9) | 168.7(2) |
| O(23)–Ni(1)–N(2) | 89.8(2) | O(21)–Ni(5)–N(10) | 167.9(2) |
| O(3)–Ni(2)–O(21) | 77.4(1) | N(9)–Ni(5)–N(10) | 78.9(2) |
| O(3)–Ni(2)–N(4) | 177.4(2) | O(2)–Ni(6)–OM(26) | 172.7(1) |
| O(9)–Ni(2)–O(21) | 165.9(1) | O(14)–Ni(6)–N(12) | 167.9(2) |
| O(21)–Ni(2)–N(4) | 100.4(1) | O(22)–Ni(6)–N(11) | 170.3(2) |
| O(23)–Ni(2)–N(3) | 167.0(2) | OM(26)–Ni(6)–N(12) | 90.3(2) |
| O(1)–Ni(3)–N(6) | 176.5(1) | N(11)–Ni(6)–N(12) | 77.8(2) |
| O(8)–Ni(3)–O(17) | 168.3(1) | Ni(1)–O(23)–Ni(2) | 110.7(2) |
| O(8)–Ni(3)–N(6) | 91.1(1) | Ni(1)–O(23)–Ni(3) | 110.2(2) |
| O(23)–Ni(3)–N(5) | 168.1(2) | Ni(1)–O(2)–Ni(6) | 103.2(2) |
| N(5)–Ni(3)–N(6) | 79.1(2) | Ni(1)–O(14)–Ni(6) | 99.4(2) |
| O(1)–Ni(4)–OW(24) | 173.4(1) | Ni(2)–O(3)–Ni(5) | 103.0(2) |
| O(12)–Ni(4)–N(7) | 167.8(2) | Ni(2)–O(21)–Ni(5) | 100.3(2) |
| O(17)–Ni(4)–N(7) | 91.3(1) | Ni(3)–O(1)–Ni(4) | 102.3(2) |
| O(17)–Ni(4)–N(8) | 168.7(1) | Ni(3)–O(17)–Ni(4) | 100.4(2) |

 © 2007 Wiley-VCH Verlag GmbH & Co. KGaA, Weinheim 

relatively solubility, lattice energy, crystallization kinetics and nature of the cation of the base, amongst others, determine the identity of the isolated product.

Two features of the reactions deserve comments. First, the reaction mixtures which lead to **1**–**3** should be filtered before crystallization to remove $Na_2SO_4$ or $Li_2SO_4$ which are insoluble in MeOH; the filtration is not necessary for the preparation of pure **3**. The products also need to be washed with a small amount of $H_2O$ to ensure complete removal of the alkali sulfate. Second, the addition of counter anions such as $ClO_4^-$ and $PF_6^-$ (for the isolation of potentially existing cationic species) and the crystallization method have no influence on the identity of the products.

The IR spectra of air-dried samples of complexes **1**, **2** and **3** exhibit a shoulder at 3430–3400 $cm^{-1}$ and one broad band of medium intensity at 3410–3255 $cm^{-1}$ assignable to ν(OH) vibrations of $OH^-$, (py)C(R)NOH, $H_2O$ and/or MeOH. Complexes **1**–**3** have $C_1$ symmetry at their sulfato ligands. The bands at about 1180–1150, 1130 and 1030 $cm^{-1}$ are therefore attributed[20] to the $\nu_3$ modes, while the bands at about 690, 630 and 590 $cm^{-1}$ are assigned[20] to the $\nu_4$ modes with the higher wavenumber band being superimposed by ligands' vibrations. The band at 1652 (**1**) and ca. 1600 (**2**, **3**) is assigned to the oximate ν(C=N) vibrational mode;[9d] in **2** and **3** this band may also have an aromatic stretch character. The appearance of many bands in the 1200–1000 $cm^{-1}$ region and possible overlap with the sulfato stretching vibration renders exact assignments of the two expected[14c] ν(N–O) modes difficult; a strong band at 1070 (**1**) and ca. 1050 (**2**, **3**) $cm^{-1}$ is a serious candidate for this vibration.[14a,14b]

## Description of Structures

Partially labelled plots of the hexanuclear molecules present in **1**·2.53 MeOH·1.60 $H_2O$, **2**·3.2 MeOH·1.5 $H_2O$ and **3**·3 $H_2O$ are shown in Figures 3, 7 and 8, respectively. Selected interatomic distances and angles are listed in Tables 1, 2 and 3. Tables 4, 5 and 6 summarize intracluster hydrogen bonding data for the three complexes. The molecu-

Table 2. Selected interatomic distances [Å] and angles [°] for $[Ni_6(SO_4)_4(OH)\{(py)C(ph)NO\}_3\{(py)C(ph)NOH\}_3(MeOH)_3]$·3.2 MeOH·1.5 $H_2O$ (**2**·3.2 MeOH·1.5 $H_2O$).

| | | | |
|---|---|---|---|
| Ni(1)···Ni(3) | 5.967(9) | Ni(3)–OM(2) | 2.088(5) |
| Ni(1)···Ni(4) | 5.994(9) | Ni(3)–N(41) | 2.086(6) |
| Ni(2)···Ni(5) | 3.293(9) | Ni(3)–N(42) | 2.047(6) |
| Ni(2)···Ni(6) | 3.306(9) | Ni(4)–O(21) | 2.064(5) |
| Ni(3)···Ni(4) | 5.977(9) | Ni(4)–O(72) | 2.034(5) |
| Ni(5)···Ni(6) | 3.301(9) | Ni(4)–O(91) | 2.094(5) |
| Ni(1)–O(1) | 2.057(5) | Ni(4)–OM(3) | 2.095(6) |
| Ni(1)–O(71) | 2.077(5) | Ni(4)–N(51) | 2.070(8) |
| Ni(1)–O(82) | 2.020(5) | Ni(4)–N(52) | 2.082(7) |
| Ni(1)–OM(1) | 2.108(6) | Ni(5)–O(11) | 2.087(5) |
| Ni(1)–N(31) | 2.069(7) | Ni(5)–O(61) | 2.005(6) |
| Ni(1)–N(32) | 2.067(6) | Ni(5)–O(81) | 2.062(9) |
| Ni(2)–O(1) | 2.081(5) | Ni(5)–O(102) | 2.059(5) |
| Ni(2)–O(61) | 2.016(6) | Ni(5)–N(1) | 2.047(6) |
| Ni(2)–O(71) | 2.135(5) | Ni(5)–N(2) | 2.053(6) |
| Ni(2)–O(101) | 2.077(5) | Ni(6)–O(21) | 2.088(5) |
| Ni(2)–N(21) | 2.065(6) | Ni(6)–O(61) | 2.005(6) |
| Ni(2)–N(22) | 2.047(6) | Ni(6)–O(91) | 2.116(5) |
| Ni(3)–O(11) | 2.067(5) | Ni(6)–O(103) | 2.069(5) |
| Ni(3)–O(81) | 2.070(5) | Ni(6)–N(11) | 2.045(6) |
| Ni(3)–O(92) | 2.032(5) | Ni(6)–N(12) | 2.076(6) |
| O(1)–Ni(1)–OM(1) | 173.6(2) | N(51)–Ni(4)–N(52) | 78.3(3) |
| O(71)–Ni(1)–O(82) | 89.7(2) | O(11)–Ni(5)–N(2) | 177.2(2) |
| O(71)–Ni(1)–N(32) | 169.2(2) | O(61)–Ni(5)–O(102) | 93.0(2) |
| O(82)–Ni(1)–N(31) | 168.0(2) | O(61)–Ni(5)–N(1) | 167.8(3) |
| N(31)–Ni(1)–N(32) | 78.1(3) | O(61)–Ni(5)–N(2) | 89.8(2) |
| O(1)–Ni(2)–O(71) | 78.36(19) | O(81)–Ni(5)–O(102) | 167.2(2) |
| O(1)–Ni(2)–O(101) | 89.17(19) | O(21)–Ni(6)–O(91) | 78.15(18) |
| O(1)–Ni(2)–N(22) | 176.4(2) | O(21)–Ni(6)–N(12) | 177.3(2) |
| O(61)–Ni(2)–N(21) | 167.1(3) | O(61)–Ni(6)–N(11) | 167.2(3) |
| O(71)–Ni(2)–O(101) | 166.8(2) | O(61)–Ni(6)–N(12) | 89.9(2) |
| O(11)–Ni(3)–O(81) | 80.46(18) | O(91)–Ni(6)–O(103) | 166.20(19) |
| O(11)–Ni(3)–OM(2) | 173.1(2) | Ni(1)–O(1)–Ni(2) | 101.8(3) |
| O(81)–Ni(3)–N(41) | 90.1(2) | Ni(1)–O(71)–Ni(2) | 99.2(3) |
| O(81)–Ni(3)–N(42) | 167.9(2) | Ni(2)–O(61)–Ni(5) | 109.6(3) |
| O(92)–Ni(3)–N(41) | 168.0(2) | Ni(2)–O(61)–Ni(6) | 110.6(3) |
| O(21)–Ni(4)–OM(3) | 171.0(2) | Ni(3)–O(11)–Ni(5) | 100.4(3) |
| O(72)–Ni(4)–O(91) | 90.3(2) | Ni(3)–O(81)–Ni(5) | 99.6(3) |
| O(72)–Ni(4)–N(51) | 171.0(2) | Ni(4)–O(21)–Ni(6) | 102.0(3) |
| O(91)–Ni(4)–N(52) | 169.2(3) | Ni(4)–O(91)–Ni(6) | 100.1(3) |

 © 2007 Wiley-VCH Verlag GmbH & Co. KGaA, Weinheim 

Table 3. Selected interatomic distances [Å] and angles [°] for one of the crystallographically independent hexanuclear molecules of complex $[Ni_6(SO_4)_4(OH)\{(py)C(ph)NO\}_3\{(py)C(ph)NOH\}_3(H_2O)_3]\cdot 3H_2O$ (**3**·3 $H_2O$).

| | | | |
|---|---|---|---|
| Ni(1)···Ni(2) | 3.313(4) | Ni(3)–O(23) | 2.013(3) |
| Ni(1)···Ni(3) | 3.320(4) | Ni(3)–N(5) | 2.066(4) |
| Ni(2)···Ni(3) | 3.307(4) | Ni(3)–N(6) | 2.061(3) |
| Ni(4)···Ni(5) | 6.000(4) | Ni(4)–O(1) | 2.089(3) |
| Ni(4)···Ni(6) | 5.978(4) | Ni(4)–O(12) | 2.034(3) |
| Ni(5)···Ni(6) | 6.019(4) | Ni(4)–O(17) | 2.109(3) |
| Ni(1)–O(2) | 2.105(4) | Ni(4)–OW(24) | 2.055(3) |
| Ni(1)–O(7) | 2.070(3) | Ni(4)–N(7) | 2.080(4) |
| Ni(1)–O(14) | 2.109(3) | Ni(4)–N(8) | 2.100(4) |
| Ni(1)–O(23) | 2.023(3) | Ni(5)–O(3) | 2.092(3) |
| Ni(1)–N(1) | 2.070(4) | Ni(5)–O(18) | 2.015(3) |
| Ni(1)–N(2) | 2.069(4) | Ni(5)–O(21) | 2.062(3) |
| Ni(2)–O(3) | 2.084(3) | Ni(5)–OW(25) | 2.157(4) |
| Ni(2)–O(9) | 2.083(3) | Ni(5)–N(9) | 2.050(8) |
| Ni(2)–O(21) | 2.133(3) | Ni(5)–N(10) | 2.004(8) |
| Ni(2)–O(23) | 2.013(3) | Ni(6)–O(2) | 2.083(3) |
| Ni(2)–N(3) | 2.057(4) | Ni(6)–O(14) | 2.101(4) |
| Ni(2)–N(4) | 2.057(4) | Ni(6)–O(22) | 2.003(4) |
| Ni(3)–O(1) | 2.083(3) | Ni(6)–OW(26) | 2.085(4) |
| Ni(3)–O(8) | 2.081(3) | Ni(6)–N(11) | 2.064(4) |
| Ni(3)–O(17) | 2.116(3) | Ni(6)–N(12) | 2.086(5) |
| O(2)–Ni(1)–N(2) | 177.2(1) | N(7)–Ni(4)–N(8) | 77.4(2) |
| O(7)–Ni(1)–O(14) | 164.5(1) | O(3)–Ni(5)–OW(25) | 175.2(2) |
| O(14)–Ni(1)–N(1) | 93.0(2) | O(18)–Ni(5)–O(21) | 88.9(2) |
| O(23)–Ni(1)–N(1) | 166.1(2) | O(18)–Ni(5)–N(9) | 169.0(3) |
| O(23)–Ni(1)–N(2) | 88.7(1) | O(21)–Ni(5)–N(10) | 165.5(3) |
| O(3)–Ni(2)–O(21) | 77.9(1) | N(9)–Ni(5)–N(10) | 78.5(3) |
| O(3)–Ni(2)–N(4) | 177.4(1) | O(2)–Ni(6)–OW(26) | 172.8(1) |
| O(9)–Ni(2)–O(21) | 165.5(1) | O(14)–Ni(6)–N(12) | 169.4(2) |
| O(21)–Ni(2)–N(4) | 101.8(1) | O(22)–Ni(6)–N(11) | 172.9(2) |
| O(23)–Ni(2)–N(3) | 167.2(1) | OW(26)–Ni(6)–N(12) | 87.9(2) |
| O(1)–Ni(3)–N(6) | 177.5(1) | N(11)–Ni(6)–N(12) | 78.1(2) |
| O(8)–Ni(3)–O(17) | 166.9(1) | Ni(1)–O(23)–Ni(2) | 110.3(2) |
| O(8)–Ni(3)–N(6) | 91.8(1) | Ni(1)–O(23)–Ni(3) | 110.7(2) |
| O(23)–Ni(3)–N(5) | 167.1(1) | Ni(1)–O(2)–Ni(6) | 102.6(2) |
| N(5)–Ni(3)–N(6) | 78.7(1) | Ni(1)–O(14)–Ni(6) | 101.8(2) |
| O(1)–Ni(4)–OW(24) | 170.2(1) | Ni(2)–O(3)–Ni(5) | 101.6(2) |
| O(12)–Ni(4)–N(7) | 174.2(2) | Ni(2)–O(21)–Ni(5) | 101.0(2) |
| O(17)–Ni(4)–N(7) | 91.4(2) | Ni(3)–O(1)–Ni(4) | 102.8(2) |
| O(17)–Ni(4)–N(8) | 168.2(2) | Ni(3)–O(17)–Ni(4) | 101.0(2) |

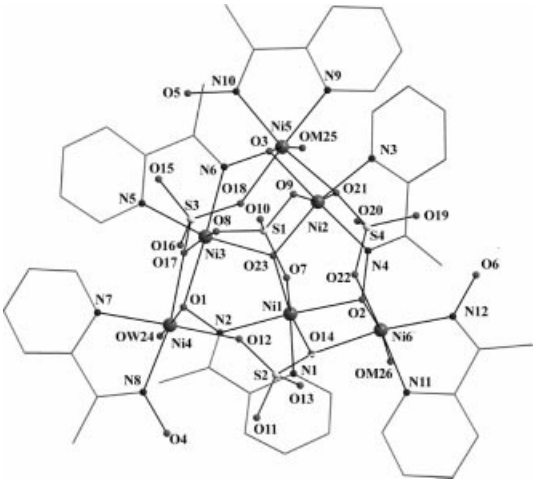


Figure 3. Partially labelled plot of the hexanuclear molecule present in complex **1**·2.53 MeOH·1.60 $H_2O$. The hydrogen atoms have been omitted for clarity.

lar structures of the three complexes are similar in many aspects and, thus, only the structure of the representative complex **1**·2.53 MeOH·1.60 $H_2O$ will be described in detail.

Table 4. Details for the intramolecular hydrogen bonds in complex $[Ni_6(SO_4)_4(OH)\{(py)C(Me)NO\}_3\{(py)C(Me)NOH\}_3(MeOH)_2(H_2O)]\cdot 2.53\,MeOH\cdot 1.60\,H_2O$ (**1**·2.53 MeOH·1.60 $H_2O$).[a]

| D–H···A | D···A [Å] | H···A [Å] | DHA [°] |
|---|---|---|---|
| O(4)–H(O4)···O(11) | 2.569 | 1.638 | 168.9 |
| O(5)–H(O5)···O(15) | 2.558 | 1.486 | 175.1 |
| O(6)–H(O6)···O(19) | 2.583 | 1.755 | 172.0 |
| OM(26)–H(OM26)···O(13) | 2.626 | 1.826 | 162.6 |
| OW(24)–HB(OW24)···O(16) | 2.666 | 1.721 | 157.0 |
| OM(25)–H(OM25)···O(20) | 2.618 | 1.966 | 148.3 |
| OM(30)[b]–H(OM30)···O(10) | 2.658 | 1.588 | 162.8 |
| OW(31)[c]–HA(OW31)···O(13) | 2.872 | 1.838 | 164.6 |
| OW(24)–HA(O24W)···OW(31) | 2.725 | 1.760 | 167.2 |

[a] A = acceptor; D = donor. [b] Atom OM(30) [not shown in Figure 3] belongs to lattice methanol. [c] Atom OW(31) [not shown in Figure 3] belongs to lattice water.

 © 2007 Wiley-VCH Verlag GmbH & Co. KGaA, Weinheim 

Table 5. Details for the intramolecular hydrogen bonds in complex $[Ni_6(SO_4)_4(OH)\{(py)C(ph)NO\}_3\{(py)C(ph)NOH\}_3(MeOH)_3]\cdot 3.2\,MeOH\cdot 1.5\,H_2O$ (**2**·3.2 MeOH·1.5 $H_2O$).[a]

| D–H···A | D···A [Å] | H···A [Å] | DHA [°] |
|---|---|---|---|
| OM(1)–H(OM1)···O(73) | 2.658 | 1.859 | 151.0 |
| OM(2)–H(OM2)···O(83) | 2.650 | 1.836 | 169.2 |
| OM(3)–H(OM3)···O(94) | 2.647 | 2.022 | 125.1 |
| O(31)–H(O31)···O(84) | 2.560 | 1.747 | 171.0 |
| O(41)–H(O41)···O(93) | 2.583 | 1.800 | 159.2 |

[a] A = acceptor; D = donor.

Table 6. Details for the intramolecular hydrogen bonds in one of the two crystallographically independent hexanuclear molecules of complex $[Ni_6(SO_4)_4(OH)\{(py)C(ph)NO\}_3\{(py)C(ph)NOH\}_3(H_2O)_3]\cdot 3\,H_2O$ (**3**·3 $H_2O$).[a]

| D–H···A | D···A [Å] | H···A [Å] | DHA [°] |
|---|---|---|---|
| O(4)–H(O4)···O(13) | 2.558(7) | 1.77 | 154.6 |
| O(5)–H(O5)···O(15) | 2.654(8) | 1.82 | 177.4 |
| O(5A)–H(O5A)···O(15) | 2.388(11) | 1.59 | 157.1 |
| O(6)–H(O6)···O(20) | 2.547(8) | 1.71 | 172.8 |
| O(6)–H(O6)···O(20A) | 2.468(11) | 1.65 | 162.5 |
| O(23)–H(O23)···O(22) | 3.001(5) | 2.46 | 123.6 |
| O(23)–H(O23)···O(12) | 3.134(3) | 2.59 | 123.5 |

[a] A = acceptor; D = donor.

In the following the binding modes of the various ligands will be often described using Harris notation.[21] Occasionally we shall use the widely approved notation based on the Greek letters μ and η.

Complex **1**·2.53 MeOH·1.60 $H_2O$ crystallizes in the monoclinic space group $P2_1/n$. Its structure consists of hexanuclear $[Ni_6(SO_4)_4(OH)\{(py)C(Me)NO\}_3\{(py)C(Me)NOH\}_3(MeOH)_2(H_2O)]$ molecules, and MeOH and $H_2O$ solvate molecules; the latter two will not be further discussed. If we assume that the nitrogen atoms of the $\mu_3$ oximate groups and the terminal oxygen atoms of the 3.2100 sulfato ligands (Figure 4) contribute to the core formation, the molecule of **1** contains the $[Ni_6(\mu_3\text{-}OH)(\mu_3\text{-}SO_4)_3(\mu_3\text{-}ONR)_3]^{2+}$ core; an alternative description of the core (using only the bridging oxygen atoms) is $[Ni_6(\mu_3\text{-}OH)(\mu\text{-}OR')_3(\mu\text{-}OR'')_3]^{2+}$, where R′ = $SO_3$ and R″ = NC(py)(Me). The topology of the core consists of six $Ni^{II}$ ions arranged as two parallel (Figure 5), near-equilateral triangular subunits, one "small" and the other "large". The metal ions in the small triangle [defined by Ni(1), Ni(2) and Ni(3)] are held together by the $\mu_3$-$OH^-$ ligand [O(23)] and one $\eta^1{:}\eta^1{:}\eta^1{:}\mu_3$ (or 3.1110,[21] Figure 2) sulfato group. Each $Ni_2$ edge is additionally bridged by one diatomic oximate group from one 3.211 (py)C(Me)$NO^-$ ligand (Figure 6). Each $Ni_2$ edge of the large triangle [defined by Ni(4), Ni(5) and Ni(6)] is bridged by two oxygen atoms of one $\eta^1{:}\eta^2{:}\mu_3$ (or 3.2100, Figure 4) sulfato ligand. Each apex of the small triangular unit is linked to an apex of the large triangular unit by two monoatomic oxygen bridges from one 3.2100 $SO_4^{2-}$ ion and one 3.211 (py)C(Me)$NO^-$ ligand, and to another apex of the large triangle by the diatomic oximate group of one 3.211 pyridyloximate ligand already used to bridge a $Ni_2$ edge of the small triangle. One bidentate chelating (py)-C(Me)NOH molecule (1.011, Figure 6) and one terminal solvate ligand [MeOH at Ni(5) and Ni(6), $H_2O$ at Ni(4)] complete six-coordination at each metal center of the large triangle.

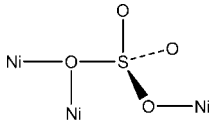


$\eta^1{:}\eta^2{:}\mu_3$, 3.2100

Figure 4. The new $\eta^1{:}\eta^2{:}\mu_3$ (3.2100) coordination mode of the $SO_4^{2-}$ ion which has been crystallographically identified in complexes **1**–**3**.

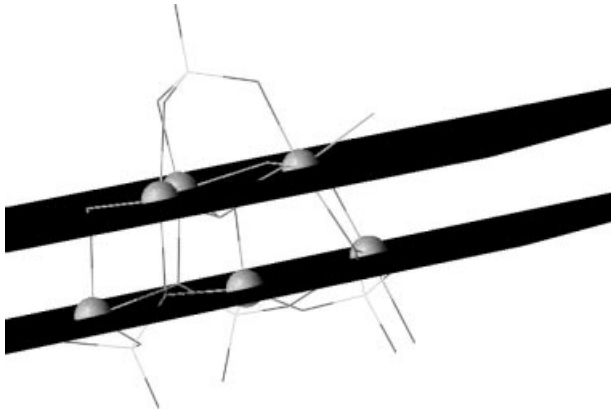

Figure 5. A view of **1** emphasizing the parallel $Ni_3$ planes.

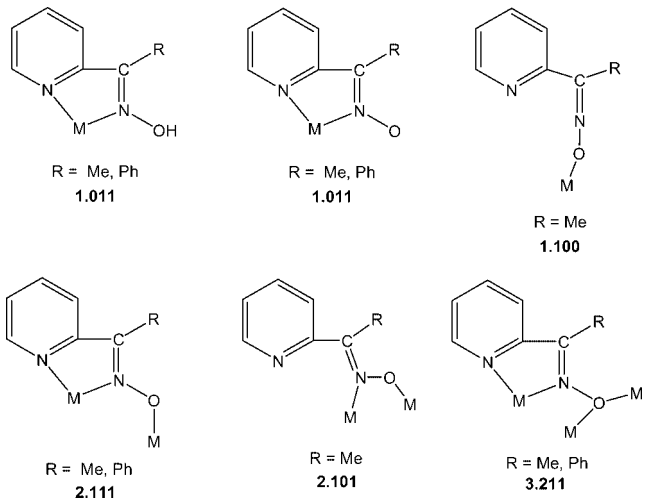


Figure 6. The up to now crystallographically established coordination modes of the ligands (py)C(ph)NOH, (py)C(ph)$NO^-$, (py)-C(Me)NOH and (py)C(Me)$NO^-$, and the Harris notation[21] that describes these modes. The 3.211 ligation mode of (py)C(Me)$NO^-$ is new and has identified for the first time in complex **1**.

Using the perspective view of Figure 5, the $\mu_3$-OH oxygen atom O(23) is 0.633 Å below the $Ni_3$ plane that it bridges [Ni(1)Ni(2)Ni(3)], i.e. the hydroxido ligand is between the almost parallel planes (dihedral angle: 0.6°) defined by the two triangular subunits. The distance between the

 © 2007 Wiley-VCH Verlag GmbH & Co. KGaA, Weinheim 

planes is 2.182 Å. The small triangle can be viewed as an inverse 9-metallacrown-3 subunit.[9i]

The $Ni^{II}\cdots Ni^{II}$ separations within the small triangular unit are in the narrow 3.293(4)–3.304(4) Å range; those within the large one are in the 5.947(4)–6.000(4) Å range. A distorted octahedral environment is created about each metal center. The Ni–$O_{sulfato}$ bond lengths are typical.[15c,18,22] The Ni–O bond lengths for the bridging sulfate oxygen atoms are longer than the Ni–O distance exhibited by the terminal oxygen atom from the same sulfato ligand.

There is a large amount of hydrogen bonding in **1**·2.53 MeOH·1.60 $H_2O$. We will briefly comment on the intramolecular hydrogen bonds, see Table 4. Each (py)C(Me)NOH oxime group is strongly intramolecularly hydrogen-bonded to an uncoordinated O atom from an 3.2100 sulfato ligand. The other uncoordinated O atom of each 3.2100 sulfato ligand also acts as acceptor; the donors for these hydrogen bonds are the MeOH and $H_2O$ ligands. The sulfato O(13) atom participates in two hydrogen bonds; of interest is also the fact that the lattice water oxygen atom OW(31) acts both as a donor and as an acceptor.

The structures of the hexanuclear molecules present in complexes **2**·3.2 MeOH·1.5 $H_2O$ (Figure 7) and **3**·3 $H_2O$ (Figure 8) are very similar to the structure of **1** except that: (i) The (py)C(Me)NOH/(py)C(Me)$NO^-$ ligands of **1** are replaced by (py)C(ph)NOH/(py)C(ph)$NO^-$ ligands in **2** and **3**, and (ii) the peripheral MeOH and $H_2O$ ligands of **1** are replaced by three terminal MeOH ligands in **2** and three terminal $H_2O$ ligands in **3**. Note that there are two crystallographically independent hexanuclear molecules in **3**·3 $H_2O$, but their bond lengths and angles differ only marginally. The three compounds also differ in the lattice solvate molecules that are present.

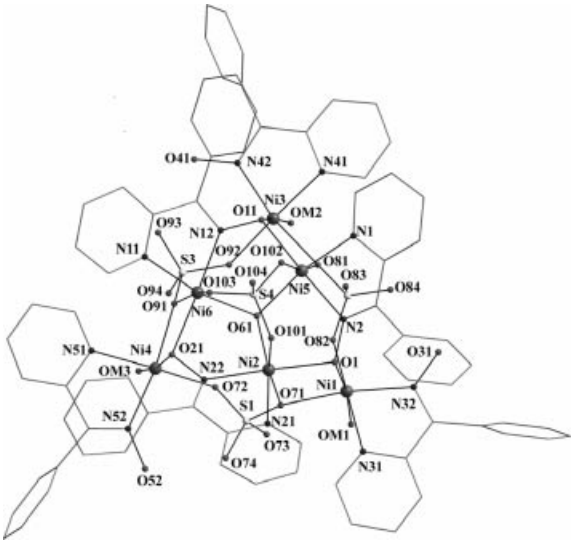


Figure 7. Partially labelled plot of the hexanuclear molecule present in complex **2**·3.2 MeOH·1.5 $H_2O$. The hydrogen atoms have been omitted for clarity.

The ligands (py)C(Me)NOH, (py)C(Me)$NO^-$, (py)C(ph)NOH and (py)C(ph)$NO^-$ have been observed in numerous ligation modes over the years.[12] Because most of their

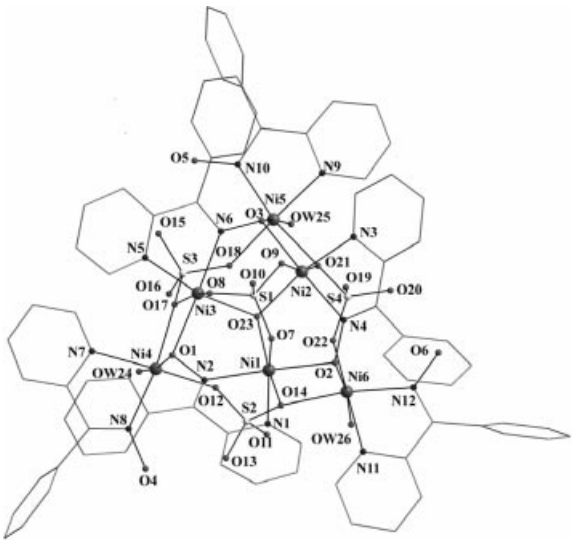


Figure 8. Partially labelled plot of one of the two, crystallographically independent hexanuclear molecules present in complex **3**·3 $H_2O$. The hydrogen atoms have been omitted for clarity.

complexes were reported only recently, we felt it timely to collect the structurally characterized non-organometallic, metal complexes of these ligands in Tables 7 and 8, together with the cores of the polynuclear complexes and the coordination modes of (py)C(R)NOH/(py)C(R)$NO^-$ (R = Me, Ph). Inspection of Tables 7 and 8 clearly shows that: (i) the complexes **1**–**3** are amongst the highest-nuclearity clusters of any metal identified with the (py)C(R)$NO^-$ ligands, (ii) the 2.111 coordination mode is the most common for the bridging (py)C(R)$NO^-$ ligands, and (iii) the 3.211 mode of (py)C(Me)$NO^-$ observed in **1** is new, i.e. it has not been characterized before, while this mode is rare in the complexes containing bridging (py)C(ph)$NO^-$ ligands.

Complexes **1**–**3** join a rather small, but growing family of $Ni^{II}_6$ complexes bearing N- and/or O-donors and possessing the metal ions in various topologies, such as hexagons, Chinese-lantern-like objects and face-shared distorted dicubanes in which one of the corners of each cubane is missing.[24] Complexes **1**–**3** are the highest-nuclearity sulfato nickel(II) clusters which have been structurally characterized.

## Magnetic Studies

Solid-state dc magnetic susceptibility measurements were performed on polycrystalline samples of the representative complexes **1** and **2**, under a constant field of 0.04 T in the temperature range 2.0–300 K. The $\chi_M T$ vs. $T$ plots for the two complexes are shown in Figure 9. The complexes exhibit a very similar magnetic behavior. The $\chi_M T$ values at room temperature are 7.39 $cm^3 mol^{-1}$ K for **1** and 7.50 $cm^3 mol^{-1}$ K for **2**, close to the expected value of 7.59 $cm^3 mol^{-1}$ K for six non-interacting $S = 1$ centers assuming $g = 2.25$. As the temperature is lowered, the $\chi_M T$ product for both compounds experiences a slight decrease in the 300 to ca. 75 K range, followed by a sharper decline

 © 2007 Wiley-VCH Verlag GmbH & Co. KGaA, Weinheim 

Table 7. Formulae, coordination modes of the ligands and cores for the structurally characterized metal complexes of (py)C(Me)NOH and/or (py)C(Me)NO$^-$.

| Complex[a] | Coordination modes[b] | Core[c] | Ref. |
|---|---|---|---|
| $[Mn^{III}_3O(O_2CMe)_3\{(py)C(Me)NO\}_3]$ | 2.111 | $[Mn^{III}_3(\mu_3\text{-}O)]^{7+}$ | [10h,10n] |
| $[Mn^{III}_3O(O_2CEt)_3\{(py)C(Me)NO\}_3]$ | 2.111 | $[Mn^{III}_3(\mu_3\text{-}O)]^{7+}$ | [10h,10n] |
| *fac*-$[Co^{III}\{(py)C(Me)NO\}_3]$ | 1.011 | | [14a] |
| $[NiBr_2\{(py)C(Me)NOH\}_2]$ | 1.011 | | [23a] |
| $[Ni\{(py)C(Me)NO\}\{(py)C(Me)NOH\}(H_2O)_2]^+$ [d] | 1.011, 1.011 | | [23a,23b] |
| $[Ni_6(SO_4)_4(OH)\ \{(py)C(Me)NO\}_3\{(py)C(Me)NOH\}_3(MeOH)_2(H_2O)]$ | 3.211, 1.011 | $[Ni_6(\mu_3\text{-}OH)(\mu_3\text{-}SO_4)_3(\mu_3\text{-}ONR)_3]^{2+}$ [e] | this work |
| $[ZnCl_2\{(py)C(Me)NOH\}_2]$ | 1.011 | | [23c] |
| $[Zn_4(OH)_2Cl_2\{(py)C(Me)NO\}_4]$ | 2.111 | $[Zn_4(\mu\text{-}OH)_2]^{6+}$ | [23c] |
| $[Zn(NO_3)_2\{(py)C(Me)NOH\}_2]$ | 1.011 | | [23d] |
| $[Rh^{III}Cl_2\{(py)C(Me)NO\}\{(py)C(Me)NOH\}]$ | 1.011, 1.011 | | [23e] |
| $[Pt^{II}\{(py)C(Me)NO\}_2]$ | 1.011 | | [23f] |
| $n$-$Bu_8Sn_4O_2\{(py)C(Me)NO\}_4$ | 1.100, 2.101 | $[Sn^{IV}_4(\mu_3\text{-}O)_2]^{12+}$ | [23g] |
| $[Et_8Sn_4O_2\{(py)C(Me)NO\}_4]$ | 1.100, 2.101 | $[Sn^{IV}_4(\mu_3\text{-}O)_2]^{12+}$ | [23g] |
| $[Me_8Sn_4O_2\{(py)C(Me)NO\}_4]$ | 1.100, 2.111 | $[Sn^{IV}_4(\mu_3\text{-}O)_2]^{12+}$ | [23h] |
| $[Ph_3Sb\{(py)C(Me)NO\}_2]$ | 1.100 | | [23i] |

[a] Counterions and lattice solvent molecules have been omitted. [b] Using Harris notation[21] (see also Figure 6). [c] Only for the polynuclear complexes; the nitrogen atoms of the $\mu_3$ oximate groups and the terminal oxygen atoms of the 3.2100 sulfato ligands are considered as contributors to the cores. [d] Both the nitrate and perchlorate salts have been structurally characterized. [e] Another representation of the core could be $[Ni_6(\mu_3\text{-}OH)(\mu\text{-}OR')_3(\mu\text{-}OR'')_3]^{2+}$, where R′– = –$SO_3$ and R″– = –NC(py)(Me).

Table 8. Formulae, coordination modes of the ligands and cores for the structurally characterized metal complexes of (py)C(ph)NOH and/or (py)C(ph)NO$^-$.

| Complex[a] | Coordination modes[b] | Core[c] | Ref. |
|---|---|---|---|
| $[Mn(O_2CPh)_2\{(py)C(ph)NOH\}_2]$ | 1.011 | | [10c] |
| $[Mn^{II}_4Mn^{III}_4(OH)_2O_2(O_2CPh)_{10}\{(py)C(ph)NO\}_4]$ | 2.111 | $[Mn^{II}_4Mn^{III}_4(\mu_4\text{-}O)_2(\mu_3\text{-}OH)_2]^{14+}$ | [10c] |
| $[Mn^{II}_3Mn^{IV}O(N_3)(O_2CPh)_3\{(py)C(ph)NO\}_4]$ | 2.111 | $[Mn^{II}_3Mn^{IV}(\mu_4\text{-}O)(\eta^1\text{:}\ \mu_2\text{-}N_3)]^{7+}$ | [10i] |
| $[Mn^{III}_3O(O_2CMe)_3\{(py)C(ph)NO\}_3]$ | 2.111 | $[Mn^{III}_3(\mu_3\text{-}O)]^{7+}$ | [10n] |
| $[Co^{II}Co^{III}_2\{(py)C(ph)NO\}_6]^{2+}$ | 2.111 | $[Co^{II}Co^{III}_2(\mu\text{-}ONR)_6]^{2+}$ | [14a] |
| *mer*-$[Co^{III}\{(py)C(ph)NO\}_3]$ | 1.011 | | [14a] |
| $[Ni_4(O_2CMe)_4\{(py)C(ph)NO\}_4(MeOH)_2]$ | 3.211 | $[Ni_4(\mu_3\text{-}ONR)_4]^{4+}$[d] | [10p] |
| $[Ni_6(SO_4)_4(OH)\{(py)C(ph)NO\}_3\{(py)C(ph)NOH\}_3(MeOH)_3]$ | 3.211, 1.011 | $[Ni_6(\mu_3\text{-}OH)(\mu_3\text{-}SO_4)_3(\mu_3\text{-}ONR)_3]^{2+}$[e] | this work |
| $[Ni_6(SO_4)_4(OH)\{(py)C(ph)NO\}_3\{(py)C(ph)NOH\}_3(H_2O)_3]$ | 3.211, 1.011 | $[Ni_6(\mu_3\text{-}OH)(\mu_3\text{-}SO_4)_3(\mu_3\text{-}ONR)_3]^{2+}$[e] | this work |

[a] Counterions and lattice solvent molecules have been omitted. [b] Using Harris notation[21] (see also Figure 6). [c] Only for the polynuclear complexes; the nitrogen atoms of the $\mu_3$ oximate groups and the terminal oxygen atoms of the 3.2100 sulfato ligands are considered as contributors to the cores. [d] Another representation of the core could be $[Ni_4(\mu\text{-}OR')_4]^{4+}$. [e] Another representation of the core could be $[Ni_6(\mu_3\text{-}OH)(\mu\text{-}OR')_3(\mu\text{-}OR'')_3]^{2+}$, where R′ = $SO_3$ and R″ = NC(py)(ph).

at lower temperatures and reaching the values of 2.37 (**1**) and 3.14 (**2**) $cm^3\,mol^{-1}\,K$ at 2.0 K. The data indicate an overall antiferromagnetic behavior. Magnetization experiments performed at 2.0 K (Figure 10) show a continuous increase of $M$ as the field increases, reaching a non-saturated value close to five electrons under an external field of 5 T.

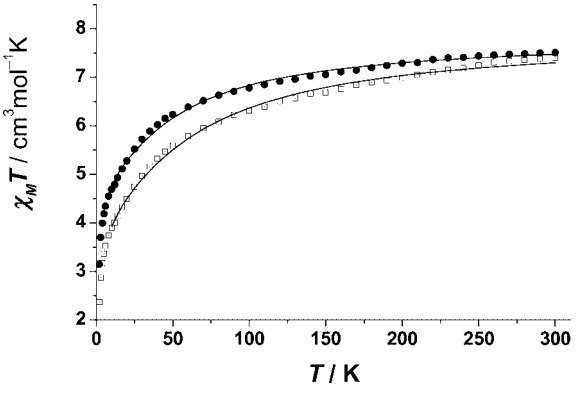


Figure 9. $\chi_M T$ vs. $T$ plots for complexes **1** (open squares) and **2** (open circles). The solid lines represent the best fit to the data as described in the text.

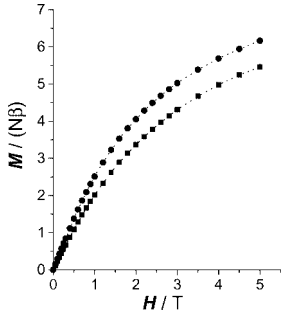


Figure 10. Magnetization plots for compounds **1** (filled squares) and **2** (filled circles) at 2 K. The dashed lines are guides for the eye.

Close inspection of the very similar molecular structures reveals that there are four different superexchange pathways and thus four different kinds of $J$ values: $J_1$ is associated (from now onwards the numbering scheme that will be used

 © 2007 Wiley-VCH Verlag GmbH & Co. KGaA, Weinheim 

is the same with that used in the real structure of **1**, see Figure 3) with the Ni(1)···Ni(2), Ni(2)···Ni(3) and Ni(1)···Ni(3) interactions through the central hydroxido bridge, a triatomic part of the 3.1110 sulfato ligand and one diatomic oximate group from a 3.211 (py)C(Me)NO$^-$ ligand; $J_2$ is associated with the Ni(1)···Ni(6), Ni(2)···Ni(5) and Ni(3)···Ni(4) interactions, each through a double ($\mu$-$O_{sulfato}$)/($\mu$-$O_{oximate}$) pathway; $J_3$ is associated with the Ni(1)···Ni(4), Ni(2)···Ni(6) and Ni(3)···Ni(5) interactions, each through one diatomic oximate group from a 3.211 (py)C(Me)NO$^-$ ligand (the Ni–O–N–Ni torsion angles are close to 90°); and finally $J_4$ is associated with the Ni(4)···Ni(5), Ni(5)···Ni(6) and Ni(4)···Ni(6) interactions, each through a single triatomic part of one 3.2100 sulfato ligand. If we consider that the six Ni$^{II}$ ions occupy the apices of a very distorted octahedron, the superexchange pathways are along the twelve edges. The spin Hamiltonian for such a system is given by Equation (1).

$$H = -J_1(S_1\cdot S_2 + S_1\cdot S_3 + S_2\cdot S_3) - J_2(S_1\cdot S_6 + S_2\cdot S_5 + S_3\cdot S_4) - J_3(S_1\cdot S_4 + S_2\cdot S_6 + S_3\cdot S_5) \quad (1)$$

$$H = -J_4(S_4\cdot S_5 + S_4\cdot S_6 + S_5\cdot S_6)$$

To avoid a vast parameterization, we decided to attempt to fit the susceptibility data using a simpler 2-$J$ model. In order to decide the best way to reduce the number of the coupling constants, we have performed the following analysis of the above mentioned "octahedral" model. It is known that the superexchange Ni–O–X–O–Ni interactions mediated by tetrahedral anions with electronegative central atoms, e.g. $SO_4^-$, $ClO_4^-$, $PO_4^{3-}$, are negligible.[18] Assuming $J_4 = 0$, the spin Hamiltonian can be expressed in the form of Equation (2) and the resulting new, simpler interaction scheme is shown in Figure 11. In Figure 12 we show some selected simulations of the magnetic response of the "octahedral" model, performed by means of the program CLUMAG.[25]

$$H = -J_1(S_1\cdot S_2 + S_1\cdot S_3 + S_2\cdot S_3) - J_2(S_1\cdot S_6 + S_2\cdot S_5 + S_3\cdot S_4) - J_3(S_1\cdot S_4 + S_2\cdot S_6 + S_3\cdot S_5) \quad (2)$$

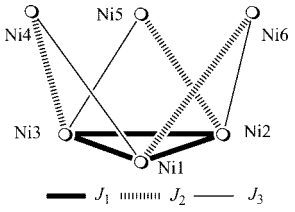


Figure 11. A 3-$J$ exchange-interaction pattern corresponding to the Hamiltonian of Equation (2) for the hexanuclear clusters reported in this work. The Hamiltonian of Equation (3) follows the same scheme assuming $J_2 = J_3$. The exchange pathways corresponding to $J_1$, $J_2$ and $J_3$ are described in the text. The numbering scheme used for the Ni$^{II}$ ions is the same with that used in the solution of the structure of **1**·2.53 MeOH·1.60 $H_2O$. Atoms Ni(1), Ni(2), Ni(3), Ni(4), Ni(5) and Ni(6) of the shown interaction scheme correspond to atoms Ni(2), Ni(5), Ni(6), Ni(4), Ni(3) and Ni(1), respectively, of the structure of **2**·3.2 MeOH·1.5 $H_2O$ (Figure 7).

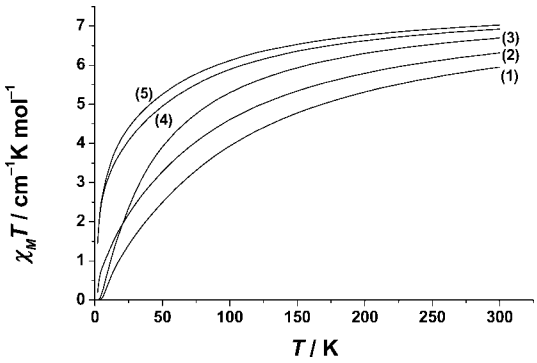


Figure 12. Calculated $\chi_M T$ vs. $T$ curves for a spin system similar to that of **1**–**3** and for various sets of the $J$ constants. A detailed description of the curves (1)–(5) is given in the text.

Curve (1) represents the behavior of a system on the basis of the Hamiltonian of Equation (1) in the case of $J_1 = J_2 = J_3 = J_4 = -20$ cm$^{-1}$ and $g = 2.25$. This system has a well-defined $S = 0$ ground state as can be seen in Figure 13. Removing the interaction in one of the octahedral faces, i.e. $J_4 = 0$, with $J_1 = J_2 = J_3 = -20$ cm$^{-1}$ and $g = 2.25$, and applying the Hamiltonian of Equation (2), we obtained curve (2); the system has a new $S = 0$ ground state (Figure 13). Curve (3) of Figure 12 is the result of the calculation with the parameters $J_1 = -20$ cm$^{-1}$, $J_2 = -10$ cm$^{-1}$, $J_3 = -5$ cm$^{-1}$ and $g = 2.25$. Again the system has an $S = 0$ ground state (Figure 13). As it is clearly evident in Figure 12, in these three cases the $\chi_M T$ value tends to zero at low temperatures by contrast with the experimental behavior of **1** and **2**, see Figure 9. More interesting are plots/curves (4) and (5) of Figure 12, obtained applying the sets $J_1 = -20$ cm$^{-1}$, $J_2 = -5$ cm$^{-1}$, $J_3 = -5$ cm$^{-1}$ and $J_1 = -20$ cm$^{-1}$, $J_2 = -5$ cm$^{-1}$, $J_3 = 0$ cm$^{-1}$, respectively. For these simulations in which $J_1 >> J_2$, $J_3$, the $\chi_M T$ product does not strongly tend to zero at low temperatures (in agreement with the experimental data, see Figure 9); this is a consequence of the close "distances" of the $S = 0$, 1, 2, 3 states in the energy spectrum, see Figure 13 for the $J_1 = -20$ cm$^{-1}$, $J_2 = -5$ cm$^{-1}$, $J_3 = -5$ cm$^{-1}$ case, plot (4). It is important to realize that the relative values of $J_2$ and $J_3$ become poorly relevant and it is not reliable to try to fit separately these two coupling constants. It should be mentioned at this point that any calculation assuming $J_1 << J_2$, $J_3$ gives $\chi_M T$ products that clearly tend to a value close to zero, and such a situation can not be assumed for **1** and **2**.

On the basis of the above calculations, we decided to apply the spin Hamiltonian of Equation (3), where $J_1$ is the coupling constant for the interactions within the small triangle [defined by Ni(1), Ni(2) and Ni(3) in **1**] and $J_2$ is a common coupling constant associated with the six interactions between the small triangle and the three peripheral Ni$^{II}$ ions [Ni(4), Ni(5) and Ni(6) in **1**]. The best-fit parameters are $J_1 = -20.5$ cm$^{-1}$, $J_2 = -2.3$ cm$^{-1}$, $g = 2.29$ for **1** and $J_1 = -17.0$ cm$^{-1}$, $J_2 = -1.9$ cm$^{-1}$, $g = 2.30$ for **2**. The agreement factor, defined as $R = \Sigma[(\chi_M)_{calcd.} - (\chi_M)_{obsd.}]^2/\Sigma[(\chi_M)_{obsd.}]^2$ was $1.1 \times 10^{-4}$ and $8.1 \times 10^{-5}$ for **1** and **2**, respectively, see Figure 9. Looking at the energy of the $S =$

 © 2007 Wiley-VCH Verlag GmbH & Co. KGaA, Weinheim 

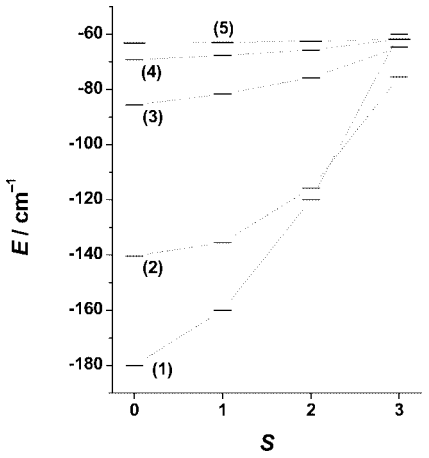


Figure 13. Energy levels for the $S = 0, 1, 2, 3$ states in the following cases: Plot (1) refers to $J_1 = J_2 = J_3 = J_4 = 20\ cm^{-1}$; plot (2) refers to $J_1 = J_2 = J_3 = -20\ cm^{-1}$; plot (3) refers to $J_1 = -20\ cm^{-1}$, $J_2 = -10\ cm^{-1}$, $J_3 = -5\ cm^{-1}$; plot (4) refers to $J_1 = -20\ cm^{-1}$, $J_2 = -5\ cm^{-1}$, $J_3 = -5\ cm^{-1}$; plot (5) refers to $J_1 = -20.5\ cm^{-1}$, $J_2 = J_3 = -2.3\ cm^{-1}$, $g = 2.29$, set of parameters resulting from the fitting procedure for **1** based on the Hamiltonian of Equation (3).

0, 1, 2, 3 levels [plot (5) in Figure 13], we realize that these spin levels are very close, i.e. with a very narrow range of less than $1.5\ cm^{-1}$, in good agreement with the magnetization data (Figure 10). Upon increasing the external field, the close non-zero spin levels give a non-saturated magnetization at 2 K as a result of the partial population of levels up to $S = 3$. The next lower $S = 4$ level is $26\ cm^{-1}$ higher in energy, excluding a magnetization corresponding to more than six unpaired electrons, as it is experimentally observed.

$$H = -J_1(S_1 \cdot S_2 + S_1 \cdot S_3 + S_2 \cdot S_3) - J_2(S_1 \cdot S_6 + S_2 \cdot S_5 + S_3 \cdot S_4 + S_1 \cdot S_4 + S_2 \cdot S_6 + S_3 \cdot S_5) \quad (3)$$

The bridging =N–O$^-$ group is known to be very efficient in mediating a strong antiferromagnetic interaction, which is provided by an orbital exchange pathway essentially of σ nature.[14c] The antiferromagnetic $J_1$ coupling is consistent with its mediation mainly by two types of bridges, a single-atom $\mu_3$-OH$^-$ group with a Ni–O(H)–Ni angle of ca. 110° and a diatomic =N–O$^-$ linkage. The non-planarity of the Ni–O–N–Ni moiety (noticeable torsion angle) reduces the antiferromagnetism, giving rise to moderate antiferromagnetic coupling.[24b] The sign of $J_2$ seems logical owing to its mediation by a $(\mu\text{-O})_2$ pathway with an average Ni–O–Ni angle of ca. 101° and one diatomic, non-planar =N–O$^-$ linkage; however, its magnitude can not be easily rationalized in the simple 2-$J$ model adopted.

## Conclusions and Perspectives

The initial use of the sulfate ligand in nickel(II)/2-pyridyl oximes chemistry, i.e. the study of the coordination chemistry of the *binary* $SO_4^{2-}$/(py)C(R)NOH (R = Me, Ph) "ligand blends" with nickel(II), has provided access to three hexanuclear clusters with interesting structures and magnetic features. The magnetic properties of two representative clusters have been interpreted using two exchange interactions in a simplified model.

Analogues of **1**–**3** with 2-pyridinecarbaldehyde oxime [(py)C(H)NOH] or di-2-pyridyl ketone oxime [$(py)_2$-CNOH], see Figure 1, are not known, until to date, and it is currently not evident whether the preparation and stability of such hexanuclear complexes are dependent on the particular nature of the R substituent on the oxime/oximate carbon. Clearly the $Ni^{II}/SO_4^{2-}$/(py)C(R)NOH chemistry warrants further study and expansion to other 3d-metals. Synthetic efforts are also in progress to realize a higher bridging behavior of the $SO_4^{2-}$ ion, e.g. $\mu_4$-$\mu_6$ (Figure 2) in 3d-metal/(py)C(R)NOH chemistry. Because the $\mu_3$-OH$^-$ ligand propagates antiferromagnetic exchange interactions in the small $Ni_3$ triangular unit of **1**–**2**, we are intensively pursuing our efforts to substitute the hydroxido bridge by an end-on triply bridging azido ligand ($\eta^1$:$\mu_3$ or 3.100), according to our well-developed synthetic strategy,[26] in order to introduce specifically ferromagnetic components in the superexchange Scheme. Work at the time of writing shows that most of the just mentioned perspectives are realizable.

## Experimental Section

**Materials and Physical Measurements:** All manipulations were performed under aerobic conditions using materials and solvents (Merck, Aldrich) as received. Complex $[Ni(SO_4)\{(py)C(Me)NOH\}(H_2O)_3]$ was prepared as described elsewhere.[19] Methyl 2-pyridyl ketone oxime, (py)C(Me)NOH, was synthesized by the reaction of equimolar quantities of 1-pyridin-2-ylethanone (2-acetylpyridine), (py)C(Me)O, $H_2NOH{\cdot}HCl$ and NaOEt in EtOH.[27] Elemental analyses (C, H, N) were performed by the University of Ioannina (Greece) Microanalytical Laboratory with an EA 1108 Carlo–Erba analyzer. IR spectra (4000–400 $cm^{-1}$) were recorded with a Perkin–Elmer 16 PC FT-spectrometer with samples prepared as KBr pellets. Magnetic susceptibility measurements in the 1.9–300 K range under a field of 0.5 T were performed with a Quantum Design SQUID magnetometer at the Magnetochemistry Service of the University of Barcelona. All measurements were carried out on polycrystalline samples. Data were corrected for diamagnetic contributions using Pascal's constants.

**$[Ni_6(SO_4)_4(OH)\{(py)C(Me)NO\}_3\{(py)C(Me)NOH\}_3(MeOH)_2(H_2O)]{\cdot}2.53\,MeOH{\cdot}1.60\,H_2O$ ($1{\cdot}2.53\,MeOH{\cdot}1.60\,H_2O$). Method A:** Solid NaOMe (0.033 g, 0.60 mmol) was added to a colorless solution of (py)C(Me)NOH (0.082 g, 0.60 mmol) in MeOH (25 mL); the solid soon dissolved. Solid $NiSO_4{\cdot}6H_2O$ (0.158 g, 0.60 mmol) was then added and the resultant solution was stirred for 1 h at room temperature. A small quantity of undissolved material was removed by filtration and the green filtrate layered with $Et_2O$ (50 mL). Slow mixing gave X-ray quality green crystals of the product. The crystals were collected by filtration, washed with cold $H_2O$ (1 mL), cold MeOH (2 mL) and ice-cold $Et_2O$ ($2 \times 3$ mL), and dried in air. Yield: 0.114 g (65%). The air-dried solid analyzed satisfactorily as MeOH-free ($1{\cdot}1.60\,H_2O$). $C_{44}H_{59.20}N_{12}Ni_6O_{27.60}S_4$ (1678.34): calcd. C 31.79, H 3.59, N 10.11; found C 31.45, H 3.72, N 9.98. IR data (KBr pellet): $\tilde{\nu}$ = 3430 (sh), 3406 (m, broad), 1652 (m), 1602 (s), 1562 (w), 1476 (m), 1440 (w), 1376 (w), 1334 (w), 1148 (s), 1126 (s), 1070 (s), 1036 (s), 984 (m), 782 (m), 690 (m), 628 (m), 592 (w), 484 (w), 430 (w) $cm^{-1}$.

 © 2007 Wiley-VCH Verlag GmbH & Co. KGaA, Weinheim 

**Method B:** A colorless solution of (py)C(Me)NOH (0.136 g, 1.00 mmol) in MeOH (10 mL) was slowly added to a slurry of $LiOH·H_2O$ (0.042 g, 1.00 mmol) in MeOH (5 mL); the hydroxide soon dissolved. The solution was then added to a slurry of $NiSO_4·6H_2O$ (0.263 g, 1.00 mmol) in MeOH (10 mL) and the resulting green solution was stirred for 1 h at room temperature. A small quantity of undissolved material was removed by filtration. The filtrate was allowed to stand undisturbed in a closed flask for a period of 4–5 d. Green crystals appeared which were collected by filtration, washed with cold $H_2O$ (1 mL), cold MeOH (1 mL) and ice-cold $Et_2O$ (2 mL), and dried in air. Yield: 0.123 g (42%). The dried solid was analyzed satisfactorily as **1**·1·60 $H_2O$. The identity of the product was further confirmed by IR spectroscopic comparison with the authentic sample prepared by method A.

**Method C:** A suspension of compound $[Ni(SO_4)\{(py)C(Me)NOH\}(H_2O)_3]$ (0.080 g, 0.22 mmol) in warm MeOH (25 mL) was treated with solid $LiOH·H_2O$ (0.006 g, 0.15 mmol). The mixture was stirred overnight at 30 °C, filtered to remove a few quantity of undissolved starting material, and the green solution was then allowed to stand undisturbed in a closed vial at room temperature. Green prismatic crystals formed within 12–14 h, and these were collected by filtration, washed with cold MeOH (2 × 2 mL) and dried in the air. Yield (based on the mononuclear complex): 0.026 g (40%). The product was identified by microanalyses and IR comparison with material from method A.

**$[Ni_6(SO_4)_4(OH)\{(py)C(ph)NO\}_3\{(py)C(ph)NOH\}_3(MeOH)_3]$·3.2 MeOH·1.5 $H_2O$ (2·3.2 MeOH·1.5 $H_2O$) and $[Ni_6(SO_4)_4(OH)\{(py)C(ph)NO\}_3\{(py)C(ph)NOH\}_3(H_2O)_3]$·3 $H_2O$ (3·3 $H_2O$) as a Mixture:** Solid NaOMe (0.033 g, 0.60 mmol) was added to a colorless solution of (py)C(ph)NOH (0.119 g, 0.60 mmol) in MeOH (25 mL); the solid soon dissolved. Solid $NiSO_4·6H_2O$ (0.158 g, 0.60 mmol) was then added and the resulting solution was stirred for 1 h at room temperature. A small quantity of undissolved material was removed by filtration and the orange filtrate layered with $Et_2O$ (50 mL). Slow mixing gave an approximately 1:1 mixture of greenish yellow prisms and yellow plates. The crystals were carefully collected by filtration, washed with cold $H_2O$ (0.5 mL), cold MeOH (1 mL) and ice-cold $Et_2O$ (2 × 3 mL), and dried in air. The two products were readily separable manually, and the yellow prisms and yellow plates proved by single-crystal X-ray crystallography to be complexes **2**·3.2 MeOH·1.5 $H_2O$ and **3**·3 $H_2O$, respectively. Batches of the different samples were used for analyses and characterization. Yield for **2**·3.2 MeOH·1.5 $H_2O$: 0.065 g (30%). The air-dried solid was analyzed satisfactorily as MeOH-free (**2**·1.5 $H_2O$). $C_{75}H_{73}N_{12}Ni_6O_{27.5}S_4$ (2059.96): calcd. C 43.67, H 3.57, N 8.15; found C 43.23, H 3.72, N 7.91. IR data (KBr pellet)

Table 9. Crystal data and structure refinement for $[Ni_6(SO_4)_4(OH)\{(py)C(Me)NO\}_3\{(py)C(Me)NOH\}_3(MeOH)_2(H_2O)]$·2.53 MeOH·1.60 $H_2O$ (**1**·2.53 MeOH·1.60 $H_2O$), $[Ni_6(SO_4)_4(OH)\{(py)C(ph)NO\}_3\{(py)C(ph)NOH\}_3(MeOH)_3]$·3.2 MeOH·1.5 $H_2O$ (**2**·3.2 MeOH·1.5 $H_2O$) and $[Ni_6(SO_4)_4(OH)\{(py)C(ph)NO\}_3\{(py)C(ph)NOH\}_3(H_2O)_3]$·3 $H_2O$ (**3**·3 $H_2O$).

| | **1**·2.53 MeOH·1.60 $H_2O$ | **2**·3.2 MeOH·1.5 $H_2O$ | **3**·3 $H_2O$ |
|---|---|---|---|
| Empirical formula | $C_{46.53}H_{69.32}N_{12}Ni_6O_{30.13}S_4$ | $C_{78.20}H_{85.80}N_{12}Ni_6O_{30.70}S_4$ | $C_{72}H_{70}N_{12}Ni_6O_{29}S_4$ |
| Mol. mass | 1759.40 | 2165.49 | 2047.90 |
| Colour and habit | green prisms | yellow prisms | yellow plates |
| Crystal size [mm] | 0.09 × 0.15 × 0.17 | 0.15 × 0.35 × 0.75 | 0.03 × 0.11 × 0.11 |
| Crystal system | monoclinic | monoclinic | monoclinic |
| Space group | $P2_1/n$ | $P2_1/n$ | $Cc$ |
| $a$ [Å] | 12.639(1) | 30.941(18) | 29.854(2) |
| $b$ [Å] | 41.824(2) | 17.235(9) | 17.358(12) |
| $c$ [Å] | 13.223(1) | 23.649(13) | 33.731(2) |
| $\alpha$ [°] | 90 | 90 | 90 |
| $\beta$ [°] | 102.95(1) | 97.24(2) | 96.43(2) |
| $\gamma$ [°] | 90 | 90 | 90 |
| $V$ [Å$^3$] | 6811.8(7) | 12511(12) | 17370(2) |
| $Z$ | 4 | 4 | 8 |
| $\rho_{calcd.}$ [g cm$^{-3}$] | 1.714 | 1.150 | 1.566 |
| $T$ [°C] | –173(2) | 25 | –80(2) |
| $\lambda$ [Mo-$K_\alpha$] [Å] | 0.71073 | | |
| Synchrotron [Å] | | | 0.77490 |
| $\lambda$ [Cu-$K_\alpha$] [Å] | | 1.54180 | |
| $\mu$ [mm$^{-1}$] | 1.840 | 2.140 | 1.835 |
| $F$(000) | 3616 | 4466 | 8400 |
| $2\theta_{max}$ [°] | 50.06 | 101.36 | 67.30 |
| Index ranges | $-15 \le h \le 14$ | $-31 \le h \le 29$ | $-42 \le h \le 42$ |
| | $-46 \le k \le 49$ | $-17 \le k \le 0$ | $-24 \le k \le 22$ |
| | $-15 \le l \le 15$ | $0 \le l \le 23$ | $-47 \le l \le 48$ |
| No. of reflections collected | 33882 | 13070 | 95514 |
| No. of independent reflections/$R_{int.}$ | 11105/0.0540 | 12673/0.0178 | 51324/0.0338 |
| Data with $I > 2\sigma(I)$ | 7069 | 9308 | 49155 |
| Parameters refined | 984 | 1171 | 2219 |
| $[\Delta/\sigma]_{max}$ | 0.000 | 0.003 | 0.001 |
| GOF (on $F^2$) | 0.938 | 1.055 | 1.106 |
| $[R_1]$[a] | 0.0461 | 0.0729 | 0.0534 |
| $wR_2$[b] | 0.0825 | 0.1988 | 0.1514 |
| Residuals [e Å$^{-3}$] | 1.068/–0.525 | 0.774/–0.644 | 1.149/–1.101 |

[a] $R_1 = \Sigma(|F_o| - |F_c|)/\Sigma(|F_o|)$. [b] $wR_2 = \{\Sigma[w(F_o^2 - F_c^2)^2]/\Sigma[w(F_o^2)^2]\}^{1/2}$.

 © 2007 Wiley-VCH Verlag GmbH & Co. KGaA, Weinheim 

for **2**·1.5 $H_2O$: $\tilde{\nu}$ = 3415 (sh), 3396 (m, broad), 1599 (m), 1470 (m), 1442 (m), 1341 (w), 1180 (s), 1129 (s), 1051 (s), 1028 (s), 965 (m), 792 (m), 745 (m), 706 (m), 628 (m), 595 (w), 474 (w), 432 (w) $cm^{-1}$. Yield for **3**·3 $H_2O$: 0.073 g (35%). $C_{72}H_{70}N_{12}Ni_6O_{29}S_4$ (2047.90): calcd. C 43.37, H 3.24, N 8.43; found C 43.45, H 3.14, N 8.50. IR data (KBr pellet) for **3**·3 $H_2O$: $\tilde{\nu}$ = 3401 (sh), 3255 (m, broad), 1604 (m), 1466 (m), 1442 (m), 1337 (w), 1175 (s), 1125 (s), 1048 (s), 1028 (s), 971 (m), 788 (m), 746 (m), 704 (m), 627 (m), 598 (w), 468 (m), 429 (w) $cm^{-1}$.

**$[Ni_6(SO_4)_4(OH)\{(py)C(ph)NO\}_3\{(py)C(ph)NOH\}_3(H_2O)_3]$·3 $H_2O$ (3·3 $H_2O$):** This complex was prepared pure in the form of yellow plates in a manner analogous to the above mentioned mixture, but using $LiOH·H_2O$ (0.017 g, 0.40 mmol) in place of NaOMe and $MeOH/H_2O$ (25 mL, 8:2, v/v) instead of MeOH. The yield was 0.001 g (60%). The air-dried solid analyzed satisfactorily as **3**·3 $H_2O$. The identity of the product was further confirmed by unit cell determinations of three crystals. The three individual determinations revealed a unit cell with dimensions identical to those found for the yellow plates, which resulted from the above described procedure that led to the mixture of **2**·3.2 MeOH·1.5 $H_2O$ and **3**·3 $H_2O$.

**X-ray Crystallographic Studies:** Crystals of **1**·2.53 MeOH·1.60 $H_2O$ were mounted in Paratone-N oil, crystals of **2**·3.2 MeOH·1.5 $H_2O$ in capillary filled with drops of mother liquor and crystals of **3**·3 $H_2O$ were mounted in air at low temperature. Diffraction measurements for **1**·2.53 MeOH·1.60 $H_2O$ were made with an Oxford Diffraction CCD instrument using graphite-monochromated Mo radiation. The X-ray data set for **2**·3.2 MeOH·1.5 $H_2O$ was collected with a $P2_1$ Nicolet diffractometer upgraded by Crystal Logic using graphite-monochromated Cu-$K_\alpha$ radiation, while diffraction measurements for **3**·3 $H_2O$ were made with a Bruker Platinum 200 CCD diffractometer on Station 11.3.1[28a] of the Advanced Light Source at Lawrence Berkeley National Laboratory, with wavelength on 0.77490 Å from a Silicon 111 monochromator. Complete crystal data and parameters for data collection and refinement are listed in Table 9. Unit cell dimensions were determined and refined by using 10130 (for **1**·2.53 MeOH·1.60 $H_2O$ at 100 K), 25 (for **2**·3.2 MeOH·1.5 $H_2O$ at 298 K) and 8475 (for **3**·3 $H_2O$ at 193 K) reflections in the ranges $10.44 < 2\theta < 55.66°$, $22 < 2\theta < 54°$ and $5.10 < 2\theta < 67.30°$, respectively. The crystals of **2**·3.2 MeOH·1.5 $H_2O$ had poor diffraction ability (despite their sufficient size) and the data were collected in increasing $2\theta$ shells. The data collection was terminated when about 50% of the collected shell data were unobserved. The structures were solved by direct methods using SIR92[28b] (**1**·2.53 MeOH·1.60 $H_2O$), SHELXS-86[28c] (**2**·3.2 MeOH·1.5 $H_2O$) and Bruker SHELXTL[28d] (**3**·3 $H_2O$), and refined by full-matrix least-squares techniques on $F^2$ with SHELXL-97[28e] (for **1**·2.53 MeOH·1.60 $H_2O$ and **2**·3.2 MeOH·1.5 $H_2O$) and Bruker SHELXTL[28d] (for **3**·3 $H_2O$). For all the structures the fully occupied non-hydrogen atoms were refined anisotropically. In the case of **1**·2.53 MeOH·1.60 $H_2O$ all lattice solvent molecules were refined with partial occupation factors, while in the case of **2**·3.2 MeOH·1.5 $H_2O$ the solvate molecules were refined isotropically. For the three structures, the hydrogen atoms attached to carbon atoms were placed at calculated positions. In **1**·2.53 MeOH·1.60 $H_2O$ most other hydrogen atoms were located from $\Delta F$ maps and refined isotropically. In **2**·3.2 MeOH·1.5 $H_2O$, the hydroxy hydrogen atoms of the coordinated MeOH molecules and the hydrogen atom of the bridging hydroxido ligand were located by difference maps and refined isotropically. In the structure of **3**·3 $H_2O$, the bridging hydroxido hydrogen atom was found in the difference map, while hydrogen atoms could neither be found or placed for the $H_2O$ molecules and were therefore omitted from the refinement.

CCDC-633009 (**1**·2.53 MeOH·1.60 $H_2O$), -633010 (**2**·3.2 MeOH·1.5 $H_2O$) and -633011 (**3**·3 $H_2O$) contain the supplementary crystallographic data for this paper. These data can be obtained free of charge from The Cambridge Crystallographic Data Centre via www.ccdc.cam.ac.uk/data_request/cif.

## Acknowledgments

S. P. P. thanks the European Social Fund (ESF) [Operational Program for Educational and Vocational Training II (EPEAEK II) and particularly the program PYTHAGORAS (grant no. 365.037)] for funding the above work. A. E. and G. A. thank the Ministerio de Educación y Ciencia (MEC) (CTQ2006-01759) for financial support. A. J. T. acknowledges financial support from the University of Cyprus and the Cyprus Research Promotion Foundation (Grant TEXNO/0506/06). The Advanced Light Source is supported by the Director, Office of Science, Office of Basic Energy Sciences, of the U.S. Department of Energy under Contract No. DE-AC02-05CH11231.

[1] a) B. Xu, N. D. Chasteen, *J. Biol. Chem.* **1991**, *266*, 19965–19970; b) T. G. Carrell, A. M. Tyryshkin, G. C. Dismukes, *J. Biol. Inorg. Chem.* **2002**, *7*, 2–22.
[2] A. M. Ako, I. J. Hewitt, V. Mereacre, R. Clérac, W. Wernsdorfer, C. E. Anson, A. K. Powell, *Angew. Chem. Int. Ed.* **2006**, *45*, 4926–4929.
[3] For reviews concerning SMMs, see: a) G. Christou, D. Gatteschi, D. N. Hendrickson, R. Sessoli, *MRS Bull.* **2000**, *25*, 66–71; b) D. Gatteschi, R. Sessoli, *Angew. Chem. Int. Ed.* **2003**, *42*, 268–297; c) G. Aromi, E. K. Brechin, *Struct. Bond.* **2006**, *122*, 1–67.
[4] R. E. P. Winpenny, in *Comprehensive Coordination Chemistry II* (Eds.: J. A. McCleverty, T. J. Meyer), Elsevier, Amsterdam, **2004**, vol. 7, pp. 125–175.
[5] a) T. Rojo, F. J. Romero-Salguero, J. M. Lehn, G. Baurn, D. Fenske, *Eur. J. Inorg. Chem.* **1999**, 1421–1428; b) E. Breuning, U. Ziener, J. M. Lehn, E. Wegelius, K. Rissanen, *Eur. J. Inorg. Chem.* **2001**, 1515–1521.
[6] R. W. Saalfrank, U. Reimann, M. Goritz, F. Hampel, A. Scheurer, F. W. Heinemann, M. Buschel, J. Daub, V. Schunemann, A. X. Trautwein, *Chem. Eur. J.* **2002**, *8*, 3614–3619.
[7] M. Fujita, K. Umemoto, M. Yoshizawa, N. Fujita, T. Kusukawa, K. Biradha, *Chem. Commun.* **2001**, 509–518.
[8] R. E. P. Winpenny, *J. Chem. Soc. Dalton Trans.* **2002**, 1–10.
[9] a) A. Müller, P. Kogerler, A. W. M. Dress, *Coord. Chem. Rev.* **2001**, *222*, 193–218; b) A. K. Boudalis, C. P. Raptopoulou, B. Abarca, R. Ballesteros, M. Chaldaoui, J.-P. Tuchagues, A. Terzis, *Angew. Chem. Int. Ed.* **2006**, *45*, 432–436; c) E. K. Brechin, *Chem. Commun.* **2005**, 5141–5153; d) P. Chaudhuri, E. Rentschler, F. Birkelbach, C. Krebs, E. Bill, T. Weyhermüller, U. Flörke, *Eur. J. Inorg. Chem.* **2003**, 541–555; e) A. J. Tasiopoulos, A. Vinslava, W. Wernsdorfer, K. A. Abboud, G. Christou, *Angew. Chem. Int. Ed.* **2004**, *43*, 2117–2121; f) Y.-J. Li, L. Lecren, W. Wernsdorfer, R. Clérac, *Inorg. Chem. Commun.* **2004**, *7*, 1281–1284; g) S. Accorsi, A.-L. Barra, A. Caneschi, G. Chastanet, A. Cornia, A. C. Fabretti, D. Gatteschi, C. Mortalò, E. Olivieri, F. Parenti, P. Rosa, R. Sessoli, L. Sorace, W. Wernsdorfer, L. Zobbi, *J. Am. Chem. Soc.* **2006**, *128*, 4742–4755; h) C. M. Zaleski, E. C. Depperman, C. Dendrinou-Samara, M. Alexiou, J. W. Kampf, D. P. Kessissoglou, M. L. Kirk, V. L. Pecoraro, *J. Am. Chem. Soc.* **2005**, *127*, 12862–

 © 2007 Wiley-VCH Verlag GmbH & Co. KGaA, Weinheim 

12872; i) V. L. Pecoraro, A. J. Stemmler, B. R. Gibney, J. J. Bodwin, H. Wang, J. W. Kampf, A. Barwins-Ki, *Prog. Inorg. Chem.* **1997**, *45*, 83–177; j) G. Wu, R. Clérac, W. Wernsdorfer, S. Qiu, C. E. Anson, I. J. Hewitt, A. K. Powell, *Eur. J. Inorg. Chem.* **2006**, 1927–1930; k) S. Youngme, P. Phuengphai, N. Chaichit, G. A. van Albada, O. Roubeau, J. Reedijk, *Inorg. Chim. Acta* **2005**, *358*, 849–853; l) S. Maheswaran, G. Chastanet, S. J. Teat, T. Mallah, R. Sessoli, W. Wernsdorfer, R. E. P. Winpenny, *Angew. Chem. Int. Ed.* **2005**, *44*, 5044–5049.

[10] a) C. J. Milios, E. Kefalloniti, C. P. Raptopoulou, A. Terzis, R. Vicente, N. Lalioti, A. Escuer, S. P. Perlepes, *Chem. Commun.* **2003**, 819–821; b) C. J. Milios, C. P. Raptopoulou, A. Terzis, R. Vicente, A. Escuer, S. P. Perlepes, *Inorg. Chem. Commun.* **2003**, *6*, 1056–1060; c) C. J. Milios, Th. C. Stamatatos, P. Kyritsis, A. Terzis, C. P. Raptopoulou, R. Vicente, A. Escuer, S. P. Perlepes, *Eur. J. Inorg. Chem.* **2004**, 2885–2901; d) C. J. Milios, E. Kefalloniti, C. P. Raptopoulou, A. Terzis, A. Escuer, R. Vicente, S. P. Perlepes, *Polyhedron* **2004**, *23*, 83–95; e) M. Alexiou, E. Katsoulakou, C. Dendrinou-Samara, C. P. Raptopoulou, V. Psycharis, E. Manessi-Zoupa, S. P. Perlepes, D. P. Kessissoglou, *Eur. J. Inorg. Chem.* **2005**, 1964–1978; f) Th. C. Stamatatos, S. Dionyssopoulou, G. Efthymiou, P. Kyritsis, C. P. Raptopoulou, A. Terzis, R. Vicente, A. Escuer, S. P. Perlepes, *Inorg. Chem.* **2005**, *44*, 3374–3376; g) C. J. Milios, P. Kyritsis, C. P. Raptopoulou, A. Terzis, R. Vicente, A. Escuer, S. P. Perlepes, *Dalton Trans.* **2005**, 501–511; h) Th. C. Stamatatos, D. Foguet-Albiol, C. C. Stoumpos, C. P. Raptopoulou, A. Terzis, W. Wernsdorfer, S. P. Perlepes, G. Christou, *J. Am. Chem. Soc.* **2005**, *127*, 15380–15381; i) C. J. Milios, S. Piligkos, A. R. Bell, R. H. Laye, S. J. Teat, R. Vicente, E. McInnes, A. Escuer, S. P. Perlepes, R. E. P. Winpenny, *Inorg. Chem. Commun.* **2006**, *9*, 642–645; j) Th. C. Stamatatos, A. K. Boudalis, Y. Sanakis, C. P. Raptopoulou, *Inorg. Chem.* **2006**, *45*, 7372–7381; k) Th. C. Stamatatos, J. C. Vlahopoulou, Y. Sanakis, C. P. Raptopoulou, V. Psycharis, A. K. Boudalis, S. P. Perlepes, *Inorg. Chem. Commun.* **2006**, *9*, 814–818; l) C. Papatriantafyllopoulou, C. P. Raptopoulou, A. Escuer, C. J. Milios, *Inorg. Chim. Acta* **2007**, *360*, 61–68; m) K. V. Priggouri, C. P. Raptopoulou, A. Escuer, Th. C. Stamatatos, *Inorg. Chim. Acta* **2007**, *360*, 69–83; n) Th. C. Stamatatos, D. Foguet-Albiol, C. C. Stoumpos, C. P. Raptopoulou, A. Terzis, W. Wernsdorfer, S. P. Perlepes, G. Christou, *Polyhedron*, in press; o) Th. C. Stamatatos, E. Diamantopoulou, C. P. Raptopoulou, V. Psycharis, A. Escuer, S. P. Perlepes, *Inorg. Chem.* in press; p) Th. C. Stamatatos, C. Papatriantafyllopoulou, E. Katsoulakou, C. P. Raptopoulou, S. P. Perlepes, *Polyhedron*, in press.

[11] a) M. Murugesu, K. A. Abboud, G. Christou, *Polyhedron* **2004**, *23*, 2779–2788; b) T. Afrati, C. Dendrinou-Samara, C. P. Raptopoulou, A. Terzis, V. Tangoulis, D. P. Kessissoglou, *Angew. Chem. Int. Ed.* **2002**, *41*, 2148–2150; c) A. J. Stemmler, J. W. Kampf, V. L. Pecoraro, *Inorg. Chem.* **1995**, *34*, 2271–2272.

[12] For a recent review concerning the coordination chemistry of 2-pyridyl-substituted oximes, see: C. J. Milios, Th. C. Stamatatos, S. P. Perlepes, *Polyhedron* **2006**, *25*, 134–194.

[13] a) G. Tamasi, R. Cini, *Dalton Trans.* **2003**, 2928–2936, and references cited therein; b) M. B. Salah, S. Vilminot, T. Mhiri, M. Kurmoo, *Eur. J. Inorg. Chem. Eur. J. Inorg.* **2004**, 2272–2276.

[14] a) Th. C. Stamatatos, A. Bell, P. Cooper, A. Terzis, C. P. Raptopoulou, S. L. Heath, R. E. P. Winpenny, S. P. Perlepes, *Inorg. Chem. Commun.* **2005**, *8*, 533–538; b) Th. C. Stamatatos, E. Diamantopoulou, A. Tasiopoulos, V. Psycharis, R. Vicente, C. P. Raptopoulou, V. Nastopoulos, A. Escuer, S. P. Perlepes, *Inorg. Chim. Acta* **2006**, *359*, 4149–4157; c) T. Weyhermüller, R. Wagner, S. Khanra, P. Chaudhuri, *Dalton Trans.* **2005**, 2539–2546; d) S. Khanra, T. Weyhermüller, E. Rentscler, P. Chaudhuri, *Inorg. Chem.* **2005**, *44*, 8176–8178; e) C. Dendrinou-Samara, C. M. Zaleski, A. Evagorou, J. W. Kampf, V. L. Pecoraro, D. P. Kessissoglou, *Chem. Commun.* **2003**, 2668–2669.

[15] a) M. I. Khan, S. Cevik, R. J. Doedens, *Chem. Commun.* **2001**, 1930–1931; b) J. Moriyama, H. Nishiguchi, T. Ishihara, Y. Takita, *Ind. Eng. Chem. Res.* **2002**, *41*, 32–36; c) S.-Y. Wan, Y.-Z. Li, T.-A. Okamura, J. Fian, W.-Y. Sun, N. Ueyama, *Eur. J. Inorg. Chem.* **2003**, 3783–3789; d) T. C. Ullrich, M. Blaesse, R. Huber, *EMBO J.* **2001**, *20*, 316–329; e) J. Reedijk, *Inorg. Chim. Acta* **1992**, *198–200*, 873–881.

[16] For recent reviews, see: a) A. J. L. Pombeiro, V. Yu. Kukushkin, in *Comprehensive Coordination Chemistry II* (Eds.: J. A. McCleverty, T. J. Meyer), Elsevier, Amsterdam, **2004**, vol. 1, pp. 631–637; b) A. G. Smith, P. A. Tasker, D. J. White, *Coord. Chem. Rev.* **2003**, *241*, 61–85; c) P. Chaudhuri, *Coord. Chem. Rev.* **2003**, *243*, 143–190.

[17] a) E. Abele, R. Abele, E. Lukevics, *Chem. Heterocycl. Compd.* **2003**, *39*, 825–865; b) H. Kumagai, M. Endo, M. Kondo, S. Kawata, S. Kitagawa, *Coord. Chem. Rev.* **2003**, *237*, 197–203.

[18] C. Papatriantafyllopoulou, C. G. Efthymiou, C. P. Raptopoulou, R. Vicente, E. Manessi-Zoupa, V. Psycharis, A. Escuer, S. P. Perlepes, *J. Mol. Struct.* **2007**, *829*, 176–188.

[19] C. Papatriantafyllopoulou, Ph. D. Thesis, University of Patras, **2007**.

[20] K. Nakamoto, *Infrared and Raman Spectra of Inorganic and Coordination Compounds,* 4th ed., Wiley, New York, **1986**, pp. 130–139, 248–251.

[21] R. A. Coxall, S. G. Harris, D. K. Henderson, S. Parsons, P. A. Tasker, R. E. P. Winpenny, *J. Chem. Soc. Dalton Trans.* **2000**, 2349–2356.

[22] a) V. V. Ponomarova, V. V. Komarchuk, I. Boldog, A. N. Chernega, J. Sieler, K. N. Domasevitch, *Chem. Commun.* **2002**, 436–437; b) J. N. Behera, K. V. Gopalkrishnan, C. N. R. Rao, *Inorg. Chem.* **2004**, *43*, 2636–2642; c) R. A. Coxall, L. F. Lindoy, H. A. Miller, A. Parkin, S. Parsons, P. A. Tasker, D. J. White, *Dalton Trans.* **2003**, 55–64.

[23] a) K. Riggle, T. Lynde-Kernell, E. O. Schlemper, *J. Coord. Chem.* **1992**, *25*, 117–125; b) A. Rajunen, M. Orama, H. Saarinen, *Acta Crystallogr. Sect. C* **1999**, *55*, 2075–2077; c) C. Papatriantafyllopoulou, C. P. Raptopoulou, A. Terzis, E. Manessi-Zoupa, S. P. Perlepes, *Z. Naturforsch. Teil B* **2006**, *61*, 37–46; d) R. Cibulka, I. Cisarova, J. Ondracek, F. Liska, J. Ludvik, *Collect. Czech. Chem. Commun.* **2001**, *66*, 170–184; e) T. Lynde-Kernell, E. O. Schlemper, *J. Coord. Chem.* **1988**, *16*, 347–356; f) D. W. Phelps, W. F. Little, D. J. Hodgson, *Inorg. Chem.* **1976**, *15*, 2263–2266; g) V. Sharma, R. K. Sharma, R. Bohra, R. Ratnani, V. K. Jain, J. E. Drake, M. B. Hursthouse, M. E. Light, *J. Organomet. Chem.* **2002**, *651*, 98–104; h) V. Sharma, R. K. Sharma, V. K. Jain, J. E. Drake, M. E. Light, M. B. Hursthouse, *J. Organomet. Chem.* **2002**, *664*, 66–69; i) A. Gupta, R. K. Sharma, R. Bohra, V. K. Jain, J. E. Drake, M. B. Hursthouse, M. E. Light, *Polyhedron* **2002**, *21*, 2387–2392.

[24] Representative references: a) A. Cornia, A. C. Fabretti, D. Gatteschi, G. Palyi, E. Rentschler, O. I. Shchegolikhina, A. A. Zhdanov, *Inorg. Chem.* **1995**, *34*, 5383–5387; b) Y.-B. Jiang, H.-Z. Kou, R.-J. Wang, A.-L. Cui, J. Ribas, *Inorg. Chem.* **2005**, *44*, 709–715; c) T. K. Paine, E. Rentschler, T. Weyhermüller, P. Chaudhuri, *Eur. J. Inorg. Chem.* **2003**, 3167–3178; d) S. Wörl, H. Pritzkow, I. O. Fritsky, R. Kramer, *Dalton Trans.* **2005**, 27–29; e) M. Mikuriya, K. Tanaka, N. Inoue, D. Yoshioka, J.-W. Lim, *Chem. Lett.* **2003**, *32*, 126–127; f) F. A. Cotton, B. H. C. Winquist, *Inorg. Chem.* **1969**, *8*, 1304–1312; g) X. Lin, D. M. J. Doble, A. J. Blake, A. Harrison, C. Wilson, M. Schröder, *J. Am. Chem. Soc.* **2003**, *125*, 9476–9483; h) M.-L. Tong, M. Monfort, J. M. C. Juan, X.-M. Chen, X.-H. Bu, M. Ohba, S. Kitagawa, *Chem. Commun.* **2005**, 233–235; i) R. E. P. Winpenny, *Adv. Inorg. Chem.* **2001**, *52*, 1–111.

[25] D. Gatteschi, L. Pardi, *Gazz. Chim. Ital.* **1993**, *123*, 231–238.

[26] G. S. Papaefstathiou, S. P. Perlepes, A. Escuer, R. Vicente, M. Font-Bardia, X. Solans, *Angew. Chem. Int. Ed.* **2001**, *40*, 884–886.

[27] M. Orama, H. Saarinen, J. Korvenranta, *J. Coord. Chem.* **1990**, *22*, 183–190.

 © 2007 Wiley-VCH Verlag GmbH & Co. KGaA, Weinheim 

[28] a) A. C. Thompson, H. A. Padmore, A. G. Oliver, S. J. Teat, R. S. Celestre, S. M. Clark, E. E. Domning, K. D. Franck, G. Y. Morrison, *AIP Conference Proceedings*, No. 708, USA, **2004**, pp. 482–485; b) *SIR-92*c) A. Altomare, G. Cascarano, C. Giacovazzo, A. Guagliardi, M. C. Burla, G. Polidori, M. Camalli, *J. Appl. Crystallogr.* **1994**, *27*, 435–436; G. M. Sheldrick, *SHELXS-86, Program for the Solution of Crystal Structures*, University of Göttingen, Germany; d) *Bruker AXS*, Madison, WI, USA, **2005**; e) G. M. Sheldrick, *SHELXL-97, Program for the Refinement of Crystal Structures*, University of Göttingen, Germany, **1997**.

Received: January 18, 2007
Published Online: April 10, 2007

 © 2007 Wiley-VCH Verlag GmbH & Co. KGaA, Weinheim 

DOI: 10.1002/ejic.200700092

# Conformational Analysis of One-Dimensional Coordination Polymers Based on $[Cp_2Cr_2(CO)_4(\mu,\eta^2\text{-}P_2)]$ by Solid-State Multinuclear NMR Spectroscopy and Density Functional Calculations

**Manfred Scheer,*[a] Laurence J. Gregoriades,[a] Manfred Zabel,[a] Marek Sierka,[b] Long Zhang,[c] and Hellmut Eckert*[c]**

*Dedicated to Professor Joachim Heinicke on the occasion of his 60th birthday*

**Keywords:** Chromium / Copper / Halides / Density functional calculations / NMR spectroscopy / Phosphorus

Reaction of the complex $[Cp_2Cr_2(CO)_4(\mu,\eta^2\text{-}P_2)]$ (**2**) with copper(I) halides leads to the quantitative formation of the new one-dimensional (1D) linear polymers $[CuX\{Cp_2Cr_2(CO)_4(\mu,\eta^2{:}\eta^1{:}\eta^1\text{-}P_2)\}]_n$ [X = Cl (**3**), Br (**4**), I (**5**)]. Polymers **3**–**5** are the first examples of supramolecular aggregates incorporating **2** as a connecting moiety. The solid-state structures of **3**–**5** are compared and their remarkable influence on the respective solid-state $^{31}P$ magic angle spinning (MAS) NMR spectra is interpreted with the help of density functional theory (DFT) calculations, which suggest that the $^{31}P$ chemical shifts are extremely sensitive to the position of the phosphorus atoms with respect to the cones of anisotropy of the carbonyl ligands.

(© Wiley-VCH Verlag GmbH & Co. KGaA, 69451 Weinheim, Germany, 2007)

## Introduction

The construction of well-defined supramolecular assemblies from discrete units is a field of considerable interest in contemporary chemical research.[1] Typically, different metal centres are connected by suitable N-, O- and/or S-donor-containing organic ligands as linkers. In our research group, however, we utilise organometallic $P_n$- and $As_n$-ligand complexes as connecting moieties.[2] The tetrahedrane complex $[Cp_2Mo_2(CO)_4(\mu,\eta^2\text{-}P_2)]$ (**1**),[3] for example, has proven to be a particularly versatile supramolecular building block and forms the basis of several oligomers and one-dimensional (1D) polymers isolated in our group.[2a,2d] In view of the versatility of complex **1** as a linker, we decided to investigate the coordination potential of its chromium analogue $[Cp_2Cr_2(CO)_4(\mu,\eta^2\text{-}P_2)]$ (**2**),[4] particularly due to the fact that it is less stable than **1** and readily undergoes fragmentation reactions,[5] and could thus lead to the formation of novel compounds with unusual $P_n$-ligand arrangements. We report herein the synthesis, characterisation and solid-state $^{31}P$ magic angle spinning (MAS) NMR spectral features of the new 1D polymers $[CuX\{Cp_2Cr_2(CO)_4(\mu,\eta^2{:}\eta^1{:}\eta^1\text{-}P_2)\}]_n$ [X = Cl (**3**), Br (**4**), I (**5**)], which are the first examples of supramolecular aggregates containing **2** as a linking unit. The MAS NMR spectra are interpreted with the help of density functional theory (DFT) calculations on the compounds **3**–**5** and the results obtained in a previous $^{31}P$ MAS NMR study on the analogous 1D polymers $[CuX\{Cp_2Mo_2(CO)_4(\mu,\eta^2{:}\eta^1{:}\eta^1\text{-}P_2)\}]_n$ [X = Cl (**6**), Br (**7**), I (**8**)].[2d]

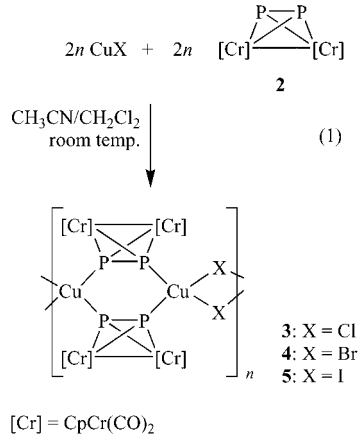


[a] Institut für Anorganische Chemie der Universität Regensburg, 93040 Regensburg, Germany
Fax: +49-941-943-4441
E-mail: mascheer@chemie.uni-regensburg.de
[b] Institut für Chemie der Humboldt-Universität zu Berlin, Unter den Linden 6, 10099 Berlin, Germany
[c] Institut für Physikalische Chemie der Westfälischen Wilhelms-Universität Münster, 48149 Münster, Germany
Fax: +49-251-832-9159
E-mail: eckerth@uni-muenster.de

 © 2007 Wiley-VCH Verlag GmbH & Co. KGaA, Weinheim 

## Results and Discussion

### Synthesis of the Products

Treatment of **2** with CuX (X = Cl, Br, I) in a mixture of $CH_3CN$ and $CH_2Cl_2$ at room temperature leads to the formation of the 1D polymers **3**–**5** [Equation (1)] as air-sensitive, moss-green microcrystalline powders. The polymers can be stored indefinitely at ambient conditions under an inert atmosphere and are insoluble in most common solvents. They are, however, soluble in trace amounts in polar solvents such as $CH_3CN$, but then apparently dissociate completely into the starting materials, as evidenced by $^{31}P$ NMR spectroscopy.

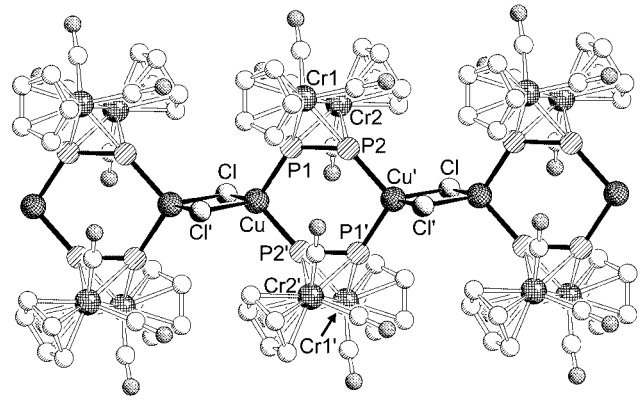


**3**

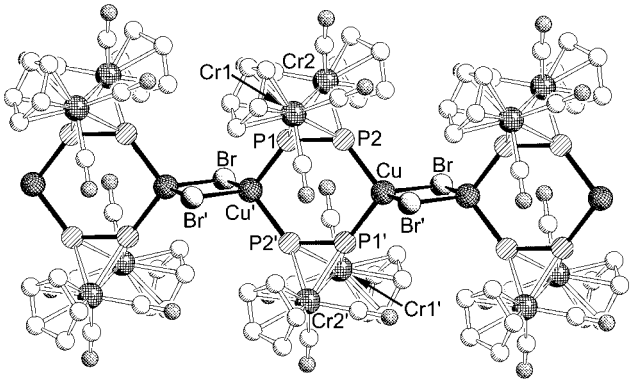


**4**

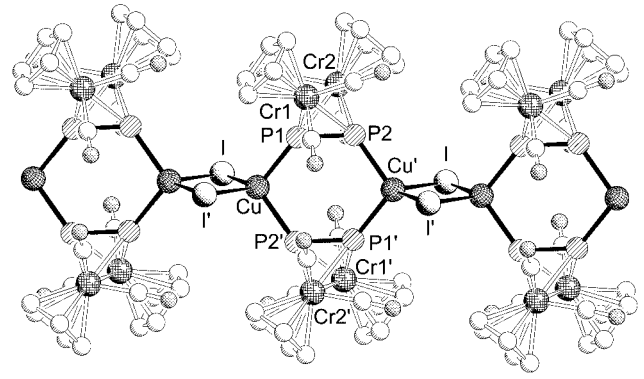


**5**

Figure 1. Portions of the structures of polymers **3**–**5** (hydrogen atoms have been omitted for clarity). See Table 1 for selected bond lengths and angles.

### X-ray Crystallographic Characterisation of the Products

Compounds **3**–**5** were characterised by X-ray crystallography; the measurement details are summarised in the Experimental Section. Their structures display a polymeric core (Figure 1) reminiscent of that in the molybdenum analogues $[CuX\{Cp_2Mo_2(CO)_4(\mu,\eta^2{:}\eta^1{:}\eta^1\text{-}P_2)\}]_n$ [X = Cl (**6**), Br (**7**), I (**8**)].[2a,2d] The $Cu^I$ centres in **3**–**5** are found in a distorted tetrahedral coordination mode and are bridged by the phosphorus atoms of **2** and the halogen atoms. As a result, structures consisting of an alternating arrangement of planar four-membered $Cu_2X_2$ rings and six-membered $Cu_2P_4$ rings in a slight chair-like conformation are formed, which are nearly orthogonal to each other. Compounds **4** and **5** and their molybdenum analogues **7** and **8** are structurally similar, whereas polymers **3** and **6** are different. Unlike the molybdenum derivative **6**, the $Cu_2P_4$ rings in the chromium analogue **3** possess an inversion centre situated at the centre of these rings.

Selected structural details for compounds **3**–**5** are listed in Table 1. The P–P bond lengths of the $Cr_2P_2$ moieties in **3** and **4** are unchanged compared to uncoordinated **2** [2.060(1) Å],[4a] whereas those in **5** are marginally longer. Although the Cu–P bond lengths are generally longer than those found in complexes of the type $[Cu_2X_2(PPh_3)_3]$[6] (X = Cl:[6a] 2.183(4)–2.245(5) Å; Br:[6b] 2.190(3)–2.260(3) Å; I:[6c] 2.219(3)–2.267(3) Å], the Cu–X bond lengths are within the ranges found in these compounds (X = Cl:[6a] 2.298(4)–2.454(4) Å; Br:[6b] 2.370(2)–2.610(2) Å; I:[6c] 2.500(2)–2.819(1) Å].

Table 1. Comparison of selected bond lengths [Å] and angles [°] in compounds **3**–**5**.

| | **3** (X = Cl) | **4** (X = Br) | **5** (X = I) |
|---|---|---|---|
| P–P | 2.061(1) | 2.061(1) | 2.073(2) |
| Cu–P | 2.289(1) | 2.297(1) | 2.323(2) |
| | 2.296(1) | 2.305(1) | 2.333(2) |
| Cu–X | 2.344(1) | 2.467(4) | 2.611(1) |
| | 2.363(1) | 2.479(4) | 2.675(1) |
| P–Cu–P | 103.17(2) | 104.07(2) | 104.95(7) |
| P1–Cu–X | 111.41(2) | 111.97(2) | 106.77(6) |
| | 114.53(2) | 112.84(2) | 116.81(6) |
| P2–Cu–X | 112.02(2) | 110.77(2) | 106.42(6) |
| | 115.58(2) | 113.81(2) | 113.17(6) |
| X–Cu–X | 100.49(2) | 103.62(2) | 108.10(4) |
| Cu–X–Cu | 79.51(2) | 76.38(1) | 71.90(3) |
| Cu···Cu···Cu | 174.86(1) | 176.48(2) | 170.50(1) |

A further interesting structural feature observed in all three polymers is that the copper atoms are alternately distributed along two parallel lines, as illustrated by the Cu···Cu···Cu angles given in Table 1 and the representation

 © 2007 Wiley-VCH Verlag GmbH & Co. KGaA, Weinheim 

of the polymers in Figure 2. Moreover, the folding angle of the $Cu_2P_4$ rings (dihedral angle between CuP1P2′ and P1P2P1′P2′ planes for **3** and **5**; dihedral angle between CuP1′P2 and P1P2P1′P2′ planes for **4**) decreases as the size of the halogen atom increases (**3**: 3.81(1)°; **4**: 2.48(1)°; **5**: 0.97(1)°].

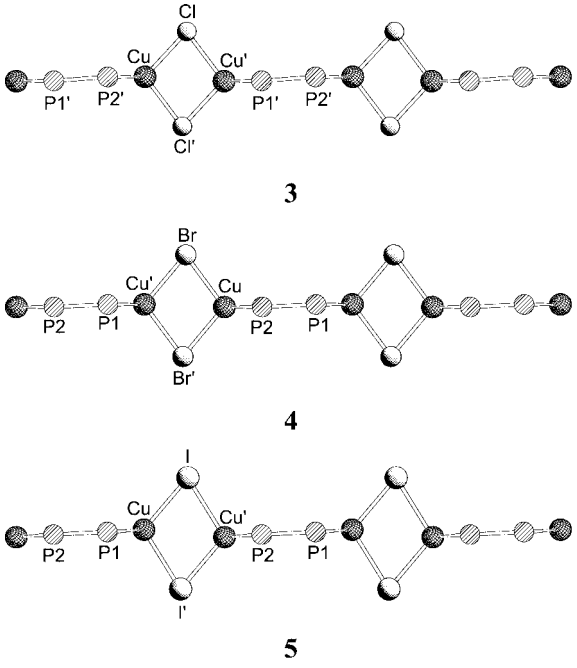


Figure 2. View of the structures of **3**–**5** perpendicular to the faces of the $Cu_2X_2$ rings, demonstrating that the copper atoms in the polymers are alternately distributed along two parallel lines (chromium atoms and their supporting ligands have been omitted for clarity).

### Spectroscopic Characterisation of the Products

Complexes **3**–**5** are soluble in $CH_3CN$ in trace amounts although they apparently dissociate completely into the starting materials according to $^{31}P$ NMR measurements. However, the fragments detected in the positive-ion ESI mass spectra of the compounds in $CH_3CN$ at room temperature (Table 2) suggest that oligomeric species are most likely also present in solution.

Table 2. Selected fragments [*m*/*z* (relative abundance in %)] detected in the positive-ion ESI mass spectra of compounds **3**–**5** in $CH_3CN$ and the proposed cations for these fragments.

| 3 (X = Cl) | 4 (X = Br) | 5 (X = I) | Proposed Cation |
|---|---|---|---|
| 1076.7(3) | 1166.6(9) | 1260.7(12) | $[(Cu_3X_2)\{Cp_2Cr_2(CO)_4P_2\}_2]^+$ |
| 1022.6(2) | 1110.5(4) | 1204.6(7) | $[(Cu_3X_2)\{Cp_2Cr_2(CO)_3P_2\}_2]^+$ |
| 978.7(16) | 1022.7(18) | 1070.6(10) | $[(Cu_2X)\{Cp_2Cr_2(CO)_4P_2\}_2]^+$ |
| 922.7(8) | 966.6(11) | 1014.6(10) | $[(Cu_2X)\{Cp_2Cr_2(CO)_3P_2\}_2]^+$ |

Solid-state $^{31}P$ MAS NMR measurements were performed for polymers **3**–**5** at room temperature; the spectra obtained are depicted in Figure 3. The chloride and bromide derivatives exhibit identical spectra and display two multiplets near $\delta$ = –100 and 80 ppm, whereas the iodide derivative displays one broad signal at $\delta$ = 46.3 ppm with

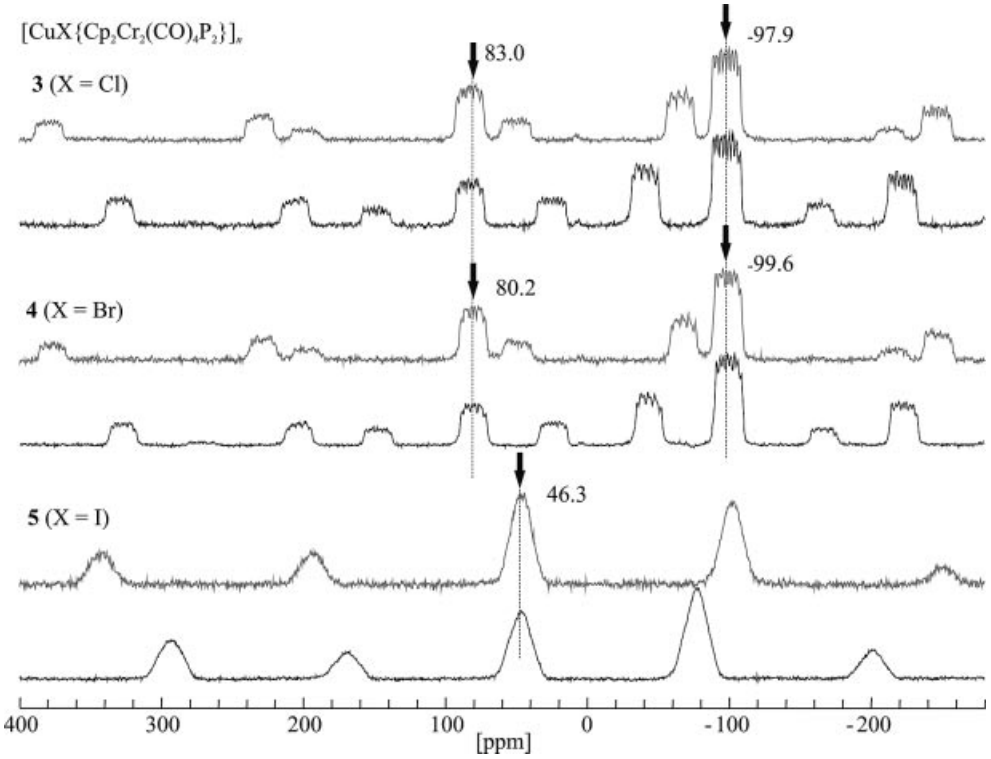


Figure 3. Solid-state $^{31}P$ MAS NMR spectra of polymers **3**–**5** [X = Cl (**3**), Br (**4**), I (**5**)], recorded with a spinning rate of 25 (bottom) and 30 kHz (top). The peaks marked with arrows are the MAS centre-bands whereas the unmarked peaks are the spinning side-bands.

 © 2007 Wiley-VCH Verlag GmbH & Co. KGaA, Weinheim 

no analysable fine structure. These spectra may seem puzzling at first sight considering the solid-state structures of polymers **3**–**5** (Figure 1) as all three polymers contain two sets of crystallographically distinct phosphorus atoms (P1 and P2), which nevertheless appear to be chemically similar. Accordingly, the severely broadened $^{31}$P NMR spectrum of the iodide derivative **5** can be interpreted in terms of two unresolved signal components. In contrast, the spectra observed for the chloride and bromide derivatives **3** and **4**, respectively, both of which exhibit two signals separated by about 180 ppm, are initially most surprising. As discussed previously,[2d] we can interpret this observation as a result of the deshielding effect exercised by the cones of anisotropy of the carbonyl ligands. A detailed examination of the structures reveals that the orientation of the P1 and P2 atoms with respect to these ligands differs and, furthermore, the average interatomic distance between the P1 atoms and the carbonyl carbon atoms of the corresponding $Cr_2P_2$ moieties in **3** and **4** [**3**: 3.128(1) Å; **4**: 3.129(1) Å] is shorter than that of the P2 atoms [**3**: 3.286(1) Å; **4**: 3.279(1) Å]. The corresponding average interatomic distances in **5** are 3.065(1) and 3.079(1) Å. Thus, in analogy to the situation previously described for the molybdenum compounds **6**–**8**,[2d] the environments of the P1 and P2 atoms in **3** and **4** are somewhat different while those of the P1 and P2 atoms in **5** are essentially identical, as suggested by the $^{31}$P MAS NMR spectra. While the spectra of **3**–**5** are astonishingly similar to those of the molybdenum analogues **6**–**8**, a satisfactory simulation of the spectrum of **3** (Figure 4) could only be obtained by including the additional effect of $^2J_{P,P}$ coupling; this coupling also manifests itself by broadening effects in the spectrum of **4** (Figure 4).

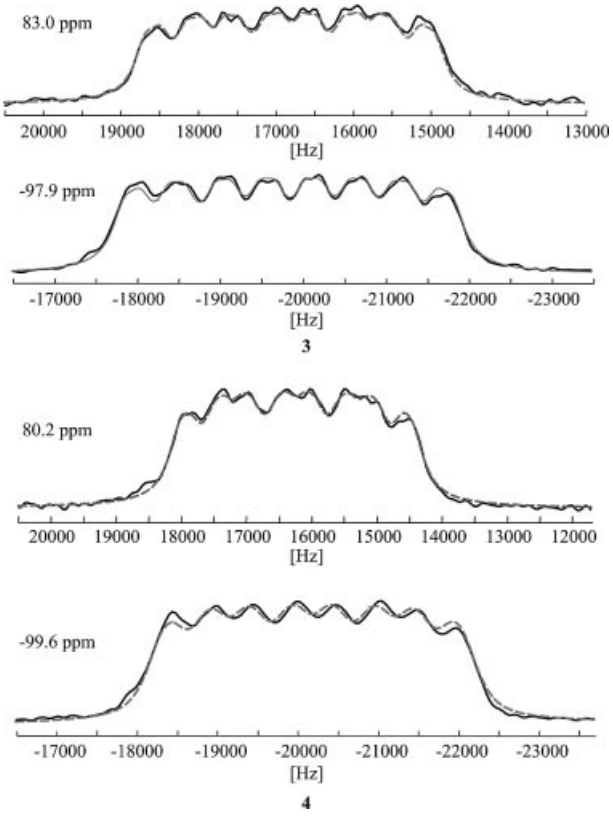


Figure 4. Comparison of the experimental (solid curve) and simulated (dashed curve) solid-state $^{31}$P MAS NMR spectra of polymers **3** and **4** (**3**: $\delta$ = 83.0 ($^1J_{Cu,P}$ = 1004, $^1J_{P,P}$ = 532, $^2J_{P,P}$ = 200 Hz, P1) and –97.9 ppm ($^1J_{Cu,P}$ = 1079, $^1J_{P,P}$ = 533, $^2J_{P,P}$ = 199 Hz, P2); **4**: $\delta$ = 80.2 ($^1J_{Cu,P}$ = 962, $^1J_{P,P}$ = 531, $^2J_{P,P}$ = 195 Hz, P1) and –99.6 ppm ($^1J_{Cu,P}$ = 1024, $^1J_{P,P}$ = 531, $^2J_{P,P}$ = 175 Hz, P2).

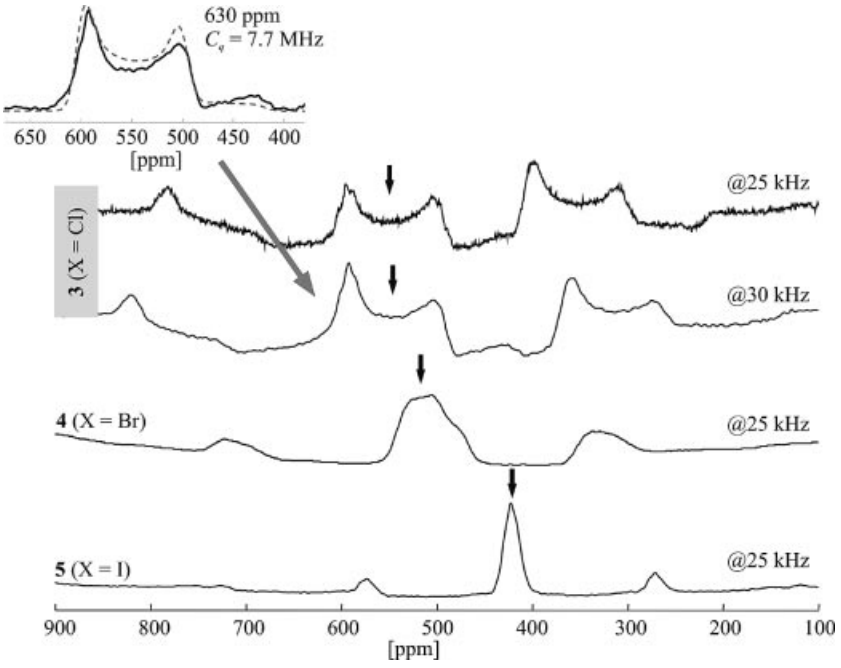


Figure 5. $^{63}$Cu MAS NMR spectra of compounds **3** (two different spinning frequencies), **4** and **5**. MAS centre-bands are labelled with black arrows. The inset compares the MAS centre-band (solid curve) to a simulated second-order quadrupolar powder pattern lineshape (dashed curve; $\eta$ = 0).

 © 2007 Wiley-VCH Verlag GmbH & Co. KGaA, Weinheim 

The low-field signals in the spectra of **3** and **4** are assigned to the P1 atoms since they are closer, on average, to the carbonyl ligands than are the P2 atoms, and therefore experience greater deshielding.

The $^{63}$Cu MAS NMR spectra of compounds **3**–**5** are presented in Figure 5. The spectrum of **5** exhibits a sharp line centred near $\delta$ = 422 ppm vs. crystalline CuI, while the MAS NMR spectra for **3** and **4** are strongly broadened by second-order quadrupolar perturbations. The $^{63}$Cu MAS NMR spectrum of **3** could be simulated with an isotropic chemical shift of $\delta$ = 630 ppm, a nuclear electric quadrupolar coupling constant of 7.7 MHz and a zero asymmetry parameter by using the dmfit routine. For **4**, the simulation of the experimental spectra yielded an isotropic chemical shift of $\delta$ = 550 ppm, and nuclear electric quadrupolar coupling constants of 5.2 and 4.8 MHz for $^{63}$Cu and $^{65}$Cu, respectively. Since the spectra of **4** were rather poorly resolved, no reliable value could be determined for the asymmetry parameter. The isotropic chemical shifts measured for the copper nuclei within the distorted $CuP_2X_2$ tetrahedral environments are consistent with those previously measured for the analogous molybdenum-based compounds[2d] and show a monotonic trend along the I → Br → Cl series. Furthermore, inspection of Table 1 reveals that the $CuX_2P_2$ tetrahedra become increasingly distorted along this series (note the significant trend of the X–Cu–X angles in particular), thereby offering a good structural rationale for the large changes observed in the $C_q$ values measured for the copper nuclei.

### Theoretical Calculations

Density functional theory (DFT) calculations were carried out on complexes **3**–**5** to support the $^{31}$P MAS NMR assignments proposed above. Full structure optimisations of the crystal structures were performed and the most important calculated structural parameters, which are in very good agreement with the experimental data (Table 1), are presented in Table 3. The calculated $^{31}$P NMR chemical shifts (Table 4) are also in very good agreement with the experimental data. For the chloride and bromide derivatives, the calculated chemical shifts of the P1 and P2 atoms are separated by about 200 ppm, whereas in the iodide derivative these shifts differ by 2 ppm. The results of the calculations thus support the deductions inferred.

Table 3. Comparison of selected calculated bond lengths [Å] and angles [°] in compounds **3**–**5**.

| | **3** (X = Cl) | **4** (X = Br) | **5** (X = I) |
|---|---|---|---|
| P–P | 2.075 | 2.077 | 2.083 |
| Cu–P | 2.252 | 2.257 | 2.278 |
| | 2.259 | 2.264 | 2.280 |
| Cu–X | 2.336 | 2.462 | 2.615 |
| | 2.352 | 2.472 | 2.651 |
| P–Cu–P | 104.52 | 105.79 | 106.79 |
| P1–Cu–X | 111.87 | 112.19 | 106.89 |
| | 115.55 | 113.84 | 117.97 |
| P2–Cu–X | 112.13 | 110.72 | 106.04 |
| | 115.24 | 113.59 | 113.53 |
| X–Cu–X | 97.79 | 110.85 | 104.81 |
| Cu–X–Cu | 82.21 | 79.15 | 75.19 |
| Cu···Cu···Cu | 174.90 | 176.48 | 169.91 |

Table 4. Calculated $^{31}$P isotropic shielding constants, $\sigma$, and chemical shifts, $\delta$ [ppm], for compounds **3**–**5**.

| | **3** | | **4** | | **5** | |
|---|---|---|---|---|---|---|
| | $\sigma$ | $\delta$ | $\sigma$ | $\delta$ | $\sigma$ | $\delta$ |
| P1 | 254.2 | 73.8 | 252.0 | 76.0 | 278.5 | 49.5 |
| P2 | 452.8 | –124.8 | 450.8 | –122.8 | 280.6 | 47.5 |

## Conclusions

The $P_2$-ligand complex **2** reacts with copper(I) halides to yield the new 1D polymers **3**–**5**. Thus, in contrast to the reactivity of complex **2** towards organometallic Lewis-acidic complexes,[5] the tetrahedrane structure of **2** remains intact upon reaction with copper(I) halides. The cores of **3**–**5** consist of an alternating arrangement of six-membered $Cu_2P_4$ and four-membered $Cu_2X_2$ [X = Cl (**3**), Br (**4**), I (**5**)] rings that are nearly orthogonal to each other. This structural motif is reminiscent of that of the 1D polymers **6**–**8**,[2a,2d] which are the molybdenum analogues of compounds **3**–**5**. Polymers **3**–**5** are the first extended assemblies incorporating **2** as a ligand and thus demonstrate the potential of **2** as a supramolecular building block.

Solid-state $^{31}$P MAS NMR measurements have been performed on the polymers **3**–**5**. The spectra of **3** and **4** display two well-separated signals, whereas only one broad signal is observed in the spectrum of **5**. Each polymer contains two sets of crystallographically distinct phosphorus atoms (P1 and P2), which, at first sight, appear chemically similar. However, inspection of the average interatomic distances between the phosphorus atoms and the carbonyl carbon atoms of the respective units of **2** has revealed that the P1 and P2 atoms in **3** and **4** are shielded to different degrees by the carbonyl ligands, while the P1 and P2 atoms in **5** are shielded to virtually the same extent. Thus, as already demonstrated for the molybdenum analogues **6**–**8**, the chemical shift of the phosphorus atoms in polymers **3**–**5** appears to be exceedingly sensitive to the position of the phosphorus atoms with respect to the cones of anisotropy of the carbonyl ligands, and this has been confirmed by DFT calculations on these compounds.

## Experimental Section

**General Remarks:** All manipulations were performed under an atmosphere of dry nitrogen using standard glove-box and Schlenk techniques. All solvents were freshly distilled from appropriate drying agents immediately prior to use. IR spectra were recorded with a Varian FTS 2000 spectrometer. Solution NMR spectra were acquired with a Bruker Avance 400 MHz spectrometer. ESI mass spectra were recorded with a Finnigan Thermoquest TSQ 7000 mass spectrometer.

**Reagents:** $[Cp_2Cr_2(CO)_4(\mu,\eta^2\text{-}P_2)]$ (**2**) was prepared according to the literature procedure.[4b] CuCl (Strem) and CuBr (Strem) were

 © 2007 Wiley-VCH Verlag GmbH & Co. KGaA, Weinheim 

purified before use, under a nitrogen atmosphere, by washing with the appropriate aqueous hydrohalic acid (half-concentrated), followed by $H_2O$, EtOH and $Et_2O$. The resulting solids were then dried at room temperature under high vacuum and stored in a dry box. CuI (Aldrich) was purified and stored in a similar manner, the only difference being that a mixture of aqueous HCl (half-concentrated) and KI was used as the first washing medium.

**Crystal Structure Analysis:** Data were collected with a STOE IPDS diffractometer. The structures were solved using SIR-97[7] and refined using SHELXL-97[8] with anisotropic displacements for non-hydrogen atoms. Hydrogen atoms were located in idealised positions and refined isotropically according to the riding model. Further details are given in Table 5.

CCDC-633372 to -633374 (for **3**–**5**, respectively) contain the supplementary crystallographic data for this paper. These data can be obtained free of charge from The Cambridge Crystallographic Data Centre via www.ccdc.cam.ac.uk/data_request/cif.

**Solid-State MAS NMR Spectroscopy:** $^{31}P$, $^{63}Cu$ and $^{65}Cu$ MAS NMR spectra were recorded at resonance frequencies of 202.5, 132.6 and 142.1 MHz, respectively, on a Bruker DSX-500 spectrometer equipped with a 2.5-mm NMR probe operating at MAS rotation frequencies of 25–30 kHz. Typical acquisition parameters for single-pulse measurements: pulse length: 3.0 μs (90° flip angle) for $^{31}P$ and 0.7 μs (30° flip angle) for $^{63,65}Cu$; recycle delay: 150 s for $^{31}P$ and 1 s for $^{63,65}Cu$; 256–512 scans for $^{31}P$ and 10000 scans for $^{63,65}Cu$. $^{31}P$ and $^{63,65}Cu$ NMR chemical shifts are referenced to 85% $H_3PO_4$ and crystalline CuI, respectively.

**Theoretical Calculations:** The following procedure was used to calculate the $^{31}P$ NMR chemical shifts. Starting from the experimental crystal structures, compounds **3**–**5** were fully optimised at the density functional theory (DFT) level using the Vienna Ab initio Simulation Package (VASP)[9,10] along with the Perdew–Wang (PW91)[11] exchange-correlation functional. The electron–ion interactions were described by the projector augmented wave (PAW) method[12] as used by Kresse and Joubert.[13] A plane-wave basis set with an energy cutoff of 300 eV along with appropriate PAW potentials was used. For the integration of the Brillouin zone, a $(1\times2\times1)$ Monkhorst–Pack grid[14] was used for **3** and **4** and a $(2\times1\times1)$ grid for **5**. Next, molecular fragments containing three $[CuX\{Cp_2Cr_2(CO)_4(\mu,\eta^2{:}\eta^1{:}\eta^1\text{-}P_2)\}]$ (X = Cl, Br, I) units terminated with single X atoms were cut out from the optimised structures. The $^{31}P$ chemical shifts were calculated for the fragments within the GIAO approach,[15] using the BP86 exchange-correlation functional,[16] SVP basis sets[17] and the Gaussian 03 program package.[18] Relativistic effective core potentials were used for iodine.[19] The $^{31}P$ chemical shifts relative to 85% $H_3PO_4$ were calculated from absolute shielding constants, $\sigma$, by using $PO(CH_3)_3$ as an internal secondary standard ($\sigma$ = 188.1) with an experimental $^{31}P$ chemical shift[20] of $\delta$ = 140 ppm relative to 85% $H_3PO_4$.

**Synthesis of 3:** A solution of CuCl (49 mg, 0.49 mmol) in $CH_3CN$ (10 mL) was carefully layered over a solution of **2** (100 mg, 0.25 mmol) in $CH_2Cl_2$ (10 mL) at room temperature. The vessel was left at room temperature in the dark and moss-green needles of **3** were deposited within a month. These were filtered, washed with $CH_3CN$ ($2\times3$ mL) and pentane ($2\times3$ mL), in that order, and dried under vacuum. Yield: 100 mg (80%); m.p. 167 °C (decomp.). $^{31}P$ MAS NMR (202.5 MHz, room temp.): $\delta$ = –97.9 (m), 83.0 ppm (m). $^{63}Cu$ MAS NMR (132.6 MHz, room temp.): $\delta$ = 630 ppm (br). Positive-ion ESI MS ($CH_3CN$, room temp.): *m/z* (%) 1076.7 (3) $[Cu_3Cl_2\{Cp_2Cr_2(CO)_4P_2\}_2]^+$, 1022.6 (2) $[Cu_3Cl_2\{Cp_2Cr_2(CO)_3P_2\}_2]^+$, 978.7 (16) $[Cu_2Cl\{Cp_2Cr_2(CO)_4P_2\}_2]^+$, 922.7 (8) $[Cu_2Cl\{Cp_2Cr_2(CO)_3P_2\}_2]^+$, 878.8 (33) $[Cu\{Cp_2Cr_2(CO)_4P_2\}_2]^+$, 864.7 (2) $[Cu_2Cl\{Cp_2Cr_2(CO)_2P_2\}_2]^+$, 822.8 (43) $[Cu\{Cp_2Cr_2(CO)_3P_2\}_2]^+$, 794.8 (1) $[Cu\{Cp_2Cr_2(CO)_{2.5}P_2\}_2]^+$, 766.8 (22) $[Cu\{Cp_2Cr_2(CO)_2P_2\}_2]^+$, 712.7 (1) $[Cu\{Cp_2Cr_2(CO)P_2\}_2]^+$, 751.8 (1) $[Cu_2Cl\{Cp_2Cr_2(CO)P_2\}_2]^+$, 695.9 (1) $[Cu_2Cl\{Cp_2Cr_2P_2\}_2]^+$, 654.7 (1) $[Cu\{Cp_2Cr_2P_2\}_2]^+$, 511.8 (60) $[Cu\{Cp_2Cr_2(CO)_4P_2\}(NCCH_3)]^+$,

Table 5. Crystallographic data for **3**–**5**.

| | **3** | **4** | **5**·*n*$CH_3CN$ |
|---|---|---|---|
| Empirical formula | $C_{14}H_{10}ClCr_2CuO_4P_2$ | $C_{14}H_{10}BrCr_2CuO_4P_2$ | $C_{16}H_{13}Cr_2CuINO_4P_2$ |
| $M_r$ | 507.16 | 551.61 | 639.66 |
| Crystal size [mm] | $0.40\times0.10\times0.06$ | $0.46\times0.08\times0.04$ | $0.30\times0.06\times0.04$ |
| $T$ [K] | 173(1) | 173(1) | 173(1) |
| $\lambda$ [Å] | 0.71073 | 0.71073 | 0.71073 |
| Crystal system | monoclinic | monoclinic | triclinic |
| Space group | $P2_1/n$ | $P2_1/n$ | $P\bar{1}$ |
| $a$ [Å] | 14.616(2) | 14.614(1) | 7.980(1) |
| $b$ [Å] | 7.909(1) | 7.943(1) | 11.485(1) |
| $c$ [Å] | 16.032(2) | 16.120(2) | 11.519(1) |
| $\alpha$ [°] | 90 | 90 | 82.06(1) |
| $\beta$ [°] | 112.10(1) | 111.72(1) | 81.06(1) |
| $\gamma$ [°] | 90 | 90 | 76.85(1) |
| $V$ [Å$^3$] | 1717.0(3) | 1738.4(3) | 1009.7(2) |
| $Z$ | 4 | 4 | 2 |
| $\rho_{calcd.}$ [g cm$^{-3}$] | 1.962 | 2.108 | 2.104 |
| $\mu$ [mm$^{-1}$] | 2.827 | 4.937 | 3.809 |
| $\theta$ range [°] | 2.98–25.86 | 2.90–25.85 | 1.80–25.90 |
| Reflections collected/unique | 23308/3303 | 14195/3347 | 6689/3006 |
| Observed reflections with [$I > 2\sigma(I)$] | 2852 | 2692 | 2225 |
| $R_{int}$ | 0.0267 | 0.0260 | 0.0998 |
| GOF on $F^2$ | 0.997 | 0.927 | 0.935 |
| Final $R$ indices [$I > 2\sigma(I)$] | $R_1$ = 0.0192 | $R_1$ = 0.0203 | $R_1$ = 0.0452 |
| | $wR_2$ = 0.0501 | $wR_2$ = 0.0475 | $wR_2$ = 0.1070 |
| $R$ indices (all data) | $R_1$ = 0.0237 | $R_1$ = 0.0281 | $R_1$ = 0.0614 |
| | $wR_2$ = 0.0513 | $wR_2$ = 0.0491 | $wR_2$ = 0.1122 |
| Max./min. $\Delta\rho$ [e Å$^{-3}$] | 0.343/–0.234 | 0.538/–0.275 | 0.979/–0.673 |

 © 2007 Wiley-VCH Verlag GmbH & Co. KGaA, Weinheim 

496.9 (2) $[Cu\{Cp_2Cr_2(CO)_2P_2\}(NCCH_3)_2]^+$, 471.6 (1) $[Cu\{Cp_2Cr_2(CO)_4P_2\}]^+$, 455.8 (100) $[Cu\{Cp_2Cr_2(CO)_2P_2\}(NCCH_3)]^+$, 442.9 (9) $[Cu\{Cp_2Cr_2P_2\}(NCCH_3)_2]^+$ or $[Cu\{Cp_2Cr_2(CO)_3P_2\}]^+$, 427.8 (17) $[Cu\{Cp_2Cr_2(CO)P_2\}(NCCH_3)]^+$. IR (KBr): $\tilde{\nu}$ = 3118 (w), 1993 (vs; CO), 1951 (vs; CO), 1914 (vs; CO), 1880 (vs; CO), 1851 (s; CO), 1424 (m), 1363 (w), 1264 (w), 1116 (w), 1062 (m), 1013 (m), 957 (w), 932 (w), 886 (m), 867 (m), 854 (s), 846 (s), 669 (w), 621 (m), 603 (m), 596 (m), 560 (s), 551 (s), 523 (m), 506 (m), 489 (m), 479 (m), 446 (w), 427 $cm^{-1}$ (w). $C_{14}H_{10}ClCr_2CuO_4P_2$ (507.17): calcd. C 33.16, H 1.99; found C 32.83, H 1.99.

**Synthesis of 4:** A solution of CuBr (70 mg, 0.49 mmol) in $CH_3CN$ (10 mL) was carefully layered over a solution of **2** (100 mg, 0.25 mmol) in $CH_2Cl_2$ (10 mL) at room temperature. The vessel was left at room temperature in the dark and moss-green needles of **4** were deposited within a month. These were filtered, washed with $CH_3CN$ (2 × 3 mL) and pentane (2 × 3 mL), in that order, and dried under vacuum. Yield: 120 mg (89%); m.p. 202 °C (decomp.). $^{31}P$ MAS NMR (202.5 MHz, room temp.): $\delta$ = –99.6 (m), 80.2 ppm (m). $^{63}Cu$ MAS NMR (132.6 MHz, room temp.): $\delta$ = 550 ppm (br). Positive-ion ESI MS ($CH_3CN$, room temp.): *m*/*z* (%) 1166.6 (9) $[Cu_3Br_2\{Cp_2Cr_2(CO)_4P_2\}_2]^+$, 1110.5 (4) $[Cu_3Br_2\{Cp_2Cr_2(CO)_3P_2\}_2]^+$, 1022.7 (18) $[Cu_2Br\{Cp_2Cr_2(CO)_4P_2\}_2]^+$, 1007.6 (2) $[Cu_2Br\{Cp_2Cr_2(CO)_3P_2\}_2(NCCH_3)]^+$, 966.6 (11) $[Cu_2Br\{Cp_2Cr_2(CO)_3P_2\}_2]^+$, 910.6 (1) $[Cu_2Br\{Cp_2Cr_2(CO)_2P_2\}_2]^+$, 878.8 (40) $[Cu\{Cp_2Cr_2(CO)_4P_2\}_2]^+$, 822.8 (17) $[Cu\{Cp_2Cr_2(CO)_3P_2\}_2]^+$, 799.5 (1) $[Cu_2Br\{Cp_2Cr_2(CO)P_2\}_2]^+$, 766.8 (6) $[Cu\{Cp_2Cr_2(CO)_2P_2\}_2]^+$, 743.6 (1) $[Cu_2Br\{Cp_2Cr_2P_2\}_2]^+$, 655.7 (2) $[Cu\{Cp_2Cr_2P_2\}_2]^+$, 599.8 (5) $[Cu_2Br\{Cp_2Cr_2(CO)_2P_2\}(NCCH_3)]^+$, 511.8 (100) $[Cu\{Cp_2Cr_2(CO)_4P_2\}(NCCH_3)]^+$, 496.8 (8) $[Cu\{Cp_2Cr_2(CO)_2P_2\}(NCCH_3)_2]^+$, 468.9 (2) $[Cu\{Cp_2Cr_2(CO)_4P_2\}]^+$, 455.8 (45) $[Cu\{Cp_2Cr_2(CO)_2P_2\}(NCCH_3)]^+$, 440.8 (9) $[Cu\{Cp_2Cr_2P_2\}(NCCH_3)_2]^+$ or $[Cu\{Cp_2Cr_2(CO)_3P_2\}]^+$, 427.8 (5) $[Cu\{Cp_2Cr_2(CO)P_2\}(NCCH_3)]^+$. IR (KBr): $\tilde{\nu}$ = 3113 (w), 1995 (vs; CO), 1951 (vs; CO), 1915 (vs; CO), 1881 (vs; CO), 1851 (s; CO), 1424 (m), 1363 (w), 1265 (w), 1116 (w), 1060 (w), 1005 (w), 956 (w), 930 (w), 886 (w), 867 (m), 852 (s), 669 (w), 620 (m), 602 (m), 596 (m), 559 (s), 550 (s), 521 (m), 504 (m), 488 (m), 478 (s), 445 $cm^{-1}$ (w). $C_{14}H_{10}BrCr_2CuO_4P_2$ (551.62): calcd. C 30.48, H 1.83; found C 30.13, H 1.81.

**Synthesis of 5·*n*$CH_3CN$:** A solution of CuI (93 mg, 0.49 mmol) in $CH_3CN$ (10 mL) was carefully layered over a solution of **2** (100 mg, 0.25 mmol) in $CH_2Cl_2$ (10 mL) at room temperature. The vessel was left at room temperature in the dark and moss-green needles of **5**·*n*$CH_3CN$ were deposited within a month. These were filtered, washed with $CH_3CN$ (2 × 3 mL) and pentane (2 × 3 mL), in that order, and dried under vacuum at room temperature. The solvent of crystallisation was not lost during the drying process. Yield: 140 mg (89%); m.p. 184 °C (decomp.). $^{31}P$ MAS NMR (202.5 MHz, room temp.): $\delta$ = 46.3 ppm (br). $^{63}Cu$ MAS NMR (132.6 MHz, room temp.): $\delta$ = 422 (br). Positive-ion ESI MS ($CH_3CN$, room temp.): *m*/*z* (%) 1260.7 (12) $[Cu_3I_2\{Cp_2Cr_2(CO)_4P_2\}_2]^+$, 1204.6 (7) $[Cu_3I_2\{Cp_2Cr_2(CO)_3P_2\}_2]^+$, 1070.6 (10) $[Cu_2I\{Cp_2Cr_2(CO)_4P_2\}_2]^+$, 1055.6 (1) $[Cu_2I\{Cp_2Cr_2(CO)_3P_2\}_2(NCCH_3)]^+$, 1014.6 (11) $[Cu_2I\{Cp_2Cr_2(CO)_3P_2\}_2]^+$, 958.6 (2) $[Cu_2I\{Cp_2Cr_2(CO)_2P_2\}_2]^+$, 878.8 (35) $[Cu\{Cp_2Cr_2(CO)_4P_2\}_2]^+$, 822.8 (17) $[Cu\{Cp_2Cr_2(CO)_3P_2\}_2]^+$, 766.7 (5) $[Cu\{Cp_2Cr_2(CO)_2P_2\}_2]^+$, 647.7 (4) $[Cu_2I\{Cp_2Cr_2(CO)_2P_2\}(NCCH_3)]^+$, 511.8 (100) $[Cu\{Cp_2Cr_2(CO)_4P_2\}(NCCH_3)]^+$, 496.8 (8) $[Cu\{Cp_2Cr_2(CO)_2P_2\}(NCCH_3)_2]^+$, 468.9 (2) $[Cu\{Cp_2Cr_2(CO)_4P_2\}]^+$, 455.8 (42) $[Cu\{Cp_2Cr_2(CO)_2P_2\}(NCCH_3)]^+$, 440.8 (8) $[Cu\{Cp_2Cr_2P_2\}(NCCH_3)_2]^+$ or $[Cu\{Cp_2Cr_2(CO)_3P_2\}]^+$, 427.8 (6) $[Cu\{Cp_2Cr_2(CO)P_2\}(NCCH_3)]^+$. IR (KBr): $\tilde{\nu}$ = 3123 (w), 3099 (w), 2254 (w; CN), 1992 (vs; CO), 1975 (vs; CO), 1918 (vs; CO), 1425 (m), 1363 (w), 1264 (w), 1116 (w), 1064 (m), 1016 (w), 927 (w), 843 (m), 833 (m), 606 (m), 599 (m), 563 (s), 540 (m), 490 (m), 425 $cm^{-1}$ (w). $C_{16}H_{13}Cr_2CuINO_4P_2$ (639.67): calcd. C 30.04, H 2.05, N 2.19; found C 29.61, H 2.05, N 2.08.

## Acknowledgments

This work was supported by the Deutsche Forschungsgemeinschaft and the Fonds der Chemischen Industrie. The authors would like to thank Prof. Joachim Sauer and the Humboldt University of Berlin for providing computing facilities, and Mrs. Petra Lugauer and Mrs. Sabine Stempfhuber for technical assistance.

[1] Recent review articles: a) W. Huang, H.-B. Zhu, S.-H. Gou, *Coord. Chem. Rev.* **2006**, *250*, 414–423; b) N. C. Gianneschi, M. S. Masar III, C. A. Mirkin, *Acc. Chem. Res.* **2005**, *38*, 825–837; c) M. Ruben, J. Rojo, F. J. Romero-Salguero, L. H. Uppadine, J.-M. Lehn, *Angew. Chem.* **2004**, *116*, 3728–3747; *Angew. Chem. Int. Ed.* **2004**, *43*, 3644–3662; d) L. Carlucci, G. Ciani, D. M. Proserpio, *Coord. Chem. Rev.* **2003**, *246*, 247–289; e) G. F. Swiegers, T. J. Malefetse, *Coord. Chem. Rev.* **2002**, *225*, 91–121.

[2] a) J. Bai, E. Leiner, M. Scheer, *Angew. Chem.* **2002**, *114*, 820–823; *Angew. Chem. Int. Ed.* **2002**, *41*, 783–786; b) J. Bai, A. V. Virovets, M. Scheer, *Angew. Chem.* **2002**, *114*, 1808–1811; *Angew. Chem. Int. Ed.* **2002**, *41*, 1737–1740; c) J. Bai, A. V. Virovets, M. Scheer, *Science* **2003**, *300*, 781–783; d) M. Scheer, L. Gregoriades, J. Bai, M. Sierka, G. Brunklaus, H. Eckert, *Chem. Eur. J.* **2005**, *11*, 2163–2169; e) M. Scheer, J. Bai, B. P. Johnson, R. Merkle, A. V. Virovets, C. E. Anson, *Eur. J. Inorg. Chem.* **2005**, 4023–4026; f) B. P. Johnson, F. Dielmann, G. Balázs, M. Sierka, M. Scheer, *Angew. Chem.* **2006**, *118*, 2533–2536; *Angew. Chem. Int. Ed.* **2006**, *45*, 2473–2475; g) L. J. Gregoriades, H. Krauss, J. Wachter, A. V. Virovets, M. Sierka, M. Scheer, *Angew. Chem.* **2006**, *118*, 4295–4298; *Angew. Chem. Int. Ed.* **2006**, *45*, 4189–4192; h) M. Scheer, L. J. Gregoriades, A. V. Virovets, W. Kunz, R. Neueder, I. Krossing, *Angew. Chem.* **2006**, *118*, 5818–5822; *Angew. Chem. Int. Ed.* **2006**, *45*, 5689–5693.

[3] a) O. J. Scherer, H. Sitzmann, G. Wolmershäuser, *J. Organomet. Chem.* **1984**, *268*, C9–C12; b) O. J. Scherer, J. Schwalb, H. Sitzmann, *Inorg. Synth.* **1990**, *27*, 224–227.

[4] a) L. Y. Goh, C. K. Chu, R. C. S. Wong, T. W. Hambley, *J. Chem. Soc., Dalton Trans.* **1989**, 1951–1956; b) L. Y. Goh, R. C. S. Wong, *Inorg. Synth.* **1992**, *29*, 247–250.

[5] a) P. Sekar, M. Scheer, A. Voigt, R. Kirmse, *Organometallics* **1999**, *18*, 2833–2837; b) P. Sekar, S. Umbarkar, M. Scheer, A. Voigt, R. Kirmse, *Eur. J. Inorg. Chem.* **2000**, 2585–2589.

[6] a) V. G. Albano, P. L. Bellon, G. Ciani, M. Manassero, *J. Chem. Soc., Dalton Trans.* **1972**, 171–175; b) H. Negita, M. Hiura, Y. Kushi, M. Kuramoto, T. Okuda, *Bull. Chem. Soc. Jpn.* **1981**, *54*, 1247–1248; c) P. G. Eller, G. J. Kubas, R. R. Ryan, *Inorg. Chem.* **1977**, *16*, 2454–2462. The relatively wide ranges quoted for the Cu–P and Cu–X bond lengths are due to the fact that the Cu atoms in the complexes $[Cu_2X_2(PPh_3)_3]$ are found in both trigonal and tetrahedral coordination modes.

[7] A. Altomare, G. Cascarano, C. Giacovazzo, A. Guagliardi, *J. Appl. Crystallogr.* **1993**, *26*, 343–350.

[8] G. M. Sheldrick, *SHELXL-97*, University of Göttingen, Germany, **1997**.

[9] G. Kresse, J. Furthmüller, *Comput. Mater. Sci.* **1996**, *6*, 15.

[10] G. Kresse, J. Furthmüller, *Phys. Rev. B* **1996**, *54*, 11169.

[11] J. P. Perdew, J. A. Chevary, S. H. Vosko, K. A. Jackson, M. R. Pederson, D. J. Singh, C. Fiolhais, *Phys. Rev. B* **1992**, *46*, 6671.

[12] P. E. Blöchl, *Phys. Rev. B* **1994**, *50*, 17953.

[13] G. Kresse, D. Joubert, *Phys. Rev. B* **1999**, *59*, 1758.

[14] H. J. Monkhorst, J. D. Pack, *Phys. Rev. B* **1976**, *13*, 5188.

[15] G. Schreckenbach, T. Ziegler, *J. Phys. Chem.* **1995**, *99*, 606–611.

[16] a) A. D. Becke, *Phys. Rev. A* **1988**, *38*, 3098–3100; b) S. H. Vosko, L. Wilk, M. Nusair, *Can. J. Phys.* **1980**, *58*, 1200–1211; c)

 © 2007 Wiley-VCH Verlag GmbH & Co. KGaA, Weinheim 

J. P. Perdew, *Phys. Rev. B* **1986**, *33*, 8822–8824; erratum: J. P. Perdew, *Phys. Rev. B* **1986**, *34*, 7406.
[17] F. Weigend, R. Ahlrichs, *Phys. Chem. Chem. Phys.* **2005**, *7*, 3297–3305.
[18] M. J. Frisch, G. W. Trucks, H. B. Schlegel, G. E. Scuseria, M. A. Robb, J. R. Cheeseman, J. A. Montgomery Jr, T. Vreven, K. N. Kudin, J. C. Burant, J. M. Millam, S. S. Iyengar, J. Tomasi, V. Barone, B. Mennucci, M. Cossi, G. Scalmani, N. Rega, G. A. Petersson, H. Nakatsuji, M. Hada, M. Ehara, K. Toyota, R. Fukuda, J. Hasegawa, M. Ishida, T. Nakajima, Y. Honda, O. Kitao, H. Nakai, M. Klene, X. Li, J. E. Knox, H. P. Hratchian, J. B. Cross, C. Adamo, J. Jaramillo, R. Gomperts, R. E. Stratmann, O. Yazyev, A. J. Austin, R. Cammi, C. Pomelli, J. W. Ochterski, P. Y. Ayala, K. Morokuma, G. A. Voth, P. Salvador, J. J. Dannenberg, V. G. Zakrzewski, S. Dapprich, A. D. Daniels, M. C. Strain, O. Farkas, D. K. Malick, A. D. Rabuck, K. Raghavachari, J. B. Foresman, J. V. Ortiz, Q. Cui, A. G. Baboul, S. Clifford, J. Cioslowski, B. B. Stefanov, G. Liu, A. Liashenko, P. Piskorz, I. Komaromi, R. L. Martin, D. J. Fox, T. Keith, M. A. Al-Laham, C. Y. Peng, A. Nanayakkara, M. Challacombe, P. M. W. Gill, B. Johnson, W. Chen, M. W. Wong, C. Gonzalez, J. A. Pople, *Gaussian 03*, Revision C.01, Gaussian, Inc., Wallingford, CT, **2004**.
[19] K. A. Peterson, D. Figgen, E. Goll, H. Stoll, M. Dolg, *J. Chem. Phys.* **2003**, *119*, 11113.
[20] D. G. Gorenski, *Phosphorus-31 NMR, Principles and Applications*, Academic Press, New York, **1984**.

Received: January 24, 2007
Published Online: May 8, 2007

 © 2007 Wiley-VCH Verlag GmbH & Co. KGaA, Weinheim 

DOI: 10.1002/ejic.200700144

# Tagging (Arene)ruthenium(II) Anticancer Complexes with Fluorescent Labels

**Fabio Zobi,[a] Beeta Balali Mood,[a] Peter A. Wood,[a] Francesca P. A. Fabbiani,[a] Simon Parsons,[a] and Peter J. Sadler*[a]**

**Keywords:** Anticancer agents / Organometallic compounds / Fluorescence / Ruthenium / Hydrolysis

Fluorescent (arene)ruthenium(II) complexes have been prepared by tagging a small fluorogenic reporter onto the chelating ligand of complexes of the type $[(\eta^6\text{-arene})RuCl(Z)]^+$ (Z = chelating ligand). Complexes $[(\eta^6\text{-}p\text{-cym})RuCl(NNO)](Cl)$ (**2**), $[(\eta^6\text{-}p\text{-cym})RuCl(\mathbf{L3})](Cl)$ (**3**) and $[(\eta^6\text{-}p\text{-cym})RuCl(\mathbf{L4})](Cl)$ (**4**) {*p*-cym = *p*-cymene, NNO = 2-[(2-aminoethyl)amino]ethanol, **L3** = 2-[(2-aminoethyl)amino]ethyl-2-(methylamino)benzoate and **L4** = *N*-{2-[(2-aminoethyl)-amino]ethyl}-2-(methylamino)benzamide} were obtained in good yield from the reaction of the Ru dimer $[(\eta^6\text{-}p\text{-cym})RuCl_2]_2$ (**1**) and the corresponding ligand. The compounds have been fully characterized and their X-ray crystal structures are reported. Compounds **3** and **4** show a photoluminescence response centered at 435 nm with partial fluorescence quenching of the fluorogenic reporters **L3** and **L4** upon coordination to the metal center. Species **2**–**4** show good solubility both in water and organic solvents. In water, **2**–**4** readily hydrolyze to form the aqua complexes. These are stable at acidic pH forming 10–15 % of the corresponding hydroxido complexes in buffered solution (25 mM HEPES) as the pH is raised to a physiological value (pH = 7.44). Under these conditions, **4** (but not **2** or **3**) undergoes a fast pH-dependent reversible intramolecular rearrangement. Experimental data and semiempirical calculations indicate that the major species arising from this transformation is a complex with a tridentate chelating ligand following deprotonation at the nitrogen atom of the amide group. Esterase-catalyzed hydrolysis of **3** liberates isatoic acid (**MIAH**) and generates **2** indicating that the complex is a substrate for the enzyme. Complexes similar to **3** may have potential for esterase-activated Ru-based prodrug delivery systems.

(© Wiley-VCH Verlag GmbH & Co. KGaA, 69451 Weinheim, Germany, 2007)

## Introduction

Organometallic ruthenium(II) complexes of the type $[(\eta^6\text{-arene})RuCl(X)(Y)]$ (where X, Y are monodentate or chelating ligands) comprise a relatively new group of anticancer compounds which are cytotoxic to cancer cells, including cisplatin-resistant cell lines.[1,2] The geometry of the complexes is generally described as pseudo-octahedral "three-legged piano-stool" in which a π-bonded arene ligand provides the seat supported by a σ-bonded chlorido and a chelating ligand which form the three legs of the stool. The arene ligand is strongly bound and stabilizes the ruthenium(II) oxidation state. It resists hydrolysis and provides a lipophilic side to the complex.[3,4] Most of the halide compounds, however, are ionic and exhibit good aqueous solubility and appear to undergo rapid aquation (substitution of bound Cl by $H_2O$).[4] Thus, while $\eta^6$-arene–$Ru^{II}$ bonds are inert toward hydrolysis, the monofunctional complexes $[(\eta^6\text{-arene})Ru^{II}(en)(Cl)]^+$ (en = ethylenediamine) readily lose their chlorido ligand and transform into the corresponding, more reactive, aquated species.[4–6]

This type of compound has continued to attract attention since it was reported by Morris et al. in 2001 that $[(\eta^6\text{-biphenyl})Ru(en)Cl][PF_6]$ is as cytotoxic to cancer cells as carboplatin.[1] Although the cellular target for (arene)ruthenium compounds and the mechanism underlying their biological effects are not yet known, much of the research has focused on the interaction of these complexes with DNA bases and oligonucleotides.[1,5–10] In the same report Morris et al. described strong and selective binding to G bases on DNA, while no inhibition of topoisomerase I or II was detected. Subsequently, Chen et al. showed that $[(\eta^6\text{-arene})Ru(en)]^{2+}$ complexes exhibit a remarkably high preference for binding to guanine N7.[5,6] Such binding is stabilized by H-bonding between the O6 of G and NH of the en ligand and strong arene–nucleobase stacking when the arene is extended, suggesting a potential DNA-binding mode, involving simultaneous arene intercalation and $Ru^{II}$ coordination.[5,6] Hydrophobic interactions were described both in solution and in the solid state, and it was suggested that it is the flexibility of the arene ligand that allows for simultaneous arene–base stacking and N7-covalent binding. The remarkable site selectivity of the complexes was further demonstrated by Novakova et al. who showed by transcription mapping experiments that in cell-free media the interaction of $[(\eta^6\text{-arene})Ru(en)]^{2+}$ complexes with DNA occurs at G N7.[11] In the same report noncovalent, hydrophobic interaction between the arene ligand and DNA was demonstrated by competitive ethidium displacement.

[a] School of Chemistry, University of Edinburgh, West Mains Road, Edinburgh EH9 3JJ, U.K.

Supporting information for this article is available on the WWW under http://www.eurjic.org or from the author.

 © 2007 Wiley-VCH Verlag GmbH & Co. KGaA, Weinheim 

Reactions of the (arene)chlorido(ethylenediamine)$Ru^{II}$ complexes with nucleotides appear to involve initial aquation of the arene complexes, and reactions of the aqua complexes with cyclic guanosine monophosphate are faster than those of the chlorido complexes.[4–6] Wang et al. showed that rates of aquation of these (arene)ruthenium anticancer agents are >20× faster than that of cisplatin. The aqua complexes behave as weak acids with p$K_a$ values for the aqua adducts ranging from 7.7 to 8.[4]

In contrast to *cis*-[$PtCl_2(NH_3)_2$], cisplatin, [($\eta^6$-arene)-Ru(en)]$^{2+}$ complexes show little binding to adenine. This is attributable to repulsive interactions between the exocyclic amino group of the base and (en)Ru $NH_2$ groups.[5,6] Replacing the neutral en by anionic acetyl acetonate as the chelating ligand changes the nucleobase specificity, and the overall affinity for adenosine was demonstrated to be greater than for guanosine.[7] The cytotoxicity of the complexes increases with the size of the arene ring system in the series arene = benzene < *p*-cymene < biphenyl < dihydroanthracene < tetrahydroanthracene which further supports a potential DNA-binding mode, involving simultaneous arene intercalation and $Ru^{II}$ coordination.[2]

Other cytotoxic (arene)Ru complexes of general formula [($\eta^6$-arene)$RuCl_2$(X)] (X = monodentate ligand) have also recently been reported, including 1,3,5-triaza-7-phosphaadamantane (PTA) and imidazole compounds described by Dyson et al.[12–16] These complexes show activity towards the TS/A mouse adenocarcinoma cancer cell line and no apparent cytotoxicity towards HBL-100 human mammary (non-tumor) cell line.[13,14] The cellular target and the mechanism underlying the biological effects for these (arene)ruthenium compounds are also not yet known. The molecules, however, exhibit a pH-dependent DNA damage such that at pH values typical of hypoxic cells DNA is damaged, whereas at pH values characteristic of healthy cells little or no damage is detected.[13,14] The complexes described by Dyson and co-workers may act by a different mechanism from those of general formula [($\eta^6$-arene)-RuCl(X)(Y)]. Loss of the arene is observed in the former complexes, and it has been suggested that single-stranded DNA may wrap around the metal center with formation of multiple coordinative N-donor bonds.[12]

In view of the importance of understanding the biological distribution of (arene)ruthenium compounds, and thus elucidating their mechanism of action, we have tagged them with a small fluorescent probe. Fluorescence microscopy has been widely used to study cellular distribution of organic drugs,[17–19] and recently it has been applied successfully to platinum complexes.[20–24] In the latter case, fluorogenic reporters of different size have been used. These range from large carboxyfluorescein diacetate,[20–22] to medium-size diaminoanthracene[23,24] to small dinitrophenyl derivatives.[20–22] Cellular uptake of labeled compounds is affected by large fluorophores, and it has been suggested that fluorescein-labeled compounds diffuse in and out of the cells and intracellular compartments at a greater rate than the parent compounds.[25]

Owing to these considerations, we have synthesized methylisatoic anhydride (**MIA**) based fluorescent derivatives of (arene)ruthenium complexes and studied their properties. The **MIA** probe was chosen for its relatively small size, a feature that we anticipated might not alter significantly the properties of the complexes. The probe has found wide applications in biochemistry, and it has been used to label a variety of biological substrates ranging from RNA and Ras-like low-molecular-weight GTP-binding proteins to relatively large enzymes like kinases and ATPases.[26–30] We report here the synthesis and characterization of **MIA**-based fluorescent derivatives of (arene)ruthenium complexes (Scheme 1). We have also studied the interaction of complexes **3** and **4** (Scheme 1) with porcine liver esterase (PLE), and we show that esterase-catalyzed hydrolysis reactions can liberate methylisatoic acid (**MIAH**) from complex **3** suggesting a possible use of similar derivatives in esterase-activated Ru-based prodrug delivery systems.

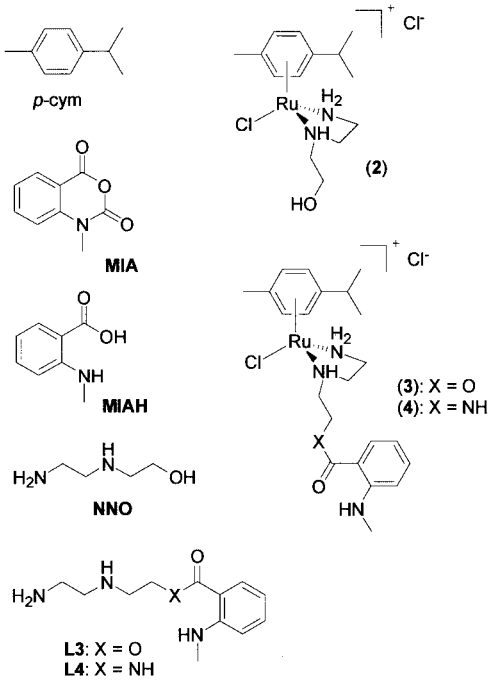


Scheme 1. Structure and abbreviations of ligands, reagents and metal complexes.

## Results and Discussion

### Synthetic Aspects and General Considerations

Reaction of the dimer [($\eta^6$-*p*-cym)$RuCl_2$]$_2$ (**1**) with 2.2 mol-equiv. of the corresponding ligand afforded the complexes [($\eta^6$-*p*-cym)RuCl(NNO)](Cl) (**2**), [($\eta^6$-*p*-cym)-RuCl(**L3**)](Cl) (**3**) and [($\eta^6$-*p*-cym)RuCl(**L4**)](Cl) (**4**) in good yields (Scheme 2). Complex **2** was first prepared for a direct conjugation reaction with **MIA**. This strategy, however, proved unsuccessful, and we were able to detect only small amounts of **3** by this route. We then proceeded by the organic synthesis of ligands (Scheme 2), and we used **2** as a

 © 2007 Wiley-VCH Verlag GmbH & Co. KGaA, Weinheim 

standard for comparison with species **3** and **4**. The compounds were characterized by $^1$H NMR spectroscopy and electrospray ionization mass spectrometry (ESI-MS). The ESI mass spectra of **2**–**4** in water, methanol or $CH_3CN$ provided parent peaks corresponding to the cations. Depending on the cone voltage, peaks corresponding to further loss of HCl were also observed. All spectra confirmed the presence of the expected products.

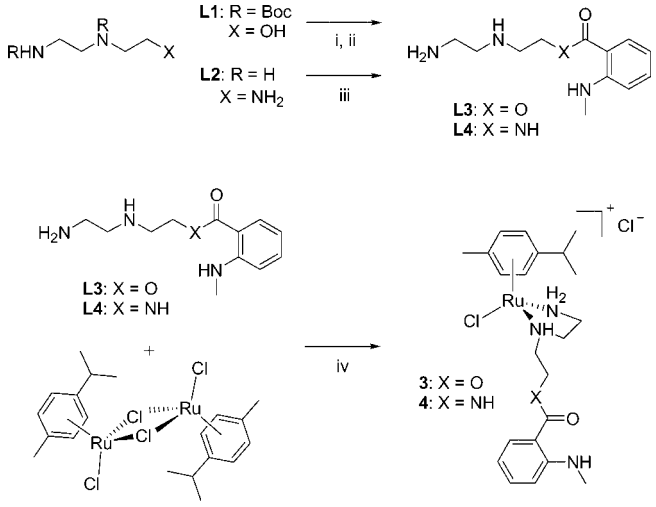


Scheme 2. Synthesis of **MIA**-related ligands and complexes. Conditions: i: **MIA**, $CH_3CN$, $K_2CO_3$, room temp. ii: TFA, $CH_2Cl_2$, room temp. iii: **MIA**, $CHCl_3$, $K_2CO_3$, room temp. iv: $CHCl_3$, room temp.

Complexes **2**–**4** showed good solubility both in water and organic solvents. The NMR spectra of compounds **3** and **4** in deuteriated chloroform contain peaks between δ = 6.5 and 8.1 ppm that correspond to the aromatic protons of the 2-(methylamino)benzoate/benzamide fragment; aliphatic proton signals are observed between δ = 2.5 and 4.7 ppm. Peaks for arene ligand protons are observed between δ = 5.4 and 5.9 ppm, with the C*H*$(CH_3)_2$ proton displaying a characteristic septet between δ = 1.7 and 2 ppm. Methyl group signals appear at δ ≈ 1.3 ppm. In water, the compounds readily form the corresponding aqua complexes. These are stable at acidic pH*, and no hydroxido species could be detected under these conditions. The p$K_a$ values of the aqua complexes also lie above 7 in agreement with values reported for similar arene species.[4,7] As the pH is raised to within the physiological range (buffered solutions, pH = 7.44) the complexes behave as weak acids forming about 10–15% of the corresponding hydroxido species. Complexes **2** and **3** are stable under these conditions for hours, but **4** slowly undergoes an intramolecular rearrangement following deprotonation at the amide nitrogen atom. This process is described in detail in the following sections. Attempts to obtain X-ray quality crystals of the aqua and hydroxido complexes were unsuccessful, but the chlorido adducts were readily crystallized from organic solvents.

## X-ray Crystallography

Crystallographic data are listed in Table 4 and selected bond lengths and angles in Table 1. The structures of the complexes **2**, **4** and **3** are shown in Figures 1, 2 and 3, respectively. All complexes have the familiar pseudo-octahedral "three-legged pianostool" geometry as described previously. Complex **2** crystallizes in space group $P\bar{1}$ with one solvent molecule of methanol and shows disorder in the methyl groups of the isopropyl substituent of *p*-cym. The disorder was modelled by allowing ½ occupancy for each of the four carbon atoms involved. The $Cl^-$ counter anion bridges the hydroxy groups of the solvent molecule and the pendent arm of the chelating ligand through two hydrogen bonds.

Table 1. Selected bond lengths [Å] and angles [°] for cations of **2**, **3** and **4**.[a]

| | **2** | **3** | **4** |
|---|---|---|---|
| Ru–Cl | 2.4257(10) | 2.4148(8) | 2.4149(18) |
| Ru–N′ | 2.125(4) | 2.132(3) | 2.115(6) |
| Ru–N′′ | 2.168(3) | 2.159(3) | 2.142(6) |
| N′–Ru–N′′ | 79.48(14) | 80.32(10) | 79.7(2) |
| N′–Ru–Cl | 83.89(10) | 82.71(8) | 85.13(17) |
| N′′–Ru–Cl | 86.92(9) | 86.88(8) | 87.83(17) |

[a] N′ and N′′ refer to the primary and secondary amine, respectively, of the chelate ligand.

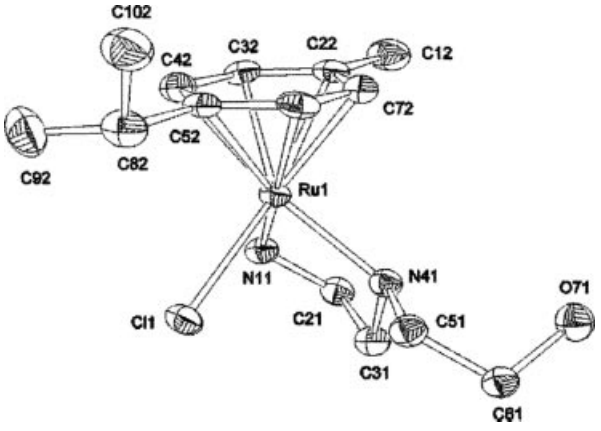


Figure 1. ORTEP diagram and atom numbering scheme for the cation of **2** (50% probability ellipsoids). The H atoms have been omitted for clarity.

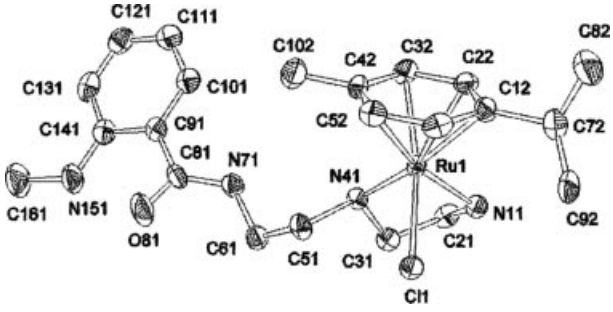


Figure 2. ORTEP diagram and atom numbering scheme for the cation of **4** (50% probability ellipsoids). The H atoms have been omitted for clarity. Two independent molecules of **4** crystallize in the same unit cell; only one is shown.

 © 2007 Wiley-VCH Verlag GmbH & Co. KGaA, Weinheim 

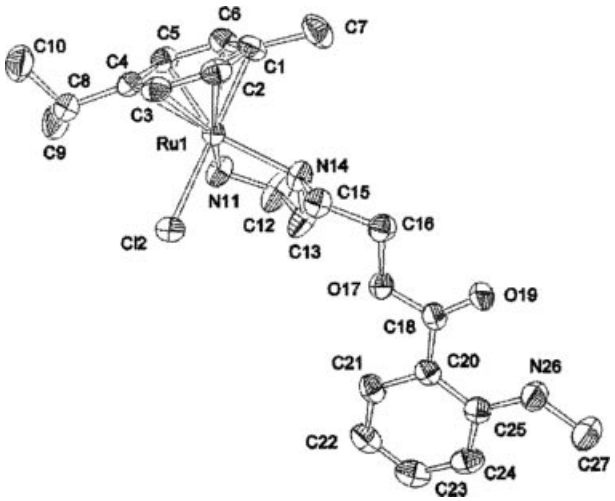


Figure 3. ORTEP diagram and atom numbering scheme for the cation of **3** (50% probability ellipsoids). The H atoms have been omitted for clarity.

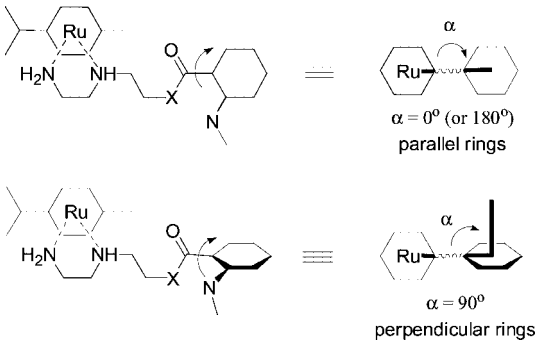


Figure 4. Schematic representation and definition of the angle $\alpha$.

Complex **4** also crystallized in space group $P\bar{1}$ with two independent molecules in the asymmetric unit. These differ by the relative orientation of the 2-(methylamino)benzamide ring with respect to the aromatic arene ring (see Figure 4). In one molecule the plane defined by the six carbon atoms of the 2-(methylamino)benzamide ring forms an angle $\alpha$ of 28° with the plane of *p*-cym, while in the other molecule the benzamide ring is rotated with an angle $\alpha$ of 47°. Three solvent molecules of chloroform co-crystallize with the complex with two $Cl^-$ counterions completing the content of the asymmetric unit. The counterions form H-bonds with NH and $NH_2$ groups of the chelating ligand.

In order to obtain crystals of **3**, the $Cl^-$ counterion had to be removed by addition of $AgClO_4$. Thus, complex **3**, as a $ClO_4^-$ salt, crystallized in space group $P2_1/n$. No solvent molecules are present in the asymmetric unit. The $ClO_4^-$ counterion shows disorder in one oxygen atom. In this case also the disorder was modelled by allowing ½ occupancy for each oxygen atom. In this structure the plane defined by the 2-(methylamino)benzoate ring is almost perpendicular to that of the *p*-cym ring ($\alpha$ = 88°, Figure 4).

For structures of the cations of **2**, **3** and **4**, metal–nitrogen and metal–chlorido bonds all fall within normal values (Table 1).[1–7] Bond lengths and distances around the metal coordination sphere are similar (within 3σ) in all three structures indicating that addition of 2-(methylamino)benzoate/benzamide has little effect on the overall coordination of the bidentate chelate. In the crystal structure of the $ClO_4^-$ salt of **3**, short van der Waals contacts are found between *p*-cym hydrogen atoms and the carbonyl oxygen atom and the $CH_3NH$ group of the 2-(methylamino)benzoate fragment of adjacent molecules. These are shown in Figure 5. Such short contacts involving coordinated arenes are becoming increasingly recognized.[31] They have also been observed in [($\eta^6$-*p*-cym)M(acac)Cl] (M = Ru or Os) complexes,[7] and it has been suggested that the weak polarization of arene ring C–H bonds may lead to interactions be-

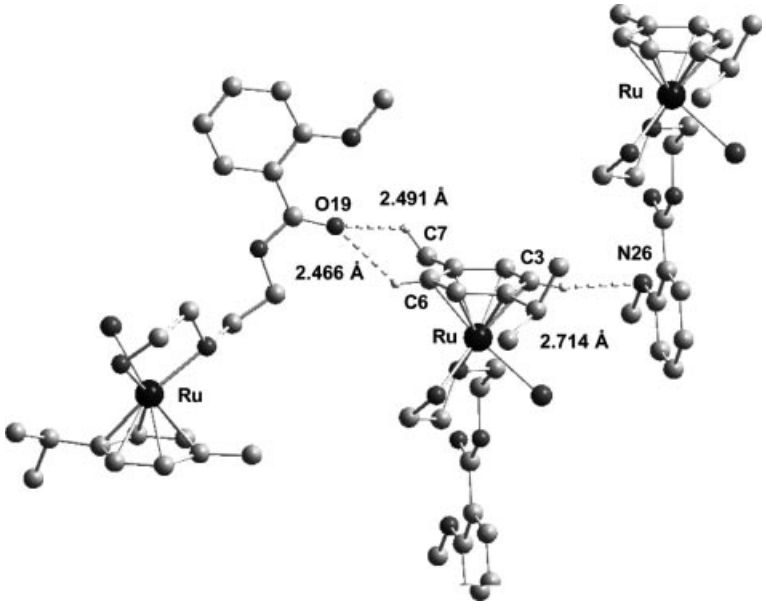


Figure 5. Short contacts involving arene hydrogen atoms of the cation in the crystal structure of **3**.

 © 2007 Wiley-VCH Verlag GmbH & Co. KGaA, Weinheim 

tween the coordinated arene and H-bond acceptors in biological target sites such as DNA or RNA.[32] It is worth noting that we found no evidence of π-stacking interactions in any of the reported structures.

Complexes **3** and **4** are the first examples of metal complexes with a pendent 2-(methylamino)benzoate/benzamide ring, thus restricting structural comparisons with similar compounds. To the best of our knowledge, the only other instance in which the same fragments have been used in coordination chemistry is in the preparation of Bosnich's type of ligands in complexes investigated for cooperative dimetallic redox reactivity. In those complexes, however, the fragment is part of a larger dinucleating ligand framework.[33–38]

### Stability in Aqueous Buffered Solutions

In water the compounds readily form the corresponding aqua complexes which are stable at acidic pH. In a buffered solution (25 mM HEPES, pH = 7.44) the complexes behave as weak acids forming about 10–15% of the corresponding hydroxido species. Complexes **2** and **3** are stable under these conditions for hours, while **4** slowly undergoes an intramolecular rearrangement following deprotonation at the amide nitrogen atom as shown in Scheme 3.

The $^1$H NMR spectrum of **4** in the buffered solution is shown in Figure 6. After ca. 15 min, three sets of *p*-cym signals were visible in the spectrum of the complex (Figure 6a). The major species is the aqua complex **4a** with *p*-cym resonances at $\delta$ = 5.52, 5.67 and 5.72 ppm. The corresponding resonances of the hydroxido species **4b** are shifted upfield to $\delta$ = 5.18 and 5.38 ppm. A third set of *p*-cym signals assigned to **4c** appears at $\delta$ = 5.15 and 5.30 ppm. Formation of **4c** was clearly evident from the time-dependent evolution of the NMR spectrum. The reaction was complete within 3 h, and the mixture thus obtained was stable for hours under these conditions. Formation of **4c** is accompanied by the appearance of a fourth species (**4d** in Figure 6). The relative integrated intensity of the signals corresponding to **4d** account for about 2% of the total *p*-cym resonances compared to 9% of the hydroxido species **4b** and 89% of **4c**. We tentatively assign these **4d** resonances to an HEPES complex of **4**. Although sulfonates are weak ligands, the assignment is reasonable given the relatively high concentration of the buffer. Moreover, it has been shown that under similar conditions, reactions of (arene)-ruthenium species with nucleotides produce ca. 1.5% of stable phosphate-bound complexes.[6] It is worth noting that the relative concentration of the hydroxido species **4b** remains unchanged during the course of the transformation indicating that the aqua complex **4a** is the reactive species.

Relative to peaks for **4a**, the NHu proton signals suffer a dramatic downfield shift for **4c**. This indicates either a strong interaction of these hydrogen atoms with nucleophilic atoms or a strong deshielding influence of the aromatic ring current of the benzamide fragment; or a combination of both. Related [($\eta^6$-arene)Ru(en)guanine]$^+$ complexes, for example, show stereospecific en NHd bonding with guanine O6, and these species in solution show a downfield shift of the chelate en NHd hydrogen signals of up to 1 ppm compared to the parent aqua complex.[5,6] It is unlikely that the observed shifts result from a partial overlap or π–π stacking of the aromatic rings, but it is possible that the shifts are also a consequence of the ring current generated by the orientation of the benzamide ring. Proton signals of the benzamide fragment show an unusual behaviour. The four non-equivalent resonances collapse into two signals, which might suggest an increased symmetry of the ring. This, however, is not possible as it would imply a complete rearrangement of the ring substituents. Therefore, we assign this to a coincidental overlap of resonances.

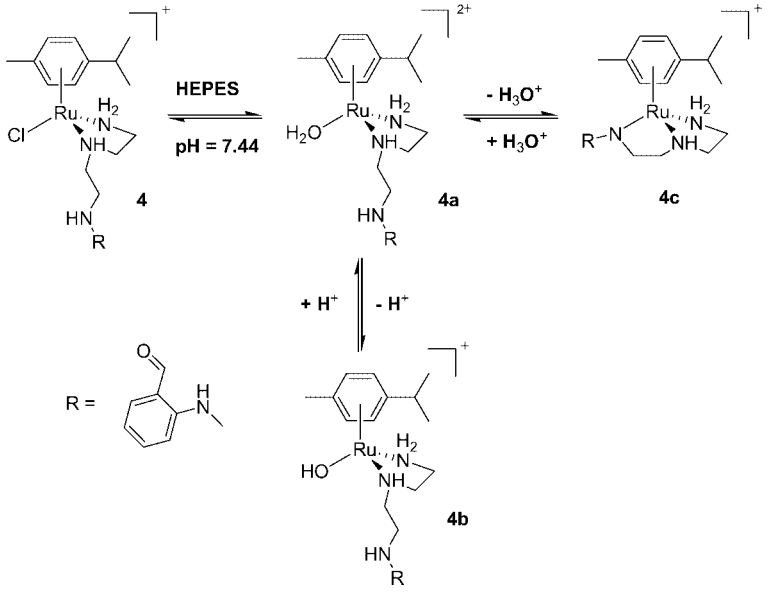


Scheme 3. Hydrolysis of **4** in buffered solution (25 mM HEPES, pH = 7.44).

 © 2007 Wiley-VCH Verlag GmbH & Co. KGaA, Weinheim 

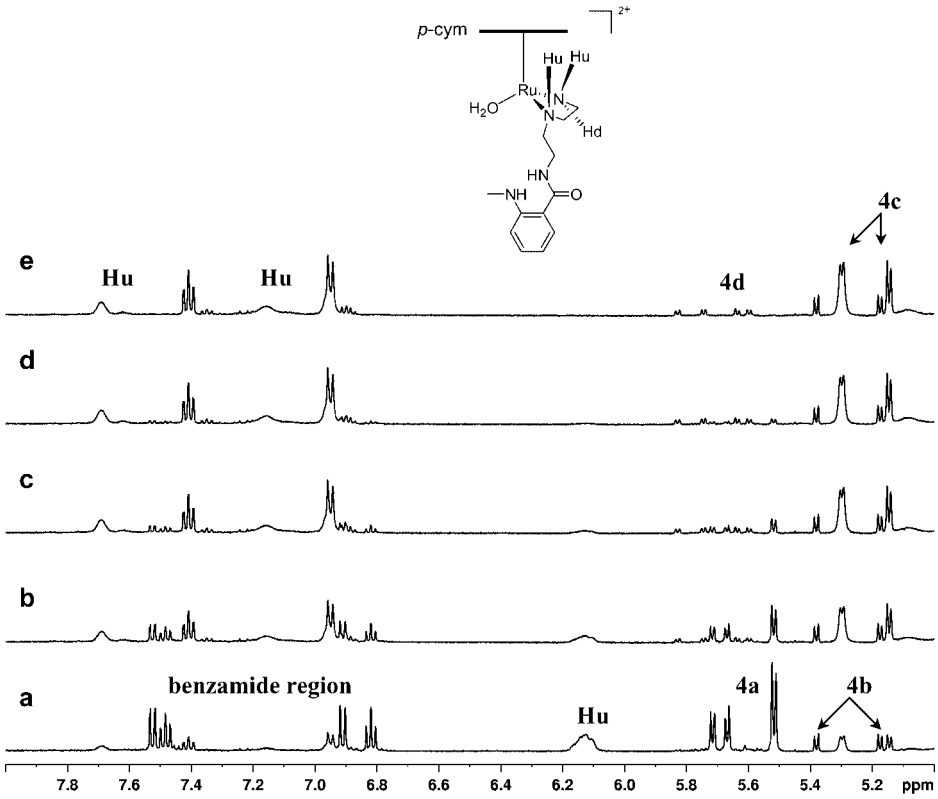


Figure 6. $^1$H NMR spectrum ($\delta$ = 5.1–7.9 ppm) of a 3 mM solution of [($\eta^6$-*p*-cym)Ru(**L4**)Cl]Cl (**4**) in HEPES buffer (25 mM, pH = 7.44). (a) After ca. 15 min; (b–d) 30-min time intervals; (e) after 3 h.

Substitution reactions of the aquated species **4a** are likely to follow the associative interchange mechanism previously described for related complexes. Wang et al. showed that aquation and anation substitution reactions of (arene)Ru species are influenced by steric hindrance of the arene ligand and that the rates of aquation of the halide complexes follow the order Cl ≈ Br > I, consistent with an associative mechanism.[4] Substituents on the *p*-cym ligand exert only minor steric effects when compared to the complexes studied by Wang et al.; however, as a π-acid ligand, *p*-cym depletes electron density on the metal center making it more electropositive. As demonstrated for [($\eta^6$-$C_6H_6$)-$Ru(H_2O)_3]^{2+}$, this electronic effect makes $Ru^{II}$ behave like an $Ru^{III}$ center in arene species,[39] thus making substitution reactions appear to occur by associative interchange mechanisms.

Changes observed in the NMR spectrum are accompanied by a transition in the UV/Vis spectrum as shown in Figure 7. Soon after dissolution of **4** in the buffer solution (pH = 7.44), the UV/Vis spectrum showed a broad d-d transition between 300 and 360 nm. Within 2 h, a relatively sharp peak at 294 nm replaced this absorption indicating that $H_2O$ is replaced by a ligand which causes a greater splitting of the metal d-orbitals. The intramolecular

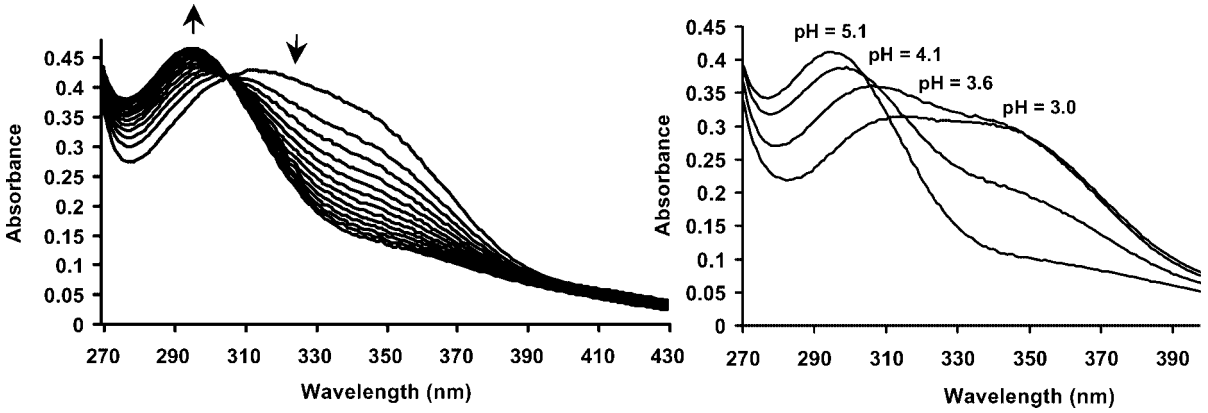


Figure 7. Left: Time evolution of the UV/Vis spectrum of a 0.5 mM solution of **4** (270–430 nm, 25 mM HEPES buffer, pH = 7.44, 5-min time intervals). Right: UV/Vis spectra of **4** at fixed pH values.

 © 2007 Wiley-VCH Verlag GmbH & Co. KGaA, Weinheim 

rearrangement of **4a** is a pH-dependent reversible process (Figure 7). Aliquots of a stock solution of **4** in water were added to 25 mM HEPES solutions, and the pH was adjusted to different values by addition of HCl. The mixtures were allowed to equilibrate at room temperature for 24 h, and their UV/Vis and ESI-MS spectra were recorded. UV/Vis analysis indicated that **4a** is stable at pH $< 3$ (Figure 7). Species **4c** began to form at pH $\approx 3.5$ and became the predominant species at higher pH values.

ESI-MS analysis confirmed this observation (Supporting Information: Figure S1). At pH $< 3.5$ only the parent peak corresponding to the cation of **4** is observed ($C_{22}H_{34}ClN_4ORu$: $m/z$ = 507.15, matching the predicted isotope pattern). At higher pH values a second peak corresponding to loss of HCl from the parent cation of **4** was also observed. This peak became the predominant signal at pH $> 4$.

### Geometry Optimization and INDO/S Analysis and Electronic Spectra

The molecular structure of **4c** was also confirmed by theoretical calculations. Molecular structures **B** and **C** were initially modeled from the crystal structure of the cation of **4** (structure **A**) and were optimized at the semiempirical level using default Hyperchem 7.5 INDO/1 functional and basis set. Structures are shown in Figure 8 and selected bond lengths are listed in Table 2. Structure **B** was chosen as a model of **4c**, while **C** (as a **4d** model) was optimized for comparison reasons. The tridentate chelate in **B** is stabilized by hydrogen bonds involving the 2-(methylamino)-benzamide ring and the Hd proton of the primary amine coordinated to the metal center. Compared to **A**, Ru–N distances increase slightly in **B** upon coordination of the deprotonated amide nitrogen atom. These results reflect an increased electron density at the metal center that weakens the σ-donor bonds of the chelate. The opposite effect is calculated for **C**, where Ru–N distances decrease (on average by 0.14 Å) by allowing HEPES to enter the Ru coordination sphere and occupy a coordination site through the sulfonate oxygen atom.

Table 2. Summary of selected INDO/1-optimized bond lengths [pm].

| | Ru–$NH_2$ | Ru–NH | Ru–X[a] |
|---|---|---|---|
| Structure **A** | 213 | 215 | 241 |
| Structure **B** | 216 | 220 | 199 |
| Structure **C** | 200 | 199 | 194 |

[a] X refers to the atom occupying the exchangeable coordination site. Thus, for structure **A**, X = Cl; for structure **B**, X = N; for structure **C**, X = O.

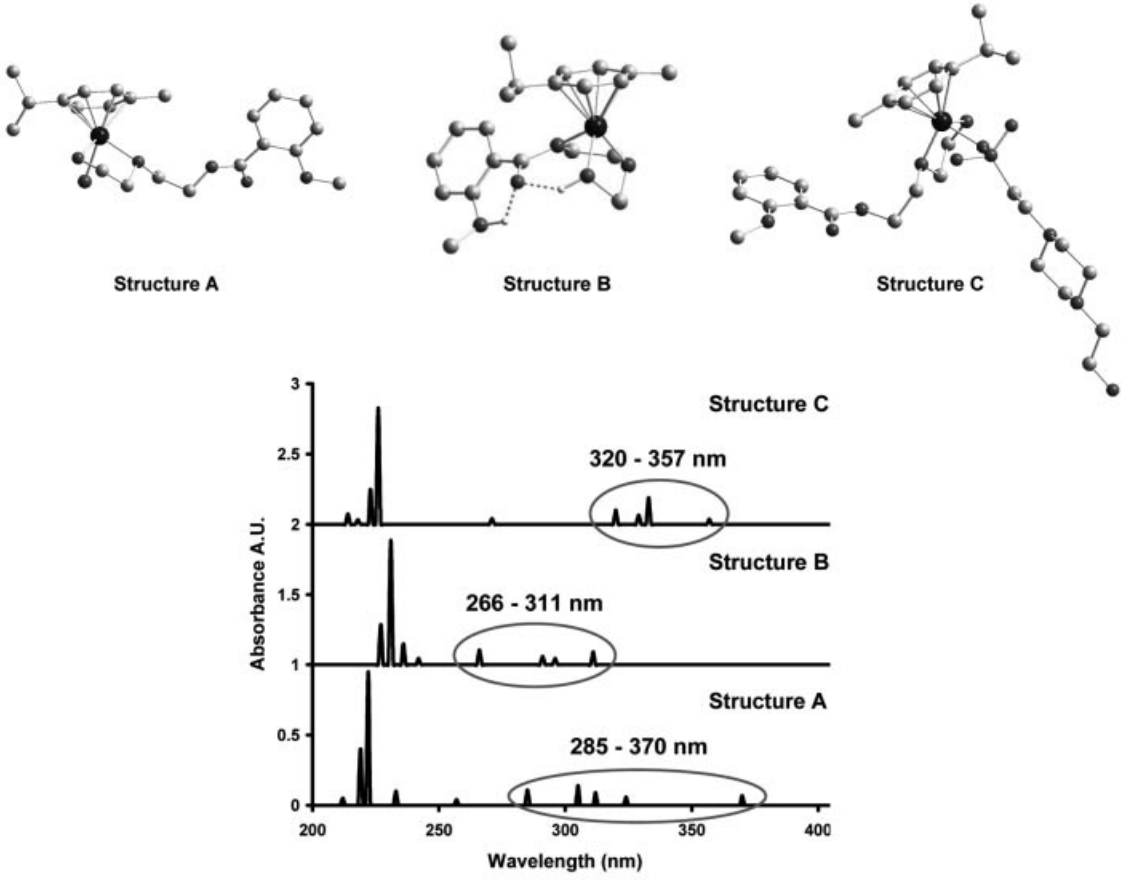


Figure 8. INDO/1-optimized geometry of structure **A** (**4**), **B** and **C** and relative predicted (gas-phase, INDO/S) spectra. Vertical bars are the predicted oscillator strengths and locations of individual computed transitions.

 © 2007 Wiley-VCH Verlag GmbH & Co. KGaA, Weinheim 

In both **B** and **C** the planarity of the arene ligand is somewhat lost compared to **A**. Both the methyl and the isopropyl group of *p*-cymene are slightly bent out of the plane defined by the six carbon atoms of the *p*-cym aromatic ring. The distortion of the arene is uniform and relatively contained in **C** with both methyl and isopropyl groups deviating from planarity by about 0.06 Å. In **B** the distortion is more pronounced and uneven with the methyl and the isopropyl substituents out of the benzene plane by 0.14 and 0.06 Å, respectively. In **A** the observed deviation is on average 0.04 Å. The net effect of these distortions is clearly visible in the predicted electronic spectra of the complexes discussed below.

Predicted absorptions of structures **A**, **B** and **C** are listed in Table 3, and spectra are shown in Figure 8. Calculations for the electronic spectra are essentially gas-phase, but the Zerner INDO parameters were obtained from solution-phase experimental data and are more likely to predict spectra where the solvent may play an important role.[40–43] In all cases calculated spectra show relatively strong transitions in the 220–235 nm region and a series of peaks of lesser intensity at longer wavelength. Overall the spectra compare well with experimental data. Complexes of the type [($\eta^6$-arene)M(X)(Y)] (M = $Ru^{II}$ or $Os^{II}$; X, Y = simple σ-donors, monodentate or chelating ligands) show a first band at 300–400 nm which is assigned to a metal d-d transition. A second band appears at around 250 nm with a shoulder at about 225 nm, and these are assigned to a d(M)→π*(X/Y) and to an arene π→π* transition, respectively.[44] The calculated spectra replicate well these features.

The loss of planarity of the arene ligand in **B** and **C** is reflected by a bathochromic shift of the π→π* transition relative to **A** (Figure 8). The degree of shift in energy can be related to the degree of arene distortion in the predicted structures. The shift is more pronounced in **B** (Δ = +9 nm) then in **C** (Δ = +5 nm). These predictions are reasonable because, while most steric effects in organic compounds cause steric inhibition of resonance which determines hypsochromic displacements in the electronic spectrum, geometry distortion tend to cause the opposite effect.[45,46] Distortion of an aromatic system raises the energy of both ground and excited states of the molecule. However, due to the greater antibonding character of the excited states their energies are less affected by distortion. Consequently, it is expected that the UV spectra would show their bands shifted bathochromically with respect to the normal, unstrained compounds of comparable structure and degree of substitution.

With respect to the d-d transition, the experimental UV/Vis spectrum of **4a** at pH = 3 (Figure 7) shows a broad absorption spanning from about 300 to 360 nm. As the pH is raised to 5.1, the transition is blueshifted with $\lambda_{max} \approx$ 294 nm. The predicted spectrum of structure **A** shows five peaks ranging from 285 to 370 nm in close agreement with the experimental spectrum of **4a** at low pH. The same d-d transition suffers two opposite shifts in the calculated spectra of **B** and **C**. A hypsochromic shift in the absorption is predicted for **B** (peaks in the range of 266–311 nm) which is consistent with the replacement of $H_2O$ or $Cl^-$ by the deprotonated amide group with stronger σ-donor character. For **C**, a bathochromic shift is predicted (peaks in the range of 320–357 nm). Of the two optimized structures, **B** shows the closest similarity to the UV/Vis spectrum of **4a** at pH = 5.1 (see Figures 8 and 9). Therefore, in agreement with experimental data, we argue that in 25 mM HEPES at pH = 7.44, **4a** undergoes deprotonation at the nitrogen atom of

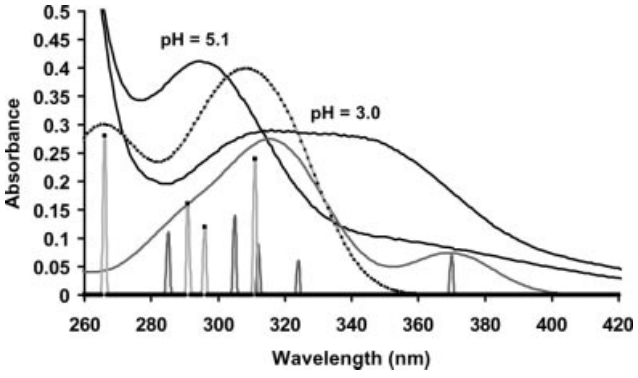


Figure 9. Experimental (black) and predicted (gas-phase, INDO/S) spectra of **4** (dark grey) and of structure **B** (light grey with squares). The vertical bars are the predicted oscillator strengths and locations of individual computed transitions. The oscillator strengths are arbitrarily scaled to match the overall spectra; they retain their correct relative intensity.

Table 3. Predicted spectra for structures **A** (cation of **4**), **B** and **C**.[a]

| Structure **A** | | Structure **B** | | Structure **C** | |
|---|---|---|---|---|---|
| Wavenumber ($\times 10^3$ $cm^{-1}$) | Oscillator strength (*f*) | Wavenumber ($\times 10^3$ $cm^{-1}$) | Oscillator strength (*f*) | Wavenumber ($\times 10^3$ $cm^{-1}$) | Oscillator strength (*f*) |
| 27.0 | 0.07 | 32.1 | 0.09 | 28.0 | 0.036 |
| 30.9 | 0.06 | 34.3 | 0.06 | 30.0 | 0.188 |
| 32.1 | 0.09 | 37.6 | 0.105 | 30.4 | 0.064 |
| 32.8 | 0.14 | 41.3 | 0.045 | 31.3 | 0.1 |
| 35.1 | 0.11 | 42.3 | 0.15 | 36.9 | 0.04 |
| 38.9 | 0.04 | 43.3 | 0.885 | 44.3 | 0.828 |
| 42.9 | 0.1 | 44.1 | 0.285 | 44.8 | 0.248 |
| 45.1 | 1.09 | | | 45.9 | 0.032 |
| 45.7 | 0.49 | | | 46.7 | 0.072 |
| 47.2 | 0.05 | | | | |

[a] Only bands for allowed transitions ($f > 0$) are listed. Energies are given to one decimal place since this is only a model system.

 © 2007 Wiley-VCH Verlag GmbH & Co. KGaA, Weinheim 

the amide group generating a complex with a tridentate chelate encompassing the $Ru^{II}$ center as depicted by structure **B**.

### Fluorescence Spectroscopy and PLE-Catalyzed Hydrolysis

In aqueous solutions (pH < 7) compounds **3** and **4** show a photoluminescence response upon excitation at 325 nm. The emission spectra of both compounds show a broad peak centered at around 435 nm. As expected, quenching of fluorescence is observed in the spectra of **3** and **4** compared to the spectra of methylisatoic acid (**MIAH**) and the corresponding free ligands **L3** and **L4** (Figure 10; Supporting Information: Figures S2 and S3). This is due to an internal heavy-atom effect. The quenching of fluorescence by heavy atoms is a phenomenon first identified as "physical quenching" by F. Perrin,[47,48] and it has been the subject of many studies.[49] Heavy atoms in the fluorophore, or in close contact with it, increase the rate of intersystem crossing (ISC) by strengthening spin-orbit coupling,[50,51] as for electronic transitions of heavy atoms. Thus, the decrease of fluorescence yield (radiative transition $S_1 \rightarrow S_0$) is explained by an increase in the probability of the competing $S_1 \rightarrow T_n$ radiationless transition of the fluorophore.

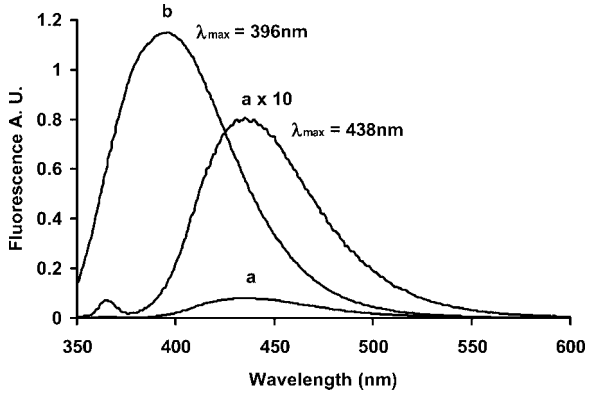


Figure 10. Fluorescence responses ($\lambda_{ex}$ = 325 nm) of a 7 μM aqueous solution of **4** (a), and of **MIAH** (b).

Complexes **3** and **4** show pH-dependent fluorescence responses (Figure 11) with maxima centered at around neutral pH. Complex **3** shows a local photoluminescence maximum at pH = 6; however, the fluorescence of the sample increases exponentially at pH > 8 due to base-catalyzed hydrolysis of the **L3** ester bond. Under these conditions, the conjugate base of **MIAH** is liberated, and the overall fluorescence of the sample increases. This observation prompted us to study the interaction of compounds **3** and **4** with porcine liver esterase (PLE) in order to determine if the complexes are substrates for this enzyme.

Ester hydrolysis by cytosolic esterases is a common strategy employed to trap photoluminescent organic sensors (most often fluorescein-type sensors) within the cell or to activate organic-based progrugs. Recently, the same strategy has being considered for possible esterase-activated metal-based prodrug delivery systems.[52] Experiments were performed in 25 mM HEPES-buffered solutions at pH = 7.44. Samples of the metal complexes were prepared in the buffer and allowed to equilibrate at room temperature for 5 h. Under these conditions, **3** hydrolyses to form the corresponding aqua (**3a**), hydroxido (**3b**) and HEPES (**3d**) complexes with relative percentage abundances of ca. 84, 14 and 2%, respectively. Complex **4**, on the other hand, is mainly present as the tridentate chelate **4c** following deprotonation at the amide nitrogen atom as described above. After the equilibration period, the enzyme was added and the interactions monitored by $^1H$ NMR and fluorescence spectroscopy.

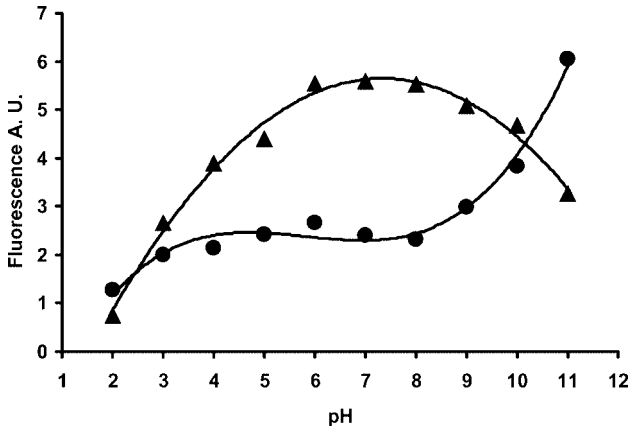


Figure 11. pH-dependent fluorescence responses ($\lambda_{ex}$ = 325 nm, $\lambda_{em}$ = 438 nm) of a 7 μM unbuffered aqueous solution of **3** (circles) and of **4** (triangles).

Treatment of **3** with PLE led to an increase in the photoluminescence intensity in its emission spectrum accompanied by a blue shift in the $\lambda_{em}$ maximum from 438 to 398 nm as shown in Figure 12. The reaction was complete after ca. 150 h of incubation, when no further spectral change could be detected. The hypsochromic shift clearly indicates hydrolysis of the **L3** ester bond and release of free **MIAH**. No change was observed in the fluorescence spectrum of **4** over the same time period. Under our experimen-

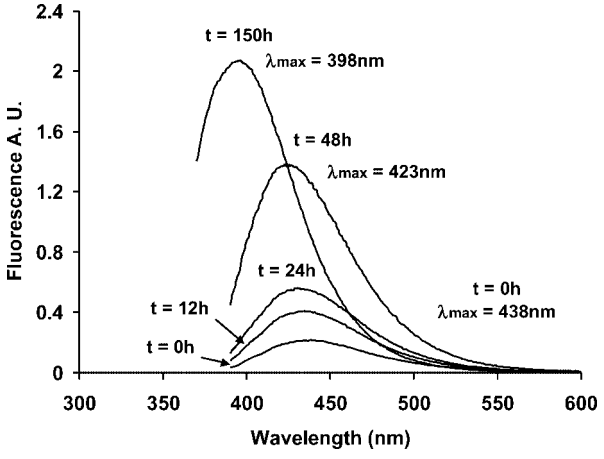


Figure 12. Fluorescence responses ($\lambda_{ex}$ = 325 nm) of a 10 μM solution of **3** (25 mM HEPES, pH = 7.44) after addition of PLE (7.5 U, incubation at 298 K).

 © 2007 Wiley-VCH Verlag GmbH & Co. KGaA, Weinheim 

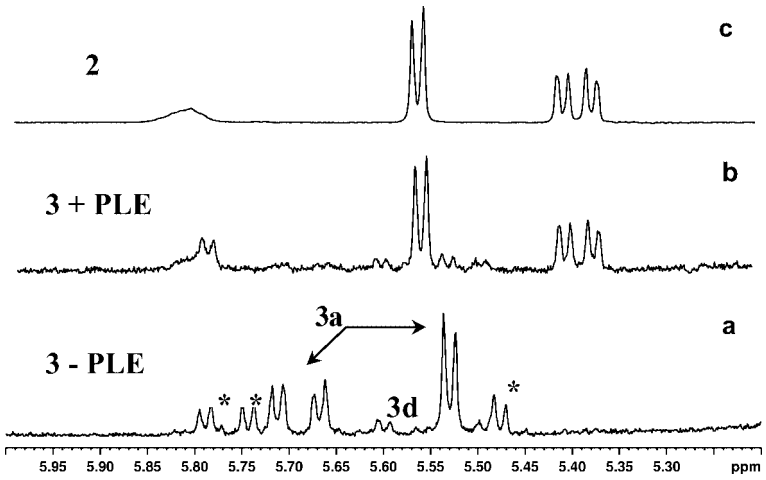


Figure 13. Low-field *p*-cym region of the $^1$H NMR spectra of a 2 mM solution of **3** in HEPES buffer (25 mM, pH = 7.44); (a) 5 h after dissolution at 298 K, (b) after 1 week incubation with PLE (15 U) at 298 K, (c) *p*-cym peaks of **2** in HEPES buffer (15 min). Asterisks indicate overlapping resonances of **3b** and **3d**.

tal conditions, PLE-catalyzed hydrolysis of the ester bond in **3** appears to be slow ($t_{1/2} \approx 40$ h) when compared to fluorophore-bearing organic molecules.[53] However, we are not aware of comparable examples involving inorganic complexes of the type we have investigated. Platinum complexes prepared by Reedijk and co-workers are all derivatized with fluorogenic reporters through amide bonds.[20–24] Their chemistry has been concentrated on reactions with guanine for comparison with the parent compounds, and they have been studied almost exclusively to elucidate their cellular distribution. Their interactions with cytosolic esterases do not appear to have been investigated.

In order to determine the fate of the ruthenium complex in the PLE-catalyzed hydrolysis of **3**, a millimolar sample of the compound was incubated with the enzyme (HEPES buffer, $D_2O$ solution, pH = 7.44) for 7 d. At the end of the incubation period, a white precipitate was detected and later identified as a 2-(methylamino)benzoate salt. The $^1$H NMR spectrum of the remaining solution was recorded and compared to the spectra of **2** and **3** in the same buffer. These are shown in Figure 13. The spectrum of **3** in the buffer revealed the presence of three species: the aqua complex (**3a**) as the major adduct, together with the hydroxido (**3b**) and HEPES (**3d**) adducts with overlapping resonances. The species distribution remained unaltered over a period of 5 h. After 1 week, a new single major set of signals was visible (Figure 13b). The peaks show the same resonances ($\delta$ = 5.38, 5.41 and 5.56 ppm) as for the *p*-cym peaks of **2** in HEPES (Figure 13c). The experimental evidence clearly indicates that esterase-catalyzed hydrolysis of **3** liberates **MIAH** and generates complex **2**. Thus, although the hydrolysis reaction appears to be slow, the results indicate that **3** is a substrate for the enzyme.

## Conclusions

We have synthesized and characterized fluorescent (arene)Ru$^{II}$ complexes of the type [($\eta^6$-arene)RuCl(Z)] (Z = chelating ligand). The compounds show interesting photoluminescent properties and may find some application in fluorescence microscopy studies aimed at elucidation of their cellular trafficking and thus provide new insights into the mechanism of action of this new class of anticancer compounds. Our results show that a fluorogenic reporter may be tagged onto these complexes either through an ester or an amide bond. If the fluorophore is linked through an ester bond, the resulting compounds may be substrates for cytosolic esterases. In this case, esterase-catalyzed hydrolysis of the reporter could potentially alter the fluorescent profile and consequently the resulting (apparent) cellular distribution of the compounds. Derivatization of the compounds through an ester bond, however, might prove useful in the design of esterase-activated Ru-based prodrug delivery systems. This is a common strategy in medicinal chemistry, as it is the case, for example, with capecitabine, an orally available prodrug of 5-deoxy-5-fluorouridine, which has recently come into clinical use for the treatment of breast and colorectal cancers.[54–57] A similar approach focussed on platinum drugs was recently suggested by Lippard.[49] Finally, tagging a reporter (or a prodrug) to (arene)Ru$^{II}$ complexes through an amide linkage is also promising; however, a spacer of proper length (> –[$CH_2$]$_2$–) must be employed. Our study indicates that if a spacer of only two carbon atoms is used, then the amide nitrogen atom readily undergoes deprotonation under physiological conditions, promoting the formation of a stable five-membered chelate ring.

## Experimental Section

**Materials:** Reagents were purchased from Aldrich and used without further purification. A porcine liver esterase (PLE) suspension was purchased from Fluka and used as supplied. [($\eta^6$-*p*-cym)-$RuCl_2$]$_2$ (**1**) was prepared according to a published procedure.[58,59]

**X-ray Crystallography:** All diffraction data were collected using a Bruker Smart Apex CCD diffractometer equipped with an Oxford

 © 2007 Wiley-VCH Verlag GmbH & Co. KGaA, Weinheim 

Table 4. Crystal structure data for complexes **2**, **3** and **4**.

| | **2** | **3** | **4** |
|---|---|---|---|
| Empirical formula | $C_{15}H_{30}Cl_2N_2O_2Ru$ | $C_{22}H_{33}Cl_2N_3O_6Ru$ | $C_{23.50}H_{35.50}Cl_{6.50}N_4ORu$ |
| Formula mass | 442.39 | 607.50 | 721.55 |
| Crystal system | triclinic | monoclinic | triclinic |
| Crystal size [mm] | $0.80 \times 0.33 \times 0.15$ | $0.22 \times 0.14 \times 0.08$ | $0.75 \times 0.15 \times 0.15$ |
| Space group | $P\bar{1}$ | $P21/n$ | $P\bar{1}$ |
| $V$ [Å$^3$] | 930.18(14) | 2530.47(12) | 3035.5(2) |
| $a$ [Å] | 9.0664(8) | 10.7840(3) | 13.9097(6) |
| $b$ [Å] | 9.8934(8) | 10.5940(3) | 15.4667(7) |
| $c$ [Å] | 11.1677(9) | 22.1650(5) | 15.7873(7) |
| $\alpha$ [°] | 109.405(5) | 90 | 80.444(3) |
| $\beta$ [°] | 90.206(6) | 92.1530(10) | 69.698(3) |
| $\gamma$ [°] | 99.447(6) | 90 | 72.812(3) |
| $T$ [K] | 150 | 150 | 150 |
| Z | 2 | 4 | 4 |
| $R$ [$F > 4\sigma(F)$][a] | 0.0498 | 0.0365 | 0.0804 |
| $R_w$[b] | 0.1384 | 0.0884 | 0.1754 |
| GOF[c] | 0.7221[d] | 0.8676[d] | 1.318 [e] |
| Max/min $\Delta\rho$ [e Å$^{-3}$] | +1.38/–2.08 | +0.98/–0.74 | +1.170/–1.219 |

[a] $R = \Sigma||F_o| - |F_c||/\Sigma|F_o|$. [b] $R_w = [\Sigma w(F_o^2 - F_c^2)^2/\Sigma wF_o^2]^{1/2}$. [c] GOF = $[\Sigma w(F_o^2 - F_c^2)^2/(n - p)]^{1/2}$ ($n$ = number of reflections, $p$ = number of parameters). $F > 4\sigma(F)$. [d] Refinement based on $F$ with ca. 5300 data. [e] Refinement based on $F$ with 12274 data.

Cryosystems low-temperature device operating at 150 K (Table 4). Absorption corrections for all data sets were performed with the multiscan procedure SADABS.[60] Structures were solved by direct methods (SHELXS or SIR92).[61,62] Complexes were refined against $F^2$ using CRYSTALS (**2** and **3**)[63] or SHELXL (**4**).[61] H-atoms were placed in idealised positions. In **2** the *i*Pr group is rotationally disordered about the pivot carbon atom (C82), and in **3** one O-atom of the perchlorate anion was modelled over two sites. The crystal of **4** was twinned. The diffraction pattern was indexed with two orientation matrices related by a twofold rotation about the (0 1 –1) reciprocal lattice direction (CELL_NOW);[64] reflections from both domains were integrated simultaneously (SAINT)[65] and used in the refinement. The twin scale factor was 0.2811(13). CCDC-634687 (**2**), -634689 (**3**) and -634688 (**4**) contain the supplementary crystallographic data for this paper. These data can be obtained free of charge from The Cambridge Crystallographic Data Centre via www.ccdc.cam.ac.uk/data_request/cif.

**NMR Spectroscopy:** $^1$H NMR spectra were acquired with Bruker DMX 500 ($^1$H, 500 MHz) or DPX 360 ($^1$H, 360 MHz) spectrometers using TBI probe-heads equipped with *z*-field gradients. Typically, $^1$H NMR spectra in $D_2O$ were acquired with water suppression by Shaka's method or with presaturation. $^1$H NMR chemical shifts were referenced internally to 1,4-dioxane ($\delta$ =3.75 ppm) for aqueous solutions, and $CHCl_3$ ($\delta$ =7.26 ppm) for [D]chloroform solutions. All data processing was carried out using XWIN-NMR version 2.0 (Bruker U.K. Ltd.).

**Mass Spectrometry:** Electrospray ionization mass spectra (ESIMS) were obtained with a Micromass Platform II mass spectrometer, and solutions were infused directly. The capillary voltage was 3.5 V, and the cone voltage was varied between 10 and 45 V, depending on sensitivity. The source temperature was 353 K. Mass spectra were recorded in a scan range of $m/z$ = 200–1200 for positive ions.

**pH Measurements:** pH measurements were carried out using a Corning 240 pH meter equipped with an Aldrich micro-combination electrode calibrated with Aldrich standard buffer solutions of pH = 4, 7, and 10. For NMR samples prepared in $D_2O$, no correction has been applied for the effect of deuterium on the glass electrode.

**Spectroscopic Measurements and Fluorometric Determinations:** All glassware was washed sequentially with 20% $HNO_3$, deionised water, and ethanol before use. Purified water was obtained from a Millipore Milli-Q water purification system. Stock solutions of reagents in water were made up to concentrations of 2 mM and kept at 4 °C in 500-μL aliquots. Portions were diluted to the required concentrations immediately prior to each experiment. Fluorescence and absorption data were measured in water and in HEPES buffer (25 mM, pH = 7.4), prepared with Millipore water. Solutions were stored in clean, dry propylene containers and were filtered before data acquisition. Fluorescence spectra were recorded from 350 to 600 nm. All measurements were performed in triplicate. Fluorescence spectroscopy measurements were performed with Perkin–Elmer LS50B or Edinburgh Instruments FS900 Fluororimeters. Excitation was set to 325 nm and emission was collected through a 350-nm cut-off filter.

**Computational Methods:** Molecular structures were initially modelled from the crystal structure of the cation of **4** and were optimized at the semiempirical INDO/1 level. A tight self-consistent-field convergence criterion ($10^{-6}$ hartree) was employed in all calculations. The electronic spectra of the complexes were calculated with the INDO/S method in the Zerner implementation[40–42,66] using the Hyperchem (version 7.5) software.[43] The ruthenium and nitrogen atomic parameters of Krogh-Jespersen et al. were used.[67] The overlap weighting factors, $f\sigma$ and $f\pi$, for INDO/S calculations were set at 1.267 and 0.585, respectively, and the number of CISs in the CIS calculations was 1250 (25 occupied and 25 unoccupied orbitals). The optical spectra of these ruthenium complexes were calculated using the SWizard program.[68,69] Half-bandwidths $\Delta_{1/2}$ were assumed to be equal to 3000 cm$^{-1}$, which is a typical half-bandwidth value for octahedral ruthenium complexes.[70]

### Synthetic Procedures

**[($\eta^6$-*p*-cym)RuCl(NNO)](Cl) (2):** [($\eta^6$-*p*-cym)$RuCl_2$]$_2$ (**1**) (100 mg, 0.16 mmol) was dissolved in $CHCl_3$ (5 mL). To this solution 2.2 mol-equiv. of 2-[(2-aminoethyl)amino]ethanol (**NNO**) was added and the mixture stirred for 12 h. A change in colour of the solution from deep red to pale yellow was observed within 10 s of addition of the ligand to **1**. The yellow precipitate was then collected by filtration, washed with ice-cold $CHCl_3$ and then three times with 5 mL of ice-cold diethyl ether. Yield: quantitative. $C_{14}H_{26}Cl_2N_2ORu$ (410.75): calcd. C 40.98, H 6.39, N 6.83; found C 40.82, H 6.09, N 6.57. $^1$H NMR (500 MHz, $CDCl_3$): $\delta$ = 1.56

 © 2007 Wiley-VCH Verlag GmbH & Co. KGaA, Weinheim 

(d, 6 H, cymene), 2.43 (s, 3 H, cymene), 2.08 (sept, 1 H, cymene), 2.99 (t, 2 H, $CH_2$), 3.18 (t, 2 H, $CH_2$), 3.49 (t, 2 H, $CH_2$), 3.56 (br., 1 H, $NH_2$), 4.06 (t, 2 H, $CH_2$), 5.04 (br., 1 H, $NH_2$), 6.63 (br., 1 H, OH), 7.33 (br., 1 H,NH) ppm. ESI MS (+ve): $m/z$ = 375 $[M]^+$. Crystals suitable for X-ray diffraction were obtained by slow diffusion of diethyl ether into a methanolic solution of the complex (typically, 5 mg of complex in 250 μL of solvent; diffusion occurred at 4 °C).

***N*,*N*′-Bis(*tert*-butoxycarbonyl)-2-[(2-aminoethyl)amino]ethanol (L1):**[71] To a solution of 2-[(2-aminoethyl)amino]ethanol (50 mmol) in THF/$H_2O$ (1:1) (300 mL), $KHCO_3$ (150 mmol) and *tert*-butoxycarbonyl anhydride ($Boc_2O$) (120 mmol) were added consecutively at 0 °C. After the reaction mixture had reached room temp., the solution was stirred overnight. The mixture was then acidified to pH = 4 by careful addition of acetic acid at 0 °C and then extracted with $CH_2Cl_2$ (4 × 200 mL). The combined organic phases were dried ($Na_2SO_4$) and concentrated under reduced pressure to give **L1** as a viscous colourless oil which crystallized on standing. **L1** was used for the next step without further purification. Yield: 6 g (60%). $^1$H NMR (360 MHz, $CDCl_3$): $\delta$ = 1.44 (s, 9 H, $CH_3$), 1.47 (s, 9 H, $CH_3$), 3.32 (m, 2 H, $CH_2$), 3.37 (m, 4 H, $CH_2$), 3.74 (m, 2 H, $CH_2$) ppm. ESI MS (+ve): $m/z$ = 343.37 $[M + K^+]$.

***N*,*N*′-Bis(*tert*-butoxycarbonyl)-2-[(2-aminoethyl)amino]ethyl-2-(methylamino)benzoate (L1′):** Boc-protected 2-[(2-aminoethyl)-amino]ethanol (0.4 g, 1.39 mmol) was dissolved in dried $CH_3CN$ (20 mL). *N*-Methylisatoic anhydride (**MIA**) (0.37 g, 2.08 mmol) was added to this solution. An excess amount of $K_2CO_3$ (2 g, 27.8 mmol) was added to the above mixture. The mixture was stirred at room temp. for 48 h, during which the reaction progress was monitored by TLC. The desired product was separated from the other possible byproducts and impurities by silica column chromatography using a solvent system of ($CH_3OH/CH_2Cl_2$, 12:88). The column was eluted with a total of 300 mL of eluent. The fractions obtained were analyzed by $^1$H NMR spectroscopy, and those containing the desired product were combined. The solvents ($CH_3OH/CH_2Cl_2$) were removed by rotary evaporation, and the resulting yellow oil was stored at 4 °C for 18 h. During storage, the product spontaneously crystallized into a light yellow solid. Yield: 277 mg (45%). $^1$H NMR (500 MHz, $CDCl_3$): $\delta$ = 1.40 (s, 18 H, $CH_3$), 2.86 (s, 3 H, $CH_3$), 3.26 (t, 2 H, $CH_2$), 3.37 (t, 2 H, $CH_2$), 3.58 (t, 2 H, $CH_2$), 4.31 (t, 2 H, $CH_2$), 4.92 (br., 1 H, NH), 5.15 (br., 1 H, NH), 6.58 (t, 1 H, aromatic), 6.63 (d, 1 H, aromatic), 7.36 (t, 1 H, aromatic), 7.48 (d, 1 H, aromatic) ppm. ESI MS (+ve): $m/z$ = 439.1 $[M]^+$, 338.1 $[M - C_5H_{10}O_2]^+$.

**2-[(2-Aminoethyl)amino]ethyl-2-(methylamino)benzoate (L3):** Boc deprotection of **L1′** was attained by dropwise addition of 15 mol-equiv. of TFA (1.28 mL, 3.45 mmol) to a solution of **L1′** (0.1 g, 0.23 mmol) in distilled $CH_2Cl_2$ (10 mL). The mixture was stirred at room temp. for 48 h and was monitored by TLC. The solvents were then removed by rotary evaporation. The crude product was re-dissolved in methanol and purified with the aid of preparative thin layer chromatography (TLC). The desired product was then extracted from preparative TLC silica by re-dissolution in methanol and stirring at room temp. for 18 h. This solution was then filtered under gravity, and all the solvents were removed from the filtrate under vacuum. The product was a dark yellow oil. Yield: 28 mg (51%). $C_{12}H_{19}N_3O_2$ (237.30): calcd. C 60.74, H 8.07, N 17.71; found C 61.03, H 8.04, N 17.38. $^1$H NMR (500 MHz, $D_2O$): $\delta$ = 2.06 (s, 1 H, $CH_3$), 3.43 (t, 2 H, $CH_2$), 3.53 (t, 2 H, $CH_2$), 3.61 (t, 2 H, $CH_2$), 4.58 (t, 2 H, $CH_2$), 6.98 (t, 1 H, aromatic), 7.09 (d, 1 H, aromatic), 7.63 (t, 1 H, aromatic), 8.07 (d, 1 H, aromatic) ppm. ESI MS (+ve): $m/z$ = 238 $[M - H]^+$.

***N*-{2-[(2-Aminoethyl)amino]ethyl}-2-(methylamino)benzamide (L4):** Typically, *N*-(2-aminoethyl)ethane-1,2-diamine (100 mg) was dissolved in $CHCl_3$ (2 mL). To this solution, **MIA** (100 mg) in $CHCl_3$ (2 mL) was added in 0.25-mL portions. Immediately after the addition of **MIA**, a white precipitate appeared. The reaction was allowed to proceed for 2 h. The white precipitate was filtered off, while the $CHCl_3$-soluble fraction was concentrated to about 3 mL and then loaded onto a preparative TLC plate. With 15% $CH_3OH$ in $CH_2Cl_2$, all the impurities contained in the starting material moved with the front, molecules derivatized with two or three **MIA** moved to the middle of the plate, while **L4** moved only a few cm from the base line. Yield: 38 mg (32%). $C_{12}H_{20}N_4O$ (236.31): calcd. C 60.99, H 8.53, N 23.71; found C 60.23, H 8.40, N 23.69. $^1$H NMR (500 MHz, $CDCl_3$): $\delta$ = 1.75 (br., $NH_2$), 2.68 (m, 2 H, $CH_2$), 2.79 (m, 2 H, $CH_2$), 2.83 (m, 5 H, $CH_2$ + $CH_3$), 3.47 (m, 2 H, $CH_2$), 6.56 (t, 1 H, aromatic), 6.64 (d, 1 H, aromatic), 6.82 (br., NH), 7.30 (t, 1 H, aromatic), 7.36 (2, 1 H, aromatic), 7.47 (br., NH) ppm. ESI MS (+ve): $m/z$ = 259.15 $[M + Na^+]$.

**[($\eta^6$-*p*-cym)RuCl(L3)](Cl) (3):** Ligand **L3**, (0.032 g, 0.13 mmol), was dissolved in $CH_3OH/CHCl_3$ (20:80) (2.4 mL). This was added dropwise to a solution of $[(\eta^6\text{-}p\text{-cym})RuCl_2]_2$ (**1**) (0.036 g, 0.059 mmol) in $CHCl_3$ (2.8 mL) to prevent any initial precipitation of the ligand. The colour of dimer solution changed from deep red to orange once all of **L3** was added. The mixture was stirred at room temp. for 40 h. During this time, a yellow precipitate developed on the sides of reaction flask, while the colour of the reaction mixture remained unchanged. Further precipitation was obtained by addition of diethyl ether (10 mL). The yellow precipitate was dried under vacuum. Yield: 22 mg (30%). $C_{22}H_{33}Cl_2N_3O_2Ru$ (543.49): calcd. C 48.62, H 6.12, N 7.73; found C 47.98, H 6.07, N 7.91. $^1$H NMR (500 MHz, $CDCl_3$): $\delta$ = 1.38 (d, 6 H, *p*-cymene), 1.74 (sept, 1 H, *p*-cymene), 2.46 (s, 3 H, *p*-cymene), 2.85–3.20 (m, 4 H, $CH_2$), 3.21 (t, 2 H, $CH_2$), 4.06 (t, 2 H, $CH_2$), 4.72 (br., 1 H, $NH_2$), 5.67–5.78 (dd, 4 H, *p*-cymene), 6.14 (br., 1 H, $NH_2$), 6.23 (br., 1 H, NH), 6.82 (t, 1 H, aromatic), 6.96 (d, 1 H, aromatic), 7.31 (br., 1 H, OH), 7.53 (t, 1 H, aromatic), 8.04 (d, 1 H, aromatic) ppm. ESI MS (+ve): $m/z$ = 508 $[M]^+$. Crystals suitable for X-ray diffraction were obtained by slow diffusion of pentane into a $CHCl_3$ solution of the complex (5 mg of complex + 2 mg of $NaClO_4$ in 250 μL of solvent; diffusion occurred at room temp.).

**[($\eta^6$-*p*-cym)RuCl(L4)](Cl) (4):** **1** (44 mg) was dissolved in $CHCl_3$ (3 mL). To this solution 2.2 mol-equiv. of **L4** (38 mg) in $CHCl_3$ (1 mL) was added and the mixture stirred for 48 h. The colour of the solution changed within 1 h from red to orange to olive-green. The reaction was monitored by $^1$H NMR spectroscopy and stopped when no further change could be observed. Diethyl ether was added to the solution depositing a yellow precipitate which was then collected by filtration and washed with diethyl ether. Yield: 68 mg (78%). $C_{22}H_{34}Cl_2N_4ORu$ (542.51): calcd. C 48.71, H 6.32, N 10.33; found C 48.08, H 5.97, N 9.98. $^1$H NMR (500 MHz, $CDCl_3$): $\delta$ = 1.22 (d, 6 H, $CH_3$, *p*-cymene), 2.08 (sept, 1 H, *p*-cymene), 2.24, (s, 3 H, $CH_3$, *p*-cymene), 2.85, (s, 3 H, $CH_3$), 3.7–2.6, (m, 8 H, $CH_2$), 5.44 (d, 1 H, *p*-cymene), 5.60 (d, 1 H, *p*-cymene), 5.65 (d, 1 H, *p*-cymene), 5.91 (d, 1 H, *p*-cymene), 6.53 (t, 1 H, aromatic), 6.59 (d, 1 H, aromatic), 7.29 (t, 1 H, aromatic), 7.99 (d, 1 H, aromatic) ppm. ESI MS (+ve): $m/z$ = 507.1 $[M]^+$. Crystals of **4** suitable for X-ray diffraction were obtained by slow diffusion of pentane into a $CHCl_3$ solution of the complex.

**Supporting Information** (see footnote on the first page of this article). Positive-ion ESI-MS spectra of a solution of **4** in 25 mM HEPES at different pH values; fluorescence response of **L3** and **L4** upon titration of 1.2 mol-equiv. of **1** (Figures S1–S3); ZINDO1/S

 © 2007 Wiley-VCH Verlag GmbH & Co. KGaA, Weinheim 

parameter files employed in the semiempirical calculations (Table S1).

## Acknowledgments

We thank the Swiss National Science Foundation (SNF; fellowship for F. Z.) for the support for this work, and Dr. Abraha Habtemariam and Dr. Ana Maria Pizarro (Edinburgh) for helpful discussions.

[1] R. E. Morris, R. E. Aird, P. del S. Murdoch, H. Chen, J. Cummings, N. D. Hughes, S. Parsons, A. Parkin, G. Boyd, D. I. Jodrell, P. J. Sadler, *J. Med. Chem.* **2001**, *44*, 3616–3621.
[2] R. E. Aird, J. Cummings, A. A. Ritchie, M. Muir, R. E. Morris, H. Chen, P. J. Sadler, D. I. Jodrell, *Br. J. Cancer* **2002**, *86*, 1652–1657.
[3] L. Dadci, H. Elias, U. Frey, A. Hoernig, U. Koelle, A. E. Merbach, H. Paulus, J. S. Schneider, *Inorg. Chem.* **1995**, *34*, 306–315.
[4] F. Wang, H. Chen, S. Parsons, I. D. H. Oswald, J. E. Davidson, P. J. Sadler, *Chem. Eur. J.* **2003**, *9*, 5810–5820.
[5] H. Chen, J. A. Parkinson, S. Parsons, R. A. Coxall, R. O. Gould, P. J. Sadler, *J. Am. Chem. Soc.* **2002**, *124*, 3064–3082.
[6] H. Chen, J. A. Parkinson, R. E. Morris, P. J. Sadler, *J. Am. Chem. Soc.* **2003**, *125*, 173–186.
[7] R. Fernández, M. Melchart, A. Habtemariam, S. Parsons, P. J. Sadler, *Chem. Eur. J.* **2004**, *10*, 5173–5179.
[8] H.-K. Liu, F. Wang, J. A. Parkinson, J. Bella, P. J. Sadler, *Chem. Eur. J.* **2006**, *12*, 6151–6165.
[9] H.-K. Liu, S. J. Berners-Price, F. Wang, J. A. Parkinson, J. Xu, J. Bella, P. J. Sadler, *Angew. Chem. Int. Ed.* **2006**, *45*, 8153–8156.
[10] F. Wang, J. Xu, A. Habtemariam, J. Bella, P. J. Sadler, *J. Am. Chem. Soc.* **2005**, *127*, 17734–17743.
[11] O. Novakova, H. Chen, O. Vrana, A. Rodger, P. J. Sadler, V. Brabec, *Biochemistry* **2003**, *42*, 11544–11554.
[12] A. Dorcier, P. J. Dyson, C. Gossens, U. Rothlisberger, R. Scopelliti, I. Tavernelli, *Organometallics* **2005**, *24*, 2114–2123.
[13] C. Scolaro, A. Bergamo, L. Brescacin, R. Delfino, M. Cocchietto, G. Laurenczy, T. J. Geldbach, G. Sava, P. J. Dyson, *J. Med. Chem.* **2005**, *48*, 4161–4171.
[14] C. Scolaro, T. J. Geldbach, S. Rochat, A. Dorcier, C. Gossens, A. Bergamo, M. Cocchietto, I. Tavernelli, G. Sava, U. Rothlisberger, P. J. Dyson, *Organometallics* **2006**, *25*, 756–765.
[15] C. A. Vock, C. Scolaro, A. D. Phillips, R. Scopelliti, G. Sava, P. J. Dyson, *J. Med. Chem.* **2006**, *49*, 5552–5561.
[16] W. H. Ang, E. Daldini, C. Scolaro, R. Scopelliti, L. Juillerat-Jeannerat, P. J. Dyson, *Inorg. Chem.* **2006**, *45*, 9006–9013.
[17] G. Arancia, A. Calcabrini, S. Meschini, A. Molinari, *Cytotechnology* **1998**, *27*, 95–111.
[18] A. A. Hindenburg, J. E. Gervasoni Jr, S. Krishna, V. J. Stewart, M. Rosado, J. Lutzky, K. Bhalla, M. A. Baker, R. N. Taub, *Cancer Res.* **1989**, *49*, 4607–4614.
[19] A. K. Larsen, A. E. Escargueil, A. Skladanowski, *Pharmacol. Ther.* **2000**, *85*, 217–229.
[20] G. V. Kalayda, G. Zhang, T. Abraham, H. J. Tanke, J. Reedijk, *J. Med. Chem.* **2005**; *48*, 5191–5202.
[21] C. Molenaar, J. M. Teuben, R. J. Heetebrij, H. J. Tanke, J. Reedijk, *J. Biol. Inorg. Chem.* **2000**, *5*, 655–665.
[22] B. A. J. Jansen, P. Wielaard, G. V. Kalayda, M. Ferrari, C. Molenaar, H. J. Tanke, J. Brouwer, J. Reedijk, *J. Biol. Inorg. Chem.* **2004**, *9*, 403–413.
[23] G. V. Kalayda, B. A. J. Jansen, C. Molenaar, P. Wielaard, H. J. Tanke, J. Reedijk, *J. Biol. Inorg. Chem.* **2004**, *9*, 414–422.
[24] G. V. Kalayda, B. A. J. Jansen, P. Wielaard, H. J. Tanke, J. Reedijk, *J. Biol. Inorg. Chem.* **2005**, *10*, 305–315.
[25] M. D. Hall, C. T. Dillon, M. Zhang, P. Beale, Z. Cai, B. Lai, A. P. J. Stampfl, T. W. Hambley, *J. Biol. Inorg. Chem.* **2003**, *8*, 726–732.
[26] K. A. Wilkinson, E. J. Merino, K. M. Weeks, *J. Am. Chem. Soc.* **2005**, *127*, 4659–4667.
[27] T. K. Nomanbhoy, D. A. Leonard, D. Manor, R. A. Cerione, *Biochemistry* **1996**, *35*, 4602–4608.
[28] J. P. Hutchinson, J. F. Eccleston, *Biochemistry* **2000**, *39*, 11348–11359.
[29] A. Y. Jan, E. F. Johnson, A. J. Diamonti, K. L. Carraway III, K. S. Anderson, *Biochemistry* **2000**, *39*, 9786–9803.
[30] S. P. Gilbert, M. L. Moyer, K. A. Johnson, *Biochemistry* **1998**, *37*, 792–799.
[31] D. Braga, F. Grepioni, G. R. Desiraju, *J. Organomet. Chem.* **1997**, *548*, 33–44.
[32] A. F. A. Peacock, A. Habtemariam, R. Fernandez, V. Walland, F. P. A. Fabbiani, S. Parsons, R. E. Aird, D. I. Jodrell, P. J. Sadler, *J. Am. Chem. Soc.* **2006**, *128*, 1739–1748.
[33] A. L. Gavrilova, B. Bosnich, *Chem. Rev.* **2004**, *104*, 349–383.
[34] A. L. Gavrilova, C. Jin Qin, R. D. Sommer, A. L. Rheingold, B. Bosnich, *J. Am. Chem. Soc.* **2002**, *124*, 1714–1722.
[35] C. Incarvito, A. L. Rheingold, A. L. Gavrilova, C. Jin Qin, B. Bosnich, *Inorg. Chem.* **2001**, *40*, 4101–4108.
[36] L. M. Liable-Sands, C. Incarvito, A. L. Rheingold, C. J. Qin, A. L. Gavrilova, B. Bosnich, *Inorg. Chem.* **2001**, *40*, 2147–2155.
[37] C. Incarvito, A. L. Rheingold, C. J. Qin, A. L. Gavrilova, B. Bosnich, *Inorg. Chem.* **2001**, *40*, 1386–1390.
[38] B. Bosnich, *Inorg. Chem.* **1999**, *38*, 2554–2562.
[39] M. Stebler-Rothlisberger, W. Hummel, P. A. Pittet, H. B. Burgi, A. Ludi, A. E. Merbach, *Inorg. Chem.* **1988**, *27*, 1358–1363.
[40] J. Ridley, M. C. Zerner, *Theor. Chim. Acta* **1976**, *42*, 223–236.
[41] M. C. Zerner, G. H. Loew, R. F. Kirchner, U. T. Mueller-Westerhoff, *J. Am. Chem. Soc.* **1980**, *102*, 589–599.
[42] W. P. Anderson, W. D. Edwards, M. C. Zerner, *Inorg. Chem.* **1986**, *25*, 2728–2732.
[43] S. I. Gorelsky, A. B. P. Lever, *J. Organomet. Chem.* **2001**, *635*, 187–196.
[44] Y. Hung, W.-J. Kung, H. Taube, *Inorg. Chem.* **1981**, *20*, 457–463.
[45] J. Kulhánek, S. Böhm, K. Palát, O. Exner, *J. Phys. Org. Chem.* **2004**, *17*, 686–693.
[46] S. Böhm, O. Exner, *Chem. Eur. J.* **2000**, *6*, 3391–3398.
[47] F. Perrin, *J. Phys. Radium* **1926**, *7*, 390–401.
[48] F. Perrin, *J. Chim. Phys.* **1928**, *25*, 531.
[49] S. K. Lower, M. A. El-Sayed, *Chem. Rev.* **1966**, *66*, 199–241.
[50] D. S. McClure, *J. Chem. Phys.* **1949**, *17*, 905–913.
[51] M. Kasha, *J. Chem. Phys.* **1952**, *20*, 71–74.
[52] D. Wang, S. J. Lippard, *Nature Rev. Drug Discovery* **2005**, *4*, 307–320.
[53] C. C. Woodroofe, A. C. Won, S. J. Lippard, *Inorg. Chem.* **2005**, *44*, 3112–3120.
[54] F. Di Costanzo, A. Sdrobolini, S. Gasperoni, *Crit. Rev. Oncol. Hematol.* **2000**, *35*, 101–108.
[55] J. L. Marshall, *Oncology* **2001**, *15*, 41–46.
[56] C. Twelves, M. Boyer, M. Findlay, J. Cassidy, C. Weitzel, C. Barker, B. Osterwalder, C. Jamieson, K. Hieke, *Eur. J. Cancer* **2001**, *37*, 597–604.
[57] M. L. H. Wang, W. K. A. Yung, M. E. Royce, D. E. Schomer, R. L. Theriault, D. F. Wogan, *Am. J. Clin. Oncol.* **2001**, *24*, 421–424.
[58] M. A. Bennett, A. K. Smith, *J. Chem. Soc., Dalton Trans.* **1974**, 233–241.
[59] R. A. Zelonka, M. C. Baird, *Can. J. Chem.* **1972**, *50*, 3063–3072.
[60] G. M. Sheldrick, University of Göttingen, Göttingen, Germany, **2006**.
[61] G. M. Sheldrick, University of Göttingen, Göttingen, Germany, **1997**.
[62] A. Altomare, G. Cascarano, C. Giacovazzo, A. Guagliardi, M. C. Burla, G. Polidori, M. Camalli, *J. Appl. Crystallogr.* **1994**, *27*, 435.
[63] P. W. Betteridge, J. R. Carruthers, R. I. Cooper, K. Prout, D. J. Watkin, *J. Appl. Crystallogr.* **2003**, *36*, 1487.

 © 2007 Wiley-VCH Verlag GmbH & Co. KGaA, Weinheim 

[64] G. M. Sheldrick, University of Göttingen, Göttingen, Germany, **2005**.
[65] Bruker-Nonius, Bruker-AXS, Madison, Wisconsin, USA, **2006**.
[66] J. Ridley, M. C. Zerner, *Theor. Chim. Acta* **1973**, *32*, 111–134.
[67] K. Krogh-Jespersen, J. D. Westbrook, J. A. Potenza, H. J. Schugar, *J. Am. Chem. Soc.* **1987**, *109*, 7025–7031.
[68] S. I. Gorelsky, SWizard program. http://www.sg-chem.net/swizard/.
[69] P. J. Hay, W. R. Wadt, *J. Chem. Phys.* **1985**, *82*, 270–283.
[70] A. B. P. Lever, *Can. J. Chem.* **2004**, *82*, 1102–1111.
[71] A different synthetic procedure was published: M. T. Schütte, P. Schumacher, C. Unger, R. Mülhaupt, F. Kratz, *Inorg. Chim. Acta* **1998**, *267*, 133–136.

Received: January 31, 2007
Published Online: May 3, 2007

 © 2007 Wiley-VCH Verlag GmbH & Co. KGaA, Weinheim 

DOI: 10.1002/ejic.200700279

# Hafnium Oxide Doped Mesostructured Silica Films

**Ralf Supplit,[a] Nicola Hüsing,*[b] Silvia Gross,[c] Sigrid Bernstorff,[d] and Michael Puchberger[a]**

**Keywords:** Mesostructured films / Ligand-assisted templating / Self-assembly / Surfactants

Hafnium oxide doped silica films with ordered mesostructures were produced with hafnium:silicon ratios between 1:60 and 1:6. A surfactant–hafnium alkoxide complex was synthesized and used as a template in a sol–gel dip-coating process. Face-centred orthorhombic, 2D centred rectangular and lamellar films were formed by evaporation-induced self-assembly (EISA). The influence of subsequent heat treatment was studied by GISAXS and TEM. The surface and in-depth molecular composition of the films was studied by XPS.

(© Wiley-VCH Verlag GmbH & Co. KGaA, 69451 Weinheim, Germany, 2007)

## Introduction

Hafnium dioxide is a ceramic material characterized by high thermal and chemical stability, high dielectric constant, good mechanical strength, catalytic properties and low electrical conductivity.[1–3] Stable porous mesostructured hafnium oxide was successfully synthesized by the groups of Sayari and Stucky by applying a surfactant templating approach[4,5] and, recently, the first mesoporous and even mesostructured thin films of crystalline hafnia were reported by using large nonionic block-copolymer templates as the structure-directing agent.[6,7]

The incorporation of hafnia in silica can lead to a noticeable improvement in the properties of $SiO_2$, for example for catalytic applications, and at the same time the problems related to the use of pure hafnium dioxide, such as high cost and low specific surface area, can be overcome. Furthermore, the binary $HfO_2$–$SiO_2$ system is appealing for the development of high-κ film to overcome limitations in the fabrication of integrated circuits.[8–10] In the past, hafnia–silica systems were developed by using conventional sol–gel processing; however a homogeneous distribution of the Hf- and Si-centres in the matrix is difficult to achieve owing to the different reaction rates of the corresponding alkoxide precursors that often result in phase separation. It is well-known that the reactivity of alkoxide precursors towards hydrolysis and condensation increases dramatically with an increase in the atomic number of the elements with the same valence: for example, silicon alkoxides < titanium alkoxides < hafnium alkoxides. Several strategies were developed to overcome the problems related to these different reactions rates, such as a modified sol–gel process based on the reaction of organically modified hafnium oxoclusters with organofunctional silanes,[11] the pyrolytic conversion of single-source precursors[12] and a chemical solution deposition approach.[13]

Highly porous, mesostructured binary $HfO_2$–$SiO_2$ films have – at least to the best of our knowledge – not been reported so far. The aim of this study is to present a synthetic strategy that allows not only precise control over the evolution of the final periodically arranged solid structure in the mixed oxide ($HfO_2$–$SiO_2$) thin film, but also a homogeneous distribution of Hf in the silica matrix even for high Hf:Si ratios. Our approach is based on a combination of ligand-assisted templating methods in which the faster reacting alkoxide (Hf-alkoxide) is coordinated to the structure-directing agent – a nonionic surfactant – in combination with a solvent evaporation-induced self-assembly approach for rapid film formation by dip-coating.

## Results and Discussion

Hafnium alkoxide/surfactant complexes were formed by the equimolar reaction of hafnium *n*-butoxide with the terminal hydroxyl group of the surfactant Brij-56 ($C_{16}EO_{10}$, decaethyleneglycol hexadecyl ether) (Scheme 1). The resulting complex (Hf–Brij) was analyzed by 2D-NMR spectroscopy.

Figure 1 shows the HSQC spectra of the product (a) compared with the unmodified surfactant (b) and with the pure hafnium butoxide (c). The dotted circle in Figure 1 (a-5) highlights a new peak at $\delta$ = 4.20 ppm ($^1$H)/69.2 ppm

[a] Institute of Materials Chemistry, Vienna University of Technology,
Getreidemarkt 9, 1060 Vienna, Austria
[b] Inorganic Chemistry I, University of Ulm,
Albert-Einstein-Allee 11, 89081 Ulm, Germany
Fax: +49-731-5022733
E-mail: nicola.huesing@uni-ulm.de
[c] CNR-ISTM, Department of Chemistry, University of Padua,
Via Marzolo, 1, Padova, Italy
[d] Sincrotone Trieste, Strada Statale 14, Km 163.5, in AREA Science Park,
34012 Basovizza, Trieste, Italy

 © 2007 Wiley-VCH Verlag GmbH & Co. KGaA, Weinheim 

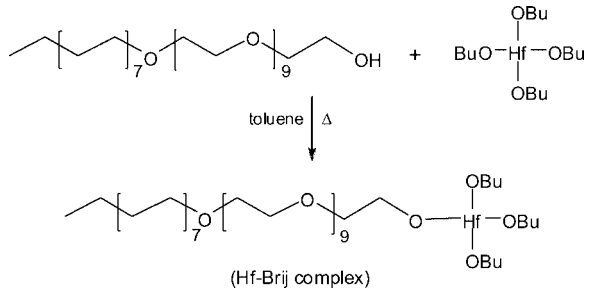


Scheme 1. Synthesis of the Hf–Brij coordination compound.

($^{13}$C) that appeared after the reaction of hafnium butoxide with Brij-56, whereas the signal at $\delta$ = 4.05 ppm ($^{1}$H)/ 69.3 ppm ($^{13}$C) [Figure 1 (a-4)], which was assigned to O-*CH*$_2$ of the butoxy groups, stayed unchanged. The new peak was assigned to the $CH_2$ group of the surfactant chain that is coordinated to the hafnium through an oxygen bridge. The TOCSY spectrum further shows that this signal correlates only to the $CH_2$ signal at $\delta$ = 3.57 ppm of the surfactant, whereas the signal at $\delta$ = 4.05 ppm correlates to signals at $\delta$ = 1.55, 1.36 and 0.95 ppm and can therefore be clearly assigned to a butoxy group.

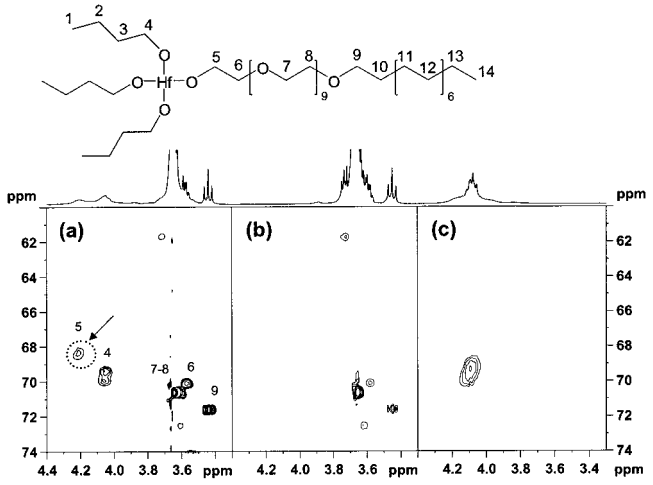


Figure 1. 2D NMR (HSQC) spectra of (a) Hf–Brij-56, (b) Brij-56 and (c) Hf(OBu)$_4$.

The Hf–Brij complex was used as the structure-directing agent in an evaporation-induced self-assembly process (EISA) to form mesostructured thin films (Figure 2).[14] The modified surfactant was added to a prehydrolyzed solution of tetraethoxysilane to form an opalescent sol. Direct addition of hafnium butoxide to such a sol would result in immediate precipitation of hafnia. This shows that the surfactant does not only serve as a structure-directing agent but also acts as an agent to control and slow down the hydrolysis and condensation rate of the alkoxide. Films were prepared by dip-coating from solutions containing different molar ratios (*M*) of the modified surfactant/tetraethoxysilane in otherwise constant composition. The resultant films were labelled Hf–Brij (*M*).

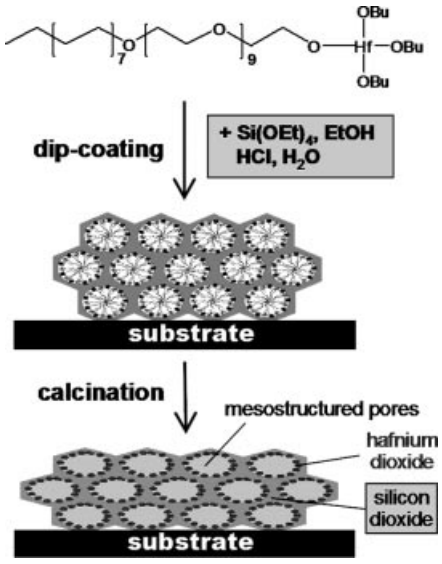


Figure 2. Schematic description of the synthetic strategy towards mesostructured hafnium oxide doped silica films.

The phase diagram of the surfactant Brij-56 shows cubic-spherical micellar, hexagonal, cubic-bicontinuous, lamellar and reversed-cubic-bicontinuous mesophases in surfactant/water mixtures with increasing concentrations of the amphiphile.[15] During the sol–gel process, the silica species replace the position of the water molecules in the hydrophilic regions of the mesophases and the volume fraction ratio of silica to amphiphile can be used to roughly predict the arising mesophases.[16] However, the systems become more complicated when mixed oxide precursors are in use, and the phase diagrams can only be used as a first guideline for the prediction of the accessible structures. When the modified surfactant is removed by calcination, it leaves the transition-metal oxide in the matrix. In this way, a silica film doped with hafnium oxide in periodically arranged mesopores is produced (Figure 2). EXAFS analysis in previous studies showed that this approach yields a molecular dispersion of the transition-metal oxide (titanium or iron) within the silica matrix without the agglomeration to nanoparticles.[17]

In the present study, a sequence of Hf oxide doped films that were prepared with different ratios (*M*) of Hf–Brij/tetraethoxysilane was analyzed by GISAXS (Figure 3). The predominant feature of the diffraction patterns is the formation of diffraction spots rather than rings, which indicates that the films are highly textured. Evaporation-induced self-assembly usually results in films with the densest crystallographic plane of the mesostructure aligned parallel to the substrate.[18] From the phase diagram of Brij-56, micellar cubic and hexagonal mesostructures are expected at low concentrations of the surfactant. During the drying and calcination processes of the films, shrinkage occurred preferentially along the direction normal to the surface plane. Because the mesostructure is aligned with respect to the substrate, this shrinkage is anisotropic and results in distortion of the mesostructure. Body-centred cubic (*Im*3*m*) struc-

 © 2007 Wiley-VCH Verlag GmbH & Co. KGaA, Weinheim 

tures transform to face-centred orthorhombic (*Fmmm*) and 2D-hexagonal (*P6m*) to 2D centred rectangular mesostructures (*C2mm*).[19–21] In agreement to that, the GISAXS analysis showed that with increasing surfactant concentrations, face-centred orthorhombic ($0.03 < M < 0.06$), 2D-centered rectangular ($M = 0.10$) and lamellar films ($M = 0.17$) were obtained. At a ratio $M = 0.12$, a biphasic film was obtained that consists of 2D-centered rectangular and lamellar mesostructures. We also found biphasic films consisting of face-centred orthorhombic as well as 2D-centered rectangular domains in the concentration range $0.06 < M < 0.10$. The existence of two phases in the same film can be attributed to a concentration gradient and inhomogeneity during EISA or to the presence of two interfaces: solid–liquid and liquid–air.

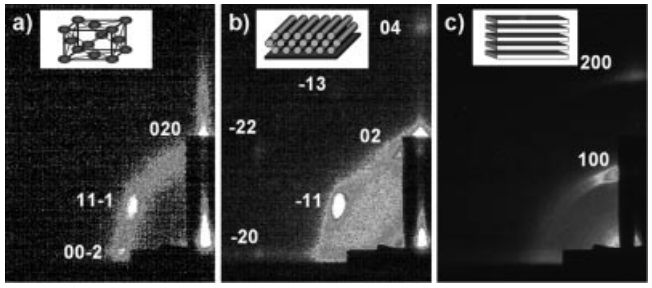


Figure 3. GISAXS pattern for Hf–Brij(0.034), Hf–Brij(0.102), Hf–Brij(0.12) and Hf–Brij(0.17) in the as-deposited state.

No structures that are derived from a bicontinuous cubic mesophase were obtained. Under certain reaction conditions (i.e. aging temperature of 45 °C), the formation of films with this mesostructure was described in the literature.[22]

In contrast, films that were prepared under the same conditions with unmodified Brij-56 did not result in the formation of an orthorhombic mesostructure. The obtained films were disordered ($M < 0.05$), 2D-centered rectangular ($0.05 < M < 0.21$) and lamellar ($0.21 < M < 0.42$). The fact that an additional mesostructure was formed under the same conditions with the hafnium alkoxide/Brij-56 complex can be explained by the larger head group volume of the modified surfactant, which increases the stability of mesostructures with a higher curvature.

The films were successively heat-treated at different temperatures and a GISAXS pattern was recorded after each step (Figure 4). The orthorhombic mesostructure had unit cell parameters of $a = 9.1$, $b = 10.2$ and $c = 12.8$ nm in the as-deposited state. After calcination at 700 °C, shrinkage was observed exclusively along the $b$ direction of the unit cell (perpendicular to the substrate) to give $a = 9.1$, $b = 6.9$ and $c = 12.9$ nm.

TEM analysis (Figure 5) of the calcined (500 °C) sample of Hf–Brij(0.034) confirmed the face-centred orthorhombic mesostructure.

The 2D-centered rectangular GISAXS pattern of Hf–Brij(0.10) (Figure 6) showed unit cell parameters of $a = 6.9$ and $b = 9.6$ nm at 25 °C. After heat treatment to 500 °C, the unit cell parameters are $a = 6.7$ and $b = 6.5$. The shrinkage (30%) occurred as expected and almost exclusively along the direction perpendicular to the substrate plane. Further heat treatment to 700 °C resulted in the destruction of the mesostructure as indicated by a strong decrease in the intensity of the 02 diffraction spot and the disappearance of the –11 and –20 spots, respectively.

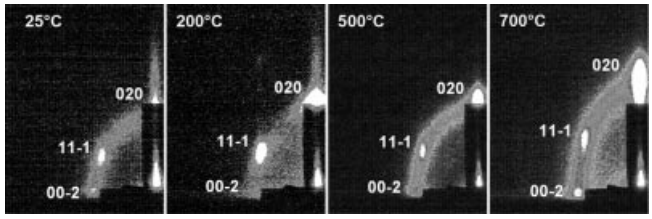


Figure 4. GISAXS series of Hf–Brij(0.034) as-deposited and successively calcined at the indicated temperatures.

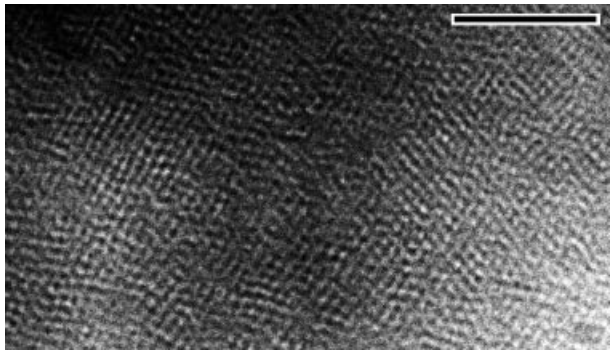

Figure 5. TEM analysis of Hf-Brij(0.034) after calcination at 450 °C; scale bar = 100 nm.

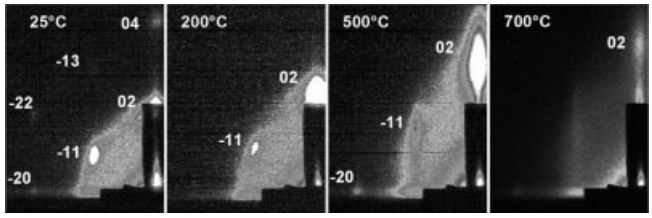


Figure 6. GISAXS series of Hf–Brij(0.10) successively calcined at the indicated temperatures.

TEM analysis of Hf–Brij(0.10) after calcination at 500 °C shows the cylindrical pores of the 2D-centered rectangular mesostructure (Figure 7).

Wide angle XRD (Figure 8) shows an amorphous network below 900 °C. Above that temperature crystallization of tetragonal hafnia occurred and the crystallite size reached approximately 10 nm at 1200 °C.[12]

The surface and in-depth composition of the Hf–Brij(0.12) sample after calcination at 450 °C was analyzed by XPS. The atomic percentages of the different elements of interest (O, Hf, C, Si) were evaluated as a function of the sputtering time, which can in turn be related to the depth of the sample.

In Figure 9 the survey spectra of the Hf–Brij(0.12) samples at the outer surface (a) and after 60 min sputtering (b) are superimposed. As it can be seen, on the surface the

 © 2007 Wiley-VCH Verlag GmbH & Co. KGaA, Weinheim 

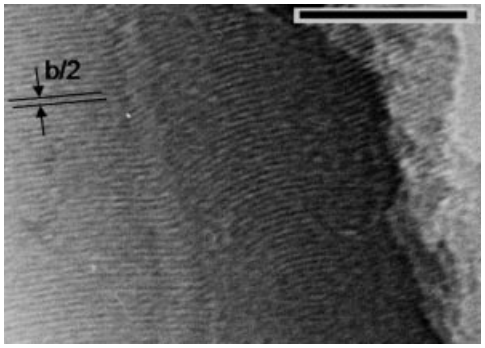


Figure 7. TEM image of Hf–Brij(0.10) after calcination at 500 °C viewed perpendicular to the unit cell *b* axis; scale bar = 100 nm.

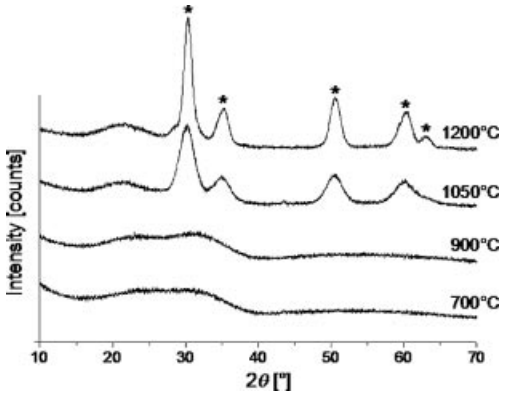


Figure 8. Temperature-dependent X-ray diffraction patterns for Hf–Brij(0.10) calcined at different temperatures. Asterisks indicate the diffraction peaks of the tetragonal hafnia phase.

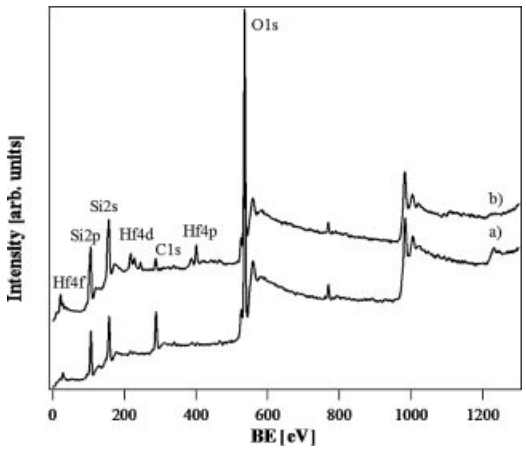


Figure 9. Superimposed survey spectra of the sample before (a) and after (b) 60 min sputtering.

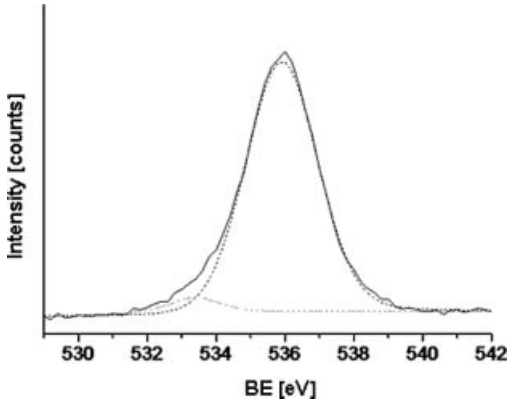


Figure 10. Deconvoluted O1s peak after 20 min sputtering.

peaks corresponding to silicon, carbon and oxygen are distinctly evident, whereas after sputtering the peaks of hafnium could also be detected. Additionally, upon sputtering, a noticeable reduction in the carbon contamination was detected, but carbon was also still present in the inner layers of the film. In addition to the survey spectra, selected spectra of the regions of interest were also acquired. The binding energies (BE) in the annealed samples were corrected for charging effects by assuming for the C1s transition a value typical for adventitious carbon (284.6 eV).[23] As it can be seen in Figure 10, the O1s peak is asymmetric and consists of two components, which could be evidenced after deconvolution. The major contribution whose value is, after charge correction, 532.9 eV, was ascribed to silica, whereas a further component at 530.6 eV (after charge correction), could be ascribed to hafnia, in agreement with the value reported in the literature.[23] Accordingly, the area intensity ratio of the two components is about 11, which is also the detected Si/Hf molar ratio.

As far as the Hf4f peak is concerned, the detected values range in the interval 17.6–18.0 and are higher than the value reported for bulk hafnia (16.7).[23] This finding is in agreement with the data reported in literature, which accounts for the shift to a higher binding energy for hafnium in a Hf–O–Si environment with respect to pure $HfO_2$.[24] Accordingly, the values detected for the $Hf4d_{5/2}$ peak, in the range 214.0–214.6 eV, are also higher than the value reported in literature (213.2 eV).[11,24]

The in-depth composition of the films, performed by sputtering analysis cycles, reveals an even distribution of the hafnium guest species in the silica host matrix. As shown in Figure 11, where the Si/Hf atomic ratios are plotted versus the sputtering time, the hafnium signal displays a uniform profile along the investigated thickness. In the outer layers, an enrichment of silicon was detected, whereas after about 20 min of sputtering the amount of hafnium gradually started to increase and the experimental Si/Hf atomic ratio ranged from 5 to 9.5, with a mean value of about 8, which is in good agreement with the nominal ratio in the starting solution (7.2). After 480 min of sputtering, the boundary between the film and the silicon substrate was reached, as the silicon peak displays two fully distinguishable components: the first at 103.9 eV, which is ascribable to the silica film, and the second at about 99.5 eV, which is attributable to the metallic silicon of the wafer substrate.

From the carbon signal, a considerable reduction in the contamination was observed after sputtering, but a significant presence of carbon (about 10% atomic) was detected along the whole film thickness, which can be ascribed to incomplete decomposition of organics upon annealing.

 © 2007 Wiley-VCH Verlag GmbH & Co. KGaA, Weinheim 

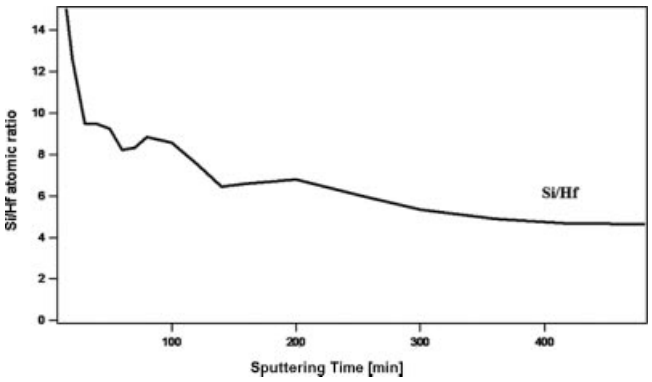


Figure 11. XPS in-depth distribution of the Si/Hf ratio.

## Conclusions

We demonstrated an effective, direct synthetic method for the preparation of mesostructured hafnium oxide doped silica films by the use of a decaethyleneglycol hexadecyl ether/hafnium butoxide complex as a structure-directing agent. By variation of the ratio between the modified surfactant:silica precursor, face-centred orthorhombic, 2D-centered rectangular and lamellar films were obtained. The influence of heat treatment on the mesostructure was investigated by GISAXS and TEM measurements. The face-centred orthorhombic mesostructure was stable at temperatures above 700 °C. The 2D-centered rectangular structure showed a somewhat lower heat stability and was already affected at that temperature. The lamellar structure was destroyed at 300 °C. The in-depth chemical composition of the film was analyzed by XPS. The measurements showed that there is a uniform distribution of the hafnium species in the silica host matrix with a concentration close to the nominal value in the starting solution.

## Experimental Section

**Materials:** Hafnium *n*-butoxide was supplied from Aldrich and used without further purification. Tetraethyl orthosilicate and Brij-56 ($C_{16}EO_{10}$) were purchased from Fluka and used as received. Toluene (99%) was obtained from Merck and distilled from calcium hydride prior to use. Ethanol (96%) was supplied by Merck.

**Methods:** The composition of the films at the surface and in the bulk was investigated by XPS. Photoelectron spectra were obtained with a Perkin–Elmer Φ5600ci spectrometer by using nonmonochromatized Al-$K_\alpha$ radiation (1486.6 eV). The spectrometer was calibrated by assuming the binding energy (BE) of the Au4f7/2 line at 83.9 with respect to the Fermi level. The standard deviation for the BE values was 0.15. The reported BE were corrected for charging effects by assigning the BE value of 284.6 eV to the C1s line of carbon. Survey scans (187.85 pass energy, 1/step, 25 ms/step) were obtained in the 0–1300 range. Detailed scans (58.7 pass energy, 0.2 eV/step, 50 ms/step) were recorded for the O1s, C1s, Hf4f, Hf4d and Si2p regions. The atomic percentages of the different species were determined by using the C1s, O1s, Hf4f and Si2p regions. In particular, after each sputtering cycle, the determination of the four atomic percentages was performed as a function of the increasing sputtering time, which was used to obtain the in-depth profiles of the various species. The atomic composition, after a Shirley-type background subtraction was evaluated by using sensitivity factors supplied by Perkin–Elmer.[23,25] Depth profiles were carried out by $Ar^+$ sputtering at 3 keV with an argon partial pressure of $5 \times 10^{-6}$ Pa. A specimen area of $2 \times 2$ mm$^2$ was sputtered. Samples were introduced directly by a fast entry lock system into the XPS analytical chamber. The assignment of the peaks was carried out by using the values reported.[23,24,26] Room-temperature grazing incidence GISAXS experiments were performed at the Austrian high-flux SAXS beam line at the synchrotron radiation centre Elettra, Trieste, Italy.[27] Films deposited on single-side polished silicon wafer substrates and subsequently calcined at different temperatures were measured at a photon energy of 8 keV and with a grazing angle $\alpha$ below 2° between the beam and the film surface. 2D-diffraction patterns were recorded with a CCD detector (Photonic Science) with a distance ($L$) of 107 cm from the sample. The recorded area is indicated by the dotted rectangle in Figure 12. The $d$ spacing was determined from the diffraction spots by analysis of the CCD images with the FIT2D program (A. P. Hammersley/ESRF). TEM images were recorded with a JEOL JEM-100CX analytical transmission electron microscope. For film samples, the surface of the film was scratched and the powder was attached to Formvar copper grids. XRD patterns were recorded with a Philips X'Pert diffractometer with a Philips PW 3040/60 (mppx) generator and a Philips PW 3050/60 goniometer. NMR spectra were recorded with a Bruker Avance 300 spectrometer equipped with a 5 mm broadband probe head and a $z$ gradient unit. 2D spectra, COSY (correlated spectroscopy), TOCSY [totally correlated spectroscopy, $T$(mix) = 120 ms] and HSQC (heteronuclear single quantum correlation), were measured with Bruker standard pulse sequences. $CDCl_3$ (99.8% euriso-top) was employed as the solvent.

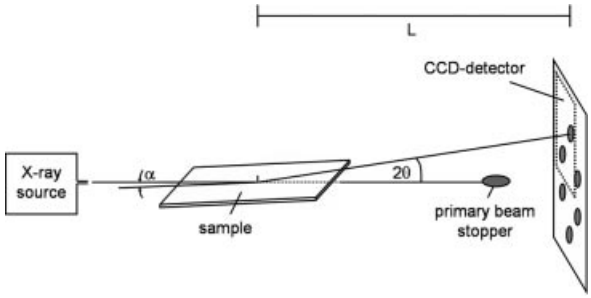


Figure 12.Setup of the GISAXS measurements.

**Synthesis of Hf-Brij56:** The reaction was carried out in a three-necked round-bottomed flask equipped with a reflux condenser and a distillation apparatus under an argon atmosphere. To remove residual water, the surfactant Pluronic-P123 was dissolved in toluene and heated to 100 °C for approximately 4 h. During that time, the toluene/water azeotrope was distilled off. The dried surfactant was then dissolved again in fresh absolute toluene. $Hf(OBu)_4$ was also dissolved in absolute toluene and added dropwise to the above prepared solution with a transition metal/surfactant molar ratio of 1:1. The mixture was stirred at 110 °C overnight. Toluene and the formed alcohol were removed by distillation and the metal-coordinated surfactants were obtained as slightly yellow or white pastes in 95% yield. $^1$H NMR (300.13 MHz, $CDCl_3$): $\delta$ = 0.82–0.95 (m, 12 H, 1-H, 14-H), 1.22–1.4 (m, 32 H, 2-H, 11-H, 12-H, 13-H), 1.55 (m, 8 H, 10-H, 3-H), 3.42 (t, $J$ = 6.8 Hz, 2 H, 9-H), 3.61 (m, 38 H, 6-H, 7-H, 8-H), 4.05 (m, 6 H, 4-H), 4.20 (m, 2 H, 5-H) ppm. $^{13}$C NMR (75.47 MHz, $CDCl_3$): $\delta$ = 14.2 (C-1, C-14), 19.1 (C-2), 22.8 (C-13), 26–32 (C-11, C-12), 29.5 (C-10), 36.8 (C-3), 69.3 (C-4), 69.2 (C-5), 70.0 (C-6), 71.7 (C-9), 70–71 (C-7, C-8) ppm.

 © 2007 Wiley-VCH Verlag GmbH & Co. KGaA, Weinheim 

**Film Preparation:** TEOS (61 mL) was prehydrolyzed in a solution containing water (4.87 mL), dilute hydrochloric acid (0.07 N, 2 mL) and ethanol (61 mL) at 60° for 90 min. This "stock" solution (8 mL) was mixed with ethanol (7 mL), HCl (0.07 N, 0.4 mL), water (0.4 mL) and different amounts of the metal-coordinated surfactant resulting in a molar ratio of Hf–Brij/TEOS/EtOH/$H_2O$/HCl = *x*:1:42:15:0.0052. Films were prepared within one hour on single-sided polished silicon wafers by dip-coating with a holding time of 30 s, a withdrawal speed of 4 mm/s at a relative humidity of 35–50%. The films were aged for at least 24 h prior to calcination. Powder samples for XRD analysis were scratched from coated glass plates after drying for 24 h at room temperature.

## Acknowledgments

The financial support of the European community for the ELETTRA synchrotron measurements is greatly acknowledged. We thank the USTEM at the Vienna University of Technology for allowing access to their TEM facilities and Berthold Stäüger from the Division of Structural Chemistry of the Institute of Chemical Technologies and Analytics, Vienna University of Technology for the XRD measurements.

[1] R. G. Simhan, *J. Non-Cryst. Solids* **1983**, *54*, 335–343.
[2] A. Paul, *J. Mater. Sci.* **1977**, *12*, 2246–2268.
[3] X. Song, A. Sayari, *Catal. Rev. Sci. Eng.* **1996**, *38*, 329–412.
[4] P. Liu, J. Liu, A. Sayari, *Chem. Commun.* **1997**, 577–578.
[5] P. Yang, D. Zhao, D. I. Margolese, B. F. Chmelka, G. D. Stucky, *Chem. Mater.* **1999**, *11*, 2813–2826.
[6] T. Brezesinski, B. Smarsly, K. Iimura, D. Grosso, C. Boissiere, H. Amenitsch, M. Antonietti, C. Sanchez, *Small* **2005**, *1*, 889–898.
[7] L. Malfatti, T. Kidchob, S. Costacurta, P. Falcaro, P. Schiavuta, H. Amenitsch, P. Innocenzi, *Chem. Mater.* **2006**, *18*, 4553–4560.
[8] Y. S. Lin, R. Puthenkovilakam, J. P. Chang, *Appl. Phys. Lett.* **2002**, *81*, 2041–2043.
[9] G. D. Wilk, R. M. Wallace, J. M. Anthony, *J. Appl. Phys.* **2000**, *87*, 484–492; G. D. Wilk, R. M. Wallace, *Appl. Phys. Lett.* **1999**, *74*, 2854–2856; G. D. Wilk, R. M. Wallace, *Appl. Phys. Lett.* **2000**, *76*, 112–114.
[10] J. P. Maria, D. Wickaksana, J. Parrette, A. I. Kingon, *J. Mater. Res.* **2002**, *17*, 1571–1579.
[11] L. Armelao, D. Bleiner, V. Di Noto, S. Gross, C. Sada, U. Schubert, E. Tondello, H. Vonmont, A. Zattin, *Appl. Surf. Sci.* **2005**, *249*, 277–294; L. Armelao, H. Bertagnolli, D. Bleiner, M. Groenewolt, S. Gross, V. Krishnan, C. Sada, U. Schubert, E. Tondello, A. Zattin, *Adv. Funct. Mater.*; DOI: 10.1002/adfm.200600458; L. Armelao, C. Eisenmenger-Sittner, M. Groenewolt, S. Gross, C. Sada, U. Schubert, E. Tondello, A. Zattin, *J. Mater. Chem.* **2005**, *15*, 1838–1848.
[12] K. V. Terry, C. G. Lugmair, T. D. Tilley, *J. Am. Chem. Soc.* **1997**, *119*, 9745–9756.
[13] D. A. Neumayer, E. Cartier, *J. Appl. Phys.* **2001**, *90*, 1801–1808.
[14] C. J. Brinker, Y. Lu, A. Sellinger, H. Fan, *Adv. Mater.* **1999**, *11*, 579–585.
[15] D. J. Mitchell, G. J. T. Tiddy, L. Waring, T. Bostock, M. P. McDonald, *J. Chem. Soc., Faraday Trans. 1* **1983**, *79*, 975–1000.
[16] P. C. A. Alberius, K. L. Frindell, R. C. Hayward, E. J. Kramer, G. D. Stucky, B. F. Chmelka, *Chem. Mater.* **2002**, *14*, 3284–3294.
[17] R. Supplit, N. Hüsing, H. Bertagnolli, M. Bauer, V. Kessler, G. A. Seisenbaeva, S. Bernstorff, S. Gross, *J. Mater. Chem.* **2006**, *16*, 4443–4453; N. Huesing, B. Launay, G. Kickelbick, S. Gross, L. Armelao, G. Bottaro, M. P. Feth, H. Bertagnolli, G. Kothleitner, *Appl. Catal. A* **2003**, *254*, 297–310.
[18] D. Grosso, F. Cagnol G. J. de A. A. Soler-Illia, E. L. Crepaldi, H. Amenitsch, A. Brunet-Bruneau, A. Bourgeois, C. Sanchez, *Adv. Funct. Mater.* **2004**, *14*, 309–322.
[19] S. Besson, C. Ricolleau, T. Gacoin, C. Jacquiod, J.-P. Boilot, *Microporous Mesoporous Mater.* **2003**, *60*, 43–49.
[20] P. Falcaro, D. Grosso, H. Amenitsch, P. Innocenzi, *J. Phys. Chem. B* **2004**, *108*, 10942–10948.
[21] M. Klotz, P.-A. Albouy, A. Ayral, C. Menager, D. Grosso, A. van der Lee, B. Cabuil, F. Babonneau, C. Guizard, *Chem. Mater.* **2000**, *12*, 1721–1728.
[22] R. C. Hayward, P. C. A. Alberius, E. J. Kramer, B. F. Chmelka, *Langmuir* **2004**, *20*, 5998–6004.
[23] K. W. Terry, C. G. Lugmair, T. D. Tilley, *J. Am. Chem. Soc.* **1997**, *119*, 9745–9756.
[24] F. Moulder, W. F. Stickle, P. E. Sobol, K. D. Bomben, *Handbook of X-ray Photoelectron Spectroscopy*, Perkin–Elmer Corporation, Eden Prairie, MN, **1991**.
[25] V. Cosnier, M. Olivier, G. Theret, B. André, *J. Vac. Sci. Technol.* **2001**, *19*, 2267–22710.
[26] D. A. Shirley, *Phys. Rev.* **1972**, *5*, 4709–4714.
[27] D. Briggs, M. P. Seah, *Practical Surface Analysis*, John Wiley & Sons, New York, **1990**.
[28] H. Amenitsch, M. Rappolt, M. Kriechbaum, H. Mio, P. Laggner, S. Bernstorff, *J. Synchrotron Radiat.* **1998**, *5*, 506–508.

Received: March 11, 2007
Published Online: May 25, 2007

 © 2007 Wiley-VCH Verlag GmbH & Co. KGaA, Weinheim 

DOI: 10.1002/ejic.200601177

# DNA Interactions Mediated by Cyclopentadienidoruthenium(II) Complexes Containing Water-Soluble Phosphanes

**Antonio Romerosa,*[a] Mustapha Saoud,[a] Tatiana Campos-Malpartida,[a] Chaker Lidrissi,[a] Manuel Serrano-Ruiz,[a] Maurizio Peruzzini,[b] Jose Antonio Garrido,[c] and Federico García-Maroto[c]**

**Keywords:** Ruthenium / Cyclopentadienyl ligands / Phosphanes / DNA / Bioinorganic chemistry

The water-soluble ruthenium(II) complexes $Na_2[RuCpX(mTPPMS)_2]$ [X = Cl (**1**), I (**2**)] and $Na_x[RuCp(mTPPMS)(PR^1{}_3)(PR^2{}_3)](OTf)_y$ [$PR^1{}_3 = PR^2{}_3 = PPh_3$ (**3**), PTA (**4**), x = y = 0; $PR^1{}_3$ = mTPPMS, $PR^2{}_3$ = PTA (**5**), x = 1, y = 0; $PR^1{}_3$ = mTPPMS, $PR^2{}_3$ = mPTA (**6**), x = y = 0; $PR^1{}_3 = PR^2{}_3$ = mTPPMS (**7**), x = 2, y = 0; $PR^1{}_3 = PPh_3$, $PR^2{}_3$ = PTA (**8**), x = y = 0; $PR^1{}_3$ = mPTA, $PR^2{}_3 = PPh_3$ (**9**), x = 0, y = 1; mTPPMS = $Ph_2P(3\text{-}OSO_2C_6H_4)^-$; PTA = 1,3,5-triaza-7-phosphaadamantane; mPTA = *N*-methyl-1,3,5-triaza-7-phosphaadamantane] have been synthesized and characterised by elemental analysis, NMR and IR spectroscopy and crystallographic methods. The X-ray crystal structure determination of $[RuCp(mTPPMS)(PPh_3)(PTA)]\cdot 2H_2O$ (**8**·$2H_2O$), which is the first half-sandwich ruthenium complex bearing three different phosphanes, has also been determined. The binding properties of these new water-soluble ruthenium complexes towards DNA and the interaction of free mTPPMS with the nucleic acid have been studied using the mobility shift assay, which has shown that both the activity of the ruthenium complexes and the possible mechanism governing the interaction with DNA are strictly dependent on the composition of the complexes.

(© Wiley-VCH Verlag GmbH & Co. KGaA, 69451 Weinheim, Germany, 2007)

## Introduction

Coordination and organometallic complexes of transition metals offer a great potential for use as anticancer agents due to their widely diverse structures and bonding modes. Change in the structural requirements and electronic properties of the metal complexes may be finely tuned to optimize the metal interaction with nucleic acid nucleobases. Ruthenium complexes have shown important biological activity and are becoming increasingly important in both bioinorganic chemistry and anticancer chemotherapy.[1–5] The water solubility of ruthenium compounds has been greatly increased by using dialkyl sulfoxide derivatives such as in [*trans*-$RuCl_4$(DMSO)Im][ImH] (NAMI-A) and [*trans*-$RuCl_4$(DMSO)dmtp][Hdmtp] (KP1019), which have recently successfully completed phase-one clinical trials,[5–12] and by the use of water-soluble phosphanes.[13,14] Work by Sadler and co-workers on the antitumor properties of organometallic piano-stool compounds[15] has shown that these complexes are effective antitumour agents and has contributed to understanding the effective mechanism ruling the interaction between the target biomolecule and the ruthenium complex.

Recently, we have reported the synthesis of the piano-stool complexes $[RuCpX(PR^1{}_3)(PR^2{}_3)]^{n+}$ (X = Cl, I; $PR^1{}_3 = PPh_3$, $PR^2{}_3$ = PTA, mPTA; $PR^1{}_3 = PR^2{}_3$ = PTA, mPTA; PTA = 1,3,5-triaza-7-phosphaadamantane; mPTA = *N*-methyl-1,3,5-triaza-7-phosphaadamantane)[16] and their interaction with DNA, which suggests a non-innocent role for the ancillary chloride ligand as the analogous germane iodide complexes are inactive towards DNA. Indeed, replacement of the chloride by a DNA fragment in the coordination sphere of the metal may result in a covalent bond between the metal and a DNA base, thus accounting for the cytotoxicity of organoruthenium species.[16b] The DNA activity of this family of complexes is further dependent on the water-soluble phosphane coordinated to the metal (PTA or mPTA), thereby suggesting that an improved interaction of the reactive {$CpRuCl(PR^1{}_3)$} fragment with DNA could be achieved by an adequate choice of the water-soluble phosphane bonded to the metal.

In order to verify this hypothesis further and to expand the number of half-sandwich $CpRu^{II}$ species bearing water-soluble phosphane ligands, we turned our attention to mTPPMS [mTPPMS = $Ph_2P(3\text{-}OSO_2C_6H_4)^-$]. This sulfonated phosphane, in spite of being one of the most popular

[a] Área de Química Inorgánica, Facultad de Ciencias, Universidad de Almería,
Almería, Spain
Fax: +34-950-015-008
E-mail: romerosa@ual.es
[b] Istituto di Chimica dei Composti Organometallici, CNR,
Via Madonna del Piano 10, 50019 Sesto Fiorentino (FI), Italy
[c] Área de Bioquímica, Facultad de Ciencias, Universidad de Almería,
Almería, Spain

 © 2007 Wiley-VCH Verlag GmbH & Co. KGaA, Weinheim 

water-soluble phosphanes for catalytic hydrogenations,[17] hydroformylations[17] and ring-opening cyclo-alkene metathesis[18] under water-containing biphasic conditions, has never been used as a water-soluble synthon of potentially bioactive organometallic or inorganic ruthenium-based complexes.

Herein, we report our recent efforts in this area and describe the synthesis and characterization of a large class of new water-soluble half-sandwich ruthenium(II) complexes supported by one, two or three mTPPMS ligands in combination with halide and/or other hydrophilic (PTA and mPTA) and hydrophobic ($PPh_3$) phosphane co-ligands [PTA = 1,3,5-triaza-7-phosphaadamantane; mPTA = *N*-methyl-1,3,5-triaza-7-phosphaadamantane; see Scheme 1]. Additionally, we have performed DNA activity studies for these complexes and compare the results with other water-soluble {CpRu} species. The results of this study show a clear dependence of the reactivity towards DNA on the kind of phosphane bonded to the metal.

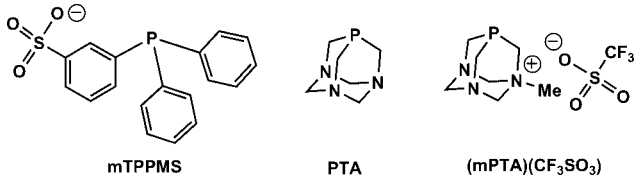


Scheme 1.

## Results and Discussion

### Synthesis and Characterization of Ruthenium Complexes 1 and 2

Complex **1** was straightforwardly obtained by substitution of the two $PPh_3$ ligands in the parent compound $[RuClCp(PPh_3)_2]$ with mTPPMS in refluxing toluene. This procedure gives **1** in much higher yield than the one described previously[19] by Suárez et al. from the direct reaction of freshly distilled CpH with $RuCl_3{\cdot}3H_2O$ and mTPPMS in refluxing ethanol. The compound obtained shows good solubility in water (41 mg mL$^{-1}$, $4.41 \times 10^{-2}$ M) as a consequence of the two mTPPMS ligands, whose presence is supported by elemental analysis and a spectroscopic investigation (see Experimental Section). Reaction of **1** with NaI or KI in MeOH at room temperature gives the quantitative formation of **2**, where the chloride ligand has been replaced by iodide (Scheme 2). Complex **2** is noticeably more stable than **1** towards oxidation and is less soluble in water, in agreement with the behaviour found for the complexes $[RuCp(PR^1{}_3)(PR^2{}_3)X]^{n+}$ (X = Cl, I; $PR^1{}_3$ = $PPh_3$, $PR^2{}_3$ = PTA, mPTA; $PR^1{}_3$ = $PR^2{}_3$ = PTA, mPTA; $n$ = 0, 1), where the iodine derivatives are always less water-soluble than the corresponding chlorides.[16] The spectroscopic properties of **2** match those of **1** and do not deserve additional comments.

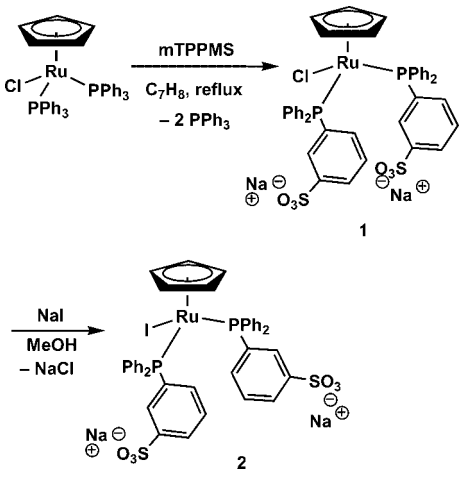


Scheme 2.

### Synthesis and Characterization of the mTPPMS Tris-Phosphane Ruthenium Complexes $Na_x[RuCp(mTPPMS)(PR^1{}_3)(PR^2{}_3)]$ [$PR^1{}_3$ = $PR^2{}_3$ = $PPh_3$ (3), PTA (4), $x$ = 0; $PR^1{}_3$ = mTPPMS, $PR^2{}_3$ = PTA (5), $x$ = 1; $PR^1{}_3$ = mTPPMS, $PR^2{}_3$ = mPTA (6), $x$ = 0; $PR^1{}_3$ = $PR^2{}_3$ = mTPPMS (7), $x$ = 2]

The reaction of $[RuCpCl(PPh_3)_2]$ with Na(mTPPMS) and $NaBF_4$, which aids chloride abstraction, in MeOH at reflux led to the substitution of the chloride ligand by mTPPMS and yielded the tris-phosphane complex $[RuCp(mTPPMS)(PPh_3)_2]$ (**3**). Similarly, the reaction of mTPPMS in MeOH with the bis-PTA derivative $[RuCpCl(PTA)_2]$ afforded the related complex $[RuCp(mTPPMS)(PTA)_2]$ (**4**) after substitution of the chloride by an mTPPMS ligand (Scheme 3). Complexes **3** and **4** were characterised by elemental analysis and conventional NMR spectroscopy. In keeping with the proposed formulation, the two complexes exhibit an $AM_2$ splitting pattern which, for **3**, results in a second-order multiplet centred at around $\delta$ = 39.6 ppm due to a fortuitous coincidence of the chemical shifts for the phosphorus atoms of both $PPh_3$ and mTPPMS which was not possible to simulate accurately. The $AM_2$ spin system is clearly visible in the spectrum of **4**, where the doublet at $\delta$ = –34.43 ppm is assigned to the two equivalent PTA P atoms while the low-field shifted triplet ($\delta$ = 49.57 ppm) is assigned to the single mTPPMS P atom.

Half-sandwich cyclopentadienidoruthenium complexes featuring three phosphane co-ligands like **3** and **4** are extremely rare and, to the best of our knowledge, are limited to the recently described complex $[RuCp(PPh_3)_2(PH_3)]Y$ (Y = $CF_3SO_3$, $PF_6$).[20] With the aim of preparing new {CpRu} complexes incorporating three tertiary phosphane co-ligands, we investigated the reaction of the bis(mTPPMS) complex **1** with additional water-soluble tertiary phosphanes. Thus, we studied the reaction of **1** with PTA, $mPTA(CF_3SO_3)$ and mTPPMS in refluxing MeOH containing $NaBF_4$. After usual workup, the new complexes $Na[RuCp(mTPPMS)_2(PTA)]$ (**5**), [RuCp(mPTA)-

 © 2007 Wiley-VCH Verlag GmbH & Co. KGaA, Weinheim 

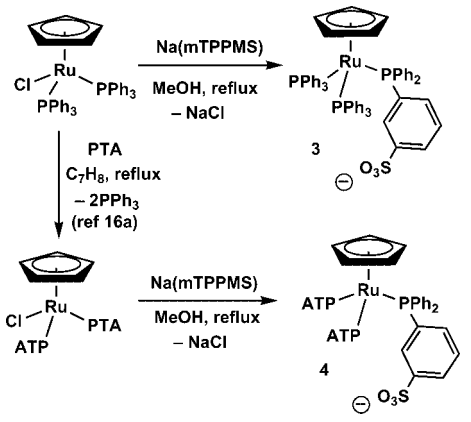


Scheme 3.

$(mTPPMS)_2$] (**6**) and $Na_2$[RuCp(mTPPMS)$_3$] (**7**) were obtained as a result of chloride substitution by PTA, mPTA and mTPPMS, respectively (Scheme 4).[21]

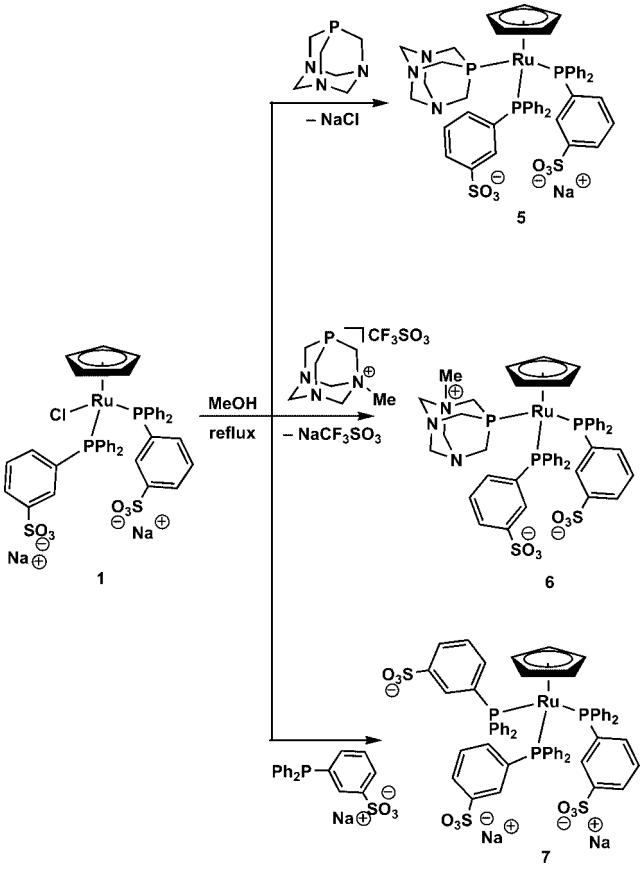


Scheme 4.

Complexes **5**–**7** were characterized by standard spectroscopic techniques. In the $^1$H NMR spectrum of **5**, the singlet due to the five Cp protons is found at $\delta$ = 4.73 ppm, which is in agreement with the chemical shift observed for complexes containing PTA.[16] A triplet at $\delta$ = –44.54 ppm (1 P) and a doublet for mTPPMS at $\delta$ = 42.22 (2 P) in the $^{31}$P{$^1$H} NMR spectrum unequivocally point to the formation of a triphosphane derivative.

Similar NMR properties were observed for **6** and **7**, which again are in agreement with the proposed formulas. Complex **6** is only moderately soluble in [D$_6$]DMSO, in which its $^{31}$P{$^1$H} NMR exhibits two broad signals for mTPPMS each corresponding to one P atom and a broad resonance integrating for one P atom with a chemical shift that is distinctive for ruthenium-bonded mPTA ($\delta$ = –29.66 ppm).[19] Steric crowding around ruthenium can be invoked to account for the magnetic inequivalency of the two mTPPMS ligands, but unfortunately the low solubility of **6** in solvents other than DMSO prevented us from performing a complete NMR investigation at low temperature, where the appearance of a distinct AMQ spin system could be anticipated.

The $^{31}$P NMR spectrum of **7**, which is the first homoleptic {CpRu} phosphane complex, is much simpler as it shows only a broad singlet at $\delta$ = 40.68 ppm with a chemical shift similar to that found for the other mTPPMS phosphane bonded to ruthenium. In the $^1$H NMR spectrum, the Cp signal for **6** falls at $\delta$ = 4.91 ppm which does not differ too much from that of **5**. In contrast, **7** shows the Cp singlet at $\delta$ = 3.96 ppm, close to that found for **3**, which only contains $PPh_3$ and mTPPMS.

### Synthesis and Characterization of the Heteroleptic Tris-Phosphane Ruthenium Complexes [RuCp(mTPPMS)(PR$^1_3$)-(PR$^2_3$)](OTf)$_x$ [PR$^1_3$ = PPh$_3$, PR$^2_3$ = PTA (8), $x$ = 0; PR$^1_3$ = mPTA, PR$^2_3$ = PPh$_3$ (9), $x$ = 1]

The reaction of [RuClCp(PPh$_3$)(PTA)][16b] with mTPPMS in refluxing MeOH led, after the usual workup, to chloride substitution and formation of [RuCp(mTPPMS)(PTA)(PPh$_3$)] (**8**). In a similar procedure, the reaction of [RuClCp(PPh$_3$)(mPTA)](CF$_3$SO$_3$) with mTPPMS gave [RuCp(mTPPMS)(PPh$_3$)(mPTA)](CF$_3$SO$_3$) (**9**; Scheme 5). Complexes **8** and **9** are the first examples of half-sandwich {CpRu} complexes containing three different phosphanes and represent a unique type of water-soluble metal complex containing two different water-soluble phosphanes along with a hydrophobic PPh$_3$ ligand. The strategy adopted here of replacing the chloride ligand in [RuClCp(PPh$_3$)(PR$_3$)]$^{n+}$ (PR$_3$ = PTA, mPTA, mTPPMS) with different water-soluble phosphanes could provide a wide range of water-soluble ruthenium complexes that share the same structural and geometric properties but may be different enough to result in a completely different interaction toward bio-molecules, particularly DNA.

The presence of three different phosphanes in **8** is clearly shown by the appearance of an AXX′ spin system in the $^{31}$P{$^1$H} NMR spectrum (Figure 1). The three doublets of doublets arise at $\delta$ = –49.30 ($^2J_{PTA,mTPPMS}$ = 41.8, $^2J_{PTA,PPh_3}$ = 38.8 Hz, PTA), 41.56 ($^2J_{PPh_3,mTPPMS}$ = 32.0, $^2J_{PPh_3,PTA}$ = 38.8 Hz, PPh$_3$) and 43.65 ppm )$^2J_{mTPPMS,PPh_3}$ = 32.0, $^2J_{mTPPMS,PTA}$ = 41.8 Hz, mTPPMS). The chemical shift of the PTA ligand in **8** is closer to that in **5** ($\delta$ = –44.54 ppm) than in **4** ($\delta$ = –34.43 ppm), which suggests that the PTA chemical shift for complexes [RuCp(PTA)(PR$^1_3$)(PR$^2_3$)]$^{n+}$

 © 2007 Wiley-VCH Verlag GmbH & Co. KGaA, Weinheim 

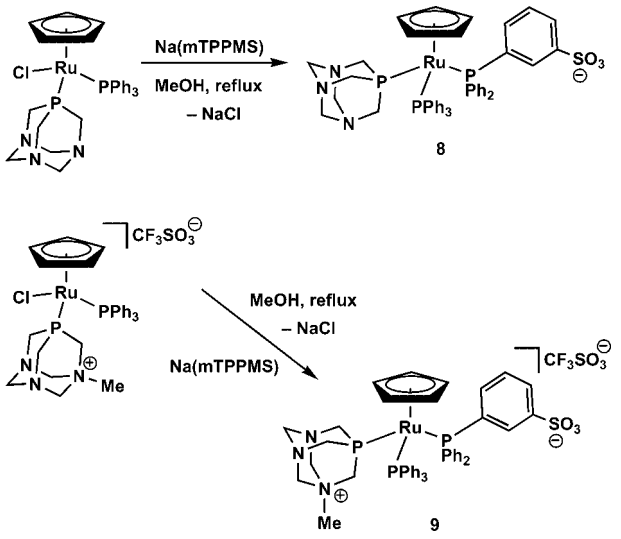


Scheme 5.

($PR^1_3$ = $PR^1_3$ = $PPh_3$, mTPPMS, PTA; $n$ = 0, 1) moves to high field as the number of mTPPMS ligands coordinated to the metal increases. The $^{31}P\{^1H\}$ NMR spectrum of **9** in $CD_3OD$, which differs from **8** by the presence of one cationic mPTA ligand instead of a neutral PTA, agrees with the proposed formula. A broad triplet at $\delta$ = –26.58 ppm is ascribed to the mPTA ligand while the fortuitous coincidence of the $PPh_3$ and mTPPMS signals is responsible for the broad resonance (two P atoms) at $\delta$ = 40.48 ppm which does not show any fine structure at –60 °C.

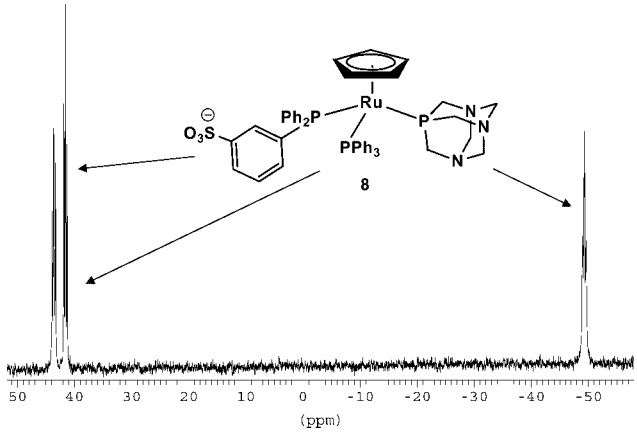


Figure 1. $^{31}P\{^1H\}$ NMR spectrum of **8** in $CDCl_3$ at 20 °C.

The $^1H$ NMR spectra of both **8** and **9** show the expected signals for both the coordinated phosphanes and the Cp ligand with the correct integral ratio. The chemical shift of the Cp group in **8** ($\delta$ = 4.86 ppm), which is shifted to low field in comparison with **1** ($\delta$ = 4.21 ppm), **2** ($\delta$ = 4.27 ppm), **3** ($\delta$ = 3.99 ppm) and **7** ($\delta$ = 3.96 ppm) but similar to that for **4** ($\delta$ = 5.00 ppm), **5** ($\delta$ = 4.73 ppm), **6** ($\delta$ = 4.91 ppm) and **9** ($\delta$ = 4.93 ppm), is worth noting. These data suggests that the resonance for the Cp protons appears at about $\delta$ = 5 ppm when PTA and/or mPTA are coordinated to the {CpRu} unit whereas it moves to high field (to around $\delta$ = 4 ppm) when mTPPMS and/or $PPh_3$ are bound to the metal.

In order to get more information on these complexes and to confirm their putative structures, we decided to undertake an X-ray diffraction study of one illustrative example of these tris-phosphane {CpRu} complexes. Crystals of **8**·$2H_2O$ were grown from a cold dilute MeOH solution and were found to be suitable for a crystallographic study. In keeping with the presence of a trio of different phosphanes coordinated to ruthenium, the asymmetric unit contains two enantiomeric ruthenium complexes and two disordered water molecules. The ruthenium atom in each enantiomer is pentahapto bonded to a cyclopentadienido ring, one $PPh_3$ and to two different water-soluble phosphanes (mTPPMS and PTA), which are coordinated to ruthenium through the apical phosphorus atom (Figure 2).[22] Remarkably, a search in the Cambridge Crystallographic Database did not find any X-ray authenticated ruthenium complexes with mTPPMS or other sulfonated phosphanes, which is quite surprising in view of the intense recent research activity aimed at preparing and studying water-soluble complexes of sulfonated phosphane ligands.

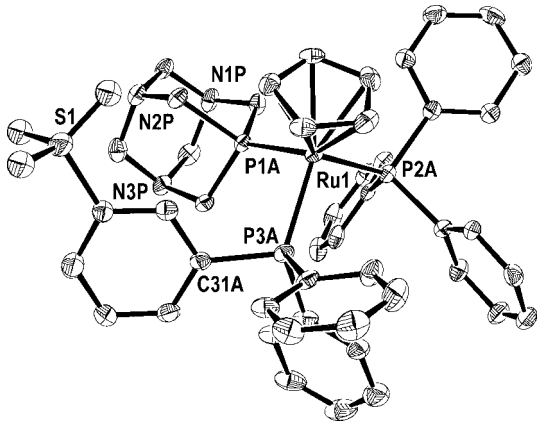


Figure 2. ORTEP view and atom numbering of compound **8**·$2H_2O$. Hydrogen atoms have been omitted for clarity.

The overall geometry of the two enantiomers of **8** is very similar to that observed for three-legged piano-stool complexes of the type $[MCpL_2X]$ and to the structures of $[RuCp(PPh_3)_2(PH_3)]PF_6$[20] and $[Ru\{\eta^5\text{-}C_5H_4C(CH_3)_2CH(PPh_2)C_5H_4N\}\{PPh_2(OCH_2CH_3)\}PPh_3]PF_6$,[23] which are the only reported examples of a {CpRu} moiety bonded to three tertiary phosphane ligands, although neither are soluble in water. The Cp rings in the pair of enantiomers are essentially planar, with the biggest deviations from the average Cp plane being 0.0084 (C1M; Ru1) and 0.0024 Å (C5N; Ru2), respectively. The $Ru–Cp_{(centroid)}$ distances are quite similar for the two enantiomeric molecules [Ru1–$Cp_{(centroid)}$ 1.883, Ru2–$Cp_{(centroid)}$ 1.886 Å] and somewhat longer than those found in $[RuClCp(PTA)_2]$ [$Ru–Cp_{(centroid)}$ 1.844 Å],[24] $[RuClCp(PPh_3)(PTA)]$ [Ru1–$Cp_{(centroid)}$ 1.845,

 © 2007 Wiley-VCH Verlag GmbH & Co. KGaA, Weinheim 

Ru2–$Cp_{(centroid)}$ 1.837 Å].[16b] The Ru–$P_{(PTA)}$ separation [Ru1–P1A 2.324(2), Ru2–P1B 2.306(3) Å] is similar to those found in other X-ray authenticated Ru–PTA derivatives,[16,22,23] while the Ru–$PPh_3$ distances [Ru1–P2A 2.370(3), Ru2–P2B 2.354(3) Å] are longer than those found in [RuClCp($PPh_3$)(PTA)] [Ru1–P1 2.302(2), Ru2–P2 2.298(3) Å].[16b]

The coordination polyhedron of each of the two enantiomers shows a distorted pseudo-octahedral geometry [P2A–Ru–P3A 101.78(10)°, P2B–Ru–P3B 101.46(9)°, P1A–Ru–P2A 94.32(10), P1A–Ru–P3A 95.12(10), P1B–Ru–P2B 93.22(9), P1B–Ru–P3B 97.46(9)], probably due to the high degree of steric repulsion between the three phosphanes.

The arrangement of enantiomeric pairs along the asymmetric unit of **8**·2$H_2O$ is supported by an evident network of hydrogen bonds. These form zigzag chains involving two disordered double water bridges that connect two oxygen atoms of the same pendent sulfonate group to a pair of N atoms (N3P, N3T) belonging to two PTA ligands from neighbouring complex molecules (Figure 3).

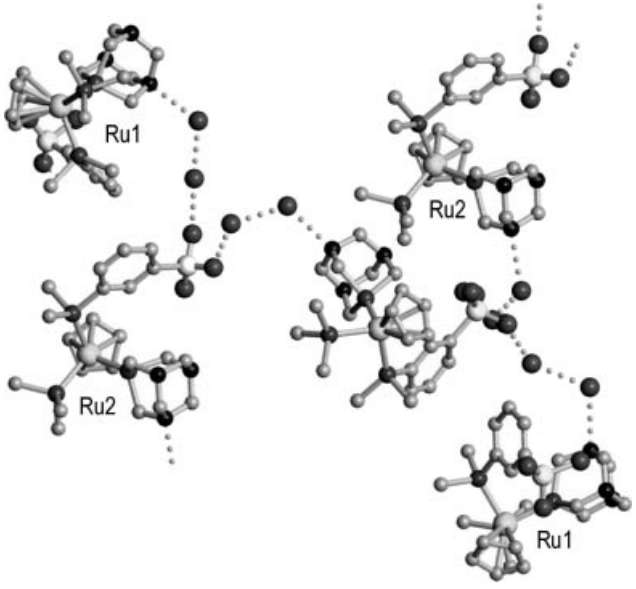


Figure 3. View of the hydrogen-bonding network of **8**·2$H_2O$. Only the *ipso* carbons of the phenyl rings of $PPh_3$ are shown, and hydrogen atoms have been omitted for clarity.

### Water Solubility and Reactivity Towards $D_2O$, $O_2$ and CO

The solubility of the new {CpRu}/mTPPMS complexes in water is summarized in Table 1 together with their stability towards hydrolysis and air. The solubility of these complexes in water may be anticipated from the presence of one, two or three water-soluble phosphanes bonded to the {CpRu} unit. However, this solubility spans a wide range of values from 0.60 mg mL$^{-1}$ for **8** and **9** to 41 mg mL$^{-1}$ for **1**. Interestingly, we did not find a direct dependence of the complex solubility on the number of water-soluble phosphanes bonded to the metal, which is puzzling. The solubility of complexes **1**, **2** and **7**, which contain only mTPPMS ligands, in water is greater than that of **3**, **4**, **5** and **6**, where mTPPMS is accompanied by $PPh_3$, PTA and mPTA, in different combinations. Furthermore, complexes **8** and **9**, which bear three different phosphanes, two of which are water-soluble, are practically insoluble in water. Although this behaviour defies any simple explanation, it is intriguing that the three more water-soluble derivatives (**1**, **2** and **7**) are the organoruthenium species that exhibit a double negative charge that is balanced by two sodium cations. The water solubility drops by one order of magnitude in **5** [$S(H_2O)_{25°C}$ = 2.5 mg mL$^{-1}$], which is a monoanion/monocation complex, and reduces slightly more in the neutral complexes **3**, **6** and **8** [$S(H_2O)_{25°C}$ < 1.0 mg mL$^{-1}$). The modest water solubility of the ionic complex **9** escapes from this rationale but is in agreement with the fact that its neutral zwitterionic character provides low solubility in water. As a general rule, the presence of $PPh_3$ in the trio of phosphanes coordinated to the {CpRu} moiety causes a severe reduction of the water solubility (see complexes **3**, **8** and **9**), although completely water-soluble combinations, such as those in **5** or **6**, are not mandatory to assure a good solubility of the related {CpRu} complexes in water, irrespective of whether they are neutral (**6**) or ionic (**5**). An interaction between oppositely charged ligands in complexes containing both mTPPMS and mPTA could lead to a lower than expected water solubility. As previously observed for other [RuCpX($PR^1_3$)($PR^2_3$)] derivatives, the water solubility of the iodide species **2** is lower than that of the chloride analogue **1**.[16,25]

Most of the complexes are stable to air in aqueous solution and can be recovered unchanged after being exposed

Table 1. Stability of complexes **1**–**9** in $D_2O$ under $O_2$ and solubility in water at 25 °C.

| Complex | Time [days] | $S(H_2O)_{25°C}$ [mg mL$^{-1}$] |
|---|---|---|
| $Na_2$[RuCpCl(mTPPMS)$_2$] (**1**) | 0.25 | 41 ($4.41\times10^{-2}$ M) |
| $Na_2$[RuCpI(mTPPMS)$_2$] (**2**) | >4[a] | 15 ($1.47\times10^{-2}$ M) |
| [RuCp(mTPPMS)($PPh_3$)$_2$] (**3**) | 0.18 | 0.9 ($8.7\times10^{-4}$ M) |
| [RuCp(mTPPMS)(PTA)$_2$] (**4**) | >4[a] | 10 ($1.2\times10^{-2}$ M) |
| Na[RuCp(mTPPMS)$_2$(PTA)] (**5**) | >4[a] | 2.5 ($2.4\times10^{-3}$ M) |
| [RuCp(mPTA)(mTPPMS)$_2$] (**6**) | >4[a] | 1.3 ($1.3\times10^{-3}$ M) |
| $Na_2$[RuCp(mTPPMS)$_3$] (**7**) | ca. 2 | 20.0 ($1.6\times10^{-3}$ M) |
| [RuCp(mTPPMS)($PPh_3$)(PTA)] (**8**) | >4[a] | 0.6 ($6.2\times10^{-4}$ M) |
| [RuCp(mTPPMS)(mPTA)($PPh_3$)]($CF_3SO_3$) (**9**) | >4[a] | 0.6 ($5.6\times10^{-4}$ M) |

[a] No reaction was observed after 4 days.

 © 2007 Wiley-VCH Verlag GmbH & Co. KGaA, Weinheim 

to visible light for more than four days at 40 °C in $D_2O$ (vide infra). In spite of the crowding at ruthenium caused by the presence of three phosphanes in a piano-stool structure, these complexes are thermally robust and do not dissociate a phosphane when refluxed in the presence of KI in EtOH or when saturated with carbon monoxide in $CDCl_3$ or $CD_3OD$ and kept at 40 °C for several hours (NMR tube experiment). Complete reaction with KI was observed only with **1** and, partially, with **7**, which gives a partial conversion to the iodide complex **2**. No reaction was observed with CO in $CD_3OD$ at 40 °C.

### Interaction of the {CpRu(mTPPMS)} Complexes with DNA

Previous studies on Pt and Ru complexes[26] have shown that modification of the electrophoretic mobility of plasmid DNA on agarose gels is commonly taken as confirmation of the presence of a direct DNA–metal interaction. The alteration of the DNA structure leads to the unwinding of the plasmid molecule holding up the migration of supercoiled DNA (SC) and slightly increasing the mobility of the open circular DNA (OC) to a point (coalescence point, CP) where both forms co-migrate. We have investigated the interaction of the new water-soluble ruthenium complexes with SC DNA using the shift mobility assay. Reactions between the ruthenium complexes and SC plasmid DNA were performed in water buffered with phosphate at pH 7.0 for 14 h at 37 °C and then samples were analyzed by electrophoresis on agarose-TAE gels. The reaction was performed in the dark even though no photochemical activation of the present ruthenium complexes has been observed, in contrast to other ruthenium complexes.[27,28]

Delay of SC DNA was observed for complexes **1**, **2**, **3** and **7**. In addition, a modest increase in the amount of OC DNA was observed, relative to untreated DNA, which indicates that some DNA cleavage may also occur. The highest activity was observed for **1** and **7** (CP at an Ri value of 6 and 5; Ri = Ru/base molar ratio) while the iodide complex **2** and complex **3**, which contains $PPh_3$, showed a lower activity against DNA (CP at Ri values of 16 and 15). No unwinding was observed with compounds containing the PTA ligands **4** and **5** at Ri values (up to 15) where the others ruthenium complexes were active (Figure 4).

The interaction of ruthenium complexes **8** and **9** with plasmidic DNA was also investigated. Although delay of SC-DNA was repeatedly observed only for **8**, a precise quantification of its activity was not possible due to the limited water solubility of this compound. Nevertheless, this result is in agreement with the DNA activity observed for other previously investigated ruthenium complexes containing mPTA which is significantly higher than that found for related species containing PTA, as observed for $[RuClCp(mPTA)(PPh_3)]^+$ vs. $[RuClCp(PTA)(PPh_3)]$.[16]

The activity of the ligand Na(mTPPMS) was also studied in a blank experiment. Interestingly, when plasmid DNA was incubated with increasing amounts of this water-soluble phosphane an increase of the relaxed form of the plasmid (OC) was obtained that was found to correlate inversely with the amount of the supercoiled form (SC). This indicates that a direct conversion of the SC into the OC form is taking place and, therefore, that mTPPMS itself is able to cleave DNA.

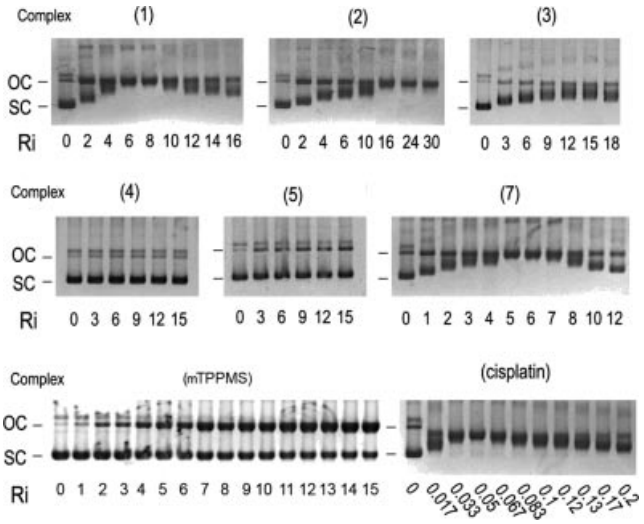


Figure 4. DNA mobility shift assay of the ruthenium complexes. Plasmid DNA was incubated with complexes $Na_2$-$[RuClCp(mTPPMS)_2]$ (**1**), $Na_2[RuCp(I)(mTPPMS)_2]$ (**2**), $[RuCp(mTPPMS)(PPh_3)_2]$ (**3**), $[RuCp(mTPPMS)(PTA)_2]$ (**4**), Na-$[RuCp(mTPPMS)_2(PTA)]$ (**5**), $Na_2[RuCp(mTPPMS)_3]$ (**7**) and the Na(mTPPMS). Ri values (Ri = Ru/base molar ratio) shown above as indicated in the Experimental Section. *cis*-$[PtCl_2(NH_3)_2]$ (cisplatin) was used as a control under the same experimental conditions.

As briefly mentioned above, only complexes **1**, **3** (less than 4 h) and **7** (ca. 2 days) react with water, probably by substitution of one ligand by a water molecule. The other ruthenium complexes (**2**, **4**, **5**, **6**, **8** and **9**) are stable in water for more than two days at 40 °C in diffuse daylight, thus suggesting that the species that interact with DNA are the unchanged ruthenium complexes. In keeping with the robustness of the $Na_x[RuCp(mTPPMS)(PR^1_3)(PR^2_3)](OTf)_y$ complexes with respect to phosphane dissociation, it is likely possible that the metal center in these complexes cannot interact directly with DNA N-nucleophiles. Many known ruthenium derivatives do not selectively interact with nucleobases and behave as intra- or interstrand cross-linking agents.[29] The interesting activity exhibited by the mTPPMS ligand towards DNA suggests that ruthenium complexes containing this ligand may be active agents for modifying DNA by a mechanism different from that usually accepted, which entails direct bonding to DNA nucleobases. Two diverse complex/DNA interaction processes can therefore be proposed for the present {CpRu(mTPPMS)} complexes. In the first mechanism an easy ligand substitution at ruthenium would allow for the interaction with DNA, whereas in the second mechanism the interaction between the metal complex and the DNA molecule might occur through a ruthenium-coordinated mTPPMS moiety without ligand dissociation. These two possible processes could act either separately or cooperatively with or without

 © 2007 Wiley-VCH Verlag GmbH & Co. KGaA, Weinheim 

a synergic effect. In the chloride complex **1**, it is conceivable that chloride, most likely exchanged with a water molecule, could be substituted by a purine base, probably coordinated through the imidazole N7 atom, as has been proposed for the related ruthenium complexes $[RuCp(L)(L')X]^{n+}$ (X = Cl, I; L = $PPh_3$, L′ = PTA, mPTA; L = L′ = PTA, mPTA).[16b] This hypothesis is supported by the lower reactivity of the iodide **2**. This complex, however, is still more active than [RuCpI(L)(L′)] (L = $PPh_3$, L′ = PTA, mPTA; L = L′ = PTA, mPTA), which do not contain mTPPMS ligands.[16b] Complex **2** might therefore also interact with DNA through a mechanism that does not involve ligand substitution at ruthenium. The two proposed DNA interaction routes could take place cooperatively for complex **7**, which displays a DNA activity similar to **1**. Complex **7** contains three mTPPMS ligands bonded to the {CpRu} unit and one phosphane is labile enough to be partially replaced by iodide through mTPPMS dissociation/water coordination. As a matter of fact, an in situ $^{31}P$ NMR experiment in $D_2O$ at 40 °C shows the appearance, together with the singlet due to unchanged **7**, of additional resonances that could be assigned to aquo complexes formed from the starting complex by water substitution of the ligands originally bonded to the metal.

Complexes **3**–**6**, **8** and **9**, which contain phosphanes that are recalcitrant to substitution, display DNA activity that is much lower than **1**, **2** and **7**. This reduced DNA activity, however, is not a consequence of their lower water solubility. For example, $S(H_2O)_{25°C}$ for the biologically active complex **3** is 0.9 mg mL$^{-1}$ whereas that for the inactive species **4** is 10 mg mL$^{-1}$. A negative influence of both PTA and mPTA on the DNA activity of mTPPMS ruthenium complexes could be hypothesized if one considers the lack of activity shown by **4** (PTA) and **5** (mPTA) with respect to the highly active **3**. Nevertheless, it is not possible to rule out that traces of free mTPPMS could be produced by a small scale dissociation of the complex. Some of the DNA modification observed may therefore be a consequence of the direct interaction of free ligand with DNA; this dissociation could also lead to a direct Ru–DNA interaction. This effect is not likely to be very significant but may be responsible for the observed single-strand break, as observed for cisplatin.

## Conclusions

A large family of new water-soluble {CpRu(mTPPMS)} complexes, namely $Na_2[RuCp(mTPPMS)_2X]$ [X = Cl (**1**), I (**2**)] and $Na_x[RuCp(mTPPMS)(PR^1_3)(PR^2_3)](OTf)_y$ [$PR^1_3$ = $PR^2_3$ = $PPh_3$ (**3**), PTA (**4**), $x = y = 0$; $PR^1_3$ = mTPPMS, $PR^2_3$ = PTA (**5**), $x = 1$, $y = 0$; $PR^1_3$ = mTPPMS, $PR^2_3$ = mPTA (**6**), $x = y = 0$; $PR^1_3$ = $PR^2_3$ = mTPPMS (**7**), $x = 2$, $y = 0$; $PR^1_3$ = $PPh_3$, $PR^2_3$ = PTA (**8**), $x = y = 0$; $PR^1_3$ = mPTA, $PR^2_3$ = $PPh_3$ (**9**), $x = 0$, $y = 1$], that contain different combinations of water-soluble (PTA, mPTA, mTPPMS) or hydrophobic ($PPh_3$) phosphanes has been synthesized and characterized. Complex **8**·2$H_2O$, which has been characterized in the solid state by X-ray diffraction analysis, is the first example of an X-ray authenticated ruthenium complex bearing three different phosphane ligands.

DNA activity tests have shown that only complexes **1**, **2**, **3** and **7** actively destabilize the duplex SC DNA structure in the dark while the rest of the tris-phosphane complexes are inactive. The ligand mTPPMS itself shows DNA activity and control experiments have indicated that a direct conversion of the SC into the OC form takes place by DNA cleavage. These results suggest that ruthenium complexes containing mTPPMS might be active agents towards DNA by a *non-dissociative mechanism* that differs from the direct bonding to DNA. Two diverse mechanisms may therefore be proposed to explain the high DNA activity of mTPPMS–Ru complexes. Besides direct DNA interaction by ligand substitution at the metal, a second process may take place by interaction between the ruthenium-coordinated mTPPMS and DNA *without ligand dissociation*. Work is in progress to obtain more extensive and precise information about the effect of the water-soluble phosphane mTPPMS on the DNA activity of this class of water-soluble ruthenium complexes.

In light of these results it may be possible to design highly DNA-active water-soluble ruthenium complexes by the appropriate combination of water-soluble phosphanes and suitable organometallic platforms, including the potentially useful {CpRu} synthon. Studies in this direction are underway in our laboratory.

## Experimental Section

**General Procedures:** All chemicals were reagent grade and were used as received from commercial suppliers, unless otherwise stated. Solvents were distilled under nitrogen from the appropriate drying agent (sodium/benzophenone for thf, sodium for toluene) prior to use. Water was doubly distilled and deoxygenated before use. All reactions and manipulations were routinely performed under a dry nitrogen atmosphere by using standard Schlenk-tube techniques. The ligands PTA, mPTA($CF_3SO_3$), Na(mTPPMS) and the complexes $[RuCpCl(PPh_3)_2]$, $[RuCpCl(PPh_3)(PTA)]$ and $[RuCpCl(PPh_3)(mPTA)](CF_3SO_3)$ were prepared as described in the literature.[16,17,30] Deuterated solvents ($CD_3OD$, [D$_6$]DMSO and $CDCl_3$) for NMR measurements (Cortec-Euriso-top) were dried with molecular sieves (0.4 nm). $^1H$ and $^{13}C\{^1H\}$ NMR spectra were recorded with a Bruker DRX300 spectrometer operating at 300.13 ($^1H$) or 75.47 MHz ($^{13}C$). Peak positions are quoted relative to tetramethylsilane and were calibrated against the residual solvent resonance ($^1H$) or the deuterated solvent multiplet ($^{13}C$). $^{31}P\{^1H\}$ spectra was recorded on the same instrument operating at 121.49 MHz and chemical shifts are quoted relative to external 85% $H_3PO_4$ with downfield values taken as positive. IR spectra were recorded for KBr discs using an IR-ATI Mattson Infinity Series spectrophotometer. Elemental analyses (C,H,N,S) were performed with a Fisons Instruments EA 1108 elemental analyser.

**Synthesis of $Na_2[RuCpCl(mTPPMS)_2]$ (1):** The sodium salt of the ligand Na(mTPPMS) (1.00 g, 2.74 mmol) was slowly added to a rapidly stirring solution of $[RuCpCl(PPh_3)_2]$ (1.00 g, 1.37 mmol) in 30 mL of toluene. After two hours refluxing, the yellow powder which separated was filtered, washed with $Et_2O$ (2 × 3 mL) and vacuum dried. The resulting compound is hygroscopic and

 © 2007 Wiley-VCH Verlag GmbH & Co. KGaA, Weinheim 

was stored under inert atmosphere. Powder, yield 1.09 g (85%). $S(H_2O)_{25°C}$ = 41 mg mL$^{-1}$ ($4.41 \times 10^{-2}$ M). $C_{41}H_{33}ClNa_2O_6P_2RuS_2$ (930.29): calcd. C 52.94, H 3.58, S 6.89; found C 52.70, H 3.72, S 6.50. IR (KBr): $\tilde{\nu}$ = 1188 cm$^{-1}$ [s, br; $\nu(SO_3)$]. $^1$H NMR (20 °C, $CD_3OD$): $\delta$ = 4.21 (s, 5 H, Cp), 7.14–8.12 (m, 28 H, $PPh_3$) ppm. $^{13}C\{^1H\}$ NMR (20 °C, $CD_3OD$): $\delta$ = 81.21 (s, Cp), 126.24–144.00 (all singlets, aromatic) ppm. $^{31}P\{^1H\}$ NMR (20 °C, $CD_3OD$): $\delta$ = 40.09 (br. s) ppm.

**Synthesis of $Na_2$[RuCpI(mTPPMS)$_2$] (2):** $Na_2$[RuClCp(mTPPMS)$_2$] (**1**) (0.1 g, 0.11 mmol) in 5 mL of MeOH was added slowly, with stirring, to a solution of NaI (0.016 g, 0.11 mmol) in 5 mL of MeOH. The resulting yellow solution was stirred for a further hour at room temperature and then its volume reduced to 1 mL under vacuum. Addition of 5 mL of $Et_2O$ gave a pale-yellow precipitate, which was filtered, washed with $Et_2O$ (2 × 2 mL) and vacuum dried. Powder, yield 0.101 g (95%). $S(H_2O)_{25°C}$ = 15 mg mL$^{-1}$ ($1.47 \times 10^{-2}$ M). $C_{41}H_{33}INa_2O_6P_2RuS_2$ (1021.9): calcd. C 48.15, H 3.25, S 6.26; found C 47.70, H 3.72, S 5.82. IR (KBr): $\tilde{\nu}$ = 1186 cm$^{-1}$ [s, br; $\nu(SO_3)$]. $^1$H NMR (20 °C, $CD_3OD$): $\delta$ = 4.27 (s, 5 H, Cp), 7.15–8.04 (m, 28 H, $PPh_3$) ppm. $^{13}C\{^1H\}$ NMR (20 °C, $CD_3OD$): $\delta$ = 81.17 (s, Cp), 125.25–143.70 (all singlets, aromatic) ppm. $^{31}P\{^1H\}$ NMR (20 °C, $CD_3OD$): $\delta$ = 38.03 (br. s) ppm.

**Synthesis of [RuCp(mTPPMS)(PPh$_3$)$_2$] (3):** Solid [RuClCp($PPh_3$)$_2$] (0.10 g, 0.14 mmol) was added to a solution of $NaBF_4$ (0.015 g, 0.138 mmol) in 50 mL of MeOH whilst stirring. After 15 min, Na(mTPPMS) (0.052 g, 0.14 mmol) was added and the mixture was heated to reflux for 1 h. The resulting yellow solution was filtered through a plug of celite and the solvent completely removed to leave a yellow solid, which was dissolved in 5 mL of $CH_2Cl_2$. This solution was filtered through a sintered glass frit and concentrated to 0.5 mL. Addition of 10 mL of $Et_2O$ yielded a yellow precipitate, which was filtered, washed with $Et_2O$ (2 × 2 mL) and vacuum dried. Powder, yield 0.12 g (83%). $S(H_2O)_{25°C}$ = 0.9 mg mL$^{-1}$ ($8.7 \times 10^{-4}$ M). $C_{59}H_{48}O_3P_3RuS$ (1031.2): calcd. C 68.66, H 4.69, S 3.10; found C 68.22, H 4.82, S 2.75. IR (KBr): $\tilde{\nu}$ = 1196 cm$^{-1}$ $\nu(SO_3)$. $^1$H NMR (20 °C, $CD_3OD$): $\delta$ = 3.99 (s, 5 H, Cp), 6.98–8.08 (m, 44 H, $PPh_3$, mTPPMS) ppm. $^{13}C\{^1H\}$ NMR (20 °C, $CD_3OD$): $\delta$ = 81.04 (s, Cp), 125.98–138.05 (all singlets, aromatic) ppm. $^{31}P\{^1H\}$ NMR (20 °C, $CD_3OD$): $\delta$ = 39.58 (br. m, $PPh_3$, mTPPMS) ppm.

**Synthesis of [RuCp(mTPPMS)(PTA)$_2$] (4):** A solution of [RuClCp(PTA)$_2$] (0.10 g, 0.19 mmol) in MeOH (15 mL) was added to solid Na(mTPPMS) (0.07 g, 0.19 mmol) and the resulting suspension refluxed for 5 h. The white precipitate that separated out was filtered while hot, washed with MeOH (3 × 5 mL) and $Et_2O$ (2 × 5 mL), and vacuum dried. Powder, yield 0.090 g (57%). $S(H_2O)_{25°C}$ = 10 mg mL$^{-1}$ ($1.2 \times 10^{-2}$ M). $C_{35}H_{43}N_6O_3P_3RuS$ (822.14): calcd. C 51.09, H 5.27, N 10.22, S 3.89; found C 50.61, H 5.42, N 9.78, S 3.35. IR (KBr): $\tilde{\nu}$ = 1197 cm$^{-1}$ $\nu(SO_3)$. $^1$H NMR (20 °C, $D_2O$): $\delta$ = 3.65–3.81 [m, 12 H, $CH_2P_{(PTA)}$], 4.27–4.38 [m, 12 H, $CH_2N_{(PTA)}$], 5.00 (s, 5 H, Cp), 7.18–7.91 (m, 14 H, aromatic) ppm. $^{13}C\{^1H\}$ NMR (20 °C, $D_2O$): $\delta$ = 55.66 [br. s, $CH_2P_{(PTA)}$], 70.29 [s, $CH_2N_{(PTA)}$], 83.78 (s, Cp), 127–136 (all singlets, aromatic) ppm. $^{31}P\{^1H\}$ NMR (20 °C, $D_2O$): $\delta$ = –34.43 (d, $^2J_{PTA,mTPPMS}$ = 34.5 Hz, 2 P, PTA), 49.57 (t, $^2J_{mTPPMS,PTA}$ = 34.5 Hz, 1 P, mTPPMS) ppm.

**Synthesis of Na[RuCp(mTPPMS)$_2$(PTA)] (5):** [RuCpCl(mTPPMS)$_2$] (**1**; 0.10 g, 0.11 mmol) and $NaBF_4$ (0.012 g, 0.11 mmol) were dissolved in 10 mL of MeOH and stirred at room temperature for 30 min before PTA (0.017 g, 0.11 mmol) was added. The suspension was refluxed for 30 min and then cooled to room temperature. Removal of the solvent under vacuum left a yellowish solid, which was mixed with 5 mL of $CH_2Cl_2$ to give a yellow suspension which was filtered and evaporated to 1 mL. Addition of $Et_2O$ (2 mL) gave a pale-yellow precipitate which was collected by filtration, washed with 2 mL of $Et_2O$ and vacuum dried. Powder, yield 0.082 g (72%). $S(H_2O)_{25°C}$ = 2.5 mg mL$^{-1}$ ($2.4 \times 10^{-3}$ M). $C_{47}H_{45}N_3NaO_6P_3RuS_2$ (1029.1): calcd. C 54.81, H 4.41, N 4.08, S 6.21; found C 54.53, H 4.52, N 3.81, S 5.83. IR (KBr): $\tilde{\nu}$ = 1194 cm$^{-1}$ $\nu(SO_3)$. $^1$H NMR (20 °C, $D_2O$): $\delta$ = 4.57–4.67 [m, 6 H, $CH_2P_{(PTA)}$], 5.23–5.31 [m, 6 H, $CH_2N_{(PTA)}$], 4.73 (s, 5 H, Cp), 7.23–8.43 (m, 15 H, aromatic) ppm. $^1$H NMR (20 °C, $CD_3OD$): $\delta$ = 4.10–4.30 [m, 6 H, $CH_2P_{(PTA)}$], 4.81–4.82 [m, 6 H, $CH_2N_{(PTA)}$], 4.35 (s, 5 H, Cp), 6.80–8.20 (m, 28 H, aromatic) ppm. $^{13}C\{^1H\}$ NMR (20 °C, DMSO): $\delta$ = 54.14 [br. s, $CH_2P_{(PTA)}$], 73.30 [s, $CH_2N_{(PTA)}$], 76.83 (s, Cp), 126–138 (all singlets, aromatic) ppm. $^{31}P\{^1H\}$ NMR (20 °C, $D_2O$): $\delta$ = –44.54 (t, $^2J_{PTA,mTPPMS}$ = 39.9 Hz, 1 P, PTA), 42.22 (d, $^2J_{mTPPMS,PTA}$ = 39.9 Hz, 2 P, mTPPMS) ppm. $^{31}P\{^1H\}$ NMR (20 °C, $CD_3OD$): $\delta$ = –49.63 (t, $^2J_{PTA,mTPPMS}$ = 38.8 Hz, 1 P, PTA), 42.80 (d, $^2J_{mTPPMS,PTA}$ = 37.0 Hz, 2 P, mTPPMS) ppm.

**Synthesis of [RuCp(mPTA)(mTPPMS)$_2$] (6):** Complex **6** was prepared following the procedure described above for **5** but replacing PTA with mPTA($CF_3SO_3$) (0.04 g, 0.11 mmol). Powder, yield 0.104 g (95%). $S(H_2O)_{25°C}$ = 1.35 mg mL$^{-1}$ ($1.3 \times 10^{-3}$ M). $C_{48}H_{47}N_3O_6P_3RuS_2$ (1020.1): calcd. C 56.46, H 4.64, N 4.12, S 6.27; found C 56.30, H 4.72, N 3.84, S 6.02. IR (KBr): $\tilde{\nu}$ = 1196, 1218 cm$^{-1}$ $\nu(SO_3)$. $^1$H NMR (20 °C, [$D_6$]DMSO): $\delta$ = 2.81 [br. s, 3 H, $CH_3N_{(mPTA)}$], 4.17 [br. m, 6 H, $CH_2P_{(mPTA)}$], 5.10 [br. m, 6 H, $CH_2N_{(mPTA)}$], 4.91 (s, 5 H, Cp), 6.74–7.82 (m, 28 H, aromatic) ppm. $^{13}C\{^1H\}$ NMR (20 °C, [$D_6$]DMSO): $\delta$ = 48.72 [s, $CH_3N_{(mPTA)}$], 51.84 [br. s, $NCH_2P_{(mPTA)}$], 59.33 [br. s, $CH_3NCH_2P_{(mPTA)}$], 68.06 [s, $NCH_2N_{(mPTA)}$], 79.11 [s, $CH_3NCH_2P_{(mPTA)}$], 86.34 (s, Cp), 128.38–148.65 (all singlets, aromatic) ppm. $^{31}P\{^1H\}$ NMR (20 °C, [$D_6$]DMSO): $\delta$ = –29.33 (br. s, 1 P, mPTA), 39.96 (br. s, 1 P, mTPPMS), 46.29 (br. s, 1 P, mTPPMS) ppm.

**Synthesis of $Na_2$[RuCp(mTPPMS)$_3$] (7):** Complex **1** (0.10 g, 0.11 mmol) and $NaBF_4$ (0.012 g, 0.11 mmol) were dissolved in MeOH (10 mL). The mixture was stirred for 15 min and then solid Na(mTPPMS) (0.04 g, 0.11 mmol) was added. The solution was then refluxed for 30 min. During this time a white precipitate formed, and this was subsequently filtered off to afford a yellow solution. Evaporation of the solvent gave a yellow powder, which was dissolved in 5 mL of $CH_2Cl_2$ and the mixture filtered and concentrated to 0.5 mL. Addition of $Et_2O$ (10 mL) gave a pale-yellow precipitate, which was filtered, washed with $Et_2O$ (2 × 2 mL) and vacuum dried. Powder, yield 0.16 g (88%). $S(H_2O)_{25°C}$ = 20.0 mg mL$^{-1}$ ($1.6 \times 10^{-3}$ M). $C_{59}H_{47}Na_2O_9P_3RuS_3$ (1236.0): calcd. C 57.28, H 3.83, S 7.76, found C 57.02, H 4.01, S 7.45. IR (KBr): $\tilde{\nu}$ = 1193 cm$^{-1}$ [s br., $\nu(SO_3)$]. $^1$H NMR (20 °C, $D_2O$): $\delta$ = 3.96 (s, 5 H, Cp), 6.66–7.70 (m, 42 H, aromatic) ppm. $^{13}C\{^1H\}$ (20 °C, $D_2O$): $\delta$ = 76.45 (s, Cp), 123.05–134.56 (all singlets, aromatic) ppm; $^{31}P\{^1H\}$ NMR (20 °C, $D_2O$): $\delta$ = 40.68 (br. s, mTPPMS) ppm.

**Synthesis of [RuCp(mTPPMS)(PPh$_3$)(PTA)]·2H$_2$O (8·2H$_2$O):** A suspension of [RuClCp($PPh_3$)(PTA)] (0.17 g, 0.25 mmol) and Na(mTPPMS) (0.10 g, 0.27 mmol) in 20 mL of methanol was heated to reflux. The mixture slowly turned pale yellow and after 1 h it was cooled to 8 °C. The crystals that separated out were filtered and dried in air. Crystals, yield 0.203 g (84%). $S(H_2O)_{25°C}$ = 0.60 mg mL$^{-1}$ [$6.2 \times 10^{-4}$ M]. $C_{47}H_{45}N_3O_3P_3RuS{\cdot}2H_2O$ (962.165): calcd. C 58.62, H 5.13, N 4.37, S 3.32; found C 58.52, H 5.22, N 4.22, S 3.10. IR (KBr): $\tilde{\nu}$ = 1197 cm$^{-1}$ $\nu(SO_3)$. $^1$H NMR (20 °C, $CDCl_3$): $\delta$ = 3.78, 3.95 [AB system, $^2J_{H_AH_B}$ = 14.0 Hz, 6 H, $CH_2P_{(PTA)}$], 4.14, 4.23 [AB system, $^2J_{H_AH_B}$ = 12.6 Hz, 6 H, $CH_2N_{(PTA)}$], 4.86 (s, 5 H, Cp), 6.97–8.60 (m, 29 H, aromatic) ppm.

 © 2007 Wiley-VCH Verlag GmbH & Co. KGaA, Weinheim 

$^{13}C\{^1H\}$ NMR (20 °C, [D$_6$]DMSO): $\delta$ = 79.12 [d, $^1J_{C,P}$ = 33.0 Hz, $CP_{(PTA)}$], 79.78 [s, $CN_{(PTA)}$], 85.33 (s, Cp), 128.67–133.55 (all singlets, aromatic) ppm. $^{31}P\{^1H\}$ NMR (20 °C, $CDCl_3$): $\delta$ = –49.30 (dd, AXX′ system, $^2J_{PTA,mTPPMS}$ = 41.8, $^2J_{PTA,PPh_3}$ = 38.8 Hz, PTA), 41.56 (dd, AXX′ system, $^2J_{PPh_3,mTPPMS}$ = 32.0, $^2J_{PPh_3,PTA}$ = 38.8 Hz, $PPh_3$), 43.65 (dd, AXX′ system, $^2J_{mTPPMS,PPh_3}$ = 32.0, $^2J_{mTPPMS,PTA}$ = 41.8 Hz, mTPPMS) ppm.

**Synthesis of [RuCp(mTPPMS)(mPTA)(PPh$_3$)](CF$_3$SO$_3$) (9):** [RuClCp($PPh_3$)(mPTA)]($CF_3SO_3$) (0.18 g, 0.23 mmol) and Na(mTPPMS) (0.1 g, 0.27 mmol) were dissolved in MeOH (30 mL) and the mixture refluxed for 12 h. The resulting yellow suspension was filtered through sintered glass and the solvent evaporated to dryness under vacuum to leave a yellow solid, which was washed and triturated with $Et_2O$ (2 × 5 mL) before being dried under vacuum. Powder, yield 0.23 g (92%). $S(H_2O)_{25°C}$ = 0.60 mg mL$^{-1}$ (5.6 × 10$^{-4}$ M). $C_{49}H_{49}F_3N_3O_6P_3RuS_2$ (1091.1): calcd. C 53.89, H 4.53, N 3.85, S 5.86; found C 53.10, H 4.72, N 5.32, S 5.52. IR (KBr): $\tilde{\nu}$ = 1194 cm$^{-1}$ $\nu(SO_3)$. $^1H$ NMR (20 °C, $CD_3OD$): $\delta$ = 3.05 [s, 3 H, $CH_3N_{(mPTA)}$], 3.37–4.61 [m, 6 H, $CH_2P_{(mPTA)}$], 4.87–5.57 [m, 6 H, $CH_2N_{(mPTA)}$], 4.93 (s, 5 H, Cp), 6.58–7.55 (m, 29 H, aromatic) ppm. $^{13}C\{^1H\}$ NMR (20 °C, $CD_3OD$): $\delta$ = 51.24 [s, $CH_3N_{(mPTA)}$], 60.33 [br., $NCH_2P_{(mPTA)}$], 68.37 [br., $CH_3NCH_2P_{(mPTA)}$], 79.26 [s, $CH_3NCH_2N_{(mPTA)}$], 79.74 [s, $NCH_2N_{(mPTA)}$], 85.8 (s, Cp), 120.28 (q, $^1J_{C,F}$ = 320.4 Hz, $OSO_2CF_3$), 128.43–138.09 (all singlets, aromatic) ppm. $^{31}P\{^1H\}$ NMR (20 °C, $CD_3OD$): $\delta$ = –26.58 (br. t, $^2J_{mPTA,mTPPMS,PPh_3}$ = 37.9 Hz, mPTA), 40.48 (br. d, $^2J_{mTPPMS,PPh_3,mPTA}$ = 33.3 Hz, $PPh_3$, mTPPMS) ppm.

**Reactions of 3–9 with KI:** In a typical procedure, a solution of the appropriate ruthenium complex **3**–**9** (approx. 0.10 mmol) dissolved in 15 mL of MeOH was treated with a slight excess of KI (0.022 g, 0.13 mmol) and brought to reflux. After 5 h, the solution was cooled and the solvents evaporated to dryness. In all cases, except **7**, the $^{31}P\{^1H\}$ NMR spectra of the crude reaction mixture confirmed that no reaction had occurred. In the case of **7**, the product obtained was a mixture of the starting material **7** (85%) and **2** (15%), which likely forms by partial replacement of one mTPPMS in **7** with iodide.

**Reactions of 3–9 with CO:** In a typical procedure, a 5-mm NMR tube was charged with about 0.10 mmol of the appropriate solid ruthenium complex **1**–**9** and around 0.5 mL of $CDCl_3$ (or $CD_3OD$ for **1**, **2** and **7**). The resulting solution was then cooled to 0 °C and dry CO was slowly bubbled through it for 2 min. The $^{31}P\{^1H\}$ NMR spectra showed no change either after one day at room temperature or one day at 40 °C.

**Stability Tests for the Ruthenium Complexes 1–9 Towards D$_2$O and O$_2$:** In a standard procedure, a 5-mm NMR tube was charged in the air with 10 mg of the appropriate ruthenium complex **1**–**9** and $D_2O$ (1.0 mL). The solution was then cooled to about 0 °C and $O_2$ was slowly bubbled through it for 2 min through a long syringe needle and then kept at 40 °C. $^{31}P\{^1H\}$ NMR monitoring showed extensive decomposition within four days only for **1**, **3** and, partially, for **7**, as indicated by the disappearance of the NMR signals and by the appearance of singlet signals that could not assigned to any known complexes apart from free mTPPMS (see also Table 1).

**DNA Mobility Shift Assay:** pBluescript KSII plasmid (3Kbp, from Stratagene; 1 μg) was added to 20 μL of 10 mM phosphate buffer solution at pH 7.0 and diluted with the appropriate amount of a freshly prepared water solution of the ruthenium complex **1**–**9** to achieve the desired stoichiometry between the nucleobase and the ruthenium complex. The reaction mixtures were then incubated for 14 h at 37 °C in the dark and 10 μL sample-aliquots were withdrawn and analysed by electrophoresis in 1% agarose-TAE gels. DNA bands were visualised by staining with ethidium bromide and photographed under UV light. The Ri value (metal to base molar ratio at the onset of the incubation) at which complete transformation of the supercoiled to relaxed form of the plasmid was registered for each active compound.

**X-ray Analysis of 8·2H$_2$O:** Crystals suitable for an X-ray diffraction study were obtained directly from the reaction mixture used to synthesize **8**. The crystals obtained were filtered off and dried in air. Data were collected at 293 K on a Bruker APEX CCD diffractometer (XDIFRACT service of the University of Almeria) using graphite-monochromated Mo-$K_\alpha$ radiation ($\lambda$ = 0.71069 Å). The unit cell parameters were obtained from least-squares refinement of 3975 reflections (4.334° < $\theta$ < 36.673°). The data were corrected for Lorentz and polarization effects. Details of crystal data and relevant information are summarized in Table 2.

Table 2. Summary of crystal data for **8**·2H$_2$O.

| | |
|---|---|
| Formula | $C_{94}H_{88}N_6O_6P_6Ru_2S_2{\cdot}2H_2O$ |
| Molecular weight | 1885.82 |
| $T$ [K] | 293 |
| $\lambda$ [Å] (Mo-$K_\alpha$ radiation) | 0.71069 |
| Cryst. dimens [mm$^3$] | 0.180 × 0.115 × 0.085 |
| Cryst. syst. | monoclinic |
| Space group | $P2_1/c$ |
| $a$ [Å] | 28.508(2) |
| $b$ [Å] | 18.358(2) |
| $c$ [Å] | 18.424(2) |
| $\beta$ [°] | 93.433(2) |
| $V$ [Å$^3$] | 9624.9(16) |
| $Z$ | 4 |
| $\rho_{calcd}$ [g cm$^{-3}$] | 1.301 |
| Absorption coefficient [mm$^{-1}$] | 0.512 |
| $F$(000) | 3888 |
| $\theta$ range | 1.32–23.27 |
| Number of reflections | 42828 |
| Number of unique reflections | 8082 |
| $R$[a] (%) | 0.0691 |
| $R_w$[b] (%) | 0.2170 |
| Goodness of fit | 1.011 |

[a] $R = \Sigma||F_o| - |F_c||/\Sigma|F_o|$. [b] $R_w = [w\Sigma(|F_o| - |F_c|)^2/\Sigma wF_o^2)]^{1/2}$.

The structure was solved using the Sir97 program.[31] Final refinement and the graphical representation were performed with SHELX-TL.[32] Refinement was done by full-matrix least-squares calculations, initially with isotropic thermal parameters. All non-hydrogen atoms and water oxygen atoms were refined anisotropically, whereas hydrogen atoms were placed at calculated positions and then refined isotropically. All of the phenyl rings were treated as rigid bodies with $D_{6h}$ symmetry and C–C distances fixed at

Table 3. Selected bond lengths [Å] and angles [°] for **8**·2H$_2$O.

| | |
|---|---|
| Ru1–P1A | 2.324(3) |
| Ru1–P2A | 2.370(3) |
| Ru1–P3A | 2.363(3) |
| Ru2–P1B | 2.306(3) |
| Ru2–P2B | 2.354(3) |
| Ru2–P3B | 2.384(3) |
| P1A–Ru1–P3A | 95.12(10) |
| P1A–Ru1–P2A | 94.32(10) |
| P3A–Ru1–P2A | 101.78(10) |
| P1B–Ru2–P2B | 93.22(9) |
| P1B–Ru2–P3B | 97.46(9) |
| P2B–Ru2–P3B | 101.46(9) |

 © 2007 Wiley-VCH Verlag GmbH & Co. KGaA, Weinheim 

1.39 Å. No significant peaks were detected in the final least-squares cycles. Selected bond lengths and angles are listed in Table 3.

CCDC-600380 contains the supplementary crystallographic data for this paper. These data can be obtained free of charge from The Cambridge Crystallographic Data Centre via www.ccdc.cam.ac.uk/data_request/cif.

## Acknowledgments

The authors would like to thank the Junta de Andalucía (PAI and Consejería de la Presidencia; grant nos. FQM-317, AM 55/04 and AM 56/04). We are also grateful to the Ministerio de Ciencia y Tecnología (MCYT) (project CTQ2006-06552/BQU.MCRTN), the European Comission Research Directorate General Human Resources and Mobility (AQUACHEM project; MRTN-CT-2003-503864) and the European Cooperation in the Field of Science and Technology (COST) Actions D17 and D29. T. C.-M. thanks Ministerio de Asuntos Exteriores y de Cooperación - Agencia Española de Cooperación Internacional (MAE-AECI) for a predoctoral fellowship. Thanks also go to Centro Nazionale di Ricerca (CNR – Short Term Mobility Program 2006) for funding the visit of A. R. to ICCOM CNR.

[1] A. C. G. Hotze, B. M. Kariuki, M. J. Hannon, *Angew. Chem. Int. Ed.* **2006**, *45*, 4839–4842.
[2] A. C. G. Hotze, E. P. L. van der Geer, S. E. Caspers, H. Kooijman, A. L. Spek, J. G. Haasnoot, J. Reedijk, *Inorg. Chem.* **2004**, *43*, 4935–4943.
[3] A. H. Velders, H. Kooijman, A. L. Spek, J. G. Haasnoot, D. de Vos, J. Reedijk, *Inorg. Chem.* **2000**, *39*, 2966–2967.
[4] M. J. Clarke, *Coord. Chem. Rev.* **2002**, *232*, 69–93.
[5] W. H. Ang, P. Dyson, *Eur. J. Inorg. Chem.* **2006**, 4003–4018.
[6] F. Frausin, V. Scarcia, M. Cocchietto, A. Furlani, B. Serli, E. Alessio, G. Sava, *J. Pharm. Exp. Therap.* **2005**, *313*, 227–233.
[7] A. F. A. Peacock, A. Habtemariam, R. Fernandez, V. Walland, F. P. A. Fabbiani, S. Parsons, R. E. Aird, D. I. Jodrell, P. J. Sadler, *J. Am. Chem. Soc.* **2006**, *128*, 1739–1748.
[8] Y. K. Yan, M. Melchart, A. Habtemariam, P. J. Sadler, *Chem. Commun.* **2005**, 4764–4776.
[9] H. M. Chen, J. A. Parkinson, S. Parsons, R. A. Coxall, R. O. Gould, P. J. Sadler, *J. Am. Chem. Soc.* **2002**, *124*, 3064–3082.
[10] F. Y. Wang, H. M. Chen, J. A. Parkinson, P. D. Murdoch, P. J. Sadler, *Inorg. Chem.* **2002**, *41*, 4509–4523.
[11] G. Sava, R. Gagliardi, A. Bergamo, E. Alessio, G. Mestroni, *Anticancer Res.* **1999**, *19*, 969–972.
[12] B. Serli, E. Zangrando, T. Gianfeffara, L. Yellowlees, E. Alessio, *Coord. Chem. Rev.* **2003**, *245*, 73–83.
[13] A. Dorcier, W. H. Ang, S. Bolaño, L. Gonsalvi, L. Juillerat-Jeannerat, G. Laurenczy, M. Peruzzini, A. D. Phillips, F. Zanobini, P. J. Dyson, *Organometallics* **2006**, *25*, 4090–4096.
[14] A. Dorcier, P. J. Dyson, C. Gossens, U. Rothlisberger, R. Scopelliti, I. Tavernelli, *Organometallics* **2005**, *24*, 2114–2123.
[15] a) S. M. Guichard, R. Else, E. Reid, B. Zeitlin, R. Aird, M. Muir, M. Dodds, H. Fiebig, P. J. Sadler, D. I. Jodrell, *Biochem. Pharmacol.* **2006**, *71*, 408–415; b) F. Y. Wang, J. J. Xu, A. Habtemariam, J. Bella, P. J. Sadler, *J. Am. Chem. Soc.* **2005**, *127*, 17734–17743.
[16] a) D. N. Akbayeva, L. Gonsalvi, W. Oberhauser, M. Peruzzini, F. Vizza, P. Brüggeller, A. Romerosa, G. Sava, A. Bergamo, *Chem. Commun.* **2003**, 264–265; b) A. Romerosa, T. Campos-Malpartida, C. Lidrissi, M. Saoud, M. Serrano-Ruiz, M. Peruzzini, J. A. Garrido-Cardenas, F. Garcia-Maroto, *Inorg. Chem.* **2006**, *45*, 1289–1298.
[17] *Aqueous-Phase Organometallic Catalysis*, 2nd ed. (Eds.: B. Cornils, W. A. Herrmann), Wiley-VCH Verlag, Weinheim, Germany, **2004**.
[18] M. Saoud, M. Peruzzini, A. Romerosa, *Organometallics* **2000**, *19*, 4005–4007.
[19] T. Suarez, B. Fontal, M. Reyes, F. Bellandi, R. Contreras, G. Leon, P. Cancines, *React. Kinet. Catal. Lett.* **2002**, *76*, 161–169.
[20] M. Di Vaira, P. Frediani, S. Seniori Costantini, M. Peruzzini, P. Stoppioni, *Dalton Trans.* **2005**, 2234–2236.
[21] The presence of $NaBF_4$ in the reaction medium is not essential but improves the product yield and favours its separation, thereby avoiding further purification steps.
[22] A. D. Phillips, L. Gonsalvi, A. Romerosa, F. Vizza, M. Peruzzini, *Coord. Chem. Rev.* **2004**, *248*, 955–993.
[23] H. Brunner, C. Valerio, M. Zabel, *New J. Chem.* **2000**, *24*, 275–279.
[24] B. J. Frost, C. A. Mebi, *Organometallics* **2004**, *23*, 5317–5323.
[25] S. Bolaño, L. Gonsalvi, F. Zanobini, F. Vizza, V. Bertolasi, A. Romerosa, M. Peruzzini, *J. Mol. Catal. A* **2004**, *224*, 61–70.
[26] T. N. Singh, C. Turro, *Inorg. Chem.* **2004**, *43*, 7260–7262.
[27] K. van der Schilden, F. Garcia, H. Kooijman, A. L. Spek, J. G. Haasnoot, J. Reedijk, *Angew. Chem. Int. Ed.* **2004**, *43*, 5668–5670.
[28] P. K. L. Fu, P. M. Bradley, D. van Loyen, H. Durr, S. H. Bossmann, C. Turro, *Inorg. Chem.* **2002**, *41*, 3808–3810.
[29] M. J. Clarke, F. C. Zhu, D. R. Frasca, *Chem. Rev.* **1999**, *99*, 2511–2533.
[30] F. Joo, J. Kovacs, A. Katho, A. C. Benyei, T. Decuir, D. J. Darensbourg, *Inorg. Synth.* **1998**, *32*, 1–45.
[31] A. Altomare, G. Cascaramo, C. Giacovazzo, A. Guagliardi, M. C. Burla, G. Polidori, M. Camalli, *J. Appl. Crystallogr.* **1994**, *27*, 435–439.
[32] G. M. Sheldrick, *SHELXTL* version 6.14; Bruker-AXS; Madison, WI **2003**.

Received: December 12, 2006
Published Online: May 3, 2007

 © 2007 Wiley-VCH Verlag GmbH & Co. KGaA, Weinheim 

DOI: 10.1002/ejic.200700021

# Solvent Control in the Protonation of [Cp*Mo(dppe)$H_3$] by $CF_3COOH$

**Pavel A. Dub,[a,b] Miguel Baya,[a] Jennifer Houghton,[a] Natalia V. Belkova,[b] Jean-Claude Daran,[a] Rinaldo Poli,*[a] Lina M. Epstein,[b] and Elena S. Shubina*[b]**

**Keywords:** Molybdenum / Hydrido ligand / Trifluoroacetato ligand / Proton transfer / Dihydrogen bonding

The outcome of the reaction between [Cp*Mo(dppe)$H_3$] [dppe = 1,2-bis(diphenylphosphanyl)ethane] and trifluoroacetic acid (TFA) is highly dependent on the solvent and the TFA/Mo ratio. The dihydride compound [Cp*Mo(dppe)$H_2$($O_2CCF_3$)] is obtained selectively when the reaction is carried out in aromatic hydrocarbons (benzene, toluene) when using less than one equivalent of TFA. The dihydride is also the end product when THF or MeCN are used as solvent, independent of the TFA/Mo ratio. In benzene/toluene the use of excess acid has a profound effect, resulting in the formation of the tetrahydrido complex [Cp*Mo(dppe)$H_4$]$^+$, which did not further evolve into the dihydrido product. Monitoring of the reaction by NMR and IR spectroscopy under different conditions (solvent, temperature, TFA/Mo ratio) reveals the rapid establishment of an equilibrium between the dihydrogen-bonded adduct, [Cp*Mo(dppe)$H_3$]···$HO_2CCF_3$, the ion-paired proton-transfer product, [Cp*Mo(dppe)$H_4$]$^+$···$^-O_2CCF_3$, and the separated ions, followed by a slower irreversible transformation to the final dihydride product with $H_2$ evolution. The activation parameters of the $H_2$ evolution and M–OR product formation were determined. Excess TFA in low-polarity solvents stabilizes the separated charged species by forming the homoconjugate anion [$CF_3COO(CF_3COOH)_n$]$^-$. The effect of the solvent on the course of the reaction can be interpreted in terms of the different polarity, H-bonding ability, and coordinating power of the various solvent molecules.

(© Wiley-VCH Verlag GmbH & Co. KGaA, 69451 Weinheim, Germany, 2007)

## Introduction

It is now well established that a common proton-transfer pathway from a proton donor HX to a transition-metal hydride complex involves the initial attack of HX on the hydride ligand with formation of a dihydrogen-bonded adduct, MH···HX, followed by proton transfer and production of a nonclassical dihydride (dihydrogen complex) product, M($\eta^2$-$H_2$)$^+$. The establishment of a hydrogen-bonded ion pair between the nonclassical cation and its counteranion increases the stability of the M($\eta^2$-$H_2$)$^+$ complex and retards its transformation into a classical polyhydride or organyloxo (X = OR) species (Scheme 1).[1]

The formation of M($\eta^2$-$H_2$)$^+$···$X^-$ ion pairs (**III**, $X^-$ = $CF_3COO^-$, $ArO^-$, $R^FO^-$), stabilized by hydrogen bonds between the dihydrogen ligand and counteranions, was detected for [CpRuH(CO)($PCy_3$)],[2,3] $PP_3MH_2$ {$PP_3$ = $P(CH_2CH_2PPh_2)_3$},[4] and [Cp*MH(dppe)] (M = Fe,[5] Ru[6]) complexes by IR and UV/Vis spectroscopy. The ion-pair stability increases with the proton-accepting ability of the anion.[3]

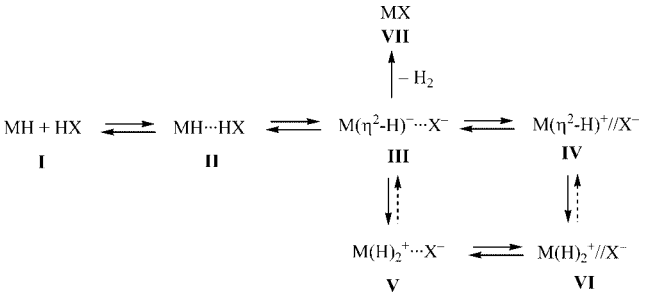


Scheme 1.

Proton transfer may also be assisted by a second molecule of the proton donor HX, depending on the acid strength. In this case, the conjugate base $X^-$ in species **III**–**VI** may be present in the form of the homoconjugate anion, $XHX^-$. We have recently shown that the irreversible isomerization of [Cp*M($\eta^2$-$H_2$)(dppe)]$^+$ complexes (M = Fe,[5] Ru[6]) into classical *trans*-dihydride species occurs upon dissociation of the M($\eta^2$-$H_2$)$^+$···$XHX^-$ ion pair (i.e., **III** to **IV**). This is indicated by the difference in temperature at which the M($\eta^2$-$H_2$)$^+$ → M$(H)_2^+$ isomerization process can occur depending on the counteranion; higher temperatures are necessary to induce isomerization in the presence of more basic anions (greater ion-pair stability). Additionally,

[a] Laboratoire de Chimie de Coordination, UPR CNRS 8241 liée par convention à l'Université Paul Sabatier et à l'Institut National Polytechnique de Toulouse,
205 Route de Narbonne, 31077 Toulouse Cedex, France
Fax: +33-561553003
E-mail: poli@lcc-toulouse.fr
[b] Nesmeyanov Institute of Organoelement Compounds, Russian Academy of Sciences,
Vavilov Street 28, 119991 Moscow, Russia
Supporting information for this article is available on the WWW under http://www.eurjic.org or from the author.

 © 2007 Wiley-VCH Verlag GmbH & Co. KGaA, Weinheim 

the isomerization rate constant does not depend on the anion nature.[7,8] In some cases, the nonclassical to classical rearrangement (**III** to **V**, or **IV** to **VI**) is a reversible process.[9]

In many cases, however, basic anions ($X^-$ = $RO^-$, $RCOO^-$) tend to displace $H_2$ from the transition-metal coordination sphere, yielding organyloxo products (i.e., **VII**). This is the case for the protonation of [(triphos)ReH$(CO)_2$],[10] [$Re(CO)H_2(NO)(PR_3)_2$],[11] and the previously mentioned [CpRuH(CO)$(PCy_3)$],[2] for which corresponding $M(\eta^2\text{-}H_2)^+X^-$ complexes could be isolated as $BF_4^-$ salts. These evolved into MX species in the presence of fluorinated alcohols or carboxylic acids. This reaction proceeds intramolecularly without the hydrogen-bonded ion-pair dissociation.[2] Most of the M–OR complexes were only characterized in solution; two examples of isolated compounds are [$ReH(OC_6H_4NO_2)(CO)(NO)(PMe_3)_2$][11] and [(triphos)$Re(CO)_2(OCOCH_2Cl)$].[10] In addition to the counteranion nature, temperature and solvent polarity could be used to control the stability of the $M(\eta^2\text{-}H_2)^+$ species and the proton-transfer equilibrium position. For example, the substantial increase in the dielectric constant of the Freon mixture ($CDCl_2F/CDF_3$, 2:1) at low temperatures was reported to assist the proton transfer to [Cp*$RuH_3(PCy_3)$], yielding [Cp*$Ru(H)_2(\eta^2\text{-}H_2)(PCy_3)]^+$-$OR^-$.[12] However, the influence of the medium on the $H_2$ release process was not studied in detail.

In contrast to all of the described systems, the protonation of the trihydridomolybdenum complex [Cp*Mo(dppe)$H_3$] gave, via the intermediate formation of a dihydrogen-bonded complex, the cationic classical tetrahydride complex [Cp*Mo(dppe)$H_4]^+$ (**V/VI**), without the detection of a nonclassical isomer, [Cp*Mo(dppe)$(\eta^2\text{-}H_2)$-$H_2]^+$ (**III/IV**). Theoretical calculations, however, located the latter complex on the proton-transfer potential energy surface, with a very low energy barrier for the intramolecular rearrangement.[13] Facile access to a nonclassical isomer is evidenced by the evolution of $H_2$ from [Cp*Mo(dppe)$H_4]^+$ at ambiet temperature. We now report new results on the protonation of [Cp*Mo(dppe)$H_3$] using trifluoroacetic acid (TFA) in various solvents of different coordinating (in particular H-bonding) ability and polarity: benzene, toluene, THF, $CH_2Cl_2$, and MeCN. These reactions led to the formation of a new hydride product with a coordinated trifluoroacetate anion. We will show how subtle changes in the protonation medium may drastically affect the reactivity of [Cp*Mo(dppe)$H_3$] and the stability of its protonation product.

## Results

Since the results of previous investigations into the protonation of [Cp*Mo(dppe)$H_3$][13–15] serve as a basis for the new findings described in this paper, we summarize here the salient points that emerge from those studies. (i) The trihydride complex has a high basicity factor ($E_j$ = $1.42 \pm 0.02$), placing it in the category of the most hydridic complexes known. (ii) As mentioned in the Introduction, the interaction with $HBF_4$ in noncoordinating or weakly coordinating solvents (diethyl ether, THF) leads directly to the tetrahydride complex [Cp*Mo(dppe)$H_4]^+$, without the detection of a nonclassical intermediate, although its presence is suggested by the theoretical calculations. (iii) [Cp*Mo(dppe)$H_4]^+BF_4^-$ is unstable and rapidly loses dihydrogen; in MeCN, this process leads to the formation of the solvent-stabilized complex [Cp*Mo(dppe)$H_2$(MeCN)]$^+$. (iv) The interaction with weaker proton donors [the fluorinated alcohols $CH_2FCH_2OH$, $CF_3CH_2OH$, and $(CF_3)_2CHOH$] in low-polarity solvents (e.g., THF, $CH_2Cl_2$) at low temperatures leads to the observation of intermediate hydrogen-bonded adducts. Infrared spectral analysis, in combination with theoretical calculations, indicates that one of the hydride ligands of [Cp*Mo(dppe)$H_3$] takes part in hydrogen bonding. (v) Proton transfer from the dihydrogen-bonded adduct yields, without the observable intervention of a second HA molecule in the rate-determining step, the tetrahydride product as a 1:1 ion-pair stabilized by a hydrogen bond between the cation and the anion, [Cp*Mo(dppe)-$H_4]^+\cdots A^-$, as established for HA = *p*-nitrophenol and $CF_3CH_2OH$. The proton-transfer reaction is equilibrated for these weaker proton donors. (vi) On a longer timescale,

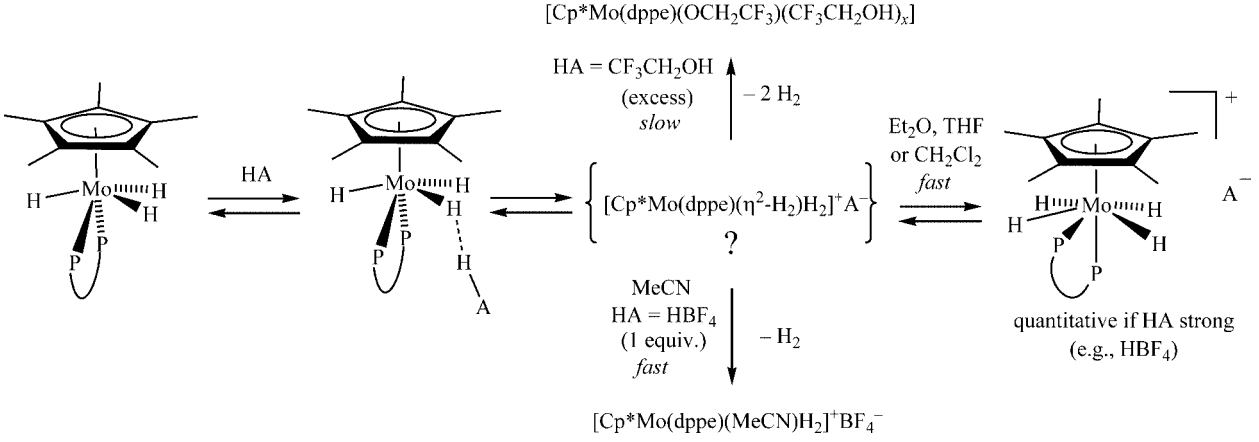


Scheme 2.

 © 2007 Wiley-VCH Verlag GmbH & Co. KGaA, Weinheim 

the tetrahydride product $[Cp^*Mo(dppe)H_4]^+$, obtained using HA = $CF_3CH_2OH$, evolves at ambient temperature by release of two $H_2$ molecules to form the hydride-free product $[Cp^*Mo(dppe)(OCH_2CF_3)]$, probably stabilized by coordination of a second alcohol molecule, $[Cp^*Mo(dppe)(OCH_2CF_3)(CF_3CH_2OH)]$. These observations are summarized in Scheme 2.

### Protonation in Benzene/Toluene: Formation of Compound $[Cp^*Mo(dppe)H_2(O_2CCF_3)]$

The room-temperature reaction between $[Cp^*Mo(dppe)H_3]$ and *strictly* 1 equiv. TFA in toluene led selectively to a new dihydride complex, $[Cp^*Mo(dppe)H_2(O_2CCF_3)]$, as seen in Equation (1). The parallel formation of free $H_2$ was confirmed by $^1H$ NMR spectroscopic monitoring (characteristic resonance at $\delta$ = 4.58 ppm). The new hydride compound was isolated and fully characterized. It is quite stable in aromatic solvents, decomposing very slowly with generation of free dppe (identified by its $^{31}P$ resonance at –12.9 ppm) and other unidentified products that do not contain hydride ligands. Ca. 13% of the product decomposed after 22 hours at room temperature.

$$[Cp^*Mo(dppe)H_3] + TFA \rightarrow [Cp^*Mo(dppe)H_2(O_2CCF_3)] + H_2 \quad (1)$$

The compound is characterized by a hydride resonance centered at –5.09 ppm, with a relative intensity corresponding to two protons, only slightly displaced relative to the hydride resonance of $[Cp^*Mo(dppe)H_3]$ at –5.16 ppm. The $^{31}P\{^1H\}$ NMR spectrum shows a resonance at 76.9 ppm, which becomes a triplet when selectively decoupled from the dppe proton resonance, confirming the presence of two hydride ligands. The shape of the hydride resonance suggests the occurrence of a dynamic process. A variable-temperature NMR investigation gave further information about this process and also provided longitudinal relaxation times for the hydride resonances. The shape of the $^1H$ resonances in the hydride region as a function of temperature is shown in Figure 1 (a). Cooling resulted in broadening and eventual decoalescence (225 K), yielding two broad resonances in a 1:1 ratio at –4.19 and –6.24 ppm. The more upfield resonance starts to resolve into a doublet at the lowest temperature, indicating coupling ($J \approx 72$ Hz) to another $I$ = 1/2 nucleus, probably one of the two phosphorus donor atoms that therefore appear to be inequivalent. This inequivalence was demonstrated by the variable-temperature $^{31}P\{^1H\}$ NMR investigation (see part b of Figure 1); decoalescence was observed at $T < 233$ K to yield two resonances in an approximate ratio of 1:1. No P–P coupling can be discerned from the spectra. The $^{31}P$ NMR data were used in a lineshape analysis, from which the activation parameters of $\Delta H^{\ddagger} = (6.4 \pm 0.4)$ kcal mol$^{-1}$ and $\Delta S^{\ddagger} = (10 \pm 2)$ cal K$^{-1}$ mol$^{-1}$ were calculated using an Eyring analysis (see electronic Supporting Information). The lineshape analysis of the $^1H$ resonance was complicated by the lack of knowledge of $J_{HP}$ data due to broadness in the low-temperature spectra, but a simulation using the rate constant obtained from the $^{31}P$ NMR spectrum and a reasonable guess for the $J_{HP}$ values gave a reasonable fit above coalescence, suggesting that the same mechanism is responsible for both H and P exchange processes. A possibility for this mechanism is illustrated in Scheme 3. The $T_1$ value for the hydride resonance remains rather high throughout the temperature range (see Supporting Information), characteristic of a classical dihydride, with a minimum of 510 ms before decoalescence. For comparison, the $T_{1min}$ of complex $[Cp^*Mo(dppe)H_4]^+$ is 174 ms for the $BF_4^-$ salt and 191 ms when obtained by proton transfer from TFE (these measurements were carried out at 400 MHz).[13]

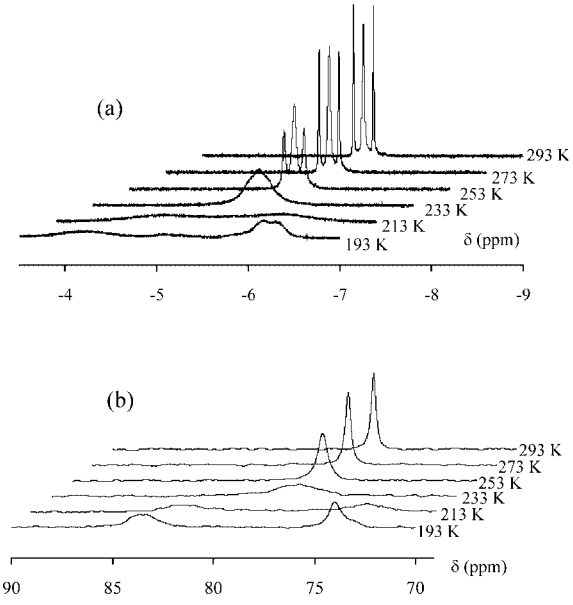


Figure 1. Variable-temperature spectra for compound $[Cp^*Mo(dppe)H_2(O_2CCF_3)]$ in $C_6D_5CD_3$: (a) $^1H$ NMR (500 MHz); (b) $^{31}P\{^1H\}$ NMR (202 MHz).

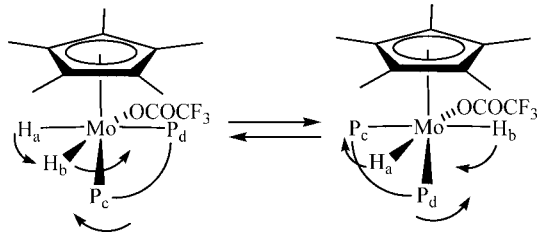


Scheme 3.

The chemical composition of the product was confirmed by single-crystal X-ray analysis. The coordination geometry, shown in Figure 2, corresponds to a rather severely distorted octahedron if the Cp* ligand is considered to occupy a single coordination position at the ring centroid. This distortion is caused by steric repulsion between the Cp* and dppe ligands and by the small size of the two hydride ligands, which force the pseudoaxial (*trans* to the Cp* ligand) phosphorus donor to move up into the wedge of the two Mo–H bonds. The CNT–Mo1–P1 angle [122.648(13)°] is greater than the CNT–Mo1–O1, CNT–Mo1–H1, and

 © 2007 Wiley-VCH Verlag GmbH & Co. KGaA, Weinheim 

CNT–Mo1–H2 angles [119.74(4)°, 98.5(10)°, and 96.9(9)°, respectively], whereas the CNT–Mo1–P2 angle [144.369(14)°] is much smaller than 180°. A similar distortion was observed in the structure of the related $[Cp^*Mo(dppe)H(MeCN)_2]^{2+}$ complex.[14] The other notable feature is the monodentate coordination of the trifluoroacetate ligand, which occupies a pseudoequatorial position *cis* to the P1 and H1 donors and *trans* to H2. The Mo1–O1 bond length [2.2008(15) Å] is unexpectedly longer than those found in other Mo monodentate carboxylate derivatives in the same or lower oxidation state, for example, 2.167(4) Å found in $[Cp^*Mo^{II}(CO)(PMe_3)_2(O_2CMe)]$,[16] 2.102(3) and 2.092(3) Å found in $[CpMo^{III}(\eta^4\text{-}C_4H_6)(O_2CCF_3)_2]$,[17] and 2.113(4) and 2.102(4) Å found in $[Cp_2Mo^{IV}(O_2CPh)_2]$.[18] Another interesting feature is the similar C8–O1 [1.249(3) Å] and C8–O2 [1.221(3) Å] distances (bond difference Δ = 0.028 Å). These are not quite as long or short, respectively, as expected for localized single and double bonds. For instance, the recently determined structure of $Ph_3CCH_2COOH$ shows clearly defined C–O [1.304(3) Å] and C=O [1.203(3) Å] bonds (Δ = 0.101 Å) with no obvious sign of hydrogen atom disorder.[19] The monodentate carboxylate C–O distances in the mentioned examples show larger differences between C=O and C–O bond lengths, although not quite as large as those found in free carboxylic acids, namely 1.277(8) Å compared with 1.212(8) Å (Δ = 0.065 Å) for $[Cp^*Mo^{II}(CO)(PMe_3)_2(O_2CMe)]$,[16] 1.276(5) and 1.255(5) Å compared with 1.200(5) and 1.192(6) Å (Δ = 0.076 and 0.063 Å, respectively) for $[CpMo^{III}(\eta^4\text{-}C_4H_6)(O_2CCF_3)_2]$,[17] and 1.281(8) and 1.300(8) Å compared with 1.208(8) and 1.210(8) Å (Δ = 0.073 and 0.090 Å, respectively) for $[Cp_2Mo^{IV}(O_2CPh)_2]$.[18] This combined evidence indicates a significant ionic contribution to the bond between the Mo center and the monodentate anion, which then continues to promote some electronic delocalization between the two C–O bonds. Other relevant structural parameters are listed in Table 1.

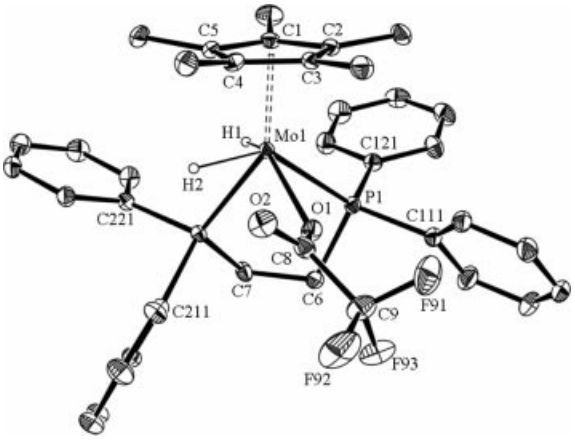


Figure 2. ORTEP view of compound $[Cp^*Mo(dppe)H_2(OCOCF_3)]$. Hydrogen atoms, except for the two hydride ligands, are omitted for clarity. The thermal ellipsoids are drawn at the 30% probability level.

Table 1. Selected bond lengths [Å] and angles [°] for compound $[Cp^*Mo(dppe)H_2(OCOCF_3)]$.

| | | | |
|---|---|---|---|
| Mo1–CNT | 1.96462(17) | Mo1–O1 | 2.2008(15) |
| Mo1–P1 | 2.5206(5) | Mo1–P2 | 2.3962(5) |
| Mo1–H1 | 1.60(3) | Mo1–H2 | 1.65(3) |
| P1–C111 | 1.833(2) | P2–C211 | 1.8459(19) |
| P1–C121 | 1.834(2) | P2–C221 | 1.828(2) |
| P1–C6 | 1.844(2) | P2–C7 | 1.849(2) |
| C6–C7 | 1.526(3) | C8–C9 | 1.547(3) |
| C8–O1 | 1.249(3) | C8–O2 | 1.221(3) |
| CNT–Mo1–O1 | 119.74(4) | | |
| P2–Mo1–P1 | 81.360(17) | H2–Mo1–H1 | 105.6(14) |
| CNT–Mo1–P1 | 122.648(13) | CNT–Mo1–P2 | 144.369(14) |
| O1–Mo1–P1 | 76.82(4) | O1–Mo1–P2 | 89.40(4) |
| CNT–Mo1–H1 | 98.5(10) | CNT–Mo1–H2 | 96.9(9) |
| O1–Mo1–H1 | 139.8(10) | O1–Mo1–H2 | 83.0(10) |
| P2–Mo1–H1 | 61.6(10) | P2–Mo1–H2 | 64.6(9) |
| P1–Mo1–H1 | 72.0(11) | P1–Mo1–H2 | 140.5(9) |

Compound $[Cp^*Mo(dppe)H_2(OCOCF_3)]$ exhibits two intense overlapping $\nu^{as}_{OCO}$ bands in the IR spectrum; the frequencies and relative intensities of which are solvent dependent (see Table 2). As the solvent polarity increases, $A_{low}/A_{high}$ decreases and $\Delta\nu = (\nu_{high} - \nu_{low})$ increases. The same behavior was observed previously for $[CpM(CO)_2(OCOR)]$ complexes (M = Fe, Ru)[20] and was explained by the presence of a Fermi resonance between the fundamental $\nu^{as}_{OCO}$ stretching vibration and an overtone or combination band of very close frequency. The larger intensity ratio observed in $CH_2Cl_2$ could be explained by the different nature of the solute–solvent interaction, since this solvent could act as a proton donor and form hydrogen bonds with the carboxyl group coordinated to the metal.

Table 2. Characteristics of the $\nu^{as}_{OCO}$ band of $[Cp^*Mo(dppe)H_2(OCOCF_3)]$ in the solid state and in solution.

| Solvent | $\nu^{as}_{OCO}$ /cm$^{-1}$ | Δν | Intensity ratio ($A_{low}/A_{high}$) |
|---|---|---|---|
| Solid (KBr) | 1700 sh, 1685 s | 15 | 1.8 |
| $C_6H_6$ | 1700 sh, 1690 | 10 | 1.2 |
| $C_6D_5CD_3$ | 1700 sh, 1690 | 10 | 1.1 |
| THF | 1702, 1690 | 12 | 1.0 |
| $CH_2Cl_2$ | 1706 sh, 1688 | 18 | 2.2 |

### Protonation in Benzene/Toluene: Evolution with Time

The $^1$H NMR spectroscopic monitoring of the $[Cp^*Mo(dppe)H_3]$–TFA reaction in $C_6D_6$ at different TFA/Mo ratios at room temperature was most enlightening. Figure 3 (a) shows the spectrum of the starting material before TFA addition.[21]

When using a 10-fold excess of TFA, the tetrahydrido complex $[Cp^*Mo(dppe)H_4]^+$ was the only observed product, see Figure 3 (b). This is characterized by a hydride triplet resonance at –3.57 ppm ($J_{HP}$ = 37.9 Hz) in the $^1$H NMR spectrum and by a $^{31}$P resonance at 72.3 ppm in $C_6D_6$, quite close to the values previously reported for the $BF_4^-$ salt in $CDFCl_2$ at –60 °C.[14] In agreement with the literature, decomposition takes place at room temperature (90% after

 © 2007 Wiley-VCH Verlag GmbH & Co. KGaA, Weinheim 

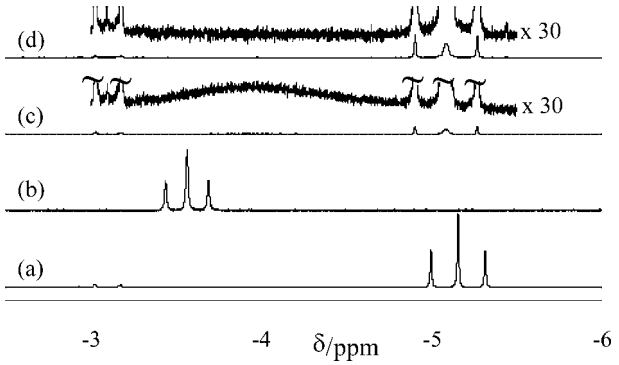


Figure 3. $^1$H NMR (300 MHz) spectroscopic monitoring of the reaction between [Cp*Mo(dppe)$H_3$] and TFA in $C_6D_6$ (290 K): (a) starting material before the TFA addition; (b) immediately after the TFA addition (10 equiv.); (c) immediately after the TFA addition (1 equiv.); (d) after 3.5 h from spectrum (c).

ca. 25 minutes), without yielding any hydride-containing product. This decomposition was not investigated in any further detail.

For the 1:1 reaction, a broad resonance was initially present in the hydride region at an intermediate position between those of the trihydride and tetrahydride complexes, in addition to the final product resonance (Figure 3, c). The position and shape of the broad resonance depends on the TFA/Mo ratio and on the temperature (vide infra). The $^{31}$P{$^1$H} NMR spectrum at room temperature exhibits two small and broadened resonances at the characteristic positions of the trihydride complex ($\delta$ = 91.4 ppm) and the tetrahydride protonation product ($\delta$ = 72.3 ppm),[22] in addition to the sharp resonance of the [Cp*Mo(dppe)$H_2$($O_2CCF_3$)] product at 76.9 ppm and a minor contaminant resonance.[21] This suggests that the broad $^1$H resonance results from a rapid degenerate exchange between the starting complex [Cp*Mo(dppe)$H_3$], which is not completely consumed, and its protonation product, [Cp*Mo(dppe)$H_4$]$^+$. This exchange will be addressed in further detail in the next section. Given the larger chemical shift difference between the $^{31}$P resonances, the shape of the $^{31}$P NMR spectrum is much closer to the slow exchange limit than that of the $^1$H NMR spectrum. After a few hours at room temperature (or upon brief warming to ca. 40 °C), the broad band disappears and the resonance corresponding to [Cp*Mo(dppe)$H_2$($OCOCF_3$)] increases in intensity (Figure 3, d). These observations reveal the presence of an equilibrium between the tetrahydride complex and the starting trihydride complex, followed by a slow irreversible conversion to the final product by $H_2$ loss.

A variable-temperature study of the reaction mixture in $C_6D_5CD_3$, carried out immediately after mixing the reagents in a 1:1 ratio, confirmed the earlier assignments. The hydride resonance of the dihydride product evolved as discussed previously (Figure 1, a), whereas the broad resonance at –3.63 ppm decoalesced at $T < 270$ K to yield two resonances at the expected positions of [Cp*Mo(dppe)$H_3$] and [Cp*Mo(dppe)$H_4$]$^+$. The incomplete protonation in the presence of a stoichiometric amount of TFA shows that the protonation process is at equilibrium using this particular proton donor. Both complexes exhibit sharp resonances when alone and also when mixed together with [Cp*Mo(dppe)$H_2$($OCOCF_3$)]. Interestingly, the hydride resonance of [Cp*Mo(dppe)$H_4$]$^+$ broadens again at $T <$ 240 K, but does not decoalesce. On the other hand, the $BF_4^-$ salt of this complex was previously reported to retain sharp lines in the $^1$H- and $^{31}$P NMR spectra down to –90 °C, indicating rapid equilibration between the inequivalent H sites.[14] This suggests that the hydride scrambling process is slowed down by hydrogen bonding between [Cp*Mo(dppe)$H_4$]$^+$ and $CF_3COO^-$.

The reaction with 3 equiv. TFA resulted in the observation of a sharp resonance at the chemical shift of the tetrahydride complex (indicating essentially complete disappearance of the starting trihydride reagent) and no significant amount of the dihydride product. The subsequent addition of 2 equiv. $Et_2NH$ to this solution led to the formation of complex [Cp*Mo(dppe)$H_2$($OCOCF_3$)] cleanly and quantitatively. When using 1.5 equiv. TFA, rather sharp resonances for the tetrahydrido complex and the final dihydrido product were initially observed by $^1$H NMR spectroscopic monitoring, but the latter was once again the only observable species remaining at the end of the reaction (ca. 30 minutes at 290 K). When using only 0.5 equiv. TFA, on the other hand, a broad resonance was again initially present, but its chemical shift was closer to that of the starting hydride complex (see Figure 4). This is as expected because the equilibrium mixture of the rapidly exchanging [Cp*Mo(dppe)$H_3$] and [Cp*Mo(dppe)$H_4$]$^+$ complexes is now richer in the former. The formation of the final dihydride product was slower (equilibrium was attained in ca. two hours at 290 K), and ca. 50% of the initial trihydride remained unreacted. As [Cp*Mo(dppe)$H_4$]$^+$ reacted to yield [Cp*Mo(dppe)$H_2$($OCOCF_3$)], the resonance corresponding to [Cp*Mo(dppe)$H_3$] sharpened. The addition of excess TFA to a solution containing [Cp*Mo(dppe)$H_2$-($OCOCF_3$)] did not lead to any reaction, in particular no tetrahydride resonance was observed under these conditions.

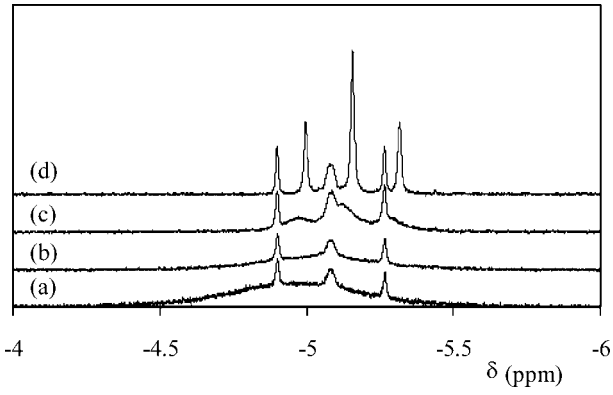


Figure 4. $^1$H NMR (300 MHz) spectroscopic monitoring of the reaction between [Cp*Mo(dppe)$H_3$] and TFA (1:0.5 ratio) in $C_6D_6$ (290 K): (a) recorded immediately; (b) after 7 min; (c) 28 min; (d) 155 min.

 © 2007 Wiley-VCH Verlag GmbH & Co. KGaA, Weinheim 

We also investigated the reaction between [Cp*Mo(dppe)$H_3$] and $CF_3COOD$ (1 equiv.) by $^1H$ NMR spectroscopy in $C_6D_5CD_3$. The reaction progressed in an essentially identical manner to that when $CF_3COOH$ was used: immediate observation of the virtual triplet at –5.25 ppm due to the final product and a broad resonance centered at ca. –3.6 ppm. The latter disappears upon brief warming to ca. 40 °C. However, the NMR spectrum shows the formation of $H_2$ and HD in ca. 3:1 ratio. This is not surprising since all hydride positions in the tetrahydride complex are readily scrambled, therefore the elimination of $H_2$ from the [Cp*Mo(dppe)$H_3$D]$^+$ cation will be statistically favored. The molybdenum product resulting from this reaction should therefore contain both H and D. The hydride resonance does not show evidence for the presence of isotopomers, probably because the isotope shift is too small. The formation of deuterated product(s), [Cp*Mo(dppe)-HD($O_2CCF_3$)] and/or [Cp*Mo(dppe)$D_2$($O_2CCF_3$)], however, was confirmed by a $^2H$ NMR-spectroscopic study, which revealed a binomial triplet resonance at –5.9 ppm with $J_{PD}$ = 7.7 Hz.

### Protonation in Other Solvents: NMR-Spectroscopic Study

The solvent has a significant effect on the course of the protonation reaction. The behavior in [$D_8$]thf is similar but not identical to that in aromatic hydrocarbons (see Figure 5); use of a (sub)stoichiometric amount of the acid initially yields a broad hydride resonance (Figure 5, b). Time evolution at these ratios leads to sharpening of the signals as the irreversible $H_2$ elimination and [Cp*Mo(dppe)-$H_2$($O_2CCF_3$)] formation takes place: a similar process to that shown in Figure 4 for the benzene solution. When the sample corresponding to Figure 5 (b) was treated with additional TFA (total 1.5 equiv.), quantitative formation of the dihydride product occurred (Figure 5, c). Use of a large excess (10 equiv.) of $CF_3COOH$ affords a sharp triplet corresponding to the tetrahydrido cation and a strong resonance for the [Cp*Mo(dppe)$H_2$($O_2CCF_3$)] product (Figure 5, d). As in $C_6D_6$ or $C_6D_5CD_3$, a broad resonance is not obtained at this ratio. However, with time, the tetrahydride resonance disappears and the dihydride resonance increases in [$D_8$]thf (Figure 5, e), whereas in the analogous benzene solution decomposition occurs without formation of the dihydride product, as stated earlier.

THF was found to be a suitable solvent in which to probe the nature of the degenerate exchange between [CpMo(dppe)$H_3$] and [Cp*Mo(dppe)$H_4$]$^+$, by repeating the protonation in the presence of $HBF_4$ instead of $CF_3COOH$ (the $BF_4^-$ salt of the tetrahydride product is soluble in THF, but precipitates from toluene or benzene). If the exchange takes place bimolecularly via a symmetrical [Cp*(dppe)-$H_3$Mo···H···Mo$H_3$(dppe)Cp*]$^+$ transition state, the lineshape of the signal will not depend on the nature of the acid. On the other hand, a unimolecular pathway involving the conjugate base of the proton donor should yield a slower exchange rate for the $BF_4^-$ sample, because this is a much weaker base than $CF_3COO^-$. The NMR-spectroscopic

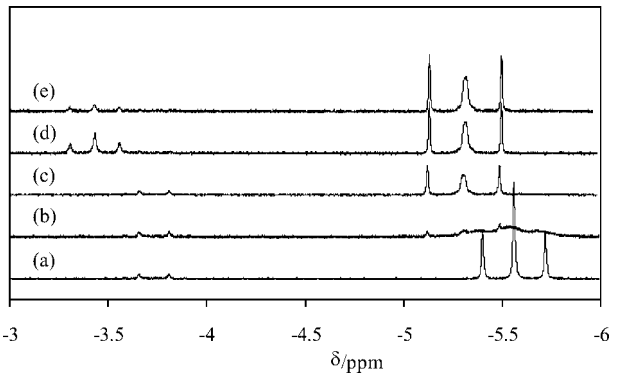


Figure 5. $^1H$ NMR (300 MHz) spectroscopic monitoring of the reaction between [Cp*Mo(dppe)$H_3$] and TFA in [$D_8$]thf (290 K): (a) before the TFA addition; (b) TFA/Mo = 0.5, 8 min; (c) further addition of 1 equiv. to sample (b): TFA/Mo = 1.5, 30 min; (d) TFA/Mo = 10, immediately after the addition; (e) after 13 min from spectrum (d). The doublet resonance at $\delta$ = –3.73 ppm belongs to the [Cp*Mo($\kappa^1$-dppe)$H_5$] contaminant.[14]

study of a 2:1 [Cp*Mo(dppe)$H_3$]/$HBF_4$ mixture provides evidence in favor of the unimolecular pathway. As seen in Figure 6, addition of 0.5 equiv. $HBF_4$ results in a decrease in the [Cp*Mo(dppe)$H_3$] resonance and the appearance of the [Cp*Mo(dppe)$H_4$]$^+$ resonance, plus a weak triplet resonance at –5.65 ppm ($J_{HP}$ = 53.5 Hz), whilst the doublet resonance of the [Cp*Mo($\kappa^1$-dppe)$H_5$] contaminant remains unchanged. The trihydride and tetrahydride complexes give separated sharp resonances, contrary to the same situation in the presence of trifluoroacetate anion in the same solvent (Figure 5, b). This clearly demonstrates that the anion determines the rate of degenerate exchange. This exchange process therefore involves the hydrogen-bonded ion pair [Cp*Mo(dppe)$H_4$]$^+$···$^-O_2CCF_3$ and the dihydrogen-bonded trihydride [Cp*Mo(dppe)$H_3$]···$HO_2CCF_3$, the latter being in further rapid equilibration with free trihydride and TFA. Analogous broadening phenomena for hydride signals as a consequence of dihydrogen bonding and equilibrated proton transfer were noted previously in other cases, although the broadening effect was limited to a few Hz in most cases.[2,23]

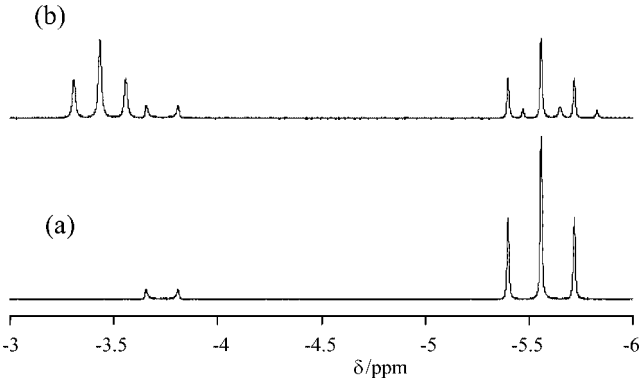


Figure 6. $^1H$ NMR-spectroscopic study of a [Cp*Mo(dppe)$H_3$]/$HBF_4$ mixture in [$D_8$]thf: (a) starting compound; (b) 21 min after the addition of 0.5 equiv. $HBF_4$. The doublet resonance at $\delta$ = –3.73 ppm belongs to the [Cp*Mo($\kappa^1$-dppe)$H_5$] contaminant.[14]

 © 2007 Wiley-VCH Verlag GmbH & Co. KGaA, Weinheim 

The new triplet resonance at –5.65 ppm in Figure 6 is assigned to complex $[Cp^*Mo(dppe)H_2(THF)]^+$. It is associated with a new $^{31}P\{^1H\}$ resonance at 70.7 ppm. For comparison, the related $[Cp^*Mo(dppe)H_2(MeCN)]^+$ complex, obtained from the protonation of $[Cp^*Mo(dppe)H_3]$ by $HBF_4$ in MeCN,[14] displays a proton resonance at –5.50 ppm ($J_{P1}$ = 51 Hz, $J_{P2}$ = 52 Hz) and a phosphorus resonance at 78.1 ppm. NMR spectroscopic monitoring shows that this resonance grows while the resonance of the tetrahydride product simultaneously decreases. Interesting features to note are (i) this cationic THF adduct is not observed in the protonation experiment with $CF_3COOH$; (ii) the rate of disappearance of the tetrahydride complex is much slower in the presence of the $BF_4^-$ anion than in the presence of the $CF_3COO^-$ anion (cf. Figure 6 with Figure 5); and (iii) conversion to the THF solvent adduct appears to be much slower than the analogous reaction in MeCN, which was reported to lead to vigorous gas evolution and quantitative production of the MeCN complex within 60 minutes.[14]

When using $CH_2Cl_2$ as the solvent, the initially formed tetrahydride complex displayed a sharper resonance, even when as little as 0.5 equiv. of the acid was used. The formation of minor amounts of $[Cp^*Mo(dppe)H_2(O_2CCF_3)]$ was also detected (ca. 10% for the 1 equiv. experiment). In this solvent, however, the interpretation of the data is difficult because of the instability of the starting material, the cationic tetrahydride intermediate, and the product (24% decomposition within one hour at room temperature).

Finally, the results of the protonation with TFA (0.5 and 1 equiv.) in $[D_3]$MeCN at room temperature are shown in Figure 7. In both cases, the immediate formation of $[Cp^*Mo(dppe)H_2(O_2CCF_3)]$ and $[Cp^*Mo(dppe)H_4]^+$ was observed. When using 0.5 equiv., the resonances corresponding to the tetrahydride complex and trihydride residual starting compound are separate and relatively sharp (see Figure 7, a): a similar situation to that seen in $CD_2Cl_2$ using TFA as the proton donor or in $[D_8]$thf using $HBF_4$. This indicates that the degenerate exchange is slow under these conditions contrary to the situations in $[D_8]$thf and $C_6D_6$ using TFA as the proton donor. In turn, this suggests that weak ion pairing occurs, if any, between the tetrahydrido cation and the trifluoroacetate anion in $[D_3]$MeCN. The conversion of the tetrahydride complex to $[Cp^*Mo(dppe)H_2(O_2CCF_3)]$ was relatively fast and quantitative, see parts b–d in Figure 7. As already noted, when the reaction was carried out in THF the final product was the trifluoroacetate compound rather than the solvent adduct $[Cp^*Mo(dppe)H_2(MeCN)]^+$ (previously shown to result from the interaction with $HBF_4$), implying that the ligand exchange shown in Equation (2) (S = THF, MeCN) is completely displaced towards the right.

A first comparison of the behavior of $[Cp^*Mo(dppe)H_4]^+$ in noncoordinating solvents confirms the complex instability, as previously shown for the $BF_4^-$ salt, leading to hydride-free decomposition products.[14] However, in the presence of either coordinating solvents or the $CF_3COO^-$ anion, efficient trapping of the 16-electron product of $H_2$ dissociation, $[Cp^*Mo(dppe)H_2]^+$, is achieved. The coordinating $CF_3COO^-$ anion is an even better trap than THF and MeCN. The nature of the solvent has a dramatic effect on two related features: (i) the ability of the $CF_3COO^-$ anion to attack the cationic complex and yield the neutral dihydride-trifluoroacetate product and (ii) the rate of degenerate exchange between $[Cp^*Mo(dppe)H_3]$ and $[Cp^*Mo(dppe)H_4]^+$. The way in which these two processes are affected by the solvent properties will be addressed in more detail in a later section.

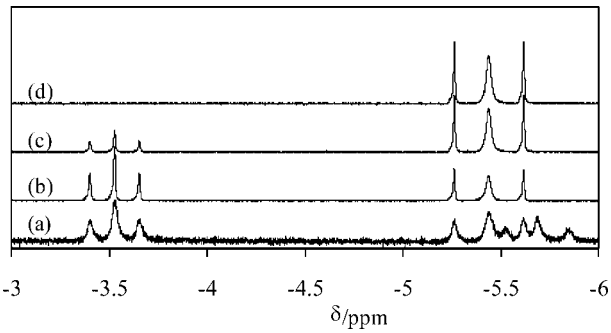


Figure 7. $^1H$ NMR-spectroscopic study of the $[Cp^*Mo(dppe)H_3]$–TFA reaction in $[D_3]$MeCN at room temperature: (a) 0.5 equiv. TFA, recorded immediately; (b) 1 equiv. TFA, recorded immediately; (c) after 9 min from spectrum (b); (d) 40 min after spectrum (b).

$$[Cp^*Mo(dppe)H_2(S)]^+ + CF_3COO^- \rightarrow [Cp^*Mo(dppe)H_2(O_2CCF_3)] + S \quad (2)$$

## IR Studies

As equilibrium positions and reaction rates are expected to strongly depend on the solvent's ability to influence hydrogen bonding and ion pairing equilibria, we considered that additional useful information could be gathered from infrared investigations, especially at low temperature where ion pairing and hydrogen bonding are favored. The dielectric permittivity, $\varepsilon$, increases at ambient temperature in the order toluene (2.4) < THF (7.8) < $CH_2Cl_2$ (8.3) << MeCN (35.9).[24] It increases substantially upon cooling for some solvents, for example, values of 15.5 for $CH_2Cl_2$[25,26] and 11.9 for THF[27,28] are recorded at 200 K, but not for others, for example, 2.47 at 240 K and 2.71 at 180 K for toluene.[26] On the other hand, these solvents have different coordinating and acid/base properties. THF is quite an efficient hydrogen-bond acceptor ($E_j$ = 1.04), better than MeCN ($E_j$ = 0.75),[29] although the latter is generally a better ligand for transition metals. Benzene and toluene are much weaker bases ($E_j$ = 0.4),[29] whereas $CH_2Cl_2$ tends to behave more like a weak proton donor than as a proton acceptor.[24] We start by presenting the spectral features of the TFA proton donor in the $\nu_{CO}$ region in various solvents, since the TFA/solvent interaction certainly plays an important role in the proton-transfer equilibria involving the hydride complex. The relevant spectra are shown in Figure 8. Two bands at similar frequencies are observed in $CH_2Cl_2$

 © 2007 Wiley-VCH Verlag GmbH & Co. KGaA, Weinheim 

and toluene (1804 and 1785 $cm^{-1}$ for the former, 1803 and 1788 $cm^{-1}$ for the latter). The higher frequency band is due to the acid monomer, whereas the lower frequency one is typically assigned to the corresponding dimer.[30] Note that the equilibrium is shifted towards the dimer in toluene, as is evident from the different relative intensities. In THF the wide, asymmetric $\nu_{CO}$ band of the acid monomer is greatly redshifted to 1780 $cm^{-1}$ because of the formation of stronger hydrogen bonds to solvent molecules. The shoulder at 1762 $cm^{-1}$ (which becomes a distinct band at 200 K) is assigned to the $CF_3COOH$ dimer. The low-frequency asymmetry of the acid bands in all solvents suggests the presence of higher order TFA associates. Thus THF can form hydrogen bonds with $CF_3COOH$, lowering the activity of the acid, which is one of the reasons for the evolution of $[Cp^*Mo(dppe)H_4]^+CF_3COO^-$ into the final dihydride product in this solvent, as will be shown later.

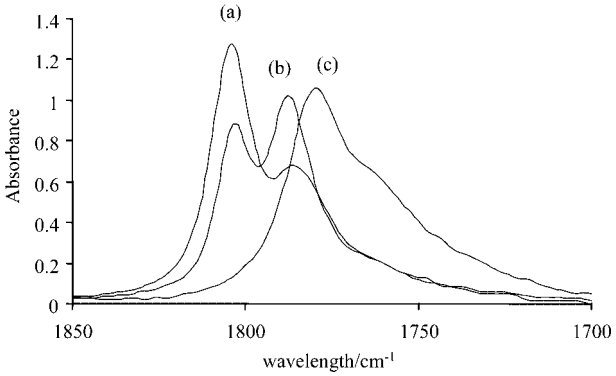


Figure 8. IR spectra of trifluoroacetic acid solutions (0.027 M, pathlength 0.04 mm) in various solvents at 290 K: (a) $CH_2Cl_2$; (b) toluene; (c) THF.

### *In Dichloromethane*

Although the starting material and products are unstable in dichloromethane at room temperature, they do not decompose at low temperatures and this solvent has many advantages for infrared studies (it is not a strong proton acceptor, therefore it does not compete with the basic hydride complexes for hydrogen bonding, and it has good solvent properties for ionic compounds). An IR spectroscopic monitoring at 200 K in the acid $\nu_{CO}$ and conjugated anion $\nu^{as}{}_{OCO}$ vibration region yielded the results shown in Figure 9. At this temperature the dihydride complex $[Cp^*Mo(dppe)H_2(O_2CCF_3)]$, which has a $\nu^{as}{}_{OCO}$ at 1692 $cm^{-1}$ (vide infra), did not form.

A tentative assignment of all observed bands is possible on the basis of previous IR studies into the interaction between $CF_3COOH$ and various bases,[30–32] in combination with the results shown in the previous section. At 200 K the acid self-association equilibrium is shifted to the dimer, exhibiting a strong band at 1780 $cm^{-1}$ with a shoulder at 1800 $cm^{-1}$ (Figure 9, b). The spectrum recorded for the solution with a $MoH_3$/TFA ratio of 1:0.5 (Figure 9, c) shows a prominent band at 1686 $cm^{-1}$ due to the $\nu^{as}{}_{OCO}$ vibration of the trifluoroacetate anion. Its relatively sharp nature and almost negligible high frequency shift relative to

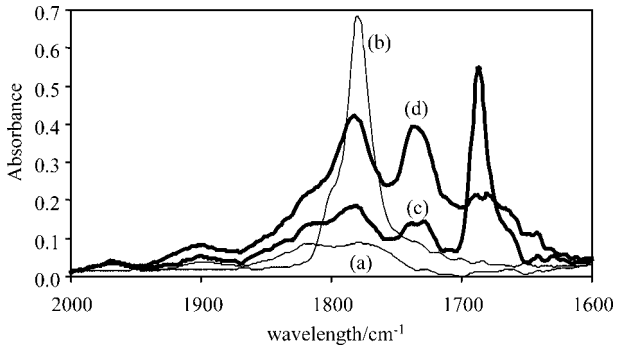


Figure 9. Low-temperature (200 K) IR spectra for the reaction between $[Cp^*Mo(dppe)H_3]$ and TFA in $CH_2Cl_2$: (a) $[Cp^*Mo(dppe)H_3]$ (0.028 M); (b) TFA (0.014 M); (c) mixture of $[Cp^*Mo(dppe)H_3]$ (0.028 M) and TFA (0.014 M); (d) mixture of $[Cp^*Mo(dppe)H_3]$ (0.028 M) and TFA (0.028 M).

the position of the free $CF_3COO^-$ anion[31,32] indicates the formation of either a weakly H-bonded contact ion pair or a solvent-separated ion pair, consistent with the relatively high polarity of $CH_2Cl_2$ at low temperatures and the poor proton-donor ability of the $[Cp^*Mo(dppe)H_4]^+$ cation. In reference to Scheme 1, this means that species **V** is extensively dissociated to **VI** or that the interaction is loose under these solvent and temperature conditions. There is no significant intensity in the region characteristic for the free homoconjugate anion, $[CF_3COO(CF_3COOH)_n]^-$. According to the literature, this species should display a low intensity, broad band with a maximum at 1630–1620 $cm^{-1}$.[33] Given the presence of an excess of the trihydride complex, most of the acid is presumably consumed and little is left to yield the homoconjugate anion. The relative intensity of the 1686 $cm^{-1}$ band indicates that the proton-transfer equilibrium is highly shifted to the tetrahydride product, and the presence of the unreacted trihydride complex is indicated by the shoulder at 1816 $cm^{-1}$ {cf. the starting spectrum of free $[Cp^*Mo(dppe)H_3]$ in Figure 9, a}. There are two additional weak bands in this spectrum. The first one at 1782 $cm^{-1}$ could be assigned to free $CH_3COOH$, but it is also consistent with a H-bonded adduct where the acid acts as a proton donor (a $CF_3COO$–H···B interaction does not significantly perturb the CO normal mode). The second band at 1736 $cm^{-1}$ indicates the presence of a H-bonded adduct where the acid acts as a proton acceptor [the $CF_3C(OH)O$···HA interaction significantly redshifts the CO normal mode].[34,35] Thus, these bands constitute evidence for the presence of a 2:1 H-bonded adduct, $[Cp^*Mo(dppe)H_3]$···$HO_2CCF_3$···$HO_2CCF_3$. The simultaneous presence of a 1:1 adduct, $[Cp^*Mo(dppe)H_3]$···$HO_2CCF_3$, cannot be established because it would also afford a band at ca. 1780 $cm^{-1}$. A general picture of the proton-transfer process can be drawn as shown in Scheme 4.

An increase in the $CF_3COOH/MoH_3$ ratio is expected to shift the hydrogen-bonding equilibrium position towards the 2:1 adduct. At the same time, equilibria involving the anionic species (either hydrogen bonded or free) are expected to shift towards the homoconjugate anion (equilibria

 © 2007 Wiley-VCH Verlag GmbH & Co. KGaA, Weinheim 

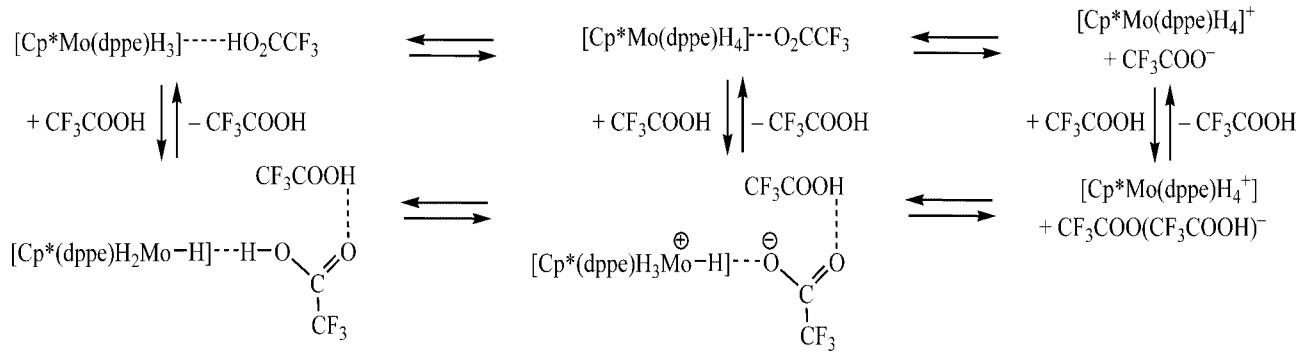


Scheme 4.

drawn vertically in Scheme 4). On the other hand, an increase in the $CF_3COOH/MoH_3$ ratio will not affect the equilibria shown horizontally in Scheme 4. Indeed, upon addition of a second 0.5 equiv. TFA (final $MoH_3$/TFA ratio of 1:1), see Figure 9d, the IR spectrum reveals a significant increase in intensity for the bands assigned to the neutral 2:1 adduct and a dramatic decrease for that assigned to the free anion. The growth of a broad shoulder at lower frequencies signals the formation of anionic aggregates, as expected.

### *In [D8]Toluene*

The low-temperature IR spectral picture in [$D_8$]toluene in the presence of a stoichiometric amount of TFA is similar to that shown in dichloromethane, see Figure 10. The band at 1742 $cm^{-1}$ observed for the 1:1 mixture (Figure 10c) is assigned to the $\nu_{CO}$ of the hydrogen-bonded complex (cf. 1736 $cm^{-1}$ in $CH_2Cl_2$), whereas the bands at 1690 and 1674 $cm^{-1}$ are assigned to the $CF_3COO^-$ anion ($\nu^{as}_{OCO}$, cf. 1686 $cm^{-1}$ in $CH_2Cl_2$). The complex pattern attained for this absorption is possibly related to the presence of different hydrogen-bonded species (hydrogen bonding should be favored more in low-polarity toluene). The anion band did not show a significant increase in intensity at greater $MoH_3$/TFA ratios (1:0.5 or 1:0.2), indicating that the proton-transfer equilibrium is shifted further towards the neutral hydrogen-bonded species in this solvent in comparison with $CH_2Cl_2$. This agrees with the results of the NMR investigation. Upon warming above 270 K, the bands corresponding to the [Cp*Mo(dppe)$H_2(O_2CCF_3)$] product at 1702 and 1690 $cm^{-1}$ quickly grow, while the shoulder at 1674 $cm^{-1}$ disappears. The final spectrum is shown in part d of Figure 10. Monitoring the growth of this band for the 1:1 reaction in $C_6H_6$ at 298 K (see Figure S3 in the Supporting Information) yielded a first-order rate constant of $(1.8 \pm 0.1)\times10^{-3}$ $s^{-1}$. In the presence of a 3–5-fold excess of acid, the broad, low intensity $\nu^{as}_{OCO}$ band of the homoconjugated anion was observed at ca. 1640 $cm^{-1}$. No formation of [Cp*Mo(dppe)$H_2(O_2CCF_3)$] was observed under these conditions, in agreement with the NMR spectroscopic data.

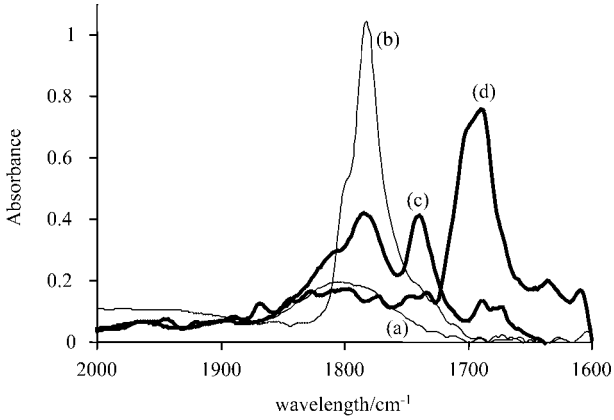


Figure 10. IR spectra for the reaction between [Cp*Mo(dppe)$H_3$] and TFA in [$D_8$]toluene: (a) [Cp*Mo(dppe)$H_3$] (0.027 M) at 200 K; (b) TFA (0.027 M) at 200 K; (c) 1:1 mixture (0.027 M) at 200 K; (d) same mixture as (c), after complete conversion at room temperature.

### *In THF*

At low temperature in this solvent and in the presence of 1 equiv. TFA, the dominant species were the neutral hydrogen-bonded complexes, as indicated by the major bands at 1784 and 1744 $cm^{-1}$ (see Figure 11, c). No significant amounts of the $CF_3COO^-$ ion were seen. This implies that proton transfer occurs to a smaller degree than in toluene. No homoconjugated anion band was observed upon raising the TFA excess to 5 equiv., in contrast to the results in aromatic hydrocarbon solution. Upon warming, the spectral changes were similar to those observed in toluene (see previous section), yielding [Cp*Mo(dppe)$H_2(O_2CCF_3)$], see Figure 11 (d). We also investigated the reverse proton-transfer reaction by mixing together [Cp*Mo(dppe)$H_4$]$^+BF_4^-$ {generated in situ at 200 K from [Cp*Mo(dppe)$H_3$] and $HBF_4$} and $CF_3COONa$ at 200 K in THF. This experiment confirms the reversible nature of the proton-transfer process and the position of equilibrium. The essentially complete disappearance of the trifluoroacetate anion $\nu^{as}_{OCO}$ bands at 1702 and 1690 $cm^{-1}$ and the growth of the $\nu_{CO}$ band at 1752 $cm^{-1}$ corresponding to the H-bonded adduct[36] were observed at 200 K in the presence of either 1

 © 2007 Wiley-VCH Verlag GmbH & Co. KGaA, Weinheim 

or 2 equiv. $[Cp^*Mo(dppe)H_4]^+BF_4^-$. Subsequent warming to 290 K led once again to $[Cp^*Mo(dppe)H_2(OCOCF_3)]$ formation.

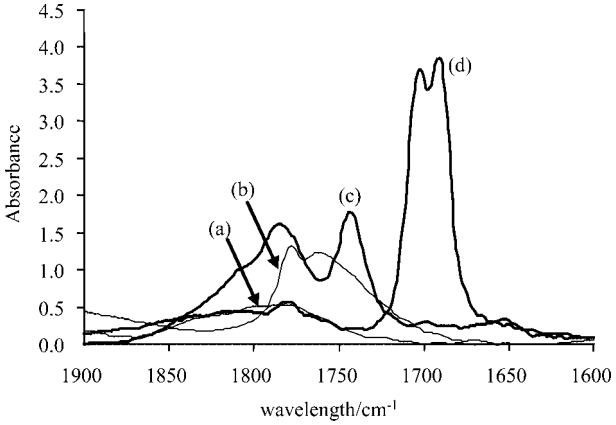


Figure 11. Low-temperature (200 K) IR spectra for the reaction of $[Cp^*Mo(dppe)H_3]$ with TFA in THF: (a) $[Cp^*Mo(dppe)H_3]$ (0.07 M); (b) TFA (0.07 M); (c) 1:1 mixture (0.07 M) at 200 K; (d) same mixture as (c), after complete conversion at room temperature.

Since the NMR-spectroscopic study shows that this conversion also occurs in the presence of excess acid, a kinetics investigation was carried out at 298 K using different TFA/Mo ratios. The reaction was found to be zero order with respect to the acid (see Table 3). Interestingly, the rate constant in THF is identical to that measured in benzene (vide supra) within experimental error. The study was also extended to different temperatures (using a TFA/Mo ratio of 1:1), with the subsequent Eyring analysis (see Supporting Information) giving the following activation parameters: $\Delta H^{\ddagger} = (31.8 \pm 0.5)$ kcal mol$^{-1}$ and $\Delta S^{\ddagger} = (36 \pm 2)$ e.u. The large positive activation entropy suggests that the transition state is dissociative in nature. At low temperatures, the rearrangement becomes too slow; for instance, reaction rate constants of $5.2 \times 10^{-8}$ and $5.8 \times 10^{-15}$ s$^{-1}$ are calculated at 250 and 200 K, respectively.

Table 3. Rate constants for the $[Cp^*Mo(dppe)H_2(O_2CCF_3)]$ formation reaction in THF; $[MoH_3] = 0.025$ M.

| $T$ /K | TFA/Mo | $k$ /10$^{-3}$ s$^{-1}$ |
|---|---|---|
| 280 | 1 | $0.064 \pm 0.0015$ |
| 290 | 1 | $0.63 \pm 0.01$ |
| 298 | 0.5 | $1.7 \pm 0.1$ |
| 298 | 1 | $1.8 \pm 0.1$ |
| 298 | 3 | $1.9 \pm 0.1$ |
| 298 | 5 | $1.80 \pm 0.05$ |
| 308 | 1 | $13.7 \pm 0.2$ |

## Discussion

The collective observations that will be detailed now are summarized in Scheme 5.

Proton transfer to $[Cp^*Mo(dppe)H_3]$, via the H-bonded adduct **A** to yield the classical tetrahydride complex, $[Cp^*Mo(dppe)H_4]^+$, **C**/**D**, is the only reaction that may occur at low temperatures. The formation of the 2:1 H-bonded adduct **A′** was also evidenced by low-temperature IR spectroscopy, but one molecule of TFA is sufficient for proton transfer to occur, as also indicated by previous ki-

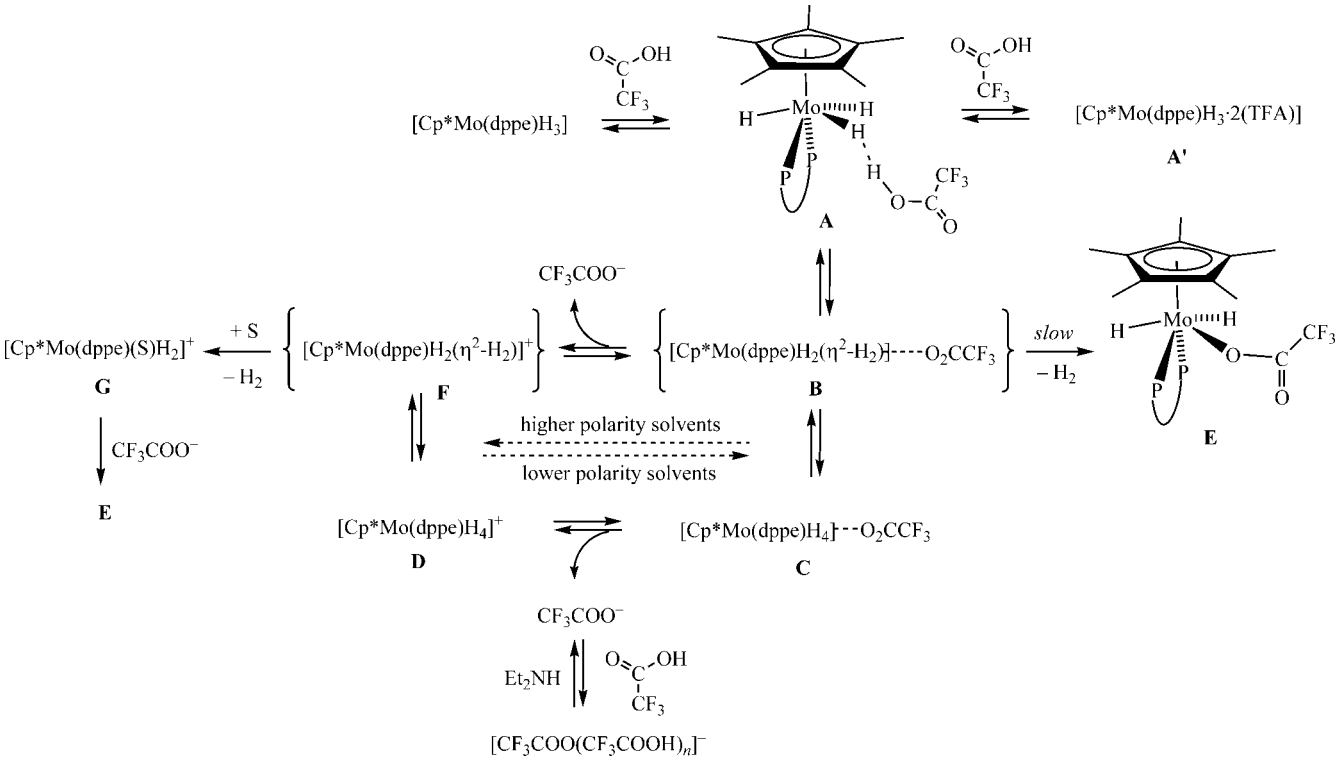


Scheme 5.

 © 2007 Wiley-VCH Verlag GmbH & Co. KGaA, Weinheim 

netics studies.[13] The proton transfer probably proceeds via a nonclassical intermediate (species **B** in Scheme 5), although we have not found any direct experimental evidence to support this proposition. Our recently reported theoretical calculations[13] indicate that the nonclassical complex lies in a very shallow minimum with a low barrier for conversion to the classical tetrahydride product, with the isomerization taking place without counteranion dissociation. The competitive dihydrogen evolution yielding [Cp*Mo(dppe)$H_2$($O_2CCF_3$)] occurs only above 250 K and is possible (in noncoordinating solvents) by the reverse reaction between **D** and $CF_3COO^-$. This forms the ion pair **C** which subsequently isomerizes to the nonclassical species **B**.

The formation of [Cp*Mo(dppe)$H_4$]$^+$ is reversible below 250 K in contrast to the irreversible formation of *trans*-Cp*$MH_2$(dppe)$^+$ (M = Fe, Ru).[6,8] One important difference between these systems is the reversibility of the nonclassical/classical isomerization for [Cp*Mo(dppe)$H_4$]$^+$ (according to the DFT calculations), whereas this process is irreversible for [Cp*M(dppe)$H_2$]$^+$ (M = Fe, Ru). However, proton transfer to the hydride ligand is less thermodynamically favorable for [Cp*Mo(dppe)$H_3$] than for [Cp*Fe(dppe)H]; a significant amount of TFA remained unreacted (in the H-bonded form) for a TFA/Mo ratio of 0.5 in $CH_2Cl_2$ at 200 K (see Figure 9), whereas it was completely consumed under the same solvent, temperature, and stoichiometry conditions in the presence of [Cp*Fe(dppe)H].[5] These results contrast with the higher basicity factor of [Cp*Mo(dppe)$H_3$] ($E_j$ = 1.42 ± 0.02)[13] relative to [Cp*Fe(dppe)H] ($E_j$ = 1.36 ± 0.02).[7] The corresponding proton transfer to [Cp*Ru(dppe)H] ($E_j$ = 1.39), however, is also an equilibrium process.[6] The basicity factor correlates with the strength of the hydrogen bond (formation enthalpy), whereas the protonation equilibrium is determined by the free energy of the proton-transfer process. Obviously, the two parameters do not necessarily correlate quantitatively.

Both the **A** ⇄ **C**/**D** equilibrium position and rate of the irreversible [Cp*Mo(dppe)$H_2$($O_2CCF_3$)] formation depend on the temperature, the solvent, and the $MoH_3$/TFA ratio. Polar solvents (e.g., dichloromethane at low temperatures, acetonitrile) weaken the hydrogen bond in **C** and lead to the formation of a solvent-separated ion pair (species **D** in Scheme 5), which stabilizes the tetrahydrido complex against the $H_2$ loss. The proton-transfer equilibrium is shifted to species **D** in $CH_2Cl_2$ even in the presence of stoichiometric amounts of the acid. Low-polarity solvents (e.g., toluene) provide less stabilization for the charged species, thus the proton-transfer equilibrium is shifted to the left when near stoichiometric amounts of the acid are used. The tetrahydride product exists as an ion pair stabilized by hydrogen bonding to the $CF_3COO^-$ anion (species **C** in Scheme 5), as reflected for instance in a reduced rate of hydride site exchange measured by $^1$H NMR spectroscopy below 240 K. The formation of hydrogen-bonded ion pairs of 1:1 composition was also confirmed for weaker proton donors.[13] At room temperature and above, the competitive irreversible $H_2$ elimination process eventually leads to the quantitative formation of the final product **E**. However, excess acid favors ion-pair dissociation through formation of the thermodynamically more stable homoconjugate anion, thereby stabilizing the proton-transfer product **D** and precluding the $H_2$ evolution.

In solvents with proton-accepting ability (THF, MeCN) the activity of the acid is reduced by hydrogen bonding with solvent molecules, formation of the homoconjugated anion is not observed, and the reaction yields **E** even in the presence of excess acid. The attainment of the same formation rate constant in THF and in benzene and the zero-order dependence on TFA agree with the proposed unimolecular generation of **E** from the same intermediate **B**. Furthermore, the large positive activation entropy is consistent with a dissociative mechanism (i.e., $H_2$ must leave before the trifluoroacetate anion can coordinate), as may be expected from the electronically saturated nature of system **B**. The rate of formation in MeCN was not determined with accuracy, but the NMR spectroscopic data in Figure 7 allow us to estimate a rate constant of ca. $2 \times 10^{-3}$ s$^{-1}$, that is, close to that determined in THF and benzene (see Table 3), if we assume a first-order decay process is in operation. The high polarity of MeCN favors proton transfer and ion-pair dissociation through the stabilization of the charge-separated species, but the instability of [Cp*Mo(dppe)$H_4$]$^+$ leads to its ultimate decomposition by $H_2$ elimination. In this case, the process may be solvent-assisted, leading to the solvent adduct **G**, as previously established by the protonation with $HBF_4$.[14] This phenomenon also occurs in THF as verified by using $HBF_4$. However, the $CF_3COO^-$ anion has a stronger coordinating power than both THF and MeCN, and the ultimate product is once again **E**.

Species **A** and **C**/**D** exhibit a dynamic exchange process, as revealed by a broad $^1$H resonance at room temperature which decoalesces at 270 K in $C_6D_5CD_3$ for the mixture containing 1 equiv. TFA. This results from the fast and direct unimolecular proton transfer involving the dihydrogen-bonded complex **A** and the H-bonded ion pair **C**. It is not possible, unfortunately, to use this information to derive an accurate value for the proton-transfer rate constant because of the complexity of the coupled equilibria and the irreversible transformation to product **E**. Assuming, however, that only species **A** and **C** are present in an approximately equimolar ratio, an activation barrier $\Delta G^{\ddagger}$ of 11.7 kcal mol$^{-1}$ may be estimated for the proton transfer in $C_6D_5CD_3$ at 270 K, from the coalescence temperature and the chemical shift difference.[37] This activation barrier is lower than that of the proton transfer by HFIP in toluene ($\Delta G^{\ddagger}_{293\,K}$ = 15.8 kcal mol$^{-1}$),[13] in agreement with the higher proton-donating ability of TFA. It is also lower than $\Delta G^{\ddagger}_{270\,K}$ for the proton transfer from HFIP to [Cp*Fe(dppe)H] in $CH_2Cl_2$ (14.7 kcal mol$^{-1}$) or from PFTB to [CpRuH(CO)($PCy_3$)] in hexane (16.1 kcal mol$^{-1}$), calculated for 270 K using the published activation parameters.[3,5] IR kinetic data (vide supra) give $\Delta G^{\ddagger}_{270\,K}$ = 22.1 kcal mol$^{-1}$ for the dihydrido-trifluoroacetate formation. The irreversibility of the $H_2$ evolution process renders [Cp*Mo(dppe)$H_2$($O_2CCF_3$)] the sole end product.

 © 2007 Wiley-VCH Verlag GmbH & Co. KGaA, Weinheim 

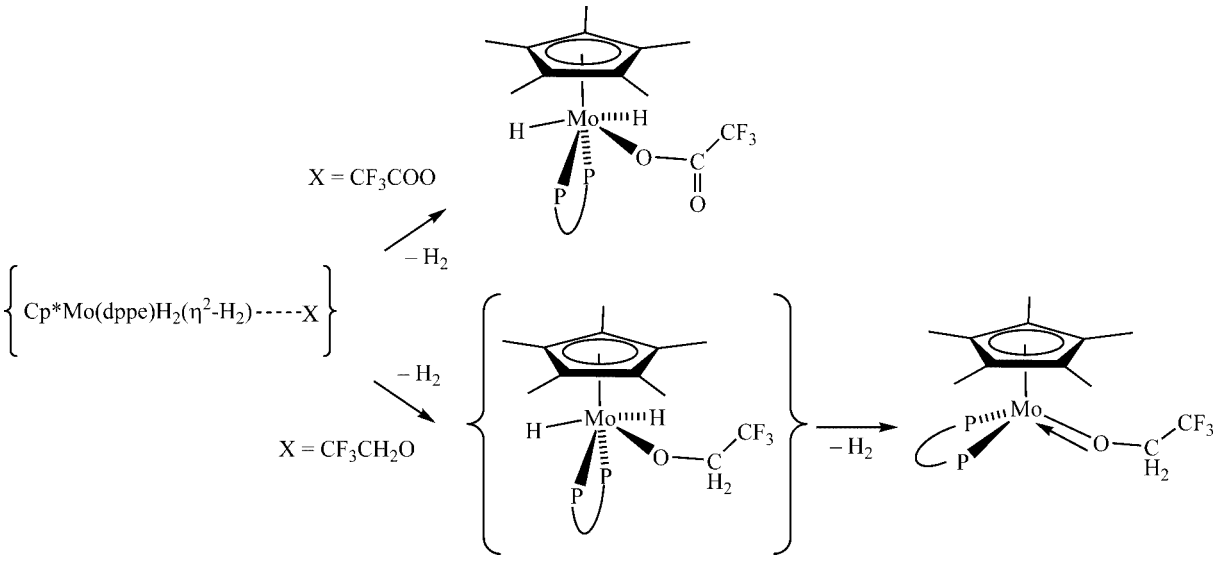


Scheme 6.

A final point of interest is a comparison between the results shown here and those reported previously for the decomposition of the proton-transfer product obtained with TFE, which led to a diamagnetic hydride-free decomposition product, $[Cp^*Mo(dppe)(OCH_2CF_3)(TFE)_x]$ ($x$ = 0 or 1). The mechanism is likely to be the same for both systems, leading to a first $H_2$ elimination assisted by the coordination of the alkoxide ligand (see Scheme 6). Why does $[Cp^*Mo(dppe)H_2(O_2CCF_3)]$ show no tendency to expel a second $H_2$ molecule and form the hypothetical compound $[Cp^*Mo(dppe)(O_2CCF_3)]$, in which the trifluoroacetate ligand would bind in a chelating fashion, whereas $[Cp^*Mo(dppe)H_4]^+(^-OCH_2CF_3)$ leads to a hydride-free product without the observation of even trace amounts of a dihydride intermediate? A possible rationalization is that the stronger π-donating ability of the oxygen lone pairs in the fluorinated alkoxide ligand may assist the elimination of the second $H_2$ molecule by stabilizing the resulting 16-electron half-sandwich $Mo^{II}$ product. By contrast, the lone pair of the trifluoroacetate oxygen donor atom is not sufficiently basic and the second oxygen atom is presumably not capable of assisting the $H_2$ elimination process, because of either thermodynamic or kinetic reasons.

## Conclusions

We explored the protonation of $[Cp^*Mo(dppe)H_3]$ by trifluoroacetic acid in various solvents which display different proton-accepting ability, polarity, and coordinating power toward transition metals: dichloromethane, benzene/toluene, THF, and MeCN. The nature of the solvent and the amount of excess acid determined the nature of the product by delicately controlling the position of the proton transfer and ion pairing equilibria. In agreement with previous investigations, the classical tetrahydrido cation was produced following the initial formation of a dihydrogen-bonded intermediate without the observation of a nonclassical tautomer (dihydrogen complex); it is stable at low temperatures and can exist as solvent-separated or contact ion pair. However, the use of suitable conditions of solvent, temperature, and hydride/acid ratio led to the selective formation of a new product, the dihydrido complex $[Cp^*Mo(dppe)H_2(O_2CCF_3)]$. The trifluoroacetate anion is a sufficiently strong ligand to coordinate to the cationic complex and saturate its coordination sphere after loss of $H_2$, even in the presence of coordinating solvent molecules such as MeCN or THF. However, it remains coordinated in a monodentate fashion and, contrary to the $CF_3CH_2O^-$ anion, is not capable of inducing the elimination of the residual hydride ligands as $H_2$ to form a hydride-free product.

## Experimental Section

**General:** All manipulations were performed under argon by standard Schlenk techniques. All solvents were dried with an appropriate drying agent (Na/benzophenone for benzene, toluene or THF; Na for pentane; $CaH_2$ for $CH_2Cl_2$) and were freshly distilled under argon prior to use. $C_6D_6$, $C_6D_5CD_3$, [$D_8$]thf, $CD_3CN$, and $CD_2Cl_2$ (Euriso-Top) for NMR spectroscopic experiments and $C_6D_5CD_3$ (Aldrich) for IR spectroscopic experiments were degassed by three freeze-pump-thaw cycles, and then purified by vacuum transfer at room temp. $[Cp^*Mo(dppe)H_3]$ was synthesized according to the literature.[14]

### Spectroscopic Studies

**NMR Investigations:** Samples of $[Cp^*Mo(dppe)H_3]$ in each solvent were prepared under argon in 5-mm NMR tubes. The $^1H$- and $^{31}P\{^1H\}$ NMR data were collected with Bruker AMX300 and Bruker AV500 spectrometers, operating at 300.1 or 500.3 MHz and 121.5 or 202.5 MHz, respectively. The temperature was calibrated using a methanol chemical-shift thermometer; the accuracy and stability was ±1 K. All samples were allowed to equilibrate at every temperature for at least 3 min. The spectra were calibrated with the residual solvent resonance ($^1H$) and with external 85% $H_3PO_4$ ($^{31}P$). The conventional inversion-recovery method (180–$\tau$–90) was

 © 2007 Wiley-VCH Verlag GmbH & Co. KGaA, Weinheim 

used to determine the variable-temperature longitudinal relaxation time $T_1$. Standard Bruker software was used for the calculation of the longitudinal relaxation time.

**IR-Spectroscopic Investigations:** The IR measurements were performed with the "Infralum 801" FTIR spectrometer using $CaF_2$ cells of 0.04-cm path length. All IR measurements were carried out by the use of a home-modified cryostat (Carl Zeiss Jena) in the 190–290 K temperature range. The cryostat modification allowed operation under an inert atmosphere and the transfer of the reagents (premixed either at low or room temp.) directly into the cell precooled to the required temperature. The accuracy of the temperature adjustment was ±1 K. This setup was used both for the variable-temperature studies and for the kinetics investigations.

**Synthesis of [Cp*Mo(dppe)H$_2$(O$_2$CCF$_3$)]:** A $CF_3COOH$ solution (9.5 μL, 0.13 mmol) in THF (3 mL) was slowly added to a solution of [Cp*Mo(dppe)$H_3$] (80 mg, 0.13 mmol) in THF (15 mL). The reaction mixture was stirred at room temp. for ca. 1.5 h. The solvent was evaporated, and the resulting solid was recrystallized from pentane. Yield: 75 mg (78%). $^1$H NMR (300.13 MHz, $C_6D_6$, 290 K): $\delta$ = –5.09 (Mo–$H_2$), 1.79 (s, 15 H, Cp*), 3.2–2.5 (m, 4 H, –$CH_2$–$CH_2$–), 7.10–7.77 (m, 20 H, Ph) ppm. $^{31}$P{$^1$H} NMR (121.5 MHz, $C_6D_6$, 290 K): $\delta$ = 76.9 (s) ppm. The $^1$H hydride and the $^{31}$P resonances decoalesce at low temperatures (see Results section). IR (KBr): $\tilde{\nu}$ = 1682 and 1702 (sh) ($\nu^{as}_{OCO}$), 1818 and 1850 (Mo–$H_2$) cm$^{-1}$. $C_{38}H_{41}F_3MoO_2P_2$ (744.6): calcd. C 61.29, H 5.56; found C 61.26, H 5.54. Crystals were grown by slow diffusion of a pentane layer into a saturated solution of the mixture containing [Cp*Mo(dppe)$H_3$] and ca. 1 equiv. of TFA in toluene.

**Kinetics of the [Cp*Mo(dppe)H$_2$(O$_2$CCF$_3$)] Formation:** The reagents were mixed at low temperature (ca. 270 K), and the solution was transferred into the cryostat. The kinetics data were obtained by following the increase of the band at 1692 cm$^{-1}$ corresponding to the [Cp*Mo(dppe)H$_2$(O$_2$CCF$_3$)] complex at the desired temperature. The first-order rates were obtained by plotting $\ln(A_\infty - A_t)$ versus time $t$.

**X-ray Analysis of Compound [Cp*Mo(dppe)H$_2$(O$_2$CCF$_3$)]:** A single crystal was mounted under inert perfluoropolyether on the tip of a glass fiber and cooled in the cryostream of the Oxford-Diffraction XCALIBUR CCD diffractometer. Data were collected using the monochromatic Mo-$K_\alpha$ radiation ($\lambda$ = 0.71073). The structure was solved by direct methods (SIR97)[38] and refined by least-squares procedures on $F^2$ using SHELXL-97.[39] All hydrogen atoms attached to carbon were introduced in the calculation in idealized positions and treated as riding models. The two hydride ligands were located in difference Fourier syntheses, and they were freely refined with isotropic thermal parameters. The molecule was drawn with the help of ORTEP32.[40] Crystal data and refinement parameters are shown in Table 4.

CCDC-632317 contains the supplementary crystallographic data for this paper. These data can be obtained free of charge from The Cambridge Crystallographic Data Centre via www.ccdc.cam.ac.uk/data_request/cif.

**Supporting Information** (see also the footnote on the first page of this article): Table of longitudinal relaxation times at different temperatures for the hydride resonance of [Cp*Mo(dppe)H$_2$(O$_2$CCF$_3$)] and figures showing IR spectra of this compound in various solvents, the IR-spectroscopic study of its formation kinetics in toluene, and an Eyring plot of the rate constants in THF.

Table 4. Crystal data and structure refinement for compound [Cp*Mo(dppe)H$_2$(O$_2$CCF$_3$)].

| | | |
|---|---|---|
| Empirical formula | $C_{38}H_{41}F_3MoO_2P_2$ | |
| Formula weight | 744.59 | |
| Temperature | 180(2) K | |
| Wavelength | 0.71073 Å | |
| Crystal system | monoclinic | |
| Space group | $P2_1/n$ | |
| Unit cell dimensions | $a$ = 11.2103(4) Å | $\alpha$ = 90° |
| | $b$ = 15.0429(7) Å | $\beta$ = 93.675(3)° |
| | $c$ = 20.1563(7) Å | $\gamma$ = 90° |
| Volume | 3392.1(2) Å$^3$ | |
| $Z$ | 4 | |
| Density (calculated) | 1.458 Mg m$^{-3}$ | |
| Absorption coefficient | 0.531 mm$^{-1}$ | |
| $F$(000) | 1536 | |
| Crystal size | 0.57 × 0.3 × 0.28 mm | |
| Theta range for data collection | 2.96–30.03° | |
| Index ranges | $-15 \le h \le 15$, $-12 \le k \le 21$, $-28 \le l \le 28$ | |
| Reflections collected | 31116 | |
| Independent reflections | 9836 [$R_{int}$ = 0.0477] | |
| Completeness to $\theta$ = 30.00° | 99.1% | |
| Absorption correction | semi-empirical from equivalents | |
| Max. / min. transmission | 0.9726 / 0.7281 | |
| Refinement method | full-matrix least-squares on $F^2$ | |
| Data / restraints / parameters | 9836 / 0 / 428 | |
| Goodness-of-fit on $F^2$ | 1.082 | |
| Final $R$ indices [$I > 2\sigma(I)$] | $R_1$ = 0.0403, $wR_2$ = 0.1022 | |
| $R$ indices (all data) | $R_1$ = 0.0480, $wR_2$ = 0.1072 | |
| Largest diff. peak and hole | 1.193 and –1.187 e Å$^{-3}$ | |

## Acknowledgments

We thank the European Commission, HYDROCHEM program (contract HPRN-CT-2002-00176) for support of this work. Additional support from the Centre National de la Recherche Scientifique (CNRS, program PICS), France, from the Russian Foundation for Basic Research (RFBR) (05-03-22001, 05-03-32415) and the Division of Chemistry and Material Sciences of RAS, Russia, is also gratefully acknowledged. N. V. B. thanks Russian Science Support Foundation for an individual grant. M. B. thanks the Ministerio de Educación y Ciencia (MEC) for a post-doctoral fellowship.

[1] N. V. Belkova, E. S. Shubina, L. M. Epstein, *Acc. Chem. Res.* **2005**, *38*, 624.
[2] N. V. Belkova, A. V. Ionidis, L. M. Epstein, E. S. Shubina, S. Gruendemann, N. S. Golubev, H. H. Limbach, *Eur. J. Inorg. Chem.* **2001**, 1753.
[3] N. Belkova, M. Besora, L. Epstein, A. Lledós, F. Maseras, E. Shubina, *J. Am. Chem. Soc.* **2003**, *125*, 7715.
[4] E. Gutsul, N. Belkova, G. Babakhina, L. Epstein, E. Shubina, C. Bianchini, M. Peruzzini, F. Zanobini, *Russ. Chem. Bull.* **2003**, *52*, 1204.
[5] N. V. Belkova, E. Collange, P. Dub, L. M. Epstein, D. A. Lemenovskii, A. Lledós, O. Maresca, F. Maseras, R. Poli, P. O. Revin, E. S. Shubina, E. V. Vorontsov, *Chem. Eur. J.* **2005**, *11*, 873.
[6] N. V. Belkova, P. A. Dub, M. Baya, J. Houghton, *Inorg. Chim. Acta* **2007**, *360*, 149.
[7] N. V. Belkova, P. O. Revin, L. M. Epstein, E. V. Vorontsov, V. I. Bakhmutov, E. S. Shubina, E. Collange, R. Poli, *J. Am. Chem. Soc.* **2003**, *125*, 11106.
[8] M. Baya, O. Maresca, R. Poli, Y. Coppel, F. Maseras, A. Lledós, N. V. Belkova, P. A. Dub, L. M. Epstein, E. S. Shubina, *Inorg. Chem.* **2006**, *45*, 10248.

 © 2007 Wiley-VCH Verlag GmbH & Co. KGaA, Weinheim 

[9] M. S. Chinn, D. M. Heinekey, *J. Am. Chem. Soc.* **1990**, *112*, 5166.
[10] E. S. Shubina, N. V. Belkova, E. V. Bakhmutova, E. V. Vorontsov, V. I. Bakhmutov, A. V. Ionidis, C. Bianchini, L. Marvelli, M. Peruzzini, L. M. Epstein, *Inorg. Chim. Acta* **1998**, *280*, 302.
[11] N. V. Belkova, E. S. Shubina, E. I. Gutsul, L. M. Epstein, I. L. Eremenko, S. E. Nefedov, *J. Organomet. Chem.* **2000**, *610*, 58.
[12] S. Gründeman, S. Ulrich, H.-H. Limbach, N. S. Golubev, G. S. Denisov, L. M. Epstein, S. Sabo-Etienne, B. Chaudret, *Inorg. Chem.* **1999**, *38*, 2550.
[13] N. V. Belkova, P. O. Revin, M. Besora, M. Baya, L. M. Epstein, A. Lledós, R. Poli, E. S. Shubina, E. V. Vorontsov, *Eur. J. Inorg. Chem.* **2006**, 2192.
[14] B. Pleune, R. Poli, J. C. Fettinger, *Organometallics* **1997**, *16*, 1581.
[15] J. Andrieu, N. V. Belkova, M. Besora, E. Collange, L. M. Epstein, A. Lledós, R. Poli, P. O. Revin, E. S. Shubina, E. V. Vorontsov, *Russ. Chem. Bull.* **2003**, *52*, 2679.
[16] J. H. Shin, D. G. Churchill, G. Parkin, *J. Organomet. Chem.* **2002**, *642*, 9.
[17] E. Le Grognec, R. Poli, P. Richard, *Organometallics* **2000**, *19*, 3842.
[18] M. A. A. F. D. C. T. Carrondo, M. J. Calhorda, M. B. Hursthouse, *Acta Crystallogr., Sect. C: Cryst. Struct. Commun.* **1987**, *43*, 880.
[19] T. Steiner, *J. Chem. Crystallogr.* **1999**, *29*, 1235.
[20] L. M. Epstein, L. N. Saitkulova, G. P. Zol'nikova, D. N. Kravtsov, *Metalloorganicheskaya Khimiya* **1991**, *4*, 1368.
[21] The starting material contains a minor amount of the [Cp*Mo($\kappa^1$-dppe)$H_5$] contaminant, which is characterized by a doublet resonance at –3.09 ppm in the $^1$H NMR spectrum and by a singlet at 57.2 ppm in the $^{31}P\{^1H\}$ NMR spectrum. This is the typical by-product of the [Cp*Mo(dppe)$H_3$] synthesis[13] and is present in variable amounts in different samples. It is rather difficult to completely remove this impurity, but its presence does not interfere with the observed transformations since it is less basic than the trihydride complex (thus is not consumed when using substoichiometric amounts of TFA), whereas it is transformed into the trihydride complex with $H_2$ evolution by an excess amount of the acid.
[22] These two resonances are sufficiently sharp for detection only on a high-field instrument ($^{31}$P resonance at 202 MHz).
[23] E. S. Shubina, N. V. Belkova, A. N. Krylov, E. V. Vorontsov, L. M. Epstein, D. G. Gusev, M. Niedermann, H. Berke, *J. Am. Chem. Soc.* **1996**, *118*, 1105.
[24] C. Reichardt, *Solvents and Solvent Effects in Organic Chemistry*, 3rd ed., WILEY-VCH, Weinheim, **2003**.
[25] S. O. Morgan, H. H. Lowry, *J. Phys. Chem.* **1930**, *34*, 2385.
[26] S. Sharif, G. S. Denisov, M. D. Toney, H.-H. Limbach, *J. Am. Chem. Soc.* **2006**, *128*, 3375.
[27] C. Carvajal, K. J. Tolle, J. Smid, M. Szwarc, *J. Am. Chem. Soc.* **1965**, *87*, 5548.
[28] D. J. Metz, A. Glines, *J. Phys. Chem.* **1967**, *71*, 1158.
[29] A. V. Iogansen, *Theor. Experim. Khim.* **1971**, *7*, 302.
[30] J. Z. Dega-Szafran, M. Grundwald-Wyspianska, M. Szafran, *Spectrochim. Acta, Ser. A* **1991**, *47*, 543.
[31] L. M. Epstein, A. N. Krylov, E. S. Shubina, *J. Mol. Struct.* **1994**, *322*, 345.
[32] E. S. Shubina, A. N. Krylov, N. V. Belkova, L. M. Epstein, A. P. Borisov, V. D. Mahaev, *J. Organomet. Chem.* **1995**, *493*, 275.
[33] W. Klemperer, G. C. Pimentel, *J. Chem. Phys.* **1954**, *22*, 1399.
[34] J. P. Castaneda, G. S. Denisov, S. Y. Kucherov, V. M. Schreiber, A. V. Shurukhina, *J. Mol. Struct.* **2003**, *660*, 25.
[35] G. V. Gusakova, G. S. Denisov, A. L. Smolyanskii, *Optika i Spektroskopiya* **1972**, *32*, 922.
[36] This band is slightly shifted relative to that obtained upon the interaction of [Cp*Mo(dppe)$H_3$] with TFA, because of the effect of the $Na^+$ and $BF_4^-$ present in solution.
[37] J. Sandström, *Dynamic NMR Spectroscopy*, Academic Press, London, **1982**.
[38] A. Altomare, M. Burla, M. Camalli, G. Cascarano, C. Giacovazzo, A. Guagliardi, A. Moliterni, G. Polidori, R. Spagna, *J. Appl. Crystallogr.* **1999**, *32*, 115.
[39] G. M. Sheldrick, *SHELXL97. Program for Crystal Structure Refinement*, University of Göttingen, Göttingen, Germany, **1997**.
[40] L. J. Farrugia, *J. Appl. Crystallogr.* **1997**, *30*, 565.

Received: January 7, 2007
Published Online: April 17, 2007

 © 2007 Wiley-VCH Verlag GmbH & Co. KGaA, Weinheim 

DOI: 10.1002/ejic.200700121

# Synthesis, Characterization and Stability of Spirodiene Complexes of Molybdenum(II): New Route to *ansa*-Molybdenocene and Ring-Functionalized Molybdenocene Compounds

**Jan Honzíček,[a] Filipe A. Almeida Paz,[b] and Carlos C. Romão*[a]**

**Keywords:** Metallocenes / Molybdenum / Spiro compounds / Functionalized cyclopentadienes / X-ray diffraction

The reactions of $[Mo(CO)_2(Cp)(NCCH_3)_2][BF_4]$ (**1**) with spiro[2.4]hepta-4,6-diene and spiro[4.4]nona-1,3-diene give the complexes $[Mo\{\eta^4\text{-}C_5H_4(CH_2)_2\}(CO)_2(Cp)][BF_4]$ (**3**) and $[Mo\{\eta^4\text{-}C_5H_4(CH_2)_4\}(CO)_2(Cp)][BF_4]$ (**4**), respectively. $[Mo\{\eta^4\text{-}C_5H_4(CH_2)_2\}(CO)_2(Cp)][BF_4]$ (**3**) is stable towards ring opening at room temperature, but its formation is accompanied by small amounts of ring-opening products $[Mo(\eta^5\text{-}C_5H_4CH_2\text{-}\eta^1\text{-}CH_2)(CO)(Cp)][BF_4]$ (**5**) and $[Mo\{\eta^5\text{-}C_5H_4(CH_2)_2\text{-}\eta^1\text{-}CO\}(CO)(Cp)][BF_4]$ (**6**). With 1,1-dimethylspiro[2.4]hepta-4,6-diene, two isomers with the formula $[Mo\{\eta^4\text{-}C_5H_4CH_2C(CH_3)_2\}(CO)_2(Cp)][BF_4]$ are formed (**7** and **8**). While the *endo*-isomer **7** is stable towards ring opening, the *exo*-isomer **8** slowly rearranges to the ring-opened product $[Mo\{\eta^5\text{-}C_5H_4C(CH_3)_2CH_2\text{-}\eta^1\text{-}CO\}(CO)(Cp)][BF_4]$ (**9**). The reaction of $[Mo(CO)_2(Ind)(NCCH_3)_2][BF_4]$ (**2**) with spiro[4.4]nona-1,3-diene also gives the diene coordinated species $[Mo\{\eta^4\text{-}C_5H_4(CH_2)_4\}(CO)_2(Ind)][BF_4]$ (**11**), which is the first example of a structurally characterized, coordinated, unsubstituted spirodiene. In contrast, reaction of **2** with spiro[2.4]hepta-4,6-diene leads directly to the *ansa*-cyclopentadienyl complex $[Mo(\eta^5\text{-}C_5H_4CH_2\text{-}\eta^1\text{-}CH_2)(CO)(Ind)][BF_4]$ (**12**). Reaction of **12** with bromine or iodine leads to the formation of Cp-substituted molybdenocene derivatives $[Mo\{\eta^5\text{-}C_5H_4(CH_2)_2X\}(CO)(Ind)X][BF_4]$ (**13**: X = Br, **14**: X = I). The compounds $[Mo(\eta^5\text{-}C_5H_4CH_2\text{-}\eta^1\text{-}CH_2)(CO)(Ind)][BF_4]$ (**12**) and $[MoBr\{\eta^5\text{-}C_5H_4(CH_2)_2Br\}(CO)(Ind)][Br]\cdot 0.5H_2O$ (**13a**) were structurally characterized, and they open the way to new functionalized molybdenocene complexes that have biological applications.

(© Wiley-VCH Verlag GmbH & Co. KGaA, 69451 Weinheim, Germany, 2007)

## Introduction

Bent metallocene complexes of the type $[M(Cp)_2X_2]$ (M = Ti, V, Nb, Mo; X = halide) have been investigated for their use in biological applications ever since their antitumor activity was discovered by Köpf and Köpf-Maier.[1] Because of the particular requirements of such applications, which include aqueous solubility and biocompatibility, considerable attention has been given in the last few years to the synthesis of modified and functionalized variants of such complexes. Substitution of halide ligands gives compounds with modified physical and chemical properties. This approach leaves the "$M(Cp)_2$" moiety unchanged, and properly chosen substituents can help in overcoming problems, such as low water solubility[2] or biological incompatibility,[3] that complicate the use of the parent compounds. Furthermore, substitution can protect the "$M(Cp)_2$" moiety during transport into the tumor cells. The active species is then generated in close proximity of or directly in the tumor cell.[4]

However, modification of the Cp rings seems to be a more promising approach towards solving of the abovementioned problems, as shown by the many results obtained in the field of bioorganometallic radiopharmaceuticals.[5] Such a modification could enable the fine tuning of cytostatic properties as was recently shown by the titanocene compounds.[6] Moreover, it allows the introduction of reactive groups that offer an anchor on which to append biologically active molecules capable of directing the final complex to the target receptors or diseased tissues.[7] This is a central issue in chemotherapy, because the treatment then becomes more effective at low doses and the damage to non-targeted and/or healthy tissues is minimized.

In the case of group IV metallocenes, a variety of ring-substituted compounds containing functional groups on one or both cyclopentadienyl rings is known,[8] thus supporting a wider range of in vitro[9] and in vivo biological tests.[10] For group V and VI metals, the quest for suitable synthetic routes is still on-going. Following our long-standing interest in the chemistry of the highly stable molybdenocene fragment, and the fact that the dichloride $[MoCl_2(Cp)_2]$ is currently under comprehensive scrutiny because of its mechanism towards antitumor action,[11] we decided to

[a] Instituto de Tecnologia Química e Biológica da Universidade Nova de Lisboa,
Av. da República, EAN, 2780-157 Oeiras, Portugal
[b] Department of Chemistry, University of Aveiro, CICECO, 3810-193 Aveiro, Portugal
Fax: +351-21-441-12-77
E-mail: ccr@itqb.unl.pt

Supporting information for this article is available on the WWW under http://www.eurjic.org or from the author.

 © 2007 Wiley-VCH Verlag GmbH & Co. KGaA, Weinheim 

explore a new suitable approach towards achieving functionalization of its rings. The introduction of alkyl substituents in one[12] or both rings has been documented.[13]

Compounds with $\eta^5$:$\eta^1$-cyclopentadienidoethyl ligands, which are derived from C–C cleavage of spirodiene compounds by the $Mo^0$ species, are potent precursors for ring-functionalized group VI metallocenes.[14] When Mo atoms are used for this purpose, the resulting *ansa* complex $[Mo(\eta^5\text{-}C_5H_4CH_2\text{-}\eta^1\text{-}CH_2)_2]$ enables the introduction of various substituents containing functional groups onto the cyclopentadienyl rings.[15] The resulting products are functionalized equally on both rings. The problem of functionalizing only one of cyclopentadienyl rings could probably be solved by the use of the *ansa* compound $[Mo(\eta^5\text{-}C_5H_4CH_2\text{-}\eta^1\text{-}CH_2)(\eta^4\text{-}C_5H_6)(CO)]$[16] that was previously synthesized from $[Mo(\eta^5\text{-}C_5H_4CH_2\text{-}\eta^1\text{-}CH_2)(CO)_3]$[17] and cyclopentadiene through a photochemical route. Unfortunately, none of these routes is very practical in the absence of metal vapor synthesis equipment or sound control of the photochemical reactions. In the present work, we propose another approach starting from the readily available $Mo^{II}$ allyl complexes $[Mo(\eta^3\text{-}C_3H_5)(CO)_2(Cp')]$ (Cp′ = Cp, Ind). These compounds, activated by $HBF_4$, as well as their stabilized counterparts $[M(CO)_2(Cp')(NCCH_3)_2][BF_4]$ (**1**: Cp′ = Cp, **2**: Cp′ = Ind) are known as strong dienophiles that could be capable of coordinating spiro[2.4]hepta-4,6-diene and spiro[4.4]nona-1,3-diene to give the $\eta^4$-diene complexes.[18] The question to be answered involved the possibility that such a coordination could activate the spirodiene ligands towards C–C cleavage and aromatization of the cyclopentadienyl ring, even in spite of the fact that the Mo center is in the +2 oxidation state; this issue was probed before, not only for Mo, but also for W, Fe, Co and Ni.[19] The following work gives an affirmative answer to this question and provides a new route to differentially substituted molybdenocene derivatives.

## Results

### Cyclopentadienyl Complexes

$[Mo(CO)_2(Cp)(NCCH_3)_2][BF_4]$ (**1**) reacts with spiro[2.4]-hepta-4,6-diene and spiro[4.4]nona-1,3-diene in $CH_2Cl_2$ at room temperature to give compounds $[Mo\{\eta^4\text{-}C_5H_4(CH_2)_2\}(CO)_2(Cp)][BF_4]$ (**3**) and $[Mo\{\eta^4\text{-}C_5H_4(CH_2)_4\}(CO)_2(Cp)][BF_4]$ (**4**), respectively. While **4** was the only product detected in its reaction mixture, for the reaction leading to **3**, two other ring-opening products were detected in the crude product. The sample collected before recrystallization contained approximately 86% of compound **3**, 7% of $[Mo(\eta^5\text{-}C_5H_4CH_2\text{-}\eta^1\text{-}CH_2)(CO)(Cp)][BF_4]$ (**5**) and 7% of $[Mo\{\eta^5\text{-}C_5H_4(CH_2)_2\text{-}\eta^1\text{-}CO\}(CO)(Cp)][BF_4]$ (**6**), as determined by $^1H$ NMR spectroscopy (see Scheme 1).

Both **3** and **4** are stable complexes in solution in the absence of strong light, and they can be recrystallized from $CH_2Cl_2/Et_2O$. This means that compounds **5** and **6** are not formed directly by decomposition of **3** but result from unclear events occurring in the initial reaction mixture. The infrared spectra of compounds **3** and **4** show two CO stretching vibrations each in the typical region for similar cationic compounds with terminal carbonyl groups (**3**: 2019, 1960 $cm^{-1}$; **4**: 2020, 1964 $cm^{-1}$).[19] $^1$NMR and $^{13}C\{^1H\}$ NMR spectra of these compounds are consistent with the $\eta^4$-coordination of the appropriate spirodiene. The resonances for the protons of the diene system are shifted to higher field upon coordination, relative to the resonances for the free ligands. Furthermore, coordination results in nonequivalent methylene groups. In the NMR spectrum of compound **3**, the signals for the protons of both methylene groups are also shifted to higher field. Nevertheless, this shift is much smaller than that recently reported for the iron(0) complex $[Fe\{\eta^4\text{-}C_5H_4(CH_2)_2\}(CO)_3]$[20] (see Table 1). We assign the resonance at higher field to the methylene protons on the external face of the coordinated spiro[2.4]hepta-4,6-diene, in accord with reported literature observations for coordinated cyclopentadienes. In fact, $[M(\eta^4\text{-}5R,5R'\text{-}C_5H_4)L_n]$ complexes, where R, R′ = $CH_2X$, systematically reveal higher field resonances for the $CH_2X$ substituent on the diene face opposite to the metal.[21] This effect is also observed in the very similar complexes $[M\{\eta^4\text{-}C_5(CH_3)_5H\}(CO)_2(Cp)]^+$ (M = Mo, W).[12a]

In compound **4**, only the protons of the methylene groups that are in neighborhood of the *ipso* carbon atom are affected by the coordination. The signals that are shifted to higher field are assigned to the methylene protons on the external face, while the signals at lower field to those on

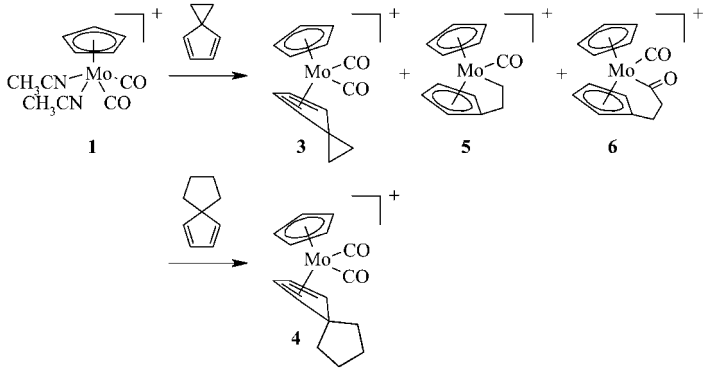


Scheme 1. Products of the reactions between compound **1** and spiro[2.4]hepta-4,6-diene and spiro[4.4]nona-1,3-diene.

 © 2007 Wiley-VCH Verlag GmbH & Co. KGaA, Weinheim 

Table 1. Chemical shifts of spiro[2.4]hepta-4,6-diene, spiro[4.4]nona-1,3-diene, and their complexes [ppm].

| | | $C_5H_4$ | $C_{ipso}$ | $CH_2$ | $CH_2$ |
|---|---|---|---|---|---|
| Spiro[2.4]hepta-4,6-diene[14b] | $^1H$ | 6.54, 6.15 | | 1.68 | |
| | $^{13}C\{^1H\}$ | 139.2, 129.1 | 37.7 | 12.5 | |
| $[Mo\{\eta^4\text{-}C_5H_4(CH_2)_2\}(CO)_2(Cp)][BF_4]$ (**3**) | $^1H$ | 6.49, 4.82 | | 1.32,[a] 0.66[b] | |
| | $^{13}C\{^1H\}$ | 96.8, 88.7 | —[c] | 28.6,[a] 14.3[b] | |
| $[Fe\{\eta^4\text{-}C_5H_4(CH_2)_2\}(CO)_3]$[20] | $^1H$ | 5.73, 2.90 | | 0.90,[a] 0.32[b] | |
| Spiro[4.4]nona-1,3-diene | $^1H$ | 6.34, 6.22 | | 1.89 | 1.72 |
| | $^{13}C\{^1H\}$ | 144.0, 128.8 | 43.6 | 32.5 | 26.1 |
| $[Mo\{\eta^4\text{-}C_5H_4(CH_2)_4\}(CO)_2(Cp)][BF_4]$ (**4**) | $^1H$ | 6.13, 5.09 | | 2.09,[a] 1.31[b] | 1.70,[a] 1.60[b] |
| | $^{13}C\{^1H\}$ | 96.4, 85.7 | 72.4 | 52.3,[a] 37.8[b] | 25.3,[a] 25.0[b] |
| $[Mo\{\eta^4\text{-}C_5H_4(CH_2)_4\}(CO)_2(Ind)][BF_4]$ (**11**) | $^1H$ | 5.30, 4.85 | | 1.83,[a] 1.10[b] | 1.57,[a] 1.44[b] |
| | $^{13}C\{^1H\}$ | 93.2, 85.2 | 71.6 | 51.9,[a] 37.1[b] | 24.9,[a] 24.7[b] |

[a] Internal face. [b] External face. [c] Not observed.

the internal face. The connectivity between the methylene groups was established by selective irradiation experiments. $^{13}C\{^1H\}$ NMR spectra of compounds **3** and **4** show that the signals for the diene carbon atoms are shifted to higher field, while the signals for the *ipso* carbon atoms and for the neighboring methylene groups appear at lower field (see Table 1). The methylene carbon atoms on the external face have resonances that are upfield relative to those for the carbon atoms on the internal face.

The ring-opening products **5** and **6** were not possible to isolate and identify separately. They were identified by NMR spectroscopy, performed on the reaction mixture containing **5** and **6** together with **3**, and their identification was based on the diastereotopic protons of the methylene groups. The connectivity between the assigned multiplets of these minor compounds was established by selective irradiation experiments (for appropriate spectra see the Supporting Information). For compound **5**, these resonances were found at $\delta$ = 2.82, 2.62, –0.41 and –0.89 ppm. The last two high field signals were assigned to the methylene group bonded to molybdenum as depicted in Scheme 1. They are in agreement with those reported for similar *ansa* alkyls such as $[Mo(\eta^5\text{-}C_5H_4CH_2\text{-}\eta^1\text{-}CH_2)_2]$.[14a] Compound **6** exhibits multiplets in its NMR spectrum at $\delta$ = 3.57–3.37 ppm (10 lines) and $\delta$ = 2.48–2.28 ppm (10 lines). These values are very similar to those reported for the compound that results from the ring opening of $[Fe\{\eta^4\text{-}C_5H_4(CH_2)_2\}(CO)_3]$ to form $[Fe(\eta^5\text{-}C_5H_4CH_2CH_2\text{-}\eta^1\text{-}CO)(CO)_2]$, which has the same kind of metal–acyl ligation proposed for **6**: $\delta$ = 3.40 (t); 2.15 ppm (t).[20] The presence of the acyl ligand could not be unequivocally established by solution IR spectroscopy because of the interference from moisture-derived absorptions and because of the low concentration of the compound. In KBr pellets, the mixture decomposed quickly.

The effect of the presence of substituents on the $sp^3$ carbon atoms of the spirodiene was studied by using 1,1-dimethyl-spiro[2.4]hepta-4,6-diene. This diene reacts with compound **1** in $CH_2Cl_2$ at room temperature (16 h) to give a 1:1:1 mixture of the *endo* **7** and *exo* isomers **8** of $[Mo\{\eta^4\text{-}C_5H_4CH_2C(CH_3)_2\}(CO)_2(Cp)][BF_4]$ and a ring-opened product (Scheme 2). The $^1H$ NMR spectra of **7** and **8** show signals for the protons in the Cp and spirodiene rings with chemical shifts similar to those found for compound **3**. Relative to the uncoordinated ligand, the resonances for the methyl protons of the *exo* isomer (**8**) and the methylene protons of the *endo* isomer (**7**) appear at higher field (**8**: $\delta$ = 0.90 ppm; **7**: $\delta$ = 0.48 ppm), which leads to the structural

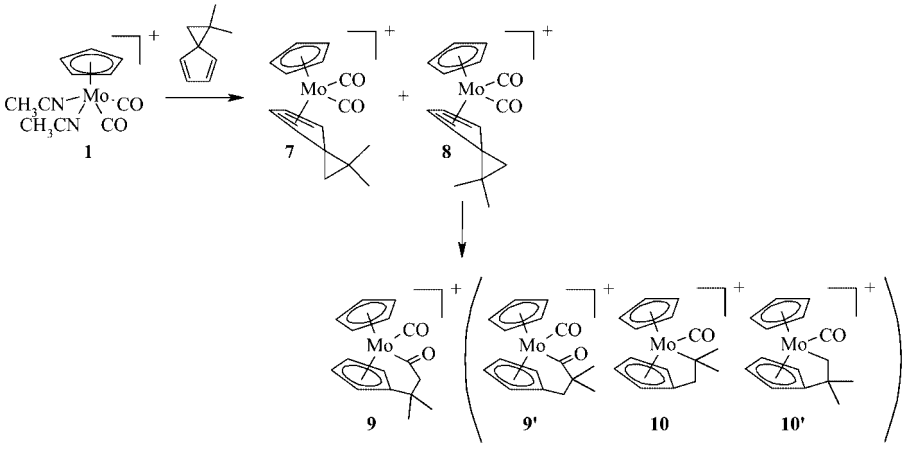


Scheme 2. Reaction of compound **1** with 1,1-dimethyl-spiro[2.4]hepta-4,6-diene.

 © 2007 Wiley-VCH Verlag GmbH & Co. KGaA, Weinheim 

assignment in Scheme 2.[21] The methyl groups of compound **7**, which are on the internal face, are not affected by coordination.

$^1$H NMR measurements of the 1:1:1 mixture in $CD_2Cl_2$, after 12 and 24 h, show exclusive activation of the *exo* isomer **8** towards ring opening (see Scheme 2). In fact, at room temperature, the resonances belonging to **7** remain unaffected, while **8** converts into a new compound, which may have one of the structures **9**, **9′**, **10**, or **10′**, as depicted in Scheme 2. The mixture of compounds **7** and the new compound, which was obtained after stirring for 24 h in $CH_2Cl_2$, is stable at room temperature, and the relative abundance of both components remains unchanged. No evidence for the formation of a second ring-opening product was observed. We were unable to isolate this new compound from the reaction mixture. Therefore, its tentative characterization relies upon the NMR spectroscopic data since solution IR spectroscopy could not conclusively identify an acyl function.

In agreement with the proposed strained *ansa* structure that would be expected from the chemistry of coordinatively activated spirodienes already exemplified by compounds **5** and **6**, the $^1$H NMR spectrum of the new compound shows diastereotopic methylene and methyl groups. The chemical shift for the methylene protons ($\delta$ = 2.22–2.12 ppm) rules out structure **10′**, since the Mo–C$H_2$ signal should appear at a much higher field. Structure **10** is not clearly compatible with the available $^1$H NMR spectroscopic data for related compounds. In fact, the C$H_2$ group at the Cp ring appears at ca. 2.5 ppm in compounds such as [Mo($\eta^5$-$C_5H_4CH_2$-$\eta^1$-$CH_2$)$_2$][15] or in **12** (see below). The more open, alternative acyl-bridged structures present the resonances for $C_5H_4$–$CH_2$ at $\delta > 3$ ppm in well-established compounds such as [Fe($\eta^5$-$C_5H_4CH_2CH_2$-$\eta^1$-CO)(CO)$_2$] (ca. 3.4 ppm)[20] or the related [Mo($\eta^5$-$C_5H_4CH_2CH_2X)_2X_2$] (X = Cl, Br, I, SPh; ca. 3.5 ppm).[15] Such chemical shift values are in agreement with those in compound **6**, which has two methylene resonances at $\delta$ = 2.22–2.12 ppm and $\delta$ = 3.57–3.37 ppm. However, since the new compound does not have any resonances in the $\delta$ = 3.5 ppm region, the formation of structure **9′** is most unlikely. Therefore, the NMR spectroscopic data is most compatible with structure **9**, although no definitive assignment is possible at present. This structure corresponds to the opening of the unhindered face of the spirodiene $C_3$ ring, which is facing the metal.

### Indenyl Compounds

[Mo(CO)$_2$(Ind)(NCCH$_3$)$_2$][BF$_4$] (**2**) was used as a starting material for the synthesis of mixed–ring molybdenocenes containing indenyl rings. Its reaction with spiro[4.4]-nona-1,3-diene gave [Mo{$\eta^4$-$C_5H_4(CH_2)_4$}(CO)$_2$(Ind)][BF$_4$] (**11**) in high yield (Scheme 3). The IR and NMR spectra of **11** are similar to those of its cyclopentadienyl counterpart **4**. In the NMR spectra of compound **11**, the signals for the spiro[4.4]nona-1,3-diene protons and carbon atoms are shifted to a higher field than those of **4**, which is in according with the higher electrophilicity of the Mo$^{II}$ center. The CO stretching vibrations of **11** occur at 2005 and 1950 cm$^{-1}$. These values are lower than those of the cyclopentadienyl counterpart **4**. The structure of **11** was confirmed by X-ray diffraction crystallography, as discussed below.

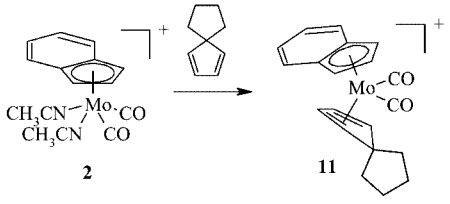


Scheme 3. Synthesis of compound **11**.

In contrast to the latter reaction, the ring-opened *ansa* compound [Mo($\eta^5$-$C_5H_4CH_2$-$\eta^1$-$CH_2$)(CO)(Ind)][BF$_4$] (**12**) was found to be the sole product of the reaction between **2** and spiro[2.4]hepta-4,6-diene (Scheme 4). The IR spectrum of this compound shows only one band in range for CO vibrations (1991 cm$^{-1}$). The $^1$H NMR spectrum shows four multiplets that are assigned to the substituted cyclopentadienyl ring, seven multiplets for the indenyl ring, and four multiplets for the ethylene bridge. The nonequivalence of the cyclopentadienyl and indenyl protons, which is caused by the low symmetry of complex **12**, is also observed in the $^{13}$C{$^1$H} NMR spectrum. The methylene protons were found to be diastereotopic, which is similar to that found for the cyclopentadienyl analog **5**. The abnormally high-field signal in the $^1$H NMR ($\delta$ = –0.07 ppm and –3.21 ppm) and $^{13}$C{$^1$H} NMR ($\delta$ = –39.3 ppm) spectra provide evidence for the bonding of the methylene group to the metal. The structural assignment of **12** was confirmed by X-ray crystallography, as discussed below.

Compound **12** is a suitable starting material for the preparation of ring-substituted compounds. Indeed, according to Scheme 4, its reactions with halogens give the compounds [Mo{$\eta^5$-$C_5H_4(CH_2)_2X$}(CO)(Ind)X][BF$_4$] (**13**: X = Br, **14**: X = I) in high yield. These compounds provide NMR spectra that are expected for compounds with $\eta^5$-bonded indenyl and substituted $\eta^5$-cyclopentadienyl rings. In compound **13**, the protons of the methylene group bonded to the cyclopentadienyl ring are diastereotopic and

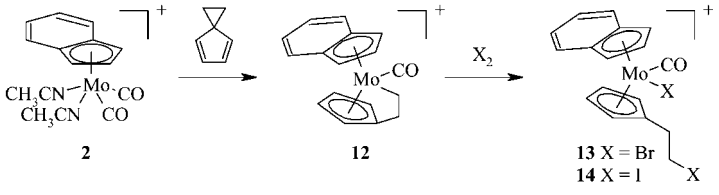


Scheme 4. Reaction of compound **2** with spiro[2.4]hepta-4,6-diene.

 © 2007 Wiley-VCH Verlag GmbH & Co. KGaA, Weinheim 

thus give rise to a six-line multiplet at $\delta$ = 3.54 ppm. In the case of compound **14**, this effect was observed for both methylene groups. The six-line multiplets are found at $\delta$ = 3.37 and 2.84 ppm. This effect is probably caused by the larger steric hindrance of iodine. The IR spectra of compounds **13** and **14** show CO stretching vibrations at 2055 and 2049 $cm^{-1}$. These values correspond to those found for analogous compounds without substituents on the cyclopentadienyl ring.[12a] These structural assignments are supported by the X-ray diffraction crystal structure obtained for compound **13**, as discussed below.

### Mass Spectrometry

Compounds **3**, **4**, **11**, **12**, **13**, and **14** were characterized by positive-ion ESI mass spectrometry. These compounds have common features and give the peaks for the parent cation $[M - BF_4]^+$ and for $[M - BF_4 - CO]^+$. As expected, the peaks for $[M - BF_4 - 2(CO)]^+$ were observed for compounds containing two carbonyl ligands (**3**, **11**). The mass spectra for the spirodiene compounds **3** and **11** and the *ansa* compound **12** contain peaks that are formed from dehydrogenation. Compounds **3** and **12** exhibit the peaks assigned to $[M - BF_4 - 2(CO) - H_2]^+$ and $[M - BF_4 - CO - H_2]^+$ in their spectra, respectively. The peaks for $[M - BF_4 - 2(CO) - H_2]^+$ and $[M - BF_4 - 2(CO) - 2H_2]^+$, which were found in the case of compound **11**, suggest the possibility of single and double dehydrogenation for the compounds that contain a chain of four methylene groups.

### X-ray Analyses of Compounds 11, 12, and 13a

The structures of $[Mo\{\eta^4\text{-}C_5H_4(CH_2)_4\}(CO)_2(Ind)][BF_4]$ (**11**), $[Mo(\eta^5\text{-}C_5H_4CH_2\text{-}\eta^1\text{-}CH_2)(CO)(Ind)][BF_4]$ (**12**), and $[MoBr\{\eta^5\text{-}C_5H_4(CH_2)_2Br\}(CO)(Ind)][Br]\cdot 0.5H_2O$ (**13a**) were determined in the solid state at 100(2) K (**11**) or at 150(2) K (**12**, **13a**) by single-crystal X-ray diffraction. Figures 1, 2, and 3 depict the crystallographically independent cationic complexes present in the crystal structures of **11**, **12**, and **13a**, respectively. Tables 2, 3, and 4 summarize the most relevant and structurally significant geometrical parameters associated with these structures. The asymmetric units of **12** and **13a** each comprise two crystallographically independent molybdenum complexes (Figures 2 and 3).

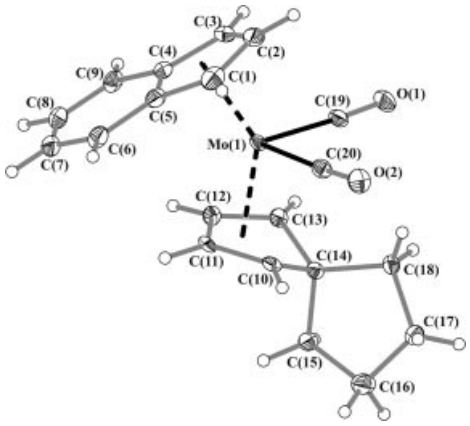


Figure 1. Schematic representation of the cationic complex $[Mo\{\eta^4\text{-}C_5H_4(CH_2)_4\}(CO)_2(Ind)]^+$ present in the crystal structure of **11**; the labeling scheme for all non-hydrogen atoms is shown. Thermal ellipsoids are drawn at the 30% probability level, and hydrogen atoms are represented as small spheres with arbitrary radii. Mo–C bonds to the $\eta^5$-indenyl and $\eta^4\text{-}C_5H_4(CH_2)_4$ organic ligands are shown as black-filled dashed bonds to the corresponding centers of gravity ($C_{g,Ind}$ and $C_{g,diene}$, respectively).

The Mo–C bonds observed for the indenyl ligands [found in the ranges 2.301(5)–2.413(4) Å, 2.254(4)–2.460(3) Å, and 2.264(3)–2.454(3) Å for structures **11**, **12**, and **13a**, respectively] are well within the range found for similar structures (38 entries in the CSD, with Mo···C interatomic distances in the range 2.24–2.50 Å; median 2.31 Å).[22] The significant spread of the interatomic Mo···C distances (magnitude of 0.26 Å for the expected range) is typical for $\eta^5$-Ind coordination. Likewise, the distances to the center of gravity, Mo···$C_{g,Ind}$, are in perfect agreement with known values for $\eta^5$-hapticity (38 entries; 1.95–2.19 Å with a median of

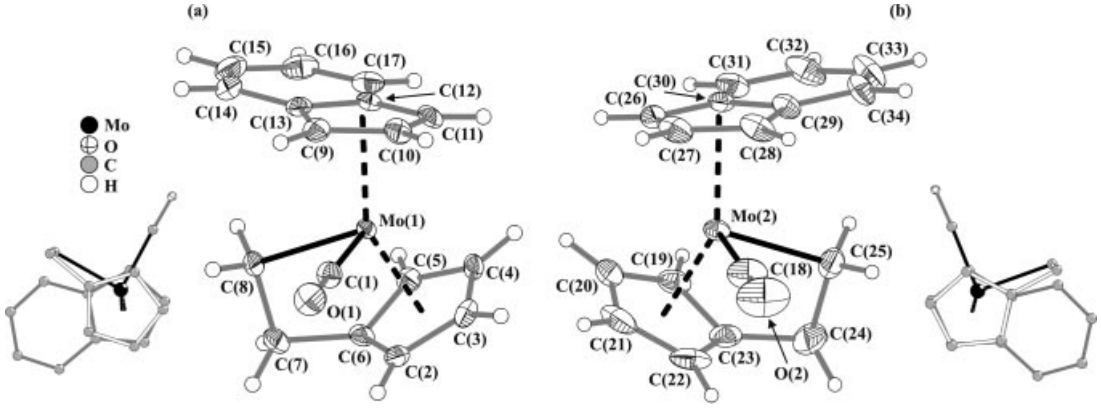


Figure 2. Schematic representation of the two crystallographically independent $[Mo(\eta^5\text{-}C_5H_4CH_2\text{-}\eta^1\text{-}CH_2)(CO)(Ind)]^+$ cationic complexes present in the crystal structure of **12** (*R* and *S* configurations); the labeling scheme for all non-hydrogen atoms is shown. Thermal ellipsoids are drawn at the 30% probability level, and hydrogen atoms are represented as small spheres with arbitrary radii. Mo–C bonds to the $\eta^5$-indenyl and $\eta^5$-cyclopentadienyl ligands are shown as black-filled dashed bonds to the corresponding centers of gravity ($C_{g,Ind}$ and $C_{g,Cp}$, respectively). The top view of each complex is represented on the side (hydrogen atoms have been omitted for clarity).

 © 2007 Wiley-VCH Verlag GmbH & Co. KGaA, Weinheim 

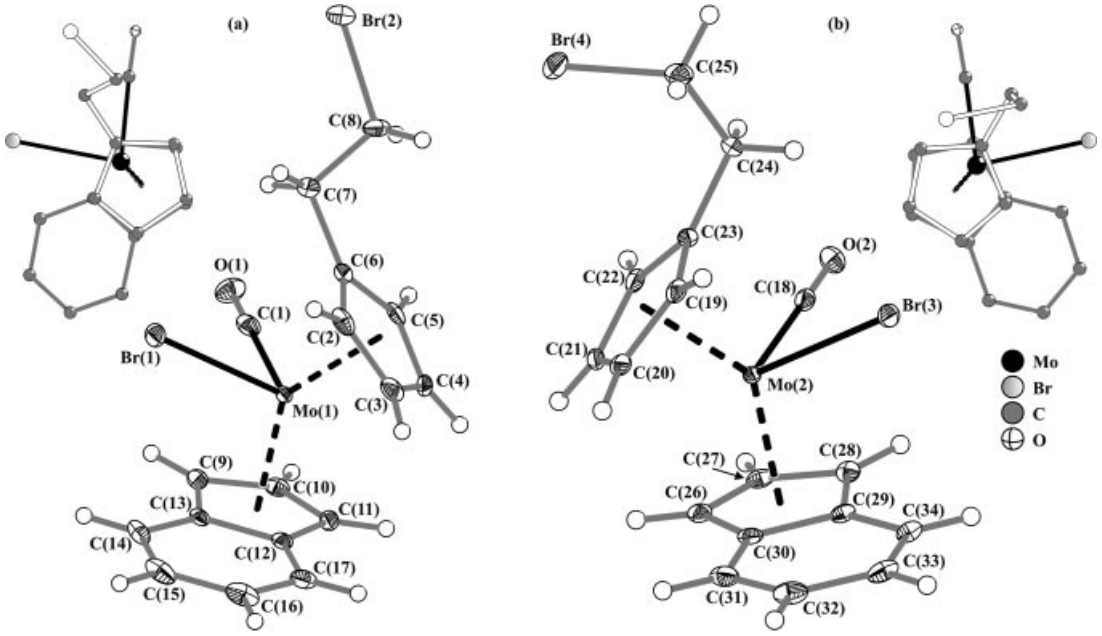


Figure 3. Schematic representation of the two crystallographically independent $[MoBr\{\eta^5\text{-}C_5H_4(CH_2)_2Br\}(CO)(Ind)]^+$ cationic complexes present in the crystal structure of **13a** (*S* and *R* configurations); the labeling scheme for all non-hydrogen atoms are shown. Thermal ellipsoids are drawn at the 30% probability level, and hydrogen atoms are represented as small spheres with arbitrary radii. Mo–C bonds to the $\eta^5$-indenyl and $\eta^5$-cyclopentadienyl ligands are shown as black-filled dashed bonds to the corresponding centers of gravity ($C_{g,Ind}$ and $C_{g,Cp}$, respectively). The top views of each complex are represented on the side (hydrogen atoms have been omitted for clarity).

Table 2. Selected bond lengths [Å] and angles [°] for the molybdenum coordination environment present in $[Mo\{\eta^4\text{-}C_5H_4(CH_2)_4\}(CO)_2(Ind)][BF_4]$ (**11**).[a,b]

| | | | |
|---|---|---|---|
| Mo(1)–C(1) | 2.301(5) | $C_{g,Ind}$···Mo(1)–C(19) | 113.63(4) |
| Mo(1)–C(2) | 2.276(5) | $C_{g,Ind}$···Mo(1)–C(20) | 112.45(5) |
| Mo(1)–C(3) | 2.304(4) | $C_{g,Ind}$···Mo(1)···$C_{g,diene}$ | 137.03(5) |
| Mo(1)–C(4) | 2.414(4) | $C_{g,diene}$···Mo(1)–C(19) | 97.28(4) |
| Mo(1)–C(5) | 2.413(4) | $C_{g,diene}$···Mo(1)–C(20) | 98.78(4) |
| Mo(1)–C(10) | 2.448(4) | C(19)–Mo(1)–C(20) | 84.96(18) |
| Mo(1)–C(11) | 2.276(4) | | |
| Mo(1)–C(12) | 2.284(4) | | |
| Mo(1)–C(13) | 2.446(4) | | |
| Mo(1)–C(19) | 1.975(5) | | |
| Mo(1)–C(20) | 1.968(4) | | |
| Mo(1)···$C_{g,Ind}$ | 2.002(2) | | |
| Mo(1)···$C_{g,diene}$ | 2.062(2) | | |

[a] $C_{g,Ind}$ – centroid of the coordinated $\eta^5$-indenyl aromatic ring [C(1) to C(5)]. [b] $C_{g,diene}$ – centroid of the coordinated $\eta^4$-diene ligand [C(10) to C(13)].

Table 3. Selected bond lengths [Å] and angles [°] for the two molybdenum coordination environments present in $[Mo(\eta^5\text{-}C_5H_4CH_2\text{-}\eta^1\text{-}CH_2)(CO)(Ind)][BF_4]$ (**12**, see Figure 2).[a,b]

| Complex (a) | | Complex (b) | |
|---|---|---|---|
| Mo(1)–C(1) | 2.002(3) | Mo(2)–C(18) | 1.973(4) |
| Mo(1)–C(2) | 2.297(3) | Mo(2)–C(19) | 2.276(4) |
| Mo(1)–C(3) | 2.291(3) | Mo(2)–C(20) | 2.290(4) |
| Mo(1)–C(4) | 2.289(3) | Mo(2)–C(21) | 2.295(4) |
| Mo(1)–C(5) | 2.276(3) | Mo(2)–C(22) | 2.284(4) |
| Mo(1)–C(6) | 2.293(3) | Mo(2)–C(23) | 2.303(4) |
| Mo(1)–C(8) | 2.271(3) | Mo(2)–C(25) | 2.273(4) |
| Mo(1)–C(9) | 2.307(3) | Mo(2)–C(26) | 2.254(4) |
| Mo(1)–C(10) | 2.274(3) | Mo(2)–C(27) | 2.275(4) |
| Mo(1)–C(11) | 2.268(3) | Mo(2)–C(28) | 2.322(3) |
| Mo(1)–C(12) | 2.377(3) | Mo(2)–C(29) | 2.460(3) |
| Mo(1)–C(13) | 2.449(3) | Mo(2)–C(30) | 2.375(3) |
| Mo(1)···$C_{g,Ind}$ | 1.995(1) | Mo(2)···$C_{g,Ind}$ | 2.000(1) |
| Mo(1)···$C_{g,Cp}$ | 1.944(1) | Mo(2)···$C_{g,Cp}$ | 1.950(1) |
| $C_{g,Ind}$···Mo(1)–C(1) | 102.81(2) | $C_{g,Ind}$···Mo(2)–C(18) | 102.41(2) |
| $C_{g,Ind}$···Mo(1)–C(8) | 108.31(1) | $C_{g,Ind}$···Mo(2)–C(25) | 107.90(4) |
| $C_{g,Ind}$···Mo(1)···$C_{g,Cp}$ | 145.43(2) | $C_{g,Ind}$···Mo(2)···$C_{g,Cp}$ | 145.46(2) |
| $C_{g,Cp}$···Mo(1)–C(1) | 105.36(3) | $C_{g,Cp}$···Mo(2)–C(18) | 105.24(1) |
| $C_{g,Cp}$···Mo(1)–C(8) | 92.13(1) | $C_{g,Cp}$···Mo(2)–C(25) | 91.31(2) |
| C(1)–Mo(1)–C(8) | 88.51(14) | C(18)–Mo(2)–C(25) | 92.4(2) |

[a] $C_{g,Ind}$ – centroid of the coordinated $\eta^5$-indenyl aromatic rings [C(9) to C(13) and C(26) to C(30)]. [b] $C_{g,Cp}$ – centroid of the coordinated $\eta^5$-cyclopentadienyl ligand [C(2) to C(6) and C(19) to C(23)].

2.03 Å). The values of the fold angle $\psi$ (3.79° for **11**, 4.41° and 4.63° for **12**, and 5.66° and 6.17° for **13a**) are also in line with this coordination mode (typically in the range 0.25–9.63° with a median of 4.40°).[23]

To the best of our knowledge, complex **11** represents the first reported crystal structure of a complex with an unsubstituted spirocyclic cyclopentadiene group. Spiro[4.4]nona-1,3-diene is coordinated in a typical $\eta^4$-coordination fashion (Figure 1), with all Mo···C distances in the range 2.276(4)–2.448(4) Å (Table 2). The corresponding four carbon atoms [C(10) to C(13)] lie almost on the same plane (maximum deviation 0.004(5) Å). This plane is perpendicular to the metal–diene centroid vector [{Mo(1)–$C_{g,diene}$}–$P_{diene}$ = 89.8(3)°; $P_{diene}$ is the diene plane]. The C–C bond lengths of the diene system [C(10)–C(11) = 1.402(7) Å; C(11)–C(12) = 1.424(6) Å; C(12)–C(13) = 1.396(7) Å] correspond to a butadiene fragment. The distance between the centroid of the diene system and molybdenum [$C_{g,diene}$–Mo(1)] is 2.062(5) Å. The spiro carbon atom [C(14)] is found to lie 0.496(4) Å out of the diene plane. The angle

 © 2007 Wiley-VCH Verlag GmbH & Co. KGaA, Weinheim 

Table 4. Selected bond lengths [Å] and angles [°] for the two molybdenum coordination environments present in [MoBr{$\eta^5$-$C_5H_4(CH_2)_2Br$}(CO)(Ind)][Br]·0.5$H_2O$ (**13a**, see Figure 3).[a,b]

| Complex (a) | | Complex (b) | |
|---|---|---|---|
| Mo(1)–C(1) | 2.019(4) | Mo(2)–C(18) | 2.005(4) |
| Mo(1)–C(2) | 2.347(3) | Mo(2)–C(19) | 2.350(3) |
| Mo(1)–C(3) | 2.369(4) | Mo(2)–C(20) | 2.379(3) |
| Mo(1)–C(4) | 2.322(3) | Mo(2)–C(22) | 2.283(3) |
| Mo(1)–C(5) | 2.288(3) | Mo(2)–C(21) | 2.316(3) |
| Mo(1)–C(6) | 2.289(3) | Mo(2)–C(23) | 2.284(3) |
| Mo(1)–C(9) | 2.264(3) | Mo(2)–C(26) | 2.291(3) |
| Mo(1)–C(10) | 2.269(3) | Mo(2)–C(27) | 2.265(3) |
| Mo(1)–C(11) | 2.308(3) | Mo(2)–C(28) | 2.271(3) |
| Mo(1)–C(12) | 2.434(3) | Mo(2)–C(29) | 2.454(3) |
| Mo(1)–C(13) | 2.443(3) | Mo(2)–C(30) | 2.426(3) |
| Mo(1)–Br(1) | 2.6077(5) | Mo(2)–Br(3) | 2.6147(4) |
| Mo(1)···$C_{g,Ind}$ | 2.006(1) | Mo(2)···$C_{g,Ind}$ | 2.002(1) |
| Mo(1)···$C_{g,Cp}$ | 1.988(1) | Mo(2)···$C_{g,Cp}$ | 1.985(1) |
| $C_{g,Ind}$···Mo(1)–C(1) | 103.95(2) | $C_{g,Ind}$···Mo(2)–C(18) | 103.82(2) |
| $C_{g,Ind}$···Mo(1)–Br(1) | 107.44(2) | $C_{g,Ind}$···Mo(2)–Br(3) | 107.52(2) |
| $C_{g,Ind}$···Mo(1)···$C_{g,Cp}$ | 136.79(2) | $C_{g,Ind}$···Mo(2)···$C_{g,Cp}$ | 136.41(2) |
| $C_{g,Cp}$···Mo(1)–C(1) | 105.00(1) | $C_{g,Cp}$···Mo(2)–C(18) | 104.77(1) |
| $C_{g,Cp}$···Mo(1)–Br(1) | 106.60(1) | $C_{g,Cp}$···Mo(2)–Br(3) | 107.12(1) |
| C(1)–Mo(1)–Br(1) | 84.59(11) | C(18)–Mo(2)–Br(3) | 85.00(10) |

[a] $C_{g,Ind}$ – centroid of the coordinated $\eta^5$-indenyl aromatic ring [C(9) to C(13) and C(26) to C(30)]. [b] $C_{g,Cp}$ – centroid of the coordinated $\eta^5$-cyclopentadienyl ligand [C(2) to C(6) and C(19) to C(23)].

between the diene plane and the plane defined by atoms C10, C13 and C14 [29.3(4)°] is smaller than that previously reported for the spirocyclic isodicyclopentadiene complex of iron(0) [36.2(3)°].[24]

The $\eta^4$-bonded spiro[4.4]nona-1,3-diene ligand is found in the less common (*exo*) conformation. So far, nine other structures (from 35 entries available in the CSD) that present the "M(Cp′)($\eta^4$-diene)LL′" (Cp′ = Cp, Cp*, Ind; M = transition metal) moiety display a similar conformation.[22]

By taking into consideration the centers of gravity of the carbon atoms connected to the molybdenum atom in **11** ($C_{g,Ind}$ and $C_{g,diene}$ for the $\eta^5$-indenyl and $\eta^4$-spiro[4.4]nona-1,3-diene molecules, respectively), we note that the Mo coordination resembles a highly distorted tetrahedron (Figure 1) in which the tetrahedral angles are significantly distorted from the ideal values and range from 84.96(18)° to 137.03(5)° (Table 2). The large angle is subtended between the centers of gravity of the C1–C5 and C10–C13 rings. The two Mo–C≡O bonds form a rather small tetrahedral angle of 84.96(18)°.

A peculiar feature of the structures of both **12** and **13a** is the presence of two crystallographically independent cationic complexes composing the asymmetric unit. As depicted in Figures 2 and 3, the two single complexes belonging to each structure are almost mirror images of each other, with only subtle differences. The slightly distinct bond lengths and angles for each pair of identical complexes are, presumably, a consequence of distinct interactions arising from the crystal packing. When viewed from above (schematic representations on the sides of Figures 2 and 3), the spatial distribution of the aromatic five-membered rings (substituted Cp versus indenyl) is not exactly identical for each pair: while in the one complex the rings are almost eclipsed (dihedral angles of about 3.9° and 1.7° for **12** and **13a**, respectively), in the other complex the substituted cyclopentadienyl ring is slightly rotated towards a staggered conformation (dihedral angles of about 14.3° and 7.5° for **12** and **13a**, respectively).

On the other hand, differences within each pair of identical complexes also arise from the intrinsic conformational flexibility associated with the aliphatic chains. This feature is particularly evident for structure **13a**, in which the two pendant arms of the substituted $\eta^5$-$C_5H_4$ rings have markedly distinct conformations and the angles between the planes containing the two aromatic rings are statistically distinct (ca. 42.0° and 44.1° for the complexes on the left and right, respectively; see Figure 3).

The two substituted cyclopentadienyl ligands of structures **12** and **13a** interact in different manners with the molybdenum centers, basically as a result of their distinct pendant arms. However, both are connected to the metallic center through the cyclopentadienyl ring, which exhibits a typical $\eta^5$-coordination fashion. The Mo···C distances for **12** and **13a** are in the ranges 2.284(4)–2.303(4) Å and 2.283(3)–2.379(3) Å, respectively, (Tables 3 and 4), which is in accord with those found from a systematic search in the CSD[22] (1628 entries for $\eta^5$-Cp: Mo–C bonds in the range 2.12–2.65 Å with median of 2.33 Å). The cyclopentadienidoethyl ($C_5H_4$–$CH_2$–$CH_2$) ligand is connected to the metallic center in **12** through the $\eta^5$-$C_5H_4$ ring and through the terminal $\eta^1$-$CH_2$ to form a *pseudo*-five-membered chelate ring (Figure 2) with an average bite angle of about 91.7° (Table 3). This value is in good agreement with those reported for the only other two related structures that contain this organic moiety found in the literature (average bite angle of 91.3°).[25] The (2-bromoethyl)cyclopentadienide ($C_5H_4$–$CH_2$–$CH_2$–Br) ligand in **13a** is exclusively bound to the molybdenum center through the $\eta^5$-$C_5H_4$ aromatic ring. A literature search reveals only one other structure that has a ligand of the type $C_5H_4$–$CH_2$–$CH_2$–X (where "X" is a halogen) bound to molybdenum: [Mo($\eta^5$-$C_5H_4CH_2CH_2I)_2$-$I_2$].[25a]

Interestingly, each crystallographically independent molybdenum center in **12** and **13a** can also be envisaged as being coordinated to four distinct moieties, which renders it as a chiral crystallographic center: in Figure 2 (structure **12**), the depicted complexes have *R* and *S* configurations (left and right, respectively), while in Figure 3 (structure **13a**), the configurations are instead *S* and *R* (left and right, respectively). It is also important to emphasize that these two crystal structures are not ideal crystal racemates, because the two geometrical isomers are not exact mirror images as previously described. Relative to **11**, the tetrahedral coordination geometries of the molybdenum centers in **12** and **13a** are significantly more distorted; while for **12**, the tetrahedral bond lengths and angles are within the ranges 1.944(1)–2.273(4) Å and 88.51(14)–145.46(2)°, respectively, for **13a**, the values are instead in the ranges 1.985(1)–2.6147(4) Å and 84.59(11)–136.79(2)°. Noteworthy is the fact that the larger tetrahedral angles for **13a** (correspond-

 © 2007 Wiley-VCH Verlag GmbH & Co. KGaA, Weinheim 

ing to the angle between the two centers of gravity of the organic moieties) are comparable to those of **11**; on the other hand, the angles that are >145° for structure **12** (see Table 3) essentially arise as a result of the geometrical constraints imposed by the five-membered chelate rings of the $\eta^5$:$\eta^1$-cyclopentadienidoethyl ligand.

The crystal packing arrangements of **12** and **13a** are essentially mediated by a considerable number of weak C–H···(O,F,Br) hydrogen bonds (not shown). In structure **13a**, and similarly to that in **11**, π–π interactions between $\eta^5$-indenyl organic ligands that belong to neighboring complexes also occur, and the water molecule of crystallization present in the crystal structure is further engaged in two strong and rather liner O–H···Br hydrogen-bonding interactions with two neighboring bromide anions (not shown): O(1 W)–H(1A)···Br(6) with $d_{D\cdots A}$ = 3.292(3) Å and ∠(DHA) = 170(3)°; O(1 W)–H(1B)···Br(5) with $d_{D\cdots A}$ = 3.268(3) Å and ∠(DHA) = 169(4)°.

## Discussion

Earlier reports on the reactivity of $Mo^0$ compounds towards spirodienes include both very reactive Mo atoms[14a] and $Mo(CO)_3(NCCH_3)_3$.[17] In both cases, the only products observed result from the opening of the cycloalkane ring and concomitant formation of one $\eta^5$-$C_5H_4$–Mo and one $\eta^1$-C–Mo bond. Similar reactivity was observed for hexamethylcyclopentadiene $C_5(CH_3)_6$, which reacts with molybdenum metal in the gas phase to give $Mo(CH_3)_2(Cp^*)_2$.[26] This formal C–C oxidative addition reaction is supported by the aromatization of the $C_5$ ring.

In the present case, the cationic $Mo^{II}$ compounds **1** and **2** are more discriminate in their reactions towards the opening of coordinated spirodienes. The less-strained spiro[4.4]-nona-1,3-diene does not undergo ring opening upon coordination to $[Mo(CO)_2(Cp')]^+$ (Cp′ = Cp, Ind), and the spirodiene complexes **4** and **11** are formed in good yield. These species are stable, and no signs of ring opening were observed. The breaking of the C–C bond takes effect only in the case of the more-strained cyclopropane ring of spiro[2.4]hepta-4,6-diene coordinated to both $[Mo(CO)_2(Cp')]^+$ fragments, but under different circumstances. Reaction of **1** with spiro[2.4]hepta-4,6-diene gives the $\eta^4$-diene compound **3** and the *ansa* compounds **5** and **6**. The last two compounds were obtained in a 1:1 molar ratio and result from ring opening of the $C_3$ ring. Each one represents a type of ring-opening product already described in the literature. In **5**, one CO group is lost and a new C–Mo bond is formed, while in **6**, the broken ring binds to a coordinated CO group instead, which results in an acyl complex. However, **5** and **6** are not formed directly from **3**. In fact, in $CH_2Cl_2$ solution and under normal laboratory light, **3** remains unchanged for at least 24 h, which is longer than the reaction time for the formation of **3**, **5**, and **6** from **1** and the spirodiene. Irradiation of a clean solution of **3** does not lead to **5**, **6**, or any tractable product. Therefore, the ring opening reaction leading to **5** and **6** takes place through pathways that are not yet clear. In contrast, the indenyl compound **2** does not form a stable or observable diene complex with spiro[2.4]hepta-4,6-diene and gives the *ansa* compound **12** selectively. Our interpretation of the above findings is depicted in Scheme 5.

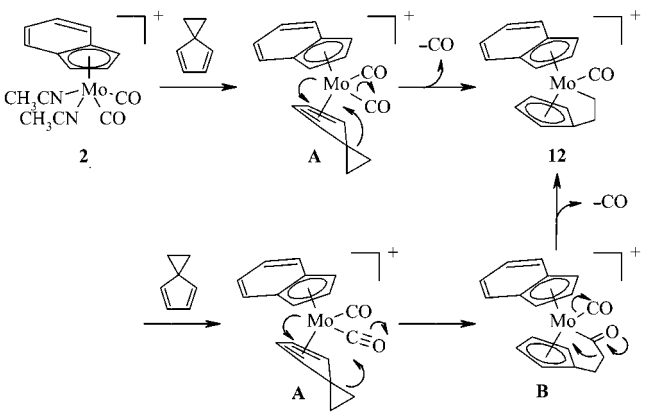


Scheme 5. Proposed pathways to compound **12** (intermediates **A** and **B** were not observed).

In both cases, a diene species should be obtained by substitution of the labile $CH_3CN$ ligands. The dienophilic character of the fragment $[Mo(CO)_2(Cp')]^+$ supports this reasoning. However, once formed, such diene complexes may have a different reactivity, which depends on the Cp′ ring present. In the case where Cp′ = Cp, complex **3** remains stable. In the case where Cp′ = Ind, the putative intermediate **A** (not observed) is expected to be much more labile towards CO loss than **3**. This is in line with the reported higher lability of $[Mo(\eta^4\text{-}C_5H_6)(CO)_2(Ind)]^+$ towards CO loss and formation of $[Mo(CO)(Cp)H(Ind)]^+$ relative to its Cp counterpart.[12a] Therefore, when intermediate **A** loses CO, the facing C–C bond of the $C_3$ ring adds across to form **12**. The alternative hypothesis that **A** undergoes C–C bond addition to CO to form **B** (not observed), which then looses CO and undergoes CO deinsertion from the acyl to lead to **12** also needs to be considered.[27] These insertion/deinsertion reactions are usually slow at the $Cp_2Mo$ fragment, but they might be favored by the indenyl over the cyclopentadienyl counterpart.

It is interesting to also note the comparison between the reactivity of spiro[2.4]hepta-4,6-diene and 1,1-dimethylspiro[2.4]hepta-4,6-diene towards the fragment $[Mo(CO)_2(Cp)]^+$. The effects of such substituents have been investigated both in coordination-assisted ring opening[28] and in the reduction of the free spiro[2.4]hepta-4,6-dienes.[29] Both substituted and unsubstituted spiro[2.4]hepta-4,6-dienes form $\eta^4$ complexes with $[Mo(CO)_2(Cp)]^+$, namely **3**, **7** and **8**. However, while **3** and **7** are stable towards subsequent ring opening, **8** slowly rearranges to a new compound. Although we have not yet been able to identify the structure of this compound, the fact that **8** reacts must mean that the substituted spirodiene is more reactive than its unsubstituted counterpart. In addition, its coordination mode also determines its reactivity, as **7** does not evolve into any ring-opening product. Since **8** has the less-hindered C–C bond

 © 2007 Wiley-VCH Verlag GmbH & Co. KGaA, Weinheim 

facing the metal, steric factors would favor the formation of **9** (or **10′** for that matter), as is most likely according to the NMR spectroscopic data available. With this view, **10′** would also have been a favorable outcome, but it was not observed. This stereochemical line of reasoning was first encountered for the reaction of 1,1-dimethyl-spiro[2.4]-hepta-4,6-diene[28] and 1-phenyl-spiro[2.4]hepta-4,6-diene[30] with $[Mo(CO)_3(NCCH_3)_3]$, which always led to the opening of the unsubstituted $C_{ipso}$–$CH_2$ bond of the $C_3$ ring. This was interpreted as the result of the preferred coordination of the substituted spirodienes having the substituents on the face opposite to the $Mo(CO)_3$ fragment, as found in **8**.[28] However, the same report reveals that for $Fe_2(CO)_9$ no such clear regioselectivity was observed, which implies that electronic factors may overrule steric considerations, as observed in the chemistry of free spirodienes. Moreover, this stereochemical argument cannot explain the selectivity that prevents the formation of **10′**. Further experimental studies supported by DFT calculations, aiming at the full characterization of the product **9** (or **10**), and the study of the activation of 1,1-dimethyl-spiro[2.4]hepta-4,6-diene by the more reactive $[Mo(CO)_2(Ind)]^+$ fragment are currently underway in our laboratories to try to understand these mechanistic details.

Regardless of the mechanistic questions, the results described mark an important step in our development of ring-functionalized molybdenocene complexes. The transformation of **12** into **13** and **14** follows the pattern previously shown by the groups of Green[14a] and Royo.[14b] The pendant bromo- and iodoalkyl substituents allow the introduction of a wide variety of functions and of bioactive molecules, as ample literature precedent has already shown. A related manipulation starting from **9** (or any of its congeners in Scheme 2) can be envisaged, thus extending the range of compounds to the bis(cyclopentadienyl)molybdenum fragment.

## Conclusions and Outlook

Spiro[2,4]hepta-4,6-dienes and spiro[2,4]nona-4,6-diene coordinate readily, to form the products in high yields, to the $[Mo(CO)_2(Cp')]^+$ fragment (Cp′ = Cp, Ind). For the Cp derivatives, ring opening only takes place with the 1,1-dimethyl-spiro[2,4]hepta-4,6-diene. In contrast, the indenyl containing fragment induces a high-yield ring opening of the unsubstituted spiro[2,4]hepta-4,6-diene, but not of spiro[2,4]nona-4,6-diene, to produce the *ansa* compound **12** from which haloalkyl-functionalized fragments are introduced onto a molybdenocene structural framework, as in compounds **13** and **14**. These are among the few examples of ring-functionalized molybdenocene derivatives capable of being manipulated for conjugation with bioactive molecules for biological and medical applications and are the first to contain differentially substituted rings. The preparation of such conjugates is presently underway and is directed towards their use as antitumor drugs.

## Experimental Section

**Methods and Materials:** All operations were performed under nitrogen by using conventional Schlenk-line techniques. The solvents were purified and dried by standard methods.[31] Spiro[2.4]hepta-4,6-diene,[14b] spiro[4.4]nona-1,3-diene,[32] 1,1-dimethyl-spiro[2.4]-hepta-4,6-diene,[33] $[Mo(CO)_2(Cp)(NCCH_3)_2][BF_4]$ (**1**),[34] and $[Mo(CO)_2(Ind)(NCCH_3)_2][BF_4]$ (**2**)[12a] were prepared according to literature procedures. Bromine and iodine (Aldrich) were used as obtained without further purification.

**Measurements:** Positive-ion electrospray ionization (ESI) mass spectra were recorded with API-ION TRAP (PO 03 MS). Samples were measured in $CH_2Cl_2$ solution. The molybdenum-containing ions had a clearly visible metal isotope pattern, which arises from the distribution: $^{92}$Mo 14.84%, $^{94}$Mo 9.25%, $^{95}$Mo 15.92%, $^{96}$Mo 16.68%, $^{97}$Mo 9.55%, $^{98}$Mo 24.13%, $^{100}$Mo 9.63%.[35] Spectra obtained were computer simulated (WSearch32 2005). Mass peaks listed refer to fragments with the isotopes $^1$H, $^{12}$C, $^{16}$O, $^{79}$Br, $^{98}$Mo, and $^{127}$I. $^1$H and $^{13}$C{$^1$H} NMR spectra were recorded in solutions at room temperature with Bruker AMX-300 spectrometer. $CDCl_3$, $CD_2Cl_2$, and [D$_6$]acetone were used as obtained (Cambridge Isotope Laboratories) without further purification. Chemical shifts are given in ppm relative to tms. IR spectra were recorded in the 4000–440 cm$^{-1}$ region (step 2 cm$^{-1}$) on a Mattson 7000 FT-IR spectrometer with KBr pellets. Spectra for compounds **3** and **4** were measured in $CH_2Cl_2$ solution with ZnS cuvettes.

**Synthesis of $[Mo\{\eta^4\text{-}C_5H_4(CH_2)_2\}(CO)_2(Cp)][BF_4]$ (3):** A solution of **1** (0.20 g, 0.52 mmol) in $CH_2Cl_2$ (25 mL) was treated with excess spiro[2.4]hepta-4,6-diene (0.14 g, 1.52 mmol). After stirring the reaction mixture for 16 h, it was concentrated in vacuo to ca. 3 mL. By adding $Et_2O$, a yellow powder precipitated (**3**). The crude product was recrystallized from $CH_2Cl_2/Et_2O$ and then from $CHCl_3/Et_2O$. Yield: 0.11 g (0.28 mmol, 54%). Positive-ion MS: *m*/*z* (%) = 311 $[M - BF_4]^+$, 283 $[M - BF_4 - CO]^+$, 255 $[M - BF_4 - 2(CO)]^+$, 253 (100) $[M - BF_4 - 2(CO) - H_2]^+$. $^1$H NMR ($CD_2Cl_2$): $\delta$ = 6.37 (t, 2 H, $C_5H_4$), 5.81 (s, 5 H, $C_5H_5$), 4.80 (t, 2 H, $C_5H_4$), 1.35 (t, $^3J_{H,H}$ = 9 Hz, 2 H, $CH_2$), 0.68 (t, $^3J_{H,H}$ = 9 Hz, 2 H, $CH_2$) ppm. $^{13}$C{$^1$H} NMR ($CD_2Cl_2$): $\delta$ = 225.1 (2 C, *C*O), 96.8 (2 C, $C_5H_4$), 94.3 (5 C, $C_5H_5$), 88.7 (2 C, $C_5H_4$), 28.6, 14.3 (2 C, $CH_2$) ppm. IR ($CH_2Cl_2$): $\tilde{\nu}$ = 2019 (s) [($\nu_a$(CO)], 1960 (s) [$\nu_s$(CO)] cm$^{-1}$.

**Synthesis of $[Mo\{\eta^4\text{-}C_5H_4(CH_2)_4\}(CO)_2(Cp)][BF_4]$ (4):** The reaction was carried out as that described for compound **3**, but with spiro[4.4]nona-1,3-diene (0.18 g, 1.50 mmol). Recrystallization of the crude product was carried out with $CH_2Cl_2/Et_2O$. Yield: 0.19 g (0.45 mmol, 86%). Positive-ion MS: *m*/*z* (%) = 339 (100) $[M - BF_4]^+$, 311 $[M - BF_4 - CO]^+$. $^1$H NMR ($CD_2Cl_2$): $\delta$ = 6.13 (t, 2 H, $C_5H_4$), 5.80 (s, 5 H, $C_5H_5$), 5.09 (t, 2 H, $C_5H_4$), 2.09 (t, $^3J_{H,H}$ = 7 Hz, 2 H, $CH_2$), 1.70 (quint, 2 H, $CH_2$), 1.60 (quint, 2 H, $CH_2$), 1.31 (t, $^3J_{H,H}$ = 7 Hz, 2 H, $CH_2$) ppm. $^{13}$C{$^1$H} NMR ($CD_2Cl_2$): $\delta$ = 227.3 (2 C, *C*O), 96.4 (2 C, $C_5H_4$), 94.5 (5 C, $C_5H_5$), 85.7 (2 C, $C_5H_4$), 72.4 ($C_{ipso}$, $C_5H_4$) 52.3, 37.8, 25.3, 25.0 (4 C, $CH_2$) ppm. IR ($CH_2Cl_2$): $\tilde{\nu}$ = 2020 (s) [$\nu_a$(CO)], 1964 (s) [$\nu_s$(CO)] cm$^{-1}$.

**Reaction of $[Mo(CO)_2(Cp)(NCCH_3)_2][BF_4]$ (1) with 1,1-Dimethyl-spiro[2.4]hepta-4,6-diene:** A solution of **1** (0.20 g, 0.52 mmol) in $CH_2Cl_2$ (25 mL) was treated with excess 1,1-dimethyl-spiro[2.4]-hepta-4,6-diene (0.18 g, 1.50 mmol). After stirring the reaction mixture for 16 h, it was concentrated in vacuo to ca. 3 mL. By adding $Et_2O$, 0.14 g of an orange powder precipitated. The NMR spectrum of this product measured immediately after dissolving the product in $CD_2Cl_2$ shows a 1:1:1 mixture of $[Mo\{endo\text{-}\eta^4\text{-}C_5H_4CH_2C(CH_3)_2\}(CO)_2(Cp)][BF_4]$ (**7**), $[Mo\{exo\text{-}\eta^4\text{-}C_5H_4CH_2C(CH_3)_2\}(CO)_2(Cp)][BF_4]$ (**8**), and $[Mo\{\eta^5\text{-}C_5H_4C(CH_3)_2\text{-}$

 © 2007 Wiley-VCH Verlag GmbH & Co. KGaA, Weinheim 

$CH_2$-$\eta^1$-CO}(CO)(Cp)][$BF_4$] (**9**). The same sample measured after 12 and 24 h shows 1:2 mixture compounds **7** and **9**. **7:** $^1$H NMR ($CD_2Cl_2$): $\delta$ = 6.33 (t, 2 H, $C_5H_4$), 5.82 (s, 5 H, $C_5H_5$), 4.86 (t, 2 H, $C_5H_4$), 1.17 (s, 2 H, $CH_2$), 0.90 (s, 6 H, $CH_3$). **8:** $^1$H NMR ($CD_2Cl_2$): 6.36 (t, 2 H, $C_5H_4$), 5.77 (s, 5 H, $C_5H_5$), 4.89 (t, 2 H, $C_5H_4$), 1.28 (s, 6 H, $CH_3$), 0.48 (s, 2 H, $CH_2$). **9:** $^1$H NMR ($CD_2Cl_2$): 6.30 (t, 2 H, $C_5H_4$), 5.71 (s, 5 H, $C_5H_5$), 5.52 (t, 2 H, $C_5H_4$), 2.24–2.12 (4-line m, 2 H, $CH_2$), 1.12 (s, 3 H, $CH_3$), 1.05 (s, 3 H, $CH_3$) ppm.

**Synthesis of [Mo{$\eta^4$-$C_5H_4(CH_2)_4$}$(CO)_2$(Ind)][$BF_4$] (11):** The reaction was carried out as that described for compound **4**, but with a solution of **2** (0.25 g, 0.57 mmol) instead of **1** in $CH_2Cl_2$. Recrystallization of the crude product was carried out with $CH_2Cl_2$/$Et_2O$. Yield: 0.22 g (0.53 mmol, 92%). Positive-ion MS: *m*/*z* (%) = 389 [M – $BF_4$]$^+$, 361 [M – $BF_4$ – CO]$^+$, 333 [M – $BF_4$ – 2(CO)]$^+$, 331 (100) [M – $BF_4$ – 2(CO) – $H_2$]$^+$, 329 [M – $BF_4$ – 2(CO) – 2$H_2$]$^+$. $^1$H NMR ($CDCl_3$): $\delta$ = 7.78–7.75 (m, 2 H, $C_9H_7$), 7.41–7.37 (m, 2 H, $C_9H_7$), 6.37 (d, 2 H, $C_9H_7$), 5.74 (t, 1 H, $C_9H_7$), 5.30 (t, 2 H, $C_5H_4$), 4.85 (t, 2 H, $C_5H_4$), 1.83 (t, $^3J_{H,H}$ = 7 Hz, 2 H, $CH_2$), 1.57 (quint, 2 H, $CH_2$), 1.44 (quint, 2 H, $CH_2$), 1.10 (t, $^3J_{H,H}$ = 7 Hz, 2 H, $CH_2$) ppm. $^{13}$C{$^1$H} NMR ($CDCl_3$): $\delta$ = 227.4 (2 C, *C*O), 130.1 (2 C, $C_9H_7$), 125.8 (2 C, $C_9H_7$), 111.9 (2$C_{ipso}$, $C_9H_7$), 95.8 (2 C, $C_9H_7$), 93.2 (2 C, $C_5H_4$), 92.4 ($C_9H_7$), 85.2 (2 C, $C_5H_4$), 71.6 ($C_{ipso}$, $C_5H_4$), 51.9, 37.1, 24.9, 24.7 (4 C, $CH_2$) ppm. IR (KBr): $\tilde{\nu}$ = 3102 (m), 2969 (m), 2878 (m), 2005 (vs) [$\nu_a$(CO)], 1950 (vs) [$\nu_s$(CO)], 1072 (br., vs) [$\nu$(BF)] cm$^{-1}$. Crystals suitable for X-ray structural analysis were prepared by carefully layering the dichloromethane solution of compound **11** with a double volume of hexane.

**Synthesis of [Mo($\eta^5$-$C_5H_4CH_2$-$\eta^1$-$CH_2$)(CO)(Ind)][$BF_4$] (12):** A solution of **2** (0.25 g, 0.57 mmol) in $CH_2Cl_2$ (25 mL) was treated with excess spiro[2.4]hepta-4,6-diene (0.14 g, 1.52 mmol). After stirring the reaction mixture for 16 h, it was concentrated in vacuo to ca. 3 mL. By adding $Et_2O$, an orange powder precipitated (**12**). The crude product was recrystallized from $CH_2Cl_2$/$Et_2O$. Yield: 0.23 g (0.55 mmol, 96%). Positive-ion MS: *m*/*z* (%) = 333 [M – $BF_4$]$^+$, 305 [M – $BF_4$ – CO]$^+$, 303 (100) [M – $BF_4$ – CO – $H_2$]$^+$. $^1$H NMR ($CD_2Cl_2$): $\delta$ = 7.79 (d, 1 H, $C_9H_7$), 7.54 (t, 1 H, $C_9H_7$), 7.42 (t, 1 H, $C_9H_7$), 7.33 (d, 1 H, $C_9H_7$), 6.31 (d, 1 H, $C_5H_4$), 6.24, 6.12 (2 × s, 2 H, $C_9H_7$), 5.45 (t, 1 H, $C_9H_7$), 5.39, 4.85, 4.82 (3 × s, 3 H, $C_5H_4$), 2.55 (6-line m, 1 H, $C_5H_4CH_2CH_2$Mo), 2.39 (6-line m, 1 H, $C_5H_4CH_2CH_2$Mo), –0.07 (5-line m, 1 H, $C_5H_4CH_2CH_2$Mo), –3.21 (7-line m, 1 H, $C_5H_4CH_2CH_2$Mo) ppm. $^{13}$C{$^1$H} NMR ($CD_2Cl_2$): $\delta$ = 226.4 (*C*O), 132.5, 131.6, 126.6, 124.7 (4 C, $C_9H_7$), 114.0, 107.9 (2$C_{ipso}$, $C_9H_7$), 97.5, 93.3, 90.7, 86.8, 86.7, 84.1, 83.3 (7 C, $C_5H_4$ and $C_9H_7$), 80.9 ($C_{ipso}$, $C_5H_4$), 19.0 ($C_5H_4CH_2CH_2$Mo), –39.3 ($C_5H_4CH_2CH_2$Mo) ppm. IR (KBr): $\tilde{\nu}$ = 3098 (m), 2947 (m), 1991 (vs) [$\nu$(CO)], 1061 (vs) [$\nu$(BF)] cm$^{-1}$. Crystals suitable for X-ray structural analysis were prepared by carefully layering the dichloromethane solution of compound **12** with a double volume of hexane.

**Synthesis of [MoBr{$\eta^5$-$C_5H_4(CH_2)_2Br$}(CO)(Cp)][$BF_4$] (13):** A solution of **12** (0.10 g, 0.24 mmol) in $CH_2Cl_2$ (15 mL) was cooled to –78 °C and then treated with excess bromine (0.10 g, 0.63 mmol). After stirring the mixture for 30 min at –78 °C, the volatiles were evaporated in vacuo. The crude product was recrystallized from $CH_2Cl_2$/$Et_2O$ to obtain **13** as a purple powder. Yield: 0.13 g (0.22 mmol, 94%). Positive-ion MS: *m*/*z* (%) = 493 [M – $BF_4$]$^+$, 465 (100) [M – $BF_4$ – CO]$^+$, 384 [M – $BF_4$ – CO – Br]$^+$. $^1$H NMR ([$D_6$]-acetone): $\delta$ = 8.02 (d, 1 H, $C_9H_7$), 7.84–7.76 (m, 2 H, $C_9H_7$), 7.60 (d, 1 H, $C_9H_7$), 6.69 (t, 1 H, $C_9H_7$), 6.47 (d, 2 H, $C_9H_7$), 6.35 (t, 1 H, $C_5H_4$), 6.27 (t, 1 H, $C_5H_4$), 6.22 (q, 1 H, $C_5H_4$), 6.03 (q, 1 H, $C_5H_4$), 3.54 (6-line m, 2 H, $C_5H_4CH_2CH_2$Br), 2.76 (t, 2 H, $C_5H_4CH_2CH_2$Br) ppm. $^{13}$C NMR ([$D_6$]acetone): $\delta$ = 218.3 (*C*O), 135.7, 135.6, 130.9, 128.7 (4 C, $C_9H_7$), 121.6, 121.5 (2$C_{ipso}$, $C_9H_7$), 112.8 ($C_{ipso}$, $C_5H_4$), 106.2, 102.3, 99.2, 94.4, 91.1, 91.0, 87.3 (7 C, $C_5H_4$ and $C_9H_7$), 33.3, 32.9 (2 C, $CH_2$) ppm. IR (KBr): $\tilde{\nu}$ = 3138 (m), 3109 (m), 3097 (m), 3063 (m), 2055 (vs) [$\nu$(CO)], 1062 (vs) [$\nu$(BF)] cm$^{-1}$.

**Synthesis of [MoBr{$\eta^5$-$C_5H_4(CH_2)_2Br$}(CO)(Ind)][Br]·0.5$H_2O$ (13a):** The reaction was carried out as that described for compound **13**, but at room temperature. The crude product was recrystallized several times from $CH_2Cl_2$/ether and acetone/ether. Crystals suitable for X-ray structural analysis were prepared by carefully layering the dichloromethane solution of compound **13a** with a double volume of hexane.

**Synthesis of [Mo{$\eta^5$-$C_5H_4(CH_2)_2I$}(CO)(Cp)I][$BF_4$] (14):** A solution of **12** (0.10 g, 0.24 mmol) in $CH_2Cl_2$ (15 mL) was cooled to –78 °C and then treated with excess iodine (0.14 g, 0.59 mmol). After stirring the mixture for 30 min at –78 °C, the volatiles were evaporated in vacuo. The crude product was washed with $Et_2O$ and then recrystallized from $CH_2Cl_2$/$Et_2O$ to obtain **14** as a purple powder. Yield: 0.15 g (0.22 mmol, 93%). Positive-ion MS: *m*/*z* (%) = 587 (100) [M – $BF_4$]$^+$, 559 [M – $BF_4$ – CO]$^+$. $^1$H NMR ([$D_6$]-acetone): $\delta$ = 7.94–7.89 (m, 2 H, $C_9H_7$), 7.76 (d, 1 H, $C_9H_7$), 7.63 (t, 1 H, $C_9H_7$), 6.68 (s, 2 H, $C_9H_7$), 6.63 (s, 2 H, $C_9H_7$), 6.44 (t, 1 H, $C_9H_7$), 6.37 (s, 1 H, $C_5H_4$), 6.28 (s, 1 H, $C_5H_4$), 6.23 (s, 1 H, $C_5H_4$), 6.13 (s, 1 H, $C_5H_4$), 3.37 (6-line m, 2 H, $C_5H_4CH_2CH_2$I), 2.84 (6-line m, 2 H, $C_5H_4CH_2CH_2$I) ppm. $^{13}$C NMR ([$D_6$]acetone): $\delta$ = 219.3 (*C*O), 135.4, 135.1, 132.4, 128.3 (4 C, $C_9H_7$), 117.9, 117.0 (2$C_{ipso}$, $C_9H_7$), 112.4 ($C_{ipso}$, $C_5H_4$), 103.3, 101.7, 98.1, 96.4, 91.0, 90.0, 86.9 (7 C, $C_5H_4$ and $C_9H_7$), 34.5 ($C_5H_4CH_2CH_2$I), 4.7 ($C_5H_4CH_2CH_2$I) ppm. IR (KBr): $\tilde{\nu}$ = 3127 (m), 3086 (m), 2049 (vs) [$\nu$(CO)], 1057 (vs) [$\nu$(BF)] cm$^{-1}$.

**X-ray Crystallography:** Suitable single-crystals of **11**, **12**, and **13a** were manually harvested from the crystallization vials and mounted on a Hampton Research CryoLoops by using FOMBLIN Y perfluoropolyether vacuum oil (LVAC 25/6) purchased from Aldrich,[36] with the help of a Stemi 2000 stereomicroscope equipped with Carl Zeiss lenses. Data were collected on a Bruker X8 Kappa APEX II charge-coupled device (CCD) area-detector diffractometer (Mo-$K_\alpha$ graphite-monochromated radiation, $\lambda$ = 0.7107 Å) controlled by the APEX2 software package[37] and equipped with an Oxford Cryosystems Series 700 cryostream that is monitored remotely by the software interface Cryopad.[38] Images were processed by using the software package SAINT+,[39] and data were corrected for absorption by the multiscan, semi-empirical method implemented in SADABS.[40] The structures were solved by using Patterson synthesis with SHELXS-97,[41] which allowed the immediate location of the central molybdenum metallic center for each complex and the Br atoms in compound **13a**. All the remaining non-hydrogen atoms were directly located with difference Fourier maps calculated from successive full-matrix, least-squares refinement cycles on $F^2$ by using SHELXL-97.[42] All non-hydrogen atoms were successfully refined by using anisotropic displacement parameters. Hydrogen atoms attached to carbon were located at their idealized positions with appropriate *HFIX* instructions in SHELXL: *43* for the aromatic hydrogen atoms associated with the Cp-substituted rings and indenyl molecules; *13* and *23* for the hydrogen atoms associated with the conjugated diene of spiro[4.4]-nona-1,3-diene and the –$CH_2$– chains, respectively. These hydrogen atoms were included in subsequent refinement cycles in riding-motion approximation with isotropic thermal displacements parameters ($U_{iso}$) fixed at 1.2 times $U_{eq}$ of the carbon atom to which they are attached.

 © 2007 Wiley-VCH Verlag GmbH & Co. KGaA, Weinheim 

Table 5. Crystal and structure refinement data for [Mo{η⁴-$C_5H_4(CH_2)_4$}(CO)$_2$(Ind)][$BF_4$] (**11**), [Mo(η⁵-$C_5H_4CH_2$-η¹-$CH_2$)(CO)(Ind)][$BF_4$] (**12**) and [MoBr{η⁵-$C_5H_4(CH_2)_2$Br}(CO)(Ind)][Br]·0.5$H_2O$ (**13a**).

| | **11** | **12** | **13a** |
|---|---|---|---|
| Formula | $C_{20}H_{19}BF_4MoO_2$ | $C_{34}H_{30}B_2F_8Mo_2O_2$ | $C_{34}H_{32}Br_6Mo_2O_3$ |
| Formula weight | 474.10 | 836.08 | 1159.94 |
| Temperature [K] | 100(2) | 150(2) | 150(2) |
| Crystal system | triclinic | monoclinic | triclinic |
| Space group | $P\bar{1}$ | $P2_1/c$ | $P\bar{1}$ |
| $a$ [Å] | 7.4845(7) | 15.2570(5) | 7.9201(2) |
| $b$ [Å] | 7.6375(8) | 8.5965(3) | 13.5129(4) |
| $c$ [Å] | 16.6146(17) | 24.2930(9) | 18.0301(4) |
| $\alpha$ [°] | 80.378(5) | – | 72.2750(10) |
| $\beta$ [°] | 82.324(5) | 96.837(2) | 81.8240(10) |
| $\gamma$ [°] | 78.153(5) | – | 73.2650(10) |
| Volume [Å$^3$] | 911.57(16) | 3163.53(19) | 1757.05(8) |
| $Z$ | 2 | 4 | 2 |
| $Z'$ | – | 2 | 2 |
| $D_c$ [g cm$^{-3}$] | 1.727 | 1.755 | 2.192 |
| $\mu$(Mo-$K_\alpha$) [mm$^{-1}$] | 0.772 | 0.872 | 7.570 |
| $F$(000) | 476 | 1664 | 1108 |
| Crystal size [mm] | 0.22 × 0.16 × 0.04 | 0.40 × 0.24 × 0.16 | 0.36 × 0.25 × 0.16 |
| Crystal type | red blocks | red blocks | red blocks |
| $\theta$ range | 3.52 to 27.48 | 3.59 to 31.63 | 3.57 to 27.48 |
| Index ranges | $-9 \le h \le 9$ | $-22 \le h \le 22$ | $-10 \le h \le 10$ |
| | $-9 \le k \le 9$ | $-12 \le k \le 12$ | $-17 \le k \le 17$ |
| | $-21 \le l \le 21$ | $-35 \le l \le 35$ | $-21 \le l \le 23$ |
| Reflections collected | 38877 | 124636 | 53608 |
| Independent reflections | 4135 | 10596 | 7997 |
| | ($R_{int}$ = 0.0313) | ($R_{int}$ = 0.0394) | ($R_{int}$ = 0.0421) |
| Data completeness [%] | 99.0 | 99.6% | 99.2% |
| Parameters | 253 | 491 | 412 |
| Final $R$ indices [$I > 2\sigma(I)$][a,b] | $R_1$ = 0.0479 | $R_1$ = 0.0477 | $R_1$ = 0.0284 |
| | $wR_2$ = 0.1257 | $wR_2$ = 0.1164 | $wR_2$ = 0.0573 |
| Final $R$ indices (all data)[a,b] | $R_1$ = 0.0522 | $R_1$ = 0.0641 | $R_1$ = 0.0426 |
| | $wR_2$ = 0.1283 | $wR_2$ = 0.1270 | $wR_2$ = 0.0607 |
| Weighting scheme[c] | $m$ = 0.0536 | $m$ = 0.0548 | $m$ = 0.0173 |
| | $n$ = 4.0207 | $n$ = 8.2897 | $n$ = 3.9398 |
| Largest diff. peak and hole [e Å$^{-3}$] | 2.462, –1.140 | 4.016, –1.414 | 1.070, –0.713 |

[a] $R_1 = \Sigma||F_o| - |F_c||/\Sigma|F_o|$. [b] $wR_2 = \{\Sigma[w(F_o^2 - F_c^2)^2]/\Sigma[w(F_o^2)^2]\}^{1/2}$. [c] $w = 1/[\sigma^2(F_o^2) + (mP)^2 + nP]$ where $P = (F_o^2 + 2F_c^2)/3$.

In structure **12**, the two $BF_4^-$ anions were found to be statistically disordered over two distinct crystallographic positions. This statistical disorder was modeled for the two anions over a central and common to the two positions B–F bond with fixed rates of occupancy of 0.80:0.20 and 0.70:0.30. Moreover, in order to ensure chemically reasonable geometries for these moieties, the B–F and F···F distances of all moieties were restrained to common (but refinable) values, which ultimately refined to 1.356(1) and 2.210(1) Å, respectively.

In structure **13a**, the two hydrogen atoms associated with the water molecule of crystallization were markedly visible from the last difference Fourier map synthesis, and were included in the final structural model, with the O–H and H···H distances restrained to 0.95(1) and 1.55(1) Å (in order to ensure a chemically reasonable geometry for this moiety) and by using a riding model with an isotropic displacement parameter fixed at *1.5* times $U_{eq}$ of the oxygen atom to which they are attached.

The last difference Fourier map synthesis showed, for **11**, the highest peak (2.462 e Å$^{-3}$) and deepest hole (–1.140 e Å$^{-3}$) located at 1.77 Å from F(2) and 0.74 Å from Mo(1), respectively; for **12**, the highest peak (4.016 e Å$^{-3}$) and deepest hole (–1.414 e Å$^{-3}$) are located at 0.70 Å from Mo(1) and 0.61 Å from Mo(2), respectively; for **13a**, the highest peak (1.070 e Å$^{-3}$) and deepest hole (–0.713 e Å$^{-3}$) are instead located at 0.94 Å from Br(6) and 0.89 Å from Mo(2), respectively. Crystallographic data and structure refinement details are summarized in Table 5.

CCDC-634114, CCDC-634115 and CCDC-634116 (for **11**, **12** and **13a**) contain the supplementary crystallographic data for this paper. These data can be obtained free of charge from The Cambridge Crystallographic Data Centre via www.ccdc.cam.ac.uk/data_request/cif.

**Supporting Information** (see footnote on the first page of this article): The composition of the compounds prepared was checked by mass spectrometry and NMR spectroscopy. Positive-ion electrospray ionization (ESI) mass spectra and $^{13}C\{^1H\}$ NMR spectra are included.

## Acknowledgments

We are grateful to *Fundação para a Ciência e Tecnologia* (FCT, Portugal) for supporting the postdoctoral project SFRH/BPD/24889/2005 and for funding the purchase of the single-crystal diffractometer. We wish to acknowledge Ana Varela Coelho for providing data from the Mass Spectrometry Service at the Instituto de Tecnologia Química e Biológica, Universidade Nova de Lisboa, Oeiras, Portugal.

 © 2007 Wiley-VCH Verlag GmbH & Co. KGaA, Weinheim 

[1] H. Köpf, P. Köpf-Maier, *Angew. Chem. Int. Ed. Engl.* **1979**, *18*, 477–478.
[2] J. B. Waern, P. Turner, M. M. Harding, *Organometallics* **2006**, *25*, 3417–3421.
[3] J. Vinklárek, H. Paláčková, J. Honzíček, J. Holubová, M. Holčapek, I. Císařova, *Inorg. Chem.* **2006**, *45*, 2156–2162.
[4] a) P. Ghosh, A. T. Kotchevar, D. D. DuMez, S. Ghosh, J. Peiterson, F. M. Uckun, *Inorg. Chem.* **1999**, *38*, 3730–3737; b) P. Ghosh, S. Ghosh, C. Navara, R. K. Narla, A. Benyumov, F. M. Uckun, *J. Inorg. Biochem.* **2001**, *84*, 241–253.
[5] a) J. Wald, R. Alberto, K. Ortner, L. Candreia, *Angew. Chem. Int. Ed.* **2001**, *40*, 3062–3066; b) R. Schibli, P. A. Schubiger, *Eur. J. Nucl. Med.* **2002**, *29*, 1529–1542.
[6] a) O. R. Allen, L. Croll, A. L. Gott, R. J. Knox, P. C. McGowan, *Organometallics* **2004**, *23*, 288–292; b) P. W. Causey, M. C. Baird, S. P. C. Cole, *Organometallics* **2004**, *23*, 4486–4494.
[7] A. Gansäuer, D. Franke, T. Lauterbach, M. Nieger, *J. Am. Chem. Soc.* **2005**, *127*, 11622–11623.
[8] Y. Qian, J. Huang, M. D. Bala, B. Lian, H. Zhang, H. Zhang, *Chem. Rev.* **2003**, *103*, 2633–2690.
[9] a) J. R. Boyles, M. C. Baird, B. G. Campling, N. Jain, *J. Inorg. Biochem.* **2001**, *84*, 159–162; b) M. Tacke, L. P. Cuffe, W. M. Gallagher, Y. Lou, O. Mendoza, H. Müller-Bunz, F.-J. K. Rehmann, N. Sweeney, *J. Inorg. Biochem.* **2004**, *98*, 1987–1994.
[10] M. C. Valadares, A. L. Ramos, F.-J. K. Rehmann, N. J. Sweeney, K. Strohfeldt, M. Tacke, M. L. S. Queiroz, *Eur. J. Pharmacol.* **2006**, *534*, 264–270.
[11] a) J. B. Waern, M. M. Harding, *J. Organomet. Chem.* **2004**, *689*, 4655–4668; b) A. Erxleben, *Inorg. Chem.* **2005**, *44*, 1082–1094; c) J. B. Waern, M. M. Harding, *Inorg. Chem.* **2004**, *43*, 206–213; d) J. L. Vera, F. R. Román, E. Meléndez, *Bioorg. Med. Chem.* **2006**, *14*, 8683–8691.
[12] a) J. R. Ascenso, C. G. Deazevedo, I. S. Gonçalves, E. Herdtweck, D. S. Moreno, M. Pessanha, C. C. Romão, *Organometallics* **1995**, *14*, 3901–3919; b) I. S. Gonçalves, E. Herdtweck, C. C. Romão, B. Royo, *J. Organomet. Chem.* **1999**, *580*, 169–177; c) T. C. Forschner, J. A. Carella II, N. J. Cooper, *Organometallics* **1989**, *9*, 2478–2483; d) T. C. Forschner, N. J. Cooper, *J. Am. Chem. Soc.* **1989**, *111*, 7420–7424; e) R. P. Hughes, S. M. Maddock, I. A. Guzei, L. M. Liable-Sands, A. L. Rheingold, *J. Am. Chem. Soc.* **2001**, *123*, 3279–3288.
[13] a) J. H. Shin, W. Savage, V. J. Murphy, J. B. Bonanno, D. G. Churchill, G. Parkin, *J. Chem. Soc., Dalton Trans.* **2001**, 1732–1753; b) J. C. Green, M. L. H. Green, C. P. Morley, *J. Organomet. Chem.* **1982**, *233*, C4–C6; c) L. Labella, A. Chernega, M. L. H. Green, *J. Chem. Soc., Dalton Trans.* **1995**, 395–402.
[14] a) A. Barretta, F. G. N. Cloke, A. Feigenbaum, M. L. H. Green, A. Gourdon, K. Prout, *J. Chem. Soc., Chem. Commun.* **1981**, 156–158; b) F. Amor, P. Royo, T. P. Spaniol, J. Okuda, *J. Organomet. Chem.* **2000**, *604*, 126–131.
[15] A. Barretta, K. S. Chong, F. G. N. Cloke, A. Feigenbaum, M. L. H. Green, *J. Chem. Soc., Dalton Trans.* **1983**, 861–864.
[16] C. G. Kreiter, M. Wenz, P. Bell, *J. Organomet. Chem.* **1990**, *394*, 195–211.
[17] P. Eilbracht, *Chem. Ber.* **1976**, *109*, 1429–1435.
[18] a) M. Bottrill, M. Green, *J. Chem. Soc., Dalton Trans.* **1977**, 2365–2371; b) J. R. Ascenso, C. G. Deazevedo, I. S. Gonçalves, E. Herdtweck, D. S. Moreno, C. C. Romão, J. Zühlke, *Organometallics* **1994**, *13*, 429–431; c) I. S. Gonçalves, C. C. Romão, *J. Organomet. Chem.* **1995**, *486*, 155–161.
[19] a) P. Eilbracht, P. Dahler, *J. Organomet. Chem.* **1977**, *127*, C48–C50; b) P. Eilbracht, U. Mayser, *Chem. Ber.* **1980**, *113*, 2211–2220; c) P. Eilbracht, P. Dahler, G. Tiedtke, *J. Organomet. Chem.* **1980**, *185*, C25–C28; d) P. Eilbracht, *Chem. Ber.* **1976**, *109*, 3136–3141.
[20] Y. T. Fu, P. C. Chao, L. K. Liu, *Organometallics* **1998**, *17*, 221–226.
[21] a) H. Müller, G. E. Herberich, *Chem. Ber.* **1971**, *104*, 2772–2780; b) H. Müller, G. E. Herberich, *Chem. Ber.* **1971**, *104*, 2780–2785.
[22] a) F. H. Allen, *Acta Crystallogr., Sect. B* **2002**, *58*, 380–388; b) F. H. Allen, W. D. S. Motherwell, *Acta Crystallogr., Sect. B* **2002**, *58*, 407–422.
[23] J. W. Faller, R. H. Crabtree, A. Habib, *Organometallics* **1985**, *4*, 929–935.
[24] L. A. Paquette, G. A. Odoherty, B. L. Miller, R. D. Rogers, A. L. Rheingold, S. L. Geib, *Organometallics* **1989**, *8*, 2167–2172.
[25] a) A. Gourdon, K. Prout, *Acta Crystallogr. Acta Crystallogr., Sect. B* **1981**, *37*, 1982–1985; b) W. Frank, C. G. Kreiter, G. J. Reiss, S. Schufft, *Acta Crystallogr., Sect. C* **1996**, *52*, 356–358.
[26] J. C. Green, M. L. H. Green, C. P. Morley, *J. Organomet. Chem.* **1982**, *233*, C4–C6.
[27] a) K. W. Barnett, *Inorg. Chem.* **1969**, *8*, 2009–2011; b) O. G. Adeyemi, N. J. Coville, *Organometallics* **2003**, *22*, 2284–2290.
[28] P. Eilbracht, W. Fassmann, W. Diehl, *Chem. Ber.* **1985**, *118*, 2314–2329.
[29] S. W. Staley, J. J. Rocchio, *J. Am. Chem. Soc.* **1969**, *91*, 1565–1566.
[30] J. Zhao, E. Herdtweck, F. E. Kuehn, *J. Organomet. Chem.* **2006**, *691*, 2199–2206.
[31] W. L. F. Armarego, D. D. Perrin, *Purification of Laboratory Chemicals*, Butterworth-Heinemann, Oxford, **1996**.
[32] M. L. H. Green, D. Ohare, *J. Chem. Soc., Dalton Trans.* **1985**, 1585–1590.
[33] I. Erden, F. P. Xu, A. Sadoun, W. Smith, G. Sheff, M. Ossun, *J. Org. Chem.* **1995**, *60*, 813–820.
[34] C. C. L. Pereira, S. S. Braga, F. A. A. Paz, M. Pillinger, J. Klinowski, I. S. Gonçalves, *Eur. J. Inorg. Chem.* **2006**, 4278–4288.
[35] R. D. Vocke, *Pure Appl. Chem.* **1999**, *71*, 1593–1607.
[36] T. Kottke, D. Stalke, *J. Appl. Crystallogr.* **1993**, *26*, 615–619.
[37] *APEX2*, *Data Collection Software Version 2.1-RC13*, Bruker AXS, Delft, The Netherlands, **2006**.
[38] *Cryopad*, *Remote Monitoring and Control, Version 1.451*, Oxford Cryosystems, Oxford, United Kingdom, **2006**.
[39] *SAINT+, Data Integration Engine Version 7.23a* © **1997–2005**, Bruker AXS, Madison, Wisconsin, USA.
[40] G. M. Sheldrick, *SADABS Version 2.01*, *Bruker/Siemens Area Detector Absorption Correction Program*, Bruker AXS, Madison, Wisconsin, USA, **1998**.
[41] G. M. Sheldrick, *SHELXS-97, Program for Crystal Structure Solution*, University of Göttingen, **1997**.
[42] G. M. Sheldrick, *SHELXL-97, Program for Crystal Structure Refinement*, University of Göttingen, **1997**.


Received: January 29, 2007
Published Online: May 10, 2007

 © 2007 Wiley-VCH Verlag GmbH & Co. KGaA, Weinheim 

DOI: 10.1002/ejic.200600802

# Activation of Aromatic, Aliphatic, and Olefinic Carbon–Fluorine Bonds Using $Cp^*_2HfH_2$

**Ryan D. Rieth,[a] William W. Brennessel,[a] and William D. Jones*[a]**

**Keywords:** Metallocenes / Hydrides / Reduction / Fluorocarbons

The hafnium hydride $Cp^*_2HfH_2$ is reacted with a series of fluorocarbons to examine the scope of C–F bond activation. Aromatic, vinylic, and aliphatic C–F bonds all show some degree of reactivity, and possible mechanisms are discussed.

(© Wiley-VCH Verlag GmbH & Co. KGaA, 69451 Weinheim, Germany, 2007)

## Introduction

Organometallic chemists have long been interested in the activation of typically inert C–F bonds using transition-metal complexes. The advantages of promoting C–F bond cleavage are both academic and practical. In one sense, the selective and predictable disruption of these interactions may result in greater synthetic utility of readily available fluorocarbons. In addition, such knowledge could have environmental ramifications, eventually leading to the destruction of harmful chlorofluorocarbons (CFCs) in the upper atmosphere. While both stoichiometric[1] and catalytic[2] C–F activation reactions have been reported using transition metals, significant efforts continue to be made to improve known methodologies and to discover new ways to cleave these strong bonds selectively with an important goal being an understanding of the mechanisms by which these transformations take place.

To date, a variety of mechanisms for C–F bond activation by transition metals have been suggested. Some of the more notable strategies involve electron transfer, electrophilic pathways, homolytic cleavage, oxidative addition, and nucleophilic routes.[3–4] While many of these mechanisms feature intermolecular interactions, several examples involve intramolecular activation,[5–6] which is oftentimes accompanied by the liberation of a small molecule such as HF.

As an example of the electron-transfer mechanism, Perutz and co-workers have suggested that an electron-rich dihydride, $Ru(dmpe)_2H_2$ (dmpe = $Me_2PCH_2CH_2PMe_2$), is capable of donating an electron to a heavily fluorinated aromatic compound, eventually leading to the formation of the observed product by the route depicted in Equation (1).[7] Similar considerations have been implicated in reactions involving Ni and Rh.[8–9]

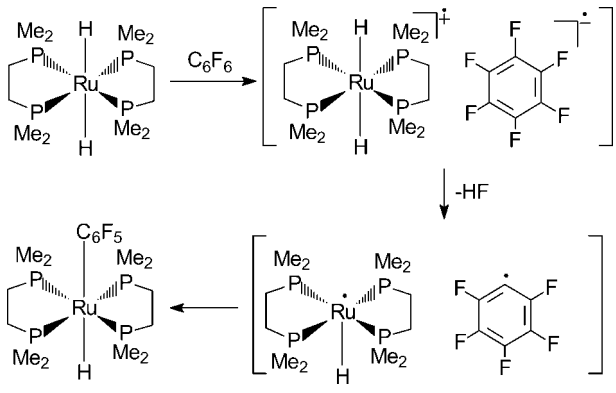


(1)

Electrophilic C–F bond activation has been suggested to occur by fluoride transfer, especially when strong Lewis acids are employed. For example, fluoride transfer from an aromatic fluorocarbon to an open coordination site in $[L_2TiMe]^+$ systems has recently been proposed by Ziegler and co-workers.[10] Rosenthal et al. have shown that cationic zirconocene complexes can abstract fluoride from perfluorophenyl groups to give Zr–F species.[11] In most cases where suggested, fluoride transfer is thought to likely occur through a cyclic transition state [Equation (2)]. Furthermore, olefinic fluorocarbons have been shown to participate in β-fluoride elimination following insertion into metal-hydride bonds, leading to the generation of a new fluorocarbon or small fluorine-containing molecule.[12–15] For perfluoroalkyl–metal complexes, α-fluoride elimination has been shown to be operative in several systems, many of which feature the use of Group 9 metals.[16] A titanium perfluoromethyl complex has also been reported, indicating that such species can be stable.[17]

[a] Department of Chemistry, University of Rochester, Rochester, New York 14627, USA
E-mail: jones@chem.rochester.edu

 © 2007 Wiley-VCH Verlag GmbH & Co. KGaA, Weinheim 

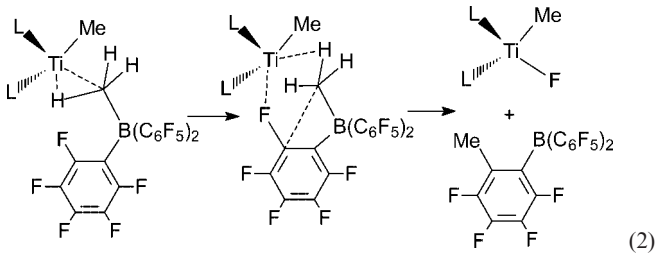


(2)

In addition to mechanisms involving the transfer of electrons or fluoride, other mechanisms that have been identified include the involvement of radical-based species in the C–F bond cleavage reactions of aliphatic fluorocarbons using $Cp^*_2ZrH_2$,[18] the oxidative addition of an aromatic C–F bond to phosphane $Ni^0$ complexes,[9,19] and the nucleophilic aromatic substitution on fluorinated aromatic species using early transition-metal complexes.[1(d),6]

As an addition to the variety of metal-based systems known to cleave C–F bonds,[3,20] the following account summarizes C–F bond activation research done using bis(pentamethylcyclopentadienyl)hafnium dihydride, $Cp^*_2HfH_2$ (**1**). The substrate scope includes aromatic, aliphatic, and olefinic compounds featuring varying steric properties and degrees of fluorination. Heterocyclic substrates are also briefly considered, and mechanistic insight into the reaction of **1** with several fluorinated alkenes is presented.

## Results and Discussion

### Synthesis of $Cp^*_2HfH_2$ and its Fluoro Derivatives

The synthesis of **1** was achieved by conversion of commercially available $Cp^*_2HfCl_2$ to $Cp^*_2HfMe_2$[21] followed by reaction with hydrogen at elevated temperature [Equation (3)]. Comparison of $^1H$ NMR spectroscopic data to known literature values for **1** confirmed that it was indeed the expected product.[22]

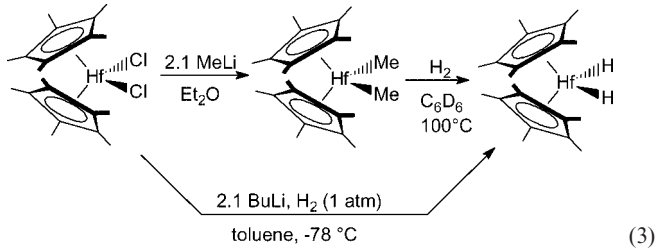


(3)

The long reaction time required for a reasonable degree of conversion can be avoided using the method reported by Bercaw, in which **1** was made directly from $Cp^*_2HfCl_2$ using *n*-butyllithium under hydrogen, a process that afforded the dried, isolated product in roughly 3 d.[22] Due to the sensitive nature of the starting hafnium complex,[23] great care was taken to prevent air and moisture from being present in any reaction using **1** as a starting material. To this end, all solvents must first be dried with purple sodium/benzophenone ketyl and then over green titanocene, formed from the reaction of $Cp_2TiCl_2$ and zinc dust in the solvent of interest.[24]

In order to obtain a general idea of how **1** reacts with fluorinated organic compounds, the starting hafnium complex was treated with several substrates, including fluorinated aromatics and olefinic compounds, aliphatic C–F bonds, and fluorinated heterocycles.

In most of the reactions, two primary metal-based products formed, $Cp^*_2HfHF$ (**2**) and $Cp^*_2HfF_2$ (**3**), as a result of either mono- or di-hydrodefluorination, respectively. Their presence in the reaction mixtures was determined by

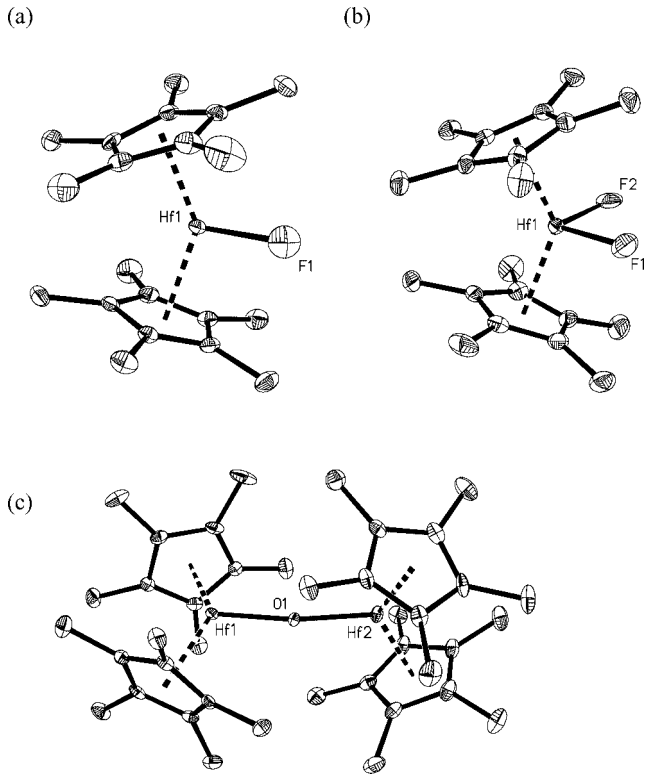


Figure 1. ORTEP diagrams of: a) **2**; b) **3**; and c) **4**. Ellipsoids are drawn at the 50% probability level. Hydrogen atoms are omitted for clarity. The fluoride ligand in **2** is disordered over two sites.

Table 1. Selected X-ray data for **2**, **3**, and **4**.

| | $Cp^*_2HfHF$ (**2**) | $Cp^*_2HfF_2$ (**3**) | $[Cp^*_2Hf]_2O$ (**4**) |
|---|---|---|---|
| Space group | $P2_1/c$ | $P2_1/n$ | $Pn$ |
| $R$(int.) | 1.65% | 3.25% | 3.02% |
| $R(\sigma)$ | 3.16% | 3.52% | 4.06% |
| $R_1$ | 4.32% | 5.02% | 2.41% |
| Cp*-Hf-Cp* | 141.7° | 137.2° | 130.9° |
| Angle[a,b,c] | 140.3° | 139.0° | 133.0° |
| Hf–O–Hf angle | N/A | N/A | 172.2(2)° |
| Hf–F or Hf–O | 1.978(6) | 2.017(4) | 1.991(3) |
| bond length[b] [Å] | 1.998(8) | 2.126(4) | 1.985(3) |

[a] Cp* represents the cyclopentadienyl centroid. [b] For the structures of **2** and **3**, two molecules were present in the asymmetric unit. Values for both structures are presented. [c] For purposes of comparison, the Cp*-Hf–Cp* angle has been reported to be 144.1° for **1**.[28]

 © 2007 Wiley-VCH Verlag GmbH & Co. KGaA, Weinheim 

Table 2. Summary of crystallographic data for **2**, **3**, and **4**.

| | **2** | **3** | **4** |
|---|---|---|---|
| Chemical formula | $C_{20}H_{31}FHf$ | $C_{20}H_{30}F_2Hf$ | $C_{40}H_{62}Hf_2O$ |
| Formula weight | 468.94 | 486.93 | 915.88 |
| Crystal system | monoclinic | monoclinic | monoclinic |
| Space group ($Z$) | $P2_1/c$ (8) | $P2_1/n$ (8) | $Pn$ (2) |
| $a$ [Å] | 15.7895(8) | 13.0151(5) | 11.0534(7) |
| $b$ [Å] | 15.4046(8) | 19.0896(8) | 10.1633(6) |
| $c$ [Å] | 16.3652(8) | 15.8115(7) | 16.5842(10) |
| $\beta$ [deg] | 109.232(1) | 107.969(1) | 103.449(1) |
| $V$ [Å]$^3$ | 3758.4(3) | 3736.8(3) | 1811.96(19) |
| $\rho_{calcd.}$ [g cm$^{-3}$] | 1.658 | 1.731 | 1.679 |
| Crystal dimensions [mm] | $0.24 \times 0.20 \times 0.10$ | $0.47 \times 0.45 \times 0.22$ | $0.50 \times 0.50 \times 0.41$ |
| Temperature [K] | 100 | 100 | 100 |
| $2\theta$ Range [deg] | 4–60 | 4–60 | 4–60 |
| Data collected | $-19 \le h \le 30$, $-15 \le k \le 15$, $-15 \le l \le 16$ | $-18 \le h \le 18$ $-26 \le k \le 26$ $-22 \le l \le 22$ | $-15 \le h \le 15$ $-14 \le k \le 14$ $-23 \le l \le 23$ |
| No. of data collected | 55625 | 55828 | 25483 |
| No. of unique data | 10862 | 10819 | 10302 |
| Agreement between equiv. data | 0.0339 | 0.0222 | 0.0302 |
| No. of observed data [$I > 2\sigma(I)$] | 9891 | 10035 | 10164 |
| No. of parameters varied | 417 | 435 | 414 |
| $\mu$ [mm$^{-1}$] | 5.556 | 5.599 | 5.754 |
| Absorption correction | empirical (SADABS) | differential (DIRDIF) | empirical (SADABS) |
| Range of transmission factors | 0.279–0.576 | 0.0983–0.292 | 0.71–0.91 |
| $R_1(F_o)$, $wR_2(F_o^2)$, all data | 0.0409, 0.0844 | 0.0235, 0.0519 | 0.0236, 0.0579 |
| $R_1(F_o)$, $wR_2(F_o^2)$, [$I > 2\sigma(I)$] | 0.0363, 0.0825 | 0.0209, 0.0508 | 0.0233, 0.0578 |
| Goodness of fit | 1.076 | 1.023 | 1.014 |

their characteristic NMR spectroscopic data. Characterization of **2** was accomplished by $^1$H and $^{19}$F NMR, as well as by $^1$H-$^{19}$F heteronuclear correlation spectroscopy. The structure of **2** was confirmed by X-ray crystallography (Figure 1).[25] Complex **3** was characterized by $^{19}$F NMR spectroscopic data, which was later confirmed through independent synthesis of the complex.[26] Further characterization was achieved through $^1$H NMR spectroscopic data[26] and X-ray crystallography (Figure 1).[25] An additional hafnium complex, $(Cp^*_2HfH)_2O$ (**4**), was isolated from a crystallization attempt of **1** and was characterized by X-ray crystallography (Figure 1) and $^1$H NMR spectroscopic data.[23,27] This compound likely arises from side reaction with adventitious water. Selected distances and angles for complexes **2**, **3**, and **4** are summarized in Table 1. Selected crystallographic data are compared in Table 2.

### Reactions of 1 with Fluoroaromatics and Fluoroaliphatics

The compounds 2- and 3-fluoropyridine both were observed to react with **1** at room temperature over the course of several hours. NMR analysis of the reaction mixtures revealed the presence of **2** and small amounts of **3** in both reactions but no free pyridine in either. In both reactions, **2** forms prior to the formation of **3**, indicating a sequential reaction of the Hf–H bond. In addition, pyridine was not observed by GC-MS analysis of the volatile materials from the reactions, suggesting that it forms strong adducts with hafnium-containing moieties in the reaction mixture. While 2-fluoropyridine reacts within a few hours, 3-fluoropyridine reacts relatively sluggishly over the course of several days.

Additional reactions using monofluorinated aromatic compounds were briefly pursued, but these experiments did not reveal the expected evidence of C–F bond cleavage. Specifically, 2- and 4-fluorobiphenyl were allowed to react with **1** for over 3 d at 120 °C without displaying C–F reactivity. In addition to reactions with monofluorinated aromatic substrates, the activation of aliphatic C–F bonds was studied using 1-fluorohexane. Initial conversion of **1** to **2** was not observed by $^{19}$F NMR until the reaction mixture was monitored after being heated to 60 °C for 44 h. The reaction was nearly complete after 20 d at 120 °C. Furthermore, hexane was also detected by $^1$H NMR spectroscopy[18] with the observed ratio of **2**:hexane being 0.4:1.0. Small amounts of **3** (5%) were also observed.

Several polyfluorinated aromatic compounds were examined. Highly symmetric substrates 1,2,4,5-tetrafluorobenzene and 2,2′,3,3′,5,5′,6,6′-octafluorobiphenyl did not participate in C–F bond cleavage after days at 120 °C. However, heating for 120 h at 100 °C produced traces of **2** or **3** in reactions involving 1,2,3,4-tetrafluorobenzene and 2,3,4,5,6-pentafluoro(allylbenzene), respectively. While longer reaction times at elevated temperatures reduced the amount of substrate relative to metal-based products, the products generated do not display NMR spectroscopic data that matches that of the expected organic products.[29]

Several perfluorinated aromatic compounds were also examined: hexafluorobenzene, octafluoronaphthalene, and decafluorobiphenyl. NMR analysis of the reactions showed that each reaction generated **2** upon heating, but that weeks at 100–120 °C are required. The observed $^{19}$F NMR chemical shift values of the organic products match known values

 © 2007 Wiley-VCH Verlag GmbH & Co. KGaA, Weinheim 

for pentafluorobenzene, 2H-heptafluoronaphthalene, and 4H-nonafluorobiphenyl.[1(d)] Additionally, 2H-heptafluoronaphthalene was observed by GC-MS analysis of the volatile materials from its respective reaction and the potential presence of 2H-nonafluorobiphenyl as the major product from its respective reaction was discounted based on previously published NMR spectroscopic data.[30] Note that $C_6F_6$ is substantially less reactive than the other perfluoroarenes.

### Reactions of 1 with Fluoroolefins

Partially fluorinated olefins investigated include 3,3,3-trifluoropropene, 1,1-difluoroethylene, hexafluoroisobutene, 3,4,4,4-tetrafluoro-3-trifluoromethyl-1-butene, α-(trifluoromethyl)styrene, and difluoromethylenecyclohexane. Reaction with 3,3,3-trifluoropropene produced **2**, **3**, 1,1-difluoropropene, and 1,1,1-trifluoropropane in a 3.7:0.5:3.4:1.0 ratio after 43 h at room temperature [Equation (4)]. However, the bulk of the conversion was observed to have occurred by $^{19}F$ NMR spectroscopy after roughly 3 min had elapsed. NMR spectroscopic data from 1,1-difluoropropene and 1,1,1-trifluoropropane match previously reported data[14] and 1,1-difluoropropene was identified by analyzing the volatile materials from the reaction by GC-MS.

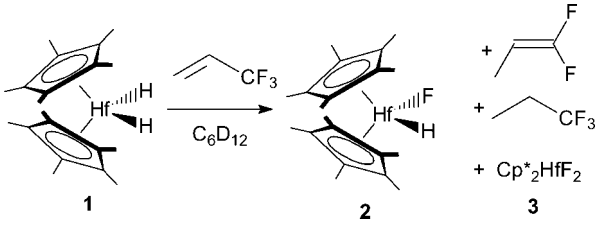

(4)

Reaction of **1** with 1,1-difluoroethylene produced **2** and a species assigned as $Cp^*_2Hf(CH_2CH_3)H$ (**5**) after 20 min at room temperature [Equation (5)]. The diagnostic $^1H$ NMR signals for **5** [$\delta$ = 11.95 (s, Hf–*H*), 0.32 (t, $-CH_2CH_3$), –0.22 (q, $-CH_2CH_3$)] are close to those reported for this complex in $C_6D_6$.[22] Furthermore, because 1-fluoroethylene[31] and free ethylene[32] were not observed, the formation of this complex can be rationalized by subsequent insertions and eliminations of 1,1-difluoroethylene and fluoroethylene into a Hf–H bond, a sequence of transformations which ultimately result in ethylene formation. This ethylene then undergoes Hf–H insertion to finally arrive at **5**.

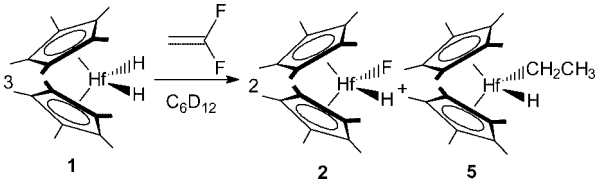

(5)

In order to alter the steric profile of the studied olefins, bulkier alkenes were then used to contrast their reactivity with that of the smaller compounds. The reaction of **1** and hexafluoroisobutene produced 1,1,3,3,3-pentafluoro-2-methyl-1-propene[14] after 50 h at room temperature [Equation (6)]. The final ratio of **2**:1,1,3,3,3-pentafluoro-2-methyl-1-propene was 1.7:1.0, according to $^{19}F$ NMR spectroscopic data.

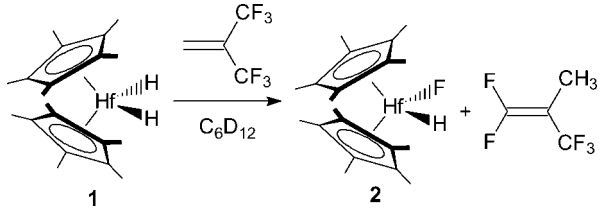

(6)

The analogous reaction using 3,4,4,4-tetrafluoro-3-trifluoromethyl-1-butene produced 1,1,1-trifluoro-2-trifluoromethyl-2-butene and 1,1,1-trifluoro-2-trifluoromethyl-2-butane, both of which could be confirmed by literature precedent [Equation (7)].[14] The reaction was allowed to proceed for 146 h at room temperature, although this time was not sufficient to completely consume **1**. The final ratio of **2**:1,1-trifluoro-2-trifluoromethyl-2-butene: 1,1,1-trifluoro-2-trifluoromethyl-2-butane obtained from $^{19}F$ NMR spectroscopic data was 11.3:7.9:1.0. The olefinic organic product was also identified by GC-MS.

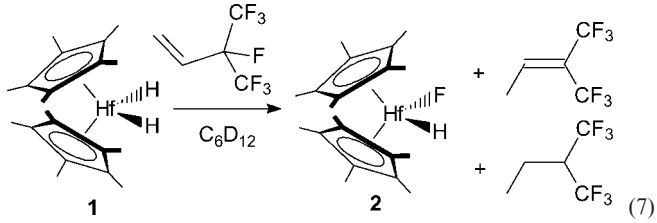

(7)

The reaction of **1** with α-(trifluoromethyl)styrene produced β,β-difluoro-α-methylstyrene, the presence of which was confirmed from previous NMR spectroscopic data [Equation (8)].[33] First evidence of the formation of **2** was observed after heating the reaction mixture for 18 h at 80 °C. **3** was first observed following 92 h of heating at 80 °C. The reaction was terminated after 163.5 h at 160 °C. On the basis of $^{19}F$ NMR spectroscopic data, the final ratio of **2**:**3**: β,β-difluoro-α-methylstyrene was 0.8:1.0: 1.5.

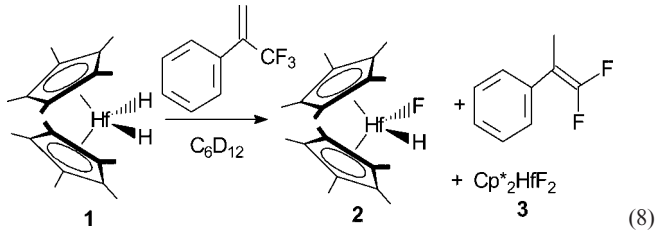

(8)

The reaction involving difluoromethylenecyclohexane was carried out in the same manner, producing **2**, **3**, and fluoromethylenecyclohexane in a 12.8:1.0: 38.0 ratio (by $^{19}F$ NMR) after 93 h of reaction at 160 °C [Equation (9)]. Initial formation of **2** was not observed until after 22 h had

 © 2007 Wiley-VCH Verlag GmbH & Co. KGaA, Weinheim 

elapsed at 120 °C. Literature values[14] were used to match obtained NMR spectroscopic data with the corresponding organic product.

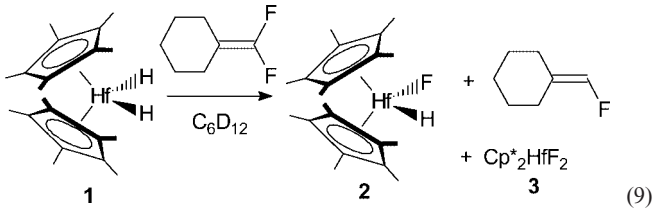


(9)

**Reactions of 1 with Perfluoroolefins**

Following the set of reactions using polyfluorinated alkenes, the perfluorinated olefins perfluoropropene and octafluorocyclopentene were used in reactions with **1**. The perfluoropropene reaction proceeded at room temperature and yielded **2** and (*E*)-1,2,3,3,3-pentafluoropropene in a 1.8:1.2 ratio (using $^{19}$F NMR spectroscopic data) after 41.5 h [Equation (10)]. The identity of the organic product was determined from previous NMR spectroscopic data[15] and conflicted with the data available for the *Z* isomer.[34]

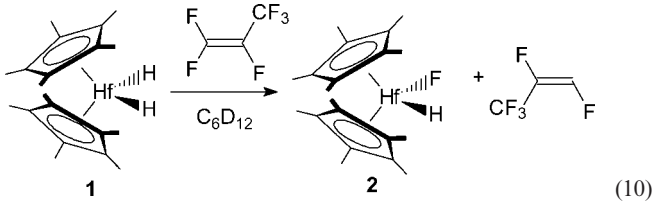


(10)

On the basis of $^{19}$F NMR spectroscopic data, the analogous reaction using octafluorocyclopentene produced a mixture of **2**, **3**, and 1H-heptafluorocyclopentene in a 41:1.0:27.4 ratio after 47 h at room temperature. Identity of the organic product was confirmed by previously obtained NMR spectroscopic data[34] and by GC-MS data obtained from the volatile materials from the reaction. Full consumption of **1** was achieved.

In an effort to understand the hydrodefluorination of octafluorocyclopentene in more detail, a stepwise C–F activation experiment was performed as follows: equimolar amounts of **1** and octafluorocyclopentene were reacted at room temperature, after which the volatile organic product (1H-heptafluorocyclopentene) was vacuum-transferred onto an additional equivalent of **1**. The first step of this reaction essentially proceeded as before, with the exception being that a small amount of a second product isomer, 4H-heptafluorocyclopentene, was observed by $^{19}$F NMR after 30 min of reaction at room temperature. The ratio of the major (expected) product to the new, minor product was 5.5:1.0. After 20 h of reaction, **1** was no longer present in the reaction mixture, and the volatile materials were vacuum-transferred to a second equivalent of **1**. The reaction was then periodically monitored by NMR spectroscopy over the course of several months (Figure 2). The reaction at room temperature afforded 1H,2H-hexafluoro-cyclopentene as the initial major organic product. However, after an extended amount of time at room temperature, 1H,2H,3H-pentafluorocyclopentene could be observed. The identity of both fluorocyclopentene products was confirmed through comparison to available NMR spectroscopic data.[34]

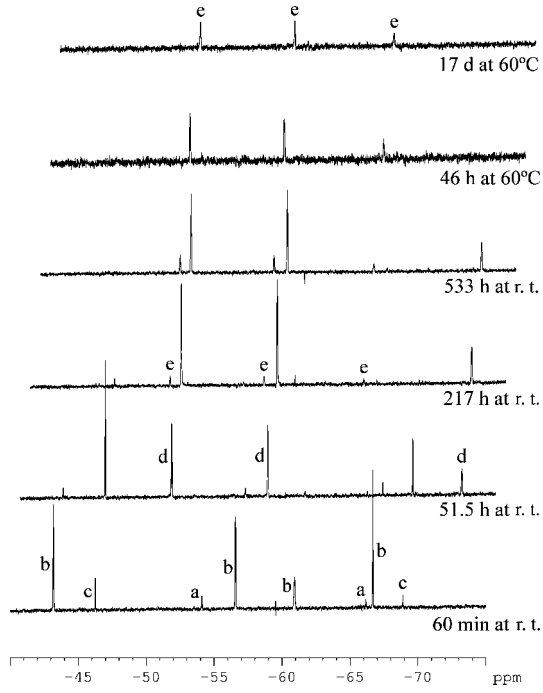


Figure 2. $^{19}$F NMR spectroscopic data for the stepwise hydrodefluorination of perfluorocyclopentene. Temperatures (°C) and allowed reaction times for the various spectra are listed in the right margin. (a = octafluorocyclopentene; b = 1H-heptafluorocyclopentene; c = 1H,2H-hexafluorocyclopentene; d = 1H,2H,3H-pentafluorocyclopentene; e = **6**).

Following a period of decreased activity, the reaction mixture was heated first to 60 °C and then to 100 °C. The relatively high temperature drastically altered the observed product distribution and even resulted in the formation of a species tentatively assigned as **6** (Scheme 1). The assignment of **6** is based largely on NMR integration values and previous observation of a similar complex involving Zr.[34]

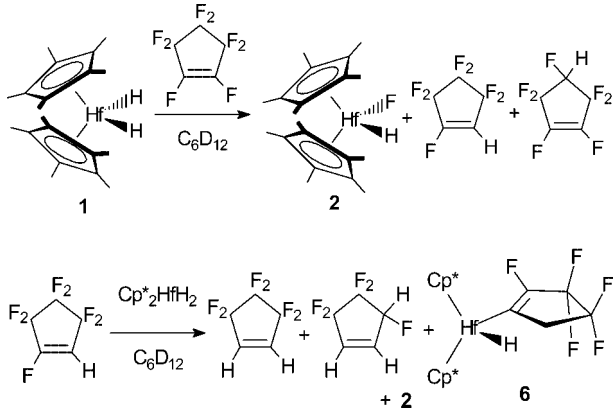


Scheme 1.

 © 2007 Wiley-VCH Verlag GmbH & Co. KGaA, Weinheim 

There appeared to be no evidence of other fluorinated cyclopentene derivatives following prolonged heating at 100 °C.[35] GC-MS analysis of the volatile materials from the reaction revealed the presence of 1H,2H,3H-pentafluorocyclopentene.

While the stepwise reaction of octafluorocyclopentene shows a preference for vinylic C–F activation over cleavage of neighboring C–F bonds, the mechanism by which the organic products are generated remains unclear. While an olefin insertion prior to β-fluoride elimination mechanism seems to be operative for other non-cyclic olefins,[4,12–15] such a process cannot be responsible for the formation of observed products in this case, because the product predicted by the mechanism is not observed [Equation (11)]. Consequently, a new mechanism must be postulated for this facile olefinic hydrogenolysis. At this point, preliminary calculations suggest a 4-center metathesis pathway between the Hf–H and C–F bond for the reaction.

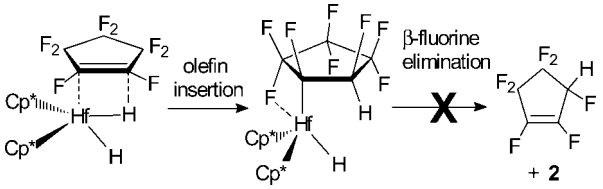


(11)

## Low-Temperature Studies

Low-temperature NMR spectroscopy was used to look for intermediates that might provide mechanistic insight into the reaction of fluorinated olefins with **1**. In particular, reactions of **1** with 3,3,3-trifluoropropene, 1,1-difluoroethylene, and 1,1-difluoropropene were studied at low temperature. Reactions were initiated at –110 °C and samples monitored in the NMR probe as they warmed to room temperature. Of the substrates examined, the reactions involving 3,3,3-trifluoropropene provided the most insight. Figure 3 shows some of the $^{19}$F NMR spectroscopic data obtained from this reaction.

The most striking aspect of the data presented in Figure 3 is the fact that some of the species observed, specifically the compounds corresponding to the peaks labeled **c** and **e**, seem to be present at low temperature but gradually vanish as the temperature is increased. One way to rationalize these observations is summarized in Equation (12) below. Assuming that insertion of the olefin into the metal-hydride bond of **1** is the initial step in the reaction, one could expect two different species – one with a branched fluoroalkyl ligand **7** and one featuring a straight-chain fluoroalkyl moiety **8** – to form. Because the NMR spectra taken from roughly –110 °C to –60 °C display only starting olefin, **1**, and two unidentified species, it seems reasonable to argue that the unassigned species may be the two insertion products, **7** and **8**. Strengthening that assertion is the fact that the signal assigned to **8** is a sharp triplet, as would be expected.

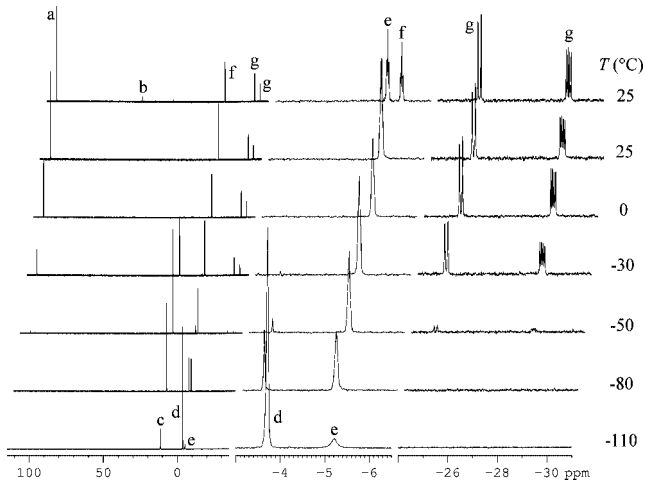


Figure 3. Variable-temperature $^{19}$F NMR spectroscopic data for the reaction of 3,3,3-trifluoropropene with **1**. The temperatures (°C) corresponding to the various spectra are given in the right margin. Regions of interest are expanded for clarity. (a = **2**, b = **3**, c = **7**, d = 3,3,3-trifluoropropene, e = **8**, f = 1,1,1-trifluoropropane, g = 1,1-difluoropropene).

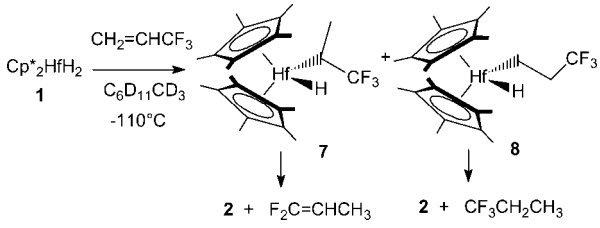


(12)

Subsequent warming of the reaction mixture results in relatively rapid disappearance of the NMR signal tentatively assigned to **7** accompanied by an appreciable increase in the signals corresponding to **2** and 1,1-difluoropropene. The β-fluoride elimination from the trifluoromethyl group is consistent with these observations. Moreover, prolonged storage of the reaction mixture at room temperature promotes the growth of the signal previously assigned to 1,1,1-trifluoropropane. Because the hydrogenated olefin signal intensity approaches that of the resonance assigned to **8**, it appears as though complex **8** may be the source of 1,1,1-trifluoropropane.

The low-temperature experiment using 3,3,3-trifluoropropene was monitored by $^{1}$H NMR in a separate trial and showed similar behavior to that observed by $^{19}$F NMR spectroscopy. Specifically, two previously unobserved signals appeared between 12–14 ppm and were tentatively assigned as the Hf–H signals from **7** ($\delta$ = 13.80 ppm) and **8** ($\delta$ = 12.90 ppm). As expected, the signal from **7** decreased quickly upon warming and was completely absent by the time the reaction was warmed to –10 °C. In addition, another resonance at $\delta$ = 0.50 ppm exhibited the same behavior and was assigned as the methyl group of **7** based on integration. The Hf–H signal from **8** along with an additional signal at –0.03 ppm (assigned to the metal-bound

 © 2007 Wiley-VCH Verlag GmbH & Co. KGaA, Weinheim 

methylene of **8** based on integration) expectedly lingered at room temperature.

While the reaction of 3,3,3-trifluoropropene with **1** appeared to successfully demonstrate that the insertion/elimination mechanism accounts for the formation of observed products, the same could not be said for the reactions of 1,1-difluoroethylene and 1,1-difluoropropene with **1**. At the current time, it appears as though the reaction involving 1,1-difluoroethylene proceeds too rapidly at low temperature to observe intermediates. In contrast, the reaction of 1,1-difluoropropene has not provided results suitable for discussion of its mechanism of reaction.

### Comparison with Reactions of Zirconium Dihydride

A comparison can be made here with the related reactivity of the zirconium analog $Cp^*_2ZrH_2$. This complex has been reported to reduce aliphatic,[36] aromatic,[1d–18] and olefinic[14–15] C–F bonds under mild conditions. It can also undergo β-fluoride elimination in fluorophenyl derivatives to generate benzyne intermediates.[37] In addition, reduction of $sp^3$ $CF_2H$–R has been reported to occur slowly with this compound. The reaction mechanisms proposed vary from free radical chain for aliphatic C–F, to nucleophilic attack for monofluoroaromatics, to insertion/β-fluoride elimination for fluoroolefins.[4] Additionally, other electrophilic titanocene[38] and zirconocene[39] complexes have been seen to cleave C–F bonds in perfluoropyridine. In general, the reactivity patterns seen with $Cp^*_2HfH_2$ mimic those of $Cp^*_2ZrH_2$, except that the hafnium complex is less reactive. Reactions proceed to give similar products either slowly, or not at all. While fewer mechanistic studies have been undertaken with hafnium, it is likely that the substrates react by similar mechanisms as in the zirconium cases.

## Experimental Section

All substrates were used as delivered without purification. Products have been characterized and unreacted starting materials have been identified primarily by comparing known $^{19}F$ NMR chemical shift values to those obtained during a given experiment (using external α,α,α-trifluorotoluene in [$D_{12}$]cyclohexane as a reference). Reported NMR spectroscopic data not referenced to external α,α,α-trifluorotoluene in [$D_{12}$]cyclohexane were converted accordingly. In some cases, $^1H$ NMR and GC-MS data were used to further confirm the identity of the organic products. NMR spectra were recorded with Bruker Avance instruments (400 or 500 MHz). GCMS data were recorded with a Shimadzu model QP2010 spectrometer. A Siemens SMART CCD area detector diffractometer equipped with an LT-2 low-temperature unit was used for X-ray crystal structure determination.

**Preparation of $Cp^*_2HfH_2$:** From dimethyl complex: $Cp^*_2HfCl_2$ (3.85 mmol; Strem) was dissolved in roughly 40 mL of diethyl ether (previously vacuum-transferred from purple sodium/benzophenone ketyl) in a nitrogen glovebox. On a Schlenk line, 2.1 equiv. of methyllithium (8.09 mmol; 1.4 M in $Et_2O$ from Aldrich) were added to the reaction mixture by syringe under positive nitrogen pressure. The reaction mixture was stirred under static nitrogen for roughly 25 h before ca. 1 mL of ACS-grade methanol was added under positive nitrogen pressure to quench the reaction. The volatile materials were removed by vacuum. Isolation of the final product was achieved by filtering a hexane mixture of crude product through celite, cooling the filtrate to –78 °C to induce crystallization, removing the mother liquor/washing the crystals with cold hexane via cannula transfer, and drying in vacuo (3.06 mmol, 80%). The second step involved placing a $C_6D_6$ solution of $Cp^*_2HfMe_2$ (0.06 mmol) under 15 psi of UHP-grade hydrogen gas (Airgas) at 100 °C. The reaction was periodically monitored by $^1H$ NMR over the course of 6 weeks, with the hydrogen being replaced many times with fresh hydrogen following several freeze-pump-thaw degassing cycles (≈ 97% final conversion to **1**). The reaction was repeated on a preparative scale with the remaining $Cp^*_2HfMe_2$. **1** was also prepared in 33% yield from the reaction of $Cp^*_2HfCl_2$ and BuLi, as described in ref.[22]. $^1H$ NMR ($C_6D_6$): $Cp^*_2HfCl_2$, $\delta$ = 1.91, s. $Cp^*_2HfMe_2$, $\delta$ = 1.80, (s, 30 H), –0.70 (s, 6 H) $Cp^*_2HfH_2$ (**1**), $\delta$ = 2.05, (s, 30 H), 15.63 (s, 2 H) ppm. $^1H$ NMR ($C_6D_{12}$): $Cp^*_2HfH_2$ (**1**), $\delta$ = 2.03, (s, 30 H), 15.37 (s, 2 H) ppm.

**Isolation of 2 and 3:** Samples of **2** and **3** were obtained from the non-volatile organometallic residue of the fluorocarbon reduction reactions. X-ray quality crystals were grown by allowing a pentane solution of the hafnium complex to evaporate into a small quantity of toluene at –30 °C in a nitrogen glovebox. X-ray quality crystals of **4** were obtained by allowing pentane vapor to diffuse into a concentrated $CH_2Cl_2$ solution of **4** at room temperature in a nitrogen glovebox. For **2**, $^1H$ NMR ($C_6D_{12}$): $\delta$ = 1.95 (s, 30 H), 10.90 (d, $J$ = 4.8 Hz, 1 H) ppm. $^{19}F$ NMR: $\delta$ = 107.8 (s) ppm. For **3**, $^1H$ NMR ($C_6D_{12}$): $\delta$ = 1.89 (s) ppm. $^{19}F$ NMR: $\delta$ = 49.7 (s) ppm. For **4**, $^1H$ NMR ($C_6D_{12}$): $\delta$ = 2.00 (s, 30 H), 2.08 (s, 30 H), 9.79 (s, 2 H) ppm.

**Reactions of 1 with Fluorocarbons:** All experiments were run in NMR tubes fitted with a Teflon™ stopper using equimolar amounts of **1** and substrate. Unless otherwise noted, twice-dried [$D_{12}$]cyclohexane was used as solvent to dissolve mixtures of the starting hafnium complex and solid substrates in a nitrogen glovebox. In reactions involving liquid substrates, ca. 10 mg of **1** was first dissolved using $C_6D_{12}$ in a nitrogen glovebox and the previously-degassed liquid substrate was added via syringe. Gaseous compounds were condensed into chilled reaction vessels using high vacuum techniques.

For reactions of 2- and 3-fluoropyridine, $^{19}F$ data[40] showed the loss of fluorocarbon reactant and the formation of **2** and small amounts of **3** (2–4%) over the course of a week at room temperature. Pyridine was not seen by $^1H$ NMR spectroscopy.[41] For reactions of 2- and 4-fluorobiphenyl, no reaction was observed at 120 °C by $^{19}F$ NMR spectroscopy.[42] Polyfluorinated aromatics showed only traces of reaction if any reaction at all after extended heating at 120 °C, as determined by monitoring the $^{19}F$ NMR spectra of these reactions. Substrates examined were 1,2,4,5-tetrafluorobenzene,[1(d)] 2,2′,3,3′,5,5′,6,6′-octafluorobiphenyl,[43] 1,2,3,4-tetrafluorobenzene,[1(d)] and 2,3,4,5,6-pentafluoro(allylbenzene).[44] In contrast, perfluorinated aromatics showed some evidence for slow reaction. $^{19}F$ NMR spectroscopic examination of reactions of hexafluorobenzene,[45] octafluoronaphthalene,[46] and decafluorobiphenyl[47] showed reduction to produce **2** after several days at 100–120 °C. Reaction of **1** with 1-fluorohexane[48] commenced only upon heating to 60 °C, and approached completion after 20 d at 120 °C.

$^{19}F$ NMR spectroscopy was used to monitor reactivity of the partially fluorinated olefins 3,3,3-trifluoropropene,[49] 1,1-difluoroethylene,[50] hexafluoroisobutene,[51] 3-trifluoromethyl-3,4,4,4-tetrafluoro-1-butene, α-(trifluoromethyl)styrene,[52] and difluoromethyl-

 © 2007 Wiley-VCH Verlag GmbH & Co. KGaA, Weinheim 

enecyclohexane,[53] as described in the text. Reactions of **1** with the perfluorinated olefins perfluoropropene[54] and octafluorocyclopentene[55] were also examined by $^{19}F$ NMR spectroscopy, but now reaction occurred quickly at room temp.

**Low-Temperature Reaction of 1 with Fluorocarbons:** Compound **1** was dissolved in [$D_{14}$]methylcyclohexane in a nitrogen glovebox. The substrate of choice was measured by achieving the appropriate pressure in a pre-calibrated glass bulb. The substrate was then condensed into the reaction vessel following degassing of the solution of **1**. Special effort was directed at keeping the NMR tube cold following transfer of the substrate, which was achieved by thawing the frozen solution of **1** in a liquid nitrogen/ethanol slush bath (–116 °C). In most instances, the NMR probe was pre-cooled to –110 °C.

1,1-Difluoropropene was obtained through the previously mentioned reaction of **1** with 3,3,3-trifluoropropene, with the exception being that the reaction was run in $C_6D_{11}CD_3$ in instances where 1,1-difluoropropene was designed to serve as a starting material in a subsequent low-temperature experiment. The volatile materials from the reaction (primarily 1,1-difluoropropene, 1,1,1-trifluoropropane, and solvent) were vacuum-transferred from this reaction onto another equivalent of **1** before thawing the reaction mixture at –116 °C. Detailed descriptions of these reactions are given in the text.

**X-ray Structure Determinations:** Single crystals of **1**, **2**, and **3** were mounted under Exxon Paratone-8277™ on glass fibers and immediately placed in a cold nitrogen stream at 100 K on the X-ray diffractometer. The X-ray intensity data (1.3 hemispheres) were collected over 6 h with a standard Siemens SMART APEX II CCD Area Detector System equipped with a normal focus molybdenum-target X-ray tube operated at 2.0 kW (50 kV, 40 mA).[56] Data were corrected for absorption using the program SADABS.[57] Space group assignments were made on the basis of systematic absences and intensity statistics by using the XPREP program (Siemens, SHELXTL 97). The structures were solved by using direct methods and refined by full-matrix least-squares on $F^2$.[58] For all of the structures, the non-hydrogen atoms were refined with anisotropic thermal parameters except for the fluoride ligand in **2**, which was disordered over two sites and refined isotropically. The Hf-bound hydride in **2** was not included in the final refinement model. There was nothing unusual about the solution or refinement of any of the structures, although the fluoride and hydride ligands in **2** were disordered (76/24 and 60/40). Compound **4** refined with a Flack parameter of 0.055(8). Further experimental details of the X-ray diffraction studies are provided in Table 2. CIF files for the structures **2**–**4** have been deposited with the CCDC.[59]

## Acknowledgments

The U. S. Department of Energy, Grant FG02-86ER13569, is gratefully acknowledged for their support of this work.

[1] Recent examples of stoichiometric C–F activation: a) D. Noveski, T. Braun, B. Neumann, A. Stammler, H. G. Stammler, *Dalton Trans.* **2004**, 4106–4119; b) R. P. Hughes, D. Zhang, L. N. Zakharov, A. L. Rheingold, *Organometallics* **2002**, *21*, 4902–4904; c) M. S. Kirkham, M. F. Mahon, M. K. Whittlesey, *Chem. Commun.* **2001**, 813–814; d) B. M. Kraft, W. D. Jones, *J. Organomet. Chem.* **2002**, *658*, 132–140.

[2] For examples of catalytic C–F activation, see: a) S. Kuhl, R. Schneider, Y. Fort, *Adv. Synth. Catal.* **2003**, *345*, 341–345; b) M. Aizenberg, D. Milstein, *J. Am. Chem. Soc.* **1995**, *117*, 8674–8675; c) M. Aizenberg, D. Milstein, *Science* **1994**, *94*, 359–361; d) J. Vela, J. M. Smith, Y. Yu, N. A. Ketterer, C. J. Flaschenriem, R. J. Lachicotte, P. L. Holland, *J. Am. Chem. Soc.* **2005**, *127*, 7857–7870; e) R. J. Young, V. V. Grushin, *Organometallics* **1999**, *18*, 294–296; f) T. Braun, R. N. Perutz, M. I. Sladek, *Chem. Commun.* **2001**, 2254–2255; g) Y. Ishii, N. Chatani, S. Yorimitsu, S. Murai, *Chem. Lett.* **1998**, 157–158.

[3] For additional discussion of these mechanisms and for examples of systems capable of C–F activation, see: J. Burdeniuc, B. Jedlicka, R. H. Crabtree, *Chem. Ber./Recueil* **1997**, *130*, 145–154.

[4] W. D. Jones, *Dalton Trans.* **2003**, 3991–3995.

[5] For examples of intramolecular C–F activation, see: a) D. Huang, K. G. Caulton, *J. Am. Chem. Soc.* **1997**, *119*, 3185–3186; b) M. Crespo, J. Granell, M. Font-Bardía, X. Solans, *J. Organomet. Chem.* **2004**, *689*, 3088–3092; c) R. P. Hughes, D. C. Lindner, A. L. Rheingold, L. M. Liable-Sands, *J. Am. Chem. Soc.* **1997**, *119*, 11544–11545; d) R. P. Hughes, J. M. Smith, *J. Am. Chem. Soc.* **1999**, *121*, 6084–6085; e) P. J. Albietz, J. F. Houlis, R. Eisenberg, *Inorg. Chem.* **2002**, *41*, 2001–2003; f) R. P. Hughes, J. M. Smith, C. D. Incarvito, K. Lam, B. Rhatigan, A. L. Rheingold, *Organometallics* **2002**, *21*, 2136–2144.

[6] P. A. Deck, M. M. Konaté, B. V. Kelly, C. Slebodnick, *Organometallics* **2004**, *23*, 1089–1097.

[7] M. K. Whittlesey, R. N. Perutz, M. Moore, *Chem. Commun.* **1996**, 787–788.

[8] B. L. Edelbach, W. D. Jones, *J. Am. Chem. Soc.* **1997**, *119*, 7734–7742.

[9] A. Steffen, M. I. Sladek, T. Braun, B. Neumann, H. G. Stammler, *Organometallics* **2005**, *24*, 4057–4064.

[10] T. Wondimagegn, Z. Xu, K. Vanka, T. Ziegler, *Organometallics* **2005**, *24*, 2076–2085.

[11] P. Arndt, U. Jäger-Fiedler, M. Klahn, W. Baumann, A. Spannenberg, V. V. Burlakov, U. Rosenthal, *Angew. Chem. Int. Ed.* **2006**, *45*, 4195–4198.

[12] B. L. Edelbach, A. K. F. Rahman, R. J. Lachicotte, W. D. Jones, *Organometallics* **1999**, *18*, 3170–3177.

[13] G. Ferrando-Miguel, H. Gérard, O. Eisenstein, K. G. Caulton, *Inorg. Chem.* **2002**, *41*, 6440–6449.

[14] B. M. Kraft, W. D. Jones, *J. Am. Chem. Soc.* **2002**, *124*, 8681–8689.

[15] E. Clot, C. Mégret, B. M. Kraft, O. Eisenstein, W. D. Jones, *J. Am. Chem. Soc.* **2004**, *126*, 5647–5653.

[16] a) M. E. Van der Boom, Y. Ben-David, D. Milstein, *J. Am. Chem. Soc.* **1999**, *121*, 6652–6656; b) R. P. Hughes, R. B. Laritchev, L. N. Zakharov, A. L. Rheingold, *J. Am. Chem. Soc.* **2005**, *127*, 6325–6334; c) C. Chiang, D. Lu, J. Huang, C. Hwang, C. Cho, L. Fan, Y. Yang, *J. Am. Chem. Soc.* **2004**, *126*, 12242–12243; d) R. P. Hughes, S. Willemsen, A. Williamson, D. Zhang, *Organometallics* **2002**, *21*, 3085–3087.

[17] F. L. Taw, B. L. Scott, J. L. Kiplinger, *J. Am. Chem. Soc.* **2003**, *125*, 14712–14713.

[18] B. M. Kraft, R. J. Lachicotte, W. D. Jones, *J. Am. Chem. Soc.* **2001**, *123*, 10973–10979.

[19] a) T. Braun, L. Cronin, C. L. Higgitt, J. E. McGrady, R. N. Perutz, M. Reinhold, *New J. Chem.* **2001**, *25*, 19–21; b) T. Braun, R. N. Perutz, *Chem. Commun.* **2002**, 2749–2757.

[20] J. L. Kiplinger, T. G. Richmond, C. E. Osterberg, *Chem. Rev.* **1994**, *94*, 373–431.

[21] L. E. Schock, T. J. Marks, *J. Am. Chem. Soc.* **1988**, *110*, 7701–7715.

[22] D. M. Roddick, M. D. Fryzuk, P. F. Seidler, G. L. Hillhouse, J. E. Bercaw, *Organometallics* **1985**, *4*, 97–104.

[23] For reaction of **1** with water, see: G. L. Hillhouse, J. E. Bercaw, *J. Am. Chem. Soc.* **1984**, *106*, 5472–5478.

[24] S. K. S. Hazari, D. Dhar, *J. Bangladesh Acad. Sci.* **1992**, *16*, 241–244.

[25] The hydride ligands were unable to be definitively located for structures **2** and **4**. Moreover, the crystal intended to contain only **2** was revealed to be a co-crystallized mixture of **2** and **3**

 © 2007 Wiley-VCH Verlag GmbH & Co. KGaA, Weinheim 

(with one monoatomic ligand site having 50% occupancy of fluorine). The data reported for **3** was isolated from a separate crystallization attempt.

[26] A. Herzog, F. Liu, H. W. Roesky, A. Demsar, K. Keller, M. Noltemeyer, F. Pauer, *Organometallics* **1994**, *13*, 1251–1256.

[27] Unsuccessful attempts to completely eliminate air and water in an attempt to crystallize **1** led to the formation of **4** in at least one instance. The undesired compound was characterized by X-ray crystallography (Figure 1) and $^1$H NMR ($C_6D_6$) data, which closely matched literature values from ref. 23.

[28] P. J. Chirik, M. W. Day, J. E. Bercaw, *Organometallics* **1999**, *18*, 1873–1881.

[29] NMR spectroscopic data for several possible organic products were consulted. $^{19}$F NMR spectroscopic data for 1,2,4-trifluorobenzene, see: a) A. M. Stuart, P. L. Coe, D. J. Moody, *J. Fluorine Chem.* **1998**, *88*, 179–184. $^{19}$F NMR spectroscopic data for 1,2,3-trifluorobenzene, see: b) G. A. Selivanova, V. F. Starichenko, V. D. Shteingarts, *Zh. Org. Khim.* **1995**, *31*, 226–232. $^1$H and $^{19}$F NMR spectroscopic data for *n*-propylpentafluorobenzene, see: c) I. Ojima, K. Kato, M. Okabe, T. Fuchikami, *J. Am. Chem. Soc.* **1987**, *109*, 7714–7720. $^1$H NMR spectroscopic data for 1-(pentafluorophenyl)-2-propanol and 1,2-epoxy-3-pentafluorophenylpropane, see: d) R. Filler, W. L. White, *J. Chem. Soc. C* **1971**, 2062–2068. 2,3,4,5- and 2,3,4,6-tetrafluoro(allylbenzene)have not been previously reported in the literature, nor have 2,3,4-, 2,3,6-, and 2,4,6-trifluoro(allylbenzene). NMR spectroscopic data for 2,3,5,6-tetrafluoro(allylbenzene)and 2,4,5-trifluoro(allylbenzene)were not available. NMR spectroscopic data for 3-pentafluorophenylpropan-1-ol has not been reported.

[30] $^{19}$F NMR spectroscopic data for 2H-nonafluorobiphenyl: D. E. Fenton, A. G. Massey, *Tetrahedron* **1965**, *21*, 3009–3018.

[31] $^1$H NMR spectroscopic data for 1-fluoroethylene: C. N. Banwell, N. Sheppard, *Mol. Phys.* **1960**, *3*, 351–369.

[32] $^1$H NMR spectroscopic data for ethylene: R. J. Abraham, M. Canton, L. Griffiths, *Magn. Reson. Chem.* **2001**, *39*, 421–431.

[33] $^{19}$F NMR spectroscopic data for β,β-difluoro-α-methylstyrene: F. J. Weigert, *J. Fluorine Chem.* **1993**, *63*, 53–58.

[34] $^1$H and $^{19}$F NMR spectroscopic data for (*Z*)-1,2,3,3,3-pentafluoropropene and X-ray structure of $Cp^*_2ZrCl(c\text{-}C_5F_5H_2)$ (Zr analog of **6**): B. M. Kraft, Ph. D. Thesis, University of Rochester, **2002**.

[35] NMR spectroscopic data for several fluorinated cyclopentene derivatives are available. $^{19}$F NMR spectroscopic data for 1H,4H-, 3H,4H-, and 3H,5H-hexafluorocyclopentene, see: a) R. Fields, M. Green, M. T. Harrison, R. N. Haszeldine, A. Jones, A. B. P. Lever, *J. Chem. Soc. A* **1970**, 49–58. $^{19}$F NMR spectroscopic data for 1H,2H,3H-pentafluorocyclopentene, see: b) W. J. Feast, D. R. A. Perry, R. Stephens, *Tetrahedron* **1966**, *22*, 433–439. $^1$H and $^{19}$F NMR spectroscopic data for 1H,2H,3H-tetrafluorocyclopentene, see: c) W. R. Dolbier, D. M. Al-Fekri, *Tetrahedron* **1987**, *43*, 39–44. $^1$H and $^{19}$F NMR spectroscopic data for 3,4- and 3,5-difluorocyclopentene, see: d) D. F. Shellhamer, M. C. Chiaco, K. M. Gallego, W. S. C. Low, B. Carter, V. L. Heasley, R. D. Chapman, *J. Fluorine Chem.* **1995**, *72*, 83–87. $^{19}$F NMR spectroscopic data for 1-fluorocyclopentene, see: e) C. J. LaFrancois, P. B. Shevlin, *Tetrahedron* **1997**, *53*, 10071–10082.

[36] B. M. Kraft, R. J. Lachicotte, W. D. Jones, *J. Am. Chem. Soc.* **2000**, *122*, 8559–8560.

[37] B. M. Kraft, R. J. Lachicotte, W. D. Jones, *Organometallics* **2002**, *21*, 727–731.

[38] a) H. M. Hoyt, F. E. Michael, R. G. Bergman, *J. Am. Chem. Soc.* **2004**, *126*, 1018–1019; b) I. M. Piglosiewicz, S. Kraft, R. Beckhaus, D. Haase, W. Saak, *Eur. J. Inorg. Chem.* **2005**, 938–945.

[39] U. Jäger-Fiedler, P. Arndt, W. Baumann, A. Spannenberg, V. V. Burlakov, U. Rosenthal, *Eur. J. Inorg. Chem.* **2005**, 2842–2849.

[40] $^{19}$F NMR spectroscopic data for 2- and 3-fluoropyridine: C. S. Giam, J. L. Lyle, *J. Am. Chem. Soc.* **1973**, *95*, 3235–3239.

[41] $^1$H NMR spectroscopic data for pyridine: A. Tamaoki, K. Takahashi, *Bull. Chem. Soc. Jpn.* **1986**, *59*, 1650–1652.

[42] $^1$H NMR spectroscopic data for 2- and 4-fluorobiphenyl: a) W. Guo, T. C. Wong, *Magn. Reson. Chem.* **1986**, *24*, 75–79. $^{19}$F NMR spectroscopic data for 2- and 4-fluorobiphenyl: b) J. Zhang, D. D. DesMarteau, *J. Fluorine Chem.* **2001**, *111*, 253–257.

[43] $^{19}$F NMR spectroscopic data for 2,2′,3,3′,5,5′,6,6′-octafluorobiphenyl: R. A. Contigiani, H. E. Bertorello, M. Martinez de Bertorello, *J. Organomet. Chem.* **1971**, *32*, 7–15.

[44] $^1$H and $^{19}$F NMR spectroscopic data for 2,3,4,5,6-pentafluoro(allylbenzene): A. Haas, J. Koehler, *J. Fluorine Chem.* **1981**, *17*, 531–537.

[45] $^{19}$F NMR spectroscopic data for hexafluorobenzene: S. Ando, T. Matsuura, *Magn. Reson. Chem.* **1995**, *33*, 639–645.

[46] $^{19}$F NMR spectroscopic data for octafluoronaphthalene: C. M. Hu, F. Long, Z. Q. Xu, *J. Fluorine Chem.* **1990**, *48*, 29–35.

[47] $^{19}$F NMR spectroscopic data for decafluorobiphenyl: G. von Fircks, H. Hausmann, V. Francke, H. Günther, *J. Org. Chem.* **1997**, *62*, 5074–5079.

[48] $^1$H NMR spectroscopic data for 1-fluorohexane: a) D. A. Flosser, R. A. Olofson, *Tetrahedron Lett.* **2002**, *43*, 4275–4279. $^{19}$F NMR spectroscopic data for 1-fluorohexane: b) G. Filipovich, G. V. D. Tiers, *J. Phys. Chem.* **1959**, *63*, 761–763.

[49] $^1$H and $^{19}$F NMR spectroscopic data for 3,3,3-trifluoropropene: M. Hanack, J. Ullmann, *J. Org. Chem.* **1989**, *54*, 1432–1435.

[50] $^{19}$F NMR spectroscopic data for 1,1-difluoroethylene: F. J. Weigert, *J. Fluorine Chem.* **1990**, *46*, 375–384.

[51] $^1$H and $^{19}$F NMR spectroscopic data for hexafluoroisobutene: S. Misaki, S. Takamatsu, *J. Fluorine Chem.* **1984**, *24*, 531–533.

[52] $^1$H and $^{19}$F NMR spectroscopic data for α-(trifluoromethyl) styrene: R. Q. Pan, X. X. Liu, M. Z. Deng, *J. Fluorine Chem.* **1999**, *95*, 167–170.

[53] $^1$H and $^{19}$F NMR spectroscopic data for difluoromethylenecyclohexane: C. M. Hu, F. L. Qing, C. X. Shen, *J. Chem. Soc., Perkin Trans. 1* **1993**, 335–338.

[54] $^{19}$F NMR spectroscopic data for perfluoropropene: M. V. Galakhov, V. A. Petrov, V. I. Bakhmutov, G. G. Belen'kii, B. A. Kvasov, L. S. German, E. I. Fedin, *Izv. Akad. SSSR, Ser. Khim.* **1985**, 306–312.

[55] $^{19}$F NMR spectroscopic data for octafluorocyclopentene: R. D. Chambers, A. R. Edwards, *J. Chem. Soc., Perkin Trans. 1* **1997**, *24*, 3623–3628.

[56] It has been noted that the integration program SAINT produces cell constant errors that are unreasonably small, because systematic error is not included. More reasonable errors might be estimated at 10 × the listed value.

[57] The SADABS program is based on the method of Blessing: R. H. Blessing, *Acta Crystallogr., Sect. A* **1995**, *51*, 33–38.

[58] Using the SHELX95 package, $R_1 = (\Sigma||F_o| - |F_c||)/\Sigma|F_o|$, $wR_2 = \{\Sigma[w(F_o^2 - F_c^2)^2]/\Sigma[w(F_o^2)^2]\}1/2$, where $w = 1/[\sigma^2(F_o^2) + (a\cdot P)^2 + b\cdot P]$ and $P = [f\cdot(\text{maximum of 0 or } F_o^2) + (1 - f)\cdot F_c^2]$.

[59] CCDC-618856 to -618858 contain the supplementary crystallographic data for this paper. These data can be obtained free of charge from The Cambridge Crystallographic Data Centre via www.ccdc.cam.ac.uk/data_request/cif.

Received: August 30, 2006
Published Online: January 4, 2007

 © 2007 Wiley-VCH Verlag GmbH & Co. KGaA, Weinheim 

DOI: 10.1002/ejic.200600811

# The Effect of Catalyst Loading in Copper-Catalyzed Cyclohexane Functionalization by Carbene Insertion

**Ana Caballero,[a] M. Mar Díaz-Requejo,[a] Swiatoslaw Trofimenko,[b] Tomás R. Belderraín,*[a] and Pedro J. Pérez*[a]**

**Keywords:** Copper / C–H activation / Homogeneous catalysis / Carbenes / N ligands

A study of the variables that affect the insertion of the :$CHCO_2Et$ group (formed from ethyl diazocetate, EDA) into the C–H bonds of cyclohexane in the presence of a $Tp^xCu$ complex as the catalyst ($Tp^x$ = trispyrazolylborate ligand) has demonstrated an anomalous effect of the catalyst loading. The use of low concentrations of catalyst produces an increase in the yield of the C–H activation product ethyl cyclohexaneacetate. This effect has also been found in the case of other less elaborated catalysts such as $[Bp^{Br3}Cu]$ or $[(bipy)_2Cu][I]$.
(© Wiley-VCH Verlag GmbH & Co. KGaA, 69451 Weinheim, Germany, 2007)

## Introduction

Diazo reagents have been employed extensively as a carbene source, initially under thermal or photochemical conditions and in the last decades with the aid of transition-metal complexes as catalysts for several transformations[1] for the transfer of the carbene unit to many saturated and unsaturated substrates (Scheme 1). Besides the desired addition or insertion products, the undesired carbene coupling side-reaction has usually been observed in the vast majority of reported systems.

It is well established that the transformations depicted in Scheme 1 take place through the intermediacy of a metallocarbene species $L_nM{=}CR^1R^2$, which is generated from the direct reaction of the catalyst $ML_n$ and the diazo compound,[1] and that this constitutes the rate-determining step of the overall process.[2,3] The transient metallocarbenoid species (MC) usually displays an electrophilic behavior,[4] which explains its reactivity towards the nucleophiles available in solution − the diazo compound or the target substrate to be functionalized. Due to its high reactivity, there are few reports in the literature in which these intermediates have been detected or isolated. In the case of copper, the first observation of one of these species under catalytic conditions is due to Straub and Hofmann.[5] Later, Warren and Dai described the preparation and structural characterization of the copper carbene complex $[(N–N)Cu{=}CPh_2]$ from the reaction of a diketiminatocopper(I) complex and $Ph_2CN_2$.[6]

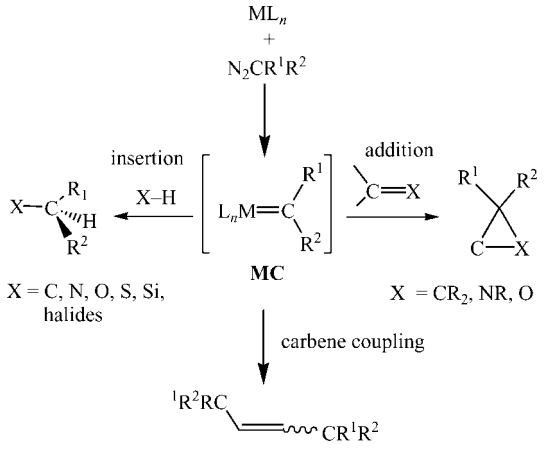


Scheme 1. Transition-metal-catalyzed carbene transfer from diazo compounds.

In recent years we have described the potential of a family of complexes of general formula $[Tp^xCu(NCMe)]$ ($Tp^x$ = homoscorpionate ligand) toward the two processes mentioned above: the addition of :$CHCO_2Et$ from ethyl diazoacetate (EDA) to multiple carbon–carbon bonds (alkenes,[7] alkynes,[8] aromatics[9]) or its insertion into single X–H bonds (alkanes,[10] amines,[11] alcohols[12]). All these transformations are accompanied by the copper-catalyzed carbene coupling reaction, which leads to the formation of diethyl fumarate and maleate in variable yields [Equation (1)]. In this contribution, we present the results obtained during the course of our investigations focused on the study of the variables that could affect the formation of these undesired by-products with the aim of its decrease or suppression. We

[a] Laboratorio de Catálisis Homogénea, Departamento de Química y Ciencia de los Materiales, Universidad de Huelva-Unidad Asociada al CSIC,
Campus de El Carmen, 21007 Huelva, Spain
[b] Department of Chemistry and Biochemistry, University of Delaware,
Newark, DE 19716, USA

 © 2007 Wiley-VCH Verlag GmbH & Co. KGaA, Weinheim 

have found an unexpected effect of the catalyst loading that affects the chemoselectivity of these transformations not only in the case of the [Tp$^x$Cu(NCMe)] catalysts but also with other less elaborated catalysts. This knowledge has allowed the enhancement of the yields of the desired products.

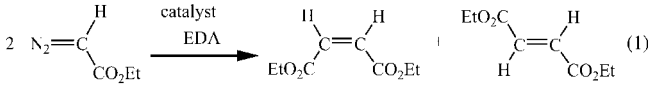


## Results and Discussion

We have previously reported[10] that the complexes [Tp$^{Br3}$Cu(NCMe)] (**1**) and [Tp$^{Ms}$Cu] (**2**) catalyze the insertion of EDA into the C–H bonds of cyclohexane (Scheme 2), leading to the formation of ethyl cyclohexaneacetate as well as diethyl fumarate (DEF) and maleate (DEM). Under the same conditions (1:20:2000 for [catalyst]:[EDA]:[$C_6H_{12}$], 0.05 mmol of catalyst) **1** and **2** gave 90 and 54% yield of ethyl cyclohexaneacetate, respectively, with DEF and DEM accounting for the remaining EDA. In order to diminish such amounts of non-desired products, we studied the effect of the following variables that could affect the chemoselectivity induced by a given catalyst: (a) the addition rate of EDA, (b) the concentration of EDA, and (c) the catalyst loading.

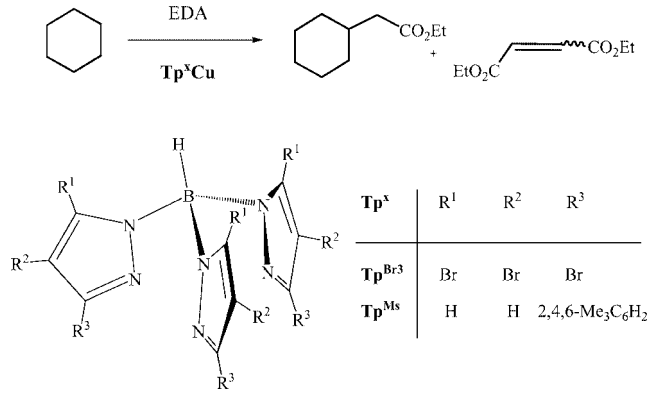


Scheme 2. [Tp$^x$Cu]-catalyzed cyclohexane functionalization by EDA insertion.

### Effect of EDA Concentration and Addition Time

The traditional experimental methodology in metal-catalyzed diazo compound decomposition usually employs a large excess of substrate with respect to the diazo compound, as well as slow addition devices to add the latter to the solution containing the catalyst and the substrate.[1,13] With this experimental design, the [diazo compound]/[catalyst] ratio in the reaction mixture can be maintained at low values, thereby minimizing the formation of DEF and DEM. To verify this common behavior, we have run a series of five experiments for the reaction of cyclohexane and EDA in the presence of **1** or **2** in which only the time employed for the addition of EDA was varied. Figure 1 (left) shows the conversion into ethyl cyclohexaneacetate obtained at the end of each experiment (determined from the NMR spectra of the crude reaction mixture). Those carried out at $t$ = 0 h were performed by adding the diazo compound in one portion, whereas the others were run with the aid of a syringe pump programmed to add the EDA (1 mmol dissolved in 10 mL of cyclohexane) over 1, 3, 6 and 12 h. An increase in the yields of the desired product was observed upon lengthening the addition time, although for the Tp$^{Ms}$-containing catalyst this increase was not as high as with the Tp$^{Br3}$ catalyst. The use of the latter in a series of experiments in which only the concentration of EDA in the feed solution was varied gave the results shown on the right-hand side in Figure 1: the lower the value of [EDA], the higher the yield of the desired product. Overall, both sets of experiments are in agreement with the mentioned effect of the [EDA]:[catalyst] ratio in the reaction mixture: a low value of this ratio enhances the yield of the desired product and decreases the yields of DEF and DEM.

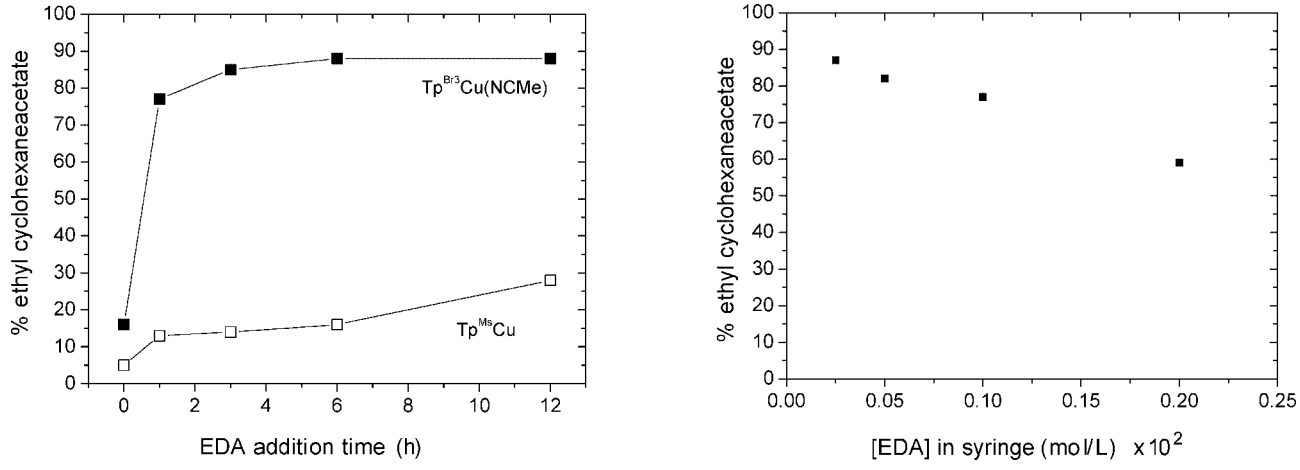


Figure 1. Variation of the yield of ethyl cyclohexaneacetate with EDA addition time (left) and the EDA concentration added from the syringe pump {[Tp$^{Br3}$Cu(NCMe)] as the catalyst}.

 © 2007 Wiley-VCH Verlag GmbH & Co. KGaA, Weinheim 

### Effect of the Catalyst Loading

Another approach to ensure the above conditions, i.e., a low [EDA]:[catalyst] ratio is to employ a higher catalyst loading at a fixed EDA concentration and addition time (6 h). Surprisingly, when we employed a fivefold amount of the catalyst (0.25 mmol instead of the 0.05 mmol in the previous experiments), we did not observe any increase in the yields of ethyl cyclohexaneacetate *but the opposite effect*. As shown in Figure 2, a certain decrease occurred with **1** (from 88 to 70%) as the catalyst, whereas no response to this variable was obtained from the experiment with **2** and the same catalyst loading (ca. 16% in both cases). We then explored the use of different catalyst loadings in the range 0.002 to 0.25 mmol, with the results displayed in Figure 2. An unexpected increase in the degree of conversion of cyclohexane and EDA into ethyl cyclohexaneacetate took place when the catalyst concentration was decreased in both cases. No EDA was detected by GC shortly after the addition was completed, which is an indication of the ease with which catalysts **1** and **2** consume the diazo compound. The main yield enhancement in the case of the $Tp^{Ms}Cu$ catalyst appeared on going from 0.01 to 0.002 mmol as the catalyst loading, which corresponds to an increase of nearly 45% (from 25 to 70%). This is a completely unexpected behavior since such an increase takes place in the direction in which the [EDA]:[catalyst] also increases, which is exactly the contrary to that found above when EDA addition time or EDA concentration were studied. It is also worth mentioning that this anomalous effect is not observed with styrene as the substrate. In this case, a similar study was carried out but no effect of the catalyst loading was observed. This is in good agreement with the fact that styrene is much more reactive than a cyclohexane C–H bond, and there is no real competition between cyclopropanation and the EDA decomposition toward diethyl fumarate and maleate.

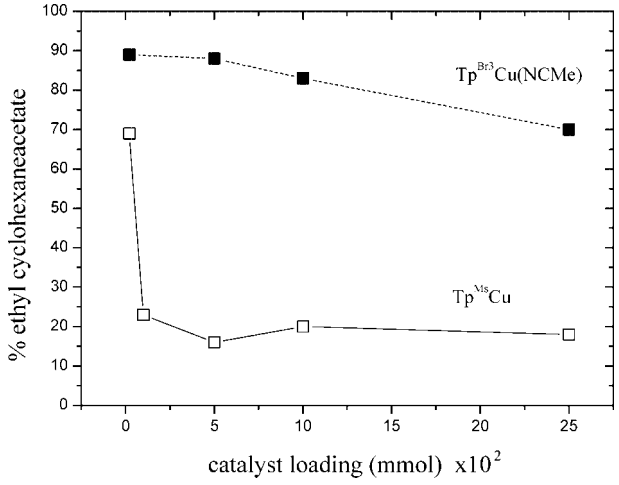


Figure 2. Effect of the catalyst loading on the yields in ethyl cyclohexaneacetate.

### Scope of this Methodology

We have not been able to find a reasonable explanation for this behavior[14] as our experimental methodology, which is based on the use of slow addition devices for EDA, prevents us from carrying out reliable kinetic studies. However, the importance of the discovery of the effect of the catalyst loading in this transformation, which gives a noticeable enhancement in the yields simply by decreasing the amount of catalyst, should be pointed out. At this point, we wondered about the extension of this proposal to other copper-based catalysts. The number of catalytic systems based on copper for the intermolecular insertion of diazo compounds into C–H bonds is very limited,[15] the highest conversions thus far being obtained with our $Tp^xCu$ system.[10] In contrast, there are more examples for the intramolecular version, including chiral catalysts that have led to moderate to high degrees of enantioselectivity.[16] The ligands bound to the copper center in these cases were preferentially bis-oxazolines and bis-imines, i.e., ligands with two nitrogen donor atoms. However, there are no reports of the use of these catalysts for the intermolecular, asymmetric insertion of diazo compounds into C–H bonds. In the search for model complexes for the above chiral systems, we decided to study the catalytic properties of the complex $[Bp^{Br3}Cu]$ (**4**), which is similar to the $[Bp^xCu]$ complexes already reported by other authors.[17] Table 1 shows the results obtained for the reaction of EDA and cyclohexane in the presence of **4**. In one-portion addition reactions, only an 8% yield of ethyl cyclohexaneacetate was observed with a 0.05 mmol catalyst loading. This yield was improved up to 13% when performing the slow addition of EDA over 3 h (entry 2). Although modest, it is worth pointing out that these data compare well with those shown in Figure 1 for **2** as the catalyst under the same conditions. Following the strategy learnt from the previous sections, we used a lower catalyst loading (0.002 mmol) of **4** and observed the desired effect: the yields were enhanced up to 36 and 49% with EDA addition times of 4 and 17 h, respectively. We find these results quite remarkable in two ways: first, they demonstrate the catalytic capability of a copper complex with a bidentate, not tridentate, $Bp^x$ ligand, with yields similar to those obtained with **2**, and secondly, they demonstrate that the steric protection assumed for the $Tp^xCu$ system seems not to be as crucial as initially supposed, and that other factors, such as the electron-withdrawing nature of the ligand and catalyst loading, could be very important at this point.

Complex **4** could be a good model for anionic chiral ligands (semicorrines, some bisoxazolines), but many others, including those referred to above, are neutral in nature. In order to check the validity of our proposal, we ran a few experiments using $[(bipy)_2Cu][I]$ (**5**) as the catalyst for the insertion of EDA into the C–H bonds of cyclohexane. We anticipated a very low catalytic activity for this complex in this reaction since (a) no electron-withdrawing groups are bonded to the metal center and (b) it appears to be coordinatively and electronically saturated. However, previous studies with this complex for the cyclopropanation of styrene have shown that bipy de-coordination takes place easily.[3a] Under our standard conditions (0.05 mmol of **5**, 1 mmol of EDA, one portion addition of the diazo ester),

 © 2007 Wiley-VCH Verlag GmbH & Co. KGaA, Weinheim 

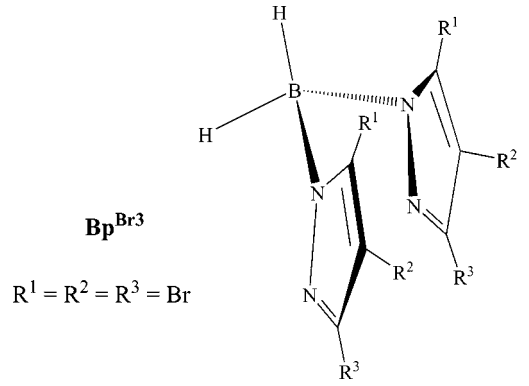


Table 1. Use of [$Bp^{Br3}$Cu] (**4**) and [$(bipy)_2$Cu][I] (**5**) as catalysts for the reaction of ethyl diazoacetate and cyclohexane.[a]

| Catalyst loading [mmol] | EDA addition time [h] | [$Bp^{Br3}$Cu][b] | [$(bipy)_2$Cu][I][b] |
|---|---|---|---|
| 0.05 | one portion | 8 | nd |
| 0.05 | 3 | 13 | – |
| 0.002 | 4 | 36 | 10 |
| 0.002 | 12 | – | 18 |
| 0.002 | 17 | 49 | – |

[a] See Experimental Section. [b] Yields calculated by NMR spectroscopy, with DEF and DEM formation accounting for 100% of EDA.

no ethyl cyclohexaneacetate was observed, with only DEF and DEM being detected at the end of the reaction. This could be enough to discard **5** (or any other complex) as a potential catalyst. However, based on our proposal, we ran two experiments with a lower catalyst loading and, with the aid of a syringe pump, with a total addition time of 4 and 12 h, the yields of the desired product increased up to 10 and 18%, respectively. Again, these results indicate that, even for very low activity and non-elaborated catalysts, the catalyst loading affects the chemoselectivity of the reaction.

## Conclusions

We have discovered that the formation of diethyl fumarate and maleate in the presence of [$Tp^x$Cu] is influenced by the catalyst loading in the opposite sense that would normally be expected. The use of very low concentrations of the [$Tp^x$Cu] catalysts causes a decrease in the formation of DEF and DEM and a concomitant increase in the yields of the desired C–H-functionalized product. These findings have been extended to copper complexes with bidentate ligands as models for other already known catalysts. We believe that these results could be extended to many already known systems for the copper-catalyzed carbene transfer from diazo compounds, thereby opening up a new perspective in the copper-catalyzed insertion of diazo compounds into C–H bonds.

## Experimental Section

**General:** $^1$H NMR spectra were run at 400 MHz and $^{13}$C NMR at 100 MHz, with $CDCl_3$ as solvent. Mass spectra were recorded with a Varian Saturn 2100T. GC analysis was performed with a Varian CP-3800. Solvents were dried and degassed before use. All reagents were purchased from Aldrich and employed without any further purification. The synthesis of the copper catalysts[7–10] was carried out as reported previously.

**General Catalytic Experiment:** [$Tp^x$Cu] (0.05 mmol) was dissolved in a mixture of $CH_2Cl_2$ (10 mL) and cyclohexane (10 mL). A solution of EDA (1 mmol) in cyclohexane (10 mL) was slowly added during the programmed time with the aid of a syringe pump, at room temperature. No EDA was detected at the end of the reaction by GC, only ethyl cyclohexaneacetate and diethyl fumarate and maleate. Other experiments were performed by adding the pure diazo compound in one portion. For those experiments carried out without cyclohexane, dichloromethane were employed as the sole solvent.

The reported yields correspond to an average of at least of two runs, and were determined in the following manner. After removal of volatiles, the crude product was investigated by $^1$H NMR spectroscopy, with a standard compound being added (tosyl chloride or styrene) to ensure that all the initial EDA was converted in the observed products. The observed ratios were compared to those from GC analysis in order to establish the response factors, which were later employed in the subsequent experiments to determine the yields. The products were identified by comparison with commercial samples (ethyl cyclohexaneacetate, diethyl fumarate and maleate) or with data already reported.

## Acknowledgments

We thank the Ministerio de Educación y Ciencia for funding (Proyecto CTQ2005-00324BQU) and reserach fellowship (A. C.). The Ramón y Cajal Programme is also thanked (M. M. D. R.).

[1] a) M. P. Doyle, *Comprehensive Organometallic Chemistry II* (Eds.: E. W. Abel, F. G. A. Stone, G. Wilkinson), Pergamon Press, Oxford, U.K., **1995**, vol 12, p. 421; b) M. P. Doyle, M. A. McKervey, T. Ye, *Modern Catalytic Methods for Organic Synthesis with Diazo Compounds*, John Wiley & Sons, New York, **1998**.
[2] M. C. Pirrung, A. T. Morehead, *J. Am. Chem. Soc.* **1996**, *118*, 8162–8163.
[3] a) M. M. Díaz-Requejo, T. R. Belderrain, M. C. Nicasio, F. Prieto, P. J. Pérez, *Organometallics* **1999**, *18*, 2601–2609; b) M. Díaz-Requejo, M. C. Nicasio, P. J. Pérez, *Organometallics* **1998**, *17*, 3051–3057.
[4] W. Kirmse, *Angew. Chem. Int. Ed.* **2003**, *42*, 1088–1093.
[5] B. F. Straub, P. Hofmann, *Angew. Chem. Int. Ed.* **2001**, *40*, 1288–1290.
[6] X. L. Dai, T. H. Warren, *J. Am. Chem. Soc.* **2004**, *126*, 10085–10094.
[7] a) M. M. Díaz-Requejo, A. Caballero, T. R. Belderrain, M. C. Nicasio, S. Trofimenko, P. J. Pérez, *J. Am. Chem. Soc.* **2002**, *124*, 978–983; b) M. M. Díaz-Requejo, T. R. Belderrain, S. Trofimenko, P. J. Pérez, *J. Am. Chem. Soc.* **2001**, *123*, 3167–3168.
[8] M. M. Díaz-Requejo, M. A. Mairena, T. R. Belderrain, M. C. Nicasio, S. Trofimenko, P. J. Pérez, *Chem. Commun.* **2001**, 1804–1805.
[9] M. E. Morilla, M. M. Díaz-Requejo, T. R. Belderrain, M. C. Nicasio, S. Trofimenko, P. J. Pérez, *Organometallics* **2004**, *23*, 293–295.
[10] a) A. Caballero, M. M. Díaz-Requejo, T. R. Belderrain, M. C. Nicasio, S. Trofimenko, P. J. Pérez, *J. Am. Chem. Soc.* **2003**, *125*, 1446–1447; b) A. Caballero, M. M. Díaz-Requejo, T. R. Belderrain, M. C. Nicasio, S. Trofimenko, P. J. Pérez, *Organometallics* **2003**, *22*, 4145–4150; c) M. M. Díaz-Requejo, T. R.

 © 2007 Wiley-VCH Verlag GmbH & Co. KGaA, Weinheim 

Belderrain, M. C. Nicasio, S. Trofimenko, P. J. Pérez, *J. Am. Chem. Soc.* **2002**, *124*, 896–897.
[11] M. E. Morilla, M. M. Díaz-Requejo, T. R. Belderrain, M. C. Nicasio, S. Trofimenko, P. J. Pérez, *Chem. Commun.* **2002**, 2998–2999.
[12] M. E. Morilla, M. J. Molina, M. M. Díaz-Requejo, T. R. Belderrain, M. C. Nicasio, S. Trofimenko, P. J. Pérez, *Organometallics* **2003**, *22*, 2914–2918.
[13] In some cases the diazo compound has been added in one portion at the beginning of the reaction. See, for example, ref.[7]
[14] The experimental data available have not been fitted into a mechanistic proposal that accounts for all them. A referee has noted that radical species could perhaps be involved in this transformation. A previous study concerning the use of [Tp*Cu] as the catalyst for carbene and nitrene transfer has shown that radicals could be responsible for the transfer only in the latter case. See: M. M. Díaz-Requejo, P. J. Pérez, M. Brookhart, J. L. Templeton, *Organometallics* **1997**, *16*, 4399–4402.
[15] a) L. T. Scott, G. J. DeCicco, *J. Am. Chem. Soc.* **1974**, *96*, 322–323; b) D. S. Wulfman, R. S. McDaniel, B. W. Peace, *Tetrahedron* **1976**, *32*, 1241–1249; c) H. V. R. Dias, R. G. Browning, S. A. Richey, C. J. Lovely, *Organometallics* **2004**, *23*, 1200–1202.
[16] H. M. L. Davies, R. E. J. Beckwith, *Chem. Rev.* **2003**, *103*, 2861–2903. See page 2865 referred to copper(I) catalysts and references cited therein.
[17] a) H. V. R. Dias, H.-L. Lu, *Inorg. Chem.* **2000**, *39*, 2246–2248; b) R. P. Houser, W. B. Tolman, *Inorg. Chem.* **1995**, *34*, 1632–1633; c) M. I. Bruce, J. D. Walsh, *Aust. J. Chem.* **1979**, *32*, 2753–2756.

Received: September 1, 2006
Published Online: December 5, 2006

 © 2007 Wiley-VCH Verlag GmbH & Co. KGaA, Weinheim 

DOI: 10.1002/ejic.200600997

# A PCP-Pincer $Ru^{II}$–Terpyridine Building Block as a Potential "Antenna Unit" for Intramolecular Sensitization

**Marcella Gagliardo,[a] Fabio Rizzo,[b,c] Martin Lutz,[d] Anthony L. Spek,[d] Gerard P. M. van Klink,[a] André E. Merbach,[e] Luisa De Cola,[c] and Gerard van Koten*[a]**

**Keywords:** Ruthenium / Lanthanides / Pincer ligands / Luminescence

The redox- and photoactive mononuclear complex [Ru(PCP)-(tpy–DTTANa$_4$)]Cl {PCP = [$C_6H_3(CH_2PPh_2)_2$-2,6]$^-$; tpy–DTTA$^{4-}$ = 4′-(2,2′:6′,2′′-terpyridine)-diethylenetriamine-*N*,*N*,*N*′′,*N*′′-tetraacetate} possesses an externally directed, vacant $N_3O_4$ polyaminocarboxylate-type binding site that coordinates to lanthanide(III) ions to give the neutral heterodinuclear $Ru^{II}$–$Ln^{III}$ complexes [Ru(PCP)(tpy–DTTA)Ln($H_2O$)$_2$] (Ln = $Gd^{3+}$, $Eu^{3+}$). The photophysical properties of solutions of the mononuclear complex [Ru(PCP)(tpy–DTTANa$_4$)]Cl were investigated in MeOH/EtOH (1:4) and compared to those of the solutions of heterodinuclear complexes [Ru(PCP)-(tpy–DTTA)Ln($H_2O$)$_2$] (Ln = $Gd^{3+}$, $Eu^{3+}$). Rigid matrix excitation at 77 K of the ππ* level of the ruthenium chromophore in the [Ru(PCP)(tpy–DTTA)Eu($H_2O$)$_2$] complex results in a weak europium(III) emission pointing to a transfer of energy from Ru→Eu as a result of the metal-to-ligand charge-transfer (MLCT) excited state of the ruthenium component to the luminescent lanthanide ion. The excited state lifetime of the europium complex is 0.2 ms in methanol solution. In deuterated solvents, the lifetime increases to 0.4 ms, which indicates that the process is solvent-dependent as a result of the strongly coordinated molecules of water that are responsible for the quenching in nondeuterated solvents.

(© Wiley-VCH Verlag GmbH & Co. KGaA, 69451 Weinheim, Germany, 2007)

## Introduction

Luminescence exerted by lanthanides is a subject that attracts considerable interest because of their potential use as components,[1] luminescent probes[2] and sensors for light amplification and frequency conversion.[3] In particular, research efforts were devoted to the design of fluorophores containing the most emissive $Eu^{III}$ and $Tb^{III}$ ions. Their long-lived emission (up to ms) in the visible spectral region, positioned away from most intrinsic fluorescence of organic or biological molecules, found a wide range of applications such as probes for clinical use (e.g. fluoroimmuno assay agents) and sensors for time-resolved microscopy.[4]

The in-principal spin-forbidden luminescence of the lanthanide ions originates from transitions within the partially filled 4f orbitals.[5] Lanthanide ions with completely filled ($Lu^{III}$) or completely unfilled ($Y^{III}$ and $La^{III}$) 4f orbitals do not show any luminescence. Characteristics of the luminescence displayed by the other ions are the line-like emission, long excited state lifetimes and the fact that the low energy of the emission is hardly affected by the environment of the ions, as the filled 5s and 5p orbitals shield the electrons in the 4f levels. In other words, the effect of the ligand field is rather small. The biggest drawback of all the lanthanide ions is their low molar absorption coefficient. A way to circumvent this problem is to use chelating ligands that are able to efficiently absorb UV and/or visible light. Upon excitation, the allowed π→π* transitions lead to the population of their excited states, which can undergo efficient energy transfer to the excited states of the lanthanide ions. Such an energy transfer in most cases occurs from the triplet-excited level of the ligands. The process is often referred to as the "antenna-effect".

Several UV-absorbing aromatic chromophores containing nitrogen and/or oxygen donor atoms (e.g. β-diketonates,[6] phenantridine,[7] bipyridine,[8] terpyridine,[9] calix[4]-arenes and *m*-terphenyl moieties[10]) as well as fluorescent dyes possessing low ππ* transitions (e.g. fluorenone dyes[11] or tetrazine[12]) were used as light-harvesting units in lanthanide complexes.

Most recently, it was demonstrated that intramolecular sensitization of lanthanide(III) ions can be achieved by

[a] Faculty of Science, Organic Chemistry and Catalysis, Utrecht University,
Padualaan 8, 3584 CH Utrecht, The Netherlands
Fax: +31-30-252-3615
E-mail: g.vankoten@chem.uu.nl
[b] Dipartimento di Chimica e Chimica Industriale, Università di Genova,
Via Dodecaneso 31, 16146 Genova, Italia
[c] Physikalisches Institut, Westfälische Wilhelms-Universität Münster,
Mendelstrasse 7, 48149, Münster, Germany
[d] Faculty of Science, Crystal and Structural Chemistry, Utrecht University,
Padualaan 8, 3584 CH Utrecht, The Netherlands
[e] Ecole Polytechnique Fédérale de Lausanne (EPFL), Laboratoire de Chimie Inorganique et Bioinorganique,
EPFL-BCH, CH-1015 Lausanne, Switzerland
Supporting information for this article is available on the WWW under http://www.eurjic.org or from the author.

 © 2007 Wiley-VCH Verlag GmbH & Co. KGaA, Weinheim 

coupling a lanthanide ion to a redox-active d block fragment that possesses broad d-d and intense charge-transfer (CT) transitions in the visible spectral region to efficiently collect photonic energy.[13] Intersystem crossing (ISC), followed by a multipolar d→4f energy transfer, leads to the sensitization of the lanthanides. One of the advantages of this approach relies on the multiplicity of the lowest excited state of the metal complexes (often the triplet states) and to the long-lived excited state lifetimes (ns versus hundreds of ns or several μs) of the metal complexes. The long-lived excited states of the donor d block allow for energy transfer processes that can be rather slow relative to the systems containing organic donor chromophores. Another interesting characteristic displayed by metal complexes is the presence of CT states in the visible region that can be selectively excited to produce sensitization of the lanthanide ions. Importantly, the energy of these states depends on the energy gap between the d and π* orbitals, for a MLCT state, and they can be modulated by choosing an appropriate metal ion, by changing the chelating ligand or by fine tuning the donating properties of the hosting ligands by introduction of electron-withdrawing or -releasing substituents (i.e. changing the HOMO and LUMO energies). However, an efficient electronic energy transfer in such polymetallic edifices requires orbital overlap between the d block excited LUMO and the 4f orbitals of the lanthanides.[14] Thus, the distance between the d and f units must be short and the linker must maximize the electronic interactions. This condition is difficult to realize because the preparation of suitable bridging ligands, as well as the introduction of two different metals, often represents a chemical challenge.

The field of heterodinuclear d/f block assemblies and the properties that can arise from metal–metal interactions is extensively reviewed.[13] Most of the systems reported to date contain low-spin $d^6$ pseudooctahedral chromophores ($Ru^{II}$, $Re^{I}$, $Ir^{III}$ and $Os^{II}$) or square-planar $Pt^{II}$ fragments that are connected to lanthanide ions by short heteroditopic bridging ligands (Scheme 1). The high-energy triplet level required for the sensitization of the europium(III) ions hampered the applicability of transition-metal-based antennae for photoexcitation of this lanthanide ion. However, recently De Cola and coworkers demonstrated the innovative use of cyclometallated $[Ir^{III}C_2N_4]$ chromophores to act as donors for the sensitization of a luminophoric $Eu^{III}$ ion.[15]

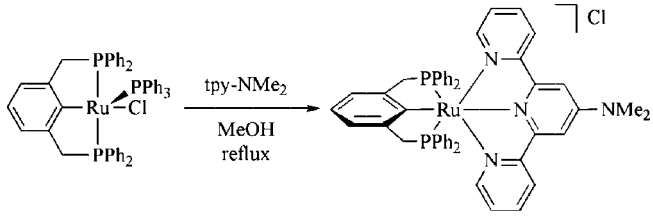


1 2

Scheme 1. Synthesis of the [Ru(PCP)(tpy–$NMe_2$)]Cl complex.

With the aim to study the potential applicability of stable, redox and photoactive bis(ortho)cyclometallated PCP-pincer $Ru^{II}$–terpyridine complexes as photosensitizers for $Eu^{III}$ ions, the synthesis of a new building block, [Ru(PCP)(tpy–DTTA$Na_4$)]Cl (vide infra; **5**, Scheme 2), was undertaken. Complex **5** contains the monoanionic, tridentate coordinating bisphosphanylaryl ligand $[C_6H_3(CH_2PPh_2)_2\text{-}2,6]^-$ (PCP) and the bifunctional chelator ligand [tpy–DTTA]$Na_4$ {tpy–$DTTA^{4-}$ = 4′-(2,2′:6′,2′′-terpyridine)diethylenetriamine-*N*,*N*,*N*′′,*N*′′-tetraacetate}. The rigid, chelating tpy–DTTA ligand with a $N_3O_4$ donor atom

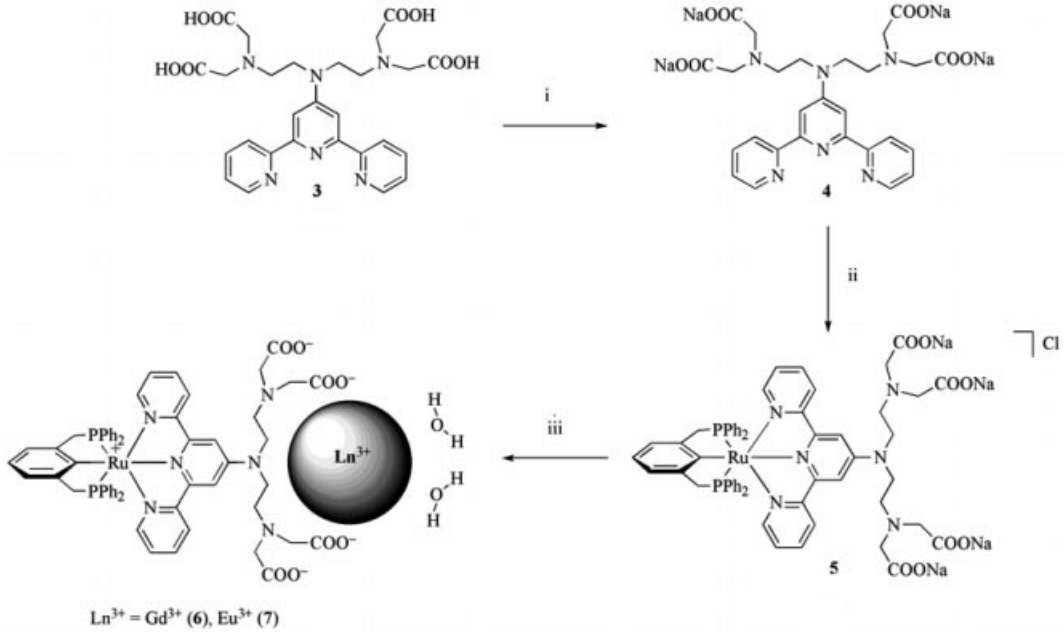


Scheme 2. Synthesis of mononuclear complex **5** and heterodinuclear complexes **6** and **7**. Reagents and conditions: i) 1 N NaOH until pH = 9.5. ii) [RuCl(PCP)($PPh_3$)], MeOH, reflux, 2 d. iii) **5**, $LnCl_3{\cdot}6H_2O$ (Ln = $Gd^{3+}$, $Eu^{3+}$), MeOH/$H_2O$, reflux, 5 h.

 © 2007 Wiley-VCH Verlag GmbH & Co. KGaA, Weinheim 

set was employed by Merbach and coworkers in the synthesis of heterometallic complexes $[M(tpy–DTTA)_2Gd_2(H_2O)_2]$ (M = $Fe^{2+}$, $Ru^{2+}$) that were investigated as MRI contrast agents.[16,17] It is of special interest to this work to demonstrate that the organometallic [Ru(PCP)(tpy–$DTTANa_4$)]Cl building block is well-suited for anchoring trivalent ions such as $Gd^{III}$ and $Eu^{III}$ to give novel heterodinuclear complexes [Ru(PCP)(tpy–DTTA)Ln$(H_2O)_2$] {Ln = $Gd^{3+}$ (**6**), $Eu^{3+}$ (**7**)}. The luminescence properties of the prepared complexes are presented and discussed.

## Results and Discussion

### Synthesis of the Monomeric Complex [Ru(PCP)(tpy–$DTTANa_4$)]Cl (5)

The ligand tpy–DTTA was prepared following the four step reaction reported by Ruloff et al.[17] Reaction[18] of [RuCl(PCP)($PPh_3$)] (**1**, Scheme 1) with an equimolar quantity of tpy–DTTA (**3**, Scheme 2) in MeOH heated at reflux afforded the desired product [Ru(PCP)(tpy–DTTA)]Cl only in low yield (< 10%). Preparation of complex [Ru(PCP)(tpy–$NMe_2$)]Cl (**2**, 63%, Scheme 1), performed under the same experimental conditions, proved unambiguously that coordination of the tpy–DTTA ligand is not hampered by the electron-donating properties of the amino substituent at the 4′-position of the tpy moiety. Synthesis of **5** involving the use of the tpy–DTTA tetrasodium salt instead of the free tetraacid was successful, which underlies the influence of the pH on the coordination properties of the tpy unit. Thus, treatment of **1** with an equimolar amount of [tpy–DTTA]$Na_4$ (**4**, Scheme 2) in refluxing methanol gave complex **5** as a dark red solid in good yield (55%). Complex **5** is stable to air and moisture and is highly soluble in water and polar solvents. The NMR spectroscopic data for **2** and **5** were as expected for their proposed six-coordinate geometry about the ruthenium centres and are similar to those of the analogous [Ru(PCP)(tpy)]Cl complex.[18]

Single-crystals of **5** suitable for X-ray analysis could not be obtained. Instead, the molecular structure of **2** was determined, which provides information concerning the effects of a 4′-$NMe_2$ substituent on both the Ru–tpy bond distances and angles.

Suitable crystals of **2** were obtained from a $CH_2Cl_2$ solution to which *n*-hexane was slowly diffused. Figure 1 depicts the molecular structure of **2** (a selection of bond lengths and angles are given in Table 1). In the solid state of **2**, a ruthenium centre, the monoanionic *P,C,P*-coordinated bisphosphanylaryl ligand and the tridentate-coordinated tpy–$NMe_2$ ligand are present. The Ru1 atom adopts a distorted octahedral coordination environment and both the PCP-pincer and tpy–$NMe_2$ ligands are coordinated in a meridional fashion. The Ru1–C1 bond length of the PCP-pincer ligand is 2.120(2) Å, whereas the two Ru–P distances are 2.3189(6) and 2.3330(5) Å, respectively.

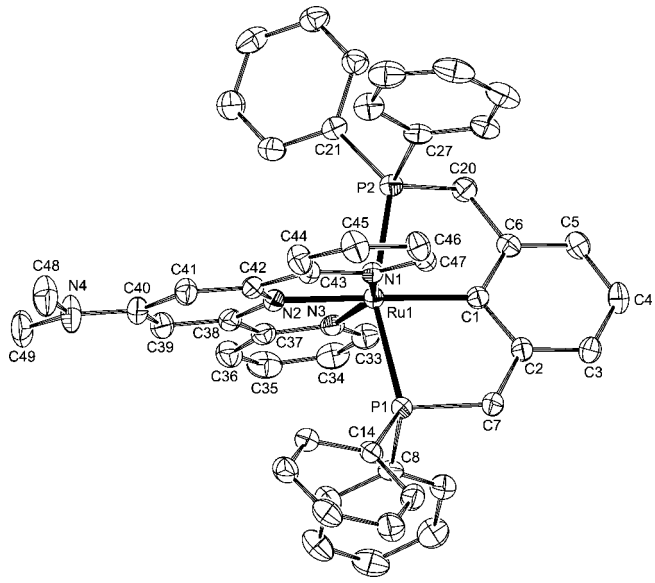


Figure 1. Displacement ellipsoid plot of **2**, drawn at the 50% probability level. Hydrogen atoms, uncoordinated chloride anions and disordered solvent molecules are omitted for clarity.

Table 1. Selected bond lengths [Å], bond angles [°] and torsion angles [°] for **2**.

| Bond Lengths [Å] | | | |
|---|---|---|---|
| Ru1–N1 | 2.0886(17) | Ru1–N2 | 2.0292(17) |
| Ru1–N3 | 2.0899(17) | Ru1–C1 | 2.120(2) |
| Ru1–P1 | 2.3189(6) | Ru1–P2 | 2.3330(5) |
| N4–C40 | 1.361(3) | N4–C48 | 1.454(3) |
| N4–C49 | 1.454(3) | | |
| **Bond Angles [°]** | | | |
| N1–Ru1–N3 | 155.85(7) | N2–Ru1–C1 | 178.40(7) |
| P1–Ru1–P2 | 157.35(2) | N1–Ru1–N2 | 78.01(6) |
| N2–Ru1–N3 | 77.86(7) | N3–Ru1–C1 | 101.25(7) |
| C1–Ru1–N1 | 102.84(7) | P1–Ru1–N1 | 89.70(5) |
| P1–Ru1–N2 | 99.37(5) | P1–Ru1–N3 | 93.16(5) |
| P1–Ru1–C1 | 79.32(6) | P2–Ru1–N1 | 91.96(5) |
| P2–Ru1–N2 | 103.07(5) | P2–Ru1–N3 | 94.49(5) |
| P2–Ru1–C1 | 78.29(6) | | |
| **Torsion Angles [°]** | | | |
| N1–C43–C42–N2 | 0.0(3) | N2–C38–C37–N3 | 0.4(3) |
| C1–C2–C7–P1 | 23.6(2) | C1–C6–C20–P2 | 24.2(2) |
| C39–C40–N4–C48 | –177.2(2) | C41–C40–N4–C49 | 175.8(2) |

The three pyridyl groups of the tpy–$NMe_2$ ligand are almost coplanar. The N1–Ru–N3 bond angle [155.85(7)°] is slightly smaller than those observed in other $Ru^{II}$–tpy complexes, which show values in the range of 156.9(5) to 159.8(1)°.[19] As commonly observed for other $Ru^{II}$–tpy complexes, geometrical constraints of the tpy backbone makes the central Ru–N2 distance [2.0292(17) Å] shorter than those of Ru–N1 [2.0886(17) Å] and Ru–N3 [2.0899(17) Å]. Analogous to what was reported for $[Ru(tpy–NMe_2)_2](PF_6)_2$,[19b] the 4′-$NMe_2$ group is approximately coplanar with the central pyridine ring of the tpy moiety [torsion angle C39–C40–N4–C48 is –177.2(2)°], which points to a planar geometry of the nitrogen atom and a high degree of π-conjugation between the $sp^2$-hybridized

 © 2007 Wiley-VCH Verlag GmbH & Co. KGaA, Weinheim 

atom of the $NMe_2$ group and with the pyridine ring. This is also apparent from the short N4–C40 distance of 1.361(3) Å and both the N4–C48 and N4–C49 bonds are 1.454(3) Å in length. Comparison of these data obtained for **2** with those reported for $[Ru(tpy\text{-}NMe_2)_2](PF_6)_2$ [$C_{tpy}$–$NMe_2$ = 1.352(14) Å; cf. 1.366(5) Å for the free tpy–$NMe_2$ ligand] reveals that in **2** the conjugation between the dimethylamino group and the central pyridine ring is slightly lower. This may indicate that the σ-donor capability of the cyclometallating PCP-pincer ligand in **2** is lower than that of the terpyridine ligands in $[Ru(tpy\text{–}NMe_2)_2](PF_6)_2$.[18]

### Synthesis of the Heteronuclear Complexes [Ru(PCP)(tpy–DTTA)Ln($H_2O$)$_2$] {Ln = $Gd^{3+}$ (6), $Eu^{3+}$ (7)}

The preparation of the lanthanide(III) complexes was straightforward. Reaction of stoichiometric amounts of **5** with the corresponding $LnCl_3{\cdot}6H_2O$ salt in a MeOH/$H_2O$ mixture afforded the NaCl-free complexes [Ru(PCP)(tpy–DTTA)Ln($H_2O$)$_2$] {Ln = $Gd^{3+}$ (**6**), $Eu^{3+}$ (**7**)} as red coloured solids in good yields after several washings with cold water. Both complexes, characterized by elemental analysis, are soluble in MeOH and DMSO and insoluble in THF, chlorinated solvents, aliphatic and aromatic solvents. In agreement with the results obtained with the analogous complex $[Ru(tpy\text{–}DTTA)_2Gd(H_2O)_2]$,[16] the solubility of **6** and **7** in water is very low. In water, **6** and **7** precipitate as light orange flocculent solids that can be recovered by centrifugation and redissolved in MeOH. A straightforward explanation for their low solubility is that the lipophilic phenyl substituents on the phosphorus centres of the PCP-pincer ligand may favour the formation of aggregates that resemble those of reverse micelle-type architectures in which the {PCP–Ru–tpy} units are at the core and the {DTTA–Gd} units are at the periphery. At the periphery of these aggregates, one carboxyl group of a $[DTTA]^{4-}$ unit may bridge a second lanthanide ion of another molecule forming an oligomeric/polymeric insoluble material. The coordinated water molecules complete the coordination sphere around each lanthanide ion leading to a nine-coordinate metal centre. Importantly, the X-ray structure of the complex $[\{C(NH_2)_3\}_3Gd(TTAHA)]{\cdot}9H_2O$ {$H_6$TTAHA = [*N*-tris(2-aminoethyl)amine-*N*′,*N*′,*N*′′,*N*′′,*N*′′′,*N*′′′-hexaacetate]}[20] revealed that two pendant arms of the tripod $[TTAHA]^{6-}$ ligand and the N-donor atoms are coordinated by the donor set $N_3O_4$ to $Gd^{3+}$. The eighth and ninth coordination sites are occupied by carboxylate oxygens belonging to the "free" pendant arm of a neighbouring complex.[20] They can be replaced by two water molecules when the complex is dissolved in water.[20]

Because the NaCl containing complexes are soluble in water, it is clear that in the presence of salt such aggregates are not formed. Coordination of the $Cl^-$ ion may compete with the coordination of the carboxyl groups (Scheme 2). Owing to the negative charge on the oxygen centres, the $N_3O_4$ pocket is able to bind the $Na^+$ cation, which results in the breakdown of the insoluble aggregates. This cooperative ion–cation bonding can be a result of the "excess" coordinating ability of the DTTA unit. Recently, Merbach and coworkers discovered that gadofullurene aggregates, whose formation may be ascribed to hydrophobic forces, can be disgregated by the addition of NaCl in aqueous solutions of $Gd@C_{60}[C(COOH)_2]_{10}$ and $Gd@C_{60}(OH)_x$ ($x \approx 27$).[21] Intercalation of the salt results in the separation of the molecules and inhibits the interactions.[21]

Interestingly, the solubility of the aggregates in water could not be improved by adding excess NaCl to aqueous solutions of NaCl-free **6** and **7**. More detailed studies are required to understand the factors that determine the solubility properties of these complexes.

Coordination of the lanthanide ions to the $[DTTA]^{4-}$ unit in **6** and **7** was investigated by infrared (IR) spectroscopy in KBr matrix. Table 2 reports the data for the bands that are most sensitive to the coordination of the lanthanide ions to the polyaminocarboxylate pendant arms of the $DTTA^{4-}$ unit. The IR spectroscopic data indicate that $O_4$-chelation of the $[DTTA]^{4-}$ unit occurs in both complexes. The asymmetric vibration mode, $\nu_{as}$(CO), of the carboxylato groups is shifted to a higher wavenumber by ca. 30 $cm^{-1}$ upon lanthanide coordination relative to the $\nu_{as}$(CO) vibration mode in parent complex **5**, which demonstrates that the carboxylato oxygens in **6** and **7** are coordinated to the lanthanide ion.[22] The symmetric vibration mode, $\nu_s$(CO), also shifts to higher wavenumbers upon coordination relative to that of **5**.

### UV/Vis Absorption Spectroscopy

The electronic spectra of mononuclear **5** and heterodinuclear **6** and **7** were recorded in MeOH at room temperature (Figure 2). Absorption maxima ($\lambda_{max}$) and molar absorption coefficients ($\varepsilon_{max}$) are summarized in Table 2. Data for complexes **2** and [Ru(PCP)(tpy)]Cl[18] are included for comparison. The UV/Vis spectra of all complexes exhibit bands

Table 2. Infrared spectral and absorption data.

| Compound | $\nu_{as}$(CO)[b] [$cm^{-1}$] | $\nu_s$(CO)[b] [$cm^{-1}$] | $\lambda_{max}$[c] [nm] ($\varepsilon_{max} \times 10^{-4}$ [$M^{-1}\,cm^{-1}$]) |
|---|---|---|---|
| [Ru(PCP)(tpy)]Cl[a] | – | – | 275 (3.7), 305 (3.9), 479 (0.8) |
| **2** | – | – | 285 (1.6), 467 (0.4) |
| **5** | $1583.80_{vs}$ | $1408.36_{s}$ | 285 (1.6), 465 (0.2) |
| **6** | $1630.89_{s}$ | $1434.53_{w}$ | 285 (1.7), 460 (0.3) |
| **7** | $1607.25_{vs}$ | $1434.43_{s}$ | 285 (1.6), 465 (0.3) |

[a] Measured at 298 K in MeCN.[15] [b] Infrared data (vs: very sharp; s: sharp; w: weak). [c] Measured at 298 K in MeOH unless otherwise specified.

 © 2007 Wiley-VCH Verlag GmbH & Co. KGaA, Weinheim 

in the UV region characteristic of the π→π* transition of the chelating ligands.[23] In the visible region, less intense, broad absorption bands are observed, which are assigned to singlet metal-to-ligand charge-transfer ($^1$MLCT) transitions from the dπ(Ru) orbitals to the π* orbitals of the tpy ligand.[23] The electronic spectra of **6** and **7** show only minor changes relative to **5**, which proves that the lanthanide ions do not substantially affect the electronic properties of the {(PCP)Ru(tpy)} moiety. The UV/Vis spectra of **5**–**7** recorded in water display similar spectroscopic features, but it must be noted that they tend to precipitate because of their low solubility in aqueous media. $^1$H NMR spectroscopic analysis in $CD_3OD$ of the precipitated solid obtained from an aqueous solution containing **7** proved, however, that the collected Ru–Eu complex is indeed **7**.

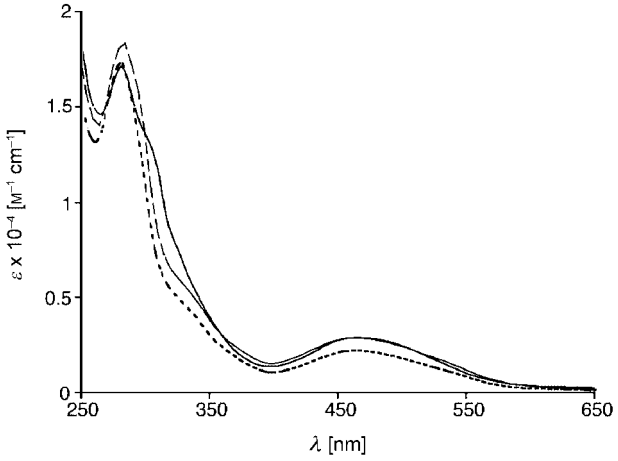


Figure 2. UV/Vis absorption spectra of mononuclear complex **5** (-----) and heterodimetallic complexes **6** (– – –) and **7** (——) measured in MeOH at 298 K.

## Emission Properties

The emissive properties of **5**–**7** were investigated in MeOH/EtOH (1:4) both at room temperature and in rigid matrix at 77 K. Emission and lifetime data recorded at 77 K are summarized in Table 3. Similar to that observed for [Ru(PCP)(tpy)]Cl and other $Ru^{II}$–tpy complexes,[24] **5** does not show emission at room temperature. This is not surprising as it is well-established that for $Ru^{II}$–tpy complexes at room temperature, a fast and efficient excited-state deactivation by nonradiative processes occurs, which is related to the population of the nonemitting metal-centred ($^3$MC) state that results from the low energy gap between the luminescent $^3$MLCT level and this state. However, **5** does not emit even at 77 K. Such a lack of emission at low temperature, contrary to what was observed for Ru–tpy analogues, could be due to the functionalization of the central pyridine ring of the tpy ligand in **5** with a tertiary amino group bearing the chelating polyaminocarboxylate units. In fact, the 4′-amino substituent is an excellent electron donor and could act as an efficient quencher both at room and low temperatures. This effect is reduced, however, once the polyaminocarboxylate unit coordinates to a lanthanide cation because the lone pair of electrons on the nitrogen atom could be involved in the coordination. In fact, at both room and low temperature, complexes **6** and **7** exhibit ruthenium-based $^3$MLCT emission at 650 and 670 nm, respectively, which is independent of the excitation wavelength. These results indicate that the coordination of the lanthanide ions indeed also involves the nitrogen atom of the amino group, which removes any possible quenching pathway. However, it cannot be excluded that some contribution to the intensity of the ruthenium-based emission also comes from the rigidification of the structure upon lanthanide ion complexation. The emission spectrum of $Ru^{II}$–$Gd^{III}$ complex **6** recorded at room temperature and at 77 K shows, aside from the ruthenium-based component, a structureless band at 440 nm (2.8 ns) and at 560 nm (200 μs). These bands were assigned on the basis of their excited lifetime to the fluorescence and phosphorescence of the ligand, respectively. It is well-known that $Gd^{III}$ promotes intersystem crossing from the singlet excited state to the corresponding triplet state (by large spin-orbit coupling induced by the heavy atom effect) and that there are no energy levels of the lanthanide ion (the energy of the lowest excited states of $Gd^{III}$ is at 32 200 $cm^{-1}$) that can accept energy from the triplet state of the ligand or from the {(PCP)Ru(tpy–DTTA)} unit. The excitation energy of the ligand-centred ππ* triplet excited state ($^3$LC) of **6**, found at 17 857 $cm^{-1}$, is still energetically suitably placed to act as a sensitizer for the luminescent $^5D_0$ of $Eu^{III}$ (17 000 $cm^{-1}$) (Figure 3, top), which allows a thermodynamically favoured energy transfer from the antenna chromophore to the lanthanide. As a result, upon excitation at 270 nm the spectrum of **7** exhibits straight lines of modest intensity that are due to transitions between the first excited state $^5D_0$ and the ground state multiplet $^7F_{1-2}$ of the $Eu^{3+}$ ion (Figure 4).

Analogously, excitation of $Ru^{II}$–$Eu^{III}$ complex **7** into the $^1$MLCT transition of the {(PCP)Ru(tpy–DTTA)} unit at 460 nm (21 739 $cm^{-1}$) produces emission from the $^5D_0$ excited state of $Eu^{III}$ (17 000 $cm^{-1}$) and from the ruthenium $^3$MLCT. The latter state, located around 14 925 $cm^{-1}$, is well below the $^5D_0$ level of europium. Thus, it can be excluded that the europium-based emission is due to an energy transfer from this state. These findings suggest that the europium emission may partly be quenched by a Eu→Ru back-energy transfer. The most likely mechanism for the sensitization of the europium ion is a partial energy transfer from the $^1$MLCT state. This mechanism would involve the direct population (upon excitation at 460 nm) of the $^1$MLCT state, fast intersystem crossing to the triplet state of the ligand, which from the Ru–Gd complex was estimated to lie between the ruthenium $^1$MLCT and the $^5D_0$ state of the europium and finally, energy transfer to the emitting lanthanide ion (Figure 3, bottom). It is interesting to note that the two excitation wavelengths (270 and 460 nm) lead to a different emission ratio between the ruthenium and the europium centres. A detailed analysis of the emissions suggests that despite the direct excitation into the ruthenium $^1$MLCT (460 nm), the ruthenium versus europium intensity is lower

 © 2007 Wiley-VCH Verlag GmbH & Co. KGaA, Weinheim 

Table 3. Emission maxima ($\lambda_{em.}$) and lifetimes ($\tau$) recorded at 77 K for complexes **6** and **7**.

| Compound | $^3$LC | | $Ru^{II}$ | | $Eu^{III}$ | |
|---|---|---|---|---|---|---|
| | $\lambda_{em.}$ [cm$^{-1}$][a] | $\tau$ [μs][c] | $\lambda_{em.}$ [cm$^{-1}$][a,b] | $\tau$ [ns][d] | $\lambda_{em.}$ [cm$^{-1}$][a,b] | $\tau$ [ms][e] | $\tau$ [ms][f] |
| **6** | 560(200) | | 650 (23.5) | | – | – | – |
| **7** | – | | 670 (34.1) | | 612 | 0.2 | 0.4 |

[a] Emission data recorded in MeOH/EtOH (1:4); $\lambda_{exc.}$ = 270 nm. [b] Emission data recorded in MeOH/EtOH (1:4); $\lambda_{exc.}$ = 460 nm. [c] Lifetime data recorded in MeOH/EtOH (1:4); $\lambda_{exc.}$ = 270 nm. [d] Lifetime data recorded in MeOH/EtOH (1:4); $\lambda_{exc.}$ = 460 nm. [e] Measurement performed in MeOH; $\lambda_{exc.}$ = 611 nm. [f] Measurement performed in dry $CD_3OD$; $\lambda_{exc.}$ = 611 nm. LC = ligand centred.

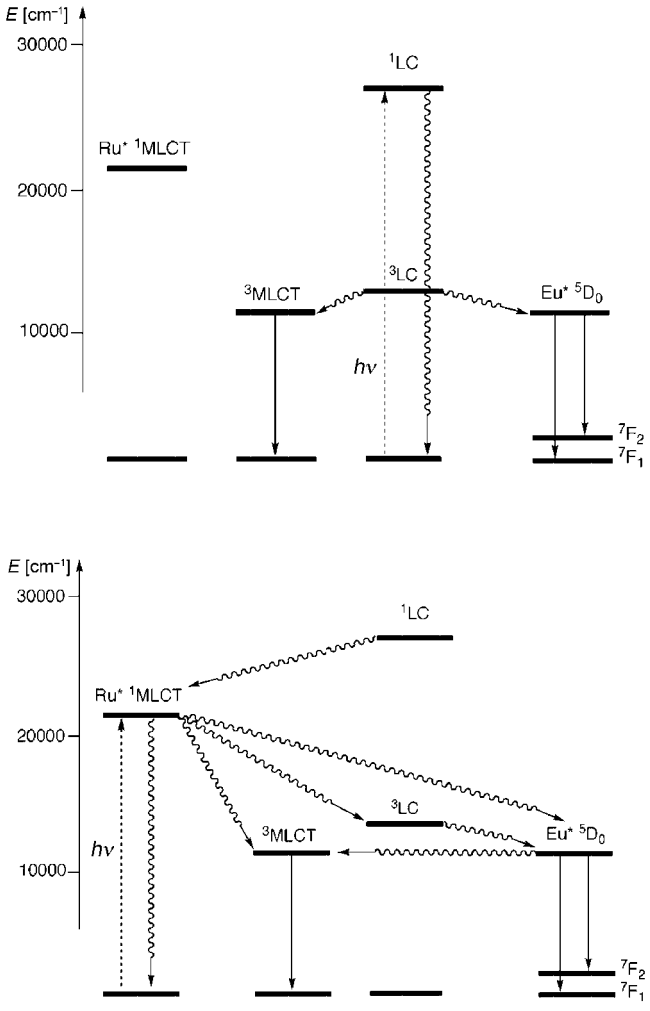


Figure 3. Energy diagram that accounts for the most important pathway for excited state deactivation of $Ru^{II}$–$Eu^{III}$ complex **7**. Top: excitation at 270 nm. Bottom: excitation at 460 nm. All radiative processes are represented with solid lines whereas the nonradiative ones are wavy.

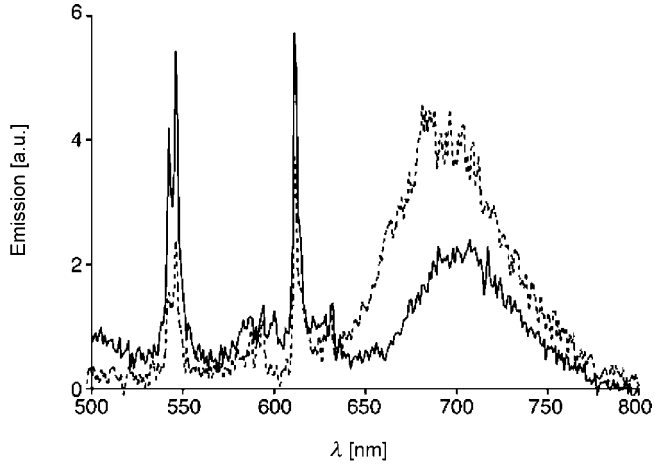


Figure 4. Emission spectral profile of $Ru^{II}$–$Eu^{III}$ complex **7** measured in MeOH/EtOH (1:4) at 77 K at $\lambda_{exc.}$ = 270 nm (– – –) and at $\lambda_{exc.}$ = 460 nm (——).

than upon excitation into the ligand-centred singlet state (270 nm). These results agree with the hypothesis that upon population of the singlet $^1$MLCT (or even of the $^3$MLCT) state, energy transfer to the $^5D_0$ of the europium is favoured more than from the ligand-localized excited states. Further support of sensitization, most likely from the $^1$MLCT, comes from the excitation spectra at low temperature. The excitation spectrum of **7** in MeOH/EtOH (1:4) at 77 K almost matches its absorption spectrum. The observed shift of the $^1$MLCT band from 460 to 400 nm is attributed to the rigid matrix, which prevents relaxation of the excited state observed at room temperature in polar solvents.

To gain more information about the quenching of the $Eu^{III}$ luminescence by its chemical environment, the lifetimes in MeOH and dry $CD_3OD$ were measured (Table 3). Monoexponential decay of the europium emission was observed in both cases. The lifetime of europium determined at 611 nm in MeOH ($\tau$ = 0.2 ms) doubled by a factor of two when the measurements were performed in dry $CD_3OD$ ($\tau$ = 0.4 ms). This solvent effect indicates that the emission intensity of the $Eu^{III}$ ion is sensitive to the number of coordinated water molecules and points to a slow exchange between the solvent and the strongly bound water molecules. The number of water molecules coordinated to the europium centre was calculated with the use of the empiric Horrocks equation[25] ($q = A\,[1/\tau(H_2O) - 1/\tau(D_2O)]$; A = 1.05 ms; uncertainty of ±0.5), which takes into account the quenching by the OH oscillators in the second coordination sphere. The estimated value of 2.5 molecules is in very good agreement with the structure of complex **7** depicted in Scheme 2, which is based on elemental analysis results. The water molecules coordinated to the lanthanide ion may exert a quenching effect on the lifetime of the $Eu^{3+}$ emission.

The Ru- and Eu-centred quantum yields ($\Phi$) for both complexes were rather low and hardly measurable, with reference to commonly used standards.

 © 2007 Wiley-VCH Verlag GmbH & Co. KGaA, Weinheim 

## Conclusions

The present work demonstrates that the inert organometallic building block [Ru(PCP)(tpy–DTTA$Na_4$)]Cl is able to coordinate gadolinium(III) and europium(III) ions to give the heterodimetallic complexes [Ru(PCP)(tpy–DTTA)-Ln($H_2O$)$_2$] (Ln = $Gd^{3+}$, $Eu^{3+}$) in good yield. Study of the photophysical properties shows that coordination of the $Gd^{III}$ cation to the mononuclear [Ru(PCP)(tpy–DTTA)]$^{3-}$ anion is accompanied by population of the triplet-excited state of the ligand and by an increase in the intensity of the ruthenium-based emission from the $^3$MLCT state. It was shown that the Ru–Eu complex exhibits sensitized visible emission upon excitation of the ππ* level and the {(PCP)-Ru(tpy–DTTA)} chromophoric unit at 470 nm, though only in rigid matrix at 77 K. The efficiency of energy transfer from $Ru^{II}$ to $Eu^{III}$ upon excitation into the $^3$LC and $^1$MLCT states was not determined because of the low intensity of the signals. However, emission lifetimes of the $Eu^{III}$ luminescence, measured in $CH_3OH$ and dry $CD_3OD$ solutions were found to be 0.2 and 0.4 ms, respectively, which confirms the presence of water coordinated to the metal ion.

The short lifetime of the $Eu^{III}$ luminescence was rationalized on the basis of a nonefficient d→f energy transfer and quenching by the coordinated water molecules. Sensitization of the $Eu^{III}$ luminescence combined with the stability of the organometallic {(PCP)Ru(tpy–DTTA)} unit in polar solvents and water encourage studies directed at the optimization of the properties (e.g. water solubility and thermodynamic stability under physiological conditions) of this class of complexes in order to produce efficient systems with properties suitable for practical applications, for example in bioassays. Notably, the complexes presented in this work are neutral. This is an important factor to take into account because positively or negatively charged molecules may lead to nonspecific binding in biological media.

## Experimental Section

**General:** All the experiments were carried out under a dry nitrogen atmosphere by using standard Schlenk techniques. Pentane and $Et_2O$ were distilled from sodium with benzophenone as an indicator. $CH_2Cl_2$ was dried with $CaH_2$. MeOH was dried with magnesium and used freshly distilled. Compounds **1**,[26] 4′-dimethylamino-2,2′:6′,2″-terpyridine,[19b] and **3**[17] were prepared according to literature procedures. All other reagents that were used are commercially available. $^1$H, $^{13}$C and $^{31}$P{$^1$H} NMR spectra were recorded at 298 K with a Varian AC200 or Varian Inova 300 spectrometer. Chemical shifts are reported relative to the residual solvent signal ($^1$H and $^{13}$C NMR spectra) or are externally referenced to 85% $H_3PO_4$ solution in water ($^{31}$P NMR spectra). Elemental microanalysis of mononuclear complexes **2** and **5** were performed by Dornis und Kolbe, Mikroanalytisches Laboratorium, Müllheim a. d. Ruhr, Germany. Elemental microanalysis of heterodinuclear complexes **6** and **7** were performed by Prof. Dr. H. Malissa and G. Reuter GmbH, Analytische Laboratorien, Lindlar, Germany.

**Electronic Spectroscopic Measurements:** UV/Vis absorption spectra were obtained with a Varian Cary 5000 spectrophotometer. Steady-state luminescence was measured in EtOH/MeOH (4:1) and in deuterated methanol at 77 K by using a Jobin Yvon Horiba Fluorolog 3 spectrofluorometer equipped with a Xe arc light source, a Spex R928P photomultiplier tube detector and double excitation and emission monochromators. Emission spectra were corrected for source intensity and detector response by using standard correction curves. For nanosecond time resolved lifetime measurements, a NanoLED-17 laser (sets at 295 nm) working with a maximum repletion rate of 1 MHz and a pulse <750 ps was used as an excitation source. The TBX Picosecond Photon Detection Module was used as the detector. Estimated errors are as follows: band maxima, ±2 nm; relative luminescence intensity, ±20%; lifetimes, ±10%.

**X-ray Crystal Structure Determination of 2:** $[C_{49}H_{43}N_4P_2Ru]Cl$ + disordered solvent, $Fw$ = 886.33 (Derived values do not contain the contribution of the disordered solvent molecules), red plate, $0.36 \times 0.21 \times 0.09$ mm$^3$, monoclinic, $C2/c$ (no. 15), $a$ = 34.5027(3), $b$ = 10.6866(1), $c$ = 24.4514(3) Å, $\beta$ = 93.4702(4)°, $V$ = 8999.10(16) Å$^3$, $Z$ = 8, $D_x$ = 1.308 g/cm$^3$ (Derived values do not contain the contribution of the disordered solvent molecules), $\mu$ = 0.52 mm$^{-1}$ (Derived values do not contain the contribution of the disordered solvent molecules). 67258 Reflections were measured with a Nonius Kappa CCD diffractometer with rotating anode (graphite monochromator, $\lambda$ = 0.71073 Å) up to a resolution of $(\sin\theta/\lambda)_{max}$ = 0.65 Å$^{-1}$ at a temperature of 150 K. An absorption correction based on multiple measured reflections was applied (0.77–0.95 correction range). Number of unique reflections: 10287 ($R_{int}$ = 0.0717). The structure was solved with automated Patterson Methods[27] and refined with SHELXL-97[28] against $F^2$ of all reflections. Non-hydrogen atoms were refined with anisotropic displacement parameters. All hydrogen atoms were introduced in geometrically idealized positions and refined with a riding model. The crystal structure contains large voids (907.4 Å$^3$/unit cell) filled with disordered solvent molecules. Their contribution to the structure factors was secured by back-Fourier transformation by using the SQUEEZE routine of the PLATON program,[29] which resulted in 328 electrons/unit cell. 516 parameters were refined with no restraints. $R1/wR2$ [$I > 2\sigma(I)$]: 0.0332/0.0809. $R1/wR2$ [all refl.]: 0.0508/0.0874. $S$ = 1.081. Residual electron density between –0.65 and 0.51 e Å$^{-3}$. Geometry calculations and checking for higher symmetry was performed with the PLATON program.[29] CCDC-634988 contains the supplementary crystallographic data for this paper. These data can be obtained free of charge from The Cambridge Crystallographic Data Centre via www.ccdc.cam.ac.uk/data_request/cif.

**[Ru(PCP)(tpy-$NMe_2$)](Cl) (2):** A solution of **1** (0.46 g, 0.5 mmol) in MeOH (15 mL) was added to a solution of 4′-$NMe_2$-2,2′:6′,2″-terpyridine (0.14 g, 0.5 mmol) in MeOH (5 mL). The reaction mixture was heated at reflux for 2 d. Subsequently, the solvent was evaporated in vacuo to give a red solid residue, stable to air and moisture, which was dissolved in $CH_2Cl_2$ (5 mL). Addition of pentane/$Et_2O$ (1:5) caused the precipitation of **2** as a red powder that was collected by filtration, washed with hexane and dried in vacuo. Yield: 0.29 g, 63%. $^1$H NMR (300.1 MHz, $CD_2Cl_2$): $\delta$ = 8.25 [d, $J_{H,H}$ = 7.0 Hz, 2 H, tpy(3, 3″)], 7.88 [s, 2 H, tpy(3′, 5′)], 7.47 [m, 2 H, tpy(4, 4″)], 7.21 [d, $J_{H,H}$ = 6.0 Hz, 2 H, tpy(6, 6″)], 7.13 (m, 3 H, ArH), 7.08 (vt, $J_{H,H}$ = 7.65 Hz, 4 H, *para*-H $PPh_2$), 6.93 (vt, $J_{H,H}$ = 7.8 Hz, 8 H, *ortho*-H $PPh_2$), 6.60 (m, 8 H, *meta*-H $PPh_2$), 6.42 [t, $J_{H,H}$ = 6.0 Hz, 2 H, tpy(5, 5″)], 3.98 (vt, $J_{H,P}$ = 4.0 Hz, 4 H, $CH_2$-P), 3.5 (s, 6 H, N-$CH_3$) ppm. $^{13}$C NMR (75.5 MHz, $CD_2Cl_2$): $\delta$ = 182.2 (d, $^3J_{C,P}$ = 17.2 Hz, $C_{ipso}$), 158.44, 154.3, 154.0, 153.1, 147.6 (vt, $J_{C,P}$ = 9.1 Hz, C-2,6), 134.4, 133.6 (vt, *ortho*-C $PPh_2$), 133.5 (vt, *meta*-C $PPh_2$), 130.6, 129.4 (dvt, $^1J_{C,P}$ = 74.8 Hz, $^{vt}J$ = 4.5 Hz, $C_{quat.}$ $PPh_2$), 129.2 (s, *para*-C $PPh_2$), 125.9, 122.7,

 © 2007 Wiley-VCH Verlag GmbH & Co. KGaA, Weinheim 

122.6 (s, C-4), 121.8 (vt, $^{vt}J_{C,P}$ = 7.9 Hz, C-3,5), 42.2 (vt, $CH_2$-P), 40.9 (s, N-$CH_3$) ppm. $^{31}P\{^1H\}$ NMR (121.4 MHz, $CD_2Cl_2$): $\delta$ = 43.4 (s, $CH_2$-P) ppm. $C_{49}H_{43}ClN_4P_2Ru$ (886.4): calcd. C 66.40, H 4.89, N 6.32; found C 66.33, H 5.04, N 6.25.

**[Ru(PCP)(tpy–DTTA)Na$_4$](Cl) (5):** Ligand **3**·7.5$H_2O$ (0.083 g, 0.12 mmol) was dissolved in distilled $H_2O$ (10 mL). Under vigorous stirring, 1 N NaOH was added drop wise until the pH of the solution was 9.5. Evaporation of water gave **4** as a white crystalline solid that was transferred into a Schlenk flask, dried in vacuo and stored under a nitrogen atmosphere prior to use. Subsequently, **1** (0.09 g, 0.1 mmol) and **4** were stirred under a nitrogen atmosphere in dry MeOH (20 mL) and heated at reflux for 2 d. The solvent was then removed in vacuo until a small residue remained. Addition of $Et_2O$ caused the precipitation of **4** as a red solid that was isolated by centrifugation, washed with hexane and cold water and dried in vacuo. Yield: 0.07 g, 55%. $^1H$ NMR (300.1 MHz, $CD_3OD$): $\delta$ = 8.68 [d, $J_{H,H}$ = 4.41 Hz, 2 H, tpy(6, 6′′)], 8.56 [d, $J_{H,H}$ = 7.71 Hz, 2 H, tpy(3, 3′′)], 8.48 [d, $J_{H,H}$ = 7.9 Hz, 2 H, tpy(5, 5′′)], 8.06 [s, 2 H, tpy(3′, 5′)], 7.98 [t, $J_{H,H}$ = 9.2 Hz, 2 H, tpy(4, 4′′)], 7.02 (m, 3 H, Ar), 7.07 (vt, $J_{H,H}$ = 7.41 Hz, 4 H, *para*-H $PPh_2$), 6.92 (vt, $J_{H,H}$ = 7.42 Hz, 8 H, *ortho*-H $PPh_2$), 6.63 (m, 8 H, *meta*-H $PPh_2$), 4.00 (br. s, 4 H, $CH_2$-P), 3.73 (br. m, 4 H), 3.65 (s, 8 H), 3.57 (br. m, 4 H) ppm. $^{13}C$ NMR (75.5 MHz, $CD_3OD$): $\delta$ = 182.9 (d, $^3J_{C,P}$ = 17.2 Hz, $C_{ipso}$), 177.97 (m, $COO^-$), 158.4, 156.7, 156.6, 154.6 (vt, C-2,6), 152.9, 148.9, 147.6, 137.48, 134.7, 133.7 (vt, *ortho*-C $PPh_2$), 131.8 (vt, *meta*-C $PPh_2$), 129.1 (dvt, $^1J_{C,P}$ = 74.8 Hz, $C_{quat.}$ $PPh_2$), 128.8 (s, *para*-C $PPh_2$), 125.7, 123.9, 123.1, 122.5 (s, C-4), 121.5 (vt, C-3,5), 105.76, 61.3, 42.4 (m, $CH_2$-P) ppm. $^{31}P\{^1H\}$ NMR (121.4 MHz, $CD_2Cl_2$): $\delta$ = 43.4 (s, $CH_2$-P) ppm. IR (KBr): $\tilde{\nu}$ = 1583.8 $(CO)_{as}$, 1408.4 $(CO)_s$ $cm^{-1}$. $C_{59}H_{53}ClN_6Na_4O_8P_2Ru$ (1264.5): calcd. C 56.04, H 4.22, N 6.65; found C 55.85, H 4.15, N 6.57.

**[Ru(PCP)(tpy–DTTA)Gd($H_2O$)$_2$] (6):** $GdCl_3$·6$H_2O$ (0.06 g, 0.16 mmol) and complex **5** (0.2 g, 1.6 mmol) were stirred together in a solution of MeOH/$H_2O$ (2:2) (20 mL) for 5 h at 70 °C. Subsequently, the volume was concentrated in vacuo. Addition of $Et_2O$ caused the precipitation of **6** as an orange solid, which was collected by centrifugation, washed several times with cold water and dried in vacuo. Yield: 0.18 g, 89%. IR: $\tilde{\nu}$ = 1615.9 $(CO)_{as}$, 1434.5 $(CO)_s$ $cm^{-1}$. $C_{59}H_{57}GdN_6O_{10}P_2Ru$ (1330.4): calcd. C 53.27, H 4.32, Gd 11.82, N 6.32, P 4.66, Ru 7.60; found C 53.11, H 4.48, Gd 11.60, N 6.34, P 4.53, Ru 7.64.

**[Ru(PCP)(tpy–DTTA)Eu($H_2O$)$_2$] (7):** Complex **7** was prepared by applying the synthetic procedure described for complex **6**. Compound **5** (0.2 g, 0.18 mmol) in MeOH/$H_2O$ (2:2) (20 mL) reacted with $EuCl_3$·6$H_2O$ (0.06 g, 0.18 mmol). Yield: 0.19 g, 83%. IR: $\tilde{\nu}$ = 1607.2 $(CO)_{as}$, 1434.4 $(CO)_s$ $cm^{-1}$. $C_{59}H_{57}EuN_6O_{10}P_2Ru$ (1325.1): calcd. C 53.48, H 4.34, Eu 11.82, N 6.34, P 4.67, Ru 7.63; found C 53.84, H 4.04, Eu 11.85, N 6.25, P 4.59, Ru 7.32.

**Supporting Information** (see footnote on the first page of this article): Excitation spectrum of **7**.

## Acknowledgments

The authors kindly acknowledge Dr. E. Cecchetto for his assistance during the emission and lifetime measurements. This work was supported by the Council for the Chemical Sciences of the Netherlands Organization for Scientific Research (CW-NWO).

[1] J. Kido, Y. Okamoto, *Chem. Rev.* **2002**, *102*, 2357–2368.
[2] J. Fang, H. You, J. Chen, J. Lin, D. Ma, *Inorg. Chem.* **2006**, *45*, 3701–3704.
[3] a) N. Sabbatini, M. Guardigli, J.-M. Lehn, *Coord. Chem. Rev.* **1993**, *123*, 201–228; b) D. Parker, J. A. G. Williams, *J. Chem. Soc., Dalton Trans.* **1996**, 3613–3628; c) A. P. de Silva, H. Q. N. Gunaratne, T. Gunnlaugsson, A. J. M. Huxley, C. P. McCoy, J. T. Rademacher, T. E. Rice, *Chem. Rev.* **1997**, *97*, 1515–1566; d) M. P. Oude Wolbers, F. C. J. M. van Veggel, F. G. A. Peters, E. S. E. van Beelen, J. W. Hofstraat, F. A. J. Geurts, D. N. Reinhoudt, *Chem. Eur. J.* **1998**, *4*, 772–780; e) D. Parker, R. S. Dickins, H. Puschmann, C. Crossland, J. A. K. Howard, *Chem. Rev.* **2002**, *102*, 1977–2010; f) L. J. Charbonnière, R. Ziessel, M. Montalti, L. Prodi, N. Zaccheroni, C. Boehme, G. Wipff, *J. Am. Chem. Soc.* **2002**, *124*, 7779–7788.
[4] a) A. Mayer, S. Neuenhofer, *Angew. Chem. Int. Ed. Engl.* **1994**, *33*, 1044–1072; b) I. D. Clark, J. P. Macmanus, A. G. Szabó, *Clin. Biochem.* **1995**, *28*, 131–135; c) A. Beeby, I. M. Clarkson, S. Faulkner, S. W. Botchway, D. Parker, A. W. Parker, J. A. G. Williams, *J. Photochem. Photobiol. B* **2000**, *57*, 83–89.
[5] G. Blasse, B. C. Grabmaier, *Luminescent Materials*, Springer, Berlin, **1994**.
[6] M. H. V. Werts, M. A. Duin, J. W. Hofstraat, J. W. Verhoeven, *Chem. Commun.* **1999**, 799–800.
[7] C. L. Maupin, D. Parker, J. A. G. Williams, J. P. Riehel, *J. Am. Chem. Soc.* **1998**, *120*, 10563–10564.
[8] S. Faulkner, A. Beeby, M.-C. Carrié, A. Dadabhoy, A. M. Kenwright, P. G. Sammes, *Inorg. Chem. Commun.* **2001**, *4*, 187–190.
[9] C. Galaup, J.-M. Couchet, S. Bedel, P. Tisnès, C. Picard, *J. Org. Chem.* **2005**, *70*, 2274–2284.
[10] M. P. Oude Wolbers, F. C. J. M. van Veggel, B. H. M. Snellink-Ruël, J. W. Hofstraat, F. A. J. Geurts, D. N. Reinhoudt, *J. Am. Chem. Soc.* **1997**, *119*, 138–144.
[11] G. A. Hebbink, L. Grave, L. A. Woldering, D. N. Reinhoudt, F. C. J. M. van Veggel, *J. Phys. Chem.* **2003**, *107*, 2483–2491.
[12] N. M. Shavaleev, S. J. A. Pope, Z. R. Bell, S. Faulkner, M. D. Ward, *Dalton Trans.* **2003**, 808–814.
[13] a) J.-C. Bünzli, C. Piguet, *Chem. Rev.* **2002**, *102*, 1897–1928; b) J.-C. Bünzli, C. Piguet, *Chem. Soc. Rev.* **2005**, *34*, 1048–1077 and references cited therein.
[14] D. L. Dexter, *J. Chem. Phys.* **1953**, *21*, 836–850.
[15] P. Coppo, M. Duati, V. N. Kozhevnikov, J. W. Hofstraat, L. De Cola, *Angew. Chem. Int. Ed.* **2005**, *44*, 1806–1810.
[16] J. Costa, R. Ruloff, L. Burai, L. Helm, A. E. Merbach, *J. Am. Chem. Soc.* **2005**, *127*, 5147–5157.
[17] R. Ruloff, G. van Koten, A. E. Merbach, *Chem. Commun.* **2004**, 842–843.
[18] M. Gagliardo, H. P. Dijkstra, P. Coppo, L. De Cola, M. Lutz, A. L. Spek, G. P. M. van Klink, G. van Koten, *Organometallics* **2004**, *23*, 5833–5840.
[19] a) M. Beley, J.-P. Collin, R. Louis, B. Metz, J.-P. Sauvage, *J. Am. Chem. Soc.* **1991**, *113*, 8521–8522; b) E. C. Constable, A. M. W. Cargill Thompson, D. A. Tocher, M. A. M. Daniels, *New J. Chem.* **1992**, *16*, 855–867; c) S. Encinas, L. Flamigni, F. Barigelletti, E. C. Constable, C. E. Housecroft, E. R. Schofield, E. Figgemeier, D. Fenske, M. Neuburger, J. G. Vos, M. Zehnder, *Chem. Eur. J.* **2002**, *8*, 137–150.
[20] R. Ruloff, R. N. Muller, D. Pubanz, A. E. Merbach, *Inorg. Chim. Acta* **1998**, *275–276*, 15–23.
[21] S. Laus, B. Sithraman, E. Tóth, R. D. Bolskar, L. Helm, S. Asokan, M. S. Wong, L. J. Wilson, A. E. Merbach, *J. Am. Chem. Soc.* **2005**, *127*, 9368–9369.
[22] V.-M. Mukkala, I. Helenius, J. Hemmilä, J. Kankare, H. Takalo, *Helv. Chim. Acta* **1993**, *76*, 1361–1378.
[23] a) J.-P. Sauvage, Collin, J.-C. Chambron, S. Guillerez, C. Coudret, V. Balzani, F. Barigelletti, L. De Cola, L. Flamigni, *Chem. Rev.* **1994**, *94*, 993–1019; b) X. Zhou, A.-M. Ren, J.-K. Feng, *J. Organomet. Chem.* **2005**, *690*, 338–347.
[24] a) M. Hissel, A. El-Ghayoury, A. Harriman, R. Ziessel, *Angew. Chem. Int. Ed.* **1998**, *37*, 1717–1720; b) J. R. Winkler, T. L. Net-

 © 2007 Wiley-VCH Verlag GmbH & Co. KGaA, Weinheim 

zel, C. Crentz, N. Sutin, *J. Am. Chem. Soc.* **1987**, *109*, 2381–2392.
[25] W. D. Horrocks, D. R. Sudnick, *Acc. Chem. Res.* **1981**, *14*, 384–392.
[26] a) T. Karlen, P. Dani, D. M. Grove, P. Steenwinkel, G. van Koten, *Organometallics* **1996**, *15*, 5687–5694; b) G. Jia, H. M. Lee, I. D. Williams, *J. Organomet. Chem.* **1997**, *534*, 173–180.
[27] P. T. Beurskens, G. Admiraal, G. Beurskens, W. P. Bosman, S. Garcia-Granda, R. O. Gould, J. M. M. Smits, C. Smykalla, *The DIRDIF99 Program System*, Technical Report of the Crystallography Laboratory, University of Nijmegen, The Netherlands, **1999**.
[28] G. M. Sheldrick, *SHELXL-97: Program for Crystal Structure Refinement*, University of Göttingen, Germany, **1997**.
[29] A. L. Spek, *J. Appl. Crystallogr.* **2003**, *36*, 7–13.

Received: October 23, 2006
Published Online: February 23, 2007

 © 2007 Wiley-VCH Verlag GmbH & Co. KGaA, Weinheim 

DOI: 10.1002/ejic.200601189

# Chelating $\eta^6$-Arene-$\eta^1$-carbene Ligands in Ruthenium Complexes

Ismail Özdemir,*[a] Serpil Demir,[a] Bekir Çetinkaya,[b] Loïc Toupet,[c] Ricardo Castarlenas,[d] Cédric Fischmeister,[d] and Pierre H. Dixneuf*[d]

**Keywords:** Ruthenium–arene / NHCs / Imidazolinylidene / Metathesis / ROMP / Polymerization

N-Heterocyclic carbene (NHC) ruthenium complexes containing a chelating NHC-$\eta^6$-arene ligand have been prepared and evaluated as precursors for ring opening metathesis polymerization (ROMP). The reaction of $[RuCl_2(p\text{-cymene})]_2$ with electron-rich olefins of the bis(imidazolinylidene) type containing at least one arylmethyl-*N* chain (aryl: 2,4,6-trimethylphenyl, 3,4,5-trimethoxyphenyl) selectively leads, upon heating, to ruthenium(II) complexes **2** containing a chelating bridged carbene $\eta^6$-arene ligand. The reaction of complexes containing an additional $ROCH_2CH_2N$ group with AgOTf leads to ionic complexes **5** with a tridentate trifunctional carbene/arene/ether ligand. The X-ray structure of $[RuCl_2\{\eta^1\text{-}CN(CH_2\{\eta^6\text{-}C_6H_2Me_3\text{-}2,4,6\})CH_2CH_2N(CH_2\{C_6H_2(OMe)_3\text{-}3,4,5\})\}]$ (**2c**) and that of the ionic ruthenium complex containing a trifunctional carbene/arene/ether ligand that provides ten electrons, $[RuCl\{\eta^1\text{-}CN(CH_2\{\eta^6\text{-}C_6H_2Me_3\text{-}2,4,6\})CH_2CH_2N(CH_2CH_2OCH_3)\}][CF_3SO_3]$ (**5e**), have been determined. The precursors **2** in the presence of AgOTf and propargyl alcohol, in order to produce an allenylidene initiator, and complexes **5** in the presence of propargyl alcohol lead to ROMP of norbornene. It is shown that initial chloride abstraction is required and that the catalyst activity is increased by using mesityl–ruthenium precursors and coordinated branched ether complexes.
(© Wiley-VCH Verlag GmbH & Co. KGaA, 69451 Weinheim, Germany, 2007)

## Introduction

Electron-releasing heterocyclic carbenes have been identified in the early days of their coordination chemistry as phosphane ligand equivalents.[1] Recently, sterically hindered N-heterocyclic carbenes (NHCs) of the 1,3-imidazolylidene and 1,3-imidazolinylidene type have been used to stabilize novel organometallic structures[2] and to generate new catalyst precursors especially in the field of C–C bond formation[3–5] and in alkene metathesis.[6] Their success in catalysis is largely due to their ability to increase the electron density at the metal site and to protect coordinatively unsaturated active metal species by their high steric hindering effect.

It is expected that when the NHC orientation is perturbed in space, the catalytic activity of the linked metal site should be largely modified. This influence has lead to the design of new chelating NHCs. Examples of bis(NHC)s,[7] mixed pyridine-carbene[8] and oxazoline-carbene[9] complexes have already been reported. We have recently shown the route to metal complexes containing mixed arene and carbene ligands providing eight electrons to the metal, and have demonstrated that the natural orientation of the carbene in these complexes is significantly modified.[10]

We now present new eight-electron bridged ($\eta^6$-arene-$\eta^1$-carbene)ruthenium complexes from related electron-rich bis(1,3-imidazolin-2-ylidene) olefins containing at least one arylmethylene group linked to a nitrogen atom. We also show that the resulting ($\eta^6$-arene-$\eta^1$-carbene)$RuCl_2$ complexes can be used to generate intermediates of the type [($\eta^6$-arene-$\eta^1$-carbene)RuCl]OTf and that these are catalyst precursors, associated to propargyl alcohol, for the polymerization of cyclic olefins by the ring opening metathesis polymerization (ROMP) process. The X-ray structure of the neutral complex $[RuCl_2\{\eta^1\text{-}CN(CH_2\{\eta^6\text{-}C_6H_2Me_3\text{-}2,4,6\})CH_2CH_2N(CH_2\{C_6H_2(OMe)_3\text{-}3,4,5\})\}]$ and those of two ionic ruthenium complexes containing di- or tridentate NHC ligands are also reported.

## Results and Discussion

The electron-rich olefins that contain one (**1a**–**1b**) or two (**1c**–**1d**) arylmethylene group(s) attached to a nitrogen atom[11] were treated with the ruthenium source $[RuCl_2(p\text{-cymene})]_2$[12] in toluene at 100 °C for 4 h in order to bring about complete conversion of $[RuCl_2(p\text{-cymene})]_2$ and substitution of the *p*-cymene ligand. The ruthenium complexes containing the bridged carbene-arene ligand were isolated as brown solids: **2a** (90%), **2b** (93%), **2c** (89%), **2d** (82%) (Scheme 1).

[a] Inönü University, Faculty of Sciences and Arts, 44069 Malatya, Turkey
[b] Ege University, Faculty of Science, Bornova 35100 Izmir, Turkey
[c] Groupe Matière Condensée et Matériaux, UMR 6626, CNRS-Université de Rennes 1, 35042 Rennes, France
[d] Institut de Sciences Chimiques, UMR 6226: CNRS-Université de Rennes 1, Catalyse et Organométalliques, Campus de Beaulieu, 35042 Rennes, France

 © 2007 Wiley-VCH Verlag GmbH & Co. KGaA, Weinheim 

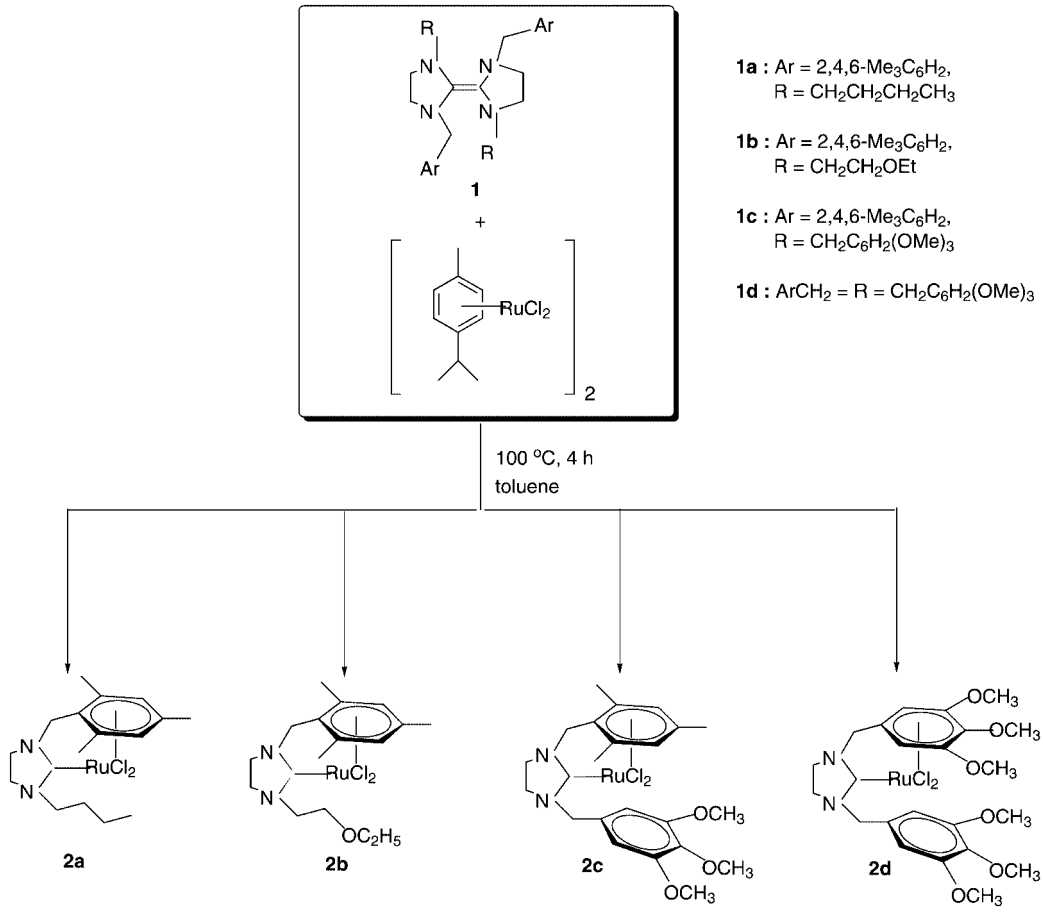


Scheme 1. Preparation of (η⁶-arene-η¹-carbene)$RuCl_2$ complexes.

The $^1H$ NMR spectra show the absence of the *p*-cymene ligand and the presence of a coordinated mesityl group in **2a**–**c** with equivalent ortho methyl groups and equivalent high-field aryl CH proton resonances at $\delta$ = 5.36–5.43 ppm (cf. $\delta$ = 6.7 ppm for **1a**–**1c**). Complex **2d** shows a coordinated aryl CH proton signal at $\delta$ = 4.78 ppm and noncoordinated aryl proton signals at $\delta$ = 6.79 ppm, whereas the aryl proton signal appears at $\delta$ = 6.90 ppm in the related olefin precursor **1d**. The coordination of the carbene carbon is evidenced by a low-field singlet in the $^{13}C$ NMR spectrum at $\delta$ = 200–201.5 ppm for **2a**–**2d**.

These syntheses show that the intramolecular displacement of the *p*-cymene ligand by the mesityl group is quantitative and rather easy. They also show (**2c**) that the coordination of the mesityl group is favoured over that of the 3,4,5-$(MeO)_3C_6H_2$ group likely because of steric repulsion between the methoxy group and the chloride ligands. The complexes **2** that do not contain an alkene-metathesis-initiating carbene are inert as catalysts for the ROMP of cyclic olefins. In order to change them into active catalysts for alkene metathesis, attempts were made to transform them into related allenylidene–ruthenium complexes according to Equation (1).[12]

$$\mathrm{LnRuCl_2} \xrightarrow[-\mathrm{AgCl}]{\mathrm{Ag^+}} \mathrm{LnRuCl}^+ \xrightarrow{\mathrm{HC{\equiv}CC(OH)Ph_2}} \mathrm{LnRuCl(=C=C=CPh_2)}^+ \quad (1)$$

Indeed, the [Ru=C=C=$CPh_2$(Cl)($PCy_3$)(*p*-cymene)]X[13] complexes were shown to be active precursors for ROMP on either thermal[14] or acid-promoted[15] transformations into indenylidene–ruthenium derivatives. The indenylidene carbene plays the role of alkene metathesis initiator in these catalyst precursors. Attempts to isolate the 16-electron ruthenium intermediates were made by the abstraction of one chloride ion from complexes **2**, before attempting allenylidene–ruthenium complex formation by addition of propargylic alcohol.

Complex **2b** and complexes **3** and **4**, analogous to **2b** and **2d**, were treated with one equivalent of AgOTf in dichloromethane at room temperature for 3 h, and the ionic complexes **5b**, **5e**, **6** were isolated in 78–85% yields (Scheme 2). The $^1H$ and $^{13}C$ NMR spectra show that the arene group remains coordinated to the metal, the (Ru=C) carbene carbon ($\delta$ = 197 ppm) is only slightly shielded relative to that in complexes **2** ($\delta$ = 200 ppm). In their $^1H$ NMR spectra at

 © 2007 Wiley-VCH Verlag GmbH & Co. KGaA, Weinheim 

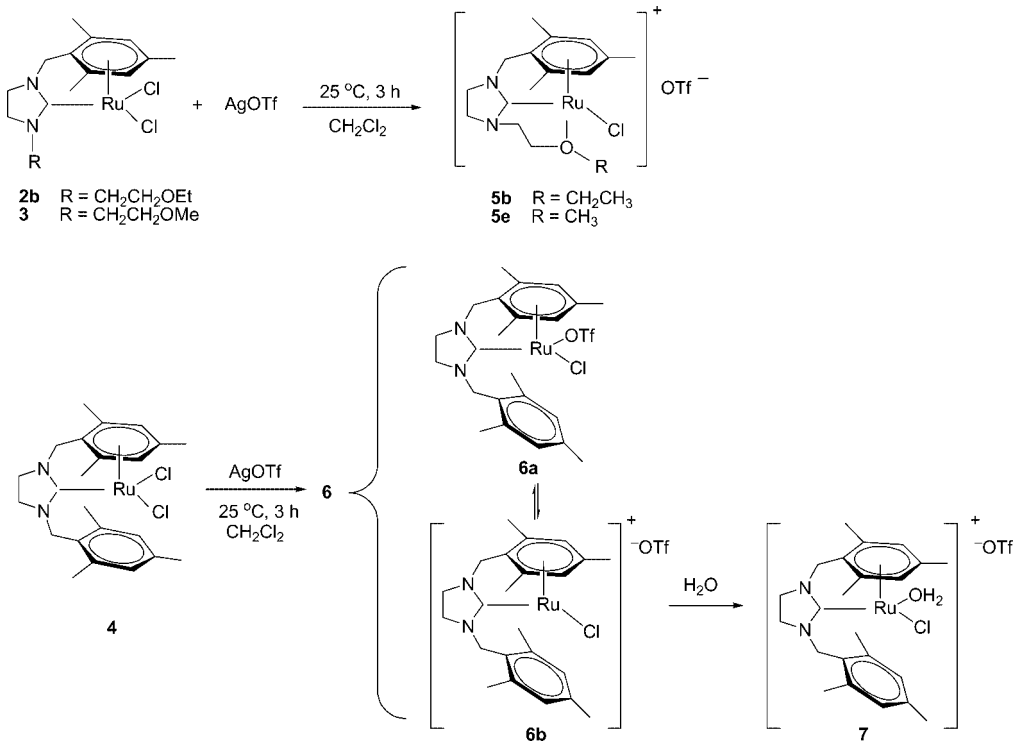


Scheme 2. Preparation of ionic mixed arene carbene ruthenium complexes **5**, **6** and **7**.

room temperature, complexes **5** show nonequivalent coordinated mesityl CH protons, which is consistent with a chiral ruthenium centre. Complex **6** is an orange solid that reacts with wet solvents to give the aquo complex **7** for which an X-ray structure has been determined (Figure 1, Table 1).[16] The nature of **6** can be understood as an 18-electron complex **6a** with a weak Ru–OTf bond in equilibrium with a 16-electron complex **6b**. The latter reacts with water in the same way that the intermediates obtained from the reaction between **2b** or **3** and AgOTf react with the ether branch to give complexes **5b** and **5e**.

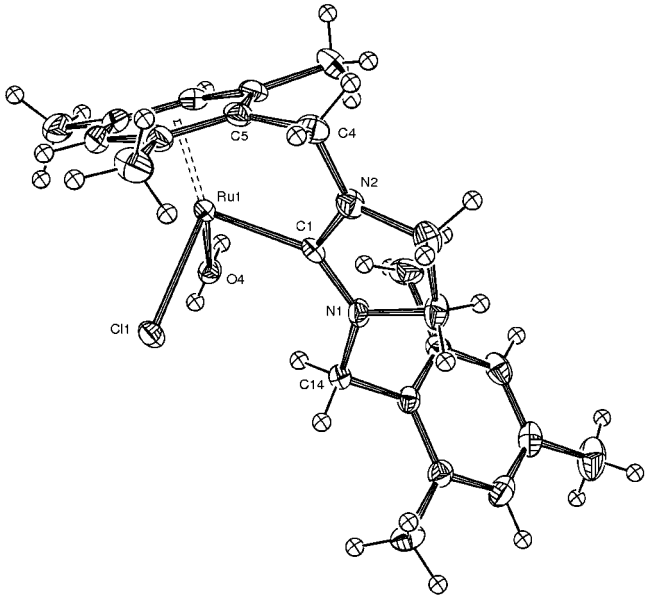


Figure 1. Molecular structure of complex **7** showing 50% ellipsoid probability. A triflate and a chloroform molecule are omitted for clarity.

Table 1. Selected bond lengths [Å] and angles [°] for the molecular structure of **7**.

| | | | |
|---|---|---|---|
| Ru1–C1 | 2.058(3) | Ru1–O4 | 2.190(2) |
| N1–C11 | 1.357(3) | Ru1–C5 | 2.107(3) |
| N2–C4 | 1.465(4) | N1–C14 | 1.458(3) |
| Ru1–Cl1 | 2.408(7) | Ru1–C6 | 2.158(3) |
| Ru1–C7 | 2.239(3) | Ru1–C8 | 2.283(3) |
| Ru1–C9 | 2.197(3) | Ru1–C10 | 2.201(3) |
| C1–Ru1–Cl1 | 82.62(7) | C1–Ru1–O4 | 95.95(9) |
| C1–Ru1–N1 | 136.23(19) | C1–Ru1–N2 | 115.1(2) |
| C1–N2–C4 | 122.9(2) | N2–C4–C5 | 106.1(2) |
| Ru1–C5–C4–N2 | 14.00 | | |

## X-ray Diffraction Study of 2c and 5e

In order to evaluate the ligand modification brought about by the abstraction of one chloride ion from complexes **2**, structural studies were carried out on a neutral complex **2c**[17] and an ionic complex **5e**[18] containing a coordinating chain.

Molecular structures of **2c** and **5e** with selected data are presented in Figure 2 with Table 2, and Figure 3 with Table 3, respectively. The structure of **2c** confirms that one of the mesityl groups is coordinated to the ruthenium atom. The structure of **5e** shows that formally a chlorine atom has been displaced by the methoxy oxygen atom and that the ligand is tricoordinate, donating ten electrons to the ruthenium atom. The mesityl–ruthenium bond length is not sig-

 © 2007 Wiley-VCH Verlag GmbH & Co. KGaA, Weinheim 

nificantly modified: the Ru–arene distance is 1.690 Å in **2c** and 1.693 Å in **5e**. By contrast, we can observe a slightly shorter carbene C–Ru bond when the NHC is tricoordinate: 1.996(3) Å in **5e** and 2.050(2) Å in **2c**.

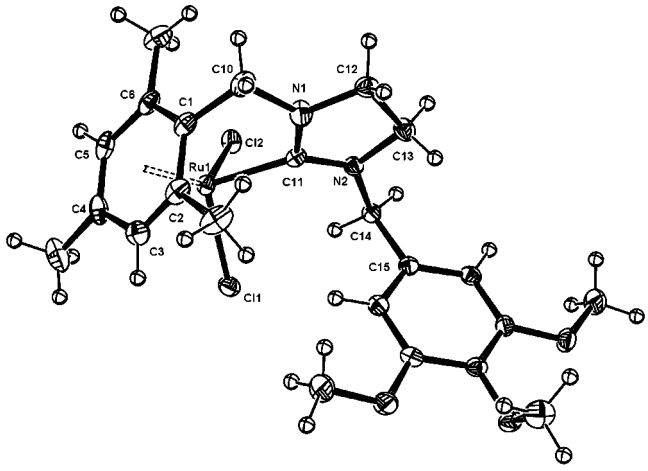


Figure 2. Molecular structure of **2c** showing 50% ellipsoid probability. A dichloromethane molecule is omitted for clarity.

Table 2. Selected bond lengths [Å] and angles [°] for the molecular structure of **2c**.

| | | | |
|---|---|---|---|
| Ru1–C11 | 2.050(2) | Ru1–C4 | 2.182(2) |
| N1–C11 | 1.357(3) | Ru1–C5 | 2.321(2) |
| N2–C11 | 1.328(3) | Ru1–C2 | 2.112(2) |
| N1–C10 | 1.452(3) | Ru1–C3 | 2.194(2) |
| Ru1–Cl1 | 2.3936(5) | Ru1–Cl2 | 2.4416(6) |
| N2–C13 | 1.474(3) | N2)–C14 | 1.458(3) |
| N1–C12 | 1.462(3) | Ru1–C6 | 2.278(2) |
| Ru1–C1 | 2.153(2) | N1–C11–N2 | 107.4(2) |
| C1–C2–C10 | 120.6(2) | N1–C10–C1 | 106.24(18) |
| N2–C14–C15 | 110.15(17) | C11–Ru1–Cl1 | 85.11(6) |
| C11–Ru1–Cl2 | 100.14(6) | N1–C11–Ru1 | 115.74(16) |
| Ru1–C1–C10–N1 | 13.99 | | |

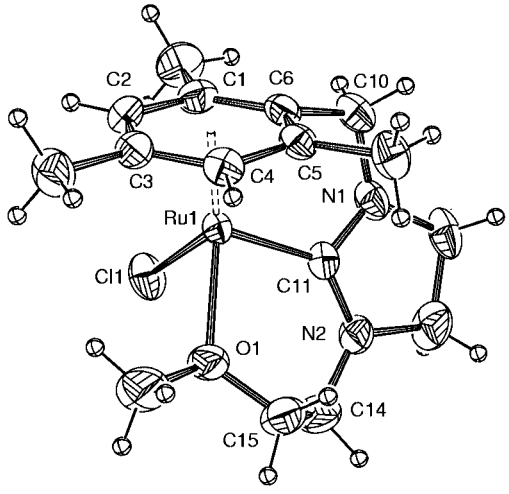


Figure 3. Molecular structure of **5e** showing 50% ellipsoid probability. A triflate molecule is omitted for clarity.

Table 3. Selected bond lengths [Å] and angles [°] for the molecular structure of **5e**.

| | | | |
|---|---|---|---|
| Ru1–C11 | 1.996(3) | Ru1–O1 | 2.175(2) |
| Ru1–C6 | 2.101(3) | Ru1–C3 | 2.330(3) |
| Ru1–C1 | 2.154(3) | Ru1–C5 | 2.197(3) |
| Ru1–C4 | 2.200(3) | Ru1–C2 | 2.274(3) |
| Ru1–Cl1 | 2.3885(8) | N1–C11 | 1.324(4) |
| N1–C10 | 1.451(5) | N2–C11 | 1.325(4) |
| N2–C14 | 1.458(5) | C6–C10 | 1.533(5) |
| C11–Ru1–O1 | 86.89(11) | N1–C11–Ru1 | 118.0(2) |
| N2–C11–Ru1 | 131.4(2) | Ru1–C6–C10–N1 | 15.3 |

## ROMP Promoted by Complexes 2 and 5

ROMP of norbornene was studied under two sets of conditions by taking into account that complexes **2** do not react with norbornene in the absence or presence of propargylic alcohol. Thus, the catalysts were generated directly from the precursors **2** by in situ treatment first with AgOTf in PhCl followed by the addition of propargylic alcohol, without isolation of the intermediate of type **5**. The resulting allenylidene or indenylidene intermediate could not be isolated, consequently the ROMP reaction was performed in situ as soon as the propargylic alcohol was added to complexes **5**, and chlorobenzene was used as solvent (conditions [a], Table 4). An analogously successful approach for the in situ generation of alkene metathesis catalysts was used for the ring closing metathesis (RCM) of dienes.[10] Another polymerization procedure was used by combining the isolated ionic complexes **5** and propargylic alcohol, $HC{\equiv}CCPh_2OH$, in order to generate the allenylidene intermediate and then the indenylidene initiator in situ

Table 4. ROMP of norbornene in PhCl catalyzed by various N-heterocyclic carbene-ruthenium intermediates in situ generated from **2** and **5**.

| Catalyst precursor | Conditions | Yield [%] | $10^{-3} \times M_n$[d] | PDI[e] | *cis* [%][f] |
|---|---|---|---|---|---|
| **2a**[a] | 15 min 80 °C | 84 | 71 | 1.8 | 41 |
| **2a**[a] | 30 min room temp. | 82 | 136 | 1.8 | 41 |
| **2b**[c] | 30 min 80 °C | 15 | 162 | 1.9 | – |
| **2c**[a] | 30 min room temp. | 78 | 68 | 1.7 | 38 |
| **2c**[a] | 15 min 80 °C | 94 | 53 | 2.2 | 39 |
| **2d**[a] | 20 min 80 °C | 74 | 76 | 1.7 | 47 |
| **2d**[a] | 480 min room temp. | 19 | 121 | 1.8 | 39 |
| **4**[b] | 420 min 80 °C | 60 | 74 | 1.8 | 23 |
| **5e**[b] | 5 min 80 °C | 71 | 60 | 1.8 | 34 |
| **5e**[b] | 480 min room temp. | 30 | 132 | 1.7 | 31 |
| **5b**[b] | 5 min 80 °C | 97 | 75 | 1.5 | 36 |
| **5b**[b] | 40 min room temp. | 95 | 54 | 1.6 | 34 |

[a] Catalyst precursor ($1.5 \times 10^{-5}$ mol), AgOTf ($1.5 \times 10^{-5}$ mol), $HC{\equiv}C{-}CPh_2(OH)$ ($1.7 \times 10^{-5}$ mol), norbornene ($4.5 \times 10^{-3}$ mol), PhCl (5 mL). [b] Catalyst precursor ($1.5 \times 10^{-5}$ mol), $HC{\equiv}C{-}CPh_2(OH)$ ($1.7 \times 10^{-5}$ mol), norbornene ($4.5 \times 10^{-3}$ mol), PhCl (5 mL). [c] Catalyst precursor ($1.5 \times 10^{-5}$ mol), norbornene ($4.5 \times 10^{-3}$ mol), PhCl (5 mL). [d] Determined by GPC in THF vs. polystyrene standards. [e] Polydispersity index $M_w/M_n$. [f] Determined by $^1$H NMR spectroscopy.

 © 2007 Wiley-VCH Verlag GmbH & Co. KGaA, Weinheim 

(conditions [b], Table 4). Precursor **2a**, under conditions [a], led to similar yields at 80 °C and room temperature, but higher molecular mass was obtained at room temperature. This indicates that a lower number of active initiators are produced at room temperature. Precursor **2b**, in the absence of AgOTf and propargylic alcohol, leads to very low activity, thus showing that the initial halide abstraction from complexes **2** is required to trigger efficient polymerization. Precursor **2c** gives a higher yield (94%) after 15 min at 80 °C, but with a broad polydispersity. Complexes **2a** and **2d** afford similar yields and polydispersity at 80 °C. However, at room temperature, precursors **2a** and **2c** with a coordinated mesityl group are much more active than **2d** with the coordinated trimethoxybenzyl group, thus showing the influence of the nature of the coordinated arene.

The ROMP, performed directly with ionic complexes **5b** and **5e**, shows that the most efficient precursor is **5b** both at room temperature and at 80 °C with high yield (>95%) and good polydispersity (PDI = 1.5). The comparison of this result to that obtained from **2b** alone indicates that the preliminary chloride ion abstraction by silver salt treatment is essential to obtain high yield and low polydispersity. The nature of the coordinated OR group, e.g. OEt or OMe, has a strong influence. The precursor **5b** (OEt) exhibits a much higher activity than **5e** (OMe).

## Conclusions

The above results show that bis(imidazolinylidene) olefins containing an arylmethyl-*N* group always displace the *p*-cymene to give ($\eta^1$-carbene-$\eta^6$-arene)$RuCl_2$ complexes upon reaction with $[RuCl_2(p\text{-cymene})]_2$. Upon chloride abstraction, these complexes containing an additional $ROCH_2CH_2$–N group lead to the tridentate carbene/arene/ether ionic complexes **5b** and **5e**. The mixed arene-NHC precursors **2** are ROMP initiators after chloride abstraction and reaction with propargylic alcohol to initially produce allenylidenes. The most active precursors **2a**, **2b** and **5b**, operate at room temperature.

## Experimental Section

Syntheses were carried out by using standard Schlenk techniques under an inert argon atmosphere with previously dried solvents. The starting complex $[RuCl_2(p\text{-cymene})]_2$ was prepared by known methods.[12] Electron-rich olefins **1** were prepared according to Lappert's procedure.[11] Infrared spectra were recorded by using KBr pellets in the range 400–4000 $cm^{-1}$ with an ATI UNICAM 2000 spectrometer. $^1H$ NMR (300 MHz) and $^{13}C$ NMR (75.5 MHz) spectra were recorded with a Bruker AM 300 WB FT spectrometer, and the chemical shifts were referenced to $CDCl_3$. Microanalyses were performed by the TÜBITAK analysis centre in Ankara.

A**[$RuCl_2${$\eta^1$-CN($CH_2${$\eta^6$-$C_6H_2Me_3$-2,4,6})$CH_2CH_2N(CH_2CH_2CH_2CH_3)$}] (2a):** A solution of the electron-rich olefin **1a** (284 mg, 0.55 mmol) and the ruthenium complex $[RuCl_2(p\text{-cymene})]_2$ (306 mg, 0.5 mmol) in degassed toluene (15 mL) was heated at 100 °C for 4 h to give **2a** in 90% yield (387 mg), after extraction into and crystallization from dichloromethane/hexane (5:20). $^1H$ NMR (300.13 MHz, $CDCl_3$): $\delta$ = 0.81 (t, $J$ = 7.4 Hz, 3 H, $CH_2CH_2CH_2CH_3$), 1.21 (hex., $J$ = 7.4 Hz, 2 H, $CH_2CH_2CH_2CH_3$), 1.42 (m, 2 H, $CH_2CH_2CH_2CH_3$), 2.11 (s, 6 H, 2 $CH_3$ Mes), 2.23 (s, 3 H, $CH_3$ Mes), 3.53 (t, $J$ = 7.6 Hz, 2 H, $CH_2CH_2CH_2CH_3$), 3.75 (s, 4 H, $NCH_2CH_2N$), 4.07 (s, 2 H, $NCH_2$ Mes), 5.38 (s, 2 H, CH Mes) ppm. $^{13}C$ NMR (75.47 MHz, $CDCl_3$): $\delta$ = 14.5 ($CH_2CH_2CH_2CH_3$), 17.2 (2 $CH_3$ Mes), 17.7 ($CH_2CH_2CH_2CH_3$), 20.1 ($CH_3$ Mes), 31.2 ($CH_2CH_2CH_2CH_3$), 47.4 ($CH_2CH_2CH_2CH_3$), 48.3 and 49.5 ($NCH_2CH_2N$), 50.0 ($NCH_2$ Mes), 88.8, 94.2, 99.4 and 100.6 ($CH_2C_6H_2Me_3$-2,4,6), 200.1 (Ru=C) ppm. $C_{17}H_{26}Cl_2N_2Ru$ (430.08): calcd. C 47.44, H 6.09, N 6.51; found C 47.47, H 6.02, N 6.39. M.p. 256–257 °C.

**[$RuCl_2${$\eta^1$-CN($CH_2${$\eta^6$-$C_6H_2Me_3$-2,4,6})$CH_2CH_2N(CH_2CH_2OCH_2CH_3)$}] (2b):** A solution of the electron-rich olefin **1b** (302 mg, 0.55 mmol) and the ruthenium complex $[RuCl_2(p\text{-cymene})]_2$ (306 mg, 0.5 mmol) in degassed toluene (15 mL) was heated at 100 °C for 4 h to give **2b** in 93% yield (415 mg) after extraction into and crystallization from dichloromethane/hexane (5:20). $^1H$ NMR (300.13 MHz, $CDCl_3$): $\delta$ = 1.07 (t, $J$ = 6.36 Hz, 3 H, $CH_2CH_2OCH_2CH_3$), 2.07 (s, 6 H, 2 $CH_3$ Mes), 2.21 (s, 3 H, $CH_3$ Mes), 3.35 (q, $J$ = 6.20 Hz, 2 H, $CH_2CH_2OCH_2CH_3$), 3.49 and 3.73 (s, 4 H, $NCH_2CH_2N$), 3.76 (m, 2 H, $CH_2CH_2OCH_2CH_3$), 3.94 (t, $J$ = 4.76 Hz, 2 H, $CH_2CH_2OCH_2CH_3$), 4.07 (s, 2 H, $NCH_2$ Mes), 5.36 (s, 2 H, CH Mes) ppm. $^{13}C$ NMR (75.47 MHz, $CDCl_3$): $\delta$ = 17.1 (2 $CH_3$ Mes), 15.7 ($CH_3$ Mes), 17.7 ($CH_2CH_2OCH_2CH_3$), 47.4 and 49.7 ($NCH_2CH_2N$), 48.6 ($NCH_2$ Mes), 52.3 ($CH_2CH_2OCH_2CH_3$), 66.4 ($CH_2CH_2OCH_2CH_3$), 72.8 ($CH_2CH_2OCH_2CH_3$), 88.8, 94.2, 99.3 and 100.8 ($CH_2C_6H_2Me_3$-2,4,6), 200.5 (Ru=C) ppm. $C_{17}H_{26}Cl_2N_2ORu$ (446.38): calcd. C 45.74, H 5.87, N 6.27; found C 45.71, H 5.90, N 6.25. M.p. 213–214 °C.

**[$RuCl_2${$\eta^1$-CN($CH_2${$\eta^6$-$C_6H_2Me_3$-2,4,6})$CH_2CH_2N(CH_2{C_6H_2(OMe)_3-3,4,5})$}] (2c):** A solution of the electron-rich olefin **1c** (420 mg, 0.55 mmol) and the ruthenium complex $[RuCl_2(p\text{-cymene})]_2$ (306 mg, 0.5 mmol) in degassed toluene (15 mL) was heated at 100 °C for 4 h to give **2c** in 89% yield (493 mg) after extraction into and crystallization from dichloromethane/hexane (5:20). $^1H$ NMR (300.13 MHz, $CDCl_3$): $\delta$ = 2.10 (s, 6 H, 2 $CH_3$ Mes), 2.26 (s, 3 H, $CH_3$ Mes), 3.52 (t, $J$ = 10.38 Hz, 2 H, $NCH_2CH_2N$), 3.67 (t, $J$ = 10.37 Hz, 2 H, $NCH_2CH_2N$), 3.74 [s, 3 H, $NCH_2C_6H_2(OMe)_3$-3,4,5], 3.76 [s, 6 H, $NCH_2C_6H_2(OMe)_3$-3,4,5], 4.05 (s, 2 H, $NCH_2$ Mes), 4.66 [s, 2 H, $NCH_2C_6H_2(OMe)_3$-3,4,5], 5.43 (s, 2 H, CH Mes), 6.67 [s, 2 H, $NCH_2C_6H_2(OMe)_3$-3,4,5] ppm. $^{13}C$ NMR (75.47 MHz, $CDCl_3$): $\delta$ = 17.3 (2 $CH_3$ Mes), 17.9 ($CH_3$ Mes), 47.6 and 49.9 ($NCH_2CH_2N$), 48.5 ($NCH_2$ Mes), 54.2 [$NCH_2C_6H_2(OMe)_3$-3,4,5], 56.9 [$NCH_2C_6H_2(OMe)_3$-3,4,5], 61.5 [$NCH_2C_6H_2(OMe)_3$-3,4,5], 89.5, 94.8, 99.9 and 101.5 ($CH_2C_6H_2Me_3$-2,4,6), 107.7, 133.3, 138.4 and 154.2 [$NCH_2C_6H_2(OMe)_3$-3,4,5], 200.9 (Ru=C) ppm. $C_{23}H_{30}Cl_2N_2O_3Ru$ (554.47): calcd. C 49.82, H 5.45, N 5.05; found C 49.85, H 5.41, N 5.12. M.p. 254–255 °C.

**[$RuCl_2${$\eta^1$-CN($CH_2${$\eta^6$-$C_6H_2(OMe)_3$-3,4,5})$CH_2CH_2N(CH_2{C_6H_2(OMe)_3-3,4,5})$}] (2d):** A solution of the electron-rich olefin **1d** (473 mg, 0.55 mmol) and the ruthenium complex $[RuCl_2(p\text{-cymene})]_2$ (306 mg, 0.5 mmol) in degassed toluene (15 mL) was heated at 100 °C for 4 h. After the mixture had been cooled to 25 °C, *n*-hexane (15 mL) was added, and the solution was cooled to –15 °C. The precipitated brown solid was filtered and recrystallized from dichloromethane/hexane (10:30). Compound **2d** was isolated in 82% yield (494 mg). $^1H$ NMR (300.13 MHz, $CDCl_3$): $\delta$ = 3.46 and 3.58 (t, $J$ = 10.38 Hz, 4 H, $NCH_2CH_2N$), 3.73 [s, 3 H, coord. $NCH_2C_6H_2(OMe)_3$-3,4,5], 3.76 [s, 6 H, coord. $NCH_2C_6H_2$-

 © 2007 Wiley-VCH Verlag GmbH & Co. KGaA, Weinheim 

(O*Me*)$_3$-*3*,4,*5*], 3.90 [s, 2 H, coord. NC*H*$_2$C$_6$H$_2$(OMe)$_3$-3,4,5], 3.94 [s, 6 H, free NCH$_2$C$_6$H$_2$(O*Me*)$_3$-*3*,4,*5*], 4.13 [s, 3 H, free NCH$_2$C$_6$H$_2$(O*Me*)$_3$-3,*4*,5], 4.66 [s, 2 H, free NC*H*$_2$C$_6$H$_2$(OMe)$_3$-3,4,5], 4.78 [s, 2 H, coord. NCH$_2$C$_6$*H*$_2$(OMe)$_3$-3,4,5], 6.79 [s, 2 H, free NCH$_2$C$_6$*H*$_2$(OMe)$_3$-3,4,5] ppm. $^{13}$C NMR (75.47 MHz, CDCl$_3$): $\delta$ = 48.2 [coord. N*C*H$_2$C$_6$H$_2$(OMe)$_3$-3,4,5], 49.7 [free N*C*H$_2$C$_6$H$_2$(OMe)$_3$-3,4,5], 52.1 and 54.6 (N*C*H$_2$*C*H$_2$N), 54.9 [coord. NCH$_2$C$_6$H$_2$(O*Me*)$_3$-3,4,5], 56.8 and 58.2 [free NCH$_2$C$_6$H$_2$(O*Me*)$_3$-3,4,5], 99.3, 107.7, 107.9 and 110.1 [coord. NCH$_2$*C*$_6$H$_2$(OMe)$_3$-3,4,5], 131.9, 137.7, 138.6 and 153.3 [free NCH$_2$*C*$_6$H$_2$(OMe)$_3$-3,4,5], 201.2 (Ru=C) ppm. $C_{23}H_{30}Cl_2N_2O_6Ru$ (602.47): calcd. C 45.85, H 5.02, N 4.65; found C 45.89, H 5.00, N 4.61. M.p. 214–215 °C.

**[RuCl{$\eta^1$-CN(CH$_2${$\eta^6$-C$_6$H$_2$Me$_3$-2,4,6})CH$_2$CH$_2$N(CH$_2$CH$_2$OCH$_2$CH$_3$)}][CF$_3$SO$_3$] (5b):** Complex **2b** (223 mg, 0.5 mmol) and silver triflate (128 mg, 0.5 mmol) in degassed $CH_2Cl_2$ were stirred for 3 h at room temperature, then filtered and crystallized from $CH_2Cl_2$/diethylether (10:20). Compound **5b** was isolated in 78% yield (218 mg). $^1$H NMR (300.13 MHz, CDCl$_3$): $\delta$ = 2.20 (t, *J* = 6.8 Hz, 3 H, CH$_2$CH$_2$OCH$_2$C*H*$_3$), 3.03 (s, 3 H, CH$_3$ Mes), 3.32 and 3.38 (s each, 3 H; 2 CH$_3$ Mes), 4.58 (t, *J* = 3.0 Hz, 2 H, CH$_2$CH$_2$OC*H*$_2$CH$_3$), 4.62 and 4.98 (m, 4 H, NC*H*$_2$C*H*$_2$N), 5.10 (m, 2 H, C*H*$_2$CH$_2$OCH$_2$CH$_3$), 5.37 (q, *J* = 12.8 Hz, 2 H, CH$_2$C*H*$_2$OCH$_2$CH$_3$), 5.84 (s, 2 H, NCH$_2$ Mes), 6.87 and 6.93 (s each, 1 H, CHMes) ppm. $^{13}$C NMR (75.47 MHz, CDCl$_3$): $\delta$ = 14.3 (CH$_3$ Mes), 15.9 (2 CH$_3$ Mes), 16.9 (CH$_2$CH$_2$OCH$_2$*C*H$_3$), 48.9 and 50.7 (N*C*H$_2$*C*H$_2$N), 66.9 (NCH$_2$ Mes), 68.5 (*C*H$_2$CH$_2$OCH$_2$CH$_3$), 83.2 (CH$_2$CH$_2$O*C*H$_2$CH$_3$), 92.7 (CH$_2$*C*H$_2$OCH$_2$CH$_3$), 93.9, 96.4, 99.9 and 102.3 (CH$_2$*C*$_6$H$_2$Me$_3$-2,4,6), 124.0 (*C*F$_3$SO$_3$), 197.7 (Ru=C) ppm. $C_{18}H_{26}ClF_3N_2O_4RuS$ (559.99): calcd. C 38.61, H 4.68, N 5.00, S 5.73; found C 38.67, H 4.61, N 5.03, S 5.71.

**[RuCl{$\eta^1$-CN(CH$_2${$\eta^6$-C$_6$H$_2$Me$_3$-2,4,6})CH$_2$CH$_2$N(CH$_2$CH$_2$OCH$_3$)}][CF$_3$SO$_3$] (5e):** Compound **5e** was prepared in the same way as **5b** and isolated in 81% yield (221 mg). $^1$H NMR (300.13 MHz, CDCl$_3$): $\delta$ = 2.33 (s, 3 H, CH$_3$ Mes), 2.38 (s, 6 H, 2 CH$_3$ Mes), 2.85 (s, 3 H, CH$_2$CH$_2$OC*H*$_3$), 3.32–4.13 (m, 8 H, NC*H*$_2$C*H*$_2$N and C*H*$_2$C*H*$_2$OCH$_3$), 4.51 (s, 2 H, NCH$_2$ Mes), 5.80 and 5.88 (each: s, 1 H, CHMes) ppm. $^{13}$C NMR (75.47 MHz, CDCl$_3$): $\delta$ = 15.9 (2 CH$_3$ Mes), 16.9 (CH$_3$ Mes), 49.3 and 58.3 (N*C*H$_2$*C*H$_2$N), 50.9 (NCH$_2$ Mes), 71.1 (*C*H$_2$CH$_2$OCH$_3$), 83.5 (CH$_2$CH$_2$O*C*H$_3$), 92.8 (CH$_2$*C*H$_2$OCH$_3$), 93.8, 96.2, 99.6 and 102.4 (CH$_2$*C*$_6$H$_2$Me$_3$-2,4,6), 124.0 (*C*F$_3$SO$_3$), 197.6 (Ru=C) ppm. $C_{17}H_{24}ClF_3N_2O_4RuS$ (545.97): calcd. C 37.40, H 4.43, N 5.13, S 5.87; found C 37.45, H 4.39, N 5.15, S 5.83. M.p. 227–228 °C.

**[RuCl{$\eta^1$-CN(CH$_2${$\eta^6$-C$_6$H$_2$Me$_3$-2,4,6})CH$_2$CH$_2$N(CH$_2${$\eta^6$-C$_6$H$_2$Me$_3$-2,4,6})}][CF$_3$SO$_3$] (6):** Compound **6** was prepared in the same way as **5b** and isolated in 85% yield (264 mg). $^1$H NMR (300.13 MHz, CDCl$_3$): $\delta$ = 2.19 (s, 12 H, coord. and free NCH$_2$C$_6$H$_2$*Me*$_3$-*2*,4,*6*), 2.29 (s, 6 H, coord. and free NCH$_2$C$_6$H$_2$*Me*$_3$-2,*4*,6), 3.77 and 4.27 (dd, *J* = 10.4 and *J* = 9.4 Hz, 4 H, NC*H*$_2$C*H*$_2$N), 4.32 (s, 2 H, coord. NC*H*$_2$C$_6$H$_2$Me$_3$-2,4,6), 4.81 (s, 2 H, free NC*H*$_2$C$_6$H$_2$Me$_3$-2,4,6), 5.71 and 5.91 (each :s, 1 H, coord. NCH$_2$C$_6$*H*$_2$Me$_3$-2,4,6), 6.80 (s, 2 H, free NCH$_2$C$_6$*H*$_2$Me$_3$-2,4,6) ppm. $^{13}$C NMR (75.47 MHz, CDCl$_3$): $\delta$ = 16.9 (coord. NCH$_2$C$_6$H$_2$*Me*$_3$-*2*,4,*6*), 17.4 (coord. NCH$_2$C$_6$H$_2$*Me*$_3$-2,*4*,6), 19.5 (free NCH$_2$C$_6$H$_2$*Me*$_3$-*2*,4,*6*), 20.0 (free NCH$_2$C$_6$H$_2$*Me*$_3$-2,*4*,6), 47.8 and 49.3 (N*C*H$_2$*C*H$_2$N), 48.0 (coord. NC*H*$_2$C$_6$H$_2$Me$_3$-2,4,6), 48.9 (free N*C*H$_2$C$_6$H$_2$Me$_3$-2,4,6), 93.7, 95.2, 97.8 and 103.4 (coord. NCH$_2$*C*$_6$H$_2$Me$_3$-2,4,6), 124.0 (*C*F$_3$SO$_3$), 128.3, 129.4, 137.9 and 138.2 (free NCH$_2$*C*$_6$H$_2$Me$_3$-2,4,6), 197.6 (Ru=C) ppm. $C_{24}H_{30}ClF_3N_2O_3RuS$ (620.07): calcd. C 46.49, H 4.87, N 4.52, S 5.17; found C 46.54, H 4.79, N 4.58, S 5.20. M.p. 242–243 °C.

**Polymerization of Norbornene by [(Arene)(NHC)RuCl$_2$)] 2:** Ruthenium complex **2** ($1.5\times10^{-5}$ mol), AgOTf ($1.5\times10^{-5}$ mol), HC≡C-CPh$_2$(OH) ($1.7\times10^{-5}$ mol), and norbornene ($4.5\times10^{-3}$ mol) were mixed in dry chlorobenzene (5 mL) under an argon atmosphere. The suspension was stirred at the desired temperature for the required time. After reaction, the resulting viscous mixture was dissolved in $CHCl_3$ (20 mL) containing 2,6-di-*tert*-butyl-4-methylphenol (BHT) (0.1%) as a radical scavenger and ethyl vinyl ether (0.3 mL). The solution was poured into methanol (300 mL) to precipitate the polymer, which was collected by filtration, dried under vacuum, and characterized by $^1$H and $^{13}$C NMR spectroscopy. Average molecular weights were determined by using GPC calibrated with polystyrene standards.

**Polymerization of Norbornene by [(Arene)(NHC)RuCl)]OTf 5:** Ruthenium complex, **5** ($1.5\times10^{-5}$ mol), HC≡C–CPh$_2$(OH) ($1.7\times10^{-5}$ mol), and norbornene ($4.5\times10^{-3}$ mol) were mixed in dry chlorobenzene (5 mL) under an argon atmosphere. The suspension was stirred at the desired temperature for the required time. After reaction, the resulting viscous mixture was treated as for polymerization with complexes **2**.

## Acknowledgments

The authors are grateful to the CNRS, Inönü University research fund (BAP 2005/42) and the European Union COST program Action D17 (003) for support.

[1] a) B. Çetinkaya, P. H. Dixneuf, M. F. Lappert, *J. Chem. Soc., Dalton Trans.* **1974**, 1827–1833; b) M. F. Lappert, *J. Organomet. Chem.* **1988**, *358*, 185–213.

[2] D. Bourissou, O. Guerret, F. P. Gabbaï, G. Bertrand, *Chem. Rev.* **2000**, *100*, 39–92.

[3] a) W. A. Herrmann, C. Köcher, *Angew. Chem.* **1997**, *109*, 2256–2282; *Angew. Chem. Int. Ed. Engl.* **1997**, *36*, 2162–2187; b) W. A. Herrmann, *Angew. Chem.* **2002**, *114*, 1342–1363; *Angew. Chem. Int. Ed.* **2002**, *41*, 1291–1309; c) W. A. Herrmann, M. Elison, J. Fischer, C. Köcher, G. R. J. Artus, *Angew. Chem.* **1995**, *107*, 2602–2605; *Angew. Chem. Int. Ed. Engl.* **1995**, *34*, 2371–2374; d) T. Weskamp, V. P. W. Böhm, W. A. Herrmann, *J. Organomet. Chem.* **1999**, *585*, 348–352; e) W. A. Herrmann, K. Öfele, D. Von Preysing, E. Herdtweck, *J. Organomet. Chem.* **2003**, *684*, 235–248; f) W. A. Herrmann, K. Öfele, D. Von Preysing, K. S. Schneider, *J. Organomet. Chem.* **2003**, *687*, 229–248; g) W. A. Herrmann, S. Schneider, K. Öfele, M. Sakamoto, E. Herdtweck, *J. Organomet. Chem.* **2004**, *689*, 2441–2449; h) W. A. Herrmann, M. Mühlhofer, Th. Strassner, A. Zeller, E. Herdtweck, *J. Organomet. Chem.* **2004**, *689*, 1418–1424; i) W. A. Herrmann, J. Schütz, *J. Organomet. Chem.* **2004**, *689*, 2995–2999.

[4] a) N. Hadei, E. A. B. Kantchev, C. J. O'Brien, M. G. Organ, *Org. Lett.* **2005**, *7*, 3805–3807; b) R. Singh, M. S. Viciu, N. Kramareva, O. Navarro, S. P. Nolan, *Org. Lett.* **2005**, *7*, 1829–1832; c) O. Navarro, R. A. Kelly, S. P. Nolan, *J. Am. Chem. Soc.* **2003**, *125*, 16194–16195; d) D. S. McGuinness, K. J. Cavell, *Organometallics* **2000**, *19*, 741–748.

[5] a) N. Gürbüz, I. Özdemir, S. Demir, B. Çetinkaya, *J. Mol. Catal. A* **2004**, *209*, 23–28; b) I. Özdemir, B. Çetinkaya, S. Demir, N. Gürbüz, *Catal. Lett.* **2004**, *97*, 37–40; c) N. Gürbüz, I. Özdemir, T. Seçkin, B. Çetinkaya, *J. Inorg. Organomet. Polym.* **2004**, *14*, 149–159; d) I. Özdemir, Y. Gök, N. Gürbüz, E. Çetinkaya, B. Çetinkaya, *Synth. Commun.* **2004**, *34*, 4135–4144; e) I. Özdemir, Y. Gök, N. Gürbüz, E. Çetinkaya, B. Çetinkaya, *Heteroat. Chem.* **2004**, *15*, 419–423; f) I. Özdemir, B. Alıcı, N. Gürbüz, E. Çetinkaya, B. Çetinkaya, *J. Mol. Catal. A* **2004**, *217*, 37–40; g) N. Gürbüz, I. Özdemir, B. Çetinkaya, *Tetrahedron Lett.* **2005**, *46*, 2273–2277; h) I. Özdemir, S. Demir, S. Yaşar, B. Çet-

 © 2007 Wiley-VCH Verlag GmbH & Co. KGaA, Weinheim 

inkaya, *Appl. Organomet. Chem.* **2005**, *19*, 55–58; i) Y. Gök, N. Gürbüz, I. Özdemir, B. Çetinkaya, E. Çetinkaya, *Appl. Organomet. Chem.* **2005**, *19*, 870–874.

[6] a) T. Weskamp, W. C. Shattenmann, M. Spiegler, W. A. Herrmann, *Angew. Chem.* **1998**, *110*, 2631–2633; *Angew. Chem. Int. Ed.* **1998**, *37*, 2490–2493; b) J. Huang, S. P. Nolan, J. L. Petersen, *J. Am. Chem. Soc.* **1999**, *121*, 2674–2678; c) M. Scholl, T. M. Trnka, J. P. Morgan, R. H. Grubbs, *Tetrahedron Lett.* **1999**, *40*, 2247–2250; d) T. Weskamp, F. J. Kohl, W. Hieringer, D. Gleich, W. A. Herrmann, *Angew. Chem.* **1999**, *111*, 2573–2576; *Angew. Chem. Int. Ed.* **1999**, *38*, 2416–2419; e) M. Scholl, S. Ding, C. W. Lee, R. H. Grubbs, *Org. Lett.* **1999**, *1*, 953–956; f) S. B. Garber, J. S. Kingsbury, B. L. Gray, A. H. Hoveyda, *J. Am. Chem. Soc.* **2000**, *122*, 8168–8179; g) S. Gessler, S. Randl, S. Blechert, *Tetrahedron Lett.* **2000**, *41*, 9973–9976; h) A. Fürstner, L. Ackermann, B. Gabor, R. Goddard, C. W. Lehmann, R. Mynott, F. Stelzer, O. R. Thiel, *Chem. Eur. J.* **2001**, *7*, 3236–3253.

[7] a) J. A. Mata, M. Poyatos, E. Peris, *Coord. Chem. Rev.*, DOI:10.1016/J.ccr.2006.06.008; b) M. Poyatos, E. Mas-Marzá, M. Sanaú, E. Peris, *Inorg. Chem.* **2004**, *43*, 1793–1798; c) J. A. Mata, A. R. Chianese, J. R. Miecznikowski, M. Poyatos, E. Peris, J. W. Faller, R. H. Crabtree, *Organometallics* **2004**, *23*, 1253–1263; d) C. H. Leung, C. D. Incarvito, R. H. Crabtree, *Organometallics* **2006**, *25*, 6099–6107; e) C. A. Quezada, J. C. Garrison, C. A. Tessier, W. J. Youngs, *J. Organomet. Chem.* **2003**, *671*, 183–186; f) M. Albrecht, J. R. Miecznikowski, A. Samuel, J. W. Faller, R. H. Crabtree, *Organometallics* **2002**, *21*, 3596–3604; g) W. A. Herrmann, J. Schwarz, *Organometallics* **1999**, *18*, 4082–4089; h) W. A. Herrmann, C. P. Reisinger, M. Spiegler, *J. Organomet. Chem.* **1998**, *557*, 93–96; i) W. A. Herrmann, J. Schwarz, M. G. Gardiner, M. Spiegler, *J. Organomet. Chem.* **1999**, *575*, 80–86; j) R. E. Douthwaite, M. L. H. Green, P. J. Silcock, P. T. Gomes, *Organometallics* **2001**, *20*, 2611–2615; k) P. L. Arnold, A. C. Scarisbrick, A. J. Blake, C. Wilson, *Chem. Commun.* **2001**, 2340–2341.

[8] a) J. A. Wright, A. A. Danopoulos, W. B. Motherwell, R. J. Carroll, S. Ellwood, *J. Organomet. Chem.* **2006**, *691*, 5204–5210; b) M. Poyatos, J. A. Mata, E. Falomir, R. H. Crabtree, E. Peris, *Organometallics* **2003**, *22*, 1110–1114; c) M. Poyatos, P. Uriz, J. A. Mata, C. Claver, E. Fernandez, E. Peris, *Organometallics* **2003**, *22*, 440–444; d) R. S. Simons, P. Custer, C. A. Tessier, W. J. Youngs, *Organometallics* **2003**, *22*, 1979–1982; e) E. Mas-Marza, E. M. Segarra, C. Claver, E. Peris, E. Fernandez, *Tetrahedron Lett.* **2003**, *44*, 6595–6599; f) A. A. Danopoulos, A. A. D. Tulloch, S. Winston, G. Eastham, M. B. Hursthouse, *Dalton Trans.* **2003**, 1009–1015; g) P. J. Barnard, M. V. Baker, S. J. Berners-Price, B. W. Skelton, A. H. White, *Dalton Trans.* **2004**, 1038–1047; h) R. H. Douthwaite, J. Houghton, B. M. Kariuki, *Chem. Commun.* **2004**, 698–699.

[9] a) S. Nanchen, A. Pfaltz, *Chem. Eur. J.* **2006**, *12*, 4550–4558; b) M. Poyatos, A. Maisse-François, S. Bellemin-Laponaz, L. H. Gade, *Organometallics* **2006**, *25*, 2634–2641; c) L. Ren, A. C. Chen, A. Decker, C. M. Crudden, *Can. J. Chem.* **2004**, *82*, 1781–1787; d) C. Bolm, T. Focken, G. Raabe, *Tetrahedron: Asymmetry* **2003**, *14*, 1733–1740; e) M.-C. Perry, X. Cui, M. T. Powell, D. R. Hou, J. H. Reibenspies, K. Burgess, *J. Am. Chem. Soc.* **2003**, *125*, 113–123.

[10] B. Çetinkaya, S. Demir, I. Özdemir, L. Toupet, D. Sémeril, C. Bruneau, P. H. Dixneuf, *Chem. Eur. J.* **2003**, *9*, 2323–2330.

[11] E. Çetinkaya, P. B. Hitchcock, H. A. Jasim, M. F. Lappert, K. Spyropoulos, *J. Chem. Soc., Perkin Trans. 1* **1992**, 561.

[12] M. A. Bennett, T. N. Huang, T. W. Matheson, A. K. Smith, *Inorg. Synth.* **1982**, *21*, 74.

[13] a) A. Fürstner, M. Liebl, C. W. Lehmann, M. Picquet, R. Kunz, C. Bruneau, D. Touchard, P. H. Dixneuf, *Chem. Eur. J.* **2000**, *6*, 1847–1857; b) M. Picquet, D. Touchard, C. Bruneau, P. H. Dixneuf, *New J. Chem.* **1999**, *23*, 141–143.

[14] M. Bassetti, F. Centola, D. Sémeril, C. Bruneau, P. H. Dixneuf, *Organometallics* **2003**, *22*, 4459–4466; R. Castarlenas, D. Sémeril, A. F. Noels, A. Demonceau, P. H. Dixneuf, *J. Organomet. Chem.* **2002**, *663*, 235–238.

[15] R. Castarlenas, P. H. Dixneuf, *Angew. Chem. Int. Ed.* **2003**, *42*, 4524–4527; R. Castarlenas, C. Vovard, C. Fischmeister, P. H. Dixneuf, *J. Am. Chem. Soc.* **2006**, *128*, 4079–4089.

[16] A few crystals suitable for X-ray structure determination were taken out of an NMR solution. Crystal data for compound **7**: $RuClC_{23}H_{32}ON_2$, $CF_3SO_3$, $CHCl_3$, $M_r$ = 757.46, triclinic, $P\bar{1}$, $a$ = 8.9960(4), $b$ = 12.9478(5), $c$ = 14.1936(6) Å, $\alpha$ = 95.034(3), $\beta$ = 89.390(3), $\gamma$ = 111.241(3)°, $V$ = 1534.6(1) Å$^3$, $Z$ = 2, $D_X$ = 1.639 Mg m$^{-3}$, $\lambda$(Mo-$K_\alpha$) = 0.71073 Å, $\mu$ = 9.80 cm$^{-1}$, $F$(000) = 768, $T$ = 120(1) K. The sample (0.21 × 0.16 × 0.14 mm) was studied with an Oxford Diffraction Xcalibur Saphir 3 diffractometer with graphite monochromatized Mo-$K_\alpha$ radiation. The data collection[19] ($2\theta_{max}$ = 54°, omega scan frames via 0.75° omega rotation and 20 s per frame, index ranges: $0 \le h \le 11$, $-16 \le k \le 16$, $-18 \le l \le 18$) gives 11443 reflections. The data leads to 6541 independent reflections, 5524 of which with $I > 2.0\sigma(I)$. The structure was solved with SIR-97,[20] which reveals the non-hydrogen atoms of the molecule. After anisotropic refinement, many hydrogen atoms may be found with a Fourier Difference. The whole structure was refined with SHELXL97[21] by the full-matrix least-squares techniques (use of $F$ square magnitude; x, $y$, $z$, $\beta_{ij}$ for Ru, Cl, C, O, S, F and N atoms, $x$, $y$, $z$ in riding mode for H atoms; 361 variables and 5524 observations with $I > 2.0\sigma(I)$; calcd. $w = 1/[\sigma^2(F_o^2) + (0.064P)^2]$ where $P = (F_o^2 + 2F_c^2)/3$ with the resulting $R$ = 0.032, $R_w$ = 0.098 and $S_w$ = 1.137, $\Delta\rho < 0.8$ e. Å$^{-3}$. Atomic scattering factors were taken from the International Tables for X-ray Crystallography.[22] CCDC-290024 contains the supplementary crystallographic data of compound **7** for this paper. These data can be obtained free of charge from The Cambridge Crystallographic Data Centre via www.ccdc.cam.ac.uk/data_request/cif.

[17] Crystal data for compound **2c**, CCDC : $C_{23}H_{30}N_2O_3Cl_2Ru$, $CH_2Cl_2$, $M_r$ = 639.39, orthorhombic, *Pbca*, $a$ = 15.1773(1), $b$ = 14.9059(1), $c$ = 23.7686(3) Å, $V$ = 5377.2(1) Å$^3$, $Z$ = 8, $D_X$ = 1.580 Mg m$^{-3}$, $\lambda$(Mo-$K_\alpha$) = 0.71073 Å, $\mu$ = 10.09 cm$^{-1}$, $F$(000) = 2608, $T$ = 110 K. The crystal (0.32 × 0.22 × 0.20 mm) was studied with a NONIUS Kappa CCD with graphite monochromatized Mo-$K_\alpha$ radiation. The cell parameters are obtained with Denzo and Scalepack[23] with 10 frames (psi rotation: 1° per frame). The data collection[24] ($2\theta_{max}$ = 54°, 297 frames via 1.5° omega rotation and 22 s per frame, index ranges: $0 \le h \le 19$, $0 \le k \le 19$, $0 \le l \le 30$) gave 52555 reflections. The data reduction with Denzo and Scalepack[23] led to 6170 independent reflections [5345 with $I > 2.0\sigma(I)$]. The structure was solved with SIR-97,[20] which revealed the non-hydrogen atoms of the structure. After anisotropic refinement, many hydrogen atoms may be found with a Fourier Difference. The whole structure was refined with SHELXL97[21] by the full-matrix least-squares techniques (use of $F$ square magnitude; x, $y$, $z$, $\beta_{ij}$ for Ru, Cl, O, N and C atoms, x, $y$, $z$ in riding mode for H atoms; 307 variables and 5345 observations with $I > 2.0\sigma(I)$; calcd. $w = 1/[\sigma^2(F_o^2) + (0.044P)^2 + 7.15P]$ where $P = (F_o^2 + 2F_c^2)/3$ with the resulting $R$ = 0.032, $R_w$ = 0.082 and $S_w$ = 1.053, $\Delta\rho < 0.70$ e Å$^{-3}$. Atomic scattering factors were taken from the International Tables for X-ray Crystallography.[22] CCDC-249335 contains the supplementary crystallographic data of compound **2c** for this paper. These data can be obtained free of charge from The Cambridge Crystallographic Data Centre via www.ccdc.cam.ac.uk/data_request/cif.

[18] Crystal data for complex **5e**: $C_{16}H_{24}N_2ORuClRu,CF_3SO_3$, $M_r$ = 545.96 monoclinic, *P*21/*c*, $a$ = 7.8439(1), $b$ = 15.6482(2), $c$ = 17.3026(2) Å, $\beta$ = 95.648(1)°, $V$ = 2113.46(5) Å$^3$, $Z$ = 4, $D_X$ = 1.716 Mg m$^{-3}$, $\lambda$(Mo-$K_\alpha$) = 0.71073 Å, $\mu$ = 10.19 cm$^{-1}$, $F$(000)= 1104, $T$ = 293 K. The crystal (0.35 × 0.33 × 0.25 mm) was studied with a NONIUS Kappa CCD with graphite monochromatized Mo-$K_\alpha$ radiation. The cell parameters are obtained with Denzo and Scalepack[23] with 10 frames (psi rotation: 1° per frame). The data collection[24] ($2\theta_{max}$ = 54°, 216 frames via

 © 2007 Wiley-VCH Verlag GmbH & Co. KGaA, Weinheim 

2.0° omega rotation and 20 s per frame, index ranges: $0 \le h \le 10$, $0 \le k \le 20$, $-22 \le l \le 22$) gives 34723 reflections. The data reduction with Denzo and Scalepack[23] led to 4849 independent reflections, 4324 of which with $I > 2.0\sigma(I)$. The structure was solved with SIR-97,[20] which revealed the non-hydrogen atoms of the molecule. After anisotropic refinement, many hydrogen atoms may be found with a Fourier Difference. The whole structure was refined with SHELXL97[21] by the full-matrix least-squares techniques (use of F square magnitude; $x$, $y$, $z$, $\beta_{ij}$ for Ru, S, F, N C and O atoms, x, $y$, $z$ in riding mode for H atoms; 263 variables and 4324 observations with $I > 2.0\sigma(I)$; calcd. $w = 1/[\sigma^2(F_o^2) + (0.07P)^2 + 2.4P]$ where $P = (F_o^2 + 2F_c^2)/3$ with the resulting $R = 0.045$, $R_w = 0.116$ and $S_w = 1.041$, $\Delta\rho < 0.96$ e Å$^{-3}$. Atomic scattering factors were taken from International Tables for X-ray Crystallography.[22] CCDC-249534 contains the supplementary crystallographic data of complex **5e** for this paper. These data can be obtained free of charge from The Cambridge Crystallographic Data Centre via www.ccdc.cam.ac.uk/data_request/cif.

[19] CrysAlis RED, Oxford Diffraction Ltd., **2004**.
[20] A. Altomare, M. C. Burla, M. Camalli, G. Cascarano, C. Giacovazzo, A. Guagliardi, A. G. G. Moliterni, G. Polidori, R. Spagna, *J. Appl. Crystallogr.* **1998**, *31*, 74–77.
[21] G. M. Sheldrick, *SHELXL-97*, Program for the Refinement of Crystal Structures, Univ. of Göttingen, Germany, **1997**.
[22] A. J. C. Kluwer, *International Tables for X-ray Crystallography*, Vol. C, Academic Publishers, Dordrecht, **1992**.
[23] a) Z. Otwinowski, W. Minor, "Processing of X-ray Diffraction Data Collected in Oscillation Mode" in *Methods in Enzymology,* **1997**, vol. 276; b) C. W. Carter, R. M. Sweet, *Macromolecular Crystallography,* Part A, Academic Press, London, pp. 307–326.
[24] Nonius, *KappaCCD Software*, Nonius HV, Delft, The Netherlands, **1999**.

Received: December 14, 2006
Published Online: March 23, 2007

 © 2007 Wiley-VCH Verlag GmbH & Co. KGaA, Weinheim 

DOI: 10.1002/ejic.200601196

# Ruthenium(II) Complexes of Thiosemicarbazones: The First Water-Soluble Complex with pH-Dependent Antiproliferative Activity

**Sanja Grguric-Sipka,[a][‡] Christian R. Kowol,[a] Seied-Mojtaba Valiahdi,[a] Rene Eichinger,[a] Michael A. Jakupec,[a] Alexander Roller,[a] Sergiu Shova,[a][‡‡] Vladimir B. Arion,*[a] and Bernhard K. Keppler*[a]**

**Keywords:** Antitumour agents / Ruthenium / N,S ligands / X-ray diffraction

Two ruthenium(II) complexes of 2-acetylpyridine $N^4$,$N^4$-dimethylthiosemicarbazone ($HL^1$) and phenanthrenequinone thiosemicarbazone ($HL^2$), namely $[Ru^{II}Cl(L^1)(PPh_3)_2]$ (**1**) and $[Ru^{II}Cl(L^2)(PPh_3)_2]$ (**2**), have been synthesised and characterised by IR, UV/Vis and NMR spectroscopy, electrospray mass spectrometry, cyclic voltammetry and X-ray crystallography. In addition, the X-ray crystal structure of $[Ru^{III}Cl_2(L^2)PPh_3]$·dmso·$1.25H_2O$ (**3**·dmso·$1.25H_2O$) is reported. The reaction of $[Ru^{II}Cl_2(dmso)_4]$ with $HL^1$ and 1,3,5-triaza-7-phosphaadamantane (PTA) gives the highly water-soluble complex $[Ru^{II}Cl(L^1)(HPTA)_2]Cl_2$·$C_2H_5OH$·$H_2O$ (**4**·$C_2H_5OH$·$H_2O$) ($S_{25°C} \geq 250$ mg/mL), which has been fully characterised. Complex **4** shows strong antiproliferative effects in low micromolar concentrations in the ovarian carcinoma cell line 41M ($IC_{50}$ = 0.87 μM) and more moderate activity in the breast cancer cell line SK-BR-3 ($IC_{50}$ = 39 μM). The activity of the compound is 6.5- and 5.4-times higher at pH = 6.0 than at pH = 7.4 in the non-small cell lung cancer cell line A549 and the colon carcinoma cell line HT-29 ($GI_{50}$ = 24 and 8.0 μM at pH = 6.0 for A549 and HT-29, respectively).
(© Wiley-VCH Verlag GmbH & Co. KGaA, 69451 Weinheim, Germany, 2007)

## Introduction

Thiosemicarbazones form a class of mixed hard-soft oxygen/nitrogen-sulfur chelating ligands that show a variety of coordination modes in metal complexes. The thiosemicarbazone can act as a monodentate ligand that binds to the metal ion through the sulfur atom[1] or as a bidentate ligand that coordinates to the metal ion through the sulfur atom and one of the nitrogen atoms of the hydrazine moiety to form a four- or a five-membered metallacycle.[2,3] The coordination capacity of thiosemicarbazones can be increased by using for their preparation aldehydes or ketones containing additional functional group(s) in position(s) suitable for chelation.[4] Beside their interesting coordination chemistry, thiosemicarbazones have a wide pharmacological spectrum of activity; their potential has been recognised to include antitumour, antiviral, antibacterial, antifungal and antimalarial properties.[5] The enzyme ribonucleotide reductase has been identified as a principal target, and thiosemicarbazones are among the most potent known inhibitors of this enzyme.[6,7] The inhibition of ribonucleotide reductase prevents the conversion of ribonucleotides into deoxyribonucleotides, which results in the impairment of DNA synthesis and repair.[8] The applicability of thiosemicarbazones as antitumour agents has been explored for over half a century,[9] the first compound of this class to enter phase II clinical trials as an antineoplastic agent being 3-aminopyridine-2-carboxaldehyde thiosemicarbazone (3-AP, triapine).[10,11] The effect of certain metals on the biological activity of thiosemicarbazones has been receiving considerable attention recently.[12–14] Although a large number of reports are available on the chemistry and biological activity of copper(II), cobalt(III), gallium(III), iron(III), platinum(II) or palladium(II) thiosemicarbazonates,[15–18] there are only a few reports on antitumour activity of the corresponding ruthenium complexes.[19,20] Interest in ruthenium was stimulated by phase I clinical trials of two ruthenium complexes, namely $(H_2im)$[*trans*-$Ru^{III}Cl_4$(Him)(dmso)] (NAMI-A; Him = imidazole) and $(H_2ind)$[*trans*-$Ru^{III}Cl_4(Hind)_2$] (KP1019; Hind = indazole), the first as an antimetastatic drug and the second as an anticancer agent against primary tumours and metastases, and in particular colon carcinomas.[21,22]

The very high cytotoxicity of our recently synthesised gallium(III) and iron(III) complexes with $N^4$-substituted α-N-heterocyclic thiosemicarbazones[23] in vitro together with the above-mentioned interest in ruthenium chemistry prompted us to synthesise novel ruthenium complexes of

[a] Institute of Inorganic Chemistry, Faculty of Chemistry, University of Vienna,
Waehringer Str. 42, 1090 Vienna, Austria
Fax: +43-1427752680
E-mail: vladimir.arion@univie.ac.at
bernhard.keppler@univie.ac.at
[‡] On sabbatical leave from the Faculty of Chemistry of the University of Belgrade.
[‡‡] On sabbatical leave from the Department of Chemistry of the Moldova State University.
Supporting information for this article is available on the WWW under http://www.eurjic.org or from the author.

 © 2007 Wiley-VCH Verlag GmbH & Co. KGaA, Weinheim 

thiosemicarbazones. We chose two ligands, 2-acetylpyridine $N^4$,$N^4$-dimethylthiosemicarbazone ($HL^1$), which shows very high cytotoxicity in the low nanomolar range and the ability to destroy the tyrosyl radical of mouse ribonucleotide reductase R2 protein,[23] and phenanthrenequinone thiosemicarbazone ($HL^2$), which is known to have antiproliferative activity in the low micromolar range.[24] The presence of the phenanthrene moiety in $HL^2$ renders this ligand capable of DNA intercalation in addition to its potential ribonucleotide reductase inhibiting properties.

Ruthenium(II) complexes with two monoanionic tridentate thiosemicarbazones are neutral species that are sparingly soluble or even insoluble in aqueous media.[25] Water solubility is required to assay the cytotoxicity in vitro, therefore we focused on the synthesis of complexes with a 1:1 metal/ligand stoichiometry. A literature survey showed that phosphorus-containing species and, in particular, triphenylphosphane often serve as ancillary ligands to complete the coordination sphere of ruthenium upon coordination of a thiosemicarbazone.[26–28] This prompted us to consider 1,3,5-triaza-7-phosphaadamantane (PTA) as a co-ligand as it is known to endow metal complexes with aqueous solubility and solubility in polar organic solvents.[29a–29e,30] The (PTA)ruthenium compounds reported so far that show antiproliferative activity are organometallic compounds derived from [Ru($\eta^6$-*p*-cymene)$Cl_2$(PTA)],[29a] some of which have been found to cause pH-dependent DNA damage.

Herein we report on the synthesis, spectroscopic characterisation and X-ray diffraction structures of three novel complexes and the pH-dependent in vitro antiproliferative activity of the first thiosemicarbazone/PTA mixed ruthenium(II) complex with high aqueous solubility.

## Results and Discussion

The reaction of [$Ru^{II}Cl_2(PPh_3)_3$] with either 2-acetylpyridine $N^4$,$N^4$-dimethylthiosemicarbazone ($HL^1$) in dry dichloromethane or phenanthrenequinone thiosemicarbazone ($HL^2$) in absolute ethanol afforded the complexes *trans*-[$Ru^{II}Cl(L^1)(PPh_3)_2$] (**1**) and *trans*-[$Ru^{II}Cl(L^2)(PPh_3)_2$] (**2**) in 41 and 80% yield, respectively. In one case the synthesis of **2** was accompanied by marginal formation of a side product, a few red crystals of which separated first on crystallisation from dimethyl sulfoxide. An X-ray diffraction study (see Supporting Information) showed that this minor species has the composition [$Ru^{III}Cl_2(L^2)PPh_3$] (**3**). Repeated crystallisation of **2** from dimethyl sulfoxide did not produce any significant amounts of **3**, thereby preventing its full characterisation. The complex *trans*-[$Ru^{II}Cl(L^1)(HPTA)_2$]$Cl_2$ (**4**) was prepared by the reaction of 2-acetylpyridine $N^4$,$N^4$-dimethylthiosemicarbazone and PTA with [$Ru^{II}Cl_2(dmso)_4$] in absolute ethanol (Figure 1). Complex **4** appears to be the first reported ruthenium(II) complex that contains a thiosemicarbazone and 1,3,5-triaza-7-phosphaadamantane (PTA) as ligands. Complexes **1** and **2** are well soluble in $CHCl_3$ but sparingly soluble in ethanol and methanol and insoluble in water, whereas complex **4** is very soluble in water ($S_{25°C} \geq 250$ mg/mL), dmso, ethanol and methanol.

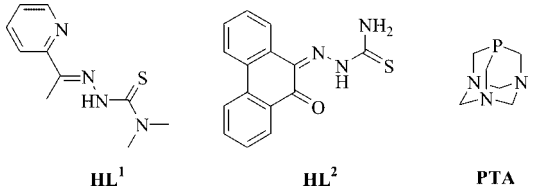


Figure 1. Structures of the ligands used.

### Spectroscopic Characterisation

Complexes **1** and **4** show two well-resolved MLCT transitions in their electronic absorption spectra. The bands at 476 (**1**) and 450 nm (**4**) can be attributed to an Ru(4dπ)→π*(py) MLCT transition, whereas the bands at 379 (**1**) and 378 nm (**4**) can be assigned to an Ru(4dπ)→π*(imine) transition.[25] The strong absorptions at 597 and 470 nm in complex **2** are assignable to a combination of MLCT bands and $Ru^{II}$ d–d bands, and the high-energy absorptions in the ultraviolet region for **1**, **2** and **4** can be attributed to intraligand π–π* transitions.

The ESI mass spectrum of complex **1** recorded in the positive mode contains a strong peak at *m*/*z* = 847 attributed to the $[M - Cl]^+$ ion and a second remarkable signal at *m*/*z* = 585 assigned to $[M - Cl - PPh_3]^+$. Complex **2** shows a low intensity peak at *m*/*z* = 942 due to the $[M + H]^+$ ion and more intense peaks at *m*/*z* = 964 and 980 attributed to $[M + Na]^+$ and $[M + K]^+$ ions, respectively. An intense signal at *m*/*z* = 906 corresponds to $[M - Cl]^+$, while that at *m*/*z* = 644 corresponds to $[M - Cl - PPh_3]^+$. The ESI mass spectrum of complex **4** contains peaks at *m*/*z* = 673 and 695, which were assigned to $[M - H]^+$ and $[M - 2H + Na]^+$, respectively. A signal at *m*/*z* = 637 is due to $[M - Cl]^+$, while that at *m*/*z* = 538 is due to $[M - H - HPTA + Na]^+$. The observed isotopic patterns fit well with the theoretical isotopic distributions.

The $^1H$ NMR spectrum of complex **1** in $CDCl_3$ shows signals attributable to the pyridine ring protons of coordinated thiosemicarbazone at $\delta$ = 8.62, 7.36, 6.86 and 6.47 ppm. The lack of any NH signal indicates the deprotonation of the ligand. Proton resonances due to the $PPh_3$ ligand are found between $\delta$ = 7.54 and 7.14 ppm. The $^{31}P$ NMR spectrum shows one resonance at $\delta$ = 30.42 ppm, thus indicating the equivalence of the two $PPh_3$ ligands in **1**. This signal is shifted only slightly downfield from that for *trans*-[RuCl(pabh)$(PPh_3)_2$] (Hpabh is a Schiff base derived from 2-pyridinecarbaldehyde and benzoylhydrazine) at $\delta$ = 27.62 ppm ($CDCl_3$).[31] Complex **2** in [$D_6$]dmso shows aromatic proton signals for the phenanthrenequinone moiety between $\delta$ = 7.19 and 8.89 ppm. The signal integrations and multiplicities are in agreement with the proposed formula, although exact assignment is not possible due to extensive overlap with resonances originating from the triphenylphosphane ligands. A singlet that can be assigned to

 © 2007 Wiley-VCH Verlag GmbH & Co. KGaA, Weinheim 

the $NH_2$ group was found at $\delta$ = 8.13 ppm. The hydrazinic NNH proton signal at $\delta$ = 14.42 ppm present in the $^1H$ NMR spectrum of the metal-free thiosemicarbazone is absent in the spectrum of the complex, thus indicating the deprotonation of the thiosemicarbazone ligand upon complexation. As for **1**, the $^{31}P$ NMR spectrum of **2** is very simple, displaying one resonance at $\delta$ = 27.36 ppm due to the equivalence of the two $PPh_3$ ligands.

Complex **4** in [$D_6$]dmso shows a signal at $\delta$ = 9.87 ppm that can be assigned to the protons of the two quaternary nitrogen atoms in the PTA ligands. As for **1**, the absence of a further NH resonance indicates the presence of a monoanionic thiosemicarbazone ligand in **4**. The pyridine ring protons occur as multiplets at $\delta$ = 8.77, 7.85, 7.67 and 7.33 ppm. The singlet due to the $N(CH_3)_2$ group is found at $\delta$ = 3.33 ppm together with the water signal. The proton resonances of the methylene groups bridging the nitrogen atoms in PTA appear as a singlet at $\delta$ = 4.62 ppm, while the resonances due to the $PCH_2N$ protons are observed as a multiplet at $\delta$ = 3.71 ppm. The $^{31}P$ NMR spectrum of **4** exhibits one singlet resonance at $\delta$ = –38.13 ppm for the two equivalent PTA ligands {cf. $\delta$ = –33.45 ppm for the two equivalent phosphorus atoms in $[RuCl(PTA)_2([9]aneS_3)]$-$CF_3SO_3$}.[29e]

The electrochemical properties of complexes **1**, **2** and **4** have been studied by cyclic voltammetry in dmso solution (0.2 M [$n$Bu$_4$N][$BF_4$]) using a glassy carbon working electrode. The cyclic voltammograms of all complexes show a single one-electron oxidation wave at $E_{1/2}$ = 0.59, 0.71 and 0.73 V vs. NHE for **1**, **2** and **4**, respectively, which can be assigned to $Ru^{II}/Ru^{III}$ electron transfer. The peak-to-peak separation ($\Delta E_p$) of 70–90 mV in complexes **1** and **2** is almost independent of the scan rate. In addition, the equality of the anodic peak current ($i_{pa}$) and the cathodic peak current ($i_{pc}$) indicates a reversible electron-transfer. The $Ru^{II}/Ru^{III}$ oxidation wave in complex **4** shows $\Delta E_p$ values of 110–130 mV in the range of scan rates from 50 to 1000 mV s$^{-1}$ and $i_{pa}/i_{pc}$ ratios close to 1. Deviations from the ideal Nernstian value of 59 mV are well documented for this type of complexes.[26] Complex **2** shows two additional irreversible reduction waves with $E_{p/2}$ values of –0.78 and –1.27 V which can be ascribed to the reduction of the thiosemicarbazone ligand. The more positive oxidation response (+140 mV) in **4** in comparison to that in **1** is in line with the poorer electron-donating ability of PTA compared to $PPh_3$.[32]

## Crystal Structures

The thiosemicarbazone ligand in **1** acts as a monoanion $(L^1)^-$ and occupies a meridional plane about the ruthenium ion, coordinating to it through pyridine nitrogen atom N1, imine nitrogen atom N2 and the thiolate sulfur atom S (Figure 2). A Cl ligand completes the square plane around the ruthenium ion. The thiosemicarbazone ligand is planar. All non-hydrogen atoms of $(L^1)^-$ lie in the crystallographic symmetry plane together with the central metal ion and the chlorido ligand. Two *trans*-positioned triphenylphosphane ligands in **1** complete the octahedron. A comparison of the bond lengths in the coordination polyhedron of **1** with those in $[Ru(HL)(PPh_3)_2Cl]^+$ [HL = 2-acetylpyridine 4-(4-tolyl)thiosemicarbazone][26] shows that the Ru–Cl bond in **1** [2.4812(13) Å] is significantly longer than in $[Ru(HL)(PPh_3)_2Cl]^+$ [2.459(2) Å]. The interatomic Ru–N1 and Ru–N2 distances of 2.092(4) and 1.976(4) Å, respectively, are similar to those in $[Ru(HL)(PPh_3)_2Cl]^+$ [2.085(5) and 1.984(5) Å, respectively], whereas the Ru–S and Ru–P bonds are shorter in **1** {2.3725(13) and 2.3747(8) Å compared to 2.386(2) and 2.399(1) Å in $[Ru(HL)(PPh_3)_2Cl]^+$}. The distribution of electron density over the thiosemicarbazide moiety in the compared complexes is different, thereby indicating the prevailing double-bond character of C8–S in $[Ru(HL)(PPh_3)_2Cl]^+$ [1.707(6) Å vs. 1.751(5) Å in **1**]. The N3–C8 bond length in **1** [1.335(7) Å] is equal within 3σ to that in $[Ru(HL)(PPh_3)_2Cl]^+$ [1.359(7) Å]. The molecules of **1** interact weakly with each other through C–H···Cl contacts, as shown in Figure S1 (Supporting Information).

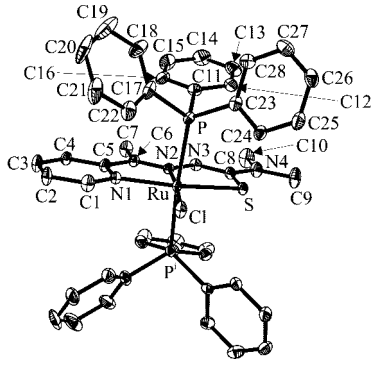


Figure 2. Perspective view of the molecule of $[Ru^{II}(L^1)(PPh_3)_2Cl]$ (**1**) with atom labelling scheme. Thermal ellipsoids are drawn at the 50% probability level, and the hydrogen atoms have been omitted for clarity. Selected bond lengths [Å] and angles [°]: Ru–N1 2.092(4), Ru–N2 1.976(4), Ru–S 2.3725(13), Ru–Cl 2.4812(13), Ru–P1 2.3747(8), S–C8 1.751(5), C8–N3 1.335(7) Å; P1–Ru–P1$^i$ 175.08(6). Symmetry code: $^i$: $-x$, $y$ + 1, $z$.

The ruthenium(II) ion in **2** is coordinated by the thiosemicarbazone anion $(L^2)^-$ through carbonyl oxygen atom O, imine nitrogen atom N1 and thiolate sulfur atom S and by the chlorido ligand in the equatorial plane. In addition, two triphenylphosphane ligands are bound in axial positions (Figure 3). Relevant bond lengths and angles are given in the legend to Figure 3. A comparison of the bond lengths of the thiosemicarbazone moiety in complex **2** with those of the metal-free thiosemicarbazone[24] shows that the S–C15 bond [1.707(4) Å] in **2** is longer than in $HL^2{\cdot}CH_3CN$ [1.681(2) Å], whereas the C15–N2 bond [1.348(9) Å] in **2** is similar to that in $HL^2{\cdot}CH_3CN$ [1.365(3) Å]. The coordination of $HL^1$ and $HL^2$ (Figure 1) to the ruthenium(II) ion in their deprotonated forms in **1** and **2**, respectively, is also indicated by the absence of counterions. The ligand in **2** has also undergone a configurational change from the (*E*) configuration found in the metal-free state[24] to a (*Z*) configuration relative to the C15–N2 bond. The phenanthrene

 © 2007 Wiley-VCH Verlag GmbH & Co. KGaA, Weinheim 

moieties in the crystal structure of **2** are stacked pairwise in an offset manner with an interplanar separation between the benzene rings (C9–C14) and (C9–C14)′ of around 3.32 Å; the distance between their centroids (X···X′) is 3.857 Å (Figure S2). The hydrogen bond between N3 as proton donor and the Cl atom of the neighbouring molecule as proton acceptor, with an N3···Cl contact of 3.490 Å, is also worthy of note.

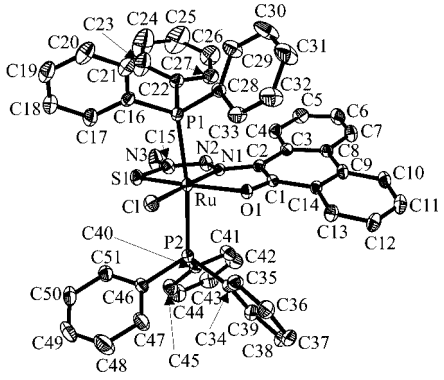


Figure 3. Perspective view of the molecule of $[Ru^{II}(L^2)(PPh_3)Cl]$ (**2**) with atom numbering scheme. Thermal ellipsoids are drawn at the 30% probability level, and the hydrogen atoms have been omitted for clarity. Selected bond lengths [Å] and angles [°]: Ru–O 2.096(2), Ru–N1 1.936(3), Ru–S 2.3608(14), Ru–P1 2.3932(10), Ru–P2 2.3824(10), Ru–Cl 2.4528(9), S–C15 1.707(4), C15–N2 1.348(9) Å; P1–Ru1–P2 170.36(3), O–Ru–S 160.96(6), N1–Ru–Cl 171.31(8).

The structure of complex **4** is shown in Figure 4. The coordination polyhedron of the ruthenium ion can be described as a distorted octahedron. As in **1**, the metal ion is coordinated in the equatorial plane by the thiosemicarbazone monoanion through pyridine nitrogen atom N1, imine nitrogen atom N2 and the thiolate sulfur atom S, and by the chlorido ligand Cl1. Both axial positions are occupied by two PTA ligands, which are bound to the ruthenium ion through phosphorus atoms P1 and P2. The Ru–$P_{(PTA)}$ separations [Ru–P1 2.3019(19), Ru–P2 2.2958(19) Å] are in the range expected for Ru–PTA complexes.[30,33] The Ru–Cl1 bond [2.4571(16) Å] is normal for Ru–PTA complexes containing chlorido co-ligands.[34] In addition, the two PTA ligands are protonated at N5 and N8, respectively, and form hydrogen bonds to Cl2 and Cl3. The S–C8 bond [1.771(6) Å] is longer than the C–S bond found in 2-acetylpyridine *N*-pyrrolidinylthiosemicarbazone [1.692(4) Å][35] and also longer than in $HL^1$ [1.720(2) Å].[36] The lengthening of this bond in **4**, along with the N2–N3 and N3–C8 bonds, indicates a significant electron delocalisation over the thiosemicarbazide moiety.[37] The Ru–N2 distance [1.979(5) Å] is slightly shorter than the Ru–N1 distance [2.081(5) Å], presumably because of steric reasons. The association of a proton with N5 of one PTA and of another one with N8 of the second PTA ligand makes the corresponding atoms good proton donors, and they are consequently involved in hydrogen bonding to the two chloride anions Cl2 and Cl3, respectively (see Figure 4).

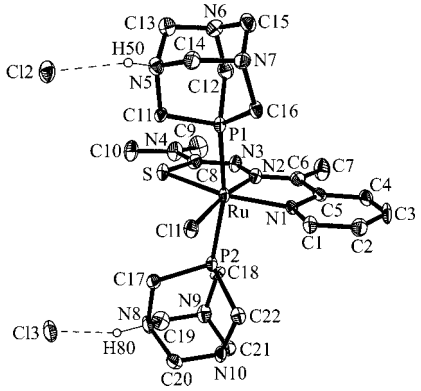


Figure 4. Perspective view of the complex $[Ru^{II}(L^1)(HPTA)_2Cl]Cl_2$ (**4**) with atom numbering scheme. Thermal ellipsoids are drawn at the 50% probability level, and the hydrogen atoms have been omitted for clarity. Selected bond lengths [Å] and angles [°]: Ru–N1 2.081(5), Ru–N2 1.979(5), Ru–S 2.3707(17), Ru–Cl1 2.4571(16), Ru–P1 2.3019(19), Ru–P2 2.2958(19), S–C8 1.771(6), C8–N3 1.303(8); P1–Ru–P2 166.05(5).

### Determination of the p$K_a$ Value

The pH of a 0.005 M aqueous solution of $[Ru^{II}Cl(L^1)(HPTA)_2]Cl_2$ (**4**) is about 3. $^{31}P$ NMR spectra of an aqueous ($D_2O$) solution of **4** were recorded at different pH* (= pD) values (from 2.11 to 11.40). We suppose that the complex exists predominantly in the monoprotonated form ($\delta$ = –37.03 ppm) at pH* = 2.11, whereas the signal of the neutral complex (with unprotonated PTA ligands) is found at $\delta$ = –48.45 ppm at pH* = 11.40 (see Figure S4, Supporting Information). At pH = 3.82 the main signal is shifted to $\delta$ = –40.02 ppm and a second, minor (< 4%) $^{31}P$ signal emerges at $\delta$ = –41.30 ppm, which increases gradually in intensity and shifts to higher frequency more sluggishly than the first peak (Figure S4). At the end of the titration (pH* = 11.40) the intensity of the second signal is 50% of the main signal. Moreover, the intensity of this second resonance increases with time. The appearance of this second $^{31}P$ resonance can be suppressed by addition of an excess of NaCl to a solution of **4** in $D_2O$. Repeated titration of a 0.15 M NaCl solution of **4** in $D_2O$ with NaOD from pH* = 3.29 to 10.30 showed that the second peak now appears first at pH = 5.16 and remains of very low intensity (< 5%) until the end of the titration (pH = 10.30). These results show that a solution of complex **4** in $D_2O$ in the pH range indicated above undergoes both protolytic reactions and hydrolysis of the $Ru^{II}$–Cl bond.

A p$K_a$ value of 4.46 for one of the axially coordinated PTA ligands in **4** was obtained from a $^{31}P$ NMR pH* titration curve in $D_2O$ (Figure 5). This value is higher than that (3.13) found from $^{31}P$ NMR titration of the coordinated PTA in $[RuCl_2(PTA)(\eta^6\text{-}p\text{-cymene})]$,[38] but lower than those reported for metal-free PTA (5.63[29c] and 6.0[39]).

The evolution of the absorption spectrum of **4** in 0.15 M NaCl aqueous solution on increasing the pH from 2.88 to 9.30 is given as Supporting Information (Figure S5) and is characterised by an isosbestic point at 445 nm.

 © 2007 Wiley-VCH Verlag GmbH & Co. KGaA, Weinheim 

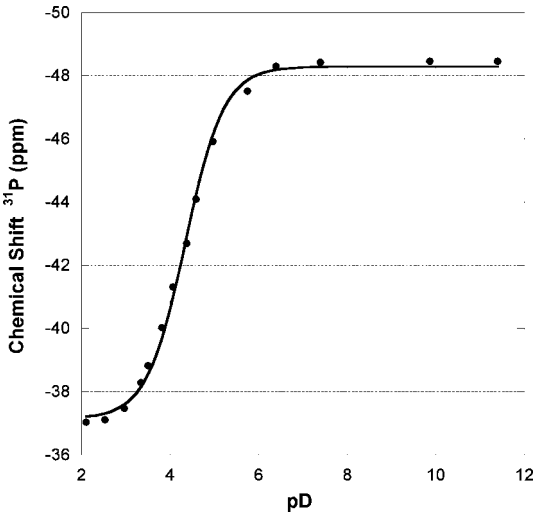


Figure 5. Plot of $\delta(^{31}P)$ vs. pD of **4**.

### Antiproliferative Activity in Cancer Cell Lines

The antiproliferative effects of compound **4** were first examined in the human cancer cell lines 41M and SK-BR-3 by means of a colourimetric microculture assay (MTT assay) with continuous exposure at pH = 7.4 for 96 h. Concentration-effect curves are presented in Figure 6A. The compound exerts strong antiproliferative effects in low micromolar concentrations in the ovarian carcinoma cell line 41M ($IC_{50}$ = 0.87 μM), while the breast cancer cell line SK-BR-3 is much less sensitive ($IC_{50}$ = 39 μM). The $IC_{50}$ values obtained in the non-small cell lung cancer cell line A549 and the colon carcinoma cell line HT-29 (Table 1) suggest that these cells are rather insensitive, but a direct comparison with the other two cell lines is not appropriate because of the different exposure times. However, experiments on the pH dependency of the antiproliferative effects, with exposure at either pH = 6.0 or 7.4 for 24 h, followed by incubation in a drug-free medium (pH = 7.4) for a further 72 h revealed that the activity of the compound is 6.5- and 5.4-times higher under slightly acidic conditions in A549 and HT-29 cells, respectively, with $IC_{50}$ values shifted towards lower micromolar concentrations (Figure 6B, Table 1). The extent of this activation clearly exceeds that of cisplatin (3.2- and 2.2-fold in A549 and HT-29 cells, respectively), while the effects of oxaliplatin are independent of the pH under the same experimental conditions.[40]

This pronounced pH dependency suggests that compound **4** may be activated preferentially in a slightly acidic environment. Such acidic conditions occur in the extracellular fluid of solid tumours as a consequence of constitutive upregulation of glycolysis (independent of oxygen supply), which is a hallmark of malignant progression that confers a growth advantage to tumour cells under the conditions of intermittent hypoxia resulting from hypovascularisation.[41,42] The altered pH gradients across cell membranes in acidic tumour regions affect the cellular drug accumulation and cytotoxicity of weakly basic chemotherapeutics such as anthracyclines, vinca alkaloids or mitoxantrone and

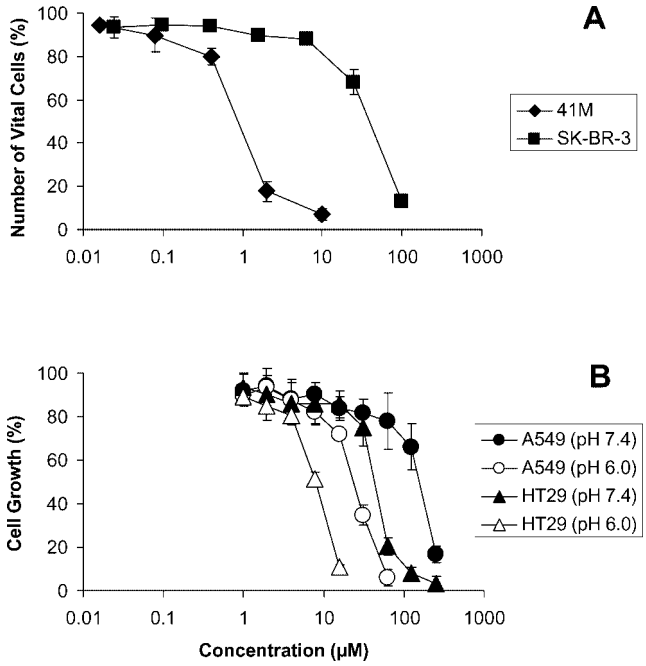


Figure 6. Antiproliferative effects of compound **4**, as determined by an MTT assay. A) Concentration-effect curves in 41M and SK-BR-3 cells (continuous exposure for 96 h). B) Concentration-effect curves (corrected for differences in growth kinetics of the corresponding controls) in A549 and HT-29 cells at pH = 7.4 and 6.0 (24 h exposure), indicating enhanced cytostatic effects in a slightly acidic medium.

Table 1. Antiproliferative effects of compound **4** in four human cancer cell lines and the pH dependency in two of these cell lines.

| Cell line | Exposure time [h] | $IC_{50}$ [μM][a] pH = 7.4 | $GI_{50}$ [μM][b] pH = 7.4 | pH = 6.0 | $GI_{50}$ ratio |
|---|---|---|---|---|---|
| 41M (ovary) | 96 | 0.87±0.09 | | | |
| SK-BR-3 (breast) | 96 | 39±5 | | | |
| A549 (lung) | 24 | 186±16 | 156±18 | 24±1 | 6.5 |
| HT29 (colon) | 24 | 47±4 | 43±4 | 8.0±0.4 | 5.4 |

[a] 50% inhibitory concentrations in the MTT assay. [b] 50% growth inhibition (corrected for differences in growth kinetics of the corresponding controls) after exposure for 24 h in the MTT assay. All values are the means with standard deviations obtained from at least three independent experiments.

may therefore contribute to the reduced chemosensitivity of acidic tumours.[43–45] On the other hand, weakly acidic drugs such as chlorambucil are more cytotoxic when the extracellular pH is slightly acidic.[44,46] These observations are consistent with ion trapping, according to which weak electrolytes that are not transported actively concentrate in the compartment where their ionised fraction is larger. Ion trapping has also been discussed as a possible explanation for the pH-dependent cellular uptake and cytotoxicity of the metal complex cisplatin, the hydrolysis products of which are in a pH-dependent equilibrium.[47] Therefore, the importance of appropriate $pK_a$ values for the design of antitumour drugs has been emphasised.[48] Furthermore, the development of prodrugs that are selectively activated in an acidic environment is being pursued as a strategy to in-

 © 2007 Wiley-VCH Verlag GmbH & Co. KGaA, Weinheim 

crease the therapeutic index by effectively killing tumour cells without impairing normal tissues.[49]

Some (PTA)ruthenium(II) complexes related to the compounds presented here have been found to induce DNA damage in isolated bacterial plasmids only at pH values less than about 7.0[50] and to exert a stronger cytotoxicity in breast cancer cells than in a non-malignant mammary gland cell line, while analogues containing methylated PTA, which is not protonated in acidic solution, do not show this kind of selectivity.[38] PTA has therefore attracted attention as a ligand that apparently confers tumour selectivity to (arene)ruthenium(II) compounds, which has been tentatively attributed to activation by protonation (assuming that the protonated form is actually the active species). While it has not been reported whether the cytotoxicity of arene–$Ru^{II}$–PTA complexes is pH-dependent, our findings with compound **4**, which exerts stronger antiproliferative effects at pH values encountered in solid tumours (6.0) than at pH values prevailing in normal tissues (7.4), support this notion. The presence of two PTA ligands in compound **4** may be favourable from this point of view and may constitute a basis for further attempts to increase tumour-selective activity. However, the pronounced decrease of p$K_a$ (from 5.6 to 3.0–3.3) resulting from the coordination of PTA to ruthenium(II) in arene–$Ru^{II}$–PTA complexes renders the possibility that ion trapping accounts for any pH-dependent cytotoxicity of this type of compounds rather unlikely[38] and raises the need for other explanations that might be completely different from previous assumptions.

In contrast to arene–$Ru^{II}$–PTA complexes, the presence of the biologically active thiosemicarbazone ligand may play a role in the activity of complex **4** even though this ligand is tightly bound to the metal centre in a tridentate manner. However, even a partial release of 2-acetylpyridine $N^4$,$N^4$-dimethylthiosemicarbazone should result in a tremendous increase in cytotoxicity because its $IC_{50}$ values of 0.22 and 2.7 nM in 41M and SK-BR-3 cells, respectively,[23] are three to four orders of magnitude below those of complex **4**. If a release of the thiosemicarbazone ligand accounts for the effects of compound **4**, it must be assumed to occur only to a very small degree.

## Conclusions

Following a known approach based on using P-containing derivatives as co-ligands, a novel highly water-soluble ruthenium(II) thiosemicarbazonate complex, namely $[Ru^{II}(L^1)(HPTA)_2Cl]Cl_2$, has been prepared. This, to the best of our knowledge, is the first ruthenium(II) complex with mixed thiosemicarbazone/PTA ligands to be isolated and characterised by X-ray crystallography. The complex shows pH-dependent antiproliferative activity in vitro in micromolar concentrations against the non-small cell lung cancer cell line A549 and the colon carcinoma cell line HT29.

## Experimental Section

**General:** All chemicals were obtained from commercial suppliers and were used without further purification. Phenanthrenequinone thiosemicarbazone,[24] 2-acetylpyridine $N^4$,$N^4$-dimethylthiosemicarbazone,[51] 1,3,5-triaza-7-phosphaadamantane (PTA)[52] and *cis*-$[RuCl_2(dmso)_4]$[53] were prepared according to published procedures. Elemental analyses were carried out at the Institute of Physical Chemistry of the University of Vienna with a Carlo Erba microanalyser. Infrared spectra were recorded with a Bruker Vertex 70 FTIR spectrometer as KBr pellets (4000–400 $cm^{-1}$). Electronic spectra were obtained with a Perkin–Elmer Lambda 650 UV/Vis spectrophotometer. Electrospray ionisation mass spectrometry was carried out in methanol with a Bruker Esquire 3000 instrument (Bruker Daltonics, Bremen, Germany). Expected and experimental isotope distributions were compared. The NMR spectra were recorded with a Bruker DPX 400 instrument using standard Bruker pulse programs. Chemical shifts for $^1H$ NMR spectra were referenced to the residual $^1H$ present in deuterated dmso and $CHCl_3$, respectively, and $^{31}P$ NMR to external $H_3{}^{31}PO_4$ in $D_2O$. Cyclic voltammograms were measured in a three-electrode cell using a 0.2-mm-diameter glassy carbon working electrode, a platinum auxiliary electrode and an $Ag|Ag^+$ reference electrode containing 0.1 M $AgNO_3$, the potential of which was corrected using an internal standard redox couple of ferrocenium/ferrocene. Measurements were performed at room temperature using an EG & G PARC 273A potentiostat/galvanostat. Deaeration of solutions was accomplished by passing a stream of argon through the solution for 5 min prior to the measurements and then maintaining a blanket of argon over the solution during the measurement. The potentials were measured in 0.2 M $[nBu_4N][BF_4]$/dmso, with $[Fe(\eta^5\text{-}C_2H_5)_2]$ ($E_{1/2}{}^{ox}$ = +0.68 V vs. NHE)[54] as internal standard, and are quoted relative to NHE.

**$[RuL^1Cl(PPh_3)_2]$ (1):** A suspension of 2-acetylpyridine $N^4$,$N^4$-dimethylthiosemicarbazone (22.3 mg, 0.1 mmol) in dry dichloromethane (5 mL) was added to a solution of $[RuCl_2(PPh_3)_3]$ (95.8 mg, 0.1 mmol) in dry dichloromethane (5 mL) and the resulting mixture was refluxed under argon for 4 h. The solution was concentrated to about 5 mL, and allowed to stand at +4 °C overnight. The product was obtained as green-brown crystals, which were filtered off, washed with *n*-hexane and dried in vacuo. Yield: 36 mg (41%). $C_{46}H_{43}ClN_4P_2RuS\cdot0.5CH_2Cl_2$ (924.86): calcd. C 60.39, H 4.80, N 6.06, S 3.47; found C 60.61, H 4.80, N 6.30, S 3.57. ESI-MS: *m*/*z* = 847 $[M - Cl^-]^+$, 585 $[M - Cl^- - PPh_3]^+$. IR: $\tilde{\nu}$ = 1522 [w, $\nu_{(C=N)}$], 1482 (m), 1391 (s), 1314 (s), 907 (w), 742 (m), 695 (s) and 516 (s, $\nu_{[Ru(PPh_3)_2]}$) $cm^{-1}$. $^1H$ NMR (400.13 MHz. $CDCl_3$): $\delta$ = 8.62 (d, $^3J_{H,H}$ = 5.1 Hz, 1 H, py), 7.54–7.51 (m, 12 H, $PPh_3$), 7.36 (m, 1 H, py), 7.24–7.21 (m, 6 H, $PPh_3$), 7.18–7.14 (m, 12 H, $PPh_3$), 6.86 (d, $^3J_{H,H}$ = 8.1 Hz, 1 H, py), 6.47 (t, $^3J_{H,H}$ = 6.2 Hz, 1 H, py), 2.70 [s, 6 H, $N(CH_3)_2$], 1.82 [s, 3 H, $C(CH_3)$] ppm. $^{31}P\{^1H\}$ (162.00 MHz; $CHCl_3$): $\delta$ = 30.42 and 26.19 [equal intensity $(PPh_3)_2$] ppm. UV/Vis ($CH_2Cl_2$): $\lambda_{max}$ ($\varepsilon$) = 599 sh (1620), 546 sh (2280), 476 (7500), 397 sh (31760), 379 (39880), 274 (47120 $M^{-1}cm^{-1}$) nm. Single crystals suitable for an X-ray diffraction study were selected directly from the reaction vessel.

**$[RuL^2Cl(PPh_3)_2]\cdot C_2H_5OH$ (2). Method a):** A suspension of phenanthrenequinone thiosemicarbazone (28.2 mg, 0.1 mmol) in dry ethanol (5 mL) was added to a suspension of $[RuCl_2(PPh_3)_3]$ (95.8 mg, 0.1 mmol) in dry ethanol (5 mL), and the resulting mixture was refluxed under argon for 4 h. The solution was concentrated to about 5 mL and allowed to stand at +4 °C overnight. The solid residue was stirred in *n*-hexane to remove the excess of ligand and triphenylphosphane, filtered off and dried in vacuo. Yield: 61 mg (65%). $C_{51}H_{40}ClN_3OP_2RuS\cdot C_2H_5OH$ (987.49): calcd. C 64.46, H 4.70, N 4.26, S 3.25; found C 64.46, H 4.36, N 4.55, S 3.34. ESI-MS: *m*/*z* = 942 $[M + H^+]^+$, 964 $[M + Na^+]^+$, 980 $[M + K^+]^+$, 906 $[M - Cl^-]^+$, 644 $[M - Cl^- - PPh_3]^+$. IR: $\tilde{\nu}$ = 1600 [s, $\nu_{(C=N)}$], 1590

 © 2007 Wiley-VCH Verlag GmbH & Co. KGaA, Weinheim 

(s), 1434 (s), 1190 (s), 743 (m), 694 (s) and 519 (s, $\nu_{[Ru(PPh_3)_2]}$) $cm^{-1}$. $^1H$ NMR (400.13 MHz, [D$_6$]dmso): $\delta$ = 8.88 (dd, $^3J_{H,H}$ = 8.3, $^4J_{H,H}$ = 1.8 Hz, 1 H, phq), 8.43 (dd, $^3J_{H,H}$ = 7.8, $^4J_{H,H}$ = 1.0 Hz, 1 H, phq), 8.35 (d, $^3J_{H,H}$ = 8.6 Hz, 1 H, phq), 8.26 (m, 1 H, phq), 8.13 (s, 2 H, $NH_2$), 7.65 (m, 1 H, phq), 7.52–7.49 (m, 12 H, $PPh_3$), 7.26–7.19 (m, 9 H, $PPh_3$ and phq), 7.14–7.11 (m, 12 H, $PPh_3$) ppm. $^{31}P\{^1H\}$ (162.00 MHz, [D$_6$]dmso): $\delta$ = 27.36 [s, 2 P, $(PPh_3)_2$]. UV/Vis ($CH_2Cl_2$): $\lambda_{max}$ ($\varepsilon$) = 597 nm (9080) , 470 (14580), 320 (13600), 268 (49330 $M^{-1}cm^{-1}$) nm. **Method b). [RuL$^2$Cl(PPh$_3$)$_2$]:** Phenanthrenequinone thiosemicarbazone (28.2 mg, 0.1 mmol) in dry ethanol (5 mL) and triphenylphosphane 76.0 mg (0.29 mmol) in dry ethanol (5 mL) were added to [$RuCl_2$(dmso)$_4$] (48.0 mg, 0.1 mmol) in dry ethanol (5 mL) and the mixture refluxed under argon for 5 h. The black solid was filtered off, washed with absolute ethanol and *n*-hexane and dried in vacuo. Yield: 79 mg (80%). $C_{51}H_{40}ClN_3OP_2RuS$ (941.42): calcd. C 65.07, H 4.28, N 4.46; found C 64.78, H 4.43, N 4.38. Single crystals suitable for X-ray data collection were obtained from a chloroform solution of **2** saturated with *n*-hexane.

**[RuL$^1$Cl(HPTA)$_2$]Cl$_2$·C$_2$H$_5$OH·H$_2$O (4·C$_2$H$_5$OH·H$_2$O):** A solution of 2-acetylpyridine $N^4$,$N^4$-dimethylthiosemicarbazone (22.3 mg, 0.1 mmol) in dry ethanol (5 mL) was added to a suspension of *cis*-[$RuCl_2$(dmso)$_4$] (44.8 mg, 0.1 mmol) in dry ethanol (5 mL), and the resulting mixture was heated at 65 °C under argon for 1 h to yield a red solution. PTA (31.6 mg, 0.2 mmol) was then added and heating was continued for a further 4 h. The green-yellow side product was separated by filtration and the red solution concentrated to about 1 mL and allowed to stand at +4 °C overnight. The red crystals formed were filtered off, washed with cold dry ethanol and dried in vacuo. Yield: 7 mg (10%). $C_{22}H_{39}Cl_3N_{10}P_2RuS{\cdot}C_2H_5OH{\cdot}H_2O$ (809.14): calcd. C 35.63, H 5.85, N 17.31, S 3.96; found C 35.09, H 5.40, N 17.49, S 4.07. ESI-MS: *m*/*z* = 673 [M – $H^+$]$^+$, 695 [M – 2 $H^+$ + $Na^+$]$^+$, 637 [M – 2 $H^+$ – $Cl^-$]$^+$, 538 [M – 2 $H^+$ – PTA + $Na^+$]$^+$. IR: $\tilde{\nu}$ = 1531 [w, $\nu_{(C=N)}$], 1503 (w), 1397 (s), 1315 (s), 768 (m), 566 (m) $cm^{-1}$. $^1H$ NMR (400.13 MHz, [D$_6$]dmso): $\delta$ = 9.87 (s, 2 H, NH), 8.77 (d, $^3J_{H,H}$ = 5.3 Hz, 1 H, py), 7.85 (m, 1 H, py), 7.67 (d, $^3J_{H,H}$ = 8.1 Hz, 1 H, py), 7.33 (m, 1 H, py), 4.62 (s, 12 H, $NCH_2N$), 3.78–3.67 (m, $^3J_{H,P}$ = 10.6 Hz, 12 H, $NCH_2P$), 3.33 [s, 6 H, $N(CH_3)_3$, below the water signal], 2.42 (s, 3 H, $CH_3$) ppm. $^{31}P\{^1H\}$ (162.00 MHz, [D$_6$]dmso): $\delta$ = –38.13 [s, 2 P, $(HPTA)_2$]. UV/Vis ($H_2O$): $\lambda_{max}$ ($\varepsilon$) = 522 sh (870), 450 (5460), 378 sh (18320), 355 (25910), 280 sh (9220), 222 sh (38930 $M^{-1}cm^{-1}$) nm. Red crystals of composition **4**·2$H_2O$ of X-ray diffraction quality were obtained by recrystallisation from ethanol.

**Determination of the p$K_a$ Values:** The pH* titration experiment was carried out in $D_2O$ at 298 K using an Ecoscan pH 6 (Eutech) pH meter equipped with a micro-combination pH electrode (Orion) for NMR tubes calibrated with buffer solution at pH = 4, 7 and 10. The pH* values were adjusted with diluted DCl and NaOD. The p$K_a$ value of the coordinated PTAs in **4** was determined by plotting the change in chemical shift of the $^{31}P$ signal against pH* and fitting the curve to the modified Henderson–Hasselbalch equation[55] ($\delta_{obs}$, $\delta_{HA}$ and $\delta_A$ are the chemical shifts for the observed, protonated and deprotonated species, respectively), by using the program KALEIDAGRAPH,[56] with the assumption that the observed values are weighted averages according to the populations of the protonated and deprotonated species.

$$\delta_{obs} = \frac{\delta_{HA} + \delta_A \cdot 10^{(pH-pK_a)}}{1+10^{(pH-pK_a)}}$$

The p$K_a$* value determined from the titration curve in Figure 5 was corrected by using the equation p$K_a$ = 0.929 p$K_a$* + 0.42 suggested by Krezel and Bal,[57] (with p$K_a$* as the p$K_a$ value determined in $D_2O$) for conversion of protonation constants, measured in $D_2O$ into constants valid for $H_2O$ solutions. The error is estimated as ±0.04 pK units for two $^{31}P$ resonances, and the mean value was taken.

**X-ray Crystallography:** X-ray diffraction measurements were performed with an X8 APEXII CCD diffractometer. Single crystals of **1**–**4** were positioned at 40, 40, 40 and 37.5 mm from the detector, respectively, and 1187, 1438, 1328 and 1320 frames were measured each for 70, 120, 50 and 10 s with a 1° scan-width. The data were processed using the SAINT software package.[58] The structures were solved by direct methods and refined by full-matrix least-squares techniques. Non-hydrogen atoms were refined with anisotropic displacement parameters. H atoms were inserted in geometrically calculated positions and refined with a riding model. The following computer programs were used: structure solution: SHELXS-97;[59] refinement: SHELXL-97;[60] molecular diagrams: ORTEP;[61] computer CPU: Pentium IV; scattering factors were taken from the literature.[62] Crystal data, data collection parameters, and structure refinement details are given in Table 2. CCDC-630689 (**1**·3$CH_2Cl_2$), -630686 (**2**), -630687 (**3**·dmso·1.25$H_2O$) and -630688 (**4**·2$H_2O$) contain the supplementary crystallographic data for this paper. These data can be obtained free of charge from The Cambridge Crystallographic Data Centre via www.ccdc.cam.ac.uk/data_request/cif.

**Cell Lines and Culture Conditions:** Human 41M (ovarian carcinoma) and SK-BR-3 (mammary carcinoma) cells were kindly provided by Lloyd R. Kelland (CRC Centre for Cancer Therapeutics, Institute of Cancer Research, Sutton, UK) and Evelyn Dittrich (General Hospital, Medical University of Vienna, Austria), respectively. Human A549 (non-small cell lung cancer) and HT29 (colon carcinoma) cells were kindly provided by Brigitte Marian (Institute of Cancer Research, Medical University of Vienna, Austria). Cells were grown in 75-$cm^2$ culture flasks (Iwaki/Asahi Technoglass, Gyouda, Japan) as adherent monolayer cultures in complete culture medium [Minimal Essential Medium (MEM) supplemented with 10% heat-inactivated fetal bovine serum, 1 mM sodium pyruvate, 4 mM L-glutamine and 1% non-essential amino acids (100×) (all purchased from Sigma–Aldrich, Vienna, Austria)]. Cultures were maintained at 37 °C in a humidified atmosphere containing 5% $CO_2$.

**Antiproliferative Activity in Cancer Cell Lines:** Antiproliferative effects were determined by means of a colourimetric microculture assay [MTT assay; MTT = 3-(4,5-dimethyl-2-thiazolyl)-2,5-diphenyl-2*H*-tetrazolium bromide]. Cells were harvested from the culture flasks by trypsinisation and seeded into 96-well microculture plates (Iwaki/Asahi Technoglass, Gyouda, Japan) in cell densities of $4 \times 10^3$ (except HT-29: $3 \times 10^3$ cells/well), in order to ensure exponential growth throughout drug exposure. After pre-incubation for 24 h, 41M and SK-BR-3 cells were exposed to serial dilutions of the test compound in 200 μL/well complete culture medium for 96 h under an atmosphere containing 5% $CO_2$. For pH-dependency experiments in A549 and HT-29 cells, the test compound was dissolved in Dulbecco's Modified Eagles Medium (DMEM) (w/o sodium hydrogencarbonate) supplemented with 10% heat-inactivated fetal bovine serum, 1 mM sodium pyruvate, 4 mM L-glutamine, 1% non-essential amino acids (100×) and sodium hydrogencarbonate in either 8.8 mM (pH = 6.0) or 39.6 mM (pH = 7.4) concentration (all purchased from Sigma–Aldrich, Vienna, Austria), and cells were exposed under an atmosphere containing 8% $CO_2$ for 24 h, followed by incubation in 200 μL/well drug-free DMEM (pH = 7.4) for a further 72 h. At the end of

 © 2007 Wiley-VCH Verlag GmbH & Co. KGaA, Weinheim 

Table 2. Crystal data and details of data collection for **1**–**4**.

| | **1**·3$CH_2Cl_2$ | **2** | **3**·dmso·1.25$H_2O$ | **4**·2$H_2O$ |
|---|---|---|---|---|
| Empirical formula | $C_{49}H_{49}Cl_7N_4P_2RuS$ | $C_{51}H_{40}ClN_3OP_2RuS$ | $C_{35}H_{33.5}Cl_2N_3O_{3.25}PRuS_2$ | $C_{22}H_{43}Cl_3N_{10}O_2P_2RuS$ |
| Formula mass | 1137.14 | 941.38 | 814.70 | 781.08 |
| Space group | $Pmn2_1$ | $P\bar{1}$ | $P2_1/c$ | $C2/c$ |
| $a$ [Å] | 18.4882(7) | 9.4527(4) | 9.8926(3) | 31.404(4) |
| $b$ [Å] | 9.3773(3) | 11.8536(7) | 17.8078(6) | 9.0952(9) |
| $c$ [Å] | 14.7549(6) | 20.2796(11) | 21.7962(7) | 25.571(3) |
| $\alpha$ [°] | | 81.177(4) | | |
| $\beta$ [°] | | 84.411(3) | 95.493(2) | 106.939(12) |
| $\gamma$ [°] | | 72.261(3) | | |
| $V$ [Å$^3$] | 2558.05(16) | 3822.1(2) | 3822.1(2) | 6986.8(14) |
| $Z$ | 2 | 2 | 4 | 8 |
| $\lambda$ [Å] | 0.71073 | 0.71073 | 0.71073 | 0.71073 |
| $\rho_{calcd.}$ [g cm$^{-3}$] | 1.476 | 1.464 | 1.417 | 1.485 |
| Crystal size [mm] | 0.18 × 0.16 × 0.14 | 0.16 × 0.07 × 0.05 | 0.34 × 0.20 × 0.18 | 0.06 × 0.06 × 0.06 |
| $T$ [K] | 100 | 296 | 100 | 100 |
| $\mu$ [cm$^{-1}$] | 81.4 | 59.7 | 73.9 | 86.6 |
| Flack parameter | –0.01(3) | | | |
| $R_1$[a] | 0.0359 | 0.0413 | 0.0539 | 0.0522 |
| $wR_2$[b] | 0.0891 | 0.1025 | 0.1631 | 0.1388 |
| GOF[c] | 1.051 | 0.997 | 1.093 | 1.058 |

[a] $R_1 = \Sigma||F_o| - |F_c||/\Sigma|F_o|$. [b] $wR_2 = \{\Sigma[w(F_o^2 - F_c^2)^2]/\Sigma[w(F_o^2)^2]\}^{1/2}$. [c] GOF = $\{\Sigma[w(F_o^2 - F_c^2)^2]/(n - p)\}^{1/2}$, where $n$ is the number of reflections and $p$ is the total number of parameters refined.

incubation, all media were replaced by 150 μL/well RPMI 1640 medium (supplemented with 10% heat-inactivated fetal bovine serum and 2 mM L-glutamine) plus 20 μL/well MTT solution in phosphate-buffered saline (5 mg/mL). After incubation for 4 h, the medium/MTT mixtures were removed and the formazan crystals formed by the mitochondrial dehydrogenase activity of vital cells were dissolved in 150 μL of dmso per well. Optical densities at 550 nm were measured with a microplate reader (Tecan Spectra Classic), using a reference wavelength of 690 nm to correct for unspecific absorption. The quantity of vital cells was expressed in terms of T/C values by comparison with untreated control microcultures, and 50% inhibitory concentrations ($IC_{50}$) were calculated from concentration-effect curves by interpolation. In order to correct for differences in growth kinetics in the pH-dependency experiments, concentration-effect curves were transformed by taking the optical densities of separate MTT-stained control microcultures at the beginning of drug exposure as zero values, and $GI_{50}$ concentrations were calculated instead of $IC_{50}$ values. Evaluation is based on the mean of at least three independent experiments, each comprising at least six microcultures per concentration level.

**Supporting Information** (see footnote on the first page of this article): Crystal packing of complexes **1** and **2**, the molecular structure of **3**, $^{31}$P NMR spectra of **4**, UV/Vis spectra of **4** at different pH values and IR spectra of **1**, **2** and **4**.

## Acknowledgments

The authors would like to thank the Austrian Science Fund (FWF), the Austrian Council for Research and Technology Development, the Austrian Research Promotion Agency (FFG), the European Cooperation in the Field of Scientific and Technical Research (COST) and the Faustus Forschung Austria Translational Drug Development AG, Vienna, Austria for financial support. We also thank Dr. Hanspeter Kählig for NMR titrations and Mag. Raffael Schuecker for helpful discussions, as well as Mag. Michael Grössl for ESI-MS measurements.

[1] T. S. Lobana, S. Khanna, R. J. Butcher, A. D. Hunter, M. Zeller, *Polyhedron* **2006**, *25*, 2755–2763.
[2] F. Basuli, M. Ruf, C. G. Pierpont, S. Bhattacharya, *Inorg. Chem.* **1998**, *37*, 6113–6116.
[3] G. Dessy, V. Fares, L. Scaramuzza, A. A. G. Tomlinson, G. De Munno, *J. Chem. Soc., Dalton Trans.* **1978**, 1549–1554.
[4] D. Kovala-Demertzi, P. N. Yadav, J. Wiecek, S. Skoulika, T. Varadinova, M. A. Demertzis, *J. Inorg. Biochem.* **2006**, *100*, 1558–1567.
[5] D. X. West, S. B. Padhye, P. B. Sonawane, *Struct. Bonding* **1991**, *76*, 1–50.
[6] E. C. Moore, A. C. Sartorelli, *Pharm. Ther.* **1984**, *24*, 439–447.
[7] E. C. Moore, A. C. Sartorelli, in *Inhibitors of Ribonucleoside Diphosphate Reductase Activity* (Eds.: J. G. Cory, A. H. Cory), Pergamon Press, Oxford, **1989**, pp. 203–215.
[8] E. C. Moore, A. C. Sartorelli, *Pharm. Ther.* **1984**, *24*, 439–447.
[9] R. W. Brockman, J. R. Thomson, M. J. Bell, H. E. Skipper, *Cancer Res.* **1956**, *16*, 167–170.
[10] L. Feun, M. Modiano, K. Lee, J. Mao, A. Marini, N. Savaraj, P. Plezia, B. Almassian, E. Colacino, J. Fischer, S. MacDonald, *Cancer Chemother. Pharmacol.* **2002**, *50*, 223–229.
[11] J. Murren, M. Modiano, C. Clairmont, P. Lambert, N. Savaraj, T. Doyle, M. Sznol, *Clin. Cancer Res.* **2003**, *9*, 4092–4100.
[12] A. Gómez Quiroga, C. Navarro Raninger, *Coord. Chem. Rev.* **2004**, *248*, 119–133.
[13] N. Farrell, *Coord. Chem. Rev.* **2002**, *232*, 1–4.
[14] U. Abram, K. Ortner, R. Gust, K. Sommer, *J. Chem. Soc., Dalton Trans.* **2000**, 735–744.
[15] M. Belicchi-Ferrari, F. Bisceglie, C. Casoli, S. Durot, I. Morgenstern-Badara, G. Pelosi, E. Pilotti, S. Pinelli, P. Tarasconi, *J. Med. Chem.* **2005**, *48*, 1671–1675.
[16] V. B. Arion, M. A. Jakupec, M. Galanski, P. Unfried, B. K. Keppler, *J. Inorg. Biochem.* **2002**, *91*, 298–305.
[17] J. Patole, S. Padhye, M. S. Moodbidri, N. Shirsat, *Eur. J. Med. Chem.* **2005**, *40*, 1052–1055.
[18] L. Otero, M. Vieites, L. Boiani, A. Denicola, C. Rigol, L. Opazo, C. Olea-Azar, J. D. Maya, A. Morello, L. Krauth-Siegel, O. E. Piro, E. Castellano, M. González, D. Gambino, H. Cerecetto, *J. Med. Chem.* **2006**, *49*, 3322–3331.

 © 2007 Wiley-VCH Verlag GmbH & Co. KGaA, Weinheim 

[19] U. K. Mazumder, M. Gupta, S. S. Karki, S. Bhattacharya, S. Rathinasamy, S. Thangavel, *Chem. Pharm. Bull.* **2004**, *52*, 178–185.
[20] F. Bregant, S. Pacor, S. Ghosh, S. K. Chattopadhyah, G. Sava, *Anticancer Res.* **1993**, *13*, 1011–1017.
[21] G. Sava, R. Gagliardi, A. Bergamo, E. Alessio, G. Mestroni, *Anticancer Res.* **1999**, *19*, 969–972.
[22] M. Galanski, V. B. Arion, M. A. Jakupec, B. K. Keppler, *Curr. Pharm. Des.* **2003**, *9*, 2078–2089.
[23] C. R. Kowol, R. Berger, R. Eichinger, A. Roller, M. A. Jakupec, P. P. Schmidt, V. B. Arion, B. K. Keppler, *J. Med. Chem.* **2007**, *50*, 1254–1265.
[24] Z. Afrasiabi, E. Sinn, S. Padhye, S. Dutta, S. Padhye, C. Newton, C. E. Anson, A. K. Powell, *J. Inorg. Biochem.* **2003**, *95*, 306–314.
[25] M. Maji, S. Ghosh, S. K. Chattopadhyay, T. C. W. Mak, *Inorg. Chem.* **1997**, *36*, 2938–2943.
[26] M. Maji, M. Chatterjee, S. Ghosh, S. Kumar Chattopadhyay, B. M. Wu, T. C. W. Mak, *J. Chem. Soc., Dalton Trans.* **1999**, 135–140.
[27] F. Basuli, S. M. Peng, S. Bhattacharya, *Inorg. Chem.* **2000**, *39*, 1120–1127.
[28] F. Basuli, S. M. Peng, S. Bhattacharya, *Inorg. Chem.* **2001**, *40*, 1126–1133.
[29] a) W. H. Ang, P. J. Dyson, *Eur. J. Inorg. Chem.* **2006**, 4003–4018; b) A. D. Phillips, L. Gonsalvi, A. Romerosa, F. Vizza, M. Peruzzini, *Coord. Chem. Rev.* **2004**, *248*, 955–993; c) W. H. Ang, E. Daldini, C. Scolaro, R. Scopelliti, L. Juillerat-Jeannerat, P. J. Dyson, *Inorg. Chem.* **2006**, *45*, 9006–9013; d) C. Scolaro, T. J. Geldbach, S. Rochat, A. Dorcier, C. Gossens, A. Bergamo, M. Cocchietto, I. Tavernelli, G. Sava, U. Rothlisberger, P. J. Dyson, *Organometallics* **2006**, *25*, 756–765; e) B. Serli, E. Zangrando, T. Gianferrata, C. Scolaro, P. J. Dyson, A. Bergamo, E. Alessio, *Eur. J. Inorg. Chem.* **2005**, 3423–3434; f) D. N. Akbayeva, L. Gonsalvi, W. Oberhauser, M. Peruzzini, F. Vizza, P. Brügeller, A. Ramerosa, G. Sava, A. Bergamo, *Chem. Commun.* **2003**, 264–265.
[30] D. J. Darensbourg, F. Joo, M. Kannisto, A. Katho, J. H. Reibenspies, D. J. Daigle, *Inorg. Chem.* **1994**, *33*, 200–208.
[31] R. Raveendran, S. Pal, *Polyhedron* **2005**, *24*, 57–63.
[32] B. J. Frost, S. B. Miller, K. O. Rove, D. M. Pearson, J. D. Korinek, J. L. Harkreader, C. A. Mebi, J. Shearer, *Inorg. Chim. Acta* **2006**, *359*, 283–288.
[33] A. Romerosa, T. Campos-Malpartida, C. Lidrissi, M. Saoud, M. Serrano-Ruiz, M. Peruzzini, J. A. Garrido-Cárdenas, F. García-Maroto, *Inorg. Chem.* **2006**, *45*, 1289–1298.
[34] B. J. Frost, C. A. Mebi, *Organometallics* **2004**, *23*, 5317–5323.
[35] A. Sreekanth, H.-K. Fun, M. R. P. Kurup, *J. Mol. Struct.* **2005**, *737*, 61–67.
[36] C. R. Kowol, V. B. Arion, B. K. Keppler, unpublished results.
[37] A. K. Nandi, S. Chaudhuri, S. K. Mazumdar, S. Ghosh, *J. Chem. Soc., Perkin Trans. 2* **1984**, 1729–1733.
[38] C. Scolaro, A. Bergamo, L. Brescacin, R. Delfino, M. Cocchietto, G. Laurenczy, T. J. Geldbach, G. Sava, P. J. Dyson, *J. Med. Chem.* **2005**, *48*, 4161–4171.
[39] K. J. Fisher, E. C. Alyea, N. A. Shahnazarian, *Phosphorus, Sulfur, Silicon Relat. Elem.* **1990**, *48*, 37–40.
[40] S-M. Valiahdi, M. A. Jakupec, B. K. Keppler, unpublished results.
[41] M. Stubbs, P. M. J. McSheehy, J. R. Griffiths, C. L. Bashford, *Mol. Med. Today* **2000**, *6*, 15–19.
[42] R. A. Gattenby, R. J. Gillies, *Nat. Rev. Cancer* **2004**, *4*, 891–899.
[43] L. E. Gerweck, S. V. Kozin, S. J. Stocks, *Br. J. Cancer* **1999**, *79*, 838–842.
[44] B. P. Mahoney, N. Raghunand, B. Baggett, R. J. Gillies, *Biochem. Pharmacol.* **2003**, *66*, 1207–1218.
[45] L. E. Gerweck, S. Vijayappa, S. Kozin, *Mol. Cancer Ther.* **2006**, *5*, 1275–1279.
[46] S. V. Kozin, P. Shkarin, L. E. Gerweck, *Cancer Res.* **2001**, *61*, 4740–4743.
[47] C. M. Laurencot, K. A. Kennedy, *Oncol. Res.* **1995**, *7*, 371–379.
[48] L. E. Gerweck, K. Seetharaman, *Cancer Res.* **1996**, *56*, 1194–1198.
[49] L. F. Tietze, T. Feuerstein, *Curr. Pharm. Des.* **2003**, *9*, 2155–2175.
[50] C. S. Allardyce, P. J. Dyson, D. J. Ellis, S. L. Heath, *Chem. Commun.* **2001**, 1396–1397.
[51] D. L. Klayman, J. P. Scovill, J. F. Bartosevich, C. J. Mason, *J. Med. Chem.* **1979**, *22*, 1367–1373.
[52] D. J. Daigle, *Inorg. Synth.* **1998**, *32*, 40–45.
[53] I. P. Evans, A. Spencer, G. Wilkinson, *J. Chem. Soc., Dalton Trans.* **1973**, 204–209.
[54] W. C. Barette Jr, H. W. Johnson Jr, D. T. Sawyer, *Anal. Chem.* **1984**, *56*, 1890–1898.
[55] Z. Szakacs, G. Hägele, R. Tyka, *Anal. Chim. Acta* **2004**, *522*, 247–258.
[56] *KALEIDAGRAPH*, version 4.03, Synergy Software, Reading, PA, **2006**.
[57] A. Krezel, W. Bal, *J. Inorg. Biochem.* **2004**, *98*, 161–166.
[58] M. R. Pressprich, J. Chambers, *SAINT + Integration Engine, Program for Crystal Structure Integration*, Bruker Analytical X-ray systems, Madison, USA, **2004**.
[59] G. M. Sheldrick, *SHELXS-97, Program for Crystal Structure Solution*, University of Göttingen, Germany, **1997**.
[60] G. M. Sheldrick, *SHELXL-97, Program for Crystal Structure Refinement,* University of Göttingen, Germany, **1997**.
[61] C. K. Johnson, Rep. ORLN-5138, Oak Ridge National Laboratory, Oak Ridge, TN, **1976**.
[62] *International Tables for X-ray Crystallography* (Ed.: A. J. C. Wilson), Kluwer Academic Press, Dordrecht, The Netherlands, **1992**, vol. C, Tables 4.2.6.8 and 6.1.1.4.

Received: December 18, 2006
Published Online: May 22, 2007

 © 2007 Wiley-VCH Verlag GmbH & Co. KGaA, Weinheim 

DOI: 10.1002/ejic.200601200

# The Role of Water in the Stereoselective Hydrogenation of 1,2-Diphenylacetylene Catalyzed by the Water-Soluble [{$RuCl_2$(*m*tppms)$_2$}$_2$]

**Gábor Kovács,[a–c] Gregori Ujaque,[a] Agustí Lledós,*[a] and Ferenc Joó*[b,c]**

**Keywords:** Alkynes / Biphasic catalysis / Density functional calculations / Hydrogenation / Reaction mechanisms

Density functional theory with dielectric continuum models was applied to describe the reaction mechanism of the stereoselective hydrogenation of phenyl-substituted alkynes with the water-soluble ruthenium complex [{$RuCl_2$(*m*tppms)$_2$}$_2$] *m*tppms [(*meta*-sulfonatophenyl)diphenylphosphane] in acidic aqueous solutions. The water solvent is modelled by the inclusion of a small cluster of three water molecules in addition to a continuum model. The possible reaction mechanisms leading to the formation of the different (*Z* and *E*) stereoisomers are computationally evaluated. It was shown that the reaction takes place in two steps; one hydrogen comes from the hydrido complex, whereas the second hydrogen is transferred from the hydroxonium ions present in the solution. The formation of the different stereoisomers is determined by the order of the two hydrogenation steps, and the analysis suggests that the formation of the (*Z*)-isomer is more favourable, which is consistent with the experimental results.
(© Wiley-VCH Verlag GmbH & Co. KGaA, 69451 Weinheim, Germany, 2007)

## Introduction

Chemo- and stereoselective reduction of carbon–carbon multiple bonds plays an important role in organic synthetic processes, both in the laboratory and in processes of industrial scale.[1] The complete hydrogenation of either double or triple carbon–carbon bonds occurs on almost all hydrogenation catalysts; however, semihydrogenation of alkyne derivatives (especially if stereoselectivity is desired) requires more sophisticated catalysts and reaction conditions.[2]

There are many examples of heterogeneous catalysts that are suitable for the conversion of alkynes into (*Z*)-alkenes, such as the Lindlar catalyst[2a] or the "P2Ni" catalytic system.[2b] Recently, Pd nanoparticles[3] and Pd catalysts supported on mesostructured silica[4] were developed as highly active and selective catalysts for partial alkyne hydrogenation. Numerous homogeneous catalytic systems are also known; however, the number of the catalysts that are selective towards the alkyne functionality in the presence of other reducible functionalities in the same molecule is more limited. Some good examples are the $Pd^0$ complexes of asymmetric bidentate nitrogen ligands,[5] cationic rhodium complexes of chelating phosphanes[6] and Cr(arene)$(CO)_3$ complexes.[7]

Aqueous and especially aqueous–organic biphasic systems have provided new prospects in organometallic catalysis,[8] since one major problem of homogeneous catalysis, that is, the separation of the catalyst from the products, can be easily solved.[8a,8b] Moreover, since the reaction in these systems takes place in the aqueous phase (the catalyst has to be water-soluble) these processes are more economical and environmentally friendly than those carried out in regular organic solvents.[8c,8d]

One of the most frequently described families of water-soluble complexes catalyzing different hydrogenation reactions are rhodium and ruthenium complexes prepared with sulfonated aromatic phosphane ligands.[1c,1d,8a] The ruthenium complex of *m*tppms [(*meta*-sulfonatophenyl)diphenylphosphane], that is [{$RuCl_2$(*m*tppms)$_2$}$_2$], was used effectively by Joó and co-workers for the selective reduction of the C=O or C=C functionalities of cinnamaldehyde in water/chlorobenzene two-phase systems, depending on reaction conditions,[9] and it has recently been reported that the aforementioned complex catalyzes the stereoselective hydrogenation of disubstituted alkynes.[10] It was found that the stereoselectivity of the reaction is mainly influenced by the pH of the aqueous solutions. In acidic solutions, the major product of the reaction is the (*Z*)-alkene, whereas under basic reaction conditions the (*E*)-isomer of the alkenes is formed in higher quantity; furthermore, a significant overreduction to the corresponding alkane was also observed.[10]

When chemo- or stereoselectivity found during aqueous-phase catalytic processes is to be explained, the unique characteristics of water have to be considered. In contrast with nonpolar organic solvents, water commonly plays the

[a] Departament de Química, Universitat Autònoma de Barcelona 08193 Bellaterra, Catalonia, Spain
[b] Insitute of Physical Chemistry, University of Debrecen P. O. Box 7, Debrecen 10, 4010 Hungary
[c] Research Group of Homogeneous Catalysis, Hungarian Academy of Sciences P. O. Box 7, Debrecen 10, 4010 Hungary
Supporting information for this article is available on the WWW under http://www.eurjic.org or from the author.

 © 2007 Wiley-VCH Verlag GmbH & Co. KGaA, Weinheim 

role of not only the solvent but that of the reactant in the catalytic cycle.[11] Water can alter the reaction pathway by interacting with the metal complex as a coordinating ligand, as a species taking part in proton-transfer reactions and, additionally, water molecules can stabilize reaction intermediates by forming hydrogen and dihydrogen bonds with different parts of the various complexes.[12] Another important feature of aqueous solutions is that the pH of the solution can be an important factor in determining chemical reactivity or selectivity.[9a,13] The pH of the solution influences both the formation of the different catalytically active species[9a] and the concentration of the reactive ions ($H_3O^+$ and $OH^-$).

Recently we published a series of papers in which, we intended to describe aqueous-phase organometallic catalytic processes by means of theoretical methods.[14,15] As a continuation of the aforementioned works, in the present study, the mechanism of the hydrogenation of 1,2-diphenylacetylene is analyzed by means of theoretical methods, with the intention of exploring the origin of the observed stereoselectivity.

## Computational Details

Complexes $[RuHCl(PH_3)_3]$ and $[RuHCl(H_2O)(PH_3)_2]$ were adopted as models for the catalytically active hydrido species. The formation of these hydrido species in aqueous solutions was already discussed when the mechanism of the selective hydrogenation of C=C functionalities in α,β-unsaturated aldehydes with the same catalytic system ($[\{RuCl_2(m\text{tppms})_2\}_2]$ catalyst in acidic aqueous solution) was considered.[15] Hence, the results regarding the formation of the appropriate catalytically active species are only summarized briefly in this paper.

We first carried out density functional theory calculations to identify the structures of the reaction intermediates of the catalytic process. In some cases, we also located the transition states corresponding to different steps of the reaction. Normal coordinate analysis has been used to verify the nature of these stationary points, and for each transition structure we calculated the intrinsic reaction coordinate (IRC) routes towards the corresponding minima. If the IRC calculations failed to reach the energy minima on the potential energy surface, we performed geometry optimizations from the final phase of the IRC path. All geometries that are presented in the article are the geometry-optimized structures of the corresponding complexes.

All DFT calculations were performed with the program package Gaussian03[16] and the B3LYP[17] combination of functionals. The LANL2DZ[18] pseudopotential was employed for the ruthenium centre, and the standard 6-31G(d) basis set was used for the other atoms.[19] For all the optimized structures, we estimated the effect of the bulk aqueous medium ($\varepsilon = 78.4$) by the application of the polarizable continuum model (PCM)[20] as implemented in Gaussian 03, thus all energies given in the text correspond to the energies taking into consideration the effect of the bulk solvent.

When solvent molecules participated in the reaction, the solvent environment was represented by a cluster of three water molecules connected by hydrogen bonds. A single water molecule is not enough to give a realistic description of the medium, since proton exchange processes that take place during the catalytic process imply transfer of charges with formation of highly reactive ions. Thus, reacting water molecules were represented by a $[(H_2O)_3]$ cluster, whereas hydroxonium ions, which are present in aqueous acidic solutions at reasonable concentration, were represented by $[(H_3O)(H_2O)_2]^+$. On the basis of earlier systematic investigations by Kovács et al.,[14,15] it can be concluded that a cluster of three water molecules represents a good compromise between a realistic description, the system size and related proportional computational time.

## Results and Discussion

As it was stated in the introduction, hydrogenation of 1,2-diphenylacetylene (Scheme 1) catalyzed by $[\{RuCl_2(m\text{tppms})_2\}_2]$ in acidic aqueous solutions always resulted in (*Z*)-stilbene [(*Z*)-1,2-diphenylethene)] with only traces of (*E*)-stilbene, and only slight overreduction to the corresponding alkane was observed.[10]

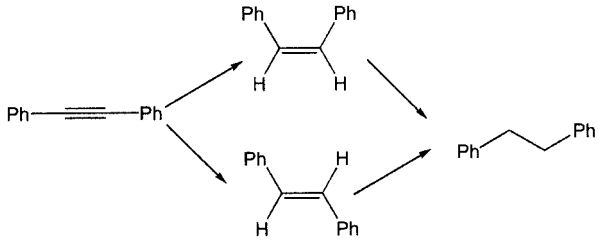


Scheme 1. Formation of products during the hydrogenation of 1,2-diphenylacetylene.

In the work to be presented, theoretical methods were applied to provide a possible mechanistic description for the formation of both (*Z*)- and (*E*)-stilbene during the hydrogenation of 1,2-diphenylacetylene in the current catalytic system and furthermore to account for the significant (*Z*)- vs. (*E*)-selectivity observed.

### The Catalytically Active Species

The formation of the catalytically active species was described in detail in one of our earlier publications, in which the mechanism of the regioselective C=C hydrogenation of α,β-unsaturated aldehydes was considered.[15] In the following section we often refer to those results, since the reaction for which a mechanism is presented proceeds in the same catalytic system.

Under acidic conditions $[RuHCl(m\text{tppms})_3]$ was detected by NMR spectroscopy to be the major species.[9] However, the spectroscopically detected complex cannot be the reactive species, since it only has a vacant position *trans* to the hydrido ligand. Thus, on the basis of QM/MM calculations

 © 2007 Wiley-VCH Verlag GmbH & Co. KGaA, Weinheim 

(in which $PPh_3$ ligands were used as models for the *m*tppms ligands) and experimental considerations, it was concluded that there were two possible pathways for the formation of a catalytically active species.[15a] One is the rearrangement of the complex to create a vacancy in the *cis* position to the hydrido ligand, and the other pathway involves the coordination of a water molecule and subsequent dissociation of a phosphane ligand. Both pathways were found to be feasible, thus the catalytic cycle was described by both possible active catalysts.[15a]

On the basis of the aforementioned considerations, the same two catalytically active species were considered in the current reaction. The models, $[RuHCl(PH_3)_3]$ (**1**) and $[RuHCl(H_2O)(PH_3)_2]$ (**1′**) for the assumed catalytically active species are shown in Figure 1.

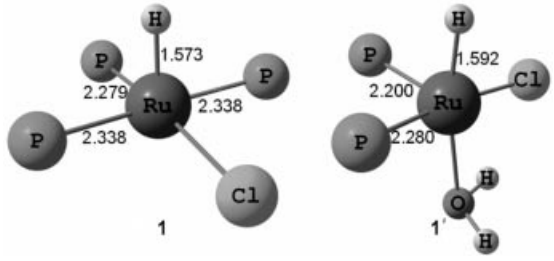


Figure 1. Optimized structures for $[RuHCl(PH_3)_3]$ (**1**) and $[RuHCl(H_2O)(PH_3)_2]$ (**1′**); the hydrogen atoms of the $PH_3$ ligands are omitted for clarity.

### Description of the Possible Reaction Mechanisms

We have calculated the possible reaction paths starting from both complex **1** and complex **1′**. Since no significant difference was found between the reaction mechanisms and energy profiles obtained for the two catalytically active species, we suppose it is enough to present the results starting from **1**. Nevertheless, the structures and energies of all stationary points obtained are available in the Supporting Information.

For the alkyne hydrogenation in the current catalytic system, three different reaction mechanisms were considered. The first step of all of them is the coordination of 1,2-diphenylacetylene to the catalytically active species and the formation of complex **2** (Figure 2). The total energy of the coordination is –3.9 kcal/mol (it has to be mentioned that this energy takes into account the fact that, prior to the coordination of the substrate, **1** has to rearrange in order to have the coordination vacancy in the *cis* position to the hydrido ligand).

Three mechanistic pathways for the semireduction of the carbon–carbon triple bond was considered:

I. Initial hydrido ligand transfer to the adjacent carbon atom with subsequent protonation of the other carbon atom by the participation of the solvent molecules (the *cis* product is formed).

II. Proton transfer from the solvent and subsequent transfer of the hydrido ligand to the other carbon atom of the triple bond (the *trans* product is formed).

III. Classical mechanism with no solvent participation (the *cis* product is formed).

#### Mechanism I

The first step of the reduction is the insertion of the carbon atom (in the *cis* position to the hydrido ligand) into the Ru–H bond, which takes place through the formation of $\mathbf{TS_{2-3}}$ (Figure 2), which lies 7.2 kcal/mol above the initial complex **2**. The product of this reaction is the intermediate **3** (lying 1.9 kcal/mol above complex **2**), in which an agostic bond is formed [*d*(C–H) = 1.16 Å, *d*(Ru–H) = 2.00 Å].

In aqueous solution, this complex can be stabilized by the coordination of a water molecule on the agostic site with an energy change of –21.4 kcal/mol. (Another mechanistic possibility is the coordination of a $H_2$ molecule instead of a $H_2O$ molecule to **3**, which will be discussed later as Mechanism III.) Considering the orientation of the phenyl groups in structure **4**, it can be seen that starting from this complex only the (*Z*)-isomer can be formed (Figure 3).

Since complex **4** does not contain either another hydrido ligand or an empty coordination site, the only possibility for the completion of the hydrogenation is the protonation of the Ru-bound carbon atom. Protonation of reasonably strong metal–carbon bonds require stronger acids, and in an aqueous phase, solvated hydroxonium ions can play that role. It was shown earlier[14a] that application of a single $H_3O^+$ as a protonating agent in the calculations represents a poor description of the real solvent environment. However, as it was mentioned in the introduction, previous studies[14,15] show that using a cluster of $[H_3O(H_2O)_2]^+$ as a representation of acidic aqueous solutions provides a good compromise between a realistic description, the system size and related proportional computational time. Hence, complex **4** and $[H_3O(H_2O)_2]^+$ were put together, and structure **5** was optimized as a minimum in the potential energy hypersurface (Figure 4), in which the acidic hydrogen of $H_3O^+$ points towards the carbon atom in order to be protonated. The transition state $\mathbf{TS_{5-6}}$ was also located as a stationary point on the potential energy surface, and it was found to lie only 1.6 kcal/mol above structure **5** in energy (Figure 4).

As a result of the protonation, (*Z*)-stilbene is formed, which remains loosely coordinated to the metal centre. The structure obtained as a result of IRC calculations and subsequent geometry optimization starting from $\mathbf{TS_{5-6}}$ is shown as structure **6** (Figure 4). The total energy change for the process **5** → **6** is hard to estimate correctly (it was calculated to be –37.9 kcal/mol), since rearrangement of the water cluster leads to the formation of a new hydrogen bond between $(H_2O)_3$ and the coordinated water molecule, the exergonicity of this step is thus surely overestimated.

The product of the protonation reaction was optimized without the water clusters (**7**), and it is shown in Figure 5. In this complex, the product (*Z*)-stilbene is still weakly co-

 © 2007 Wiley-VCH Verlag GmbH & Co. KGaA, Weinheim 

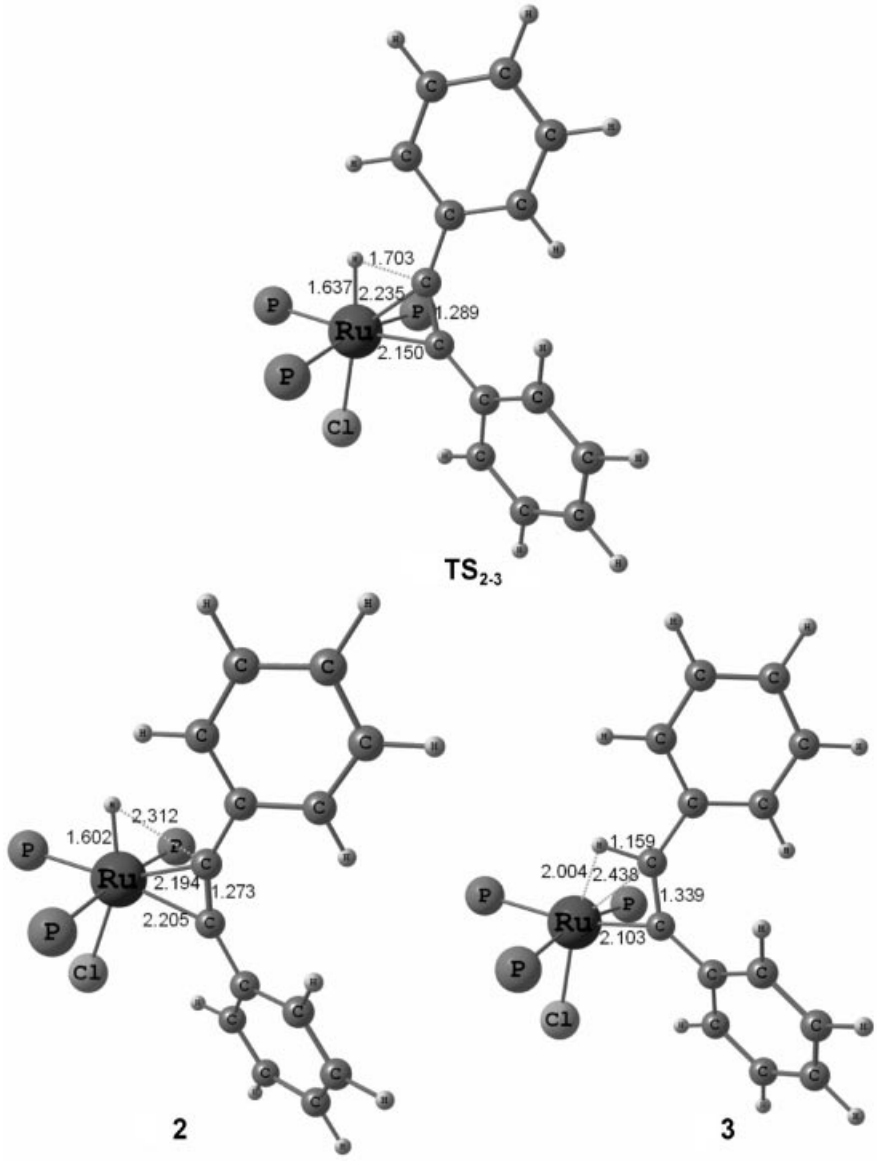


Figure 2. Optimized structures with selected bond lengths representing carbon insertion into the Ru–H bond in complex **2** (Mechanism I).

ordinated [*d*(Ru–C) = 2.65 and 2.63 Å, respectively] to the ruthenium centre. Complete decoordination of the product from **7** leads to the formation of **8** (Figure 5), with an energy change of 9.3 kcal/mol, generating an empty coordination site.

The final step of the reaction regenerates the catalytically active hydrido species. In aqueous solution, the most obvious way for this step to occur is the coordination and subsequent deprotonation of a $H_2$ molecule. It was shown in earlier studies that regeneration of the (hydrido)ruthenium is an energetically favourable reaction, since coordination of the $H_2$ molecule is an exergonic process, and the deprotonation of the coordinated $H_2$ molecule with water molecules occurs through low energy barriers.[15a]

In this case, coordination of hydrogen to complex **8** leads to complex **9** (Figure 5). The energy change for the coordination is –9.1 kcal/mol. On the basis of previous studies,[14,15] it is reasonable to assume that the deprotonation takes place by proton transfer from the dihydrogen ligand to the surrounding water molecules. In order to describe this step, we carried out calculations for a model that involves the interaction of complex **9** with a cluster of three water molecules and also for the corresponding hydrido species where the proton is transferred to the water (see structures **10** and **11** in Figure 6). The transition state for the deprotonation reaction could not be identified in these calculations because of the flat nature of the potential energy surface corresponding to structure **10**. In fact, the

 © 2007 Wiley-VCH Verlag GmbH & Co. KGaA, Weinheim 

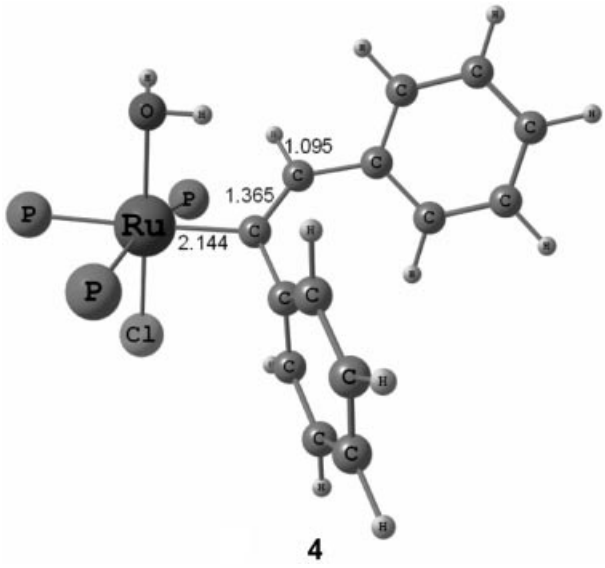


Figure 3. Optimized structure for complex **4**.

geometry optimization procedure initiated from the **9**···$(H_2O)_3$ species converged to **11** after leaving the flat part of the surface. The estimated energy difference between **10** and **11** is reasonably low (–6.2 kcal/mol) and shows that the deprotonation of the coordinated hydrogen ligand is thermodynamically favourable. It is expected that these kinds of computational difficulties could be avoided if much larger water clusters were used to represent the bulk water medium; however, larger clusters are at present computationally prohibitive.

The dissociation of a $H_2O$ molecule from the deprotonated complex and rearrangement to the most stable isomer leads to the regeneration of complex **1**, thus closing the catalytic cycle. The energy change for the last process is 3.7 kcal/mol. The reaction mechanism is summarized in Scheme 2.

### Mechanism II

Another possibility for the reduction to take place is that, after the coordination of 1,2-diphenylacetylene and formation of complex **2**, the first step of the reduction is the protonation of one carbon atom of the triple bond by the solvent environment. To explore this possible reaction pathway, $[H_3O(H_2O)_2]^+$ was used as the model for the protonating agent in aqueous solutions as in Mechanism I and in earlier projects.

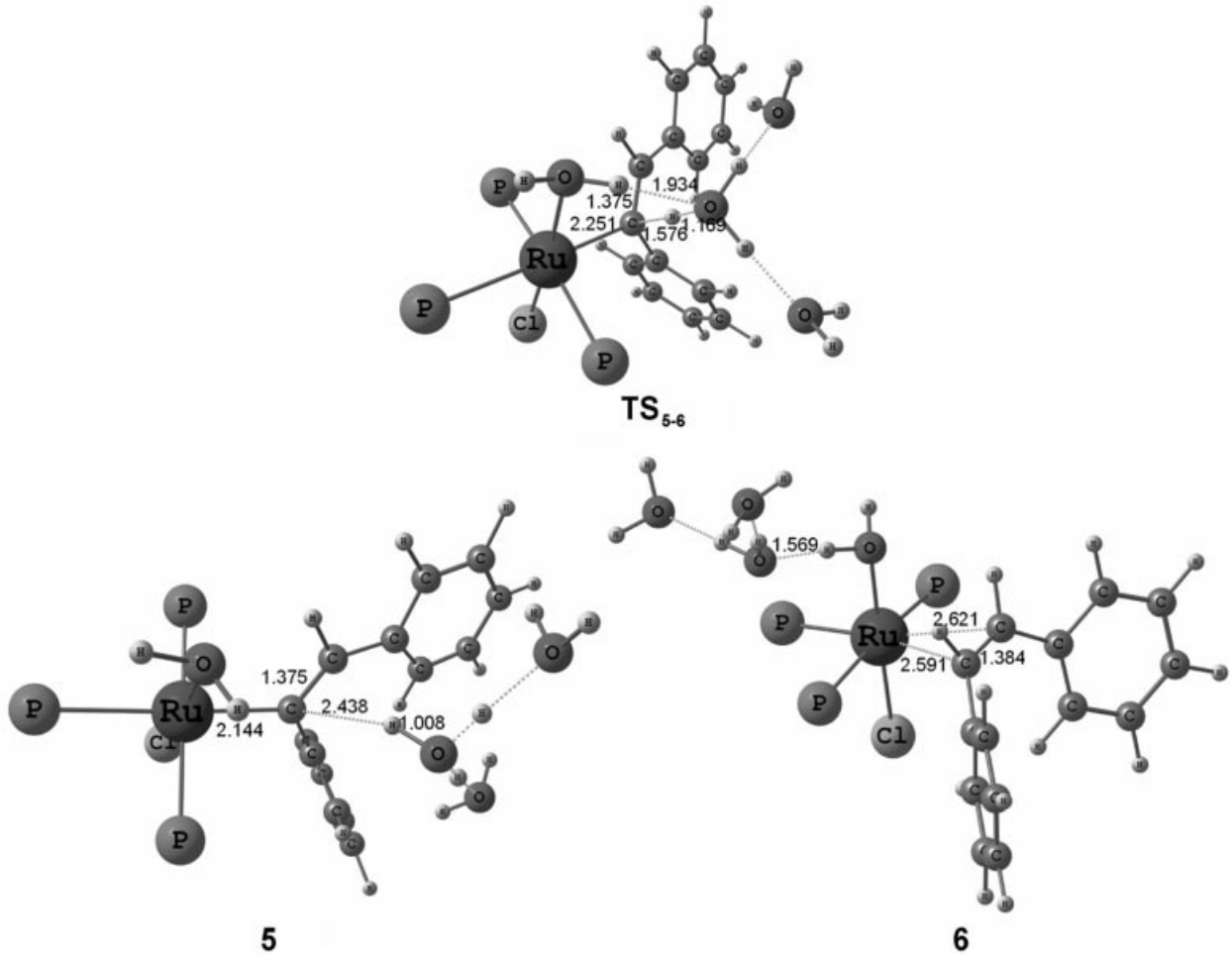


Figure 4. Optimized structures with selected bond lengths representing the protonation of the carbon atom (Mechanism I).

 © 2007 Wiley-VCH Verlag GmbH & Co. KGaA, Weinheim 

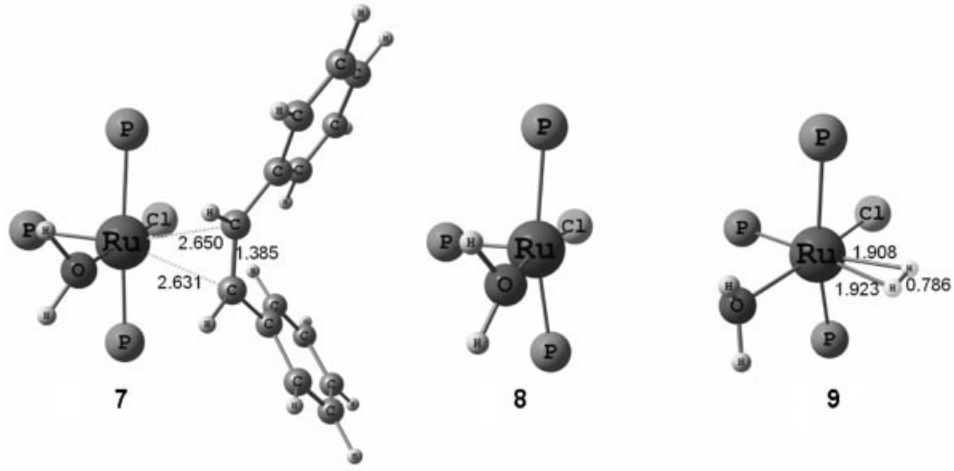


Figure 5. Optimized structures with selected bond lengths representing the decoordination of the product and subsequent coordination of a $H_2$ molecule.

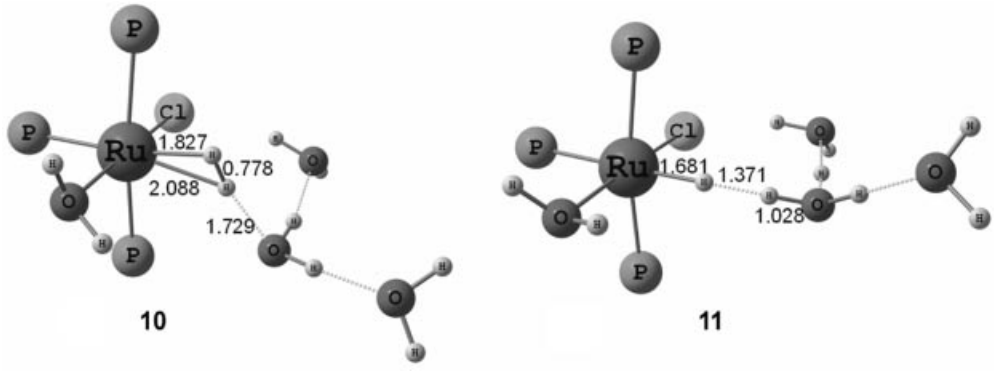


Figure 6. Optimized structures with selected bond lengths representing the deprotonation of the coordinated $H_2$ molecule.

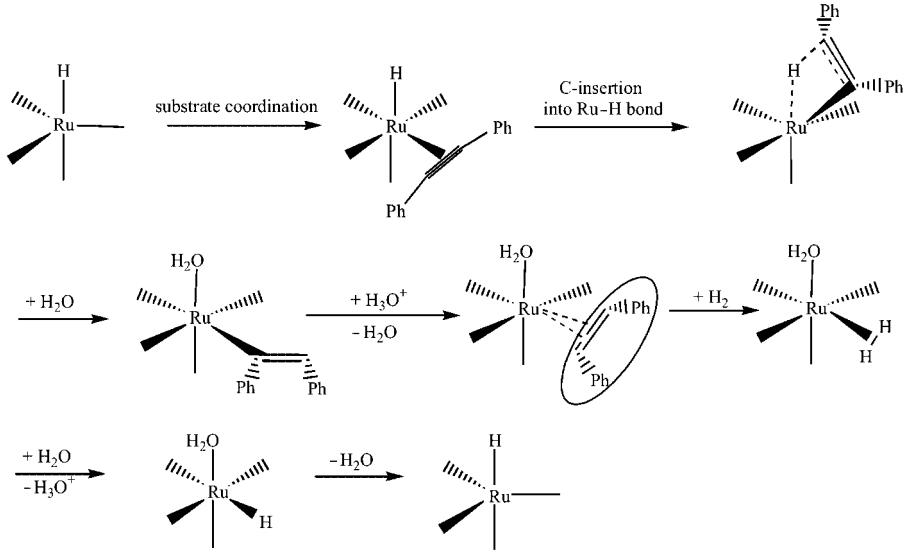


Scheme 2. Mechanism I for the reduction of 1,2-diphenylacetylene catalyzed by [{$RuCl_2$(*m*tppms)$_2$}$_2$] in acidic aqueous solutions.

Hence, $[H_3O(H_2O)_2]^+$ and complex **2** were put together in a way that the acidic hydrogen of the cluster points to the carbon atom, which is intended to be protonated, and structure **12** was optimized as a minimum (Figure 7). The transition state (**TS$_{12–13}$**) corresponding to proton transfer from $[H_3O(H_2O)_2]^+$ to the metal complex was also located as a stationary point on the potential energy surface, and the barrier for the protonation was found to be 9.6 kcal/

 © 2007 Wiley-VCH Verlag GmbH & Co. KGaA, Weinheim 

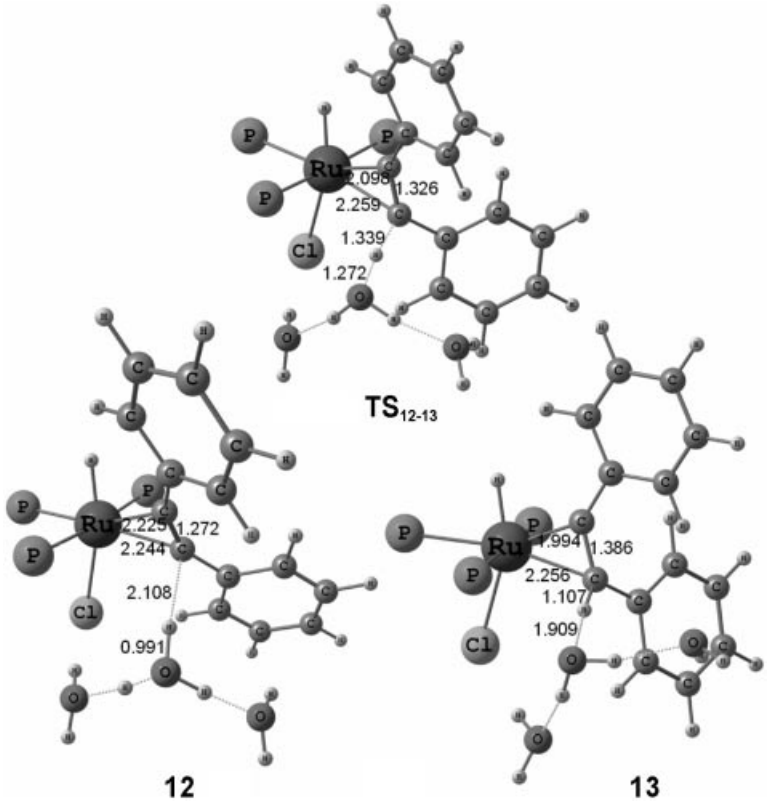


Figure 7. Optimized structures with selected bond lengths representing the protonation of the carbon in complex **12** (Mechanism II).

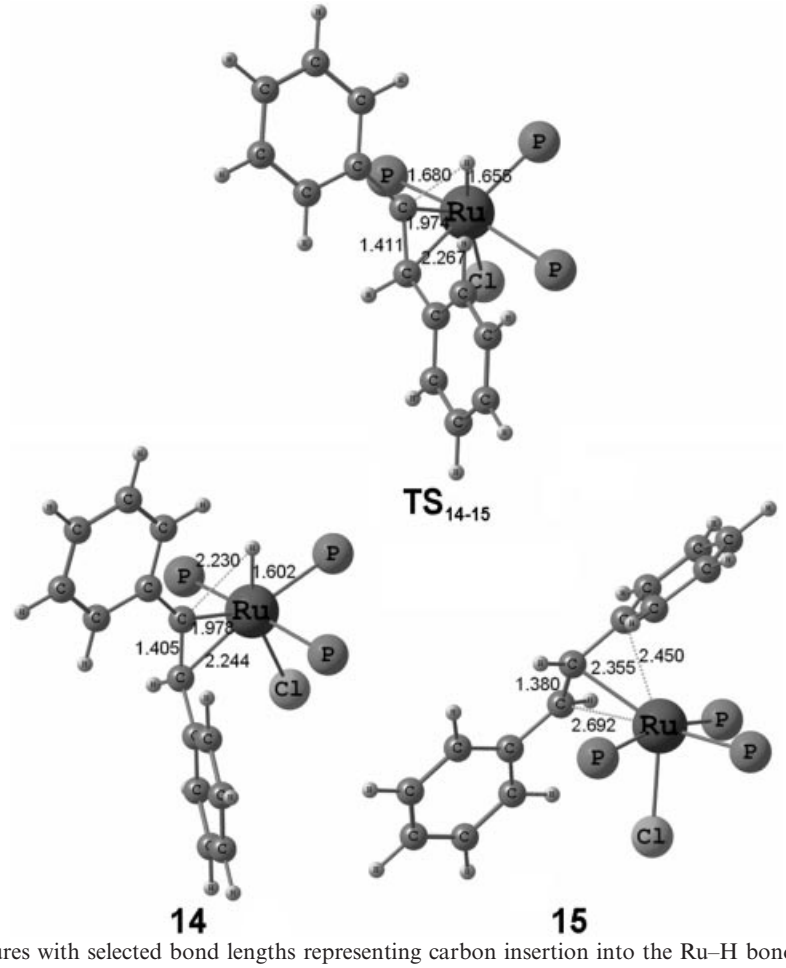


Figure 8. Optimized structures with selected bond lengths representing carbon insertion into the Ru–H bond (Mechanism II).

 © 2007 Wiley-VCH Verlag GmbH & Co. KGaA, Weinheim 

mol (Figure 7). The product of the protonation is structure **13**, which lies 1.5 kcal/mol lower in energy than structure **12** (Figure 7).

The completion of the reduction can be facilitated in this case by the transfer of the hydrido ligand to the other carbon atom. One would also think about the protonation of the other carbon, but protonation of a positively charged complex is considered to be very unfavourable. To obtain the stationary points relevant to this hydrido transfer, structure **13** was reoptimized in the absence of the water molecules, and structure **14** was optimized as the corresponding minimum (Figure 8). The transition state $\mathbf{TS_{14–15}}$ corresponding to the hydrido transfer was located on the potential energy surface, and the process can be characterized by a barrier of 9.1 kcal/mol. The steric position of the phenyl rings in structure **14** clearly indicates that in this reaction pathway only the (*E*)-isomer can be formed.

The product of the process, structure **15**, calculated from the IRC calculations contains coordinated (*E*)-stilbene (the energy change for the hydrido transfer is –31.4 kcal/mol), but in the presence of water molecules, this intermediate is converted into structure **16** (Figure 9). This complex, which contains a water molecule and (*E*)-stilbene loosely coordinated and has a similar structure to that of complex **7**, is formed from structure **15** with an energy change of –7.2 kcal/mol.

Further steps of the reaction mechanism, that is, regeneration of the catalytically active species, are the same as those in Mechanism I: decoordination of (*E*)-stilbene is followed by the coordination and subsequent deprotonation of a $H_2$ molecule. Then, decoordination of the $H_2O$ molecule regenerates the empty coordination site, which makes the coordination of another substrate molecule possible. The energy changes for these steps are the following: product dissociation: 8.4 kcal/mol, hydrogen coordination: –9.1 kcal/mol, deprotonation of $H_2$: –6.2 kcal/mol and $H_2O$ decoordination: 3.7 kcal/mol. The reaction mechanism is summarized in Scheme 3.

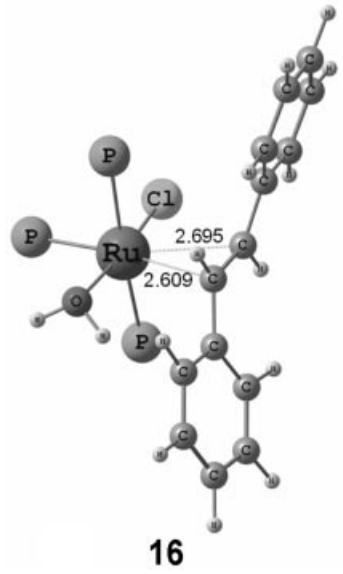


Figure 9. Optimized structure for complex **16**.

### Mechanism III

The third possible mechanism considered for the hydrogenation of 1,2-diphenylacetylene with the aforementioned Ru complex is connected to Mechanism I. As it was mentioned, complex **3**, formed by carbon insertion into the Ru–H bond, can be stabilized by the coordination of either a $H_2O$ or a $H_2$ molecule.

The coordination of a water molecule and the following reaction steps were discussed as Mechanism I. Another possibility is the coordination of a $H_2$ molecule to the complex and σ-bond metathesis between the $\eta^2$-coordinated $H_2$ and the alkyl moiety. Complex **17**, formed by the coordination of a hydrogen molecule to complex **3**, is shown in Figure 10. The energy change for the coordination is –16.0 kcal/mol. In this case the second hydrogen can come from the coordinated $H_2$ molecule. The transition state $\mathbf{TS_{17–18}}$ and the

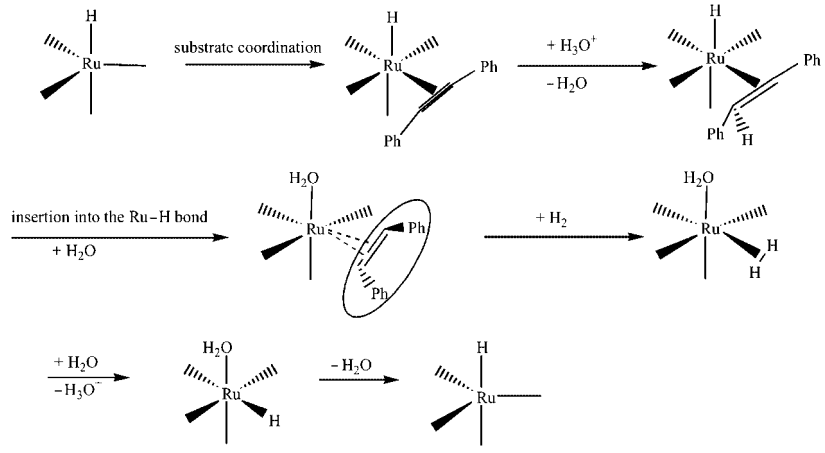


Scheme 3. Mechanism II for the reduction of 1,2-diphenylacetylene catalyzed by [{$RuCl_2$(*m*tppms)$_2$}$_2$] in acidic aqueous solutions.

 © 2007 Wiley-VCH Verlag GmbH & Co. KGaA, Weinheim 

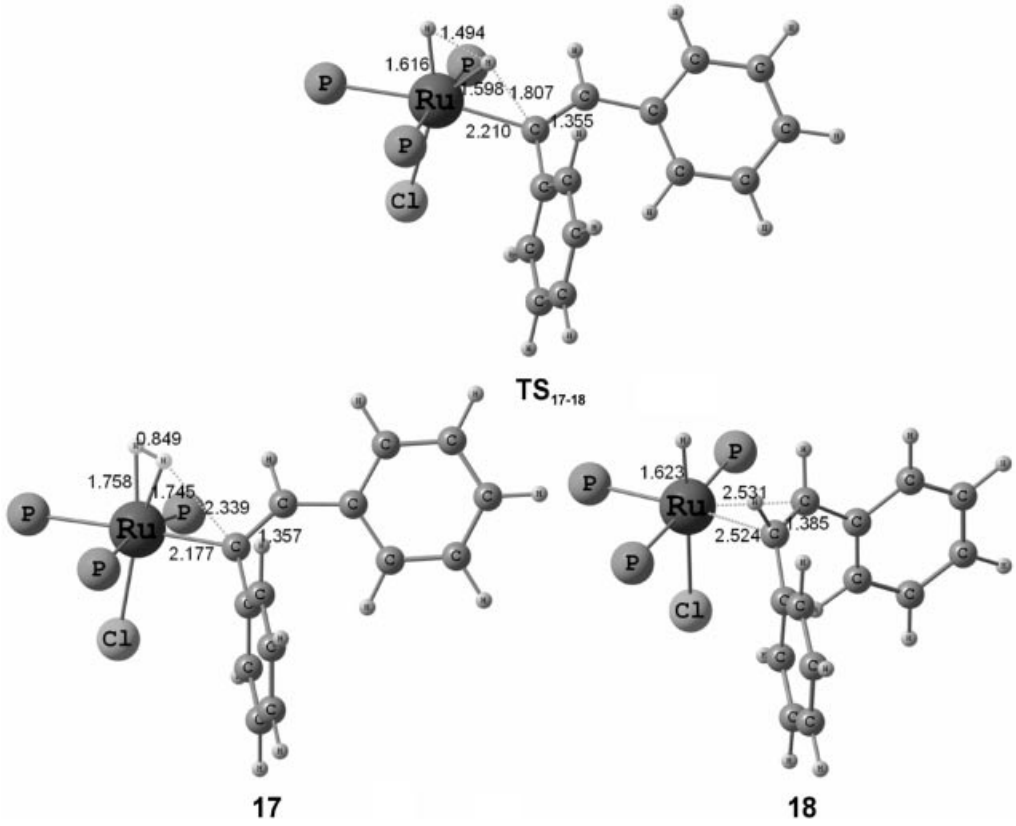


Figure 10. Optimized structures with selected bond lengths representing σ-bond metathesis in structure **17** (Mechanism III).

product of this reaction step, structure **18** (Figure 10), were obtained as stationary points. The calculated reaction barrier is 3.7 kcal/mol, whereas the energy change is –27.8 kcal/mol.

This mechanism would also facilitate the formation of the (*Z*)-product. Although the global barrier for this process is really similar to that of Mechanism I, we believe that this pathway does not play an important role in the process. The reason for this is not only that the coordination of $H_2$ to complex **2** is energetically less favourable than that of water (–21.4 vs. –16.0 kcal/mol), but also that the concentration of $H_2$ molecules in acidic aqueous solutions is well below that of water molecules. In addition, if the classic mechanism (no participation of solvent in the hydrogenation) were to act in aqueous solutions, it would not be possible to explain the selectivity as a function of pH, as it was demonstrated by Delbecq et al.,[21] and observed in our previous studies concerning the regioselective hydrogenation of α,β-unsaturated aldehydes.[15]

### Discussion and Comparison of the Proposed Mechanisms

On the basis of the energetics and other considerations, we can explain the stereoselectivity observed in the current catalytic system. Of the considered mechanisms, Mechanism I and III favour the formation of the (*Z*)-product, while Mechanism II leads to the formation of the (*E*)-product. Mechanism III was shown to be unimportant on the basis of the considerations in the end of the last section. Hence, the stereoselectivity can be explained by comparison of the energetics obtained for Mechanisms I and II.

If we consider the energy changes for the various steps of Mechanism I, it can be seen that the first step of the hydrogenation has a barrier of 7.2 kcal/mol, and after the first step coordination of a $H_2O$ molecule is energetically favourable by 21.4 kcal/mol, and in addition, the second hydrogenation step is characterized by a TS which lies only 1.6 kcal/mol over the corresponding minimum. Nevertheless, the first barrier in Mechanism II is 9.6 kcal/mol, and since the first step does not result in any coordination vacancy, no solvent coordination can give extra stabilization. In addition, the second step has a barrier of 9.1 kcal/mol. Comparing the energy values for the two mechanisms, it is quite clear that Mechanism I features more favourable energetics, thus it accounts for the stereoselectivity observed in acidic aqueous solutions.

## Concluding Remarks

Theoretical methods were applied in this work to describe the mechanism of the aqueous-phase hydrogenation of 1,2-diphenylacetylene with [{$RuCl_2$(*m*tppms)$_2$}$_2$] catalyst. Our study provided realistic mechanistic pathways for the formation of (*Z*)- and (*E*)-stilbene, and in addition the ener-

 © 2007 Wiley-VCH Verlag GmbH & Co. KGaA, Weinheim 

getics clearly accounted for the relevant stereoselectivity observed.

The mechanism of the reaction was described by the application of $PH_3$ model ligands for *m*tppms, which was proved to be a reliable substitution in earlier examinations of catalytic reactions with the same catalyst,[15] when phosphane dissociation is not considered as a reaction step. The same catalytically active species were used to provide a theoretical description for the regioselective C=C vs. C=O hydrogenation of α,β-unsaturated aldehydes in the same catalytic system, that is, using the same catalyst dissolved in acidic aqueous solution.

Since the reaction proceeds in water, the effect of the solvent had to be taken into account. In all reaction steps, the effect of the bulk solvent was estimated by the application of the polarizable continuum model (PCM/UA0), whereas in the case of the steps involving the participation of water molecules in proton transfer reactions, small clusters of water molecules were used as models for the solvent environment.

Three different mechanisms were considered for the reaction. Two of the mechanisms (Mechanism I and III) correspond to the formation of the (*Z*)-isomer, while Mechanism II results in the formation of (*E*)-stilbene. On the basis of both the energetics and experimental considerations, Mechanism I and II are thought to be feasible reaction pathways for the formation of the two stereoisomers.

In the course of both reaction mechanisms, the hydrogenation proceeds in two steps: the insertion of one carbon atom of the multiple bond to the Ru–H bond and the protonation of the other carbon atom. The two mechanisms differ in the order of the two hydrogenation steps. In the course of Mechanism I, the first step is the transfer of the hydrido ligand to the adjacent carbon atom of the coordinated substrate, and the hydrogenation is completed by the protonation of the other carbon atom of the multiple bond with hydroxonium ions, which results in the formation of (*Z*)-stilbene. Conversely, Mechanism II involves the protonation of one of the carbon atoms by the surrounding hydroxonium ions as the first step, which is followed by the insertion of the other carbon to the Ru–H bond. This latter mechanism yields the (*E*)-isomer as product. We mention that this (*E*)-isomer is the main alkene product under basic conditions; however, it is unlikely to form by the aforementioned mechanism, since the concentration of $H_3O^+$ is very low in basic solutions. We assume that $OH^-$ participation leads to reversed stereoselectivity in alkaline solutions.

The stereoselectivity observed in the reaction system was explained by the lower barriers and the more favourable energetics calculated for Mechanism I.

The calculations also highlighted again that water presents a distinct reaction environment in the case of organometallic processes, since the solvent molecules (and its ions) can take part in the reaction and make unconventional pathways possible. Water molecules can coordinate to the metal centres of the complexes, as was also considered in the course of the above investigation. In addition, water molecules can act as proton donors or acceptors, thus forming hydrogen or dihydrogen bonds with the ligands and taking part in proton transfer reactions with the metal complexes.

In summary, the present work provided a detailed mechanistic picture for the stereoselective hydrogenation of disubstituted alkynes with a water-soluble phosphane complex of ruthenium. It was found that the two important pathways corresponding to the formation of the two stereoisomers differ in the order of the two hydrogenation steps (insertion and protonation), and the calculated energetics is consistent with the experimentally observed stereoselectivity.

**Supporting Information** (see footnote on the first page of this article): Optimized geometries and thermochemistry data (total energy in the gas phase and total energy in solution in hartree units) for the species mentioned in the paper.

## Acknowledgments

We gratefully acknowledge the European Commission for funding this work through the AQUACHEM Research Training Network (Contract No. MRTN-CT-2003-503864). A. L. and G. U. acknowledge financial support from the Spanish MEC (Project No. CTQ2005-09000-CO2-01). A. L. thanks the *Generalitat de Catalunya* for a *Distinció' per a la Promoció de laRecerca Universitària*. F. J. is grateful for financial support by the National Research Fund of Hungary (Grant No. OTKA T043365).

[1] a) B. R. James, *Homogeneous Hydrogenation*, Wiley, New York **1973**; b) S. S. Kritsjánsdottír, J. R. Norton, "Acidity of Hydrido Transition Metal Complexes in Solution" in *Transition Metal Hydrides* (Ed.: A. Dedieu), VCH, Weinheim, **1992**; c) P. A. Chaloner, M. A. Esteruelas, F. Joó, L. A. Oro, *Homogeneous Hydrogenation*, Kluwer, Dordrecht, **1995**; d) M. Peruzzini, R. Poli (Eds.), *Recent Advances in Hydride Chemistry*, Elsevier, Amsterdam, **2003**.

[2] a) H. Lindlar, *Helv. Chim. Acta* **1952**, *35*, 446–456; b) J. Choi, N. M. Yoon, *Tetrahedron Lett.* **1996**, *37*, 1057–1060; c) C. A. Brown, V. K. Ahuja, *J. Org. Chem.* **1973**, *38*, 2226–2230.

[3] N. Semagina, E. Joannet, S. Parra, E. Sulman, A. Renken, L. Kiwi-Minsker, *Appl. Catal. A: Gen.* **2005**, *280*, 141–147.

[4] N. Marín-Astorga, G. Pecchi, J. Pinnavia, G. Alvez-Manoli, P. Reyes, *J. Mol. Catal. A* **2006**, *247*, 145–152.

[5] a) M. W. van Laren, C. J. Elsevier, *Angew. Chem. Int. Ed.* **1999**, *38*, 3715–3717; b) M. W. van Laren, M. A. Duin, C. Klerk, M. Naglia, D. Rogolino, P. Pelagatti, A. Bacchi, C. Pelizzi, C. J. Elsevier, *Organometallics* **2002**, *21*, 1546–1553; c) D. Evrard, K. Groison, Y. Mugnier, P. D. Harvey, *Inorg. Chem.* **2004**, *43*, 790–796.

[6] R. R. Schrock, J. A. Osborn, *J. Am. Chem. Soc.* **1976**, *98*, 2134–2143.

[7] M. Sodeoka, M. Shibasaki, *J. Org. Chem.* **1985**, *50*, 1147–1149.

[8] a) F. Joó, *Aqueous Organometallic Catalysis*, Kluwer, Dordrecht, **2001**; b) D. J. Adams, P. J. Dyson, S. J. Tavener, *Chemistry in Alternative Reaction Media*, Wiley, Chichester, **2004**; c) F. Joó, Á. Kathó, *Aqueous Phase Organometallic Catalysis* (Eds.: B. Cornils, W. A Herrmann), 2nd ed., Wiley-VCH, **2004**; d) B. Cornils, W. A. Herrmann, I. T. Horváth, W. Leitner, S. Mecking, H. Olivier-Bourbignon, D. Vogt (Eds.), *Multiphase Homogeneous Catalysis*, Wiley-VCH, Weinheim, **2005**; e) P. A. Grieco, *Organic Synthesis in Water*, Blackie, London, **1998**.

[9] a) F. Joó, J. Kovács, A. Cs. Bényei, Á. Kathó, *Angew. Chem. Int. Ed.* **1998**, *37*, 969–970; b) F. Joó, J. Kovács, A. Cs. Bényei, Á. Kathó, *Catal. Today* **1998**, *42*, 441–448.

 © 2007 Wiley-VCH Verlag GmbH & Co. KGaA, Weinheim 

[10] H. H. Horváth, F. Joó, *React. Kinet. Catal. Lett.* **2005**, *85*, 355–360.
[11] a) F. Joó, *Encyclopedia of Catalysis* (Ed.: I. T. Horváth), Wiley, New York, **2002**, vol. I; b) M. Laghmari, D. Sinou, *J. Mol. Catal.* **1991**, *66*, L15.
[12] a) N. Belkova, M. Besora, L. M. Epstein, A. Lledós, F. Maseras, E. S. Shubina, *J. Am. Chem. Soc.* **2003**, *125*, 7715–7725; b) G. Orlova, S. Scheiner, T. Kar, *J. Phys. Chem. A* **1999**, *103*, 514–520; c) H. S. Chu, Z. T. Xu, S. M. Ng, C. P. Lau, Z. Lin, *Eur. J. Inorg. Chem.* **2000**, 993–1000.
[13] F. Joó, J. Kovács, A. Cs. Bényei, L. Nádasdi, G. Laurenczy, *Chem. Eur. J.* **2001**, *7*, 193–199.
[14] a) G. Kovács, G. Schubert, F. Joó, I. Pápai, *Organometallics* **2005**, *24*, 3059–3065; b) G. Kovács, G. Schubert, F. Joó, I. Pápai, *Catal. Today* **2006**, *115*, 53–60.
[15] a) G. Kovács, G. Ujaque, A. Lledós, F. Joó, *Organometallics* **2006**, *25*, 862–872; b) A. Rossin, G. Kovács, G. Ujaque, A. Lledós, F. Joó, *Organometallics* **2006**, *25*, 5010–5023.
[16] M. J. Frisch, G. W. Trucks, H. B. Schlegel, G. E. Scuseria, M. A. Robb, J. R. Cheeseman, J. A. Montgomery Jr, T. Vreven, K. N. Kudin, J. C. Burant, J. M. Millam, S. S. Iyengar, J. Tomasi, V. Barone, B. Mennucci, M. Cossi, G. Scalmani, N. Rega, G. A. Petersson, H. Nakatsuji, M. Hada, M. Ehara, K. Toyota, R. Fukuda, J. Hasegawa, M. Ishida, T. Nakajima, Y. Honda, O. Kitao, H. Nakai, M. Klene, X. Li, J. E. Knox, H. P. Hratchian, J. B. Cross, V. Bakken, C. Adamo, J. Jaramillo, R. Gomperts, R. E. Stratmann, O. Yazyev, A. J. Austin, R. Cammi, C. Pomelli, J. W. Ochterski, P. Y. Ayala, K. Morokuma, G. A. Voth, P. Salvador, J. J. Dannenberg, V. G. Zakrzewski, S. Dapprich, A. D. Daniels, M. C. Strain, O. Farkas, D. K. Malick, A. D. Rabuck, K. Raghavachari, J. B. Foresman, J. V. Ortiz, Q. Cui, A. G. Baboul, S. Clifford, J. Cioslowski, B. B. Stefanov, G. Liu, A. Liashenko, P. Piskorz, I. Komaromi, R. L. Martin, D. J. Fox, T. Keith, M. A. Al-Laham, C. Y. Peng, A. Nanayakkara, M. Challacombe, P. M. W. Gill, B. Johnson, W. Chen, M. W. Wong, C. Gonzalez and J. A. Pople, *Gaussian 03*, Revision C.02, Gaussian Inc., Wallingford CT, **2004**.
[17] a) A. D. Becke, *J. Chem. Phys.* **1993**, *98*, 5648–5652; b) C. Lee, W. Yang, R. G. Parr, *Phys. Rev. B* **1988**, *37*, 785–789; c) P. J. Stephens, F. J. Devlin, C. F. Chabalowski, M. J. Frisch, *J. Phys. Chem.* **1994**, *98*, 11623–11627.
[18] a) P. J. Hay, W. R. Wadt, *J. Chem. Phys.* **1985**, *82*, 270–283; b) W. R. Wadt, P. J. Hay, *J. Chem. Phys.* **1985**, *82*, 284–298; c) P. J. Hay, W. R. Wadt, *J. Chem. Phys.* **1985**, *82*, 299–310.
[19] a) P. C. Hariharan, J. A. Pople, *Mol. Phys.* **1974**, *27*, 209–214; b) V. A. Rassolov, M. A. Ratner, J. A. Pople, P. C. Redfern, L. A. Curtiss, *J. Comput. Chem.* **2001**, *22*, 976–984.
[20] a) S. Miertus, E. Scrocco, J. Tomasi, *Chem. Phys.* **1981**, *55*, 117–129; b) V. Barone, M. Cossi, J. J. Tomasi, *J. Chem. Phys.* **1997**, *107*, 3210–3221.
[21] J. Joubert, F. Delbecq, *Organometallics* **2006**, *25*, 854–861.

Received: December 18, 2006
Published Online: May 8, 2007

 © 2007 Wiley-VCH Verlag GmbH & Co. KGaA, Weinheim 

DOI: 10.1002/ejic.200601235

# Metallated Phthalocyanines as the Core of Dendrimers – Synthesis and Spectroscopic Studies

**Julien Leclaire,[a] Rodolphe Dagiral,[a] Anna Pla-Quintana,[a] Anne-Marie Caminade,*[a] and Jean-Pierre Majoral*[a]**

**Keywords:** Dendrimers / Phthalocyanine / Phosphorus / UV/Vis spectroscopy / Cobalt

The complexation of a first-generation dendrimer possessing a metal-free octasubstituted phthalocyanine as its core has been carried out with copper and cobalt chlorides. In the case of the cobalt complex, the synthesis of the dendrimer has been pursued up to the eighth generation. The progressive influence of the branches upon the core has been studied with dendrimers from generation 1 to generation 7, using UV/Vis spectroscopy. These data indicate a progressive isolation of the core.

(© Wiley-VCH Verlag GmbH & Co. KGaA, 69451 Weinheim, Germany, 2007)

## Introduction

Phthalocyanines[1] possess unique physico-chemical properties, which led to widespread potential applications in various fields such as photodynamic therapy,[2] solar energy conversion,[3] various optoelectronic devices,[4] or catalysed photooxidation of pollutants.[5] The main intrinsic problem when using such compounds is their strong stacking tendency to form dimers and other aggregated species in solution,[6] which induces a significant decrease in the photosensitising efficiency. Thus, much effort has been put into synthesizing nonaggregated phthalocyanines, generally by grafting bulky substituents, which also increase the solubility. One interesting way to achieve this goal consists of grafting dendritic substituents. Several examples have been reported since the first one published in 1997.[7] The phthalocyanine core can be either free,[8] or more generally complexed by a metal (in particular zinc),[7] or connected to a silicon derivative bearing dendritic stoppers.[9] In most cases, these phthalocyanines are tetrasubstituted, and only a few publications have reported the synthesis of octasubstituted dendritic phthalocyanines.[10,11] This is surprising in view of the advantages offered by the octasubstitution over the tetrasubstitution, in particular the absence of regioisomers, and a higher steric hindrance, which should facilitate the isolation of the core (preventing aggregation), even for low-generation dendritic substituents. This observation prompted us to report the synthesis of an octasubstituted metal-free phthalocyanine, which we used as the core for growing phosphorus-containing dendritic branches[12] up to generation 5, including a water-soluble series.[13] Having in hand a series of dendrimers possessing a metal-free phthalocyanine as a core, it appeared interesting to study their complexation ability, and the consequences of the complexation upon their spectroscopic properties. We report here the synthesis and characterization of a series of dendritic phthalocyanine complexes from generation 1 to generation 8, their UV/Vis properties, and the structural information deduced from these data.

## Results and Discussion

The complexation could have been carried out with any of the generations from 0 to 5 of the dendrimer having a free phthalocyanine as a core that we have previously synthesized;[12,13] however, from a practical point of view the first generation appears to be the most suitable. Indeed, it is more soluble than generation zero, and it is sufficiently small to ascertain a quantitative complexation. We decided to study the complexation of two metals that were very rarely incorporated into the core of phthalocyanine-containing dendrimers: copper (one example of a first generation only)[14] and cobalt (one example of first and second generations).[15] In both cases the reaction is carried out with the corresponding dichloride derivatives, in the presence of triethylamine as a base in THF (Scheme 1). The complexation reaction is mainly controlled by the disappearance of the band at 3250 $cm^{-1}$ in the infra-red spectra, corresponding to the pyrrolic NH bonds. Indeed, we have previously shown that triethylamine (and even DBU) are unable to deprotonate the phthalocyanine in THF,[12] thus the absence of N–H bonds is exclusively due to the complexation.

We expected that the paramagnetism due to the presence of $Cu^{II}$ could induce an enlargement of the signals detected

[a] Laboratoire de Chimie de Coordination du CNRS,
205 route de Narbonne, 31077 Toulouse Cedex 4, France
Fax: +33-5-61553003
E-mail: caminade@lcc-toulouse.fr
majoral@lcc-toulouse.fr

 © 2007 Wiley-VCH Verlag GmbH & Co. KGaA, Weinheim 

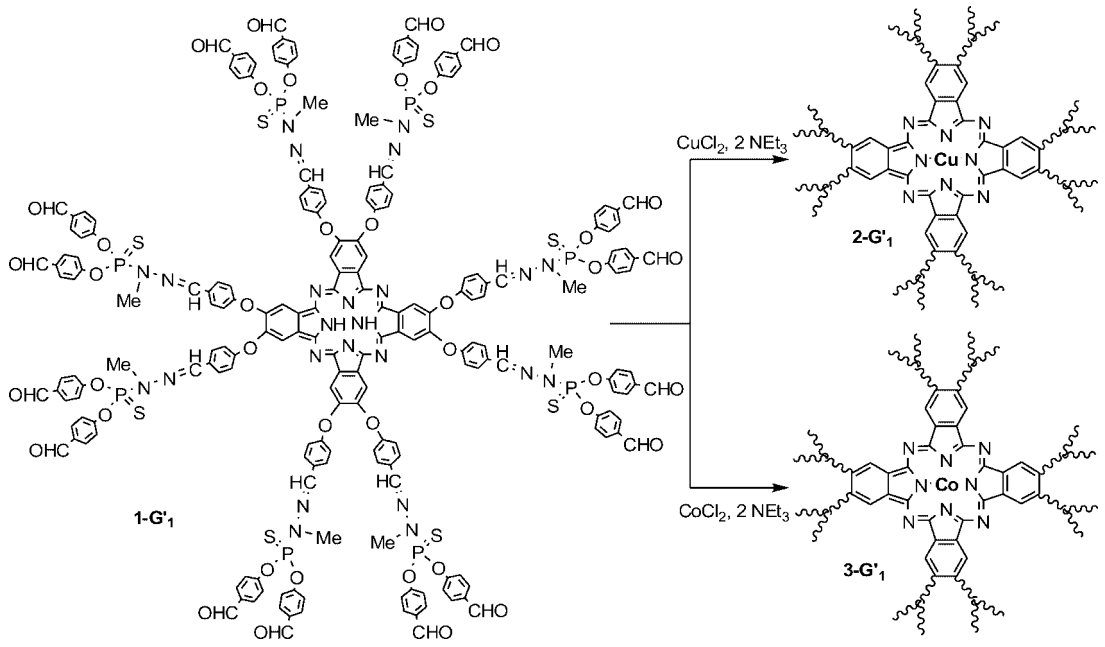


Scheme 1.

by NMR; such a phenomenon is observed and is particularly important for $^1$H NMR, as mentioned in the single existing example reported so far.[14] On the other hand, $Co^{II}$ in $CoCl_2$ is not paramagnetic, but we observed an enlargement of the NMR signals, indicating that the resulting complex is paramagnetic. No NMR spectroscopic data were reported for the single previous example of a dendritic phthalocyanine cobalt complex,[15] but such paramagnetism is known for cobalt complexes of nondendritic phthalocyanines.[16] The perturbation being less important with the cobalt complex than with the copper one, we decided to grow the dendrimer only from the cobalt complex **3-G′$_1$**, using our classical method of synthesis of phosphorus-containing dendrimers,[12,17] i.e. the repetition of condensation reactions between aldehyde endgroups and the phosphorhydrazide $H_2NNMeP(S)Cl_2$, and substitution reactions of the chlorine atoms by the sodium salt of 4-hydroxybenzaldehyde (Scheme 2). The completion of the condensation reactions is easily shown by $^1$H NMR, with the disappearance of the singlet corresponding to the aldehyde groups (also detected by $^{13}$C NMR and IR). The substitution reaction is monitored by $^{31}$P NMR, which firstly displays a signal at ca. 74 ppm, corresponding to the monosubstitution [P(S)-Cl($OC_6H_4CHO$)], as well as the signal corresponding to unreacted $P(S)Cl_2$ at $\delta$ = 63.3 ppm. Both signals disappear when the reaction has gone to completion, on behalf of the appearance of a signal at $\delta$ = 60.5 ppm. The precision of the NMR techniques to ascertain the completion of these reactions is estimated to be 0.5%. These syntheses have been carried out up to the eighth generation **3-G$_8$** [$P(S)Cl_2$ endgroups]. This is not the highest generation obtainable (no particular broadening of signals is observed); however, the series of dendrimers synthesized up to this generation is large enough to study the progressive influence of the branches upon the core, and is the largest series of dendritic phthalocyanines reported in the literature to date, thus we decided to stop at this stage.

The phthalocyanine core is a sensitive probe and sensor, thus it appeared interesting to study the UV/Vis and fluorescence properties of this family of dendritic phthalocyanine complexes. All experiments are carried out with dendrimers with aldehyde endgroups (from **3-G′$_1$** to **3-G′$_7$**), which are more stable than the $P(S)Cl_2$ endgroups. The π-π* transitions of the phthalocyanine ring should afford two types of absorption bands centred at about 300 nm (B-band) and about 670 nm (Q-band) in the UV/Vis spectra.

The B band is not very useful to study the behaviour of the core, since there is a superposition with the absorption band characteristic of the arylhydrazones constituting the branches of the dendrimers. However, this area is interesting to study the dependence of the molar absorption coefficient ($\varepsilon$) on the number of chromophoric units. We have already shown that there is a linear correlation between $\varepsilon$ and the number of aryl groups for the dendrimers built from the free phthalocyanine core, at least up to generation four.[12] The question of the linearity remains open for high generations, but plotting the measured values of $\varepsilon$ vs. the theoretical number of aryl groups gives a straight line even up to generation seven (Figure 1). Such behaviour both confirms that each arylhydrazone group is electronically independent (no overcrowding on the periphery) and that the expected number of arylhydrazones is indeed present (no large defects, even for high generations), confirming the information deduced from NMR spectroscopic data.

The Q-band of phthalocyanines is in an area where the dendritic skeleton is totally transparent, thus it is able to provide very interesting information concerning the symmetry and the environment of the core. Indeed, free neutral phthalocyanines have a $D_{2h}$ symmetry, inducing a splitting of the Q-band into two components [$Q_y(0,0)$ and $Q_x(0,0)$]

 © 2007 Wiley-VCH Verlag GmbH & Co. KGaA, Weinheim 

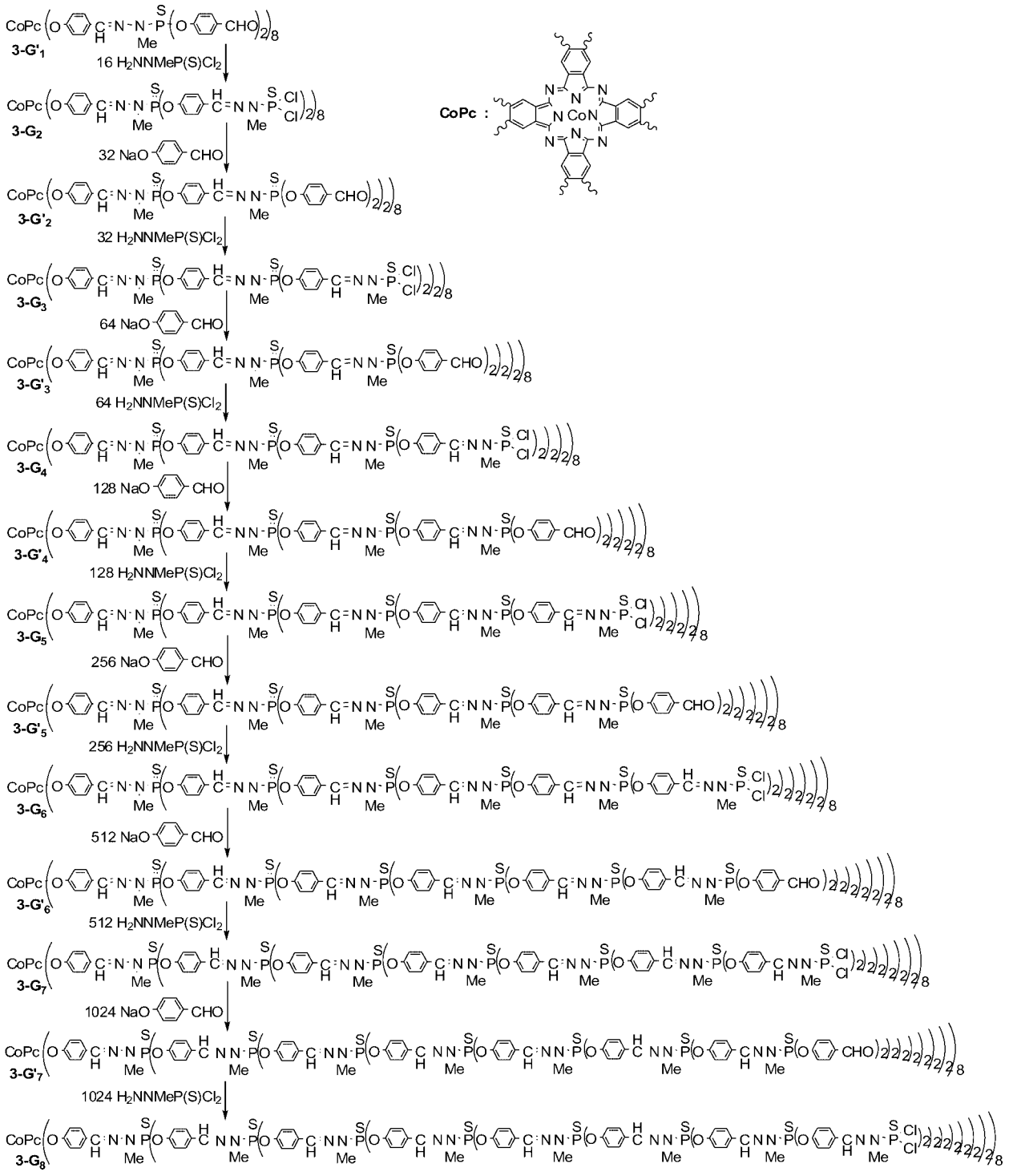


Scheme 2.

giving two main absorptions (ca. 670 and 700 nm). On the other hand, the complexation of a metal induces a $D_{4h}$ symmetry, which should give a single Q-band. The UV/Vis spectrum of the first generation **3-G′$_1$** in the area 650–700 nm displays a single band [$\lambda$ = 674 nm, Q(0,0)], accompanied as usual by a vibrational band [$\lambda$ = 610 nm, Q(0,1)] (Figure 2). However, a broad band is also clearly visible between both bands, usually attributed to an aggregation phenomenon. This attribution is confirmed by the fact that it progressively disappears when the number of the generation increases. In the spectrum corresponding to the seventh generation **3-G′$_7$** (see the insert in Figure 2), only the Q(0,0) and Q(0,1) bands are visible, and the intermediate band has totally disappeared; obviously, any aggregation is unlikely for a seventh generation in which the core should be totally protected by the branches.

 © 2007 Wiley-VCH Verlag GmbH & Co. KGaA, Weinheim 

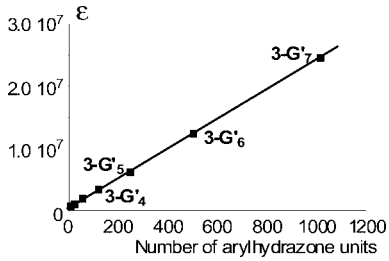


Figure 1. Variation of $\varepsilon$ ($mol^{-1}$ L $cm^{-1}$) at 268 nm with the number of arylhydrazone groups in $CHCl_3$.

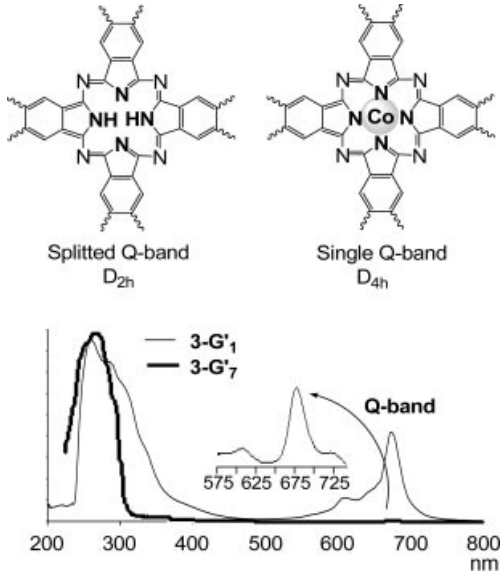


Figure 2. (top) Symmetry of free and complexed phthalocyanine cores, and spectroscopic consequences. (bottom) UV/Vis spectra of the first (**3-G′$_1$**) and seventh (**3-G′$_7$**) generations of the complexed cobalt phthalocyanine; both spectra are normalized to have the same intensity at 268 nm. The insert is an enlargement of the area of the Q-band of **3-G′$_7$** in THF.

The area of the Q-band provides other proofs of the progressive isolation of the core when the generation increases. Indeed, the value of $\varepsilon_{max}$ for the Q-band increases linearly from generation 1 to generation 5, and more smoothly from generation 5 to generation 7 (Figure 3). Such behaviour corresponds to a progressive isolation of the core, as shown by an analogous increase of $\varepsilon$ already reported for chromophores encapsulated in liposomes.[18] Furthermore, the value of $\lambda_{max}$ for the Q-band also increases linearly (bathochromic effect) from generation 1 to generation 5, and is practically constant from generation 5 to generation 7. Reichardt has proposed a relationship between solvatochromism and polarity.[19] We may interpret the bathochromic effect observed here as a consequence of the increase of the local polarity induced by the branches (constituted of arylhydrazones) towards the core. We already observed the same phenomenon for dendritic metal-free phthalocyanines up to generation 4.[12] The major (and unprecedented) information obtained here is that this increase is stopped after the fifth generation. We may interpret this phenomenon as a consequence of the steric hindrance around the core: it is already totally encapsulated by the branches of the fifth generation, and the presence of additional branches has no influence on it.

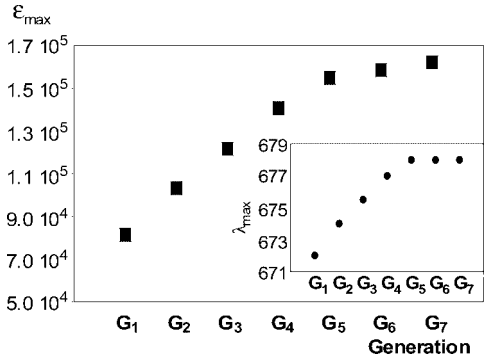


Figure 3. Variation of $\varepsilon_{max}$ of the Q-band with the generation. Insert: variation of $\lambda_{max}$ of the Q-band with the generation for compounds **3-G′$_n$** ($n$ = 1–7), in THF.

Fluorescence also might be particularly suitable to detect the variation of the response of the dendrimer core upon modifications of its local environment. Thus, we tried to study the fluorescence of the series **3-G′$_n$** in THF, via excitation at the beginning of the Q-band at 646 nm and using 3,3′-diethyloxatricarbocyanine iodide (DOTCI) in absolute ethanol as a reference.[20] However, no fluorescence is observed. Such behaviour may seem surprising; indeed, dendritic zinc phthalocyanines in organic solvents have a relatively intense quantum yield ( ≈ 0.30) even for small generations (0–2),[21] but a complete lack of fluorescence has been observed for some cobalt phthalocyanines.[22] Such behaviour is due to the unfilled d-orbitals of $Co^{II}$ that couple with the π orbital system of the phthalocyanine, providing additional and very efficient channels for π* deactivation.[22] Thus, it is not surprising to observe the absence of fluorescence in our case; indeed, this intrinsic deactivation obviously cannot be prevented by the presence of the dendritic branches, whatever the generation of the dendrimer.

## Conclusions

The synthesis of the largest series of dendritic phthalocyanines to date (up to generation 8), and the study of their spectroscopic properties provide interesting insights into the nanoenvironment around the phthalocyanine core and into the role of the dendritic branches. A progressive protection of the core can be deduced from the UV/Vis spectra as expected. The shielding effect of the branches induces an increase of the intensity ($\varepsilon$) of the Q-band specific of phthalocyanines. Furthermore, an increase of the local polarity induced by the arylhydrazone branches constituting the skeleton of the dendrimers is observed, as shown by the bathochromic shift of the Q-band. Both phenomena are observed up to generation 5, but ceased for generations 6 and 7. Such behaviour indicates that the branches of the fifth generation provide a maximum shielding and crowding of the core, and that the influence of additional layers (generations) cannot be detected by the core.

 © 2007 Wiley-VCH Verlag GmbH & Co. KGaA, Weinheim 

## Experimental Section

**General:** All manipulations were carried out with standard high vacuum and dry-argon techniques. The solvents were freshly dried and distilled (THF and ether over sodium/benzophenone, pentane and $CH_2Cl_2$ over phosphorus pentoxide). All the vessels were wrapped in aluminum foil to protect the compounds from light. Classical $^1H$, $^{13}C$, $^{31}P$ NMR spectra were recorded with Bruker AC 200, AC 250, DPX 300 or AMX 400 spectrometers. References for NMR chemical shifts are 85% $H_3PO_4$ for $^{31}P$ NMR, $SiMe_4$ for $^1H$ and $^{13}C$ NMR spectroscopy. The attribution of $^{13}C$ NMR signals has been done using $J_{mod}$, two-dimensional HMBC, and HMQC, Broad Band or CW $^{31}P$ decoupling experiments when necessary. The numbering used for NMR assignments is depicted in Figure 4. The acquisition of mass spectra (MALDI-TOF) was attempted for the higher generations with a Voyager DE-ST spectrometer (Perseptive Biosystems), but could not afford any data concerning the purity of these compounds, due to rearrangements of the hydrazone linkages, as already observed.[23] UV/Vis spectra were recorded with a Specord 205 spectrophotometer (Analytik Jena).

**Dendrimer 2-G′$_1$: 1-G′$_1$** (0.150 g, 0.036 mmol),[12] $CuCl_2$ (0.0049 g, 0.036 mmol) and triethylamine (11.6 μL, 0.083 mmol) in THF (1.5 mL) were heated at 100 °C whilst stirring in a sealed Schlenk tube for 3 h. The mixture was then cooled to room temperature and was filtered through celite. The resulting solution was evaporated to dryness to afford **2-G′$_1$** as a blue powder in 98% yield (0.149 g). $^{31}P\{^1H\}$ NMR ($CDCl_3$): $\delta$ = 60.6 (s, $P_1$) ppm. $^1H$ NMR ($CDCl_3$): $\delta$ = 3.37 (br. s, 24 H, $CH_3$-N), 7.34 (br. s, 48 H, $C_{0-1}{}^2$-H), 7.79 (br. s, 64 H, $C_{0-1}{}^3$-H, CH=N, CHPc), 9.86 (br. s, 16 H, CHO) ppm. $^{13}C\{^1H\}$ NMR ($CDCl_3$): $\delta$ = 32.8 (d, $^2J_{CP}$ = 12.6 Hz, $CH_3$-N-$P_1$), 115.2 (s, $C^2$), 117.7 (s, $C_0{}^2$, $C^1$), 122.0 (d, $^3J_{CP}$ = 4.6 Hz, $C_1{}^2$), 128.7 (s, $C_0{}^3$), 129.9 (s, $C^3$), 131.4 (s, $C_1{}^3$), 131.6 (s, $C_0{}^4$), 133.6 (s, $C_1{}^4$), 139.9 (d, $^3J_{CP}$ = 11.9 Hz, CH=N-N-$P_1$), 149.8 (s, $C^4$), 150.0 (s, $C_0{}^1$), 155.1 (d, $^2J_{CP}$ = 7.8 Hz, $C_1{}^1$), 190.8 (br. s, CHO) ppm. IR (KBr): $\tilde{\nu}$ = 1702 $cm^{-1}$ $\nu_{CHO}$. $C_{208}H_{152}CuN_{24}O_{40}P_8S_8$ (4195.5): calcd. C 59.55, H 3.65, N 8.01; found C 59.27, H 3.81, N 7.96.

**Dendrimer 3-G′$_1$: 1-G′$_1$** (0.666 g, 0.161 mmol), $CoCl_2$ (0.0209 g, 0.161 mmol) and triethylamine (49.4 μL, 0.354 mmol) in THF (6 mL) were heated at 110 °C whilst stirring in a sealed Schlenk tube for 3 h. The mixture was then cooled to room temperature overnight and was concentrated under reduced pressure. Then dichloromethane (20 mL) was added and the resulting mixture was filtered through celite. The resulting solution was evaporated to dryness to afford **3-G′$_1$** as a dark green powder in 87% yield (0.585 g). $^{31}P\{^1H\}$ NMR ($CDCl_3$): $\delta$ = 60.7 (s, $P_1$) ppm. $^1H$ NMR ($CDCl_3$): $\delta$ = 3.42 (br. s, 24 H, $CH_3$-N), 7.36 (br. s, 48 H, $C_{0-1}{}^2$-H), 7.76 (br. s, 64 H, $C_{0-1}{}^3$-H, CH=N, CHPc), 9.89 (br. s, 16 H, CHO) ppm. $^{13}C\{^1H\}$ NMR ($CDCl_3$): $\delta$ = 32.9 (br. s, $CH_3$-N), 118.0 (br. s, $C_0{}^2$), 122.1 (br. s, $C_1{}^2$), 128.6 (br. s, $C_0{}^3$), 131.5 (br. s, $C_1{}^3$), 133.8 (br. s, $C_1{}^4$), 140.0 (br. s, CH=N-N-$P_1$), 155.2 (br. s, $C_1{}^1$), 190.7 (br. s, CHO) ppm. IR (KBr): $\tilde{\nu}$ = 1702 $cm^{-1}$ $\nu_{CHO}$. $C_{208}H_{152}CoN_{24}O_{40}P_8S_8$ (4190.9): calcd. C 59.61, H 3.66, N 8.02; found C 60.36, H 3.71, N 8.07.

**General Procedures for the Synthesis of Dendrimers 3-G$_n$ and 3-G′$_n$**

**Dendrimers 3-G$_n$:** A freshly prepared solution of dichlorothiophosphorhydrazide (0.25 M in $CHCl_3$) was added dropwise to a solution of **3-G′$_{n-1}$** [0.500 g; $n$ = 2 (0.1193 mmol), $n$ = 3 (0.0526 mmol), $n$ = 4 (0.0248 mmol), $n$ = 5 (0.0121 mmol), $n$ = 6 (0.0059 mmol), $n$ = 7 (0.00296 mmol), $n$ = 8 (0.00147 mmol)] in THF (5 to 10 mL). The resulting mixture was stirred overnight then evaporated to dryness. The residue was washed with 20 mL of diethyl ether/pentane (1:1) then dried under vacuum. Dendrimers **3-G$_n$** were obtained as coloured powders from dark green for the lowest generations to light green for the highest generations.

**Dendrimers 3-G′$_n$:** 4-Hydroxybenzaldehyde sodium salt (5% excess) was added to a solution of **3-G$_n$** [0.600 g; $n$ = 2 (0.0887 mmol), $n$ = 3 (0.0409 mmol), $n$ = 4 (0.0197 mmol), $n$ = 5 (0.0097 mmol), $n$ = 6 (0.0048 mmol), $n$ = 7 (0.00239 mmol)] in THF (10 to 20 mL). The resulting mixture was stirred overnight, and then centrifuged. The solution was concentrated under reduced pressure and the residue was washed with 20 mL of THF/diethyl ether/pentane (1:2:2), then twice with 20 mL of diethyl ether/pentane (1:1). Dendrimers **3-G′$_n$** were obtained as coloured powders (from dark green for the lowest generations to light green for the highest generations) after drying under vacuum.

**3-G$_2$:** 79% Yield, 0.638 g. $^{31}P\{^1H\}$ NMR ($CDCl_3$): $\delta$ = 62.3 (br. s, $P_1$), 63.3 (br. s, $P_2$) ppm. $^1H$ NMR ($CDCl_3$): $\delta$ = 3.36 (m, 72 H, $CH_3$-N-$P_{1-2}$), 7.25 (br. s, 48 H, $C_{0-1}{}^2$-H), 7.66 (br. s, 80 H, $C_{0-1}{}^3$-H, CH=N-N-$P_{1-2}$, CHPc) ppm. $^{13}C\{^1H\}$ NMR ($CDCl_3$): $\delta$ = 31.9 (d, $^2J_{CP}$ = 12.3 Hz, $CH_3$-N-$P_2$), 33.0 (d, $^2J_{CP}$ = 13.2 Hz, $CH_3$-N-$P_1$), 115.5 (s, $C^2$), 117.6 (br. s, $C_0{}^2$, $C^1$), 121.9 (br. s, $C_1{}^2$), 128.7 (br. s, $C_0{}^3$, $C_1{}^3$), 129.8 (s, $C^3$), 131.4 (br. s, $C_0{}^4$, $C_1{}^4$), 139.7 (br. s, CH=N-N-$P_1$), 140.7 (d, $^3J_{CP}$ = 17.9 Hz, CH=N-N-$P_2$), 150.3 (br. s, $C_0{}^1$), 151.9 (br. s, $C_1{}^1$) ppm. $C_{224}H_{200}Cl_{32}CoN_{56}O_{24}P_{24}S_{24}$ (6767): calcd. C 39.76, H 2.98, N 11.59; found C 39.89, H 2.93, N 11.71.

**3-G′$_2$:** 98% Yield, 0.826 g. $^{31}P\{^1H\}$ NMR ($CDCl_3$): $\delta$ = 60.6 (s, $P_2$), 62.5 (s, $P_1$) ppm. $^1H$ NMR ($CDCl_3$): $\delta$ = 3.34 (m, 72 H, $CH_3$-N-$P_{1-2}$), 7.35 (m, 112 H, $C_{0-2}{}^2$-H), 7.5–8.5 (m, 144 H, $C_{0-2}{}^3$-H, CH=N-N-$P_{1-2}$, CHPc), 9.90 (br. s, 32 H, CHO) ppm. $^{13}C\{^1H\}$ NMR ($CDCl_3$): $\delta$ = 33.0 (br. s, $CH_3$-N-$P_{1-2}$), 118.2 (br. s, $C_0{}^2$, $C^1$), 121.9 (br. s, $C_{1-2}{}^2$), 128.3 (s, $C_0{}^3$, $C_1{}^3$), 129.2 (s, $C^3$), 131.5 (s, $C_2{}^3$), 132.1 (br. s, $C_0{}^4$, $C_1{}^4$), 133.7 (br. s, $C_2{}^4$), 139.7–140.1 (m, CH=N-N-$P_{1-2}$), 151.5 (br. s, $C_0{}^1$, $C_1{}^1$), 155.1 (br. s, $C_2{}^1$), 190.8 (s, CHO) ppm. IR (KBr): $\tilde{\nu}$ = 1702 $cm^{-1}$ $\nu_{CHO}$. $C_{448}H_{360}CoN_{56}O_{88}P_{24}S_{24}$ (9508): calcd. C 56.59, H 3.82, N 8.25; found C 56.31, H 3.91, N 8.23.

**3-G$_3$:** 81% Yield, 0.624 g. $^{31}P\{^1H\}$ NMR ($CDCl_3$): $\delta$ = 62.2 (br. s, $P_{1,2}$), 63.2 (br. s, $P_3$) ppm. $^1H$ NMR ($CDCl_3$): $\delta$ = 3.33 (m, 168 H, $CH_3$-N-$P_{1-3}$), 7.25 (m, 112 H, $C_1{}^2$-H), 7.4–8.2 (m, 176 H, $C_{1-2}{}^3$-H, CH=N-N-$P_{1-3}$, CHPc) ppm. $^{13}C\{^1H\}$ NMR ($CDCl_3$): $\delta$ = 31.7 (d, $^2J_{CP}$ = 12.9 Hz, $CH_3$-N-$P_3$), 32.9 (d, $^2J_{CP}$ = 11.1 Hz, $CH_3$-N-$P_{1-2}$), 121.7 (s, $C_{1-2}{}^2$), 128.2 (s, $C_0{}^3$, $C_1{}^3$), 128.5 (s, $C_2{}^3$), 131.3 (s, $C_{1-2}{}^4$), 140.5 (m, CH=N-N-$P_{1-3}$), 151.6 (s, $C_{1-2}{}^1$) ppm. $C_{480}H_{456}Cl_{64}CoN_{120}O_{56}P_{56}S_{56}$ (14660): calcd. C 39.33, H 3.14, N 11.47; found C 39.98, H 3.19, N 11.48.

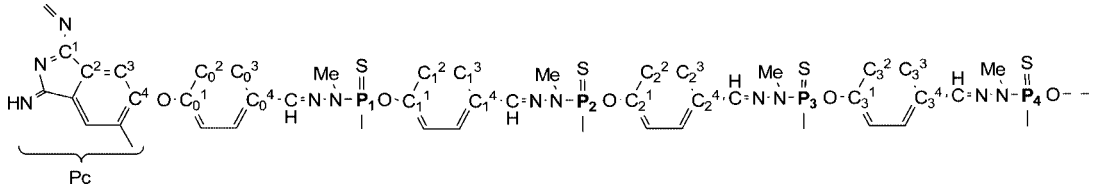


Figure 4. Numbering used for NMR assignments.

 © 2007 Wiley-VCH Verlag GmbH & Co. KGaA, Weinheim 

**3-G′$_3$:** 78% Yield, 0.643 g. $^{31}P\{^1H\}$ NMR ($CDCl_3$): $\delta$ = 60.5 (s, $P_3$), 62.4 (s, $P_2$), 62.8 (s, $P_1$) ppm. $^1H$ NMR ($CDCl_3$): $\delta$ = 3.33 (br. s, 168 H, $CH_3$-N-$P_{1-3}$), 6.5–7.4 (m, 240 H, $C_{0-3}{}^2$-H), 7.4–8.4 (m, 304 H, $C_{0-3}{}^3$-H, CH=N-N-$P_{1-3}$, CHPc), 9.93 (br. s, 64 H, CHO) ppm. $^{13}C\{^1H\}$ NMR ($CDCl_3$): $\delta$ = 33.0 (br. s, $CH_3$-N-$P_{1-3}$), 121.9 (br. s, $C_{1-3}{}^2$), 128.3 (s, $C_{0-2}{}^3$), 131.5 (s, $C_3{}^3$), 131.8 (s, $C_{1-2}{}^4$), 133.6 (s, $C_3{}^4$), 139.0–140.5 (m, CH=N-N-$P_{1-3}$), 151.5 (br. s, $C_{1-2}{}^1$), 155.1 (br. s, $C_3{}^1$), 190.8 (s, CHO) ppm. IR (KBr): $\tilde{\nu}$ = 1702 $cm^{-1}$ $\nu_{CHO}$. $C_{928}H_{776}CoN_{120}O_{184}P_{56}S_{56}$ (20142): calcd. C 55.34, H 3.88, N 8.35; found C 55.37, H 3.84, N 8.29.

**3-G$_4$:** 86% Yield, 0.650 g. $^{31}P\{^1H\}$ NMR ($CDCl_3$): $\delta$ = 62.2 (s, $P_3$), 62.4 (s, $P_2$), 62.6 (s, $P_1$), 63.3 (s, $P_4$) ppm. $^1H$ NMR ($CDCl_3$): $\delta$ = 3.35 (br. d, $^3J_{HP}$ = 9.4 Hz, 360 H, $CH_3$-N-$P_{1-4}$), 7.25 (m, 240 H, $C_{0-3}{}^2$-H), 7.64 (m, 368 H, $C_{0-3}{}^3$-H, CH=N-N-$P_{1-4}$, CHPc) ppm. $^{13}C\{^1H\}$ NMR ($CDCl_3$): $\delta$ = 31.8 (d, $^2J_{CP}$ = 13.8 Hz, $CH_3$-N-$P_4$), 33.9 (d, $^2J_{CP}$ = 12.5 Hz, $CH_3$-N-$P_{1-3}$), 121.9 (s, $C_{1-3}{}^2$), 128.3 (s, $C_{0-2}{}^3$), 128.7 (s, $C_3{}^3$), 131.5 (s, $C_3{}^4$), 132.1 (s, $C_{1-2}{}^4$), 138.7–139.5 (m, CH=N-N-$P_{1-3}$), 140.7 (d, $^3J_{CP}$ = 18.6 Hz, CH=N-N-$P_4$), 151.4 (br. s, $C_{1-2}{}^1$), 151.8 (br. s, $C_3{}^1$) ppm. $C_{992}H_{968}Cl_{128}CoN_{248}O_{120}P_{120}S_{120}$ (30446): calcd. C 39.14, H 3.20, N 11.41; found C 39.21, H 3.17, N 11.58.

**3-G′$_4$:** 99% Yield, 0.808 g. $^{31}P\{^1H\}$ NMR ($CDCl_3$): $\delta$ = 60.5 (s, $P_4$), 62.4 (s, $P_3$), 62.7 (s, $P_2$), 62.9 (s, $P_1$) ppm. $^1H$ NMR ($CDCl_3$): $\delta$ = 3.32 (br. s, 360 H, $CH_3$-N-$P_{1-4}$), 6.5–7.4 (m, 496 H, $C_{0-4}{}^2$-H), 7.4–8.4 (m, 624 H, $C_{0-4}{}^3$-H, CH=N-N-$P_{1-4}$, CHPc), 9.89 (br. s, 128 H, CHO) ppm. $^{13}C\{^1H\}$ NMR ($CDCl_3$): $\delta$ = 32.9 (d, $^2J_{CP}$ = 13.1 Hz, $CH_3$-N-$P_4$), 33.1 (br. d, $^2J_{CP}$ = 12 Hz, $CH_3$-N-$P_{1-3}$), 121.9 (s, $C_{1-4}{}^2$), 128.3 (s, $C_{0-3}{}^3$), 131.5 (s, $C_4{}^3$), 131.8 (s, $C_3{}^4$), 132.1 (br. s, $C_{1-2}{}^4$), 133.6 (s, $C_4{}^4$), 139.0–139.4 (m, CH=N-N-$P_{1-3}$), 139.6 (d, $^3J_{CP}$ = 17.3 Hz, CH=N-N-$P_4$), 151.5 (br. s, $C_{1-3}{}^1$), 155.1 (br. d, $^2J_{CP}$ = 7 Hz, $C_4{}^1$), 190.8 (s, CHO) ppm. IR (KBr): $\tilde{\nu}$ = 1702 $cm^{-1}$ $\nu_{CHO}$. $C_{1888}H_{1608}CoN_{248}O_{376}P_{120}S_{120}$ (41410): calcd. C 54.76, H 3.91, N 8.39; found C 54.81, H 3.90, N 8.39.

**3-G$_5$:** 93% Yield, 0.696 g. $^{31}P\{^1H\}$ NMR ($CDCl_3$): $\delta$ = 62.1 (s, $P_4$), 62.4 (s, $P_3$), 62.7 (s, $P_{1-2}$), 63.2 (s, $P_5$) ppm. $^1H$ NMR ($CDCl_3$): $\delta$ = 3.33 (br. s, 744 H, $CH_3$-N-$P_{1-5}$), 7.22 (br. s, 496 H, $C_{0-4}{}^2$-H), 7.64 (br. s, 752 H, $C_{0-4}{}^3$-H, CH=N-N-$P_{1-5}$, CHPc) ppm. $^{13}C\{^1H\}$ NMR ($CDCl_3$): $\delta$ = 31.9 (d, $^2J_{CP}$ = 12.4 Hz, $CH_3$-N-$P_5$), 33.1 (d, $^2J_{CP}$ = 13.0 Hz, $CH_3$-N-$P_{1-4}$), 121.9 (s, $C_{1-4}{}^2$), 128.3 (s, $C_{1-3}{}^3$), 128.7 (s, $C_4{}^3$), 131.5 (s, $C_4{}^4$), 132.1 (s, $C_{1-3}{}^4$), 139.1 (m, CH=N-N-$P_{1-4}$), 140.7 (d, $^3J_{CP}$ = 17.6 Hz, CH=N-N-$P_5$), 151.4 (br. s, $C_{1-3}{}^1$), 151.8 (br. d, $^2J_{CP}$ = 5 Hz, $C_4{}^1$) ppm. $C_{2016}H_{1992}Cl_{256}CoN_{504}O_{248}P_{248}S_{248}$ (62018): calcd. C 39.04, H 3.24, N 11.38; found C 39.21, H 3.28, N 11.19.

**3-G′$_5$:** 97% Yield, 0.788 g. $^{31}P\{^1H\}$ NMR ($CDCl_3$): $\delta$ = 60.5 (s, $P_5$), 62.4 (s, $P_4$), 62.7 (br. s, $P_{1-3}$) ppm. $^1H$ NMR ($CDCl_3$): $\delta$ = 3.31 (br. s, 744 H, $CH_3$-N-$P_{1-5}$), 6.5–7.4 (m, 1008 H, $C_{0-5}{}^2$-H), 7.4–8.4 (m, 1264 H, $C_{0-5}{}^3$-H, CH=N-N-$P_{1-5}$, CHPc), 9.89 (br. s, 256 H, CHO) ppm. $^{13}C\{^1H\}$ NMR ($CDCl_3$): $\delta$ = 32.9 (d, $^2J_{CP}$ = 13.1 Hz, $CH_3$-N-$P_5$), 33.0 (d, $^2J_{CP}$ = 12 Hz, $CH_3$-N-$P_{1-4}$), 121.9 (s, $C_{1-5}{}^2$), 128.3 (s, $C_{1-4}{}^3$), 131.5 (s, $C_5{}^3$), 131.8 (s, $C_4{}^4$), 132.1 (s, $C_{1-3}{}^4$), 133.6 (s, $C_5{}^4$), 138.9–139.2 (m, CH=N-N-$P_{1-4}$), 139.7 (d, $^3J_{CP}$ = 14.4 Hz, CH=N-N-$P_5$), 151.4 (m, $C_{1-4}{}^1$), 155.1 (br. d, $^2J_{CP}$ = 7.9 Hz, $C_5{}^1$), 190.8 (s, CHO) ppm. IR (KBr): $\tilde{\nu}$ = 1703 $cm^{-1}$ $\nu_{CHO}$. $C_{3808}H_{3272}CoN_{504}O_{760}P_{248}S_{248}$ (83947): calcd. C 54.48, H 3.93, N 8.41; found C 54.62, H 3.83, N 8.41.

**3-G$_6$:** 90% Yield, 0.671 g. $^{31}P\{^1H\}$ NMR ($CDCl_3$): $\delta$ = 62.1 (s, $P_5$), 62.4 (s, $P_4$), 62.7 (br. s, $P_{1-3}$), 63.2 (s, $P_6$) ppm. $^1H$ NMR ($CDCl_3$): $\delta$ = 3.34 (br. s, 1512 H, $CH_3$-N-$P_{1-6}$), 7.22 (br. s, 1008 H, $C_{0-5}{}^2$-H), 7.65 (br. s, 1520 H, $C_{0-5}{}^3$-H, CH=N-N-$P_{1-6}$, CHPc) ppm. $^{13}C\{^1H\}$ NMR ($CDCl_3$): $\delta$ = 31.9 (d, $^2J_{CP}$ = 12.6 Hz, $CH_3$-N-$P_6$), 33.1 (d, $^2J_{CP}$ = 12.6 Hz, $CH_3$-N-$P_{1-5}$), 121.9 (s, $C_{1-5}{}^2$), 128.3 (s, $C_{1-4}{}^3$), 128.7 (s, $C_5{}^3$), 131.5 (s, $C_5{}^4$), 132.1 (s, $C_{1-4}{}^4$), 139.1 (d, $^3J_{CP}$ = 16.7 Hz, CH=N-N-$P_{1-5}$), 140.7 (d, $^3J_{CP}$ = 18.6 Hz, CH=N-N-$P_6$), 151.3 (br. s, $C_{1-4}{}^1$), 151.8 (br. s, $C_5{}^1$) ppm. $C_{4064}H_{4040}Cl_{512}CoN_{1016}O_{504}P_{504}S_{504}$ (125162): calcd. C 39.00, H 3.25, N 11.37; found C 39.17, H 3.21, N 11.50.

**3-G′$_6$:** 91% Yield, 0.737 g. $^{31}P\{^1H\}$ NMR ($CDCl_3$): $\delta$ = 60.5 (s, $P_6$), 62.3 (s, $P_5$), 62.7 (br. s, $P_{1-4}$) ppm. $^1H$ NMR ($CDCl_3$): $\delta$ = 3.32 (br. s, 1512 H, $CH_3$-N-$P_{1-6}$), 6.5–7.4 (m, 2032 H, $C_{0-6}{}^2$-H), 7.4–8.5 (m, 2544 H, $C_{0-6}{}^3$-H, CH=N-N-$P_{1-6}$, CHPc), 9.86 (br. s, 512 H, CHO) ppm. $^{13}C\{^1H\}$ NMR ($CDCl_3$): $\delta$ = 32.9 (d, $^2J_{CP}$ = 12.8 Hz, $CH_3$-N-$P_6$), 33.0 (d, $^2J_{CP}$ = 12 Hz, $CH_3$-N-$P_{1-5}$), 121.9 (s, $C_{1-6}{}^2$), 128.3 (s, $C_{1-5}{}^3$), 131.5 (s, $C_6{}^3$), 131.8 (s, $C_5{}^4$), 132.1 (s, $C_{1-4}{}^4$), 133.6 (s, $C_6{}^4$), 139.1–139.3 (m, CH=N-N-$P_{1-5}$), 139.7 (d, $^3J_{CP}$ = 14.1 Hz, CH=N-N-$P_6$), 151.1–151.8 (m, $C_{1-5}{}^1$), 155.1 (d, $^2J_{CP}$ = 7.0 Hz, $C_6{}^1$), 190.8 (s, CHO) ppm. IR (KBr): $\tilde{\nu}$ = 1702 $cm^{-1}$ $\nu_{CHO}$. $C_{7648}H_{6600}CoN_{1016}O_{1528}P_{504}S_{504}$ (169021): calcd. C 54.35, H 3.94, N 8.42; found C 54.77, H 3.86, N 8.61.

**3-G$_7$:** 93% Yield, 0.692 g. $^{31}P\{^1H\}$ NMR ($CDCl_3$): $\delta$ = 62.0 (s, $P_6$), 62.3 (s, $P_5$), 62.5 (br. s, $P_{1-4}$), 63.2 (s, $P_7$) ppm. $^1H$ NMR ($CDCl_3$): $\delta$ = 3.33 (br. s, 3048 H, $CH_3$-N-$P_{1-7}$), 7.21 (br. s, 2032 H, $C_{0-6}{}^2$-H), 7.64 (br. s, 3056 H, $C_{0-6}{}^3$-H, CH=N-N-$P_{1-7}$, CHPc) ppm. $^{13}C\{^1H\}$ NMR ($CDCl_3$): $\delta$ = 31.9 (d, $^2J_{CP}$ = 12.6 Hz, $CH_3$-N-$P_7$), 33.1 (d, $^2J_{CP}$ = 12.3 Hz, $CH_3$-N-$P_{1-6}$), 121.9 (s, $C_{1-6}{}^2$), 128.3 (s, $C_{1-5}{}^3$), 128.7 (s, $C_6{}^3$), 131.4 (s, $C_6{}^4$), 132.1 (s, $C_{1-5}{}^4$), 139.1 (m, CH=N-N-$P_{1-6}$), 140.7 (d, $^3J_{CP}$ = 18.9 Hz, CH=N-N-$P_7$), 151.3 (br. s, $C_{1-5}{}^1$), 151.8 (br. d, $^2J_{CP}$ = 6 Hz, $C_6{}^1$) ppm. $C_{8160}H_{8136}Cl_{1024}CoN_{2040}O_{1016}P_{1016}S_{1016}$ (251450): calcd. C 38.98, H 3.26, N 11.36; found C 40.01, H 3.19, N 11.31.

**3-G′$_7$:** 93% Yield, 0.753 g. $^{31}P\{^1H\}$ NMR ($CDCl_3$): $\delta$ = 60.5 (s, $P_7$), 62.4 (s, $P_6$), 62.7 (br. s, $P_{1-5}$) ppm. $^1H$ NMR ($CDCl_3$): $\delta$ = 3.31 (br. s, 3048 H, $CH_3$-N-$P_{1-7}$), 6.5–7.4 (m, 4080 H, $C_{0-7}{}^2$-H), 7.4–8.5 (m, 5104 H, $C_{0-7}{}^3$-H, CH=N-N-$P_{1-7}$, CHPc), 9.85 (br. s, 1024 H, CHO) ppm. $^{13}C\{^1H\}$ NMR ($CDCl_3$): $\delta$ = 32.9 (d, $^2J_{CP}$ = 12.4 Hz, $CH_3$-N-$P_7$), 33.0 (d, $^2J_{CP}$ = 12 Hz, $CH_3$-N-$P_{1-6}$), 121.9 (s, $C_{1-7}{}^2$), 128.3 (s, $C_{1-6}{}^3$), 131.5 (s, $C_7{}^3$), 131.8 (s, $C_6{}^4$), 132.1 (s, $C_{1-5}{}^4$), 133.6 (s, $C_7{}^4$), 138.8–139.2 (m, CH=N-N-$P_{1-6}$), 139.7 (d, $^3J_{CP}$ = 15.8 Hz, CH=N-N-$P_7$), 151.1–151.8 (m, $C_{1-6}{}^1$), 155.1 (br. d, $^2J_{CP}$ = 5 Hz, $C_6{}^1$), 190.8 (s, CHO) ppm. IR (KBr): $\tilde{\nu}$ = 1702 $cm^{-1}$ $\nu_{CHO}$. $C_{15328}H_{13256}CoN_{2040}O_{3064}P_{1016}S_{1016}$ (339167): calcd. C 54.28, H 3.94, N 8.43; found C 54.96, H 4.02, N 8.44.

**3-G$_8$:** 90% Yield, 0669 g. $^{31}P\{^1H\}$ NMR ($CDCl_3$): $\delta$ = 62.1 (s, $P_7$), 62.4 (s, $P_6$), 62.6 (br. s, $P_{1-5}$), 63.2 (s, $P_8$) ppm. $^1H$ NMR ($CDCl_3$): $\delta$ = 3.32 (br. s, 6120 H, $CH_3$-N-$P_{1-8}$), 7.21 (br. s, 4080 H, $C_{0-7}{}^2$-H), 7.63 (br. s, 6128 H, $C_{0-7}{}^3$-H, CH=N-N-$P_{1-8}$, CHPc) ppm. $^{13}C\{^1H\}$ NMR ($CDCl_3$): $\delta$ = 31.9 (d, $^2J_{CP}$ = 12.6 Hz, $CH_3$-N-$P_8$), 33.1 (d, $^2J_{CP}$ = 12.6 Hz, $CH_3$-N-$P_{1-7}$), 121.9 (s, $C_{1-7}{}^2$), 128.3 (s, $C_{1-6}{}^3$), 128.7 (s, $C_7{}^3$), 131.5 (s, $C_7{}^4$), 132.0 (s, $C_{1-6}{}^4$), 139.1 (br. d, $^3J_{CP}$ = 13.8 Hz, CH=N-N-$P_{1-7}$), 140.7 (d, $^3J_{CP}$ = 18.4 Hz, CH=N-N-$P_8$), 151.3 (br. d, $^2J_{CP}$ = 6 Hz, $C_{1-6}{}^1$), 151.8 (d, $^2J_{CP}$ = 6.7 Hz, $C_7{}^1$) ppm. $C_{16352}H_{16328}Cl_{2048}CoN_{4088}O_{2040}P_{2040}S_{2040}$ (504026): calcd. C 38.97, H 3.27, N 11.36; found C 39.99, H 3.12, N 11.21.

## Acknowledgments

Thanks are due to the Fundación Ramón Areces for a grant to A. P.-Q., and to the CNRS for financial support.

[1] C. C. Leznoff, A. B. P. Lever (Eds.), *Phthalocyanines. Properties and Applications*, VCH Publishers, New York, **1989**, vol. 1; **1993**, vols. 2 and 3; **1996**, vol. 4 .
[2] H. Ali, J. E. van Lier, *Chem. Rev.* **1999**, *99*, 2379–2450.

 © 2007 Wiley-VCH Verlag GmbH & Co. KGaA, Weinheim 

[3] M. K. Nazeeruddin, R. Humphry-Baker, M. Grätzel, B. A. Murrer, *Chem. Commun.* **1998**, 719–720.
[4] Z. Bao, A. J. Lovinger, J. Brown, *J. Am. Chem. Soc.* **1998**, *120*, 207–208.
[5] B. Meunier, A. Sorokin, *Acc. Chem. Res.* **1997**, *30*, 470–476.
[6] M. T. M. Choi, P. P. S. Li, D. K. P. Ng, *Tetrahedron* **2000**, *56*, 3881–3887.
[7] M. Kimura, K. Nakada, Y. Yamaguchi, K. Hanabusa, H. Shirai, N. Kobayashi, *Chem. Commun.* **1997**, 1215–1216.
[8] M. Brewis, G. J. Clarkson, A. M. Holder, N. B. McKeown, *Chem. Commun.* **1998**, 969–970.
[9] M. Brewis, G. J. Clarkson, V. Goddard, M. Helliwell, A. M. Holder, N. B. McKeown, *Angew. Chem. Int. Ed.* **1998**, *37*, 1092–1094.
[10] M. Kimura, H. Narikawa, K. Ohta, K. Hanabusa, H. Shirai, N. Kobayashi, *Chem. Mater.* **2002**, *14*, 2711–2717.
[11] C. A. Kernag, D. V. McGrath, *Chem. Commun.* **2003**, 1048–1049.
[12] J. Leclaire, R. Dagiral, S. Fery-Forgues, Y. Coppel, B. Donnadieu, A. M. Caminade, J. P. Majoral, *J. Am. Chem. Soc.* **2005**, *127*, 15762–15770.
[13] J. Leclaire, Y. Coppel, A. M. Caminade, J. P. Majoral, *J. Am. Chem. Soc.* **2004**, *126*, 2304–2305.
[14] J. Y. Jaung, *Bull. Korean Chem. Soc.* **2004**, *25*, 1453–1454.
[15] M. Kimura, Y. Sugihara, T. Muto, K. Hanabusa, H. Shirai, N. Kobayashi, *Chem. Eur. J.* **1999**, *5*, 3495–3500.
[16] S. Güner, M. K. Sener, H. Dinçer, Y. Köseoglu, S. Kazan, M. B. Koçak, *J. Magn. Magn. Mater.* **2006**, *300*, e530–e533.
[17] N. Launay, A. M. Caminade, R. Lahana, J. P. Majoral, *Angew. Chem. Int. Ed. Engl.* **1994**, *33*, 1589–1592.
[18] S. Dahli, J. J. Cosa, M. Bishop, D. Phillips, *Langmuir* **1996**, *12*, 293–300.
[19] C. Reichardt, *Chem. Rev.* **1994**, *94*, 2319–2358.
[20] A. Georges, G. Patonay, *Talanta* **1997**, *45*, 285–289.
[21] A. C. H. Ng, X. Y. Li, D. K. P. Ng, *Macromolecules* **1999**, *32*, 5292–5298.
[22] A. V. Nikolaitchick, M. A. J. Rodgers, *J. Phys. Chem. A* **1999**, *103*, 7597–7605.
[23] J. C. Blais, C. O. Turrin, A. M. Caminade, J. P. Majoral, *Anal. Chem.* **2000**, *72*, 5097–5105.

Received: December 22, 2006
Published Online: April 26, 2007

 © 2007 Wiley-VCH Verlag GmbH & Co. KGaA, Weinheim 

DOI: 10.1002/ejic.200700007

# Zirconium(IV) Tris(phosphinoamide) Complexes as a Tripodal-Type Metalloligand: A Route to Zr–M (M = Cu, Mo, Pt) Heterodimetallic Complexes

**Takashi Sue,[a] Yusuke Sunada,[a,b] and Hideo Nagashima*[a,b]**

**Keywords:** Phosphinoamide / Heterodimetallic / Tripodal ligands

Treatment of $ZrCl_4$ with 3 equiv. of Li($PPh_2NR$) (R = *t*Bu, *i*Pr) gives tris(phosphinoamide)zirconium complexes, $(PPh_2NR)_3$-ZrCl [R = *t*Bu (**1a**), *i*Pr (**1b**)], in high yield. Crystal structures of **1a**,**b** show that three phosphorus atoms are coordinated to the zirconium center in the solid state, whereas variable temperature NMR studies indicate a reversible coordination/dissociation process of three phosphorus atoms in the solution state. Reaction of **1a**,**b** with CuCl give rise to the formation of Zr–Cu heterodimetallic complexes, $ClCu(Ph_2PNR)_3$-ZrCl [R = *t*Bu (**2a**), *i*Pr (**2b**)]. The molecular structures of **2a**,**b** show that the Cu atom adopts a pseudotetrahedral coordination geometry with tripodal phosphorus moieties and a chlorine atom, whereas the ligand arrangement around the Zr atom is trigonal bipyramidal with the linear Cl–Zr–Cu axis at the apical site. A Zr–Mo heterodimetallic complex, $(CO)_3$-$Mo(Ph_2PNiPr)_3ZrCl$ (**3**), is synthesized from **1b** and $Mo(CO)_3$-$(CH_3CN)_3$, in which the ligands around the Mo center are arranged octahedrally, and three phosphorus moieties are coordinated in the *fac*-$P_3$ fashion. The reaction of **1b** with a square planar $Pt^{II}$ precursor, such as $(COD)PtCl_2$, is unique and gives ($\kappa^2$-$Ph_2PNiPr$)$Pt(Ph_2PNiPr)_2ZrCl_3$ (**4**), which is the first example of a Zr–Pt zwitterionic heterodimetallic complex. The reaction involves intramolecular migration of two chlorine atoms from Pt to Zr as well as that of a $Ph_2PNiPr$ moiety from Zr to Pt.

(© Wiley-VCH Verlag GmbH & Co. KGaA, 69451 Weinheim, Germany, 2007)

## 1. Introduction

It is well-known in coordination chemistry that ligand design is important for the synthesis of transition-metal complexes with unique structures and properties. Phosphanes are one of the most investigated ligands, especially in their application to homogeneous catalysis. Numerous monodentate and bidentate phosphane ligands have been developed, and their ligation to appropriate transition metals has contributed to the opening of new aspects in catalytic transformations of organic molecules and polymers.[1] Electronic and steric effects of these phosphane ligands are well-documented by using Tolman's $\chi$ values and cone angles for monodentate phosphanes and bite angles for bidentate phosphane ligands.[2] Thus, the chemical properties of most transition-metal complexes having monodentate and/or bidentate phosphane ligands are predictable in modern organometallic chemistry. Although relatively little has been studied compared with chemistry of mono- and bidentate phosphane ligands, tridentate phosphane ligands have attracted the attention of organometallic chemists as a result of their special structural and chemical properties.[3] Tridentate tertiary phosphane ligands can be classified into two types according to their preferred coordination geometries: one is the *fac*-$P_3$ (tripodal) coordination mode, whereas the other is the *mer*-$P_3$ coordination mode. The phosphane 1,1,1-tris[(diphenylphosphanyl)methyl]ethane (triphos) is the best-known *fac*-$P_3$ tripodal-type phosphane ligand for transition metals.[4] For instance, treatment of triphos with CuCl or $Mo(CO)_3(CH_3CN)_3$ reportedly gives (triphos)CuCl[4a] or (triphos)$Mo(CO)_3$, respectively.[4b] These examples clearly demonstrate that the tripodal ligands rigidly coordinate to a single transition-metal center in the *fac*-$P_3$ fashion so as to stabilize the mononuclear transition-metal complexes with tetrahedral and octahedral coordination geometries. This feature is different from the *mer*-$P_3$ ligands that are often used to stabilize a multimetallic framework, which bridges over the dual metals by virtue of its structural flexibility.

An interesting recent development used to control the electronic properties of the phosphane ligand is the introduction of a Lewis acid center in the ligand backbone.[5] As shown in Figure 1, the "amphoteric ligand" reported by Labinger is a typical example, in which both the Lewis acidic $R_2Al$ moieties and Lewis basic $R_2P$ units are included in one molecule; unique reactivity of the aluminum phosphinoamide $Ph_2PNtBuAlEt_2$ was discovered in the reaction with several transition-metal carbonyls.[6,7] The bi-

[a] Graduate School of Engineering Sciences, Kyushu University
Kasuga, Fukuoka, 816-8580 Japan
[b] Institute for Materials Chemistry and Engineering,
Kasuga, Fukuoka, 816-8580 Japan
E-mail: nagasima@cm.kyushu-u.ac.jp

Supporting information for this article is available on the WWW under http://www.eurjic.org or from the author.

 © 2007 Wiley-VCH Verlag GmbH & Co. KGaA, Weinheim 

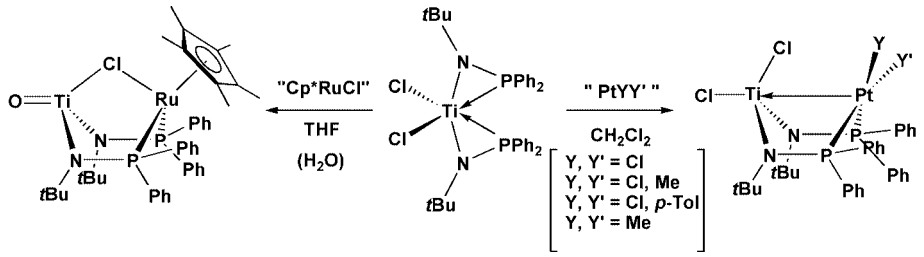


Scheme 1.

dentate version of the amphoteric ligand was lately reported by Bourissou and coworkers who reported the synthesis of diphosphanylborane ($o$-$i$Pr$_2$P-C$_6$H$_3$)$_2$B(Ph) and its ligation to the RhCl moiety in the reaction with [Rh(nbd)Cl]$_2$.[8,9] We reported earlier a titanium version of bidentate amphoteric ligands, (Ph$_2$PNR)$_2$TiCl$_2$ (R = $t$Bu, $i$Pr), which are good precursors to Ti–Pt and Ti–Ru heterodimetallic complexes, YY′Pt(Ph$_2$PN$t$Bu)$_2$TiCl$_2$ (Y, Y′ = Cl; Y = Me, Y′ = Cl; Y = $p$-Tol, Y′ = Cl; Y, Y′ = Me) and Cp*Ru(μ-Cl)(Ph$_2$PN$t$Bu)$_2$Ti = O as shown in Scheme 1.[10] The Ti–Pt complexes have a trigonal bipyramidal titanium and a square planar platinum center,[10a] whereas the Ti–Ru complex has titanium and ruthenium atoms with trigonal bipyramidal and tetrahedral geometries, respectively.[10b] Synthesis of a tridentate amphoteric ligand was examined by the design of the *fac*-P$_3$ tripodal-type compounds containing a cyclopentadienyl or tris(pyrazolyl)hydroborate zirconium moiety in the molecule; Cp*Zr(OCH$_2$PPh$_2$)$_3$ or TpZr(OCH$_2$PPh$_2$)$_3$ acts as a tripodal-like ligand in Cp*Zr(OCH$_2$PPh$_2$)$_3$Ni(CO), Cp*Zr(OCH$_2$PPh$_2$)$_3$RhMe, and TpZr(OCH$_2$PPh$_2$)$_3$Mo(CO)$_3$.[11]

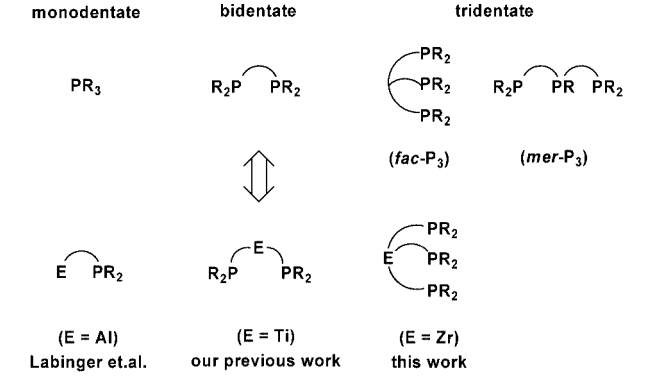


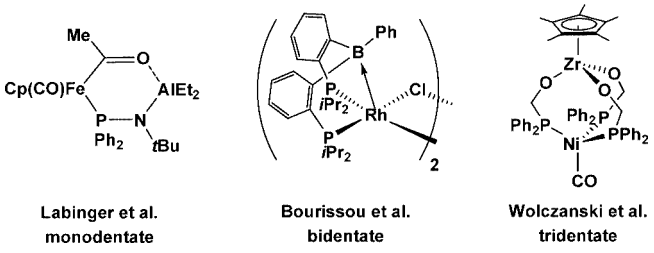


Figure 1. Monodentate, bidentate, and tridentate phosphorus ligands containing a Lewis acidic center.

We were interested in the fact that the cyclopentadienyl group in previous examples of the *fac*-P$_3$ tripodal-type amphoteric ligands reduced the Lewis acidity of the zirconium center. As described above, we synthesized the titanium phosphinoamides as a bidentate amphoteric ligand, which was successfully ligated to organoruthenium or platinum species to give the corresponding Ti–Ru and Ti–Pt complexes. Of interest are the structures of these heterodimetallic complexes: the Ti–Ru compound has a bridging chlorine atom, whereas the existence of a Pt→Ti dative bond is suggested from the crystal structure of the Ti–Pt complexes. The Lewis acidity of the titanium center is probably the reason for these structural features. In this context, we examined the synthesis of (PPh$_2$NR)$_3$TiCl (R = $i$Pr, $t$Bu) by the reaction of TiCl$_4$ with 3 equiv. of LiNRPPh$_2$; however, (PPh$_2$NR)$_2$TiCl$_2$ was the only product at room temperature and only a small amount of the species assignable to the desired (PPh$_2$NR)$_3$TiCl (R = $i$Pr, $t$Bu) was detectable by NMR spectroscopy when the reaction mixture was heated at 70 °C. In sharp contrast, the reaction of 3 equiv. of lithium phosphinoamide with ZrCl$_4$ successfully led to the formation of tris(phosphinoamide)zirconium, (PPh$_2$NR)$_3$ZrCl [R = $t$Bu (**1a**), $i$Pr (**1b**)]. In this paper, we describe the preparation, molecular structure, and solution dynamics of **1a**,**b** and their coordination behavior to several late transition metals. The heterodimetallic complexes ClCu(Ph$_2$PNR)$_3$ZrCl and (CO)$_3$Mo(Ph$_2$PN$i$Pr)$_3$ZrCl showed that these zirconium phosphinoamides behave as a *fac*-P$_3$ tripodal ligand which effectively stabilizes the late-transition-metal complexes with tetrahedral and octahedral geometries. A unique reaction involving complicated intermetallic ligand rearrangement occurred in the reaction of **1b** with (COD)PtCl$_2$, which afforded a zwitterionic dimetallic complex, ($\kappa^2$-Ph$_2$PN$i$Pr)Pt(Ph$_2$PN$i$Pr)$_2$ZrCl$_3$ (**4**).

## 2. Results and Discussion

### 2.1 Synthesis and Characterization of Tris(phosphinoamide)-zirconium Complexes (Ph$_2$PN$t$Bu)$_3$ZrCl (1a) and (Ph$_2$PN$i$Pr)$_3$ZrCl (1b)

Treatment of 3 equiv. of Li(Ph$_2$PNR) (R = $t$Bu, $i$Pr) with zirconium tetrachloride in THF afforded tris(phosphinoamide)zirconium complexes, (Ph$_2$PNR)$_3$ZrCl [R = $t$Bu (**1a**), $i$Pr (**1b**)], in 86 and 84% yield, respectively, as colorless crys-

 © 2007 Wiley-VCH Verlag GmbH & Co. KGaA, Weinheim 

tals (Scheme 2). A single $^{31}P$ NMR resonance appeared for **1a**,**b** at –11.8 and –12.0 ppm, respectively, which were 34.4 and 46.5 ppm shifted to higher field relative to that of the phosphinoamide ligands $Ph_2PNHtBu$ and $Ph_2PNHiPr$.[12] Although dynamic behavior was observed, as described later in detail, $^1H$ and $^{13}C$ NMR spectroscopy clearly showed signals assignable to $Ph_2P$ and *t*Bu or *i*Pr groups. The molecular structures of **1a**,**b** were determined by X-ray diffraction analysis and are shown in Figure 2; representative bond lengths and angles for **1a**,**b** are summarized in Table 1. The asymmetric unit of **1a** contains three crystallographically independent but chemically equivalent molecules. Ambiguous value of the Flack parameter (0.42) suggests the structure of **1a** is inversion twinned, which is sometimes seen in a trigonal space group. There is a threefold axis along with the Zr–Cl bond in the solid-state structure of all three independent molecules of **1a**. One of the molecular structures of **1a** is described in Figure 2. Three phosphinoamide ligands are connected to the zirconium center by a Zr–N bond and all of the three phosphorus moieties are coordinated. Both **1a**,**b** assume a distorted tetrahedral geometry with one chlorine atom and three centers of the N–P bonds. In the solid-state structure, all three phosphorus atoms are oriented away from the chlorine atom, and no isomer was found in the crystal. The N–P bond lengths are comparable to those seen in Eisen's zirconium tetrakis(phosphinoamide) complex, $Zr(Ph_2PNPh)_4$,[13] our previously reported titanium complexes, $(Ph_2PNR)_2TiCl_2$ (R = *t*Bu, *i*Pr), and other known phosphinoamide or related complexes.[14] The Zr–N bond lengths around 2.15 Å are slightly longer than those found in previously reported zirconium amide complexes,[15] whereas the Zr–P bond lengths are somewhat shorter than those of known zirconium phosphane complexes.[16]

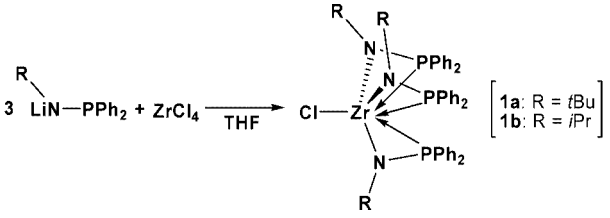


Scheme 2.

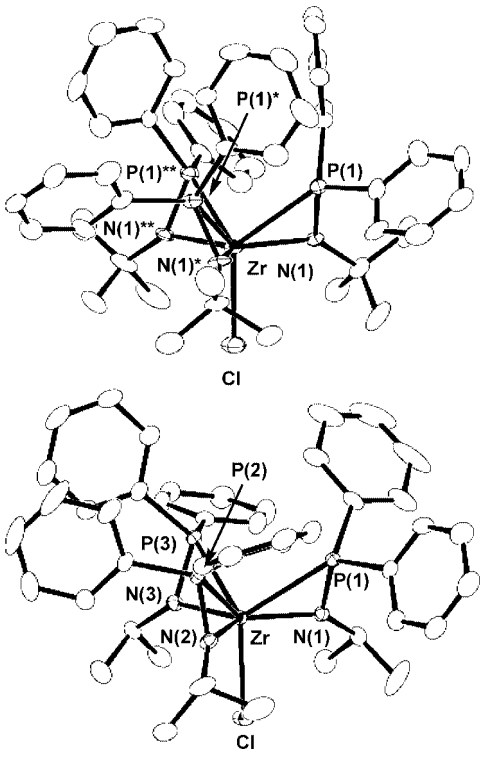


Figure 2. Molecular structures of $(Ph_2PNtBu)_3ZrCl$ (**1a**) (top) $(Ph_2PNiPr)_3ZrCl$ (**1b**) (bottom) with 50% probability ellipsoids. Hydrogen atoms are omitted for clarity.

Although all of the three phosphorus atoms are bonded with the zirconium center in the solid state, NMR spectroscopic studies suggested a dynamic coordination/dissociation process of these three phosphorus atoms that is similar to that of titanium phosphinoamide, $(Ph_2PNR)_2TiCl_2$,[10a] and $Zr(Ph_2PNPh)_4$.[13] In a representative example, $^1H$ NMR spectra of **1a** are dependent on the temperature measured: at room temperature, three broad signals at $\delta$ = 6.99–7.17 ppm and one singlet at $\delta$ = 1.47 ppm were seen, which are assignable to the protons of the Ph group and the methyl portion of the *t*Bu group. At –90 °C, the spectrum consists of six signals at $\delta$ = 6.53 (m, 2 H), 6.66 (t, 2 H), 6.95 (t, 1 H), 7.20 (t, 2 H), 7.24 (m, 2 H), and 7.29 (t, 1 H) ppm and a slightly broadened singlet at $\delta$ = 1.37 ppm, which are assignable to two sets of phenyl signals

Table 1. Representative bond lengths and angles for **1a**,**b**.

| Bond lengths [Å] | | | Bond angles [°] | | |
|---|---|---|---|---|---|
| | **1a** | **1b** | | **1a** | **1b** |
| Zr–Cl(1) | 2.505(2) [2.488(2), 2.525(2)] | 2.4865(9) | Cl–Zr–N(1) | 91.09(13) [91.07(12), 89.70(11)] | 86.28(7) |
| Zr–N(1) | 2.183(6) [2.181(4), 2.180(3)] | 2.150(2) | Cl–Zr–N(2) | | 86.18(8) |
| Zr–N(2) | | 2.137(2) | Cl–Zr–N(3) | | 93.81(8) |
| Zr–N(3) | | 2.101(2) | N(1)–Zr–N(2) | 120.0(2) [119.9(2), 120.2(2)] | 133.29(10) |
| Zr–P(1) | 2.626(2) [2.617(2), 2.608(2)] | 2.6659(9) | N(1)–Zr–N(3) | | 117.07(10) |
| Zr–P(2) | | 2.6577(9) | N(2)–Zr–N(3) | | 109.40(10) |
| Zr–P(3) | | 2.6516(9) | N(1)–Zr–P(1) | 38.87(14) [39.22(13), 39.21(12)] | 38.09(7) |
| N(1)–P(1) | 1.654(5) [1.662(5), 1.656(4)] | 1.645(2) | N(2)–Zr–P(2) | | 38.30(8) |
| N(2)–P(2) | | 1.648(3) | N(3)–Zr–P(3) | | 38.64(7) |
| N(3)–P(3) | | 1.656(2) | | | |

 © 2007 Wiley-VCH Verlag GmbH & Co. KGaA, Weinheim 

of the *ortho*-, *meta*-, *para*-, *meta*-, *ortho*-, and *para* protons, respectively, and a signal for the *t*Bu group. $^1$H NMR spectroscopic resonances due to the phenyl moieties were unequivocally assigned by a $^1$H–$^1$H selective decoupling measurement. The spectrum is explained by the existence of three magnetically equivalent phosphinoamide ligands, in which two phenyl groups bonded with each phosphorus atom are inequivalent. Similar variable temperature NMR studies of **1b** also showed dynamic behavior; two signals due to the Ph group [$\delta$ = 7.12–7.17 (m, 12 H), 7.22–7.26 (m, 18 H) ppm] appeared at room temperature, which were broadened at –90 °C to show three broad signals. Similarly, the methyl and methine signals of the *i*Pr group were gradually broadened at lower temperatures, and only a single set of broad signals was seen even at –90 °C. Because **1b** is not very soluble in $CD_2Cl_2$ at low temperatures, the well-resolved spectra below –90 °C, in which two doublets due to the inequivalent methyl groups should appear, were unable to be obtained because of technical problems. These spectral changes are consistent with the fact that phosphorus atoms are coordinated to the zirconium center at lower temperatures, whereas reversible dissociation takes place at higher temperatures in solution states; this is favorable for the possible usage of **1** as a tripodal metalloligand as described later.[17]

In close analogy to these results, Eisen and coworkers reported the preparation and structure determination of $Zr(Ph_2PNPh)_4$, which also showed dynamic behavior in variable temperature NMR studies.[13] The four phosphinoamide ligands are bonded to the zirconium atom by Zr–N and Zr←P bonds in the solid state. In solution, the coordination of the phosphorus atoms is reversible. Although the synthetic method of Eisen's complex is similar to that of **1**, neither $Zr(Ph_2PN$*t*$Bu)_4$ nor $Zr(Ph_2PN$*i*$Pr)_4$ was detected in our experiments. As a representative experiment, $ZrCl_4$ was treated with 4 equiv. of $Li(Ph_2PN$*i*$Pr)$ in THF at room temperature overnight; $^1$H and $^{31}$P NMR spectra of the crude product showed the formation of **1b** as a single product; $Zr(Ph_2PN$*i*$Pr)_4$ was not detected. This is presumably attributable to the steric bulkiness of the *t*Bu and *i*Pr groups, which prevents the reaction of **1** to the corresponding zirconium tetrakis(phosphinoamide). It should be noted that we have never seen the formation of $(Ph_2PNR)_2ZrCl_2$ (R = *t*Bu, *i*Pr) even in the reaction of $ZrCl_4$ with less than 2 equiv. of $Li(Ph_2PNR)$, though Zhang et al. recently reported the synthesis of bis(phosphinoamide)zirconium complexes, $(Ph_2PNR)_2ZrCl_2$ (R = *t*Bu, Ph), by the reaction of 2 equiv. of $Li(Ph_2PNR)$ (R = *t*Bu, Ph) with $ZrCl_4$; no detailed spectroscopic data were described.[18] Repeated attempts to reproduce the result of Zhang were unsuccessful. In a typical example, 2 equiv. of $Li(Ph_2PN$*t*$Bu)$ was reacted with $ZrCl_4$ in THF from which only complex **1a** was obtained in 30~50% yield and unreacted $ZrCl_4$ was recovered as a THF adduct. This is interesting in comparison with our previous result that the reaction of $TiCl_4$ with 2 equiv. of $Li(Ph_2PNR)$ resulted in the exclusive formation of $(Ph_2PNR)_2TiCl_2$.

### 2.2 Use of 1 as a Tripodal-Type Metalloligand: Construction of Zr–Cu and Zr–Mo Heterodimetallic Complexes $ClCu(Ph_2PNR)_3ZrCl$ [R = *t*Bu (2a), *i*Pr (2b)] and $(CO)_3Mo(Ph_2PN$*i*$Pr)_3ZrCl$ (3)

As described above, the fluxional behavior of **1** in the variable temperature $^1$H NMR spectroscopic studies suggested that **1** was a *fac*-$P_3$ tripodal-type metalloligand. It is known that the *fac*-$P_3$ tripodal-type is suitable as the ligand of complexes with tetrahedral or octahedral geometry.[3] As a representative model of a tetrahedral complex, $Cu^I$ complexes were prepared. Treatment of **1** with 1 equiv. of CuCl in $CH_3CN$ at room temperature afforded Zr–Cu heterodimetallic complexes, $ClCu(Ph_2PNR)_3ZrCl$ [R = *t*Bu (**2a**), *i*Pr (**2b**)], as yellow crystals in 78 and 82% yield, respectively (Scheme 3). The products were unequivocally characterized by NMR spectroscopy, in which no dynamic behavior was visible in the temperature range from –90 to 30 °C. In a typical example, the $^1$H NMR spectrum of **2a** gave signals due to the *ortho*-, *meta*-, and *para* protons of six magnetically equivalent Ph groups in an integral ratio of 12:12:6, and one singlet at $\delta$ = 1.50 ppm, which is assignable to the methyl protons of the *t*Bu group. In the $^{13}$C NMR spec-

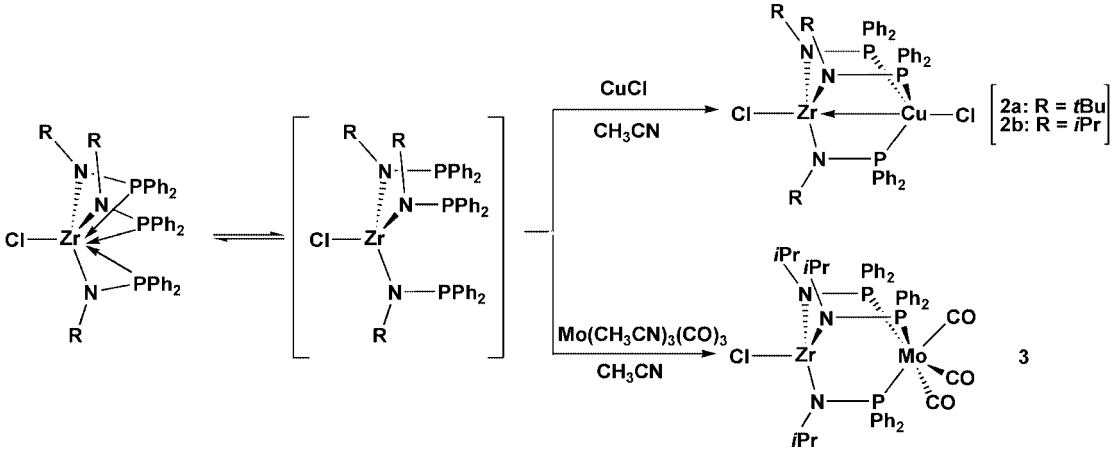


Scheme 3.

 © 2007 Wiley-VCH Verlag GmbH & Co. KGaA, Weinheim 

trum, four signals at $\delta$ = 127.9 (*meta*-Ph), 129.5 (*para*-Ph), 132.8 (*ortho*-Ph), and 134.5 (*ipso*-Ph) ppm are observed, which are assignable to the six magnetically equivalent phenyl groups, along with two signals at $\delta$ = 34.8 ($CMe_3$) and 61.8 ($CMe_3$) ppm due to the three magnetically equivalent *t*Bu groups. This clearly demonstrates the $C_{3v}$ symmetry of the molecule. A singlet appeared at $\delta$ = –30.6 ppm in the $^{31}P$ NMR spectrum of **2a**; peak broadening due to the interaction with the quadrupolar copper center is good evidence of the coordination of three phosphorus moieties to the Cu atom. Spectral data of **2b** is analogous to those of **2a** in the points that three $Ph_2PN$*i*Pr ligands are magnetically equivalent (the integral ratio of methyl and methine protons of *i*Pr and three Ph protons is 18:3:12:12:6) and broadening of the $^{31}P$ NMR spectroscopic resonance ($\delta$ = –11.2 ppm) is ascribed to the coordination of the phosphorus moiety to the copper center. The $C_{3v}$ symmetric structure deduced from these spectroscopic features is confirmed by X-ray diffraction analysis of **2a**,**b** of which the ORTEP drawings are shown in Figure 3, and selected bond lengths and angles are summarized in Table 2.

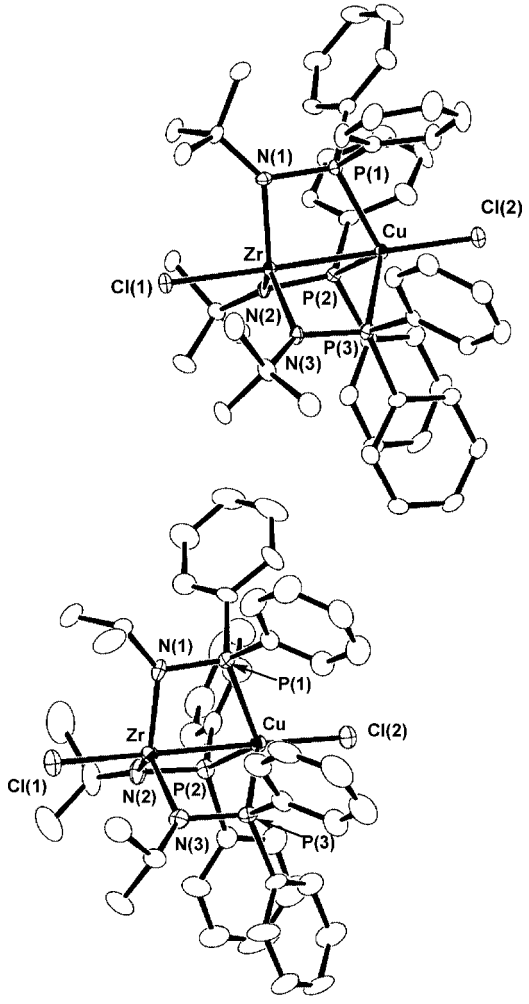


Figure 3. Molecular structures of $ClCu(Ph_2PNtBu)_3ZrCl$ (**2a**) (top) and $ClCu(Ph_2PNiPr)_3ZrCl$ (**2b**) (bottom) with 50% probability ellipsoids. Hydrogen atoms are omitted for clarity.

The asymmetric unit of **2b** contains two crystallographically independent but chemically equivalent molecules. Bond lengths and angles of the second molecule are given in brackets in Table 2. The molecular structures show that two metal centers are linked by three phosphinoamide ligands. The zirconium center adopts a trigonal bipyramidal coordination geometry with the three nitrogen atoms in the basal position and the Cl(1)–Zr–Cu as the apical axis. The sum of the equatorial angles around the zirconium atom is ca. 357 °. Alternatively, the geometry around the copper is distorted tetrahedrally because of the effective stabilization of tetrahedral geometry given by tripodal-type $P_3$ coordination. The Cl(1)–Zr–Cu–Cl(2) axis is arranged linearly, the bent angles of Cl(1) and Cl(2) from the Zr–Cu axis are 0.77(2)° and 3.12(4)°, respectively, in **2a**. The N–P bond lengths of **2a**,**b** are approximately 0.1 Å shorter than the normal N–P single bonds, but comparable to those of starting zirconium complexes **1a**,**b**, which reflect the partial N–P double bond character. This was supported by the sum of the three angles at the N atom (359.3–359.9°), which is close to the theoretical value of 360° for the planar $sp^2$-hybridized nitrogen atom. The shorter bond lengths of N–P were also observed in our Ti–Pt and Ti–Ru phosphinoamide complexes,[10] $Zr(Ph_2PNPh)_4$,[13] and related complexes.[14] The Cu–P [2.3126(12)–2.3626(11) Å] bond lengths are slightly longer than those of (triphos)CuCl (2.282–2.299 Å),[4e] but comparable to related copper phosphane complexes such as $(PPh_3)_3CuCl$ (2.348 Å).[19]

Reaction of **1b** with an octahedrally arranged molybdenum precursor led to the formation of Zr–Mo heterodimetallic complex **3** (Scheme 3). In **3**, ligands around the molybdenum center are arranged octahedrally, to which the zirconium phosphinoamide moieties are coordinated in a facial coordination mode. Treatment of **1b** with $Mo(CO)_3(CH_3CN)_3$ in $CH_2Cl_2$ at room temperature resulted in the replacement of the $CH_3CN$ ligands by three phosphorus atoms of **1b** to give a Zr–Mo heterodimetallic complex, $(CO)_3Mo(Ph_2PNiPr)_3ZrCl$ (**3**), in 70% yield as pale yellow crystals. The $^1H$ NMR spectrum of **3** showed signals for three magnetically equivalent $Ph_2PNiPr$ moieties, which indicates the $C_{3v}$ symmetric structure of **3** in solution. No dynamic behavior was observed in variable temperature NMR spectroscopic experiments. The $^{31}P$ NMR spectrum of **3** showed a singlet at $\delta$ = 36.3 ppm, which is low-field shifted by ca. 20 ppm relative to $(triphos)Mo(CO)_3$ ($\delta$ =16.8 ppm). The IR spectrum of **3** shows characteristic C≡O stretching bands at 1987 and 1913 $cm^{-1}$, which is 50–70 $cm^{-1}$ shifted to higher frequencies relative to those of $(triphos)Mo(CO)_3$ (1937, 1844 $cm^{-1}$).[4b] The back-donation from molybdenum to the $\pi^*$ orbital of CO in **3** is apparently weaker than that in $(triphos)Mo(CO)_3$. There are two possible explanations for this: one is direct through-space interaction between Lewis acidic Zr and Mo atoms; the other is through-bond interaction by way of the Zr–N–P–Mo bond.[20]

The molecular structure determined by X-ray diffraction analysis is depicted in Figure 4, and representative bond lengths and angles are summarized in Table 2.The two

 © 2007 Wiley-VCH Verlag GmbH & Co. KGaA, Weinheim 

Table 2. Representative bond lengths and angles for dimetallic complexes.

| Bond lengths [Å] | | | | | Bond angles [°] | | | | |
|---|---|---|---|---|---|---|---|---|---|
| | **2a** | **2b**[a] | **3** | **4** | | **2a** | **2b**[a] | **3** | **4** |
| Zr–M | 2.6069(7) | 2.6854(6) [2.6790(6)] | 2.9741(5) | 2.964(4) | Cl(1)–Zr–M | 179.23(2) | 178.93(3) [176.01(3)] | 180 | 163.01(4) |
| Zr–Cl(1) | 2.4314(11) | 2.4026(10) [2.4048(13)] | 2.4427(12) | 2.390(2) | Zr–M–Cl(2) | 176.88(4) | 174.99(3) [174.43(3)] | | |
| Zr–Cl(2) | | | | 2.506(2) | N(1)–Zr–N(2) | 118.44(14) | 116.79(13) [116.00(13)] | 119.66(9) | 99.8(2) |
| Zr–Cl(3) | | | | 2.4936(14) | N(1)–Zr–N(3) | 120.34(14) | 118.90(14) [118.76(11)] | 119.72(10) | |
| Zr–N(1) | 2.149(2) | 2.100(3) [2.085(3)] | 2.114(2) | 2.140(3) | N(2)–Zr–N(3) | 120.29(12) | 121.04(14) [121.65(12)] | 119.68(8) | |
| Zr–N(2) | 2.156(4) | 2.108(4) [2.114(3)] | 2.115(2) | 2.181(4) | P(1)–M–P(2) | 85.94(3) | 83.48(3) [82.94(3)] | 100.16(2) | 101.03(4) |
| Zr–N(3) | 2.157(3) | 2.107(3) [2.108(2)] | 2.113(2) | | P(1)–M–P(3) | 84.92(2) | 81.59(2) [82.50(3)] | 100.20(2) | 106.94(4) |
| M–P(1) | 2.3626(11) | 2.3146(10) [2.3126(12)] | 2.5787(5) | 2.2439(11) | P(2)–M–P(3) | 83.22(3) | 80.85(3) [80.51(2)] | 100.17(2) | 145.57(12) |
| M–P(2) | 2.3356(12) | 2.3306(12) [2.3265(9)] | 2.5796(8) | 2.3270(11) | Zr–N(1)–P(1) | 93.1(2) | 98.5(2) [99.0(2)] | 99.08(8) | 102.2(2) |
| M–P(3) | 2.3408(12) | 2.3458(11) [2.3576(10)] | 2.5783(7) | 2.2548(11) | Zr–N(2)–P(2) | 95.0(2) | 99.8(2) [99.4(2)] | 99.08(8) | 105.0(2) |
| N(1)–P(1) | 1.665(3) | 1.666(3) [1.667(3)] | 1.671(2) | 1.641(4) | Zr–N(3)–P(3) | 95.3(2) | 99.6(2) [99.0(2)] | 99.08(8) | |
| N(2)–P(2) | 1.649(3) | 1.671(3) [1.674(3)] | 1.671(2) | 1.641(4) | | | | | |
| N(3)–P(3) | 1.659(3) | 1.668(3) [1.668(3)] | 1.671(2) | 1.615(4) | | | | | |

[a] The asymmetric unit of **2b** consists of two crystallographically independent but chemically equivalent molecules. Bond lengths and angles of the second molecule are given in brackets.

metal centers are connected by three phosphinoamide bridges and three phosphorus atoms are coordinated to the molybdenum center in a *fac*-$P_3$ fashion. The Mo–P bond lengths of **3** [2.5783(7)–2.5796(8) Å] are slightly longer relative to those found in previously reported (triphos)-$Mo(CO)_3$ [2.516(1) Å],[4b] whereas C–O bond lengths of 1.140(3) Å are comparable to those of (triphos)-$Mo(CO)_3$ [1.155(3) Å].[4b] The Mo–Zr and Mo–P distances suggest that the above-described shift of the $\tilde{\nu}$(C≡O) band to higher frequencies can be better explained by through-bond interactions.

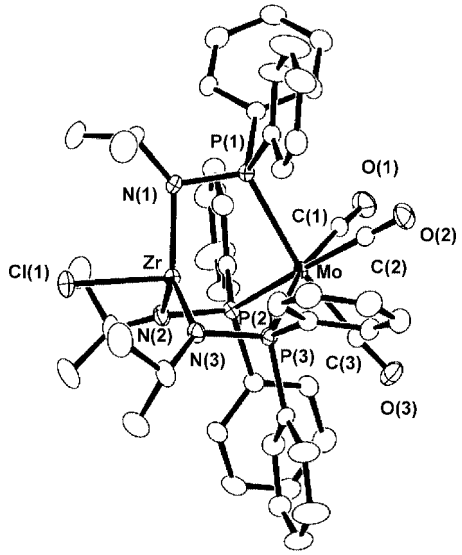


Figure 4. Molecular structure of $(CO)_3Mo(Ph_2PNiPr)_3ZrCl$ (**3**) with 50% probability ellipsoids. Hydrogen atoms are omitted for clarity.

### 2.3 Construction of Zr–Pt Heterodimetallic Complexes with the Use of $Pt^{II}$ Precursors that Do Not Provide Suitable Coordination Geometries for *fac*-$P_3$ Ligands

In the above-described two types of heterodimetallic complexes, the zirconium phosphinoamides act as the *fac*-$P_3$ tripodal-type ligand. The tetrahedral geometry of the $Cu^I$ and octahedral structure of the $Mo^0$ are suitable for the *fac*-$P_3$ tripodal-type coordination. One question concerns the fate of the zirconium phosphinoamides in the reaction with the second metal complex fragment that does not have the appropriate coordination geometry for the *fac*-$P_3$ tripodal-type coordination. To resolve this question, we chose a square-planar arranged $Pt^{II}$ precursor as the reactant in the reaction with **1**. Treatment of **1b** with $(COD)PtCl_2$ in $CH_2Cl_2$ at room temperature for 1 h afforded a novel Zr–Pt heterodimetallic complex, ($\kappa^2$-$Ph_2PNiPr$)$Pt(Ph_2PNiPr)_2$-$ZrCl_3$(**4**) in 75% yield (Scheme 4). The $^{31}P$ NMR spectrum of **4** showed the presence of three different phosphorus atoms with a satellite signal due to the coupling with $^{195}Pt$, $\delta$ = 12.9 ($J_{P,P}$ = 6.7, 286 Hz, $J_{Pt,P}$ = 3153 Hz), 3.4 ($J_{P,P}$ = 6.7, 13.9 Hz, $J_{Pt,P}$ = 3403 Hz), and –32.5 ppm ($J_{P,P}$ = 13.9, 286 Hz, $J_{Pt,P}$ = 1578 Hz). In contrast to the $C_{3v}$ symmetric structures of the Zr–Cu and Zr–Mo complexes giving a sin-

 © 2007 Wiley-VCH Verlag GmbH & Co. KGaA, Weinheim 

gle $^{31}P$ NMR spectroscopic resonance, the $^{31}P$ NMR spectrum of **4** clearly demonstrates that three $Ph_2PNiPr$ ligands in **4** are magnetically inequivalent and the complex has no symmetry. The nonsymmetric structure of **4** is also supported by the $^1H$ NMR spectrum of **4**; in a typical example, there exists three doublets at $\delta$ = 0.71, 1.15, and 1.45 ppm, which are due to the methyl protons of the *i*Pr group. It is noteworthy that one of them ($\delta$ =0.71 ppm) is significantly shifted to a higher field (vide infra).

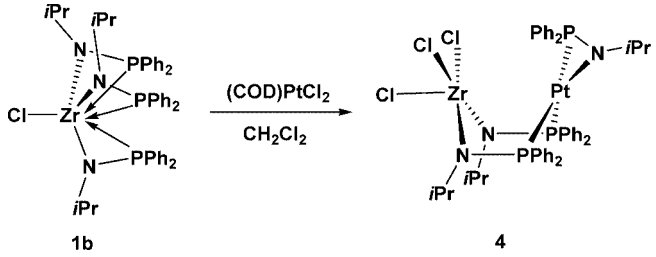


Scheme 4.

The molecular structure of **4** was established by X-ray study. Figure 5 shows the ORTEP view of **4** and selected bond lengths and angles of **4** are listed in Table 2. Two metal centers are linked by two phosphinoamide bridges in a boat form similar to Ti–Pt and Ti–Ru phosphinoamide complexes. Ligand arrangement around the zirconium atom is pseudooctahedral with two nitrogen atoms and two chlorine atoms at the basal plane and Cl(1) and Pt at the apical position. Geometry around the platinum atom is distorted square planar with the Pt atom out of the plane defined by P(1), P(2), and the center of N(3)–P(3) (ca. 0.077 Å). A similar distorted structure was also observed in $YY'Pt(Ph_2PNtBu)_2TiCl_2$ complexes in which the Pt atom is out of the plane by ca. 0.181–0.328 Å. The N(3)–P(3) bond length of 1.615(4) Å is ca. 0.03 Å shorter than those of the bridging phosphinoamide ligands, which indicates that there is a slightly increased double bond character of the N(3)–P(3) bond. The ligand arrangement indicates that **4** is formally considered to have a zwitterionic form with $Zr^{IV-}$ and $Pt^{II+}$ centers. To the best of our knowledge, this is the first example of a zwitterionic Zr–Pt heterodimetallic complex. The molecular structure provided clues for understanding the NMR spectroscopic data, which included three magnetically inequivalent methyl and methine signals of the *i*Pr group that were observed in the $^1H$ NMR spectrum and three $^{31}P$ NMR spectroscopic resonances with different chemical shifts and $^{31}P$–$^{195}Pt$ coupling constants. The nonsymmetric structure of **4** is reasonable in giving three doublets at $\delta$ = 0.71, 1.15, and 1.45 ppm that are due to the methyl protons of the *i*Pr group. An unusual upfield shift of one of the three doublets due to the methyl group in the *i*Pr moieties can be ascribed to the methyl proton of the *i*Pr of $\kappa^2$-coordinated phosphinoamide moiety, which is effectively shielded by one of the phenyl rings of the $PPh_2$ group of the bridging phosphinoamide ligand. The signal at $\delta$ = 3.4 ppm in the $^{31}P$ NMR spectrum is *trans* to the N atom of the $\kappa^2$-coordinated phosphinoamide and the other two are *trans* to each other. The value of each coupling constant is consistent with this interpretation.

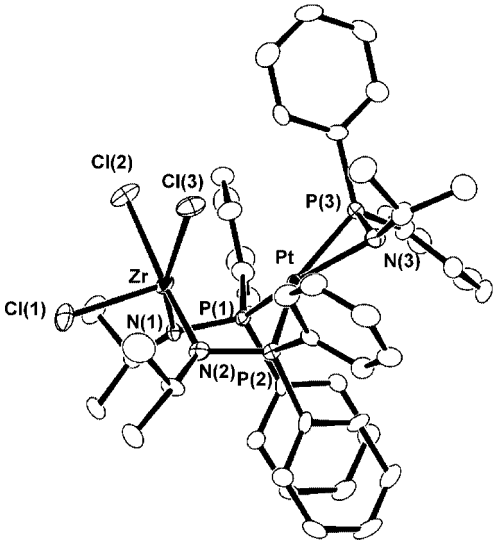


Figure 5. Molecular structure of ($\kappa^2$-$Ph_2PNiPr$)$Pt(Ph_2PNiPr)_2$-$ZrCl_3$(**4**) with 50% probability ellipsoids. Hydrogen atoms are omitted for clarity.

This unusual ligand rearrangement in the reaction of **1b** with a square planar platinum complex fragment provided some mechanistic insight. The reaction is likely to occur intramolecularly and the ligand migration is internuclear. The dimetallic structure of **4**, in which the Zr and Pt exist close enough to exchange their individual ligands, is the key to accomplish the rearrangement. The possible mechanism is illustrated in Scheme 5. Three phosphorus atoms of zirco-

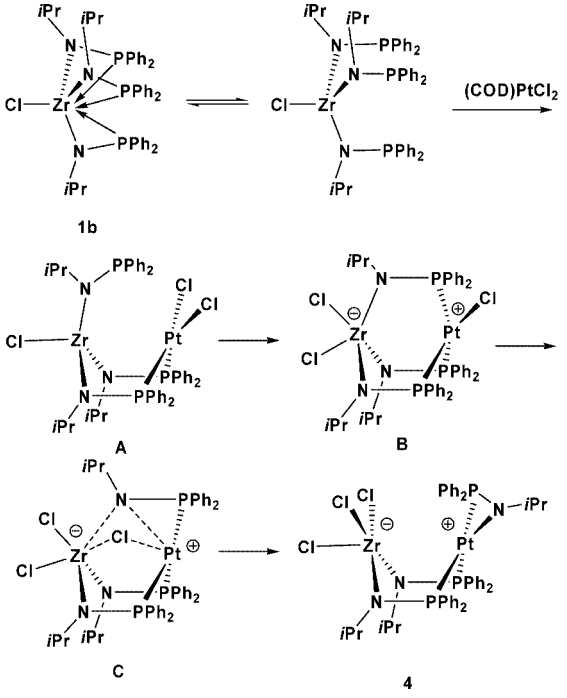


Scheme 5.

 © 2007 Wiley-VCH Verlag GmbH & Co. KGaA, Weinheim 

nium phosphinoamide **1b** reversibly dissociate to their uncoordinated forms in solution and two of them react with a square-planar $Pt^{II}$ species to form **A**. Coordination of the remaining phosphorus atom to the $Pt^{II}$ center results in internuclear migration of a chlorine atom from Pt to Zr to give zwitterionic intermediate **B**. The tricyclic structure of **B** generates significant ring strain that triggers the cleavage and recombination of the Zr–N and Pt–Cl bonds to form **4**. These results clearly demonstrate that zirconium phosphinoamides **1a**,**b** behave as *fac*-$P_3$ tripodal-type metalloligands in the reaction with transition metals that are able to attain a tetrahedral or octahedral geometry while coordinated to the metal center with a square planar structure. This geometry is unfavorable for the coordination of the tripodal-type ligand and as such an internuclear ligand arrangement is induced to release the ring strain of the primarily formed intermediates.

## 3. Concluding Remarks

As described above, we attained success in the preparation of tris(phosphinoamide)zirconium complexes, $(Ph_2PNR)_3ZrCl$ [R = *t*Bu (**1a**), *i*Pr (**1b**)], which reacted with a second metal complex fragment to form heterodimetallic complexes, $ClCu(Ph_2PNR)_3ZrCl$ (**2**) and $(CO)_3Mo(Ph_2PN{\it i}Pr)_3ZrCl$ (**3**). In the Zr-Cu and Zr-Mo complexes, the coordination geometry around the late-transition-metal center is defined as pseudotetrahedral and octahedral, respectively, owing to the effective coordination of they $P_3$-moiety of **1** in the tripodal fashion. The reaction of **1b** with square planar arranged $(COD)PtCl_2$ is unique and gives a zwitterionic heterodimetallic complex ($\kappa^2$-$Ph_2PN{\it i}Pr)Pt(Ph_2PN{\it i}Pr)_2ZrCl_3$ (**4**); this reaction involves intramolecular migration of two chlorine atoms from Pt to Zr as well as that of a $iPrNPPh_2$ moiety from Zr to Pt. In heterodimetallic complexes **2**–**4**, the Lewis acidic zirconium and the late-transition-metal atoms are closely located; this realized the internuclear ligand arrangement seen in the formation of **4**. The driving force for the rearrangement can be attributed to the fact that the hard chlorine atom preferred the hard zirconium center, whereas the soft phosphinoamide ligand preferred the soft platinum atom. Of interest is the possible dative interaction of the late transition metal to the zirconium atom. As reported earlier, we proposed the Ti←Pt interaction in the $YY'Pt(Ph_2PN{\it t}Bu)_2TiCl_2$ complexes from the crystal structures. There is an occupied $d_{z^2}$ orbital in the platinum atom, and this possibly interacted with the Lewis acidic titanium center. The Ti←Pt bond lengths decrease in the order $Cl_2Pt(Ph_2PN{\it t}Bu)_2TiCl_2$ [2.8358(6) Å] > $MeClPt(Ph_2PN{\it t}Bu)_2TiCl_2$ [2.7547(10) Å] > $Me_2Pt(Ph_2PN{\it t}Bu)_2TiCl_2$ [2.6860(11) Å]; this is explained by assuming that the higher electron dense platinum complex moiety can make a stronger dative bond interaction. The molecular structure of **2** revealed that the Zr–Cu bond length of **2a** [2.6069(7) Å] is slightly shorter than the sum of the van der Waals radii of Zr and Cu (ca. 2.74 Å)[21] (ca. 95% of the sum of the radii). In contrast, the Zr–Mo and Zr–Pt distances of 2.9741(5) and 2.964(4) Å in complexes **3** and **4**, respectively, are nearly identical to the sum of the van der Waals radii of Zr–Mo and Zr–Pt (ca. 3.05 Å)[21] (98 and 97% of the sum of the radii, respectively). The Rh–B interaction is proposed in Bourissou's complex, $\{[(o\text{-}{\it i}Pr_2P\text{-}C_6H_3)_2B(Ph)]RhCl\}_2$, from chemical shifts of the $^{11}B$ NMR spectroscopic resonance and the Rh–B distance found from X-ray crystallography. This was supported by DFT calculations {BP86/[CEP-31G(Rh), 6-31G*(other elements)]}, in which bonding interaction was observed at the HOMO of the complex.[8] However, our preliminary theoretical calculations (single-point calculation of the structure of **2a**/HF/LanL2DZ) did not provide clear evidence for the bonding interaction at the HOMO level. Thus, further theoretical studies with a higher functional level, including those of **3**, **4**, previously reported Ti–Pt heterodimetallic complexes, and related complexes, should be performed to discuss metal–metal interactions.

In summary, **1** is useful as a metalloligand for the formation of Zr–M heterodimetallic compounds, though the coordination mode of **1** was dependent on the preferred coordination environment of the second transition–metal centers. Current efforts are directed towards the synthesis of novel heterodimetallic complexes with several second transition-metal complex fragments having other coordination geometries. Their systematic results, including structural properties and dynamic behaviors, are expected to open the way to construct novel heterodimetallic complexes with unique structures, electronic properties, and reactivities.

## Experimental Section

**General:** Manipulation of air- and moisture-sensitive organometallic compounds was carried out under a dry argon atmosphere by using standard Schlenk tube techniques associated with a high-vacuum line, or with the nitrogen filled glove box. All solvents were distilled from appropriate drying reagents prior to use (THF, hexane; $Ph_2CO$/Na, $CH_3CN$, $CH_2Cl_2$; $CaH_2$). $^1H$, $^{13}C$, and $^{31}P$ NMR spectra were recorded with a JEOL Lambda 600 or a Lambda 400 spectrometer at ambient temperature unless otherwise noted. $^1H$, $^{13}C$, and $^{31}P$ NMR chemical shifts ($\delta$ values) were given in ppm relative to the solvent signal ($^1H$, $^{13}C$) or standard resonances ($^{31}P$; external 85% $H_3PO_4$). IR spectra were recorded with a JASCO FT/IR-550 spectrometer. Melting points were measured with a Yanaco SMP3 micro melting point apparatus. Elemental analyses were performed by the Elemental Analysis Center, Faculty of Science, Kyushu University, or with a Perkin–Elmer 2400/CHN analyzer. Starting materials, phosphinoamide,[12] $[Mo(CO)_3(CH_3CN)_3]$,[22] and $(COD)PtCl_2$[23] were synthesized by the method reported in the literature.

**$(Ph_2PNR)_3ZrCl$ [R = *t*Bu (1a), *i*Pr (1b)]:** In a 100-mL Schlenk tube, $Ph_2PNH{\it t}Bu$ (2589 mg, 10.06 mmol) was dissolved in THF (30 mL). A hexane solution of *n*BuLi (1.56 M, 6.5 mL, 10.14 mmol) was added to the solution at –78 °C, and the solution was slowly warmed to room temperature. After stirring at room temperature for 3 h, the mixture was cooled to –78 °C and a THF (15 mL) solution of $ZrCl_4$ (800 mg, 3.43 mmol) was added dropwise. The slightly yellow solution turned off white in color and a white solid precipitated. After 12 h, all of the volatiles were removed under

 © 2007 Wiley-VCH Verlag GmbH & Co. KGaA, Weinheim 

vacuum, and the formed crude product was dissolved in $CH_2Cl_2$ (20 mL). The insoluble materials were filtered off through a G3 filter, and the resulting filtrate was concentrated to a volume of 5 mL. Hexane (20 mL) was added to this supersaturated $CH_2Cl_2$ solution. The desired product was obtained as colorless crystals in 86% yield (2580 mg, 2.88 mmol). In a similar fashion, **1b** was obtained in 84% yield as colorless crystals. **1a**: M.p. 108 °C (dec). $^1H$ NMR (600 MHz, $CD_2Cl_2$): $\delta$ = 1.47 (s, 27 H, *t*Bu), 6.99–7.17 (br., 30 H, Ph) ppm. $^{13}C$ NMR (150 MHz, $CD_2Cl_2$): $\delta$ = 34.1 ($CMe_3$), 60.0 (m, $CMe_3$), 127.5 (m, *meta*-Ph), 128.8 (*para*-Ph), 133.4 (m, *ortho*-Ph), 136.75 (*ipso*-Ph) ppm. $^{31}P\{^1H\}$ NMR (243 MHz, $CD_2Cl_2$): $\delta$ = –11.8 (s) ppm. $C_{48}H_{57}ClN_3P_3Zr$ (895.59): calcd. C 64.37, H 6.42, N 4.69; found C 64.14, H 6.42, N 4.45. **1b**: M.p. 107–108 °C (dec). $^1H$ NMR (600 MHz, $CD_2Cl_2$): $\delta$ = 1.20 [d, $J_{H,H}$ = 6.6 Hz, 18 H, $(CH_3)_2CH$], 3.89 [sept, $J_{H,H}$ = 6.6 Hz, 3 H, $(CH_3)_2CH$], 7.12–7.17 (m, 12 H, *meta*-Ph), 7.22–7.26 (m, 18 H, *ortho* and *para*-Ph) ppm. $^{13}C$ NMR (150 MHz, $CD_2Cl_2$): $\delta$ = 26.8 [$(CH_3)_2CH$], 53.2 [$(CH_3)_2CH$], 128.1 (*meta*-Ph), 129.3 (*para*-Ph), 133.4 (m, *ortho*-Ph), 136.9 (m, *ipso*-Ph) ppm. $^{31}P\{^1H\}$ NMR (243 MHz, $CD_2Cl_2$): $\delta$ = –12.0 (s) ppm.$C_{45}H_{51}ClN_3P_3Zr$ (853.51): calcd. C 63.32, H 6.02, N 4.92; found C 63.34, H 6.52, N 5.40.[24]

**$ClCu(Ph_2PNR)_3ZrCl$ [R = *t*Bu (2a), *i*Pr (2b)]:** A 20-mL Schlenk tube was charged with **1a** (44 mg, 0.050 mmol) and CuCl (5 mg, 0.051 mmol), and the atmosphere was replaced by argon. The mixture was dissolved in $CH_3CN$ (5 mL). The color of the solution changed immediately from colorless to yellow, from which a yellow precipitate was separated. After removal of the solvent in vacuo, the solid was washed with hexane (3 × 2 mL). The crude product was dissolved in warm $CH_2Cl_2$, and the insoluble materials (unreacted CuCl) were filtered off. The filtrate was cooled to –30 °C to form yellow microcrystals of **2a** in 78% yield (38 mg, 0.038 mmol). In a similar fashion, **1b** was obtained in 82% yield as yellow microcrystals. **2a**: M.p. 116–117 °C (dec). $^1H$ NMR (600 MHz, $CD_2Cl_2$): $\delta$ = 1.50 (s, 27 H, *t*Bu), 6.96 (t, *J* = 7.4 Hz, 12 H, *meta*-Ph), 7.15 (t, *J* = 7.4 Hz, 6 H, *para*-Ph), 7.42 (br., 12 H, *ortho*-Ph) ppm. $^{13}C$ NMR (150 MHz, $CD_2Cl_2$): $\delta$ = 34.8 ($CMe_3$), 61.8 (m, $CMe_3$), 127.9 (*meta*-Ph), 129.5 (*para*-Ph), 132.8 (*ortho*-Ph), 134.5 (m, *ipso*-Ph) ppm. $^{31}P\{^1H\}$ NMR (243 MHz, $CD_2Cl_2$): $\delta$ = –30.6 (br) ppm. $C_{48}H_{57}Cl_2CuN_3P_3Zr$ (994.59): calcd. C 57.97, H 5.78, N 4.22; found C 57.51, H 5.94, N 4.32. **2b**: M.p. 117–118 °C (dec). $^1H$ NMR (600 MHz, $CD_2Cl_2$): $\delta$ = 1.38 [d, $J_{H,H}$ = 6.6 Hz, 18 H, $(CH_3)_2$-CH], 3.85 [m, 3 H, $(CH_3)_2CH$], 6.98 (t, $J_{H,H}$ = 7.7 Hz, 12 H, *meta*-Ph), 7.19 (t, $J_{H,H}$ = 7.7 Hz, 6 H, *para*-Ph), 7.34 (br., 12 H, *ortho*-Ph) ppm. $^{13}C$ NMR (150 MHz, $CD_2Cl_2$): $\delta$ = 27.2 [$(CH_3)_2CH$], 53.2 [$(CH_3)_2CH$], 128.1 (*meta*-Ph), 130.0 (*para*-Ph), 133.7 (m, *ortho*-Ph), 134.8 (m, *ipso*-Ph) ppm. $^{31}P\{^1H\}$ NMR (243 MHz, $CD_2Cl_2$): $\delta$ = –11.2 (br) ppm. $C_{45}H_{51}Cl_2CuN_3P_3Zr$ (952.52): calcd. C 56.74, H 5.40, N 4.41; found C 56.87, H 5.80, N 4.59.

**$(CO)_3Mo(Ph_2PNiPr)_3ZrCl$ (3):** A 20-mL Schlenk tube was charged with **1b** (428 mg, 0.501 mmol) and $Mo(CO)_3(CH_3CN)_3$ (155 mg, 0.511 mmol), and the atmosphere was replaced by argon. The mixture was dissolved in $CH_2Cl_2$ (5 mL), and the solution was stirred at room temperature for 1 h. The color of the reaction mixture changed from yellow to red. The solution was kept at –30 °C to form pale yellow microcrystals of **3** in 70% yield (365 mg, 0.353 mmol). M.p. 227–228 °C (dec). $^1H$ NMR (600 MHz, $CD_2Cl_2$): $\delta$ = 1.11 [d, $J_{H,H}$ = 6.8 Hz, 18 H, $(CH_3)_2CH$], 3.67 [m, 3 H, $(CH_3)_2CH$], 7.25–7.28 (m, 12 H, *meta*-Ph), 7.36–7.41 (m, 18 H, *para* and *ortho*-Ph) ppm. $^{13}C$ NMR (150 MHz, $CD_2Cl_2$): $\delta$ = 26.0 [$(CH_3)_2CH$], 53.0 [$(CH_3)_2CH$], 128.9 (m, *meta*-Ph), 129.8 (*para*-Ph), 133.4 (m, *ortho*-Ph), 138.0 (m, *ipso*-Ph), 218.3 (m, CO) ppm. $^{31}P\{^1H\}$ NMR (243 MHz, $CD_2Cl_2$): $\delta$ = 36.3 (s) ppm. IR (KBr pellet): $\tilde{\nu}$ = 1987 (C≡O), 1913 (C≡O) $cm^{-1}$.$C_{48}H_{51}Cl_2MoN_3O_3P_3Zr$ (1033.49): calcd. C 55.78, H 4.97, N 4.07; found C 55.48, H 4.91, N 4.00.

**($\kappa^2$-$Ph_2PNiPr$)$Pt(Ph_2PNiPr)_2ZrCl_3$ (4):** A 20-mL Schlenk tube was charged with **1b** (50 mg, 0.059 mmol) and $(COD)PtCl_2$ (21 mg, 0.056 mmol), and the atmosphere was replaced by argon. The mixture was dissolved in $CH_2Cl_2$ (5 mL), and the solution was stirred at room temperature for 1 h. The color of the reaction mixture changed from yellow to red. The solution was cooled to –30 °C to form pale yellow crystals of **4** in 75% yield (47 mg, 0.042 mmol). M.p. 126–128 °C (dec). $^1H$ NMR (600 MHz, $CD_2Cl_2$): $\delta$ = 0.71 [d, $J_{H,H}$ = 6.8 Hz, 6 H, $(CH_3)_2CH$], 1.15 [d, $J_{H,H}$ = 6.0 Hz, 6 H, $(CH_3)_2CH$], 1.45 [d, $J_{H,H}$ = 6.0 Hz, 6 H, $(CH_3)_2CH$], 2.97 [m, 1 H, $(CH_3)_2CH$], 3.47 [m, 1 H, $(CH_3)_2CH$], 3.62 [m, 1 H, $(CH_3)_2CH$], 6.75–6.80 (m, 4 H, Ph), 6.90–6.97 (m, 4 H, Ph), 7.07–7.12 (m, 2 H, Ph), 7.13–7.17 (m, 4 H, Ph), 7.22–7.27 (m, 2 H, Ph), 7.37–7.42 (m, 4 H, Ph), 7.51–7.60 (m, 10 H, Ph) ppm. $^{13}C$ NMR (150 MHz, $CD_2Cl_2$): $\delta$ = 25.2 [$(CH_3)_2CH$], 25.8 [$(CH_3)_2CH$], 27.0 [$(CH_3)_2CH$], 49.2 [$(CH_3)_2CH$], 54.2 [$(CH_3)_2CH$], 54.7 [$(CH_3)_2CH$], 127.5 (Ph), 128.2 (Ph), 129.0 (Ph), 130.5 (Ph), 130.7 (Ph), 133.0 (Ph), 133.1 (Ph), 133.4 (Ph), 134.1 (Ph) ppm. $^{31}P\{^1H\}$ NMR (243 MHz, $CD_2Cl_2$): $\delta$ = 12.9 (dd, $J_{P,P}$ = 6.7, 286 Hz, $J_{Pt,P}$ = 3153 Hz), 3.4 (dd, $J_{P,P}$ = 6.7, 13.9 Hz, $J_{Pt,P}$ = 3403 Hz), –32.5 (dd, $J_{P,P}$ = 13.9, 286 Hz, $J_{Pt,P}$ = 1578 Hz) ppm.$C_{45}H_{51}Cl_3N_3P_3PtZr$ (1119.51): calcd. C 48.28, H 4.59, N 3.75; found C 48.14, H 4.66, N 3.68.

Table 3. Crystallographic data for zirconium phosphinoamides.

| | **1a** | **1b** |
|---|---|---|
| Empirical formula | $C_{48}H_{57}ClN_3P_3Zr$ | $C_{45}H_{51}ClN_3P_3Zr$ |
| Formula weight | 895.59 | 853.51 |
| Crystal system | trigonal | monoclinic |
| Lattice type | primitive | primitive |
| Space group | P3 (#143) | $P2_1/n$ (#14) |
| *a* [Å] | 19.4576(14) | 11.293(2) |
| *b* [Å] | 19.4576(14) | 16.724(3) |
| *c* [Å] | 10.8143(10) | 22.575(4) |
| *α* [°] | 90 | 90 |
| *β* [°] | 90 | 93.930(2) |
| *γ* [°] | 120 | 90 |
| Volume [Å$^3$] | 3545.7(5) | 4253.6(12) |
| *Z* value | 3 | 4 |
| $D_{calcd.}$ [g cm$^{-3}$] | 1.258 | 1.333 |
| *F*(000) | 1404.00 | 1776.00 |
| $\mu$(Mo-$K_\alpha$) [cm$^{-1}$] | 4.249 | 4.686 |
| Crystal color, habit | colorless, prism | colorless, platelet |
| Crystal dimensions [mm] | 0.15 × 0.05 × 0.02 | 0.25 × 0.15 × 0.08 |
| No. observations (all reflections) | 10782 | 9605 |
| No. variables | 506 | 529 |
| Reflection/parameter ratio | 21.31 | 18.16 |
| *R* (all reflections) | 0.0825 | 0.0705 |
| $R_1$ [$I > 2.00\sigma(I)$][a] | 0.0757 | 0.0466 |
| $wR_2$ (all reflections)[b] | 0.1890 | 0.1494 |
| GOF | 1.114 | 1.006 |
| Flack parameter | 0.42(5) | |
| Max shift/error in final cycle | 0.000 | 0.000 |
| Maximum peak in final diff. map [e Å$^{-3}$] | 4.30 | 1.23 |
| Minimum peak in final diff. map [e Å$^{-3}$] | –0.75 | –0.76 |

[a] $R_1 = \Sigma||F_o| - |F_c||/\Sigma|F_o|$. [b] $wR_2 = [\Sigma\{w(F_o^2 - F_c^2)^2\}/\Sigma\{w(F_o^2)^2\}]^{1/2}$.

 © 2007 Wiley-VCH Verlag GmbH & Co. KGaA, Weinheim 

Table 4. Crystallographic tables for the heterodimetallic complexes.

| | **2a** | **2b** | **3** | **4** |
|---|---|---|---|---|
| Empirical formula | $C_{48}H_{57}Cl_2N_3P_3CuZr$ | $C_{45}H_{51}ClN_3P_3CuZr{\cdot}CH_2Cl_2$ | $C_{48}H_{57}ClO_3N_3P_3MoZr{\cdot}1/4C_6H_6$ | $C_{45}H_{51}Cl_3N_3P_3PtZr$ |
| Formula weight | 994.59 | 987.96 | 1033.49 | 1119.51 |
| Crystal system | triclinic | triclinic | trigonal | monoclinic |
| Lattice type | primitive | primitive | *R*-centered | primitive |
| Space group | $P\bar{1}$ (#2) | $P\bar{1}$ (#2) | $R\bar{3}$ (#148) | $P2_1/n$ (#14) |
| *a* [Å] | 10.968(2) | 10.9996(12) | 14.516(3) | 11.539(2) |
| *b* [Å] | 11.948(2) | 21.564(2) | 14.516(3) | 23.527(4) |
| *c* [Å] | 19.980(4) | 21.801(2) | 39.098(7) | 16.727(3) |
| *α* [°] | 79.863(9) | 66.326(3) | 90 | 90 |
| *β* [°] | 84.577(9) | 83.226(4) | 90 | 92.090(2) |
| *γ* [°] | 63.397(7) | 85.984(4) | 120 | 90 |
| Volume [Å$^3$] | 2304.2(7) | 4701.4(8) | 7135(2) | 4538.1(13) |
| *Z* value | 2 | 4 | 6 | 4 |
| $D_{calcd.}$ [g cm$^{-3}$] | 1.433 | 1.396 | 1.477 | 1.638 |
| *F*(000) | 1028.00 | 2028.00 | 3240.00 | 2224.00 |
| $\mu$(Mo-$K_\alpha$) [cm$^{-1}$] | 9.443 | 9.799 | 6.839 | 36.137 |
| Crystal color, habit | yellow, chip | yellow, block | yellow, block | yellow, chip |
| Crystal dimensions [mm] | 0.20 × 0.08 × 0.05 | 0.20 × 0.18 × 0.10 | 0.20 × 0.15 × 0.05 | 0.20 × 0.09 × 0.08 |
| No. observations (all reflections) | 10146 | 20685 | 3630 | 10368 |
| No. variables | 580 | 1024 | 194 | 506 |
| Reflection/parameter ratio | 17.49 | 20.20 | 18.71 | 20.49 |
| *R* (all reflections)[a] | 0.0765 | 0.0733 | 0.0403 | 0.0515 |
| $R_1$ [$I > 2.00\sigma(I)$][b] | 0.0535 | 0.0572 | 0.0379 | 0.0454 |
| $wR_2$ (all reflections) | 0.1675 | 0.1359 | 0.0942 | 0.0855 |
| GOF | 1.005 | 1.067 | 1.125 | 1.223 |
| Max shift/error in final cycle | 0.000 | 0.001 | 0.000 | 0.002 |
| Maximum peak in final diff. map [e Å$^{-3}$] | 1.62 | 1.13 | 0.80 | 3.73 |
| Minimum peak in final diff. map [e Å$^{-3}$] | –0.92 | –1.58 | –1.07 | –1.43 |

[a] $R_1 = \Sigma||F_o| - |F_c||/\Sigma|F_o|$. [b] $wR_2 = [\Sigma\{w(F_o^2 - F_c^2)^2\}/\Sigma\{w(F_o^2)^2\}]^{1/2}$.

**X-ray Data Collection and Reduction:** Single crystals of all complexes were grown from $CH_2Cl_2$/pentane. X-ray crystallography was performed with a Rigaku Saturn CCD area detector with graphite monochromated Mo-$K_\alpha$ radiation ($\lambda$ = 0.71070A). The reflection data were collected at 123(2) K by using ω scan in the $\theta$ range of $3.1 \leq \theta \leq 27.5°$ (**1a**), $3.0 \leq \theta \leq 27.5°$ (**1b**), $3.0 \leq \theta \leq 27.5°$ (**2a**), $3.1 \leq \theta \leq 27.5°$ (**2b**), $3.1 \leq \theta \leq 27.5°$ (**3**), $3.1 \leq \theta \leq 27.5°$ (**4**). The data obtained were processed with Crystal-Clear (Rigaku) on a Pentium computer, and were corrected for Lorentz and polarization effects. The structures was solved by direct methods (SIR 97[25] for **1a**,**b**, and **2b**, SIR 92[26] for **2a**, **3**, and **4**) and expanded by using Fourier techniques.[27] The non-hydrogen atoms were refined anisotropically, and the hydrogen atoms by using the riding model. The final cycle of full-matrix least-squares refinement on $F^2$ was based on 10782 observed reflections and 563 variable parameters for **1a**, 9605 observed reflections and 529 variable parameters for **1b**, 10146 observed reflections and 580 variable parameters for **2a**, 20685 observed reflections and 1113 variable parameters for **2b**, 10383 observed reflections and 599 variable parameters for **3**, and on 10368 observed reflections and 556 variable parameters for **4**. Neutral atom scattering factors were taken from Cromer and Waber.[28] All calculations were performed with the CrystalStructure[29,30] crystallographic software package. Details of the final refinement are summarized in Tables 3 and 4, and the numbering scheme employed is shown in Figures 2, 3, 4, and 5 which was drawn with ORTEP at 50% probability ellipsoids. Unsatisfactory quality of the crystal in the crystallographic analysis of **1a** provided two large residual densities near the Zr atom. However, the data obtained are reliable enough to discuss the atom connectivity, bond lengths, and angles. CCDC-632038 (**1a**), -632039 (**1b**), -632040 (**2a**), -632041 (**2b**), -632042 (**3**), and -632043 (**4**) contain the supplementary crystallographic data for this paper. These data can be obtained free of charge from The Cambridge Crystallographic Data Centre via www.ccdc.cam.au.uk/data_request/cif.

**Supporting Information** (see footnote on the first page of this article): Variable temperature NMR spectroscopic data (**1a**,**b**) and $^1$H, $^{13}$C, and $^{31}$P NMR spectroscopic data (**1a**,**b**, **2a**,**b**, **3**, **4**).

## Acknowledgments

This work was supported by the Ministry of Education, Culture, Sports, Science and Technology, Japan by Grant-in-Aid for Scientific Research on Priority Areas (No. 15036253 and 16033246), "Reaction Control of Dynamic Complexes".

[1] a) P. Dierkes, P. W. N. M. van Leeuwen, *J. Chem. Soc., Dalton Trans.* **1999**, 1519–1529; b) P. W. N. M. van Leeuwen, P. C. J. Kamer, J. N. H. Reek, P. Dierkes, *Chem. Rev.* **2000**, *100*, 2741–2770; c) Z. Freixa, P. W. N. M. van Leeuwen, *Dalton Trans.* **2003**, 1890–1901; d) T. Appleby, J. D. Woollins, *Coord. Chem. Rev.* **2002**, *235*, 121–140; e) D. M. A. Minahan, W. E. Hill, C. A. McAuliffe, *Coord. Chem. Rev.* **1984**, *55*, 31–54; f) R.

 © 2007 Wiley-VCH Verlag GmbH & Co. KGaA, Weinheim 

Noyori, *Angew. Chem. Int. Ed.* **2002**, *41*, 2008–2022; g) R. Noyori, T. Ohkuma, *Angew. Chem. Int. Ed.* **2001**, *40*, 40–73.

[2] C. A. Tolman, *Chem. Rev.* **1977**, *77*, 313–348.

[3] H. A. Mayer, W. C. Kaska, *Chem. Rev.* **1994**, *94*, 1239–1272.

[4] a) S. Gambarotta, S. Strologo, C. Floriani, A. Chiesi-Villa, C. Guastini, *Organometallics* **1984**, *3*, 1444–1445; b) O. Walter, T. Klein, G. Huttner, L. Zsolnai, *J. Organomet. Chem.* **1993**, *458*, 63–81; c) A. Muth, O. Walter, G. Huttner, A. Asam, L. Zsolnai, Ch. Emmerrich, *J. Organomet. Chem.* **1994**, *468*, 149–163; d) L. Sacconi, S. Midollini, *J. Chem. Soc., Dalton Trans.* **1972**, 1213–1216; e) D. J. Fife, H. J. Mueh, C. F. Campana, *Acta Crystallogr., Sect. C: Cryst. Struct. Commun.* **1993**, *49*, 1714–1716; f) A. F. Kowalski, M. T. Ashby, *J. Am. Chem. Soc.* **1995**, *117*, 12639–12640.

[5] It is well-known that the reaction of a Lewis acidic boron center with an appropriate anion gives the corresponding borate. Peters et al. described the synthesis of a new type of bidentate and *fac*-$P_3$ tripodal phosphanes containing a borate anion, bis or tris[(diphenylphosphanyl)methyl]borate such as $[Ph_nB(CH_2PPh_2)_{4-n}]^-$ ($n$ = 1, 2). They successfully ligate to various transition metals such as Fe, Co, Ni, Pd and Pt complex fragments. Seea) S. J. Thomas, J. C. Peters, *J. Am. Chem. Soc.* **2001**, *123*, 5100–5101; b) T. A. Betley, J. C. Peters, *Angew. Chem. Int. Ed.* **2003**, *42*, 2385–2389; c) J. C. Thomas, J. C. Peters, *Inorg. Chem.* **2003**, *42*, 5055–5073; d) T. A. Betley, J. C. Peters, *Inorg. Chem.* **2003**, *42*, 5074–5084; e) J. C. Thomas, J. C. Peters, *J. Am. Chem. Soc.* **2003**, *125*, 8870–8888; f) C. C. Lu, J. C. Peters, *J. Am. Chem. Soc.* **2004**, *126*, 15818–15832; g) C. C. Lu, J. C. Peters, *J. Am. Chem. Soc.* **2002**, *124*, 5272–5273; h) see ref.[9b]; i) J. C. Peters, J. C. Thomas, J. A. Dupont, C. G. Riordan, *Inorg. Synth.* **2004**, *34*, p., 8; j) S. D. Brown, M. P. Mehn, J. C. Peters, *J. Am. Chem. Soc.* **2005**, *127*, 13146–13147; k) C. C. Lu, C. T. Saouma, M. W. Day, J. C. Peters, *J. Am. Chem. Soc.*, DOI: 10.1021/ja06043 58; l) S. D. Brown, J. C. Peters, *J. Am. Chem. Soc.* **2005**, *127*, 1913–1923; m) C. C. Lu, J. C. V. Peters, *Inorg. Chem.* **2006**, *45*, 8597–8607; n) J. Li, P. I. Djurovich, B. D. Alleyne, M. Yousufuddin, N. N. Ho, J. C. Peters, R. Bau, M. E. Thompson, *Inorg. Chem.* **2005**, *44*, 1713–1727; o) D. M. Jenkins, J. C. Peters, *J. Am. Chem. Soc.* **2005**, *127*, 7148–7165; p) J. C. Peters, J. D. Feldman, T. D. Tilley, *J. Am. Chem. Soc.* **1999**, *121*, 9871–9872; q) C. M. Thomas, N. P. Mankad, J. C. Peters, *J. Am. Chem. Soc.* **2006**, *128*, 4956–4957; r) C. M. Thomas, J. C. Peters, *Organometallics* **2005**, *24*, 5858–5867; s) J. Li, P. I. Djurovich, B. D. Alleyne, M. Yousufuddin, N. N. Ho, J. C. Thomas, J. C. Peters, R. Bau, M. E. Thompson, *Inorg. Chem.* **2005**, *44*, 1713–1727; t) M. T. Whited, E. Rivard, J. C. Peters, *Chem. Commun.* **2006**, 1613–1615; u) I. R. Shapiro, D. M. Jenkins, J. C. Thomas, M. W. Day, J. C. Peters, *Chem. Commun.* **2001**, 2152–2153; v) A. A. Barney, A. F. Heyduk, D. G. Nocera, *Chem. Commun.* **1999**, 2379–2380.

[6] a) J. A. Labinger, J. N. Bonfiglio, D. L. Grimmett, S. T. Masuo, E. Shearin, J. S. Miller, *Organometallics* **1983**, *2*, 733–740; b) H. H. Karsch, A. Appelt, F. H. Kohler, G. Muller, *Organometallics* **1985**, *4*, 231–238; c) O. T. Beachley Jr, C. Tessier-Youngs, *Organometallics* **1983**, *2*, 796–801; d) F. Thomas, S. Schluz, M. Nieger, K. Nattinen, *Chem. Eur. J.* **2002**, *8*, 1915–1924; e) D. F. Clemens, D. H. H. Sisler, W. S. Brey, *Inorg. Chem.* **1966**, *5*, 527–533.

[7] For other Lewis acid containing monodentate ligands, see: S. Bontemps, G. Bouhadir, K. Miqueu, D. Bourissou, *J. Am. Chem. Soc.* **2006**, *128*, 12056–12057.

[8] S. Bontemps, G. Gornitzka, G. Bouhadir, K. Miqueu, D. Bourissou, *Angew. Chem. Int. Ed.* **2006**, *45*, 1611–1614.

[9] For other Lewis acid containing bidentate ligands, see: a) L. Turculet, J. D. Feldman, T. D. Tilley, *Organometallics* **2004**, *23*, 2488–2502; b) C. Thomas, J. C. Peters, *Polyhedron* **2004**, *23*, 2901–2913.

[10] a) H. Nagashima, T. Sue, T. Oda, A. Kanemitsu, T. Matsumoto, Y. Motoyama, Y. Sunada, *Organometallics* **2006**, *25*, 1987–1994; b) Y. Sunada, T. Sue, T. Matsumoto, H. Nagashima, *J. Organomet. Chem.* **2006**, *691*, 3176–3182.

[11] a) G. S. Ferguson, P. T. Wolczanski, L. Párkányi, M. C. Zonnevylle, *Organometallics* **1988**, *7*, 1967–1979; b) G. S. Ferguson, P. T. Wolczanski, *Organometallics* **1985**, *4*, 1601–1605; c) O. Kühl, S. Joachim, J. Sieler, E. Hey-Hawkins, *Polyhedron* **2001**, *20*, 2171–2177.

[12] H. H. Sisler, N. L. Smith, *J. Org. Chem.* **1961**, *26*, 611–613.

[13] O. Kuhl, T. Koch, F. B. Somoza Jr, P. C. Junk, E. Hey-Hawkins, D. Plat, M. S. Eisen, *J. Organomet. Chem.* **2000**, *604*, 116–125.

[14] a) M. T. Gamer, P. W. Roesky, *Inorg. Chem.* **2004**, *43*, 4903–4906; b) P. W. Roesky, *Inorg. Chem.* **2006**, *45*, 798–802; c) N. Poetschke, M. Nieger, M. A. Khan, E. Niecke, M. T. Ashby, *Inorg. Chem.* **1997**, *36*, 4087–4093; d) P. W. Roesky, *Heteroat. Chem.* **2002**, *13*, 514–520; e) M. T. Gamer, P. W. Roesky, *Inorg. Chem.* **2005**, *44*, 5963–5965; f) C. Qi, S. Zhang, J. Sun, *J. Organomet. Chem.* **2005**, *690*, 2941–2946; g) T. K. Panda, M. T. Gamer, P. W. Roesky, *Inorg. Chem.* **2006**, *45*, 910–916; h) P. W. Roesky, M. T. Gamer, N. Marinos, *Chem. Eur. J.* **2004**, *10*, 3537–3542; i) P. W. Roesky, M. T. Gamer, M. Puchner, A. Greiner, *Chem. Eur. J.* **2002**, *8*, 5265–5271; j) D. Fenske, B. Maczek, K. Maczek, *Z. Anorg. Allg. Chem.* **1997**, *623*, 1113–1120.

[15] a) C. Airoldi, D. C. Bradley, H. Chudzynska, M. B. Hursthouse, K. M. A. Malik, P. R. Raithby, *J. Chem. Soc., Dalton Trans.* **1980**, 2010–2015; b) X. Yu, S. Bi, I. A. Guzei, Z. Liu, Z.-L. Xue, *Inorg. Chem.* **2004**, *43*, 7111–7119; c) P. Renner, C. Galka, H. Memmler, U. Kauper, L. H. Gade, *J. Organomet. Chem.* **1999**, *591*, 71–77; d) see also ref.[15a]

[16] a) M. D. Fryzuk, H. D. Williams, S. J. Rettig, *Inorg. Chem.* **1983**, *22*, 863–868; b) F. A. Cotton, P. A. Kibala, *Acta Crystallogr., Sect. C: Cryst. Struct. Commun.* **1991**, *47*, 270–272.

[17] One of the reviewers suggested that the dynamic behavior observed here could also be interpreted as the twisting of the phosphinoamide ligand without dissociation of the phosphorus moiety from the Zr center. Although this possibility could not be ruled out, we consider the coordination/dissociation process of the phosphinoamide ligands to be reasonable for the following reasons. First, a similar process was also proposed in the solution dynamics of $Zr(Ph_2PNPh)_4$ and $(Ph_2PNR)_2TiCl_2$. Second, the facile reaction with CuCl and other complex fragments suggests the existence of uncoordinated phosphorus atoms in solution.

[18] C. Qi, S. Zhang, J. Sun, *Appl. Organomet. Chem.* **2006**, *20*, 138–141.

[19] J. T. Gill, J. J. Mayerle, P. S. Wekker, D. F. Lewis, D. A. Ucko, D. J. Barton, *Inorg. Chem.* **1976**, *15*, 1155–1168.

[20] One reviewer suggested that the CO stretching vibration in the IR spectrum could also be shifted as a result of the geometric constrains given by the tripodal phosphorus ligand. This cannot be ruled out.

[21] a) F. A. Cotton, G. Wilkinson, P. L. Gaus (Eds.), *Basic Inorganic Chemistry*, 3rd ed., John Wiley & Sons, New York, **1995**, pp. 60–61; b) A. Bondi, *J. Phys. Chem.* **1964**, *68*, 411–451; c) R. D. Shannon, *Acta Crystallogr., Sect. A* **1976**, *32*, 751–767.

[22] D. P. Tate, W. R. Knipple, J. M. Augl, *Inorg. Chem.* **1962**, *1*, 433–434.

[23] H. C. Clark, L. E. Manzer, *J. Organomet. Chem.* **1973**, *59*, 411–428.

[24] The extreme moisture sensitivity of the complex prevented its exact elemental analysis even though we used our best techniques, including sample preparation in a glove box, weight measurement in a glove bag, and elemental analysis as soon as the weight measurement was complete.

[25] A. Altomare, M. Burla, M. Camalli, G. Cascarano, C. Giacovazzo, A. Guagliardi, A. Moliterni, G. Polidori, R. Spagna, *SIR97*, **1999**.

[26] A. Altomare, G. Cascarano, C. Giacovazzo, A. Guagliardi, M. Burla, G. Polidori, M. Camalli, *SIR92*, **1994**.

 © 2007 Wiley-VCH Verlag GmbH & Co. KGaA, Weinheim 

[27] P. T. Beurskens, G. Admiraal, G. Beurskens, P. W. Bosman, R. de Gelder, R. Israel, J. M. M. Smits, *The DIRDIF-99 Program System: Technical Report of the Crystallography Laboratory*, University of Nijmegen, Nijmegen, The Netherlands, **1999**.
[28] D. T. Cromer, J. T. Waber, *International Tables for X-ray Crystallography*, Kynoch Press, Birmingham, U. K., **1974**, vol. 4.
[29] *Crystal Structure 3.8: Crystal Structure Analysis Package*, Rigaku and Rigaku/MSC, 9009 New Trails Dr., The Woodlands, Texas, 77381 USA, **2000**–**2006**.
[30] J. R. Carruthers, J. S. Rollett, P. W. Betteridge, D. Kinna, L. Pearce, A. Larsen, E. Gabe, *CRYSTALS Issue 11*, Chemical Crystallography Laboratory, Oxford, U. K., **1999**.

Received: January 3, 2007
Published Online: May 15, 2007

 © 2007 Wiley-VCH Verlag GmbH & Co. KGaA, Weinheim 

DOI: 10.1002/ejic.200700044

# Transfer Hydrogenation Reactions Catalyzed by Free or Silica-Immobilized $[RuCl_2(ampy)\{RN(CH_2PPh_2)_2\}]$ Complexes

**Alessandro Del Zotto,*[a] Carla Greco,[a,b] Walter Baratta,[a] Katia Siega,[a] and Pierluigi Rigo[a]**

**Keywords:** Ruthenium / Transfer hydrogenation / Heterogeneous catalysis / Silica / Ketones

The complexes *cis*-$[RuCl_2(ampy)\{R^1N(CH_2PPh_2)_2\}]$ [ampy = (2-aminomethyl)pyridine, $R^1$ = $C_6H_5$ or $(CH_3CH_2O)_3Si(CH_2)_3$] showed very high catalytic activity in the homogeneous transfer hydrogenation of acetophenone (TOF > 300000 $h^{-1}$) with the use of 2-propanol as the hydrogen donor and in the presence of sodium isopropoxide. The ligand $(CH_3CH_2O)_3Si(CH_2)_3N(CH_2PPh_2)_2$ (ATM) was prepared in high yield by reacting (3-aminopropyl)triethoxysilane, paraformaldehyde, and diphenylphosphane in toluene heated at 80 °C. The $-N(CH_2PPh_2)_2$ function was attached to the surface of three different kinds of silica by means of two alternative methods. Thus, MA-Si-150 and mesoporous MA-Si-MCM-41 were prepared by the reaction of the inorganic matrix with ATM, whereas MA-Si-60 was synthesized by reaction of the commercially available 3-aminopropyl-functionalized silica gel with HCHO and $PHPh_2$ in refluxing toluene. The $-(CH_2)_3N(CH_2PPh_2)_2$ functionalized inorganic materials were used to anchor the $RuCl_2(ampy)$ moiety; thus, three different silica-immobilized versions of the *cis*-$[RuCl_2(ampy)(ATM)]$ complex were obtained. The silica-anchored complexes were tested in the transfer hydrogenation of acetophenone, which was found to be fast and quantitative; the effect of the nature of the silica support on the activity of the catalyst was almost negligible. It was possible to reuse the catalytic system for a second cycle without a decrease in the activity, but the efficiency of the catalyst considerably diminished in successive reuses.

(© Wiley-VCH Verlag GmbH & Co. KGaA, 69451 Weinheim, Germany, 2007)

## Introduction

The catalytic transfer hydrogenation of ketones has recently emerged as a useful and convenient method to prepare secondary alcohols, including chiral compounds.[1] Several transition-metal complexes have been found to catalyze the reduction of ketones by using 2-propanol as a hydrogen donor or the system formic acid/triethylamine. In particular, significant results were obtained, mainly by Noyori and co-workers, using ruthenium(II) complexes with monotosylated diamines[2] or amino alcohols.[3] These catalysts, as well as those based on rhodium and iridium with the same type of ligands, have been largely investigated in recent years by several research groups.[4] Many efforts have been made to design highly efficient catalysts but, for large-scale applications, increasing activity and productivity of the catalytic reactions is still a target of primary importance as is the ability to separate, recover, and recycle the catalyst.

Recently, we reported the synthesis of a series of phosphanyl–$Ru^{II}$ complexes bearing the (2-aminomethyl)pyridine (ampy)[5–8] ligand or the related 6-(4′-methylphenyl)-2-pyridylmethylamine ligand,[9,10] and examined their ability to catalyze the reduction of ketones. Among complexes with the ampy ligand, exceptionally high catalytic activity was observed for complexes also bearing diphosphane ligands (Figure 1) with the *cis* isomer showing higher efficiency. TOF values up to $4 \times 10^5$ $h^{-1}$ and *ee* values up to 94% with the use of chiral diphosphane ligands were obtained.[7] The analogous species with two triphenylphosphane ligands was less active;[7] however, they seemed to be suitable precursors for the anchoring of the $RuCl_2(ampy)$ moiety to a solid support. The grafting of a complex active in the homogeneous phase to an inert solid support is find-

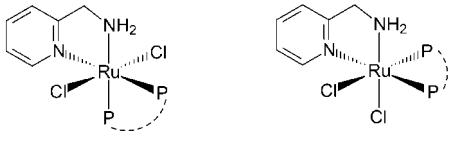


Figure 1. $Ru^{II}$–ampy complexes efficient in transfer hydrogenation.

[a] Dipartimento di Scienze e Tecnologie Chimiche, Università di Udine
Via Cotonificio 108, 33100 Udine, Italy
E-mail: alessandro.delzotto@uniud.it
[b] Serichim s.r.l.
P. le Marinotti 1, 33050 Torviscosa, Udine, Italy

 © 2007 Wiley-VCH Verlag GmbH & Co. KGaA, Weinheim 

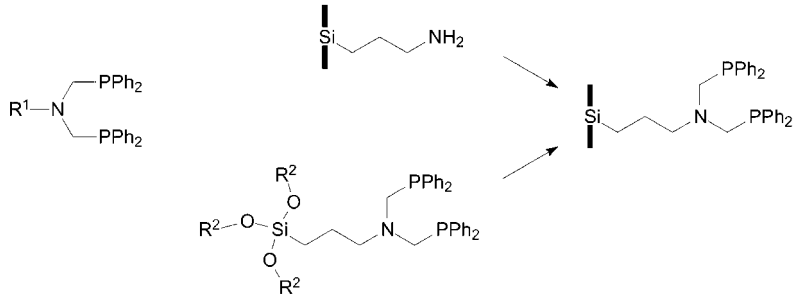

Scheme 1.

ing fast growing interest because the use of immobilized catalysts can provide a significant improvement to overcome the problems of separation and recycling of the catalyst. Silica is the most common support for the heterogenization of molecular catalysts[11] owing to its high stability, inertness, and low cost, all of which render this matrix attractive for medium-scale synthesis and industrial applications. However, the use of catalysts immobilized on inorganic supports for the transfer hydrogenation of ketones is still rare.

With the very active *cis*-[$RuCl_2$(ampy)(dppp)][7] [dppp = 1,3-bis(diphenylphosphanyl)propane] complex in mind, we turned our attention to the $R^1N(CH_2PPh_2)_2$ ligand (Scheme 1), which is topologically analogous to dppp, easily prepared, and used to anchor the $RuCl_2$(ampy) moiety to a solid support. A suitable choice for the $R^1$ group, as in the case of $(OR^2)_3Si(CH_2)_3$–, allows the diphosphane to be conveniently grafted onto a silica support. Alternatively, the $–N(CH_2PPh_2)_2$ function linked to the inorganic matrix can be obtained by reacting a suitable amino-functionalized silica with $H_2CO$ and $PPh_2H$ (Scheme 1).

Similar $Ru^{II}$-functionalized silicas, where the metal is surrounded by a $Cl_2N_2P_2$ donor set, were prepared by Kumar and Ghosh starting from supports with ethylenediamino arms.[12] Such catalytic systems were successfully applied to the hydrogenation of carbonyl compounds. Furthermore, Reek, van Leeuwen, and co-workers used silica-immobilized $Ru^{II}$ complexes for the asymmetric reduction of acetophenone where the metal was anchored to the inert support by chelation to an aminoalcohol moiety.[13] Finally, Tu and co-workers investigated the asymmetric transfer hydrogenation of different prochiral ketones by using $Ru^{II}$ complexes immobilized on amorphous or mesoporous silicas functionalized through chiral diamine arms.[14]

In this paper, we present the preparation and characterization of the $Ru^{II}$ complexes [$RuCl_2$(ampy){$R^1N(CH_2PPh_2)_2$}] [$R^1$ = $C_6H_5$ or $(CH_2)_3Si(OCH_2CH_3)_3$] as well as of three different $–N(CH_2PPh_2)_2$ functionalized silicas along with the corresponding $Ru^{II}$ derivatives containing the $RuCl_2$(ampy) moiety. Furthermore, the catalytic application of both free and immobilized complexes to the transfer hydrogenation of acetophenone by using 2-propanol as the hydrogen source is reported and discussed.

## Results and Discussion

### Synthesis and Characterization of the Diphosphanes and Diphosphanyl-Functionalized Silicas

Following a known synthetic method,[15] the diphosphane (3-{bis[(diphenylphosphanyl)methyl]amino}propyl)-triethoxysilane (ATM) was obtained as a colorless oil by reacting (3-aminopropyl)triethoxysilane with paraformaldehyde and diphenylphosphane in a 1:2.5:2 molar ratio in toluene heated at 80 °C [Equation (1)]. Unreacted paraformaldehyde was easily eliminated by filtration after dissolving the crude product in ethyl ether. The product, which was isolated in high yield, showed a single resonance at $\delta$ = –28.0 ppm in the $^{31}P\{^1H\}$ NMR spectrum and a clean $^1H$ NMR spectrum, which confirmed its very high purity.

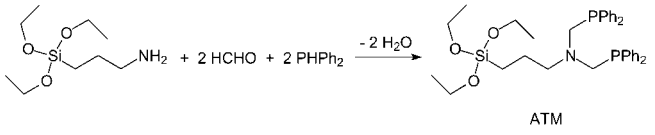


(1)

As the morphology of the inorganic support (surface area and porosity) as well as the distance between the catalytic sites could influence the activity of the anchored transition-metal complex,[11] we prepared three different silica-immobilized versions of the ATM ligand. The first one was synthesized according to Equation (2) by starting from the commercially available 3-aminopropyl-functionalized silica gel (mean pore size: 60 Å, surface area: 550 $m^2 g^{-1}$, loading: 1 $mmol g^{-1}$), which was heated at reflux in toluene for 48 h together with HCHO and $PHPh_2$. The product, 3-{bis-[(diphenylphosphanyl)methyl]amino}propyl-functionalized silica gel (MA-Si-60) was obtained as a white cream powder, which was characterized by elemental analysis (C, H, N, P), TGA measurements, and CP-MAS $^{31}P$ NMR spectroscopy. The latter confirmed the presence of the anchored diphosphane function (broad singlet at $\delta$ = –25.3 ppm). Two minor broad signals centered at $\delta$ = 20.3 and 30.8 ppm, within the range for the P=O resonances, and a shoulder on the high-field signal were indicative of the formation of small amounts of products resulting from the oxidation of the ligand.[16] Furthermore, from the elemental analysis of ni-

 © 2007 Wiley-VCH Verlag GmbH & Co. KGaA, Weinheim 

trogen and phosphorus, it was possible to determine 0.86 and 0.70 mmol $g^{-1}$ loading, respectively. The relative P/N molar ratio (1.6) is lower than that expected (2.0) for total conversion of the $–NH_2$ functions to $–N(CH_2PPh_2)_2$. This finding could be reasonably explained in terms of a material still showing about 20% of the amine function unchanged. The possibility of formation of $HNCH_2PPh_2$ functions on the inorganic surface seems to be excluded by the NMR spectroscopic data, though the presence of both $–NHCH_2PPh_2$ and $–N(CH_2PPh_2)_2$ groups cannot be excluded as the resonances of the P nuclei could be superimposed. It should be noted that no appreciable variation in the loading was observed when the reaction time was increased, whereas a lower value (0.49 mmol $g^{-1}$, based on P analysis) was determined when the reaction was stopped after 24 h. Two further preparations of MA-Si-60 confirmed the good reproducibility of the synthesis.

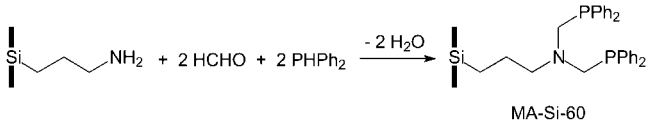


(2)

Two other 3-{bis[(diphenylphosphanyl)methyl]amino}-propyl-functionalized silicas, namely, MA-Si-150 and MA-Si-MCM-41, were conveniently prepared starting from Davisil silica with a 150 Å mean pore size and a surface area of 300 $m^2 g^{-1}$ and MCM-41 mesoporous silica with a surface area of 1000 $m^2 g^{-1}$, respectively. Both were obtained by combining ATM and the appropriate matrix in toluene heated at 80 °C according to Equation (3). As per MA-Si-60, the two products were characterized by elemental analysis. The calculated loading, based on phosphorus, was 0.46 mmol $g^{-1}$ for MA-Si-150 and 0.59 mmol $g^{-1}$ for MA-Si-MCM-41. As observed for MA-Si-60, the syntheses of MA-Si-150 and MA-Si-MCM-41 showed very good reproducibility. Compounds MA-Si-60, MA-Si-150, and MA-Si-MCM-41 were also characterized by TGA measurements, which were run under an atmosphere of argon in the temperature range 20–800 °C. From 20 to ca. 250 °C, all samples showed about 5% weight loss due to water release, whereas the progressive weight decrease above 250 °C was attributed to organic material release only. Thus, in the range 250–800 °C, MA-Si-60, MA-Si-150, and MA-Si-MCM-41 lost 24, 15, and 20% of their weight, respectively. These data, combined with the relative amounts of $–(CH_2)_3NH_2$ and $–(CH_2)_3N(CH_2PPh_2)_2$ groups, present in each material, calculated from the P/N molar ratio, allowed MA-Si-60, MA-Si-150, and MA-Si-MCM-41 to be obtained following the loading 0.64, 0.39, and 0.50 mmol $g^{-1}$, respectively. Such values are lower than those obtained from the elemental analysis of phosphorus.

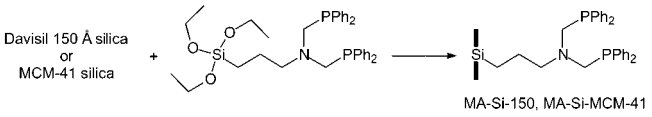


(3)

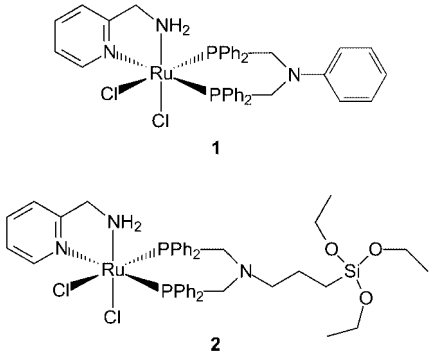


Figure 2. $Ru^{II}$–ampy complexes with the ligands $PhN(CH_2PPh_2)_2$ and ATM.

## Synthesis of the Ruthenium(II)–ampy Complexes

The synthesis of the six-coordinate *cis*-$[RuCl_2(ampy)\{R^1N(CH_2PPh_2)_2\}]$ [$R^1 = C_6H_5$ **1**, $R^1 = (CH_2)_3Si(OCH_2CH_3)_3$ **2**] (Figure 2) complexes was carried out as described previously for analogous compounds starting from $[RuCl_2(PPh_3)_3]$, ampy, and the diphosphane in a 1:1:1 molar ratio.[7] The complexes precipitated spontaneously as sand yellow microcrystals from hot solutions of toluene and were almost insoluble in common solvents. However, acceptable quality $^{31}P\{^1H\}$ NMR spectra were recorded from saturated $CD_2Cl_2$ solutions. The spectra of **1** and **2** appeared as AB spin systems with a coupling constant of about 45 Hz; the doublets of **1** were centered at $\delta$ = 39.7 and 43.2 ppm and those of **2** at $\delta$ = 37.8 and 45.9 ppm. As the NMR spectroscopic parameters agree with those found for the *cis*-$[RuCl_2(ampy)(dppp)]$[7] complex, we propose for complexes **1** and **2** the same stereochemistry to that shown by *cis*-$[RuCl_2(ampy)(dppp)]$, with P-*trans*-Cl and P-*trans*-N(pyridine) arrangements. As a matter of fact, this represents the common stable geometry shown by several complexes bearing ampy and different diphosphane ligands with $C_3$ and $C_4$ backbones.[7]

## Synthesis and Characterization of Silica-Immobilized Ruthenium(II) Complexes

As depicted in Equation (4), by reacting the appropriate functionalized silica and the *trans,cis*-$[RuCl_2(PPh_3)_2(ampy)]$ complex in boiling 2-propanol, three different $Ru^{II}$-based immobilized catalysts, namely, Ru-MA-Si-60, Ru-MA-Si-150, and Ru-MA-Si-MCM-41, were prepared. The catalysts were thoroughly washing with dichloromethane to eliminate all traces of physisorbed metal–organic species from the inert support. All materials appeared as yellow to yellow–orange microcrystalline solids, which were characterized by

 © 2007 Wiley-VCH Verlag GmbH & Co. KGaA, Weinheim 

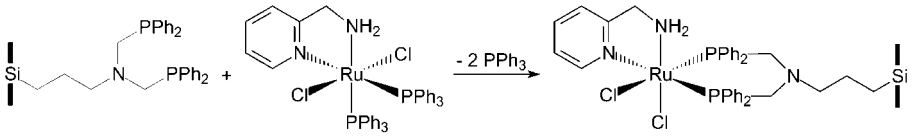


(4)

elemental analysis (C, H, N, Ru) and TGA measurements in the range 20–800 °C to assess the metal loading. The yield of the reaction (based on ruthenium), was generally high (88, 91, and 84% for Ru-MA-Si-60, Ru-MA-Si-150, and Ru-MA-Si-MCM-41, respectively). The calculated loading values were 0.35, 0.29, and 0.33 mmol $g^{-1}$ of complex, in the respective order. To address the reaction to the formation of the *cis* dichloro isomer immobilized on silica, the reagents were heated at reflux and allowed to react for 2 h. In the case of Ru-MA-Si-60, a $^{31}P$ CP/MAS NMR spectroscopic investigation was undertaken. The spectrum showed, in addition to signals due to uncoordinated diphosphane and the corresponding oxide, two signals at $\delta$ = 47 and 53 ppm. The rather large line width may be the reason for the lack of observable coupling between the two inequivalent P nuclei. The NMR measurements are in agreement with the presence of a unique $Ru^{II}$ species immobilized on the inert support.

### Transfer Hydrogenation of Acetophenone in the Homogeneous Phase

The metal-catalyzed transfer hydrogenation of ketones was accomplished by using 2-propanol as the hydrogen donor heated at reflux [Equation (5)]. It is well-documented that the presence of a strong base as a cocatalyst enhances the rate of the reaction.[17] Accordingly, all catalytic tests were run in the presence of sodium 2-propoxide generated by dissolution of metallic sodium into the alcohol.

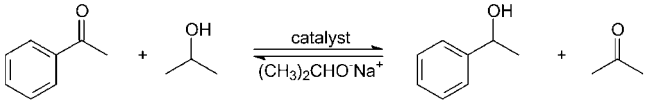


(5)

As complexes **1** and **2** showed only partial solubility in 2-propanol, even when heated at reflux and in catalytic conditions, we turned our attention to in situ prepared catalytic systems. Thus, the catalytic reactions were carried out with the use of a 0.1 M solution of acetophenone in 2-propanol in the presence of 0.05 mol-% of the *cis,cis*-[$RuCl_2(PPh_3)_2$(ampy)] complex, 0.06 mol-% of the appropriate $R^1N(CH_2PPh_2)_2$ ligand, and 2 mol-% of $(CH_3)_2CHO^-Na^+$ (substrate/Ru/base = 2000:1:40) under reflux conditions. $^{31}P$ NMR spectroscopic monitoring of a dilute $CDCl_3$ solution containing *trans,cis*-[$RuCl_2(PPh_3)_2$(ampy)] and the ligand ATM in a 1:1 molar ratio showed that on increasing the temperature the $PPh_3$ ligands are completely replaced by the diphosphane ligand and that after prolonged heating the only Ru-containing species detectable in solution was complex **2**. Analogous results were obtained by monitoring the *trans,cis*-[$RuCl_2(PPh_3)_2$(ampy)]/[$C_6H_5N(CH_2PPh_2)_2$] system, for which the exclusive formation of **1** was observed. These findings confirm that the in situ prepared catalytic systems effectively correspond to isolated complexes **1** and **2**, which are obtained in almost insoluble form in refluxing toluene.

A comparison of the catalytic efficiency of the complexes bearing $R^1N(CH_2PPh_2)_2$ ligands with that of isostructural *cis*-[$RuCl_2$(ampy)(dppp)] shows that the modification of the diphosphane by substitution of the central carbon atom of the P–C–C–C–P skeleton with a N–$R^1$ moiety has only a little influence on the activity of the relative ruthenium complex. As a matter of fact, by using complexes **1** and **2**, the catalytic reduction of acetophenone was completed (98%) within 1 min (Table 1, Entries 1 and 2), and the corresponding very high TOF values (>300000 $h^{-1}$ at 50% conversion) were of the same magnitude to that found for *cis*-[$RuCl_2$(ampy)(dppp)] (220000 $h^{-1}$).[7]

### Transfer Hydrogenation of Acetophenone in the Heterogeneous Phase

All three silica-immobilized ruthenium complexes were examined as catalysts in the transfer hydrogenation of acetophenone. Standard reactions were carried out by using 500:1 and 20:1 acetophenone/Ru and $(CH_3)_2CHO^-Na^+$/Ru molar ratios, respectively, at the reflux temperature of 2-propanol (82 °C). The results are collected in Table 1. Although, as expected, the immobilized complexes were much less active than their counterparts in the homogeneous phase, a quantitative conversion of the substrate into 1-phenylethanol was observed within 90 min (Table 1, Entries 3–5), and the results showed that the nature of the inorganic support played an almost negligible role on the performance of the catalyst. An analogous behavior was observed for ruthenium complexes anchored on mesoporous MCM-41 and MCM-48 and amorphous silicas.[12] The concentration of the strong base is crucial for the activity of the supported complex. In fact, a decrease in the $(CH_3)_2CHO^-Na^+$/Ru molar ratio from 20:1 to 5:1 resulted in a 94% conversion achieved in 8 h by using Ru-MA-Si-MCM-41 (Table 1, Entry 6). It should be stressed that the stability of the functionalized silicas Ru-MA-Si-60, Ru-MA-Si-150, and Ru-MA-Si-MCM-41, as well as that of the precursor 3-aminopropyl-functionalized silica gel, towards $(CH_3)_2CHO^-Na^+$ was analyzed. All samples, after treatment with a 20-fold excess of base for 2 h at 100 °C showed a 15–20% reduction in the linked organic moiety (based on nitrogen analysis). These results are in agreement with the metal

 © 2007 Wiley-VCH Verlag GmbH & Co. KGaA, Weinheim 

Table 1. Catalytic transfer hydrogenation of acetophenone with the use of silica-supported complexes at 82 °C.

| Entry[a] | Catalyst | S/C[b] | B/C[c] | Yield[d] [%] | Time [min] |
|---|---|---|---|---|---|
| 1 | *cis*,*cis*-[$RuCl_2(PPh_3)_2$(ampy)]/$PhN(CH_2PPh_2)_2$[e] | 2000 | 40 | 98 | 1[f] |
| 2 | *cis*,*cis*-[$RuCl_2(PPh_3)_2$(ampy)]/ATM[e] | 2000 | 40 | 98 | 1[g] |
| 3 | Ru-MA-Si-60 | 500 | 20 | 97 | 90 |
| 4 | Ru-MA-Si-150 | 500 | 20 | 99 | 90 |
| 5 | Ru-MA-Si-MCM-41 | 500 | 20 | 99 | 90 |
| 6 | Ru-MA-Si-MCM-41 | 500 | 5 | 94 | 480 |
| 7 | Ru-MA-Si-150 | 500 | 20 | 99 | 90 |
| 7(1) | – | – | – | 99 | 240 |
| 7(2) | – | – | – | 12 | 1440 |
| 8 | Ru-MA-Si-150 | 100 | 20 | 99 | 60 |
| 8(1) | – | – | – | 98 | 60 |
| 8(2) | – | – | – | 98 | 720 |
| 8(3) | – | – | – | 82 | 1440 |
| 9 | Ru-MA-Si-MCM-41[h] | 500 | 20 | 6 | 720 |

[a] The values reported in parenthesis for Entries 7 and 8 indicate the successive reuses of the catalyst. [b] Substrate/catalyst(Ru) molar ratio. [c] Base/catalyst molar ratio. [d] The yield of 1-phenylethanol was determined by GC. [e] Reaction run in the homogeneous phase, Ru/ligand, 1:1.2 molar ratio. [f] TOF = 320000 $h^{-1}$ (turnover frequency = mol of acetophenone converted to 1-phenylethanol per mole of catalyst per hour at 50% conversion). [g] TOF = 340000 $h^{-1}$. [h] At 40 °C.

leaching measured after the first use of the catalyst (see below).

Recycling tests were run on all three silica-immobilized ruthenium complexes with the use of both the 500:1 and the 100:1 substrate/ruthenium molar ratios. As almost identical results were observed with the three different silica supports, only those obtained with the representative Ru-MA-Si-150 catalyst are presented in Table 1. By using a high substrate/ruthenium molar ratio, such as 500:1, the activity of the recycled catalyst in the second run resulted reduced [Table 1, Entries 7 and 7(1)], although complete conversion of acetophenone into 1-phenylethanol was achieved. In the next reuse, only low amounts of product were obtained, which indicates that there is a breakdown in the catalytic system [Table 1, Entry 7(2)]. The measurements were repeated by using a lower substrate/ruthenium molar ratio (100:1). As can be seen in Table 1 [Entries 8–8(3)], the efficiency of the catalyst was apparently retained in the first reuse, but then it drastically decreased; however, in the third run the substrate underwent complete transformation into 1-phenylethanol. It should be stressed that in each successive catalytic trial, the recovered catalyst was mixed not only with acetophenone and solvent, but also with a 20-fold excess of $(CH_3)_2CHO^-Na^+$ with respect to the amount of ruthenium effectively present. It is important to note that the efficiency of the catalyst did not appreciably fade from the first to the second use. This finding should be compared with the observed breakdown in the activity of complexes **1** and **2**, as well as of all similar derivatives,[7] when reused as homogeneous catalysts.

As decomposition processes should be reduced by working at low temperature, the catalytic potential of Ru-MA-Si-MCM-41 was verified at 40 °C. In this case, the reaction proceeded at an extremely low rate as only 6% conversion was observed after 12 h (Table 1, Entry 9). ICP MS measurements carried out on both Ru-MA-Si-150 and Ru-MA-Si-MCM-41 systems treated at 100 °C for 2 h in the presence of a strong excess of $(CH_3)_2CHO^-Na^+$ (20:1 with respect to the metal) indicated that for both samples about 15% of the ruthenium present in the immobilized catalyst was released into the solution. Not surprisingly, analogous results concerning the metal leaching were obtained by measuring the ruthenium amount in solution after the first catalytic trial. By contrast, an almost negligible metal leaching (<2%) was measured in the successive reuse of the catalyst. Thus, as the activity of the immobilized complex remained unchanged from the first to the second use, one can conclude that the ruthenium released into the solution is present in a catalytically inactive form. It should be noted that $^{31}P$ NMR spectroscopic measurements run on the recovered solutions did not give any useful information about the decomposition pattern of the catalyst. The neat decline of the efficiency of the catalyst in the successive reuses can be ascribed to a decomposition of the structure of the supported metal complex.

## Conclusions

We have shown that the *cis*-[$RuCl_2$(ampy)-{$R^1N(CH_2PPh_2)_2$}] complexes are highly efficient homogeneous catalysts in the transfer hydrogenation of acetophenone with 2-propanol and that they may have great potential for a broad application in the reduction of carbonyl compounds. We have also demonstrated that the anchoring of the $RuCl_2$(ampy) moiety to a silica support can be easily accomplished when the surface of the inorganic matrix is prior functionalized with $-N(CH_2PPh_2)_2$ arms. Such a modification of the support was done by two alternative pathways, which allowed the syntheses of three different mesoporous or amorphous silicas and of the relative immobilized ruthenium(II) complexes. These systems have shown to be catalytically active in the transfer hydrogenation of acetophenone, which is rapidly and quantitatively transformed into 1-phenylethanol. Recovery and recycling of the inorganic material still resulted in good catalytic perform-

 © 2007 Wiley-VCH Verlag GmbH & Co. KGaA, Weinheim 

ance but only for the first reuse as decomposition of the catalyst limited successive reuses.

## Experimental Section

**General:** All reagents were purchased from Aldrich and used without further purification. Commercial reagent grade solvents were dried according to standard methods and freshly distilled under an atmosphere of argon before use. All syntheses and manipulations were carried out under an atmosphere of argon by using either standard Schlenk or glove box techniques. The diphosphane $PhN(CH_2PPh_2)_2$[15b] and the complexes $[RuCl_2(PPh_3)_3]$,[18] *trans*,*cis*-$[RuCl_2(PPh_3)_2(ampy)]$,[7] and *cis*,*cis*-$[RuCl_2(PPh_3)_2(ampy)]$[7] were synthesized according to literature procedures. The solution of $(CH_3)_2CHO^-Na^+$ in 2-propanol used in the catalytic trials was prepared by dissolving 46 mg of freshly cut Na into 20 mL of solvent and kept under an atmosphere of argon in the dark. The $^1H$ and $^{31}P$ NMR spectra in solution (at 200.13 and 81.02 MHz, respectively) were recorded with a Bruker AC 200 F QNP spectrometer. The $^1H$ chemical shifts were referenced to $SiMe_4$, whereas positive $^{31}P$ NMR chemical shifts are reported downfield from 85% $H_3PO_4$ as an external standard. The NMR characterization of solid samples was performed with a Bruker AC 200 spectrometer equipped for solid state analysis. Samples were spun at 7000 Hz in 7 mm diameter zirconia rotors with Kel-F caps. $^{31}P$ SPE MAS NMR spectra were obtained at 80.90 MHz by using a single pulse experiment and high-power proton decoupling, with 120 s relaxing delay. $^{31}P$ NMR chemical shifts were externally calibrated with respect to solid triphenylphosphane at $\delta = -7.2$ ppm and were referenced to 85% $H_3PO_4$. The GC analyses of the catalytic mixtures were run with a Fisons GC 8000 Series gas chromatograph equipped with a Supelco PTA-5 column [30 m long, 0.53 mm i.d., coated with a 3.0 μm poly(5% diphenyl-95% dimethylsiloxane) film] Injector temperature was kept at 250 °C and the column temperature was programmed from 50 °C to 170 °C with a gradient of 8 °C min$^{-1}$. The elemental analyses (C, H, N) were carried out at the Microanalytical Laboratory of the Dipartimento di Scienze e Tecnologie Chimiche, Università di Udine, with a Carlo Erba 1106 elemental analyzer. Phosphorus and ruthenium quantitative determination were carried out at the Dipartimento di Scienze e Tecnologie Chimiche and the Dipartimento di Scienze Agrarie e Ambientali, Università di Udine by using a Varian Vista MPX axial Inductively Coupled Plasma-Optical Emission spectrometer (for the determination of P) and a Spectro Analytical Instruments Spectromass 2000 Type MSDIA10B Inductively Coupled Plasma Mass spectrometer (for the determination of Ru). Samples (20 mg) were digested on a microwave apparatus MILESTONE Mega 1200 by use of 1 mL of 65% $HNO_3$, 0.4 mL of 30% $H_2O_2$ and 0.1 mL of 40% HF with a mineralization program at 650 W for 20 min in Teflon vessels. Thermogravimetric analyses were performed by using a TA Instrument (Waters) TGA Q500 apparatus. Weight loss was measured in the range 20–800 °C with a heating rate of 10 °C min$^{-1}$, under an argon atmosphere.

**(3-{Bis[(diphenylphosphanyl)methyl]amino}propyl)triethoxysilane (ATM):** A mixture of (3-aminopropyl)triethoxysilane (0.89 g, 4.0 mmol), paraformaldehyde (0.30 g, 10 mmol) and diphenylphosphane (1.49 g, 8.0 mmol) was stirred in toluene (20 mL) and heated at 80 °C for 1 h with complete dissolution of solid paraformaldehyde. The solvent was removed under vacuum. The resulting oil was treated with ethyl ether (20 mL), the mixture was filtered, and the product was recovered from the solution as a colorless oil by elimination of the solvent under vacuum. Yield: 2.18 g (88%). $^1H$ NMR (200 MHz, $CDCl_3$, 295 K): $\delta$ = 7.1–7.5 (m, 20 H, *phenyl*), 3.73 (q, $J_{H,H}$ = 7.0 Hz, 6 H, $CH_2CH_3$), 3.55 (d, $J_{P,H}$ = 3.3 Hz, 4 H, $NCH_2P$), 2.82 (m, 2 H, $CH_2CH_2N$), 1.48 (m, 2 H, $CH_2CH_2CH_2$), 1.16 (t, $J_{H,H}$ = 7.0 Hz, 9 H, $CH_3$), 0.46 (m, 2 H, $CH_2Si$) ppm. $^{13}C\{^1H\}$ NMR (50 MHz, $CDCl_3$, 295 K): $\delta$ = 138.2 (d, $J_{C,P}$ = 12.8 Hz, $C^i$), 133.0 (d, $J_{C,P}$ = 18.3 Hz, $C^o$), 128.3 ($C^p$), 128.2 (d, $J_{C,P}$ = 8.5 Hz, $C^m$), 59.2 (t, $J_{C,P}$ = 9.2 Hz, $CH_2CH_2N$), 58.6 (dd, $J_{C,P}$ = 5.5, 9.1 Hz, $NCH_2P$), 58.2 ($CH_2CH_3$), 19.7 ($CH_2CH_2CH_2$), 18.3 ($CH_2CH_3$), 7.6 ($CH_2Si$) ppm. $^{31}P\{^1H\}$ NMR (81 MHz, $CDCl_3$, 295 K): $\delta$ = –28.0 ppm.

***cis*-[$RuCl_2$(ampy){$PhN(CH_2PPh_2)_2$}] (1):** $[RuCl_2(PPh_3)_3]$ (384 mg, 0.40 mmol) and 2-(aminomethyl)pyridine (45 mg, 0.42 mmol) were mixed in toluene (15 mL), and the slurry was heated at reflux for 2 h. The ligand $PhN(CH_2PPh_2)_2$ (196 mg, 0.40 mmol) was then added, and the mixture was heated at reflux for another 20 h. Upon cooling, a sand yellow powder precipitated, which was isolated by filtration, washed with ethyl ether, and dried under reduced pressure. Yield: 225 mg (73%). $C_{38}H_{37}Cl_2N_3P_2Ru$ (769.66): calcd. C 59.30, H 4.85, N 5.46; found C 59.23, H 4.66, N 5.31. $^{31}P\{^1H\}$ NMR (81 MHz, $CD_2Cl_2$): $\delta$ = 39.7 (d, $J_{P,P}$ = 44.7 Hz), 43.2 (d, $J_{P,P}$ = 44.7 Hz) ppm.

***cis*-[$RuCl_2$(ampy)(ATM)] (2):** As for **1**, but with the use of the ATM ligand instead of $PhN(CH_2PPh_2)_2$. Sand yellow solid. Yield: 246 mg (68%). $C_{41}H_{53}Cl_2N_3O_3P_2RuSi$ (897.90): calcd. C 54.84, H 5.95, N 4.68; found C 54.01, H 5.92, N 4.59. $^{31}P\{^1H\}$ NMR (81 MHz, $CD_2Cl_2$): $\delta$ = 37.8 (d, $J_{P,P'}$ = 46.2 Hz), 45.9 (d, $J_{P,P'}$ = 46.2 Hz) ppm.

**Preparation of 3-{Bis[(diphenylphosphanyl)methyl]amino}propyl-Functionalized Silica Gels**

**MA-Si-60 from Silica with 60 Å Mean Pore Size:** A mixture of 3-aminopropyl-functionalized silica gel (60 Å mean pore size) (1.00 g, 1.0 mmol of amine), paraformaldehyde (90 mg, 3.0 mmol), and diphenylphosphane (465 mg, 2.5 mmol) was stirred in toluene (20 mL) and heated at reflux for 48 h. A cream white product was recovered by filtration, washed with ethyl ether, and dried under vacuum. Yield: 1.15 g. Composition found: C 19.90, H 2.30, N 1.21, P 4.32. TGA analysis (20–800 °C, under argon): $\Delta w$ = 24% (water loss excluded).

**MA-Si-150 from Silica with 150 Å Mean Pore Size:** A mixture of Davisil silica gel (150 Å mean pore size) (510 mg), which was activated by heating at 150 °C under vacuum for 15 h, and ATM (302 mg) was stirred in toluene (10 mL) and heated at 110 °C for 20 h. The pale yellow mixture was cooled, filtered, washed with toluene, dichloromethane, ethanol, and ethyl ether, and finally dried under reduced pressure to obtain a cream white solid. Yield: 782 mg. Composition found: C 13.01, H 1.56, N 0.77, P 2.83. TGA analysis (20–800 °C, under argon): $\Delta w$ = 14% (water loss excluded).

**MA-Si-MCM-41 from MCM-41 Mesoporous Silica:** A mixture of MCM-41 mesoporous silica gel (440 mg) which was activated by treatment at 150 °C under vacuum for 2 h, and ATM (310 mg) was stirred in toluene (10 mL) and heated at 110 °C for 18 h. After cooling, the mixture was filtered, and the white solid was washed with toluene, dichloromethane, ethanol, and ethyl ether. The white product was then dried under reduced pressure. Yield: 714 mg. Composition found: C 19.87, H 2.21, N 0.96, P 3.64. TGA analysis (20–800 °C, under argon): $\Delta w$ = 20% (water loss excluded).

**Synthesis of Silica-Supported $Ru^{II}$ Complexes**

**$Ru^{II}$ Complex Supported on MA-Si-60 Silica (Ru-MA-Si-60):** A suspension of silica MA-Si-60 (100 mg) and *trans*,*cis*-$[RuCl_2(PPh_3)_2(ampy)]$ (32 mg) was heated at reflux in 2-propanol (5 mL) for 2 h.

 © 2007 Wiley-VCH Verlag GmbH & Co. KGaA, Weinheim 

After cooling, the mixture was filtered, and the solid was carefully washed with 2-propanol, dichloromethane (until the discarded solvent resulted colorless), and ethyl ether to give a yellow powder, which was dried under reduced pressure. Yield: 102 mg. Composition found: C 21.29, H 2.47, N 1.55, Ru 3.48. TGA analysis (20–800 °C, under argon): $\Delta w$ = 20% (water loss excluded).

**$Ru^{II}$ Complex Supported on MA-Si-150 Silica (Ru-MA-Si-150):** Ru-MA-Si-150 was prepared as indicated above for Ru-MA-Si-60 from silica MA-Si-150 (100 mg) and *trans*,*cis*-[$RuCl_2(PPh_3)_2$(ampy)] (26 mg). The isolated product is a yellow powder. Yield: 92 mg. Composition found: C 15.38, H 1.70, N 1.10, Ru 3.22. TGA analysis (20–800 °C, under argon): $\Delta w$ = 16% (water loss excluded).

**$Ru^{II}$ Complex Supported on MA-Si-MCM-41 Silica (Ru-MA-Si-MCM-41):** Ru-MA-Si-MCM-41 was prepared as indicated above for Ru-MA-Si-60 from functionalized mesoporous silica MA-Si-MCM-41 (100 mg) and *trans*,*cis*-[$RuCl_2(PPh_3)_2$(ampy)] (32 mg). The product is a yellow–orange microcrystalline powder. Yield: 99 mg. Composition found: C 20.95, H 2.18, N 1.34, Ru 3.41. TGA analysis (20–800 °C, under argon): $\Delta w$ = 20% (water loss excluded).

**Studies on the Stability of the Functionalized Silicas Towards Sodium Isopropoxide:** A 25-mL Schlenk was charged with silica (3-aminopropyl-functionalized silica gel, MA-Si-60, MA-Si-150, or MA-Si-MCM-41) (15 mg), 2-propanol (10 mL), and the suitable amount of a 0.1 M solution of $(CH_3)_2CHO^-Na^+$ in 2-propanol to obtain a 1:20 molar ratio between the organic function linked to silica and base. The mixture was warmed under an atmosphere of argon, at 100 °C for 2 h. After cooling, the solid was filtered off, washed with 2-propanol and dichloromethane, dried, and analyzed (C, H, N).

**Catalytic Transfer Hydrogenation of Acetophenone in Homogeneous Phase:** Two solutions containing (a) acetophenone and (b) *cis*,*cis*-[$RuCl_2(PPh_3)_2$(ampy)]/ATM were prepared as follows: (a) a 50-mL Schlenk was charged with acetophenone (240 μL, 2 mmol) and 2-propanol (19 mL), and the vessel was put into an oil bath at 100 °C; (b) a 10-mL Schlenk was charged with *cis*,*cis*-[$RuCl_2(PPh_3)_2$(ampy)] (4.0 mg, 5 μmol), ATM (6.8 mg, 10 μmol), 2-propanol (3 mL), and $(CH_3)_2CHO^-Na^+$ (0.1 M in 2-propanol, 2 mL). The mixture was then gently warmed until complete dissolution of the complex was achieved. Finally, 1 mL of solution (b) was added to solution (a) kept at reflux, with immediate starting of the catalytic reaction. For the GC analysis of the reaction mixture, 0.2 mL of the solution was extracted by means of a syringe, cooled, mixed with ethyl ether (2 mL), and the resulting suspension was passed through a microcolumn filled with silica gel to eliminate any inorganic material.

**General Procedure for the Transfer Hydrogenation of Acetophenone with Silica-Supported Catalysts:** Under an argon atmosphere, a 25-mL Schlenk was charged with the silica-anchored ruthenium(II) complex ($10^{-3}$ mmol of metal). Then, 2-propanol (10 mL) and $(CH_3)_2CHONa$ (0.1 M in 2-propanol, 0.2 mL) were added and the mixture was heated at reflux. Finally, by addition of acetophenone (0.5 mmol) the catalytic reaction started. Samples for the GC analysis were prepared as indicated above.

**General Procedure for Recycling of Silica-Supported Catalysts:** The mixture recovered after the first catalytic trial was centrifuged, and the solution was discarded. The solid was washed with dichloromethane and 2-propanol and vacuum dried. It was then weighed and transferred into a 25-mL Schlenk, which was charged under an atmosphere of argon, with 2-propanol and $(CH_3)_2CHO^-Na^+$ (0.1 M in 2-propanol). The mixture was warmed to reflux, and the catalytic reaction was started by the addition of acetophenone. Amounts of solvent, base, and substrate were based on the weight of the recovered catalyst to maintain a constant substrate/metal/base ratio. Analogous procedures were adopted for successive reuses of the catalysts.

## Acknowledgments

The authors are indebted to Federchimica, Rome, Italy for a fellowship to C. G. We thank Prof. C. de Leitenburg, Dr. F. Tubaro, and Mr. P. Polese (Dipartimento di Scienze e Tecnologie Chimiche, University of Udine) for carrying out TGA measurements, ICP-MS, and elemental analyses, respectively. We also thank Dr. A. Sassi (Dipartimento di Processi Chimici dell′Ingegneria, University of Padua) and Dr. M. Contin (Dipartimento di Scienze Agrarie e Ambientali, University of Udine) for performing solid state NMR and ICP-OE measurements, respectively.

[1] a) G. Zassinovich, G. Mestroni, S. Gladiali, *Chem. Rev.* **1992**, *92*, 1051–1069; b) R. Noyori, S. Hashiguchi, *Acc. Chem. Res.* **1997**, *30*, 97–102; c) R. Noyori, M. Yamakawa, S. Hashiguchi, *J. Org. Chem.* **2001**, *66*, 7931–7944; d) J.-E. Bäckvall, *J. Organomet. Chem.* **2002**, *652*, 105–111; e) S. E. Clapham, A. Hadzovic, R. H. Morris, *Coord. Chem. Rev.* **2004**, *248*, 2201–2237; f) S. Gladiali, E. Alberico, *Chem. Soc. Rev.* **2006**, *35*, 226–236; g) J. S. M. Samec, J.-E. Bäckvall, P. G. Andersson, P. Brandt, *Chem. Soc. Rev.* **2006**, *35*, 237–248; h) T. Ikariya, K. Murata, R. Noyori, *Org. Biomol. Chem.* **2006**, *4*, 393–406.

[2] a) S. Hashiguchi, A. Fujii, J. Takehara, T. Ikariya, R. Noyori, *J. Am. Chem. Soc.* **1995**, *117*, 7562–7563; b) A. Fujii, S. Hashiguchi, N. Uematsu, T. Ikariya, R. Noyori, *J. Am. Chem. Soc.* **1996**, *118*, 2521–2522; c) K.-J. Haack, S. Hashiguchi, A. Fujii, T. Ikariya, R. Noyori, *Angew. Chem. Int. Ed. Engl.* **1997**, *36*, 285–288; d) K. Matsumura, S. Hashiguchi, T. Ikariya, R. Noyori, *J. Am. Chem. Soc.* **1997**, *119*, 8738–8739; e) M. Yamakawa, H. Ito, R. Noyori, *J. Am. Chem. Soc.* **2000**, *122*, 1466–1478; f) T. Ohkuma, N. Utsumi, K. Tsutsumi, K. Murata, C. Sandoval, R. Noyori, *J. Am. Chem. Soc.* **2006**, *128*, 8724–8725.

[3] a) J. Takehara, S. Hashiguchi, A. Fujii, S. Inoue, T. Ikariya, R. Noyori, *Chem. Commun.* **1996**, 233–234; b) D. A. Alonso, D. Guijarro, P. Pinho, O. Temme, P. G. Andersson, *J. Org. Chem.* **1998**, *63*, 2749–2751; c) S. J. M. Nordin, P. Roth, T. Tarnai, D. A. Alonso, P. Brandt, P. G. Andersson, *Chem. Eur. J.* **2001**, *7*, 1431–1436; d) K. Everaere, A. Mortreux, M. Bulliard, J. Brussee, A. van der Gen, G. Nowogrocki, J.-F. Carpentier, *Eur. J. Org. Chem.* **2001**, 275–291.

[4] a) K. Murata, T. Ikariya, R. Noyori, *J. Org. Chem.* **1999**, *64*, 2186–2187; b) J. Mao, D. C. Baker, *Org. Lett.* **1999**, *1*, 841–843; c) A. Patti, S. Pedotti, *Tetrahedron: Asymmetry* **2003**, *14*, 597–602; d) H. Brunner, F. Henning, *Monatsh. Chem.* **2004**, *135*, 885–897; e) X. Wu, J. Liu, X. Li, A. Zanotti-Gerosa, F. Hancock, D. Vinci, J. Ruan, J. Xiao, *Angew. Chem. Int. Ed.* **2006**, *45*, 6718–6722; f) N. A. Cortez, R. Rodriguez-Apodaca, G. Aguirre, M. Parra-Hake, T. Cole, R. Somanathan, *Tetrahedron Lett.* **2006**, *47*, 8515–8518; g) S. P. Tanis, B. R. Evans, J. A. Nieman, T. T. Parker, W. D. Taylor, S. E. Heasley, P. M. Herrinton, W. R. Perrault, R. A. Hohler, L. A. Dolak, M. R. Hester, E. P. Seest, *Tetrahedron: Asymmetry* **2006**, *17*, 2154–2182; h) D. S. Matharu, D. J. Morris, G. J. Clarkson, M. Wills, *Chem. Commun.* **2006**, 3232–3234; i) D. J. Morris, A. M. Hayes, M. Wills, *J. Org. Chem.* **2006**, *71*, 7035–7044; j) X. Wu, X. Li, M. McConville, O. Saidi, J. Xiao, *J. Mol. Catal. A* **2006**, *247*, 153–158; k) J. Hannedouche, P. Peach, D. J. Cross, J. A. Kenny, I. Mann, I. Houson, L. Campbell, T. Walsgrove, M. Wills, *Tetrahedron* **2006**, *62*, 1864–1876; l) I. Schiffers, T. Rantanen, F. Schmidt, W. Bergmans, L. Zani, C. Bolm, *J. Org. Chem.* **2006**, *71*, 2320–2331; m) X. Li, J. Blacker, I. Houson, X. Wu, J. Xiao, *Synlett* **2006**, 1155–1160; n) C. C. Watts, P. Thoniyot, F. Cappuccio, J. Verhagen, B. Gallagher, B. Singaram, *Tetrahedron:*

 © 2007 Wiley-VCH Verlag GmbH & Co. KGaA, Weinheim 

*Asymmetry* **2006**, *17*, 1301–1307; o) R. V. Wisman, J. G. de Vries, B. J. Deelman, H. J. Heeres, *Org. Process Res. Dev.* **2006**, *10*, 423–429.
[5] W. Baratta, A. Del Zotto, G. Esposito, A. Sechi, M. Toniutti, E. Zangrando, P. Rigo, *Organometallics* **2004**, *23*, 6264–6272.
[6] W. Baratta, P. Da Ros, A. Del Zotto, A. Sechi, E. Zangrando, P. Rigo, *Angew. Chem. Int. Ed.* **2004**, *43*, 3584–3588.
[7] W. Baratta, E. Herdtweck, K. Siega, M. Toniutti, P. Rigo, *Organometallics* **2005**, *24*, 1660–1669.
[8] W. Baratta, J. Schütz, E. Herdtweck, W. A. Herrmann, P. Rigo, *J. Organomet. Chem.* **2005**, *690*, 5570–5575.
[9] W. Baratta, G. Chelucci, S. Gladiali, K. Siega, M. Toniutti, M. Zanette, E. Zangrando, P. Rigo, *Angew. Chem. Int. Ed.* **2005**, *44*, 6214–6219.
[10] W. Baratta, M. Bosco, G. Chelucci, A. Del Zotto, K. Siega, M. Toniutti, E. Zangrando, P. Rigo, *Organometallics* **2006**, *25*, 4611–4620.
[11] a) E. Lindner, T. Schneller, F. Auer, H. A. Mayer, *Angew. Chem. Int. Ed.* **1999**, *38*, 2155–2174; b) C. E. Song, S.-g. Lee, *Chem. Rev.* **2002**, *102*, 3495–3524; c) Z.-l. Lu, E. Lindner, H. A. Mayer, *Chem. Rev.* **2002**, *102*, 3543–3578; d) D. E. De Vos, M. Dams, B. F. Sels, P. A. Jacobs, *Chem. Rev.* **2002**, *102*, 3615–3640; e) R. Chen, R. P. J. Bronger, P. C. J. Kamer, P. W. N. M. van Leeuwen, J. N. H. Reek, *J. Am. Chem. Soc.* **2004**, *126*, 14557–14566; f) M. Heitbaum, F. Glorius, I. Escher, *Angew. Chem. Int. Ed.* **2006**, *45*, 4732–4762; g) A. Sakthivel, F. M. Pedro, A. S. T. Chiang, F. E. Kühn, *Dalton Trans.* **2006**, 320–326.
[12] a) A. Ghosh, R. Kumar, *J. Catal.* **2004**, *228*, 386–396; b) A. Ghosh, R. Kumar, *Microporous Mesoporous Mater.* **2005**, *87*, 33–44.
[13] A. J. Sandee, D. G. I. Petra, J. N. H. Reek, P. C. J. Kramer, P. W. N. M. van Leeuwen, *Chem. Eur. J.* **2001**, *7*, 1202–1208.
[14] a) P.-N. Liu, P.-M. Gu, F. Wang, Y.-Q. Tu, *Org. Lett.* **2004**, *6*, 169–172; b) P.-N. Liu, P.-M. Gu, J.-G. Deng, Y.-Q. Tu, Y.-P. Ma, *Eur. J. Inorg. Chem.* **2005**, 3221–3227.
[15] a) L. Maier, *Helv. Chim. Acta* **1965**, *48*, 1034–1039; b) A. L. Balch, M. M. Olmstead, S. P. Rowley, *Inorg. Chim. Acta* **1990**, *168*, 255–264.
[16] J. A. Davies, S. Dutremez, A. A. Pinkerton, *Inorg. Chem.* **1991**, *30*, 2380–2387.
[17] a) A. Aranyos, G. Csjernyik, K. J. Szabó, J. E. Bäckvall, *Chem. Commun.* **1999**, 351–352; b) O. Pàmies, J. E. Bäckvall, *Chem. Eur. J.* **2001**, *7*, 5052–5058.
[18] T. A. Stephenson, G. Wilkinson, *J. Inorg. Nucl. Chem.* **1966**, *28*, 945–951.

Received: January 13, 2007
Published Online: May 4, 2007

 © 2007 Wiley-VCH Verlag GmbH & Co. KGaA, Weinheim 

DOI: 10.1002/ejic.200700091

# Pyridine Carboxylate Complexes of $Mo^{II}$ as Active Catalysts in Homogeneous and Heterogeneous Polymerization

**Maria Vasconcellos-Dias,[a] Carla D. Nunes,*[a] Pedro D. Vaz,[a] Paula Ferreira,[b] and Maria José Calhorda*[a]**

**Keywords:** Molybdenum / Lamellar materials / Polymerization / Heptacoordination / Catalysis / ROMP

New lamellar materials intercalated with molybdenum(II) complexes with potential catalytic properties were prepared by a stepwise procedure. The lamellar material was first calcined at 823 K for four hours to eliminate all the carbonate ions; the layered structure was reconstructed after treatment with a solution of either pycH (pyridine-2-carboxylic acid) or $pydcH_2$ (pyridine-2,6-dicarboxylic acid) in a KOH solution of dmf at 343 K. Impregnation with a solution of the organometallic precursor $[Mo(CO)_3I_2(NCCH_3)_2]$ led to substitution of the nitrile groups by two pyridine ligands. All the materials were characterized by powder X-ray diffraction, FTIR, and $^{13}C$ CP MAS and $^{27}Al$ MAS solid-state NMR spectroscopy. Similar $Mo^{II}$ complexes were also prepared by using pycH or $pydcH_2$ and characterized by elemental analysis as well as FTIR and $^1H$ and $^{13}C$ solution NMR spectroscopy. These new materials and the complexes of pyc or pydc ligands containing 4.54 wt.-% and 6.33 wt.-% of Mo respectively, catalyze the ring-opening-metathesis polymerization of norbornene and the polymerization of styrene at 333 K, their performance increasing upon the addition of methylalumoxane (MAO) as cocatalyst.

(© Wiley-VCH Verlag GmbH & Co. KGaA, 69451 Weinheim, Germany, 2007)

## 1. Introduction

Heterogeneous catalysis allows an easy separation of the products of a given reaction from the catalyst, being therefore favored in many industrial processes. The combination of organometallic complexes and a selected support has received much attention in recent years owing to the new perspectives it opens, since the first are known for their capabilities in selective and efficient promotion of many reactions in solution, while the latter optimize recovery and recycling of the catalysts.[1,2]

The choice of the supporting material and the incorporation of the organometallic precursor must be handled with care. In particular, porous materials are very promising candidates for such purposes, as they offer a large surface area inside the pores, but they must be designed by taking into consideration the need to afford a stable (and reactive) material without blocking the pores, so that the reaction can proceed and a good contact between the reactants is promoted.

Layered materials such as clays have been successfully used as hosts for the intercalation of other species. Layered double hydroxides (LDH), available as minerals or from synthesis and known as anionic clays, are very versatile. They can be thought of as descending from a $M(OH)_2$ hydroxide, such as $Mg(OH)_2$, with a structure built from layers of $Mg(OH)_6$ edge-sharing octahedra; if some of these $Mg^{2+}$ dications are replaced by $M^{3+}$ cations, the layers become positively charged, and anions are needed to balance this charge. They occupy, along with water molecules, the space between layers, and can be exchanged with other anions, organic or inorganic. Hydrotalcite (HTC) is an anionic clay from this family, based on Mg and Al cations, but a wide range of compositions $[M^{2+}_{1-x}M^{3+}_x(OH)_2](A^{m-})_{x/m}\cdot nH_2O$ ($M^{2+}$ = $Mg^{2+}$, $Zn^{2+}$, $Ni^{2+}$, etc., $M^{3+}$ = $Al^{3+}$, $Cr^{3+}$, $Ga^{3+}$, etc.) is possible.[3,4]

A rich intercalation chemistry can be obtained not only from the anion exchange process, but also from the substitution of the di- and trivalent cations in the layers. When sizes are not too different, the initial type of structure (brucite) does not change. The value of $x$, measuring the amount of $M^{3+}$ relative to ($M^{3+}$ + $M^{2+}$), is related to the distance between layers. This distance changes when other anions are introduced, although the layered structure is able to swell in the case of large anions, making space available between layers. Among the possible strategies for exchanging anions, rehydration of a calcined precursor has proved advantageous compared to direct anion exchange,[3] as competition between anions can be more efficiently pre-

[a] Departamento de Química e Bioquímica, CQB, Faculdade de Ciências da Universidade de Lisboa,
1749-016 Lisboa, Portugal
Fax: +351-217500088
E-mail: mjc@fc.ul.pt
cmnunes@fc.ul.pt
[b] Departamento de Engenharia Cerâmica e do Vidro, CICECO, Universidade de Aveiro,
Campus de Santiago, 3810-193 Aveiro, Portugal
Supporting information for this article is available on the WWW under http://www.eurjic.org or from the author.

 © 2007 Wiley-VCH Verlag GmbH & Co. KGaA, Weinheim 

vented as long as carbonate, the anion found in the minerals, is excluded. Several groups have worked along these lines, intercalating organic and inorganic anions, from simple to complicated biological ones.[3–5] In another interesting route, the synthesis of the double hydroxide is carried out in the presence of the anions chosen to belong to the final structure.[6,7]

These anions, despite their origin, can undergo several reactions, namely coordination to a metal center, provided that suitable functional groups are present. The calcined HTC itself has also been shown to catalyze reactions such as the aziration of oxiranes.[8] In this work, we studied the intercalation of pyridine-2-carboxylate and pyridine-2,6-dicarboxylate in a Mg/Al HTC and the reaction of the supported anions with a $Mo^{II}$ precursor $[Mo(CO)_3I_2(NCCH_3)_2]$ (**1**), in order to evaluate the catalytic activity of the final materials in the heterogeneous polymerization of olefins. This was compared with the catalytic activity of the homogeneous analogue in the same reaction and the activity of related $Mo^{II}$ complexes supported in other matrices.[9]

## 2. Results and Discussion

### 2.1. Characterization of the Complexes

The precursor complex $[Mo(CO)_3I_2(NCCH_3)_2]$ (**1**)[10] was allowed to react with two equivalents of either pycH or $pydcH_2$ (Scheme 1), affording the complexes formulated as $[Mo(CO)_3I_2(pycH)_2]$ (**2**) and $[Mo(CO)_3I_2(pydcH_2)_2]$ (**3**), respectively, as outlined in Scheme 2.[11,12]

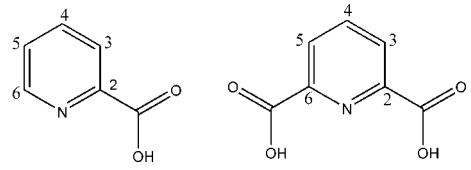


Scheme 1.

The $^1H$ NMR spectrum of $[Mo(CO)_3I_2(pycH)_2]$ (**2**) shows clear differences from those of the precursor complex **1** and the pycH ligand, namely the absence of a resonance at ca. 2.0 ppm assigned to the acetonitrile ligands of **1**, reflecting the loss of both acetonitrile ligands.

The four signals of the 6-H, 4-H, 3-H, and 5-H atoms (see numbering in Scheme 1) of the coordinated pycH ligand are observed at 8.99, 8.71, 8.66, and 8.37 ppm, respectively, clearly shifted relative to the corresponding signals in the free ligand at 8.76, 8.03, 8.10, and 7.67 ppm. The downfield shift experienced by the signals of the complexed ligand can be explained by the coordination to the electron-rich Mo center. The $^{13}C$ NMR spectrum confirms the above observations. Indeed, in the coordinated pycH, the resonances at 149.5, 144.2, 142.4, 131.3 and 129.0 ppm are assigned to the C-6, C-4, C-2, C-5, and C-3 atoms of the pyridine ring, while the carboxylate carbon atom appears at $\delta$ = 161.2 ppm. These values are shifted relative to those for the free ligand by small [149.4 ppm (C-6), 124.6 ppm (C-3)] and large amounts [137.4 (C-4), 148.4 (C-2), 126.7 (C-5), 166.1 ppm (carboxylate carbon)]. All these values are collected in Table 1.

The FTIR spectrum of $[Mo(CO)_3I_2(pycH)_2]$ (**2**) also reveals the absence of the $\nu_{C\equiv N}$ stretching modes at ca. 2300 $cm^{-1}$ (Table 2). Another strong evidence for the substitution of the nitrile ligands is the strong redshift (lower wavenumbers) experienced by the $\nu_{C\equiv O}$ modes relative to the bands in complex **1**. The appearance of four bands at 2018, 1959, 1900, and 1845 $cm^{-1}$, assigned to the $\nu_{C\equiv O}$ modes, when only three were expected, was ascribed to the existence of another isomer in the solid. This situation has also been reported previously for the parent compound (Figure 1).[13] In order to evaluate the possible fluxionality between both isomers, complex **2** was dissolved in methanol, and the vibrational spectrum of this solution was recorded. The four bands are still visible in solution, as shown in Figure S1 in the Supporting Information, and are reflected in the difference spectrum compared with that of $[Mo(CO)_3I_2(pycH)_2]$ (**2**).

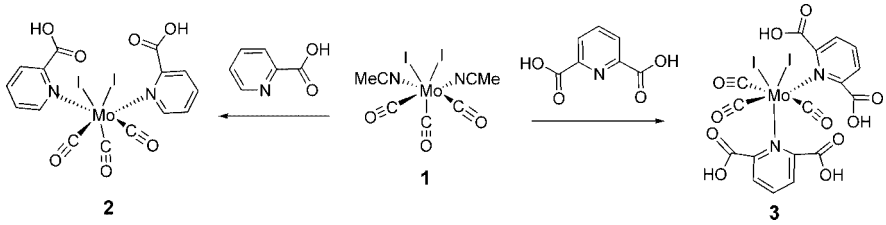


Scheme 2.

Table 1. $^1H$ and $^{13}C$ NMR chemical shifts [ppm] for the ligands pycH and $pydcH_2$, and the complexes **2** and **3**.

| | 3-H | 4-H | 5-H | 6-H | C-2 | C-3 | C-4 | C-5 | C-6 | COOH |
|---|---|---|---|---|---|---|---|---|---|---|
| pycH | 8.10 | 8.03 | 7.67 | 8.76 | 148.4 | 124.6 | 137.4 | 126.7 | 149.4 | 166.1 |
| **2** | 8.66 | 8.71 | 8.37 | 8.99 | 142.4 | 129.0 | 144.2 | 131.3 | 149.5 | 161.2 |
| $pydcH_2$ | 8.28 | 8.23 | 8.28 | – | 148.0 | 127.4 | 139.2 | 127.4 | 148.0 | 165.4 |
| **3** | 8.39 | 8.27 | 8.39 | – | 150.2 | 130.0 | 141.2 | 130.0 | 150.2 | 167.1 |

 © 2007 Wiley-VCH Verlag GmbH & Co. KGaA, Weinheim 

Table 2. FTIR wavenumbers of the $\nu_{C\equiv O}$, $\nu_{C=O}$, and $\nu_{C=N}$ modes for the ligands pycH and $pydcH_2$, and the complexes **1**, **2**, and **3**.

| Complex or ligand | $\nu_{C\equiv O}$ [$cm^{-1}$] | $\nu_{C=O}$ [$cm^{-1}$] | $\nu_{C=N}$ [$cm^{-1}$] |
|---|---|---|---|
| $[Mo(CO)_3I_2(NCCH_3)_2]$ (**1**) | 2017 (vs), 1924 (broad, vs) | – | – |
| pycH | – | 1722 (vs) | 1609 (vs), 1596 (vs) |
| $pydcH_2$ | – | 1701 (vs) | 1468 (s), 1416 (s) |
| $[Mo(CO)_3I_2(pycH)_2]$ (**2**) | 2018 (m), 1959 (s), 1900 (s), 1845 (s) | 1740 (s) | 1654 (s), 1612 (m) |
| $[Mo(CO)_3I_2(pydcH_2)_2]$ (**3**) | 2071 (s), 2011 (s), 1943 (s) | 1696 (vs) | 1458 (m), 1413 (m) |

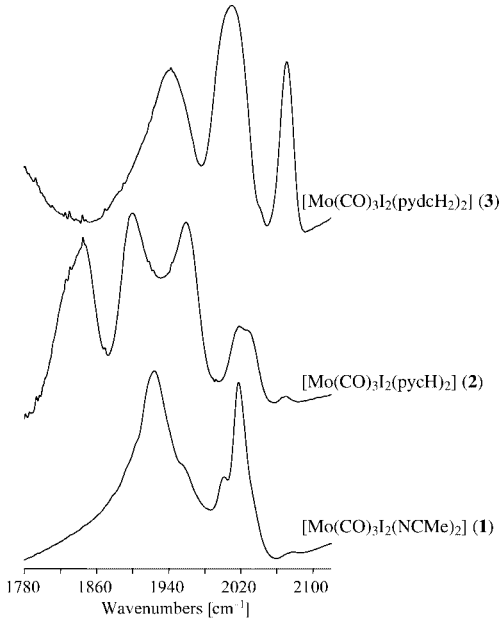


Figure 1. FTIR spectra of $[Mo(CO)_3I_2(NCCH_3)_2]$ (**1**), $[Mo(CO)_3I_2(pycH)_2]$ (**2**), and $[Mo(CO)_3I_2(pydcH_2)_2]$ (**3**).

The vibrational spectrum of complex **3** also supports its formulation as $[Mo(CO)_3I_2(pydcH_2)_2]$. The FTIR spectrum of $[Mo(CO)_3I_2(pydcH_2)_2]$ (**3**) shows only three narrow bands assignable to a single isomer, a fact that can be explained by the larger bulk of the two nitrogen ligands. They are slightly shifted relative to those of the precursor complex **1**. The $\nu_{C=O}$ mode of the $pydcH_2$ ligand shifts from 1701 $cm^{-1}$ (in the free ligand) to 1696 $cm^{-1}$ in complex **3**, while two bands assigned to the $\nu_{C=N}$ mode at 1468 ($\nu_{sym}$) and 1416 $cm^{-1}$ ($\nu_{asym}$) in the free ligand undergo a redshift to 1458 and 1413 $cm^{-1}$, respectively, after binding.

In what concerns the ligand, the major changes should involve the $\nu_{C=N}$ of the ring and $\nu_{C=O}$ of the COOH group. The band at 1740 $cm^{-1}$ ($\nu_{C=O}$ modes of the COOH group) in **2** shows a small blueshift of ca. 18 $cm^{-1}$, suggesting no involvement in hydrogen bonding. The $\nu_{C=N}$ modes of the free pycH ligand (1596 and 1609 $cm^{-1}$) shift upon complexation to 1612 and 1654 $cm^{-1}$, respectively.

The most relevant spectroscopic features of complex **2** are summarized in Table 2, as well as the corresponding data for complex **3**, the precursor complex **1**, and the ligands pycH and $pydcH_2$.

The $^1H$ NMR spectrum of complex $[Mo(CO)_3I_2(pydcH_2)_2]$ (**3**) is similar to the one described for **2**, with resonances at $\delta$ = 8.39 (3-H, 5-H) and 8.27 ppm (4-H), shifted to higher $\delta$ values relative to those observed for the free ligand ($\delta$ = 8.28 ppm for 3-H and 5-H; 8.23 ppm for 4-H). The pyridine signals in the $^{13}C$ NMR spectrum appear at 150.2, 141.2, and 130.0 ppm, being assigned to C-2/C-6, C-4, and C-3/C-5, respectively, while the COOH carbon is observed at $\delta$ = 167.1 ppm. All the signals are shifted downfield in comparison with free $pydcH_2$ [148.0 (C-2/C-6); 139.2 (C-4), and 127.4 ppm (C-3/C-5); COOH 165.4 ppm].

### 2.2. Intercalation of the Ligands and the Organometallic Fragment in Hydrotalcite

Prior to the intercalation experiments, the commercial HTC (**4**) lamellar material was submitted to a calcination process at 823 K for 4 h to eliminate the $CO_3^{2-}$ anions in the interlayer region, as described previously.[8] The structure of the lamellar material collapses, but it is rebuilt in the following step, when the deprotonated ligands pyc and pydc are intercalated inside the intergallery space by using dmf at 343 K.[6] This procedure made possible the preparation of composite materials HTC–pyc (**5**) and HTC–pydc (**6**), containing the anions in the interlayer space, according to Scheme 3.

The results of elemental analyses of materials **5** and **6** show that the C/N mol ratios are 5.6 and 6.6, respectively, which are slightly higher than the expected values, 5.2 in pyc and 6.0 in pydc. On the other hand, the C/H mol ratios are 3.4 and 2.6, much lower than the expected values of 7.2 and 6.0. This suggests that incorporation of some carbonate during reconstruction of the layered structure leading to a multiphase sample does not take place.[14] Instead, the high content of hydrogen may be explained by the uptake of OH groups. On the basis of the amount of nitrogen for the two materials **5** and **6**, the contents of pyc and pydc ligands incorporated are 57% and 63%, respectively.

These functionalized materials were then allowed to react with the organometallic precursor **1** in dry $CH_2Cl_2$ for 24 h at room temperature, affording the new materials HTC–pyc–Mo (**7**) and HTC–pydc–Mo (**8**) after filtration and drying. The molybdenum loadings for the organometallic composite materials **7** and **8** were found to be 4.54 wt.-% and 6.3 wt.-% (0.43 mmol $g^{-1}$ and 0.66 mmol $g^{-1}$), respectively, showing that higher metal quantities were incorporated in comparison to immobilization in a mesoporous support.[9] These results indicate the coordination of the available supported ligands to molybdenum to form 2:1 complexes, such as **2** and **3**.

All the new materials were characterized by powder XRD, FTIR, and solid-state $^{13}C$ and $^{27}Al$ NMR spectroscopic techniques.

 © 2007 Wiley-VCH Verlag GmbH & Co. KGaA, Weinheim 

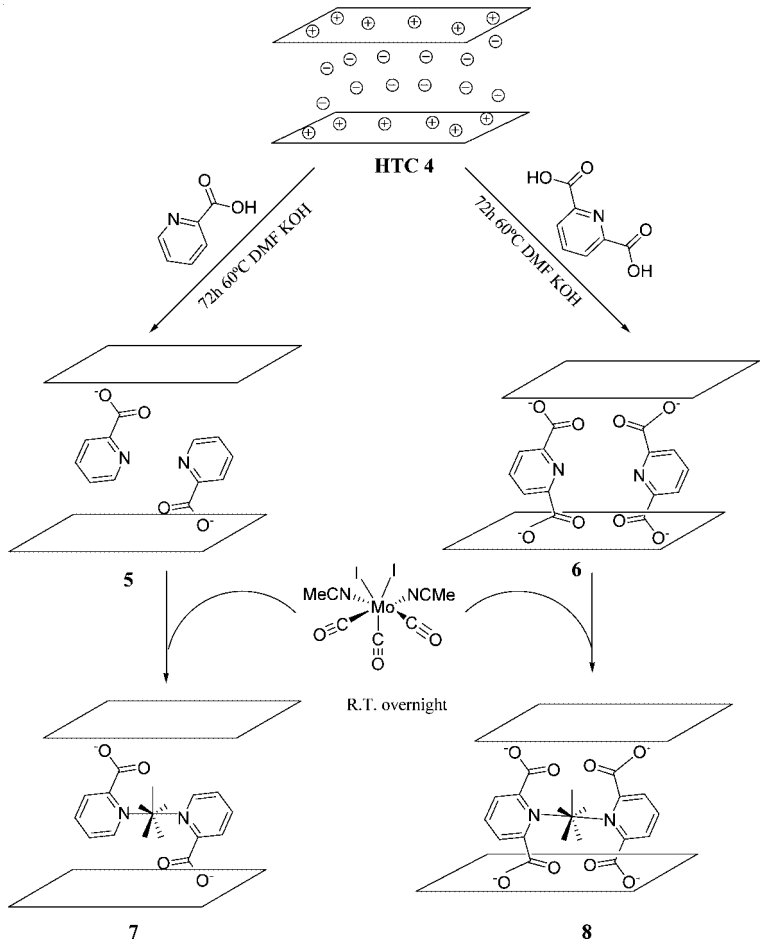


Scheme 3.

The powder XRD patterns obtained for these lamellar materials are typical of this type of reasonably well-ordered materials, exhibiting sharp and symmetric 003 reflections (Figure 2).[15]

The peaks were indexed to a rhombohedral symmetry. There was evidence of $Al(OH)_3$ in the lamellar materials, arising from the presence of gibbsite, at $2\theta$ = 17.5, 28.9, and 39.2°. The calculated *d* parameters were 15.3 Å for the lamellar material **5** and 12.2 Å for material **6**. The 15.3 Å value found for material **5** corresponds to a gallery height of 10.5 Å, assuming the HTC sheets to be 4.8 Å thick.[3] Considering the longest dimension of the pycH guest to be approximately 8.8 Å, the value estimated for benzoate,[3] the XRD results suggest that a bilayer-like structure is assembled within the gallery. Furthermore, since the gallery height is only slightly superior to the size of the guest, the bilayer arrangement might consist of superimposed guest molecules, as schematized in Figure 3. Similar proposals have already been discussed by some authors.[3,15]

In the case of material **6**, the gallery height was found to be 7.4 Å. Assuming the length of the $pydcH_2$ guest (similar to a terephthalate anion) to be 9.9 Å, it is most likely that the molecules cannot be upright. They may either lie in a

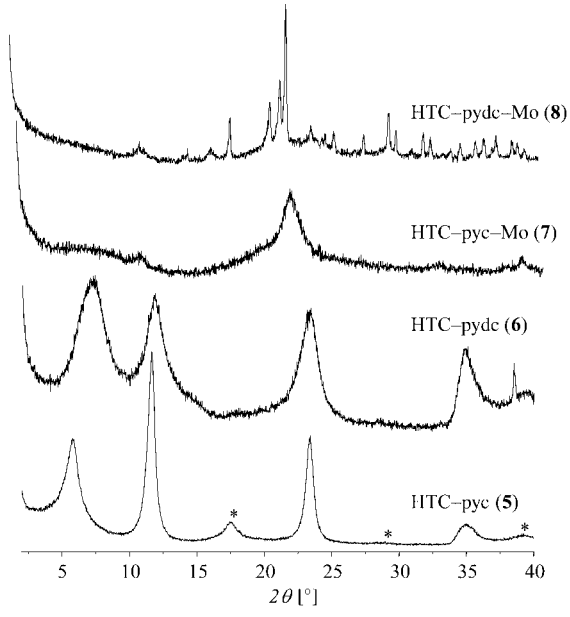


Figure 2. Powder XRD patterns of HTC–pyc (**5**), HTC–pydc (**6**), HTC–pyc–Mo (**7**), and HTC–pydc–Mo (**8**); * denotes peaks from gibbsite.

 © 2007 Wiley-VCH Verlag GmbH & Co. KGaA, Weinheim 

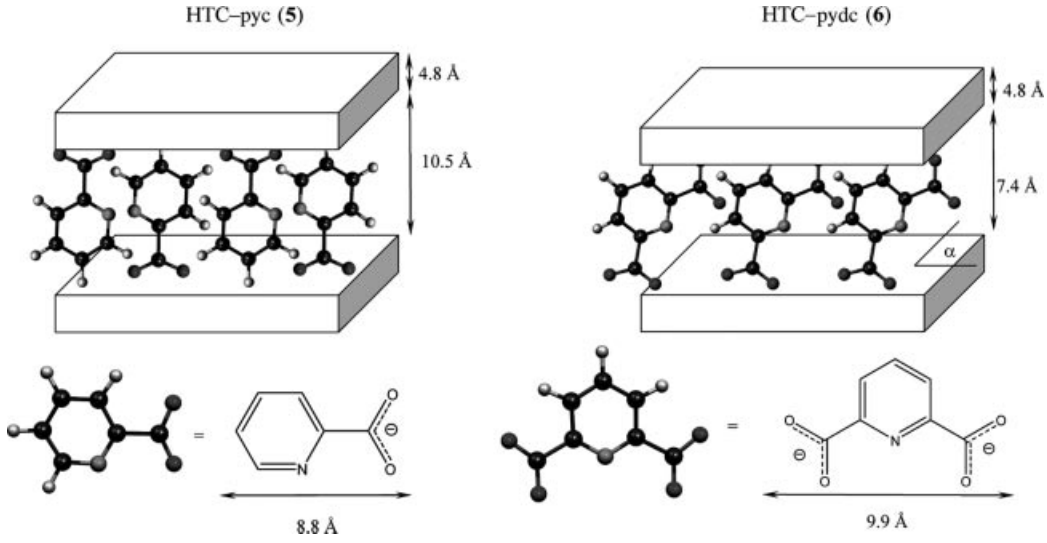


Figure 3. Models for the interlayer arrangement of the guest species of the materials HTC–pyc (**5**) and HTC–pydc (**6**); a color version of this figure is part of the Supporting Information.

horizontal arrangement, such as described in previous works,[3,15] or prefer tilted positions, up to a maximum tilt angle of 48° ($\alpha$ in Figure 3). This is also supported by the large full width at half height of the diffraction peaks.[15] The XRD patterns of materials **5** and **6** are very similar in terms of the number and positions of peaks, and differ mainly in the band width: broader peaks are observed for material **6**.

For materials **7** and **8**, obtained after treatment with complex **1**, the 001 reflections are significantly reduced in intensity. These changes can be attributed to a marked increase in the electron density at the midpoint of the interlayers due to the presence of the Mo centers at a high loading (4–6 wt.-%). This is in line with previous reports.[16,17] It is also possible, according to other reports, that the structure has partially disrupted owing to exfoliation, especially in material **8**.[18]

The FTIR spectrum of the HTC host material is similar to that of other materials of the same type. In the high-frequency region (4000–2000 $cm^{-1}$), it is dominated by broad bands at about 3400 $cm^{-1}$, assigned to the O–H stretches of weakly hydrogen-bonded water molecules and layer hydroxy groups. Some carbonate groups, from the air and humidity, may be responsible for the band at around 1400 $cm^{-1}$.The derivatized materials HTC–pyc (**5**) and HTC–pydc (**6**), resulting from the treatment of HTC with pyc and pydc anions, respectively, showed new bands in their vibrational spectra relative to the host material HTC. For HTC–pyc (**5**), a band at 3458 $cm^{-1}$ is assigned to the O–H stretches of the structure of HTC and water molecules, as described above, the bands at 1598 and 1594 $cm^{-1}$, to the $\nu_{C=N}$ of the pyridine ring, and the band at 1632 $cm^{-1}$ to the $\nu_{C=O}$ group of the carboxylate group of the ligand. Some of these bands show a deviation relative to the free ligand, because the ligand is deprotonated and held inside the gallery of the material. For HTC–pydc (**6**), it is possible to assign the bands at 2982 and 2977 $cm^{-1}$ to the $\nu_{C-H}$ of the ring and the $\nu_{C=N}$ mode of the pyridine ring at 1439 and 1376 $cm^{-1}$ (at 1468 and 1416 $cm^{-1}$ in the free ligand). The band at 1607 $cm^{-1}$ can be assigned to the $\nu_{C=O}$ mode of the ligand (1701 $cm^{-1}$ in the free ligand). The small changes observed in the bands of both composite materials suggest that the structures of the anionic ligands were not affected during immobilization in the material.

Treatment of the composite materials **5** and **6** with the organometallic complex $[Mo(CO)_3I_2(NCCH_3)_2]$ led to the new materials HTC–pyc–Mo (**7**) and HTC–pydc–Mo (**8**). In the composite material **7**, the vibrations of the carbonyl groups ($\nu_{C\equiv O}$) at 2022, 1950, and 1880 $cm^{-1}$ are shifted relative to those of complex **2**, probably as a result of specific host–guest interactions between the $Mo(CO)_3$ core and the layers of the HTC-derivatized host material. The $\nu_{C=N}$ modes of the pyridine ring appear at 1640 and 1630 $cm^{-1}$. These values are higher than those for the free ligand (1609 and 1596 $cm^{-1}$) and are close to those for complex **2**, indicating chelation to the metal center. The same trends are observed in HTC–pydc–Mo (**8**), with the $\nu_{C\equiv O}$ modes of the $Mo(CO)_3$ fragment at 2037, 1955, and 1892 $cm^{-1}$, and the $\nu_{C=N}$ modes of the pyridine ring at 1442 and 1395 $cm^{-1}$, values slightly lower than those for the free ligand (1468 and 1416 $cm^{-1}$), and close to the values for complex **3**. No bands that might be assigned to the $\nu_{C\equiv N}$ modes, observed at 2304 and 2277 $cm^{-1}$ in the precursor **1**, corresponding to the acetonitrile ligands, were detected in either HTC–pyc–Mo (**7**) or HTC–pydc–Mo (**8**).

The $^{13}C$ CP MAS NMR spectra of the lamellar materials **5**–**8** (Figure 4) exhibit several resonances in the $120 < \delta < 150$ ppm range assigned to carbon atoms of the pyridine ring, and a single peak in the $160 < \delta < 170$ ppm range assigned to the carboxylate carbon atoms. These results indicate that the ligands are inside the interlamellar space of hydrotalcite for materials **5** and **6**. The sharp signals ob-

 © 2007 Wiley-VCH Verlag GmbH & Co. KGaA, Weinheim 

served for material **5** are similar to those found in solution for the pycH ligand, and can therefore be assigned: 124.7 (C-3), 128.0 (C-5), 139.8 (C-2), 146.6 (C-4), and 150.9 (C-6), and 170.1 ppm (*C*OO$^-$ group). In material **6**, the spectrum is not so well resolved. Three peaks at $\delta$ = 125.1, 139.2, and 150.2 ppm are attributed to the pyridine ring of the pydc ligand, and another at $\delta$ = 170.5 ppm for the *C*OO$^-$ group.

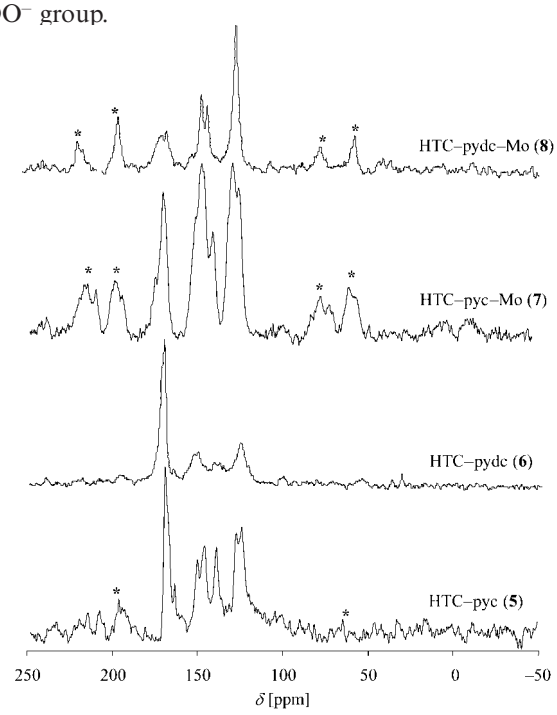


Figure 4. $^{13}$C CP MAS NMR spectra for the materials HTC–pyc (**5**), HTC–pydc (**6**), HTC–pyc–Mo (**7**), and HTC–pydc–Mo (**8**); * denotes spinning side bands.

In materials **7** and **8**, no resonances of the acetonitrile ligands of precursor **1** are detected, and signals from the C≡O ligands are not visible, since they have a long relaxation time. On the other hand, the signals of the pyc ligand in **7** are not as clear as in the precursor **5**: 170.3 (*C*OO$^-$ group), 124.9 (C-3), 128.6 (C-5), 140.4 (C-2), and 147.0 ppm (C-4), whereas C-6 is convoluted with C-4. In material **8**, only three signals are resolved, namely the signals of the pyridine ring at $\delta$ = 127.1, 143.9, and 147.2 ppm, and that of the COO$^-$ group at $\delta$ = 167.4 ppm, as also observed for material **6**.

The $^{27}$Al MAS NMR spectra of all the lamellar materials are very similar. A sharp peak is observed at ca. 9 ppm, with a broad downfield shoulder, assigned to octahedral aluminum. Similar spectra are described in the literature.[19] The first site, corresponding to the sharp peak, displays a distribution of isotropic chemical shifts and is probably due to the presence of a range of slightly different local Al environments generated by the random insertion of Al in the layers. The low-frequency shoulder corresponds essentially to undistributed Al species, but it has an average quadrupole coupling constant that is larger than that of the first site. This has been ascribed previously to small clusters of Al atoms in the brucite-like layers.[7]

### 2.3. Polymerization Catalytic Studies

Following the interest in the study of olefin polymerization catalyzed by Mo$^{II}$ and W$^{II}$ systems over the last years,[11–15] complex **1** has been tested for ring-opening-metathesis polymerization (ROMP) catalysis of norbornene and norbornadiene (NBE and NBD, respectively; polyNBE and polyNBD denote the corresponding polymer product).[11] ROMP of NBD has been successfully carried out by complexes $[Mo(CO)_3(NCCH_3)_2X_2]$ at room temperature for X = Br, while for X = I, a cocatalyst such as $ZrCl_4$ or $AlCl_3$ is required in order to initiate polymerization.[11] Recently, some of these Mo$^{II}$ and W$^{II}$ complexes immobilized in a MCM–41 material have also shown weak activity towards the ROMP reactions of NBE and NBD.[9] MAO has been successfully used as a cocatalyst in heterogeneous clay/metal systems as described in previous publications addressing olefin polymerization.[20,21]

In the present work, complexes **2** and **3** as well as materials **7** and **8** were tested for ROMP catalysis of NBE and polymerization of styrene (STY) at 333 K, and the results are collected in Table 3. The effect of addition of a cocatalyst (MAO) on the catalytic performance and the nature of the polymer were also checked. Complexes **2** and **3** show comparable activities towards both olefins, stressing that there is no beneficial effects of using either pycH or $pydcH_2$ ligands. This same trend is observed when MAO is used.

In absence of the cocatalyst, the composite materials **7** and **8** are slightly more active catalysts for the polymerization reaction of STY than the homogeneous counterparts **2** and **3**, while the results are comparable in the case of ROMP of NBE. The presence of aluminum in the sheets of the host material may contribute to a higher Lewis acidity and therefore induce a more efficient catalysis. This situation has already been discussed previously.[9,22–24]

Neither the calcined HTC host material nor the derivatized materials **5** and **6** possess catalytic activity towards the polymerization reactions of the olefins, indicating that the active species must contain molybdenum.

For all metal-containing catalysts and in the absence of the cocatalyst, the polymerization of STY is easier to accomplish than ROMP of NBE. Nevertheless, when MAO is used, the performances are boosted, more significantly for NBE than for STY, and polymer yields of polyNBE are higher than those found for polySTY. In fact, addition of MAO increases the yield of polySTY by an average factor of 3, while for polyNBE this factor reaches an average of 27.5. This general increase in yield is expected because of the role of MAO as a radical initiator, promoting the formation of the initial active species that binds to the metal center where the propagation and/or termination steps occur.

Another interesting factor is the local structure of the polymer, as homotactic isomers are preferred, namely in the case of polySTY, because of their industrial importance.[22,23] For polyNBE, a reasonable *cis* content is achieved in all the catalytic processes, but the *cis* content rises significantly in the presence of MAO. Thus, addition

 © 2007 Wiley-VCH Verlag GmbH & Co. KGaA, Weinheim 

Table 3. Results for the polymerization reactions of NBE and STY initiated by isolated and immobilized $[Mo(CO)_3I_2(L)_2]$ complexes at 333 K.

| Catalyst | Cocatalyst | PolyNBE | | PolySTY | |
|---|---|---|---|---|---|
| | | Yield [%] | *cis* [%] | Yield [%] | *syndio* [%] |
| $[Mo(CO)_3I_2(pycH)_2]$ (**2**) | – | 3 | 50 | 9 | 20 |
| | MAO | 99 | 50 | 31 | 20 |
| $[Mo(CO)_3I_2(pydcH_2)_2]$ (**3**) | – | 3 | 45 | 8 | 62 |
| | MAO | 91 | 60 | 24 | 65 |
| HTC–pyc–Mo (**7**) | – | 4 | 33 | 23 | 22 |
| | MAO | 95 | 44 | 60 | 65 |
| HTC–pydc–Mo (**8**) | – | 4 | 38 | 25 | 47 |
| | MAO | 94 | 56 | 61 | 42 |
| MCM–DAB–Mo[a] | – | 36 | – | – | – |
| | MAO | 59 | – | – | – |

[a] DAB = $(OEt)_3Si(CH_2)_3N{=}C(Ph){-}C(Ph){=}N(CH_2)_3Si(OEt)_3$, Mo = $MoBr_2(CO)_3$; from ref.[9]

of MAO is helpful not only in terms of reaction initiation, but also in directing the formation of homotactic polymer structures.

In the case of polySTY, the trend in the percentage of the syndiotactic polymer structure is not as clear, and MAO does not seem to influence the percentage of homotactic structures very much. As a general rule, and despite some good values of syndiotactic polymer yield (see Table 3, entries 3, 4, and 6), there is a general tendency towards the preparation of *syndio*-rich atactic polymers.

All the species described above exhibit higher catalytic activities towards the ROMP of NBE than the related $Mo^{II}$ and $W^{II}$ complexes immobilized in a MCM–41 material (Table 3, last entry).

## 3. Conclusions

The intercalation of heptacoordinate halocarbonylmolybdenum(II) complexes in organic–inorganic hybrid clay materials was successfully accomplished by first intercalating carboxylic acid derivatives of pyridine, under basic conditions, into the interlayer spacing of previously calcined hydrotalcite clay and subsequently introducing an organometallic fragment. This scheme was confirmed by several analytical techniques. For instance, FTIR spectra exhibited the bands assigned to $\nu_{C\equiv O}$ modes, reflecting the incorporation of the organometallic *fac*-$Mo(CO)_3$ core, and others showing the coordination of Mo to the pyridine ligand. Powder X-ray diffraction patterns, on the other hand, revealed the reconstruction of the HTC layered structure.

The catalytic activity in the ROMP reaction of NBE and polymerization of STY improves upon going from the homogeneous-phase complexes **2** and **3** to the corresponding heterogenized catalysts (**7** and **8**). In general, the conversions are higher for STY than for NBE. When MAO is added as a cocatalyst, the polymer yields are increased for both, so that the only obvious advantage of the heterogeneous catalysts seems to be the ease of separation.

A high content of *cis* polymer is detected for polyNBE, and the *cis* content increases when the reaction is carried out in the presence of MAO. There is no such simple trend for polySTY. The local structures of the polySTY may be better defined as *syndio*-rich atactic polymer chains.

## Experimental Section

**General:** All preparations and manipulations were performed by using standard Schlenk techniques under nitrogen. Commercial grade solvents were dried and deoxygenated by standard procedures ($Et_2O$ over Na/benzophenone ketyl; $CH_2Cl_2$, dmf, and $CH_3CN$ over $CaH_2$), distilled under nitrogen, and kept over 4 Å molecular sieves (3 Å for $CH_3CN$). Picolinic acid (pycH), pyridine-2,6-dicarboxylic acid ($pydcH_2$), methyl alumoxane (MAO), and Mg,Al-hydrotalcite (HTC) were purchased from Aldrich Co. Prior to the intercalation experiments, commercial hydrotalcite was calcined (823 K for 4 h) in order to eliminate all the carbonate anions.[8] The precursor organometallic complex $[Mo(CO)_3I_2(NCCH_3)_2]$ (**1**) was also prepared according to literature methods.[10]

Powder XRD data were collected with a Phillips PW1710 diffractometer by using graphite-filtered Cu-$K_\alpha$ radiation. FTIR spectra were measured with a Nicolet Nexus 6700 FTIR spectrometer by using KBr pellets (for complexes) in the transmission mode and also with diffuse reflectance (for clay materials). Solution spectra were measured in a liquid cell with KBr windows and by using dry methanol as solvent. All FTIR spectra were measured with 2 $cm^{-1}$ resolution.

$^1H$ and $^{13}C$ solution NMR spectra were obtained at 400.13 MHz and 100.62 MHz, respectively, with a Bruker Avance 400 spectrometer by using $CD_3OD$ as solvent. Chemical shifts are quoted in ppm from TMS.

$^{27}Al$ and $^{13}C$ solid-state NMR spectra were recorded at 104.26 MHz and 100.62 MHz, respectively, with a (9.4 T) Bruker Avance 400P spectrometer. $^{13}C$ solid-state NMR spectra were also recorded at 125.76 MHz with a Bruker Avance 500P spectrometer. $^{27}Al$ MAS NMR spectra were acquired by using short and powerful radio-frequency pulses (0.6 μs, corresponding to π/12 pulses), a spinning rate of 14 kHz, and a recycle delay of 1 s. Chemical shifts are quoted in ppm relative to $[Al(H_2O)_6]^{3+}$. $^{13}C$ CP MAS NMR spectra were recorded with a 4.5-μs $^1H$ 90° pulse, 2-ms contact time, a spinning rate of 8 kHz, and 4-s recycle delays. Chemical shifts are quoted in ppm from TMS. Microanalyses were performed at the University of Vigo and the University of Aveiro.

**Catalytic Studies:** The complexes and materials reported herein were tested in the ROMP of norbornene (NBE) and polymerization of styrene (STY) under a $N_2$ atmosphere at 333 K and by using toluene as solvent. The catalytic reactions with complexes **2** and **3** were carried out by using a catalyst/olefin mol ratio of 1:200. In the studies with the composite materials **7** and **8**, a Mo/olefin mol ratio of 1:200 (based on the metal loadings as determined by ICP–

 © 2007 Wiley-VCH Verlag GmbH & Co. KGaA, Weinheim 

AES) was used. For the catalytic reaction with MAO as cocatalyst, the Mo/Al/olefin mol ratio was 1:3:200. In a typical experiment, a certain amount of the materials containing olefin (18.5 mmol) was mixed in toluene (10 mL) at 333 K. All the reactions were stopped after 48 h. This was accomplished by separating the catalysts by filtration, followed by the addition of methanol to the toluene solution in order to precipitate the polymer. The polymers were precipitated by addition of methanol at the end of the reaction, i.e., after 48 h and upon catalyst separation. The solid polymer was separated by filtration, and the polymers were dried in vacuo before being weighed. The yields were calculated on the basis of the initial weight of olefin used. The identification of the polymers was accomplished by $^1$H NMR spectroscopy, and the *cis* content (NBE) and tacticity (STY) were estimated from $^1$H and $^{13}$C NMR spectroscopic data.[24,25–29]

**Preparation of the Complexes $[Mo(CO)_3I_2L_2]$ (L = pycH or pydcH$_2$) (2, 3):** A solution of $[Mo(CO)_3I_2(NCCH_3)_2]$ (**1**) (0.50 mmol, 258 mg) in $CH_2Cl_2$ (10 mL) was treated with a solution of the ligand pycH or pydcH$_2$ (1 mmol; 123 or 167 mg) in $CH_2Cl_2$ (5 mL). The resulting solution was stirred for 14 h at room temperature. The desired complex precipitated, and the solvent was filtered off. The complex was then washed with hexane and dried under vacuum.

**$[Mo(CO)_3I_2(pycH)_2]$ (2):** Yield: 92%. $C_{15}H_{10}I_2MoN_2O_7$ (680.00): calcd. C 26.49, H 1.48, N 4.12; found C 26.05, H 1.62, N 4.27. IR (KBr): $\tilde{\nu}$ = 3094 (m), 3052 (w), 2069 (vw), 2018 (m), 1959 (m), 1900 (m), 1845 (m), 1740 (s), 1654 (s), 1612 (vs), 1576 (m), 1559 (m), 1460 (s), 1340 (m), 1294 (s), 1206 (m), 1166 (m), 1092 (m), 962 (m), 757 (vs), 708 (m), 690 (m), 656 (w), 448 (w) cm$^{-1}$. $^1$H NMR (400.13 MHz, $CDCl_3$, room temp.): $\delta$ = 8.99 (d, $J_{5,6}$ = 5.6 Hz, 1 H, pyc), 8.71 (t, $J_{4,5}$ = 8.0 Hz, 1 H, pyc), 8.66 (d, $J_{3,4}$ = 7.6 Hz, 1 H, pyc), 8.37 (t, $J_{5,6}$ = 6.6 Hz, 1 H, pyc) ppm. $^{13}$C NMR (100.62 MHz, $CDCl_3$, room temp.): $\delta$ = 161.2 (COOH), 149.5 (C-6), 144.2 (C-4), 142.4 (C-2), 131.7 (C-5), 129.0 (C-3) ppm.

**$[Mo(CO)_3I_2(pydcH_2)_2]$ (3):** Yield: 96%. $C_{17}H_{10}I_2MoN_2O_{11}$ (768.02): calcd. C 26.59, H 1.31, N 3.65; found C 26.09, H 1.26, N 3.44. IR (KBr): $\tilde{\nu}$ = 3447(w), 3068 (w), 2901 (w), 2624 (w), 2546 (w), 2071 (w), 2011 (m), 1943 (m), 1696 (vs), 1654 (s), 1575 (m), 1458 (m), 1413 (m), 1331 (m), 1298 (m), 1266 (m), 1176 (w), 1080 (m), 997 (m), 915 (m), 855 (m), 752 (s), 702 (s), 648(s) cm$^{-1}$. $^1$H NMR (400.13 MHz, $CDCl_3$, room temp.): $\delta$ = 8.27 (d, $J_{3,4}$ = 7.2 Hz, 1 H, pydc), 8.39 (d, $J_{4,5}$ = 7.6 Hz, 2 H, pydc) ppm. $^{13}$C NMR (100.62 MHz, $CDCl_3$, room temp.): $\delta$ = 167.1 (COOH), 150.2 (C-2, C-6), 141.2 (C-4), 130.0 (C-3, C-5) ppm.

**Preparation of the Materials HTC–L (L = pyc or pydc) (5, 6):** A mixture of pycH (7.30 mmol) or pydcH$_2$ (3.60 mmol) in freshly distilled dmf (10 mL) and deionized water (20 mL) with NaOH (1 equiv. for pycH or 2 equiv. for pydcH$_2$) was stirred until complete solubilization. This solution was then added to a suspension of calcined HTC (1.00 g) in freshly distilled dmf (25 mL) at 343 K, and the reaction mixture was stirred at the same temperature for 48 h. All the manipulations were carried out under a $N_2$ atmosphere to prevent the uptake of carbonate anions. The resulting material was then filtered off, washed with deionized water (3 × 20 mL), and dried in a desiccator under vacuum.

**HTC–pyc (5):** Elemental analysis found: C 13.65, H 4.05, N 2.41. IR (KBr) $\tilde{\nu}$ = : 3458 (vs), 1632 (s), 1598 (s), 1476 (m), 1374 (s), 1293 (w) cm$^{-1}$. $^{13}$C NMR CP MAS NMR: $\delta$ = 124.7 (C-3), 128.0 (C-5), 139.8 (C-2), 146.6 (C-4), 150.9 (C-6), 170.1 (COOH) ppm. $^{27}$Al MAS NMR: $\delta$ = 9.47 ppm.

**HTC–pydc (6):** Elemental analysis found: C 10.19, H 3.98, N 1.55. IR (KBr): $\tilde{\nu}$ = 2982 (vs), 2977 (vs), 2907 (s), 1607 (s), 1563 (s), 1439 (m), 1376 (vs), 1269 (w), 1174 (w), 1083 (w), 957 (m), 771 (s), 676 (s), 566 (m), 450 (s) cm$^{-1}$. $^{13}$C NMR CP MAS NMR: $\delta$ = 125.1 (C-3, C-5), 139.2 (C-4), 150.2 (C-2, C-6), 170.5 (COOH) ppm. $^{27}$Al MAS NMR: $\delta$ = 9.28 ppm.

**Preparation of the Materials HTC–L–Mo (L = pyc or pydc) (7, 8):** A solution of $[Mo(CO)_3I_2(NCCH_3)_2]$ (**1**) (0.34 g, 0.65 mmol) in dry $CH_2Cl_2$ (5 mL) was added to a suspension of the HTC intercalated material HTC–L (**4** or **5**) (1.00 g) in dry $CH_2Cl_2$ (20 mL). The reaction mixture was stirred under a $N_2$ atmosphere at room temperature for 24 h. The resulting material was then filtered off, washed with $CH_2Cl_2$ (2 × 20 mL), and dried in a desiccator under vacuum.

**HTC–pyc–Mo (7):** Elemental analysis found: C 7.36, H 2.66, Mo 4.54, N 1.32. IR (KBr) $\tilde{\nu}$ = 3460 (vs), 2972 (w), 2947 (w), 2875 (w), 1950 (m), 1640 (s), 1630 (s), 1480 (m), 1380 (m), 1300 (w), 962 (m), 679 (s), 447 (s) cm$^{-1}$. $^{13}$C CP MAS NMR: $\delta$ = 124.7 (C-3), 128.0 (C-5), 139.8 (C-2), 146.6 (C-4), 150.9 (C-6), 170.1 (COOH) ppm. $^{27}$Al MAS NMR: $\delta$ = 9.97 ppm.

**HTC–pydc–Mo (8):** Elemental analysis found: C 5.19, H 3.14, Mo 6.33, N 0.96. IR (KBr): $\tilde{\nu}$ = 3480 (m), 2180 (m), 2180 (w), 2037 (vw), 1955 (vw), 1892 (vw), 1680 (vs), 1617 (vs), 1442 (m), 1395 (s), 1294 (m), 1198 (w), 1084 (m) cm$^{-1}$. $^{13}$C CP MAS NMR: $\delta$ = 127.1 (C-3, C-5), 143.9 (C-4), 147.2 (C-2, C-6), 164.66 (COOH) ppm. $^{27}$Al MAS NMR: $\delta$ = 9.67 ppm.

**Supporting Information** (see footnote on the first page of this article): FTIR spectra of $[Mo(CO)_3I_2(NCCH_3)_2]$ (**1**), $[Mo(CO)_3I_2(pycH)_2]$ (**2**), complex **2** in MeOH solution and the difference spectrum of complex **2** and MeOH; color version of Figure 3.

## Acknowledgments

C. D. N. and P. D. V. thank Fundação para a Ciência e a Tecnologia (FCT) for research grants (SFRH/BPD/14512/2003) and (SFRH/BPD/14903/2004), respectively. The authors are grateful to FCT and FEDER for grant POCTI/QUI/44654/2002.

[1] M. H. Valkenberg, W. F. Hölderich, *Catal. Rev.* **2002**, *44*, 321–374.
[2] A. Taguchi, F. Schüth, *Microporous Mesoporous Mater.* **2005**, *77*, 1–45.
[3] a) S. P. Newman, W. Jones, *New J. Chem.* **1998**, *22*, 105–115 and the references cited therein; b) S. P. Newman, S. J. Williams, P. V. Coveney, W. Jones, *J. Phys. Chem. B* **1998**, *102*, 6710–6719 and the references cited therein.
[4] A. I. Khan, D. O'Hare, *J. Mater. Chem.* **2002**, *12*, 3191–3198.
[5] J.-C. Dupin, H. Martinez, C. Guimon, E. Dumitriu, I. Fechete, *Applied Clay Sci.* **2004**, *27*, 95–106.
[6] S. Gago, M. Pillinger, A. A. Valente, T. M. Santos, J. Rocha, I. S. Gonçalves, *Inorg. Chem.* **2004**, *43*, 5422–5431.
[7] S. Gago, M. Pillinger, T. M. Santos, J. Rocha, I. S. Gonçalves, *Eur. J. Inorg. Chem.* **2004**, 1389–1395.
[8] G. Negrón, N. Guerrra, L. Lomas, R. Gaviño, J. Cárdenas, *ARKIVOC* **2003**, *xi*, 179–184.
[9] J. Gimenez, C. D. Nunes, P. D. Vaz, A. A. Valente, P. Ferreira, M. J. Calhorda, *J. Mol. Catal. A: Chem.* **2006**, *256*, 90–98.
[10] P. K. Baker, S. G. Fraser, E. M. Keys, *J. Organomet. Chem.* **1986**, *309*, 319–321.
[11] C. D. Nunes, M. Pillinger, A. A. Valente, J. Rocha, A. D. Lopes, I. S. Gonçalves, *Eur. J. Inorg. Chem.* **2003**, 3870–3877 and references cited therein.
[12] C. D. Nunes, M. Pillinger, A. A. Valente, A. D. Lopes, I. S. Gonçalves, *Inorg. Chem. Commun.* **2003**, *6*, 1228–1233.
[13] P. K. Baker, M. B. Hursthouse, A. I. Karaulov, A. J. Lavery, K. M. A. Malik, D. J. Muldoon, A. Shawcross, *J. Chem. Soc., Dalton Trans.* **1994**, 3493–3498.

 © 2007 Wiley-VCH Verlag GmbH & Co. KGaA, Weinheim 

[14] S. Carlino, *Solid State Ionics* **1997**, 73–84.
[15] J.-C. Dupin, H. Martinez, C. Guimon, E. Dumitriu, I. Fechete, *Applied Clay Sci.* **2004**, *27*, 95–106.
[16] P. Beaudot, M. E. De Roy, J. P. Basse, *Chem. Mater.* **2004**, *16*, 935–945.
[17] S. Gago, M. Pillinger, R. A. Sá Ferreira, L. D. Carlos, T. M. Santos, I. S. Gonçalves, *Chem. Mater.* **2005**, *17*, 5803–5809.
[18] R. Ma, Z. Liu, L. Li, N. Iyi, T. Sasaki, *J. Mater. Chem.* **2006**, *16*, 3809–3813.
[19] J. Rocha, M. del Marco, V. Rives, M. A. Ulibarri, *J. Mater. Chem.* **1999**, *9*, 2499–2503.
[20] S. Ray, G. Galgali, A. Lele, S. Sivaram, *J. Polym. Sci., Part A: Polym. Chem.* **2004**, *43*, 304–318.
[21] S. Bruzaud, Y. Grohens, S. Ilinca, J.-F. Carpentier, *Macromol. Mater. Eng.* **2005**, *290*, 1106–1114.
[22] D. Jamanek, A. Woyna, W. Skupiński, *Appl. Organomet. Chem.* **2002**, *16*, 575–579.
[23] F. Bao, R. Ma, X. Lü, G. Gui, Q. Wu, *Appl. Organomet. Chem.* **2006**, *20*, 32–38.
[24] H. Rahiala, I. Beurroies, T. Eklund, K. Hakala, R. Gougeon, P. Trens, J. B. Rosenholm, *J. Catal.* **1999**, *188*, 14–23.
[25] M. Al-Jahdali, P. K. Baker, A. J. Lavery, M. Meehan, D. J. Muldoon, *J. Mol. Catal. A* **2000**, *159*, 51–62.
[26] P. K. Baker, M. A. Beckett, B. M. Stiefvater-Thomas, *J. Mol. Catal. A* **2003**, *193*, 77–81.
[27] T. Szymanska-Buzar, T. Glowiak, I. Czelusniak, *J. Organomet. Chem.* **2001**, *640*, 72–78.
[28] T. Szymanska-Buzar, T. Glowiak, I. Czelusniak, *Polyhedron* **2002**, *21*, 2505–2513.
[29] I. Czelusniak, T. Szymanska-Buzar, *Appl. Catal., A* **2004**, *277*, 173–182.

Received: January 24, 2007
Published Online: May 9, 2007

 © 2007 Wiley-VCH Verlag GmbH & Co. KGaA, Weinheim 

DOI: 10.1002/ejic.200700112

# Gold(I) and Palladium(II) Thiolato Complexes Containing Water-Soluble Phosphane Ligands

Elena Vergara,[a] Susana Miranda,[b] Fabian Mohr,[c] Elena Cerrada,[a] Edward R. T. Tiekink,[d] Pilar Romero,[a] Aránzazu Mendía,*[b] and Mariano Laguna*[a]

**Keywords:** Phosphane ligands / Palladium / Gold / Thiolato complexes

Water-soluble gold(I) and palladium(II) complexes containing different thiolates and the phosphanes 1,3,5-triaza-7-phosphaadamantane (PTA) and 3,7-diacetyl-1,3,7-triaza-5-phosphabicyclo[3.3.1]nonane (DAPTA) are described. The complexes were characterised by spectroscopic techniques including 2D NMR experiments, and the complexes $[Au(S_2CNEt_2)(PTA)]$, *trans*-$[Pd(SC_5H_4N)_2(PTA)_2]$ and *trans*-$[Pd(SC_5H_4N)_2(DAPTA)_2]$ were additionally characterised by X-ray crystallography; the latter complex is one of the few structurally characterised DAPTA complexes.
(© Wiley-VCH Verlag GmbH & Co. KGaA, 69451 Weinheim, Germany, 2007)

## Introduction

Water as a solvent for chemical transformations is experiencing a renaissance which has mainly been driven by environmental and, to some extent, economical concerns. The use of water as a solvent, however, requires the development of new catalysts or reagents that are compatible (stable) and soluble in water.[1,2] Gold thiolato complexes dispersed in different solvents, including natural resins, have been used as a gold source for decorating ceramic tiles and glasses after heating.[3] Because these dispersions are liquid, they are commonly referred to as "liquid gold" and, when other late transition metals are involved, the name "liquid precious metal" is used. To avoid the use of toxic and volatile solvents, there is an increasing interest in the development of water-soluble "liquid metals" and thus for water-soluble thiolato complexes.[4] The main strategy employed in this area is either the use of thiolato ligands with solubilising groups or the replacement of traditional phosphane ligands with other water-soluble analogues such as the mono-, di- and tri-sulfonated triphenylphosphanes.[4] Herein, we describe the use of the water-soluble phosphanes 1,3,5-triaza-7-phosphaadamantane (PTA) and 3,7-diacetyl-1,3,7-triaza-5-phosphabicyclo[3.3.1]nonane (DAPTA). PTA was first prepared about thirty years ago[5] and some gold complexes were studied by Fackler Jr.[6–9] and some of us.[10–13] A review and recent reports of new coordination modes of this ligand illustrate the rich and varied coordination chemistry displayed by this compound.[13–16] The diacetate derivative of PTA known as DAPTA has only been reported recently[17] and to date only a very limited number of complexes with this ligand have been described.[11,17]

In this paper we report the synthesis and structures of some water-soluble gold(I) and palladium(II) complexes containing PTA and DAPTA with various thiolato ligands.

## Results and Discussion

### Gold Complexes

The thiolato gold(I) complexes $[Au(SR)(PR'_3)]$ (SR = various thiolato derivatives as shown in Scheme 1; $PR'_3$ = PTA, DAPTA) were easily prepared in good yields by treating the complexes $[AuCl(PR'_3)]$ with the thiol derivatives in the presence of base (Scheme 1). The complexes [AuCl(PTA)][6] and [AuCl(DAPTA)] were prepared by replacement of tetrahydrothiophene (tht) from [AuCl(tht)] with the appropriate phosphane.

The thiolato complexes were characterised by spectroscopic techniques and in the case of $[Au(S_2CNEt_2)(PTA)]$ by X-ray diffraction. All of the $[Au(SR)(PR'_3)]$ complexes reported here show singlet resonances in their $^{31}P\{^1H\}$ NMR spectra displaced to a lower field relative to those of the free phosphanes.[5,17] The $^1H$ NMR spectra of the phosphane resonances merit some comments. The N$CH_2$P resonances appear as doublets in free PTA and as singlets in the thiolato derivatives, whilst the N$CH_2$N resonances appear as singlets in free PTA and as an AB system in the thiolato complexes. This behaviour has been observed in

[a] Departamento de Química Inorgánica, Instituto de Ciencia de Materiales de Aragón, Universidad de Zaragoza – C.S.I.C, 50009 Zaragoza, Spain
[b] Departamento de Quimica, Facultad de Ciencias, Universidad de Burgos, 09001 Burgos, Spain
[c] Fachbereich C – Anorganische Chemie, Bergische Universität Wuppertal, Wuppertal, 42119, Germany
[d] Department of Chemistry, University of Texas at San Antonio, One UTSA Circle, Texas 78249-0698, USA

 © 2007 Wiley-VCH Verlag GmbH & Co. KGaA, Weinheim 

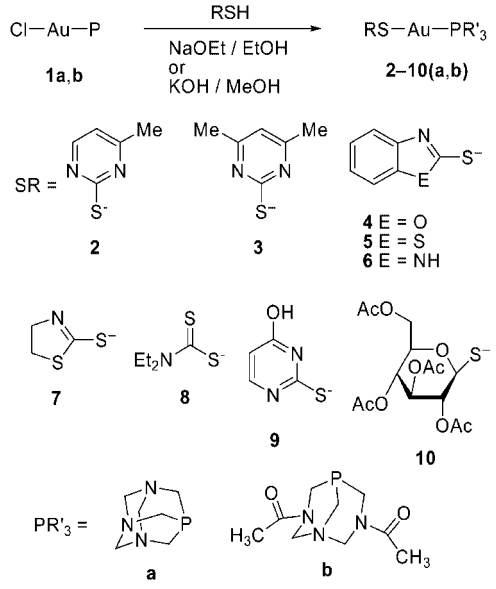


Scheme 1.

other PTA gold derivatives and was confirmed by 2D NMR spectroscopic techniques in the palladium complexes.[18] The $^1$H NMR spectra of the DAPTA thiolato derivatives are much more complicated and show a similar pattern to that of the free ligand (Figure 1a). The assignment of the originally reported $^1$H NMR spectrum of DAPTA[17] is incorrect so we provide a corrected assignment for all the signals on the basis of various 2D NMR methods here. The N*CH*$_2$P signals of DAPTA appear as five resonances, four of which integrate as one proton and the other as two protons, which is due to the nonsymmetry of the compound. Further assignment of these signals was conducted by $^1$H-, $^{13}$C- and $^1$H–$^{31}$P{$^1$H} HSQC experiments. The latter, in addition to the $^1$H{$^{31}$P} NMR spectrum (Figure 1b), show that all these protons are coupled with the phosphorus atom, although some of them with very small coupling constants.

The $^1$H–$^{13}$C HSQC spectrum permits the assignment of the resonances of each of the diastereotopic methylene protons, one pair at $\delta$ = 5.25 (dd) and 3.20 (dt) ppm, the other at $\delta$ = 4.28 (d) and 3.79 (ddd) ppm. The third methylene N*CH*$_2$P is not diastereotopic, hence it appears as a doublet at $\delta$ = 3.51 ppm. In addition, $^1$H–$^1$H homodecoupling experiments point to some coupling between protons of different methylene groups. The two N*CH*$_2$N methylene groups are diastereotopic and appear at $\delta$ = 5.79(d) and 3.95(d) ppm and the other at $\delta$ =4.93(d) and 4.53(d) ppm. The mass spectra of the gold(I) thiolato complexes show in all cases the parent peak, which confirms the proposed stoichiometry. In some cases higher mass adducts formed by the addition of Au(PTA) or Au(DAPTA) fragments can be observed, which is typical behaviour in mass spectra of thiolate gold(I) complexes.[19,20]

The water solubility of complexes **2** and **7** are quite high at 115 g/L for **2a**, 125 g/L for **2b**, 42 g/L for **7a** and 51 g/L for **7b**. The rest of complexes that are insoluble in water

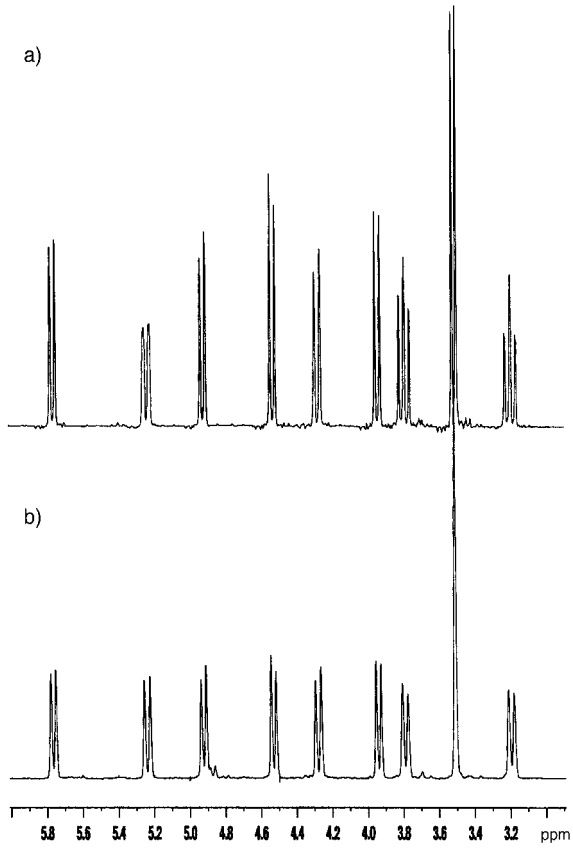


Figure 1. $^1$H NMR spectrum showing the $CH_2$ region of DAPTA; a) P coupled spectrum, b) P decoupled spectrum.

tend to be quite soluble in MeOH or MeOH/$H_2O$ mixtures. The solid gold(I) thiolato complexes are stable at room temperature but start to decompose around 200 °C and ultimately give metallic gold at ca. 750–800 °C as shown by thermal analysis experiments. Attempts to grow single crystals of any of the water-soluble complexes proved unsuccessful, in part owing to the decomposition of the solutions that occurred over a period of 1–2 weeks. However, we were successful in obtaining X-ray quality crystals of the *N*,*N*-diethyldithiocarbamate complex [Au($S_2CNEt_2$)(PTA)], the molecular structure of which is shown in Figure 2.

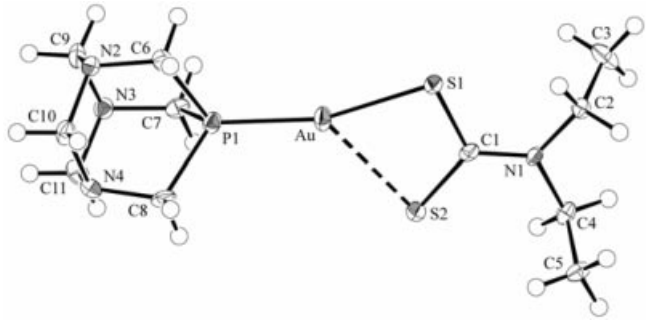


Figure 2. Molecular structure of [Au($S_2CNEt_2$)(PTA)]. Ellipsoids show 50% probability levels. Bond lengths [Å] and angles [°]: Au–P1 2.2310(14), Au–S1 2.3840(13), Au···S2 2.7806(15); S1–Au–P1 163.54(5), S2···Au–P1 126.96(5).

 © 2007 Wiley-VCH Verlag GmbH & Co. KGaA, Weinheim 

To a first approximation, the molecule of [Au($S_2CNEt_2$)(PTA)] comprises a linear gold atom geometry defined by the S1 and P1 atoms. The relatively close approach of the S2 atom [Au–S2 2.7806(15) Å] is responsible for the significant distortion away from the ideal linear geometry, the angle P1–Au–S1 measures 163.54(5)°. There are several related monophosphane gold(I) dithiocarbamate structures available in the literature[21] and these, along with related xanthate ($S_2COR$)[22] and dithiocarboxylate ($S_2CR$)[23] structures, feature significantly more linear geometries at the gold atom as the S2 atom forms Au···S2 distances greater than 3.0 Å in these structure. Thus, the structure of [Au($S_2CNEt_2$)(PTA)] is exceptional. For the dithiocarbamate structures,[21] the Au–S1, Au···S2 and Au–P1 distances fall in the ranges 2.3256(16)–2.3388(1), 3.0150(2)–3.1068(11) and 2.2430(14)–2.2600(4) Å, respectively. It is evident that the Au–P1 distance is significantly shorter in [Au($S_2CNEt_2$)(PTA)], which is consistent with the strong σ bonding ability of this ligand. This interaction pushes the S1 atom away from the gold centre and allows close approach of the S2 atom.

### Palladium Complexes

The chlorido palladium(II) complexes *cis*-[$PdCl_2$(PTA)$_2$] (**11a**) and *cis*-[$PdCl_2$(DAPTA)$_2$] (**11b**) were easily prepared by reacting $PdCl_2$ directly with stoichiometric quantities of the corresponding phosphanes. The *cis* geometry can be deduced from the presence of two ν(Pd–Cl) and ν(Pd–P) bands in the far-IR spectrum. This is consistent with the *cis* geometry of *cis*-[$PdCl_2$(PTA)$_2$], which was structurally characterised.[24,25] Thiolato palladium(II) complexes are easily prepared from the above dichlorido precursor complexes by reaction with the thiol derivatives in the presence of base. This synthetic approach was previously used by us[26] in the preparation of new palladium(II) and platinum(II) complexes showing novel thiolate coordination modes. The palladium thiolato complexes [Pd(SR)$_2$(PR′$_3$)$_2$] (SR = 2-$SC_5H_4N$, 2-$SC_4H_3N_2$ and PR′$_3$ = PTA, DAPTA) were prepared in good yields and were characterised by various spectroscopic techniques as well as X-ray crystallography (Scheme 2). The [Pd(SR)$_2$(PR′$_3$)$_2$] complexes show only one ν(Pd–P) and ν(Pd–S) band in the far-IR spectrum, which suggests a *trans* configuration about the palladium. This was indeed confirmed by an X-ray crystallographic study of *trans*-[Pd(2-$SC_5H_4N$)$_2$(PTA)$_2$] (**12a**) and *trans*-[Pd(2-$SC_5H_4N$)$_2$(DAPTA)$_2$] (**12b**). Molecular structures of these two complexes are shown in Figures 3 and 4, respectively.

The $^{31}P\{^1H\}$ NMR singlet resonances of the complexes are shifted to a higher field than those of the chlorido derivatives; furthermore, there is little difference in the chemical shift between the 2-pyridine and 2-pyrimidine derivatives. Like in the above-mentioned gold(I) complexes, the $^1H$ NMR spectra show singlet resonances due to equivalent $NCH_2P$ protons of the PTA ligand as well as the AB system assigned to the $NCH_2N$ protons. The DAPTA complexes show geminal H–H coupling for the $NCH_2N$ and $NCH_2P$ protons and, in addition, the P–H and H–H coupling patterns are identical to those observed in the free ligand. In addition, the mass spectra LSIMS+ agree with the mononuclear structures of the four thionate derivatives. No peaks due to any aggregation of metal–phosphane fragments comparable to gold(I) derivatives **1**–**10** are observed.

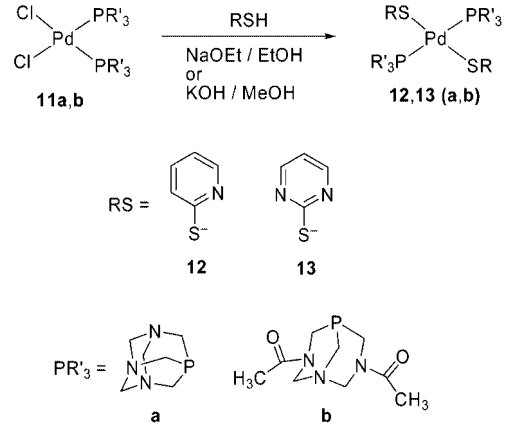


Scheme 2.

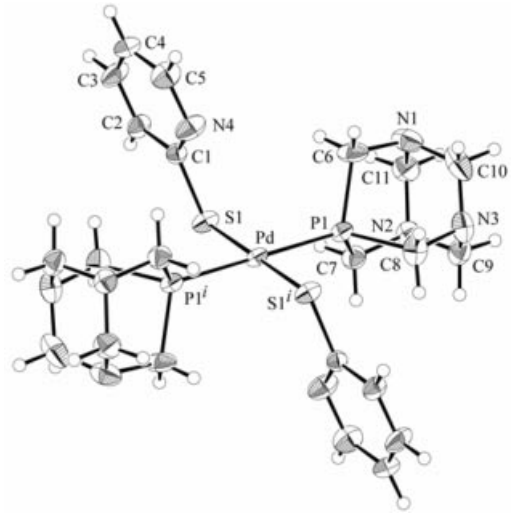


Figure 3. Molecular structure of *trans*-[Pd($SC_5H_4N$)$_2$(PTA)$_2$]. Ellipsoids show 35% probability levels. Primed atom related by the symmetry operation *i*: 1 – *x*, 1 – *y*, 1 – *z*. Selected bond lengths [Å] and angles [°]: Pd–S1 2.3411(13), Pd–P1 2.2832(13), S1–C1 1.745(5); S1–Pd–P1 87.44(5).

Compounds **12**–**13** did not show any sign of decomposition even after several months at room temperature. They are insoluble in solvents such as methanol, ethanol, acetone and hexane, and they are partially soluble in $CH_2Cl_2$, $CHCl_3$, DMSO and $H_2O$. The solubility in $H_2O$ is similar for all four complexes and is about 10 g/L. It is known that incorporation of the highly water-soluble DAPTA ligand into the coordination sphere of group 10 metal centres leads to water insoluble compounds.[17] We show here that the combination of thiolate and triazaphosphane ligands is a good ligand combination for the synthesis of water-soluble compounds of this group with attractive properties for new applications.

 © 2007 Wiley-VCH Verlag GmbH & Co. KGaA, Weinheim 

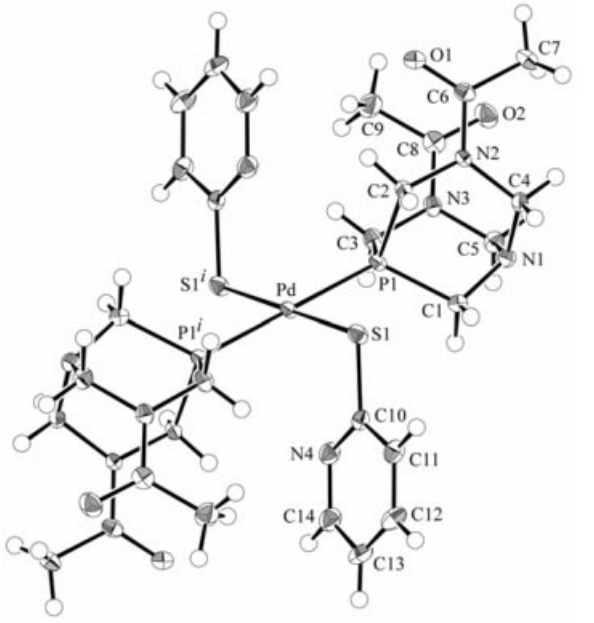


Figure 4. Molecular structure of *trans*-[Pd($SC_5H_4N$)$_2$(DAPTA)$_2$]. Ellipsoids show 50% probability levels. Primed atom related by the symmetry operation *i*: 1 – *x*, 1 – *y*, 1 – *z*. Selected bond lengths [Å] and angles [°]: Pd–S1 2.3421(4), Pd–P1 2.2962(4), S1–C1 1.7536(18); S1–Pd–P1 87.092(16).

The palladium atom in *trans*-[Pd($SC_5H_4N$)$_2$(PTA)$_2$] (**12a**) lies on a crystallographic centre of inversion and lies within a *trans* $N_2S_2$ donor set that defines a square-planar geometry. The structure of *trans*-[Pd($SC_5H_4N$)$_2$(DAPTA)$_2$] (**12b**) is virtually identical to that just described, which allows the differences in chemistry, and shows virtually the same geometric parameters about the palladium save for the Pd–P1 bond length that is longer than that in *trans*-[Pd($SC_5H_4N$)$_2$(PTA)$_2$]. In each case, the pyridine nitrogen atom is directed towards the central palladium atom but the Pd···N4 separations of 3.307(5) and 3.1564(16) Å are not considered to represent significant bonding interactions. Arguably, the most closely related complex in the literature available for comparison is that of *trans*-[Pd($SC_5H_5$)$_2${P(H)$Cy_2$}$_2$][27] for which two independent centrosymmetric molecules comprise the asymmetric unit. Here, the two Pd–S bond lengths are 2.3366(2) and 2.3393(17) Å, with Pd–P of 2.3056(18) and 2.3121(18) Å. These distances are shorter and longer, respectively, than those found in each of *trans*-[Pd($SC_5H_4N$)$_2$(PTA)$_2$] and *trans*-[Pd($SC_5H_4N$)$_2$(DAPTA)$_2$]. There are no analogous *trans*-$PdN_2S_2$ structures containing either PTA or DAPTA in the crystallographic literature. However, a protonated form of PTA is found in the crystal structure of *trans*-[Pd($NCS$)$_2$($PTAH$)$_2$]($NCS$)$_2$[28] with Pd–S and Pd–P distances of 2.3509(8) and 2.2940(8) Å, respectively, in the centrosymmetric molecule. Both of these distances are longer than the analogous bonds in *trans*-[Pd($SC_5H_4N$)$_2$(PTA)$_2$]. In the crystal structure of *trans*-[Pd($SC_5H_4N$)$_2$(PTA)$_2$], molecules associate through C–H···S interactions to form a chain motif along the *a* direction. From symmetry, each molecule forms two donor and two acceptor C–H···S interactions with geometric parameters: C7–H7a···S1$^{ii}$ = 2.74 Å, C7···S1$^{ii}$ = 3.663(5) Å and angle at H7a of 160°; *ii*: –*x*, 1 – *y*, 1 – *z*. By contrast, a three-dimensional architecture is found in the crystal structure of [Pd($SC_5H_4N$)$_2$(DAPTA)$_2$] owing to the presence of C–H···O interactions. The O1 atom is bifurcated and forms interactions with the H1b and H5a atoms. The geometric parameters defining these interactions are C1–H1b···O1$^{ii}$ = 2.47 Å, C1···O1$^{ii}$ = 3.357(2) Å and angle at H1b of 152° for *ii*: *x*, 3/2 – *y*, –1/2 + *z*; the parameters for the C5–H5a···O1$^{ii}$ interaction are 2.48 Å, 3.359(2) Å and 151°, respectively.

As commented for the gold complexes, the palladium derivatives were analysed by thermogravimetric analysis showing decomposition to metal (gold or palladium) around 750 °C. This behaviour permits their use as "liquid metal" when deposited on tiles and heated around 800 °C. The water solubility avoids the use of toxic organic solvents for this purpose. As an alternative to thermally induced decomposition, the use of a YAG laser beam focused on the complexes also leads to metal deposition as recently reported by some of us and others.[29,30] The development and optimisation of better metal deposition conditions are in progress.

## Conclusions

We report here water-soluble thiolato complexes of gold(I) and palladium(II) that could be used for the preparation of "liquid metals" for metallic deposition. The structures of some derivatives were determined by X-ray crystallography and show a pseudolinear coordination of gold(I) in [Au($S_2CNEt_2$)(PTA)] and *trans* square-planar coordination of palladium in *trans*-[Pd($SC_5H_4N$)$_2$(PTA)$_2$] and *trans*-[Pd($SC_5H_4N$)$_2$(DAPTA)$_2$]; the latter complex is one of the few structurally characterised examples of a compound containing DAPTA.

## Experimental Section

**General:** NMR spectra were recorded with 400 MHz Varian Inova or 400 or 500 MHz Bruker Avance spectrometers. Chemical shifts are quoted relative to external TMS ($^1$H, $^{13}$C) or 85% $H_3PO_4$ ($^{31}$P). FAB mass spectra were measured with a Micromass Autospec spectrometer in positive ion mode by using NBA as matrix. IR spectra were recorded as KBr or polyethylene disks with Nicolet Impact 410 or JASCO FTIR (far-IR) spectrometers. Elemental analyses were obtained in-house by using a LECO CHNS-932 microanalyser. The phosphanes PTA,[31] DAPTA[17] and [AuCl(tht)][32] as well as [AuCl(PTA)][6] were prepared according to published methods.

**DAPTA:** $^1$H NMR (500 MHz, $CDCl_3$, 25 °C): $\delta$ = 2.03 (s, 3 H, CO*Me*), 2.02 (s, 3 H, CO*Me*), 3.20 (dt, $J_{H,H} \approx J_{P,H}$ = 15.2 Hz, $^4J_{H,H}$ = 2.5 Hz, 1 H, NC$H_2$P), 3.51 (d, $J_{P,H}$ = 11.4 Hz, 2 H, NC$H_2$P), 3.79 (ddd, $^2J_{H,H}$ = 15.4 Hz, $J_{P,H}$ = 14.7 Hz, $^4J_{H,H}$ = 2.8 Hz 1 H, NC$H_2$P), 3.95 (d, $J_{H,H}$ = 14.0 Hz, 1 H, NC$H_2$N), 4.28 (d, $J_{H,H}$ = 15.4 Hz, 1 H, NC$H_2$P), 4.53 (d, $J_{H,H}$ = 13.8 Hz, 1 H, NC$H_2$N), 4.93 (d, $J_{H,H}$ = 13.8 Hz, 1 H, NC$H_2$N), 5.25 (dd, $J_{H,H}$ = 15.2 Hz, $J_{P-H}$ = 2.0 Hz, 1 H, NC$H_2$P), 5.79 (d, $J_{H,H}$ = 14.0 Hz, 1 H,

 © 2007 Wiley-VCH Verlag GmbH & Co. KGaA, Weinheim 

NC$H_2$N) ppm. $^{31}P\{^1H\}$ NMR (202 MHz, $CDCl_3$, 25 °C): $\delta$ = –81.06 ppm. MS EI: *m/z* = 143 [M – 2$CH_3CO$]$^+$, 186 [M – $CH_3CO$]$^+$, 229 [M]$^+$, 230 [M + H]$^+$.

**Preparation of [AuCl(DAPTA)] (1b):** To a solution of [AuCl(tht)] (0.500 g, 1.56 mmol) in $CH_2Cl_2$ (ca. 50 mL) was added DAPTA (0.357 g, 1.56 mmol). After stirring the mixture for ca. 2 h, the solid products were isolated by filtration, washed with $CH_2Cl_2$ and $Et_2O$ and dried in vacuo. Yield: 99%, colourless solid. $^1H$ NMR (400 MHz, [D$_6$]acetone, 25 °C): $\delta$ = 2.05 (s, 3 H, CO*Me*), 2.08 (s, 3 H, CO*Me*), 3.84 (d, *J* = 15.7 Hz, 1 H, NC$H_2$P), 4.12 (s, 2 H, NC$H_2$P), 4.24 (d, *J* = 14.1 Hz, 1 H, NC$H_2$N), 4.42 (dt, *J* = 15.7, 2.6 Hz, 1 H, NC$H_2$P), 4.79 (d, *J* = 14.2 Hz, 1 H, NC$H_2$N), 4.97 (dd, *J* = 15.2, 7.9 Hz, 1 H, NC$H_2$P), 5.05 (d, *J* = 14.2 Hz, 1 H, NC$H_2$N), 5.54 (dd, *J* = 15.6, 9.5 Hz, 1 H, NC$H_2$P), 5.63 (d, *J* = 14.0 Hz, 1 H, NC$H_2$N) ppm. $^{31}P\{^1H\}$ NMR (162 MHz, [D$_6$]acetone, 25 °C): $\delta$ = –25.65 ppm. FAB MS: *m/z* = 426 [M – Cl]$^+$, 462 [M]$^+$, 655 [M – Cl + DAPTA]$^+$, 887 [M + AuDAPTA]$^+$. $C_9H_{16}AuClN_3O_2P$ (461.6): calcd. C 23.42, H 3.49, N 9.10; found C 24.01, H 3.31, N 9.21.

**Preparation of [Au(SR)(PR′$_3$)] Complexes:** To a solution of KOH (0.022 g, 0.385 mmol) in MeOH (ca. 10 mL) containing the thiol compound (0.308 mmol) was added [AuCl(PR′$_3$)] (PR′$_3$ = PTA, DAPTA) (0.100 g, 0.257 mmol). After stirring the mixture for ca. 20 h, the solid products were isolated by filtration, washed with $H_2O$, MeOH and $Et_2O$ and dried in vacuo. In some cases, the [Au(SR)(P)] complexes were soluble in MeOH so a different work up procedure was used. The solution was evaporated to dryness in vacuo, and the residue was extracted with $CH_2Cl_2$ (3 × 10 mL). The combined extracts were passed through Celite and concentrated in vacuo to ca. 5 mL. Addition of pentane or $Et_2O$ precipitated the products, which were isolated by filtration and dried in air.

**[Au(SMepyrim)(PTA)] (2a):** Yield: 49%, colourless solid. $^1H$ NMR (400 MHz, [D$_6$]DMSO, 25 °C): $\delta$ = 2.26 (s, 3 H, Me), 4.36 (s, 6 H, C$H_2$P), 4.40 (d, *J* = 13.1 Hz, 3 H, C$H_2$N), 4.50 (d, *J* = 13.1 Hz, 3 H, C$H_2$N), 6.85 (d, *J* = 5.3 Hz, 1 H, pyrim-H$^5$), 8.18 (d, *J* = 5.1 Hz, 1 H, pyrim-H$^6$) ppm. $^{31}P\{^1H\}$ NMR (162 MHz, [D$_6$]DMSO, 25 °C): $\delta$ = –48.29 ppm. FAB MS: *m/z* = 480 [M]$^+$, 833 [M + AuPTA]$^+$. $C_{11}H_{17}AuN_5PS$ (479.3): calcd. C 27.57, H 3.58, N 14.61; found C 27.50, H 3.75, N 14.30.

**[Au(SMepyrim)(DAPTA)] (2b):** Yield: 63%, colourless solid. $^1H$ NMR (400 MHz, $CDCl_3$, 25 °C): $\delta$ = 2.08, 2.09 (s, 3 H, DAPTA-Me), 2.39 (s, 3 H, Me), 3.75 (dd, *J* = 16.0, 6.3 Hz, 1 H, NC$H_2$P), 4.03 (s, 2 H, NC$H_2$P), 4.04 (d, *J* = 15.2 Hz, 1 H, NC$H_2$N), 4.35 (m, 1 H, NC$H_2$P), 4.64 (d, *J* = 14.1 Hz, 1 H, NC$H_2$N), 4.80 (m, 1 H, NC$H_2$P), 4.90 (d, *J* = 13.9 Hz, 1 H, NC$H_2$N), 5.64 (dd, *J* = 15.2, 7.4 Hz, 1 H, NC$H_2$P). 5.74 (d, *J* = 14.2 Hz, 1 H, NC$H_2$N), 6.75 (d, *J* = 5.3 Hz, 1 H, pyrim-H$^5$), 8.19 (d, *J* = 5.3 Hz, 1 H, pyrim-H$^6$) ppm. $^{31}P\{^1H\}$ NMR (162 MHz, $CDCl_3$, 25 °C): $\delta$ = –24.88 ppm. FAB MS: *m/z* = 552 [M]$^+$, 978 [M + AuDAPTA]$^+$. $C_{15}H_{24}AuN_5O_2PS$ (551.4): calcd. C 30.50, H 3.84, N 12.70; found C 30.41, H 3.79, N 12.64.

**[Au(SMe$_2$pyrim)(PTA)] (3a):** Yield: 89%, colourless solid. $^1H$ NMR (400 MHz, $D_2O$, 25 °C): $\delta$ = 2.50 (s, 6 H, Me), 4.55 (s, 6 H, C$H_2$P), 4.93 (d, *J* = 12.9 Hz, 3 H, C$H_2$N), 4.86 (d, *J* = 12.9 Hz, 3 H, C$H_2$N), 7.12 (s, 1 H, pyrim-H$^5$) ppm. $^{31}P\{^1H\}$ NMR (162 MHz, $D_2O$, 25 °C): $\delta$ = –35.73 ppm. FAB MS: *m/z* = 494 [M]$^+$, 857 [M + AuPTA]$^+$. $C_{12}H_{19}AuN_5PS$ (493.3): calcd. C 29.22, H 3.88, N 14.20; found C 29.12, H 3.77, N 14.55.

**[Au(SMe$_2$pyrim)(DAPTA)] (3b):** Yield: 57%, colourless solid. $^1H$ NMR (400 MHz, $CDCl_3$, 25 °C): $\delta$ = 2.10 (s, 6 H, DAPTA-Me), 2.35 (s, 6 H, Me), 3.72 (d, *J* = 15.4 Hz, 1 H, NC$H_2$P), 4.01 (s, 2 H, NC$H_2$P), 4.08 (d, *J* = 13.7 Hz, 1 H, NC$H_2$N), 4.32 (d, *J* = 15.4 Hz, 1 H, NC$H_2$P), 4.66 (d, *J* = 14.7 Hz, 1 H, NC$H_2$N), 4.75 (dd, *J* = 15.0, 9.5 Hz, 1 H, NC$H_2$P), 4.93 (d, *J* = 15.1 Hz, 1 H, NC$H_2$N), 5.65 (dd, *J* = 16.3, 7.3 Hz, 1 H, NC$H_2$P), 5.77 (d, *J* = 14.2 Hz, 1 H, NC$H_2$N), 6.60 (s, 1 H, pyrim-H$^5$) ppm. $^{31}P\{^1H\}$ NMR (162 MHz, $CDCl_3$, 25 °C): $\delta$ = –24.82 ppm. FAB MS: *m/z* = 566 [M]$^+$, 991 [M + AuDAPTA]$^+$. $C_{16}H_{26}AuN_5O_2PS$ (565.4): calcd. C 31.87, H 4.10, N 12.39; found C 31.82, H 3.99, N 12.18.

**[Au(benzoxazole)(PTA)] (4a):** Yield: 85%, pale yellow solid. $^1H$ NMR (400 MHz, $CDCl_3$, 25 °C): $\delta$ = 4.37 (s, 6 H, C$H_2$P), 4.50 (d, *J* = 10.7 Hz, 3 H, C$H_2$N), 4.53 (d, *J* = 10.7 Hz, 3 H, C$H_2$N), 7.10 (m, 2 H, benzoxazole-H$^2$,H$^3$), 7.34 (d, *J* = 7.8 Hz, 1 H, benzoazole-H$^1$), 7.46 (d, *J* = 7.8 Hz, 1 H, benzoazole-H$^4$) ppm. $^{31}P\{^1H\}$ NMR (162 MHz, $CDCl_3$, 25 °C): $\delta$ = –52.00 ppm. FAB MS: *m/z* = 505 [M]$^+$, 858 [M + AuPTA]$^+$. $C_{13}H_{16}AuN_4OPS$ (504.3): calcd. C 30.96, H 3.20, N 11.11; found C 30.95, H 3.25, N 11.30.

**[Au(benzoxazole)(DAPTA)] (4b):** Yield: 60%, colourless solid. $^1H$ NMR (400 MHz, $CDCl_3$, 25 °C): $\delta$ = 2.05 (s, 6 H, DAPTA-Me), 3.61 (d, *J* = 16.2 Hz, 1 H, NC$H_2$P), 3.91 (s, 2 H, NC$H_2$P), 4.01 (d, *J* = 14.3 Hz, 1 H, NC$H_2$N), 4.19 (d, *J* = 15.6 Hz, 1 H, NC$H_2$P), 4.58 (d, *J* = 14.3 Hz, 1 H, NC$H_2$N) ppm. 4.71 (dd, *J* = 15.9, 10.1 Hz, 1 H, NC$H_2$P), 4.88 (d, *J* = 14.1 Hz, 1 H, NC$H_2$N), 5.65 (dd, *J* = 15.7, 7.9 Hz, 1 H, NC$H_2$P), 5.72 (d, *J* = 14.4 Hz, 1 H, NC$H_2$N), 7.08–7.17 (m, 2 H, benzoxazole-H$^2$,H$^3$), 7.27–7.34 (m, 2 H, benzoazole-H$^1$,H$^4$) ppm. $^{31}P\{^1H\}$ NMR (162 MHz, $CDCl_3$, 25 °C): $\delta$ = –26.28 ppm. FAB MS: *m/z* = 577 [M]$^+$, 1003 [M + AuDAPTA]$^+$. $C_{16}H_{21}AuN_4O_3PS$ (576.4): calcd. C 33.28, H 3.67, N 9.70; found C 33.36, H 3.53, N 10.06.

**[Au(Sbenzothiazole)(PTA)] (5a):** Yield: 74%, pale yellow solid. $^1H$ NMR (400 MHz, [D$_6$]DMSO, 25 °C): $\delta$ = 4.42 (s, 6 H, C$H_2$P), 4.52 (d, *J* = 12.6 Hz, 3 H, C$H_2$N), 4.40 (d, *J* = 12.6 Hz, 3 H, C$H_2$N), 7.21 (dt, *J* = 7.1, 1.3 Hz, 1 H, benzothiaz-H$^3$), 7.33 (dt, *J* = 7.1, 1.3 Hz, 1 H, benzothiaz-H$^2$), 7.62 (dd, *J* = 8.1, 0.8 Hz, 1 H, benzothiaz-H$^4$), 7.76 (dd, *J* = 8.1, 0.8 Hz, 1 H, benzothiaz-H$^1$) ppm. $^{31}P\{^1H\}$ NMR (162 MHz, [D$_6$]DMSO, 25 °C): $\delta$ = –48.23 ppm. FAB MS: *m/z* = 521 [M]$^+$, 874 [M + AuPTA]$^+$. $C_{13}H_{16}AuN_4PS_2$ (520.3): calcd. C 30.01, H 3.10, N 10.77; found C 29.99, H 2.90, N 11.11.

**[Au(Sbenzothiazole)(DAPTA)] (5b):** Yield: 68%, colourless solid. $^1H$ NMR (400 MHz, $CDCl_3$, 25 °C): $\delta$ = 2.07 (s, 6 H, DAPTA-Me), 3.75 (d, *J* = 16.0 Hz, 1 H, NC$H_2$P), 3.99 (s, 2 H, NC$H_2$P), 4.03 (d, *J* = 14.4 Hz, 1 H, NC$H_2$N), 4.27 (d, *J* = 15.6 Hz, 1 H, NC$H_2$P), 4.57 (d, *J* = 14.0 Hz, 1 H, NC$H_2$N), 4.77 (dd, *J* = 15.6, 9.7 Hz, 1 H, NC$H_2$P), 4.87 (d, *J* = 14.0 Hz, 1 H, NC$H_2$N), 5.66 (dd, *J* = 16.0, 7.4 Hz, 1 H, NC$H_2$P), 5.73 (d, *J* = 14.0 Hz, 1 H, NC$H_2$N), 7.20 (dt, *J* = 8.2, 0.8 Hz, 1 H, benzothiaz-H$^3$), 7.32 (dt, *J* = 7.4, 1.2 Hz, 1 H, benzothiaz-H$^2$), 7.58 (d, *J* = 7.4 Hz, 1 H, benzothiaz-H$^4$), 7.71 (d, *J* = 8.2 Hz, 1 H, benzothiaz-H$^1$) ppm. $^{31}P\{^1H\}$ NMR (162 MHz, $CDCl_3$, 25 °C): $\delta$ = –28.76 ppm. FAB MS: *m/z* = 593 [M]$^+$, 1018 [M + AuDAPTA]$^+$. $C_{16}H_{20}AuN_4O_2PS_2$ (592.4): calcd. C 32.44, H 3.40, N 9.46; found C 31.94, H 3.40, N 9.46.

**[Au(Sbenzimidazole)(PTA)] (6a):** Yield: 81%, colourless solid. $^1H$ NMR (400 MHz, [D$_6$]DMSO, 25 °C): $\delta$ = 4.28 (s, 6 H, C$H_2$P), 4.45 (d, *J* = 12.9 Hz, 3 H, C$H_2$N), 4.35 (d, *J* = 12.9 Hz, 3 H, C$H_2$N), 6.98 (dd, *J* = 5.8, 3.0 Hz, 2 H, benzimidaz), 7.24 (br. s, 2 H, benzimidaz), 12.22 (br. s, 1 H, N*H*) ppm. $^{31}P\{^1H\}$ NMR (162 MHz, [D$_6$]-DMSO, 25 °C): $\delta$ = –49.90 ppm. FAB MS: *m/z* = 405 [M]$^+$, 857 [M + AuPTA]$^+$. $C_{13}H_{17}AuN_5PS$ (503.3): calcd. C 31.02, H 3.40, N 13.91; found C 30.96, H 3.41, N 13.70.

**[Au(Sbenzimidazole)(DAPTA)] (6b):** Yield: 58%, colourless solid. $^1H$ NMR (400 MHz, $CDCl_3$, 25 °C): $\delta$ = 2.06 (s, 6 H, DAPTA-

 © 2007 Wiley-VCH Verlag GmbH & Co. KGaA, Weinheim 

Me), 3.60 (d, *J* = 16.1 Hz, 1 H, NC*H*$_2$P), 3.85 (s, 2 H, NC*H*$_2$P), 4.02 (d, *J* = 14.3 Hz, 1 H, NC*H*$_2$N), 4.18 (d, *J* = 15.6 Hz, 1 H, NC*H*$_2$P), 4.60 (d, *J* = 14.3 Hz, 1 H, NC*H*$_2$N), 4.70 (dd, *J* = 15.9, 10.1 Hz, 1 H, NC*H*$_2$P), 4.89 (d, *J* = 14.1 Hz, 1 H, NC*H*$_2$N), 5.64 (dd, *J* = 15.7, 7.9 Hz, 1 H, NC*H*$_2$P), 5.71 (d, *J* = 14.4 Hz, 1 H, NC*H*$_2$N), 7.08–7.17 (m, 2 H, benzoimidazole-H$^2$,H$^3$), 7.27–7.34 (m, 2 H, benzoazole-H$^1$,H$^4$) ppm. $^{31}P\{^1H\}$ NMR (162 MHz, $CDCl_3$, 25 °C): $\delta$ = –27.26 ppm. FAB MS: *m*/*z* = 576 $[M]^+$, 1002 $[M + AuDAPTA]^+$. $C_{16}H_{21}AuN_5O_2PS$ (575.4): calcd. C 33.40, H 3.68, N 12.17; found C 33.57, H 3.85, N 12.35.

**[Au(Sthiazoline)(PTA)] (7a):** Yield: 63%, pale yellow solid. $^1H$ NMR (400 MHz, $[D_6]$DMSO, 25 °C): $\delta$ = 3.30 (t, *J* = 8.1 Hz, 2 H, thiazoline), 4.09 (t, *J* = 8.1 Hz, 2 H, thiazoline), 4.36 (s, 6 H, C*H*$_2$P), 4.53 (d, *J* = 12.9 Hz, 3 H, C*H*$_2$N), 4.37 (d, *J* = 12.9 Hz, 3 H, C*H*$_2$N) ppm. $^{31}P\{^1H\}$ NMR (162 MHz, $[D_6]$DMSO, 25 °C): $\delta$ = –48.62 ppm. FAB MS: *m*/*z* = 473 $[M]^+$, 826 $[M + AuPTA]^+$. $C_9H_{16}AuN_4PS_2$ (472.3): calcd. C 22.89, H 3.41, N 11.86; found C 22.95, H 3.27, N 12.25.

**[Au(Sthiazoline)(DAPTA)] (7b):** Yield: 65%, colourless solid. $^1H$ NMR (400 MHz, $CDCl_3$, 25 °C): $\delta$ = 2.11, 2.12 (s, 3 H, DAPTA-Me), 3.43 (t, *J* = 7.8 Hz, 2 H, thiazoline), 3.72 (d, *J* = 14.4 Hz, 1 H, NC*H*$_2$P), 4.01 (s, 2 H, NC*H*$_2$P), 4.09 (d, *J* = 13.4 Hz, 1 H, NC*H*$_2$N), 4.20 (t, *J* = 8.1 Hz, 2 H, thiazoline), 4.30 (d, *J* = 16.2 Hz, 1 H, NC*H*$_2$P), 4.69 (d, *J* = 14.4 Hz, 1 H, NC*H*$_2$N), 4.76 (m, 1 H, NC*H*$_2$P), 4.94 (d, *J* = 14.1 Hz, 1 H, NC*H*$_2$N), 5.63 (dd, *J* = 15.2, 6.8 Hz, 1 H, NC*H*$_2$P), 5.77 (d, *J* = 14.1 Hz, 1 H, NC*H*$_2$N) ppm. $^{31}P\{^1H\}$ NMR (162 MHz, $CDCl_3$, 25 °C): $\delta$ = –32.74 ppm. FAB MS: *m*/*z* = 545 $[M]^+$, 970 $[M + AuDAPTA]^+$. $C_{12}H_{20}AuN_4O_2PS_2$ (544.4): calcd. C 26.48, H 3.70, N 10.29; found C 26.40, H 3.43, N 10.86.

**[Au(Et$_2$dtc)(PTA)] (8a):** Yield: 83%, pale yellow solid. $^1H$ NMR (400 MHz, $CDCl_3$, 25 °C): $\delta$ = 1.29 (t, *J* = 9.1 Hz, 6 H, C*H*$_3$CH$_2$), 3.84 (q, *J* = 7.1 Hz, 4 H, CH$_3$C*H*$_2$), 4.27 (s, 6 H, C*H*$_2$P), 4.56 (d, *J* = 13.4 Hz, 3 H, C*H*$_2$N), 4.48 (d, *J* = 13.4 Hz, 3 H, C*H*$_2$N) ppm. $^{31}P\{^1H\}$ NMR (162 MHz, $CDCl_3$, 25 °C): $\delta$ = –52.92 ppm. FAB MS: *m*/*z* = 502 $[M]^+$, 856 $[M + AuPTA]^+$. $C_{11}H_{22}AuN_4PS_2$ (502.4): calcd. C 26.30, H 4.41, N 11.15; found C 26.24, H 4.16, N 11.35. X-ray quality crystals were obtained by slow diffusion of hexane into a $CH_2Cl_2$ solution of the complex.

**[Au(Et$_2$dtc)(DAPTA)] (8b):** Yield: 52%, yellow solid. $^1H$ NMR (400 MHz, $CDCl_3$, 25 °C): $\delta$ = 1.30 (t, *J* = 9.1 Hz, 6 H, C*H*$_3$CH$_2$), 2.09 (s, 6 H, DAPTA-Me), 3.70 (d, *J* = 16.2 Hz, 1 H, NC*H*$_2$P), 3.85 (q, *J* = 7.1 Hz, 4 H, CH$_3$C*H*$_2$), 4.05 (s, 2 H, NC*H*$_2$P), 4.10 (d, *J* = 14.3 Hz, 1 H, NC*H*$_2$N), 4.32 (d, *J* = 15.6 Hz, 1 H, NC*H*$_2$P), 4.73 (d, *J* = 14.3 Hz, 1 H, NC*H*$_2$N), 4.80 (dd, *J* = 15.9, 10.1 Hz, 1 H, NC*H*$_2$P), 4.97 (d, *J* = 14.1 Hz, 1 H, NC*H*$_2$N), 5.60 (dd, *J* = 15.7, 7.9 Hz, 1 H, NC*H*$_2$P), 5.78 (d, *J* = 14.4 Hz, 1 H, NC*H*$_2$N) ppm. $^{31}P\{^1H\}$ NMR (162 MHz, $CDCl_3$, 25 °C): $\delta$ = –31.44 ppm. FAB MS: *m*/*z* = 574 $[M]^+$, 1000 $[M + AuDAPTA]^+$. $C_{14}H_{26}AuN_4O_2PS_2$ (574.5): calcd. C 29.27, H 4.56, N 9.75; found C 29.82, H 4.52, N 9.98.

**[Au(thiouracil)(PTA)] (9a):** Yield: 64%, colourless solid. $^1H$ NMR (400 MHz, $[D_6]$DMSO, 25 °C): $\delta$ = 4.36 (s, 6 H, C*H*$_2$P), 4.41 (d, *J* = 12.9 Hz, 3 H, C*H*$_2$N), 4.49 (d, *J* = 12.9 Hz, 3 H, C*H*$_2$N), 5.86 (d, *J* = 6.3 Hz, 1 H, thiouracil), 7.53 (d, *J* = 6.0 Hz, 1 H, thiouracil), 12.12 (br. s, 2 H, NH) ppm. $^{31}P\{^1H\}$ NMR (162 MHz, $[D_6]$DMSO, 25 °C): $\delta$ = –48.99 ppm. IR (KBr disk): $\tilde{\nu}$ = 3413 (N–H), 1688 (C=O) $cm^{-1}$. FAB MS: *m*/*z* = 482 $[M]^+$. $C_{10}H_{16}AuN_5OPS$ (482.3): calcd. C 24.90, H 3.34, N 14.52; found C 25.04, H 3.15, N 14.30.

**[Au(thiouracil)(DAPTA)] (9b):** Yield: 65%, colourless solid. $^1H$ NMR (400 MHz, $D_2O$, 25 °C): $\delta$ = 2.09 (s, 6 H, DAPTA-Me), 3.82 (d, *J* = 15.5 Hz, 1 H, NC*H*$_2$P), 4.01 (s, 2 H, NC*H*$_2$P), 4.25 (d, *J* = 14.1 Hz, 1 H, NC*H*$_2$N), 4.34 (d, *J* = 15.6 Hz, 1 H, NC*H*$_2$P), 5.10 (d, *J* = 14.2 Hz, 1 H, NC*H*$_2$N), 5.37 (dd, *J* = 15.9, 10.1 Hz, 1 H, NC*H*$_2$P), 5.49 (d, *J* = 14.1 Hz, 1 H, NC*H*$_2$N), 5.64 (dd, *J* = 15.7, 7.9 Hz, 1 H, NC*H*$_2$P), 5.71 (d, *J* = 14.4 Hz, 1 H, NC*H*$_2$N), 6.08 (d, *J* = 7.04 Hz, 1 H, thiouracil), 7.66 (d, *J* = 7.04 Hz, 1 H, thiouracil) ppm. $^{31}P\{^1H\}$ NMR (162 MHz, $D_2O$, 25 °C): $\delta$ = –29.81 ppm. FAB MS: *m*/*z* = 556 $[M]^+$, 982 $[M + AuDAPTA]^+$. $C_{16}H_{21}AuN_5O_2PS$ (555.3): calcd. C 28.12, H 3.81, N 12.61; found C 28.30, H 3.85, N 12.35.

**[Au(Sglucosetetraacetate)(PTA)] (10a):** A mixture of [AuCl(PTA)] (0.100 g, mmol), 1-thio-β-D-glucose tetraacetate (0.094 g, mmol) and $K_2CO_3$ (0.036 g, mmol) in EtOH (10 mL) and water (10 mL) was stirred for ca. 18 h. The solvents were removed under reduced pressure, and the solid residue was extracted with acetone and filtered through Celite. The addition of pentane to the filtrate afforded the colourless product, which was isolated by filtration and dried in air. Yield: 79%, colourless solid. $^1H$ NMR (400 MHz, $[D_6]$-acetone, 25 °C): $\delta$ = 1.83, 1.88, 1.92, 1.94 (s, 3 H, Me), 3.80 (ddd, *J* = 9.8, 4.5, 2.3 Hz, 1 H, H$^5$), 4.00 (dd, *J* = 12.4, 2.4 Hz, 1 H, C*H*$_2$), 4.13 (dd, *J* = 12.1, 4.5 Hz, 1 H, C*H*$_2$), 4.38 (s, 6 H, C*H*$_2$P), 4.46 (d, *J* = 12.9 Hz, 3 H, C*H*$_2$N), 4.50 (d, *J* = 12.9 Hz, 3 H, C*H*$_2$N), 4.75 (t, *J* = 9.3 Hz, 1 H, H$^2$), 4.93 (t, *J* = 9.9 Hz, 1 H, H$^4$), 4.97–5.05 (m, 2 H, H$^1$, H$^3$) ppm. $^{31}P\{^1H\}$ NMR (162 MHz, $[D_6]$-acetone, 25 °C): $\delta$ = –49.18 ppm. $C_{20}H_{31}AuN_3O_9PS$ (717.5): calcd. C 33.48, H 4.35, N 5.86; found C 33.34, H 4.25, N 6.09.

***cis*-[PdCl$_2$(DAPTA)$_2$] and *cis*-[PdCl$_2$(DAPTA)$_2$]:** To a suspension of $[PdCl_2]$ (0.099 g, 0.56 mmol) in $CH_2Cl_2$ (ca. 20 mL) was added PR′$_3$ = PTA (0.177 g, 1.13 mmol) or DAPTA (0.259 g, 1.13 mmol). After stirring the mixture for ca. 24 h, the yellow solid products were isolated by filtration, washed with $CH_2Cl_2$ and dried in vacuo.

***cis*-[PdCl$_2$(PTA)$_2$] (11a):** Yield: 96%, yellow solid. $^1H$ NMR (400 MHz, $D_2O$, 25 °C): $\delta$ = 4.58 (s, 12 H, NC*H*$_2$P), 4.63 (d, *J* = 12 Hz, 6 H, NC*H*$_2$N), 4.57 (d, *J* = 12 Hz, 6 H, NC*H*$_2$N) ppm. $^{31}P\{^1H\}$ NMR (162 MHz, $D_2O$, 25 °C): $\delta$ = –21.6 (s) ppm. IR (nujol): $\tilde{\nu}$ = 281, 271 (Pd–P), 307, 286 (Pd–Cl) $cm^{-1}$. FAB MS: *m*/*z* = 457 $[M – Cl]^+$. $C_{12}H_{24}Cl_2N_6P_2Pd$ (491.3): calcd. C 29.32, H 4.92, N 17.09; found C 29.73, H 4.76, N 16.85.

***cis*-[PdCl$_2$(DAPTA)$_2$] (11b):** Yield: 93%, yellow solid. $^1H$ NMR (400 MHz, $CDCl_3$, 25 °C): $\delta$ = 2.08 (s, 3 H, DAPTA-Me), 2.09 (s, 3 H, DAPTA-Me), 2.39 (s, 6 H, DAPTA-Me), 3.75 (dd, *J* = 16.0, 6.3 Hz, 2 H, NC*H*$_2$P), 4.03 (s, 4 H, NC*H*$_2$P), 4.04 (d, *J* = 15.2 Hz, 2 H, NC*H*$_2$N), 4.35 (m, 2 H, NC*H*$_2$P), 4.64 (d, *J* = 14.1 Hz, 2 H, NC*H*$_2$N), 4.80 (m, 2 H, NC*H*$_2$P), 4.90 (d, *J* = 13.9 Hz, 2 H, NC*H*$_2$N), 5.64 (dd, *J* = 15.2, 7.4 Hz, 2 H, NC*H*$_2$P), 5.74 (d, *J* = 14.2 Hz, 2 H, NC*H*$_2$N) ppm. $^{31}P\{^1H\}$ NMR (162 MHz, $CDCl_3$, 25 °C): $\delta$ = –34.20 ppm. IR (nujol): $\tilde{\nu}$ = 277, 245 (Pd–P), 366, 311 (Pd–Cl) $cm^{-1}$. FAB MS: *m*/*z* = 601 $[M – Cl]^+$, 637 $[M]^+$. $C_{18}H_{32}Cl_2N_6O_4P_2Pd$ (635.8): calcd. C 34.01, H 5.07, N 13.22; found C 33.84, H 4.99, N 12.92.

**Preparation of *trans*-[Pd(SR)$_2$(PR′$_3$)$_2$] Complexes:** To a solution of the sodium salt of the thiol derivatives (prepared in situ from the thiol and NaOEt) in absolute EtOH was added *cis*-$[PdCl_2(PR'_3)_2]$ (PR′$_3$ = PTA, DAPTA). After stirring the mixture for ca. 24 h, the resulting precipitates were isolated by filtration and washed well with absolute EtOH and dried in air.

***trans*-[Pd(SPy)$_2$(PTA)$_2$] (12a):** Yield: 82%, yellow solid. $^1H$ NMR (400 MHz, $CDCl_3$, 25 °C): $\delta$ = 4.14 (s, 12 H, C*H*$_2$P), 4.35 (m, 12 H, C*H*$_2$N), 6.85 (dt, *J* = 6.0, 1.0 Hz, 2 H, Py-H$^5$), 7.30 (dt, *J* = 7.7, 1.0 Hz, 2 H, Py-H$^4$), 7.56 (d, *J* = 8.0 Hz, 2 H, Py-H$^3$), 8.25 (d, *J* = 5.0 Hz, 2 H, Py-H$^6$) ppm. $^{31}P\{^1H\}$ NMR (162 MHz, $CDCl_3$,

 © 2007 Wiley-VCH Verlag GmbH & Co. KGaA, Weinheim 

Table 1. Crystallographic parameters and refinement details for [Au($S_2CNEt_2$)(PTA)], *trans*-[Pd($SC_5H_4N$)$_2$(PTA)$_2$] and *trans*-[Pd($SC_5H_4N$)$_2$-(DAPTA)$_2$].

| Parameter | [Au($S_2CNEt_2$)(PTA)] | *trans*-[Pd($SC_5H_4N$)$_2$(PTA)$_2$] | *trans*-[Pd($SC_5H_4N$)$_2$(DAPTA)$_2$] |
|---|---|---|---|
| Formula | $C_{11}H_{22}AuN_4PS_2$ | $C_{22}H_{32}N_8P_2PdS_2$ | $C_{28}H_{40}N_8O_4P_2PdS_2$ |
| *Fw* | 502.38 | 641.02 | 785.14 |
| Crystal system | orthorhombic | triclinic | monoclinic |
| Space group | $P2_12_12_1$ | $P\bar{1}$ | $P2/_1c$ |
| *a* [Å] | 7.2450(3) | 6.3722(14) | 9.9858(2) |
| *b* [Å] | 7.9897(4) | 10.393(2) | 10.4425(2) |
| *c* [Å] | 27.1870(13) | 11.117(2) | 15.5161(3) |
| *α* [°] | 90 | 65.422(3) | 90 |
| *β* [°] | 90 | 78.909(4) | 100.468(2) |
| *γ* [°] | 90 | 72.698(3) | 90 |
| *V* [Å$^3$] | 1573.73(13) | 637.2(2) | 1591.04(5) |
| *Z* | 4 | 1 (dimer) | 2 (dimer) |
| *μ* [cm$^{-1}$] | 9.708 | 1.047 | 0.865 |
| $D_X$ [g/cm$^3$] | 2.120 | 1.670 | 1.639 |
| No. indep. reflns | 3742 | 2222 | 5133 |
| No obs. reflns with $I>2\sigma(I)$ | 3304 | 1816 | 3913 |
| *R* (obs. data) | 0.034 | 0.035 | 0.025 |
| *a* in weighting scheme | 0.030 | 0.057 | 0.040 |
| $R_w$ (all data) | 0.068 | 0.114 | 0.072 |
| CCDC No. | 634748 | 634749 | 634750 |

25 °C): $\delta$ = –57.20 ppm. IR (nujol): $\tilde{\nu}$ = 392 (Pd–S), 254 (Pd–P) cm$^{-1}$. FAB MS: m/z = 530 [M – SPy]$^+$, 484 [M – PTA]$^+$. $C_{22}H_{33}N_8P_2PdS_2$ (641.0): calcd. C 41.22, H 5.03, N 17.48; found C 40.77, H 4.91, N 17.04.

***trans*-[Pd(SPy)$_2$(DAPTA)$_2$] (12b):** Yield: 66%, pale yellow solid. $^1$H NMR (400 MHz, $CDCl_3$, 25 °C): $\delta$ = 1.84 (s, 6 H, DAPTA-Me), 2.05 (s, 6 H, DAPTA-Me), 3.66 (d, *J* = 15.7 Hz, 2 H, NC$H_2$P), 3.73 (d, *J* = 15.1 Hz, 2 H, NC$H_2$P), 3.88 (d, *J* = 14.1 Hz, 2 H, NC$H_2$N), 3.94 (d, *J* = 15.7 Hz, 2 H, NC$H_2$P), 4.17 (d, *J* = 15.4 Hz, 2 H, NC$H_2$P), 4.50 (d, *J* = 13.8 Hz, 2 H, NC$H_2$N), 4.59 (d, *J* = 15.6 Hz, 2 H, NC$H_2$P), 4.87 (d, *J* = 13.9 Hz, 2 H, NC$H_2$N), 5.63 (d, *J* = 15.6 Hz, 2 H, NC$H_2$P), 5.71 (d, *J* = 14.1 Hz, 2 H, NC$H_2$N), 6.92 (t, *J* = 6.0 Hz, 2 H, SPy-H$^5$), 7.35 (dt, *J* = 7.8, 1.3 Hz, 2 H, Py-H$^4$), 7.52 (d, *J* = 7.8, 1.3 Hz, 4 H, SPy-H$^3$), 8.32 (d, *J* = 4.3 Hz, 2 H, Py-H$^6$) ppm. $^{31}$P{$^1$H} NMR (162 MHz, $CDCl_3$, 25 °C): $\delta$ = –35.60 ppm. IR (nujol): $\tilde{\nu}$ = 364 (Pd–S), 271 (Pd–P) cm$^{-1}$. FAB MS: *m/z* = 556 [M – DAPTA]$^+$, 674 [M – SPy]$^+$, 785 [M]$^+$. $C_{28}H_{40}N_8O_4P_2PdS_2$ (785.2): calcd. C 42.83, H 5.14, N 14.27; found C 42.82, H 5.18, N 13.74.

***trans*-[Pd(SPyrim)$_2$(PTA)$_2$] (13a):** Yield: 75%, cream coloured solid. $^1$H NMR (400 MHz, $CDCl_3$, 25 °C): $\delta$ = 4.22 (s, 12 H, C$H_2$P), 4.41 (m, 12 H, C$H_2$N), 6.85 (t, *J* = 4.5 Hz, 2 H, pyrim-H$^5$), 8.35 (d, *J* = 4.5 Hz, 4 H, pyrim-H$^4$, H$^6$) ppm. $^{31}$P{$^1$H} NMR (162 MHz, $CDCl_3$, 25 °C): $\delta$ = –57.13 ppm. IR (nujol): $\tilde{\nu}$ = 392 (Pd–S), 256 (Pd–P) cm$^{-1}$. FAB MS: m/z = 374 [M – PTA – SPyrim]$^+$, 486 [M – PTA]$^+$, 531 [M – SPyrim]$^+$. $C_{20}H_{30}N_{10}P_2PdS_2$ (643.0): calcd. C 37.36, H 4.70, N 21.78; found C 37.20, H 4.88, N 21.52.

***trans*-[Pd(SPyrim)$_2$(DAPTA)$_2$] (13b):** Yield: 80%, pale yellow solid. $^1$H NMR (400 MHz, $CDCl_3$, 25 °C): $\delta$ = 1.74 (s, 6 H, DAPTA-Me), 2.05 (s, 6 H, DAPTA-Me), 3.72 (dd, *J* = 15.4, 2.5 Hz, 2 H, NC$H_2$P), 3.76 (d, *J* = 15.4 Hz, 2 H, NC$H_2$P), 3.93 (d, *J* = 14.1 Hz, 2 H, NC$H_2$N), 4.09 (d, *J* = 15.4 Hz, 2 H, NC$H_2$P), 4.26 (dd, *J* = 15.7, 2.2 Hz, 2 H, NC$H_2$P), 4.58 (d, *J* = 14.1 Hz, 2 H, NC$H_2$N), 4.62 (d, *J* = 15.7 Hz, 2 H, NC$H_2$P), 4.89 (d, *J* = 14.0 Hz, 2 H, NC$H_2$N), 5.66 (d, *J* = 15.7 Hz, 2 H, NC$H_2$P), 5.73 (d, *J* = 13.9 Hz, 2 H, NC$H_2$N), 6.93 (t, *J* = 4.8 Hz, 2 H, Spyrim-H$^5$), 8.47 (d, *J* = 4.8 Hz, 4 H, Spyrim-H$^4$,H$^6$) ppm. $^{31}$P{$^1$H} NMR (162 MHz, $CDCl_3$, 25 °C): $\delta$ = –37.10 ppm. IR (nujol): $\tilde{\nu}$ = 370 (Pd–S), 262 (Pd–P) cm$^{-1}$. FAB MS: m/z = 446 [M – SPyrim – DAPTA]$^+$, 558 [M – DAPTA]$^+$, 675 [M – SPyrim]$^+$. $C_{26}H_{38}N_{10}O_4P_2PdS_2$ (787.1): calcd. C 39.67, H 4.87, N 17.79; found C 39.13, H 5.01, N 17.87.

**Crystallography:** Intensity data for [Au($S_2CNEt_2$)(PTA)] (**8a**), *trans*-[Pd($SC_5H_4N$)$_2$(PTA)$_2$] (**12a**) and *trans*-[Pd($SC_5H_4N$)$_2$-(DAPTA)$_2$] (**12b**) were measured at 293, 230 and 293 K, respectively, with a Xcalibur Oxford Diffraction in the case of **12b** and on a Bruker CCD for **8a** and **12a** fitted with Mo-$K_\alpha$ radiation so that $\sigma_{max}$ was 28.4, 25.0 and 32.2°, respectively. The structures were solved by heavy-atom methods (SHELXS97) [33] and refinement was on $F^2$ (SHELXL97)[33] with the use of data that was corrected for absorption effects with an empirical procedure,[34] with non-hydrogen atoms modelled with anisotropic displacement parameters, with hydrogen atoms in their calculated positions, and by using a weighting scheme of the form $w = 1/[\sigma^2(F_o^2) + (aP)^2]$ where $P = (F_o^2 + 2F_c^2)/3$. Disorder was noted in the structure of [Au($S_2CNEt_2$)(PTA)] so that two distinct positions were determined for the gold atom. Refinement showed that the major component had a site occupancy factor = 0.807(3). The absolute configuration of [Au($S_2CNEt_2$)(PTA)] was determined on the basis of differences in Friedel pairs included in the data sets and confirmed by the near zero value of the Flack parameter [i.e. –0.003(7)].[35] A residual electron density peak of 1.12 e/Å$^3$ was noted in the final difference map for *trans*-[Pd($SC_5H_4N$)$_2$(DAPTA)$_2$], this was located between the Pd and S1 atoms. Molecular structures are shown in Figures 1, 2 and 3 and were generated with ORTEP.[36] Data analyses were performed with PLATON.[37] Crystallographic data and refinement details are given in Table 1. These data can be obtained free of charge from The Cambridge Crystallographic Data Centre via www.ccdc.cam.ac.uk/data_request/cif.

## Acknowledgments

We thank the Ministerio de Ciencia y Tecnologia (Spain) and FEDER (CTQ2005-08099-CO3-01), as well as the Junta de Castilla y Leon and the University of Burgos (BU033A06 and 112-541A-487.01) for financial support. F. M thanks the University of Burgos for a visiting fellowship and E. V. is grateful to the CSIC for a I3P research grant.

 © 2007 Wiley-VCH Verlag GmbH & Co. KGaA, Weinheim 

[1] B. Cornils, W. A. Herrmann, *Aqueous-Phase Organometallic Catalysis Concepts and Applications*, Wiley-VCH, Weinheim, **1998**.
[2] F. Joó, *Aqueous Organometallic Catalysis*, Kluver Academic Publishers, Dordrecht, **2001**.
[3] P. T. Bishop, *Gold Bull.* **2002**, *35*, 89–98, and references therein.
[4] A. Shultz, N. Giesecke, European patent, **1998**, 0 857707.
[5] D. J. Daigle, A. B. Peperman Jr, S. L. Vail, *J. Heterocycl. Chem.* **1974**, *11*, 407.
[6] Z. Assefa, B. G. McBurnett, R. J. Staples, J. P. Fackler Jr, B. Assmann, K. Angermaier, H. Schmidbaur, *Inorg. Chem.* **1995**, *34*, 75–83.
[7] Z. Assefa, B. G. McBurnett, R. J. Staples, J. P. Fackler Jr, *Inorg. Chem.* **1995**, *34*, 4965–4972.
[8] J. M. Forward, J. P. Fackler Jr, R. J. Staples, *Organometallics* **1995**, *14*, 4194–4198.
[9] Z. Assefa, J. M. Forward, T. A. Grant, R. J. Staples, B. E. Hanson, A. A. Mohamed, J. P. Fackler Jr, *Inorg. Chim. Acta* **2003**, *352*, 31–45.
[10] F. Mohr, E. Cerrada, M. Laguna, *Organometallics* **2006**, *25*, 644–648.
[11] F. Mohr, S. Sanz, E. R. T. Tiekink, M. Laguna, *Organometallics* **2006**, *25*, 3084–3087.
[12] S. Sanz, L. Jones, F. Mohr, M. Laguna, *Organometallics* **2007**, *26*, 952–957.
[13] F. Mohr, L. R. Falvello, M. Laguna, *Eur. J. Inorg. Chem.* **2006**, 3152–3154.
[14] A. D. Phillips, L. Gonsalvi, A. Romerosa, F. Vizza, M. Peruzzini, *Coord. Chem. Rev.* **2004**, *248*, 955–993.
[15] B. J. Frost, C. M. Bautista, R. Huang, J. Shearer, *Inorg. Chem.* **2006**, *45*, 3481–3483.
[16] C. Lidrissi, A. Romerosa, M. Saoud, M. Serrano-Ruiz, L. Gonsalvi, M. Peruzzini, *Angew. Chem. Int. Ed.* **2005**, *44*, 2568–2572.
[17] D. J. Darensbourg, C. G. Ortiz, J. W. Kamplain, *Organometallics* **2004**, *23*, 1747–1754.
[18] J. Ruiz, N. Cutillas, F. López, G. Lopez, D. Bautista, *Organometallics* **2006**, *25*, 5768–5773.
[19] M. C. Gimeno, P. G. Jones, A. Laguna, M. Laguna, R. Terroba, *Inorg. Chem.* **1994**, *33*, 3932–3938.
[20] E. Cerrada, P. G. Jones, A. Laguna, M. Laguna, *Inorg. Chem.* **1996**, *35*, 2995–3000.
[21] a) J. G. Wijnhoven, W. P. Bosman, P. T. J. Beurskens, *J. Cryst. Mol. Struct.* **1972**, *2*, 7–15; b) S. Y. Ho, E. R. T. Tiekink, *Acta Crystallogr., Sect. E* **2001**, *57*, m603–m604; c) S. Y. Ho, E. R. T. Tiekink, *Acta Crystallogr., Sect. E* **2002**, *58*, m86–m87; d) S. Y. Ho, E. R. T. Tiekink, *Z. Kristallogr. - New Cryst. Struct.* **2002**, *217*, 359–360; e) S. Y. Ho, E. R. T. Tiekink, *Z. Kristallogr. - New Cryst. Struct.* **2004**, *219*, 73–74; f) S. Y. Ho, E. R. T. Tiekink, *Z. Kristallogr. - New Cryst. Struct.* **2005**, *220*, 343–344.
[22] a) E. R. T. Tiekink, I. Haiduc, *Prog. Inorg. Chem.* **2005**, *54*, 127–319; b) D. de Vos, S. Y. Ho, E. R. T. Tiekink, *Bioinorg. Chem. Applns.* **2004**, *2*, 141–154.
[23] S. Y. Ho, E. R. T. Tiekink, *Z. Kristallogr.* **2004**, *219*, 513–518.
[24] a) E. C. Alyea, G. Ferguson, S. Kannan, *Polyhedron* **1998**, *17*, 2727–2732; b) E. C. Alyea, G. Ferguson, S. Kannan, *Chem. Commun.* **1998**, 345–346.
[25] D. J. Darensbourg, T. J. Decuir, N. W. Stafford, J. R. Robertson, J. D. Draper, J. H. Reibenspies, *Inorg. Chem.* **1997**, *36*, 4218–4226.
[26] A. Mendia, E. Cerrada, F. J. Arnáiz, M. Laguna, *Dalton Trans.* **2006**, 609–616.
[27] M. Pasquali, F. Marchetti, P. Leoni, T. Beringhelli, G. D'Alfonso, *Gazz. Chim. Ital.* **1993**, *123*, 659–664.
[28] A. M. M. Meij, S. Otto, A. Roodt, *Acta Crystallogr., Sect. C* **2003**, *59*, m352–m364.
[29] E. Muñoz, M. de Val, M. L. Ruiz-Gonzalez, C. López-Gascón, M. L. Sanjuán, M. T. Martinez, J. M. Gonzalez-Calbet, G. F. de la Fuente, M. Laguna, *Chem. Phys. Lett.* **2006**, *420*, 86–89.
[30] R. Heathcote, J. A. S. Howell, N. Jennings, D. Cartlidge, L. Cobden, S. Coles, M. Hursthouse, *Dalton Trans.* **2007**, 1309–1315.
[31] D. J. Daigle, *Inorg. Synth.* **1998**, *32*, 40.
[32] R. Uson, A. Laguna, M. Laguna, *Inorg. Synth.* **1989**, *26*, 85–91.
[33] G. M. Sheldrick, *SHELXS97 and SHELXL97*, University of Göttingen, Germany, **1997**.
[34] G. M. Sheldrick, *SADABS*, University of Göttingen, Germany, **2001**.
[35] H. D. Flack, *Acta Crystallogr., Sect. A* **1983**, *39*, 876–881.
[36] C. K. Johnson, *ORTEP II*, Report ORNL-5136, Oak Ridge National Laboratory, Oak Ridge, TN, **1976**.
[37] A. L. Spek, *PLATON: A Multipurpose Crystallographic Tool*, Utrecht University, The Netherlands, **2006**.

Received: January 27, 2007
Published Online: May 22, 2007

 © 2007 Wiley-VCH Verlag GmbH & Co. KGaA, Weinheim 

DOI: 10.1002/ejic.200700115

# Photoinitiation of Acrylate Polymerization with (Arene)chromium Complexes

E. Peter Kündig,*[a] Long-He Xu,[a] Mikhail Kondratenko,[a] Allan F. Cunningham Jr.,*[b] and Martin Kunz[b]

**Keywords:** Acrylate polymerization / Photoinitiators / Arene complexes / Chromium / Radiation curing

Photoinitiation of acrylate polymerization by [Cr($\eta^6$-arene)-$(CO)_3$] complexes in the presence of an organic chloro compound was investigated. For the bimolecular system, a good correlation between activity and metal–arene and metal–carbonyl bond strength was observed. The highest efficiency was found for an initiator in which the organic chloro compound was tethered to the complexed arene: [Cr($\eta^6$-$C_6H_5CH_2OCOCCl_3$)$(CO)_3$]. The initial steps of the photoinitiation were probed and provided evidence for metal–arene bond cleavage in an Cr($\eta^2$-acrylate)($\eta^6$-arene)$(CO)_2$ complex. (© Wiley-VCH Verlag GmbH & Co. KGaA, 69451 Weinheim, Germany, 2007)

## Introduction

Photoinitiated polymerization, commonly termed radiation curing, is an important industrial process employed for the fabrication of a wide variety of products ranging from floor coatings to integrated circuit boards. Among the advantages of this technology are lower energy costs and the concomitant reduction in the use of organic solvents, issues of ever-increasing importance.[1]

One of the key elements in a radiation-curable system is the photoinitiator.[2] Most of the commercially available photoinitiators are organic compounds which absorb in the UV and near-UV regions of the electromagnetic spectrum. Prompted by a potential further reduction in energy costs through the use of standard light sources and the increased availability of visible-light lasers which are required for technically advanced applications, efforts to develop photoinitiators sensitive to visible light have multiplied. In this domain, transition-metal organometallic chemistry offers special opportunities, as most organometallic compounds absorb in the visible region because of the partial occupation of the metal d orbitals. In addition, the absorption characteristics of such complexes can be manipulated by modifying the nature of the metal-bound ligands.[2] The commercialization of two organometallic photoinitiators, Irgacure 784, a titanocene suitable for the polymerization of acrylate-based systems with the argon laser, and Irgacure 261, a ferrocenium salt which provides a Lewis acid upon irradiation and is used to cure epoxy resins, attest to the viability of this approach.[3,4]

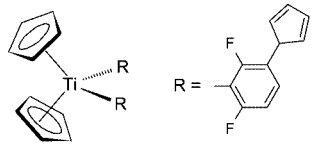


Irgacure 784

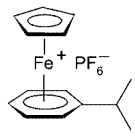


Irgacure 261

The photochemistry of a large number of organometallic compounds under varying conditions has been investigated, and, in some cases, the generation of radicals or acidic species has been observed.[3,5] One well-documented example is the combination of carbonylmetal complexes with carbon tetrachloride, which serves to photoinitiate the polymerization of acrylates via the production of the trichloromethyl radical. Whereas the initial work of Bamford and coworkers concentrated on the homoleptic carbonylmetal complexes, decacarbonyldimanganese and decacarbonyldirhenium,[6] it was later extended to include organometallic derivatives of manganese[7] and (arene)tricarbonylchromium complexes.[8]

An abbreviated version of the mechanism of radical production proposed by Bamford for the bimolecular photoinitiator composed of (benzene)tricarbonylchromium (**1**) and carbon tetrachloride is shown in Scheme 1. Irradiation of **1** in the presence of methyl methacrylate (mma) is presumed to give rise to an exciplex of the acrylate and **1**, which undergoes further transformation to the (mma)chromium complexes **2** and **3**. The former, being at best a 16-electron complex when one assumes coordination of both the double bond and the ketone of mma to the metal, can interact directly with carbon tetrachloride and thereby provide an initiating trichloromethyl radical and, formally, a chromium(I) species. In the case of complex **3**, ligand dissociation, which also occurs in the dark but is greatly accelerated by irradiation, must precede radical generation, unless, of course, through-space electron transfer can occur. Accord-

[a] Department of Organic Chemistry, University of Geneva, 30 quai Ernest Ansermet, 1211 Geneva, Switzerland
[b] Ciba Specialty Chemicals, Ltd., 4002 Basel, Switzerland

 InterScience © 2007 Wiley-VCH Verlag GmbH & Co. KGaA, Weinheim 

ing to this mechanism, the formation of one initiating radical is accompanied by the liberation of one molecule of arene. Indeed, this is observed experimentally in that the quantum yield for decomposition of the arene complex is indistinguishable from the quantum yield for initiation of polymerization. In addition, these quantities are dependent on the nature of the arene complex: the stronger the arene–chromium bond, the slower the rate of polymerization (and decomposition).

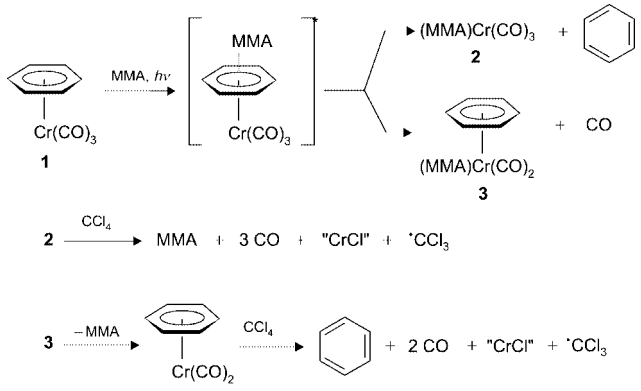


Scheme 1. Mechanism proposed by Bamford for the photoinitiation of methyl methacrylate (MMA) polymerization in the presence of [Cr(benzene)(CO)$_3$] (**1**)/$CCl_4$.[6]

A major drawback of the (arene)tricarbonylchromium/carbon tetrachloride photoinitiator system, from an industrial viewpoint, is the use of the highly volatile and carcinogenic carbon tetrachloride as coinitiator. Furthermore, the intermolecular nature of the radical production requires the use of a great excess of this component. One approach toward the resolution of both of these problems is to attach a functional group capable of producing radicals upon reduction directly to chromium. In addition to decreasing the volatility of the system, the presence of an intramolecularly bound coinitiator should lead to an increase in photoinitiator activity, since a high effective concentration of the coinitiator in the vicinity of the metal is assured. We have analyzed this approach and now report our results on the design, synthesis, and reactivity of a new class of unimolecular organometallic photoinitiators.

## Results and Discussion

### Bimolecular Photoinitiators

Initial work was aimed at the identification of an appropriate substitute for carbon tetrachloride which would exhibit similar reactivity in the presence of (benzene)tricarbonylchromium (**1**). On the basis of literature reports of the photoinitiator activity of decacarbonyldimanganese and ethyl trichloroacetate,[9] and the crosslinking of poly(vinyl trichloroacetate) with this carbonylmetal complex,[9a,10] phenalkyl trichloroacetates were targeted as potential coinitiators. The presence of a phenyl group was desired in order to allow introduction of the tricarbonylchromium moiety by using well-documented methodology.[11,12]

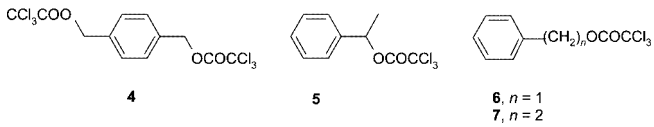


**4** **5** **6**, $n = 1$ **7**, $n = 2$

Synthesis of the trichloroacetates **4**–**7** was carried out by the reaction of the corresponding alcohols with trichloroacetyl chloride and pyridine in dichloromethane.[13] The coinitiator activity of these acetates in the presence of **1** was assessed under typical industrial conditions. The photoinitiator system to be tested was added to a clear lacquer consisting of a mixture of polyfunctional acrylates and vinylpyrrolidinone (for details, see Exp. Sect.). A 60–70-μm layer of the resulting formulation was applied to a sheet of aluminum, then covered first with a polyester foil and finally with a 21-step optical wedge. The sample was then placed at a distance of 30 cm from a 4-kW Xenon lamp and irradiated for 20 s. The reactivity of the various photoinitiator combinations, quantified as the number of completely hardened (cured) steps after development in ethanol, is shown in Figure 1. It should be noted at this point that a difference of two steps corresponds to a twofold increase in reactivity; i.e., the transmittance of light at step 1 is two times that at step 3. It is evident that even **1** alone is a photoinitiator, albeit of very low activity (step 0, which is 100% transparent, is cured). Given the fact that dissolved oxygen is present in the formulation and that one component of the formulation contains hydroxy groups (dipentaerythritol monohydroxypentacrylate), the unimolecular photoinitiator activity of the complexes may be due to oxidative ligand exchange rather than radical polymerization of the acrylate units. Wagner and Purbrick[14] previously reported that **1** promotes the photochemical crosslinking of polymers containing pendant hydroxy groups in the presence of oxygen. The formation of O–$Cr^{III}$ bonds between polymer molecules was suggested to account for this observation (Scheme 2).

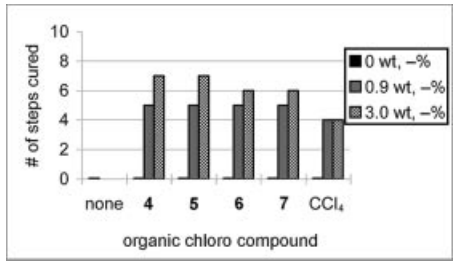


Figure 1. Reactivity of 0.3 wt.-% **1** in the presence of organic chlorides **4**–**7** and $CCl_4$ (0, 0.9, and 3.0 wt.-%) in a clear lacquer. 20-s irradiation with a 4-kW Xenon lamp through a 21-step optical wedge.

The addition of an organic chloro compound results in a substantial increase in activity. The most efficient coinitiators are the bis(trichloroacetate) **4** and 2-phenethyl trichloroacetate (**5**). They are 1.5 to 3 times more reactive than carbon tetrachloride over the concentration range studied (increase of 1–3 cured steps, Figure 1). The increased reactivity of the trichloroacetates can be ascribed to the forma-

 © 2007 Wiley-VCH Verlag GmbH & Co. KGaA, Weinheim 

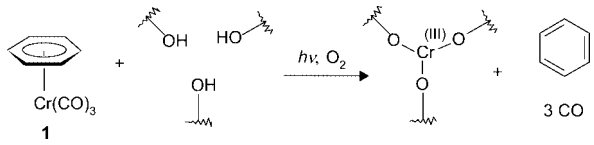


Scheme 2. Formation of $Cr^{III}$ species from the reaction of **1** with polymers containing pendant hydroxy groups in the presence of oxygen.

tion of a resonance-stabilized α-carbonyloxy radical. In the absence of **1**, all the trichloroacetates as well as carbon tetrachloride were inactive. As expected from the work of Bamford discussed previously, enhanced reactivity is observed for all the trichloroacetates when **1** is replaced with the chlorobenzene complex **8**, which has a weaker chromium–arene bond (Figure 2). In this case, however, trichloroacetates **4**, **6**, and **7** are twice as effective as **5** (increase of 2 cured steps). Surprisingly, carbon tetrachloride exhibits more or less the same coinitiator activity with both complexes. This may indicate that the rate-determining step in the case of carbon tetrachloride is its reaction with the active chromium species to provide the trichloromethyl radical rather than the generation of the latter from **1** or **8**.

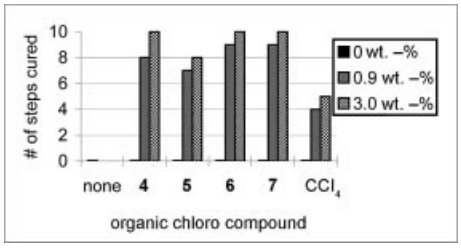


Figure 2. Reactivity of 0.3 wt.-% **8** in the presence of organic chlorides **4**–**7** and $CCl_4$ (0, 0.9, and 3.0 wt.-%) in a clear lacquer. 20-s irradiation with a 4-kW Xenon lamp through a 21-step optical wedge.

It is apparent from the order of reactivity that neither the nature of the tether between the phenyl and trichloroacetate groups nor the number of trichloroacetate groups per molecule has a significant effect on the rate of polymerization.

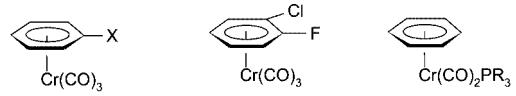


**8**, X = Cl **9**, X = F
**10**, X = $CF_3$ **11**, X = $COCH_3$
**12**, X = $OCH_3$

**13**

**14**, R = OPh
**15**, R = Ph

At this point, the influence of the arene substituent of the chromium complex upon its activity in the presence of **4** was investigated. Other than **13**, which was obtained via lithiation of **9** followed by treatment with hexachloroethane,[15] all complexes were prepared by direct ligand exchange in hexacarbonylchromium [11] or tricarbonyl(naphthalene)chromium.[16] With the exception of **14**, which can cure 2 steps, crosslinking of the formulation is negligible when the complexes are employed alone (at 100% transmittance, 0 steps). The superior photoinitiator activity of **14** may be connected to the lower oxidative stability of the 16-electron chromium fragment resulting from loss of carbon monoxide. In contrast, the phosphane complex **15**, which could formally yield a similar unsaturated fragment, does not undergo direct photodissociation of carbon monoxide.[17] When **4** is present, the highest reactivity is observed for the halogenated complexes **13** and **9** (9 steps). In general, complexes containing one electron-withdrawing group exhibit higher reactivity than that of the parent benzene complex **1**. The anisole complex **12** is about as active as **1**, whereas the phosphane- and phosphite-substituted complexes **14** and **15** are less reactive than **1** (Figure 3).

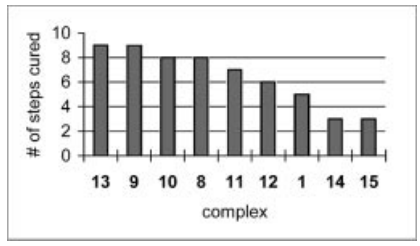


Figure 3. Reactivity of 0.9 wt.-% **4** and 0.3 wt.-% [Cr(arene)$(CO)_3$] complexes in a clear lacquer. 20-s irradiation with a 4-kW Xenon lamp through a 21-step optical wedge.

The results obtained with the (arene)tricarbonylchromium complexes are in accord with those of Bamford: reactivity increases with decreasing arene–chromium bond strength. Although the absolute bond strengths of all the complexes employed in this study are not reported in the literature, the bond strengths are directly related to the energy of the HOMOs of the complexes and, in turn, their oxidation potentials and their carbonyl stretching frequencies.[18] In fact, very good correlation is obtained between νCO and the number of steps cured. A higher carbonyl stretching frequency, indicative of a lower M–CO bond strength, results in higher reactivity. As proposed by Bamford, this can be explained by the more facile substitution of the arene or CO by acrylate, thus leading to higher concentrations of the active intermediates **2** and **3** (Scheme 1). It should be noted, however, that the photochemical generation of species related to **2** from (arene)tricarbonylchromium is not expected to be an important pathway as irradiation of (arene)tricarbonylchromium leads almost exclusively to loss of CO.[17a]

The effect of substituting a carbonyl ligand of **1** with phosphane or phosphite is a marked decrease in bimolecular photoinitiator activity. The combinations of complexes **14** and **15** with **4** exhibit the lowest reactivity of all the systems studied. Inspection of the carbonyl stretching frequencies indicates that these compounds have the strongest chromium–carbonyl bonds (νCO: 1915 and 1857 $cm^{-1}$ for **14** and 1890 and 1831 $cm^{-1}$ for **15** vs. 1974 and 1894 $cm^{-1}$ for **1**), which is consistent with the mechanism based on initial carbonyl dissociation. Given that the drastic decrease in carbonyl stretching frequency is due to direct resonance of the phosphorus ligand with the carbonyl ligands through the metal atom and not to interactions with the benzene substituent, it is difficult to compare these complexes with the tricarbonyl series. There are indications, however, that the arene–chromium bond in such complexes is also

 © 2007 Wiley-VCH Verlag GmbH & Co. KGaA, Weinheim 

stronger than that in **1**. For example, arene exchange reactions with dicarbonyl(naphthalene)(triphenylphosphane)-chromium have not been successful,[19] whereas arene exchange in tricarbonyl(naphthalene)chromium is a well-proven, widely applied, mild method for the synthesis of (arene)tricarbonylchromium complexes.[12,16,20]

### Unimolecular Photoinitiators

Having defined the factors affecting the bimolecular generation of radicals from (arene)chromium complexes and phenalkyl trichloroacetates, we then focused our attention on the synthesis and reactivity of the following unimolecular system: the tricarbonylchromium complexes of phenalkyl trichloroacetates. Of initial interest was the effect of the distance between the phenyl and trichloroacetate functionalities on the photoinitiating efficiency. The required complexes were prepared in two steps by starting from the phenalkyl alcohols. Ligand exchange of hexacarbonylchromium with the alcohols provided the complexes **16a**–**d** which were acetylated under standard conditions to afford complexes **17a**–**d** (Scheme 3).

These compounds were then evaluated in the acrylate formulation at a concentration of 0.3 wt.-% as described previously (Figure 4). The most active photoinitiator is the benzyl trichloroacetate complex **17a** (11 steps) which is 1.5 times more effective than the bimolecular combinations of 0.3 wt.-% **8** and 3.0 wt.-% organic chloride. Upon lengthening the chain by one carbon, as in **17b**, a fourfold decrease in activity results. Although the replacement of the ethylene bridge in **17b** by a propylene bridge (in **17c**) again causes a reduction in activity, further increases in chain length are without effect. It is interesting to note that the advantage of attaching the coinitiator directly to the chromium complex is lost when the methylene tether is longer than two carbons: the photoinitiator activity of **17c** and **17d** are exactly the same as that of the bimolecular combination of **1** and 0.9 wt.-% **4** or **6** (Figure 1). The fact that addition of 0.9 wt.-% of the bis(trichloroacetate) **4** to formulations containing the photoinitiators **17** leads to a slight increase in activity in almost all cases may indicate that decomplexation of the arene occurs prior to radical generation.

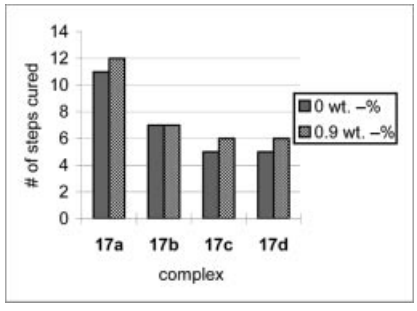


Figure 4. Reactivity of 0.3 wt.-% **17a**–**d** alone or with 0.9 wt.-% **4** in a clear lacquer. 20-s irradiation with a 4-kW Xenon lamp through a 21-step optical wedge.

Retaining the basic structure of complex **17a** as a template, two general strategies were employed in an attempt to enhance the photoinitiator activity of this class of compounds: (1) monitoring the orientation and number of trichloroacetate functionalities and (2) substitution of the arene moiety. With the first strategy, it is clear that the trichloroacetate group must be in proximity to the metal center to allow the generation of initiating radicals. Therefore, any interaction or structural constraint that forces these groups into a *syn* geometry should also result in higher reactivity.

With this in mind, we undertook the synthesis of the derivatives of **17a** having methyl substitution at the benzyl carbon. The higher steric volume of the methyl group should lead compounds such as **19a** and **19b** to exhibit preferred conformations in which the acetate functionality resides on the same face of the arene as the tricarbonylchromium moiety.

Unfortunately, these two compounds were unstable and could not be evaluated in the acrylate-based lacquer. Although the arene complexes **18a** and **18b** could be obtained in good yields, their subsequent reactions with trichloroacetyl chloride led, in the first case, to an oil which decomposed at room temperature and, in the second case, to elimination to afford the methylstyrene complex **20** (Scheme 4).[21] A derivative with the desired structural constraint was found in the *syn*-1-tetrahydronaphthol complex *syn*-**21**.[22] Reaction with trichloroacetyl acetate furnished the desired trichloroacetate **22** in 93% yield. Attempted trichloroacetylation of the corresponding *anti* isomer (*anti*-**21**) led to decomposition via the metal-stabilized benzyl cation.[23] The assessment of **22** in the acrylate lacquer revealed that the structural constraint has little effect on the photoinitiator activity (Figure 5). It is feasible that the advantage gained by this modification is offset by the deactivating influence of the additional alkyl group.

Neither does the increase in the number of trichloroacetate groups of the photoinitiator have a measurable effect on its activity. Bis(trichloroacetate) **24**, prepared via the complexed diol **23**, exhibits the same activity as **17a** (11

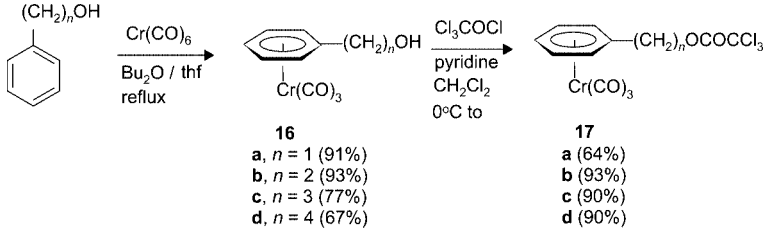


**16**
**a**, *n* = 1 (91%)
**b**, *n* = 2 (93%)
**c**, *n* = 3 (77%)
**d**, *n* = 4 (67%)

**17**
**a** (64%)
**b** (93%)
**c** (90%)
**d** (90%)

Scheme 3. Synthesis of $Cr(CO)_3$ complexes of phenalkyl trichloroacetates.

 © 2007 Wiley-VCH Verlag GmbH & Co. KGaA, Weinheim 

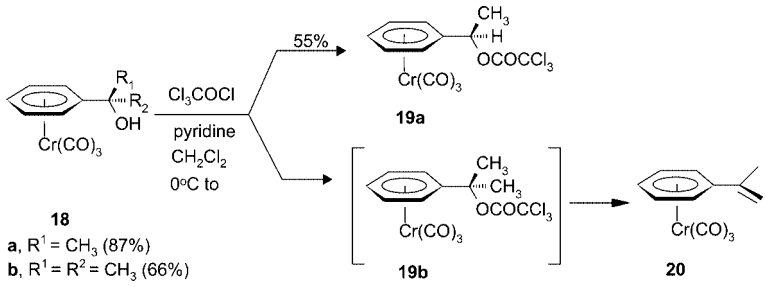


Scheme 4. Attempted synthesis of α-methylated analogs of **17a**.

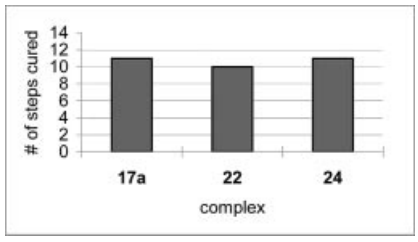


Figure 5. Reactivity of 0.3 wt.-% [Cr(arene)(CO)$_3$] complexes **17a**, **22**, and **24** in a clear lacquer. 20-s irradiation with a 4-kW Xenon lamp through a 21-step optical wedge.

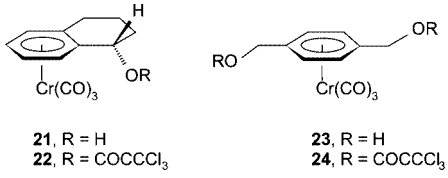


steps, Figure 5). This is in accord with results obtained with the bimolecular photoinitiator systems which show that the coinitiator activity of **4** and **6** are approximately the same.

Since the bimolecular activity of the chromium complexes exhibited a strong dependence on the nature of the arene substituent, it was hoped that the activity of **17a** could be modified in the same fashion. The di- and trisubstituted tricarbonylchromium complexes **25** and **26** were prepared as usual. The direct reaction of *o*-chlorobenzyl alcohol with $Cr(CO)_6$ afforded complex **27a**[24] in low yield (19%). Protection of the alcohol functionality as its *tert*-butyldimethylsilyl ether prior to complexation gave a slightly improved yield of **27b** (27%) and, using [$Cr(CO)_3$-(naphthalene)] as the Cr(CO)3 source, this yield was raised to 40%.[16a] The complexes were then converted into their respective trichloroacetates **28**–**30** and compared to **17a** as photoinitiators in the acrylate lacquer. In contrast to the bimolecular photoinitiators, a slight decrease in activity was observed upon introduction of an *ortho*-methoxy or an *ortho*-chlorine substituent in **17a**: both **29** and **30** allow the curing of only 10 steps vs. 11 steps for **17a** (Figure 6). A further erosion of activity is found when a second alkoxy group is introduced: the catechol derivative **28** is four times less reactive than **17a**. Apparently, the upper limit of reactivity is already attained with complex **18a**. This could imply that the rate-determining step of radical production, at high levels of activity, is the interaction of the trichloroacetate with the metal fragment. With complexes of lower activity, the rate of radical production would be defined by the rate of ligand dissociation.

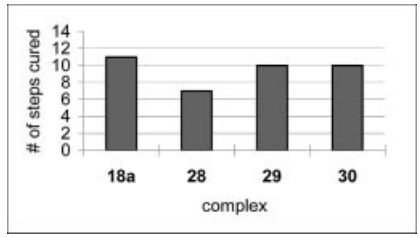


Figure 6. Reactivity of 0.3 wt.-% [Cr(arene)(CO)$_3$] complexes **18a**, **28**–**30** in a clear lacquer. 20-s irradiation with a 4-kW Xenon lamp through a 21-step optical wedge.

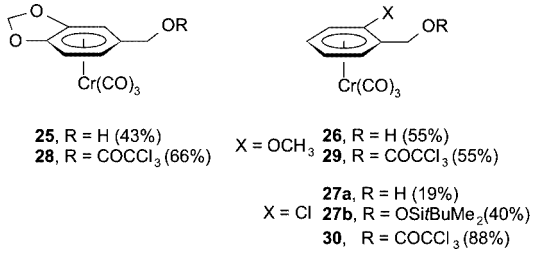


Having established that complex **17a** possessed optimum reactivity and synthetic accessibility, we then probed its photochemistry in the absence of polymerizable acrylates with the goal of identifying the initiating species. It is important to note that the test results obtained with the series of phenalkyl trichloroacetate complexes **17a**–**17d** can be rationalized in terms of initial carbonyl loss or arene loss. Dissociation of a carbonyl ligand would allow direct coordination of a chlorine atom of the trichloroacetate to chromium (Scheme 5, path a). Subsequent oxidation and fragmentation would engender an unstable 17-electron $Cr^I$ arene complex containing a carboxydichloromethyl radical. As the energetics of the intramolecular interaction is clearly dependent upon the chain length, one would expect the highest reactivity with **17a**, as is observed. Likewise, postulating initial arene dissociation, the trichloroacetate moiety of **17a** would remain closer to the metal than in **17b**–**d** which have longer methylene chains.

First attempts to trap a radical intermediate were carried out in benzene solution in the presence of excess methyl 2-*tert*-butyl-2-propenoate (**31**).[25] Acrylate **31** has previously been employed to identify the initiating radicals for a

 © 2007 Wiley-VCH Verlag GmbH & Co. KGaA, Weinheim 

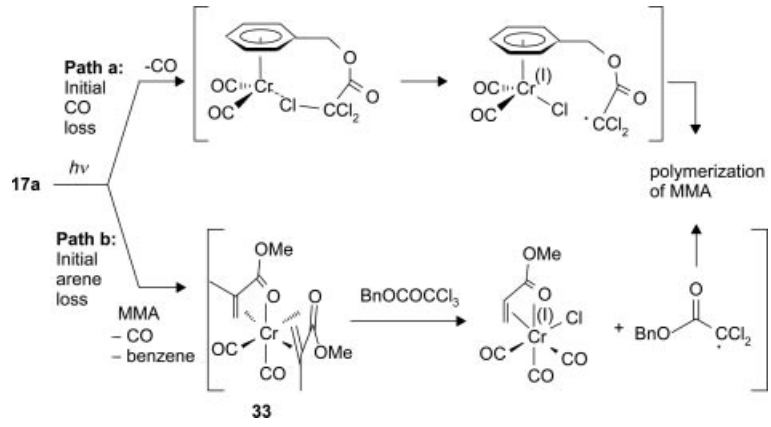


Scheme 5. Possible pathways of radical generation by irradiation of the Cr complex **17a** in methyl methacrylate.

**31** **32**

number of photoinitiators, as radical addition to **31** does not lead to polymerization.[26] Irradiation of a 0.25-M solution of **17a** containing 4 equiv. **31** at 350 nm (four lamps of 24 W each) in a Rayonet apparatus for 12 h led to the isolation of one new product, the benzyl chloride complex **32** in 17% yield along with 19% recovered starting material.

No trace of a radical addition product to **31** could be detected. An analogous result was obtained upon photolysis of **17a** in the absence of **31**. At a concentration of 0.25 M, **32** was obtained in 41% yield after irradiation for 2 d, whereas only a trace of **32** could be detected at a concentration of 0.08 M. These results show that **31** does not play a role in the formation of complex **32** and that it is unlikely that **32** is formed from **17a** by an intramolecular process. These results then appear to rule out path a (Scheme 5).

The failure to trap any radical species in the aforementioned photolysis of **17a** and **32** suggests that the polymerizable acrylate is an important component of this photoinitiator system. The role of the acrylate may be to displace the arene from the chromium complex, thereby generating an intermediate (a diacrylate complex of chromium, e.g. **33**) which is more reactive toward the organic halide (path b). This process is initiated by the loss of CO and olefin coordination of mma. Slippage of the arene from the $\eta^6$ to the $\eta^4$ coordination mode concomitant with $\eta^4$ coordination of mma leads to an intermediate that should readily undergo further association of mma with liberation of benzene. Photoinitiation of polymerization via initial loss of CO was dismissed by Bamford in order to explain the higher rates of decomposition of **1** (evolution of benzene) in mma as compared to isooctane *in the absence of an organic chloro compound* ($CCl_4$). It is unclear whether these observations are related to the generation of initiating radicals. In any event, it can been readily seen that the enhanced arene formation reported could also arise from the mode of substitution of arene by mma shown in Scheme 5, path b.

Neither the direct irradiation of **17a** in the presence of methyl methacrylate (mma) or methyl acrylate (ma) nor the two-step procedure based on cyclooctene[27] afforded the desired alkene complexes. Turning to the parent complex **1**, mma again yielded no isolable complex. However, as communicated earlier from this laboratory,[28] the two-step procedure, when combined with the use of ma, gave the acrylate complex **34** in good yield. The acrylate ligand strongly labilizes the metal–arene bond, presumably by a haptotropic rearrangement as shown in Scheme 6. The arene ligand in **34** is more labile than the acrylate, and **34** undergoes arene exchange at ambient temperature.[28] Mono- and dihapto ligands displace first the arene, and then the acrylate. An example pertinent to the subject of the present investigation is the reaction of **34** with 1,3-cyclohexadiene at ambient temperature to give [$Cr(CO)_2(\eta^4$-1,3-cyclohexadiene$)_2$] (**35**) in high yield.[28–30]

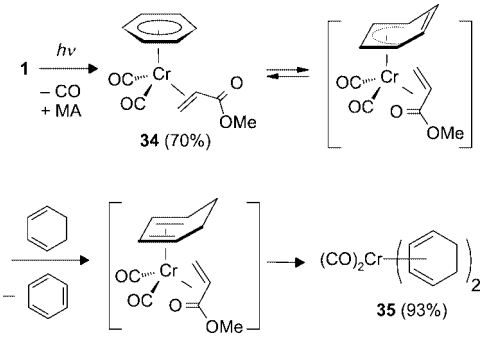


Scheme 6. Substitution of both benzene and methyl acrylate in **1** by cycohexadiene to give **35**.

The reactivity of **34** was then assayed under various conditions. In the absence of the organic chloro compound **4** in the dark, no polymerization of ma was observed. Nonetheless, after 3 h at room temp. complex **34** could no longer be detected, and this indicates an exchange of benzene for ma as previously noted by Bamford. Upon addition of **4** to the solution of **34** in ma in the absence of light, rapid polymerization of ma occurred. In contrast, the combination of **4** with complex **1** does not lead to polymerization in the absence of irradiation.

 © 2007 Wiley-VCH Verlag GmbH & Co. KGaA, Weinheim 

This provides substantial evidence for the intermediacy of an acrylate complex in the photopolymerization of acrylates with the arene chromium complex/organic chloro compound initiator system. Photoinitiation starts by CO substitution for an acrylate. The acrylate ligand, which can interconvert between an $\eta^2$ and an $\eta^4$ binding mode, renders the arene–metal bond labile. Arene displacement leads to a reactive intermediate, e.g. **33**, which can reduce suitable organic chlorides, thereby generating initiating radicals. Incorporation of the organic chloro compound in the chromium complex results in a more efficient photoinitiator, as the essential components remain in close proximity throughout the initiating process.

## Experimental Section

All manipulations involving organometallic compounds were carried out under an atmosphere of purified nitrogen by using an inert gas/vacuum double manifold and standard Schlenk techniques. Solvents for the preparation of chromium complexes were dried and distilled under nitrogen immediately before use. Methyl acrylate was purified by washing twice with NaOH (5% aq.) to remove inhibitors, then twice with water, and then dried with $CaCl_2$, $Na_2CO_3$, $MgSO_4$, and finally distilled from CaH. Complexes **8**,[11] **9**,[11] **10**,[31] **12**,[11] **14**,[32] **15**[33] were prepared as described in the literature. A high pressure Hg-lamp (Philipps-125W) was used for the synthesis of phosphane- or phosphitechromium complexes. Photolysis of methyl acrylate in the presence of a chromium complex was carried out for mechanistic investigations by using a photochemical reactor (Rayonet-CAT NO RPR-100) equipped with RPR-3500 Å lamps (Southern New England Ultraviolet Company, USA). Analytical and preparative TLC: Merck silica gel 60 $F_{254}$ plates. Flash column chromatography: silica gel 60, (Merck). M.p.: Büchi 510, not corrected. IR: Mattson Polaris or Perkin–Elmer 1650 FT-IR spectrometer, NaCl solution cells. $^1$H and $^{13}$C-NMR: Bruker 400 MHz or Varian-XL-200 spectrometer. MS: Varian CH 4 or SM 1, 70 eV; high-resolution MS (HRMS): VG analytical 7070E mass spectrometer.

**4-(2,2,2-Trichloroacetoxymethyl)benzyl Trichloroacetate (4):** To a mixture of 1,4-phenylenedimethanol (690 mg, 5 mmol) and pyridine (988 mg, 12.5 mmol) in dry $CH_2Cl_2$ (80 mL) was added dropwise trichloroacetyl chloride (2.0 g, 11 mmol) at 0 °C. The resulting mixture was stirred at room temp. for 1 h before removing the solvent. The residue was purified by chromatography on silica gel (pentane/diethyl ether 2/1) to give **4** as a white solid (1.56 g, 76%). M.p. 82–84 °C. IR ($CH_2Cl_2$): $\tilde{\nu}$ = 1766, 1227, 982, 831, 685 cm$^{-1}$. $^1$H NMR (400 MHz, $CDCl_3$): $\delta$ = 5.37 (s, 4 H, $CH_2$), 7.44 (s, 4 H, ArH) ppm. $^{13}$C NMR (100 MHz, CDC $l_3$): $\delta$ = 70.1, 89.7, 128.6, 134.6, 161.8 ppm. MS: *m*/*z* (%) = 428 (4) $[M]^+$, 393 (4), 335 (4), 281 (12), 265 (100), 231 (5), 119 (17), 104 (42), 91 (25), 77 (11), 36 (8), 28 (4). $C_{12}H_8Cl_6O_4$ (428.91): calcd. C 33.60, H 1.88; found C 33.61, H 1.88.

**Tricarbonyl(4-hydroxymethylphenylmethanol)chromium (23):**[34] Under $N_2$, a degassed mixture of (4-hydroxymethylphenyl)methanol (1.38 g, 10 mmol) and (naphthalene)tricarbonylchromium (2.64 g, 10 mmol) in thf (50 mL) was heated for 15 h at 60 °C. Solvent removal followed by chromatography on silica gel with diethyl ether and recrystallization in toluene afforded **23** (2.49 g, 90%). IR ($CH_2Cl_2$): $\tilde{\nu}$ = 1969, 1892 cm$^{-1}$. $^1$H NMR (400 MHz, $CD_3COCD_3$): $\delta$ = 4.43 (s, 4 H, $CH_2$), 4.66 (s, 2 H, OH), 5.73 (s, 4 H, ArH) ppm. $^{13}$C NMR (100 MHz, [$D_6$]Acetone): $\delta$ = 62.1, 92.6, 112.5, 233.7 ppm. MS: *m*/*z* (%) = 274 (20) $[M]^+$, 218 (6), 190 (22), 172 (20), 104 (100), 78 (12), 52 (50), 28 (40). $C_{11}H_{10}CrO_5$ (274.19): calcd. C 48.19, H 3.68; found C 48.18, H 3.65.

**General Procedure for the Synthesis of Chromium Complexes (Method A11) Tricarbonyl($\eta^6$-1,2,3,4-tetrahydro-1-naphthol)chromium(0) (*syn*-21):**[22] A degassed solution of 1,2,3,4-tetrahydro-1-naphthol (2.25 g, 15.20 mmol), $Cr(CO)_6$ (4.00 g, 18.17 mmol), and thf (4 mL) in $Bu_2O$ (80 mL) was heated under reflux (oil bath $T$ = 160 °C) for 40 h. After cooling to room temperature, the solution was filtered through Celite, then evaporated under reduced pressure. The yellow solid was recrystallized from $CH_2Cl_2$/hexane to give 2.85 g *syn*-**21**. The mother liquor was concentrated, and the residue chromatographed on silica gel (diethyl ether/hexane = 1:1) to give two fractions (0.61 g *syn*-**21** and 0.27 g *anti*-**21**). The total yield was 86%, and the ratio *syn*/*anti* was 93:7. Complex *syn*-**21**: IR ($CH_2Cl_2$): $\tilde{\nu}$ = 1963, 1885 cm$^{-1}$. $^1$H NMR (200 MHz, $CDCl_3$): $\delta$ = 1.55–2.20 (m, 5 H, OH and $CH_2$), 2.45–2.85 (m, 2 H, $PhCH_2$), 4.40–4.65 (m, 1 H, CHOH), 5.00–5.25 (m, 2 H, ArH), 5.50 (t, $J$ = 6.2 Hz, 1 H, ArH), 5.82 (d, $J$ = 6.4 Hz, 1 H, ArH) ppm. $^{13}$C NMR (50 MHz, $CDCl_3$): $\delta$ = 19.2, 27.5, 32.1, 66.6, 89.0, 90.2, 93.5, 95.1, 112.8, 113.8, 233.3 ppm.

***anti*-21:** $^1$H NMR (200 MHz, $CDCl_3$): $\delta$ = 1.45–2.20 (m, 4 H, $CH_2$), 2.45–2.85 (m, 3 H, OH and $PhCH_2$), 4.45–4.68 (br, 1 H, CHOH), 5.20 (d, $J$ = 6.2 Hz, 1 H, ArH), 5.24 (t, $J$ = 5.8 Hz, 1 H, ArH), 5.33 (t, $J$ = 6.2 Hz, 1 H, ArH), 5.66 (d, $J$ = 5.8 Hz, 1 H, ArH) ppm. $^{13}$C NMR (50 MHz, $CDCl_3$): $\delta$ = 18.1, 28.0, 31.5, 67.0, 91.1, 92.2, 93.6, 94.4, 108.7, 110.0, 233.1 ppm.

**Method B16b (Complex 27b):** A degassed mixture of (2-chlorobenzyloxy)-*tert*-butyldimethylsilane (2.05 g, 8 mmol) and naphthalenetricarbonylchromium (1.06 g, 4 mmol) in thf/diethyl ether (5 mL, 4:1) was heated in a Carius tube with an o-ring tap for 22 h at 70 °C. Solvent removal followed by chromatography on silica gel (hexane/diethyl ether) afforded **27b** (628 mg, 40%). IR ($CH_2Cl_2$): $\tilde{\nu}$ = 1910, 1978 cm$^{-1}$. $^1$H NMR (200 MHz, $C_6D_6$): $\delta$ = 0.04 (s, 3 H, SiMe), 0.09 (s, 3 H, SiMe), 0.97 (s, 9 H, *t*Bu), 4.14 (t, $J$ = 6.3 Hz, 1 H, ArH), 4.29 (t, $J$ = 6.3 Hz, 1 H, ArH), 4.46 (s, 2 H, CH2), 4.66 (d, $J$ = 6.3 Hz, 1 H, ArH), 5.37 (d, $J$ = 6.3 Hz, 1 H, ArH) ppm.

**Method C: Tricarbonyl($\eta^6$-1-chloro-2-fluorobenzene)chromium(0) (13):**[15] *n*BuLi (1.57 N in hexane, 0.70 mL, 1.1 mmol) was added dropwise to a solution of complex **9** (0.232 g, 1.0 mmol) in thf (10 mL) at –78 °C. The solution was slowly warmed to –45 °C over 45 min. After recooling to –78 °C, hexachloroethane (1.19 g, 5.0 mmol) was added, and the reaction mixture was warmed to room temp. over a period of 3 h. After concentration of the solution, the residue was dissolved in diethyl ether, washed with water, then dried with $MgSO_4$. Removal of volatiles and chromatography on silica gel yielded complex **13** (180 mg, 68%). IR ($CH_2Cl_2$): $\tilde{\nu}$ = 1986, 1914 cm$^{-1}$. $^1$H NMR (200 MHz, $C_6D_6$): $\delta$ = 3.57–3.66 (m, 1 H, ArH), 3.87–3.97 (m, 1 H, ArH), 4.30–4.38 (m, 1 H, ArH), 4.58–4.65 (m, 1 H, ArH) ppm. $^{13}$C NMR (100 MHz, $C_6D_6$): $\delta$ = 78.9 (d, $J$ = 21.0 Hz), 86.1, 89.7 (d, $J$ = 6.6 Hz), 92.5, 100.4, 141.9 (d, $J$ = 265 Hz), 230.7 ppm.

Complexes **16a**–**d**, **18a**,**b**, **25**, and **26** were obtained by method A.

**($\eta^6$-Benzyl alcohol)tricarbonylchromium(0) (16a):**[35] IR (diethyl ether): $\tilde{\nu}$ = 1972, 1896 cm$^{-1}$. $^1$H NMR (400 MHz, $C_6D_6$): $\delta$ = 1.40–1.70 (br, 1 H, OH), 3.83 (s, 2 H, $CH_2OH$), 4.37 (t, $J$ = 5.6 Hz, 1 H, ArH), 4.53 (t, $J$ = 5.6 Hz, 2 H, ArH), 4.67 (d, $J$ = 5.6 Hz, 2 H, ArH) ppm. $^{13}$C NMR (100 MHz, $C_6D_6$): $\delta$ = 62.8, 90.8, 91.4, 92.9, 111.8, 233.5 ppm.

**Tricarbonyl($\eta^6$-2-phenylethanol)chromium(0) (16b):**[36] IR (diethyl ether): $\tilde{\nu}$ = 1969, 1896 cm$^{-1}$. $^1$H NMR (200 MHz, $C_6D_6$): $\delta$ = 0.63–

 © 2007 Wiley-VCH Verlag GmbH & Co. KGaA, Weinheim 

0.75 (br, 1 H, OH), 1.98 (t, $J$ = 6.0 Hz, 2 H, $PhCH_2$), 3.16 (t, $J$ = 6.0 Hz, 2 H, $CH_2OH$), 4.25–4.60 (m, 5 H, ArH) ppm. $^{13}C$ NMR (100 MHz, $C_6D_6$): $\delta$ = 37.9, 62.6, 90.6, 93.4, 110.4, 233.7 ppm.

**Tricarbonyl(η⁶-3-phenylpropan-1-ol)chromium(0) (16c):** IR (diethyl ether): $\tilde{\nu}$ = 1970, 1896 $cm^{-1}$. $^1H$ NMR (400 MHz, $C_6D_6$): $\delta$ = 0.75–1.05 (br, 1 H, OH), 1.34 (m, 2 H, $CH_2$), 2.05 (t, $J$ = 8.0 Hz, 2 H, $PhCH_2$), 3.15–3.25 (br, 2 H, $CH_2OH$), 4.36 (t, $J$ = 6.3 Hz, 1 H, ArH), 4.46 (d, $J$ = 6.3 Hz, 2 H, ArH), 4.58 (t, $J$ = 6.3 Hz, 2 H, ArH) ppm. $^{13}C$ NMR (100 MHz, $C_6D_6$): $\delta$ = 31.3, 33.8, 61.2, 90.2, 92.6, 93.7, 113.9, 233.5 ppm.

**Tricarbonyl(η⁶-4-phenylbutan-1-ol)chromium(0) (16d):** Yellow oil. IR (diethyl ether): $\tilde{\nu}$ = 1971, 1896 $cm^{-1}$. $^1H$ NMR (200 MHz, $C_6D_6$): $\delta$ = 0.85–1.40 (br, 5 H, OH and $CH_2$), 1.75–2.05 (m, 2 H, $PhCH_2$), 3.10–3.40 (m, 2 H, $CH_2OH$), 4.20–4.65 (m, 5 H, ArH) ppm. $^{13}C$ NMR (100 MHz, $C_6D_6$): $\delta$ = 62.8, 90.8, 91.4, 93.0, 111.8, 233.5 ppm.

**Tricarbonyl(η⁶-1-phenylethanol)chromium(0) (18a):**[37] Yellow oil. IR ($C_6H_6$): $\tilde{\nu}$ = 1968, 1892 $cm^{-1}$. $^1H$ NMR (200 MHz, $C_6D_6$): $\delta$ = 1.18 (d, $J$ = 6.5 Hz, 3 H, $CH_3$), 2.65–2.75 (br, 1 H, OH), 4.18–4.50 (br, 1 H, CHOH), 4.53–4.77 (m, 4 H, ArH), 5.25 (d, $J$ = 6.5 Hz, 1 H, ArH) ppm. $^{13}C$ NMR (50 MHz, $C_6D_6$): $\delta$ = 25.2, 67.6, 90.8, 91.3, 92.5, 92.7, 92.9, 116.5, 118.0, 233.9 ppm.

**Tricarbonyl(η⁶-2-phenyl-2-propanol)chromium(0) (18b):** Yellow oil. IR ($CH_2Cl_2$): $\tilde{\nu}$ = 1967, 1888 $cm^{-1}$. $^1H$ NMR (200 MHz, $C_6D_6$): $\delta$ = 1.16 (s, 6 H, $CH_3$), 1.59 (s, 1 H, OH), 4.43 (t, $J$ = 6.2 Hz, 2 H, ArH), 4.55 (t, $J$ = 6.2 Hz, 1 H, ArH), 5.05 (d, $J$ = 6.2 Hz, 2 H, ArH) ppm. $^{13}C$ NMR (100 MHz, $C_6D_6$): $\delta$ = 31.3, 70.3, 91.0, 91.7, 93.4, 121.4, 233.8 ppm.

**(η⁶-1,3-Benzo[1,3]dioxol-5-methanol)tricarbonylchromium(0) (25):**[38] Yellow oil. $^1H$ NMR (200 MHz, $C_6D_6$): $\delta$ = 1.40–1.65 (br, 1 H, OH), 3.60–3.80 (br, 2 H, $CH_2OH$), 4.20 (d, $J$ = 5.9 Hz, 1 H, ArH), 4.72 (d, $J$ = 5.9 Hz, 1 H, ArH), 4.91 (s, 2 H, $OCH_2O$), 5.09 (s, 1 H, ArH) ppm. $^{13}C$ NMR (50 MHz, $C_6D_6$): $\delta$ = 62.7, 75.9, 76.5, 84.4, 100.3, 106.3, 129.6, 233.7 ppm.

**Tricarbonyl(η⁶-2-methoxybenzyl alcohol)chromium(0) (26):**[39] IR (diethyl ether): $\tilde{\nu}$ = 1966, 1890 $cm^{-1}$. $^1H$ NMR (200 MHz, $C_6D_6$): $\delta$ = 1.45–1.85 (br, 1 H, OH), 2.91 (s, 3 H, $OCH_3$), 3.80–4.25 (m, 3 H, $CH_2OH$ and ArH), 4.34 (d, $J$ = 6.2 Hz, 1 H, ArH), 4.64 (t, $J$ = 6.2 Hz, 1 H, ArH), 5.30 (d, $J$ = 5.7 Hz, 1 H, ArH) ppm.

**General Procedure for the Synthesis of Trichloroacetate Derivatives: Tricarbonyl(η⁶-1,2,3,4-tetrahydro-1-naphthyl trichloroacetate)chromium(0) (22):** To a mixture of complex **21** (1.34 g, 4.70 mmol) and $Et_3N$ (0.86 mL, 6.12 mmol) in $CH_2Cl_2$ was added dropwise trichloroacetyl chloride (0.58 mL, 5.10 mmol) at 0 °C. The resulting mixture was stirred at room temp. for 1 h, then poured into water, and extracted with $CH_2Cl_2$. The organic solution was dried with $MgSO_4$ and then concentrated. The residue was purified by chromatography on silica gel (diethyl ether/hexane = 1–2:2) to give 1.89 g (94%) of **22** as a light yellow crystalline solid. M.p. 81.0–81.5 °C. IR (hexane): $\tilde{\nu}$ = 1982, 1920, 1908, 1766 $cm^{-1}$. $^1H$ NMR (400 MHz, $CDCl_3$): $\delta$ = 1.75 (m, 4 H, $CH_2$), 2.60–2.90 (m, 2 H, $PhCH_2$), 5.05 (d, $J$ = 6.6 Hz, 1 H, ArH), 5.09 (t, $J$ = 6.6 Hz, 1 H, ArH), 5.50 (t, $J$ = 6.6 Hz, 1 H, ArH), 5.56 (d, $J$ = 6.6 Hz, 1 H, ArH), 5.80 (dd, $J$ = 6.6, 6.8 Hz, 1 H, PhCHOH) ppm. $^{13}C$ NMR (50 MHz, $C_6DCl_3$): $\delta$ = 18.3, 27.5, 27.9, 73.6, 87.6, 88.8, 92.9, 94.7, 104.1, 111.9, 161.8, 232.1 ppm.

**1-Phenethyl Trichloroacetate (5):** IR ($CH_2Cl_2$): $\tilde{\nu}$ = 1763, 1496, 1453, 1248, 1059, 883, 828 $cm^{-1}$. $^1H$ NMR (400 MHz, $CDCl_3$): $\delta$ = 1.60 (d, $J$ = 6.8 Hz, 3 H, $CH_3$), 5.90 (q, $J$ = 6.8 Hz, 1 H, OCH), 7.20–7.35 (m, 5 H, ArH) ppm. $^{13}C$ NMR (100 MHz, $CDCl_3$): $\delta$ = 21.8 78.2, 99.3, 126.0, 128.6, 128.7, 139.5 161.1 ppm.

**Benzyl Trichloroacetate (6):** IR ($CH_2Cl_2$): $\tilde{\nu}$ = 1766, 1498, 1456, 1228, 965, 829.0 $cm^{-1}$. $^1H$ NMR (400 MHz, $CDCl_3$): $\delta$ = 5.37 (s, 2 H, $PhCH_2O$), 7.30–7.45 (m, 5 H, ArH) ppm. $^{13}C$ NMR (100 MHz, $CDCl_3$): $\delta$ = 70.7, 99.3, 128.3, 128.8, 129.0, 133.7, 161.8 ppm.

**(η⁶-Benzyl trichloroacetate)tricarbonylchromium(0) (17a):** Yellow solid. M.p. 98.50–100 °C. IR (hexane): $\tilde{\nu}$ = 1987, 1923, 1774 $cm^{-1}$. $^1H$ NMR (200 MHz, $C_6D_6$): $\delta$ = 4.10–4.37 (br, 5 H, ArH and $CH_2O$), 4.37–4.56 (br, 2 H, ArH) ppm. $^{13}C$ NMR (50 MHz, $C_6D_6$): $\delta$ = 68.9, 91.6, 92.0, 93.1, 100.9, 161.5, 232.2 ppm. $C_{12}H_7Cl_3CrO_5$ (389.54): calcd. C 37.00, H 1.81; found C 37.15, H 1.81.

**Tricarbonyl(η⁶-phenethyl trichloroacetate)chromium(0) (17b):** Yellow solid. M.p. 85.5–86.0 °C. IR (diethyl ether): $\tilde{\nu}$ = 1973, 1900, 1772 $cm^{-1}$. $^1H$ NMR (400 MHz, $C_6D_6$): $\delta$ = 1.90 (t, $J$ = 6.0 Hz, 2 H, $PhCH_2$), 3.96 (t, $J$ = 6.0 Hz, 2 H, $CH_2O$), 4.16–4.55 (m, 5 H, ArH) ppm. $^{13}C$ NMR (100 MHz, $C_6D_6$): $\delta$ = 33.7, 68.5, 90.1, 91.5, 92.6, 93.2, 107.1, 161.5, 233.1 ppm. $C_{13}H_9Cl_3CrO_5$ (403.57): calcd. C 38.69, H 2.25; found C 38.66, H 2.21.

**Tricarbonyl(η⁶-3-phenylpropyl trichloroacetate)chromium(0) (17c):** Yellow solid. M.p. 57.50–58.0 °C. IR (diethyl ether): $\tilde{\nu}$ = 1973, 1900, 1791 $cm^{-1}$. $^1H$ NMR (400 MHz, $C_6D_6$): $\delta$ = 1.17–1.40 (br, 2 H, $CH_2$), 1.70–1.98 (br, 2 H, $PhCH_2$), 3.58–3.87 (br, 2 H, $CH_2O$), 4.15–4.42 (br, 3 H, ArH), 4.42–4.68 (br, 2 H, ArH) ppm. $^{13}C$ NMR (100 MHz, $C_6D_6$): $\delta$ = 29.1, 30.8, 67.8, 90.2, 92.1, 93.4, 111.3, 161.8, 233.4 ppm. $C_{14}H_{11}Cl_3CrO_5$ (417.59): calcd. C 40.27, H 2.65; found C 40.30, H 2.65.

**Tricarbonyl(η⁶-4-phenylbutyl trichloroacetate)chromium(0) (17d):** Yellow oil. IR (diethyl ether): $\tilde{\nu}$ = 1971, 1896, 1770 $cm^{-1}$. $^1H$ NMR (200 MHz, $C_6D_6$): $\delta$ = 0.70–1.40 (br, 4 H, $CH_2$), 1.50–2.00 (br, 2 H, $PhCH_2$), 3.45–4.00 (br, 2 H, $CH_2O$), 4.15–4.43 (br, 3 H, ArH), 4.43–4.85 (br, 2 H, ArH) ppm. $^{13}C$ NMR (50 MHz, $C_6D_6$): $\delta$ = 27.0, 27.5, 34.2, 68.6, 90.2, 92.2, 93.6, 112.6, 161.9, 233.5 ppm. MS: $m/z$ (%) = 430 (85) $[C_{13}H_9Cl_3CrO_6]^{+\cdot}$, 346 (18), 311 (14), 236 (100), 117 (16), 91 (100), 52 (53). HRMS: $m/z$ calcd. for $C_{15}H_{13}Cl_3CrO_5$ 429.9233; found 429.9268.

**Tricarbonyl(η⁶-1-phenethyl trichloroacetate)chromium(0) (19a):** Yellow oil. IR ($CH_2Cl_2$): $\tilde{\nu}$ = 1974, 1898, 1767 $cm^{-1}$. $^1H$ NMR (200 MHz, $C_6D_6$): $\delta$ = 1.14 (d, $J$ = 3.98 Hz, 3 H, $CH_3$), 4.20–5.50 (m, 6 H, ArH and CHO) ppm. $^{13}C$ NMR (50 MHz, $C_6D_6$): $\delta$ = 20.3, 75.6, 90.6, 91.1, 91.2, 91.5, 92.6, 107.8, 160.7, 232.4 ppm.

**Tricarbonyl(η⁶-α-methylstyrene)chromium(0) (20):** IR ($CH_2Cl_2$): $\tilde{\nu}$ = 1968, 1891 $cm^{-1}$. $^1H$ NMR (400 MHz, $C_6D_6$): $\delta$ = 1.65 (dd, $J$ = 0.8, 1.4 Hz, 3 H, $CH_3$), 4.40–4.50 (m, 3 H, ArH), 4.70–4.78 (m, 2 H, ArH), 4.78 (d, $J$ = 1.4 Hz, 1 H, C=$CH_2$), 5.02 (d, $J$ = 0.8 Hz, 1 H, C=$CH_2$) ppm. $^{13}C$ NMR (100 MHz, $C_6D_6$): $\delta$ = 20.4, 90.3, 91.7, 91.8, 109.2 114.3, 139.6, 233.4 ppm.

**Tricarbonyl[4-(2,2,2-trichloroacetoxymethyl)benzyl trichloroacetate]chromium(0) (24):** Yellow solid. M.p. 98.5–100 °C. IR ($C_6H_6$): $\tilde{\nu}$ = 1979, 1912, 1770 $cm^{-1}$. $^1H$ NMR (400 MHz, $CDCl_3$): $\delta$ = 5.14 (s, 4 H), 5.53 (s, 4 H) ppm. $^{13}C$ NMR (100 MHz, $CDCl_3$): $\delta$ = 68.4, 89.3, 91.8, 100.8, 161.6, 230.5 ppm. MS: $m/z$ (%) = 564 (1) $[M]^+$, 438 (2), 265 (8), 139 (40), 104 (100), 52 (15), 28 (36). $CrC_{15}H_8Cl_6O_7$ (564.94): calcd. C 31.89, H 1.43; found 31.86, H 1.42.

**(η⁶-Benzo[1,3]dioxol-5-ylmethyl trichloroacetate)tricarbonylchromium(0) (28):** Yellow crystals. M.p. 75 °C (decomp.). IR ($CH_2Cl_2$): $\tilde{\nu}$ = 1971, 1894, 1768 $cm^{-1}$. $^1H$ NMR (200 MHz, $CDCl_3$): $\delta$ = 4.92 (d, $J$ = 12.2 Hz, 1 H, $CH_2O$), 5.01 (d, $J$ = 12.2 Hz, 1 H, $CH_2O$), 5.11 (d, $J$ = 6.3 Hz, 1 H, ArH), 5.50 (d, $J$ = 6.3 Hz, 1 H, ArH), 5.65 (s, 1 H, ArH), 5.77 (s, 1 H, $OCH_2O$), 6.00 (s, 1 H, $OCH_2O$) ppm. $^{13}C$ NMR (50 MHz, $C_6D_6$): $\delta$ = 69.4, 71.4, 75.8, 78.0, 88.0, 95.3, 95.3, 101.5, 129.2, 129.8, 162.1, 232.4 ppm.

 © 2007 Wiley-VCH Verlag GmbH & Co. KGaA, Weinheim 

**Tricarbonyl(η⁶-2-methoxybenzyl trichloroacetate)chromium(0) (29):** Yellow solid. M.p. 95 °C (decomp.). IR (diethyl ether): $\tilde{\nu}$ = 1975, 1902, 1770 $cm^{-1}$. $^1H$ NMR (200 MHz, $C_6D_6$): $\delta$ = 2.4–3.15 (br, 3 H, $OCH_3$), 3.52–4.20 (br, 2 H, $PhCH_2O$), 4.20–5.40 (br, 4 H, ArH) ppm. $^{13}C$ NMR (50 MHz, $C_6D_6$): $\delta$ = 55.4, 65.0, 73.0, 84.2, 89.9, 90.1, 94.2, 97.0, 142.5, 161.5, 232.4 ppm. MS: *m*/*z* (%) = 418 (1.62) $[C_{13}H_9Cl_3CrO_6]^{+\cdot}$, 257 (2.39), 173 (3.89), 157 (3.13), 121 (100), 91 (50.95), 52 (45.6). HRMS: *m*/*z* calcd. for $C_{13}H_9Cl_3CrO_6$ 417.8955; found 417.8893.

**Tricarbonyl(η⁶-2-chlorobenzyl trichloroacetate)chromium(0) (30):** IR (diethyl ether): $\tilde{\nu}$ = 1985, 1920, 1773 $cm^{-1}$. $^1H$ NMR (200 MHz, $C_6D_6$): $\delta$ = 3.90–4.16 (m, 1 H, ArH), 4.40–4.44 (m, 1 H, ArH), 4.47 (d, *J* = 12.5 Hz, 1 H, $PhCH_2O$), 4.79 (d, *J* = 12.5 Hz, 1 H, $PhCH_2O$), 4.69–4.86 (m, 1 H, ArH) ppm. $^{13}C$ NMR (50 MHz, $C_6D_6$): $\delta$ = 66.7, 87.3, 89.9, 90.7, 93.0, 94.4, 97.5, 113.8, 161.2, 230.9 ppm.

**Evaluation of Photoinitiator Reactivity in an Acrylate Formulation:** A base formulation of the following composition was prepared: 50 g Actylan 200 (urethane acrylate, Akcros), 10 g Sartomer SR 399 (dipentaerythritol monohydroxypentaacrylate), 15 g TPGDA (Tripropyleneglycol diacrylate), 10 g TMPTA (Trimethylolpropane triacrylate), 15 g *N*-vinylpyrrolidone, 0.3 g BYK 300 (silicon resin for scratch resistance, 50% polymer in a mixture of xylene/butanol).

The photoinitiator component(s) were incorporated into a portion of the base formulation by stirring at 60 °C. The formulation was coated on an 300 μm aluminum foil with an electrical applicator equipped with a 100-μm wire-wound rod. The resulting film was successively laminated with a 76-μm Mylar foil, which serves as an oxygen barrier, a Stouffer 21-step optical wedge, which allows the determination of the relative reactivity of the photoinitiator systems, and a UV-transparent polyester foil, and then fixed on a vacuum table. Broad-band exposure was performed with a 4-kW Xenon lamp at a distance of 30 cm with a fixed dose of 291 mJ $cm^{-2}$. After exposure, the laminated foils were removed, and the film was developed in an ultrasonic bath of ethanol for 10 s. The number of fully cured steps, which serves as a measure of reactivity, was determined after drying for 5 min at 40 °C. Step 0 of the Stouffer optical wedge is 100% transparent. From step 1 to step 21, the transparency decreases from 89.13 to 0.09%, whereby every 2 steps corresponds to a halving of the transparency. Thus, a photoinitiator system which can cure 10 steps is twice as reactive as one which effects the curing of 8 steps.

**Irradiation of Complex 17a to Give (η⁶-Benzyl chloride)tricarbonylchromium (32):**[40] A solution of **17a** (0.385 g, 0.99 mmol) in benzene (5 mL) was irradiated in a Rayonet photoreactor (Four 3500 Å lamps) until complete disappearance of starting material (2 d, followed by TLC). The reaction mixture was filtered (Celite) and concentrated. Chromatography on silica gel (eluent hexane/EtOAc = 5:1) afforded complex **32** as a yellow solid (0.107 g, 41%). 1H NMR (200 MHz, $C_6D_6$): $\delta$ = 3.47 (s, 2 H, $CH_2Cl$), 4.15–4.40 (m, 5 H, ArH) ppm. MS: *m*/*z* (%) = 262 (11) $[M^+]$, 178 (26), 143 (8), 91 (100), 52 (60). HRMS: *m*/*z* calcd. for $C_{10}H_7ClCrO_3$ 261.9489; found 261.9477.

**(η⁶-Benzene)dicarbonyl(η²-methyl acrylate)chromium(33b):** Following a literature method,[27] a solution of (η⁶-benzene)(η²-*cis*-cyclooctene)$Cr(CO)_2$ was prepared by photolysis (Philips, HPK 125) of complex **1** (0.642 g, 3 mmol) in benzene (200 mL)/cyclooctene (16 mL). Methyl acrylate (270 μL, 3 mmol) was added to the reaction mixture after completion of the irradiation. After 16 h, the mixture was filtered through Celite. Volatiles were removed in vacuo. The residue was taken up in hexane/benzene (20:1) and recrystallized at –40 °C to give red-orange crystals of **33b** (0.586 g, 72%). M.p. 82–83 °C. IR (hexane): $\tilde{\nu}$ = 1948 (s), 1896 (s), 1704 (m) $cm^{-1}$. 1H NMR ($C_6D_6$, 200 MHz): $\delta$ = 4.35 (s, 6 H, $C_6H_6$), 3.56 (s, 3 H, $OCH_3$), 2.93 (dd, *J* = 11.3, 7.7 Hz, 1 H, C=C*H*-$CO_2$Me), 2.76 (dd, *J* = 11.3, 0.8 Hz, 1 H, $CH_2$=C), 2.37 (dd, *J* = 7.7, 0.8 Hz, 1 H, $CH_2$=C) ppm. 13C NMR ($C_6D_6$, 50 MHz): $\delta$ = 246.6, 245.9, 177.2, 95.9, 50.1, 41.4, 38.6 ppm. MS: *m*/*z* (%) = 272 (0.4) $[M^+]$, 186(4), 158(7), 130(18), 78(100), 52(65). $C_{12}H_{12}CrO_4$ (272.22): calcd. C 52.95, H 4.44; found C 52.72, H 4.36.

## Acknowledgments

Support of this work by the Swiss National Science Foundation (grant to E. P. K.) and by Ciba Specialty Chemicals (Fellowship to L. H. X.) is gratefully acknowledged.

[1] Selected refs: a) J. Benkhoff, K. Dietliker, T. Jung, K. Powell, E. Sitzmann, *Asia Pacific Coat. J.* **2006**, *19*, 38; b) R. S. Davidson, R. J. Holman, *Rev. Prog. Col.* **2003**, *33*, 46; c) C. Decker, *J. Appl. Polym. Sci.* **1998**, *70*, 2269; d) A. B. Scranton, C. N. Bowman, R. W. Peiffer (Eds.), *Photopolymerization: Fundamentals and Applications*, ACS Symposium Series, No. 673, American Chemical Society, Washington, DC, **1997**; e) *Radiation Curing in Polymer Technology and Science* (Eds.: J. P. Fouassier, J. P. Rabek), Elsevier Applied Science London and New York, **1993**; f) S. P. Pappas (Ed.), *Radiation Curing: Science and Technology*, Plenum Press, New York, **1992**.

[2] a) K. Dietliker, *A Compilation of Photoinitiators Commercially Available for UV Today*, SITA Technology Ltd., Edinburgh, **2002**; b) J. V. Crivello, K. Dietliker *Photoinitiators for Free Radical Cationic and Anionic Photopolymerisation, Vol. III* in the series *Chemistry and Technology of UV and EB Formulation for Coatings, Inks and Paints,* John Wiley and Sons/SITA Technology Ltd., London **1998**; c) B. M. Monroe, G. C. Weed, *Chem. Rev.* **1993**, *93*, 435.

[3] Irgacure 784 and Irgacure 261 are trademarks of Ciba Specialty Chemicals Ltd., Basel.

[4] For reviews on inorganic and organometallic photoinitiators see: a) J. P. Fouassier, X. Allonas, D. Burget, *Prog. Org. Coatings* **2003**, *47*, 16; b) C. Kutal, *Coord. Chem. Rev.* **2001**, *211*, 353; c) J. Jakubiak, J. F. Rabek, *Polimery* **1999**, *44*, 447; d) A. F. Cunningham Jr, V. Desobry in *Radiation Curing in Polymer Science and Technology, Vol. II* (Eds.: J. P. Fouassier, J. F. Rabek), Elsevier Applied Science London, **1993**, p. 323.

[5] a) V. Jakubek, A. J. Lees, *Inorg. Chem.* **2004**, *43*, 6869.

[6] a) C. H. Bamford, *Pure Appl. Chem.* **1973**, *34*, 173; b) C. H. Bamford in *Reactivity, Mechanism and Structure in Polymer Chemistry* (Eds.: A. D.Jenkins, A. Ledwith), Wiley, New York, **1974**, p. 52.

[7] C. H. Bamford, S. U. Mullik, *J. Chem. Soc. Faraday Trans. 1* **1979**, *75*, 2562.

[8] a) C. H. Bamford, K. G. Al-Lamee, C. J. Konstantinov, *J. Chem. Soc. Faraday Trans. 1* **1977**, *73*, 1406; b) C. H. Bamford, K. G. Al-Lamee, *J. Chem. Soc. Faraday Trans. 1* **1984**, *80*, 2175.

[9] a) C. H. Bamford, R. W. Dyson, C. G. Eastmond, D. Whittle, *Polymer (Lond.)* **1969**, *16*, 759; b) C. H. Bamford, C. G. Eastmond, D. Whittle, *Polymer (Lond.)* **1969**, *16*, 771; c) J. Ashworth, C. H. Bamford, E. G. Smith, *Polymer* **1972**, *13*, 57.

[10] a) C. H. Bamford, R. W. Dyson, C. G. Eastmond, *J. Polym. Sci. C* **1970**, *16*, 2425.

[11] C. A. L. Mahaffy, P. L. Pauson, *Inorg. Synth.* **1979**, *19*, 154.

[12] a) E. P. Kündig, *Transition Metal Arene π-Complexes in Organic Synthesis and Catalysis, Vol. 7*, Springer, Heidelberg, **2004**; b) E. P. Kündig, S. Pache, *Sci. Synth.* **2003**, *2*, 153.

[13] K. Saigo, M. Usui, K. Kikuchi, E. Shimada, T. Mukaiyama, *Bull. Chem. Soc (Japan)* **1977**, *50*, 1863.

 © 2007 Wiley-VCH Verlag GmbH & Co. KGaA, Weinheim 

[14] a) H. M. Wagner, M. D. Purbrick, *J. Photogr. Sci.* **1981**, *29*, 230; b) H. M. Wagner, M. D. Purbrick, British Patent 2176796, issued to Kodak Ltd., priority 6.17.85.
[15] M. E. Wright, *Organometallics* **1989**, *8*, 407.
[16] a) J. A. Morley, N. F. Woolsey, *J. Org. Chem.* **1992**, *57*, 6487; b) E. P. Kündig, C. Perret, S. Spichiger, G. Bernardinelli, *J. Organomet. Chem.* **1985**, *286*, 183; c) B. Deubzer, H. P. Fritz, C. G. Kreiter, K. Öfele, *J. Organomet. Chem.* **1967**, *7*, 289.
[17] a) W. Strohmeier, H. Hellmann, *Chem. Ber.* **1963**, *96*, 2859; b) E. P. Kündig, C. Dupré, B. Bourdin, A. Cunningham Jr, D. Pons, *Helv. Chim. Acta* **1994**, *77*, 421.
[18] A. D. Hunter, V. Mozol, S. D. Tsai, *Organometallics* **1992**, *11*, 2251.
[19] P. Nirchio, J. D. Wink, *Organometallics* **1991**, *10*, 2499.
[20] Selected examples: a) U. Englert, C. Hu, A. Salzer, E. Alberico, *Organometallics* **2004**, *23*, 5419; b) K. Kamikawa, T. Sakamoto, Y. Tanaka, M. Uemura, *J. Org. Chem.* **2003**, *68*, 9356; c) G. Bernardinelli, S. Gillet, E. P. Kündig, R. Liu, A. Ripa, L. Saudan, *Synthesis* **2001**, 2040; d) K. Kamikawa, T. Watanabe, A. Daimon, M. Uemura, *Tetrahedron* **2000**, *56*, 2325; e) A. Quattropani, G. Bernardinelli, E. P. Kündig, *Helv. Chim. Acta* **1999**, *82*, 90; f) M. V. Troutman, D. H. Appella, S. L. Buchwald, *J. Am. Chem. Soc.* **1999**, *121*, 4916; g) T. J. J. Muller, M. Ansorge, K. Polborn, *J. Organomet. Chem.* **1999**, *578*, 252; h) A. J. Pearson, A. V. Gontcharov, *J. Org. Chem.* **1998**, *63*, 152; i) D. Schinzer, U. Abel, P. G. Jones, *Synlett* **1997**, 632; j) E. P. Kündig, J. Leresche, L. Saudan, G. Bernardinelli, *Tetrahedron* **1996**, *52*, 7363.
[21] I. U. Khand, C. A. L. Mahaffy, P. L. Pauson, *J. Chem. Res. (S)* **1978**, 352.
[22] a) D. E. F. Gracey, W. R. Jackson, W. B. Jennings, T. R. B. Mitchell, *J. Chem. Sc.* **1969**, 1204; b) S. G. Davies, C. L. Goodfellow, *J. Organomet. Chem.* **1988**, *340*, 195; c) H. G. Schmalz, B. Millies, J. W. Bats, G. Dürner, *Angew. Chem. Int. Ed. Engl.* **1992**, *21*, 631.
[23] S. G. Davies, T. D. McCarthy, in *Comprehensive Organometallic Chemistry II, Vol. 12* (Eds.: E. W. Abel, F. G. A. Stone, G. Wilkinson), Pergamon Press, Oxford, **1995**, p. 1039.
[24] a) S. Top, G. Jaouen, J. Gillois, C. Baldoli, S. Maiorana, *J. Chem. Soc. Chem. Commun.* **1988**, 1284; b) S. G. Davies, C. L. Goodfellow, *J. Organomet. Chem.* **1989**, *370*, C5.
[25] a) L. H. Xu, E. P. Kündig, *Helv. Chim. Acta* **1994**, *77*, 1480; b) J. W. Crawford, *J. Chem. Soc.* **1953**, 2658.
[26] a) V. Desobry, K. Dietliker, R. Hüsler, W. Rutsch, H. Löliger, *Poly. Paint Colour J.* **1988**, *178*, 913; b) V. Desobry, K. Dietliker, L. Misev, M. Rembold, G. Rist, W. Rutsch in *Radiation Curing of Polymeric Materials* (Eds.: C. E. Hoyle, J. F. Kinstle), American Chemical Society, Washington, D. C., **1990**, p. 92.
[27] K. R. Plowman, I. S. Butler, A. M. English, *Inorg. Synth.* **1982**, *XXI*, 2.
[28] E. P. Kündig, M. Kondratenko, P. Romanens, *Angew. Chem. Int. Ed. Engl.* **1998**, *37*, 3146.
[29] E. P. Kündig, G. Bernardinelli, M. Kondratenko, F. Robvieux, P. T. Romanens, *Helv. Chim. Acta* **2003**, *86*, 4169.
[30] $[Cr(CO)_2(\eta^4\text{-}1,3\text{-cyclohexadiene})_2]$ is a catalyst for the [6+2] cycloaddition between cycloheptatriene and activated olefins: E. P. Kündig, F. Robvieux, M. T. Kondratenko, *Synthesis* **2002**, 2053.
[31] a) J. A. Heppert, M. A. Morgenstern, D. M. Scherubel, F. Takusagawa, M. R. Shaker, *Organometallics* **1988**, *7*, 1715; b) F. Van Meurs, J. M. Van der Toorn, H. Van Bekkum, *J. Organomet. Chem.* **1976**, *113*, 341.
[32] P. A. Brown, H. J. Lyons, A. R. Manning, *Inorg. Chim. Acta* **1970**, *4*, 428.
[33] W. Strohmeyer, F. J. Müller, *Chem. Ber.* **1969**, *102*, 3608.
[34] M. R. Domingo, A. Irving, Y.-H. Liao, J. R. Moss, A. Nash, *J. Organomet. Chem.* **1993**, *443*, 233.
[35] a) B. Nicholls, M. C. Whiting, *J. Chem. Soc.* **1959**, 551; b) J. Blagg, S. G. Davies, C. L. Goodfellow, K. H. Sutton, *J. Chem. Soc. Perkin Trans. 1* **1990**, 1133.
[36] a) W. R. Jackson, C. M. McMullen, *J. Chem. Soc.* **1965**, 1170; b) J. Lebibi, J. Brocard, D. Couturier, *Bull. Soc. Chim. Fr.* **1982**, 357.
[37] a) F. Effenberger, K. Schoellkopf, *Chem. Ber.* **1985**, *118*, 4356; b) J. Blagg, S. G. Davies, C. L. Goodfellow, K. H. Sutton, *J. Chem. Soc. Perkin Trans. 1* **1987**, 1805; c) J. Gillois, D. Buisson, R. Azerad, G. Jaouen, *J. Chem. Soc. Chem. Commun.* **1988**, 1224; d) J. A. Heppert, J. Aubé, M. E. Thomas-Miller, M. L. Milligan, F. Takusagawa, *Organometallics* **1990**, *9*, 727.
[38] S. Top, G. Jaouen, C. Baldoli, P. DelButtero, S. Maiorana, *J. Organomet. Chem.* **1991**, *413*, 125.
[39] R. Dabard, A. Meyer, *C. R. Hebd. Seances Acad. Sci., Ser. C* **1967**, *264*, 903.
[40] a) J. D. Holmes, D. A. K. Jones, R. Pettit, *J. Organomet. Chem.* **1965**, *4*, 324; b) V. Galamb, G. Palyi, F. Ungvary, L. Marko, R. Boese, G. Schmid, *J. Am. Chem. Soc.* **1986**, *108*, 3344; c) S. E. Gibson, G. A. Schmid, *J. Chem. Soc.* **1997**, 865.

Received: January 28, 2007
Published Online: May 11, 2007

 © 2007 Wiley-VCH Verlag GmbH & Co. KGaA, Weinheim 

DOI: 10.1002/ejic.200700235

# Generation of [2×2] Grid Metallosupramolecular Architectures from Preformed Ditopic Bis(acylhydrazone) Ligands and through Component Self-Assembly

**Xiao-Yu Cao,[a] Jack Harrowfield,[a] Jonathan Nitschke,[a][‡] Juan Ramírez,[a] Adrian-Mihail Stadler,[a] Nathalie Kyritsakas-Gruber,[b] Augustin Madalan,[a] Kari Rissanen,[c] Luca Russo,[c] Gavin Vaughan,[d] and Jean-Marie Lehn*[a]**

*Dedicated to Professor Neil Bartlett on the occasion of his 75th birthday*

**Keywords:** Grids / Ditopic acylhydrazones / Component assembly / Crystal structures

Ditopic bis(acylhydrazone) ligands, derived from the reactions of carbohydrazides with 2-phenylpyrimidine-4,6-dicarbaldehyde and designed for grid formation with octahedrally coordinating transition-metal ions, exhibit a varied coordination chemistry depending upon the degree of their deprotonation. The neutral acylhydrazones are relatively poor ligands and are seemingly involved in multiple, labile complexation equilibria varying with the solvent and the particular metal salt in solution; nevertheless, grid complexes of different forms can be isolated in the solid state. Although only limited study has been made of the singly deprotonated ligands, grid species appear to be much more readily isolated. With the doubly deprotonated ligands, grid formation is strongly favoured in both the solution and solid states. As a consequence, the grid structures form spontaneously in the presence of a base by self-assembly from their components without need to preform the ditopic ligands. Extensive structural studies have been carried out both to establish the grid structures and to analyse the nature of the supramolecular interactions possible for neutral and charged grid species.
(© Wiley-VCH Verlag GmbH & Co. KGaA, 69451 Weinheim, Germany, 2007)

## Introduction

Metallosupramolecular chemistry has developed a wide range of fascinating multicomponent coordination architectures generated by self-assembly from suitably designed ligands and specific metal ions.[1–12] The structure of the ligand bears the molecular information, as a message in molecules, that is processed through the coordination algorithm of the metal ion. Grid-type metallosupramolecular entities are of special interest, as they represent regularly positioned arrays of metal ions that may display novel optical, electronic and magnetic properties.[8,12,13] In particular, [2×2] tetranuclear grids have been extensively studied by our group.[8] We describe here developments towards classes of [2×2] grids presenting novel structural and functional characteristics.

[a] Laboratoire de Chimie Supramoléculaire, Institut de Science et d'Ingénierie Supramoléculaires, Université Louis Pasteur, 8 allée Gaspard Monge, Strasbourg, 67083, France
[b] Service de Cristallographie, Institut Le Bel, Université Louis Pasteur, 4 rue Blaise Pascal, Strasbourg, 67083, France
[c] Nanoscience Centre, Department of Chemistry, University of Jyväskylä, P. O. Box 35, 40014 JYU, Finland
[d] European Synchrotron Radiation Facility (ESRF), B. P. 220, 38043, Grenoble, France
[‡] Present address: Departement de Chimie Organique, Université de Genève, 30 Quai Ernest Ansermet, 1211 Genève, Switzerland

### Design Features

The "parent" [2×2] grid architectures incorporate ditopic ligands based on pyridine (py) and pyrimidine (pym) groups in a py-py-pym-py-py sequence amounting to two tridentate terpyridine-type coordination centres (structure **L**).[8] Replacement of a py group by an isosteric hydrazone unit presents considerable synthetic advantages as well as other novel properties. It may be achieved by condensation of a central pyrimidine-4,6-dicarbaldehyde with either a pyridine-2-hydrazine or a hydrazide (Figure 1, routes leading to products **A** and **B**, respectively), thus generating ditopic ligands incorporating two hydrazone functions as central groups of two tridentate metal coordination centres. Ligands containing two unsubstituted hydrazone units (Figure 1) possess two ionisable sites[12,14–19] that may serve to modulate (i) the coordination properties of the ligands, (ii)

 © 2007 Wiley-VCH Verlag GmbH & Co. KGaA, Weinheim 

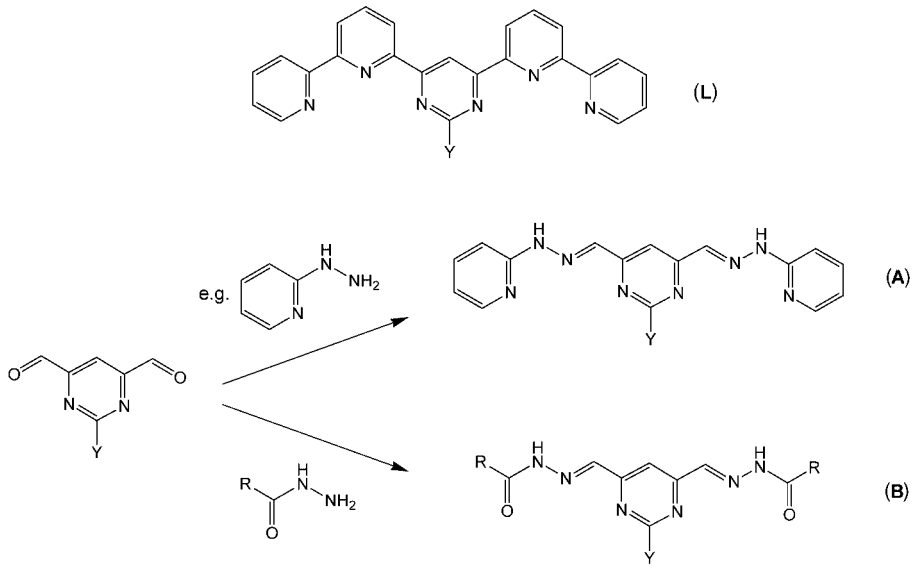


Figure 1. The parent [2×2] grid-forming bis(bipyridyl)pyrimidine ligand **L** and synthetic pathways to isosteric hydrazone (**A**) and acylhydrazone (**B**) analogues. Note that the bis(tridentate) form shown is but one of the configurations possible for such ligands.

the optical electronic and magnetic properties of the grid complexes, as well as (iii) the communication between external effectors and the metal centres.

In addition, the py-hydrazone ligands (**A** in Figure 1) may be fitted with side chains that will extend along the axis perpendicular to the mean plane of the four metal cations in the grid,[20] whereas for the grids formed from acylhydrazone ligands (**B** in Figure 1), the R side chains extend laterally. Thus, grid formation from these two types of ligands results in multiple "axial" and "lateral" functionalisation. Furthermore, the acylhydrazone groups may also bear axial side chains, resulting in grids presenting a total of sixteen substituents that can be of two different types.

Finally, the hydrazone-based ligands need not to be preformed, as they may form directly from their components and the metal ions in a single overall process in the course of the self-organisation of the grid architecture (Figure 2). Component self-assembly has a long history in coordination chemistry involving carbonyl condensation reactions.[21] Multicomponent/multinuclear self-assembly has been shown to take place in the spontaneous build-up of another type of [2×2] grid[22] and has been further exploited recently.[11]

Grid-type complexes formed from hydrazone-containing ligands display several features of great interest: (i) easy synthetic access from preformed ligands or by component

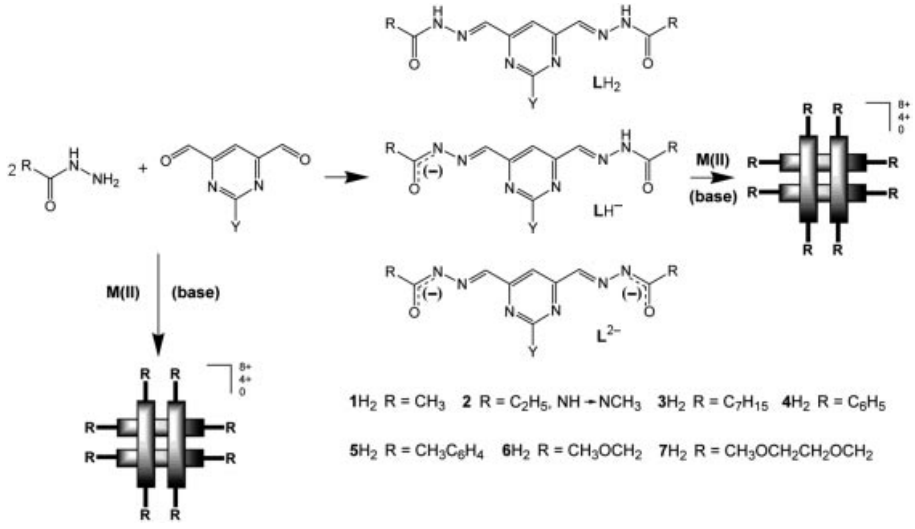


Figure 2. Formation and ionisation of a bis(acylhydrazone) derived from a pyrimidinedicarbaldehyde, with an idealised representation of the laterally functionalised grid, which may be formed by complexation either from the preformed ligand or by reaction with its constituents. Only the bis(tridentate) form of the ligand is shown. The seven particular acylhydrazones studied in the present work are listed (Y = phenyl in all cases).

 © 2007 Wiley-VCH Verlag GmbH & Co. KGaA, Weinheim 

self-assembly; (ii) multiple functionalisation; (iii) response to external effectors. We have undertaken studies towards the exploration and the exploitation of these different aspects of the potentialities offered by such grid complexes of the [2×2] type as well as of other types.

The readily ionised ligands of type **B** (Figure 2) provide functionalised grid complexes, giving rise to quartets of pairs of "lateral" functional groups. Crystal structure determinations on a range of these complexes with $M^{II}$ transition-metal ions give indications of a variety of labile interactions possible in grid systems, which might be exploited in supramolecular chemistry.

## Results and Discussion

### 1. Bis(acylhydrazone) Ligand Synthesis and Characterisation

The neutral, protonated forms of the bis(acylhydrazone) ligands presently described have all been obtained by double-condensation reactions of 2-phenylpyrimidine-4,6-dicarbaldehyde with carbohydrazides (designated henceforth as acylhydrazines). It is possible to conduct these reactions with a much greater variety of acylhydrazines, work which will be the subject of other publications,[23] and, of course, to vary the nature of the dicarbaldehyde. Characterisation of the reactions between the phenylpyrimidinedicarbaldehyde and acylhydrazines in homogeneous solution is complicated by the low solubility of the products in most solvents, as well as by changes in the form of the dicarbaldehyde in different solvents (Figure 3). The dicarbaldehyde, as obtained directly from the partially aqueous final synthetic medium,[24] is hydrated to a degree and thus present as a mixture of forms, even though it does crystallise well from diethyl ether. In aprotic solvents such as chloroform or acetonitrile, the $^1$H NMR spectrum shows predominantly peaks attributable to the true aldehyde only (even in the presence of low concentrations of water present in the undried solvents), whereas in methanol only an extremely weak –CHO signal of the aldehyde species can be discerned, and the bulk (99%) of the compound appears to be present as its bis(hemiacetal), giving rise to a CH resonance at $\delta$ = 5.54 ppm, a similar weak resonance at $\delta$ = 5.53 ppm along with the aldehyde peak at $\delta$ = 10.09 ppm, consistent with the presence of ca. 1% mono(hemiacetal)monoaldehyde. We presume that, in the absence of an acid catalyst, further reactions to give acetal species must be very slow.

Fortunately, the hemiacetals are labile, since addition of an acylhydrazine to a methanol solution of the dicarbaldehyde results in the appearance of new peaks corresponding to hydrazide-*N* addition products within the time required for mixing the reagents and recording the spectrum. Typically after a period of some tens of minutes at room temperature for 2:1 molar mixtures of acylhydrazine and dicarbaldehyde, the bis(acylhydrazone) derivatives of the dicarbaldehyde begin to precipitate from such solutions, indicating that elimination reactions of the addition intermediates are also relatively rapid. The insolubility of the bis(acylhydrazone) is commonly such that it is the material precipitated even from solutions in which the molar ratio of reactants is 1:1. Consistent with an inhibition of the reaction by acetal formation in methanol, product precipitation occurs much sooner (within a few minutes) in acetonitrile. In the particular case of benzoylhydrazine, the initial precipitate obtained from acetonitrile solvent appears to be amorphous and even oily but slowly (over days) transforms largely into clusters of pale yellow needles, indicating that the immediate product could be a mixture of stereoisomers.[25,26] A further indication of this is that, in the presence of some $M^{II}$ ions (M = Mn, Zn), the precipitate, which still does not contain the metal ions, deposits more slowly and appears to be entirely crystalline. Perhaps this is because the precipitation of one form is retarded by complexation, even though complexation by both stereoisomers is well-established for simple acylhydrazones,[26,27] and (see below) at least two forms are still present in the precipitate. Up to the point of precipitation in solutions not containing

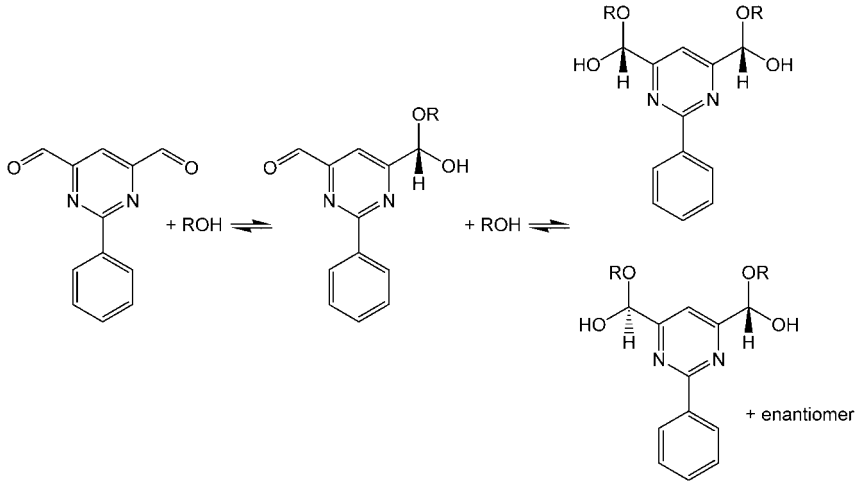


Figure 3. Hydrate (R = H) and hemiacetal (R = alkyl) formation reactions of 2-phenylpyrimidine-4,6-dicarbaldehyde.

 © 2007 Wiley-VCH Verlag GmbH & Co. KGaA, Weinheim 

metal ions, strong signals near $\delta$ = 5.7 ppm are consistent with the fact that addition intermediates are the dominant solution species, at least two being apparent.

For the hydrazides derived from methoxy- and methoxyethoxyacetic acid, solvents can be found in which all components stay soluble up to the point of homogeneous equilibrium. Here, at concentrations of ca. $5 \times 10^{-3}$ mol L$^{-1}$, NMR spectroscopy shows that small but detectable concentrations of species containing a tetrahedral methine centre are present even after several days at room temperature in acetonitrile, and over relatively short time periods (at least 1 h) in this solvent, the methoxyacetyl system seems simply to be involved in an addition equilibrium where a significant fraction of dicarbaldehyde is present. The addition of a metal ion such as $Zn^{II}$ to a mixture of acylhydrazine and dicarbaldehyde has multiple effects, including an initial release of dicarbaldehyde, presumably as a consequence of coordination of the acylhydrazine reactant, though ultimately there is a modest acceleration of the formation of the acylhydrazone. The situation is simpler in dimethyl sulfoxide solvent, where an addition equilibrium appears to be very rapidly established and is then very slowly displaced towards the elimination products (hydrazones) unless $Zn^{II}$ is added, in which case, for the addition of one molar equivalent, the spectrum changes over a period of minutes at ambient temperature towards that of the "free" bis(acylhydrazone) in this solvent. If $Ga^{III}$ is used as catalyst, the reaction seems to be complete within the time of mixing of the reagents. Thus, it can be deduced that there is efficient Lewis acid catalysis of acylhydrazone formation in dmso.

The solids that precipitate commonly from preparative mixtures can be dissolved in solvents such as dmso and do not show $^1$H spectral resonances near $\delta$ = 5.7 ppm, nor do they appear to react with the low concentrations of water present in such solvents. In most cases, however, at least two NH resonances of different intensity are detectable, indicating that stereoisomers are present (Figure 4). For related grid-forming ligands derived from thiocarbonodihydrazide,[19b] it has been established by a crystallographic study that the most readily crystallised isomer is not that ultimately found in the grid complexes, intramolecular hydrogen bonding being suggested as a factor favouring the form observed. That the proton complex of the anionic ligand has coordination characteristics very different from those of its transition-metal complexes is hardly surprising and has, of course, a great number of precedents.

While isomerism of acylhydrazones is usually considered to be associated with configuration about the hydrazone C=N bond, restricted rotation about the acyl-C–N bond is also possible; furthermore, there is evidence that intermolecular hydrogen bonding can give rise to multiple species in solution.[28] For bis(acylhydrazone)s, *E*/*Z* isomerisation about the hydrazone bond could give rise to at least three isomeric forms, and in several of the present hydrazones (e.g. **1**H$_2$, R = CH$_3$) the $^1$H NMR spectra show multiple NH (and other) resonances consistent with the presence of at least two forms. For the ligand **6**H$_2$ (R = CH$_3$OCH$_2$), one NH resonance is strongly dominant, but there are pairs of methyl and methylene peaks of similar intensity, indicating that this molecule is largely in the (*E*,*Z*) form. This may also apply for the ligand **5**H$_2$ (R = CH$_3$C$_6$H$_4$), for which the spectrum shows two sets of resonances of very different intensity, although for the closely related benzoylhydrazine derivative **4**H$_2$ (R = C$_6$H$_5$), the $^1$H NMR spectrum in [D$_6$]-

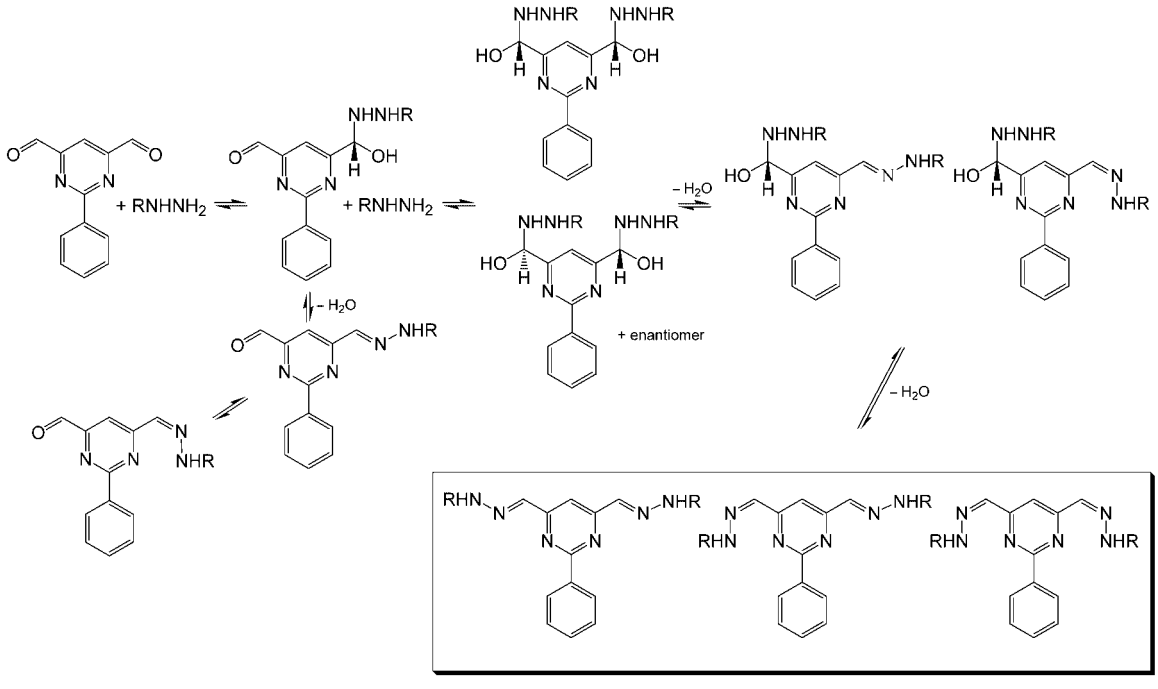


Figure 4. Species possibly present in reaction mixtures formed from 2-phenylpyrimidine-4,6-dicarbaldehyde and acylhydrazines in non-nucleophilic solvents; each stereoisomer may, of course, have other conformations than those shown.

 © 2007 Wiley-VCH Verlag GmbH & Co. KGaA, Weinheim 

dmso shows a single, relatively sharp NH resonance ($\delta$ = 12.40 ppm), and the NOESY spectrum (Figure 5) can be interpreted in terms of a single conformation of the (*E*,*E*) isomer. Thus, the correlation between the NH protons, C, and the CH=N protons, B, establishes the (*E*) configuration of the hydrazone link, while the correlation of C with the aromatic protons, D, is consistent with the (*E*) configuration of the amide bond. Assuming that a *trans* conformation of the unsaturated-N substituents on the C(aromatic)–C(hydrazone) single bond would be favoured, the configuration deduced for this molecule is that shown in Figure 5.

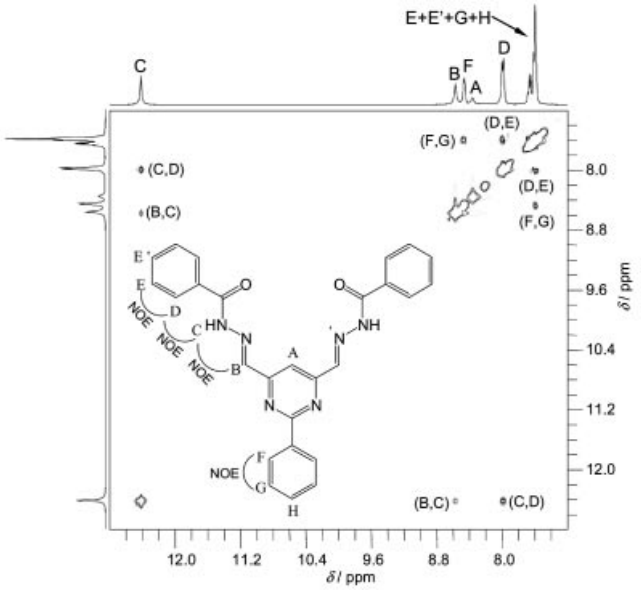


Figure 5. $^1$H-NOESY spectrum (300 MHz, [D$_6$]dmso) for the compound **4**H$_2$; the observed correlations and the configuration deduced are shown in the inset.

This conclusion is supported by the NOESY spectrum of ligand **2** (Figure 6), which shows several important similarities to that of **4**H$_2$. A crystal structure determination for ligand **2** (Figure 7) has established not only proton locations consistent with the spectrum, but has also shown the anticipated arrangement about the C(aromatic)–C(hydrazone) single bonds. The correlation (B,C) between the methyl protons, C, and the hydrazone proton, B, is in agreement with the (*E*) configuration of the C=N hydrazone bond and with an *s-trans* conformation of the N–N bond substituents. Moreover, a correlation (B,F) between the hydrazone proton, B, and the phenyl protons, F, on C2 and C2′ confirms the *s-trans* conformation of the bond connecting the hyz group to the pym ring. The correlation (A,D) between the pyrimidine proton, A, on C5 and the methylene protons, D, suggests the *s-cis* conformation of the amide bond, a difference from the conformation in **4**H$_2$, which may be attributable to both steric and electronic differences between phenyl and ethyl substituents. The weak correlation (A,B) between the pyrimidine proton, A, on C5 and the hydrazone, B, shows that, in solution, the *s-trans* conformation of the C(aromatic)–C(hydrazone) bond is partially twisted because of the steric hindrance between the two acyl arms of the ligand.

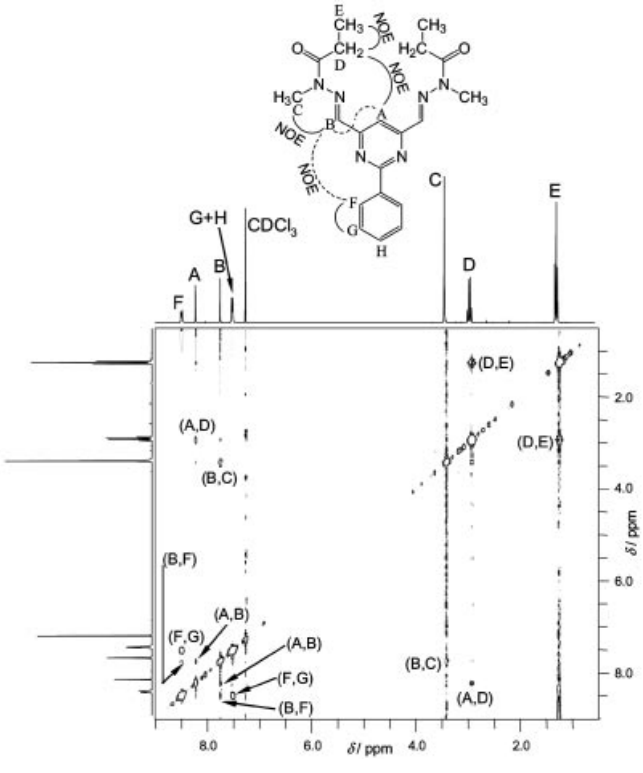


Figure 6. $^1$H-NOESY spectrum (300 MHz, $CDCl_3$) of compound **2**; proton correlations and the deduced configuration of the molecule are shown in the inset.

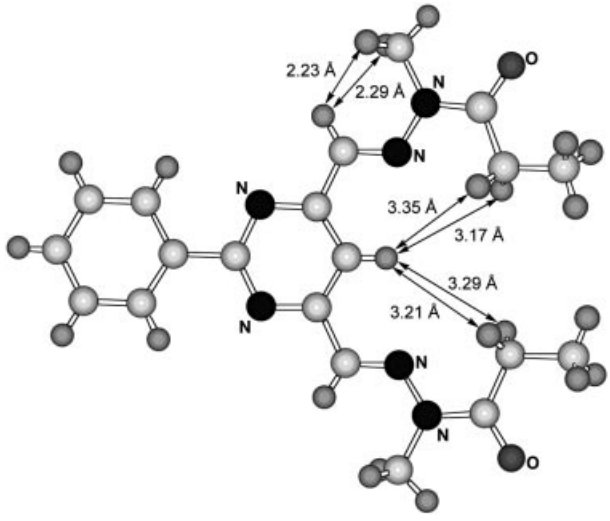


Figure 7. One molecule of **2** as found in the crystal lattice. Several intramolecular H···H separations are indicated.

## 2. Complexation of the Bis(acylhydrazone) Ligands

As the first transition-metal series provides a number of labile M$^{II}$ species commonly showing octahedral coordination but with a variety of electronic properties, the most readily available members, viz. Mn$^{II}$, Fe$^{II}$, Co$^{II}$, Ni$^{II}$, Cu$^{II}$

 © 2007 Wiley-VCH Verlag GmbH & Co. KGaA, Weinheim 

and $Zn^{II}$, were chosen for our initial investigations. $Mn^{II}$ proved to be complicated to study, presumably because of both the relatively low stability of its complexes, as reflected by its position in the Irving–Williams series,[29] and its susceptibility to undergo multiple oxidation processes, even though mass spectra provided evidence that the expected grids were the initial products of synthesis. The present focus is therefore upon the remaining five metal ions, although $Cu^{II}$ also provided some difficulties. In view of its diamagnetism, and hence the feasibility of recording high-resolution NMR spectra, $Zn^{II}$ was generally chosen as the first metal ion to be investigated, though of course it was not expected to necessarily give the most stable complexes. As anticipated and confirmed by structural and spectroscopic studies, the bis(acylhydrazone) ligands do generate 2×2 grid complexes.

### *(a) Complex Formation from the Preformed Bis(acylhydrazone) Ligands*

A limited degree of binding of the neutral ligands to $M^{II}$ ions even in pure methanol or acetonitrile solvents is suggested by the fact that acylhydrazones dissolve quite readily in these solvents when, for example, the metal triflate is added, to give appreciably coloured solutions. In the case of ligand $\mathbf{7}H_2$ (R = $CH_3OCH_2CH_2OCH_2$), which shows some solubility in $CH_3CN$, addition of one equivalent $Zn^{II}$ causes significant changes in the $^1H$ NMR spectrum, and in general the spectra of mixtures of the neutral ligands with $Zn^{II}$ vary somewhat with the metal ion concentration. Nevertheless, the spectra are poorly resolved and complex, showing slow, minor changes over time, indicating that several species may be present, and evaporation of the solvent generally results in reprecipitation of the free ligand. If, however, the initial reaction mixture containing $Zn^{II}$ (as its triflate) is immediately diluted with a poorly ligating solvent such as diethyl ether, the colour changes from pale yellow to red, presumably indicating some degree of metal complexation, and ultimately both yellow (ligand) and red crystalline materials deposit from the solution. If nitromethane is used as the solvent for the reaction, complexation of the acylhydrazone appears to be more favoured than in acetonitrile, in that the solution formed has a clear red colour, but at least for bis(benzoylhydrazone) it is still the free acylhydrazone which precipitates most readily from the solution. This precipitation can be inhibited by increasing the amount of $Zn(CF_3SO_3)_2$ present, ultimately enabling the deposition of a red 2:1 complex. In the $^1H$ NMR spectrum of this species in acetonitrile (in which the ligand itself is completely insoluble), the *ortho* protons of the central phenyl ring appear to have undergone strong shielding, which is consistent with the binding of metal ions and the resulting rotation of the phenyl group. More interesting is the observation that with tetrafluoroborate in place of triflate, a 1:1 complex precipitates, as it does in the case of $Ni^{II}$ when perchlorate is the associated anion. Note, however, that $Ni^{II}$ does not guarantee success in the isolation of a neutral ligand complex, as, while $Ni(BF_4)_2$ and ligand $\mathbf{3}H_2$ (R = $C_7H_{15}$) dissolve in boiling methanol to give an orange solution, it is the ligand which precipitates on cooling, and with $Ni(NO_3)_2$ and ligand $\mathbf{4}H_2$, the red complex which precipitates contains partly deprotonated ligand.

Overall, these observations indicate that there is a delicate balance of various solvent- and anion-dependent equilibria, including acid dissociation, involved in the interactions of neutral acylhydrazones with $M^{II}$ transition-metal ions, complications which of course are undesirable in relation to the ultimate goal of using the complexes in solution chemistry. Both of the 1:1 complexes referred to above have the form of grids in the solid state (see crystallographic discussion) but they are nonetheless quite different, the Ni species having only the (*E*,*E*) form of the ligand while the Zn species has a 1:1 mixture of (*E*,*E*) and (*Z*,*Z*) isomers.

In contrast to the behaviour in neutral media, when a base such as triethylamine is added to the reaction mixtures, rapid changes occur, and for the $Zn^{II}$ systems, the $^1H$ NMR spectra indicate the presence of distinctly different species after the addition of one and two molar equivalents of the base. The effects of adding more than two equivalents are negligible, and the final spectra are in fact identical with those obtained on dissolving the structurally characterised neutral grid species (see below) obtained by precipitation from preparative mixtures of similar composition. It is thus assumed that the species present in solution are also tetranuclear grids. In the high-resolution spectra that can be obtained with the $Zn^{II}$ complexes, those at room temperature reflect a higher symmetry than would be expected for a grid having exactly the same structure as in the solid but that this is a reflection of site-exchange processes is indicated by the fact that at –40° in $CHCl_3$, the acetylhydrazone dianion complex shows aromatic resonances consistent with restricted rotation of the central (pyrimidine) phenyl group, giving rise to a distinction between "inner" and "outer" *ortho* and *meta* proton sites.[30]

### *(b) Complex Formation by Component Self-Assembly*

In the absence of any added base in moderately polar and ligating solvents such as methanol or acetonitrile, the reaction between the phenylpyrimidinedicarbaldehyde and acylhydrazines in the presence of one molar equivalent of various $M^{II}$ ions as their triflates leads commonly, as noted above, to the precipitation of the metal-free acylhydrazone. Nonetheless, the colour of the reaction medium prior to precipitation is indicative of some degree of complexation, and although the development of this colour in methanol and acetonitrile occurs over a time period similar to that required for precipitation of the acylhydrazone in the absence of the metal, in dimethyl sulfoxide it is clear that there is an efficient metal ion catalysis of hydrazone formation. When a base such as triethylamine is incorporated in the reaction mixtures, metal ion catalysis (template effect) appears to be important in all solvents, as very rapid reactions (extensive within the time of mixing) occur to give the same neutral complex species as those obtained from reactions with the preformed ligand in basic media. An advantage of performing the syntheses in this "one pot" manner is that a good solvent for all components is much more readily

 © 2007 Wiley-VCH Verlag GmbH & Co. KGaA, Weinheim 

found than for the reactions involving preformed ligands, so that precipitation of the product from a homogeneous solution occurs easily.

### 3. General Chemistry of the Grid Systems

As many of the neutral (grid) complexes show appreciable solubility in solvents in which the parent bis(acylhydrazone)s are completely insoluble, it is possible to recover the ligand from neutral complexes by their protonation upon acidification in solution. When the complex $[Zn_4(\mathbf{1})_4]$, for example, is dissolved in methanol, in which it forms an orange solution, and acetic acid is added, the colour is instantly discharged, and the neutral ligand rapidly precipitates. Significantly, the $^1$H NMR spectrum of this material is identical with that of the "preformed" ligand, indicating it to be a mixture of species and, since the crystal structure of the neutral grid shows the presence of a single isomer of the dianionic ligand, this suggests that isomerisation of the neutral ligand is very rapid. Support for this conclusion is offered by the fact that the water-soluble complex $[Zn_4(\mathbf{6})_4]$ (R = $CH_3OCH_2$), when dissolved in $D_2O$, shows two sharp singlet resonances for the methyl and methylene protons, each of which become at least three peaks when acetic acid is added.

We thus conclude that ligand isomerisation cannot constitute a kinetic barrier to the formation of complexes. (It may be noted here that attempts to separate *E*/*Z* isomers of acylhydrazones by flash chromatography have been unsuccessful.[31]) Also significant is the fact that the use of a strong acid such as HCl to protonate the neutral complexes does not lead to precipitation of the neutral ligand, but instead to its hydrolysis, indicating that it should be possible to find conditions where all components (acylhydrazine, dicarbaldehyde and metal ion complexes) are in labile equilibrium.

Although neutral grid complexes do not generally show high solubility in apolar solvents, most dissolve readily in pyridine or, to a lesser extent, both in methanol and in dimethyl sulfoxide. Interestingly, the grids are frequently more soluble in a mixed solvent (protic + aprotic) than in either of its components. Preferential solubility in particular solvents results from the appropriate choice of acyl group; for example, the heptanoylhydrazine derivatives are moderately soluble in dichloromethane, the benzoylhydrazine derivatives in acetone and the tolylhydrazine complexes in benzene (and in dichloromethane but not in toluene), while the methoxy- and methoxyethoxyacetylhydrazine derivatives show some solubility in water. Acetonitrile is a useful solvent for the syntheses, both of the ligands and of their complexes, since the reactants are generally quite soluble and the desired products insoluble (while byproducts such as triethylammonium triflate are soluble), but, as indicated in the Experimental Section, a variety of simple approaches can be used successfully, and wherever either of the solvents methanol or acetonitrile has been used, it may certainly be substituted by the other. The successful synthesis of the neutral grids depends on the facile deprotonation of the coordinated acylhydrazone, and although no direct measurements of the acidity constants of the coordinated acylhydrazones used here have been made, triethylamine, in various solvents including water, sufficed to completely deprotonate ligands $\mathbf{1}H_2$ and $\mathbf{3}H_2$–$\mathbf{7}H_2$ when bound to first-row transition-metal(II) ions, indicating that the bound ligands are significantly stronger acids than the triethylammonium ion. This deduction is supported by the fact that the use of $^1$H NMR to monitor the titration of 1:1 mixtures of $Zn^{II}$ and various ligands with triethylamine showed shifts of the triethylamine protons consistent with complete protonation up to the point of addition of a full two equivalents of the base. Independent measurements[32] on water-soluble grids formed by pyrimidinedicarbaldehyde bis(acylhydrazone) derivatives indicate that the first ligand proton is quite acidic, and that the second is removed at pH ≈ 7.

### 4. Crystal Structures of Acylhydrazone Complexes

Basic crystallographic data for all the complexes presently studied are summarised in Table 2, Table 3 and Table 4. Disorder associated with lattice solvent molecules, grid substituents and (in some cases) anions was a common problem, and not all the structures are of equivalent quality. In all cases, however, the nature of the metal aggregate has been established with certainty. Not all crystals obtained proved suitable for an X-ray structure determination, so that the following discussion is presented more in terms of identified grid types than in terms of the systematic variation of the ligands and metals, though certainly some ligand and metal effects are taken into consideration.

#### *(a) Complexes of the Non-Deprotonated Ligands*

##### *(i) $[Ni_4(4H_2)_4](ClO_4)_8$*

The reaction between acetonitrile-solvated $Ni^{II}$ perchlorate and ligand $\mathbf{4}H_2$ (R = $C_6H_5$) in nitromethane provides a crystalline complex which may be formulated on the basis of its structure determination as $[Ni_4(\mathbf{4}H_2)_4](ClO_4)_8 \cdot 8H_2O \cdot 4CH_3NO_2$. (Elemental analysis of the dried bulk material is consistent with a formulation in which only one molecule of nitromethane of solvation is present.) The cation present in the lattice (Figure 8) is a 2×2 grid species of a form very similar to those formed with neutral hydrazone ligands[8,18,33] and remarkably similar to grids formed by the deprotonated acylhydrazones described below. It is thus a useful reference point for the whole of the present discussion.

As viewed perpendicular to the mean plane of the $Ni_4$ unit, it appears that this unit is very close to a square, but in fact there is a significant distortion towards a "butterfly" form reflected in the fact that the centroids of the two Ni···Ni diagonals are separated by 0.685 Å. This can be seen largely as a consequence of the fact that the metal–donor-atom array for a given ligand unit does not have the idealised geometry[34] shown in Figure 6, but instead is such

 © 2007 Wiley-VCH Verlag GmbH & Co. KGaA, Weinheim 

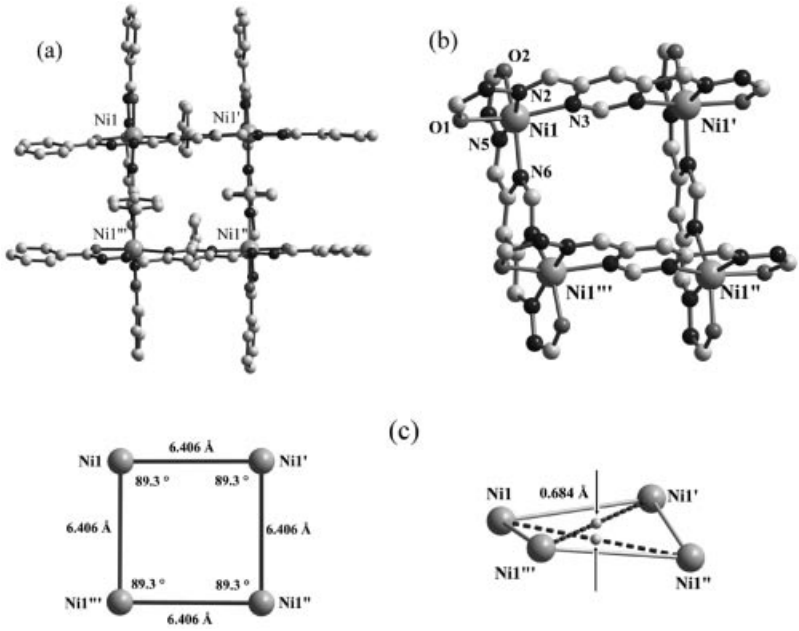


Figure 8. (a) A view of the full grid unit perpendicular to the $Ni_4$ plane and (b) a view of the grid in perspective, without phenyl substituents, to show the metal ion coordination; (c) aspects of the geometry of the $Ni_4$ unit.

that the Ni–N(hydrazide) vectors are slightly inclined to one another (here at 15°). This can be accommodated and allows six-coordination of the metal (by binding of a second ligand) by displacing two metal atoms in the same direction out of the idealised square which would be formed if the incline was 0°. As will be seen in considering other grids (see ahead), however, this is perhaps not the only factor of influence (Figure 9).

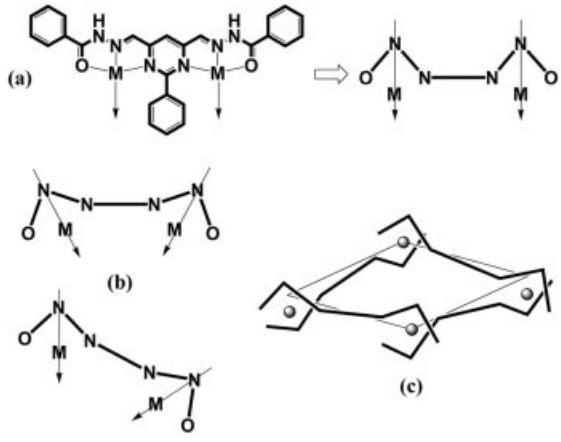


Figure 9. (a) An idealised structural representation of a metal-bound ditopic acylhydrazone and its schematic equivalent, showing parallel orientation of the M–N(hydrazide) vectors. (b) Schematic representations, with exaggerated inclination, of an actual metal-bound ditopic acylhydrazone, shown both in a form where the M···M vector is horizontal and where the O···N(inner) vector is horizontal. (c) Schematic representation of a grid formed by a real acylhydrazone, the metal atoms (grey spheres) located relative to a perfect square.

$Ni^{II}$-donor atom bond lengths (Table 1) reflect the expected weaker donor ability of the pyrimidine-*N* atom relative to the hydrazide-*N* atom, and C–N and C–O bond lengths within the hydrazide unit indicate significant delocalisation and hence an enhanced donor ability of the hydrazide-*O* atom relative to a simple carbonyl-*O* atom. While it is conceivable that the bound ligand is in fact deprotonated and that $H_3O^+$ and not $H_2O$ is present in the lattice, each uncoordinated hydrazide-*N* atom has a short contact to oxygen (ca. 2.7–3.2 Å), suggesting that it is indeed protonated, nevertheless involved in strong hydrogen bonding. The oxygen atoms involved in these contacts, interestingly, are those of perchlorate anions and not of water molecules. Unfortunately, the quality of the structure (from a twinned crystal) and disorder of both perchlorate and water entities militate against a detailed analysis of the hydrogen bonding.

When viewed down *a*, for example, the lattice can be considered to be made up of layers of cations, water and some of the perchlorate anions, alternating with layers of perchlorate anions and water. Thus, direct interactions between grid units do not give rise to a three-dimensional array, but within the sheets of cations (parallel to the *ab* plane), there is an interlocking of grid units as a result of face-to-face interactions of the terminal phenyl rings (any edge-to-face contacts being very remote). Note that, as in several analogous hydrazone complexes, each phenyl group attached to a pyrimidine ring lies within the grid and is parallel to two flanking ligand units at a distance of ca. 3.5 Å, suggesting its involvement in intramolecular stacking. The phenyl group loses its plane of symmetry perpendicular to the ring plane, so that the two *ortho* and the two *meta* protons are nonequivalent, as also seen in the solution NMR spectra of certain other complexes.[30]

Though various $Ni^{II}$ salts react with ligand $\mathbf{4}H_2$ to give isolable red complexes, not all of which prove to contain the undeprotonated ligand, with most of the other metal ions studied this is not so, and the free ligand is the material

 © 2007 Wiley-VCH Verlag GmbH & Co. KGaA, Weinheim 

Table 1. Metal–donor-atom bond lengths in acylhydrazone grids, $[M_4(\mathbf{L}H_n)_4]^{4n+}$.

| Metal | Ligand | M–N(hydrazide) /Å | M–N(pyrimidine) /Å | M–O /Å |
|---|---|---|---|---|
| $Ni^{II}$ | $\mathbf{4}H_2$ | 1.978(7), 2.006(5) | 2.151(5), 2.167(6) | 2.066(5), 2.092(5) |
| $Zn^{II}$ | $\mathbf{4}H_2$ | 2.122(5), 2.138(5)[a,b] | 2.170(5), 2.169(5)[a,b] | 2.147(4), 2.137(4)[a,b] |
| | | 2.105(5), 2.095(5)[b,d] | 2.171(6), 2.169(6)[b,d] | 2.134(5), 2.127(5)[b,d] |
| | | 2.183(5), 2.142(5)[a,c] | | 2.038(4), 2.024(4)[a,c] |
| | | 2.133(5), 2.133(5)[c,d] | | 2.099(4), 2.094(5)[c,d] |
| $Co^{II}$ | $\mathbf{4}H^-$ | 2.02(1), 2.07(1) | 2.17(1), 2.21(1) | 2.058(9), 2.14(1) |
| | | 2.02(1), 2.06(1) | 2.19(1), 2.24(1) | 2.05(1), 2.15(1) |
| | | 2.05(1), 2.07(1) | 2.19(1), 2.21(1) | 2.03(1), 2.16(1) |
| | | 2.05(1), 2.08(1) | 2.16(1), 2.27(1) | 2.06(1), 2.119(9) |
| $Ni^{II}$ | $\mathbf{4}H^-$ | 1.989(4), 1.980(4) | 2.199(5), 2.171(5) | 2.062(4), 2.082(4) |
| | | 2.018(4), 1.981(4) | 2.168(4), 2.175(5) | 2.039(4), 2.120(4) |
| | | 1.994(5), 1.993(4) | 2.190(5), 2.172(4) | 2.060(5), 2.077(4) |
| | | 1.977(4), 1.989(4) | 2.169(5), 2.175(5) | 2.063(5), 2.093(4) |
| $Co^{II}$ | $\mathbf{1}^{2-}$ | 2.037(4), 2.051(4) | 2.186(4), 2.211(4) | 2.083(4), 2.090(3) |
| $Ni^{II}$ | $\mathbf{1}^{2-}$ | 1.993(4), 1.997(4) | 2.179(5), 2.182(5) | 2.059(4), 2.072(4) |
| | | 1.991(4), 1.993(4) | 2.182(5), 2.189(5) | 2.067(4), 2.069(4) |
| $Zn^{II}$ | $\mathbf{1}^{2-}$ | 2.060(6), 2.064(6) | 2.228(6), 2.249(6) | 2.115(5), 2.127(6) |
| | | 2.072(6), 2.087(6) | 2.245(6), 2.256(6) | 2.108(6), 2.116(6) |
| $Fe^{II}$ | $\mathbf{3}^{2-}$ | 2.085(3), 2.103(3) | 2.198(2), 2.271(3) | 2.095(2), 2.113(2) |
| $Co^{II}$ | $\mathbf{3}^{2-}$ | 2.038(3), 2.041(3) | 2.217(3), 2.238(3) | 2.085(3), 2.090(3) |
| $Ni^{II}$ | $\mathbf{3}^{2-}$ | 1.990(5), 1.992(4) | 2.191(5), 2.218(5) | 2.067(4), 2.073(4) |
| $Cu^{II}$ | $\mathbf{3}^{2-}$ | 1.927(3), 1.969(3) | 2.198(3), 2.591(4) | 2.024(3), 2.211(3) |
| | | 1.933(4), 1.973(3) | 2.220(3), 2.454(3) | 2.028(3), 2.165(8) |
| $Zn^{II}$ | $\mathbf{3}^{2-}$ | 2.057(3), 2.059(3) | 2.245(3), 2.334(3) | 2.106(3), 2.138(3) |
| | | 2.030(3), 2.033(3) | 2.268(3), 2.554(4) | 2.064(3), 2.146(2) |

[a] Terminal Zn atoms: Zn–N($CH_3CN$) 2.0589(5), Zn–O(water) 2.052(4) Å. [b] (*E*,*E*) Ligand. [c] (*Z*,*Z*) Ligand. [d] Zn atoms bridged by $[BF_4]^-$: Zn–F 1.975(5), 1.980(5) Å.

preferentially precipitated from nearly all solutions containing equimolar amounts of $Mn^{II}$, $Fe^{II}$, $Co^{II}$ and $Zn^{II}$. With $Cu^{II}$, there is obviously complexation, but the product appears to undergo slow decomposition and no crystals suitable for structure determination were isolated. With $Zn^{II}$, a method was finally found to isolate a crystalline complex, and its structure provides an intriguing contrast with that of the $Ni^{II}$ complex described above.

### *(ii) $Zn^{II}$ Complex of $4H_2$*

The $Zn(BF_4)_2$ complex of $\mathbf{4}H_2$ may be formulated as $[Zn_8(E,E\text{-}\mathbf{4}H_2)_4(Z,Z\text{-}\mathbf{4}H_2)_4(OH_2)_2(CH_3CN)_2(BF_4)_2](BF_4)_{14}\cdot 7C_6H_6\cdot 3CH_3CN\cdot 3H_2O$. The stoichiometric unit (Figure 10) is a double grid, tetrafluoroborate anions serving as the links between two identical $Zn_4$ grid units. The grids, however, are very different from those seen in the $Ni^{II}$ complex, in that the $Zn_4$ are of a rectangular, and not square, shape each being very close to planar and involving pairs of $\mathbf{4}H_2$ in their (*E*,*E*) and (*Z*,*Z*) forms. Each metal ion is thus bound to one site of an (*E*,*E*) ligand and one site of a (*Z*,*Z*) ligand, and it is because the latter site is only didentate that the Zn centres achieve six-coordination by binding either monodentate ($H_2O$, $CH_3CN$) or bridging didentate ($[BF_4]^-$) co-ligands. (This observation raises interesting prospects for rearrangements of complexes of the ligands by changes in the oxidation state of a metal, for example, Cu, where the different oxidation states have different preferred coordination geometry.) The combination of convergent, tridentate donor sites on one ligand (*E*,*E*) with divergent, didentate sites on the other (*Z*,*Z*) presumably explains the fact that the $Zn_4$ unit here is essentially planar. The $Zn^{II}$ centres bridged by the (*Z*,*Z*) ligand are quite remote (Figure 10), indicating that paramagnetic metal ions in the same structure would be unlikely to show significant magnetic interactions.

In its (*Z*,*Z*) form, the three phenyl groups of bound $\mathbf{4}H_2$ are placed in proximity, with similar orientations away from the coordinated metal sites. In the double $Zn_4$ array of the $Zn^{II}$ complex, this means that the upper and lower surfaces parallel to the $Zn_4$ planes consist essentially of arrays of phenyl groups, since it is the (*Z*,*Z*) ligands which form the exterior faces. Unsurprisingly, there is strong interpenetration of these arrays from different double-grid units, which is consistent with the fact that π-stacking plays a significant role in the lattice assembly. Though the (*E*,*E*) ligands appear less accessible for intermolecular contacts, the fact that, in this configuration, the terminal phenyl groups project laterally rather than axially allows significant "slipped" overlap between staggered arrays of one set of these ligands, while the other set has at most remote contacts between the terminal carbon atoms but is involved in stacking with the lattice benzene molecules. The lattice water and acetonitrile molecules, as well as the $[BF_4]^-$ anions, are involved also in various contacts between themselves and with aromatic rings, so that the full gamut of weak forces appearing to be operative is highly complicated.

Although its crystal structure has not been determined, it is worth noting that a 2:1 complex of $\mathbf{4}H_2$, $Zn_2(\mathbf{4}H_2)(CF_3SO_3)_4\cdot 2H_2O\cdot CH_3CN$, is readily isolated. While it is perhaps surprising that the binding of two cations does not lead to facile acid dissociation of the ligand, it may be that repulsion between the cationic centres is relieved by adopt-

 © 2007 Wiley-VCH Verlag GmbH & Co. KGaA, Weinheim 

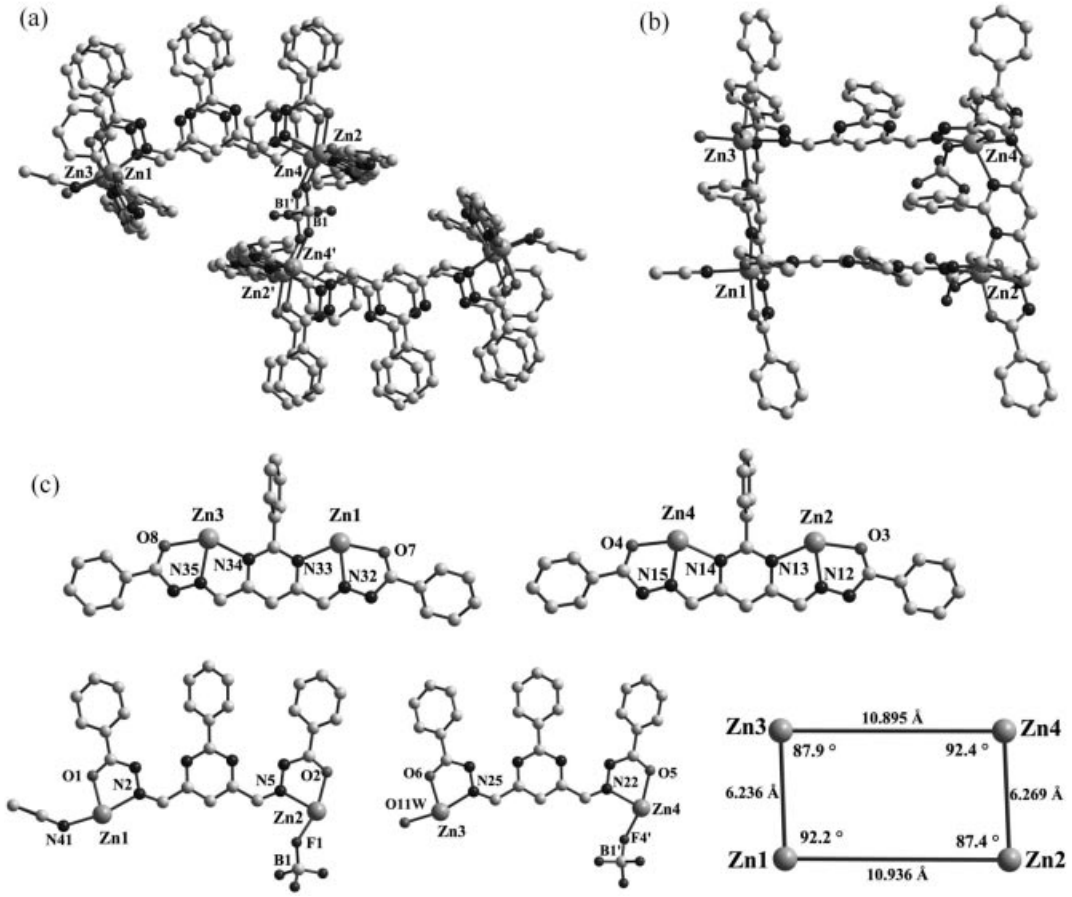


Figure 10. (a) A view of the "double-grid" unit and (b) an approximately orthogonal view of one rectangular grid; (c) geometry of the $Zn_4$ unit and views, perpendicular to the mean plane of the pyrimidine ring, of the two types of ligand unit [lower: (*Z*,*Z*); upper: (*E*,*E*)] found in each rectangle.

ing the (*E*,*E*) configuration seen in the 1:1 complex and which places the two metals at positions quite remote from one another, thus minimising the effect of the second metal on the hydrazide NH proton influenced more closely by the first metal.

### *(b) Complexes Containing Partly Deprotonated Ligands*

#### *(i) $[Co_4(\mathbf{4}H)_4](BF_4)_4$*

While rational syntheses based on monodeprotonation of the acylhydrazones are presumably possible, the first complex of this type was isolated from a reaction medium (involving ligand $\mathbf{4}H_2$) to which no base was deliberately added, a result which parallels those concerning several thioacylhydrazone analogues,[19] although it has proved difficult to reproduce. Under conditions of formally correct stoichiometry, it appears to be the complex $[Co_4(\mathbf{4})_2(\mathbf{4}H)_2](BF_4)_2$ which precipitates. The crystal selected from the initial preparation was characterised by a single-crystal X-ray diffraction study, from which the composition $[Co_4(\mathbf{4}H)_4](BF_4)_4{\cdot}7CH_3CN$ was deduced, as well as the presence of a quadruply charged $[2\times2]Co_4^{II}$ grid species (Figure 11), very similar in form, including the "butterfly" nature of the $M_4$ unit, to that seen in the complex $[Ni_4(\mathbf{4}H_2)_4](ClO_4)_8{\cdot}8H_2O{\cdot}4CH_3NO_2$ (Figure 8). While the structure is somewhat more complicated to analyse than those of related neutral $M^{II}$ complex species incorporating fully deprotonated ligands, there are some remarkable similarities between them all (see ahead). Assuming the residual proton of $\mathbf{4}H^-$ to be localised on one N-centre, isomeric forms of the grid are possible, and thus it is unfortunate that NH protons were not located in the structure solution. However, a view of the cationic grid unit shows that each ligand unit is unsymmetrical, with a significant but different twisting distortion of one hydrazide entity on each, so that the idealised isomeric form is that of $S_4$ symmetry shown also in Figure 11. The actual symmetry of the lattice is such that the grid units have no symmetry and thus all four Co atoms are nonequivalent. In agreement with the fact that the bent ends of the ligands are the sites of protonation, the Co–O bond lengths (Table 1) are greater than those for the less distorted units, though comparison (ahead) with data for fully deprotonated complexes of $Co^{II}$ indicates that the overall effect of protonation/deprotonation on bond lengths is quite slight and may not be simply related to differences in the formal charge assigned to the donor atoms. Further-

 © 2007 Wiley-VCH Verlag GmbH & Co. KGaA, Weinheim 

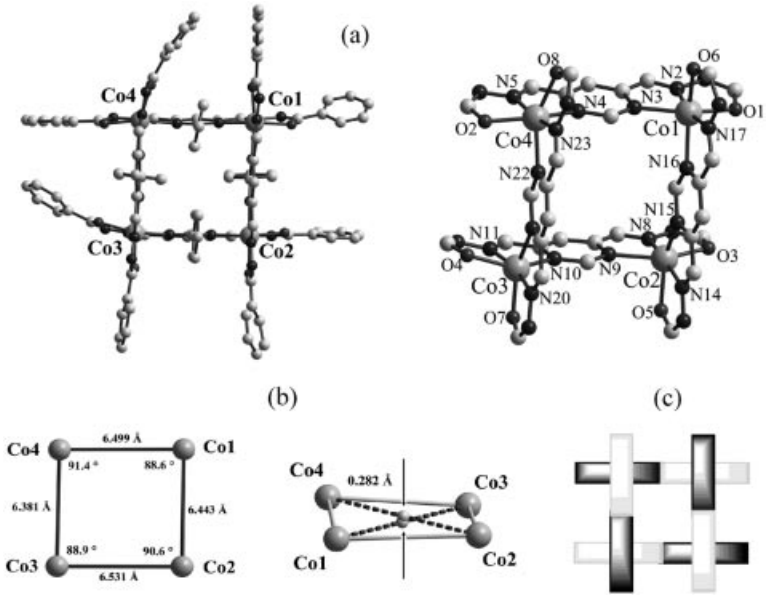


Figure 11. (a) Approximately orthogonal views of the grid unit present in $[Co_4(\mathbf{4}H)_4](BF_4)_4 \cdot 7CH_3CN$; (b) aspects of the geometry of the $Co_4$ unit and (c) the idealised representation of the grid in terms of ligand units that are unsymmetrical because of partial deprotonation.

more, given that force constants for bond stretching and bending for light elements considerably exceed those for transition-metal–donor-atom bonds,[33] it is reasonable that it is the ligand which imposes nearly a fixed coordination geometry on the metal.

A feature of the lattice of $[Co_4(\mathbf{4}H)_4](BF_4)_4 \cdot 7CH_3CN$, which is not found in that of $[Ni_4(\mathbf{4}H_2)_4](ClO_4)_8 \cdot 8H_2O \cdot 4CH_3NO_2$ presumably because of the need to accommodate a greater number of anions, is the three-dimensionality of the interactions between grids, a feature rather commonly observed in neutral grids. Every grid in the lattice of $[Co_4(\mathbf{4}H)_4](BF_4)_4 \cdot 7CH_3CN$ can be considered to be surrounded tetrahedrally by four others in a way which involves a kind of "slipped stacking" of pairs of hydrazone ligands from separate grids, so that every (grid)$(grid)_4$ unit has idealised $S_4$ symmetry (Figure 12). This extended tetrahedral interlocking of grids gives rise to a lattice which, when viewed down *c*, for example, appears to consist of columns composed of grids in alternating, inverted pairs separated by channels into which protrude the "bent" ends of the ligands and which contain partially disordered $[BF_4]^-$ anions and acetonitrile solvent as well. Some anions and solvents can also be considered to be located within the grid columns, and in both environments there are numerous contacts to aromatic entities.

### *(ii)* $[Ni_4(\mathbf{4})_{2.5}(\mathbf{4}H)_{1.5}](NO_3)_{1.5} \cdot CH_3OH \cdot 0.5(C_2H_5)_2O$

The isolation of a complex of a deprotonated thiohydrazone ligand by use of the metal nitrate in methanol has been suggested[19d] to be a consequence of the consumption of acid by a (metal-catalysed) reduction of nitrate by the solvent. Though this seems less likely for acetonitrile, the

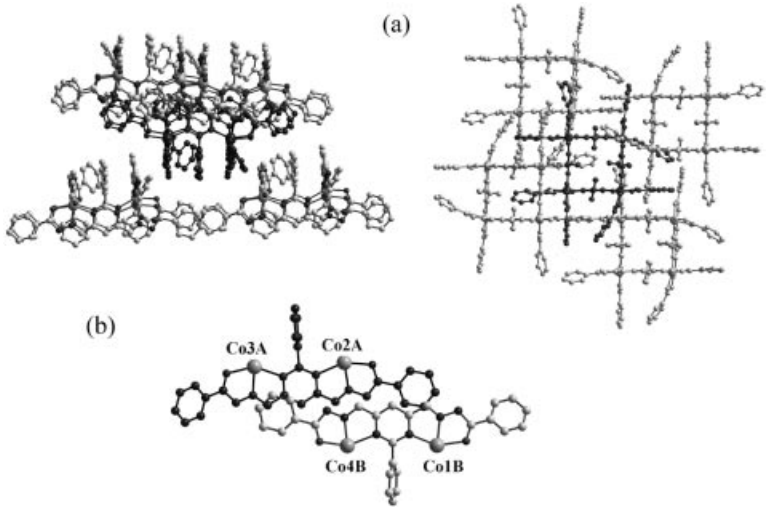


Figure 12. (a) Orthogonal views of a grid unit (atoms in black) and its environment of four other grids; (b) atom contacts within the proximal ligand units of separate grids.

 © 2007 Wiley-VCH Verlag GmbH & Co. KGaA, Weinheim 

presently isolated complex of ligand $\mathbf{4}H_2$ with $Ni(NO_3)_2$ was recrystallised from methanol, and both needle and plate-like crystals were apparent in the product mass. As with the $Co^{II}$ complex above, analysis of the bulk product corresponded to a composition, $[Ni_4(\mathbf{4})(\mathbf{4}H)_3](NO_3)_3$, which is different from that deduced from solution of the crystal structure for a selected plate-like crystal. Perhaps the simplest explanation of all the present results, including the isolation of true complexes of the uncharged ligands from the most (Brønsted) acidic solvent, nitromethane, is that coordination of the ligand results in partial dissociation and the formation of multiple species related by proton loss in solution, and various species precipitate, depending upon subtle aspects of lattice interactions. The solid-state structure of the material, which was assigned the composition $[Ni_4(\mathbf{4})_{2.5}(\mathbf{4}H)_{1.5}](NO_3)_{1.5}\cdot CH_3OH\cdot 0.5(C_2H_5)_2O$ (presumably indicating it to be a mixture of different protonated forms) on the basis of its structure solution, shows various similarities to that of $[Co_4(\mathbf{4}H)_4](BF_4)_4\cdot 7CH_3CN$, including the bending of a terminal phenyl group unit (Figure 13) and the tetrahedral coordination of one grid unit by four others involving close contacts of atoms within parallel ligand planes of separate grids. Perhaps in reflection of the higher degree of ligand deprotonation, the $Ni_4$ unit is closer to a true square than that in the complex of the undeprotonated ligand.

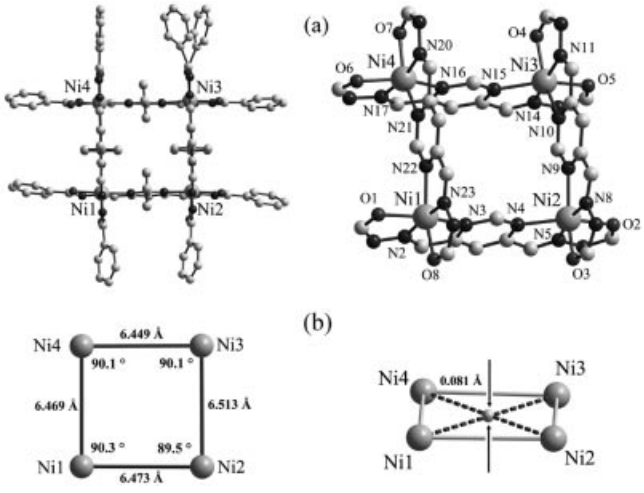


Figure 13. (a) Orthogonal views of the cationic grid unit in$[Ni_4(\mathbf{4})_{2.5}(\mathbf{4}H)_{1.5}](NO_3)_{1.5}$; (b) aspects of the geometry of the $Ni_4$ unit of the grid.

### *(c) Complexes of the Doubly Deprotonated Ligands*

Structural studies within the group of ligands presently described have been limited to the $Co^{II}$, $Ni^{II}$ and $Zn^{II}$ complexes of ligand $\mathbf{1}H_2$ and the $Fe^{II}$, $Co^{II}$, $Ni^{II}$, $Cu^{II}$ and $Zn^{II}$ complexes of ligand $\mathbf{3}H_2$. All are confirmed to be [2×2] grids, but significant variations in both the grid core and the lattice interactions are seen.

*Neutral Grids of Ligand* $\mathbf{1}^{2-}$

A common feature of the Co, Ni and Zn complexes of $\mathbf{1}^{2-}$ is the high degree of hydration of the solids.

*(i) [$Co_4(\mathbf{1})_4$] Complex:* From the structure determination, the $Co^{II}$ complex is formulated as $[Co_4(\mathbf{1})_4]\cdot 8CH_3OH\cdot 16H_2O$ and contains a familiar grid unit with a butterfly-form $Co_4$ aggregate and with Co–N and Co–O bond lengths all very similar on average to those of $[Co_4(\mathbf{4}H)_4](BF_4)_4\cdot 7CH_3CN$. There is also a similarity to this complex in that the lattice can be regarded as involving tetrahedrally connected grid units, though the slipped stacking observed here is associated also with bridging of grids by water molecules forming hydrogen bonds to hydrazide-*N* and acetyl-*O* atoms of essentially orthogonal ligands of adjacent grids. Disorder in the solvent molecule array makes any detailed interpretation of its nature difficult, but it is clear that hydrogen bonding plays a major role in the assembly of the lattice.

*(ii) [$Ni_4(\mathbf{1})_4$] Complex:* The structure of $[Ni_4(\mathbf{1})_4]\cdot \approx 18H_2O$ (Figure 14) displays several significant differences from that of the Co complex, which may be to some extent dependent upon their differences in solvation, although the grid unit is overall very similar, despite the twofold and not fourfold symmetry associated with its different space group. The distortion of the $Ni_4$ unit from planarity, as measured by the distance between the centroids of the diagonals (0.216 Å vs. 0.925 Å for the Co species) is considerably smaller, and this is associated with a packing of the grid units which reflects their twofold symmetry in that although each grid is surrounded by four others in an essentially tetrahedral array (involving, once again, "slipped stacking" of parallel ligand units), two neighbours are slightly more remote than the others, so that the lattice, when viewed down *a*, has the appearance of being built up from staggered double-layers of grids. Despite its partial disorder, the water molecule array clearly involves hydrogen bonding to all the hydrazide-*N* and acetyl-*O* atoms of every grid as well as water–water interactions (Figure 15), forming chains that link the grids additionally to any stacking, and perhaps it is the importance of this extensive set of interactions that results in the distortion of the intergrid stacking (relative to that in the Co complex). Another possible consequence is

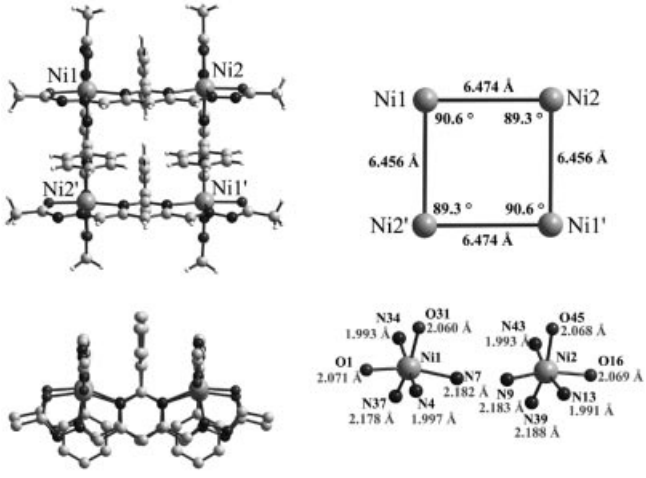


Figure 14. Structure and geometry of the grid unit present in $[Ni_4(\mathbf{1})_4]\cdot \approx 18H_2O$.

 © 2007 Wiley-VCH Verlag GmbH & Co. KGaA, Weinheim 

the fact that grids lying along the columns seen end-on down *a* are now close enough for contacts to occur between the acetyl-$CH_3$ groups and the acetyl-*O* atoms (C···O 3.66 Å). (For coplanar grid units of the Co structure, these atoms are >4 Å apart.) Other adjacent grids in the Ni complex have acetyl-$CH_3$/acetyl-$CH_3$ and acetyl-$CH_3$/phenyl-*C* contacts of also ca. 3.7 Å.

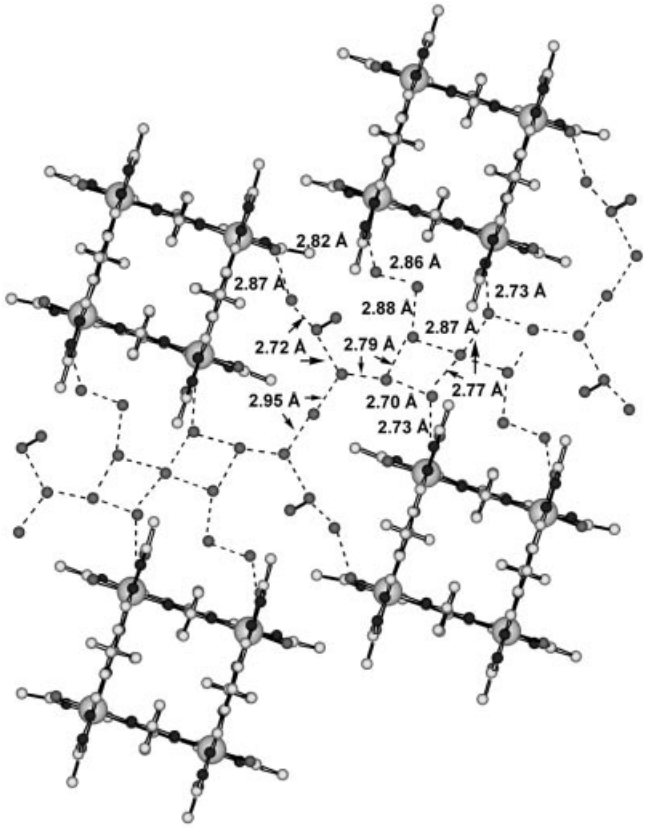


Figure 15. A partial view of the hydrogen bond network present in $[Ni_4(\mathbf{1})_4]\cdot\approx 18H_2O$.

*(iii) [$Zn_4(\mathbf{1})_4$] Complex*: The structure of $[Zn_4(\mathbf{1})_4]\cdot\approx 18H_2O$ is practically isostructural with that of its Ni analogue. Metal–donor-atom bonds are slightly longer to $Zn^{II}$ than to $Ni^{II}$, but the distortion of the $Zn_4$ unit from planarity (diagonal centroid separation 0.191 Å) is marginally smaller. Evidence for intergrid interactions is the same, so that again it appears that hydrogen bonding to the apolar grid is an important interaction.

### *Neutral Grids of Ligand $\mathbf{3}^{2-}$*

Complexes of the ligand $\mathbf{3}^{2-}$ make up the most nearly complete series of metallogrid complexes structurally characterised. All five metals (Fe, Co, Ni, Cu, Zn) studied form the expected $[2\times2]M_4^{II}$ grids, but with some significant differences in structure both within the series and between their analogues in the series formed by $\mathbf{1}^{2-}$. Introduction of a $C_7H_{15}$ "tail" in $\mathbf{3}^{2-}$ in place of the methyl group of $\mathbf{1}^{2-}$ leads to a much lower degree of hydration of the $[M_4(\mathbf{3})_4]$ series, where either tetra- (Fe, Co, Ni) or di- (Cu, Zn) hydrates are formed. The retained water molecules act in isolation to form bridges, again involving hydrazide-*N* and acyl-*O* acceptors, between grids. Across the $[M_4(\mathbf{3})_4]$ series, there is remarkably little variation in M–O and M–N(pyrimidine) distances ($Cu^{II}$ excepted – see below) and only the M–N(hydrazide) bond lengths show the variations expected on the basis of changes in effective nuclear charge across the transition-metal group. For the Co, Ni and Zn complexes of $\mathbf{3}^{2-}$ and $\mathbf{1}^{2-}$, there are no significant differences in analogous M–O and M–N bond lengths, but considerable differences are found in the distortions of the $M_4$ units from planarity. Thus, in all $[M_4(\mathbf{3})_4]$ complexes, the diagonal–centroid separations are ca. 1 Å and do not diminish dramatically across the series, as seems to be the case for the $\mathbf{1}^{2-}$ complexes. The origins of this difference are obscure, especially given that despite such an "internal" difference, "externally" all the grids (from both ligands) display similar properties in that they form very similar lattices (space group differences accommodated). A particular common feature is the tetrahedral coordination of any one grid by four others, associated in all cases with a seeming stacking of ligand units and, given its persistence, indicating that, whatever the nature of the interactions giving rise to these contacts, they are an important means of association of acylhydrazone grids.

The $Fe^{II}$, $Co^{II}$ and $Ni^{II}$ complexes of ligand $\mathbf{3}^{2-}$ are isostructural, while the analogous $Zn^{II}$ complex crystallises in a cell of lower symmetry associated with a lower degree of hydration. Useful for more detailed consideration of the $[M_4(\mathbf{3})_4]$ structures is the form of $[Cu_4(\mathbf{3})_4]\cdot 2H_2O$, which, although unique as a structurally characterised grid, provides a lattice that may be considered to be the "Rosetta Stone" for the interpretation of all the present structures. In the molecular grid unit $[Cu_4\mathbf{3}_4]$ (Figure 16), several features of the geometry differ markedly from those of the Co, Ni and Zn grids. One that does not is the geometry of the binding portion of the ligand, indicating that bond lengths and bond angles about the metals must be the primary means of adapting to any degree of metal–ligand misfit. Thus, for a ligand intended to generate grids with octahedral units by coordinating metal ions, it is unsurprising, given the well-known tendency of $Cu^{II}$ to adopt strongly tetragonally distorted octahedral geometry (and generally to readily lose one or two of its six ligands), to find that the $Cu^{II}$ coordination geometry in the present complex is very irregular (Figure 17), involving in particular considerable variation (up to ca. 0.4 Å) in the Cu–N(pyrimidine) distances.

As discussed earlier, the outer donor atoms of a given tritopic site cannot generally lie at the same distance from the metal as the central donor while also giving bond angles of π/2. Thus, distortion of some kind is inherent in grid formation, and it is certainly well-known that it can become very marked in grids larger than the [2×2] type.[8,33,35] Hence, the form of the Cu grid here may express the way in which any grid must tend to distort in order to achieve the most efficient coordination of the ligand. While all the

 © 2007 Wiley-VCH Verlag GmbH & Co. KGaA, Weinheim 

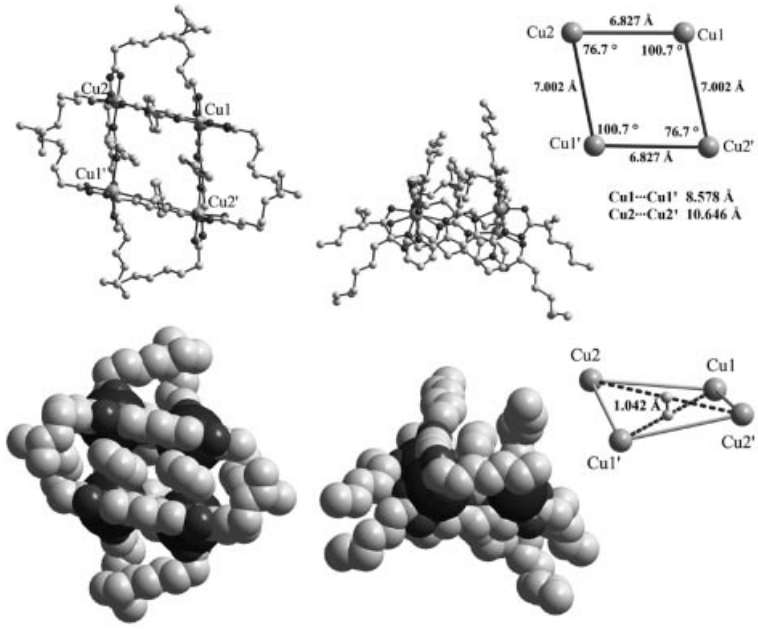


Figure 16. Views and various features of the geometry of the grid unit present in the lattice of $[Cu_4\mathbf{3}_4]\cdot 2H_2O$. The projection of the $Cu_4$ unit is given with Cu(1)···Cu(1′) along *x* and Cu(2)···Cu(2′) along *y*, although the two axes are not coplanar.

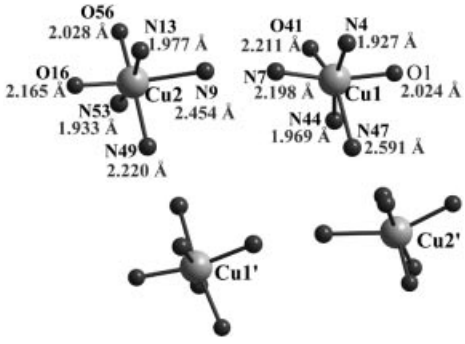


Figure 17. Donor atom distribution about the $Cu^{II}$ centres of a grid unit.

grids formed by the $C_7$-functionalised ligand involve a "butterfly" form of the $M_4$ unit, with $Cu^{II}$ this is associated also with a marked "extrusion" (Figure 16), which results in very different diagonal Cu···Cu distances (possibly influencing magnetic properties, for example). Significantly, however, even with $Cu^{II}$, there is no change in the system which is great enough to result in an apparent change in the form of the metal–ligand aggregate formed.

Thus, outside the grid units, the lattice of $[Cu_4\mathbf{3}_4]\cdot 2H_2O$ is of very similar appearance (Figure 18) to those of the other metal complexes; kinked $C_7$ substituents occupy the space between grids, each of which is surrounded tetrahedrally by four other grids. (The alkyl chain conformations differ, but this presumably corresponds to a very small energy difference.) The specific location and quantity of the lattice water in the $Cu^{II}$ complex, however, may be associated with the distorted form of the $Cu_4$ grid. It is apparent (Figure 19) that the water molecules lie essentially within the columns of grids which run parallel to *c* and they are in fact not in positions where they can bridge grids lying in separate columns, as is the case in the Co compound lattice, for example. Thus, hydrogen bond bridging of grids (Figure 20) occurs in one dimension only (i.e. along *c*), where it

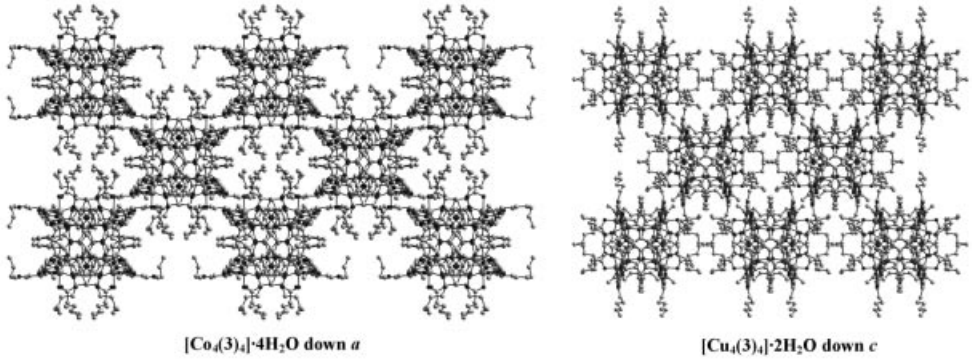


Figure 18. Comparison illustrating the grossly similar forms of the lattices of the Co and Cu complexes.

 © 2007 Wiley-VCH Verlag GmbH & Co. KGaA, Weinheim 

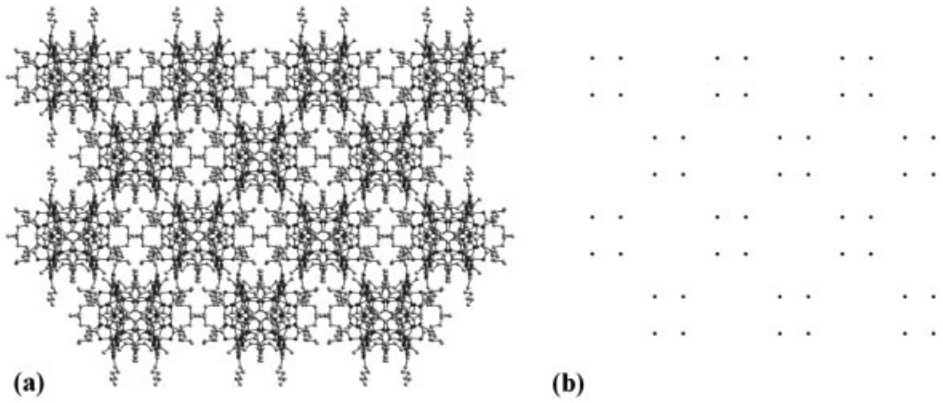


Figure 19. Partial views of the lattice of $[Cu_4\mathbf{3}_4]\cdot 2H_2O$ (down *c*) showing (a) all atoms and (b) water molecule oxygen atoms only.

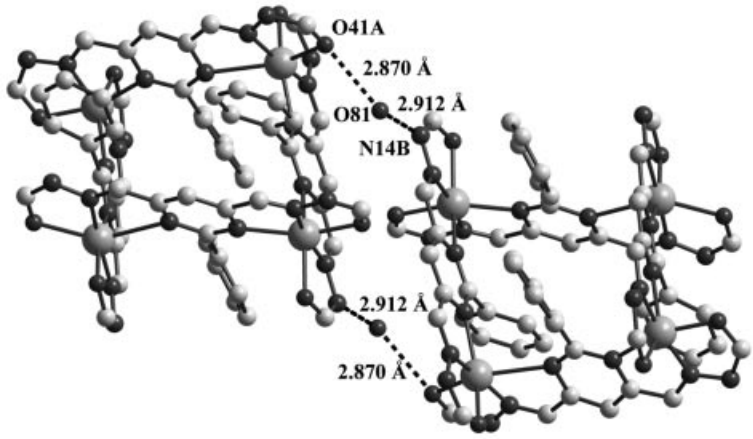


Figure 20. Adjacent $Cu_4$ grids with their shorter edges at the closest position, showing water molecules that form bridges between the two grids.

brings the shorter edges of the grid units into proximity. Longer edge pairs are also present, but their proximity does not seem to be directly assisted by hydrogen bonding. Perhaps the length of the edges keeps hydrogen-bond-acceptor sites too remote to be efficiently bridged by a single water molecule, while "aromatic–aromatic" contacts are maintained (Figure 21), which is perhaps again consistent with their provision of a more important contribution to the lattice energy and structure.

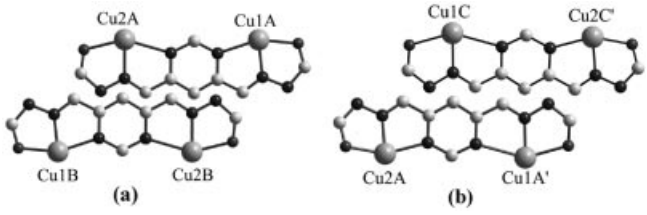


Figure 21. Atom contacts of 3.6 Å or less between ligand atoms in (a) the shorter edges of two adjacent grids and (b) the longer edges of two adjacent grids.

### *(d) Properties of the Grid Complexes*

Crucial to the extension of the chemistry of bis(acylhydrazone) ligands presently studied is the knowledge of the exact conditions under which metallogrid species are stable. Clearly, the several crystal structures obtained here inspire confidence in the belief that in the solid state, certainly with doubly deprotonated ligands, grid species are present. In solution, the situation is less certain in general, although NMR spectroscopy of $Zn^{II}$ complexes again indicates the presence of grids (at $[Zn^{II}] \approx 10^{-3}$ mol L$^{-1}$) only when the ligands are doubly deprotonated. Nonetheless, most of the neutral grid complexes can be subjected to adsorption (silica) chromatography without decomposition, indicating that all of them retain at least the grid stoichiometry in solution (in solvents such as dichloromethane containing ca. 10% methanol). The most direct evidence of the form of paramagnetic species in solution, particularly that of those for which crystal structures have not been obtained, is provided by MALDI-TOF mass spectrometry, though of course this establishes most directly the stoichiometry and not the structure. Here, in a relatively strongly coordinating solvent like tetrahydrofuran, there is evidence that the grids begin to undergo extensive dissociation at concentrations below $10^{-4}$ mol L$^{-1}$.

In regard to possible applications, the properties of grid complexes of importance include not only their redox, elec-

 © 2007 Wiley-VCH Verlag GmbH & Co. KGaA, Weinheim 

tronic and magnetic behaviour,[8] but also the supramolecular chemistry which may be mediated by their substituents. The crystal structures reported here show that, despite their symmetrical and thus apolar nature, neutral grids derived from acylhydrazones are good hydrogen bond acceptors, in view of the presence of charged sites in the deprotonated ligands, and are prone to stacking interactions involving the delocalised ligand entities. Differing substituents derived from the acid hydrazide moieties have a marked influence on the interactions of the grids with the medium, viz. upon their solubility, and in the particular case of the grid derived from methoxyethoxyacetohydrazide, the detection of $Na^+$ adducts by mass spectrometry indicates that metal ion coordination by appropriate side chains is possible.

Different transition-metal ions must endow their grids with different redox, spectroscopic and magnetic properties, and while detailed studies of the magnetism of the complexes are still in progress, $^1$H NMR spectroscopy shows that the $Fe^{II}$ complexes are in mixed-spin states at room temperature (in solution). Fluorescence apparent for the $Zn^{II}$ grids is quenched in all the open-shell transition-metal ion grids, though the exact mechanism of deactivation is yet to be established. All the grids show strong absorption in the visible region, with features that vary not only with the metal, but also with the acyl-unit substituents. That the acylhydrazone-derived grids may show very different redox behaviour from the grids derived from pyridylhydrazones is indicated by the difficulty experienced in obtaining a $Co^{III}$ complex of the benzoylhydrazone $\mathbf{4}H_2$. While $Co^{II}$ complexes of pyridylhydrazones are very sensitive to atmospheric oxygen under basic conditions and readily give tetra-$Co^{III}$ grids,[8] the $Co^{II}$ complex of $\mathbf{4}^{2-}$ is insensitive to oxygen or hydrogen peroxide, and appears to undergo only partial oxidation by $Ce^{IV}$ to give a mixed-valence $Co^{III}$-$Co^{II}$ grid.

## Conclusions

The grid complexes presently characterised are related to but differ significantly from those derived from both bis(hydrazone)s of 2-phenylpyrimidine-4,6-dicarbaldehyde and thiocarbonylbis(hydrazone)s. Bis(acylhydrazone)s, as neutral ligands, appear to be poorer chelators than the analogous neutral bis(hydrazone)s, but they are more easily deprotonated, enhancing their donor properties and thus providing, with $M^{II}$ ions, a family of neutral grids with lateral substituents which may be very readily varied over a wide range. Compared to thiocarbonylbis(hydrazone)s, their metal-chelating sites are considerably more widely separated [especially in their (*Z*,*Z*) form], so that different electronic and magnetic interactions within the metal ion quartet of the grids are expected.

The present structural studies show that some aspects of grid geometry, in particular the distortion of the $M_4$ unit from planarity, are remarkably sensitive to minor variations in the ligand structure. The geometry of the chelating sites of the ligands, in contrast, is insensitive to both its substituents and to the bound metal ion, and it is clear that accommodation of the requirements of a grid array is largely achieved through the flexibility of the metal ion coordination environment. A feature of nearly all the grid lattices presently studied is the association of grid units in pseudo-tetrahedral arrays, where ligands of different grids lie parallel and with numerous atom contacts $< 3.5$ Å, which is presumably indicative of a type of stacking interaction. Another common feature is hydration of the formally apolar grid units through hydrazide-*N* and acyl-*O* hydrogen bond acceptor sites. Finally, a remarkable feature resides in the efficient self-assembly of the grid structures in the presence of a base directly from their organic components and the metal ions (see also ref.[22]).

## Experimental Section

**Reagents and Equipment:** Although a literature synthesis of 2-phenylpyrimidine-4,6-dicarbaldehyde exists,[24a] the compound was presently prepared by an adaptation of an alternative literature method for partial oxidation of azaaromatic methyl groups[24b] applied to 4,6-dimethyl-2-phenylpyrimidine[36] and developed by Dr. J.-L. Schmitt. The procedure is detailed below. 1-methyl-1-propionylhydrazine was obtained as described in the literature.[37] Acetohydrazide, benzohydrazide, 4-toluohydrazide and heptanohydrazide were obtained from Aldrich Chemicals and used as received. Methoxyacetyl- and methoxyethoxyacetyl chlorides were obtained commercially (Lancaster) and converted into the hydrazides by reaction with excess hydrazine. All solvents and chemicals used in the syntheses were reagent grade and were used without further purification or drying. Dimethyl sulfoxide (dmso) solvates of metal triflates and tetrafluoroborates used as reactants in various complex ion syntheses were prepared by precipitation (at least twice) of the (commercial) anhydrous or hydrated salts from dmso by the addition of ethanol/diethyl ether. For $[Cu(dmso)_6](CF_3SO_3)_2$, the presence of the hexakis(solvent) species in the solid was confirmed by a crystal structure determination.[38] $[Ni(CH_3CN)_6](ClO_4)_2$ was prepared as described in the literature.[39] Iron(II) ascorbate was purchased from Sigma Chemicals.

Solution $^1$H (400 MHz) and $^{13}$C (100 MHz) NMR spectra were recorded with a Bruker Ultrashield Avance 400 instrument, using residual solvent proton resonances as internal references for the $^1$H NMR spectra and the solvent $^{13}$C peaks as references for the $^{13}$C NMR spectra. The atom numbering used in assignments of the NMR peaks is shown in Figure 22. Mass spectra [MALDI-TOF and electrospray (ESMS)] were provided by the Service de Spectrometrie de Masse, Université Louis Pasteur. MALDI-TOF spectra of neutral grid species in all cases provided $[M + H]^+$ peaks. Elemental microanalyses (C,H,N) were provided by the Service d'Ana-

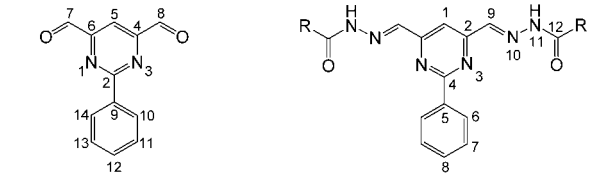


Figure 22. Atom numbering used in description of the NMR spectra.

 © 2007 Wiley-VCH Verlag GmbH & Co. KGaA, Weinheim 

lyses, Université Louis Pasteur, all samples being gently dried by storage in an unevacuated desiccator containing concentrated $H_2SO_4$ as desiccant for at least 3 d.

**Synthesis**

**(a) 2-Phenylpyrimidine-4,6-dicarbaldehyde:** A stirred solution of 4,6-dimethyl-2-phenylpyrimidine (5.08 g; 27.6 mmol), iodine (14.02 g; 53.2 mmol) and trifluoroacetic acid (8.0 mL; 103.8 mmol) in deoxygenated dmso (200 mL) was heated, under argon, at 150 °C for 135 min. After cooling to ambient temperature, further manipulations were conducted under the normal atmosphere. A solution of $Na_2S_2O_3{\cdot}5H_2O$ (31.6 g; 127.3 mmol) in water (100 mL) was added, causing discharge of the $I_2$ colour, after which the solution was neutralised by the addition of saturated $NaHCO_3$ solution. The product was extracted into $CH_2Cl_2$ ($6 \times 100$ mL) and the combined extracts dried with $MgSO_4$ before being taken to dryness in vacuo. The dmso remaining in the orange residue was removed by high-vacuum distillation, and the product was then crystallised from diethyl ether as pale yellow needles. Yield: 4.06 g (19.2 mmol, 80%). M.p. 123.5 °C. $^1$H NMR ($CDCl_3$): $\delta$ = 10.18 (s, 2 H, 7,8-H), 8.60 (d, $^3J$ = 7.9 Hz, 2 H, 10,14-H), 8.12 (s, 1 H, 5-H), 7.58 (m, 3 H, 11,12,13-H) ppm. $^{13}$C NMR ($CDCl_3$): $\delta$ = 192.13 (C-7,8), 166.76 (C-2), 160.25 (C-4,6), 135.50 (C-9), 128.60, 128.93 (C-10,14, C-11,13), 132.17 (C-12), 109.97 (C-5) ppm.

**(b) Bis(acylhydrazone)s of 2-Phenylpyrimidine-4,6-dicarbaldehyde, RCONR′N=CHC$_{10}$H$_6$N$_2$CH=NNR′COR**

**(i) R = CH$_3$, R′ = H (1H$_2$):** Solutions of 2-phenylpyrimidine-4,6-dicarbaldehyde (250 mg) in $CH_3CN$ (10 mL) and acetohydrazide (190 mg) in $CH_3CN$ (10 mL) were mixed to give a pale yellow solution. Within 30 s, the solution became turbid, and after 5 min, formation of a granular but not obviously crystalline pale yellow precipitate was extensive. After 12 h, the well-settled precipitate was separated from the colourless supernatant, washed with $CH_3CN$ and diethyl ether, and dried in vacuo. Yield: 280 mg (80%). $C_{16}H_{16}N_6O_2{\cdot}^1/_4H_2O$ (327.85): calcd. C 58.51, H 4.99, N 25.63; found C 58.7, H 4.85, N 25.2%. M.p. > 310 °C (decomp.). $^1$H NMR ([D$_6$]dmso): $\delta$ = 11.93, 11.91, 11.83 (NH), 8.41 (m, br), 8.24, 8.20, 8.17, 8.10, 8.09, 8.07, 8.05, 7.57, 2.28, 2.27, 2.04 ppm. $^{13}$C NMR ([D$_6$]dmso): $\delta$ = 172.5, 172.4, 166.3, 166.2, 163.8, 161.2, 160.8, 143.9, 143.4, 141.1, 140.6, 136.4, 131.1, 128.7, 127.8, 108.1, 107.8, 54.8, 21.7, 20.2, 19.9 ppm. ESMS: *m*/*z* (%) = 325.24 (100) [M + H]$^+$.

**(ii) R = C$_2$H$_5$, R′ CH$_3$ (2):** 2-Phenylpyrimidine-4,6-dicarbaldehyde (421 mg) and 1-methyl-1-propionylhydrazine (405 mg) were dissolved in ethanol (35 mL), and the solution was stirred at room temperature for 24 h as a yellow precipitate formed. The precipitate was collected, washed with ethanol and dried under vacuum. Yield: 443 mg (59%). The compound was recrystallised from $CHCl_3$ by addition of $CH_3CN$. M.p. 231–232 °C. $^1$H NMR ($CDCl_3$): $\delta$ = 8.49–8.46 (m, 2 H), 8.24 (s, 1 H), 7.77 (s, 2 H), 7.51–7.50 (m, 3 H), 2.93 (q, $J$ = 7.6 Hz, 4 H), 1.25 (t, $J$ = 7.6 Hz, 6 H) ppm. $^{13}$C NMR ($CDCl_3$): $\delta$ = 176.2, 165.3, 161.7, 137.2, 137.1, 131.3, 128.9, 128.5, 108.3, 28.5, 27.2, 9.6 ppm. ESMS: *m*/*z* (%) = 381.30 (100) {[M + H]$^+$ = [$C_{20}H_{24}N_6O_2$ + H]$^+$}.

**(iii) R = C$_7$H$_{15}$, R′ = H (3H$_2$):** Essentially the same procedure as described for the synthesis of **1**H$_2$ was followed, except that ethanol (20 mL) was used as solvent in the reaction of 2-phenylpyrimidine-4,6-dicarbaldehyde (273 mg) and heptanohydrazide (469 mg), the acylhydrazone precipitating as an almost white solid. Yield: 478 mg (75%). The compound was recrystallised from boiling acetonitrile (or methanol) by cooling on ice. $C_{28}H_{40}N_6O_2$ (492.66): calcd. C 68.26, H 8.18, N 17.06; found C 68.6, H 8.10, N 17.1%. M.p. 225–227 °C. $^1$H NMR ([D$_6$]dmso): $\delta$ = 11.85 (br., 2 H), 8.43 (m, 2 H), 8.25 (m, 1 H), 8.09 (m, 2 H), 7.58 (br. m, 3 H), 2.68 (m, 2 H), 2.31 (m, 2 H), 1.63 (m, 4 H), 1.32 (m, 16 H), 0.86 (m, 6 H) ppm. $^{13}$C NMR ($CDCl_3$): $\delta$ = 174.8, 169.3, 163.9, 161.3, 160.9, 143.9, 143.6, 141.0, 140.5, 136.5, 131.2 128.7, 127.8, 108.2, 107.3, 34.3, 31.8, 31.2, 28.8, 28.7, 28.5, 28.4, 24.8, 24.2, 24.0, 22.1, 13.9$_2$,13.8$_8$ ppm. ESMS: *m*/*z* (%) = 492.30 (100) [M + H]$^+$.

**(iv) R = C$_6$H$_5$, R′ = H (4H$_2$):** Solutions of 2-phenylpyrimidine-4,6-dicarbaldehyde (50 mg) in $CH_3CN$ (3 mL) and benzohydrazide (64 mg) in $CH_3CN$ (2 mL) were mixed to give a pale yellow solution. Within 2 min, deposition of pale yellow, globular material commenced, and, on continued standing, this material transformed into clusters of pale yellow needles. After 12 h, the solid was collected, washed with $CH_3CN$ and dried in air. Yield: 98 mg (93%). Use of methanol as a solvent gave essentially the same result, though initiation of the precipitation was slower (ca. 30 min). The compound was recrystallised from pyridine by addition of acetonitrile. $C_{26}H_{20}N_6O_2{\cdot}^1/_2H_2O$ (457.49): calcd. C 68.26, H 4.63, N 18.37; found C 68.4, H 4.74, N 18.1%. M.p. 286–287 °C. $^1$H NMR ([D$_6$]-dmso): $\delta$ = 12.40 (s, 2 H), 8.56 (s, 2 H), 8.45 (t, $^3J$ = 3.6 Hz, 2 H), 8.35 (s, 1 H), 7.98 (d, $^3J$ = 7.2 Hz, 4 H) 7.67–7.62 (m, 3 H), 7.62–7.53 (m, 6 H) ppm. $^{13}$C NMR ([D$_6$]dmso): $\delta$ = 164.0, 163.6, 161.3, 145.7, 136.5, 132.8, 132.3, 131.2, 128.8, 128.6, 127.9, 108.9 ppm. ESMS: *m*/*z* (%) = 449.10 (100) [M + H]$^+$.

**(v) R = 4-CH$_3$C$_6$H$_4$, R′ = H (5H$_2$):** The procedure used for ligand **3**H$_2$ was followed for the reaction of 2-phenylpyrimidine-4,6-dicarbaldehyde (223 mg) and toluohydrazide (331 mg), the acylhydrazone again precipitating as an almost white solid which was recrystallised from pyridine by addition of acetonitrile. Yield: 364 mg (73%). $C_{28}H_{24}N_6O_2$ (476.53): calcd. C 70.57, H 5.08, N 17.64; found C 70.5, H 4.69, N 17.6%. M.p. 287–288 °C. $^1$H NMR ([D$_6$]-dmso): $\delta$ = 14.59 (w), 12.39 (w), 12.34, 8.56, 8.46, 8.34, 8.22 (w), 8.21 (w), 7.90, 7.89, 7.81 (w), 7.79 (w), 7.59, 7.40, 7.38, 7.33 (w), 7.31 (w), 2.44 (w), 2.41 ppm. $^{13}$C NMR ([D$_6$]dmso): $\delta$ = 164.0, 163.4, 161.3, 158.2, 145.4, 142.5, 136.5, 136.1, 131.6, 131.2, 129.9, 129.8, 129.4, 129.2, 128.8, 128.2, 127.9, 127.7, 114.9, 108.8, 104.5, 104.4, 21.1$_3$, 21.0$_9$ ppm. ESMS: *m*/*z* (%) = 477.2 (100) [M + H]$^+$.

**(vi) R = CH$_3$OCH$_2$, R′ = H (6H$_2$):** $CH_3OCH_2CONHNH_2$ (21 mg) in $CH_3CN$ (1 mL) and 2-phenylpyrimidine-4,6-dicarbaldehyde (22 mg) in $CH_3CN$ (1 mL) were mixed to give a slightly cloudy, pale yellow solution, which was filtered (the cloudiness appearing to be due to traces of acid impurity in the hydrazide) before being mixed with a solution of $[Ga(dmso)_6](CF_3SO_3)_3$ (5 mg; ca. 0.1 molar equivalent) in $CH_3CN$ (1 mL). The colour of the mixture changed to a deeper yellow, and within 5 min, deposition of the product commenced. (In the absence of $Ga^{III}$, no precipitate forms within at least 2 h.) After 1 h, the solid was collected and washed with $CH_3CN$ and diethyl ether. Yield: 30 mg (75%). The compound was recrystallised from hot thf by addition of an equal volume of diethyl ether after cooling. $C_{18}H_{20}N_6O_4{\cdot}^1/_2H_2O$ (393.40): calcd. C 54.96, H 5.38, N 21.36; found C 54.9, H 5.1, N 21.8%. M.p. 238–239 °C. $^1$H NMR ([D$_6$]dmso): $\delta$ = 11.93 (NH) (two very weak peaks at $\delta$ = 13.86 and 12.00 ppm may also be NH resonances), 8.43 (s, br.), 8.39 (m, br.), 8.20, 8.01 (t, $^3J$ = 15 Hz), 7.55 (s, br.), 4.49, 4.08, 3.39, 3.35 ppm. $^{13}$C NMR ([D$_6$]dmso): $\delta$ = 171.6, 166.9, 164.4, 161.7, 161.1, 146.3, 146.0, 142.3, 141.6, 136.8, 131.7, 129.2, 128.3, 109.4, 108.9, 108.7, 71.5, 69.4, 59.3, 59.0 ppm. ESMS: *m*/*z* (%) = 385.29 (100) [M + H]$^+$.

**(vii) R = CH$_3$OCH$_2$CH$_2$OCH$_2$, R′ = H (7H$_2$):** The relatively high solubility of the product in most organic solvents made its direct precipitation from the volume of solvent required to dissolve the reactants rather inefficient. Hence, 2-phenylpyrimidine-4,6-dicarb-

 © 2007 Wiley-VCH Verlag GmbH & Co. KGaA, Weinheim 

aldehyde (40 mg) and methoxyethoxyacetohydrazide (82 mg) were allowed react in acetonitrile (5 mL) for 2 h before the solvent was removed under vacuum. The pale yellow residue was then dissolved in the minimum volume of boiling acetonitrile and the solution cooled on ice to provide clusters of pale yellow needles. These were recrystallised similarly. Yield: 57 mg (64%). $C_{22}H_{28}N_6O_6 \cdot {}^1/_2H_2O$ (481.51): calcd. C 54.88, H 6.07, N 17.45; found C 54.8, H 6.2, N 17.6%. M.p. 165–166 °C. $^1$H NMR ($CD_3CN$): $\delta$ = 10.66, 9.82, 8.50, 8.24, 8.15, 7.92, 7.56, 4.62, 4.17, 3.74, 3.60, 3.55, 3.43, 3.33 ppm. $^{13}$C NMR ($CDCl_3$): $\delta$ = 168.4, 167.9, 166.9, 164.7, 162.9, 161.0, 158.1, 147.4, 146.0, 137.7, 136.9, 136.2, 131.7, 131.1, 129.1, 128.8$_3$, 128.7$_7$, 128.6, 128.3, 124.6, 115.0, 111.3, 71.6, 71.5, 71.4, 71.1, 71.0, 70.1, 70.0, 59.1, 58.8 ppm. ESMS: *m*/*z* (%) = 473.36 (100) $[M + H]^+$.

**(c) Metal Ion Complexes of the Bis(acylhydrazone) Ligands**

**(i) R = $CH_3$, R′ = H (1H$_2$)**

**Zn$^{II}$ Complex (Zn/L 1:1) of the Doubly Deprotonated Ligand, [Zn$_4$(1)$_4$]·23H$_2$O:** Solutions of $[Zn(dmso)_6](BF_4)_2$ (730 mg) and $CH_3CONHNH_2$ (180 mg) in $CH_3CN$ (5 mL) and of 2-phenylpyrimidine-4,6-dicarbaldehyde (215 mg) in $CH_3CN$ (5 mL) were mixed to give a clear yellow solution from which no precipitate formed (cf. ligand synthesis). Addition of triethylamine (0.3 mL) caused immediate precipitation of a canary yellow solid which, after 12 h, was collected by filtration, washed with $CH_3CN$ and diethyl ether and dried in air. Yield: 424 mg (85%). The crude product was dissolved in methanol (40 mL), filtered to remove a small amount of gelatinous material and reprecipitated by the addition of diethyl ether. $[Zn_4(\mathbf{1})_4]\cdot 23H_2O\cdot CH_3OH = C_{65}H_{106}N_{24}O_{32}Zn_4$ (1997.3): calcd. C 39.09, H 5.35, N 16.83; found C 39.3, H 4.4, N 16.9%. M.p. > 250 °C (decomp.). $^1$H NMR ([D$_6$]dmso): $\delta$ = 7.60 (t, $^3J$ = 7.7 Hz, 1 H, 8-H), 7.52 (s, 1 H, 1-H), 7.51 (s, 2 H, 9,9′-H), 7.09 (t, $^3J$ = 7.7 Hz, 2 H, 7,7′-H), 6.28 (d, $^3J$ = 7.3 Hz, 2 H, 6,6′-H), 1.82 (s, 6 H, $CH_3$) ppm. (A large water peak was also observed, as expected from the high degree of hydration of the solid.) $^{13}$C NMR ([D$_6$]dmso): $\delta$ = 181.7, 165.1, 158.4, 136.1, 133.4, 130.0, 128.0, 125.2, 117.8, 22.5 ($CH_3$) ppm. MS (MALDI-TOF): *m*/*z* (%) = 1551.1 (100) $[M + H]^+$.

**Other M$^{II}$ Complexes (M/L 1:1) of the Doubly Deprotonated Ligand, [M$_4$(1)$_4$]·*n*H$_2$O:** The following synthesis illustrates an alternative to the above, in which the preformed diacylhydrazone is used as a reactant. A solution of KO*t*Bu (71 mg) in dry methanol (5 mL) was slowly added to a stirred slurry of **1**H$_2$ (99 mg) in dry $CH_2Cl_2$ (20 mL) to give a yellow solution. This was mixed with a solution of $[M(dmso)_6](CF_3SO_3)_2$ (254 mg for M = Zn, with the appropriate slightly different amounts for M = Co and Ni) in dry methanol (5 mL), causing a marked intensification of the colour (dark red-brown for Co, deep yellow-brown for Ni and orange for Zn) and some precipitation. After stirring the mixture for 1 h, the solvents were removed under vacuum and the residues crystallised from methanol as above. Yields were essentially quantitative.

**M = Co$^{II}$:** $[Co_4(\mathbf{1})_4]\cdot 23H_2O = C_{64}H_{102}Co_4N_{24}O_{31}$ (1939.4): C 39.64, H 5.30, N 17.33; found C 39.6, H 4.95, N 17.4%. M.p. >250 °C (decomp.). MS (MALDI-TOF) *m*/*z* (%) = 1526.3 (100).

**M = Ni$^{II}$:** $[Ni_4(\mathbf{1})_4]\cdot 22H_2O = C_{64}H_{100}N_{24}Ni_4O_{30}$ (1920.4): calcd. C 40.02, H 5.25, N 17.50; found C 40.1, H 5.01, N 17.8%. M.p. >250 °C (decomp.). MS (MALDI-TOF): *m*/*z* (%) = 1523.2 (100).

**(ii) R = $C_2H_5$, R′ = $CH_3$ (2):** This acylhydrazone appears to be a rather poor ligand, and no solid transition-metal complexes were readily obtained from it.

**(iii) R = $C_7H_{15}$, R′ = H (3H$_2$):** All complexes (M/L 1:1) containing the doubly deprotonated ligand were obtained as described above (for ligand **1**H$_2$) by using KO*t*Bu to deprotonate the preformed ligand. Again, yields appeared to be essentially quantitative. $[Fe(dmso)_6](CF_3SO_3)_2$ was used as the reactant for the synthesis of the Fe$^{II}$ complex.

**Fe$^{II}$ Complex [Fe$_4$(3)$_4$]·3H$_2$O:** $C_{112}H_{158}Fe_4N_{24}O_{11}$ (2240.0): calcd. C 60.05, H 7.11, N 15.00; found C 59.7, H 7.21, N 14.9%. M.p. >250° (decomp.). MS (MALDI-TOF): *m*/*z* (%) = 2187.0 (100).

**Co$^{II}$ Complex [Co$_4$(3)$_4$]·11H$_2$O:** $C_{112}H_{174}Co_4N_{24}O_{19}$ (2396.5): calcd. C 56.13, H 7.32, N 14.03; found C 56.0, H 7.03, N 13.7%. M.p. >250 °C (decomp.). MS (MALDI-TOF): *m*/*z* (%) = 2199.8 (100).

**Ni$^{II}$ Complex [Ni$_4$(3)$_4$]·11H$_2$O·2CH$_2$Cl$_2$:** $C_{114}H_{178}Cl_2N_{24}Ni_4O_{19}$ (2565.4): calcd. C 53.37, H 6.99, N 13.10; found C 53.4, H 7.33, N 13.1%. M.p. >250 °C (decomp.). MS (MALDI-TOF): *m*/*z* (%) = 2198.9 (100).

**Cu$^{II}$ Complex [Cu$_4$(3)$_4$]·2H$_2$O:** $C_{112}H_{156}Cu_4N_{24}O_{10}$ (2252.9): calcd. C 59.71, H 6.98, N 14.92; found C 60.0, H 7.04, N 15.1%. M.p. >250 °C (decomp.). MS (MALDI-TOF): *m*/*z* (%) = 2217.4 (100).

**Zn$^{II}$ Complex [Zn$_4$(3)$_4$]·4.5H$_2$O:** $C_{112}H_{161}N_{24}O_{12.5}Zn_4$ (2323.2): calcd. C 57.90, H 6.99, N 14.47; found C 57.9, H 7.07, N 14.8%. M.p. >250 °C (decomp.). $^1$H NMR ($CDCl_3$): $\delta$ = 7.62 (t, $^3J$ = 7.5 Hz, 1 H, 8-H), 7.37 (s, 2 H, 9-H), 7.13 (t, $^3J$ = 7.5 Hz, 2 H, 7,7′-H), 6.80 (s, 1 H, 1-H), 6.50 (d, $^3J$ = 6.9 Hz, 2 H, 6,6′-H), 2.19 (m, 4 H), 1.50 (m, 4 H), 1.20 (m, 16 H), 0.82 (t, $^3J$ = 6.6 Hz, 6 H, $CH_3$) ppm. $^{13}$C NMR ($CDCl_3$): $\delta$ = 186.4, 165.9, 159.1, 137.2, 132.6, 130.5, 128.3, 126.3, 116.5, 37.2, 31.9, 29.8, 29.2, 26.9, 22.7, 14.2 ppm. MS (MALDI/TOF): *m*/*z* (%) = 2225.8 (100) $[M + H]^+$.

**(iv) R = $C_6H_5$, R′ = H (4H$_2$)**

**Attempted Synthesis of the Co$^{II}$ Complex (Co/L 1:1) of the Singly Deprotonated Ligand:** Triethylamine (10 mg, viz. 1 mL of a solution of 0.1 g of the amine in 10 mL of $CH_3CN$) was added to a yellow solution of 2-phenylpyrimidine-4,6-dicarbaldehyde (22 mg) in $CH_3CN$ (1 mL), causing the colour to become brownish, though immediate addition of a solution of benzohydrazide (27 mg) in $CH_3CN$ (1 mL) caused a return to pale yellow. Without delay, a solution of $[Co(dmso)_6](BF_4)_2$ (70 mg) in $CH_3CN$ (1 mL) was added, producing a deep brown-red solution from which small, dark red crystals began to deposit within 30 s. After 12 h, the precipitate was collected and washed on the filter with $CH_3CN$ and then diethyl ether. Yield: 18 mg (33%). The complex was recrystallised from chloroform (in which it is only moderately soluble) by the addition of acetonitrile. $[Co_4(\mathbf{4})_2(\mathbf{4H})_2](BF_4)_2 = C_{104}H_{74}B_2Co_4F_8N_{24}O_8$ (2197.3): calcd. C 56.85, H 3.39, N 15.30; found C 56.8, H 3.9, N 15.4%. Note that a single crystal drawn from the initial reaction product was found, as a result of the solution of its structure by X-ray crystallography, to have the composition $[Co_4(\mathbf{4H})_4](BF_4)_4\cdot 7CH_3CN$.

**Co$^{II}$ Complex (Co/L 1:1) of the Doubly Deprotonated Ligand:** The procedure above was repeated except that the quantity of triethylamine added (20 mg) was doubled. Here, copious precipitation of a dark red solid occurred immediately, though again 12 h was allowed for equilibration. The final precipitate was collected and washed with acetonitrile followed by diethyl ether on the filter. Yield: 48 mg (89%). The complex was recrystallised from chloroform by the addition of acetonitrile. $[Co_4(\mathbf{4})_4]\cdot 7H_2O = C_{104}H_{86}Co_4N_{24}O_{15}$ (2147.77): calcd. C 58.16, H 4.04, N 15.65; found C 58.2, H 4.2, N 15.0%. MS (MALDI/TOF): *m*/*z* (%) = 2022.2 (100) $[M + H]^+$.

**Ni$^{II}$ Complexes (Ni/L 1:1) of the Undeprotonated and Partly Deprotonated Ligand:** (a) Ligand **4**H$_2$ (42.4 mg) and $[Ni(CH_3CN)_6]$-

 © 2007 Wiley-VCH Verlag GmbH & Co. KGaA, Weinheim 

$(ClO_4)_2$ (47.7 mg) were stirred at room temperature with anhydrous $CH_3NO_2$ (8 mL) until a clear red solution was obtained. Stirring was continued for another 3 h before diisopropyl ether was added to cause precipitation of the red complex. $[Ni_4(\mathbf{4}H_2)_4](ClO_4)_8 \cdot CH_3NO_2 = C_{105}H_{83}Cl_8N_{25}Ni_4O_{42}$ (2885.3): calcd. C 43.70, H 2.90, N 12.13; found C 43.9, H 3.6, N 12.2%. Note that a single crystal drawn from the reaction mixture was assigned the composition $[Ni_4(\mathbf{4}H_2)_4](ClO_4)_8 \cdot 8H_2O \cdot 4CH_3NO_2$ on the basis of the solution of its X-ray structure determination. (b) $[Ni(OH_2)_6](NO_3)_2$ (29 mg) and 2-phenylpyrimidine-4,6-dicarbaldehyde (23 mg) were dissolved in $CH_3CN$ (2 mL), giving a yellow-green solution. $C_6H_5CONHNH_2$ (27 mg) in $CH_3CN$ (1 mL) was then added, an initial pale violet precipitate dissolving readily on agitation of the mixture. Within 30 s, a yellow precipitate commenced to form from the yellow solution, but on continued agitation, the solution became dark red, and the precipitate transformed into a red-brown solid. After 2 h, the solid was collected by filtration and washed with $CH_3CN$ and diethyl ether. Yield: 28 mg (48%). The complex was recrystallised from methanol by the addition of diethyl ether. Slow crystallisation by vapour diffusion of diisopropyl ether into a methanol solution provided a mixture of plate- and needle-like crystals. The synthesis can equally well be conducted in methanol, in which case no precipitates form, but a reaction time of at least 3 h is required at room temperature before the product can be precipitated by the addition of ether. Elemental analyses indicated that the complex in fact contains the ligand in both its doubly and singly deprotonated forms. $[Ni_4(\mathbf{4})(\mathbf{4}H)_3](NO_3)_3 \cdot 4CH_3OH = C_{108}H_{93}N_{27}Ni_4O_{21}$ (2339.9): calcd. C 55.44, H 4.01, N 16.16; found C 55.7, H 4.2, N 16.7%.

**$Zn^{II}$ Complex (Zn/L 1:1) of the Undeprotonated Ligand:** 2-Phenylpyrimidine-4,6-dicarbaldehyde (23 mg), $C_6H_5CONHNH_2$ (27 mg) and $Zn(BF_4)_2$ (23 mg) were dissolved in $CH_3CN$ (5 mL) to give a red solution, which was then taken to dryness under vacuum. The residue was dissolved in a mixture of $CH_3CN$ (1 mL) and $CH_3NO_2$ (2 mL), giving a deep red solution which was then diluted with benzene (10 mL). On keeping the mixture in a sealed flask, small red plates slowly deposited within a few hours, to be followed over a period of several days by yellow crystals of free ligand. One of the red crystals was selected for a crystal structure determination, from which it was assigned the composition $[Zn_8(E,E\text{-}\mathbf{4}H_2)_4(Z,Z\text{-}\mathbf{4}H_2)_4(OH_2)_2(CH_3CN)_2(BF_4)_2](BF_4)_{14} \cdot 7C_6H_6 \cdot 3CH_3CN \cdot 3H_2O$.

**$Zn^{II}$ Complex (Zn/L 2:1) of the Undeprotonated Ligand:** A filtered solution of $C_6H_5CONHNH_2$ (27 mg) and $Zn(CF_3SO_3)_2$ (75 mg) in $CH_3NO_2$ (3 mL) was mixed with a filtered solution of 2-phenylpyrimidine-4,6-dicarbaldehyde (22 mg) in $CH_3NO_2$ (2 mL), giving a bright yellow solution which developed a red-orange colour within 5 min. Slow deposition of small, red-orange crystals commenced shortly thereafter. After 48 h, the crystals were collected, washed with diethyl ether and dried in air. Yield: 65 mg (52%). The complex was recrystallised from acetonitrile by vapour diffusion of diethyl ether, forming clusters of fine, red needles. $Zn_2(\mathbf{4}H_2)(CF_3SO_3)_4 \cdot 2H_2O \cdot CH_3CN = C_{31}H_{27}F_{12}N_7O_{16}S_4Zn_2$ (1241.7): calcd. C 30.68, H 2.17, N 7.83; found C 30.7, H 3.1, N 7.8%. $^1H$ NMR ($CD_3CN$): $\delta$ = 12.58 (s, br., 2 H, NH), 8.61 (s, 2 H, 9,9′-H), 8.45 (s, 1 H, 1-H), 8.01 (d, $^3J$ = 8 Hz, 4 H), 7.76 (m, 3 H), 7.62 (t, $^3J$ = 8 Hz, 4 H), 7.49 (t, $^3J$ = 8 Hz, 2 H), 7.42 (s, br., 2 H) ppm.

**Attempted Formation of the $Zn^{II}$ Complex (Zn/L 1:1) of the Singly Deprotonated Ligand:** The procedure described above for preparation of the $Co^{II}$ analogue was repeated with $[Zn(dmso)_6](CF_3SO_3)_2$ (83 mg) substituted for $[Co(dmso)_6](BF_4)_2$. A copious, dark-red, seemingly crystalline precipitate formed immediately and 12 h at room temperature was then allowed for equilibration before the solid was collected and washed with acetonitrile and diethyl ether. Yield: 34 mg. Microscopic examination indicated contamination of this crude product with a few crystals of the bis(acylhydrazone). The complex was recrystallised from $CHCl_3$ by addition of $CH_3CN$, microanalysis then indicating that it was in fact the complex of the doubly deprotonated ligand. $[Zn_4(\mathbf{4})_4] \cdot 4H_2O = C_{104}H_{80}N_{24}O_{12}Zn_4$ (2119.5): calcd. C 58.94, H 3.80, N 15.86; found C 59.3, H 3.9, N 15.9%. M.p. >250 °C (decomp.).

**$Zn^{II}$ Complex (Zn/L 1:1) of the Doubly Deprotonated Ligand:** The procedure described above for preparation of the $Co^{II}$ analogue was repeated with $[Zn(dmso)_6](CF_3SO_3)_2$ (83 mg) substituted for $[Co(dmso)_6](BF_4)_2$. A bright red precipitate formed immediately, though again 12 h was allowed for full equilibration. The solid was collected and washed with acetonitrile and diethyl ether. Yield: 45 mg (84%). The complex was recrystallised from $CHCl_3$ by addition of $CH_3CN$. $[Zn_4(\mathbf{4})_4] \cdot 5H_2O = C_{104}H_{82}N_{24}O_{13}Zn_4$ (2137.5): calcd. C 58.44, H 3.87, N 15.73; found C 58.3, H 3.5, N 15.3%. M.p. >250 °C (decomp.). $^1H$ NMR ($CD_3OD/CD_2Cl_2$ 1:4): $\delta$ = 7.80 (m, 5 H, phenyl 2-protons superimposed on H-8); 7.73 (s, 2 H, 9-H); 7.43 (s, 1 H, 1-H); 7.40 (t, $^3J$ = 8 Hz, 2 H, phenyl 4-protons); 7.27 (t, $^3J$ = 8 Hz, 4 H, phenyl 3-protons); 7.14 (t, 2 H, 7,7′-H); 6.42 (d, $^3J$ = 8 Hz, 2 H, 6,6′-H) ppm. $^{13}C$ NMR ($C_2D_5OD/CD_2Cl_2$ 1:4): $\delta$ = 175.0, 156.8, 132.9, 132.5, 129.6, 128.4, 127.3, 126.7, 126.5, 126.4, 126.3, 123.9, 115.7 ppm. MS (MALDI-TOF): *m/z* (%) = 2048.3 (100) $[M + H]^+$.

**Other $M^{II}$ Complexes (M/L 1:1) of the Doubly Deprotonated Ligand**

**M = Fe:** $Fe^{II}$ ascorbate (43 mg, 5% excess) was dissolved in water (0.5 mL) and added to a solution of benzohydrazide (27 mg) in $CH_3CN$ (3 mL) to give a deep violet solution. 2-phenylpyrimidine-4,6-dicarbaldehyde (22 mg) in $CH_3CN$ (1 mL) was added and the mixture allowed stand for 5 min. The oily, violet precipitate which formed was redissolved by the addition of water (2 mL) before triethylamine (20 mg) was added, causing the solution to gain a deep yellow-brown colour and brown crystals to commence depositing. After 2 h, the crystals were collected and washed with water, acetonitrile and diethyl ether, then air dried. Yield: 39 mg (74%). The complex was recrystallised from ethanol/$CH_2Cl_2$ (1:10) by adding an equal volume of ethanol and allowing the $CH_2Cl_2$ to evaporate out. $[Fe_4(\mathbf{4})_4] \cdot 6H_2O = C_{104}H_{84}Fe_4N_{24}O_{14}$ (2117.4): calcd. C 59.00, H 4.00, N 15.88; found C 59.2, H 3.7, N 16.2%. MS (MALDI-TOF): *m/z* (%) = 2010.4 (100) $[M + H]^+$.

**M = Ni:** Benzohydrazide (54 mg) and $[Ni(dmso)_6](CF_3SO_3)_2$ (164 mg) were dissolved in $CH_3CN$ (2 mL), forming a blue solution. Triethylamine (40 mg) was added, followed by a solution of 2-phenylpyrimidine-4,6-dicarbaldehyde (43 mg) in $CH_3CN$ (2 mL). An amorphous, deep yellow-brown precipitate formed immediately. After 12 h, by which time the precipitate was obviously crystalline, this was collected and washed with a little acetonitrile (slightly soluble) and then ether. Yield: 82 mg (73%). The complex was recrystallised from boiling ethanol (20 mL) by cooling to room temperature, very slow deposition of small, brown, rod-like crystals ensuing. $[Ni_4(\mathbf{4})_4] \cdot 2CH_3CN \cdot 9H_2O = C_{108}H_{96}N_{26}Ni_4O_{17}$ (2265.0): calcd. C 57.27, H 4.27, N 16.08; found C 57.1, H 4.0, N 16.1%. MS (MALDI-TOF): *m/z* (%) = 2021.3 (80) $[M + H]^+$.

**M = Cu:** Benzohydrazide (54 mg) and $[Cu(dmso)_6](CF_3SO_3)_2$ (164 mg) were dissolved in $CH_3CN$ (2 mL), forming a blue solution. Triethylamine (40 mg) was added (causing a colour change to brownish-green), followed by a solution of 2-phenylpyrimidine-4,6-dicarbaldehyde (43 mg) in $CH_3CN$ (2 mL). An amorphous, dark brown precipitate formed immediately. Again, the mixture was allowed stand for 12 h before the precipitate was collected and washed with acetonitrile (slightly soluble) and ether. Yield: 88 mg

 © 2007 Wiley-VCH Verlag GmbH & Co. KGaA, Weinheim 

(82%). The complex was recrystallised from ethanol/$CH_2Cl_2$ (1:10) by slow evaporation of the filtered solution. $[Cu_4(\mathbf{4})_4]\cdot 6H_2O$ = $C_{104}H_{84}Cu_4N_{24}O_{14}$ (2148.1): calcd. C 58.15, H 3.94, N 15.65; found C 58.1, H 3.7, N 15.2%. MS (MALDI-TOF): *m*/*z* (%) = 2041.3 (5) $[M + H]^+$.

**(v) R = 4-$CH_3C_6H_4$, R′ = H (5H$_2$)**

**Cu$^{II}$ Complex (Cu/L 1:1) of the Doubly Deprotonated Ligand:** $[Cu(dmso)_6](CF_3SO_3)_2$ (166 mg), 2-phenylpyrimidine-4,6-dicarbaldehyde (44 mg) and 4-$CH_3C_6H_4CONHNH_2$ (60 mg) were dissolved together in $CH_3CN$ (5 mL), the initially green solution developing a deep red colour within 60 s. Precipitation of a red-brown solid with a metallic sheen rapidly ensued but, before this was extensive, triethylamine (50 mg) was added, causing the precipitate to become a darker red and to become more voluminous. After 15 min, the precipitate was well-settled and the supernatant retained only a pale yellow colour. The precipitate was collected, washed with $CH_3CN$ then diethyl ether, and air-dried. Yield: 86 mg (75%). It was recrystallised from the minimum volume (ca. 20 mL) of EtOH/$CH_2Cl_2$ (1:10) by adding EtOH (10 mL) after filtration and allowing the $CH_2Cl_2$ to evaporate out. $[Cu_4(\mathbf{5})_4]\cdot 7H_2O$ = $C_{112}H_{102}Cu_4N_{24}O_{15}$ (2278.3): calcd. C 59.04, H 4.51, N 14.75; found C 59.1, H 4.4, N 14.8%. MS (MALDI-TOF): *m*/*z* (%) = 2153.5 (10) $[M + H]^+$.

**Zn$^{II}$ Complex (Zn/L 1:1) of the Doubly Deprotonated Ligand:** The method using the preformed ligand deprotonated by KO*t*Bu was used to provide the orange complex, which was recrystallised from a 1:1 mixture of $CH_3OH$ and $CH_2Cl_2$ by adding an equal volume of $CH_3CN$ and then allowing the $CH_2Cl_2$ to evaporate out. $C_{112}H_{152}N_{24}O_8Zn_4\cdot 12H_2O$ (2375.8): calcd. C 56.62, H 4.75, N 14.15; found C 56.3, H 4.09, N 14.2%. M.p. >250 °C (decomp.). $^1$H NMR ($CDCl_3$ + $CD_3OD$, 1:1): $\delta$ = 7.67 (t, $^3J$ = 7.3 Hz, 1 H, 8-H), 7.64 (d, $^3J$ = 8.0 Hz, 4 H, tolyl-2-protons), 7.59 (s, 2 H, 9,9′-H), 7.23 (s, 1 H, 1-H), 7.03 (t, $^3J$ = 7.7 Hz, 2 H, 7,7′-H), 7.01 (d, $^3J$ = 8.0 Hz, 4 H, tolyl-3-protons), 6.34 (d, $^3J$ = 7.3 Hz, 2 H, 6,6′-H), 2.26 (s, 6 H, $CH_3$) ppm. $^{13}$C NMR ($CDCl_3$): $\delta$ = 177.1, 166.3, 158.9, 152.8, 142.1, 137.6, 132.9, 131.0, 129.7, 128.2, 126.6, 116.1, 107.9, 73.5, 69.3, 32.1, 30.6, $29.9_5$, $29.9_2$, $29.8_7$, 29.8, 29.7, $29.6_4$, $29.5_6$, 29.5, $26.3_3$, $26.3_0$, 22.86, 22.9, $14.2_7$, $14.2_5$ ppm. MS (MALDI-TOF): *m*/*z* (%) = 2161.3 (100) $[M + H]^+$.

As an alternative synthesis, solutions of $Zn(BF_4)_2\cdot$6dmso (70 mg) and 4-$CH_3C_6H_4CONHNH_2$ (30 mg) in $CH_3CN$ (1 mL) and of 2-phenylpyrimidine-4,6-dicarbaldehyde (22 mg) in $CH_3CN$ (1 mL) were mixed to give an initially pale yellow solution, which developed a deep orange colour over 2 min. Triethylamine (30 mg) was then added to give immediately a red precipitate, which was collected by filtration and washed with acetonitrile and diethyl ether. Yield: 43 mg (59%). This was recrystallised by dissolution in the minimum volume (ca. 20 mL) of 1:1 ethanol/$CH_2Cl_2$, filtration and slow evaporation of the filtrate.

**(vi) R = $CH_3OCH_2$, R′ = H (6H$_2$)**

**Zn$^{II}$ Complex (Zn/L 1:1) of the Doubly Deprotonated Ligand:** $CH_3OCH_2CONHNH_2$ (42 mg) and $Zn(BF_4)_2\cdot$6dmso (120 mg) were dissolved in $CH_3CN$ (2 mL) and added to a solution of 2-phenylpyrimidine-4,6-dicarbaldehyde (43 mg) in $CH_3CN$ (2 mL) to give a clear, yellow solution. Triethylamine (50 mg, excess) was added to produce an immediate bright orange precipitate which settled within 5 min, leaving a pale yellow supernatant. After 1 h, the precipitate was collected, washed with $CH_3CN$ and diethyl ether and dried in air. Yield: 65 mg (64%). The crude product was dissolved in boiling $CH_3OH$ (10 mL), filtered to remove a small amount of brownish, gelatinous material, and the filtrate diluted with an equal volume of diethyl ether to produce small orange crystals. $C_{72}H_{72}N_{24}O_{16}Zn_4\cdot 11H_2O$ (1989.2): calcd. C 43.47, H 4.76, N 16.75; found C 43.5, H 4.4, N 16.8%. M.p. >255 °C (about this temperature, the sample shrinks and its colour lightens but there is no obvious melting). $^1$H NMR ($D_2O$): $\delta$ = 7.78 (m, br.), 7.73 (s), 7.28 (m, br.), 3.91 (s, 2 H), 3.21 (s, 3 H) ppm. $^{13}$C NMR ($D_2O$ + ca. 10% $CD_3OD$): $\delta$ = 181.6, 166.6, 159.8, 138.9, 136.7, 132.9, 130.0, 121.2, 72.1, 59.5 ppm. MS (MALDI-TOF): no peaks above *m*/*z* 897 were detectable.

Table 2. Crystal and refinement data.

| Compound | Ligand **2** | $[Ni_4(\mathbf{4}H_2)_4](ClO_4)_8\cdot 12H_2O$ | $[Zn_8(\mathbf{4}H_2)_8](BF_4)_{16}\cdot 7C_6H_6\cdot 5CH_3CN\cdot 5H_2O$ | $[Co_4(\mathbf{4}H)_4](BF_4)_4\cdot 7CH_3CN$ |
|---|---|---|---|---|
| Chemical formula | $C_{20}H_{24}N_6O_2$ | $C_{104}H_{104}Cl_8N_{24}Ni_4O_{52}$ | $C_{260}H_{227}B_{16}F_{64}N_{53}O_{23}Zn_8$ | $C_{118}H_{97}B_4Co_4F_{16}N_{31}O_8$ |
| $M$/g mol$^{-1}$ | 380.5 | 3184.4 | 6374.1 | 2660.2 |
| Crystal system | triclinic | tetragonal | monoclinic | monoclinic |
| Space group | $P\bar{1}$ | $I4_2d$ | $P2_1/n$ | $P2_1/c$ |
| $a$ /Å | 7.7940(2) | 17.835(3) | 18.581(5) | 22.0163(4) |
| $b$ /Å | 10.7990(3) | 17.835(3) | 22.001(5) | 24.0465(4) |
| $c$ /Å | 23.9020(6) | 52.461(11) | 33.559(8) | 22.9922(5) |
| $\alpha$ /° | 88.312(2) | 90 | 90 | 90 |
| $\beta$ /° | 87.627(2) | 90 | 95.163(12) | 99.531(5) |
| $\gamma$ /° | 76.929(1) | 90 | 90 | 90 |
| $V$ /Å$^3$ | 1957.6 | 16687(5) | 13663(6) | 12004.4(4) |
| Z | 1 | 4 | 2 | 4 |
| $D_{calcd.}$ /g cm$^{-3}$ | 1.291 | 1.268 | 1.545 | 1.470 |
| $\lambda$ /Å | 0.71073 (Mo-$K_\alpha$) | 0.71073 (Mo-$K_\alpha$) | 0.38745 (Synchrotron) | 0.71073 (Mo-$K_\alpha$) |
| $\mu$ /mm$^{-1}$ | 0.087 | 0.65 | 0.432 | 0.639 |
| $F$(000) | 808 | 6112 | 6444 | 5432 |
| $T$ /K | 173(2) | 173(2) | 120(2) | 173(2) |
| $R_{int}$ | 0.027 | 0.051 | 0.064 | 0.08 |
| $R_1$ | 0.057 | 0.109 | 0.089 | 0.103 |
| $wR_2$ | 0.185 | 0.267 | 0.2395 | 0.129 |
| GOF | 0.813 | 1.028 | 1.042 | 1.167 |
| $\Delta\rho_{min}$ /e Å$^{-3}$ | –0.26 | –0.55 | –1.56 | –0.17 |
| $\Delta\rho_{max}$ /e Å$^{-3}$ | 0.23 | 0.81 | 1.03 | 1.42 |
| CCDC # | 637552 | 637553 | 637554 | 637555 |

 © 2007 Wiley-VCH Verlag GmbH & Co. KGaA, Weinheim 

**(vii) R = $CH_3OCH_2CH_2OCH_2$, R′ = H ($7H_2$)**

**$Zn^{II}$ Complex (Zn/L 1:1) of the Doubly Deprotonated Ligand:** Again, this was prepared from the preformed ligand by using KO*t*Bu as base. The orange product was recrystallised from $CH_3CN$ by addition of diethyl ether. $C_{88}H_{104}N_{24}O_{24}Zn_4 \cdot 13H_2O$ (2377.7): calcd. C 44.45, H 5.51, N 14.14; found C 44.3, H 5.03, N 14.4%. M.p. >250 °C (decomp.). $^1H$ NMR ($CD_3CN$): $\delta$ = 7.64 (t, $^3J$ = 7.6 Hz, 1 H, 8-H); 7.51 (s, 2 H, 9-H); 7.25 (s, 1 H, 1-H); 7.17 (t, $^3J$ = 7.6 Hz, 2 H, 7,7′-H); 6.39 (d, $^3J$ = 7.2 Hz, 2 H, 6,6′-H); 3.95 (s, 4 H, $COCH_2O$); 3.46 (m, 4 H, $CH_2CH_2$); 3.39 (m, 4 H, $CH_2CH_2$); 3.22 (s, 6 H, $CH_3$) ppm. $^{13}C$ NMR ($CD_3CN$): $\delta$ = 182.6, 173.7, 166.7, 159.8, 137.5, 136.2, 131.6, 129.6, 126.7, 72.4, 71.8, 70.9, 58.7 ppm. MS (MALDI-TOF): *m*/*z* (%) = 2144.4 (100).

**Crystallography**

**(a) Growth of Crystals for Structure Determination** (formulae indicate the composition determined from the structure solutions): Bis(acylhydrazone) (**2**) crystals were obtained by liquid diffusion of $CH_3CN$ into a solution of **2** in $CHCl_3$. $[Ni_4(\mathbf{4}H_2)_4](ClO_4)_8 \cdot 8H_2O \cdot 4CH_3NO_2$ crystals were obtained by vapour diffusion of di-

Table 3. Crystal and refinement data.

| Compound | $[Ni_4(\mathbf{4})_4](NO_3)_{1.5} \cdot CH_3OH \cdot 0.5Et_2O \cdot 4H_2O$ | $[Co_4(\mathbf{1})_4] \cdot 8CH_3OH \cdot 16H_2O$ | $[Ni_4(\mathbf{1})_4] \cdot (\approx 18H_2O)$ | $[Zn_4(\mathbf{1})_4] \cdot (\approx 18H_2O)$ |
|---|---|---|---|---|
| Chemical formula | $C_{107}H_{90.5}N_{25.5}Ni_4O_{18}$ | $C_{72}H_{120}Co_4N_{24}O_{32}$ | $C_{64}H_{92}N_{24}Ni_4O_{26}$ | $C_{64}H_{92}N_{24}O_{26}Zn_4$ |
| $M$/g mol$^{-1}$ | 2248.83 | 2069.6 | 1840.0 | 1873.2 |
| Crystal system | triclinic | tetragonal | monoclinic | monoclinic |
| Space group | $P\bar{1}$ | $I4_1/a$ | $C2/c$ | $C2/c$ |
| $a$ /Å | 16.1617(4) | 19.8830(7) | 16.489(3) | 16.669(3) |
| $b$ /Å | 18.0510(4) | 19.8830(7) | 25.581(5) | 25.573(5) |
| $c$ /Å | 21.3102(5) | 25.2440(7) | 20.524(4) | 20.493(4) |
| $\alpha$ /° | 89.621(1) | 90 | 90 | 90 |
| $\beta$ /° | 73.838(1) | 90 | 110.29(3) | 109.96(3) |
| $\gamma$ /° | 72.380(2) | 90 | 90 | 90 |
| $V$ /Å$^3$ | 5670.6(3) | 9979.8(6) | 8120(3) | 8226(3) |
| Z | 2 | 4 | 4 | 4 |
| $D_{calcd.}$ /g cm$^{-3}$ | 1.311 | 1.356 | 1.505 | 1.513 |
| $\lambda$ /Å | 0.71073 (Mo-$K_\alpha$) | 0.71073 (Mo-$K_\alpha$) | 0.71073 (Mo-$K_\alpha$) | 0.71073 (Mo-$K_\alpha$) |
| $\mu$ /mm$^{-1}$ | 0.728 | 0.741 | 1.004 | 1.242 |
| $F$(000) | 2297 | 4144 | 3837 | 3883 |
| $T$ /K | 173(2) | 173(2) | 173(2) | 173(2) |
| $R_{int}$ | 0.10 | 0.054 | 0.088 | 0.089 |
| $R_1$ | 0.086 | 0.078 | 0.080 | 0.107 |
| $wR_2$ | 0.2185 | 0.211 | 0.156 | 0.246 |
| GOF | 0.984 | 1.002 | 1.080 | 1.089 |
| $\Delta\rho_{min}$ /e Å$^{-3}$ | –0.64 | –0.37 | –1.49 | –0.82 |
| $\Delta\rho_{max}$ /e Å$^{-3}$ | 0.98 | 0.67 | 1.51 | 1.74 |
| CCDC # | 637556 | 637557 | 637558 | 637559 |

Table 4. Crystal and refinement data.

| Compound | $[Fe_4(\mathbf{3})_4] \cdot 4H_2O$ | $[Co_4(\mathbf{3})_4] \cdot 4H_2O$ | $[Ni_4(\mathbf{3})_4] \cdot 4H_2O$ | $[Cu_4(\mathbf{3})_4] \cdot 2H_2O$ | $[Zn_4(\mathbf{3})_4] \cdot 2H_2O$ |
|---|---|---|---|---|---|
| Chemical formula | $C_{112}H_{160}Fe_4N_{24}O_{12}$ | $C_{112}H_{160}Co_4N_{24}O_{12}$ | $C_{112}H_{160}N_{24}Ni_4O_{12}$ | $C_{112}H_{156}Cu_4N_{24}O_{10}$ | $C_{112}H_{156}N_{24}O_{10}Zn_4$ |
| $M$/g mol$^{-1}$ | 2258.0 | 2270.4 | 2269.5 | 2252.8 | 2256.1 |
| Crystal system | tetragonal | tetragonal | tetragonal | monoclinic | monoclinic |
| Space group | $I4_1/a$ | $I4_1/a$ | $I4_1/a$ | $I2/a$ | $C2/c$ |
| $a$ /Å | 21.184(1) | 21.215(3) | 21.167(3) | 19.949(4) | 29.3560(6) |
| $b$ /Å | 21.184(1) | 21.215(3) | 21.167(3) | 25.296(5) | 25.4480(8) |
| $c$ /Å | 25.391(3) | 25.231(5) | 25.163(5) | 22.233(4) | 20.0720(5) |
| $\alpha$ /° | 90 | 90 | 90 | 90 | 90 |
| $\beta$ /° | 90 | 90 | 90 | 91.77(3) | 130.919(2) |
| $\gamma$ /° | 90 | 90 | 90 | 90 | 90 |
| $V$ /Å$^3$ | 11394.5(15) | 11356(3) | 11274(3) | 11214(4) | 11330.6(5) |
| Z | 4 | 4 | 4 | 4 | 4 |
| $D_{calcd.}$ /g cm$^{-3}$ | 1.312 | 1.328 | 1.337 | 1.334 | 1.323 |
| $\lambda$ /Å | 0.31840 (Synchrotron) | 0.71073 (Mo-$K_\alpha$) | 0.71073 (Mo-$K_\alpha$) | 0.71073 (Mo-$K_\alpha$) | 0.71073 (Mo-$K_\alpha$) |
| $\mu$ /mm$^{-1}$ | 0.303 | 0.644 | 0.728 | 0.817 | 0.904 |
| $F$(000) | 4768 | 4816 | 4832 | 4768 | 4768 |
| $T$ /K | 180(2) | 173(2) | 173(2) | 173(2) | 173(2) |
| $R_{int}$ | 0.159 | 0.055 | 0.103 | 0.095 | 0.066 |
| $R_1$ | 0.0825 | 0.067 | 0.088 | 0.067 | 0.077 |
| $wR_2$ | 0.212 | 0.169 | 0.181 | 0.138 | 0.157 |
| GOF | 1.055 | 1.095 | 1.095 | 1.051 | 1.017 |
| $\Delta\rho_{min}$ /e Å$^{-3}$ | –1.12 | –0.66 | –0.68 | –0.71 | –0.74 |
| $\Delta\rho_{max}$ /e Å$^{-3}$ | 0.73 | 1.80 | 1.89 | 1.34 | –0.70 |
| CCDC # | 637560 | 637561 | 637562 | 637563 | 637564 |

 © 2007 Wiley-VCH Verlag GmbH & Co. KGaA, Weinheim 

isopropyl ether into a $CH_3NO_2$ solution. A $[Zn_8(E,E\text{-}\mathbf{4}H_2)_4(Z,Z\text{-}\mathbf{4}H_2)_4(OH_2)_2(CH_3CN)_2(BF_4)_2](BF_4)_{14}\cdot 7C_6H_6\cdot 3CH_3CN\cdot 3H_2O$ crystal was selected from the mixture of products obtained as described above. A $[Co_4(\mathbf{4}H)_4](BF_4)_4\cdot 7CH_3CN$ single crystal was selected from the mass obtained on one occasion when the ligand and metal ion were subjected to reaction in the absence of any deliberately added base. $[Ni_4(\mathbf{4})_{2.5}(\mathbf{4}H)_{1.5}](NO_3)_{1.5}\cdot CH_3OH\cdot 0.5(C_2H_5)_2O$ single crystals, as a mixture of needles and plates, were grown by vapour diffusion of diethyl ether into a methanol solution of the complex. All variously solvated complexes $[M_4(\mathbf{1})_4]$, M = $Co^{II}$, $Ni^{II}$, $Zn^{II}$, were crystallised by slow evaporation of methanol solutions in air. All variously hydrated complexes $[M_4(\mathbf{3})_4]$, M = $Fe^{II}$, $Co^{II}$, $Ni^{II}$, $Cu^{II}$, $Zn^{II}$, were crystallised by liquid-liquid diffusion of $CH_3CN$ into $CHCl_3$ solutions.

**(b) Structure Determination:** The structures were determined under various conditions on various instruments in Jyväskäla, Strasbourg and Grenoble (European Synchrotron Radiation Facility). Basic information for each structure is given in Tables 2, 3 and 4.

CCDC-637552–637565 contain the supplementary crystallographic data for this paper. These data can be obtained free of charge from The Cambridge Crystallographic Data Centre via www.ccdc.cam.ac.uk/data_request/cif.

## Acknowledgments

A. M. acknowledges financial support of a Marie Curie Intra-European Fellowship (Project 023627). J. R. thanks CONACyT de Mexicò (registro 113226) for a predoctoral fellowship.

[1] J.-M. Lehn, *Supramolecular Chemistry – Concepts and Perspectives,* VCH, Weinheim, **1995**, Ch. 9 in particular.
[2] M. Fujita, *Chem. Soc. Rev.* **1998**, *27*, 417–425.
[3] D. L. Caulder, K. N. Raymond, *Acc. Chem. Res.* **1999**, *32*, 975–982.
[4] G. F. Swiegers, T. F. Malafetse, *Chem. Rev.* **2000**, *100*, 3483–3538.
[5] M. Albrecht, *Chem. Rev.* **2001**, *101*, 3457–3497.
[6] J.-C. G. Bünzli, C. Piguet, *Chem. Rev.* **2002**, *102*, 1897–1928.
[7] S. R. Seidel, P. J. Stang, *Acc. Chem. Res.* **2002**, *35*, 922–983.
[8] M. Ruben, J. Rojo, F. J. Romero-Salguero, L. H. Uppadine, J.-M. Lehn, *Angew. Chem. Int. Ed.* **2004**, *43*, 3644–3662.
[9] P. J. Steel, *Acc. Chem. Res.* **2005**, *38*, 243–250.
[10] N. Morohashi, F. Narumi, H. Nobuhiko, T. Hattori, S. Miyano, *Chem. Rev.* **2006**, *106*, 5291–5316.
[11] J. R. Nitschke, *Acc. Chem. Res.* **2007**, *40*, 103–112.
[12] a) S. A. Parsons, L. K. Thompson, S. K. Dey, C. Wilson, J. A. K. Howard, *Inorg. Chem.* **2006**, *45*, 8832–8834; b) S. K. Dey, L. K. Thompson, L. N. Dawe, *Chem. Commun.* **2006**, 4967–4969 and the references cited therein to the extensive work of this group.
[13] M. Ruben, J.-M. Lehn, P. Müller, *Chem. Soc. Rev.* **2006**, *35*, 1056–1067.
[14] K. M. Gardinier, R. G. Khoury, J.-M. Lehn, *Chem. Eur. J.* **2000**, *6*, 4124–4131.
[15] C. M. Armstrong, P. V. Berhnardt, P. Chin, D. R. Richardson, *Eur. J. Inorg. Chem.* **2003**, 1145–1156.
[16] M. Ruben, J.-M. Lehn, G. B. M. Vaughan, *Chem. Commun.* **2003**, 1338–1339.
[17] L. H. Uppadine, J.-P. Gisselbrecht, J.-M. Lehn, *Chem. Commun.* **2004**, 718–719.
[18] M. Barboiu, M. Ruben, G. Blasen, N. Kyritsakas, E. Chacko, M. Dutta, O. Radekovich, K. Lenton, D. J. R. Brook, J.-M. Lehn, *Eur. J. Inorg. Chem.* **2006**, 784–792.
[19] For grid complexes containing ionised hydrazone groups derived from thiocarbonodihydrazide, see: a) C.-Y. Duan, Z.-H. Liu, X.-Z. You, T. C. W. Mak, *Chem. Commun.* **1997**, 381–382; b) C. He, C.-Y. Duan, C.-J. Fang, Y.-J. Liu, Q.-J. Meng, *J. Chem. Soc., Dalton Trans.* **2000**, 1207–1212; c) G. Han, G. Dong, C.-Y. Duan, H. Mo, Q.-J. Deng, *New J. Chem.* **2002**, *26*, 1371–1377; d) M. A. Ali, P. V. Bernhardt, C. L. Kiem, A. H. Mirza, *Aust. J. Chem.* **2004**, *57*, 409–413. For grid complexes incorporating ionised amide groups see, for instance, J. Klingele, J. F. Boas, J. R. Pilbrow, B. Moubaraki, K. S. Murray, K. J. Berry, K. A. Hunter, G. B. Jameson, P. D. W. Boyd, S. Brooker, *Dalton Trans.* **2007**, 633–645.
[20] P. Tielmann, A. Marchal, J.-M. Lehn, *Tetrahedron Lett.* **2005**, *46*, 6349–6353.
[21] a) L. F. Lindoy, *Quart. Rev. Chem. Soc.* **1971**, *25*, 379–391; b) D. StC. Black in *Comprehensive Coordination Chemistry* (Eds.: G. Wilkinson, R. D. Gillard, J. A. McCleverty), Pergamon Press, Oxford, **1987**, vol. 1, ch. 7.4, pp. 415–462.
[22] J. R. Nitschke, J.-M. Lehn, *Proc. Natl. Acad. Sci. USA* **2003**, *100*, 11970–11974.
[23] J-M. Lehn et al., manuscripts in preparation.
[24] a) ($SeO_2$ oxidation): T. Sakamoto, T. Sakasai, H. Yamanaka, *Chem. Pharm. Bull.* **1981**, *29*, 2485–2490; b) ($I_2$/dmso oxidation): A. Angeloff, J.-C. Daran, J. Bernadou, B. Meunier, *Eur. J. Inorg. Chem.* **2000**, 1985; E. Vismara, F. Fontana, F. Minisci, *Gazz. Chim. Ital.* **1987**, *117*, 136; A. Markovac, C. L. Stevens, A. B. Ash, B. E. Hackley Jr, *J. Org. Chem.* **1970**, *35*, 841.
[25] G. Palla, G. Predieri, P. Domiano, C. Vignali, W. Turner, *Tetrahedron* **1986**, *42*, 3649–3654.
[26] P. Pelagatti, M. Carcelli, F. Franchi, C. Pelizzi, A. Bacchi, A. Fochi, H.-W. Frühauf, K. Goubitz, K. Vrieze, *Eur. J. Inorg. Chem.* **2000**, 463–475.
[27] S. Sen, P. Talukder, G. Rosair, S. Mitra, *Struct. Chem.* **2005**, *16*, 605–610.
[28] A. M. Barreto Bastos, A. F. de Carvalho Alcântara, H. Beraldo, *Tetrahedron* **2005**, *61*, 7045–7053.
[29] L. H. Gade, *Koordinationschemie*, Wiley-VCH, Weinheim, **1998**, p. 87.
[30] J. Rojo, F. J. Romero-Salguero, J.-M. Lehn, G. Baum, D. Fenske, *Eur. J. Inorg. Chem.* **1999**, 1421–1428.
[31] J. Qin, G. K. Friestad, *Tetrahedron* **2003**, *59*, 6393–6402.
[32] J-M. Lehn, J. Ramírez, unpublished.
[33] G. S. Hanan, C. R. Arana, J.-M. Lehn, G. Baum, D. Fenske, *Chem. Eur. J.* **1996**, *2*, 1292–1302.
[34] P. Comba, T. W. Hambley, *Molecular Mechanics*, Wiley-VCH, Weinheim, **2001**, p. 20.
[35] a) E. Breuning, G. S. Hanan, F. J. Romero-Salguero, A. M. Garcia, P. N. W. Baxter, J.-M. Lehn, E. Wegelius, K. Rissanen, H. Nierengarten, A. van Dorsselaer, *Chem. Eur. J.* **2002**, *8*, 3458–3466; b) M. Barboiu, G. Vaughan, R. Graff, J.-M. Lehn, *J. Am. Chem. Soc.* **2003**, *125*, 10257–10265 and references cited therein.
[36] C. A. C. Haley, P. Maitland, *J. Chem. Soc.* **1951**, 3155–3159.
[37] a) R. L. Hinman, D. L. Fulton, *J. Am. Chem. Soc.* **1958**, *80*, 1895–1900; b) M. J. Wanner, M. Koch, G.-J. Koonen, *J. Med. Chem.* **2004**, *47*, 6875–6883.
[38] (A. De Cian) $[Cu(dmso)_6](CF_3SO_3)_2$, $C_{14}H_{36}CuF_6O_{12}S_8$, $M_r$ 830.45, triclinic, space group $P\bar{1}$, $a$ 8.4430(3), $b$ 9.6000(3), $c$ 11.4400(5) Å, $\alpha$ 66.407(1), $\beta$ 81.202(1), $\gamma$ 89.780(3)°, 173(2) K, $Z$ = 1, $R_1$ 0.051, $wR_2$ 0.128; CCDC 637565.
[39] A. E. Wickenden, R. A. Krause, *Inorg. Chem.* **1965**, *4*, 404–407.

Received: February 22, 2007
Published Online: May 23, 2007

 © 2007 Wiley-VCH Verlag GmbH & Co. KGaA, Weinheim

**The EUChemSoc Societies have taken the significant step into the future by merging their traditional journals, to form two leading chemistry journals, the *European Journal of Inorganic Chemistry* and the *European Journal of Organic Chemistry.* Three further EUChemSoc Societies (Austria, Czech Republic and Sweden) are Associates of the two journals.**

## COVER PICTURE

**The cover picture shows** the 5-metallacrown-5 complex, which is obtained by the self-assembly of five copper(II) ions, five 2-picolinehydroximate ligands (picha) and the central mercury(II) ion. The (15-metallacrown-5)$Hg^{II}$ and -$Pb^{II}$ complexes have been obtained in the crystalline form as pyridine adducts $[HgCu_5(picha)_5(py)_7](NO_3)_2$ and $[PbCu_5(picha)_5(py)_6](NO_3)_2$ (axial pyridine molecules are not shown). Unlike the analogous lanthanide(III) derivatives, which are essentially flat, the presented 15-metallacrown-5 system is dome-shaped, although not as convex as the shell of the turtle Gubi (shown in the background). Gubi is the favorite pet of the daughter of one of the authors. Details are discussed in the article by J. Lisowski et al. on p. 3015 ff.

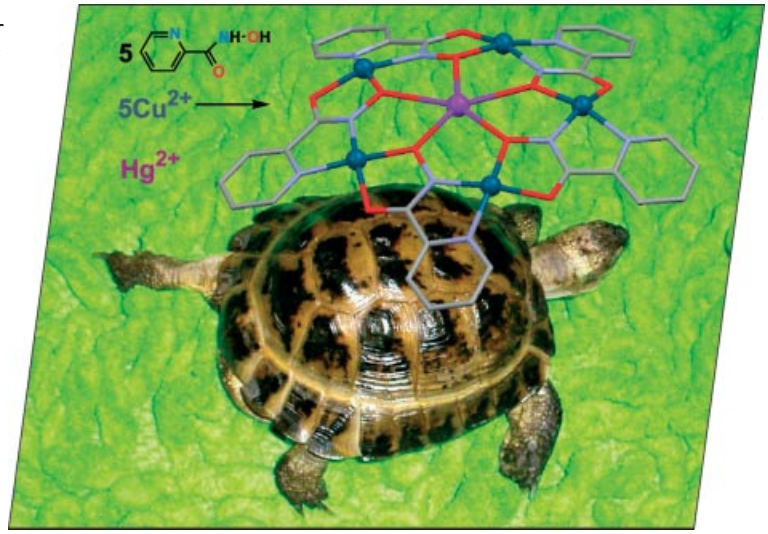


 © 2007 Wiley-VCH Verlag GmbH & Co. KGaA, Weinheim

**The EUChemSoc Societies have taken the significant step into the future by merging their traditional journals, to form two leading chemistry journals, the *European Journal of Inorganic Chemistry* and the *European Journal of Organic Chemistry.* Three further EUChemSoc Societies (Austria, Czech Republic and Sweden) are Associates of the two journals.**

## COVER PICTURE

**The cover picture shows** the 5-metallacrown-5 complex, which is obtained by the self-assembly of five copper(II) ions, five 2-picolinehydroximate ligands (picha) and the central mercury(II) ion. The (15-metallacrown-5)$Hg^{II}$ and -$Pb^{II}$ complexes have been obtained in the crystalline form as pyridine adducts $[HgCu_5(picha)_5(py)_7](NO_3)_2$ and $[PbCu_5(picha)_5(py)_6](NO_3)_2$ (axial pyridine molecules are not shown). Unlike the analogous lanthanide(III) derivatives, which are essentially flat, the presented 15-metallacrown-5 system is dome-shaped, although not as convex as the shell of the turtle Gubi (shown in the background). Gubi is the favorite pet of the daughter of one of the authors. Details are discussed in the article by J. Lisowski et al. on p. 3015 ff.

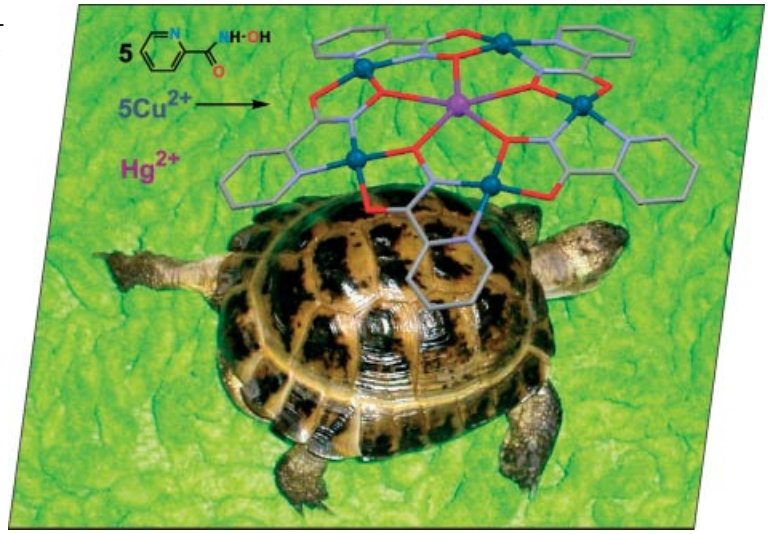


 © 2007 Wiley-VCH Verlag GmbH & Co. KGaA, Weinheim 

# CONTENTS

## MICROREVIEW


### Coordination Rectangle, Prism, Tube

**C.-L. Chen, J.-Y. Zhang, C.-Y. Su* ..... 2997–3010**

Coordination Assemblies of Metallacyclic, Prismatic and Tubular Molecular Architectures Based on the Non-rigid Ligands

**Keywords:** Metallacycle / Coordination prism / Coordination tube / Non-rigid ligand / Molecular architecture



Recent progresses in self-assembly of coordination molecular architectures showing polygonal, prismatic and tubular structures on the basis of the semi-rigid or flexible ligands have been introduced. Four assembly routes depending on the symmetry interactions between specific ligands and metal ions are outlined: a) molecular clips + metal ions of $C_n$ symmetry; b) multipodal ligands + metal ions of $C_2$ symmetry; c) molecular clips + protected metal ions of restrained $C_n$ symmetry and d) multicomponent self-assembly.


## SHORT COMMUNICATION


### Osmium-Rhodium Clusters

**J. Po-Kwan Lau, Y.-J. Gu, W.-T. Wong* ..... 3011–3014**

High-Yield Synthesis of a New Layered High-Nuclearity Carbonyl Osmium-Rhodium Cluster Complex – Synthesis, Structural Characterization, and Electrochemistry of $[PPN][Os_9Rh_3(\mu\text{-}CO)_2(CO)_{26}]$


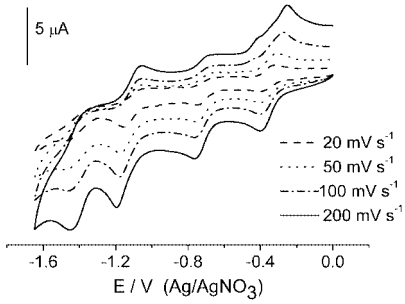



**Keywords:** Osmium / Rhodium / High-nuclearity clusters / Electrochemistry



A direct and high-yield synthetic route for a novel dodecanuclear osmium-rhodium mixed-metal cluster is presented. The redox properties of the cluster were examined, and it was found that the anion behaves as an "electron reservoir".


## FULL PAPERS


### Metallacrowns

**S. H. Seda, J. Janczak, J. Lisowski* ..... 3015–3022**

Synthesis and Structural Characterisation of Copper(II) 15-Metallacrown-5 Complexes with $Pb^{II}$, $Hg^{II}$, $Ag^{I}$, $Na^{I}$ and $Y^{III}$ Central Metal Ions


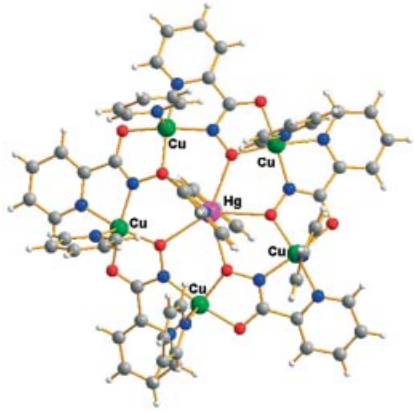



**Keywords:** Metallamacrocyles / Hydroxamic acids / Lead / Mercury / Copper / Crystal structure



New copper(II) 15-metallacrown-5 complexes $[MCu_5L_5]X_n$ {$H_2L$ is 2-picoline- or (*S*)-phenylalaninehydroxamic acid and M is the central metal ion} have been characterised. The X-ray crystal structures of the $Pb^{II}$ and $Hg^{II}$ derivatives show that the 15-metallacrown-5 ring can adopt a distorted conformation in order to adjust to the size of central metal ion.

## High-Valent Oxidoiron(IV) Systems

An empty low-lying 3σ* orbital is responsible for the catalytic activity of oxidoiron(IV) compounds in alkane hydroxylation. We study the influence of the ligand environment on the spin state and catalytic activity of simple systems, correlating these properties to the strength of the electron donation from the ligands, and in particular, we prove that systems with *weak* equatorial and axial donor ligands show superior catalytic activity.

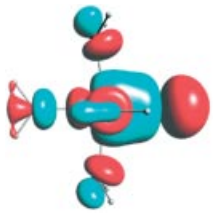

**L. Bernasconi,* M. J. Louwerse, E. J. Baerends* ..... 3023–3033**

The Role of Equatorial and Axial Ligands in Promoting the Activity of Non-Heme Oxidoiron(IV) Catalysts in Alkane Hydroxylation

**Keywords:** Density functional calculations / Fenton reaction / Alkanes / Hydroxylation / High-valent oxidoiron(IV) systems / Push effect

## Organoruthenium(II) Complexes

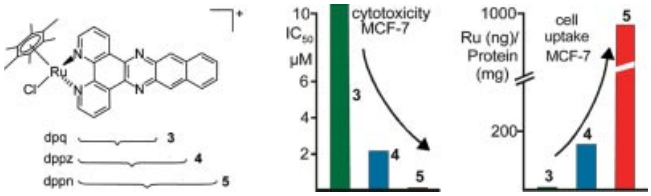


The DNA binding of polypyridyl (pp) complexes such as **3**–**5** has been studied by spectroscopic and viscometric techniques. Intercalation is observed for dpq and dppz complexes but not for chloro complexes with smaller (phen,tap) or larger (dppn) ligands. The cytotoxicities of the complexes correlate with the level of cellular ruthenium uptake in the order of increasing ligand size.

**S. Schäfer, I. Ott, R. Gust, W. S. Sheldrick* ..... 3034–3046**

Influence of the Polypyridyl (pp) Ligand Size on the DNA Binding Properties, Cytotoxicity and Cellular Uptake of Organoruthenium(II) Complexes of theType $[(\eta^6\text{-}C_6Me_6)Ru(L)(pp)]^{n+}$ [L = Cl, $n$ = 1; L = $(NH_2)_2CS$, $n$ = 2]

**Keywords:** Ruthenium / Iridium / DNA / Antitumour agents / Arene ligands

## Iron(II) Spin Crossover

Parity effect and anion influence found at the spin-crossover behaviour of iron(II) coordination polymers and visualised by systematic magnetic and magneto-optical investigations are based on structural variations.

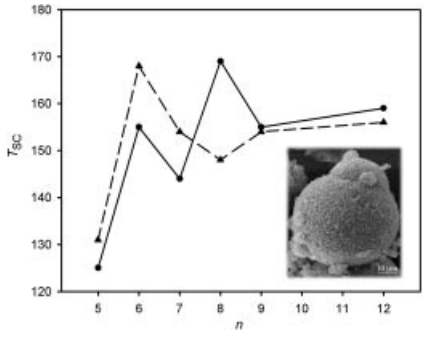


**A. Absmeier, M. Bartel, C. Carbonera, G. N. L. Jameson, F. Werner, M. Reissner, A. Caneschi, J.-F. Létard, W. Linert* ..... 3047–3054**

Mutual Influence of Spacer Length and Noncoordinating Anions on Thermal and Light-Induced Spin-Crossover Properties of Iron(II)–α,ω-Bis(tetrazol-1-yl)alkane Coordination Polymers

**Keywords:** Iron(II) / Magnetic properties / Coordination polymers / Photomagnetism / Spin crossover

## Metallacyclic Antitumour Agents

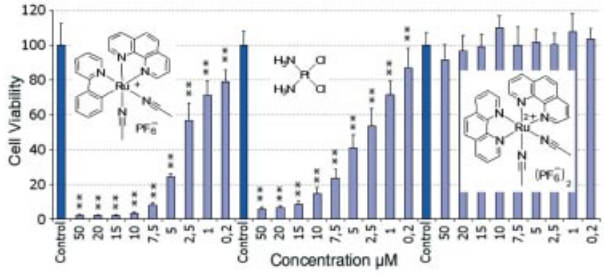


Several cycloruthenated compounds have been evaluated for their in vitro cytotoxicity against a series of human and murine tumor cells. Some of these organometallic compounds that contain a chemically stable Ru-C σ bond stabilized by intramolecular coordination of a nitrogen atom displayed interesting in vitro cytotoxic activities against tumor cells of the same order of magnitude as cisplatin.

**L. Leyva, C. Sirlin,* L. Rubio, C. Franco, R. Le Lagadec, J. Spencer, P. Bischoff, C. Gaiddon, J.-P. Loeffler, M. Pfeffer* ..... 3055–3066**

Synthesis of Cycloruthenated Compounds as Potential Anticancer Agents

**Keywords:** Bioinorganic chemistry / Ruthenium / Metallacycles / Antitumor agents

 © 2007 Wiley-VCH Verlag GmbH & Co. KGaA, Weinheim 

# CONTENTS


## Ion Exchange Kinetics

**E. Pasgreta, R. Puchta, A. Zahl, R. van Eldik* ..... 3067–3076**

Ligand Exchange Processes on Solvated Lithium Cations, V. Complexation by Cryptands in Acetone as Solvent

**Keywords:** Lithium / Cryptands / Acetone / Exchange mechanism

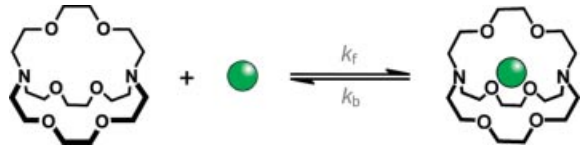


$^7$Li NMR was used to study $Li^+$ exchange between the cryptands C222 and C221 and acetone as solvent, as a function of ligand-to-metal mol ratio, temperature and pressure. The reported activation parameters suggest that the exchange reaction follows an associative interchange mechanism.

## Organometal(IV) Halides with $AlMe_3$

**D. Zhang* ..... 3077–3082**

Facile Formation of Hexacyclic $[Al_3O_2Cl]$ Aluminum and Alkoxide-Bridged Titanium Complexes: Reactions of $AlMe_3$ with $[Ti(L)Cl_2]$ [L = 2,2′-Methylenebis(6-*tert*-butyl-4-methylphenolato)]

**Keywords:** Aluminum complexes / Titanium complexes / Trimethylaluminum

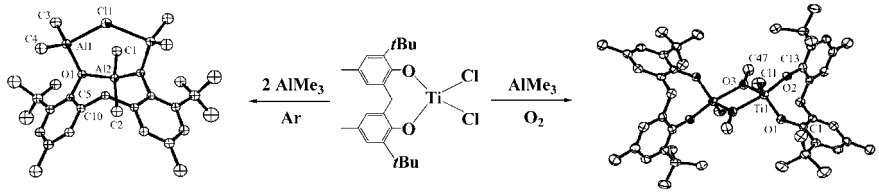


The dichloride titanium complex $[Ti(L)Cl_2]$ [L = 2,2′-methylenebis(6-*tert*-butyl-4-methylphenolato)] (**1**) reacted with $AlMe_3$ in a 1:2 ratio under argon to give the trimetallic compound $[(L)(AlMe_2)_3(\mu_2\text{-}Cl)]$ (**2**) with a symmetrical six-membered ring $[Al_3(\mu_2\text{-}O)_2(\mu_2\text{-}Cl)]$, while the reaction of 1 equiv. $AlMe_3$ under $O_2$ afforded the oxygen-insertion product $[\{(L)TiCl\}_2(\mu_2\text{-}OMe)_2]$ (**4**) with a five-coordinate metal center.

## Stabilized Ylides

**L. Braun, G. Kehr, T. Blömker, R. Fröhlich, G. Erker* ..... 3083–3090**

Preferred Phosphorus Ylide Formation Upon Alkylation of Lithiobis(diphenylphosphanyl)acetonitrile

**Keywords:** Chelates / Phosphane ligands / Carbanions / Ylides / Alkylation

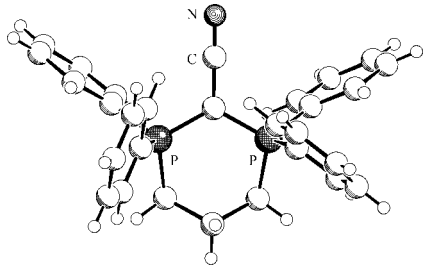


The reaction of lithiobis(diphenylphosphanyl)acetonitrile, which exhibits an unusual monomeric structure in the crystal form, with a variety of alkyl halides proceeds exclusively by alkylation at phosphorus to yield mono- or dialkylated ylidic products.

## Chiral-at-Phosphorus Complexes

**M. J.-L. Tschan, G. Süss-Fink,* F. Chérioux, B. Therrien ..... 3091–3100**

Dinuclear (Arene)ruthenium Complexes Containing a Chiral-at-Phosphorus Phosphanido Bridge

**Keywords:** Arene ligands / Ruthenium / Tethered complexes / P ligands / Hydride ligands

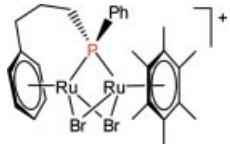


The cation $[(\eta^6\text{-arene})Ru_2(\mu_2\text{-}H)_3]^+$ reacts with $PPh_2(CH_2)_3Ph$ to give the phosphanido complex $[(\eta^6\text{-arene})Ru_2\{\mu_2\text{-}PPh(CH_2)_3Ph\}(\mu_2\text{-}H)_2]^+$ which, upon heating in bromobenzene, converts into $[(\eta^6\text{-arene})Ru_2\{\mu_2\text{-}PPh(CH_2)_3\text{-}\eta^6\text{-}Ph\}(\mu_2\text{-}Br)_2]^+$, the first chiral-at-phosphorus diruthenium complex.


 © 2007 Wiley-VCH Verlag GmbH & Co. KGaA, Weinheim 

## Macrocycles

Nicholas-type reaction strategies are used to promote the formation of a range of large crown-type macrocycles incorporating coordinated 1,3-diynes and a range of unsaturated donor units.

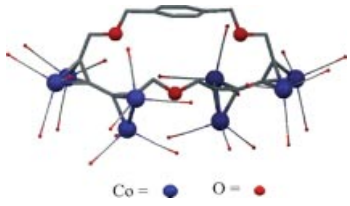


**L. J. Hope-Weeks,* M. J. Mays, G. A. Solan* ..... 3101–3114**

Coordinated 1,3-Diyne Diols as Organometallic Building Blocks for Large Macrocycles Containing Oxygen and Unsaturated Donor Units

**Keywords:** Macrocycles / Cobalt complexes / Oxygen / Alkynes / Nicholas reaction

## Dimetallic $Pt^{II}/Ag^{I}$ Complexes

A series of alkynyl platinum(II) complexes *trans*-[Pt(C≡$CCH_2R)_2(PPh_3)_2$] and *cis*-[Pt(C≡$CCH_2R)_2$(dppe)] containing C-bonded propargyl derivatives of 2-hydroxypyridine, 2-pyridinethiol, 2-hydroxy-4-methylquinoline, phthalimide and pyrazole were prepared and shown to act as organometallic ligands to form mixed-metal $Pt^{II}/Ag^{I}$ complexes.

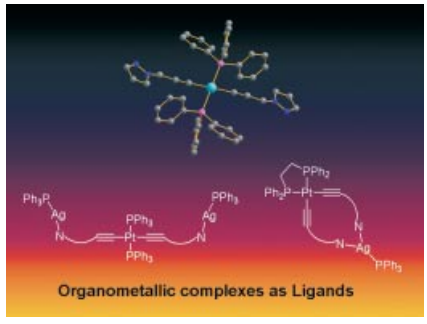


**F. Mohr,* A. Mendía,* M. Laguna ..... 3115–3123**

Platinum(II) Alkynyl Complexes Containing *N*- and *S*-Propargylated Ligands: Synthesis, Structures and Formation of $Pt^{II}/Ag^{I}$ Coordination Compounds

**Keywords:** Platinum / Alkynes / Silver / Dimetallic / Coordination complexes

## Chiral Palladacycles

A novel phosphapalladacycle was prepared from the ligand (diphenylmethyl)diphenylphosphane in the optically active form. This phosphapalladacycle was noted to behave differently with respect to the analogous phosphapalladacycle prepared from (diphenylmethyl)di-*tert*-butylphosphane in terms of palladacycle conformational flexibility, regioselectivity and stability of the Pd–C bond.

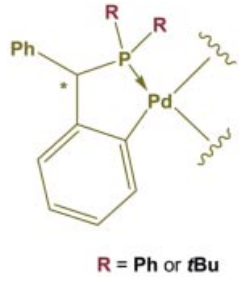


**J. K.-P. Ng, S. Chen, G.-K. Tan, P.-H. Leung* ..... 3124–3134**

Substituent Effects on the Stereoelectronic and Chemical Properties of a Novel Phosphapalladacycle

**Keywords:** Palladium / Phosphane ligands / Chirality / NMR spectroscopy / Substituent effects

**If not otherwise indicated in the article, papers in issue 18 were published online on June 18, 2007**

 © 2007 Wiley-VCH Verlag GmbH & Co. KGaA, Weinheim 

# SPOTLIGHTS …

## *Gas Absorption*

J.-M. Chen, W. Wei, X.-L. Feng, T.-B. Lu*

**$CO_2$ Fixation and Transformation by a Dinuclear Copper Cryptate under Acidic Conditions**

*Chem. Asian J.*
DOI: **10.1002/asia.200700042**

**A crypt for carbon**: There exists a dinuclear copper cryptate that can take up atmospheric $CO_2$ in weakly acidic media. The resulting μ-$O_2$COH-bridged complex (shown) can be converted into carbonate monoesters in alcohol. The mechanisms of these processes are suggested based on the results of X-ray analysis, solution studies, and DFT calculations.

## *FRET-Based Screening*

Z. Cheng, M. Miskolzie, R. E. Campbell*

**In Vivo Screening Identifies a Highly Folded β-Hairpin Peptide with a Structured Extension**

*ChemBioChem*
DOI: **10.1002/cbic.200600565**

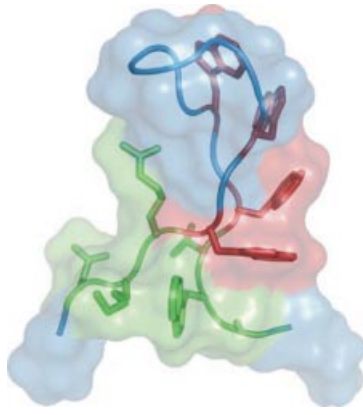

**Like finding a hairpin in the haystack**. We have used an in vivo FRET-based screening method to identify highly folded β-hairpin peptides in large libraries. An NMR structure reveals that a cross-strand cation–π interaction helps stabilize the most highly folded β-hairpin.

## *Bond Theory*

K. Brandhorst, J. Grunenberg*

**Characterizing Chemical Bond Strengths Using Generalized Compliance Constants**

*ChemPhysChem*
DOI: **10.1002/cphc.200700038**

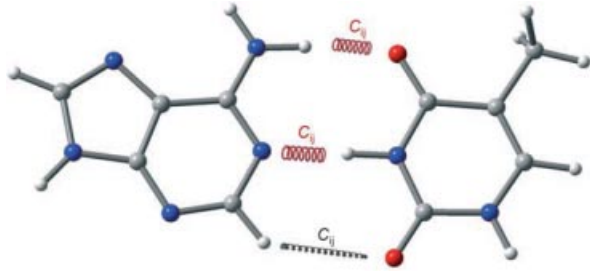


**How strong is it**? The determination of bond strength is a nontrivial task with often controversial results. In this viewpoint, the authors make a case for the utilization of generalized compliance constants as valid bond-strength descriptors for the comparison of next-neighbor interactions in covalent bonds and for noncovalent interactions such as hydrogen bonds and agostic interactions.

## *Receptor Ligands*

G. Jiang, Y. Xu, Y. Fujiwara, T. Tsukahara, R. Tsukahara, J. Gajewiak, G. Tigyi, G. D. Prestwich*

**α-Substituted Phosphonate Analogues of Lysophosphatidic Acid (LPA) Selectively Inhibit Production and Action of LPA**

*ChemMedChem*
DOI: **10.1002/cmdc.200600280**

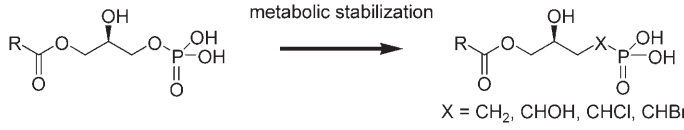


**Metabolically stabilized**: We present the total synthesis and pharmacological characterization of α-substituted phosphonate analogues of LPA. The compounds include isoform-selective agonists and antagonists for the LPA GPCRs, and also include potent inhibitors of lysophospholipase D, a key enzyme involved in LPA biosynthesis.

 © 2007 Wiley-VCH Verlag GmbH & Co. KGaA, Weinheim 

# … ON OUR SISTER JOURNALS

**The insulating role** of 1,4-disubstituted bicyclo[2,2,2]octane has been examined in a theoretical study on bis-ferrocenyl model compounds. Two prototypes of electron-fuelled molecular motors have been synthesized, incorporating either conjugated or insulating spacers between the central core and the ferrocene terminal electroactive groups (see figure).

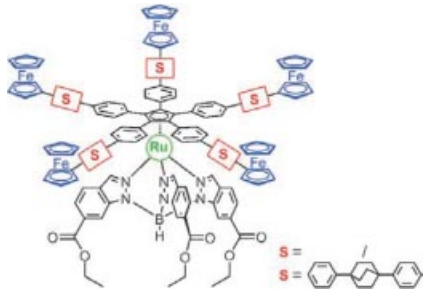


*Molecular Motors*

G. Vives, A. Gonzalez, J. Jaud, J.-P. Launay, G. Rapenne*

**Synthesis of Molecular Motors Incorporating *para*-Phenylene-Conjugated or Bicyclo[2,2,2]octane-Insulated Electroactive Groups**

*Chem. Eur. J.*
DOI: **10.1002/chem.200700223**

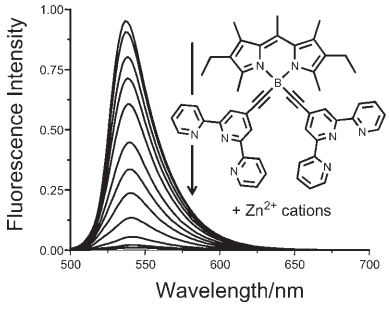


Equipping bodipy dyes with terpyridine (terpy) units leads to two distinct types of self-assembled structures: In the presence of zinc(II) cations, the terpy units facilitate formation of the corresponding dinuclear complexes. In certain solvents, those dyes bearing B-ethynylpyrene residues assemble into π-stacked structures that fluoresce at longer wavelength.

*Dye Photochemistry*

A. Harriman,* L. J. Mallon, B. Stewart, G. Ulrich, R. Ziessel*

**Boron Dipyrromethene Dyes Bearing Ancillary 2,2′:6′,2″-Terpyridine Coordination Sites**

*Eur. J. Org. Chem.*
DOI: **10.1002/ejoc.200700190**

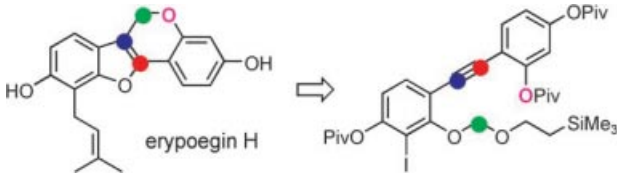


**Fighting back**: A concise route to the pterocarpene derivative erypoegin H, a natural product endowed with considerable activity against a range of methicillin-resistant *Staphyllococcus aureus* strains and vancomycin-resistant enterococci, has been developed. The key step in the synthesis is a $PtCl_2$-catalyzed carboalkoxylation reaction of an alkyne (see retrosynthesis; Piv = pivaloyl).

*Natural Products*

A. Fürstner,* E. K. Heilmann, P. W. Davies

**Total Synthesis of the Antibiotic Erypoegin H and Cognates by a $PtCl_2$-Catalyzed Cycloisomerization Reaction**

*Angew. Chem. Int. Ed.*
DOI: **10.1002/anie.200700895**

On these pages, we feature a selection of the excellent work that has recently been published in our sister journals. If you are reading these pages on a computer, click on any of the items to read the full article. Otherwise please see the DOIs for easy online access through Wiley InterScience.

 © 2007 Wiley-VCH Verlag GmbH & Co. KGaA, Weinheim 

DOI: 10.1002/ejic.200700187

# Coordination Assemblies of Metallacyclic, Prismatic and Tubular Molecular Architectures Based on the Non-rigid Ligands

**Chun-Long Chen,[a] Jian-Yong Zhang,[a] and Cheng-Yong Su*[a,b]**

**Keywords:** Metallacycle / Coordination prism / Coordination tube / Non-rigid ligand / Molecular architecture

This microreview covers recent advances in the assembly of coordination molecular architectures showing cyclic, prismatic and tubular structures based on the semi-rigid or flexible ligands. Four assembly routes are outlined depending on the symmetry interactions between specific ligands and metal ions.
(© Wiley-VCH Verlag GmbH & Co. KGaA, 69451 Weinheim, Germany, 2007)

[a] MOE Laboratory of Bioinorganic and Synthetic Chemistry, State Key Laboratory of Optoelectronic Materials and Technologies, School of Chemistry and Chemical Engineering, Sun Yat-Sen University,
Guangzhou 510275, China
Fax: +86-20-8411-5178
E-mail: cesscy@mail.sysu.edu.cn
[b] State Key Laboratory of Applied Organic Chemistry, Lanzhou University,
Lanzhou 730000, China

## 1. Introduction

During the past decades, great attentions have been paid to control the self-assembly of metallasupramolecular species, and numerous discrete molecular architectures with different shapes and functionalities have been synthesized in an effort to approach the ambitious goal: rational prediction and design.[1] Usually, the coordination assemblies can be classified into two main branches: infinite coordination

*Chun-Long Chen was born in 1979 in Jiangxi, China. He got his Ph.D degree from Sun Yat-Sen University in 2005 under the supervision of Professor Cheng-Yong Su and Professor Bei-Sheng Kang. His research interests are mainly focused on self-assembly of coordination supramolecular species and their dynamic behavior in solution. He was a visiting scholar in Hans-Conrad zur Loye's group at University of South Carolina (Sep. 2004-Jul. 2005), where he was engaged in the design and synthesis of rigid ligands and their coordination chemistry. He is currently doing post-doctoral research with Dr. Nathaniel L. Rosi at University of Pittsburgh.*

*Jian-Yong Zhang was born in 1974 in Henan, China. He obtained his master's degree from Nankai University in 1999 with Prof. Shansheng Xu and his PhD from National University of Singapore in 2003 under the supervision of Prof. T. S. Andy Hor on rhenium complexes for nuclear medicine, followed by one-year postdoctoral experience at the Institut de Recherches sur la Catalyse – CNRS, France, with Prof. Liliane G. Hubert-Pfalzgraf on molecular precursors for inorganic materials. Further three-year post-doc experience was gained at the Queen's University of Belfast, UK, with Dr. Stuart L. James on coordination cages and polymers. He joined Sun Yat-Sen University in 2006 and is currently an associate professor. His research interests include catalysis, supramolecular chemistry and materials chemistry.*

*Cheng-Yong Su was born in 1968 in Inner Mongolia, China. He earned his Ph.D degree in Chemistry from Lanzhou University in 1996 under the supervision of Professor Min-Yu Tan in the field of Rare Earth chemistry. He joined Professor Wolfgang Kaim's group at Stuttgart University as an Alexander von Humboldt Research Fellow in 2001, and moved to the University of South Carolina in 2002 working with Professor Hans-Conrad zur Loye as a Postdoctoral Fellow for one and half years. He became Associate Professor in 1998 at Sun Yat-Sen University and was promoted to Professor in 2004. He is the author or co-author of over 100 peer reviewed publications and has research interests in coordination crystal engineering, molecular architectures and supramolecular chemistry.*

 © 2007 Wiley-VCH Verlag GmbH & Co. KGaA, Weinheim 

polymers and discrete molecular architectures. The field of coordination polymers continues to expand exponentially because of their potential applications in the areas of catalysis, chirality, conductivity, luminescence, magnetism, spin-transition (spin-crossover), non-linear optics (NLO) and porosity or zeolitic behaviors. On the other hand, interests in the design and construction of discrete molecular architectures have also experienced extraordinary progress not only because of their intrinsic aesthetic appeals but also due to their various potentials for being used as sensors, probes, catalysts, containers and in basic host-guest chemistry.

On the base of some well-documented strategies, such as Molecular Library Model,[1a,1b] Symmetry Interaction Model,[1c,1d] Directional-Bonding Approach,[1a] Weak-Link Synthetic Approach,[1e] and so on, various discrete molecular architectures with desired shapes and concomitant properties have been synthesized. However, most of these approaches relate to high symmetric molecules, such as polygons and polyhedra. The ligands therein used are usually rigid or specifically multifunctional, and the coordination geometry of metal center sometimes needs protecting. In contrast, using of non-rigid (semi-rigid or flexible) ligands to construct well-shaped molecular architectures is far less common, partly due to the less predictable assembly process. However, the incorporation of flexible components may endow the molecular architectures with potential advantages, for example, a "breathing" ability in the solid state and adaptive recognition properties as a functional of coexisting guest or counterions. Furthermore, flexibility of the non-rigid ligand can afford a good opportunity to investigate the details of the self-assembly process and provide more information for the directional synthesis of target supramolecular complexes. For instance, the flexibility of the ligand can lead to the formation of both discrete macrocycles and infinite polymeric structures on the basis of the conformational freedom of the connecting fragment, and the conversion between these two types of structures could be related by the concept of ring-opening isomerism.[2] Most important, deliberate design of non-rigid ditopic ligands can afford organic "molecular clips" which make it easy to construct relatively lower-symmetric molecular architectures of rectangular or prismatic shapes following a ligand-directed symmetry-interaction approach.[3]

We have long been involving in the synthesis of cyclic, tubular or cage-like metallasupramolecules through design of the specified semi-rigid or flexible ligands with benzimidazolyl or quinolyl as terminal groups and rigid arenes or flexible alkenes as spacers. Given the availability of different coordination modes provided by the designed ligands, we have synthesized a diverse array of discrete structures ranging from simple binuclear cyclic $M_2L_2$, prismatic $M_3L_2$, $M_2L_3$ or $M_2L_4$, to tubular $M_4L_4$ molecular architectures. The present microreview will mainly concentrate on recent progress in the assembly of the prismatic coordination structures by using of the non-rigid ligands, involving some related examples of macrocyclic and tubular molecules on the basis of the results from our and other groups, but avoid covering comprehensive literature examples.

## 2. Design Approaches

Several general strategies have been developed for construction of the discrete coordination molecular architectures.[1] The directional-bonding or molecular library approaches[1a,1e] are efficient for building up molecular polygons or polyhedra based on rigid ligands, the symmetry-interaction approach[1a–1d] is a powerful tool to elegant shapes and architectures like helicates, tetrahedral and adamantoid structures through multibranched chelating ligands, the molecular paneling approach is used by Fujita et al.[1b] to assemble large 3D assemblies, and the weak-link approach is mainly developed by Mirkin et al.[1e] to prepare supramolecular architectures from flexible ligands. However, none of above strategies are characteristic of prismatic structures.

In contrast to the highest symmetric polyhedral structures which possessing multiple *n*-fold rotation axes, the right prisms are composed of two regular *n*-gons perpendicular to a sole *n*-fold rotation axis, such as trigonal and tetragonal prisms, therefore, showing relatively lower symmetry. The even lower symmetric oblique prisms only contain two polygonal bases in parallel and several lateral parallelograms without actual *n*-fold rotation axis. On the other hand, a lot of dimeric cage structures possessing apparent $D_{nh}$ symmetry also show prismatic shape without the strict lateral parallelograms. The common feature of these structures is the absence of multiple *n*-fold rotation ($n \geq 3$) symmetry but having two parallel *n*-gons. If such structures are open ended (two bases of the prisms are not closed), tubular structures are formed. Similar symmetry relationship between the polyhedral and prismatic structures can also be found between polygonal and rectangular structures.

To achieve convergent assembly of molecular prisms by preventing appearance of more than one *n*-fold axes during the self-assembly process, more deliberate predesign and judicious choice of the components are required. One of constructive approaches proposed by Stang and co-workers is to design a "molecular clip": two parallel coordination sites are facing in the same direction, which allows for the assembly e.g. of a molecular rectangle by using rigid bipyridyl bridging ligands[4a,4b] or of trigonal prisms by using tritopic ligands with pyridyl subunits.[4c] Taking advantages of such a design principle, we have proposed a ligand-directed symmetry-interaction approach,[3] relying on synthesis of shape-defined "organic molecular clips" which display a coordination directing mode similar to Stang's organometallic clips, thereby facilitate modular assembly of prismatic architectures. On the basis of known examples from our and other groups, the following routes for assembly of coordination prismatic cages and related structures could be outlined:

### 2.1 Molcular Clips + Metal Ions of $C_n$ Symmetry

As shown in Scheme 1 a molecular clip can be a ditopic semi-rigid ligand possessing two coordinating arms which must take the *cis* conformation. Because the molecular clip

 © 2007 Wiley-VCH Verlag GmbH & Co. KGaA, Weinheim 

has a symmetry no higher than 2-fold, combination of the molecular clips with two axial centers will give rise to rectangle or *n*-gonal prisms determined by *n*-fold symmetry of the axial centers ($C_n$). That is, two linearly coordinating metal ions will connect two clips to form a rectangular-shaped structure, while two triangularly coordinating metal ions can lead to the formation of a trigonal prism, and further, a tetragonal prism may be generated by using two metal ions which prefer a square-planar coordination environment. The shape and size of the assembled molecules are determined by the size of the ligands and preferred coordination of the metal ions.

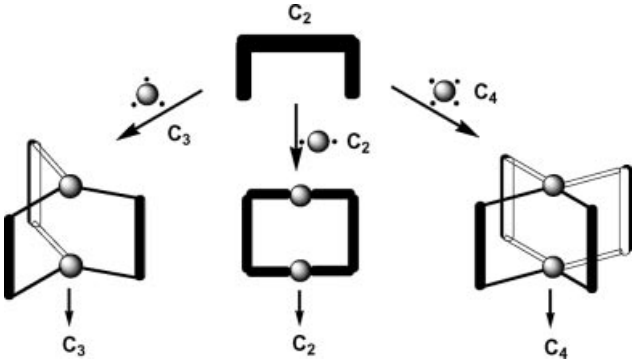


Scheme 1. Assembly of rectangular or prismatic structures from molecular clips and metal ions of $C_n$ symmetry.

### 2.2 Multipodal Ligands + Metal Ions of $C_2$ Symmetry

A complementary approach to construct compositionally different but topologically identical prismatic molecules compared to route 2.1 is shown in Scheme 2. In this route, a multipodal ligand which contains more than two legs connecting with the basal core and pointing in the same direction (*cis* conformation) is used to determine the *n*-fold rotation axis. In combination of the metal ions with $C_2$ symmetry, *n*-gonal prismatic structures are readily available depending on the size and shape of the ligands. One of the advantages of this route is that assembly of the coordination prisms with higher $C_n$ symmetry ($n \geq 5$) become feasible. This is hard for route 2.1 due to absence of metal ions with coordination geometry having $C_5$ or higher rotation symmetry.

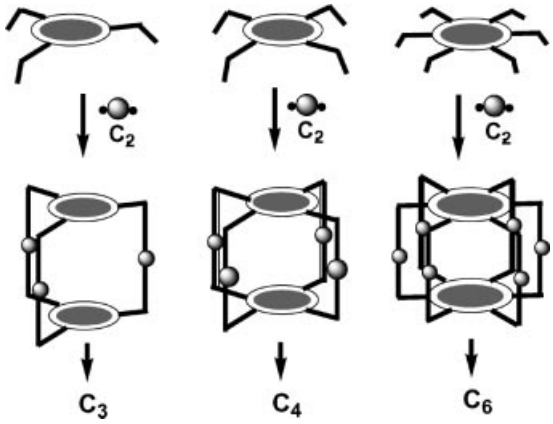


Scheme 2. Assembly of prismatic structures from multipodal ligands and metal ions of $C_2$ symmetry.

### 2.3 Molcular Clips + Protected Metal Ions of Restrained $C_n$ Symmetry

Another route to construct rectangular and prismatic molecular architectures is to use selected symmetry of metal ions with protected coordination geometry. For example, the octahedral metal ions are known to provide versatile coordination symmetry, however, it is a surprise that their potential application in construction of molecular prisms has so far been mainly realized in tetragonal prisms. As depicted in Scheme 3, the utilization of four equatorial sites can afford a $C_4$ tetragonal node, while a $C_3$ trigonal node can be produced if three *fac*-coordination sites are blocked. Even further, if only two opposite coordination sites are kept free while all other occupied, a linear node of $C_2$ symmetry is obvious. Such symmetry restrained metal ions interact with the appropriate molecular clips can lead to formation of tetragonal prism, dicapped trigonal prisms and molecular rectangles, respectively. Therefore, octahedral metal ions could become an abundant source to construct

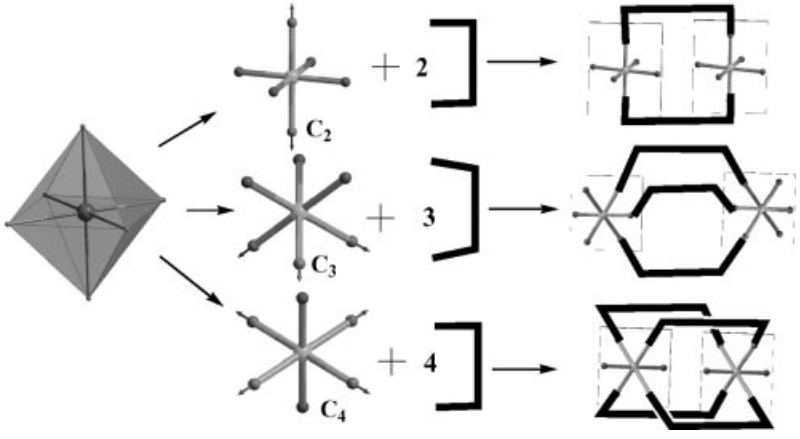


Scheme 3. Assembly of rectangular or prismatic structures from molecular clips and blocked octahedral metal ions.

 © 2007 Wiley-VCH Verlag GmbH & Co. KGaA, Weinheim 

rectangular or prismatic molecular architectures following the ligand-directed symmetry-interaction approach if their $C_n$ symmetry can be properly retained.[5] Similarly, the metal ions of square pyramidal geometry could provide $C_4$ symmetry if the apical site is blocked, and the trigonal bipyramidal geometry could give rise to $C_3$ symmetry if two axial sites are protected.

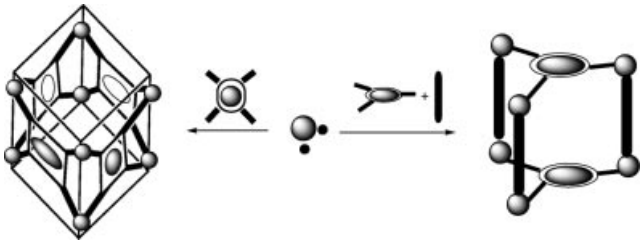

Scheme 4. Representative of multicomponent assembly of a molecular tube or a trigonal prism.

### 2.4 Multicomponent Self-Assembly

By contrast to above approaches for construction of discrete molecular architectures based on $C_n$ symmetry, deliberate design of prismatic architecture has long been achieved from multiple components self-assembly as depicted in Scheme 4.

This approach is mainly characteristic of the rigid ligands. The pioneering work in this field includes Lehn's cylindrical structures[6] assembled from tetrapyridine and hexaphenylhexaazatriphenylene derivatived multidentate compounds involving two triangular ligands and three ditopic linear ligands. However, the flexible tetrapyridine ligand containing the $CH_2CH_2$ spacer was found to be able to result in the similar trigonal structure.[6c] Fujita and co-workers have reported a series of prismatic architectures based on the self-assembly of tridentate panel-like ligand, bidentate pillar ligand and *cis*-capped $Pd^{II}$ or $Pt^{II}$ ions.[7a–7c] Because the ligands are normally "self-select",[7a,7c] the template has been found necessary for the formation of such prismatic structures. Moreover, thus constructed molecular architectures are usually kinetically stable once formed and remain stable to a certain extent even after the template was removed.

It is interesting that formation of tubular structures sometimes takes benefit from such a multicomponent assemble process.[7d] As shown in Scheme 4, if the ligands oc-

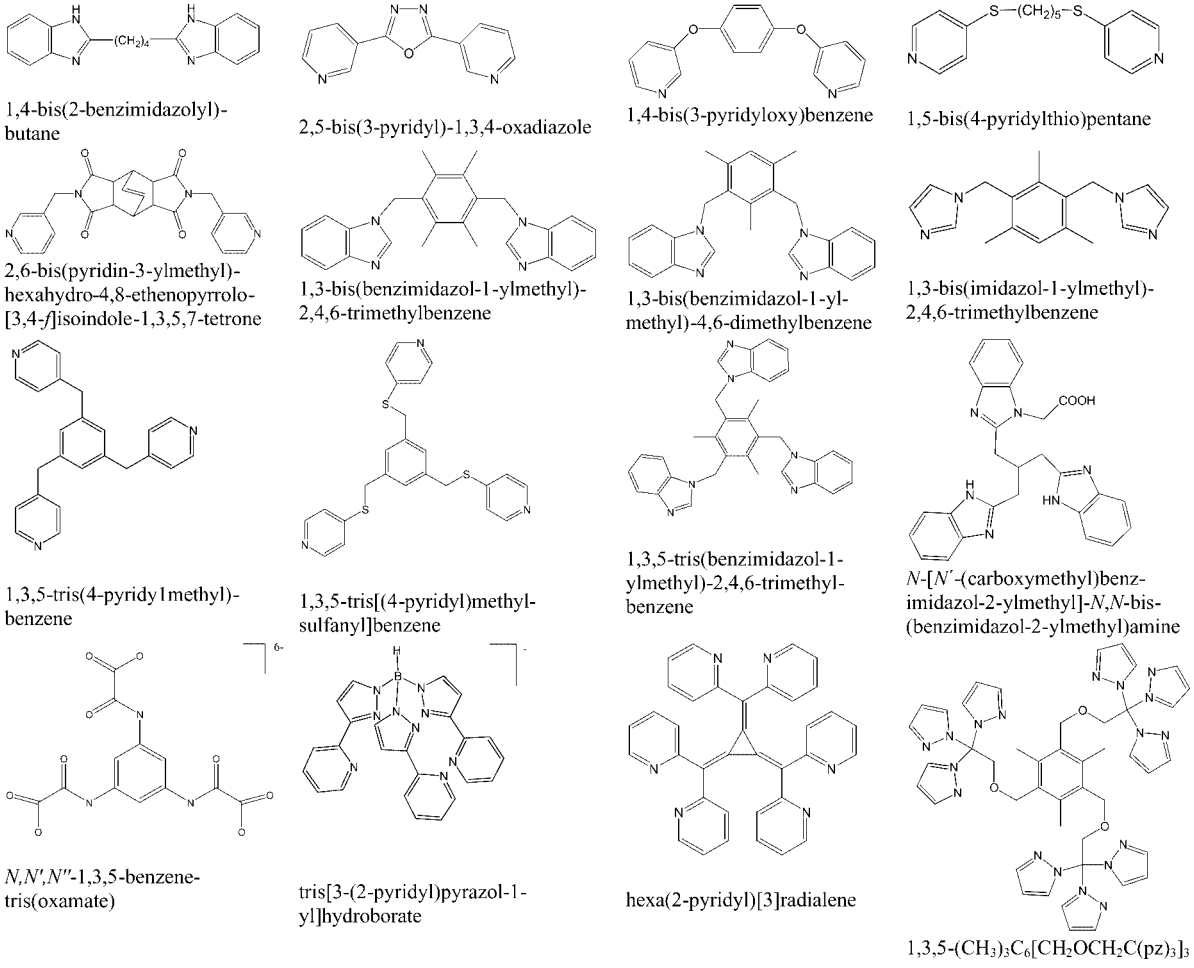


Scheme 5. Part of the mentioned ligands.

 © 2007 Wiley-VCH Verlag GmbH & Co. KGaA, Weinheim 

cupying the bases of the prisms are absent, the prismatic structure becomes open-ended, thus turning into tubular architectures keeping the shape of the prisms.

It should be noticed that there are other routes besides above four have also appeared in the literature. On the other hand, these approaches sometimes may also result in formation of helical structures, such as double-stranded, triple-stranded and even quadruple-stranded helicates,[1d,8] which sometimes become ambiguous to be distinguishable from the prismatic structures. However, for the molecular architectures having well-shaped structure or even possessing apparent $C_{n\mathrm{h}}$ or $D_{n\mathrm{h}}$ symmetry which incompatible with the helical sense, it is inappropriate to describe them as helicates. In this microreview, we mainly focus on apparently regular molecular architectures. A few obvious helicates are only mentioned selectively. In many cases, the structures may not possess the exact crystallographically imposed $C_n$ symmetry thus deviating from the right prisms, or only keeping the overall prismatic shapes. Part of organic ligands mentioned in the following discussion are listed in Scheme 5.

## 3. Cyclic Molecular Architectures

### 3.1 $M_2L_2$ Metallacycles and Rectangles Based on Non-Rigid Ligands

Design and synthesis of cyclic molecular architecture has attracted extensive interests in several research fields, including materials chemistry and molecular nanotechnology. Dinuclear metallacycles may represent the most productive cyclic molecular architectures, partly owing to the fact that the closed $M_2L_2$ motif is the smallest metallacyclic species hence the most thermodynamically favored one predominant over other larger species in solution. As early examples of such structures, flexible long-chain diphosphanes $Ph_2P(CH_2)_nPPh_2$ ($n \geq 3$) have been shown to generally give rise to dinuclear ring structures on reaction with equivalent amounts of silver(I) or copper(I) salts, containing terminal or bridging anions.[9] Depending on the different conformations of the non-rigid ligands, $M_2L_2$ cyclic molecules can display varied shapes like molecular rectangles, molecular rhombus and dinuclear helicates as shown in Scheme 6. Usually, when the non-rigid ligand contains two terminal coordinating arms which adopt a *cis* conformation and point to the same direction, the ligand can act as a "molecular clip" to react with metal ions to form $M_2L_2$ rectangles. While the angular ligand turning in the middle can react with two metal ions to assemble an $M_2L_2$ molecule showing rhombic structure. On the contrary, if the conformation of the non-rigid ligand is changed from *cis* to *trans*, the ligand can twist along two metal axes to form dinuclear helicate. For example, Hannon et al. designed a series of bis(pyridylimine) Schiff-base ligands from methyldianiline, which offer sufficient flexibility for two strands to wrap around the two metal centers while impose the same stereochemistry at both centers. Reaction of these ligands with $Cu^{I}$ or $Ag^{I}$ ions afforded various dinuclear helicates.[10]

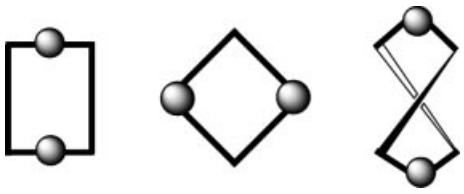

Scheme 6. Schematic view of the rectangular, rhombic or dinuclear helical $M_2L_2$ metallacycles.

Compared to the well developed higher symmetric $M_4L_4$ square, molecular rectangles may be able to exhibit improved selectivity and sensitivity with respect to molecular recognition and separation.[4] However, preparation of molecular rectangles based on the rigid ligands is still challengeable, because simply mixing two ligands of different lengths and *cis*-protected metal corners usually forms two types of molecular squares instead of molecular rectangles due to the enthalpic reason.[11] Alternatively, Stang and coworkers creatively designed an organometallic "clip" which anchors two metal corners on each side of a rigid ligand and opens two labile coordination sites in a nearly parallel fashion ready for connecting the second rod-like dipotic ligand.[4a] Similarly, clever design of semi-rigid ligand possessing two co-facial directing coordination groups could provide analogous "organic molecular clips" which facilitate a ligand-directed symmetry-interaction approach[3] for fabrication of rectangular structures as demonstrated in route 2.1 and 2.3.

Early examples matching such design approach can be found in a series of cofacial dinuclear complexes formed from bis(β-diketone) and bis(β-ketoenamine) ligands.[12a–12d] The well-defined size and shape of these complexes show inner cavity where small guest molecules are able to be hosted. Latter examples include Mirkin's neutral $Re^{I}$ macrocycles of the phosphanylthioether ligands,[12e] Cotton's molecular loops composed of two dimetal *cis*-$Mo_2(DAniF)_2^{2+}$ units (DAniF = *N*,*N*′-di-*p*-anisylformamidinate) linked by two dicarboxylate dianions,[12f] Chung's $Ag^{I}$ metallosupramolecules of the flexible 2-pyridyl ligands,[12g] and Fujita's rhombic structure consisting of two angular dipyridyl ligands and *cis*-protected metal ions.[12h]

We designed a series of semi-rigid and flexible ligands containing two (benz)imidazolyl or quinolyl terminal coordinating groups.[13] The flexibility of the methylene -$CH_2$- groups endow the ligands conformational freedom and, when induced by the symmetry interaction from properly selected metal ions, they behavior as molecular "clips" to assemble dinuclear metallocycles showing the rectangular structures. The shape and size of these molecular rectangles could be adjusted by modifying the structures of the ligands, thereby imposing distinguishable nature of the cavity and ability of hosting small molecules or counterions (Figure 1).[3] In addition, many dinuclear macrocycles based on the non-rigid ligands have good solubility, thus giving a chance to investigate their solution dynamics and the potential mechanism of self-assembly by means of NMR and ESI-MS techniques. For example, in complexes

 © 2007 Wiley-VCH Verlag GmbH & Co. KGaA, Weinheim 

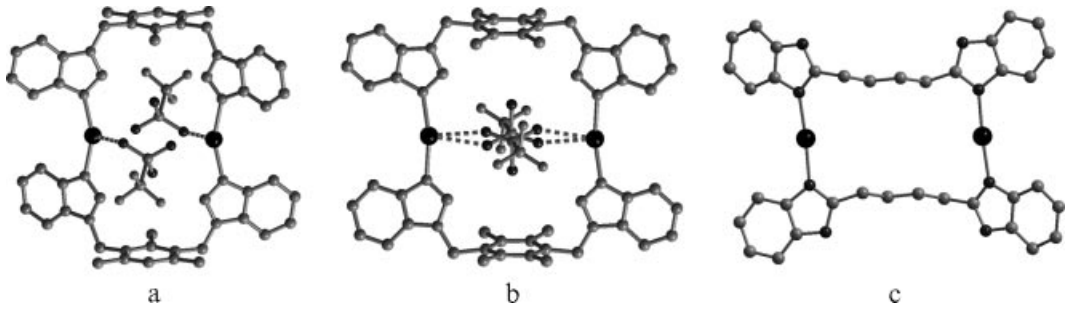


Figure 1. Rectangular structures formed in complexes (a) $[Ag_2\mathbf{L^1}_2](CF_3SO_3)_2$ [$\mathbf{L^1}$ = 1,3-bis(benzimidazol-1-ylmethyl)-2,4,6-trimethylbenzene],[3] (b) $[Ag_2\mathbf{L^2}_2](CF_3SO_3)_2$ [$\mathbf{L^2}$ = 1,4-bis(benzimidazol-1-ylmethyl)-2,3,5,6-tetramethylbenzene][3] and (c) $[Ag_2(C4BIm)_2](CF_3CO_2)_2$.[13a]

$[Ag_2(C4BIm)_2](CF_3CO_2)_2$ [C4BIm = 1,4-bis(2-benzimidazolyl)butane][13a] as shown in Figure 1, c, the solution dynamics study showed that equilibria among the $[Ag_2(C4BIm)_2]^{2+}$ dication and other potential oligomers were established via a solvent-assisted dissociative exchange mechanism. The calculated metal–ligand exchange barrier from VT-$^1$H NMR results was comparable with the energy of a strong hydrogen bond, which accounts for the reason that why the formation of $Ag^I$ complexes are very unpredictable and can be easily affected by various subtle factors and why astonishingly diversified structures and topologies could be obtained from $Ag^I$ and quite similar ligands, namely, supramolecular isomerism.[13a]

### 3.2 $M_nL_n$ ($n \geq 3$) Metallacycles Based on Non-Rigid Ligands

The directional-bonding approach has been usually used to predetermine the larger cyclic molecules, and various structures with a wide range of sizes, shapes and desirable physical properties have been obtained through careful selection of the metal starting material, coordinatively inert directing ligands or bridging ligands.[1] Theoretically, multinuclear cyclic molecular architectures can be synthesized via the systematic combination of ditopic building blocks and metals conforming to required angles as shown in Scheme 7, in which the regular models of polygons, such as triangles, squares, pentagon, hexagons an so on, could be developed.

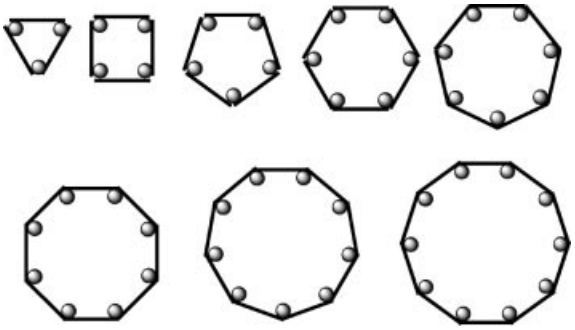

Scheme 7. Schematic view of the metallacycles varying from triangle to decagon.

However, there are many subtle factors which can influence the final formation of the cyclic molecules based on the non-rigid ligands, so precise control of the polygonal shape and size is often difficult. Nevertheless, Puddephatt et al.[14a] reported a cationic molecular triangle [{Pt($Bu_2$-bipy)[μ-4-$NC_5H_4C(NO)NH$-4-$C_5H_4N$]}$_3$]$^{6+}$ which was assembled from the *cis*-blocked platinum(II) unit ($Bu_2$-bipy)-$Pt^{2+}$ and the unsymmetrical bis(pyridine) ligand 4-$NC_5H_4C(NO)NH$-4-$C_5H_4N$ (Figure 2, a), while a neutral molecular triangle [*cis*-$Mo_2(DAniF)_2]_3$(*trans*-1,4-$O_2CC_6H_{10}CO_2)_3$ (DAniF = *N*,*N*′-di-*p*-anisylformamidinate) containing metal–metal bound units derived from paddlewheel complexes was obtained by Cotton et al.[14b] The square $M_4L_4$ molecules are rather common for the rigid ligands, but still remain rare for the non-rigid ligands. One example can be found in a nickel(II)-based cationic molecular square $[Ni(HL)]_4^{4+}$ which was achieved via self-assembly from a pentadentate N4S ligand bis[phenyl(2-pyridyl)methanone] thiocarbazone ($H_2L$).[14c] The ligand was believed to be "conformationally rigid" and its multidentate character made it possible to use the octahedral metal ion for formation of square structure. A similar example is a zinc(II)-based square complex assembled from a linear-spacer-bridged bis(pyrrol-2-ylmethyleneamine) ligand. The structure possesses a $D_4$ geometry with two pyrrol-2-ylmethyleneamine units adopt a *trans* arrangement resulting in inner dimensions of 8.7 × 8.7 Å[14d] as shown in Figure 2, b.

It is usually believed that, for the $M_nL_n$ macrocyclic structures, when the value *n* becomes larger, the discrete macrocycles becomes more thermodynamically disfavored in solution. However, the flexibility of the ligands sometimes may facilitate formation of multinuclear macrocyclic $M_nL_n$ ($n \geq 4$) with the aid of template guest. Known examples may be found from a series of $M_6L_6$ assemblies,[15] such as the chiral $Ag_6L_6$ from a completely stereospecific self-assembly of a semi-rigid bipyridine derivative with fused pinene group,[15a] neutral molecular $Pd_6L_6$ hexagons by using of flexible carboxylic acid modified ditertiary phosphanes $\kappa^3$-$P_2O$-terdentate ligands,[15b] $Fe_6L_6$ hexameric ferric wheels from reaction of various *N*-substituted diethanolamines.[15c] Even larger metallacycles[16] include [30]-metallacrown-10 compounds $[Mn(C_{14}H_9N_2O_3)(CH_3OH)]_{10}\cdot 5CH_2Cl_2\cdot 16CH_3OH\cdot H_2O$ and $[Fe(C_{14}H_9N_2O_3)(CH_3OH)]_{10}\cdot$

 © 2007 Wiley-VCH Verlag GmbH & Co. KGaA, Weinheim 

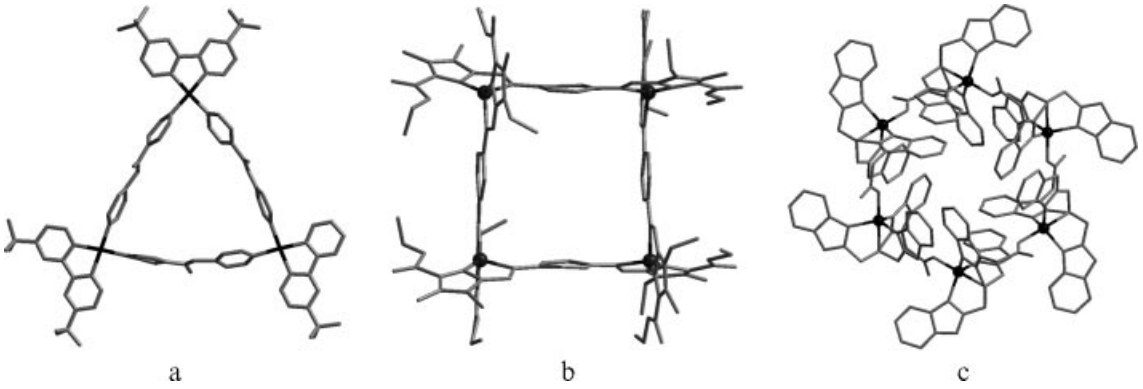


Figure 2. (a) A cationic molecular triangle $[\{Pt(Bu_2\text{-bipy})[\mu\text{-}4\text{-}NC_5H_4C(NO)NH\text{-}4\text{-}C_5H_4N]\}_3]^{6+}$,[14a] (b) a zinc(II)-based square complex assembled from a bis(pyrrol-2-ylmethyleneamine) ligand,[14d] and (c) a hexanuclear cationic metallamacrocycle $[Cu_6(Acntb)_6](ClO_4)_6\cdot 6H_2O$.[15d]

$3CH_2C_{12}\cdot 12.5CH_3OH\cdot 5H_2O$ with a pentadentate ligand *N*-phenylsalicylhydrazidate,[16a] [36]metallacrown-12 $Ni^{II}$ compound $[Ni(C_{13}H_9N_3O_2)(CH_3OH)]_{12}$ from a pentadentate Schiff-base ligand salicylaldehyde 2-pyridinecarboxylhydrazone,[16b] 36-membered dodecanuclear $Mn^{II}$ metalladiazamacrocycle $[Mn_{12}(tpeshz)_{12}(dmf)_{12}]$ (H3tpeshz = *N*-*trans*-2-pentenoylsalicylhydrazide)[16c] and $[Mn_{12}(chxshz)_{12}(MeOH)_{12}]$ (H3chxshz = *N*-cyclohexanoylsalicylhydrazide),[16d] and a chiral luminescent $Au_{16}$ ring $[(dppm)_2Au_4(pipzdtc)]_4(PF_6)_8$ assembled from achiral components dppm [bis(diphenylphosphanyl)methane] and $K_2$(pipzdtc) (piperazine-1,4-dicarbodithiolate).[16e]

We have modified a versatile $C_3$-symmetric ligand, tris(2-benzimidazolylmethyl)amine (ntb), by introducing one acetic acid group to get a new unsymmetric tripodal ligand *N*-[*N*′-(carboxymethyl)benzimidazol-2-ylmethyl]-*N*,*N*-bis(benzimidazol-2-ylmethyl)amine (HAcntb). Reaction of this ligand with $Cu(ClO_4)_2$ afforded a nanometer-sized hexanuclear cationic metallamacrocycle $[Cu_6(Acntb)_6](ClO_4)_6\cdot 6H_2O$ as shown in Figure 2, c.[15d] Each $Cu^{II}$ ion is coordinated by three imino-nitrogen atoms and the apical amino-nitrogen atom form the same ligand, and one oxygen atom of the branching methylenecarboxylate group from another ligand, thus linking six $Cu^{II}$ ions to a hexameric structure possessing a crystallographically imposed –3 symmetry.

As mentioned above, one of the disadvantages by using non-rigid ligand is the difficulty of the controlling the size of the target macrocycles. A typical example is the assembly of a series of chiral molecular polygons, ranging from triangle to octagon, with $[cis\text{-}(PEt_3)_2PtCl_2]$ and the same enantiopure 6,6′-bis(alkynyl)-1,1′-binaphthalene.[17] The limited conformational flexibility of the bridging ligand is believed the key to the facile one-pot self-assembly of six polygons of different size, which were able to be purified by silica gel column chromatography in varied yield. Another problem by using non-rigid ligand is the difficulty of determining the shape of the molecules. In many cases, so called circular helicates were obtained. For example, Steel et al. obtained an $M_3L_3$ trinuclear metallacycles[18a] by exploiting a semi-rigid ligand 1,3-bis(8-quinolyloxymethyl)-benzene to react with $AgCF_3SO_3$, and Hannon et al. reported a $Cu^{I}$ trinuclear helicate[18b] by utilizing semi-rigid bis(pyridylimine) Schiff-base ligands based on 4,4′-methylenebis(2,6-dimethylaniline). Moreover, different polygons can interconvert into each other by guest- or counterion-induced interactions which favor one over another during the assembly process. For example, Stang et al.[19a] reported an equilibrium mixture of triangular and square assemblies which was established in solution when the flexible, ditopic donor unit, *trans*-bis(4-pyridyl)ethylene, was treated with the ditopic acceptor unit, $cis\text{-}(Me_3P)_2Pt(OTf)_2$, in a 1:1 ratio. Such equilibrium is dependent on water and anions, and selective crystallization of either of the two species can be accomplished via the appropriate choice of solvents and ratio of anions. Similarly, Lehn and co-workers demonstrated that a linear trinuclear triple helicate could be converted to a pentagonal $M_5L_5$ in the presence of a template chloride anion while hexagonal $M_6L_6$ in the presence of a sulfate anion.[19b]

## 4. Prismatic Molecular Architectures

Design and assembly of prismatic molecular architectures, especially for those possessing an internal cavity capable of entrapping guest molecules, has been receiving great interests in recent years because of the prospective applications in host-guest chemistry, molecular recognition, catalysis, biology (drug delivery), and materials science (molecular devices). This section will give some examples according to the *n*-gonal bases of the prismatic structures.

### 4.1 Trigonal Prismatic Cages

#### *4.1.1 Assembled via Route 2.1*

Two three-connected metal ions locating at two bases and three ditopic ligands acting as lateral edges are required by this approach. The $Ag^{I}$ ion is a good candidate which is well known to display flexible coordination geometry vary-

 © 2007 Wiley-VCH Verlag GmbH & Co. KGaA, Weinheim 

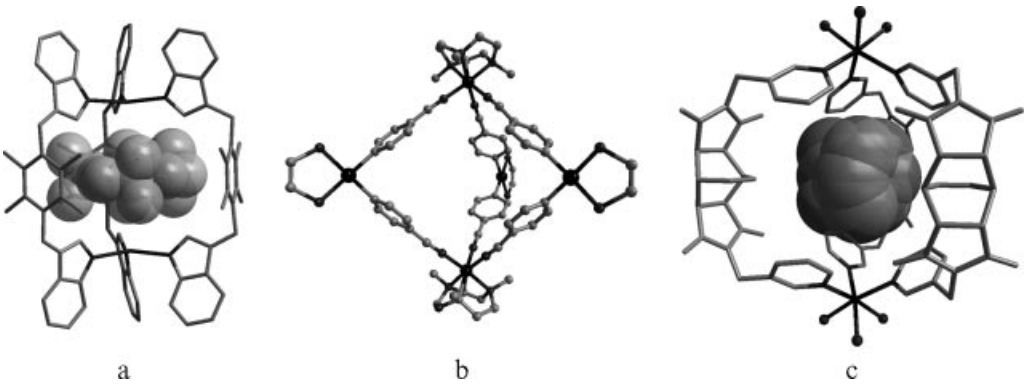


Figure 3. (a) Trigonal prismatic structures in complex $[Ag_2\mathbf{L^2}_3](CF_3SO_3)_2$,[21a] (b) trigonal-bipyramidal cage in complex $[[(Me_3tacn)Rh(CCPy)_3]_2[(DCPE)Pt]_3]$[22b] and (c) dicapped trigonal prismatic cage in complex $[Zn_2\mathbf{L^3}_3(H_2O)_6]\cdot(CF_3SO_3)_4\cdot CHCl_3$.[5] Guest molecules are shown in space-filling mode.

ing from two-coordinate linear to six-coordinate octahedral geometry.[20] When taking the triangular coordination geometry, $Ag^I$ ion can be utilized as trigonal node to assemble trigonal prisms in combination with three clip-like bis(monodentate) ligands. For example, we have prepared a ligand 1,4-bis(benzimidazol-1-ylmethyl)2,3,5,6-tetramethylbenzene (**L²**) which reacts with $AgCF_3SO_3$ in a 2:3 ratio to afforded a trigonal prismatic cage $[Ag_2\mathbf{L^2}_3](CF_3SO_3)_2$ as shown in Figure 3, a.[21a] The three ligands adopted the *cis* conformations with the nitrogen donor atoms from the benzimidazole rings pointing to the same direction, thus behaving as molecular "clip". The entire cationic prism exhibits an unusual $S_3$ symmetry. Steel et al.[21b] reported a similar structure which was described as a helicate. Another example of trigonal prism with trigonal geometric metal ions at the bases has been synthesized by Johnson and coworkers.[21c] In this case they used three dithiol ligands and two $As^{III}$ metal ions and the trigonal prism was close to a $C_{3h}$ symmetry.

### *4.1.2 Assembled via Route 2.3*

If metal ions of higher coordination numbers are used for such a purpose, the metal centers have to be protected to degrade the symmetry to $C_n$ according to the route 2.3. For instance, when the metal ions take the tetrahedral coordination geometry, one of four coordination sites has to be occupied by a monodentate anion or auxiliary ligand. By utilizing diphosphane ligand 1,2-bis(diphenylphosphanyl)-acetylene (dppa) to react with $Ag^I$ ions in a 2:3 ratio, a trigonal prism with tetrahedral geometric $Ag^I$ atoms at bases was obtained by James et al., in which the fourth coordination sites was taken by oxygen from anion $CF_3SO_3^-$ or $NO_3^-$, and the three P atoms from diphosphane ligands took the other three coordination sites.[22a] Another interesting example is the trigonal-bipyramidal supramolecular cage constructed by Youngs et al.[22b] where they used the well protected octahedral $Rh^{II}$ and square $Pt^{II}$ ions as shown in Figure 3, b. The reaction of 4-ethynyl-pyridine with the facially protected $(Me_3tacn)RhCl_3$ in the presence of *tert*-butyllithium afforded the octahedral complex $(Me_3tacn)Rh(CCPy)_3$, further reaction of this unit with three corner restricted *cis*-$(DCPE)Pt(NO_3)_2$ resulted in the mixed-metal-containing trigonal bipyramidal $[[(Me_3tacn)Rh(CCPy)_3]_2((DCPE)Pt)_3]$. From another point of view, this structure can be described as an assembly of three angular metal-containing ligands with two facially protected octahedral metal ions, showing a shape analogous to the trigonal prism.

We have prepared a semi-rigid conformational adaptive ligand, 2,6-bis(pyridin-3-ylmethyl)hexahydro-4,8-ethenopyrrolo[3,4-*f*]isoindole-1,3,5,7-tetrone (**L³**), which can react with the octahedral $Zn^{II}$ ion to afford a complex $[Zn_2\mathbf{L^3}_3(H_2O)_6]\cdot(CF_3SO_3)_4\cdot CHCl_3$[5] as shown in Figure 3, c. Two $Zn^{II}$ ions in this complex are coordinated by three different ligands and three water molecules, resulting in a N3O3 environment where three N and three O atoms are arranged in a *fac*-conformation allowing of a *3*-fold rotation symmetry $C_3$, thus the $[M_2\mathbf{L^3}_3]^{4+}$ cationic motif displays a dicapped trigonal prismatic structure (Figure 3, c) containing a trigonal cage in which a disordered $CHCl_3$ guest molecule is hosted. The molecule possesses an exact $C_{3h}$ point symmetry with a $C_3$ rotation axis passing through two $Zn^{II}$ atoms and a mirror plan bisecting the molecule.[5]

It should be noted that routes 2.1 and 2.3 are also applicable to rigid ligands providing the ligands are ditopic and exhibit the molecular clip character. For instance, Du et al.[23a] obtained a trigonal prism $[Cu_2(\mathbf{L^4})_3(CH_3CN)_2](ClO_4)_2$ [**L⁴** = 2,5-bis(3-pyridyl)-1,3,4-oxadiazole] in which one coordination site of each distorted tetrahedral $Cu^I$ center is occupied by N atom of an acetonitrile solvent, and the other three coordination sites join three different ligands acting as a 3-connecting node. Each trigonal prismatic cation hosts one water guest inside the cavity. Moreover, the bases of the trigonal prism can also be provided by different metal ions. Catalano et al. reported two mixed-metal trigonal prisms $[AuPdTl(P_2phen)_3](PF_6)_2$ and $[AuPtTl(P_2phen)_3](PF_6)_2$, where one basal site was taken by $Au^I$, and the other by $Pd^0$ or $Pt^0$. One $Tl^I$ ion was encapsulated inside via metal–metal interactions.[23b]

 © 2007 Wiley-VCH Verlag GmbH & Co. KGaA, Weinheim 

A combination of two six-coordinate metal ions and three flexible bis(bidentate) ligands can also follows route 2.1 to give $M_2L_3$ molecular architecture, however, in most cases the ligands are twisted and the structures are actually dinuclear triple-stranded helicates[24] which fall out the scope of this review.

### *4.1.3 Assembled via Route 2.2*

Alternatively, the two bases of the trigonal prism can also be provided by non-metal planes. As shown in Scheme 3, tripodal ligands can be exploited in the assembly of trigonal prism following route 2.2, where the trigonal prism is generated in combination with three bridging metal ions. The tripodal ligands could be based on an aromatic ring, macrocycle, or even B atomic core having three *cis*,*cis*,*cis* conformational coordinating legs.

#### *4.1.3.1 From Tri(monodentate) Tripodal Ligands Based on Aromatic Core*

By using of the inherent $C_3$ symmetry of benzene ring, Fujita and co-workers designed one semi-rigid tripodal ligand 1,3,5-tris(4-pyridylmethyl)benzene and firstly described the formation of a trigonal prismatic structure having $M_3L_2$ components with two tripodal ligands bridged by three palladium atoms.[25] By changing the donor group 4-pyridyl to 1-imidazolyl, Sun and co-workers synthesized some new types of tripodal ligands and obtained a series of $M_3L_2$ trigonal prisms composed of two tripodal ligands and three bridging tetrahedral geometric zinc ions[25b] or linear coordinated silver ions.[25c–25e] Their results indicated that the frameworks of these prisms were mainly determined by the nature of the tripodal ligand and geometric need of the metal ions, independent of the anions and the solvents. A similar trigonal prism was also reported by Lindoy et al.,[25f] where they combine a flexible tripodal ligand 1,3,5-tris[(4-pyridyl)methylsulfanyl]benzene with three silver(I) ions affording an $M_3L_2$ prismatic structure.

Similarly, based on the inherent $C_3$ symmetry of mesitylene core, we have designed a semi-rigid tri(monodentate) tripodal ligand 1,3,5-tris(benzimidazol-1-ylmethyl)-2,4,6-trimethylbenzene with 1-benzimidazolyl as coordination donor groups. Reaction of this tripodal ligand with $AgBF_4$, $AgClO_4$ or CuI resulted in a series of $M_3L_2$ trigonal prismatic cages which comprising two *syn*-conformational tripodal ligands jointed by three linearly coordinated metal ions with six benzimidazolyl legs nearly perpendicular to the central mesitylene cores (Figure 4, a).[3,26a] It was found that the assembly processes were not significantly affected by the counteranions, metal-to-ligand ratio or the solvent used, and the guest molecules encapsulated inside the cages showed diversified shapes and sizes varying from the spherical anion $BF_4^-$, $ClO_4^-$ to the planar $Cu_2I_4^{2-}$ coordination motif. To enlarge the inner cavity, the three legs of such tri(monodentate) tripodal ligand can be elongated. Ahn et al. have prepared a ligand containing three extended 4-pyridine legs with mesitylene or 1,3,5-triethylbenzene as cores. Two homochiral trigonal prisms were obtained from two tripodal ligands bridged by three $Pd^{II}$ ions. Since these prisms had internal binding sites, the authors believed that these cages could recognize organoammonium ions, or even chiral guests.[26b]

#### *4.1.3.2 From Tri(bidentate) or Tri(tridentate) Tripodal Ligands Based on Aromatic Core*

To assemble the trigonal prismatic structures by using the tri(monodentate) tripodal ligands, three metal ions with only two free coordination sites are required, such as linear coordinated $Ag^I$ or $Cu^I$ ions. The metal ion of higher coordination number needs proper blocking. Such restriction can be released by using tri(bidentate) or tri(tridentate) tripodal ligands. Journaux et al.[27a] designed a tripodal ligands *N*,*N*′,*N*′′-1,3,5-benzenetris(oxamate) with oxamate group as coordination donor. Two ligands adopted a tris(*N*,O-bidentate) coordination mode to generate a trigonal prism in which each $Cu^{II}$ ions was coordinated by two nitrogen atoms and two oxygen atoms in the equatorial plane. Similarly, Reger et al.[27b] designed a tri(tridentate) tripodal ligand $1,3,5\text{-}(CH_3)_3C_6[CH_2OCH_2C(pz)_3]_3$ (pz = pyrazolyl ring). Since each arm of this flexible tripodal ligand has three potential coordination donors, so many metal ions with different coordination geometry can be used to assembly $M_3L_2$ trigonal prism. Reaction of this ligand with $AgBF_4$ gave rise to a trigonal prismatic cage of composition $\{[Ag_3L_2(CH_3CN)](BF_4)_3\}\cdot(CH_3CN)_4$, in which all arms take a bidentate coordination mode to join three four coordinating $Ag^I$ ions. One $CH_3CN$ guest molecule was encapsulated inside the trigonal prism (Figure 4, b).

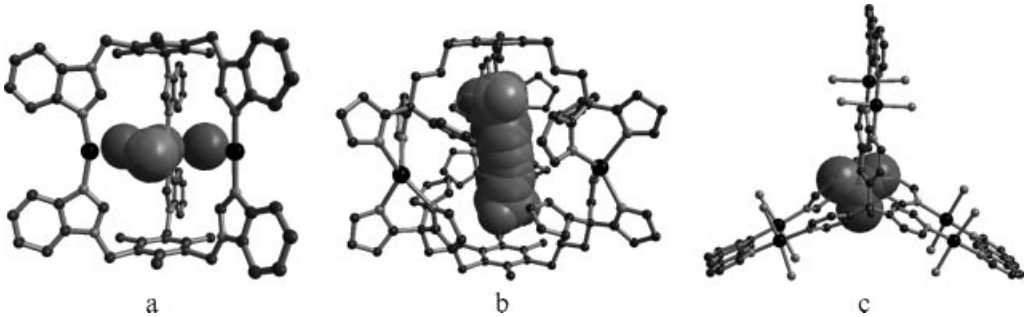


Figure 4. Representative trigonal prismatic structures assembled from (a) a tri(monodentate) tripodal ligand,[3] (b) a tri(tridentate) tripodal ligand[27b] and (c) an $sp^3$ C atom based tripodal ligand.[28d]

 © 2007 Wiley-VCH Verlag GmbH & Co. KGaA, Weinheim 

*4.1.3.3 From Tripodal Ligands Based on Non-Aromatic Core*

Alternatively, tripodal ligand could also contains a non-aromatic core, such as cavitand moiety, $sp^3$ C or B atoms etc.[28] Shinkai et al. obtained a trigonal prism via $Pd^{II}$-pyridine interactions when they used the tripodal ligand based on homooxacalix[3] as starting material, in which the [60] fullerene can be encapsulated inside the cavity.[28a] A variety of tripodal organic ligands or metal-containing ligands with $sp^3$ C, adamantane, Si or P=O as central cores have been synthesized by Stang and co-workers. Reaction of these ligands with predesigned metal-containing "clip" or organic "clip" afforded various trigonal structures (Figure 4, c).[28b–28d] Ward et al. synthesized an $M_3L_2$ structure by using tri-chelating hexadentate ligand tris[3-(2-pyridyl)-pyrazol-1-yl]hydroborate based on B center, in which each $Cu^I$ ion is four coordinated by two *N*,*N*′-bidentate arms from two ligands.[25e] Torres et al. also reported an $M_3L_2$ trigonal cage based on subphthalocyanine which is a 14 π-electron aromatic macrocycle combining three *N*-fused diiminoisoindole units around a boron atom.[25f]

## 4.2 Tetragonal Prismatic Cages

### *4.2.1 Assembled via Route 2.1*

Metal ions preferring square-planar coordination geometry can be utilized to assemble tetragonal prisms through route 2.1 when the four coordination sites in the same plane are taken by four bis(monodentate) ligands with *cis* conformation.[29] The $Pd^{II}$ and $Pt^{II}$ ions are the mostly used square-planar geometric metal ions in the literature, and the coordination flexible $Cu^{II}$ ion sometimes is also used in the construction of tetragonal prism when it adopts square-planar coordination geometry. One of the earliest papers in this area is reported by Steel and co-workers,[29a] where they synthesized a coordinatively saturated tetragonal cage by using the ligand 1,4-bis(3-pyridyloxy)benzene and $Pd^{II}$ ion. One hexafluorophosphate anion was encapsulated inside the cage acting as a bridging ligand via the weak Pd···F interactions. However, this structure exhibits the helical sense and described by authors as the quadruply stranded helicate. A more regular trigonal prism was fabricated by Fujita et al.[29b] when they used a rigid bis(pyridyl) ligand to react with $Pd(NO_3)_2$ at a ratio of 2:1, in which each tetragonal prismatic cage encapsulated a nitrate ion inside its cavity. An isomorphous tetragonal structure based on $Pt^{II}$ ion was reported by Chand et al. in modified reaction conditions.[29c] Similar tetragonal prism based square-planar $Pd^{II}$ ions was also assembled from a semi-rigid ligand 1,3-bis(imidazol-1-ylmethyl)-2,4,6-trimethylbenzene (bitmb), in which the two square planar geometric $Pd^{II}$ ions were bridged by four bitmb ligands in *cis*-conformation.[29d] By exploiting some bis(amidopyridine) ligands to react with $[PdCl_2(PhCN)_2]$, Puddephatt at al. obtained a series of dipalladium(II) tetragonal prisms (Figure 5, a), these prismatic complexes exhibited remarkable host–guest chemistry. The encapsulated guest molecules could vary from anions, neutral molecules to cations, depending on the conformation of the bis(amidopyridine) ligands.[30]

### *4.2.2 Assembled via Route 2.3*

The metal ions adopting the square-pyramidal or octahedral coordination geometries can be used to assemble tetragonal prisms if the apical positions were blocked by auxiliary ligands or counterions. In this route, the metal ions usually involve $Co^{II}$, $Zn^{II}$, $Ni^{II}$, $Cu^{II}$ and so on.[31] One of the early tetragonal prisms constructed following this way is the $Cu^{II}$ prism synthesized by Atwood and co-workers,[31a] in which the two octahedral $Cu^{II}$ ions are bridged by four semi-rigid bis(monodentate) ligands and two coordinated water molecules occupy the axial positions. Later they reported an isomorphous tetragonal structure by using six-coordinate $Co^{II}$ ion instead of $Cu^{II}$.[31b] From the reaction of a semi-rigid ligand 3,5-bis(benzimidazol-1-ylmethyl)-1,4-dimethoxyl-2,6-dimethylbenzene with $Co(BF_4)_2 \cdot 6H_2O$ in the presence of solvent $CH_3CN$, Amouri et al.[31c] obtained a coordinatively unsaturated cobalt-based $M_2L_4$ cage, in which each $Co^{II}$ ion adopted a square-pyramidal coordination geometry. The four equatorial positions were occupied by four benzimidazolyl arms and the solvent molecule $CH_3CN$ coordinated to $Co^{II}$ ions at the axial position. The anion $BF_4^-$ was encapsulated inside through weak interactions with the metal centers. Similar tetragonal prisms have also been synthesized by Bu et al.[31d] when they used a flexible ligand 1,5-bis(4-pyridylthio)pentane to react with $Co(ClO_4)_2 \cdot 6H_2O$ or $Zn(ClO_4)_2 \cdot 6H_2O$.

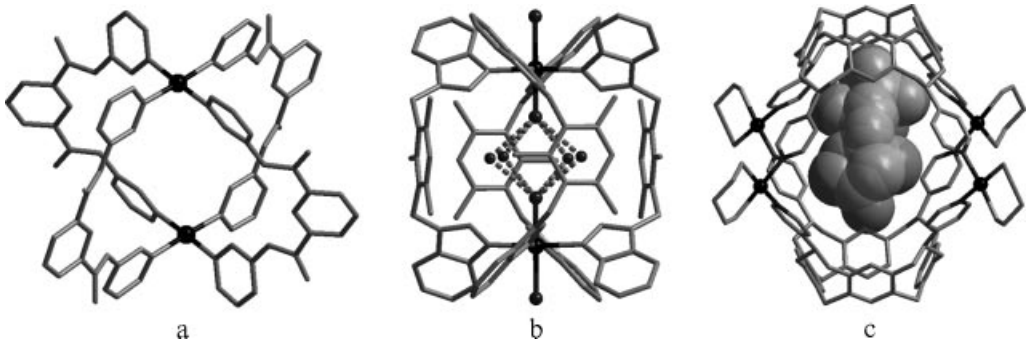


Figure 5. Representative tetragonal prismatic structures assembled with (a) square planar $Pd^{II}$ ion,[30a] (b) octahedral $Ni^{II}$ ion[3] and (c) cavitand-based tetrapodal ligand[33c] (phenyl groups are omitted).

 © 2007 Wiley-VCH Verlag GmbH & Co. KGaA, Weinheim 

We have prepared a semi-rigid ligand 1,3-bis(benzimidazol-1-ylmethyl)-2,4,6-trimethylbenzene (bbimms) which reacted with $Cu(ClO_4)_2$ to afford a right prismatic cage complex.[3,21a] Four ligands take *cis* conformation to bridge two copper(II) ions to form the prism within which resides an axially disordered perchlorate anion. There is crystallographically imposed $C_4$ axis passing through the two $Cu^{II}$ atoms and a $\sigma_h$ mirror across the center of the molecule, resulting in an $S_4$ symmetry of the box. Along the $C_4$ axis the perchlorate anions are arranged alternately inside and outside the box to generate a one-dimensional multicompartmental column. Moreover, we found that metal halide compounds like $NiCl_2$ and $CoCl_2$ were good candidates for providing four open equatorial sites. The halide atoms are usually retained after metal ions coordinate with the bis(monodentate) ligands, so metal halide can be ideally used to assembly tetragonal prisms. From the reaction of mbbimb ligand with $NiCl_2{\cdot}6H_2O$, we obtained a neutral $S_4$ symmetric tetragonal prismatic cage as shown in Figure 5, b. In this complex, the two $Ni^{II}$ ions are held by the benzimidazolyl arms from four $C_4$-symmetrically arranged ligands via four equivalent Ni–N bonds with the octahedral coordination geometry completed by two axial chloride ions. There are four *4*-fold symmetrically arranged water molecules was hosted inside the cage via weak O–H···Cl hydrogen bonds. Similar tetragonal prismatic cages based on metal halide were also reported by Hong et al.[31e] when they used a flexible ligand 1,3-bis(pyrid-4-ylthio)propan-2-one to react with $CoCl_2{\cdot}6H_2O$ or $CoBr_2{\cdot}6H_2O$, where only one halide anion ligated to metal ions at the apical position to complete a distorted square-pyramidal coordination geometry.

#### *4.2.3 Assembled via Route 2.2*

Similar to trigonal prisms described above, tetragonal prismatic structures can also be assembled from two tetrapodal ligands and four bridging metal ions through route 2.2. Four legs of the tetrapodal ligand could be monodentate, bidentate or tridentate. As a consequence, four metal ions with two, four or six coordination sites available are required, respectively.

Although various tetrapodal ligands based on the aromatic ring are available in literature, successful application of route 2.2 to assembly of tetragonal prismatic structure is still rare.[32] However, Brisbois et al.[32] obtained one organometallic tetragonal complex when they used tetradentate ligand based on cyclobutadienyl core to react with ethylenediamine palladium(II) nitrate, in which the two organometallic tetrapodal ligands CpCo-tetrakis(3-pyridyl)cyclobutadiene were bridged by four *cis*-protected $Pd^{II}$ ions. On the other hand, Shinkai and co-workers[32b] have exploited porphyrin-based tetrapodal ligands containing four pyridyl donor groups to react with the *cis*-protected $Pd^{II}$ ions, leading to formation of dimeric capsules. The $^1H$ NMR spectral studies indicate that such self-assembled molecular capsules have a highly symmetrical $D_{4h}$ structure as well as a large inside cavity.

Even more tetrapodal ligands have been synthesized on the basis of cavitand or calix[4]arene moieties with substituted pyridyl or cyano groups as coordination donors.[33] The first tetragonal cage based on cavitand ligand was reported by Dalcanale et al.,[33a] in which the two tetracyanocavitand derivatives were connected by four square-planar $Pd^{II}$ or $Pt^{II}$ ions. Afterwards, a series of similar enlarged prismatic cages have been reported by them or others through design of related deepened cavitand precursors via introduction of an appropriate coordinating group on the resorcinarene skeleton (Figure 5, c).[33b–33e] Hong et al.[33f] designed cavitand ligand via introduction of four flexible 4-pyridylmethyl groups at the upper rims and assembled $Pd^{II}$ and $Pt^{II}$ cages, while Harrison et al.[33g] synthesized similar prisms by using cavitand ligand with four flexible methyliminodiacetic acids attached to its upper rims. The cage was formed from two ligands connected by four six-coordinate $Co^{II}$ ions.

### 4.3. Multigonal Prismatic Cages

The coordination prismatic structures with two bases of *n*-gons ($n \geq 5$) are heretofore rather rare. One of the reasons is that the metal ions with $C_n$ ($n \geq 5$) symmetric coordination sites locating in the same plane remain very unusual, so the routes 2.1 and 2.3 are not applicable for such a purpose. The routes 2.3 and 2.4 are potentially practicable for construction of e.g. pentagonal or hexagonal-prismatic structures, however, it was found difficult to maintain $C_n$ ($n \geq 5$) symmetry during self-assembly process. For example, pentapodal[34a] and hexapodal[27b] ligands have been prepared to react with the two-connecting metal ions, nevertheless, assembly of pentagonal or hexagonal prismatic structures were not successful due to failure to prevent intramolecular metal chelation or conformational isomerization.

One example close to a hexagonal-prismatic structure was reported by Steel and co-workers.[34b] They synthesized an $M_6L_2$ cage by using the ligand hexa(2-pyridyl)[3]radialene (**L**$^5$) to react with silver tetrafluoroborate. In this complex, two ligands both adopt a hexapodal hexadentate coordination mode, connected by six bridging $Ag^I$ ions to result in a hexapodal prismatic metallosupramolecule with an encapsulated $\mu_3$-fluorido anion (Figure 6).

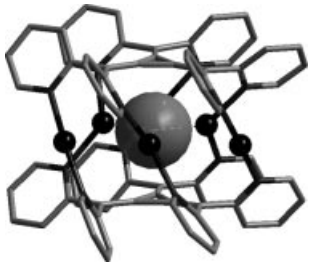

Figure 6. A representative hexagonal prismatic structure assembled with a hexapodal ligand **L**$^5$.[34b]

 © 2007 Wiley-VCH Verlag GmbH & Co. KGaA, Weinheim 

## 5. Tubular Molecular Architectures

In contrast to the well-developed inorganic nanotubes and organic nanotubular molecular architectures, the field of inorganic-organic hybrid coordination nanotubes remains largely unexplored in spite of the fast moving developments in the area of inorganic-organic hybrid materials. Recently, designing and constructing of tubular structures by utilizing coordination chemistry has been realized to be a useful approach, and a number of coordination polymers containing tubular channels have been synthesized.[35] However, the discrete coordination tubular molecular architectures remain rather uncommon. Depending on the deliberately protected angular coordination environments displayed by metal atoms and the judicious choice of the multidentate ligands, construction of coordination tubes via multicomponent assembly route 2.4 is feasible in the aid of template effect of the guest molecules. Initial work in this topic was reported by Fujita and co-workers.[36] They synthesized one discrete coordination tube by using rigid oligo(3,5-pyridine)s ligand and *cis*-protected $Pd^{II}$ ions, in which the four ligands were bridged by $Pd^{II}$ ions to encircle into tube, and the rod-like guests was the essential template of the formation of such coordination nanotubes (Figure 7, a). The tube dissociated into its components by the removal of the guest molecule and again re-associated by the addition of guest molecule.[36a] The length of thus formed tubes could be controlled just by elongating the ligand with increasing the numbers of pyridine nuclei.[36b] However, the solubility of the ligand became poorer when the ligand had more rigid rings, therefore they further introduced methylene ($CH_2$) groups to design flexible long tape-shape ligand, and successfully extended the length of similar coordination nanotube to 3.5 nm.[36c] Another longer coordination tube based on $Pd^{II}$ was also reported by them when they used one semi-rigid tetrapodal ligand having four terpyridines arms to react with $Pd^{II}$ ions, in which the two tetrapodal ligands were circled into a 3.0 nm open tube as a result of the coordination of terpyridines with $Pd^{II}$ ions.[36d]

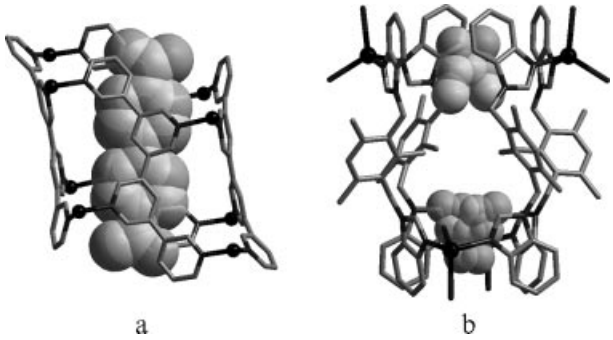


Figure 7. Tubular structures assembled with (a) a tetrakis(3,5-pyridine) ligand[36b] and (b) a *trans*-conformational ditopic semi-rigid ligand.[36e]

Based on the fact that the ditopic semi-rigid ligand is able to display either *cis*- or *trans*-conformation depending on the orientation of the two coordinating arms, we synthesized a discrete tubular tetramers $[Hg_4Cl_8(bbimms)_4]$ [bbimms = 1,3-bis(benzimidazol-1-ylmethyl)-2,4,6-trimethylbenzene] when we reacted the semi-rigid ligand bbimms with $HgCl_2$ which favors bent coordination geometry. The neutral molecular tube was generated by self-cyclization of four $[HgCl_2(bbimms)]$ subunits whose orientation alternates successively up and down (Figure 7, b), and the guest molecules DMSO or DMF played an important role in the formation and stabilization of the tubular structures. The interior cavity of the tube was approximately $4.6 \times 8.6 \times 16.8$ Å after consideration of the van der Waals radii. Furthermore, the neutral tubes were aligned to resemble a pipeline and that these pipelines were arranged into a three-dimensional columnar architecture.[36e]

## Concluding Remarks

In summary, well-shaped discrete molecular architectures are able to be constructed by using non-rigid ligands in contrast to the usually favored rigid ligands. Appropriate design and control of the donor groups and conformations of the semi-rigid or flexible ligands facilitate formation of relatively lower symmetric metallacyclic, prismatic and tubular structures in comparison to the higher symmetric polygonal or polyhedral structures. According to the distinguished nature of the non-rigid ligands and symmetry modification of metal ions, four assembly routes are available to direct formation of rectangular, prismatic and tubular architectures which are inherently related through the rotation symmetry. However, it should be noticed that the non-rigid ligands often display conformation freedom, for example, facile conversion between *cis* conformation and *trans* conformation of the ditopic semi-rigid ligands, which make it possible to generate coordination polymers instead of discrete molecular architectures. Therefore, vast effort is still needed to fully understand various subtle factors that influence the formation of closed molecular architectures as well as the shape stability and cavity size.

## Acknowledgments

The author gratefully acknowledges all the co-authors cited in the joint publications. This work has been supported by the National Science Funds for Distinguished Young Scholars of China (Grant 20525310), the NSF of China (Grant 20673147) and Guangdong Province (Grant 04205405), and RFDP of the Education Ministry of China.

[1] a) S. Leininger, B. Olenyuk, P. J. Stang, *Chem. Rev.* **2000**, *100*, 853–908; b) M. Fujita, K. Umemoto, M. Yoshizawa, N. Fujita, T. Kusukawa, K. Biradha, *Chem. Commun.* **2001**, 509–518; c) D. L. Caulder, K. N. Raymond, *J. Chem. Soc., Dalton Trans.* **1999**, 1185–1200; d) R. L. Paul, Z. R. Bell, J. C. Jeffery, J. A. McCleverty, M. D. Ward, *Proc. Natl. Acad. Sci. USA* **2002**, *99*, 4883–4888; e) B. J. Holliday, C. A. Mirkin, *Angew. Chem. Int. Ed.* **2001**, *40*, 2022–2043.
[2] C.-Y. Su, A. M. Goforth, M. D. Smith, H.-C. zur Loye, *Inorg. Chem.* **2003**, *42*, 5685–5692.
[3] C.-Y. Su, Y.-P. Cai, C.-L. Chen, M. D. Smith, W. Kaim, H.-C. zur Loye, *J. Am. Chem. Soc.* **2003**, *125*, 8595–8613.

 © 2007 Wiley-VCH Verlag GmbH & Co. KGaA, Weinheim 

[4] a) C. J. Kuehl, C. L. Mayne, A. M. Arif, P. J. Stang, *Org. Lett.* **2000**, *2*, 3727–3729; b) C. J. Kuehl, S. D. Huang, P. J. Stang, *J. Am. Chem. Soc.* **2001**, *123*, 9634–9641; c) C. J. Kuehl, Y. K. Kryschenko, U. Radhakrishnan, S. R. Seidel, S. D. Huang, P. J. Stang, *Proc. Natl. Acad. Sci. USA* **2002**, *99*, 4932–9636.

[5] Z.-M. Liu, Y. Liu, S.-R. Zheng, Z.-Q. Yu, M. Pan, C.-Y. Su, *Inorg. Chem.* **2007**, *46*, http://dx.doi.org/10.1021/ic062270+.

[6] a) P. Baxter, J.-M. Lehn, A. DeCian, J. Fischer, *Angew. Chem. Int. Ed. Engl.* **1993**, *32*, 69–72; b) A. Marquis-Rigault, A. Dupont-Gervais, P. N. W. Baxter, A. V. Dorsselaer, J.-M. Lehn, *Inorg. Chem.* **1996**, *35*, 2307–3210; c) P. N. W. Baxter, J.-M. Lehn, G. Baum, D. Fenske, *Chem. Eur. J.* **1999**, *5*, 102–112; d) A. M. Garcia, D. M. Bassani, J.-M. Lehn, G. Baum, D. Fenske, *Chem. Eur. J.* **1999**, *5*, 1234–1238.

[7] a) K. Kumazawa, K. Biradha, T. Kusukawa, T. Okano, M. Fujita, *Angew. Chem. Int. Ed.* **2003**, *42*, 3909–3913; b) M. Yoshizawa, K. Ono, K. Kumazawa, T. Kato, M. Fujita, *J. Am. Chem. Soc.* **2005**, *127*, 10800–10801; c) M. Yoshizawa, J. Nakagawa, K. Kumazawa, M. Nagao, M. Kawano, T. Ozeki, M. Fujita, *Angew. Chem. Int. Ed.* **2005**, *44*, 1810–1813; d) Y. Yamanoi, Y. Sakamoto, T. Kusukawa, M. Fujita, S. Sakamoto, K. Yamaguchi, *J. Am. Chem. Soc.* **2001**, *123*, 980–981; e) J. Zhang, P. W. Miller, M. Nieuwenhuyzen, S. L. James, *Chem. Eur. J.* **2006**, *12*, 2448–2453 and references cited therein.

[8] a) M. Albrecht, *Chem. Rev.* **2001**, *101*, 3457–3497; b) C. Piguet, G. Bernardinelli, G. Hopfgartner, *Chem. Rev.* **1997**, *97*, 2005–2062; c) Y.-P. Cai, C.-Y. Su, C.-L. Chen, Y.-M. Li, B.-S. Kang, A. S. C. Chan, W. Kaim, *Inorg. Chem.* **2003**, *42*, 163–168.

[9] a) S. Kitagawa, M. Kondo, S. Kawata, S. Wada, M. Maekawa, M. Munakata, *Inorg. Chem.* **1995**, *34*, 1455–1465; b) E. R. T. Tiekink, *Acta Crystallogr., . Sect. C* **1990**, *46*, 1933–1934; c) D. M. Ho, R. Bau, *Inorg. Chem.* **1983**, *21*, 4073–4079; d) S. P. Neo, Z.-Y. Zhou, T. C. W. Mak, T. S. A. Hor, *Inorg. Chem.* **1995**, *34*, 520–523; e) R. N. Yang, Y. M. Hou, B. Y. Xue, D. M. Wang, D. M. Jin, *Transition Met. Chem.* **1996**, *21*, 28–30; f) F. Caruso, M. Camalli, H. Rimml, L. M. Venanzi, *Inorg. Chem.* **1995**, *34*, 673–679.

[10] a) M. J. Hannon, C. L. Painting, N. W. Alcock, *Chem. Commun.* **1999**, 2023–2024; b) M. J. Hannon, L. J. Childs, *Supramol. Chem.* **2004**, *16*, 7–22.

[11] P. Thanasekaran, R.-T. Liao, Y.-H. Liu, T. Rajendran, S. Rajagopal, K.-L. Lu, *Coord. Chem. Rev.* **2005**, *249*, 1085–1110.

[12] a) A. W. Maverick, S. C. Buckingham, Q. Yao, J. R. Bradbury, G. G. Stanley, *J. Am. Chem. Soc.* **1986**, *108*, 7430–7431; b) A. W. Maverick, F. E. Klavetter, *Inorg. Chem.* **1984**, *23*, 4129–4130; c) A. W. Maverick, M. L. Ivie, J. H. Waggenspack, F. R. Fronczek, *Inorg. Chem.* **1990**, *29*, 24032409; d) J. R. Bradbury, J. L. Hampton, D. P. Martone, A. W. Maverick, *Inorg. Chem.* **1989**, *28*, 2392–2399; e) F. M. Dixon, A. H. Eisenberg, J. R. Farrell, C. A. Mirkin, L. M. Liable-Sands, A. L. Rheingold, *Inorg. Chem.* **2000**, *39*, 3432–3433; f) F. A. Cotton, C. Lin, C. A. Murillo, *Inorg. Chem.* **2001**, *40*, 472–477; g) D. M. Shin, I. S. Lee, Y.-A. Lee, Y. K. Chung, *Inorg. Chem.* **2003**, *42*, 2977–2982; h) M. Fujita, M. Aoyagi, F. Ibukuro, K. Ogura, K. Yamaguchi, *J. Am. Chem. Soc.* **1998**, *120*, 611–612.

[13] a) C.-L. Chen, H.-Y. Tan, J.-H. Yao, Y.-Q. Wan, C.-Y. Su, *Inorg. Chem.* **2005**, *44*, 8510–8520; b) C.-Y. Su, X.-P. Yang, S. Liao, T. C. W. Mak, B.-S. Kang, *Inorg. Chem. Commun.* **1999**, *2*, 383–385; c) Y.-P. Cai, C.-Y. Su, H.-X. Zhang, Z.-Y. Zhou, L.-X. Zhu, A. S. C. Chan, H.-Q. Liu, C.-L. B.-S. Kang, *Z. Anorg. Allg. Chem.* **2002**, *628*, 2321–2328; d) C.-Y. Su, S. Liao, H.-L. Zhu, B.-S. Kang, X.-M. Chen, H.-Q. Liu, *J. Chem. Soc., Dalton Trans.* **2000**, 1985–1993.

[14] a) Z. Qin, M. C. Jennings, R. J. Puddephatt, *Chem. Commun.* **2001**, 2676–2677; b) F. A. Cotton, C. Lin, C. A. Murillo, *Inorg. Chem.* **2001**, *40*, 575–577; c) C. He, C.-Y. Duan, C.-J. Fang, Y.-J. Liu, Q.-J. Meng, *J. Chem. Soc., Dalton Trans.* **2000**, 1207–1212; d) Z. Wu, Q. Chen, S. Xiong, B. Xin, Z. Zhao, L. Jiang, J. S. Ma, *Angew. Chem. Int. Ed.* **2003**, *42*, 3271–3274.

[15] a) O. Mamula, A. von Zelewsky, G. Bernardinelli, *Angew. Chem. Int. Ed.* **1998**, *37*, 289–293; b) M. R. J. Elsegood, M. B. Smith, P. M. Staniland, *Inorg. Chem.* **2006**, *45*, 6761–6770; c) R. W. Saalfrank, C. Deutscher, S. Sperner, T. Nakajima, A. M. Ako, E. Uller, F. Hampel, F. W. Heinemann, *Inorg. Chem.* **2004**, *43*, 4372–4382; d) C.-Y. Su, X.-P. Yang, B.-S. Kang, T. C. W. Mak, *Angew. Chem. Int. Ed.* **2001**, *40*, 1725–1728.

[16] a) S.-X. Liu, S. Lin, B.-Z. Lin, C.-C. Lin, J.-Q. Huang, *Angew. Chem.* **2001**, *113*, 1118–1121; b) Y. Bai, D.-B. Dang, C.-Y. Duan, Y. Song, Q.-J. Meng, *Inorg. Chem.* **2005**, *44*, 5972–5974; c) R. P. John, K. Lee, M. S. Lah, *Chem. Commun.* **2004**, 260–2661; d) R. P. John, J. Park, D. Moon, K. Lee, M. S. Lah, *Chem. Commun.* **2006**, 3699–3701; e) S.-Y. Yu, Z.-X. Zhang, E. C.-C. Cheng, Y.-Z. Li, V. W.-W. Yam, H.-P. Huang, R. Zhang, *J. Am. Chem. Soc.* **2005**, *127*, 17994–17995.

[17] H. Jiang, W. Lin, *J. Am. Chem. Soc.* **2003**, *125*, 8084–8085.

[18] a) M. R. A. Al-Mandhary, P. J. Steel, *Inorg. Chem. Commun.* **2002**, *5*, 954–955; b) L. J. Childs, N. W. Alcock, M. J. Hannon, *Angew. Chem. Int. Ed.* **2002**, *41*, 4244–4247.

[19] a) M. Schweiger, S. R. Seidel, A. M. Arif, P. J. Stang, *Inorg. Chem.* **2002**, *41*, 2556–2559; b) B. Hasenknopf, J.-M. Lehn, N. Boumediene, A. Dupont-Gervais, A. V. Dorsselaer, B. Kneisel, D. Fenske, *J. Am. Chem. Soc.* **1997**, *119*, 10956–10962.

[20] C.-L. Chen, B.-S. Kang, C.-Y. Su, *Aust. J. Chem.* **2006**, *59*, 3–18.

[21] a) C.-Y. Su, Y.-P. Cai, C.-L. Chen, H.-X. Zhang, B.-S. Kang, *J. Chem. Soc., Dalton Trans.* **2001**, 359–361; b) B. J. O'Keefe, P. J. Steel, *Inorg. Chem. Commun.* **2000**, *3*, 473–475; c) W. J. Vickaryous, R. Herges, D. W. Johnson, *Angew. Chem. Int. Ed.* **2004**, *43*, 5831–5833.

[22] a) E. Lozano, M. Nieuwenhuyzen, S. L. James, *Chem. Eur. J.* **2001**, *7*, 2644–2651; b) J. C. Garrison, M. J. Panzner, P. D. Custer, D. V. Reddy, P. L. Rinaldi, C. A. Tessier, W. J. Youngs, *Chem. Commun.* **2006**, 4644–4646.

[23] a) M. Du, X.-J. Zhao, J.-H. Guo, *Inorg. Chem. Commun.* **2005**, *8*, 1–5; b) V. J. Catalano, M. A. Malwitz, *J. Am. Chem. Soc.* **2004**, *126*, 6560–6561.

[24] a) C. Uerpmann, J. Malina, M. Pascu, G. J. Clarkson, V. Moreno, A. Rodger, A. Grandas, M. J. Hannon, *Chem. Eur. J.* **2005**, *11*, 1750–1756; b) F. Tuna, M. R. Lees, G. J. Clarkson, M. J. Hannon, *Chem. Eur. J.* **2004**, *10*, 5737–5750; c) D. Guo, K.-J. Pang, C.-Y. Duan, C. He, Q.-J. Meng, *Inorg. Chem.* **2002**, *41*, 5978–5985; d) A. Lützen, M. Hapke, J. Griep-Raming, D. Haase, W. Saak, *Angew. Chem. Int. Ed.* **2002**, *41*, 2086–2089.

[25] a) M. Fujita, S. Nagao, N. Ogura, *J. Am. Chem. Soc.* **1995**, *117*, 1649–1650; b) W.-Y. Sun, J. Xie, K.-B. Yu, *Chem. Lett.* **2001**, 342–343; c) W.-Y. Sun, J. Fan, T.-a. Okamura, J. Xie, K.-B. Yu, N. Ueyama, *Chem. Eur. J.* **2001**, *7*, 2557–2562; d) J. Fan, W.-Y. Sun, T.-a. Okamura, J. Xie, W.-T. Tang, N. Ueyama, *New J. Chem.* **2002**, *26*, 199–201; e) J. Fan, H.-F. Zhu, T.-a. Okamura, W.-Y. Sun, W.-X. Tang, N. Ueyama, *Chem. Eur. J.* **2003**, *9*, 4724–4731; f) D. J. Bray, L.-L. Liao, B. Antonioli, K. Gloe, L. F. Lindoy, J. C. McMurtrie, G. Wei, X.-Y. Zhang, *Dalton Trans.* **2005**, 2082–2083.

[26] a) C.-Y. Su, Y.-P. Cai, C.-L. Chen, F. Lissner, B.-S. Kang, W. Kaim, *Angew. Chem. Int. Ed.* **2002**, *41*, 3371–3375; b) J. Kim, D. Ryu, Y. Sei, K. Yamaguchi, K. H. Ahn, *Chem. Commun.* **2006**, 1136–1138.

[27] a) X. Ottenwaelder, J. Cano, Y. Journaux, E. Rivière, C. Brennan, M. Nierlich, R. Ruiz-García, *Angew. Chem. Int. Ed.* **2004**, *43*, 850–852; b) D. L. Reger, R. F. Semeniuc, M. D. Smith, *Inorg. Chem.* **2003**, *42*, 8137–8139.

[28] a) A. Ikeda, M. Yoshimura, H. Udzu, C. Fukuhara, S. Shinkai, *J. Am. Chem. Soc.* **1999**, *121*, 4296–4297; b) Y. K. Kryschenko, S. R. Seidel, D. C. Muddiman, A. I. Nepomuceno, P. J. Stang, *J. Am. Chem. Soc.* **2003**, *125*, 9647–9652; c) H.-B. Yang, K. Ghosh, N. Das, P. J. Stang, *Org. Lett.* **2006**, *8*, 3991–3994; d) C. J. Kuehl, Y. K. Kryschenko, U. Radhakrishnan, S. R. Seidel, S. D. Huang, P. J. Stang, *Proc. Natl. Acad. Sci. USA* **2002**, *99*, 4932–4936; e) P. L. Jones, J. C. Jeffery, J. P. Maher, J. A. McCle-


 © 2007 Wiley-VCH Verlag GmbH & Co. KGaA, Weinheim 

verty, P. H. Rieger, M. D. Ward, *Inorg. Chem.* **1997**, *36*, 3088–3095; f) C. G. Claessens, T. Torres, *J. Am. Chem. Soc.* **2002**, *124*, 14522–14523.

[29] a) D. A. McMorran, P. J. Steel, *Angew. Chem. Int. Ed.* **1998**, *37*, 3295–3927; b) D. K. Chand, K. Biradha, M. Fujita, *Chem. Commun.* **2001**, 1652–1653; c) D. K. Chand, C. Balaji, R. Manivannan, J. Athilakshmi, *Tetrahedron Lett.* **2006**, *47*, 2867–2869; d) H.-K. Liu, J. Hu, T.-W. Wang, X.-L. Yu, J. Liu, B.-S. Kang, *J. Chem. Soc., Dalton Trans.* **2001**, 3534–3540.

[30] a) N. Yue, Z. Q. Qin, M. C. Jennings, D. J. Eisler, R. J. Puddephatt, *Inorg. Chem. Commun.* **2003**, *6*, 1269–1271; b) N. L. S. Yue, D. J. Eisler, M. C. Jennings, R. J. Puddephatt, *Inorg. Chem.* **2004**, *43*, 7671–7681; c) N. L. S. Yue, D. J. Eisler, M. C. Jennings, R. J. Puddephatt, *Inorg. Chem. Commun.* **2005**, *8*, 31–33.

[31] a) L. J. Barbour, G. W. Orr, J. L. Atwood, *Nature* **1998**, *393*, 671–673; b) L. J. Barbour, G. W. Orr, J. L. Atwood, *Chem. Commun.* **2000**, 859–860; c) H. Amouri, L. Mimassi, M. N. Rager, B. E. Mann, C. Guyard-Duhayon, L. Raehm, *Angew. Chem. Int. Ed.* **2005**, *44*, 4543–4546; d) Y.-B. Xie, J.-R. Li, C. Zhang, X.-H. Bu, *Cryst. Growth Des.* **2005**, *5*, 1743–1749; e) B. L. Wu, D. Q. Yuan, B. Y. Lou, H. Han, C. P. Liu, C. X. Zhang, M. C. Hong, *Inorg. Chem.* **2005**, *44*, 9175–9184.

[32] a) S. C. Johannessen, R. G. Brisbois, *J. Am. Chem. Soc.* **2001**, *123*, 3818–3819; b) A. Ikeda, M. Ayabe, S. Shinkai, S. Sakamoto, K. Yamaguchi, *Org. Lett.* **2002**, *2*, 3707–3710.

[33] a) P. Jacopozzi, E. Dalcanale, *Angew. Chem. Int. Ed.* **1997**, *36*, 613–615; b) N. Cuminetti, M. H. K. Ebbing, P. Rrados, J. d. Mendoza, E. Dalcanale, *Tetrahedron Lett.* **2001**, *42*, 527–530; c) L. Pirondini, D. Bonifazi, B. Cantadori, P. Braiuca, M. Campagnolo, R. De Zorzi, S. Geremia, F. Diederichd, E. Dalcanale, *Tetrahedron* **2006**, *62*, 2008–2015; d) F. Fochi, P. Jacopozzi, E. Wegelius, K. Rissanen, P. Cozzini, E. Marastoni, E. Fisicaro, P. Manini, R. Fokkens, E. Dalcanale, *J. Am. Chem. Soc.* **2001**, *123*, 7539–7552; e) R. Pinalli, V. Cristini, V. Sottili, S. Geremia, M. Campagnolo, A. Caneschi, E. Dalcanale, *J. Am. Chem. Soc.* **2004**, *126*, 6516–6517; f) S. J. Park, D. M. Shin, S. Sakamoto, K. Yamaguchi, Y. K. Chung, M. S. Lah, J.-I. Hong, *Chem. Eur. J.* **2005**, *11*, 235–241; g) R. G. Harrison, J. L. Burrows, L. D. Hansen, *Chem. Eur. J.* **2005**, *11*, 5881–5888; h) F. A. Cotton, P. Lei, C. Lin, C. A. Murillo, X. Wang, S.-Y. Yu, Z.-X. Zhang, *J. Am. Chem. Soc.* **2004**, *126*, 1518–1525.

[34] a) Z. L. Zhong, A. Ikeda, M. Ayabe, S. Shinkai, S. Sakamoto, K. Yamaguchi, *J. Org. Chem.* **2001**, *66*, 1002–1008; b) P. J. Steel, C. J. Sumby, *Chem. Commun.* **2002**, 322–323.

[35] a) W.-G. Lu, C.-Y. Su, T.-B. Lu, L. Jiang, J.-M. Chen, *J. Am. Chem. Soc.* **2006**, *128*, 34–35; b) M. Hong, Y. Zhao, W. Su, R. Cao, M. Fujita, Z. Zhou, A. S. C. Chan, *Angew. Chem. Int. Ed.* **2000**, *39*, 2468–2470.

[36] a) M. Aoyagi, K. Biradha, M. Fujita, *J. Am. Chem. Soc.* **1999**, *121*, 7457–7458; b) M. Aoyagi, S. Tashiro, M. Tominaga, K. Biradha, M. Fujita, *Chem. Commun.* **2002**, 2036–2037; M. Aoyagi, S. Tashiro, M. Tominaga, K. Biradha, M. Fujita, *Chem. Commun.* **2002**, 2038–2039; c) T. Yamaguchi, S. Tashiro, M. Tominaga, M. Kawano, T. Ozeki, M. Fujita, *J. Am. Chem. Soc.* **2004**, *126*, 10818–10819; d) S. Tashiro, M. Tominaga, T. Kusukawa, M. Kawano, S. Sakamoto, K. Yamaguchi, M. Fujita, *Angew. Chem. Int. Ed.* **2003**, *42*, 3267–3270; e) C.-Y. Su, M. D. Smith, H.-C. zur Loye, *Angew. Chem. Int. Ed.* **2003**, *42*, 4085–4089.

Received: February 9, 2007
Published Online: May 23, 2007

 © 2007 Wiley-VCH Verlag GmbH & Co. KGaA, Weinheim 

DOI: 10.1002/ejic.200700074

# High-Yield Synthesis of a New Layered High-Nuclearity Carbonyl Osmium-Rhodium Cluster Complex – Synthesis, Structural Characterization, and Electrochemistry of [PPN][$Os_9Rh_3(\mu\text{-}CO)_2(CO)_{26}$]

**Jasmine Po-Kwan Lau,[a] Yan-Juan Gu,[a] and Wing-Tak Wong*[a]**

**Keywords:** Osmium / Rhodium / High-nuclearity clusters / Electrochemistry

A direct and high-yield synthetic route for a novel dodecanuclear osmium-rhodium mixed-metal cluster is presented. The redox properties of the cluster were examined, and it was found that the anion behaves as an "electron reservoir".

(© Wiley-VCH Verlag GmbH & Co. KGaA, 69451 Weinheim, Germany, 2007)

## Introduction

The synthesis and isolation of the first heteronuclear carbonyl transition-metal complexes in the 1960s[1–3] had a great impact on the field of mixed-metal cluster chemistry. A large number of articles have appeared within the last 20 years that have reported the preparation and characterization of high-nuclearity mixed-metal clusters. The interest in these clusters is due to their fascinating metal core, potential application in catalysis,[4] and ability to act as an electron reservoir, and more recently, as valuable precursors to support nanocatalysts and nanosized metal particles.[5] To date, the majority of high-nuclearity mixed-metal clusters have been achieved by the use of redox coupling reactions between an anionic carbonyl compound and cationic metal electrophiles.[6–8] However, high-nuclearity Os-Rh mixed-metal clusters that have been achieved by a similar approach are rare.[9] We recently established a facile and reliable route for preparing such species in high yield by the simple thermolysis of a neutral Os-Rh cluster, [$Os_3Rh(\mu\text{-}H)_3(CO)_{12}$]. The high yields of the cluster allowed an electrochemical study of the complex and revealed the ability of the cluster to function as an "electron reservoir" that permits the uptake and release of electrons without significant cluster breakdown. We now report the synthesis, structural characterization, and electrochemical study of the novel high-nuclearity osmium-rhodium mixed-metal cluster [PPN][$Os_9Rh_3(\mu\text{-}CO)_2(CO)_{26}$] ([PPN]**1**). The metal framework in **1** is observed for the first time for an $M_{12}$ system.

[a] Department of Chemistry, the University of Hong Kong, Pokfulam Road, Hong Kong, China
Fax: +852-25472933
E-mail: wtwong@hkucc.hku.hk

## Results and Discussion

The high-nuclearity Os-Rh mixed-metal cluster anion **1** was isolated as a $[PPN]^+$ salt with a 60% yield from the thermolysis of a neutral Os-Rh cluster, [$Os_3Rh(\mu\text{-}H)_3(CO)_{12}$], in *n*-heptane for 2 h (see Scheme 1), together with a number of uncharacterized cluster species in very low quantity. The complex was characterized by spectroscopic methods and by a single-crystal X-ray diffraction study. The arrangement of the metal center of **1** can be described as two fused octahedra that share a common equatorial Rh–Rh edge. Two additional osmium atoms cap the faces of these octahedra in such a way that one adjacent triangular face is capped at the opposite ends of the fused bioctahedral structure (Figure 1). The Rh(1)–Rh(2) bond length [2.781(2) Å] is comparable to other apical-equatorial Rh–Rh distances observed within the compound and those bond lengths that have been observed for other trirhodium faces in osmium-rhodium mixed-metal clusters.[9] The structure of **1** contains 28 carbonyl ligands, and two of them are μ-bridging across the same apical-apical Rh–Os bond (Figure 2). The Rh(3)–Os(9) [2.632(8) Å] distance is slightly shorter than the average apical-equatorial Rh–Os bond [2.672(2) Å] of the cluster but much shorter than all other equatorial-equatorial Rh–Os distances in the molecule. A short Os–Os bond is observed between the apices of the fused octahedra. The Os(2)–Os(3) distance [2.626(1) Å] is shorter than the remaining Os–Os bonds, whose lengths range from 2.721(4) to 2.868(1) Å in the compound and are comparable to the normal average Os–Os distance in other osmium clusters.[10,11] To the best of our knowledge, the metal arrangement in complex **1** has not been observed in an $M_{12}$ system. Essentially, a similar framework structure is adopted by other homo- and heterometallic decanuclear clusters, such as [$Ru_8Pt_2(CO)_{23}(\mu_3\text{-}H)_2$],[12] [$Ru_{10}C_2(CO)_{24}$]$^{2-}$,[13] [$Ru_{10}C_2(\mu\text{-}\eta^2\text{:}\eta^2\text{-}C_3H_4)$]$^{2-}$,[14] [$Ga_{10}${Si-

 © 2007 Wiley-VCH Verlag GmbH & Co. KGaA, Weinheim 

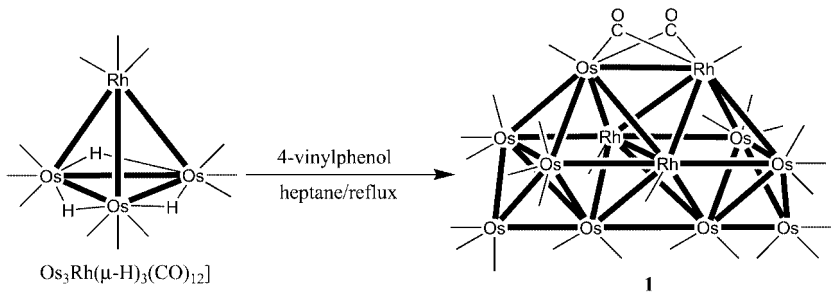


Scheme 1.

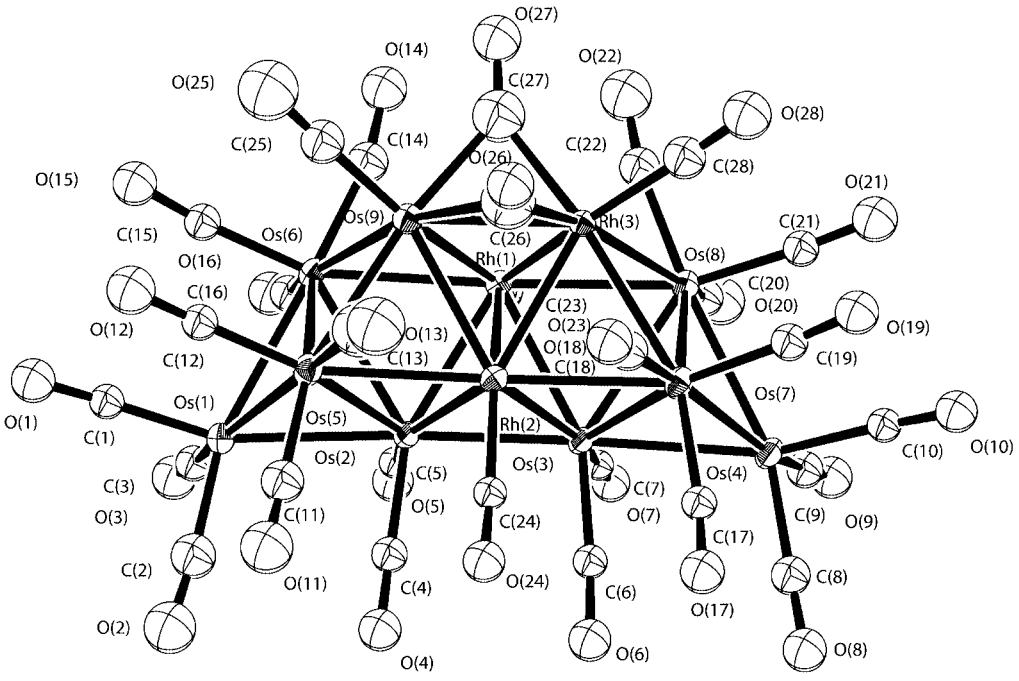


Figure 1. Molecular structure of the anion $[Os_9Rh_3(\mu\text{-}CO)_2(CO)_{26}]^-$ of **1** with the atom numbering scheme; selected bond lengths [Å] and angles [°]: Os(1)–Os(2) 2.793(1), Os(1)–Os(5) 2.815(1), Os(1)–Os(6) 2.847(2), Os(2)–Os(3) 2.626(1), Os(2)–Os(5) 2.833(1), Os(2)–Os(6) 2.825(1), Os(2)–Rh(1) 2.669(2), Os(3)–Os(7) 2.818(1), Os(3)–Os(8) 2.814(1), Os(3)–Rh(1) 2.670(2), Os(3)–Rh(2) 2.682(2), Os(4)–Os(7) 2.799(1), Os(4)–Os(8) 2.826(1), Os(5)–Os(6) 2.868(1), Os(5)–Os(9) 2.721(4), Os(5)–Rh(2) 2.799(2), Os(6)–Os(9) 2.783(3), Os(6)–Rh(1) 2.808(2), Os(7)–Os(8) 2.868(1), Os(7)–Rh(2) 2.783(2), Os(7)–Rh(3) 2.800(8), Os(8)–Rh(1) 2.801(2), Os(8)–Rh(3) 2.950(7), Os(9)–Rh(2) 2.734(4), Os(9)–Rh(3) 2.632(8), Rh(1)–Rh(2) 2.781(2), Rh(1)–Rh(3) 2.806(6), Rh(2)–Rh(3) 2.684; Rh(2)–Rh(1)–Rh(3) 57.4(2), Rh(1)–Rh(2)–Rh(3) 61.8(1), Rh(1)–Rh(3)–Rh(2) 60.8(2).

$(SiMe_3)_3\}_6]$,[15] and $Os_{10}(CO)_{24}\{Au(PPh_2R)\}_4]$[10] (R = Ph or Me). Cluster **1** contains 31 short contacts, and has an overall electron count of 156. This electron count cannot be obtained by the application of any of the usual electron counting schemes.[16,17] This is not entirely unexpected, as it is common for rhodium to have a stable 16-electron configuration.

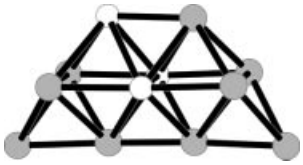

Figure 2. Metal core geometry of $[PPN][Os_9Rh_3(\mu\text{-}CO)_2(CO)_{26}]$ (**1**) (Os in grey and Rh in white).

To investigate the redox properties of this new mixed-metal cluster anion, a cyclic voltammetry of **1** in $CH_2Cl_2$ with *n*-tetrabutylammonium hexafluorophosphate (TBAHFP) as the supporting electrolyte at room temperature was carried out, the result of which is depicted in Figure 3. The electrochemical data are summarized in Table 1. Cluster **1** exhibits four successive reversible cathodic waves at $E_{pc}$ = –0.34, –0.72, –1.12, and –1.42 V, and two irreversible anodic waves at 0.71 and 0.80 V vs. $Ag/AgNO_3$, which is similar to that observed in the high-nuclearity osmium-palladium mixed-metal cluster $[PPN]_2[Os_{18}Pd_3(\mu\text{-}C)_2(CO)_{42}]$.[8] The four successive reversible cathodic waves reveal that the anionic charge of the cluster itself does not prevent it from accepting more electrons and releasing them reversibly. This suggests that cluster **1** can act as an electron reservoir, and has the ability to gain or lose electrons with-

 © 2007 Wiley-VCH Verlag GmbH & Co. KGaA, Weinheim 

out significant decomposition. Controlled potential coulometry was performed at –0.53 V for **1**, indicating that each redox process consumes one electron per molecule. With regard to oxidation, two irreversible anodic waves were also observed, and this oxidation process is believed to lead to the breakdown of the cluster.

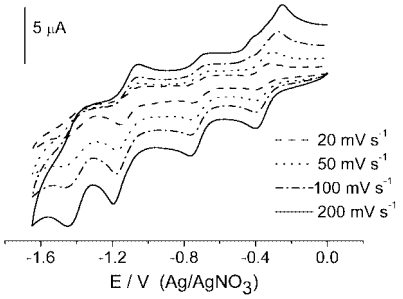


Figure 3. Cyclic voltammogram of [PPN][$Os_9Rh_3(\mu\text{-}CO)_2(CO)_{26}$] in $CH_2Cl_2$ containing 0.1 M $t$Bu$_4$NPF$_6$ in $CH_2Cl_2$; glass carbon electrode, platinum auxiliary electrode and Ag/$AgNO_3$ reference electrode; scan rate that varied from 20 to 200 mV s$^{-1}$.

Table 1. Electrochemical data[a] for cluster **1**.

| Reduction [V][b,c] | | Oxidation [V][b] | |
|---|---|---|---|
| $E_{pc1}$ | (–0.34) | $E_{pa1}$ | 0.71 |
| $E_{pc2}$ | (–0.72) | $E_{pa2}$ | 0.80 |
| $E_{pc3}$ | (–1.12) | | |
| $E_{pc4}$ | (–1.42) | | |

[a] Ca. $10^{-3}$ M cluster in 0.1 M $t$Bu$_4$NPF$_6$ in $CH_2Cl_2$ at 298 K, the working electrode was a glassy carbon electrode, the auxiliary electrode was a platinum electrode, and the reference electrode was Ag/$AgNO_3$ (0 V) under the same conditions, calibrated with ferroence. The scan rate was 100 mV s$^{-1}$. [b] $E_{pa}$ and $E_{pc}$ are the anodic and cathodic potential, respectively. [c] The values in parentheses are the $E_{1/2}$, half-wave potential values.

It is noteworthy that the average separation ($\Delta E_{av}$) between the formal electrode potentials of the consecutive redox couples observed in **1** is significantly smaller than those found in the dodecanuclear metal clusters that have been reported (see Table 2). An estimated value of $\Delta E_{av}$ for an $M_{12}$ cluster that is based on the nuclearity should be around 0.6 V.[24] The number of cluster valence electrons (CVE) found in **1** is 156 and is fewer than 158, as predicted by the Condensed Polyhedron Electrons (CPE) theory.[17] However, the observed CVE for other $M_{12}$ clusters that have been reported are all higher than the expected electron count using the CPE approach. The intrinsic electron deficiency of **1** may allow for the uptake of more electrons and a smaller $\Delta E_{av}$.

## Conclusions

The formation of a high-yield synthesis of high-nuclearity osmium-rhodium mixed-metal cluster by thermolysis of the neutral cluster [$Os_3Rh(\mu\text{-}H)_3(CO)_{12}$] has been developed. An unprecedented metal skeleton of this $M_{12}$ system is observed. The electrochemical studies revealed four reversible redox couples with unusually smaller separations for this cluster anion.

## Experimental Section

**Synthesis:** All manipulations were carried out under nitrogen with dry deoxygenated solvents. Thermolysis of [$Os_3Rh(\mu\text{-}H)_3(CO)_{12}$] (200 mg, 0.2 mmol) in $n$-heptane (50 mL) for 2 h led to a dark brown suspension upon stirring. The solution was then filtered to remove the black residue, and the filtrate was reduced under reduced pressure to 3 mL. An excess amount of [$N(PPh_3)_2Cl$] (110 mg, 0.5 mmol) in MeOH (3 mL) was added to the solution. TLC separation using $n$-hexane/$CH_2Cl_2$ (2:1, v/v) as an eluent afforded the [$Os_9Rh_3(\mu\text{-}CO)_2(CO)_{26}]^-$ salt (337 mg, 0.12 mmol, 60%) with an uncharacterized red brown complex in very small quantities. Black crystals of compound [PPN]**1** were obtained by slow concentration of an octane/$CH_2Cl_2$ solution mixture at –20 °C for 5–7 d in the presence of excess [PPN]$^+$ salts. $C_{64}H_{30}NO_{28}Os_9Rh_3$ (3281.45): calcd. C 22.99, H 0.90, N 0.42, P 1.85; found C 22.90, H 0.88, N 0.45, P 1.90. IR [$CH_2Cl_2$, ν(CO)]: $\tilde{\nu}$ = 2068 (vs), 2035 (vs), 2026 (m), 1610 (w) cm$^{-1}$. MS (FAB, +ve): 2804 (calcd. 2804). $^1$H NMR (400 MHz, $CD_2Cl_2$): $\delta$ = 7.50 (m, 24 H, Ph), 7.52 (m, 6 H, Ph) ppm.

**Crystallographic Data for 1:** [$C_{28}O_{28}Os_9Rh_3{\cdot}C_{36}H_{30}NP_2$]·0.5($CH_2Cl_2$), $M$ = 3385.86, triclinic, space group $P\bar{1}$ (#2), $a$ = 17.115(5), $b$ = 16.146(6), $c$ = 19.686(7) Å, $\alpha$ = 104.32(4), $\beta$ = 102.55(1), $\gamma$ = 99.07(1)°, $V$ = 3843(3) Å, $Z$ = 2, $D_{calcd.}$ = 2.926 g/cm$^3$, $T$ = 298 K, $F(000)$ = 3030.00, Mo-$K_\alpha$ radiation ($\lambda$ = 0.7107 Å), $\mu$(Mo-$K_\alpha$) = 155.8 cm$^{-1}$, crystal dimensions 0.25 × 0.30 × 0.35 mm. 9566 observed diffraction data [$I > 1.50\sigma(I)$] and $R_{int}$ = 0.055. The structure was solved by Patterson methods and expanded by using Fourier difference techniques,[18] and refined by full-matrix least-squares analysis on $F$ to $R$ = 0.056, $Rw$ = 0.058, and $\omega = 1/\sigma^2(F_o)$. All metal atoms were refined anisotropically and the other non-hydrogen atoms were refined isotropically. The hydrogen atoms were generated in their ideal positions and were included in the structure factor calculations using the riding mode. The osmium atoms Os(9) and Os(10) were found to be disordered in a 50:50 amount with the Rh(4) and Rh(3) atoms at the apices of the fused bioctahedra, respectively. Refinement converged with 50% occupancy of each atom type at each of the two sites. A highly disordered dichloromethane molecule was also present with 50% occupancy. All calculations were performed with a computer using the program package Crystal Structure.[19] CCDC-297120 contains the

Table 2. Summary of the relationship between the number of valence electrons and the average separation between the formal electrode potentials of consecutive redox couples.

| Structure | CVE[a] | CPE[b] | $\Delta E_{av}$ [V] | No. of redox couple peaks | Ref. |
|---|---|---|---|---|---|
| **1** | 156 | 158 | 0.37 | 4 | this work |
| [$Co_{10}Rh_2(N)_2(CO)_{24}]^{2-}$ | 168 | 162 | 0.53 | 3 | [20] |
| [$Fe_6Ni_6(N)_2(CO)_{24}]^{2-}$ | 168 | 160 | 0.53 | 3 | [21] |
| [$Fe_6Pd_6H(CO)_{24}]^{3-}$ | 160 | 158 | 0.75 | 3 | [22] |
| [$Ir_{12}(\mu\text{-}CO)_5(CO)_{19}]^{2-}$ | 158 | 154 | 0.58 | 3 | [23] |

[a] Cluster Valence Electrons. [b] Expected valence electron count based on the Condensed Polyhedral Electron Count.

 © 2007 Wiley-VCH Verlag GmbH & Co. KGaA, Weinheim 

supplementary crystallographic data for this paper. These data can be obtained free of charge from The Cambridge Crystallographic Data Centre via www.ccdc.cam.ac.uk/data_request/cif.

## Acknowledgments

We gratefully acknowledge the financial support of the Research Grants Council of Hong Kong and the University of Hong Kong. J. P.-K. L. and Y.-J. G. acknowledge the receipt of postgraduate studentships (2003–2006), administrated by the University of Hong Kong.

[1] E. W. Albel, A. Singh, G. Wilkinson, *J. Chem. Soc.* **1960**, 1321–1324.
[2] R. B. King, P. M. Treichel, F. G. A. Stone, *Chem. Ind. (London)* **1961**, 747–748.
[3] J. F. Tilney-Bassett, *Proc. Chem. Soc., London* **1960**, 419.
[4] B. C. Gates, *Chem. Rev.* **1995**, *95*, 511–522; *Catalysis by Di- and Polynuclear Metal Cluster Complexes* (Eds: R. D. Adams, F. A. Cotton), Wiley-VCH, New York, **1998**; N. Toshima, T. Yonezawa, *New J. Chem.* **1998**, *22*, 1179–1201; *Metal Clusters in Chemistry* (Eds: P. Braunstein, L. A. Oro, P. R. Raithby), Wiley-VCH, New York, **1999**.
[5] J. M. Thomas, B. F. G. Johnson, R. Raja, G. Sankar, P. A. Midgley, *Acc. Chem. Res.* **2003**, *36*, 20–30.
[6] V. Dearing, S. R. Drake, L. H. Gade, B. F. G. Johnson, J. Lewis, M. McParthin, H. R. Powell, *J. Chem. Soc., Dalton Trans.* **1992**, 921–931.
[7] B. F. G. Johnson, J. Lewis, W. J. H. Nelson, P. R. Raithby, M. D. Vargas, *J. Chem. Soc., Chem. Commun.* **1983**, 608–610.
[8] K.-F. Yung, W.-T. Wong, *Angew. Chem. Int. Ed.* **2003**, *42*, 553–555.
[9] S. Y.-W. Hung, W.-T. Wong, *Chem. Commun.* **1997**, 2099–2100.
[10] Z. Akhter, S. L. Ingham, J. Lewis, P. R. Raithby, *Angew. Chem. Int. Ed. Engl.* **1996**, *35*, 992–993.
[11] B. F. G. Johnson, J. Lewis, *Inorg. Synth.* **1971**, *13*, 92–95.
[12] R. D. Adams, Z. Li, J.-C. Li, W. Wu, *Organometallics* **1992**, *11*, 4001–4009.
[13] H. C.-M. Tai, J. R. Shapley, *J. Am. Chem. Soc.* **1982**, *104*, 7347–7349.
[14] K. Lee, J. Shapley, *Organometallics* **1998**, *17*, 4030–4036.
[15] R. B. King, *J. Organomet. Chem.* **2002**, *646*, 146–152.
[16] D. M. P. Mingos, *Acc. Chem. Res.* **1984**, *17*, 311–319.
[17] D. M. P. Mingos, *J. Chem. Soc., Chem. Commun.* **1983**, 706–708.
[18] DIRDIF99: P. T. Beurskens, G. Admiroal, G. Beurskens, W. P. Bosman, R. de Gelder, R. Isrel, J. M. M. Smits, *Technical Report of the Crystallography Laboratory*, University of Nijimegen, **1999**.
[19] Crystal Structure Analysis Package, Rigaku and Rigaku/MSC, USA, **2000**–**2003**.
[20] M. Costa, R. Della, A. Fumagalli, F. Laschi, S. Losi, P. Macchi, A. Sironi, P. Zanello, *Inorg. Chem.* **2007**, *46*, 552–560.
[21] R. D. Pergola, M. Bruschi, F. F. de Biani, A. Fumagali, L. Garlaschelli, F. Laschi, M. Manassero, M. Sansoni, P. Zanello, *C. R. Chim.* **2005**, *8*, 1850–1855.
[22] E. Brivio, A. Ceriotti, R. D. Pergola, L. Garlaschelli, F. Demartin, M. Manassero, M. Sansoni, P. Zanello, F. Laschi, B. T. Heaton, *J. Chem. Soc., Dalton Trans.* **1994**, 3237–3242.
[23] R. D. Pergola, F. Demartin, L. Garlaschelli, M. Manassero, S. Martinengo, N. Masciocchi, P. Zanello, *Inorg. Chem.* **1993**, *32*, 3670–3674.
[24] F. F. de Biani, C. Femoni, M. C. Iapalucci, G. Longoni, P. Zanello, A. Ceriotti, *Inorg. Chem.* **1999**, *38*, 3721–3724.

Received: January 22, 2007
Published Online: May 11, 2007

 © 2007 Wiley-VCH Verlag GmbH & Co. KGaA, Weinheim 

DOI: 10.1002/ejic.200600881

# Synthesis and Structural Characterisation of Copper(II) 15-Metallacrown-5 Complexes with $Pb^{II}$, $Hg^{II}$, $Ag^{I}$, $Na^{I}$ and $Y^{III}$ Central Metal Ions

**Sabry Hamed Seda,[a] Jan Janczak,[b] and Jerzy Lisowski*[a]**

**Keywords:** Metallamacrocyles / Hydroxamic acids / Lead / Mercury / Copper / Crystal structure

The new copper(II) 15-metallacrown-5 complexes with the central metal ions $Pb^{II}$, $Hg^{II}$, $Ag^{I}$, $Na^{I}$ and $Y^{III}$, with the formula $[MCu_5L_5]X_n$ {$H_2L$ is 2-picolinehydroxamic acid or (*S*)-phenylalaninehydroxamic acid and $X^-$ is $NO_3^-$ or $Cl^-$}, have been synthesised and characterised by NMR and UV/Vis spectroscopy, electrospray mass spectrometry and elemental analysis. The $Pb^{II}$- and $Hg^{II}$ 15-metallacrown-5 complexes were obtained in the crystalline form as pyridine adducts $[PbCu_5(picha)_5(py)_6](NO_3)_2{\cdot}3(py)$ and $[HgCu_5(picha)_5(py)_7](NO_3)_2{\cdot}2(py)$ and their X-ray crystal structures were determined. In both complexes, each peripheral $Cu^{II}$ ion of the metallacrown is coordinated by one pyridine molecule bonded in the axial position. In the case of the $Pb^{II}$ derivative, one additional axial pyridine molecule is bound to the central metal ion, while in the case of the $Hg^{II}$ derivative, two axial pyridine ligands are bound to the central $Hg^{II}$ ion. The relative stability of the copper(II) 15-metallacrown-5 complexes with various central metal ions was determined on the basis of competition reactions. The relative preference of the 15-metallacrown-5 system for the central metal ion follows the series $Na^{I}$, $Ag^{I}$ < lanthanide(III), $Hg^{II}$ < $Pb^{II}$.

(© Wiley-VCH Verlag GmbH & Co. KGaA, 69451 Weinheim, Germany, 2007)

## Introduction

The bridging properties of aminohydroximate ligands are the basis for the formation of cyclic polynuclear complexes called metallacrowns,[1] which are inorganic analogues of crown ethers. In particular, the geometric requirements of the α-aminohydroximates, that form only five-membered chelate rings, result in a pentagonal arrangement of the 15-metallacrown-5 system (Figure 1), as observed in the interesting heteropolynuclear copper(II)–lanthanide(III) complexes[2–5] such as $[LnCu_5(picha)_5](NO_3)_3$ and $[LnCu_5(pheha)_5](NO_3)_3$, {where Ln is the lanthanide(III) ion, picha is the 2-picolinehydroxamic acid dianion and pheha is the (*S*)-phenylalaninehydroxamic acid dianion (Figure 2)} or analogous uranyl(VI) and calcium(II) complexes.[6] These complexes, which contain five copper(II) ions and which were discovered by the Pecoraro group, are assembled in the presence of an additional central metal ion, i.e. $Ln^{3+}$, $UO_2^{2+}$ or $Ca^{2+}$, and they correspond to complexed forms of crown ethers. In contrast, without the additional metal template, the same α-aminohydroxamic acids form the $[Cu_5L_4]X_2$ 12-metallacrown-4 complexes.[7,8] Analogous 15-metallacrown-5 lanthanide(III) complexes in which the peripheral $Cu^{II}$ ions are replaced by $Ni^{II}$ ions[9] or the α-aminohydroximate ligand is replaced by mandelohydroximate[10] (Figure 2) are also known. The high stability and preferred binding of $UO_2^{2+}$ over $Ca^{2+}$ by the copper(II) 15-metallacrown-5 complexes were studied in the context of the sequestering of the toxic uranyl ions and the biological importance of hydroxamic acids.[8a] The α-aminohydroxamic acids alone were also studied as possible sequestering agents for toxic lead(II) ions.[11]

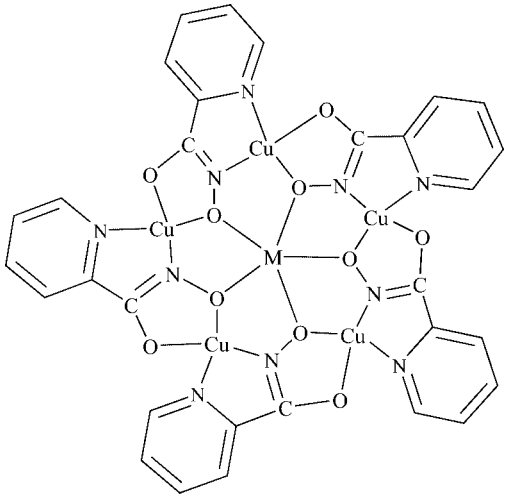

Figure 1. The structure of the $[MCu_5(picha)_5]^{n+}$ 15-metallacrown-5 complex. Axial ligands are omitted.

In this contribution, we present the synthesis, spectroscopic and structural characterisation of $[MCu_5L_5]X_n$ 15-

[a] Department of Chemistry, University of Wrocław,
14 F. Joliot-Curie, 50-383 Wrocław, Poland
Fax: +48-71-3282-348
E-mail: jurekl@wchuwr.chem.uni.wroc.pl
[b] Institute of Low Temperature and Structure Research, Polish Academy of Sciences,
P. O. Box 1410, 50-950 Wrocław, Poland

Supporting information for this article is available on the WWW under http://www.eurjic.org or from the author.

 © 2007 Wiley-VCH Verlag GmbH & Co. KGaA, Weinheim 

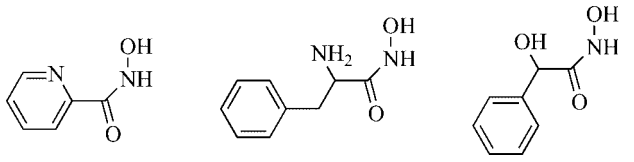

Figure 2. 2-Picoline-, phenylalanine- and mandelohydroxamic acids.

metallacrown-5 complexes (Figure 1) with new central metal ions [M = $Pb^{II}$, $Hg^{II}$, $Ag^{I}$, $Na^{I}$ or $Y^{III}$, L = picha or pheha, X = $NO_3^-$ or $Cl^-$] and demonstrate the high stability of the 15-metallacrown-5 complexes of toxic lead(II) and mercury(II) metal ions.

## Results and Discussion

### X-ray Crystal Structure of the $[PbCu_5(picha)_5(py)_6](NO_3)_2 \cdot 3(py)$ Complex

The slow diffusion of diethyl ether into a pyridine solution of the $[PbCu_5(picha)_5](NO_3)_2 \cdot 3H_2O$ complex results in the formation of crystals of the pyridine adduct $[PbCu_5(picha)_5(py)_6](NO_3)_2 \cdot 3(py)$. The asymmetric unit of this complex contains the cationic complex $[PbCu_5(picha)_5(py)_6]^{2+}$ (Figure 3). The 15-metallacrown-5 system formed by five $Cu^{II}$ ions and five bridging 2-picolinehydroximate anions in this complex is less planar (the deviation of the atoms from the mean equatorial plane ranges from –1.061 Å for C43 to +0.804 Å for O41) relative to that in other copper(II) 15-metallacrown-5 complexes.[2–6] The buckling of the metallacrown most likely results from the relatively large size of the $Pb^{II}$ ion. Two of the 2-picolinehydroximate fragments are tilted with respect to the plane formed by the remaining three 2-picolinehydroximate ligands in such a way that the diameter of the ring formed by the five hydroximate oxygen atoms increases. The cavity radius of the metallacrown is 1.15 Å and matches well with the radius of the six-coordinate $Pb^{II}$ ion (1.19 Å). Each copper(II) ion is equatorially coordinated by two O atoms [the Cu–O distances range from 1.908 to 1.989(3) Å] and two N atoms [the Cu–N distances range from 1.941 to 2.030(3) Å] of the two neighbouring 2-picolinehydroximate ligands and one axial pyridine molecule [the Cu–$N_{py}$ distances range from 2.289 to 2.416(4) Å]. Thus, the complex has a pseudo fivefold symmetry. In this way, all five copper(II) ions exhibit identical coordination environments, in contrast to previously reported copper(II) 15-metallacrown-5 complexes,[2–6] which exhibit a variation in the axial donor sets of the copper(II) ions. The $Pb^{II}$ ion is coordinated in the centre of the metallacrown by five hydroximate oxygen atoms [the Pb–O distances range from 2.491 to 2.590(3) Å] and is additionally coordinated by one axial pyridine molecule with a Pb–$N_{py}$ bond length of 2.493(3) Å. Interestingly, this pyridine molecule and all five pyridine molecules coordinated to the $Cu^{II}$ ions are positioned on the same side of the macrocycle. Moreover, the pyridine-rich faces of the neighbouring complex cations related by an inversion centre are directed towards each other, which results in the formation of layers of pyridine molecules almost parallel to the (020) crystallographic plane (see Figure 4). In the unit cell, two of the three additional pyridine solvate molecules are located on the other side of the 15-metallacrown-5 core and one of the two is located almost perpendicularly to the core and is oriented with the N atom pointing towards the Cu4 atom [the Cu4···$N_{py}$ contact is 2.752(3) Å]. The third pyridine solvate molecule is located in the same plane as the coordinated pyridine molecules.

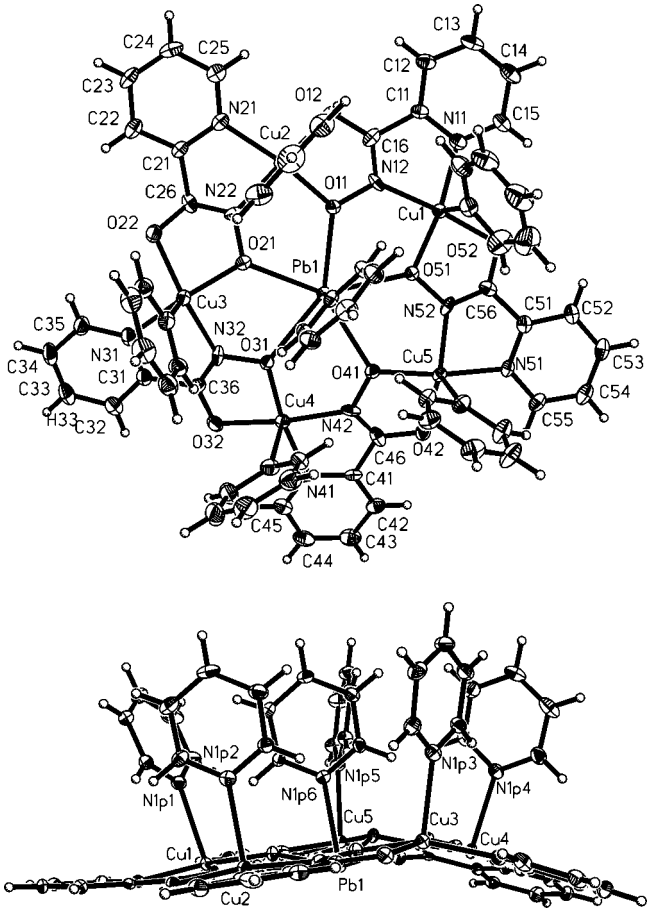





Figure 3. Top and side view of the $[PbCu_5(picha)_5(py)_6]^{2+}$ complex cation.

The $Pb^{II}$ ion adopts a pentagonal-pyramidal geometry, which is similar to that observed in a related nickel(II) 15-metallacrown-5 complex.[9] This geometry is relatively rare for lead(II) complexes.[12,13] The arrangement of the donor atoms around the $Pb^{II}$ ion is hemi-directed, in accord with the presence of the stereochemically active lone pair of electrons.[14] The $Pb^{II}$ ion is slightly displaced by 0.476(2) Å from the mean plane formed by the five hydroximate oxygen atoms in a direction away from the bound pyridine ligand. As a result of this displacement towards the open face, the $Pb^{II}$ ion adopts an umbrella-like structure.[12,13] The displacement of the $Pb^{II}$ ion towards the stereochemically active lone pair and the resulting distortion of the pentagonal pyramid is in accord with the VSEPR model, which predicts the privileged position of the lone pair.[15]

 © 2007 Wiley-VCH Verlag GmbH & Co. KGaA, Weinheim 

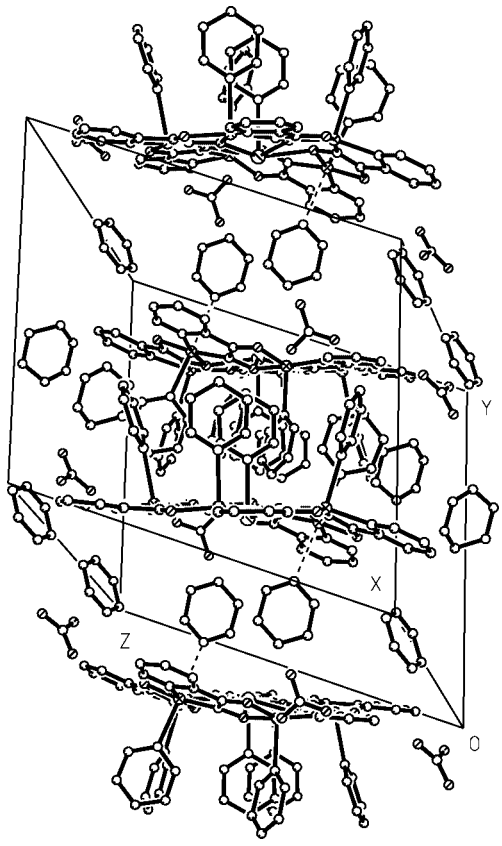


Figure 4. View of the crystal packing of $[PbCu_5(picha)_5(py)_6](NO_3)_2 \cdot 3(py)$ showing layers of pyridine molecules almost parallel to the (020) crystallographic plane.

### X-ray Crystal Structure of the $[HgCu_5(picha)_5(py)_7](NO_3)_2 \cdot 2(py)$ Complex

The slow diffusion of diethyl ether into a pyridine solution of the $[HgCu_5(picha)_5](NO_3)_2 \cdot 5H_2O$ complex also results in the formation of a pyridine adduct, $[HgCu_5(picha)_5(py)_7](NO_3)_2 \cdot 2(py)$. The asymmetric unit of this crystal contains the cationic complex $[HgCu_5(picha)_5(py)_7]^{2+}$ (Figure 5). The central $Hg^{II}$ ion is positioned almost exactly in the least-squares plane of the five oxygen donor atoms of the metallacrown [deviation from this plane is equal to 0.071(3) Å]. This ion is seven-coordinate – the five equatorial oxygen atoms of the metallacrown [the Hg–O distances range from 2.533 to 2.568(2) Å] and the two nitrogen atoms of the axially coordinated pyridine molecules [the two Hg–$N_{py}$ distances are equal to 2.175(3) and 2.182(3) Å] define a pentagonal-bipyramidal geometry. While several mercury(II) complexes of highly distorted pentagonal-bipyramidal geometry are known,[16] the discussed complex presents the first example of $Hg^{II}$ complexes that forms an almost regular pentagonal bipyramid with a fivefold symmetry (Supporting Information, Table S1). Each copper(II) ion in $[HgCu_5(picha)_5(py)_7]^{2+}$ is equatorially coordinated by two O atoms [the Cu–O distances range from 1.914 to 1.994(2) Å] and two N atoms [the Cu–N distances range from 1.928 to 2.043(3) Å] of the two neighbouring 2-picolinehydroximate ligands and one axial pyridine molecule [the Cu–$N_{py}$ distances range from 2.256 to 2.275(3) Å]. Similarly, as in the lead(II) complex discussed above, all the pyridine molecules axially coordinated to the $Cu^{II}$ ions are positioned on the same side of the metallacrown.

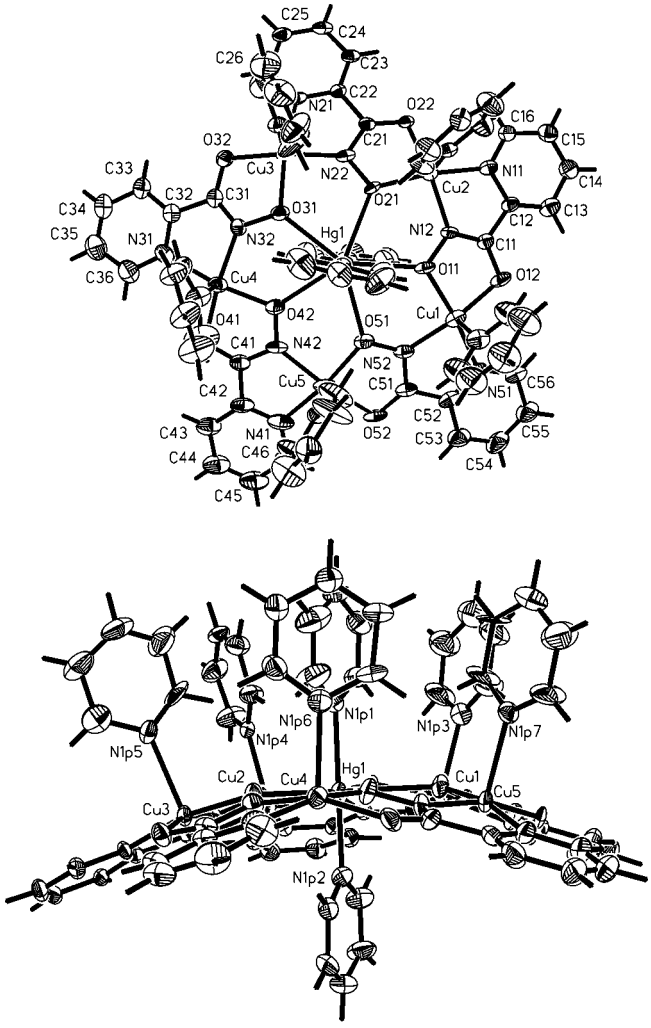


Figure 5. Top and side view of the $[HgCu_5(picha)_5(py)_7]^{2+}$ complex cation.

The deviation of the copper(II) 15-metallacrown-5 system from planarity in this complex is the largest for this class of compounds. The metallacrown adjusts itself to the size of the central $Hg^{II}$ ion by adopting a distinctive bowl shape. The cavity radius of the metallacrown further increases to 1.20 Å, which reflects the large effective size of the central mercury(II) ion. A search of the Cambridge Structural Database (Version 5.24) for Hg complexes containing a similar $N_2O_5$ donor set yields only one complex, bis[(μ2-trifluoroacetato-*O*,*O*,*O*′)-(trifluoroacetato-*O*,*O*′)pyridinemercury(II)] with a highly distorted pentagonal-bipyramidal geometry.[16a] The latter complex contains five equatorially coordinated oxygen atoms and two axially coordinated pyridine molecules with Hg–O distances that range from 2.55 to 2.87 Å and an average Hg–$N_{py}$ distance of 2.12 Å. These values, which are somewhat similar to those observed in $[HgCu_5(picha)_5(py)_7](NO_3)_2 \cdot 2(py)$, indi-

 © 2007 Wiley-VCH Verlag GmbH & Co. KGaA, Weinheim 

cate that the effective "equatorial" radius of mercury(II) in this type of environment is substantially larger than the 1.02 and 1.14 Å reported for six- and eight-coordinate mercury(II) complexes, respectively.[17] Even longer bonds with equatorial donor atoms are found in mercury(II) complexes that have other donor sets and that exhibit a distorted pentagonal-bipyramidal geometry.[16] Thus, the seven-coordinate mercury(II) ion is large enough to push aside the aminohydroximate ligands and force the 15-metallacrown-5 system to adopt a bowl shape. The variation in the cavity radius reflects the flexibility of the copper(II) 15-metallacrown-5 ring in adjusting to the geometric requirements of the central metal ion.

In the unit cell, the pyridine solvate molecules are located in the hole between the cationic $[HgCu_5(picha)_5(py)_7]^{2+}$ complexes related by an inversion centre and translation (see Supporting Information, Figure S1). The two charge-compensating nitrate anions are also located in this hole. The pyridine-rich faces of the neighbouring complex cations related by an inversion centre form a layer of pyridine molecules almost parallel to the (230) crystallographic plane.

### Synthesis and Solution Characterization of the $[MCu_5L_5]X_n$ Complexes

The 15-metallacrown-5 complexes with the $Pb^{II}$, $Hg^{II}$, $Ag^{I}$, $Na^{I}$ and $Y^{III}$ central metal ions can be obtained in high yields in a straightforward synthesis based on the self assembly of α-aminohydroxamic acid, $Cu^{II}$ ions and the central metal ion in the presence of base. The NMR spectroscopic and ESI MS analyses of the crude reaction mixtures show that the 15-metallacrown-5 complex is the main product. In the case of the $Ag^{I}$ complex, the product isolated in the synthesis based on stoichiometric amounts of substrates exhibits small amounts of other complexes, and the use of excess $Ag^{I}$ ions was necessary for the isolation of the pure product. It is interesting to note the profound differences in product formation when NaOH or KOH was used in the reaction with α-aminohydroxamic acid and $Cu^{II}$ ions. While the smaller sodium cation templates the formation of the 15-metallacrown-5 ring, the potassium cation is too big to fit in the centre of this metallacrown, and the 12-metallacrown-4 complex with a central $Cu^{II}$ ion is therefore formed.[7]

The identities of the new copper(II) 15-metallacrown-5 complexes, $[NaCu_5(picha)_5](NO_3)$, $[AgCu_5(picha)_5](NO_3)$, $[PbCu_5(picha)_5](NO_3)_2$, $[PbCu_5(pheha)_5](NO_3)_2$, $[HgCu_5(picha)_5](NO_3)_2$ and $[YCu_5(pheha)_5]Cl_3$, are confirmed by positive mode ESI MS analysis in methanol/DMSO solutions. The spectra of the two lead(II) complexes exhibit peaks at $m/z$ = 1266 and 602 corresponding to the $\{[PbCu_5(picha)_5](NO_3)\}^+$ and $[PbCu_5(picha)_5]^{2+}$ species, respectively (Supporting Information, Figure S2), or a peak at $m/z$ = 707 corresponding to $[PbCu_5(pheha)_5]^{2+}$ (Supporting Information, Figure S3). The ESI-MS spectrum of the mercury(II) complex reveals peaks at $m/z$ = 1260 and 599 corresponding to $\{[HgCu_5(picha)_5](NO_3)\}^+$ and $[HgCu_5(picha)_5]^{2+}$, respectively, in addition to the signals of unidentified species that are formed by rearrangement of the starting complex in diluted solution. In the case of the yttrium(III) complex, signals at $m/z$ = 1368, 666 and 432 corresponding to the $\{[YCu_5(pheha)_5](Cl)_2\}^+$, $\{[YCu_5(pheha)_5](Cl)\}^{2+}$ and $[YCu_5(pheha)_5]^{3+}$ species, respectively, were observed in its spectrum, while only one signal is observed for both the silver(I) and sodium(I) 15-metallacrown-5 complexes; $m/z$ = 1107 for $[AgCu_5(picha)_5]^+$ and $m/z$ = 1021 for $[NaCu_5(picha)_5]^+$.

The positions of copper(II) d–d bands of the discussed 15-metallacrown complexes are sensitive to the type of central metal ion. This effect may reflect changes in axial ligation and/or in the degree of distortion from the ideal geometry (e.g. square pyramidal) of the copper(II) ions, which results from the slightly different buckling of the 15-metallacrown-5 system in each complex. The UV/Vis spectra of DMSO solutions of the $Na^{I}$, $Hg^{II}$ and $Pb^{II}$ complexes derived from picolinehydroxamic acid show bands at 558, 592 and 622 nm, respectively, and the spectra of the $Pb^{II}$ and $Yb^{III}$ complexes derived from (*S*)-phenylalaninehydroxamic acid exhibit d–d bands at 547 and 573 nm, respectively.

The $^1H$ NMR spectra of the $[D_6]$DMSO solutions of the 15-metallacrown-5 complexes derived from 2-picolinehydroxamic acid each exhibit four signals (Figure 6), while those of the derivatives of (*S*)-phenylalaninehydroxamic acid show six non-exchangeable signals (Supporting Information, Figure S4) in addition to two proton-exchangeable signals, in accord with the presence of diastereotopic $CH_2$ and $NH_2$ groups. The $^1H$ NMR signals can be tentatively assigned on the basis of linewidth analysis. In paramagnetic complexes with dominant dipolar and Curie relaxation mechanisms, the linewidths are inversely proportional to the sixth power of the proton–metal distance.[18] On this basis, the broadest and most-downfield-shifted $^1H$ NMR signals of the $[MCu_5(picha)_5](NO_3)_x$ complexes can be assigned to the protons at position 6 of the picoline ring, the two signals in the 20–40 ppm region correspond to those at positions 3 and 5 and the relatively narrow signals around 10 ppm correspond to those at position 4. In the case of the $Pb^{II}$ derivative, this assignment was confirmed by the observation of correlations between the signals for the protons at positions 3 and 4 and between the signals for those at positions 5 and 4 (in other cases, the nuclear relaxation was too fast to observe the expected COSY correlations). In the case of the $[MCu_5(pheha)_5]X_n$ complexes, the most-downfield-shifted $^1H$ NMR signals correspond to the protons at the α position, the next two signals correspond to those at the β positions, the three relatively narrow signals around 7 ppm are assigned to the protons of the phenyl ring and the two very broad upfield-shifted signals to the $NH_2$ protons. The two upfield-shifted signals disappear after addition of $D_2O$ because they correspond to exchangeable protons. The signals for the two diastereotopic β protons are well separated as expected for paramagnetic complexes. The $^1H$ NMR spectral patterns of the discussed $[MCu_5L_5]^{n+}$ complexes are very similar to those of the anal-

 © 2007 Wiley-VCH Verlag GmbH & Co. KGaA, Weinheim 

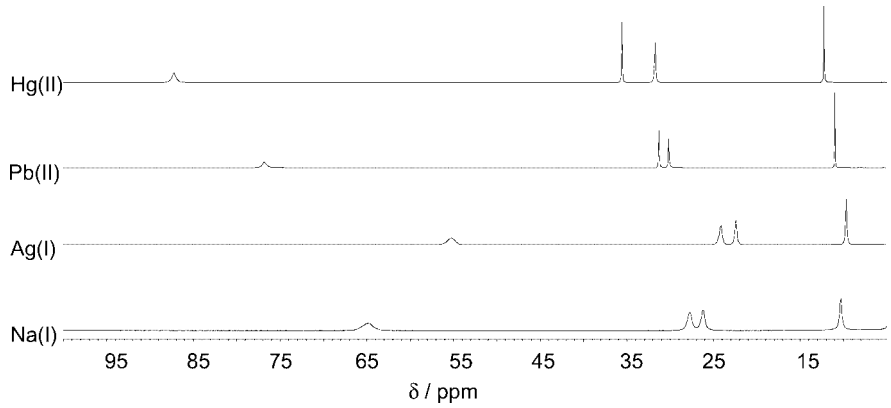


Figure 6. $^1$H NMR spectra (298 K) of [D$_6$]DMSO solutions of the [NaCu$_5$(picha)$_5$](NO$_3$), [AgCu$_5$(picha)$_5$](NO$_3$), [PbCu$_5$(picha)$_5$](NO$_3$)$_2$ and [HgCu$_5$(picha)$_5$](NO$_3$)$_2$ 15-metallacrown-5 complexes.

ogous $[MNi_5L_5]^{n+}$ and $[Cu_5L_4]^{2+}$ complexes,[7,9] which is in accord with the dominant contact contribution to the isotropic (paramagnetic) shifts of the aminohydroximate ligand. The upfield paramagnetic shifts of the $NH_2$ protons probably reflect sizeable dipolar contributions to the isotropic shift or spin polarisation effects,[18] which lead to a different sign of the contact shift of the $NH_2$ protons relative to those of other ligand protons.

The simple NMR spectra of the metallacrown complexes, in terms of the number of lines expected for a single α-aminohydroximate ligand, may arise as a result of two possibilities: (i) the presence of a single, pure complex of high symmetry with equivalent aminohydroximate ligands, or (ii) the presence of kinetically labile complexes of low symmetry or a mixture of labile complexes. In the latter case, the dissociation and rearrangement of the metallacrown complexes may lead to fast ligand exchange on the NMR time scale and observation of only one set of averaged signals. However, in the present case this situation can be excluded, since separate NMR signals for various α-aminohydroximate complexes are indeed observed for solutions of crude reaction mixtures or for the less-pure preparations of the discussed metallacrowns. Similarly, separate signals for the two ligand types are observed for the solutions containing mixtures of two 15-metallacrown-5 complexes with different central metal ions. Thus, the simplicity of the observed NMR spectra proves that only one complex with a high, effective fivefold symmetry is present in each case.

$^1$H NMR spectroscopy was used to compare the relative stabilities of the 15-metallacrown-5 complexes with various central metal ions. In the competition experiments, the additional metal salt was combined with the [D$_6$]DMSO solutions of the 15-metallacrown-5 complexes, and the $^1$H NMR spectra recorded over a period of time were used to monitor the exchange of the central metal ion. In the case of copper(II) 15-metallacrown-5 complexes with $Na^I$ or $Ag^I$ central metal ions, the addition of one equivalent of Pb(NO$_3$)$_2$ resulted in the disappearance of the $^1$H NMR signals corresponding to the starting complexes $[NaCu_5(picha)_5]^+$ or $[AgCu_5(picha)_5]^+$ and the appearance of new four signals at positions identical to those observed for [D$_6$]DMSO solution of [PbCu$_5$(picha)$_5$](NO$_3$)$_2$. The reaction was relatively fast (the transformation was completed after 15 min) and no intermediate was detected. Similarly, after 5 d at 323 K, complete conversion of the $Na^I$- or $Ag^I$ 15-metallacrown-5 complexes into $[LnCu_5(picha)_5]^{3+}$ (Ln = La, Sm) was observed after addition of one equivalent of the nitrate salt of a light lanthanide(III) ion (Figure 7, Supporting Information, Figure S5). The final spectra were identical to those of the independently synthesised $[LnCu_5(picha)_5]^{3+}$ complexes. In the same reaction with heavier lanthanide(III) ions (Ln = Sm, Yb), a small amount of the pentanuclear $[Cu_5(picha)_4]^{2+}$ 12-metallacrown-4 complex[7] was formed, which was detected in the final NMR spectra (Supporting Information, Figures S6 and S7). The slightly different behaviour of the heavy and light lanthanide(III) ions is related to the higher stability of the copper(II) 15-metallacrown-5 complex with the lighter lanthanide(III) ions.[7] The preference for the larger (lighter) lanthanide ions can be further confirmed by competition reactions between lanthanide(III) 15-metallacrown-5 derivatives and various lanthanide(III) salts. Addition of one equivalent of La(NO$_3$)$_3$·6H$_2$O or Sm(NO$_3$)$_3$·6H$_2$O to a DMSO solution of $[YbCu_5(picha)_5]^{3+}$ results in the gradual growth of a new signals corresponding to $[LaCu_5(picha)_5]^{3+}$ or $[SmCu_5(picha)_5]^{3+}$, respectively (Supporting Information, Figures S8 and S9). A partial conversion was obtained after the solution was heated for 55 d at 323 K (70% of the starting complex was converted in the case of $La^{III}$ and 63% in the case of $Sm^{III}$). The reverse reactions were not observed in analogous $^1$H NMR measurements. These observations indicate that the exchange of the lanthanide(III) ions is very slow, and equilibrium is not reached in these experiments. A similar situation was observed for the reaction of lanthanide(III) 15-metallacrown-5 complexes with the lead(II) nitrate. The partial (40–70%) conversion of the $[LnCu_5(picha)_5]^{3+}$ complex into $[PbCu_5(picha)_5]^{2+}$ was observed (Figure 8, Supporting Information, Figures S10–S12). Partial conversion of $[LnCu_5(picha)_5]^{3+}$ into the corresponding mercury(II) 15-metallacrown-5 complex, $[HgCu_5(picha)_5]^{2+}$, was also observed in the reaction with the mer-

 © 2007 Wiley-VCH Verlag GmbH & Co. KGaA, Weinheim 

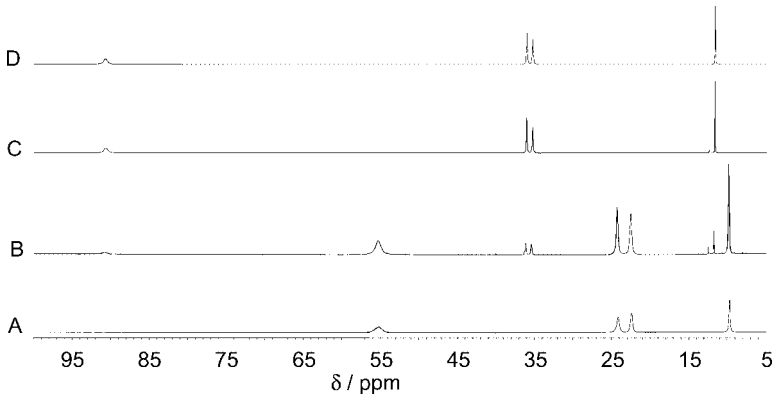


Figure 7. The $^1$H NMR spectra ([D$_6$]DMSO, 298 K) of: (A) the $[AgCu_5(picha)_5]^+$ complex, (B) $[AgCu_5(picha)_5]^+$ treated at 323 K with 1 equiv. $Sm(NO_3)_3{\cdot}6H_2O$ for 1 h, (C) for 5 d, (D) the $[SmCu_5(picha)_5]^{3+}$ complex.

cury(II) nitrate. In this case, however, a more complicated behaviour was observed – the subsequent decomposition of the resulting complex upon prolonged heating.

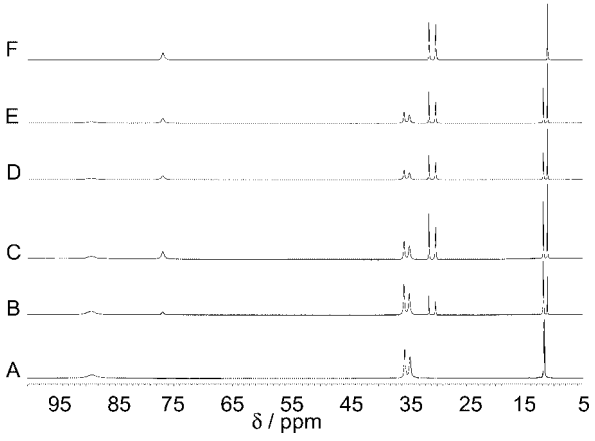


Figure 8. The $^1$H NMR spectra ([D$_6$]DMSO, 298 K) of: (A) the $[LaCu_5(picha)_5]^{3+}$ complex, (B) $[LaCu_5(picha)_5]^{3+}$ treated at 323 K with 1 equiv. $Pb(NO_3)_2$ for 1 d, (C) for one week, (D) for two weeks, (E) for one month, (F) the $[PbCu_5(picha)_5]^{2+}$ complex.

It should also be noted that the copper(II) 15-metallacrown-5 system is more stable than the copper(II) 12-metallacrown-4 system. The ring system of the 15-metallacrown-5 complex with the central $Pb^{II}$ or $Hg^{II}$ metal ion is not destroyed in pyridine solutions, while the 12-metallacrown-4 ring of $[Cu_5(picha)_4](NO_3)_2$ is destroyed by the competing pyridine ligand.[7] Further, the $[Cu_5(picha)_4]^{2+}$ complex is converted into $[MCu_5(picha)_5]^{n+}$ complexes after the addition of $Ag^I$, $Pb^{II}$ or $Hg^{II}$ nitrate, as indicated by $^1$H NMR spectra.

## Conclusions

We have shown that the copper(II) 15-metallacrown-5 system is well suited for the binding of a variety of relatively large metal ions in the centre of the metallacrown. In particular, the heavy metal ions lead(II) and mercury(II) form stable complexes of this type. In pyridine solution, these complexes form pyridine adducts, $[HgCu_5(picha)_5(py)_7](NO_3)_2$ and $[PbCu_5(picha)_5(py)_6](NO_3)_2$, in which the pyridine molecules are bound to the $Cu^{II}$ ions on the same side of the metallacrown. The 15-metallacrown-5 ring can adopt a buckled conformation in order to adjust to the size and coordination requirements of the central metal ion. The relative preference of the 15-metallacrown-5 system for the central metal ion follows the series $Na^I$, $Ag^I$ < lanthanide(III), $Hg^{II}$ < $Pb^{II}$. This series indicates that both electronic factors (preference for the metal ions that form strong bonds with the nitrogen and oxygen donor atoms) and geometric factors (preference for the larger metal ions) influence the stability of the formed complexes.

## Experimental Section

### Reagents and Materials

2-Picolinehydroxamic acid ($H_2$picha) and (*S*)-phenylalaninehydroxamic acid ($H_2$pheha) were prepared as reported previously.[4] All lanthanide(III) nitrates were obtained from Aldrich Chemical Co., $Cu(NO_3)_2{\cdot}3H_2O$, $Cu(CH_3COO)_2{\cdot}H_2O$, NaOH, $Pb(NO_3)_2$, $Hg(NO_3)_2{\cdot}H_2O$, pyridine and methanol (obtained from POCH) were of analytical grade and used without further purification.

### Synthesis

**$[NaCu_5(picha)_5](NO_3){\cdot}3H_2O$:** NaOH (0.095 g, 2.39 mmol) was added to a methanolic solution (25 mL) of 2-picolinehydroxamic acid (0.165 g, 1.19 mmol), and the resultant mixture was stirred for 10 min until a clear solution was obtained. A methanolic solution (10 mL) of $Cu(NO_3)_2{\cdot}3H_2O$ (1.19 mmol, 0.288 g) was added, and a brown precipitate, which appeared immediately, was separated. The product was recrystallised from methanol to give a deep brown complex $[NaCu_5(picha)_5](NO_3){\cdot}3H_2O$ (90 mg, 33% yield). $C_{30}H_{26}Cu_5N_{11}NaO_{16}$ (1137.31): calcd. C 31.70, H 2.30, N 13.56; found C 31.38, H 1.99, N 13.48%. $^1$H NMR (DMSO): $\delta$ = 9.90, 25.60, 27.42, 64.13 ppm; ($CD_3OD$): $\delta$ = 10.29, 26.19, 27.70, 64.82 ppm.

**$[AgCu_5(picha)_5](NO_3){\cdot}5H_2O$:** Solid NaOH (0.048 g, 1.19 mmol) was added to a solution of 2-picolinehydroxamic acid (0.165 g, 1.19 mmol) in methanol (25 mL), and the resultant clear solution was stirred for 10 min. $Cu(NO_3)_2{\cdot}3H_2O$ (0.144 g, 0.597 mmol) and solid $Ag(NO_3)$ (0.041 g, 0.238 mmol) were then added, and a brown precipitate started to appear. The solution mixture was stirred for 2 d. The obtained brown precipitate was filtered and dissolved in

 © 2007 Wiley-VCH Verlag GmbH & Co. KGaA, Weinheim 

methanol again. Addition of a second portion of $Ag(NO_3)$ (0.02 g) to the methanol solution resulted in the formation of a brown-black precipitate, which was filtered and dried (81 mg 27% yield). $C_{30}H_{30}AgCu_5N_{11}O_{18}$ (1258.22): calcd. C 28.63, H 2.4, N 12.25; found C 28.49, H 2.38, N 12.35. $^1$H NMR (DMSO): $\delta$ = 9.66, 22.38, 24.11, 55.25 ppm.

**$[PbCu_5(picha)_5](NO_3)_2\cdot 3H_2O$:** 2-picolinehydroxamic acid (0.082 g, 0.60 mmol) was added to a methanolic solution (25 mL) of $Cu(CH_3COO)_2\cdot H_2O$ (0.120 g, 0.60 mmol), and the resultant deep brown solution was stirred for 10 min. A hot methanolic solution (10 mL) of $Pb(NO_3)_2$ (0.040 g, 0.12 mmol) was then added, and the green solution was left to stir overnight. The volume was reduced by a rotary evaporator, and the brown precipitate was filtered and dried (102 mg, 62% yield). $C_{30}H_{26}Cu_5N_{12}O_{19}Pb$ (1383.53): calcd. C 26.04, H 1.89, N 12.15; found C 26.17, H 1.72, N 12.19%. $^1$H NMR (DMSO): $\delta$ = 10.98, 31.15, 31.27, 76.79 ppm.

**$[PbCu_5(pheha)_5](NO_3)_2\cdot 5H_2O$:** $Cu(CH_3COO)_2\cdot H_2O$ (0.120 g, 0.60 mmol) was dissolved in methanol (25 mL), (*S*)-phenylalaninehydroxamic acid (0.107 g, 0.60 mmol) was added, and the mixture was stirred for 15 min. A hot methanolic solution (10 mL) of $Pb(NO_3)_2$ (0.040 g, 0.12 mmol) was then added, and the green solution was left to stir for 2 h. After evaporation of solvent, a brown precipitate was obtained (117 mg, 60% yield). $C_{45}H_{60}Cu_5N_{12}O_{21}Pb$ (1629.96): calcd. C 33.15, H 3.71, N 10.31; found C 32.96, H 3.60, N 10.31%. $^1$H NMR (DMSO): $\delta$ = 6.87, 7.00, 7.15, 7.90, 14.20, 21.52, –83.61, –98.96 ppm.

**$[HgCu_5(picha)_5](NO_3)_2\cdot 5H_2O$:** $Cu(CH_3COO)_2\cdot H_2O$ (0.120 g, 0.60 mmol) was dissolved in methanol (25 mL), 2-picolinehydroxamic acid (0.082 g, 0.60 mmol) was added, and the resultant solution was stirred for 15 min. A hot methanolic solution (10 mL) of $Hg(NO_3)_2$ (0.041 g, 0.12 mmol) was then added dropwise whilst stirring, and the resultant solution was heated at reflux overnight. The green-orange product that formed was filtered, washed with methanol and dried (91 mg, 54% yield). $C_{30}H_{30}Cu_5HgN_{12}O_{21}$ (1412.83): calcd. C 25.49, H 2.14, N 11.89; found C 25.65, H 1.76, N 11.55%. $^1$H NMR (DMSO): $\delta$ = 12.24, 31.74, 35.53, 87.25 ppm.

**$[YCu_5(pheha)_5]Cl_3\cdot 12H_2O$:** (*S*)-phenylalaninehydroxamic acid (0.107 g, 0.60 mmol) was added to a stirred solution of $Cu(CH_3COO)_2\cdot H_2O$ (0.120 g, 0.60 mmol) in $H_2O$ (25 mL). An aqueous solution (10 mL) of $YCl_3$ (0.033 g, 12 mmol) was added dropwise whilst stirring, and the colour of the mixture changed from green to deep blue. The mixture was left to stir overnight. Deep blue crystals of the complex were obtained (87 mg, 45% yield) upon slow evaporation of the solvent. $C_{45}H_{74}Cl_3Cu_5N_{10}O_{22}Y$ (1620.12): calcd. C 33.35, H 4.60, N 8.30; found C 33.06, H 4.60, N, 8.64%. $^1$H NMR ($CD_3OD$): $\delta$ = 7.05, 7.26, 7.34, 9.69, 16.64, 30.38 ppm.

**$[LnCu_5(picha)_5](NO_3)_3$ Complexes:** These were synthesised as described previously.[4,7]

### $^1$H NMR, ESI-MS and UV/Vis Measurements

The $^1$H NMR spectra were collected on a Bruker AMX 500 spectrometer. The spectra were calibrated by using solvent signals as reference. The gradient-COSY spectra were acquired with 256 × 1K data points and zero-filled to 1K×1K matrix. The positive-mode ESI-MS spectra were measured with a Finnigan MAT TSQ 700 triple stage quadrupole mass spectrometer equipped with an electrospray ionization (ESI) source and with a Micromass LCT (TOF) instrument. The UV/Vis absorption spectra were measured with a CARY 5 spectrophotometer. The elemental analyses were carried out on a Perkin–Elmer 2400 CHN elemental analyzer.

### X-ray Data Collection and Structure Determination

X-ray intensity data for both crystals were collected by using graphite monochromated Mo-$K_\alpha$ radiation on a four-circle κ-geometry KUMA KM-4 diffractometer with a two-dimensional area CCD detector at 100(2) K. The ω-scan technique with $\Delta\omega$ = 0.75° for each image was used for the data collection; 960 images for six different runs covering about 98% of the Ewald sphere were performed. Initially the lattice parameters were refined on about 150 reflections obtained from 40 images for eight runs with different orientations in the reciprocal space. Finally, the lattice parameters were refined by least-squares methods based on all the reflections with $I > 2\sigma(F^2)$. One image was used as a standard for monitoring

Table 1. Crystal data for the $[PbCu_5(picha)_5(py)_6](NO_3)_2\cdot 3(py)$ and $[HgCu_5(picha)_5(py)_7](NO_3)_2\cdot 2(py)$ complexes.[a]

| Formula | $(C_{60}H_{50}N_{16}O_{10}Cu_5\ Pb)(NO_3)_2\cdot 3(C_5H_5N)$ | $(C_{65}H_{55}N_{17}O_{10}Cu_5Hg)(NO_3)_2\cdot 2(C_5H_5N)$ |
|---|---|---|
| Molecular weight | 2041.37 | 2034.77 |
| Crystal system | Triclinic | Triclinic |
| Space group | $P\bar{1}$ | $P\bar{1}$ |
| *a*, *b*, *c* [Å] | 15.676(3), 16.030(3), 17.978(3) | 13.419(3), 15.077(3), 21.671(4) |
| $\alpha$, $\beta$, $\gamma$ [°] | 72.29(3), 74.19(3), 79.06(3) | 89.56(3), 93.84(3), 93.32(3) |
| Volume, *V* [Å$^3$] | 3883.7(15) | 4367.9(12) |
| *Z* | 2 | 2 |
| Temperature [K] | 100(2) | 100(2) |
| $D_{calcd.}$ [g cm$^{-3}$] | 1.746 | 1.546 |
| $D_{obs.}$ (floatation) [g cm$^{-3}$] | 1.74 | 1.54 |
| Radiation, Mo-$K_\alpha$ [Å] | 0.71073 | 0.71073 |
| Index range | $-20 \le h \le 20$, $-21 \le k \le 19$, $-22 \le l \le 22$ | $-17 \le h \le 17$, $-19 \le k \le 19$, $-28 \le l \le 26$ |
| Reflections collected | 24344 | 26103 |
| Independent reflections | 17793 ($R_{int}$ = 0.0214) | 20822 ($R_{int}$ = 0.0609) |
| Observed reflections [$I > 2\sigma(I)$] | 14514 | 12327 |
| Abs. coeff., $\mu$ [mm$^{-1}$] | 3.586 | 3.019 |
| Correction | Lorenz and polarisation, absorption | Lorenz and polarisation, absorption |
| $T_{min}$, $T_{max}$ | 0.327, 0.678 | 0.526, 0.684 |
| $R(F^2 > \sigma)$ | 0.0365 | 0.0701 |
| $wR(F^2$ all reflections) | 0.0903 | 0.1771 |
| *S* | 1.005 | 1.074 |
| $\Delta\rho$ [e Å$^{-3}$] | –0.941, +1.544 | –1.050, +1.832 |

[a] $R = \Sigma||F_o| - |F_c||/\Sigma F_o$; $wR(F^2) = \{\Sigma[w(F_o^2 - F_c^2)^2]/\Sigma wF_o^4\}^{1/2}$; $w^{-1} = [\sigma^2(F_o^2) + (0.0560P)^2]$ for the Pb compound and $w^{-1} = [\sigma^2(F_o^2) + (0.105P)^2]$ for the Hg compound, $P = (F_o^2 + 2F_c^2)/3$.

 © 2007 Wiley-VCH Verlag GmbH & Co. KGaA, Weinheim 

the stability of the crystals as well as for monitoring the data collection after every 40 images, and no correction on the relative intensity variation was necessary. Integration of the intensities and correction for Lorenz and polarisation effects were performed with a KUMA KM-4 CCD program system.[19] The face-indexed analytical absorption was calculated with the SHELXTL program.[20] The structures were solved by direct methods by using SHELXS of the SHELXL97 program.[21] The structures were refined with anisotropic thermal parameters for all non-hydrogen atoms. Difference Fourier maps gave electron density concentrations located approximately for all hydrogen atom positions; these positions were idealised (HFIX 43 for all H atoms of the pyridyl rings with isotropic thermal parameters of $1.2U_{eq}$ of the carbon atoms joined directly to the hydrogen atoms). Final difference Fourier maps showed no peaks of chemical significance. Details of the data collection parameters and final agreement factors are presented in Table 1. Selected bond lengths are listed in the Supporting Information, Table S1. CCDC-620938 and -620939 contains the supplementary crystallographic data for the $[PbCu_5(picha)_5(py)_6](NO_3)\cdot 3(py)$ and $[HgCu_5(picha)_5(py)_7](NO_3)\cdot 2(py)$ complexes, respectively. These data can be obtained free of charge from The Cambridge Crystallographic Data Centre via www.ccdc.cam.ac.uk/datarequest/cif.

**Supporting Information** (see footnote on the first page of this article): Figure S1 – crystal packing of the $[HgCu_5(picha)_5(py)_7](NO_3)\cdot 2(py)$ complex, Figures S2 and S3 – ESI MS spectra of $Pb^{II}$ derivatives, Figures S4–S12 – NMR spectra, and Table S1 – selected geometrical parameters for the $[PbCu_5(picha)_5(py)_6](NO_3)\cdot 3(py)$ and $[HgCu_5(picha)_5(py)_7](NO_3)\cdot 2(py)$ complexes are presented.


[1] J. J. Bodwin, A. D. Cutland, R. G. Malkani, V. L. Pecoraro, *Coord. Chem. Rev.* **2001**, *216*, 489.

[2] a) A. D. Cutland, R. G. Malkani, J. W. Kampf, V. L. Pecoraro, *Angew. Chem. Int. Ed.* **2000**, *39*, 2689; b) A. J. Stemmler, A. Barwinski, M. J. Baldwin, V. Yung, V. L. Pecoraro, *J. Am. Chem. Soc.* **1996**, *118*, 11962.

[3] a) A. D. Cutland, J. A. Halfen, J. W. Kampf, V. L. Pecoraro, *J. Am. Chem. Soc.* **2001**, *123*, 6211; b) A. D. Cutland-Van Nord, J. W. Kampf, V. L. Pecoraro, *Angew. Chem. Int. Ed.* **2002**, *41*, 4668; c) C. M. Zaleski, E. C. Depperman, J. W. Kampf, M. L. Kirk, V. L. Pecoraro, *Inorg. Chem.* **2006**, *45*, 10022.

[4] A. J. Stemmler, J. W. Kampf, M. L. Kirk, B. H. Atasi, V. L. Pecoraro, *Inorg. Chem.* **1999**, *38*, 2807.

[5] T. N. Parac-Vogt, A. Pacco, P. Nockemann, S. Laurent, R. N. Muller, M. Wickleder, G. Meyer, L. Vander Elst, K. Binnemans, *Chem. Eur. J.* **2006**, *12*, 204.

[6] A. J. Stemmler, J. W. Kampf, V. L. Pecoraro, *Angew. Chem. Int. Ed. Engl.* **1996**, *35*, 2841.

[7] S. H. Seda, J. Janczak, J. Lisowski, *Inorg. Chim. Acta* **2006**, *359*, 1055.

[8] a) T. N. Parac-Vogt, A. Pacco, C. Görller-Walrand, K. Binnemans, *J. Inorg. Biochem.* **2005**, *99*, 497; b) A. Pacco, T. N. Parac-Vogt, E. van Basien, K. Pierloot, C. Görller-Walrand, K. Binnemans, *Eur. J. Inorg. Chem.* **2005**, 3303; c) M. Careri, F. Dallavalle, M. Tegoni, I. Zagnoni, *J. Inorg. Biochem.* **2003**, *93*, 174; d) M. Tegoni, F. Dallavalle, B. Belosi, M. Remelli, *Dalton Trans.* **2004**, 1329.

[9] S. H. Seda, J. Janczak, J. Lisowski, *Inorg. Chem. Commun.* **2006**, *9*, 792.

[10] T. N. Parac-Vogt, A. Pacco, P. Nockeman, Y.-F. Yuan, C. Görller-Walrand, K. Binnemans, *Eur. J. Inorg. Chem.* **2006**, 1466.

[11] D. Batka, E. Farkas, *J. Inorg. Biochem.* **2006**, *100*, 2.

[12] B. Sui, W. Zhao, G. Ma, T. Okamura, J. Fan, Y.-Z. Li, S.-H. Tang, W.-Y. Sun, N. Ueyama, *J. Mater. Chem.* **2004**, *14*, 1631.

[13] M. Yamami, H. Furutachi, T. Yokoyama, H. Okawa, *Inorg. Chem.* **1998**, *37*, 6832.

[14] L. Shimoni-Livny, J. P. Glusker, C. W. Bock, *Inorg. Chem.* **1998**, *37*, 1853.

[15] R. J. Gillespie, *Chem. Soc. Rev.* **1992**, *21*, 59–69.

[16] a) J. Halfpenny, R. W. H. Small, F. G. Thorpe, *Acta Crystallogr., Sect. B* **1978**, *34*, 3075; b) M. A. Harvey, S. Baggio, M. T. Garland, R. Baggio, *Aust. J. Chem.* **2001**, *54*, 711; c) G. Webber, *Acta Crystallogr., Sect. B* **1980**, *36*, 2779; d) K. Onan, J. Rebek, T. Costello, L. Marshal, *J. Am. Chem. Soc.* **1983**, *105*, 6759; e) J. Rebek, T. Costello, L. Marshal, R. Wattley, R. C. Gadwood, *J. Am. Chem. Soc.* **1985**, *107*, 7481; f) A. M. Costero, E. Monrabal, C. Andreu, R. Martinez-Manez, J. Soto, M. Padilia-Tosta, T. Pardo, L. E. Ochano, J. M. Amigo, *J. Chem. Soc., Dalton Trans.* **2000**, 361; g) V. Y. Komarov, E. A. Ukraintseva, D. V. Soldatov, G. D. Enright, P. S. Galkin, R. Luboradzki, J. Lipkowski, *J. Inclusion Phenom. Macrocyclic Chem.* **2004**, *50*, 227; h) K. A. Byriel, K. R. Dunster, L. R. Gahan, C. H. L. Kennard, J. L. Latten, *Inorg. Chim. Acta* **1992**, *196*, 35; i) K. Kubo, N. Kato, A. Mori, H. Takeshita, *Acta Crystallogr., Sect. C* **2000**, *56*, 644; j) R. D. Rodgers, A. H. Bond, J. L. Wolf, *J. Coord. Chem.* **1993**, *29*, 187; k) L. E. Ochando, J. M. Amigo, A. M. Costero, M. Pitarch, T. Debaerdemaeker, *Cryst. Res. And Technol.* **1996**, *31*, 37; l) A. M. Costero, C. Andreu, E. Monrabal, A. Tortajada, L. E. Ochando, J. M. Amigo, *Tetrahedron* **1996**, *52*, 12499; m) A. Bashal, M. McPartlin, B. P. Murphy, H. R. Powell, S. Walker, *J. Chem. Soc., Dalton Trans.* **1994**, 1383; n) A. M. Costero, M. Pitarch, C. Andreu, L. E. Ochando, J. M. Amigo, *Tetrahedron* **1996**, *52*, 669.

[17] R. D. Shannon, *Acta Crystallogr., Sect. A* **1976**, *32*, 751.

[18] a) I. Bertini, C. Luchinat, *Coord. Chem. Rev.* **1996**, *150*, 1; b) J. A. Peters, J. Huskens, D. J. Raber, *J. Prog. NMR Spectrosc.* **1996**, *28*, 283.

[19] KUMA Diffraction, *KUMA KM-4 CCD Program Package, Ver. 163*, Wrocław, Poland, **2000**.

[20] G. M Sheldrick, *SHELXTL Program*, Siemens Analytical X-ray Instrument Inc., Madison WI, **1991**.

[21] G. M. Sheldrick, *SHELXL-97, Program for the Solution and Refinement of Crystal Structures*, University of Göttingen, Göttingen, Germany, **1997**.


Received: September 21, 2006
Published Online: February 21, 2007

 © 2007 Wiley-VCH Verlag GmbH & Co. KGaA, Weinheim 

DOI: 10.1002/ejic.200601238

# The Role of Equatorial and Axial Ligands in Promoting the Activity of Non-Heme Oxidoiron(IV) Catalysts in Alkane Hydroxylation

**Leonardo Bernasconi,*[a] Manuel J. Louwerse,[a] and Evert Jan Baerends*[a]**

**Keywords:** Density functional calculations / Fenton reaction / Alkanes / Hydroxylation / High-valent oxidoiron(IV) systems / Push effect

The key electronic structural feature of the $FeO^{2+}$ moiety, which determines its activity as an alkane hydroxylation catalyst, is the presence of low-lying acceptor orbitals, namely the $3\sigma^\star$ $3d_{z^2}$–$2p_z$ antibonding orbital. Both the energetic position of this orbital and the spin state of the system (which in turn also affects the $3\sigma^\star$ energy) depend on the surrounding ligands. We present results of density functional theory (DFT) calculations performed on a series of gas-phase complexes of composition $[FeO(H_2O)_n(L)_{5-n}]^{2+}$ ($n$ = 4, 1, 0) derived from the recently characterised aqueous $[FeO(H_2O)_5]^{2+}$ by substitution of ligand water molecules with L = $NH_3$, $CH_3CN$, $H_2S$ and $BF_3$. The calculations reveal that the high-spin (quintet) state is favoured by the weaker σ-donating equatorial ligands, which is consistent with the literature. The high-spin configuration is more reactive because of significant exchange stabilisation of the crucial $3\sigma^\star\uparrow$ orbital. Once the quintet state is formed by a judicious choice of *equatorial* ligands, the reactivity can be fine-tuned by modulating the energy of the $3\sigma^\star$ orbital by varying the nature of the *axial* ligand. A linear relation between the σ-donor properties of the axial ligand (estimated from the magnitude of the orbital interaction between the σ lone pair and the $3\sigma^\star$ orbital) and the activation barrier for the abstraction reaction is observed, and is related to a "push effect" of the σ donors that destabilises the $3\sigma^\star$ orbital. We propose that species with enhanced activation properties for hydrogen abstraction relative to $[FeO(H_2O)_5]^{2+}$ might be obtainable by either replacing the axial ligand with a σ donor weaker than $H_2O$ or by preventing ligands from coordinating to iron in an axial position.

(© Wiley-VCH Verlag GmbH & Co. KGaA, 69451 Weinheim, Germany, 2007)

## I. Introduction

The identification of high-valent transition-metal-ion intermediates in several enzymatic oxidation processes of biosynthetic and metabolic relevance[1–7] has been one of the key achievements in understanding mechanisms responsible for the in vivo activation and reduction of molecular oxygen. Among the most common cofactors of enzymes involved in oxidative processes, copper, manganese and iron, the latter is by far the most widespread.[8–14] Reactions mediated by iron-containing oxygenases have been studied for over 30 years,[15,16] and high-valent (oxido)$Fe^{IV}$ (ferryl) intermediates were recognised early in compounds I and II of catalases and peroxidases.[17–22] The highly reactive nature of these intermediates hampers their isolation as stable species, and spectroscopic methods, often along with theoretical studies, are thus important sources of information on their structure and mechanistic properties.

High-valent metal states have also been postulated in intermediates of various non-heme-iron–protein catalysed processes. Only recently, however, has the involvement of a ferryl species been conclusively proved, specifically in the catalytic cycle of the taurine/α-ketoglutarate dioxygenase (TauD) enzyme.[23–25] This compound has an S = 2 (quintet) ground state,[26] at variance with the S = 1 (triplet) state invariably observed in model porphyrin and non-porphyrin systems, a fact that has been related to the local geometry of the metal coordination environment.[27] A number of biomimetic polydentate non-heme ligands, such as 1,4,8,11-tetramethyl-1,4,8,11-tetraaza-cyclotetradecane (TMC)[28,29] and *N*,*N*-bis(2-pyridylmethyl)-*N*-bis(2-pyridyl)methylamine (N4Py),[30] capable of stabilising high-valent iron states have been synthesised and extensively studied since 2000.[31,32] Various ferryl complexes with room-temperature lifetimes that range from seconds to days have been generated and identified spectroscopically and, to date, three of them have been characterised crystallographically.[29,31,33,34]

An important issue is the presence and role of different spin states of oxidoiron complexes. The presence of different spin states is a key element in the work on two-state reactivity (mostly of $FeO^+$) by Schröder, Shaik, Schwarz and co-workers.[35–37] Various computational studies of S = 2 (oxido)$Fe^{IV}$ systems have appeared (e.g. refs.[38–42]). Schöneboom et al.[43] have applied DFT and various correlated ab initio methods to five-coordinate $C_{4v}$ $[FeO]^{2+}$ com-

[a] Theoretische Chemie, Vrije Universiteit Amsterdam,
De Boelelaan 1083, 1081 HV Amsterdam, The Netherlands
Fax: +31-20-598-7629
E-mail: L.Bernasconi@few.vu.nl
EJ.Baerends@few.vu.nl

 © 2007 Wiley-VCH Verlag GmbH & Co. KGaA, Weinheim 

plexes. In subsequent work,[44] Neese examined in detail the interplay between triplet and quintet states on the structure, energy and spectroscopic properties of $[FeO(NH_3)_5]^{2+}$ by using (hybrid) DFT and multireference configuration interaction methods. The main factor governing the relative stability of the triplet vs. quintet ground state in this simple system was found to be the strength of the equatorial ligand field. The triplet state was found to be lower in energy in the equilibrium geometry having a distance of $R(FeN_{eq})$ = 2.062 Å between the metal centre and the equatorial N atoms, whereas a lower-energy quintet state was found at larger distances [$R(FeN_{eq})$ = 2.203 Å]. Very little influence from the *axial* ligand on the triplet–quintet separation was observed. Furthermore, the length and strength of the $Fe^{IV}$–O bond was found to be similar for the two spin states. On the basis of DFT calculations, it has also been observed that an S = 1 → S = 2 spin transition would radically change the spectroscopic properties of a $[FeO(TMC)(X)]^{2+}$ species, yet leave the nature of the $Fe^{IV}O$ bond essentially unmodified.[42,45]

Although the S = 1 → S = 2 spin transition has but little effect on the stability of the $Fe^{IV}$–O bond, this phenomenon has important implications for the *catalytic activity* of $Fe^{IV}O$-containing species. In general, non-heme enzymes (typically S = 2) are more reactive than heme ones (typically S = 1). The fact that in non-heme iron enzymes the metal ion is in a high-spin state while heme enzymes as well as all known synthetic $Fe^{IV}O$ complexes (with the exception of $[FeO(H_2O)_5]^{2+}$) are low-spin[16] is explained by the *weaker ligand field* in the non-heme systems. Although it is well recognised that high-spin complexes are more reactive than the low-spin ones, a straightforward explanation seems to be lacking still; we will address this issue in the present work (cf. also ref.[46]).

Not only the equatorial ligands, but also the axial ligand *trans* to the oxido ligand affects the reactivity. A classical example of the influence of the axial ligand on the activity of metal centres in enzymes is the *push effect* in the dioxygen cleavage reaction catalysed by cytochrome P450,[47–50] to yield the elusive Compound I.[3,13,43,51–53] A strong electron donation from the thiolate ligand in the proximal site of heme was first proposed in 1976[47] to be solely responsible for the highly efficient O–O breaking ability of P450. Although experimental findings have provided some support for this hypothesis,[48,50] a complete model for the catalytic activity of P450 is currently still lacking,[54] and various additional factors (e.g. the presence of potassium ions or specific amino acid residues in the vicinity of the heme site, hydrogen bonds with a proximal cysteine ligand, involvement of a reductase enzyme promoting the electron transfer) may contribute to the regulation of its activity. Isolating and characterising the role of axial ligand effects in the catalytic activity may therefore provide insight into the relative importance of the different factors promoting reactions catalysed by FeO-containing enzymes.

In studying activation effects on hydrogen atom abstraction from weak C–H bonds induced by substitution of the *axial* NCMe with $CF_3COO^-$ in the synthetic S = 1 complex $[FeO(TMC)(NCMe)]^{2+}$, Rohde and Que[28] advanced the hypothesis that this ligand substitution may be able to induce a weakening of the ligand field and provide access to the more reactive S = 2 surface. This study of $[FeO(TMC)(CF_3COO)]^+$, a subsequent one devoted to similar non-heme complexes with anionic ligands, $[FeO(TMC)(NCS)]^+$ and $[FeO(TMC)(N_3)]^+$,[55] and the recent theoretical work of Kamachi et al.,[56] devoted to activation effects in the first step of the cyclohexane hydroxylation reaction induced by anionic ligands coordinated to an $Fe^{IV}O$ porphyrin π-cation radical, confirm the remarkable importance of axial ligands in modulating the activity of oxidoiron complexes in organic oxidations.

$[FeO(H_2O)_5]^{2+}$ has attracted considerable attention from a theoretical perspective, because of its controversial role in the chemistry of the Fenton reaction (oxidation by a mixture of ferrous salts and hydrogen peroxide). The important intermediate in this reaction is either a free hydroxyl radical, as proposed in the 1930s by Haber and Weiss,[57] or the ferryl ion, as proposed by Bray and Gorin.[58]. Ever since, the issue has been the subject of much debate: see the original work of Groves et al.[59,60] and for reviews refs.[15,61–63] and references cited therein. DFT calculations[38,64] and first-principles molecular dynamics[64–66] have shown that the formation of the ferryl ion is thermodynamically favourable in the gas phase and viable in aqueous solution at room temperature. Experimentally, $[FeO(H_2O)_5]^{2+}$ has been obtained by reaction of $[Fe(H_2O)_5]^{2+}$ with $O_3$ in acidic aqueous solution, and it has been found to be stable over a period of about 10 seconds.[67–69] To date, this is the only known synthetic S = 2 ferryl complex. Buda et al.[38,41] and Louwerse and Baerends[46] presented detailed analyses of the electronic structure of this complex and of the factors governing its reactivity in hydrogen abstraction from methane and methanol. The effect of solvation on reaction barriers was also studied.[46,70,71] The essential results of these studies is that the reactivity of $[FeO(H_2O)_5]^{2+}$ in hydrogen abstraction from a simple alkane or alcohol is a one-electron phenomenon involving the empty $3\sigma^*\uparrow$ orbital of $[FeO(H_2O)_5]^{2+}$, and that solvation affects the reactivity strongly by changing the energy of the latter orbital. The importance of the $3\sigma^*\uparrow$ orbital has also been recognised in the work of Decker et al.[72]

In the present work we analyse the effects of ligand substitution in simple gas-phase systems of composition $[FeO(H_2O)_n(L)_{5-n}]^{2+}$, with L = $NH_3$, $CH_3CN$, $H_2S$ and $BF_3$. As for the precursor species $[FeO(H_2O)_5]^{2+}$, in these systems the metal ion is surrounded by a distorted octahedral coordination environment of $C_{2v}$ symmetry, with four equatorial ligands in roughly planar geometry and one axial ligand in the *trans* position to the oxide ion (Figure 1). The aim of this study is to gauge the relative importance of axial vs. equatorial ligands in: (a) favouring either a low (S = 1) or high (S = 2) spin state; (b) influencing the ability of the system to abstract a hydrogen atom from a methane molecule. We also address the issue of the origin of the higher reactivity in S = 2 vs. S = 1 complexes in alkane hydroxylation.

 © 2007 Wiley-VCH Verlag GmbH & Co. KGaA, Weinheim 

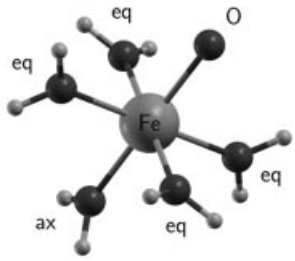


Figure 1. The structure of $[FeO(H_2O)_5]^{2+}$. Equatorial and axial ligands are indicated. O is the O(oxido) atom.

The paper is organised as follows. In Section II, details of the calculations are given. In Section IIIA, we study the role of equatorial and axial ligands in influencing the relative stabilities of high- and low-spin states of the compounds $[FeO(H_2O)_n(NH_3)_{5-n}]^{2+}$. In Section IIIB, we analyse the hydrogen atom transfer reaction from a methane molecule to each of the latter compounds (corresponding to the first step in $Fe^{IV}O$-catalysed aliphatic hydroxylation[15]). We verify the more reactive nature of high-spin complexes, which has experimentally often been observed. Here it is explained as being caused by the strong exchange stabilisation of the crucial $3\sigma^* \uparrow$ acceptor orbital in high-spin complexes with weak equatorial ligand fields. In Section IIIC, we study the manner in which the energy of the latter orbital can be modified by varying the nature of the axial ligand in (high-spin) compounds of composition $[FeO(H_2O)_4(L_{ax})]^{2+}$. The $3\sigma^* \uparrow$ orbital is pushed up by stronger σ donors at the axial coordination site, which leads to reduced reactivity. This effect in the high-spin complexes is opposite to the *push effect* that has been identified in the *low-spin* $Fe^{IV}O$ porphyrin π-cation radical. Our findings are summarised in Section IV. The general rules emerging from our study are, first, that weak-field equatorial ligands are needed to obtain the high-spin state, in order to enhance the good acceptor properties (electrophilic nature) of $[L_5FeO]^{2+}$ through stabilisation of the acceptor orbital, and second, that even higher efficiency of hydrogen atom transfer from methane than in reactions involving $[FeO(H_2O)_5]^{2+}$ might be achievable by occupying the axial coordination site with a weaker donor ligand (or even an electron acceptor), or by leaving it unoccupied and enforcing a square-planar equatorial coordination for iron.

## II. Computational Details

Calculations were performed by using ADF[73–75] with a QZ4P basis set for iron and a TZ2P basis set for all other atoms. All electrons were treated explicitly. Relativistic effects were included by using the Zero-Order Regular Approximation (ZORA).[76] In the majority of the calculations exchange-correlation effects were described at the BLYP[77,78] level of theory. Standard generalised gradient corrections (GGAs), as well as the local density approximation, are known to disfavour high-spin states in $Fe^{II}$ and $Fe^{III}$ complexes, as opposed to hybrid and some *meta*-GGA functionals.[79–81] For this reason, in determining the most stable spin state for the ground state of each of the complexes examined, we performed additional full geometry optimisation by using the OPBE functional, a combination of the OPTX[82] and the PBE[83] functionals. OPBE has been shown to yield spin state relative stabilities comparable to hybrid and *meta*-GGA prescriptions.[81,84] Convergence criteria for geometry optimisations were $5 \times 10^{-4}$ hartree in the total energy, $5 \times 10^{-3}$ hartree Å$^{-1}$ in the gradients, $5 \times 10^{-3}$ Å in bond lengths and 0.25° in bond and dihedral angles.

## III. Results and Discussion

### A. Ligand-Induced Spin Transition in $[FeO(H_2O)_n(NH_3)_{5-n}]^{2+}$

Detailed discussions of the electronic structure of $[FeO]^{2+}$ and of its "microsolvated" counterpart $[FeO(H_2O)_5]^{2+}$ (**1**) are given in refs.[38,41,46,72] The characteristic one-electron spectrum of $[FeO(H_2O)_5]^{2+}$ in its quintet ground state (Figure 2) shows significant stabilisation of the majority of ↑ spin orbitals, caused by the exchange field generated by four unpaired ↑ electrons. For the $d_{xy}\uparrow$ / $d_{xy}\downarrow$ pair, there are additional sources for the especially large gap (see below). Overlap of 3d and O(oxido) 2p orbitals leads to bonding/antibonding pairs of σ symmetry ($2\sigma$: $d_{z^2}+p_z$, doubly occupied; $3\sigma^*$: $d_{z^2}-p_z$, virtual) and π symmetry ($1\pi$: $d_{xz,yz}+p_{x,y}$, doubly occupied; $2\pi^*$: $d_{xz,yz}-p_{x,y}$, singly occupied). The d orbitals of δ symmetry, $d_{x^2-y^2}$ and $d_{xy}$, cannot mix by symmetry with O $2p_z$ orbitals, they are one hundred percent d (in $FeO^{2+}$) and Fe–O nonbonding. The $d_{xy}/d_{x^2-y^2}$ pair with ↑ spin (both singly occupied) are degenerate in bare $[FeO]^{2+}$, but the degeneracy is lifted in the $[FeO(H_2O)_5]^{2+}$ complex by antibonding interactions of the $d_{x^2-y^2}$ orbital with the σ lone pairs of the equatorial water molecules and by bonding interactions of the $d_{xy}$ with their π lone pairs.[41] These contributions bring about a difference in energy of 2.69 eV between the occupied orbitals $d_{xy}\uparrow$ and $d_{x^2-y^2}\uparrow$. The gap between the corresponding unoccupied orbitals $d_{xy}\downarrow$ and $d_{x^2-y^2}\downarrow$ is much smaller (1.13 eV),

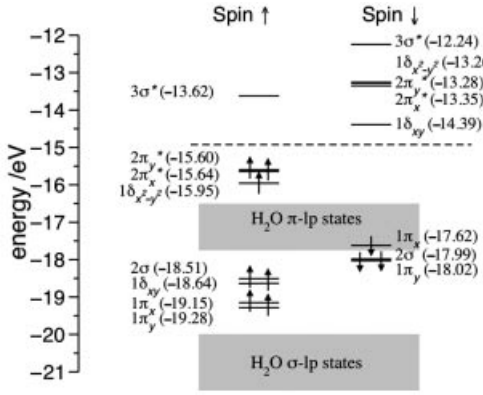


Figure 2. BLYP Kohn–Sham one-particle energies (in parentheses) of $[FeO(H_2O)_5]^{2+}$. The *z* axis is parallel to the Fe–O bond. Shaded areas represent the energy regions spanned by π ($1b_2$) and σ ($2a_1$) lone pairs of the water molecules. The dashed line separates occupied from virtual states (Cf. ref.[46]).

 © 2007 Wiley-VCH Verlag GmbH & Co. KGaA, Weinheim 

since they are both above the water lone pairs and are both pushed up (only the $d_{xy}\downarrow$ less so by the weaker π interactions than the $d_{x^2-y^2}\downarrow$ by the stronger σ interactions). Nevertheless, the fact that $d_{xy}\uparrow$ is pushed down, on top of being stabilised by the exchange field of the excess ↑ spin electrons, and that the $d_{xy}\downarrow$ is pushed up, on top of being less stabilised by the exchange field, leads to the particularly large gap of 4.25 eV between this ↑/↓ pair. These orbital interactions with the water lone pairs also explain the different nodal structure of the two spin components of the $d_{xy}$ orbital (Figure 3): the $d_{xy}\uparrow$ component, which clearly exhibits the in-phase mixing with water π lone pairs and the $d_{xy}\downarrow$ component, which has out-of-phase mixing with those lone pairs.

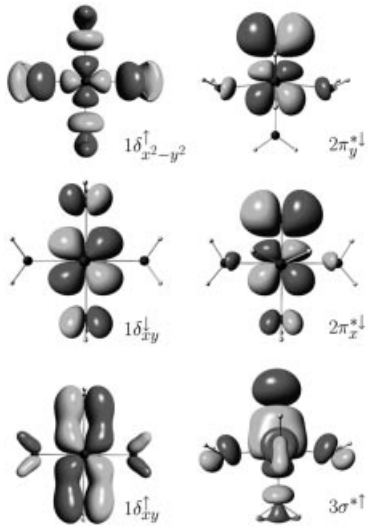


Figure 3. Selected Kohn–Sham orbitals of $[FeO(H_2O)_5]^{2+}$. Nonbonding $1\delta_{x^2-y^2}\uparrow$ and $1\delta_{xy}\downarrow$ orbitals are involved in the composition-induced transition from the quintet to the triplet ground state, in which they act as the donor and acceptor of one electron, respectively. Antibonding $2\pi_{x,y}^*\downarrow$ and $3\sigma^*\uparrow$ orbitals, which are empty in both spin states, regulate the attitude of the $Fe^{IV}O$ towards accepting electrons from a substrate and determine the reaction pathway in H-atom abstraction from a hydrocarbon. In the three plots on the left, the *z* axis [parallel to the Fe–O(oxido) bond] is perpendicular to the plane of the page, and the axial water molecule is not visible. In the plots on the right, the *z* axis is along the vertical and the axial ligand is in the lower part of each plot.

We consider now the substitution of the ligand water molecules with ammonia molecules to yield axially monosubstituted $[FeO(H_2O)_4(NH_3)]^{2+}$ (**1a**), equatorially substituted $[FeO(NH_3)_4(H_2O)]^{2+}$ (**1b**) and the fully ammoniated complex $[FeO(NH_3)_5]^{2+}$ (**1c**). The Kohn–Sham levels for these complexes are shown in Figure 4. The monosubstituted complex **1a** was found to possess a quintet ground state, albeit the difference in energy between quintet and triplet was found to decrease in comparison to the all-water complex **1** (Table 1). In accordance with ref.,[81] we found the BLYP functional to underestimate the absolute value of the quintet–triplet energy difference as compared to OPBE. The two did, however, yield a ground state with the same multiplicity in all complexes. For **1b** and **1c**, the triplet state appears to be preferred, although the difference in energy between the two spin states, particularly in the fully ammoniated system, is small. So, we find here that, in agreement with the results of ref.[44], the spin state of the complex is almost completely determined by the nature of the equatorial ligands: electron donating ligands in the equatorial position favour the low-spin triplet state.

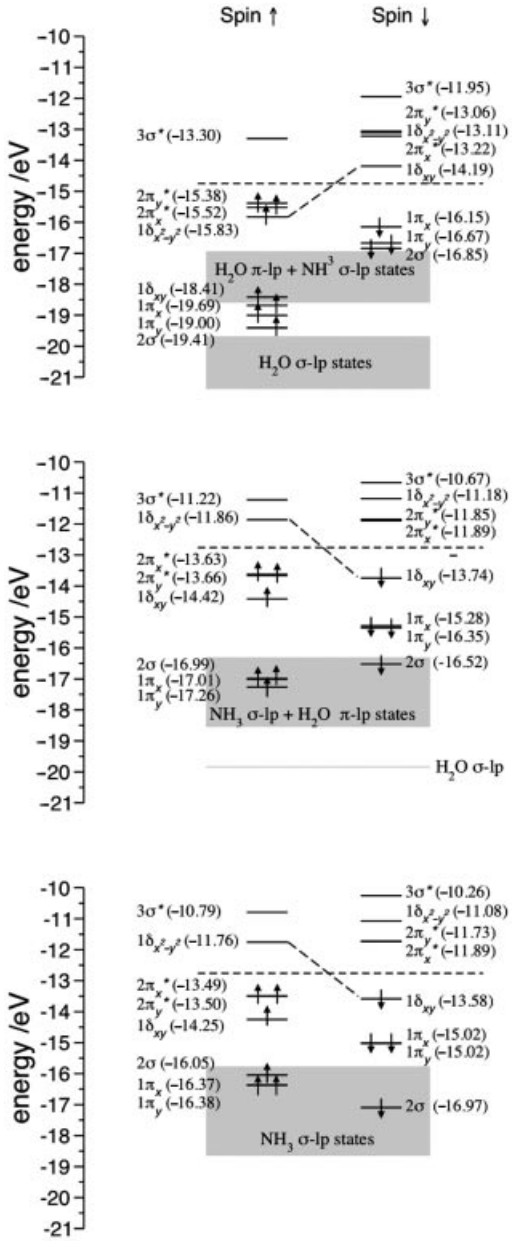


Figure 4. Kohn–Sham energy levels of axially (*top*), equatorially (*centre*) and fully $NH_3$-substituted $[FeO(H_2O)_n(NH_3)_{5-n}]^{2+}$ ($n$ = 4, 1, 0) complexes. The first system is in a quintet ground state, the second and third in a triplet. Oblique dashed lines indicate the energy difference between $1\delta_{x^2-y^2}\uparrow$ and $1\delta_{xy}\downarrow$ orbitals. See main text for details.

The reason is simple. Equatorial substitution selectively affects the energy of orbitals extending in the *xy* plane. Since the σ lone pair of $NH_3$ is more electron-donating than

 © 2007 Wiley-VCH Verlag GmbH & Co. KGaA, Weinheim 

Table 1. Second and third columns: differences between quintet (S = 2) and triplet (S = 1) ground state energies of $[FeO(H_2O)_n(NH_3)_{5-n}]^{2+}$. The data refer to fully optimised geometries for each spin state. Fourth through eighth column: BLYP energies of selected Kohn–Sham spin orbitals in the ground state with the most stable spin multiplicity (S = 2 for **1** and **1a**, S = 1 for **1b** and **1c**). *o* and *e* indicate occupied and empty orbitals, respectively. Note the change in occupations in going from **1a** to **1b**. All values are in eV.

| | | BLYP | OPBE | $1\delta_{x^2-y^2}\uparrow$ | $2\pi_x^*\uparrow$ | $2\pi_y^*\uparrow$ | $1\delta_{xy}\downarrow$ | $3\sigma^*\uparrow$ |
|---|---|---|---|---|---|---|---|---|
| **1** | $[FeO(H_2O)_5]^{2+}$ | –0.280171 | –1.131758 | –15.95 *o* | –15.64 *o* | –15.60 *o* | –14.39 *e* | –13.62 *e* |
| **1a** | $[FeO(H_2O)_4(NH_3)]^{2+}$ | –0.206509 | –0.697896 | –15.83 *o* | –15.52 *o* | –15.38 *o* | –14.19 *e* | –13.30 *e* |
| **1b** | $[FeO(H_2O)(NH_3)_4]^{2+}$ | 0.523687 | 0.139269 | –11.86 *e* | –13.63 *o* | –13.66 *o* | –13.74 *o* | –11.22 *e* |
| **1c** | $[FeO(NH_3)_5]^{2+}$ | 0.443386 | 0.049770 | –11.76 *e* | –13.49 *o* | –13.50 *o* | –13.58 *o* | –10.79 *e* |

the σ lone pair of $H_2O$, an orbital like $d_{x^2-y^2}$ with antibonding σ interactions with the ligands is strongly destabilised, and the $d_{x^2-y^2}\uparrow$ moves in the orbital spectrum close to the $3\sigma^*\uparrow$ orbital (Figure 5). It actually becomes so high-lying that it loses its electron to the empty, now lower-lying ↓ spin orbital $d_{xy}\downarrow$. It should be noted that the effect of equatorial $NH_3$ substitution is different for the $d_{xy}$ orbitals of ↑ and ↓ spin. The $d_{xy}\uparrow$ loses the pushing down effect of the higher-lying π lone pairs of the equatorial waters and moves up, like $d_{x^2-y^2}\uparrow$ did; the $d_{xy}\downarrow$ loses the pushing up effect of the lower-lying water π lone pairs and moves down, so that it even more readily accepts the electron of the destabilised $d_{x^2-y^2}\uparrow$ orbital. Electron transfer from $d_{x^2-y^2}\uparrow$ to $d_{xy}\downarrow$ entails a spin flip, with the effect that the stabilising exchange field for the ↑ spin orbitals becomes smaller, which provides an additional relative destabilisation of $d_{x^2-y^2}\uparrow$ with respect to $d_{xy}\downarrow$. This spin flip leaves only two unpaired ↑ spin electrons in the $2\pi^*$ orbitals, hence a triplet state. We note that finally the $d_{xy}\uparrow$ and $d_{xy}\downarrow$, which are both occupied, have now a much reduced gap (ca. 0.7 eV) relative to the initial gap of 4.2 eV. The remaining gap reflects the remaining exchange stabilisation of the two excess ↑ spins in the $2\pi^*$ orbitals. Since electron transfer from the $d_{x^2-y^2}\uparrow$ to the $d_{xy}\downarrow$ orbital occurs between orbitals with nonbonding Fe–O character, the stability of the $Fe^{IV}O$ bond is barely affected.[42,44,45] This is confirmed by the change in the $Fe^{IV}O$ bond length of no more than ≈0.02 Å as a function of composition and/or spin state (Table 2). The spin flip has, nevertheless, a crucial effect on the reactivity, because of the loss of (part of) the exchange stabilisation of the $3\sigma^*\uparrow$ orbital. The role of the $3\sigma^*\uparrow$ orbital in the reactivity is discussed in the following sections.

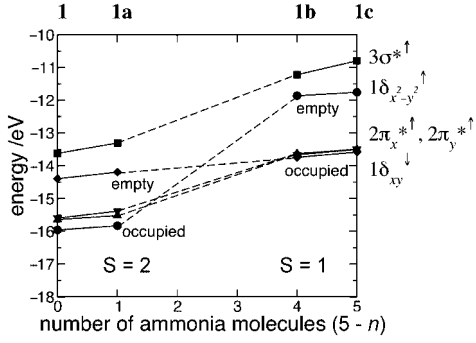


Figure 5. Energy of selected spin orbitals of $[FeO(H_2O)_n(NH_3)_{5-n}]^{2+}$ as a function of the number of ammonia molecules, 5–*n*, in the complex. Lines are guides for the eye.

Substitution of only the axial water molecule in **1** with ammonia has a very moderate destabilising effect (upshift of 0.1–0.3 eV) for all orbitals of π and δ symmetry (Figure 5), consistent with the fact that their wavefunctions have zero overlap with the σ lone pair of the axial $NH_3$. Replacement of the axial water molecule with ammonia does, however, more visibly affect orbitals with lobes along the *z* axis (the Fe–O bond axis) like 2σ, which is pushed down by the higher-lying $NH_3$ lone pair by ca. 1 eV, and the $3\sigma^*$ orbital, which is pushed up by ca. 0.3 eV. In fact, the overall orbital energy pattern is little affected by substitution of only the axial water molecule, and this substitution is not in itself able to induce a transition from high- to low-spin multiplicity, although a destabilisation of the S = 2 state vs. S = 1 is observed, possibly caused by small changes in the geometry of the equatorial ligand environment (Table 2). In either spin state, the effects of axial ligands on the energy

Table 2. Selected bond lengths [Å] in $[FeO(H_2O)_n(NH_3)_{5-n}]^{2+}$ (*n* = 5, 4, 1, 0) complexes. All geometries have been optimised in both high- and low-spin states. Subscripts ax and eq refer to ligands in axial and equatorial positions, respectively. For equatorial distances, averages over four values are reported.

| | | $\langle O_{eq}–Fe\rangle$ | | $O_{ax}–Fe$ | | $\langle N_{eq}–Fe\rangle$ | | $N_{ax}–Fe$ | | Fe–O | |
|---|---|---|---|---|---|---|---|---|---|---|---|
| | | S = 1 | S = 2 | S = 1 | S = 2 | S = 1 | S = 2 | S = 1 | S = 2 | S = 1 | S = 2 |
| **1** | $[FeO(H_2O)_5]^{2+}$ | 2.000 | 2.106 | 2.117 | 2.091 | – | – | – | – | 1.627 | 1.621 |
| **1a** | $[FeO(H_2O)_4(NH_3)]^{2+}$ | 2.018 | 2.121 | – | – | – | – | 2.173 | 2.147 | 1.641 | 1.636 |
| **1b** | $[FeO(H_2O)(NH_3)_4]^{2+}$ | – | – | 2.215 | 2.153 | 2.079 | 2.232 | – | – | 1.633 | 1.627 |
| **1c** | $[FeO(NH_3)_5]^{2+}$ | – | – | – | – | 2.087 | 2.244 | 2.221 | 2.173 | 1.647 | 1.641 |

 © 2007 Wiley-VCH Verlag GmbH & Co. KGaA, Weinheim 

of the 3σ* orbital (pushing up by stronger donors) will have a similar effect on the reactivity. This will be discussed in Section III C. Overall, the S = 2 → S = 1 spin conversion upon equatorial $NH_3$ substitution has the effect of raising the axial 3σ* ↑ orbital away from the vicinity of the Fermi energy. This fact will be shown to bear remarkable consequences on the electron-acceptor properties of the coordinated $[FeO]^{2+}$ group.

### B. Ligand Effects on Hydrogen Abstraction from Methane

Alkane hydroxylation by the $[Fe^{IV}O]^{2+}$ species follows a *rebound mechanism*.[15,59,60,70] First, one hydrogen atom is abstracted from the substrate to yield $[Fe^{III}OH]^{2+}$ and a carbon radical. The latter then collapses onto the hydroxy oxygen. It has been emphasised that the ability of $[Fe^{IV}O]^{2+}$ to promote hydrogen abstraction is directly connected to its electrophilic character: the FeO···HR bond is established by electron donation out of the RH bonding orbitals into a low-lying acceptor orbital on $[Fe^{IV}O]^{2+}$.[46,72] The empty 3σ* ↑ orbital lies 2 eV above the HOMO $2\pi_x$* ↑ and 0.3 eV below the next occupied $2\pi_x$* ↓ orbital, and it has a lobe extending on the oxygen side of the $Fe^{IV}O$ group (Figure 3). Its energy and shape thus make it an ideal acceptor for the electron of the incoming hydrogen atom. Its unusual stability, in spite of being an antibonding Fe $3d_{z^2}$–O $2p_z$ combination, originates (apart from the 2+ charge on $FeO^{2+}$ and the stabilising exchange field in particular in the high-spin state) from an in-phase overlap of O $2p_z$ with the equatorial torus of the Fe $3d_{z^2}$. This contribution attenuates the antibonding character of the orbital (cf. Figure 5 in ref.[46]). Analysis of the interaction between $[FeO(H_2O)_5]^{2+}$ and various substrate molecules ($CH_4$, $CH_3OH$, $H_2O$) has indeed shown that the 3σ* ↑ orbital plays a cardinal role in driving hydrogen abstractions in the gas phase, in aqueous solution and possibly in other media.[46] In all these cases, the abstraction reaction was found to follow an identical pattern, involving as first step the formation of a $[FeO(H_2O)_5]^{2+}$–substrate encounter complex. The bonding energy of the complex, ranging from 9 ($CH_4$) to 70 ($CH_3OH$) kJ mol$^{-1}$, reflects the amount of interaction between the donor orbital (HOMO) of the substrate and the 3σ* ↑ orbital of $[FeO(H_2O)_5]^{2+}$. In the case of methane, the in-phase combination of one of the $T_2$ molecular orbitals and the latter has 89% $T_2$ and 11% 3σ* ↑ character. This situation corresponds to a partial, if small, transfer of an electron from the donor to the acceptor. In the more tightly bound methanol complex, the mixing of donor and 3σ* ↑ in their bonding combination is 55–45%, indicating that the electron is almost equally shared between the donor orbital and the 3σ* ↑ orbital. In both the methane and methanol complexes, the donor orbital is essentially a C–H σ bond. Partial promotion of an electron to the 3σ* ↑ orbital thus results in a weakening of this bond. Since the overall reaction brings about the net transfer of one electron from the substrate to $[FeO(H_2O)_5]^{2+}$ via a concerted bond breaking (substrate–H) and bond formation (H–$OFe^{IV}$),[15] partial electron transfer in the reactants corresponds to a starting electronic structure more similar to the transition state, hence to a lower activation barrier. The stronger the electron-sharing interaction between the substrate molecule and $[FeO(H_2O)_5]^{2+}$ in the encounter complex, the more facile is then the abstraction of the hydrogen atom from the substrate.

We show in Figure 6 the abstraction barriers for the reaction of $CH_4$ with the axially, equatorially and fully ammoniated complexes **1a**, **1b**, **1c**. The energy of the 3σ* ↑ orbital is 0.32 (in **1a**), 2.4 (in **1b**) and 2.8 eV (in **1c**) higher than that in the nonammoniated complex **1** (Table 1). These complexes are representative of (a) an S = 2 system (the complex **1a**) with moderate 3σ* ↑ destabilisation (as compared to the all-water complex **1**), and (b) two S = 1 systems (the complexes **1b** and **1c**) with large and comparable 3σ* ↑ destabilisation. Reaction profiles were obtained by (unconstrained) preliminary optimisation of the encounter complex followed by constrained reduction of the O(oxido)–H distance. For each value of the constraint, a full geometry optimisation was carried out. The reaction barrier for hydrogen abstraction is defined here as the difference in total energy between the transition state (at the maximum of each curve) and the energy of the reactant complex. We computed barriers of 54, 111 and 103 kJ mol$^{-1}$ for **1a** + $CH_4$, **1b** + $CH_4$ and **1c** + $CH_4$, respectively. These should be compared to the value for the **1** + $CH_4$ abstraction reaction, 23 kJ mol$^{-1}$.[46] Overall, a decrease in the reaction rate is therefore observed in the sequence **1** > **1a** > **1b** ≈ **1c**.

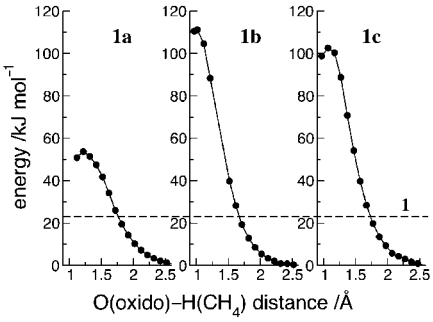


Figure 6. Energy barriers for C–H bond cleavage in axially (**1a**), equatorially (**1b**) and fully (**1c**) $NH_3$-substituted $[FeO(H_2O)_5]^{2+}$. The total energy of the $[FeO(H_2O)_n(NH_3)_{5-n}]^{2+} + CH_4$ complex is represented here as a function of the constrained O(oxido)–H distance. The energy of the reactant complex is taken as the zero point of the energy scale. The dashed line indicates the barrier height for $[FeO(H_2O)_5]^{2+}$ (**1**, see ref.[46]).

The transition to the triplet ground state as a result of equatorial substitution (i.e. going from **1** to **1b**) raises the height of the barrier roughly by a factor of four. Substitution of the axial water molecule, both in **1** and **1b** has, by contrast, only a moderate effect. This trend mirrors the moderate destabilisation of the 3σ* ↑ orbital, 0.3 eV (**1** → **1a**) and 0.4 eV (**1b** → **1c**), to be compared to the much larger effect of equatorial substitution and spin flip, e.g.

 © 2007 Wiley-VCH Verlag GmbH & Co. KGaA, Weinheim 

2.5 eV for **1a** → **1c**. We do, however, observe that, although the destabilisation of the 3σ*↑ orbital is moderate in both **1** → **1a** and **1b** → **1c**, the latter substitution (axial ligand) results in a much larger increase in the reaction barrier. This is the only case in which no correlation is observed between 3σ*↑ energy and reaction barrier, and this indicates that in triplet compounds the reactivity is no longer *exclusively* determined by the 3σ*↑ orbital alone. The ability of the 3σ*↑ orbital to act as an electron accepting orbital (AO) depends in the first place on its energy relative to the donating orbital (DO) of the substrate. The energy of AO and the DO should be compared in the same conditions (geometry, overall charge, etc.) as in the starting reactant complex. A second factor contributing to the AO–DO interaction is the spatial distribution of the 3σ*↑ orbital. Since the electron transfer occurs at the oxygen side of the Fe–O group and the 3σ*↑ orbital arises from a combination of the Fe $3d_{z^2}$ and the $2p_z$ orbital of O(oxido), the large contribution from the latter (ca. 50%) results in enhanced in-phase overlap of 3σ*↑ with the DO.

For a given substrate, the variation of the energy of the 3σ*↑ orbital in the $[L_5FeO]^{2+}$ complex caused by ligand replacement or other environmental changes provides a qualitative index of reactivity. An upward shift of the 3σ*↑ orbital results in larger activation barriers. The changes that induce a rise in the orbital energy of 3σ*↑ lead to a concomitant reduction of the amplitude of the 3σ*↑ orbital at the oxido side. Axial substitution pushes the $3d_{z^2}$ up directly, and equatorial substitution does so indirectly by causing a spin flip and a weaker exchange field. The relative contributions of the Fe $3d_{z^2}$ to the AO 3σ*↑ therefore increase along the sequence **1** → **1a** → **1b** → **1c**, varying as 37%, 42%, 52%, 51%, and those of the O(oxido) $2p_z$ diminish in the sequence 48%, 30%, 25%, 23%, respectively. So there is a progressive localisation of the orbital on the metal centre and a consequent decrease in the ability to overlap with the DO on the O(oxido) side. Both factors, the higher orbital energy of the 3σ*↑ orbital and the decreasing amplitude at the oxido side, work in the same direction in increasing the activation barrier.

We observe that this model, using only the 3σ*↑ AO and the C–H bonding orbital as the DO, applies strictly only to those $FeO^{2+}$ complexes in which 3σ*↑ is the only important acceptor orbital. This only holds for a quintet ground state. The S = 2 → S = 1 transition not only destabilises 3σ*↑, decreasing its electron accepting ability, but it also opens an alternative electron-transfer channel through the now lower lying $2\pi_x$*↓ and $2\pi_y$*↓ orbitals (Figure 5, **1b** and **1c**). An incoming DO might then interact with the 3σ*↑ and $2\pi_{x,y}$*↓ orbitals simultaneously, leading to an Fe–O–H angle that is considerably smaller than the 180° we have observed in the quintet state.[46] The proximity of the empty $2\pi_{x,y}$*↓ orbitals even in the quintet state, will make the energy surface of the reactant complex, and probably also that of the transition state, rather flat with respect to the Fe–O–H angle.

### C. Axial Ligand Influence on Reactivity

We showed in the previous sections that: (1) the spin state of a complex $[FeO(L_{eq})_4(L_{ax})]^{2+}$ is determined by the nature of the equatorial ligands ($L_{eq}$) alone; (2) the quintet ground state is more reactive than the triplet in hydrogen abstractions; (3) the reactivity of the quintet ground state is driven by the transfer of an electron to a low-lying 3σ*↑ orbital; (4) the axial ligand ($L_{ax}$) regulates the reactivity of the complex by inducing relatively minor (few tenths of an eV) shifts in the energy of the 3σ*↑ orbital. Here we address the issue of how the last effect can be directed to tuning the reactivity of an $Fe^{IV}$–O complex in C–H bond cleavage.

We examined a series of simple systems $[FeO(H_2O)_5]^{2+}$, by substitution of either the axial or the equatorial ligand water molecules with $CH_3CN$ and $H_2S$, but carrying the same charge. Similar to the $[FeO(H_2O)_n(NH_3)_{5-n}]^{2+}$ complexes described above, a transition to a triplet ground state was observed for $L_{eq} = CH_3CN$, irrespective of the nature of $L_{ax}$. The situation is far less clear in the $H_2S$-substituted complexes, where differences in energy between the quintet and triplet states after equatorial substitution are within 0.02 eV. In both $CH_3CN$ and $H_2S$ complexes, however, replacement of only the axial ligand was not sufficient to favour the triplet over the quintet state, similar to $NH_3$ substitution, OPBE quintet–triplet energy differences being ≈0.4 and ≈0.2 eV in the $CH_3CN$ and $H_2S$ complexes respectively. In particular, we observed an overall change of no more than ≈0.2 eV in the energy difference between $1\delta_{xy}$↓ and $1\delta_{x^2-y^2}$↑ as a result of the replacement of the axial ligand (Table 3).

Replacement of the axial ligand in $[FeO(H_2O)_4(L_{ax})]^{2+}$ was found to decrease slightly the energy of the 3σ*↑ orbital in the case of $H_2S$ (–0.06 eV) and to increase it by 0.72 eV in the case of $CH_3CN$. The relative 3σ*↑ contri-

Table 3. BLYP Kohn–Sham orbital energies (in eV) for optimised complexes of composition $[FeO(H_2O)_4(L_{ax})]^{2+}$, where $L_{ax}$ indicates the axial ligand. Values for $[FeO(H_2O)_5]^{2+}$ are from ref.[46]

| | $1\delta_{x^2-y^2}$↑ | $2\pi_x$*↑ | $2\pi_y$*↑ | 3σ*↑ | $1\delta_{xy}$↓ | $1\delta_{x^2-y^2}$↓ | $2\pi_x$*↓ | $2\pi_y$*↓ |
|---|---|---|---|---|---|---|---|---|
| $[FeO(H_2O)_5]^{2+}$ | –15.95 | –15.64 | –15.60 | –13.62 | –14.39 | –13.26 | –13.35 | –13.28 |
| $[FeO(H_2O)_4(NH_3)]^{2+}$ | –15.83 | –15.52 | –15.38 | –13.30 | –14.19 | –13.11 | –13.22 | –13.06 |
| $[FeO(H_2O)_4(H_2S)]^{2+}$ | –15.70 | –15.54 | –14.85 | –13.68 | –14.27 | –13.12 | –13.32 | –13.25 |
| $[FeO(H_2O)_4(CH_3CN)]^{2+}$ | –15.23 | –15.07 | –15.07 | –12.90 | –13.66 | –12.57 | –12.84 | –12.83 |
| $[FeO(H_2O)_4(BF_3)]^{2+}$ | –16.15 | –16.03 | –15.98 | –14.13 | –14.58 | –13.44 | –13.71 | –13.65 |
| $[FeO(H_2O)_4(o)]^{2+}$ | –16.64 | –16.64 | –16.48 | –14.78 | –15.19 | –13.91 | –14.32 | –14.13 |

 © 2007 Wiley-VCH Verlag GmbH & Co. KGaA, Weinheim 

bution to the in-phase $3\sigma^* \uparrow -e_z$ orbital combination is very similar in the $H_2O$ and $H_2S$ complexes (11 and 10% respectively) as well as in the $CH_3CN$ and $NH_3$ complexes (both 7%). C–H cleavage reaction barriers vary according to the sequence $[FeO(H_2O)_4(H_2S)]^{2+} \approx [FeO(H_2O)_5]^{2+} < [FeO(H_2O)_4(CH_3CN)]^{2+} < [FeO(H_2O)_4(NH_3)]^{2+}$. This mirrors the total amount of $3\sigma^* \uparrow -e_z$ orbital interaction in the reactant complex and, to a lesser extent, the absolute energy of the $3\sigma^* \uparrow$ orbital. The initial $3\sigma^* \uparrow -e_z$ orbital interaction is a good index of reactivity, since in all complexes the transition state is characterised by an equal distribution of the electron between the DO and the AO (Table 4), which will be obtained more readily if the starting point is more strongly mixed. The overall height of the activation barrier is therefore correlated with the contribution of the $3\sigma^* \uparrow$ orbital to the $CH_4$–$[FeO(H_2O)_4(L_{ax})]^{2+}$ charge-transfer state; the larger this quantity the lower the activation energy.

Table 4. Percentage $3\sigma^* \uparrow$ character in the in-phase $3\sigma^* \uparrow -e_z$ overlap for methane complexes ($3\sigma^* \uparrow$ %) in the reactant complex (RC) and transition state (TS) geometries. Percentage contribution of σ lone pair (or $e_1$ in $[FeO(H_2O)_4(BF_3)]^{2+}$ to $3\sigma^* \uparrow$ (Ax σ-lp). C–H bond-cleavage barrier ($\Delta E_{TS}$, in kJ mol$^{-1}$) for hydrogen abstraction from $CH_4$. Values for $[FeO(H_2O)_5]^{2+}$ are from ref.[46]

| | $3\sigma^* \uparrow$ % | | Ax σ-lp% | $\Delta E_{TS}$ |
|---|---|---|---|---|
| | RC | TS | | |
| $[FeO(H_2O)_5]^{2+}$ | 11 | 46 | 1.71 | 23 |
| $[FeO(H_2O)_4(NH_3)]^{2+}$ | 7 | 52 | 4.95 | 54 |
| $[FeO(H_2O)_4(H_2S)]^{2+}$ | 10 | 49 | 1.94 | 25 |
| $[FeO(H_2O)_4(CH_3CN)]^{2+}$ | 7 | 49 | 3.06 | 41 |
| $[FeO(H_2O)_4(BF_3)]^{2+}$ | 25 | 54 | <1 | 7 |
| $[FeO(H_2O)_4(o)]^{2+}$ | 34 | 48 | 0 | 1 |

We have verified that a stronger σ-donating axial ligand decreases the ability of a $[FeO(H_2O)_4(L_{ax})]^{2+}$ complex to promote C–H bond breaking, and that a ligand with a σ-donating character comparable to that of water ($H_2S$) leaves it virtually unchanged.[85] It is therefore reasonable to expect that a ligand with no σ-donor character might be able to revert the trend in reactivity observed above and yield an even higher reactivity than that obtained with all-water ligands. For this reason we studied the compound $[FeO(H_2O)_4(BF_3)]^{2+}$, where as before the electron-deficient $BF_3$ ligand occupies the axial position. Although this species was found to be stable in the gas phase, we do not address here the issue of its stability either with respect to $[FeO(H_2O)_5]^{2+}$ or as a solvated species. The $BF_3$ molecule coordinates to the metal centre through one of the fluorine atoms with a Fe–F–B angle of 141.1°. The $3\sigma^* \uparrow$ orbital (Figure 7) exhibits a nodal structure analogous to the one observed in $[FeO(H_2O)_5]^{2+}$; one of the B–F bonding orbitals of $BF_3$ replaces the σ lone pair of $H_2O$, and its energy is 0.51 eV lower than that in the latter species. For this system, we computed a C–H dissociation barrier of only 7 kJ mol$^{-1}$, which is consistent with the large $3\sigma^* \uparrow$ stabilisation.

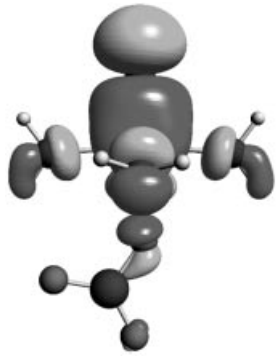

Figure 7. The $3\sigma^* \uparrow$ orbital in $[FeO(H_2O)_4(BF_3)]^{2+}$. The $BF_3$ molecule axially coordinated to $Fe^{IV}$ is in the lower portion of the figure. The orientation is as in Figure 3, right column. Note that the $C_3$ axis of the $BF_3$ ligand is not perpendicular to the $z$ axis, and one of the B–F bonds is roughly oriented toward the metal centre.

Finally, we consider a hypothetical $[FeO(H_2O)_4(o)]^{2+}$ complex in which the axial ligand is removed, and the O–Fe–O angles (where O stands for the oxygen atoms of the remaining ligands) are constrained to their values as in $[FeO(H_2O)_5]^{2+}$. Owing to the absence of an antibonding combination with orbitals of the axial ligand, the energy of the $3\sigma^* \uparrow$ orbital is further lowered relative to the $BF_3$ complex to 1.16 eV below its value in $[FeO(H_2O)_5]^{2+}$. The C–H bond cleavage occurs with virtually no barrier, the activation energy being lower than 1 kJ mol$^{-1}$. In the reactant complex, the DO of $CH_4$ carries a substantial $3\sigma^* \uparrow$ character (34%, vs. 53% $e_z$ character), which is roughly three times as much as that in the $[FeO(H_2O)_5]^{2+} + CH_4$ complex.

In Figure 8 we show activation barriers as a function of the percentage σ lone pair character of the axial ligand (or the $e_1$ orbital in the case of $BF_3$) in the $3\sigma^* \uparrow$ orbital. The latter quantity can be taken as measure of the overall "push" (or destabilisation) experienced by the $3\sigma^* \uparrow$ orbital because of the presence of a σ-donating ligand. For the S = 2 complexes considered in this work, this quantity varies from 0 (for $[FeO(H_2O)_4(o)]^{2+}$) to 4.95% (for $[FeO(H_2O)_4(NH_3)]^{2+}$), and the C–H activation barriers are shown here to depend on it linearly (with a correlation coefficient ≈0.98).

It is interesting to observe that Rohde and Que[28] have found that the axial NCMe ligand in $[FeO(TMC)(L_{ax})]^{2+}$ leads to lower reactivity than the axial carboxylate ligand $CF_3COO^-$. These are low-spin complexes because of equatorial nitrogen donor coordination by the TMC ligand, and the carboxylate substitution may, as suggested by the authors, lead to relative stabilisation of the high-spin S = 2 state, so that the latter becomes more easily accessible (possibly along the reaction path, in a two-state reactivity process). We do indeed find the difference between the S = 1 ground state and the S = 2 state in **1c** to be very small (BLYP) or vanishing (OPBE). However, we should note that the experimental observation corresponds to the expected effect of a weaker ligand field from the carboxylate than from the NCMe ligand, leading to reduced destabilisa-

 © 2007 Wiley-VCH Verlag GmbH & Co. KGaA, Weinheim 

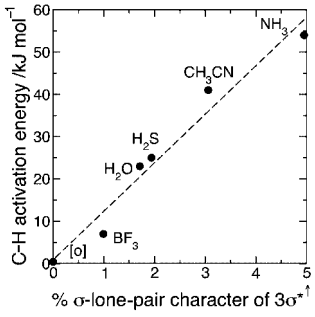


Figure 8. C–H bond-cleavage energy as a function of percentage σ lone pair contribution to the 3σ*↑ orbital in isolated $[FeO(H_2O)_4(L_{ax})]^{2+}$ complexes. The nature of $L_{ax}$ is indicated, and [o] represents the complex with removed axial ligand. The dashed line (with slope 11.47 kJ mol$^{-1}$ and intercept 0.89 kJ mol$^{-1}$) has been obtained by linear regression from the calculated values.

tion of the 3σ*↑ orbital. Overall, the activation effect observed in ref.[28] is therefore fully consistent with the molecular orbital model of reactivity described here.

## IV. Conclusions

We have highlighted the electronic structural features explaining the extraordinary reactivity of the $[Fe^{IV}O]^{2+}$ group in the oxidation of aliphatic C–H bonds: (a) a very low-lying acceptor orbital interacts with the C–H bonding orbital which acts as a donor; (b) in high-spin complexes, the energy of the 3σ*↑ acceptor orbital is lowered by the exchange field of the excess ↑ spin electrons, leading to enhanced reactivity.

The empty 3σ*↑ orbital ($3d_{z^2}$–$2p_z$) is the most important acceptor orbital, being low-lying and having a large amplitude at the oxido ligand. We have detailed that the non-bonding electrons in the dδ orbitals $3d_{x^2-y^2}$ and $3d_{xy}$ (perpendicular to the Fe–O axis) are not just spectator electrons. When a ligand-induced switching occurs from the unpaired spin electron configuration $(3d_{x^2-y^2}\uparrow)^1(3d_{xy}\uparrow)^1$ to the spin-paired configuration $(3d_{xy})^2$, the lowering of the spin multiplicity from S = 2 to S = 1 makes the exchange field of the unpaired spin up electrons considerably less stabilising, and the empty 3σ*↑ shifts up. It then less readily accepts electrons from the C–H bonding orbital, hence the low-spin state S = 1 will require a higher activation energy in the hydrogen abstraction step. The spin state is determined by the ligand environment, in particular by the equatorial ligand field acting on the $d_{x^2-y^2}$ orbital. We analysed a series of compounds of composition $[FeO(L_{eq})_4(L_{ax})]^{2+}$ derived from $[FeO(H_2O)_5]^{2+}$ (S = 2) by substitution of water with ligands with enhanced or decreased σ-donor capability. For all complexes, there are two possible ground states of different spin multiplicity (quintet or triplet) lying close in energy. The quintet ground state was found to be more stable for $[FeO(H_2O)_5]^{2+}$ and all the systems in which only the axial water molecule is replaced. The triplet ground state is favoured by the stronger σ-donating ligands (e.g. $L_{eq} = NH_3$). These ligands push the $3d_{x^2-y^2}\uparrow$ up, so that it becomes favourable for it to shed its electron into the originally empty $3d_{xy}\downarrow$, where it can pair up with the electron in the $3d_{xy}\uparrow$.

Whereas the equatorial ligands have the most important effect, determining the spin state, the *axial* ligand (*trans* to the oxido ligand) directly interacts with the crucial acceptor orbital 3σ*↑ and affects its energy and shape. Therefore, the catalytic properties can be fine-tuned by varying the σ-donor properties of the *axial* ligand alone. Changes in the orbital energy of ≈1 eV or less may result in variations of up to 100 kJ mol$^{-1}$ in the C–H bond cleavage activation barrier. We also proved that axial ligands with decreased σ-donor ability enhance the catalytic properties of $[FeO(H_2O)_5]^{2+}$-derived systems by decreasing the energy of the 3σ*↑ orbital and favouring its overlap with a suitable donor orbital of the substrate. We also proved the existence of a linear relation between the magnitude of the mixing between 3σ*↑ and the axial-ligand orbital responsible for its destabilisation. The effect of the *axial* ligand can be optimally tuned by modifying its σ-donor properties. In the absence of σ donation (as in the hypothetical $[FeO(H_2O)_4(o)]^{2+} + CH_4$ system), C–H bond cleavage occurs almost spontaneously.

In summary, the optimal electronic properties for C–H bond activation and hydroxylation require a high-spin state, which is favoured by equatorial ligands with a weak ligand field, such as $H_2O$. A weak axial ligand field is similarly favourable, once the high-spin state is stabilised by a suitable equatorial field. These findings are consistent with the high catalytic activity of non-heme enzymes with flexible ligand environments and oxygen donor ligands rather than nitrogen lone pairs, such as TauD. The 2-His 1-carboxylate facial triad in the active site of the latter system consists of an equatorial ligand set with one nitrogen donor; the other equatorial ligands are oxygen based (e.g. $H_2O$). The remaining histidine ligand coordinates the metal centre through a nitrogen donor in the axial site, a situation that is, according to our analysis, not optimal. A carboxylate ligand instead of a nitrogen donor in the axial position would in principle be more favourable, which is also in accordance with the results of ref.[28] The insights gained in this work may be helpful in devising catalytic species for homogeneous alkane hydroxylation with superior activation properties, as well as in understanding the mechanistic role of oxidation intermediates containing high-valent metal centres with $[FeO(H_2O)_5]^{2+}$-like coordination and supported by a protective framework, such as zeolites[86] and oxygenated EDTA–Fe complexes in aqueous solution.[87–89]

## Acknowledgments

This work was supported by the Dutch National Research School Combination "Catalysis by Design" (NRSC-C). Computer resources were provided by the Netherlands' Scientific Research Council (NOW) through a grant from the Stichting Nationale Computerfaciliteiten (NCF).

 © 2007 Wiley-VCH Verlag GmbH & Co. KGaA, Weinheim 

[1] A. Ghosh, *J. Inorg. Biochem.* **2006**, *100*, 419–420.
[2] G. T. Babcock, *Proc. Natl. Acad. Sci. USA* **1999**, *96*, 12971–12973.
[3] T. Omura, *Biochem. Biophys. Res. Com.* **1999**, *266*, 690–698.
[4] W. L. Smith, D. L. DeWitt, R. M. Garavito, *Annu. Rev. Biochem.* **2000**, *69*, 145–182.
[5] F. D'Agnillo, A. I. Alayash, *Free Radical Biol. Med.* **2002**, *33*, 1153–1164.
[6] R. K. Behan, M. T. Green, *J. Inorg. Biochem.* **2006**, *100*, 448–459.
[7] A. V. Nemukhin, I. A. Topol, R. E. Cachau, S. K. Burt, *Theor. Chem. Acc.* **2006**, *115*, 348–353.
[8] A. L. Feig, S. J. Lippard, *Chem. Rev.* **1994**, *94*, 759–805.
[9] L. Que Jr, R. Y. N. Ho, *Chem. Rev.* **1996**, *96*, 2607–2624.
[10] B. J. Wallar, J. D. Lipscomb, *Chem. Rev.* **1996**, *96*, 2625–2657.
[11] E. I. Solomon, T. C. Brunold, M. I. Davis, J. N. Kemsley, S.-K. Lee, N. Lehnert, F. Neese, A. J. Skulan, Y.-S. Yang, J. Zhou, *Chem. Rev.* **2000**, *100*, 235–349.
[12] T. D. H. Bugg, *Tetrahedron* **2003**, *59*, 7075–7101.
[13] I. G. Denisov, T. M. Makris, S. G. Sligar, I. Schlichting, *Chem. Rev.* **2005**, *105*, 2253–2277.
[14] S. Shaik, D. Kumar, S. P. de Visser, A. Altun, W. Thiel, *Chem. Rev.* **2005**, *105*, 2279–2328.
[15] J. T. Groves, *J. Inorg. Biochem.* **2006**, *100*, 434–447.
[16] A. Bassan, M. R. A. Blomberg, T. Borowski, P. E. M. Siegbahn, *J. Inorg. Biochem.* **2006**, *100*, 727–743.
[17] P. G. Debrunner, *Hyperfine Interact.* **1990**, *53*, 21–36.
[18] R. Rutter, M. Valentine, M. P. Hendrich, L. P. Hager, P. G. Debrunner, *Biochemistry* **1983**, *22*, 4769–4774.
[19] R. Rutter, L. P. Hager, H. Dhonau, M. Hendrich, M. Valentine, P. Debrunner, *Biochemistry* **1984**, *23*, 6809–6816.
[20] C. E. Schulz, P. W. Devaney, H. Winkler, P. G. Debrunner, N. Doan, R. Chiang, R. Rutter, L. P. Hager, *FEBS Lett.* **1979**, *103*, 102–105.
[21] C. E. Schulz, R. Rutter, J. T. Sage, P. G. Debrunner, L. P. Hager, *Biochemistry* **1984**, *23*, 4743–4754.
[22] H.-P. Hersleth, U. Ryde, P. Rydberg, C. H. Görbitz, K. K. Andersson, *J. Inorg. Biochem.* **2006**, *100*, 460–476.
[23] J. C. Price, E. W. Barr, B. Tirupati, J. M. Bollinger Jr, C. Krebs, *Biochemistry* **2003**, *42*, 7497–7508.
[24] J. C. Price, E. W. Barr, T. E. Glass, C. Krebs, J. M. Bollinger Jr, *J. Am. Chem. Soc.* **2003**, *125*, 13008–13009.
[25] D. A. Proshlyakov, T. F. Henshaw, G. R. Monterosso, M. J. Ryle, R. P. Hausinger, *J. Am. Chem. Soc.* **2004**, *126*, 1022–1023.
[26] P. J. Riggs-Gelasco, J. C. Price, R. B. Guyer, J. H. Brehm, E. W. Barr, J. M. Bollinger Jr, C. Krebs, *J. Am. Chem. Soc.* **2004**, *126*, 8108–8109.
[27] C. Krebs, J. C. Price, J. Baldwin, L. Saleh, M. T. Green, J. M. Bollinger Jr, *Inorg. Chem.* **2005**, *44*, 742–757.
[28] J.-U. Rohde, L. Que Jr, *Angew. Chem. Int. Ed.* **2005**, *44*, 2255–2258.
[29] J.-U. Rohde, J.-H. In, M. H. Lim, W. W. Brennessel, M. R. Bukowski, A. Stubna, E. Münck, W. Nam, L. Que Jr, *Science* **2003**, *299*, 1037–1039.
[30] J. Kaizer, E. J. Klinker, N. Y. Oh, J.-U. Rohde, W. J. Song, A. Stubna, J. Kim, E. Münck, W. Nam, L. Que Jr, *J. Am. Chem. Soc.* **2004**, *126*, 472–473.
[31] X. Shan, L. Que Jr, *J. Inorg. Biochem.* **2006**, *100*, 421–433.
[32] M. M. Conradie, J. Conradie, A. Ghosh, *J. Inorg. Biochem.* **2006**, *100*, 620–626.
[33] E. J. Klinker, J. Kaizer, W. W. Brennessel, N. L. Woodrum, C. J. Cramer, L. Que Jr, *Angew. Chem. Int. Ed.* **2005**, *44*, 3690–3694.
[34] M. R. Bukowski, K. D. Koehntop, A. Stubna, E. L. Bominaar, J. A. Halfen, E. Münck, W. Nam, L. Que Jr, *Science* **2005**, *310*, 1000–1002.
[35] N. Harris, S. Shaik, D. Schröder, H. Schwarz, *Helv. Chim. Acta* **1999**, *82*, 1784–1797.
[36] S. Shaik, M. Filatov, D. Schröder, H. Schwarz, *Chem. Eur. J.* **1998**, *4*, 193–199.
[37] D. Schröder, S. Shaik, H. Schwarz, *Acc. Chem. Res.* **2000**, *33*, 139–145.
[38] F. Buda, B. Ensing, M. C. M. Gribnau, E. J. Baerends, *Chem. Eur. J.* **2001**, *7*, 2775–2783.
[39] A. Ghosh, E. Tangen, H. Ryeng, P. R. Taylor, *Eur. J. Inorg. Chem.* **2004**, *23*, 4555–4560.
[40] A. Bassan, M. R. A. Blomberg, P. E. M. Siegbahn, *Chem. Eur. J.* **2003**, *9*, 106–115.
[41] F. Buda, B. Ensing, M. C. M. Gribnau, E. J. Baerends, *Chem. Eur. J.* **2003**, *9*, 3436–3444.
[42] A. Decker, J.-U. Rohde, L. Que Jr, E. I. Solomon, *J. Am. Chem. Soc.* **2004**, *126*, 5378–5379.
[43] J. C. Schöneboom, F. Neese, W. Thiel, *J. Am. Chem. Soc.* **2005**, *127*, 5840–5853.
[44] F. Neese, *J. Inorg. Biochem.* **2006**, *100*, 716–726.
[45] N. Lehnert, R. Y. N. Ho, L. Que Jr, E. I. Solomon, *J. Am. Chem. Soc.* **2001**, *123*, 8271–8290.
[46] M. J. Louwerse, E. J. Baerends, *Phys. Chem. Chem. Phys.* **2007**, *9*, 156–166.
[47] J. H. Dawson, R. H. Holm, J. R. Trudell, G. Barth, R. E. Linder, E. Bunnenberg, C. Djerassi, S. C. Tang, *J. Am. Chem. Soc.* **1976**, *98*, 3707–3709.
[48] J. H. Dawson, M. Sono, *Chem. Rev.* **1987**, *87*, 1255–1276.
[49] J. H. Dawson, *Science* **1988**, *240*, 433–439.
[50] M. Sono, M. P. Roach, E. D. Coulter, J. H. Dawson, *Chem. Rev.* **1996**, *96*, 2841–2887.
[51] T. M. Makris, K. von Koenig, I. Schlichting, S. G. Sligar, *J. Inorg. Biochem.* **2006**, *100*, 507–518.
[52] V. Guallar, R. A. Friesner, *J. Am. Chem. Soc.* **2004**, *126*, 8501–8508.
[53] A. Altun, V. Guallar, R. A. Friesner, S. Shaik, W. Thiel, *J. Am. Chem. Soc.* **2006**, *128*, 3924–3925.
[54] C. Limberg, *Angew. Chem. Int. Ed.* **2003**, *42*, 5932–5954.
[55] C. V. Sastri, M. J. Park, T. Ohta, T. A. Jackson, A. Stubna, M. S. Seo, J. Lee, J. Kim, T. Kitagawa, E. Münck, L. Que Jr, W. Nam, *J. Am. Chem. Soc.* **2005**, *127*, 12494–12495.
[56] T. Kamachi, T. Kouno, W. Nam, K. Yoshizawa, *J. Inorg. Biochem.* **2006**, *100*, 751–754.
[57] F. Haber, J. Weiss, *Naturwiss.* **1932**, *51*, 948–950.
[58] W. C. Bray, M. H. Gorin, *J. Am. Chem. Soc.* **1932**, *54*, 2124–2125.
[59] J. T. Groves, M. Van Der Puy, *J. Am. Chem. Soc.* **1974**, *96*, 5274–5275.
[60] J. T. Groves, G. A. McClusky, *J. Am. Chem. Soc.* **1976**, *98*, 859–861.
[61] P. Wardman, L. P. Candeias, *Radiat. Res.* **1996**, *145*, 523–531.
[62] H. B. Dunford, *Coord. Chem. Rev.* **2002**, *233*, 311–318.
[63] F. Gozzo, *J. Mol. Catal. A* **2001**, *171*, 1–22.
[64] B. Ensing, F. Buda, P. Blöchl, E. J. Baerends, *Phys. Chem. Chem. Phys.* **2002**, *4*, 3619–3627.
[65] B. Ensing, F. Buda, P. Blöchl, E. J. Baerends, *Angew. Chem. Int. Ed.* **2001**, *40*, 2893–2895.
[66] B. Ensing, E. J. Baerends, *J. Phys. Chem. A* **2002**, *106*, 7902–7910.
[67] T. Løgager, J. Holcman, K. Sehested, T. Pedersen, *Inorg. Chem.* **1992**, *31*, 3523–3529.
[68] O. Pestovsky, A. Bakac, *J. Am. Chem. Soc.* **2004**, *126*, 13757–13764.
[69] O. Pestovsky, S. Stoian, E. L. Bominaar, X. Shan, E. Münck, L. Que Jr, A. Bakac, *Angew. Chem. Int. Ed.* **2005**, *44*, 6871–6874.
[70] B. Ensing, F. Buda, M. C. M. Gribnau, E. J. Baerends, *J. Am. Chem. Soc.* **2004**, *126*, 4355–4365.
[71] M. J. Louwerse, P. Vassilev, E. J. Baerends, *J. Phys. Chem. A*, submitted.
[72] A. Decker, M. D. Clay, E. I. Solomon, *J. Inorg. Biochem.* **2006**, *100*, 697–706.
[73] *ADF2005.01*, SCM, Theoretical Chemistry, Vrije Universiteit Amsterdam, The Netherlands; http://www.scm.com.
[74] E. J. Baerends, D. E. Ellis, P. Ros, *Chem. Phys.* **1973**, *2*, 41–51.


 © 2007 Wiley-VCH Verlag GmbH & Co. KGaA, Weinheim 

[75] C. Fonseca Guerra, J. G. Snijders, G. te Velde, E. J. Baerends, *Theor. Chem. Acc.* **1998**, *99*, 391–403.
[76] E. van Lenthe, E. J. Baerends, J. G. Snijders, *J. Chem. Phys.* **1994**, *101*, 9783–9792.
[77] A. Becke, *Phys. Rev. A* **1988**, *38*, 3098–3100.
[78] C. Lee, W. Yang, R. G. Parr, *Phys. Rev. B* **1988**, *37*, 785–789.
[79] A. Fouqueau, S. Mer, M. E. Casida, L. M. L. Daku, A. Hauser, T. Mineva, F. Neese, *J. Chem. Phys.* **2004**, *120*, 9473–9486.
[80] A. Fouqueau, M. E. Casida, L. M. L. Daku, A. Hauser, F. Neese, *J. Chem. Phys.* **2005**, *122*, 044110.
[81] M. Swart, A. R. Groenhof, A. W. Ehlers, K. Lammertsma, *J. Phys. Chem. A* **2004**, *108*, 5479–5483.
[82] N. C. Handy, A. J. Cohen, *Mol. Phys.* **2001**, *99*, 403–412.
[83] J. P. Perdew, K. Burke, M. Ernzerhof, *Phys. Rev. Lett.* **1996**, *77*, 3865–3868.
[84] A. R. Groenhof, M. Swart, A. W. Ehlers, K. Lammertsma, *J. Phys. Chem. A* **2005**, *109*, 3411–3417.
[85] As previously observed, the preference for a quintet ground state is not as marked in $[FeO(H_2O)(H_2S)]^{2+}$ as it is in $[FeO(H_2O)_5]^{2+}$. In practice, this factor may hamper the catalytic activity of the former system.
[86] G. I. Panov, A. K. Uriarte, M. A. Rodkin, V. I. Sobolev, *Catal. Today* **1998**, *41*, 365–385.
[87] T. Mizuta, J. Wang, K. Miyoshi, *Inorg. Chim. Acta* **1995**, *230*, 119–125.
[88] S. Seibig, R. van Eldik, *Inorg. Chem.* **1997**, *36*, 4115–4120.
[89] L. Bernasconi, E. J. Baerends, in preparation.

Received: December 22, 2006
Published Online: May 10, 2007

 © 2007 Wiley-VCH Verlag GmbH & Co. KGaA, Weinheim 

DOI: 10.1002/ejic.200700206

# Influence of the Polypyridyl (pp) Ligand Size on the DNA Binding Properties, Cytotoxicity and Cellular Uptake of Organoruthenium(II) Complexes of the Type $[(\eta^6\text{-}C_6Me_6)Ru(L)(pp)]^{n+}$ [L = Cl, $n$ = 1; L = $(NH_2)_2CS$, $n$ = 2]

**Sven Schäfer,[a] Ingo Ott,[b] Ronald Gust,[b] and William S. Sheldrick*[a]**

**Keywords:** Ruthenium / Iridium / DNA / Antitumour agents / Arene ligands

The DNA binding of polypyridyl (pp) ($\eta^6$-hexamethylbenzene)ruthenium(II) complexes of the type $[(\eta^6\text{-}C_6Me_6)RuCl(pp)](CF_3SO_3)$ (pp = phen, tap, dpq, dppz, dppn) **1**–**5** and $[(\eta^6\text{-}C_6Me_6)Ru\{(NH_2)_2CS\}(pp)](CF_3SO_3)_2$ (pp = dpq, dppz, dppn) **6**–**8** has been studied by UV/Vis spectroscopy, circular dichroism and viscosity measurements. Complexes **3**–**5**, **7** and **8** are potent cytotoxic agents towards the human cancer cell lines MCF-7 and HT-29. Stable intercalative binding into CT DNA is indicated for the dpq and dppz complexes by large increases $\Delta T_m$ of 12–25 °C in the DNA thermal denaturation temperature for $r$ = [complex]/[DNA] = 0.1. Large viscosity increases for DNA in the presence of **3** and **4** are also in accordance with this binding mode as are the pronounced hypochromic UV/Vis shifts for the $\pi$–$\pi^*$ transitions of the dppz ligands of **4** and **7** in the range 360–400 nm. A small $\Delta T_m$ value of 2 °C and effectively unchanged viscosity suggest that Ru–N (nucleobase) coordinative binding is thermodynamically preferred for the larger polypyridyl ligand of **5** under equilibrium conditions, as is also the case for the small ligands phen and tap in complexes **1** and **2**. CD spectra indicate that the B DNA conformation is essentially retained for interaction with the chloro complexes **1**–**5** but that very significant distortions occur for the thiourea complexes **6**–**8**. The in vitro cytotoxicities of the chloro complexes **3**–**5** are dependent on the size of the polypyridyl ligand with $IC_{50}$ values increasing in the order dppn < dppz < dpq: for instance $IC_{50}$ values of 11.1, 2.12, and 0.13 μM were determined for **3**–**5** towards MCF-7. These values correlate well with the cellular uptake efficiency which increases from 1.1 over 146.6 to 906.7 ng(Ru)/mg (protein) within the series **3**–**5**.
(© Wiley-VCH Verlag GmbH & Co. KGaA, 69451 Weinheim, Germany, 2007)

## Introduction

The intercalation of transition metal polypyridyl complexes into DNA has been a topic major bioinorganic interest in the past two decades and continues to receive much attention.[1–3] We have recently established that organometallic half-sandwich compounds of the types $[(\eta^5\text{-Cp*})Ir(amino\ acid\text{-}\kappa S)(dppz)]^{n+}$ ($n$ = 1–3, dppz = dipyrido[3,2-*a*:2′,3′-*c*]phenazine)[4–6] and $[(\eta^6\text{-arene})Ru(amino\ acid\text{-}\kappa S)(dppz)]^{n+}$ ($n$ = 1–3, arene = $C_6H_6$, $Me_3C_6H_3$, $C_6Me_6$),[7] with a thioether-coordinated methionine-containing amino acid or peptide, exhibit strong intercalative binding into DNA. In these complexes and in $[(\eta^5\text{-Cp*})Ru(dppz)(NO)](CF_3SO_3)_2$,[8] the magnitudes of the binding constants $K_b$ ($8.8\times10^4$ to $5.5\times10^6$ M$^{-1}$) are clearly dependent on the overall cation charge $n$ (1–3), i.e. on additional electrostatic interactions with the negatively charged phosphodiester backbone of DNA.

This finding is in accordance with the results of Sartorius and Schneider[9] for heterocyclic derivatives with positively charged ammonium groups in their side chains. These authors also found that the intercalation binding strength is essentially a function of the size of the aromatic system, independent of heteroatoms or the presence of local positive charges within such planar moieties. Sterical considerations suggest that such a simple size dependence will be unlikely for the side-on intercalation mode (Figure 1) established by 2D-NOESY[7] for the interaction of $[(\eta^6\text{-}C_6Me_6)Ru(Ac\text{-}met\text{-}OH\text{-}\kappa S)(dppz)]^{2+}$ (Ac-met-OH = *N*-acetyl-L-methionine) with the hexanucleotide $d(GTCGAC)_2$. Inspection of Figure 1 indicates, for instance, that increasing the surface area and length of the polypyridyl ligand by replacing dppz with dppn (benzo[*i*]dipyrido[3,2-*a*:2′,3′-*c*]phenazine) might favour this type of intercalation by enabling additional stacking with the adenine and cytosine bases of the left-hand strand. On the other hand, inevitable close non-bonding contacts between atoms of the additional six-membered ring of dppn and DNA riboses could prevent a suitable alignment of the polypyridyl ligand.

To establish whether there is, indeed, an optimum polypyridyl ligand (pp) for side-on intercalation of $(\eta^6\text{-}C_6Me_6)Ru^{II}$ complexes, we have now studied the DNA binding

[a] Lehrstuhl für Analytische Chemie, Ruhr-Universität Bochum, 44780 Bochum
Fax: +49-234-3214420
E-mail: william.sheldrick@ruhr-uni-bochum.de
[b] Institut für Pharmazie, Freie Universität Berlin, Königin-Luise-Str. 2–4, 14195 Berlin
E-mail: ottingo@zedat.fu-berlin.de

 © 2007 Wiley-VCH Verlag GmbH & Co. KGaA, Weinheim 

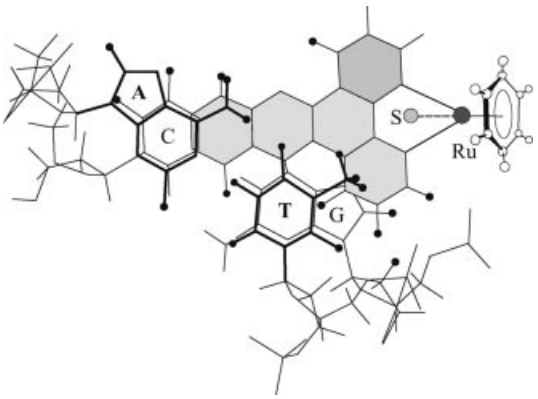


Figure 1. Schematic illustration of the side-on intercalation of [($\eta^6$-$C_6Me_6$)Ru(Ac-met-OH-κ*S*)(dppz)]$^{2+}$ into the $G_1T_2/C_6A_5$ sequence of the hexanucleotide d(GTCGAC)$_2$.[7]

properties of compounds of the type [($\eta^6$-$C_6Me_6$)RuCl(pp)]-($CF_3SO_3$)$_2$ (**1**–**5**) with the diimine ligands phen (1,10-phenanthroline), tap (1,4,5,8-tetraazaphenanthrene), dpq (dipyrido[3,2-*f*:2′,3′-*h*]quinoxaline), dppz and dppn (Scheme 1). The preparation of [($\eta^6$-$C_6Me_6$)RuCl(phen)]Cl has recently been reported by Süss–Fink et al.,[10] who studied the hydrolytic potential of the corresponding dicationic aqua complex [($\eta^6$-$C_6Me_6$)Ru($H_2O$)(phen)]($BF_4$)$_2$ for transfer hydrogenation reactions in aqueous solution. Both dppz and dppn have been confirmed as intercalating ligands in their $Re^I$ complexes such as [*fac*-Re(CO)$_3$(pp)(pyridine)]($CF_3SO_3$),[11–13] which exhibit steric requirements similar to the half-sandwich polypyridyl ($\eta^6$-$C_6Me_6$)$Ru^{II}$ complexes. As polypyridyl ligand intercalation and chloride substitution by purine nucleobases might be expected to compete as possible DNA binding modes for complexes **1**–**5**, three thiourea complexes [($\eta^6$-$C_6Me_6$)Ru{($NH_2$)$_2$CS}(pp)] ($CF_3SO_3$)$_2$ (pp = dpq, dppz, dppn) **6**–**8** were also investigated (Scheme 2). The *trans*-sited thiourea ligands in the metallointercalator [Pt(bpy){($NH_2$)$_2$CS}$_2$]$Cl_2$ remain coordinated on DNA interaction and have been shown to play effectively no role in DNA binding.[14] As they are *cis*-sited relative to the polypyridyl ligands, additional N–H···O hydrogen bonding interactions to DNA could be possible for complexes **6**–**8**.

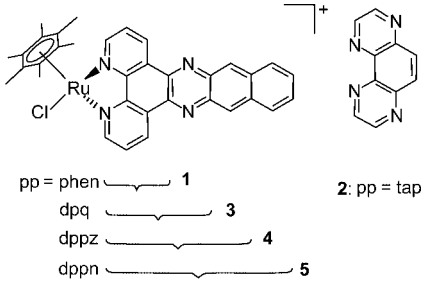


Scheme 1

Arene ruthenium(II) complexes have been shown to exhibit promising anticancer activity.[15,16] The first report appeared in 1990 when the amino acidato complex [($\eta^6$-$C_6H_6$)-RuCl(L-H-Pro-O-κ$^2$*N*,*O*)] (H-Pro-OH = L-proline) was found to be significantly active in vivo towards mouse P388 leukaemia cells (T/C = 125% for a dosis 0.68 mg kg$^{-1}$) but inactive in vitro towards L1210 cells.[17] The in vitro cytotoxic properties of [($\eta^6$-arene)$Ru^{II}$] complexes with phosphane,[16,21] sulfoxide[18–20] and chelating diamine or diimine ligands[15,22] have been investigated in recent years. Compounds of the latter type [($\eta^6$-arene)RuCl(LL′)]($PF_6$) (LL′ = diamine or diimine) with extended polycyclic arenes (e.g. tetrahydroanthracene) and LL′ = ethylenediamine are most active towards A2780 human ovarian cancer cells, whereas those with polar substituents on the arene or with aromatic diimine ligands such as bpy or phen, exhibit considerably reduced activity.[23] As DNA is considered to be a possible target for ($\eta^6$-arene)$Ru^{II}$ compounds,[15] we considered it to be of interest to also study the in vitro cytotoxity of complexes **3**–**5**, **7** and **8** with the extended polypyridyl ligands dpq, dppz and dppn, and to establish whether this can be correlated with the mode and strength of DNA binding and/or with cellular uptake. The human cell lines MCF-7 (breast cancer) and HT-29 (colon cancer) were selected for cytotoxicity studies.

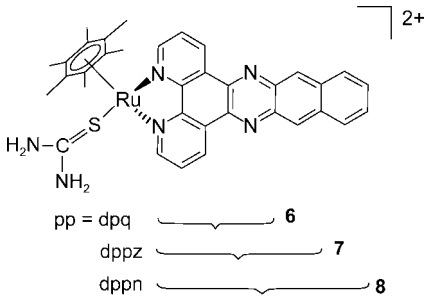


Scheme 2

## Results and Discussion

### Synthesis of 1–8 and Structures of 1 and 3

The compounds of the type [($\eta^6$-$C_6Me_6$)RuCl(pp)]-($CF_3SO_3$) **1**–**5** (pp = phen, tap, dpq, dppz, dppn) were prepared by refluxing the solvent complex [($\eta^6$-$C_6Me_6$)-RuCl(acetone)$_2$] ($CF_3SO_3$) with the appropriate polypyridyl ligand (pp) in $CH_3OH/CH_2Cl_2$ for 2 h.

[($\eta^6$-$C_6Me_6$)RuCl(acetone)$_2$]$^+$ can be obtained in situ by addition of two equivalents of Ag($CF_3SO_3$) to a solution of the dimeric complex [{($C_6Me_6$)$RuCl_2$}$_2$] in acetone and subsequent filtration of the precipitated AgCl after stirring in the dark for 0.5 h. Following removal of the remaining chloride ligand by analogous treatment of complexes **3**–**5** with a second equivalent of Ag($CF_3SO_3$) in acetone, addition of thiourea to the resulting in situ complexes [($\eta^6$-$C_6Me_6$)Ru(acetone)(pp)]$^{2+}$ affords [($\eta^6$-$C_6Me_6$)Ru(pp)-{($NH_2$)$_2$CS}] ($CF_3SO_3$)$_2$ **6**–**8** (pp = dpq, dppz, dppn) after refluxing the reaction mixture for 2 h in $CH_3OH/CH_2Cl_2$. All the complexes were characterised by $^1$H and $^{13}$C NMR

 © 2007 Wiley-VCH Verlag GmbH & Co. KGaA, Weinheim 

Table 1. Crystal and refinement data for **1** and **3**.

| | **1** | **3** |
|---|---|---|
| Empirical formula | $C_{25}H_{26}ClF_3N_2O_3RuS$ | $C_{26}H_{26}ClF_3N_4O_3RuS$ |
| $M$ | 628.06 | 680.10 |
| Measurement temperature [K] | 293(2) | 109(2) |
| Crystal system | monoclinic | monoclinic |
| Space group | $P2_1/c$ | $P2_1/c$ |
| $a$ [Å] | 8.9278(5) | 14.3922(13) |
| $b$ [Å] | 11.5314(6) | 11.6752(9) |
| $c$ [Å] | 24.0047(12) | 15.4171(11) |
| $\beta$ [°] | 97.981(4) | 96.469(7) |
| $V$ [Å$^3$] | 2447.3(2) | 2574.1(4) |
| $Z$ | 4 | 4 |
| $F$(000) | 1272.0 | 1376.0 |
| $\rho_{calcd.}$ [g/cm$^{-3}$] | 1.705 | 1.755 |
| Crystal size [mm] | $0.22 \times 0.13 \times 0.04$ | $0.17 \times 0.10 \times 0.02$ |
| Radiation | Mo-$K_\alpha$ | Mo-$K_\alpha$ |
| $\mu$ [mm$^{-1}$] | 0.890 | 0.856 |
| $2\theta_{max}$ [°] | 25.0 | 27.5 |
| $h,k,l$ ranges | –10/10, –13/13, –28/28 | –18/18, –15/15, –20/20 |
| Collected reflections | 30680 | 36744 |
| Unique reflections | 4298 | 5875 |
| Observed reflections [$I > 2\sigma(I)$] | 3992 | 3795 |
| $R_1$ [$I > 2\sigma(I)$] | 0.048 | 0.051 |
| $wR_2$ [all data] | 0.080 | 0.094 |
| $S$ (goodness-of-fit) | 1.154 | 1.045 |
| max./min. $\Delta\rho$(e Å$^{-3}$) | 0.72/–0.74 | 0.92/–0.98 |

and positive-ion LSIMS and gave satisfactory microanalyses. The structures of complexes **1** and **3** were determined by X-ray structural analysis (Table 1) and their respective cations are depicted in Figures 2 and 3. Complex **1** exhibits an interplanar angle of 54.1° between its benzene and polypyridyl ring systems, complex **2** a much larger angle of 75.2°. The individual $[(\eta^6\text{-}C_6Me_6)RuCl(pp)]^+$ cations pack with parallel polypyridyl ligands in their respective lattices.

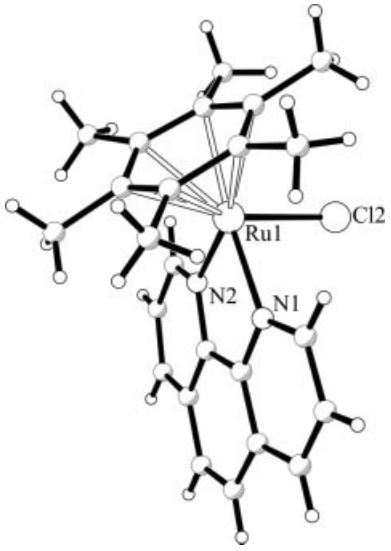


Figure 2. Molecular structure of the cations of $[(\eta^6\text{-}C_6Me_6)RuCl(phen)](CF_3SO_3)$ (**1**). Selected bond lengths [Å] and angles [°]: Ru1–Cl2 2.401(1) Ru1–N1 2.107(3), Ru1–N2 2.098(3), Ru1–C 2.194(3) – 2.251(3), N1–Ru1–N2 77.7(1), N1–Ru1–Cl2 85.08(8) N2–Ru1–Cl2 84.71(8).

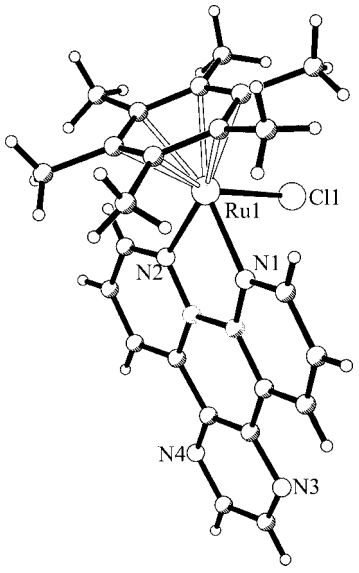


Figure 3. Molecular structure of the cations of $[(\eta^6\text{-}C_6Me_6)RuCl(dpq)](CF_3SO_3)$ (**3**). Selected bond lengths [Å] and angles [°]: Ru1–Cl1 2.408(1) Ru1–N1 2.109(4), Ru1–N2 2.101(4), Ru1–C 2.192(2) – 2.204(2), N1–Ru1–N2 77.1(1), N1–Ru1–Cl1 82.9(1) N2–Ru1–Cl1 84.7(1).

## DNA Binding Studies

### *UV/Vis Absorption and Thermal Denaturation Studies for 1–8*

Following an incubation period of 5 min, UV/Vis spectra for the buffered solutions of **1**–**4**, **6** and **7** (pH 7.2, 10 mM phosphate) with CT DNA at $r = 0.1$ {$r$ = [complex]/[DNA] with DNA concentration in mol/L (nucleotide)} exhibit no

 © 2007 Wiley-VCH Verlag GmbH & Co. KGaA, Weinheim 

further significant changes, thereby indicating that achievement of equilibrium conditions is relatively rapid. A pronounced decrease in absorbance at about 364 and 383 nm and bathochromic shifts of about 5 nm are indicative of possible dppz intercalation into the biopolymer for complexes **4** and **7**. The time dependence of these changes is illustrated for the chloro complex **4** in part a of Figure 4.

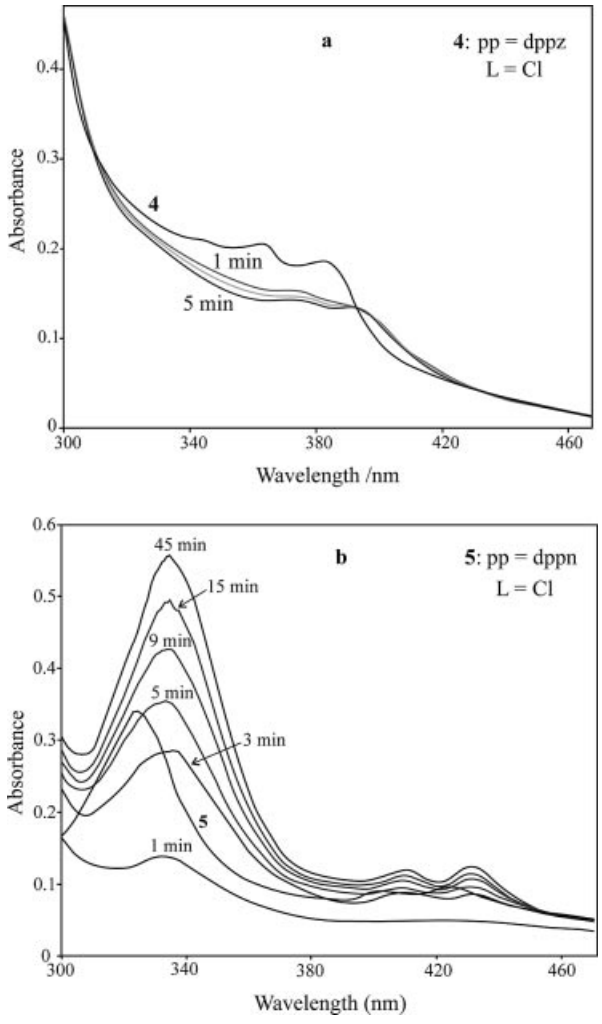


Figure 4. Time dependence of the UV/Vis spectra of complexes **4** and **5** (both 20 μM) in a 10 mM phosphate buffer (pH = 7.2) with CT DNA (200 μM). Times are given in minutes for individual curves.

Hypochromic shifts $\Delta A/A$ of respectively –28% and –16% at 364 nm are observed for **4** and **7** and indicate that the nature of the DNA interaction must be similar for both the dppz complexes. On mixing with CT DNA, the UV/Vis spectrum of the dppn complex **5** initially exhibits even more pronounced hypo- and bathochromic shifts for the spin-allowed π–π* transitions at about 327, 403 and 425 nm. Part b of Figure 4 depicts the $\Delta A/A$ value of –59% at 336 nm and the associated red shift of about 9 nm after 1 min. These initial spectral changes are followed by an increase in the absorbance values over the next 45 min to reach a maximum value of +63% at 336 nm. The original absorbance values of the complex are reached within 5 min after mixing. In similarity to complex **5** (Figure 4, b), significant decreases in $\Delta A/A$ are also observed for the dppn complex **8** at 327, 403 and 425 nm on initial mixing with DNA and these are followed by large increases with equilibrium being achieved within 15 min. The respective initial and final values of $\Delta A/A$ at the first maximum are –29% and +49%. No effective changes in absorption in the range 300–420 nm were recorded for the complexes **1** (pp = phen), **2** (pp = tap) and **3** (pp = dpq) on mixing with CT DNA. The UV/Vis spectra for all complex/[DNA] reaction mixtures exhibit no significant changes over a period of 36 h after equilibrium is achieved.

Thermal denaturation studies for CT DNA can provide simple a means of gauging the efficacy of polypyridyl intercalation for organometallic complexes[4–7] such as **1**–**8**, provided that electrostatic and hydrogen-bonding interactions with the biopolymer may be regarded as remaining effectively unchanged by pp ligand variation. The $\Delta T_m$ values listed in Table 2 for the monocations of **1**–**5** and the dications of **6**–**8** were recorded under equilibrium conditions in a phosphate buffer, (pH = 7.2) for $r = 0.1$ and are indicative of strong DNA intercalation for the dppz ligand of **4** ($\Delta T_m$ = 20 °C), and **7** ($\Delta T_m$ = 25 °C). In contrast, the DNA melting temperature remains effectively unchanged on treatment with complexes **1**, **2** and **5** [$\Delta T_m$ = 0 (phen), +2 (tap), +2 °C (dppn)]. A similar $\Delta T_m$ value of –2 °C has also been reported for $[(\eta^6\text{-}C_6H_6)RuCl(en)]^+$ (en = ethylenediamine),[22] which preferentially coordinates DNA guanine nucleobases at their endocyclic nitrogen atoms N7. The small $\Delta T_m$ value of only + 2 °C is more surprising for the larger dppn ligand with its much more extensive aromatic surface area, but in accordance with the previously discussed UV/Vis studies (Figure 4, b), which indicate an absence of dppn intercalation under equilibrium conditions. Relatively large increases in $T_m$ of 14° and 12 °C are, however, observed for the dpq complexes **3** and **6** respectively, suggesting that this polypyridyl ligand could also participate in intercalative DNA binding. The significant increase in $\Delta T_m$ for the dicationic complexes **7** and **8** [$\Delta T_m$ changes: +5 (dppz), +6 °C (dppn)] in comparison to the monocationic species **4** and **5** may be caused by the increased strength of the electrostatic interactions with the biopolymer but the possibility of N–H···X (X = O, N) hydrogen bonding involving the thiourea

Table 2. Melting temperature shifts $\Delta T_m$, for the interaction of complexes $[(\eta^6\text{-}C_6Me_6)Ru(L)(pp)]^{n+}$ ($n$ = 1, 2) **1**–**8** with CT DNA ($r = 0.1$) in a 10 mM phosphate buffer at pH = 7.2 after incubation for 60 min.

| Complex | pp | L | | $\Delta T_m$[°C] |
|---|---|---|---|---|
| 1 | phen | Cl | 1 | 0 |
| 2 | tap | Cl | 1 | 2 |
| 3 | dpq | Cl[a] | 1 | 14 |
| 4 | dppz | Cl[a] | 1 | 20 |
| 5 | dppn | Cl | 1 | 2 |
| 6 | dpq | $(NH_2)_2CS$ | 2 | 12 |
| 7 | dppz | $(NH_2)_2CS$ | 2 | 25 |
| 8 | dppn | $(NH_2)_2CS$ | 2 | 8 |

[a] Aquation can lead to the dications $[(\eta^6\text{-}C_6Me_6)Ru(H_2O)(pp)]^{2+}$ as intercalating species after incubation (pp = dpq, dppz).

 © 2007 Wiley-VCH Verlag GmbH & Co. KGaA, Weinheim 

amino functions and DNA acceptor atoms X cannot be ruled out. Interestingly a small relative decrease in $\Delta T_m$ of –2 °C is observed for the dicationic dpq complex **6** in comparison to its chloro analogue **3**.

### *Circular Dichroism Studies for 1–8*

The high $\Delta T_m$ values recorded for the dppz complexes **4** and **7** in comparison to the dppn complexes **5** and **8** suggest that dppz may offer a close to optimum aromatic surface area for side-on intercalation into B DNA[7] (Figure 1) and that dppn may be too long and its surface area too extensive for effective DNA binding in this mode. Characteristic changes in the observed circular dichroism (CD) spectra of DNA provide a convenient means of monitoring conformational changes for the biopolymer.[7,24,25] As depicted in Figure 5, a negative band at 246 nm caused by the helical B conformation and a positive band at 275 nm due to base stacking are observed for CT DNA.[26] Addition of the phen and tap complexes **1** and **2** at a 1:10 complex/[DNA] molar ratio leads to only minor spectral changes, thereby indicating little distortion of the B helix following the formation of Ru–N bonds to DNA nucleobases. The spectra of Figure 5 and the CD spectra for the other complexes exhibited no significant changes during a period of 36 h following equilibrium achievement. Complex/[DNA] solutions remained clear and opalescence was not observed. The depicted spectra were all recorded after 24 h.

Although aromatic molecules often generate CD bands between 300 and 400 nm on interaction with DNA, the appearance of these signals is generally not of relevance for the assignment of the binding mode. This is because the observed induced circular dichroism is caused by a rigid orientation of the molecule with respect to the double helix and this can result from surface or groove binding in addition to intercalation. The dppz complexes **4** and **7** do, however, exhibit characteristic negative CD bands with molar elipticities [$\theta$] of $-4.1 \times 10^{-3}$ and $-1.9 \times 0^{-3}$ deg cm$^2$ mol$^{-1}$ at $\lambda$ = 300 nm (Figure 6) and we have previously established[6] that the appearance of such bands in the range 290–340 nm is, indeed characteristic for intercalating organometallic dppz complexes. The observed wavelength range corresponds with that of the broad π–π* absorption maximum at $\lambda_{max}$ = 280 nm of the complexes themselves. A small but significant increase in [$\theta$] for the positive CD band at 272 nm for **4** may be attributed to additional stabilisation of base stacking in the helix due to dppz intercalation. Whereas the molar ellipticity for the positive band at 268 nm is also similar for the analogous thiourea complex **7**, a dramatic decrease in the negative value of [$\theta$] for the band at 243 nm is apparent in the latter case. This implies a significant change in the original B helical conformation due possibly to both the twofold positive charge and the participation of thiourea amino functions in hydrogen bonding to the biopolymer.

The CD spectra for 1:10 mixtures of the dpq complexes **3** and **6** with CT DNA (Figure 7) also provide evidence for intercalation. When compared to the CD spectrum of CT DNA alone, a broadening and apparent splitting of the positive CD band are ascertainable for the **3**/DNA mixture and, to a lesser extent, the **6**/DNA mixture. As complexes **3** and **6** exhibit absorption maxima for spin-allowed MLCT π–π* transitions at $\lambda_{max}$ 261 and 284 nm, the appearance of the positive band in the range 270–295 nm could be due to a spectral overlap with a negative CD contribution due to intercalating dpq ligands. This interpretation would correlate with the large $\Delta T_m$ values of 14 and 12 °C registered for these dpq complexes. The decrease in the negative value of the molar ellipticity [$\theta$] for the band at 243 nm is less pronounced for **6** than for the analogous dppz complex **7**, but once again indicates that significant changes in the B DNA conformation must have taken place.

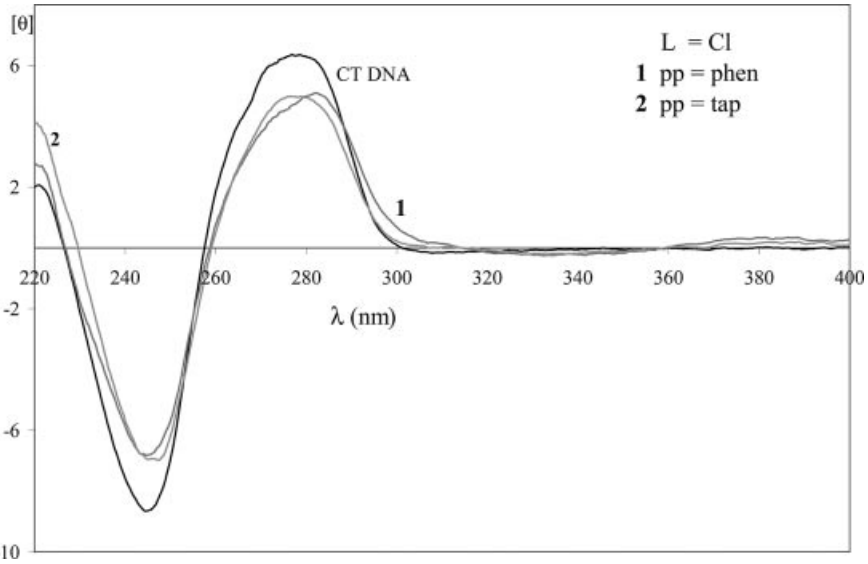


Figure 5. CD spectra of CT DNA and mixtures of **1** (pp = phen) and **2** (pp = tap) with CT DNA ($r$ = 0.1) in a 10 mM phosphate buffer (pH = 7.2) after 24 h incubation.

 © 2007 Wiley-VCH Verlag GmbH & Co. KGaA, Weinheim 

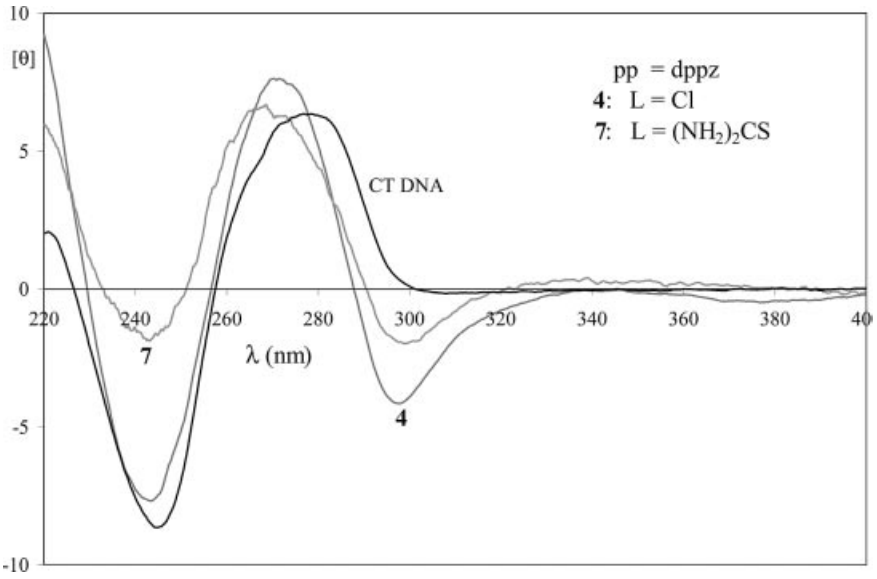


Figure 6. CD spectra of CT DNA and mixtures of **4** and **7** (pp = dppz) with CT DNA ($r$ = 0.1) in a 10 mM phosphate buffer (pH = 7.2) after 24 h incubation.

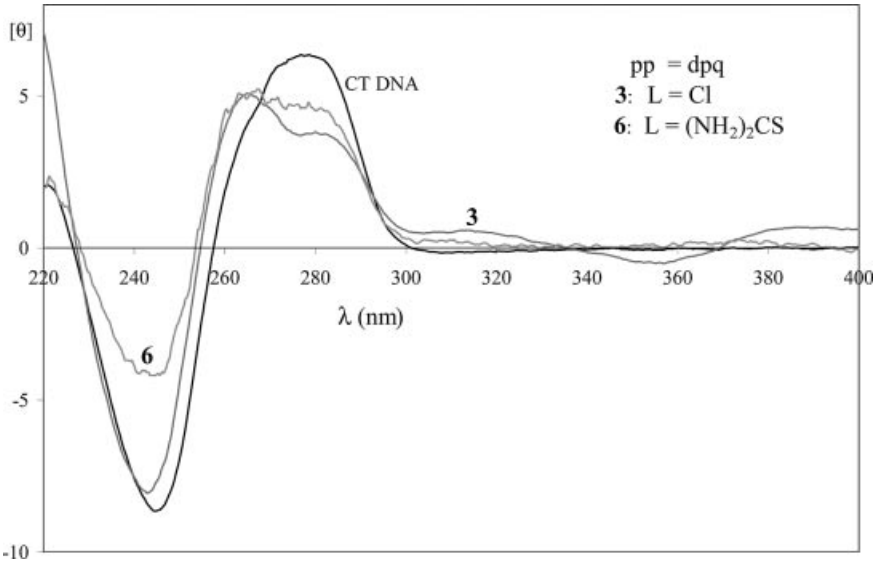


Figure 7. CD spectra of mixtures of **3** and **6** (pp = dpq) with CT DNA ($r$ = 0.1) in a 10 mM phosphate buffer (pH = 7.2) after 24 h incubation.

Both the large increase in $\Delta A/A$ of +63% at 327 nm and the minimal increase in the DNA melting temperature of +2 °C are in accordance with an absence of dppn intercalation for **5**/DNA mixtures under equilibrium conditions. The CD spectrum for such a mixture after 24 h incubation (Figure 8) is closely similar to those registered for the coordinatively bonded phen and tap complexes **1** and **2**. These observations contrast dramatically with other intercalation studies for transition metal complexes, which have established strong intercalative binding for this polypyridyl ligand.[11–13,27] For instance, a binding constant $K_b$ = $7.8 \times 10^4$ M$^{-1}$ and site size $s$ of 1.4 have very recently been determined for the complex [Ir(dppn)(ppy)$_2$] ($PF_6$) (Hppy = 2-phenylpyridine).[27] This $K_b$ value is significantly larger than that of $2.0 \times 10^4$ M$^{-1}$ ($s$ = 1.3) obtained for the analogous dppz complex, in accordance with similar findings for rhenium(I) complexes.[11–13] In agreement with the conclusions of Sartorius and Schneider,[9] it seems likely that an enhanced, presumably end-on intercalative binding affinity results from the larger planar surface area of the dppn ligand in comparison to dppz. Intercalative DNA binding has also recently been confirmed for the complexes [Ru(bpy)$_2$(ppip)]$^{2+}$ and [Ru(phen)$_2$(ppip)]$^{2+}$ [ppip = 2-(4′-phenoxyphenyl)imidazo[4,5-*f*][1,10]phenanthroline],[28] whose ppip ligand is even longer than dppn. The apparent lack of intercalation for **5** under equilibrium conditions must, therefore, be attributed to the preferred side-on mode of ($\eta^6$-arene)Ru$^{II}$ complexes.[7] It is possible that a kinetically favoured end-on intercalation may lead to the initial dramatic decrease in $\Delta A/A$ of –59% at 327 nm for the **5**/

 © 2007 Wiley-VCH Verlag GmbH & Co. KGaA, Weinheim 

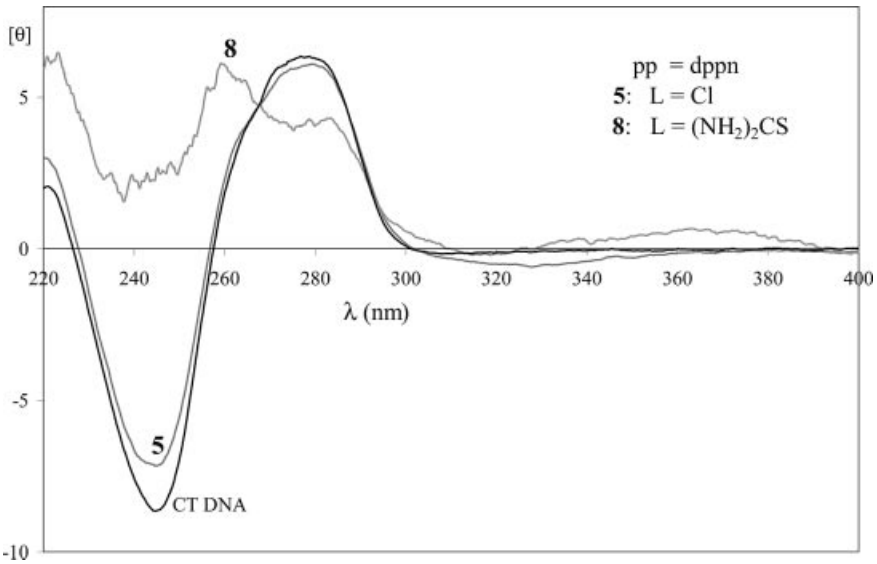


Figure 8. CD spectra of mixtures of **5** and **8** (pp = dppn) with CT DNA ($r$ = 0.1) in a 10 mM phosphate buffer (pH = 7.2) after 24 h incubation.

DNA mixture but that a subsequent rearrangement to a side-on mode with increased base overlap is no longer possible. Support for this line of reasoning is provided by the CD spectrum of the **8**/DNA mixture (Figure 8), for which the stability of the Ru–S (thiourea) bond will be expected to prevent a ligand-substitution reaction and resulting Ru–N (nucleobase) binding. The disappearance of the negative DNA CD band at about 246 nm on the addition of the non-coordinating thiourea complex **8** now implies, in contrast to **5**, DNA damage and complete loss of the original B-helix conformation.

### *Viscosity Measurements on 3–5*

Intercalation of aromatic ligands such as dppz between adjacent nucleobase pairs leads to a lengthening and stiffening of the double helix and these structural changes are reflected in an increase in DNA viscosity.[29,30] The CD spectra of mixtures of the chloro complexes **3**–**5** (pp = dpq, dppz, dppn) with CT DNA suggest that the B conformation of the double helix remains essentially unperturbed in each case, independent of whether the interaction is predominantly intercalative or coordinative. These systems were therefore selected for viscometric titrations and Figure 9 illustrates the dependence of the DNA viscosity on the logarithmic function $\ln(1+r)$ with $r$ = [complex]/[DNA] for complexes **3**–**5**. The slopes of +2.23 and +3.13 for **3** and **4** correlate well with the observed $\Delta T_m$ value of +14 and +20 °C and confirm DNA lengthening and thereby intercalation. In contrast, a small decrease in viscosity is observed for the dppn complex **5** in accordance with its small $\Delta T_m$ value of +2 °C and the positive $\Delta A/A$ values at equilibrium, which are in accordance with coordinative binding following substitution of the chloride ligand.

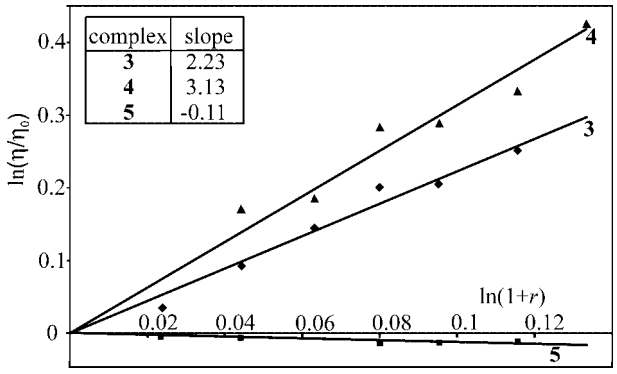


Figure 9. Viscometric titration of sonicated DNA with the complexes **3**–**5** (pp = dpq, dppz, dppn; X = Cl) in a 10 mM phosphate buffer (pH = 7.2): η = reduced viscosity of the DNA solution in the presence of a complex, $\eta_o$ = the reduced viscosity of the DNA solution without the complex, $r$ = [complex]/[DNA].

It is interesting to compare the DNA binding studies on **3**–**5** with our contrasting recent results for the analogous $(\eta^5\text{-}C_5Me_5)Ir^{III}$ complexes $[(\eta^5\text{-}C_5Me_5)IrCl(pp)](CF_3SO_3)$ (pp = dpq, dppz, dppn),[31] for which chloride substitution will be several orders of magnitude more rapid.[32] Whereas a very small increase is observed for the DNA viscosity (slope = +0.16) on mixing with the $(\eta^5\text{-}C_5Me_5)Ir^{III}$ dpq complex, significant decreases (slopes –1.63 and –1.42) occur for the dppz and dppn complexes. As the $\Delta T_m$ values of respectively +2, +7 and +2 °C are modest for the $(\eta^5\text{-}C_5Me_5)Ir^{III}$ complexes and the UV/Vis and CD spectra for their reaction mixtures with CT DNA also provide no evidence for intercalation, it is reasonable to conclude that coordinative Ir–N7 binding to the DNA purine bases must be predominant. The viscosity decreases for the dppz and dppn complexes may be due to kinking or bending of the

 © 2007 Wiley-VCH Verlag GmbH & Co. KGaA, Weinheim 

double helix[33,34] caused by hydrophobic interactions with the DNA surface and associated polypyridyl stacking.

### DNA Binding Parameters for 4

Binding constants $K_b$ in the range $7.3 \times 10^5$ to $5.5 \times 10^6$ M$^{-1}$ have been determined for least-squares fits to UV/Vis titration data of complexes of the type $[(\eta^6\text{-}C_6Me_6)\text{-}Ru(dppz)(peptide\text{-}\kappa S)]^{n+}$ ($n$ = 2, 3) with CT DNA using the hypochromic absorption shifts at $\lambda_{max}$ = 364 nm and the non-cooperative non-specific binding model of Bard and Thorp.[35,36] The corresponding site sizes $s$ between 2.3 and 5.1 are in accordance with intercalative binding.[7] It is interesting to compare these parameters with those now obtained for the dppz complexes **4** and **7**. UV/Vis spectra were recorded for buffered 20 μM solutions of **4** and **7** at pH 7.2 following a 60 min incubation with increasing quantities of CT DNA (10–300 μM). An isosbestic point at 399 nm is in each case in accordance with a simple equilibrium distribution between DNA-bound and free $(\eta^6\text{-}C_6Me_6)Ru^{II}$ complex. Figure 10 depicts the least-squares fit to absorbance values recorded for complex **4** at 383 nm, which afforded a $K_b$ value of 2.0(5) $10^6$ M$^{-1}$ and a site size $s$ of 1.42(8). The analogous binding parameters for the thiourea complex **7** are 6(3) $10^6$ M$^{-1}$ for $K_b$ and 1.55(6) for s. These binding constants are much higher than those of $1.6 \times 10^5$ and $1.5 \times 10^5$ reported for the monocationic complex cations $[(\eta^6\text{-}C_6Me_6)\text{-}Ru(AcH_{-1}cysOH\text{-}\kappa S)(dppz)]^+$ and $[(\eta^6\text{-}C_6Me_6)Ru(HglyglyH_{-1}cysOH\text{-}\kappa S)(dppz)]^+$ (HcysOH = L-cysteine, HglyOH = glycine) but similar to those of $7.3 \times 10^5$–$5.5 \times 10^6$ M$^{-1}$ previously observed for complex di- and trications of this type (e.g. peptide = AcmetOH, $H_2$metOMe).[7] The DNA melting temperature increases of 10.4 and 9.4 °C are also much lower for the former monocationic species, whereas the typical $\Delta T_m$ values in the range 18.2–18.5 °C for the latter cations are close to that of 20 °C recorded for **4**. These findings suggest that aquation of the original chloride complex $[(\eta^6\text{-}C_6Me_6)RuCl(dppz)]^+$ may take place during the incubation period and that the intercalation data may correspond to the aqua dication $[(\eta^6\text{-}C_6Me_6)Ru(dppz)(H_2O)]^{2+}$. A similar line of reasoning applies to the dpq complex **3**, whose $\Delta T_m$ value of 14 °C is close to that of 12 °C recorded for the dications of **6**. The higher $K_b$ value for complex **7** in comparison to **4** may be due to additional hydrogen bonding involving the thiourea ligands.

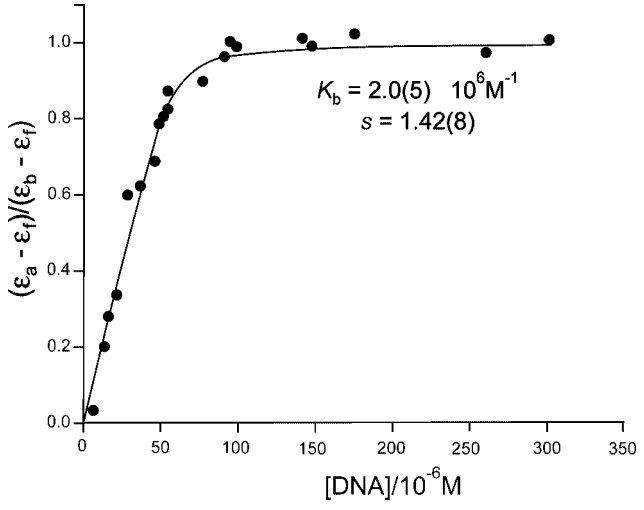


Figure 10. Best least-squares fit to the model of Bard and Thorp[34,35] for the UV/Vis titration data complex **4** with CT DNA.

### Cytotoxicity Studies

Table 3 lists the in vitro cytotoxicity of selected $[(\eta^6\text{-}C_6Me_6)Ru^{II}]$ and $[(\eta^5\text{-}C_5Me_5)Ir^{III}]$ complexes against selected human cancer cell lines MCF-7 (breast cancer) and HT-29 (colon cancer). It is apparent for the $[(\eta^6\text{-}C_6Me_6)\text{-}Ru^{II}]$ chloro complexes **3**–**5** that their cytotoxicity is directly correlated to the surface area of the polypyridyl ligand. The $IC_{50}$ values vary in the following order: dppn < dppz < dpq. A similar partial trend (dppn < dppz) can be discerned for the $IC_{50}$ values of the thiourea complexes **7** and **8** towards the HT-29 cell line and to a lesser extent towards MCF-7. Comparison of the observed cytotoxicities for the monocationic and dicationic dppn complexes **5** and **8** suggests that the overall cation charge may also play a role.

On taking our DNA binding studies into account, a number of ways may be proposed in which the polypyridyl ligand could influence the cytotoxicity of this class of compound:

(1) Extending the size of the polypyridyl ligand will confer lipophilic character to the complexes and thereby enhance their uptake into cells. A lower cation charge should likewise favour increased cellular uptake.

(2) Complex recognition and initial kinetically favoured intercalation into the DNA double helix will likewise be enhanced by an increase in the surface area and length of the polypyridyl ligand.

(3) When initial intercalation is followed by substitution of ligand L (or $H_2O$ if aquation has previously taken place), the size of the polypyridyl ligand may influence the degree of distortion of the B DNA conformation caused by coordinative M–N (nucleobase) binding (M = Ru, Ir) or by surface binding.

Inspection of Table 3 indicates that the MCF-7 $IC_{50}$ values for the dppz complexes $[(\eta^6\text{-}C_6Me_6)RuCl(dppz)]^+$ (**4**), $[(\eta^6\text{-}C_6Me_6)Ru(dppz)\{(H_2N)_2CS\}]^{2+}$ (**7**) and $[(\eta^5\text{-}C_5Me_5)\text{-}IrCl(dppz)]^+$ are effectively independent of the nature of the metal or the ligand L. Whereas both **4** and **7** exhibit stable side-on intercalative binding into DNA, relatively rapid Ir–N (nucleobase) coordination is observed for the $(\eta^5\text{-}C_5Me_5)\text{-}Ir^{III}$ complex following initial intercalation.[31] These observations suggest that cell uptake and kinetically favoured DNA intercalation as a rapid recognition process may play the key roles in determining the potency of such organometallic polypyridyl complexes. It is interesting to note, in this respect, that compounds of the type $[(\eta^6\text{-arene})RuCl(en)]^+$ containing polycyclic aromatic coligands have been found to be more potent than the analogous $\eta^6$-benzene or $\eta^6$-cymene complexes.[15,23] In striking contrast to such ($\eta^6$-ar-

 © 2007 Wiley-VCH Verlag GmbH & Co. KGaA, Weinheim 

Table 3. $IC_{50}$ values (μM)[a] for organometallic polypyridyl (pp) complexes of the types $[(\eta^6\text{-}C_6Me_6)RuL(pp)]^{n+}$ and $[(\eta^6\text{-}C_5Me_5)IrL(pp)]^{n+}$ [L = Cl, $n$ = 1; L = $(NH_2)_2$ CS, $n$ = 2].

| Complex | Arene | N,N′-Chelating ligand | L | MCF-7 $IC_{50}$ | HT-29 $IC_{50}$ |
|---|---|---|---|---|---|
| (i) $Ru^{II}$ complexes | | | | | |
| 3 | $C_6Me_6$ | dpq | Cl | 11.1 (1.0) | 30.3 (5.6) |
| 4 | $C_6Me_6$ | dppz | Cl | 2.1 (0.6) | 2.5 (0.6) |
| 5 | $C_6Me_6$ | dppn | Cl | 0.13 (0.02) | 0.4 (0.1) |
| 7 | $C_6Me_6$ | dppz | $(NH_2)_2$ CS | 2.5 (0.1) | 6.7 (1.2) |
| 8 | $C_6Me_6$ | dppn | $(NH_2)_2$ CS | 2.1 (0.1) | 1.4 (0.4) |
| (ii) $Ir^{III}$ complexes | | | | | |
| | $C_5Me_5$ | en[37a] | Cl | > 100 | |
| | $C_5Me_5$ | phen[37b] | Cl | > 100 | |
| | $C_5Me_5$ | dppz[31] | Cl | 2.3 (0.4) | 7.4 (0.9) |
| | $C_5Me_5$ | dppn[31] | $(NMe_2)_2$CS | 0.17 (0.02) | 0.41 (0.16) |
| (iii) | Cisplatin | | | 2.0 (0.3) | 7.0 (2.0) |

[a] Towards the human cancer cell lines MCF-7 (breast cancer) and HT-29 (colon cancer); the values between brackets represent the standard errors.

ene)$Ru^{II}$ compounds, the $IC_{50}$ values for the polypyridyl complexes of Table 3 appear, however, to be independent of the lability of the M–L bond. The low $IC_{50}$ values for the complex $[(\eta^5\text{-}C_5Me_5)Ir\{(NMe_2)CS\}(dppn)](CF_3SO_3)_2$[31] in comparison to **8** may result from its increased lipophilicity owing to the presence of $(NMe_2)_2CS$ ligands rather than thiourea.

These structure–activity relations suggest that initial DNA recognition and intercalation[38] rather than kinetically controlled coordinative Ru–N(DNA) binding could be of central importance in determining the cytotoxicity of organometallic polypyridyl complexes. It is, therefore, of interest to compare our results with those recently obtained for other metallointercalators. Like the dppz complexes of Table 3, $[Pt(4\text{-}Bu\text{-}ppy)(dppz)](CF_3SO_3)$ is a potent cytotoxic agent and exhibits $IC_{50}$ values some 10 and 40 times lower than cisplatin towards the human cell lines KB-3–1 and KB-V1.[39] In contrast, the dirhodium(II) complexes *cis*-$[Rh_2(\mu\text{-}O_2CCH_3)_2(pp)(O_2CCH_3\text{-}\kappa O)(CH_3OH\text{-}\kappa O)]^+$ (pp = dppz,dppn) are about 4 to 7 times less cytotoxic towards Hs-27 human skin cells than the parent paddlewheel compound *cis*-$[Rh_2(\mu\text{-}O_2CCH_3)_4]$.[40,41] The structure-activity studies on these and other dirhodium complexes are of particular relevance for the present investigation because their $IC_{50}$ values were shown to be related to the lability of the equatorial ligands in the $Rh_2$ core rather than to the size of the polypyridyl ligand.

## Cellular Uptake

In order to evaluate the influence of the cellular uptake on the results of the cytotoxicity experiments we quantified the ruthenium concentration in tumour cells exposed to **3**–**5**, **7** and **8** by atomic absorption spectroscopy. On the basis of the data depicted in Figure 11, it can be concluded that the Ru uptake increases dramatically in the order dpq < dppz < dppn and is much higher for monocationic than for dicationic species with the same polypyridyl ligand, which is in good agreement with the results from the cytotoxicity studies. Accordingly, the highest uptakes of 906.7(1.5) and 1054.7(94.5) ng Ru/mg protein were observed for the monocationic dppn compound **5** with MCF-7 and HT-29 cells, respectively. The dicationic dppn complex **8** exhibited significantly lower cellular ruthenium levels, which were even lower than those found for the monocationic dppz complex **4**. Incubation with the dicationic dppz complex **7** led to decreased cellular ruthenium concentrations in comparison to dppn complex **8** and the monocationic dpq complex **3** was accumulated at the lowest levels with values of only 1.1(1.1) and 11.8(8.5) ng Ru/mg protein being recorded for the cell lines MCF-7 and HT-29. The increase in cellular uptake efficiency with increasing lipophilicity of the ligands is more pronounced for the monocationic series of complexes (**3** << **4** << **5**) than for the dicationic compounds (**7** < **8**). It is apparent that ligand hydrophobicity outweighs the influence of the number of positive charges.

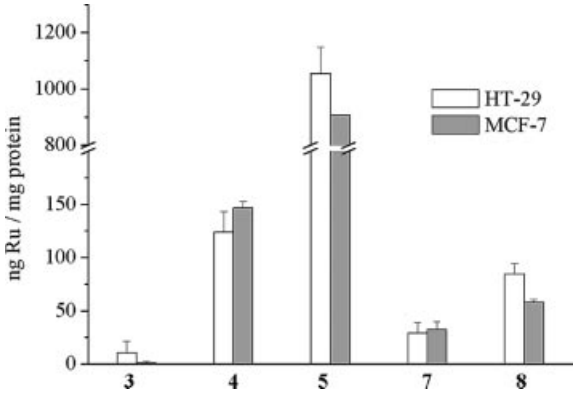


Figure 11. Cellular ruthenium levels in HT-29 and MCF-7 tumour cells after exposure to 10 μM of the complexes for 4 h ($n$ = 2). In some cases the error bars are hidden behind the columns.

The outstanding result is the extraordinarily high uptake of dppn complex **5** which is approximately one order of magnitude higher than the average uptake of the other Ru complexes. Interestingly, this is in good agreement with the significantly lower $IC_{50}$ values of **5** compared to **3**, **4**, **7** and

 © 2007 Wiley-VCH Verlag GmbH & Co. KGaA, Weinheim 

the second dppn complex **8**. Additional experiments using only 1.0 μM instead of 10 μM solutions of **5** resulted in ruthenium levels [59.1(5.5) ng Ru/mg protein in MCF-7 and 74.5(10.2) ng Ru/mg protein in HT-29 cells] in the range observed for the other compounds at 10 μM. In contrast, the ruthenium content of the samples was found to be below the limit of detection on exposure to 1.0 μM solutions **3**, **4**, **7** and **8**. As compound **3** was barely detectable at 10 μM concentration a higher dosage for this compound was applied for sake of comparison. As expected 100 μM solutions of **3** afforded clearly detectable cellular ruthenium levels of 219.3(80.0) ng Ru/mg protein in MCF-7 and 287.9(43.1) ng Ru/mg protein in HT-29 cells.

Comparison of the cytotoxicity data of Table 3 and the cellular uptake data of Figure 11 indicates that the antiproliferative effects of the complexes were slightly more pronounced in MCF-7 cells than in HT-29 cells (with the exception of **8**) but that the cellular uptake was similar in both tumour cell types. On the basis of distinct cellular parameters (such as cell volume and cell protein content) of MCF-7[42] and HT-29[43] cells, the molar cellular ruthenium concentrations can be estimated from the observed ng/mg values. According to this procedure, 1.0 ng ruthenium per 1.0 mg cell protein correspond to a complex concentration of 1.1 μM in MCF-7 but to 2.0 μM in HT-29 cells. Therefore, the effective molar ruthenium concentrations are higher in HT-29 cells than in MCF-7 cells. Other differences between the two tumour cell types (e.g. the generally faster growth of HT-29 cells) or the intracellular distribution of the complexes will probably play an important role in determining the observed antiproliferative effects. MCF-7 cells are also more sensitive towards the platinum complex cisplatin than HT-29 cells. A decreased activity for cisplatin in colon cancer cells is an established fact, for which resistance phenomena have been made responsible.[44] The uptake of ruthenium indazole complexes such as *trans*-(Hind)[$RuCl_4$-$(ind)_2$] (ind = indazole), KP1019, into HT-29 cells has been reported.[45] In these experiments, a 30 min incubation with 100 μM of the agents resulted in up to 120–160 ng ruthenium being observed per $10^6$ cells. Based on the fact that 1.0 mg cell protein of HT-29 cells correspond to approximately $5.6 \times 10^6$ cells,[43] the values for the indazole complexes are within the same order of magnitude to those reported in this study, e.g. 188 ng Ru/$10^6$ cells for 10 μM concentrations of **5** or 51.4 ng Ru/$10^6$ cells for 100 μM concentrations of **3** in HT-29 cells. It is worth noting, however, that the uptake of **5** was recorded for a tenfold lower complex concentration in comparison to KP1019.

## Conclusions

We have demonstrated that the DNA binding of polypyridyl organoruthenium complexes of the types [($\eta^6$-$C_6Me_6$)-RuCl(pp)]($CF_3SO_3$) and [($\eta^6$-$C_6Me_6$)Ru{$(NH_2)_2CS$}(pp)]-($CF_3SO_3$)$_2$ is governed by both the size of the polypyridyl ligand and the lability of the Ru–L bond [L = Cl, $(NH_2)_2$-CS]. Whereas stable intercalative binding is observed for the dpq complexes **3**, **4** (L = Cl), **6** and **7** [L = $(NH_2)_2CS$], substitution of the chloride ligand leads to preferred Ru–N (DNA) coordinative binding for both smaller (**1**, phen; **2**, tap) and larger (**5**, dppn) polypyridyl ligands. The significant increase in $\Delta T_m$ and DNA viscosity on going from dpq in **3** to dppz in **4** suggest that the latter ligand may offer a close to optimum size for side-on intercalation. In contrast, the cytotoxicity of such compounds appears to be governed mainly by the size of the polypyridyl ligands with $IC_{50}$ values varying in the following order dppn < dppz < dpq. The cellular uptake increases in the order dpq < dppz < dppn and $n = 2 < n = 1$ ($n$ = cation charge) and is in good agreement with the observed $IC_{50}$ values. To the best of our knowledge [($\eta^5$-$C_5Me_5$)IrCl(dppz)]($CF_3SO_3$) and [($\eta^5$-$C_5Me_5$)Ir{$(NMe_2)_2CS$}(dppn)]($CF_3SO_3$)$_2$ are the first organoiridium(III) complexes with proven in vitro cytotoxicity towards cancer cell lines.

## Experimental Section

**General:** UV/Vis spectra were recorded with an Analytik Jena SPECORD 200 spectrometer and CD spectra with a Jasco J-715 instrument in the range 220–400 nm for 1:10 complex/[DNA] mixtures [complex = 20 μM, DNA concentration in M(nucleotide) = 200 μM] in a 10 mM phosphate buffer at pH 7.2. LSIMS spectra (LSIMS = liquid secondary ion mass spectrometry) were registered for the mass range $m/z < 3000$ with a Fisons VG Autospec employing a caesium ion gun (voltage 17 kV) and 3-nitrobenzyl alcohol as the liquid matrix. A Bruker DRX 400 was employed for the registration of $^1H$ and $^{13}C$ NMR spectra with chemical shifts reported as $\delta$ values relative to the signal of the deuterated solvent. $^{13}C$ NMR signals for the $CF_3SO_3$ anions of **1**–**8** were observed in the range $\delta$ = 121.8–122.8 ppm (q) and are not listed for individual complexes. Elemental analyses were performed on a Vario EL of Elementar Analysensysteme GmbH. $RuCl_3 \cdot xH_2O$ and $Ag(CF_3SO_3)$ was obtained from Chempur, 1,10-phenanthroline from J. T. Baker, hexamethylbenzene, thiourea and $(Me_2N)_2CS$ from Acros, and calf thymus DNA (CT DNA) from Sigma. The starting compounds [{($\eta^6$-$C_6Me_6$)RuCl(μ-Cl)}$_2$],[46] tap,[47] dpq,[48] dppz[49] and dppn[11] were prepared in accordance with literature procedures. All solvents were analytical reagents grade (J. T. Baker) and were dried and distilled before use. [($\eta^5$-$C_5Me_5$)IrCl(pp)]($CF_3SO_3$) (pp = phen, dppz) and [($\eta^5$-$C_5Me_5$)IrCl(en)]($CF_3SO_3$) were prepared described previously.[31,37]

**[($\eta^6$-$C_6Me_6$)RuCl(phen)]($CF_3SO_3$) (1):** Two equivalents of $Ag(CF_3SO_3)$ (25.7 mg, 0.1 mmol) were added to [{($C_6Me_6$)-$RuCl_2$}$_2$] (34.0 mg, 0.05 mmol) and stirred in the dark for 0.5 h in 10 mL acetone. Filtration of the resulting AgCl precipitate and subsequent solvent removal under vacuum afforded [($C_6Me_6$)Ru-Cl(acetone)$_2$]($CF_3SO_3$), which was stirred with the ligand phen (18.0 mg, 0.1 mmol) in $CH_3OH/CH_2Cl_2$ (1:1, 10 mL) at 55 °C for 2 h. Following volume reduction of the resulting clear solution to 2 mL and addition of $CH_3OH$ (3 mL), the product was precipitated with diethyl ether, washed and dried in vacuo. Yield: 62% (39 mg). $C_{25}H_{26}ClF_3N_2O_3RuS$ (628.1): calcd. C 47.8, H 4.2, N 4.4, S 5.1; found C 47.4, H 4.4, N 4.3, S 5.2. LSIMS: $m/z$ (%) = 593 (2) [M – Cl]$^+$, 479 (100) [M – OTf]$^+$, 444 (10) [M – Cl – OTf]$^+$. $^1H$ NMR (400 MHz, [D$_6$]DMSO, 25 °C): $\delta$ = 2.33 (s, 18 H, C$H_3$ $C_6Me_6$), 8.16 (m, 2 H, phen), 8.23 (s, 2 H, phen), 8.80 (dd, 2 H, phen), 9.41 (dd, 2 H, phen) ppm. $^{13}C$ NMR ([D$_6$]DMSO): $\delta$ = 15.8 (C$CH_3$

 © 2007 Wiley-VCH Verlag GmbH & Co. KGaA, Weinheim 

$C_6Me_6$), 97.2 ($CCH_3$ $C_6Me_6$), 127.6, 128.8, 131.9, 139.7, 147.2, 154.8 (phen) ppm.

**[(η⁶-$C_6Me_6$)RuCl(tap)]($CF_3SO_3$) (2):** Preparation as for **1** with the ligand tap (18.2 mg, 0.1 mmol). Yield: 70% (44 mg). $C_{23}H_{26}ClF_3N_4O_3RuS$ (630.1): calcd. C 43.9, H 3.8, N 8.9, S 5.1; found C 43.6, H 3.8, N 8.9, S 5.1. LSIMS: *m/z* (%) = 631 (1) [M + H]$^+$, 595 (1) [M – Cl]$^+$, 481 (100) [M – OTf]$^+$, 446 (15) [M – Cl – OTf]$^+$. $^1$H NMR (400 MHz, [D$_6$]DMSO, 25 °C): $\delta$ = 2.31 (s, 18 H, $CH_3C_6Me_6$), 8.61 (s, 2 H, tap), 9.45 (d, 2 H, tap), 9.51 (d, 2 H, tap) ppm. $^{13}$C NMR ([D$_6$]DMSO): $\delta$ = 16.0 ($CCH_3$ $C_6Me_6$), 98.7 ($CCH_3$ $C_6Me_6$), 133.7, 146.9, 148.9, 150.9 (tap) ppm.

**[(η⁶-$C_6Me_6$)RuCl(dpq)]($CF_3SO_3$) (3):** Preparation as for **1** with the ligand dpq (23.2 mg, 0.1 mmol). Yield: 46% (31 mg). $C_{27}H_{26}ClF_3N_4O_3RuS$ (680.1): calcd. C 47.7, H 3.9, N 8.2, S 4.7; found C 47.3, H 3.9, N 8.2, S 4.4. LSIMS: *m/z* (%) = 635 (1) [M – Cl]$^+$, 531 (100) [M – OTf]$^+$, 496 (15) [M – Cl – OTf]$^+$. $^1$H NMR (400 MHz, [D$_6$]DMSO, 25 °C): $\delta$ = 2.13 (s, 18 H, $CH_3$ $C_6Me_6$), 8.30 (m, 2 H, dpq), 9.33 (s, 2 H, dpq), 9.46 (d, 2 H, dpq), 9.61 (d, 2 H, dpq) ppm. $^{13}$C NMR ([D$_6$]DMSO): $\delta$ = 15.2 ($CCH_3$ $C_6Me_6$), 95.5 ($CCH_3$ $C_6Me_6$), 127.6, 128.5, 134.7, 138.9, 146.7, 146.9, 155.0 (dpq) ppm.

**[(η⁶-$C_6Me_6$)RuCl(dppz)]($CF_3SO_3$) (4):** Preparation as for **1** with the ligand dppz (28.2 mg, 0.1 mmol). Yield: 45% (33 mg). $C_{31}H_{28}ClF_3N_4O_3RuS$ (730.2): calcd. C 51.0, H 3.9, N 7.7, S 4.4; found C 50.6, H 3.8, N 7.3, S 4.2. LSIMS: *m/z* (%) = 581 (100) [M – OTf]$^+$, 545 (15) [M – Cl – OTf]$^+$. $^1$H NMR (400 MHz, [D$_6$]-DMSO, 25 °C): $\delta$ = 2.18 (s, 18 H, $CH_3$ $C_6Me_6$), 8.19 (m, 2 H, dppz), 8.34 (m, 2 H, dppz) 8.49 (m, 2 H, dppz) 9.46 (dd, 2 H, dppz), 9.71 (dd, 2 H, dppz) ppm. $^{13}$C NMR ([D$_6$]DMSO): $\delta$ = 17.0 ($CCH_3$ $C_6Me_6$), 97.4 ($CCH_3$ $C_6Me_6$), 128.9, 130.3, 130.5, 133.6, 136.1, 140.7, 143.0, 149.3, 156.2 (dppz) ppm.

**[(η⁶-$C_6Me_6$)RuCl(dppn)]($CF_3SO_3$) (5):** Preparation as for **1** with the ligand dppn (33.2 mg, 0.1 mmol). Yield: 74% (58 mg). $C_{35}H_{30}ClF_3N_4O_3RuS$ (780.2): calcd. C 53.9, H 3.9, N 7.2, S 4.1; found C 53.9, H 3.8, N 7.1, S 4.2. LSIMS: *m/z* (%) = 631 (100) [M – OTf]$^+$, 596 (10) [M – Cl – OTf]$^+$. $^1$H NMR (400 MHz, [D$_6$]DMSO, 25 °C): $\delta$ = 2.14 (s, 18 H, $CH_3$ $C_6Me_6$), 7.73 (m, 2 H, dppn), 8.29 (m, 2 H, dppn), 8.39 (m, 2 H, dppn), 9.16 (s, 2 H, dppn), 9.40 (dd, 2 H, dppn), 9.64 (dd, 2 H, dppn) ppm. $^{13}$C NMR ([D$_6$]DMSO): $\delta$ = 15.2 ($CCH_3$ $C_6Me_6$), 95.5 ($CCH_3$ $C_6Me_6$), 127.87, 127.89, 127.91, 128.5, 129.6, 134.5, 135.0, 137.8, 140.0, 148.8, 155.1 (dppn) ppm.

**[(η⁶-$C_6Me_6$)Ru(dpq){$(NH_2)_2CS$}]($CF_3SO_3$)$_2$ (6):** An equivalent of $Ag(CF_3SO_3)$ (25.7 mg, 0.1 mmol) was added to a solution of [{($C_6Me_6$)$RuCl_2$}$_2$] (34.0 mg, 0.05 mmol) in 10 mL acetone and stirred in the dark for 0.5 h. Filtration of the precipitate AgCl and subsequent solvent removal under vacuum afforded [($C_6Me_6$)Ru-Cl(acetone)$_2$] ($CF_3SO_3$), which was stirred with the ligand dpq (23 mg, 0.1 mmol) at 55 °C for 2 h. Following solvent removal, the resulting residue of complex 3 was dissolved in 10 mL acetone and treated with a further equivalent of $Ag(CF_3SO_3)$. After stirring in the dark for 0.5 h, filtration of AgCl and solvent removal, the remaining solid was dissolved in 10 mL of a 1:1 $CH_3OH/CH_2Cl_2$ mixture and treated with thiourea (7.6 mg, 0.1 mmol). The solution was then refluxed for 12 h and subsequently reduced in volume to 2 mL. Following addition of 2 mL of $CH_3OH$, the product was precipitated by addition of diethyl ether, washed and dried in vacuo. Yield: 44% (38 mg). $C_{29}H_{30}F_6N_6O_6RuS_3$ (869.8): calcd. C 40.0, H 3.5, N 9.7, S 11.1; found C 39.6, H 3.2, N 9.5, S 10.9. LSIMS: *m/z* (%) = 722 (4) [M – OTf]$^+$, 645 (45) [M – OTf – thiourea]$^+$. $^1$H NMR (400 MHz, [D$_6$]DMSO, 25 °C): $\delta$ = 2.10 (s, 18 H, $CH_3$ $C_6Me_6$), 7.1 (br., 4 H, thiourea), 8.32 (m, 2 H, dpq), 9.24 (d, 2 H, dpq), 9.37 (s, 2 H, dpq), 9.61 (d, 2 H, dpq) ppm. $^{13}$C NMR ([D$_6$]DMSO): $\delta$ = 15.4 ($CCH_3$ $C_6Me_6$), 97.7 ($CCH_3$ $C_6Me_6$), 128.4, 129.1, 134.9, 139.4, 147.0, 147.3, 156.0 (dpq), 174.4 (thiourea) ppm.

**[(η⁶-$C_6Me_6$)Ru(dppz){$(NH_2)_2CS$}]($CF_3SO_3$)$_2$ (7):** Preparation as for **6** with the ligand dppz (29.1 mg, 0.1 mmol). Yield: 63% (58 mg). $C_{33}H_{32}F_6N_6O_6RuS_3$ (919.9): calcd. C 43.1, H 3.5, N 9.1, S 10.5; found C 42.9, H 3.8, N 8.8, S 10.2. LSIMS: *m/z* (%) = 943 (2) [M + Na]$^+$, 771 (12) [M – OTf]$^+$, 695 (7) [M – OTf – thiourea]$^+$, 621 (10) [M – 2OTf]$^+$, 546 (35) [M – 2OTf – thiourea]$^+$. $^1$H NMR (400 MHz, [D$_6$]DMSO, 25 °C): $\delta$ = 2.12 (s, 18 H, $CH_3$ $C_6Me_6$), 7.1 (br., 4 H, thiourea), 8.21 (m, 2 H, dppz), 8.32 (m, 2 H, dppz) ppm. 8.53 (m, 2 H, dppz), 9.23 (d, 2 H, dppz), 9.71 (d, 2 H, dppz). $^{13}$C NMR ([D$_6$]DMSO): $\delta$ = 15.7 ($CCH_3$), 97.8 ($CCH_3$), 128.6, 129.7, 129.8, 133.3, 135.2, 140.0, 142.2, 148.5, 156.1 (dppz), 174.4 (thiourea) ppm.

**[(η⁶-$C_6Me_6$)Ru(dppn)] {$(NH_2)_2CS$}($CF_3SO_3$)$_2$ (8):** Preparation as for **6** with the ligand dppn (32.0 mg, 0.1 mmol). Yield: 47% (46 mg). $C_{37}H_{34}F_6N_6O_6RuS_3$ (970.0): calcd. C 45.8, H 3.5, N 8.7, S 9.9; found C 46.2, H 3.3, N 8.5, S 10.1. LSIMS: *m/z* (%) = 821 (4) [M – OTf]$^+$, 744 (3) [M – 2OTf – thiourea]$^+$ [M – OTf – thiourea]$^+$ 596 (7). $^1$H NMR (400 MHz, [D$_6$]DMSO, 25 °C): $\delta$ = 2.13 (s, 18 H, $CH_3$ $C_6Me_6$), 7.2 (br., 4 H, thiourea), 7.82 (m, 2 H, dppn), 8.31 (m, 2 H, dppn), 8.48 (m, 2 H, dppn) 9.19 (m, 2 H, dppn), 9.25 (s, 2 H, dppn), 9.69 (m, 2 H, dppn) ppm. $^{13}$C NMR ([D$_6$]DMSO): $\delta$ = 15.7 ($CCH_3$), 97.8 ($CCH_3$), 128.3, 128.5, 128.8, 129.0, 130.1, 135.0, 135.3, 138.2, 141.1, 149.0, 156.1 (dppn) 174.4 (thiourea) ppm.

**X-ray Structural Analysis of 1 and 3:** Crystal and refinement data are summarised in Table 1. Intensity data were collected with an Oxford Diffraction Sapphire-CCD diffractometer at 293 K (**1**) and 109 K (**3**) using 1° $\omega$ scans and Mo-$K_\alpha$ radiation ($\lambda$ = 0.71073 Å). The data were corrected for absorption by the Gauss method and solved by direct methods with SHELX97. Refinement against $F^2$ was performed by SHELXL97[50] with anisotropic temperature factors for non-hydrogen atoms and protons at geometrically calculated positions as riding atoms.

CCDC-635848 to -635849 contain the supplementary crystallographic data for **1** and **3** and may be obtained free of charge at www.ccdc.cam.ac.uk/conts/retrieving.html or from the Cambridge Crystallographic Data Centre, 12 Union Road, Cambridge CB2 1EZ, UK; Fax: +44-1223/336-033; E-mail: deposit@ccdc.cam.ac.uk.

**DNA Binding Studies of 1–8:** The thermal denaturation temperature $T_m$ of 1:10 complex/DNA mixtures [DNA concentration = M(nucleotide)] were determined in a 10 mM phosphate buffer at pH = 7.2. Melting curves were recorded at 2 °C steps for the wavelength 260 nm with an Analytik Jena SPECORD 200 spectrometer equipped with a Peltier temperature controller. $T_m$ values were calculated by determining the midpoints of melting curves from the first-order derivatives. The experimental $\Delta T_m$ values of Table 2 are estimated to be accurate within ±1 °C. Concentrations of CT DNA were determined spectrophotometrically using the molar extinction coefficient $\varepsilon_{260}$ = 6600 M$^{-1}$ cm$^{-1}$.[51]

All electronic absorption titrations were performed at 293 K. After sonication, buffered solutions of CT DNA gave a UV absorbance ration $A_{260}/A_{280}$ of ca. 1.90, indicating that the DNA was sufficiently free of proton.[52] 20 μM solutions of the individual metal complexes were treated with DNA over a range of molarities 20 to 300 μM (nucleotide). All UV/Vis spectra were measured after equilibration, i.e. no further change in the monitored absorbance. Titration curves were constructed from the fractional change in absorbance as a function of DNA concentration according to the

 © 2007 Wiley-VCH Verlag GmbH & Co. KGaA, Weinheim 

model of Bard and Thorp[35,36] for non-cooperative non specific binding for one type of discrete DNA binding site.

Equation (1) was used to fit the absorption data by least-squares refinement of binding constants ($K_b$) and site sizes ($s$) with $b = 1 + K_bC_t + K_b$ [DNA]/2$s$, where $\varepsilon_a$ is the extinction coefficient of the complex in the absence of DNA, $\varepsilon_b$ the extinction coefficient of the complex when fully bound to DNA (i.e. no absorption change on further addition of DNA), $K_b$ the equilibrium constant in $M^{-1}$, $C_t$ the total metal complex concentration, [DNA] the DNA concentration in M(nucleotide) and $s$ the binding site size. Values of $\varepsilon_b$ were obtained by extrapolation from the $y$ intercept of plots of $\varepsilon_a/\varepsilon_f$ vs. 1/[DNA]. The $K_b$ and $s$ values of Table 2 are those for the best least-squares fits to the individual UV/Vis titration curves using the program ORIGIN 6.0.

$$(\varepsilon_a - \varepsilon_f)/(\varepsilon_b - \varepsilon_f) = (b - \{b^2 - 2K^2_bC_t[\text{DNA}]/s\}^{1/2})/2K_bC_t \quad (1)$$

**Viscosity Measurements:** Viscosities for complex/sonicated DNA mixtures were determined using a Cannon–Ubbelhode Semi-micro dilution viscometer (Series No 75, Cannon Instrument Co) held at a constant temperature of 25 °C in a water bath. The viscometer contained 2 mL of 0.4 mM sonicated DNA solution in a 10 mM phosphate buffer (pH = 7.2). 0.2 mM complex solutions also containing sonicated DNA at the same concentration as in the viscometer (0.4 mM) were added in increments of 100 μL from a micropipet. Solutions were passed through filters to remove particulate material prior to use. Reduced viscosities $\eta_O$ were calculated by literature methods[29] and plotted as $\ln(\eta/\eta_O)$ ($\eta_O$ = reduced viscosity of the DNA solution in the absence of complex) against $\ln(1+r)$ for rod-like DNA (approximately 600 base pairs).

**Cell Culture:** MCF-7 breast cancer and HT-29 human colon carcinoma cells were maintained in 10% (v/v) fetal calf serum containing cell culture medium (minimum essential medium eagle supplemented with 2.2 g $NaHCO_3$, 110 mg/L sodium pyruvate and 50 mg/L gentamicin sulfate adjusted to pH 7.4) at 37 °C: 5% $CO_2$ and passaged twice a week according to standard procedures.

**Cytotoxicity Measurements:** The antiproliferative effects of the compounds were determined following an established procedure.[53] In short, cells were suspended in cell culture medium (HT-29: 2850 cells/mL, MCF-7: 10000 cells/mL), and 100 μL aliquots thereof were plated in 96 well plates and incubated at 37 °C: 5% $CO_2$ for 48 h (HT-29) or 72 h (MCF-7). Stock solutions of the compounds in DMSO were freshly prepared and diluted with cell culture medium to the desired concentrations (final DMSO concentration: 0.1% v/v). The medium in the plates was replaced with medium containing the compounds in graded concentrations (six replicates). After further incubation for 72 h (HT-29) or 96 h (MCF-7) the cell biomass was determined by crystal violet staining and the $IC_{50}$ values were determined as those concentrations causing 50% inhibition of cell proliferation. Results were calculated from 2–3 independent experiments.

**Cellular Uptake:** For cellular uptake studies, cells were grown until at least 70% confluency in 175-$cm^2$ cell culture flasks. Stock solutions of the complexes in DMSO were freshly prepared and diluted with cell culture medium to the desired concentrations (final DMSO concentration: 0.1% v/v, final complex concentrations: 1.0 and 10 μM). The cell culture medium of the cell culture flasks was replaced with 10 mL of the cell culture medium solutions containing the compounds and the flasks were incubated at 37 °C:5% $CO_2$ for 4 h. The culture medium was removed, the cell layer washed with 10 mL PBS (phosphate buffered saline pH 7.4), treated with 2–3 mL trypsin solution (0.05% trypsin, 0.02% EDTA in PBS) and incubated for 2 min at 37 °C:5% $CO_2$ after removal of the trypsin solution. Cells were resuspended in 10 mL PBS and isolated by centrifugation (room temperature, 2000 g, 5 min). The cell pellets were resuspended in 1.0 mL twice distilled water, lysed by use of a sonotrode and appropriately diluted with twice distilled water. The ruthenium content of the samples was determined by AAS (see below) and the protein content by the Bradford method. Results were calculated as ng ruthenium per mg cellular protein from the data obtained in 2 independent experiments.

**AAS Measurements:** A Vario 6 graphite furnace atomic absorption spectrometer (AnalytikJena AG) was used for ruthenium quantification. Ru was detected at a wavelength of 349.9 nm with a bandpass of 1.2 nm. A deuterium lamp was used for background correction. Standards for calibration purposes were prepared as aqueous dilutions of a commercially available ruthenium standard stock solution [Acros, 1 mg/mL ruthenium in HCl (5%)]. To each 160 μL sample or standard solution 20 μL Triton X-100 (1%) and 40 μL HCl (1 N) were added. A volume of 25 μL thereof was injected into the graphite tubes. Drying, pyrolysis and atomization in the graphite furnace was performed according to the conditions listed in Table 4. The detection limit for the method was 4.8 μg Ru $L^{-1}$. The mean AUC (area under curve) absorptions of duplicate injections were used throughout the study.

Table 4. Graphite furnace program for AAS measurements.

| Step | Temperature [°C] | Ramp [°C/s] | Hold [s] |
|---|---|---|---|
| drying | 90 | 10 | 40 |
| drying | 105 | 7 | 30 |
| drying | 120 | 15 | 20 |
| drying | 500 | 50 | 30 |
| pyrolysis | 900 | 200 | 20 |
| AZ (zeroing) | 900 | 0 | 6 |
| atomisation | 2200 | maximum | 4 |
| tube cleaning | 2600 | 1000 | 6 |

## Acknowledgments

Financial support of this work in Bochum and Berlin by the Deutsche Forschungsgemeinschaft (DFG) within the research group FOR 630 "Biological function of Organometallic Compounds" is gratefully acknowledged. We are also grateful to Heike Scheffler and Manuela Winter for technical support.

[1] B. Nordén, P. Lincoln, B. Åkerman, E. Tuite, in *Metal Ions in Biological Systems* (Eds.: A. Sigel, H. Sigel) Marcel Dekker, New York, **1996**, *33*, 177.
[2] K. E. Erkkila, D. T. Odom, J. K. Barton, *Chem. Rev.* **1999**, *99*, 2777–2795.
[3] C. Metcalfe, J. A. Thomas, *Chem. Soc. Rev.* **2003**, *32*, 215–224.
[4] D. Herebian, W. S. Sheldrick, *J. Chem. Soc., Dalton Trans.* **2002**, 966–974.
[5] R. Stodt, S. Gençaslan, A. Frodl, C. Schmidt, W. S. Sheldrick, *Inorg. Chim. Acta* **2003**, *355*, 242–253.
[6] S. Gençaslan, W. S. Sheldrick, *Eur. J. Inorg. Chem.* **2005**, 3840–3849.
[7] A. Frodl, D. Herebian, W. S. Sheldrick, *J. Chem. Soc., Dalton Trans.* **2002**, 3664–3673.
[8] T. K. Schoch, J. L. Hubbard, C. R. Zoch, G.-B. Yi, M. Sørlie, *Inorg. Chem.* **1996**, *35*, 4383.
[9] J. Sartorius, H.-J. Schneider, *J. Chem. Soc., Perkin Trans. 2* **1997**, *2*, 2319–2327.
[10] J. Canivet, L. Karmazin-Brelot, G. Süss-Fink, *J. Organomet. Chem.* **2005**, *690*, 3202 –3211.

 © 2007 Wiley-VCH Verlag GmbH & Co. KGaA, Weinheim 

[11] V. W.-W. Yam, K. K.-W. Lo, K.-K. Cheung, R. Y.-C. Kong, *J. Chem. Soc., Chem. Commun.* **1995**, 1191–1193.
[12] V. W.-W. Yam, K. K.-W. Lo, K.-K. Cheung, R. Y.-C. Kong, *J. Chem. Soc., Dalton Trans.* **1997**, 2067–2072.
[13] K. K.-W. Lo, R. Y.-C. Kong, *Organometallics* **2004**, *23*, 3062–3070.
[14] M. Cusumano, M. L. Di Pietro, A. Giannetto, P. A. Vainiglia, *J. Inorg. Biochem.* **2005**, *99*, 560–565.
[15] Y. W. Yan, M. Melchart, A. Habtemarian, P. J. Sadler, *Chem. Commun.* **2005**, 4764 –4776.
[16] P. J. Dyson, G. Save, *Dalton Trans.* **2006**, 1929–1933.
[17] W. S. Sheldrick, S. Heeb, *Inorg. Chim. Acta* **1990**, *168*, 93–100; S. Heeb, Dissertation, University of Kaiserslautern **1990**, pp110–113.
[18] Y. N. Vashisht Gopal, D. Jayaraju, A. K. Kandapi, *Biochemistry* **1999**, *38*, 4382–4388.
[19] Y. N. Vashisht Gopal, N. Konura, A. K. Kandapi, *Arch. Biochem. Biophys.* **2002**, *401*, 53–62.
[20] L. A. Huxham, E. L. S. Cheu, B. O. Patrick, B. R. James, *Inorg. Chim. Acta* **2003**, *352*, 238–246.
[21] C. S. Allardyce, P. J. Dyson, D. J. Ellis, S. L. Heath, *Chem. Commun.* **2001**, 1396 –1397.
[22] R. E. Morris, R. E. Aird, P. del S. Murdoch, H. M. Chen, J. Cummings, N. D. Hughes, S. Parsons, A. Parkin, G. Boyd, D. I. Jodrell, P. J. Sadler, *J. Med. Chem.* **2001**, *44*, 3616–3621.
[23] A. Habtemarian, M. Melchert, R. Fernandez, S. Parsons, I. D. H. Oswald, A. Prakin, F. P. A. Fabbiani, J. E. Davidson, A. Dawson, R. E. Aird, D. I. Jodrell, P. J. Sadler, *J. Med. Chem.* **2006**, *49*, 6858–6868.
[24] V. Brabec, V. Kleinwächter, J.-L. Butour, N. P. Johnson, *Biophys. Chem.* **1990**, *35*, 129–141.
[25] D. M. Gray, in: *Circular Dichroism and the Conformational Analysis of Biomolecules* (Ed.:G. D. Fasman), Plenum Press, New York. **1996**, 469–500.
[26] W. C. Johnson, in: *Circular Dichroism: Principles and Applications, 2nd Edition* (Eds.: N. Berova, K. Nakanishi, R. W. Woody), VCH Publishers, New York **2000**, 523–540.
[27] K. K.-W. Lo, C.-K. Chung, N. Zhu, *Chem. Eur. J.* **2006**, *12*, 1500–1512.
[28] L.-F. Tan, H. Chao, H. Li, Y.-J. Liu, B. Sun, W. Wei, L.-N. Ji, *J. Inorg. Biochem.* **2005**, *99*, 513–520.
[29] G. Cohen, H. Eisenberg, *Biopolymers* **1966**, *4*, 429–440.
[30] D. Suh, J. B. Chaires, *Bioorg. Med. Chem.* **1995**, *3*, 723–728.
[31] S. Schäfer, W. S. Sheldrick, *J. Organomet. Chem.* **2007**, *692*, 1300–1309.
[32] L. Dadci, H. Elias, U. Frey, A. Hörnig, U. Koelle, A. E. Merbach, H. Paulus, J. S. Schneider, *Inorg. Chem.* **1995**, *34*, 306–315.
[33] A. Raja, V. Rajendrian, P. Uma Masheswari, R. Balamunrugam, C. A. Kilner, M. A. Halcrow, M. Palaniandavar, *J. Inorg. Biochem.* **2005**, *99*, 1717–1732.
[34] B. Selvakumar, V. Rajendrian, P. Uma Mashesuari, H. Stoeckli-Evans, M. Palaniandavar, *J. Inorg. Biochem.* **2006**, *100*, 316–330.
[35] M. T. Carter, M. Rodriguez, A. J. Bard, *J. Am. Chem. Soc.* **1989**, *111*, 8901–8911.
[36] S. R. Smith, G. A. Neyhart, W. A. Karlsbeck, H. H. Thorp, *New J. Chem.* **1994**, *18*, 397–406.
[37] a) M. Scharwitz, T. van Almsick, W. S. Sheldrick, *Acta Crystallogr., Sect. E* **2007**, *63*, m1469–m1470; b) M. Scharwitz, S. Schäfer, T. van Almsick, W. S. Sheldrick, *Acta Crystallogr., Sect. E* **2007**, *63*, m1111–m1113.
[38] J. S. Ren, T. C. Jenkins, J. B. Chaires, *Biochemistry* **2000**, *39*, 8439–8447.
[39] C.-M. Che, M. Yang, K.-H. Wong, H.-L. Chan, W. Lam, *Chem. Eur. J.* **1999**, *5*, 3350 –33346.
[40] A. M. Angeles-Boza, P. M. Bradley, P. K.-L. Fu, S. E. Wicke, J. Bacsa, K. R. Dunbar, C. Turro, *Inorg. Chem.* **2004**, *43*, 8510–8519.
[41] A. M. Angeles-Boza, H. T. Chifotides, J. D. Aguirre, A. Chouai, P. K.-L. Fu, K. R. Dunbar, C. Turro, *J. Med. Chem.* **2006**, *49*, 6841–6847.
[42] R. Gust, B. Schnurr, R. Krauser, G. Bernhardt, M. Koch, B. Schmid, E. Hummel, H. Schoenenberger, *J. Cancer Res. Clin. Oncol.* **1998**, *124*, 585–597.
[43] I. Ott, H. Scheffler, R. Gust, *ChemMedChem* **2007**, *2*, 702–707.
[44] Z. H. Siddik, *Oncogene* **2003**, *22*, 7265–7279.
[45] S. Kapitza, M. Pongratz, M. A. Jakupec, P. Heffeter, W. Berger, L. Lackinger, B. K. Keppler, B. Marian, *J. Cancer Res. Clin. Oncol.* **2005**, *131*, 101–110.
[46] M. A. Bennett, T.-N. Huang, T. W. Matheson, A. K. Smith, *Inorg. Synth.* **1980**, *10*, 74–80.
[47] P. Crochet, B. Demerseman, C. Rocaboy, D. Schleyer, *Organometallics* **1996**, *15*, 3048–3061.
[48] J. G. Collins, A. D. Sleemann, J. R. Aldrich-Wright, I. Greguric, T. W. Hambley, *Inorg. Chem.* **1998**, *37*, 3133–3141.
[49] A. Delgadillo, P. Romo, A. M. Leiva, B. Loeb, *Helv. Chim. Acta* **2003**, *86*, 2110–2120.
[50] G. M. Sheldrick, *SHELXS97 and SHELXL97*, Göttingen, Germany, **1997**.
[51] H.-Q. Liu, T.-C. Cheung, S.-M. Peng, C.-M. Che, *J. Chem. Soc., Chem. Commun.* **1995**, 1787–1788.
[52] J. Marmur, *J. Mol. Biol.* **1961**, *3*, 208–218.
[53] I. Ott, K. Schmidt, B. Kircher, P. Schumacher, T. Wiglenda, R. Gust, *J. Med. Chem.* **2005**, *48*, 622–629.

Received: February 14, 2007
Published Online: May 10, 2007

 © 2007 Wiley-VCH Verlag GmbH & Co. KGaA, Weinheim 

DOI: 10.1002/ejic.200601096

# Mutual Influence of Spacer Length and Noncoordinating Anions on Thermal and Light-Induced Spin-Crossover Properties of Iron(II)–α,ω-Bis(tetrazol-1-yl)-alkane Coordination Polymers

**Alina Absmeier,[a,b] Matthias Bartel,[a,c] Chiara Carbonera,[b] Guy N. L. Jameson,[d] Franz Werner,[a] Michael Reissner,[e] Andrea Caneschi,[c] Jean-François Létard,[b] and Wolfgang Linert*[a]**

**Keywords:** Iron(II) / Magnetic properties / Coordination polymers / Photomagnetism / Spin crossover

The influence of noncoordinating anions is analysed in an extension of our systematic investigations into iron(II) spin-crossover coordination polymers. We present here ditetrazole complexes of iron(II) tetrafluoroborate where the two tetrazole moieties are separated by alkylene spacers. The number of carbon atoms in the spacer (*n*) was varied between *n* = 5–10, 12, and the complexes were compared with their $ClO_4^-$ analogues. Pronounced magnetic and magneto-optical differences were found in the comparison of the two series. A chain-type arrangement in the complexes' crystal structures is proposed with decreased interactions between iron centres as *n* increases, leading to more gradual spin transitions. When *n* = 5–7 the smaller tetrafluoroborate causes the spin transitions of the respective complexes to occur at higher temperatures than those of the equivalent perchlorate series. Both series exhibit a parity effect, but at *n* = 8 the parity effect reverses for tetrafluoroborate. With increasing *n*, however, iron–iron interactions seem to fade away and a limiting value of $T_{SC}$ = 160 K is approached by both series.

(© Wiley-VCH Verlag GmbH & Co. KGaA, 69451 Weinheim, Germany, 2007)

## Introduction

Interest in multifunctional spin-crossover (SC) compounds within more complicated structural frameworks has increased dramatically in recent years,[1–3] leading to the discovery of exciting magnetic and photomagnetic properties. These investigations have yielded 1D,[4–8] 2D[9] and 3D[10–15] coordination polymers using iron(II) as the SC species. Our group has focused its recent research efforts on ditetrazole ligands with varying length alkylene spacer groups between the coordinating tetrazole groups, hereafter referred to as *n*ditz (see Figure 1). Within this family, short spacers (two carbon atoms) lead to 1D chain networks,[4] whilst four carbon atoms lead to 3D networks.[16,17] To build these frameworks not only is the number of carbon atoms (*n*) in the bridging alkylene groups in the ditetrazole ligand important, but the noncoordinating anion is also important. Anions are also believed to influence the SC behaviour of coordination compounds, varying spin transition temperatures and cooperative effects associated with the sharpness and hysteresis of the transition.[7,18–22]

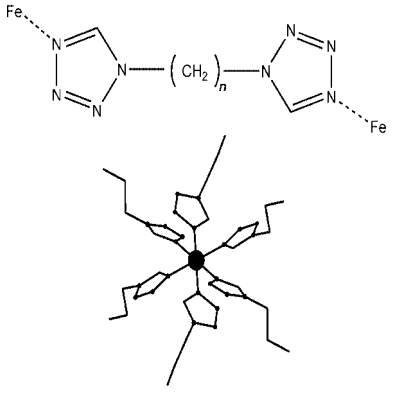


Figure 1. The ditetrazole ligand used and the octahedral geometry around iron(II).

In a previous investigation[23] we reported detailed magneto-optical data for a series (*n* = 4–9) using perchlorate as the anion, which showed an interesting dependence between the magneto-optical properties and the parity of the alky-

[a] Institute of Applied Synthetic Chemistry, Vienna University of Technology,
Getreidemarkt 9/163-AC, 1060 Vienna, Austria
Fax: +43-1-58801-16299
E-mail: wlinert@mail.zserv.tuwien.ac.at
[b] Institut de Chimie de la Matière Condensée de Bordeaux, UPR CNRS No 9048, Université Bordeaux 1, Groupe des Sciences Moléculaires,
87 Av. du Doc. A. Schweitzer, 33608 Pessac, France
[c] LAMM, Dipartimento di Chimica & UdR INSTM, Università di Firenze,
Via della Lastruccia 3, 50019 Sesto F.no, Italy
[d] Department of Chemistry, University of Otago,
P. O. Box 56, Dunedin, New Zealand
[e] Institute for Solid State Physics, Vienna University of Technology,
Wiedner Hauptstraße 8–10/138, 1040 Vienna, Austria

 © 2007 Wiley-VCH Verlag GmbH & Co. KGaA, Weinheim 

lene spacer. In order to compare and contrast the results obtained for the perchlorates,[23] we synthesised an analogous series ($n$ = 5–9) of complexes with the tetrafluoroborate anion and extended both series up to $n$ = 12. Tetrafluoroborate is known to be of similar size, geometry and chemical hardness to perchlorate. Indeed, the estimated ionic radii are 2.29 Å for $BF_4^-$ and 2.37 Å for $ClO_4^-$.[24] Furthermore, the polymers were identically prepared and this minimised differences. We did not want to change the structure of the complexes considerably by using bigger, softer and geometrically different anions such as $PF_6^-$ or $SbF_6^-$ because then a direct comparison would be unsound. We present here a comparison of the magneto-optical properties and provide tentative structural information based on comparative X-ray powder diffraction (XRPD) studies of the two series. As seen from preliminary inspections of X-ray patterns, $[Fe(4ditz)_3](BF_4)_2$ and $[Fe(4ditz)_3](ClO_4)_2$ adopt completely different structures when compared with the complexes with longer spacers and are therefore excluded from this report and will be presented in a separate paper. Taking into consideration the small decrease in diameter in going from $ClO_4^-$ to $BF_4^-$, the difference in properties are far greater than anticipated.

## Results and Discussion

### Powder Diffraction

As it was impossible to grow single crystals of the title materials, the microcrystalline samples were investigated by XRPD. The homologous series $[Fe(n\text{ditz})_3](X)_2\cdot EtOH$ ($n$ = 5–10, 12; X = $BF_4^-$, $ClO_4^-$) are characterised as follows (Figure 2): (i) The perchlorate compounds[23] show a higher degree of crystallinity compared with that of the tetrafluoroborates. (ii) The diffractograms are very similar in shape. (iii) The reflection with the longest d-spacing is the strongest and is shifted systematically to lower diffraction angles with increasing alkyl chain length. (iv) The reflections broaden with increasing $n$ and level off to background at $2\theta \approx 35°$, while the half-widths of the longest ones are more or less conserved. (v) All phases form very thin platelike microcrystallites with a thickness of a fraction of a micrometer.

Point (ii) lets us conclude that the phases exhibit more or less the same basic structure. The reflection broadening can be explained by size effects due to the extremely thin plates. As the largest crystallographic axis is usually the direction of the lowest crystal growth rate, the base plane of the microplates lies perpendicular to the longest cell axis. The reflection with the largest d-spacing, showing a steady shift as $n$ increases, can be regarded as this axis (possibly of higher order) that mirrors the increasing number of methylene groups in the ligands. Powder indexing of the phase $[Fe(5ditz)_3](BF_4)_2\cdot EtOH$, with the positions of the first 20 reflections determined using the DICVOL program,[25] yielded a preliminary solution in the monoclinic crystal system (pseudohexagonal): $a$ = 10.99, $b$ = 20.37, $c$ = 10.07 Å, $\alpha = \gamma = 90$, $\beta$ = 126.1°, $V$ = 1822 Å$^3$, $M_{20}$ = 13, which is in

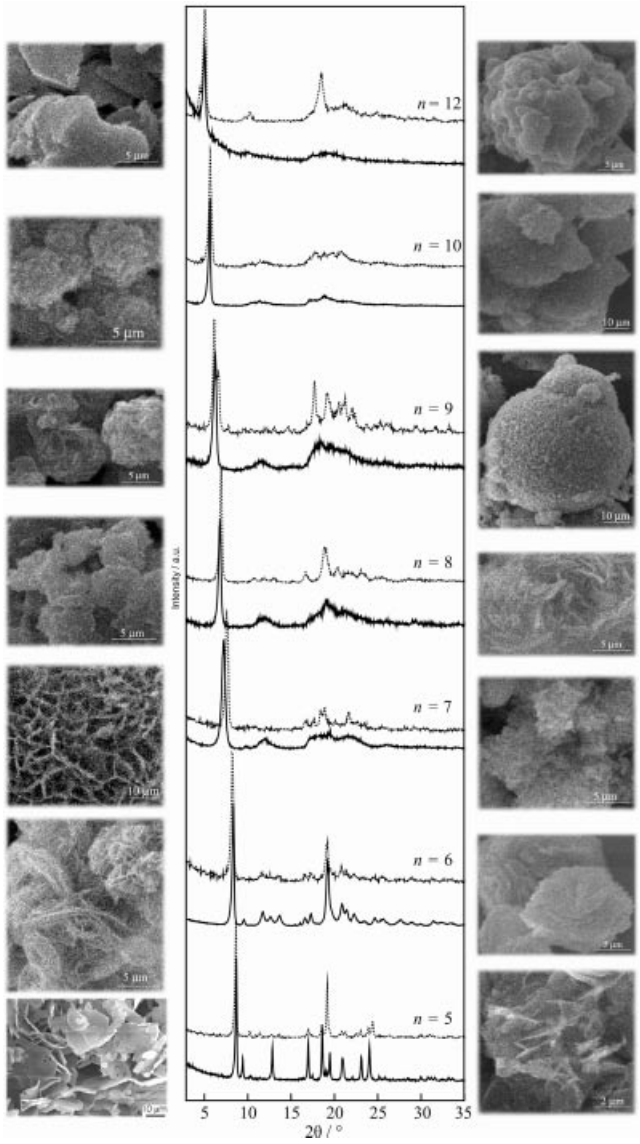


Figure 2. Comparison of the $[Fe(n\text{ditz})_3](BF_4)_2\cdot EtOH$ ($n$ = 5–10, 12; solid) series' X-ray powder patterns ($\lambda$ = Cu-$K_{\alpha 1,2}$) with those of the corresponding perchlorates (upper lines), flanked by the corresponding SEM images ($BF_4^-$ left, $ClO_4^-$ right).

accordance with a unit cell content of $Z$ = 2. This metric can be regarded as a distorted variant of the trigonal symmetry found for $[Fe(2ditz)_3](BF_4)_2$[4] with comparable lattice parameters: $a = b$ = 10.380(1), $c$ = 14.953(3) Å, $V$ = 1395.3(3) Å$^3$ [at 296(2) K, the shortened $c$ axis is caused by the ethylene spacer]. Therefore we tend to describe the pentylene- to dodecylene-ditetrazole complex series in a chain-type arrangement as well. The higher order complexes are suspected to crystallise in the triclinic system which, however, is not possible to confirm from the low-quality powder patterns. Calculating the unit cell volumes for the phases under investigation, assuming the monoclinic cell from earlier and setting the $b$ axis length to $d\times 2$ of the longest line (i.e., the 020 reflection), results in unit cell contents $Z$ ca. 2, which again is in accordance with the $[Fe(2ditz)_3](BF_4)_2$ complex. In Figure 3 an idealised tenta-

 © 2007 Wiley-VCH Verlag GmbH & Co. KGaA, Weinheim 

tive structural proposition is depicted. The ligands, linked together by iron(II), are stretched out and aligned parallel in a hexagonal close-packed manner with the counterions in between the chains. Increases in the alkylene spacer length will expand the unit cell in the crystallographic direction of the chains, leaving the other two untouched. Additionally, the voids between them become larger and are likely to be filled with presumably disordered and nonstoichiometric amounts of solvent molecules. As the interaction between the chains is weak [the Coulomb forces between the positively charged iron(II) and $BF_4^-$ will diminish with increasing *n*], stacking faults are favoured by longer spacers, and additional reflection broadening is likely to be observed.

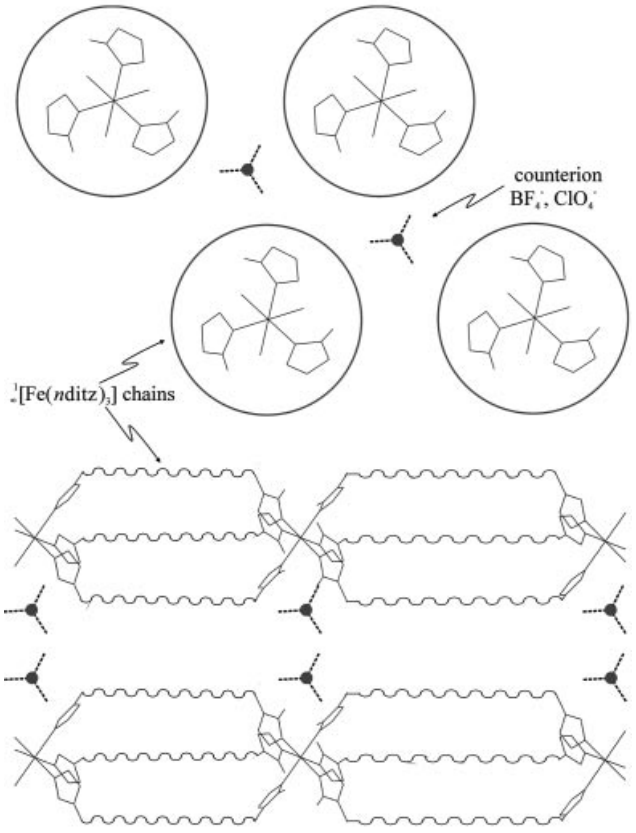


Figure 3. Tentative basic structural model of the $[Fe(nditz)_3](X)_2 \cdot EtOH$ ($n$ = 5–10, 12; X = $BF_4^-$, $ClO_4^-$) phases viewed along the $[Fe(nditz)_3]^{2+}$ chains (circled, top) and the perpendicular direction (bottom). The orientation and geometry of the complex is presumed arbitrarily.

## Optical Properties

As expected, all members of the series show a thermochromic effect associated with a spin transition, that is, from white in the HS state at room temperature to violet in the LS state at lower temperatures. The result of a typical temperature-dependent reflectivity experiment, which is a preliminary test for the LIESST (light-induced excited spin-state trapping) measurement (see below), is illustrated in Figure 4, using $[Fe(5ditz)_3](BF_4)_2$ as an example. No significant differences are found between the $BF_4^-$ and $ClO_4^-$ series. The spectra shown are measured within the range 450–900 nm at particular temperatures between 10 and 290 K and clearly show the presence of the expected d-d transitions of an octahedrally coordinated $Fe^{II}$ complex: the $^5T_2 \rightarrow {}^5E$ band at 830 nm when HS and the $^1A_1 \rightarrow {}^1T_1$ band at 570 nm when LS. The second LS transition, $^1A_1 \rightarrow {}^1T_2$, normally observable at 370 nm, is not within the range of the instrument. In addition, we recorded the change in intensity of both HS and LS bands as a function of temperature under constant light irradiation (see inset in Figure 4) by following changes in the reflectivity occurring at $(830 \pm 2.5)$ and $(550 \pm 2.5)$ nm.

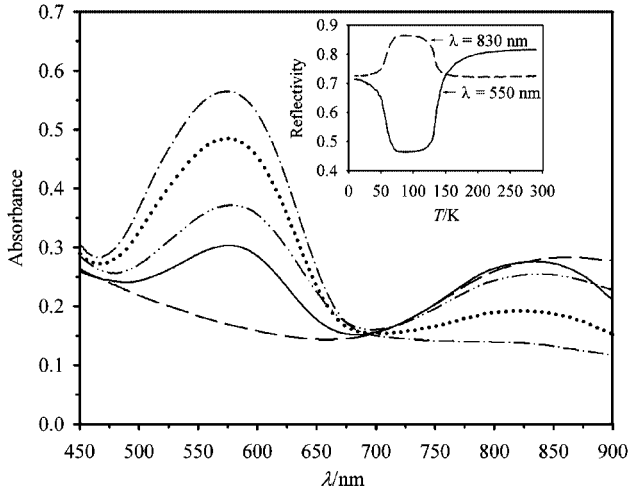


Figure 4. Reflectivity measurements of $[Fe(5ditz)_3](BF_4)_2$ as a function of temperature. Absorbance spectra at 280 K (– –), 140 K (– · · –), 80 K (– · –), 60 K (···) and 10 K (–) are shown. The inset reports the reflectivity followed at $(550 \pm 2.5)$ and $(830 \pm 2.5)$ nm.

For all compounds, at room temperature only the HS band is visible, whilst at 80 K only the LS transition is observable. Below 80 K, however, the reflectivity experiment demonstrates the existence of a photoinduced phenomenon at the surface. In fact, at low temperatures the sample was seen to bleach (see Figure 4 and inset), indicating the occurrence of a LS/HS photoconversion through the LIESST effect. For each compound, we calculated the amount of photobleached fraction (%Irr-Surface; reported in Table 1) relative to the value found at room temperature. However, similar to the previously published $ClO_4^-$ analogues,[23] the higher the $T_{SC}$, the lower the level of the light-induced LS/HS transformation as described by the inverse energy-gap law by Hauser[26] and the $T(LIESST)/T_{SC}$ relation introduced by Letard.[27] Magneto-optical parameters of $[Fe(nditz)_3](X)_2$ where $n$ = 10, 12 and X = $BF_4^-$, $ClO_4^-$ were not measured.

 © 2007 Wiley-VCH Verlag GmbH & Co. KGaA, Weinheim 

Table 1. Spin transition, reflectivity and LIESST parameters of the discussed complexes.

| | X = $BF_4^-$ | | | | X = $ClO_4^-$[a] | | | |
|---|---|---|---|---|---|---|---|---|
| $[Fe(n\text{ditz})_3](X)_2$ | $T_{SC}$/K | $T$(LIESST)/K | %Irr-Surface[b] | %Irr-Bulk[c] | $T_{SC}$/K[d] | $T$(LIESST)/K | %Irr-Surface[b] | %Irr-Bulk[c] |
| 5 | 131 | 58 | 71 | 84 | 125 | 52 | 64 | 72 |
| 6 | 164 | _[e] | 34 | 25 | 155 | _[e] | 42 | 43 |
| 7 | 154 | 58 | 47 | 71 | 144 | 51 | 42 | 57 |
| 8 | 148 | 52 | 47 | 55 | 169 | _[e] | 14 | 13 |
| 9 | 154 | 50[f] | 50 | 36 | 155 | 37 | 26 | 47 |
| 10[g] | 150 | – | – | – | 160 | – | – | – |
| 12[g] | 156 | – | – | – | 159 | – | – | – |

[a] Data taken from ref.[23] [b] Percentage of the sample photobleached. [c] Percentage conversion to the metastable high spin state by irradiation at 10 K. [d] $T_{SC}$ is the temperature of the spin transition estimated from the maximum in the first derivative of the $\chi_M T$ vs. $T$ plot. [e] No minimum in $d(\chi_M T)/d(T)$ observable. [f] No minimum in $d(\chi_M T)/d(T)$ observable: estimated from the obtained relaxation curve of the LIESST experiment. [g] No magneto-optical data available.

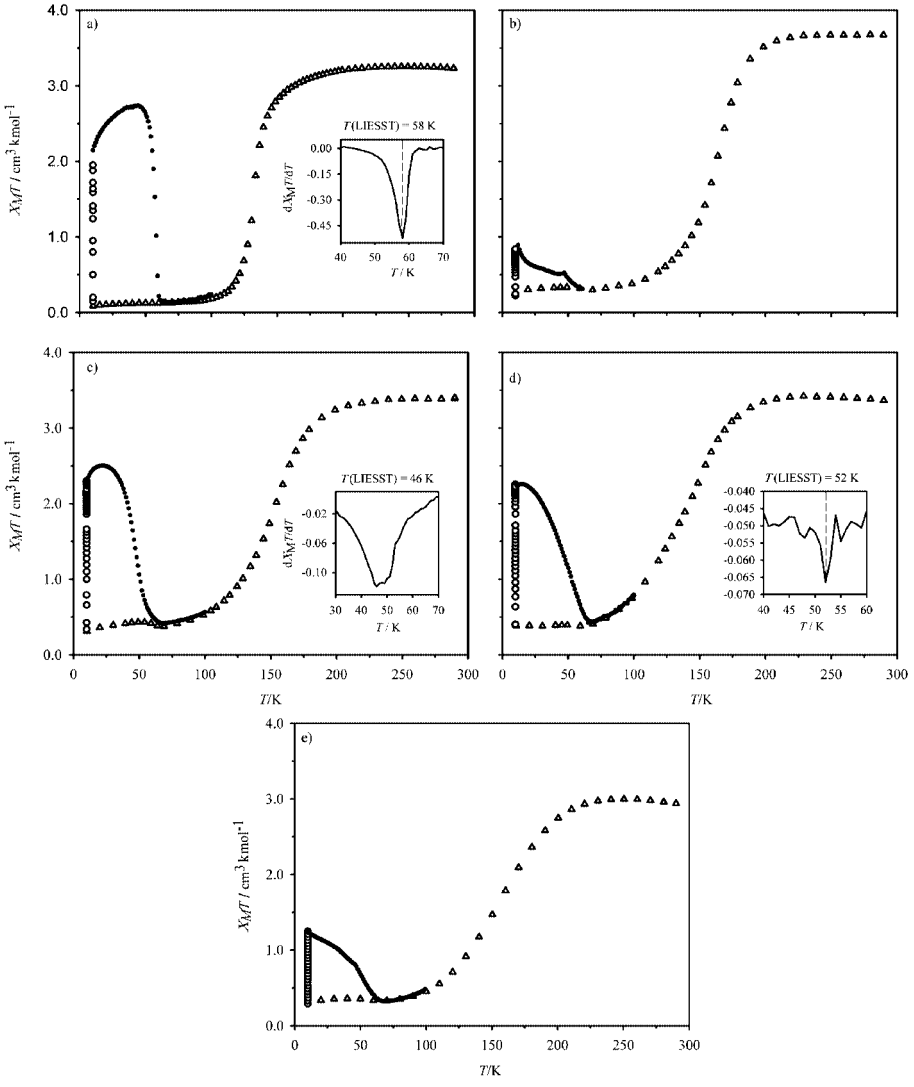


Figure 5. Temperature dependence of $\chi_M T$ for (a) $[Fe(5ditz)_3](BF_4)_2$, (b) $[Fe(6ditz)_3](BF_4)_2$, (c) $[Fe(7ditz)_3](BF_4)_2$, (d) $[Fe(8ditz)_3](BF_4)_2$, (e) $[Fe(9ditz)_3](BF_4)_2$. (Δ) Data recorded without irradiation; (○) data recorded during irradiation at 10 K; (●) $T$(LIESST) measurement, data recorded in the warming mode with the laser turned off after irradiation for one hour. The existence of a small anomaly at around 50 K on the $T$(LIESST) curve corresponds to a remnant oxygen contamination even if particular precaution was taken to purge the SQUID cavity for one hour at room temperature.

 © 2007 Wiley-VCH Verlag GmbH & Co. KGaA, Weinheim 

### Magnetic and Photomagnetic Properties

Susceptibility curves were measured between 10 and 300 K for all compounds, and the obtained curves depicting $\chi_M T$ versus $T$, where $\chi_M$ is the molar magnetic susceptibility and $T$ is the temperature, are shown in Figure 5. The temperature of the thermal spin transition, $T_{SC}$, estimated from the maximum in the first derivative of the $\chi_M T$ versus $T$ plot, is given in Table 1. Photomagnetic measurements were carried out as previously published,[23] and this procedure allowed the quantification of $T$(LIESST) (see Table 1), which is determined by the minimum of the $d(\chi_M T)/d(T)$ versus $T$ curve recorded during thermal-induced relaxation.[28] Figure 5 shows the photomagnetic behaviour, and Table 1 shows for each compound the percentage of photoconversion obtained by irradiation at 10 K relative to the magnetic value recorded at room temperature where a pure HS state is assumed (%Irr-Bulk).

All compounds {$[Fe(n\text{ditz})_3](X)_2$, $n$ = 5–10, 12; X = $BF_4^-$, $ClO_4^-$} undergo a complete spin transition between 100 and 220 K (see Figure 5, a–e) and reach a $\chi_M T$ product close to 3.3 $cm^3 \cdot K \cdot mol^{-1}$, in agreement with the theoretically expected value for HS $Fe^{II}$ compounds at room temperature.

At low temperatures in some of the curves, a residual magnetisation is observed yielding a $\chi_M T$ value up to 0.4 $cm^3 \cdot K \cdot mol^{-1}$, which might be caused by thermally inactive HS iron(II) or traces of iron(III). Comparison of the new magnetic data with the perchlorate data shows a similar trend for $n$ = 5–7. The SC curves themselves are all very similar with the $[Fe(5ditz)_3](BF_4)_2$ transition curve a little steeper. The temperatures of transition, $T_{SC}$, are all higher for $BF_4^-$ than for $ClO_4^-$. The %Irr-Surface and %Irr-Bulk values show a similar relationship with $n$ but the actual values are different, suggesting a similar relationship with parity. There is, however, a variation when $n$ is changed from 7 to 8. Here $T_{SC}$ of $[Fe(8ditz)_3](BF_4)_2$ is lower and the transition itself is a lot more gradual than its perchlorate analogue, while %Irr-Surface and %Irr-Bulk are significantly higher. This reversal of the parity dependence at this point suggests that the smaller $BF_4^-$ causes a change in the arrangement of the alkyl chains. By $n$ = 9, the transition is very gradual and almost exactly the same in both cases ($T_{SC}$ = 154 K for $BF_4^-$ and 155 K for $ClO_4^-$). The lowered $\chi_M T$ value at high temperature for the $BF_4^-$ complex is caused by LS $Fe^{II}$ or LS $Fe^{III}$ impurities. $[Fe(10ditz)_3](ClO_4)_2$ has a flatter magnetic curve than that of the $BF_4^-$ analogue but $T_{SC}$ is 10 K higher (see Figure 6). However by $n$ = 12, the transitions are remarkably similar again (see Figure 6). This might be because any further changes in the arrangement of the alkyl chains would now be insignificant with respect to the greater separation of the iron centres.

The larger iron–iron distances and disorder should lead to a concomitant decrease in cooperativity between iron centres until the transition can be described by a simple Boltzmann distribution. This behaviour is supported by the magnetic properties around the transition temperature. The slope at the inflection point of the transition curves ($T_{SC}$) is plotted in Figure 7. It can be seen that the spin transition curves become more gradual with increasing $n$ as expected. This lends further support to the suggestion that all compounds in the series produce a chain-type arrangement, as proposed in the XRPD section.

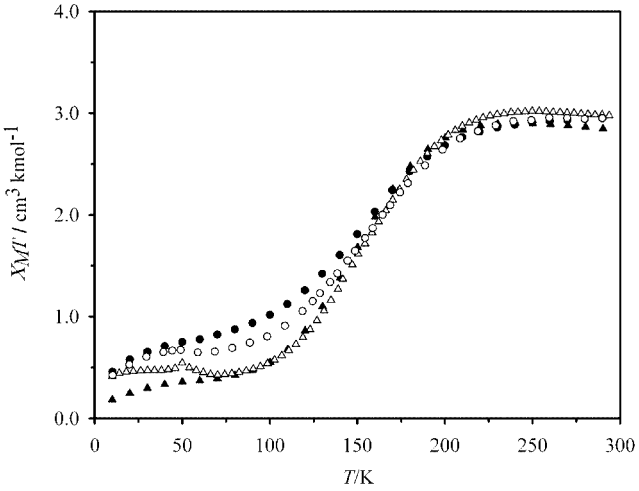


Figure 6. Temperature dependence of $\chi_M T$ for (a) $[Fe(10ditz)_3](BF_4)_2$ (▲) and $[Fe(10ditz)_3](ClO_4)_2$ (●) and b) $[Fe(12ditz)_3](BF_4)_2$ (Δ) and $[Fe(12ditz)_3](ClO_4)_2$ (○), in the heating mode. The existence of a small anomaly at around 50 K on the curves almost certainly corresponds to a remnant oxygen contamination.

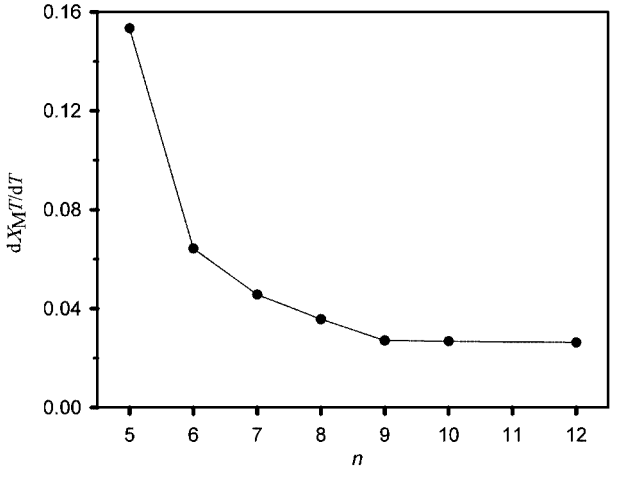


Figure 7. The slope of the $\chi_M T$ curves of the $BF_4^-$ series at the transition temperature ($T_{SC}$) for $n$ = 5–10, 12, in the heating mode. The line connecting the points has no physical meaning and is intended only as a guide.

## Conclusions

We present here a detailed study of a homologous series of iron(II) SC coordination polymers using $BF_4^-$ as the counteranion and compare this data with our previous study of closely related compounds[23] using the same ligands but with $ClO_4^-$ as the counteranion. By changing the anion to $BF_4^-$, we observed that the structure has changed slightly and thus altered the SC behaviour. As indicated by XRPD, the phases seem to adopt a 1D polymer by forming

 © 2007 Wiley-VCH Verlag GmbH & Co. KGaA, Weinheim 

chains, arranged approximately in a hexagonal close-packed manner. The longer the alkylene spacer, the higher the disorder of the infinite 1D network as indicated by severe reflection broadening.

In Figure 8, $T_{SC}$ versus $n$ is shown for the $BF_4^-$ and the $ClO_4^-$ series. Both curves show a zigzag behaviour with decreasing amplitude, reaching a similar end point. Indeed, $[Fe(12ditz)_3](ClO_4)_2$ has a $T_{SC}$ = 159 K and $[Fe(12ditz)_3](BF_4)_2$ has a $T_{SC}$ = 156 K. This suggests that as the alkylene spacer is lengthened, $T_{SC}$ eventually reaches a limiting value of 160 K. It is, however, obvious that the tetrafluoroborates show a reversal in the parity effect as $n$ is increased from 7 to 8. This suggests that at this length the alkylene chains are differently arranged. In contrast, the perchlorates show a parity effect up to $n$ = 12[23] (see Figure 8).

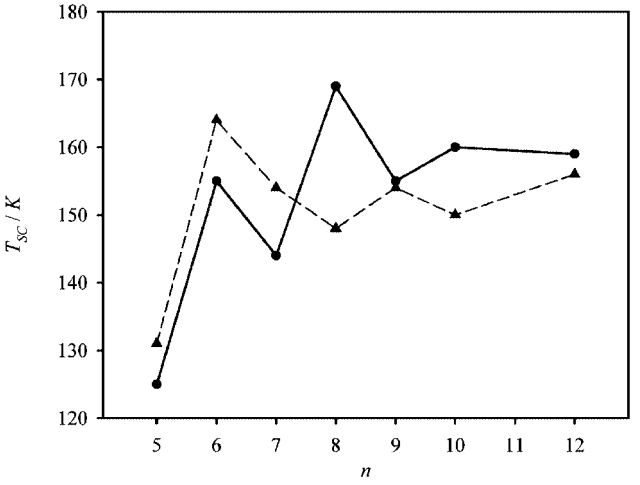


Figure 8. Comparison of $T_{SC}$ as a function of the number of carbon atoms ($n$) in the spacer of the ditetrazole ligands for the $BF_4^-$ (▲) and $ClO_4^-$ (●) series.

Chemical intuition would suggest more or less identical results for such similar noncoordinating anions like perchlorate and tetrafluoroborate. In spite of this, our investigations on these two related series clearly show that there is a anion dependence, especially in terms of their magneto-optical behaviour. Furthermore, the pronounced dependence of $T_{SC}$ upon the parity of the spacer length which was found in the perchlorate series is also found, with alterations, in the tetrafluoroborate over the whole series (see Figure 8). Eventually, however, both series reach the same limiting value of $T_{SC}$ at high $n$ when orientation is insignificant with respect to the separation of the iron centres. As far as we can derive from our studies, the choice of the ligand system represents the fundamental requirement to obtain a SC compound, but the impact of the noncoordinating anion seems to be of similar importance. With this in mind, the interest is now focused on complexes in which the interaction of anion and ligand leads to optimised systems where the spin transition and cooperativity can be systematically tuned to be used for future applications of new materials with interesting magneto-optical features.

## Experimental Section

**Chemicals and Standard Physical Characterisation:** Iron(II) tetrafluoroborate hexahydrate was obtained from Aldrich. All other chemicals were standard reagent grade and used as supplied. Elemental analyses (C, H and N) were performed in the laboratories of Dr. Roman Boca (Slovenská Vyská Scola Technicá v Bratislava, Chemitechothenologická Fakulta, Radlinského 9, 81237 Bratislava, Slovakia). Mid-range FTIR spectra of the compounds were recorded as KBr pellets within the range of 4400–450 $cm^{-1}$ using a Perkin–Elmer 16PC FTIR spectrometer. Pellets were obtained by pressing the powdered mixture of the samples in KBr in vacuo using a hydraulic press applying a pressure of 10000 $kg \cdot cm^{-2}$ for 5 min.

**Synthesis of the Complexes:** The general synthetic pathway and the synthesis of the ligands used [1,*n*-bis(tetrazol-1-yl)alkane; $n$ = 5–10, 12] has been previously reported.[17,23,29,30] Note that the 1,11-bis(tetrazol-1-yl)undecan has not yet been synthesised. The respective ligand (*n*ditz, 1 mmol) was dissolved in reagent grade ethanol ($n$ = 5–10, 12). While the solution cooled down to 40 °C, iron(II) tetrafluoroborate hexahydrate or iron(II) perchlorate hexahydrate (0.33 mmol) and a small amount of ascorbic acid to keep the iron as iron(II) were diluted in ethanol (5 mL). This solution was slowly added to the dissolved ligand, and the resulting mixture was stirred for 4 h. The precipitate was filtered off, and the obtained powder was dried with $P_2O_5$. It has so far proved impossible to grow single crystals by any of the standard methods including H-tube slow diffusion or slow cooling.

**Elemental Analyses and Mid-FTIR**

**$[Fe(5ditz)_3](BF_4)_2$:** Yield: 0.16 g (59%). $C_{21}H_{36}B_2F_8FeN_{24}$ (854.14): calcd. C 29.53, H 4.25, N 39.36; found C 29.30, H 4.18, N 37.66. Mid-FTIR: $\tilde{\nu}$ = 3146 (C–H stretching vibration, ν, of the aromatic tetrazole ring), 2949, 2933 and 2862 ($\nu_{C-H}$ of the aliphatic C–H in the butylene spacer), 1506, 1370 ($\nu_{N=N}$, $\nu_{C-N}$), 1183, 1109 ($\nu_{C=N}$, $\nu_{N-N}$, $\nu_{C-N}$) $cm^{-1}$.

**$[Fe(6ditz)_3](BF_4)_2$:** Yield: 0.15 g (50%). $C_{24}H_{42}B_2F_8FeN_{24}$ (896.22): calcd. C 32.16, H 4.72, N 37.51; found C 31.41, H 4.78, N 36.15. Mid-FTIR: $\tilde{\nu}$ = 3148 ($\nu_{C-H}$ of the aromatic tetrazole ring), 2938 and 2862 ($\nu_{C-H}$ of the aliphatic C–H in the butylene spacer), 1506, 1372 ($\nu_{N=N}$, $\nu_{C-N}$), 1182, 1102 ($\nu_{C=N}$, $\nu_{N-N}$, $\nu_{C-N}$) $cm^{-1}$.

**$[Fe(7ditz)_3](BF_4)_2$:** Yield: 0.19 g (61%). $C_{27}H_{48}B_2F_8FeN_{24}$ (938.31): calcd. C 34.56, H 5.16, N 35.83; found C 34.00, H 5.18, N 35.72. Mid-FTIR: $\tilde{\nu}$ = 3147 ($\nu_{C-H}$ of the aromatic tetrazole ring), 2940 and 2862 ($\nu_{C-H}$ of the aliphatic C–H in the butylene spacer), 1507, 1375 ($\nu_{N=N}$, $\nu_{C-N}$), 1173, 1108 ($\nu_{C=N}$, $\nu_{N-N}$, $\nu_{C-N}$) $cm^{-1}$.

**$[Fe(8ditz)_3](BF_4)_2$:** Yield: 0.18 g (55%). $C_{30}H_{54}B_2F_8FeN_{24}$ (980.39): calcd. C 36.75, H 5.55, N 34.29; found C 36.84, H 5.58, N 33.63. Mid-FTIR: $\tilde{\nu}$ = 3148 ($\nu_{C-H}$ of the aromatic tetrazole ring), 2936 and 2859 ($\nu_{C-H}$ of the aliphatic C–H in the butylene spacer), 1507, 1368 ($\nu_{N=N}$, $\nu_{C-N}$), 1183, 1102 ($\nu_{C=N}$, $\nu_{N-N}$, $\nu_{C-N}$) $cm^{-1}$.

**$[Fe(9ditz)_3](BF_4)_2$:** Yield: 0.25 g (72%). $C_{33}H_{60}B_2F_8FeN_{24}$ (1022.47): calcd. C 38.77, H 5.91, N 32.88; found C 38.95, H 5.83, N 31.96. Mid-FTIR: $\tilde{\nu}$ = 3148 ($\nu_{C-H}$ of the aromatic tetrazole ring), 2933 and 2857 ($\nu_{C-H}$ of the aliphatic C–H in the butylene spacer), 1507, 1375 ($\nu_{N=N}$, $\nu_{C-N}$), 1174, 1108 ($\nu_{C=N}$, $\nu_{N-N}$, $\nu_{C-N}$) $cm^{-1}$.

**$[Fe(10ditz)_3](BF_4)_2$:** Yield: 0.24 g (69%). $C_{36}H_{66}B_2F_8FeN_{24}$ (1064.55): calcd. C 40.62, H 6.25, N 31.58; found C 40.83, H 6.03, N 31.41. Mid-FTIR: $\tilde{\nu}$ = 3145 ($\nu_{C-H}$ of the aromatic tetrazole ring), 2929 and 2851 ($\nu_{C-H}$ of the aliphatic C–H in the butylene spacer), 1504, 1372 ($\nu_{N=N}$, $\nu_{C-N}$), 1177, 1098 ($\nu_{C=N}$, $\nu_{N-N}$, $\nu_{C-N}$) $cm^{-1}$.

 © 2007 Wiley-VCH Verlag GmbH & Co. KGaA, Weinheim 

**$[Fe(12ditz)_3](BF_4)_2$:** Yield: 0.26 g (67%). $C_{42}H_{72}B_2F_8FeN_{24}$ (1148.71): calcd. C 44.15, H 6.35, N 29.42; found C 44.08, H 6.90, N 28.08. Mid-FTIR: $\tilde{\nu}$ = 3141 ($\nu_{C-H}$ of the aromatic tetrazole ring), 2917 and 2852 ($\nu_{C-H}$ of the aliphatic C–H in the butylene spacer), 1501, 1383 ($\nu_{N=N}$, $\nu_{C-N}$), 1176, 1096 ($\nu_{C=N}$, $\nu_{N-N}$, $\nu_{C-N}$) $cm^{-1}$.

**$[Fe(10ditz)_3](ClO_4)_2$:** Yield: 0.20 g (55%). $C_{36}H_{66}Cl_2FeN_{24}O_8$ (1089.84): calcd. C 39.68, H 6.10, N 30.85; found C 39.03, H 5.60, N 29.23. Mid-FTIR: $\tilde{\nu}$ = 3136 ($\nu_{C-H}$ of the aromatic tetrazole ring), 2917 and 2850 ($\nu_{C-H}$ of the aliphatic C–H in the butylene spacer), 1508, 1383 ($\nu_{N=N}$, $\nu_{C-N}$), 1178, 1088 ($\nu_{C=N}$, $\nu_{N-N}$, $\nu_{C-N}$) $cm^{-1}$.

**$[Fe(12ditz)_3](ClO_4)_2$:** Yield: 0.28 g (71%). $C_{42}H_{72}Cl_2FeN_{24}O_8$ (1167.94): calcd. C 43.19, H 6.21, N 28.78; found C 42.57, H 6.63, N 28.01. Mid-FTIR: $\tilde{\nu}$ = 3139 ($\nu_{C-H}$ of the aromatic tetrazole ring), 2922 and 2851 ($\nu_{C-H}$ of the aliphatic C–H in the butylene spacer), 1504, 1375 ($\nu_{N=N}$, $\nu_{C-N}$), 1175, 1094 ($\nu_{C=N}$, $\nu_{N-N}$, $\nu_{C-N}$) $cm^{-1}$.

**X-ray Powder Diffraction:** The samples were gently ground and placed on flat-plate single-crystal silicon sample holders by the slurry technique with cyclohexane (Merck, p.a.) as elutriating liquid. Powder patterns were recorded with a Philips X'Pert diffractometer in Bragg–Brentano geometry using Cu-$K_{\alpha 1,2}$ radiation.

**Reflectivity Measurements:** Reflectivity of the samples was investigated by using a custom-built reflectivity set-up equipped with a CVI spectrometer, which allowed the collection of both the reflectivity spectra within the range of 450–900 nm at a given temperature and the following of the temperature dependence of the signal at a selected wavelength (±2.5 nm) at 5–290 K. The experiment was performed directly using a thin layer of the powdered sample without any dispersion in a matrix.[31]

**Magnetic Susceptibility and Magneto-Optical Measurements:** Magnetic measurements were completed with two SQUID magnetometers: (i) SQUID Cryogenix S600 magnetometer with an applied field of 1 T and (ii) MPMS-55 Quantum Design SQUID magnetometer with an operating field of 2 T within the temperature range of 2–300 K and with a cooling/heating speed of 10 $K \cdot min^{-1}$ in the settle mode at atmospheric pressure. Further measurements were made with a 9 T-PPMS-system from Quantum Design VSM operating with a field of 1 T. All magnetic measurements were performed using powder samples weighing ca. 12 mg. The data were corrected for the magnetisation of the sample holder and for diamagnetic contributions, estimated from Pascal's constants.

The photomagnetic measurements were performed using a Spectra Physics Series 2025 $Kr^+$ laser ($\lambda$ = 532 nm) coupled by an optical fibre to the cavity of the SQUID magnetometer previously described in ref.[27] The laser light power at the sample was adjusted to 5 $mW \cdot cm^{-2}$. Bulk attenuation of light intensity was limited as much as possible by the preparation of a thin layer of compound. It is noteworthy that there was no change in the data due to sample heating upon laser irradiation. The weight of these thin layer samples (approximately 0.2 mg) was obtained by comparison of the measured thermal spin-crossover curve with another curve of a more accurately weighed sample of the same compound.

## Acknowledgments

The financial support of the Austrian Science Foundation, FWF project 19335-N17, the Italian Ministero dell'Università e della Ricerca through project FIRB RBNE033KMA, and the European Community for NE "MAGMAnet" NMP3-CT-2005-515767 projects is gratefully acknowledged. Furthermore, we want to thank the European Cooperation in the Field of Science and Technology (COST) for granting A. A. a "Short Term Scientific Mission" in Bordeaux D14 and D35. Additionally, M. B. carried out research in Florence within the Marie Curie Training site LAMM (MOL-MAG-MEST-CT-2004-504204). We wish to thank the Vienna University of Technology for funding under the "Innovatives Projekt NovMat". We also wish to thank Prof. K. Mereiter (TU Vienna) for the collection of the XRPD data, Dr. M. Grunert (University of Mainz) for producing $[Fe(12ditz)_3](BF_4)_2$, Prof. G. Hilscher (TU Vienna) for SQUID measurements on the same sample, Mrs. K. Poppenberger (TU Vienna) and Mr. Y. Hasegawa (Aoyama-Gakuin University) for the SEM measurements.

[1] C. Janiak, *Dalton Trans.* **2003**, 2781–2804.
[2] Y. Garcia, V. Niel, M. C. Munoz, J. A. Real, *Spin Crossover in 1D, 2D and 3D Polymeric Fe(II) Networks* in *Topics in Current Chemistry*, vol. 233: *Spin Crossover in Transition Metal Compounds I*, Springer, Berlin, Heidelberg, **2004**.
[3] J. A. Real, A. B. Gaspar, M. C. Munoz, *Dalton Trans.* **2005**, 2062–2079.
[4] J. Schweifer, P. Weinberger, K. Mereiter, M. Boca, C. Reichl, G. Wiesinger, G. Hilscher, P. J. van Koningsbruggen, H. Kooijman, M. Grunert, W. Linert, *Inorg. Chim. Acta* **2002**, *339*, 297–306.
[5] K. Yoneda, K. Adachi, S. Hayami, Y. Maeda, M. Katada, A. Fuyuhiro, S. Kawata, S. Kaizaki, *Chem. Commun.* **2006**, 45–47.
[6] V. Ksenofontov, A. B. Gaspar, J. A. Real, P. Gütlich, *J. Chem. Phys. Lett. B* **2001**, *105*, 12266–12271.
[7] O. Roubeau, M. A. Gomez, E. Balskus, J. J. A. Kolnaar, J. J. G. Haasnoot, J. Reedijk, *New J. Chem.* **2001**, *25*, 144–150.
[8] S. Hayami, G. Juhasz, Y. Maeda, T. Yokoyama, O. Sato, *Inorg. Chem.* **2005**, *44*, 7289–7291.
[9] R. Bronisz, *Inorg. Chem.* **2005**, *44*, 4463–4465.
[10] Y. Garcia, O. Kahn, L. Rabardel, B. Chansou, L. Salmon, J. P. Tuchagues, *Inorg. Chem.* **1999**, *38*, 4663–4670.
[11] V. Niel, J. M. Martinez-Agudo, M. C. Munoz, A. B. Gaspar, J. A. Real, *Inorg. Chem.* **2001**, *40*, 3838–3839.
[12] V. Niel, A. L. Thompson, M. C. Munoz, A. Galet, A. E. Goeta, J. A. Real, *Angew. Chem. Int. Ed.* **2003**, *42*, 3760–3763.
[13] A. Galet, V. Niel, M. C. Munoz, J. A. Real, *J. Am. Chem. Soc.* **2003**, *125*, 14224–14225.
[14] G. Molnár, V. Niel, J.-A. Real, L. Dubrovinsky, A. Bousseksou, J. J. McGarvey, *J. Phys. Chem. B* **2003**, *107*, 3149–3155.
[15] V. Niel, A. L. Thompson, A. E. Goeta, C. Enachescu, A. Hauser, A. Galet, M. C. Munoz, J. A. Real, *Chem. Eur. J.* **2005**, *11*, 2047–2060.
[16] C. M. Grunert, J. Schweifer, P. Weinberger, W. Linert, K. Mereiter, G. Hilscher, M. Muller, G. Wiesinger, P. J. van Koningsbruggen, *Inorg. Chem.* **2004**, *43*, 155–165.
[17] P. J. van Koningsbruggen, Y. Garcia, H. Kooijman, A. L. Spek, J. G. Haasnoot, O. Kahn, J. Linares, E. Codjovi, F. Varret, *J. Chem. Soc., Dalton Trans.* **2001**, 466–471.
[18] B. J. Kennedy, A. C. McGrath, K. S. Murray, B. W. Skelton, A. H. White, *Inorg. Chem.* **1987**, *26*, 483–495.
[19] M. Yamada, H. Hagiwara, H. Torigoe, N. Matsumoto, M. Kojima, F. Dahan, J.-P. Tuchagues, N. Re, S. Iijima, *Chem. Eur. J.* **2006**, *12*, 4536–4549.
[20] M. Yamada, M. Ooidemizu, Y. Ikuta, S. Osa, N. Matsumoto, S. Iijima, M. Kojima, F. Dahan, J.-P. Tuchagues, *Inorg. Chem.* **2003**, *42*, 8406–8416.
[21] V. A. Money, J. Elhaik, I. R. Evans, M. A. Halcrow, J. A. K. Howard, *Dalton Trans.* **2004**, 65–69.
[22] V. Ksenofontov, H. Spiering, S. Reiman, Y. Garcia, A. B. Gaspar, N. Moliner, J. A. Real, P. Gütlich, *Chem. Phys. Lett.* **2001**, *348*, 381–386.
[23] A. Absmeier, M. Bartel, C. Carbonera, G. N. L. Jameson, P. Weinberger, A. Caneschi, K. Mereiter, J.-F. Létard, W. Linert, *Chem. Eur. J.* **2006**, *12*, 2235–2243.
[24] M. Ue, *J. Electrochem. Soc.* **1994**, *141*, 3336–3342.
[25] A. Boultif, D. Louër, *J. Appl. Crystallogr.* **1991**, *24*, 987–993.

 © 2007 Wiley-VCH Verlag GmbH & Co. KGaA, Weinheim 

[26] A. Hauser, *Coord. Chem. Rev.* **1991**, *111*, 275–290.
[27] a) J.-F. Létard, P. Guionneau, O. Nguyen, J. S. Costa, S. Marcén, G. Chastanet, M. Marchivie, L. Capes, *Chem. Eur. J.* **2005**, *11*, 4582–4589; b) J.-F. Létard, *J. Mater. Chem.* **2006**, *16*, 2550–2559.
[28] J.-F. Létard, L. Capes, G. Chastanet, N. Moliner, S. Létard, J.-A. Real, O. Kahn, *Chem. Phys. Lett.* **1999**, *313*, 115–120.
[29] P. L. Franke, J. G. Hasnoot, A. P. Zuur, *Inorg. Chim. Acta* **1982**, *59*, 5–9.
[30] C. M. Grunert, P. Weinberger, J. Schweifer, C. Hampel, A. F. Stassen, K. Mereiter, W. Linert, *J. Mol. Struct.* **2005**, *733*, 41–52.
[31] C. Carbonera, A. Dei, C. Sangregorio, J.-F. Létard, *Chem. Phys. Lett.* **2004**, *396*, 198–201.

Received: November 21, 2006
Published Online: May 15, 2007

 © 2007 Wiley-VCH Verlag GmbH & Co. KGaA, Weinheim 

DOI: 10.1002/ejic.200601149

# Synthesis of Cycloruthenated Compounds as Potential Anticancer Agents

**Lida Leyva,[a] Claude Sirlin,*[a] Laura Rubio,[b] Cecilia Franco,[b] Ronan Le Lagadec,[b] John Spencer,[c] Pierre Bischoff,[d] Christian Gaiddon,[e] Jean-Philippe Loeffler,[e] and Michel Pfeffer*[a]**

**Keywords:** Bioinorganic chemistry / Ruthenium / Metallacycles / Antitumor agents

A library of 19 cycloruthenated derivatives is constructed by making use of the well-known cyclometalation reaction. Their geometries are modified in a straightforward manner by addition of either mono- or bidentate ligands, such as bipyridine, phenanthroline, 1,2-bis(diphenylphosphanyl)ethane, dimethylphenylphosphane, triphenylphosphane, and 1,3,5-triaza-7-phosphatricyclo[3.3.1.1]decane (PTA) ligands, to cationic cycloruthenated centers. The antitumor properties of the compounds thus obtained are investigated in order to compare them with recently reported ruthenium complexes and cisplatin. $IC_{50}$ values against mammalian cells (A-172, HCT-116, and RDM-4) are determined for the library compounds and some of them, such as those derived from orthoruthenated phenylpyridine and a bidentate N,N ligand, display activity of the same order of magnitude as cisplatin.

(© Wiley-VCH Verlag GmbH & Co. KGaA, 69451 Weinheim, Germany, 2007)

## Introduction

It is now well established that metal complexes can be considered as pharmaceuticals for therapeutic or diagnostic use.[1] Since the fortuitous discovery of their anticancer properties in the 1960s, platinum compounds have been recognized as very powerful anticancer drugs that have helped to revolutionize cancer therapy.[2] Consequently, cisplatin is currently one of the three most widely used drugs in chemotherapy and is highly effective in treating ovarian and testicular cancers. It also contributes to the treatment of many other cancers. Despite these facts, it presents two major disadvantages, namely its severe toxicity, especially nephrotoxicity, neurotoxicity, and emetogenesis, and its limited applicability to a narrow range of tumors as several tumors are naturally resistant or have developed resistance.[2c] In order to improve cancer therapies, new platinum and non-platinum containing entities such as metallocenes, titanium(IV) and gold(I) complexes, and gallium(III) salts have been considered as alternatives to cisplatin.[1b,1c]

[a] Institut de Chimie de Strasbourg, CNRS – Université Louis Pasteur,
4, rue Blaise Pascal, 67000 Strasbourg, France
[b] Instituto de Quimica, Universidad National Autonoma de Mexico,
Circuito Exterior, Ciudad Universitaria, Coyoacan, 04510 Mexico DF, Mexico
[c] School of Science, University of Greenwich,
Chatham Maritime, Kent ME4 4TB, UK
[d] Laboratoire d'Altérations Génetiques des Cancers et Réponse thérapeutique, UPRES EA-3430, IRCAD, Hôpitaux Universitaires,
1, place de l'Hôpital, Strasbourg, France
[e] Laboratoire de Signalizations Moléculaires et Neurodégénerescence, U 692, INSERM – Université Louis Pasteur,
11, rue Human, Strasbourg, France

In this respect, special attention has been paid to the application of ruthenium compounds in chemotherapy since such complexes are often able to display properties similar to those of platinum and iron in that they have analogous ligand-exchange abilities to platinum complexes and are less toxic than platinum, presumably because they can mimic iron in the course of binding to serum transferrin or albumin. Since rapidly dividing cells have a greater requirement for iron, these cells will increase the number of transferrin receptors at their surface, thereby sequestering more metal-loaded receptors. As the drug becomes targeted toward cancer cells, its toxicity should be reduced.[3] Some noticeable progress has been made recently whereby several teams have developed new organometallic or coordination complexes based on ruthenium(III) for this purpose.[4] Recently, $[ImH]^+[Ru(Im)(Me_2SO)Cl_4]^-$ (NAMI-A; Im = imidazole) and $[IndH]^+[Ru(Ind)_2Cl_4]^-$ (KP1019; Ind = 1*H*-indazole) have successfully completed phase I clinical trials as antimetastatic drugs[5] and have been shown to be precursors of $Ru^{II}$ complexes in vivo. Following on from these results a growing number of research groups have studied the biological activities of related ruthenium(II) complexes. Thus, Sadler et al. have found that some areneruthenium(II) complexes exhibit interesting in vitro and in vivo anticancer activities,[6] and Dyson et al. have studied related complexes and determined their antibiotic and antiviral activities.[7] Similarly, Reedijk et al. have established the high cytotoxicity of a series of bis(2-phenylazopyridine)ruthenium(II) complexes against A2780 human ovarian carcinoma cell lines.[8]

Some of us have recently reported that organometallic cycloruthenated compounds, such as those formed by the direct cyclometalation (involving a CH activation reaction)

 © 2007 Wiley-VCH Verlag GmbH & Co. KGaA, Weinheim 

of a nitrogen-containing ligand, can interact with biological molecules. Indeed, these organometallic species can be used as very efficient mediators of electron transfer to or from oxidized or reduced active sites of redox enzymes.[9] We thus reasoned that these molecules might have potential anticancer applications, as was shown recently for related cyclopalladated or cycloplatinated complexes.[10] Given that most metal complexes that have been previously tested for antitumor activity contain ligands that are only weakly bound to the metal via a heteroatom (N, O, S) to metal coordination bond, it is very likely that at some point in the process these ligands can dissociate from the metal in an in vivo context. In contrast to previous work, we were interested in assessing the behavior towards tumor cells of related complexes in which a ligand is bound to a metal by strong covalent bonds such as, for instance, a C–M σ bond stabilized by intramolecular coordination of an heteroatom, a bonding scheme that is typical of cyclometalated compounds. We reasoned that these cyclometalated ligands might remain attached to the metal throughout the biological process, whereas more labile ligands such as halides or solvents can dissociate and enable DNA binding. These stable ligands may additionally impart useful physical properties to the organometallic moiety (fluorescence or phosphorescence for instance), thus enabling the metal and ligand to be traced in the cells and in vivo. Other reasons for studying compounds with monoanionic bidentate ligands strongly bound to the metal center include: (i) the complexes obtained with only neutral ligands will be monocationic whereas the corresponding compounds having a neutral bidentate chelate will lead to dicationic species under similar conditions, and (ii) the electronic behavior (electrophilicity or nucleophilicity) of the ruthenium center will be significantly modified as compared to that of $Ru^{II}$ complexes containing neutral bidentate ligands. This might shed light upon its mechanism of interaction with cell-based macromolecules such as DNA or proteins, for instance. Previous studies of the reactivity of cycloruthenated complexes towards various nucleophilic or electrophilic reagents[11] have shown that, depending on the reaction conditions, the metallacyclic unit of these compounds is rather inert and that the existence of the cycloruthenated ligand is able to stabilize the whole complex. We thus decided to evaluate the biological activity of some of these compounds and were delighted to observe that they indeed display interesting properties as antitumor agents in vitro.[12] In this paper we wish to disclose the synthesis and characterization together with some further biological results that we have established in this area with cycloruthenated compounds.

## Synthesis and Characterization of the Cycloruthenated Compounds

The library of organoruthenium compounds employed in this study is shown in Scheme 1. Most starting cycloruthenated materials were obtained by the well-known cyclometalation reaction involving a C–H bond activation at an early stage of the procedure. The cycloruthenation of *N*,*N*-dimethyl(phenylmethyl)amine and the 2-phenylpyridine ligands to afford the starting materials **1** and **2** has been described elsewhere.[13]

Complexes **3** and **4** were synthesized more than a decade ago by the same cyclometalation reaction, although a transmetalation reaction using orthomercuriated derivatives of *N*,*N*-dimethylbenzylamine and (*R*)- or (*S*)-*N*,*N*-dimethyl(1-phenylethyl)amine, respectively, have been shown to be more efficient for obtaining these chloride derivatives.[14]

Compounds **5**–**8** were obtained by adding one equivalent of the required phosphane ligand {$PMe_2Ph$, $PPh_3$, or 1,3,5-triaza-7-phosphatricyclo[3.3.1.1]decane (PTA)[15]} at room temperature to solutions of **1** (to afford **5**) or **2** (to afford **6**, **7**, and **8**). Similar yields of product were obtained in dichloromethane, acetonitrile, and methanol.

The compounds were characterized by elemental analysis as well as by $^1H$ and $^{31}P$ NMR spectroscopy. Thus, a $^4J_{P,H}$ coupling constant was observed for the signal of the $\eta^6$-benzene ligand in **5**, thereby providing evidence for the *trans* geometry of the phosphane and the metalated arene. A chiral version of this compound has been reported previously along with its crystal structure.[16] The $^1H$ and $^{31}P$ NMR spectra of **6**, **7**, and **8** reveal that these compounds exist as only one regioisomer. The acetonitrile ligands gave rise to two signals in a 1:2 ratio and both of them show a $^5J_{P,H}$ coupling of 1.3–1.8 Hz. This clearly indicates the presence of two nonequivalent acetonitrile molecules located *trans* to each other at the ruthenium atom; the third one and the phosphane ligand are in the same plane as the orthoruthenated phenylpyridine unit. However, spectroscopic investigations were not helpful in determining the position of the phosphane ligand with respect to the C–N chelate in these complexes. The single-crystal X-ray diffraction analysis of **7** and **8** (see Figures 1 and 2, respectively, for ORTEP drawings of the cations) revealed that the geometry of the complexes was as predicted from the NMR spectroscopic data.

The identification of the atoms of the C–N chelate bound to Ru from the X-ray structure was, however, ambiguous, although the analysis of the lengths of the Ru–N bond of the Ru-NCMe units allowed us to establish unambiguously that the phosphorus atom is *trans* to the carbon atom of the chelate in both **7** and **8**. The Ru–N4 bond (2.029 Å) in **7** and Ru–N3 bond (2.024 Å) in **8** are typical of acetonitrile ligands bound to Ru *trans* to N, as can be verified from X-ray diffraction data of related compounds (see Table 1). Indeed, when the acetonitrile ligand is *trans* to C, the Ru–N distance is usually around 0.1 Å longer (see compounds **2** and **9**). Consequently, the phosphane ligands must be located *trans* to the carbon atom in **7** and **8**, and this fact is further highlighted by the longer Ru–P bonds [2.458(1) and 2.395(1) Å, respectively] than in any other $Ru^{II}$ complex studied in this paper [average: 2.367(1) Å]. This lengthening of the Ru–N and Ru–P bonds is expected for such bonds *trans* to a carbon atom, which is known to exert a larger *trans* influence than a nitrogen atom.[17]

As the positions *trans* to the carbon and *trans* to the nitrogen atom are identical here as far as their steric con-

 © 2007 Wiley-VCH Verlag GmbH & Co. KGaA, Weinheim 

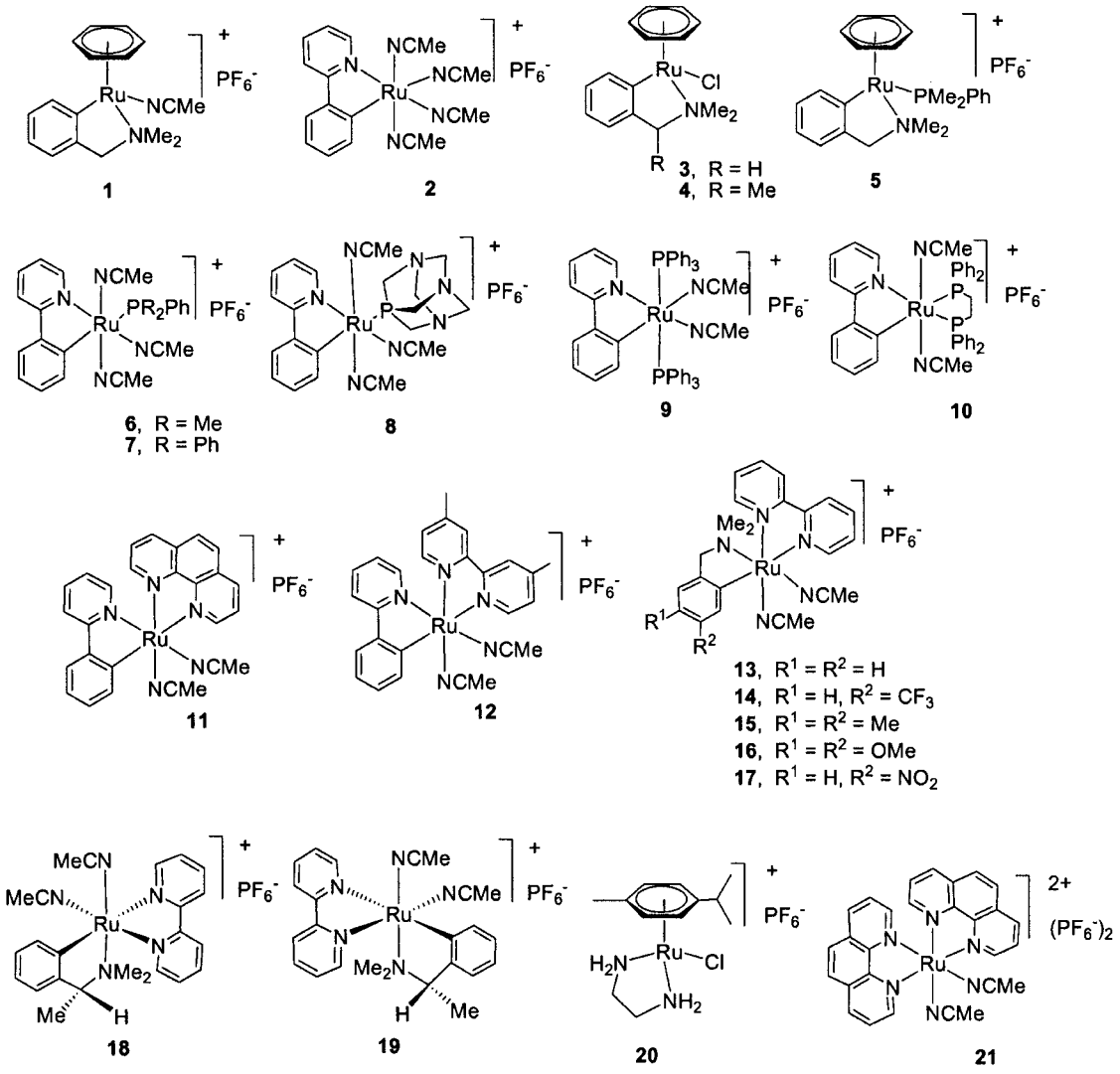


Scheme 1.

straints are concerned, the location of the phosphanes is very likely to be the result of a larger *trans* effect[17] of the phenyl group of the C–N chelate bonded to Ru through a C–Ru σ bond as compared to that of the pyridine unit of the same chelate. This result is in line with what was found recently when bidentate bipyridine or phenanthroline ligands were coordinated to the same compound **2** (in **12** and **11**) and for which one nitrogen atom was also coordinated *trans* to the Ru–C bond. The position of the $PPh_3$ and the PTA ligands *trans* to the carbon atom was, however, not expected as there are plenty of examples in the literature of the coordination of phosphane ligands in similar cyclometalated compounds of palladium for which it has been shown that the phosphane is indeed very reluctant to coordinate to the palladium atom *trans* to the carbon atom.[20] It was thus not unreasonable to expect the phosphane ligands to be bound to Ru in any position except the one *trans* to C. Complexes **7** and **8** are likely to be formed under kinetic control.

When two equivalents of phosphane were added to **2** in refluxing acetonitrile and the mixture stirred for 24 h a different reaction took place as we observed the formation of **9** due to the substitution of two acetonitrile ligands on the ruthenium atom by two triphenylphosphanes. The positions occupied by these latter ligands seemed to be symmetrical as only one signal is observed for the two phosphorus atoms in the $^{31}P$ NMR spectrum. In contrast to the previous case, the signals of the acetonitrile protons did not display any $J_{H,P}$ coupling with the phosphorus atoms, thereby suggesting that these ligands are located *trans* to the N and the C atoms of the phenylpyridine chelate, respectively. The structure of **9** was ascertained by an X-ray diffraction study on a single crystal.[21] The results are displayed in Figure 3, which shows an ORTEP view of the cationic part of **9**. It is at once apparent that the two phosphane ligands are located in a mutual *trans* arrangement. The Ru–P, Ru–C, and Ru–N bond lengths are in the expected range for such bonds.

 © 2007 Wiley-VCH Verlag GmbH & Co. KGaA, Weinheim 

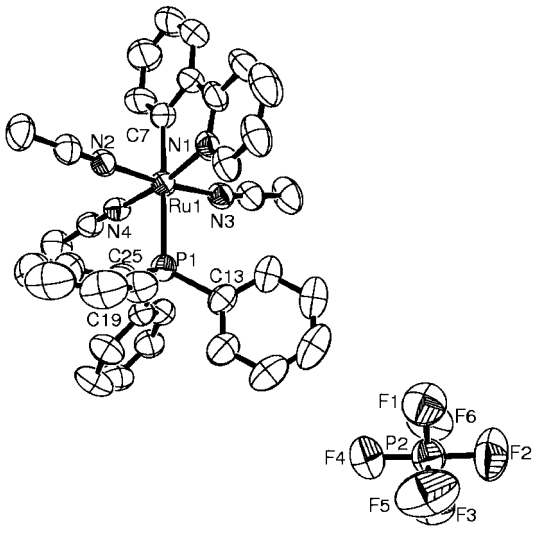


Figure 1. ORTEP view of compound **7**. Selected bond distances [Å] and angles [°]: Ru1–N2 2.009(3), Ru1–N(4) 2.026(3), Ru1–N3 2.039(3), Ru1–C7 2.049(4), Ru1–N1 2.088(3), Ru1–P1 2.458(1); N2–Ru1–N4 87.89(11), N2–Ru1–N3 172.84(11), N4–Ru1–N3 91.65(11), N2–Ru1–C7 87.63(12), N4–Ru1–C7 92.85(13), N3–Ru1–C7 85.26(12), N2–Ru1–N1 87.46(10), N4–Ru1–N1 171.53(11).

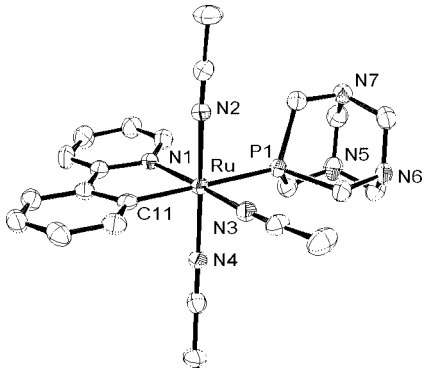


Figure 2. ORTEP view of the cation of **8**. Selected bond distances [Å] and angles [°]: Ru1–N2 2.013(2), Ru1–N4 2.022(2), Ru1–N3 2.024(2), Ru1–C11 2.068(3), Ru1–N1 2.087(2), Ru1–P1 2.395(1); N2–Ru1–N4 175.34(8), N2–Ru1–N3 88.70(8), N4–Ru1–N3 87.91(7), N2–Ru1–C11 90.75(8), N4–Ru1–C11 90.75(8), N3–Ru1–C11 95.46(9), N2–Ru1–N1 89.66(7), N4–Ru1–N1 93.41(7).

Adding one equivalent of 1,2-bis(diphenylphosphanyl)-ethane (dppe) to **2** in acetonitrile under the same conditions as for the synthesis of **9** afforded **10** in yields of up to 60%. Whereas the $^{31}P$ NMR spectrum of **10** shows an AB-type pattern for two nonequivalent phosphorus atoms ($^3J_{P,P}$ = 8 Hz), the signal of the acetonitrile protons is a singlet with no $J_{H,P}$ coupling visible. This situation clearly indicates that the acetonitrile ligands are located *trans* to each other. This was confirmed by the X-ray diffraction study of a single crystal of **10**, an ORTEP view of which is shown in Figure 4. We note that the Ru–C(8) and Ru–N(1) bond lengths are elongated by 5% (approx. 0.1 Å) relative to related compounds due to the large *trans* influence of the phosphorus atoms. The distances and angles of the other parts of the molecules are as expected.

Table 1. Ru–N bond lengths of Ru–NCMe units in various cycloruthenated complexes.

| | Ru–N [Å] | Atom or ligands *trans* to N | Ref. |
|---|---|---|---|
| **1** | 2.058(2) | $\eta^6$-benzene | [18] |
| | 2.055(6), 2.034(4) | N (PhPy)[a] | |
| **2**[b] | 2.154(6), 2.162(6) | C (PhPY) | [19] |
| | 2.019(5), 2.009(4) | N (MeCN) | |
| | 2.015(5), 2.009(4) | N (MeCN) | |
| | 2.026(3) | N (PhPy) | |
| **7** | 2.039(3) | N (MeCN) | this work |
| | 2.009(3) | N (MeCN) | |
| | 2.024(2) | N (PhPy) | |
| **8** | 2.013(2) | N (MeCN) | this work |
| | 2.022(2) | N (MeCN) | |
| **9** | 2.026(3) | N (PhPy) | |
| | 2.134(3) | C (PhPY) | this work |
| **10** | 2.001(6) | N (MeCN) | |
| | 2.001(6) | N (MeCN) | this work |
| **11** | 1.989(5) | N (PhPy) | |
| | 2.002(4) | N(phen)[c] | [19] |
| **16** | 2.005(7) | N [3,4-$(OMe)_2$dmba][d] | |
| | 2.045(7) | N(bipy)[e] | [18] |
| **18**–**19** | 2.017(5), 2.009(5) | N [(*R*,*S*)-1-PEA][f] | |
| | 2.001(5), 2.012(4) | N(bipy) | this work |

[a] PhPy = orthometalated 2-phenylpyridine. [b] This compound exists in two different forms, although the molecular structure of each is identical. [c] phen = phenanthroline. [d] dmba = orthometalated *N*,*N*-dimethylbenzylamine. [e] bipy = 2,2′-bipyridine. [f] PEA = orthometalated phenylethylamine.

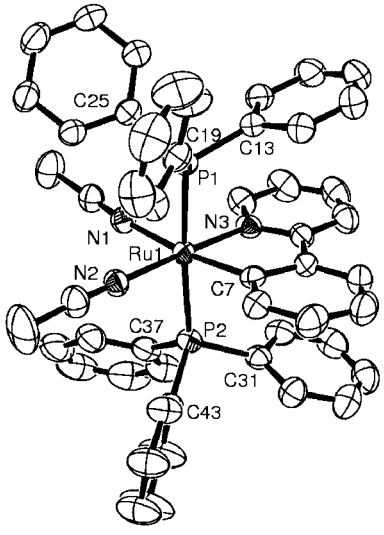


Figure 3. ORTEP view of the cationic part of compound **9**. Selected bond distances [Å] and angles [°]: Ru1–N2 2.026(3), Ru1–N3 2.065(3), Ru1–C7 2.058(4), Ru1–N1 2.134(3), Ru1–P1 2.3765(9), Ru1–P2 2.3781(9); N2–Ru1–P1 92.94(8), N2–Ru1–N3 177.20(10), P2–Ru1–N3 88.73(7), N2–Ru1–C7 101.57(12), N1–Ru1–C7 171.72(11), N3–Ru1–C7 79.22(12), N2–Ru1–N1 86.19(10).

The remaining compounds of our library of cycloruthenated compounds (see Scheme 1) that do not contain a phosphane ligand (**11**–**19**) have either been described earlier (**11**[19] and **13**–**17**[18]) or were synthesized by following similar procedures (**12** as **11** and **18**, **19** as **13**) Compounds **18** and **19** are chiral versions of **13** with the two opposite

 © 2007 Wiley-VCH Verlag GmbH & Co. KGaA, Weinheim 

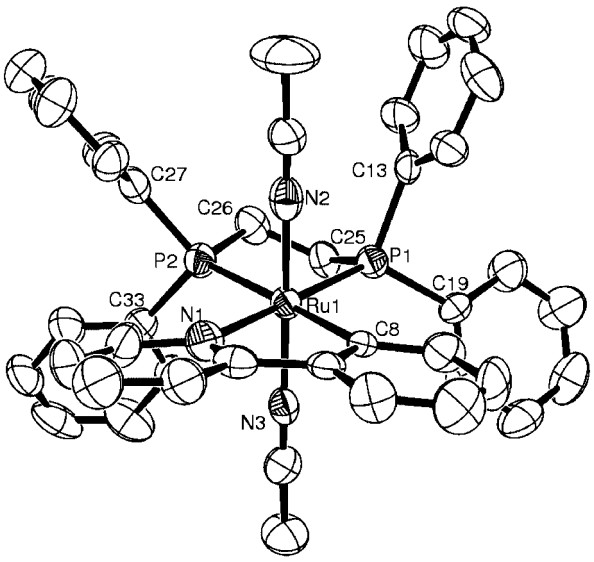


Figure 4. ORTEP view of the cationic part of compound **10**. Selected bond distances [Å] and angles [°]: Ru1–N3 2.001(6), Ru1–N2 2.001(6), Ru1–C8 2.096(6), Ru1–N1 2.118(5), Ru1–P1 2.343(2), Ru1–P2 2.373(2); N3–Ru1–N2 175.9(2), P1–Ru1–P2 83.08(6), C8–Ru1–N1 77.6(2), C8–Ru1–P1 100.42(17), N1–Ru1–P2 98.86(18).

configurations at the benzylic fragment of the cycloruthenated ligand. The starting materials for the synthesis of **18** and **19**, namely $[(\eta^6\text{-}C_6H_6)Ru\{C_6H_4\text{-}2\text{-}(R)\text{-}CHMeNMe_2\}(NCMe)]PF_6$ and $[(\eta^6\text{-}C_6H_6)Ru\{C_6H_4\text{-}2\text{-}(S)\text{-}CHMeNMe_2\}(NCMe)]PF_6$ respectively, were obtained by a direct cyclometalation of the corresponding (*R*)- or (*S*)-1,1-*N*,*N*-dimethyl(phenylethyl)amine, respectively.[12] Due to the chirality at the ruthenium center these two complexes were a mixture of diastereomers with a diastereomeric excess (*de*) of 48% in favor of the ($R_C$,$S_{Ru}$) and ($S_C$,$R_{Ru}$) isomers rather than the ($R_C$,$R_{Ru}$) and ($S_C$,$S_{Ru}$) isomers, respectively.

We will only describe the synthesis and characterization of **18** from $[(\eta^6\text{-}C_6H_6)Ru\{C_6H_4\text{-}2\text{-}(R)\text{-}CHMeNMe_2\}(NCMe)]PF_6$ as **19** displays exactly the same behavior. The $\eta^6$-benzene ligand was removed by adding one equivalent of bipyridine in acetonitrile and stirring at room temperature for 12 h, which led to good yields of **18**. The $^1$H NMR spectra indicated that this complex also exists as diastereomers, with the *de* having dropped to 22%. Thus, **18** is a mixture of two diastereomers (**18maj** and **18min**).

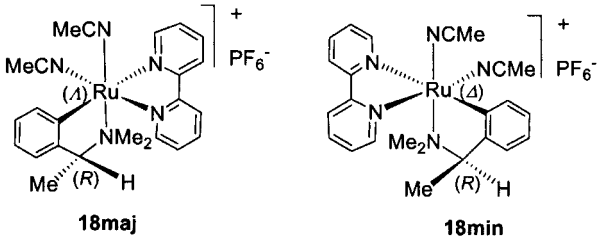


Crystallization from $CH_2Cl_2/Et_2O$ afforded crystals that consisted mainly of the major isomer **18maj**, with a *de* value of 98.5% (note that the mother liquor from which these crystals were obtained now has a *de* = 0% as a result of the removal of part of the major diastereomer). Redissolution of this compound did not cause any change in its *de*, even after several days at room temperature. Moreover, the composition of the initial mixture of diastereomers in $CD_3CN$ did not vary with temperature in the range –40 to 55 °C. These data allowed us to conclude that these diastereomers, in contrast to their pseudo-tetrahedral counterpart $[(\eta^6\text{-}C_6H_6)Ru\{C_6H_4\text{-}2\text{-}(R)\text{-}CHMeNMe_2\}(NCMe)]PF_6$, are very likely to be rigid in solution such that their epimerization, if it takes place at all, should occur at much higher temperatures. An X-ray diffraction study was performed for each of the complexes. An ORTEP of **18**, together with some typical distances and angles, is given in Figure 5; the data for **19**, which are obviously identical to those of **18**, have been deposited.

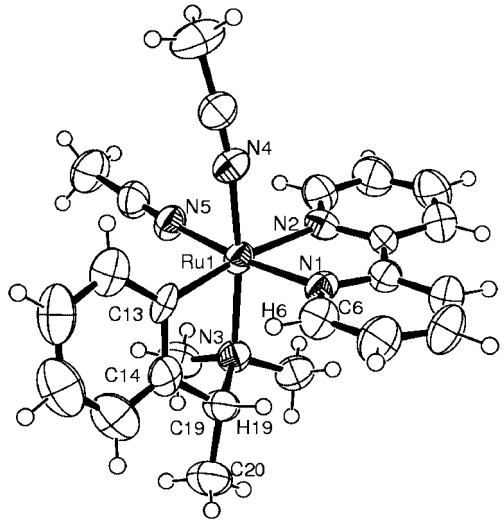


Figure 5. ORTEP view of the cationic part of compound **18**. Selected bond distances [Å] and angles [°]: Ru1–N3 2.175(5), Ru1–N4 2.018(5), Ru1–N5 2.001(5), Ru1–C13 2.027(6), Ru1–N1 2.057(5), Ru1–N2 2.148(5); N2–Ru1–N1 78.16(19), N2–Ru1–N3 96.69(18), N3–Ru1–C13 78.4(2), N4–Ru1–N5 84.5(2), N4–Ru1–N3 172.4(2).

It is immediately clear that the structure is similar to that of the *N*,*N*-dimethylbenzylamine derivatives as one of the bipyridine nitrogen atoms is linked to Ru *trans* to the C atom of the C–N chelate. The configuration at the ruthenium metal is such that the major diastereomer has a *lambda* (Λ)[22] configuration at the ruthenium atom associated with an *R* configuration at the carbon atom, whereas a *delta* (Δ) configuration was found for the other derivative which has an *S* configuration at the benzylic carbon atom. In order to verify that the crystal selected for the X-ray diffraction study was indeed the major isomer, we recorded its $^1$H NMR spectra. The 2D NOESY spectrum shows that there is an interaction between the benzylic proton and the *ortho* H [on C(6)] of the bipyridine [they are around 2.53 Å apart; see HC(19)···HC(6) in Figure 5]. This cannot be the case in the minor isomer as the C–N chelate must have rotated by 180° around the Ru–C bond, which places the benzylic proton away from the bipyridine one.

 © 2007 Wiley-VCH Verlag GmbH & Co. KGaA, Weinheim 

## Solubility and Stability of the Complexes

### Solubilities

Except for **8**, most of the cycloruthenated compounds are poorly soluble in pure water. For instance, complex **11** has a solubility in water of only 0.1 mM. However, all of them are sufficiently soluble in DMSO, MeCN, or alcohols (methanol, ethanol). The samples for in vitro tests were obtained from 50.0 mM solutions of the ruthenium complexes in pure DMSO or MeCN, which were then sequentially diluted with the required amount of cell culture media in order to obtain the solutions to be studied, whose concentration ranged from 0.2 to 50 μM. These solutions were assimilated to water solutions of our compounds. In marked contrast to the other compounds, **8** has a sufficiently high solubility in water (3.2 mM) that its characterization by $^1$H NMR spectroscopy in $D_2O$ proved possible. This latter study showed that the MeCN ligands are not displaced by water since a $^5J_{P,H}$ coupling was observed for the signals of the acetonitrile ligands.

As compound **11** gave some of the best results with respect to in vitro activity, we studied the behavior of solutions of this complex in water. Because of its insufficient aqueous solubility we could not follow the behavior of such solutions by NMR spectroscopy. Nevertheless, we found that the MeCN ligands were not displaced by $CD_3OD$ or [$D_6$]acetone.

### Stabilities

We initially verified that the UV/Vis spectrum of a $10^{-4}$ M solution of **11** in pure $CH_3CN$ did not change with time (after 48 h). This somewhat predictable result proved that the C–N chelate is not labile in this medium. The same spectrum and the same stability over a 24 h period were observed for $10^{-4}$ M solutions of **11** obtained from either a $CH_3CN$ solution or a DMSO solution of this compound to which water, buffered at pH 7, was added. This result highlighted the fact that the behavior of solutions of **11** in water is not dependent upon the solvent used to obtain their mother solutions. No changes were observed in the UV/Vis spectra when the pH of the solution was increased to 9 or when sodium chloride (150 mM) was added to the water solution at pH 7. Moreover, no significant changes were observed for any of these solutions after 48 h in the dark.

We also found that the stability of aqueous solutions of **11** changed dramatically when they were irradiated with an halogen lamp (approx. 150 W) for up to 20 minutes as we observed the disappearance of the absorptions at 400 and 450 nm together with the appearance of a new absorption at around 366 nm. Ryabov et al. have recently reported a related study of the behavior of a methanol solution of **11**, which they found to be photosensitive,[19] and they suggested that the MeCN ligand is substituted by methanol upon irradiation. It is very likely that our water solution of **11** behaves similarly to give an aquo species that is more prone to oxidation as we observed a UV/Vis spectrum that is very similar to that described in MeOH. We also checked that a solution used for in vitro tests irradiated as above had a lower antitumor activity than the nonirradiated one (see Table 2 below).

## Biological Effects

### In Vitro Cell Growth Inhibition

To evaluate the antitumor potential of the various ruthenium-derived compounds we analyzed their effect on cell proliferation. A-172 cells derived from a human glioblastoma were treated with different doses of complexes from our library or with cisplatin and the cells' viability was determined by measuring a specific cellular enzymatic activity of the remaining living cells after 48 h. We next studied the effect of these compounds on other cell lines derived from adenocarcinoma (HCT-116) and lymphoma (RDM-4) and evaluated their $IC_{50}$ values. The results obtained with the three different cell lines are summarized in Table 2.

Table 2. $IC_{50}$ [μM] values of the cycloruthenated complexes compared with those of reference compounds (cisplatin, **20**, and **21**) for three cell lines.

| | Tumor cell line | | | Ref. | Names used in ref.[12] |
|---|---|---|---|---|---|
| | A-172 | HCT-116 | RDM-4 | | |
| cisplatin | 3.9±0.2 | 3±2 | 3±2 | [12] | |
| **2** | >50 | >50 | > 50 | [12] | RDC8 |
| **3** | >50 | >50 | > 50 | [12] | RDC3 |
| **4** | >50 | >50 | > 50 | | |
| **5** | 4.8±0.2 | 3±2 | 30±10 | [12] | RDC6 |
| **6** | 1.7±03 | 3±2 | 10±5 | [12] | RDC9 |
| **8** | >50 | >50 | – | this work | |
| **9** | 15±2 | 5±2 | – | this work | |
| **10** | 3±2 | 7±2 | – | this work | |
| **11**[b] | 1.9±0.2 | 3±2 | 10±5 | [12] | RDC11 |
| **12** | 3±2 | 3±2 | 10±5 | this work[a] | RDC12 |
| **13** | 12±2 | 10±5 | 10±5 | this work | |
| **14** | 6±2 | 6±2 | – | this work | |
| **15** | 9±2 | 3±2 | – | this work | |
| **16** | >50 | >50 | 30±10 | this work | |
| **17** | 15±2 | 15±5 | 30±10 | this work | |
| **18** | >50 | 20±5 | – | this work | |
| **19** | >50 | 20±5 | – | this work | |
| **20** | 5±2 | 20±5 | – | this work | |
| **21** | >50 | >50 | – | this work | |

[a] The $IC_{50}$ values reported for this compound in ref.[12] are erroneous. [b] The $IC_{50}$ values obtained for solutions of **11** irradiated with visible light are about twice as high as those for solutions protected from light (the data given here are for solutions of **11** protected from light).

We first tested the complexes **3**–**5** that are structurally related to **20**,[6] which is known to inhibit the growth of A-2780 human ovarian cancer cells. The $IC_{50}$ values for **3** and **4** show that these species are inactive, whereas **5** displayed a good activity. According to the above classification, **20** displays a moderate $IC_{50}$ value of 5–20 μM with our cell lines.

 © 2007 Wiley-VCH Verlag GmbH & Co. KGaA, Weinheim 

In order to mimic the anticancer behavior of cisplatin we then turned our attention to ruthenium-containing species that have two mutually *cis* and potentially aquatable coordination sites for binding to DNA. We thus selected alternative cycloruthenated compounds containing from two to four MeCN ligands on Ru. Complex **2**, which has four acetonitrile ligands bound to the ruthenium atom, was found to be inactive. However, substitution of these MeCN ligands with either 2,2′-bipyridine (bipy), phenanthroline (phen), or phosphane or diphosphane ligands significantly improved its activity. This increased activity for the bipy or phen derivatives might be related to the fact that ruthenium complexes containing bipyridine or phenanthroline are known to be cytotoxic due to their potential for intercalation.[1g] Compounds **5**–**15** thus displayed good to medium activities, with the exception of **8**, which displayed a disappointingly low activity with two cell lines (see Table 2). This low activity is not correlated to the instability of the complex towards oxygen as we verified that only 15% of the compound is oxidized in water solution after 48 h [$^1$H and $^{31}$P NMR spectra indicated the presence of O=P($CH_2$-N-$CH_2$)$_3$[23]]. Note, however, that the two MeCN ligands do not have to be mutually *cis*, as **9** and **10**, which have two MeCN ligands that are *cis* and *trans* to each other, respectively, displayed similarly good activities

As this stage, we checked whether the presence of a Ru–C bond has a significant effect on the activity of such compounds. Indeed, we found that **21**,[24] which is structurally closely related to **11**, displayed no activity. We note, however, that **21** has a double positive charge on the Ru atom whereas **11** has only a single charge. The increased activity on going from **21** to **11** might thus be due to the presence of the Ru–C bond but also to a larger lipophilicity for **11** as compared to **21**.

The putative target of the cycloruthenated compounds is DNA, which is a chiral molecule. As a consequence we prepared and tested the two enantiomeric complexes **18** and **19**, which both consist of a mixture of diastereomers with a *de* of 98.5 (see above), in order to observe potential chiral recognition. Unfortunately, these two complexes were found to be only poorly active and no conclusion could be drawn.

We were also interested in examining the effect of the electronic properties of the metalated phenyl unit upon the activity. The trifluoromethyl-substituted compound **14** and the dimethyl-substituted complex **15** were found to be as efficient as **13**, whereas the dimethoxy and nitro derivatives (**16** and **17**, respectively) are less active. These data did not allow us to correlate the activity of the organoruthenium compounds to the electronic nature of the cyclometalated ligand.

### Induction of G1 Arrest and Apoptosis

To understand the effect of our compounds on cell growth we examined their effect on the cell cycle by FACS (Fluorescence Activated Cell Sorter) analysis. Treatment of RDM-4 cell lines with 15 μM of **6** or **11** (near to the approximate $IC_{50}$ value) led to a marked increase in the number of cells in the G0/G1 phase. On the other hand, treatment with 45 μM of **6** or **11** (total inhibiting concentration) led to the formation of hypodiploid particles that created an important sub-G1 phase. The number of cells accumulated in the sub-G1 phase was lower than 10% at 24 h, but exceeded 50% at 48 h and reached 60% at 72 h. These results show that cycloruthenated compounds are able to both induce a G1 cell-cycle arrest and DNA fragmentation, which suggests induction of apoptosis.

To further analyze the characteristics of cell death induced by cycloruthenated compounds we performed immunocytochemistry experiments to assess the status of the nucleus and the possible activation of caspase 3, a protease induced by, and involved in, the apoptotic process. A-172 cells were treated with cisplatin, **6**, or **11** for 24 or 48 h. After fixation, the cells were labeled with an antibody that recognizes the active fragment of caspase 3. The nuclei were stained with Hoechst colorant. The cells treated with cisplatin or cycloruthenated compounds showed nuclei alterations, such as fragmentation or condensation. Moreover, we observed that cycloruthenated compounds stimulate Bax protein levels, which suggests that these compounds induce apoptosis by a mitochondrial pathway.[12] However, it is possible that other apoptotic pathways involving Fas and/or caspase 8 might still operate.

## Conclusions

A series of cycloruthenated complexes, some of which have been synthesized and characterized for the first time here, have been tested for their biological activities. Some of these compounds induce cytostatic and cytotoxic effects on mammalian tumor cells at least as effectively as cisplatin. Taking into account all of the results we have not yet been able to determine the nature of the particular pharmacophore. Cellular studies have shown that several ruthenium-derived compounds lead to $G_1$ arrest and induce apoptosis in various tumor lines of glioblastoma, neuroblastoma, and lymphoma. Several investigations are currently underway to improve the potential use of these substances as a cancer treatment. These include the determination of their in vivo toxicity and efficiency and the evaluation of the DNA-drug interaction at the molecular level.

## Experimental Section

**Chemicals:** All reactions were performed in Schlenk tubes under argon. Further workup, chromatography over standardized alumina, and crystallization were also performed under argon. We note, however, that our compounds are stable in air as solids once isolated, whereas solutions are stable for up to 48 h. Solvents were dried and distilled under argon prior to use: diethyl ether and *n*-hexane over sodium/benzophenone, dichloromethane and acetonitrile over calcium hydride. Mass spectra were recorded with a JEOL JMS-SX102A instrument with *m*-nitrobenzyl alcohol as the matrix. $^1$H and $^{13}$C NMR spectra were recorded with FT-Bruker AC 300 and ARX 500 spectrometers operating at 300.13 and 500.14 MHz

 © 2007 Wiley-VCH Verlag GmbH & Co. KGaA, Weinheim 

for $^1H$ and 75.47 and 125.77 MHz for $^{13}C$, respectively. 2D COSY and $^1H/^{13}C$ HSQC sequences were used to help the assignments of the $^1H$ and $^{13}C$ spectra. The chemical shifts are referenced to the residual solvent peaks; chemical shifts ($\delta$) and coupling constants ($J$) are expressed in ppm and Hz, respectively. Elemental analyses were performed by the Service de Microanalyse de l'Institut de Chimie, Strasbourg (France); the presence of crystallization solvent in some compounds was ascertained by $^1H$ NMR spectroscopy.

**[Ru(η⁶-C₆H₆){2-(CH₂NMe₂-κ*N*)-C₆H₄-κ*C*¹}(PMe₂Ph)]PF₆ (5):** A yellow solution of complex **1** (0.08 g, 0.156 mmol) and $PMe_2Ph$ (0.023 mL, 0.162 mmol) was stirred in $CH_2Cl_2$ (10 mL) for 3 h at room temperature. The reaction mixture was concentrated in vacuo and washed with *n*-hexane. The yellow residue was dissolved in a minimum amount of $CH_2Cl_2$ (1 mL) and a yellow solid was precipitated by the addition of *n*-hexane (0.09 g, 95% yield). $C_{23}H_{23}F_6NP_2Ru\cdot 1/2CH_2Cl_2$ (632.91): calcd. C 44.13, H 4.69, N 2.19; found C 44.30, H 4.59, N 2.16. $^1H$ NMR ($CD_3CN$): $\delta$ = 7.75 (dt, $^3J$ = 7.5 Hz, 1 H, $H^6$), 7.39 (tdd, $^3J$ = 7.5, $^4J$ = 1.7 Hz, 1 H, $H^p$), 7.22 (td, $^3J$ = 8.0, $^4J$ = 2.0 Hz, 2 H, $H^m$), 7.08 (tdd, $^3J$ = 7.1 Hz, 1 H, $H^4$ or $H^5$), 7.00–6.88 (m, 3 H, $H^o$ and $H^4$ or $H^5$), 6.72 (d, $^3J$ = 7.5 Hz, 1 H, $H^3$), 5.74 (d, $^3J_{H,P}$ = 1.1 Hz, 6 H, $C_6H_6$), 2.85 and 2.43 (AB, $^2J$ = 14.5 Hz, 2 H, $CH_2$), 2.77 (d, $^4J_{H,P}$ = 1.1 Hz, 3 H, NMe), 2.66 (s, 3 H, NMe), 1.99 (d, $^2J$ = 9.3 Hz, 3 H, PMe), 1.50 (d, $^2J$ = 9.7 Hz, 3 H, PMe) ppm. $^{31}P\{^1H\}$ NMR ($CD_3CN$): $\delta$ = 6.37 (s, 1 P, $PMe_2Ph$), –142.97 (sept, $^1J_{P,F}$ = 711 Hz, 1 P, $PF_6$) ppm.

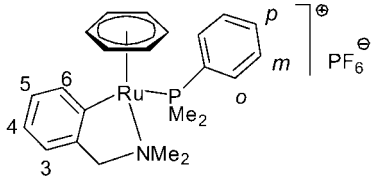


**[Ru(C₆H₄-2-C₅H₄N)(PMe₂Ph)(NCMe)₃]PF₆ (6):** Dimethylphenylphosphane (0.031 mL, 0.22 mmol) was added to a solution of compound **2** (0.124 g, 0.22 mmol) in MeCN (5 mL) and the solution was stirred at room temp. for 18 h. The yellowish-green solution was then filtered through $Al_2O_3$ with MeCN as eluent. A yellow fraction was collected and concentrated in vacuo. The powder thus formed was dissolved in a minimum amount of MeCN/$Et_2O$. After addition of *n*-hexane **6** was obtained as a yellow powder (0.122 g, 84% yield). $C_{25}H_{28}F_6N_4P_2Ru$ (662.07): calcd. C 45.39, H 4.27, N 8.47; found C 45.35, H 4.49, N 8.33. $^1H$ NMR ($CD_3CN$): $\delta$ = 8.39 (ddd, $^3J$ = 5.8, $^4J$ = 1.6, $^5J$ = 0.8 Hz, 1 H, $H^{12}$), 8.08 (dddd, $^3J$ = 7.1, $^4J_{H,P}$ = 4.7, $^4J$ = 1.3, $^5J$ = 0.5 Hz, 1 H, $H^5$), 7.89 (d, $^3J$ = 8.1 Hz, 1 H, $H^9$), 7.80 (d, $^3J$ = 7.8 Hz, 1 H, $H^8$), 7.71–7.63 (m, 3 H, $H^{10}$ and $H^o$), 7.53–7.49 (m, 2 H, $H^m$), 7.44 (t, $^3J$ = 7.4 Hz, 1 H, $H^p$), 7.20 (td, $^3J$ = 7.3, $^4J$ = 1.4 Hz, 1 H, $H^6$), 7.06 (td, $^3J$ = 7.5, $^4J$ = 1.4 Hz, 1 H, $H^7$), 6.92 (ddd, $^3J$ = 7.3, $^3J$ = 5.8, $^4J$ = 1.5 Hz, 1 H, H11), 2.33 (d, $^5J_{H,P}$ = 1.7 Hz, 3 H, NCMe), 1.97 (d, $^5J_{H,P}$ = 1.8 Hz, 6 H, 2 NCMe), 1.86 (d, $^2J_{H,P}$ = 5.8 Hz, 6 H, $PMe_2$) ppm. $^{13}C\{^1H\}$ NMR ($CD_3CN$): $\delta$ = 185.5 ($C^4$), 170.2 ($C^2$), 156.6 ($C^{12}$), 147.1 ($C^3$), 138.0 ($C^5$), 137.5 ($C^{10}$), 131.0 ($C^o$), 129.6 and 129.7 ($C^m$), 129.3 and 129.2 ($C^6$ and $C^p$), 124.4 ($C^8$ and $C^{ipso}$), 123.6 (N*C*Me), 122.9 ($C^7$), 122.3 ($C^{11}$), 119.4 ($C^9$), 13.55 and 13.41 ($PMe_2$), 4.31 and 3.99 (NC*Me*) ppm. $^{31}P\{^1H\}$ NMR ($CD_3CN$): $\delta$ = –7.08 (s, 1 P, $PMe_2$), –144.40 (sept, $^1J_{P,F}$ = 704.6 Hz, 1 P, $PF_6$) ppm.

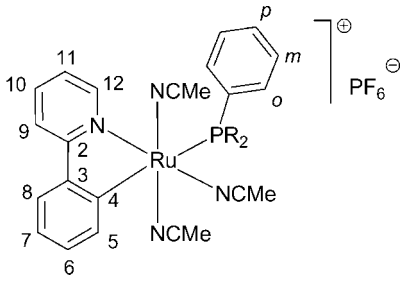


***trans*-[Ru(C₆H₄-2-C₅H₄N)(PPh₃)(NCMe)₃]PF₆ (7):** Complex **2** (0.200 g, 0.35 mmol) and $PPh_3$ (0.093 g, 0.35 mmol) were dissolved in 30 mL of acetonitrile and stirred at room temperature for 72 h. The solvent was then removed in vacuo and the product was purified by column chromatography over $Al_2O_3$ using dichloromethane as eluent. A yellow fraction was collected and the solvent was removed in vacuo. The solid was dissolved in a mixture of $CH_3CN$/$CH_2Cl_2$ (1:1) and slow diffusion of $Et_2O$ into this solution afforded **7** as yellow crystals, which were filtered off, washed three times with $Et_2O$, and dried in vacuo. Yield: 0.172 g (62%). $C_{35}H_{32}F_6N_4P_2Ru$ (785.66): calcd. C 53.51, H 4.11, N 7.13; found C 53.62, H 4.33, N 7.11. $^1H$ NMR ($CD_3CN$): $\delta$ = 8.50 (d, $^3J$ = 5.8 Hz, 1 H, $H^{12}$), 8.10 (ddd, $^3J$ = 7.4, $^4J$ = 4.6, $^5J$ = 1.2 Hz, 1 H, $H^5$), 7.94 (d, $^3J$ = 8 Hz, 1 H, $H^9$), 7.85 (dd, $^3J$ = 7.7, $^4J$ = 1.3 Hz, 1 H, $H^8$), 7.70 (ddd, $^3J$ = 8.1, $^4J$ = 7.4, $^5J$ = 1.4 Hz, 1 H, $H^{10}$), 7.64–7.59 (m, 6 H, $PPh_3$), 7.49–7.44 (m, 9 H, $PPh_3$), 7.24 (tt, $^3J$ = 7.4, $^4J$ = 1.4 Hz, 1 H, $H^6$ or $H^7$), 7.10 (td, $^3J$ = 7.4, $^4J$ = 1.4 Hz, 1 H, $H^6$ or $H^7$), 6.76 (ddd, $^3J$ = 7.4, $^4J$ = 5.8, $^5J$ = 1.4 Hz, 1 H, $H^{11}$), 2.00 (s, $^5J_{H,P}$ = 1.3 Hz, 3 H, $CH_3CN$), 1.82 (s, $^5J_{H,P}$ = 1.3 Hz, 6 H, $CH_3CN$) ppm. $^{31}P$ NMR ($CD_3CN$): $\delta$ = 27.35 (s, $PPh_3$), –144.03 (sept, $^1J$ = 706 Hz, $PF_6$) ppm. MS ($FAB^+$): *m/z* (%) 641 (13) $[M + H]^+$, 600 (3) $[M + H – MeCN]^+$, 559 (12) $[M + H – 2MeCN]^+$, 518 (68) $[M + H – 3MeCN]^+$. 379 (100) $[M + H – PPh_3]^+$, 338 (60) $[M + H – PPh_3 – MeCN]^+$, 297 (65) $[M + H – PPh_3 – 2MeCN]^+$, 256 (28) $[M + H – PPh_3 – 3MeCN]^+$.

***trans*-[Ru(C₆H₄-2-C₅H₄N)(PTA)(NCMe)₃]PF₆ (8):** PTA was synthesized as described in the literature.[23] One equivalent of PTA (0.35 g, 2.2 mmol) was added to an orange solution of **2** (1.26 g, 2.16 mmol) in MeOH (300 mL). The yellow solution thus obtained was stirred at room temperature for about 4 h and then dried in vacuo. The resulting yellow powder was dissolved in $CH_2Cl_2$. This solution was washed two times with half its volume of water and dried with $MgSO_4$. *Caution*: this procedure is aimed at removing the impurities that are soluble in water; however, this should be done rapidly in order to avoid oxidation of the product and to limit its dissolution in water. The $CH_2Cl_2$ was then removed in vacuo and the powder thus formed dissolved in $CH_3CN$ to which $Et_2O$ was added. This afforded yellow microcrystals of **8** (80 mg, 22% yield). $C_{23}H_{29}F_6N_7P_2Ru$ (680.53): calcd. C 40.59, H 4.30, N 14.41; found C 40.68, H 4.38, N 14.22. $^1H$ NMR ($D_2O$, 400 MHz): $\delta$ = 8.55 (d, $^3J$ = 5.6 Hz, 1 H, $H^{12}$), 8.17 (ddd, $^3J$ = 7, $^3J_{H,P}$ = 4.9, $^4J$ = 1 Hz, 1 H, $H^5$), 8.03 (d, $^3J$ = 8 Hz, 1 H, $H^9$), 7.98 (d, $^3J$ = 8 Hz, 1 H, $H^8$), 7.85 (td, $^3J$ = 8, $^4J$ = 1.2 Hz, 1 H, $H^{10}$), 7.41 (dd, $^3J \approx$ 7.3, $^1J$ = 1 Hz, 1 H, $H^6$), 7.26 (td, $^3J$ = 7.3, $^4J$ = 1 Hz, 1 H, $H^7$), 7.19 (ddd, $^3J$ = 7.2, $^3J$ = 5.6, $^4J$ = 1.2 Hz, 1 H, $H^{11}$), 4.60 (s, 6 H, $NCH_2N$), 4.42 (d, $^2J_{H,P}$ = 3.2 Hz, 6 H, $PCH_2$), 2.6 (d, $^5J_{H,P}$ = 1.6 Hz, 3 H, $NCCH_3$ equatorial), 2.03 (d, $^5J_{H,P}$ = 1.6 Hz, 6 H, $NCCH_3$ apical) ppm. $^{13}C\{^1H\}$ NMR: $\delta$ = 157.5 ($C^{12}$), 137.5 ($C^{10}$), 137.2 ($C^5$), 130 ($C^6$), 125 ($C^8$), 124.4 ($C^7$), 123.3 ($C^{11}$), 119.8 ($C^9$), 72 (d, $J_{C,P}$ = 7 Hz, $NCH_2N$), 49 (s, $J_{C,P}$ = 6 Hz, $PCH_2$), 3.8 ($NCCH_3$), 3.4 ($NCCH_3$) ppm. $^{31}P\{^1H\}$ NMR ($CD_3CN$, 300 MHz): $\delta$ = –68.4 (s, 1 P, PTA), –143.4 (sept, $^1J_{P,F}$ = 706 Hz, 1 P, $PF_6$) ppm.

 © 2007 Wiley-VCH Verlag GmbH & Co. KGaA, Weinheim 

***trans*-[Ru($C_6H_4$-2-$C_5H_4N$)($PPh_3$)$_2$($NCMe$)$_2$]$PF_6$ (9):** Complex **2** (0.200 g, 0.35 mmol) and $PPh_3$ (0.186 g, 0.71 mmol) were dissolved in 30 mL of acetonitrile and refluxed for 24 h. The solvent was then removed in vacuo and the product was purified by column chromatography over $Al_2O_3$ using dichloromethane as eluent. A yellow fraction was collected and the solvent was removed in vacuo. The solid was dissolved in a mixture of $CH_3CN/CH_2Cl_2$ (1:1) and slow diffusion of $Et_2O$ into this mixture afforded **9** as yellow crystals, which were filtered off, washed three times with $Et_2O$, and dried in vacuo. Yield: 0.190 g (54%). $C_{31}H_{44}F_6N_3P_3Ru$ (766.68): calcd. C 61.15, H 4.40, N 4.17; found C 61.15, H 4.59, N 4.47. $^1$H NMR ($CD_3CN$): $\delta$ = 7.95 (dd, $^3J$ = 5.9, $^4J$ = 0.7 Hz, 1 H, H$^{12}$), 7.26 (d, $^3J$ = 7.4 Hz, 1 H, H$^5$), 7.4–7.0 (m, 33 H, $PPh_3$, H$^8$, H$^9$ and H$^{10}$), 6.75 (td, $^3J$ = 7.4 Hz, 1 H, H$^6$ or H$^7$), 6.67 (td, $^3J$ = 7.4, $^4J$ = 1.5 Hz, 1 H, H$^7$ or H$^6$), 6.47 (td, $^3J$ = 5.8, $^4J$ = 1.4 Hz, 1 H, H$^{11}$), 2.14 (s, 3 H, $CH_3CN$), 1.96 (s, 3 H, $CH_3CN$) ppm. $^{13}$C{$^1$H} NMR ($CD_3CN$): $\delta$ = 180.9 (C$^4$), 167.1 (C$^2$ or C$^3$), 152.5 (C$^{12}$), 146.5 (C$^3$ or C$^2$), 141.4 (C$^5$), 135.4 (C$^{10}$ or C$^8$), 134.3 (t, $J_{C,P}$ = 5.2 Hz, C$^o$), 132.7 ($J_{C,P}$ = 19 Hz, C$^{ipso}$), 130.2 (s, C$^p$), 128.8 (t, $J_{C,P}$ = 8 Hz, C$^m$), 128.7 (C$^6$), 123.7 (C$^8$ or C$^{10}$), 122.15 (C$^{11}$), 120.9 (C$^7$), 119.09 (C$^9$), 30.9 (*Me*NC) ppm. $^{31}$P NMR ($CD_3CN$): $\delta$ = 35.3 (s, $PPh_3$), –143.4 (sept, $^1J_{P,F}$ = 710 Hz, $PF_6$) ppm. MS (FAB$^+$): *m/z* (%) 821 (20) [M – MeCN]$^+$, 780 (95) [M – 2MeCN]$^+$, 518 (100) [M – 2MeCN – $PPh_3$]$^+$, 256 (9) [M – 2MeCN – 2$PPh_3$]$^+$.

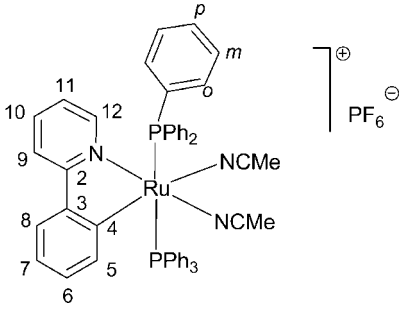


***cis*-[Ru($C_6H_4$-2-$C_5H_4N$)(dppe)($NCMe$)$_2$]$PF_6$ (10):** Complex **2** (0.200 g, 0.355 mmol) and dppe ($Ph_2PC_2H_4PPh_2$; 0.141 g, 0.355 mmol) were dissolved in 30 mL of methanol to yield a yellow solution. This solution was refluxed for 19 h. The solvent was then evaporated in vacuo and the product filtered through $Al_2O_3$ using dichloromethane as eluent. A yellow fraction was collected and concentrated. Diethyl ether was then added to precipitate the product as an amorphous yellow solid. This solid was filtered off, washed three times with diethyl ether, and dried in vacuo. Yellow crystals were obtained by slow diffusion of $Et_2O$ into a concentrated solution of **10** in $CH_2Cl_2/CH_3CN$ (1:1) at room temperature. Yield: 0.143 g (46%). $C_{41}H_{38}F_6N_3P_3Ru{\cdot}CH_2Cl_2$ (955.67): calcd. C 52.17, H 4.40, N 4.55; found C 52.31, H 4.55, N 4.71. $^1$H NMR ($CD_3CN$): $\delta$ = 8.07 (d, $^3J$ = 8.2 Hz, 1 H, H$^{12}$), 7.95–7.85 (m, 3 H, H$^8$, H$^5$ and H$^9$), 7.65–7.35 (m, 21 H, $PPh_2$ + H$^{10}$), 7.07–7.01 (m, 2 H, H$^6$ and H$^7$), 6.88 (ddd, $^3J$ = 7.3, $^3J$ = 6.0, $^4J$ = 1.3 Hz, 1 H, H$^{11}$), 2.69 (m, 4 H, $CH_2$), 1.50 (d, $^5J_{H,P}$ = 1.1 Hz, 6 H, $CH_3CN$) ppm. $^{13}$C{$^1$H} NMR ($CD_3CN$): $\delta$ = 167.9 (d, $J_{C,P}$ = 6 Hz, C$^4$), 156.4 (d, $J_{C,P}$ = 7.4 Hz, C$^{12}$), 148.4 (s, C$^2$ or C$^3$), 144.7 (d, $J_{C,P}$ = 4.7 Hz, C$^9$), 138.9 (s, C$^8$ or C$^6$),134.8 (d, $J_{C,P}$ = 26 Hz, C$^{ipso}$), 134.2 (d, $J_{C,P}$ = 40 Hz, C$^{ipso}$), 133.7 (d, $J_{C,P}$ = 9 Hz, C$^o$), 133.5 (d, $J_{C,P}$ = 10 Hz, C$^o$), 131.1 (d, $J_{C,P}$ = 6.7 Hz, C$^p$), 129.9 (d, $J_{C,P}$ = 8 Hz, C$^m$), 129.4 (d, $J_{C,P}$ = 9 Hz, C$^m$), 129.1 (d, $J_{C,P}$ = 5.7 Hz, C$^{10}$), 125.5 (s, C$^6$ or C$^8$), 125.1 (d, $J_{C,P}$ = 3 Hz, C$^3$ or C$^2$), 123.5 (s, C$^7$ or C$^{11}$), 123.2 (s, C$^{11}$ or C$^7$), 120.2 (s, C$^5$), 32.6 (dd, $J_{C,P}$ = 30, $J_{C,P}$ = 18 Hz, $CH_2$), 29.2 (dd, $J_{C,P}$ = 25, $J_{C,P}$ = 10 Hz, $CH_2$), 4.02 (s, *Me*NC) ppm. $^{31}$P NMR ($CD_3CN$): $\delta$ = 68.41 (s, $PPh_2$), 43.64 (s, $PPh_2$), –143.3 (sept, $J_{P,F}$ = 706 Hz, $PF_6$) ppm. MS (FAB$^+$): *m/z* (%) 736 [M]$^+$, 654 (100) [M – 2MeCN]$^+$.

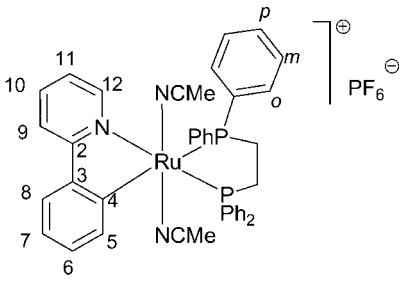


**[Ru($C_6H_4$-2-$C_5H_4N$)(4,4′-diMe-2,2′-bipy)($NCMe$)$_2$]$PF_6$ (12):** 4,4′-Dimethyl-2,2′-bipyridine (4,4′-diMe-2,2′-bipy; 0.033 g, 0.181 mmol) was added to a solution of **2** (0.102 g, 0.181 mmol) in $CH_2Cl_2$ (13 mL) and the solution was stirred at room temp. for 2 days. The course of the reaction was followed by $^1$H NMR spectroscopy. The solvent was then removed in vacuo and the product was dissolved in a minimum of MeCN/$Et_2O$. Hexane (30 mL) was added and the mixture was left to stand for 3 days to give a dark-brown powder (yield: 0.116 g, 96%). $C_{27}H_{26}F_6N_5PRu$ (666.56): calcd. C 48.65, H 3.93, N 10.51; found C 48.24, H 4.07, N 10.60. $^1$H NMR ($CD_3CN$): $\delta$ = 9.18 (d, $^3J$ = 5.5 Hz, 1 H, H$^{6'}$), 8.30 (s, 1 H, H$^{3'}$), 8.21 (ddd, $^3J$ = 7.4, $^4J$ = 1.3, $^5J$ = 0.5 Hz, 1 H, H$^{12}$), 8.09 (s, 1 H, H$^{3''}$), 7.85–7.81 (m, 2 H, H$^5$ and H$^9$), 7.68–7.66 (m, 2 H, H$^{5'}$ and H$^{6''}$), 7.52 (ddd, $^3J$ = 8.2, $^3J$ = 7.4, $^4J$ = 1.6 Hz, 1 H, H$^{10}$), 7.44 (ddd, $^3J$ = 5.7, $^4J$ = 1.6, $^5J$ = 0.8 Hz, 1 H, H$^8$), 7.24 (td, $^3J$ = 7.3, $^4J$ = 1.3 Hz, 1 H, H$^{11}$), 7.05 (ddd, $^3J$ = 7.7, $^3J$ = 7.2, $^4J$ = 1.3 Hz, 1 H, H$^6$), 6.85 (dd, $^3J$ = 5.9, $^4J$ = 1.8 Hz, 1 H, H$^{5''}$), 6.73 (ddd, $^3J$ = 7.3, $^3J$ = 5.7, $^4J$ = 1.5 Hz, 1 H, H$^7$), 2.64 and 2.34 (2 × s, 6 H, $CH_3$), 2.21 and 2.19 (2 × s, 6 H, NCMe) ppm. $^{13}$C{$^1$H} NMR ($CD_3CN$): $\delta$ = 300 MHz: 193.5 (C$^4$), 169.5 (C$^2$), 159.95, 155.9, 154.5 (C$^{5'}$ or C$^{6''}$), 151.5 (C$^8$), 150.4 (C$^{6'}$), 149.5, 148.1, 146.7, 138.8 (C$^{12}$), 136.2 (C$^{10}$), 129.0 (C$^{11}$), 128.5 (C$^{6''}$ or C$^{5'}$), 126.9 (C$^{5''}$), 124.6–124.3 (C$^{3'}$ + C$^{3''}$ + C$^9$ or C$^5$), 121.8 (C$^7$), 121.2 (C$^6$), 118.6 (C$^5$ or C$^9$), 21.27 (Me), 20.75 (Me), 4.2 (*Me*CN), 3.9 (*Me*CN) ppm.

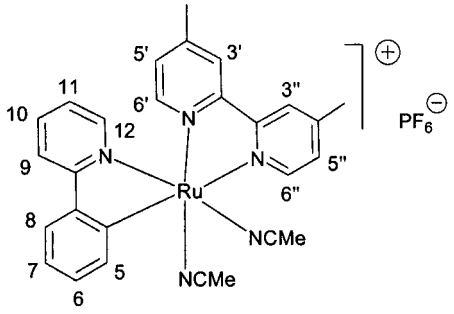


**[Ru(2,2′-bipyridine){(*R*)-2-(CHMeN$Me_2$-κ*N*)-$C_6H_4$-κ$C^1$}($NCMe$)$_2$]$PF_6$ (18):** A solution of [($\eta^6$-$C_6H_6$)Ru{(*R*)-2-(CHMeN$Me_2$)$C_6H_4$}($NCMe$)]$PF_6$ (0.100 g, 0.19 mmol) and 2,2′-bipyridine (0.030 g, 0.19 mmol) in 15 mL of acetonitrile was stirred at room temp. for 12 h. The resulting deep purple solution was evaporated to dryness and the residue (whose *de* was 22%) was purified by column chromatography over $Al_2O_3$ using dichloromethane as an eluent. The purple band was collected and the solvents evaporated to dryness. Slow diffusion of diethyl ether into a concentrated solution of the purple solid in $CH_2Cl_2$/MeCN (1:1) gave dark purple crystals of **18** with a *de* of 98.5%. The *de* of

 © 2007 Wiley-VCH Verlag GmbH & Co. KGaA, Weinheim 

**18maj** vs. **18min** was determined by comparing the intensity of the benzylic proton of the minor isomer with the intensity of the satellite signal of the same proton coupled to $^{13}C$ of the major isomer. Yield: 0.064 g (53%). $C_{24}H_{28}F_6N_5PRu$ (632.55): calcd. C 45.57, H 4.46, N 11.07; found C 45.59, H 4.51, N 10.93. $^1H$ NMR ($CD_3CN$): **18maj**: $\delta$ = 9.33 (ddd, $^3J$ = 5.3, $^4J$ = 1.5, $^5J$ = 0.7 Hz, 1 H, H$^{6''}$), 8.44 (d, $^3J$ = 8.2 Hz, 1 H, H$^{3''}$), 8.31 (d, $^3J$ = 7.9 Hz, 1 H, H$^{3'}$), 8.18 (ddd, $^3J$ = 5.6, $^4J$ = 1.5, $^5J$ = 0.6 Hz, 1 H, H$^{6'}$), 8.08 (ddd, $^3J$ = 9.1, $^3J$ = 7.6, $^4J$ = 1.5 Hz, 1 H, H$^{4''}$), 7.79 (m, 2 H, H$^{4'}$ and H$^6$), 7.73 (ddd, $^3J$ = 7.5, $^3J$ = 5.2, $^4J$ = 1.1 Hz, 1 H, H$^{5''}$), 7.17 (td, $^3J$ = 6.5, $^4J$ = 1 Hz, 1 H, H$^{5'}$), 7.07 (m, 1 H, H$^5$), 6.92 (m, 2 H, H$^3$ and H$^4$), 3.40 (q, $^3J$ = 6.7 Hz, 1 H, CH), 2.41 (s, 3 H, $CH_3CN$), 2.16 (s, 3 H, $NCH_3$), 2.06 (s, 3 H, $CH_3CN$), 1.49 (s, 3 H, $NCH_3$), 1.18 (d, $^3J$ = 6.7 Hz, 3 H, $CH_3$) ppm; **18min**: $\delta$ = 9.35 (m, 1 H, H$^{6''}$), 8.71 (dd, H6′), 8.43 (d 1 H, H$^{3''}$), 8.31 (d, 1 H, H$^{3'}$), 8.08 (ddd, 1 H, H$^{4''}$), 7.90 (dd, $^3J$ = 7.2, $^4J$ = 1.2 Hz, 1 H, H$^6$), 7.79 (m, 2 H, H$^{4'}$), 7.73 (ddd, 1 H, H$^{5''}$), 7.23 (ddd, 1 H, H$^{5'}$) 7.17 (td, 1 H, H$^5$), 6.94 (m, 1 H, H$^4$), 6.86 (d, 1 H, H$^3$), 4.09 (q, $^3J$ = 6.7 Hz, 1 H, CH), 2.46 (s, 3 H, $CH_3CN$), 2.31 (s, 3 H, $NCH_3$), 2.07 (s, 3 H, $CH_3CN$), 1.27 (d, $^3J$ = 6.7 Hz, 3 H, $CH_3$), 1.13 (s, 3 H, $NCH_3$) ppm. $^{13}C\{^1H\}$ NMR ($CD_3CN$): **18maj**: $\delta$ = 183.6, 159.7, 155.9, 153.4 (C6′′), 151.0, 150.4 (C6′), 137.0 (C4′ or C6), 136.0 (C4′′), 134.9 (C4′ or C6), 126.7 (C5′), 125.5 (C5′′), 124.8 (C5), 122.9 (C3′), 122.8 (C3 or C4), 120.4 (C3 or C4), 120.3, 118.0, 70.1 (*C*HMe), 46.5 and 45.7 ($NMe_2$), 9.9 ($CHCH_3$), 3.8 and 3.1 ($NCCH_3$) ppm. MS (FAB$^+$): *m/z* (%) 633 (8) [M$^+$ + $PF_6^-$ + H]$^+$, 488 (24) [M]$^+$, 447 (12) [M – MeCN]$^+$, 406 (88) [M – 2MeCN]$^+$.

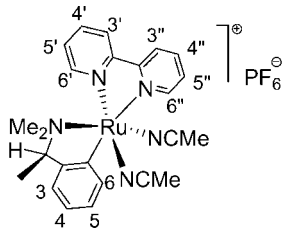


**[Ru(2,2′-bipyridine){(*S*)-2-(CHMeNMe$_2$-κ*N*)-C$_6$H$_4$-κ*C*$^1$}(NCMe)$_2$]-PF$_6$ (19):** The synthesis and spectroscopic data were the same as for **18**. $C_{24}H_{28}F_6N_5PRu$ (632.55): calcd. C 45.57, H 4.46, N 11.07; found C 45.65, H 4.54, N 10.91

**X-ray Diffraction Studies of Compounds 7–10, 18, and 19:** Crystals of the various compounds were obtained according to the crystallization procedure described for each compound (Table 3). Diffraction intensities data were collected with a SMART Apex diffractometer equipped with a graphite-monochromated Mo-$K_\alpha$ radiation source and CCD area detector, at room temperature. The

Table 3. Crystal data and structure refinement.

| | **7** | **8** | **9** |
|---|---|---|---|
| Empirical formula | $C_{36}H_{32}F_6N_4OP_2Ru$ | $C_{25}H_{32}F_6N_8P_2Ru$ | $C_{51}H_{44}F_6N_3P_3Ru$ |
| Formula weight | 813.67 | 721.60 | 1006.87 |
| Crystal system | monoclinic | monoclinic | monoclinic |
| Space group | $P2_1/n$ | $P2_1/c$ | $P2_1/c$ |
| *a* [Å] | 12.4740(8) | 11.8140(2) | 16.796(1) |
| *b* [Å] | 24.6128(15) | 15.6510(3) | 15.938(1) |
| *c* [Å] | 13.9723(8) | 16.7910(4) | 17.377(1) |
| *α* [°] | 90 | 90 | 90 |
| *β* [°] | 111.242(1) | 102.598(1) | 90.677(1) |
| *γ* [°] | 90 | 90 | 90 |
| *Z* | 4 | 4 | 4 |
| Flack's parameter | | | |
| Final *R* indices [$I > 2\sigma(I)$] | *R*1 = 0.0413 | *R*1 = 0.0428 | *R*1 = 0.0424 |
| | *wR*2 = 0.0917 | *wR*2 = 0.0978 | *wR*2 = 0.0969 |
| *R* indices (all data) | *R*1 = 0.0610 | *R*1 = 0.0796 | *R*1 = 0.0564 |
| | *wR*2 = 0.0965 | *wR*2 = 0.1115 | *wR*2 = 0.1017 |
| Goodness-of-fit on $F^2$ | 0.906 | 1.003 | 0.951 |
| Largest diff. peak and hole [e Å$^{-3}$] | 0.627 and –0.229 | 0.901 and –0.767 | 0.644 and –0.437 |
| | **10** | **18** | **19** |
| Empirical formula | $C_{42}H_{40}Cl_2F_6N_3P_3Ru$ | $C_{24}H_{28}F_6N_5PRu$ | $C_{24}H_{28}F_6N_5PRu$ |
| Formula weight | 965.63 | 632.55 | 632.55 |
| Crystal system | monoclinic | tetragonal | tetragonal |
| Space group | $P2_1/n$ | $P4_3$ | $P4_1$ |
| *a* [Å] | 11.7961(12) | 8.4853(3) | 8.4835(3) |
| *b* [Å] | 16.3996(16) | 8.4853(3) | 8.4835(3) |
| *c* [Å] | 22.226(2) | 37.630(3) | 37.615(3) |
| *α* [°] | 90 | 90 | 90 |
| *β* [°] | 90.341(2) | 90 | 90 |
| *γ* [°] | 90 | 90 | 90 |
| *Z* | 4 | 4 | 4 |
| Flack's parameter | | –0.03(4) | –0.02(5) |
| Final *R* indices [$I > 2\sigma(I)$] | *R*1 = 0.0607 | *R*1 = 0.0423 | *R*1 = 0.0460 |
| | *wR*2 = 0.0905 | *wR*2 = 0.0803 | *wR*2 = 0.1083 |
| *R* indices (all data) | *R*1 = 0.1468 | *R*1 = 0.0485 | *R*1 = 0.0508 |
| | *wR*2 = 0.1064 | *wR*2 = 0.0825 | *wR*2 = 0.1114 |
| Goodness-of-fit on $F^2$ | 0.784 | 1.059 | 1.020 |
| Largest diff. peak and hole [e Å$^{-3}$] | 0.882 and –0.484 | 0.710 and –0.520 | 0.603 and –0.533 |

 © 2007 Wiley-VCH Verlag GmbH & Co. KGaA, Weinheim 

data collected were processed to produce conventional intensity data with the SAINT plus program. The intensity data were corrected for Lorentz and polarization effects, no absorption correction was applied. The structures were solved by direct methods, completed by a subsequent difference Fourier synthesis map, and refined by full-matrix least-squares procedures on $F^2$. All non-hydrogen atoms were refined anisotropically. The crystal structures have solvents of crystallization, which were refined isotropically in two or three major contributors. In the case of compound **7**, the molecule of methanol was refined in three positions with major contributors. Hydrogen atoms could not be refined due to the high level of disorder. The $PF_6$ anions are in special positions and the fluorine atoms are distorted and were modeled and refined anisotropically in two major contributors. Hydrogen atom positions were calculated and included in the final cycle of refinement. All calculations were performed with the SHELXTL (6.10) program package.[25] CCDC-617638 to -617642 and CCDC-629738 (for **7**, **9**, **10**, **18**, **19**, and **8**, respectively) contain the supplementary crystallographic data for this paper. These data can be obtained free of charge from the Cambridge Crystallographic Data Center at http://www.ccdc.ac.uk.data/cif.

**Cell-Proliferation Assays:** The ruthenium samples for in vitro tests were obtained from 50.0 mM solutions of the ruthenium complexes in pure DMSO, which were then sequentially diluted with the required amount of cell culture media in order to obtain study solutions with a concentration ranging from 0.2 to 50 μM. A-172 and HCT-116 cells were obtained from American Type Cell Culture Collection. RDM-4, a murine T lymphoma, was obtained from Dr. D. Oth (Institut Armand Frappier, Laval des Rapides, Québec, Canada). Cells were grown in 96-well plates and treated at 70% confluence. The medium was removed after 48 h and MTT (0.5 mg mL$^{-1}$) in DMEM (Dulbecco's Modified Eagle Medium) was added for 1 h. The medium was removed again and 0.04% HCl in 2-propanol was added to solubilize the crystals. Absorption differences were quantified with an Elisa plate reader (Metertech USA) at 490–650 nm. The experiments were repeated between two and five times, and the mean deviation was determined by considering the extreme values found over all experiments.

**Cell-Cycle Analysis and Apoptosis Assays:** Hypodiploid DNA was measured as described according to Nicoletti.[26] Briefly, $10^6$ cells were centrifuged and fixed in 1 mL of cold 70% ethanol at 4 °C for one hour, washed once with PBS (Phosphate Buffered Saline) and EDTA (2 mM), and re-suspended in 1 mL of PBS containing 0.25 mg Rnase A, 2 mM EDTA and 0.1 mg of propidium iodide. Cells were analyzed after incubation at 37 °C for 30 min in the dark. The fluorescence of 10,000 cells was analyzed using a FACS scan flow cytometer and CellQuest software (Becton Dickinson, San José, CA).

## Acknowledgments

The Université Louis Pasteur and the Ministère de l'Education Nationale are thanked for a student fellowship (to L. L.), the Centre National de la Recherche Scientifique (CNRS), Institut National de la Santé et de la Recherche Médicale (INSERM), the Consejo Nacional de Ciencia y Tecnología (CONACYT) (project numbers 34293-E and 40135-Q), and the Agence Nationale de la Recherche (ANR-05-EMPB-019-01/02) are thanked for partial support of the work. We are grateful to Ms. B. Wieczoreck and K. Küpfer for their help in the synthesis and characterization of **11**. X-ray diffraction studies were performed by Dr. Simon Hernandez and Dr. Ruben Alfredo Toscano (UNA Mexico; compounds **7**, **9**, **10**, **18**, and **19**) and by Dr. A. de Cian (ULP Strasbourg, compound **8**).

[1] a) C. Orvig, M. J. Abrams, *Chem. Rev.* **1999**, *99*, 2201–2204; b) M. J. Clarke, F. Zhu, D. R. Frasca, *Chem. Rev.* **1999**, *99*, 2511–2534; c) Z. Guo, P. J. Sadler, *Angew. Chem. Int. Ed.* **1999**, *38*, 1512–1531; d) Y. K. Yan, M. Melchart, A. Habtemariam, P. J. Sadler, *Chem. Commun.* **2005**, 4764–4776; e) U. Schatzschneider, N. Metzler-Nolte, *Angew. Chem. Int. Ed.* **2006**, *45*, 1504–1507; f) A. R. Timerbaev, C. G. Hartinger, S. S. Aleksenko, B. K. Keppler, *Chem. Rev.* **2006**, *106*, 2224–2248; g) W. H. Ang, P. J. Dyson, *Eur. J. Inorg. Chem.* **2006**, 4003–4018; h) P. J. Dyson, G. Sava, *Dalton Trans.* **2006**, 1929–1933; i) D. Wang, S. J. Lippard, *Nat. Rev. Drug Discov.* **2005**, *4*, 307–320; j) *Bioorganometallics, Biomolecules, Labelling, Medicine* (Ed.: G. Jaouen), John Wiley & Sons, **2005**; k) *Metallotherapeutic Drugs and Metal-Based Diagnostic Agents: The Use of Metals in Medicine* (Eds.: M. Gielen, E. R. T. Tiekink), John Wiley & Sons, **2005**.

[2] a) *Platinum and Other Metal Coordination Compounds in Cancer Chemotherapy* (Eds.: H. M. Pinto, J. H. Schornagel), Plenum, New York, **1996**; b) *Cisplatin: Chemistry and Biochemistry of a Leading Anticancer Drug* (Ed.: B. Lippert), Wiley-VCH, Weinheim, **1999**; c) E. Wong, C. M. Giandomenico, *Chem. Rev.* **1999**, *99*, 2451–2466; d) E. R. Jamieson, S. J. Lippard, *Chem. Rev.* **1999**, *99*, 2467–2498.

[3] a) C. S. Allardyce, P. J. Dyson, *Platinum Met. Rev.* **2001**, *45*, 62–69; b) M. J. Clarke, *Coord. Chem. Rev.* **2003**, *236*, 209–233.

[4] a) H. Depenbrock, S. Schmelcher, R. Peter, B. K. Keppler, G. Weirich, T. Block, J. Rastetter, A. R. Hanauske, *Eur. J. Cancer* **1997**, *33*, 2404–2410; b) M. A. Jakupec, E. Reisner, A. Eichinger, M. Pongratz, V. B. Arion, M. Galanski, C. G. Hartinger, B. K. Keppler, *J. Med. Chem.* **2005**, *48*, 2831–2837 and references cited therein.

[5] a) G. Sava, A. Bergamo, *Int. J. Oncol.* **2000**, *17*, 353; b) J. M. Rademaker-Lakhai, D. van den Bongard, D. Pluim, J. H. Beijnen, J. H. Schellens, *Clin. Cancer Res.* **2004**, *10*, 3717–3727; c) C. G. Hartinger, S. Zorbas-Seifried, M. A. Jakupec, B. Kynast, H. Zorbas, B. K. Keppler, *J. Inorg. Biochem.* **2006**, *100*, 891–904.

[6] a) R. E. Morris, R. E. Aird, P. del S. Murdoch, H. Chen, J. Cummings, N. D. Hughes, S. Parsons, A. Parkin, G. Boyd, D. I. Jodrell, P. J. Sadler, *J. Med. Chem.* **2001**, *44*, 3616–3621; b) R. E. Aird, J. Cummings, A. A. Ritchie, M. Muir, R. E. Morris, H. Chen, P. J. Sadler, D. I. Jodrell, *Br. J. Cancer.* **2002**, *86*, 1652–1657.

[7] C. S. Allardyce, P. J. Dyson, D. J. Ellis, P. A. Salter, R. Scopelliti, *J. Organomet. Chem.* **2003**, *668*, 35–42.

[8] A. C. G. Hotze, M. Baca, A. H. Velders, B. A. J. Jansen, H. Kooijman, A. L. Spek, J. G. Haasnoot, J. Reedijk, *J. Med. Chem.* **2003**, *46*, 1743–1750.

[9] a) A. D. Ryabov, V. Sukharev, L. Alexandrova, R. Le Lagadec, M. Pfeffer, *Inorg. Chem.* **2001**, *40*, 6529–6532; b) A. D. Ryabov, V. Sukharev, L. Alexandrova, R. Le Lagadec, M. Pfeffer, *Inorg. Chem.* **2003**, *42*, 6598–6600; c) A. D. Ryabov, V. S. Kurova, E. V. Ivanova, R. Le Lagadec, L. Alexandrova, *Anal. Chem.* **2005**, *77*, 1132–1139; d) R. Le Lagadec, L. Alexandrova, H. Estevez, M. Pfeffer, V. Laurinavicius, J. Razumiene, A. D. Ryabov, *Eur. J. Inorg. Chem.* **2006**, 2735–2738.

[10] a) A. Gómez-Quiroga, C. Navarro-Ranninger, *Coord. Chem. Rev.* **2004**, *248*, 119–133 and references cited therein b) G. L. Edwards, D. S. C. Black, G. B. Deacon, L. P. G. Wakelin, *Can. J. Chem.* **2005**, *83*, 969–979; c) C. Bincoletto, I. L. S. Tersariol, C. R. Oliveira, S. Dreher, D. M. Fausto, M. A. Soufen, F. D. Nascimento, A. C. F. Caires, *Bioorg. Med. Chem.* **2005**, *13*, 3047–3055 and references cited therein.

[11] a) H. C. L. Abbenhuis, M. Pfeffer, J. P. Sutter, A. de Cian, J. Fischer, L. H. Ji, J. H. Nelson, *Organometallics* **1993**, *12*, 4464–4472; b) W. Ferstl, I. K. Sakodinskaya, N. Beydoun-Sutter, G. Le Borgne, M. Pfeffer, A. D. Ryabov, *Organometallics* **1997**, *16*, 411–418; c) M. Pfeffer, J. P. Sutter, E. P. Urriolabeitia, *Bull. Soc. Chim. Fr.* **1997**, *134*, 947–954; d) V. Ritleng, M. Pfeffer, C. Sirlin, *Organometallics* **2003**, *22*, 347–354.

 © 2007 Wiley-VCH Verlag GmbH & Co. KGaA, Weinheim 

[12] C. Gaiddon, P. Jeannequin, P. Bischoff, M. Pfeffer, C. Sirlin, J. P. Loeffler, *J. Pharmacol. Exp. Ther.* **2005**, *315*, 1403–1411.
[13] S. Fernandez, M. Pfeffer, V. Ritleng, C. Sirlin, *Organometallics* **1999**, *18*, 2390–2394.
[14] S. Attar, J. H. Nelson, J. N. Fischer, A. de Cian, J. P. Sutter, M. Pfeffer, *Organometallics* **1995**, *14*, 4559–4569.
[15] C. Scolaro, A. Bergamo, L. Brescacin, R. Delfino, M. Cochietto, G. Laurenczy, T. J. Gelbach, G. Sava, P. J. Dyson, *J. Med. Chem.* **2005**, *48*, 4161–4171.
[16] V. Ritleng, P. Bertani, M. Pfeffer, C. Sirlin, J. Hirschinger, *Inorg. Chem.* **2001**, *40*, 5117–5122.
[17] *Advanced Inorganic Chemistry, 5th ed.* (Eds.: F. A. Cotton, G. Wilkinson), Wiley-Interscience, New York, **1988**, p. 1299–1300.
[18] R. Le Lagadec, L. Rubio, L. Alexandrova, R. A. Toscano, E. V. Ivanova, R. Meskys, V. Laurinavicius, M. Pfeffer, A. D. Ryabov, *J. Organomet. Chem.* **2004**, *689*, 4820–4832.
[19] A. D. Ryabov, R. Le Lagadec, H. Estevez, R. A. Toscano, S. Hernandez, L. Alexandrova, V. S. Kurova, A. Fischer, C. Sirlin, M. Pfeffer, *Inorg. Chem.* **2005**, *44*, 1626–1634.
[20] a) J. Dehand, J. Jordanov, M. Pfeffer, M. Zinsius, *C. R. Acad. Sci. Paris* **1975**, *281*, 651–654; b) J. Vicente, J. A. Abad, A. D. Frankland, M. C. Ramírez de Arellano, *Chem. Eur. J.* **1999**, *5*, 3066–3075 and references cited therein.
[21] The X-ray diffraction study was performed on single crystals obtained from a sample that was synthesized in MeOH instead of MeCN. This explains why one disordered molecule of MeOH was found in this structure.
[22] See *IUPAC, Nomenclature of Inorganic Chemistry, Recommendations* (Ed.: G. J. Leigh), Blackwell Scientific Publications, Oxford, **1990**.
[23] D. J. Aigle, *Inorg. Synth.* **1998**, *32*, 40–45.
[24] G. M. Brown, R. W. Callahan, T. J. Meyer, *Inorg. Chem.* **1975**, *14*, 1915–1921.
[25] G. M. Sheldrick, *SHELXTL (Version 6.10)*, Bruker AXS Inc., Madison, Wisconsin, USA, **2000**.
[26] I. Nicoletti, G. Migliorati, M. C. Pagliacci, F. Grignani, C. Riccardi, *J. Immunol. Methods* **1991**, *139*, 271.

Received: December 5, 2006
Published Online: May 10, 2007

 © 2007 Wiley-VCH Verlag GmbH & Co. KGaA, Weinheim 

DOI: 10.1002/ejic.200601169

# Ligand Exchange Processes on Solvated Lithium Cations: Complexation by Cryptands in Acetone as Solvent[‡]

Ewa Pasgreta,[a] Ralph Puchta,[a,b] Achim Zahl,[a] and Rudi van Eldik*[a]

**Keywords:** Lithium / Cryptands / Acetone / Exchange mechanism

Kinetic studies on $Li^+$ exchange between the cryptands C222 and C221 and acetone as solvent were performed as a function of ligand-to-metal ratio, temperature and pressure using $^7Li$ NMR spectroscopy. Temperature and pressure dependence measurements were performed in the presence of an excess of $Li^+$. The rate and activation parameters for the exchange process are: C222: $k_{298} = (1.7 \pm 0.5) \times 10^3$ $s^{-1}$, $\Delta H^{\#} = 24 \pm 1$ $kJ\,mol^{-1}$ and $\Delta S^{\#} = -105 \pm 4$ $J\,K^{-1}\,mol^{-1}$; C221: $k_{298} = 2.24 \pm 0.09$ $s^{-1}$, $\Delta H^{\#} = 29 \pm 2$ $kJ\,mol^{-1}$ and $\Delta S^{\#} = -141 \pm 5$ $J\,K^{-1}\,mol^{-1}$. The influence of pressure on the exchange rate is insignificant for both ligands, such that the activation volume is around zero within the experimental error limits. The reported activation parameters suggest that the exchange of $Li^+$ between solvated and chelated ions follows an associative interchange mechanism.

(© Wiley-VCH Verlag GmbH & Co. KGaA, 69451 Weinheim, Germany, 2007)

## Introduction

Following the work of Pedersen on two-dimensional crowns, Lehn and co-workers developed in the late 1960s a range of three-dimensional, polycyclic ligand systems which they named cryptands (Greek: *cryptos* = cave).[1] Until today this class of compounds has been intensively explored and extended in different directions[2] in terms of cavity size,[3,4] donor atoms,[5] and metalla-topomers.[6] Because cryptands readily form complexes with a wide range of metal ions and $NH_4^+$,[7] provided the ion involved is not too large to be contained in the macrocyclic cavity,[8] they find their application in various areas like catalysis, medicine, biomimetic research,[9,10] and as receptors[11] and electrides.[12] Studies on the complexes (cryptates) formed between alkali-metal ions and cryptands, have revealed a substantial understanding of the effects of metal-ion size and cryptand-cavity size on the structure, stability and lability of cryptates, and the mechanism of the cryptate complex-formation processes.[13,14] Such selective complexation has led to many biological and chemical studies.

Kinetic studies on macrocyclic complex-formation reactions with alkali cations not only result in important information on the rates and mechanisms of complex-formation reactions, but also lead to a better understanding of the high selectivity of these ligands toward different cations. The broad impact of such studies spans from the theory of complexation to cation transport through membranes, and makes the ability to control cation selectivity via tactical structural changes in the complexing agent of prime importance.[10] Polyoxo macrobicyclic diamines, represented by the structure in Figure 1, are able to form metal-ion complexes in which the metal ion is located in the cavity of the macromolecule and two nitrogen donors along with the oxygen donors participate in binding the metal cation. All complexes have a 1:1 stoichiometry with the metal ion positioned at the center of the ligand cavity.[13]

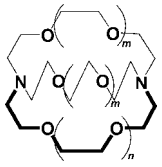


Figure 1. Chelate structures: C211: $m = 0$, $n = 1$; C221: $m = 1$, $n = 0$; C222: $m = 1$, $n = 1$.

In case of crown ethers and cryptands in non-aqueous solutions, the rates of complex-formation ($k_f$) with alkali-metal cations are in general diffusion-controlled and, consequently, the complexation selectivities are governed by the decomplexation rates ($k_d$).[15] These reactions have received significant attention, initially from Lehn and co-workers and more recently from Popov et al.[16,17] and Lincoln et al.[18] Many examples have been included in a series of review articles.[19,20] It has been reported that ligand structure and solvent properties have considerable effects on the reaction rates, activation parameters, and exchange mechanism

[‡] Part V. Part IV: E. Pasgreta, R. Puchta, A. Zahl, R. van Eldik, *Eur. J. Inorg. Chem.*, in press.

[a] Institute for Inorganic Chemistry, University of Erlangen-Nürnberg,
Egerlandstr. 1, 91058 Erlangen, Germany
E-mail: vaneldik@chemie.uni-erlangen.de
[b] Computer Chemistry Center, University of Erlangen-Nürnberg, Nägelsbachstr. 25, 91052 Erlangen, Germany

Supporting information for this article is available on the WWW under http://www.eurjic.org or from the author.

 © 2007 Wiley-VCH Verlag GmbH & Co. KGaA, Weinheim 

of cations between the solvated and complexed sites. We have now extended our earlier studies[21] on $Li^+$ exchange reactions to acetone as solvent.

Non-aqueous solvents and their mixtures combined with $Li^+$ are often used in secondary lithium batteries.[22] $Li^+$ in acetone is also known to catalyze Diels–Alder-reactions[23] and the ene reaction.[24] The behavior of $Li^+$-ions in different solvents is therefore an important research area.[25–27] A variety of studies on solutions of $Li^+$ in acetone have been mainly studied experimentally[26,28] and some theoretically,[29,30] as well as for solvent/acetone combinations[27] or chelator/acetone combinations.[27,31] In this contribution, we focus on acetone as a solvent and the competition between solvated and endohedral complexed $Li^+$, report kinetic parameters for the exchange of $Li^+$ between solvated and complexed states in acetone under ambient and elevated pressure conditions, and discuss the mechanistic implications.

## Results and Discussion

### Spectroscopic and Kinetic Observations

In preliminary experiments we investigated the $Li^+$ exchange in different solvents. In water and methanol the exchange process was too fast to be studied by $^7Li$ NMR (only a single signal was observed). The process became slower in acetonitrile, and in acetone two completely separated signals were observed at low temperature. We, therefore, investigated $Li^+$ exchange between the selected cryptands and acetone as solvent. A similar system was also investigated before by Popov et al.[17] Although they reported a significantly negative value for the activation entropy, they suggested the operation of a dissociative exchange mechanism. We realized that it would be worth to perform a reinvestigation of this system in acetone in order to clarify this apparent discrepancy, in particular by means of high pressure $^7Li$ NMR spectroscopy.

Initially, a series of $^7Li$ NMR measurements for the $Li^+$–cryptand system in acetone were performed. For each of the cryptands C222, C221 and C211, molar ratio dependent measurements were performed by variation of both the cryptand/$Li^+$ and $Li^+$/cryptand molar ratios. The results enabled us to observe the distribution of particular species on variation of the concentration ratio. Basically, two signals of varying intensity were observed in the $^7Li$ NMR spectra that refer to solvated $Li^+$ and $Li^+$ bound inside the cryptand cavity. In case of the smallest chelate C211, however, an additional signal appeared which can be ascribed to $Li^+$ bound outside the cryptand and being partially solvated. In the case of $Li(C211)^+$, the complex is very stable and almost no exchange takes place. A detailed study of the observed rate constant, $k_{obsd.}$, for the exchange of $Li^+$ as a function of temperature and pressure was therefore undertaken only for C221 and C222. The lithium exchange reaction between cryptand and acetone was studied for three solutions with different ligand-to-metal ratios in the presence of an excess of $Li^+$.

Three signals can be observed in Figure 2, viz. one coming from the reference ($\delta$ = 5.8 ppm) and the other two from the exchanging sites ($\delta$ = 9.0 ppm for solvated $Li^+$ and 6.6 ppm for complexed $Li^+$). At low temperature the signals are sharp and completely separated due to very slow or no exchange. Because the formation constant for $Li(C221)^+$ is very high,[13] the concentration of bound lithium equals the amount of cryptand added. At ca. 283 K, the signals start to broaden and the exchange process takes place. The linear temperature dependence for the temperature range in which exchange takes place can be seen in Figure 5. In the case of C222 (Figure 3), the exchange process is faster due to the larger cavity of the cryptand. The signals that refer to solvated and complexed Li cation (8.7 and 6.8 ppm, respectively at 223 K) coalescence at ca. 263 K and at high temperature (>313 K) only one sharp signal at 7.7 ppm was observed as a consequence of a very fast exchange process. An accurate temperature dependence for C222 over a large temperature range can be observed in Figure 6.

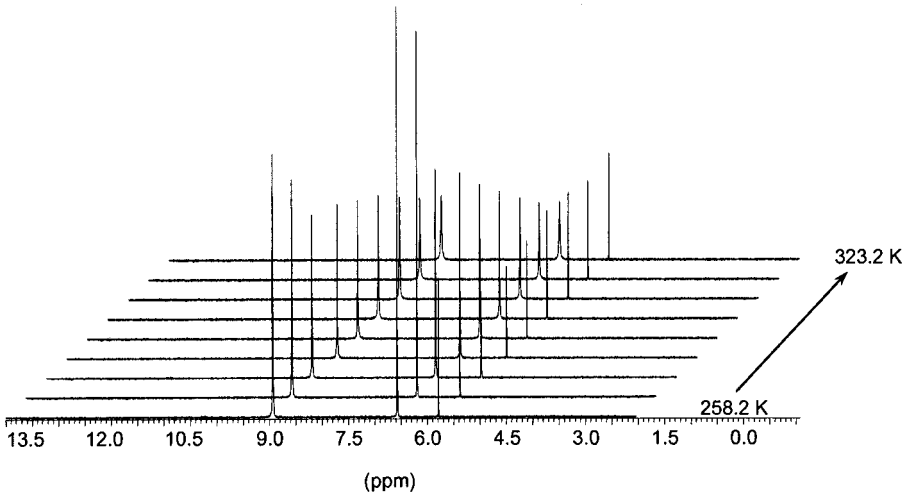


Figure 2. $^7Li$ NMR spectra recorded as a function of temperature for the mol ratio C221/$LiClO_4$ = 0.5.

 © 2007 Wiley-VCH Verlag GmbH & Co. KGaA, Weinheim 

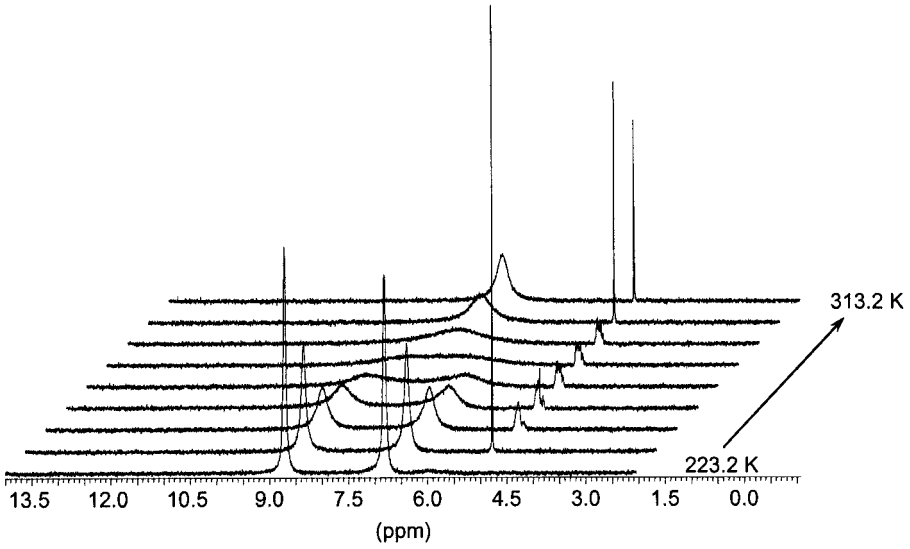


Figure 3. $^{7}$Li NMR spectra recorded as a function of temperature for the mol ratio C222/$LiClO_4$ = 0.5.

The rate of the exchange reaction increased not only with increasing cavity size of the cryptand but also with increasing concentration of the chelate, as can be recognized from the shape of the signals at 223 K in Figure 4 and from the values of $k_{obsd.}$ in Table 1 (see Figure 5 and Figure 6). A summary of the all the measured rate constants are given in Tables S1 and S2 (see Supporting Information).

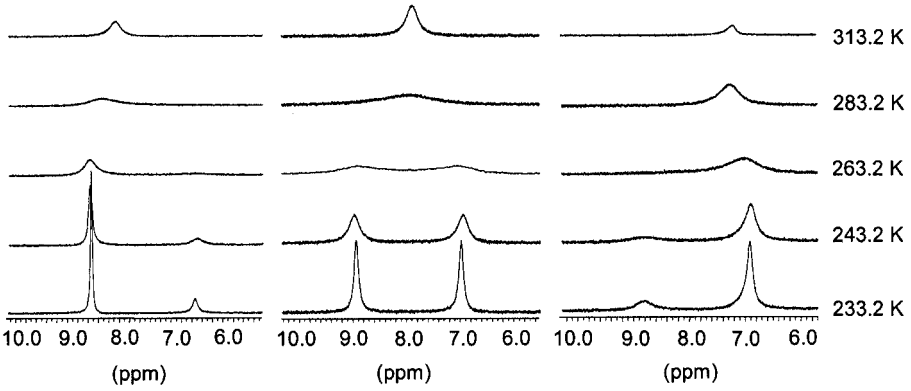


Figure 4. $^{7}$Li NMR spectra of C222 and $LiClO_4$ in acetone. Temperature dependence for the sample ratios C222/$LiClO_4$ = 0.25, 0.5 and 0.75, respectively.

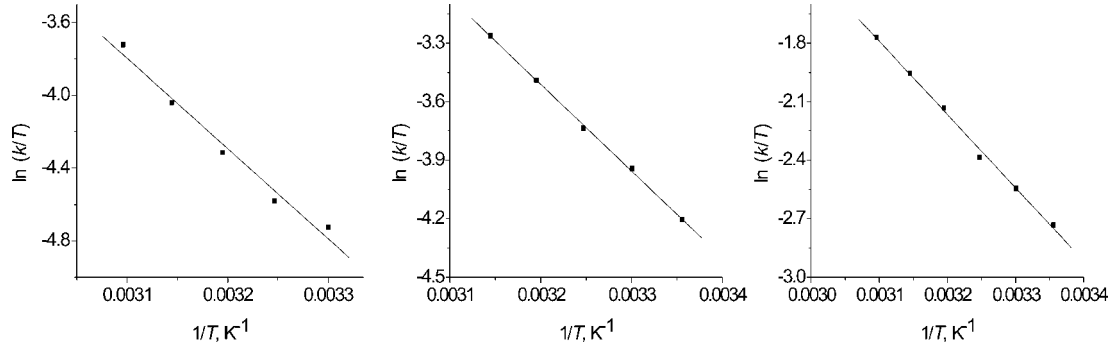


Figure 5. Eyring plots for $k_{obsd.}$ as a function of temperature for C221 in the temperature range in which exchange was observed for the concentration ratios C221/$LiClO_4$ = 0.5, 0.65 and 0.8, respectively.

 © 2007 Wiley-VCH Verlag GmbH & Co. KGaA, Weinheim 

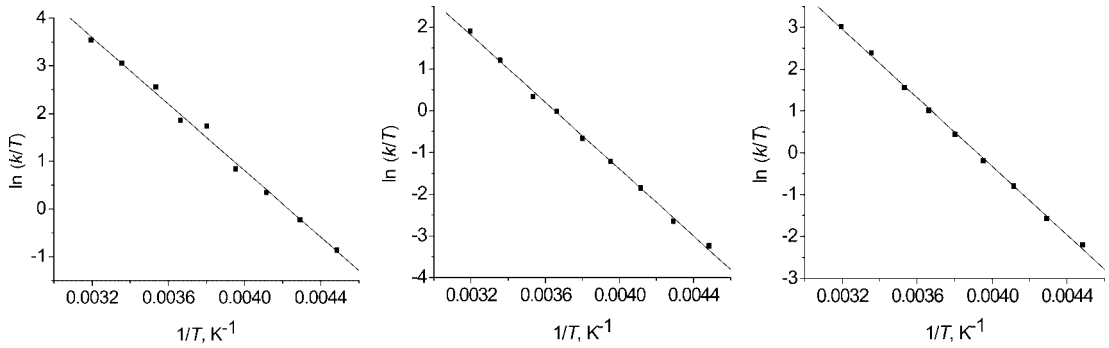


Figure 6. Eyring plots for $k_{obsd.}$ as a function of temperature for C222 for the concentration ratios C222/$LiClO_4$ = 0.25, 0.5 and 0.75, respectively.

Table 1. Values of the observed rate constants ($k_{obsd.}$) and activation parameters calculated from the line-shape analysis for the exchange of $Li^+$ between solvated and chelated sites at 25 °C.

| Molar ratio [L]/[$Li^+$] C221 | $k_{obsd.}^{298}$ [$s^{-1}$] | $\Delta H^{\#}$ [kJ $mol^{-1}$] | $\Delta S^{\#}$ [J $K^{-1}$ $mol^{-1}$] |
|---|---|---|---|
| 0.5 | 2.10 ± 0.04 | 41 ± 3 | –102 ± 12 |
| 0.65 | 4.5 ± 0.1 | 37 ± 1 | –109 ± 3 |
| 0.8 | 19.4 ± 0.8 | 31 ± 1 | –116 ± 4 |
| C222 | | | |
| 0.25 | 1001 ± 20 | 33.3 ± 0.5 | –76 ± 1 |
| 0.5 | 3263 ± 98 | 34.1 ± 0.4 | –64 ± 1 |
| 0.75 | 6346 ± 254 | 29 ± 1 | –75 ± 2 |

## Suggested Exchange Mechanism

Two mechanisms should be considered for the decomplexation processes of cryptand–alkali-metal complexes: unimolecular (dissociative) and bimolecular (associative) cation exchange. The solvent plays a major role in the unimolecular mechanism and this mechanism is therefore favored in strong donor solvents.[20]

Lincoln et al.[18] investigated many similar systems where the $Li^+$ cation was exchanged between different cryptands or crown ethers and common solvents. In case of crown ethers and cryptands in non-aqueous solutions, the rates of formation ($k_c$) for their interaction with alkali-metal cations are generally diffusion controlled and, consequently, the complexation selectivities are governed by the decomplexation rates ($k_d$). They proposed the operation of a monomolecular mechanism for the decomplexation of $Li^+$ from the cryptand, notwithstanding the fact that decomplexation is characterized by very negative activation entropies.

According to Popov et al.,[17] there are two possible mechanisms that need to be considered for the exchange of $Li^+$ cation between the solvated and the complexed sites, viz. bimolecular (associative) (*I*) and unimolecular (dissociative) (back reaction in II) cation exchange processes, where S presents solvent and L the employed chelate.[17,32] (In this description we have added the terms "associative" and "dissociative" because this is implied by the mechanistic interpretation offered by the authors.)

$$*Li(S)^+ + Li(L)^+ \underset{k_{-1}}{\overset{k_1}{\rightleftharpoons}} Li(S)^+ + *Li(L)^+ \quad (I)$$

$$Li(S)^- + L \underset{k_{-2}}{\overset{k_2}{\rightleftharpoons}} Li(L)^+ + S \quad (II)$$

At equilibrium:

$k_1[*Li(S)][Li(L)] = k_{-1}[*Li(L)][Li(S)]$

$k_2[Li(S)][L] = k_{-2}[Li(L)][S]$

Therefore see Equations (1) and (2)

$$-\frac{d}{dt}[Li(S)] = k_{obsd.}[Li(S)] = k_1[Li(S)][Li(L)] + k_{-2}[Li(L)][S] \quad (1)$$

$$k_{obsd.} = k_1[Li(L)] + \frac{k_{-2}[Li(L)][S]}{[Li(S)]} \quad (2)$$

An alternative form of Equation (2) is Equation (3), which was used to fit the data in Figure 7 and Figure 9.

$$\frac{k_{obsd.}}{[Li(S)]} = k_1 + k_{-2}' \cdot \frac{1}{[Li(S)]} \quad (3)$$

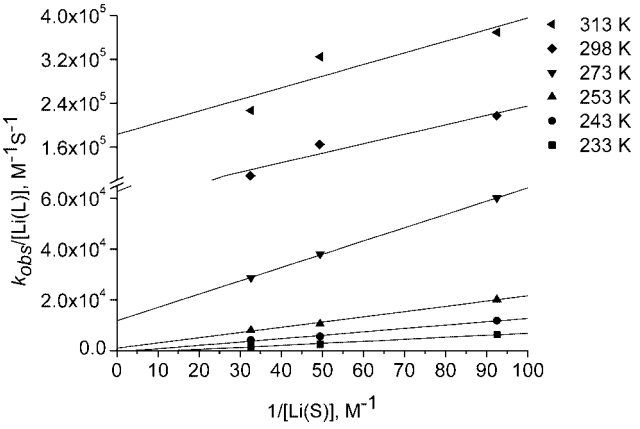


Figure 7. Plots of $k_{obsd.}$/[Li(L)] vs. 1/[Li(S)] for C222 as a function of temperature.

Plots of $k_{obsd.}$/[Li(L)] vs. 1/[Li(S)] were found to be linear with varying slopes ($k_{-2}' = k_{-2}$[S]) and intercepts ($k_1$) (see Figure 7 and Figure 8). The plots indicate that both path-

 © 2007 Wiley-VCH Verlag GmbH & Co. KGaA, Weinheim 

ways compete with each other and the competition is controlled by temperature and the nature of the cryptand. In the case of C222 (Figure 7), the plots at low temperature exhibit no meaning intercept, whereas the plots at high temperature exhibit very large intercepts. Thus the contribution from $k_1$ increases significantly with temperature. In the case of C221 (Figure 8), all the plots exhibit almost no intercept, such that the exchange process is mainly controlled by $k_{-2}$. The corresponding Eyring plots are shown in Figure 9 and Figure 10, respectively, and the thermal activation parameters are summarized in Table 2.

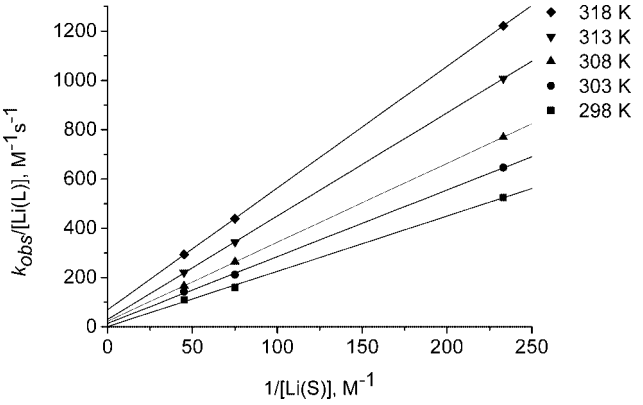


Figure 8. Plots of $k_{obsd.}$/[Li(L)] vs. 1/[Li(S)] for C221 as a function of temperature.

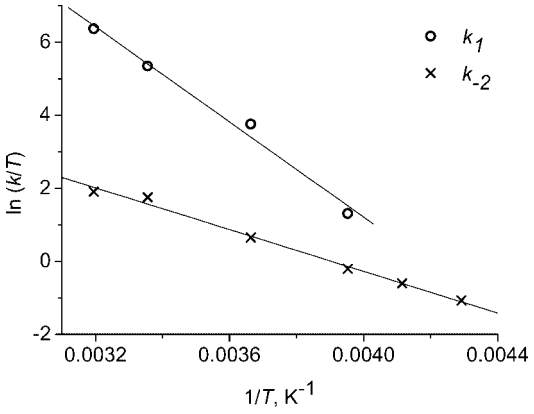


Figure 9. Eyring plots for $k_1$ and $k_{-2}$ as a function of temperature for C222.

The activation parameters derived from the temperature dependence of $k_1$ are rather inaccurate due to the large error limits of the intercepts and the reported activation entropy has no mechanistic meaning. On the basis of the values of $k_{-2}$ and the significantly negative activation entropies obtained for this pathway, the activation parameters support an associative type of exchange process. $k_{-2}$ for C222

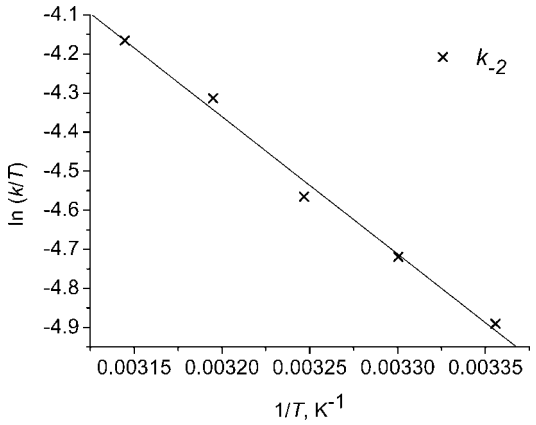


Figure 10. Eyring plot for $k_{-2}$ as a function of temperature for C221.

is almost three orders of magnitude larger than for C221. Furthermore, the activation parameters are very similar to those obtained directly from the values of $k_{obsd.}$ as a function of temperature. This would be in a good agreement with that postulated by Lincoln, who assumed that only the decomplexation process contributes to the observed reaction under the given experimental conditions. The negative activation entropies found for the decomplexation reactions of both C221 and C222 strongly suggest that attack of the solvent on the complexes $Li^+$ must play an important role in the decomplexation process, i.e. decomplexation follows an associative mechanism (see theoretical calculations).

The reported activation parameters are within the range of those reported by Popov et al. for closely related systems.[17] However, it should be pointed out that they used a different rate law than the one proposed by Shchori et al.[33] and the one used in the present study, which complicates a direct comparison of the reported activation parameters. Nevertheless, although they proposed another mechanism, the values of the activation parameters obtained from their study are very similar to ours, as shown in Table 3.

Table 3. Comparison of activation parameters.

| | $k_b$ [$s^{-1}$] | $\Delta H^{\#}$ [kJ $mol^{-1}$] | $\Delta S^{\#}$ [J $K^{-1}$ $mol^{-1}$] |
|---|---|---|---|
| Popov et al.[28] | 794 ± 42 | 20 ± 1 | –121 ± 3 |
| This work | 1724 ± 484 | 24 ± 1 | –105 ± 4 |

It is reasonable to expect that solvents such as acetonitrile, acetone and γ-butyrolactone, due to their similar properties as expected from their rather similar Gutmann donor numbers ($DN$ = 14.1, 17.0 and 18.0, respectively,[34]) should coordinate to $Li^+$ in a similar way and should have a similar influence on the exchange mechanism. This obser-

Table 2. Thermal activation parameters obtained from the values of $k_1$ and $k_{-2}$ as a function of temperature.

| Chelate | $k_1^{298}$ [$M^{-1}$ $s^{-1}$] | $k_{-2}^{298}$ [$s^{-1}$] | $\Delta H^{\#}$ [kJ $mol^{-1}$] | $\Delta S^{\#}$ [J $K^{-1}$ $mol^{-1}$] |
|---|---|---|---|---|
| C221 | | 2.24 ± 0.09 | 29 ± 2 | –141 ± 5 |
| C222 | | (1.7 ± 0.5) × $10^3$ | 24 ± 1 | –105 ± 4 |
| C222 | (6 ± 3) × $10^4$ | | 54 ± 4 | +29 ± 15 |

 © 2007 Wiley-VCH Verlag GmbH & Co. KGaA, Weinheim 

vation corresponds to that reported by Shamsipur et al.[35] for the exchange of $Li^+$ between C221 and acetonitrile/nitromethane mixtures. In all solvent mixtures used, $Li^+$ exchange was found to occur through an associative mechanism, as expected for weakly donor solvents (*DN* = 14.1 and 2.7 for acetonitrile and nitromethane, respectively).

### High Pressure $^7$Li NMR Measurements

Additional mechanistic information on the intimate nature of the exchange mechanism can in principle be obtained from the effect of pressure on the $Li^+$ exchange process.[36] A systematic pressure dependence study was performed to determine the volume of activation for the $Li^+$ exchange process for both chelates. Pressure-dependent NMR spectra were recorded for each sample over the pressure range of 0.1 to 150 MPa at 313.2 K. The higher temperature had to be chosen, because in the case of C221 the exchange process hardly occurs at room temperature, whereas in the case of C222 the signals are broad at room temperature due to coalescence and it was difficult to observe line broadening that resulted from increasing pressure. There are two signals to be seen in Figure 11: one for the solvated Li at 8.8 ppm and the one for Li complexed by C221 at 6.5 ppm. It can be observed that there is a very small difference in the shape of the NMR spectra recorded at various pressures. The same effect was observed for the second ligand, C222 (Figure 12), where only one signal appears due to the fast exchange. Its shape almost does not change with the varying pressure for any of the three samples. The rate constants calculated for each pressure were very similar within the experimental error limits and resulted in a practically zero value for $\Delta V^{\#}_{obsd.}$ for both ligands, which points to a concerted interchange type of exchange mechanism.[37] In terms of an interchange mechanism, bond formation and bond cleavage occur in a concerted fashion without the formation of a distinct intermediate of higher or lower coordination number. In addition, decomplexation will be accompanied by charge creation due to the release of $Li^+$, which in turn will lead to an increase in electrostriction which will offset the intrinsic volume changes.

### Theoretical Calculations

For the closely related γ-butyrolactone and $Li^+$/γ-butyrolactone high level ab initio studies were recently performed by Rey et al.[38] For acetone and $Li^+$/acetone only Hartree–Fock calculations were performed.[30] In our DFT calculations we found that the $Li^+$ cation coordinates to the carbonyl oxygen with an almost co-linear configuration relative to the carbon–oxygen bond, as for γ-butyrolactone. This configuration holds for clusters of up to four molecules and also in the solid phase, where a tetrahedral first solvation (coordination) sphere was found (see Table 4).[31]

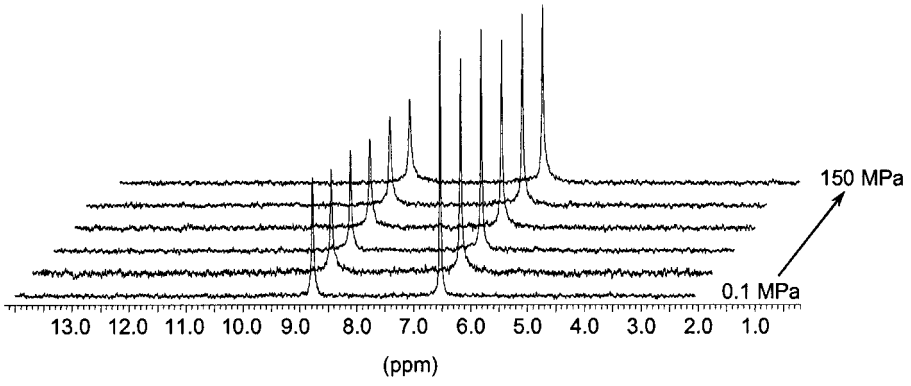


Figure 11. $^7$Li NMR spectra recorded as a function of pressure at 313.2 K for the mol ratio C221/$LiClO_4$ = 0.5.

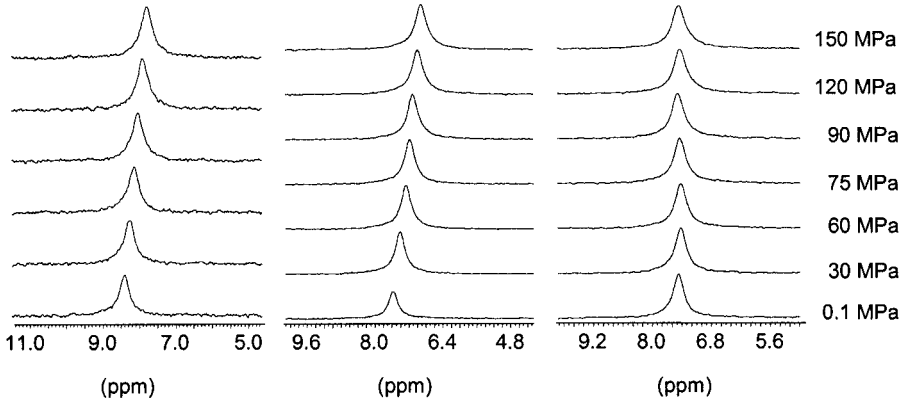


Figure 12. $^7$Li NMR spectra of C222 and $LiClO_4$ in acetone. Pressure dependence for the sample ratios C222/$LiClO_4$ = 0.25, 0.5, and 0.75, respectively, at 313.2 K.

 © 2007 Wiley-VCH Verlag GmbH & Co. KGaA, Weinheim 

Table 4. Calculated bond length for $Li^+$ solvated in acetone.

| Bond length [Å] | PG | B3LYP/D95Vp | B3LYP/6-311+G** |
|---|---|---|---|
| $[Li(acetone)]^+$ | $C_2$ | 1.77 | 1.75 |
| $[Li(acetone)_2]^+$ | $D_2$ | 1.81 | 1.79 |
| $[Li(acetone)_3]^+$ | $D_3$ | 1.88 | 1.86 |
| $[Li(acetone)_4]^+$ | $C_1$ | 1.96 (averaged) | 1.96 (averaged) |

Experimentally, a decrease in the cavity size of the cryptands hampers the exchange of $Li^+$ between the cryptand and the solvent. We were able to observe it in the case of γ-butyrolactone and again we can see it in the present case. The improved binding of $Li^+$ in a smaller cavity is visible from the structure and the following model reaction [Equation (4)] that describes the energy required for the dechelation process. Application of the CPCM solvent model strengthens this trend significantly (see Table 5).

$$[Li \subset Cryptand]^+ + 4\ solvent \rightarrow [Li(solvent)_4]^+ + Cryptand \quad (4)$$

Table 5. Dechelation energy, $E_{dechelation}$, for the reaction outlined in Equation (4).[a]

| Acetone | C222 | C221 | C211 |
|---|---|---|---|
| $E_{dechelation}$ (DFT) [kcal/mol] | –8.6 | +2.0 | +3.0 |
| $E_{dechelation}$ (CPCM) [kcal/mol] | +5.4 | +13.6 | +20.4 |
| γ-Butyrolactone | C222 | C221 | C211 |
| $E_{dechelation}$ (DFT) [kcal/mol][21] | –16.8 | –11.6 | –5.3 |

[a] DFT: RB3LYP/D95Vp, CPCM: RB3LYP(CPCM)/D95Vp//RB3LYP/D95Vp.

In agreement with previous studies by Wipff et al.,[3] we also found only a limited flexibility for the investigated cryptands in our DFT calculations, therefore all cryptands were calculated within the highest possible symmetry (Table 5). We recently demonstrated that reaction (4) is a valuable tool to determine ion selectivity as a function of the ionic radii[39] and to examine cavity size of the cryptands as a variable.[21,40]

In agreement with the experimental kinetic data, the smaller cryptand binds $Li^+$ better and slows down its exchange rate (Table 2). On comparing the calculated Li–O and Li–N bond lengths of the three structures with the bond length in $[Li(OH_2)_4]^+$ and $[Li(NH_3)_4]^+$, the trend can easily be understood (see Table 6 and Figure 11). In C222, $Li^+$ is four-fold weakly coordinated in a trigonal-pyramidal shape by one Li–N and three Li–O interactions all clearly elongated (0.2 and 0.1 Å, respectively). The $Li^+$ cation in C221 is five-fold coordinated (distorted trigonal-bipyramidal structure) by one nitrogen and four oxygen bonds all extended by around 0.15 Å. The coordinating bonds in $[Li \subset C211]^+$ are even more extended, but the Li–O bonds form a somewhat distorted tetrahedral coordination sphere for the lithium monocation, while the stronger elongated Li–N bonds form a kind of second coordination sphere. Therefore, the lithium ion can formally adopt a six-coordinate state, which strongly supports the proposed associative character of the decomplexation process that involves binding of external solvent molecules as suggested by the very negative activation entropies. A comparison of the calculated and X-ray bond lengths shows a good agreement. A comparison between the calculated data for γ-butyrolactone and acetone shows the same trend for both solvents. $Li^+$ is better coordinated in the smaller cavities of the smaller cryptands, as expected.

To draw a conclusion on solvation abilities from a direct comparison of the dechelating energies in acetone and γ-butyrolactone, is risky. The calculated dechelating energies can not be considered as a proof of the rule of Madrakian et al., that there is an inverse relationship between the stability of the complexes and the solvating ability of the solvent.[31] The different values can be attributed to the different number of non-hydrogen atoms in both solvents. Acetone has only four non-hydrogen atoms, while γ-butyrolactone has six and can therefore stabilize charge much better.

## Conclusions

It can be concluded from the results of the present study that for the $Li^+$ exchange process between C222, C221 and acetone as solvent, two pathways, viz. bimolecular (associative) and unimolecular (dissociative) compete with each other. The pressure dependence of the exchange process suggests the operation of a pure interchange mechanism, whereas the negative activation entropy values favor an associative interchange process for the decomplexation reaction. The basic idea of an interchange process involves concerted bond formation and bond cleavage, which is in agreement with the consideration that acetone is a rather weak

Table 6. Calculated (RB3LYP/D95Vp) and X-ray bond lengths (in Å).

| *d* [Å] | C222 | C221 | C211 | $[Li(OH_2)_4]^+$ | $[Li(acetone)_4]^+$ | $[Li(NH_3)_4]^+$ |
|---|---|---|---|---|---|---|
| Li–O | 2.14 | 2.06, 2.08, 2.10 | 2.14, 2.11 | 1.95 | 1.96 | – |
| Li–N | 2.22 | 2.28 | 2.38 | – | – | 2.13 |
| PG | $C_3$ | $C_1$ | $C_2$ | $T$ | $C_1$ | $C_1$ |
| X-ray | | [41] | [42] | [43] | [44] | [45] |
| Li–O | – | 1.99<br>2.06<br>2.10 | 2.17<br>2.08 | 1.96 | 1.94, 1.91, 1.93, 1.95 | – |
| Li–N | – | 2.40<br>2.44 | 2.29 | – | – | 2.08 |

 © 2007 Wiley-VCH Verlag GmbH & Co. KGaA, Weinheim 

donor. The results are in good agreement with that expected on the basis of a systematic comparison with data reported in the literature for solvents of similar donor strength.

## Experimental Section

**General Procedures:** The preparation of test solutions was carried out under Ar or $N_2$ using standard Schlenk techniques, under an Ar in a glove box, or under vacuum. Lithium perchlorate (Aldrich, battery grade) was vacuum-dried at 120 °C for 48 h and then stored under dry nitrogen. The cryptands C222 (purchased from Fluka), C221 and C211 (purchased from Aldrich) were dried under vacuum for 48 h and stored under dry nitrogen. Acetone (Acros, extra dry, water < 50 ppm) was used as received. Solutions of $LiClO_4$, C222, C221 and C211 in acetone were prepared under dry nitrogen. For the $^7$Li NMR measurements the solutions were sealed in 5-mm NMR tubes under Ar. In order to study the kinetics of the exchange of $Li^+$ between C222 and C221 and acetone as solvent, three solutions of different concentration ratio were prepared for each system. The concentration of lithium perchlorate in each solution was kept constant at 0.04 M, whereas the concentration of ligand was varied between 0.01 M and 0.032 M. In this way the measurements were always performed in the presence of an excess of $Li^+$.

**$^7$Li NMR Spectroscopy:** Variable-temperature and variable-pressure Fourier transform $^7$Li NMR spectra were recorded at a frequency of 155 MHz with a Bruker Avance DRX 400WB spectrometer equipped with a superconducting BC-94/89 magnet system. Spinning tubes (5 mm) were used with a 1-mm o.d. melting point capillary inserted coaxially in the spinning tube and filled with an external reference solution (1 M $LiClO_4$ in acetonitrile). The temperature dependence measurements were performed over a wide as possible temperature range for each system. We did not use a temperature calibration by insertion of a capillary filled with methanol (low temperature calibration) or ethylene glycol (high temperature calibration) into the sample tube, as the corresponding signals of these solvents would disturb the NMR spectra in the region of interest. In such a case a temperature-calibrated NMR probe has to be used in order to determine the temperature of the sample accurately.

Methanol was used for the low-temperature calibration of the NMR probe, whereas ethylene glycol was used for high-temperature calibration. The actual sample temperature can be calculated from the chemical shift differences. If there is any difference between the sample temperature and the temperature detected by the thermocouple of the probe, the probe can be calibrated by using standard Bruker Topspin software.

A homemade high-pressure probe described in the literature[46] was used for the variable-pressure experiments which were conducted at a selected temperature and at ambient, 30, 60, 75, 90, 120 and

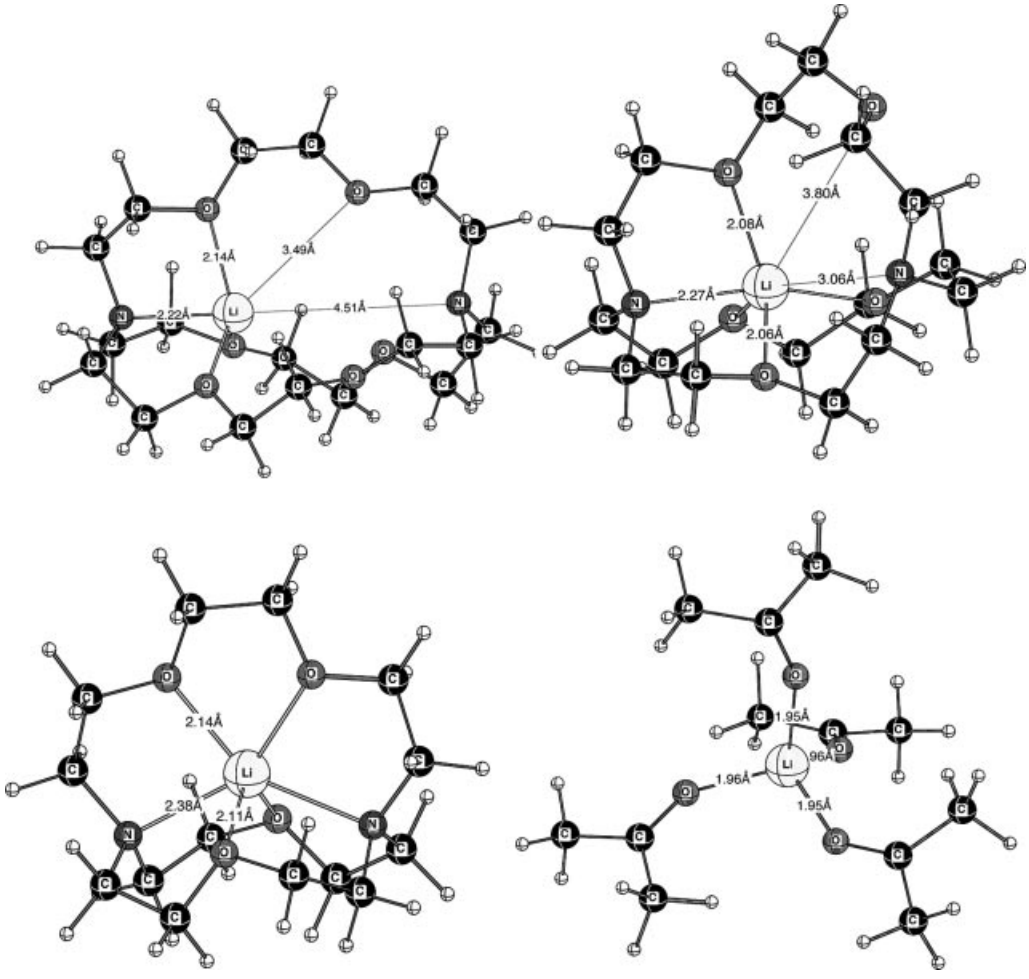


Figure 13. Optimized structures for $[Li \subset C222]^+$, $[Li \subset C221]^+$, $[Li \subset C211]^+$ and $[Li(acetone)_4]^+$.

 © 2007 Wiley-VCH Verlag GmbH & Co. KGaA, Weinheim 

150 MPa pressure. A standard 5-mm NMR tube cut to a length of 45 mm was used for the sample solution. The high-pressure NMR tube was sealed with a MACOR plug and an O-ring made of VITON. The plug and O-ring were shown to be stable in the employed solvent. The pressure was transmitted by the movable MACOR piston to the sample, and the temperature of the sample was controlled with a Pt-100 resistor. The probe itself was externally heated with a thermostatted circulating fluid that was pumped through a double helix that was cut into the outer surface of the autoclave. Because the sample is embedded in the high-pressure transmitting fluid that serves as a thermostating bath, a reliable temperature setting is guaranteed.

For a typical kinetic run, 0.8 mL of solution was transferred under Ar to a Wilmad screw-cap NMR tube equipped with a poly(tetrafluoroethylene) septum. All test samples were prepared in the same way.

**Programs:** The line widths of the NMR signals were obtained by fitting Lorentzian functions to the experimental spectra using the NMRICMA 2.7 program[47] for Matlab.[48] The adjustable parameters were the resonance frequency, intensity, line width and baseline. Complete line-shape analysis based on the Kubo–Sack formalism using modified Bloch equations[49] was also performed with NMRICMA 2.7 to extract rate constants from experimental spectra. The temperature and pressure dependent $^{7}$Li line widths and chemical shifts employed in the line shape analysis were extrapolated from low temperatures where no exchange-induced modification occurred.

**Quantum Chemical Calculations:** All structures were optimized with the B3LYP[50] and the basis set D95Vp,[51] or with 6-311+G** with no constrains other than symmetry, and confirmed to be minima by computation of vibrational frequencies. Relative energies were corrected for zero point vibrational energy differences (Figure 13). The D95V basis set, augmented with polarisation functions (D95Vp), was used.[52] If not otherwise mentioned, calculations were done without a solvent model. The influence of bulk solvent was probed using the CPCM[53] formalism and water as solvent, i.e., B3LYP(CPCM)/D95Vp//B3LYP/D95Vp. The Gaussian 03 suite of programs was used throughout.[54]

**Supporting Information** (see also the footnote on the first page of this article): Two tables with values of the observed rate constants ($k_{obs}$) calculated from the line shape analysis for the exchange of $Li^+$ between solvated and chelated sites for two cryptands.

## Acknowledgments

This work was supported by the European Commission Training and Mobility of Researchers Network (HPRN-CT-2000-19, "Solvation Dynamics and Ionic Mobility in Conventional and Polymer Solvents") and the Deutsche Forschungsgemeinschaft (SFB 583 on Redox-active Metal Complexes). We would like to thank Dr. Lothar Helm (EPFL Lausanne) for introducing E. P. to the software NMRICMA 2.7, Dr. Nico van Eikema Hommes for helpful discussions, Michael Galle for preliminary calculations, Prof. Tim Clark for hosting this work in the CCC and the Regionales Rechenzentrum Erlangen (RRZE) for a generous allotment of computer time.

[1] a) B. Dietrich, J. M. Lehn, J. P. Sauvage, *Tetrahedron Lett.* **1969**, *34*, 2889–2892; b) B. Dietrich, J. M. Lehn, J. P. Sauvage, *Tetrahedron Lett.* **1969**, *34*, 2885–2888.

[2] a) J. M. Lehn, *Acc. Chem. Res.* **1978**, *11*, 49–57; b) J. M. Lehn, *Angew. Chem.* **1988**, *100*, 91–116.

[3] G. Wipff, J. M. Wurtz, *New J. Chem.* **1989**, *13*, 807–820.

[4] X. X. Zhang, R. M. Izatt, K. E. Krakowiak, J. S. Bradshaw, *Inorg. Chim. Acta* **1997**, *254*, 43–47.

[5] J. M. Lehn, F. Montavon, *Helv. Chim. Acta* **1976**, *59*, 1566–1583.

[6] a) R. Puchta, V. Seitz, N. J. R. van Eikema Hommes, R. W. Saalfrank, *J. Mol. Model.* **2000**, *6*, 126–132; b) R. W. Saalfrank, A. Dresel, V. Seitz, S. Trummer, F. Hampel, M. Teichert, D. Stalke, C. Stadler, J. Daub, V. Schunemann, A. X. Trautwein, *Chem. Eur. J.* **1997**, *3*, 2058–2062; c) R. W. Saalfrank, V. Seitz, D. L. Caulder, K. N. Raymond, M. Teichert, D. Stalke, *Eur. J. Inorg. Chem.* **1998**, *9*, 1313–1317; d) R. W. Saalfrank, V. Seitz, F. W. Heinemann, C. Gobel, R. Herbst-Irmer, *J. Chem. Soc., Dalton Trans.* **2001**, *5*, 599–603.

[7] B. Dietrich, J. P. Kintzinger, J. M. Lehn, B. Metz, A. Zahidi, *J. Phys. Chem.* **1987**, *91*, 6600–6606.

[8] L. F. Lindoy, *The Chemistry of Macrocyclic Ligand Complexes*, Cambridge University Press, Cambridge, **1992**, p. 269.

[9] a) M. Farahbakhsh, H. Schmidt, D. Rehder, *Chem. Ber./Recueil* **1997**, *130*, 1123–1127; b) C. E. Housecroft, *Cluster Compounds of Main Group Elements*, VCH, Weinheim, Germany, **1996**, p. 94; c) M. Kirch, J. M. Lehn, *Angew. Chem.* **1975**, *87*, 542–543; d) J. M. Lehn, F. Montavon, *Helv. Chim. Acta* **1978**, *61*, 67–82; e) W. E. Morf, W. Simon, *Helv. Chim. Acta* **1971**, *54*, 2683–2704; f) M. J. Pregel, E. Buncel, *J. Am. Chem. Soc.* **1993**, *115*, 10–14; g) W. Simon, W. E. Morf, P. C. Meier, *Struct. Bond.* **1973**, *16*, 113–160.

[10] J. M. Lehn, J. P. Sauvage, *J. Chem. Soc., Chem. Commun.* **1971**, *9*, 440–441.

[11] K. Severin, *Coord. Chem. Rev.* **2003**, *245*, 3–10.

[12] R. H. Huang, M. J. Wagner, D. J. Gilbert, K. A. Reidy-Cedergren, D. L. Ward, M. K. Faber, J. L. Dye, *J. Am. Chem. Soc.* **1997**, *119*, 3765–3772.

[13] J. M. Lehn, J. P. Sauvage, *J. Am. Chem. Soc.* **1975**, *97*, 6700–6707.

[14] G. Wipff, P. Kollman, *Nouv. J. Chim.* **1985**, *9*, 457–465.

[15] B. G. Cox, J. Garcia-Rosas, H. Schneider, *J. Am. Chem. Soc.* **1981**, *103*, 1054–1059.

[16] R. R. Rhinebarger, A. I. Popov, *Polyhedron* **1988**, *7*, 1341–1347; A. J. Smetana, A. I. Popov, *J. Solution Chem.* **1980**, *9*, 183–196.

[17] M. Shamsipur, A. I. Popov, *J. Phys. Chem.* **1986**, *90*, 5997–5999.

[18] a) A. Abou-Hamdan, S. F. Lincoln, *Inorg. Chem.* **1991**, *30*, 462–466; b) P. Clarke, J. M. Gulbis, S. F. Lincoln, E. R. T. Tiekink, *Inorg. Chem.* **1992**, *31*, 3398–3404; c) P. Clarke, S. F. Lincoln, E. R. T. Tiekink, *Inorg. Chem.* **1991**, *30*, 2747–2751; d) S. F. Lincoln, A. Abou-Hamdan, *Inorg. Chem.* **1990**, *29*, 3584–3589; e) S. F. Lincoln, T. Rodopoulos, *Inorg. Chim. Acta* **1991**, *190*, 223–229; f) S. F. Lincoln, T. Rodopoulos, *Inorg. Chim. Acta* **1993**, *205*, 23–30; g) S. F. Lincoln, A. K. W. Stephens, *Inorg. Chem.* **1991**, *30*, 3529–3534; h) A. K. W. Stephens, R. S. Dhillon, S. E. Madbak, S. L. Whitbread, S. F. Lincoln, *Inorg. Chem.* **1996**, *35*, 2019–2024.

[19] a) R. M. Izatt, J. S. Bradshaw, S. A. Nielsen, J. D. Lamb, J. J. Christensen, D. Sen, *Chem. Rev.* **1985**, *85*, 271–339; b) R. M. Izatt, J. S. Bradshaw, K. Pawlak, R. L. Bruening, B. J. Tarbet, *Chem. Rev.* **1992**, *92*, 1261–1354; c) R. M. Izatt, K. Pawlak, J. S. Bradshaw, R. L. Bruening, *Chem. Rev.* **1995**, *95*, 2529–2586.

[20] R. M. Izatt, K. Pawlak, J. S. Bradshaw, R. L. Bruening, *Chem. Rev.* **1991**, *91*, 1721–1785.

[21] E. Pasgreta, R. Puchta, M. Galle, N. van Eikema Hommes, R. van Eldik, *J. Inclusion Phenom. Macrocyclic Chem.* **2007**, *58*, 81–88.

[22] a) K. Sonoda, M. Deguchi, H. Koshina, M. Armand, C. Michot, M. Gauthier, *Proc. Electrochem. Soc.* **2003**, 512–517; b) N. Takami, M. Sekino, T. Ohsaki, M. Kanda, M. Yamamoto, *J. Power Sources* **2001**, *97–98*, 677–680.

[23] *Spec. Issue*: S. T. Handy, P. A. Grieco, C. Mineur, L. Ghosez, *Synlett* **1995**, 565–567.

 © 2007 Wiley-VCH Verlag GmbH & Co. KGaA, Weinheim 

[24] W. J. Kinart, E. Sniec, I. Tylak, C. M. Kinart, *Phys. Chem. Liq.* **2000**, *38*, 193–201.
[25] a) J. Barthel, R. Buchner, E. Wismeth, *J. Solution Chem.* **2000**, *29*, 937–954; b) J. Barthel, H. J. Gores, R. Neueder, A. Schmid, *Pure Appl. Chem.* **1999**, *71*, 1705–1716; c) F. Croce, A. D'Aprano, C. Nanjundiah, V. R. Koch, C. W. Walker, M. Salomon, *J. Electrochem. Soc.* **1996**, *143*, 154–159; d) K. Matsubara, R. Kaneuchi, N. Maekita, *J. Chem. Soc., Faraday Trans.* **1998**, *94*, 3601–3605; e) J. M. Alia, H. G. M. Edwards, *Vib. Spectrosc.* **2000**, *24*, 185–200; f) G. Kumar, Janakiraman, N. Namboodiri, Gangadharan, Saminathan, Kanagaraj, N. Sharief, *J. Chem. Eng. Data* **1991**, *36*, 467–470; g) R. Puchta, M. Galle, N. van Eikema Hommes, E. Pasgreta, R. van Eldik, *Inorg. Chem.* **2004**, *43*, 8227–8229; h) D. Spångberg, K. Hermansson, *Chem. Phys.* **2004**, *300*, 165–176.
[26] a) S. Himeno, M. Takamoto, T. Ueda, R. Santo, A. Ichimura, *Electroanalysis* **2004**, *16*, 656–660; b) M. Hojo, H. Hasegawa, N. Hiura, *J. Phys. Chem.* **1996**, *100*, 891–896.
[27] E. Karkhaneei, M. H. Zebrajadian, M. Shamsipur, *J. Inclusion Phenom. Macrocyclic Chem.* **2001**, *40*, 309–312.
[28] a) J. M. Alia, Y. Diaz de Mera, H. G. M. Edwards, F. J. Garcia, E. E. Lawson, *J. Mol. Struct.* **1997**, *408–409*, 439–450; b) M. Chabanel, D. Legoff, K. Touaj, *J. Chem. Soc., Faraday Trans.* **1996**, *92*, 4199–4205; c) M. Hojo, H. Hasegawa, Y. Morimoto, *Anal. Sci.* **1996**, *12*, 521–524; d) J. Barthel, R. Neueder, H. Poepke, H. Wittmann, *J. Solution Chem.* **1999**, *28*, 489–503; e) V. D. Kiselev, E. A. Kashaeva, N. A. Luzanova, A. I. Konovalov, *Thermochim. Acta* **1997**, *303*, 225–228; f) Y. Kameda, N. Kudoh, S. Suzuki, T. Usuki, O. Uemura, *Bull. Chem. Soc. Jpn.* **2001**, *74*, 1009–1014.
[29] R. J. Blint, *J. Electrochem. Soc.* **1995**, *142*, 696–702.
[30] R. L. Jarek, T. D. Miles, M. L. Trester, S. C. Denson, S. K. Shin, *J. Phys. Chem. A* **2000**, *104*, 2230–2237.
[31] T. Madrakian, A. Afkhami, J. Ghasemi, M. Shamsipur, *Polyhedron* **1996**, *15*, 3647–3652.
[32] E. Shchori, J. Jagur-Grodzinski, M. Shporer, *J. Am. Chem. Soc.* **1973**, *95*, 3842–3846.
[33] E. Shchori, J. Jagur-Grodzinski, Z. Luz, M. Shporer, *J. Am. Chem. Soc.* **1971**, *93*, 7133–7138.
[34] Y. Marcus, *Chem. Soc. Rev.* **1993**, *22*, 409–416.
[35] M. Shamsipur, E. Karkhaneei, A. Afkhami, *J. Coord. Chem.* **1998**, *44*, 23–32.
[36] a) A. V. Davis, D. Fiedler, G. Seeber, A. Zahl, R. van Eldik, K. N. Raymond, *J. Am. Chem. Soc.* **2006**, *128*, 1324–1333; b) R. van Eldik, C. D. Hubbard, *Chemistry at Extreme Conditions*, Elsevier, Amsterdam, **2005**, p. 109–164; c) M. Wolak, R. van Eldik, *J. Am. Chem. Soc.* **2005**, *127*, 13312–13315; d) A. Zahl, R. van Eldik, M. Matsumoto, T. W. Swaddle, *Inorg. Chem.* **2003**, *42*, 3718–3722; e) J. R. Rustad, A. G. Stack, *J. Am. Chem. Soc.* **2006**, *128*, 14778–14779.
[37] L. Helm, A. E. Merbach, *Chem. Rev.* **2005**, *105*, 1923–1959.
[38] M. Masia, R. Rey, *J. Phys. Chem. B* **2004**, *108*, 17992–18002.
[39] M. Galle, R. Puchta, N. J. R. van Eikema Hommes, R. van Eldik, *Z. Phys. Chem.* **2006**, *220*, 511–523.
[40] R. Puchta, R. van Eldik, *Eur. J. Inorg. Chem.* **2007**, 1120–1127.
[41] S. Choua, H. Sidorenkova, T. Berclaz, M. Geoffroy, P. Rosa, N. Mezailles, L. Ricard, F. Mathey, P. Le Floch, *J. Am. Chem. Soc.* **2000**, *122*, 12227–12234.
[42] D. Moras, R. Weiss, *Acta Crystallogr., Sect. B: Struct. Sci.* **1973**, *29*, 400–403.
[43] W. Meske, D. Babel, *Z. Anorg. Allg. Chem.* **1998**, *624*, 1751–1755.
[44] F. A. Cotton, L. M. Daniels, C. A. Murillo, H. C. Zhou, *Inorg. Chim. Acta* **2000**, *300–302*, 319–327.
[45] N. Scotti, U. Zachwieja, H. Jacobs, *Z. Anorg. Allg. Chem.* **1997**, *623*, 1503–1505.
[46] A. Zahl, A. Neubrand, S. Aygen, R. van Eldik, *Rev. Sci. Instrum.* **1994**, *65*, 882–886.
[47] L. Helm, A. Borel *NMRICMA 2.7*, University of Lusanne, **2000**.
[48] *Matlab*, version 5.3.1., Mathworks Inc., **1999**.
[49] J. A. Pople, W. G. Schneider, H. J. Bernstein, *High-Resolution Nuclear Magnetic Resonance*, McGrow-Hill Book Co., New York, **1959**, p. 513.
[50] a) A. D. Becke, *J. Chem. Phys.* **1993**, *98*, 5648–5652; b) C. Lee, W. Yang, R. G. Parr, *Phys. Rev. B: Condens. Matter* **1988**, *37*, 785–789; c) P. J. Stephens, F. J. Devlin, C. F. Chabalowski, M. J. Frisch, *J. Phys. Chem.* **1994**, *98*, 11623–11627.
[51] a) T. H. Dunning Jr, P. J. Hay, *Modern Theoretical Chemistry*, Plenum, New York, **1976**, vol. 3, p. 1–28; b) S. Huzinaga, J. Andzelm, M. Klobukowski, E. Radzio-Andzelm, Y. Sakai, H. Tatewaki, *Gaussian basis sets for molecular calculations*, Elsevier, Amsterdam, **1984**.
[52] a) The performance of the computational level employed in this study is well documented, see for example: M. Galle, R. Puchta, N. van Eikema Hommes, R. van Eldik, *Z. Phys. Chem.* **2006**, *220*, 511–523; R. Puchta, N. J. R. van Eikema Hommes, R. Meier, R. van Eldik, *Dalton Trans.* **2006**, *28*, 3392–3395; S. Klaus, H. Neumann, H. Jiao, A. Jacobi von Wangelin, D. Goerdes, D. Struebing, S. Huebner, M. Hateley, C. Weckbecker, K. Huthmacher, T. Riermeier, M. Beller, *J. Organomet. Chem.* **2004**, *689*, 3685–3700; R. W. Saalfrank, C. Deutscher, H. Maid, A. M. Ako, S. Sperner, T. Nakajima, W. Bauer, F. Hampel, B. A. Hess, N. J. R. van Eikema Hommes, R. Puchta, F. W. Heinemann, *Chem. Eur. J.* **2004**, *10*, 1899–1905; A. Scheurer, H. Maid, F. Hampel, R. W. Saalfrank, L. Toupet, P. Mosset, R. Puchta, N. J. R. van Eikema Hommes, *Eur. J. Org. Chem.* **2005**, *12*, 2566–2574; C. F. Weber, R. Puchta, N. J. R. van Eikema Hommes, P. Wasserscheid, R. van Eldik, *Angew. Chem.* **2005**, *117*, 6187–6192; C. F. Weber, R. Puchta, N. J. R. van Eikema Hommes, P. Wasserscheid, R. van Eldik, *Angew. Chem. Int. Ed. Engl.* **2005**, *44*, 6033–6038; b) R. Puchta, M. Galle, N. J. R. van Eikema Hommes, *Z. Naturforsch., Teil B* **2006**, *61*, 1327–1334.
[53] a) V. Barone, M. Cossi, *J. Phys. Chem. A* **1998**, *102*, 1995–2001; b) M. Cossi, N. Rega, G. Scalmani, V. Barone, *J. Comput. Chem.* **2003**, *24*, 669–681.
[54] M. J. Frisch, G. W. Trucks, H. B. Schlegel, G. E. Scuseria, M. A. Robb, J. R. Cheeseman, J. A. Montgomery Jr, T. Vreven, K. N. Kudin, J. C. Burant, J. M. Millam, S. S. Iyengar, J. Tomasi, V. Barone, B. Mennucci, M. Cossi, G. Scalmani, N. Rega, G. A. Petersson, H. Nakatsuji, M. Hada, M. Ehara, K. Toyota, R. Fukuda, J. Hasegawa, M. Ishida, T. Nakajima, Y. Honda, O. Kitao, H. Nakai, M. Klene, X. Li, J. E. Knox, H. P. Hratchian, J. B. Cross, V. Bakken, C. Adamo, J. Jaramillo, R. Gomperts, R. E. Stratmann, O. Yazyev, A. J. Austin, R. Cammi, C. Pomelli, J. W. Ochterski, P. Y. Ayala, K. Morokuma, G. A. Voth, P. Salvador, J. J. Dannenberg, V. G. Zakrzewski, S. Dapprich, A. D. Daniels, M. C. Strain, O. Farkas, D. K. Malick, A. D. Rabuck, K. Raghavachari, J. B. Foresman, J. V. Ortiz, Q. Cui, A. G. Baboul, S. Clifford, J. Cioslowski, B. B. Stefanov, G. Liu, A. Liashenko, P. Piskorz, I. Komaromi, R. L. Martin, D. J. Fox, T. Keith, M. A. Al-Laham, C. Y. Peng, A. Nanayakkara, M. Challacombe, P. M. W. Gill, B. Johnson, W. Chen, M. W. Wong, C. Gonzalez, J. A. Pople, *Gaussian 03, Revision B.03, Gaussian Inc.*, Wallingford, CT, **2004**.

Received: December 11, 2006
Published Online: May 10, 2007

 © 2007 Wiley-VCH Verlag GmbH & Co. KGaA, Weinheim 

DOI: 10.1002/ejic.200601227

# Facile Formation of Hexacyclic [$Al_3O_2Cl$] Aluminum and Alkoxide-Bridged Titanium Complexes: Reactions of $AlMe_3$ with [$Ti(L)Cl_2$] [L = 2,2′-Methylenebis(6-*tert*-butyl-4-methylphenolato)]

**Dao Zhang*[a]**

**Keywords:** Aluminum complexes / Titanium complexes / Trimethylaluminum

The titanium dichloride complex [(L)$TiCl_2$] [L = 2,2′-methylenebis(6-*tert*-butyl-4-methylphenolato)] (**1**) reacted with trimethylaluminum ($AlMe_3$) in a 1:2 ratio to give a trimetallic aluminum complex of the composition [(L)$(AlMe_2)_3(\mu$-Cl)] (**2**) with a symmetric six-membered ring [$Al_3(\mu_2$-O)$_2(\mu_2$-Cl)] and a four-coordinate aluminum center in the solid state. The reaction of 1 equiv. $AlMe_3$ gave [(L)TiMeCl] (**3**), which could absorb $O_2$ gas to afford the oxygen-insertion product [{(L)-$TiCl\}_2(\mu$-$OMe)_2$] (**4**) with a five-coordinate metal center. Upon reaction of $H_2L$ with $AlMe_3$, the binuclear, four-coordinate adduct [{(L)$AlMe\}_2$] (**5**) was formed. Complex **4** supported on $MgCl_2$ and activated with aluminum alkyls reveals high catalytic activity for ethylene polymerization to produce polymers with molecular weight distributions of ca. 3.1.
(© Wiley-VCH Verlag GmbH & Co. KGaA, 69451 Weinheim, Germany, 2007)

## Introduction

Reactions of organometal(IV) halides with alkyls of group 13 elements, especially those of aluminum, have attracted much interest because of their inherent fundamental chemistry as well as their potential applications. The methylation of a metallocene(IV) chloride is assumed to be the first step of activation of a polymerization catalyst and one of the first well-defined products is Tebbe's reagent, [$Cp_2Ti(\mu_2$-$CH_2)(\mu_2$-Cl)$AlMe_2$], derived from $Cp_2TiMe_2$ and $AlMe_3$.[1] Later, methyl nonmetallocene transition-metal complexes could be conveniently prepared with the Jordan amido/alkyl exchange protocol using $AlMe_3$, a technique primarily utilized with complexes of the metallocene type.[2] Several novel aluminum-containing clusters, [$(Cp^*M)_3Al_6$-$Me_8(CH)_5(CH_2)_2$] (M = Zr, Hf),[3] [($t$$Bu_3PN$)$Ti(\mu$-Me)$(\mu_4$-C)-$(AlMe_2)_2]_2$,[4] and [$Cp^*_4Y_4(\mu_2$-$CH_3)_2\{(CH_3)Al(\mu_2$-$CH_3)_2\}_4$-$(\mu_4$-$CH)_2$],[5] have been developed by the reactions of the corresponding metal complexes with $AlMe_3$ that could perform the abstraction of hydrogen from methyl groups. Nevertheless, such clusters, particularly those bearing two or more different metals, are very rare because of the limitations inherent in available synthetic methods. Moreover, a surprisingly facile transmetalation of the multidentate ligands from a transition metal such as zirconium or iron to aluminum was reported by using $AlR_3$ (R = Me or Et).[6,7]

As part of an ongoing project whose aim is to study the chemistry of olefin polymerization catalysis, some novel metal catalysts have been designed and successfully pre-

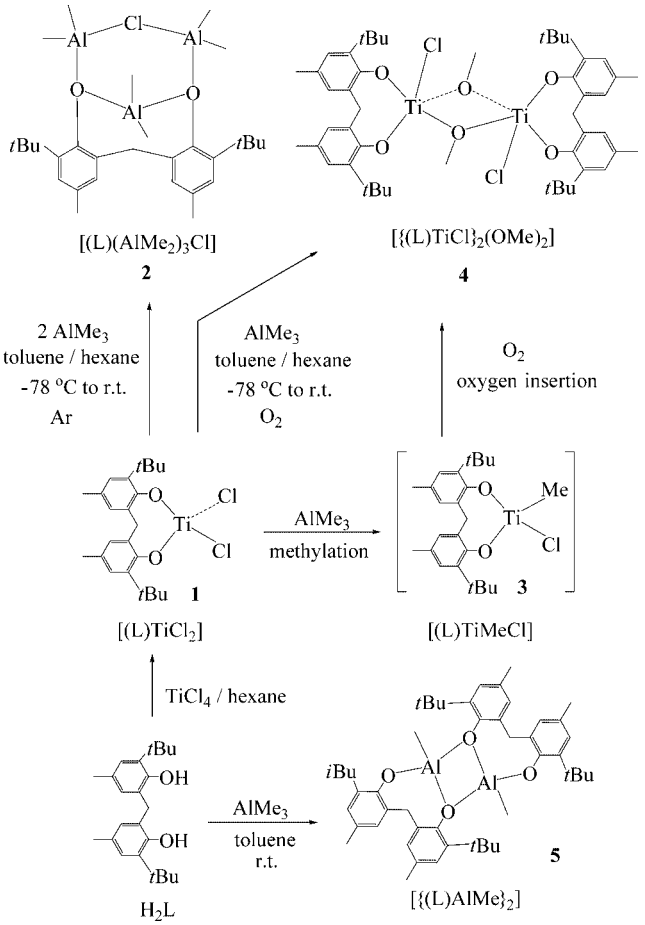


Scheme 1. Synthesis of aluminum and titanium complexes **2**–**5** using $AlMe_3$.

[a] Department of Chemistry, Fudan University, Shanghai 200433, P. R. China
Fax: +86-21-65641740
E-mail: daozhang@fudan.edu.cn

 © 2007 Wiley-VCH Verlag GmbH & Co. KGaA, Weinheim 

pared.[8] Our goal is to create highly active, single-site heterogeneous systems for the ethylene polymerization process. Some titanium complexes supported on $MgCl_2$, which is a widely used support in conventional Z–N catalysts, and activated with aluminum alkyls are highly effective ethylene polymerization catalysts.[9] Especially the interaction of titanium compounds with aluminum derivatives was of great interest to us for understanding the high activity of titanium aryloxides in the ethylene polymerization process.[10]

In the present report, we aim to present the synthesis and structures of an unexpected trimetallic, hexacyclic aluminum and alkoxide-bridged titanium complex by the reaction of trimethylaluminum with $[(L)TiCl]_2$ [(L) = 2,2′-methylenebis(6-*tert*-butyl-4-methylphenolato)] (**1**) (Scheme 1). To the best of our knowledge, such examples have never been demonstrated. Ethylene polymerization with an alkoxide-bridged titanium complex supported on $MgCl_2$ and activated with alkylaluminum compounds is also included.

## Results and Discussion

Reaction of $AlMe_3$ solved in toluene with **1** at a 2:1 molar ratio at room temp. leads to a color change from red to dark brown, and the air- and moisture-sensitive complex, $[(L)(AlMe_2)_3Cl]$ (**2**), is formed as dark green crystals and isolated by filtration in 31% yield after the reaction solution is cooled to –20 °C overnight. Compound **2** does not react further with $AlMe_3$, even not at 100 °C in [$D_8$]toluene, and is soluble and stable in benzene and toluene.

The $^1H$ (see Figure 1) and $^{13}C$ NMR spectra of **2** are in good agreement with the crystal structure obtained from X-ray diffraction techniques. The alkyl groups attached to the metal centers are not equivalent and are in the expected chemical shift ranges; both the $^1H$ and $^{13}C$ signals are shifted distinctly from the starting $AlMe_3$. $^1H$ NMR spectroscopic data for **2** reveals the presence of three different methyl ($AlMe_2$) environments at $\delta$ = –1.19, –0.52, and 0.17 ppm in [$D_6$]benzene ($\delta$ = –1.26, –0.57, and 0.12 ppm in [$D_8$]toluene) with integral intensity ratios of 3:6:9 (Figure 1). Also observed is one set of resonances for the L ligand. These observations suggest that compound **2** has the same structure in solution and in the solid state.

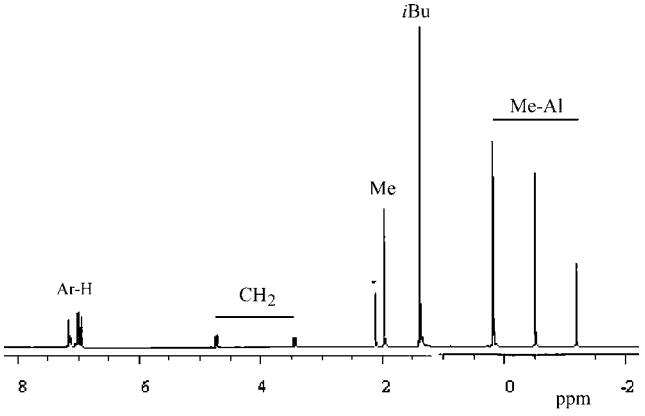


Figure 1. $^1H$ NMR spectra of **2** (containing toluene marked with *) in [$D_6$]benzene.

In the solid state, compound **2** forms unexpected trinuclear aluminum molecules in which there are no titanium atoms, indicating that transmetalation occurs (Figure 2 and Table 1). The central, nearly symmetrical, hexacyclic $[Al_3(\mu_2\text{-}O)_2(\mu_2\text{-}Cl)]$ is composed of three aluminum atoms, one bridging chlorine, and two bridging oxygen atoms [O(1), O(1A)] of the L ligand. This type of bridging has been rarely observed in phenolate aluminum compounds. Each aluminum atom is coordinated in a distorted tetrahedral fashion by oxygen [O(1), O(1A)] of the L ligands or chloride besides two methyl groups. The Al–O bond lengths are similar to those found in other structures of four-coordinate aluminum aryloxides.[11] The Al–Cl distance of 2.321(2) Å lies in the range of 2.2695(17)–2.3224(11) Å observed for other chlorine-bridged aluminum complexes with multidentate aryloxide ligands linked by three different spacers.[12]

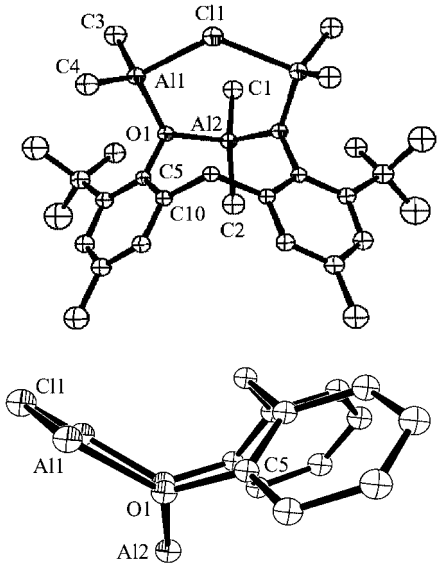


Figure 2. Molecular structure of **2**.

Table 1. Selected bond lengths [Å] and angles [°] for **2**.

| | | | |
|---|---|---|---|
| Cl(1)–Al(1) | 2.321(2) | Al(1)–O(1) | 1.855(5) |
| Al(1)–C(3) | 1.954(6) | Al(1)–C(4) | 1.935(8) |
| Al(2)–O(1) | 1.890(5) | Al(2)–C(1) | 1.929(7) |
| Al(2)–C(2) | 1.96(1) | O(1)–C(5) | 1.436(5) |
| C(5)–C(10) | 1.397(7) | C(10)–C(11) | 1.521(8) |
| O(1)–Al(1)–C(3) | 115.4(3) | O(1)–Al(1)–C(4) | 111.5(2) |
| O(1)–Al(1)–Cl(1) | 99.9(1) | C(3)–Al(1)–C(4) | 119.3(3) |
| C(3)–Al(1)–Cl(1) | 102.3(2) | C(4)–Al(1)–Cl(1) | 105.3(3) |
| O(1)–Al(2)–C(1) | 106.6(2) | O(1)–Al(2)–C(2) | 108.2(2) |
| C(1)–Al(2)–C(2) | 123.8(5) | C(5)–O(1)–Al(1) | 117.1(4) |
| C(5)–O(1)–Al(2) | 114.9(3) | Al(1)–O(1)–Al(2) | 126.6(2) |
| C(10)–C(5)–O(1) | 116.3(5) | C(11)–C(10)–C(5) | 123.4(4) |

However, treatment of **1** with precisely 1 equiv. $AlMe_3$ in [$D_6$]benzene in a J-Young tube under argon resulted in the formation of an unidentified mixture ($^1H$ NMR), and no [(L)TiMeCl] (**3**) could be isolated. Interestingly, the same reaction carried out under $O_2$ affords small amount of yellow, very thin, needle-like crystals of $\{[(L)TiCl]_2(\mu\text{-}OMe)_2\}$ (**4**). The formation of **4** clearly indicates the insertion of

 © 2007 Wiley-VCH Verlag GmbH & Co. KGaA, Weinheim 

dioxygen into "M–R" bonds of the resultant intermediate titanium complex **3**.[13] The presence of ν(Ti–Cl) frequencies at ca. 419 $cm^{-1}$ in the IR spectra of **4** indicates characteristic modes for terminally coordinated chlorine. The methoxy groups bridging the two titanium centers are equivalent, giving rise to one singlet at $\delta$ = 4.12 ppm in the $^1H$ NMR spectra. Also, one set of resonances due to the (L) ligand, slightly shifted from that detected for **1**, was observed.

The X-ray crystal structure of **4** (Figure 3 and Table 2) shows that the binuclear molecule contains a core of two internal aluminum atoms linked by oxygen atoms from the two OMe groups. The remaining two chlorine atoms are bonded terminally to the titanium atoms. Two boat-conformation L ligands are bonded similarly, having two oxygen atoms in the same titanium coordination sphere. The coordination sphere around the titanium center can be described as distorted square pyramidal, the oxygen atoms of the L ligand [O(1), O(2)] and of two bridging OMe groups [O(3), O(3A)] forming the equatorial plane, while the chlorine atom [Cl(1)] occupies the apical sites. As expected, the average Ti–μ-O (methoxo) distance of 1.962(2) Å is significantly longer than the terminal ones [av. 1.788(3) Å] but similar to those observed in $[(tritox)_2Ti_2(\mu\text{-}OMe)_2Me_2]$ [2.015(10) Å].[13a] The Ti–Cl distance of 2.2599(1) Å is shorter than that detected in [(tbmp)Ti ($\eta^5$-$C_5H_5$)Cl] [2.343(2)] and $Ti(tmbp)Cl_2$ [2.236(2) Å] (tmbp = 2,2′-thiobis(4-methyl-6-*tert*-butylphenoxo)[14] and is only surpassed by the values of 2.252(2) and 2.237(2) Å found in $[(tbop)_2Ti_3(OEt)_2Cl_6]$.[15]

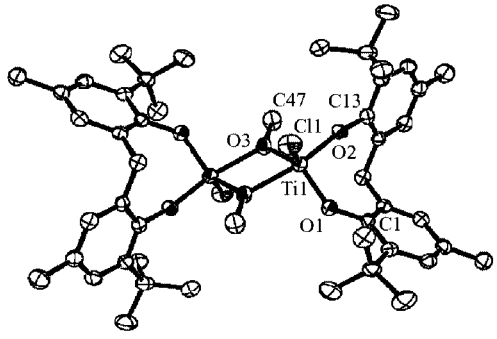


Figure 3. Molecular structure of **4**.

Table 2. Selected bond lengths [Å] and angles [°] for **4**.

| | | | |
|---|---|---|---|
| Ti(1)–Cl(1) | 2.259(1) | Ti(1)–O(1) | 1.805(2) |
| Ti(1)–O(2) | 1.776(2) | Ti(1)–O(3) | 1.962(2) |
| Cl(1)–Ti(1)–O(1) | 112.52(8) | Cl(1)–Ti(1)–O(2) | 98.95(9) |
| Cl(1)–Ti(1)–O(3) | 121.75(8) | O(1)–Ti(1)–O(2) | 98.0(1) |
| O(1)–Ti(1)–O(3) | 122.2(1) | O(2)–Ti(1)–O(3) | 92.1(1) |
| Cl(2)–Ti(2)–O(4) | 112.67(8) | C(1)–O(1)–Ti(1) | 140.9(2) |
| C(13)–O(2)–Ti(1) | 155.4(3) | C(47)–O(3)–Ti(1) | 129.6(2) |

The reaction of $H_2L$ and $AlMe_3$ in an equimolar ratio in toluene as well as in *n*-hexane leads to formation of the dimer $\{[(L)AlMe]_2\}$ (**5**) in good yield.[12d] There is no OH resonance in the $^1H$ NMR spectrum, indicating a loss of hydroxy protons. The methyl groups attached to the metal centers are equivalent and are in the expected chemical shift ranges; both the $^1H$ and $^{13}C$ signals are shifted slightly from the starting $AlMe_3$.

Crystals of **5** suitable for X-ray structure determination were obtained from hexane/toluene. The molecular structure of **5** is shown in Figure 4, and selected bond lengths and angles are listed in Table 3. Crystals of **5** comprise a centrosymmetric dimer with a planar $Ti_2O_2$ core. The titanium atoms in **4** have tetrahedral geometry. The two Al–O(aryloxo) distances of 1.693(1) and 1.856(1) Å are in the expected range for $Al^{III}$ complexes with facially coordinated bis(aryloxo) ligands. The Ti–C(methyl) distance of 1.941(3) Å is typical for $Ti_2O_2$ moieties and similar to those observed in $[(tritox)_2Ti_2(\mu\text{-}OMe)_2Me_2]$ [2.063(10) Å][13a] and $[(L)TiMe_2]$ [2.090(9) and 2.030(10) Å].[16]

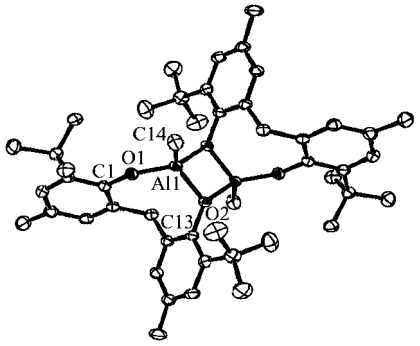


Figure 4. Molecular structure of **5**.

Table 3. Selected bond lengths [Å] and angles [°] for **5**.

| | | | |
|---|---|---|---|
| Al(1)–O(1) | 1.693(1) | Al(1)–O(2) | 1.856(1) |
| Al(1)–C(14) | 1.941(3) | O(1)–Al(1)–O(2) | 108.93(6) |
| O(1)–Al(1)–C(14) | 108.1(1) | O(2)–Al(1)–C(14) | 125.64(8) |
| C(1)–O(1)–Al(1) | 158.2(2) | C(13)–O(2)–Al(1) | 124.8(1) |

Titanium complex **4** was tested in an ethylene polymerization process. The catalyst was prepared in *n*-hexane by milling a slurry of $[MgCl_2(thf)_2]$ with **4** (the molar ratio is 10:1) and $AlEt_2Cl$ as the cocatalyst (see Exp. Sect.). Prior to the polymerization, ethylene was passed through the suspension of the catalyst. Then, MAO was added to the catalyst and dispersed in the prepolymer to form a highly active catalyst. Thus, the polymerization of ethylene was performed in a two-step process. The aim of the first step (very low Al:Ti molar ratio, normal pressure of monomer, very low rate of polymerization) was to prepare granules of polymer containing dispersed catalyst. These granules acted as a "microreactor" in the second step of polymerization with a high rate (Granular Reactor Technology). This method gave PE yields twice as high as those obtained with the one-stage activation process. The ethylene polymerization results and polymer characterization data are summarized in Table 4.

 © 2007 Wiley-VCH Verlag GmbH & Co. KGaA, Weinheim 

Table 4. Results of ethylene polymerization.[a]

| Entry | Complex | $T$ [°C] | Activity[b] | $M_w/M_n$ |
|---|---|---|---|---|
| 1 | **4** | 50 | 123 | 3.08 |
| 2 | **4** | 70 | 149 | 3.11 |
| 3[c] | **4** | 50 | 278 | n.d.[d] |
| 4 | $Cp_2TiCl_2$ | 50 | 108 | 2.94 |

[a] Polymerization conditions: MAO (Al:Ti = 4000) as the cocatalyst, ethylene pressure: $P_{gauge}$ = 70 psi, 0.5 h. [b] kg PE $g^{-1}$ Ti $h^{-1}$. [c] Ethylene pressure is $P_{gauge}$ = 100 psi. [d] Not determined.

For comparison of catalyst activities, titanocene dichloride ($Cp_2TiCl_2$) was used as a reference under the same conditions (Table 1, entry 4). It turned out that the catalysts based on complex **4** (entries 1–3) exhibited comparable catalytic activity (about 120 kg PE $g^{-1}$Ti $h^{-1}$) for ethylene polymerization. This is compared with the titanocene catalyst, and much less than that originally reported for [(tbmp)-$TiX_2$]/MAO (820 kg PE/g of Ti h for X = Cl and 677 kg PE/g of Ti h for X = O*i*Pr; 20 °C, 3 MPa, 1 μmmol catalyst)[17] and [$(tbop)_2Ti_3(OEt)_2Cl_6$]/MAO (353 kg PE/g of Ti h; 50 °C, 0.5 MPa, 1 μmmol catalyst)[15] systems. The molecular weights ($M_w$) of the polyethylene produced range from 9.18 to $11.97 \times 10^5$, and the molecular weight distributions ($M_w/M_n$) are narrower than those reported for ethylene polymerization with catalysts.[18,19] It would appear that, for polymerization of ethylene, activation of systems based on complex **4** affords a single well-defined active species. This indicates that the cocatalyst does not abstract the ligand L from the titanium center to the aluminum. The nature of the active center in the catalyst based on the L–titanium complexes is currently being investigated.

## Conclusions

In contrast to methylation of some organometal chlorides with $AlMe_3$, the unexpected transmetalation reaction of the corresponding titanium chloride complex **1** with $AlMe_3$ in a 1:2 ratio occurs with the generation of trialuminum complex **2** with a symmetrical, hexacyclic [$Al_3(\mu_2\text{-}O)_2$-($\mu_2$-Cl)] core. The reaction of **1** with $AlMe_3$ in an equimolar ratio affords the methoxy-bridged dimeric titanium chloride complex **4**, which suggests the formation of the monomethyl titanium complex **3** that easily absorbs $O_2$ to give an oxygen-insertion product. Treatment of $H_2$mbmp with $AlMe_3$ leads to the formation of the dimeric methyl titanium complex **5**. Complex **4** supported on $MgCl_2$ and activated with aluminum alkyls is highly effective as an ethylene polymerization catalyst. The narrow molecular weight distribution for this system suggests the operation of a well-defined, heterogeneous single-site catalyst.

## Experimental Section

**General Considerations:** All operations were carried out under a dry argon atmosphere, using standard Schlenk techniques. All of the solvents were distilled under dinitrogen from the appropriate drying agents prior to use. [$D_6$]Benzene and [$D_8$]toluene were distilled from K metal and degassed by three freeze-pump-thaw cycles prior to use. The $TiCl_4$, $AlMe_3$ solution (1.0 M in hexane), and MAO compounds were obtained from the Aldrich Chemical Co. and were used without further purification unless stated otherwise. 2,2′-Methylenebis(6-*tert*-butyl-4-methylphenol) [$H_2$(L)] and [Ti(L)-$Cl_2$] (**1**) were synthesized according to literature methods.[20] $^1$H and $^{13}$C NMR spectra were recorded with a JEOL Lambda-500 spectrometer. Chemical shifts are reported in parts per million. Elemental analyses were measured with Yanaco MT-6 and MSU-32 microanalyzers. Infrared spectra were recorded with a Perkin–Elmer 180 spectrophotometer in Nujol mulls.

**Synthesis of [(L)($AlMe_2$)$_3$($\mu$-Cl)] (2):** $AlMe_3$ (1.0 M $Me_3Al$, 0.82 mL in hexane, 0.82 mmol) was added to a toluene/hexane solution (10/40 mL) of Ti(L)$Cl_2$ (**1**) (188 mg, 0.41 mmol) at –78 °C. The mixture was slowly warmed to room temp., and the color of the solution changed from red to brown-yellow and finally dark brown. After the resulting solution was stirred for another 8 h, the blue precipitate was separated by filtration. The clear solution was cooled to –20 °C for about one week to afford **2** as dark green crystals in 31% yield (46 mg based on $AlMe_3$). $^1$H NMR (500 MHz, $C_6D_6$): $\delta$ = –1.19 (s, 3 H, $CH_3$-Al), –0.52 (s, 6 H, $CH_3$-Al), 0.17 (s, 9 H, $CH_3$-Al), 1.38 (s, 18 H, $C(CH_3)_3$), 1.97 (s, 6 H, $CH_3$), 2.11 (s, 3 H, toluene), 3.45 (d, $J_{H\text{-}H}$ = 13.65 Hz, $CH_2$), 4.73 (d, $J_{H\text{-}H}$ = 13.65 Hz, $CH_2$), 6.96 (s, 2 H, Ar), 7.00–7.13 (m, 5 H, toluene), 7.16 (s, 2 H, Ar) ppm. $^1$H NMR (500 MHz, $C_7D_8$): $\delta$ = –1.26 (s, 3 H, $CH_3$-Al), –0.57 (s, 6 H, $CH_3$-Al), 0.12 (s, 3 H, $CH_3$-Al), 0.13 (s, 6 H, $CH_3$-Al), 1.40 (s, 18 H, $C(CH_3)_3$), 2.01 (s, 6 H, $CH_3$), 2.14 (s, toluene), 3.38 (d, $J_{H\text{-}H}$ = 13.65 Hz, $CH_2$), 4.66 (d, $J_{H\text{-}H}$ = 13.65 Hz, $CH_2$), 6.94 –7.12 (m, H-Ar, toluene) ppm. $^{13}$C NMR (126 MHz, $C_6D_6$): $\delta$ = 147.35, 140.60, 137.84, 135.23, 134.69, 130.32, 129.28, 129.18, 128.51, 128.29, 128.10, 127.91, 125.64, 35.68, 34.48, 32.75, 21.36, 20.85, –2.85, –6.00, –7.42, –8.75 ppm. $C_{29}H_{48}Al_3ClO_2$ (545.09): calcd. C 63.90, H 8.88; found C 63.77, H 8.91.

**Synthesis of [{(L)TiCl}$_2$($\mu$-OMe)$_2$] (4):** $AlMe_3$ (1.0 equiv. $AlMe_3$, 1.64 mL in hexane, 1.64 mmol) was added to a toluene/hexane solution (10/40 mL) of [(L)$TiCl_2$] (**1**) (0.375 g, 0.82 mmol) at –78 °C. The mixture was slowly warmed to room temp., and the color of the solution changed from red to orange. After the resulting solution was stirred for another 8 h under a dioxygen atmosphere, the precipitate was separated by filtration. The clear solution was cooled to –35 °C for about one week to afford orange crystals in 21% yield. $^1$H NMR (500 MHz, $C_6D_6$): $\delta$ = 1.47 (s, 9 H, $CH_3$), 1.52 (s, 9 H, $CH_3$), 2.05 (s, 3 H, $CH_3$), 2.08 (s, 3 H, $CH_3$), 3.42 (d, $J_{H\text{-}H}$ = 14.0 Hz, $CH_2$), 3.95 (d, $J_{H\text{-}H}$ = 14.0 Hz, $CH_2$), 4.12 (s, 6 H), 6.87 (s, 1 H, Ar), 6.92 (s, 3 H, Ar), 6.70 (s, 2 H, Ar) ppm. $^{13}$C NMR (126 MHz, $C_6D_6$): $\delta$ = 161.73, 161.52 ($\Delta\delta$ = 0.208, O-$C_{Ar}$), 136.44, 136.37, 136.01, 135.28, 133.17, 133.06, 129.28, 129.02, 128.97, 128.51, 128.41, 128.30, 128.10, 127.91, 126.11, 126.08, 69.81, 64.56, 35.38, 35.22, 35.16, 34.65, 30.32, 30.21, 21.05, 21.01 ppm. $C_{48}H_{66}Cl_2O_6Ti_2$ (905.67): calcd. C 63.66, H 7.35; found C 63.91, H 7.42.

**Synthesis of {[(L)$AlMe]_2$} (5):** Complex **5** was prepared by using a modification of the technique used in ref.[12d]. $AlMe_3$ (1.0 equiv. $AlMe_3$, 1.5 mL in hexane, 1.5 mmol) was added to a toluene/hexane solution (10/15 mL) of $H_2$L (0.5 g, 1.5 mmol) at –78 °C. The mixture was slowly warmed to room temp. and a white solid appeared. After the resulting mixture was stirred for another 8 h, the precipitate was separated by filtration and washed with hexane to give 0.29 g of **5** as a white solid in 52% yield. $^1$H NMR (500 MHz, $C_6D_6$): $\delta$ = 0.144 (s, 3 H, Al-$CH_3$), 1.37 (s, 9 H, $CH_3$), 1.40 (s, 9 H, $CH_3$), 1.84 (s, 3 H, $CH_3$), 2.32 (s, 3 H, $CH_3$), 3.69 (d, $J_{H\text{-}H}$ = 12.95 Hz, $CH_2$), 4.69 (d, $J_{H\text{-}H}$ = 12.95 Hz, $CH_2$), 6.88 (s, 1 H, Ar),

 © 2007 Wiley-VCH Verlag GmbH & Co. KGaA, Weinheim 

7.04 (s, 1 H, Ar) ppm. $^{13}C$ NMR (126 MHz, $C_6D_6$): $\delta$ = 161.73, 161.52 ($\Delta\delta$ = 0.208, O-$C_{Ar}$), 136.44, 136.37, 136.01, 135.28, 133.17, 133.06, 129.28, 129.02, 128.97, 128.51, 128.41, 128.30, 128.10, 127.91, 126.11, 126.08, 69.81, 64.56, 35.38, 35.22, 35.16, 34.65, 30.32, 30.21, 21.05, 21.01 ppm. $C_{48}H_{66}Al_2O_4$ (761.00): calcd. C 75.76, H 8.74; found C 75.67, H 8.71.

**Ethylene Polymerization:** To a slurry of [$MgCl_2(thf)_2$] (10 mmol) in *n*-hexane milled under argon in a glass mill (250 mL capacity, with 20 balls) at room temp. for 10 h, were added the titanium compound **4** (1 mmol) and *n*-hexane (50 mL). After the mixture was milled for an additional 24 h, the sample of precatalyst suspension (containing 0.01 mmol of titanium) was activated with $AlEt_2Cl$ (the molar ratio Al:Ti is 150) for 15 min at 50 °C under argon. Prior to polymerization, ethylene was passed through the suspension of the catalyst (10 mL) in a Schlenk ampoule for 15 min at room temp. and normal pressure, and the prepolymer was obtained. Then, MAO was added to the catalyst and dispersed in the prepolymer to form a highly active catalyst. The polymerization of ethylene was carried out in *n*-hexane at 50 or 70 °C in a stainless steel reactor (1 L), equipped with a stirrer, at $P_{gauge}$ = 70 or 100 psi pressure. The polymerization was quenched with a solution of HCl (5% in methanol) and dried under vacuum. The molecular weight ($M_w$) and molecular weight distribution ($M_w/M_n$) of the polypropylenes were determined by GPC in 1,2,4-trichlorobenzene using standard polystyrenes as a reference.

**X-ray Crystal Structure Determination:** A suitable crystal was immersed in mineral oil and mounted on a nylon loop in a random orientation under a cold stream of dry nitrogen (Rigaku GNNP low-temperature device). Diffraction experiments were performed with Mo-$K_\alpha$ radiation ($\lambda$ = 0.71070 Å) in a Rigaku CCD diffractometer. The data were collected in a hemisphere in 720 frames with 20–40-s exposure times (4.0° < 2$\theta$ < 45–55°). The data were processed by using CrystalClear (Rigaku) processing packages.[21] The structures were determined by routine heavy-atom and Fourier methods by using SHELXS 97[22] and refined by full-matrix least-squares with the non-hydrogen atoms with anisotropic and hydrogen with fixed isotropic thermal parameters of 0.07 Å by means of the SHELXL 97[23] program. The hydrogen atoms were partially located from difference electron-density maps, and the rest were fixed at predetermined positions. Scattering factors were from common sources.[24] Some details of data collection and refinement are given in Table 5.

Table 5. Summary of data collection and structure refinement details for **2**, **4**, and **5**.

| Compound | **2** | **4** | **5** |
|---|---|---|---|
| Formula | $C_{29}H_{48}Al_3ClO_2$ | $C_{56}H_{85}Cl_2O_6Ti_2$ | $C_{30}H_{39}AlO_2$ |
| $F_w$ | 545.09 | 1020.99 | 458.62 |
| Temp. [K] | 173 | 173 | 173 |
| Crystal system | monoclinic | monoclinic | triclinic |
| Space group | *Cm* (#8) | $P\bar{1}$ (#2) | $P\bar{1}$ (#2) |
| *a* [Å] | 11.677(8) | 9.787(3) | 9.209(3) |
| *b* [Å] | 20.261(11) | 12.689(4) | 11.613(3) |
| *c* [Å] | 9.214(6) | 25.294(8) | 14.466(5) |
| $\alpha$ [°] | 90 | 73.659(10) | 73.496(12) |
| $\beta$ [°] | 121.886(8) | 78.020(12) | 87.58(1) |
| $\gamma$ [°] | 90 | 76.319(12) | 66.038(10) |
| *V* [Å$^3$] | 1850.9(20) | 2895.2(17) | 1350.8(7) |
| *Z* | 4 | 2 | 2 |
| $D_{calcd.}$ [g cm$^{-3}$] | 1.956 | 1.171 | 1.127 |
| $\mu$ (Mo-$K_\alpha$) [mm$^{-1}$] | 3.87 | 4.12 | 0.98 |
| No. of unique reflections | 2180 | 12712 | 5898 |
| $R_1/wR_2$ [a] | 0.090/0.144 | 0.076/0.161 | 0.057/0.172 |
| GOF | 1.053 | 1.035 | 1.001 |
| Min./max. electron density [e Å$^3$] | –0.60/0.86 | –0.66/1.20 | –0.44/0.51 |

[a] Definitions: $R_1 = \Sigma||F_o| - |F_c||/\Sigma|F_o|$, $wR_2 = [\Sigma w(F_o^2 - F_c^2)^2/\Sigma w(F_o^2)^2]^{1/2}$.

CCDC-631721 (for **2**), -631722 (for **4**), and -631723 (for **5**) contain the supplementary crystallographic data for this paper. These data can be obtained free of charge from The Cambridge Crystallographic Data Centre via www.ccdc.cam.ac.uk/data_request/cif.

## Acknowledgments

Financial support by the National Science Foundation of China (Grant No. 20671021) is gratefully acknowledged. The author thanks Dr. A. Wells for the ethylene polymerization tests. The author also thanks Prof. Dr. H. Kawaguchi for his preview.

[1] F. N. Tebbe, G. W. Parshall, G. S. Reddy, *J. Am. Chem. Soc.* **1978**, *100*, 3611–3613.
[2] a) I. Kim, R. F. Jordan, *Macromolecules* **1996**, *29*, 489–491; b) G. M. Diamond, R. F. Jordan, J. L. Petersen, *J. Am. Chem. Soc.* **1996**, *118*, 8024–8033; c) B. Thiyagarajan, R. F. Jordan, V. G. Young Jr, *Organometallics* **1999**, *18*, 5347–5359.
[3] a) A. Herzog, H. W. Roesky, Z. Zak, M. Noltemeyer, *Angew. Chem. Int. Ed. Engl.* **1994**, *33*, 967–968; b) A. Herzog, H. W. Roesky, F. Jäger, A. Steiner, M. Noltemeyer, *Organometallics* **1996**, *15*, 909–917.
[4] J. E. Kickham, F. Guérin, D. W. Stephan, *J. Am. Chem. Soc.* **2002**, *124*, 11486–11494.
[5] H. M. Dietrich, H. Grove, K. W. Törnroos, R. Anwander, *J. Am. Chem. Soc.* **2006**, *128*, 1458–1459.
[6] S. B. Cortright, J. N. Coalter III, M. Pink, J. N. Johnston, *Organometallics* **2004**, *23*, 5885–5888.
[7] J. Scott, S. Gambarotta, I. Korobkov, Q. Knijnenburg, B. De Bruin, P. H. M. Budzelaar, *J. Am. Chem. Soc.* **2005**, *127*, 17204–17206.
[8] a) D. Zhang, G. Jin, N. Hu, *Chem. Commun.* **2002**, 574–575; b) D. Zhang, G. Jin, *Eur. J. Inorg. Chem.* **2003**, 1570–1576; c) D. Zhang, G. Jin, *Organometallics* **2003**, *22*, 2851–2854; d) D. Zhang, G. Jin, L. Weng, F. S. Wang, *Organometallics* **2004**, *23*, 3270–3275; e) D. Zhang, G. Jin, *J. Polym. Sci., Part A: Polym. Chem.* **2004**, *42*, 1018–1024; f) D. Zhang, G. Jin, *Appl. Catal., A* **2004**, *262*, 85–91; g) D. Zhang, G. Jin, *App. Catal., A* **2004**, *262*, 13–18; h) D. Zhang, G. Jin, *Inorg. Chem. Commun.* **2006**, *9*, 1322–1325.
[9] a) K. Soga, M. Kaminaka, *Macromol. Chem. Phys.* **1993**, *194*, 1745–1755; b) G. Satyanarayana, S. Sivaram, *Macromolecules* **1993**, *26*, 4712–4714; c) S. S. Sarma, S. Sivaram, *Macromol. Chem. Phys.* **1997**, *198*, 495–503.
[10] For recent reviews, see: a) M. Shibasaki, N. Yoshikawa, *Chem. Rev.* **2002**, *102*, 2187–2210; b) D. C. Bradley, R. C. Mehrotra, I. P. Rothwell, A. Singh, *Alkoxo and Aryloxo Derivatives of Metals*, Academic Press, London, **2001**; c) P. D. Knight, P. Scott, *Coord. Chem. Rev.* **2003**, *242*, 125–143; d) H. Kawaguchi, T. Matsuo, *J. Organomet. Chem.* **2004**, *689*, 4228–4243.
[11] a) M. D. Healy, J. W. Ziller, A. R. Barron, *J. Am. Chem. Soc.* **1990**, *112*, 2949–2954; b) A. J. S. Son, M. G. Thorn, P. E. Fanwick, I. P. Rothwell, *Organometallics* **2003**, *22*, 2318–2324; c) D. G. Hendershot, M. Barber, R. Kumar, J. P. Oliver, *Organometallics* **1991**, *10*, 3302–3309; d) J. Lewinski, J. Zachara, I. Justyniak, *Organometallics* **1997**, *16*, 4597–4605; e) J. A. Francis, S. G. Bott, A. R. Barron, *J. Chem. Soc., Dalton Trans.* **1998**, 3305–3310; f) H. Schumann, M. Frick, B. Heymer, F. Girgsdies, *J. Organomet. Chem.* **1996**, *512*, 117–126.
[12] a) A. I. Cottone, M. J. Scott, *Organometallics* **2000**, *19*, 5254–5256; b) W. Braune, J. Okuda, *Angew. Chem. Int. Ed.* **2003**, *42*, 64–68; c) C. Lin, L. Yan, F. Wang, Y. Sun, C. Lin, *J. Organomet. Chem.* **1999**, *587*, 151–159; d) I. Taden, H. C. Kang, W. Massa, T. P. Spaniol, J. Okuda, *Eur. J. Inorg. Chem.* **2000**, 441–445.

 © 2007 Wiley-VCH Verlag GmbH & Co. KGaA, Weinheim 

[13] The reaction of $O_2$ with "M–R" bonds of IVB metal complexes has been reported. See: a) T. V. Lubben, P. T. Wolczanski, *J. Am. Chem. Soc.* **1987**, *109*, 424–435; b) T. V. Lubben, P. T. Wolczanski, *J. Am. Chem. Soc.* **1985**, *107*, 701–703; c) S.-J. Kim, D. W. Choi, Y. J. Lee, B. H. Chae, J. Ko, S. O. Kang, *Organometallics* **2004**, *23*, 559–567.
[14] Z. Janas, L. B. Jerzykiewicz, S. Przybylak, R. L. Richards, P. Sobota, *Organometallics* **2000**, *19*, 4252–4257.
[15] a) Z. Janas, L. B. Jerzykiewicz, P. Sobota, K. Szczegot, D. Wioeniewska, *Organometallics* **2005**, *24*, 3987–3994; b) Z. Janas, B. J. Jerzykiewicz, K. Przybylak, P. Sobota, K. Szczegot, *Eur. J. Inorg. Chem.* **2004**, 1639–1645.
[16] C. Floriani, F. Corazza, W. Lesueur, A. Chiesi-Villa, C. Guastini, *Angew. Chem. Int. Ed. Engl.* **1989**, *28*, 66–67.
[17] a) T. Miyataka, K. Mizunuma, Y. Seki, M. Kakugo, *Makromol. Chem. Rapid Commun.* **1989**, *10*, 349–352; b) T. Miyatake, K. Mizunuma, Y. Seki, M. Kakugo, *Macromol. Symp.* **1993**, *66*, 203–214.
[18] A. J. van der Linden, C. J. Schaverien, N. Meijboom, C. Ganter, A. G. Orpen, *J. Am. Chem. Soc.* **1995**, *117*, 3008–3021.
[19] P. Sobota, K. Przybylak, J. Utko, L. B. Jerzykiewicz, A. J. L. Pombeiro, M. F. C. Guedes da Silva, K. Szczegot, *Chem. Eur. J.* **2001**, *7*, 951–958.
[20] a) F. Corazza, C. Floriani, A. Chiesi-Villa, C. Guastini, *Inorg. Chem.* **1991**, *30*, 145–148; b) J. Okuda, S. Fokken, H. C. Kang, W. Massa, *Chem. Ber.* **1995**, *128*, 221–227; c) L. Porri, A. Ripa, P. Colombo, E. Miano, S. Capelli, S. V. Meille, *J. Organomet. Chem.* **1996**, *514*, 213–217; d) R. D. J. Froese, D. G. Musaev, T. Matsubara, K. Morokuma, *J. Am. Chem. Soc.* **1997**, *119*, 7190–7196; e) R. D. J. Froese, D. G. Musaev, T. Matsubara, K. Morokuma, *Organometallics* **1999**, *18*, 373–379.
[21] a) *CrystalClear Software Package*, Rigaku and Molecular Structure Corp; b) J. W. Pflugrath, *Acta Crystallogr., Sect. D* **1999**, *55*, 1718–1725.
[22] G. M. Sheldrick, *SHELXS 97*, Program for the solution of crystal structures, University of Göttingen, Germany, **1990**.
[23] G. M. Sheldrick, *SHELXL 97*, Program for refining crystal structures, University of Göttingen, Germany, **1997**.
[24] D. T Cromer, J. T. Waber *International Tables for X-ray Crystallography*, Kynoch Press, Birmingham, **1974**, vol. IV, p. 99, 149.

Received: December 22, 2006
Published Online: May 10, 2007

 © 2007 Wiley-VCH Verlag GmbH & Co. KGaA, Weinheim 

DOI: 10.1002/ejic.200700082

# Preferred Phosphorus Ylide Formation Upon Alkylation of Lithiobis(diphenylphosphanyl)acetonitrile

**Leonie Braun,[a] Gerald Kehr,[a] Tobias Blömker,[a][‡] Roland Fröhlich,[a][‡] and Gerhard Erker*[a]**

*Dedicated to Professor Rolf Gleiter on the occasion of his 70th birthday*

**Keywords:** Chelates / Phosphane ligands / Carbanions / Ylides / Alkylation

Deprotonation of the readily available chelate phosphane bis(diphenylphosphanyl)acetonitrile (**6**) leads to stabilized carbanion system **7**. Lithiobis(diphenylphosphanyl)acetonitrile (**7**) features a unique thf-stabilized monomeric structure in the crystal form with a short cyanonitrogen–Li contact. Alkylation of **7** with *n*-alkyl bromides (R–Br, R = ethyl, *n*-propyl, *n*-butyl, *n*-hexyl) takes place selectively at one phosphorus atom to yield stabilized ylides **8a**–**d** (two examples characterized by X-ray diffraction). Treatment of **7** with the more reactive alkylation agents methyl iodide or benzyl bromide results in alkylation at both phosphorus atoms to give delocalized bis(phosphonium)ylides **9a**,**b** (both characterized by X-ray diffraction). Similarly, the reaction of **7** with 1,3-dibromopropane or 1,4-dibromobutane yields six- and seven-membered heterocyclic bis(phosphonium)ylides **10a**,**b**, respectively. The spectroscopic characterization and X-ray crystal structure analysis again indicate the presence of delocalized $Ph_2RP–C(CN)–PRPh_2$ substructures.
(© Wiley-VCH Verlag GmbH & Co. KGaA, 69451 Weinheim, Germany, 2007)

## Introduction

A variety of structural alternatives has been discussed for α-lithiated acetonitrile derivatives.[1] From a number of experimental studies complemented by spectroscopic and theoretical investigations it seemed clear that the majority of $RCHCN^-$ systems favored dimeric structures of type **1** in the solid state, which are characterized by the presence of a central $N_2Li_2$ four-membered heterocyclic arrangement (Figure 1).[2–6]

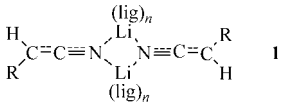


**1**

Figure 1. Preferred dimeric structures of lithiated acetonitrile derivatives.

We recently observed a monomeric structure of a lithiated acetonitrile example, namely lithiobis(diphenylphosphanyl)acetonitrile (**7**, see below).[7a] Phosphorus substituted ylides such as **2** or **3** are very interesting multifunctionalized organophosphorus compounds. Their structural and chemical features have attracted considerable interest.[7–10] Investigations in this field have led to the discovery of extended systems such as **4** or **5** (Figure 2).[8c,11–12]

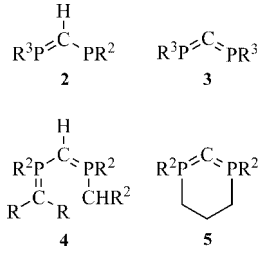


Figure 2. Examples of *P*-substituted phosphorus ylides.

We have now combined the chemistry of the $Li[(Ph_2P)_2CCN]$ system (**7**) with that of the P-stabilized ylides. This followed from a very typical reaction mode that is characteristic of **7**, namely its preferred alkylation at phosphorus upon treatment with a variety of alkyl halide electrophiles with the formation of new cyano-functionalized phosphorus ylides derived from the framework of **7**. A detailed description of some of this work is presented in this account.

## Results and Discussion

We previously showed that bis(diphenylphosphanyl)acetonitrile (**6**, dppmCN)[13] was readily obtained from the reaction of acetonitrile with chlorodiphenylphosphane in the

[a] Universität Münster, Organisch-Chemisches Institut, Corrensstrasse 40, 48149 Münster, Germany
Fax: +49-251-83-36503
E-mail: erker@uni-muenster.de
[‡] X-ray crystal structure analyses

 © 2007 Wiley-VCH Verlag GmbH & Co. KGaA, Weinheim 

presence of a strong base. System **6** has served as a chelate ligand for metal complex formation. The in situ generated Pd(dppmCN) catalyst was shown to give very high activities in a Suzuki–Miyaura carbon–carbon coupling reaction.[14]

The deprotonation of dppmCN (**6**) was cleanly effected by treatment with *n*-butyllithium (Scheme 1).[7a] The resulting lithiobis(diphenylphosphanyl)acetonitrile product (**7**) was characterized by X-ray diffraction.[15–17] System **7** features a shortened C1–C2 [1.386(3) Å] bond and the C2–N linkage [1.162(3) Å] is lengthened relative to that reported for **6**[6] [cf. C1–C2 1.462(3) Å, C2–N 1.148(3) Å]. In **7**, the C1–P bonds are markedly shortened [1.784(2) Å, 1.775(2) Å] relative to the P1–C(Ar) bonds in **7** [1.835(2)–1.845(2) Å] and those reported in the literature for **6**[6] [1.874(2) Å, 1.895(2) Å]. These characteristic data indicate some electronic delocalization in **7**, including the pair of phosphorus groups. Most remarkably, system **7** is monomeric in the solid state – quite different from the preferred dimeric structures of its congeners **1** – with a N–Li contact of 1.957(4) Å. Figure 3 shows a view of the molecular structure of **7**.

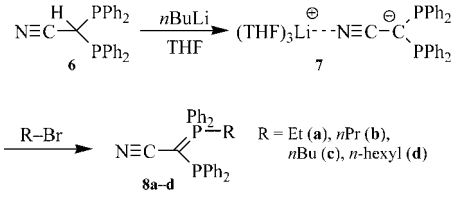


Scheme 1.

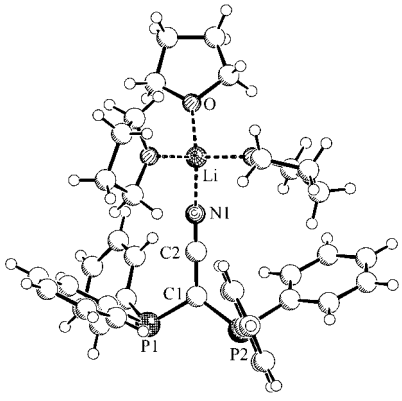


Figure 3. A view of the molecular structure of **7**.

Compound **7** is attacked by primary *n*-alkyl bromide electrophiles exclusively at one of the phosphorus atoms with clean formation of the respective ylide products (**8a**–**d**, R = ethyl, *n*-propyl, *n*-butyl, *n*-hexyl). Spectroscopically, the products are characterized by the observation of two very different $^{31}$P NMR spectroscopic phosphorus resonances. The ylidic phosphorus signal is shifted substantially to positive $\delta$ values relative to its neutral precursor **6** or its anionic precursor **7** (for details see Table 1). The central carbon atom C1 consequently features two very different $^{1}J_{P,C}$ coupling constants (e.g. **8a**: $\delta$ = 6.92 ppm, $^{1}J_{P,C}$ = 128.0, 28.9 Hz).

Table 1. Selected spectroscopic data of ylide products **8a**–**d**.[a]

| | **8a** ($C_2H_5$) | **8b** ($nC_3H_7$) | **8c** ($nC_4H_9$) | **8d** ($nC_6H_{13}$) |
|---|---|---|---|---|
| $\delta$(3-H) | 2.71 | 2.65 | 2.68 | 2.66 |
| $\delta$(4-H) | 1.23 | 1.64 | 1.58 | 1.59 |
| $\delta(^{13}C1)$ | 6.9 | 7.4 | 7.4 | 7.3 |
| $^{1}J_{P,C}$ | 128.0, 28.9 | 128.2, 29.3 | 128.0, 28.5 | 128.1, 28.8 |
| $\delta(^{13}C{\equiv}N)$ | 125.0 | 125.0 | 125.0 | 125.1 |
| $^{2}J_{P,C}$ | 13.1, 0.8 | 13.0, 1.0 | 13.0, 1.1 | 12.9, 1.1 |
| $\delta(^{13}C3)$ | 19.1 | 27.6 | 25.3 | 25.6 |
| $^{1}J_{P,C}$ | 62.5, 9.9 | 60.7, 9.3 | 60.8, 9.2 | 60.9, 9.8 |
| $\delta(^{31}P1)$ | 29.3 | 27.0 | 26.9 | 26.9 |
| $\delta(^{31}P2)$ | –19.2 | –19.0 | –19.5 | –19.5 |
| $^{2}J_{P,P}$ | 140.8 | 141.2 | 140.8 | 142.0 |
| $\tilde{\nu}$(C≡N) | 2137 | 2148 | 2133 | 2151 |

[a] NMR spectra in $CD_2Cl_2$, $\delta$ [ppm], $J$ [Hz]; IR spectra in KBr, $\tilde{\nu}$ [$cm^{-1}$].

Compounds **8a**,**c** both exhibit very similar structures (Table 2). Therefore, only example **8c** (R = *n*-butyl) is described here in detail (Figure 4 and Table 2). Single crystals suitable for X-ray crystal structure analysis were obtained by the slow evaporation of solvent from a toluene/dichloromethane solution of functionalized ylide **8c**.

Table 2. Selected structural parameters of ylide products **8a**,**c**.[a]

| | **8a** (ethyl) | **8c** (*n*-butyl) |
|---|---|---|
| C2–N1 | 1.155(3) | 1.151(3) |
| C1–C2 | 1.409(3) | 1.412(3) |
| C1–P1 | 1.793(2) | 1.790(2) |
| C1–P2 | 1.728(2) | 1.721(2) |
| P1–C1–P2 | 121.0(1) | 118.8(1) |
| P1–C3 | 1.816(2) | 1.809(2) |

[a] Bond lengths [Å]; angles [°].

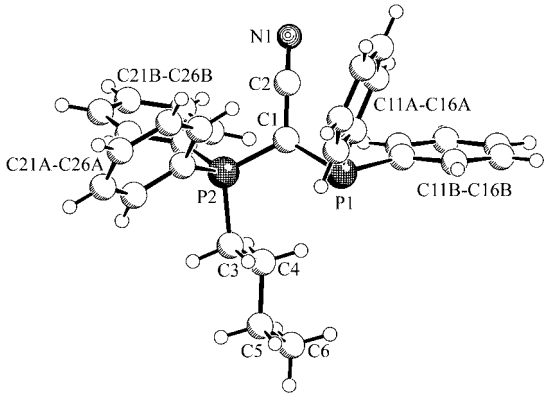


Figure 4. Molecular geometry of **8c**.

Compound **8c** features a central $sp^2$ hybridized planar tricoordinate ylidic carbon center (C1) to which a cyano substituent and a pair of differently substituted phosphorus atoms are bonded (Figure 4). The C1–C≡N unit is linear [angle C1–C2–N1 178.6(2)°]. Relative to the reference molecule bis(diphenylphosphanyl)acetonitrile (**6**), the C≡N bond in **8c** is slightly longer at 1.151(3) Å [cf. **6**: 1.148(2) Å] and the adjacent C1–C2 linkage is shorter [**8c**: 1.412(3) Å, cf. **6**: 1.462(2) Å], which indicates some conjugative stabilization of the adjacent ylide moiety [P2–C1: 1.721(2) Å]. Consequently, the remaining C1–P1 bond [1.790(2) Å] is

 © 2007 Wiley-VCH Verlag GmbH & Co. KGaA, Weinheim 

markedly longer. The bond angles at C1 amount to 118.8(1)° (P1–C1–P2), 117.4(1)° (P2–C1–C2), and 121.5(1)° (P1–C1–C2) and the *n*-butyl substituent angle at P2 is 112.5(1)° [C1–P2–C3; P2–C3: 1.809(2) Å]. The remaining P–C aryl bond lengths at the tetracoordinate phosphorus atom P2 [P2–C21A: 1.812(2) Å, P2–21B: 1.810(2) Å] are slightly shorter relative to the P–C(aryl) bonds of its tricoordinate congener P1 [P1–C11A: 1.837(2) Å, P1–C11B: 1.835(2) Å].

The reaction of anion **7** takes a slightly different course when more reactive alkyl halide electrophiles are employed. Thus, treatment of **7** with methyl iodide results in the formation of a bisalkylated product (**9a**) (Scheme 2). In this case, a methyl group becomes attached at each phosphorus atom.[8c,11] Formally, the product may be regarded as a cyano-stabilized phosphorus ylide that is further stabilized by a newly formed phosphonium cation substituent. In reality, it appears that a delocalized bis(phosphonium)ylide is formed. In solution, this led to the observation of a single $^{31}$P NMR spectroscopic resonance at $\delta$ = 21.7 ppm and there is a single [P]–$CH_3$ $^1$H NMR spectroscopic signal at $\delta$ = 2.40 ppm.

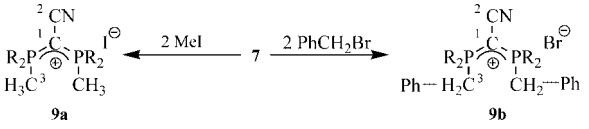


Scheme 2.

The $^{13}$C NMR spectrum of **9a** features a binominal triplet resonance of the central carbon atom C1 at $\delta$ = 5.6 ppm with a $^1J_{P,C}$ = 117.1 Hz. The corresponding C≡N $^{13}$C NMR spectroscopic signal was located at $\delta$ = 119.4 ppm. Both the P–$CH_3$ and the P–$C_{ipso}$(aryl) $^{13}$C NMR spectroscopic signals ($\delta$ = 14.6 and 122.6 ppm) have a more complicated appearance due to nonfirst-order splitting of the respective $^{13}$C/$^{31}$P NMR spin systems (for further details see Table 3 and the Experimental Section).

Table 3. Selected spectroscopic data of compounds **9** and **10**.[a].

| | **9a** ($CH_3$) | **9b** ($CH_2$Ph) | **10a** $(CH_2)_3$ | **10b** $(CH_2)_4$ |
|---|---|---|---|---|
| $\delta$($^{31}$P1/ $^{31}$P2) | 21.7 | 23.9 | 18.3 | 28.8 |
| $\delta$($^{13}$C1) | 5.6 | 3.2 | 3.2 | 4.7 |
| $^1J_{PC}$ | 117.1 | 117.3 | 103.8 | 108.9 |
| $\delta$($^{13}$C2) | 119.4 | 120.4 | 119.1 | 119.8 |
| $^2J_{PC}$ | 3.9 | 4.8 | [c] | 2.3 |
| $\delta$($^{13}$C3) | 14.6 | 36.6 | 21.5 | 24.7 |
| $\delta$(*i*-Ph$^P$)[b] | 122.6 | 119.4 | 123.4 | 123.6 |
| $\delta$(*o*-Ph$^P$)[b] | 132.8 | 134.0 | 133.1 | 132.9 |
| $\delta$(*m*-Ph$^P$)[b] | 130.4 | 129.9 | 130.2 | 130.3 |
| $\delta$(*p*-Ph$^P$)[b] | 134.8 | 134.6 | 134.6 | 134.6 |
| $\tilde{\nu}$(C≡N) | 2160 | 2159 | 2166 | 2157 |

[a] NMR spectra in $CD_2Cl_2$, $\delta$ [ppm], *J* [Hz]; IR in KBr, $\tilde{\nu}$ [$cm^{-1}$]. [b] Tentative absolute assignment. [c] Singlet structure with $\nu_{1/2}$ ca. 2 Hz.

The reaction of **6** with benzyl bromide takes a similar course. We isolated doubly benzylated bis(phosphonium)ylide product **9b** from the reaction mixture in close to quantitative yield. Product **9b** exhibits similar spectroscopic features (Table 3). Both products **9a**,**b** were characterized by X-ray diffraction. Single crystals of **9a** were obtained by the slow evaporation of a saturated toluene/dichloromethane solution. Single crystals of **9b** were similarly obtained from dichloromethane.

Compound **9a** exhibits a delocalized bis(phosphonium)ylide-type structure with well separated cations and anions (Figure 5). In the crystal form, a chiral conformation is adopted. Nevertheless, the pair of C1–P1 and C1–P2 bonds is almost equal in length [1.734(4) Å, 1.751(4) Å]. The system features a distorted U-shaped conformation ranging from the aryl *ipso*-carbon C11B through P1, C1, and P2 to the methyl carbon atom C4 (Figure 5). The C1–C2(N) bond of **9a** is short [1.413(6) Å], which is a structural indication of CN stabilization of the central ylidic moiety. The conformation of the central section of the molecule is characterized by dihedral angles 104.3(3)° (C3–P1–C1–P2), –34.6(4)° (P1–C1–P2–C4), –80.2° (C3–P1–C1–C2), and 149.9° (C2–C1–P2–C4). The C1–C2–N1 unit is close to linear [178.7(5)°].

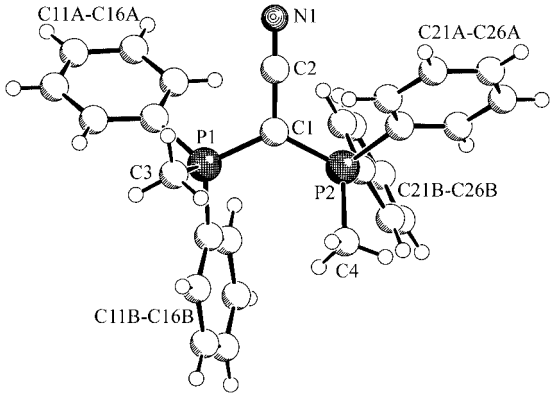


Figure 5. Molecular structure of **9a** (only the cation is depicted).

Compound **9b** features an overall structure that is similar to **9a**. Again, the P–C($sp^2$) bond lengths are similar to each other (Table 4) and both the C1–C2 and the adjacent C2–N1 bonds are rather short. Compound **9b** exhibits a slightly different conformation. The trio of aryl and alkyl substituents at the phosphorus atoms are arranged such that they are oriented close to the staggered position along the hypothetical P1···P2 axis. Both benzyl groups are pointing away from the core of molecule **9b** in this geometrical arrangement (Figure 6).

The reaction of anionic reagent **7** with 1,3-dibromopropane takes a similar course. Alkylation at both phosphorus atoms yields ylidic product **10a** (87%, isolated) (Scheme 3). The NMR spectra of **10a** point to a similar delocalized bis(phosphonium)ylide structure as it was found for **9a**,**b**. Compound **10a** features a single $^{31}$P NMR spectroscopic resonance at $\delta$ = 18.3 ppm and a single set of $^1$H/$^{13}$C NMR phenyl spectroscopic resonances (Table 3 and the Experimental Section). The bridging trimethylene unit appears to be symmetrical in solution, and in the $^1$H NMR spectrum it resonates as a 4 H multiplet at $\delta$ = 3.50 ppm ([P]–$CH_2$) and a 2 H signal at $\delta$ = 2.45 ppm (–$CH_2$–).

 © 2007 Wiley-VCH Verlag GmbH & Co. KGaA, Weinheim 

Table 4. Selected structural parameters of compounds **9a**,**b** and **10a**,**b**.[a]

| | **9a** ($CH_3$) | **9b** ($CH_2Ph$) | **10a** $(CH_2)_3$ | **10b** $(CH_2)_4$ |
|---|---|---|---|---|
| C2–N1 | 1.151(6) | 1.148(3) | 1.157(4) | 1.150(4) |
| C1–C2 | 1.413(6) | 1.410(3) | 1.410(4) | 1.410(4) |
| C1–C2–N1 | 178.7(5) | 179.0(3) | 179.5(4) | 179.1(3) |
| P1–C1 | 1.734(4) | 1.751(2) | 1.744(3) | 1.748(2) |
| P2–C1 | 1.751(4) | 1.747(2) | 1.731(3) | 1.745(2) |
| P1–C3 | 1.787(5) | 1.820(2)[b] | 1.800(3) | 1.786(3) |
| P2–C4 | 1.793(4) | 1.823(2)[c] | 1.803(3)[d] | 1.801(3)[e] |
| P1–C1–P2 | 126.9(2) | 126.4(1) | 121.9(2) | 128.3(2) |
| P1–C1–C2 | 115.7(3) | 117.1(2) | 118.5(2) | 116.4(2) |
| P2–C1–C2 | 117.2(3) | 115.7(1) | 118.3(2) | 115.3(2) |

[a] Bond lengths [Å]; angles [°]. [b] P1–C11. [c] P2–C41 (Figure 6). [d] P2–C5 (Figure 7). [e] P2–C6 (see Figure 6).

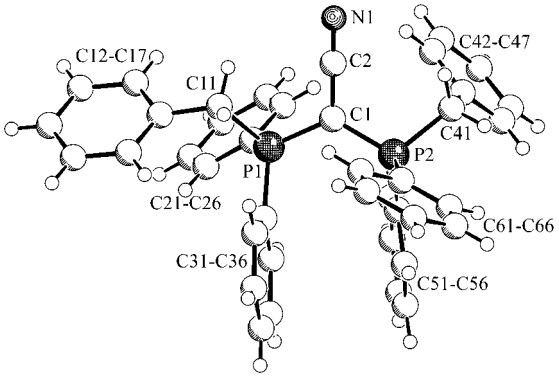


Figure 6. A projection of the molecular geometry of compound **9b** in the crystal form (only the cation is shown).

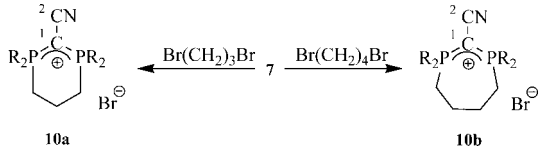


Scheme 3.

The corresponding $^{13}C$ NMR spectroscopic signals were observed at $\delta$ = 21.5 ppm (C3/C5) and $\delta$ = 17.0 ppm (t, $^3J_{P,C}$ = 6.0 Hz, C-4). As expected, the central ylidic carbon atom resonance shows up as a binominal triplet due to coupling with a pair of symmetry-equivalent phosphorus neighbors ($\delta$ = 3.2 ppm, $^1J_{P,C}$ = 103.8 Hz), and the adjacent nitrile carbon atom resonance appears at $\delta$ = 119.1 ppm (s, $\nu_{1/2}$ ca. 2 Hz).

The reaction of **7** with 1,4-dibromobutane proceeds analogously to yield product **10b** (73% isolated). Compound **10b** also seems to be a delocalized stabilized ylide. It features spectroscopic data similar to **10a** (Table 3).

Single crystals for X-ray crystal structure analyses of compounds **10a**,**b** were obtained by slow evaporation of the solvent from toluene/dichloromethane solutions. The structure of **10a** features a six-membered heterocycle (Figure 7). It contains a delocalized P1–C2–P2 unit with a pair of close-to-equal P–C bond lengths (Table 4). The corresponding C1–C2 bond length is in the typical range [1.410(4) Å] as is the adjacent C2–N1 linkage [1.157(4) Å]. The coordination geometry around the central ylidic carbon atom C1 is trigonal planar (for bond angles, see Table 4). The endocyclic saturated trimethylene unit of **10a** exhibits a typical staggered conformation.

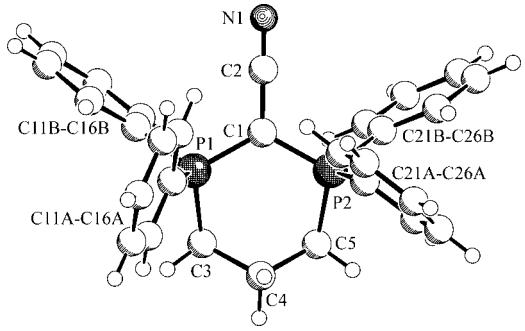


Figure 7. Molecular structure of **10a** (cation only).

The bonding parameters of the P1–C(CN)–P2 unit of seven-membered heterocyclic compound **10b** are similar to those of **10a**. In this case, the P1–C1 [1.748(2) Å] and P–C2 [1.745(2) Å] bonds are in fact almost identical in length as it is expected for a delocalized stabilized bis(phosphonium)-ylide structure. Again, the P–C(aryl) vectors are oriented close to the eclipsed conformation along the hypothetical P1···P2 connection and the P1–C3 [1.786(3) Å] and P2–C6 [1.801(3) Å] vectors are arranged close to parallel to each other. The remaining connecting tetramethylene unit of compound **10b** adopts an all-staggered conformation (Figure 8).

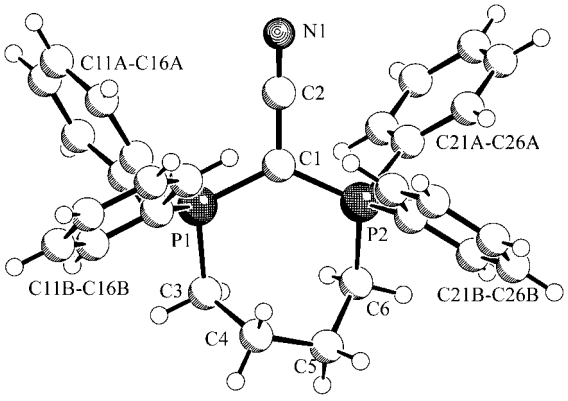


Figure 8. A view of the molecular structure of compound **10b** (cation only).

## Conclusions

We have shown that the chelate phosphane bis(diphenylphosphanyl)acetonitrile (dppmCN, **6**) is readily deprotonated by treatment with, for example, *n*-butyllithium to selectively yield monoanionic system **7**. Lithiobis(diphenylphosphanyl)acetonitrile (**7**) features a unique monomeric thf-stabilized structure in the crystal form that contains a delocalized P–C(CN)–P moiety and a short contact of the lithium cation to the nitrile nitrogen at the opposite end of the system. Nevertheless, the alkylation with a variety of alkyl ha-

 © 2007 Wiley-VCH Verlag GmbH & Co. KGaA, Weinheim 

lide electrophiles very selectively takes place only at phosphorus. In each of the examples studied and described here, the –CN nitrogen atom as well as the "carbanionic" $P_2C1$ carbon center was left untouched by these reagents under the applied reaction conditions.[18] In some cases, selective alkylation at one of the two phosphorus centers was observed, which resulted in the formation of phosphorus ylides that are stabilized by the cyano substituent and the $–PR_2$ group at the ylidic carbon atom. Upon treatment with more strongly electrophilic reagents such as methyl iodide or benzyl bromide, twofold alkylation at phosphorus was observed, which led to the formation of apparently delocalized bis(phosphonium)ylide structures. Treatment of **7** with difunctional α,ω-dibromoalkanes led to analogous cyclic bis(phosphonium)ylide products. We assume that the subsequent P–C bond-forming step was favored because it took place intramolecularly. Now that such highly stabilized ylidic systems have become so easily available and their structure and spectroscopic features investigated and characterized, it will be interesting to learn their specific chemical properties and their potential synthetic use.

## Experimental Section

**General Information:** Most reactions were carried out under an inert atmosphere (argon) in Schlenk-type glassware or in a glove box. Solvents were dried and distilled under an atmosphere of argon prior to use. NMR spectra were recorded with Bruker AC 200 FT ($^1$H: 200 MHz, $^{13}$C: 50.3 MHz, $^{31}$P: 81 MHz), Varian Inova 500 ($^1$H: 499.8 MHz, $^{13}$C: 126 MHz), or Unity Plus 600 ($^1$H: 600 MHz, $^{13}$C: 151 MHz, $^{31}$P: 242.5 MHz) spectrometers. Most NMR assignments were supported by additional 2D experiments. The assignment of $J_{P,H}$ or $J_{P,C}$ was made by $^1$H{$^{31}$P} or $^{13}$C{$^1$H,$^{31}$P} NMR decoupling experiments. Melting points were determined with a DSC 2010 (TA-Instruments) apparatus. IR spectra were obtained with a Varian 3100 FT-IR (ECALIBUR Serie) spectrometer. MS (ESI) spectra were measured with a Micromass QuatroLC-Z mass spectrometer. GC was performed with a Hewlett Packard HP 6890 Series GC System. X-ray crystal structure data sets were collected with a Nonius KappaCCD diffractometer with Mo-radiation and equipped with a rotating anode generator. The following programs were used for data analysis: data collection, COLLECT;[19] data reduction, Denzo-SMN;[20] absorption correction, SORTAV[21] and Denzo;[22] structure solution, SHELXS-97;[23] structure refinement, SHELXL-97;[24] graphics, SCHAKAL.[25] CCDC-629968, -629969, and -631598 to -631602 contain the supplementary crystallographic data for this paper. These data can be obtained free of charge from The Cambridge Crystallographic Data Centre via www.ccdc.cam.ac.uk/data_request/cif.

**Preparation of Lithiobis(diphenylphosphanyl)acetonitrile (7):** Bis(diphenylphosphanyl)acetonitrile (3.26 g, 7.96 mmol) was dissolved in dry tetrahydrofuran (50 mL) and cooled to –78 °C. After the addition of *n*-butyllithium (1.6 M in hexane, 5.47 mL, 8.76 mmol), the reaction mixture was warmed to room temperature and stirred overnight. The solvent was removed in vacuo, and the residue was suspended in pentane (40 mL). The product was collected by filtration, washed with pentane (3 × 40 mL), and dried in vacuo (white solid, yield: 3.68 g, 73%). M.p. 144 °C (DSC). $^1$H NMR (600 MHz, $C_6D_6$/tdf, 298 K): $\delta$ = 7.40 (m, 8 H, *o*-Ph), 7.06 (m, 8 H, *m*-Ph), 6.99 (m, 4 H, *p*-Ph), 3.54 (br. s, 12 H, thf), 1.68 (br. s, 12 H, thf) ppm. $^{13}$C{$^1$H} NMR (151 MHz, $C_6D_6$/TDF, 298 K): $\delta$ = 147.2 (m, *i*-Ph), 133.1 (m, *o*-Ph), 129.4 (t, $^2J_{P,C}$ = 3.3 Hz, CN), 127.6 (m, *m*-Ph), 126.3 (s, *p*-Ph), 68.1 (m, thf), 26.3 (m, thf), 15.5 (t, $^2J_{P,C}$ = 13.5 Hz, C-1) ppm. $^{31}$P{$^1$H} NMR (81 MHz, $C_6D_6$/tdf, 298 K): $\delta$ = 2.7 (s) ppm. FTIR (KBr): $\tilde{\nu}$ = 3043, 2968, 2878, 2107, 2066, 1478, 1429, 1040, 744, 695, 560, 508 cm$^{-1}$. $C_{26}H_{20}LiNP_2$·3thf (631.66): calcd. C 72.26, H 7.02, N 2.22; found C 71.53, H 6.85, N 2.11. X-ray crystal structure analysis of **7**: formula $C_{26}H_{20}NP_2Li$·$(C_4H_8O)_3$, $M$ = 631.62, light yellow crystal 0.25 × 0.25 × 0.20 mm, $a$ = 9.658(1), $b$ = 18.516(1), $c$ = 19.627(1) Å, $\beta$ = 96.27(1)°, $V$ = 3488.9(4) Å$^3$, $\rho_{calcd.}$ = 1.202 g cm$^{-3}$, $\mu$ = 0.161 mm$^{-1}$, empirical absorption correction ($0.961 \le T \le 0.969$), $Z$ = 4, monoclinic, space group $P2_1/c$ (No. 14), $\lambda$ = 0.71073 Å, $T$ = 198 K, $\omega$ and $\phi$ scans, 23326 reflections collected ($\pm h$, $\pm k$, $\pm l$), [(sin$\theta$)/$\lambda$] = 0.66 Å$^{-1}$, 8344 independent ($R_{int}$ = 0.059) and 5029 observed reflections [$I \ge 2\sigma(I)$], 410 refined parameters, $R$ = 0.057, $wR_2$ = 0.147, max. residual electron density 0.41 (–0.30) e Å$^{-3}$, hydrogen atoms calculated and refined as riding atoms.

**General Procedure for the Reaction of 7 with Alkyl Bromides:** Lithium cyanobis(diphenylphosphanyl)methanide·$(thf)_3$ (**7**, 1 equiv.) was dissolved in dry tetrahydrofuran (50 mL). After the addition of the respective alkyl halide (4 or 6 equiv.) the solution was stirred at room temperature overnight. The solvent was removed in vacuo, and the residue was suspended in dichloromethane (50 mL). The precipitate was filtered off and washed with dichloromethane (3 × 20 mL). The organic phases were combined, and the volatilities were removed in vacuo. The obtained crude product was suspended in pentane (40 mL), collected by filtration, washed with pentane, and then dried in vacuo.

**8a:** The reaction of **7** (0.50 g, 0.79 mmol) with bromoethane (0.35 g, 0.24 mL, 3.21 mmol) yielded **8a** as a white solid (0.24 g, 69%). M.p. 129 °C (DSC). $^1$H NMR (600 MHz, $CD_2Cl_2$, 298 K): $\delta$ = 7.67 (m, $^3J_{P-1,H}$ = 12.1 Hz, 4 H, *o*-Ph$^1$), 7.63 (m, $^5J_{P-1,H}$ = 1.8 Hz, 2 H, *p*-Ph$^1$), 7.52 (m, $^4J_{P-1,H}$ = 2.9 Hz, 4 H, *m*-Ph$^1$), 7.45 (m, $^3J_{P-2,H}$ = 7.8 Hz, 4 H, *o*-Ph$^2$), 7.32 (m, $^4J_{P-2,H}$ = 1.5 Hz, 4 H, *m*-Ph$^2$), 7.30 (m, 2 H, *p*-Ph$^2$), 2.71 (dq, $^2J_{P-1,H}$ = 12.2 Hz, $^3J_{H,H}$ = 7.4 Hz, $PCH_2$), 1.23 (td, $^3J_{P-1,H}$ = 18.4 Hz, $^3J_{H,H}$ = 7.4 Hz, $CH_3$) ppm. $^{13}$C{$^1$H} NMR (126 MHz, $CD_2Cl_2$, 298 K): $\delta$ = 141.1 (dd, $^1J_{P-2,C}$ = 8.5 Hz, $^3J_{P-1,C}$ = 7.2 Hz, *i*-Ph$^2$), 133.04 (dd, $^2J_{P-1,C}$ = 9.2 Hz, $^4J_{P-2,C}$ = 1.5 Hz, *o*-Ph$^1$), 133.03 (d, $^4J_{P-1,C}$ = 2.9 Hz, *p*-Ph$^1$), 132.7 (d, $^2J_{P-2,C}$ = 19.6 Hz, *o*-Ph$^2$), 129.4 (d, $^3J_{P-1,C}$ = 12.0 Hz, *m*-Ph$^1$), 128.5 (d, $^3J_{C,P-2}$ = 6.8 Hz, *m*-Ph$^2$), 128.2 (s, *p*-Ph$^2$), 127.0 (dd, $^1J_{P-1,C}$ = 86.7 Hz, $^2J_{P-1,C}$ = 2.6 Hz, *i*-Ph$^1$), 125.0 (dd, $^2J_{P-1,C}$ = 13.1 Hz, $^2J_{P-2,C}$ = 0.8 Hz, C≡N), 19.1 (dd, $^1J_{P-1,C}$ = 62.5 Hz, $^3J_{P-2,C}$ = 9.9 Hz, $CH_2$), 6.96 (dd, $^2J_{P-1,C}$ = 4.9 Hz, $^4J_{P-2,C}$ = 2.9 Hz, $CH_3$), 6.92 (dd, $^1J_{P-1,C}$ = 128.0 Hz, $^1J_{P-2,C}$ = 28.9 Hz, P=C) ppm. $^{31}$P{$^1$H} NMR (202 MHz, $CD_2Cl_2$, 298 K): $\delta$ = 29.3 (d, $^2J_{P-1,P-2}$ = 140.8 Hz, P-1), –19.2 (d, $^2J_{P-2,P-1}$ = 140.8 Hz, P-2) ppm. FTIR (KBr): $\tilde{\nu}$ = 3058, 2957, 2137, 1429, 1261, 1100, 1025, 800, 695, 564 cm$^{-1}$. MS (EI, 70 eV): $m/z$ (%) = 437.2 (72) $[M]^+$, 408.1 (100) $[M - CH_2CH_3]^+$, 360 (17) $[M - C_6H_5]^+$, 262.1 (16), 185.1 (23) $[M - C_{12}H_{10}P]^+$, 183.0 (29) $[C_{12}H_8P]^+$. $C_{28}H_{25}NP_2$ (437.46): calcd. C 76.88, H 5.76, N 3.20; found C 76.43, H 5.71, N 3.11. X-ray crystal structure analysis of **8a**: formula $C_{28}H_{25}NP_2$, $M$ = 437.43, colorless crystal 0.30 × 0.30 × 0.20 mm, $a$ = 9.602(1), $b$ = 15.189(1), $c$ = 15.789(1) Å, $\beta$ = 100.05(1)°, $V$ = 2267.4(3) Å$^3$, $\rho_{calcd.}$ = 1.281 g cm$^{-3}$, $\mu$ = 0.208 mm$^{-1}$, empirical absorption correction ($0.941 \le T \le 0.960$), $Z$ = 4, monoclinic, space group $P2_1/n$ (No. 14), $\lambda$ = 0.71073 Å, $T$ = 198 K, $\omega$ and $\phi$ scans, 15000 reflections collected ($\pm h$, $\pm k$, $\pm l$), [(sin$\theta$)/$\lambda$] = 0.67 Å$^{-1}$, 5441 independent ($R_{int}$ = 0.043) and 4049 observed reflections [$I \ge 2\sigma(I)$], 281 refined parameters, $R$ = 0.045, $wR_2$ = 0.112, max. residual electron density

 © 2007 Wiley-VCH Verlag GmbH & Co. KGaA, Weinheim 

0.33 (–0.38) e Å$^{-3}$, hydrogen atoms calculated and refined as riding atoms.

**8b:** The reaction of **7** (1.00 g, 1.58 mmol) with 1-bromopropane (0.78 g, 0.58 mL, 6.34 mmol) yielded **8b** as a white solid (0.66 g, 93%). M.p. 122 °C (DSC). $^1$H NMR (499.8 MHz, $CD_2Cl_2$, 298 K): $\delta$ = 7.67 (m, $^3J_{P-1,H}$ = 12.1 Hz, 4 H, *o*-Ph$^1$), 7.62 (m, $^5J_{P-1,H}$ = 1.8 Hz, 2 H, *p*-Ph$^1$), 7.52 (m, $^4J_{P-1,H}$ = 2.9 Hz, 4 H, *m*-Ph$^1$), 7.45 (m, $^3J_{P-2,H}$ = 7.7 Hz, 4 H, *o*-Ph$^2$), 7.32 (m, $^4J_{P-2,H}$ = 1.7 Hz, 4 H, *m*-Ph$^2$), 7.30 (m, $^5J_{P-2,C}$ = 0.5 Hz, 2 H, *p*-Ph$^2$), 2.65 (m, $^2J_{P-1,H}$ = 12.1 Hz, $PCH_2$), 1.64 (m, $^3J_{P-1,H}$ = 16.6 Hz, 2 H, $CH_2$), 1.03 (td, $^3J_{H,H}$ = 7.4 Hz, $^4J_{P-1,H}$ = 1.6 Hz, 3 H, $CH_3$) ppm. $^{13}$C{$^1$H} NMR (126 MHz, $CD_2Cl_2$, 298 K): $\delta$ = 141.1 (dd, $^1J_{P-2,C}$ = 8.5 Hz, $^3J_{P-1,C}$ = 7.2 Hz, *i*-Ph$^2$), 133.00 (d, $^4J_{P-1,C}$ = 2.9 Hz, *p*-Ph$^1$), 132.99 (dd, $^2J_{P-1,C}$ = 9.4 Hz, $^4J_{P-2,C}$ = 1.6 Hz, *o*-Ph$^1$), 132.7 (d, $^2J_{P-2,C}$ = 19.7 Hz, *o*-Ph$^2$), 129.4 (d, $^3J_{P-1,C}$ = 12.0 Hz, *m*-Ph$^1$), 128.4 (d, $^3J_{C,P-2}$ = 6.8 Hz, *m*-Ph$^2$), 128.2 (s, *p*-Ph$^2$), 127.3 (dd, $^1J_{P-1,C}$ = 86.7 Hz, $^2J_{P-1,C}$ = 2.4 Hz, *i*-Ph$^1$), 125.0 (dd, $^2J_{P-1,C}$ = 13.0 Hz, $^2J_{P-2,C}$ = 1.0 Hz, C≡N), 27.6 (dd, $^1J_{P-1,C}$ = 60.7 Hz, $^3J_{P-2,C}$ = 9.3 Hz, $PCH_2$), 16.7 (dd, $^2J_{P-1,C}$ = 3.8 Hz, $^4J_{P-2,C}$ = 3.2 Hz, $CH_2$), 15.6 (d, $^3J_{P-1,C}$ = 17.1 Hz, $CH_3$), 7.4 (dd, $^1J_{P-1,C}$ = 128.2 Hz, $^1J_{P-2,C}$ = 29.3 Hz, P=C) ppm. $^{31}$P{$^1$H} NMR (202 MHz, $CD_2Cl_2$, 298 K): $\delta$ = 27.0 (d, $^2J_{P-1,P-2}$ = 141.2 Hz, P-1), –19.0 (d, $^2J_{P-1,P-2}$ = 141.2 Hz, P-2) ppm. $^1$H,$^{31}$P ghmbc (499.8/202 MHz, $CD_2Cl_2$, 298 K): $^{31}$P/$^1$H, $\delta$ = 27.0/7.67, 7.62, 7.52, 2.65, 1.64, 1.03 (P-1/*o*, *p*, *m*-Ph$^1$, $PCH_2$, $CH_2$, $CH_3$); –19.0/7.45 (P-2/*o*-Ph$^2$) ppm. FTIR (KBr): $\tilde{\nu}$ = 3055, 2963, 2873, 2148, 1436, 1172, 1118, 1070, 955, 803, 69 cm$^{-1}$. MS (EI, 70 eV): *m*/*z* (%) = 451.2 (30) $[M]^+$, 408.1 (68) $[M - C_3H_7]^+$, 374.2 (6) $[M - C_6H_5]^+$, 262.1 (32), 185.1 (39) $[M - C_{12}H_{10}P]^+$, 183.0 (100) $[C_{12}H_8P]^+$.

**8c:** The reaction of **7** (1.00 g, 1.58 mmol) with 1-bromobutane (0.87 g, 0.68 mL, 6.33 mmol) yielded **8c** as a white solid (0.55 g, 75%). M.p. 134 °C (DSC). $^1$H NMR (600 MHz, $CD_2Cl_2$, 298 K): $\delta$ = 7.68 (m, 4 H, *o*-Ph$^1$), 7.63 (m, 2 H, *p*-Ph$^1$), 7.52 (m, 4 H, *m*-Ph$^1$), 7.46 (m, 4 H, *o*-Ph$^2$), 7.33 (m, 4 H, *m*-Ph$^2$), 7.31 (m, 2 H, *p*-Ph$^2$), 2.68 (m, $PCH_2$), 1.58 (m, 2 H, $PCH_2CH_2$), 1.43 (m, 2 H, $CH_2CH_3$), 0.87 (t, $^3J_{H,H}$ = 7.3 Hz, 3 H, $CH_3$) ppm. $^{13}$C{$^1$H} NMR (151 MHz, $CD_2Cl_2$, 298 K): $\delta$ = 141.1 (dd, $^1J_{P-2,C}$ = 8.6 Hz, $^3J_{P-1,C}$ = 7.4 Hz, *i*-Ph$^2$), 132.96 (d, $^4J_{P-1,C}$ = 3.2 Hz, *p*-Ph$^1$), 132.95 (dd, $^2J_{P-1,C}$ = 9.2 Hz, $^4J_{P-2,C}$ = 1.6 Hz, *o*-Ph$^1$), 132.7 (d, $^2J_{P-2,C}$ = 19.7 Hz, *o*-Ph$^2$), 129.4 (d, $^3J_{P-1,C}$ = 11.9 Hz, *m*-Ph$^1$), 128.4 (d, $^3J_{C,P-2}$ = 6.8 Hz, *m*-Ph$^2$), 128.2 (s, *p*-Ph$^2$), 127.3 (dd, $^1J_{P-1,C}$ = 86.8 Hz, $^2J_{P-1,C}$ = 2.4 Hz, *i*-Ph$^1$), 125.0 (dd, $^2J_{P-1,C}$ = 13.0 Hz, $^2J_{P-2,C}$ = 1.1 Hz, C≡N), 25.3 (dd, $^1J_{P-1,C}$ = 60.8 Hz, $^3J_{P-2,C}$ = 9.2 Hz, $PCH_2$), 24.8 (t, $^2J_{P-1,C}$ = $^4J_{P-2,C}$ = 3.5 Hz, $PCH_2CH_2$), 24.3 (d, $^3J_{P-1,C}$ = 15.9 Hz, $CH_2CH_3$), 13.6 ($CH_3$), 7.4 (dd, $^1J_{P-1,C}$ = 128.0 Hz, $^1J_{P-2,C}$ = 28.5 Hz, P=C) ppm (assignment made by comparison with the NMR spectroscopic data of **8a**,**b**). $^{31}$P{$^1$H} NMR (81 MHz, $CD_2Cl_2$, 298 K): $\delta$ = 26.9 (d, $^2J_{P-1,P-2}$ = 140.8 Hz, P-1), –19.5 (d, $^2J_{P-1,P-2}$ = 140.8 Hz, P-2) ppm. FTIR (KBr): $\tilde{\nu}$ = 3050, 2957, 2923, 2867, 2133, 1628, 1433, 1261, 1103, 976, 800, 748, 688 cm$^{-1}$. MS (EI, 70 eV): *m*/*z* (%) = 465.2 (66) $[M]^+$, 408.1 (100) $[M - C_3H_7]^+$, 388.0 (15) $[M - C_6H_5]^+$, 262.1 (54) $[P(C_6H_5)_3]^+$, 185.1 (39) $[M - C_{12}H_{10}P]^+$, 183.0 (100) $[C_{12}H_8P]^+$, 108.0 (25) $[PC_6H_5]^+$. X-ray crystal structure analysis of **8c**: formula $C_{30}H_{29}NP_2$, $M$ = 465.48, light yellow crystal 0.50 × 0.30 × 0.15 mm, $a$ = 10.493(1), $b$ = 14.584(1), $c$ = 17.167(1) Å, $\beta$ = 97.95(1)°, $V$ = 2601.8(3) Å$^3$, $\rho_{calcd.}$ = 1.188 g cm$^{-3}$, $\mu$ = 0.185 mm$^{-1}$, empirical absorption correction (0.913 ≤ $T$ ≤ 0.973), $Z$ = 4, monoclinic, space group $P2_1/n$ (No. 14), $\lambda$ = 0.71073 Å, $T$ = 198 K, $\omega$ and $\phi$ scans, 18706 reflections collected ($\pm h$, $\pm k$, $\pm l$), [(sin$\theta$)/$\lambda$] = 0.67 Å$^{-1}$, 6292 independent ($R_{int}$ = 0.038) and 5226 observed reflections [$I \geq 2\sigma(I)$], 299 refined parameters, $R$ = 0.049, $wR_2$ = 0.142, max. residual electron density 1.01 (–0.33) e·Å$^{-3}$, hydrogen atoms calculated and refined as riding atoms.

**8d:** The reaction of **7** (0.50 g, 0.79 mmol) with 1-bromohexane (0.52 g, 0.44 mL, 3.14 mmol) yielded **8d** as a white solid (0.33 g, 85%). M.p. 155 °C (DSC). $^1$H NMR (600 MHz, $CD_2Cl_2$, 298 K): $\delta$ = 7.68 (m, 4 H, *o*-Ph$^1$), 7.63 (m, 2 H, *p*-Ph$^1$), 7.52 (m, 4 H, *m*-Ph$^1$), 7.45 (m, 4 H, *o*-Ph$^2$), 7.32 (m, 4 H, *m*-Ph$^2$), 7.31 (m, 2 H, *p*-Ph$^2$), 2.66 (m, $PCH_2$), 1.59 (m, 2 H, $PCH_2CH_2$), 1.39 (m, 2 H, $PCH_2CH_2CH_2$), 1.22 (m, 4 H, $CH_2CH_2CH_3$), 0.84 (m, 3 H, $CH_3$) ppm. $^{13}$C{$^1$H} NMR (151 MHz, $CD_2Cl_2$, 298 K): $\delta$ = 141.1 (dd, $^1J_{P-2,C}$ = 8.5 Hz, $^3J_{P-1,C}$ = 7.3 Hz, *i*-Ph$^2$), 132.97 (d, $^4J_{P-1,C}$ = 2.9 Hz, *p*-Ph$^1$), 132.96 (dd, $^2J_{P-1,C}$ = 9.3 Hz, $^4J_{P-2,C}$ = 1.5 Hz, *o*-Ph$^1$), 132.7 (d, $^2J_{P-2,C}$ = 19.9 Hz, *o*-Ph$^2$), 129.4 (d, $^3J_{P-1,C}$ = 12.0 Hz, *m*-Ph$^1$), 128.4 (d, $^3J_{C,P-2}$ = 6.8 Hz, *m*-Ph$^2$), 128.2 (s, *p*-Ph$^2$), 127.3 (dd, $^1J_{P-1,C}$ = 86.7 Hz, $^2J_{P-1,C}$ = 2.6 Hz, *i*-Ph$^1$), 125.1 (dd, $^2J_{P-1,C}$ = 12.9 Hz, $^2J_{P-2,C}$ = 1.1 Hz, C≡N), 31.4 (d, $^4J_{P-1,C}$ = 0.8 Hz, $CH_2CH_2CH_3$), 30.8 (d, $^3J_{P-1,C}$ = 15.6 Hz, $PCH_2CH_2CH_2$), 25.6 (dd, $^1J_{P-1,C}$ = 60.9 Hz, $^3J_{P-2,C}$ = 9.8 Hz, $PCH_2$), 22.70 ($CH_2CH_3$), 22.66 (dd, $^2J_{P-1,C}$ = 4.0 Hz, $^4J_{P-2,C}$ = 3.1 Hz, $PCH_2CH_2$), 14.1 ($CH_3$), 7.3 (dd, $^1J_{P-1,C}$ = 128.1 Hz, $^1J_{P-2,C}$ = 28.8 Hz, P=C) ppm (assignment made by comparison with the NMR spectroscopic data of **8a**,**b**). $^{31}$P{$^1$H} NMR (81 MHz, $CD_2Cl_2$, 298 K): $\delta$ = 26.9 (d, $^2J_{P-1,P-2}$ = 142.0 Hz, P-1), –19.5 (d, $^2J_{P-2,P-1}$ = 142.0 Hz, P-2) ppm. FTIR (KBr): $\tilde{\nu}$ = 3057, 2961, 2931, 2859, 2151, 1436, 1260, 1184, 1100, 1017, 804, 744, 718, 691, 549 cm$^{-1}$. MS (EI, 70 eV): *m*/*z* (%) = 493.2 (63) $[M]^+$, 408.1 (100) $[M - C_6H_{13}]^+$, 262.1 (67) $[P(C_6H_5)_3]^+$, 186.1 (53) [M(408) – $C_{12}H_{10}P]^+$, 108.0 (26) $[PC_6H_5]^+$.

**9a:** The reaction of **7** (0.70 g, 1.11 mmol) with methyl iodide (0.95 g, 0.41 mL, 6.69 mmol) yielded **9a** as a white solid (0.48 g, 76%). M.p. 221 °C (DSC). $^1$H NMR (600 MHz, $CD_2Cl_2$, 298 K): $\delta$ = 7.72 (m, 4 H, *p*-Ph), 7.67 (m, 8 H, *o*-Ph), 7.58 (m, 8 H, *m*-Ph), 2.40 (m, 6 H, $CH_3$) ppm. $^{13}$C{$^1$H} NMR (151 MHz, $CD_2Cl_2$, 298 K): $\delta$ = 134.8 (*p*-Ph), 132.8 (m, *o*-Ph), 130.4 (m, *m*-Ph), 122.6 (m, *i*-Ph), 119.4 (t, $^2J_{P,C}$ = 3.9 Hz, C≡N), 14.6 (m, $CH_3$), 5.6 (t, $^1J_{P,C}$ = 117.1 Hz, P=C) ppm. $^{31}$P{$^1$H} NMR (81 MHz, $CD_2Cl_2$, 298 K): $\delta$ = 21.7 ppm. FTIR (KBr): $\tilde{\nu}$ = 3050, 2957, 2885, 2160, 1435, 1105, 1049, 886, 747, 689 cm$^{-1}$. MS (EI, 70 eV): *m*/*z* (%) = 438 (9) $[M]^+$, 423 (47) $[M - CH_3]^+$, 408.1 (32) $[M - 2CH_3]^+$, 360 (17) $[M - C_6H_5]^+$, 262.1 (14), 185.1 (46) $[M - C_{12}H_{10}P]^+$, 183.0 (42) $[C_{12}H_8P]^+$. $C_{28}H_{26}INP_2$ (565.37): calcd. C 59.48, H 4.64, N 2.48; found C 59.31, H 4.68, N 2.34. X-ray crystal structure analysis of **9a**: formula $C_{28}H_{26}INP_2$, $M$ = 565.34, colorless crystal 0.25 × 0.25 × 0.10 mm, $a$ = 9.596(1), $b$ = 9.803(1), $c$ = 13.891(1) Å, $\alpha$ = 88.18(1), $\beta$ = 77.69(1), $\gamma$ = 84.98(1)°, $V$ = 1271.7(2) Å$^3$, $\rho_{calcd.}$ = 1.476 g cm$^{-3}$, $\mu$ = 11.193 mm$^{-1}$, empirical absorption correction (0.166 ≤ $T$ ≤ 0.401), $Z$ = 2, triclinic, space group $P\bar{1}$ (No. 2), $\lambda$ = 1.54178 Å, $T$ = 223 K, $\omega$ and $\phi$ scans, 15740 reflections collected ($\pm h$, $\pm k$, $\pm l$), [(sin$\theta$)/$\lambda$] = 0.60 Å$^{-1}$, 4481 independent ($R_{int}$ = 0.040) and 4413 observed reflections [$I \geq 2\sigma(I)$], 291 refined parameters, $R$ = 0.047, $wR_2$ = 0.139, max. residual electron density 1.93 (–0.91) e·Å$^{-3}$ close to I, hydrogen atoms calculated and refined as riding atoms.

**9b:** The reaction of **7** (0.30 g, 0.47 mmol) with benzyl bromide (0.50 g, 0.34 mL, 2.92 mmol) yielded **9b** as a white solid (0.23 g, 73%). M.p. 182 °C (DSC). $^1$H NMR (600 MHz, $CD_2Cl_2$, 298 K): $\delta$ = 7.60 (m, 4 H, *p*-Ph$^P$), 7.35 (m, 2 H, *p*-Ph), 7.33 (m, 8 H, *m*-Ph$^P$), 7.27 (m, 8 H, *o*-Ph$^P$), 7.24 (m, 4 H, *m*-Ph), 7.03 (m, 4 H, *o*-Ph), 4.34 (m, 4 H, $CH_2$) ppm. $^{13}$C{$^1$H} NMR (151 MHz, $CD_2Cl_2$, 298 K): $\delta$ = 134.6 (m, *p*-Ph$^P$), 134.0 (m, *o*-Ph$^P$), 131.6 (m, *o*-Ph), 129.9 (m, *m*-Ph$^P$), 129.2 (*m*-Ph), 129.0 (*p*-Ph), 128.6 (*i*-Ph, assigned by $^1$H,$^{13}$C ghmbc experiment), 120.4 (t, $^2J_{P,C}$ = 4.8 Hz, C≡N),

 © 2007 Wiley-VCH Verlag GmbH & Co. KGaA, Weinheim 

119.4 (m, *i*-$Ph^P$), 36.6 (m, $CH_2$), 3.2 (t, $^1J_{P,C}$ = 117.3 Hz, P=C) ppm. $^{31}P\{^1H\}$ NMR (81 MHz, $CD_2Cl_2$, 298 K): $\delta$ = 23.9 ppm. FTIR (KBr): $\tilde{\nu}$ = 3050, 3009, 2854, 2781, 2159, 1434, 1149, 1104, 1047, 833, 782, 743, 691, 582 $cm^{-1}$. MS (EI, 70 eV): *m*/*z* (%) = 589 (1) $[M]^+$, 499 (12) $[M - CH_2(C_6H_5)]^+$, 408.1 (32) $[M - 2CH_2(C_6H_5)]^+$, 360 (17) $[M - C_6H_5]^+$, 262.1 (14), 183.0 (77) $[C_{12}H_8P]^+$, 91 (100) $[CH_2(C_6H_5)]^+$. $C_{40}H_{34}BrNP_2$ (670.57): calcd. C 71.65, H 5.11, N 2.09; found C 70.91, H 5.07, N 1.87. X-ray crystal structure analysis of **9b**: formula $C_{40}H_{34}BrNP_2 \cdot CH_2Cl_2$, $M$ = 755.46, colorless crystal 0.50 × 0.35 × 0.25 mm, $a$ = 10.323(1), $b$ = 18.641(1), $c$ = 19.633(1) Å, $\beta$ = 104.19(1)°, $V$ = 3662.7(4) $Å^3$, $\rho_{calcd.}$ = 1.370 $g\,cm^{-3}$, $\mu$ = 3.923 $mm^{-1}$, empirical absorption correction ($0.244 \le T \le 0.441$), $Z$ = 4, monoclinic, space group $P2_1/c$ (No. 14), $\lambda$ = 1.54178 Å, $T$ = 223 K, $\omega$ and $\phi$ scans, 28553 reflections collected ($\pm h$, $\pm k$, $\pm l$), [(sin$\theta$)/$\lambda$] = 0.58 $Å^{-1}$, 5911 independent ($R_{int}$ = 0.041) and 5588 observed reflections [$I \ge 2\,s(I)$], 424 refined parameters, $R$ = 0.037, $wR_2$ = 0.100, max. residual electron density 0.58 (–0.51) e·$Å^{-3}$, hydrogen atoms calculated and refined as riding atoms.

**10a:** The reaction of **7** (0.30 g, 0.47 mmol) with 1,3-dibromopropane (0.39 g, 0.20 mL, 1.93 mmol) yielded **10a** as a white solid (0.22 g, 88%). M.p. 128 °C (DSC). $^1H$ NMR (600 MHz, $CD_2Cl_2$, 298 K): $\delta$ = 7.88 (m, 8 H, *o*-Ph), 7.72 (m, 4 H, *p*-Ph), 7.61 (m, 8 H, *m*-Ph), 3.50 (m, 4 H, $PCH_2$), 2.45 (m, 2 H, $CH_2$) ppm. $^{13}C\{^1H\}$ NMR (151 MHz, $CD_2Cl_2$, 298 K): $\delta$ = 134.6 (m, *p*-Ph), 133.1 (m, *o*-Ph), 130.2 (m, *m*-Ph), 123.4 (m, *i*-Ph), 119.1 (C≡N), 21.5 (m, $PCH_2$), 17.0 (t, $^3J_{P,C}$ = 6.0 Hz, $CH_2$), 3.2 (t, $^1J_{P,C}$ = 103.8 Hz, P=C) ppm. $^{31}P\{^1H\}$ NMR (81 MHz, $CD_2Cl_2$, 298 K): $\delta$ = 18.3 (s) ppm. FTIR (KBr): $\tilde{\nu}$ = 3054, 3014, 2884, 2166, 1435, 1156, 1108, 1041, 995, 849, 722, 688 $cm^{-1}$. MS (EI, 70 eV): *m*/*z* (%) = 450 (100) $[M]^+$, 408 (22) $[M - C_3H_6]^+$, 262.1 (27), 183.0 (86) $[C_{12}H_8P]^+$, 108 (34) $[C_6H_5P]^+$. $C_{29}H_{26}BrNP_2$ (530.38): calcd. C 65.67, H 4.94, N 2.64; found C 65.70, H 5.40, N 2.30. X-ray crystal structure analysis of **10a**: formula $C_{29}H_{26}NP_2Br \cdot 1/2\ C_7H_8$, $M$ = 576.43, colorless crystal 0.40 × 0.35 × 0.07 mm, $a$ = 9.714(1), $b$ = 16.270(1), $c$ = 10.062(1) Å, $\alpha$ = 107.84(1), $\beta$ = 92.61(1), $\gamma$ = 101.18(1)°, $V$ = 1475.7(2) $Å^3$, $\rho_{calcd.}$ = 1.297 $g\,cm^{-3}$, $\mu$ = 1.522 $mm^{-1}$, empirical absorption correction ($0.581 \le T \le 0.901$), $Z$ = 2, triclinic, space group $P\bar{1}$ (No. 2), $\lambda$ = 0.71073 Å, $T$ = 198 K, $\omega$ and $\phi$ scans, 15825 reflections collected ($\pm h$, $\pm k$, $\pm l$), [(sin$\theta$)/$\lambda$] = 0.67 $Å^{-1}$, 7092 independent ($R_{int}$ = 0.053) and 5386 observed reflections [$I \ge 2\sigma(I)$], 337 refined parameters, $R$ = 0.071, $wR_2$ = 0.218, max. residual electron density 1.72 (–0.69) e·$Å^{-3}$ close to Br, bromine atom and the toluene solvent molecule are disordered and refined with split positions, hydrogen atoms calculated and refined as riding atoms.

**10b:** The reaction of **7** (0.50 g, 0.79 mmol) with 1,4-dibromobutane (0.68 g, 0.38 mL, 3.15 mmol) yielded **10b** as a white solid (0.27 g, 63%). M.p. 146 °C (DSC). $^1H$ NMR (600 MHz, $CD_2Cl_2$, 298 K): $\delta$ = 7.83 (m, 8 H, *o*-Ph), 7.76 (m, 4 H, *p*-Ph), 7.66 (m, 8 H, *m*-Ph), 3.34 (m, 4 H, $PCH_2$), 2.02 (m, 4 H, $CH_2$) ppm. $^{13}C\{^1H\}$ NMR (151 MHz, $CD_2Cl_2$, 298 K): $\delta$ = 134.6 (*p*-Ph), 132.9 (m, *o*-Ph), 130.3 (m, *m*-Ph), 123.6 (m, *i*-Ph), 119.8 (t, $^2J_{P,C}$ = 2.3 Hz, C≡N), 24.7 (m, $PCH_2$), 21.5 (m, $CH_2$), 4.7 (t, $^1J_{P,C}$ = 108.9 Hz, P=C) ppm. $^{31}P\{^1H\}$ NMR (81 MHz, $CD_2Cl_2$, 298 K): $\delta$ = 28.8 (s) ppm. FTIR (KBr): $\tilde{\nu}$ = 2911, 2875, 2852, 2835, 2799, 2157, 1479, 1433, 1400, 1163, 1150, 1107, 1051, 992, 821, 748, 719, 689, 554, 525, 508 $cm^{-1}$. MS (EI, 70 eV): *m*/*z* (%) = 464 (54) $[M]^+$, 408 (7) $[M - C_4H_8]^+$, 262.1 (28), 183.0 (100) $[C_{12}H_8P]^+$, 108 (55) $[C_6H_5P]^+$. $C_{30}H_{28}BrNP_2$ (544.41): calcd. C 66.19, H 5.18, N 2.57; found C 66.14, H 4.95, N 2.42. X-ray crystal structure analysis of **10b**: formula $C_{30}H_{28}NP_2Br$, $M$ = 544.38, colorless crystal 0.40 × 0.30 × 0.20 mm, $a$ = 10.659(1), $b$ = 11.425(1), $c$ = 12.583(1) Å, $\alpha$ = 115.27(1), $\beta$ = 99.22(1), $\gamma$ = 99.03(1)°, $V$ = 1323.5(2) $Å^3$, $\rho_{calcd.}$ = 1.366 $g\,cm^{-3}$, $\mu$ = 3.392 $mm^{-1}$, empirical absorption correction ($0.344 \le T \le 0.550$), $Z$ = 2, triclinic, space group $P\bar{1}$ (No. 2), $\lambda$ = 1.54178 Å, $T$ = 223 K, $\omega$ and $\phi$ scans, 18436 reflections collected ($\pm h$, $\pm k$, $\pm l$), [(sin$\theta$)/$\lambda$] = 0.59 $Å^{-1}$, 4515 independent ($R_{int}$ = 0.027) and 4483 observed reflections [$I \ge 2\sigma(I)$], 307 refined parameters, $R$ = 0.040, $wR_2$ = 0.118, max. residual electron density 0.43 (–0.88) e·$Å^{-3}$, hydrogen atoms calculated and refined as riding atoms.

## Acknowledgments

Financial support from the Deutsche Forschungsgemeinschaft and the Fonds der Chemischen Industrie is gratefully acknowledged.

[1] J. Kaneti, P. v. R. Schleyer, T. Clark, A. J. Kos, G. W. Spitznagel, J. G. Andrade, J. B. Moffat, *J. Am. Chem. Soc.* **1986**, *108*, 1481–1492.
[2] Review: G. Boche, *Angew. Chem.* **1989**, *101*, 286–306; *Angew. Chem. Int. Ed. Engl.* **1989**, *28*, 277–297.
[3] a) G. Boche, K. Harms, M. Marsch, *J. Am. Chem. Soc.* **1988**, *110*, 6925–6926; b) G. Boche, M. Marsch, K. Harms, *Angew. Chem.* **1986**, *98*, 373–374; *Angew. Chem. Int. Ed. Engl.* **1986**, *25*, 373–374.
[4] D. Enders, J. Kirchhoff, P. Gerdes, D. Mannes, G. Raabe, J. Runsink, G. Boche, M. Marsch, H. Ahlbrecht, H. Sommer, *Eur. J. Org. Chem.* **1998**, 63–72.
[5] a) R. Scott, J. Granander, G. Hilmersson, *J. Am. Chem. Soc.* **2004**, *126*, 6798–6805; b) R. Sott, J. Granander, G. Hilmersson, *Chem. Eur. J.* **2002**, *8*, 2081–2087; c) P. R. Carlier, J. D. Madura, *J. Org. Chem.* **2002**, *67*, 3832–3840; d) R. Koch, B. Wiedel, E. Anders, *J. Org. Chem.* **1996**, *61*, 2523–2529; e) P. R. Carlier, B. L. Lucht, D. B. Collum, *J. Am. Chem. Soc.* **1994**, *116*, 11602–11603; f) C. Lambert, P. v. R. Schleyer, U. Pieper, D. Stalke, *Angew. Chem.* **1992**, *104*, 78–79; *Angew. Chem. Int. Ed. Engl.* **1992**, *31*, 77–79.
[6] B. Ledig, M. Marsch, K. Harms, G. Boche, *Z. Kristallogr.* **1999**, *214*, 511–512.
[7] a) K. Issleib, H. P. Abicht, *J. Prakt. Chem.* **1970**, *312*, 456–465; b) K. Issleib, R. Lindner, *Justus Liebigs Ann. Chem.* **1966**, *699*, 40–52.
[8] a) R. Tonner, F. Öxler, B. Neumüller, W. Petz, G. Frenking, *Angew. Chem.* **2006**, *118*, 8206–8211; *Angew. Chem. Int. Ed.* **2006**, *45*, 8038–8042; b) G. E. Hardy, J. I. Zink, W. C. Kaska, J. C. Baldwin, *J. Am. Chem. Soc.* **1978**, *100*, 8001–8002; c) A. T. Vincent, P. J. Wheatley, *J. Chem. Soc., Dalton Trans.* **1972**, 617–622; d) F. Ramitez, N. B. Desai, B. Hansen, N. Mckelvin, *J. Am. Chem. Soc.* **1961**, *83*, 3539–3540.
[9] a) H. Schmidbaur, G. Haßlberger, U. Dreschler, U. Schubert, C. Kappenstein, A. Frank, *Angew. Chem.* **1979**, *91*, 437–438; *Angew. Chem. Int. Ed. Engl.* **1979**, *18*, 408–409; b) H. Schmidbaur, O. Gasser, C. Krüger, J. C. Sekutowski, *Chem. Ber.* **1977**, *110*, 3517–3527; c) O. Gasser, H. Schmidbaur, *J. Am. Chem. Soc.* **1975**, *97*, 6281–6282.
[10] C. N. Matthews, G. H. Birum, *Acc. Chem. Res.* **1969**, *2*, 373–379.
[11] H. Schmidbaur, U. Dreschler, B. Zimmer-Gasser, D. Neugebauer, U. Schubert, *Chem. Ber.* **1980**, *113*, 902–911.
[12] H. Schmidbaur, T. Costa, B. Milewski-Mahrla, U. Schubert, *Angew. Chem.* **1980**, *92*, 557–558; *Angew. Chem. Int. Ed. Engl.* **1980**, *19*, 555–556.
[13] H. Schmidbaur, personal communication.
[14] a) L. Braun, P. Liptau, G. Kehr, J. Ugolotti, R. Fröhlich, G. Erker, *Dalton Trans.* **2007**, 1409–1415; b) L. Braun, G. Kehr, R. Fröhlich, G. Erker, *Inorg. Chim. Acta* **2007**, in press; c) Y.-F. Yu, A. Wojcicki, M. Calligarist, G. Nardin, *Organometallics* **1986**, *5*, 47–53.
[15] A. Schmidpeter, G. Burget, *Angew. Chem.* **1985**, *97*, 602–603; *Angew. Chem. Int. Ed. Engl.* **1985**, *24*, 580–581.

 © 2007 Wiley-VCH Verlag GmbH & Co. KGaA, Weinheim 

[16] For a comparison, see: H. H. Karsch, G. Grauvogel, P. Mikulcik, P. Bissinger, G. Müller, *J. Organomet. Chem.* **1994**, *465*, 65–71; H. H. Karsch, B. Deubelly, G. Müller, *J. Organomet. Chem.* **1988**, *352*, 47–59; H. H. Karsch, G. Müller, *J. Chem. Soc., Chem. Commun.* **1984**, 569–570.
[17] For other examples of P-stabilized carbanions, see, for example: K. Izod, *Coord. Chem. Rev.* **2002**, *227*, 153–173.
[18] a) For a comparison, see: J. Ruiz, F. Marquínez, V. Riera, M. Vivanco, S. García-Granda, M. R. Díaz, *Chem. Eur. J.* **2002**, *8*, 3872–3878; b) J. Ruiz, F. Marquínez, V. Riera, M. Vivanco, S. García-Granda, M. R. Díaz, *Angew. Chem.* **2000**, *112*, 1891–1893; *Angew. Chem. Int. Ed.* **2000**, *39*, 1821–1823; c) J. Ruiz, V. Riera, M. Vivanco, S. García-Granda, M. R. Díaz, *Organometallics* **1998**, *17*, 4562–4567; d) J. Ruiz, V. Riera, M. Vivanco, M. Lanfranchi, A. Tiripicchio, *Organometallics* **1998**, *17*, 3835–3837; e) J. Ruiz, V. Riera, M. Vivanco, S. García-Granda, M. A. Salvadó, *Organometallics* **1996**, *15*, 1079–1081.
[19] COLLECT, data collection software, Nonius B.V., **1998**.
[20] Z. Otwinowski, W. Minor, *Methods Enzymol.* **1997**, *276*, 307–326.
[21] a) R. H. Blessing, *Acta Crystallogr. Sect. A* **1995**, *51*, 33–37; b) R. H. Blessing, *J. Appl. Crystallogr.* **1997**, *30*, 421–426.
[22] Z. Otwinowski, D. Borek, W. Majewski, W. Minor, *Acta Crystallogr. Sect. A* **2003**, *59*, 228–234.
[23] G. M. Sheldrick, *Acta Crystallogr. Sect. A* **1990**, *46*, 467–473.
[24] G. M. Sheldrick, *SHELXL-97*, University of Göttingen, **1997**.
[25] E. Keller, *SCHAKAL*, University of Freiburg, **1997**.

Received: January 23, 2007
Published Online: May 11, 2007

 © 2007 Wiley-VCH Verlag GmbH & Co. KGaA, Weinheim 

DOI: 10.1002/ejic.200601174

# Dinuclear (Arene)ruthenium Complexes Containing a Chiral-at-Phosphorus Phosphanido Bridge

**Mathieu J.-L. Tschan,[a] Georg Süss-Fink,*[a] Frédéric Chérioux,[b] and Bruno Therrien[a]**

*Dedicated to Professor Hans-Ludwig Krauss on the occasion of his 80th birthday*

**Keywords:** Arene ligands / Ruthenium / Tethered complexes / P ligands / Hydride ligands

The unsaturated diruthenium cation $[(\eta^6\text{-}C_6Me_6)(\eta^6\text{-}p\text{-}i\text{PrMeC}_6H_4)Ru_2(\mu_2\text{-}H)_3]^+$ reacts with $PPh_2(CH_2)_3Ph$ to give the phosphanido complex $[(\eta^6\text{-}C_6Me_6)(\eta^6\text{-}p\text{-}i\text{PrMeC}_6H_4)Ru_2\{\mu_2\text{-}PPh(CH_2)_3Ph\}(\mu_2\text{-}H)_2]^+$ (**1**), which contains a stereogenic phosphorus atom in the bridge, and benzene. Heating of **1** in bromobenzene gives the first chiral-at-phosphorus diruthenium complex $[(\eta^6\text{-}C_6Me_6)Ru_2\{\mu_2\text{-}PPh(CH_2)_3\text{-}\eta^6\text{-}Ph\}(\mu_2\text{-}Br)_2]^+$ (**3**) due to the replacement of the *p*-cymene ligand by the phenyl group at the pendant arm and hydrido bridges by bromido bridges. The single-crystal X-ray structure analysis of [**3**][$BF_4$] reveals a racemic mixture of both enantiomers ($R_P$)-**3** and ($S_P$)-**3** in the crystal. Similarly, the reaction of $[(\eta^6\text{-}C_6Me_6)(\eta^6\text{-}p\text{-}i\text{PrMeC}_6H_4)Ru_2(\mu_2\text{-}H)_3]^+$ and the enantiopure phosphane (*R*)-$PPh_2(CH_2)_2CHMePh$ yields the complex $[(\eta^6\text{-}C_6Me_6)(\eta^6\text{-}p\text{-}i\text{PrMeC}_6H_4)Ru_2\{\mu_2\text{-}(R)\text{-}PPh(CH_2)_2CHMePh\}(\mu_2\text{-}H)_2]^+$ (**4**) as a mixture of diastereomers. An optically active mixture (*de* = 4 %) of phosphanido-bridged complexes $[(\eta^6\text{-}C_6Me_6)Ru_2\{\mu_2\text{-}(R)\text{-}PPh(CH_2)_2CHMe\text{-}\eta^6\text{-}Ph\}(\mu_2\text{-}Br)_2]^+$ (**6**), containing the ($R_C$,$S_P$) and ($R_C$,$R_P$) diastereomers, is obtained upon heating of **4** in bromobenzene. The molecular structure of [**6**][$BF_4$] reveals that the two diastereomers ($R_C$,$S_P$)-**6** and ($R_C$,$R_P$)-**6** exist as two conformers. The non-chiral-at-phosphorus analogues $[(\eta^6\text{-}C_6Me_6)_2Ru_2\{\mu_2\text{-}PPh(CH_2)_3Ph\}(\mu_2\text{-}H)_2]^+$ (**2**) and $[(\eta^6\text{-}C_6Me_6)_2Ru_2\{\mu_2\text{-}(R)\text{-}PPh(CH_2)_2CHMePh\}(\mu_2\text{-}H)_2]^+$ (**5**) have also been synthesized and structurally characterized by single-crystal X-ray structure analyses of [**2**][$BF_4$] and [**5**][$BF_4$].

(© Wiley-VCH Verlag GmbH & Co. KGaA, 69451 Weinheim, Germany, 2007)

## Introduction

(Arene)ruthenium complexes, in spite of their venerable history, have not lost their fascination thanks to their rich and diversified chemistry.[1] An increasing number of catalytic reactions involving (arene)ruthenium complexes, such as transfer hydrogenation reactions,[2] alkene metathesis[3] or Diels–Alder reactions,[4] have contributed to the steadily growing interest in these complexes, which owe their fertility and versatility mainly to the stability of the arene–ruthenium bond. The complete loss of the arene ligand can be an undesired side-reaction during a catalytic process, although the stability of the (arene)ruthenium moiety can be increased by arene ligands containing chelating substituents.[5] The synthesis of such (arene)ruthenium complexes can be achieved by intramolecular arene ligand exchange at the ruthenium atom, which works only if either an electron-poor arene ligand is replaced by an electron-rich one[6] or if the reaction can take advantage of the chelate effect.[5] Thus, examples of tethered (arene)ruthenium complexes containing oxygen,[7] phosphorus,[5,6,8] sulfur[9] and carbon or nitrogen[10] donor atoms have been reported.

Recently, we found that the unsaturated dinuclear cation $[(\eta^6\text{-}C_6Me_6)_2Ru_2(\mu_2\text{-}H)_3]^+$ reacts with tertiary phosphanes such as $PPh_3$ and $PPhMe_2$ to give the phosphanido-bridged complexes $[(\eta^6\text{-}C_6Me_6)_2Ru_2(\mu_2\text{-}PR_2)(\mu_2\text{-}H)_2]^+$ (R = Ph, Me) and benzene.[11] The reaction proceeds by P–C activation intermediates containing a bridging phenyl ligand, $[(\eta^6\text{-}C_6Me_6)_2Ru_2(\mu_2\text{-}PR_2)(\mu_2\text{-}Ph)(\mu_2\text{-}H)]^+$ (R = Ph, Me), and the phenyl derivative is isolated as the tetrafluoroborate salt. This P–C bond-cleavage reaction occurs even in the case of trialkylphosphanes such as P*n*$Bu_3$ and P*n*$Oct_3$ to give the cations $[(\eta^6\text{-}C_6Me_6)_2Ru_2(\mu_2\text{-}PR_2)(\mu_2\text{-}H)_2]^+$ (R = *n*Bu, *n*Oct) and the corresponding olefin and dihydrogen.[11] The diphenylphosphanido derivative $[(\eta^6\text{-}C_6Me_6)_2Ru_2(\mu_2\text{-}PPh_2)(\mu_2\text{-}H)_2]^+$ turned out to be a highly selective catalyst for hydrogenation of carbon–carbon double bonds.[12]

The mixed dinuclear (arene)trihydridoruthenium complex $[(\eta^6\text{-}C_6Me_6)(\eta^6\text{-}p\text{-}i\text{PrMeC}_6H_4)Ru_2(\mu_2\text{-}H)_3]^+$, which we synthesized recently,[13] reacts with phosphanes in the same way as its symmetrical analogue, $[(\eta^6\text{-}C_6Me_6)_2Ru_2(\mu_2\text{-}H)_3]^+$, although, because of the asymmetry of the diruthenium backbone, the reaction with mixed phosphanes allows

[a] Institut de Chimie, Université de Neuchâtel,
Case postale 158, 2009 Neuchâtel, Suisse
Fax: +41-32-718-2511
E-mail: georg.suess-fink@unine.ch
[b] Laboratoire FEMTO-ST/LPMO, CNRS UMR 6174,
32 Avenue de l'Observatoire, 25044 Besançon cedex, France

 © 2007 Wiley-VCH Verlag GmbH & Co. KGaA, Weinheim 

the synthesis of phosphanido-bridged diruthenium complexes that are chiral at the phosphorus atom. Moreover, the use of mixed phosphanes containing a phenyl substituent at the end of a pendant arm should give access to tethered P-chiral diruthenium complexes.

In this paper, we report the synthesis of the first tethered chiral-at-phosphorus diruthenium complex, $[(\eta^6\text{-}C_6Me_6)Ru_2\{\mu_2\text{-}PPh(CH_2)_3\text{-}\eta^6\text{-}Ph\}(\mu_2\text{-}Br)_2]^+$ (**3**), which was obtained as a racemic mixture by heating of $[(\eta^6\text{-}C_6Me_6)(\eta^6\text{-}p\text{-}i\text{PrMeC}_6H_4)Ru_2\{\mu_2\text{-}PPh(CH_2)_3Ph\}(\mu_2\text{-}H)_2]^+$ (**1**) in bromobenzene. The enantiopure phosphane (*R*)-$PPh_2(CH_2)_2$-CHMePh, reported by Zenneck et al.,[8c] gave an optically active mixture of the diastereomeric complexes ($R_C$,$S_P$)- and ($R_C$,$R_P$)-$[(\eta^6\text{-}C_6Me_6)Ru_2\{\mu_2\text{-}(R)\text{-}PPh(CH_2)_2CHMe\text{-}\eta^6\text{-}Ph\}(\mu_2\text{-}Br)_2]^+$ (**6**).

## Results and Discussion

The dinuclear trihydrido complex $[(\eta^6\text{-}C_6Me_6)(\eta^6\text{-}i\text{PrMeC}_6H_4)Ru_2(\mu_2\text{-}H)_3]^+$ reacts with the mixed phosphane $PPh_2(CH_2)_3Ph$, which was recently reported by Wright et al.,[5] to give the phosphanido-bridged complex $[(\eta^6\text{-}C_6Me_6)(\eta^6\text{-}p\text{-}i\text{PrMeC}_6H_4)Ru_2\{\mu_2\text{-}PPh(CH_2)_3Ph\}(\mu_2\text{-}H)_2]^+$ (**1**; Scheme 1). The reaction was carried out at 55 °C in dichloromethane solution, and the yield of [**1**][$BF_4$] can be increased from 30% to 38% by performing the reaction under hydrogen pressure (3 bar). The reason for the use of hydrogen in this reaction is the conversion of the intermediate $[(\eta^6\text{-}C_6Me_6)(\eta^6\text{-}p\text{-}i\text{PrMeC}_6H_4)Ru_2\{\mu_2\text{-}PPh(CH_2)_3Ph\}(\mu_2\text{-}Ph)(\mu_2\text{-}H)]^+$, which was observed by mass spectrometry in accordance with the fully characterized analogue $[(\eta^6\text{-}C_6Me_6)_2Ru_2(\mu_2\text{-}PPh_2)(\mu_2\text{-}Ph)(\mu_2\text{-}H)]^+$,[11] into **1** by reaction with $H_2$.

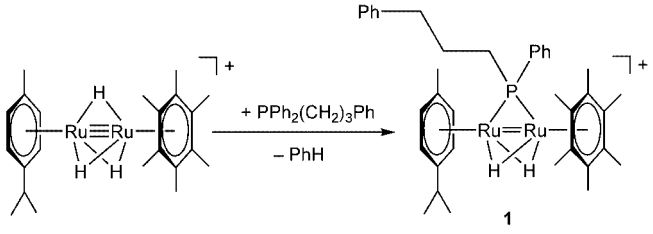


Scheme 1. Synthesis of $[(\eta^6\text{-}C_6Me_6)(\eta^6\text{-}p\text{-}i\text{PrMeC}_6H_4)Ru_2\{\mu_2\text{-}PPh(CH_2)_3Ph\}(\mu_2\text{-}H)_2]^+$ (**1**).

Complex **1** possesses a stereogenic phosphanido bridge and was obtained as a racemic mixture since the nucleophilic attack of the phosphane occurs at one of the two ruthenium atoms and none of the two P–$C_{(aryl)}$ bonds is preferentially cleaved. The two hydrido ligands in **1** are diastereotopic, as seen by the $^1$H NMR spectrum, which exhibits two doublets of doublets in the hydride region at $\delta$ = –14.65 (dd, $^2J_{H,H}$ = 2.8, $^2J_{H,P}$ = 28 Hz, 1 H) and –16.06 (dd, $^2J_{H,H}$ = 2.8, $^2J_{H,P}$ = 31 Hz, 1 H) ppm. The two enantiomers of **1** are shown in Figure 1.

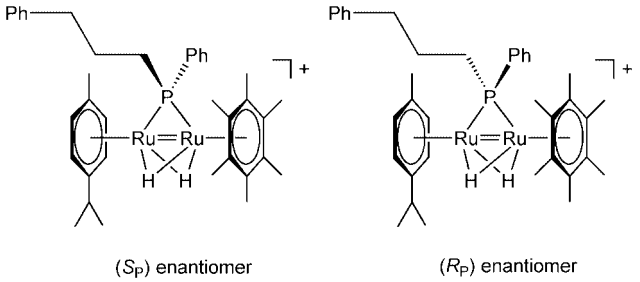


Figure 1. The two enantiomers of $[(\eta^6\text{-}C_6Me_6)(\eta^6\text{-}p\text{-}i\text{PrMeC}_6H_4)Ru_2\{\mu_2\text{-}PPh(CH_2)_3Ph\}(\mu_2\text{-}H)_2]^+$ (**1**).

As we failed to obtain crystals of [**1**][$BF_4$] suitable for X-ray structure analysis, we synthesized an achiral analogue of **1** containing two hexamethylbenzene ligands. The cation $[(\eta^6\text{-}C_6Me_6)_2Ru_2\{\mu_2\text{-}PPh(CH_2)_3Ph\}(\mu_2\text{-}H)_2]^+$ (**2**) is accessible in the same way as **1** from $PPh_2(CH_2)_3Ph$ and $[(\eta^6\text{-}C_6Me_6)_2Ru_2(\mu_2\text{-}H)_3]^+$ (Scheme 2). The reaction was carried out under the same conditions as for **1** ($CH_2Cl_2$, 55 °C, 3 bar $H_2$) and, in this case, the yield of the reaction was much higher (85%). Dark-red crystals of [**2**][$BF_4$] suitable

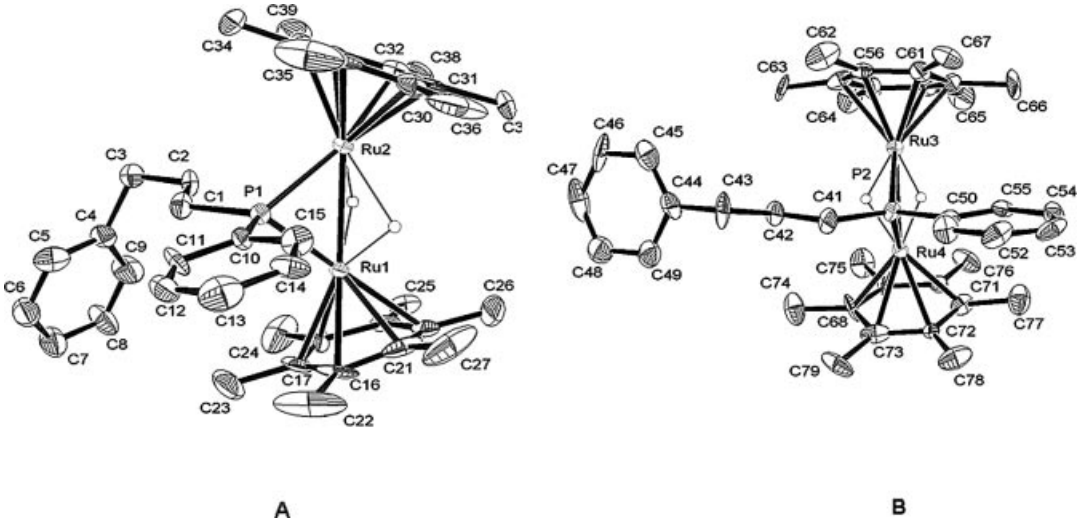


Figure 2. Molecular structure of the two independent molecules of cation **2** (anions, solvent molecules, and hydrogen atoms, except for the hydrido ligands, have been omitted for clarity).

 © 2007 Wiley-VCH Verlag GmbH & Co. KGaA, Weinheim 

for X-ray structure analysis were obtained by slow diffusion of hexane into a concentrated dichloromethane solution of [**2**][$BF_4$]. The molecular structure of cation **2** is shown in Figure 2.

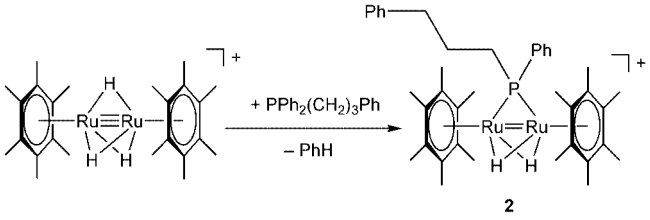


2

Scheme 2. Synthesis of [($\eta^6$-$C_6Me_6$)$_2$$Ru_2${$\mu_2$-PPh$(CH_2)_3$Ph}($\mu_2$-H)$_2$]$^+$ (**2**).

The single-crystal X-ray structure analysis for cation **2** reveals a PPh$(CH_2)_3$Ph moiety and two hydrido ligands bridging the two ruthenium atoms, with each ruthenium atom also being coordinated to an $\eta^6$-$C_6Me_6$ ligand. The Ru–Ru distances [2.670(2) and 2.767(2) Å] are similar to those expected for a ruthenium–ruthenium double bond. Two independent molecules are observed in the crystal structure of [**2**][$BF_4$], with the major difference between them being the conformation of the P$(CH_2)_3$Ph unit (see Figure 2). Thus, the C1–C2–C3–C4 torsion angle in molecule **A** is 170(3)° (*anti* conformation), while in molecule **B** the C41–C42–C43–C44 torsion angle is –69(2)° (*syn* conformation). These two molecules adopt a pairwise arrangement in the unit cell of [**2**][$BF_4$], as shown in Figure 3. The presence of a bridging PPh$(CH_2)_3$Ph ligand forces the arene moieties to adopt a tilted geometry. The two $C_6Me_6$ arene ligands are not parallel to each other, and the angles between the $C_6Me_6$ planes are 34.9(2)° and 34.4(4)° for molecules **A** and **B**, respectively.

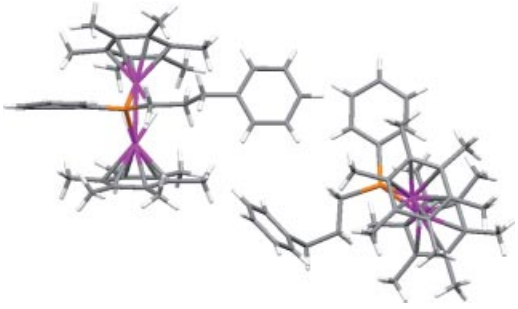

Figure 3. Pairwise arrangement of *anti*-**2** (molecule **A**) and *syn*-**2** (molecule **B**) in the unit cell of [**2**][$BF_4$].

The arene exchange reaction between the *p*-cymene ligand and the phenyl substituent in the pendant arm of the phosphanido ligand in [($\eta^6$-$C_6Me_6$)($\eta^6$-*p*-*i*PrMe$C_6H_4$)-$Ru_2${$\mu_2$-PPh$(CH_2)_3$Ph}($\mu_2$-H)$_2$]$^+$ (**1**) is achieved by heating of [**1**][$BF_4$] at 150 °C in bromobenzene. The reaction leads to the dibromo complex [($\eta^6$-$C_6Me_6$)$Ru_2${$\mu_2$-PPh$(CH_2)_3$-$\eta^6$-Ph}($\mu_2$-Br)$_2$]$^+$ (**3**; Scheme 3), and the reaction requires more forcing conditions than in the case of [($\eta^6$-*p*-*i*PrMe$C_6H_4$)-$Ru${$PPh_2(CH_2)_3$Ph}$Cl_2$].[5] Replacement of the $C_6M_6$ ligand is not observed.

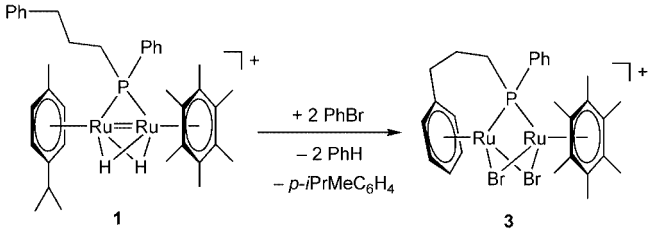


1 3

Scheme 3. Synthesis of [($\eta^6$-$C_6Me_6$)$Ru_2${$\mu_2$-PPh$(CH_2)_3$-$\eta^6$-Ph}($\mu_2$-Br)$_2$]$^+$ (**3**).

The surprising substitution of the two hydrido bridges in **1** by two bromido bridges in **3** that occurs during arene ligand exchange was confirmed by NMR monitoring: on comparing the $^1$H NMR spectra of [**1**][$BF_4$] and [**3**][$BF_4$] it becomes clear that both the *p*-cymene signals and the hydride signals have disappeared and that coordination of the $\eta^6$-$C_6H_5$ substituent of the pendant arm gives rise to three new signals at $\delta$ = 6.25 (m, 2 H, *H-ortho*), 5.43 (t, $^3J_{H,H}$ = 4.8 Hz, 1 H, *H-para*), and 5.04 (m, 2 H, *H-meta*) ppm. As expected, the three methylene groups in the ligand arm give rise to two signals each because the $CH_2$ protons are diastereotopic (Figure 4). In contrast to **1** and **2**, the $^4J_{P,H}$ coupling (1 Hz) for **3**, which gives rise to a doublet at $\delta$ = 1.94 ppm, is visible for the methyl protons of the $\eta^6$-$C_6Me_6$ ligand, presumably due to the almost parallel arrangement of the two $\eta^6$-arene ligands. A similar $^4J_{P,H}$ coupling has been observed in the mononuclear complexes [($\eta^6$-$C_6Me_6$)-Ru(CO)(P$Me_3$)Me]$^+$,[14] [($\eta^6$-$C_6Me_6$)Ru(P$R_3$)$Me_2$], and [($\eta^6$-$C_6Me_6$)Ru(P$R_3$)(OCO$CF_3$)Me] (P$R_3$ = P$Me_3$, P$Ph_3$, P$Me_2$Ph).[15] In accordance with the presence of two bromido ligands, the ESI mass spectrum of [**3**][$BF_4$] shows a parent peak at *m*/*z* = 752. The molecular structure of this complex was finally confirmed by single-crystal X-ray analysis.

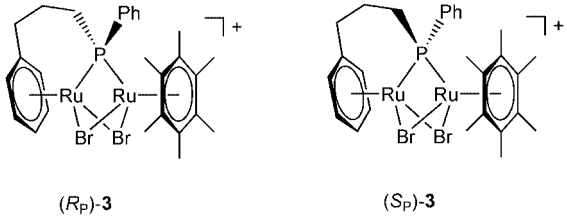


($R_P$)-**3** ($S_P$)-**3**

Figure 4. The two enantiomers ($R_P$)-**3** and ($S_P$)-**3**.

Dark-orange crystals of [**3**][$BF_4$] suitable for an X-ray structure analysis were obtained by slow diffusion of diethyl ether into a concentrated acetone solution of [**3**][$BF_4$]. Two enantiomers are observed independently in the asymmetric unit of [**3**][$BF_4$] (see Figure 5).

The ruthenium atoms in [**3**][$BF_4$] are in a distorted octahedral geometry in which the two metal centers are bridged by a tethered phosphanido and two bromido ligands. The Ru–Br bond lengths [ranging from 2.552(1) to 2.586(1) Å] and Ru–Br–Ru angles [ranging from 82.16(4) to 82.90(4)°] are similar to those found in other dinuclear ($\eta^6$-arene)-ruthenium complexes bridged by bromine atoms, for example [$Ru_2$($\eta^6$-1,3,5-$C_6H_3Et_3$)$_2$($\mu_2$-Br)$_3$][$Re_2(CO)_6$($\mu_2$-Br)$_3$] and [$Ru_2$($\eta^6$-*p*-*i*PrMe$C_6H_4$)$_2$($\mu_2$-Br)$_3$][$Re_2(CO)_6$($\mu_2$-Br)$_3$].[16] The

 © 2007 Wiley-VCH Verlag GmbH & Co. KGaA, Weinheim 

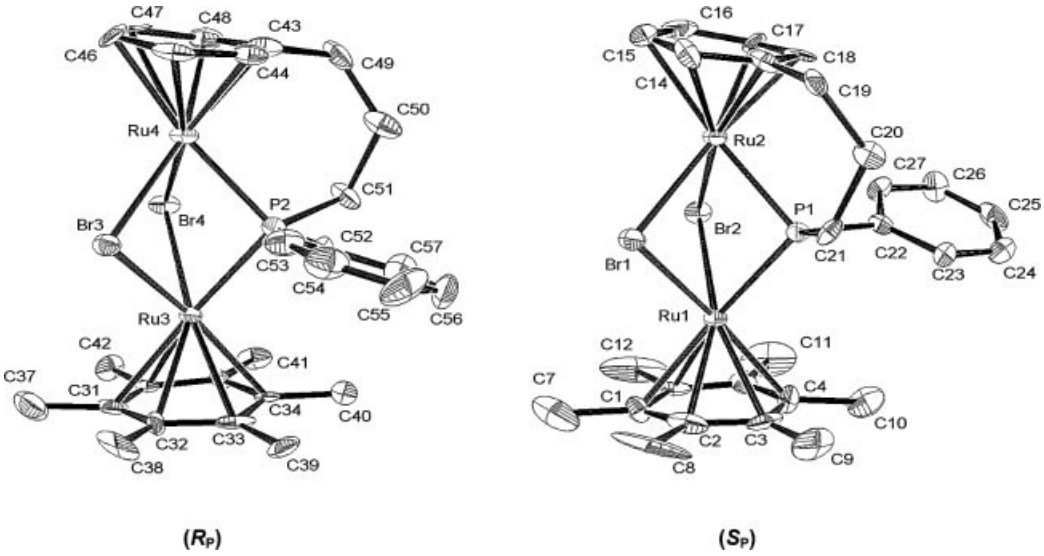


Figure 5. Molecular structure of the two independent enantiomers of cation **3** (anions and hydrogen atoms have been omitted for clarity).

Ru–Ru distances [3.3973(3) and 3.3764(3) Å] are well outside the range (2.28–2.95 Å) for a metal–metal single bond.[17] The phenyl rings of the η⁶-arene ligands are almost parallel, with an angle between the two planes of 8.8(7)° in ($R_P$)-**3** and 9.8(7)° in ($S_P$)-**3**. The *p*-cymene ligand in [**1**][$BF_4$] is replaced by the phenyl ring of the pendant arm of the phosphanido ligand upon formation of [**3**][$BF_4$], which gives rise to a six-membered metallacycle. Both enantiomers of **3** show a chair-like conformation for the six-membered metallacycles (see Figure 6).

Figure 6. Capped-stick representation of the chair-like conformation observed in cations ($R_P$)-**3** and ($S_P$)-**3**.

In order to obtain a mixture of diastereomers instead of a racemic mixture of enantiomers we decided to treat [(η⁶-$C_6Me_6$)(η⁶-*p*-*i*PrMe$C_6H_4$)$Ru_2$(μ₂-H)₃]⁺ with the enantiopure phosphane (*R*)-$PPh_2(CH_2)_2$CHMePh, which contains a stereogenic carbon center and is similar to the achiral analogue $PPh_2(CH_2)_3$Ph. Given the fact that racemization of the stereogenic carbon atom in this ligand was not observed during the synthesis of [$RuCl_2${η¹-(*R*)-$PPh_2(CH_2)_2$-CHMe-η⁶-Ph}],[8c] we can assume that the ($R_C$) configuration of (*R*)-$PPh_2(CH_2)_2$CHMePh also does not change in the reaction with the dinuclear trihydrido complex.

The trihydrido complex [(η⁶-$C_6Me_6$)(η⁶-*p*-*i*PrMe$C_6H_4$)-$Ru_2$(μ₂-H)₃]⁺ reacts with the enantiopure phosphane (*R*)-$PPh_2(CH_2)_2$CHMePh to give the cation [(η⁶-$C_6Me_6$)(η⁶-*p*-*i*PrMe$C_6H_4$)$Ru_2${μ₂-(*R*)-PPh$(CH_2)_2$CHMePh}(μ₂-H)₂]⁺ (**4**), which was obtained as a mixture of the two diastereomers ($R_C$,$R_P$)-**4** and ($R_C$,$S_P$)-**4** (Scheme 4). The reaction was carried out in dichloromethane at 55 °C under hydrogen (3 bar). The yield of 38% is similar to that for the synthesis of **1**. Unfortunately, we were not able to separate the two diastereomers either by crystallization or by chromatography on silica gel.

As no X-ray quality crystals of [**4**][$BF_4$] could be obtained, we treated the enantiopure phosphane (*R*)-$PPh_2(CH_2)_2$CHMePh with the bis(hexamethylbenzene) analogue [(η⁶-$C_6Me_6$)$_2Ru_2$(μ₂-H)₃]⁺ to obtain [(η⁶-$C_6Me_6$)$_2$-$Ru_2${μ₂-(*R*)-PPh$(CH_2)_2$CHMePh}(μ₂-H)₂]⁺ (**5**; Scheme 5).

The dark-red crystals of [**5**][$BF_4$] obtained by slow diffusion of diethyl ether into a concentrated solution of

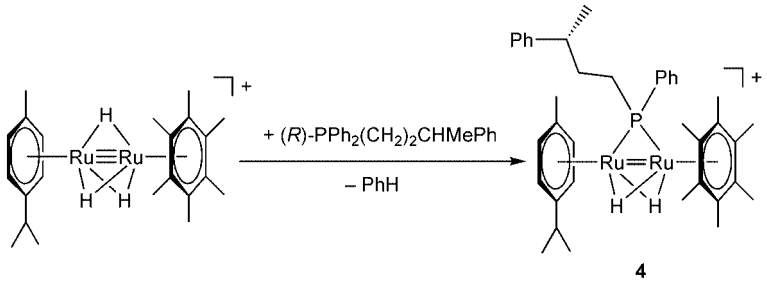


Scheme 4. Synthesis of [(η⁶-$C_6Me_6$)(η⁶-*p*-*i*PrMe$C_6H_4$)$Ru_2${μ₂-(*R*)-PPh$(CH_2)_2$CH-MePh}(μ₂-H)₂]⁺ (**4**).

 © 2007 Wiley-VCH Verlag GmbH & Co. KGaA, Weinheim 

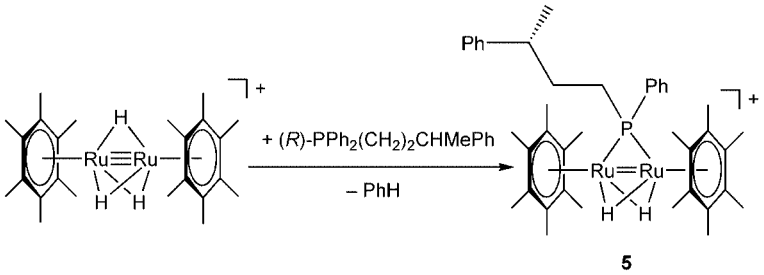


Scheme 5. Synthesis of $[(\eta^6\text{-}C_6Me_6)_2Ru_2\{\mu_2\text{-}(R)\text{-}PPh(CH_2)_2CHMePh\}(\mu_2\text{-}H)_2]^+$ (**5**).

[**5**][$BF_4$] in dichloromethane were found to be suitable for X-ray analysis. The molecular structure of cation **5** was confirmed by X-ray crystal structure analysis of its tetrafluoroborate salt (Figure 7).

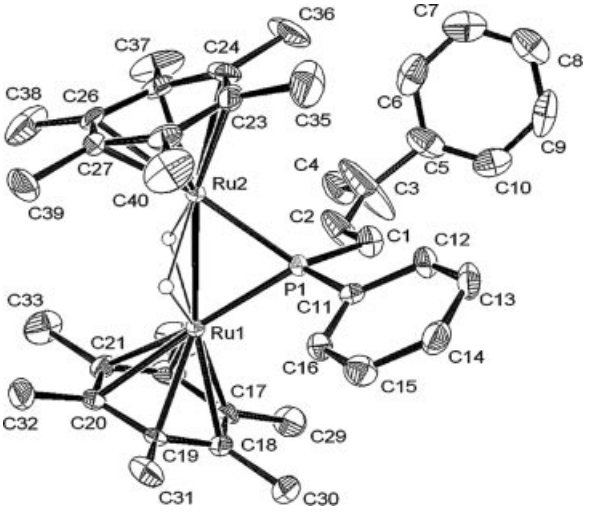


Figure 7. Molecular structure of cation **5** (anion and hydrogen atoms other than the hydrido ligands have been omitted for clarity).

The centrosymmetric space group $P2_1/c$ of [**5**][$BF_4$] suggests a racemic mixture of ($R_C$) and ($S_C$) enantiomers of **5** in the crystal. However, the stereogenic carbon atom (C3 in Figure 7) in **5** is highly disordered, as demonstrated by the exceptionally stretched ellipsoid along the C–H axis in the ORTEP plot (Figure 7), which may give rise to a centrosymmetric space group despite retention of the ($R_C$) configuration. The Ru–Ru distance [2.6346(8) Å] is similar to those observed in [**2**][$BF_4$] and remains within the range of a ruthenium–ruthenium double bond. As in [**2**][$BF_4$], the presence of a bridging phosphanido ligand forces the arene moieties to adopt a tilted geometry. The angle between the two $C_6Me_6$ planes is 38.8(2)°.

As the question of the enantiomeric purity of **5** could not be solved by X-ray crystallography because of the centrosymmetric space group ($P2_1/c$) and disorder problems, we used circular dichroism to find out whether or not the stereogenic carbon center in the side-chain has racemized during the synthesis of **5**, despite the known enantiostability of (*R*)-$PPh_2(CH_2)_2CHMePh$.[8c] Although the concentration-dependent CD signal at 350 nm (Figure 8) shows **5** to be optically active, which suggests that the stereogenic carbon center has (*R*) configuration, we cannot exclude partial racemization during the synthesis of this compound.

As in the case of **1**, the ligand exchange reaction between *p*-cymene and the phenyl substituent on the pendant arm

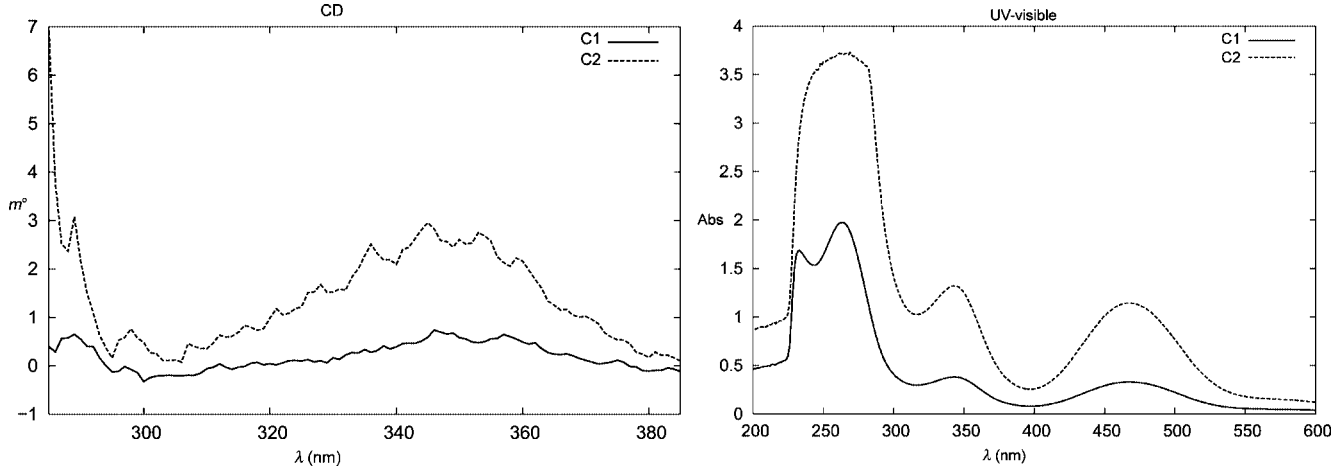


Figure 8. CD (left) and UV/Vis (right) spectra of [**5**][$BF_4$] recorded in $CH_2Cl_2$ at two different concentrations ($c_1 = 5.05 \times 10^{-4}$ M, $c_2 = 1.67 \times 10^{-3}$ M), $m° = 10^{-3}°$.

 © 2007 Wiley-VCH Verlag GmbH & Co. KGaA, Weinheim 

was achieved by heating of $[(\eta^6\text{-}C_6Me_6)(\eta^6\text{-}p\text{-}i\text{PrMeC}_6H_4)\text{-}Ru_2\{\mu_2\text{-}(R)\text{-}PPh(CH_2)_2CHMePh\}(\mu_2\text{-}H)_2]^+$ (**4**) at 150 °C in bromobenzene. This reaction also leads to the dibromido derivative $[(\eta^6\text{-}C_6Me_6)Ru_2\{\mu_2\text{-}(R)\text{-}PPh(CH_2)_2CHMe\text{-}\eta^6\text{-}Ph\}(\mu_2\text{-}Br)_2]^+$ (**6**; Scheme 6), which was obtained as a mixture of ($R_C$,$S_P$) and ($R_C$,$R_P$) diastereomers (Figure 9).

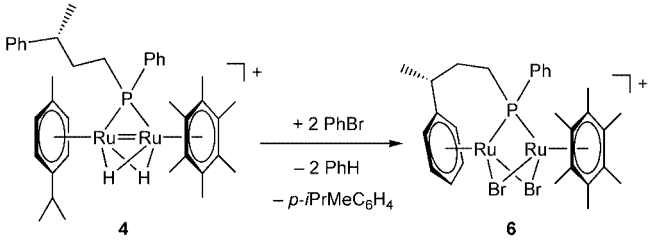


Scheme 6. Synthesis of $[(\eta^6\text{-}C_6Me_6)Ru_2\{\mu_2\text{-}(R)\text{-}PPh(CH_2)_2CHMe\text{-}\eta^6\text{-}Ph\}(\mu_2\text{-}Br)_2]^+$ (**6**).

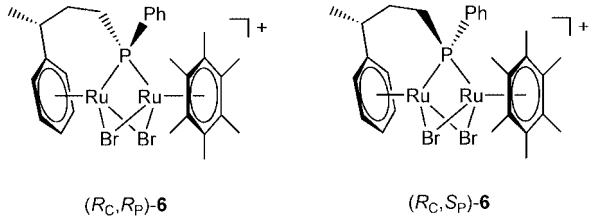


Figure 9. The two diastereomers ($R_C$,$R_P$)-**6** and ($R_C$,$S_P$)-**6**.

Single crystals suitable for an X-ray structure analysis were obtained by slow diffusion of diethyl ether into a concentrated acetone solution of [**6**][$BF_4$]. Examination of the structure with PLATON[18] revealed an ambiguity over the choice of the space group ($P1$ or $P\bar{1}$). Expecting a chiral molecule, resolution was performed in the noncentrosymmetric group $P1$. The structure was refined to convergence with a Flack parameter of 0.23(2). Both diastereomers, ($R_C$,$R_P$)-**6** and ($R_C$,$S_P$)-**6**, show the two ruthenium atoms to be in a distorted octahedral geometry in which the metal

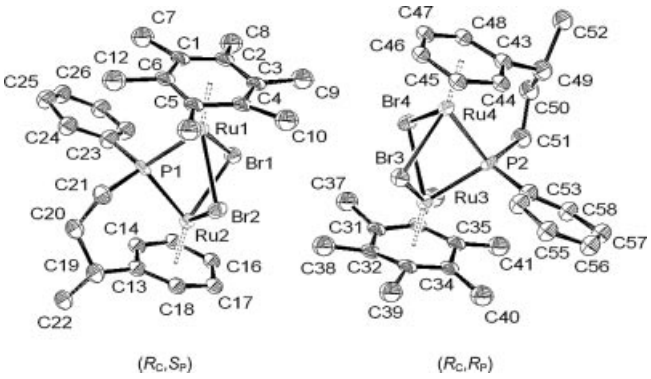


Figure 10. The molecular structure of the diastereomers of cation **6** (anions, solvent molecules, and hydrogen atoms have been omitted for clarity).

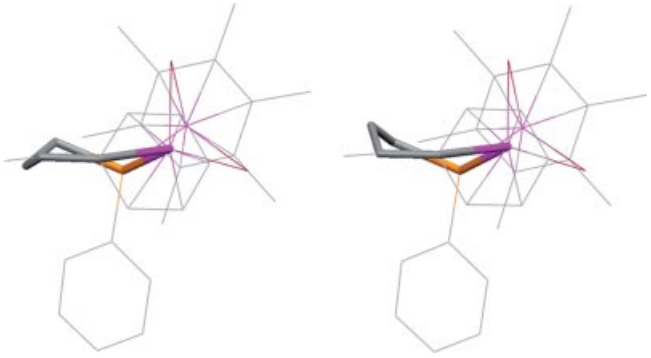

Figure 11. The chair-like (left) and half-twist-like (right) conformations in cation **6**.

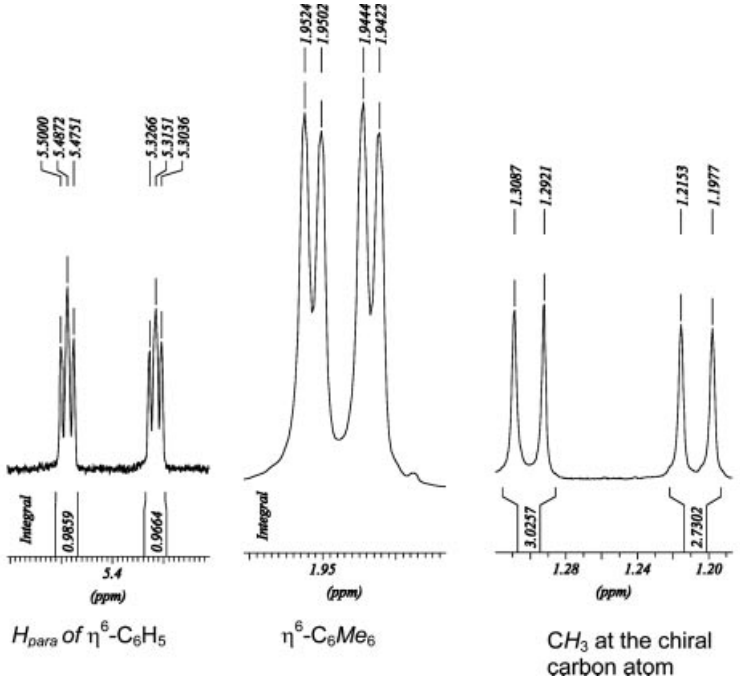


Figure 12. Selected $^1$H NMR signals ([$D_6$] acetone) of the diastereomeric mixture of [**6**][$BF_4$].

 © 2007 Wiley-VCH Verlag GmbH & Co. KGaA, Weinheim 

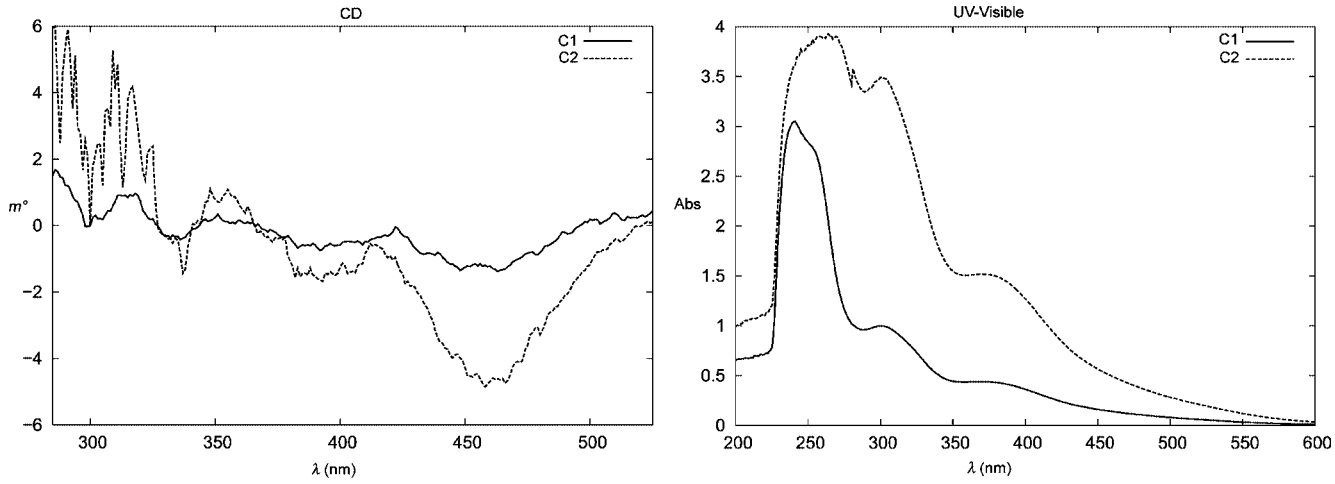


Figure 13. CD and UV/Vis spectra of [**6**][$BF_4$] at two different concentrations ($c_1 = 5.86 \times 10^{-4}$ M, $c_2 = 2.05 \times 10^{-3}$ M).

centers are bridged by a tethered phosphanido and two bromido ligands (Figure 10). The Ru–Br bond lengths (average 2.572 Å) and the Ru–Br–Ru angles (average 82.15°) are similar to those found in [**3**][$BF_4$]. Similarly, the Ru–Ru distances [identical at 3.380(2) Å] are similar to those observed in [**3**][$BF_4$]. The two $\eta^6$-arene ligands are almost parallel to each other in both molecules, with an angle between the two aromatic planes of 10.2(4)° for the ($R_C$,$S_P$) and 12.1(4)° for the ($R_C$,$R_P$) isomer. Replacement of the *p*-cymene ligand by a phenyl ring at the pendant arm of the phosphanido ligand in [**6**][$BF_4$] generates a six-membered metallacycle upon coordination. Surprisingly, two conformations are observed for the six-membered metallacycle, a chair-like ($R_C$,$S_P$) and a half-twist-like ($R_C$,$R_P$) conformation for the diastereomers of **6** (Figure 11).[19]

The two diastereomers ($R_C$,$S_P$)-**6** and ($R_C$,$R_P$)-**6** are distinguishable in the $^1$H NMR spectrum, which shows two doublets of almost equal intensity for the $\eta^6$-$C_6Me_6$ protons at $\delta$ = 1.95 and 1.94 ppm. As in **3**, the $^4J_{P,H}$ coupling (0.9 Hz) is also observable for the methyl protons of the $\eta^6$-$C_6Me_6$ ligand in **6** since the two arene ligands in this complex are almost parallel to each other. Accordingly, two signals are observed for the *para* protons of the $\eta^6$-$C_6H_5$ ligand [$\delta$ = 5.48 (t) and 5.31 ppm (t)] and for the methyl substituent at the stereogenic carbon atom [$\delta$ = 1.29 (d) and 1.20 (d) ppm]. The integration of the $^1$H NMR signals suggests that both diastereomers are present in almost equal quantities, with a slight excess of one (52:48; Figure 12). This diastereoselectivity (*de* = 4%) was confirmed by circular dichroism: The CD spectrum of [**6**][$BF_4$] in dichloromethane, recorded at two different concentrations, indeed shows a small concentration-dependent CD signal centered at 460 nm (Figure 13).

## Conclusions

We have synthesized several chiral-at-phosphorus phosphanidodiruthenium complexes and shown that an intramolecular ligand exchange between one arene ligand at the ruthenium atom and a phenyl substituent in the side-arm of the phosphanido bridge leads to chiral tethered derivatives. Introduction of a stereogenic carbon atom in the pendant arm of the phosphanido bridging ligand gives rise to the formation of diastereomeric complexes.

## Experimental Section

**General Remarks:** All manipulations were carried out under nitrogen using standard Schlenk techniques. All solvents were degassed with nitrogen prior to use. The silica gel (type G) used for preparative thin-layer chromatography was purchased from Macherey–Nagel GmbH. The phosphanes were synthesized according to previously described methods.[5,8c] The starting compounds [($\eta^6$-$C_6Me_6$)($\eta^6$-*p*-*i*PrMe$C_6H_4$)$Ru_2$($\mu_2$-H)$_3$][$BF_4$][13] and [($C_6Me_6$)$_2Ru_2$($\mu_2$-H)$_3$][$BF_4$][20] were synthesized according to previously described methods. Bromobenzene (puriss.) was purchased from Fluka, stored under nitrogen, and dried with molecular sieves (4 Å). Deuterated NMR solvents were purchased from Cambridge Isotope Laboratories, Inc. NMR spectra were recorded with a Bruker 400 MHz spectrometer. Mass spectra were recorded by Prof. Titus Jenny at the University of Fribourg. Microanalyses were carried out in the Laboratory of Pharmaceutical Chemistry at the University of Geneva.

**Synthesis of [($\eta^6$-$C_6Me_6$)($\eta^6$-*p*-*i*PrMe$C_6H_4$)$Ru_2${$\mu_2$-PPh($CH_2$)$_3$Ph}-($\mu_2$-H)$_2$][$BF_4$] [1][$BF_4$]:** [($\eta^6$-$C_6Me_6$)($\eta^6$-*p*-*i*PrMe$C_6H_4$)$Ru_2$($\mu_2$-H)$_3$]-[$BF_4$] (230 mg, 0.39 mmol) was dissolved in dichloromethane (250 mL) in a pressure Schlenk tube and the phosphane $PPh_2$-($CH_2$)$_3$Ph (178 mg, 0.58 mmol) was added. The solution was then flushed and pressurized with hydrogen (3 bar) and stirred at 55 °C under hydrogen pressure for 18 h. After cooling to room temperature, the solvent was evaporated to dryness and the brown product obtained was purified by preparative thin-layer chromatography on silica gel (acetone/dichloromethane, 1:10). The product was extracted from the silica with acetone from the brown band, and evaporation of the solvent gave the pure product (yield: 38%, 120 mg, 0.15 mmol). $^1$H NMR (400 MHz, [$D_6$]acetone, 25 °C): $\delta$ = 7.32–7.20 (m, 8 H, *H*-Ph), 7.04 (m, 2 H, *H*-Ph), 6.03 (t, $^3J_{H,H}$ = 5 Hz, 2 H, *H*-Ar *p*-cymene), 5.72 (d, $^3J_{H,H}$ = 5.9 Hz, 1 H, *H*-Ar *p*-cymene), 5.65 (d, $^3J_{H,H}$ = 6.2 Hz, 1 H, *H*-Ar *p*-cymene), 2.73 (m, 2 H, PPhC$H_2$C$H_2$C$H_2$Ph), 2.57 (m, 3 H, *H*-*i*Pr, PPhC$H_2$C$H_2$C$H_2$Ph), 2.11 [s, 18 H, $C_6$(Me)$_6$], 2.02 (s, 3 H,

 © 2007 Wiley-VCH Verlag GmbH & Co. KGaA, Weinheim 

$CH_3C_6H_4iPr$), 1.27 [t, $^3J_{H,H}$ = 7 Hz, 6 H, $CH(CH_3)_2$] 0.89 (m, 2 H, $PPhCH_2CH_2CH_2Ph$), –14.65 (dd, $^2J_{H,H}$ = 2.8, $^2J_{H,P}$ = 28 Hz, 1 H, hydride), –16.06 (dd, $^2J_{H,H}$ = 2.8, $^2J_{H,P}$ = 31 Hz, 1 H, hydride) ppm. $^{13}C\{^1H\}$ NMR (100 MHz, [D$_6$]acetone, 25 °C): $\delta$ = 142.7 (*C*-Ar), 142.1 (*C*-Ar), 132.67 (*C*-Ar), 132.5 (*C*-Ar), 129.6 (*C*-Ar), 129.6 (*C*-Ar), 129.4 (*C*-Ar), 129.3 (*C*-Ar), 129.2 (*C*-Ar), 128.37 (*C*-Ar), 128.2 (*C*-Ar), 126.7 (*C*-Ar), 99.2 (Me*i*Pr$C_6H_4$), 97.4 [$C_6$(Me)$_6$], 97.2 (Me*i*Pr$C_6H_4$), 85.3 (Me*i*Pr$C_6H_4$), 84.6 (Me*i*Pr$C_6H_4$), 82.8 (Me-*i*Pr$C_6H_4$), 81.5 (Me*i*Pr$C_6H_4$), 37.1 (d, $J_{C,P}$ = 18 Hz, $CH_2$), 32.7 ($CH_2$), 31.7 (d, $J_{C,P}$ = 6.4 Hz, $CH_2$), 23.7 [$CH(CH_3)_2$], 23.7 [$CH(CH_3)_2$], 20.3 ($C_6H_4CH_3$), 17.5 [$C_6(CH_3)_6$] ppm. $^{31}P\{^1H\}$ NMR (160 MHz, [D$_6$]acetone, 25 °C): $\delta$ = 114.62 (s) ppm. MS (ESI): *m*/*z* = 728 $[M + H]^+$. $C_{37}H_{50}BF_4PRu_2$ (814.71): calcd. C 54.54, H 6.18; found C 54.51, H 6.20.

**Synthesis of [($\eta^6$-$C_6Me_6$)$_2$Ru$_2${$\mu_2$-PPh(CH$_2$)$_3$Ph}($\mu_2$-H)$_2$][BF$_4$] [2][BF$_4$]:** [($\eta^6$-$C_6Me_6$)$_2$Ru$_2$($\mu_2$-H)$_3$][BF$_4$] (150 mg, 0.24 mmol) was dissolved in dichloromethane (200 mL) in a pressure Schlenk tube and the phosphane $PPh_2(CH_2)_3Ph$ (93 mg, 0.30 mmol) was added. The solution was then flushed and pressurized with hydrogen (3 bar) and stirred at 55 °C under hydrogen pressure for 18 h. After cooling to room temperature, the solvent was evaporated to dryness and the brown product obtained was purified by preparative thin-layer chromatography on silica gel (acetone/dichloromethane, 1:10). The product was extracted with acetone from the brown band, and evaporation of the solvent gave the pure product (yield: 85%, 172 mg, 0.20 mmol). Crystals suitable for X-ray structure analysis were obtained by diffusion of diethyl ether into a concentrated dichloromethane solution of [**2**][BF$_4$]. $^1H$ NMR (400 MHz, [D$_6$]acetone, 25 °C): $\delta$ = 7.38–7.20 (m, 8 H, *H*-Ph), 6.95 (m, 2 H, *H*-Ph), 2.78 (t, $^3J_{H,H}$ = 7.4 Hz, 2 H, $PPhCH_2CH_2CH_2Ph$), 2.55 (m, 2 H, $PPhCH_2CH_2CH_2Ph$), 2.17 [s, 18 H, $C_6(CH_3)_6$], 0.86 (m, 2 H, $PPhCH_2CH_2CH_2Ph$), –15.18 (dd, $^2J_{H,H}$ = 3, $^2J_{H,P}$ = 28 Hz, 1 H, hydride), –16.50 (dd, $^2J_{H,H}$ = 3, $^2J_{H,P}$ = 30 Hz, 1 H, hydride) ppm. $^{13}C\{^1H\}$ NMR (100 MHz, [D$_6$]acetone, 25 °C): $\delta$ = 142.4 (*C*-Ar), 132.1 (*C*-Ar), 132.0 (*C*-Ar), 128.9 (*C*-Ar), 128.8 (*C*-Ar), 128.0 (*C*-Ar), 127.9 (*C*-Ar), 126.3 (*C*-Ar), 96.9 [$C_6$(Me)$_6$], 36.7 (d, $J_{C,P}$ = 20 Hz, $CH_2$), 31.8 ($CH_2$), 31.52 (d, $J_{C,P}$ = 12 Hz, $CH_2$), 17.4 [$C_6(CH_3)_6$] ppm. $^{31}P\{^1H\}$ NMR (160 MHz, [D$_6$]acetone, 25 °C): $\delta$ = 101.73 (s) ppm. MS (ESI): *m*/*z* 756 $[M + H]^+$. $C_{39}H_{56}BF_4PRu_2$ (844.78): calcd. C 55.45, H 6.68; found C 55.39, H 6.61.

**Synthesis of [($\eta^6$-$C_6Me_6$)Ru$_2${$\mu_2$-PPh(CH$_2$)$_3$-$\eta^6$-Ph}($\mu_2$-Br)$_2$][BF$_4$] [3][BF$_4$]:** [($\eta^6$-$C_6Me_6$)($\eta^6$-*p*-*i*PrMe$C_6H_4$)Ru$_2${$\mu_2$-PPh(CH$_2$)$_3$Ph}($\mu_2$-H)$_2$][BF$_4$] (120 mg, 0.15 mmol) was dissolved in bromobenzene (25 mL) that had been dried with molecular sieves (4 Å) and saturated with nitrogen prior to use. The solution was heated at 150 °C for 20 h. After cooling to room temperature, the solvent was evaporated to dryness in a trap-to-trap apparatus. The brown-red product obtained was purified by preparative thin-layer chromatography on silica gel (acetone/dichloromethane, 1:10). The product was extracted with acetone from the lowest major orange band ($R_f$ = 0.4). Evaporation of the solvent gave the pure product (yield: 30%, 38 mg, 0.045 mmol). Crystals suitable for X-ray structure analysis were obtained by slow diffusion of diethyl ether into a concentrated acetone solution of [**3**][BF$_4$]. $^1H$ NMR (400 MHz, [D$_6$]acetone, 25 °C): $\delta$ = 7.96 (br., 2 H, P-*Ph*), 7.53 (m, 3 H, P-*Ph*), 6.25 (m, 2 H, *H-ortho* $\eta^6$-*Ph*), 5.43 (t, $^3J_{H,H}$ = 4.8 Hz, 1 H, *H-para* $\eta^6$-*Ph*), 5.04 (m, 2 H, *H-meta* $\eta^6$-*Ph*), 3.44 (m, 1 H, $CH_2$), 3.05 (td, $^3J_{H,H}$ = 3.7, $^2J_{H,H}$ = 15.3 Hz, 1 H, $CH_2$), 2.58 (m, 1 H, $CH_2$), 2.38 (m, 1 H, $CH_2$), 1.98 (m, 1 H, $CH_2$), 1.94 [d, $^4J_{P,H}$ = 1 Hz, 18 H, $C_6(CH_3)_6$], 1.40 (m, 1 H, $CH_2$) ppm. $^{13}C\{^1H\}$ NMR (100 MHz, [D$_6$]acetone, 25 °C): $\delta$ = 136.6 (P-*Ph*), 136.4 (P-*Ph*), 130.6 (P-*Ph*), 130.6 (P-*Ph*), 129.2 (P-*Ph*), 129.1 (P-*Ph*), 99.2 ($\eta^6$-*Ph*), 94.9 ($\eta^6$-*Ph*), 93.8 [$C_6(CH_3)_6$], 84.9 ($\eta^6$-*Ph*), 82.0 ($\eta^6$-*Ph*), 81.7 ($\eta^6$-*Ph*), 72.5 ($\eta^6$-*Ph*), 30.2 (d, $J_{C,P}$ = 33 Hz, $CH_2$), 24.5 (d, $J_{C,P}$ = 7 Hz, $CH_2$), 20.2 (d, $J_{C,P}$ = 16 Hz, $CH_2$), 15.3 [$C_6(CH_3)_6$] ppm. $^{31}P\{^1H\}$ NMR (160 MHz, [D$_6$]acetone, 25 °C): $\delta$ = –14.53 (s) ppm. MS (ESI): *m*/*z* = 752 $[M + H]^+$. $C_{27}H_{34}BBr_2F_4PRu_2$ (838.29): calcd. C 38.68, H 4.08; found C 38.75, H 4.16.

**Synthesis of [($\eta^6$-$C_6Me_6$)($\eta^6$-*p*-*i*PrMe$C_6H_4$)Ru$_2${$\mu_2$-(*R*)-PPh(CH$_2$)$_2$-CHMePh}($\mu_2$-H)$_2$][BF$_4$] [4][BF$_4$]:** Synthesis of this complex followed the procedure described for [**1**][BF$_4$] but with [($\eta^6$-$C_6Me_6$)($\eta^6$-*p*-*i*PrMe$C_6H_4$)Ru$_2$($\mu_2$-H)$_3$][BF$_4$] (260 mg, 0.44 mmol) and (*R*)-$PPh_2(CH_2)_2CHMePh$ (210 mg, 0.66 mmol) as starting materials. The product was extracted from the brown band with acetone, and evaporation of the solvent gave the pure product (yield: 38%, 138 mg, 0.17 mmol). $^1H$ NMR (400 MHz, [D$_6$]acetone, 25 °C): $\delta$ = 7.32 (m, 16 H, *H*-Ph), 6.98 (m, 4 H, *H*-Ph β of P), 6.09 (d, $^3J_{H,H}$ = 6 Hz, 1 H, *p*-*i*PrMe$C_6H_4$), 6.04 (d, $^3J_{H,H}$ = 5.4 Hz, 1 H, *p*-*i*PrMe$C_6H_4$), 5.98 (d, $^3J_{H,H}$ = 5.4 Hz, 1 H, *p*-*i*PrMe$C_6H_4$), 5.95 (d, $^3J_{H,H}$ = 6 Hz, 1 H, *p*-*i*PrMe$C_6H_4$), 5.75 (d, $^3J_{H,H}$ = 6 Hz, 1 H, *p*-*i*PrMe$C_6H_4$), 5.70 (t, $^3J_{H,H}$ = 6.6 Hz, 1 H, *p*-*i*PrMe$C_6H_4$), 5.64 (d, $^3J_{H,H}$ = 5.8 Hz, 1 H, *p*-*i*PrMe$C_6H_4$), 2.88 [m, 2 H, $MeC_6H_4CH(CH_3)_2$], 2.7–2.2 [m, 6 H, $PhCH(CH_3)CH_2CH_2PPh_2$], 2.13 [s, 18 H, $C_6(CH_3)_6$], 2.06 [s, 18 H, $C_6(CH_3)_6$], 2.02 [s, 3 H, $MeC_6H_4CH(CH_3)_2$], 1.98 [s, 3 H, $MeC_6H_4CH(CH_3)_2$], 1.28 [m, 18 H, $MeC_6H_4CH(CH_3)_2$, $PhCH(CH_3)CH_2CH_2PPh_2$], 1.25–0.7 [m, 4 H, $PhCH(CH_3)CH_2CH_2PPh_2$], –14.68 (td, $^2J_{H,H}$ = 2.8, $^2J_{H,P}$ = 27.6 Hz, 2 H, hydride), –16.04 (dd, $^2J_{H,H}$ = 2.8, $^2J_{H,P}$ = 30.7 Hz, 1 H, hydride), –16.10 (dd, $^2J_{H,H}$ = 2.8, $^2J_{H,P}$ = 30.9 Hz, 1 H, hydride) ppm. $^{13}C\{^1H\}$ NMR (100 MHz, [D$_6$]acetone, 25 °C): $\delta$ = 147.2 (*C*-Ar), 147.2 (*C*-Ar), 141.7 (*C*-Ar), 141.5 (*C*-Ar), 132.2 (*C*-Ar), 132.1 (*C*-Ar), 129.2 (*C*-Ar), 129.2 (*C*-Ar), 128.8 (*C*-Ar), 128.8 (*C*-Ar), 127.9 (*C*-Ar), 127.8 (*C*-Ar), 127.5 (*C*-Ar), 127.3 (*C*-Ar), 126.6 (*C*-Ar), 113.3 (*C*-Ar), 98.8 (Me*i*Pr$C_6H_4$), 98.3 (Me*i*Pr$C_6H_4$), 97.1 [$C_6(CH_3)_6$], 97.0 [$C_6(CH_3)_6$], 96.8 (Me*i*Pr$C_6H_4$), 85.2 (Me*i*Pr$C_6H_4$), 84.8 (Me*i*Pr$C_6H_4$), 84.2 (Me*i*Pr$C_6H_4$), 83.9 (Me*i*Pr$C_6H_4$), 82.9 (Me*i*Pr$C_6H_4$), 81.2 (Me*i*Pr$C_6H_4$), 81.1 (Me*i*Pr$C_6H_4$), 41.1 (*C*HMe), 40.9 (d, $J_{C,P}$ = 4.3 Hz, $CH_2$), 38.2 (d, $J_{C,P}$ = 21 Hz, $CH_2$), 32.3 [$CH(CH_3)_2$], 23.3 [$CH(CH_3)$], 23.3 [$CH(CH_3)_2$], 21.5 [$CH(CH_3)_2$], 21.2 ($C_6H_4CH_3$), 20.0 [$CH(CH_3)$],17.2 [$C_6(CH_3)_6$], 17.2 [$C_6(CH_3)_6$] ppm. $^{31}P\{^1H\}$ NMR (160 MHz, [D$_6$]acetone, 25 °C): $\delta$ = 114.82 (s), 114.73 (s) ppm. MS (ESI): *m*/*z* = 742 $[M + H]^+$. $C_{38}H_{54}BF_4PRu_2$ (830.75): calcd. C 54.93, H 6.55; found C 55.09, H 6.72.

**Synthesis of [($\eta^6$-$C_6Me_6$)$_2$Ru$_2${$\mu_2$-(*R*)-PPh(CH$_2$)$_2$CHMePh}($\mu_2$-H)$_2$][BF$_4$] [5][BF$_4$]:** Synthesis of this complex followed the procedure described for [**2**][BF$_4$] but with [($\eta^6$-$C_6Me_6$)$_2$Ru$_2$($\mu_2$-H)$_3$][BF$_4$] (100 mg, 0.16 mmol) and (*R*)-$PPh_2(CH_2)_2CHMePh$ (57 mg, 0.18 mmol) as starting materials. The product was extracted from the brown band with acetone, and evaporation of the solvent gave the pure product (yield: 86%, 117 mg, 0.14 mmol). Crystals suitable for X-ray structure analysis were obtained by slow diffusion of diethyl ether into a concentrated acetone solution of [**5**][BF$_4$]. $^1H$ NMR (400 MHz, [D$_2$]dichloromethane, 25 °C): $\delta$ = 7.36–7.17 (m, 8 H, *H*-Ph), 6.75 (m, 2 H, *H*-Ph), 2.76 [q, $^3J_{H,H}$ = 7 Hz, 1 H, $PhCH(CH_3)(CH_2)_2PPh_2$], 2.40–2.10 [m, 2 H, $PhCH(CH_3)CH_2CH_2PPh_2$], 2.13 [s, 18 H, $C_6(CH_3)_6$], 2.05 [s, 18 H, $C_6(CH_3)_6$], 1.29 [d, $^3J_{H,H}$ = 7 Hz, 3 H, $PPhCH(CH_3)CH_2CH_2Ph$] 0.65 [m, 2 H, $PPhCH(CH_3)CH_2CH_2Ph$], –15.28 (dd, $^2J_{H,H}$ = 3, $^2J_{H,P}$ = 28.1 Hz, 1 H, hydride), –16.67 (dd, $^2J_{H,H}$ = 3, $^2J_{H,P}$ = 31.3 Hz, 1 H, hydride) ppm. $^{13}C\{^1H\}$ NMR (100 MHz, [D$_6$]acetone, 25 °C): $\delta$ = 147.3 (*Ph*), 140.8 (*Ph*), 132.1 (*Ph*), 132.0 (*Ph*), 128.9 (*Ph*), 128.8 (*Ph*), 128.0 (*Ph*), 127.9 (*Ph*), 127.3 (*Ph*), 126.6 (*Ph*), 96.9 [$C_6$-$(CH_3)_6$], 41.1 (d, $J_{C,P}$ = 18 Hz, $CH_2$), 41.0 (*C*H), 38.2 (d, $J_{C,P}$ = 8 Hz, $CH_2$), 21.2 [$CH(CH_3)$] 17.4 [$C_6(CH_3)_6$], 17.3 [$C_6(CH_3)_6$] ppm. $^{31}P\{^1H\}$ NMR (160 MHz, [D$_6$]acetone, 25 °C): $\delta$ = 102.33 (s) ppm.

 © 2007 Wiley-VCH Verlag GmbH & Co. KGaA, Weinheim 

Table 1. Crystallographic and selected experimental data for [**2**][$BF_4$]·0.5$CH_2Cl_2$, [**3**][$BF_4$], [**5**][$BF_4$], and [**6**][$BF_4$]·$(CH_3)_2CO$.

| | [**2**][$BF_4$]·0.5$CH_2Cl_2$ | [**3**][$BF_4$] | [**5**][$BF_4$] | [**6**][$BF_4$]·$(CH_3)_2CO$ |
|---|---|---|---|---|
| Empirical formula | $C_{39.5}H_{55}BClF_4PRu_2$ | $C_{27}H_{34}BBr_2F_4PRu_2$ | $C_{40}H_{56}BF_4PRu_2$ | $C_{31}H_{42}BBr_2F_4OPRu_2$ |
| Formula mass | 885.21 | 838.28 | 856.77 | 910.39 |
| Crystal system | orthorhombic | triclinic | monoclinic | triclinic |
| Space group | $Pca2_1$ | $P\bar{1}$ | $P2_1/c$ | $P1$ |
| Crystal color and shape | red block | orange plate | red plate | red block |
| Crystal size | 0.85 × 0.28 × 0.12 | 0.48 × 0.20 × 0.07 | 0.40 × 0.28 × 0.10 | 0.46 × 0.28 × 0.12 |
| $a$ [Å] | 18.7393(15) | 10.4799(11) | 10.756(2) | 10.4690(9) |
| $b$ [Å] | 20.0175(10) | 16.6813(17) | 20.776(4) | 11.3906(9) |
| $c$ [Å] | 20.8971(18) | 18.038(2) | 17.745(4) | 15.5091(13) |
| $\alpha$ [°] | | 99.150(15) | | 95.506(10) |
| $\beta$ [°] | | 105.969(14) | 104.29(3) | 101.751(10) |
| $\gamma$ [°] | | 102.461(12) | | 110.354(9) |
| $V$ [Å$^3$] | 7838.8(10) | 2879.1(5) | 3842.7(13) | 1669.4(2) |
| $Z$ | 8 | 4 | 4 | 2 |
| $T$ [K] | 173(2) | 173(2) | 173(2) | 173(2) |
| $D_c$ [g cm$^{-3}$] | 1.500 | 1.934 | 1.481 | 1.811 |
| $\mu$ [mm$^{-1}$] | 0.926 | 3.923 | 0.874 | 3.393 |
| Scan range [°] | $4.62 < 2\theta < 54.18$ | $3.92 < 2\theta < 51.96$ | $4.74 < 2\theta < 51.64$ | $4.32 < 2\theta < 51.98$ |
| Unique reflections | 11455 | 9529 | 5612 | 10511 |
| Reflections used [$I > 2\sigma(I)$] | 2657 | 3436 | 3860 | 8765 |
| $R_{int}$ | 0.0766 | 0.0739 | 0.0484 | 0.0495 |
| Final $R$ indices [$I > 2\sigma(I)$][a] | 0.0464, $wR_2$ 0.0713 | 0.0467, $wR_2$ 0.0748 | 0.0511, $wR_2$ 0.1468 | 0.0635, $wR_2$ 0.1659 |
| $R$ indices (all data) | 0.2138, $wR_2$ 0.1234 | 0.1615, $wR_2$ 0.0899 | 0.0789, $wR_2$ 0.1620 | 0.0760, $wR_2$ 0.2010 |
| Goodness-of-fit | 0.469 | 0.672 | 1.033 | 1.096 |
| Max/min $\Delta\rho$/e [Å$^{-3}$] | 0.441, –0.499 | 1.225, –1.183 | 0.763, –0.845 | 1.640, –3.755 |

[a] Structures were refined on $F_o^2$: $wR_2 = \{\Sigma[w(F_o^2 - F_c^2)^2]/\Sigma w(F_o^2)^2\}^{1/2}$, where $w^{-1} = [\Sigma(F_o^2) + (aP)^2 + bP]$ and $P = [\max(F_o^2,0) + 2F_c^2]/3$.

MS (ESI): $m/z$ = 770 [M + H]$^+$. $C_{40}H_{56}BF_4PRu_2$ (856.79): calcd. C 56.07, H 6.58; found C 56.03, H 6.51.

**Synthesis of [(η$^6$-$C_6Me_6$)$Ru_2${μ$_2$-(*R*)-PPh($CH_2$)$_2$CHMe-η$^6$-Ph}(μ$_2$-Br)$_2$][$BF_4$] [6][$BF_4$]:** Synthesis of this complex followed the procedure described for [**3**][$BF_4$] but with [(η$^6$-$C_6Me_6$)(η$^6$-*p*-*i*PrMe-$C_6H_4$)$Ru_2${μ$_2$-(*R*)-PPh($CH_2$)$_2$CHMePh}(μ$_2$-H)$_2$][$BF_4$] (110 mg, 0.13 mmol) as starting material. The product was extracted from the lowest main orange band ($R_f$ = 0.4) with acetone and evaporation of the solvent gave the pure product (yield: 40%, 45 mg, 0.053 mmol). Crystals suitable for X-ray structure analysis were obtained by slow diffusion of diethyl ether into a concentrated acetone solution of [**6**][$BF_4$]. $^1$H NMR (400 MHz, [D$_6$]acetone, 25 °C): $\delta$ = 7.97 (br., 4 H, P-*Ph*), 7.54 (m, 6 H, P-*Ph*), 6.25 (m, 4 H, η$^6$-*Ph*), 5.47 (t, $^3J_{H,H}$ = 4.9 Hz, 1 H, η$^6$-*Ph*), 5.30 (t, $^3J_{H,H}$ = 4.5 Hz, 1 H, η$^6$-*Ph*), 5.05 (m, 4 H, η$^6$-*Ph*), 3.52 (m, 1 H, C*H*$_2$), 3.27 (m, 1 H, C*H*$_2$), 2.98 (m, 1 H, C*H*), 2.70–2.0 (m, 5 H, C*H*, C*H*$_2$), 1.95 [d, $^4J_{P,H}$ = 0.9 Hz, 18 H, $C_6(CH_3)_6$], 1.94 [d, $^4J_{P,H}$ = 0.9 Hz, 18 H, $C_6(CH_3)_6$], 1.64 (m, 1 H, C*H*$_2$), 1.52 (m, 1 H, C*H*$_2$), 1.29 (d, $^3J_{H,H}$ = 6.6 Hz, 3 H, C*H*$_3$), 1.20 (d, $^3J_{H,H}$ = 7 Hz, 3 H, C*H*$_3$) ppm. $^{13}$C{$^1$H} NMR (100 MHz, [D$_6$]acetone, 25 °C): $\delta$ = 137.6 (P-*Ph*), 137.6 (P-*Ph*), 134.0 (br., P-*Ph*), 132.6 (P-*Ph*), 132.0 (P-*Ph*), 131.7 (P-*Ph*), 130.2, 130.2 (br., P-*Ph*), 130.0 (P-*Ph*), 129.9 (P-*Ph*), 129.3 (P-*Ph*), 128.5 (P-*Ph*), 99.0 (η$^6$-*Ph*), 96.1 (η$^6$-*Ph*), 94.9 [*C*$_6$(CH$_3$)$_6$], 90.7 (η$^6$-*Ph*), 90.3 (η$^6$-*Ph*), 83.8 (η$^6$-*Ph*), 82.2 (η$^6$-*Ph*), 81.9 (η$^6$-*Ph*), 78.1 (η$^6$-*Ph*), 75.0 (η$^6$-*Ph*), 73.5 (η$^6$-*Ph*), 72.7 (η$^6$-*Ph*), 39.1 (*C*H$_2$), 34.2 (d, $J_{C,P}$ = 15 Hz, *C*H$_2$), 31.8 (*C*H), 29.1, 24.5 [CH(*C*H$_3$)], 23.5, 20.0, 16.4 [$C_6(CH_3)_6$] ppm. $^{31}$P{$^1$H} NMR (160 MHz, [D$_6$]acetone, 25 °C): $\delta$ = –8.71 (s), –9.82 (s) ppm. MS (ESI): $m/z$ = 766 [M + H]$^+$. $C_{28}H_{36}BBr_2F_4PRu_2$ (852.31): calcd. C 39.45, H 4.26; found C 39.65, H 4.45.

**X-ray Crystallographic Study:** Crystals of [**2**][$BF_4$]·0.5$CH_2Cl_2$, [**3**][$BF_4$], [**5**][$BF_4$], and [**6**][$BF_4$]·$(CH_3)_2CO$ were mounted individually on a Stoe Image Plate Diffraction system equipped with a φ circle goniometer, using graphite-monochromated Mo-$K_\alpha$ radiation ($\lambda$ = 0.71073 Å). Data were collected in the φ range 0–200°, with increments of 1.2°, 1.5°, 1.0° and 1.0°, respectively, in the 2$\theta$ range from 2.0–26° ($D_{max}$–$D_{min}$ = 12.45–0.81 Å). The structures were solved by direct methods using the program SHELXS-97.[21] Refinement and all further calculations were carried out using SHELXL-97.[22] The H atoms were included in calculated positions and treated as riding atoms using the SHELXL default parameters in all cases. The non-H atoms were refined anisotropically, using weighted full-matrix least squares on $F^2$. Crystallographic details are summarized in Table 1. Figures 2, 5, 7, and 10 were drawn with ORTEP,[23] while Figures 3, 6, and 11 were produced with the program MERCURY.[24] CCDC-629980 ([**2**][$BF_4$]·0.5$CH_2Cl_2$), -629981 ([**3**][$BF_4$]), -629982 ([**5**][$BF_4$]), and -629983 {[**6**][$BF_4$]·$(CH_3)_2CO$} contain the supplementary crystallographic data for this paper. These data can be obtained free of charge from The Cambridge Crystallographic Data Centre via www.ccdc.cam.ac.uk/data_request/cif.

## Acknowledgments

Financial support from the Fond National Suisse de la Recherche Scientifique is gratefully acknowledged. The authors are also indebted to the Johnson Mathey Technology Centre for a loan of ruthenium trichloride hydrate and to Professor H. Stoeckli-Evans for free access to X-ray facilities.

[1] a) M. A. Bennett, *Comprehensive Organometallic Chemistry II*, Pergamon Press, Oxford, **1995**, vol. 7, p. 549; b) H. Le Bozec, D. Touchard, P. H. Dixneuf, *Adv. Organomet. Chem.* **1989**, *29*, 163–247.

[2] a) K. J. Haack, S. Hashigushi, A. Fujii, T. Ikariya, R. Noyori, *Angew. Chem.* **1997**, *109*, 297–300; *Angew. Chem. Int. Ed. Engl.* **1997**, *36*, 285–288; b) R. Noyori, M. Yamakawa, S. Hashigushi, *J. Org. Chem.* **2001**, *66*, 7931–7944; c) D. G. I. Petra, J. N. H.

 © 2007 Wiley-VCH Verlag GmbH & Co. KGaA, Weinheim 

Reek, J. W. Handgraaf, E. J. Meijer, P. Dierkes, P. C. J. Kramer, J. Brussee, H. E. Schoemaker, P. W. N. M. van Leeuwen, *Chem. Eur. J.* **2000**, *6*, 2818–2829; d) S. Ogo, T. Abura, Y. Watanabe, *Organometallics* **2002**, *21*, 2964–2969; e) S. Ogo, K. Uehara, T. Abura, Y. Watanabe, S. Fukuzumi, *Organometallics* **2004**, *23*, 3047–3052; f) J. Canivet, L. Karmazin-Brelot, G. Süss-Fink, *J. Organomet. Chem.* **2005**, *690*, 3202–3211; g) J. Canivet, G. Labat, H. Stoeckli-Evans, G. Süss-Fink, *Eur. J. Inorg. Chem.* **2005**, 4493–4500; h) J. Hannedouche, G. J. Clarkson, M. Wills, *J. Am. Chem. Soc.* **2004**, *126*, 986–987; i) D. J. Cross, I. Houson, A. M. Kawamoto, M. Wills, *Tetrahedron Lett.* **2004**, *45*, 843–846; j) D. Sterk, M. S. Stephan, B. Mohar, *Tetrahedron Lett.* **2004**, *45*, 535–537; k) K. Everaere, A. Mortreux, M. Bulliard, J. Brussee, A. van der Gen, G. Nowogrocki, J.-F. Carpentier, *Eur. J. Org. Chem.* **2001**, 275–291; l) A. M. Maj, K. M. Pietrusiewicz, I. Suisse, F. Agbossou, A. Mortreux, *J. Organomet. Chem.* **2001**, *626*, 157–160; m) K. Everaere, A. Mortreux, J.-F. Carpentier, *Adv. Synth. Catal.* **2003**, *345*, 67–77.

[3] a) D. Jan, L. Delaude, F. Simal, A. Demonceau, *J. Organomet. Chem.* **2000**, *606*, 55–64; b) R. Castarlenas, M. Eckert, P. H. Dixneuf, *Angew. Chem.* **2005**, *117*, 2632–2635; *Angew. Chem. Int. Ed.* **2005**, *44*, 2576–2579.

[4] J. W. Faller, A. Lavoie, *J. Organomet. Chem.* **2001**, *630*, 17–22.

[5] P. D. Smith, A. H. Wright, *J. Organomet. Chem.* **1998**, *559*, 141–147.

[6] B. Therrien, T. R. Ward, M. Pilkington, C. Hoffman, F. Gilardoni, J. Weber, *Organometallics* **1998**, *17*, 330–337.

[7] a) Y. Miyaki, T. Onishi, I. Kurosawa, *Inorg. Chim. Acta* **2000**, *300–302*, 369–377; b) G. Marconi, H. Baier, F. W. Heinemann, P. Pinto, H. Pritzkow, U. Zenneck, *Inorg. Chim. Acta* **2003**, *352*, 188–200; c) T. Ohnishi, Y. Miyaki, H. Asano, H. Kurosawa, *Chem. Lett.* **1999**, *28*, 809–810.

[8] a) B. Therrien, T. R. Ward, *Angew. Chem.* **1999**, *111*, 418–421; *Angew. Chem. Int. Ed.* **1999**, *38*, 405–408; b) B. Therrien, A. König, T. R. Ward, *Organometallics* **1999**, *18*, 1565–1568; c) P. Pinto, G. Marconi, F. W. Heinemann, U. Zenneck, *Organometallics* **2004**, *23*, 374–380; d) K. Umezawa-Vizzini, I. Y. Guzman-Jimenez, K. H. Whitmire, T. R. Lee, *Organometallics* **2003**, *22*, 3059–3065; e) J. W. Faller, P. P. Fontaine, *Organometallics* **2005**, *24*, 4132–4138; f) V. Cadierno, J. Diez, J. Garcia-Alvarez, J. Gimeno, *Chem. Commun.* **2004**, 1820–1821; g) J. W. Faller, D. G. D′Alliessi, *Organometallics* **2003**, *22*, 2749–2757; h) P. D. Smith, T. Geldrich, M. B. Hursthouse, *J. Organomet. Chem.* **2002**, *659*, 1–9; i) K. Umezawa-Vizzini, T. R. Lee, *Organometallics* **2003**, *22*, 3066–3076; j) P. Pinto, A. W. Götz, G. Marconi, B. A. Hess, A. Marinetti, F. W. Heinemann, U. Zenneck, *Organometallics* **2006**, *25*, 2607–2616.

[9] R. Y. C. Shin, G. K. Tan, L. L. Koh, L. Y. Goh, *Organometallics* **2004**, *23*, 6293–6298.

[10] a) T. J. Geldbach, G. Laurenczy, R. Scopelliti, P. J. Dyson, *Organometallics* **2006**, *25*, 733–742; b) A. M. Hayes, D. J. Morris, G. J. Clarkson, M. Wills, *J. Am. Chem. Soc.* **2005**, *127*, 7318–7319; c) H. Brunner, C. Valerio, M. Zabel, *New J. Chem.* **2000**, *24*, 275–279.

[11] M. J.-L. Tschan, F. Chérioux, L. Karmazin-Brelot, G. Süss-Fink, *Organometallics* **2005**, *24*, 1974–1981.

[12] M. J.-L. Tschan, G. Süss-Fink, F. Chérioux, B. Therrien, *Chem. Eur. J.* **2007**, *13*, 292–299.

[13] L. Vieille-Petit, G. Süss-Fink, B. Therrien, T. R. Ward, H. Stoeckli-Evans, G. Labat, L. Karmazin-Brelot, A. Neels, T. Bürgi, R. G. Finke, C. M. Hagen, *Organometallics* **2005**, *24*, 6104–6119.

[14] H. Werner, R. Werner, *J. Organomet. Chem.* **1979**, *174*, C67–C69.

[15] H. Werner, H. Kletzin, *J. Organomet. Chem.* **1982**, *228*, 289–300.

[16] A. C. da Silva, H. Piotrowski, P. Mayer, K. Polborn, K. Severin, *J. Chem. Soc. Dalton Trans.* **2000**, 2960–2963.

[17] K. Mashima, A. Mikami, A. Nakamura, *Chem. Lett.* **1992**, 1795–1798.

[18] A. L. Spek, *J. Appl. Crystallogr.* **2003**, *36*, 7–13.

[19] F. A. Carey, R. J. Sundberg, *Advanced Organic Chemistry Part A: Structure and Mechanisms*, 2nd ed., Plenum Press, New York **1984**, p. 113.

[20] M. Jahncke, G. Meister, G. Rheinwald, H. Stoeckli-Evans, G. Süss-Fink, *Organometallics* **1997**, *16*, 1137–1143.

[21] G. M. Sheldrick, *Acta Crystallogr., Sect. A* **1990**, *46*, 467–473.

[22] G. M. Sheldrick, *SHELXL-97*, University of Göttingen, Germany **1999**.

[23] L. J. Farrugia, *J. Appl. Crystallogr.* **1997**, *30*, 565.

[24] I. J. Bruno, J. C. Cole, P. R. Edgington, M. Kessler, C. F. Macrae, P. McCabe, J. Pearson, R. Taylor, *Acta Crystallogr., Sect. B* **2002**, *58*, 389–397.

Received: December 11, 2006
Published Online: June 6, 2007

 © 2007 Wiley-VCH Verlag GmbH & Co. KGaA, Weinheim 

DOI: 10.1002/ejic.200700113

# Coordinated 1,3-Diyne Diols as Organometallic Building Blocks for Large Macrocycles Containing Oxygen and Unsaturated Donor Units

**Louisa J. Hope-Weeks,*[a] Martin J. Mays,[b] and Gregory A. Solan*[c]**

**Keywords:** Macrocycles / Cobalt complexes / Oxygen / Alkynes / Nicholas reaction

The acid-catalysed reaction of [{$Co_2(CO)_6$(μ-η²-$HOCH_2C_2$-)}$_2$] (**1a**) with a range of alkyl diols has been examined as means of preparing large crown-type macrocycles (up to twenty eight-membered) containing at least one coordinated 1,3-diyne unit, multiple oxygen atoms and a variety of soft donor units. Thus, interaction of **1a** with $HOCH_2(CH_2)_nCH_2OH$, allows access to the monomeric cyclised complexes [{$Co_2(CO)_6$}$_2${*cyclo*-μ-η²:μ-η²-$CH_2C_2C_2CH_2OCH_2(CH_2)_nCH_2O$}] (**3a**: $n = 2$, **3b**: $n = 3$, **3c**: $n = 4$) along with the dimeric cyclised species [{$Co_2(CO)_6$}$_2$-{*cyclo*-μ-η²:μ-η²-$CH_2C_2C_2CH_2OCH_2(CH_2)_nCH_2O$}]$_2$ (**4a**: $n = 2$, **4b**: $n = 3$, **4c**: $n = 4$). Introduction of additional oxygen donor atoms into the macrocycle can be achieved by reaction of **1a** with the glycols, $HO(CH_2CH_2O)_nH$, to afford exclusively monomeric [{$Co_2(CO)_6$}$_2${*cyclo*-μ-η²:μ-η²-$CH_2C_2C_2CH_2O(CH_2CH_2O)_n$}] (**5a**: $n = 3$, **5b**: $n = 4$). On the other hand, treatment of **1a** with the 1,3-diyne-linked alkyl diols, $HOCR_2C{\equiv}CC{\equiv}CCR_2OH$, furnishes the more rigid monomeric [{$Co_2(CO)_6$}$_2$-{*cyclo*-μ-η²:μ-η²-$CH_2C_2C_2CH_2OCR_2C_2C_2CR_2O$}] [**6a**: R = H, **6b**: R = Me] and dimeric macrocycles [{$Co_2(CO)_6$}$_2$-{*cyclo*-μ-η²:μ-η²-$CH_2C_2C_2CH_2OCR_2C_2C_2CR_2O$}]$_2$ [**7a**: R = H, **7b**: R = Me], whereas the use of the alkynyl- or aryl-linked alkyl diols, $HOCH_2(L)CH_2OH$, affords the unsymmetrical dimeric [{$Co_2(CO)_6$}$_2$-{*cyclo*-μ-η²:μ-η²-$CH_2C_2C_2CH_2$}$_2$O{$OCH_2(L)CH_2O$}] [**8a**: L = –C≡C–, **8b**: L = 1,4-$C_6H_4$] and symmetrical dimeric species [{$Co_2(CO)_6$}$_2$-{*cyclo*-μ-η²:μ-η²-$CH_2C_2C_2CH_2OCH_2(L)CH_2O$}]$_2$ [**9a**: L = –C≡C–, **9b**: L = 1,4-$C_6H_4$]. Also isolated as a by-product from all the above reactions is the self-dimerised macrocycle [{$Co_2(CO)_6$}$_2$-{*cyclo*-μ-η²:μ-η²-$CH_2C_2C_2CH_2O$}]$_2$ (**2**) which can itself be synthesised more directly by treating **1a** with catalytic quantities of $HBF_4{\cdot}OEt_2$. Single crystal X-ray diffraction studies have been performed on **2**, **3a**, **5a**, **7a**, **8a**, **8b** and **9a**.

(© Wiley-VCH Verlag GmbH & Co. KGaA, 69451 Weinheim, Germany, 2007)

## Introduction

Recent years have seen a surge of interest in the application of the acid-catalysed Nicholas reaction (both intra- and intermolecular)[1] to promote the formation of both carbocyclic and heteroatom-containing medium to large ring systems.[1d,2–6,9–11] This can, in part, be attributed to the connection the resultant materials have to either natural products,[2,4] bio-inorganic hosts,[7] molecular sensors[7] or to nanomaterials.[8] With regard to intermolecular reactions, the reactivity of hexacarbonyldicobalt-coordinated monoyne diols, [{$Co_2(CO)_6$(μ-η²-$HOCR_2C{\equiv}CR_2OH$)}] (R = H, hydrocarbyl), towards a range of nucleophiles has been extensively investigated by Went and co-workers and allows access to a rich variety of medium to large macrocycles containing an assortment of donor functionalities.[3] On the other hand, the use of the more extended bis(hexacarbonyldicobalt)-coordinated diyne diols (and ethers) has received less attention with a few reports focusing on the reactivity of organo-linked diyne derivatives.[4–6] In our programme, we have found that the less flexible and conjugated 1,3-diyne diol, [{$Co_2(CO)_6$(μ-η²-$HOCH_2C_2$-)}$_2$] (**1a**, Figure 1), can also serve as a pre-organised building block for the assembly of ring systems including large thio- and mixed S,O-macrocycles.[9,10] Significantly, the use of the more bulky [{$Co_2(CO)_6$(μ-η²-$HOCMe_2C_2$-)}$_2$] (**1b**) inhibits an intermolecular reaction and instead generates a strained seven-membered ring carbocycle via an intramolecular pathway.[11]

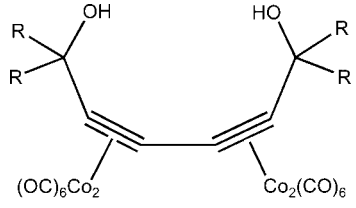


R = H (**1a**), Me (**1b**)

Figure 1. Bis[$Co_2(CO)_6$]-coordinated diyne-diol **1**.

As an extension to our work in this area, we have been interested in employing the Nicholas reaction to generate crown-type macrocycles that can additionally incorporate soft donor groups such as 1,3-diynes, alkynes and aryls groups. To this end we have targeted a family of alkyl diols,

[a] Department of Chemistry and Biochemistry, Texas Tech University,
Lubbock, TX 79409-1061, USA
[b] Department of Chemistry,
Lensfield Road, Cambridge CB2 1EW, UK
[c] Department of Chemistry, University of Leicester,
University Road, Leicester LE1 7RH, UK
E-mail: gas8@leicester.ac.uk

 © 2007 Wiley-VCH Verlag GmbH & Co. KGaA, Weinheim 

$HOCR_2$-linker-$CR_2OH$ (linker = alkyl, glycol, 1,3-diynyl, alkynyl, aryl; R = H, Me), as potential nucleophiles for the acid-catalysed reaction with the less sterically encumbered **1a**. Herein, we report full details of our findings from this study.

## Results and Discussion

### 1. Reactions of 1a with Alkyl Diols

The reaction of $[\{Co_2(CO)_6(\mu\text{-}\eta^2\text{-}HOCH_2C_2\text{-})\}_2]$ (**1a**) with one equivalent of $HOCH_2(CH_2)_nCH_2OH$ ($n$ = 2–4) in dichloromethane at –78 °C in the presence of $HBF_4{\cdot}OEt_2$ gave the self-dimerised product $[\{Co_2(CO)_6\}_2\{cyclo\text{-}\mu\text{-}\eta^2\text{:}\mu\text{-}\eta^2\text{-}CH_2C_2C_2CH_2O\}]_2$ (**2**), the monomeric cyclised complexes $[\{Co_2(CO)_6\}_2\{cyclo\text{-}\mu\text{-}\eta^2\text{:}\mu\text{-}\eta^2\text{-}CH_2C_2C_2CH_2OCH_2(CH_2)_nCH_2O\}]$ (**3a**: $n$ = 2, **3b**: $n$ = 3, **3c**: $n$ = 4) and the dimeric cyclised species $[\{Co_2(CO)_6\}_2\{cyclo\text{-}\mu\text{-}\eta^2\text{:}\mu\text{-}\eta^2\text{-}CH_2C_2C_2CH_2OCH_2(CH_2)_nCH_2O\}]_2$ (**4a**: $n$ = 2, **4b**: $n$ = 3, **4c**: $n$ = 4) in high combined yield (Scheme 1). Complex **2** can also be obtained by stirring **1a** in dichloromethane in the presence of $HBF_4{\cdot}OEt_2$. The complexes **2**–**4** have been characterised by FAB mass spectrometry and by $^1H$ and $^{13}C$ NMR and IR spectroscopy (see Table 1 and experimental section). Satisfactory microanalytical data were obtained for all complexes. In addition, the complexes **2** and **3a** have been the subject of single-crystal X-ray diffraction studies.

Suitable crystals of **2** and **3a** for the X-ray determination were grown from dichloromethane by slow diffusion of hexane at 0 °C. Perspective views of **2** and **3a** are depicted in Figures 2 and 3; selected bond lengths and angles are listed in Tables 2 and 3. The molecular structure of **2** contains a crystallographic centre of symmetry which lies at the midpoint of the C(18)–C(13A) and C(13)–C(18A) alkynic bonds. The structure itself is based on a fourteen-membered 1,8-dioxacyclotetradeca-3,5,10,12-tetrayne ring with the two diyne units each coordinated by two $Co_2(CO)_6$ units in an $\eta^2$:$\eta^2$ fashion. The $Co_2C_2$ cores adopt the expected tetrahedral arrangements with the bond parameters falling within the normal range.[12–14] Within each coordinated diyne unit the two $Co_2C_2$ units are disposed in a pseudo *cis* configuration [torsion angle C(16)–C(17)–C(18)–C(13A) 36.5°] with the C≡C–$CH_2$ *bend-back* angles[15] [C(15)–C(16)–C(17) 141.5(2), C(18A)–C(13)–C(14) 144.5(2)°] similar to those observed in related acyclic cobalt–alkyne complexes;[12,13] the mean C≡C–$CH_2$ angle is 141.31°.[16]

Complex **3a** crystallises with two discrete independent molecules (A and B in Table 3) within its asymmetric unit. The main difference between the two molecules is the presence of some disorder within the O(16)–C(17)–C(18)–C(19)

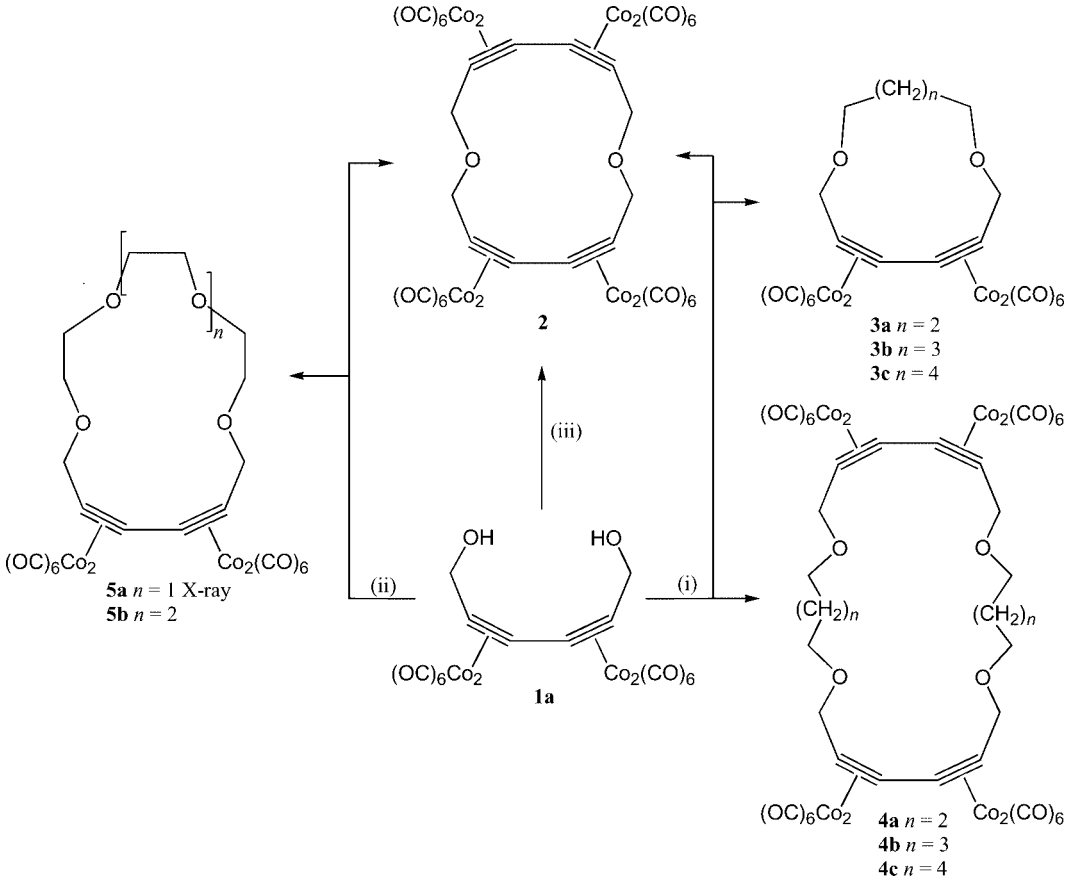


Scheme 1. Reagents and conditions; (i) $HOCH_2(CH_2)_nCH_2OH$, $HBF_4{\cdot}OEt_2$ (cat.), –78 °C, $CH_2Cl_2$; (ii) $HO(CH_2CH_2O)_nH$, $HBF_4{\cdot}OEt_2$ (cat.), –78 °C, $CH_2Cl_2$; (iii) $HBF_4{\cdot}OEt_2$ (cat.), –78 °C, $CH_2Cl_2$.

 © 2007 Wiley-VCH Verlag GmbH & Co. KGaA, Weinheim 

Table 1. Spectroscopic and analytical data for the new complexes **2**–**9**.

| | $\nu$(CO) [cm$^{-1}$][a] | $^1$H NMR [$\delta$][b] | FAB mass spectrum | Microanalysis [%][c] | |
|---|---|---|---|---|---|
| | | | | C | H |
| **2** | 2025 (s), 2062 (s), 2083 (s), 2100 (m) | 4.93 (s, 8 H, $CCH_2O$) | $M^+$ (1328), $M^+ - n$CO ($n$ = 1–24) | 32.65 (32.56) | 0.71 (0.61) |
| **3a** | 2027 (s), 2063 (vs), 2083 (s), 2101 (m) | 4.67 (s, 4 H, $CCH_2O$), 3.57 [br. s, 4 H, $OCH_2(CH_2)_2CH_2O$], 1.67 [br. s, 4 H, $OCH_2(CH_2)_2CH_2O$] | $M^+$ (736), $M^+ - n$CO ($n$ = 1–12) | 36.02 (35.90) | 1.66 (1.64) |
| **3b** | 2024 (s), 2059 (vs), 2082 (s), 2100 (m) | 4.68 (s, 4 H, $CCH_2O$), 3.48 [br. s, 4 H, $OCH_2(CH_2)_3CH_2O$], 1.5–1.3 [m, 6 H, $OCH_2(CH_2)_3CH_2O$] | $M^+$ (750), $M^+ - n$CO ($n$ = 1–12) | 37.01 (36.81) | 1.91 (1.87) |
| **3c** | 2023 (s), 2058 (vs), 2082 (s), 2102 (m) | 4.57 (s, 4 H, $CCH_2O$), 3.57 [m, 4 H, $OCH_2(CH_2)_4CH_2O$], 1.5–1.3 [m, 8 H, $OCH_2(CH_2)_4CH_2O$] | $M^+$ (764), $M^+ - n$CO ($n$ = 1–12) | 37.24 (37.73) | 2.14 (2.11) |
| **4a** | 2024 (s), 2059 (vs), 2081 (s), 2101 (m) | 4.66 (s, 8 H, $CCH_2O$), 3.73 [br. s, 8 H, $OCH_2(CH_2)_2CH_2O$], 1.70 [br. s, 8 H, $OCH_2(CH_2)_2CH_2O$] | $M^+$ (1472), $M^+ - n$CO ($n$ = 1–24) | 36.08 (35.90) | 1.76 (1.64) |
| **4b** | 2025 (s), 2059 (vs), 2082 (m), 2101 (m) | 4.67 (s, 8 H, $CCH_2O$), 3.60 [m, 8 H, $OCH_2(CH_2)_3CH_2O$], 1.6–1.4 [m, 12 H, $OCH_2(CH_2)_3CH_2O$] | $M^+$ (1500), $M^+ - n$CO ($n$ = 1–24) | 37.05 (36.81) | 2.01 (1.87) |
| **4c** | 2025 (s), 2058 (vs), 2082 (s), 2101 (m) | 4.59 (s, 8 H, $CCH_2O$), 3.51 [m, 8 H, $OCH_2CH_2(CH_2)_2CH_2CH_2O$], 1.55 [br. s, 8 H, $CH_2CH_2(CH_2)_2CH_2CH_2O$], 1.29 [br. s, 8 H, $CH_2CH_2(CH_2)_2CH_2CH_2O$] | $M^+$ (1528), $M^+ - n$CO ($n$ = 1–24) | 36.92 (37.73) | 2.05 (2.11) |
| **5a** | 2026 (s), 2062 (vs), 2084 (s), 2102 (m) | 4.82 (s, 4 H, $CCH_2O$), 3.8–3.5 [m, 12 H, $O(CH_2CH_2O)_3$] | $M^+$ (796), $M^+ - n$CO ($n$ = 1–12) | 36.22 (36.21) | 1.96 (2.03) |
| **5b** | 2025 (s), 2059 (vs), 2082 (s), 2101 (m) | 4.77 (s, 4 H, $CCH_2O$), 3.8–3.6 [m, 16 H, $O(CH_2CH_2O)_4$] | $M^+$ (840), $M^+ - n$CO ($n$ = 1–12) | 37.34 (37.17) | 2.22 (2.40) |
| **6a** | 2027 (s), 2059 (vs), 2084 (s), 2102 (m) | 4.95 (s, 4 H, $CCH_2O$), 4.33 (s, 4 H, $CCH_2O$) | $M^+$ (756), $M^+ - n$CO ($n$ = 1–12) | 38.41 (38.13) | 1.31 (1.07) |
| **6b** | 2030 (s), 2057 (vs), 2084 (s), 2093 (w), 2102 (w) | 4.96 (s, 4 H, $CCH_2O$), 1.41 (s, 12 H, $CH_3$) | $M^+$ (812), $M^+ - n$CO ($n$ = 1–12) | – | – |
| **7a** | 2027 (s), 2058 (vs), 2084 (s), 2103 (m) | 4.74 (s, 8 H, $CCH_2O$), 4.42 (s, 8 H, $CCH_2O$) | $M^+$ (1512), $M^+ - n$CO ($n$ = 1–24) | 38.48 (38.13) | 1.01 (1.07) |
| **7b** | 2030 (s), 2061 (vs), 2083 (s), 2102 (w) | 4.12 (s, 8 H, $CCH_2O$), 1.23 (s, 24 H, $CH_3$) | $M^+$ (1624), $M^+ - n$CO ($n$ = 1–24) | 40.76 (39.93) | 1.42 (1.29) |
| **8a** | 2015 (sh), 2031 (m), 2056 (m), 2065 (vs), 2085 (m), 2102 (m) | 5.10 (s, 4 H, $CCH_2O$), 4.79 (s, 4 H, $CCH_2O$), 4.39 (s, 4 H, $CCH_2O$) | $M^+$ (1396), $M^+ - n$CO ($n$ = 1–24) | 35.66 (35.89)[d] | 1.45 (1.33)[d] |
| **8b** | 2024 (s), 2035 (m), 2058 (s), 2064 (vs), 2083 (s), 2101 (m) | 7.37 (br. s, 4 H, Ph), 4.86 (s, 4 H, $CCH_2O$), 4.54 (s, 4 H, $CCH_2O$), 4.09 (s, 4 H, $CCH_2O$) | $M^+$ (1448), $M^+ - n$CO ($n$ = 1 – 24) | 36.12 (36.50) | 1.22 (1.11) |
| **9a** | 2029 (s), 2061 (s), 2085 (s), 2103 (m) | 4.74 (s, 8 H, $CCH_2O$), 4.42 (s, 8 H, $CCH_2O$) | $M^+$ (1464), $M^+ - n$CO ($n$ = 1–24) | 36.07 (36.10) | 1.22 (1.10) |
| **9b** | 2027 (s), 2059 (vs), 2083 (s), 2102 (w) | 7.5–7.3 (m, 8 H, Ph), 4.50 (s, 8 H, $CCH_2O$), 4.48 (s, 8 H, $CCH_2O$) | $M^+$ (1568), $M^+ - n$CO ($n$ = 1–24) | 39.79 (39.83) | 1.68 (1.54) |

[a] $CH_2Cl_2$ solution, 0.5 mm NaCl cells. [b] $^1$H NMR chemical shifts in ppm relative to $SiMe_4$ ($\delta$ = 0.0 ppm), coupling constants in Hz in $CDCl_3$ at 293 K. [c] Calculated values shown in parentheses. [d] Calculated values include 0.5 hexane.

section of the ring in molecule A which is absent in B. The molecular structure consists of a twelve-membered 1,6-dioxacyclododeca-8,10-diyne macrocyclic ring with the diyne section coordinated by two $Co_2(CO)_6$ units and linked at each end by a $CH_2OCH_2CH_2CH_2CH_2OCH_2$ chain. The $Co_2C_2$ cores adopt the expected tetrahedral arrangements with the metal–metal bonds of each being located almost perpendicular to the corresponding alkyne vectors and their lengths falling in the expected ranges.[12–14] Inspection of the C≡C–C≡C torsion angle within the coordinated 1,3-diyne section of the macrocycle also reveals some differences between the independent molecules [torsion angle C(14)–C(13)–C(24)–C(23) 50.7° (molecule A), 44.2° (molecule B)] with the mean value ca. 11° larger than that in **2**. The *bend back* angles within and between molecules are similar [140.7(3), 140.2(3) (molecule A) vs. 138.6(3), 140.4(4)° (molecule B)] and as with **2** comparable with those found in related non-cyclic 1,3-diyne cobalt carbonyl complexes.[12,13]

The IR spectra of **2**–**4** reveal terminal carbonyl bands with patterns similar to that for **1a**[17] and to other bis(hexacarbonyldicobalt)-protected 1,3-diyne complexes.[13] In their FAB mass spectra, molecular ions are clearly visible along with fragmentation peaks corresponding to the loss of carbonyl groups from the corresponding molecular ion. In the $^1$H NMR spectra of **2**–**4**, the protons for the methylene groups adjacent to both an alkynic carbon atom and an oxygen atom are seen as singlets in the range $\delta$ = 4.57–4.93 while the aliphatic chain $CH_2$ groups in **3** and **4** are seen more upfield. Due to the high degree of symmetry as

 © 2007 Wiley-VCH Verlag GmbH & Co. KGaA, Weinheim 

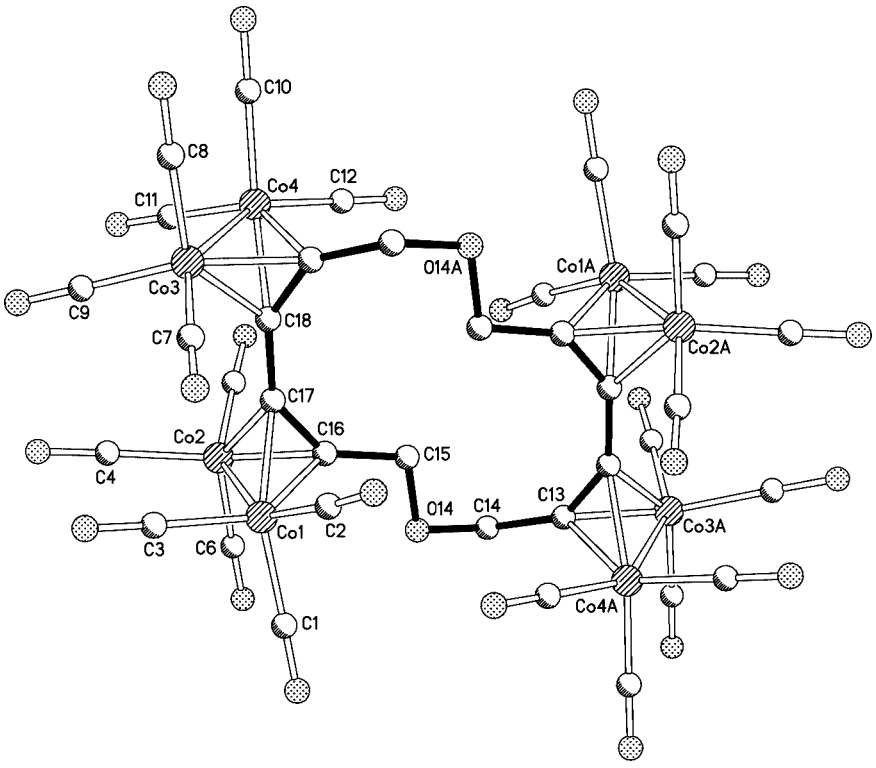


Figure 2. Molecular structure of **2** with partial atom labeling Scheme; all hydrogen atoms have been omitted for clarity.

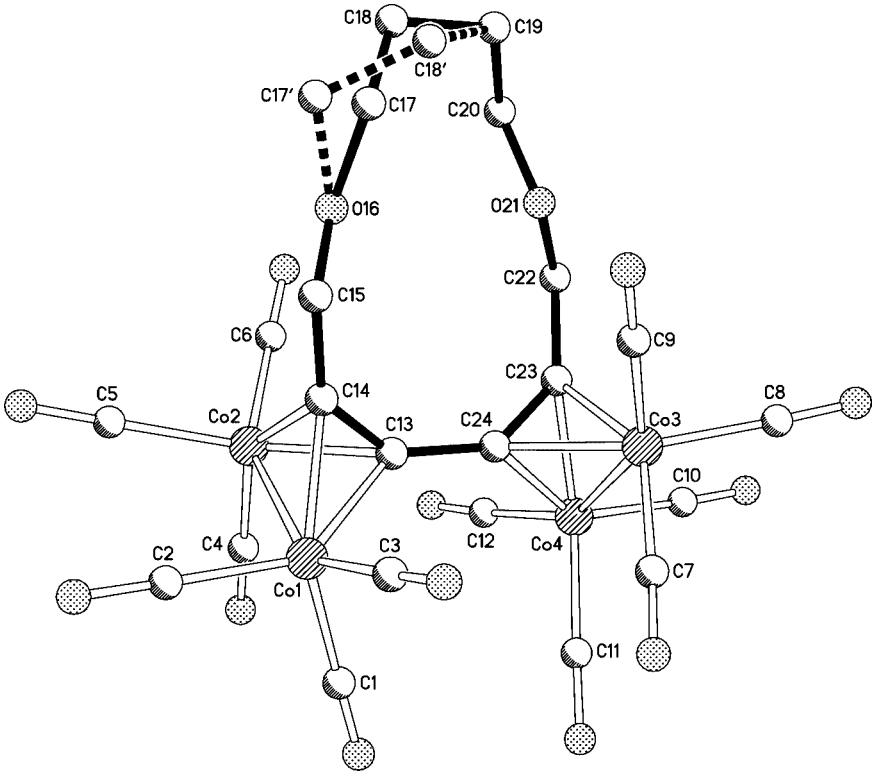


Figure 3. Molecular structure of **3a** with partial atom labeling scheme; all hydrogen atoms have been omitted for clarity (the dotted line indicates the disordered moiety).

 © 2007 Wiley-VCH Verlag GmbH & Co. KGaA, Weinheim 

Table 2. Selected bond lengths [Å] and angles (°) for **2**.[a]

| Bond lengths | | | |
|---|---|---|---|
| C(13)–C(14) | 1.497(3) | C(18)–C(13A) | 1.362(3) |
| C(14)–O(14) | 1.426(2) | Co(1)–Co(2) | 2.4700(3) |
| C(15)–O(14) | 1.419(2) | Co(3)–Co(4) | 2.4626(4) |
| C(15)–C(16) | 1.479(3) | Co–C(carbonyl) | 1.787(2)–1.831(2) |
| C(16)–C(17) | 1.363(3) | C–O(carbonyl) | 1.125(3)–1.140(2) |
| C(17)–C(18) | 1.432(3) | Co–C(alkyne) | 1.941(2)–1.980(2) |
| Bond angles | | | |
| C(18A)–C(13)–C(14) | 144.5(2) | C(15)–C(16)–C(17) | 141.5(2) |
| C(13)–C(14)–O(14) | 115.29(15) | C(16)–C(17)–C(18) | 143.5(2) |
| C(14)–O(14)–C(15) | 110.86(14) | C(17)–C(18)–C(13A) | 145.4(2) |
| O(14)–C(15)–C(16) | 110.9(2) | | |

[a] Atoms with suffix A are generated by symmetry ($-x$, $1-y$, $-z$).

Table 3. Selected bond lengths [Å] and angles (°) for **3a**.

| Bond lengths | Molecule A | Molecule B |
|---|---|---|
| C(13)–C(14) | 1.353(4) | 1.350(4) |
| C(14)–C(15) | 1.482(4) | 1.484(4) |
| C(15)–O(16) | 1.406(4) | 1.427(3) |
| O(16)–C(17) | 1.521(7) | 1.433(4) |
| C(17)–C(18) | 1.549(8) | 1.499(5) |
| C(18)–C(19) | 1.408(6) | 1.535(5) |
| C(19)–C(20) | 1.486(5) | 1.489(5) |
| C(20)–O(21) | 1.370(4) | 1.414(4) |
| O(21)–C(22) | 1.431(4) | 1.415(4) |
| C(22)–C(23) | 1.477(4) | 1.479(4) |
| C(23)–C(24) | 1.353(4) | 1.352(4) |
| C(24)–C(13) | 1.420(4) | 1.426(4) |
| Co(1)–Co(2) | 2.4588(5) | 2.4646(5) |
| Co(3)–Co(4) | 2.4717(5) | 2.4692(5) |
| Co–C(carbonyl) | 1.787(2)–1.831(2) | 1.787(2)–1.831(2) |
| C–O(carbonyl) | 1.125(3)–1.140(2) | 1.125(3)–1.140(2) |
| Co–C(alkyne) | 1.941(2)–1.980(2) | 1.941(2)–1.980(2) |
| Bond angles | | |
| C(13)–C(14)–C(15) | 140.2(3) | 140.4(3) |
| C(14)–C(15)–O(16) | 107.6(2) | 108.1(2) |
| C(15)–O(16)–C(17) | 107.9(3) | 112.9(2) |
| O(16)–C(17)–C(18) | 104.3(5) | 113.3(3) |
| C(17)–C(18)–C(19) | 116.1(5) | 115.2(3) |
| C(18)–C(19)–C(20) | 113.6(4) | 116.1(3) |
| C(19)–C(20)–O(21) | 109.2(3) | 110.1(3) |
| C(20)–O(21)–C(22) | 113.1(3) | 112.4(4) |
| O(21)–C(22)–C(23) | 106.7(3) | 108.9(2) |
| C(22)–C(23)–C(24) | 140.7(3) | 138.6(3) |
| C(23)–C(24)–C(13) | 141.5(3) | 141.2(3) |

well as the quadrupole broadening due to $^{59}$Co, the NMR spectroscopic data for monomeric **3** and its respective dimer **4** are virtually indistinguishable.

## 2. Reaction of 1a with Glycols

With the intent of introducing additional hard oxygen donor functionality into the macrocycle, the reaction of **1a** with two types of glycol was examined. Thus, treatment of **1a** with one equivalent of $HO(CH_2CH_2O)_nH$ ($n$ = 3, 4) in dichloromethane at –78 °C in the presence of $HBF_4{\cdot}OEt_2$ gave the monomeric cyclised complexes [$\{Co_2(CO)_6\}_2$-{*cyclo*-μ-η$^2$:μ-η$^2$-$CH_2C_2C_2CH_2O(CH_2CH_2O)_n$}] (**5a**: $n$ = 3, **5b**: $n$ = 4) in high yield (Scheme 1). As with the reactions of **1a** with $HO(CH_2)_nOH$ (vide supra), **2** was isolated as a minor by-product in each case. Both new complexes have been characterised by mass spectrometry and by $^1$H, $^{13}$C NMR and IR spectroscopy (see Table 1 and Experimental section). Satisfactory microanalytical data were obtained for both **5a** and **5b**. In addition, **5a** has been the subject of a single-crystal X-ray diffraction study.

Single crystals of **5a** suitable for the X-ray determination were grown from hexane by slow evaporation at 0 °C. A view of the structure is depicted in Figure 4; selected bond lengths and angles are given in Table 4. The structure consists of a sixteen-membered 1,4,7,10-tetraoxacyclohexadeca-12,14-diyne ring with the two methylene end groups of the coordinated $CH_2C{\equiv}C{-}C{\equiv}CCH_2$ moiety linked by a triethyleneglycol-derived tether. Within the $Co_2C_2$ tetrahedral cores there are no unusual structural features, with all bond lengths and angles falling in the expected ranges.[12–14] The relative disposition of the two $Co_2C_2$ fragments can be described as pseudo *cis* [torsion angle C(14)–C(15)–C(16)–C(17) 45.6°] while the two $CH_2$–C≡C *bend back* angles are comparable [C(13)–C(14)–C(15) 142.05(19) vs. C(16)–C(17)–C(18) 140.9(2)°]. An approximation of the cavity size can be made by studying the non-bonding oxygen–oxygen separations [O(13)···O(14) 2.916, O(13)···O(15) 4.730, O(13)···O(16) 5.240, O(14)···O(16) 4.800 Å] which can be compared to the non-bonding O–O separations of 4.362, 3.012 and 2.971 Å in 12-crown-4.[18]

The $^1$H NMR spectra of **5a** and **5b** are similar with the methylene protons on the $OCH_2$ groups adjacent to the alkynic carbons taking the form of a singlet at ca. 4.80 while the $OCH_2CH_2O$ protons are seen as multiplets in the range $\delta$ = 3.82–3.56. The $^{13}$C NMR spectra are also similar but differ with two resonances seen for the methylene carbons

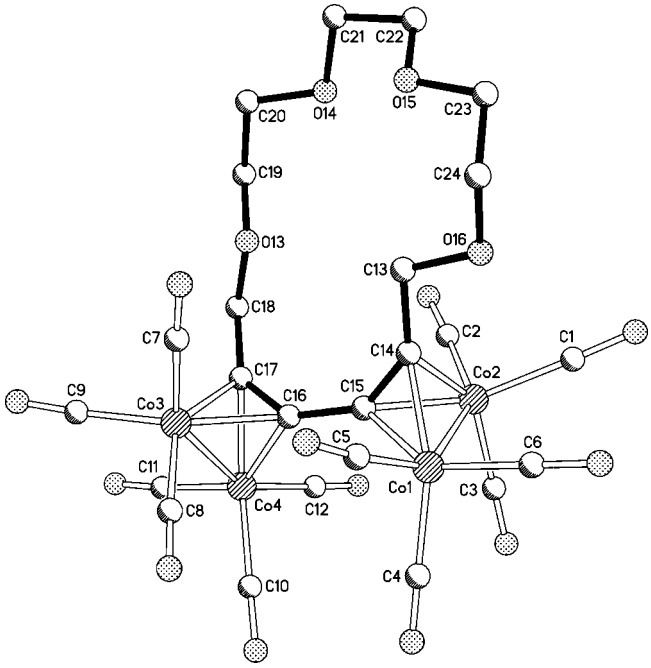


Figure 4. Molecular structure of **5a** with partial atom labeling scheme; all hydrogen atoms have been omitted for clarity.

 © 2007 Wiley-VCH Verlag GmbH & Co. KGaA, Weinheim 

Table 4. Selected bond lengths [Å] and angles (°) for **5a**.

| Bond lengths | | | |
|---|---|---|---|
| C(13)–C(14) | 1.480(3) | C(22)–O(15) | 1.413(3) |
| C(14)–C(15) | 1.358(3) | O(15)–C(23) | 1.415(3) |
| C(15)–C(16) | 1.429(3) | C(23)–C(24) | 1.493(3) |
| C(16)–C(17) | 1.352(3) | C(24)–O(16) | 1.430(2) |
| C(17)–C(18) | 1.485(3) | O(16)–C(13) | 1.421(2) |
| C(18)–O(13) | 1.410(3) | Co(1)–Co(2) | 2.4710(4) |
| O(13)–C(19) | 1.424(3) | Co(3)–Co(4) | 2.4715(4) |
| C(19)–C(20) | 1.494(3) | Co–C(carbonyl) | 1.784(3)–1.828(3) |
| C(20)–O(14) | 1.412(3) | C–O(carbonyl) | 1.129(3)–1.141(3) |
| O(14)–C(21) | 1.426(3) | Co–C(alkyne) | 1.938(2)–1.976(2) |
| C(21)–C(22) | 1.488(3) | | |
| **Bond angles** | | | |
| C(13)–C(14)–C(15) | 142.05(19) | C(20)–O(14)–C(21) | 111.76(17) |
| C(14)–C(15)–C(16) | 141.5(2) | O(14)–C(21)–C(22) | 107.82(19) |
| C(15)–C(16)–C(17) | 141.9(2) | C(21)–C(22)–O(15) | 107.6(2) |
| C(16)–C(17)–C(18) | 140.9(2) | C(22)–O(15)–C(23) | 112.92(18) |
| C(17)–C(18)–O(13) | 109.19(18) | O(15)–C(23)–C(24) | 109.23(19) |
| C(18)–O(13)–C(19) | 111.21(17) | C(23)–C(24)–O(16) | 113.51(19) |
| O(13)–C(19)–C(20) | 109.8(2) | C(24)–O(16)–C(13) | 113.91(15) |
| C(19)–C(20)–O(14) | 109.00(19) | O(16)–C(13)–C(14) | 108.79(17) |

in **5a** while four are present in **5b**. Confirmation of the monomeric nature of **5a** and **5b** is revealed in their FAB mass spectra with molecular ion peaks along with fragmentation peaks corresponding to the loss of carbonyl groups from the parent ion evident.

It is uncertain why an additional dimeric species is not formed in any of the reactions of **1a** with glycols in a manner similar to that seen for the reaction of **1a** with aliphatic diols (vide supra). It would seem likely that the presence of oxygen donors within the glycolic-based nucleophile could lead to a weak Co–O interaction in an intermediate (or transition state) which would favour monomeric ring closure. Indeed, such an Co–O interaction has previously been proposed to explain the high monomer to dimer ratio observed during the reaction of **1a** with dithioethers.[9b]

### 3. Reaction of 1a with Diynyl-, Alkynyl- or Aryl-Linked Alkyl Diols

In order to introduce a soft donor into the macrocycle we have also targeted the reactions of alkyl diols that contain alkynyl or aryl linking units. Accordingly, the reaction of **1a** with one equivalent of the 1,3-diyne-linked alkyl diols, $HOCR_2C{\equiv}CC{\equiv}CCR_2OH$, was initially examined and found to furnish, in addition to trace quantities of **2**, monomeric [$\{Co_2(CO)_6\}_2$-{*cyclo*-μ-$\eta^2$:μ-$\eta^2$-$CH_2C_2C_2CH_2OCR_2C_2C_2CR_2O$}] [**6a**: R = H, **6b**: R = Me] and dimeric macrocycles [$\{Co_2(CO)_6\}_2${*cyclo*-μ-$\eta^2$:μ-$\eta^2$-$CH_2C_2C_2CH_2OCR_2C_2C_2CR_2O$}]$_2$ [**7a** R = H, **7b** R = Me] in high combined yield (Scheme 2).

As with **3** and **4**, the similarity of the spectroscopic data for monomeric **6** with the corresponding dimeric **7** meant unequivocal identification by NMR and IR spectroscopy proved problematic (see Table 1). Nevertheless, the incorporation of the uncoordinated 1,3-diyne into the macrocycle could be confirmed by the presence of two different types of methylene protons in the $^1$H NMR spectra of **6a** and **7a**, while the equivalent methyl protons in **6b** and **7b** are seen as singlets (see Table 1). In the FAB mass spectra of **6** and **7**, however, the complexes could be readily distinguished, with molecular ion peaks corresponding to monomeric and dimeric species along with fragmentation peaks that match to the loss of twelve or twenty-four successive carbonyl groups, respectively.

In order to identify unambiguously the new complexes the structure of one such complex, **7a**, was determined by a single-crystal X-ray diffraction study. Suitable crystals for the study could be grown from dichloromethane by slow diffusion of hexane at 0 °C. Selected bond lengths and angles are given in Table 5 and a view of the molecular structure is depicted in Figure 5.

The molecular structure of **7a** sits on a crystallographic centre of symmetry which lies between the alkynic bonds C(13)–C(14A) and C(13A)–C(14). The structure confirms the molecule is comprised of four $Co_2(CO)_6$ units and is bridged by a twenty-eight-membered 1,8,15,22-tetraoxacycloicosaocta-3,5,10,12,17,19,24,26-octayne ring. The geometric parameters of the pseudo-tetrahedral $Co_2C_2$ cores are unexceptional. As expected the *bend back* angles for the non-coordinated diyne are close to one hundred and eighty degrees [C(18)–C(19)–C(20) 177.2(3), C(21)–C(22)–C(23) 173.4°] while the coordinated ones [C(15)–C(16)–C(17) 141.2(2), C(24)–C(13)–C(14A) 138.3(2)°] fall in a range similar to previously reported acyclic cobalt-bound diyne complexes.[12–14] The two uncoordinated diyne chains adopt a parallel relative conformation with the C(22) and C(22A) separation being 3.748 Å. Examination of the coordinated C≡C–C≡C torsion angles (40.2°) reveals the $Co_2C_2$ units to be disposed in a pseudo *cis* configuration.

The reaction of the shorter alkynyl- or aryl-linked alkyl diols, $HOCH_2(L)CH_2OH$ (L = –C≡C–, 1,4-$C_6H_4$) with **1a** has also been examined. Thus treatment of **1a** with one equivalent of $HOCH_2(L)CH_2OH$ (L = –C≡C–, 1,4-$C_6H_4$), in the presence of $HBF_4{\cdot}OEt_2$, affords the unsymmetrical dimeric [$\{Co_2(CO)_6\}_2${*cyclo*-μ-$\eta^2$:μ-$\eta^2$-$CH_2C_2C_2CH_2$}$_2$O-{$OCH_2(L)CH_2O$}] [**8a**: L = –C≡C–, **8b**: L = 1,4-$C_6H_4$] and symmetrical dimeric species [$\{Co_2(CO)_6\}_2${*cyclo*-μ-$\eta^2$:μ-$\eta^2$-$CH_2C_2C_2CH_2OCH_2(L)CH_2O$}]$_2$ [**9a**: L = –C≡C–, **9b**: L = 1,4-$C_6H_4$] in high combined yields (Scheme 2). Also isolated in trace quantities is the self-dimerised species **2** but there is no evidence for any monomeric species (cf. reactions of **1a** with diynyl-linked alkyl diols).

The FAB mass spectra of **8** and **9** give molecular ion peaks along with fragmentation peaks consistent with the proposed dimeric structures (see Table 1). In the IR spectra for **9** four terminal carbonyl bands are seen in a pattern similar to that observed for the other symmetrical monomeric (**3**, **5**, **6**) or dimeric (**2**, **4**, **7**) species prepared in this work. In the case of **8a** and **8b**, however, the terminal carbonyl regions are more complicated with greater than four bands evident and consistent with the dicobalt units now being in non-equivalent environments. The unsymmetrical nature of **8a** and **8b** is further supported by the $^1$H NMR spectra which show three singlets for the inequivalent methylene protons, this inequivalence also being reflected in the $^{13}$C NMR spectra with three singlets observed for the corresponding methylene carbon atoms.

 © 2007 Wiley-VCH Verlag GmbH & Co. KGaA, Weinheim 

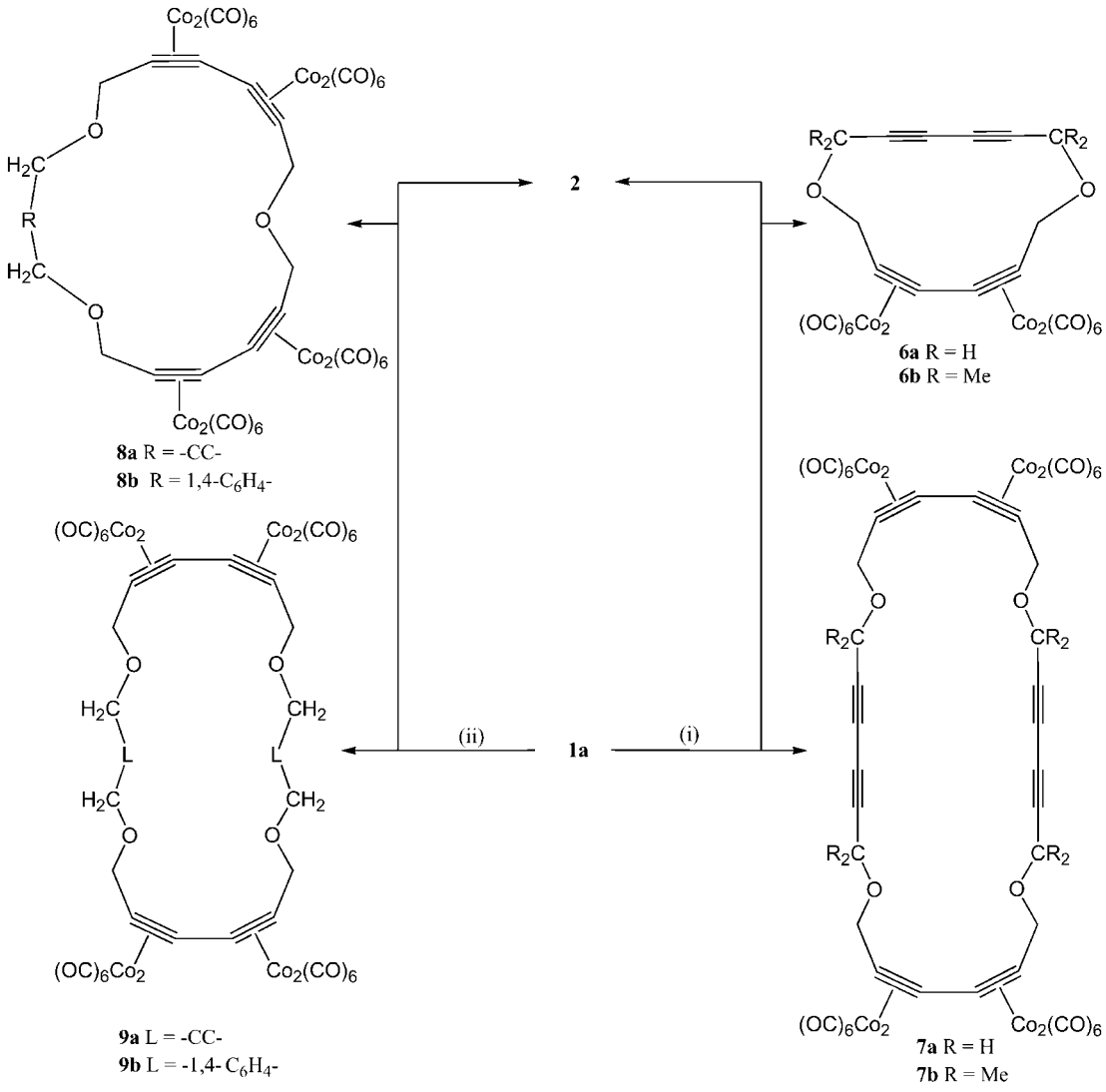


Scheme 2. Reagents and conditions; (i) $HOCR_2C_2C_2CR_2OH$, $HBF_4{\cdot}OEt_2$ (cat.), –78 °C, $CH_2Cl_2$; (ii) $HOCH_2$-L-$CH_2OH$, $HBF_4{\cdot}OEt_2$ (cat.), –78 °C, $CH_2Cl_2$.

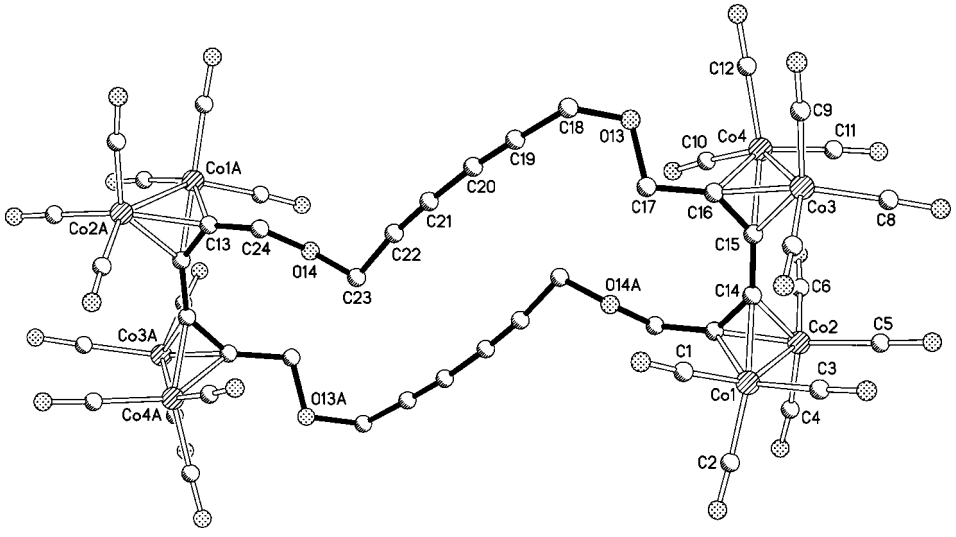


Figure 5. Molecular structure of **7a** with partial atom labeling scheme; all hydrogen atoms have been omitted for clarity.

 © 2007 Wiley-VCH Verlag GmbH & Co. KGaA, Weinheim 

Table 5. Selected bond lengths [Å] and angles (°) for **7a**.[a]

| Bond lengths | | | |
|---|---|---|---|
| C(13A)–C(14) | 1.353(3) | C(22)–C(23) | 1.471(4) |
| C(14)–C(15) | 1.434(3) | C(23)–O(14) | 1.417(3) |
| C(15)–C(16) | 1.358(3) | O(14)–C(24) | 1.422(3) |
| C(16)–C(17) | 1.476(3) | C(24)–C(13) | 1.479(3) |
| C(17)–O(13) | 1.426(3) | Co(1)–Co(2) | 2.4701(5) |
| O(13)–C(18) | 1.422(3) | Co(3)–Co(4) | 2.4700(5) |
| C(18)–C(19) | 1.463(4) | Co–C(carbonyl) | 1.788(3)–1.831(3) |
| C(19)–C(20) | 1.196(3) | C–O(carbonyl) | 1.128(3)–1.139(3) |
| C(20)–C(21) | 1.376(3) | Co–C(alkyne) | 1.935(2)–1.968(2) |
| C(21)–C(22) | 1.195(4) | | |
| **Bond angles** | | | |
| C(13A)–C(14)–C(15) | 140.0(2) | C(19)–C(20)–C(21) | 175.3(3) |
| C(14)–C(15)–C(16) | 140.3(2) | C(20)–C(21)–C(22) | 176.4(3) |
| C(15)–C(16)–C(17) | 141.2(2) | C(21)–C(22)–C(23) | 173.4(3) |
| C(16)–C(17)–O(13) | 108.49(19) | C(22)–C(23)–O(14) | 114.8(2) |
| C(17)–O(13)–C(18) | 112.56(19) | C(23)–O(14)–C(24) | 112.9(2) |
| O(13)–C(18)–C(19) | 113.9(2) | O(14)–C(24)–C(13) | 107.12(19) |
| C(18)–C(19)–C(20) | 177.2(3) | C(24)–C(13)–C(14A) | 138.3(2) |

[a] Atoms with suffix A are generated by symmetry ($-x + 1/2, -y + 1/2, -z$).

Confirmation of the proposed structural types was obtained from single-crystal X-ray diffraction studies that were performed on **8a**, **8b** and **9a**. Suitable crystals of each complex could be grown form dichloromethane solution by diffusion of hexane at 0 °C. Views of **8a**, **8b** and **9a** are shown in Figure 6, Figure 7 and Figure 8; selected bond lengths are angles are listed in Table 6, Table 7 and Table 8.

The molecular structure of **8a** sits on a crystallographic centre of symmetry which lies at the centre of O(13) and the mid-point of the C(21)···C(21A) and C(22)···C(22A) vectors within the phenyl ring; no such centre of symmetry is apparent in **8a**. The structures of **8a** and **8b** are similar and reveal nineteen- (**8a**) and twenty-one-membered (**8b**) macrocyclic rings with one methylene end-group in each $\{Co_2(CO)_6\}_2$(*cyclo*-μ-η$^2$:μ-η$^2$-$CH_2C_2C_2CH_2$) unit linked by an oxygen atom and the other by a $OCH_2C{\equiv}CH_2O$ (**8a**) or by a $OCH_2C_6H_4CH_2O$ (**8b**) moiety. The $Co_2C_2$ cores, as in related structures, adopt pseudo tetrahedral geometries with all bond lengths within the cores falling in the expected

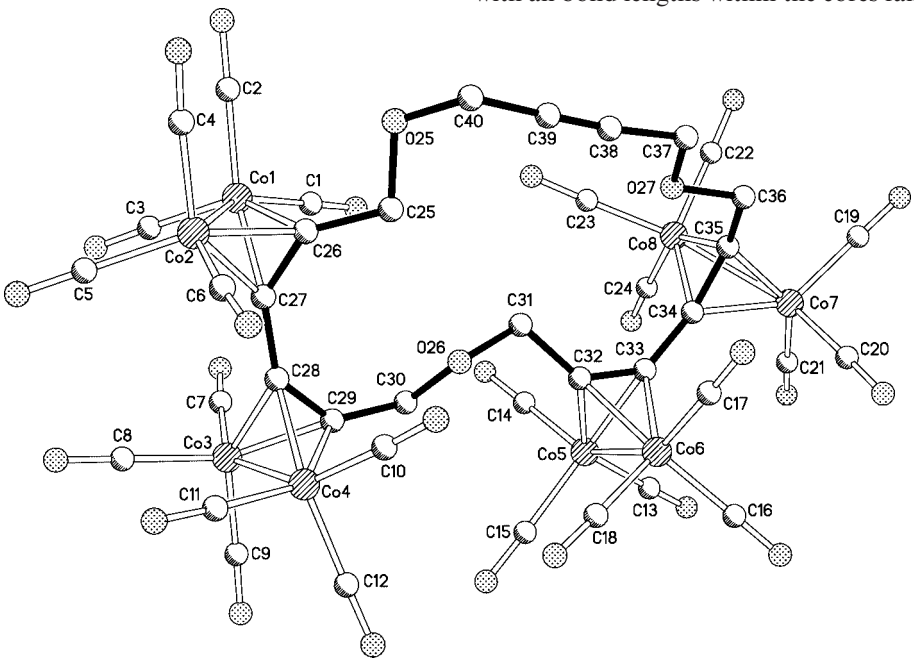


Figure 6. Molecular structure of **8a** with partial atom labeling scheme; all hydrogen atoms have been omitted for clarity.

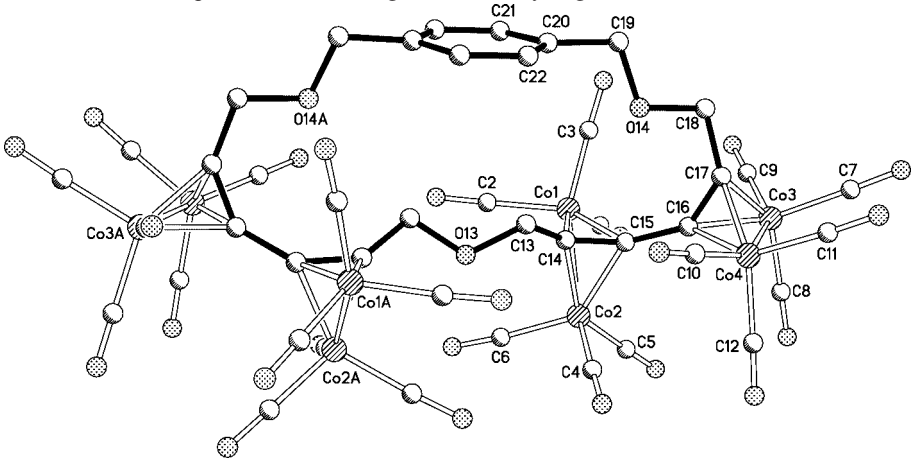


Figure 7. Molecular structure of **8b** with partial atom labeling scheme; all hydrogen atoms have been omitted for clarity.

 © 2007 Wiley-VCH Verlag GmbH & Co. KGaA, Weinheim 

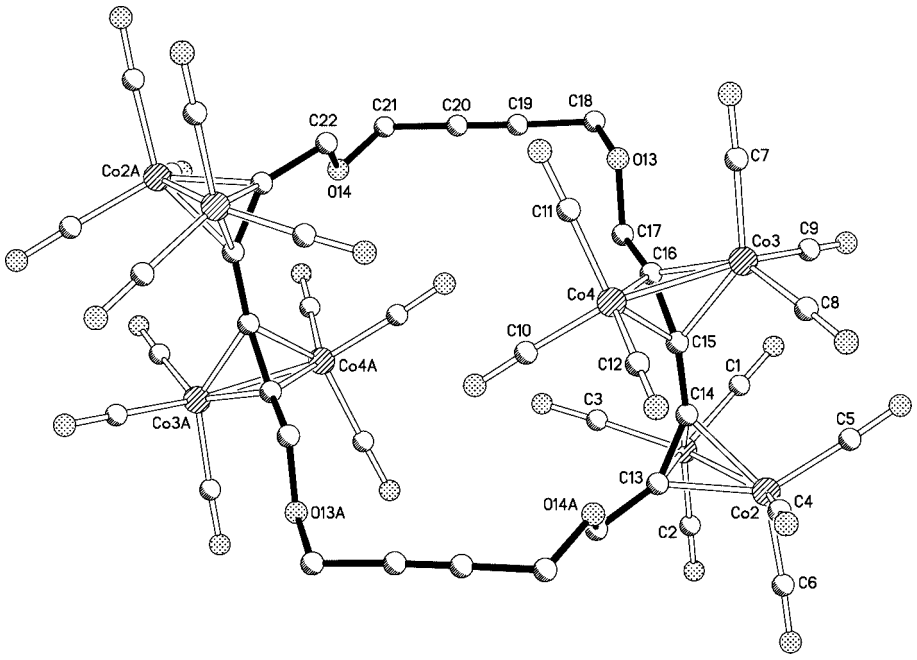


Figure 8. Molecular structure of **9a** with partial atom labeling scheme; all hydrogen atoms have been omitted for clarity.

Table 6. Selected bond lengths [Å] and angles (°) for **8a**.

| Bond lengths | | | |
|---|---|---|---|
| C(25)–C(26) | 1.475(5) | C(36)–O(27) | 1.422(4) |
| C(25)–O(25) | 1.421(4) | O(27)–C(37) | 1.427(4) |
| C(26)–C(27) | 1.349(4) | C(37)–C(38) | 1.456(5) |
| C(27)–C(28) | 1.432(4) | C(38)–C(39) | 1.195(5) |
| C(28)–C(29) | 1.351(5) | C(39)–C(40) | 1.464(5) |
| C(29)–C(30) | 1.484(5) | C(40)–O(25) | 1.420(4) |
| C(30)–O(26) | 1.415(4) | Co(1)–Co(2) | 2.4699(7) |
| O(26)–C(31) | 1.425(4) | Co(3)–Co(4) | 2.4661(6) |
| C(31)–C(32) | 1.492(5) | Co(5)–Co(6) | 2.4674(7) |
| C(32)–C(33) | 1.352(5) | Co(7)–Co(8) | 2.4758(6) |
| C(33)–C(34) | 1.430(5) | Co–C(carbonyl) | 1.782(4)–1.825(5) |
| C(34)–C(35) | 1.353(5) | C–O(carbonyl) | 1.122(5)–1.140(5) |
| C(35)–C(36) | 1.482(5) | Co–C(alkyne) | 1.936(3)–1.967(3) |
| **Bond angles** | | | |
| O(25)–C(25)–C(26) | 109.7(3) | C(33)–C(34)–C(35) | 141.1(3) |
| C(25)–C(26)–C(27) | 139.8(3) | C(34)–C(35)–C(36) | 139.0(3) |
| C(26)–C(27)–C(28) | 140.1(3) | C(35)–C(36)–O(27) | 109.1(3) |
| C(27)–C(28)–C(29) | 138.8(3) | C(36)–O(27)–C(37) | 109.9(3) |
| C(28)–C(29)–C(30) | 137.0(3) | O(27)–C(37)–C(38) | 110.5(3) |
| C(29)–C(30)–O(26) | 108.5(3) | C(37)–C(38)–C(39) | 174.6(4) |
| C(30)–O(26)–C(31) | 113.7(3) | C(38)–C(39)–C(40) | 178.8(4) |
| O(26)–C(31)–C(32) | 115.2(3) | C(39)–C(40)–O(25) | 114.2(3) |
| C(31)–C(32)–C(33) | 136.0(3) | C(40)–O(25)–C(25) | 112.0(3) |
| C(32)–C(33)–C(34) | 139.9(3) | | |

ranges for this class of compounds.[12–14] The $CH_2$–C≡C *bend back* angles reveal some differences between structures with the angle involving the O-linked methylene groups in **8a** being more strained than the $OCH_2C{\equiv}CCH_2O$-linked ones [C(28)–C(29)–C(30) 137.0(3), C(31)–C(32)–C(33) 136.0(3)° vs. C(34)–C(35)–C(36) 139.0(3), C(25)–C(26)–C(27) 139.8(3)°]. By contrast, in **8b** the $OCH_2C_6H_4CH_2O$-linked methylene groups are more strained [C(16)–C(17)–C(18) 135.1(2) vs. C(13)–C(14)–C(15) 142.0(2)°]. As with

Table 7. Selected bond lengths [Å] and angles (°) for **8b**.[a]

| Bond lengths | | | |
|---|---|---|---|
| C(13)–O(13) | 1.406(3) | C(19)–C(20) | 1.501(4) |
| C(13A)–O(13) | 1.406(3) | C(20)–C(21) | 1.369(4) |
| C(13)–C(14) | 1.484(3) | C(21)–C(22A) | 1.379(4) |
| C(14)–C(15) | 1.350(3) | C(20)–C(22) | 1.367(4) |
| C(15)–C(16) | 1.420(3) | Co(1)–Co(2) | 2.4705(5) |
| C(16)–C(17) | 1.350(3) | Co(3)–Co(4) | 2.4698(5) |
| C(17)–C(18) | 1.489(3) | Co–C(carbonyl) | 1.779(4)–1.827(3) |
| C(18)–O(14) | 1.426(3) | C–O(carbonyl) | 1.125(3)–1.141(3) |
| O(14)–C(19) | 1.430(3) | Co–C(alkyne) | 1.941(2)–1.986(2) |
| **Bond angles** | | | |
| O(13)–C(13)–C(14) | 109.80(19) | C(17)–C(18)–O(14) | 107.7(2) |
| C(13)–C(14)–C(15) | 142.0(2) | C(18)–O(14)–C(19) | 110.97(18) |
| C(14)–C(15)–C(16) | 140.6(2) | O(14)–C(19)–C(20) | 108.9(2) |
| C(15)–C(16)–C(17) | 138.7(2) | C(13A)–O(13)–C(13) | 117.6(3) |
| C(16)–C(17)–C(18) | 135.1(2) | | |

[a] Atoms with suffix A are generated by symmetry ($-x$, $y$, $1/2 - z$).

Table 8. Selected bond lengths [Å] and angles (°) for **9a**.[a]

| Bond lengths | | | |
|---|---|---|---|
| C(13)–C(22A) | 1.486(3) | C(20)–C(21) | 1.477(3) |
| C(13)–C(14) | 1.349(3) | C(21)–O(14) | 1.424(3) |
| C(14)–C(15) | 1.430(3) | O(14)–C(22) | 1.428(3) |
| C(15)–C(16) | 1.356(3) | Co(1)–Co(2) | 2.4786(4) |
| C(16)–C(17) | 1.484(3) | Co(3)–Co(4) | 2.4689(4) |
| C(17)–O(13) | 1.417(3) | Co–C(carbonyl) | 1.790(3)–1.830(3) |
| O(13)–C(18) | 1.429(3) | C–O(carbonyl) | 1.125(3)–1.136(3) |
| C(18)–C(19) | 1.473(3) | Co–C(alkyne) | 1.936(2)–1.976(2) |
| C(19)–C(20) | 1.185(3) | | |
| **Bond angles** | | | |
| C(13)–C(14)–C(15) | 143.03(19) | C(18)–C(19)–C(20) | 176.7(2) |
| C(14)–C(15)–C(16) | 141.7(2) | C(19)–C(20)–C(21) | 177.1(2) |
| C(15)–C(16)–C(17) | 139.6(2) | C(20)–C(21)–O(14) | 114.04(19) |
| C(16)–C(17)–O(13) | 109.32(18) | C(21)–O(14)–C(22) | 112.74(19) |
| C(17)–O(13)–C(18) | 112.27(17) | O(14)–C(22)–C(13A) | 107.41(19) |
| O(13)–C(18)–C(19) | 113.82(18) | C(14)–C(13)–C(22A) | 139.0(2) |

[a] Atoms with suffix A are generated by symmetry ($-x$, $-y$, $1 - z$).

 © 2007 Wiley-VCH Verlag GmbH & Co. KGaA, Weinheim 

previous structures in this work the two $Co_2C_2$ units within each coordinated diyne are disposed in a pseudo *cis* configuration [torsion angle C(26)–C(27)–C(28)–C(29) 39.6°, C(32)–C(33)–C(34)–C(35) 46.0° (**8a**); C(14)–C(15)–C(16)–C(17) 47.8° (**8b**)].

As with **8b**, the molecular structure of **9a** sits on a crystallographic centre of symmetry which lies in this case between bonds C(13)–C(22A) and C(13A)–C(22). The structure comprises a twenty-four-membered 1,6,13,18-tetraoxacycloicosatetra-3,8,10,15,20,22-hexayne ring containing two uncoordinated alkyne moieties and two coordinated diyne groups. Within the $Co_2C_2$ tetrahedral cores there are no unusual features with all bond lengths and angles falling in the expected ranges.[12–14] In contrast to previous struc-

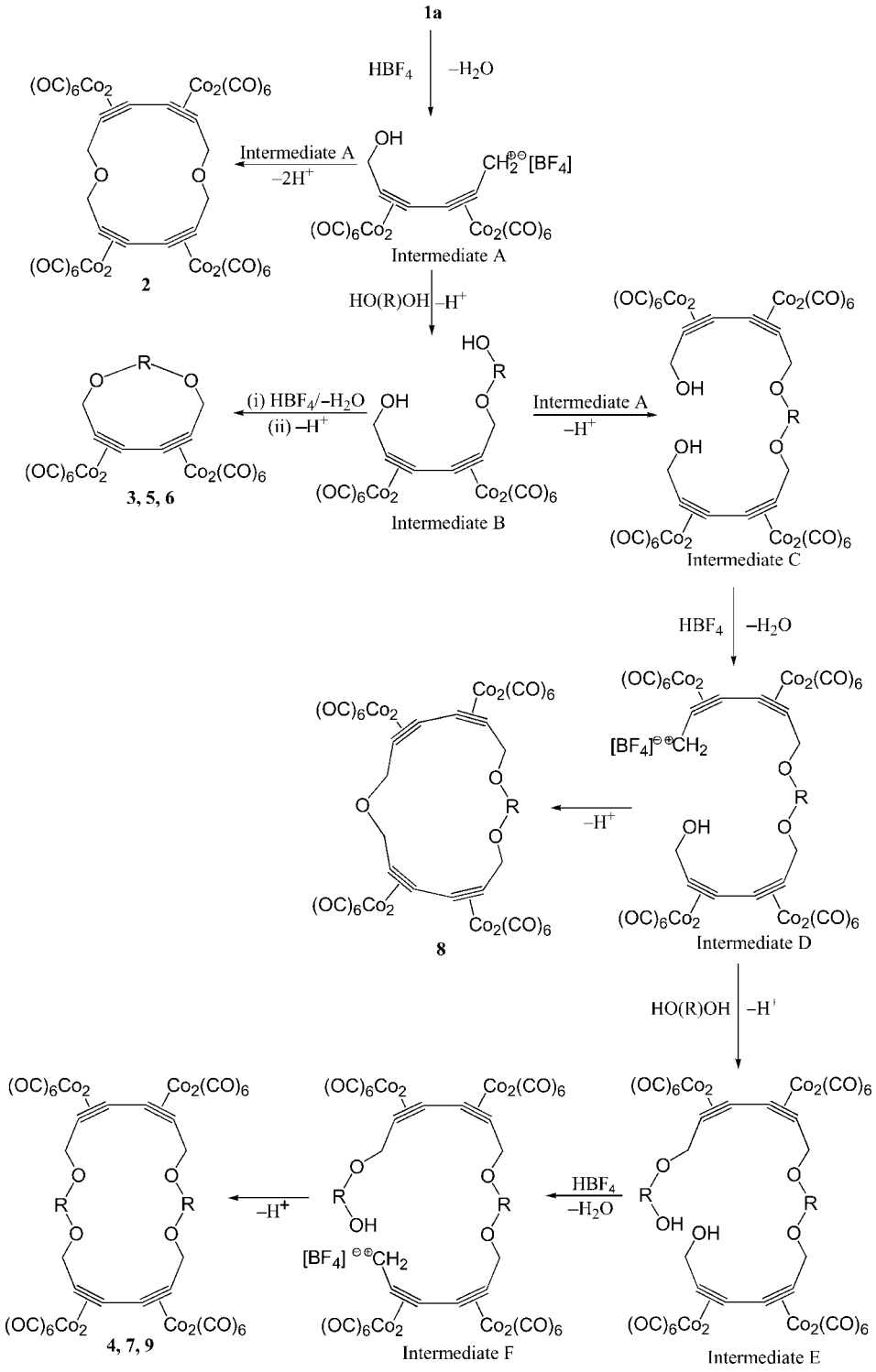


Scheme 3. Proposed pathway for the formation of **2**–**9** (R = linking unit).

 © 2007 Wiley-VCH Verlag GmbH & Co. KGaA, Weinheim 

tures determined in this work, the relative disposition of the two $Co_2C_2$ fragments on each diyne unit can be best described as pseudo *trans* [torsion angle C(13)–C(14)–C(15)–C(16) 101.7°] while the two $CH_2$–C≡C *bend back* angles are comparable [139.6(2) vs. 139.0(2)°].

The formation of the unsymmetrical complexes **8** was unexpected but could be used as some indirect evidence that the Nicholas reaction chemistry outlined here occurs via sequential functionalisation at the α carbon atoms and not by a dication (e.g., $[\{Co_2(CO)_6(\mu\text{-}\eta^2\text{-}CH_2C_2\text{-})\}_2]^{2+}$).[6d,17c,19] Indeed, we have shown elsewhere that a mono-functionalised derivative can be isolated on treatment of **1a** with PhSH which can in turn be converted to a di-functionalised derivative with the same or with a different thiol-based nucleophile.[20] With these observations in mind a possible pathway for the formation of the macrocyclic complexes **2**–**9** is shown in Scheme 3.

The initial step for all products proceeds by the formation of the propargylium monocation (intermediate A) when can then can either undergo nucleophilic attack with one end of the alkyl diol, HO(R)OH to form intermediate B or undergo self dimerisation to give **2**. Intermediate B can then follow one of two pathways; for complexes **3**, **5** and **6** the generation of the cationic species derived from B results in ring closure via an intramolecular reaction. The second pathway is for intermediate B to act as nucleophile and to react with A to form intermediate C. Intermediate C can then in turn follow, via cationic intermediate D, one of two pathways to afford unsymmetrical **8** or symmetrical **4**, **7** and **9**. It would seem likely that formation of **8** would be preferred with shorter chain R groups (i.e., $CH_2C{\equiv}CCH_2$ or $CH_2C_6H_4CH_2$) allowing closer proximity of the intramolecular reactive partners in D. Complexes **4**, **7** and **9** are formed when D elects to undergo intermolecular nucleophilic attack with HO(R)OH to give intermediate E. Ring closure is achieved by the intramolecular reaction resulting from generation of cationic intermediate F and nucleophilic attack by the remaining hydroxy group on the chain.

## 4. Conclusions

Our systematic study has showed that the alkyl diols, $HOCR_2$-linker-$CR_2OH$ (linker = alkyl, glycol, 1,3-diynyl, alkynyl, aryl; R = H, Me), can all act as effective nucleophiles on reaction with **1a** to generate crown-type macrocycles containing between and twelve and twenty eight atoms in high yields. In all cases the presence of trace quantities of the self-dimerised product **2** indicates a competitive reaction pathway that was not observed in our previous study of the reactions of thiol-based nucleophiles with **1a**.[9] The nature of the linker in the alkyl diol plays a key role in determining the monomer to dimer ratio, with monomeric **5** being uniquely favoured when **1a** is treated with glycols while with alkynyl- or aryl-linked alkyl diols solely the dimeric products **8**, **9** result; with alkyl- or 1,3-diyne-linked alkyl diols mixtures of both monomeric (**3**, **6**) and dimeric species (**4**, **7**) can be isolated. The identification of unsymmetrical dimeric species **8** when alkynyl- or aryl-linked alkyl diols nucleophiles are employed represents an unexpected observation.

## Experimental Section

**General Remarks:** Unless otherwise stated all experiments were carried out under dry, oxygen-free nitrogen, using standard Schlenk line techniques and solvents freshly distilled from appropriate drying agent.[21] NMR spectra were recorded in $CDCl_3$ with a Bruker DRX 400 spectrometer with TMS as an external standard for $^1H$ and $^{13}C$ spectra at ambient temperature. Infrared spectra were recorded in dichloromethane solution in 0.5-mm NaCl solution cells, with a Perkin–Elmer 1710 Fourier Transform Spectrometer. FAB (Fast atom bombardment) mass spectra were recorded with a Kratos MS 890 instrument using 3-nitrobenzyl alcohol as matrix. Elemental analyses were performed by the Microanalytical Department at the University of Cambridge. Preparative TLC was carried out on 1-mm silica plates prepared at the University of Cambridge. Column chromatography was performed on Kieselgel 60 (70–230 mesh ASTM). All products are listed in order of decreasing $R_f$. The reagents, 1,4-butanediol, 1,5-pentanediol, 1,6-hexanediol, triethylene glycol, tetraethylene glycol, tetrafluoroboric acid (54 wt.-% in diethyl ether), 1,4-benzenedimethanol, 2-butyne-1,4-diol, 2,4-hexadiyne-1,6-diol and 2,7-dimethyl-3,5-octadiyne-2,7-diol were obtained from Aldrich Chemical Co. and used without further purification. Complex $[\{Co_2(CO)_6(\mu\text{-}\eta^2\text{-}HOCH_2C_2\text{-})\}_2]$ (**1a**) was prepared by the literature method.[17]

**Reaction with $HOCH_2(CH_2)_2CH_2OH$:** Six drops of $HBF_4{\cdot}OEt_2$ were added to a stirred solution of **1a** (0.50 g, 0.733 mmol) and $HOCH_2(CH_2)_2CH_2OH$ (0.07 mL, 0.764 mmol) in dichloromethane (150 mL) at –78 °C. The solution was warmed to room temperature and after 6 h an excess of sodium hydrogen carbonate was added. All volatiles were removed on the rotary evaporator, the residue taken up in hexane and the suspension filtered through a plug of magnesium sulfate. The filtrate was adsorbed onto silica, the silica pumped dry and added to the top of a chromatography column. Elution with hexane/dichloromethane (8:1) afforded orange crystalline **2** (0.10 g, 10%) and **3a** (0.15 g, 28%). Further elution of the column with hexane/dichloromethane (6:1) yielded red crystalline **4a** (0.42 g, 39%). **Complex 2:** $^{13}C\{^1H\}$ NMR ($CDCl_3$, 75 MHz): $\delta$ = 199.4 (CO), 96.6 (C≡C), 72.4 ($OCH_2$) ppm. **Complex 3a:** $^{13}C\{^1H\}$ NMR ($CDCl_3$, 75 MHz): $\delta$ = 199.6 (CO), 92.6, 82.6 (C≡C), 72.3, 71.6 ($OCH_2$), 29.7 [$OCH_2(CH_2)_2CH_2O$] ppm. **Complex 4a:** $^{13}C\{^1H\}$ NMR ($CDCl_3$, 75 MHz): $\delta$ = 191.5, 189.8 (CO), 99.2 (C≡C), 71.3, 70.9 ($OCH_2$), 29.7, 26.8 [$OCH_2(CH_2)_2CH_2O$] ppm.

**Reaction with $HOCH_2(CH_2)_3CH_2OH$:** Six drops of $HBF_4{\cdot}OEt_2$ were added to a stirred solution of **1a** (0.50 g, 0.733 mmol) and $HOCH_2(CH_2)_3CH_2OH$ (0.08 mL, 0.763 mmol) in dichloromethane (150 mL) at –78 °C. The solution was warmed to room temperature and after 6 h an excess of sodium hydrogen carbonate was added. All volatiles were removed on the rotary evaporator, the residue taken up in hexane and the suspension filtered through a plug of magnesium sulfate. The filtrate was adsorbed onto silica, the silica pumped dry and added to the top of a chromatography column. Elution with hexane/dichloromethane (8:1) afforded orange crystalline **2** (0.05 g, 5%). Further elution of the column with hexane/dichloromethane (6:1) yielded red crystalline **3b** (0.15 g, 28%) and then with hexane/dichloromethane (4:1), orange crystalline **4b** (0.32 g, 29%). **Complex 3b:** $^{13}C\{^1H\}$ NMR ($CDCl_3$, 75 MHz): $\delta$ =

 © 2007 Wiley-VCH Verlag GmbH & Co. KGaA, Weinheim 

196.5 (CO), 98.8 (C≡C), 71.6, 69.8 ($OCH_2$), 26.7, 23.5 [$OCH_2(CH_2)_3CH_2O$] ppm. **Complex 4b:** $^{13}C\{^1H\}$ NMR ($CDCl_3$, 75 MHz): $\delta$ = 199.6 (CO), 94.3 (C≡C), 72.8, 71.4 ($OCH_2$), 24.3, 23.5 [$OCH_2(CH_2)_3CH_2O$] ppm.

**Reaction with $HOCH_2(CH_2)_4CH_2OH$:** Six drops of $HBF_4{\cdot}OEt_2$ were added to a stirred solution of **1a** (0.50 g, 0.733 mmol) and $HOCH_2(CH_2)_4CH_2OH$ (0.09 g, 0.762 mmol) in dichloromethane (150 mL) at –78 °C. The solution was warmed to room temperature and after 6 h an excess of sodium hydrogen carbonate was added. All volatiles were removed on the rotary evaporator, the residue taken up in hexane and the suspension filtered through a plug of magnesium sulfate. The filtrate was adsorbed onto silica, the silica pumped dry and added to the top of a chromatography column. Elution with hexane/dichloromethane (8:1) afforded orange crystalline **2** (0.10 g, 10%). Further elution of the column with hexane/dichloromethane (7:1) yielded red crystalline **3c** (0.31 g, 55%) and then with hexane/dichloromethane (4:1), orange crystalline **4c** (0.31 g, 28%). **Complex 3c:** $^{13}C\{^1H\}$ NMR ($CDCl_3$, 75 MHz): 198.9 (CO), 98.7 (C≡C), 71.3, 70.1 ($OCH_2$), 26.7 [$OCH_2(CH_2)_4CH_2O$]. **Complex 4c:** $^{13}C\{^1H\}$ NMR ($CDCl_3$, 75 MHz): $\delta$ = 198.9 (CO), 96.8 (C≡C), 74.2, 71.3 ($OCH_2$), 29.6, 25.9 [$OCH_2(CH_2)_4CH_2O$] ppm.

**Reaction with $HO(CH_2CH_2O)_3H$:** Four drops of $HBF_4{\cdot}OEt_2$ were added to a stirred solution of **1a** (0.50 g, 0.733 mmol) and $HO(CH_2CH_2O)_3H$ (0.10 mL, 0.749 mmol) in dichloromethane (150 mL) at –78 °C. The solution was warmed to room temperature and after 12 h an excess of sodium hydrogen carbonate was added. All volatiles were removed on the rotary evaporator, the residue taken up in hexane and the suspension filtered through a plug of magnesium sulfate. The filtrate was adsorbed onto silica, the silica pumped dry and added to the top of a chromatography column. Elution with hexane/dichloromethane (8:1) afforded orange crystalline **2** (0.05 g, 5%). Further elution of the column with dichloromethane yielded deep red crystalline **5a** (0.49 g, 83%). **Complex 5a:** $^{13}C\{^1H\}$ NMR ($CDCl_3$, 75 MHz): $\delta$ = 195.6 (CO), 101.2, 82.6 (C≡C), 72.4, 71.8 ($OCH_2$) ppm.

**Reaction with $HO(CH_2CH_2O)_4H$:** Four drops of $HBF_4{\cdot}OEt_2$ were added to a stirred solution of **1a** (0.50 g, 0.733 mmol) and $HO(CH_2CH_2O)_4H$ (0.13 mL, 0.753 mmol) in dichloromethane (150 mL) at –78 °C. The solution was warmed to room temperature and after 12 h an excess of sodium hydrogen carbonate was added. All volatiles were removed on the rotary evaporator, the residue taken up in hexane and the suspension filtered through a plug of magnesium sulfate. The filtrate was adsorbed onto silica, the silica pumped dry and added to the top of a chromatography column. Elution with hexane/dichloromethane (8:1) afforded orange crystalline **2** (0.10 g, 10%). Further elution of the column with dichloromethane afforded red crystalline **5b** (0.25 g, 40%). **Complex 5b:** $^{13}C\{^1H\}$ NMR ($CDCl_3$, 75 MHz): $\delta$ = 199.0 (CO), 98.8, 83.4 (C≡C), 72.0, 71.4, 71.0, 70.8 ($OCH_2$) ppm.

**Reaction with $HOCH_2C{\equiv}CC{\equiv}CCH_2OH$:** Six drops of $HBF_4{\cdot}OEt_2$ were added to a stirred solution of **1a** (0.50 g, 0.733 mmol) and $HOCH_2C{\equiv}CC{\equiv}CCH_2OH$ (0.080 g, 0.736 mmol) in dichloromethane (150 mL) at room temperature. After 16 h of stirring an excess of sodium hydrogen carbonate was added. All volatiles were removed on the rotary evaporator, the residue taken up in hexane and the suspension filtered through a plug of magnesium sulfate. The filtrate was adsorbed onto silica, the silica pumped dry and added to the top of a chromatography column. Elution with hexane/dichloromethane (8:1) afforded orange crystalline **2** (0.04 g, 4%). Further elution of the column with hexane/dichloromethane (3:1) gave deep red crystalline **6a** (0.18 g, 32%) and then with hexane/dichloromethane (2:1), deep red crystalline **7a** (0.18 g, 32%). **Complex 6a:** $^{13}C\{^1H\}$ NMR ($CDCl_3$, 75 MHz): $\delta$ = 194.3 (CO), 98.4, 91.2 (C≡C), 73.2, 71.2 ($OCH_2$) ppm. **Complex 7a:** $^{13}C\{^1H\}$ NMR ($CDCl_3$, 75 MHz): $\delta$ = 198.7 (CO), 101.2, 82.6 (C≡C), 74.6, 71.2 ($OCH_2$) ppm.

**Reaction with $HOC(Me)_2C{\equiv}CC{\equiv}CC(Me)_2OH$:** Six drops of $HBF_4{\cdot}OEt_2$ were added to a stirred solution of **1a** (0.50 g, 0.733 mmol) and $HOC(Me)_2C{\equiv}CC{\equiv}CC(Me)_2OH$ (0.081 g, 0.736 mmol) in dichloromethane (150 mL) at room temperature. After 16 h of stirring an excess of sodium hydrogen carbonate was added. All volatiles were removed on the rotary evaporator, the residue taken up in hexane and the suspension filtered through a plug of magnesium sulfate. The filtrate was adsorbed onto silica, the silica pumped dry and added to the top of a chromatography column. Elution with hexane/dichloromethane (8:1) afforded orange crystalline **2** (0.04 g, 4%). Further elution of the column with hexane/dichloromethane (4:1) gave red crystalline **6b** (0.16 g, 27%) and then with hexane/dichloromethane (2:1), orange crystalline **7b** (0.41 g, 34%). **Complex 6b:** $^{13}C\{^1H\}$ NMR ($CDCl_3$, 75 MHz): $\delta$ = 198.9 (CO), 96.4, 82.4 (C≡C), 72.6 [$OC(CH_3)_2$], 28.4 ($CH_3$) ppm. **Complex 7b:** $^{13}C\{^1H\}$ NMR ($CDCl_3$, 75 MHz): $\delta$ = 198.9 (CO), 98.6, 84.2 (C≡C), 72.5 [$OC(CH_3)_2$], 26.9 ($CH_3$) ppm.

**Reaction with $HOCH_2C{\equiv}CCH_2OH$:** Six drops of $HBF_4{\cdot}OEt_2$ were added to a stirred solution of **1a** (0.50 g, 0.733 mmol) and $HOCH_2C{\equiv}CCH_2OH$ (0.065 g, 0.755 mmol) in dichloromethane (150 mL) at room temperature. After 16 h of stirring an excess of sodium hydrogen carbonate was added. All volatiles were removed on the rotary evaporator, the residue dissolved in hexane and the solution filtered through a plug of magnesium sulfate. The filtrate was adsorbed onto silica, the silica pumped dry and added to the top of a chromatography column. Elution with hexane/dichloromethane (8:1) afforded orange crystalline **2** (0.04 g, 4%). Further elution of the column with hexane/dichloromethane (4:1) gave deep red crystalline **8a** (0.24 g, 23%) and then with hexane/dichloromethane (3:1), deep red crystalline **9a** (0.52 g, 48%). **Complex 8a:** $^{13}C\{^1H\}$ NMR ($CDCl_3$, 75 MHz): $\delta$ = 199.9 (CO), 104.2, 94.3, 89.6 (C≡C), 74.3, 72.4, 68.2 ($CH_2$) ppm. **Complex 9a:** $^{13}C\{^1H\}$ NMR ($CDCl_3$, 75 MHz): $\delta$ = 194.5 (CO), 94.2, 92.6 (C≡C), 74.8, 73.2 ($OCH_2$) ppm.

**Reaction with $HOCH_2(C_6H_4)CH_2OH$:** Six drops of $HBF_4{\cdot}OEt_2$ were added to a stirred solution of **1a** (0.50 g, 0.733 mmol) and $HOCH_2(C_6H_4)CH_2OH$ (0.11 g, 0.796 mmol) in dichloromethane (150 mL) at room temperature. After 16 h of stirring an excess of sodium hydrogen carbonate was added. All volatiles were removed on the rotary evaporator, the residue dissolved in hexane and the solution filtered through a plug of magnesium sulfate. The filtrate was adsorbed onto silica, the silica pumped dry and added to the top of a chromatography column. Elution with hexane/dichloromethane (8:1) afforded orange crystalline **2** (0.04 g, 4%). Further elution of the column with hexane/dichloromethane (4:1) yielded deep red crystalline **8b** (0.42 g, 40%) and then with hexane/dichloromethane (3:1), deep red crystalline **9b** (0.39 g, 34%). **Complex 8b:** $^{13}C\{^1H\}$ NMR ($CDCl_3$, 75 MHz): $\delta$ = 199.0 (CO), 137.7, 129.3 (Ph), 101.2, 97.9, 92.7 (C≡C), 73.7, 72.6, 71.7 ($OCH_2$) ppm. **Complex 9b:** $^{13}C\{^1H\}$ NMR ($CDCl_3$, 75 MHz): $\delta$ = 198.9 (CO), 137.6, 127.9 (Ph), 99.7, 92.7 (C≡C), 72.8, 70.6 ($OCH_2$) ppm.

**Crystallographic Studies:** Single crystal X-ray diffraction data for **2**, **3a**, **5a**, **7a**, **8a**, **8b** and **9a** were collected using a Nonius-Kappa CCD diffractometer, equipped with an Oxford Cryosystems cyrostream and employing Mo-$K_\alpha$ ($\lambda$ = 0.71073 Å) irradiation from a sealed tube X-ray source. Cell refinement, data collection and data

 © 2007 Wiley-VCH Verlag GmbH & Co. KGaA, Weinheim 

reduction were performed with the programs DENZO[22] and COLLECT[23] and multi-scan absorption corrections were applied to all intensity data with the program SORTAV.[24] All structures were solved and refined with the programs SHELXS97 and SHELXL97,[25] respectively. Hydrogen atoms were included in calculated positions (C–H = 0.96 Å) riding on the bonded atom with isotropic displacement parameters set to $1.5U_{eq}$(C) for methyl H atoms and $1.2U_{eq}$(C) for all other H atoms. Details of the data collection, refinement and crystal data are listed in Table 9.

CCDC-634737 (for **2**), -634738 (for **3a**), -634739 (for **5a**), -634740 (for **7a**), -63741 (for **8a**), -63743 (for **8b**) and -63742 (for **9a**) contain

Table 9. Crystallographic and data processing parameters for **2**, **3a**, **5a**, **7a**, **8a**, **8b** and **9a**.[a]

| Complex | **2** | **3a** | **5a** | **7a** |
|---|---|---|---|---|
| Formula | $C_{36}H_8Co_8O_{26}$ | $C_{22}H_{12}Co_4O_{14}$ | $C_{24}H_{16}Co_4O_{16}$ | $C_{48}H_{16}Co_8O_{28}$ |
| $M$ | 1327.86 | 736.04 | 796.09 | 1512.05 |
| Crystal size [mm$^3$] | 0.16×0.16×0.14 | 0.23×0.18×0.18 | 0.16×0.14×0.07 | 0.23×0.11×0.02 |
| Temperature [K] | 180(2) | 218(2) | 180(2) | 180(2) |
| Crystal system | triclinic | monoclinic | triclinic | monoclinic |
| Space group | $P\bar{1}$ | $P2_1/c$ | $P\bar{1}$ | $C2/c$ |
| $a$ [Å] | 9.1421(2) | 10.5931(2) | 9.3341(3) | 30.6875(9) |
| $b$ [Å] | 9.7436(2) | 29.3338(6) | 10.8973(4) | 9.7804(3) |
| $c$ [Å] | 13.8812(3) | 18.0644(2) | 16.0019(5) | 18.9422(3) |
| $\alpha$ [°] | 81.4780(10) | 90 | 87.727(2) | 90 |
| $\beta$ [°] | 75.7070(10) | 102.1540(10) | 77.193(2) | 93.862(2) |
| $\gamma$ [°] | 68.0840(10) | 90 | 73.997(2) | 90 |
| $V$ [Å$^3$] | 1109.47(4) | 5487.44(16) | 1525.26(9) | 5672.3(3) |
| $Z$ | 1 | 8 | 2 | 4 |
| $D_c$ [Mg·m$^{-3}$] | 1.987 | 1.782 | 1.733 | 1.771 |
| $F$(000) | 648 | 2912 | 792 | 2976 |
| $\mu$(Mo-$K_\alpha$)[mm$^{-1}$] | 3.005 | 2.443 | 2.209 | 2.366 |
| Reflections collected | 29146 | 41586 | 18340 | 22382 |
| Independent reflections | 5084 | 12431 | 6923 | 6445 |
| $R_{int}$ | 0.0572 | 0.0641 | 0.0475 | 0.0650 |
| Restraints/parameters | 0/316 | 3/710 | 0/397 | 0/379 |
| Final $R$ indices | $R_1$ = 0.0273 | $R_1$ = 0.0419 | $R_1$ = 0.0334 | $R_1$ = 0.0364 |
| [$I>2\sigma(I)$] | $wR_2$ = 0.0639 | $wR_2$ = 0.0917 | $wR_2$ = 0.0609 | $wR_2$ = 0.0848 |
| All data | $R_1$ = 0.0374 | $R_1$ = 0.0775 | $R_1$ = 0.0581 | $R_1$ = 0.0519 |
| | $wR_2$ = 0.0674 | $wR_2$ = 0.1043 | $wR_2$ = 0.0683 | $wR_2$ = 0.0923 |
| Goodness of fit on $F^2$ (all data) | 1.070 | 1.041 | 1.009 | 1.027 |
| Complex | **8a** | **8b** | **9a** | |
| Formula | $C_{40}H_{12}Co_8O_{27}$·0.5$C_6H_{14}$ | $C_{44}H_{16}Co_8O_{27}$ | $C_{44}H_{16}Co_8O_{28}$ | |
| $M$ | 1439.02 | 1448.01 | 1464.01 | |
| Crystal size [mm$^3$] | 0.18×0.16×0.09 | 0.23×0.14×0.05 | 0.16×0.14×0.05 | |
| Temperature [K] | 220(2) | 180(2) | 180(2) | |
| Crystal system | triclinic | monoclinic | triclinic | |
| Space group | $P\bar{1}$ | $C2/c$ | $P\bar{1}$ | |
| $a$ [Å] | 10.6824(2) | 15.6580(5) | 8.9576(3) | |
| $b$ [Å] | 15.9498(5) | 10.3968(2) | 10.3831(4) | |
| $c$ [Å] | 17.1603(5) | 33.3519(11) | 15.6330(4) | |
| $\alpha$ [°] | 74.682(2) | 90 | 104.052(2) | |
| $\beta$ [°] | 80.721(2) | 97.216(2) | 96.197(2) | |
| $\gamma$ [°] | 73.670(2) | 90 | 107.097(2) | |
| $V$ [Å$^3$] | 2694.21(13) | 5386.5(3) | 1322.69(8) | |
| $Z$ | 2 | 4 | 1 | |
| $D_c$ [Mg·m$^{-3}$] | 1.774 | 1.786 | 1.838 | |
| $F$(000) | 1418 | 2848 | 720 | |
| $\mu$(Mo-$K_\alpha$)[mm$^{-1}$] | 2.484 | 2.486 | 2.533 | |
| Reflections collected | 28377 | 14546 | 15323 | |
| Independent reflections | 12158 | 5984 | 6052 | |
| $R_{int}$ | 0.0534 | 0.0528 | 0.0541 | |
| Restraints/parameters | 5/688 | 0/357 | 0/361 | |
| Final $R$ indices | $R_1$ = 0.0437 | $R_1$ = 0.0363 | $R_1$ = 0.0335 | |
| [$I>2\sigma(I)$] | $wR_2$ = 0.0988 | $wR_2$ = 0.0789 | $wR_2$ = 0.0733 | |
| All data | $R_1$ = 0.0731 | $R_1$ = 0.0607 | $R_1$ = 0.0469 | |
| | $wR_2$ = 0.1125 | $wR_2$ = 0.0873 | $wR_2$ = 0.0791 | |
| Goodness of fit on $F^2$ (all data) | 1.011 | 0.978 | 1.041 | |

[a] Data in common: graphite-monochromated Mo-$K_\alpha$ radiation, $\lambda$ = 0.71073 Å; $R_1 = \Sigma||F_o| - |F_c||/\Sigma|F_o|$, $wR_2 = [\Sigma w(F_o^2 - F_c^2)^2/\Sigma w(F_o^2)^2]1/2$, $w^{-1} = [\sigma^2(F_o)^2 + (aP)^2]$, $P = [\max.(F_o^2,0) + 2(F_c^2)]/3$, where a is a constant adjusted by the program; goodness of fit = $[\Sigma(F_o^2 - F_c^2)2/(n-p)]^{1/2}$ where $n$ is the number of reflections and $p$ the number of parameters.

 © 2007 Wiley-VCH Verlag GmbH & Co. KGaA, Weinheim 

the supplementary crystallographic data for this paper. These data can be obtained free of charge from The Cambridge Crystallographic Data Centre via www.ccdc.cam.ac.uk/data_request/cif.

## Acknowledgments

We acknowledge the financial support of the Engineering and Physical Sciences Research Council (EPSRC) (L. J. H.-W) and Dstl. Fort Halstead (L. J. H.-W). The help of the EPSRC mass spectrometry service, Swansea is gratefully acknowledged. Dr John E. Davies is thanked for crystal structure determinations.

[1] For reviews see: a) G. G. Melikyan, K. M. Nicholas, in *Modern Acetylene Chemistry* (Eds.: P. J. Stang, F. Diederich), VCH, Weinheim, **1995**, chapter 4, pp. 99–139; b) A. J. M. Caffyn, K. M. Nicholas, in *Comprehensive Organometallic Chemistry II* (Eds.: E. W. Abel, F. G. A. Stone, G. Wilkinson), Pergamon, Oxford, **1995**, vol. 12, chapter 7, pp. 685–702; c) K. M. Nicholas, *Acc. Chem. Res.* **1987**, *20*, 207–214; d) B. J. Teobald, *Tetrahedron* **2002**, *58*, 4133–4170.

[2] a) M. Isobe, R. Nishizawa, S. Hosokawa, T. Nishikawa, *Chem. Commun.* **1998**, 2665–2676; b) N. Ortega, T. Martin, V. S. Martin, *Org. Lett.* **2006**, *8*, 871–873 and refs therein; c) C. Mukai, S. Yamaguchi, Y. Sugimoto, N. Miyakoshi, E. Kasamatsu, M. Hanaoka, *J. Org. Chem.* **2000**, *65*, 6761–6765.

[3] a) A. Gelling, G. F. Mohmand, J. C. Jeffery, M. J. Went, *J. Chem. Soc., Dalton Trans.* **1993**, 1857–1862; b) A. Gelling, J. C. Jeffery, D. C. Povey, M. J. Went, *J. Chem. Soc., Chem. Commun.* **1991**, 349–351; c) F. Demirhan, A. Gelling, S. Irisli, J. C. Jeffery, S. N. Salek, O. S. Senturk, M. J. Went, *J. Chem. Soc., Dalton Trans.* **1993**, 2765–2773; d) F. Demirhan, S. Irisli, S. N. Salek, O. S. Senturk, M. J. Went, J. C. Jeffery, *J. Organomet. Chem.* **1993**, *453*, C30–C31; e) S. C. Bennett, J. C. Jeffery, M. J. Went, *J. Chem. Soc., Dalton Trans.* **1994**, 3171–3176.

[4] E. Alvaro, M. C. de la Torre, M. A. Sierra, *Chem. Commun.* **2006**, 985–987.

[5] G. G. Melikyan, M. A. Khan, K. M. Nicholas, *Organometallics* **1995**, *14*, 2170–2172.

[6] a) R. Guo, J. R. Green, *Chem. Commun.* **1999**, 2503–2504; b) R. Gibe, J. R. Green, G. Davidson, *Org. Lett.* **2003**, *5*, 1003–1005; c) R. Gibe, J. R. Green, *Chem. Commun.* **2002**, 1550–1551; d) R. Guo, J. R. Green, *Synlett* **2000**, 746–748.

[7] See for example: a) R. M. Izatt, K. Pawlak, J. S. Bradshaw, R. L. Breuning, *Chem. Rev.* **1991**, *91*, 1721–1785; b) L. F. Lindoy, *Pure Appl. Chem.* **1997**, *69*, 2179–2186; c) F. Neve, M. Ghedini, M. Francescangeil, *Liq. Cryst.* **1996**, *21*, 625–630; d) A. J. Blake, A. Taylor, M. Schröder, *J. Chem. Soc., Chem. Commun.* **1993**, 1097–1098.

[8] P. I. Dosa, C. Erben, V. S. Iyer, K. P. C. Vollhardt, I. M. Wasser, *J. Am. Chem. Soc.* **1999**, *121*, 10430–10431.

[9] a) J. E. Davies, L. J. Hope-Weeks, M. J. Mays, P. R. Raithby, *Chem. Commun.* **2000**, 1411–1412; b) L. J. Hope-Weeks, M. J. Mays, A. D. Woods, *J. Chem. Soc., Dalton Trans.* **2002**, 1812–1819.

[10] R. C. J. Atkinson, L. J. Hope-Weeks, M. J. Mays, G. A. Solan, *J. Organomet. Chem.* **2007**, *692*, 2076–2085.

[11] V. B. Golovko, L. J. Hope-Weeks, M. J. Mays, M. McPartlin, A. M. Sloan, A. D. Woods, *New J. Chem.* **2004**, *28*, 527–534.

[12] a) X.-N. Chen, J. Zhang, S.-L. Wu, Y.-Q. Yin, W.-L. Wang, J. Sun, *J. Chem. Soc., Dalton Trans.* **1999**, 1987–1992; b) C. E. Housecroft, B. F. G. Johnson, M. S. Khan, J. Lewis, P. R. Raithby, M. E. Robson, D. A. Wilkinson, *J. Chem. Soc., Dalton Trans.* **1992**, 3171–3178.

[13] a) V. B. Golovko, M. J. Mays, A. D. Woods, *New J. Chem.* **2002**, *26*, 1706–1708; b) B. F. G. Johnson, J. Lewis, P. R. Raithby, D. A. Wilkinson, *J. Organomet. Chem.* **1991**, *408*, C9–C12; c) E. Champeil, S. M. Draper, *J. Chem. Soc., Dalton Trans.* **2001**, 1440–1447; d) M. B. Nielsen, N. F. Utesch, N. N. P. Moonen, C. Boudon, J.-P. Gisselbrecht, S. Concilio, S. P. Piotto, P. Seiler, P. Gunter, M. Gross, F. Diederich, *Chem. Eur. J.* **2002**, *8*, 3601–3613; e) M. I. Bruce, B. W. Skelton, M. E. Smith, A. H. White, *Aust. J. Chem.* **1999**, *52*, 431–435; f) Q.-L. Suo, L.-M. Han, Y.-B. Wang, J.-H. Ye, N. Zhu, X.-B. Leng, J. Sun, *J. Coord. Chem.* **2004**, *57*, 1591–1601.

[14] B. J. Rausch, R. Gleiter, F. Rominger, *J. Chem. Soc., Dalton Trans.* **2002**, 2219–2226.

[15] For use of the $CH_2$–C≡C *bend-back* angles as an indicator of strain present in alkyne-/diyne-containing macrocycles see refs. 3b, 9, 10.

[16] Calculated from a CCDC search, F. H. Allen, O. Kennard, *Chem. Design Automation News* **1993**, *8*, 31.

[17] a) G. F. Mohmand, K. Thiele, M. J. Went, *J. Organomet. Chem.* **1994**, *471*, 241–248; b) A. Osella, L. Milone, C. Nervi, M. Ravera, *Eur. J. Inorg. Chem.* **1998**, 1473–1477; c) Amouri, C. Da Silva, B. Malezieux, R. Andres, J. Vaissermann, M. Gruselle, *Inorg. Chem.* **2000**, *39*, 5053–5058.

[18] P. Groth, *Acta Chem. Scand. Ser. A* **1978**, *32*, 279–280.

[19] a) S. C. Bennet, M. A. Philipis, M. J. Went, *J. Chem. Soc., Chem. Commun.* **1994**, 225–239; b) G. G. Melikyan, A. Deravakian, S. Myer, S. Yadegar, K. I. Hardcastle, J. Ciurash, P. J. Toole, *J. Organomet. Chem.* **1999**, *578*, 68–75.

[20] L. J. Hope-Weeks, M. J. Mays, C. Paredes, G. A. Solan, *Can. J. Chem.* **2007**, submitted.

[21] W. L. F. Armarego, D. D. Perrin, "*Purification of Laboratory Chemicals*", Butterworth Heinemann, 4th ed., **1996**.

[22] Z. Otwinowski, W. Minor, *Methods Enzymol.* **1997**, *276*, 307–326.

[23] R. Hooft, *COLLECT*, Nonius BV, Delft, The Netherlands, **1998**.

[24] R. H. Blessing, *Acta Crystallogr., Sect. A* **1995**, *51*, 33–38.

[25] G. M. Sheldrick, *SHELXS97 and SHELXL97*, University of Göttingen, Germany, **1997**.

Received: January 28, 2007
Published Online: May 10, 2007

 © 2007 Wiley-VCH Verlag GmbH & Co. KGaA, Weinheim 

DOI: 10.1002/ejic.200700157

# Platinum(II) Alkynyl Complexes Containing *N*- and *S*-Propargylated Ligands: Synthesis, Structures and Formation of $Pt^{II}/Ag^{I}$ Coordination Compounds

**Fabian Mohr,*[a,b] Aránzazu Mendía,*[b] and Mariano Laguna[c]**

**Keywords:** Platinum / Alkynes / Silver / Dimetallic / Coordination complexes

Alkylation of 2-hydroxypyridine, 2-pyridinethiol, 2-hydroxy-4-methylquinoline, phthalimide and pyrazole with propargyl bromide gave a series of alkynes in high yield. These alkynes were reacted with the chloroplatinum(II) compounds *trans*-$[PtCl_2(PPh_3)_2]$ and *cis*-$[PtCl_2(dppe)]$ to afford the respective *trans*- and *cis*-bis(alkynyl)platinum(II) complexes, which were characterised by spectroscopic analysis and by X-ray diffraction. The platinum(II) complexes containing the thiopyridyl- and pyrazolyl-substituted alkynes react with 1 or 2 equiv. of $[Ag(NO_3)(PPh_3)]$ to give dimetallic $Pt^{II}/Ag^{I}$ complexes.

(© Wiley-VCH Verlag GmbH & Co. KGaA, 69451 Weinheim, Germany, 2007)

## Introduction

Platinum(II) alkynyl complexes have been known for many years, but since the discovery of their luminescence and nonlinear optical (NLO) properties the field has experienced rapid growth.[1–5] Numerous platinum(II) alkynyl complexes have been synthesised by a variety of different routes and some complexes have been structurally characterised.[6,7] O-Propargylated compounds, in particular those derived from bisphenols, have been extensively used as C-donor ligands in the supramolecular assembly of gold(I) polymers, macrocycles and catenanes;[8–13] however, no examples of their use as ligands in other transition-metal complexes have been reported. Whereas the preparation, some organic transformations and applications of selected *N*-propargylated compounds have been published,[14–17] the organometallic chemistry of these species acting as C-donor ligands is a relatively unexplored field. Silver alkynyl complexes of various propargylamines have been used as alkyne transfer reagents in the synthesis of analogues of the opium derivative cotarnine.[18] Similarly, gold(I) phosphane complexes containing *N*-propargylphthalimide have been used to transfer the Au-phosphane moiety to tetra- and penta-iron clusters.[19] A series of alkynyl tin and silicon complexes containing C-coordinated *N*-propargylpyrazole have been prepared from the lithium salt.[20] Alkynyl complexes of mercury containing *N*-propargylated acridone are strongly fluorescent and have been used as sensitive sensors for the detection of organomercury compounds in water or biological systems.[21,22] *S*-Propargylated compounds are even less well-studied; their preparation and some organic chemistry of only a small number of compounds has been reported.[23,24] The only known example of a metal-containing derivative of an *S*-propargylated compound is the tin complex of propargylthiotriazole, which was patented as a fungicide.[25] In light of this lack of organometallic chemistry of *N*- and *S*-propargylated compounds, we wished to pursue our interest in metal alkynyl complexes[26–28] and the chemistry of platinum complexes with N,S-donor ligands[29] by preparing and structurally characterising some platinum(II) alkynyl complexes of various *N*- and *S*-propargylated compounds.

## Results and Discussion

The tautomerism of 2-hydroxypyridine has been studied both experimentally and computationally in great detail by various groups. Spectroscopic data indicates that the hydroxy form is the major tautomer in the gas phase.[30–32] In the solid state, however, the formation of hydrogen bonded dimers seems to favour the 2-pyridone tautomers.[33] Similarly, we found, by $^1H$ and $^{13}C$ NMR spectroscopy in acetone, that 2-hydroxypyridine and 2-pyridinethiol exist exclusively as the 2-pyridone and 2-pyridinethione tautomers, respectively. Upon reaction of these compounds with propargyl bromide in the presence of base in acetone, these two starting materials gave two different propargylated products. In the case of 2-hydroxypyridine, the *N*-propargylated product ($R^1CH_2C{\equiv}CH$) was obtained, whereas from 2-pyridinethiol the *S*-propargylated compound ($R^2CH_2C{\equiv}CH$)

[a] Fachbereich C – Anorganische Chemie, Bergische Universität Wuppertal,
42119 Wuppertal, Germany
Fax: +49-202-439-3053
E-mail: fmohr@uni-wuppertal.de
[b] Departamento de Química, Facultad de Ciencias, Universidad de Burgos,
09001 Burgos, Spain
[c] Departamento de Química Inorgánica, Instituto de Ciencia de Materiales de Aragón, Universidad de Zaragoza-C.S.I.C,
50009 Zaragoza, Spain

 © 2007 Wiley-VCH Verlag GmbH & Co. KGaA, Weinheim 

was isolated (Scheme 1). We calculated the relative energies of each of the four possible propargylated isomers using density functional theory (DFT) methods. In the case of 2-hydroxypyridine, the *N*-propargylated compound is 8.8 kcal/mol more stable than the O-propargylated tautomer. In contrast, for 2-pyridinethione the *S*-propargylated species is 2.5 kcal/mol more stable than the *N*-propargylated tautomer (Figure 1). These computational results are in agreement with our, and previously reported, experimental observations.[16,23] In addition to the two alkynes discussed above, the previously reported *N*-propargylated compounds derived from 2-hydroxy-4-methylquinoline,[14] phthalimide[17] and pyrazole[15] (designated as $R^nCH_2C{\equiv}CH$; $n$ = 3–5) were prepared similarly (Scheme 2). In our hands, the procedure using $K_2CO_3$ in acetone was much simpler in terms of work up (filtration and evaporation of acetone) than the previously described methods. *N*-Alkylation in $R^1CH_2CCH$ and $R^3CH_2CCH$ is evident from their NMR- (particularly $^{13}C$) and IR spectra. The methylene carbon signal in the $^{13}C$ NMR spectra of these two compounds is shifted by ca. 17 ppm downfield relative to that of the *S*-propargyl derivative $R^2CH_2CCH$. Similarly, although less pronounced, the $NCH_2$ proton signals of $R^1CH_2CCH$ and $R^3CH_2CCH$ are shifted ca. 2 ppm downfield relative to the $SCH_2$ resonance of $R^2CH_2CCH$, which is consistent with the difference in electronegativity of sulfur and nitrogen. Further evidence for *N*-propargylation is seen in the IR spectra of $R^1CH_2CCH$ and $R^3CH_2CCH$, which show strong C=O absorption bands.

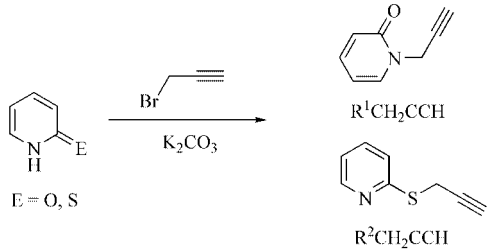


Scheme 1.

These alkynes react with the dichloroplatinum(II) complexes *trans*-$[PtCl_2(PPh_3)_2]$ and *cis*-$[PtCl_2(dppe)]$ [dppe = $Ph_2P(CH_2)_2PPh_2$] in the presence of $Et_2NH$ and a catalytic amount of [CuI][34–36] to afford the air- and water-stable alkynyl platinum(II) complexes *trans*-$[Pt(C{\equiv}CCH_2R)_2(PPh_3)_2]$ ($R^1$ = **1**, $R^2$ = **3**, $R^3$ = **5**, $R^4$ = **7**, $R^5$ = **9**) and *cis*-$[Pt(C{\equiv}CCH_2R)_2(dppe)]$ ($R^1$ = **2**, $R^2$ = **4**, $R^3$ = **6**, $R^4$ = **8**, $R^5$ = **10**), respectively, in high yields (Scheme 3). Complexes **1**–**10** were characterised spectroscopically including $^1H$ and $^{31}P\{^1H\}$ NMR spectroscopy, mass spectrometry, IR spectroscopy and elemental analysis. The $^{31}P\{^1H\}$ NMR spectra of complexes **1**–**10** show sharp singlet resonances with Pt satellites having $J_{Pt-P}$ values of ca. 2600 and 2300 Hz for the *trans* and *cis* isomers, respectively, which indicates the presence of a single species in solution. In principle, there are two possible configurations of the R groups for all but complexes **7** and **8**, namely the *exo–exo* and *endo–exo* configurations as illustrated for complex **2** in Figure 2. The $^1H$

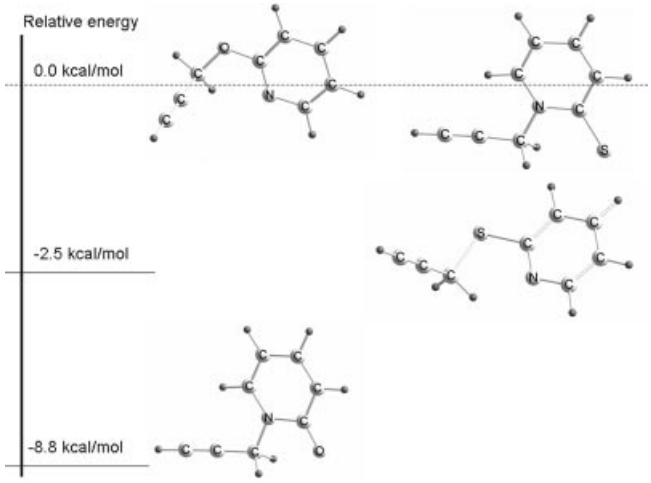


Figure 1. DFT optimised structures of the propargylated tautomers of 2-propargyloxypyridine and 2-propargylthiopyridine showing the energy differences between the two forms.

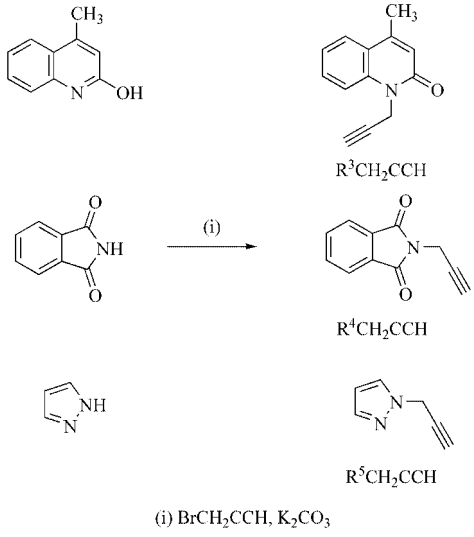


Scheme 2.

NMR spectrum of complex **2** in $CDCl_3$ at room temperature shows only one set of signals (doublets and triplets) for the R substituents, which indicates that rotation about the C–N bond is rapid in solution on the NMR timescale. Lowering the temperature to –80 °C has no effect on the appearance of the $^1H$ NMR spectrum, which suggests that any of the possible conformations rapidly interconvert in solution. In the solid-state structures, however, the *endo–exo* configuration is found. It is worth mentioning here that some of

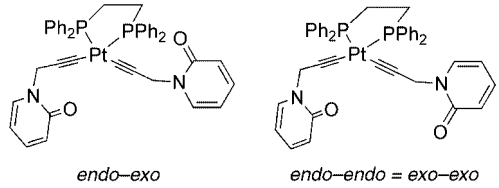


Figure 2. Illustration of the isomeric configurations of the pyridone substituents in complex **2**.

 © 2007 Wiley-VCH Verlag GmbH & Co. KGaA, Weinheim 

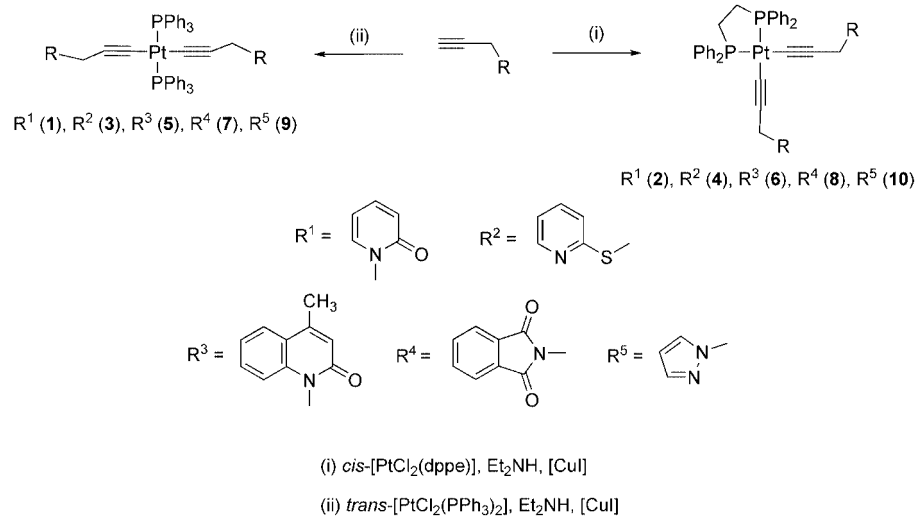


Scheme 3.

these complexes hold water tenaciously, as is evident from $H_2O$ signals in the $^1H$ NMR spectra and confirmed by elemental analysis. Even prolonged drying under high vacuum does not seem to remove this solvated water. The LSIMS mass spectra of all ten complexes show molecular ion peaks whose isotopic distributions match the expected patterns. The solid-state structures of the complexes *trans*-[Pt(C≡C$CH_2R^1$)$_2$($PPh_3$)$_2$] (**1**), *cis*-[Pt(C≡C$CH_2R^1$)$_2$(dppe)] (**2**), *trans*-[Pt(C≡C$CH_2R^3$)$_2$($PPh_3$)$_2$] (**5**), *trans*-[Pt(C≡C$CH_2R^5$)$_2$($PPh_3$)$_2$] (**9**) and *cis*-[Pt(C≡C$CH_2R^5$)$_2$(dppe)] (**10**) were determined by single-crystal X-ray diffraction. The molecular structure of **1** (Figure 3) consists of a platinum atom coordinated by two triphenylphosphane ligands and two acetylide molecules in a *trans* geometry. The coordination about the platinum atom is square planar, and the angle subtended at the Pt centre is 92.90(14)°. The Pt–C, Pt–P and C≡C bond lengths [1.998(5), 2.3163(12) and 1.201(7) Å, respectively] are very similar to those observed in other *trans*-bis(triphenylphosphane)platinum(II) acetylide complexes such as *trans*-[Pt(C≡C$C_6H_4$-4-$NH_2$)$_2$($PPh_3$)$_2$] [Pt–P = 2.310(1), Pt–C = 2.005(4) and C≡C = 1.206(6) Å][37] or *trans*-[Pt{C≡C$C_6H_4$-4-SC(O)Me}$_2$($PPh_3$)$_2$] [Pt–P = 2.3177(15), Pt–C = 2.027(6) and C≡C = 1.179(9) Å].[38] A unique feature of the solid-state structure of complex **1** is the presence of a hydrogen-bonding interaction between the alkyne ligand carbonyl group oxygen atom and a *meta* hydrogen of one of the $Ph_3P$ phenyl rings with a H···O=C distance of ca. 2.7 Å, a distance typically found in weak hydrogen-bonding interactions.[39] The molecular structure of *cis* complexes **2** (Figure 4) and **10** (Figure 5) consist of a distorted [P–Pt–C angle ca. 173°] square planar platinum centre to which one dppe unit and two C-bonded alkyne molecules are coordinated in a mutually *cis* arrangement. The Pt–C and Pt–P bond lengths (see Table 1) are similar to those of the *trans* derivative (see above) and also similar to other *cis* platinum alkynyl complexes including *cis*-[Pt(C≡CH)$_2$(dppe)] [Pt–C = 2.025(5), Pt–P = 2.2851(12) and C≡C = 1.164(8) Å][40] and *cis*-[Pt(C≡CC≡CH)$_2$(dppe)] [Pt–C = 2.20(1), Pt–P = 2.269(3) and C≡C = 1.218(6) Å].[41]

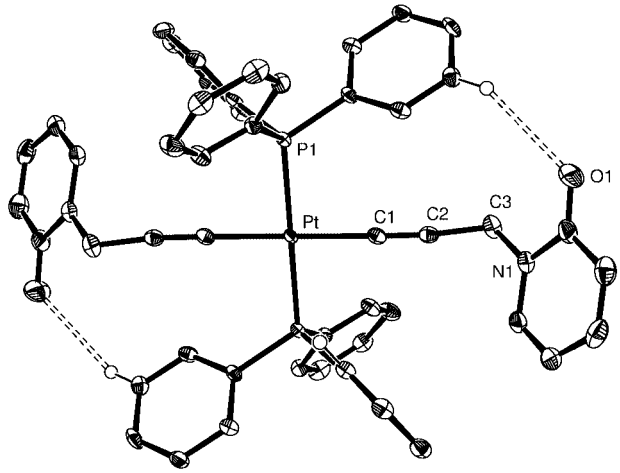


Figure 3. Molecular structure of *trans*-[Pt(C≡C$CH_2R^1$)$_2$($PPh_3$)$_2$] (**1**). Thermal ellipsoids show 50% probability levels. Hydrogen atoms (except those involved in H-bonding interactions) omitted for clarity.

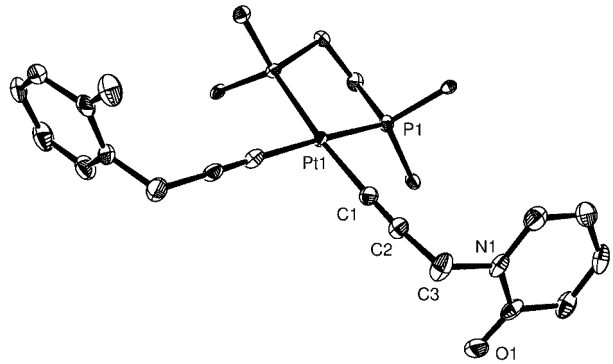


Figure 4. Molecular structure of *cis*-[Pt(C≡C$CH_2R^1$)$_2$(dppe)] (**2**). Thermal ellipsoids show 50% probability levels. Hydrogen atoms have been omitted for clarity and only the *ipso* carbon atoms of the phenyl groups are shown.

 © 2007 Wiley-VCH Verlag GmbH & Co. KGaA, Weinheim 

Table 1. Selected structural parameters for complexes **1**, **2**, **5**, **9** and **10**.

| | **1** | **2** | **5** | **9** | **10** |
|---|---|---|---|---|---|
| P–Pt–C angle [°] | 92.90(14) | 173.96(14) | 88.39(12) | 93.12(17) | 173.64(18), 174.7(2) |
| Pt–C [Å] | 1.998(5) | 2.018(5) | 2.013(4) | 2.006(6) | 2.046(8), 2.060(7) |
| Pt–P [Å] | 2.3163(14) | 2.2823(13) | 2.2872(13) | 2.2896(15) | 2.2802(18), 2.2807(17) |
| C≡C [Å] | 1.201(7) | 1.168(7) | 1.190(6) | 1.191(9) | 1.135(10), 1.114(9) |

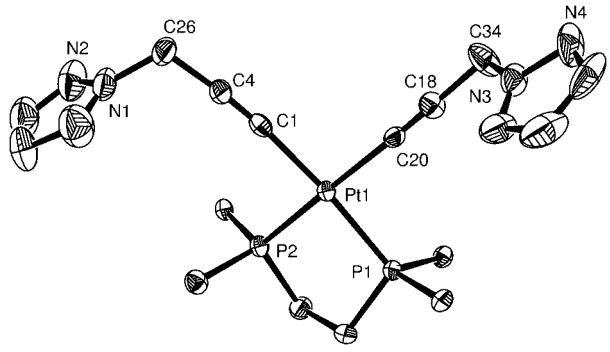


Figure 5. Molecular structure of *cis*-[Pt(C≡CCH$_2$R$^5$)$_2$(dppe)] (**10**). Thermal ellipsoids show 50% probability levels. Hydrogen atoms have been omitted for clarity and only the *ipso* carbon atoms of the phenyl groups are shown.

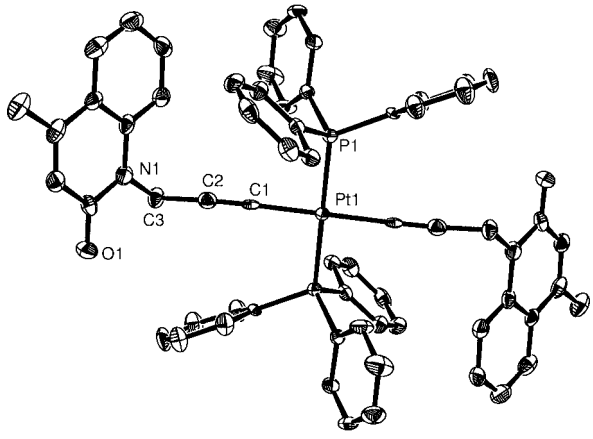


Figure 6. Molecular structure of *trans*-[Pt(C≡CCH$_2$R$^3$)$_2$(PPh$_3$)$_2$] (**5**). Thermal ellipsoids show 50% probability levels. Hydrogen atoms have been omitted for clarity.

As a consequence of the *trans* effect, the C≡C bond lengths in *cis* complexes **2** [1.1687(7) Å] and **10** [1.135(10) and 1.114(9) Å] are slightly shorter than those of the *trans* complexes. The other two *trans* complexes **5** (Figure 6) and **9** (Figure 7) are structurally very similar to complex **1**, although with slightly longer Pt–P distances. For comparison, important structural data for the *trans* and *cis* complexes is summarised in Table 1.

The platinum(II) complexes containing the alkynes R$^2$CH$_2$C≡CH and R$^5$CH$_2$C≡CH (**3**, **4**, **9** and **10**) possess an uncoordinated nitrogen atom which could allow theses compounds to act as organometallic ligands to give heterodimetallic species upon coordination to other metals. Indeed, *trans* complexes **3** and **9** react with 2 equiv. of [Ag-

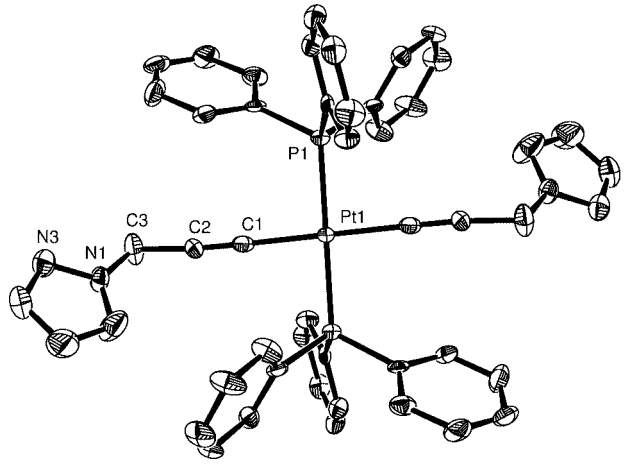


Figure 7. Molecular structure of *trans*-[Pt(C≡CCH$_2$R$^5$)$_2$(PPh$_3$)$_2$]·2CHCl$_3$ (**9**). Thermal ellipsoids show 50% probability levels. Hydrogen atoms and CHCl$_3$ of solvation have been omitted for clarity.

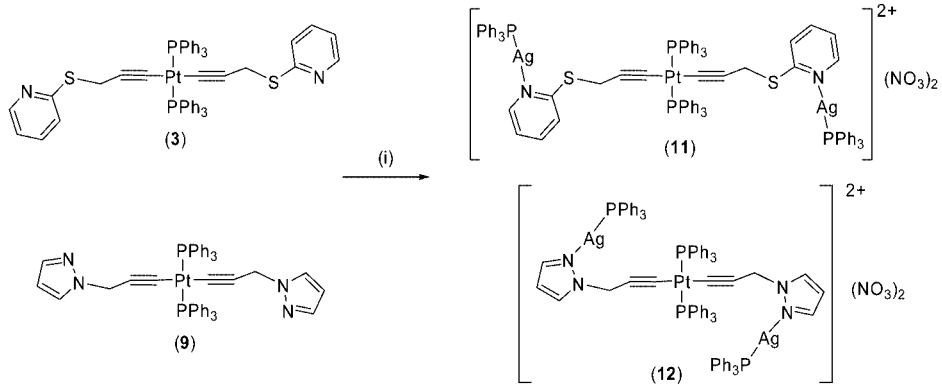


Scheme 4.

 © 2007 Wiley-VCH Verlag GmbH & Co. KGaA, Weinheim 

$(NO_3)(PPh_3)$] to give the cationic platinum(II)/silver(I) complexes *trans*-[Pt(C≡CCH$_2$R$^n$)$_2$($PPh_3$)$_2$($AgPPh_3$)$_2$]($NO_3$)$_2$ (*n* = 2, **11**; *n* = 5, **12**) (Scheme 4). The reaction of complexes **3** and **9** with only 1 equiv. of [Ag($NO_3$)$PPh_3$] gave mixtures of products which were not analysed further. NMR spectroscopic data of these mixtures seems to indicate the presence of both starting material (i.e. complex **3** or **9**) as well as dimetallic complexes **11** or **13**. Clearly, the *trans* geometry does not allow the system to bend in such a manner that a macrocyclic complex incorporating only one silver ion can be formed. Similarly, *cis* complexes **4** and **10** react with either 1 or 2 equiv. of the silver compound to give the heterodimetallic compounds *cis*-[Pt(C≡CCH$_2$R$^n$)$_2$(dppe)($AgPPh_3$)]$NO_3$ (*n* = 2, **13**; *n* = 5, **14**) or *cis*-[Pt(C≡CCH$_2$R$^n$)$_2$(dppe)($AgPPh_3$)$_2$]($NO_3$)$_2$ (*n* = 2, **15**; *n* = 5, **16**), respectively (Scheme 5). Complexes **11**–**16** were characterised spectroscopically; attempts to grow X-ray quality crystals so far have failed as the stability of these compounds in solution is limited. The $^{31}P\{^1H\}$ NMR spectra of complexes **11**–**16** consist of a singlet resonance with $^{195}Pt$ satellites due to the Pt–phosphane unit and, at room temperature, a very broad (almost invisible) signal for the Ag–$PPh_3$ moiety. At –80 °C, this broad signal is resolved into a pair of doublets arising from coupling of the phosphorus nucleus to both the $^{109}Ag$ and $^{107}Ag$ isotopomers (Figure 8). The $^{195}Pt$–$^{31}P$ coupling constants of dimetallic Pt/Ag macrocycles **13**–**14** are ca. 100 Hz larger than those of the "free-ligand" Pt complexes, consistent with a change of angle about the platinum centre

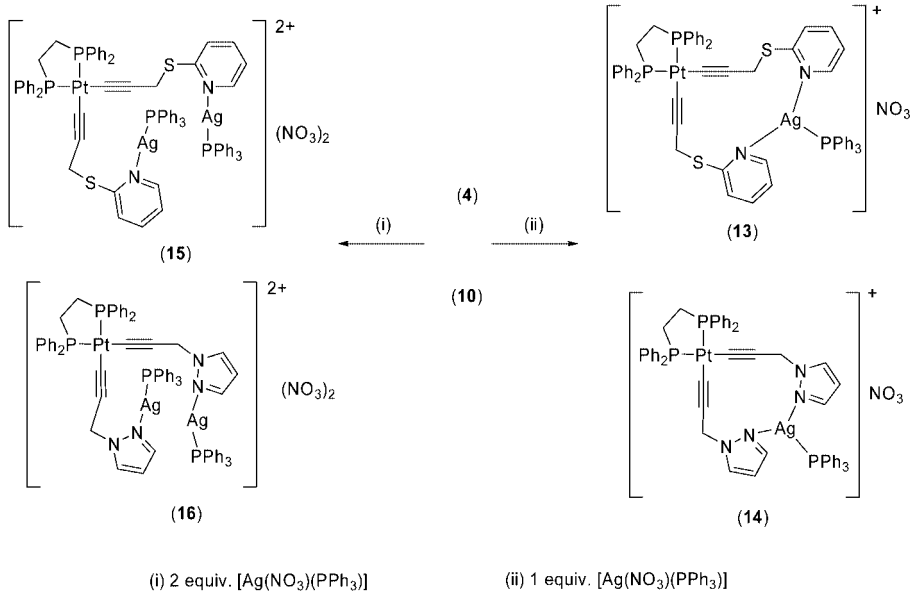


Scheme 5.

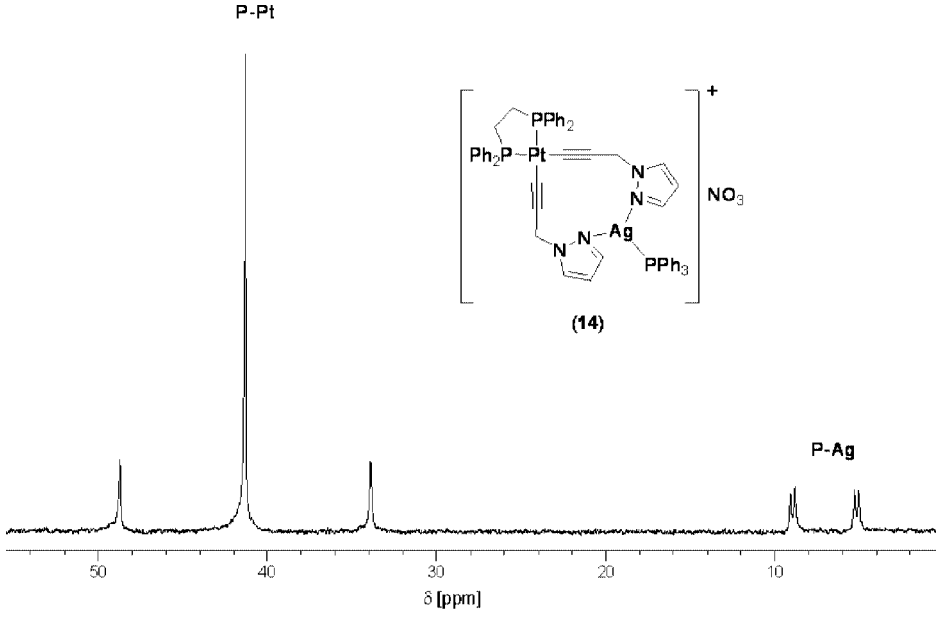


Figure 8. $^{31}P\{^1H\}$ NMR (162 MHz) spectrum of *cis*-[Pt(C≡CCH$_2$R$^5$)$_2$(dppe)($AgPPh_3$)]$NO_3$ (**14**) in $CD_2Cl_2$ at –80 °C.

 © 2007 Wiley-VCH Verlag GmbH & Co. KGaA, Weinheim 

consistent with the expected "tweezer-motion" of the alkyne substituents to coordinate to the silver atom. The possibility that the silver ions are coordinated to the triple bond rather than the N atom can be disproved from the IR data; the C≡C stretching frequency of both the "free" and "coordinated" Pt complexes are almost identical. Complexes **11**–**16** represent examples of complexes in which an organometallic compound acts as metalloligand. Some examples of such metalloligands include the alkynyl gold(I) macrocycles and [2]catenanes containing pyridyl and bipyridyl backbones that are coordinated to a $Pt^{IV}$ centre,[42] the pyrazolyl- and pyridyl-substituted ferrocenes that are N-coordinated to various Au and Ag species,[43,44] the alkynyl-functionalised bis(pyrazolyl)methane derivatives containing Au/Pd and Pt/Pd[45] and various supramolecular assemblies based on the M–C≡C (4-$C_6H_4N$) (M = Pt, Ru) unit.[40,46–48]

## Conclusion

We have shown that various *N*- and *S*-propargylated compounds form platinum(II) alkynyl complexes in high yields and that these compounds can act as N-donor ligands to $Ag^{I}$ ions. In the case of *cis*-Pt complexes, dimetallic macrocycles are formed. Further work on the use of these organometallic ligands is currently in progress.

## Experimental Section

**General:** NMR spectra were recorded with a 400 MHz Varian Inova spectrometer. Chemical shifts are quoted relative to external TMS ($^1$H, $^{13}$C) or 85% $H_3PO_4$ ($^{31}$P). LSIMS mass spectra were measured with a Micromass Autospec spectrometer in positive ion mode by using NBA as matrix. IR spectra were recorded with a Nicolet Impact 410 instrument. Elemental analyses were obtained in-house by using a LECO CHNS-932 microanalyser. *N*-Propargyl-2-pyridone, 2-propargylthiopyridine, *N*-propargyl-4-methyl-2-quinolidone, *N*-propargylphthalimide and 2-propargylpyrazole were prepared by modified literature procedures.[14–17,23] Spectroscopic data of these alkynes is given here since only very few details have been previously reported. The $Pt^{II}$ phosphane complexes *trans*-[$PtCl_2(PPh_3)_2$] and *cis*-[$PtCl_2$(dppe)] were prepared by the reaction of [$PtCl_2(NCMe)_2$] with appropriate amounts of the phosphanes. The silver(I) complex [$Ag(NO_3)(PPh_3)$] was prepared by a literature procedure.[49] All other reagents and solvents were obtained commercially and used as received. DFT calculations were carried out with the PRIRODA software package incorporating relativistic Stevens, Basch, Krauss basis sets.[50,51] Geometries were fully optimised and the located minima were confirmed by the absence of imaginary frequencies.

**Preparation of the Alkynes:** A mixture of the appropriate NH or SH derivatives (2-pyridone, 2-hydroxy-4-methylquinoline, phthalimide and 2-pyridinethiol), $K_2CO_3$ (excess) and propargyl bromide (1.6 equiv.) was heated at reflux in acetone for ca. 8 h. The cooled mixture was filtered, and the filtrate was evaporated to dryness. The resulting crude products were purified by chromatography on silica gel using $CH_2Cl_2$ as eluent.

**Preparation of the [Pt(C≡CR)$_2$(P)] Complexes:** A mixture of the alkyne (0.228 mmol), [$PtCl_2$(P)] (0.098 mmol), [CuI] (5 mg) in $Et_2NH$ (5 mL) and EtOH (5 mL) was heated at reflux for ca. 1 h. The solid products were isolated by filtration, washed with $H_2O$, EtOH and $Et_2O$ and dried in vacuo.

***N*-Propargyl-2-pyridone (R$^1$CH$_2$C≡CH):** Yield: 2.10 g (75%), dark orange oil. $^1$H NMR (400 MHz, $CDCl_3$): $\delta$ = 2.27 (t, $J$ = 2.5 Hz, 1 H, ≡CH), 4.74 (d, $J$ = 2.5 Hz, 2 H, $NCH_2$), 6.22 (dt, $J$ = 6.6, 1.3 Hz, 1 H, H$^5$), 6.55 (dd, $J$ = 9.1, 0.8 Hz, 2 H, H$^3$), 7.33 (m, 1 H, H$^4$), 6.61 (ddd, $J$ = 6.8, 2.0, 0.5 Hz, 1 H, H$^6$) ppm. $^{13}$C NMR (100 MHz, $CDCl_3$): $\delta$ = 37.45 ($NCH_2$), 75.21 (C≡CH), 76.73 (C≡CH), 106.24 (C5), 120.32 (C3), 135.74 (C4), 139.68 (C6), 161.80 (C2) ppm.

***trans*-[Pt(C≡CR$^1$)$_2$(PPh$_3$)$_2$] (1):** Yield: 0.258 g (83%), pale brown solid. $^1$H NMR (400 MHz, $CDCl_3$): $\delta$ = 4.01 (t, $J$ = 1.8 Hz, 4 H, $NCH_2$), 5.61 (dt, $J$ = 6.8, 1.5 Hz, 2 H, H$^5$), 6.33 (ddd, $J$ = 8.8, 2.0, 0.5 Hz, 2 H, H$^3$), 6.88 (dd, $J$ = 6.8, 2.0 Hz, 2 H, H$^6$), 7.12 (dt, $J$ = 6.6, 2.0 Hz, 2 H, H$^4$), 7.31–7.44 (m, 18 H, *p*-, *m*-$Ph_3$P), 7.70–7.77 (m, 12 H, *o*-$Ph_3$P) ppm. $^{31}$P{$^1$H} NMR (162 MHz, $CDCl_3$): $\delta$ = 18.89 ($J_{Pt,P}$ = 2619 Hz) ppm. IR (KBr disk): $\tilde{\nu}$ = 2135 (C≡C), 1657 (C=O) cm$^{-1}$. FAB MS: $m/z$ = 984 [M + H]$^+$. $C_{52}H_{42}N_2O_2P_2Pt$ (983.9): calcd. C 63.48, H 4.30, N 2.85; found C 63.03, H 4.32, N 3.02. X-ray quality crystals were grown by slow diffusion of $Et_2O$ into a $CH_2Cl_2$ solution of the complex.

***cis*-[Pt(C≡CR$^1$)$_2$(dppe)] (2):** Yield: 0.242 g (75%), colourless solid. $^1$H NMR (400 MHz, $CDCl_3$): $\delta$ = 2.30–2.48 (m, 4 H, $PCH_2CH_2P$), 4.76 (t, $J$ = 6.6 Hz, 4 H, $NCH_2$), 5.81 (dt, $J$ = 6.6, 1.2 Hz, 2 H, H$^5$), 6.42 (d, $J$ = 8.6 Hz, 2 H, H$^3$), 7.19 (m, 2 H, H$^4$), 7.38–7.51 (m, 12 H, *p*-, *m*-$Ph_2$P), 7.80–7.88 (m, 8 H, *o*-$Ph_2$P), 7.89 (dd, $J$ = 7.0, 1.9 Hz, 2 H, H$^6$) ppm. $^{31}$P{$^1$H} NMR (162 MHz, $CDCl_3$): $\delta$ = 43.23 ($J_{Pt,P}$ = 2316 Hz) ppm. IR (KBr disk): $\tilde{\nu}$ = 2137 (C≡C), 1652 (C=O) cm$^{-1}$. FAB MS: $m/z$ = 858 [M + H]$^+$. $C_{42}H_{36}N_2O_2P_2Pt$ (857.8): calcd. C 58.81, H 4.23, N 3.27; found C 58.88, H 4.24, N 3.35. X-ray quality crystals were grown by slow diffusion of $Et_2O$ into a $CH_2Cl_2$ solution of the complex.

**2-Propargylthiopyridine (R$^2$CH$_2$C≡CH):** Yield: 2.01 g (75%), yellow oil. $^1$H NMR (400 MHz, $CDCl_3$): $\delta$ = 2.18 (t, $J$ = 2.7 Hz, 1 H, ≡CH), 3.94 (d, $J$ = 2.7 Hz, 2 H, $SCH_2$), 7.00 (ddd, $J$ = 7.4, 4.7, 0.8 Hz, 1 H, H$^5$), 7.20 (d, $J$ = 8.2 Hz, 1 H, H$^3$), 7.49 (ddd, $J$ = 9.4, 7.4, 1.9 Hz, 1 H, H$^4$), 8.44 (ddd, $J$ = 5.1, 1.9, 1.1 Hz, 1 H, H$^6$) ppm. $^{13}$C NMR (100 MHz, $CDCl_3$): $\delta$ = 18.11 ($SCH_2$), 70.40 (C≡CH), 80.01 (C≡CH), 119.80 (C5), 121.93 (C3), 136.05 (C4), 149.44 (C6), 156.96 (C26) ppm. *Caution*: On several occasions this alkyne decomposed spontaneously producing large amounts of extremely malodorous fumes and black soot.

***trans*-[Pt(C≡CR$^2$)$_2$(PPh$_3$)$_2$] (3):** Yield: 0.260 g (81%), pale yellow solid. $^1$H NMR (400 MHz, $CDCl_3$): $\delta$ = 3.19 (s, 4 H, $SCH_2$), 6.74 (d, $J$ = 8.6 Hz, 2 H, H$^3$), 6.80 (t, $J$ = 5.8 Hz, 2 H, H$^5$), 7.11 (dt, $J$ = 7.8, 1.6 Hz, 2 H, H$^4$), 7.28–7.40 (m, 18 H, *p*-, *m*-$Ph_3$P), 7.66–7.77 (m, 12 H, *o*-$Ph_3$P), 8.25 (d, $J$ = 4.7 Hz, 2 H, H$^6$) ppm. $^{31}$P{$^1$H} NMR (162 MHz, $CDCl_3$): $\delta$ = 19.47 ($J_{Pt,P}$ = 2662 Hz) ppm. IR (KBr disk): $\tilde{\nu}$ = 2125 (C≡C) cm$^{-1}$. FAB MS: $m/z$ = 1016 [M + H]$^+$. $C_{52}H_{42}N_2O_2P_2PtS_2{\cdot}H_2O$ (1033.2): calcd. C 60.39, H 4.29, N 2.71; found C 59.94, H 4.28, N 3.02.

***cis*-[Pt(C≡CR$^2$)$_2$(dppe)] (4):** Yield: 0.134 g (40%), pale yellow solid. $^1$H NMR (400 MHz, $CDCl_3$): $\delta$ = 2.31 (m, 4 H, $PCH_2CH_2P$), 3.99 (t, $J$ = 7.0 Hz, 4 H, $SCH_2$), 6.75 (dt, $J$ = 5.1, 1.6 Hz, 2 H, H$^5$), 7.06–7.15 (m, 4 H, H$^3$, H$^4$), 7.28–7.41 (m, 12 H, *p*-, *m*-$Ph_2$P), 7.79–7.89 (m, 8 H, *o*-$Ph_2$P), 8.24 (ddd, $J$ = 5.1, 2.7, 12 Hz, 2 H, H$^6$) ppm. $^{31}$P{$^1$H} NMR (162 MHz, $CDCl_3$): $\delta$ = 41.43 ($J_{Pt,P}$ = 2305 Hz) ppm. IR (KBr disk): $\tilde{\nu}$ = 2128 (C≡C) cm$^{-1}$. FAB MS: $m/z$ = 890 [M + H]$^+$. $C_{42}H_{36}N_2O_2P_2PtS_2{\cdot}1/2H_2O$ (898.1): calcd. C 56.12, H 4.15 N 3.12; found C 55.83, H 4.11, N 3.34.

 © 2007 Wiley-VCH Verlag GmbH & Co. KGaA, Weinheim 

***N*-Propargyl-4-methyl-2-quinolidone ($R^3CH_2C{\equiv}CH$):** Yield: 1.36 g (55%), brown solid. $^1H$ NMR (400 MHz, $CDCl_3$): $\delta$ = 2.33 (t, $J$ = 2.6 Hz, 1 H, ≡CH), 2.47 (s, 3 H, Me), 5.11 (d, $J$ = 2.6 Hz, 2 H, $NCH_2$), 6.60 (s, 1 H, $H^3$), 7.29 (t, $J$ = 7.7 Hz, 1 H, $H^6$), 7.53 (d, $J$ = 8.1 Hz, 1 H, $H^5$), 7.61 (dt, $J$ = 7.3, 1.3 Hz, 1 H, $H^7$), 7.72 (dd, $J$ = 8.1, 1.3 Hz, 1 H, $H^8$) ppm. $^{13}C$ NMR (100 MHz, $CDCl_3$): $\delta$ = 19.01 (Me), 31.28 ($NCH_2$), 72.22 (C≡CH), 78.16 (C≡CH), 114.86 (C3), 120.68 (C8), 121.63 (C10), 122.29 (C6), 125.33 (C5), 130.53 (C7), 138.35 (C9), 147.23 (C4), 161.02 (C2) ppm.

***trans*-[Pt(C≡CR$^3$)$_2$(PPh$_3$)$_2$] (5):** Yield: 0.225 g (64%), tan solid. $^1H$ NMR (400 MHz, $CDCl_3$): $\delta$ = 2.40 (s, 6 H, Me), 4.36 (s, 4 H, $NCH_2$), 6.40 (s, 2 H, $H^3$), 6.82 (d, $J$ = 8.2 Hz, 2 H, $H^5$), 6.94 (t, $J$ = 8.2 Hz, 2 H, $H^6$), 7.02 (t, $J$ = 7.4 Hz, 2 H, $H^7$), 7.13–7.24 (m, 18 H, *p*-, *m*-$Ph_3P$), 7.51 (dd, $J$ = 7.8, 0.8 Hz, 2 H, $H^8$), 7.54–7.62 (m, 12 H, *o*-$Ph_3P$) ppm. $^{31}P\{^1H\}$ NMR (162 MHz, $CDCl_3$): $\delta$ = 19.79 ($J_{Pt,P}$ = 2663 Hz) ppm. IR (KBr disk): $\tilde{\nu}$ = 2128 (C≡C), 1652 (C=O) cm$^{-1}$. FAB MS: $m/z$ = 1112 [M + H]$^+$. $C_{62}H_{50}N_2O_2P_2Pt{\cdot}2H_2O$ (1147.3): calcd. C 64.84, H 4.74, N 2.44; found C 64.56, H 4.70, N 2.84.

***cis*-[Pt(C≡CR$^3$)$_2$(dppe)] (6):** Yield: 0.245 g (66%), tan solid. $^1H$ NMR (400 MHz, $CDCl_3$): $\delta$ = 2.23 (m, 4 H, $PCH_2CH_2P$), 2.38 (s, 6 H, Me), 5.15 (s, 4 H, $NCH_2$), 5), 6.43 (s, 2 H, $H^3$), 7.05 (t, $J$ = 7.4 Hz, 2 H, $H^7$), 7.10–7.22 (m, 10 H, *m*-$Ph_2P$, $H^6$), 7.23–7.32 (m, 4 H, *p*-$Ph_2P$), 7.52 (d, $J$ = 7.8 Hz, 2 H, $H^8$), 7.57–7.72 (m, 10 H, *o*-$Ph_2P$, $H^5$) ppm. $^{31}P\{^1H\}$ NMR (162 MHz, $CDCl_3$): $\delta$ = 41.62 ($J_{Pt,P}$ = 2295 Hz) ppm. IR (KBr disk): $\tilde{\nu}$ = 2138 (C≡C), 1650 (C=O) cm$^{-1}$. FAB MS: $m/z$ = 986 [M + H]$^+$. $C_{52}H_{44}N_2O_2P_2Pt{\cdot}H_2O$ (1003.3): calcd. C 62.20, H 4.62, N 2.79; found C 61.98, H 4.45, N 3.04.

***N*-Propargylphthalimide ($R^4CH_2C{\equiv}CH$):** Yield: 1.29 g (65%), pale yellow oil. $^1H$ NMR (400 MHz, $CDCl_3$): $\delta$ = 2.22 (t, $J$ = 2.3 Hz, 1 H, ≡CH), 4.44 (d, $J$ = 2.3 Hz, 2 H, $NCH_2$), 7.73 (m, 2 H, arom), 7.87 (m, 2 H, arom) ppm. $^{13}C$ NMR (100 MHz, $CDCl_3$): $\delta$ = 26.93 ($NCH_2$), 71.46 (C≡CH), 77.12 (C≡CH), 123.52, 131.90, 134.17 (arom) ppm.

***trans*-[Pt(C≡CR$^4$)$_2$(PPh$_3$)$_2$] (7):** Yield: 0.286 g (82%), ivory solid. $^1H$ NMR (400 MHz, $CDCl_3$): $\delta$ = 3.75 (s, 4 H, $NCH_2$), 7.11–7.31 (m, 18 H, *p*-, *m*-$Ph_3P$), 7.60–7.76 (m, 20 H, *o*-$Ph_3P$, arom) ppm. $^{31}P\{^1H\}$ NMR (162 MHz, $CDCl_3$): $\delta$ = 19.56 ($J_{Pt,P}$ = 2646 Hz) ppm. IR (KBr disk): $\tilde{\nu}$ = 1231 (C≡C), 1713 (C=O) cm$^{-1}$. FAB MS: $m/z$ = 1088 [M + H]$^+$. $C_{58}H_{42}N_2O_4P_2Pt{\cdot}H_2O$ (1105.2): calcd. C 62.97, H 4.01, N 2.53; found C 62.98, H 4.17, N 2.85.

***cis*-[Pt(C≡CR$^4$)$_2$(dppe)] (8):** Yield: 0.148 g (41%), colourless solid. $^1H$ NMR (400 MHz, $CDCl_3$): $\delta$ = 2.28 (m, 4 H, $PCH_2CH_2P$), 4.50 (t, $J$ = 7.0 Hz, 4 H, $NCH_2$), 7.14–7.25 (m, 12 H, *p*-, *m*-$Ph_2P$), 7.54–7.80 (m, 16 H, *o*-$Ph_3P$, arom) ppm. $^{31}P\{^1H\}$ NMR (162 MHz, $CDCl_3$): $\delta$ = 42.01 ($J_{Pt,P}$ = 2289 Hz) ppm. IR (KBr disk): $\tilde{\nu}$ = 2140 (C≡C), 1709 (C=O) cm$^{-1}$. FAB MS: $m/z$ = 962 [M + H]$^+$. $C_{49}H_{39}N_2O_4P_2Pt{\cdot}H_2O$ (994.2): calcd. C 59.14, H 4.16, N 2.82; found C 59.10, H 4.17, N 3.06.

**2-Propargylpyrazole ($R^5CH_2C{\equiv}CH$):** Yield: 1.31 g (42%), pale yellow oil. $^1H$ NMR (400 MHz, $CDCl_3$): $\delta$ = 2.49 (t, $J$ = 2.7 Hz, 1 H, ≡CH), 4.94 (d, $J$ = 2.3 Hz, 2 H, $NCH_2$), 6.29 (t, $J$ = 2.3 Hz, 1 H, Pz-$H^4$), 7.53 (d, $J$ = 1.6 Hz, 1 H, Pz-$H^5$), 7.59 (d, $J$ = 2.3 Hz, 1 H, Pz-$H^3$) ppm. $^{13}C$ NMR (100 MHz, $CDCl_3$): $\delta$ = 41.65 ($NCH_2$), 74.83 (C≡CH), 76.98 (C≡CH), 106.39 (C4), 129.02 (C5), 140.23 (C3) ppm.

***trans*-[Pt(C≡CR$^5$)$_2$(PPh$_3$)$_2$] (9):** Yield: 0.312 g (83%), colourless solid. $^1H$ NMR (400 MHz, $CDCl_3$): $\delta$ = 4.22 (s, 4 H, $NCH_2$), 5.48 (br. s, 2 H, Pz-$H^4$), 6.54 (br. s, 2 H, Pz-$H^5$), 7.27 (br. s, 2 H, Pz-$H^3$), 7.31–7.44 (m, 18 H, *p*-, *m*-$Ph_3P$), 7.70–7.80 (m, 12 H, *o*-$Ph_3P$) ppm. $^{31}P\{^1H\}$ NMR (162 MHz, $CDCl_3$): $\delta$ = 20.12 ($J_{Pt,P}$ = 2641 Hz) ppm. IR (KBr disk): $\tilde{\nu}$ = 2138 (C≡C) cm$^{-1}$. FAB MS: $m/z$ = 853 [M + H]$^+$. $C_{48}H_{40}N_4P_2Pt$ (929.9): calcd. C 61.99, H 4.34, N 6.03; found C 61.56, H 4.35, N 5.82. X-ray quality crystals were grown by slow diffusion of $Et_2O$ into a $CHCl_3$ solution of the complex.

***cis*-[Pt(C≡CR$^5$)$_2$(dppe)] (10):** Yield: 0.137 g (71%), tan solid. $^1H$ NMR (400 MHz, $CDCl_3$): $\delta$ = 2.30–2.48 (m, 4 H, $PCH_2CH_2P$), 5.01 (t, $J$ = 7.0 Hz, 4 H, $NCH_2$), 5.90 (br. s, $J$ = 1.2 Hz, 2 H, Pz-$H^4$), 7.22 (br. s, 2 H, Pz-$H^5$), 7.34 (br. s, 2 H, Pz-$H^3$), 7.36–7.50 (m, 12 H, *p*-, *m*-$Ph_2P$), 7.79–7.90 (m, 8 H, *o*-$Ph_2P$) ppm. $^{31}P\{^1H\}$ NMR (162 MHz, $CDCl_3$): $\delta$ = 43.00 ($J_{Pt,P}$ = 2315 Hz) ppm. IR (KBr disk): $\tilde{\nu}$ = 2140 (C≡C) cm$^{-1}$. FAB MS: $m/z$ = 804 [M + H]$^+$. $C_{38}H_{34}N_4P_2Pt$ (803.7): calcd. C 56.79, H 4.26, N 6.97; found C 56.63, H 4.27, N 7.04.

**Preparation of Heterodimetallic Pt$^{II}$/Ag$^{I}$ Complexes:** To a solution of the Pt complex in $CH_2Cl_2$ (7 mL) was added either 1 or 2 equiv. of solid [Ag($NO_3$)($PPh_3$)]. After stirring for ca. 1 h, the solution was passed through Celite and concentrated in vacuo. Addition of $Et_2O$ precipitated the complexes, which were isolated by filtration and dried in air.

***trans*-[Pt(C≡CR$^2$)$_2$(PPh$_3$)$_2$(AgPPh$_3$)$_2$](NO$_3$)$_2$ (11):** Yield: 0.038 g (81%), ivory solid. $^1H$ NMR (400 MHz, $CD_2Cl_2$): $\delta$ = 3.21 (s, 4 H, $SCH_2$), 6.81–6.99 (m, 4 H, $H^3$, $H^5$), 7.23–7.76 (m, 62 H, $Ph_3P$, $H^4$), 8.05 (m, 2 H, $H^6$) ppm. $^{31}P\{^1H\}$ NMR (162 MHz, $CD_2Cl_2$, –80 °C): $\delta$ = 17.67 ($J_{Pt,P}$ = 2524 Hz), 11.07 (d, $J_{^{109}Ag,P}$ = 538, $J_{^{107}Ag,P}$ = 465 Hz) ppm. IR (KBr disk): $\tilde{\nu}$ = 2126, 2054 (C≡C), 1398 (N=O), 1294 ($NO_2$) cm$^{-1}$. FAB MS: $m/z$ = 1385 [M – $AgPPh_3$]$^+$, 1123 [M – Ag – 2$Ph_3P$]$^+$. $C_{88}H_{72}Ag_2N_4O_6P_4PtS_2{\cdot}CH_2Cl_2$ (1965.3): calcd. C 54.39, H 3.80, N 2.85; found C 53.99, H 3.95, N 2.93.

***trans*-[Pt(C≡CR$^5$)$_2$(PPh$_3$)$_2$(AgPPh$_3$)$_2$](NO$_3$)$_2$ (12):** Yield: 0.040 g (78%), ivory solid. $^1H$ NMR (400 MHz, $CD_2Cl_2$): $\delta$ = 4.30 (s, 4 H, $NCH_2$), 6.10 (t, $J$ = 2.2 Hz, 2 H, Pz-$H^4$), 6.97 (d, $J$ = 1.5 Hz, 2 H, Pz), 7.14 (d, $J$ = 1.5 Hz, 2 H, Pz), 7.22–7.72 (m, 60 H, $Ph_3P$) ppm. $^{31}P\{^1H\}$ NMR (162 MHz, $CD_2Cl_2$, –80 °C): $\delta$ = 29.88 ($J_{Pt,P}$ = 2520 Hz), 11.18 (d, $J_{^{109}Ag,P}$ = 540, $J_{^{107}Ag,P}$ = 463 Hz) ppm. IR (KBr disk): $\tilde{\nu}$ = 2138, 2083 (C≡C), 1384 (N=O), 1297 ($NO_2$) cm$^{-1}$. $C_{84}H_{70}Ag_2N_6O_6P_4Pt{\cdot}1/2CH_2Cl_2$ (1836.7): calcd C 55.26, H 3.90, N 4.58; found C 55.39, H 4.12, N 4.62.

***cis*-[Pt(C≡CR$^2$)$_2$(dppe)(AgPPh$_3$)]NO$_3$ (13):** Yield: 0.035 g (83%), tan solid. $^1H$ NMR (400 MHz, $CD_2Cl_2$): $\delta$ = 2.39–2.57 (m, 4 H, $PCH_2CH_2P$), 3.77 (s, 4 H, $SCH_2$), 6.90 (t, $J$ = 4.4 Hz, 2 H, Py), 6.97 (d, $J$ = 7.7 Hz, 4 H, Py), 7.27–7.79 (m, 37 H, $Ph_2P$, $Ph_3P$, Py), 8.31 (d, $J$ = 4.0 Hz, 2 H, $H^6$) ppm. $^{31}P\{^1H\}$ NMR (162 MHz, $CD_2Cl_2$, –80 °C): $\delta$ = 40.13 ($J_{Pt,P}$ = 2433 Hz), 11.10 (d, $J_{^{109}Ag,P}$ = 541, $J_{^{107}Ag,P}$ = 469 Hz) ppm. IR (KBr disk): $\tilde{\nu}$ = 2098 (C≡C), 1384 (N=O) cm$^{-1}$. FAB MS: $m/z$ = 997 [M – $Ph_3P$]$^+$. $C_{60}H_{51}AgN_3O_3P_3PtS_2{\cdot}CH_2Cl_2$ (1407.0) C 52.07, H 3.80 N 2.98; found C 52.06, H 4.00, N 3.09.

***cis*-[Pt(C≡CR$^5$)$_2$(dppe)(AgPPh$_3$)]NO$_3$ (14):** Yield: 0.026 g (78%), ivory solid. $^1H$ NMR (400 MHz, $CD_2Cl_2$): $\delta$ = 2.41–2.60 (m, 4 H, $PCH_2CH_2P$), 4.76 (s, 4 H, $NCH_2$), 6.21 (t, $J$ = 2.2 Hz, 2 H, Pz-$H^4$), 7.12–7.83 (m, 39 H, $Ph_2P$, $Ph_3P$, Pz) ppm. $^{31}P\{^1H\}$ NMR (162 MHz, $CD_2Cl_2$, –80 °C): $\delta$ = 41.29 ($J_{Pt,P}$ = 2400 Hz), 6.97 (d, $J_{^{109}Ag,P}$ = 653, $J_{^{107}Ag,P}$ = 566 Hz) ppm. IR (KBr disk): $\tilde{\nu}$ = 2120 (C≡C), 1336 (N=O) cm$^{-1}$. $C_{56}H_{49}AgN_5O_3P_3Pt{\cdot}CH_2Cl_2$ (1320.8): calcd. C 51.83, H 3.89, N 5.30; found C 51.71, H 4.04, N 4.94.

***cis*-[Pt(C≡CR$^2$)$_2$(dppe)(AgPPh$_3$)$_2$](NO$_3$)$_2$ (15):** Yield: 0.041 g (76%), tan solid. $^1H$ NMR (400 MHz, $CD_2Cl_2$): $\delta$ = 2.40–2.59 (m, 4 H, $PCH_2CH_2P$), 3.74 (s, 4 H, $SCH_2$), 6.81 (m, 2 H, Py), 7.07 (m, 2 H, Py), 7.28–7.76 (m, 52 H, $Ph_2P$, $Ph_3P$, Py), 8.10 (m, 2 H, $H^6$)

 © 2007 Wiley-VCH Verlag GmbH & Co. KGaA, Weinheim 

Table 2. Crystal data and refinement details for complexes **1**, **2**, **5**, **9** and **10**.

| | **1** | **2** | **5** | **9** | **10** |
|---|---|---|---|---|---|
| Empirical formula | $C_{52}H_{40}N_2O_2P_2Pt$ | $C_{42}H_{36}N_2O_2P_2Pt$ | $C_{62}H_{50}N_2O_2P_2Pt$ | $C_{50}H_{42}N_4Cl_6P_2Pt$ | $C_{38}H_{34}N_4P_2Pt$ |
| Formula mass | 981.89 | 857.76 | 1112.07 | 1168.61 | 803.72 |
| Crystal system | triclinic | monoclinic | triclinic | triclinic | orthorhombic |
| Space group | $P\bar{1}$ | $C2/c$ | $P\bar{1}$ | $P\bar{1}$ | $Pbca$ |
| $a$ [Å] | 9.0466(6) | 14.973(6) | 9.783(4) | 8.277(2) | 17.6036(17) |
| $b$ [Å] | 10.5428(6) | 18.366(7) | 10.836(5) | 12.177(3) | 13.4388(13) |
| $c$ [Å] | 11.3405(7) | 12.819(5) | 13.091(5) | 12.714(3) | 28.890(3) |
| $\alpha$ [°] | 96.486(1) | 90 | 104.27(4) | 73.332(5) | 90 |
| $\beta$ [°] | 106.646(1) | 104.474(8) | 104.14(3) | 79.273(6) | 90 |
| $\gamma$ [°] | 90.901(1) | 90 | 108.94(3) | 82.584(5) | 90 |
| $V$ [Å$^3$] | 1028.34(19) | 3413(2) | 1189.9(9) | 1202.2(5) | 6834.5(11) |
| $Z$ | 1 | 4 | 1 | 1 | 1 |
| $\rho_{calcd.}$ [Mg/m$^3$] | 1.586 | 1.669 | 1.552 | 1.614 | 1.562 |
| $\mu$ [mm$^{-1}$] | 3.535 | 4.245 | 3.065 | 3.358 | 4.232 |
| $F(000)$ | 490 | 1704 | 560 | 580 | 3184 |
| $\theta$ limits [°] | 1.89–28.83 | 1.79–25.00 | 1.72–25.00 | 1.69–25.00 | 1.41–28.13 |
| Measured reflections | 6692 | 16271 | 11140 | 11602 | 63837 |
| Unique reflections | 3728 | 2997 | 4042 | 4209 | 7983 |
| Parameters | 268 | 222 | 314 | 286 | 406 |
| GOF on $F^2$ | 0.755 | 1.182 | 1.160 | 1.084 | 1.004 |
| $R_1$ [$I > 2\sigma(I)$] | 0.0384 | 0.0254 | 0.0240 | 0.0354 | 0.0487 |
| $wR_2$ (on $F^2$, all data) | 0.0811 | 0.0792 | 0.0707 | 0.1116 | 0.1521 |
| $\Delta\rho_{min/max}$ [e/Å$^3$] | 2.142 and –1.392 | 0.728 and –1.204 | 0.750 and –0.582 | 0.710 and –0.979 | 0.964 and –3.012 |
| CCDC deposition code | 634848 | 634849 | 634850 | 634851 | 634052 |

ppm. $^{31}P\{^1H\}$ NMR (162 MHz, $CD_2Cl_2$, –80 °C): $\delta$ = 41.70 ($J_{Pt,P}$ = 2389 Hz), 11.14 (d, $J_{^{109}Ag,P}$ = 593, $J_{^{107}Ag,P}$ = 468 Hz) ppm. IR (KBr disk): $\tilde{\nu}$ = 2097 (C≡C), 1384 (N=O) cm$^{-1}$. FAB MS: $m/z$ = 997 [M – Ag – $2Ph_3P$]$^+$. $C_{78}H_{66}Ag_2N_4O_6P_4PtS_2 \cdot 1/2CH_2Cl_2$ (1796.7): calcd. C 52.48, H 3.76 N 3.12; found C 52.42, H 3.99, N 3.13.

***cis*-[Pt(C≡CR$^5$)$_2$(dppe)(AgPPh$_3$)]NO$_3$ (16):** Yield: 0.041 g (73%), ivory solid. $^1H$ NMR (400 MHz, $CD_2Cl_2$): $\delta$ = 2.40–2.57 (m, 4 H, $PCH_2CH_2P$), 4.79 (s, 4 H, $NCH_2$), 6.26 (t, $J$ = 2.2 Hz, 2 H, Pz-H$^4$), 7.28–7.73 (m, 54 H, $Ph_2P$, $Ph_3P$, Pz) ppm. $^{31}P\{^1H\}$ NMR (162 MHz, $CD_2Cl_2$, –80 °C): $\delta$ = 41.20 ($J_{Pt,P}$ = 2416 Hz), 11.07 (d, $J_{^{109}Ag,P}$ = 540, $J_{^{107}Ag,P}$ = 468 Hz) ppm. IR (KBr disk): $\tilde{\nu}$ = 2097 (C≡C), 1384 (N=O) cm$^{-1}$. FAB MS: $m/z$ = 911 [M – $Ph_3P$]$^+$. $C_{74}H_{64}Ag_2N_6O_6P_4Pt \cdot 1/2CH_2Cl_2$ (1710.5): calcd. C 52.31, H 3.83, N 4.91; found C 52.21, H 4.18, N 4.92.

**X-ray Crystallography:** Crystals of complex **1** (colourless block, 0.09 × 0.12 × 0.21 mm), **2** (colourless block, 0.10 × 0.10 × 0.20 mm), **5** (yellow prism 0.10 × 0.20 × 0.20 mm), **9**·2CHCl$_3$ (colourless prism, 0.20 × 0.30 × 0.50 mm) and **10** (colourless prism, 0.60 × 0.10 × 0.10 mm) were mounted in oil on a glass fibre. Data was collected at 100 K (293 K for complex **10**) by using a Bruker Apex CCD diffractometer with graphite-monochromated Mo-$K_\alpha$ radiation ($\lambda$ = 0.71073 Å). Data reduction and absorption corrections were applied by using SADABS.[52] The structures were solved by direct methods and refined to $F_o^2$ by using full-matrix least-squares.[53] All hydrogen atoms were placed in calculated positions and refined as riding on their respective carbon atoms. Crystallographic and refinement details are collected in Table 2.

CCDC-634848, -634849, -634850, -634851 and -634052 (for compounds **1**, **2**, **5**, **9** and **10**, respectively) contain the supplementary crystallographic data for this paper. These data can be obtained free of charge from The Cambridge Crystallographic Data Centre via www.ccdc.cam.ac.uk/data_request/cif.

## Acknowledgments

We wish to thank the Spanish Ministry for Education and Science, Junta de Castilla y León as well as the University of Burgos for generous financial support (grant numbers BQU2005-0899, BU033A06 and 112-541A-487.01). F. M. thanks the University of Burgos for a visiting fellowship.

[1] V. W. W. Yam, C. K. Hui, K. M. C. Wong, N. Zhu, K. K. Cheung, *Organometallics* **2002**, *21*, 4326–4334.
[2] W. Y. Wong, G. L. Lu, K. H. Choi, *J. Organomet. Chem.* **2002**, *659*, 107–116.
[3] V. W. W. Yam, K. K. W. Lo, K. M. C. Wong, *J. Organomet. Chem.* **1999**, *578*, 3–30.
[4] M. P. Cifuentes, M. A. Humphrey, *J. Organomet. Chem.* **2004**, *689*, 3968–3981.
[5] C. E. Powell, M. G. Humphrey, *Coord. Chem. Rev.* **2004**, *248*, 725–756.
[6] G. K. Anderson in *Comprehensive Organometallic Chemistry II* (Ed.: E. W. Abel, F. G. A. Stone, G. Wilkinson), Pergamon, Oxford, **1995**.
[7] U. Belluco, R. Bertani, R. A. Michelin, M. Mozzon, *J. Organomet. Chem.* **2000**, *600*, 37–55.
[8] M. A. MacDonald, R. J. Puddephatt, *Organometallics* **2000**, *19*, 2194–2199.
[9] C. P. McArdle, J. J. Vittal, R. J. Puddephatt, *Angew. Chem. Int. Ed.* **2000**, *39*, 3819–3822.
[10] M. C. Irwin, J. J. Vittal, R. J. Puddephatt, *Organometallics* **1997**, *16*, 3541–3547.
[11] R. J. Puddephatt, *Chem. Commun.* **1998**, 1055–1062.
[12] R. J. Puddephatt, *Coord. Chem. Rev.* **2001**, *216–217*, 313–332.
[13] G. Jia, R. J. Puddephatt, J. D. Scott, J. J. Vittal, *Organometallics* **1993**, *12*, 3565–3574.
[14] C. E. Pawloski (Dow Chemical Company), US 3624089, **1971**.
[15] E. Diez-Barra, A. de la Hoz, A. Loupy, A. Sanchez-Migallon, *Heterocycles* **1994**, *38*, 1367–1374.
[16] A. Casaschi, R. Grigg, J. M. Sansano, *Tetrahedron* **2001**, *57*, 607–615.

 © 2007 Wiley-VCH Verlag GmbH & Co. KGaA, Weinheim 

[17] J. F. Valliant, P. Schaffer, *J. Inorg. Biochem.* **2001**, *85*, 43–51.
[18] L. Y. Ukhin, I. R. Gol′ding, V. G. Kartsev, *Chem. Nat. Compd.* **2004**, *40*, 156–159.
[19] G. Ferguson, J. F. Gallagher, A. M. Kelleher, T. R. Spalding, F. T. Deeney, *J. Organomet. Chem.* **2005**, *690*, 2888–2894.
[20] B. Wrackmeyer, O. I. Tok, M. H. Bhatti, K. Shahid, S. Ali, *Z. Naturforsch.* **2003**, *58b*, 607–612.
[21] F. Bolletta, D. Fabbri, M. Lombardo, L. Prodi, C. Trombini, N. Zaccheroni, *Organometallics* **1996**, *15*, 2415–2417.
[22] M. Lombardo, I. Vassura, D. Fabbri, C. Trombini, *J. Organomet. Chem.* **2005**, *690*, 588–593.
[23] R. Abele, E. Abele, K. Rubina, O. Dzenitis, P. Arsenyan, I. Shestakova, A. Nesterova, I. Domracheva, J. Popelis, S. Grinberga, E. Lukevics, *Chem. Heterocycl. Compd.* **2002**, *38*, 867–872.
[24] C. R. Johnson, A. Nakanishi, N. Nakanishi, K. Tanaka, *Tetrahedron Lett.* **1975**, *16*, 2865–2868.
[25] H. R. Krüger, U. Schröer, D. Baumert, H. Joppien (Schering AG), DE 2936951, **1981**.
[26] L. A. Méndez, J. Jiménez, E. Cerrada, F. Mohr, M. Laguna, *J. Am. Chem. Soc.* **2005**, *127*, 852–853.
[27] F. Mohr, E. Cerrada, M. Laguna, *Organometallics* **2006**, *25*, 644–648.
[28] F. Mohr, S. Sanz, E. R. T. Tiekink, M. Laguna, *Organometallics* **2006**, *25*, 3084–3087.
[29] A. Mendía, S. Miranda, M. Laguna, unpublished results.
[30] J. S. Kwiatkowski, J. Leszczynski, *J. Mol. Struct.* **1996**, *376*, 325–342.
[31] J. S. Kwiatkowski, J. Leszczynski, *Theochem* **1994**, *312*, 201–213.
[32] A. Dkhissi, L. Houben, J. Smets, L. Adamowicz, G. Maes, *J. Mol. Struct.* **1999**, *484*, 215–227.
[33] I. Alkorta, J. Elguero, *J. Org. Chem.* **2002**, *67*, 1515–1519.
[34] K. Sonogashira, T. Yatake, Y. Tohda, S. Takahashi, N. Hagihara, *J. Chem. Soc., Chem. Commun.* **1977**, 291–292.
[35] K. Sonogashira, Y. Fujikuta, T. Yatake, N. Toyoshima, S. Takahashi, N. Hagihara, *J. Organomet. Chem.* **1978**, *145*, 101–108.
[36] A. Fehn, F. Achenbach (Wacker Chemie GmbH), DE19943102, **2001**.
[37] A. J. Deeming, G. Hogarth, M. Y. Lee, M. Saha, S. P. Redmond, H. Phetmung, A. G. Orpen, *Inorg. Chim. Acta* **2000**, *309*, 109–122.
[38] M. Mayor, C. von Hänisch, H. B. Weber, J. Reichert, D. Beckmann, *Angew. Chem. Int. Ed.* **2002**, *41*, 1183–1186.
[39] T. Steiner, G. Desiraju, *Chem. Commun.* **1998**, 891–892.
[40] M. Janka, G. K. Anderson, N. P. Rath, *Organometallics* **2004**, *23*, 4382–4390.
[41] M. I. Bruce, K. Costuas, J. F. Halet, B. C. Hall, P. J. Low, B. K. Nicholson, B. W. Skelton, A. H. White, *J. Chem. Soc., Dalton Trans.* **2002**, 383–398.
[42] N. C. Habermehl, F. Mohr, D. J. Eisler, M. C. Jennings, R. J. Puddephatt, *Can. J. Chem.* **2006**, *84*, 111.123.
[43] E. M. Barranco, M. C. Gimeno, A. Laguna, M. D. Villacampa, *Inorg. Chim. Acta* **2005**, *358*, 4177–4182.
[44] E. M. Barranco, O. Crespo, M. C. Gimeno, P. G. Jones, A. Laguna, C. Sarroca, *J. Chem. Soc., Dalton Trans.* **2001**, 2523–2529.
[45] F. Mohr, E. Cerrada, M. Laguna, *Dalton Trans.* **2006**, 5567–5573.
[46] J. L. Zuo, E. Herdtweck, F. E. Kühn, *J. Chem. Soc., Dalton Trans.* **2002**, 1244–1246.
[47] J. A. Whiteford, C. V. Lu, P. J. Stang, *J. Am. Chem. Soc.* **1997**, *119*, 2524–2533.
[48] Y. K. Kryschenko, S. R. Seidel, A. M. Arif, P. J. Stang, *J. Am. Chem. Soc.* **2003**, *125*, 5193–5198.
[49] R. A. Stein, C. Knobler, *Inorg. Chem.* **1977**, *16*, 242–245.
[50] D. N. Laikov, *Chem. Phys. Lett.* **1997**, *281*, 151–156.
[51] D. N. Laikov, Y. A. Ustynyuk, *Russ. Chem. Bull.* **2005**, *54*, 820–826.
[52] G. M. Sheldrick, *SADABS version 2.03*, University of Göttingen, **2002**.
[53] G. M. Sheldrick, *SHELXTL-NT 6.1*, University of Göttingen, **1998**.

Received: February 2, 2007
Published Online: May 14, 2007

 © 2007 Wiley-VCH Verlag GmbH & Co. KGaA, Weinheim 

DOI: 10.1002/ejic.200700171

# Substituent Effects on the Stereoelectronic and Chemical Properties of a Novel Phosphapalladacycle

Joseph Kok-Peng Ng,[a] Shuli Chen,[b] Geok-Kheng Tan,[a] and Pak-Hing Leung*[b]

**Keywords:** Palladium / Phosphane ligands / Chirality / NMR spectroscopy / Substituent effects

A novel phosphapalladacycle was prepared by direct cyclopalladation of the ligand (diphenylmethyl)diphenylphosphane (**2**). The corresponding μ-chloro five-membered phosphapalladacycle **3** was obtained by heating a toluene solution of **2** and $Pd(OAc)_2$ followed by chloride ion metathesis. An optical resolution procedure was then employed by separation of the (*S*)-prolinato derivatives **4** by fractional crystallization followed by treatment with dilute hydrochloric acid to yield both enantiopodes of the dimers **3** in the optically active forms. The current phosphapalladacycle was noted to display different properties with respect to the analogous phosphapalladacycle prepared from (diphenylmethyl)di-*tert*-butylphosphane. For instance, the phosphapalladacycle based on the (diphenylmethyl)di-*tert*-butylphosphane was shown to be conformationally rigid. In contrast, the analogous five-membered phosphapalladacycle of phosphane **2** was noted to exist in both the δ and λ conformations in the solid state, while a flattened conformation was observed in solution. In addition, the (diphenylmethyl)di-*tert*-butylphosphane-based phosphapalladacycle was noted to exhibit a much more improved regioselectivity towards ancillary ligands such as (*S*)-prolinate and triphenylphosphane than **2**. Furthermore, the μ-chloro dimer **3** of the current palladacycle was shown to be lacking in thermodynamic stability of the Pd–C bond that was noted for the *t*Bu analogue. In contrast, the Pd–C bonds of dimer **3** were immediately ruptured in the presence of concentrated HCl to give rise to the binuclear complex **5**, in which the phosphane was coordinated in the $\eta^1$-P coordination mode.

(© Wiley-VCH Verlag GmbH & Co. KGaA, 69451 Weinheim, Germany, 2007)

## Introduction

Metal complexes of phosphorus-based ligands have played central roles in organometallic and synthetic chemistry.[1] In particular, the chiral forms of these metal complexes have also continued to be invaluable as agents in catalytic asymmetric syntheses.[2] Suitable forms of these ligands may be transformed to give rise to palladacycles.[3–5] The latter (or cyclopalladated complexes) are a well-known class of compounds in organometallic chemistry, and they can be derived from ligands containing other heteroatom donors such as nitrogen and sulfur, apart from those of phosphorus. The syntheses and applications of many of these cyclopalladated complexes are currently being reported.[6] The properties of a ligand could be enhanced as a result of cyclopalladation. For instance, Lewis demonstrated that while a cyclopalladated triarylphosphite was effective as a catalyst for halogenating C=C bonds, the same task could not be accomplished by its non-cyclopalladated analogue.[7] Since then, the synthetic utilities of these systems as homogeneous catalysts were further illustrated.[3a–3j,5a–5e,8]

We have previously contributed to the field of palladacycle chemistry by the exploitation of chiral, nitrogen-based palladacycles for the syntheses of optically active phosphanes of various functionalities.[9] To further improve the synthetic efficiency of these invaluable phosphanes in terms of enhanced chemo-, regio-, diastereo- and enantioselectivities, it is essential to develop new variants of this palladacycle motif. Apart from modifying the organic framework of the cyclopalladated ligand,[8m,9d,9e] we have explored the possibility of replacing the original nitrogen atom with its phosphorus and arsenic congeners.[4] The work reported herein serves to describe the development and characteristics of a new phosphorus-based palladacycle that was prepared in the optically active form. The palladacycle was constructed from the ligand (diphenylmethyl)diphenylphosphane and reveals features that are characteristically different from that of the structurally analogous (diphenylmethyl)di-*tert*-butylphosphane.[10]

## Results and Discussion

### Synthesis of the Phosphapalladacycle in the Optically Active Form

The preparation of the prochiral phosphane **2** was based on the reported procedure that was applied to the synthesis

[a] Department of Chemistry, National University of Singapore
Kent Ridge, Singapore 119260
[b] Division of Chemistry and Biological Chemistry, Nanyang Technological University
Singapore 637616

 © 2007 Wiley-VCH Verlag GmbH & Co. KGaA, Weinheim 

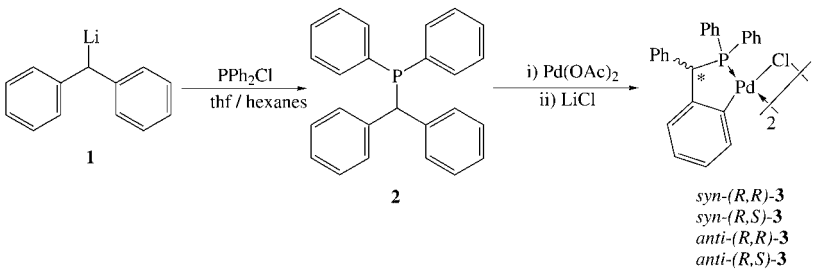


Scheme 1. Synthesis of compounds **2** and **3**.

of its *t*Bu analogue,[11] i.e. treatment of (diphenylmethyl)-lithium (**1**) with the corresponding chlorodiphenylphosphane (Scheme 1), which afforded the product as a white solid. Earlier attempts had failed to synthesize **2** by the more common methods of halide displacement from either (a) chlorodiphenylphosphane with a Grignard reagent or (b) an alkyl halide by using sodium diphenylphosphanide, which was found to be efficient for structurally analogous phosphanes.[4] The structure of compound **2** was confirmed by the doublet resonance of the α-CH proton in the $^1$H NMR spectrum ($CDCl_3$). This proton spin couples with the $^{31}$P nucleus with $^2J_{P,H}$ = 6.8 Hz. Importantly, this doublet resonance is crucial as an indicator of the successful merging of the diphenylmethyl and diphenylphosphanyl skeletons.

As illustrated in Scheme 1, treatment of the phosphane **2** with palladium(II) acetate followed by chloride ion metathesis led to the chloro-bridged dimeric complex **3** of the phosphapalladacycle. Complex **3** was thus isolated as air-stable pale yellow blocks in 61% yield. The dimer was detected by $^{31}$P NMR spectroscopy ($CDCl_3$) as a series of overlapping peaks at $\delta$ = 70.4–70.8 ppm at room temperature (300 K). However, upon cooling to 223 K, the resonance was reproduced as four resolved singlets at $\delta$ = 70.7, 70.8, 70.9 and 71.4 ppm. This supports the chiral and racemic nature of the phosphapalladacycle in solution, which is exemplified by the presence of the six equilibrating isomers, namely, the chiral *syn*- and *anti*-(*R*,*R*)/(*S*,*S*) and the achiral, *meso syn*- and *anti*-(*R*,*S*) isomers.

In the solid state, an X-ray diffraction study of **3** revealed that the complex was crystallized as the achiral, *meso-anti* isomer. The molecular structure is presented in Figure 1. The structure consists of a symmetrical plane that bisects the ClCl axis, each half of the dimer being the mirror image of the other. Moreover, the central four-membered {$Pd_2(\mu$-$Cl)_2$}cycle is flat, and its four atoms form a perfect plane. The stereogenic states of the two α-C atoms are manifested by the attachments of four different substituents. *ortho*-Palladation generates diastereotopicity on the two PPh rings. One of them is considered "axial", since its P1–$C_{ipso}$ bond subtends an angle of 18.5° with the normal to the m.c.pl. (mean coordination plane), while the value of 62.4° applies to the equivalent bond of the "equatorial" PPh ring.

Addition of the chiral ligand, (*S*)-prolinate, to the dimer **3** gave rise to a mixture of two pairs of diastereomeric derivatives **4** (Scheme 2). The presence of the two extra isomers was a consequence of geometric (*E*,*Z*) isomerism resulting from the nonsymmetrical nature of the (*S*)-prolinate. Four singlets were therefore present in the $^{31}$P NMR spectrum ($CDCl_3$). The racemic (and therefore chiral) nature of the phosphapalladacycle was emphasized by categorizing the four singlets into two pairs of resonances with overall equal intensities. These were observed at $\delta$ = 62.7, 71.0 and 64.4, 72.1 ppm with relative intensities of 4:9 and 3:10 correspondingly.

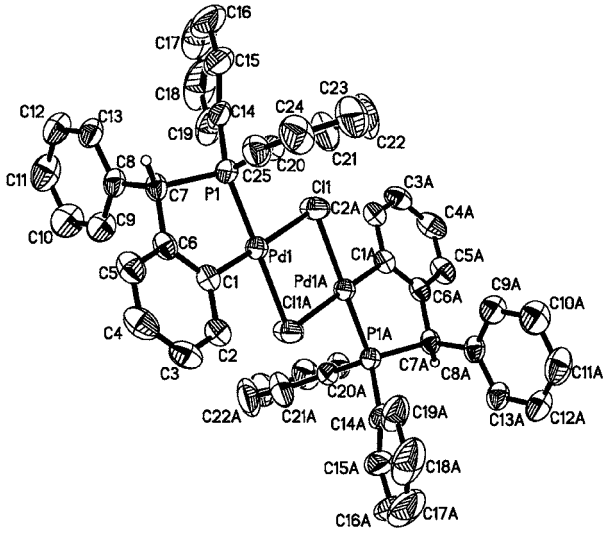


Figure 1. X-ray molecular structure of *meso*-**3**. Selected bond lengths [Å] and bond angles [°]: Pd1–C1, 2.017(3); Pd1–P1, 2.183(1); Pd1–Cl1, 2.441(1); Pd1–Cl1A, 2.407(1); C1–Pd1–P1, 79.43(8); C1–Pd1–Cl1, 174.43(8); C1–Pd1–Cl1A, 97.87(8); P1–Pd1–Cl1, 96.95(3); Cl1–Pd1–Cl1A, 97.87(8); Pd1–Cl1–Pd1A, 94.39(3).

The separation of the two enantiomeric forms of the phosphapalladacycle was then accomplished by the slow fractional crystallization of the mixture of four diastereomers from a solution of $CH_2Cl_2$/diethyl ether. The (*R*,*S*)- and (*S*,*S*)-**4** complexes were obtained sequentially in 59 and 77% yields. The absolute configurations of these derivatives were determined from their X-ray molecular structures. These are presented in Figure 2 and Figure 3 for (*R*,*S*)-**4** and (*S*,*S*)-**4** [as the (*Z*)-isomers], respectively, while the selected bond lengths and bond angles are presented in Table 1. Their absolute configurations were confirmed from

 © 2007 Wiley-VCH Verlag GmbH & Co. KGaA, Weinheim 

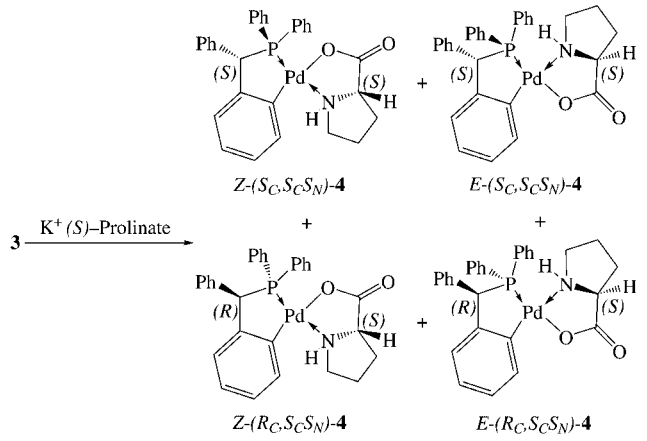


Scheme 2. Formation of (*S*)-prolinate derivatives **4**.

their respective Flack parameters of 0.02(3) and 0.04(4). Like the previously reported (*S*)-prolinate complexes, the secondary stereogenic nitrogen atom from the (*N*,*O*) chelate was noted to adopt the (*S*) configuration in both diastereomers.[9e,12] Both diastereomers are presented as the (*Z*) geometrical isomer and they are noted to have similar bond lengths and bond angles.

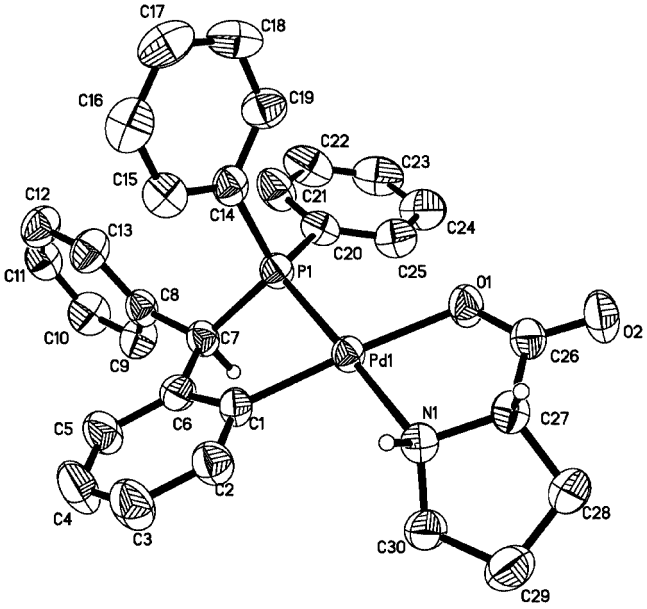

Figure 2. X-ray molecular structure of *Z*-($R_C$,$S_CS_N$)-**4**.

The two optical antipodes of the chloro dimer **3** were then readily obtained by mixing the respective (*S*)-prolinate derivatives **4** with 1 M HCl. Thus, (*R*,*R*)-**3** was isolated as a yellowish-green amorphous powder in quantitative yield (Scheme 3), with $[a]_D$ = –382° ($CH_2Cl_2$). Notably, such acid treatment did not lead to any loss of optical activity, as verified from the $^{31}P$ NMR spectroscopic data of the (*S*)-prolinate complexes **4**, obtained by a re-derivatization of the optically resolved forms of **3**. At room temperature (300 K), the $^{31}P\{^1H\}$ spectra ($CDCl_3$) of the optically resolved dimers **3** had an apparent broad singlet at $\delta$ = 70.8–70.9 ppm. The variable temperature (VT) $^{31}P\{^1H\}$ NMR spectra of (*R*,*R*)-**3**, summarized in Figure 4, indicate that the appearance of the NMR resonance signals is temperature-dependent, as an additional singlet emerges upon cooling. This resonance is shifted progressively downfield relative to the parent signal. The effect is completely reversible, so that warming the NMR sample causes the signal to coalesce with the latter, albeit rather weakly shifted upfield. The appearance of two sets of singlets indicates the existence of the *syn* and *anti* regioisomers that are possible within the dimeric nature of **3**. The fact that other signals originating from the achiral, *meso syn*- and *anti*-(*R*,*S*) iso-

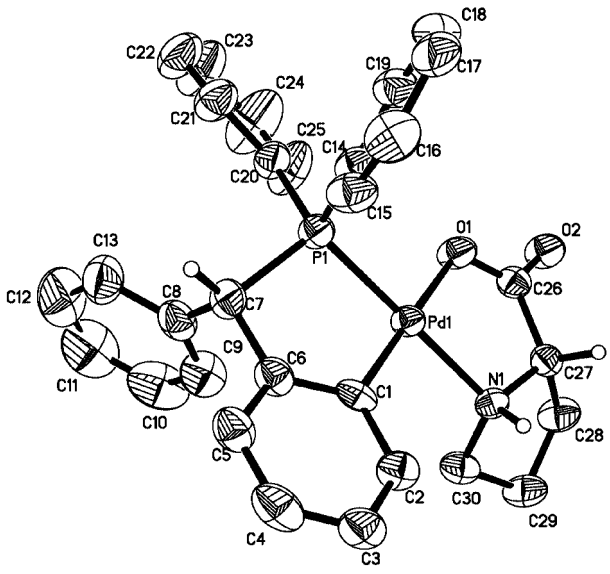

Figure 3.. -ray molecular structure of *Z*-($S_C$,$S_CS_N$)-**4**.

Table 1. Selected bond lengths [Å] and angles [°] of (*Z*)-($R_C$,$S_CS_N$)- and (*Z*)-($S_C$,$S_CS_N$)-**4**.

| *Z*-($R_C$,$S_CS_N$)-**4** | | *Z*-($S_C$,$S_CS_N$)-**4** | |
|---|---|---|---|
| Pd1–C1 | 2.006(4) | Pd1–C1 | 2.015(4) |
| Pd1–O1 | 2.083(3) | Pd1–O1 | 2.084(3) |
| Pd1–N1 | 2.118(3) | Pd1–N1 | 2.095(4) |
| Pd1–P1 | 2.219(1) | Pd1–P1 | 2.203(1) |
| P1–C7 | 1.845(4) | P1–C7 | 1.849(5) |
| C6–C7 | 1.513(6) | C6–C7 | 1.518(7) |
| C1–C6 | 1.408(5) | C1–C6 | 1.406(6) |
| P1–C20 | 1.823(4) | P1–C20 | 1.815(5) |
| P1–C14 | 1.826(5) | P1–C14 | 1.814(5) |
| C7–C8 | 1.514(6) | C7–C8 | 1.495(7) |
| C1–Pd1–O1 | 177.1(2) | C1–Pd1–O1 | 178.9(2) |
| C1–Pd1–N1 | 97.5(1) | C1–Pd1–N1 | 97.9(2) |
| O1–Pd1–N1 | 80.5(1) | O1–Pd1–N1 | 81.1(1) |
| C1–Pd1–P1 | 80.8(1) | C1–Pd1–P1 | 81.0(1) |
| O1–Pd1–P1 | 101.20(8) | O1–Pd1–P1 | 99.9(1) |
| N1–Pd1–P1 | 178.3(1) | N1–Pd1–P1 | 178.7(1) |
| C7–P1–Pd1 | 101.1(1) | C7–P1–Pd1 | 103.5(2) |
| C6–C7–P1 | 103.8(3) | C6–C7–P1 | 102.5(3) |
| C1–C6–C7 | 117.2(4) | C1–C6–C7 | 118.6(4) |
| C6–C1–Pd1 | 120.7(3) | C6–C1–Pd1 | 120.8(3) |
| C26–C27–C28 | 113.2(4) | C26–C27–C28 | 114.7(4) |
| N1–C30–C29 | 104.7(4) | N1–C30–C29 | 105.0(4) |

 © 2007 Wiley-VCH Verlag GmbH & Co. KGaA, Weinheim 

mers were not observed (but were present for the unresolved parent dimer) points to a good degree of optical purity for the obtained (*R*,*R*)-**3**.

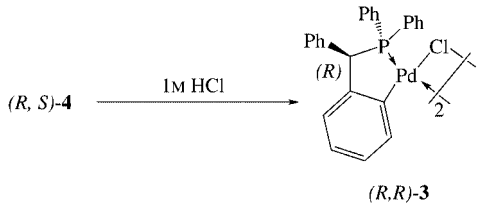


Scheme 3. Regeneration of the dimer **3** in the optically active form.

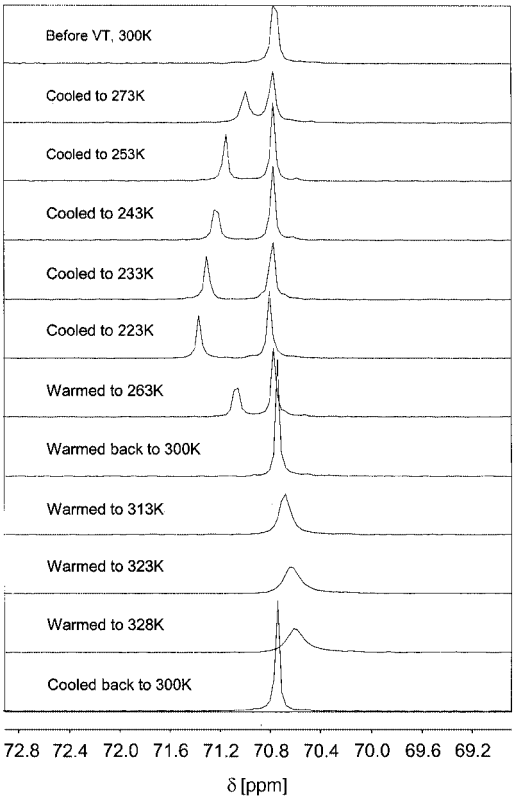


Figure 4. VT $^{31}$P NMR spectra of (*R*,*R*)-**3**.

### Substituent Effects on Phosphapalladacycle Characteristics

While the palladacycle obtained from (diphenylmethyl)-di-*tert*-butylphosphane structurally resembles the current one (the two differ only in terms of the substituents on the phosphorus atom), the properties of the two systems were noticeably dissimilar. First, the replacement of the *t*Bu$_2$P with the Ph$_2$P group seems to evoke a conformational flexibility on the phosphapalladacycle ring. Comparison of the *meso*-**3**, (*R*,*S*)- and (*S*,*S*)-**4** molecular structures (Figure 1, Figure 2 and Figure 3) reveals the possibility of the ring to adopt either one of the two conformational states. This is because in *meso*-**3** and (*S*,*S*)-**4**, the phenyl substituent at the stereogenic α-C atom is noted to adopt the axial orientation, as indicated by the respective angles of 7.0 and 9.5° subtended by this substituent to the normal of the m.c.pl. On the other hand, this angle was found to be 96.8° (or 83.2° as the adjacent angle) for (*R*,*S*)-**4** and as such, the phenyl substituent at the α-C atom is considered equatorially disposed. The possibility of the α-C phenyl substituent to adopt two different orientations indicates a lack of crucial intrachelate steric interactions to enforce it to permanently adopt an axial orientation. The absence of such an interaction is due to the rotational ability of this substituent along the C7–C8 bond. Evidently, this could be supported by the diversification of the angle between the mean planes of this phenyl substituent and the palladated {C(1–6)} phenylene ring by 24.6° from 99.2° in *meso*-**3** to 74.6° in ($S_C S_C$)-**4**, despite the common axial disposition of their α-C phenyl substituents. It should be noted from the structure of ($R_C S_C$)-**4** that, when the substituent is equatorially disposed, the mean plane of this phenyl ring is almost perpendicular to that of the palladated phenylene ring, at 83.1°. When the α-C phenyl substituent is in this rotameric state, any unfavourable steric repulsion with the palladated ring may thus be effectively minimized. In support of this statement, the shortest distance between the two aromatic rings, i.e. that between the H5 and H13 protons, at 3.350 Å, may be mentioned. A separation of this magnitude for these two atoms far exceeds the sum of van der Waals radii for two hydrogen atoms (2.4 Å) and is considered too large to generate any kind of instability to the conformational state of the phosphapalladacycle ring when the α-C phenyl substituent is equatorially disposed. For comparison, a close interaction of this kind at 2.148–2.234 Å between the α-C proton and the nearest proton of the palladated naphthylene ring was found for the conformationally rigid *ortho*-palladated [1-(1′-naphthyl)ethyl]diphenylphosphane system.[4a] In other words, in the current phosphapalladacycle, the prevention of any unfavourable steric contacts between the two aromatic rings may be accomplished simply by the adoption of a suitable rotameric state for the equatorially disposed α-C phenyl substituent or by the alternate axial orientation of this substituent. In contrast, the solid state studies of the *t*Bu-based phosphapalladacycle (*S*)-**7** revealed an axial orientation of the α-C phenyl substituent.[10] The alternate equatorially disposed orientation of this substituent was prevented by the close interaction of this phenyl ring with the *t*Bu groups or the H5 atom of the palladated phenyl ring. Any form of steric relief that could be brought about by the adoption of a certain rotameric state of this phenyl ring seems remote, since it is surrounded by three groups in this conformational state.

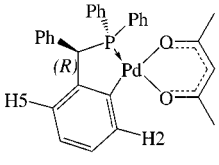


(*R*)-**6**

The lack of conformational rigidity of the current –PPh$_2$ based phosphapalladacycle is not restricted to the solid state but extends to solution. This was observed in the 2D $^1$H-$^1$H NOESY NMR spectrum (Figure 5) of the β-dike-

 © 2007 Wiley-VCH Verlag GmbH & Co. KGaA, Weinheim 

tonate derivative, (*R*)-**6**, which was obtained as an amorphous powder, with $[\alpha]_{436} = -1123°$ ($CH_2Cl_2$), from the direct treatment of the dimer (*R*,*R*)-**3** with sodium acetylacetonate in acetone. From its $^1H$ NMR spectrum ($CDCl_3$), two visibly distinguished sets of *ortho*-, *meta*- and *para*-PPh protons appear, as the two PPh rings are diastereotopic. Assignment of the signals was made by a combination of $^1H\{^{31}P\}$, 2D $^1H$-$^1H$ COSY and NOESY NMR spectroscopic experiments. The four aromatic protons of the *ortho*-palladated ring form a spin system, as observed from the COSY data. The most upfield aromatic signal was assigned to the H5 proton, in recognition of its NOE contact (interaction C) with the α-CH proton. The latter spin couples with the adjacent $^{31}P$ nucleus and was presented as a simple doublet resonance ($^2J_{P,H}$ = 13.3 Hz). A rather unexpected long-range coupling with the $^{31}P$ nucleus was detected for the H2 proton, the corresponding coupling constant being a rather significant 4.0 Hz. The five aromatic protons of the α-C phenyl substituent are collectively represented as an extensively overlapping multiplet at $\delta$ = 7.00–7.05 ppm. The 2D $^1H$-$^1H$ NOESY NMR spectrum points to a rather flattened palladacycle ring in which each PPh ring was observed to distinctly interact through NOE with only either the methine proton or the phenyl ring at the stereogenic α-C centre (interactions A and D). Such a conformational picture may be satisfied by either one of the two Newman representations in Figure 6.

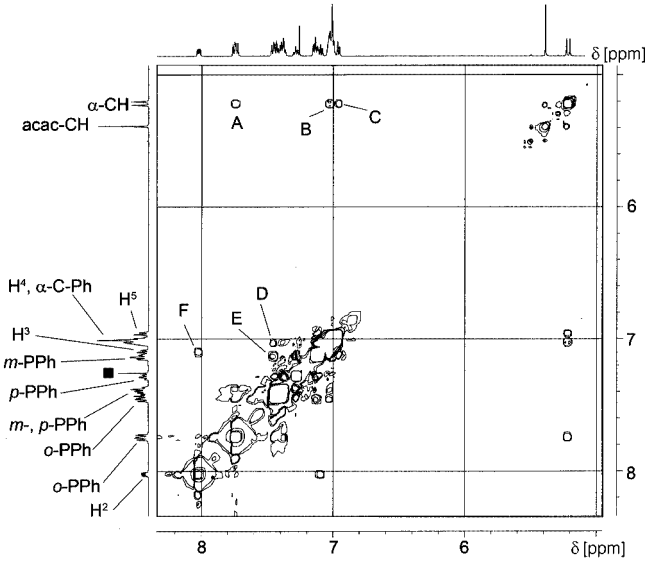


Figure 5. Expanded 2D $^1H$-$^1H$ NOESY NMR spectrum of (*R*)-**6** ($CDCl_3$). Selected NOE interactions: A: α-CH–*o*-PPh; B: α-CH–*o*-Ph of α-CPh; C: α-CH–H5; D: *o*-PPh–*o*-Ph of α-CPh; E: *o*-PPh–*m*-PPh; F: H2–H3. Solvent signal: ■, $CDCl_3$.

In contrast, the phosphapalladacycle ring of the $tBu_2P$ equivalent is conformationally rigid, on the basis of a similar 2D $^1H$-$^1H$ NOESY NMR study performed on the analogous β-diketonate complex **7** (whose preparation was reported earlier[10]) containing the (*S*) configuration at the α-C centre. The aromatic signals in its $^1H$ NMR spectrum may be divided into two separate sets of spin patterns accounting for a total of nine aromatic protons. One of these

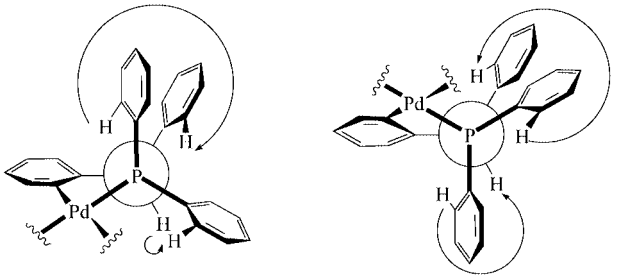


Figure 6. Newman projections for two possible flattened palladacycle conformations for complex (*R*)-**6**. Curved arrows depict NOE contacts.

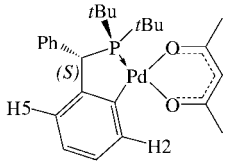


(*S*)-**7**

comprises the four protons (H2–H5) of the *ortho*-palladated phenylene ring, while the other set of signals is representative of the remaining five aromatic protons belonging to the α-C phenyl substituent. The most upfield aromatic signal was assigned the H5 proton on account of its NOE contact with the α-C methine proton from the 2D $^1H$-$^1H$ NOESY NMR spectrum (Figure 7 and Figure 8). Among the (H2–H5) set of aromatic protons, such an NOE interaction is only possible for this proton, given its closest proximity to the α-CH proton. The remaining three aromatic protons of the same set may next be unambiguously assigned by using the H5 proton as a starting point by considering either (i) the coupling information from the COSY data or (ii) the negative, off-diagonal, i.e. NOE signals among these protons from the NOESY NMR spectrum.

As an added peculiarity, the spectral pattern of the five aromatic protons of the α-C phenyl substituent corresponds to a rather complicated ABCDE spin system, in which both *ortho* protons are chemically nonequivalent on the NMR time scale, a characteristic that is also shared by the *meta* protons. The detection of an off-diagonal, opposite-phased EXSY signal (signal I, in Figure 8) between the two *ortho* protons in the 2-D $^1H$-$^1H$ NOESY NMR spectrum points to the exchangeability between these two protons, which may be provided by the rotational capability of the $C^{\alpha}$–$C^{i}$ bond of the phosphapalladacycle, but such capability must be rather restricted even in solution to allow a differentiation and hence signal-doubling of both *ortho* protons (as well as the *meta* protons).

In the expanded 2-D $^1H$-$^1H$ NOESY NMR spectrum (Figure 7), NOE contacts were observed between the α-CH protons and both sets of the *t*Bu substituents (interactions C and D). Moreover, similar interactions between the two *ortho* protons of the α-C phenyl substituent and only one of the two available *t*Bu substituents were noted (interactions A and B). Consequently, these NOE patterns, together with the absence of similar NOE contacts between the α-C

 © 2007 Wiley-VCH Verlag GmbH & Co. KGaA, Weinheim 

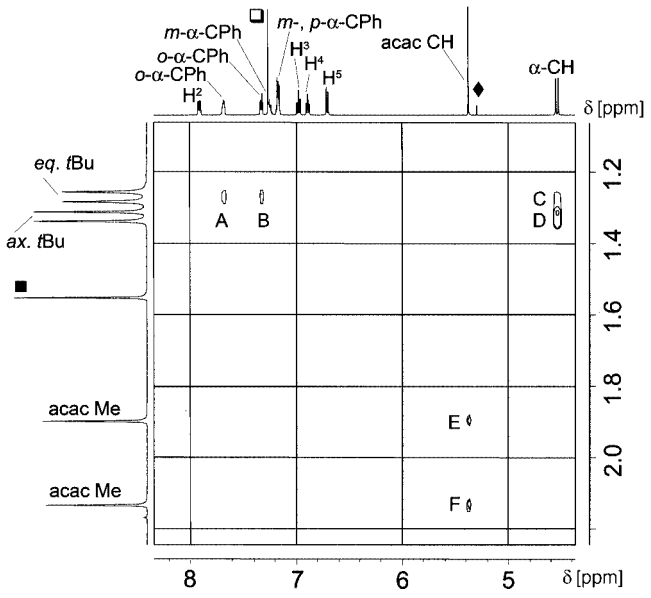


Figure 7. Expanded 2D $^1$H-$^1$H NOESY NMR spectrum of (*S*)-**7** ($CDCl_3$). Aliphatic–aromatic NOE interactions: A: equatorial *t*Bu–*o*-α-Ph; B: equatorial *t*Bu–*o*-α–Ph; C: equatorial *t*Bu–α–CH; D: axial *t*Bu–α–CH; E: acac CH–acac Me; F: acac CH–acac Me. Solvent signals: ■, $H_2O$, ♦, $CH_2Cl_2$, □, $CDCl_3$.

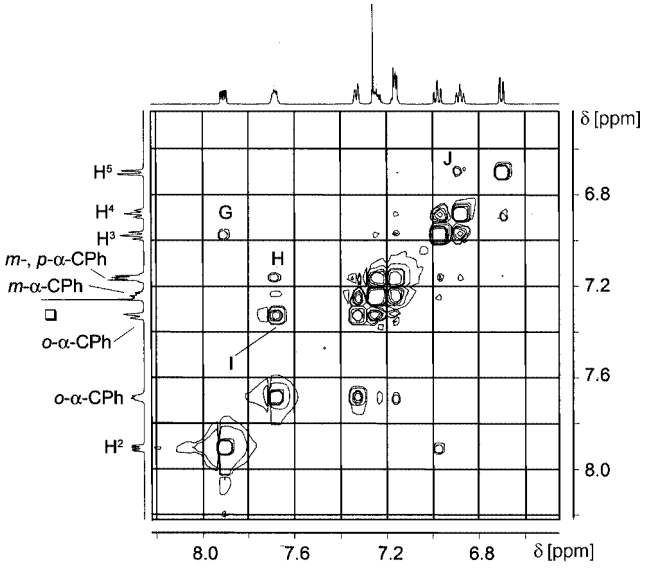


Figure 8. Expanded 2D $^1$H-$^1$H NOESY NMR spectrum of (*S*)-**7** ($CDCl_3$). Selected aromatic–aromatic NOE interactions: G: H2–H3; H: *o*-α-Ph–*m*-α-Ph; J: H4–H5. EXSY signal: I: *o*-α-Ph–*o*-α-Ph. Solvent signal: □, $CDCl_3$.

phenyl *ortho* protons and the remaining *t*Bu group (i.e. the axially disposed *t*Bu group; the other *t*Bu group must be the equatorially disposed one) must be known in support of the λ conformation and the rigid state of the phosphapalladacycle with (*S*) absolute configuration in solution. As a comparison, this set of NOE interactions is impossible for the case of the δ conformation for the same absolute (*S*) configuration at the α-C centre, as illustrated by the by the Sawhorse and Newman projections along the P–α-C bond in Figure 9.

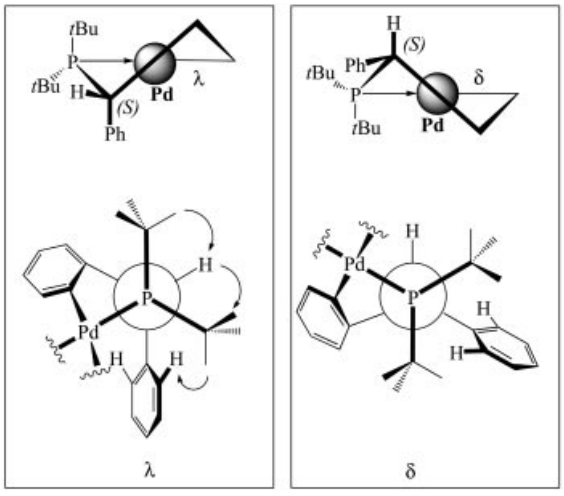


Figure 9. Sawhorse and Newman projections for the λ and δ conformations for complex (*S*)-**7** ($CDCl_3$). Curved arrows depict NOE contacts.

A mentionable observation among these aromatic signals is the presence of the long-range $^1$H–$^{31}$P spin-spin couplings for the H2 and H4 protons. A rather significant coupling constant of 3.9 Hz over four bonds was found for the former, while a coupling constant of 2.1 Hz over possibly five bonds was detected for the latter. Such a phenomenon is unusual, when similar couplings for the other two aromatic protons belonging to the same phenylene ring do not exist. A similar feature was also noted for the corresponding H2 proton in (*R*)-**6**.

The large steric bulk of the *t*Bu groups has resulted in a better regioselectivity with respect to the coordination of arriving ancillary ligands to the palladacycle. This was noted in the reaction of the chloro-bridged dimer **8** with (*S*)-prolinate, in which the strong degree of regioselectivity is evident from the product distribution of 99:1 and 98:2 (*E*/*Z*) for its (*S*,*S*) and (*R*,*S*) derivatives, correspondingly.[10] Furthermore, compound **8** reacted with triphenylphosphane to give the *trans* isomer (±)-**9** exclusively (Scheme 4). This is far superior with respect to the current phosphapalladacycle **3**, which generated a mixture of *cis* and *trans* isomers (±)-**10** in 1.1:1 ratio. Both geometrical isomers were readily distinguished from each other by a consideration of the $^2J_{P,P}$ coupling constants. These were determined to be 29.0 Hz for *cis*-**10** and were more pronounced at 418.1 and 390.6 Hz for *trans*-(±)-**10** and *trans*-(±)-**9**, respectively. For *trans*-(±)-**9**, only one set of signals was observed in its $^1$H NMR spectrum expectedly and the *trans*-(*P*, *P*) geometry was further inferred from the relatively high-field position of the phenylene aromatic proton at $\delta$ = 6.24 ppm. The best evidence for this geometry was provided by its molecular structure. The structure (with the accompanying numbering scheme) is presented in Figure 10. The chiral nature of the phosphapalladacycle is obvious from the stereogenic α-C atom, by the *ortho*-palladation of only one of the two available phenyl rings (i.e. the C1–C6 phenyl ring) on the phosphane moiety. Analysis of the extent of the tetrahedral distortion on the central Pd atom reveals that it is located in

 © 2007 Wiley-VCH Verlag GmbH & Co. KGaA, Weinheim 

a highly congested environment: the dihedral angle between the {P1–Pd1–C1} and {Cl1–Pd1–P2} planes has a large value of 23.0°. Such a large value is probably an indication of the need to relieve steric repulsion due to the presence of the phosphapalladacycle bulky *t*Bu substituents and the $PPh_3$ phenyl rings. The overcrowding around the central Pd atom was further demonstrated by the mean vertical displacement of 0.2483 Å from planarity of the five atoms of the m.c.pl.

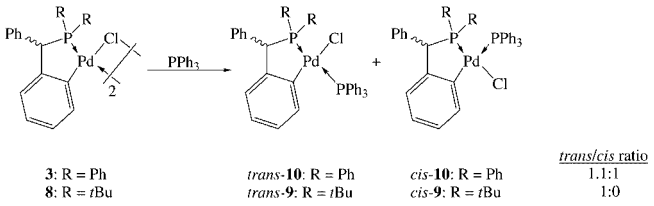


Scheme 4. Formation of triphenylphosphane adducts (±)-**9** and (±)-**10**.

Notably, the current $Ph_2P$-based phosphapalladacycle also discloses a profound difference in the Pd–C bond reactivity. To recall, the Pd–C bond of the *t*$Bu_2P$ analogue was noted to be only kinetically unstable and the phosphapalladacycle ring opens and closes reversibly by Pd–C bond cleavage in refluxing acetone containing concentrated HCl.[10] This effect was attributed to the thermodynamic stability imparted to the palladacycle by the steric influence of the bulky *t*Bu substituents. In stark contrast to its *t*$Bu_2P$ analogue, the presence of a few drops of concentrated HCl in a $CDCl_3$ solution of the chloro dimer **3** led to a permanent ring opening of the phosphapalladacycle by cleavage of the Pd–C bond (Scheme 5). The transformation was immediate, as observed from the colour change from pale yellow to orange-red. The fact that the Pd–C bond cleavage of the current phosphapalladacycle was permanent was affirmed by the possibility to even isolate the binuclear product **5** from this procedure and perform an X-ray diffraction study. From Figure 11, the complex has an overall *anti* structure that reveals the occupation of both diagonally opposite terminal ends of the dimer by two additional chloride ligands. Moreover, the $\eta^1$-P type of coordination mode adopted by the phosphane ligand is apparent here. Unlike the *ortho*-palladated structure, however, the central four-membered $\{Pd_2(\mu\text{-}Cl)_2\}$cycle is not planar, since each Pd atom deviates from planarity by an angle of 6.45°. It is worth mentioning that the P–Pd bond has weakened as a result of palladacycle ring opening. This bond length has increased from 2.1832(7) Å in the *ortho*-palladated structure

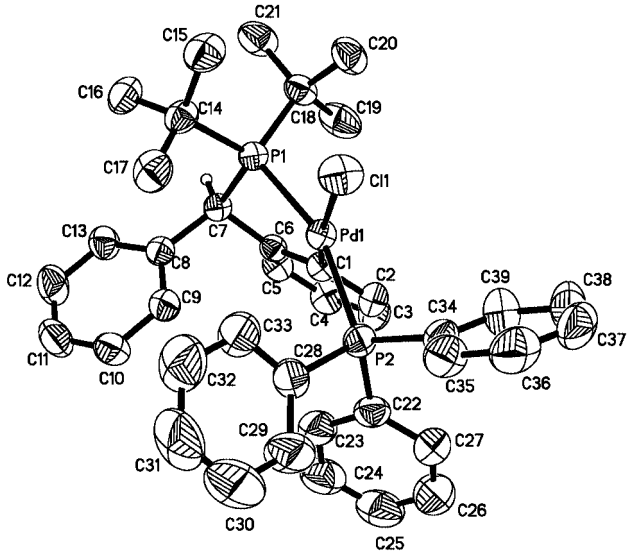


Figure 10. X-ray molecular structure of *trans*-(±)-**9**. Selected bond lengths [Å] and bond angles [°]: Pd1–P1, 2.295(1); Pd1–C1; 2.014(2); Pd1–O1, 2.375(1); Pd1–Cl1, 2.3878(5); C1–Pd1–P1, 80.41(5); C1–Pd1–P2, 96.99(5); P1–Pd1–P2, 161.01(2); C1–Pd1–Cl1, 167.63(5); P1–Pd1–Cl1, 97.77(2); P2–Pd1–Cl1, 88.63(2).

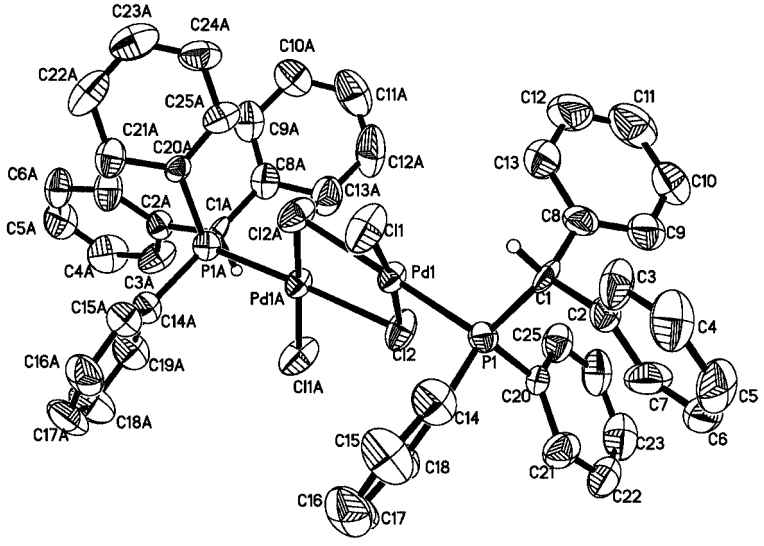


Figure 11. X-ray molecular structure of compound **5**. Selected bond lengths [Å] and bond angles [°]: Pd1–P1, 2.237(3); Pd1–Cl1, 2.260(3); Pd1–Cl2, 2.323(3); Pd1–Cl2A, 2.414(3); P1–Pd1–Cl2, 96.5(1); P1–Pd1–Cl1, 86.9(1); P1–Pd1–Cl2A, 177.4(1); Cl1–Pd1–Cl2, 171.9(1), Cl2–Pd1–Cl2A, 85.8(1); Cl1–Pd1–Cl2A, 90.7(1).

 © 2007 Wiley-VCH Verlag GmbH & Co. KGaA, Weinheim 

**3** to 2.237(3) Å in the monodentate state. Thus, the possibility of stabilizing the P–Pd bond as a result of *ortho*-palladation is noteworthy. The P–C bond strengths have not varied significantly, however.

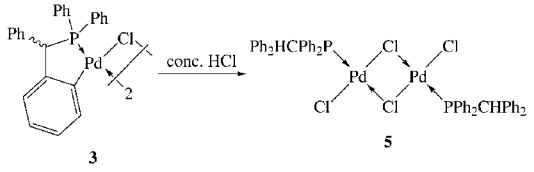


**3** **5**

Scheme 5. Permanent Pd–C bond cleavage to generate the achiral binuclear dimer **5**.

## Conclusions

The novel palladacycle based on the ligand (diphenylmethyl)diphenylphosphane was prepared in the optically active forms by optical resolution of its (*S*)-prolinate derivatives. This palladacycle was shown to display properties which were different from those of its bulkier analogue, the (diphenylmethyl)di-*tert*-butylphosphane-based palladacycle. First, the five-membered ring of the current palladacycle assumes both available conformations in solution and in the solid state. From solid-state X-ray structure studies, the conformational flexibility of this system was directly attributed to the absence of intrachelate interactions in either the λ or the δ conformations. Second, the bulkiness of the *t*Bu groups also brings about a more improved regioselectivity with respect to the coordination of ancillary triphenylphosphane and (*S*)-prolinate ligands for the latter palladacycle. Third, in the absence of such steric effects originating from the *t*Bu groups, the Pd–C bond of the former does not possess the type of thermodynamic stability that was observed for the latter. Currently, both palladacycles are being tested in various asymmetric applications.

## Experimental Section

**General:** Reactions involving air-sensitive compounds were performed under a positive pressure of argon. Routine $^1$H NMR spectra were recorded at 300 MHz or 500 MHz with a Bruker ACF 300 or Bruker AMX 500 NMR spectrometer. All the $^{31}$P{$^1$H} NMR spectra were recorded at 120 MHz or 202 MHz with a Bruker ACF 300 or Bruker AMX 500 NMR spectrometer. Unless stated otherwise, all NMR spectroscopic experiments were performed at room temperature (300 K). Melting points were determined with a Büchi melting point B-545 apparatus and are uncorrected. Optical rotations were measured on the specified solution in 1-dm or 0.1-dm cells at 25 °C with a Perkin–Elmer Model 341 polarimeter. Elemental analyses were performed by the Elemental Analysis Laboratory of the Department of Chemistry at the National University of Singapore.

**(Diphenylmethyl)diphenylphosphane (2):** A solution of (diphenylmethyl)lithium was prepared by syringing *n*-BuLi in hexanes (3.7 mL, 5.9 mmol, 1.6 M) into a thf solution (5 mL) of diphenylmethane (1.00 g, 5.94 mmol) and allowing the mixture to stir at room temperature for 3 h. The freshly prepared, intensely red solution of (diphenylmethyl)lithium was then added dropwise to an ice-chilled thf solution (5 mL) of chlorodiphenylphosphane (0.98 g, 4.46 mmol) with rapid stirring. The addition led to an immediate decolourization of the (diphenylmethyl)lithium reagent. When decolourization was no longer observed upon further addition of the (diphenylmethyl)lithium reagent, the addition was discontinued, the ice-bath was removed, and the mixture was allowed to stir at room temperature for a further 30 min. It was then concentrated to dryness, washed with freshly deoxygenated water (20 mL) and extracted with $CH_2Cl_2$ (3 × 50 mL). The organic extracts were combined, dried with $MgSO_4$ and filtered. The product was finally obtained as a white solid upon removal of solvents by distillation and further drying under reduced pressure. Yield: 1.54 g (98.0%). $^1$H NMR (300 MHz, $CDCl_3$): $\delta$ = 4.63 (d, $^2J_{P,H}$ = 6.8 Hz, 1 H, $Ph_2CH$), 7.03–7.26 (m, 20 H, aromatic protons) ppm. $^{31}$P{$^1$H} NMR (121 MHz, $CDCl_3$): $\delta$ = –3.2 (s) ppm.

**Di-μ-chlorobis{[(diphenylphosphanyl)(phenyl)methyl]phenyl-*C*$^2$,*P*}-dipalladium(II) (3):** The phosphane **2** (1.57 g, 4.46 mmol) and palladium(II) acetate (1.00 g, 4.46 mmol) were suspended in toluene (100 mL), and the reacting mixture was stirred at 50 °C for 2 h to give a deep reddish brown mixture with deposition of palladium black. The mixture was concentrated to dryness by using a rotary evaporator to yield a crude reddish-black residue. $^{31}$P{$^1$H} NMR (121 MHz, $CDCl_3$): $\delta$ = 68.4 (s) ppm. The residue was then suspended in acetone (15 mL), to which a solution of lithium chloride (0.50 g, 11.8 mmol) in acetone/methanol (1:3, v/v) was added. The mixture was then stirred for 90 min, concentrated to dryness and re-suspended in $CH_2Cl_2$. This suspension was filtered through a plug of Celite to yield an orange solution, which was further washed with water (40 mL). The organic extract was concentrated and chromatographed on a silica gel column from which the chloro dimer was eluted as a pale yellowish-green fraction by using $CH_2Cl_2$–hexanes (1:2, v/v). Crystallization from $CH_2Cl_2$/diethyl ether yielded pale yellow blocks; m.p. (decomp.) 232–236 °C. Yield: 1.36 g (61.3%). $C_{50}H_{40}Cl_2P_2Pd_2$ (986.52): calcd. C 60.9, H 4.1; found C 60.6, H 4.1. $^1$H NMR (300 MHz, $CDCl_3$): $\delta$ = 5.27 (d, $^2J_{P,H}$ = 13.6 Hz, 1 H, α-CH), 6.98–8.11 (br. overlapping m, 19 H, aromatic protons) ppm. $^{31}$P{$^1$H} NMR (121 MHz, $CDCl_3$): $\delta$ = 70.4, 70.6, 70.8 (br. overlapping s) ppm; (223 K) four sets of signals at $\delta$ = 70.7 (s), 70.8 (s), 70.9 (s) and 71.4 (s) ppm.

***sym*-Dichlorodi-μ-chlorobis[(diphenylmethyl)diphenylphosphane]dipalladium(II) (5):** To a $CH_2Cl_2$ solution (3 mL) of the racemic complex **3** (0.11 g, 0.12 mmol) was added an excess of conc. HCl (30 μL, 37% wt/wt, spec. gravity 1.19) with a micropipette. The mixture was allowed to stir vigorously for 1 h at room temperature, after which it was diluted with water (5 mL) and $CH_2Cl_2$ (20 mL). The orange-red organic layer was separated and was washed with water (2 × 5 mL) and dried with $MgSO_4$. The excess $CH_2Cl_2$ was removed, from which the product was obtained as fine orange-red crystals from $CH_2Cl_2$/hexanes exhibiting low solubility; m.p. (decomp.) 231–233 °C. Yield: 0.088 g (72.7%). $C_{50}H_{42}Cl_4P_2Pd_2$ (1059.44): calcd. C 56.7, H 4.0; found C 56.3, H 4.3. $^1$H NMR (300 MHz, $CDCl_3$): $\delta$ = 6.35 (d, $^2J_{P,H}$ = 15.6 Hz, 1 H, α-CH), 7.19–7.48 (m, 20 H, aromatic protons) ppm. $^{31}$P{$^1$H} NMR (121 MHz, $CDCl_3$): $\delta$ = 36.8 (s) ppm.

**Chloro{[(±)-(diphenylphosphanyl)(phenyl)methyl]phenyl-*C*$^2$,*P*}-(triphenylphosphane)palladium(II) [(±)-10]:** Triphenylphosphane (0.012 g, 0.045 mmol) was added to a $CH_2Cl_2$ solution (3 mL) of the dimer **3** (0.022 g, 0.022 mmol), and the mixture was stirred for 30 min, after which the pale yellow solution was concentrated in vacuo, and the product was obtained as pale yellow crystals in $CH_2Cl_2$/hexanes; m.p. 200–202 °C. Yield: 0.020 g (58.8%).

 © 2007 Wiley-VCH Verlag GmbH & Co. KGaA, Weinheim 

$C_{43}H_{35}ClP_2Pd$ (755.55): calcd. C 68.4, H 4.7; found C 68.5, H 4.4. $^1H$ NMR (300 MHz, $CDCl_3$) two sets of signals in 1:0.87 ratio for both geometric isomers in favour of the *cis* isomer, $\delta$ = 5.16 (br. d, $^2J_{P,H}$ = 13.7 Hz, 1 H, α- CH of *trans* isomer), 5.31 (d, $^2J_{P,H}$ = 13.3 Hz, 1 H, α-CH of *cis* isomer), 6.32–8.61 (aromatic protons of both isomers) ppm. $^{31}P\{^1H\}$ NMR (202 MHz, $CDCl_3$) two sets of signals in 1:0.87 ratio for both geometric isomers in favour of the *cis* isomer, $\delta$ = 18.1 (d, $^2J_{P,P}$ = 29.0 Hz, $PPh_3$ of *cis* diastereomer), 26.6 (d, $^2J_{P,P}$ = 418.1 Hz, $PPh_3$ of *trans* diastereomer), 58.6 (d, $^2J_{P,P}$ = 418.1 Hz, palladacycle P of *trans* diastereomer), 71.0 (d, $^2J_{P,P}$ = 29.0 Hz, palladacycle P of *cis* diastereomer) ppm.

**[(*S*)-Prolinato-*N*,*O*]{(±)-1-[(diphenylphosphanyl)(phenyl)methyl]-phenyl-*C*$^2$,*P*}palladium(II) (4):** A methanol solution (9 mL) of potassium (*S*)-prolinate (0.312 g, 0.680 mmol) was added to the dimer **3** (1.00 g, 1.02 mmol) suspended in $CH_2Cl_2$ (10 mL), and the mixture was stirred for 1 h at room temperature. The resulting white suspension was concentrated to dryness, re-suspended in $CH_2Cl_2$ (8 mL), washed with water (2 × 10 mL) and dried with $MgSO_4$. The colourless solution was then concentrated to dryness by using a rotary evaporator and was further dried at 70 °C in vacuo for 3 h to yield a flaky white solid; m.p. (decomp.) 225–227 °C. $[\alpha]_D$ = +107°, $[\alpha]_{578}$ = +114°, $[\alpha]_{546}$ = +129°, $[\alpha]_{436}$ = +263°, $[\alpha]_{365}$ = +636° (*c* 1.1, $CH_2Cl_2$). Yield: 1.15 g (99.1%). $C_{30}H_{28}NO_2PPd$ (571.93): calcd. C 63.0, H 4.9, N 2.5; found C 62.5, H 5.1, N 2.7. $^1H$ NMR ($CDCl_3$, 500 MHz) four sets of signals in the ratio of 0.4:0.3:0.9:1.0, $\delta$ = 1.32–1.44 [overlapping m, γ-H of *E*-(*R*,*S*)- and *E*-(*S*,*S*)-diastereomers], 1.75 [m, γ-H of *E*-(*S*,*S*)-diastereomer], 1.81–1.86 [overlapping m, γ-H of *Z*-(*S*,*S*)-diastereomer, γ-H of *E*- and *Z*-(*R*,*S*)-diastereomers], 2.02–2.41 [series of m, γ-H of *Z*-(*S*,*S*)-and *Z*-(*R*,*S*)-diastereomers, both β-H of *E*-(*R*,*S*)-diastereomers, both β-Hs of *E*-(*S*,*S*)-diastereomers, β-H of *Z*-(*R*,*S*)-diastereomer, both β-H of *Z*-(*S*,*S*)-diastereomers, δ-H of *E*-(*S*,*S*)-diastereomer, N-H of *E*-(*R*,*S*)-diastereomer], 2.44–2.61 [series of m, β-H of *Z*-(*R*,*S*)-diastereomer, δ-H of *E*-(*R*,*S*)-diastereomer, δ-H of *E*-(*S*,*S*)-diastereomer, N-H of *E*-(*S*,*S*)-diastereomer], 2.80 [m, δ-H of *E*-(*R*,*S*)-diastereomer], 3.35 [m, δ-H of *Z*-(*R*,*S*)-diastereomer], 3.41–3.51 [overlapping m, both δ-Hs of *Z*-(*S*,*S*)-diastereomer], 3.55 [δ-H of *Z*-(*R*,*S*)-diastereomer], 3.61–3.69 [overlapping m, N-H of both *Z*-(*R*,*S*)- and *Z*-(*S*,*S*)-diastereomers], 3.92 [m, α-H of *E*-(*R*,*S*)-diastereomer], 3.99 [m, α-H of *E*-(*S*,*S*)-diastereomer], 4.14 [m, α-H of *Z*-(*S*,*S*)-diastereomer], 4.22 [m, α-H of *Z*-(*R*,*S*)-diastereomer], 5.08 [d, $^2J_{P,H}$ = 13.9 Hz, palladacycle α-H of *Z*-(*S*,*S*)-diastereomer], 5.20 [d, $^2J_{P,H}$ = 13.0 Hz, palladacycle α-H of *Z*-(*R*,*S*)-diastereomer], 5.40 [d, $^2J_{P,H}$ = 12.5 Hz, palladacycle α-H of *E*-(*S*,*S*)-diastereomer], 5.49 [d, $^2J_{P,H}$ = 12.5 Hz, palladacycle α-H of *E*-(*R*,*S*)-diastereomer], 6.71 [d, $^2J_{H,H}$ = 7.49 Hz, *o*-α-Ph of *E*-(*R*,*S*)-diastereomer], 6.74 [d, $^2J_{H,H}$ = 7.77 Hz, 2-H of *E*-(*R*,*S*)-diastereomer], 6.78 [m, *o*-α-Ph of *E*-(*S*,*S*)-diastereomer], 6.85 [d, $^2J_{H,H}$ = 6.94 Hz, 5-H of *E*-(*S*,*S*)-diastereomer], 6.93–7.58 [series of m, aromatic protons of all four diastereomers], 7.72–7.85 [partially overlapping m, *o*-PPh of *Z*-(*R*,*S*)-, *o*-PPh of *E*-(*R*,*S*)-and *o*-PPh of *E*-(*S*,*S*)-diastereomers], 8.10–8.15 [partially overlapping m, 2-H proton of *E*-(*R*,*S*)- and *E*-(*S*,*S*)-diastereomers] ppm. $^{31}P\{^1H\}$ NMR ($CDCl_3$, 202 MHz) four signals in relative intensities of 4:3:9:10, $\delta$ = 62.7 (s), 64.4 (s), 71.0 (s) and 72.1 (s) ppm respectively.

**Separation of ($R_C$,$S_C$$S_N$) and ($S_C$,$S_C$$S_N$) Diastereomers**

**Isolation of ($R_C$,$S_C$$S_N$)-(Prolinato-*N*,*O*){[(diphenylphosphanyl)-(phenyl)methyl]phenyl-*C*$^2$,*P*}palladium(II) [($R_C$,$S_C$$S_N$)-4]:** Diethyl ether was slowly added at regular intervals to a moderately concentrated $CH_2Cl_2$ solution of the above 1:1 mixture of both diastereomers (1.168 g, 2.04 mmol), from which the less soluble diastereomer ($R_C$,$S_C$$S_N$)-**4** was isolated after two days as colourless blocks with 97.1% *de* (from $^{31}P\{^1H\}$ NMR spectroscopic data), which gradually desolvated upon standing at room temperature; m.p. 191–193 °C. $[\alpha]_D$ = –109°, $[\alpha]_{578}$ = –114°, $[\alpha]_{546}$ = –131°, $[\alpha]_{436}$ = –242°, $[\alpha]_{365}$ = –397° (*c* 1.1, $CH_2Cl_2$). Yield: 0.34 g (59.0%, based on the theoretical yield of one diastereomer). $C_{30}H_{28}NO_2PPd$ (571.93): calcd. C 63.0, H 4.9, N 2.5; found C 63.0, H 4.8, N 2.6. $^1H$ NMR ($CDCl_3$, 500 MHz) two sets of signals in 1:0.28 ratio in favour of the *E*-isomer, $\delta$ = 1.41 (m, 1 H, γ-H of *E*-isomer), 1.77–1.87 (overlapping m, γ-H of both isomers), 2.04–2.14 (overlapping m, γ-H of *Z*-isomer, β-H of *E*-isomer), 2.19–2.39 (overlapping m, β-H of *Z*-isomer, β-H and N-H of *E*-isomer), 2.45–2.56 (overlapping m, β-H of *Z*-isomer, δ-H of *E*-isomer), 2.80 (m, 1 H, δ-H of *E*-isomer), 3.36 (m, 1 H, δ-H of *Z*-isomer), 3.56 (br. overlapping m, 2 H, δ-H and N-H of *Z*-isomer), 3.93 (m, 1 H, prolinate α-H of *E*-isomer), 4.21 (m, 1 H, prolinate α-H of *Z*-isomer), 5.20 (d, $^2J_{P,H}$ = 13.0 Hz, 1 H, palladacycle α-H of *Z*-isomer), 5.46 (d, $^2J_{P,H}$ = 12.5 Hz, 1 H, palladacycle α-H of *E*-isomer), 6.70 (d, $^3J_{H,H}$ = 7.7 Hz, 2 H, *o*-α-Ph of *E*-isomer), 6.73 (d, $^3J_{H,H}$ = 7.4 Hz, 1 H, 5-H of *E*-geometrical isomer), 6.92–7.46 (m, aromatic protons of both geometric isomers), 7.52–7.58 (overlapping m, aromatic protons of both geometric isomers), 7.73 (ddd, $^3J_{H,H}$ = 8.5Hz, $^4J_{H,H}$ = 1.6 Hz, $^3J_{P,H}$ = 11.1 Hz, 2 H, *o*-PPh of *Z*-isomer), 7.81 (ddd, $^3J_{H,H}$ = 8.0 Hz, $^4J_{H,H}$ = 1.6 Hz, $^3J_{P,H}$ = 11.0 Hz, 2 H, *o*-PPh of *E*-isomer), 8.13 (ddd, $^3J_{H,H}$ = 7.7 Hz, $^4J_{H,H}$ = 1.1 Hz, $J_{P,H}$ = 4.0 Hz, 1 H, 2-H of *E*-isomer) ppm. $^{31}P\{^1H\}$ NMR ($CDCl_3$, 202 MHz) two signals with relative intensities of 2.8:10, $\delta$ = 64.5 (s, *Z*-isomer), 72.2 (s, *E*-isomer) ppm.

**Isolation of ($S_C$,$S_C$$S_N$)-(Prolinato-*N*,*O*){[(diphenylphosphanyl)-(phenyl)methyl]phenyl-*C*$^2$,*P*}palladium(II) [($S_C$,$S_C$$S_N$)-4]:** Subsequent slow evaporation of the remaining mother liquor above afforded the more soluble diastereomer ($S_C$,$S_C$$S_N$)-**4** as large colourless blocks with 91.0% *de* (from $^{31}P\{^1H\}$ NMR spectroscopic data); m.p. (decomp.) 272–274 °C. $[\alpha]_D$ = +303°, $[\alpha]_{578}$ = +318°, $[\alpha]_{546}$ = +369°, $[\alpha]_{436}$ = +728°, $[\alpha]_{365}$ = +1580° (*c* 1.1, $CH_2Cl_2$). Yield: 0.45 g (76.8%, based on the theoretical yield of one diastereomer). $C_{30}H_{28}NO_2PPd$ (571.93): calcd. C 63.0, H 4.9, N 2.5; found C 63.2, H 4.7, N 2.6. $^1H$ NMR ($CDCl_3$, 500 MHz) two sets of signals in 1: 0.43 ratio in favour of the *E*-isomer, $\delta$ = 1.34 (m, 1 H, γ-H of *E*-isomer), 1.75 (m, 1 H, γ-H of *E*-isomer), 1.85 (m, 1 H, γ-H of *Z*-isomer), 2.08–2.13 (overlapping m, γ-H of *Z*-isomer, β-H and δ-H of *E*-isomer), 2.23 (m, 1 H, β-H of *E*-isomer), 2.38 (overlapping m, 2 H, both β-H of *Z*-isomer), 2.50–2.61 (overlapping m, 2 H, δ-H and N-H of *E*-isomer), 3.43–3.52 (overlapping m, 2 H, both δ-H protons of *Z*- isomer), 3.65 (br. m, 1 H, N-H of *Z*-isomer), 4.00 (m, 1 H, prolinate α-H of *E*-isomer), 4.14 (m, 1 H, prolinate α-H of *Z*-isomer), 5.08 (d, $^2J_{P,H}$ = 13.8 Hz, 1 H, palladacycle α-H of *Z*-isomer), 5.40 (d, $^2J_{P,H}$ = 12.7 Hz, 1 H, palladacycle α-H of *E*-isomer), 6.78 (m, 2 H, *o*-α-Ph), 6.85 (d, $^3J_{H,H}$ = 7.3 Hz, 1 H, 5-H of *E*-isomer), 7.00–7.58 (overlapping m, aromatic protons of both geometric isomers), 7.78 (ddd, $^3J_{H,H}$ = 8.1 Hz, $^4J_{H,H}$ = 1.4 Hz, $^3J_{P,H}$ = 10.9 Hz, 2 H, *o*-PPh of *E*-geometrical isomer), 8.10 (ddd, $^3J_{H,H}$ = 7.8 Hz, $^4J_{H,H}$ = 1.4 Hz, $J_{P,H}$ = 4.1 Hz, 1 H, 2-H of *E*-geometrical isomer) ppm. $^{31}P\{^1H\}$ NMR ($CDCl_3$, 202 MHz) two sets of signals with relative intensities of 4.3:10 in favour of the *E*-isomer, $\delta$ = 62.7 (s, *Z*-geometrical isomer), 71.1(s, *E*-geometrical isomer) ppm.

**(*R*,*R*)-di-μ-Chlorobis{[(diphenylphosphanyl)(phenyl)methyl]phenyl-*C*$^2$,*P*}dipalladium(II) [(*R*,*R*)-3]:** Dilute HCl (10 mL, 1 M) was added to a $CH_2Cl_2$ solution (10 mL) of the diastereomer ($R_C$,$S_C$$S_N$)-**4** (0.2347 g, 0.410 mmol), and the resulting solution was vigorously stirred for 5 min at room temperature. The aqueous layer was separated, and the procedure was repeated once with the same amount of HCl. The organic layer was then removed, washed with water (2 × 10 mL), dried with $MgSO_4$ and the solvents evaporated to dry-

 © 2007 Wiley-VCH Verlag GmbH & Co. KGaA, Weinheim 

ness in vacuo to afford the (*R*,*R*)-**3** as a greenish-yellow powder (attempts to crystallize the product by using a variety of solvents have been unsuccessful thus far); m.p. (decomp.) 196–200 °C. $[\alpha]_D$ = –382°, $[\alpha]_{578}$ = –400°, $[\alpha]_{546}$ = –468°, $[\alpha]_{436}$ = –946° (*c* 0.5, $CH_2Cl_2$). Yield: 0.20 g (99.0%). $C_{50}H_{40}Cl_2P_2Pd_2$ (986.52): calcd. C 60.9, H 4.1; found C 61.2, H 4.0. $^1$H NMR ($CDCl_3$, 300 MHz): $\delta$ = 5.22 (d, $^2J_{P,H}$ = 13.7 Hz, 1 H, α-CH), 6.89–8.03 (br. overlapping m, 19 H, aromatic protons) ppm. $^{31}P\{^1H\}$ NMR (121 MHz, $CDCl_3$): $\delta$ = 70.8 (s), (253 K) 2 sets of signals with relative intensities of 1: 0.65, $\delta$ = 70.8 (s), 71.1(s) ppm.

**(*S*,*S*)-di-μ-Chlorobis{[(diphenylphosphanyl)(phenyl)methyl]phenyl-*C*$^2$,*P*}dipalladium(II) [(*S*,*S*)-3]:** Dilute HCl (7 mL, 1 M) was added to a $CH_2Cl_2$ solution (10 mL) of the ($S_C$, $S_CS_N$)-**4** (0.1642 g, 0.287 mmol), and the resulting solution was vigorously stirred for 5 min at room temperature. The aqueous layer was separated, and the procedure was repeated once with the same amount of HCl. The organic layer was next removed, washed with water (2 × 10 mL), dried with $MgSO_4$ and the solvents evaporated to dryness in vacuo to afford the (*S*,*S*)-**3** as a greenish-yellow powder; m.p. (decomp.) 198–202 °C. $[\alpha]_D$ = +368°, $[\alpha]_{578}$ = +384°, $[\alpha]_{546}$ = +446°, $[\alpha]_{436}$ = +908° (*c* 0.5, $CH_2Cl_2$). Yield: 0.141 g (99.5%). $C_{50}H_{40}Cl_2P_2Pd_2$ (986.52): calcd. C 60.9, H 4.1; found C 60.9, H 3.9. $^1$H NMR ($CDCl_3$, 300 MHz): $\delta$ = 5.22 (d, $^2J_{P,H}$ = 13.7 Hz, 1 H, α-CH), 6.89–8.03 (br. overlapping m, 19 H, aromatic protons) ppm. $^{31}P\{^1H\}$ NMR (121 MHz, $CDCl_3$): $\delta$ = 70.9 (s) ppm.

**(*R*)-(Acetylacetonato-*O*,*O*′){1-[(diphenylphosphanyl)(phenyl)methyl]-phenyl-*C*$^2$,*P*}dipalladium(II) [(*R*)-6]:** To an acetone solution (3 mL) of the dimer (*R*,*R*)-**3** (0.139 g, 0.141 mmol) was added Na acac·$H_2O$ (0.040 g, 0.282 mmol), and the mixture was vigorously stirred at room temperature for 2 h until a white suspension was obtained. The suspension was filtered through a short plug of Celite, and the colourless solution was concentrated to dryness in vacuo to yield a white amorphous powder; m.p. 86–89 °C. $[\alpha]_{436}$ = –1123°, $[\alpha]_{365}$ = –2397° (*c* 0.7, $CH_2Cl_2$). Yield: 0.089 g (56.7%). $C_{30}H_{27}O_2PPd$ (556.92): calcd. C 64.7, H 4.9; found C 64.9, H 4.8. $^1$H NMR ($CDCl_3$, 500 MHz): $\delta$ = 1.84 (s, 3 H, acac-Me), 2.15 (s, 3 H, acac-Me), 5.22 (d, $^2J_{P,H}$ = 13.3 Hz, 1 H, α-CH), 5.39 (s, 1 H, acac-CH), 6.96 (dd, $^3J_{H,H}$ = 7.6 Hz, $^4J_{H,H}$ = 1.42 Hz, 1 H, 5-H), 7.00–7.05 (m, 6 H, 4-H, *o*-Ph, *m*-Ph, *p*-Ph protons of α-C-Ph substituent), 7.09 (m, 1 H, 3-H), 7.13 (m, 2 H, *m*-PPh), 7.29 (dtt, $^3J_{H,H}$ = 7.4 Hz, $^4J_{H,H}$ = 1.29Hz, $^5J_{P,H}$ = 2.1 Hz, 1 H, *p*-PPh), 7.45 (ddd, $^3J$(H,H) = 8.5, $^4J_{H,H}$ = 1.3, $^3J_{P,H}$ = 11.5 Hz, 2 H, *o*-PPh), 7.74 (dddd, $^3J_{H,H}$ = 8.0 Hz, $^4J_{H,H}$ = 1.8 Hz, $^4J_{H,H}$ = 1.3 Hz, $^3J_{P,H}$ = 11.2 Hz, 2 H, *o*-PPh), 8.02 (ddd, $^3J_{H,H}$ = 7.8 Hz, $^4J_{H,H}$ = 1.3 Hz, $J_{P,H}$ = 4.0 Hz, 1 H, 2-H) ppm. $^{31}P\{^1H\}$ NMR ($CDCl_3$, 202 MHz): $\delta$ = 66.4 (s) ppm.

**Chloro{(±)-1-[(di-*tert*-butylphosphanyl)(phenyl)methyl]phenyl-*C*$^2$,*P*}(triphenylphosphane)palladium(II) [(±)-9]:** Triphenylphosphane (0.069 g, 0.262 mmol) was added to a $CH_2Cl_2$ solution of the corresponding chloro dimer **3** (0.108 g, 0.119 mmol), and the resulting mixture was allowed to stir for 16 h under a positive pressure of argon. The product was isolated as pale yellow blocks from $CH_2Cl_2$/hexanes upon slow crystallization; m.p. 216–217 °C. Yield: 0.145 g (85.3%). $C_{39}H_{43}ClP_2Pd$ (715.57): calcd. C 65.5, H 6.1; found C 65.4, H 6.1. $^1$H NMR ($CDCl_3$, 500 MHz): $\delta$ = 1.21 (d, $^3J_{P,H}$ = 12.8 Hz, 9 H, axial *t*Bu), 1.40 (d, $^3J_{P,H}$ = 13.1 Hz, 9 H, equatorial *t*Bu), 4.54 (dd, $^2J_{P,H}$ = 11.7 Hz, $^4J_{P,H}$ = 5.1 Hz, 1 H, α-CH), 6.24 (m, 1 H, 2-H), 6.64–6.71 (m, 2 H, 3-H, 4-H), 6.80 (dd, $^3J_{H,H}$ = 7.6 Hz, $^4J_{H,H}$ = 1.4 Hz, 1 H, 5-H), 6.94 (br. dd, $^3J_{H,H}$ = $^3J_{H,H}$ = 7.5 Hz, 1 H, *m*-α-Ph), 7.17 (m, 1 H, *p*-α-Ph), 7.24–7.40 (m, *m*-$PPh_3$, *p*-$PPh_3$, *o*-α-Ph, *m*-α-Ph, signals of free $PPh_3$), 7.70 (m, 6 H, *o*-$PPh_3$), 8.46 (br. d, $^3J_{H,H}$ = 7.8 Hz, 1 H, *o*-α-Ph) ppm. $^{31}P\{^1H\}$ NMR (202 MHz, $CDCl_3$): $\delta$ = –5.0 (*s*, free $PPh_3$), 24.8 (d, $^2J_{P,P}$ = 390.6 Hz, coordinated $PPh_3$), 100.5 (d, $^2J_{P,P}$ = 390.6 Hz, palladacycle P), four overlapping sets of signals at 111.8, 111.9, 112.1, 112.2 (s, signals of racemic dimer) ppm.

**X-ray Diffraction Studies of the Complexes *meso*-3, (*Z*)-($R_C$,$S_CS_N$)-4, (*Z*)-($S_C$, $S_CS_N$)-4, 5 and *trans*-(±)-9:** Crystal data for these five complexes and a summary of the crystallographic analyses are given in Table 2. Diffraction data were collected on a Siemens SMART CCD diffractometer with Mo-$K_\alpha$ radiation (graphite monochromator) by using $\omega$-scans. SADABS absorption corrections were applied, and refinements by full-matrix least-squares were based on SHELXL 93.[13] All non-hydrogen atoms were refined anisotropically. Hydrogen atoms were introduced at fixed distance from carbon atoms and were assigned fixed thermal parameters.

CCDC-634583 (for *meso*-**3**), -634584 [for (*Z*)-($R_C$,$S_CS_N$)-**4**], -634585 [for (*Z*)-($S_C$,$S_CS_N$)-**4**], -634586 (for **5**), and -634587 [for *trans*-(±)-**9**] contain the supplementary crystallographic data for this paper. These data can be obtained free of charge from The Cambridge Crystallographic Data Centre via www.ccdc.cam.ac.uk/data_request/cif.

Table 2. Crystallographic data for complexes *meso*-**3**, *Z*-($R_C$,$S_CS_N$)-**4**, *Z*-($S_C$,$S_CS_N$)-**4**, **5** and *trans*-(±)-**9**.

| | *meso*-**3** | *Z*-($R_C$,$S_CS_N$)-**4** | *Z*-($S_C$,$S_CS_N$)-**4** | **5** | *trans*-(±)-**9** |
|---|---|---|---|---|---|
| Formula | $C_{50}H_{40}Cl_2P_2Pd_2$ | $C_{30}H_{28}NO_2PPd$ | $C_{30}H_{28}NO_2PPd$ | $C_{50}H_{42}Cl_4P_2Pd_2$ | $C_{39}H_{43}ClP_2Pd$ |
| *M* | 986.46 | 571.90 | 571.90 | 1059.38 | 715.52 |
| Space group | $I4_1/a$ | $P2_1$ | $P2_12_12_1$ | $C2/c$ | $P2_1/n$ |
| Crystal system | Tetragonal | Monoclinic | Orthorhombic | Monoclinic | Monoclinic |
| *a* [Å] | 29.912(2) | 9.866(2) | 8.7813(7) | 10.4912(14) | 12.4345(5) |
| *b* [Å] | 29.912(2) | 9.1675(18) | 9.6673(7) | 16.715(2) | 15.4637(6) |
| *c* [Å] | 10.5243(14) | 14.831(3) | 31.100(3) | 25.710(3) | 19.4561(8) |
| α [°] | 90 | 90 | 90 | 90 | 90 |
| β [°] | 90 | 107.856(4) | 90 | 93.834(4) | 106.7020(10) |
| γ [°] | 90 | 90 | 90 | 90 | 90 |
| *V* [Å$^3$] | 9416.6(16) | 1276.9(5) | 2640.1(4) | 4498.5(11) | 3583.3(2) |
| *Z* | 8 | 2 | 4 | 4 | 4 |
| *T* [K] | 223(2) | 293(2) | 223(2) | 295(2) | 295(2) |
| λ [Å] | 0.71073 | 0.71073 | 0.71073 | 0.71073 | 0.71073 |
| μ [mm$^{-1}$] | 0.977 | 0.817 | 0.790 | 1.143 | 0.707 |
| $R_1$ (obs. data) | 0.0370 | 0.0382 | 0.0519 | 0.0810 | 0.0360 |
| $wR_2$ (obs. data) | 0.0983 | 0.0876 | 0.1029 | 0.1541 | 0.0853 |
| Flack parameter | – | 0.02(3) | 0.04(4) | – | – |

 © 2007 Wiley-VCH Verlag GmbH & Co. KGaA, Weinheim 

## Acknowledgments

We thank the National University of Singapore for the financial support of this research and the award of a research scholarship to J. K.-P. N. We also thank the Nanyang Technological University for the research scholarship to S. C.

[1] B. Cornils, W. A. Herrmann (Eds.), *Applied Homogenous Catalysis with Organometallic Compounds*, VCH, Weinheim, **1996**.

[2] a) G. W. Parshall, S. D. Ittel, *Homogenous Catalysis: The Applications and Chemistry of Catalysis by Soluble Transition Metal Complexes*, 2nd ed., Wiley, New York, **1992**; b) R. Noyori, *Asymmetric Catalysis in Organic Synthesis*, Wiley-Interscience, New York, **1994**; c) I. Ojima (Ed.), *Catalytic Asymmetric Synthesis*, Wiley-VCH, New York, **2000**.

[3] a) W. A. Herrmann, C. Brossmer, K. Öfele, C.-P. Reisinger, T. Priermeier, M. Beller, H. Fischer, *Angew. Chem. Int. Ed. Engl.* **1995**, *34*, 1844–1848; b) W. A. Herrmann, C.-P. Reisinger, K. Öfele, C. Broßmer, M. Beller, H. Fischer, *J. Mol. Catal. A* **1996**, *108*, 51–56; c) J. M. Brunel, A. Heumann, G. Buono, *Angew. Chem. Int. Ed.* **2000**, *39*, 1946–1949; d) M. Castella, F. Calahorra, D. Sainz, D. Velasco, *Org. Lett.* **2001**, *3*, 541–544; e) B. L. Shaw, S. D. Perera, E. A. Staley, *Chem. Commun.* **1998**, 1361–1362; f) M. Ohff, A. Ohff, M. E. van der Boom, D. Milstein, *J. Am. Chem. Soc.* **1997**, *119*, 11687–11688; g) K. Kiewel, Y. Liu, D. E. Bergbreiter, G. A. Sulikowski, *Tetrahedron Lett.* **1999**, *40*, 8945–8948; h) J. M. Longmire, X. Zhang, M. Shang, *Organometallics* **1998**, *17*, 4374–4378; i) B. S. Williams, P. Dani, M. Lutz, A. L. Spek, G. van Koten, *Helv. Chim. Acta* **2001**, *84*, 3519–3530; j) D. Morales-Morales, R. E. Cramer, C. M. Jensen, *J. Organomet. Chem.* **2002**, *654*, 44–50; k) V. V. Dunina, O. N. Gorunova, L. G. Kuz′mina, M. V. Livantsov, Y. K. Grishin, *Tetrahedron: Asymmetry* **1999**, *10*, 3951–3961; l) V. V. Dunina, O. N. Gorunova, M. V. Livantsov, Y. K. Grishin, L. G. Kuz′mina, N. A. Kataeva, A. V. Churakov, *Tetrahedron: Asymmetry* **2000**, *11*, 3967–3984.

[4] a) J. K.-P. Ng, G.-K. Tan, J. J. Vittal, P.-H. Leung, *Inorg. Chem.* **2003**, *42*, 7674–7682; b) J. K.-P. Ng, Y. Li, G.-K. Tan, L.-L. Koh, J. J. Vittal, P.-H. Leung, *Inorg. Chem.* **2005**, *44*, 9874–9886.

[5] a) D. A. Albisson, R. B. Bedford, S. E. Lawrence, P. N. Scully, *Chem. Commun.* **1998**, 2095–2096; b) F. Miyazaki, K. Yamaguchi, M. Shibasaki, *Tetrahedron Lett.* **1999**, *40*, 7379–7383; c) R. B. Bedford, S. M. Draper, N. Scully, S. L. Welch, *New J. Chem.* **2000**, *24*, 745–747; d) D. Morales-Morales, C. Grause, K. Kasaoka, R. Redón, R. E. Cramer, C. M. Jensen, *Inorg. Chim. Acta* **2000**, *300–302*, 958–963; e) R. B. Bedford, S. L. Welch, *Chem. Commun.* **2001**, 129–130; f) V. I. Sokolov, L. A. Bulygina, O. Y. Borbulevych, O. V. Shishkin, *J. Organomet. Chem.* **1999**, *582*, 246–251; g) L. L. Troitskaya, S. T. Ovseenko, Y. L. Slovokhotov, I. S. Neretin, V. I. Sokolov, *J. Organomet. Chem.* **2002**, *642*, 191–194.

[6] J. Dupont, C. S. Consorti, J. Spencer, *Chem. Rev.* **2005**, *105*, 2527–2571.

[7] L. N. Lewis, *J. Am. Chem. Soc.* **1986**, *108*, 743–749.

[8] a) M. Beller, H. Fischer, W. A. Herrmann, K. Öfele, C. Brossmer, *Angew. Chem. Int. Ed. Engl.* **1995**, *34*, 1848–1849; b) B. L. Shaw, S. D. Perera, E. A. Staley, *Chem. Commun.* **1998**, 1361–1362; c) M. Beller, T. H. Riermeier, *Eur. J. Inorg. Chem.* **1998**, 29–35; d) D. Morales-Morales, R. Redón, C. Yung, C. M. Jensen, *Chem. Commun.* **2000**, 1619–1620; e) M. Ohff, A. Ohff, D. Milstein, *Chem. Commun.* **1999**, 357–358; f) H. Weissman, D. Milstein, *Chem. Commun.* **1999**, 1901–1902; g) D. E. Bergbreiter, P. L. Osburn, Y.-S. Liu, *J. Am. Chem. Soc.* **1999**, *121*, 9531–9538; h) D. E. Bergbreiter, P. L. Osburn, A. Wilson, E. M. Sink, *J. Am. Chem. Soc.* **2000**, *122*, 9058–9064; i) A. S. Gruber, D. Zim, G. Ebeling, A. L. Monteiro, J. Dupont, *Org. Lett.* **2000**, *2*, 1287–1290; j) X. Gai, R. Grigg, M. I. Ramzan, V. Sridharan, S. Collard, J. E. Muir, *Chem. Commun.* **2000**, 2053–2054; k) S. F. Kirsch, L. E. Overman, *J. Am. Chem. Soc.* **2005**, *127*, 2866–2867; l) L. E. Overman, T. P. Remarchuk, *J. Am. Chem. Soc.* **2002**, *124*, 12–13; m) P.-H. Leung, K.-H. Ng, Y. Li, A. J. P. White, D. J. Williams, *Chem. Commun.* **1999**, 2435–2436; n) S. Gosiewska, S. H. Martinez, M. Lutz, A. L. Spek, G. van Koten, R. J. M. K. Gebbink, *Eur. J. Inorg. Chem.* **2006**, 4600–4607.

[9] a) Y. Qin, H. Lang, J. J. Vittal, G.-K. Tan, S. Selvaratnam, A. J. P. White, D. J. Williams, P.-H. Leung, *Organometallics* **2003**, *22*, 3944–3950; b) X. Liu, K. F. Mok, P.-H. Leung, *Organometallics* **2001**, *20*, 3918–3926; c) G. He, S.-K. Loh, J. J. Vittal, K. F. Mok, P.-H. Leung, *Organometallics* **1998**, *17*, 3931–3936; d) Y. X. Li, K. H. Ng, S. Selvaratnam, G. K. Tan, J. J. Vittal, P.-H. Leung, *Organometallics* **2003**, *22*, 834; e) Y. X. Li, S. Selvaratnam, J. J. Vittal, P.-H. Leung, *Inorg. Chem.* **2003**, *42*, 3229–3236.

[10] J. K.-P. Ng, S. Chen, G.-K. Tan, P-H. Leung, *Inorg. Chem.*, DOI: 10.1021/ic0702320, submitted.

[11] H. Grüetzmacher in *Synthetic Methods of Organometallic and Inorganic Chemistry*, *Vol. 3: Phosphorus, Arsenic, Antimony and Bismuth* (Ed.: H. H. Karsch), Georg Thieme Verlag, Stuttgart, **1996**, pp. 85–88.

[12] a) R. Urban, R. Krämer, S. Mihan, K. Polborn, B. Wagner, W. Beck, *J. Organomet. Chem.* **1996**, *517*, 191–200; b) V. V. Dunina, E. D. Razmyslova, L. G. Kuz′mina, A. V. Churakov, M. Y. Rubina, Y. K. Grishin, *Tetrahedron: Asymmetry* **1999**, *10*, 3147–3155.

[13] G. M. Sheldrick, *SHELXL 93, Program for Crystal Structure*, University of Göttingen, Germany **1993**.

Received: February 5, 2007
Published Online: May 10, 2007

 © 2007 Wiley-VCH Verlag GmbH & Co. KGaA, Weinheim

**The EUChemSoc Societies have taken the significant step into the future by merging their traditional journals, to form two leading chemistry journals, the *European Journal of Inorganic Chemistry* and the *European Journal of Organic Chemistry.* Three further EUChemSoc Societies (Austria, Czech Republic and Sweden) are Associates of the two journals.**

## COVER PICTURE

**The cover picture shows** the electro-induced core interconversions in three dinuclear manganese tris(2-methylpyridyl)amine (tpa) complexes. The mono-(μ-oxo) mono-(μ-acetato) $[Mn_2^{III,III}(O)(O_2CCH_3)(tpa)_2]^{3+}$ and the bis-(μ-oxo) $[Mn_2^{IV,IV}(O)_2(tpa)_2]^{4+}$ complexes are selectively and quasi-quantitatively generated by sequential exhaustive electrochemical two-electron oxidations of the bis-(μ-acetato) $[Mn_2^{II,II}(O_2CCH_3)_2(tpa)_2]^{2+}$ complex. At each step one acetato bridge is substituted by an oxo bridge coming from the deprotonation of one residual water molecule in the solvent. The background picture shows some cyclic voltammograms recorded during this study. Details are discussed in the article by M.-N. Collomb et al. on p. 3179 ff. We thank Dr. Damien Jouvenot for the design of the cover picture.

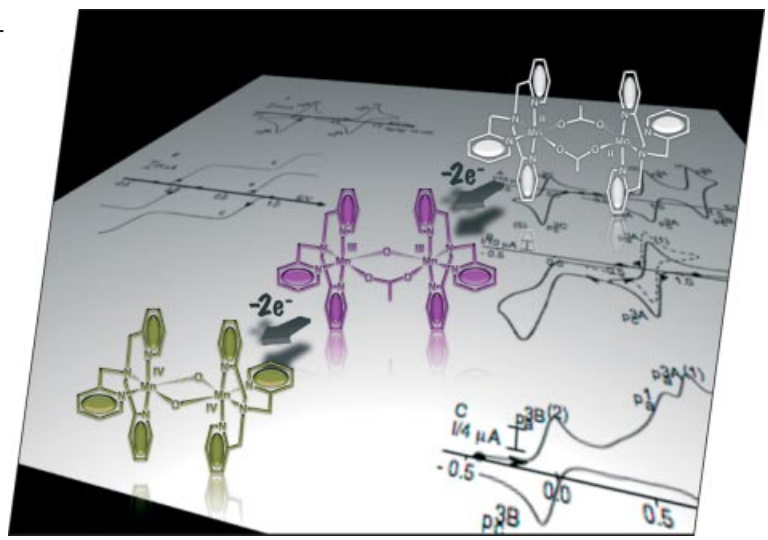


 © 2007 Wiley-VCH Verlag GmbH & Co. KGaA, Weinheim 

# CONTENTS

## MICROREVIEW

### Steric Manipulation

**A. A. Trifonov* ..... 3151–3167**

Reactions of Ytterbocenes with Diimines: Steric Manipulation of Reductive Reactivity

**Keywords:** Lanthanides / Diimines / Reductive reactivity / N,N ligands / Redox tautomerism

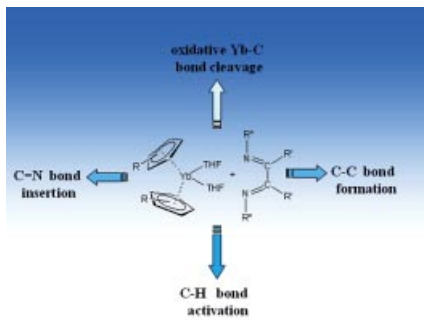


Reactions of ytterbocenes with diimines are found to be strongly influenced by the steric crowding in the coordination sphere of the metal atom and the coordination capacities of π-aromatic ligands. The reactions may occur with oxidation of the ytterbium atom as well as with retention of its oxidation state. C–C bond formation, C–H bond activation, C=N bond insertion, and oxidative Yb–C bond cleavage processes are documented.

## SHORT COMMUNICATIONS

### Charge Density Determination

**D. Förster, S. Scheins, P. Luger, D. Lentz,* W. Preetz ..... 3169–3172**

Electron Density and Bonding in Borates: An Experimental Study of Tetrabutylammonium Heptahydridohexaborate, $[(C_4H_9)_4N][B_6H_7]$

**Keywords:** Charge density / Borates / Topological analysis

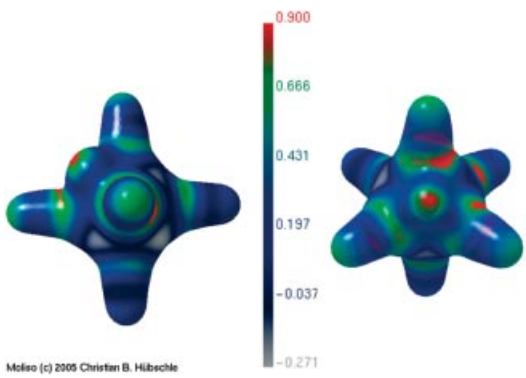


The charge density of $[B_6H_7]^-$ has been determined from high-resolution X-ray diffraction data. The electrostatic potential provides information about its reactivity.

### Flexible Coordination Modes

**I. J. S. Fairlamb,* S. Tommasi, B. E. Moulton, W. Zheng, Z. Lin, A. C. Whitwood ..... 3173–3178**

Conformational Flexibility in a Carbobicyclic Diphosphinite Ligand

**Keywords:** Ligands / Bite angle / Transspanning / Palladium / Binuclear complexes

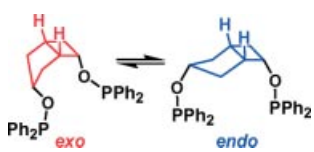


The conformational flexibility of FLEXIphosO is demonstrated experimentally for the first time. Variable bite angles can be accessed using carbobicyclic backbone structures for bidentate ligands.

 © 2007 Wiley-VCH Verlag GmbH & Co. KGaA, Weinheim 

EurJIC European Journal of Inorganic Chemistry

# FULL PAPERS

## Dinuclear Manganese Complexes

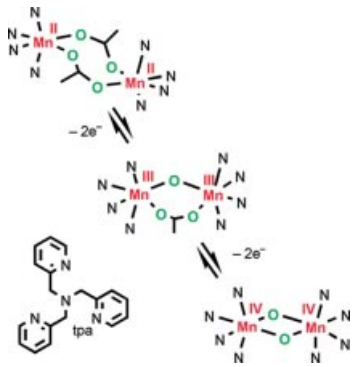


The electro-induced interconversion of the bis(μ-acetato) dinuclear manganese(II,II) complex $[Mn_2(O_2CCH_3)_2(tpa)_2]^{2+}$ into the corresponding mono-(μ-oxo) mono-(μ-acetato) $Mn_2^{III,III}$ and bis(μ-oxo) $Mn_2^{IV,IV}$ complexes has been investigated in $CH_3CN$. The isolation and characterization of the $Mn_2^{III,III}$ complex is also reported.

**M.-N. Collomb,* C. Mantel, S. Romain, C. Duboc, J.-C. Leprêtre, J. Pécaut, A. Deronzier** ..... **3179–3187**

Redox-Induced μ-Acetato and μ-Oxo Core Interconversions in Dinuclear Manganese Tris(2-methylpyridyl)amine (tpa) Complexes: Isolation and Characterization of $[Mn_2^{III}(\mu\text{-}O)(\mu\text{-}O_2CCH_3)(tpa)_2]^{3+}$

**Keywords:** Manganese / Electrochemistry / N ligands / Bridging ligands

## Iron(III) Spin Crossover

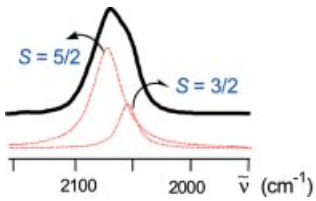


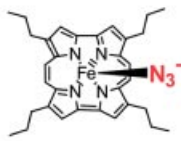


Magnetic characterization of the azide complex of iron(III) porphycene indicates that this complex is in mixed $S = 5/2$, 3/2 states. The IR stretching band of the coordinating azide was found to split into the 2049- and 2066-$cm^{-1}$ bands, demonstrating that the two spin isomers are not quantum-mechanically admixed but in thermal equilibrium. The minimum lifetime of the spin isomers was estimated to be 0.3 ps.

**S. Neya,* A. Takahashi, H. Ode, T. Hoshino, M. Hata, A. Ikezaki, Y. Ohgo, M. Takahashi, H. Hiramatsu, T. Kitagawa, Y. Furutani, H. Kandori, N. Funasaki, M. Nakamura** ..... **3188–3194**

Magnetic and Infrared Properties of the Azide Complex of (2,7,12,17-Tetrapropylporphycenato)iron(III): A Novel Admixing Mechanism of the $S = 5/2$ and $S = 3/2$ States

**Keywords:** Macrocyclic ligands / Iron / Electronic structure / Spin crossover / Azides / IR spectroscopy

## Bridging Thione Ligands

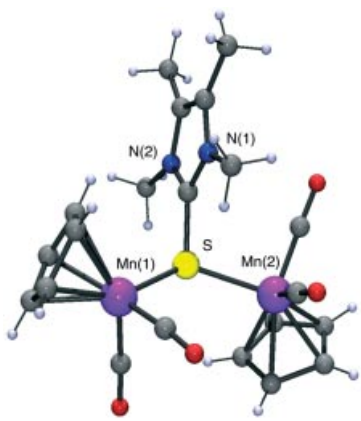


Photolysis of $[CpMn(CO)_3]$ in the presence of 1,3,4,5-tetramethylimidazoline-2-thione produced a bridging thione complex, $[\{CpMn(CO)_2\}_2(\mu\text{-}SC_3N_2Me_4)]$, which has an unprecedented geometry featuring a pyramidal sulfur atom and long Mn···Mn distance. Photoreaction of $[M(CO)_6]$ with the thione yielded mononuclear complexes $[M(CO)_5(SC_3N_2Me_4)]$ (M = Mo, W).

**K. Saito, Y. Kawano,* M. Shimoi*** ..... **3195–3200**

Syntheses and Structures of Molybdenum, Tungsten, and Manganese Complexes of a Cyclic Thiourea, $[M(CO)_5(SC_3N_2Me_4)]$ (M = Mo, W) and $[\{CpMn(CO)_2\}_2(\mu\text{-}SC_3N_2Me_4)]$

**Keywords:** Imidazolinethiones / Manganese / Molybdenum / Thioureas / Tungsten

## Biomineralization

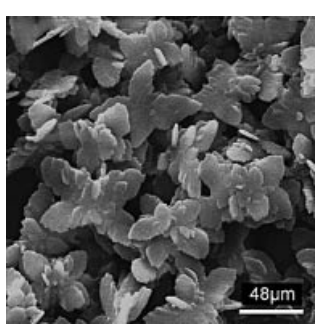


The formation of flower-like crystals of calcium oxalate monohydrate is induced by *E. coli* and its secretions. The true role of *E. coli* in the formation of urinary stones is explored in a new line of research.

**L. Chen, Y. H. Shen,* R. Jia, A. J. Xie,* B. Huang, X. B. Cheng, Q. F. Zhang, R. Y. Guo** ..... **3201–3207**

The Role of *Escherichia coliform* in the Biomineralization of Calcium Oxalate Crystals

**Keywords:** Urolithiasis / *Escherichia coliform* / Calcium oxalate / Nucleation and growth / Biomineralization

 © 2007 Wiley-VCH Verlag GmbH & Co. KGaA, Weinheim 

# CONTENTS

## Cyclopalladation

**M. Bröring,* C. Kleeberg, E. Cónsul Tejero ..... 3208–3216**

Syntheses, Structures and Coordination Modes of Acetatopalladium(II) Complexes with 1,3-Bis(2-arylimino)isoindoline Ligands of Different Steric Influence

**Keywords:** Cyclometalation / Isoindoline ligands / Polynuclear complexes / Palladium / Coordination modes

A comparative study on palladium complexes of bai ligands with different steric hindrance revealed that different coordination modes (*NNN* vs. *CNN* coordination) are possible in the system. The outcome of the metallation reaction was found to depend on a number of factors like solubility of the products, stoichiometry of metal precursor and charge compensation.

## Ligand Encapsulation

**V. Lozan, P. Y. Solntsev, G. Leibeling, K. V. Domasevitch,* B. Kersting* ..... 3217–3226**

Tetranuclear Nickel Complexes Composed of Pairs of Dinuclear $LNi_2$ Fragments Linked by 4,4′-Bipyrazolyl, 1,4-Bis(4′-pyrazolyl)benzene, and 4,4′-Bipyridazine: Synthesis, Structures, and Magnetic Properties

**Keywords:** Macrocyclic ligands / Bipyrazolate ligands / Nickel / Polynuclear complexes / Magnetic properties

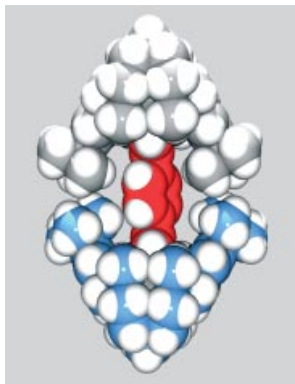

The ability of 4,4′-bipyrazolate type ligands to link dinuclear $LNi_2$ units has been examined. The formation of the $Ni_4$ complexes depends critically on the steric bulkiness of the supporting ligand L and the length of the organic spacer between the connecting heterocycles. The ability of the bipyrazolate moiety to transmit magnetic exchange interactions has also been examined.

## Quadrant Effects

**C. Bachmann, R. Gutmann, G. Czermak, A. Dumfort, S. Eller, M. Fessler, H. Kopacka, K.-H. Ongania, P. Brüggeller* ..... 3227–3239**

The Influence of Steric Pressure on the Structure of Homodimetallic Rhodium(I) and Iridium(I) Complexes Containing a Bis(bidentate) Phosphane Ligand

**Keywords:** X-ray diffraction / Chelates / Phosphane ligands / Iridium / Rhodium

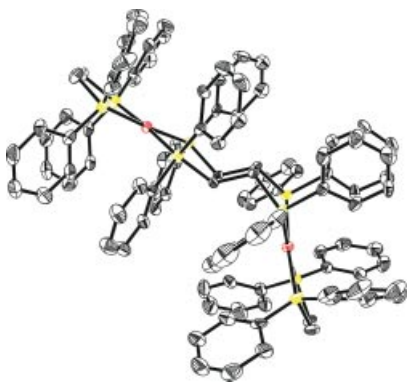

Fifteen novel homodimetallic $Rh^I$ and $Ir^I$ complexes containing *cis*,*trans*,*cis*-1,2,3,4-tetrakis(diphenylphosphanyl)cyclobutane ligands were prepared. The solid-state structures of seven of these new compounds were determined to study the influence of steric pressure. The onset of this steric pressure also changes the quadrant effect.

## Metal–Metal Bonds

**I. Bytheway, C. S. Griffith, G. A. Koutsantonis,* B. W. Skelton, A. H. White ..... 3240–3246**

A Linear Ru-Tl-Ru Complex Obtained from Halide Abstraction: An Example of Metal-Dative Bonding

**Keywords:** Ruthenium / Thallium / AIM calculations / Metal–metal bond

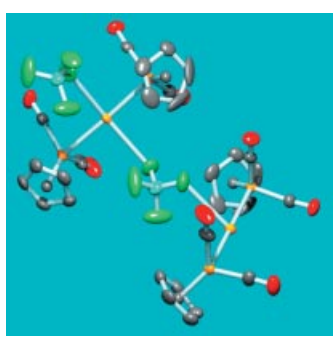

Complexes containing ruthenium–thallium bonds are reported. One containing a linear Ru–Tl–Ru vector was prepared by halide abstraction from a ruthenium chloride complex using $TlBF_4$. The bonding in this monocation was rationalised using AIM theroretical calculations which inferred $Ru^0–Tl^I–Ru^0$ as the best description.

 © 2007 Wiley-VCH Verlag GmbH & Co. KGaA, Weinheim 

## $Ni^{II}/Ni^{III}$ Chemistry

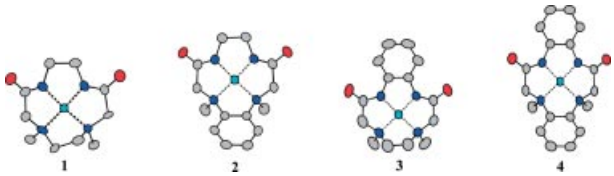


This work shows the design and synthesis of four novel macrocyclic ligands and their square-planar $Ni^{II}$ complexes **1**−**4**. The attainable redox potential for $Ni^{II}$ complexes (>0.6 V vs. SCE) allowed us to oxidize them electrochemically or chemically to generate an unstable "green species" that show distinct features in the absorption spectrum and exhibit anisotropic EPR spectrum. These findings strongly point out that the unstable green species is a $Ni^{III}$ species.

**S. K. Sharma, S. Upreti, R. Gupta* ..... 3247−3259**

Effect of Ligand Architecture on the Structure and Properties of Square-Planar Nickel(II) Complexes of Amide-Based Macrocycles

**Keywords:** Nickel complexes / Macrocyclic ligands / Electrochemistry

## Polymerization Catalysts

New lanthanide borohydride complexes supported by bulky guanidinate ligands $[(Me_3Si)_2NC(N\text{-}Cy)_2]_2Ln(\mu\text{-}BH_4)_2Li(THF)_2$ (Ln = Nd, Sm, Yb) initiate the ring-opening polymerization of racemic lactide, providing atactic polymers with a good degree of control, i.e. controlled molecular weights and relatively narrow polydispersities ($1.09 < M_w/M_n < 1.77$).

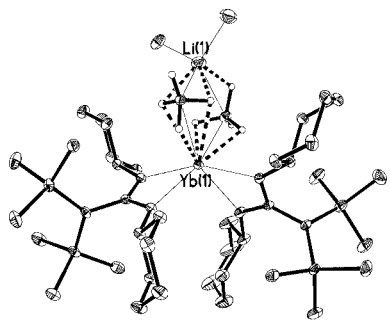


**G. G. Skvortsov, M. V. Yakovenko, P. M. Castro, G. K. Fukin, A. V. Cherkasov, J.-F. Carpentier,* A. A. Trifonov* ..... 3260−3267**

Lanthanide Borohydride Complexes of Bulky Guanidinate Ligands $[(Me_3Si)_2NC(N\text{-}Cy)_2]_2Ln(\mu\text{-}BH_4)_2Li(THF)_2$ (Ln = Nd, Sm, Yb): Synthesis, Structure and Catalytic Activity in Lactide Polymerization

**Keywords:** Lanthanides / Borohydrides / Guanidinates / N ligands / Lactides / Polymerization

## Unsymmetrical (Phthalocyaninato)$Cu^{II}$

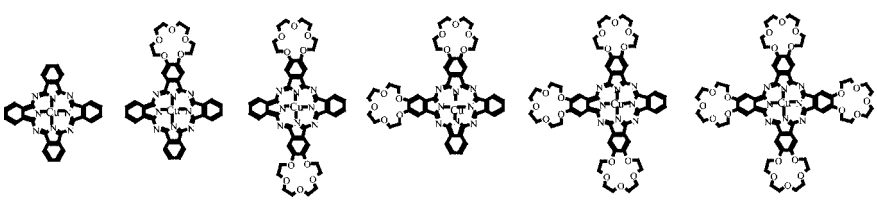

A series of unsymmetrical (phthalocyaninato)copper(II) complexes containing different numbers of 15-crown-5 groups at the peripheral positions have been prepared. The effects of the substituent number and molecular symmetry on the spectra and supramolecular structure formation in solution have been systematically investigated.

**N. Sheng, Y. Zhang, H. Xu, M. Bao, X. Sun,* J. Jiang* ..... 3268−3275**

(Phthalocyaninato)copper(II) Complexes Fused with Different Numbers of 15-Crown-5 Moieties − Synthesis, Spectroscopy, Supramolecular Structures, and the Effects of Substituent Number and Molecular Symmetry

**Keywords:** Phthalocyanines / Crown ether / Supramolecular chemistry / Molecular symmetry

## Lanthanide Complexes

Pentadentate hydrazone-type ligands based on semicarbazone or SAMP are prepared and used for the coordination of lanthanide(III) salts. A series of achiral as well as chiral coordination compounds is thus obtained and characterized.

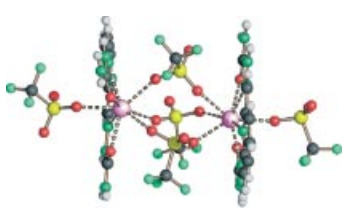

**M. Albrecht,* S. Mirtschin, O. Osetska, S. Dehn, D. Enders, R. Fröhlich, T. Pape, E. F. Hahn ..... 3276−3287**

Pentadentate Ligands for the 1:1 Coordination of Lanthanide(III) Salts

**Keywords:** Hydrazone / Lanthanides / Coordination compounds / Chelating ligands / Helical compounds

**If not otherwise indicated in the article, papers in issue 19 were published online on June 21, 2007**

 © 2007 Wiley-VCH Verlag GmbH & Co. KGaA, Weinheim

**The EUChemSoc Societies have taken the significant step into the future by merging their traditional journals, to form two leading chemistry journals, the *European Journal of Inorganic Chemistry* and the *European Journal of Organic Chemistry.* Three further EUChemSoc Societies (Austria, Czech Republic and Sweden) are Associates of the two journals.**

## COVER PICTURE

**The cover picture shows** the electro-induced core interconversions in three dinuclear manganese tris(2-methylpyridyl)amine (tpa) complexes. The mono-(μ-oxo) mono-(μ-acetato) $[Mn_2^{III,III}(O)(O_2CCH_3)(tpa)_2]^{3+}$ and the bis-(μ-oxo) $[Mn_2^{IV,IV}(O)_2(tpa)_2]^{4+}$ complexes are selectively and quasi-quantitatively generated by sequential exhaustive electrochemical two-electron oxidations of the bis-(μ-acetato) $[Mn_2^{II,II}(O_2CCH_3)_2(tpa)_2]^{2+}$ complex. At each step one acetato bridge is substituted by an oxo bridge coming from the deprotonation of one residual water molecule in the solvent. The background picture shows some cyclic voltammograms recorded during this study. Details are discussed in the article by M.-N. Collomb et al. on p. 3179 ff. We thank Dr. Damien Jouvenot for the design of the cover picture.

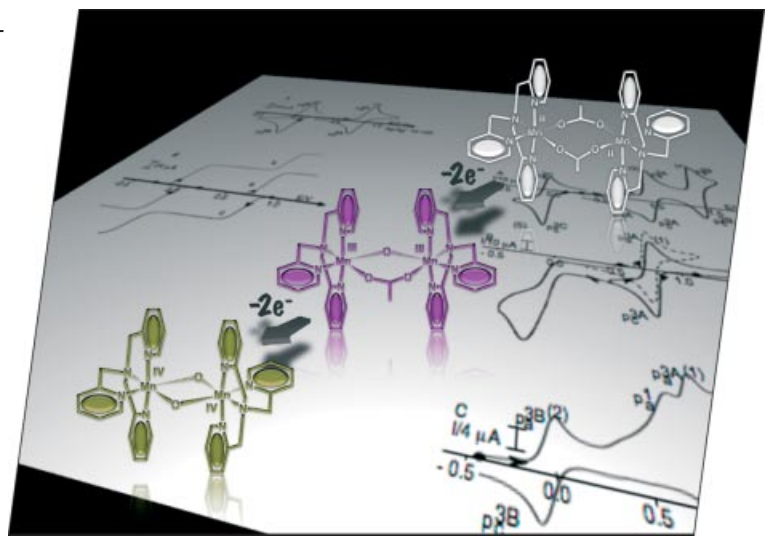


 © 2007 Wiley-VCH Verlag GmbH & Co. KGaA, Weinheim 

# SPOTLIGHTS …

## *Porphyrins*

H. Hata, S. Yamaguchi, G. Mori, S. Nakazono, T. Katoh, K. Takatsu, S. Hiroto, H. Shinokubo,* A. Osuka*

**Regioselective Borylation of Porphyrins by C–H Bond Activation under Iridium Catalysis to Afford Useful Building Blocks for Porphyrin Assemblies**

*Chem. Asian J.*
DOI: **10.1002/asia.200700086**

**The bor-on the ring**: A boryl group can be selectively introduced at sterically uncongested positions in the aryl groups of porphyrin substrates whose peripheral β-positions are sterically hindered. This method can be applied to a variety of monomeric and oligomeric functional porphyrins, hence offering an efficient route to elaborate multiporphyrin-based molecular constructs. pinB = pinacolboryl.

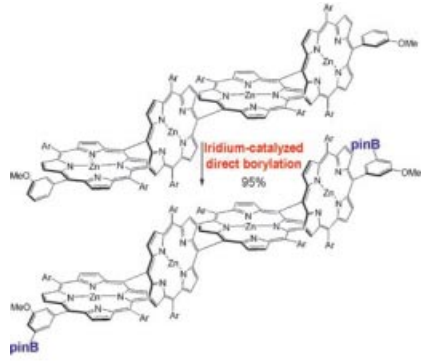


## *Amyloid β-Peptide*

T. Takahashi,* K. Ohta, H. Mihara

**Embedding the Amyloid β-Peptide Sequence in Green Fluorescent Protein Inhibits Aβ Oligomerization**

*ChemBioChem*
DOI: **10.1002/cbic.200700108**

**Against a green background**. We have embedded the amyloid β-peptide (Aβ) sequence into the green fluorescent protein (GFP) structure to generate a pseudo-Aβ surface on the β-barrel (see figure); this construct was highly active in inhibiting Aβ oligomerization. One GFP variant (P13H), which mimicked the parallel β sheets of Aβ, was found to bind Aβ with high affinity and inhibit Aβ oligomerization, even though the concentration of P13H was lower than that of Aβ.

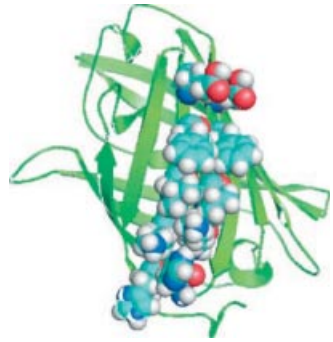

## *Graft Polymerization*

M. Chen, W. H. Briscoe, S. P. Armes, H. Cohen, J. Klein*

**Robust, Biomimetic Polymer Brush Layers Grown Directly from a Planar Mica Surface**

*ChemPhysChem*
DOI: **10.1002/cphc.200700131**

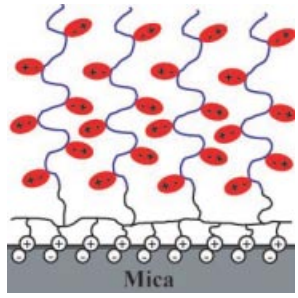


**Robust polymer brushes** are grown from a planar mica surface (see figure) using atom-transfer radical polymerization. The brushes are characterized by X-ray photoelectron spectroscopy, X-ray reflectometry, atomic force microscopy, optical interferometry, and surface forces.

## *Inhibitor Design*

I. Bichlmaier, M. Kurkela, T. Joshi, A. Siiskonen, T. Rüffer, H. Lang, M. Finel, J. Yli-Kauhaluoma*

**Potent Inhibitors of the Human UDP-Glucuronosyltransferase 2B7 Derived from the Sesquiterpenoid Alcohol Longifolol**

*ChemMedChem*
DOI: **10.1002/cmdc.200600246**

**The overlapping substrate selectivities** of promiscuous metabolic enzymes such as UGTs make the design of selective inhibitors difficult. The results of this study indicate that the phenyl-substituted longifolol derivate (shown) is a potent and selective inhibitor of UGT2B7, the key enzyme involved in drug glucuronidation. The tricyclic framework is presumably responsible for isoform selectivity, the phenyl group prevents glucuronidation of the hydroxy group, which itself promotes solubility.

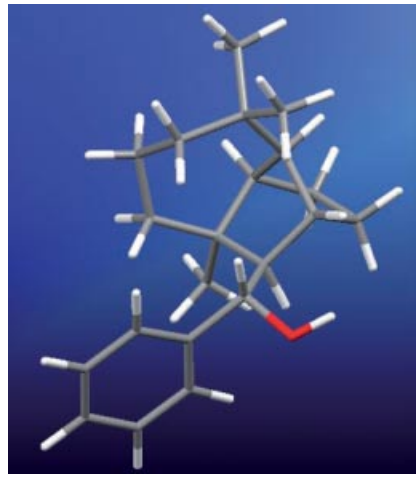

 © 2007 Wiley-VCH Verlag GmbH & Co. KGaA, Weinheim 

EurJIC European Journal of Inorganic Chemistry

**Dynamic exchange between three symmetry-equivalent binding sites** is observed for precatalysts of allylic alkylations (see scheme). The third ligating unit in the $C_3$-chiral stereodirecting ligands leads to superior catalyst performance compared to the bisoxazoline analogues.

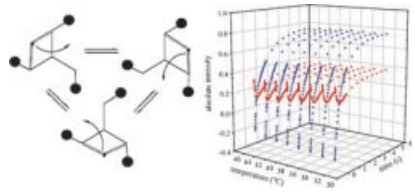

*Asymmetric Catalysis*

C. Foltz, M. Enders, S. Bellemin-Laponnaz,* H. Wadepohl, L. H. Gade*

**Using a Tripod as a Chiral Chelating Ligand: Chemical Exchange Between Equivalent Molecular Structures in Palladium Catalysis with 1,1,1-Tris(oxazolinyl)ethane ("Trisox")**

*Chem. Eur. J.*
DOI: **10.1002/chem.200700307**

*Asymmetric Catalysis*

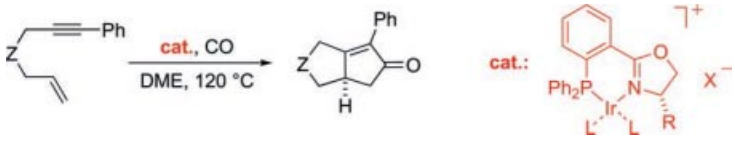


Iridium complexes derived from chiral phosphane–oxazolines (phox ligands) are efficient catalysts for intramolecular Pauson–Khand reactions. Under optimized conditions high yields and enantioselectivities of > 90% *ee* were obtained with 2 mol-% of catalyst. The influence of the CO pressure and the anion were studied. The structure of a dicarbonyl(phox)iridium complex was determined by X-ray analysis.

Z.-L. Lu, E. Neumann, A. Pfaltz*

**Asymmetric Catalytic Intramolecular Pauson–Khand Reactions with Ir(phox) Catalysts**

*Eur. J. Org. Chem.*
DOI: **10.1002/ejoc.200700330**

*Tryptophan Fluorescence*

**Kind of blue**: Tryptophan residues embedded in rigid and hydrophobic protein matrices, like azurin and domain 1 of a transhydrogenase (dI), yield blue-shifted emission spectra with vibrational fine structure. These features are typical for emission from the $^1L_b$ state of indole, and not the $^1L_a$ state. Nevertheless, these proteins are found to emit from $^1L_a$, except for a mutant of domain 1 (dI.M97V), which features the most blue-shifted protein emission ever reported.

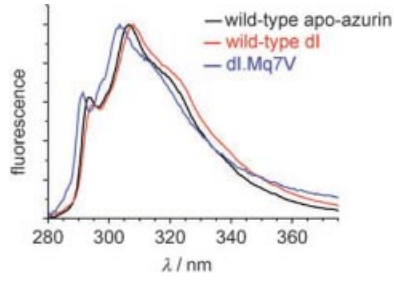


*Tryptophan Fluorescence*

J. Broos,* K. Tveen-Jensen, E. de Waal, B. H. Hesp, J. B. Jackson,* G. W. Canters, P. R. Callis

**The Emitting State of Tryptophan in Proteins with Highly Blue-Shifted Fluorescence**

*Angew. Chem. Int. Ed.*
DOI: **10.1002/anie.200700839**

On these pages, we feature a selection of the excellent work that has recently been published in our sister journals. If you are reading these pages on a computer, click on any of the items to read the full article. Otherwise please see the DOIs for easy online access through Wiley InterScience.

 © 2007 Wiley-VCH Verlag GmbH & Co. KGaA, Weinheim 

DOI: 10.1002/ejic.200601209

# Reactions of Ytterbocenes with Diimines: Steric Manipulation of Reductive Reactivity

**Alexander A. Trifonov*[a]**

*Dedicated to Prof. G. A. Abakumov on the occasion of his 70th birthday*

**Keywords:** Lanthanides / Diimines / Reductive reactivity / N,N ligands / Redox tautomerism

This review is devoted to the investigation of reactions of ytterbocenes with diimines. These reactions are found to be strongly influenced by the steric crowding in the coordination sphere of the metal atom and the coordination capacities of π-aromatic ligands coordinated to the ytterbium. The reactions may occur with oxidation of the ytterbium atom as well as with retention of its oxidation state. C–C bond formation, C–H bond activation, C=N bond insertion, and oxidative Yb–C bond cleavage processes are documented for reactions of ytterbocenes with diimines. Steric overcrowding of the coordination sphere of the ytterbium atom can induce "extra" reducing ability of ytterbocenes and allow them to act not only as one- but also as two-electron reductants with respect to diimines.
(© Wiley-VCH Verlag GmbH & Co. KGaA, 69451 Weinheim, Germany, 2007)

## 1. Introduction

Diimino ligands appeared in transition-metal chemistry in the late 1960s and have turned out to be a promising coordination environment able to provide unusual structures and unique reactivity.[1] The high catalytic activity of the diimino complexes of late transition metals in olefin polymerization has demonstrated the high potential of this ligand system in catalysis.[2] The permanent attention for diimines is mainly roused by the diversity of their redox and coordination properties. The lone electron pair at nitrogen atoms and the π electrons of the C=N bonds allow the diimine molecule to act both as a N-donor and as a π-electron donor ligand in a variety of coordination modes. The redox-active diimine molecule can coordinate metal atoms in high oxidation states as a neutral ligand[3] (Scheme 1, A), but also, due to its pronounced electron affinity (for example, the reduction potential of *t*BuN=CH–CH=N*t*Bu is $E^0_{SCE}$ = 1.822 V),[4] it can oxidize electropositive metals accepting one or two electrons, thus forming a radical anion (Scheme 1, B)[5] or dianion (Scheme 1, C).[6]

The diimine ligands were introduced into organolanthanide chemistry in the works of Cloke and Edelmann in the 1980s and allowed the synthesis of isolable lanthanide complexes.[7] The known compounds could be divided into two main groups based on the reduction state and the coordination mode of the diimino ligand. The first group is presented by homo- and hetero-ligated compounds containing the diimine radical anion coordinated to the lanthanide atom by two nitrogen atoms (Scheme 1, B).[7a–7f] The second group consists of complexes coordinated by the doubly reduced enediamido fragment 2σ:π-bonded to the central metal atom (Scheme 1, C).[7g,7h]

The redox-active character of diimines and the low energy of their π* orbitals[8] makes their complexes with lanthanide metals of two stable oxidation states promising ob-

[a] G. A. Razuvaev Institute of Organometallic Chemistry of the Russian Academy of Sciences,
Tropinina 49, 603950, Nizhny Novgorod, GSP-445, Russia
Fax: +7-8312-621497
E-mail: trif@imoc.sinn.ru

*Alexander Trifonov was born in Gorky (Nizhny Novgorod), Russia in 1962. In 1979–1984 he studied chemistry at the State University of Gorky and in 1984 received his diploma degree. During his PhD studies he worked at the Institute of Organometallic Chemistry of Russian Academy of Sciences (Nizhny Novgorod) under the supervision of Prof. M. N. Bochkarev and in 1989 received his PhD. He did postdoctoral studies at the Technical University of Berlin (Prof. H. Schumann, 1991), Université de Paris-Sud (Prof. H. Kagan, 1993–1995), and Mainz University (Prof. J. Okuda, 1999–2000). After returning to the Institute of Organometallic Chemistry, he defended the second thesis in 2003 and in 2004 became head of the Laboratory of Coordination Chemistry. Since 2005 he has been a professor of chemistry of Nizhny Novgorod State University. His research interests lie in the area of the synthesis of organometallic and coordination compounds of rare earth metals and their application in homogeneous catalysis and material chemistry.*

 © 2007 Wiley-VCH Verlag GmbH & Co. KGaA, Weinheim 

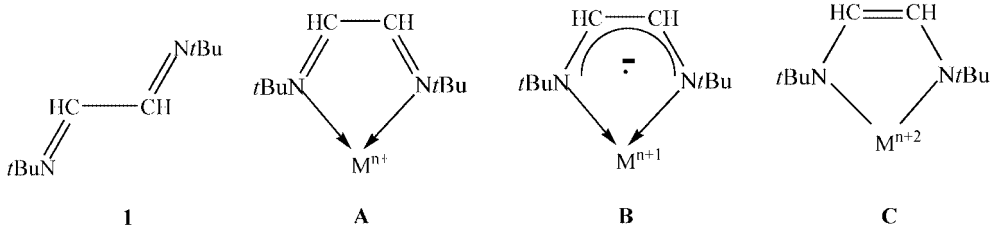


Scheme 1.

jects with respect to investigation of intramolecular metal–ligand electron transfers. Ytterbium seems to be the most advantageous candidate for this purpose due to a rather low $Yb^{II} \rightleftharpoons Yb^{III}$ transformation potential (for comparison, reduction potentials of $M^{III}/M^{II}$ in aqueous solution vs. SHE: Eu, –0.35; Yb, –1.15; Sm, –1.55 V).[9] Diamagnetism of the divalent ytterbium (electron configuration $Yb^{II}$ $4f^{14}$) complexes and moderate paramagnetism of its trivalent species (electron configuration $Yb^{III}$ $4f^{13}$, $\mu$ = 3.29–4.45 $\mu_B$)[10] makes NMR spectroscopy applicable for the investigation of ytterbium compounds in both oxidation states. On the other hand, noticeable differences in the magnetic properties of the $Yb^{II}$ and $Yb^{III}$ derivatives[10] allow easy estimation of the ytterbium atom oxidation state by means of magnetochemistry. Moreover, complexes of trivalent ytterbium emitting in the near-infrared region and containing conjugated diimino ligands which can act as sensitizers are of great interest because of potential applications in optoelectronic devices and medical diagnosis.[11] Compounds that undergo easy and reversible redox transformations by intramolecular electron transfer provoked by low-energy external excitations are of potential interest for the construction of molecular switches.

Complexes of trivalent ytterbium containing radical-anionic diimine ligands are promising models for investigation of metal–ligand bonding to provide a ground for a deeper understanding of the electronic structure of f-metal compounds and the contribution of f-electrons in a bonding interaction. The first tris(diazabutadiene) derivative of trivalent ytterbium ($t$BuNCHCHN$t$Bu)$_3$Yb containing three radical-anionic diimine ligands has demonstrated a complex temperature-dependent magnetic behavior which allowed us to suggest the existence of redox tautomerism.[7f] In order to gain insight into the nature of bonding in diimino complexes of f-elements, we focused on the synthesis of mixed-ligand $Yb^{III}$ compounds containing one paramagnetic ligand. The reactions of ytterbocenes with diimines were chosen as a synthetic approach to this class of compounds, and systematic investigation of these reactions has unexpectedly discovered a very rich and often unpredictable reactivity. The differences in reactivity as a function of steric crowding in the coordination sphere of the metal atom, coordination capacities of the π-aromatic ligands bound to ytterbium, and their tendency towards haptotropic rearrangements allow an expansion of ytterbocene reductive chemistry and the revelation of new types of reactions and complexes.

The review is mainly focused on the ytterbium derivatives since there is far less known about the diimine complexes of samarium and ytterbium. Work on this subject is being pursued at the moment.

## 2. Reactions Resulting in the Formation of Diimino Complexes $[Cp_2Yb^{III}(L^{\cdot-})]$ and $[Cp_2Yb^{II}(L^0)]$ (Cp = $C_5H_5$, $C_5MeH_4$, $C_5Me_5$, $C_9H_7$, $C_9H_6CH_2$, $C_{13}H_9$; L = RN=CH–CH=NR, bipy)

The *N*,*N*′-di-*tert*-butyl-1,4-diazabutadiene (**1**) was the first and remains the most widely employed diazabutadiene ligand in organolanthanide chemistry. Ytterbocenes $[Cp_2Yb(THF)_2]$ {Cp = $C_5H_5$ (**2**), $C_5Me_5$ (**3**), $C_9H_7$ (**4**), $C_9H_6CH_2$ (**5**), $C_{13}H_9$ (**6**)} reacted with **1** in a similar way, and the reactions afforded sandwich complexes of trivalent ytterbium containing the radical anion of diazabutadiene $[Cp_2Yb(t$BuNCHCHN$t$Bu$^{\cdot-})]$ {Cp = $C_5H_5$ (**7**),[12] $C_5Me_5$ (**8**),[13] $C_9H_7$ (**9**),[14] $C_9H_6CH_2$ (**10**),[14] $C_{13}H_9$ (**11**)[15]} (Scheme 2). It is worthy to note that **1** oxidized complex **2** at room temperature in THF solution, while compounds **3**–**6** did not react with **1** in THF. This is proven by the $^1$H NMR spectra of the reaction mixtures of **3**–**6** and **1** in [$D_8$]-thf which show superposition of the spectra of the diamagnetic $Yb^{II}$ complexes and of free diazabutadiene. In contrast, $^1$H NMR spectroscopy indicates paramagnetism of the product formed in the reaction of **2** and **1** in THF, thus giving evidence for the oxidation of the ytterbium atom to $Yb^{III}$ oxidation state. The reactions of complexes **3**–**6** with **1** occurred only in toluene media at 60 °C and resulted in the formation of the complexes **8**–**11** (Scheme 2).

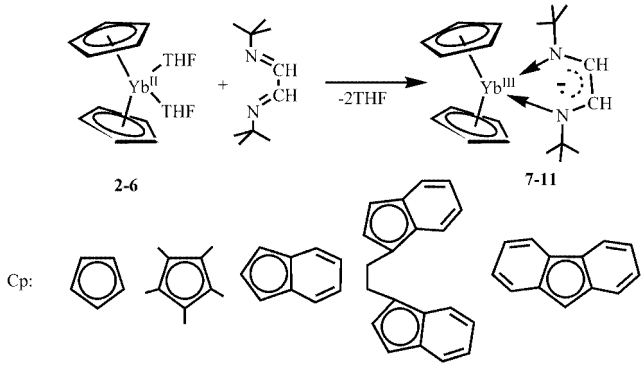


Scheme 2.

 © 2007 Wiley-VCH Verlag GmbH & Co. KGaA, Weinheim 

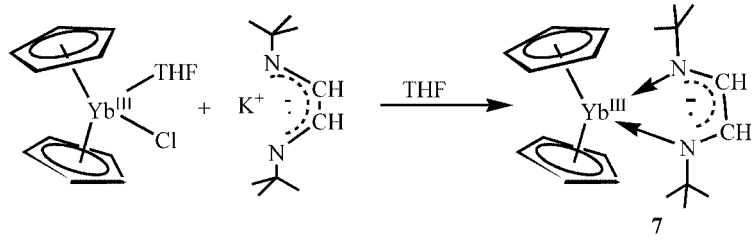


$$2(C_5H_5)_2YbCl(THF) + Na^+{}_2(t\text{BuNCHCHN}t\text{Bu}^{2-}) \xrightarrow{THF} (C_5H_5)_2Yb(t\text{BuNCHCHN}t\text{Bu}) + (C_5H_5)_2Yb(THF)_2 + 2NaCl$$

**7**

Scheme 3.

Complex **7** was also obtained by the metathesis reaction of equimolar amounts of $[(C_5H_5)_2YbCl(THF)]$ and $(t\text{BuNCHCHN}t\text{Bu}^{-})K^+$ (Scheme 3). An attempt to synthesize a dinuclear compound containing two $[(C_5H_5)_2Yb]$ moieties linked by a μ-bridging enediamido fragment by the reaction of a twofold molar excess of $[(C_5H_5)_2YbCl(THF)]$ with $Na^+{}_2(t\text{BuNCHCHN}t\text{Bu}^{2-})$ afforded a mixture of complex **7** and $[(C_5H_5)_2Yb(THF)_2]$ (Scheme 3).[12]

The bulkier 1,4-bis(2,6-diisopropylphenyl)-1,4-diaza-1,3-butadiene (**12**) also reacted with ytterbocenes $[(C_9H_7)_2Yb(THF)_2]$ and $[(C_5MeH_4)_2Yb(THF)_2]$ in toluene, affording the derivatives of trivalent ytterbium coordinated by the radical anion of diazadiene $[(C_9H_7)_2Yb(i\text{Pr}_2C_6H_3NCHCHNC_6H_3i\text{Pr}_2)]$ (**13**)[16] and $[(C_5MeH_4)_2Yb(i\text{Pr}_2C_6H_3NCHCHNC_6H_3i\text{Pr}_2)]$ (**14**), respectively (Scheme 4).[17]

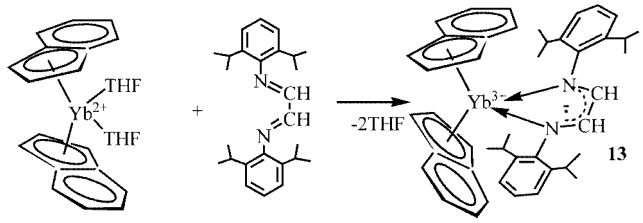


Scheme 4.

The structures of complexes **7**–**10**, **13**, **14** have been determined by X-ray diffraction studies which revealed that in all compounds, the ytterbium atom is $\eta^5$-coordinated by the two "cyclopentadienyl" units and the two nitrogen atoms of the radical-anionic diazabutadiene ligand, and it adopts the geometry of a distorted tetrahedron (Figures 1, 2, 3, 4, 5, and 6).

The Yb–$Cp_{Centr.}$ distances in complexes **7**–**10**, **13**, **14** (Table 1) are shorter than those in the starting $Yb^{II}$ complexes.[18] The shortening of the Yb–$Cp_{Centr.}$ distances in complexes **7**–**10**, **13**, **14** compared with those in the starting ytterbocenes indicates the oxidation of the ytterbium atom from $Yb^{II}$ to $Yb^{III}$.[19] However, in all cases the magnitude of the shortening is considerably less than that expected on the basis of the difference in the ionic radii of $Yb^{II}$ and $Yb^{III}$ (0.155 Å) and obviously results from reciprocal repul-

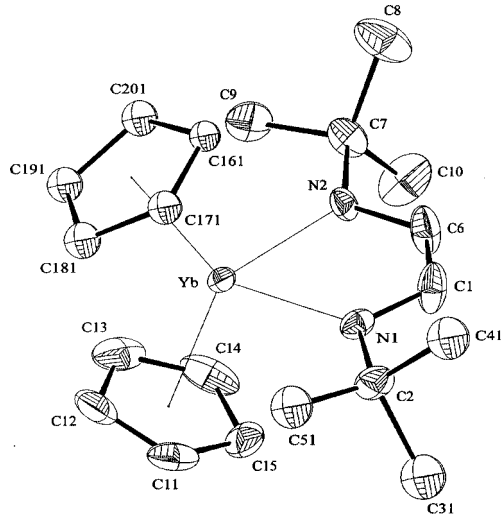


Figure 1. Molecular structure of complex $[(C_5H_5)_2Yb(t\text{BuNCHCHN}t\text{Bu})]$ (**7**).

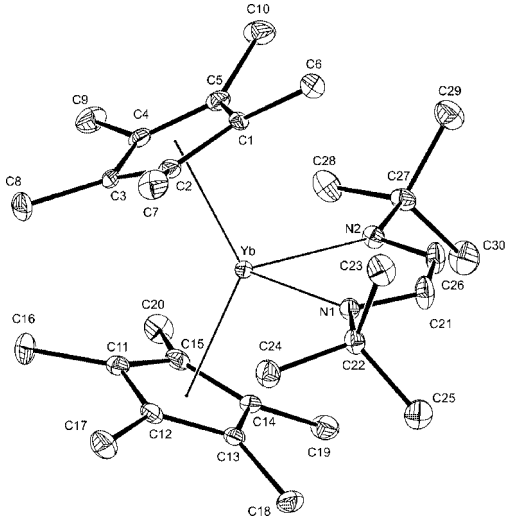


Figure 2. Molecular structure of complex $[(C_5Me_5)_2Yb(t\text{BuNCHCHN}t\text{Bu})]$ (**8**).

 © 2007 Wiley-VCH Verlag GmbH & Co. KGaA, Weinheim 

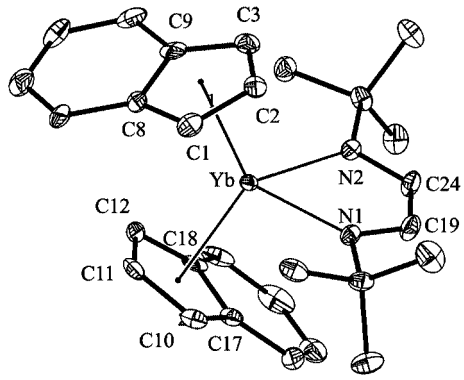


Figure 3. Molecular structure of complex $[(C_9H_7)_2Yb(t\text{BuNCH-CHN}t\text{Bu})]$ (**9**).

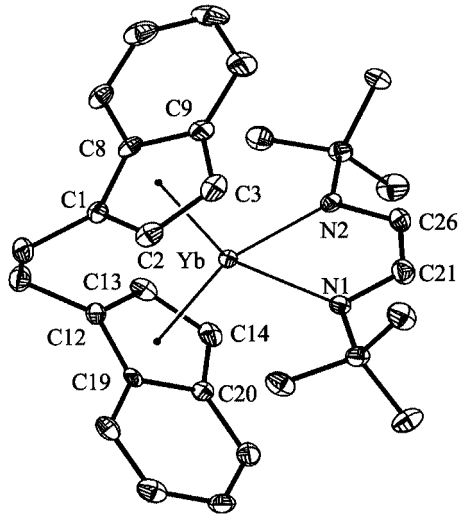


Figure 4. Molecular structure of complex $[(C_9H_6CH_2)_2Yb(t\text{Bu-NCHCHN}t\text{Bu})]$ (**10**).

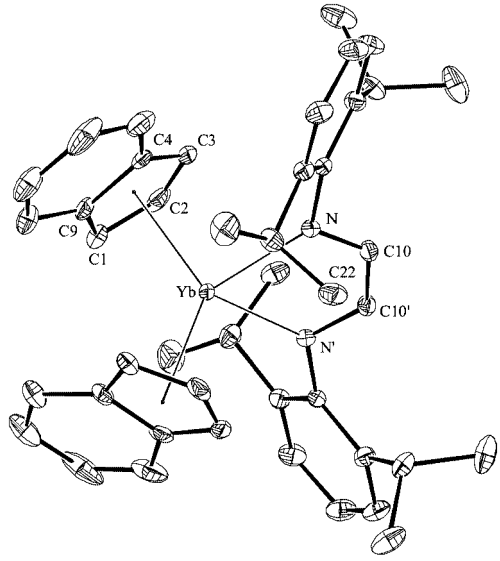


Figure 5. Molecular structure of complex $[(C_9H_7)_2Yb(i\text{Pr}_2\text{-}C_6H_3NCHCHNC_6H_3i\text{Pr}_2)]$ (**13**).

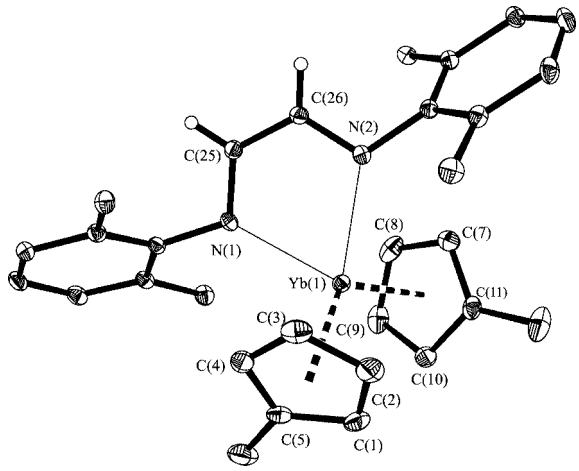


Figure 6. Molecular structure of complex $[(C_5MeH_4)_2Yb(i\text{Pr}_2\text{-}C_6H_3NCHCHNC_6H_3i\text{Pr}_2)]$ (**14**). The methyl carbon atoms of the *i*Pr groups are omitted.

sion of the π-aromatic ligands coordinated to the ytterbium atom and the diazabutadiene ligand. The Yb–$Cp_{Centr.}$ bond lengths observed in the related complexes **7**–**10** increase as a function of the bulkiness of the $\eta^5$-coordinated ligand and become the maximum for the pentamethylcyclopentadienyl ligand, reflecting its highest steric demand in the series of synthesized compounds. The same tendency is also observed for Yb–N bond lengths in complexes **7**–**10** (Table 1). Comparison of the bonding situation in complexes **9** and **13**, containing the same indenyl ligands but different diazadienes, shows that the replacement of the *tert*-butyl radical by bulkier 2,6-diisopropylphenyl in the diazadiene molecule results in noticeable lengthening of the Yb–N bonds. The bond lengths within the diazabutadiene ligand of compounds **7**–**10**, **13**, **14** indicate its radical-anionic character. An electron transfer from the ytterbium atom to the LUMO of the ligand is expected to cause delocalization of the charge over the whole conjugated NCCN fragment which involves changes in the bond lengths. Compared with the N=C and C–C bond lengths in the parent free diazadiene molecules,[20,21] the N=C bonds in the diazadiene ligands of complexes **7**–**10**, **13**, **14** are substantially elongated, while the C–C bonds are shortened and close to the values of aromatic C–C bonds.[22] The structural parameters of complexes **7**–**10**, **13**, **14** are in agreement with the trivalent oxidation state of the ytterbium atom and the radical-anionic character of the diazadiene ligand. Unexpectedly, the complexes **7**–**11**, **13**, **14** in the solid state as well as in toluene solutions are ESR silent in the temperature range 173 to 300 K. This fact is attributable either to a substantial broadening of the signal of the diazadiene radical anion in the field of the paramagnetic $Yb^{III}$ ion or to antiferromagnetic coupling of the spin carriers. The IR and UV/Vis spectra of complexes **7**–**11**, **13**, **14** identify the diazabutadiene ligand as a radical anion. The complexes **7**–**11**, **13**, **14** are paramagnetic with the values of the effective magnetic moments in the region 3.0–4.8 $\mu_B$ (300 K), giving evidence for the trivalent oxidation state of the ytterbium atom.[10]

 © 2007 Wiley-VCH Verlag GmbH & Co. KGaA, Weinheim 

Table 1. Values of effective magnetic moments ($\mu_{eff}$, $\mu_B$, 300 K), and selected bond lengths [Å] and bond angles [°] for complexes [$Cp_2Yb(t$BuNCHCHN$t$Bu$^{-}$)].

| Complex | | Ref. | $\mu_{eff}$ [$\mu_B$] 300 K | Bond lengths [Å] and bond angles [°] C–N[a] | C–C[a] | Yb–N | Yb–$Cp_{Centr.}$ | $Cp_{Centr.}$–Yb–$Cp_{Centr.}$ |
|---|---|---|---|---|---|---|---|---|
| [$(C_5H_5)_2$Yb($t$BuNCHCHN$t$Bu)] | **7** | [12] | 4.80 | 1.31(2) 1.30(2) | 1.40(2) | 2.306(9)<br>2.309(9) | 2.324(7)<br>2.334(4) | 128.1(2) |
| [$(C_5Me_5)_2$Yb($t$BuNCHCHN$t$Bu)] | **8** | [13] | 4.1 | 1.339(4) 1.326(5) | 1.398(5) | 2.385(3)<br>2.394(3) | 2.414(2)<br>2.401(2) | 130.27(6) |
| [$(C_9H_7)_2$Yb($t$BuNCHCHN$t$Bu)] | **9** | [14] | 3.4 | 1.323(8) 1.309(8) | 1.412(9) | 2.318(5)<br>2.335(5) | 2.383(3)<br>2.376(3) | 125.44(11) |
| [$(C_9H_6CH_2)_2$Yb($t$BuNCHCHN$t$Bu)] | **10** | [14] | 3.0 | 1.324(7) 1.331(6) | 1.420(7) | 2.321(4)<br>2.343(5) | 2.371(2)<br>2.383(2) | 120.05(8) |
| [$(C_{13}H_9)_2$Yb($t$BuNCHCHN$t$Bu)] | **11** | [15] | 4.8 | – | – | – | – | – |
| [$(C_9H_7)_2$Yb($i$Pr$_2$C$_6$H$_3$NCHCHNC$_6$H$_3i$Pr$_2$)] | **13** | [16] | 3.4 | 1.330(4) | 1.412(7) | 2.381(3) | 2.376(2) | 124.9(6) |
| [$(C_5MeH_4)_2$Yb($i$Pr$_2$C$_6$H$_3$NCHCHNC$_6$H$_3i$Pr$_2$)] | **14** | [17] | 4.06 | 1.338(2) 1.335(2) | 1.395(2) | 2.3577(14)<br>2.3926(13) | 2.332(2)<br>2.331(2) | 127.27(2) |

[a] C–N and C–C bond lengths within the NCCN fragment.

Magnetic measurements of crystalline samples of complexes **9**, **10**,[14] **13**,[16] **14**[17] in the temperature range 2–300 K show a similar shape of the plots of $1/\chi$ versus $T$ and $\mu$ versus $T$ with nonlinear dependence as a function of temperature. The effective magnetic moments of the complexes **9**, **10**, **13** increase from 1.50–1.60 $\mu_B$ at 2 K to 3.0–3.4 $\mu_B$ at 300 K. The values of the effective magnetic moments of **9**, **10**, **13** in benzene solution at 300 K, estimated according to the published procedure,[23] are in agreement with the data obtained for the crystalline samples by the SQUID method. Trivalent ytterbium is paramagnetic with an electron configuration of $4f^{13}$, and the expected magnetic moment of $Yb^{III}$ complexes is 3.8 $\mu_B$ at 5–30 K and 4.5 $\mu_B$ at 90–300 K.[24] For complexes containing noninteracting spins, their contribution to the molar magnetic susceptibility is additive. A $Yb^{III}$ complex additionally containing a radical anion, as is suggested for **9**, **10**, **13**, should show a magnetic moment of 4.2 $\mu_B$ in the temperature range of 5–30 K and 4.8 $\mu_B$ in the temperature range of 90–300 K, provided that the spins of the two unpaired electrons do not interact. However, the experimental values of the magnetic moments obtained for **9**, **10**, **13** are considerably lower than the expected values which can be caused either by redox tautomerism between paramagnetic [$(C_9H_7)_2Yb^{III}(L^{-})$] and diamagnetic [$(C_9H_7)_2Yb^{II}(L^0)$] molecules or by antiferromagnetic coupling of the two unpaired electrons in [$(C_9H_7)_2Yb^{III}(L^{-})$] (L = diazadiene). Antiferromagnetic coupling between trivalent rare earth ions and paramagnetic semiquinone ligands was found to be dominating for the series of complexes Ln(DTBSQ)$(HBPz_3)_2$ (Ln = Er, Tb, Dy, Yb; DTBSQ = 3,5-di-*tert*-butylsemiquinone; $HBPz_3$ = hydrotrispyrazolylborate).[25] Hatfield and co-workers have described a strong exchange coupling between the lanthanide ions and the phthalocyaninato ligand radical in bis(phthalocyaninato)lanthanide sandwich compounds ($Pc^{2-}$) $Ln^{III}(Pc^{1-})$ (Ln = Gd, Tb, Dy, Ho, Er, Tm, Yb, Lu). The value of the room-temperature magnetic moment for the trivalent ytterbium antiferromagnetically coupled with an organic radical anion was calculated as 3.46 $\mu_B$.[26] The value of the magnetic moment (4.06 $\mu_B$) observed at 300 K for complex **14** suggests that both ferro- and antiferromagnetic coupled states of $Yb^{3+}$ and the radical anion are present at room temperature. The analysis of the plots $1/\chi$ versus $T$ and $\mu$ versus $T$ suggests that an antiferromagnetic spin interaction is a plausible reason for the low magnetic moments, however the available data do not allow definite exclusion of the existence of redox tautomers for **9**, **10**, **13**, **14**.

Complexes **8**–**10**, **13** have demonstrated uncommon solvent-mediated intramolecular redox transformations in solutions.[13,14,16] Complexes **8**–**10**, **13** in the crystalline state as well as in nonsolvating solvents (aromatic or aliphatic hydrocarbons) exist as paramagnetic derivatives of trivalent ytterbium coordinated by the diazadiene radical anion [$(R)_2Yb^{III}(L^{-})$] (R = $C_5Me_5$, $C_9H_7$, $-CH_2C_9H_6$; L = diazadiene), while in solvating solvents (THF) these compounds are diamagnetic. $^1$H NMR, UV/Vis spectroscopy, and magnetic measurements proved the diamagnetism of complexes **8**–**10**, **13** in THF solutions and therefore the divalent oxidation state of the ytterbium atom. Moreover, recrystallization of complexes **8**–**10**, **13** from THF/hexane mixtures allowed the recovery of the parent ytterbocene in good yields. Dissolution of **8**–**10**, **13** in THF caused displacement of the radical-anionic diazadiene ligand by THF molecules. This process implies an electron transfer from the diazadiene radical anion to the ytterbium ion, resulting in the oxidation of the ligand to neutral diazadiene and reduction of $Yb^{III}$ to $Yb^{II}$ followed by substitution of the neutral diazadiene ligand by THF molecules (Scheme 5).[14,16]

One can suppose that steric repulsion of the bulky indenyl, pentamethylcyclopentadienyl, and diazadiene ligands is decisive for the examined reactions and the elongation and weakening of the Yb–N bonds in complexes **8**–**10**, **13**. Hence, the energy of the Coulomb interaction between the $[(R)_2Yb^{III}]^+$ cationic species and the radical anion of diazadiene is comparable with that of the coordination bonds between $R_2Yb^{II}$ and THF molecules, and as a result the diazadiene ligand redox substitution becomes feasible.

Unlike complexes **8**–**10**, **13**, compound [$Cp_2Yb$($t$BuNCHCHN$t$Bu)] (**7**) did not undergo a reductive substitution process and remained paramagnetic in THF solutions.[12] Such a distinction in solution redox behavior is

 © 2007 Wiley-VCH Verlag GmbH & Co. KGaA, Weinheim 

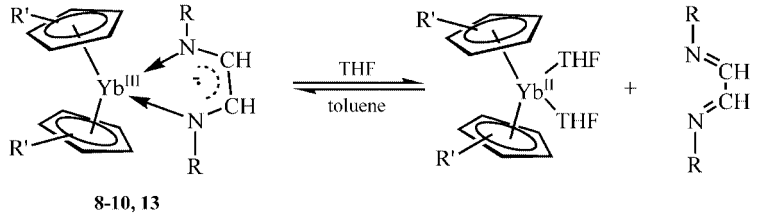


Scheme 5.

obviously caused by the structural difference of **7** and namely by the Yb–N bond lengths which are the shortest in the series of related compounds (Table 1). The shorter contact between cationic and anionic moieties in complex **7** should result in an increase in the energy of the Coulomb interaction, and the energy consumption for the reductive substitution of the diazadiene ligand can not be overcome by formation of coordination ytterbium–oxygen bonds. A similar behavior towards THF was described by Evans and co-workers for decamethylsamarocene complexes with aromatic polycyclic ligands.[27] However, unlike complexes **8**–**10**, **13**, the samarium derivatives can not be regenerated by removal of THF and addition of aromatic or aliphatic solvents.

Distinctions in the reductive reactivity of metallocene derivatives of divalent samarium and europium toward diimines from that of ytterbium compounds are defined by the $Ln^{II}/Ln^{III}$ transformation potentials characteristic for these elements. The reducing capacity of $Ln^{II}$ compounds increases in the triad Eu < Yb < Sm (for comparison, reduction potentials $M^{III}/M^{II}$ in aqueous solution vs. SHE: Eu, –0.35; Yb, –1.15; Sm, –1.55 V).[9a] Decamethylsamarocene easily reduced *N*,*N*′-di-*tert*-butyl-1,4-diazabutadiene, affording the derivative of trivalent samarium coordinated by the radical anion of diazadiene $(C_5Me_5)_2Sm^{III}$-(*t*BuNCHCHN*t*Bu$^{-\cdot}$) (**15**),[7c] whereas the reaction of the europium analogue $(C_5Me_5)_2Eu(Et_2O)$ resulted in the formation of the adduct with the neutral diazadiene ligand $(C_5Me_5)_2Eu^{II}$(*t*BuNCHCHN*t*Bu$^0$) (**16**).[28] On the other hand, the diazadiene $(C_6F_5)N{=}C(Me){-}C(Me){=}N(C_6F_5)$ possessing higher electron affinity oxidized $(C_5Me_5)_2Eu(Et_2O)$ in toluene solution at room temperature to the trivalent europium complex $(C_5Me_5)_2Eu^{III}\{C_6F_5NC(Me)C(Me)NC_6F_5^{-\cdot}\}$ (**17**) (Scheme 6).[28] The difference in the oxidation state of the europium atom in complexes **16** and **17** is undoubtedly proven by the metric parameters and magnetic measurements of the compounds.

Solvent-mediated reversible intramolecular redox reaction, analogous to that previously described for ytterbium compounds,[13,14,16] was reported for complex **17**.

The reactivity of metallocene-type complexes of trivalent lanthanides containing the radical anion of diazadiene is poorly investigated. Complexes **7**–**11**, **13** are inactive in olefin polymerization. Reaction of complex **7** with 9-fluorenone in a 1:1 molar ratio in THF was found to occur with oxidation of the diazadiene radical anion, abstraction of

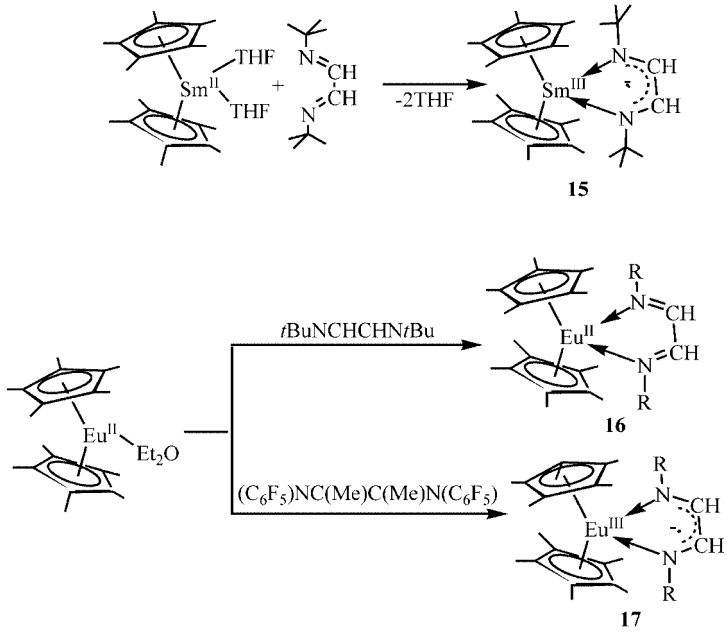


Scheme 6.

 © 2007 Wiley-VCH Verlag GmbH & Co. KGaA, Weinheim 

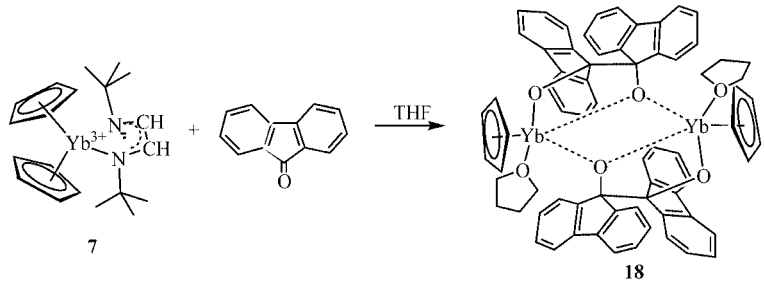


Scheme 7.

one cyclopentadienyl ring, pinakol condensation, and formation of the dimeric $Yb^{III}$ complex [CpYb($\mu^2$-$OC_{13}H_8$–$C_{13}H_8O$)(THF)]$_2$ (**18**) (Scheme 7).[13] An X-ray diffraction study of complex **18** has revealed that two [CpYb(THF)] moieties are linked by two 9,9-difluorenyldialcoxo ligands (Figure 7).

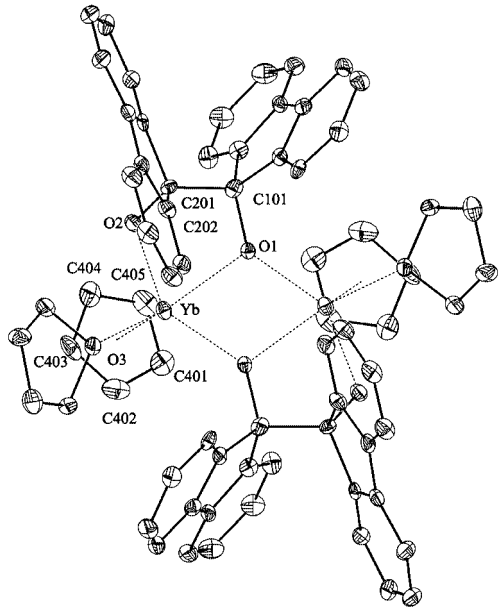


Figure 7. Molecular structure of complex [CpYb($\mu^2$-$OC_{13}H_8$–$C_{13}H_8O$)(THF)]$_2$ (**18**).

2,2′-Bipyridine (bipy), which has a virtually planar structure and contains a N=C–C=N fragment, can be considered as a diimine ligand. The reduction potential of bipy (–2.18 V)[29] is noticeably lower than that of 1,4-di-*tert*-butyl-1,4-diazabuta-1,3-diene (–1.822 V),[4] and bipyridine derivatives of ytterbium have promise from the standpoint of possible redox tautomeric transformations. Andersen and co-workers have investigated reactions of ytterbocenes bearing cyclopentadienyl ligands with different substituents [Cp′′$_2$Yb($Et_2O$)] {Cp′′ = $C_5Me_5$, $C_5Me_4H$, 1,3-$(Me_3C)_2$-$C_5H_3$, 1,3-$(Me_3Si)_2C_5H_3$} with 2,2′-bipyridine (bipy) and phenanthroline (phen), which afforded complexes [Cp′′$_2$Yb(L)] (L = bipy, phen).[30,31] The various ytterbocenes interacted differently with bipy and phenanthroline depending on the steric and electronic properties of the substituents on the cyclopentadienyl ligands, which also influence the extent of paramagnetism of the resultant compounds [Cp′′$_2$Yb(L)]. The electron-withdrawing $SiMe_3$ groups make the metal more electropositive thus stabilizing the $Yb^{II}$ oxidation state; the derived ytterbocene did not reduce bipy and phen, and the reactions afforded the adducts with neutral L [Cp′′$_2$$Yb^{II}$($L^0$)]. The ytterbocenes containing electron-donating alkyl groups (pentamethyl, tetramethyl, *t*Bu) on the cyclopentadienyl rings tend to reduce bipy and phen, affording paramagnetic $Yb^{III}$ complexes containing a bipy radical anion [Cp′′$_2$$Yb^{III}$($L^{-\cdot}$)] (Scheme 8).

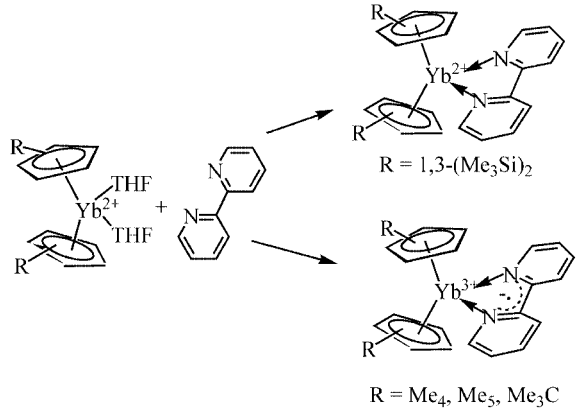


Scheme 8.

The measured magnetic moments of obtained complexes, which are less than those expected for complexes [Cp′′$_2$$Yb^{III}$($L^{-\cdot}$)] containing two noninteracting paramagnetic centers, are explained by electron exchange model for spin coupling between $Yb^{III}$ and the single unpaired electron in the anion radical $L^{-\cdot}$. The extent of paramagnetism of paramagnetic complexes [$(C_5Me_5)_2$Yb(bipy-X)] with 4,4′-disubstituted bipyridines (X = Me, $Me_3C$, OMe, Ph, $CO_2Me$, $CO_2Et$) was found to be dependent on the substituents on the bipyridine ligands. The values of $\chi$ and $\mu_{eff}$ at 400 K increase in the series OMe < H < $CO_2R$ (R = Me, Et) ≤ Ph and correlate with the electron-withdrawing properties of the substituents.[32]

Unusual for substituted ytterbocene bipyridine adducts, rapid exchange (on the NMR time scale) between the complex [{1,2,4-$(Me_3C)_3C_5H_2$}$_2$Yb(bipy)] and free 2,2′-bipyr-

 © 2007 Wiley-VCH Verlag GmbH & Co. KGaA, Weinheim 

idine was observed in [$D_8$]toluene in a wide range of temperatures, thus indicating fluxional behavior in solution (Scheme 9).[31]

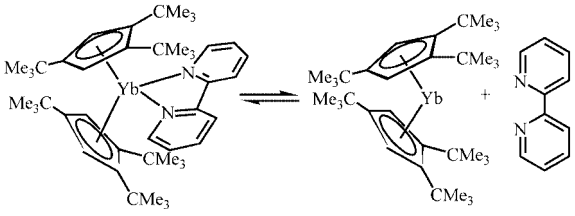

Scheme 9.

The electrochemical studies of complexes [$(C_5Me_5)_2$Yb(L)] (L = bipy, phen) have demonstrated that stabilization of their respective LUMOs of diimine ligands and destabilization of metal f-orbitals favors the spontaneous ground-state charge-transfer process. The spectroscopic data from the f-f transition region for [$(C_5Me_5)_2$Yb(L)] indicate that the f-orbital splitting in these compounds is not sensitive to the differences in the electronic structures of bipy and phen. The separation between the ligand-based oxidation wave ($L^{0/-}$) and the metal-based reduction wave ($Yb^{III/II}$) in the adducts [$(C_5Me_5)_2$Yb(L)] is 0.79 V for both bipy and phen derivatives. In the spectra of complexes [$(C_5Me_5)_2$Yb(L)] previously unreported, the near-IR bands have been assigned to ligand($\pi^*$)-to-metal(f-orbital) charge-transfer transitions. The Raman spectra give evidence of the radical-anionic nature of the diimine ligands in these complexes.[33]

The bis(indenyl) derivative [$(C_9H_7)_2$Yb(THF)$_2$] (**4**) reacted with bipy in THF at room temperature to yield the $Yb^{II}$ complex [$(C_9H_7)_2Yb^{II}(bipy^0)$] (**19**). This is consistent with the lower electron-donating ability of the indenyl ligand compared with that of the pentamethylcyclopentadienyl ligand that results in lower reducing capacity of complex **4**. Surprisingly despite the higher electron affinity of diazadiene **1**, it did not react with complex **4** in THF media, while the reaction with bipy immediately afforded compound **19** in good yield. Obviously that can be attributed to the higher steric demand of the ligand **1**. Magnetic measurement, $^1$H NMR, IR, and UV/Vis spectra of **19** indicate that the complex is a diamagnetic adduct with neutral bipy. The X-ray diffraction analysis of complex **19** has revealed that the crystals contain two crystallographically independent molecules. The Yb–C bond lengths indicate the divalent state of the ytterbium atom. The most essential difference of the two crystallographically independent molecules **19** are the dihedral angles between the planes of the pyridine rings: 11.2(8)° and 4.8(8)°.[16] The torsion angle between the planes of the pyridine rings serves as an indicator of the electronic state of the bipy ligand in the complex. This angle in free bipy and in complexes with the neutral bipy ligand is in the region 10–17°;[29,30] the electron transfer to the highest occupied molecular orbital of the bipy molecule leads to a change in its geometry, including its flattening due to partial double bonding between two C atoms at positions 2 and 2′. Hence, the presence of two crystallographically independent molecules, which differ in the geometric parameters of the bipy ligand, could be considered as evidence for the existence of redox isomers of **19**. However, the identity of the Yb–C bond lengths and the geometry of the bipy ligands in both molecules **19** rules out the existence of redox isomers. Apparently, the difference in the dihedral angles of the bipy ligands in two crystallographically independent molecules is associated not with the electronic state but with steric restrictions caused by the mutual arrangement of the indenyl and bipy ligands. Furthermore, in one of the molecules, the six-membered fragments of the indenyl ligands are located above each pyridine ring of the bipyridine ligand (Figure 8).

Therefore, an increase in the dihedral angle between the pyridine rings should result in close contacts between indenyl and bipy ligands and consequently in the increase in the energy of nonbonded repulsions.

## 3. Reactions Resulting in C–C Bond Formation

As mentioned earlier, the Yb–N bond lengths and the reversibility of the intramolecular metal–ligand electron transfer can be regulated by tuning the steric demand of the ligands coordinated to the ytterbium atom and the substituents at the nitrogen atoms of the diimine molecule. However, successive increase in the π-aromatic ligand size in the series $C_5MeH_4$, $C_9H_7$, $C_{13}H_9$ led (in the case of fluor-

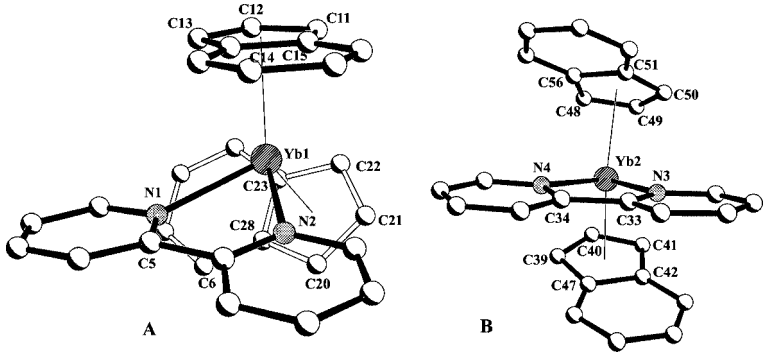


Figure 8. Two crystallographically independent molecules of complex [$(C_9H_7)_2Yb^{II}(bipy^0)$] (**19**).

 © 2007 Wiley-VCH Verlag GmbH & Co. KGaA, Weinheim 

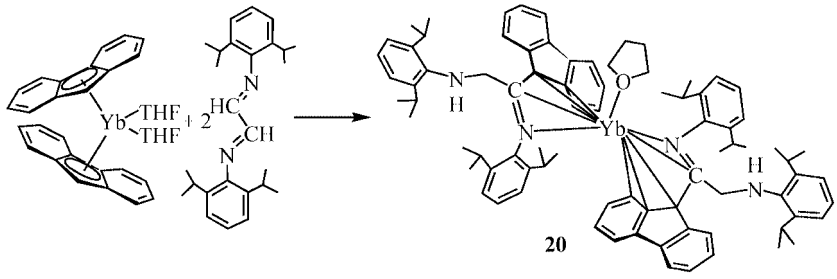


Scheme 10.

enyl) to a dramatic change in the pathway of the reaction of 1,4-bis(2,6-diisopropylphenyl)-1,4-diaza-1,3-butadiene (**12**) with a related ytterbocene. Unlike the previously mentioned reactions of ytterbocenes with diimines, the reaction of the bis(fluorenyl) complex $[(C_{13}H_9)_2Yb(THF)_2]$ with bulkier **12** under the same conditions did not occur with oxidation of the ytterbium atom but resulted in the formation of the unusual $Yb^{II}$ derivative $[Yb\{\eta^5\text{-}C_{13}H_8C(=N\text{–}C_6H_3iPr_2\text{-}2,6)CH_2NHC_6H_3iPr_2\text{-}2,6\}_2(THF)]$ (**20**) which was isolated in 80% yield (Scheme 10).[34]

The $Yb^{II}$ cation is $\eta^5$-coordinated by two novel monoanionic multifunctional ligands $\{C_{13}H_8C(=N\text{–}C_6H_3iPr_2\text{-}2,6)CH_2NHC_6H_3iPr_2\text{-}2,6\}^-$ arising from unprecedented coupling of the allylic carbon atom of the fluorenyl ligand with the imino carbon atom of the diazadiene **12** (Figure 9).

The C–C bond formation in **20** also implies migration of the two H atoms initially bonded to the coupled carbon atoms and acquisition of these hydrogen atoms by the second imino group which results in the hydrogenated $–CH_2–NH–$ fragment. In the course of the reaction, the coordination mode of the fluorenyl ligand to the Yb atom changes from the $\eta^5$-type in the starting complex $[(C_{13}H_9)_2Yb(THF)_2]$,[15] to a rather unusual $\eta^3$-type by one carbon atom of the five-membered ring and two carbon atoms of the six-membered ring. The $\eta^2$-coordination of the imino group to the Yb atom results in formation of the planer $\eta^5$-bonded heteropentadienyl frame. The bonding situation gives evidence of a delocalized π system in the heteropentadienyl fragment. The arrangement around the ytterbium atom in **20** determines the geometry of the heteropentadienyl bent sandwich complex.

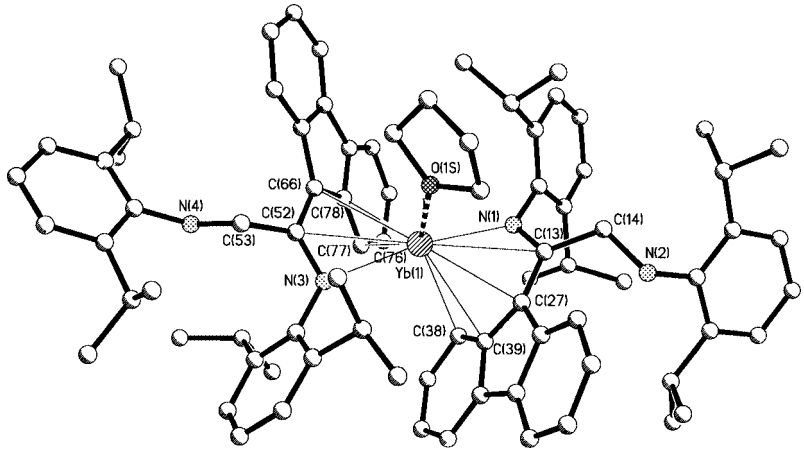


Figure 9. Molecular structure of complex $[Yb\{\eta^5\text{-}C_{13}H_8C(=N\text{–}C_6H_3iPr_2\text{-}2,6)CH_2NHC_6H_3iPr_2\text{-}2,6\}_2(THF)]$ (**20**).

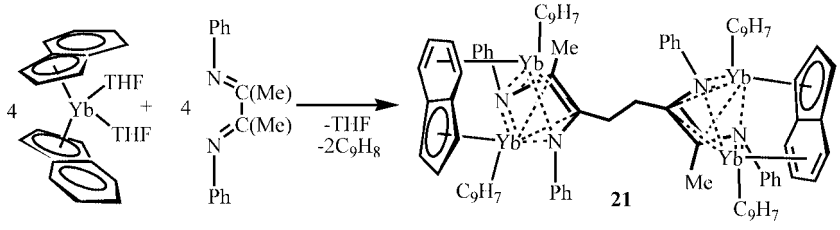


Scheme 11.

 © 2007 Wiley-VCH Verlag GmbH & Co. KGaA, Weinheim 

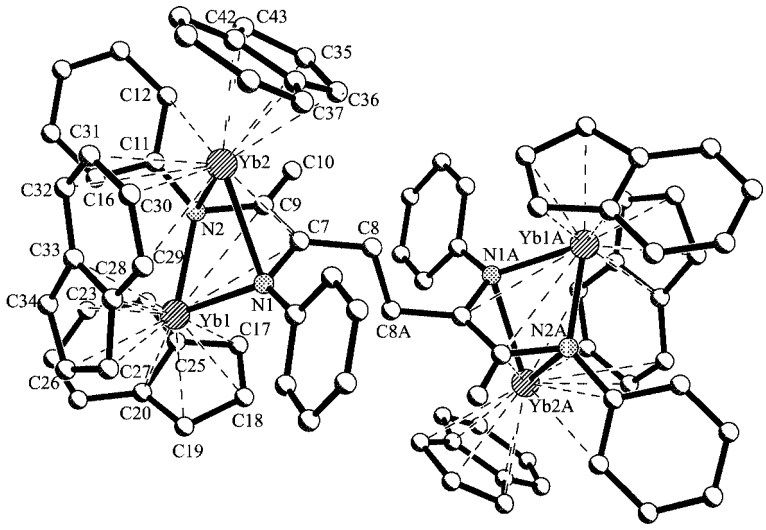


Figure 10. Molecular structure of complex $[Yb_2(\mu\text{-}\eta^5{:}\eta^4\text{-}C_9H_7)(\eta^5\text{-}C_9H_7)_2\{\mu\text{-}\eta^4{:}\eta^4\text{-}PhNC(CH_2)=C(Me)NPh\}]_2$ (**21**).

Another example of C–C bond formation was documented for the reaction of bis(indenyl)ytterbium complex $[(C_9H_7)_2Yb(THF)_2]$ with an equimolar amount of the diazabutadiene PhN=C(Me)–C(Me)=NPh. The reaction occurred with reductive diimine coupling and afforded the tetranuclear complex $[Yb_2(\mu\text{-}\eta^5{:}\eta^4\text{-}C_9H_7)(\eta^5\text{-}C_9H_7)_2\{\mu\text{-}\eta^4{:}\eta^4\text{-}PhNC(CH_2)=C(Me)NPh\}]_2$ (**21**) (Scheme 11).[35]

The reaction is accompanied by indene formation which obviously arises as a product of partial cleavage of Yb–indenyl bonds and hydrogen abstraction by the indenyl radical from a molecule of solvent or diimine. The molecule of **21** has a tetranuclear core which consists of two dinuclear units $[Yb_2(\mu\text{-}\eta^5{:}\eta^4\text{-}C_9H_7)(\eta^5\text{-}C_9H_7)_2\{\mu\text{-}\eta^4{:}\eta^4\text{-}PhNC(CH_2)=C(Me)NPh\}]$ connected by the $CH_2$–$CH_2$ bridge, as a result of hydrogen abstraction from one of the methyl radicals at the imino group of the diazadiene ligand and coupling of these methylene carbon atoms (Figure 10).

The dinuclear fragments are assembled due to unusual bridging $\mu\text{-}\eta^5{:}\eta^4$-coordination of the indenyl ligand and $\mu\text{-}\eta^4{:}\eta^4$-coordination of the diimine ligand. Each ytterbium atom in complex **20** is coordinated by two indenyl ligands but in different ways. One ytterbium atom of the dinuclear unit is $\eta^5$-bound with two cyclopentadienyl fragments of two indenyl ligands, while the second ytterbium atom is coordinated by the five- and six-membered rings in $\eta^5$- and $\eta^4$-fashion, respectively. Coordination of the six-membered ring leads to noticeable distortion of its planarity. Such $\mu$-bridging coordination of indenyl ligands is rather rare[36] and, to the best of our knowledge, has never been described for organolanthanides. The *ipso*- and *ortho*-carbon atoms of one of the phenyl rings of the diimine ligand are also involved in metal–ligand bonding through $\eta^2$-coordination to the ytterbium atom. The average Yb–C($C_5$-indenyl) and Yb–N bond lengths in **21** are somewhat different for the ytterbium atoms within a dinuclear unit. Complex **21** is paramagnetic with the experimental value of the effective magnetic moment 2.6 $\mu_B$ (293 K), which is intermediate between the average $\mu_{eff}$ value reported for $Yb^{III}$ derivatives and that of diamagnetic $Yb^{II}$ compounds.[10] Thus both the X-ray analysis data and magnetic measurements provide evidence that complex **21** is a mixed-valent compound containing both $Yb^{II}$ and $Yb^{III}$ atoms. The bonding situation within the NCCN fragment of **21** is consistent with a dianionic character of the diimino ligand. The double C–C bond of a doubly reduced enediamido moiety also participates in a dinuclear core formation, coordinating to both ytterbium atoms in $\eta^2$-fashion. The length of the carbon–carbon bond formed in the reaction is characteristic for ordinary C–C σ bonds.[22]

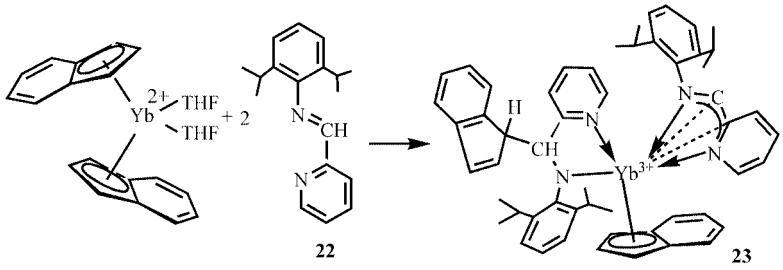


Scheme 12.

 © 2007 Wiley-VCH Verlag GmbH & Co. KGaA, Weinheim 

Iminopyridines containing a conjugated NCCN fragment might be considered as diimino ligands. Formation of a C–C bond resulted from N=C bond insertion into the Yb–($\eta^5$-$C_9H_7$) bond which was observed in the reaction of bis(indenyl) derivative [$(C_9H_7)_2Yb(THF)_2$] with a twofold molar excess of *N*-2,6-diisopropylphenylimino-2-pyridine (**22**) (THF, 20 °C), which led to formation of the $Yb^{III}$ complex [Yb($\eta^5$-$C_9H_7$){N(2,6-*i*$Pr_2C_6H_3$)CH($C_9H_7$)($C_5H_5N$)}-{$\eta^4$-2,6-*i*$Pr_2C_6H_3$NCH($C_5H_5N$)}] (**23**) (Scheme 12).[37]

Paramagnetism of complex **23** ($\mu_{eff}$ = 4.3 $\mu_B$, 293 K) indicates the trivalent oxidation state of the ytterbium atom.[10] Compound **23** is a half-sandwich complex in which the coordination sphere of the Yb atom is set up by an $\eta^5$-coordinated $C_9H_7$ anion, two nitrogen atoms of an amido-pyridinato ligand, and two nitrogen atoms of an iminopyridine radical anion (Figure 11).

The chelating amido-pyridinato ligand arises from insertion of the N=C bond of iminopyridine **22** into the Yb–($\eta^5$-$C_9H_7$) bond. This insertion results in Yb–$C_9H_7$ bond cleavage and formation of Yb–N and C–C bonds. To the best of our knowledge this is the sole example of such an insertion. The amido-pyridinato ligand is bound to the Yb atom by one covalent and one coordination bond. The bond angles about the methyne carbon atom of the amido-pyridinato ligand prove that, unlike the related carbon in the parent **22**, it adopts $sp^3$ hybridization. The geometric parameters within the planar NCCN fragment of the iminopyridine ligand in **22** give evidence of its reduced radical-anionic character. Formation of the amido-pyridinato ligand in complex **22** obviously implies rearrangement of the coordination fashion of one of the indenyl ligands in the $(C_9H_7)_2Yb$ fragment from $\eta^5$ to $\eta^1$ and subsequent insertion of the N=C bond of the iminopyridine molecule coordinated to the ytterbium atom into the Yb–$C_9H_7$ bond (Scheme 13).

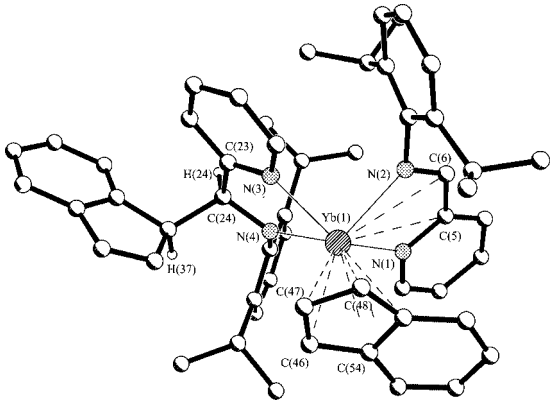


Figure 11. Molecular structure of complex [Yb($\eta^5$-$C_9H_7$){N(2,6-*i*$Pr_2C_6H_3$)CH($C_9H_7$)($C_5H_5N$)}{$\eta^4$-2,6-*i*$Pr_2C_6H_3$NCH($C_5H_5N$)}] (**23**).

## 4. Reactions Resulting in C–H Bond Activation

In order to evaluate the influence of the steric and electronic properties of the diimine on the pathway of its reaction with ytterbocenes, the bis(fluorenyl) compound [$(C_{13}H_9)_2Yb(THF)_2$] was treated with the bulky diimine *i*$Pr_2C_6H_3$N=C(Me)C(Me)=N$C_6H_3$*i*$Pr_2$ (**23**) bearing two methyl substituents at the imino carbon atoms (in contrast to diimine **12**). It was found that replacement of the imino hydrogen atoms by two methyl radicals dramatically influenced the reaction pathway and led to formation of the novel half-sandwich $Yb^{II}$ derivative [Yb($\eta^5$-$C_{13}H_9$){2,6-*i*$Pr_2C_6H_3$–N=C($CH_3$)–C($CH_2$)=N–$C_6H_3$*i*$Pr_2$-2,6}(THF)] (**24**) (Scheme 14).[34]

The compound is diamagnetic, corresponding to the $Yb^{II}$ oxidation state. The coordination sphere of the ytterbium atom in **24** is set up by one fluorenyl ligand coordinated in $\eta^5$-fashion, two nitrogen atoms of the novel monoanionic ligand {2,6-*i*$Pr_2C_6H_3$–N=C($CH_3$)–C($CH_2$)=N–$C_6H_3$*i*$Pr_2$-2,6}$^-$ (resulting from proton abstraction from the methyl radical at the imino group of the parent diimine), and one THF molecule (Figure 12).

Unlike the geometry of the diimine radical anions in $Yb^{III}$ complexes exhibiting redistribution of the bond lengths characteristic of the delocalized NCCN π system, the geometry of the monoanionic ligand in **24** indicates a partial double bonding and delocalization of the negative charge only in the NCC fragment (Scheme 15).[34] Flat geometry of the methylene carbon atom (the sum of the bond angles is 359.8°) in this fragment and the C–C bond length give evidence for $sp^2$ hybridization of this carbon atom.

Concentration of the negative charge on the N atom of the $NCCH_2$ fragment results in shortening of the respective Yb–N bond and nonequivalence of the Yb–N bonds. Partial double C–C bonding in the $NCCH_2$ fragment becomes evident also from NMR spectra of **24** which indicate that the two methylene protons become diastereotopic. The geometry of the $NCCH_2$ fragment may be formally presented as the result of the existence and interconversion of two resonance forms of complex **24** (Scheme 15). Isolation of fluorene from the reaction in nearly quantitative yield

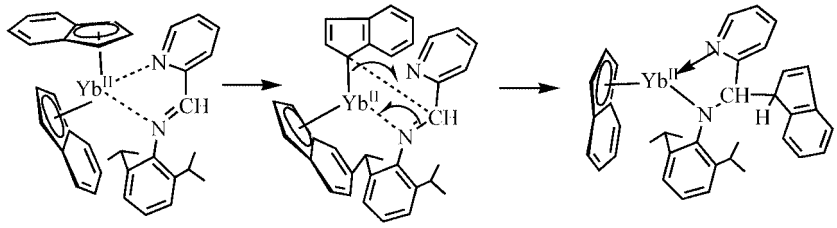


Scheme 13.

 © 2007 Wiley-VCH Verlag GmbH & Co. KGaA, Weinheim 

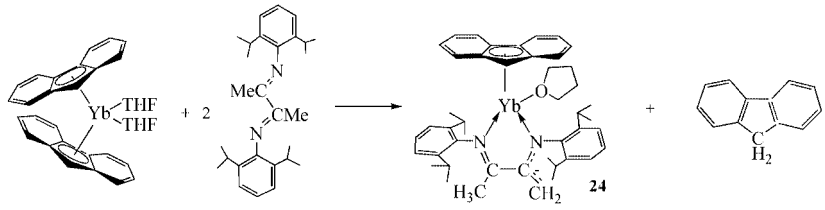


Scheme 14.

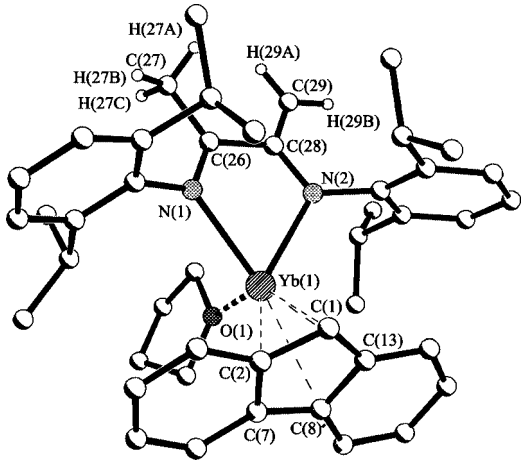


Figure 12. Molecular structure of complex [Yb(η$^5$-$C_{13}H_9$){2,6-*i*Pr$_2$C$_6$H$_3$–N=C(CH$_3$)–C(CH$_2$)=N–C$_6$H$_3$*i*Pr$_2$-2,6}(THF)] (**24**).

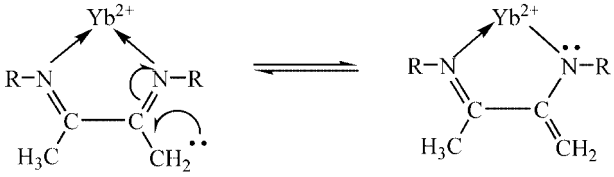


Scheme 15.

proves that the fluorenyl anion (or radical) is responsible for the proton abstraction from **23** and formation of the monoanionic diimino ligand.

The previously mentioned reaction of the formation of complex **21** (Scheme 11) also implies the stage of C–H bond activation. It is noteworthy that the substituents at the imino carbon atoms of the diimine molecule strongly influence their reactions with ytterbocenes. Thus the diimine *i*Pr$_2$C$_6$H$_3$N=CHCH=NC$_6$H$_3$*i*Pr$_2$ (**12**) easily oxidized complex [(C$_{13}$H$_9$)$_2$Yb(THF)$_2$], and the reaction afforded complex [(C$_9$H$_7$)$_2$Yb$^{III}$(*i*Pr$_2$C$_6$H$_3$NCHCHNC$_6$H$_3$*i*Pr$_2^{\cdot-}$)] (**13**),[16] while the analogue bearing two methyl groups at the imino carbon atoms *i*Pr$_2$C$_6$H$_3$N=C(Me)C(Me)=NC$_6$H$_3$*i*Pr$_2$ (**23**) did not react with the same ytterbocene even after continuous heating in toluene at 60 °C.[38]

## 5. Reactions Resulting in Yb–C Bond Cleavage

Yb–C bond cleavage was observed in several reactions of ytterbocenes with diazadienes and iminopyridines and was always accompanied by oxidation of the ytterbium atom to the trivalent state. This type of reactivity has never been documented for the reactions with bipy or phen.

The reaction of [(C$_9$H$_7$)$_2$Yb(THF)$_2$] with diimine PhN=C(Me)–C(Me)=NPh in equimolar amounts was mentioned to afford a tetranuclear mixed-valent ytterbium complex [Yb$_2$(μ-η$^5$:η$^4$-C$_9$H$_7$)(η$^5$-C$_9$H$_7$)$_2${μ-η$^4$:η$^4$-PhNC(CH$_2$)=C(Me)NPh}]$_2$ (**21**) that resulted from reductive diimine coupling. The same reaction in 1:2 molar ratio resulted in formation of the dinuclear mixed-valent complex [Yb$_2$(μ-η$^5$:η$^4$-C$_9$H$_7$)(η$^5$-C$_9$H$_7$)$_2${μ-η$^4$:η$^4$-PhNC(Me)=C(Me)NPh}] (**25**) (Scheme 16).[35] The reaction occurred with partial cleavage of the Yb–C bonds and was accompanied by indene formation.

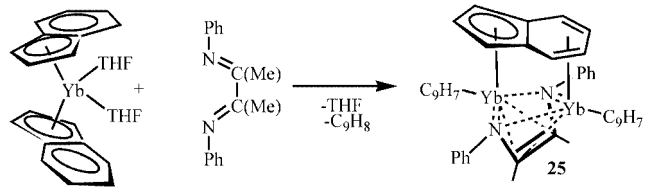


Scheme 16.

Complex **25** is paramagnetic. The effective magnetic moment found for **25** ($\mu_{eff}$ = 2.7 $\mu_B$ at 293 K) is intermediate between the average $\mu_{eff}$ value reported for Yb$^{III}$ derivatives (4.3 $\mu_B$) and that of diamagnetic Yb$^{II}$ compounds[10] and provides evidence of different oxidation states of ytterbium atoms. Assembling of the dinuclear species of **25** becomes possible due to the unusual bridging μ-η$^5$:η$^4$-coordination of the indenyl ligand and μ-η$^4$:η$^4$-coordination of the doubly reduced diimine ligand (Figure 13).

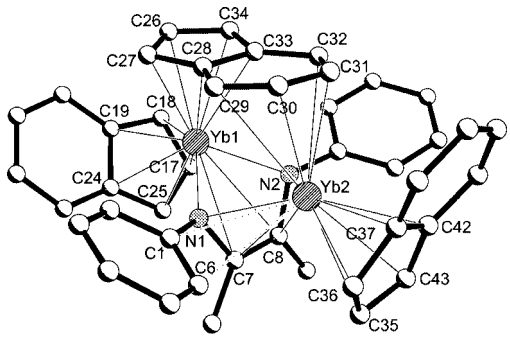


Figure 13. Molecular structure of complex [Yb$_2$(μ-η$^5$:η$^4$-C$_9$H$_7$)(η$^5$-C$_9$H$_7$)$_2${μ-η$^4$:η$^4$-PhNC(Me)=C(Me)NPh}] (**25**).

 © 2007 Wiley-VCH Verlag GmbH & Co. KGaA, Weinheim 

Cleavage of the Yb–C bonds occurred in the reactions of ytterbocenes containing bulky cyclopentadienyl ligands $[Cp^*_2Yb(THF)_2]$ {$Cp^* = C_5Me_5$ (**26**), $C_5Me_4H$ (**27**)} with 1,4-bis(2,6-diisopropylphenyl)-1,4-diaza-1,3-butadiene (**12**). The reductive reactivity of ytterbocenes in their reactions with **12** has been found to be strongly dependent on steric crowding in the coordination sphere of the ytterbium atom. Unlike the previously described reaction of complex $[(C_5MeH_4)_2Yb(THF)_2]$ which resulted in formation of the $Yb^{III}$ derivative with the radical anion of diimine $[(C_5MeH_4)_2Yb(iPr_2C_6H_3NCHCHNC_6H_3iPr_2)]$ (**14**), interactions of ytterbocenes **26** and **27** containing bulkier polymethylated cyclopentadienyl ligands with **12** under similar conditions resulted in elimination of one Cp* ring, oxidation of the ytterbium atom, and formation of the mono(cyclopentadienyl) $Yb^{III}$ complex $[(Cp^*)Yb^{III}(iPr_2C_6H_3NCH{=}CHNC_6H_3iPr_2^{2-})(THF)]$ {$Cp^* = C_5Me_5$ (**28**), $C_5Me_4H$ (**29**)} (Scheme 17).[17]

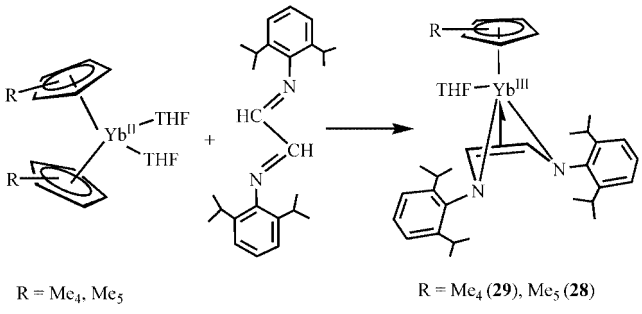


Scheme 17.

Consequently, depending on the steric crowding in the coordination sphere of the metal atom, ytterbocenes can act as both one- and two-electron reductants in their reactions with diimines. Obviously, complexes $[Cp^*_2Yb(THF)_2]$ demonstrate sterically induced reductive reactivity,[39] and double reduction of **12** becomes possible due to oxidation of the $Yb^{II}$ to $Yb^{III}$ and oxidation of one Cp* anion.

In complexes **28** and **29** the coordination sphere of the $Yb^{III}$ is set up by a $\eta^5$-coordinated Cp* ligand, the dianion of diazabutadiene which is bonded in $\eta^4$-fashion, and one THF molecule (Figures 14 and 15).

The geometry of the planar NCCN fragment in **28** and **29** is consistent with a dianionic character of the diimino ligand. The bonding situation within the diimino ligand and its coordination mode in **28** and **29** is different from those observed for the radical-anionic ligand in **14**. The C=C bond of a doubly reduced enediamido moiety NCCN also participates in metal–ligand bonding and is coordinated to the ytterbium atom in $\eta^2$-fashion. The Yb–N bond lengths in **28** and **29** are remarkably shorter than those in compound **14**, thus indicating a different type of metal–ligand bonding which may be considered in these complexes as $2\sigma{:}\pi$.

The investigation of the magnetic properties of **28** has been performed in a wide range of temperatures. Complex **28** is a very attractive object for investigation of redox tautomeric transformations since both forms {$[(C_5Me_5)Yb^{III}(DAD^{2-})(THF)]$ and $[(C_5Me_5)Yb^{II}(DAD^{\cdot-})(THF)]$} (DAD = $iPr_2C_6H_3NCH{=}CHNC_6H_3iPr_2$) contain a single paramagnetic center, and spin antiferromagnetic coupling can be excluded. The magnetic moment of **28** at 300 K is 4.41 $\mu_B$ which is close to the calculated free $Yb^{III}$ ion value for a $^2F_{7/2}$ multiplet.[24c] The magnetic moment of **28** at 2 K of 2.03 $\mu_B$ is too low for $Yb^{III}$ and is more compatible with the magnetic moments observed for organic radical anions with $S = ½$ (1.73 $\mu_B$). The field dependence of the magnetization performed at 2 K for sample **28** was satisfactory fitted with the Brilloun function with $S = ½$. However, the value of the saturation magnetization at 50 kOe of 1.21 $\mu_B$ is slightly higher than the expected value for a free radical with $S = ½$ and $g = 2.0023$. Such magnetic behavior may be attributed to temperature-induced redox tautomeric transformations of two forms of complex **28** (Scheme 18).

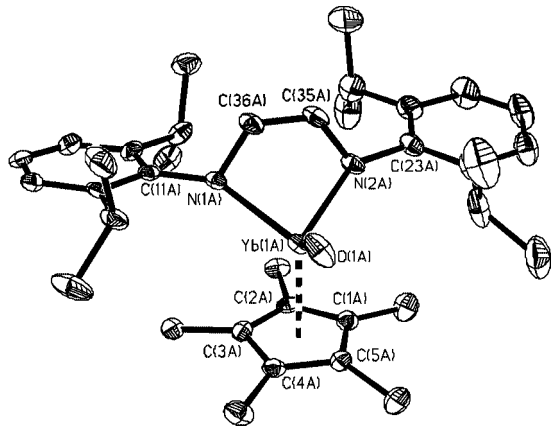


Figure 14. Molecular structure of complex $[(C_5Me_5)Yb^{III}(iPr_2C_6H_3NCH{=}CHNC_6H_3iPr_2^{2-})(THF)]$ (**28**). The methylene groups of the THF molecule are omitted.

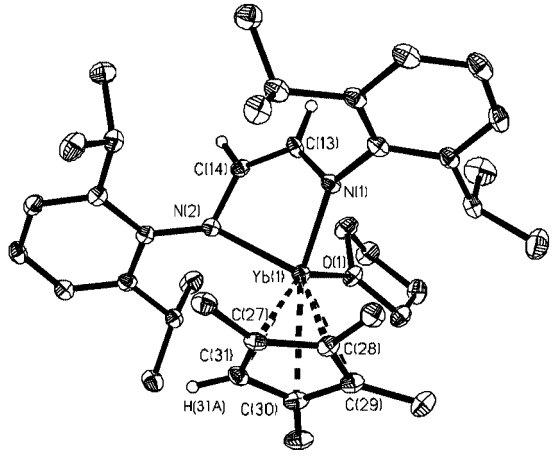


Figure 15. Molecular structure of complex $[(C_5Me_4H)Yb^{III}(iPr_2C_6H_3NCH{=}CHNC_6H_3iPr_2^{2-})(THF)]$ (**29**).

 © 2007 Wiley-VCH Verlag GmbH & Co. KGaA, Weinheim 

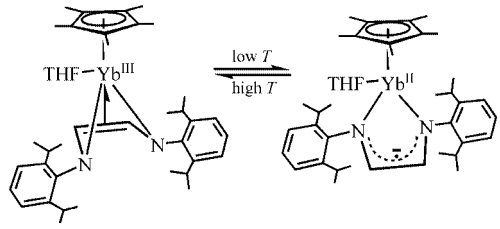


Scheme 18.

To the best of our knowledge, complexes **28** and **29** are the first examples of a terminal $\eta^4$-coordination mode of the diimine dianion to a lanthanide atom. In the organolanthanide complexes previously reported, dianionic diimino ligands adopted a μ-bridging coordination mode bonding two homo- or heterometallic centers (Scheme 19) in **30**, **31**,[7a,7g] **32**,[40] **33**.[41]

Replacement of the indenyl ligand by a bulkier fluorenyl analogue in a ytterbocene molecule switched the pathway of the reaction with *N*-(2,6-diisopropylphenyl)imino-2-pyridine (**22**) from C–C bond formation to Yb–C bond cleavage.[37] The reaction of the complex $[(C_{13}H_9)_2Yb(THF)_2]$ with **22** under similar conditions resulted in cleavage of all $\eta^5$-Yb–$C_{13}H_9$ bonds, oxidation of the Yb atom to the trivalent state, and formation of the tris(iminopyridine) compound $[\{2,6\text{-}i\text{Pr}_2C_6H_5NCH(C_5H_5N)^{-\bullet}\}_3Yb^{III}]$ (**34**) (Scheme 20).

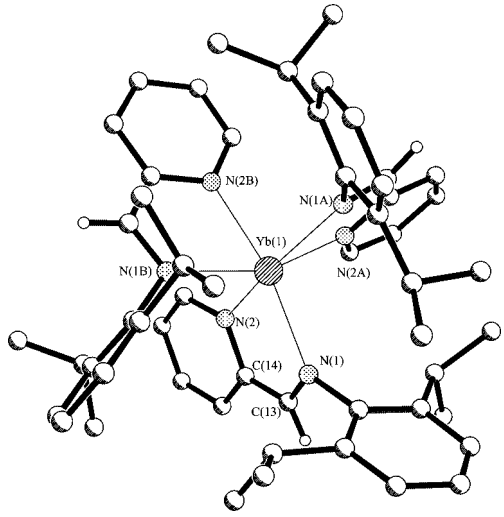


Figure 16. Molecular structure of complex $[\{2,6\text{-}i\text{Pr}_2C_6H_5\text{-}NCH(C_5H_5N)^{-\bullet}\}_3Yb^{III}]$ (**34**).

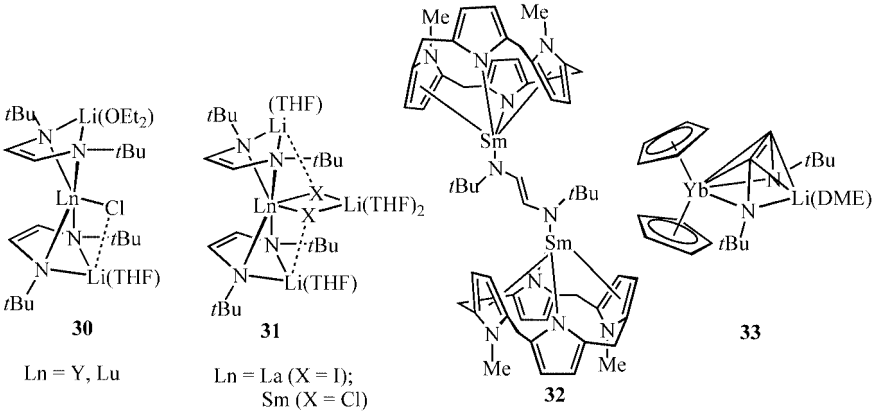


Scheme 19.

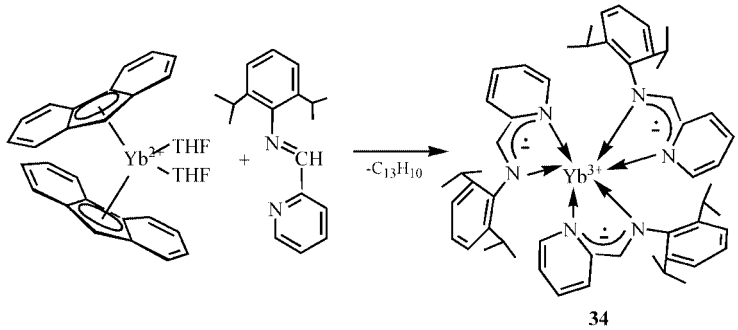


Scheme 20.

 © 2007 Wiley-VCH Verlag GmbH & Co. KGaA, Weinheim 

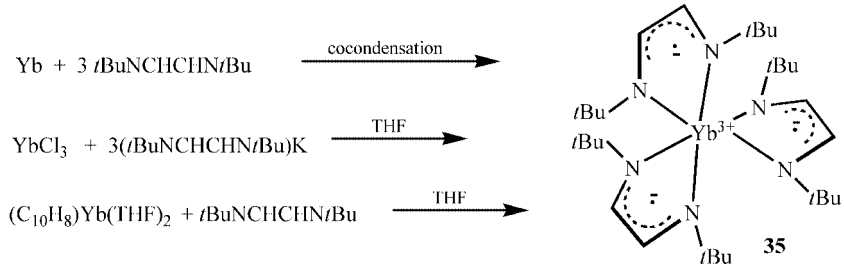


Scheme 21.

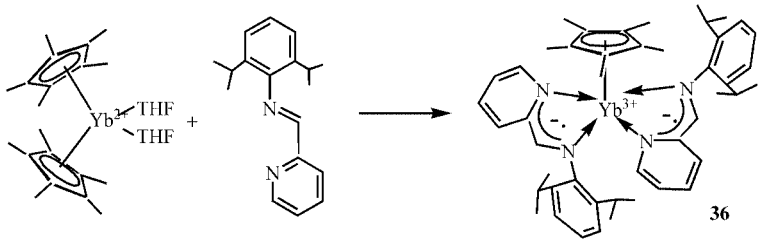


Scheme 22.

The magnetic moment of complex **34** (3.74 $\mu_B$, 293 K) gives evidence of the trivalent oxidation state of the ytterbium atom. The $Yb^{III}$ atom in **34** is coordinated by three chelating iminopyridine ligands bound by two nitrogen atoms (Figure 16).

The Yb–N bond lengths in **34** are comparable to the appropriate distances in $Yb^{III}$ complexes with radical-anionic diimine ligands. The bonding situation within the planar diimino fragment is consistent with the radical-anionic form of the iminopyridine ligand. Previously we synthesized a related tris(diazabutadiene) complex of trivalent ytterbium [(*t*BuNCHCHN*t*Bu)$_3$Yb] (**35**) in which the $Yb^{III}$ atom is coordinated by three radical anions of diazabutadiene (Scheme 21).[7f]

The nature as well as the coordination environment of the ytterbium atom in both complexes **34** and **35** is very similar; nevertheless, the value of the magnetic moment of **35** (5.78 $\mu_B$, 293 K) is much higher than that of **34** (3.74 $\mu_B$, 293 K). The low-temperature magnetic investigation of complex **35** suggested the existence of temperature-induced redox tautomeric transformations for this compound.[7f]

'Complex [$(C_5Me_5)_2Yb(THF)_2$] containing the pentamethylcyclopentadienyl ligand, which has the highest steric demand in the series of the studied compounds, reacted with *N*-2,6-diisopropylphenylimino-2-pyridine (**22**) in a different way. The reaction of [$(C_5Me_5)_2Yb(THF)_2$] with a twofold molar excess of **22** under similar conditions occurred with abstraction of one Cp* ring, oxidation of the ytterbium atom, and afforded a novel half-sandwich complex of trivalent ytterbium [$(C_5Me_5)Yb^{III}${2,6-*i*Pr$_2$C$_6$H$_3$NCH(C$_5$H$_5$N)$^{-\cdot}$}$_2$] (**36**) (Scheme 22).[37] The value of the magnetic moment of complex **36** (3.71 $\mu_B$, 293 K) is consistent with the trivalent oxidation state of the ytterbium atom.[10] In complex **36** the ytterbium atom is coordinated by one $C_5Me_5$ ligand in $\eta^5$-fashion and two iminopyridine radical anions. Both chelating iminopyridine radical anions in **36** are bound to the ytterbium atom through two coordination Yb–N bonds (Figure 17). Complex **36** is the first example of a half-sandwich lanthanide compound containing two radical-anionic ligands.

## 6. Conclusions

The pathway of reactions of ytterbocenes with diimines is strongly influenced by the steric crowding in the coordination sphere of the metal atom created by both π-aromatic ligands and substituents at the nitrogen atoms of the diimine molecule. Moreover, coordination capacities and a tendency of π-aromatic ligands coordinated to the ytterbium atom for haptotropic rearrangements ($\eta^5$–$\eta^3$–$\eta^1$) play a crucial role in the modification of the reactivity of ytterbocenes toward diimines. These reactions may occur with oxidation of the ytterbium atom as well as with retention of its oxidation state. C–C bond formation, C–H bond activation, C=N bond insertion, and oxidative Yb–C bond cleavage processes were documented for reactions of ytterbocenes with diimines. Steric overcrowding of the coordination sphere of the ytterbium atom can induce "extra" reducing ability of ytterbocenes and allow them to act not only as one- but also as two-electron reductants with respect to diimines. Fine tuning of the Yb–N bond length in complexes [$Cp_2Yb^{III}(L^{-\cdot})$] (L = diimine) by means of regulation of both steric and electronic properties of Cp and L ligands provides control of intramolecular metal–ligand electron transfer. Complexes [$Cp_2Yb^{III}(L^{-\cdot})$] and [$CpYb^{III}(L^{2-})$-(THF)] are promising objects for the investigation of spin

 © 2007 Wiley-VCH Verlag GmbH & Co. KGaA, Weinheim 

coupling and temperature-induced redox tautomerism which provide a ground for exploring bonding models and electronic structure of compounds of f-transition metals.

## Acknowledgments

This work was supported by the Russian Foundation for Basic Research (Grant No. 05-03-32390), Program of the Presidium of the Russian Academy of Science (RAS), and RAS Chemistry and Material Science Division. A. T. thanks the Russian Foundation for science support.

[1] G. van Koten, K. Vrieze, *Adv. Organomet. Chem.* **1982**, *21*, 151–239.
[2] J. P. Britovsek, V. C. Gibson, D. F. Wass, *Angew. Chem. Int. Ed.* **1999**, *38*, 428–447.
[3] a) K. Vrieze, *J. Organomet. Chem.* **1986**, *300*, 307–326; b) H. Bock, H. tom Dieck, *Chem. Ber.* **1967**, *100*, 228–246; c) J. Scholz, B. Richter, R. Goddar, K. Krueger, *Chem. Ber.* **1993**, *126*, 57–61.
[4] H. tom Dieck, I. W. Renk, *Chem. Ber.* **1971**, *104*, 110–130.
[5] a) M. G. Gardner, G. R. Hanson, F. C. Lee, C. L. Raston, *Inorg. Chem.* **1994**, *33*, 2456–2461; b) F. G. N. Cloke, C. I. Dalby, M. J. Henderson, P. B. Hitchcock, C. H. L. Kennard, R. N. Lamb, C. L. Raston, *J. Chem. Soc. Chem. Commun.* **1990**, 1394–1396; c) K.-H. Thiele, V. Lorenz, G. Thiele, P. Zoennchen, J. Scholz, *Angew. Chem.* **1994**, *106*, 1461–1463; *Angew. Chem. Int. Ed. Engl.* **1994**, *33*, 1372–1373.
[6] a) H. tom Dieck, J. Rieger, G. Fendesack, *Inorg. Chim. Acta* **1990**, *177*, 191–197; b) W. A. Hermann, M. Denk, W. Scherer, F.-R. Klingan, *J. Organomet. Chem.* **1993**, *444*, C21–C24; c) B. Richter, J. Scholz, J. Sieler, K.-H. Thiele, *Angew. Chem.* **1995**, *107*, 2865–2867; *Angew. Chem. Int. Ed. Engl.* **1995**, *34*, 2867–2869; d) F. G. N. Cloke, G. R. Hanson, M. J. Henderson, P. B. Hitchcock, C. L. Raston, *J. Chem. Soc. Chem. Commun.* **1989**, 1002–1003; e) J. Scholz, M. Dlikan, D. Stroehl, A. Dietrich, H. Schumann, K.-H. Thiele, *Chem. Ber.* **1990**, *123*, 2279–2285; f) J. Scholz, A. Dietrich, H. Schumann, K.-H. Thiele, *Chem. Ber.* **1991**, *124*, 1035–1039.
[7] a) F. G. N. Cloke, H. C. de Lemos, A. A. Sameh, *J. Chem. Soc. Chem. Commun.* **1986**, 1344–1345; b) F. G. N. Cloke, *Chem. Soc. Rev.* **1993**, *22*, 17–21; c) A. Recknagel, M. Noltemeyer, F. T. Edelmann, *J. Organomet. Chem.* **1991**, *410*, 53–61; d) A. Scholz, K.-H. Thiele, J. Scholz, R. Weimann, *J. Organomet. Chem.* **1995**, *501*, 195–200; e) P. Poremba, F. T. Edelmann, *J. Organomet. Chem.* **1997**, *549*, 101–104; f) M. N. Bochkarev, A. A. Trifonov, F. G. N. Cloke, C. I. Dalby, P. T. Matsunaga, R. A. Andersen, H. Schumann, J. Loebel, H. Hemling, *J. Organomet. Chem.* **1995**, *486*, 177–182; g) H. Goerls, B. Neumueller, A. Scholz, J. Scholz, *Angew. Chem.* **1995**, *107*, 372–375; *Angew. Chem. Int. Ed. Engl.* **1995**, *34*, 673–676; h) J. Scholz, H. Goerls, H. Schumann, R. Weimann, *Organometallics* **2001**, *20*, 4394–4402.
[8] J. Reinhold, R. Benedix, P. Birner, H. Hennig, *Inorg. Chim. Acta* **1979**, *33*, 209–213.
[9] a) L. R. Morss, *Chem. Rev.* **1976**, *76*, 827–841; b) R. G. Finke, S. R. Keenan, D. A. Shirardi, P. L. Watson, *Organometallics* **1986**, *5*, 598–601; c) A. M. Bond, G. B. Deacon, R. H. Newnham, *Organometallics* **1986**, *5*, 2312–2316.
[10] W. J. Evans, M. A. Hozbor, *J. Organomet. Chem.* **1987**, *326*, 299–306.
[11] a) J.-C. G. Bünzli, C. Piguet, *Chem. Soc. Rev.* **2005**, *34*, 1048–1077; b) A. Døssing, *Eur. J. Inorg. Chem.* **2005**, 1425–1434; c) T. Gunnlaugsson, J. P. Leonard, *Chem. Commun.* **2005**, 3114–3131; d) K. Kuriki, Y. Koike, *Chem. Rev.* **2002**, *102*, 2347–2356; e) J. Kido, Y. Okamoto, *Chem. Rev.* **2002**, *102*, 2357–2368.
[12] A. A. Trifonov, E. N. Kirillov, M. N. Bochkarev, H. Schumann, S. Muehle, *Russ. Chem. Bull.* **1999**, *48*, 382–384.
[13] A. A. Trifonov, Yu. A. Kurskii, M. N. Bochkarev, S. Muehle, S. Dechert, H. Schumann, *Russ. Chem. Bull.* **2003**, *52*, 601–606.
[14] A. A. Trifonov, E. A. Fedorova, V. N. Ikorskii, S. Dechert, H. Schumann, M. N. Bochkarev, *Eur. J. Inorg. Chem.* **2005**, 2812–2818.
[15] A. A. Trifonov, E. N. Kirillov, S. Dechert, H. Schumann, M. N. Bochkarev, *Eur. J. Inorg. Chem.* **2001**, 2509–2514.
[16] A. A. Trifonov, E. A. Fedorova, G. K. Fukin, V. N. Ikorskii, Yu. A. Kurskii, S. Dechert, H. Schumann, M. N. Bochkarev, *Russ. Chem. Bull.* **2004**, *53*, 2736–2743.
[17] A. A. Trifonov, I. A. Borovkov, E. A. Fedorova, G. K. Fukin, J. Larionova, N. O. Druzhkov, V. K. Cherkasov, *Chem. Eur. J.*, DOI: 10.1002/chem.200601481.
[18] a) G. B. Deacon, P. I. MacKinnon, T. W. Hambley, J. C. Taylor, *J. Organomet. Chem.* **1983**, *259*, 91–97; b) T. D. Tilley, R. A. Andersen, B. Spencer, A. Zalkin, *Inorg. Chem.* **1982**, *21*, 2647–2649; c) A. V. Khvostov, B. M. Bulychev, V. K. Belsky, A. I. Sizov, *J. Organomet. Chem.* **1999**, *584*, 164–170; d) J. Z. Jin, Z. S. Jin, W. Q. Chen, Y. Zhang, *Chinese J. Struct. Chem. (Jiegou Huaxue)* **1993**, *12*, 241–245.
[19] R. D. Schannon, *Acta Crystallogr., Sect. A* **1976**, *32*, 751–767.
[20] C. J. M. Huige, A. L. Spek, J. L. de Boer, *Acta Crystallogr., Sect. C* **1985**, *41*, 113–116.
[21] T. V. Laine, M. Klinga, A. Maaninen, E. Aitola, M. Leskelä, *Acta Chem. Scand.* **1999**, *53*, 968–973.
[22] F. A. Allen, O. Konnard, D. G. Watson, L. Brammer, G. Orpen, R. Taylor, *J. Chem. Soc. Perkin Trans. 1* **1987**, 1–19.
[23] a) D. F. Evans, *J. Chem. Soc.* **1959**, 2003–2005; b) D. F. Evans, G. V. Fazakerley, R. F. Phillips, *J. Chem. Soc. A* **1971**, 1931–1934.
[24] a) M. Gerloch, E. C. Constable, *Transition Metal Chemistry*, VCH, Weinheim, **1995**; b) E. A. Boudreaux, L. N. Mulay, *Theory and Applications of Molecular Paramagnetism*, Wiley Interscience, New York, **1976**; c) R. D. L. Carlin, *Magnetochemistry*, Springer-Verlag, Berlin, **1986**.
[25] A. Caneschi, A. Dei, D. Gatteschi, S. Poussereau, L. Sorace, *Dalton Trans.* **2004**, 1048–1055.
[26] K. L. Trojan, J. L. Kendall, K. D. Kepler, W. E. Hatfield, *Inorg. Chim. Acta* **1992**, *198–200*, 795–803.
[27] a) W. J. Evans, T. A. Ulibarri, J. W. Ziller, *J. Am. Chem. Soc.* **1990**, *112*, 219–223; b) W. J. Evans, S. L. Gonzales, J. W. Ziller, *J. Am. Chem. Soc.* **1994**, *116*, 2600–2608.
[28] J. A. Moore, A. H. Cowley, J. C. Gordon, *Organometallics* **2006**, *25*, 5207–5209.
[29] M. N. Chisholm, J. C. Huffman, I. P. Rothwell, *J. Am. Chem. Soc.* **1981**, *103*, 4945–4947.
[30] M. Schultz, J. M. Boncella, D. J. Berg, T. Don Tilley, R. A. Andersen, *Organometallics* **2002**, *21*, 460–472.
[31] M. D. Walter, M. Schultz, R. A. Andersen, *New J. Chem.* **2006**, *30*, 238–246.
[32] M. D. Walter, D. J. Berg, R. A. Andersen, *Organometallics* **2006**, *25*, 3228–3237.
[33] R. E. Da Re, C. J. Kuehl, M. G. Brown, R. C. Rocha, E. D. Bauer, K. D. John, D. E. Morris, A. P. Shreve, J. L. Sarrao, *Inorg. Chem.* **2003**, *42*, 5551–5559.
[34] A. A. Trifonov, E. A. Fedorova, G. K. Fukin, N. O. Druzhkov, M. N. Bochkarev, *Angew. Chem. Int. Ed.* **2004**, *43*, 5045–5048; *Angew. Chem.* **2004**, *116*, 5155–5158.
[35] A. A. Trifonov, E. A. Fedorova, G. K. Fukin, E. V. Baranov, N. O. Druzhkov, M. N. Bochkarev, *Chem. Eur. J.* **2006**, *12*, 2752–2757.
[36] a) K. Jonas, W. Rüsseler, C. Krüger, E. Raabe, *Angew. Chem. Int. Ed. Engl.* **1986**, *25*, 928–929; b) M. I. Bruce, B. W. Skelton, A. H. White, N. N. Zaitseva, *Inorg. Chem. Commun.* **1999**, *2*, 17–20; c) S. Sun, C. A. Dullaghan, G. B. Carpenter, A. L. Ri-

 © 2007 Wiley-VCH Verlag GmbH & Co. KGaA, Weinheim 

eger, P. H. Rieger, D. A. Sweigart, *Angew. Chem. Int. Ed. Engl.* **1995**, *34*, 2540–2542; d) A. Eisenstadt, F. Frolow, A. Efraty, *J. Chem. Soc. Chem. Commun.* **1982**, 642–644.
[37] A. A. Trifonov, E. A. Fedorova, I. A. Borovkov, G. K. Fukin, E. V. Baranov, J. Larionova, N. O. Druzhkov, *Organometallics*, DOI: 10.1021/om070073s.
[38] I. A. Borovkov, A. A. Trifonov, unpublished results.
[39] a) W. J. Evans, B. L. Davis, *Chem. Rev.* **2002**, *102*, 2119–2136; b) W. J. Evans, *J. Organomet. Chem.* **2002**, *647*, 2–11.
[40] J. Wang, R. I. J. Amos, A. S. P. Frey, M. Gardiner, M. Hilder, P. C. Junk, *Organometallics* **2005**, *24*, 2259–2261.
[41] A. A. Trifonov, L. N. Zakharov, M. N. Bochkarev, Yu. T. Struchkov, *Russ. Chem. Bull.* **1994**, *43*, 145–148.

Received: December 19, 2006
Published Online: June 12, 2007

 © 2007 Wiley-VCH Verlag GmbH & Co. KGaA, Weinheim 

DOI: 10.1002/ejic.200700444

# Electron Density and Bonding in Borates: An Experimental Study of Tetrabutylammonium Heptahydridohexaborate, $[(C_4H_9)_4N][B_6H_7]$

**Diana Förster,[a] Stephan Scheins,[a] Peter Luger,[a] Dieter Lentz,*[b] and Wilhelm Preetz[c]**

**Keywords:** Charge density / Borates / Topological analysis

An experimental study of a high-resolution X-ray data set of the *closo*-boranate $[B_6H_7]^-$ was performed. The charge density distribution and its topological properties were analyzed according to the "Atoms in Molecules" theory of R. W. Bader. The $[B_6H_7]^-$ anion forms an octahedral boron cage with one of the six faces capped by an additional proton. The unusual bonding situation of the threefold capping hydrogen atom is of special interest and is discussed in detail. Three new B–H bonds form, while the B–B bonds in the capped boron triangle vanish. The reactivity of the $[B_6H_7]^-$ anion is visualized by the electrostatic potential.

(© Wiley-VCH Verlag GmbH & Co. KGaA, 69451 Weinheim, Germany, 2007)

## Results and Discussion

The very stable $[B_nH_n]^{2-}$ anions form *closo* clusters with spherical aromaticity.[1,2] $[B_6H_6]^{2-}$, $[B_7H_7]^{2-}$, $[B_8H_8]^{2-}$ and $[B_{10}H_{10}]^{2-}$ can be protonated forming stable monoanions.[3,4] The structures of $[B_6H_7]^-$ and $[B_{10}H_{11}]^-$ have been determined by X-ray diffraction[3] and nonempirical calculations.[5–7] During our experimental charge density studies of compounds with multi-center two-electron bonds like $B_2H_6$[8] we became interested in the charge-density distribution $\rho(\mathbf{r})$ and its topological analysis of $[B_6H_6]^{2-}$ and $[B_6H_7]^-$.[9] Herein, we report on the results of a study based on a high-resolution low-temperature X-ray diffraction experiment of $[Bu_4N]^+[B_6H_7]^-$, where the $[B_6H_7]^-$ anion crystallizes with one tetrabutylammonium cation in the asymmetric unit. Figure 1 shows the structure of the $[B_6H_7]^-$ anion and its numbering scheme.[10]

A multipole refinement based on the Hansen–Coppens formalism[14] and a topological analysis were performed using the program package XD.[15] A known problem in X-ray structure solution and charge-density analysis is the determination of the position of the hydrogen atoms. Thus, in this study the terminal hydrogen atoms $H_{term}$ of the borate were fixed at neutron distances, taken from neutron diffraction data of decaborane.[16] Mebel et al. published a theoretical study of the structure and migrational non-rigidity of the $[B_6H_7]^-$ anion (Gaussian80, SCF/4-31G).[5] They found five stable states whose total energy levels are very close together. The global minimum has $C_{3v}$ symmetry. A geometry optimization of the title anion was performed (Gaussian98,[17] B3LYP/6-311G**), starting at experimental geometry which converged with a $C_s$ symmetry as depicted in Figure 2. Therefore, the anion packed with

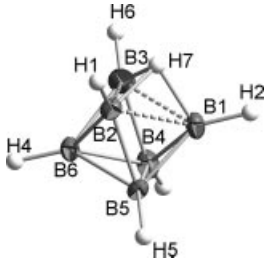


Figure 1. The structure and labeling scheme of the $[B_6H_7]^-$ anion; Diamond[11] drawing.

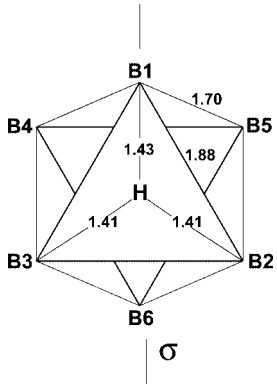


Figure 2. Symmetry scheme of the $[B_6H_7]^-$ ion according to the geometry optimization. View from above the capped boron triangle.

[a] Institut für Chemie und Biochemie/Kristallographie der Freien Universität Berlin,
Fabeckstr. 36a, 14195 Berlin, Germany
[b] Institut für Chemie und Biochemie/Anorganische Chemie der Freien Universität Berlin,
Fabeckstr. 34–36, 14195 Berlin, Germany
Fax: +49-30-838-53310
E-mail: lentz@chemie.fu-berlin.de
[c] Institut für Anorganische Chemie, Christian-Albrechts-Universität,
Olshausenstr. 40 (Otto-Hahn-Platz 6/7), 24098 Kiel, Germany

 © 2007 Wiley-VCH Verlag GmbH & Co. KGaA, Weinheim 

$[Bu_4N]^+$ in $P2_1/n$ presents a local energy minimum. The B–$H_{term}$ distances obtained by ab initio calculations correspond exactly to neutron values of $B_{10}D_{14}$, while the theoretical optimized B–B distances differ only in the fourth decimal place from the experimental results of $[B_6H_7]^-$. Thus, it seemed to be justified to fix the bond lengths to the capping hydrogen atom, B–H7 to the corresponding values of the ab initio calculation (at 1.41 Å from B2 and B3, and 1.43 Å from B1, see Figure 2) for the multipole refinement.

The topological analysis of the charge density was carried out using the formalism of the theory of "atoms in molecules" (AIM) developed by Bader.[12,13] The values of the electron density $\rho_{bcp}$ and the Laplacian $\nabla^2\rho_{bcp}$ at the bond critical points (bcp) enable a quantitative description of the bonds. They are given in Table 1. The topological parameters of the capping bonds B–$H_{cap}$ and the region they influence reveal several interesting aspects.

Bond critical points can be found on all B–B contacts except those capped by the hydrogen atom. Thus, the capping of the triangular face results in the loss of three covalent bonds [distances B1–B2 1.867(1) Å, B2–B3 1.863(1) Å and B3–B1 1.874(1) Å], so that four-membered rings are formed by H7 and three boron atoms, e.g. B1–H7–B3–B4, characterized by ring critical points (rcp) located in the center. The experimentally derived bond topological properties are in very good agreement with the theoretical ones. For the B–B bonds the mean deviation for $\rho_{bcp}$ and $\nabla^2\rho_{bcp}$ between theory and experiment is 0.05(2) e Å$^{-3}$ and 0.5(3) e Å$^{-5}$, even for the ring critical points the deviation is small, 0.05(1) e Å$^{-3}$ and 0.17(2) e Å$^{-5}$. In case of the B–H bonds the differences between theory and experiment are slightly higher. For terminal B–$H_{term}$ bonds it is 0.05(3) e Å$^{-3}$ and 7.0(8) e Å$^{-5}$, while the capping B–$H_{cap}$ bonds differ by 0.10(2) e Å$^{-3}$ in $\rho_{bcp}$ and 1.6(8) e Å$^{-5}$ in the Laplacian values.

Figure 3 shows the contour line Laplacian diagram of the capped boron plane B1–B2–B3 (left) compared to the plane spanned by the atoms B4–B5–B6 (right). In contrast to the capped plane the uncapped one shows shared interaction on the B–B bonds, indicated by a charge concentration on the B–B bond path, bordered furthermore by the zero Laplace line (black). As a consequence of the missing bcp values, the coordination number of B1, B2 and B3 is 4, while B4, B5 and B6 are bonded to five neighboring atoms.

Table 1. Topological properties of $[B_6H_7]^-$.

| Bond | Bond length $r$ [Å] | $\rho$ [e/Å$^3$] exp. | theor. | $\nabla^2\rho$ [e/Å$^5$] exp. | theor. |
|---|---|---|---|---|---|
| Triangle B–B bonds; 2e-3c bonds | | | | | |
| B1–B4 | 1.7066(6) | 0.93(2) | 0.90 | –4.3(2) | –3.9 |
| B1–B5 | 1.7037(7) | 0.93(2) | 0.90 | –3.9(3) | –4.1 |
| B2–B5 | 1.7071(6) | 0.97(2) | 0.90 | –4.9(2) | –3.9 |
| B2–B6 | 1.7081(6) | 0.92(3) | 0.89 | –3.6(4) | –3.8 |
| B3–B4 | 1.7112(9) | 1.00(3) | 0.90 | –4.6(3) | –3.9 |
| B3–B6 | 1.7098(7) | 0.95(3) | 0.89 | –4.5(3) | –3.8 |
| B4–B5 | 1.7284(7) | 0.90(3) | 0.86 | –3.5(4) | –2.8 |
| B4–B6 | 1.7276(6) | 0.94(3) | 0.86 | –3.8(3) | –2.9 |
| B5–B6 | 1.7224(6) | 0.91(4) | 0.87 | –3.7(3) | –3.0 |
| av. all[a] | 1.714(9) | 0.94(3) | 0.89(2) | –4.1(5) | –3.6(5) |
| Terminal B–$H_{term}$ bonds; 2e-2c bonds | | | | | |
| B1–H1 | 1.19 | 1.13(1) | 1.15 | –9.8(2) | –3.5 |
| B2–H2 | 1.19 | 1.16(1) | 1.15 | –9.6(2) | –3.5 |
| B3–H3 | 1.19 | 1.16(1) | 1.15 | –9.5(2) | –3.4 |
| B4–H4 | 1.19 | 1.21(2) | 1.13 | –10.4(2) | –2.6 |
| B5–H5 | 1.19 | 1.21(2) | 1.13 | –10.5(2) | –2.6 |
| B6–H6 | 1.19 | 1.19(2) | 1.13 | –10.4(2) | –2.6 |
| av. all[a] | | 1.18(6) | 1.14(1) | –10.0(4) | –3(4) |
| Capping B–$H_{cap}$ bonds; 2e-4c bonds | | | | | |
| B1–H7 | 1.43 | 0.70(1) | 0.63 | 0.2(3) | –0.2 |
| B2–H7 | 1.41 | 0.75(2) | 0.63 | –2.5(3) | –0.3 |
| B3–H7 | 1.41 | 0.75(1) | 0.63 | –2.5(2) | –0.3 |
| av. all[a] | | 0.73(2) | 0.63(0) | –1.7(10) | –0.3(1) |
| Ring critical points in the capped B(1)–B(2)–B(3) plane | | | | | |
| B1–H7–B2–B5 | | 0.66(2) | 0.61 | 0.8(2) | 0.8 |
| B1–H7–B3–B4 | | 0.64(2) | 0.60 | 1.3(2) | 0.8 |
| B2–H7–B3–B6 | | 0.68(2) | 0.61 | 0.7(2) | 0.7 |

[a] av. is the average of the values in the column.

Figure 4 shows the bending of the bond paths which is most pronounced for the B–$H_{cap}$ bonds curved into the interior of the $B_6$ cage (see Figure 4, right). This results in longer bond-path lengths in comparison to the atomic distances, which is 0.002 Å for the B–B bonds and up to 0.2 Å for the B–$H_{cap}$ bonds.

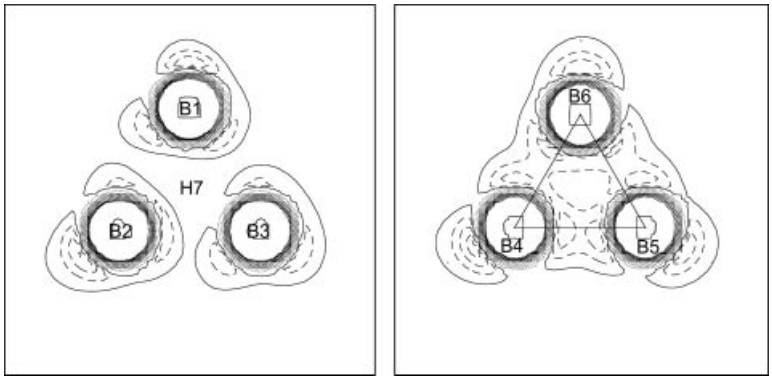


Figure 3. Contour line diagram of the Laplacian (dotted lines positive values, dashed lines negative, solid line zero Laplacian) of the capped B1–B2–B3 plane (left) and the uncapped B4–B5–B6 plane on the opposite side of the molecule (right).

 © 2007 Wiley-VCH Verlag GmbH & Co. KGaA, Weinheim 

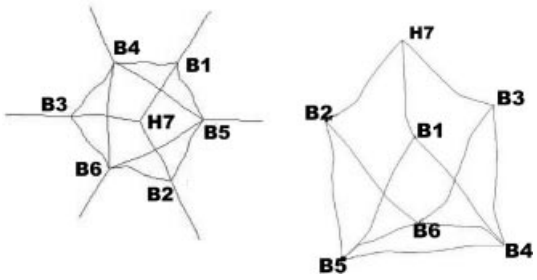


Figure 4. Bond paths of the title compound. Left: View from above the capped boron triangle, capping hydrogen atom in the center of the figure. Right: Side view, capping hydrogen atom on top of the figure.

The electrostatic potential (esp) was calculated by using the method of Su and Coppens[18] on the basis of experimental data. This calculation considers a $[B_6H_7]^-$ ion extracted from the crystal but still containing the polarization effects induced by intermolecular interactions. Figure 5 displays the electrostatic potential, mapped onto the isoelectron-density surface at $\rho(\mathbf{r}) = 0.5 e Å^{-3}$. The positive potential (red) is concentrated around the boron atoms and the negative potential around the terminal hydrogen atoms. There is a gradient of polarization between the hydrogen atoms. Thereby the terminal hydrogen atoms of the capped triangle are less polarized (green) than the hydrogen atoms on the opposite site of the molecule (blue). The remarkable effect of the capping H7 atom is also shown in the esp value. It shows a positive potential (red), indicating the reactivity of this hydrogen atom towards nucleophilic attack. $[B_6H_7]^-$ is very unstable and reacts in basic solution immediately by emitting a proton to form $[B_6H_6]^{2-}$.

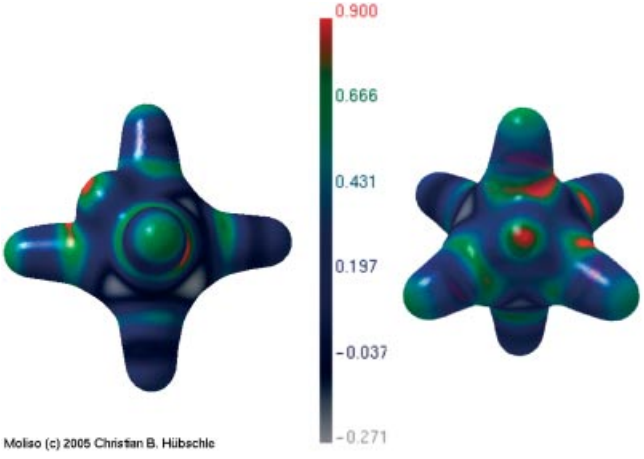


Figure 5. Electrostatic potential of the title compound; generated with the MolIso program.[19] Left: View from above the capped boron triangle, capping hydrogen atom in the center of the figure. Right: View from a terminal hydrogen atom of the non-capped triangle, capping hydrogen atom on top of the figure.

## Acknowledgments

This work was supported by the Deutsche Forschungsgemeinschaft, DFG, (SPP 1178, grant Lu 222/28-1 and Le 423/13-1).

[1] R. B. King, *Chem. Rev.* **2001**, *101*, 1119.
[2] Z. Chen, R. B. King, *Chem. Rev.* **2005**, *105*, 3613.
[3] S. G. Shore, E. J. M. Hamilton, A. N. Bridges, J. Bausch, J. A. Krause-Bauer, D. Dou, J. Liu, S. Liu, H. Hall, E. A. Meyers, K. E. Vermillion, *Inorg. Chem.* **2003**, *42*, 1175; W. Preetz, A. Heinrich, J. Thiesing, *Z. Naturforsch., Teil B* **1988**, *50*, 623; P. A. Wegner, D. M. Adams, F. J. Callabretta, L. T. Spada, R. G. Unger, *J. Am. Chem. Soc.* **1973**, *95*, 7513; D. M. Vinitskii, V. L. Lagun, K. A. Solntsev, N. T. Kuznetsov, I. Yu. Kuznetsov, *Koord. Khim.* **1985**, *11*, 1504; V. I. Privalov, V. P. Tarasov, M. A. Meladze, D. M. Vinitskii, K. A. Solntsev, Yu. A. Buslaev, N. T. Kuznetsov, *Russ. J. Inorg. Chem. (Engl. Transl.)* **1986**, *31*, 633; V. N. Mustyasta, N. A. Votinova, K. A. Solntsev, N. T. Kuznetsov, *Dokl. Chem. Proc. Sov. Acad. Sci. (Engl. Transl.)* **1988**, *301*, 245; J. Baurmeister, A. Franken, W. Preetz, *Z. Naturforsch., Teil B* **1995**, *50*, 623.
[4] N. T. Kuznetsov, K. A. Solntsev, *Chemistry of Inorganic Hydrides* (Ed.: N. T. Kuznetsov), Nauka Publ., Moskow, **1990**, p. 5.
[5] A. M. Mebel, O. P. Charkin, I. Yu. Kuznetsov, K. A. Solntsev, N. T. Kuznetsov, *Russ. J. Inorg. Chem. (Engl. Transl.)* **1988**, *33*, 958.
[6] A. M. Mebel, O. P. Charkin, K. A. Solntsev, N. T. Kuznetsov, *Russ. J. Inorg. Chem. (Engl. Transl.)* **1988**, *33*, 1292; A. M. Mebel, O. P. Charkin, K. A. Solntsev, N. T. Kuznetsov, *Chemistry of Inorganic Hydrides* (Ed.: N. T. Kuznetsov), Nauka Publ., Moskow, **1990**, p. 43; A. M. Mebel, O. P. Charkin, I. Yu. Kuznetsov, K. A. Solntsev, N. T. Kuznetsov, *Russ. J. Inorg. Chem. (Engl. Transl.)* **1989**, *34*, 156.
[7] M. L. McKee, M. Bühl, O. P. Charkin, P. v. R. Schleyer, *Inorg. Chem.* **1993**, *32*, 4549; M. Bühl, A. M. Mebel, O. P. Charkin, P. v. R. Schleyer, *Inorg. Chem.* **1992**, *31*, 3769; A. M. Mebel, O. P. Charkin, M. Bühl, P. v. R. Schleyer, *Inorg. Chem.* **1993**, *32*, 463; A. M. Mebel, O. P. Charkin, P. v. R. Schleyer, *Inorg. Chem.* **1993**, *32*, 469.
[8] C. B. Hübschle, M. Messerschmidt, D. Lentz, P. Luger, *Z. Anorg. Allg. Chem.* **2004**, *630*, 1313.
[9] W. Preetz, G. Peters, *Eur. J. Inorg. Chem.* **1999**, *11*, 1831.
[10] Crystals of $[Bu_4N][B_6H_7]$ were obtained by crystallization from methanol. Empirical formula: $[(C_4H_9)_4N][B_6H_7]$; formula mass [g mol$^{-1}$]: 314.37; crystal system: monoclinic; space group: $P2_1/n$ (no. 14); $Z = 4$; temperature: 98 K; cell parameters: $a$ = 8.611(1) Å, $b$ = 17.112(2) Å, $c$ = 15.151(2) Å, $\beta$ = 99.309(5)°, $V$ = 2203.1(5) Å$^3$; density: 0.9478(2) g cm$^{-3}$; $\lambda$ = 0.71073 Å; $2\theta_{max.}$ = 102.85°; 162395 reflections, 23027 unique reflections; completeness: 92.0%; redundancy: 7.0; $R(F^2)_{int.}$ = 0.039, $R(F)_{mul}$ = 0.026; residual density: –0.16/0.21 e Å$^{-3}$. CCDC-637977 contains the supplementary crystallographic data for this paper. These data can be obtained free of charge from The Cambridge Crystallographic Data Centre via www.ccdc.cam.ac.uk/data_request/cif.
[11] *DIAMOND*, version 3.1, Crystal Impact GbR, Bonn, Germany, **2006**.
[12] R. F. W. Bader, *Atoms in Molecules*, Claredon, Oxford, **1994**; R. F. W. Bader in *The Encyclopedia of Computational Chemistry* (Eds.: P. von R. Schleyer, N. L. Alinger, T. Clark, J. Gasteiger, P. A. Kollman, H. F. Schaefer III, P. R. Schreiner), Wiley, Chichester, **1998**.
[13] R. F. W. Bader, P. L. A. Popelier, T. A. Keith, *Angew. Chem.* **1994**, *106*, 647; *Angew. Chem. Int. Ed. Engl.* **1994**, *33*, 620.
[14] N. K. Hansen, P. Coppens, *Acta Crystallogr., Sect. A* **1978**, *34*, 909.
[15] T. Koritsánszky, S. Howard, P. Macchi, C. Gatti, L. J. Farrugia, R. P. Mallinson, A. Volkow, Z. W. Su, T. Richter, N. K. Hansen, *XD, A Computer Program Package for Multipole Refinement and Analysis of Electron Densities from Diffraction Data*, User Manual, Freie Universität Berlin, **2004**.
[16] A. Tippe, W. C. Hamilton, *Inorg. Chem.* **1969**, *8*, 464.

 © 2007 Wiley-VCH Verlag GmbH & Co. KGaA, Weinheim 

[17] M. J. Frisch, G. W. Trucks, H. B. Schlegel, G. E. Scuseria, M. A. Robb, J. R. Cheeseman, V. G. Zakrzewski, J. A. Montgomery Jr, R. E. Stratmann, J. C. Burant, S. Dapprich, J. M. Millam, A. D. Daniels, K. N. Kudin, M. C. Strain, O. Farkas, J. Tomasi, V. Barone, M. Cossi, R. Cammi, B. Mennucci, C. Pomelli, C. Adamo, S. Clifford, J. Ochterski, G. A. Petersson, P. Y. Ayala, Q. Cui, K. Morokuma, D. K. Malick, A. D. Rabuck, K. Raghavachari, J. B. Foresman, J. Cioslowski, J. V. Ortiz, A. G. Baboul, B. B. Stefanov, G. Liu, A. Liashenko, P. Piskorz, I. Komaromi, R. Gomperts, R. L. Martin, D. J. Fox, T. Keith, M. A. Al-Laham, C. Y. Peng, A. Nanayakkara, C. Gonzalez, M. Challacombe, P. M. W. Gill, B. Johnson, W. Chen, M. W. Wong, J. L. Andres, C. Gonzalez, M. Head-Gordon, E. S. Replogle, and J. A. Pople, *Gaussian98*, Revision A.7, Gaussian Inc., Pittsburgh, PA, **1998**.
[18] Z. W. Su, P. Coppens, *Acta Crystallogr., Sect. A* **1992**, *48*, 188.
[19] C. B. Hübschle, P. Luger, *J. Appl. Crystallogr.* **2006**, *39*, 901.
Received: February 23, 2007
Published Online: May 30, 2007

 © 2007 Wiley-VCH Verlag GmbH & Co. KGaA, Weinheim 

DOI: 10.1002/ejic.200700484

# Conformational Flexibility in a Carbobicyclic Diphosphinite Ligand

**Ian J. S. Fairlamb,*[a] Simona Tommasi,[a] Benjamin E. Moulton,[a] Wenxu Zheng,[b] Zhenyang Lin,[b] and Adrian C. Whitwood[a]**

**Keywords:** Ligands / Bite angle / Trans-spanning / Palladium / Binuclear complexes

An unsymmetrical bicyclo[3.2.0]heptanyl diphosphinite ligand, FLEXIphosO, shows flexible coordination modes to palladium centres. The X-ray crystal structure for [$Pd^0_2$-(P,P′)$_3$] has been determined which reveals that the bicyclic backbone of the FLEXIphosO ligand exists in an *exo*-envelope conformation. The change in conformation stands in stark contrast to that observed in mononuclear neutral and cationic palladium(II) complexes containing the FLEXIphosO ligand, where an *endo*-envelope is observed in solution and in the solid-state. Theoretical studies provide an insight into the relative stability of palladium(0) complexes containing the FLEXIphosO ligand. Another large spanning angle ligand, SPANphos, does not form a similar palladium(0) dimer complex under identical reaction conditions, highlighting the unusual behaviour of the FLEXIphosO ligand.

(© Wiley-VCH Verlag GmbH & Co. KGaA, 69451 Weinheim, Germany, 2007)

## Introduction

Bidentate phosphorus ligands are commonly used in coordination chemistry, synthesis and catalysis. The majority of these are rigid and on coordination to a transition metal possess a defined bite angle, a structural feature that is important in key steps in many transition metal-catalysed processes. The global complexity of the complete catalytic cycles of these reactions leads one to anticipate that bidentate ligands that can alter their bite angle could be beneficial to individual steps that are intrinsically different, e.g. oxidative addition and transmetallation, leading to an overall more efficient process. Although this proposition remains a significant challenge, it is evident that the identification of ligands that are capable of energetically accessible geometrical changes will be useful in addressing a key evolution in the design of efficient dynamic ligands. Ligands such as dioxop,[1] bisbi,[2] triptycene,[3] TRANSphos,[4] TRAP,[5] dppf,[6] xantphos,[7] and others[8] offer *cis* and *trans* coordination modes in square-planar complexes. SPANphos, a second generation variant of Xantphos developed by van Leeuwen and co-workers,[9] exhibits interesting catalytic properties in methanol carbonylation,[10] a facile *cis* to *trans* coordination mode switch, as well as the ability to form bimetallic complexes. Further additions to these ligand classes would be useful, particularly structures that utilise conformational changes imposed by a carbobicyclic skeleton – a potentially beneficial structural facet that has rarely been employed in ligand design strategies.[11] In this report we present evidence showing that the bicyclo[3.2.0]-heptanyl ligand **1**, B[3.2.0]DPO[12] renamed as FLEXIphosO[13] (Figure 1), can undergo a conformational change on coordination to $Pd^0$. Our previous studies[14] have established that **1** exhibits an exclusive *cis*-coordination mode in neutral and cationic $Pd^{II}$ and $Pt^{II}$ complexes, e.g. **2**–**4**, where

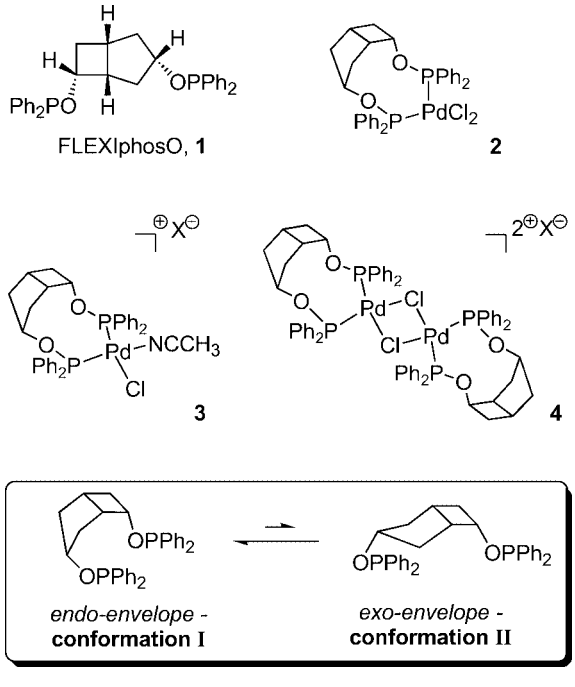


Figure 1. Bicyclo[3.2.0]heptanyl ligand and palladium complexes.

[a] Department of Chemistry, University of York, Heslington, York, YO10 5DD, U.K.
Fax: +44-1904-434091
E-mail: ijsf1@york.ac.uk
[b] Department of Chemistry, The Hong Kong University of Science and Technology, Clear Water Bay, Kowloon, Hong Kong, P. R. China

Supporting information for this article is available on the WWW under http://www.eurjic.org or from the author.

 © 2007 Wiley-VCH Verlag GmbH & Co. KGaA, Weinheim 

the ligand backbone possesses an *endo*-envelope conformation (**I**). Crucially, theoretical calculations support a conformational change from **I** to **II**, the latter an *exo*-envelope, for the stabilisation of cationic $[Pd^{II}(H)L_2]$ species, which are proposed key intermediates in 1,6-diene cycloisomerization reactions.[15] Direct experimental evidence for the existence of conformation **II** is presented in this communication.

## Results and Discussion

Generally, new bidentate ligands are often coordinated to $Pd^{II}$, $Pt^{II}$ and $Rh^{I}$, perhaps due to their ease of preparation, stability and purification. Low oxidation state metal complexes are less often prepared, e.g. $Pd^0$, leading us to investigate the complexation of **1** to $Pd^0$. The reaction of **1** with $[Pd_2(dba)_3]$ (**1**/Pd = 1:1) in $CD_2Cl_2$ at 25 °C affords one species as evidenced by $^{31}P$ NMR spectroscopy. Complexes **5a** (thermodynamic) and **5b** (kinetic) represent the most likely products. Two broad signals at {P1: $\delta$ = 108.1 and P2: $\delta$ = 109.8 (br. s); $\Delta\nu_{1/2}$ = 40 Hz} suggests **5a** as the product. The pseudo-molecular ion ($MH^+$ = *m*/*z* 837.1853; calculated 837.1873) was confirmed by APCI-ESI MS, exhibiting a correct isotopic distribution against calculated values for $C_{48}H_{45}O_3P_2Pd_1$. Repeats of this experiment resulted in the appearance of a minor species, possessing several phosphorus environments, as shown by $^{31}P$ NMR spectroscopy. The presence of excess **1** relative to Pd accounts for the formation of this species, confirmed by the reaction of ca. 3 equiv. of **1** with $[Pd_2(dba)_3]$, which affords this species as the major component[16] (Scheme 1). Two sharp singlets in the $^{31}P$ NMR spectrum are observed at $\delta$ = 108.8 and $\delta$ = 116.6, as well as two sets of multiplets, the first collected between $\delta$ = 107.7–110.1 and the second between $\delta$ = 112.4–115.6. The $^{31}P$ NMR spectrum appears to be complicated by ligand **1** being unsymmetrical. The two sharp singlets could be attributed to either **5b** or **5c**. However, the multiplets could only arise through consideration of the possible isomeric forms **5c** and **5cc** (Figure 2).

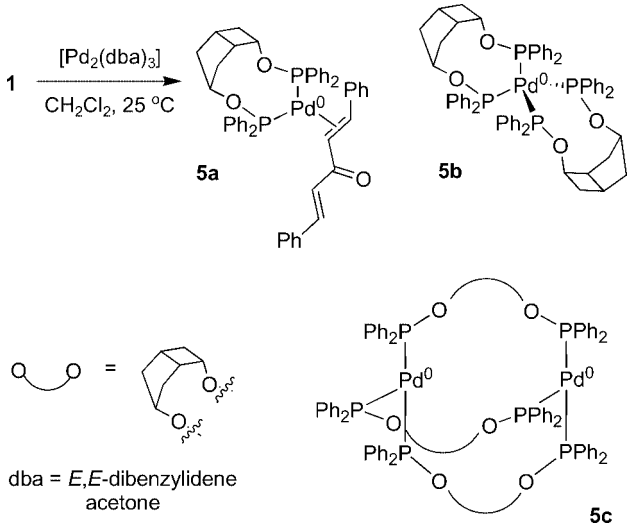


Scheme 1. Synthesis of $Pd^0$ complexes containing ligand **1**.

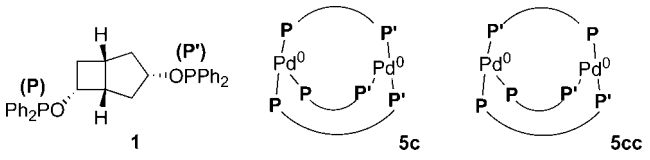


Figure 2. Isomeric forms of $[Pd_2(FLEXIphosO)_3]$ complex (**5c**/**5cc**).

Simulation of the $^{31}P$ NMR spectrum for this mixture of compounds using the gNMR package confirmed that the muliplets were attributable to an isomeric form **5cc**, e.g. a six-spin system (Figure 3). The large $^2J_{PP}$ couplings (about 100–127 Hz) and small chemical shift differences between the phosphorus substituents in each of the cyclobutyl and cyclopentyl rings leads to pronounced second order effects, complicating the appearance of the $^{31}P$ NMR spectrum (Table 1 and Figure 3). The phosphorus environments in **5cc** are inequivalent due to the phosphinite group in the cyclobutyl ring in fragment (Pd1–P,P′,P′) breaking the overall symmetry, which directly affects the spin-spin coupling pattern for the other fragment (Pd2–P,P,P′). The larger $^2J$(P,P′) couplings are observed in the (Pd1–P,P′,P′) fragment between P (environment D) and both P′ groups (environments B and C; 123.7 and 126.8 Hz, respectively). In

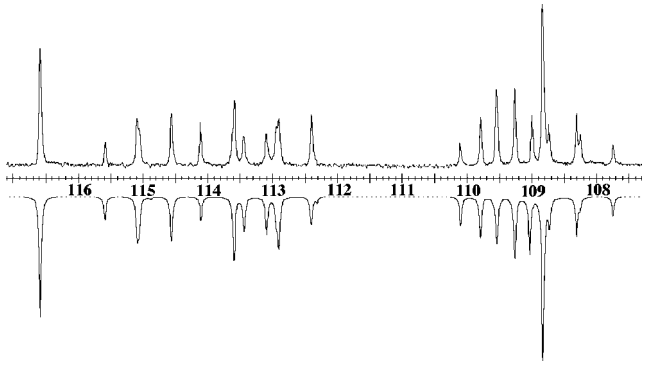


Figure 3. Experimental (upper) and simulated (lower) $^{31}P$ NMR spectra for **5c**/**5cc**.

Table 1. Simulated $^{31}P$ NMR spectroscopic data for complex **5cc**.

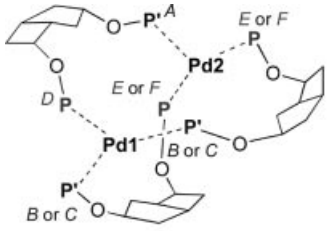


| P environment | $\delta$ | $J_A$ | $J_B$ | $J_C$ | $J_D$ | $J_E$ |
|---|---|---|---|---|---|---|
| A | 109.3 | | | | | |
| B | 109.5 | 0 | | | | |
| C | 108.4 | 0 | 116.0 | | | |
| D | 113.6 | 0 | 123.7 | 126.8 | | |
| E | 112.9 | 107.8 | 0 | 0 | 0 | |
| F | 115.0 | 108.7 | 0 | 0 | 0 | 100.4 |

 © 2007 Wiley-VCH Verlag GmbH & Co. KGaA, Weinheim 

contrast there is a smaller $^2J_{P',P'}$ coupling between B and C (is 116 Hz). Smaller couplings are seen in the (Pd2–P,P,P′) fragment, with P′ (environment A) coupling with both P groups (environments E and F; 107.8 and 108.7, respectively). As with the first fragment, the two similar phosphorus environments, in this case E and F, exhibit a $^2J_{P,P}$ coupling of 100.4 Hz. Isomer **5c** is much more straightforward, exhibiting only two singlets at $\delta$ = 108.8 and $\delta$ = 116.6, due to $C_{3v}$ symmetry. Attributing these singlets to **5b** has been ruled out on the basis that this species is undetected by APCI-ESI MS, whilst **5a** and **5c** are. It is interesting to note that [**5c**]$^+$ is produced as a stable ion on ionizing **5a** by this technique, highlighting the gas-phase stability of this species.

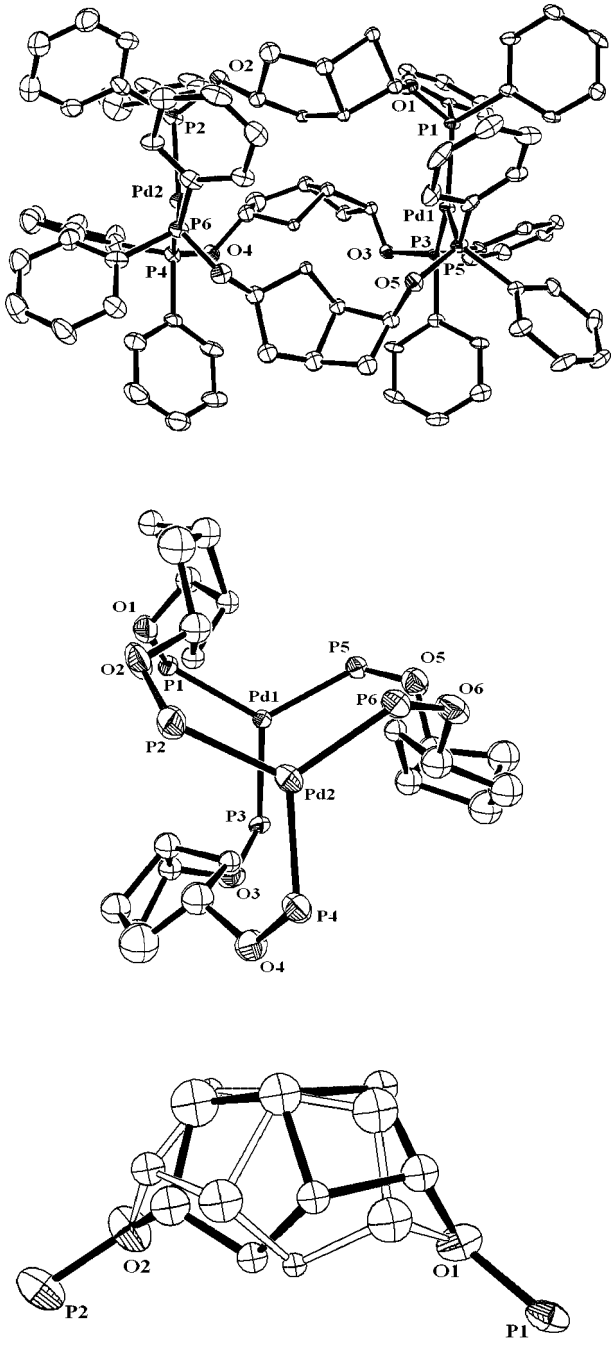


Figure 4. X-ray structure of complex **5c/5cc** (H atoms and $CH_2Cl_2$ omitted for clarity). Top structure: each ligand oriented in the same direction. Middle structure: phosphorus phenyl groups omitted. Bottom structure: showing the two orientations of the bicyclo[3.2.0]heptanyl structure in the ligand backbone. Selected bond lengths [Å] and angles [°]: O(1)–P(1) 1.632(6); O(2)–P(2) 1.624(6); O(3)–P(3) 1.641(6); O(4)–P(4) 1.637(6); O(5)–P(5) 1.631(6); O(6)–P(6) 1.618(6); P(1)–Pd(1) 2.294(2); P(2)–Pd(2) 2.284(2); P(3)–Pd(1) 2.295(2); P(4)–Pd(2) 2.284(2); P(5)–Pd(1) 2.289(2); P(6)–Pd(2) 2.275(2); P(5)–Pd(1)–P(1) 121.50(8); P(5)–Pd(1)–P(3) 119.89(8); P(1)–Pd(1)–P(3) 118.46(8); P(6)–Pd(2)–P(2) 117.98(9); P(6)–Pd(2)–P(4) 121.24(8); P(2)–Pd(2)–P(4) 120.08(9).

Layering a dichloromethane solution of the mixture of **5c** and **5cc**, under an inert atmosphere,[17] with diethyl ether (1:5, v/v) produced dark red crystals suitable for analysis by X-ray diffraction, which revealed the dimeric structure as a mixture of these isomeric forms (Figure 4).

The dimeric complex contains three bridging ligands and as ligand **1** is unsymmetrical it is found in two positions, which has been modelled with a 2:1 occupancy. The complex crystallizes with one molecule of dichloromethane. There is no evidence for a Pd–Pd bond in this structure and the total electron count for each metal is 16-electrons. The Pd(1)–Pd(2) distance is 7.191 Å. The average phosphorus–palladium bond length is slightly different for each Pd atom {Pd(1)–P 2.293(2) Å; Pd(2)–P 2.284(2) Å}, as is the average oxygen–phosphorus bond length around each Pd centre {O–P for Pd(1) 1.635(6); O–P for Pd(2) 1.626(6)}. The $PdP_3$ fragments are near eclipsed, and if one considers isomer **5c** possesses $C_{3v}$ symmetry.

Of particular interest is the observation that this complex is isostructural with $[Pd^0{}_2(dba)_3{\cdot}CH_2Cl_2]$.[18] In the latter complex, each $Pd^0$ centre is coordinated by three alkenes, with the dba acting as a bridging ligand {the Pd(1)–Pd(2) bond length is 3.194 Å in this complex}.[18c] The dimeric complex is a rare example of a phosphorus variant of this ubiquitous dimeric $Pd^0$ alkenyl complex. Two more closely related $[Pd^0{}_2(P,P)_3]$ complexes are known, where P,P = bis(diphenylphosphanyl)methane[19] and bis(diphenoxy)-*N*-methylphospazane.[20] In each of these complexes, the Pd···Pd bond length is 2.959(2) and 2.855(2), respectively. Moreover, these ligands possess small spanning angle ligands, whereas ligand **1** exhibits a much larger angle.

## Theoretical Studies

To study the geometric properties and relative stabilities of the species illustrated in Scheme 1, theoretical calculations were performed at the Becke3LYP level of DFT theory on the model complexes in which the phenyl groups were replaced by hydrogens.

As discussed above, the reaction of **1** with $[Pd_2(dba)_3]$ (**1**/Pd = 1:1) in $CH_2Cl_2$ affords **5a** initially. The absence of **5b** experimentally is intriguing. Bidentate phosphane ligands usually give this type of complex as the kinetic product.[21] To compare the relative stability of **5a** and **5b**, the reaction energy for Equation (1) was calculated.

 © 2007 Wiley-VCH Verlag GmbH & Co. KGaA, Weinheim 

**5b** + dba → **5a** + FLEXIphosO (1)

The calculations reveal that the reaction energy $\Delta E$ is –0.5 kcal/mol. Once the phenyl groups are employed in the calculations, **5b** is expected to be even less favoured due to its relatively more congested structure. Experimentally an excess of dba may further tip the balance in favour of **5a**, more so than seen for other types of phosphanes. In the presence of a slight excess of ligand **1** relative to Pd, the reaction actually gives the dimeric complex **5c**; again **5b** is not formed. To study the relative stability of **5c**, the reaction energy for Equation (2) was calculated.

2 **5a** + FLEXIphosO (**1**) → **5c** + 2 dba (2)

The reaction energy $\Delta E$ was calculated to be –4.5 kcal/mol, confirming the experimental observation that the dimeric complex **5c** is the only species in the presence of a slight excess of **1** relative to Pd.

Since both the *endo*- and *exo*-envelope conformations for the free ligand are possible, it is interesting to assess how the stability of the complexes changes with the variation of the ligand's conformation. Both **5a** and **5b** shown in Scheme 1 have an *endo*-envelope conformation of ligand **1**. We were able to locate their conformational isomers **5a′** and **5b′** in which the ligand shows an *exo*-envelope conformation (Figure 5). **5a′** and **5b′** were found to be less stable by 2.7 and 4.8 kcal mol$^{-1}$ than **5a** and **5b**, respectively. **5c** has an *exo*-envelope conformation of the ligand. Crucially, its *endo*-envelope conformational isomer **5c′** does not correspond to a local minimum on the potential energy surface.

In a previous study on related complexes with ligand **1** containing a $Pd^{II}$ metal centre,[12] we found that when the ligand offers a *cis* coordination mode only the *endo*-envelope conformational isomer exists; when the ligand offers a *trans* coordination mode only the *exo*-envelope conformational isomer exists. In the $Pd^{II}$ complexes studied, the geometry around the metal centre is square-planarly-based and the P–Pd–P bite angles are forced to be close to either 90° or 180°.

The trigonal planar geometry of $Pd^0L_3$ complexes and the tetrahedral geometry of $Pd^0L_4$ complexes allows ligand **1** to show its binding flexibility since the P–Pd–P bite angles are no longer limited to those close to either 90° or 180°. Therefore, in the mononuclear $Pd^0$ complexes shown in Scheme 1, both the *endo*- and *exo*-envelope conformations of ligand **1** are local minima on the potential energy surface.

In the dimeric palladium complex **5c**, the long distance between the two phosphorus atoms in each of the three bridging ligands, a situation similar to that when ligand **1** offers a *trans* coordination mode in $Pd^{II}$ complexes, forces each ligand to adopt the *exo*-envelope conformation.

A final note is that in addition to **5c**, the calculations show that the dimeric complex can easily access the isomeric form **5cc** as shown in Figure 2, considering the (P,P′) structure of the ligand. The isomers **5c** and **5cc** share comparable stability. The difference in energy between **5c** and **5cc** is only 0.3 kcal/mol, implying that both **5c** and **5cc** coexist in solution, a finding supported by the $^{31}P$ NMR spectroscopic studies. In the calculated structures the distance between the two Pd atoms is 6.58 Å in **5c** and 6.60 Å in **5cc**.

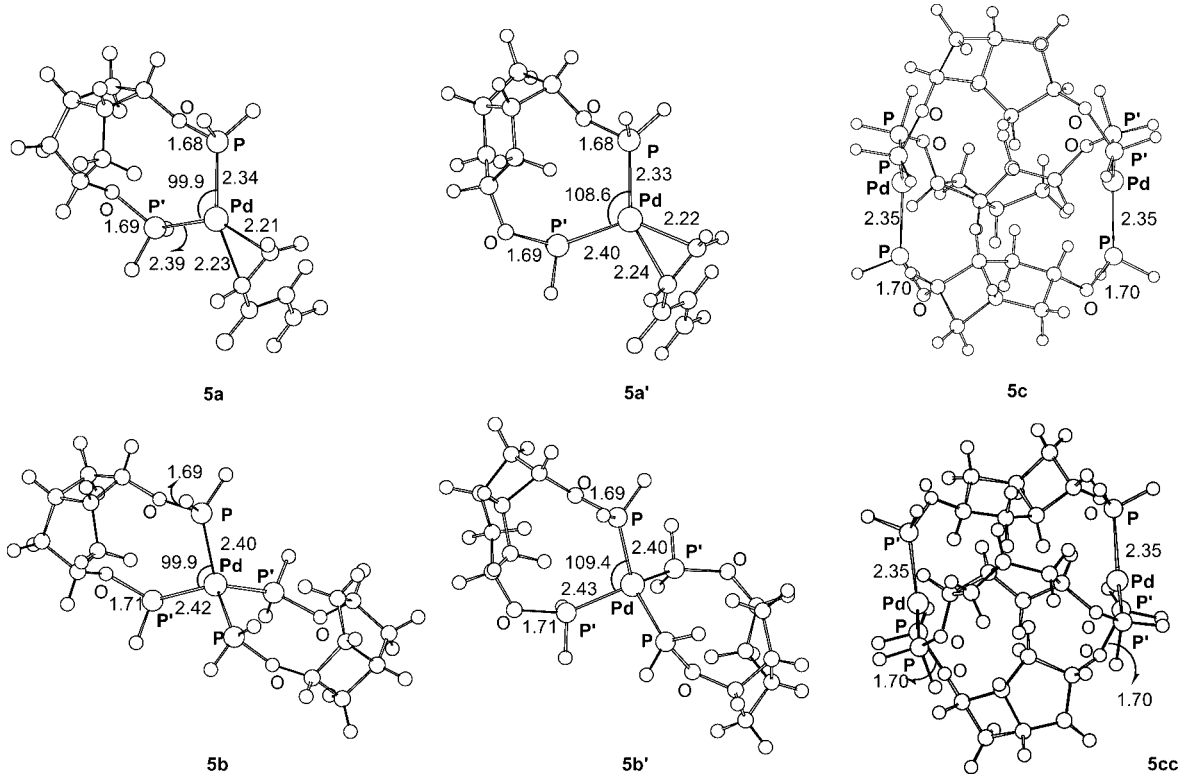


Figure 5. Calculated structures for the model $Pd^0$ complexes. The bond lengths are given in angstrom and the bond angles in degrees.

 © 2007 Wiley-VCH Verlag GmbH & Co. KGaA, Weinheim 

It is clear that there is no interaction between these two atoms. The long P–P′ distance (≈ 6.7 Å) in each ligand can only be accessed via the *exo* conformation. In the solid state, the phenyl groups cause significant lengthening (to 7.191 Å). All the P–O and Pd–P bonds in two isomers are about 1.70 and 2.35 Å respectively, which are longer than that found in the solid-state structure of **5c**.

We envisaged that other ligands possessing large bite angles would allow for the preparation of similar complexes. The reaction of SPANphos **6** with $[Pd_2(dba)_3]$ (**1**/Pd = 1:1) in $CD_2Cl_2$ at 25 °C was monitored by $^{31}P$ NMR spectroscopy which showed one very broad signal at $\delta$ = 22.7–24.8, characterized as [Pd(**6**)($\eta^2$-dba)] (**7**), the pseudo-molecular ion ($MH^+$ = *m*/*z* 1045.3135; calculated 1045.3125) was confirmed by APCI-ESI MS, exhibiting a correct isotopic distribution against calculated values for $C_{64}H_{61}O_3P_2Pd_1$ (Scheme 2). The same reaction with excess SPANphos (ca. 3 equiv.) affords once again this complex, in addition to free ligand ($\delta$ = –16.2 ppm). It is interesting to note that ligand **6** does form rhodium dimer complexes of the type $[Rh_2(\mu\text{-}Cl)_2(\mathbf{6})(CO)_2]$, where the ligand exhibits a conformational change in the bichroman backbone.[9a,10] Molecular models suggest that unfavourable steric factors may explain why $[Pd_2(\mathbf{6})_3]$ is not formed under similar conditions to ligand **1**.

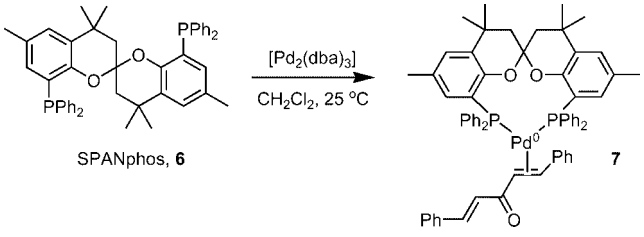


Scheme 2. Synthesis of a $Pd^0$ complex containing SPANphos.

## Conclusions

In summary, the bicyclo[3.2.0]heptanyl ligand **1**, renamed as FLEXIphosO, shows flexible coordination modes[22] to transition metal centres. The influence of substituents on this bicyclic ring system is currently being assessed in our laboratories. We envisage that other carbobicyclic compounds will exhibit similar behaviour. Finally, conformational flexibility is a structural facet that could readily be exploited in transition metal–ligand catalyst design.

## Experimental Section

**NMR Experiments:** All reactions were conducted in a dry box ($O_2$ and $H_2O$ levels < 0.5 ppm). A typical experiment: $[Pd_2(dba)_3]$ (5 mg) was added to ligand **1** (1 equiv.) in $CD_2Cl_2$ (0.5 mL) at 25 ± 0.5 °C. The mixture was stirred for 0.5 h, and then filtered through Celite™ (pipette and glass wool used); the filtrate was analysed directly by NMR spectroscopy. The ratio of **1**/Pd and solvent was changed according to the details supplied in the main text. Similar experiments were performed for the SPANphos ligand **6**. It should be noted that all the phosphane–palladium–alkene complexes are air sensitive.

**Crystallography:** X-ray quality single crystals of **5c/5cc** were grown layering a $CH_2Cl_2$ solution containing the complex with diethyl ether (1:5, v/v) in a dry-box, which gave dark red crystals. The X-ray diffraction experiment was carried out on a Bruker Smart Apex diffractometer with Mo-$K_\alpha$ radiation ($\bar{\lambda}$ = 0.71073 Å) using a SMART CCD camera. The low temperature of the crystal was maintained with a Cryostream (Oxford Cryosystems) open-flow gas cryostat. The reflection intensities were corrected for absorption by a semi-empirical method based on the intensities of Laue equivalents and multiple measurements of identical reflections. The structures were solved by the Patterson and Fourier technique and refined by full-matrix least-squares against $F^2$ of all reflections, using SHELXTL software. The atoms of the bicyclo[3.2.0]heptanyl ring systems (x3) are disordered over two positions (50:50), as depicted in Figure 2. **Crystal data**: $C_{94}H_{92}Cl_2O_6P_6Pd_2$, $M$ = 1787.20, triclinic, $a$ = 12.1575(15), $b$ = 12.2884(16), $c$ = 32.357(4) Å, $U$ = 4184.9(9) Å$^3$, $\alpha$ = 81.132(3), $\beta$ = 79.892(3), $\gamma$ = 61.929(2), $T$ = 110(2) K, space group = $P\bar{1}$, $Z$ = 2, $\mu$(Mo–$K_a$) = 0.663 mm$^{-1}$, 15636 reflections measured, 8992 unique ($R_{int}$ = 0.0358) which were used in all calculations. Final $R1$ = 0.0627 and $wR(F^2)$ = 0.1595 (all data). CCDC-642869 contains the supplementary crystallographic data for this paper. These data can be obtained free of charge from The Cambridge Crystallographic Data Centre via www.ccdc.cam.ac.uk/data_request/cif.

**APCI-ESI MS Experiments:** Bruker MicroTOF from Bruker Daltonics, Bremen, Germany. ESI was performed by injecting a 5 µl of the sample prepared in a dry-box (50 µg in $CH_2Cl_2$/MeOH; 95:5 v/v) into a stream of 200 µl/min methanol on a LC system Agilent 1200 (capillary 4500V; nebulizer 1.3 Bar; dry gas 8 L min$^{-1}$; dry temp. 180 °C).

**Theoretical Calculations:** Density functional theory calculations were performed at the B3LYP level using Gaussian 03.

**Supporting Information** (see also the footnote on the first page of this article): The $^{31}P$ NMR spectroscopic data for all the palladium complexes described in this paper. X-ray data for complex **5c/5cc** and the computational details and Cartesian coordinates for the calculated structures (depicted in Figure 5) are included.

## Acknowledgments

We are grateful to The Royal Society, Engineering and Physical Sciences Research Council (EPSRC) and Stylacats for funding and Astra-Zeneca for an unrestricted research award. Prof. P. van Leeuwen, Dr. Z. Freixa and Ms N. Goetz (ICIQ, Tarragona, Spain) are thanked for helpful discussions and providing SPANphos. Drs. J. M. Lynam and T. A. Dransfield have provided valuable assistance with gNMR and MS, respectively, and Dr. M. Bandini (Bologna, Italy) is thanked for supporting an exchange visit for S. T.

[1] J. M. Brown, P. A. Chaloner, G. Descotes, R. Glaser, D. Lafont, D. Sinou, *J. Chem. Soc. Chem. Commun.* **1979**, 611.
[2] a) T. J. Devon, G. W. Phillips, T. A. Puckette, J. L. Stavinoha, J. J. Vanderbilt, US Pat., 4, 694,109, **1987** (to Eastman Kodak), see also: *Chem. Abstr.* **1988**, *108*, 7890; b) M. R. Eberhard, K. M. Heslop, A. G. Orpen, P. G. Pringle, *Organometallics* **2005**, *24*, 335.
[3] a) O. Grossman, C. Azerraf, D. Gelman, *Organometallics* **2006**, *25*, 375; b) C. Azerraf, O. Grossman, D. Gelman, *J. Organomet. Chem.* **2007**, *692*, 761.

 © 2007 Wiley-VCH Verlag GmbH & Co. KGaA, Weinheim 

[4] N. J. DeStefano, D. K. Johnson, L. M. Venanzi, *Helv. Chim. Acta* **1976**, *59*, 2683.
[5] M. Sawamura, H. Hamashima, Y. Ito, *Tetrahedron: Asymmetry* **1991**, *2*, 593.
[6] H. Kawano, Y. Nishimura, M. Onishi, *Dalton Trans.* **2003**, 1808.
[7] M. Kranenburg, Y. E. M. van der Burgt, P. C. J. Kamer, P. W. N. M. van Leeuwen, *Organometallics* **1995**, *14*, 3081.
[8] a) R. A. Leising, J. J. Grzybowski, K. J. Takeuchi, *Inorg. Chem.* **1988**, *27*, 1020; b) N. Lewanzik, T. Oeser, J. Blumel, J. A. Gladysz, *J. Mol. Catal. A* **2006**, *254*, 20; c) A. J. Nawara, T. Shima, F. Hampel, J. A. Gladysz, *J. Am. Chem. Soc.* **2006**, *128*, 4962; d) L. K. Knight, Z. Freixa, P. W. N. M. van Leeuwen, J. N. H. Reek, *Organometallics* **2006**, *25*, 954; e) R. C. Smith, J. D. Protasiewicz, *Organometallics* **2004**, *23*, 4215.
[9] a) C. Jiménez-Rodríguez, F. X. Roca, C. Bo, J. Benet-Buchholz, E. C. Escudero-Adán, Z. Freixa, P. W. N. M. van Leeuwen, *Dalton Trans.* **2006**, 268; b) Z. Freixa, M. S. Beentjes, G. D. Batema, C. B. Dieleman, G. P. F. van Strijdonck, J. N. H. Reek, P. C. J. Kamer, J. Fraanje, K. Goubitz, P. W. N. M. van Leeuwen, *Angew. Chem. Int. Ed.* **2003**, *42*, 1284.
[10] Z. Freixa, P. C. J. Kamer, M. Lutz, A. L. Spek, P. W. N. M. van Leeuwen, *Angew. Chem. Int. Ed.* **2005**, *44*, 4385.
[11] C. A. Bessel, P. Aggarwal, *Chem. Rev.* **2001**, *101*, 1031.
[12] a) N. Derrien, C. B. Dousson, S. M. Roberts, U. Berens, M. Burk, M. J. Ohff, *Tetrahedron: Asymmetry* **1999**, *10*, 3341; b) B. Adger, U. Berens, M. J. Griffiths, M. J. Kelly, R. McCague, J. A. Miller, C. F. Palmer, S. M. Roberts, R. Selke, U. Vitinus, G. Ward, *Chem. Commun.* **1997**, 1713.
[13] Ligand **1** has been renamed as FLEXIphosO, with approval from Professor Stanley M. Roberts.
[14] I. J. S. Fairlamb, S. Grant, A. C. Whitwood, J. Whitthall, A. S. Batsanov, J. C. Collings, *J. Organomet. Chem.* **2005**, *690*, 4462.
[15] I. J. S. Fairlamb, S. Grant, S. Tommasi, J. M. Lynam, M. Bandini, H. Dong, Z. Lin, A. C. Whitwood, *Adv. Synth. Catal.* **2006**, *348*, 2515.
[16] APCI-ESI MS analysis confirmed a molecular ion at 1702.32, which is $C_{93}H_{90}O_6P_6Pd_2$, confirmed by comparison with the calculated isotopic distribution; an accurate mass determination for this ion was not attainble.
[17] The $Pd^0$ dimer complex is air sensitive and degrades to give palladium nanoparticles within minutes in the presence of air.
[18] a) C. G. Pierpont, M. C. Mazza, *J. Chem. Soc. Chem. Commun.* **1973**, 207; b) T. Ukai, H. Kawazura, Y. Ishii, J. J. Bonnet, J. A. Ibers, *J. Organomet. Chem.* **1974**, *65*, 253; c) K. Selvakumar, M. Valentini, M. Wörle, P. S. Pregosin, A. Albinati, *Organometallics* **1999**, *18*, 1207.
[19] R. U. Kirss, R. Eisenberg, *Inorg. Chem.* **1989**, *28*, 3372.
[20] M. S. Balakrishna, S. S. Krishnamurthy, R. Murugavel, M. Nethaji, I. I. Mathews, *J. Chem. Soc. Dalton Trans.* **1993**, 477.
[21] L. S. Hegedus, In *Transition Metals in the Synthesis of Complex Organic Molecules*, University Science Books, Mill Valley, CA (USA), **1994**.
[22] Balakrishna and co-workers have reported that a diphosphinite of *syn*-1,4-cyclohexane shows flexible coordination modes (for mono-nuclear $Pd^{II}/Pt^{II}$ complexes a boat conformation is preferred; for a $Ru^{II}$ dimer a chair conformation is preferred), see: M. S. Balakrishna, P. P. George, S. M. Mobin, *Polyhedron* **2005**, *24*, 475.

Received: April 12, 2007
Published Online: Juni 1, 2007

 © 2007 Wiley-VCH Verlag GmbH & Co. KGaA, Weinheim 

DOI: 10.1002/ejic.200601089

# Redox-Induced μ-Acetato and μ-Oxo Core Interconversions in Dinuclear Manganese Tris(2-methylpyridyl)amine (tpa) Complexes: Isolation and Characterization of $[Mn_2^{III}(\mu\text{-}O)(\mu\text{-}O_2CCH_3)(tpa)_2]^{3+}$

**Marie-Noëlle Collomb,*[a] Claire Mantel,[a,b] Sophie Romain,[a] Carole Duboc,[b] Jean-Claude Leprêtre,[a] Jacques Pécaut,[c] and Alain Deronzier[a]**

**Keywords:** Manganese / Electrochemistry / N ligands / Bridging ligands

The electrochemical properties of the bis(μ-acetato) complex $[Mn_2^{II}(O_2CCH_3)_2(tpa)_2]^{2+}$ ($\mathbf{1}^{2+}$) [tpa = tris(2-methylpyridyl)-amine] in an organic medium ($CH_3CN$) have been studied. Two successive controlled potential oxidations of a solution of $\mathbf{1}^{2+}$ at 0.7 and 1.1 V vs. $Ag/Ag^+$ (10 mM) allow the selective and nearly quantitative formation of the mono-(μ-oxo) mono-(μ-acetato) complex $[Mn_2^{III}(O)(O_2CCH_3)(tpa)_2]^{3+}$ ($\mathbf{2}^{3+}$) and the bis(μ-oxo) complex $[Mn_2^{IV}(O)_2(tpa)_2]^{4+}$ ($\mathbf{3}^{4+}$), respectively. These results show that each substitution of an acetate group by an oxo group is caused by an overall two-electron oxidation of the corresponding dimanganese complex. The associated electrochemical back transformations were also investigated. Complex $\mathbf{2}^{3+}$, which possesses a rare mono-(μ-oxo) mono-(μ-acetato) motif, has been isolated and characterized by X-ray crystallography. This complex crystallizes in the monoclinic system, space group $P2_1/n$ with $a$ = 11.9899(17), $b$ = 35.050(5), $c$ = 12.3952(18) Å, $\beta$ = 101.218(6)°, $Z$ = 4.

(© Wiley-VCH Verlag GmbH & Co. KGaA, 69451 Weinheim, Germany, 2007)

## Introduction

Much effort has been directed towards the chemistry of binuclear manganese complexes with oxo- and/or acetato-bridged cores due to their relevance to biological systems such as the manganese catalases (Mn Cat) and the oxygen-evolving complex (OEC) of photosystem II (PSII).[1–3] The active centers are a di- (MnCat) or a tetranuclear (OEC) manganese complex where oxidation states II, III, and IV are implicated during the enzymatic catalytic cycles. The MnCat switches between the $Mn_2^{II}$ and $Mn_2^{III}$ forms during the catalysis, and only these two oxidation states are able to catalyze the disproportionation of $H_2O_2$ at extremely high rates.[1] Recent structural characterizations[4–7] of the oxidized $Mn_2^{III}$ form reveal a Mn–Mn separation of 3.03 to 3.4 Å and that the two metal centers are triply bridged by a $\mu_{1,3}$-carboxylate group of a glutamate (or aspartate) residue and two oxygen atoms, possibly one oxo and one hydroxo. EXAFS studies suggest that the Mn–Mn separation is significantly longer in the reduced $Mn_2^{II}$ form of the enzyme (3.4 to 3.7 Å), such that both bridging oxygen atoms come from water and/or hydroxide.[8]

In contrast, the exact structure of the active center in PSII, as well as the mechanism of water oxidation, remain elusive.[2,9–15] During the catalytic cycle it is known that the tetranuclear manganese cluster in PSII cycles through five increasingly oxidized states, denoted as $S_0$–$S_4$. The most oxidized state, $S_4$, is unstable and relaxes back to $S_0$ with the release of $O_2$. On the basis of XAS and EPR data, it is generally accepted that the oxidation states in $S_1$ and $S_2$ are $Mn_2^{III}Mn_2^{IV}$ and $Mn^{III}Mn_3^{IV}$, respectively.[2,16] XAS studies have also provided evidence for the existence of Mn–(μ-O)$_2$–Mn (Mn–Mn distance of 2.7 Å) and Mn–(μ-O)–Mn (Mn–Mn distance of 3.3 Å) moieties in the tetramer,[17,18] while the recent crystal structures of PSII[19–23] suggest that the four metallic ions of the OEC are organized in a "3 + 1" fashion.

The oxidation state changes in both MnCat and PSII enzymes are accompanied by structural changes involving the groups bridging the Mn atoms. For example, the significant structural changes that occur during the $S_0 \rightarrow S_1$ and $S_2 \rightarrow S_3$ transitions in PSII have been identified as a deprotonation of a μ-hydroxo bridge and the formation of a third Mn–(μ-O)$_2$–Mn unit, respectively.[2,14] In addition, as suggested recently, the combination of bidentate carboxylate ligands and mono- or di-oxo bridges could enhance the stability of the cation arrangement and facilitate rearrangement of the μ-oxo bridges during the S-state cycle.[23]

[a] Laboratoire d'Electrochimie Organique et de Photochimie Rédox, Université Joseph Fourier, CNRS UMR 5630, Institut de Chimie Moléculaire de Grenoble (ICMG), FR CNRS 2607, Grenoble 1,
B. P. 53, 38041 Grenoble Cedex 9, France
Fax: +33-4-76514267
E-mail: Marie-Noelle.Collomb@ujf-grenoble.fr
[b] The Grenoble High Magnetic Field Laboratory, CNRS UPR 5021,
B. P. 166, 38042 Grenoble Cedex 9, France
[c] DRFMC-Service de Chimie Inorganique et Biologique, Laboratoire Coordination et Chiralité, CEA-Grenoble,
38054 Grenoble Cedex, France

 © 2007 Wiley-VCH Verlag GmbH & Co. KGaA, Weinheim 

μ-Acetato/μ-hydroxo or μ-oxo bridging ligand changes in relation to Mn oxidation have been reported for synthetic binuclear Mn complexes with multidentate ancillary N and/or O ligands.[24–34] Electrochemistry is a convenient way to investigate these kinds of redox-induced structural changes, and we have previously demonstrated the efficiency of the electrochemically induced core interconversion in an organic medium ($CH_3CN$) for the tris(μ-acetato) complex $[Mn_2^{II}(O_2CCH_3)_3(bpea)_2]^+$ [bpea = *N*,*N*-bis(2-methylpyridyl)ethylamine].[28,29] The mono-(μ-oxo) $[Mn_2^{III}(O)(O_2CCH_3)_2(bpea)_2]^{2+}$ and bis(μ-oxo) $[Mn_2^{IV}(O)_2(O_2CCH_3)(bpea)_2]^{3+}$ complexes have been selectively and quantitatively generated by an exhaustive electrochemical oxidation of $[Mn_2^{II}(O_2CCH_3)_3(bpea)_2]^+$. In order to evaluate the influence of the structure of the complex on the efficiency of the electrochemical process, we report here a similar study conducted with the bis(μ-acetato) complex $[Mn_2^{II}(O_2CCH_3)_2(tpa)_2]^{2+}$ ($\mathbf{1}^{2+}$) [tpa = tris(2-methylpyridyl)amine]. This latter complex contains tetradentate amino ligands instead of tridentate ones and only two acetate bridging ligands instead of three. The electrochemical synthesis of the mono-(μ-oxo) mono-(μ-acetato) complex $[Mn_2^{III}(O)(O_2CCH_3)(tpa)_2]^{3+}$ ($\mathbf{2}^{3+}$) and the redox properties of the bis(μ-oxo) complex $[Mn_2^{III,IV}(O)_2(tpa)_2]^{3+}$ ($\mathbf{3}^{3+}$) are also reported. Complexes $\mathbf{1}(TCNQ)_2\cdot CH_3CN$, $\mathbf{3}(BPh_4)_2$, and $\mathbf{3}(S_2O_6)_{3/2}\cdot 7H_2O$[35–37] have been structurally and spectroscopically characterized previously, and the electrochemical properties of $\mathbf{3}^{3+}$ have been briefly studied in $CH_3CN$.[37,38] In contrast, complex $\mathbf{2}^{3+}$, which possesses a rare mono-(μ-oxo) mono-(μ-acetato) motif,[39–41] has not been isolated previously and we report here its characterization by X-ray crystallography.

## Results

### Synthesis and Crystal Structure of $[Mn_2^{III}(\mu\text{-}O)(\mu\text{-}O_2CCH_3)(tpa)_2](PF_6)_3$ $[\mathbf{2}(PF_6)_3]$

This complex was obtained by preparative electrolysis of a concentrated solution of $\mathbf{1}^{2+}$ in $CH_3CN$ containing 0.1 M $Bu_4NPF_6$. Slow diffusion of diethyl ether into this solution leads to single crystals of $\mathbf{2}(PF_6)_3\cdot CH_3CN$ in good yield (see Experimental Section). The structure of this complex was determined by X-ray diffraction. Figure 1 shows the structure of the $[Mn_2^{III}(\mu\text{-}O)(\mu\text{-}O_2CCH_3)(tpa)_2]^{3+}$ cation and the atom labelling scheme; Table 1 summarises important bond lengths and angles. Each manganese atom exhibits a highly distorted octahedral geometry and is bound by four nitrogen atoms from a single tpa ligand and two oxygen atoms, one from the bridging oxo group and the other from the bridging acetate.

The $\{Mn_2(O)(O_2CCH_3)\}^{3+}$ core of the complex yields a Mn···Mn distance of 3.253(3) Å. To the best of our knowledge, only four other crystallographically characterized complexes possess this type of core. In $[Mn_2^{III}(O)(O_2CCH_3)(bispicen)_2]^{3+}$ [bispicen = *N*,*N*′-bis(2-methylpyridyl)ethane-1,2-diamine] and $[Mn_2^{III}(O)(O_2CCH_3)(bispicMe_2en)_2]^{3+}$ [bispicMe$_2$en = *N*,*N*′-dimethyl-*N*,*N*′-bis(2-methylpyridyl)ethane-1,2-diamine],[39] the Mn···Mn distances are 3.276(3) and 3.292(14) Å, respectively, whereas in $[Mn_2^{III}(O)(O_2CCH_3)(tmima)_2]^{2+}$ [tmima = tris(1-methylimidazol-2-yl)methylamine][40] and $[Mn_2^{III}(O)(O_2CCH_3)(bpia)_2]^{3+}$ [bpia = bis(picolyl)(*N*-methylimidazol-2-yl)amine][41] the two manganese ions are separated by 3.250(1) and 3.2544(8) Å, respectively. Compared to the other crystallographically characterized dimanganese tpa complexes, the Mn···Mn distance in $\mathbf{2}^{3+}$ is significantly longer than those found in the bis(μ-oxo) complexes at the (III,III) and (III,IV) oxidation level [2.656(2) Å ($\mathbf{3}^{2+}$)[36] and 2.643(1) Å ($\mathbf{3}^{3+}$)[37]] and shorter than that in the bis(μ-acetato) complex [4.154(1) Å ($\mathbf{1}^{2+}$)].[35] A noticeable compression of the bond

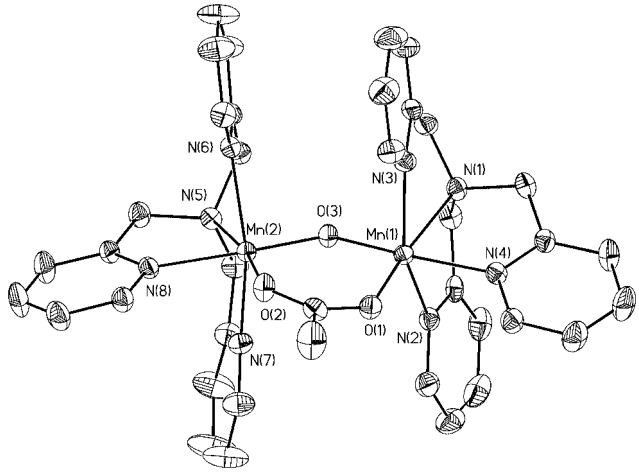


Figure 1. ORTEP view of the cation $[Mn_2^{III}(O)(O_2CCH_3)(tpa)_2]^{3+}$ ($\mathbf{2}^{3+}$).

Table 1. Selected bond lengths [Å] and angles [°] for $\mathbf{2}(PF_6)_3\cdot CH_3CN$.

| | | | |
|---|---|---|---|
| Mn(1)–Mn(2) | 3.253(3) | | |
| Mn(1)–N(1) | 2.187(3) | Mn(2)–N(5) | 2.168(3) |
| Mn(1)–N(2) | 2.163(3) | Mn(2)–N(6) | 2.193(3) |
| Mn(1)–N(3) | 2.194(3) | Mn(2)–N(7) | 2.201(3) |
| Mn(1)–N(4) | 2.048(3) | Mn(2)–N(8) | 2.058(3) |
| Mn(1)–O(1) | 1.987(2) | Mn(2)–O(2) | 1.987(2) |
| Mn(1)–O(3) | 1.778(2) | Mn(2)–O(3) | 1.786(2) |
| Mn(1)–O(3)–Mn(2) | 131.82(3) | | |
| N(1)–Mn(1)–N(2) | 78.68(11) | N(5)–Mn(2)–N(6) | 75.85(11) |
| N(1)–Mn(1)–N(3) | 75.38(11) | N(5)–Mn(2)–N(7) | 78.27(11) |
| N(1)–Mn(1)–N(4) | 80.80(11) | N(5)–Mn(2)–N(8) | 80.82(11) |
| N(2)–Mn(1)–N(3) | 154.00(11) | N(6)–Mn(2)–N(7) | 153.91(11) |
| N(2)–Mn(1)–N(4) | 83.87(11) | N(6)–Mn(2)–N(8) | 89.71(11) |
| N(3)–Mn(1)–N(4) | 90.22(12) | N(7)–Mn(2)–N(8) | 82.93(12) |
| O(1)–Mn(1)–O(3) | 98.29(11) | O(2)–Mn(2)–O(3) | 98.49(11) |
| O(1)–Mn(1)–N(1) | 166.49(12) | O(2)–Mn(2)–N(5) | 170.68(12) |
| O(1)–Mn(1)–N(2) | 109.05(11) | O(2)–Mn(2)–N(6) | 105.87(11) |
| O(1)–Mn(1)–N(3) | 96.08(11) | O(2)–Mn(2)–N(7) | 99.15(11) |
| O(1)–Mn(1)–N(4) | 88.90(11) | O(2)–Mn(2)–N(8) | 89.99(11) |
| O(3)–Mn(1)–N(1) | 92.45(11) | O(3)–Mn(2)–N(5) | 90.65(11) |
| O(3)–Mn(1)–N(2) | 91.42(11) | O(3)–Mn(2)–N(6) | 89.72(11) |
| O(3)–Mn(1)–N(3) | 91.45(11) | O(3)–Mn(2)–N(7) | 93.85(11) |
| O(3)–Mn(1)–N(4) | 172.40(11) | O(3)–Mn(2)–N(8) | 171.32(11) |

 © 2007 Wiley-VCH Verlag GmbH & Co. KGaA, Weinheim 

lengths along the $N_{pyridine}$(4 or 8)–Mn–$O_{oxo}$(3) axis is observed in $\mathbf{2}^{3+}$ due to the Jahn–Teller effect expected for a high-spin $d^4$ $Mn^{III}$ ion. Although this kind of distortion is rarely observed for a $Mn^{III}$ ion, a similar tetragonal compression occurs in the four other complexes with the same core.[39–41] The Mn–$O_{oxo}$–Mn angle of 131.82(3)° in $\mathbf{2}^{3+}$ is comparable to those found in the four other complexes (130.9° < Mn–$O_{oxo}$–Mn < 133°). The Mn–$O_{oxo}$ bond lengths of 1.778(2) and 1.786(2) Å and the Mn–$O_{acetate}$ distance of 1.987(3) Å in $\mathbf{2}^{3+}$ are consistent with the corresponding bond lengths reported for the parent complexes [1.784(3) < Mn–$O_{oxo}$ < 1.801(3) Å and 1.90(3) < Mn–$O_{carb}$ < 2.042(4) Å].[39–41] The Mn–$N_{pyridine}$(4 and 8) bonds [2.048(3) and 2.058(3) Å] *trans* to the oxo group are considerably shorter than the other Mn–$N_{pyridine}$ bond lengths due to the compression of the octahedron [Mn(1)–N(2) 2.163(3), Mn(1)–N(3) 2.194(3), Mn(2)–N(6) 2.193(3), Mn(2)–N(7) 2.201(3) Å]. The distortions from octahedral geometry observed around the Mn ions are also due to the spatially constrained nature of the tetradentate tpa ligand, as revealed by the values of the $N_{amine}$–Mn–$N_{pyridine}$ intraligand angles, which range between 75.38° and 90.22° (Table 1); the theoretical value is 90°.

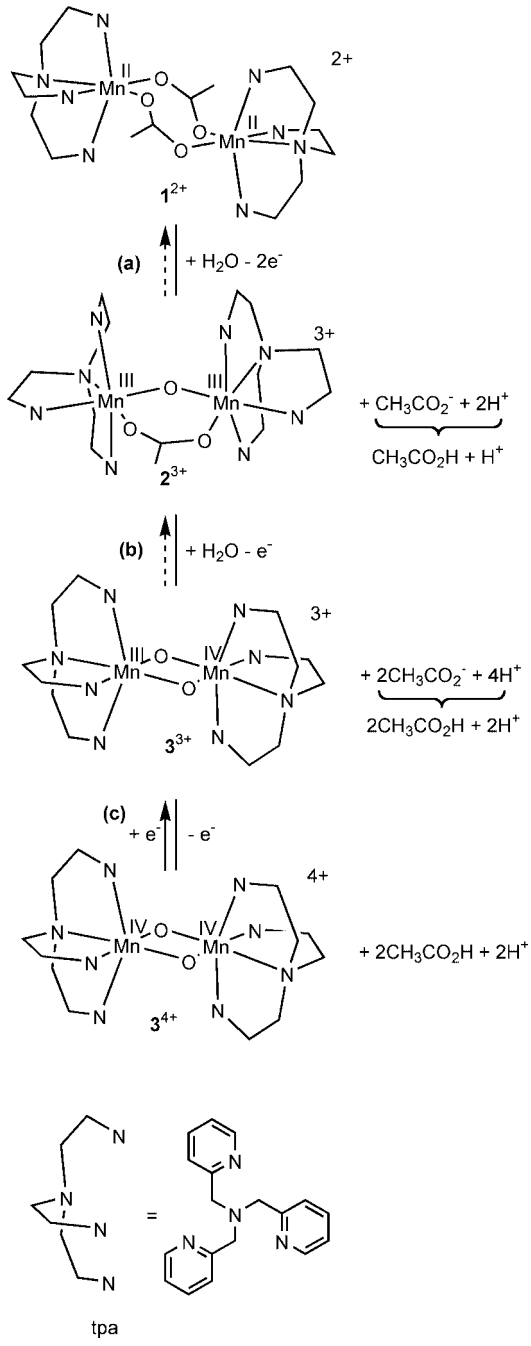


Scheme 1. Electrochemical interconversions of dinuclear manganese tpa complexes.

## Electrochemistry

As we will see, the oxidation of $\mathbf{1}^{2+}$ in $CH_3CN$ is a fully irreversible process that leads first to the mono-(μ-oxo)/mono-(μ-acetato) complex $\mathbf{2}^{3+}$ and then the bis(μ-oxo) complex $\mathbf{3}^{4+}$ (Scheme 1). For a better understanding of the processes involved, the electrochemical behavior of $\mathbf{3}^{3+}$ is first presented, and then those of complexes $\mathbf{2}^{3+}$ and $\mathbf{1}^{2+}$. All the potentials are referenced to an Ag/0.01 M $AgNO_3$ reference electrode in $CH_3CN$ + 0.1 M $Bu_4NClO_4$. Potentials referred to this system can be converted to the ferrocene/ferrocenium couple by subtracting 87 mV, or to SCE or NHE by adding 298 or 548 mV, respectively.[42]

### *Electrochemical Behavior of $[Mn_2^{III,IV}(O)_2(tpa)_2](ClO_4)_3$ [$3(ClO_4)_3$]*

As previously observed by Suzuki et al.,[38] the cyclic voltammogram of a $CH_3CN$ solution of $\mathbf{3}^{3+}$ in the presence of 0.1 M $Bu_4NClO_4$ (Figure 2, A) displays a single reversible oxidation wave at $E^{3A}_{1/2}$ = 0.77 V ($E^{3A}_{pa}$ = 0.80 and $E^{3A}_{pc}$ = 0.74 V; $\Delta E_p$ = 60 mV) and one reversible reduction wave at $E^{3B}_{1/2}$ = –0.05 V ($E^{3B}_{pc}$ = –0.08 and $E^{3B}_{pa}$ = –0.02 V; $\Delta E_p$ = 60 mV) corresponding to Equations (1) and (2), respectively.

$$[Mn_2^{III,IV}(O)_2(tpa)_2]^{3+} \rightleftharpoons [Mn_2^{IV,IV}(O)_2(tpa)_2]^{4+} + e^- \quad (1)$$
$$\mathbf{3}^{3+} \qquad\qquad \mathbf{3}^{4+}$$

$$[Mn_2^{III,IV}(O)_2(tpa)_2]^{3+} + e^- \rightleftharpoons [Mn_2^{III,III}(O)_2(tpa)_2]^{2+} \quad (2)$$
$$\mathbf{3}^{3+} \qquad\qquad \mathbf{3}^{2+}$$

Exhaustive electrolyses of solutions of this complex confirm the excellent stability of the $Mn_2^{III,III}$ ($\mathbf{3}^{2+}$) and $Mn_2^{IV,IV}$ ($\mathbf{3}^{4+}$) species. Exhaustive reduction of a solution of $\mathbf{3}^{3+}$ at –0.2 V consumes one electron per molecule of complex and leads to the quasi-quantitative formation of the one-electron-reduced species $\mathbf{3}^{2+}$ (yield: 97%). The yield is calculated from the relative height of the two waves [Equation (2)] of the voltammograms at a rotating disc electrode before and after reduction (Figure 2, B).

 © 2007 Wiley-VCH Verlag GmbH & Co. KGaA, Weinheim 

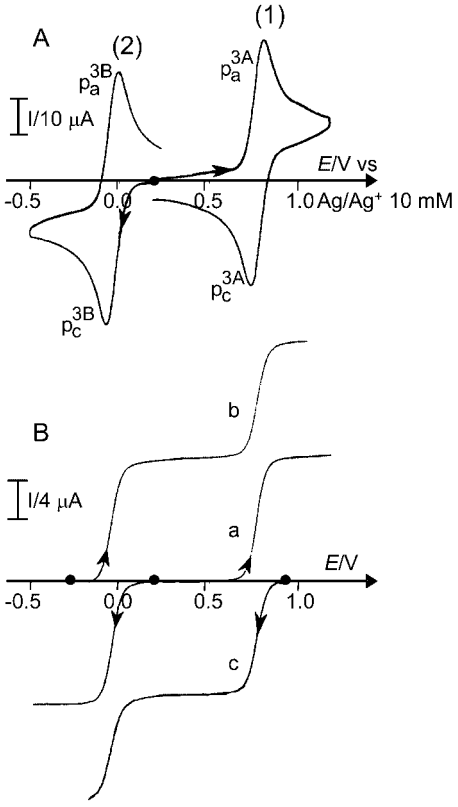


Figure 2. (A) Cyclic voltammograms at a Pt electrode (diameter: 5 mm) of a 0.72 mM solution of $\mathbf{3}^{3+}$ in $CH_3CN$ + 0.1 M $Bu_4NClO_4$; sweep rate: 100 mV s$^{-1}$; (B) voltamperograms at a Pt rotating disc electrode (diameter: 0.2 mm); rotation speed: 600 min$^{-1}$; sweep rate: 10 mV s$^{-1}$: (a) solution (A), (b) solution (A) after exhaustive reduction at –0.2 V (formation of $\mathbf{3}^{2+}$), and (c) after exhaustive oxidation of a solution of a 0.72 mM of $\mathbf{3}^{3+}$ in $CH_3CN$ + 0.1 M $Bu_4NBF_4$ at 0.9 V (formation of $\mathbf{3}^{4+}$). The numbers in parentheses correspond to the equation number in the text.

On the other hand, as previously reported,[38] exhaustive oxidation of a solution of $\mathbf{3}^{3+}$ at 0.9 V in $CH_3CN$ in the presence of 0.1 M $Bu_4NClO_4$ leads to the formation of a green precipitate corresponding to $\mathbf{3}^{4+}$. However, we were able to prevent the precipitation of $\mathbf{3}^{4+}$ by using $Bu_4NBF_4$ as supporting electrolyte instead of $Bu_4NClO_4$. This complex is formed in solution with a 95% yield after one electron has been consumed per molecule (Figure 2B). Figure 3 displays the absorption spectra of the different species in the visible region. The green (III,IV) complex $\mathbf{3}^{3+}$ (spectrum a) shows three bands in the visible region at 444 ($\varepsilon$ = 1490 M$^{-1}$ cm$^{-1}$), 560 (760), and 658 nm (620) and one band in the UV region at 258 nm (36850). The green (IV,IV) complex $\mathbf{3}^{4+}$ (spectrum c) exhibits three visible bands at 418, 534 and 642 nm. This spectrum is similar to that obtained by Suzuki et al.[38] after redissolution of the green precipitate of $[Mn_2^{IV,IV}(O)_2(tpa)_2](ClO_4)_4$ in $CH_3CN$ in the absence of supporting electrolyte [418 (6000), 534 (1032), and 642 nm (1084)]. The pale-yellow (III,III) complex (spectrum b) does not exhibit any well-resolved bands in the visible region.[36]

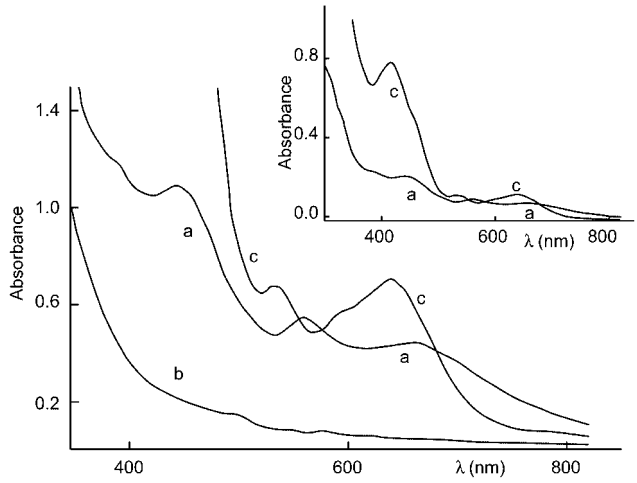


Figure 3. Visible absorption spectra of a 0.72 mM solution of $\mathbf{3}^{3+}$ in $CH_3CN$ + 0.1 M $Bu_4NClO_4$: (a) initial solution, (b) solution (a) after exhaustive reduction at –0.2 V, and (c) after exhaustive oxidation of a 0.72 mM solution of $\mathbf{3}^{3+}$ in $CH_3CN$ + 0.1 M $Bu_4NBF_4$ at 0.9 V; $l$ = 1 cm; inset: $l$ = 2 mm.

### *Electrochemical Behavior of $[Mn_2^{III}(O)(O_2CCH_3)(tpa)_2](PF_6)_3\cdot CH_3CN$ [2(PF$_6$)$_3$·CH$_3$CN]*

Figure 4 shows the visible absorption spectrum of $\mathbf{2}^{3+}$. This pale purple/red complex exhibits two visible absorption bands at 494 ($\varepsilon$ = 520 M$^{-1}$ cm$^{-1}$) and 532 nm (440) corresponding to d-d transitions and a broad absorption band centerd at 720 nm (185). This spectrum is similar to those reported for other complexes possessing the same $\{Mn_2(O)(O_2CCH_3)\}^{3+}$ core.[39–41] The cyclic voltammogram of this complex in $CH_3CN$ containing 0.1 M $Bu_4NBF_4$ (scan rate of 100 mV s$^{-1}$) displays three waves at $E_{1/2}^{2A}$ = 0.95 V ($E_{pa}^{2A}$ = 1.00 and $E_{pc}^{2A}$ = 0.90 V; $\Delta E_p$ = 100 mV),

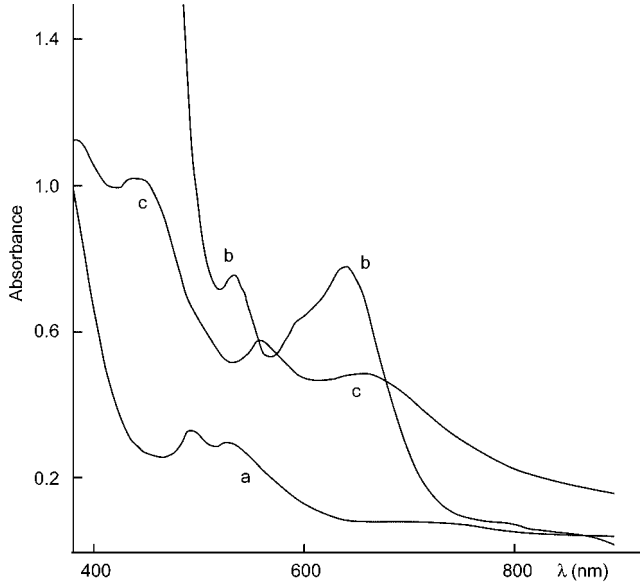


Figure 4. Visible absorption spectra of a 0.77 mM solution of $\mathbf{2}^{3+}$ in $CH_3CN$ + 0.1 M $Bu_4NBF_4$: (a) initial solution, (b) solution (a) after exhaustive oxidation at 1.15 V, and (c) solution (b) after exhaustive reduction at 0.6 V; $l$ = 1 cm.

 © 2007 Wiley-VCH Verlag GmbH & Co. KGaA, Weinheim 

$E_{1/2}^{2B}$ = 1.45 V ($E_{pa}^{2B}$ = 1.49 and $E_{pc}^{2B}$ = 1.41 V; $\Delta E_p$ = 80 mV); $E_{1/2}^{2C}$ = –0.07 V ($E_{pc}^{2C}$ = –0.12 and $E_{pa}^{2C}$ = –0.02 V; $\Delta E_p$ = 100 mV; Figure 5, A). The two oxidation waves are reversible and are attributed to the redox couples $Mn_2^{III,III/III,IV}$ and $Mn_2^{III,IV/IV,IV}$ [Equations (3) and (4), respectively].

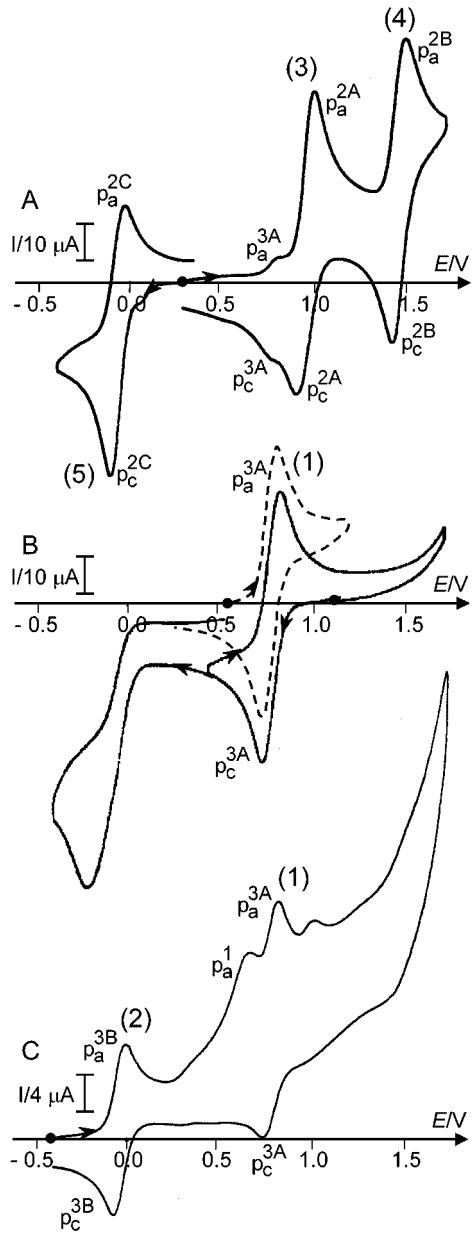


Figure 5. (A) Cyclic voltammograms at a Pt electrode (diameter: 5 mm) of a 0.77 mM solution of $\mathbf{2}^{3+}$ in $CH_3CN$ + 0.1 M $Bu_4NBF_4$; scan rate: 100 mV $s^{-1}$; (B) solution (A) after exhaustive oxidation at 1.15 V [curve (–), formation of $\mathbf{3}^{4+}$], then exhaustive reduction at 0.6 V [curve (----), formation of $\mathbf{3}^{3+}$], and (C) after exhaustive reduction of a 0.3 mM solution of $\mathbf{2}^{3+}$ at –0.4 V (formation of $\mathbf{1}^{2+}$ and $\mathbf{3}^{2+}$); scan rate: 100 mV $s^{-1}$. The numbers in parentheses correspond to the equation number in the text.

The reduction wave, which is only partially reversible at that scan rate, is associated with the redox states $Mn_2^{III,III/III,II}$ [Equation (5)].

$$[Mn_2^{III}(O)(O_2CCH_3)(tpa)_2]^{3+} \rightleftharpoons [Mn_2^{III,IV}(O)(O_2CCH_3)(tpa)_2]^{4+} + e^- \quad (3)$$
$$\mathbf{2}^{3+} \qquad\qquad \mathbf{2}^{4+}$$

$$[Mn_2^{III,IV}(O)(O_2CCH_3)(tpa)_2]^{4+} \rightleftharpoons [Mn_2^{IV}(O)(O_2CCH_3)(tpa)_2]^{5+} + e^- \quad (4)$$
$$\mathbf{2}^{4+} \qquad\qquad \mathbf{2}^{5+}$$

$$[Mn_2^{III}(O)(O_2CCH_3)(tpa)_2]^{3+} + e^- \rightleftharpoons [Mn_2^{III,II}(O)(O_2CCH_3)(tpa)_2]^{2+} \quad (5)$$
$$\mathbf{2}^{3+} \qquad\qquad \mathbf{2}^{2+}$$

The additional reversible wave with low intensity located at $E_{1/2}^{3A}$ = 0.77 V corresponds to an impurity of about 8% of the bis(μ-oxo) complex $\mathbf{3}^{3+}$ present in the sample (see below). None of the oxidized or reduced species of $\mathbf{2}^{3+}$ are stable over the timescale of a controlled potential electrolysis.

Exhaustive oxidation of a solution of $\mathbf{2}^{3+}$ at a potential of 1.15 V consumes about two electrons per molecule of complex and leads to the quasi-quantitative formation of the di-μ-oxo $Mn_2^{IV,IV}$ complex $\mathbf{3}^{4+}$. The formation of this complex is the result of the instability of the one-electron-oxidized form of $\mathbf{2}^{3+}$ $[Mn_2^{III,IV}(O)(O_2CCH_3)(tpa)_2]^{4+}$ [Equation (3)], which reacts with residual water in the solvent[25–29,43] to form the binuclear complex $\mathbf{3}^{3+}$ by substitution of one acetato bridge by an oxo bridge [Equation (6)].

$$[Mn_2^{III,IV}(O)(O_2CCH_3)(tpa)_2]^{4+} + H_2O \rightleftharpoons [Mn_2^{III,IV}(O)_2(tpa)_2]^{3+} + CH_3CO_2^- + 2\,H^+ \quad (6)$$
$$\mathbf{2}^{4+} \qquad\qquad \mathbf{3}^{3+}$$

However, since $\mathbf{3}^{3+}$ is more easily oxidizable than $\mathbf{2}^{3+}$ ($E_{1/2}^{3A}$ = 0.77 and $E_{1/2}^{2A}$ = 0.95 V, respectively), $\mathbf{3}^{3+}$ is oxidized to $\mathbf{3}^{4+}$ at the electrolysis potential used for the oxidation of $\mathbf{2}^{2+}$ [$E$ = 1.15 V; Equation (1)]. Equation (7) summarises the overall reaction.

$$[Mn_2^{III}(O)(O_2CCH_3)(tpa)_2]^{3+} + H_2O \rightleftharpoons [Mn_2^{IV}(O)_2(tpa)_2]^{4+} + CH_3CO_2^- + 2\,H^+ + 2e^- \quad (7)$$
$$\mathbf{2}^{3+} \qquad\qquad \mathbf{3}^{4+}$$

It should be noted that if one of the two protons released is trapped by the acetate anion released, the other one does not interact with $\mathbf{3}^{4+}$ since the formation of this complex is quasi-quantitative, as estimated by electrochemistry and by visible absorption spectroscopy (Figure 4, spectrum b). The cyclic voltammogram obtained after oxidation (Figure 5, B) shows the one-electron reversible wave at $E_{1/2}^{3A}$ = 0.77 V which is typical of the electroactivity of $\mathbf{3}^{4+}$, $[Mn_2^{IV,IV}/$

 © 2007 Wiley-VCH Verlag GmbH & Co. KGaA, Weinheim 

$Mn_2^{III,IV}$ couple; Equation (1)] and is followed by a second irreversible system at –0.21 V corresponding to the reduction of $\mathbf{3}^{3+}$. The irreversibility of this latter system is due to the presence of both acetate anions and protons released during the oxidation in solution [Equation (7)].

Indeed, under these particular conditions the reduction of the electrolyzed solution of $\mathbf{3}^{4+}$ at –0.4 V (three electrons consumed per initial molecule of $\mathbf{2}^{3+}$) does not lead selectively to the complex $\mathbf{3}^{2+}$ but to an equimolar mixture of complexes $\mathbf{3}^{2+}$ and $\mathbf{1}^{2+}$, as for the direct reduction of the initial solution of $\mathbf{2}^{3+}$ at this potential (see below). If the electrolyzed solution of $\mathbf{3}^{4+}$ is reduced at 0.6 V (consumption of about one electron per molecule of initial complex $\mathbf{2}^{3+}$), $\mathbf{3}^{3+}$ is obtained [Equation (1), Figure 5, B (dashed curve].

Exhaustive reduction of a solution of complex $\mathbf{2}^{3+}$ at a controlled potential of –0.4 V consumes one electron per molecule of complex. The resulting cyclic voltammogram (Figure 5, C) corresponds to the superimposition of the activity of complexes $\mathbf{3}^{2+}$ and $\mathbf{1}^{2+}$ (see below). The respective amount of both complexes was estimated from the height of the different waves at the rotating disc electrode and corresponds, for each complex, to half of the initial concentration of $\mathbf{2}^{3+}$. The reduction mechanism of $\mathbf{2}^{3+}$ involves the initial formation of the unstable species $\mathbf{2}^{2+}$ [Equation (5)] which undergoes a disproportionation reaction to give the stable final species $\mathbf{1}^{2+}$ and $\mathbf{3}^{2+}$ [Equation (8)].

$$[Mn_2^{II,III}(O)(O_2CCH_3)(tpa)_2]^{2+} \rightleftharpoons \underset{\mathbf{2}^{2+}}{} \quad (8)$$

$$\tfrac{1}{2}\,[Mn_2^{II}(O_2CCH_3)_2(tpa)_2]^{2+} + \tfrac{1}{2}\,[Mn_2^{III}(O)_2(tpa)_2]^{2+}$$
$$\mathbf{1}^{2+} \qquad\qquad \mathbf{3}^{2+}$$

Equation (9) summarises the overall process.

$$[Mn_2^{III}(O)(O_2CCH_3)(tpa)_2]^{3+} + e^- \rightleftharpoons \underset{\mathbf{2}^{3+}}{} \quad (9)$$

$$\tfrac{1}{2}\,[Mn_2^{II}(O_2CCH_3)_2(tpa)_2]^{2+} + \tfrac{1}{2}\,[Mn_2^{III}(O)_2(tpa)_2]^{2+}$$
$$\mathbf{1}^{2+} \qquad\qquad \mathbf{3}^{2+}$$

The two oxidation waves of $\mathbf{2}^{3+}$ [Equations (3) and (4)] appear to be more reversible than those of $[Mn_2^{III}(O)(O_2CCH_3)_2(bpea)_2]^{2+}$ at the same scan rate.[29] This shows that the rate of formation of the bis(μ-oxo) complex $\mathbf{3}^{3+}$ is slower than that of $[Mn_2^{III,IV}(O)_2(O_2CCH_3)(bpea)_2]^{2+}$ due to the greater stability of $[Mn_2^{III,IV}(O)(O_2CCH_3)(tpa)_2]^{4+}$ compared to $[Mn_2^{III,IV}(O)(O_2CCH_3)_2(bpea)_2]^{3+}$.

### *Electrochemical Behavior of $[Mn_2^{II}(O_2CCH_3)_2(tpa)_2](PF_6)_2$ [1(PF$_6$)$_2$]*

The cyclic voltammogram of a solution of $\mathbf{1}^{2+}$ in $CH_3CN$ containing 0.1 M $Bu_4NBF_4$ displays a first irreversible oxidation peak at $E_{pa}^{1}$ = 0.70 V corresponding to the oxidation of the metallic centers of the complex (Figure 6, A). This oxidation leads to the formation of $\mathbf{2}^{3+}$, as evidenced by the presence of its two partially reversible oxidation waves at $E_{1/2}^{2A}$ = 0.95 and $E_{1/2}^{2B}$ = 1.45 V, which follow the irreversible oxidation peak at 0.70 V, and by the irreversible reduction peak at –0.04 V in the reverse scan. Complex $\mathbf{3}^{3+}$, which is formed during the oxidation of $\mathbf{2}^{3+}$ at $E_{pa}^{2A}$ = 1.0 V, is also detected in the cyclic voltammogram by the presence of its first reduction peak at $E_{pc}^{3A}$ = 0.73 V. This electro-induced transformation is faster than the oxidation of $\mathbf{2}^{3+}$ into $\mathbf{3}^{3+}$ since the oxidation peak of $\mathbf{1}^{2+}$ is fully irreversible even for higher scan rates of up to 500 mV s$^{-1}$.

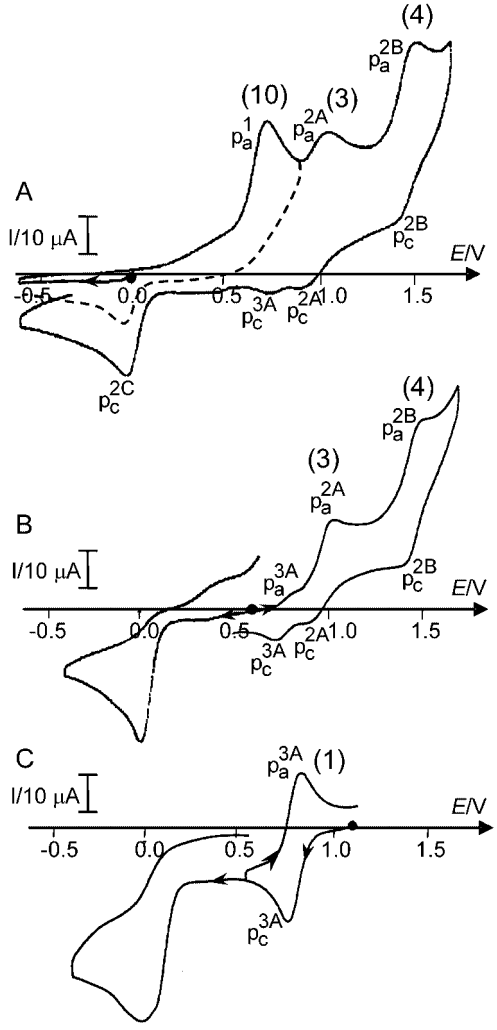


Figure 6. Cyclic voltammograms at a Pt electrode (diameter: 5 mm) of (A) a 0.45 mM solution of $\mathbf{1}^{2+}$ in $CH_3CN$ + 0.1 M of $Bu_4NClO_4$; (B) solution (A) after exhaustive oxidation at 0.7 V (formation of $\mathbf{2}^{3+}$), and (C) solution (B) after exhaustive oxidation at 1.10 V (formation of $\mathbf{3}^{4+}$); scan rate: 100 mV s$^{-1}$. The numbers in parentheses correspond to the equation number in the text.

As expected, exhaustive oxidation of a solution of $\mathbf{1}^{2+}$ at 0.7 V consumes two electrons per molecule of complex and leads mainly to the formation of $\mathbf{2}^{3+}$ (yield: 90%). The resulting cyclic voltammogram displays the typical activity of this complex (Figure 6, B). However, a small amount of $\mathbf{3}^{3+}$ is also formed during the oxidation process (about 8%), as

 © 2007 Wiley-VCH Verlag GmbH & Co. KGaA, Weinheim 

attested by the presence of its reversible oxidation wave at $E^{3A}_{1/2}$ = 0.77 V. This explains why the same amount of this complex is present in the sample of $\mathbf{2}^{3+}$ isolated from electrolyzed solutions.

The processes involved in the oxidation of $\mathbf{1}^{2+}$ are summarized in Equation (10) [Scheme 1(a)].

$$\underset{\mathbf{1}^{2+}}{[Mn_2^{II}(O_2CCH_3)_2(tpa)_2]^{2+}} + H_2O \rightleftharpoons \underset{\mathbf{2}^{3+}}{[Mn_2^{III}(O)(O_2CCH_3)(tpa)_2]^{3+}} + CH_3CO_2^- + 2\,H^+ + 2\,e^- \quad (10)$$

As for the oxidation of $\mathbf{2}^{3+}$ into $\mathbf{3}^{4+}$ [Equation (7)], the oxidation of $\mathbf{1}^{2+}$ into $\mathbf{2}^{3+}$ leads to the dissociation of one acetate anion and the formation of an oxo bridge between the two manganese ions by deprotonation of a water molecule from the solvent.

Subsequent electrolysis at 1.10 V results in the quantitative formation of $\mathbf{3}^{4+}$ after the exchange of two additional electrons per molecule of the initial complex $\mathbf{1}^{2+}$ [Equation (7)] [Scheme 1 (b)]. The cyclic voltammogram of the resulting green solution (Figure 6, C), as well as the visible absorption spectrum, are typical of a solution of $\mathbf{3}^{4+}$. It should be noted that $\mathbf{3}^{4+}$ can be generated directly, with the same yield, by a four-electron oxidation of $\mathbf{1}^{2+}$ at 1.10 V [Equation (11); Scheme 1 (a–c)].

$$\underset{\mathbf{1}^{2+}}{[Mn_2^{II}(O_2CCH_3)_2(tpa)_2]^{2+}} + 2\,H_2O \rightleftharpoons \underset{\mathbf{3}^{4+}}{[Mn_2^{IV}(O)_2(tpa)_2]^{4+}} + 2\,CH_3CO_2^- + 4\,H^+ + 4\,e^- \quad (11)$$

The reaction in Equation (10) is an overall reversible process, therefore a controlled-potential reduction of the electrochemically generated solution of $\mathbf{2}^{3+}$ at –0.6 V completely restores the initial amount of $\mathbf{1}^{2+}$ [Scheme 1 (a)] after the consumption of two electrons per molecule of initial $\mathbf{1}^{2+}$. Likewise, the initial amount of $\mathbf{1}^{2+}$ can also be obtained by a controlled-potential reduction of the electrochemically generated solution of $\mathbf{3}^{4+}$ at –0.6 V [Equation (11); Scheme 1 (a–c)] after consumption of 3.8 electrons per molecule of $\mathbf{1}^{2+}$.

## Discussion and Conclusion

We have systematically investigated the redox properties of three different cores $\{Mn_2^{II}(\mu\text{-}O_2CCH_3)_2\}$, $\{Mn_2^{III}(\mu\text{-}O)(\mu\text{-}O_2CCH_3)\}$, and $\{Mn_2^{III}(\mu\text{-}O)_2\}/\{Mn_2^{III,IV}(\mu\text{-}O)_2\}/\{Mn_2^{IV,IV}(\mu\text{-}O)_2\}$ with the same terminal ligand (tpa) and studied possible core interconversions between the various oxidation levels of manganese. Oxidation of the $\{Mn_2^{II}(\mu\text{-}O_2CCH_3)_2\}$ complex $\mathbf{1}^{2+}$ is fully irreversible and mainly leads to $\{Mn_2^{III}(\mu\text{-}O)(\mu\text{-}O_2CCH_3)\}$ ($\mathbf{2}^{3+}$). Further oxidation of $\mathbf{2}^{3+}$ yields the $\{Mn_2^{IV,IV}(\mu\text{-}O)_2\}$ complex $\mathbf{3}^{4+}$ quantitatively (Scheme 1). The rate of the electroinduced transformation of $\mathbf{1}^{2+}$ into $\mathbf{2}^{3+}$ is faster than that of $\mathbf{2}^{3+}$ into $\mathbf{3}^{4+}$, as shown by the shape of the cyclic voltammograms of $\mathbf{1}^{2+}$ and $\mathbf{2}^{3+}$, which attests to the greater instability of a $(\mu\text{-}O_2CCH_3)_2$ species at the $Mn_2^{II,III}$ oxidation level than that of a $(\mu\text{-}O)(\mu\text{-}O_2CCH_3)$ at the $Mn_2^{III,IV}$ oxidation level. In addition, $\mathbf{2}^{3+}$ and $\mathbf{3}^{4+}$ can be selectively generated owing to a good separation of the two two-electron oxidation waves [the oxidation potentials of $\mathbf{1}^{2+}$ and $\mathbf{2}^{3+}$ are 0.70 and 0.95 V vs. $Ag/Ag^+$ (10 mM), respectively]. The oxidation potential of $\mathbf{3}^{3+}$ (0.77 V) is located between the oxidation potentials of $\mathbf{1}^{2+}$ and $\mathbf{2}^{3+}$. These transformations ($\mathbf{1}^{2+}$ into $\mathbf{2}^{3+}$ and $\mathbf{2}^{3+}$ into $\mathbf{3}^{4+}$) are chemically reversible by reduction processes, although the two steps are not separated. Indeed, $\mathbf{1}^{2+}$ is directly and entirely regenerated by reduction of $\mathbf{3}^{4+}$ (or $\mathbf{3}^{3+}$). These core interconversions under oxidative and reductive conditions obviously occur concomitantly with protonation/deprotonation reactions at the bridging oxo groups.

We have also isolated and crystallographically characterized a new binuclear manganese complex in the tpa series ($\mathbf{2}^{3+}$), which shows that the (III,III) oxidation state in the tpa series is stable with two types of cores: a bis(μ-oxo) and a mono-(μ-oxo) mono-(μ-acetato). The difference in Mn···Mn separation across the four binuclear tpa compounds is 1.50 Å [$\{Mn_2^{II}(O_2CCH_3)_2\}$ 4.154(1), $\{Mn_2^{III}(O)(O_2CCH_3)\}$ 3.253, $\{Mn_2^{III}(O)_2\}$ 2.656(2), $\{Mn_2^{III,IV}(O)_2\}$ 2.643(1) Å].

These electrochemical and crystallographic results are in agreement with the hypothesis of the presence of one oxo bridge for the active site of MnCat in the $Mn_2^{III,III}$ oxidation state.

We are currently evaluating the ability of these tpa complexes to disproportionate hydrogen peroxide in order to compare their efficiencies to those of the parent bpea complexes. Indeed, although the electrochemical behavior of the bpea and tpa complexes are quite similar, the oxidation potentials of the bpea complexes are clearly lower (about 160–190 mV) than those of the tpa complexes owing to the presence of an additional acetate bridge, which has a more pronounced electron-donor character than that of pyridine. In addition, the rate of formation of the $Mn_2^{III,IV}$ complex $\mathbf{3}^{3+}$ by oxidation of the $Mn_2^{III,III}$ complex $\mathbf{2}^{3+}$ is slower than that of the tpa derivative. A different catalytic efficiency may therefore be expected for these two kinds of complexes.

## Experimental Section

**Materials:** Acetonitrile (Rathburn, HPLC grade) was used as received and stored under argon in a glovebox. Tetra-*n*-butylammonium perchlorate ($Bu_4NClO_4$), tetra-*n*-butylammonium tetrafluoroborate ($Bu_4NBF_4$), and tetra-*n*-butylammonium hexafluorophosphate ($Bu_4NPF_6$) were purchased from Fluka and used as received.

Tris(2-pyridylmethyl)amine (tpa) and the complex $\mathbf{3}(ClO_4)_3$ were synthesized according to previously described methods.[38]

**$[Mn_2^{II}(O_2CCH_3)_2(tpa)_2](PF_6)_2$ [$\mathbf{1}(PF_6)_2$]:** A solution of $MnSO_4{\cdot}H_2O$ (38.2 mg, 0.227 mmol) in water (5 mL) was added to

 © 2007 Wiley-VCH Verlag GmbH & Co. KGaA, Weinheim 

a solution of tpa (66 mg, 0.227 mmol) in methanol (5 mL). After 25 min of stirring, a solution of $NaCH_3CO_2$ (19 mg, 0.227 mmol) in water (1 mL) was added. The resulting colorless solution was stirred at room temperature for 15 min. After addition of solid $KPF_6$ (82.2 mg, 0.446 mmol) the solution was evaporated to dryness and the yellow-white residue redissolved in $CH_3CN$. The solution was filtered to remove insoluble white $K_2SO_4$ and the filtrate was then evaporated to dryness. The colorless residue obtained was then redissolved in dichloromethane and the resulting solution filtered to remove a white powder corresponding to excess $KPF_6$. The filtrate was then evaporated to dryness and a pale-yellow powder corresponding to **1**$(PF_6)_2$ was obtained. Yield: 150 mg (60%). These crystals analyzed satisfactorily as $[Mn_2^{II}(\mu\text{-}O_2CCH_3)_2(tpa)_2](PF_6)_2$. $C_{40}H_{42}F_{12}Mn_2N_8O_4P_2$ (1098.6): calcd. C 43.71, H 3.85, N 10.2; found C 43.66, H3.91, N 10.12. IR (KBr): $\tilde{\nu}$ = 3428 $cm^{-1}$ (m), 1605 (s), 1580 (s), 1505 (w), 1484 (m), 1444 (s), 1353 (w), 1294 (m), 1269 (w), 1158 (m), 1122 (w), 1100 (m), 1053 (m), 1017 (m), 840 (vs), 764 (s), 639 (m), 557 (s), 500 (w), 415 (w).

**$[Mn_2^{III}(O)(O_2CCH_3)(tpa)_2](PF_6)_3$ [2$(PF_6)_3$]:** This complex was synthesized by an electrochemical procedure. Exhaustive oxidation of a 4.5 mM solution of **1**$(PF_6)_2$ in 12 mL of $CH_3CN$ containing 0.1 M $Bu_4NPF_6$ as supporting electrolyte at 0.80 V on a platinum plate led to formation of a red-purple solution corresponding to the complex $\mathbf{2}^{3+}$. Red-purple crystals of **2**$(PF_6)_3{\cdot}CH_3CN$ suitable for X-ray diffraction were grown after one day by slow vapor diffusion of diethyl ether into this solution. These were filtered, washed with $CH_2Cl_2$, and dried under air. Yield: 53.9 mg (85%). These crystals analyzed satisfactorily as **2**$(PF_6)_3$. $C_{38}H_{39}Mn_2N_8O_3P_3F_{18}$ (1200): calcd. C 37.93, H3.24, N 9.51; found C 38.00, H 3.25, N 9.33. IR (KBr): $\tilde{\nu}$ = 3445 $cm^{-1}$ (vs), 1609 (s), 1574 (w), 1531 (w), 1487 (w), 1445 (s), 1295 (m), 1163 (m), 1101 (m), 1063 (m), 1032 (m), 1023 (m), 839 (vs), 761 (m), 707 (m), 678 (m), 661 (m), 614 (m), 557 (s), 414 (w). UV/Vis ($CH_3CN$): $\lambda_{max}$ ($\varepsilon$) = 256 nm (20640 $M^{-1}cm^{-1}$), 289 (10910, sh), 380 (1160, sh), 494 (410), 532 (350), 720 (150).

**Spectroscopy:** Infrared spectra were recorded with a Perkin–Elmer Spectrum GX FTIR spectrometer. Electronic absorption spectra were recorded with a Cary 50 Varian spectrophotometer. Initial and electrolyzed solutions were transferred into a conventional cuvette cell in a glovebox. The cell was inserted into an optical translator connected to the spectrophotometer through a fiber optic system (Photonetics Spectrofip System). The optical fibers pass through the wall of the dry box via seals.

**Electrochemical Measurements:** All electrochemical measurements were run under argon in a dry glovebox at room temperature. Cyclic voltammetry (CV) and controlled potential electrolysis experiments were performed using an EG&G PAR model 173 potentiostat equipped with a PAR model universal programmer and a PAR model 179 digital coulometer. The electrolyte was a 0.1 M solution of $Bu_4NClO_4$, $Bu_4NBF_4$, or $Bu_4NPF_6$ in $CH_3CN$. A standard three-electrode electrochemical cell was used. Potentials were referred to an Ag/10 mM $AgNO_3$ reference electrode in $CH_3CN$ (+0.1 M $Bu_4NClO_4$). The working electrodes were 5-mm-diameter platinum disks polished with 2-μm diamond paste for cyclic voltammetry [$E_{pa}$: anodic peak potential; $E_{pc}$: cathodic peak potential; $E_{1/2} = (E_{pa} + E_{pc})/2$; $\Delta E_p = E_{pa} - E_{pc}$] and 2-mm-diameter disks for rotating disk electrode experiments (RDE). Exhaustive electrolyses were carried out with a 5 $cm^2$ platinum cylinder or a 10×10×4 $mm^3$ carbon felt electrode (RCV, 2000, 65 mg $cm^{-3}$, from Le Carbone Lorraine). The counter electrode was a Pt wire in $CH_3CN$ (+0.1 M $Bu_4NClO_4$, $Bu_4NBF_4$, or $Bu_4NPF_6$).

**Crystal-Structure Determination of 2$(PF_6)_3{\cdot}CH_3CN$:** A crystal of **2**$(PF_6)_3{\cdot}CH_3CN$ of dimensions 0.5×0.4×0.08 $mm^3$ was selected. Diffraction data were collected with a Bruker SMART diffractometer with Mo-$K_\alpha$ radiation. All calculations were performed using the SHELXTL computer program.[44] The structure was solved by direct methods and refined by full-matrix least-squares fits on $F^2$. The crystallographic data are summarized in Tables 1 and 2.

Table 2. Principal crystallographic data and parameters for $[Mn_2^{III}(O)(O_2CCH_3)(tpa)_2](PF_6)_3{\cdot}CH_3CN$ [**2**$(PF_6)_3{\cdot}CH_3CN$].

| | |
|---|---|
| Compound | $[Mn_2^{III}(O)(O_2CCH_3)(tpa)_2](PF_6)_3{\cdot}CH_3CN$ |
| Chemical formula | $C_{40}H_{42}F_{18}Mn_2N_9O_3P_3$ |
| Formula weight | 1241.62 |
| Crystal system | monoclinic |
| Space group | $P2_1/n$ |
| $a$ [Å] | 11.9899(17) |
| $b$ [Å] | 35.050(5) |
| $c$ [Å] | 12.3952(18) |
| $\beta$ [°] | 101.218(6) |
| $V$ [Å$^3$] | 5109.5(13) |
| $T$ [K] | 223(2) |
| $\lambda$ [Å] | 0.71073 |
| Density [mg m$^{-3}$] | 1.614 |
| $Z$ | 4 |
| $\mu$ [mm$^{-1}$] | 0.701 |
| $F$(000) | 2504 |
| Reflections collected | 10619 |
| $R_1$[a] | 0.0514 |
| $wR_2$[b] | 0.1048 |

[a] $R_1 = \Sigma||F_o| - |F_c||/\Sigma|F_o|$. [b] $wR = [\Sigma w(|F_o| - |F_c|)^2/\Sigma wF_o^2]^{1/2}$.

CCDC-625212 contains the supplementary crystallographic data for this paper. These data can be obtained free of charge from the Cambridge Crystallographic Data Center via www.ccdc.cam.ac.uk/datarequest/cif.

## Acknowledgments

The authors acknowledge Dr. J.-M. Latour from the Laboratoire de Physicochimie des Métaux en Biologie, DRDC, UMR 5155 CEA-CNRS-UJF, CEA-Grenoble for a gift of **3**$(ClO_4)_3$. This research was supported by the COST D21 program.

[1] J. Wu, J. E. Penner-Hahn, V. L. Pecoraro, *Chem. Rev.* **2004**, *104*, 903 and references cited therein.
[2] S. Mukhopadhyay, S. K. Mandal, S. Bhaduri, W. H. Armstrong, *Chem. Rev.* **2004**, *104*, 3981 and references cited therein.
[3] D. C. Weatherburn, S. Mandal, S. Mukhopadhyay, S. Bahduri, L. F. Lindoy, Manganese, in *Comprehensive Coordination Chemistry II* (Eds.: J. A. McCleverty, T. J. Meyer), Elsevier Pergamon, Oxford, **2004**, vol. 5, p. 1.
[4] S. Antonyuk, V. Melik-Adamyan, A. Popov, V. Lamzin, P. Hempstead, P. Harrison, P. Artymyuk, V. Barynin, *Crystallogr.* **2000**, *45*, 105.
[5] M. M. Whittaker, V. V. Barynin, T. Igarashi, J. W. Whittaker, *Eur. J. Biochem.* **2003**, *270*, 1102.
[6] V. V. Barynin, P. D. Hempstead, A. A. Vagin, S. V. Antonyuk, W. R. Melik-Adamyan, V. S. Lamzin, P. M. Harrison, P. J. Artymiuk, *J. Inorg. Biochem.* **1997**, *67*, 196 and references cited therein.
[7] V. V. Barynin, M. M. Whittaker, S. V. Antonyuk, V. S. Lamzkin, P. M. Harrison, P. J. Artymiuk, J. W. Whittaker, *Structure* **2001**, *9*, 725 and references cited therein.
[8] T. L. Stemmer Jr, T. M. Sossong, J. I. Goldstein, D. E. Ash, T. E. Elgren Jr, D. M. Kurtz, J. E. Penner-Hahn, *Biochemistry* **1997**, *36*, 9847.
[9] B. Kok, B. Forbush, M. McGloin, *Photochem. Photobiol.* **1970**, *11*, 457.

 © 2007 Wiley-VCH Verlag GmbH & Co. KGaA, Weinheim 

[10] P. Joliot, G. Barbieri, R. Chabaud, *Photochem. Photobiol.* **1969**, *10*, 309.
[11] M. Haumann, P. Liebisch, C. Müller, M. Barra, M. Grabolle, H. Dau, *Science* **2005**, *310*, 1019.
[12] J. E. Penner-Hahn, C. Yocum, *Science* **2005**, *310*, 982.
[13] J. P. McEvoy, J. A. Gascon, V. S. Batista, G. W. Brudvig, *Photochem. Photobiol.* **2005**, *4*, 940.
[14] M. Haumann, C. Müller, P. Liebisch, L. Iuzzolino, J. Dittmer, M. Grabolle, T. Neisius, W. Meyer-Klaucke, D. Dau, *Biochemistry* **2005**, *44*, 1894 and references cited therein.
[15] J. P. McEvoy, G. W. Brudvig, *Chem. Rev.* **2006**, *106*, 4457.
[16] R. D. Britt, J. M. Peloquin, K. A. Campbell, *Annu. Rev. Biophys. Biomol. Struct.* **2000**, *29*, 463.
[17] P. Glatzel, U. Bergmann, J. Yano, H. Visser, J. H. Robblee, W. Gu, F. M. F. de Groot, G. Christou, V. L. Pecoraro, S. P. Cramer, V. K. Yachandra, *J. Am. Chem. Soc.* **2004**, *126*, 9946 and references cited therein.
[18] V. K. Yachandra, K. Sauer, M. P. Klein, *Chem. Rev.* **1996**, *96*, 2927.
[19] A. Zouni, H.-T. Witt, J. Kern, P. Fromme, N. Krauβ, W. Saenger, P. Orth, *Nature* **2001**, *409*, 739.
[20] N. Kamiya, J.-R. Shen, *Proc. Natl. Acad. Sci. USA* **2003**, *100*, 98.
[21] K. N. Ferreira, T. M. Iverson, K. Maghlaoui, J. Barber, S. Iwata, *Science* **2004**, *303*, 1831.
[22] J. Kern, B. Loll, A. Zouni, W. Saenger, K.-D. Irrgang, J. Biesiadka, *Photosynth. Res.* **2005**, *84*, 153.
[23] B. Loll, J. Kern, W. Saenger, A. Zouni, J. Biesiadka, *Nature* **2005**, *438*, 1040.
[24] T. Tanase, S. J. Lippard, *Inorg. Chem.* **1995**, *34*, 4682.
[25] S. Mahapatra, P. Das, R. Mukherjee, *J. Chem. Soc., Dalton Trans.* **1993**, 217.
[26] S. Mahapatra, T. K. Lal, R. Mukherjee, *Inorg. Chem.* **1994**, *33*, 1579.
[27] T. K. Lal, R. Mukherjee, *Inorg. Chem.* **1998**, *37*, 2373.
[28] M.-N. Collomb Dunand-Sauthier, A. Deronzier, I. Romero, *J. Electroanal. Chem.* **1997**, *436*, 219.
[29] I. Romero, L. Dubois, M.-N. Collomb, A. Deronzier, J.-M. Latour, J. Pécaut, *Inorg. Chem.* **2002**, *41*, 1795.
[30] A. E. M. Boelrijk, S. V. Khangulov, G. C. Dismukes, *Inorg. Chem.* **2000**, *39*, 3009.
[31] L. Dubois, R. Caspar, L. Jacquamet, P.-E. Petit, M.-F. Charlot, C. Baffert, M.-N. Collomb, A. Deronzier, J.-M. Latour, *Inorg. Chem.* **2003**, *42*, 4817.
[32] L. P. Nielsen, M. Mortensen, S. Kjaergaard Knudsen, K.-L. Lund, M.-N. Collomb, C. Baffert, A. Deronzier, J.-M. Latour, N. Thorup, C. J. KcKenzie, *Dalton Trans.* **2003**, 1765.
[33] C. Hureau, S. Blanchard, M. Nierlich, G. Blain, E. Rivière, J.-J. Girerd, E. Anxolabéhères-Mallart, G. Blondin, *Inorg. Chem.* **2004**, *43*, 4415.
[34] A. Magnuson, P. Liebisch, J. Högblom, M. F. Anderlund, R. Lomoth, W. Meyer-Klaucke, M. Haumann, H. Dau, *J. Inorg. Biochem.* **2006**, *100*, 1234.
[35] H. Oshio, E. Ino, I. Mogi, T. Ito, *Inorg. Chem.* **1993**, *32*, 5697.
[36] Y. Hitomi, A. Ando, H. Matsui, T. Ito, T. Tanaka, S. Ogo, T. Funabiki, *Inorg. Chem.* **2005**, *44*, 3473.
[37] D. K. Towle, C. A. Botsford, D. J. Hodgson, *Inorg. Chim. Acta* **1988**, *141*, 167.
[38] M. Suzuki, S. Tokura, M. Suhara, A. Uehara, *Chem. Lett.* **1988**, 1763.
[39] N. Arulsamy, J. Glerup, A. Hazell, D. J. Hodgson, C. J. McKenzie, H. Toftlund, *Inorg. Chem.* **1994**, *33*, 3023.
[40] K. J. Oberhausen, R. J. O'Brien, J. F. Richardson, R. M. Buchanan, R. Costa, J.-M. Latour, H.-L. Tsai, D. N. Hendrickson, *Inorg. Chem.* **1993**, *32*, 4561.
[41] M. U. Triller, W.-Y. Hsieh, V. L. Pecoraro, A. Rompel, B. Krebs, *Inorg. Chem.* **2002**, *41*, 5544.
[42] V. V. Pavlishchuk, A. W. Addison, *Inorg. Chim. Acta* **2000**, *298*, 97.
[43] M. M. Morrison, D. T. Sawyer, *Inorg. Chem.* **1978**, *17*, 333.
[44] G. M. Sheldrick, *SHELXTL-Plus*, vers. 5.1, Structure Determination Software Programs, Bruker-AXS Inc., Madison, WI, **1998**.

Received: November 20, 2006
Published Online: March 20, 2007

 © 2007 Wiley-VCH Verlag GmbH & Co. KGaA, Weinheim 

DOI: 10.1002/ejic.200601183

# Magnetic and Infrared Properties of the Azide Complex of (2,7,12,17-Tetrapropylporphycenato)iron(III): A Novel Admixing Mechanism of the $S$ = 5/2 and $S$ = 3/2 States

**Saburo Neya,*[a] Akihiro Takahashi,[a] Hirotaka Ode,[a] Tyuji Hoshino,[a] Masayuki Hata,[a] Akira Ikezaki,[b] Yoshiki Ohgo,[b] Masashi Takahashi,[c] Hirotsugu Hiramatsu,[d] Teizo Kitagawa,[d] Yuji Furutani,[e] Hideki Kandori,[e] Noriaki Funasaki,[f] and Mikio Nakamura[b]**

**Keywords:** Macrocyclic ligands / Iron / Electronic structure / Spin crossover / Azides / IR spectroscopy

The five-coordinate ferric azide complex of 2,7,12,17-tetrapropylporphyrcene [Fe(TPrPc)$N_3$] was characterized with proton NMR, electron paramagnetic resonance (EPR), Mössbauer, and IR techniques. The paramagnetic NMR showed the pyrrole-H signal that exhibits anomalous *anti*-Curie type of 1/$T$-dependence over a 310–190 K range. The EPR of the solid sample resolved a signal with $g$ = 5.42, 5.40, and 2.00 at 5 K. The quadrupole splitting parameter of the Mössbauer spectrum was 2.20 mm s$^{-1}$ at 290 K, and the magnetic moment was 4.70 $\mu_B$ at 290 K for the microcrystalline sample. These results suggest that [Fe(TPrPc)$N_3$] is not pure high-spin ($S$ = 5/2) but a spin mixture of the $S$ = 5/2, 3/2 states. The azide in [Fe(TPrPc)$N_3$] exhibited split IR bands ascribed to the two spin isomers at 2066 and 2049 cm$^{-1}$. The 2049-cm$^{-1}$ band, assigned to the $S$ = 3/2 species, was reversibly intensified with decreasing temperature. The IR results demonstrate that the $S$ = 3/2, 5/2 states are not quantum-mechanically admixed but in thermal equilibrium. The thermodynamic parameters associated with the spin equilibrium, $\Delta H$ = –3 990 cal mol$^{-1}$ and $\Delta S$ = –16.5 cal mol$^{-1}$ K$^{-1}$, were obtained from the NMR shift analysis, and the population of the $S$ = 3/2 isomer was calculated to be 0.19 at 293 K. A minimum lifetime of the two spin isomers was estimated to be 0.3 ps with IR.

(© Wiley-VCH Verlag GmbH & Co. KGaA, 69451 Weinheim, Germany, 2007)

## Introduction

Understanding of hemoprotein function is aided by the elucidation of the structure of the prosthetic group. There is a general consensus that heme is not always rigid but flexible and can deform easily. Nonplanar heme deformation in a crowded protein matrix is suggested to be functionally important.[1] Porphyrin molecular shape can be artificially changed with organic synthesis by rearranging the tetrapyrrole array.[2] A typical example is 2,7,12,17-tetrapropylporphycene (TPrPc; Scheme 1), discovered by Vogel et al. in 1987.[3] The macrocycle consists of a rectangular tetrapyrrole, in marked contrast with the square porphyrin. The modified tetrapyrrole extensively alters the physicochemical properties of parent porphyrin. TPrPc exhibits characteristic light absorption spectra[2,3] and redox properties.[4]

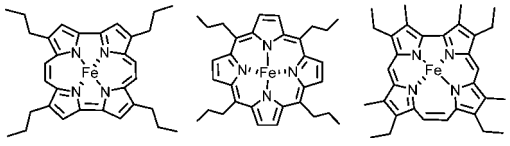


Scheme 1. Structure of the Fe$^{III}$ complex of the porphyrinoids. The coordinating azide ion is omitted for clarity.

Among the exogenous heme ligands, azide ion ($N_3^-$) occupies a distinctive position to induce a thermal equilibrium between the high- ($S$ = 5/2) and low-spin ($S$ = 1/2) states in ferric hemoprotein.[5] The equilibrium was analyzed to monitor the heme–globin interactions.[6,7] The spin-state equilibrium of azide hemoprotein has been well reproduced with six-coordinate model hemes.[8–12] In contrast, the five-coordinate ferric heme [Fe(porphyrinato)$N_3$] is a typical high-spin complex.[10,11] The X-ray analysis for [Fe(TPP)-

[a] Department of Physical Chemistry, Graduate School of Pharmaceutical Sciences, Chiba University,
Inage-Yayoi, Chiba 263-8522, Japan
E-mail: sneya@p.chiba-u.ac.jp
[b] Department of Chemistry, School of Medicine, Toho University,
Omorinishi, Ota-ku, Tokyo 143-8540, Japan
[c] Department of Chemistry, Faculty of Science, Toho University, Funabashi, Chiba 274-8510, Japan
[d] Center for Integrative Bioscience, Okazaki National Institutes, Okazaki, Aichi 444-8787, Japan
[e] Department of Materials Science and Engineering, Nagoya Institute of Technology,
Showa-ku, Nagoya 466-8555, Japan
[f] Department of Physical Chemistry, Kyoto Pharmaceutical University,
Yamashina, Kyoto 607-8414, Japan

 © 2007 Wiley-VCH Verlag GmbH & Co. KGaA, Weinheim 

$N_3$] (TPP, *meso*-tetraphenylporphyrinato) provided structural rationale for the high-spin state in five-coordinate azide heme.[11]

The coordination core in porphycene is contracted.[2,3] Recent spectroscopic investigations suggest that the narrower metallo cavity in porphycene affects the magnetic properties of the central iron(III) atom. The five-coordinate ferric chloride complex of porphycene, for instance, exhibits some intermediate-spin ($S$ = 3/2) character,[13,14] whereas the corresponding iron porphyrin is pure high-spin. In six-coordinate ferric porphycene with axial azide/imidazole, the high-spin population is lost, whereas the corresponding porphyrin is 15% high-spin.[6] The unique structure of the corrphycene molecule suggests that the azide complex of ferric iron porphycene [Fe(TPrPc)$N_3$] is likely to exhibit an unusual behavior. We found that [Fe(TPrPc)$N_3$] has magnetic properties, which are intermediate between the $S$ = 5/2 and 3/2 states, in marked contrast with the pure $S$ = 5/2 state of the corresponding iron porphyrins. Although the mixed-spin $S$ = 5/2, 3/2 compounds have been extensively elucidated with various physical methods,[15,16] there has apparently been no IR spectroscopic report for this system. We demonstrate here that IR spectroscopy, when applied to [Fe(TPrPc)$N_3$], discloses a novel picture of the spin admixing.

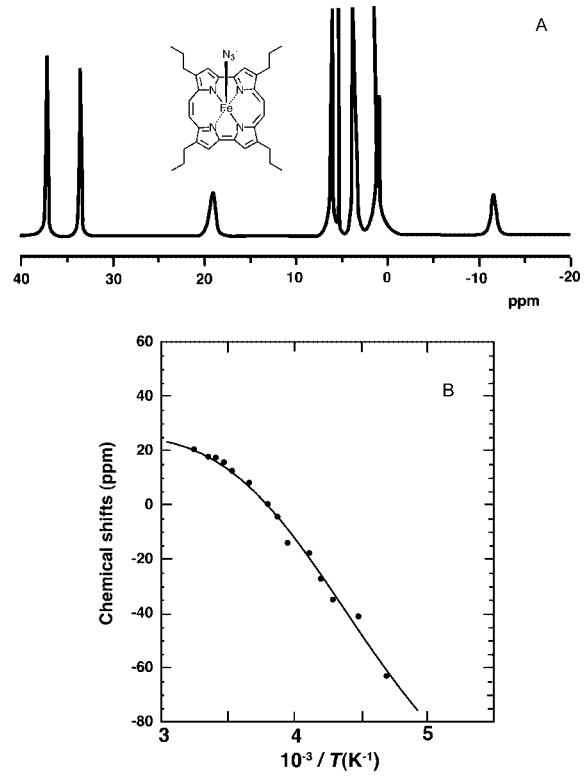


Figure 1. Proton NMR spectroscopy. (A) [Fe(TPrPc)$N_3$] in $CD_2Cl_2$ at 300 K. (B) The Curie plots for the pyrrole-H signal. The solid curve is theoretical fit calculated with the equation in the text.

## Results

### $^1$H NMR and EPR

We recorded the $^1$H NMR of [Fe(TPrPc)$N_3$] to elucidate the magnetic anomaly inferred from the unique structure. Figure 1 shows the NMR spectrum recorded in $CD_2Cl_2$. The α-$CH_2$, β-$CH_2$, and γ-$CH_3$ signals of the *n*-propyl substituents were observed at 37.2, 33.6, 6.1, 6.0, and 3.6 ppm, respectively. The ethene-bridge proton was located at –11.6 ppm, and pyrrole-H was at $\delta$ = 19.1 ppm. The assignment is based on the peak intensity and iron–proton distance. The methylene doublets come from the magnetic anisotropy brought about by iron displacement from the porphycene plane (diastereotropic effect), and indicate the five-coordinate state.[17] The five-coordinate structure is supported from the pyrrole-H shift at $\delta$ = 19 ppm because the six-coordinate high-spin heme iron exhibits the pyrrole-H shift at about 65 ppm.[17] The 1/$T$ dependence of these signals is irregular. The protons in the propyl groups and ethene bridges do not follow the Curie law to exhibit curved plots. The Curie plots of the pyrrole-H are especially anomalous. The signal shifted to –30 ppm at 200 K beyond the diamagnetic region (Figure 1, part B). The behavior of the pyrrole-H closely resembles that of [Fe(TPP)$ClO_4$][18] and [Fe(TPrPc)X] (X = Cl, Br, I),[13] which are in the mixed-spin $S$ = 5/2, 3/2 state. The nonlinear Curie behaviors suggest that [Fe(TPrPc)$N_3$] is not pure high spin.

Figure 2 displays the EPR spectrum of solid [Fe(TPrPc)-$N_3$] at 5 K. The spectrum shows nearly axial-symmetric signals with $g$ = 5.42, 5.40, and 2.00. These $g$-values were determined from the theoretical simulation. The split $g_\perp$ signals are consistent with the lower symmetry of the porphycene. The $g_\perp$ = 5.42 is between $g_\perp$ = 6 and 4 for the typical $S$ = 5/2 and 3/2 species, respectively.[19,20] A similar spectrum with $g$ = 5.82, 5.78, and 2.00 was obtained in toluene at 5 K (result not shown). Another notable EPR observation is the considerable temperature dependence. The EPR

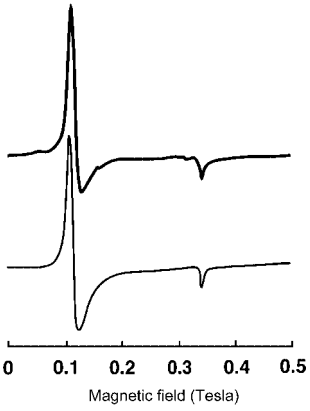


Figure 2. The EPR spectra of microcrystalline [Fe(TPrPc)$N_3$] at 5 K. The upper spectrum is the observed spectrum, and the lower is a simulation with $g$ = 5.42, 5.40, and 2.00.

 © 2007 Wiley-VCH Verlag GmbH & Co. KGaA, Weinheim 

spectrum broadened out above 10 K and no signals were detected at 77 K. This is in contrast with ordinary ferric high-spin heme with well-defined EPR signals at liquid nitrogen temperature.[20]

### Analysis of NMR Isotropic Shift

Unusual NMR behavior of the pyrrole-H signal (Figure 1) and the characteristic EPR (Figure 2) suggest a magnetic anomaly for [Fe(TPrPc)$N_3$]. The paramagnetic shift was analyzed on the basis of the two-spin model. The observed pyrrole-H shift $\delta$ consists of the diamagnetic and isotropic contributions.[17] A 9.6-ppm diamagnetic of the pyrrole-H shift was adopted from the metal-free TPrPc.[3] Then we obtain $\delta - 9.6 = a\delta_A + (1 - a)\delta_B$, where $\delta_A = A/T$ and $\delta_B = B/T$ are the isotropic shifts of the two paramagnetic components **A** and **B**. The constants $A$ and $B$ define, respectively, the slope of the straight lines in the Curie plots for **A** and **B**, and $a$ and $(1 - a)$ represent fractions of the two components. It follows that the isotropic shift is $\delta - 9.6 = a(A/T) + (1 - a)(B/T)$ and that the equilibrium constant is $K = [\mathbf{A}]/[\mathbf{B}] = a/(1 - a) = [A - T(\delta - 9.6)]/[T(\delta - 9.6) - B]$. The van't Hoff equation, $\ln K = -\Delta H/RT + \Delta S/R$, is modified for the NMR analysis into the following form:

$$\ln\frac{A-T(\delta-9.6)}{T(\delta-9.6)-B}=-\frac{\Delta H}{R}\frac{1}{T}+\frac{\Delta S}{R}$$

The pyrrole-H shift $\delta$ was analyzed by fitting the temperature profiles for [Fe(TPrPc)$N_3$] (Figure 1, part B) to the van't Hoff formalism. For this end, the parameters $A$ and $B$ were varied at $\delta = 10$ ppm $K^{-1}$ intervals in a realistic ($A$, $B$) = (40000 to 5000, –1500 to –50000) region, and an ($A$, $B$) set that gives rise to the best linear plots was looked for. The computer program that was originally used for the analysis of the thermochromism[21] and isotropic shift[22] of azide hemoprotein was employed. The best linear plot, with a correlation coefficient 0.99579, was obtained at ($A$, $B$) = (7940, –22660), corresponding to $\Delta H = -3990$ cal $mol^{-1}$ and $\Delta S = -16.5$ cal $mol^{-1}$ $K^{-1}$. From these thermodynamic values, an equilibrium constant $K = [\mathbf{A}]/[\mathbf{B}] = 19{:}81$ at 295 K and the midpoint of transition $T_c = \Delta H/\Delta S = 242$ K were determined. The solid curve for the pyrrole-H shift in Figure 1 represents the theoretical fit calculated with these parameters.

### Mössbauer

We examined the Mössbauer of [Fe(TPrPc)$N_3$] to ascertain further the anomalies inferred from the above NMR and EPR. The Mössbauer spectra of a powder sample are shown in Figure 3. The isomer shift $\delta_{Fe}$ is 0.19 mm $s^{-1}$ and quadrupole splitting $\Delta E_q$ is 2.20 mm $s^{-1}$ at 290 K. These values are temperature dependent, and gradually changed to $\delta_{Fe} = 0.26$ mm $s^{-1}$ and $\Delta E_q = 2.68$ mm $s^{-1}$ at 77 K.

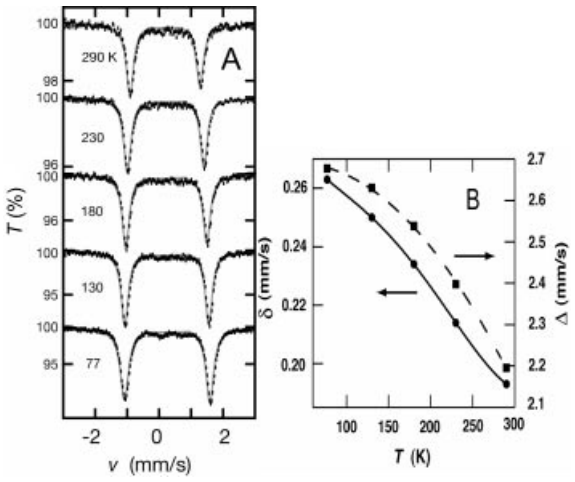


Figure 3. The solid-state Mössbauer spectra of [Fe(TPrPc)$N_3$]. (A) Observed spectra at the indicated temperatures. (B) Temperature dependence of quadrupole splitting $\Delta E_q$ and isomer shift $\delta_{Fe}$.

### Magnetic Susceptibility

The magnetic moment provides the direct and quantitative evaluation of the spin configuration of metal complexes. Figure 4 shows the magnetic susceptibility of microcrystalline [Fe(TPrPc)$N_3$] recorded over a 5–300 K range. The effective magnetic moment 4.80 $\mu_B$ at 290 K gradually fell down to 4.06 $\mu_B$ at 50 K. The values are intermediate between 5.92 and 3.87 $\mu_B$, expected for the pure $S = 5/2$ and 3/2 states, respectively.[5]

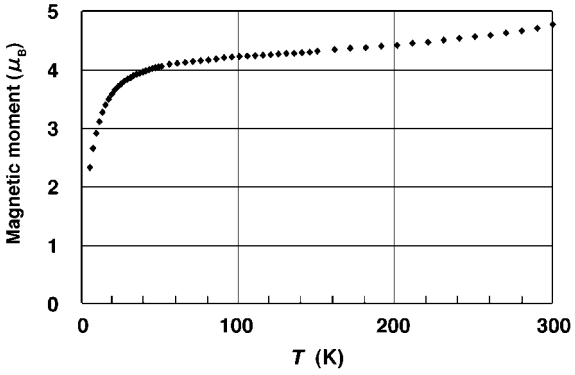


Figure 4. Temperature dependence of the effective magnetic moments of microcrystalline [Fe(TPrPc)$N_3$].

### IR Spectra

Several iron-bound ligands of heme exhibit sufficiently intense vibrational bands. The antisymmetric IR stretching band of the azide is observed around 2030 $cm^{-1}$.[6–9] Figure 5 compares the IR spectra of the azide in [Fe(TPrP)$N_3$], [Fe(corrphycenato)$N_3$], and [Fe(TPrPc)$N_3$]. In the spectra of the former two compounds, single bands with a half-height width $\Delta\nu_{1/2} = 18$ $cm^{-1}$ were observed at 2060 $cm^{-1}$. The spectral profile is in agreement with those observed for azide complexes of protohemin (2065 $cm^{-1}$, $\Delta\nu_{1/2} = 19$ $cm^{-1}$)[7,10] and another iron corrphycene (2058 $cm^{-1}$,

 © 2007 Wiley-VCH Verlag GmbH & Co. KGaA, Weinheim 

$\Delta\nu_{1/2}$ = 16 cm$^{-1}$).[23] The single IR bands for [Fe(TPrP)$N_3$] and [Fe(corrphycenato)$N_3$] suggest their pure high-spin ($S$ = 5/2) state. On the other hand, the azide band of porphycene [Fe(TPrPc)$N_3$] at 2062 cm$^{-1}$ is not symmetric and somewhat broader, with a shoulder around 2040 cm$^{-1}$ (Figure 5, part C). The curve analysis resolved two peaks at 2066 cm$^{-1}$ ($\Delta\nu_{1/2}$ = 28 cm$^{-1}$) and 2049 cm$^{-1}$ ($\Delta\nu_{1/2}$ = 18 cm$^{-1}$) with an integrated intensity ratio of $I_{2049}/I_{2066}$ = 24/76. The IR spectrum was temperature-dependent, the 2049-cm$^{-1}$ peak being notably intensified with an isosbestic point at 2055 cm$^{-1}$ upon cooling (Figure 6). The transition was fully reversible. We recorded the IR spectrum in the solid state to examine the consistency with EPR and Mössbauer spectra. Figure 7 shows the IR spectrum of [Fe(TPrPc)$N_3$] in solid state. The bands were also identified at 2027 cm$^{-1}$ ($\Delta\nu_{1/2}$ = 18 cm$^{-1}$) and 2012 cm$^{-1}$ ($\Delta\nu_{1/2}$ = 15 cm$^{-1}$) with $I_{2012}/I_{2027}$ = 26/74.

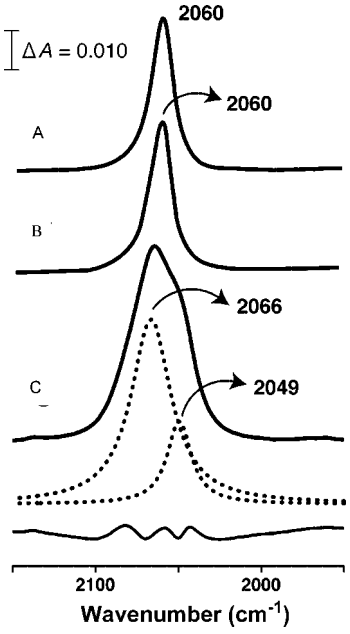


Figure 5. The IR absorption of iron-bound azide at 295 K. The iron concentration is about 2 mM in chloroform. (A) [Fe(TPrP)$N_3$], (B) [Fe(etiocorrphycenato)$N_3$], and (C) [Fe(TPrPc)$N_3$]. The broken curves in (C) are from Gaussian fitting. The half-height widths of the 2066- and 2049-cm$^{-1}$ bands are 29 and 18 cm$^{-1}$, respectively. The lowest curve in (C) is the residual.

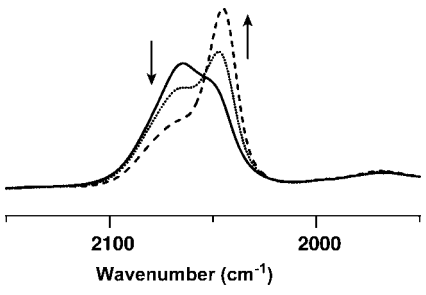


Figure 6. The IR absorption spectra of [Fe(TPrPc)$N_3$] in chloroform. Temperature decreases (295, 254, and 216 K) as indicated by the arrows.

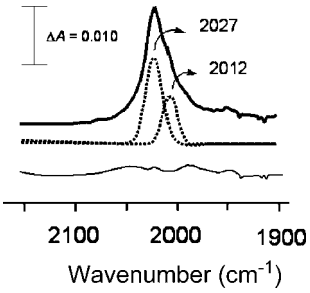


Figure 7. The IR absorption spectra of solid [Fe(TPrPc)$N_3$] at 295 K.

## Discussion

### Magnetic Anomalies in [Fe(TPrPc)$N_3$]

[Fe(TPrPc)$N_3$] exhibits several magnetic anomalies. The pyrrole-H shift does not follow the Curie law (Figure 1). The NMR behavior parallels that reported for [Fe(TPP)-$ClO_4$][18] and [Fe(TPrPc)X] (X = Br, Cl, I).[13] The NMR similarity suggests that [Fe(TPrPc)$N_3$] is predominantly high-spin, with an appreciable intermediate-spin ($S$ = 3/2) character. The pyrrole-H shift of 19 ppm (Figure 1) supports the mixing of the $S$ = 3/2 state because the signal resonates at 48 and –30 ppm for the five-coordinate ferric porphyrin in the $S$ = 5/2 and $S$ = 3/2 states, respectively.[17,18] The strong upfield bias of this signal at lower temperature indicates the $S$ = 3/2 ground state. Mixing of the $S$ = 3/2 state in [Fe(TPrPc)$N_3$] is supported from the EPR spectrum with $g_\perp$ = 5.42 (Figure 2). The quadrupole splitting $\Delta E_q$ = 2.20 mm s$^{-1}$ at 290 K (Figure 3) is also intermediate between those of the typical $S$ = 5/2 ($\Delta E_q$ = 0.8 ± 0.2) and $S$ = 3/2 complexes ($\Delta E_q$ = 3.2 ± 0.3).[24] Quantitative support for the $S$ = 5/2, 3/2 assignment comes from the magnetic moment of 4.8–4.1 $\mu_B$ over a 300–20 K range. On the basis of these physical results, we assign a mixed $S$ = 5/2, 3/2 state to [Fe(TPrPc)$N_3$].

As the ranking of azide in the spectrochemical[25] and magnetochemical[19] series is comparable with halides, a pure $S$ = 5/2 state, which is ordinarily found in [Fe(porphyrinato)X] (X = halides), may be expected for [Fe(TPrPc)$N_3$] as well. Contrary to the expectation, [Fe(TPrPc)$N_3$] is not pure high-spin. We note similar deviation from the pure high-spin state in [Fe(TPrPc)X] (X = Cl, Br, I)[13] and the all-alkyl porphycene derivatives.[14] The X-ray analyses of free base TPrPc[3] and relevant iron(III) porphyrins[26–28] provide the structural account for the mixing of the $S$ = 3/2 state. Porphycene has a narrower coordination core.[3] The narrower metallo cavity in TPrPc results in a shorter Fe–N(pyrrole) bond and strengthens the equatorial ligand field of the iron. Under the circumstances, the $d_{x^2-y^2}$ orbital of high-spin iron is destabilized to induce the $S$ = 3/2 state. Thus, the mixed $S$ = 3/2 state in [Fe(TPrPc)$N_3$] is achieved with the synchronization of the core contraction[3,26–28] and a moderately small ligand-field splitting parameter of azide.[19,25]

 © 2007 Wiley-VCH Verlag GmbH & Co. KGaA, Weinheim 

### IR Spectra

The most characteristic observation for [Fe(TPrPc)$N_3$] is the split IR bands of the coordinating azide (Figure 5, part C). This is in contrast with the single azide band in [Fe(TPrP)$N_3$] (2060 $cm^{-1}$; Figure 5, part A) or [Fe(proto-porphyrinato)$N_3$] (2064 $cm^{-1}$).[7,10] It may be possible, however, that the 2049-$cm^{-1}$ band in [Fe(TPrPc)$N_3$] is from a plausible contaminant, a di-azide species. Contamination with di-azide species is set aside because a bis-azide hemin displays the two IR bands at about 2035 and 2015 $cm^{-1}$.[12] In addition, the proton NMR spectrum of [Fe(TPrPc)$N_3$] (Figure 1) shows a single pyrrole-H peak at $\delta$ = 19 ppm to rule out the sample contamination. It is possible that the 2049-$cm^{-1}$ peak is from a trace amount of the sodium azide, which is NMR invisible, suspended in the chloroform. This possibility is eliminated because the IR band of sodium azide in chloroform is at 2170 $cm^{-1}$.[7] It might also be possible that the split IR bands in [Fe(TPrPc)$N_3$] come from an equilibrium between five-coordinate [Fe(TPrPc)$N_3$] and six-coordinate [Fe(TPrPc)$N_3$($H_2O$)], where the iron-bound water molecule comes from a trace amount of residual water in chloroform. This possibility is unlikely because a reference porphyrin [Fe(TPrP)$N_3$] (Figure 5, part A), measured in the same lot of chloroform, exhibits a single band. As porphycene has a rectangular molecule with a $C_2$ symmetry, one may claim that the two IR bands in [Fe(TPrPc)-$N_3$] arise from the rotational isomers of azide about the azide–iron bond. The possibility is also eliminated because [Fe(etiocorrphycenato)$N_3$] (Figure 5, part B) and [Fe{bis(ethoxycarbonyl)corrphycenato}$N_3$][23] exhibit single azide bands despite their trapezoidal molecular shape. The prospect of Fermi resonance[29] for the split azide bands may be neglected because no sharp signal occurred at 1024 $cm^{-1}$, and because the 2049-$cm^{-1}$ band is markedly intensified at lower temperature. Thus the two IR bands in [Fe(TPrPc)$N_3$] reflect a real magnetic anomaly of the iron.

Another notable observation is that the IR peak width is different between the 2049- ($\Delta\nu_{1/2}$ = 18 $cm^{-1}$) and 2066-$cm^{-1}$ ($\Delta\nu_{1/2}$ = 28 $cm^{-1}$) bands (Figure 5). The notably larger line width of the latter may reflect increased orientation variability of the azide about the iron–azide bond because the IR band width of iron-bound azide has been demonstrated to increase with increasing ligand fluctuation.[30] Consistent with this proposal, the IR bands of the solid [Fe(TPrPc)$N_3$] in Figure 7, that is, $\Delta\nu_{1/2}$ = 18 $cm^{-1}$ (2027 $cm^{-1}$) and 15 $cm^{-1}$ (2012 $cm^{-1}$), are narrower owing to a decreased ligand motion in the solid.

### Novel View Emerged from IR

It has been proposed for the ferric porphyrin with a mixed-spin $S$ = 5/2, 3/2 system that the two states are quantum-mechanically admixed through the spin-orbit coupling and that the admixed state has a new discrete ground state.[15,16] The spin mixing has been proposed to occur in hemoproteins like cytochrome $c'$ and horseradish peroxidase.[16] NMR, EPR, and Mössbauer results for the model compounds of cytochrome $c'$ are apparently consistent with the quantum mechanical model.[19,26–28] In the proton NMR of [Fe(TPP)$ClO_4$][18,19] and [Fe(TPrPc)X] (X = Cl, Br, I),[13] the single pyrrole-H peaks shift far-upfield at lower temperature. The EPR and Mössbauer do not exhibit the two signals from the spin isomers. Present NMR, EPR, and Mössbauer results for [Fe(TPrPc)$N_3$] parallel those reported for [Fe(TPP)$ClO_4$] and [Fe(TPcPc)X].[13,18,19]

IR, on the other hand, resolves two azide peaks for [Fe(TPrPc)$N_3$] (Figure 5, part C). This observation demonstrates that the $S$ = 5/2 and 3/2 states are not quantum-mechanically admixed but that they coexist separately. Based on the NMR, EPR, and Mössbauer results indicating dominance of the $S$ = 3/2 species at lower temperature, we assign the 2049-$cm^{-1}$ IR peak, which prevails at 216 K, to the $S$ = 3/2 isomer and the 2066-$cm^{-1}$ band to the $S$ = 5/2 isomer. Population of the $S$ = 3/2 species is estimated to be 0.21 at 20 °C on the assumption that the two magnetic isomers have closely similar extinction coefficients in the IR spectrum. The equilibrium is more quantitatively evaluated from the pyrrole-H shift in Figure 1. We now assign the **A** and **B** states assumed in the NMR analysis to the $S$ = 3/2 and $S$ = 5/2 states, respectively. Fractions of the $S$ = 3/2 isomer, calculated with the $\Delta H$ and $\Delta S$ for the NMR analysis, are 0.20 (293 K), 0.43 (254 K), and 0.72 (216 K). These values are in good agreement with 0.24 (293 K), 0.43 (254 K), and 0.61 (216 K) estimated from the solution IR (Figure 6). The IR spectrum of the solid in Figure 7 resolves two IR bands. Existence of the two spin isomers in the IR spectrum is consistent with the implication from EPR, Mössbauer, and magnetic susceptibility, which were measured for the solid sample (Figures 2–4).

We emphasize that IR resolves the two spin isomers of [Fe(TPrPc)$N_3$] while EPR, NMR, and Mössbauer do not. Why does IR alone discriminate the spin isomers? The conflict is explained by realizing the timescale of the applied spectroscopic methods. The approximate timescales of IR, EPR, NMR, and Mössbauer are $10^{-13}$, $10^{-4}$–$10^{-8}$, $10^{-1}$–$10^{-9}$, and $10^{-7}$ $s^{-1}$, respectively.[31] IR has excellent temporal resolution over EPR, NMR, and Mössbauer, which observe the time-averaged structures. Consequently, we can discern with IR the thermal spin-state equilibrium and the quantum mechanical mixing in the mixed $S$ = 5/2, 3/2 system. Increase of the 2049-$cm^{-1}$ peak and concomitant decrease of the 2066-$cm^{-1}$ band with decreasing temperature, accompanied with the 2054-$cm^{-1}$ isosbestic point (Figure 6), demonstrate that the $S$ = 5/2 and $S$ = 3/2 isomers are in a thermal equilibrium. This is in marked contrast with the claim that a homogeneous $S$ = 5/2, 3/2 state in the ferric heme iron is solely created by quantum mechanical spin-orbit coupling.[16]

A closely related coexistence of two spin isomers has been reported for ferric azide heme in a mixed $S$ = 5/2, 1/2 system where the two states are in a thermal equilibrium. IR distinguishes the $S$ = 5/2, 1/2 spin isomers of the azide hemes[9,10,21] and hemoproteins,[7,8] while NMR and EPR do not. Unfortunately, IR has been scarcely applied to the mixed $S$ = 5/2, 3/2 heme. Strong IR absorption of the iron-

 © 2007 Wiley-VCH Verlag GmbH & Co. KGaA, Weinheim 

bound azide in [Fe(TPrPc)$N_3$] provides a unique opportunity to make use of the vibration spectroscopy to the mixed $S$ = 5/2, 3/2 heme. IR resolves the $S$ = 5/2, 3/2 isomers, demonstrating that the $S$ = 3/2 and 5/2 states of [Fe(TPrPc)$N_3$] are not uniformly admixed but slowly interchanging on the IR timescale. From the peak separation of 17 $cm^{-1}$ and the relationship $\tau = 1/(2\pi\Delta\nu)$, where $\Delta\nu$ = (light velocity) × (peak separation),[31] we can estimate a minimum lifetime $\tau$ = 0.3 ps for the two magnetic isomers.

### Unified View of the Spin Mixing in Iron(III)

The ferric heme iron adopts either $S$ = 5/2, 3/2, or 1/2 state depending on the axial ligand and/or macrocycle conformation. Mixing of the three spin states is frequently observed. The thermal mixing of the $S$ = 5/2, 1/2 states or spin crossover of ferric hemes and hemoproteins has been established.[5–10] Recently, Nakamura et al. have found a novel type of spin crossover between the $S$ = 3/2 and 1/2 states for the saddle-shaped ferric porphyrins.[32–34] The deformed iron porphyrin is magnetically inhomogeneous with independent $S$ = 3/2 and 1/2 components in the mixed $S$ = 3/2, 1/2 system. An analogous thermal mixing of the $S$ = 3/2, 1/2 isomers has been reported for a non-heme complex of bis(*o*-iminobenzoquinonato)iron(III) by Chun et al.[35] Thus, the spin mixing in the $S$ = 5/2, 1/2 and $S$ = 3/2, 1/2 systems occurs through thermal spin crossover. Present IR analysis for [Fe(TPrPc)$N_3$] demonstrates that the $S$ = 5/2 and 3/2 states are not quantum-mechanically admixed but in a thermal equilibrium. This situation parallels those found in the $S$ = 5/2, 1/2[5–10] and $S$ = 3/2, 1/2[32–34] systems. The temperature-dependent changes of the EPR, NMR, and Mössbauer for [Fe(TPrPc)$N_3$] are thus interpreted to reflect the spin crossover. In view of the IR elucidation for [Fe(TPrPc)$N_3$], the quantum chemical admixing of the two ground states is unlikely for this complex. We therefore point out the possibility that the three types of magnetic mixing among the $S$ = 5/2, 3/2, and 1/2 states in ferric heme could be commonly described in terms of thermal spin crossover between the two magnetic isomers. The general distinction of the quantum-mechanical or thermal mixing of the spin states, however, is still to be established by further case-by-case analyses.

## Experimental Section

**TPrPc, [Fe(TPrPc)$N_3$], and Related Macrocycles:** 2,7,12,17-Tetrapropylporphycene (TPrPc) was prepared by the method of Vogel et al.[3] The ferric chloride complex [Fe(TPrPc)Cl][36] was purified with silica-gel column chromatography with chloroform/methanol (97:3, v/v) mixture. The [Fe(TPrPc)Cl] in benzene was vigorously mixed overnight with aqueous sodium azide (5 M)[7] overnight to furnish [Fe(TPrPc)$N_3$]. The sample was recrystallized from hexane/dichloromethane. $C_{32}H_{36}FeN_7$: calcd. C 66.90, H 6.31, N 16.89; found C 67.15, H 6.12, N 17.02. Formation of [Fe(TPrPc)$N_3$] was also confirmed with the $^1$H NMR spectrum where the hyperfine-shifted pyrrole-H signal ($\delta$ = 28.2 ppm in $CDCl_3$) of [Fe(TPrPc)Cl] was replaced with the new signal ($\delta$ = 24.3 ppm) from [Fe(TPrPc)$N_3$].

*meso*-Tetrapropylporphyrin (TPrP, Scheme 1) and the iron chloride [Fe(TPrP)Cl] were obtained according to the literature methods.[37,38] The azide complex [Fe(TPrP)$N_3$] was derived from the chloride compound after the ligand exchange as carried out for [Fe(TPrPc)$N_3$]; the sample was recrystallized from hexane/dichloromethane. Synthesis of [Fe(etiocorrphycenato)$N_3$] (Scheme 1) has been reported.[6]

**Spectroscopic Measurements:** $^1$H NMR spectra at 300 MHz were recorded with a JEOL LA300 with a temperature variation unit, and chemical shifts were referenced to tetramethylsilane. The X-band electron paramagnetic resonance (EPR) spectra were recorded with a Bruker E500 spectrometer equipped with an Oxford helium cryostat. IR spectra were obtained on a Nicolet Avatar spectrometer at a 2-$cm^{-1}$ resolution with a 50-μm cell, and apodized with a Happe–Genzel function. IR spectra at low temperature were obtained on a Digilab FTS-7000 spectrometer equipped with an Oxford cooling unit.[38] The IR spectrum of the solid material was recorded after evaporation of concentrated sample in dichloromethane over the $CaF_2$ disk. $^{57}$Fe Mössbauer spectra were measured on a Wissel–Mössbauer spectrometer system. The sample was kept in a gas-flow cryostat and $^{57}$Co(Rh) source was kept at room temperature. Isomer shifts $\delta_{Fe}$ were referenced to α-iron at room temperature. The solid-state magnetic susceptibilities were measured over a 5–300 K range at 1 T with a Quantum Design MPMS-7 SQUID magnetometer. The data were corrected for both the diamagnetism of the basket and molecule Pascal's constants.

## Acknowledgments

We thank the Research Center for Molecular-Scale Nanoscience and the Institute for Molecular Science for assistance in obtaining the EPR and magnetic moment. This work was supported by grants-in-aid from the Japanese Society for the Promotion of Science for "Basic Scientific Research" (grant number 18590094) and "Initiatives for Attractive Education for Graduate Schools".

[1] J. A. Shelnutt, X.-Z. Song, J.-G. Ma, S.-L. Jia, W. Jentzen, C. J. Medforth, *Chem. Soc. Rev.* **1998**, *27*, 31–41.
[2] J. L. Sessler, A. Gebauer, E. Vogel in *The Porphyrin Handbook* (Eds.: K. M. Kadish, K. M. Smith, R. Guilard), Academic Press, San Diego, CA, **2000**, vol. 2, pp. 1–54.
[3] E. Vogel, M. Balci, K. Pramod, P. Koch, J. Lex, O. Ermer, *Angew. Chem. Int. Ed. Engl.* **1987**, *26*, 928–931.
[4] C. Bernard, Y. L. Mest, J. P. Gisselbrecht, *Inorg. Chem.* **1998**, *37*, 181–190.
[5] T. Iizuka, T. Yonetani, *Adv. Biophys.* **1970**, *1*, 157–182.
[6] S. Neya, C. K. Chang, D. Okuno, T. Hoshino, M. Hata, N. Funasaki, *Inorg. Chem.* **2005**, *44*, 1193–1195.
[7] S. McCoy, W. S. Caughey, *Biochemistry* **1970**, *9*, 2387–2393.
[8] J. O. Alben, L. Y. Fager, *Biochemistry* **1972**, *11*, 842–847.
[9] S. Neya, S. Hada, N. Funasaki, J. Umemura, T. Takenaka, *Biochim. Biophys. Acta* **1985**, *827*, 157–163.
[10] S. Neya, I. Morishima, *J. Am. Chem. Soc.* **1982**, *104*, 5068–5661.
[11] Y. Zhang, W. A. Hallows, W. J. Ryan, J. G. Jones, G. B. Carpenter, D. A. Sweigart, *Inorg. Chem.* **1994**, *33*, 3306–3312.
[12] M. K. Ellison, H. Nasri, Y.-M. Xia, J.-C. Marchon, C. E. Schulz, P. G. Debrunner, W. R. Scheidt, *Inorg. Chem.* **1997**, *36*, 4804–4811.
[13] K. Rachlewicz, L. Latos-Grażyński, E. Vogel, Z. Ciunik, L. B. Jerzykiewicz, *Inorg. Chem.* **2002**, *41*, 1979–1988.
[14] Y. Ohgo, S. Neya, T. Ikeue, M. Takahashi, M. Takeda, N. Funasaki, M. Nakamura, *Inorg. Chem.* **2002**, *41*, 4627–4629.

 © 2007 Wiley-VCH Verlag GmbH & Co. KGaA, Weinheim 

[15] M. M. Maltempo, P.-I. Ohlsson, K.-G. Paul, L. Petersson, A. Ehrenberg, *Biochemistry* **1979**, *18*, 2935–2941.
[16] M. M. Maltempo, T. H. Moss, *Q. Rev. Biophys.* **1976**, *9*, 181–215.
[17] H. M. Goff in *Iron Porphyrins, Part I* (Eds.: A. B. P. Lever, H. B. Gray), Addison-Wesley, London, **1983**, pp. 237–281.
[18] a) E. Goff, H. Shimomura, *J. Am. Chem. Soc.* **1980**, *102*, 31–37; b) T. Sakai, Y. Ohgo, A. Hoshino, T. Ikeue, M. Saitoh, M. Takahashi, M. Nakamura, *Inorg. Chem.* **2004**, *43*, 5034–5043.
[19] D. R. Evans, C. A. Reed, *J. Am. Chem. Soc.* **2000**, *122*, 4660–4667.
[20] W. E. Blumberg, *Methods Enzymol.* **1981**, *76*, 312–329.
[21] S. Neya, S. Hada, N. Funasaki, J. Umemura, T. Takenaka, *Biochim. Biophys. Acta* **1985**, *828*, 241–246.
[22] S. Neya, N. Funasaki, *Biochemistry* **1986**, *25*, 1221–1226.
[23] S. Neya, M. Tsubaki, H. Hori, T. Yonetani, N. Funasaki, *Inorg. Chem.* **2001**, *40*, 1220–1225.
[24] J. R. Sams, T. B. Tsin in *The Porphyrins* (Ed.: D. Dolphin), Academic Press, New York, **1979**, vol. 4, pp. 425–478.
[25] E. König, *Coord. Chem. Rev.* **1968**, *3*, 471–495.
[26] C. A. Reed, T. Mashiko, S. P. Bentley, M. E. Kastner, W. R. Scheidt, K. Spartalian, G. Lang, *J. Am. Chem. Soc.* **1979**, *101*, 2948–2958.
[27] W. R. Scheidt, D. K. Geiger, Y. Reed, C. A. J. Lee, G. Lang, *Inorg. Chem.* **1987**, *26*, 1039–1045.
[28] G. P. Gupta, G. Lang, Y. J. Lee, W. R. Scheidt, K. Shelly, C. A. Reed, *Inorg. Chem.* **1987**, *26*, 3022–3030.
[29] D. C. Harris, M. D. Bertolucci, *Symmetry and Spectroscopy: An Introduction to Vibrational and Electronic Spectroscopy*, Dover, New York, **1978**, pp. 164–167.
[30] R. Maurus, R. Bogumil, N. T. Nguyen, A. G. Mauk, G. Brayer, *Biochem. J.* **1998**, *332*, 67–74.
[31] D. F. Shriver, P. W. Atkins, C. H. Langford, *Inorganic Chemistry*, 2nd ed., Oxford University Press, Oxford, **1994**, pp. 111–113.
[32] T. Ikeue, Y. Ohgo, M. Yamaguchi, M. Takahashi, M. Takeda, M. Nakamura, *Angew. Chem. Int. Ed.* **2001**, *40*, 2617–2620.
[33] Y. Ohgo, T. Ikeue, M. Nakamura, *Inorg. Chem.* **2002**, *41*, 1698–1700.
[34] Y. Ohgo, T. Ikeue, M. Takahashi, M. Takeda, M. Nakamura, *Eur. J. Inorg. Chem.* **2004**, 98–809.
[35] H. Chun, E. Bill, T. Weyhermüller, K. Wieghardt, *Inorg. Chem.* **2003**, *42*, 5612–5620.
[36] A. D. Adler, F. Longo, F. Kampas, J. Kim, *J. Inorg. Nucl. Chem.* **1970**, *32*, 2443–2445.
[37] S. Neya, N. Funasaki, *J. Heterocycl. Chem.* **1997**, *34*, 689–690.
[38] H. Kandori, Y. Furutani, K. Shimono, Y. Shichida, N. Kamo, *Biochemistry* **2001**, *40*, 15693–15698.

Received: December 13, 2006
Published Online: May 15, 2007

 © 2007 Wiley-VCH Verlag GmbH & Co. KGaA, Weinheim 

DOI: 10.1002/ejic.200700089

# Syntheses and Structures of Molybdenum, Tungsten, and Manganese Complexes of a Cyclic Thiourea, $[M(CO)_5(SC_3N_2Me_4)]$ (M = Mo, W) and $[\{CpMn(CO)_2\}_2(\mu\text{-}SC_3N_2Me_4)]$

**Kazuya Saito,[a] Yasuro Kawano,*[a] and Mamoru Shimoi*[a]**

**Keywords:** Imidazolinethiones / Manganese / Molybdenum / Thioureas / Tungsten

Photolysis of $[CpMn(CO)_3]$ in the presence of 1,3,4,5-tetramethylimidazoline-2-thione, $SC_3N_2Me_4$ (**1**), produced a thione-bridged dinuclear complex, $[\{CpMn(CO)_2\}_2(\mu\text{-}SC_3N_2Me_4)]$ (**2**). Compound **2** shows unprecedented geometry of the Mn–S–Mn framework, featuring a pyramidal sulfur atom and long Mn···Mn distance. Photoreaction of $[M(CO)_6]$ (M = Mo, W) with **1** afforded mononuclear complexes $[M(CO)_5(SC_3N_2Me_4)]$ [M = Mo (**3**), W (**4**)]. In compounds **2**–**4**, the C–S bond of the thione ligand is stretched on coordination because of the polarization of the metal–ligand linkage. (© Wiley-VCH Verlag GmbH & Co. KGaA, 69451 Weinheim, Germany, 2007)

## Introduction

*N*-Heterocyclic carbenes (NHC) have proved to be excellent ligands in transition-metal complexes.[1–4] NHCs also form various adducts with *p*-block element fragments to give compounds with a formula of $E–C(NR)_2(CR')_2$, where E = $BX_3$, $AlX_3$, $GeI_2$, $SnCl_2$, $CH_2$, S, Se, and so forth.[4,5] The sulfur adducts, imidazolinethiones (cyclic thioureas), are employed as precursors of NHCs.[6] They are also components of tris(mercaptoimidazolyl)hydroborate ligands, which attract considerable attention because of their face-capping character and strong electron-donating ability, and are applied to enzyme models.[7] It is thus increasingly important to better understand the coordinating ability of imidazolinethiones. However, few examples of their transition-metal complexes have been reported.[8–10] In this paper, we describe the reaction of 1,3,4,5-tetramethylimidazoline-2-thione (**1**)[6] with $[CpMn(CO)_3]$, which produces a dinuclear complex that involves a rare bridging thione ligand, $[\{CpMn(CO)_2\}_2(\mu\text{-}SC_3N_2Me_4)]$ (**2**). The syntheses and structures of molybdenum and tungsten derivatives, $[M(CO)_5(SC_3N_2Me_4)]$ [M = Mo (**3**), W (**4**)], are also reported here.

## Results and Discussion

### Synthesis of a Thione-Bridged Dinuclear Manganese Complex $[\{CpMn(CO)_2\}_2(\mu\text{-}SC_3N_2Me_4)]$ (2)

Irradiation of $[CpMn(CO)_3]$ with **1** in a 2:1 ratio produced a red solution. Its $^1H$ NMR spectrum exhibited three singlet resonances at $\delta$ = 1.11, 3.13, and 4.41 ppm, and their relative intensity was 6:6:5. This suggests formation of a mononuclear thione complex, $[CpMn(CO)_2(SC_3N_2Me_4)]$. However, cooling the solution afforded a small amount of $[\{CpMn(CO)_2\}_2(\mu\text{-}SC_3N_2Me_4)]$ (**2**) as red needles. Probably, the thione ligand is labile in solution, and a $[CpMn(CO)_2]$ fragment generated is reversibly coordinated to the sulfur atom of another molecule of $[CpMn(CO)_2(SC_3N_2Me_4)]$ to provide the dimer **2**, which precipitates on cooling [Equation (1)]. Indeed, when crystals of **2** were dissolved in $[D_6]$-benzene, the solution showed the $^1H$ NMR spectrum of the monomer.

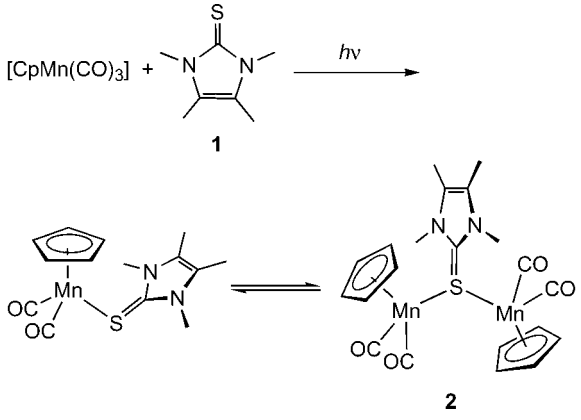


(1)

The molecular structure of **2** is displayed in Figure 1, and key geometrical parameters are given in Table 1. Two $[CpMn(CO)_2]$ moieties are bridged by the imidazolinethione ligand. The Mn(1)–S and Mn(2)–S bond lengths are 2.3343(15) and 2.3495(11) Å, respectively. These values are similar to those of $[Mn_2(\mu\text{-}SMe)_2(\mu\text{-}CO)(PMe_3)_2$-

[a] Department of Basic Science, Graduate School of Arts and Sciences, University of Tokyo,
Meguro-ku, Tokyo 153-8902, Japan
Fax: +813-5454-6567
E-mail: ckawano1@mail.ecc.u-tokyo.ac.jp
cshimoi@mail.ecc.u-tokyo.ac.jp

 © 2007 Wiley-VCH Verlag GmbH & Co. KGaA, Weinheim 

$(CO)_4$] (av. 2.331 Å).[11] Cationic dinuclear manganese thiolates, [{(MeCp)Mn$(CO)_2$}$_2$(μ-SR)][$PF_6$] (**5**, R = *i*Pr, *t*Bu; MeCp = $\eta^5$-$MeC_5H_4$), have substantially shorter Mn–S bonds [2.242(2)–2.267(1) Å].[12] The Mn–S bonds of "inidene" complexes, [{CpMn$(CO)_2$}$_2${μ-S($C_6H_4$X)}][$PF_6$] (**6**, X = H, $NO_2$), are even shorter [2.177(3)–2.218(3) Å] because of their multiple bond character.[12,13]

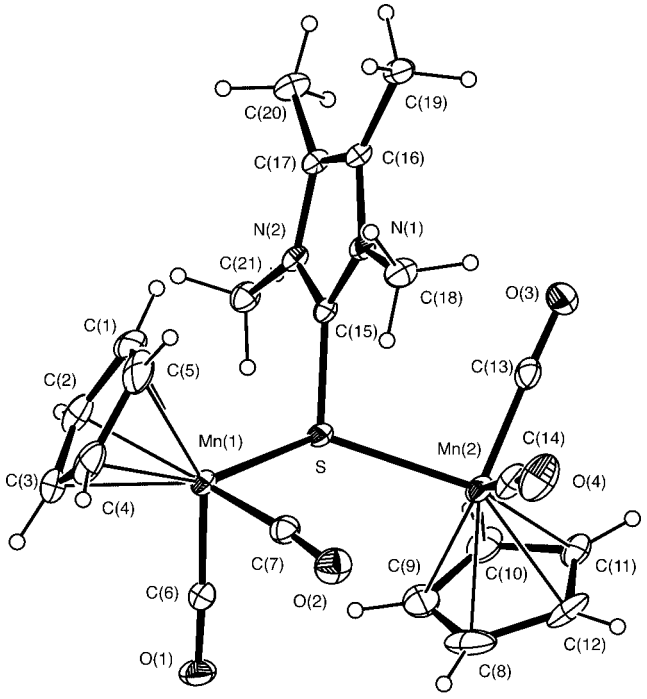


Figure 1. ORTEP drawing of [{CpMn$(CO)_2$}$_2$(μ-$SC_3N_2Me_4$)] (**2**) (30% thermal ellipsoids).

Table 1. Selected bond lengths [Å] and angles [°] for [{CpMn$(CO)_2$}$_2$(μ-S=$CN_2Me_2C_2Me_2$)] (**2**).

| Bond lengths [Å] | | | |
|---|---|---|---|
| Mn(1)–S(1) | 2.3343(15) | Mn(2)–S(1) | 2.3495(11) |
| Mn(1)–C(6) | 1.764(3) | Mn(1)–C(7) | 1.773(3) |
| Mn(2)–C(13) | 1.767(3) | Mn(2)–C(14) | 1.779(3) |
| CNT(1)–Mn(1)[a] | 1.785 | CNT(2)–Mn(2)[a] | 1.787 |
| C(6)–O(1) | 1.163(3) | C(7)–O(2) | 1.158(4) |
| C(13)–O(3) | 1.167(4) | C(14)–O(4) | 1.159(4) |
| S(1)–C(15) | 1.740(3) | C(15)–N(1) | 1.348(3) |
| C(15)–N(2) | 1.344(3) | C(16)–N(1) | 1.389(3) |
| C(17)–N(2) | 1.393(3) | C(16)–C(17) | 1.357(4) |
| **Bond angles [°]** | | | |
| Mn(1)–S–Mn(2) | 126.79(3) | C(15)–S–Mn(1) | 110.05(10) |
| C(15)–S–Mn(2) | 106.08(9) | CNT(1)–Mn(1)–S[a] | 124.20 |
| CNT(1)–Mn(1)–C(6)[a] | 123.13 | CNT(1)–Mn(1)–C(7)[a] | 125.75 |
| C(6)–Mn(1)–S | 88.22(10) | C(7)–Mn(1)–S | 96.13(10) |
| C(6)–Mn(1)–C(7) | 88.85(13) | CNT(2)–Mn(2)–S[a] | 117.68 |
| CNT(2)–Mn(2)–C(13)[a] | 124.16 | CNT(2)–Mn(2)–C(14)[a] | 123.38 |
| C(13)–Mn(2)–S | 94.56(10) | C(14)–Mn(2)–S | 99.92(11) |
| C(13)–Mn(2)–C(14) | 90.20(14) | N(1)–C(15)–S | 129.4(2) |
| N(2)–C(15)–S | 123.73(19) | N(2)–C(15)–N(1) | 106.8(2) |
| C(15)–N(1)–C(16) | 109.7(2) | C(15)–N(2)–C(17) | 109.9(2) |
| C(17)–C(16)–N(1) | 106.9(2) | C(16)–C(17)–N(2) | 106.7(2) |

[a] CNT: the centroid of the cyclopentadinyl ring.

The bridging sulfur atom is pyramidalized. The sum of the bond angles around this atom is 343°, indicating the existence of a lone electron pair at the sulfur atom. The Mn(1)···Mn(2) interatomic distance is 4.1878(18) Å, and the Mn(1)–S–Mn(2) bond angle is 126.79(3)°. These indicate the absence of bonding interaction between the two metal atoms. Thus, the structure of **2** features a pyramidal sulfur atom and long Mn···Mn separation. This is an unprecedented geometry of the Mn–S–Mn framework (see Scheme 1). Thiolates **5** contain a pyramidal sulfur atom, but they have a Mn–Mn single bond.[12] The intermetallic bond length is 2.906(1) (R = *i*Pr) or 2.962(1) Å (R = *t*Bu). In contrast, the inidene complex **6** (X = $NO_2$) includes a planar sulfur atom and long Mn···Mn distance (4.032 and 4.046 Å; two independent molecules are present in the asymmetric unit).[12] Complex [$Mn_2$(μ-SMe)$_2$(μ-CO)-$(PMe_3)_2(CO)_4$] has pyramidal sulfur atoms and a Mn–Mn single bond (2.581 Å).[11]

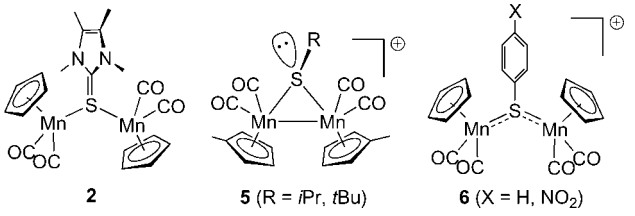


Scheme 1.

The C–S bond of the imidazolinethione ligand is stretched on coordination to the manganese atoms. The C(15)–S bond length is 1.740(3) Å, which is significantly longer than that of free **1**, 1.690(2) Å.[14] This is probably due to the pronounced polarization of the metal–ligand linkage (canonical structures **B** and **C**, Scheme 2), which is induced by the capability to take positive charge into the imidazole ring of the thione ligand. Through this polarization, the C–S moiety carries a single bond character. The imidazole ring is almost perpendicular with respect to the Mn–Mn vector. This is also consistent with the canonical structures **B** and **C**. If the sulfur–manganese interaction was composed of coordination of the lone electron pair on $sp^2$-sulfur (Scheme 2, **A**), the imidazole ring would be expected to be nearly parallel to the Mn–Mn vector.

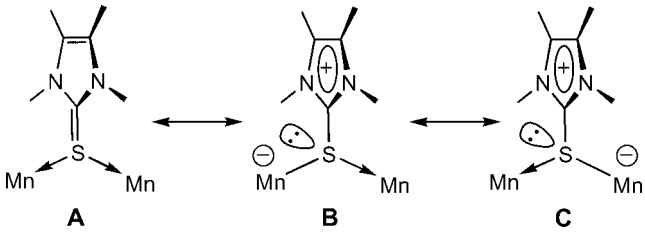


Scheme 2.

Creighton and co-workers have reported the reaction of an imidazolinethione with $CuCl_2$. During the reaction, $Cu^{II}$ is reduced to afford a dimeric $Cu^{I}$ complex **7** (Scheme 3), which contains bridging imidazolinethione ligands and a short Cu–Cu contact [2.914(1) Å].[15]

 © 2007 Wiley-VCH Verlag GmbH & Co. KGaA, Weinheim 

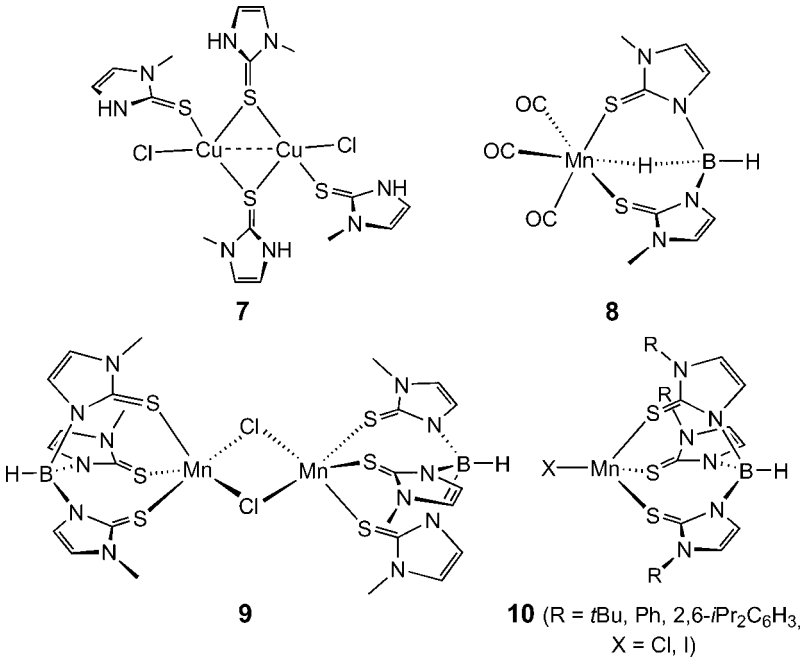


Scheme 3.

Several manganese complexes containing a bis- or tris-(mercaptoimidazolyl)hydroborate ligand have been reported (**8**–**10**, Scheme 3).[16,17] The crystal structures of **9** and **10** were determined, and it was shown that they had Mn–S bond lengths of 2.435(3)–2.569(8) Å and S–C bond lengths of 1.707(2)–1.721(2) Å.[17] Compound **2** has a shorter Mn–S bond and a longer C–S bond than **9** and **10**. Hence, the thione ligand polarizes very strongly in **2**, probably because the charge separation concentrates in one imidazolinethione unit.

### Synthesis of Group 6 Metal Complexes $[M(CO)_5(SC_3N_2Me_4)]$ [M = Mo (3), W (4)]

Group 6 metal complexes of chalcogenoimidazolines have been synthesized by Kuhn and co-workers. Thione, selone, and tellone, $E{=}C(N\mathit{i}Pr)_2(CMe)_2$ (E = S, Se, Te), react with $[M(CO)_6]$ or $[M(CO)_5(thf)]$ to produce the corresponding mononuclear chalcogenoimidazoline complexes.[8] Chromium derivatives $[Cr(CO)_5\{E{=}C(N\mathit{i}Pr)_2(CMe)_2\}]$ (**11**, E = S, Se, Scheme 4) were crystallographically characterized. However, with regard to tetramethylimidazoline derivatives, only the tellone complex $[W(CO)_5\{TeC_3N_2Me_4\}]$ has been documented.[8] Does the use of sterically less demanding **1** influence the number of metal fragments in the product, as observed in the formation of **2**? To clarify this point, we carried out the reaction of **1** with $[M(CO)_6]$ (M = Mo, W) under photolytic conditions.

Photoreactions of $[M(CO)_6]$ with **1** proceeded smoothly and gave yellow solutions, from which the thione complexes $[M(CO)_5(SC_3N_2Me_4)]$ [M = Mo (**3**), W (**4**)] were isolated as analytically pure crystals [76% for **3** and 33% for **4**, Equation (2)]. No evidence for the formation of dimeric species was obtained.

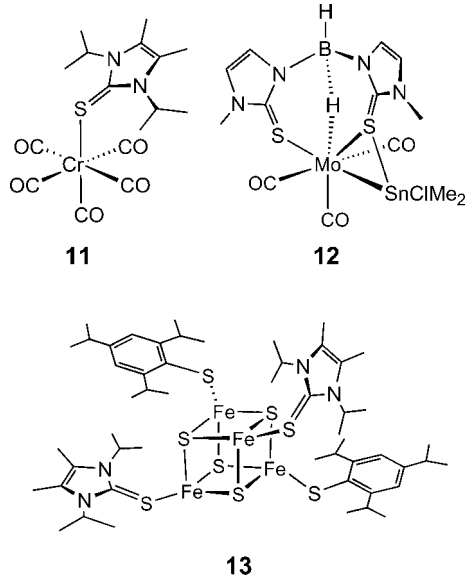


Scheme 4.

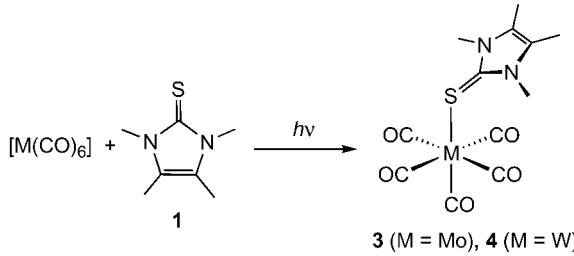


(2)

Figures 2 and 3 display the crystal structures of compounds **3** and **4**. The important bond lengths and angles are listed in Tables 2 and 3. Although the molecular struc-

 © 2007 Wiley-VCH Verlag GmbH & Co. KGaA, Weinheim 

tures of **3** and **4** are quite similar, the two compounds are not isomorphous. Crystals of **3** contain two crystallographically independent molecules in the asymmetric unit. However, their structures are essentially the same. The two molecules of **3** are associated through π-stacking of the imidazole rings. The separation between the five-membered rings is 3.3–3.6 Å. In **3** and **4**, the $[M(CO)_5]$ unit is coordinated to the cyclic thione ligand through a M–S dative bond to form an octahedral geometry. As a whole, their structures are akin to Kuhn's complex **11**.[8] They also resemble that of a methyleneimidazoline complex, $[Mo(CO)_5(CH_2{=}C_3N_2Me_4)]$,[18] whose ligand, an ylidic olefine, is isoelectronic with **1**. The M–S bond lengths are 2.6084(11) Å and 2.6113(11) Å in **3**, and 2.6146(14) Å in **4**. In compound **12** (Scheme 4), one thione unit of the bis(mercaptoimidazolyl)dihydroborate bridges the molybdenum center and tin atom with a long Mo–S bond length of 2.631(3) Å. The interatomic distance between the molybdenum and sulfur of the other ("terminal") thione moiety is 2.51(2) Å.[19]

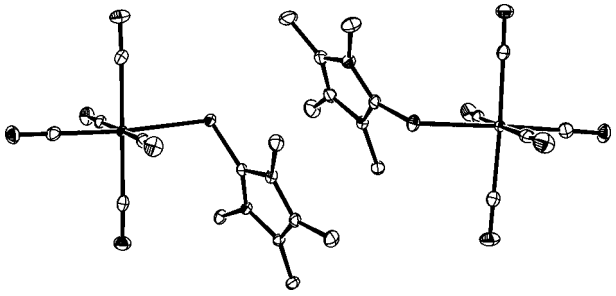

Figure 2. ORTEP drawing of $[Mo(CO)_5(SC_3N_2Me_4)]$ (**3**) (50% thermal ellipsoids). Hydrogen atoms have been omitted for clarity.

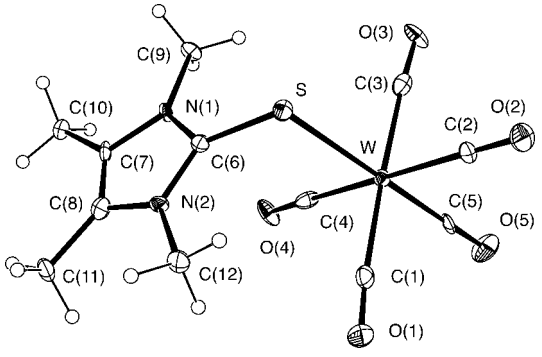


Figure 3. ORTEP drawing of $[W(CO)_5(SC_3N_2Me_4)]$ (**4**) (50% thermal ellipsoids).

The imidazolinethione ligand is connected to the central metal, directing the face of the heterocycle to the $[M(CO)_5]$ fragment. This is in sharp contrast to a chromium–thioacetone complex $[Cr(CO)_5(S{=}CMe_2)]$[20] and a mercury derivative $[HgCl_2(SC_3N_2H_4)_2]$,[21] in which the thione ligand directs the edge of the molecular plane to the metal. Such geometry of **3** and **4** suggests $sp^3$ hybridization of the sulfur atom caused by the greatly polarized M–S–C linkage (canonical structure **E**, Scheme 5). Indeed, the M–S–C bond angles are 108.31(7) and 109.40(7)° in **3**, and 103.29(16)° in **4**, which are close to the tetrahedral angle. As expected, the C=S bond is elongated. The C–S interatomic distances are 1.719(2) and 1.717(2) in **3** and 1.731(5) Å in **4** [that of free **1** is 1.690(2) Å].[14] Such phenomena are also found in **11**

Table 2. Selected bond lengths [Å] and angles [°] for $[Mo(CO)_5(S{=}C_3N_2Me_4)]$ (**3**).

| Bond lengths [Å] | | | |
|---|---|---|---|
| Molecule A | | | |
| Mo(1)–S(1) | 2.6084(11) | Mo(1)–C(1) | 2.071(2) |
| Mo(1)–C(2) | 2.026(2) | Mo(1)–C(3) | 2.044(2) |
| Mo(1)–C(4) | 2.072(2) | Mo(1)–C(5) | 1.971(2) |
| C(1)–O(1) | 1.132(3) | C(2)–O(2) | 1.141(3) |
| C(3)–O(3) | 1.141(3) | C(4)–O(4) | 1.128(3) |
| C(5)–O(5) | 1.148(3) | S(1)–C(6) | 1.719(2) |
| C(6)–N(1) | 1.355(2) | C(6)–N(2) | 1.348(2) |
| C(7)–N(1) | 1.397(2) | C(8)–N(2) | 1.389(2) |
| C(7)–C(8) | 1.353(2) | | |
| Molecule B | | | |
| Mo(2)–S(2) | 2.6113(11) | Mo(2)–C(13) | 2.066(2) |
| Mo(2)–C(14) | 2.050(2) | Mo(2)–C(15) | 2.037(2) |
| Mo(2)–C(16) | 2.062(2) | Mo(2)–C(17) | 1.971(2) |
| C(13)–O(6) | 1.139(3) | C(14)–O(7) | 1.139(3) |
| C(15)–O(8) | 1.143(3) | C(16)–O(9) | 1.134(3) |
| C(17)–O(10) | 1.150(3) | S(2)–C(18) | 1.717(2) |
| C(18)–N(3) | 1.349(2) | C(18)–N(4) | 1.351(2) |
| C(19)–N(3) | 1.399(2) | C(20)–N(4) | 1.389(2) |
| C(19)–C(20) | 1.352(3) | | |
| **Bond angles [°]** | | | |
| Molecule A | | | |
| C(1)–Mo(1)–S(1) | 85.34(7) | C(2)–Mo(1)–S(1) | 91.61(6) |
| C(3)–Mo(1)–S(1) | 94.20(7) | C(4)–Mo(1)–S(1) | 90.58(6) |
| C(5)–Mo(1)–S(1) | 174.83(5) | C(6)–S(1)–Mo(1) | 108.31(7) |
| N(1)–C(6)–S(1) | 126.04(14) | N(2)–C(6)–S(1) | 127.50(13) |
| N(1)–C(6)–N(2) | 106.21(15) | C(6)–N(1)–C(7) | 109.82(15) |
| C(6)–N(2)–C(8) | 110.24(15) | C(8)–C(7)–N(1) | 106.70(16) |
| C(7)–C(8)–N(2) | 107.03(15) | | |
| Molecule B | | | |
| C(13)–Mo(2)–S(2) | 86.10(7) | C(14)–Mo(2)–S(2) | 89.10(7) |
| C(15)–Mo(2)–S(2) | 96.60(6) | C(16)–Mo(2)–S(2) | 88.27(7) |
| C(17)–Mo(2)–S(2) | 175.09(5) | C(18)–S(2)–Mo(2) | 109.40(7) |
| N(3)–C(18)–S(2) | 128.29(14) | N(4)–C(18)–S(2) | 125.50(14) |
| N(3)–C(18)–N(4) | 106.07(16) | C(18)–N(3)–C(19) | 109.95(16) |
| C(18)–N(4)–C(20) | 110.36(15) | C(20)–C(19)–N(3) | 106.78(17) |
| C(19)–C(20)–N(4) | 106.83(17) | | |

Table 3. Selected bond lengths [Å] and angles [°] for $[W(CO)_5(S{=}C_3N_2Me_4)]$ (**4**).

| Bond lengths [Å] | | | |
|---|---|---|---|
| W(1)–S(1) | 2.6146(14) | W(1)–C(1) | 2.040(4) |
| C(1)–O(1) | 1.145(6) | C(2)–O(2) | 1.151(6) |
| C(3)–O(3) | 1.151(6) | C(4)–O(4) | 1.160(6) |
| C(5)–O(5) | 1.166(5) | S(1)–C(6) | 1.731(5) |
| C(6)–N(1) | 1.353(5) | C(6)–N(2) | 1.351(6) |
| C(7)–N(1) | 1.390(5) | C(8)–N(2) | 1.377(6) |
| C(7)–C(8) | 1.341(6) | | |
| **Bond angles [°]** | | | |
| C(1)–W(1)–S(1) | 90.77(12) | C(2)–W(1)–S(1) | 90.82(14) |
| C(3)–W(1)–S(1) | 90.02(12) | C(4)–W(1)–S(1) | 91.22(15) |
| C(5)–W(1)–S(1) | 178.00(13) | C(6)–S(1)–W(1) | 103.51(15) |
| N(1)–C(6)–S(1) | 125.9(4) | N(2)–C(6)–S(1) | 127.5(3) |
| N(2)–C(6)–N(1) | 106.6(4) | C(6)–N(1)–C(7) | 109.5(4) |
| C(6)–N(2)–C(8) | 109.1(3) | C(8)–C(7)–N(1) | 106.5(4) |
| C(7)–C(8)–N(2) | 108.3(4) | | |

 © 2007 Wiley-VCH Verlag GmbH & Co. KGaA, Weinheim 

[the C–S bond length is 1.737(5) Å][8] and a rhodium complex [RhCl(cod)($SC_3N_2Me_4$)] [1.725(2) Å].[9] An iron–sulfur cluster **13** includes two imidazolinethione ligands, whose C–S bond lengths are 1.689(14) and 1.719(16), respectively.[10]

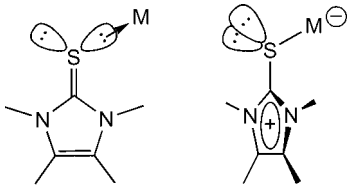


Scheme 5.

The strong donating ability of the thione ligand leads to enhancement of back-donation to the *trans* carbonyl ligand. The bond lengths between the metal and *trans*-carbonyl carbon atoms are 1.969(2) and 1.967(2) Å for **3**, and 1.966(5) Å for **4**. These are substantially shorter than the metal–*cis*-carbonyl bonds. The averages of the separations between the metal and *cis* carbonyls are 2.05 and 2.04 Å for **3** and **4**, respectively. In fact, the infrared spectra of **3** and **4** showed carbonyl stretching bands that are low-frequency shifted relative to $[M(CO)_6]$.

## Experimental Section

All manipulations were carried out under high vacuum or dry nitrogen. Reagent-grade hexane, THF, and toluene were distilled under nitrogen from sodium-benzophenone ketyl just before use. $[D_6]$-benzene was dried with potassium mirrors before use and transferred into NMR tubes under vacuum. $SC_3N_2Me_4$ (**1**) was prepared according to the literature.[6] $[Mo(CO)_6]$ (Strem), $[W(CO)_6]$ (Aldrich), and $[CpMn(CO)_3]$ (Strem) were used as purchased. $^1H$ and $^{13}C$ NMR spectra were recorded with a JEOL α-500 spectrometer. IR spectra were recorded with a JASCO FTIR-350 spectrometer. Mass spectra were measured with a JEOL JMS-S600H spectrometer.

**Syntheses of $[\{CpMn(CO)_2\}_2(\mu\text{-}SC_3N_2Me_4)]$ (2):** A solution of $[CpMn(CO)_3]$ (80 mg, 0.040 mmol) and **1** (31 mg, 0.020 mg) in hexane (4 mL) and THF (1 mL) mixture was irradiated with a 450-W medium-pressure Hg arc lamp for 1 h. Removal of volatiles, extraction of the residue with toluene, and cooling of the extract afforded **2** as red needles in small amounts. $^1H$ NMR (500 MHz, $[D_6]$benzene): $\delta$ = 1.11 (s, 6 H, CMe), 3.13 (s, 6 H, NMe), 4.41 (br., 5 H) ppm. This spectrum is consistent with a mononuclear complex, $[CpMn(CO)_2(SC_3N_2Me_4)]$.

**Syntheses of $[Mo(CO)_5(SC_3N_2Me_4)]$ (3):** A dichloromethane solution of $[Mo(CO)_6]$ (85 mg, 0.32 mmol) and **1** (46 mg, 0.30 mmol) was irradiated at 8 °C for 1 h with stirring using a 450-W medium pressure Hg lamp. The resulting yellow solution was concentrated to about 1 mL and diluted with hexane (4 mL). Cooling the solution to –25 °C provided **2** (90 mg, 0.23 mmol, 76%) as yellow-gray crystals. $^1H$ NMR (500 MHz, $[D_6]$benzene): $\delta$ = 1.09 (s, 6 H, CMe), 2.92 (s, 6 H, NMe) ppm. $^{13}C$ NMR (125 MHz, $[D_6]$benzene): $\delta$ = 7.96 (CMe), 31.9 (NMe), 122.6 (ring-C), 158.6 (C=S), 206.5, 213.7 (CO) ppm. IR (Nujol mull): $\tilde{\nu}$ = $\nu$(CO) 2066, 1987, 1912, 1872 $cm^{-1}$. MS (70 eV): $m/z$ (%) = 393 ($[M^+]$), 156 ($[SC_3N_2Me_4^+]$). $C_{12}H_{12}MoN_2O_5S$ (392.24): calcd. C 36.75, H 3.08, N 7.14; found C 36.59, H 3.10, N 6.96.

**Syntheses of $[W(CO)_5(SC_3N_2Me_4)]$ (4):** The synthesis of **4** was conducted in a similar manner to that of **3**. The yield of yellow crystals

Table 4. Crystal data for compounds **2**, **3**, and **4**.

| | **2** | **3** | **4** |
|---|---|---|---|
| Empirical formula | $C_{21}H_{22}Mn_2N_2O_4S$ | $C_{12}H_{12}MoN_2O_5S$ | $C_{12}H_{12}N_2O_5SW$ |
| Formula mass | 508.35 | 408.24 | 480.15 |
| Crystal color | red | yellow-gray | yellow |
| Temperature [K] | 153(2) | 153(2) | 153(2) |
| Wavelength | 0.71073 | 0.71073 | 0.71073 |
| Crystal system | triclinic | triclinic | monoclinic |
| Space group | $P\bar{1}$ | $P\bar{1}$ | $C2/c$ |
| $a$ [Å] | 8.945(5) | 10.827(6) | 20.494(9) |
| $b$ [Å] | 9.911(6) | 11.281(6) | 6.474(4) |
| $c$ [Å] | 13.650(7) | 14.582(6) | 24.651(11) |
| $\alpha$ [°] | 107.69(2) | 111.07(2) | 90 |
| $\beta$ [°] | 92.521(19) | 99.989(19) | 112.932(14) |
| $\gamma$ [°] | 109.35(2) | 106.31(2) | 90 |
| $V$ [Å$^3$] | 1073.6(10) | 1518.4(13) | 3012(2) |
| $Z$ | 2 | 4 | 8 |
| $D_{calcd}$ [Mg m$^{-3}$] | 1.573 | 1.786 | 1.588 |
| Abs. coeff. [mm$^{-1}$] | 1.303 | 1.031 | 5.872 |
| $F$(000) | 520 | 806 | 1368 |
| Crystal size [mm] | 0.25 × 0.20 × 0.08 | 0.60 × 0.40 × 0.30 | 0.50 × 0.15 × 0.10 |
| $\theta$ range [°] | 3.12–27.46 | 3.08–27.47 | 3.30–27.48 |
| Index ranges | $-11 \le h \le 11$,<br>$-12 \le k \le 12$,<br>$-17 \le l \le 15$ | $0 \le h \le 14$,<br>$-14 \le k \le 13$,<br>$-18 \le l \le 18$ | $0 \le h \le 26$,<br>$0 \le k \le 8$,<br>$-31 \le l \le 29$ |
| Independent reflections | 10625 | 6874 | 3434 |
| No. of parameters | 275 | 387 | 194 |
| Gof on $F^2$ | 1.086 | 1.138 | 1.066 |
| Final $R$ indices [$I > 2\sigma(I)$] | $R_1$ = 0.0414, $wR_2$ = 0.1194 | $R_1$ = 0.0253, $wR_2$ = 0.0941 | $R_1$ = 0.0357, $wR_2$ = 0.1170 |
| $R$ indices (all data) | $R_1$ = 0.0540, $wR_2$ = 0.1371 | $R_1$ = 0.0271, $wR_2$ = 0.0999 | $R_1$ = 0.0366, $wR_2$ = 0.1206 |
| Largest diff. peak and hole [e Å$^{-3}$] | 0.883 and –0.616 | 0.487 and –1.535 | 1.520 and –2.902 |

 © 2007 Wiley-VCH Verlag GmbH & Co. KGaA, Weinheim 

of **4** was 33%. $^1$H NMR (500 MHz, [D$_6$]benzene): $\delta$ = 1.00 (s, 6 H, CMe), 2.91 (s, 6 H, NMe) ppm. $^{13}$C NMR (125 MHz, [D$_6$]benzene): $\delta$ = 7.91 (CMe), 31.8 (NMe), 123.0 (ring-C), 157.3 (C=S), 199.6, 201.6 (CO) ppm. IR (Nujol mull): $\tilde{\nu}$ = $\nu$(CO) 2064, 1980, 1899, 1864 cm$^{-1}$. MS (70 eV): *m*/*z* (%) = 480 ([M$^+$]), 156 ([$SC_3N_2Me_4^+$]). $C_{12}H_{12}N_2O_5SW$ (480.14): calcd. C 30.02, H 2.51, N 5.83; found C 30.20, H 2.71, N 5.59.

**X-ray Crystal Structure Determination:** Crystals of **2**, **3**, and **4** (Table 4) were grown by cooling their solutions. Intensity data were collected with a Rigaku RAPID imaging plate diffractometer using graphite-monochromated Mo-$K_\alpha$ radiation ($\lambda$ = 0.71073 Å). Data collection was carried out at –120 °C. Crystal data, data collection parameters, and convergence results are listed in Table 4.

Numerical absorption corrections were applied on the crystal shapes. The structures of all complexes were solved by the direct method and refined on $F^2$. All non-hydrogen atoms were located and refined applying anisotropic temperature factors. Coordinates of hydrogen atoms were idealized with the use of riding models. Calculations were performed using the program package SHELX 97.[22]

CCDC-634432 (for **2**), -634433 (for **3**), and -634434 (for **4**) contain the supplementary crystallographic data for this paper. These data can be obtained free of charge from the Cambridge Crystallographic Data Centre via www.ccdc.cam.ac.uk/data_request/cif

## Acknowledgments

This work was financially supported by the Japanese Ministry of Education, Science, Sports, and Culture (Grant-in Aid for Special Project Research, number 15036215).

[1] A. J. Arduengo III, R. L. Harlow, M. Kline, *J. Am. Chem. Soc.* **1991**, *113*, 361–363.
[2] D. Bourissou, O. Guerret, F. P. Gabba, G. Bertrand, *Chem. Rev.* **2000**, *100*, 39–91.
[3] C. J. Carmalt, A. H. Cowley, *Adv. Inorg. Chem.* **2000**, *50*, 1–32.
[4] W. A. Herrmann, C. Koecher, *Angew. Chem. Int. Ed. Engl.* **1997**, *36*, 2162–2187.
[5] For example: a) N. Kuhn, H. Bohnen, J. Kreutzberg, D. Bläser, R. Boese, *J. Chem. Soc., Chem. Commun.* **1993**, 1136–1137; b) W. A. Hermann, C. Köcher, L. J. Goossen, G. R. J. Artus, *Chem. Eur. J.* **1996**, *2*, 1627–1636; c) M. D. Francis, D. E. Hibbs, M. B. Hursthouse, C. Jones, N. A. Smithies, *J. Chem. Soc., Dalton Trans.* **1998**, 3249–3254; d) A. J. Arduengo III, H. V. R. Dias, J. C. Calabrese, F. Davidson, *J. Am. Chem. Soc.* **1992**, *114*, 9724–9725; e) X.-W. Li, J. Su, G. H. Robinson, *Chem. Commun.* **1996**, 2683–2684; f) A. J. Arduengo III, H. V. R. Dias, J. C. Calabrese, F. Davidson, *Inorg. Chem.* **1993**, *32*, 1541–1542; g) N. Kuhn, T. Kratz, D. Bläser, R. Boese, *Chem. Ber.* **1995**, *128*, 245–250; h) A. Schäfer, M. Weidenbrush, W. Saak, S. Pohl, *J. Chem. Soc., Chem. Commun.* **1995**, 1157–1158; i) N. Kuhn, G. Henkel, T. Kratz, J. Kreutzberg, R. Boese, A. H. Maulitz, *Chem. Ber.* **1993**, *126*, 2041–2045.
[6] N. Kuhn, T. Kratz, *Synthesis* **1993**, 561–562.
[7] a) J. Reglinski, M. Garner, I. D. Cassidy, P. A. Slavin, M. D. Spicer, D. R. Armstrong, *J. Chem. Soc., Dalton Trans.* **1999**, 2119–2126; b) M. Garner, J. Reglinski, I. Cassidy, M. D. Spicer, A. R. Kennedy, *Chem. Commun.* **1996**, 1975–1976; c) I. R. Crossley, A. F. Hill, E. R. Humphrey, M. K. Smith, *Organometallics* **2006**, *25*, 2242–2247; d) M. M. Ibrahim, J. Seebacher, G. Steinfeld, H. Vahrenkamp, *Inorg. Chem.* **2005**, *44*, 8531–8538.
[8] N. Kuhn, R. Fawzi, T. Kratz, M. Steimann, *Phosphorus Sulfur Silicon* **1996**, *108*, 107–119.
[9] A. Neveling, G. R. Julius, S. Cronje, C. Esterhuysen, H. G. Raubenheimer, *Dalton Trans.* **2005**, 181–192.
[10] M. Harmjanz, C. Junghans, U. A. Opitz, B. Bahlmann, S. Pohl, *Z. Naturforsch., B: Chem. Sci.* **1996**, *51*, 1040–1048.
[11] L. J. Lyons, M. H. Tegen, K. J. Haller, D. H. Evans, P. M. Treichel, *Organometallics* **1988**, *7*, 357–365.
[12] P. Lau, H. Braunwarth, G. Huttner, D. Günauer, K. Evertz, W. Imhof, C. Emmerich, L. Zsolnai, *Organometallics* **1991**, *10*, 3861–3873.
[13] H. Braunwarth, G. Huttner, L. Zsolnai, *Angew. Chem. Int. Ed. Engl.* **1988**, *27*, 698–699.
[14] N. Kuhn, J. Fahl, R. Fawzi, M. Steimann, *Z. Kristallogr. - New Cryst. Struct.* **1998**, *213*, 434.
[15] J. R. Creighton, D. J. Gardiner, A. C. Gorvin, C. Gutterridge, A. R. W. Jackson, E. S. Raper, P. M. A. Sherwood, *Inorg. Chim. Acta* **1985**, *103*, 195–205.
[16] P. J. Bailey, A. Dawson, C. McCormack, S. A. Moggach, I. D. H. Oswald, S. Parsons, D. W. H. Rankin, A. Turner, *Inorg. Chem.* **2005**, *44*, 8884–8898.
[17] S. Senda, Y. Ohki, T. Hirayama, D. Toda, J. L. Chen, T. Matsumoto, H. Kawaguchi, K. Tatsumi, *Inorg. Chem.* **2006**, *45*, 9914–9925.
[18] N. Kuhn, H. Bohnen, D. Bläser, R. Boese, *Chem. Ber.* **1994**, *127*, 1405–1407.
[19] M. R. St.-J. Foreman, A. F. Hill, M. K. Smith, N. Tshabang, *Organometallics* **2005**, *24*, 5224–5226.
[20] B. A. Karchar, R. A. Jacobson, *J. Organomet. Chem.* **1977**, *132*, 387–393.
[21] G. Pavlović, Z. Popović, Ž. Soldin, D. Matković-Čalogović, *Acta Crystallogr., Sect. C: Cryst. Struct. Commun.* **2000**, *56*, 61–63.
[22] a) G. M. Sheldrick, *SHELXS-97*, University of Göttingen, **1997**; b) G. M. Sheldrick, *SHELXL-97*, University of Göttingen, **1997**.

Received: January 24, 2007
Published Online: May 23, 2007

 © 2007 Wiley-VCH Verlag GmbH & Co. KGaA, Weinheim 

DOI: 10.1002/ejic.200700212

# The Role of *Escherichia coliform* in the Biomineralization of Calcium Oxalate Crystals

**Long Chen,[a] Yuhua Shen,*[a] Rong Jia,[b] Anjian Xie,*[a,c] Bei Huang,[b] Xiaobin Cheng,[b] Qingfeng Zhang,[a] and Ruiyong Guo[b]**

**Keywords:** Urolithiasis / *Escherichia coliform* / Calcium oxalate / Nucleation and growth / Biomineralization

The influence of the common bacterium *Escherichia coliform* (*E. coli*) on the nucleation and growth of calcium oxalate (CaOxa) in aqueous solution is studied in order to determine its role in the biomineralization of urinary stones. The results show that CaOxa crystals obtained in the presence of *E. coli* transform more quickly from calcium oxalate dihydrate (COD) into calcium oxalate monohydrate (COM), and they become even larger, than in the absence of the bacterium. On decreasing the concentration of chemical reagents, in other words increasing the ratio bacterium/CaOxa, except for the more rapid phase transition from COD to COM, the CaOxa particles obtained become larger and more regular with a hexagonal morphology. This suggests that *E. coli* accelerates the crystallization of COM, which is the most stable crystal phase of CaOxa and the major component of urinary stones. Transmission electron microscopy (TEM) images, electron diffraction (ED) patterns, and Fourier-transform IR (FTIR) spectra show that the biomineralization process of CaOxa crystals takes place both inside and outside the bacterium, which implies that it is induced by both intracellular biomolecules and the bioorganic secretions of the bacteria. Sodium dodecyl sulfate polyacrylamide gel electrophoresis (SDS-PAGE) data and UV/Vis spectra show that the proteins bound to the crystal surface with a molecular weight of around 26.5 kDa have tyrosine, tryptophan, or phenylalanine residues. The zeta potential and FTIR spectra are used to investigate the mineralization mechanism of CaOxa with *E. coli* and show that, the negatively charged biomolecules inside and outside the bacterium interact with $Ca^{2+}$ ions to provide nucleation sites and then act as modifiers to induce the nucleation, growth, and aggregation of COM crystals. Therefore, we infer that *E. coli* mineralizes calcium oxalate and plays a role in the formation of urinary stones.

(© Wiley-VCH Verlag GmbH & Co. KGaA, 69451 Weinheim, Germany, 2007)

## Introduction

Urolithiasis is a common disease affecting millions throughout the world that remains a serious health concern due to its severe symptoms, such as great pain and urinary-tract obstruction and infection. At present, stones are mainly treated by surgery or extracorporeal shock wave lithotripsy followed by prolonged antibiotic treatment and oral citrate, although these remedies are unsatisfactory because of a high rate of recurrence. No effective drugs or treatment methods for this stubborn disease are currently available, therefore many studies on the mechanism of stone formation have been performed in recent years in the search for such treatments and methods. A number of questions still remain, however, regarding the factors that promote and inhibit stone formation, some of which are somewhat controversial.[1]

A urinary stone is a product of abnormal biomineralization whose principal mineral component is calcium oxalate monohydrate (COM),[2,3] which is the thermodynamically most stable phase of CaOxa. The other two phases of CaOxa, namely calcium oxalate trihydrate (COT) and calcium oxalate dihydrate (COD), rarely form stones as they are unstable and are more easily excreted in the urine than COM. In these stones, inorganic crystals are always mixed with organic matrices such as lipids, carbohydrates, and proteinaceous materials, and studies have shown that, although these organic materials account for only about 2% of the total mass, they play a very important role in the stone-formation process.[4,5] To better understand the role of organic matrices in urinary stone formation, Langmuir monolayers,[6–12] vesicles,[13] biomolecules,[14] etc., have all been used to induce the nucleation and growth of COM crystals. Our groups have recently studied the crystal growth of CaOxa in a reverse microemulsion of *p*-octyl polyethylene glycol phenyl ether (OP)/isooctyl alcohol (IOA)/cyclohexane/water containing different kinds of amino acids, and found that the type of amino acid, the pH, and surfactant can all influence the formation of CaOxa

[a] School of Chemistry and Chemical Engineering, Anhui University,
Hefei 230039, P. R. China
Fax: +86-551-510-7342
E-mail: s_yuhua@163.com
anjx@163.com
[b] School of Life Science, Anhui University,
Hefei 230039, P. R. China
[c] Key Laboratory of Environment-Friendly Polymer Materials of Anhui Province,
Hefei 230039, P. R. China

 © 2007 Wiley-VCH Verlag GmbH & Co. KGaA, Weinheim 

crystals.[15] We have also investigated crystal growth of CaOxa induced by octadecanoic acid/octadecylamine monolayers influenced by different concentrations of human serum albumin, and obtained different morphologies of CaOxa crystals with three kinds of phases.[16] We have also successfully inhibited the phase transition from COT to COM with 1,2-bis(*O*-aminophenoxy)ethane-*N*,*N*,*N*,*N*-tetraacetic acid.[16]

Some microorganisms, especially nanobacteria, have been reported to be involved in the formation of urinary stones. Nanobacteria are very tiny bacteria that range from 80–500 nm in size which have been isolated from renal stones[17,18] and have been shown to mineralize calcium and phosphate even under physiological conditions.[19,20] Cuerpo et al., for example, have found that when these bacteria are injected intravenously they accumulate in the kidney and produce apatite,[21,22] which suggests that the kidney is a preferred site for mineralization by these tiny bacteria, and Shiekh et al. have investigated the effects of intravenous administration of nanobacteria on the kidneys of Wistar rats and have found evidence for their inflammatory infiltration and accumulation in the cortex; in addition, small uniform renal calcification was seen on the surface of renal tubules.[23] These studies have therefore shown that nanobacteria may act as biomineralization centers for the initiation of kidney stones and play a contributory role in urolithiasis. Instead of promoting the formation of stone, oxalate-eating bacteria such as *Oxalobacter formigenes* can degrade oxalate and prevent the occurrence of CaOxa urolithiasis.[24,25]

The common bacterium *Escherichia coliform* (*E. coli*) is often found in urinary stones and it could damage the protective anti-adhesive GAG layer and cause crystal retention or alter urine composition in such a way that favors stone formation.[26,27] It has also been found that *E. coli* plays an important role in urinary-tract infections.[28] However, to date, there is no report of its true role in the biomineralization of urinary stones. In the present study, we report that *E. coli* can induce the nucleation, growth, and aggregation of CaOxa by biomolecules internally or externally and promote the formation of COM with a regular morphology, which suggests that it plays a contributory role in the biomineralization of urinary stones. This may help our further understanding of the stone-formation mechanism and lead to a method for the prevention and treatment of urolithiasis. In addition, it is also significant for the synthesis of inorganic materials with different morphologies.

## Results and Discussion

SEM images of CaOxa particles obtained after an aging time of 5 h in the absence and presence of *E. coli* are shown in Figure 1; the corresponding XRD patterns are shown in Figure 2. It can clearly be seen that the CaOxa particles obtained under these two conditions have different sizes and crystal phases. Without the bacterium, quasi-hexagonal or irregular CaOxa particles with an average diagonal of about 150 nm (shown in Figure 1a) are obtained. The corresponding XRD patterns (shown in Figure 2a) display diffraction peaks at 14.22°, 15.08°, 19.90°, 24.44°, 30.20°, 31.66°, and 32.02°, which can be indexed to the (*hkl*) indices (200), (211), and (411) of a COD phase (JCPDS card number 17-541), and the ($\bar{1}$01), (020), ($\bar{2}$02), and (121) indices of a COM phase (JCPDS card number 20-231), respectively. This indicates that the crystals obtained are a mixture of COM and COD. Figure 1b shows that hexagonal or rhombic particles with an average diagonal of about 300 nm are obtained in the presence of *E. coli* (0.5 wt.-%) that are larger than those formed without the bacterium. The XRD patterns (Figure 2b) show that they are all COM. These results imply that *E. coli* promotes the crystallization of COM and influences the size and morphology of the product.

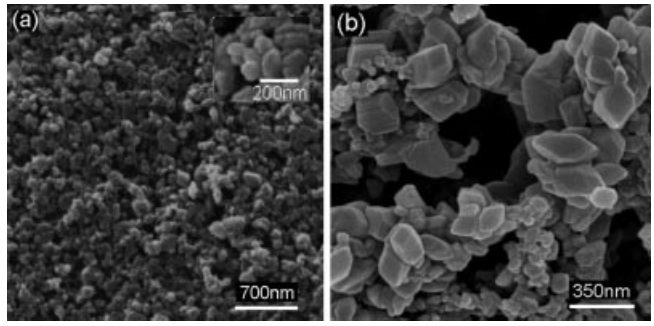


Figure 1. SEM images of CaOxa precipitates obtained in different systems after 5 h of reaction: (a) without *E. coli*, (b) with *E. coli* (0.5 wt.-%). The inset in (a) is a magnification.

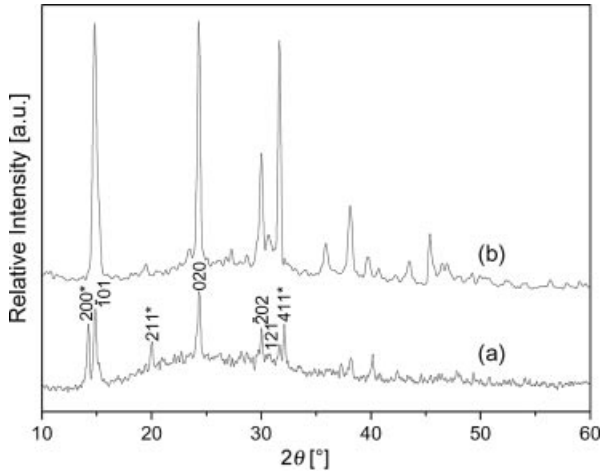


Figure 2. XRD patterns of CaOxa precipitates obtained in different systems after 5 h of reaction: (a) without *E. coli*, (b) with *E. coli* (0.5 wt.-%). The peaks of COD are labeled with an asterisk.

In order to investigate the influence of aging time and the ratio bacterium/chemical reagents on the formation of CaOxa, SEM images (Figure 3) and XRD patterns (Figure 4) of the products formed in two systems at different reaction times were recorded. At a CaOxa concentration of $2.5 \times 10^{-2}$ M the mass ratio bacteria/CaOxa is 1.56:1 (*E. coli*: 0.5 wt.-%) and the morphologies of CaOxa particles obtained transform from predominantly bipyramidal to predominantly hexagonal, although the sizes show no obvious

 © 2007 Wiley-VCH Verlag GmbH & Co. KGaA, Weinheim 

changes (range from 100–600 nm) after aging for between 5 min and 3 d (shown in Figure 3a–d). The corresponding XRD patterns show that the CaOxa obtained has two phases including COD and COM (shown in Figure 4a–d). If $I_D$ and $I_M$ are defined as the intensity of the characteristic diffraction peaks of COD (200) and COM ($\bar{1}01$), the percentage of COD in the mixture can be calculated from the equation $\%COD = I_D/(I_M + I_D)$.[29] With aging times of 5 min, 30 min, 3 h, and 3 d, the percentage of COD in the products is 55.6%, 52.7%, 26.5%, and 0.02%, respectively. This clearly shows that the amount of COD in the crystals decreases gradually and almost disappears with an increase of aging time, which suggests that thermodynamically unstable COD changed into stable COM with time.

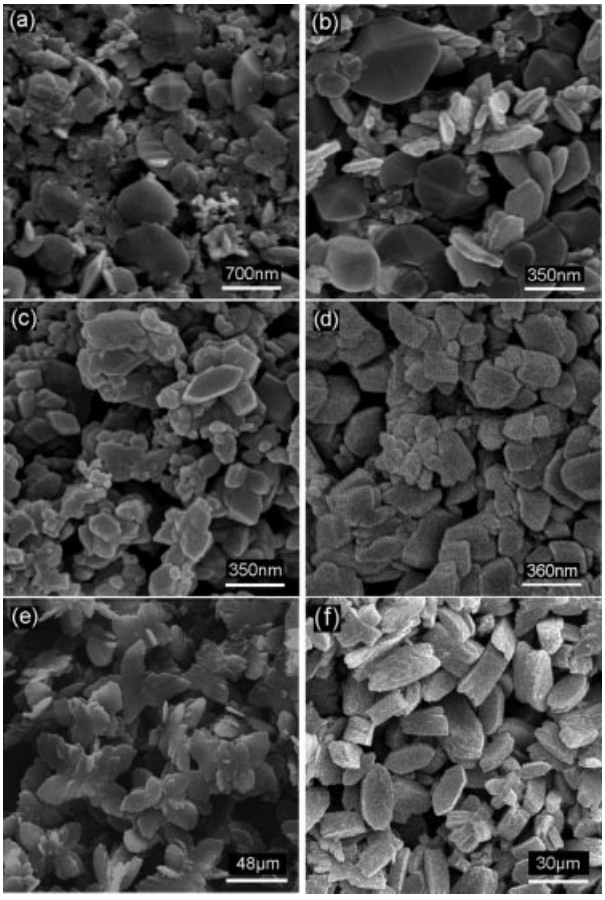


Figure 3. SEM images of CaOxa precipitates obtained in two systems at different reaction times: (a)–(d) concentration of CaOxa of $2.5 \times 10^{-2}$ M with aging times of 5 min, 30 min, 3 h, and 3 d, respectively, with 0.5 wt.-% *E. coli*; (e), (f) concentration of CaOxa of $2.5 \times 10^{-3}$ M and aging times of 3 h and 3 d, respectively, with 0.5 wt.-% *E. coli*.

Decreasing the concentration of CaOxa to $2.5 \times 10^{-3}$ M increased the mass ratio bacteria/CaOxa (15.6:1) and the sizes and morphologies of the CaOxa particles obtained also changed. It can be seen from Figure 3e, taken after 3 h, that flower-like CaOxa particles were obtained. Every "petal" of the "flower" is quasi-hexagonal with a mean diagonal of around 30 μm. The corresponding XRD patterns show that they are all COM crystals (Figure 4e). To the

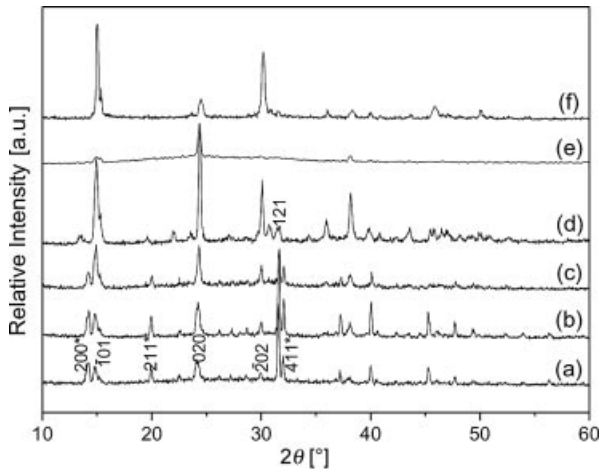


Figure 4. XRD patterns of CaOxa precipitates obtained in two systems at different reaction times: (a)–(d) concentration of CaOxa of $2.5 \times 10^{-2}$ M with aging times of 5 min, 30 min, 3 h, and 3 d, respectively, with 0.5 wt.-% *E. coli*; (e), (f) concentration of CaOxa of $2.5 \times 10^{-3}$ M and aging times of 3 h and 3 d, respectively, with 0.5 wt.-% *E. coli*. The peaks labeled with an asterisk correspond to COD.

best of our knowledge the general morphology of COM is hexagonal, therefore the "flowers" probably form due to the aggregation of several single hexagonal COM particles. This suggests that *E. coli* influences the growth and aggregation of CaOxa. When the aging time was increased to 3 d mainly hexagonal CaOxa particles with an average diagonal of around 30 μm were obtained (Figure 3f). Compared with those formed after 3 h, these particles are isolated with no apparent change in size. The XRD results show that they are also COM (Figure 4f), although the strongest diffraction peak is ($\bar{1}01$) instead of (020), which implies that the bacterium (*E. coli*) influences the crystallization process.

It can be seen from the above results that the CaOxa particles obtained become larger, more regular, and aggregate more easily with an increase in the bacteria/CaOxa ratio and that, at the same aging time (3 h), the phase transition from COD to COM is more rapid. This further suggests that *E. coli* accelerates the crystallization of COM and makes the particles become larger. Larger COM particles form urinary stones more easily because they are more difficult to excrete, therefore we can speculate that *E. coli* plays an important role in the biomineralization process of urinary stones. In addition, it can also be speculated from the above results that a higher concentration of CaOxa does not always result in a risk of urinary stones.

TEM images of the products obtained by drying the reacting solution containing $2.5 \times 10^{-3}$ M CaOxa and 0.5 wt.-% *E. coli* after aging for 12 h were recorded in order to explore the details of nucleation and growth of COM induced by *E. coli* (see Figure 5). It can clearly be seen that there are many uniform spindle-shaped particles in the CaOxa-centered area (Figure 5a), which were proved by their electron diffraction (ED) pattern (Figure 5c) to be COM crystals. When examined carefully, these crystals are found to be enclosed by light shells. We infer that the light

 © 2007 Wiley-VCH Verlag GmbH & Co. KGaA, Weinheim 

materials on the crystal surface are the bioorganic secretions of the bacterium. In addition, many light, rod-like bacteria (*E. coli*) can be seen in the bacteria-centered area (Figure 5b). The darker parts seen in the bodies of some bacteria were shown from their ED patterns (Figure 5d) to be COM crystals. This suggests that $Ca^{2+}$ and $C_2O_4^{2-}$ ions can enter into the cells of the bacteria and form COM crystals due to inducement by intracellular biomolecules. In other words, the bacteria can control the nucleation and growth of COM crystals in their interior. In order to confirm the TEM results, the FTIR spectrum of CaOxa crystals obtained from the solution after the same reaction time was determined (Figure 6). It can be seen from this spectrum that the symmetric and antisymmetric oxalate C=O stretching bands are located at 1618 and 1321 $cm^{-1}$, respectively. Very importantly, the band located at 1640 $cm^{-1}$ (amide I) shows that the CaOxa obtained contains *E. coli* proteins. The surface-bound proteins released from the COM crystals grown in the presence of *E. coli* were removed by treatment with NaOCl and analyzed by 10% sodium dodecyl sulfate polyacrylamide gel electrophoresis (SDS-PAGE) at pH = 8.2. The data show that the surface-bound proteins have a molecular weight of about 26.5 kDa (lane 2, Figure 7a). The UV/Vis spectrum of the surface-bound proteins is shown in Figure 7b. The peak at 210 nm was assigned to the strong absorption of the peptide bonds of the protein in the extract, which arises from an n–π* transition of the C=O group. The absorption at 280 nm is due to the π–π* transition of the tyrosine, tryptophan, or phenylalanine residues of the proteins. Two enzymes in urine, namely sialidase and urokinase, are thought to play a role in urolithiasis. Sialidase is responsible for the conversion of urinary mucosubstances into mineralizable matrix and urokinase regulates the urinary uromucoid concentration. du Toit et al.[30] have found that *E. coli* can inhibit urokinase and stimulate sialidase activity, which leads to the formation of a mineralizable stone matrix. They also suggested that *E. coli* might cause urolithiasis by producing matrix substances that increase crystal adherence to the epithelium.[31] The average concentration of *E. coli* in the urine of patients with a urinary tract infection or urolithiasis is about $10^6$ cells/mL,[32,33] which is very close to the experimental levels found by du Toit et al.[30] It can be speculated that the CaOxa surface-bound proteins with a molecular weight of about 26.5 kDa are probably the urokinase inhibitor and sialidase stimulator synthesized by *E. coli* during incubation.[30] Except for altering the excretion of the two enzymes, these proteins could also act as matrices for stone formation. Further investigations are in progress to determine the sequences of the proteins and the nature of the interaction of the proteins with the different crystallographic faces of CaOxa crystals. Taken together, these results suggest that the bacteria and their secretions participate in the crystallization of CaOxa, which means that *E. coli* can mineralize calcium and oxalate both intracellularly and with their bioorganic secretions. Previous studies have shown that nanobacteria can mineralize calcium and phosphate and act as crystallization centers during the formation of urinary stones,[21–23] therefore we speculate that *E. coli* probably also acts as a nucleus in the biomineralization of urinary stones.

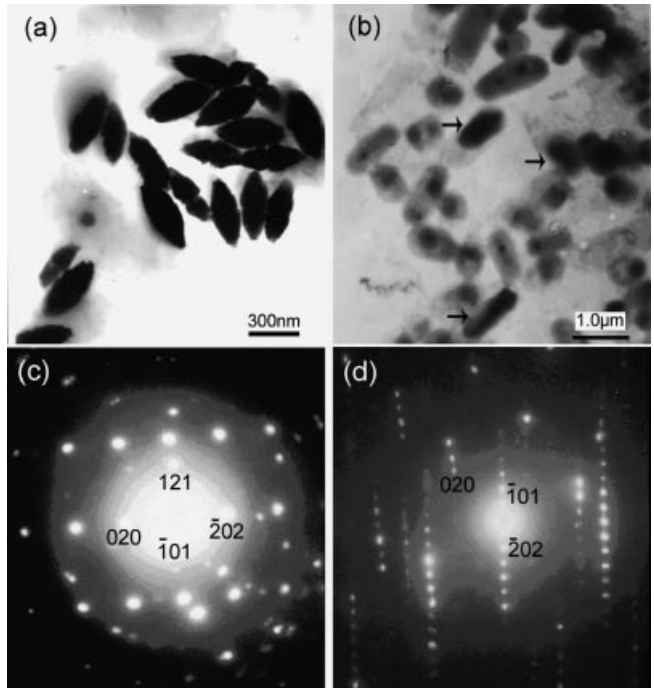


Figure 5. TEM images of the products obtained by drying the reaction solution containing $2.5 \times 10^{-3}$ M CaOxa and 0.5 wt.-% *E. coli* after aging for 12 h [(a): CaOxa-centered area; (b): bacteria-centered area] and electron-diffraction (ED) patterns of the crystals obtained [(c): CaOxa-centered area; (d): bacteria-centered area]. The arrows in (b) point to CaOxa crystals grown in cells of *E. coli*.

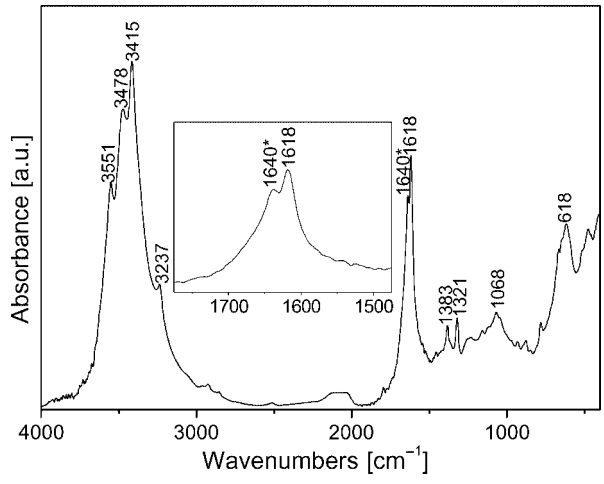


Figure 6. FTIR spectrum of CaOxa particles obtained from the reaction solution containing $2.5 \times 10^{-3}$ M CaOxa and 0.5 wt.-% *E. coli* after aging for12 h. The inset shows the magnification of the bands located at 1618 and 1640 $cm^{-1}$. The peak labeled with an asterisk is the amide I band of the *E. coli* proteins.

To the best of our knowledge, the cell walls of *E. coli* are composed of lipopolysaccharide and peptidoglycan, which is a polymer of glucide and protein with a polysaccharide structure, 30% of whose subunits (*N*-acetylglucosamines and *N*-acetylmuramic acids) interlace together to form a

 © 2007 Wiley-VCH Verlag GmbH & Co. KGaA, Weinheim 

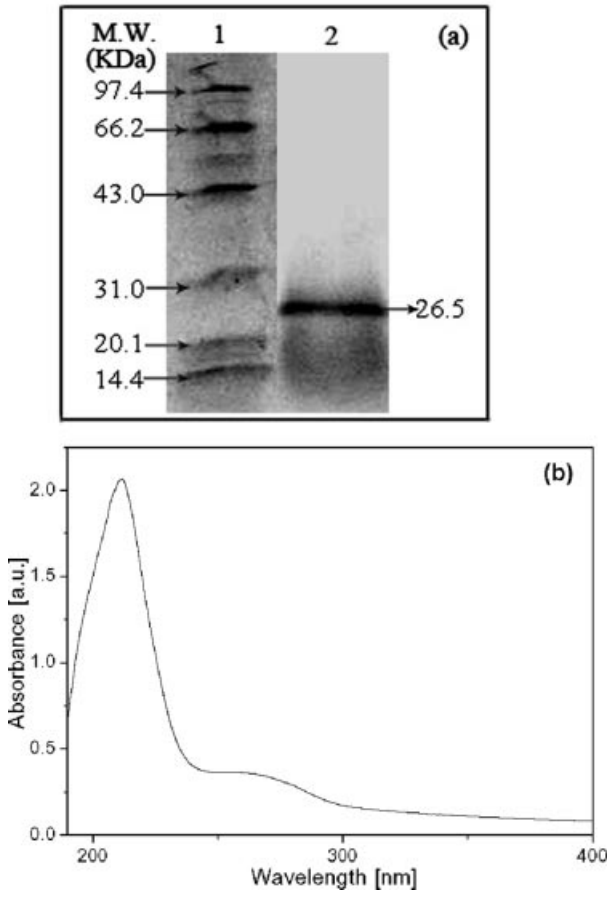


Figure 7. (a) SDS-PAGE data showing the proteins that were originally bound to the surface of the COM crystals grown in the presence of *E. coli*. Lane 1 shows standard protein molecular weight markers with the corresponding molecular weights, in kDa, indicated by arrows. Lane 2 corresponds to the protein bands in the *E. coli* secretions obtained by treatment of COM crystals grown in the presence of *E. coli* with NaOCl. (b) UV/Vis spectrum of the proteins obtained by treatment of COM crystals grown in the presence of *E. coli* with NaOCl.

relatively loose structure with many bare electronegative groups, which could attract and combine with $Ca^{2+}$ ions to provide nucleation sites. In addition, proteins and other biomolecules present in the cell could also interact with $Ca^{2+}$ ions. $C_2O_4^{2-}$ anions would then be attracted to the $Ca^{2+}$-enriched environment and the crystal nucleus of CaOxa would form. Growth of CaOxa crystals would then be controlled by the cell walls or the biomolecules in the bacterial cells.

Bacteria can produce many extracellular proteins such as enzymes, etc.;[34] therefore, we also studied the secretions of *E. coli* in detail by means of zeta potential and FTIR measurements to clarify the interaction between the bacteria and CaOxa. The zeta potential of *E. coli* secretions in aqueous solution shows a peak at about –137 mV (Figure 8), which implies that they are negatively charged and could therefore strongly attract and enrich $Ca^{2+}$ through electrostatic interactions to provide nucleation sites for CaOxa crystals.

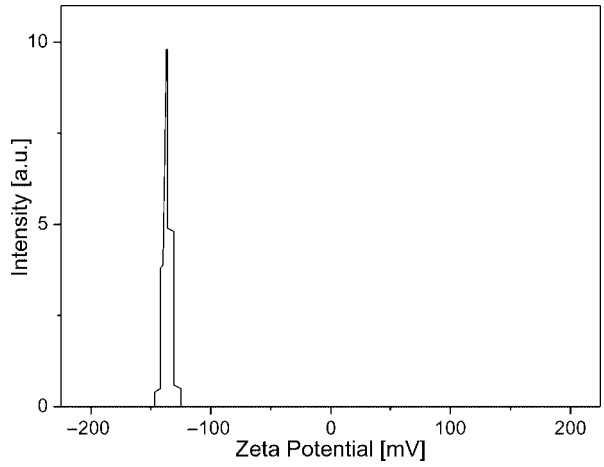


Figure 8. Zeta potential of the *E. coli* secretions in aqueous solution (*E. coli*: 0.5 wt.-%).

Figure 9 shows the FTIR spectra of *E. coli* and its secretions in the absence and presence of $CaCl_2$. Figure 9a clearly shows that their principal components are mainly proteins, and the main bands at 1640, 1543, and 1401 $cm^{-1}$ can be assigned to amide I ($\nu_{C=O}$), II ($\delta_{N-H}$), and III ($\nu_{C-N}$) absorptions, respectively. In the spectrum in Figure 9b, which was recorded in the presence of $Ca^{2+}$, the amide I band is shifted by 6 $cm^{-1}$ to lower frequencies and the amide II band has disappeared, which indicates that there are strong interactions between $Ca^{2+}$ ions and the proteins secreted by *E. coli*. In order to obtain more detailed information, the secondary structures of the proteins with and without $Ca^{2+}$ ions were studied by recording the second derivative followed by a curve fitting (shown in Figure 10a, b).[35] In the absence of $Ca^{2+}$ ions, the bands located at 1641, 1632, 1623, and 1614 $cm^{-1}$ were assigned to a β-sheet, that at 1677 $cm^{-1}$ to a β-turn, those at 1669 and 1661 $cm^{-1}$ to an α-helix, and that at 1652 $cm^{-1}$ to a random coil of a protein secondary structure. In the presence of $Ca^{2+}$ ions, however, the bands attributed to the β-sheet are found at 1690, 1641, 1631, 1622, 1613, and 1603 $cm^{-1}$, that for the β-turn at 1678 $cm^{-1}$, those for the α-helix at 1669 and 1662 $cm^{-1}$, and that for the random coil at 1653 $cm^{-1}$. The percentages of β-sheet, β-turn, α-helix and random coil of *E. coli* proteins in the absence and presence of $Ca^{2+}$ ions change from 53.5%, 14.2%, 13.4%, and 18.9% in the former case to 62.4%, 8.8%, 11.3%, and 17.5% in the latter. This indicates that, compared with that of the proteins, the percentage of β-sheet of protein-$Ca^{2+}$ compounds increases while the percentage of β-turn, α-helix, and random coil all significantly decreased, which suggests that the interaction between $Ca^{2+}$ and proteins makes the conformation of the proteins become more ordered. These ordered proteins could influence the nucleation, growth, and aggregation of CaOxa crystals.

 © 2007 Wiley-VCH Verlag GmbH & Co. KGaA, Weinheim 

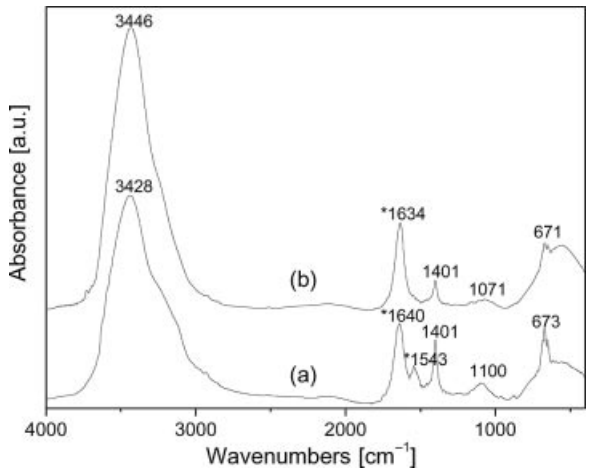


Figure 9. FTIR spectra of (a) *E. coli* aqueous solution (*E. coli*: 0.5 wt.-%) and (b) *E. coli*/$CaCl_2$ aqueous solution (*E. coli*: 0.5 wt.-%; $CaCl_2$: $5 \times 10^{-3}$ M). The amide I and II bands of the *E. coli* proteins are labeled with an asterisk.

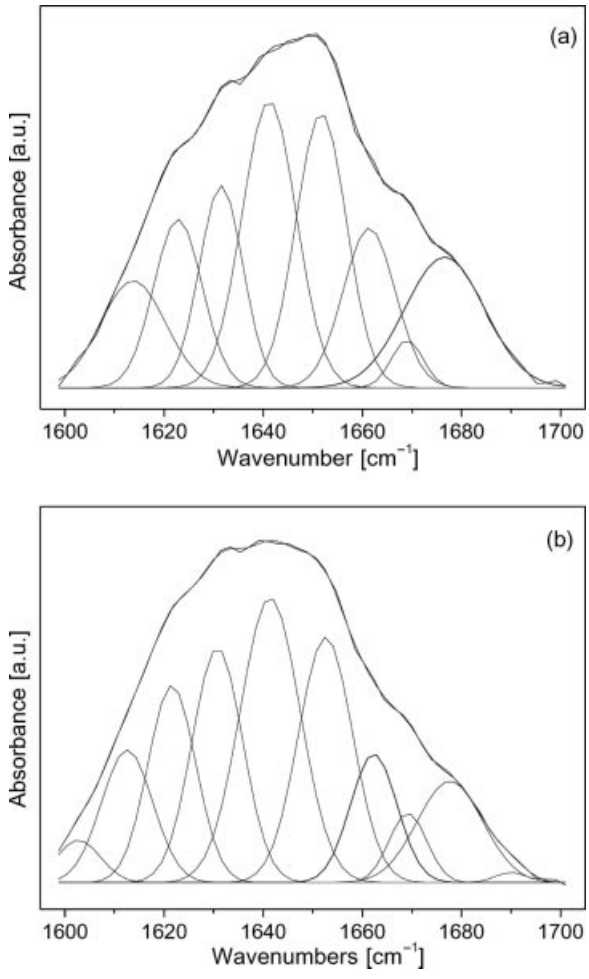


Figure 10. Second derivative and Gaussian curve fitting of the bands between 1600 and 1700 $cm^{-1}$ (amide I of proteins) for (a) *E. coli* proteins and (b) *E. coli* protein-$Ca^{2+}$ complexes.

According to the Gibbs–Thomson formula of classic nucleation theory,[36] the nucleation and growth of CaOxa induced by *E. coli* could be explained by thermodynamic Equation (1), where $J$ and $S$ are the nucleation rate and supersaturation, respectively, and A and B are constants.

$$J = A\exp[-B(\ln S)^{-2}] \quad (1)$$

We can see from this equation that the rate of nucleation increases with an increase of supersaturation. The interaction between *E. coli* proteins and $Ca^{2+}$ ions concentrates these ions around the negatively charged groups of the proteins, which results in an increased supersaturation of CaOxa in this region. As a result, the nucleation rate of CaOxa is increased and the electronegative and ordered proteins also direct the growth of the nucleus and promote the formation of COM crystals. The bacteria therefore accelerate the nucleation and growth of COM crystals.

The above results imply that the common bacterium *E. coli* could also induce the nucleation and growth of CaOxa crystals and accelerate the crystallization of COM when it infects the urinary tract, which means that *E. coli* plays an important role in biomineralization and promotes the formation of urinary stones.

## Conclusions

Investigation of the influence of *E. coli* on the nucleation and growth of CaOxa crystals in aqueous solution has shown that this bacterium accelerates the formation of COM crystals and makes the particles become larger. When the concentration of CaOxa is decreased, the ratio bacteria/CaOxa increases, the COM crystals obtained become more regular and larger, and the phase transition from COD to COM occurs more rapidly. TEM and FTIR results have shown that the nucleation and growth of CaOxa crystals are induced by intracellular biomolecules and bacterial secretions. SDS-PAGE data and UV/Vis spectroscopy have shown that the surface-bound proteins with a molecular weight of about 26.5 kDa contain tyrosine, tryptophan, or phenylalanine residues. The formation mechanism of CaOxa in the presence of *E. coli* has also been discussed. It is likely that the negatively charged *E. coli* proteins interact strongly with $Ca^{2+}$ ions and make the secondary structure of these proteins more ordered. These ordered proteins induce the nucleation and growth of CaOxa crystals. *E. coli* is therefore likely to play an important role in biomineralization and promote the formation of urinary stone.

## Experimental Section

**Materials and Instruments:** Chloroform, anhydrous ethanol, and acetone were all purchased from Shanghai Chemical Reagent Company (Shanghai, China) and were all analytically pure. Anhydrous calcium chloride, sodium hydroxide, hydrochloric acid, and sodium oxalate ($Na_2Oxa$) were obtained commercially and were also analytically pure. All the above reagents were used without further purification. Doubly distilled water was used in all experiments. Bacteria (*E. coli*) were cultivated on beef peptone culture medium after 48 h incubation at 37 °C in our laboratory. Fourier transform infrared

 © 2007 Wiley-VCH Verlag GmbH & Co. KGaA, Weinheim 

spectra were recorded with a Nicolet 870 instrument with a resolution of 4 $cm^{-1}$ in the wavenumber range from 400 to 4000 $cm^{-1}$ using the KBr pellet technique. X-ray diffraction patterns were recorded with a DX-2000 diffractometer using Cu-$K_\alpha$ radiation at a scan rate of 0.06° in $2\theta$ per second. Scanning electron microscopy was performed with a Hitachi X-650 instrument at an accelerating voltage of 20 kV. Transmission electron microscopy and selected-area electron diffraction studies of the CaOxa particles were carried out with a JEM model 100SX electron microscope from Japan Electron Co. at an accelerating voltage at 200 kV. A UV/Vis double beam spectrophotometer (Beijing Purkinje General Instrument Co., Ltd, China) and a zeta potentiometer (Malvern Instruments Limited) were also used.

**Methods:** In a typical experiment, the appropriate amount of *E. coli* was added to a $5\times10^{-2}$ or $5\times10^{-3}$ M aqueous solution of $CaCl_2$ (40 mL), and this solution was mixed with the same concentration and volume of an aqueous $Na_2Oxa$ solution. The reaction solution was airproofed and kept at a temperature of 35±1 °C for between 5 min and 72 h after stirring for 30 s. The concentration of *E. coli* in the reaction solution was kept constant at 0.5 wt.-% and the pH of the solution was adjusted to about 7.0. Control experiments were carried out under the same conditions without addition of bacteria. The size and the morphology of the precipitates obtained were examined by scanning electron microscopy (SEM), while their crystalline phases were examined by X-ray powder diffraction (XRD). The zeta potential of an aqueous *E. coli* (0.5 wt.-%) solution was measured to determine the nature of the charge of the bacterial secretions. A drop of an aqueous *E. coli* solution (*E. coli*: 0.5 wt.-%) with and without $CaCl_2$ ($CaCl_2$: $5\times10^{-3}$ M) was placed on a KBr crystal after aging for 1 h at a temperature of 35±1 °C and dried before recording the FTIR spectra to determine the composition of the *E. coli* secretion and the interaction between the *E. coli* secretion and $Ca^{2+}$ ions. A drop of reaction solution (*E. coli*: 0.5 wt.-%; CaOxa: $2.5\times10^{-3}$ M) was placed on a copper grid after aging for 12 h at a temperature of 35 ± 1 °C and dried before recording the TEM image and SAED patterns in order to investigate the influence of the bacterium on the growth of CaOxa crystals. The particles obtained by centrifuging the reaction solution (after aging for 12 h) were washed with doubly distilled water and dried for FTIR spectroscopic determination. To identify the proteins bound to the calcium oxalate crystals that are possibly responsible for the crystal shape and type control, the CaOxa crystals obtained in the presence of bacteria were washed thoroughly after aging for 72 h and then treated with 4% sodium hypochlorite (NaOCl) solution. The free proteins detached from the COM crystals in solution were separated by centrifugation and analyzed by 10% SDS-PAGE at pH = 8.2 and UV/Vis spectroscopy.

## Acknowledgments

This work was supported by the National Science Foundation of China (20471001, 20671001), the Important Project of Anhui Provincial Education Department (ZD2007004-1), and the Specific Project for Talents of Science and Technology of the Universities of Anhui Province (2005 hbz03).

[1] S. Atanassova, K. Neykov, I. Gutzow, *J. Cryst. Growth* **2000**, *212*, 233–238.
[2] E. L. Prien, E. L. Prien, *Am. J. Med.* **1968**, *45*, 654–672.
[3] A. Smesko, R. P. Singh, A. C. Lanzalaco, G. H. Nancollas, *Colloids Surf.* **1988**, *30*, 361–371.
[4] S. R. Khan, R. L. Hackett, *J. Urol.* **1993**, *150*, 239–245.
[5] W. H. Boyce, F. K. Garvey, *J. Urol.* **1956**, *76*, 213–227.
[6] S. Whipps, S. R. Khan, F. J. O'Palko, R. Backov, D. R. Talham, *J. Cryst. Growth* **1998**, *192*, 243–249.
[7] R. Backov, S. R. Khan, C. Mingotaud, K. Byer, C. M. Lee, D. R. Talham, *J. Am. Soc. Nephrol.* **1999**, *10*, S359–S363.
[8] R. Backov, C. M. Lee, S. R. Khan, C. Mingotaud, G. E. Fanucci, D. R. Talham, *Langmuir* **2000**, *16*, 6013–6019.
[9] S. R. Khan, P. A. Glenton, R. Backov, D. R. Talham, *Kidney Int.* **2002**, *62*, 2062–2072.
[10] I. O. Benítez, D. R. Talham, *Langmuir* **2004**, *20*, 8287–8293.
[11] I. O. Benítez, D. R. Talham, *J. Am. Chem. Soc.* **2005**, *127*, 2814–2815.
[12] J. M. Ouyang, S. P. Deng, *Dalton Trans.* **2003**, 2846–2851.
[13] J. M. Ouyang, L. Duan, J. H. He, B. Tieke, *Chem. Lett.* **2003**, *32*, 268–269.
[14] L. J. Wang, S. R. Qiu, W. Zachowicz, X. Y. Guan, J. J. DeYoreo, G. H. Nancollas, J. R. Hoyer, *Langmuir* **2006**, *22*, 7279–7285.
[15] Y. H. Shen, W. J. Yue, A. J. Xie, S. K. Li, Z. Qian, *Colloids Surf., B* **2005**, *45*, 120–124.
[16] Y. H. Shen, W. J. Yue, A. J. Xie, Z. Q. Lin, F. Z. Huang, *Colloids Surf., A* **2004**, *234*, 35–41.
[17] M. Khullar, S. K. Sharma, S. K. Singh, P. Bajwa, F. A. Sheikh, M. Sharma, *Urol. Res.* **2004**, *32*, 190–195.
[18] N. Ciftcioglu, M. Bjorklund, K. Kuorikoski, K. Bergstrom, E. O. Kajander, *Kidney Int.* **1999**, *56*, 1893–1898.
[19] E. O. Kajander, M. Bjorklund, N. Ciftcioglu, *Proc. SPIE.-Int. Soc. Opt. Eng.* **1998**, *3441*, 86–94.
[20] N. Ciftcioglu, M. Bjorklund, E. O. Kajander, *Proc. SPIE.-Int. Soc. Opt. Eng.* **1998**, *3441*, 105–111.
[21] E. G. Cuerpo, E. O. Kajander, N. Ciftcioglu, F. L. Castellano, C. Correa, J. Gonzalez, F. Mampaso, F. Liano, E. G. de Gabiola, A. E. Barrilero, *Arch. Esp. Urol.* **2000**, *53*, 291–303.
[22] K. K. Akerman, J. T. Kuikka, N. Ciftcioglu, J. Parkkinen, K. A. Bergstrom, I. Kuronen, E. O. Kajander, *Proc. SPIE.-Int. Soc. Opt. Eng.* **1997**, *3111*, 436–442.
[23] F. A. Shiekh, M. Khullar, S. K. Singh, *Urol. Res.* **2006**, *34*, 53–57.
[24] C. Kwak, H. K. Kim, E. C. Kim, M. S. Choi, H. H. Kim, *Eur. Urol.* **2003**, *44*, 475–481.
[25] R. Kumar, M. Mukherjee, M. Bhandari, A. Kumar, H. Sidhu, R. D. Mittal, *Eur. Urol.* **2002**, *41*, 318–322.
[26] A. Edin-Liljegren, L. Grenabo, H. Hedelin, J. Larsson, S. Pettersson, *Scand. J. Urol. Nephrol.* **1993**, *27*, 163–167.
[27] A. Edin-Liljegren, L. Rodin, L. Grenabo, H. Hedelin, *Scand. J. Urol. Nephrol.* **2001**, *35*, 106–111.
[28] N. S. Morris, D. J. Stickler, R. J. McLean, *World J. Urol.*. **1999**, *17*, 345–350.
[29] M. Donnet, N. Jongen, J. Lemaitre, P. Bowen, *J. Mater. Sci. Lett.* **2000**, *19*, 749–750.
[30] P. J. du Toit, C. H. van Aswegen, P. L. Steyn, A. Pols, D. J. du Plessis, *Urol. Res.* **1992**, *20*, 393–397.
[31] P. Bassi, *Stone Formation*, in *Handbook of Biomineralization – Medical and Clinical Aspects* (Eds: M. Epple, E. Bauerlein), Wiley-VCH, Weinheim, Germany, **2007**, pp. 329–348.
[32] J. K. Lim, N. W. Gunther, H. Zhao, D. E. Johnson, S. K. Keay, H. L. T. Mobley, *Infect. Immun.* **1998**, *66*, 3303–3310.
[33] T. A. Kanellopoulos, P. J. Vassilakos, M. Kantzis, A. Ellina, F. Kolonitsiou, D. A. Papanastasiou, *Eur. J. Pediatr.* **2005**, *164*, 355–361.
[34] G. Butland, J. M. Peregrín-Alvarez, J. Li, W. H. Yang, X. C. Yang, V. Canadien, A. Starostine, D. Richards, B. Beattie, N. Krogan, M. Davey, J. Parkinson, J. Greenblatt, A. Emili, *Nature* **2005**, *433*, 531–537.
[35] A. E. Andreeva, I. R. Karamancheva, *J. Mol. Struct.* **2001**, *565–566*, 177–182.
[36] Y. H. Shen, A. J. Xie, L. C. Huang, F. Z. Huang, Z. X. Chen, D. Ma, *Synth.. React.. Inorg. Met.-Org. Chem.* **2005**, *35*, 359–364.

Received: February 15, 2007
Published Online: May 29, 2007

 © 2007 Wiley-VCH Verlag GmbH & Co. KGaA, Weinheim 

DOI: 10.1002/ejic.200700286

# Syntheses, Structures and Coordination Modes of Acetatopalladium(II) Complexes with 1,3-Bis(2-arylimino)isoindoline Ligands of Different Steric Influence

**Martin Bröring,*[a] Christian Kleeberg,[a] and Esther Cónsul Tejero[a]**

**Keywords:** Cyclometalation / Isoindoline ligands / Polynuclear complexes / Palladium / Coordination modes

Acetatopalladium(II) complexes of four different 1,3-bis(2-arylimino)isoindoline ligands (bai's) with different degrees of steric congestion have been prepared and were characterized by NMR and XRD with respect to nuclearity and coordination mode. In particular, the propensity for heteroaryl ring rotation and C–H activation has been investigated. Palladium(II) ions bind to bai ligands in different coordination modes, either as classical Werner-type *N*,*N*,*N* bonded complexes or—after pyridyl ring rotation and C–H activation—as carbometalated *C*,*N*,*N* chelates. In the latter case two (bai•)-Pd(OAc) subunits have been found to dimerize via two bridging Pd(OAc) moieties in the solid and in solution. These stable and electroneutral tetranuclear species are of low solubility in non-donor solvents, but break up into soluble dinuclear species of unknown composition upon the addition of DMSO, azide or cyanide. Attempts to activate C–C bonds by this strategy were not successful. Surprisingly, the exchange of the terminal pyridines by pyrimidines does not result in the formation of oligonuclear or oligomeric species. Besides the degree of steric hindrance, three more factors, solubility of the products, stoichiometry of metal precursor and charge compensation, have been identified to govern the outcome of the metalation of these bai ligands.

(© Wiley-VCH Verlag GmbH & Co. KGaA, 69451 Weinheim, Germany, 2007)

## Introduction

Palladacycles[1] constitute an important class of organometallic species. Despite their historical role in the development of organometallic chemistry,[2] cyclometallated palladium(II) compounds have found entry in many different fields like organic synthesis, catalysis, and material science.[3] In addition, many of the nowadays indispensable palladium-promoted organic transformations are considered to proceed via palladacyclic intermediates.[4]

1,3-Bis(2-arylimino)isoindolines (bai) are monoanionic, meridonal tridentate *N*,*N*,*N* ligands[5] that were first introduced in the 1950s.[6] Palladium(II) complexes of such bai ligands like **1** and others are known as classical coordination compounds,[7] and their catalytic capabilities in the hydrogenation of alkenes have been demonstrated.[8] In a recent study it was described that steric strain applied to the coordination unit of such classical (bai)Pd complexes by well-situated terminal methyl groups results in an intriguing reactivity, i.e. pyridine ring rotation and C–H activation of the heteroaromatic ligand, to yield the carbopalladated 1,3-bis(6-methylpyridyl-2-imino)isoindoline (6-Me-bpi*) species **2** (Figure 1).[9] This report tempted us to investigate the reactivity of palladium(II) ions on bai ligands of different steric influence and to compare their behaviour with a class of related meridonal-tridentate *N*,*N*,*N* ligands, the α,ω-dimethyltripyrrins,[10] that we had studied before. In a first attempt we were able to show, that the stoichiometry of the palladium precursor added to the bai ligand is responsible for the outcome of the reaction, i.e. the formation of a Werner-type or a cyclopalladated product, if the steric hindrance is equal for the N- and the C donor positions.[11] We have now extended the study to ligands with different degrees of intramolecular strain, and report here about the results of our work.

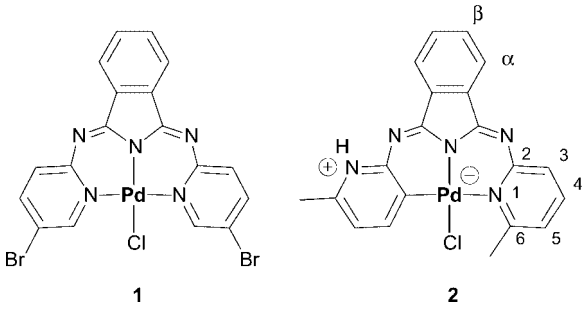


**1** **2**

Figure 1. *N*,*N*,*N* vs. *C*,*N*,*N* binding mode of unstrained and strained (bpi)PdCl derivatives **1**[7a)] and **2**.[9]

[a] Fachbereich Chemie, Philipps-Universität Marburg, Hans-Meerwein-Straße, 35032 Marburg, Germany
Fax: +49-6421-282-5653
E-mail: Martin.Broering@chemie.uni-marburg.de

Supporting information for this article is available on the WWW under http://www.eurjic.org or from the author.


© 2007 Wiley-VCH Verlag GmbH & Co. KGaA, Weinheim

## Results and Discussion

### Preparation of 1,3-Bis(2-arylimino)isoindolines H(bai) 8–11

The preparation of the 1,3-bis(2-arylimino)isoindolines H(bai) **8**–**11** used in this study is presented in Scheme 1. In general, symmetric H(bai) derivatives can be prepared by a method introduced by Siegl[5a)] upon treatment of phthalodinitrile **3** with a heteroarylamine $ArNH_2$ **4**–**7** and calcium chloride in 1-butanol (Scheme 1). **8** and **9** had been prepared by this approach before.[5a] The new compounds **10** and **11** form in yields of 62% and 7%, and were analyzed by elemental analyses and HRMS, respectively. The low yield was obtained for H(4-Me-bpmi) **11** after 7 d at reflux and is a result of the fair reactivity of aminopyrimidine **7**. Only one successful attempt for the preparation of H(bpmi) derivatives had been described in literature so far.[5j]

The interpretation of the spectroscopic properties of **10** and **11** is straightforward and proofs that the new derivatives behave very similar to other known H(bai) species.[5a)] The NMR spectra show $C_{2v}$ symmetric species in solution and are typically governed by the large number of signals arising from the different aromatic C–H groups. These congested spectra can easily be interpreted after separation in three subspectra. The signals of the methyl group protons typically appear between $\delta$ = 2 and 3 ppm (2.42 and 2.43 ppm for **10**, 2.58 ppm for **11**). The second subspectrum concerns the α- and β protons of the central $C_6H_4$ moiety, which lead to two multiplets for **10** and **11** at 8.05/7.65 and 8.10/7.68 ppm, respectively. The other signals at 7.46/6.86 ppm and 8.62/6.96 ppm belong to the C–H protons of the terminal heterocycles, i.e. the pyridines in **10** and the pyrimidines in **11**. A similar signal pattern is also found for all (bai)$Pd^{II}$(OAc) complexes in this study. For the free base ligands **10** and **11**, however, another broad signal indicating a NH function appears at $\delta$ = 12.3 and 13.3 ppm, respectively.

### Formation of Mono- and Tetranuclear Species 12 and 13 from H(bai) 8 and 9

The complex (bpi)Pd(OAc) **12** was prepared from 1,3-bis(pyridyl-2-imino)isoindoline H(bpi)[5a)] (**8**) and palladium acetate in methanol and precipitates from the reaction mixture as an orange, microcrystalline powder in a yield of 76% (Scheme 2). The constitution $C_{20}H_{15}N_5PdO_2$ was confirmed by combustion analysis and MALDI-MS.

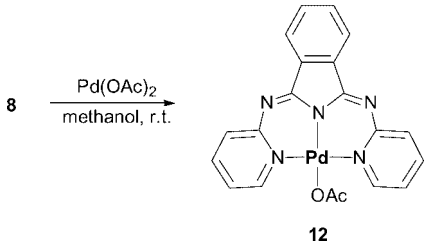


Scheme 2. Preparation of (bpi)Pd(OAc) **12**.

$^1H$ and $^{13}C$ NMR spectra of **12** are in agreement with a compound of $C_2$ symmetry. The acetato ligand can be detected by characteristic signals for the methyl protons and for the carbon atoms at 2.15, 24.8 and 172.7 ppm, respectively. The assumed Werner-type *N*,*N*,*N* coordination of the palladium ion was established by a X-ray crystallographic analysis. A suitable crystal ($CH_2Cl_2$ solvate) grew from a dichloromethane solution at –40 °C. Selected bond lengths and angles are summarized in Table 1 (with Figure 2). Table 2 gives crystallographic details. The molecular structure of **12** is shown in Figure 3.

The molecular structure of **12** confirms the solution spectra and shows a palladium(II) ion coordinated to three nitrogen atoms N1, N2 and N3 of the bpi ligand at distances of 2.038(5), 1.946(5) and 2.037(5) Å. The fourth coordination site is occupied by the O1 donor atom of the acetate moiety in a distance of 2.034(3) Å. The central Pd–N2 bond is markedly shorter than the other two. Literature proposes

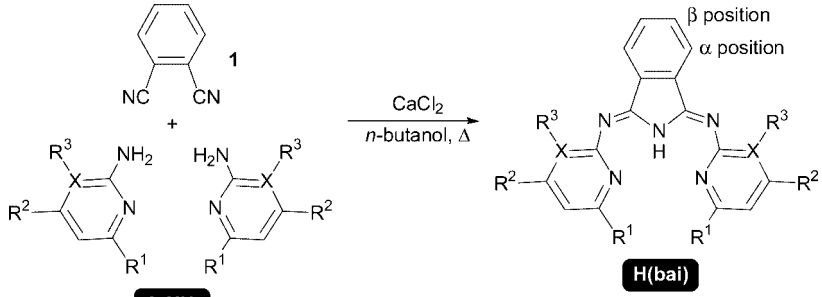


| | $ArNH_2$ | H(bai) |
|---|---|---|
| X = C; $R^1$,$R^2$,$R^3$ = H | **4** | **8** |
| X = C; $R^1$ = Me; $R^2$,$R^3$ = H | **5** | **9** |
| X = C; $R^1$,$R^3$ = Me; $R^2$ = H | **6** | **10** |
| X = N; $R^1$ = Me; $R^2$,$R^3$ = H | **7** | **11** |

Scheme 1. Preparation of H(bai) ligands **8**–**11**.

 © 2007 Wiley-VCH Verlag GmbH & Co. KGaA, Weinheim 

Table 1. Selected structural data for **12**, **13**, **14** and **15**.[a]

| Compound | **12** | **13** | **14 A**[b] | **14 B**[b] | **15** |
|---|---|---|---|---|---|
| N1–Pd1 | 2.038(5) | 2.174(7) | 2.083(4) | 2.070(4) | 2.048(2) |
| N2–Pd1 | 1.946(5) | 1.987(9) | 1.949(4) | 1.954(4) | 1.958(2) |
| N3–Pd1/C*–Pd1 | 2.037(5) | 1.975(9) | 2.080(4) | 2.090(4) | 2.060(2) |
| O1–Pd1 | 2.034(3) | 2.054(7) | 2.053(3) | 2.045(3) | 2.033(2) |
| N3–Pd2 | – | 2.010(9) | – | – | – |
| N5–Pd2 | – | 2.079(8) | – | – | – |
| O2–Pd2 | – | 2.029(7) | – | – | – |
| O3–Pd2 | – | 1.977(6) | – | – | – |
| N1–Pd1–N2 | 89.87(19) | 90.1(3) | 89.15(15) | 89.98(15) | 89.31(10) |
| N1–Pd1–N3/C* | 169.29(19) | 170.3(3) | 164.71(14) | 166.81(14) | 178.81(10) |
| N1–Pd1–O1 | 91.27(17) | 92.7(3) | 90.36(12) | 89.33(12) | 92.27(9) |
| N2–Pd1–N3/C* | 89.91(19) | 90.6(4) | 90.20(16) | 90.36(16) | 89.80(10) |
| N2–Pd1–O1 | 174.58(17) | 169.6(3) | 160.27(14) | 160.66(14) | 177.59(9) |
| N3/C*–Pd1–O1 | 89.94(17) | 88.4(3) | 95.34(13) | 94.66(13) | 88.60(9) |
| N3–Pd2–N5 | – | 65.0(3) | – | – | – |
| N3–Pd2–O2 | – | 173.3(3) | – | – | – |
| N3–Pd2–O3 | – | 101.4(3) | – | – | – |
| N5–Pd2–O2 | – | 108.3(3) | – | – | – |
| N5–Pd2–O3 | – | 166.3(3) | – | – | – |
| O2–Pd2–O3 | – | 85.2(3) | – | – | – |

[a] Unified numbering scheme used for all compounds, see Figure 2. [b] A and B correspond to distinct molecules in the unit cell.

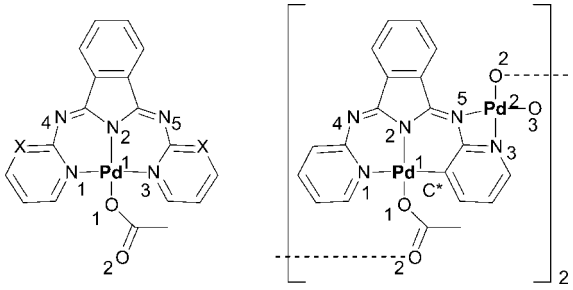


Figure 2. Unified numbering scheme adapted for use in crystallographic determinations.

the increased ionic character of this bond to be responsible for this observation[7a)] that is due to a largely localized negative charge at N2. The deviation of the angles N1–Pd–

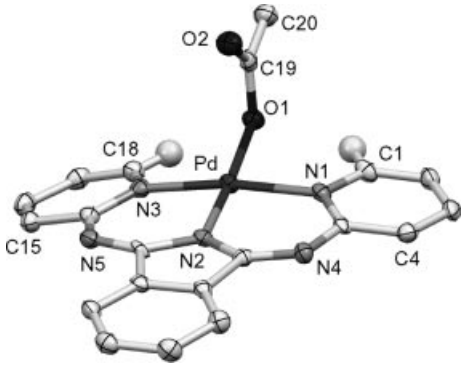


Figure 3. Molecular structure of (bpi)Pd(OAc) **12** in the solid state (most hydrogen atoms omitted for clarity; ellipsoids are set at the 50% probability level).

Table 2. Crystallographic details.

| Compound | **12**×$CH_2Cl_2$ | **13** | **14** | **15**×$CHCl_3$ |
|---|---|---|---|---|
| Formula | $C_{21}H_{17}Cl_2N_5O_2Pd$ | $C_{24}H_{21}N_5O_4Pd_2$ | $C_{24}H_{23}N_5O_2Pd$ | $C_{21}H_{18}Cl_3N_7O_2Pd$ |
| $M_r$ /g mol$^{-1}$ | 548.70 | 656.26 | 519.87 | 613.17 |
| Space group | $P2_1/n$ | $C2/c$ | $Pn$ | $P2_1/n$ |
| $a$ /Å | 12.0777(12) | 15.442(3) | 12.0930(11) | 14.0418(14) |
| $b$ /Å | 10.9337(11) | 17.764(4) | 12.8156(11) | 8.1576(6) |
| $c$ /Å | 16.0578(19) | 18.220(4) | 14.3969(13) | 20.894(2) |
| β /° | 103.415(13) | 97.69(3) | 107.903(10) | 103.288(12) |
| $V$ /Å$^3$ | 2062.6(4) | 4953.0(17) | 2123.2(3) | 2329.3(4) |
| $Z$ | 4 | 8 | 4 | 4 |
| $d_{calcd.}$ /g cm$^{-3}$ | 1.767 | 1.760 | 1.626 | 1.749 |
| Crystal size /mm$^3$ | 0.48 × 0.24 × 0.12 | 0.23 × 0.19 × 0.05 | 0.20 × 0.16 × 0.12 | 0.46 × 0.11 × 0.04 |
| $\mu$(Mo-$K_\alpha$) /mm$^{-1}$ | 1.189 | 1.492 | 0.907 | 1.176 |
| 2$\theta$ limits /° | 4.0–51.8 | 4.0–50.4 | 4.36–51.96 | 3.96–52.12 |
| Measured reflections | 15071 | 7808 | 16264 | 17818 |
| Independent reflections | 3648 | 4232 | 8067 | 4525 |
| Observed reflections[a] | 2781 | 2368 | 7015 | 3242 |
| No. parameters | 281 | 320 | 588 | 338 |
| $R_1$[b] ($R_1$ all data) | 0.0683 | 0.0988 | 0.0331 | 0.0485 |
| $wR_2$[c] ($wR_2$ all data) | 0.1384 | 0.1509 | 0.0531 | 0.0697 |
| Max. / min. peaks | 1.788 / –1.497 | 1.937/ –1.445 | 0.592/–0.408 | 0.609/–0.461 |

[a] Observation criterion: $I > 2\sigma(I)$. [b] $R_1 = \Sigma||F_o| - |F_c||/\Sigma|F_o|$. [c] $wR_2 = \{\Sigma[w(F_o^2 - F_c^2)^2]/\Sigma[w(F_o^2)^2]\}1/2$.

 © 2007 Wiley-VCH Verlag GmbH & Co. KGaA, Weinheim 

N3 and N2–Pd–O1 of 10.7° and 5.4°, respectively, from 180° reveal a non-planar coordination of the $d^8$ $Pd^{II}$ ion that obviously derives from steric interactions between the acetato donor O1 and the terminal protons at C1,18. With 2.208 and 2.212 Å the O1···H distances are found to undercut the van der Waals limit by up to 15.1%.[12] For **1** and **2** which contain the larger chlorido ligand instead of the acetate oxygen atom the N2–Pd–Cl angle is found steeper at 167.74 and 165.13°, respectively, but with a similar degree of X···H and/or X···$CH_3$ interaction of 16.3–20.2% below the van der Waals limit. The bpi ligand of **12** displays a non-planar, convex conformation with twists of the pyridyl and isoindole ring mean squares planes from the N1,N2,N3 plane of 10.82°, 14.42° and 4.34°, respectively. Similar twists are unknown for related tripyrrin complexes and allow bai ligands to better adapt to coordinative requirements by a higher degree of conformational flexibility.

The reaction of H(6-Me-bpi) **9** with two equivalents of palladium(II) acetate also proceeds under the slow formation of a solid precipitate. The product **13** that is obtained after filtration and excessive washing with methanol in 46% yield, however, shows a lower solubility and an entirely different constitution than (bpi)Pd(OAc) **12**. From mass spectra and combustion analytical data the presence of a tetranuclear dimer can be concluded. As will be shown by XRD and NMR studies the constitution of the product **13** is that of a carbopalladated tetranuclear dimer as displayed in Scheme 3. **13** forms very selectively even if less than the stoichiometric amount of palladium acetate is used, and it is reasonable to assume that the low solubility of the tetranuclear dimer efficiently supports the selective formation of the unexpected product. A similar behaviour has been observed with the 4,6-Me2-bpi derivative,[11] if two (or more) equivalents of palladium acetate are employed.

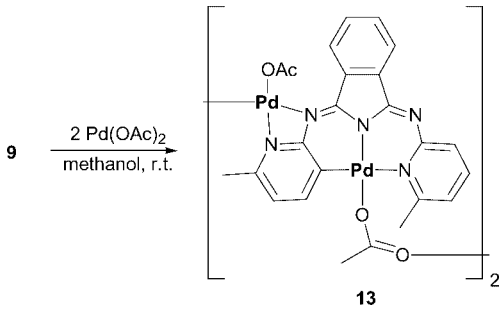


Scheme 3. Formation of [(6-Me-bpi*)$_2$Pd$_4$(OAc)$_4$] **13**.

A crystal of **13** suitable for a X-ray crystallographic analysis was obtained from a solution in chloroform by layering with *n*-hexane and diffusion at room temperature. **13** crystallizes as a solvate, presumably a dihydrate, in the monoclinic system, space group *C*2/*c*, with $Z = 8$. Due to the severe disorder the solvent was removed using the SQUEEZE command in PLATON. The molecular structure of **13** contains two identical monomeric subunits and is presented in Figure 4. Selected bond lengths and angles are given in Table 1. Table 2 summarizes crystallographic details.

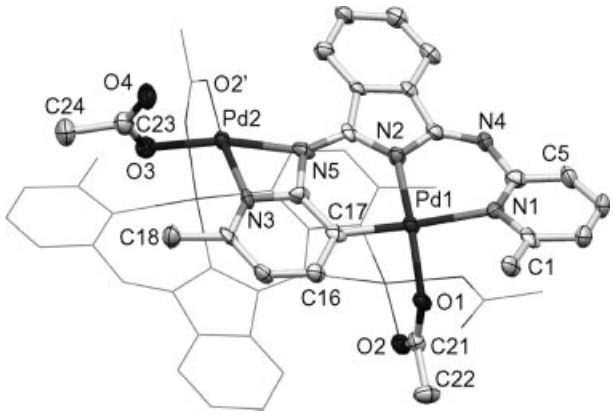


Figure 4. Molecular structure of (6-Me-bpi*)$_2$Pd$_4$(OAc)$_4$ **13** in the solid state (hydrogen atoms omitted for clarity; ellipsoids are set at the 50% probability level).

Complex **13** is a dimer of a palladium complex of a C-H activated 6-Me-bpi ligand, referred to as 6-Me-bpi*. The monomeric (6-Me-bpi*)Pd$_2$(OAc) subunits are doubly bridged by two bidentate acetato ligands which occupy one coordination site on each type of palladium ion, the central ion Pd1 and the peripheral ion Pd2, with Pd–O distances of 2.054(7) and 2.029(7) Å. Besides the acetate coordination the peripheral $Pd^{II}$ ion is bound to N3 and N5 in distances of 2.010(9) and 2.079(8) Å, respectively, and with a narrow N3–Pd2–N5 angle of 65.0(3)°. The fourth coordination site of the distorted square-planar Pd2 ion is saturated by a terminal acetate in a distance of 1.977(6) Å. The *C*,*N*,*N* coordination of the Pd1 atom of **13** is identical to the one recently reported for the mononuclear H[(6-Me-bpi*)PdCl] **2**.[9] Instead of a second palladium ion coordinated to N3 and N5, however, **2** contains a proton at N3 for charge balance. For this reason as well as for the geometrical differences of the bridging coordination modes of chlorido vs. acetato ligands precedent **2** lacks the ability for dimerization via intermolecular coordinative interactions and thus remains monomeric. With the exception of nuclearity, however, the metrics of **2** and **13** as determined by XRD are very similar.

The (6-Me-bpi*)Pd subunits of **13** are stacked above each other in an antiparallel orientation and in a distance of about 3.157 Å. The correlation (Pd–N1) > (Pd–N2) seen above for the Werner-type complex **12** is retained in **13**, and the *trans* influence of the C* donor opposite to N1 is clearly visible in the elongated Pd–N1 bond of 2.174(7) Å. The carbon atom C17 of the inverted pyridine moiety binds to Pd1 in a distance of 1.975(7) Å. The conformation of the 6-Me-bpi* ligand is convex as in **12** but unsymmetric in the predictable sense that the *N* bound pyridine ring with the methyl group close to the acetate O1 atom shows a large tilt of 18.82° while the *C* bonded pyridine ring with the methyl group turned away from the acetato ligand tilts only slightly by 9.78° with respect to the N1,N2,C* plane. The distances O1···H16 and O1···$CH_3$ of 2.362 and 2.764 Å are 9.2% and 18.7% below the van der Waals limit and therefore again in a range that appears typical for this class of

 © 2007 Wiley-VCH Verlag GmbH & Co. KGaA, Weinheim 

compounds. With the exception of the remaining rotational freedom of the terminal acetates the tetranuclear and dimeric morphology of **13** is very rigid, so that the poor solubility of this compound can be rationalized from its structure.

The $^1$H NMR spectrum of **13** in $CD_2Cl_2$ shows a characteristic signal at $\delta$ = 5.51 ppm that was assigned to a proton situated at the C–H activated pyridyl residue (H5) by H,H COSY spectroscopy (see ESI, Figure S1). As the molecular structure of **13** reveals, this proton is situated directly above the aromatic $C_6H_4$ moiety of the isoindoline subunit of the symmetry equivalent monomer in a distance of about 3.3 Å. The high field shift observed for this signal is a consequence from the aromatic ring current of the benzene moiety, and H5 can thus be regarded a probe for the degree of aggregation. The $^1$H NMR spectra proof that the dimeric nature of **13** is not broken up in non-donor solvents like $CH_2Cl_2$ but largely resemble those found in the solid state. The XRD and NMR results of **13** resemble those observed before for a related 4,6-$Me_2$-bpi derivative.[11]

### Investigations of the Formation and Deaggregation of the Tetranuclear Species 13

While for **9** only the tetranuclear cage compound **13** could be isolated in substance, it was possible to isolate a Werner-type complex like **11** with the 4,6-$Me_2$-bpi ligand, depending on the stoichiometry of the metallation agent.[11] Obviously, the steric hindrance for C–H activation is higher for the 4,6-$Me_2$-bpi complex and leads to an increased kinetic stabilization of a mononuclear Werner-type species. In order to gain insight into the elemental steps of the formation of **13** the reaction between H(6-Me-bpi) **9** and two equivalents of $Pd(OAc)_2$ was carried out in deuterated methanol and investigated by $^1$H NMR spectroscopy. The mixture became turbid after a hour, and a spectrum was recorded which clearly showed the presence of two major and one minor species (Figure 5). One of the major as well as the minor species could be identified as the free base ligand H(6-Me-bpi) **9** and as a tetranuclear dimer similar to or identical with **13**, which seems to be present already in its saturation concentration. The remaining signals indicate the presence of a new, $C_2$ symmetric compound with a higher solubility, presumably the Werner-type complex (6-Me-bpi)Pd(OAc). Unfortunately all attempts to isolate this species failed, and **13** was obtained after work-up as the sole product. The study shows that the pyridine rotation and the C–H activation step occur *after* the initial metalation of **9**, and that the kinetic stability of the Werner-type intermediate (6-Me-bpi)Pd(OAc) in the presence of excess $Pd^{II}$ ions is not sufficient to prevent the concurring precipitation of **13**. With respect to the exclusive formation of the Werner-type compound from the unhindered ligand **8** this result supports the hypothesis of strain-induced C–H activation[9] and proofs the labilizing influence of steric strain on the kinetic stability of *N*,*N*,*N* bound species. Further insight into the C–H activation step and/or the pyridine ring inversion, however, could not be obtained. Especially the role of the solvent for the observed pyridin ring rotation/cyclometallation reaction remains unclear, since all attempts to metallate different bai ligands with palladium(II) acetate in solvents other than methanol yielded mixtures of several unassigned compounds.

A second set of $^1$H NMR spectroscopic experiments was devoted to the deaggregation of **13** and the possible determination of the structures of dinuclear fragments of **13**. The experiments were carried out using a) a donor solvent ([$D_6$]-DMSO), b) a donor anion in a donor solvent ($NaN_3$ in [$D_6$]DMSO), and c) a donor anion in a non-donor solvent ([$n$Bu$_4$N]CN in $CD_2Cl_2$; see ESI for selected details from $^1$H-NMR and H,H-COSY spectra obtained from these experiments).

If the $^1$H NMR spectrum of **13** is measured in [$D_6$]-DMSO a major compound with $C_s$ symmetry and without signals for aromatic C–H groups below a chemical shift of 6.9 ppm is detected, indicating a monomeric species in solution. In addition, a number of poorly resolved signals appear and indicate the presence of several side products. An

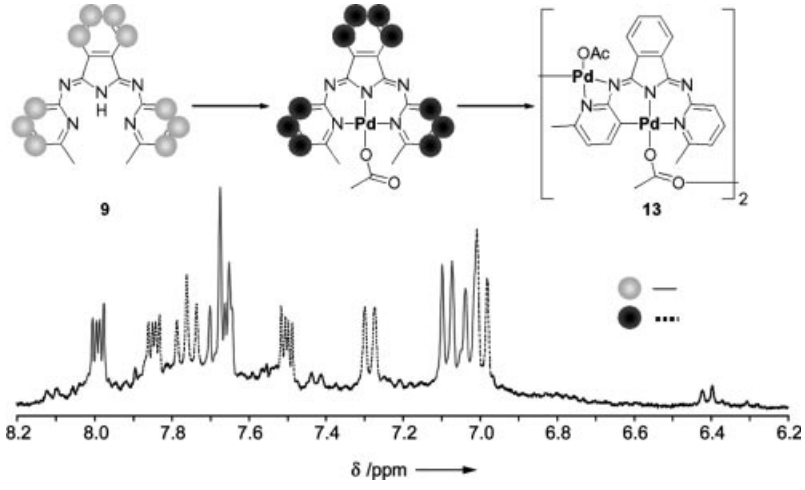


Figure 5. Details from the $^1$H NMR spectroscopic reaction control of the metalation of **9** (400 MHz, [D4]MeOH) and identification of the Werner-type monomeric species (6-Me-bpi)Pd(OAc).

 © 2007 Wiley-VCH Verlag GmbH & Co. KGaA, Weinheim 

exact description of the molecular structure of the monomeric species, however, or a decision about whether one or two palladium ions are bound to the 6-Me-bpi* ligand, can not be given from the spectrum.

Upon the addition of excess sodium azide to the solution of **13** in [$D_6$]DMSO the spectrum clearifies and now displays the presence of one major and one minor compound which are both monomeric in nature and show both $C_s$ symmetry (presumably isomers). In addition only one singlet for an acetate species is present at $\delta$ = 1.64 ppm. This value is characteristic for a weakly bound acetate (e.g. NaOAc in [$D_6$]DMSO: 1.57 ppm) and suggests complete exchange for azido ligands.

A similar $^1$H NMR spectrum with a major and a minor form and a single signal for acetate protons at $\delta$ = 1.78 ppm was obtained from **13** in deuterated dichloromethane upon the addition of tetra-*n*-butylammonium cyanide. Directly after the addition a colour change from orange to yellow was observed. After several hours a yellow solid formed and precipitated from this solution. The solid is insoluble in most solvents, but is slowly taken up in pyridine with an intense yellow colour. The formation and reactivity of the insoluble final product may be explained by the polymerization of a dinuclear fragment [(6-Me-bpi*)$Pd_2$CN]$^+$ via μ-cyanido ligands.

### Metalation Behaviour of New bai Ligands H(bai) 10 and 11

The ease of C–H activation promoted by a simple steric stimulation as in **13** tempted us to use the same stimulus for a C–C activation reaction. Similar reactions have been studied before in pincer complexes with other noble metals like ruthenium, iridium and others.[13] Towards this goal the suitably substituted H(3,6-$Me_2$-bpi) **10** was designed and employed in the reaction with palladium acetate under standard conditions (Scheme 4). Even upon prolonged heating, however, only the Werner-type complex **14** was formed and could be isolated in 21% yield. Elemental analysis and mass spectra confirmed the constitution $C_{24}H_{23}N_5O_2Pd$ of **14**.

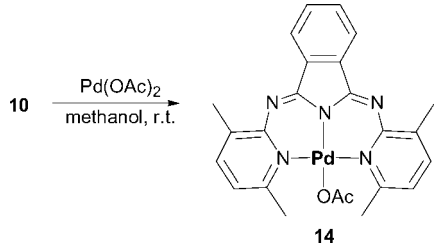


Scheme 4. Preparation of (3,6-$Me_2$-bpi)Pd(OAc) **14**.

The $C_2$ symmetry of the product can be derived from the proton and carbon NMR spectra. Support for the assignments was obtained by a X-ray crystallographic analysis. Two similar molecules **A** and **B** are present in the unit cell of which only the parameters of molecule **A** will be discussed. The molecular structure of **14A** is shown in Figure 6. Selected bond lengths and angles for both molecules are summarized in Table 1. Table 2 gives crystallographic details for the structure determination.

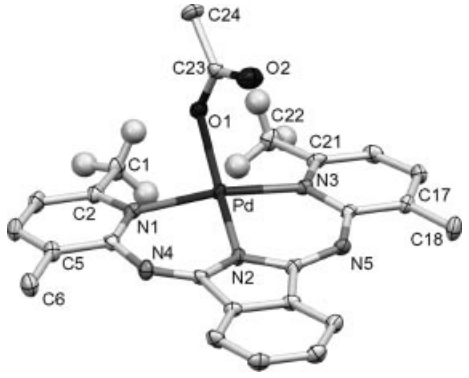


Figure 6. Molecular structure of (3,6-$Me_2$-bpi)Pd(OAc) **14** (molecule **A**) in the solid state (most hydrogen atoms omitted for clarity; ellipsoids are set at the 50% probability level).

The result from the crystallographic analysis of **14** shows the expected distortion of the coordination sphere of the palladium(II) ion by non-linear N1–Pd–N3 and N2–Pd–O1 angles of 164.71° and 160.27°, respectively. These angles correspond to a pseudoplanar conformation of the 3,6-$Me_2$-bpi ligand[10b)] and indicate repulsive interactions between the terminal methyl groups of the bpi subunit and the O1 donor atom of the acetate group. Other than the bpi ligand in **12**, however, the 3,6-$Me_2$-bpi ligand of **14** shows no convex distortion but rather a conformation, in which the mean squares plane of the isoindole subunit is about 0.3–0.5 Å underneath the (almost) coplanar mean squares plane of both pyridyl moieties. This arrangement results in additional space for the acetate O1 donor atom which is located in distances of 2.792(6) and 2.845(6) Å, i.e. 17.9% and 16.3% below the van der Waals limit, from the terminal methyl groups. Very similar values of 16.0% and 18.1% have been obtained from the related mononuclear (4,6-$Me_2$-bpi)Pd(OAc) described earlier.[11] In both cases, an additional fraction of intramolecular strain is distributed to the Pd–N1 and Pd–N3 bonds as judged by their elongations of about 0.04 Å with respect to **12**. Obviously, the system contains sufficient resources to compensate for intramolecular strain, so that a process that requires a significantly larger activation energy than the C($sp^2$)–H activation is not sufficiently promoted by this approach.

Of particular interest was the question of why the C–H activation of **13** does not occur on the site of the peripheral $Pd^{II}$ ion and without pyridyl ring rotation. In particular it is unclear, whether the pyridyl rotation/C–H activation step is necessary for the coordination of a second palladium ion (as could be suggested from the inertness of **12** towards additional $Pd(OAc)_2$), or if the coordination of a second ion ($Pd^{II}$ for **13** and the 4,6-$Me_2$-bpi precedent, $H^+$ for **2**) to an initially formed kinetic product, i.e. the signals of a Werner-type *N*,*N*,*N*-bonded complex seen in the NMR experiment (Figure 5) or the isolated mononuclear 4,6-$Me_2$-bpi complex, assists in this process. To answer this question

 © 2007 Wiley-VCH Verlag GmbH & Co. KGaA, Weinheim 

the bis(pyrimidyl) derivative **11** was designed. The kinetic *and* the thermodynamic product of the reaction of **11** with a first equivalent of $Pd(OAc)_2$ must be identical due to the inability of **11** to undergo a C–H activation process, and should already exhibit two heteroaryl termini with two methyl groups and two *N* donor atoms pointing outwards. Thus, as the final product, a di- or trinuclear complex or an aggregate thereof should be expected.

**11** was metalated under standard conditions and a new, yellow compound **15** separated from the reaction mixture (Scheme 5). Elemental analysis and mass spectra indicate the exclusive formation of a mononuclear compound. Surprisingly, neither a two- or threefold metalation nor a di- or oligomerization occurs despite the presence of excessive palladium acetate. $^1H$ and $^{13}C$ NMR spectroscopic data for **15** again suggests the formation of a $C_2$ symmetric species. Whether both methyl termini point in- or outwards could be clearified in favour of the latter scenario by a X-ray diffraction study.

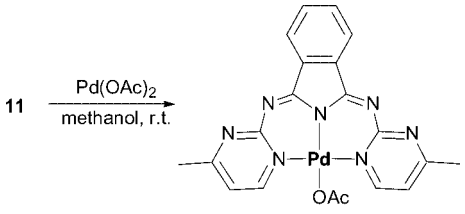


**15**

Scheme 5. Preparation of (6-Me-bpmi)Pd(OAc) **15**.

Yellow needles of **15** suitable for the XRD investigation were obtained by diffusion of *n*-hexane into a $CHCl_3$ solution at room temperature. The molecular structure of **15** is shown in Figure 7. Selected bond lengths and angles are summarized in Table 1. Table 2 gives crystallographic details.

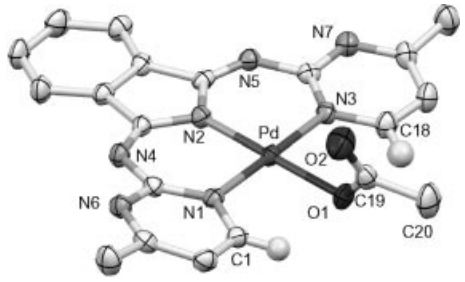


Figure 7. Molecular structure of (6-Me-bpmi)Pd(OAc) **15** in the solid state (most hydrogen atoms omitted for clarity; ellipsoids are set at the 50% probability level).

Complex **15** resides in the expected conformation for a mononuclear chelate, in that the methyl substituents of both pyrimidine rings point outwards. Other than for **12** the coordination environment of the $Pd^{II}$ ion of **15** is close to planar, and the N1–Pd–N3– and N2–Pd–O1–angles are almost linear with 178.81(10)° and 177.59(9)°, respectively. Related values in the (trpy)Pd series usually indicate a *helical* conformation of the organic chelate ligand.[10a,10b,10f,10g] For **15** a new conformation, the concave twist (with respect to the orientation of the acetate group; Figure 7), is observed. With angles between mean squares planes of the pyrimidine(N1) and pyrimidine(N3) subunits and the N1,N2,N3 plane of only 11.06(15)° and 3.36(15)°, respectively, the heterocycles are only slightly tilted away. The Pd–N (1.958(2)–2.060(2) Å] and Pd–O1 distances (2.033(2) Å] are intermediate to those observed for the bpi complexes **12** and **14**, and the typical shortness of the Pd–N2 bond is observed for **15**, too. **15** is thus another example for the structural diversity of bai complexes.

Two rationals may be considered for the exclusive formation of a mononuclear and monomeric species in the reaction of **11** with palladium acetate. First, the outwards pointing methyl groups might interfere with the coordination of a second equivalent of the metal carrier, and secondly, **15** is devoid of a ionic trigger. The first argument appears improbable due to the fact that the same steric encumbrance is present at the peripheral coordination site of the tetranuclear dimer **13**. For the second, more probable argument one has to consider that the monomeric and mononuclear species from **13**, $[(6\text{-Me-bpi*})Pd(OAc)]^-$, which is the formal *C* bonded analog of **15**, carries a negative charge that promotes the binding of another cation.

## Conclusions

In summary we have prepared a set of related (bai)-$Pd^{II}$(OAc) complexes and characterized them in solution and in the solid state with respect to their propensity for intramolecular C–H and C–C activation in dependence of intramolecular strain. In the majority of cases classical, though strained Werner type coordination compounds were found. Despite their constitution from $sp^2$ centres the bai ligands show a remarkable flexibility that allows to adapt smoothly to coordinative constraints and dissipates much of the strain energy to the ligand backbone. As a second coordination mode C–H activation has been observed in a tetranuclear dimer. This outcome of the metalation reaction appears feasible if the rotation of one pyridyl ring is sufficiently supported by the sterics. The comparative study with a pyrimidine derived ligand unraveled, that the binding of a second palladium(II) ion occurs most probably *after* the C–H activation step and becomes a favourable process mainly due to charge balance. Thus the second cation supports the selective formation of a cyclopalladated product mainly indirectly by the formation of a neutral dimer with a low solubility.

## Experimental Section

**General:** All reagents and solvents were purchased from commercial sources. Reagents were used as received. Solvents were dried by standard methods and stored under an argon atmosphere. NMR spectra were obtained on a Bruker ARX 300 or DRX 400 spectrometer in the solvents indicated below. Mass spectra were recorded on a VG Tribid or a Varian CH7 (EI, 70 eV), a Bruker Biflex IV (MALDI), a Qstar Pulsar i (HR-MALDI) or a Ionspec Ultima (ESI) instrument. *m*/*z* values are given for the most abun-

 © 2007 Wiley-VCH Verlag GmbH & Co. KGaA, Weinheim 

dant isotopes only. UV/Vis spectra were measured on a Shimadzu UV1601PC in the range from 200–1100 nm. For X-ray crystallographic measurements an IPDS-I (Stoe) was used. All structures were solved using "*SHELXS*, Program for Crystal Structure Determination"[14] and refined with "*SHELXL*, Program for Crystal Structure Refinement".[15] The solvent in the structure of **13** was removed using the program SQUEEZE in PLATON.[16] CCDC-639805 to -639808 contain the supplementary crystallographic data for this paper. These data can be obtained free of charge from The Cambridge Crystallographic Data Centre via www.ccdc.cam.ac.uk/datarequest/cif.

**Syntheses of 1,3-Bis(arylimino)isoindolines H(bai) 10 and 11. General Procedure:** Phthalodinitrile (**1**) (2.56 g, 20 mmol), heterocyclic amine **6** or 7 (50 mmol) and anhydrous calcium chloride (0.22 g, 2 mmol) are suspended in 1-butanol and heated to reflux for 44 h (**10**) or 168 h (**11**). The solvent is removed in vacuo to leave a yellowish residue. For **10** this solid is extracted with dichloromethane, filtered and recrystallized by the addition of *n*-hexane to leave a yellow solid. For **11** chromatography on silica with THF/pentane (1:3, then 2:1), followed by recrystallization from THF/pentane (1:1) produces a clean, yellow material.

**1,3-Bis(3,6-dimethyl-2-pyridylimino)isoindoline (10):** Yield 4.40 g (62%), m.p. 140–142 °C. $^1$H NMR (300 MHz, $CD_2Cl_2$, 25 °C): $\delta$ = 2.42 (s, 6 H, $CH_3$), 2.43 (s, 6 H, $CH_3$), 6.86 (d, $^3J$ = 7.6 Hz, 2 H, 5-$CH_{Py}$), 7.46 (d, $^3J$ = 7.6 Hz, 2 H, 4-$CH_{Py}$), 7.62–7.68 (m, 2 H, β-CH), 8.02–8.07 (m, 2 H, α-CH), 12.3 (s br, 1 H, NH) ppm. $^{13}$C{$^1$H} NMR (75 MHz, $CD_2Cl_2$, 25 °C): $\delta$ = 17.2, 24.1, 119.5, 122.2, 126.9, 131.5, 136.0, 139.2, 151.8, 154.2, 158.2 ppm. MS (EI): *m*/*z* = 355 [M$^+$], 249 ([M – $C_7H_8N$]$^+$), 235 ([M – $C_7H_8N_2$]$^+$). UV/Vis ($CH_2Cl_2$): $\lambda_{max}$ = 237, 286, 384 nm. $C_{22}H_{21}N_5$ (355.436): calcd. C 74.34, H 5.96, N 19.70; found C 74.18, H 5.82, N 19.43.

**1,3-Bis(4-methyl-2-pyrimidinylimino)isoindoline (11):** Yield 0.50 g (7%), m.p. >200 °C. $^1$H NMR (300 MHz, $CD_2Cl_2$, 25 °C): $\delta$ = 2.58 (s, 6 H, $CH_3$), 6.96 (d, $^3J$ = 5.1 Hz, 2 H, 5-$CH_{Pm}$), 7.67–7.70 (m, 2 H, β-CH), 8.08–8.12 (m, 2 H, α-CH), 8.62 (d, $^3J$ = 5.1 Hz, 2 H, 4-$CH_{Pm}$), 13.3 (s br, 1 H, NH) ppm. $^{13}$C{$^1$H} NMR (75 MHz, $CD_2Cl_2$, 25 °C): $\delta$ = 24.3, 116.5, 123.1, 132.5, 135.8, 156.4, 157.5, 165.1, 168.8 ppm. HRMS (ESI) calcd. for $C_{18}H_{15}N_7Na$: 352.1281; obs. 352.1281, Δ = 0.0 mmu. UV/Vis ($CH_2Cl_2$): $\lambda_{max}$ = 265, 337, 350 nm.

**Syntheses of Acetatopalladium(II) Chelates 12–15. General Procedure:** H(bai) **8**–**11** (0.1 mmol) and palladium acetate (44.9 mg, 0.2 mmol) are suspended in methanol (3 mL) and stirred at ambient temperature under a blanket of argon for 16 h. A solid separates, which is collected by filtration and washed extensively with methanol to leave the product as a red to orange solid.

**(bpi)Pd(OAc) 12:** Yield 35.3 mg (76%), m.p. >200 °C. $^1$H NMR (300 MHz, $CD_2Cl_2$, 25 °C): $\delta$ = 2.15 (s, 3 H, OAc), 7.13 (t, $^3J$ = 6.3 Hz, 2 H, $CH_{Py}$), 7.55–7.98 (m, 4 H, $CH_{Py}$, α-CH), 7.58–7.63 (m, 4 H, $CH_{Py}$, β-CH), 8.89 (m, 2 H, $CH_{Py}$) ppm. $^{13}$C{$^1$H} NMR (75 MHz, $CD_2Cl_2$, 25 °C): $\delta$ = 24.8, 120.4, 122.4, 127.5, 131.7, 138.3, 139.7, 148.4, 152.1, 145.0, 172.7 ppm. MS (MALDI): *m*/*z* = 404 [[M – OAc]$^+$]. UV/Vis ($CH_2Cl_2$): $\lambda_{max}$ = 241, 330, 434, 463 nm. $C_{20}H_{15}N_5O_2Pd$ (463.79): calcd. C 51.79, H 3.26, N 15.10; found C 51.60, H 3.25, N 15.07.

**(6-Me-bpi*)$_2$Pd$_4$(OAc)$_4$ (13):** Yield 30.2 mg (46%), m.p. >200 °C. $^1$H NMR (400 MHz, $CD_2Cl_2$, 25 °C): $\delta$ = 1.33 (s, 3 H, $CH_3$), 1.98 (s, 3 H, $CH_3$), 2.30 (s, 3 H, $CH_3$), 3.04 (s, 3 H, $CH_3$), 5.51 (d, $^3J$ = 8.3 Hz, 1 H, 5-$CH_{Py}$), 7.10 (d, $^3J$ = 7.6 Hz, 1 H, $CH'_{Py}$), 7.15 (d, $^3J$ = 8.3 Hz, 1 H, 1 H, 4-$CH_{Py}$), 7.32 (m, 1 H, β/β′-CH), 7.43 (d, $^3J$ = 7.3 Hz, 1 H, $CH'_{Py}$), 7.51 (m, 1 H, β/β′-CH), 7.67 (d, $^3J$ = 8.0 Hz, 1 H, α/α′-CH), 7.76 (t, $^3J$ = 7.6 Hz, 1 H, 4-$CH'_{Py}$), 7.87 (d, $^3J$ = 7.3 Hz, 1 H, α/α′-CH) ppm. $^1$H NMR (300 MHz, [D$_6$]DMSO, 25 °C): $\delta$ = 1.78 (s, 2 H), 1.91 (s, 2 H), 1.99 (s, 2 H), 2.87 (s, 3 H, $CH_3$), 3.19 (s, 3 H, $CH_3$), 6.94 (d, $^3J$ = 6.6 Hz, 1 H, $CH_{Py}$), 7.14 (d, $^3J$ = 7.3 Hz, 1 H, $CH'_{Py}$), 7.38 (d, $^3J$ = 8.0 Hz, 1 H, $CH'_{Py}$), 7.68–7.76 (m, 2 H, β,β′-CH), 7.87 (t, $^3J$ = 6.5 Hz, 1 H, $CH'_{Py}$), 8.02 (d, $^3J$ = 7.3 Hz, 1 H, α/α′-CH), 8.13 (d, $^3J$ = 6.6 Hz, 1 H, $CH_{Py}$), 9.13 (d, $^3J$ = 6.6 Hz, 1 H, α/α′-CH), 11.94 (br.s, 1 H) ppm. $^{13}$C{$^1$H} NMR (100 MHz, $CD_2Cl_2$, 25 °C): $\delta$ = 19.3, 21.9, 25.4, 26.2, 116.6, 118.1, 121.9, 122.5, 123.8, 124.0, 128.4, 130.9, 134.2, 138.3, 144.4, 154.9, 160.0, 182.3; due to the low solubility of the compound the signals for two quarternary carbon atoms were not detected ppm. MS (MALDI): *m*/*z* = 1253 ([M – OAc]$^+$), 598 ([M/2 – OAc]$^+$), 432 ([(6-Me-bpi*)Pd]$^+$). UV/Vis ($CH_2Cl_2$): $\lambda_{max}$ = 237, 306, 359, 458, 489 nm. $C_{48}H_{42}N_{10}O_8Pd_4$ (1312.59): calcd. C 43.92, H 3.23, N 10.67; found C 43.70, H 3.43, N 10.53.

**(3,6-Me$_2$-bpi)Pd(OAc) (14):** Yield 10.9 mg (21%), m.p. >200 °C. $^1$H NMR (300 MHz, $CD_2Cl_2$, 25 °C): $\delta$ = 1.76 (s, 3 H, OAc), 2.59 (s, 6 H, $CH_3$), 2.60 (s, 6 H, $CH_3$), 6.84 (d, $^3J$ = 7.6 Hz, 2 H, $CH_{Py}$), 7.51–7.56 (m, 2 H, β-CH), 7.57–7.92 (m, 2 H, α-CH), 7.59 (d, $^3J$ = 7.3 Hz, 2 H, $CH_{Py}$) ppm. $^{13}$C{$^1$H} NMR (75 MHz, $CD_2Cl_2$, 25 °C): $\delta$ = 17.8, 23.5, 26.8, 121.3, 122.2, 129.6, 130.9, 137.7, 140.2, 152.6, 154.7, 159.2, 176.7 ppm. HRMS (ESI) calcd. for $C_{22}H_{20}N_5Pd$: 460.0754; obs. 460.0757, Δ = 0.3 mmu. UV/Vis ($CH_2Cl_2$): $\lambda_{max}$ = 240, 376, 505, 537 nm. $C_{24}H_{23}N_5O_2Pd$ (519.89): calcd. C 55.45, H 4.46, N 13.47; found C 54.88, H 4.30, N 13.39.

**(6-Me-bpmi)Pd(OAc) (15):** Yield 35.6 mg (72%), m.p. >200 °C. $^1$H NMR (300 MHz, $CDCl_3$, 25 °C): $\delta$ = 2.12 (s, 3 H, OAc), 2.65 (s, 6 H, $CH_3$), 6.99 (d, $^3J$ = 6.2 Hz, 2 H, *5*-$CH_{Pm}$), 7.60–8.63 (m, 2 H, β-CH), 8.15–8.18 (m, 2 H, α-CH), 8.87 (d, $^3J$ = 6.2 Hz, 2 H, *4*-$CH_{Pm}$) ppm. $^{13}$C{$^1$H} NMR (75 MHz, $CDCl_3$, 25 °C): $\delta$ = 24.5, 24.6, 116.4, 123.5, 132.3, 137.6, 154.9, 156.1, 160.2, 172.0, 177.9 ppm. MS (MALDI): *m*/*z* 434 ([M – OAc]$^+$). HRMS (MALDI) calcd. for $C_{18}H_{14}N_7Pd$: 434.0345; obs. 434.03437, Δ = 0.2 mmu. UV/Vis ($CH_2Cl_2$): $\lambda_{max}$ = 344, 420, 444 nm. $C_{20}H_{17}N_7O_2Pd{\cdot}CHCl_3$ (613.19): calcd. C 41.13, H 2.96, N 15.99; found C 41.09, H 2.90, N 16.14.

## Acknowledgments

Support for this work by the Deutsche Forschungsgemeinschaft (DFG) is gratefully acknowledged.

[1] J. Dupont, C. S. Consorti, J. Spencer, *Chem. Rev.* **2005**, *105*, 2527–2572.

[2] a) A. C. Cope, R. W. Siekman, *J. Am. Chem. Soc.* **1965**, *87*, 3272–3273; b) A. C. Cope, E. C. Friedrich, *J. Am. Chem. Soc.* **1968**, *90*, 909–913.

[3] a) G. W. Parshall, *Acc. Chem. Res.* **1970**, *3*, 139–144; b) J. Dehand, M. Pfeffer, *Coord. Chem. Rev.* **1976**, *18*, 327–358; c) M. I. Bruce, *Angew. Chem.* **1977**, *89*, 75–89; *Angew. Chem. Int. Ed. Engl.* **1977**, *16*, 73–86; d) I. Omae, *Chem. Rev.* **1979**, *79*, 287–321; e) I. Omae, *Coord. Chem. Rev.* **1982**, *42*, 245–257; f) E. C. Constable, *Polyhedron* **1984**, *3*, 1037–1057; g) G. R. Newkome, W. E. Puckett, V. K. Gupta, G. E. Kiefer, *Chem. Rev.* **1986**, *86*, 451–489; h) M. Pfeffer, *Pure Appl. Chem.* **1992**, *64*, 335–342; i) P. Steenwinkel, R. A. Gossage, G. van Koten, *Chem. Eur. J.* **1998**, *4*, 759–762; j) W. A. Herrmann, V. P. W. Bohm, C. P. Reisinger, *J. Organomet. Chem.* **1999**, *576*, 23–41; k) M. Albrecht, G. van Koten, *Angew. Chem.* **2001**, *113*, 3866–3898; *Angew. Chem. Int. Ed.* **2001**, *40*, 3750–3781; l) J. Dupont, M. Pfeffer, J. Spencer, *Eur. J. Inorg. Chem.* **2001**, 1917–1927; m) R. B. Bedford, *Chem. Commun.* **2003**, 1787–1796; n) M. E. van der Boom, D. Milstein, *Chem. Rev.* **2003**, *103*, 1759–1792;

 © 2007 Wiley-VCH Verlag GmbH & Co. KGaA, Weinheim 

o) R. B. Bedford, C. S. J. Cazin, D. Holder, *Coord. Chem. Rev.* **2004**, *248*, 2283–2321; p) I. Omae, *Coord. Chem. Rev.* **2004**, *248*, 995–1023; q) I. P. Beletskaya, A. V. Cheprakov, *J. Organomet. Chem.* **2004**, *689*, 4055–4082.
[4] G. Dyker, *Chem. Ber./Recueil* **1997**, *130*, 1567–1578.
[5] a) W. O. Siegl, *J. Org. Chem.* **1977**, *42*, 1872–1878; b) F. A. Chavez, P. K. Mascharak, *Acc. Chem. Res.* **2000**, *33*, 539–545; c) O. P. Anderson, A. la Cour, A. Dodd, A. D. Garrett, M. Wicholas, *Inorg. Chem.* **2003**, *42*, 4513–4515; d) E. Balogh-Hergovich, G. Speier, M. Réglier, M. Giorgi, E. Kuzmann, A. Vértes, *Eur. J. Inorg. Chem.* **2003**, 1735–1740; e) M. B. Meder, L. H. Gade, *Eur. J. Inorg. Chem.* **2004**, 2716–2722; f) M. B. Meder, B. A. Siggelkow, L. H. Gade, *Z. Anorg. Allg. Chem.* **2004**, *630*, 1962–1968; g) E. Balogh-Hergovich, G. Speier, M. Réglier, M. Giorgi, E. Kuzmann, A. Vértes, *Inorg. Chem. Commun.* **2005**, *8*, 457–459; h) M. Wicholas, A. D. Garrett, M. Gleaves, A. M. Morris, M. Rehm, O. P. Anderson, A. La Cour, *Inorg. Chem.* **2006**, *45*, 5804–5811. Other coordination modes have occasionally been reported, see for example i) D. M. Baird, K. Y. Shih, J. H. Welch, R. D. Bereman, *Polyhedron* **1989**, *8*, 2359–2365; j) D. M. Baird, K. Y. Shih, *Polyhedron* **1991**, *10*, 229–235; k) O. P. Anderson, A. la Cour, A. Dodd, A. D. Garrett, M. Wicholas, *Inorg. Chem.* **2003**, *42*, 122–127.
[6] a) J. A. Elvidge, R. P. Linstead, *J. Chem. Soc.* **1952**, 5000–5007; b) J. A. Elvidge, R. P. Linstead, *J. Chem. Soc.* **1952**, 5008–5015; c) P. F. Clark, J. A. Elvidge, R. P. Linstead, *J. Chem. Soc.* **1953**, 3593–3602.
[7] a) B. A. Siggelkow, M. B. Meder, C. H. Galka, L. H. Gade, *Eur. J. Inorg. Chem.* **2004**, 3424–3435; b) M. Meder, C. H. Galka, L. H. Gade, *Monatsh. Chem.* **2005**, *136*, 1693–1706; c) B. A. Siggelkow, L. H. Gade, *Z. Anorg. Allg. Chem.* **2005**, *631*, 2575–2584; d) M. B. Meder, I. Haller, L. H. Gade, *Dalton Trans.* **2005**, 1403–1415.
[8] B. A. Siggelkow, M. B. Meder, C. H. Galka, L. H. Gade, *Eur. J. Inorg. Chem.* **2004**, 3424–3435.
[9] B. L. Dietrich, J. Egbert, A. M. Morris, M. Wicholas, O. P. Anderson, S. M. Miller, *Inorg. Chem.* **2005**, *44*, 6476–6481.
[10] a) M. Bröring, C. D. Brandt, *Chem. Commun.* **2001**, 499–500; b) M. Bröring, C. D. Brandt, *J. Chem. Soc. Dalton Trans.* **2002**, 1391–1395; c) M. Bröring, C. D. Brandt, *Chem. Commun.* **2003**, 2156–2157; d) M. Bröring, C. D. Brandt, S. Stellwag, *Chem. Commun.* **2003**, 2344–2345; e) M. Bröring, C. D. Brandt, S. Link, *Inorg. Chim. Acta* **2005**, *358*, 3122–3134; f) M. Bröring, S. Prikhodovski, C. D. Brandt, E. Cónsul Tejero, *Z. Anorg. Allg. Chem.* **2007**, *633*, 458–464; g) M. Bröring, S. Prikhodovski, S. Köhler, *Acta Crystallogr., Sect. C* **2007**, *63*, m68–m70.
[11] M. Bröring, C. Kleeberg, *Dalton Trans.* **2007**, 1101–1103.
[12] A. Bondi, *J. Phys. Chem.* **1964**, *68*, 441–451.
[13] See e.g.: a) B. Rybtchinski, D. Milstein, *Angew. Chem.* **1999**, *111*, 918–932; *Angew. Chem. Int. Ed.* **1999**, *38*, 870–883; b) M. Gandelman, A. Vigalok, L. Konstantinovsky, D. Milstein, *J. Am. Chem. Soc.* **2000**, *122*, 9848–9849; c) R. M. Gauvin, H. Rozenberg, L. J. W. Shimon, D. Milstein, *Organometallics* **2001**, *20*, 1719–1724; d) B. Rybtchinski, S. Oevers, M. Montag, A. Vigalok, H. Rozenberg, J. M. L. Martin, D. Milstein, *J. Am. Chem. Soc.* **2001**, *123*, 9064–9077.
[14] G. M. Sheldrick, *SHELXS-97, Program for Crystal Structure Determination*, University of Göttingen, **1997**.
[15] G. M. Sheldrick, *SHELXL-97, Program for Crystal Structure Refinement*, University of Göttingen, **1997**.
[16] A. L. Spek, *Acta Crystallogr., Sect. A* **1990**, *46*, C-34.

Received: March 13, 2007
Published Online: May 29, 2007

 © 2007 Wiley-VCH Verlag GmbH & Co. KGaA, Weinheim 

DOI: 10.1002/ejic.200700317

# Tetranuclear Nickel Complexes Composed of Pairs of Dinuclear $LNi_2$ Fragments Linked by 4,4′-Bipyrazolyl, 1,4-Bis(4′-pyrazolyl)benzene, and 4,4′-Bipyridazine: Synthesis, Structures, and Magnetic Properties

**Vasile Lozan,[a] Pavlo Y. Solntsev,[b] Guido Leibeling,[c] Konstantin V. Domasevitch,*[b] and Berthold Kersting*[a]**

**Keywords:** Macrocyclic ligands / Bipyrazolate ligands / Nickel / Polynuclear complexes / Magnetic properties

The ability of the ligands 4,4′-bipyrazolyl ($H_2bpz$), 1,4-bis(4′-pyrazolyl)benzene ($H_2bpzb$), and 4,4′-bipyridazine (*bpdz*) to link two dioctahedral $LNi_2$ units has been examined. The following complexes were prepared: $[L^1Ni^{II}_2(Hbpz)][BPh_4]$ (**6**$[BPh_4]$), $[L^1Ni^{II}_2(bpdz)][ClO_4]_2$ (**7**$[ClO_4]_2$), $[(L^1Ni^{II}_2)_2(bpzb)][BPh_4]_2$ (**8**$[BPh_4]_2$), and $[(L^2Ni^{II}_2)_2(bpz)][BPh_4]_2$ (**9**$[BPh_4]_2$), where $(L^1)^{2-}$ and $(L^2)^{2-}$ represent macrocyclic hexaaza-dithiophenolate ligands. All complexes have been characterised by UV/Vis spectroscopy, IR spectroscopy, and X-ray crystallography. Whereas $(Hbpz)^-$ and *bpdz* in **6**$[BPh_4]_2$ and **7**$[ClO_4]_2$ act as bidentate ligands coordinating to only one $[LNi_2]^{2+}$ unit, in **8**$[BPh_4]_2$ and **9**$[BPh_4]_2$ the $(bpzb)^{2-}$ and $(bpz)^{2-}$ units are tetradentate linkers. This is qualitatively explained in terms of the absence or presence of steric repulsions between the *t*Bu groups of the supporting ligands and the length of the coligands. The structures of the tetranuclear complexes differ mainly in the distance between the center of the Ni···Ni axes of the isostructural $[LNi_2]$ units {14.040(1) Å in **8**$[BPh_4]_2$, 9.184(1) Å in **9**$[BPh_4]_2$}. The two $Ni_2$-pyrazolato planes in **9**$[BPh_4]_2$ are coplanar. An analysis of the temperature-dependent magnetic susceptibility data for **9**$[BPh_4]_2$ reveals the presence of weak ferromagnetic exchange interactions between the $Ni^{II}$ ions in the binuclear $[L^2Ni_2]$ subunits with values for the magnetic exchange constant $J_1$ of 23.97 $cm^{-1}$ ($\mathbf{H} = -2JS_1S_2$). The exchange coupling across the dipyrazolato bridge is less than 0.1 $cm^{-1}$, suggesting that no significant interdimer exchange coupling occurs in **9**$[BPh_4]_2$.

(© Wiley-VCH Verlag GmbH & Co. KGaA, 69451 Weinheim, Germany, 2007)

## Introduction

The coordination chemistry of the potentially quadridentate ligands 4,4′-bipyrazolyl ($H_2bpz$)[1,2] and its derivative 3,3′,5,5′-tetramethyl-4,4′-bipyrazolyl ($H_2Me_4bpz$)[3–6] has been studied in some detail, primarily due to their capability to form porous coordination polymers with potential uses as solid sorbents, ion exchangers or heterogeneous catalysts.[7–11] In this context, a large body of work has been carried out concerning the formation of polypyrazolate-based coordination networks with open framework structures.[12,13] It is surprising that such ligands have not yet been used in the construction of discrete polynuclear complexes. The oligonuclear $Pd_3$ and $Pd_4$ complexes reported by Yu et al. may serve as rather rare examples of this class of compounds.[14]

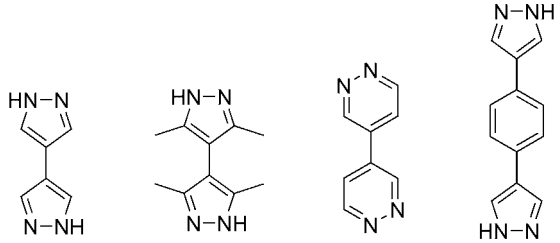


$H_2bpz$ $H_2Me_4bpz$ *bpdz* $H_2bpzb$

In previous work, we described a series of dinuclear transition-metal complexes of the macrocyclic $N_6S_2$ ligands $L^1$ and $L^2$ (Scheme 1).[15,16] These complexes have a rich coordination chemistry since the $[L^1M_2]^{2+}$ fragments are able to coordinate a large variety of coligands such as $Cl^-$,[15] $OH^-$,[17] $NO_2^-$, $NO_3^-$, $N_3^-$,[18] $BH_4^-$,[19] $ClO_4^-$, $ReO_4^-$, $SO_4^{2-}$, $MoO_4^{2-}$,[20] $MoO_3(OMe)^-$,[21] and various carboxylate anions.[16,22,23]

The magnetic properties of an isostructural series of bioctahedral $[L^1M^{II}_2(OAc)]^+$ complexes have also been reported.[24] In the $Mn^{II}_2$, $Fe^{II}_2$ and $Co^{II}_2$ complexes of this

[a] Institut für Anorganische Chemie, Universität Leipzig, Johannisallee 29, 04103 Leipzig
Fax: +49-341-973-6199
E-mail: b.kersting@uni-leipzig.de
[b] Inorganic Chemistry Department, Kiev University, Volodimirska Street 64, Kiev 01033, Ukraine
E-mail: dk@anorgchemie.univ.kiev.ua
[c] Institut für Anorganische Chemie, Georg-August-Universität Göttingen, 37077 Göttingen, Germany

Supporting information for this article is available on the WWW under http://www.eurjic.org or from the author.

 © 2007 Wiley-VCH Verlag GmbH & Co. KGaA, Weinheim 

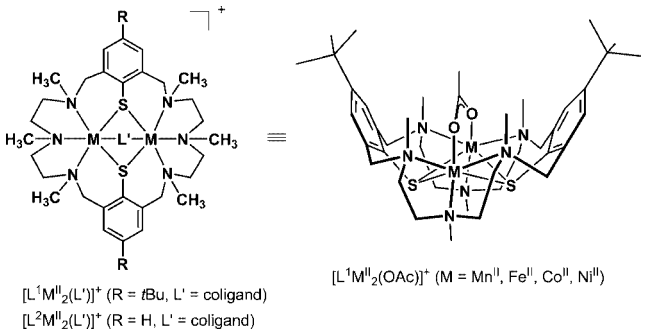


Scheme 1. Dinuclear complexes of the hexaaza-dithiophenolate ligands $(L^1)^{2-}$ and $(L^2)^{2-}$.

series intramolecular antiferromagnetic exchange interactions are present with $J$ values of –5.1, –10.6, and –2.0 $cm^{-1}$ ($\mathbf{H} = -2J\mathbf{S}_1\mathbf{S}_2$). For the corresponding $Ni^{II}_2$ complex, however, a ferromagnetic exchange interaction is observed ($J$ = +6.4 $cm^{-1}$). In view of the strong interest in the targeted design of molecular-based magnetic materials using high-spin molecules of higher nuclearity,[25–31] we have initiated a study on the synthesis of complexes in which pairs of exchange coupled $[L^1Ni_2]$ units are linked by 4,4′-bipyrazole ($H_2bpz$) and 1,4-bis(4-pyrazolyl)-benzene ($H_2bpzb$). The neutral ligand 4,4′-bipyridazine (*bpdz*) was also included in this study. We report herein the results of our investigation together with the single-crystal X-ray structure determination of the complexes $[L^1Ni^{II}_2(Hbpz)][BPh_4]$ (**6**[$BPh_4$]), $[L^1Ni^{II}_2(bpdz)][ClO_4]_2$ (**7**[$ClO_4$]$_2$), $[(L^1Ni^{II}_2)_2(bpzb)][BPh_4]_2$ (**8**[$BPh_4$]$_2$), and $[(L^2Ni^{II}_2)_2(bpz)][BPh_4]_2$ (**9**[$BPh_4$]$_2$). The results of temperature-dependent magnetic susceptibility measurements on $[(L^2Ni^{II}_2)_2(bpz)][BPh_4]_2$ (**9**[$BPh_4$]$_2$) are also described.

## Results and Discussion

### Synthesis of Ligands and Complexes

Of the N-heterocycles used in this study, only 4,4′-bipyrazolyl ($H_2bpz$) was reported previously.[1,2] Scheme 2 depicts the syntheses of the new compounds $H_2bpzb$ and *bpdz*. The Diels–Alder reaction of bright-red 1,2,4,5-tetrazine (**1**) with *cis*-/*trans*-1,4-bis(dimethylamino)butadiene (**2**) in a 2.1:1 ratio is accompanied by a vigorous evolution of dinitrogen and affords after thermal elimination of dimethylamine and recrystallization from methanol colourless 4,4′-bipyridazine (*bpdz*) in reasonable yields (39%). The route to $H_2bpzb$ began with a Vilsmeyer–Haack-type reaction of *p*-phenylenediacetic acid **3** with $POCl_3$/DMF to give the bis(trimethinium) salt **4**, which was isolated as its perchlorate salt.[32] Hydrolysis of **4** followed by treatment of the resulting tetraaldehyde **5** (not isolated) with hydrazine furnished the new dipyrazole derivative $H_2bpzb$ as thin white needles in good overall yield (78%). The new compounds were of sufficient purity for metal complex syntheses.

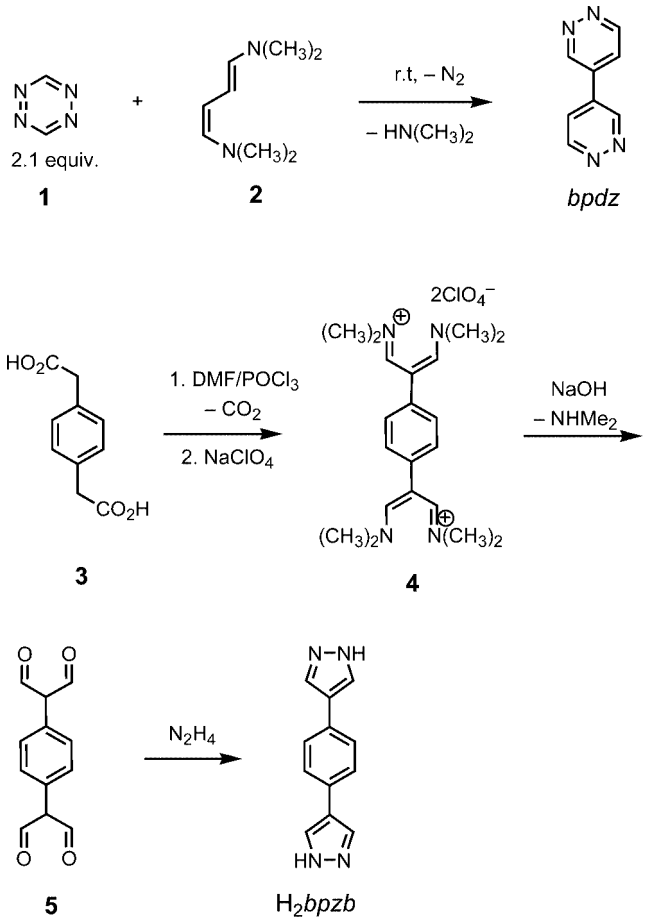


Scheme 2. Synthesis of the heterocycles $H_2bpzb$ and *bpdz*.

Attempts to link two $[L^1Ni_2]^{2+}$ units by a $(bpz)^{2-}$ dianion did not meet with any success. Treatment of $[L^1Ni_2Cl][ClO_4]$ with triethylammonium 4,4-bipyrazolate in methanol in varying molar ratios resulted always in the formation of the green 1:1 complex $[(L^1)Ni_2(Hbpz)][ClO_4]$ (**6**[$ClO_4$]), presumably as a result of the sterically demanding *tert*-butyl groups. Nickel complexes of the neutral *bpdz* ligand were found to be inaccessible from $[L^1Ni_2Cl][ClO_4]$. The substitution reaction succeeded only with the more labile perchlorato complex $[L^1Ni_2(ClO_4)][ClO_4]$, but again only 1:1 complexes formed. Thus, treatment of a dark green acetonitrile solution of $[L^1Ni_2(ClO_4)][ClO_4]$ with *bpdz* produced a brown-yellow solution, from which brown crystals of $[L^1Ni_2(bpdz)][ClO_4]_2$ (**7**[$ClO_4$]$_2$) could be isolated in 80% yield.

It was clear at this stage that tetranuclear $Ni_4$ complexes would only be accessible with longer bipyrazolyls or with less bulky $LNi_2$ precursor subunits. Indeed, reaction of $[L^1Ni_2Cl][ClO_4]$ with a 0.5 molar equivalent of $(bpzb)^{2-}$ (prepared in situ from $H_2bpzb$ and $NEt_3$) in methanol followed by addition of an exess of $LiClO_4$ and recrystallization from acetonitrile affords the green complex $[(L^1Ni_2)_2(bpzb)][ClO_4]_2$ (**8**[$ClO_4$]$_2$) in 76% yield. Similarly, reaction of $[L^2Ni_2Cl][ClO_4]$ with half a molar equivalent of $(bpz)^{2-}$ in methanol followed by addition of an excess of $LiClO_4$ fur-

 © 2007 Wiley-VCH Verlag GmbH & Co. KGaA, Weinheim 

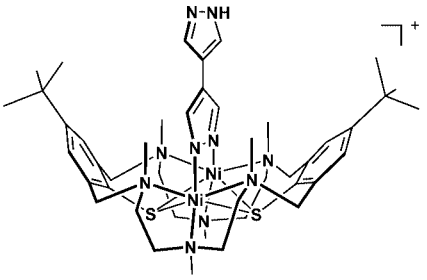

$[L^1Ni_2(Hbpz)]^+$ (**6**)

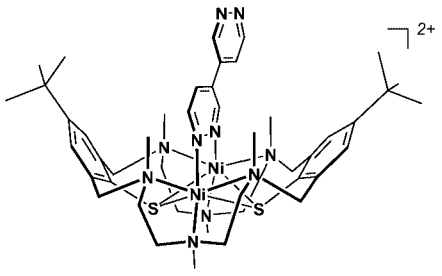

$[L^1Ni_2(bpdz)]^+$ (**7**)

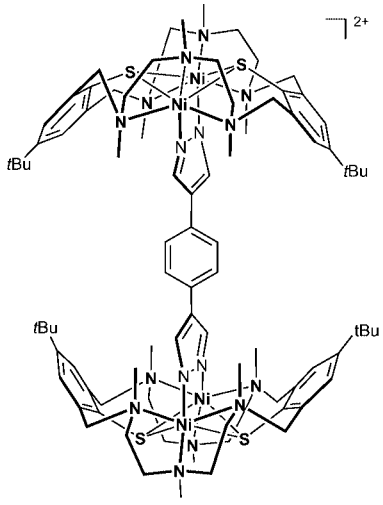

$[(L^1Ni)_2(bpzb)]^{2+}$ (**8**)

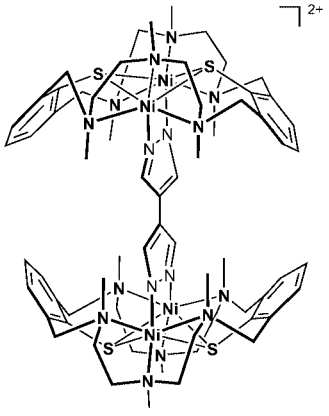

$[(L^2Ni)_2(bpz)]^{2+}$ (**9**)

nished the tetranuclear species $[(L^2Ni_2)_2(bpz)][ClO_4]_2$ (**9**$[ClO_4]_2$) as a dark-green, air-stable solid. Complexes **8** and **9** were also isolated as tetraphenylborate salts.

All compounds gave satisfactory elemental analyses and were characterized by IR spectroscopy and UV/Vis spectroscopy, and compounds **6**$[BPh_4]\cdot 1.5MeCN$, **7**$[ClO_4]_2\cdot 3MeCN$, **8**$[BPh_4]_2\cdot 6MeCN\cdot 2H_2O$, and **9**$[BPh_4]_2\cdot 2CH_2Cl_2$ also by X-ray structure analysis.

## Characterization of the Complexes

### *Spectroscopic Characterization. IR and UV/Vis Spectroscopy*

The infrared spectra of all compounds display the bands expected for the macrocyclic ligands and counterions, but were not informative with respect to the conformations of the supporting or coligands. Only the band at 3385 $cm^{-1}$ in the IR spectrum of **6**$[BPh_4]$ can be attributed to the N–H stretching vibration of the protonated pyrazole moiety. The electronic absorption spectra of the nickel complexes have been recorded in the 300–1600 nm range in acetonitrile solution. The spectra of the pyrazolato complexes **6**, **8** and **9** display two weak absorption bands around 640 and 1190 nm typical of octahedral $Ni^{II}$ ($S = 1$) ions. The observed values closely compare with those of $[L^1Ni_2(pz)]^+$ (*pz* = pyrazolate)[18] indicative of $\mu_{1,2}$-bridging pyrazolate functions and pseudo-octahedral $N_4S_2$ coordination environments around the Ni atoms. The UV/Vis spectrum of the bipyridazine complex **7**$[ClO_4]$ is similar but not identical with that of **6**$[BPh_4]$, displaying two weak bands at 608 and 1100 nm. The corresponding absorptions in previously reported $[L^1Ni_2(pydz)]^{2+}$ (*pydz* = pyridazine)[18] were observed at 615 and 1095 nm. The slight differences in the position of the d-d transitions indicate that each complex retains its integrity in solution.

## X-ray Crystallography

Single-crystals of **6**$[BPh_4]\cdot 1.5MeCN$ were obtained by slow evaporation of a 1:1 acetonitrile/ethanol solution of **6**$[BPh_4]$. The crystal structure is composed of dinuclear $[L^1Ni_2(Hbpz)]^+$ cations, tetraphenylborate anions, and acetonitrile molecules of solvent of crystallization. An Ortep plot of the structure of complex **6** is depicted in Figure 1. Selected bond lengths and angles are summarized in Table 1. The bipyrazolato ligand acts only as a bidentate ligand towards one dinuclear $[L^1Ni^{II}_2]^{2+}$ unit through the ring atoms N(7) and N(8). The atoms N(9) and N(10) remain uncoordinated, but the hydrogen atom bonded to N(9) is involved in a hydrogen bonding interaction with an adjacent acetonitrile solvate molecule [N(9)···N(11)

 © 2007 Wiley-VCH Verlag GmbH & Co. KGaA, Weinheim 

2.975 Å]. The distance between the N atom of the acetonitrile and N(10) is 3.652 Å. The corresponding C–C, C–N, and N–N distances of the two five membered rings of the $(bpz)^{2-}$ dianion do not deviate significantly from each other; the largest difference being in the N–N bonds [N(7)–N(8) 1.384(2) Å, N(9)–N(10) 1.329(2) Å]. Note that the two heterocycles are not strictly coplanar. The dihedral angle between the two five-membered rings is 25.6°. The C(40)–C(42) bond is of length 1.472(2) Å indicative of a C–C single bond. The $[L^1Ni_2]^{2+}$ subunits in **6** and the compounds described below are structurally very similar, and the Ni–N and Ni–S distances lie within very narrow ranges (Table 1). The Ni···Ni distance is at 3.373(1) Å, which is nearly identical with that in $[L^1Ni_2(pz)][BPh_4]$ [3.389(1) Å].[18] Overall, this structure clearly shows that the bipyrazolate moiety cannot link two $[L^1Ni_2]^{2+}$ units. This can be attributed to the steric demand of the *t*Bu groups which hinder the formation of a tetranuclear complex. This assumption is nicely corroborated by the crystal structure determination of **9**$[BPh_4]_2$.

Figure 2 shows the structure of the dinuclear $Ni^{II}_2$ complex **7** in crystals of **7**$[ClO_4]_2$·3MeCN. Again, the 4,4′-bipyridazine ligand acts only as a bidentate group coordinating to only one bioctahedral $[L^1Ni_2]^{2+}$ entity through the ring nitrogen atoms N(7) and N(8). Metal complexes of 4,4′-bipyridazine have not been reported previously. The average $Ni–N_{pyridazine}$ bond length of 2.159(2) Å is significantly longer than the $Ni–N_{pyrazolate}$ distance in **6** [2.043(2) Å], implying that the neutral bipyridazine binds more weakly to the dinuclear $[L^1Ni_2]^{2+}$ fragment in **7** than

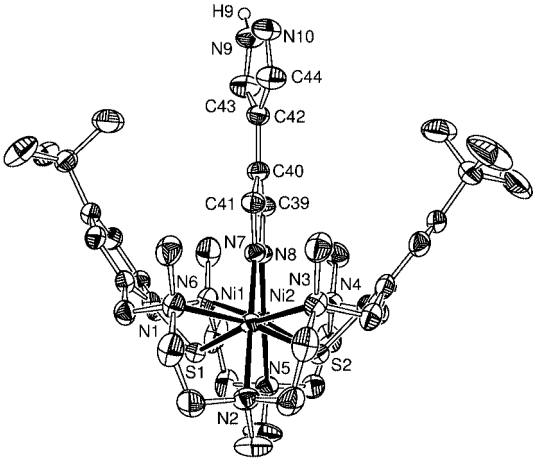


Figure 1. ORTEP representation of the structure of the $[L^1Ni^{II}_2(Hbpz)]^+$ cation in crystals of **6**$[BPh_4]$·1.5MeCN. Ellipsoids are represented at the 50% probability level. Hydrogen atoms except H(9) have been omitted for clarity.

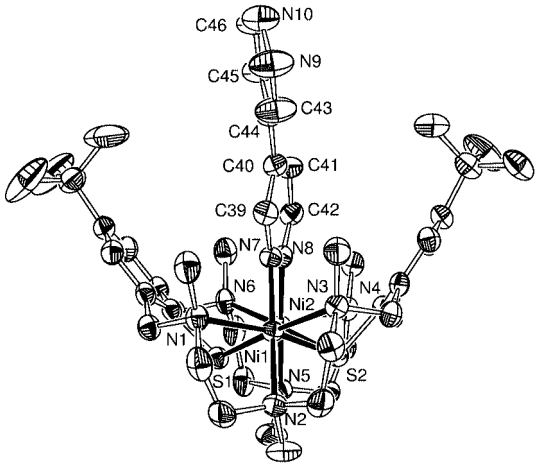


Figure 2. Structure of the $[L^1Ni^{II}_2(bpdz)]^{2+}$ dication in crystals of **7**$[ClO_4]_2$·3MeCN with thermal ellipsoids at the 50% probability level. Hydrogen atoms are omitted for reasons clarity.

Table 1. Selected bond lengths [Å] and angles [°] in **6**–**9**.

| | **6**$[BPh_4]$·1.5MeCN | **7**$[ClO_4]_2$·3MeCN | **8**$[BPh_4]_2$·6MeCN·$2H_2O$ | **9**$[BPh_4]_2$·$2CH_2Cl_2$ |
|---|---|---|---|---|
| Ni(1)–N(7) | 2.050(2) | 2.149(3) | 2.065(2) | 2.037(2) |
| Ni(1)–N(1) | 2.316(2) | 2.352(3) | 2.276(2) | 2.430(2) |
| Ni(1)–N(2) | 2.178(2) | 2.125(3) | 2.186(2) | 2.170(2) |
| Ni(1)–N(3) | 2.307(2) | 2.255(3) | 2.279(2) | 2.206(2) |
| Ni(1)–S(1) | 2.4682(7) | 2.435(1) | 2.4692(5) | 2.5020(5) |
| Ni(1)–S(2) | 2.4844(9) | 2.4846(9) | 2.4878(5) | 2.4493(5) |
| Ni(2)–N(8) | 2.036(2) | 2.168(3) | 2.091(2) | 2.005(2) |
| Ni(2)–N(4) | 2.319(2) | 2.410(3) | 2.247(2) | 2.211(2) |
| Ni(2)–N(5) | 2.167(2) | 2.128(3) | 2.236(2) | 2.142(2) |
| Ni(2)–N(6) | 2.293(2) | 2.202(3) | 2.300(2) | 2.435(2) |
| Ni(2)–S(1) | 2.4958(8) | 2.4533(9) | 2.3983(5) | 2.5307(5) |
| Ni(2)–S(2) | 2.4754(7) | 2.434(1) | 2.4967(5) | 2.4553(5) |
| Ni–N | 2.208(2) | 2.224(3) | 2.210(2) | 2.205(2) |
| Ni–S | 2.4810(7) | 2.452(1) | 2.4630(5) | 2.4843(5) |
| Ni···Ni | 3.373(1) | 3.401(1) | 3.349(1) | 3.373(1) |
| $Ni–Ni^{cent}$/$Ni–Ni^{cent}$[a] | – | – | 14.040(1) | 9.184(1) |
| $N–M–N_{cis}$[b] | 90.73(8) | 90.5(1) | 90.69(6) | 90.33(6) |
| $N–M–N_{trans}$[b] | 176.63(7) | 176.2(1) | 177.04(6) | 175.70(6) |
| $S–M–N_{cis}$[b] | 90.83(7) | 91.22(8) | 91.06(5) | 91.13(2) |
| $S–M–N_{trans}$[b] | 170.27(6) | 171.03(8) | 170.22(5) | 171.43(5) |
| S–M–S[b] | 81.62(3) | 81.28(3) | 80.46(2) | 82.10(2) |
| M–S–M[b] | 85.65(2) | 87.83(3) | 85.68(2) | 85.53(2) |

[a] Distance between center of the Ni···Ni axes of the $Ni_2$ units. [b] Average values.

 © 2007 Wiley-VCH Verlag GmbH & Co. KGaA, Weinheim 

does the charged pyrazolato ligand in **6**. A similar behaviour has been noted previously for $[L^1Ni_2(pydz)]^{2+}$ and $[L^1Ni_2(pz)]$.[18] As in **6**, the coordination of the pyridazine ring to the $Ni^{II}$ ions results in a slight elongation of the N–N bond length [N(7)–N(8) = 1.336(2) Å vs. N(9)–N(10) 1.366(2) Å]. Likewise, the two six-membered rings are also tilted by 25.2° with respect to each other. The Ni···Ni distance is at 3.401(1) Å.

Complex **8**$[BPh_4]_2$·6MeCN·$2H_2O$ crystallizes in the triclinic space group $P\bar{1}$ with six cocrystallized acetonitrile and two water molecules. The $[(L^1Ni_2)_2(bpzb)]^{2+}$ complex is centrosymmetric (Figure 3). Selected bond lengths and angles are summarized in Table 1. The structure of **8** unambiguously confirms the ability of the deprotonated 1,4-bis(4′-pyrazolyl)-benzene to link two $[L^1Ni^{II}_2]^{2+}$ units. The four six-coordinate Ni atoms are arranged in a rectangular fashion, the Ni···Ni distances being 3.349(1) Å [Ni(1)···Ni(2)] and 14.040(1) Å [Ni(1)···Ni(2′)], respectively. Note that the $Ni_2$pyrazolato planes are coplanar with each other, but that the central aromatic ring is slightly twisted out of this plane ($\tau$ = 23.8°). The metal–ligand bond lengths within the $[L^1Ni_2(pyrazolato)]^{2+}$ units reveal no anomalities and are very similar to those in **6** [Table 1]. There are no significant intermolecular interactions between the $Ni_4$ complexes. The shortest intermolecular Ni···Ni distance is at 7.806[1] Å.

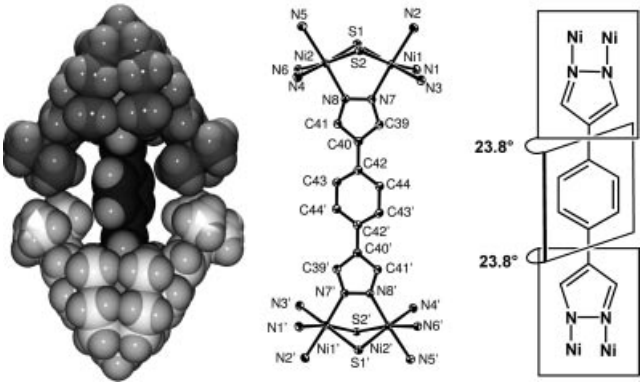


Figure 3. Left: Van der Waals plot of the $[(L^1Ni^{II}_2)_2(bpzb)]^{2+}$ dication in crystals of **8**$[BPh_4]_2$·6MeCN·$2H_2O$. Middle: ORTEP representation of the core structure of **8** with the atom labeling Scheme. Ellipsoids are represented at the 50% probability level. Symmetry code used to generate equivalent atoms: $1 - x$, $1 - y$, $1 - z$ (′). Right: Mutual orientation of the $Ni_2$pyrazolato planes in **8**.

Crystals of **9**$[BPh_4]_2$·$2CH_2Cl_2$ are triclinic, space group $P\bar{1}$. Ortep views of the structure of the dication **9** and the central core are provided in Figure 4. A selection of the most important bond lengths is given in Table 1. Again, **9** exhibits crystallographically imposed inversion symmetry. In striking contrast to **6**, the bipyrazolate moiety in **9** behaves as a tetradentate bridging ligand joining two binuclear $[L^2Ni_2]$ subunits, most likely as a consequence of the absence of the *tert*-butyl groups in $(L^2)^{2-}$. The bipyrazolate ligand assumes a planar conformation and the $Ni_2N_2$ planes are only slightly folded with respect to the bipyrazolato plane (folding angle: 165.4°). The Ni···Ni distance of 3.448(1) Å is the same as that in **6**. The distance *d* between the center of the Ni···Ni axes of the binuclear subunits amounts to 9.184(1) Å, which is significantly smaller than the corresponding distance in **8**. The bond lengths and angles around the Ni atoms within the $[L^2Ni_2]^{2+}$ unit reveal no unusual features. The average Ni–S, Ni–$N_{amine}$ and Ni–$N_{pyrazolato}$ distances are at 2.018(3), 2.291(3), and 2.517(1) Å, respectively. Virtually the same distances are seen in **6**. A large number of polymeric metal complexes containing bipyrazolato ligands have been structurally characterized;[2–7] to the best of our knowledge, **9** is the first discrete species of $(bpz)^{2-}$. Overall, this structure clearly shows that two bioctahedral $[L^2Ni_2]^{2+}$ units can be linked by bipyrazolate dianions.

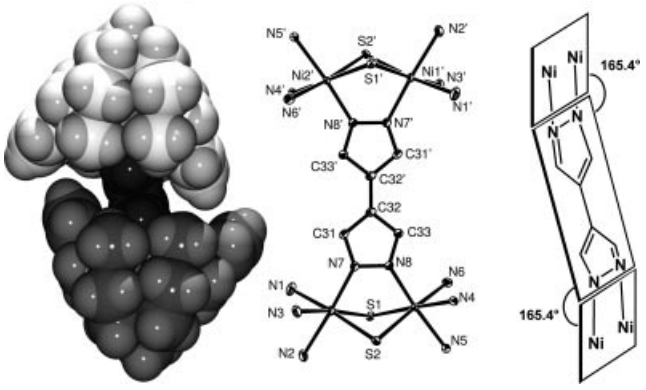


Figure 4. Left: van der Waals plot of the $[(L^2Ni^{II}_2)_2(\mu\text{-bipyrazolato})]^{2+}$ dication in crystals of **9**$[BPh_4]_2$·$2CH_2Cl_2$. Middle: ORTEP representation of the core structure of **9** with the atom labeling Scheme. Ellipsoids are represented at the 50% probability level. Symmetry code used to generate equivalent atoms: $1 - x$, $2 - y$, $- z$ (′). Right: Tilting of the $Ni_2$pyrazolato planes in **9**.

## Magnetic Properties of 9$[BPh_4]_2$

To gain insight into the electronic structure of **9**$[BPh_4]_2$ variable-temperature magnetic susceptibility data were measured between 2.0 and 295 K by using a SQUID magnetometer in an applied external magnetic field of 0.2 T. Figure 5 shows a plot of the temperature dependence of the effective magnetic moment for **9**$[BPh_4]_2$. The effective magnetic moment increases from 6.75 $\mu_B$ at 295 K to a maximum value of 7.59 $\mu_B$ at 22 K. On lowering the temperature further the magnetic moment decreases to 6.97 $\mu_B$ at 2.0 K. Although the effective magnetic moment at 22 K is smaller than expected for the spin-only value of 9.84 $\mu_B$ for $S_T$ = 4 resulting from the ferromagnetic coupling of four $Ni^{II}$ ions ($S_i$ = 1, $g$ = 2.20), it is larger than the value of 6.22 $\mu_B$ calculated for four noninteracting $Ni^{II}$ ions. This behaviour indicates the presence of weak ferromagnetic exchange interactions between the $Ni^{II}$ ions in the binuclear subunits but negligible – if any – coupling across the bipyrazolate bridge. This is not surprising, considering the long distance between the nickel(II) ions.

 © 2007 Wiley-VCH Verlag GmbH & Co. KGaA, Weinheim 

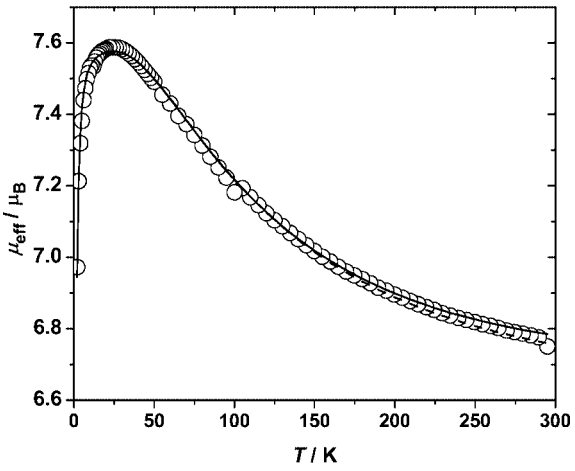


Figure 5. Temperature dependence of $\mu_{eff}$ (per tetranuclear complex) for **9**$[BPh_4]_2$. The full line represents the best theoretical fit to Equation (1). The dashed line represents the best fit to the dimer model in Equation (3).

The magnetic susceptibility data were fitted to Equation (1), where $\chi_{tetra}$ and $\chi_{mono}$ refer to the molar susceptibilities of a $Ni_4$ complex and a fraction $\rho$ of a mononuclear nickel(II) impurity with Curie constant $C = Ng^2\mu_B^2/3kT$.

$$\chi = \chi_{tetra}(1 - \rho) + 4\chi_{mono}\rho \quad (1)$$

The molar magnetic susceptibility $\chi_{tetra}$ was derived from the appropriate spin-Hamiltonian Equation (2) including the isotropic HDVV exchange, the single-ion zero-field splitting and the single-ion Zeeman interaction by a full-matrix diagonalization approach.

$$H = -2J_1(\hat{S}_1 \cdot \hat{S}_2 + \hat{S}_3 \cdot \hat{S}_4) - 2J_2(\hat{S}_1 \cdot \hat{S}_3 + \hat{S}_1 \cdot \hat{S}_4 + \hat{S}_2 \cdot \hat{S}_3 + \hat{S}_2 \cdot \hat{S}_4) + \sum_{i=1}^{4}[D_i(\hat{S}_{iz}^2 - \tfrac{1}{3}S_i(S_i+1)) + g_i\mu_B S_{i\tau}B_\tau] \ (\tau = x, y, z) \quad (2)$$

In this model $J_1$ represents the exchange interaction between the $Ni^{2+}$ ions within the dinuclear subunit, whereas $J_2$ describes the interaction across the bipyrazolate moiety. The $D$ and $g$ values were considered to be identical for all of the four $Ni^{2+}$ ions. Notice that D represents an effective zero-field splitting parameter, since in Equation (2) and Equation (4) the zero-field splitting tensors of all ions are assumed to be collinear. The least-squares fitting of the experimental data over the full temperature range led to $J_1$ = +24.0(1) $cm^{-1}$, $J_2$ = –0.001(5) $cm^{-1}$, $g$ = 2.19(1), $D$ = 4.8(2) $cm^{-1}$, and $\rho$ = 0.02(1)%. The inclusion of the $D$ parameter improves the low-temperature fit significantly, but it represents by no means an accurate value since temperature-dependent magnetic susceptibility measurements are not very appropriate for the determination of the sign and magnitude of $D$.[33,34] However, this analysis establishes clearly that magnetic exchange interactions via the dipyrazolate moiety are not significant ($J_2 < 0.1$ $cm^{-1}$) and that the magnetic properties of complex **9** are solely based on the exchange couplings in the binuclear $[L^2Ni_2(pyrazolate)]^+$ subunits. Therefore, we also tried to simulate the temperature dependence of the magnetic data by using an isotropic dimer model [Equation (3)] for two $Ni^{II}$ ($S$ = 1) ions based on the Hamiltonian in [Equation (4)].

$$\chi = 2[\chi_{dim}(1 - \rho) + 2\chi_{mono}\rho] \quad (3)$$

$$H = -2JS_1S_2 + \sum_{i=1}^{2}(D_i(\hat{S}_{zi}^2 - 1/3(S_i(S_i+1)) + g_i\mu_B S_{i\tau}B_\tau)) \ (\tau = x, y, z) \quad (4)$$

The magnetic data could be reproduced equally well by this approach (Figure 5), yielding $J_1$ = +24.14 $cm^{-1}$, $g$ = 2.19, $D$ = 4.85 $cm^{-1}$, and $\rho$ = 0.020%. Again, this analysis reveals a weak ferromagnetic coupling between the two $Ni^{II}$ ions. All of these values are in excellent agreement with those reported for other dinuclear nickel(II) complexes of $(L^1)^{2-}$ providing further support for the absence of significant interdimer exchange coupling in **9**$[BPh_4]_2$.[18,24]

It should be noted that there is much interest in the distance-dependence of superexchange interactions between paramagnetic transition metal ions bridged by extended organic spacer ligands. Thus, a large number of dicarboxylato-bridged copper(II) dimers with Cu···Cu separations of 5 to 15 Å have been prepared and their magnetic properties have been determined.[35–41] The magnetic exchange interactions decrease rapidly with increasing Cu···Cu separations and the experimentally determined $J$ values approach the values predicted by the Coffman–Buettner relation [$|J| \leq 1$ $cm^{-1}$ for $d$(M···M) $\geq$ 9 Å].[42] This finding also applies to other paramagnetic metal ions than Cu.[43] The observations made for the nickel(II) complexes presented herein are in good agreement with the reported trend. It is also worth mentioning that the coplanarity of the two $Ni_2$pyrazolato planes in **9** does not strengthen the magnetic exchange interactions via the bipyrazolate moiety.

## Conclusions

In summary, we presented the synthesis of two new heterocyclic $N_4$-ligands and the first members of a new class of tetranuclear nickel(II) complexes in which pairs of dinuclear $LNi_2$ fragments are united by $(bpz)^{2-}$ and $(bpzb)^{2-}$ groups. The isolation of the two dinuclear complexes **6** and **7** clearly show that the ease of formation of a tetranuclear cluster depends critically on two factors: (*i*) the length of the bridging coligand and (*ii*) the steric demand of the supporting ligand. If one pays attention to these two factors one can readily prepare higher nuclearity clusters such as **8** and **9**. These exist as stable and discrete complexes in solution and in the solid state as ascertained by various spectroscopic methods and X-ray crystallography. The $Ni_4$ complexes are well separated from each other in the solid state. The magnitude of the exchange interaction $J_2$ across the bipyrazolate was found to be less than 0.1 $cm^{-1}$, suggesting that no interdimer exchange coupling occurs in **9**. In this

 © 2007 Wiley-VCH Verlag GmbH & Co. KGaA, Weinheim 

sense the $LNi_2^{2+}$ fragments are ideally suited to screen novel extended bridging ligands for their ability to transmit magnetic exchange interactions between paramagnetic transitions metal ions.

## Experimental Section

**General Remarks:** Solvents and reagents were of reagent grade quality and used as received unless otherwise specified. The compounds 4,4′-bipyrazol,[2] $[L^1Ni^{II}_2Cl][ClO_4]$,[15] $[L^1Ni^{II}_2(ClO_4)][ClO_4]$,[20] and $[L^2Ni^{II}_2(Cl)][ClO_4]$[16] were prepared according to the literature procedures. Melting points were determined in capillaries and are uncorrected. IR spectra were measured on a Bruker VECTOR 22 FT-IR spectrophotometer as KBr pellets, electronic absorption spectra on a Jasco V-570 UV/Vis/near IR spectrophotometer. Elemental analysis were performed on a Vario EL analyzer (Elementaranalysensysteme GmbH). All metal complexes crystallize with solvent molecules (see crystal structures), but slowly lose their solvent molecules of crystallization upon standing in air. This is why the observed microanalytical data do not fit exactly with the calculated values (for the solvent-free compounds). Temperature-dependent magnetic susceptibility measurements on powdered solid samples were carried out on a SQUID magnetometer (MPMS Quantum Design) over the temperature range 2.0 –293 K. The magnetic field applied was 0.20 Tesla. The observed susceptibility data were corrected for underlying diamagnetism by using Pascal's constants.

***Safety Note: Caution!*** *Perchlorate salts of transition metal complexes are potentially hazardous and may explode. Only small quantities should be prepared and handled with great care.*

**4,4′-Bipyridazine (*bpdz*):** A solution of 12.31 g (0.15 mol) 1,2,4,5-tetrazine (**1**) in 150 mL of dry 1,4-dioxane was added dropwise for a period of 40 min to a stirred solution of 10.09 g (0.072 mol) of *cis-trans*-1,4-bis(dimethylamino)butadiene (**2**) in 60 mL of dry 1,4-dioxane. The immediate evolution of nitrogen gas and discoloration were accompanied with a pronounced exothermic effect. After the addition was completed, the red-brown reaction mixture was stirred at 80 °C for 4 h (elimination of dimethylamine) and then left overnight at room temp. The precipitate was filtered, washed with 5 mL $CH_2Cl_2$ and twice crystallized from methanol with charcoal yielding a pure product (4.44 g, 39%) as thin colorless needles. $^1$H NMR (400 MHz, [D$_6$]DMSO): $\delta$ = 9.77 (s, 2 H, 3-CH), 9.37 (d, 2 H, 6-CH), 8.23 (dd, 2 H, 5-CH) ppm. $C_8H_6N_4$ (158.16): calcd. C 60.75, H 3.82, N 35.43; found C 60.44, H 3.89, N 35.17.

**1,4-Bis(4′-pyrazolyl)benzene. Intermediate 4:** 11.2 mL (0.12 mol) $POCl_3$ was added dropwise to 45 mL of dry DMF at 5–10 °C with constant stirring. The mixture was stirred for an additional hour at room temp. Then 3.88 g (20.0 mmol) solid *p*-phenylenediacetic acid (**3**) was added at once and the clear solution formed was stirred for 4 h at 90–95 °C and then at room temperature overnight. The resulting black mixture was poured on 100 g crushed ice. After decomposition of the excess Vilsmeyer reagent a saturated solution of 15.0 g $NaClO_4$ was added with stirring. The resulting nearly white crystalline deposit of the bis(trimethinium) diperchlorate (**4**[$ClO_4$]$_2$) was filtered and washed with two 15 mL portions of water. The yield was 8.21 g (79.5%). This compound was used in the next step without further purification. **Intermediate 5:** 8.22 g (15.6 mmol) of the perchlorate salt **4**[$ClO_4$]$_2$ were added to a warm solution of 3.45 g (86 mmol) NaOH in 20 mL water, and the mixture was heated with stirring for 7–8 min (bath temperature 90 °C) until total dissolution of the organic salt was observed. The yellow-colored mixture was cooled to room temp., diluted with 10 mL water and 10% HCl solution was added to pH = 5, leading to precipitation of the tetraaldehyde **5**. Then 5.0 mL hydrazine hydrate was added at once with stirring, which effects dissolution of **5** and after 15–20 min stirring at room temp. the dipyrazole $H_2$*bpzb* deposits as thin white needles. The mixture was left overnight and filtered to yield 3.22 g (98.5%) of the product. This compound was used for the preparation of the metal complexes without further purification.

**$[L^1Ni_2(H$*bpz*$)][ClO_4]$ (6[$ClO_4$]):** To a solution of $H_2$*bpz* (13.8 mg, 0.103 mmol) in methanol (30 mL) was added triethylamine (20 mg, 0.20 mmol). Complex $[L^1Ni_2Cl][ClO_4]$ (194 mg, 0.210 mmol) was added and the resulting yellow solution was stirred for 12 h. A solution of $LiClO_4 \cdot 3H_2O$ (160 mg, 1.00 mmol) in methanol (2 mL) was then added. After further stirring for 12 h, the green precipitate was filtered, washed with cold ethanol, and dried in air. Yield: 80 mg (76%). M.p. 363–365 °C (decomp.). IR (KBr): $\tilde{\nu}$ = 3394 (m), 2961 (s), 2867 (s), 1629 (w), 1463 (s), 1394 (w), 1363 (w), 1311 (w), 1265 (w), 1236 (w), 1203 (w), 1151 (m), 1078 [vs, $\nu_3(ClO_4^-)$], 1057 (s), 1041 (s), 1008 (w), 914 (m), 882 (w), 825 (m), 754 (w), 657 (w), 626 [m, $\nu_4(ClO_4^-)$], 563 (w), 535 (w), 492 (w), 461 (w), 418 (w). UV/Vis ($CH_3CN$): $\lambda_{max}$/nm ($\varepsilon$/M$^{-1}$ cm$^{-1}$) = 385 (1064), 634 (13), 1187 (24).

**$[L^1Ni_2(H$*bpz*$)][BPh_4]$ (6[$BPh_4$]):** To a solution of **6**[$ClO_4$] (102 mg, 0.100 mmol) in methanol (50 mL) was added a solution of $NaBPh_4$ (342 mg, 1.00 mmol) in methanol (50 mL). The reaction mixture was allowed to stir for 3 h. The green product was filtered, washed with ethanol, and dried in air to give 113 mg (91%) of **6**[$BPh_4$] as a green, air-stable, microcrystalline powder. M.p. 295–297 °C (decomp.). IR (KBr): $\tilde{\nu}$ = 3384 (m), 3123 (w), 3054 (m), 3032 (m), 2963 (s), 2858 (s), 1944 (w), 1877 (w), 1815 (w), 1764 (w), 1622 (w), 1580 (w), 1524 (w), 1462 (s), 1425 (m), 1393 (m), 1363 (m), 1309 (w), 1265 (m), 1235 (m), 1201 (w), 1169 (w), 1151 (w), 1126 (w), 1075 (m), 1040 (s), 1006 (w), 928 (w), 912 (m), 881 (w), 824 (m), 733 [s, $\nu(BPh_4^-)$], 704 [s, $\nu(BPh_4^-)$], 628 (m), 611 (m), 562 (w), 534 (w), 492 (w), 467 (w), 430 (w), 417 (w). UV/Vis ($CH_3CN$): $\lambda_{max}$/nm ($\varepsilon$/M$^{-1}$ cm$^{-1}$) = 382 (1037), 634 (14), 1182 (24). $C_{68}H_{89}BN_{10}Ni_2S_2$ (1238.83): calcd. C 65.93, H 7.24, N 11.31, S 5.18; found C 65.50, H 7.53, N 11.00, S 4.96. Single crystals of **6**[$BPh_4$]·1.5MeCN suitable for X-ray structure analysis were grown by slow evaporation of an ethanol/acetonitrile solution of **6**[$BPh_4$]. These crystals slowly lose the solvent molecules of solvent of crystallization at ambient temperature and become turbid.

**$[L^1Ni_2($*bpdz*$)][ClO_4]_2$ (7[$ClO_4$]$_2$):** To a solution of $[L^1Ni_2Cl][ClO_4]$ (92 mg, 0.10 mmol) in methanol (30 mL) was added solid Pb($ClO_4$)$_2$ (80 mg, 0.20 mmol). The color of the reaction mixture immediately turned from yellow to dark green. The reaction mixture was stirred for 5 min, filtered off from $PbCl_2$, and to the dark-green filtrate was added a solution of *bpdz* (7.9 mg, 0.050 mmol) in acetonitrile (5 mL) to give a brown-yellow solution. The solution was kept at room temperature for three days during which time brown crystals separated. These were isolated by filtration, washed with a little amount of cold methanol, and dried in air. Yield: 91 mg (80%). M.p. 297–298 °C (decomp.). IR (KBr): $\tilde{\nu}$ = 3433 (m), 2962 (s), 2868 (s), 2250 (w), 2017 (w), 1603 (w), 1581 (m), 1464 (s), 1395 (m), 1364 (m), 1310 (m), 1267 (m), 1235 (m), 1199 (w), 1094 [vs, $\nu_3(ClO_4^-)$], 912 (m), 887 (m), 850 (w), 824 (s), 755 (w), 688 (w), 669 (w), 624 [s, $\nu_4(ClO_4^-)$], 566 (w), 538 (w), 494 (w), 440 (w), 414 (w) cm$^{-1}$. UV/Vis ($CH_3CN$): $\lambda_{max}$/nm ($\varepsilon$/M$^{-1}$ cm$^{-1}$) = 608 (47), 1094 (51). $C_{46}H_{70}Cl_2N_{10}Ni_2O_8S_2$ (1143.53): calcd. C 48.31, H 6.17, N 12.25, S 5.61; found C 48.25, H 5.98, N 11.95, S 5.32. The crystals of **7**[$ClO_4$]$_2$·3MeCN used for an X-ray structure determination were picked from the mother liquor.

 © 2007 Wiley-VCH Verlag GmbH & Co. KGaA, Weinheim 

**[($L^1Ni_2$)$_2$(*bpzb*)][$ClO_4$]$_2$ (**8**[$ClO_4$]$_2$):** To a solution of $H_2$*bpzb* (21 mg, 0.10 mmol) in methanol (50 mL) and triethylamine (20 mg, 0.20 mmol) was added solid [$L^1Ni_2Cl$][$ClO_4$] (184 mg, 0.200 mmol). The mixture was stirred for 3 d during which time the colour of the suspension changed from yellow to green. A solution of $LiClO_4 \cdot 3H_2O$ (320 mg, 2.00 mmol) in methanol (10 mL) was added. After stirring for 1 d, the green precipitate was collected by filtration, washed several times with cold ethanol and dried in air. Yield: 150 mg (76%). M.p. 342–343 °C (decomp.). IR (KBr): $\tilde{\nu}$ = 3431 (s), 2962 (s), 2866 (s), 1630 (w), 1579 (w), 1462 (s), 1395 (w), 1363 (w), 1310 (w), 1266 (w), 1233 (m), 1201 (w), 1150 (m), 1121 (s), 1077 [vs, $\nu(ClO_4^-)$], 1057 (s), 1041 (s), 1000 (w), 956 (w), 928 (w), 913 (w), 881 (w), 826 (m), 807 (w), 754 (w), 625 [m, $\nu_4(ClO_4^-)$], 564 (w), 535 (w), 493 (w), 413 (w) $cm^{-1}$. UV/Vis ($CH_3CN$): $\lambda_{max}$/nm ($\varepsilon$/$M^{-1}cm^{-1}$) = 380 (4989), 627 (57), 1195 (132).

**[($L^1Ni_2$)$_2$(*bpzb*)][$BPh_4$]$_2$ (**8**[$BPh_4$]$_2$):** To a solution of **8**[$ClO_4$]$_2$ (198 mg, 0.100 mmol) in methanol (50 mL) was added a solution of $NaBPh_4$ (684 mg, 2.00 mmol) in methanol (10 mL). The reaction mixture was allowed to stir for 1 h, and the volume of the solution reduced in vacuo to about 30 mL. The green product was filtered, washed with ethanol and dried in air to give 189 mg (78%) of **8**[$BPh_4$]$_2$ as a green, air-stable, microcrystalline powder. M.p. 350–351 °C (decomp.). IR (KBr): $\tilde{\nu}$ = 3435 (s), 3054 (m), 3027 (m), 2963 (s), 2866 (s), 1636 (w), 1579 (w), 1480 (m), 1462 (s), 1395 (w), 1363 (w), 1310 (w), 1266 (w), 1233 (m), 1201 (w), 1169 (w), 1152 (w), 1122 (w), 1108 (w), 1076 (m), 1056 (m), 1042 (s), 1000 (w), 956 (w), 928 (w), 912 (w), 881 (w), 825 (s), 733 [s, $\nu(BPh_4^-)$], 704 [s, $\nu(BPh_4^-)$], 629 (w), 612 (m), 564 (w), 535 (w), 492 (w), 445 (w) $cm^{-1}$. UV/Vis ($CH_3CN$): $\lambda_{max}$/nm ($\varepsilon$/$M^{-1}cm^{-1}$) = 381 (4626), 631 (53), 1190 (112). $C_{136}H_{176}B_2N_{16}Ni_4S_4$ (2419.62): calcd. C 67.51, H 7.33, N 9.26, S 5.30; found C 66.92, H 7.39, N 9.15, S 4.82. Single crystals of **8**[$BPh_4$]·6MeCN·$2H_2O$ suitable for X-ray structure analysis were grown by slow evaporation of an ethanol/acetonitrile solution of **8**[$BPh_4$].

**[($L^2Ni_2$)$_2$(*bpz*)][$ClO_4$]$_2$ (**9**[$ClO_4$]$_2$):** To a solution of $H_2$*bpz* (13.4 mg, 0.100 mmol) in methanol (30 mL) was added triethylamine (20 mg, 0.20 mmol). Complex [$L^2Ni_2Cl$][$ClO_4$] (162 mg, 0.200 mmol) was slowly added resulting in the immediate formation of a green precipitate. After the addition was complete, further $LiClO_4 \cdot 3H_2O$ (320 mg, 2.00 mmol) dissolved in methanol (2 mL) was added, and stirring was continued for additional 12 h. The green product was collected by filtration, washed several times with cold methanol, and dried in air. Yield: 123 mg (73%). M.p. 340–341 °C (decomp.). IR (KBr): $\tilde{\nu}$ = 3521 (m), 2969 (s), 2855 (s), 2245 (w), 2017 (w), 1628 (w), 1587 (m), 1487 (s), 1454 (s), 1435 (s), 1396 (m), 1364 (w), 1350 (w), 1298 (m), 1268 (s), 1254 (m), 1200 (w), 1170 (m), 1095 [vs, $\nu_3(ClO_4^-)$], 1042 (s), 999 (m), 956 (w), 916 (s), 897 (w), 828 (s), 806 (m), 764 (s), 727 (w), 670 (m), 655 (w), 623 [s, $\nu_4(ClO_4^-)$], 566 (w), 537 (w), 489 (w), 462 (w), 433 (w), 412 (w) $cm^{-1}$. UV/Vis ($CH_3CN$): $\lambda_{max}$/nm ($\varepsilon$/$M^{-1}cm^{-1}$) = 294 (23213), 380 (3785), 635 (66), 1178 (91).

**[($L^2Ni_2$)$_2$(*bpz*)][$BPh_4$]$_2$ (**9**[$BPh_4$]$_2$):** To a warm solution of **9**[$ClO_4$]$_2$ (168 mg, 0.100 mmol) in methanol (50 mL) was added a solution of $NaBPh_4$ (342 mg, 1.00 mmol) in methanol (100 mL). The reaction mixture was allowed to stir for 3 h. The green microcrystalline precipitate was filtered, washed with ethanol and dried in air yielding 186 mg (88%) of **9**[$BPh_4$]$_2$ as a green powder. M.p. 335–336 °C (decomp.). IR (KBr): $\tilde{\nu}$ = 3523 (w), 3054 (m), 2984 (s), 2854 (s), 2247 (w), 1634 (w), 1586 (m), 1484 (m), 1463 (s), 1435 (s), 1396 (m), 1364 (m), 1350 (w), 1337 (w), 1297 (m), 1267 (s), 1255 (m), 1200 (w), 1169 (m), 1095 (s), 1075 (s), 1041 (s), 998 (m), 956 (m), 916 (s), 896 (m), 827 (s), 806 (m), 761 (s), 732 [s, $\nu(BPh_4^-)$], 704 [s, $\nu(BPh_4^-)$], 669 (m), 623 (s), 612 (m), 565 (w), 536 (w), 488 (w), 465 (w), 433 (w), 412 (w) $cm^{-1}$. UV/Vis ($CH_3CN$): $\lambda_{max}$/nm ($\varepsilon$/$M^{-1}cm^{-1}$) = 294 (27244), 376 (4504), 637 (63), 1183 (111). $C_{114}H_{140}B_2N_{16}Ni_4S_4$ (2119.09): calcd. C 64.61, H 6.66, N 10.58, S 6.05; found C 62.79, H 6.81, N 11.43, S 5.92. Single crystals of **9**[$BPh_4$]$_2$·$2CH_2Cl_2$ suitable for X-ray structure analysis were grown by recrystallization from dichloromethane.

**Collection and Reduction of X-ray Data:** Suitable single crystals of **6**[$BPh_4$]·1.5MeCN, **7**[$ClO_4$]$_2$·3MeCN, **8**[$BPh_4$]$_2$·6MeCN·$2H_2O$, and **9**[$BPh_4$]$_2$·$2CH_2Cl_2$ were selected and mounted on the tip of a glass fibre using perfluoropolyether oil. The data sets were collected at 213(2) K using a STOE IPDS-2T diffractometer. Graphite-mono-

Table 2. Crystallographic data for complexes **6**[$BPh_4$]·1.5MeCN, **7**[$ClO_4$]$_2$·3MeCN, **8**[$BPh_4$]$_2$·6MeCN·$2H_2O$, and **9**[$BPh_4$]$_2$·$2CH_2Cl_2$.

| Compound | **6**[$BPh_4$]·1.5MeCN | **7**[$ClO_4$]$_2$·3MeCN | **8**[$BPh_4$]$_2$·6MeCN·$2H_2O$ | **9**[$BPh_4$]$_2$·$2CH_2Cl_2$ |
|---|---|---|---|---|
| Formula | $C_{71}H_{93.50}BN_{11.50}Ni_2S_2$ | $C_{52}H_{79}Cl_2N_{13}Ni_2O_8S_2$ | $C_{148}H_{198}B_2N_{22}Ni_4O_2S_4$ | $C_{116}H_{144}B_2Cl_4N_{16}Ni_4S_4$ |
| $M_r$ [g/mol] | 1300.42 | 1266.72 | 2701.98 | 2288.97 |
| Space group | $P\bar{1}$ | $P\bar{1}$ | $P\bar{1}$ | $P\bar{1}$ |
| *a* [Å] | 12.5151(13) | 13.2202(9) | 13.9142(4) | 12.2969(5) |
| *b* [Å] | 16.2376(14) | 15.6825(10) | 16.0978(5) | 15.3907(6) |
| *c* [Å] | 18.270(2) | 16.7954(10) | 18.6102(6) | 15.5812(7) |
| *a* [°] | 98.745(12) | 74.250(8) | 108.658(2) | 73.445(3) |
| *β* [°] | 95.316(12) | 69.252(8) | 107.475(2) | 80.928(3) |
| *γ* [°] | 103.121(11) | 66.228(8) | 102.448(3) | 79.567(3) |
| *V* [Å$^3$] | 3542.4(6) | 2946.2(3) | 3536.1(2) | 2762.2(2) |
| *Z* | 2 | 2 | 1 | 1 |
| $d_{calcd.}$ g/cm$^3$ | 1.219 | 1.428 | 1.269 | 1.376 |
| Cryst. size [mm] | 0.30 × 0.25 × 0.25 | 0.27 × 0.24 × 0.18 | 0.30 × 0.30 × 0.15 | 0.30 × 0.20 × 0.15 |
| $\mu$(Mo-$K_\alpha$) [mm$^{-1}$] | 0.639 | 0.864 | 0.643 | 0.900 |
| $\theta$ limits [°] | 2.37–28.04 | 5.84–25.98 | 3.31–33.29 | 3.36–28.00 |
| Measured reflections | 24520 | 23694 | 59533 | 19250 |
| Independent reflections | 15783 | 10610 | 23987 | 13319 |
| Observed reflections[a] | 10159 | 5881 | 18472 | 11233 |
| Number of parameters | 778 | 727 | 845 | 659 |
| $R_1$[b] ($R_1$ all data) | 0.0399 (0.0571) | 0.0417 (0.0826) | 0.0526 (0.0713) | 0.0370 (0.0443) |
| $wR_2$[c] ($wR_2$ all data) | 0.1111 (0.1142) | 0.0874 (0.0932) | 0.1383 (0.1478) | 0.1092 (0.1121) |
| Max., min. peaks, [e/Å$^3$] | 0.994, –0.751 | 0.602, –0.570 | 1.105, –1.256 | 1.349, –1.563 |

[a] Observation criterion: $I > 2\sigma(I)$. [b] $R_1 = \Sigma||F_o| - |F_c||/\Sigma|F_o|$. [c] $wR_2 = \{\Sigma[w(F_o^2 - F_c^2)^2]/\Sigma[w(F_o^2)^2]\}^{1/2}$.

 © 2007 Wiley-VCH Verlag GmbH & Co. KGaA, Weinheim 

chromated Mo-$K_\alpha$ radiation ($\lambda$ = 0.71073 Å) was used throughout. The data were processed with the program STOE X-AREA.[44] Selected details of the data collection and refinement are given in Table 2. The structures were solved by direct methods[45] and refined by full-matrix least-squares techniques on the basis of all data against $F^2$ using SHELXL-97.[46] PLATON was used to search for higher symmetry.[47] All non-hydrogen atoms were refined anisotropically. H atoms were placed at calculated positions and refined as riding atoms with isotropic displacement parameters.

Some of the solvate molecules in **6** and **7** were found to be disordered or only partially occupied. In the crystal structure of **6**$[BPh_4]_2$·1.5MeCN the occupancy factor of one MeCN was reduced to 0.5. In the crystal structure of **7**$[BPh_4]_2$·6MeCN·$2H_2O$ the water molecule was found to be disordered over two sites. The respective orientations were refined by using a split atom model to give site occupancy factors of 0.59(1) [O(1a)] and 0.41(1) [for O(1b)]. Water hydrogen atoms were not included in the refinement. Graphics were produced with Ortep3 for Windows.[48]

CCDC-641207 (for **2**), -641208 (for **3**), -641209 (for **4**), and -641210 (for **5**) contain the supplementary crystallographic data for this paper. These data can be obtained free of charge from the Cambridge Crystallographic Data Centre via www.ccdc.cam.ac/data_request/cif.

**Supporting Information** (see also the footnote on the first page of this article): Experimental and calculated magnetic values susceptibility data for **9**$[BPh_4]_2$.

## Acknowledgments

We sincerely thank the Deutsche Forschungsgemeinschaft (DFG) (priority program 1137 "Molecular Magnetism") for funding of this work. We are grateful to Prof. Dr. F. Meyer for providing facilities for magnetic susceptibility measurements.

[1] S. Trofimenko, *J. Org. Chem.* **1964**, *29*, 3046–3049.
[2] I. Boldog, J. Sieler, A. N. Chernega, K. V. Domasevitch, *Inorg. Chim. Acta* **2002**, *338*, 69–77.
[3] P. E. Kruger, G. D. Fallon, B. Moubaraki, K. S. Murray, *J. Chem. Soc., Chem. Commun.* **1992**, 1926–1927.
[4] a) V. V. Ponomarova, V. V. Komarchuk, I. Boldog, A. N. Chernega, J. Sieler, K. Domasevitch, *Chem. Commun.* **2002**, 436–437; b) I. Boldog, E. B. Rusanov, J. Sieler, S. Blaurock, K. V. Domasevitch, *Chem. Commun.* **2003**, 740–741; c) E. B. Rusanov, V. V. Ponomarova, V. V. Komarchuk, H. Stoeckli-Evans, E. Fernandez-Ibanez, F. Stoeckli, J. Sieler, K. V. Domasevitch, *Angew. Chem.* **2003**, *115*, 2603–2605; *Angew. Chem. Int. Ed.* **2003**, *42*, 2499–2501.
[5] J.-P. Zang, S. Horike, S. Kitagawa, *Angew. Chem.* **2007**, *119*, 907–910; *Angew. Chem. Int. Ed.* **2007**, *46*, 889–892.
[6] J. He, Y.-G. Yin, T. Wu, D. Li, X.-C. Huang, *Chem. Commun.* **2006**, 2845–2847.
[7] a) M. Eddaoudi, D. B. Moler, H. Li, B. Chen, T. M. Reineke, M. O'Keeffe, O. M. Yaghi, *Acc. Chem. Res.* **2001**, *34*, 319–330; b) M. Eddaoudi, J. Kim, J. B. Wachter, H. K. Chae, M. O'Keeffe, O. M. Yaghi, *J. Am. Chem. Soc.* **2001**, *123*, 4368–4369; c) J. L. C. Rowsell, A. R. Millward, K. S. Park, O. M. Yaghi, *J. Am. Chem. Soc.* **2004**, *126*, 5666–5667; d) T. J. Barton, L. M. Bull, W. G. Klemperer, D. A. Loy, B. McEnaney, M. Misono, P. A. Monson, G. Pez, G. W. Scherer, J. C. Vartuli, O. M. Yaghi, *Chem. Mater.* **1999**, *11*, 2633–2656.
[8] C. N. R. Rao, S. Natarajan, A. Choudhury, S. Neeraj, A. A. Ayi, *Acc. Chem. Res.* **2001**, *34*, 80–87.
[9] B. Moulton, M. J. Zaworotko, *Chem. Rev.* **2001**, *101*, 1629–1658.
[10] S. Kitagawa, S. Noro, T. Nakamura, *Chem. Commun.* **2006**, 701–707.
[11] S. Kitagawa, R. Kitaura, S. Noro, *Angew. Chem.* **2004**, *116*, 2388–2430; *Angew. Chem. Int. Ed.* **2004**, *43*, 2334–2375.
[12] I. Boldog, E. B. Rusanov, A. N. Chernega, J. Sieler, K. V. Domasevitch, *Angew. Chem.* **2001**, *113*, 3543–3546; *Angew. Chem. Int. Ed.* **2001**, *40*, 3435–3438.
[13] K. V. Domasevitch, I. Boldog, *Acta Crystallogr., Sect. C* **2005**, *61*, 373–376.
[14] S. Y. Yu, H.-P. Huang, S.-H. Liu, Q. Jia, Y.-Z. Li, B. Wu, Y. Sei, K. Yamaguchi, Y.-J. Pan, H.-W. Ma, *Inorg. Chem.* **2005**, *44*, 9471–9488.
[15] B. Kersting, G. Steinfeld, *Chem. Commun.* **2001**, 1376–1377.
[16] a) G. Steinfeld, V. Lozan, B. Kersting, *Angew. Chem.* **2003**, *115*, 2363–2365; *Angew. Chem. Int. Ed.* **2003**, *42*, 2261–2263; b) S. Käss, T. Gregor, B. Kersting, *Angew. Chem.* **2006**, *118*, 107–110; *Angew. Chem. Int. Ed.* **2006**, *45*, 101–104.
[17] M. H. Klingele, G. Steinfeld, B. Kersting, *Z. Naturforsch., Teil B* **2001**, *56*, 901–907.
[18] J. Hausmann, M. H. Klingele, V. Lozan, G. Steinfeld, D. Siebert, Y. Journaux, J. J. Girerd, B. Kersting, *Chem. Eur. J.* **2004**, *10*, 1716–1728.
[19] Y. Journaux, V. Lozan, J. Hausmann, B. Kersting, *Chem. Commun.* **2006**, 83–84.
[20] V. Lozan, B. Kersting, *Eur. J. Inorg. Chem.* **2007**, 1436–1443.
[21] V. Lozan, B. Kersting, *Inorg. Chem.* **2006**, *45*, 5630–5634.
[22] B. Kersting, *Angew. Chem.* **2001**, *113*, 4110–4112; *Angew. Chem. Int. Ed.* **2001**, *40*, 3988–3990.
[23] B. Kersting, G. Steinfeld, *Inorg. Chem.* **2002**, *41*, 1140–1150.
[24] Y. Journaux, T. Glaser, G. Steinfeld, V. Lozan, B. Kersting, *Dalton Trans.* **2006**, 1738–1748.
[25] *Magnetism: Molecules to Materials* (Eds.: J. S. Miller, M. Drillon), Wiley-VCH, Weinheim, **2001**.
[26] E. Coronado, P. Delhaes, D. Gatteschi, J. S. Miller (Eds.), *Molecular magnetism: From Molecular Assmblies to Devices*, NATO ASI Series, Kluwer, Dordrecht, The Netherlands, **1995**, vol. 321.
[27] S. P. Watton, P. Fuhrmann, L. E. Pence, A. Caneschi, A. Cornia, G. L. Abbati, S. J. Lippard, *Angew. Chem.* **1997**, *109*, 2917–2919; *Angew. Chem. Int. Ed. Engl.* **1997**, *36*, 2774–2776.
[28] J. Larionova, M. Gross, M. Pilkington, H. Andres, H. Stoeckli-Evans, H. U. Güdel, S. Decurtins, *Angew. Chem.* **2000**, *112*, 1667–1672; *Angew. Chem. Int. Ed.* **2000**, *39*, 1605–1609.
[29] A. L. Dearden, S. Parsons, R. E. P. Winpenny, *Angew. Chem.* **2001**, *113*, 155–158; *Angew. Chem. Int. Ed.* **2001**, *40*, 151–154.
[30] S. Demeshko, G. Leibeling, S. Dechert, F. Meyer, *Dalton Trans.* **2006**, 3458–3465.
[31] B. Kersting, G. Steinfeld, D. Siebert, *Chem. Eur. J.* **2001**, *7*, 4253–4258.
[32] C. C. Barton, G. F. Daves, G. Franceschi, *J. Chem. Soc., Perkin Trans.* **1980**, 643–647.
[33] T. Beissel, T. Glaser, F. Kesting, K. Wieghardt, B. Nuber, *Inorg. Chem.* **1996**, *35*, 3936–3947.
[34] K. K. Nanda, A. W. Addison, N. Paterson, E. Sinn, L. K. Thompson, U. Sakaguchi, *Inorg. Chem.* **1998**, *37*, 1028–1036.
[35] T. R. Felthouse, E. J. Laskowski, D. N. Hendrickson, *Inorg. Chem.* **1977**, *16*, 1077–1089.
[36] a) M. Julve, M. Verdaguer, A. Gleizes, M. Philoche-Levisalles, O. Kahn, *Inorg. Chem.* **1984**, *23*, 3808–3818; b) S. Alvarez, M. Julve, M. Verdaguer, *Inorg. Chem.* **1990**, *29*, 4500–4507.
[37] M. Verdaguer, J. Gouteron, S. Jeannin, Y. Jeannin, O. Kahn, *Inorg. Chem.* **1984**, *23*, 4291–4296.
[38] a) E. G. Bakalbassis, C. A. Tsipis, J. Mrozinski, *Inorg. Chem.* **1985**, *24*, 4231–4233; b) E. G. Bakalbassis, J. Mrozinski, C. A. Tsipis, *Inorg. Chem.* **1986**, *25*, 3684–3690; c) C. E. Xanthopoulos, M. P. Sigalas, G. A. Katsoulos, C. A. Tsipis, A. Terzis, M. Mentzafos, A. Hountas, *Inorg. Chem.* **1993**, *32*, 5433–5436.
[39] P. Chaudhuri, K. Oder, K. Wieghardt, S. Gehring, W. Haase, B. Nuber, J. Weiss, *J. Am. Chem. Soc.* **1988**, *110*, 3657–3658.

 © 2007 Wiley-VCH Verlag GmbH & Co. KGaA, Weinheim 

[40] K. S. Burger, P. Chaudhuri, K. Wieghardt, B. Nuber, *Chem. Eur. J.* **1995**, *1*, 583–589.
[41] C. Erasmus, W. Haase, *Spectrochim. Acta, Ser. A* **1994**, *50*, 2189–2195.
[42] R. E. Coffman, G. R. Buettner, *J. Phys. Chem.* **1979**, *83*, 2387–2392.
[43] J. Cano, G. De Munno, J. L. Sanz, R. Ruiz, J. Faus, F. Lloret, M. Julve, A. Caneschi, *J. Chem. Soc., Dalton Trans.* **1997**, 1915–1923.
[44] *XAREA*, Stoe & Cie, Darmstadt, Germany, **2001**.
[45] G. M. Sheldrick, *Acta Crystallogr., Sect. A* **1990**, *46*, 467–473.
[46] G. M. Sheldrick, *SHELXL-97*, Computer program for crystal structure refinement, University of Göttingen, Göttingen, Germany, **1997**.
[47] Spek, A. L. *PLATON – A Multipurpose Crystallographic Tool*, Utrecht University, Utrecht, The Netherlands, **2000**.
[48] L. J. Farrugia, *J. Appl. Crystallogr.* **1997**, *30*, 565.
Received: March 22, 2007
Published Online: May 22, 2007

 © 2007 Wiley-VCH Verlag GmbH & Co. KGaA, Weinheim 

DOI: 10.1002/ejic.200601210

# The Influence of Steric Pressure on the Structure of Homodimetallic Rhodium(I) and Iridium(I) Complexes Containing a Bis(bidentate) Phosphane Ligand

**Christian Bachmann,[a] Rene Gutmann,[a] Georg Czermak,[a] Alexander Dumfort,[a] Sylvia Eller,[a] Markus Fessler,[a] Holger Kopacka,[a] Karl-Hans Ongania,[b] and Peter Brüggeller*[a]**

**Keywords:** X-ray diffraction / Chelates / Phosphane ligands / Iridium / Rhodium

Fifteen novel homodimetallic $Rh^I$ and $Ir^I$ complexes containing the bis(bidentate) phosphane ligand *cis*,*trans*,*cis*-1,2,3,4-tetrakis(diphenylphosphanyl)cyclobutane (dppcb) were prepared and characterized by NMR spectroscopy ($^1H$, $^{13}C\{^1H\}$, $^{31}P\{^1H\}$), mass spectrometry, IR spectroscopy, elemental analyses and melting points. Furthermore, the solid-state structures of seven of these new compounds were fully determined by single-crystal X-ray diffraction analyses to study the influence of steric pressure. The precursor complex $[Rh_2(\eta^4\text{-cod})_2(dppcb)]X_2$ (**1**), $X^- = BF_4^-$, $PF_6^-$, $SbF_6^-$, completely characterized by its X-ray structure, smoothly reacts with mono- or bidentate ligands containing phosphorus or nitrogen donor atoms. Thus, monophosphanes and monophosphites produce compounds of the structure type $[Rh_2L_4(dppcb)](SbF_6)_2$ [L = $PMe_2Ph$, **2**; $PMePh_2$, **3**; $P(OMe)_3$, **5**; $P(OPh)_3$, **6**]. The X-ray structures of **3** and **6** show that $PMePh_2$ and $P(OPh)_3$ are capable of compensating steric interactions. The treatment of **1** with diphosphanes leads to the structure type $[Rh_2L_2(dppcb)](SbF_6)_2$ [L = bis(diphosphanyl)-methane, dppm, **7**; bis(diphenylphosphanyl)amine, dppam, **8**; 1,2-bis(diphenylphosphanyl)ethane, dppe, **9**; *cis*-1,2-bis(diphenylphosphanyl)ethene, *cis*-dppen, **10**]. The X-ray structures of **8**, **9** and **10** clearly indicate the onset of steric pressure as a consequence of mechanical coupling, which results in two different coordination moieties for homodimetallic species **9** and **10**. Under steric pressure, the quadrant effects of dppcb and dppe become comparable to $Rh^I$ complexes. The use of mono- or bidentate ligands containing nitrogen donor atoms leads to the compounds $[Rh_2(pyridine)_4(dppcb)](SbF_6)_2$ (**11**), $[Rh_2(2,2'\text{-bipyridine})_2(dppcb)](SbF_6)_2$ (**12**) and $[Rh_2(1,10\text{-phenanthroline})_2(dppcb)](SbF_6)_2$ (**13**). The crystal structures of **1** and the novel complex $[Ir_2(\eta^4\text{-cod})_2(dppcb)]X_2$ (**14**), $X^- = BF_4^-$, $SbF_6^-$, are isomorphous. However, it was only possible to produce restricted examples of derivatives of **14** owing to the reluctance of **14** to release cod. Thus, monophosphanes lead to the five-coordinate species $[Ir_2(\eta^4\text{-cod})_2(PMe_2Ph)_2(dppcb)](BF_4)_2$ (**15**), whereas the four-coordinate compound $[Ir_2(PMePh_2)_4(dppcb)](BF_4)_2$ (**16**) is formed by using the sterically more demanding ligand $PMePh_2$ instead of $PMe_2Ph$.
(© Wiley-VCH Verlag GmbH & Co. KGaA, 69451 Weinheim, Germany, 2007)

## Introduction

Only recently was it shown that the efficiency of catalysts containing bidentate or bis(bidentate) phosphanes is strongly determined by the flexibility of their backbones.[1–3] This influence of the backbone can be seen in different catalytic applications like the copolymerization of carbon monoxide and ethene,[1] the oxidative carbonylation of styrene[2] and the Schulz–Flory oligomerization of ethene.[3] The common feature of these different kinds of homogeneous catalysis is that square-planar complexes are thought to be responsible for the catalytic activity.[1–3] By contrast, it is well-known that in the case of hydroformylation the catalytically active species is a trigonal bipyramidal hydrido rhodium complex, which usually contains two phosphorus donor ligands.[4] Because the whole catalytic cycle for the hydroformylation reaction consists of five-coordinate species,[4] the enlargement in the coordination number relative to the above square planar catalysts certainly increases the steric pressure.[5]

In this context, steric pressure is defined as the sum of intramolecular steric interactions keeping the coordination geometry and/or conformation of a certain complex virtually intact.[5] This means that the onset of steric pressure enforcing intramolecular contact approaches also changes the quadrant effect[1–3] in square planar species because the quadrant diagrams usually depend on the spatial distributions of the phenyl groups present in bidentate or bis(bidentate) phosphanes (see below, Figure 3). A certain intramolecular steric pressure only allows distinct spatial distri-

[a] Institut für Allgemeine, Anorganische und Theoretische Chemie, Universität Innsbruck,
Innrain 52a, 6020 Innsbruck, Austria
E-mail: Peter.Brueggeller@uibk.ac.at
[b] Institut für Organische Chemie, Universität Innsbruck,
Innrain 52a, 6020 Innsbruck, Austria

 © 2007 Wiley-VCH Verlag GmbH & Co. KGaA, Weinheim 

butions of these phenyl rings and hence controls the quadrant effect. Thus, steric pressure is important to determine the structure of the resultant complexes and steers their catalytic activity by the quadrant effect.[1–3]

Therefore, in this work, the onset of steric pressure is studied in a series of X-ray structures of novel square planar homodimetallic $Rh^I$ species containing the bis(bidentate) phosphane *cis*,*trans*,*cis*-1,2,3,4-tetrakis(diphenylphosphanyl)cyclobutane (dppcb) prepared in our laboratory.[6] It seemed to us especially interesting to see if the rigidity of the backbone of dppcb is enough to provide the same usual quadrant effect,[1–3] which shows one axial and one equatorial phenyl group at each phosphorus centre, even under "steric pressure". In the case of dppcb, the onset of intramolecular steric interactions leads to excellent photochemical and photophysical properties of six-coordinate homodimetallic $Ru^{II}$ compounds.[7,8] However, in general, sterically congested five-coordinate complexes of $Rh^I$ are rare and/or unstable towards the loss of the fifth ligand.[9] In contrast, a typical situation for carbonylation catalysis is that starting square planar compounds lead to five-coordinate species.[9,10] Therefore, a subtle choice of the steric requirements of further ligands should make it possible to observe a change in the usual conformation of the cyclobutane backbone of dppcb also in square planar $Rh^I$ complexes, which would result in a different quadrant effect. This study should shed light on the question of whether there is sufficient flexibility in the ligand backbone of dppcb to allow easy access to all intermediates in the catalytic carbonylation cycle.[11]

## Results and Discussion

### Synthesis of Complexes

$[Rh_2(\eta^4\text{-cod})_2(dppcb)]X_2$ (**1**), $X^- = BF_4^-$, $PF_6^-$, $SbF_6^-$ (Figure 4), was prepared by a reported procedure for the in situ generation of a coordinatively unsaturated species $[Rh(\eta^4\text{-cod})(acetone)_2]X$ from the chlorido-bridged dirhodium complex $[RhCl(\eta^4\text{-cod})]_2$.[12] Treatment of $[Rh(\eta^4\text{-cod})(acetone)_2]X$ with dppcb leads to **1** in excellent yield. The use of different anions was necessary, as only the $BF_4^-$ salt yielded single crystals suitable for X-ray structure analysis, $PF_6^-$ is the only innocent counterion under the planned catalytic hydroformylation conditions, and only the $SbF_6^-$ form of **1** produced further derivatives in excellent yield. The exchange of these anions was carried out by utilizing the corresponding silver salt.[12]

The apparent simple cod substitution from **1** makes it a suitable precursor complex.[13] Thus, **1** smoothly reacts with the monophosphane $PMe_2Ph$ to give $[Rh_2(PMe_2Ph)_4(dppcb)](SbF_6)_2$ (**2**, see Figure 1). However, in the case of the sterically more demanding monophosphane $PMePh_2$, not only the main product (Figure 1) $[Rh_2(PMePh_2)_4(dppcb)](SbF_6)_2$ (**3**) was formed, but also the known homoleptic complex[12b] $[Rh(PMePh_2)_4](SbF_6)$ (**4**), which was produced in a side reaction and isolated in a pure form (Figure 1). The formation of homoleptic species depending on the steric demands of the involved ligands is typical for this kind of reaction.[13] However, the use of the sterically congested monophosphane $PPh_3$ and **1** leads to a fast equilibrium between the different compounds as evidenced from the resulting $^{31}P\{^1H\}$ NMR spectrum; no product could be isolated.

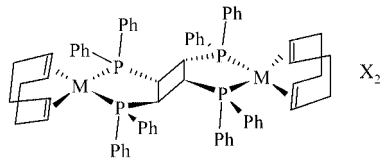

**1**: M = Rh; X = $BF_4$, $PF_6$, $SbF_6$
**14**: M = Ir; X = $BF_4$, $SbF_6$

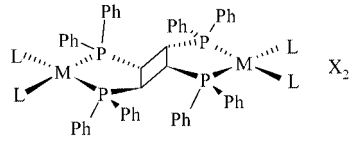

M = Rh; X = $SbF_6$; **2**: L = $P(CH_3)_2Ph$, **3**: L = $P(CH_3)Ph_2$, **5**: L = $P(OCH_3)_3$, **6**: L = $P(OPh)_3$
M = Ir; X = $BF_4$; **16**: L = $P(CH_3)Ph_2$

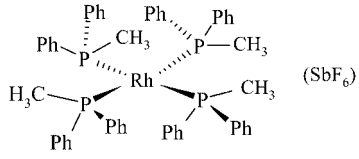

**4**

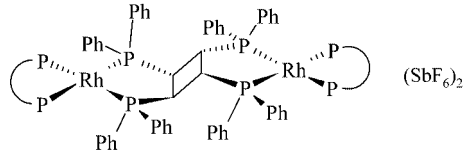

P P = **7**: dppm, **8**: dppam, **9**: dppe, **10**: *cis*-dppen

Figure 1. Structure types observed in Rh and Ir complexes.

Phosphanes can be sterically and electronically modified.[14] Because the propensity for incremental tuning is crucially important in catalysis,[14] we successfully extended the reaction sequence above to phosphites, diphosphanes and mono- and bidentate nitrogen ligands (see complexes **5**–**13** in Figures 1 and 2). Only this synthetic effort made it possible to obtain a series of X-ray structures containing increasingly sterically more-demanding ligands and to study their fine tuning of the conformation of dppcb. It was especially hoped that the onset of steric pressure could lead to different coordination units within these homodimetallic species.

In the case of $Ir^I$, the analogous reaction sequence leading to **1** was unsuccessful. However, as observed previously[15] for a comparable synthesis, it was possible to perform the direct reaction of dppcb with the chlorido-bridged

 © 2007 Wiley-VCH Verlag GmbH & Co. KGaA, Weinheim 

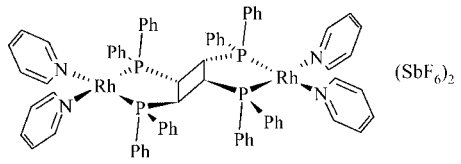


**11**

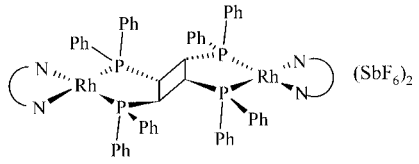


N N = **12**: bpy, **13**: phen

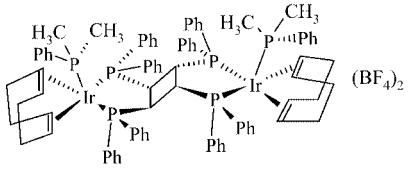


**15**

Figure 2. Structure types observed in Rh and Ir complexes.

diiridium complex $[IrCl(\eta^4\text{-cod})]_2$ and $[Ir_2Cl_2(\eta^4\text{-cod})_2$-(dppcb)] resulted in excellent yield. Subsequent treatment with AgX produced $[Ir_2(\eta^4\text{-cod})_2(dppcb)]X_2$ (**14**), $X^-$ = $BF_4^-$, $SbF_6^-$ (see Figure 1).[15]

Analogous to **1**, only the $BF_4^-$ salt of **14** yielded single crystals that were suitable for X-ray structure analysis; the crystal structures of **1** and **14** are isomorphous. However, synthetic difficulties appeared when **14** was used as a precursor complex for further derivatives in its $BF_4^-$ as well as $SbF_6^-$ forms. Similar observations were made when other chelating ligands were treated with iridium precursor complexes and even under harsh conditions it was not possible to displace the remaining cod ligand; decomposition occurred instead.[11] This is in agreement with the higher degree of metal-to-cod bonding and back-bonding in the iridium complexes than in the rhodium complexes and hence with the greater stability of the Ir–cod compounds.[16] Because the ligand exchange reactions observed in $Rh^I$ and $Ir^I$ systems are likely to proceed by associative mechanisms,[13] **14** smoothly reacts with the monophosphane $PMe_2Ph$ to give the five-coordinate species $[Ir_2(\eta^4\text{-cod})_2(PMe_2Ph)_2$-$(dppcb)](BF_4)_2$ (**15**, see Figure 2). Pentacoordinated structures containing cod are well-known for $Ir^I$;[17] they are much more stable than the $Rh^I$ complexes (compare analogous complexes **2** and **15** in Figures 1 and 2).

However, the greater steric pressure of $PMePh_2$ leads to the displacement of cod in **14** and the four-coordinate compound $[Ir_2(PMePh_2)_4(dppcb)](BF_4)_2$ (**16**, Figure 1) is formed.

Interestingly, the substitutional lability of 1,5-cod versus triorganophosphane ligands does not play any role in the clean synthesis of **1** or **14**, though this lability is consistent with predictions that are based on hard–soft acid–base theory where the soft olefin ligand is replaced preferentially by a soft triorganophosphane donor.[18] However, as a consequence of the intrinsic problem of pentacoordination in the $Ir^I$ case it was not possible to obtain the same series of complexes as for those of $Rh^I$, which reflected increasing steric pressure.

## Comparison of the Quadrant Effects in Complexes of dppe and dppcb

Conformations and quadrant diagrams for M(dppe) and $M_2$(dppcb) complexes are shown in Figure 3.[19] The conformation adopted by the phenyl groups in dppe complexes is noticeably different from that for the dppcb ligand. In terms of the quadrant effect, the steric crowding provided by the phenyl groups is diagonally disposed with respect to the coordination plane in the dppe derivatives. By contrast, this steric crowding is usually concentrated on one side of the coordination plane in the dppcb complexes owing to spatial distributions of the phenyl substituents on the phosphorus donors so that the two axial phenyl rings are located on the same side of the coordination plane.[2,19] However, it is clear that the conformations shown in Figure 3 are only the borderline cases.

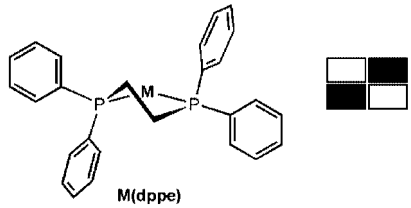


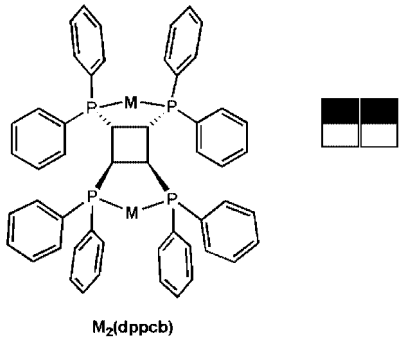


Figure 3. Quadrant effects in complexes of dppe and dppcb.

Especially for $M_2$(dppcb), a centrosymmetric structure is depicted where each coordination unit contains two axial and two equatorial phenyl groups. This conformation is typical for homodimetallic species of dppcb without steric pressure.[1–3,6,20] The distances of the *ipso* carbon atoms of the phenyl substituents from the coordination planes clearly define axial, equatorial and diagonal dispositions (see Figure 3). Thus, the influence of the onset of steric pressure on the idealized $M_2$(dppcb) conformation in Figure 3 can be directly measured.

 © 2007 Wiley-VCH Verlag GmbH & Co. KGaA, Weinheim 

### Isomorphous X-ray Structures of $[M_2(\eta^4\text{-cod})_2(dppcb)](BF_4)_2$ [M = Rh (1), Ir (14)]

It is well-known that the time-averaged preferred conformations of the five-membered metallarings in complexes of type **1** (see Figure 1) are dictated by the nature of the bidentate or bis(bidentate) phosphane ligand.[2] The X-ray structure of **1** (see Figure 4) clearly reveals that only the phenyl groups attached to P(2) show axial and equatorial spatial distributions with respect to the coordination plane.

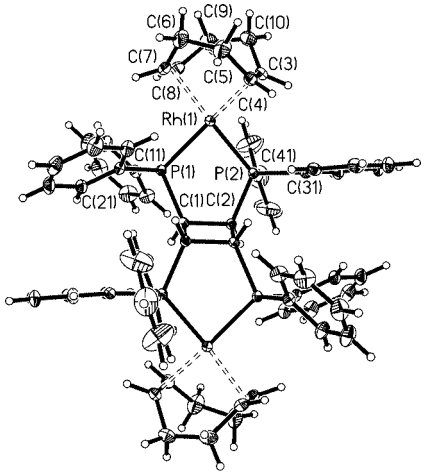


Figure 4. View of the cation of $[Rh_2(\eta^4\text{-cod})_2(dppcb)](BF_4)_2$ (**1**). The atom labelling scheme is shown.

The diagonal disposition of the phenyl substituents at P(1) is characteristic of dppe.[2,19,21] This difference is shown by the deviations of the four *ipso* carbon atoms C(11), C(21), C(31) and C(41) of –1.177(4), 1.650(4), 0.187(5) and –2.079(5) Å, respectively, from the coordination plane defined by the atoms Rh(1), P(1) and P(2) and the centres of gravity of the cod double bonds (see Figure 4).[22] The largest deviations for C(21) of 1.650(4) Å and for C(41) of –2.079(5) Å indicate that the diagonal quadrants are more hindered (see Figures 3 and 4). Obviously the steric pressure introduced by cod is already enough to change the usual quadrant effect of $M_2$(dppcb) in Figure 3. The atoms and centres of gravity ($C_g$) defining the coordination plane are tetrahedrally distorted, as shown by the deviations from this plane: Rh(1) 0.038(2) Å, P(1) 0.267(2) Å, P(2) –0.289(2) Å, $C_{g1}$ 0.284(3) Å, $C_{g2}$ –0.301(3) Å.

It was shown that short intramolecular contacts due to steric pressure in homodimetallic complexes of dppcb change their photochemical and photophysical properties.[7,8] In the case of **1**, this steric pressure is clearly responsible for the observed unusual quadrant effect. Thus, in **1** the shortest intramolecular contact between the phenyl rings along a *trans* axis of the cyclobutane ring is C(22)···H(46B) of 2.988 Å. Furthermore, the hydrogen atoms attached to the double bonds of cod (see Figure 4) also show pronounced intramolecular interactions with adjacent phenyl groups: H(3A)···H(42A) 2.980 Å, H(4A)···H(36A) 2.475 Å, H(7A)···H(22A) 2.764 Å, H(8A)···H(12A) 2.558 Å. As a consequence, the C=C bonds of the cod ring are not coordinated perpendicular to the P(1)–Rh(1)–P(2) plane and a dihedral angle of 22.5(1)° with the $C_{g1}$–Rh(1)–$C_{g2}$ plane occurs. In **1**, the distortion from an ideal square-planar coordination is larger than that in $[Rh(\eta^4\text{-cod})\{CH_2P(C_6H_4\text{-}SiMe_2CH_2CH_2C_6F_{13}\text{-}p)_2\}_2](BPh_4)$ with a corresponding dihedral angle of 13.1°,[21] though the steric crowding of the latter complex is considerable. A further indication of steric pressure in **1** is the significantly different Rh–C distances,[21,23] where selected bond lengths and angles of **1** and **14** are given in Table 1.

Table 1. Selected bond lengths [Å] and angles [°] for **1** and **14**.

| Compound **1** | | Compound **14** | |
|---|---|---|---|
| Rh(1)–P(1) | 2.2797(7) | Ir(1)–P(1) | 2.2775(13) |
| Rh(1)–P(2) | 2.2671(7) | Ir(1)–P(2) | 2.2815(13) |
| Rh(1)–C(3) | 2.264(3) | Ir(1)–C(3) | 2.192(6) |
| Rh(1)–C(4) | 2.227(3) | Ir(1)–C(4) | 2.242(6) |
| Rh(1)–C(7) | 2.276(3) | Ir(1)–C(7) | 2.200(5) |
| Rh(1)–C(8) | 2.234(3) | Ir(1)–C(8) | 2.225(6) |
| C(3)–C(4) | 1.368(5) | C(3)–C(4) | 1.360(11) |
| C(7)–C(8) | 1.361(6) | C(7)–C(8) | 1.396(9) |
| P(1)–Rh(1)–P(2) | 83.65(2) | P(1)–Ir(1)–P(2) | 84.45(4) |

However, these Rh–C distances are significantly shorter than in *cis*-$[Rh(\eta^4\text{-cod})\{Me_2Si(\mu\text{-}NtBu)_2PCH_2\}_2](BF_4)$ with an average Rh–C distance of 2.305(6) Å.[14] The latter long rhodium–carbon bonds were interpreted in terms of an increased steric repulsion between the bis(phosphane) and the cyclooctadiene moieties.[14] Obviously, in **1** the steric pressure is efficiently released by a suitable distortion of the square-planar coordination together with a suitable spatial distribution of the phenyl substituents leading to an unusual quadrant effect for homodimetallic species of dppcb.

The structures of **1** and **14** fulfill the criteria of the same ligands, the same coordination number and geometry, isomorphous crystal lattices and equal experimental conditions, and, therefore, allow an exact comparison of their geometric features.[24] The quadrant effect in **14**, given by the deviations of the four *ipso* carbon atoms C(11), C(21), C(31) and C(41) of –1.169(5), 1.647(5), 0.217(6) and –2.080(5) Å, respectively, from the coordination plane defined as above, is nearly identical to **1**. The same is true for the tetrahedral distortion of the coordination plane, as shown by the deviations from this plane: Ir(1) 0.032(2) Å, P(1) 0.272(2) Å, P(2) –0.289(2) Å, $C_{g1}$ 0.297(3) Å, $C_{g2}$ –0.311(3) Å and the resulting dihedral angle defined as above of 23.0(1)°. Also, the steric pressure of **14** is comparable to **1** (see above): C(22)···H(46B) 2.982 Å, H(3A)···H(42A) 2.908 Å, H(4A)···H(36A) 2.417 Å, H(7A)···H(22A) 2.729 Å, H(8A)···H(12A) 2.602 Å. However, the mean value of the significantly shorter Ir–C distances (see Table 1) of 2.196(4) Å in **14** is significantly shorter than the corresponding parameter of 2.231(2) Å in **1**. Analogously, the mean value of the significantly longer Ir–C distances of 2.234(4) Å is significantly shorter than the corresponding parameter of 2.270(2) Å in **1**.

Olefins such as cod are generally considered to be rather weakly binding ligands.[11] However, the possibility of a preorganization of the metal binding site leads to the formation of especially stable complexes and the olefin is not dis-

 © 2007 Wiley-VCH Verlag GmbH & Co. KGaA, Weinheim 

placed in the catalytically active species.[11] It was shown above in the cases of **1** and **14** that a reorganization of dppcb, which results in the coordination of cod, produces a suitable quadrant effect and a tetrahedrally distorted coordination sphere that are responsible for the tighter binding of cod. As a consequence, the C=C bond lengths of cod are elongated in these complexes, which is normal for diene complexes of this type.[16] The mean values of the cod double bond lengths are 1.365(4) Å in **1** and 1.378(7) Å in **14**. Thus, the bond lengthening in the iridium complex is slightly more pronounced, which is in agreement with its higher degree of metal-to-ligand bonding and back-bonding.[16] This is in line with the significantly longer mean value of the M–centroid distances of 2.145(2) Å in **1** relative to the corresponding parameter of 2.105(4) Å in **14**. Though the M–cod *trans* influence is smaller than the M–C *trans* influence of organic groups,[25] the significantly longer M–centroid mean value in **1** produces a significantly shorter mean value of the M–P bond lengths of 2.2734(5) Å in **1** versus 2.2795(9) Å in **14**. The use of weakly bonded olefins as leaving groups is wide-spread for rhodium catalysts.[26] The M–C distances in **1** and **14** are located within the typical range of 2.1–2.3 Å.[15,17,18,27] However, the significantly longer mean value of the M–centroid distances in **1** than in **14** nicely corresponds to the fact that cod is easily displaced in the case of **1**, whereas difficulties appear using **14** as a precursor complex as a result of the five-coordinate species that still contains cod.

### X-ray Structures of $[Rh_2(PMePh_2)_4(dppcb)](SbF_6)_2$ (3), $[Rh(PMePh_2)_4](SbF_6)$ (4) and $[Rh_2\{P(OPh)_3\}_4(dppcb)](SbF_6)_2$ (6)

To confirm the observation that steric pressure changes the quadrant effect in homodimetallic species of dppcb such as **1** and **14**, a series of X-ray structures showing increasing steric pressure were analyzed. Figure 5 clearly shows that in **3** the phenyl rings at P(1) are diagonally disposed with respect to the coordination plane, whereas the phenyl groups attached to P(2) show axial and equatorial spatial distributions. This means that the quadrant effect in **3** is similar to **1** and **14** (compare with Figure 4). In all cases, this influence on the quadrant effect by conformational restraints can be referred to as mechanical coupling in analogy to the concept of molecular mechanics strain energy.[28] As in the field of molecular mechanics, mechanical coupling refers to the energy terms associated with bond stretches, bond angle bends, torsional deformations, van der Waals and electrostatic interactions.[28]

Obviously, the steric pressure imposed by cod in **1** and **14** is comparable to two $PMePh_2$ moieties in **3**. Thus, the deviations of the four *ipso* carbon atoms C(11), C(21), C(31) and C(41) from the coordination plane defined by the atoms Rh(1), P(1), P(2), P(3) and P(4) are –1.175(6), 1.534(5), 0.237(5) and –2.022(6) Å, respectively (see Figure 5). These deviations are almost identical to the corresponding parameters of **1** and **14** (see above), where the largest deviations for C(21) of 1.534(5) Å and for C(41) of –2.022(6) Å again indicate that the diagonal quadrants are more hindered. Also, in **3** the coordination plane is tetrahedrally distorted, as shown by the deviations from this plane: Rh(1) 0.008(1) Å, P(1) 0.303(1) Å, P(2) –0.305(1) Å, P(3) 0.261(1) Å, P(4) –0.267(1) Å.

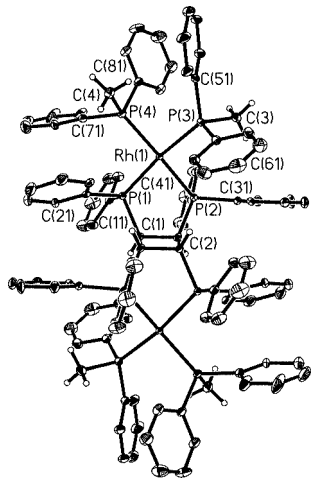


Figure 5. View of the cation of $[Rh_2(PMePh_2)_4(dppcb)](SbF_6)_2$ (**3**). The atom labelling scheme is shown. Hydrogen atoms attached to the phenyl rings are omitted for clarity.

Although alternative ligand conformations are undoubtedly accessible in solution, the solid-state structures presented in this work exhibit trends which are consistent with steric effects exerting an important influence on reactivity.[19] In the case of **3**, the occurrence of steric pressure leads to isolable side product **4**. The evidence of steric crowding in **3**, which is comparable to **1** and **14**, again stems from short intramolecular contact approaches. Thus, the shortest intramolecular contact between the phenyl rings along a *trans* axis of the cyclobutane ring is C(33)···H(22B) of 3.080 Å. The shortest intramolecular contact between the dppcb and $PMePh_2$ moieties is H(46A)···H(86A) of 2.449 Å and the shortest intramolecular contact between the $PMePh_2$ moieties is H(4B)···C(56) of 2.554 Å. As in the cases of **1** and **14**, the steric pressure in **3** is partly released by a dihedral angle of 20.7(1)° between the P(1)–Rh(1)–P(2) and P(3)–Rh(1)–P(4) planes.

The formation of homoleptic complexes such as **4** is typical for the reaction type leading to **3**.[13] In general, the amount of tetrahedral distortion in cations $[(phosphane)_4Rh]^+$ can be rationalized as a compromise between the preferred square planar arrangement of a $d^8$ transition-metal centre and the steric repulsion of the four $PR_2$ groups.[13] In Figure 6 this tetrahedral distortion can be clearly seen for **4**.

The crystal structure of **4** consists of two slightly different conformations and shows dihedral angles defined as above between *cis* P–Rh–P planes of 34.5(1)° and 31.2(1)°, respectively. The Rh–P bond lengths in the two conformations of **4** are significantly shorter than the Rh–$PMePh_2$ distances in **3** (see Table 2). This is in line with a better release of steric pressure in **4** than in **3**, where also the elec-

 © 2007 Wiley-VCH Verlag GmbH & Co. KGaA, Weinheim 

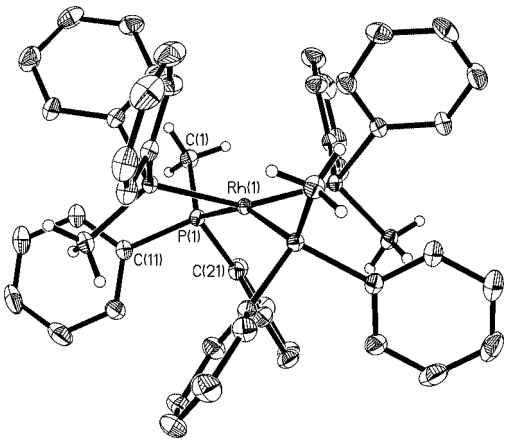


Figure 6. View of the cation of one conformation of $[Rh(PMePh_2)_4](SbF_6)$ (**4**). The atom labelling scheme is shown. Hydrogen atoms attached to the phenyl rings are omitted for clarity.

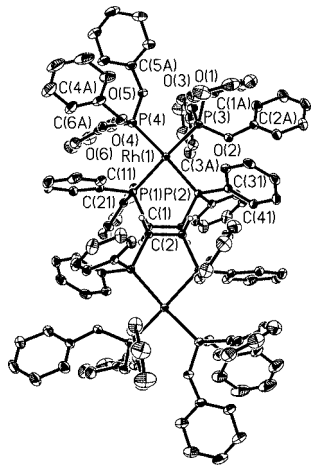


Figure 7. View of the cation of $[Rh_2\{P(OPh)_3\}_4(dppcb)](SbF_6)_2$ (**6**). The atom labelling scheme is shown. Hydrogen atoms attached to the phenyl rings are omitted for clarity.

tronic bite angle effect of dppcb could play a part.[4] The Rh–P bond lengths of **4** are in between the average of the equatorial Rh–P bond lengths of 2.308 Å and the corresponding axial parameter of 2.337(2) Å in the distorted trigonal bipyramidal $[RhH(PMePh_2)_4]$.[29] Distortions of the square planar structure like in **4** for example, also in the case of chlorotris(triphenylphosphane)rhodium(I), are well-known.[18]

It was recognized that the quadrant effect in **1**, **3** and **14** is nearly identical and shows axial and equatorial phenyl rings attached to one phosphorus atom and diagonally disposed phenyl groups attached to the other. However, further enhancement in the steric pressure as a result of the introduction of $P(OPh)_3$ leads to a change in the quadrant effect in **6**. Thus, in **6** the deviations of the four *ipso* carbon atoms C(11), C(21), C(31) and C(41) from the coordination plane defined by the atoms Rh(1), P(1), P(2), P(3) and P(4) are 0.620(5), –1.945(5), 1.480(5) and –1.394(6) Å, respectively (see Figure 7). This means that in contrast to **1**, **3** and **14**, no typical equatorial phenyl ring is present in **6** and, rather, the spatial distributions of the phenyl substituents resemble pseudoequatorial, pseudoaxial and diagonal dispositions, respectively.[22] However, the largest deviations for C(21) of –1.945(5) Å and for C(31) of 1.480(5) Å are still in line with more hindered diagonal quadrants as in the cases **1**, **3** and **14** (see Figures 3 and 7). In **6**, the coordination plane is again tetrahedrally distorted, where the deviations from this plane are: Rh(1) 0.028(1) Å, P(1) –0.180(1) Å, P(2) 0.163(1) Å, P(3) –0.171(1) Å, P(4) 0.160(1) Å.

For comparable (diphosphane)rhodium compounds it was found that structures determined by X-ray methods in the solid state and structures characterizing the ensembles of molecules in solution are congruent within the limits of error.[30] This means that a change in the quadrant effect observed in the solid state is important for active catalysts derived from precatalysts such as **1**. Also, in **6** short intramolecular contact approaches are responsible for the observed conformation leading to a change in the quadrant effect compared with **1**, **3** and **14**. The shortest intramolecular contact between the phenyl rings along a *trans* axis of the cyclobutane ring is C(34)···H(26B) of 2.910 Å. The shortest intramolecular contact between the dppcb and $P(OPh)_3$ moieties is H(16A)···H(6BA) of 2.591 Å and the shortest intramolecular contact between the $P(OPh)_3$ moieties is H(1BA)···H(4BA) of 2.604 Å. However, the dihedral angle of 12.4(1)° between the P(1)–Rh(1)–P(2) and P(3)–Rh(1)–P(4) planes in **6** is significantly smaller than the corresponding parameters in **1**, **3** and **14**. This means that the steric pressure in **6** is better released by a change in the quadrant effect of dppcb than by a strong tetrahedral distortion of the coordination plane.

### X-ray Structures of $[Rh_2(dppam)_2(dppcb)](SbF_6)_2$ (8), $[Rh_2(dppe)_2(dppcb)](SbF_6)_2$ (9) and $[Rh_2(cis\text{-}dppen)_2(dppcb)](SbF_6)_2$ (10)

To the best of our knowledge, the X-ray structures of **8**–**10** are the first X-ray structural characterizations of rhodi-

Table 2. Selected bond lengths [Å] and angles [°] for **3**, **4** and **6**.

| Compound **3** | | Compound **6** | | Compound **4** | |
|---|---|---|---|---|---|
| Rh(1)–P(1) | 2.2838(14) | Rh(1)–P(1) | 2.3259(10) | Rh(1)–P(1) | 2.3278(7) |
| Rh(1)–P(2) | 2.3021(14) | Rh(1)–P(2) | 2.3349(9) | Rh(2)–P(2) | 2.3325(7) |
| Rh(1)–P(3) | 2.3576(14) | Rh(1)–P(3) | 2.2674(11) | P(1)–Rh(1)–P(1A) | 92.631(7) |
| Rh(1)–P(4) | 2.3454(13) | Rh(1)–P(4) | 2.2550(10) | P(2)–Rh(2)–P(2A) | 92.145(6) |
| P(1)–Rh(1)–P(2) | 81.18(5) | P(1)–Rh(1)–P(2) | 83.83(3) | | |
| P(3)–Rh(1)–P(4) | 92.67(5) | P(3)–Rh(1)–P(4) | 91.30(4) | | |

 © 2007 Wiley-VCH Verlag GmbH & Co. KGaA, Weinheim 

um(I) complexes with two different chelating phosphanes. Of course, the difficulty in preparing and crystallizing these compounds stems from a further enhancement of steric pressure. As a consequence, dppcb could show the ability to form different coordination sites within homodimetallic species. This may have implications for their potential use as dimetallic catalysts, comparable to the ability of dimetallic systems with $M_2P_4$ units containing bis[{(diphenylphosphanyl)ethyl}phenylphosphanyl]methane to move between open and closed bridged forms.[25] Indeed, Figures 8, 9 and 10 clearly show that the stronger steric pressure in **9** and **10**, which contain 5–5–4–5–5-membered ring systems compared with **8** that contains a 4–5–4–5–4-membered ring system, produces two different coordination sites in **9** and **10**, respectively. As all X-ray structures presented in this study show no strong intermolecular contacts or no obvious packing effect, we may assume as a first approximation that the forces on the molecule in solution are of the same order of magnitude as those in the solid.[31] Though the crystallographic restraints are strong for structures **1**, **3**, **6**, **8** and **14** because of the presence of centres of symmetry in the middle of the cyclobutane rings, this means that centrosymmetric conformations are also available in solution for these structures. By contrast, it seems likely that **9** and **10** crystallizing in different space groups not only show noncentrosymmetric structures in the solid state, but also in solution.

Interestingly, the quadrant effect of dppcb in **8** is similar to **1**, **3** and **14**. Thus, the phenyl groups attached to one phosphorus atom show axial and equatorial spatial distributions, whereas a diagonal disposition occurs for the phenyl substituents of the other phosphorus atom (see Figure 8).

This is clearly reflected in the deviations of the four *ipso* carbon atoms C(11), C(21), C(31) and C(41) of –0.164(5), 1.912(5), 1.368(5) and –1.253(5) Å, respectively, from the coordination plane defined by the atoms Rh(1), P(1), P(2), P(3) and P(4). However, the largest deviations for C(21) of 1.912(5) Å and for C(31) of 1.368(5) Å concentrate the steric crowding now on one side of the coordination plane (see Figures 3 and 8). The atoms defining this least-squares plane are again tetrahedrally distorted, as shown by the deviations from this plane: Rh(1) 0.025(1) Å, P(1) 0.185(1) Å, P(2) –0.196(1) Å, P(3) 0.213(1) Å, P(4) –0.226(1) Å and the resulting dihedral angle defined as above of 16.9(1)°. Also, in this case short intramolecular contacts indicate steric crowding. The shortest contacts are 3.199 Å for H(22A)···

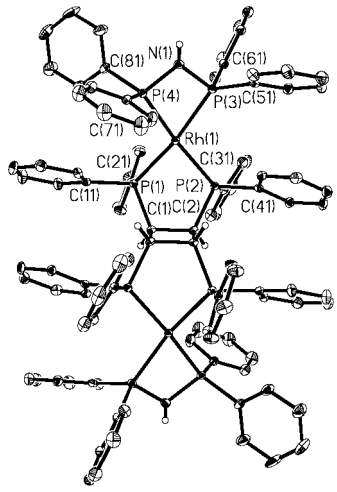


Figure 8. View of the cation of $[Rh_2(dppam)_2(dppcb)](SbF_6)_2$ (**8**). The atom labelling scheme is shown. Hydrogen atoms attached to the phenyl rings are omitted for clarity.

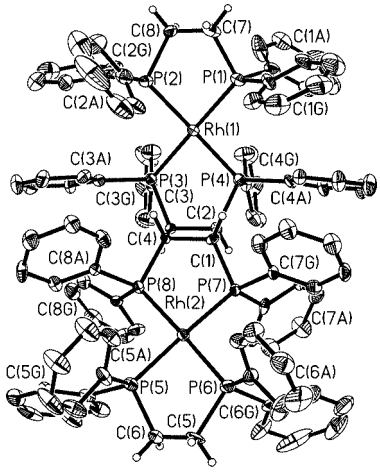


Figure 9. View of the cation of $[Rh_2(dppe)_2(dppcb)](SbF_6)_2$ (**9**). The atom labelling scheme is shown. Hydrogen atoms attached to the phenyl rings are omitted for clarity.

Table 3. Selected bond lengths [Å] and angles [°] for **8**, **9** and **10**.

| Compound **8** | | Compound **9** | | Compound **10** | |
|---|---|---|---|---|---|
| Rh(1)–P(1) | 2.2860(10) | Rh(1)–P(1) | 2.314(4) | Rh(1)–P(1) | 2.305(3) |
| Rh(1)–P(2) | 2.2909(10) | Rh(1)–P(2) | 2.289(4) | Rh(1)–P(2) | 2.302(3) |
| Rh(1)–P(3) | 2.3124(10) | Rh(1)–P(3) | 2.303(4) | Rh(1)–P(5) | 2.287(3) |
| Rh(1)–P(4) | 2.2937(10) | Rh(1)–P(4) | 2.317(4) | Rh(1)–P(6) | 2.293(3) |
| N(1)–H(3) | 0.74(4) | Rh(2)–P(5) | 2.323(4) | Rh(2)–P(3) | 2.294(3) |
| P(1)–Rh(1)–P(2) | 82.42(4) | Rh(2)–P(6) | 2.314(4) | Rh(2)–P(4) | 2.282(3) |
| P(3)–Rh(1)–P(4) | 69.90(4) | Rh(2)–P(7) | 2.289(4) | Rh(2)–P(7) | 2.303(3) |
| | | Rh(2)–P(8) | 2.287(4) | Rh(2)–P(8) | 2.310(3) |
| | | P(1)–Rh(1)–P(2) | 83.64(16) | P(1)–Rh(1)–P(2) | 80.97(10) |
| | | P(3)–Rh(1)–P(4) | 81.12(13) | P(5)–Rh(1)–P(6) | 83.70(13) |
| | | P(5)–Rh(2)–P(6) | 82.56(15) | P(3)–Rh(2)–P(4) | 86.35(10) |
| | | P(7)–Rh(2)–P(8) | 86.63(13) | P(7)–Rh(2)–P(8) | 83.48(11) |

 © 2007 Wiley-VCH Verlag GmbH & Co. KGaA, Weinheim 

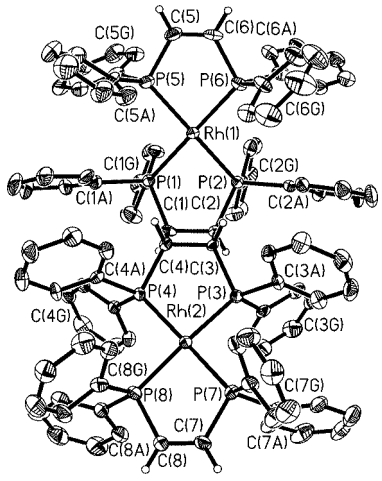


Figure 10. View of the cation of $[Rh_2(cis\text{-dppen})_2(dppcb)](SbF_6)_2$ (**10**). The atom labelling scheme is shown. Hydrogen atoms attached to the phenyl rings are omitted for clarity.

H(46B) along a *trans* axis of the cyclobutane ring and 2.540 Å for H(36A)···H(62A) between the dppcb and dppam moieties. However, the small four-membered chelate ring angle P(3)–Rh(1)–P(4) of only 69.90(4)° (see Table 3) moves the phenyl groups of dppam away from the rhodium centre, which reduces the overall steric pressure of **8**. In contrast to **9** and **10**, this could still allow a centrosymmetric conformation for **8**. Compound **8** shows only very weak hydrogen bonds between the located N–H hydrogen atoms of dppam and the $SbF_6^-$ counterions. This is nicely confirmed by the shorter N–H bond length of 0.74(4) Å (see Table 3) than in comparable complexes of dppam with strong hydrogen bonds (0.78–0.79 Å).[32] Furthermore, it is also in agreement with the values of **8** for $\nu$(N–H) and $\delta$(N–H) of 3330 and 1266 $cm^{-1}$, respectively.[33] It is well-known that π–π stacking of phenyl rings might play a role in tuning organometallic reactivity.[19] Though no crystallographic restraints influence the X-ray structures of **9** and **10**, these alignments of the phenyl groups can be seen in several cases in Figures 9 and 10.

Obviously, the steric pressure is so enormous in **9** and **10** that it is necessary to minimize steric tensions through this effect. This has dramatic consequences on the conformations of **9** and **10**. The envelope-foldings, defined as the angles between the least-squares planes through the chelating phosphorus and backbone carbon atoms of dppcb and through the chelating phosphorus atoms of dppcb and the rhodium atoms, are usually orientated towards the cyclobutane rings: 20.6(1)°, **1**; 30.7(1)°, **3**; 16.5(1)°, **6**; 31.8(1)°, **8**; 20.4(1)°, **14**. The same effect is present in **9** and **10** with regard to the Rh(1) atom: 38.1(2)°, **9**; 36.8(2)°, **10**. However, the analogous envelope-foldings for the Rh(2) centres in **9** and **10** are orientated away from the cyclobutane rings: 10.0(2)°, **9**; 11.8(2)°, **10**. This inverse envelope-folding is rare for homodimetallic species of dppcb and indicative of strong steric pressure.[7]

Indeed, the quadrant effects of dppcb become completely different for the two unequal coordination units of **9** and **10**, respectively (see Figures 9 and 10). In the cases of **9** and **10**, the phenyl rings attached to the phosphorus atoms of dppcb coordinating to the Rh(1) atoms show pseudoaxial and pseudoequatorial spatial distributions, as indicated by the deviations of the four *ipso* carbon atoms from the coordination planes defined as above: **9**, C(3A) –0.541(5) Å, C(3G) 1.653(5) Å, C(4A) –0.514(5) Å, C(4G) 1.670(5) Å; **10**, C(1A) –0.755(4) Å, C(1G) 1.619(4) Å, C(2A) –0.359(5) Å, C(2G) 1.786(5) Å. In both cases the steric crowding is concentrated on one side of the coordination plane as a result of the largest deviations for C(3G) of 1.653(5) Å and for C(4G) of 1.670(5) Å in the case of **9** and for C(1G) of 1.619(4) Å and for C(2G) of 1.786(5) Å in the case of **10** (see Figures 3, 9 and 10). In contrast, the phenyl substituents attached to the phosphorus atoms of dppcb coordinating to the Rh(2) centres unequivocally show diagonal dispositions, where the corresponding parameters are: **9**, C(7A) 1.599(5) Å, C(7G) –1.270(5) Å, C(8A) –1.373(5) Å, C(8G) 1.511(5) Å; **10**, C(3A) –1.116(5) Å, C(3G) 1.667(5) Å, C(4A) –1.446(4) Å, C(4G) 1.402(4) Å. The largest deviations corresponding to the Rh(2) centre in **9** for C(7A) of 1.599(5) Å and for C(8G) of 1.511(5) Å again concentrate the steric crowding on one side of the coordination plane (see Figures 3 and 9).

Interestingly, the analogous largest deviations in **10** for C(3G) of 1.667(5) Å and for C(4A) of –1.446(4) Å are in line with more hindered diagonal quadrants (see Figures 3 and 10). However, in **9** and **10** all deviations from the least-squares coordination planes are below 0.08 Å, as also indicated by the resulting small dihedral angles defined as above: **9**, at Rh(1) 3.3(2)°, at Rh(2) 1.8(2)°; **10**, at Rh(1) 7.4(2)°, at Rh(2) 5.0(2)°. Again, short intramolecular contacts are responsible for the observed unusual conformations. The shortest intramolecular contacts along a *trans* axis of the cyclobutane rings are 2.778 Å for C(4A)···H(7FA) in **9** and 2.916 Å for C(2A)···H(3HA) in **10**. Furthermore, the shortest intramolecular contacts are 2.310 Å for H(2HA)···H(3LA) between the dppcb and dppe moieties and 2.635 Å for H(6HA)···H(2FA) between the dppcb and *cis*-dppen moieties.

Obviously, the significantly larger five-membered chelate ring angles of dppe and *cis*-dppen in **9** and **10** relative to dppam in **8** (see Table 3) move the phenyl groups of dppe and *cis*-dppen towards the rhodium centres. This leads to overall steric pressures in **9** and **10**, which cannot be released within centrosymmetric conformations. Interestingly, though no crystallographic restraints are present, the cyclobutane rings of **9** and **10** are completely planar within statistical significance, which further confirms the similarity of the solid state to the solution structures, as discussed above. Both **9** and **10** show significantly different chelate angles of dppcb for the two unequal coordination units: **9**, 81.12(13)° and 86.63(13)°; **10**, 80.97(10)° and 86.35(10)° (see Table 3). This means that under steric pressure the chelate angles may also change, which is, beside the quadrant effect, another important feature for catalytic cycles.[19]

 © 2007 Wiley-VCH Verlag GmbH & Co. KGaA, Weinheim 

### Investigation of 1–3 and 5–16 in the Solution State

All compounds **1**–**3** and **5**–**16** show sharp doublets in the rhodium cases that are due to $^1J_{Rh,P}$ couplings and sharp single peaks in the iridium cases for the dppcb resonances in the $^{31}P\{^1H\}$ NMR spectra at ambient temperature. This indicates equivalent phosphorus atoms of dppcb for all complexes. Cooling the sample down to 178 K only leads to broadened signals. This behaviour is typical for dppcb conformations with planar cyclobutane rings,[34] in contrast to folded cyclobutane ring conformations.[6] Because planar cyclobutane rings were also observed in the X-ray structures of **1**, **3**, **6**, **8**, **9**, **10** and **14** independent of crystallographic constraints, this nicely confirms the fact that the solid-state and solution structures are identical. The structure types shown in Figures 1 and 2 are not only determined by these X-ray structures, but also their $^1J_{Rh,P}$ values of dppcb are consistent with the proposed *trans* influence series for $Rh^I$ species.[12a] Typically, nitrogen-containing ligands such as those in **11**–**13** exert a weak *trans* influence, which leads to $^1J_{Rh,P}$ parameters of 162–180 Hz. In **1** cod shows a stronger *trans* influence with $^1J_{Rh,P}$ of 154 Hz, which is characteristic of cod.[12b] In this series, the two ligand types with the highest *trans* influence, phosphanes and phosphites,[12a] produce $^1J_{Rh,P}$ values for dppcb of 129–137 Hz. A similar range of 121–135 Hz was observed for the corresponding $^1J_{Rh,P}$ parameters of the mono- and diphosphanes in **2**, **3** and **7**–**10**. The phosphites in **5** and **6** show larger $^1J_{Rh,P}$ values of 199 Hz and 234 Hz, respectively, which is also in agreement with earlier results.[12a] The range of $^2J_{P,P_{trans}}$ parameters of 234–267 Hz is typical for phosphanes, where also in this case the $^2J_{P,P_{trans}}$ values for phosphites of 364 Hz in **5** and 380 Hz in **6** are larger.[12a]

In **9** and **10**, the two different coordination units interchange with one another, with the asymmetric isomer being the more stable one. This leads to a coalescence of the $^{31}P\{^1H\}$ NMR signals for dppcb as well as for those of dppe and *cis*-dppen, which cannot be resolved at low temperatures. This effect is comparable to the conformational isomerisation of [(κ-$PMes_2CH_2CH(OH)CH_2$-κ-$PPh_2$]-Rh(η⁴-cod)]⁺, where $\delta$ and $\lambda$ isomers interchange with one another, with the $\lambda$ isomer being the more stable one.[30] In this complex, the mesityl groups at the $PMes_2$ entity behave as coupled rotors, their rotation is only possible in the transformation between the $\delta$ and $\lambda$ forms.[30] In an analogous manner, the phenyl groups at the $PPh_2$ entities in **9** and **10** behave as coupled rotors, their rotation is only possible in the transformation between pseudoaxial and pseudoequatorial spatial distributions and diagonal dispositions of the phenyl rings of dppcb (see Figures 9 and 10). This is clearly confirmed by the observed π–π stacking interactions in **9** and **10** and could be regarded as a "mechanical molecular machine".[30] These conformational properties will control the stereochemical result of reactions mediated by chelate compounds of dppcb.[35]

## Summary

The series of X-ray structures presented in this work indicates that steric pressure changes the quadrant effect. It clearly proves that the rigid cyclobutane backbone of dppcb does not play any role in determining the quadrant effect, if homodimetallic $Rh^I$ complexes of dppcb are under steric pressure. Depending on the kind and magnitude of steric pressure, both borderline cases typical for the M(dppe) and $M_2$(dppcb) quadrant effects in Figure 3 are observed. In consequence of which, dppcb and dppe show no differentiation between their distributions of equatorial–equatorial and equatorial–axial geometric isomers for the five-coordinate intermediates in the case of catalytic hydroformylation.[36] However, the regioselectivity of hydroformylation is governed by a complex web of electronic and steric effects that have so far defied unravelling.[19] Nevertheless, excellent progress was made in realizing when and how regioselectivity and enantioselectivity are controlled within a catalytic hydroformylation cycle.[37] Our work shows that it is not enough to study the quadrant effects of precatalysts such as **1**,[38] but it is also necessary to realize how the steric pressure varies during the catalytic cycle. Predictions solely based on X-ray structures of precatalysts such as **1** could be misleading. The occurrence of two different coordination units in **9** and **10** also seems to be of some importance for rhodium-catalysed tandem reactions.[39]

## Experimental Section

**Reagents and General Procedures:** The ligand dppcb was prepared as described earlier.[6] $[RhCl(\eta^4\text{-cod})]_2$, $[IrCl(\eta^4\text{-cod})]_2$, AgX ($X^-$ = $BF_4^-$, $PF_6^-$, $SbF_6^-$) and dry solvents of purissimum grade quality were obtained from Fluka. Mono- and diphosphanes, phosphites and nitrogen-containing ligands were purchased from Strem. A Schlenk apparatus and oxygen-free, dry Ar were used in the syntheses of all complexes. Solvents were degassed by several freeze–pump–thaw cycles prior to use. All reactions were carried out at ambient temperature.

**Instrumentation:** Fourier-mode $^1H$, $^{13}C\{^1H\}$ and $^{31}P\{^1H\}$ NMR spectra were obtained with a Bruker DPX-300 spectrometer (internal deuterium lock) at 298 K. Positive chemical shifts are downfield from the standards: TMS for the $^1H$ and $^{13}C\{^1H\}$ resonances and 85% $H_3PO_4$ for the $^{31}P\{^1H\}$ resonances. Owing to the restricted solubility of compounds **1**–**16**, the $^{13}C\{^1H\}$ NMR spectra in $CD_2Cl_2$ are rather insensitive to structural variations, where only the $^{13}C\{^1H\}$ NMR resonances of the phenyl rings are clearly resolved in the range 128–136 ppm as multiplets.

**$[Rh_2(\eta^4\text{-cod})_2(dppcb)]X_2$ (1), $X^- = BF_4^-$, $PF_6^-$, $SbF_6^-$:** $[RhCl(\eta^4\text{-cod})]_2$ (40 mg, 0.081 mmol) was dissolved in acetone (5 mL) and $AgBF_4$ (32 mg, 0.162 mmol) also dissolved in acetone (1 mL) was added with vigorous stirring. The reaction mixture was stirred for 3 h, and the formed AgCl was filtered off. To this solution, dppcb (64 mg, 0.081 mmol) was added with vigorous stirring. The dark orange solution was stirred for 15 min, and the solvent was then completely removed. The orange residue was washed with diethyl ether (5 mL) and dried in vacuo. Red crystals were recrystallized from $CH_2Cl_2$. Yield: 0.125 g (91%). M.p. 255 °C (dec.). $^1H$ NMR (300 MHz, $CD_2Cl_2$, 25 °C): $\delta$ = 6.5–8.0 (m, 40 H, Ph), 4.92 [s, 8 H,

 © 2007 Wiley-VCH Verlag GmbH & Co. KGaA, Weinheim 

C*H* (cod)], 4.30 [br. s, 4 H, C*H* (cyclobutane)], 2.41 [s, 16 H, C$H_2$ (cod)] ppm. $^{31}P\{^1H\}$ NMR (121.495 MHz, $CH_2Cl_2$, 25 °C): $\delta$ = 72.9 (d, $^1J_{Rh,P}$ = 154 Hz) ppm. MS (FAB+): *m*/*z* (*m*/$z_{calcd.}$) = 1302.0 (1301.7) $[M - BF_4]^+$, 607.7 (607.5) $[M - BF_4]^{2+}$. $C_{68}H_{68}B_2F_8P_4Rh_2 \cdot 3.68CH_2Cl_2$ (1701.07): calcd. C 50.61, H 4.47; found C 50.72, H 4.53. Single crystals suitable for X-ray structure analysis with the composition $[Rh_2(\eta^4\text{-cod})_2(dppcb)](BF_4)_2 \cdot 3.68CH_2Cl_2$ were obtained by slow evaporation of a $CH_2Cl_2$ solution of the orange residue under a dry atmosphere of Ar at ambient temperature. $[Rh_2(\eta^4\text{-cod})_2(dppcb)]X_2$, $X^- = PF_6^-$, $SbF_6^-$, were prepared in an analogous manner showing yields of 82 and 90%, respectively.

**$[Rh_2(PMe_2Ph)_4(dppcb)](SbF_6)_2$ (2):** $[Rh_2(\eta^4\text{-cod})_2(dppcb)](SbF_6)_2$ (160 mg, 0.0950 mmol) was dissolved in $CH_2Cl_2$ (8 mL) and $PMe_2Ph$ (53 mg, 0.380 mmol) was added by syringe with vigorous stirring. The reaction mixture was stirred for 1 h. In the meantime, the colour of the solution changed from orange into golden brown. The solvent was completely removed, the yellow residue was washed with diethyl ether (5 mL) and dried in vacuo. A yellow powder was recrystallized from $CH_2Cl_2$. Yield: 0.163 g (85%). M.p. 198 °C (dec.). $^1H$ NMR (300 MHz, $CD_2Cl_2$, 25 °C): $\delta$ = 6.4–8.1 (m, 60 H, Ph), 4.31 [br. s, 4 H, C*H* (cyclobutane)], 1.08 (br. m, 24 H, C$H_3$) ppm. $^{31}P\{^1H\}$ NMR (121.495 MHz, $CH_2Cl_2$, 25 °C): $\delta$ = 76.5 (dd, $^1J_{Rh,P}$ = 129 Hz, $^2J_{P,P_{trans}}$ = 234 Hz, dppcb), –6.9 (dd, $^1J_{Rh,P}$ = 129 Hz, $^2J_{P,P_{trans}}$ = 234 Hz, $PMe_2Ph$) ppm. MS (FAB+): *m*/*z* (*m*/$z_{calcd.}$) = 1786.9 (1786.9) $[M - SbF_6]^+$, 775.5 (775.6) $[M - SbF_6]^{2+}$. $C_{84}H_{88}F_{12}P_8Rh_2Sb_2$ (2022.644): calcd. C 49.88, H 4.39; found C 49.97, H 4.46.

**$[Rh_2(PMePh_2)_4(dppcb)](SbF_6)_2$ (3):** Procedure as per that of **2**. Yield: 85%. M.p. 151–154 °C. $^1H$ NMR (300 MHz, $CD_2Cl_2$, 25 °C): $\delta$ = 6.3–8.2 (m, 80 H, Ph), 4.28 [br. s, 4 H, C*H* (cyclobutane)], 1.10 (br. m, 12 H, C$H_3$) ppm. $^{31}P\{^1H\}$ NMR (121.495 MHz, $CH_2Cl_2$, 25 °C): $\delta$ = 75.1 (dd, $^1J_{Rh,P}$ = 137 Hz, $^2J_{P,P_{trans}}$ = 234 Hz, dppcb), 6.6 (dd, $^1J_{Rh,P}$ = 129 Hz, $^2J_{P,P_{trans}}$ = 234 Hz, $PMePh_2$) ppm. MS (FAB+): *m*/*z* (*m*/$z_{calcd.}$) = 2035.1 (2035.1) $[M - SbF_6]^+$, 899.8 (899.7) $[M - SbF_6]^{2+}$. $C_{104}H_{96}F_{12}P_8Rh_2Sb_2 \cdot 2CH_2Cl_2$ (2440.76): calcd. C 52.16, H 4.13; found C 52.29, H 4.25. Single crystals suitable for X-ray structure analysis with the composition $[Rh_2(PMePh_2)_4(dppcb)](SbF_6)_2 \cdot 2CH_2Cl_2$ were obtained by slow evaporation of a $CH_2Cl_2$ solution of **3** under an Ar atmosphere at ambient temperature.

**$[Rh_2\{P(OMe)_3\}_4(dppcb)](SbF_6)_2$ (5):** Procedure as per that of **2**. Yield: 82%. M.p. 215 °C (dec.). $^1H$ NMR (300 MHz, $CD_2Cl_2$, 25 °C): $\delta$ = 6.5–8.0 (m, 40 H, Ph), 4.30 [br. s, 4 H, C*H* (cyclobutane)], 3.20–3.50 (m, 36 H, OC$H_3$) ppm. $^{31}P\{^1H\}$ NMR (121.495 MHz, $CH_2Cl_2$, 25 °C): $\delta$ = 78.2 (dd, $^1J_{Rh,P}$ = 129 Hz, $^2J_{P,P_{trans}}$ = 364 Hz, dppcb), 117.0 [dd, $^1J_{Rh,P}$ = 199 Hz, $^2J_{P,P_{trans}}$ = 364 Hz, $P(OMe)_3$] ppm. MS (FAB+): *m*/*z* (*m*/$z_{calcd.}$) = 1730.8 (1730.7) $[M - SbF_6]^+$, 747.4 (747.5) $[M - SbF_6]^{2+}$. $C_{64}H_{80}F_{12}O_{12}P_8Rh_2Sb_2$ (1966.43): calcd. C 39.09, H 4.10, O 9.76; found C 39.15, H 4.20, O 9.53.

**$[Rh_2\{P(OPh)_3\}_4(dppcb)](SbF_6)_2$ (6):** Procedure as per that of **2**. Yield: 82%. M.p. 95–98 °C. $^1H$ NMR (300 MHz, $CD_2Cl_2$, 25 °C): $\delta$ = 6.1–8.5 (m, 100 H, Ph), 4.33 [br. s, 4 H, C*H* (cyclobutane)] ppm. $^{31}P\{^1H\}$ NMR (121.495 MHz, $CH_2Cl_2$, 25 °C): $\delta$ = 76.1 (dd, $^1J_{Rh,P}$ = 129 Hz, $^2J_{P,P_{trans}}$ = 380 Hz, dppcb), 112.0 [dd, $^1J_{Rh,P}$ = 234 Hz, $^2J_{P,P_{trans}}$ = 380 Hz, $P(OPh)_3$] ppm. MS (FAB+): *m*/*z* (*m*/$z_{calcd.}$) = 2475.2 (2475.4) $[M - SbF_6]^+$. $C_{124}H_{104}F_{12}O_{12}P_8Rh_2Sb_2 \cdot 4.26CH_2Cl_2$ (3072.97): calcd. C 50.13, H 3.69, O 6.25; found C 50.25, H 3.85, O 6.10. Single crystals suitable for X-ray structure analysis with the composition $[Rh_2\{P(OPh)_3\}_4(dppcb)](SbF_6)_2 \cdot 4.26CH_2Cl_2$ were obtained by slow evaporation of a $CH_2Cl_2$ solution of **6** under an Ar atmosphere at ambient temperature.

**$[Rh_2(dppm)_2(dppcb)](SbF_6)_2$ (7):** $[Rh_2(\eta^4\text{-cod})_2(dppcb)](SbF_6)_2$ (100 mg, 0.0593 mmol) was dissolved in $CH_2Cl_2$ (10 mL) and dppm (46 mg, 0.119 mmol) was added in solid form with vigorous stirring. The reaction mixture was stirred for 1 h and a clear orange solution was obtained. The solvent was completely removed, the yellow residue was washed with diethyl ether (5 mL) and dried in vacuo. A yellow powder was recrystallized from $CH_2Cl_2$. Yield: 0.106 g (80%). M.p. 250–253 °C. $^1H$ NMR (300 MHz, $CD_2Cl_2$, 25 °C): $\delta$ = 6.5–8.0 (m, 80 H, Ph), 4.30 [br. s, 4 H, C*H* (cyclobutane)], 2.22 (br. m, 4 H, C$H_2$P) ppm. $^{31}P\{^1H\}$ NMR (121.495 MHz, $CH_2Cl_2$, 25 °C): $\delta$ = 79.7 (dd, $^1J_{Rh,P}$ = 137 Hz, $^2J_{P,P_{trans}}$ = 259 Hz, dppcb), –18.5 (dd, $^1J_{Rh,P}$ = 121 Hz, $^2J_{P,P_{trans}}$ = 259 Hz, dppm) ppm. MS (FAB+): *m*/*z* (*m*/$z_{calcd.}$) = 2238.1 (2237.8) $[M - H]^+$, 2003.4 (2003.1) $[M - SbF_6]^+$. $C_{102}H_{88}F_{12}P_8Rh_2Sb_2$ (2238.84): calcd. C 54.72, H 3.96; found C 54.83, H 4.03.

**$[Rh_2(dppam)_2(dppcb)](SbF_6)_2$ (8):** Procedure as per that of **7**. Yield: 87%. M.p. 275–278 °C. $^1H$ NMR (300 MHz, $CD_2Cl_2$, 25 °C): $\delta$ = 6.0–8.3 (m, 80 H, Ph), 4.29 [br. s, 4 H, C*H* (cyclobutane)] ppm. $^{31}P\{^1H\}$ NMR (121.495 MHz, $CH_2Cl_2$, 25 °C): $\delta$ = 78.5 (dd, $^1J_{Rh,P}$ = 137 Hz, $^2J_{P,P_{trans}}$ = 267 Hz, dppcb), 45.9 (dd, $^1J_{Rh,P}$ = 121 Hz, $^2J_{P,P_{trans}}$ = 267 Hz, dppam) ppm. IR (KBr): $\tilde{\nu}$ = 3330 (m) (N–H), 1266 (m) (N–H) $cm^{-1}$. MS (FAB+): *m*/*z* (*m*/$z_{calcd.}$) = 2240.2 (2239.9) $[M - H]^+$, 2005.1 (2005.1) $[M - SbF_6]^+$. $C_{100}H_{86}F_{12}N_2P_8Rh_2Sb_2$ (2240.81): calcd. C 53.60, H 3.87, N 1.25; found C 53.73, H 3.93, N 1.15. Single crystals suitable for X-ray structure analysis with the composition $[Rh_2(dppam)_2(dppcb)](SbF_6)_2$ were obtained by slow evaporation of a $CH_2Cl_2$ solution of **8** under an Ar atmosphere at 277 K.

**$[Rh_2(dppe)_2(dppcb)](SbF_6)_2$ (9):** Procedure as per that of **7**. Yield: 83%. M.p. 140 °C (dec.). $^1H$ NMR (300 MHz, $CD_2Cl_2$, 25 °C): $\delta$ = 6.5–8.1 (m, 80 H, Ph), 4.31 [br. s, 4 H, C*H* (cyclobutane)], 2.25 (br. m, 8 H, C$H_2$P) ppm. $^{31}P\{^1H\}$ NMR (121.495 MHz, $CH_2Cl_2$, 25 °C): $\delta$ = 81.7 (dd, $^1J_{Rh,P}$ = 137 Hz, $^2J_{P,P_{trans}}$ = 241 Hz, dppcb), 54.3 (dd, $^1J_{Rh,P}$ = 131 Hz, $^2J_{P,P_{trans}}$ = 241 Hz, dppe) ppm. MS (FAB+): *m*/*z* (*m*/$z_{calcd.}$) = 2267.2 (2266.9) $[M]^+$, 2031.5 (2031.2) $[M - SbF_6]^+$. $C_{104}H_{92}F_{12}P_8Rh_2Sb_2 \cdot 3.85CH_2Cl_2$ (2593.845): calcd. C 49.94, H 3.87; found C 49.99, H 3.95. Single crystals suitable for X-ray structure analysis with the composition $[Rh_2(dppe)_2(dppcb)](SbF_6)_2 \cdot 3.85CH_2Cl_2$ were obtained by slow evaporation of a $CH_2Cl_2$ solution of **9** under an Ar atmosphere at ambient temperature.

**$[Rh_2(cis\text{-dppen})_2(dppcb)](SbF_6)_2$ (10):** Procedure as per that of **7**. Yield: 78%. M.p. 205–207 °C. $^1H$ NMR (300 MHz, $CD_2Cl_2$, 25 °C): $\delta$ = 6.5–8.1 (m, 80 H, Ph), 6.30 (br. m, 4 H, PC*H*C*H*P), 4.32 [br. s, 4 H, C*H* (cyclobutane)] ppm. $^{31}P\{^1H\}$ NMR (121.495 MHz, $CH_2Cl_2$, 25 °C): $\delta$ = 76.8 (dd, $^1J_{Rh,P}$ = 129 Hz, $^2J_{P,P_{trans}}$ = 259 Hz, dppcb), 66.2 (dd, $^1J_{Rh,P}$ = 135 Hz, $^2J_{P,P_{trans}}$ = 259 Hz, *cis*-dppen) ppm. MS (FAB+): *m*/*z* (*m*/$z_{calcd.}$) = 2262.0 (2261.8) $[M - H]^+$, 2027.5 (2027.1) $[M - SbF_6]^+$. $C_{104}H_{88}F_{12}P_8Rh_2Sb_2 \cdot 5.16CH_2Cl_2$ (2701.066): calcd. C 48.54, H 3.67; found C 48.64, H 3.73. Single crystals suitable for X-ray structure analysis with the composition $[Rh_2(cis\text{-dppen})_2(dppcb)](SbF_6)_2 \cdot 5.16CH_2Cl_2$ were obtained by slow evaporation of a $CH_2Cl_2$ solution of **10** under an Ar atmosphere at ambient temperature.

**$[Rh_2(pyridine)_4(dppcb)](SbF_6)_2$ (11):** $[Rh_2(\eta^4\text{-cod})_2(dppcb)](SbF_6)_2$ (100 mg, 0.0593 mmol) was dissolved in $CH_2Cl_2$ (7.5 mL) and pyridine (19 mg, 0.237 mmol) was added by syringe with vigorous stirring. The reaction mixture was stirred for 10 min and a clear, yellow solution was obtained. The solvent was then completely removed, and the yellow residue was washed with diethyl ether (5 mL) and

 © 2007 Wiley-VCH Verlag GmbH & Co. KGaA, Weinheim 

dried in vacuo. A yellow powder was recrystallized from $CH_2Cl_2$. Yield: 0.083 g (78%). M.p. 240–243 °C. $^1H$ NMR (300 MHz, $CD_2Cl_2$, 25 °C): $\delta$ = 8.2–9.4 (m, 20 H, pyridine), 6.6–8.1 (m, 40 H, Ph), 4.30 [br. s, 4 H, C*H* (cyclobutane)] ppm. $^{31}P\{^1H\}$ NMR (121.495 MHz, $CH_2Cl_2$, 25 °C): $\delta$ = 91.3 (d, $^1J_{Rh,P}$ = 178 Hz) ppm. MS (FAB+): *m*/*z* (*m*/$z_{calcd.}$) = 656.2 (656.5) [M – H – $SbF_6$]$^{2+}$. $C_{72}H_{64}F_{12}N_4P_4Rh_2Sb_2$ (1786.538): calcd. C 48.41, H 3.61, N 3.14; found C 48.53, H 3.73, N 3.07.

**[$Rh_2$(2,2′-bipyridine)$_2$(dppcb)]($SbF_6$)$_2$ (12):** Procedure as per that of **11** with a reaction time of 2 h. The dark red powder was recrystallized from $CH_2Cl_2$. Yield: 77%. M.p. 270 °C (dec.). $^1H$ NMR (300 MHz, $CD_2Cl_2$, 25 °C): $\delta$ = 8.1–9.3 (m, 16 H, bipyridine), 6.5–8.2 (m, 40 H, Ph), 4.35 [br. s, 4 H, C*H* (cyclobutane)] ppm. $^{31}P\{^1H\}$ NMR (121.495 MHz, $CH_2Cl_2$, 25 °C): $\delta$ = 95.4 (d, $^1J_{Rh,P}$ = 162 Hz) ppm. MS (FAB+): *m*/*z* (*m*/$z_{calcd.}$) = 1547.1 (1546.8) [M – $SbF_6$]$^+$, 1391.0 (1390.6) [M – bipyridine – $SbF_6$]$^+$, 655.2 (655.5) [M – $SbF_6$]$^{2+}$. $C_{72}H_{60}F_{12}N_4P_4Rh_2Sb_2$ (1782.506): calcd. C 48.52, H 3.39, N 3.14; found C 48.61, H 3.47, N 3.05.

**[$Rh_2$(1,10-phenanthroline)$_2$(dppcb)]($SbF_6$)$_2$ (13):** Procedure as per that of **11** with a reaction time of 40 min. The dark red powder was recrystallized from $CH_2Cl_2$.Yield: 81%. M.p. 260 °C (dec.). $^1H$ NMR (300 MHz, $CD_2Cl_2$, 25 °C): $\delta$ = 8.3–9.5 (m, 16 H, phenanthroline), 6.4–8.3 (m, 40 H, Ph), 4.45 [br. s, 4 H, C*H* (cyclobutane)] ppm. $^{31}P\{^1H\}$ NMR (121.495 MHz, $CH_2Cl_2$, 25 °C): $\delta$ = 95.9 (d, $^1J_{Rh,P}$ = 180 Hz) ppm. MS (FAB+): *m*/*z* (*m*/$z_{calcd.}$) = 1594.0 (1593.8) [M – H – $SbF_6$]$^+$, 678.9 (679.0) [M – H – 2$SbF_6$]$^{2+}$. $C_{76}H_{60}F_{12}N_4P_4Rh_2Sb_2$ (1830.55): calcd. C 49.87, H 3.30, N 3.06; found C 49.95, H 3.41, N 3.01.

**[$Ir_2$($\eta^4$-cod)$_2$(dppcb)]$X_2$ (14), $X^-$ = $BF_4^-$, $SbF_6^-$:** [IrCl($\eta^4$-cod)]$_2$ (100 mg, 0.149 mmol) was dissolved in toluene (7 mL) and dppcb (118 mg, 0.149 mmol) was added with vigorous stirring. The reaction mixture was stirred for 6 h, and the formed yellowish precipitate was filtered off. The precipitate was washed with toluene (10 mL) and dried in vacuo. The obtained yellowish powder was suspended in $CH_2Cl_2$/DMF (5:2, 20 mL). To this suspension was slowly added $AgBF_4$ (58 mg, 0.298 mmol) dissolved in $CH_2Cl_2$/DMF (5:2, 5 mL). Immediately an intense red solution formed. This solution was stirred for several minutes, the solvent was completely removed and the residue dried in vacuo. The residue was then suspended in $CH_2Cl_2$ (20 mL) and the suspension was stirred for 45 min. The formed AgCl was filtered off, the solvent of the resulting dark red solution was completely removed and the red–brown residue was dried in vacuo. Red–brown crystals were recrystallized from $CH_2Cl_2$. Yield: 0.210 g (75%). M.p. 225 °C (dec.). $^1H$ NMR (300 MHz, $CD_2Cl_2$, 25 °C): $\delta$ = 6.4–8.1 (m, 40 H, Ph), 4.90 [s, 8 H, C*H* (cod)], 4.25 [br. s, 4 H, C*H* (cyclobutane)], 2.43 [s, 16 H, C$H_2$ (cod)] ppm. $^{31}P\{^1H\}$ NMR (121.495 MHz, $CH_2Cl_2$, 25 °C): $\delta$ = 63.5 (s) ppm. MS (FAB+): *m*/*z* (*m*/$z_{calcd.}$) = 1480.3 (1480.3) [M – $BF_4$]$^+$. $C_{68}H_{68}B_2F_8Ir_2P_4$·3.68$CH_2Cl_2$ (1879.69): calcd. C 45.80, H 4.04; found C 45.95, H 4.10. Single crystals suitable for X-ray structure analysis with the composition [$Ir_2$($\eta^4$-cod)$_2$(dppcb)]($BF_4$)$_2$·3.68$CH_2Cl_2$ were obtained by slow evaporation of a $CH_2Cl_2$ solution of the red–brown residue under a dry Ar atmosphere at ambient temperature. [$Ir_2$($\eta^4$-cod)$_2$(dppcb)]($SbF_6$)$_2$ was prepared in an analogous manner with a yield of 67%.

**[$Ir_2$($\eta^4$-cod)$_2$($PMe_2Ph$)$_2$(dppcb)]($BF_4$)$_2$ (15):** Procedure as per that of **2** with 2 equiv. of the monophosphane. Yield: 67%. M.p. 168–170 °C. $^1H$ NMR (300 MHz, $CD_2Cl_2$, 25 °C): $\delta$ = 6.4–8.1 (m, 50 H, Ph), 4.80 [s, 8 H, C*H* (cod)], 4.26 [br. s, 4 H, C*H* (cyclobutane)], 2.35 [s, 16 H, C$H_2$ (cod)], 0.95 (br. s, 12 H, C$H_3$) ppm. $^{31}P\{^1H\}$ NMR (121.495 MHz, $CH_2Cl_2$, 25 °C): $\delta$ = 36.3 (s, dppcb), –52.4 (s, $PMe_2Ph$) ppm. MS (FAB+): *m*/*z* (*m*/$z_{calcd.}$) = 1843.1 (1843.4) [M]$^+$, 1479.4 (1479.3) [M – H – $BF_4$ – 2$PMe_2Ph$]$^+$. $C_{84}H_{90}B_2F_8Ir_2P_6$ (1843.44): calcd. C 54.73, H 4.92; found C 54.85, H 4.98.

**[$Ir_2$($PMePh_2$)$_4$(dppcb)]($BF_4$)$_2$ (16):** Procedure as per that of **2**. Yield: 68%. M.p. 145–147 °C. $^1H$ NMR (300 MHz, $CD_2Cl_2$, 25 °C): $\delta$ = 6.3–8.2 (m, 80 H, Ph), 4.29 [br. s, 4 H, C*H* (cyclobutane)], 1.05 (br. s, 12 H, C$H_3$) ppm. $^{31}P\{^1H\}$ NMR (121.495 MHz, $CH_2Cl_2$, 25 °C): $\delta$ = 63.0 (d, $^2J_{P,P_{trans}}$ = 255 Hz, dppcb), –3.1 (d, $^2J_{P,P_{trans}}$ = 255 Hz, $PMePh_2$) ppm. MS (FAB+): *m*/*z* (*m*/$z_{calcd.}$) = 2065.6 (2065.9) [M + H – $BF_4$]$^+$, 1865.4 (1865.7) [M + H – $BF_4$ – $PMePh_2$]$^+$. $C_{104}H_{96}B_2F_8Ir_2P_8$ (2151.74): calcd. C 58.05, H 4.50; found C 58.19, H 4.61.

**X-ray Crystallography:** Details of the crystals and data collections are summarized in Tables 4 and 5. In the cases of **4** and **8**, the data collections were performed with a Nonius Kappa CCD diffractometer with the use of combined $\phi$–$\omega$ scans. Cell refinement, data reduction and the empirical absorption correction were done by Denzo and Scalepack programs.[40] In the cases of **1**, **3**, **6**, **9**, **10** and **14**, all data were collected with a Siemens P4 diffractometer by using $\omega$ scans. Cell refinement and data reduction were done by the software of the Siemens P4 diffractometer,[41] and the empirical

Table 4. Crystallographic data for **1**, **14**, **3** and **4**.

| Compound | **1** | **14** | **3** | **4** |
|---|---|---|---|---|
| Empirical formula | $C_{68}H_{68}B_2F_8P_4Rh_2$·3.68$CH_2Cl_2$ | $C_{68}H_{68}B_2F_8Ir_2P_4$·3.68$CH_2Cl_2$ | $C_{104}H_{96}F_{12}P_8Rh_2Sb_2$·2$CH_2Cl_2$ | $C_{52}H_{52}F_6P_4RhSb$ |
| Formula mass | 1701.07 | 1879.69 | 2436.73 | 1139.49 |
| Crystal system | triclinic | triclinic | triclinic | tetragonal |
| Space group | $P\bar{1}$ | $P\bar{1}$ | $P\bar{1}$ | $I4_1/a$ |
| *a* [Å] | 13.068(2) | 13.054(4) | 12.590(4) | 16.0493(4) |
| *b* [Å] | 13.442(2) | 13.422(3) | 14.504(3) | |
| *c* [Å] | 13.686(2) | 13.713(4) | 16.947(2) | 38.0415(6) |
| $\alpha$ [°] | 108.23(1) | 108.13(1) | 69.94(1) | |
| $\beta$ [°] | 96.30(1) | 96.66(1) | 71.86(1) | |
| $\gamma$ [°] | 118.95(1) | 118.80(1) | 68.72(1) | |
| *V* [Å]$^3$ | 1896.9(6) | 1896.2(10) | 2646.2(11) | 9798.7(4) |
| *Z* | 1 | 1 | 1 | 8 |
| *T* [K] | 298(2) | 298(2) | 298(2) | 298(2) |
| Measured reflections | 9056 | 8364 | 10399 | 5621 |
| Independent reflections | 7978 | 7357 | 7566 | 5378 |
| Final $R_1$, $wR_2$ [$I > 3\sigma(I)$ **1**, **14**, **3**; $I > 2\sigma(I)$ **4**] | 0.0392<br>0.1037 | 0.0367<br>0.0931 | 0.0436<br>0.1013 | 0.0344<br>0.0747 |

 © 2007 Wiley-VCH Verlag GmbH & Co. KGaA, Weinheim 

Table 5. Crystallographic data for **6**, **8**, **9** and **10**.

| Compound | **6** | **8** | **9** | **10** |
|---|---|---|---|---|
| Empirical formula | $C_{124}H_{104}F_{12}O_{12}P_8Rh_2Sb_2 \cdot 4.26CH_2Cl_2$ | $C_{100}H_{86}F_{12}N_2P_8Rh_2Sb_2$ | $C_{104}H_{92}F_{12}P_8Rh_2Sb_2 \cdot 3.85CH_2Cl_2$ | $C_{104}H_{88}F_{12}P_8Rh_2Sb_2 \cdot 5.16CH_2Cl_2$ |
| Formula mass | 3063.67 | 2240.81 | 2593.845 | 2691.41 |
| Crystal system | triclinic | triclinic | monoclinic | monoclinic |
| Space group | $P\bar{1}$ | $P\bar{1}$ | $P2_1$ | $P2_1/n$ |
| $a$ [Å] | 13.496(3) | 13.1051(3) | 13.9880(10) | 17.148(3) |
| $b$ [Å] | 16.922(2) | 14.1135(3) | 30.376(4) | 31.557(5) |
| $c$ [Å] | 18.541(2) | 14.9161(3) | 14.342(3) | 22.126(4) |
| $\alpha$ [°] | 64.06(1) | 73.281(1) | | |
| $\beta$ [°] | 85.44(1) | 68.345(1) | 107.80(1) | 92.16(1) |
| $\gamma$ [°] | 69.93(1) | 66.887(1) | | |
| $V$ [Å]$^3$ | 3564.0(11) | 2325.18(9) | 5802.2(15) | 11965(4) |
| $Z$ | 1 | 1 | 2 | 4 |
| $T$ [K] | 298(2) | 218(2) | 298(2) | 298(2) |
| Measured reflections | 16436 | 18256 | 14111 | 21099 |
| Independent reflections | 14420 | 9347 | 12251 | 15536 |
| Final $R_1$, $wR_2$ [$I > 3\sigma(I)$ **6**, **9**, **10**; $I > 2\sigma(I)$ **8**] | 0.0437<br>0.1192 | 0.0316<br>0.0736 | 0.0531<br>0.1269 | 0.0617<br>0.1514 |

absorption corrections were based on $\psi$ scans of nine reflections, respectively ($\chi$ = 78 to 102°, 360° scans in 10° steps in $\psi$).[42] All structure determination calculations were carried out with SHELXTL NT 5.10 including SHELXS-97[43] and SHELXL-97.[44] Final refinements on $F^2$ were carried out with anisotropic thermal parameters for all non-hydrogen atoms in all cases. For **8**, the protons attached to the nitrogen atom of dppam and the cyclobutane ring were located and isotropically refined with fixed $U$. All other hydrogen atoms were included using a riding model with isotropic $U$ values depending on the $U_{eq}$ of the adjacent carbon atoms. The $CH_2Cl_2$ solvent molecules in **1**, **3**, **6**, **9**, **10** and **14** are disordered. Tables 1, 2 and 3 contain selected bond lengths and bond angles of all eight structures.

CCDC-628190 to -628197 contain the supplementary crystallographic data for this paper. These data can be obtained free of charge from The Cambridge Crystallographic Data Centre via www.ccdc.cam.ac.uk/datarequest/cif.

## Acknowledgments

R. G., G. C. and A. D., and S. E., and M. F. thank the University of Innsbruck for post doctoral, PhD and diploma grants, respectively. This research was also financially supported by the Fonds zur Förderung der wissenschaftlichen Forschung, Vienna, Austria and the Tiroler Wissenschaftsfonds, Innsbruck, Austria. P. B. thanks Claudio Bianchini and Werner Oberhauser for helpful discussions.

[1] C. Bianchini, H. M. Lee, A. Meli, W. Oberhauser, F. Vizza, P. Brüggeller, R. Haid, C. Langes, *Chem. Commun.* **2000**, 777–778.
[2] C. Bianchini, G. Mantovani, A. Meli, W. Oberhauser, P. Brüggeller, T. Stampfl, *J. Chem. Soc., Dalton Trans.* **2001**, 690–698.
[3] C. Bianchini, L. Gonsalvi, W. Oberhauser, D. Sémeril, P. Brüggeller, R. Gutmann, *Dalton Trans.* **2003**, 3869–3875.
[4] Z. Freixa, P. W. N. M. van Leeuwen, *Dalton Trans.* **2003**, 1890–1901.
[5] H. A. Mayer, W. C. Kaska, *Chem. Rev.* **1994**, *94*, 1239–1272.
[6] W. Oberhauser, C. Bachmann, T. Stampfl, R. Haid, C. Langes, H. Kopacka, A. Rieder, P. Brüggeller, *Inorg. Chim. Acta* **1999**, *290*, 167–179.
[7] R. Haid, R. Gutmann, T. Stampfl, C. Langes, G. Czermak, H. Kopacka, K.-H. Ongania, P. Brüggeller, *Inorg. Chem.* **2001**, *40*, 7099–7104.
[8] R. Gutmann, G. Czermak, A. Dumfort, W. E. van der Veer, B. Hong, H. Kopacka, K.-H. Ongania, T. Bechtold, P. Brüggeller, *Inorg. Chem. Commun.* **2005**, *8*, 319–322.
[9] I. O. Koshevoy, O. V. Sizova, S. P. Tunik, A. Lough, A. J. Poë, *Eur. J. Inorg. Chem.* **2005**, 4516–4520.
[10] B. Cornils, W. A. Herrmann, R. Schlögl, C.-H. Wong, *Catalysis from A to Z*, Wiley-VCH, Weinheim, **2000**, pp. 279–282.
[11] P. Maire, F. Breher, H. Schönberg, H. Grützmacher, *Organometallics* **2005**, *24*, 3207–3218.
[12] a) J. J. Gambaro, W. H. Hohman, D. W. Meek, *Inorg. Chem.* **1989**, *28*, 4154–4159; b) R. R. Schrock, J. A. Osborn, *J. Am. Chem. Soc.* **1971**, *93*, 2397–2407.
[13] R. Fornika, C. Six, H. Görls, M. Kessler, C. Krüger, W. Leitner, *Can. J. Chem.* **2001**, *79*, 642–648.
[14] I. Schranz, G. R. Lief, S. J. Midstokke, L. Stahl, *Inorg. Chem.* **2002**, *41*, 6919–6927.
[15] J. P. Cahill, A. P. Lightfoot, R. Goddard, J. Rust, P. J. Guiry, *Tetrahedron: Asymmetry* **1998**, *9*, 4307–4312.
[16] F. Läng, F. Breher, D. Stein, H. Grützmacher, *Organometallics* **2005**, *24*, 2997–3007.
[17] C. Laporte, C. Böhler, H. Schönberg, H. Grützmacher, *J. Organomet. Chem.* **2002**, *641*, 227–234.
[18] Z. Duan, M. J. Hampden-Smith, E. N. Duesler, A. L. Rheingold, *Polyhedron* **1994**, *13*, 609–623.
[19] L. Gonsalvi, H. Adams, G. J. Sunley, E. Ditzel, A. Haynes, *J. Am. Chem. Soc.* **2002**, *124*, 13597–13612.
[20] a) W. Oberhauser, T. Stampfl, R. Haid, C. Langes, C. Bachmann, H. Kopacka, K.-H. Ongania, P. Brüggeller, *Polyhedron* **2001**, *20*, 727–740; b) W. Oberhauser, T. Stampfl, C. Bachmann, R. Haid, C. Langes, H. Kopacka, K.-H. Ongania, P. Brüggeller, *Polyhedron* **2000**, *19*, 913–923.
[21] E. de Wolf, A. L. Spek, B. W. M. Kuipers, A. P. Philipse, J. D. Meeldijk, P. H. H. Bomans, P. M. Frederik, B.-J. Deelman, G. van Koten, *Tetrahedron* **2002**, *58*, 3911–3922.
[22] C. Bianchini, P. Brüggeller, C. Claver, G. Czermak, A. Dumfort, A. Meli, W. Oberhauser, E. García Suárez, *Dalton Trans.* **2006**, 2964–2973.
[23] M. J. Burk, J. E. Feaster, W. A. Nugent, R. L. Harlow, *J. Am. Chem. Soc.* **1993**, *115*, 10125–10138.
[24] W. Oberhauser, C. Bachmann, T. Stampfl, R. Haid, C. Langes, A. Rieder, P. Brüggeller, *Polyhedron* **1998**, *17*, 3211–3220.
[25] P. Nair, G. K. Anderson, N. P. Rath, *Organometallics* **2003**, *22*, 1494–1502.

 © 2007 Wiley-VCH Verlag GmbH & Co. KGaA, Weinheim 

[26] H. Schumann, O. Stenzel, S. Dechert, F. Girgsdies, J. Blum, D. Gelman, R. L. Halterman, *Eur. J. Inorg. Chem.* **2002**, 211–219.
[27] J. L. Bookham, D. M. Smithies, M. Thornton-Pett, *J. Chem. Soc., Dalton Trans.* **2000**, 975–980.
[28] D. G. McCollum, G. P. A. Yap, A. L. Rheingold, B. Bosnich, *J. Am. Chem. Soc.* **1996**, *118*, 1365–1379.
[29] D. Zhao, R. Bau, *Inorg. Chim. Acta* **1998**, *269*, 162–166.
[30] A. Frick, V. Schulz, G. Huttner, *Eur. J. Inorg. Chem.* **2002**, 3129–3147.
[31] A. Martín, A. G. Orpen, *J. Am. Chem. Soc.* **1996**, *118*, 1464–1470.
[32] G. Liehr, G. Szucsányi, J. Ellermann, *J. Organomet. Chem.* **1984**, *265*, 95–106.
[33] a) P. Bhattacharyya, R. N. Sheppard, A. M. Z. Slawin, D. J. Williams, J. D. Woollins, *J. Chem. Soc., Dalton Trans.* **1993**, 2393–2400; b) R. Haid, R. Gutmann, G. Czermak, C. Langes, W. Oberhauser, H. Kopacka, K.-H. Ongania, P. Brüggeller, *Inorg. Chem. Commun.* **2003**, *6*, 61–67.
[34] a) T. Stampfl, G. Czermak, R. Gutmann, C. Langes, H. Kopacka, K.-H. Ongania, P. Brüggeller, *Inorg. Chem. Commun.* **2002**, *5*, 490–495; b) T. Stampfl, R. Haid, C. Langes, W. Oberhauser, C. Bachmann, H. Kopacka, K.-H. Ongania, P. Brüggeller, *Inorg. Chem. Commun.* **2000**, *3*, 387–392.
[35] V. Schulz, A. Frick, G. Huttner, *Eur. J. Inorg. Chem.* **2002**, 3111–3128.
[36] C. Bianchini, W. Oberhauser, A. Orlandini, C. Giannelli, P. Frediani, *Organometallics* **2005**, *24*, 3692–3702.
[37] C. P. Casey, S. C. Martins, M. A. Fagan, *J. Am. Chem. Soc.* **2004**, *126*, 5585–5592.
[38] Preliminary catalytic hydroformylation experiments of 1-hexene to yield the corresponding linear and branched aldehydes by using $[Rh_2(\eta^4\text{-cod})_2(dppcb)](PF_6)_2$ (**1**) as a precatalyst exhibited good activity and moderate regioselectivity in *n*-heptanal.
[39] N.-W. Tseng, J. Mancuso, M. Lautens, *J. Am. Chem. Soc.* **2006**, *128*, 5338–5339.
[40] Z. Otwinowski, W. Minor in *Methods in Enzymology Vol. 276: Macromolecular Crystallography, Part A* (C. W. Carter Jr, R. M. Sweet, Eds.), Academic Press, New York, **1997**, pp. 307–326.
[41] *SHELXTL*, version 4.2, Siemens Analytical X-ray Instruments, Madison, WI, **1991**.
[42] A. C. T. North, D. C. Phillips, F. S. Mathews, *Acta Crystallogr., Sect. A* **1968**, *24*, 351–359.
[43] G. M. Sheldrick, *Acta Crystallogr., Sect. A* **1990**, *46*, 467–473.
[44] G. M. Sheldrick, *SHELXL-97: Program for Refinement of Crystal Structures*, University of Göttingen, Germany, **1997**.

Received: December 19, 2006
Published Online: May 23, 2007

 © 2007 Wiley-VCH Verlag GmbH & Co. KGaA, Weinheim 

DOI: 10.1002/ejic.200700025

# A Linear Ru-Tl-Ru Complex Obtained from Halide Abstraction: An Example of Metal-Dative Bonding

**Ian Bytheway,[a] Christopher S. Griffith,[a][‡] George A. Koutsantonis,*[a] Brian W. Skelton,[a] and Allan H. White[a]**

**Keywords:** Ruthenium / Thallium / AIM calculations / Metal–metal bond

The simple abstraction of chloride ion from $[RuCl(CO)_2(\eta\text{-}C_5H_5)]$ using $[TlBF_4]$ proved problematic, unexpectedly giving a new complex containing linear Ru–Tl–Ru. The complex, $[\{Ru(CO)_2(\eta\text{-}C_5H_5)\}_2(\mu\text{-}Tl)(F\text{–}BF_2\text{–}F)]_\infty$, was polymeric, as determined by a single-crystal X-ray diffraction experiment, in which the thallium centres are bridged by the anions. In an effort to compare the nature of the Tl–Ru bonds, an additional complex was prepared by the reaction of $Tl^{3+}$ ions with $[Ru(CO)_2(\eta\text{-}C_5H_5)]^-$. The resulting neutral complex, $[\{Ru(CO)_2(\eta\text{-}C_5H_5)\}_3(\mu\text{-}Tl)]$, was also structurally characterised. Quantum chemical calculations of $[\{Ru(CO)_2(\eta\text{-}C_5H_5)\}_2(\mu\text{-}Tl)][BF_4]$ suggest that the Tl–Ru bond has ionic character with integrated atomic charges showing that the metal–metal bonding is best represented as $Ru^0$–$Tl^I$–$Ru^0$.
(© Wiley-VCH Verlag GmbH & Co. KGaA, 69451 Weinheim, Germany, 2007)

## Introduction

Interactions between closed-shell metals and their ions has spawned the field of "metallophilicity"[1–4] which is attracting increasing interest with respect to the photophysical properties of the resulting complexes.[5–8] Additionally there is an interest in the coordination chemistry of low-valent group 13, particularly those transition-metal complexes containing "naked" group 13 atoms as bridging ligands,[9] the thesis being that these atoms should display very strong π-acceptor properties.

In recent work, we have been pursuing the chemistry of the $Ru(CO)_2(\eta\text{-}C_5H_5)$ fragment in various guises[10–19] and have observed that protonation of $[\{Ru(CO)_2(\eta\text{-}C_5H_5)\}_2(\mu\text{-}C{\equiv}C)]$ gave the unexpected trinuclear complex, $[\{Ru(CO)_2(\eta\text{-}C_5H_5)\}_3(\mu\text{-}C{\equiv}C)]^+$.[16] This reaction was irreproducible, but the nature of the product suggested that a more rational and dependable route to its synthesis was the addition of the metal electrophile $[Ru(CO)_2(\eta\text{-}C_5H_5)(solvent)]^+$ to $[\{Ru(CO)_2(\eta\text{-}C_5H_5)\}_2(\mu\text{-}C{\equiv}C)]$. The unusual chemistry encountered in the attempted syntheses of such *solvento* cations is described below.

## Results and Discussion

The synthesis of $[Ru(thf)(CO)_2(\eta\text{-}C_5H_5)](BF_4)$ (**1**) by chloride abstraction from the electron-poor complex, $[Ru(CO)_2(\eta\text{-}C_5H_5)Cl]$ (**2**), using $[AgBF_4]$ was attempted but the reaction, surprisingly, proved to be problematic. The precipitation of a grey/white material, presumably $[AgCl]_n$, was observed at reflux in thf and the reaction monitored by infrared spectroscopy for 12 h, beyond which the infrared spectrum of the reaction mixture changed minimally. Two new ν(CO) absorptions at 2019 and 2073 $cm^{-1}$ were observed along with those attributable to residual **2**. Recrystallisation of the reaction mixture gave material which appeared to correspond to **1**, contaminated (ca. 5%) with **2**. The analogous abstraction of the halide ions from $[Fe(CO)_2(\eta\text{-}C_5R_5)X]$ (R = H, Me; X = Cl, I) complexes by silver ion in donor solvents is well known, giving the corresponding *solvento* cation,[20–22] although the preparation of complex **1**, to the best of our knowledge, is unreported. Our attempts to use this material in further reactions proved unsuccessful.

The alternative halide-abstraction reagent, $[TlBF_4]$, was employed in the attempted removal of the chloride ion from **2**, but instead of the expected *solvento* cation the reaction gave a moderate yield of the 1D polymer, $[\{Ru(CO)_2(\eta\text{-}C_5H_5)\}_2(\mu\text{-}Tl)(F\text{–}BF_2\text{–}F)]_\infty$ (**3**), the connectivity of which was determined by a single-crystal X-ray structural determination.

The FAB mass spectrum of complex **3** consisted of a base peak at *m*/*z* 651 corresponding to $[M]^+$. The $^1H$ NMR spectrum had the expected singlet resonance at $\delta$ = 5.54 ppm assigned to $Ru(\eta\text{-}C_5H_5)$, and is comparable to the resonance reported for the complex $[Ru(CO)_2(\eta\text{-}C_5H_5)(MeCN)][PF_6]$.[23] The $^{19}F$ NMR spectrum contains a single, broad resonance at $\delta$ = 151.72 ppm, which is inconsistent with the solid-state structure where two fluorine environments are observed suggesting that the polymeric

[a] Chemistry, M313, School of Biomedical, Biomolecular and Chemical Sciences, University of Western Australia, 35 Stirling Highway, Crawley, Perth, WA 6009, Australia
Fax: +61-8-6488-7247
E-mail: gak@chem.uwa.edu.au
[‡] Present address: Institute for Materials and Engineering Sciences, Australian Nuclear Science and Technology Organisation, New Illawarra Rd, Lucas Heights NSW 2234, Australia

 InterScience © 2007 Wiley-VCH Verlag GmbH & Co. KGaA, Weinheim 

structure arises from cation–anion contacts imposed to some extent by close packing contraints. The fluxional nature of the complex in solution is highlighted by the infrared spectrum where the three absorptions at 2024, 1999 and 1971 $cm^{-1}$ do not imply an exclusive, relative synclinal orientation of the two cyclopentadienyl ligands as defined by the solid-state structure. In spite of the apparent stability of **3** in the solid state, inconsistent microanalytical results were obtained.

Given the dearth of complexes with Ru–Tl complexes in the literature we decided to add to the examples extant with the reaction of $[Ru(CO)_2(\eta\text{-}C_5H_5)]^-$[24] and $TlCl_3{\cdot}4H_2O$ which gave $[\{Ru(CO)_2(\eta\text{-}C_5H_5)\}_3(\mu_3\text{-}Tl)]$ (**4**) in moderate yield. The infrared spectrum of **4** contains three strong υ(CO) absorptions at 1998, 1972 and 1929 $cm^{-1}$, reminiscent of the infrared spectrum of $[\{Ru(CO)_2(\eta\text{-}C_5H_5)\}_3(\mu_3\text{-}In)]$.[25] The FAB mass spectrum does not contain a molecular ion but resembles that for complex **3** with an ion assigned to $[\{Ru(CO)_2(\eta\text{-}C_5H_5)\}_2(Tl)]^+$ at *m*/*z* 651. The $^1H$ NMR spectrum contains a doublet centred at $\delta$ = 4.69 ppm attributed to coupling of the $^{205}Tl$ nuclei to $Ru(\eta\text{-}C_5H_5)$ ($^3J_{TlH}$ = 7.9 Hz).

The complexes $[\{M(CO)_x(\eta\text{-}C_5H_5)\}_3(\mu_3\text{-}Tl)]$ (M = Cr, *x* = 3, **5**;[26] M = Mo, *x* = 3, **6**;[26,27] M = W, *x* = 3, **7**;[26] M = Fe, *x* = 2, **8**.[28]) are examples of complexes analogous to **4**, although the oxidation state of the thallium in these examples is formally $Tl^{III}$. Complex **6** has also been prepared from the reaction of $Tl(C_5H_5)$ and $Mo(CO)_6$.[27]

A similar $^2J_{TlH}$ coupling was not observed for complexes **3**, **6**[27] or the complexes $[TlR_2\{M(CO)_2(\eta\text{-}C_5H_5)\}]$ (R = Me, M = Mo; R = Me, M = W; R = Et, M = Mo).[29,30] However, Whitmire and co-workers[28] observed a $^3J_{TlH}$ coupling constant of 26 Hz for **8** and, in accord with these workers, the pair of doublets centered at $\delta$ = 85.1 and 202.7 ppm in the $^{13}C$ NMR spectrum of **4** is assigned to the coupling of the $^{205}Tl$ nuclei to $Ru(\eta\text{-}C_5H_5)$ ($^2J_{TlC}$ = 7.8 Hz) and Ru–CO ($^2J_{TlC}$ = 279.3 Hz). These assignments imply a single $\{Ru(CO)_2(\eta\text{-}C_5H_5)\}$ environment in solution which is inconsistent with the solid-state structures and suggests that the $(\eta\text{-}C_5H_5)$ environments are exchanging on the NMR time-scale.

The most relevant literature precedent for **3** is the anion produced in the reaction between $[RuBr(CO)_3(\eta^3\text{-}C_3H_5)]$ and Tl(*closo*-1,2-$Me_2$-3,1,2-$TlC_2B_9H_9$), viz. $Tl[\{Ru(CO)_2(\eta^5\text{-}7,8\text{-}Me_2\text{-}7,8\text{-}C_2B_9H_9)\}_2(\mu\text{-}Tl)]$, which was isolated as the $[NEt_4]^+$ salt, **9**, after metathesis, along with a small amount of the neutral tricarbonyl, $[Ru(CO)_3(\eta^5\text{-}7,8\text{-}Me_2\text{-}7,8\text{-}C_2B_9H_9)]$.[31] Most notable in the difference between the compound reported here, **3**, and complex **9** is that the former contains the bridging Tl in a cation while the latter is more typically an anion. The bonding can be described as purely ionic, involving two anionic $Ru^{II}$ centres and the $Tl^+$ cation, as has been postulated for a number of transition-metal salts containing $Tl^+$.[31] However, in the light of what the authors considered as relatively short Ru–Tl bonds, it was suggested that a significant covalent interaction might be imparting stability, leading to short Ru–Tl distances in complex **9**, through filled 4d and empty 5p orbitals of suitable symmetry on Ru and the filled 6s and empty 6p orbitals on the thallium atom, based on assertions suggested for the bonding in $[Ir_2(\mu\text{-}Tl)\{\mu\text{-}(PPh_2CH_2)_2AsPh\}_2Cl(CO)_2]^+$.[32] We have explored the bonding in **3** in more detail using ab initio calculations and these will be discussed below.

### Solid State Structures of $[\{Ru(CO)_2(\eta\text{-}C_5H_5)\}_2(\mu\text{-}Tl)(F\text{–}BF_2\text{–}F)]$ (3) and $[\{Ru(CO)_2(\eta\text{-}C_5H_5)\}_3(\mu_3\text{-}Tl)]$ (4)

The results of the single-crystal structural determinations of complexes **3** and **4** are presented in Figure 1 and Figure 2 with interatomic parameters collected in Table 1 and details of the determinations in Table 5. Preliminary examination of the Tl–Ru bond lengths present in **3**, suggested they appeared to be very short when compared to the sum of the metallic radii of the two metals (3.03 Å).[33] In the complexes, $[\{Mn(CO)_2(\eta\text{-}C_5H_4R)\}_2(\mu\text{-}E)]$ (E = Ge, R = $CH_3$; E = Pb, R = H), this comparison of the bond lengths has been used as the prime indicator of multiple bond character between the main and transition-metal centres,[34–37] the most relevant example of this type of complex to **3** being $[\{Cr(CO)_5\}_2(\mu\text{-}Tl)]^-$.[38] Surprisingly, there exist only two crystallographically characterised complexes containing a Tl–Ru bond, the high nuclearity ruthenium carbido clus-

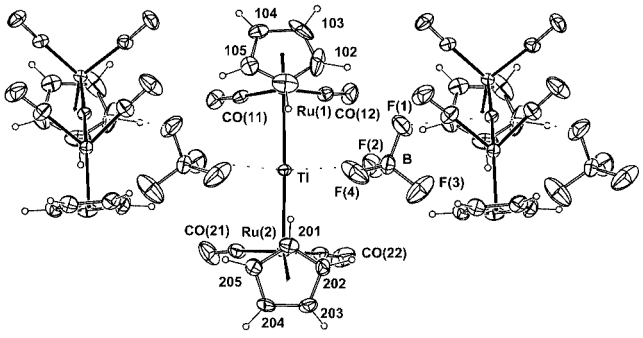


Figure 1. A section of the polymeric strand of **3**.

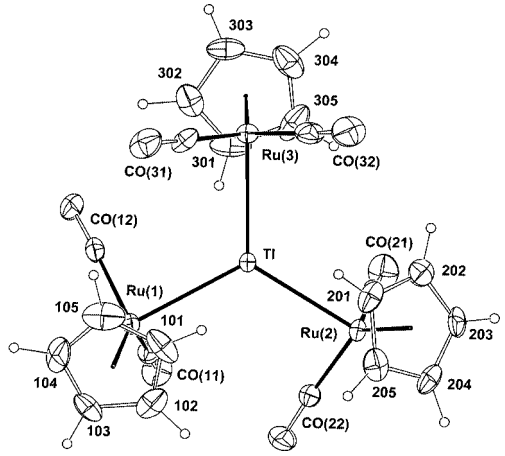


Figure 2. Molecular structure of **4**.

 © 2007 Wiley-VCH Verlag GmbH & Co. KGaA, Weinheim 

ter,[39] $[\{Ru_6(C)(CO)_{16}\}_2(\mu\text{-}Tl)]^-$, with Tl–Ru bond lengths between 2.775(3)–2.875(2) Å and anionic $[NEt_4][\{Ru(CO)_2(\eta^5\text{-}7,8\text{-}Me_2\text{-}7,8\text{-}C_2B_9H_9)\}_2(\mu\text{-}Tl)]$ (**9**),[31] Tl–Ru 2.5994(4) Å.

Table 1. Selected interatomic distances [Å] and angles [°] in compounds **3** ands **4**.[a]

| Distances | **3** | **4** |
|---|---|---|
| Ru(1)–Tl | 2.6298(7) | 2.7327(8) |
| Ru(2)–Tl | 2.6260(7) | 2.7198(8) |
| Ru(3)–Tl | – | 2.7089(8) |
| Ru(1)–C(11),C(12) | 1.870(9), 1.88(1) | 1.84(1), 1.90(1) |
| Ru(2)–C(21),C(22) | 1.89(1), 1.86(1) | 1.86(1), 1.856(9) |
| Ru(3)–C(31),C(32) | – | 1.86(1), 1.84(1) |
| Ru(1)–cp(100) | $1.88_8$ | |
| Ru(2)–cp(200) | $1.89_9$ | |
| Ru(3)–cp(300) | | |
| C(n1)–O(*n*1) | 1.12(1), 1.12(2) | 1.16(1), 1.12(1) |
| C(n2)–O(*n*2) | 1.12(2), 1.18(2) | 1.16(1), 1.15(1) |
| C(n3)–O(*n*3) | | 1.15(2), 1.16(1) |
| Angles | | |
| Ru(1)–Tl–Ru(2) | 176.98(3) | 120.04(2) |
| Ru(1)–Tl–Ru(3) | – | 117.39(3) |
| Ru(2)–Tl–Ru(3) | – | 122.57(3) |
| C(*n*1)–Ru(*n*)–C(*n*2) | 93.6(5), 91.2(6) | 88.8(4), 90.9(4), 89.3(5) |
| Ru(1)–C(1*m*)–O(1*m*) | 177(1), 174.7(9) | 177.4(8), 178(1) |
| Ru(2)–C(2*m*)–O(2*m*) | 176(1), 176.5(9) | 178.2(9), 176.0(7) |
| Ru(3)–C(3*m*)–O(3*m*) | – | 178.6(9), 179(1) |

[a] Carbonyls C,O (*n* = 1–3) are attached to Ru(*n*) [*n* = 1, 2, (3)]; C,O [1, 2, (3)*m*] designate carbonyls *m* = 1, 2, (3) attached to Ru[1, 2, (3)].

The successful synthesis and structural determination of complex **4** gave another suitable complex containing Tl–Ru single bonds for comparison against that of **3** and as such will be discussed here. Complex **3** crystallises in the monoclinic centrosymmetric space group $P2_1/c$, a single formula unit, devoid of crystallographic symmetry, comprising the asymmetric unit of the structure. The structure of **3** comprises an essentially one-dimensional polymeric strand with a repeating unit consisting of one cation and one anion. The close contact of a fluorine atom from the tetrafluoroborate anion of the repeating unit and that of an adjacent repeating unit with the thallium atom of the cation [2.88(1), 2.92(1) Å] results in the observed polymeric structure. The anion B–F(1–4) are 1.38, 1.39, 1.32, 1.34(2) Å, suggesting a distinction between the interacting and non-interacting F–B distances, but that may be impacted by lack of libration correction. F(1)–B–F(2) and F(3)–B–F(4) are enlarged above the tetrahedral norm to 112(1), 120(2)°.

The cation comprises two $\{Ru(CO)_2(\eta\text{-}C_5H_5)\}$ groups coordinated to a central thallium atom such that the Ru–Tl–Ru vector is essentially linear [176.98(3) °]. The geometries about the two Ru atoms are unremarkable but the relative synclinal orientation of the fragments is intriguing given that this stereochemistry places the two cyclopentadienyl ligands at the intuitively unfavourable point of least separation. Presumably the steric requirements of the cations is such that this orientation offers the most favourable crystal packing situation as well as allowing the maximum intermolecular anion-cation contacts. The Tl–Ru bond lengths of 2.6298(7) Å [Ru(1)] and 2.6260(7) Å [Ru(2)] seem unusually "short" in comparison to the sum of the two metallic radii (3.05 Å).[33] However, a recent structural determination of a similar complex, $[\{Ru(CO)_2(\eta^5\text{-}7,8\text{-}C_2B_9H_9)\}_2(\mu\text{-}Tl)][NEt_4]$[31] gave a significantly shorter distance of 2.5994(4) Å. In this anionic complex the Ru–Tl–Ru vector is appreciably bent at 165.67(2)°.

The $Tl_3Ru$ complex **4** crystallises in the centrosymmetric space group $P\bar{1}$; a single molecule, devoid of crystallographic symmetry, together with one half of the toluene molecule of solvation, which lies disordered about a crystallographic inversion centre, comprises the asymmetric unit of the structure. The molecular structure of **4** is shown in Figure 2, together with the numbering scheme used; pertinent bond lengths and angles are presented in Table 1.

The determination shows that the complex consists of a central thallium atom surrounded by three $\{Ru(CO)_2(\eta\text{-}C_5H_5)\}$ groups. The geometry about the thallium atom is trigonal planar, as is evident from the sum of the three ∠ Ru–Tl–Ru being equal to 360°, with the thallium atom located only 0.012(1) Å out of the $Ru_3$ plane. The measured Tl–Ru bond lengths are 2.7327(8) [Ru(1)], 2.7198(8) [Ru(2)] and 2.7089(8) Å [Ru(3)], which are significantly elongated from those measured for **3** by ca. 0.09 Å and 0.133 Å for **9** but "short" compared to the sum of the metallic radii.[33] The large steric bulk of the $\{Ru(CO)_2(\eta\text{-}C_5H_5)\}$ groups appears to be accommodated around the central thallium atom by rotation about the Tl–Ru vectors resulting in two of the cyclopentadienyl ligands orientated on the same side of the $TlRu_3$ plane with the remaining cyclopentadienyl ligand in a relative anticlinal orientation. The overall arrangement of the $\{Ru(CO)_2(\eta\text{-}C_5H_5)\}$ groups is comparable to that observed in the solid-state structure of the triiron thallium complex **8**;[28] presumably the Tl–Ru bond rotations play some part in the solution process which results in the equivalence observed in the $^1H$ and $^{13}C$ NMR solution spectra. Similar rotation about the M–Ga vectors of $[\{M(CO)_3(\eta\text{-}C_5H_5)\}_3(\mu_3\text{-}Ga)]$ (M = Mo **5**,[40] W **6**[41]) has been discussed previously.[42] The (carborane)$Ru(CO)_2$ units in **9** are mutually twisted and seem to allow even closer approach of the Ru and Tl centres.

With these observations in mind, elongation of the Tl–Ru bond lengths for **4** with respect to **3** and **9** may only be consequent on the steric congestion about the thallium atom and not on the presence of any multiple bonding in complex **3**. This situation is a reminder that the assignment of multiple bonding in these and other systems, based purely on structural data, is fraught with uncertainty.

### Quantum Chemical Calculations of $[\{Ru(CO)_2(\eta\text{-}C_5H_5)\}_2(\mu\text{-}Tl)(F\text{–}BF_2\text{–}F)]_\infty$ (3)

In order to probe the nature of the bonding in **3**, quantum-chemical calculations were performed on $[\{Ru(CO)_2(Cp)\}_2Tl]^+$ at the geometry observed from the single-crystal X-ray structural determination of **3** to obtain the total charge density distribution, $\rho(r)$, for analysis using the

 © 2007 Wiley-VCH Verlag GmbH & Co. KGaA, Weinheim 

theory of Atoms in Molecules (AIM).[43] To produce $\rho(r)$ amenable to study by AIM, all electron basis sets were used in conjuction with the Hartree–Fock method.

Within the theory of AIM, bonds are defined in terms of lines of maximum charge density connecting given nuclei, such that each line passes through a saddle point. The collection of these bond paths as well as other topological features of $\rho(r)$ is termed the molecular graph. For **3** the molecular graph is comprised of 2 Ru–Tl, 14 Ru–C, 4 C–O, 10 C–C and 10 C–H bond critical points. As predicted, ring critical points were located at the centre of each cyclopentadienyl ring and cage critical points located between each ruthenium and cyclopentadienyl ligand. The location of these bond critical points indicated that the utilised basis sets were adequate for the purpose of describing the total $\rho$ present within the solid-state structure of **3**. Bond critical point data are summarised in Table 2.

Table 2. Average values, in atomic units, of $\rho(r)$ and $\nabla^2\rho(r)$ at various bond critical points in **3**.

| Bond | $\rho(r)$ | $\nabla^2\rho(r)$ |
|---|---|---|
| Ru–Tl | 0.065 | 0.12 |
| Ru–C (CO) | 0.15 | 0.63 |
| Ru–C (Cp) | 0.079 | 0.22 |
| C–O | 0.45 | 0.56 |
| C–C | 0.27 | –0.91 |

Inspection of $\rho(r)$ at the ruthenium and thallium bond critical points shows these values are relatively small and possess positive Laplacians [$\nabla^2\rho(r)$], also evident from Figure 3 is the depletion of charge in the Ru–Tl internuclear regions, tending to indicate that the charges of the ruthenium and thallium nuclei are contracted and best described as "closed shell" or ionic.[43] The interatomic surface separating the ruthenium and thallium atoms is also shown.

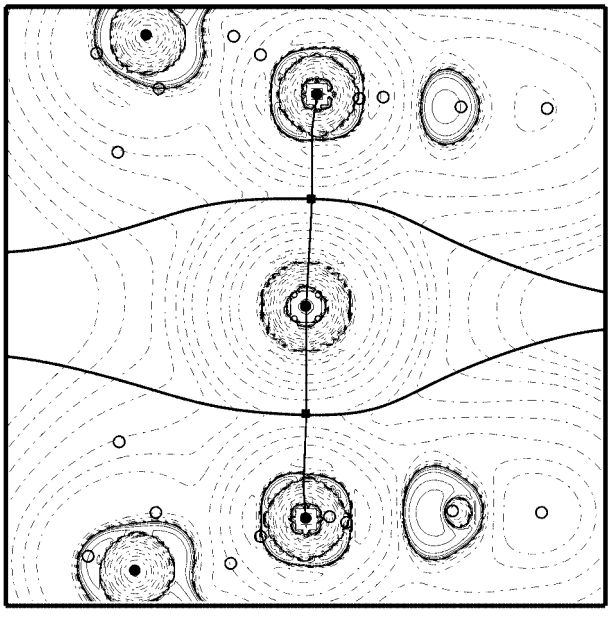

Figure 3. Plot of $\nabla^2\rho(r)$ for **3**, in a plane containing the metal nuclei. Full contours denote regions where charge is concentrated ($\nabla^2\rho(r) < 0$) and broken contours denote regions where charge is depleted ($\nabla^2\rho(r) > 0$). The bond paths joining the Ru and Tl nuclei are superimposed, and the bond critical point is denoted by the filled square. The interatomic surface separating Ru and Tl is also shown.

Similar depletion of charge in the internuclear region of a metal–metal bond has recently received experimental verification for the molecules $[Co_2(CO)_6(AsPh_3)_2]$[44] and $[Mn_2(CO)_{10}]$.[45]

Although the implied ionic nature of the Ru–Tl interaction suggested that multiple metal–metal bonding was absent in **3**, further clarification of the interaction by determination of the atomic populations for each metal nucleus was sought. Two separate methodologies were employed for these calculations:

1) integration of the calculated charge density within the zero-flux surface for each atom;[43]

2) use of the Natural Bond Orbital scheme (NBO).[46,47]

Atomic populations calculated by both methods are presented in Table 3 and support the initial calculations that the Ru–Tl bonding interaction is best described as ionic with no support for any metal–metal multiple bonding but there is substantial donation of electron density from the Ru atoms to the Tl centre. Importantly, the NBO analysis yields electron configurations of $6s^{1.5}\ 6p^{0.6}$ for thallium and $5s^{0.4}\ 4d^{7.4}$ for both ruthenium atoms. Thus, one can consider a dative interaction from the Ru to the Tl as a description of the bonding in **3**.

Table 3. Net atomic populations ($q$), calculated for both the experimental and optimised geometries of **3**.

| Method | All electrons | | B3LYP/LANL2DZ | |
|---|---|---|---|---|
| | Experimental geometry | | 0° | 180° |
| $q$ | Integrated | NBO | NBO | NBO |
| Tl | 1.32[a] | 0.74 | 1.03 | 1.03 |
| Ru | 0.16 | 0.16 | –0.25 | –0.25 |
| CO | –0.10 | 0.07 | 0.16 | 0.15 |
| Cp | –0.11 | –0.17 | –0.08 | –0.07 |

[a] This value obtained by difference from the other integrated populations.

The observed synclinal orientation of the {$Ru(CO)_2(\eta$-$C_5H_5)$} fragments in complex **3** was noted in the solid-state structure and so optimisation of this and the anticlinal stereochemistry was undertaken at the B3LYP/LANL2DZ level of theory. The calculated bond lengths and angles at these orientations were found to be closely similar to the experimental data (Table 4).

Surprisingly, the difference in energy of the two orientations was calculated at 5 kJ/mol, in favour of the anticlinal geometry, and one may have regarded that this orientation would be the most favoured based purely upon steric considerations. Observation of the synclinal stereochemistry in the solid-state structure, coupled with the rather small energy difference calculated between the syn- and anticlinal orientations, suggests that the stereochemistry may be purely a result of crystal packing effects or, perhaps, stabilisation by the tetrafluoroborate counter-anions. Additionally,

 © 2007 Wiley-VCH Verlag GmbH & Co. KGaA, Weinheim 

Table 4. Selected experimental and calculated bond lengths [Å] and angles (°) for **3**.

| | Experimental | Calculated geometry 0° | 180° |
|---|---|---|---|
| Bond length | | | |
| Tl–Ru | 2.6279 | 2.743 | 2.740 |
| Ru–C (CO) | 1.875 | 1.898 | 1.897 |
| Ru–C ($Cp_c$) | 1.885 | 2.001 | 2.000 |
| C–O | 1.135 | 1.178 | 1.178 |
| Bond angle | | | |
| Ru–Tl–Ru | 176.98 | 177.97 | 180.00 |
| Ru–C–O | 175.98 | 178.50 | 176.70 |
| Tl–Ru–C (CO) | 88.23 | 88.98 | 89.20 |
| Tl–Ru–C ($Cp_c$) | 120.0 | 121.80 | 120.98 |
| (CO) C–Ru–C (CO) | 92.40 | 92.80 | 92.84 |
| ($Cp_c$) C–Ru–C (CO) | 122.5 | 126.50 | 126.70 |

NBO charges obtained for both optimised geometries also suggest that thallium is unipositive (see Table 3).

The chemistry which results in the formation of **3** can represented by the following equation:

$$2[RuCl(CO)_2(\eta\text{-}C_5H_5)] + 4Tl(BF_4)_4 \rightarrow [\{Ru(CO)_2(\eta\text{-}C_5H_5)\}_2(\mu_2\text{-}Tl)][BF_4] + 2TlCl + Tl(BF_4)_3$$

The reaction presumably proceeds by oxidation of thallous ions to give formally zero-valent ruthenium that then combines with the available $Tl^+$ ions to give the products. However, this intrepretation is a little problematic given that it suggests that highly oxidising $Tl^{III}$ will co-exist with highly reduced ruthenium species.

## Conclusions

We have shown that so-called simple halide abstraction reactions can be problematic but some TlRu complexes are readily prepared by nucleophilic substitution of transition metal halides. Ab initio calculations have helped rationalise both the bonding within the linear Ru–Tl–Ru complex and the observation of solid state packing effects within the crystal structure of complex, **3**, and suggesting that the Tl atom is a significant acceptor of electron density in the linear Ru–Tl–Ru complex. Additionally, it is clear that bond lengths alone are no arbiter of multiple bonding

## Experimental Section

**General Remarks:** Manipulations of oxygen- and moisture-sensitive compounds were performed under high purity argon using standard Schlenk techniques or in a dry box (Miller Howe).

Infrared spectra were recorded with a Bio-Rad FTS 45 or 40 FTIR spectrometer. $^1H$ and $^{13}C$ NMR spectra were acquired with Varian Gemini 200 or Bruker ARX 500 spectrometers. $^{31}P$ NMR spectra were acquired with a Bruker ARX 500 spectrometer. $^1H$ and $^{13}C$ NMR spectra were referenced with respect to incompletely deuterated solvent signals. Mass spectra were obtained with a VG AutoSpec spectrometer employing a Fast Atom Bombardment (FAB) ionisation source in all samples unless otherwise specified. Elemental analyses were performed by The Research School of Chemistry Microanalytical Unit, Australian National University, ACT. *n*-Hexane and toluene were dried with sodium metal and distilled from sodium benzophenone ketyl under argon. Distilled solvents were stored over sodium or potassium mirrors until use.

**$[\{Ru(CO)_2(\eta\text{-}C_5H_5)\}_2(\mu\text{-}Tl)][BF_4]$(3):** A solution of $RuCl(CO)_2(\eta\text{-}C_5H_5)$ (100 mg, 0.388 mmol) and $TlBF_4$ (112 mg, 0.385 mmol) in tetrahydrofuran (30 mL) was heated at reflux (48 h) till the infrared absorption at 2023 $cm^{-1}$ became constant. The reaction mixture was filtered, the solution volume reduced (to ca. 20 mL), then added dropwise to diethyl ether (50 mL) to give a pale yellow precipitate. Recrystallisation ($CH_2Cl_2$/$Et_2O$) gave **3** (60 mg, 42%) as yellow rods. $C_{14}H_{10}BF_4O_4Ru_2Tl$ (735.56): calcd. C 21.85, H 1.37; found C 22.21, H 0.83. FABMS: *m*/*z* (%) = 651 (35) [$M^+$]. IR ($CH_2Cl_2$): $\tilde{\nu}$ = 2024 (m), 1999 (m), 1971 [m (CO)] $cm^{-1}$. $^1H$ NMR (500 MHz, [$D_6$]acetone, 25 °C): $\delta$ = 5.54 [s, ($\eta$-$C_5H_5$)] ppm. $^{19}F$ NMR (470 MHz, [$D_6$]acetone, 25 °C): $\delta$ = 151.7 (s, $BF_4$) ppm.

**$[\{Ru(CO)_2(\eta\text{-}C_5H_5)\}_3(\mu\text{-}Tl)]$(4)·0.5$C_6H_5CH_3$:** A solution of freshly prepared $Na[Ru(CO)_2(\eta\text{-}C_5H_5)]$ (0.674 mmol) in tetrahydrofuran was added to a stirred solution of $TlCl_3$ (70 mg, 0.224 mmol) in tetrahydrofuran (15 mL), then heated at reflux (2 h). The solvent was removed in vacuo and the residues extracted with toluene (2 × 30 mL) to give a blood-red solution. Reduction of the solution volume (to ca. 50 mL) and addition of hexane gave red crystals of **4** at –35 °C (119 mg, 61%). IR ($C_7H_7$): $\tilde{\nu}$ = ν(CO) = 1998 m, 1972 (s), 1929 [m (CO)] $cm^{-1}$. $^1H$ NMR (200 MHz, [$D_6$]benzene, 25 °C): $\delta$ = 4.69 [d, $^2J_{TlH}$ = 7.9 Hz, ($\eta$-$C_5H_5$)] ppm. $^{13}C$ NMR (50.3 MHz, [$D_6$]benzene, 25 °C): $\delta$ = 202.7 (d, $^2J_{TlC}$ = 279.3 Hz, Ru-CO), 85.1 [d, $J_{TlH}$ = 7.8 Hz, ($\eta$-$C_5H_5$)] ppm. FABMS: *m*/*z* (%) = 651 (35) [$M^+$ – {$Ru(CO)_2(\eta$-$C_5H_5)$}]. $C_{21}H_{15}O_6Ru_3Tl$ (871.24): calcd. C 28.95, H 1.74; found C 28.39, H 1.67.

**X-ray Crystallographic Study:** Full spheres of CCD area-detector diffractometer data were measured (Bruker AXS instrument, ω-scans, *T* ca. 300 K; monochromatic Mo-$K_\alpha$ radiation, $\lambda$ = 0.7107$_3$ Å) yielding $N_{t(otal)}$ reflections, these merging to *N* unique ($R_{int}$ quoted) after "empirical"/multiscan absorption correction (proprietary software). $N_o$ with $F > 4\sigma(F)$ were considered "observed"

Table 5. Crystallographic structure determinations of [{$Ru(CO)_2(\eta$-$C_5H_5)$}$_2$($\mu$-Tl)][$BF_4$] (**3**) and [{$Ru(CO)_2(\eta$-$C_5H_5)$}$_3$($\mu$-Tl)] (**4**).

| Compound | **3** | **4** |
|---|---|---|
| Formula | $C_{14}H_{10}BF_4O_4Ru_2Tl$ | $C_{24.5}H_{19}O_6Ru_3Tl$ |
| $M_r$ | 735.56 | 917.01 |
| Crystal system | monoclinic | triclinic |
| Space group | $P2_1/c$ (No. 14) | $P\bar{1}$ (No. 2) |
| *a* [Å] | 12.023(1) | 7.5367(4) |
| *b* [Å] | 12.996(1) | 9.6907(5) |
| *c* [Å] | 13.163(1) | 18.841(1) |
| $\alpha$ [°] | – | 94.321(4) |
| $\beta$ [°] | 113.239(1) | 95.88(1) |
| $\gamma$ [°] | – | 104.672(1) |
| *V* [Å$^3$] | 1889.9(5) | 1316.8(1) |
| $D_{calcd.}$ [g cm$^{-3}$] | 2.585 | 2.312 |
| *Z* | 4 | 2 |
| $\mu_{Mo}$ [cm$^{-1}$] | 101.4 | 78.2 |
| Dimension [mm] | 0.20 × 0.10 × 0.08 | 0.45 × 0.22 × 0.08 |
| $T_{min./max.}$ | 0.59 | 0.47 |
| $2\theta_{max.}$ [°] | 58 | 58 |
| $N_t$ | 21923 | 14368 |
| $N(R_{int})$ | 4772(0.036) | 6376(0.046) |
| $N_o$ | 3681 | 5813 |
| *R* | 0.043 | 0.038 |
| $R_w$ | 0.062 | 0.041 |

 © 2007 Wiley-VCH Verlag GmbH & Co. KGaA, Weinheim 

and used in the full-matrix least-squares refinements, refining anisotropic thermal parameter forms for the non-hydrogen atoms ($x$, $y$, $z$, $U_{iso})_H$ being constrained at estimated values. Conventional residuals $R$, $R_w$ on $|F|$ are cited at convergence {reflection weights: $[\sigma^2(F) + 0.0004F^2]^{-1}$}. Neutral atom complex scattering factors were employed within the Xtal 3.7 program system.[48] Pertinent data are given in Table 5 and Figure 1 and Figure 2, the latter showing 20% probability amplitude displacement envelopes for the non-hydrogen atoms, hydrogen atoms having arbitrary radii of 0.1 Å.

CCDC-116532 and -116533 contain the supplementary crystallographic data for this paper. These data can be obtained free of charge from The Cambridge Crystallographic Data Centre via www.ccdc.cam.ac.uk/data_request/cif.

**Theoretical Calculations:** Ab initio calculations were performed with the Gaussian 94 software package.[49] The experimental geometry was used for the calculation of a Hartree–Fock all-electron wave function. The Huzinaga[50] basis sets with uncontracted outer d-shells were used for Ru [432211/4211/321] and Tl [4322211/422211/4211/3] while standard 3-21G basis sets[49] were used for C, O and H atoms. Optimized geometries were obtained using the B3LYP functional[51,52] as implemented in Gaussian 94[49,53] in conjunction with the LANL2DZ effective core potentials for Ru and Tl[54] and D95V all-electron basis sets[55] for C,O and H. The MORPHY98 program[56] was used to search for critical points in the total charge density[57] and to calculate integrated atomic populations.[58] Orbital occupancies and charges were also obtained using the natural bond orbital (NBO) program[46,47] implemented in Gaussian 94.

## Acknowledgments

C. S. G. was the holder of a Australian Postgraduate Award.

[1] A. Hamel, N. W. Mitzel, H. Schmidbaur, *J. Am. Chem. Soc.* **2001**, *123*, 5106.
[2] H. Schmidbaur, *Gold. Bull.* **2000**, *33*, 3.
[3] P. Pyykko, W. Schneider, A. Bauer, A. Bayler, H. Schmidbaur, *Chem. Commun.* **1997**, 1111.
[4] H. Schmidbaur, A. Hamel, N. W. Mitzel, A. Schier, S. Nogai, *Proc. Natl. Acad. Sci. USA* **2002**, *99*, 4916.
[5] Q.-M. Wang, Y.-A. Lee, O. Crespo, J. Deaton, C. Tang, H. J. Gysling, M. C. Gimeno, C. Larraz, M. D. Villacampa, A. Laguna, R. Eisenberg, *J. Am. Chem. Soc.* **2004**, *126*, 9488.
[6] E. J. Fernandez, A. Laguna, J. M. Lopez-De-Luzuriaga, M. Monge, P. Pyykko, N. Runeberg, *Eur. J. Inorg. Chem.* **2002**, 750.
[7] V. W.-W. Yam, K. M.-C. Wong, N. Zhu, *Angew. Chem. Int. Ed.* **2003**, *42*, 1400.
[8] V. W.-W. Yam, *C. R. Chim.* **2005**, *8*, 1194.
[9] S. Aldridge, *Angew. Chem. Int. Ed.* **2006**, *45*, 8097.
[10] C. S. Griffith, G. A. Koutsantonis, B. W. Skelton, A. H. White, *Chem. Commun.* **1998**, *7*, 1805.
[11] L. T. Byrne, J. P. Hos, G. A. Koutsantonis, B. W. Skelton, A. H. White, *J. Organomet. Chem.* **2000**, *598*, 28.
[12] C. S. Griffith, G. A. Koutsantonis, B. W. Skelton, A. H. White, *Chem. Commun.* **1998**, 1805.
[13] L. T. Byrne, C. S. Griffith, J. P. Hos, G. A. Koutsantonis, B. W. Skelton, A. H. White, *J. Organomet. Chem.* **1998**, *565*, 259.
[14] L. T. Byrne, C. S. Griffith, G. A. Koutsantonis, B. W. Skelton, A. H. White, *J. Chem. Soc., Dalton Trans.* **1998**, 1575.
[15] C. S. Griffith, G. A. Koutsantonis, B. W. Skelton, A. H. White, *J. Organomet. Chem.* **2003**, *670*, 198.
[16] C. S. Griffith, G. A. Koutsantonis, B. W. Skelton, A. H. White, *Chem. Commun.* **2002**, 2174.
[17] L. T. Byrne, J. P. Hos, G. A. Koutsantonis, B. W. Skelton, A. H. White, *J. Organomet. Chem.* **1999**, *592*, 95.
[18] C. S. Griffith, G. A. Koutsantonis, B. W. Skelton, A. H. White, *Angew. Chem. Int. Ed.* **2005**, *44*, 3038.
[19] C. S. Griffith, G. A. Koutsantonis, B. W. Skelton, A. H. White, *J. Organomet. Chem.* **2005**, *690*, 3410.
[20] D. L. Reger, C. J. Coleman, *J. Organomet. Chem.* **1977**, *131*, 153.
[21] M. Rosenblum, *Acc. Chem. Res.* **1974**, *7*, 122.
[22] A. S. Batsanov, O. S. Manole, Y. T. Struchkov, G. P. Zol'nikova, D. N. Kravtsov, *Metalloorg. Khim.* **1993**, *6*, 213.
[23] A. Jungbauer, H. Behrens, *Z. Naturforsch., Teil B* **1978**, *33*, 1083.
[24] T. Blackmore, M. I. Bruce, F. G. A. Stone, *J. Chem. Soc. A* **1968**, 2158.
[25] J. C. Calabrese, L. M. Clarkson, T. B. Marder, N. C. Norman, N. J. Taylor, *J. Chem. Soc., Dalton Trans.* **1992**, 3525.
[26] J. Burlitch, T. W. Theyson, *J. Chem. Soc., Dalton Trans.* **1974**, 828.
[27] J. Rajaram, J. A. Ibers, *Inorg. Chem.* **1973**, *12*, 1313.
[28] J. W. v. Hal, L. B. Alemany, K. H. Whitmire, *Inorg. Chem.* **1997**, *36*, 3152–3159.
[29] B. Walther, R. Mahrwald, C. Jahn, W. Klar, *Z. Anorg. Allg. Chem.* **1976**, *423*, 144.
[30] B. Walther, C. Rockstroh, *J. Organomet. Chem.* **1972**, *44*, C4.
[31] J. C. Jeffery, P. A. Jelliss, Y.-H. Liao, F. G. A. Stone, *J. Organomet. Chem.* **1998**, *551*, 27.
[32] A. L. Balch, J. K. Nagle, M. M. Olmstead, P. E. Reedy Jr, *J. Am. Chem. Soc.* **1987**, *109*, 4123.
[33] A. F. Wells, *Structural Inorganic Chemistry*, 5th edn. ed., Clarendon Press, Oxford, **1984**.
[34] W. A. Herrmann, H.-J. Kneuper, E. Herdweck, *Angew. Chem. Int. Ed. Engl.* **1985**, *24*, 1062.
[35] W. A. Herrmann, *Angew. Chem. Int. Ed. Engl.* **1986**, *25*, 56.
[36] W. A. Herrmann, H.-J. Kneuper, E. Herdweck, *Chem. Ber.* **1989**, *122*, 445.
[37] W. Gade, E. Weiss, *J. Organomet. Chem.* **1981**, *213*, 451.
[38] B. Schiemenz, G. Huttner, *Angew. Chem. Int. Ed. Engl.* **1993**, *105*, 1840.
[39] G. B. Ansell, M. A. Modrick, J. S. Bradley, *Acta Crystallogr., Sect. C* **1984**, *40*, 1315.
[40] L. M. Clarkson, W. Clegg, D. C. R. Hockless, N. C. Norman, T. B. Marder, *J. Chem. Soc., Dalton Trans.* **1991**, 2229.
[41] A. J. Conway, P. B. Hitchcock, J. D. Smith, *J. Chem. Soc., Dalton Trans.* **1975**, 1945.
[42] R. M. Campbell, L. M. Clarkson, W. Clegg, D. C. R. Hockless, N. L. Pickett, N. C. Norman, *Chem. Ber.* **1992**, *125*, 55.
[43] R. F. W. Bader, *Atoms in Molecules: A Quantum Theory*, Oxford University Press, Oxford, **1990**.
[44] P. Macchi, D. M. Proserpio, A. Sironi, *J. Am. Chem. Soc.* **1998**, *120*, 13429.
[45] R. Bianchi, G. Gervasio, D. Marabello, *Inorg. Chem.* **2000**, *39*, 2360.
[46] E. D. Glendening, A. E. Reed, J. E. Carpenter, F. Weinhold, NBO 3.1, **1995**.
[47] A. E. Reed, L. A. Curtis, F. Weinhold, *Chem. Rev.* **1988**, *88*, 899.
[48] S. R. Hall, D. J. du Boulay, R. Olthof-Hazekamp, *Xtal 3.7 User's Manual*, University of Western Australia, **2001**.
[49] M. J. Frisch, G. W. Trucks, H. B. Schlegel, P. M. W. Gill, B. G. Johnson, M. A. Robb, J. R. Cheeseman, T. Keith, G. A. Petersson, J. A. Montgomery, K. Raghavachari, M. A. Al-Laham, V. G. Zakrzewski, J. V. Ortiz, J. B. Foresman, J. Cioslowski, B. B. Stefanov, A. Nanayakkara, M. Challacombe, C. Y. Peng, P. Y. Ayala, W. Chen, M. W. Wong, J. L. Andres, E. S. Replogle, R. Gomperts, R. L. Martin, D. J. Fox, J. S. Binkley, D. J. Defrees, J. Baker, J. P. Stewart, M. Head-Gordon, C. Gonzalez, J. A. Pople, *Gaussian94*, Rev. B.1, Gaussian Inc., Pittsburgh, **1995**.

 © 2007 Wiley-VCH Verlag GmbH & Co. KGaA, Weinheim 

[50] J. Andzelm, S. Huzinaga, M. Klobukowski, E. Radzio-Andzelm, Y. Sakai, H. Tatewaki, *Gaussian Basis Sets for Molecular Calculations*, Elsevier, Amsterdam, **1984**.
[51] A. D. Becke, *Phys. Rev. A* **1988**, *38*, 3098.
[52] C. Lee, W. Yang, R. G. Parr, *Phys. Rev. B: Condens. Matter* **1988**, *37*, 785.
[53] P. J. Stephens, F. J. Devlin, C. F. Chabalowski, M. J. Fisch, *J. Phys. Chem.* **1994**, *98*, 11623.
[54] P. J. Hay, W. R. Wadt, *J. Chem. Phys.* **1985**, *82*, 299.
[55] T. H. Dunning Jr, P. J. Hay, *Modern Theoretical Chemistry*, Plenum, New York, **1976**.
[56] P. L. A. Popelier, R. G. A. Bone, *MORPHY98*, A Topological Analysis Program, UMIST.
[57] P. L. A. Popelier, *Comput. Phys. Commun.* **1996**, *93*, 212.
[58] P. L. A. Popelier, *Mol. Phys.* **1996**, *87*, 1169

Received: January 9, 2007
Published Online: May 23, 2007

 © 2007 Wiley-VCH Verlag GmbH & Co. KGaA, Weinheim 

DOI: 10.1002/ejic.200700122

# Effect of Ligand Architecture on the Structure and Properties of Square-Planar Nickel(II) Complexes of Amide-Based Macrocycles

**Savita K. Sharma,[a] Shailesh Upreti,[b] and Rajeev Gupta*[a]**

**Keywords:** Nickel complexes / Macrocyclic ligands / Electrochemistry

The present work discusses the design and synthesis of four novel macrocyclic ligands and their $Ni^{II}$ complexes. All four ligands ($H_21^{EN}$, $H_22^{EN}$, $H_23^{OP}$, $H_24^{OP}$) are designed to provide an identical donor-environment composed of two deprotonated anionic amide-*N* coordination and two neutral amine-*N* coordination and an identical 12-membered macrocyclic ring around the nickel center. The $Ni^{II}$ complexes (**1**, **2**, **3**, and **4** of doubly deprotonated ligands $[1^{EN}]^{2-}$, $[2^{EN}]^{2-}$, $[3^{OP}]^{2-}$, and $[4^{OP}]^{2-}$, respectively) are prepared and thoroughly characterized. The coordination geometry around the $Ni^{II}$ center is square planar as determined by the single crystal structure analyses. The average $Ni–N_{amide}$ bond lengths are shorter by ca. 0.1 Å than the average $Ni–N_{amine}$ distances while the average $N_{amide}–Ni–N_{amide}$ angles are shorter by ca. 4° than the average $N_{amine}–Ni–N_{amine}$ angles. The $Ni^{II}$ ion is housed quite tightly within the aperture of the macrocycle as seen by the short Ni–N bond lengths and a very small displacement (0.11–0.17 Å) of the Ni center out of the $N_4$ basal plane. The detailed $^1H$ and $^{13}C$ NMR studies on the diamagnetic Ni–complexes reveal that the solid state conformation of the complexes **1**–**4** is retained in the solution. The $Ni^{III/II}$ potential is fairly positive (>0.6 V vs. SCE) for all four complexes, while the complexes with phenylene as part of the ligand also show the oxidation(s) of the ring(s) (>1.1 V vs. SCE). Coulometric measurements confirm both responses as $1e^-$ process. Electrochemical or chemical oxidation at the 1st potential results in the generation of an unstable "green species" that show distinct features in the absorption spectrum and exhibit anisotropic EPR spectrum. These findings strongly point out that the unstable green species is a $Ni^{III}$ species. The 2nd and/or 3rd oxidation is centered on the phenylene ring(s) and lead to an immediate decomposition.
(© Wiley-VCH Verlag GmbH & Co. KGaA, 69451 Weinheim, Germany, 2007)

## Introduction

The interest in the nickel coordination complexes supported with amide ligands has always attracted synthetic chemists due to many reasons. One of them is to stabilize nickel ions in high oxidation states to gain knowledge about such species in general and to further use them as oxidizing agents.[1] Secondly, the recent developments in spectroscopic and/or structural identification of the nickel species in the catalytic cycle of several enzymes, for example, [NiFe]-hydrogenases,[2] Ni-dependent superoxide dismutase,[3] acetyl-coenzyme A synthase[4] and Ni-tetrahydrocorphinoid cofactor ($F_{430}$) of methyl-coenzyme M reductase[5] has reignited the interests in the area of bioinorganic model studies of nickel ion. In fact, the identification of deprotonated carboxamido-*N* coordination in a number of Ni-enzymes has challenged the synthetic chemists to design the low-molecular weight models to understand the structure and function of the native enzymes. A latest case is the emergence of quite interesting synthetic systems to model the active site structure of Acetyl coenzyme A synthase/carbon monoxide dehydrogenase (ACS/CODH).[6] Also, $Ni^{II}$ in conjunction with oligopeptides has found to cause DNA cleavage in the presence of suitable oxidants; $Ni^{III}$ and/or $Ni^{IV}$ species have been postulated for this cleavage.[7] In this context, as well as in order to develop better oxidizing systems, emphasis should be to achieve a high oxidation state of the nickel ion. The redox properties of a nickel center can be fine-tuned by the use of strong donor groups in a constrained environment in conjunction with the incorporation of non-innocent ligand features that also participate in the redox properties.

Amide-based macrocyclic ligands possess interesting oligopeptide features of the biologically important moieties and serve as effective ligands for early and late transition metal ions.[8,9] Extensive research has been devoted in understanding the nickel coordination chemistry with amide-based azamacrocyclic ligands;[8] however, studies have mainly been limited to the solution generated species in most of the instances with structural information limited to handful examples. Such studies have primarily been targeted to understand the effective placement of the nickel ion within the aperture or the cavity of the macrocycle with

[a] Department of Chemistry, University of Delhi, Delhi 110007, India
Fax: +91-11-2766-6605
E-mail: rgupta@chemistry.du.ac.in
[b] Department of Chemistry, Indian Institute of Technology, Delhi, New Delhi, 110016, India
Supporting information for this article is available on the WWW under http://www.eurjic.org or from the author.

 © 2007 Wiley-VCH Verlag GmbH & Co. KGaA, Weinheim 

the emphasis on the 13-and 14-membered dioxotetraamines (see Scheme 1). The pioneering work of Kimura and Kodama[10] has resulted in a number of important conclusions, for example, 13-membered macrocycle, dioxo[13]-aneN$_4$ ideally house the low-spin Ni$^{II}$ ion tightly compared to the analogous 14-membered, dioxo[14]aneN$_4$ and 15-membered, dioxo[15]aneN$_4$ macrocycles. In continuation, they also show that the macrocyclic ring size (13...15-membered) has a profound effect on the redox potential of the Ni$^{II}$/Ni$^{III}$ couple. Lampeka and Gavrish[11,12] have further progressed this work and recently shown the crystal structures of the Ni$^{II}$ complexes with dioxo[13]aneN$_4$ and dioxo[14]aneN$_4$ ligands. Both Ni complexes, as anticipated earlier, are square planar and the solid-state structures have shown to be retained in solution by the proton NMR studies. In spite of the importance anticipated for the 12-membered macrocycles (such as small size of the macrocyclic aperture and tight chelation), surprisingly, the chemistry has not been explored. A possible explanation for the expansion of the chemistry of 13-membered or higher macrocycle is the readily accessibility of such ligands via the aminolysis reaction of malonic esters with variable polyamines.[8] Moreover, it was always anticipated that a tiny 12-membered macrocycle may not be able to accommodate a transition metal ion. In fact, Martell and co-workers[13] have shown few 2:1 sandwich metal complexes of a very similar amide ligand (1,4,7,10-tetraazacyclododecane-2,9-dione), where M$^{II}$ (M = Co, Ni, and Cu) ion is in between two ligands. This is to be noted, however, that these complexes were synthesized and isolated at neutral pH. These literature precedents have laid the foundation of our present work and we have commenced a systematic synthetic investigation to shed light on the effect of the ligand architecture imposed by the macrocyclic ligands on the properties of coordination complexes. Herein, we report the design and synthesis of four novel macrocyclic ligands and their coordination chemistry towards Ni$^{II}$ ion. These ligands have been designed to keep two important parameters identical; basic donor-environment around the nickel center, and the size of macrocycle which is 12-membered in all four cases. This is followed by the understanding of the effect of ligand planarity and non-innocent feature(s) on the structural, spectroscopic, and redox properties of the nickel center.

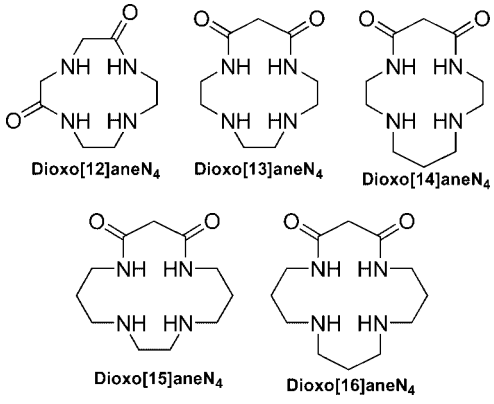


Scheme 1.

## Results and Discussion

### Ligand Design and Synthesis

The macrocyclic ligands ($H_21^{EN}$, $H_22^{EN}$, $H_23^{OP}$, and $H_24^{OP}$) are designed to simultaneously provide two amide and two amine coordinations to the metal center. Moreover, the ligands are intended to afford an identical primary coordination environment to the metal center. The only difference between these four ligands is the subtle alteration in the backbone of the ligands. For example, $H_22^{EN}$ differ from $H_21^{EN}$ by the involvement of one phenylene unit in the framework of the macrocycle, whereas $H_24^{OP}$ differ from $H_21^{EN}$ by the incorporation of two such units. These ligands are synthesized in two steps starting from the corresponding primary diamines (Scheme 2).

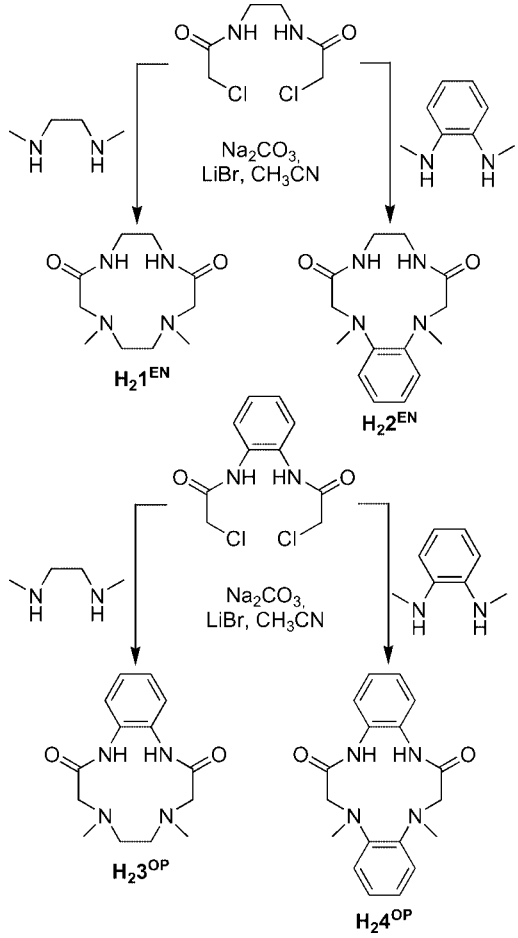


Scheme 2. Synthesis of ligands.

In the first step, the diamine is converted into the respective bis(chloroacetamide) by treating with two equiv. of chloroacetyl chloride.[14] In the next step, the bis(chloroacetamide) is treated with the corresponding secondary amine to afford the desired ligand. It is worth mentioning here that during the synthesis of these ligands, LiBr was used as a templating agent.[15] Interestingly, the synthetic attempts were unsuccessful without the addition of LiBr as templating agent. The utilization of a templating agent is well known in the literature for the synthesis of macrocyclic

 © 2007 Wiley-VCH Verlag GmbH & Co. KGaA, Weinheim 

ligands from simple crown-ethers to more complex molecules.[16] All new ligands are thoroughly characterized using various spectroscopic measurements and give satisfactory microanalysis results.

### Synthesis and Characterization of Metal Complexes

All $Ni^{II}$ complexes, **1**–**4**, were synthesized as follows: DMF solution of the respective ligand was first deprotonated with solid NaH under $N_2$ atmosphere followed by the addition of $NiCl_2$ as the metal source. The complex **1** can, however, be synthesized in better yield by treating the methanolic solution of the ligand $H_21^{EN}$ with 2 equiv. of NaOH followed by the addition of the $Ni(OAc)_2$ salt. Usual workup and recrystallization (vapor diffusion of diethyl ether to a MeCN solution of complexes) afforded highly crystalline material in moderate recrystallized yield (ca. 40%). All complexes are deep yellow to orange-yellow in color.

In the FTIR spectra, the absence of ν(N–H) stretching frequency confirms the deprotonated nature of the amide ligands. A bathochromic shift in the C=O stretching frequency was observed for all complexes compared to the free ligand and prove that the deprotonated N-amide group is coordinated to the Ni ion.[17] In addition, complex **2** also has water as solvent of crystallization which shows the ν(OH)[17] absorption in the region of 3300–3400 $cm^{-1}$ (cf. crystal structure). Solution conductivity data[18] confirm the non-electrolytic nature of all $Ni^{II}$ complexes, whereas the elemental analyses results authenticate the purity of the bulk samples. In the electrospray mass spectra, molecular ion peak corresponding to the complexes, **1**, **2**, **3**, and **4** were obtained at 285.05 (**1** + $H^+$), 333.27 (**2** + $H^+$), 333.05 (**3** + $H^+$), and 381.35 (**4** + $H^+$), respectively, and assert the integrity of the metal complexes in the solution.

### Crystal Structure Studies

All $Ni^{II}$ complexes have been structurally characterized and the molecular structures of the complexes are shown in Figures 1, 2, 3, and 4, while the important crystallographic

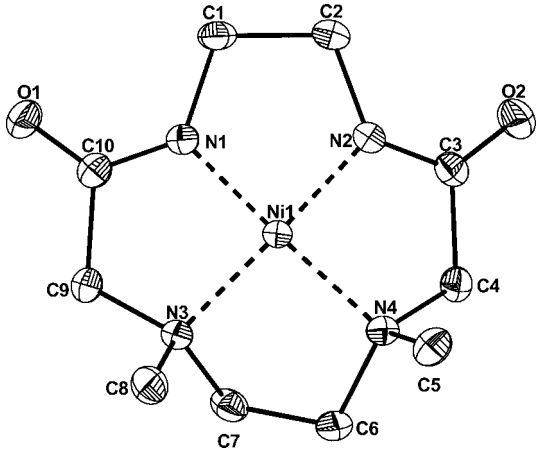


Figure 1. Molecular structure of complex **1** (thermal ellipsoid are drawn at 30% probability level). Hydrogen atoms, solvent molecule are omitted for clarity.

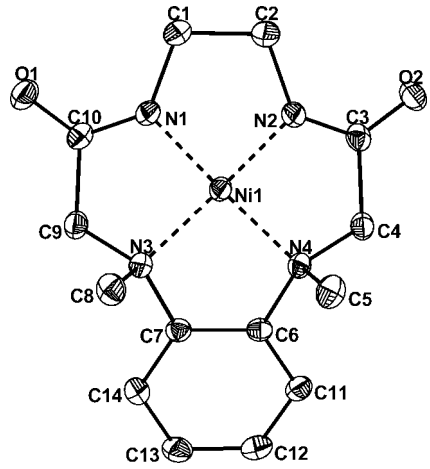


Figure 2. Molecular structure of complex **2** (thermal ellipsoid are drawn at 30% probability level). Hydrogen atoms, solvent molecule are omitted for clarity.

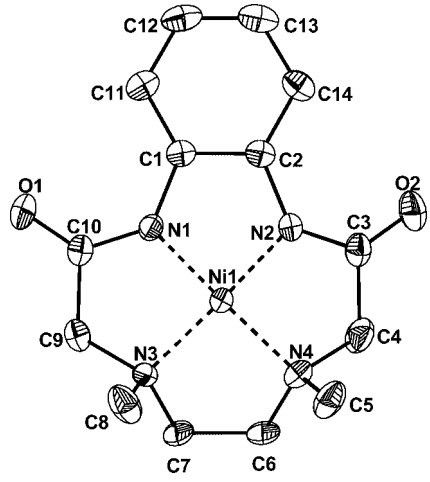


Figure 3. Molecular structure of complex **3** (thermal ellipsoid are drawn at 30% probability level). Hydrogen atoms are omitted for clarity. The atoms C6 and C7 were occupying two crystallographically independent positions and only the atoms with site occupancy factor of 0.8 are shown for clarity.

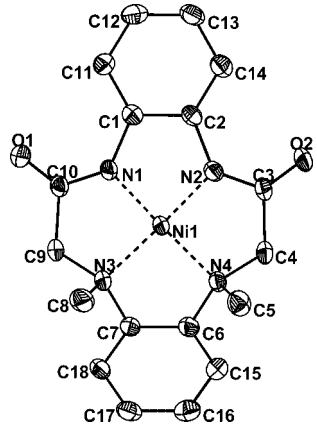


Figure 4. Molecular structure of complex **4** (thermal ellipsoid are drawn at 30% probability level). Hydrogen atoms are omitted for clarity.

 © 2007 Wiley-VCH Verlag GmbH & Co. KGaA, Weinheim 

and structural parameters are presented in Tables 1, 2 and S1 (for the latter see electronic supporting information). The coordination geometry around the $Ni^{II}$ center is square planar in all four complexes. The $Ni^{II}$ ion is simultaneously coordinated by two deprotonated amidic-*N* atoms and two tertiary amine-*N* atoms. In all four complexes $Ni^{II}$ ion is surrounded by four five-membered chelate rings. In all cases, the bond angles formed by the lateral chelate rings about the Ni center are close to the ideal value of 90° for a perfect square-planar complex; however, the bond angle involving two anionic $N_{amide}$ has a slightly smaller value of ca. 88° which is compensated by a little higher angle (ca. 92°) for the chelate ring involving two $N_{amine}$. The methyl groups on the tertiary nitrogen centers are located on one side of the plane in all cases. This is in contrast to a number of examples where relative position of the N–H or N–R groups results in the occurrence of the geometrical isomers.[11] The lateral 5-membered chelate rings [–C(O)–$CH_2$– fragment] in all complexes are adopting the envelope conformation.[11,19] Both carbon atoms in these rings are present on the same side of $N_{amide}$–Ni–$N_{amine}$ plane with larger displacement of the carbon atoms connected to the amine nitrogens ($sp^3$ centers).

For complex **1**, the average Ni–$N_{amide}$ bond length is ca. 1.81 Å, while the average Ni–$N_{amine}$ bond length is ca. 1.91 Å. The difference of 0.1 Å may be attributed to the anionic coordination from the deprotonated amidic nitrogens compared to the neutral amine nitrogen donors. The N(1)–Ni–N(2) bond angle of 87.40° is smaller than the N(3)–Ni–N(4) bond angle of 92.36°. The observed difference of ca. 5° between the two bond angles explains the tight chelate formation from the two anionic amidate nitrogens. The other two angles (ca. 89°) involving lateral five-membered rings are similar to each other. Another interesting feature of the structure is the orientation of the carbon centers of the –$CH_2CH_2$– fragments of the amine part of the macrocyclic ligand which is adapting *gauche* conformation.[11]

Table 1. Crystallographic data for [Ni($1^{EN}$)] (**1**), [Ni($2^{EN}$)] (**2**), [Ni($3^{OP}$)] (**3**), and [Ni($4^{OP}$)] (**4**).

| Complex | [$Ni^{II}$($1^{EN}$)] (**1**·$CH_3CN$) | [$Ni^{II}$($2^{EN}$)] (**2**·$H_2O$) | [$Ni^{II}$($3^{OP}$)] (**3**) | $Ni^{II}$($4^{OP}$)] (**4**) |
|---|---|---|---|---|
| Empirical formula | $C_{12}H_{21}N_5O_2Ni$ | $C_{14}H_{20}N_4O_3Ni$ | $C_{14}H_{18}N_4O_2Ni$ | $C_{18}H_{18}N_4O_2Ni$ |
| Formula mass | 326.03 | 351.03 | 333.01 | 381.05 |
| $T$ [K] | 298 | 298 | 298 | 298 |
| Crystal system | triclinic | orthorhombic | monoclinic | triclinic |
| Space group | $P\bar{1}$ | $P2_12_12_1$ | $P2_1/n$ | $P\bar{1}$ |
| Color, shape | yellow, needle | yellow, plate | yellow, block | yellow, block |
| $a$ [Å] | 8.684(3) | 8.998(8) | 8.9315(9) | 11.676(3) |
| $b$ [Å] | 9.095(5) | 10.562(2) | 10.319(1) | 11.739(4) |
| $c$ [Å] | 9.449(7) | 16.411(3) | 15.502(6) | 13.271(5) |
| $\alpha$ [°] | 100.771(2) | | | 78.597(4) |
| $\beta$ [°] | 98.061(3) | | 101.237(2) | 69.901(5) |
| $\gamma$ [°] | 92.061(2) | | | 80.854(6) |
| $V$ [Å$^3$] | 724.4(7) | 1559.7(14) | 1401.3(6) | 1666.3(10) |
| $Z$ | 2 | 4 | 4 | 4 |
| $D_{calcd.}$ [g cm$^{-3}$] | 1.495 | 1.496 | 1.578 | 1.515 |
| Absorption coefficient [mm$^{-1}$] | 1.348 | 1.262 | 1.394 | 1.184 |
| $R$[a] | 0.0386 | 0.0244 | 0.0403 | 0.0520 |
| $R_w$[b] | 0.0874 | 0.0601 | 0.1003 | 0.1415 |
| GOF on $F^2$ | 1.000 | 1.072 | 1.132 | 1.139 |

[a] $R = \Sigma||F_o| - |F_c||/\Sigma|F_o|$. [b] $R_w = \{[\Sigma(|F_o|^2|F_c|^2)^2]\}^{1/2}$.

Table 2. Selected bond lengths and angles for [Ni($1^{EN}$)] (**1**), [Ni($2^{EN}$)] (**2**), [Ni($3^{OP}$)] (**3**), and [Ni($4^{OP}$)] (**4**).

| Bond length | [$Ni^{II}$($1^{EN}$)] (**1**) | [$Ni^{II}$($2^{EN}$)] (**2**) | [$Ni^{II}$($3^{OP}$)] (**3**) | [$Ni^{II}$($4^{OP}$)] (**4**)[a] |
|---|---|---|---|---|
| Ni1–N1 | 1.806(3) | 1.822(4) | 1.801(2) | 1.812(4), 1.824(4) |
| Ni1–N2 | 1.808(3) | 1.813(3) | 1.805(2) | 1.803(4), 1.817(4) |
| Ni1–N3 | 1.904(2) | 1.910(3) | 1.889(2) | 1.901(4), 1.896(4) |
| Ni1–N4 | 1.908(3) | 1.910(4) | 1.890(2) | 1.896(4), 1.897(4) |
| C3–O2 | 1.232(4) | 1.260(3) | 1.224(4) | 1.232(6), 1.230(6) |
| C10–O1 | 1.232(4) | 1.253(3) | 1.227(4) | 1.229(6), 1.237(5) |
| Bond angles | | | | |
| N1–Ni1–N2 | 87.40(11) | 87.90(12) | 87.24(10) | 87.33(18), 87.60(17) |
| N3–Ni1–N4 | 92.36(11) | 92.08(12) | 92.44(11) | 92.00(17), 91.89(16) |
| N1–Ni1–N3 | 89.57(11) | 89.76(12) | 89.65(11) | 89.90(17), 89.47(16) |
| N2–Ni1–N4 | 88.83(11) | 89.05(12) | 89.86(10) | 89.71(18), 89.78(17) |
| N1–Ni1–N4 | 171.31(12) | 170.43(9) | 172.09(11) | 171.97(17), 169.59(16) |
| N2–Ni1–N3 | 166.93(11) | 172.31(7) | 173.26(11) | 171.76(18), 172.51(16) |

[a] There are two independent molecules in the asymmetric unite cell. Metric parameters are reported for both independent molecules.

 © 2007 Wiley-VCH Verlag GmbH & Co. KGaA, Weinheim 

The average Ni–$N_{amide}$ and Ni–$N_{amine}$ distances at ca. 1.81 Å and 1.91 Å, respectively, for complex **2** are identical to **1**. The other distances and angles are comparable to that of **1**. However, the amine carbon centers emerging from the 1, 2-diaminobenzene are now planar as a result of the involvement of a rigid phenylene unit. Interestingly the carbon centers of the $–CH_2CH_2–$ fragments connected to the amide part of the macrocyclic ligand are now adopting a partial *gauche* conformation.[11] Moreover, the unit cell has a water molecule which is hydrogen bonded to the amide oxygen atoms from two different molecules of **2**. The consequence is the formation of a zig–zag chain with alternate arrangement of complex **2** and $H_2O$ (Figure S1).

The average bond lengths for **3** are simialr to that of **1** and **2**. The $–CH_2CH_2–$ fragment of the amine part is now adopting envelope conformation[11,19] in contrast to the gauche conformation of **1**. Moreover, the incorporation of the phenylene group as part of the macrocyclic backbone resulted in a more planar arrangement of the chelate involving two amidic nitrogens than in case of **1** and **2** (cf. Table S1).

In line with other three complexes, the bond lengths and angles for the complex **4** are also comparable. Interestingly, due to the involvement of the phenylene groups both from the amide part of the macrocyclic backbone as well as the amine part of the macrocyclic backbone, the attached carbon centers have become co-planar as can be seen by their respective angles. However, the molecule as a whole is non-planar and adopts a saucer shaped conformation (lateral view, Figure S2).

The average Ni–$N_{amide}$ bond lengths of the present complexes are shortest among the reported examples having a similar coordination environment.[10f,10g,11,12] For example, the average Ni–$N_{amide}$ bond lengths for the $Ni^{II}$ complexes of the ligands, dioxo[13]ane$N_4$ and dioxo[14]ane$N_4$ are 1.839 and 1.889 Å, respectively.[11] In fact, the average Ni–$N_{amide}$ bond lengths distance of the complexes reported in this work are 0.04–0.05 Å shorter than the mentioned examples. This is worth to mention here that the average Ni–$N_{amide}$ bond lengths of a $Ni^{III}$ complex of a tetraamide ligand of Collins[20] is ca. 1.84 Å which is 0.04 Å longer than our complexes.

The deviation of the $Ni^{II}$ ion from the coordination basal plane (defined by N1, N2, N3, and N4) is an indication of the optimal placement of the metal ion within the macrocyclic aperture. This out of $N_4$ basal plane displacement is maximum for the **1** (0.170 Å) and minimum for the **4** (0.110 Å) with other two complexes **2** and **3** have intermediate values. These numbers suggest that the $Ni^{2+}$ ion is most tightly and optimally placed in **4** (Table S1).

The angles between the various planes are presented in Table S1. In general, the plane involving $N_{amide}$ centers (N1 and N2) are comparatively planar due to the enhanced delocalization in the amidate fragment. The angle between the plane comprising both $N_{amide}$ (Ni1, N1, C1, C2, and N2) and the plane involving both $N_{amine}$ (Ni1, N4, C6, C7, and N3) is quite significant. This value varies from 23.62° to 28.70° in all four cases and explains the reason for a saucer-shaped structure of the complexes (lateral view, Figure S2). Similarly, the angle between planes involving lateral carbon centers varies from 30.27° for **3** to 40.29° for **1** and points out towards the envelope conformation.

### Absorption Spectral Studies

The absorption spectra of **1**–**4** complexes in MeCN are displayed in Figure 5. All complexes are deep yellow in color and their absorption spectra display distinct features for the four-coordinate square planar $Ni^{II}$ ion. Complexes **1**–**4**, display the $\lambda_{max}$ within a small range of 436 to 444 nm, thus indicating a similar electronic environment created by the ligand around the Ni ion. The observed similarity between the absorption features of complexes is also reflected in their very similar solid state crystal structures (vide supra) as well as NMR spectra (vide infra). High energy features are observed below 310 nm and could tentatively be assigned as intra-ligand transitions. The absorption spectral features of $Ni^{II}$ complexes of macrocyclic ligands have been subjected to detailed investigations to understand the ligand planarity and the placement of the Ni center in the cavity of the macrocycle.[8,10a,21] It has been suggested that the lower the $\lambda_{max}$ value for the $Ni^{II}$ complex better the fitting of the $Ni^{II}$ center inside the macrocyclic cavity. Comparing the $\lambda_{max}$ values of the $Ni^{II}$ complexes, it is clear that the complexes **1** and **2** differ marginally with each other, while the complexes **3** and **4** indicate an almost identical placement. These data indicate that in the solution state the $Ni^{II}$ ion is most optimally placed within the basal plane provided by the ligand framework in the following order: **1**, **2**, **3** ≈ **4**.

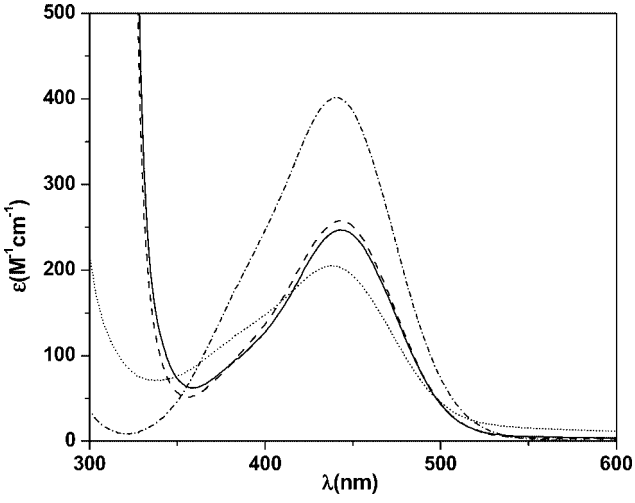


Figure 5. UV/Vis spectra of $Ni^{II}$ complexes in $CH_3CN$: complex **1** (-·-·-·-·), complex **2** (——), complex **3** (----), and complex **4** (·····).

In order to analyze the binding affinity of the axial ligands towards the present square planar $Ni^{II}$ complexes, **1**–**4** were titrated with few potential monodentate ligands [$Cl^–$, pyridine, 4-(dimethylamino)pyridine]. No change in the absorbance maximum was observed for any of the four complexes. This experiment rules out the binding affinity of

 © 2007 Wiley-VCH Verlag GmbH & Co. KGaA, Weinheim 

such ligands towards nickel complexes. For the similar reason, absorption spectra were also recorded in better coordinating solvent, for example, DMF, DMSO, and $H_2O$ (Figure S3, S4, and S5). The $\lambda_{max}$ was observed in a narrow range (430–444 nm) for all four complexes, thus again eliminates the possibility of the solvent coordination. A shoulder at ca. 380 nm was also noticed for all complexes; the intensity of this shoulder was found to vary with the solvent of study.

### Nuclear Magnetic Resonance Studies

To investigate the solution state structures of the nickel complexes, their $^1H$ and $^{13}C$ NMR spectroscopic studies were performed (Figures S6, S7, S8, S9 and Table 3, Table S2). $^1H$ NMR spectra of all complexes were recorded in [$D_6$]DMSO as well as in $CD_3CN$ and are very similar. All complexes, **1**–**4** are diamagnetic with $S = 0$ ground state as displayed by their diamagnetic NMR spectra. Assignments of the signals have been made through the consideration of the relative peak areas and comparison with free ligand spectrum. However, in the case of complex **1**, 2D {$^1H$-$^{13}C$} correlation spectrum was also performed to accurately assign various signals (Figure S10). The $^1H$ NMR spectra of all complexes are quite interesting and deserve special attention. The twisting of the $–CH_2CH_2–$ fragment (of the *N*,*N*′-dimethylethylenediamine part) results in the different chemical environment of the protons attached to these carbon centers. Two sets of H signals were observed as multiplets for complex **1** and **3** at 2.67 and 3.76; and 2.74 and 3.86 ppm, respectively (labeled as proton *a* and *c*, respectively). The $–CH_2CH_2–$ fragment of the deprotonated amide backbone was also twisted and resulted in the appearance of the multiplets at $\delta = 2.67$ and 3.21 ppm (labeled as proton *a* and *b*, respectively) for **1**, and 2.78 and 3.22 ppm for **2**, respectively. Coincidently, for complex **1**, one of the $–CH_2–$ group's proton signals (labeled as proton *a*) were observed at the same position suggesting a similar chemical environment. The most interesting aspect of the spectra of all complexes **1**–**4** is the observation of the AB-type coupling (or geminal coupling) between the protons attached to the $–C(O)CH_2–$ fragment.[11,12] The signals for the pair of protons from the $–C(O)CH_2–$ fragment (*d* and *e*) appear at $\delta = 3.07$ and 4.00 ppm for **1**, 3.70 and 4.15 for **2**, 3.12 and 4.13 ppm for **3**, and 3.89 and 4.43 ppm for **4**. The geminal coupling constant, $J(H^dH^e)$ for complexes **1** and **3** was 15.9 Hz, while a value of ca. 15.5 Hz was observed for **2** and **4**, respectively. The observation of the AB-type coupling in these complexes suggests the rigid nature of the macrocyclic ligands that places protons *d* and *e* in different chemical environment. In general, the $^1H$ NMR spectra of the transition metal complexes of azamacrocyclic ligands are complicated due to the "frozen" conformation of the chelate rings[11,12] and the spectra of **1**, **2**, **3**, and **4**

Table 3. $^1H$ NMR data of [$Ni^{II}(1^{EN})$] (**1**), [$Ni^{II}(2^{EN})$] (**2**), [$Ni^{II}(3^{OP})$] (**3**), and [$Ni^{II}(4^{OP})$] (**4**).[a]

| Proton | [$Ni^{II}(1^{EN})$] (**1**) | [$Ni^{II}(2^{EN})$] (**2**) | [$Ni^{II}(3^{OP})$] (**3**) | [$Ni^{II}(4^{OP})$] (**4**) |
|---|---|---|---|---|
| | 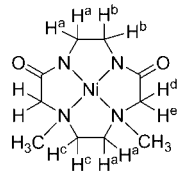 | 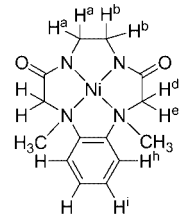 | 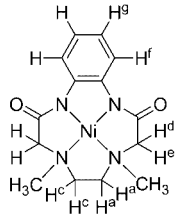 | 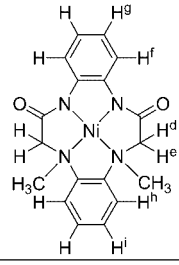 |
| a | 2.67, m (2.66, m) | 2.78, m (2.73, m) | 2.74, m (2.80, m) | – |
| b | 3.21, m (3.25, m) | 3.22, m (3.23, m) | – | – |
| c | 3.76, m (3.69, m) | – | 3.86, m (3.89, m) | – |
| d | 3.07, d, $J = 15.9$[b] (3.08, d, $J = 15.9$[b]) | 3.70, d, $J = 15.5$[b] (3.58, d, $J = 15.6$[b]) | 3.12, d, $J = 15.9$[b] (3.28, d, $J = 16.2$[b]) | 3.89, d, $J = 15.5$[b] (3.80, d, $J = 15.3$[b]) [3.86, d, $J = 15.14$[b]] |
| e | 4.00, d, $J = 15.9$[b] (3.90, d, $J = 15.9$[b]) | 4.15, d, $J = 15.5$[b] (4.13, d, $J = 15.3$[b]) | 4.13, d, $J = 15.9$[b] (4.14, d, $J = 15.9$[b]) | 4.43, d, $J = 15.6$[b] (4.42, d, $J = 15.5$[b]) [4.51, d, $J = 15.12$[b]] |
| f | – | – | 7.41, m (7.56, m) | 7.55, m (7.62, m) [7.76, m] |
| g | – | – | 6.54, m (6.70, m) | 7.55, m (7.44, m) [7.49, m] |
| h | – | 7.47, m (7.36, m) | – | 6.67, m (7.30, m) [7.25, m] |
| i | – | 7.47, m (7.26, m) | – | 6.67, m (6.65, m) [6.85, m] |
| $-CH_3$ | 2.49, s (2.45, s) | 2.87, s (2.79, s) | 2.52, s (2.64, s) | 3.01, s (3.00, s) [3.06, s] |

[a] Spectra are recorded in [$D_6$]DMSO. Parentheses ( ) and square brackets [ ] indicate values of spectra recorded in $CD_3CN$ and $CDCl_3$, respectively. Abbreviations: s = singlet; d = doublet; m = multiplet. [b] Geminal coupling constant.

 © 2007 Wiley-VCH Verlag GmbH & Co. KGaA, Weinheim 

are no exception. Conformational rigidity of such systems results from the fact that the inversion of the chelate rings requires a change of the configuration of the coordinated amine nitrogen atom(s). The complex nature of the $^1$H NMR spectra of **1**–**4** is most likely arising due to the macrocyclic nature of the coordinated ligand. The inherent strain of the macrocyclic ligand have caused few of the carbon centers to be out of the plane as also observed in the crystal structure determination (vide supra).

In contrast to the proton NMR spectra, the $^{13}$C NMR spectra of **1**–**4** are quite straight forward (Table S2, Figure S9). Even though proton NMR spectra reflected the complexity arising due to the non-planarity of few carbon centers that resulted in the different chemical environment for the attached protons, the carbon NMR spectra were averaged out. A close similarity in the $^{13}$C chemical shifts of identical carbon centers was observed for all complexes. For example, the methyl C signals were observed in a close range of 47–52 ppm. Similarly, the chemical shift for the carbon centers of *N*,*N*′-dimethylethylenediamine part (labeled as *d*) were seen at $\delta \approx 60$ ppm for **1** and **3**.

There was no evidence of any paramagnetic species in the NMR spectra, which show that the Ni$^{II}$ complexes retain their square-planar geometry in solution. This observation also corroborate the identical conclusion drawn from the absorption spectral studies that the Ni$^{II}$ complexes of the present ligands do not bind various axial ligands [Cl$^-$, pyridine, 4-(dimethylamino)pyridine, or solvents, etc.].

## Electrochemical Studies

Cyclic voltammetric (CV) and controlled potential electrolysis (coulometric) studies were performed for all four Ni$^{II}$ samples to investigate the extent of stabilization of the Ni$^{III}$ state as well as the possible ligand oxidation.[22] In addition, the CV results will also help in understanding the accessibility of the higher oxidation states and the effect of the ligand architecture on the redox potential. The electrochemical data for complexes **1**–**4** are summarized in Table 4.

### *Electrochemistry in CH$_3$CN*

The 1$^{st}$ oxidation process for all complexes is displayed in Figure 6, while the complete oxidation range is shown for complex **4** (Figure 7). In $CH_3CN$, for 1$^{st}$ oxidation, each complex undergo 1e$^-$ oxidation in the potential range of 0.61–0.83 V (vs. SCE). The one electron nature of each redox response has been confirmed by the controlled potential electrolysis experiments. The peak-to-peak separation ($\Delta E_p$) for the 1$^{st}$ response, for complexes **1**–**4** are in the range of 60–100 mV and point out towards reversible to quasi-reversible nature of the responses (Table 4). For comparison, the redox potential for the complex, [Ni(dioxo[12]-aneN$_4$)] is 0.62 V[10b] (vs. SCE in $H_2O$) while Ni complexes of 13- and 14-analogues appear at higher potential (> 0.80 V, Table 4).[10b–10e,10g] No reduction wave was observed in the potential range studied (–2.0 V for $CH_3CN$ and –2.2 V for DMF vs. SCE).

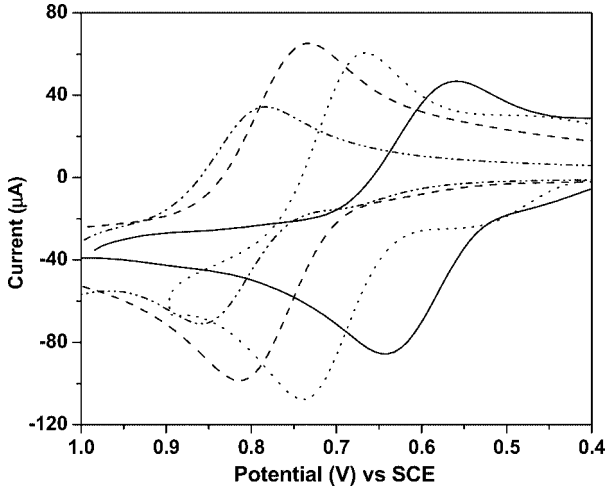


Figure 6. Cyclic voltammograms of Ni$^{II}$ complexes in $CH_3CN$: complex **1** (——), complex **2** (----), complex **3** (·····), and complex **4** (-·-·-·-·).

The complex **1** show only one oxidation response at 0.61 V ($\Delta E_p$ = 90 mV), as expected for the Ni$^{II}$ complex of a perfect innocent ligand. On the other hand, rest of the

Table 4. Cyclic voltammetric data[a] for [Ni(1$^{EN}$)] (**1**), [Ni(2$^{EN}$)] (**2**), [Ni(3$^{OP}$)] (**3**), and [Ni(4$^{OP}$)] (**4**) and comparison with literature examples.

| Complex | $E_1$ [V] in $CH_3CN$ ($\Delta E_p$ [mV]); $n$[c] | $E_2$ [V] in $CH_3CN$ ($E_{pa}$); $n$[c] | $E_3$ [V] in $CH_3CN$ ($E_{pa}$); $n$[c] | $E_1$ [V] in DMF[b] ($\Delta E_p$ [mV]) | $E_2$ [V] in DMF[b] ($E_{pa}$) | Ref. |
|---|---|---|---|---|---|---|
| [Ni(1$^{EN}$)] (**1**) | 0.61 (90); 0.94 | – | – | 0.53 (100) | – | this work |
| [Ni(2$^{EN}$)] (**2**) | 0.78 (100); 0.96 | 1.88; 1.91 | – | 0.67 (110) | – | this work |
| [Ni(3$^{OP}$)] (**3**) | 0.71 (70); 1.00 | 1.10; 1.98 | – | 0.67 (80) | 1.13 | this work |
| [Ni(4$^{OP}$)] (**4**) | 0.83 (73); 1.02 | 1.13; 1.96 | 1.32; 2.9 | 0.78 (90) | 1.20 | this work |
| [Ni(dioxo[12]aneN$_4$)][d] | 0.62 (100) | | | | | [10b] |
| [Ni(dioxo[13]aneN$_4$)][d] | 0.90 (80) | | | | | [10b,d,e,g] |
| [Ni(dioxo[14]aneN$_4$)][d] | 0.80 (80) | | | | | [10b,c] |
| [Ni(dioxo[15]aneN$_4$)][d] | 0.62 (100) | | | | | [10b] |

[a] Conditions: Complex ca. 1 mM solution, TBAP as supporting electrolyte as ca. 100 mM solution, potential vs. SCE, glassy carbon as working electrode, Pt as auxiliary electrode, scan rate = 100 mV/s. [b] Pt as working electrode, other conditions are identical. [c] Coulombic $n$ (number of electron(s) taking part in the oxidation process). [d] in water with $Na_2SO_4$ as supporting electrolyte and glassy carbon as working electrode.

 © 2007 Wiley-VCH Verlag GmbH & Co. KGaA, Weinheim 

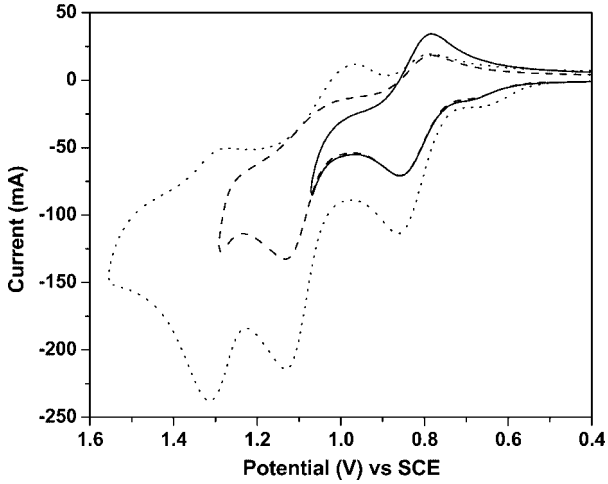


Figure 7. Cyclic voltammogram of complex **4** in $CH_3CN$.

complexes, **2**, **3**, and **4** display oxidation waves corresponding to both metal as well as the ligand oxidation(s). The extent of the non-innocent feature(s) increases in the following order: **1** > **2** ≈ **3** > **4**. The complex **2** display oxidation waves at 0.78 and 1.88 V ($E_{pa}$), which we assign as the $Ni^{III/II}$ response and irreversible ligand oxidation, respectively. The similar responses for the complex **3** were observed at 0.71 and 1.1 V ($E_{pa}$), respectively. For complex **3**, the occurrence of the ligand oxidation potential at much lower potential is most likely due to the involvement of the ring π–current in resonance with the nickel *d*-electrons. The complex **4** exhibits three oxidation peaks at 0.83 V, 1.13 ($E_{pa}$), and 1.32 ($E_{pa}$) V, while the 1st one is metal-centered, the other two processes are ligand-centered. It has been found that the ligands incorporating 1,2-diaminobenzene ring are susceptible to oxidation, generating a cation radical.[22c,23,24] Based on these literature reports we tentatively assign the redox processes observed at >1.1 V located on the ligand π-system.[24f,24g]

A comparison of the stepwise redox potential values of the $[Ni(Ligand)]^+/[Ni(Ligand)]$ ($E_1$) and $[Ni(Ligand)]^{2+}/[Ni(Ligand)]^+$ ($E_2$) couples for all four complexes, **1**–**4** allows the establishment of the nature of the singly, doubly, and in one case triply oxidized species along the present series of the complexes. The four different ligands used in the present study differ only by the placement of the amine and amide fragments within the ethylene or *o*-phenylene part that coordinate to the nickel ion. For example, the ligand $H_2\mathbf{1}^{EN}$ is an innocent one while the other three ligands have at least one non-innocent feature, either in the form of extended π-conjugated *o*-phenylenediamidate fragment or *N*,*N*′-dimethyl-*o*-phenylenediamine fragment. The significant shift in the $E_1$ potentials of complexes **1**–**4** toward more positive values according to $[\mathbf{1}^{EN}]^{2-} < [\mathbf{3}^{OP}]^{2-} < [\mathbf{2}^{EN}]^{2-} < [\mathbf{4}^{OP}]^{2-}$ clearly indicates that the 1st oxidation is metal-centered, leading to a $Ni^{III}$ species. The destabilization of the trivalent oxidation state by increasing the π-conjugated *o*-phenylene fragment(s) is attributed to the poor donor capacity of such ligands due to the delocalization of the negative charge on the deprotonated amide groups into the attached phenylene fragment.[25,26]

In contrast, the $E_2$ value for the second oxidation, for complexes and **3** and **4**, appear at ca. 1.1 V and does not vary upon changing the ligand. This situation is more consistent with ligand-centered oxidation at the *o*-benezenediamidate fragment, generating the $Ni^{III}$-*o*-benzosemiquinonediimine π-cation species.[25] The almost identical potential for $E_2$ (except for complex **2**) rules out metal-centered oxidation as that would have resulted in altered potential due to the ligand field effect. For complex **2**, an irreversible response was observed at a very high potential (ca. 1.9 V vs. SCE). We tentatively assign this response as the oxidation of the *o*-phenylene-*N*,*N*′-dimethyldiamine fragment. The reason for very high positive potential could be due to the non-conjugation of the $sp^3$-based fragment with Ni center. Interestingly, a 3rd potential ($E_3$) for the complex **4** was noticed as an irreversible process at ca. 1.3 V vs. SCE. We again assign this redox process based at the *N*,*N*′-dimethyl-*o*-phenylenediamine fragment. However, why this oxidation appears at a lower potential than the complex **2** is not clear to us.

### *Electrochemistry in DMF*

CV studies were also carried out in DMF to understand the effect of a more polar and better coordinating solvent. A comparative CV plot is shown in Figure 8 while the data are presented in Table 4. As can be seen from the Table 4, the $Ni^{III}/Ni^{II}$ potential are between the range of 0.53 V, lowest for complex **1**, and 0.78 V, highest for complex **4**. A similar trend has been observed before in $CH_3CN$. However, in general, the $Ni^{III}$ state is more stabilized by 40 mV for complex **3** to 110 mV for **2** in DMF than in MeCN. This investigation reveals that the $Ni^{III}$ state of the complexes is better stabilized due to the enhanced solvation, as the polarity of the solvent increased. Ligand-centered oxidation ($E_{pa}$) for complexes, **3** and **4** were observed at 1.13 and

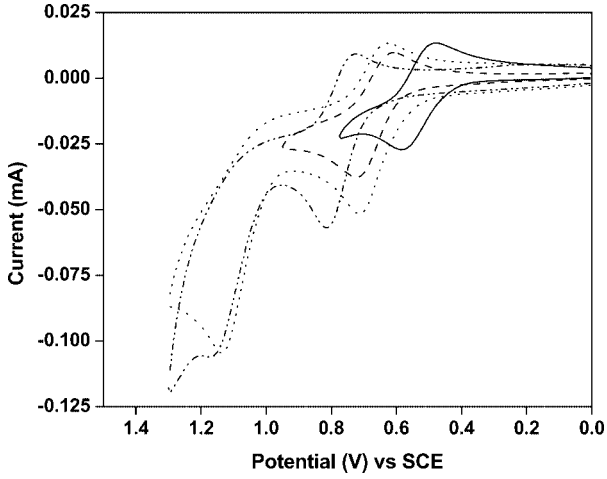


Figure 8. Cyclic voltammograms of $Ni^{II}$ complexes in DMF: complex **1** (——), complex **2** (----), complex **3** (·····), and complex **4** (-·-·-·-).

 © 2007 Wiley-VCH Verlag GmbH & Co. KGaA, Weinheim 

1.20 V, respectively, as noted before in MeCN. The observed potentials are consistent with the oxidation of *o*-benzenediamidate fragment, generating the $Ni^{III}$-*o*-benzosemiquinonediimine π-cation species. Finally, the oxidation of the *N*,*N*′-dimethyl-*o*-phenylenediamine fragment was not observed within the solvent limit.

### *Electrochemical Oxidation and Spectroscopic Characterization of the Oxidized Species*

The singly oxidized forms of complexes, **1**–**4** were generated electrochemically in $CH_3CN$ solution and characterized by the absorption and EPR spectroscopy. The electrochemical oxidation of the solution containing the respective $Ni^{II}$ complex generated a metastable green to greenish-brown species which was stable enough to record the absorption (Figure 9) and the EPR spectra (Figure 10).

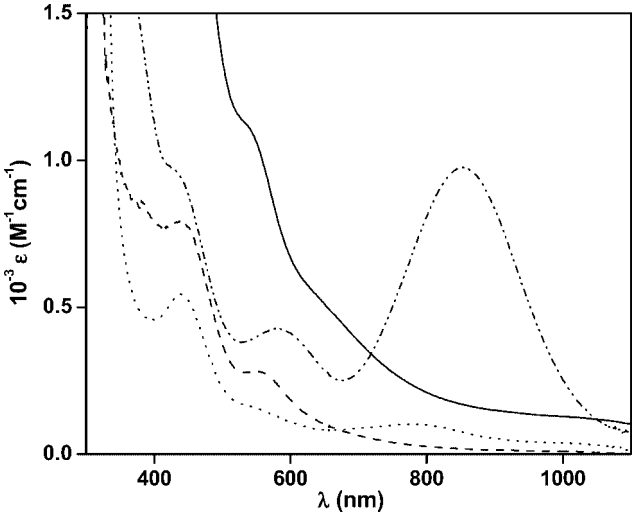


Figure 9. Absorption spectra of electrochemically generated $[\mathbf{1}^{Ox}]^+$, $[\mathbf{2}^{Ox}]^+$, $[\mathbf{3}^{Ox}]^+$, and $[\mathbf{4}^{Ox}]^+$ in $CH_3CN$: complex $[\mathbf{1}^{Ox}]^+$ (——), complex $[\mathbf{2}^{Ox}]^+$ (----), complex $[\mathbf{3}^{Ox}]^+$ (-·-·-·-), and complex $[\mathbf{4}^{Ox}]^+$ (·····).

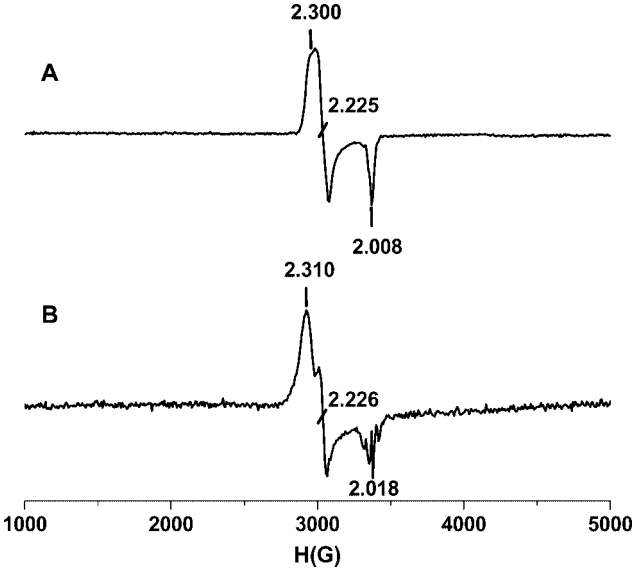


Figure 10. EPR spectra of electrochemically generated $[\mathbf{2}^{Ox}]^+$ (A) and $[\mathbf{3}^{Ox}]^+$ (B) species in $CH_3CN$ at 100 K.

The absorption spectra of these oxidized complexes have rich features and are dominated by a string of charge-transfer bands having ε values in the range of 200–1000 $M^{-1}cm^{-1}$. For complex **1**, the oxidized species $[\mathbf{1}^{Ox}]^+$ was generated after oxidizing the solution at 0.8 V vs. SCE and resulted in a brownish-green colored solution. This solution displays broad features at ca. 1000, ca. 660 and ca. 540 nm and justifies its brownish-green color. The $[\mathbf{2}^{Ox}]^+$ was generated after setting the potential at 0.95 V vs. SCE and produced a green solution with $\lambda_{max}$ at 555 and 437 nm. An intense deep green solution resulted when the complex **3** was oxidized at 0.90 V. Here, an exceptionally intense peak with $\lambda_{max}$ at 855 nm (ε ca. 1000 $M^{-1}cm^{-1}$) was noticed along with two weak features at 580 and ca. 430 nm. Qualitatively, this oxidized species was also the most stable one. We believe that the close proximity of the *o*-benzenediamidate fragment with the $Ni^{III}$ center has helped in the delocalization of the unpaired spin onto the ligand's π orbitals. This enhanced delocalization has resulted in the better stability of the green species as well as the occurrence of the intense and broad absorption features in the visible region. In contrast, a less stable pale-green species resulted after the oxidation at 1.0 V for complex **4**. For $[\mathbf{4}^{Ox}]^+$, the absorption features were observed at ca. 1020, 780, ca. 550, and 440 nm. By a purely qualitative comparison, the oxidized species $[\mathbf{2}^{Ox}]^+$ and $[\mathbf{4}^{Ox}]^+$ are more unstable than the other two species, $[\mathbf{1}^{Ox}]^+$ and $[\mathbf{3}^{Ox}]^+$. The most probable reason is that the incorporation of the non-planar *N*,*N*′-dimethyl-*o*-phenylenediamine fragment in the complexes, **2** and **4** (cf. crystal structures) may have increased the distortion at the nickel center and diminish the possibility of the delocalization of the unpaired spin accumulated on the $Ni^{III}$ ion.

The $Ni^{II}$ complexes of various macrocyclic ligands listed in Scheme 1 have also been reported for their ability to stabilize the $Ni^{III}$ state. The electrochemical or chemical oxidation of the aqueous solution resulted in the generation of a "brown" species that displays transitions in the UV region, 300–360 nm.[10b,10d,27,28] The nature of these transitions has been suggested to be charge transfer. A six-coordinate species has been suggested with solvent molecules serving as the axial ligands. Recently, Journaux and Garcia have reported a solution generated $Ni^{III}$ species of a tetradentate tetraamide ligand.[25c] For this systems, the $\lambda_{max}$ for the $Ni^{III}$ species was observed at 910 with a shoulder at 760 nm. The observed similarity between the $Ni^{III}$ species of Journaux and Garcia to that of our systems suggest a similar electronic chromophore.[25c]

The solution generated oxidized species, $[\mathbf{1}^{Ox}]^+$ – $[\mathbf{4}^{Ox}]^+$, display anisotropic signals in their X-band EPR spectra. The EPR spectra of the singly oxidized $Ni^{III}$ –complexes, $[\mathbf{2}^{Ox}]^+$ and $[\mathbf{3}^{Ox}]^+$ in the frozen $CH_3CN$ solution at 100 K are shown in Figure 10. The spectra consist of a rhombic signal characteristic of a four-coordinate square-planar $Ni^{III}$ (a $d^7$ low-spin system) with an $S = 1/2$ ground state. The individual *g* values for $[\mathbf{1}^{Ox}]^+$ and $[\mathbf{2}^{Ox}]^+$ are 2.360, 2.167, and 2.005 and 2.300, 2.225, and 2.008, while for the $[\mathbf{3}^{Ox}]^+$ and $[\mathbf{4}^{Ox}]^+$ are 2.310, 2.226, and 2.018, and 2.205, 2.188, and 2.006, respectively. The large rhombicity and the

 © 2007 Wiley-VCH Verlag GmbH & Co. KGaA, Weinheim 

high average $g$ values ($g_{avg} = (g_1 + g_2 + g_3)/3$; 2.177, 2.178, 2.185, and 2.133, for $[\mathbf{1^{Ox}}]^+$, $[\mathbf{2^{Ox}}]^+$, $[\mathbf{3^{Ox}}]^+$, $[\mathbf{4^{Ox}}]^+$, respectively) unambiguously indicates that the oxidation is located on the Ni center, thereby confirming the $Ni^{III}$ nature of the singly oxidized species.[25] In case ligand oxidation had occurred, the resulting cation-radical would likely to exhibit an isotropic EPR spectrum with g value close to the free electron value of 2.002.[25a,25b] Moreover, the presence of three distinct signals ($g_1$, $g_2$, and $g_3$) in the spectrum also rules out the existence of a 5-or 6-coordinate species in solution as that would give an axial signal with $g_\perp > g_\parallel$. In fact, the solution generated $Ni^{III}$ species of the dioxo[14]-ane$N_4$ ligand displays $g_\perp$ at 2.23 and $g_\parallel$ at 2.02 with $g_\perp > g_\parallel$.[28] These findings along with the absorption spectroscopic data strongly suggest that the present Ni complexes remain four-coordinated. The observation of the three different g values at 2.193, 2.080, and 2.006 for the $Ni^{III}$ species reported by the Journaux and Garcia, are quite similar to the present systems, thus again indicating a similar electronic structure. In fact, these authors have suggested that the unpaired electron occupies a π-type metal 3d orbital and thus attesting the metal-centered oxidation rather than the ligand-centered oxidation.[25c]

Our efforts to characterize the doubly oxidized species were unsuccessful owing to very unstable nature of the respective species. The electrochemical oxidation at the 2nd (for **2**, **3** and **4**) and 3rd potential (for **4** only) immediately lead to the decomposition of the transiently generated species. It is to be noted, however, that all these redox processes were $1e^-$ in nature as determined by the coulometry.

### Chemical Oxidation and Vindication of Electrochemical Findings

The accessible redox potentials (cf. Table 4) of the complexes **1**–**4** and the successful electrochemical generation of the singly oxidized forms, $[\mathbf{1^{Ox}}]^+$ – $[\mathbf{4^{Ox}}]^+$, prompted us to try chemical oxidation. A number of $1e^-$ oxidants were attempted (for example, $(NH_4)_2[Ce(NO_3)_6]$, $[NO]BF_4$, and AgOTf),[29] however, a mixture of species and decomposed products avoided the clear conversion, until a rather uncommon oxidant, $Cu(OTf)_2$ was used. The redox potential of the $Cu(OTf)_2$ in $CH_3CN$ is 0.8 V vs. SCE[29] and clearly seem to cause oxidation at the first oxidation potential of the complexes **1**–**4**. Indeed, addition of 1.2 equiv. of the $Cu(OTf)_2$ to a $CH_3CN$ solution of the respective $Ni^{II}$ complex, resulted in a clean $1e^-$ oxidation. The chemical oxidation of the solution containing the respective Ni complex generated a green to greenish-brown species as observed electrochemically before. The UV/Vis spectra of the chemically oxidized form were recorded and found to be identical as shown in Figure 9. EPR spectra of the oxidized species were not attempted due to the possible contamination from the unreacted $Cu(OTf)_2$.

## Conclusions

The presented work demonstrates the syntheses and characterization of four novel square-planar $Ni^{II}$ complexes with amide-amine-based macrocyclic ligands. The important findings of the present study are summarized as follows:

(1) To the best of our knowledge, for the first time a systematic investigation has been carried out to understand the structural, spectroscopic and redox properties of the $Ni^{II}$ ion in a set of 12-membered macrocyclic ligands.

(2) Crystal structures show a very tight binding of the Ni ion by the macrocyclic ligand in all four cases. Some of the Ni–$N_{amide}$ bond lengths are the shortest amongst the literature examples.

(3) The occurrence of the geminal coupling for few protons in the proton NMR spectra clearly depict the inherent strain present in the macrocycle of the $Ni^{II}$ complexes.

(4) The low-valent $Ni^{II}$ complexes are capable of undergoing one, two and in one case three $1e^-$ oxidations that are successively metal-and ligand-centered, as revealed by the trend observed in the formal redox potentials on changing the ligand along the present series of the complexes.

(5) The $Ni^{III}$ species were generated in solution both electrochemically and chemically [after oxidizing with $Cu(OTf)_2$] and shown to have rich spectroscopic features.

(6) The unstable $1e^-$ oxidized species are concluded to be $Ni^{III}$ species by the absorption spectra and their anisotropic EPR spectra typical for a $Ni^{III}$ ion in a square-planar geometry.

(7) The $2e^-$ and $3e^-$ oxidations, which are ligand-centered, lead to immediate decomposition, and prevented us to characterize this species.

## Experimental Section

**Materials and Reagents:** All reagents were obtained from commercial sources and used as received. *N*,*N*′-Dimethylformamide (DMF) was dried and distilled from 4-Å molecular sieves and stored over sieves. Acetonitrile (MeCN) was dried by distillation from anhydrous $CaH_2$. Diethyl ether was dried by refluxing over sodium metal wires under inert atmosphere. Tetrahydrofuran (THF) was dried by refluxing and distilling from sodium metal and benzophenone. Ethyl alcohol ($C_2H_5OH$) and methyl alcohol ($CH_3OH$) were distilled from magnesium ethoxide and magnesium methoxide, respectively. Chloroform ($CHCl_3$) and dichloromethane ($CH_2Cl_2$) were purified by washing with 5% aqueous sodium carbonate solution followed by water and finally dried with anhydrous $CaCl_2$, before a final reflux and distillation. Petroleum ether (boiling range: 60–80 °C) and hexanes (boiling range: 60–80 °C) were dried by refluxing and distilling over sodium metal wires. *N*,*N*′-bis(chloroacetyl)ethylenediamine and *N*,*N*′-bis(chloroacetyl)-*o*-phenylenediamine were prepared according to a published procedure.[14]

### Ligand Syntheses

**$H_2\mathbf{1}^{EN}$:** LiBr (0.8 g, 9 mmol), $Na_2CO_3$ (4.0 g, 40 mmol) and *N*,*N*′-bis(chloroacetyl)ethylenediamine (1.0 g, 5 mmol) were taken in MeCN (140 mL) and the mixture was refluxed with stirring for 1 h. To this was added *N*,*N*′-dimethylethylenediamine (0.4 g, 5 mmol) dissolved in MeCN (20 mL). The resulting mixture was refluxed whilst stirring for an additional 48 h. The mixture was cooled, filtered and the solvent was removed under reduced pressure to afford a semi-mass. The crude product was further purified by column

 © 2007 Wiley-VCH Verlag GmbH & Co. KGaA, Weinheim 

chromatography using silica gel (100–200 mesh) with 10% MeOH/$CHCl_3$ ($R_f$ = 0.45). A white product was obtained after purification. Yield 0.15 g (16%). An analytically pure product (in ca. 75% yield) can also be obtained by recrystallizing the crude product by layering the $CHCl_3$ solution with the petroleum ether (boiling range: 60–80 °C). $C_{10}H_{20}N_4O_2$ (228.30): calcd. C 52.61, H 8.83, N 24.54; found C 52.95, H 8.82, N 24.34. M.p. 170–174 °C. $^1$H NMR (300 MHz, $CDCl_3$, 25 °C): $\delta$ = 2.38 (s, 6 H, $CH_3$), 2.50 (s, 4 H, $–CH_2CH_2–$), 2.96 [s, 4 H,$–CH_2C(O)$-], 3.48 (m, 4 H, $–CH_2CH_2–$), 7.2 [s (broad), 2 H, NH] ppm. FT-IR (KBr disk): $\tilde{\nu}$ = 3310, 2940, 2840, 2820, 2781, 1651 cm$^{-1}$. MS (EI$^+$, *m*/*z*): calcd. for $C_{10}H_{20}N_4O_2$ 228.30, found 228.58.

**$H_22^{EN}$:** This ligand was synthesized in a similar manner as that of $H_21^{EN}$ with following reagents: LiBr (0.51 g, 5.8 mmol), $Na_2CO_3$ (2.49 g, 23.52 mmol), *N*,*N*′-bis(chloroacetyl)ethylenediamine (0.63 g, 2.94 mmol), and *N*,*N*′-dimethyl-*o*-phenylenediamine (0.4 g, 2.94 mmol). The crude product was recrystallized by layering the $CHCl_3$ layer with hexanes. Yield 0.250 g (30%). $C_{14}H_{20}N_4O_2$ (277.34): calcd. C 60.85, H 7.30, N 20.28; found C 60.79, H 7.18, N 19.68. M.p. 164–165 °C. $^1$H NMR (300 MHz, $CDCl_3$, 25 °C): $\delta$ = 2.85 (s, 6 H, $CH_3$), 2.78 (s, 4 H, $–CH_2–CH_2–$), 3.56 [s, 4 H, $–CH_2–C(O)–$], 7.2–7.4 (m, 4 H, arom.), 9.5 [s (broad), 2 H, NH] ppm. FT-IR (KBr disk): $\tilde{\nu}$ = 3233, 3050, 2866, 1664 cm$^{-1}$. MS (EI$^+$, *m*/*z*): calcd. for $C_{14}H_{20}N_4O_2$ 277.34, found 277.344.

**$H_23^{OP}$:** This ligand was synthesized in a similar manner as that of $H_21^{EN}$. However, this time following reagents were used: LiBr (0.7 g, 8 mmol), $Na_2CO_3$ (4.0 g, 32 mmol), *N*,*N*′-bis(chloroacetyl)-*o*-phenylenediamine (1.0 g, 4 mmol), and *N*,*N*′-dimethylethylenediamine (0.4 g, 4 mmol). The crude product was recrystallized from $CHCl_3$ solution after layering with the petroleum ether (boiling range: 60–80 °C). Yield 0.90 g (95%). $C_{14}H_{20}N_4O_2$ (276.34): calcd. C 60.85, H 7.30, N 20.28; found C 60.49, H 7.42, N 20.61. M.p. 164–165 °C. $^1$H NMR (300 MHz, $CDCl_3$, 25 °C): $\delta$ = 2.45 (s, 6 H, $CH_3$), 2.64 (m, 4 H, $–CH_2–CH_2$), 3.16 [s, 4 H, $–CH_2C(O)–$], 7.21 (m, 2 H, arom.), 7.60 (m, 2 H, arom.), 9.48 [s (broad), 2 H, NH] ppm. FT-IR (KBr disk): $\tilde{\nu}$ = 3221, 2942, 2833, 1674 cm$^{-1}$. MS (EI$^+$, *m*/*z*): calcd. for $C_{14}H_{20}N_4O_2$ 276.34, found 276.38.

**$H_24^{OP}$:** Using the aforementioned procedure, the ligand $H_24^{OP}$, was synthesized with following reagents: LiBr (1.3 g, 14.8 mmol), $Na_2CO_3$ (6.3 g, 59 mmol), *N*,*N*′-bis(chloroacetyl)-*o*-phenylenediamine (1.93 g, 7.4 mmol), and *N*,*N*′-dimethyl-*o*-phenylenediamine (1.0 g, 7.4 mmol). The crude product was recrystallized from $CHCl_3$ solution after layering with the petroleum ether (boiling range: 60–80 °C) or hexanes. Yield 1.0 g (42%). $C_{18}H_{20}N_4O_2$ (324.38): calcd. C 66.65, H 6.21, N 17.27; found C 66.7, H 6.15, N 16.98. M.p. 178–184 °C. $^1$H NMR (300 MHz, $CDCl_3$, 25 °C): $\delta$ = 2.95 (s, 6 H, $CH_3$), 3.72 [s, 4 H, $–CH_2C(O)$-], 7.12 (m, 4 H, arom.), 7.22 (m, 4 H, arom.), 7.52 [s (broad), 2 H, NH] ppm. FT-IR (KBr disk): $\tilde{\nu}$ = 3317, 3221, 2942, 2833, 1689 cm$^{-1}$. MS (EI$^+$, *m*/*z*): calcd. for $C_{18}H_{20}N_4O_2$ 324.38, found 324.60.

### Syntheses of Metal Complexes

**[$Ni^{II}(1^{EN})$] (1) Method A:** The ligand $H_21^{EN}$ (0.10 g, 0.44 mmol) was dissolved in DMF (10 mL) under magnetic stirring and solid NaH (0.023 g, 0.96 mmol) was added under nitrogen atmosphere. The resulting mixture was stirred until $H_2$ evolution was ceased. To this mixture was added a solution of $NiCl_2$ (0.057 g, 0.44 mmol) dissolved in DMF (5 mL). The resulting deep yellow solution was stirred for 3 h at room temperature. The solvent was evaporated under reduced pressure and the crude compound was isolated after washing with diethyl ether. The crude compound was dissolved in MeCN (15 mL) and passed through celite pad in a medium porosity frit. The filtrate was concentrated to 1/3$^{rd}$ of its original volume and the diffusion of diethyl ether resulted in deep yellow crystalline product in a day. The product was filtered and dried under vacuum. Yield 0.040 g (35%).

**Method B:** The ligand $H_21^{EN}$ (0.10 g, 0.439 mmol) was dissolved in MeOH (5 mL) and treated with solid NaOH (0.035 g, 0.88 mmol) under magnetic stirring. A solution of $Ni(OAc)_2$ dissolved in MeOH (6 mL) was added dropwise to the ligand solution. The resulting straw yellow solution was stirred for 2 h at room temperature. The solvent was removed under reduced pressure and the crude compound was isolated after washing with diethyl ether. The recrystallization was achieved by dissolving the crude compound in MeCN and diffusing diethyl ether. The highly crystalline deep yellow product was filtered, washed with diethyl ether and dried under vacuum. Yield 0.050 g (40%). $C_{10}H_{18.5}N_4O_{2.25}Ni$ (including $0.25H_2O$, 284.97): calcd. C 41.49, H 6.40, N 19.36; found C 41.56, H 6.39, N 19.03. FT-IR (KBr disk): $\tilde{\nu}$ = 3400, 2984, 2948, 2905, 2859, 2808, 1607 cm$^{-1}$. Conductivity ($CH_3CN$, ca. 1 mM solution, 298 K): $\Lambda_M$ = 2 $\Omega^{-1}$ cm$^2$ mol$^{-1}$. UV/Vis [$\lambda_{max}$, nm ($\varepsilon$, M$^{-1}$cm$^{-1}$)] (in $CH_3CN$): 230 sh (18200), 260 sh (6100), 436 (390). UV/Vis [$\lambda_{max}$, nm ($\varepsilon$, M$^{-1}$cm$^{-1}$)] (in DMF): 440 (400). UV/Vis [$\lambda_{max}$, nm ($\varepsilon$, M$^{-1}$cm$^{-1}$)] (in DMSO): 440 (570). UV/Vis [($\lambda_{max}$, nm ($\varepsilon$, M$^{-1}$cm$^{-1}$)] (in $H_2O$): 435 (140). MS (EI$^+$, *m*/*z*): calcd. for $C_{10}H_{18}N_4O_2Ni$ 284.08, found 285.05 (**1** + H$^+$). $^1$H NMR ([D$_6$]DMSO, 300 MHz, 25 °C): $\delta$ = 2.49 (s, 6 H, $–CH_3$), 2.67 (m, 4 H, $–CH_2–$), 3.07 (d, 2 H, $–CH_2C(O)–$), 3.21 (m, 2 H, $–CH_2–$), 3.76 (m, 2 H, $–CH_2–$), 4.00 (d, 2 H, $–CH_2C(O)–$) ppm. $^1$H NMR ($CD_3CN$, 300 MHz, 25 °C): $\delta$ = 2.45 (s, 6 H, $–CH_3$), 2.66 (m, 4 H, $–CH_2–$), 3.08 (d, 2 H, $–CH_2C(O)–$), 3.25 (m, 2 H, $–CH_2–$), 3.69 (m, 2 H, $–CH_2–$), 3.90 (d, 2 H, $–CH_2C(O)–$) ppm. $^{13}$C NMR ([D$_6$]DMSO, 300 MHz, 25 °C): $\delta$ = 48.21 ($–CH_3$), 49.07 ($–CH_2CH_2–$), 60.70 ($–CH_2CH_2–$), 69.66 ($–C(O)CH_2–$), 175.14 (C=O) ppm.

**[$Ni^{II}(2^{EN})$] (2):** This complex was synthesized following the method **A** (yield 45%) or **B** (yield 35%) for complex **1**. $C_{14}H_{19}N_4O_{2.5}Ni$ (including $0.5H_2O$, 333.01): calcd. C 46.70, H 5.83, N 15.56; found C 46.51, H 5.83, N 15.32. FT-IR (KBr disk): $\tilde{\nu}$ = 3400, 2935, 2866, 1598 cm$^{-1}$. Conductivity ($CH_3CN$, ca. 1 mM solution, 298 K): $\Lambda_M$ = 12 $\Omega^{-1}$ cm$^2$ mol$^{-1}$. UV/Vis [$\lambda_{max}$, nm ($\varepsilon$, M$^{-1}$cm$^{-1}$)] (in $CH_3CN$): 241 (7560), 440 (270). UV/Vis [$\lambda_{max}$, nm ($\varepsilon$, M$^{-1}$cm$^{-1}$)] (in DMF): 440 (270). UV/Vis [$\lambda_{max}$, nm ($\varepsilon$, M$^{-1}$cm$^{-1}$)] (in DMSO): 438 (200). UV/Vis [$\lambda_{max}$, nm ($\varepsilon$, M$^{-1}$cm$^{-1}$)] (in $H_2O$): 430 (190). MS (EI$^+$, *m*/*z*): calcd. for $C_{14}H_{18}N_4O_2Ni$ 332.08, found 333.27 (**2** + H$^+$). $^1$H NMR ([D$_6$]DMSO, 300 MHz, 25 °C): $\delta$ = 2.78 (m, 2 H, $–CH_2–$), 2.87 (s, 6 H, $–CH_3$), 3.22 (m, 2 H, $–CH_2–$), 3.70 (d, 2 H, $–CH_2C(O)–$), 4.15 (d, 2 H, $–CH_2C(O)–$), 7.47 (m, 4 H, arom. H) ppm. $^1$H NMR ($CD_3CN$, 300 MHz, 25 °C): $\delta$ = 2.73 (m, 2 H, $–CH_2–$), 2.79 (s, 6 H, $–CH_3$), 3.23 (m, 2 H, $–CH_2–$), 3.58 (d, 2 H, $–CH_2C(O)–$), 4.13 (d, 2 H, $–CH_2C(O)–$), 7.26 (m, 2 H, arom. H), 7.36 (m, 2 H, arom. H) ppm. $^{13}$C NMR ([D$_6$]DMSO, 300 MHz, 25 °C): $\delta$ = 48.23 ($–CH_3$), 51.34 ($–CH_2CH_2–$), 70.03 ($–C(O)CH_2–$), 123.75 (Ar-h), 129.83 (Ar-g), 149.14 (Ar-f), 172.47 (C=O) ppm.

**[$Ni^{II}(3^{OP})$] (3):** A similar procedure as that of **1** was followed and the product was isolated as deep yellow blocks. Yield from method **A**: 42%. Yield from method **B**: 37%. $C_{14}H_{18}N_4O_2Ni$ (333.01): calcd. C 50.50, H 5.41, N 16.83; found C 50.53, H 5.33, N 16.62. FT-IR (KBr disk): $\tilde{\nu}$ = 2933, 1619, 1601 cm$^{-1}$. Conductivity ($CH_3CN$, ca. 1 mM solution, 298 K): $\Lambda_M$ = 10 $\Omega^{-1}$ cm$^2$ mol$^{-1}$. UV/Vis [$\lambda_{max}$, nm ($\varepsilon$, M$^{-1}$cm$^{-1}$)] (in $CH_3CN$): 271 (1300), 291 (11360), 444 (325). UV/Vis [$\lambda_{max}$, nm ($\varepsilon$, M$^{-1}$cm$^{-1}$)] (in DMF): 292 (18200), 441 (370). UV/Vis [$\lambda_{max}$, nm ($\varepsilon$, M$^{-1}$cm$^{-1}$)] (in DMSO): 441 (250). UV/Vis [$\lambda_{max}$, nm ($\varepsilon$, M$^{-1}$cm$^{-1}$)] (in $H_2O$): 437 (350). MS (EI$^+$, *m*/*z*): calcd. for $C_{14}H_{18}N_4O_2Ni$ 332.08, found 333.06 (**3** + H$^+$). $^1$H NMR ([D$_6$]DMSO, 300 MHz, 25 °C): $\delta$ = 2.52 (s, 6H $–CH_3$), 2.74 (m, 2

 © 2007 Wiley-VCH Verlag GmbH & Co. KGaA, Weinheim 

H, $-CH_2-$), 3.12 (d, 2 H, $-CH_2C(O)-$), 3.86 m, 2 H, $-CH_2-$), 4.13 (d, 2 H, $-CH_2C(O)-$), 6.54 (m, 2 H, Ar-g), 7.41 (m, 2 H, Ar-f) ppm. $^1$H NMR ($CD_3CN$, 300 MHz, 25 °C): $\delta$ = 2.64 (s, 6H $-CH_3$), 2.80 (m, 2 H, $-CH_2-$), 3.28 (d, 2 H, $-CH_2C(O)-$), 3.89 (m, 2 H, $-CH_2-$), 4.14 (d, 2 H, $-CH_2C(O)-$), 6.70 (m, 2 H, Ar-g), 7.56 (m, 2 H, Ar-f) ppm. $^{13}$C NMR ([D$_6$]DMSO, 300 MHz, 25 °C): $\delta$ = 47.68 ($-CH_3$), 59.72 ($-CH_2CH_2-$), 69.50 ($-C(O)CH_2-$), 119.15 (Ar-k), 120.30 (Ar-j), 142.36 (Ar-i), 171.60 (C=O) ppm.

**[Ni$^{II}$(4$^{OP}$)] (4):** This complex was also synthesized in an analogous method and the recrystallized product was isolated as orange-yellow crystals in 38% from method **A** and 30% from method **B**. $C_{18}H_{18}N_4O_2Ni$ (380.69): calcd. C 56.79, H 4.77, N 14.7; found C 56.78, H 4.85, N 14.63. FT-IR (KBr disk): $\tilde{\nu}$ = 3006, 2935, 1632 cm$^{-1}$. Conductivity ($CH_3CN$, ca. 1 mM solution, 298 K): $\Lambda_M$ = 2 $\Omega^{-1}$ cm$^2$ mol$^{-1}$. UV/Vis [$\lambda_{max}$, nm ($\varepsilon$, M$^{-1}$ cm$^{-1}$)] (in $CH_3CN$): 265 (17000), 290 (13000), 443 (250). UV/Vis [$\lambda_{max}$, nm ($\varepsilon$, M$^{-1}$ cm$^{-1}$)] (in DMF): 291 (10600), 441 (200). UV/Vis [$\lambda_{max}$, nm ($\varepsilon$, M$^{-1}$ cm$^{-1}$)] (in DMSO): 441 (250). UV/Vis [$\lambda_{max}$, nm, qualitative (in $H_2O$)]: 438. MS (EI$^+$, *m*/*z*): calcd. for $C_{18}H_{18}N_4O_2Ni$ 380.08, found 381.35 (**4** + H$^+$). $^1$H NMR ($CD_3CN$, 300 MHz, 25 °C): $\delta$ = 3.00 (s, 6 H, $-CH_3$), 3.80 (d, 2 H, $-CH_2C(O)-$), 4.42 (d, 2 H, $-CH_2C(O)-$), 6.65 (m, 2 H, Ar-i), 7.30 (m, 2 H, Ar-h), 7.44 (m, 2 H, Ar-g), 7.62 (m, 2 H, Ar-f) ppm. $^1$H NMR ([D$_6$]DMSO, 300 MHz, 25 °C): $\delta$ = 3.01 (s, 6 H, $-CH_3$), 3.89 (d, 2 H, $-CH_2C(O)-$), 4.43 (d, 2 H, $-CH_2C(O)-$), 6.67 (m, 4 H, Ar-H), 7.55 (m, 4 H, Ar-H) ppm. $^1$H NMR ($CDCl_3$, 300 MHz, 25 °C): $\delta$ = 3.06 (s, 6 H, $-CH_3$), 3.86 (d, 2 H, $-CH_2C(O)-$), 4.51 (d, 2 H, $-CH_2C(O)-$), 6.85 (m, 2 H, Ar-i), 7.25 (m, 2 H, Ar-h), 7.49 (m, 2 H, Ar-g), 7.76 (m, 2 H, Ar-f) ppm. $^{13}$C NMR ([D$_6$]DMSO, 300 MHz, 25 °C): $\delta$ = 51.81 ($-CH_3$), 70.33 ($-C(O)CH_2-$), 119.41 (Ar-k), 121.09 (Ar-j), 123.59 (Ar-h), 129.94 (Ar-g), 142.46 (Ar-i), 148.81 (Ar-f), 170.63 (C=O) ppm.

**Physical Measurements:** The conductivity measurements were done in organic solvents using the digital conductivity bridge from Popular Traders, India (model number: PT-825). The elemental analysis data were obtained from Elementar Analysen Systeme GmbH Vario EL-III instrument. The NMR measurements were done using either Hitachi R-600 FT NMR (60 MHz) or an Avance Bruker (300 MHz) instrument. The infra-red spectra (either as KBr pellet or as a mull in mineral oil) were recorded using the Perkin–Elmer FTIR 2000 spectrometer. The absorption spectra were recorded using the Perkin–Elmer Lambda-25 spectrophotometer. The mass spectra were obtained on a Jeol SX102/DA-6000 instrument.

**Electrochemical Measurements:** Cyclic voltammetric experiments were performed by using a PAR model 370 electrochemistry system consisting of M-174A polarographic analyzer, M-175 universal programmer, and RE 0074 X-Y recorder or a CH instruments electrochemical analyzer (Model No. 600B Series). The cell contained a glassy carbon (PAR model G0021) or a Beckman Pt (M-39273) working electrode, a Pt wire auxiliary electrode, and a saturated calomel electrode (SCE) as reference electrode. A salt bridge (containing supporting electrolyte, tetra-*n*-butylammonium perchlorate (TBAP) dissolved in either MeCN or DMF) was used to connect the SCE with the electrochemistry solution.[30] For constant potential electrolysis experiments a Pt-mesh was used as the working electrode. The solutions were ca. 1 mM in complex and ca. 0.1 M in supporting electrolyte, tetra-*n*-butylammonium perchlorate (TBAP). Under our experimental conditions, the $E_{1/2}$ values (in Volts) for the couple Fc$^+$/Fc were 0.40 in MeCN vs. SCE.

**Crystal Structure Determination:** X-ray diffraction studies of crystal mounted on a capillary were carried out on a Bruker AXS SMART-APEX diffractometer with a CCD area detector ($K_\alpha$ radiation, $\lambda$ = 0.71073 Å, monochromator: graphite).[31] Frames were collected at $T$ = 293 as well as at $T$ = 100 K by $\omega$, $\phi$ and $2\theta$ rotation at 10 s per frame with SAINT.[32] The measured intensities were reduced to $F^2$ and corrected for absorption with SADABS.[33] Structure solution, refinement, and data output were carried out with the SHELXTL program.[33] Non-hydrogen atoms were refined anisotropically. All hydrogen atoms were placed in geometrically calculated positions by using a riding model. For complex **3**, disorder was observed for the C6 and C7 atoms of the amine fragment. These atoms (C6 and C7) were occupying two crystallographically independent positions which could be located from the additional residual electron density. The site occupancy factors were refined with the help of free variable PART instruction. Refinement of the site occupancy factors (SOFs) for the disordered atoms C6 and C7 gave the value 0.81 (2) this factor was thereafter fixed at 0.80. The occupancy factor of the other possible set of positions (C6D/C7D) was 0.20. A structure model based on a statistically disordered C atom improved the accuracy of C–C bonds of interest. H atoms have been omitted from the disordered part. Table 1 contains necessary crystallographic details.

CCDC-635113 to -635116 (for **1**–**4**) contain the supplementary crystallographic data for this paper. These data can be obtained free of charge from The Cambridge Crystallographic Data Centre via www.ccdc.cam.ac.uk/data_request/cif.

**Supporting Information** (see also the footnote on the first page of this article): Crystal packing diagram of complex **2** (Figure S1); lateral view of the crystal structures of the complexes **1**, **2**, **3**, and **4** (Figure S2); absorption spectra for complexes **1**, **2**, **3**, and **4** recorded in DMF (Figure S3), DMSO (Figure S4), and $H_2O$ (Figure S5); $^1$H NMR spectra of complexes **1**, **2**, **3**, and **4** in [D$_3$]MeCN (Figure S6) and in [D$_6$]DMSO (Figure S7), $^1$H NMR spectra of complex **4** in $CDCl_3$ (Figure S8) and $^{13}$C NMR spectra of complexes **1**, **2**, **3**, and **4** in [D$_6$]DMSO (Figure S9); 2D {$^1$H-$^{13}$C} NMR spectrum of complex **1** (Figure S10); Plane and displacement parameters (Table S1); and $^{13}$C NMR spectroscopic data (Table S2).

## Acknowledgments

Authors (RG) thank the Department of Science and Technology (DST), New Delhi, India for the financial support, Professors R. Ramanan and A. K. Ganguli from Indian Institute of Technology, New Delhi, India for the crystallographic help, and DST-FIST funded single crystal diffraction facility at IIT-Delhi for data collection. We express our deepest gratitude to Professor R. Mukherjee and his research group at IIT - Kanpur for extending their laboratory facilities for the detailed electrochemical studies. Reviewer's suggestions during the revision stage were very helpful.

[1] a) J. D. Koola, J. K. Kochi, *Inorg. Chem.* **1987**, *26*, 908; b) H. Yoon, C. J. Burrows, *J. Am. Chem. Soc.* **1988**, *110*, 4087; c) T. R. Wagler, C. J. Burrows, *Tetrahedron Lett.* **1988**, *29*, 5091; d) B. Dangel, M. Clarke, J. Haley, D. Sames, R. Polt, *J. Am. Chem. Soc.* **1997**, *119*, 10865; e) T. R. Wagler, Y. Fang, C. J. Burrows, *J. Org. Chem.* **1989**, *54*, 1584.

[2] a) R. Cammack, *Adv. Inorg. Chem.* **1988**, *32*, 297; b) J. J. G. Moura, I. Moura, M. Teixeira, A. V. Xavier, G. D. Fauque, J. Legall, *Met. Ions Biol. Syst.* **1988**, *23*, 285.

[3] H.-D. Youn, E.-J. Kim, J.-H. Roe, Y. C. Hah, S.-O. Kang, *Biochem. J.* **1996**, *318*, 889.

[4] P. A. Lindahl, *Biochemistry* **2002**, *41*, 2097.

[5] U. Ermler, W. Grabarse, S. Shima, M. Goubeaud, R. K. Thauer, *Science* **1997**, *278*, 1457.

[6] a) M. L. Golden, M. V. Rampersad, J. H. Reibenspies, M. Y. Darensbourg, *Chem. Commun.* **2003**, 1824; b) Q. Wang, A. J.

 © 2007 Wiley-VCH Verlag GmbH & Co. KGaA, Weinheim 

Blake, E. S. Davies, E. J. L. McInnes, C. Wilson, M. Schroder, *Chem. Commun.* **2003**, 3012; c) R. Krishnan, J. K. Voo, C. G. Riordan, L. Zahkarov, A. L. Rheingold, *J. Am. Chem. Soc.* **2003**, *125*, 4422; d) R. C. Linck, C. W. Spahn, T. B. Rauchfuss, S. R. Wilson, *J. Am. Chem. Soc.* **2003**, *125*, 8700; e) R. Krishnan, C. G. Riordan, *J. Am. Chem. Soc.* **2004**, *126*, 4484; f) T. C. Harrop, M. M. Olmstead, P. K. Mascharak, *Chem. Commun.* **2004**, 1744; g) T. C. Harrop, M. M. Olmstead, P. K. Mascharak, *J. Am. Chem. Soc.* **2004**, *126*, 14714.

[7] a) E. C. Long, *Acc. Chem. Res.* **1999**, *32*, 827; b) C. Harford, S. Narindrasorasak, B. Sarkar, *Biochemistry* **1996**, *35*, 4271.

[8] E. Kimura, *J. Coord. Chem.* **1986**, *15*, 1 and references cited therein.

[9] a) G. D. Santis, L. Fabbrizzi, M. Licchelli, P. Pallavicini, *Coord. Chem. Rev.* **1992**, *120*, 237; b) D. W. Margerum, G. D. Ovens, in *Metal ions in Biological Systems, Ed.* H. Sigel, M. Dekker, New York, **1981**, *12*, 75; c) J. S. Rybka, D. W. Margerum, *Inorg. Chem.* **1980**, *19*, 2784; d) P. K. Mascharak, *Coord. Chem. Rev.* **2002**, *225*, 201; e) D. S. Marlin, M. M. Olmstead, P. K. Mascharak, *Inorg. Chem.* **1999**, *38*, 3258; f) F. A. Chavez, M. M. Olmstead, P. K. Mascharak, *Inorg. Chem.* **1997**, *36*, 6323; g) T. J. Collins, R. D. Powell, C. Slebodnick, E. S. Uffelman, *J. Am. Chem. Soc.* **1991**, *113*, 8419; h) J. M. Workman, R. D. Powell, A. D. Procyk, T. J. Collins, D. F. Bocian, *Inorg. Chem.* **1992**, *31*, 1548; i) L. Fabbrizzi, *Comments Inorg. Chem.* **1985**, *4*, 33; j) L. Fabbrizzi, T. A. Kaden, A. Perotti, B. Seghi, L. Siegfried, *Inorg. Chem.* **1986**, *25*, 321; k) R. W. Hay, P. R. Norman, *Transition Met. Chem.* **1980**, *5*, 232; l) R. W. Hay, R. Bembi, W. Sommerville, *Inorg. Chim. Acta* **1982**, *59*, 147; m) R. W. Hay, M. P. Pujari, F. McLaren, *Inorg. Chem.* **1984**, *23*, 3033.

[10] a) M. Kodama, T. Yatsunami, E. Kimura, *J. Chem. Soc. Dalton Trans.* **1979**, 1783; b) M. Kodama, E. Kimura, *J. Chem. Soc. Dalton Trans.* **1981**, 694; c) E. Kimura, A. Sakonaka, R. Machida, *J. Am. Chem. Soc.* **1982**, *104*, 4255; d) E. Kimura, T. Koike, R. Machida, R. Nagai, M. Kodama, *Inorg. Chem.* **1984**, *23*, 4181; e) X. H. Bu, D. L. An, X. C. Cao, Y. T. Chen, M. Shionoya, E. Kimura, *Polyhedron* **1996**, *15*, 161; f) X. H. Bu, X. C. Cao, Z. H. Zhang, Z. A. Zhu, Y. T. Chen, M. Shionoya, E. Kimura, *Polyhedron* **1996**, *15*, 1203; g) X. H. Bu, D. L. An, Z. A. Zhu, Y. T. Chen, M. Shionoya, E. Kimura, *Polyhedron* **1997**, *16*, 179.

[11] Y. D. Lampeka, S. P. Gavrish, R. W. Hay, T. Eisenblatter, P. Lightfoot, *J. Chem. Soc. Dalton Trans.* **2000**, 2023.

[12] S. P. Gavrish, Y. D. Lampeka, P. Lightfoot, *Inorg. Chim. Acta* **2004**, *357*, 1023.

[13] a) D. Kong, X. Ouyang, A. E. Martell, A. Clearfield, *Inorg. Chem. Commun.* **2003**, *6*, 317; b) J. Gao, J. H. Reibenspies, Y. Sun, A. E. Martell, *Helv. Chim. Acta* **2003**, *86*, 563.

[14] H.-J. Krugar, G. Peng, R. H. Holm, *Inorg. Chem.* **1991**, *30*, 734.

[15] A. Grenz, S. Ceccarelli, C. Bolm, *Chem. Commun.* **2001**, 1726.

[16] J. W. Steed, J. L. Atwood, in *Supramolecular Chemistry*, John Wiley & Sons Ltd., **2000**, chapter 3.

[17] K. Nakamoto in *Infrared and Raman Spectra of Inorganic and Coordination Compounds*, John Wiley & Sons, **1986**.

[18] W. J. Geary, *Coord. Chem. Rev.* **1971**, *7*, 81.

[19] P. Comba, S. P. Gavrish, R. W. Hay, P. Hilfenhaus, Y. D. Lampeka, P. Lightfoot, A. Peters, *Inorg. Chem.* **1999**, *38*, 1416.

[20] T. J. Collins, T. R. Nichols, E. S. Uffelman, *J. Am. Chem. Soc.* **1991**, *113*, 4708.

[21] L. Fabbrizzi, *J. Chem. Soc. Dalton Trans.* **1979**, 1857.

[22] a) M. Ray, D. Ghosh, Z. Shirin, R. Mukherjee, *Inorg. Chem.* **1997**, *36*, 3568; b) A. K. Patra, R. Mukherjee, *Inorg. Chem.* **1999**, *38*, 1388; c) A. K. Patra, M. Ray, R. Mukherjee, *Inorg. Chem.* **2000**, *39*, 652; d) A. K. Singh, R. Mukherjee, *Dalton Trans.* **2005**, 2886.

[23] a) M. Ray, S. Mukherjee, R. Mukherjee, *J. Chem. Soc. Dalton Trans.* **1990**, 3635; b) M. Ray, R. Mukherjee, *Polyhedron* **1992**, *11*, 2929.

[24] a) C.-M. Che, W.-H. Leung, C.-K. Li, H.-Y. Cheng, S.-M. Peng, *Inorg. Chim. Acta* **1992**, *196*, 43; b) S.-T. Mak, V. W.-W. Yam, C.-M. Che, T. C. W. Mak, *J. Chem. Soc. Dalton Trans.* **1990**, 2555; c) W.-H. Leung, J.-X. Ma, V. W.-W. Yam, C.-M. Che, C.-K. Poon, *J. Chem. Soc. Dalton Trans.* **1991**, 1071; d) S.-T. Mak, W.-T. Wong, V. W.-W. Yam, T.-F. Lai, C.-M. Che, *J. Chem. Soc. Dalton Trans.* **1991**, 1915; e) T. J. Collins, D. R. Powell, C. Slebodnick, E. S. Uffelman, *J. Am. Chem. Soc.* **1991**, *113*, 8419; f) S.-M. Peng, C.-T. Chen, D.-S. Liaw, C.-I. Chen, Y. Wang, *Inorg. Chim. Acta* **1985**, *101*, L31; g) S.-M. Peng, D.-S. Liaw, *Inorg. Chim. Acta* **1986**, *113*, L11.

[25] a) A. Aukauloo, X. Ottenwaelder, R. Ruiz, S. Poussereau, Y. Pei, Y. Journaux, P. Fleurat, F. Volatron, B. Cervera, M. C. Munoz, *Eur. J. Inorg. Chem.* **1999**, 1067; b) X. Ottenwaelder, R. Ruiz, R. Ruiz-Garcia, G. Blondin, R. Carasco, J. Cano, D. Lexa, Y. Journaux, A. Aukauloo, *Chem. Commun.* **2004**, 504; c) X. Ottenwaelder, A. Aukauloo, Y. Journaux, R. Carasco, J. Cano, B. Cervera, I. Castro, S. Curreli, M. C. Munoz, A. L. Rosello, B. Soto, R. Ruiz-Garcia, *Dalton Trans.* **2005**, 2516; d) R. Carasco, J. Cano, X. Ottenwaelder, A. Aukauloo, Y. Journaux, R. Ruiz-Garcia, *Dalton Trans.* **2005**, 2527.

[26] a) R. Ruiz, C. S. Barland, A. Aukauloo, E. Anxolabehere-Mallart, Y. Journaux, J. Cano, M. C. Munoz, *J. Chem. Soc. Dalton Trans.* **1997**, 745; b) B. Cervera, J. L. Sanz, M. J. Ibanez, G. Vila, F. LLoret, M. Julve, R. Ruiz, X. Ottenwaelder, A. Aukauloo, S. Poussereau, Y. Journaux, M. C. Munoz, *J. Chem. Soc. Dalton Trans.* **1998**, 781.

[27] Y. D. Lampeka, S. P. Gavrish, *Polyhedron* **2000**, *19*, 2533.

[28] L. Fabbrizzi, A. Poggi, *J. Chem. Soc. Chem. Commun.* **1980**, 646.

[29] N. G. Connelly, W. E. Geiger, *Chem. Rev.* **1996**, *96*, 877.

[30] D. T. Sawyer, J. L. Roberts Jr, *Experimental Electrochemistry for Chemists*, Wiley, New York, 1974.

[31] *SMART: Bruker Molecular Analysis Research Tool*, Version 5.618, Bruker Analytical X-ray Systems, **2000**.

[32] *SAINT-NT*, Version 6.04, Bruker Analytical X-ray Systems, **2001**.

[33] *SHELXTL-NT*, Version 6.10, Bruker Analytical X-ray Systems, **2000**.

Received: January 30, 2007
Published Online: May 29, 2007

 © 2007 Wiley-VCH Verlag GmbH & Co. KGaA, Weinheim 

DOI: 10.1002/ejic.200700123

# Lanthanide Borohydride Complexes of Bulky Guanidinate Ligands $[(Me_3Si)_2NC(N\text{-}Cy)_2]_2Ln(\mu\text{-}BH_4)_2Li(THF)_2$ (Ln = Nd, Sm, Yb): Synthesis, Structure and Catalytic Activity in Lactide Polymerization

**Grigorii G. Skvortsov,[a] Marina V. Yakovenko,[a] Pascal M. Castro,[b] Georgy K. Fukin,[a] Anton V. Cherkasov,[a] Jean-François Carpentier,*[b] and Alexander A. Trifonov*[a]**

**Keywords:** Lanthanides / Borohydrides / Guanidinates / N ligands / Lactides / Polymerization

A series of new lanthanide borohydride complexes supported by bulky guanidinate ligands $[(Me_3Si)_2NC(N\text{-}Cy)_2]_2Ln(\mu\text{-}BH_4)_2Li(THF)_2$ [Ln = Nd (**1**), Sm (**2**), Yb (**3**)] was synthesized by the reaction of related tris(borohydride)s $Ln(BH_4)_3(THF)_2$ with a twofold molar excess of $[(Me_3Si)_2NC(N\text{-}Cy)_2]Li$ in toluene at 65 °C. The complexes were isolated after recrystallization from hexane in 66, 64, and 68 % yield, respectively. X-ray diffraction studies revealed that compounds **1**–**3** are heterodimetallic complexes that have two borohydride ligands μ-bridging the lanthanide and lithium atoms. Those compounds, especially neodymium complex **1**, act as monoinitiators for the ring-opening polymerization of racemic lactide, providing atactic polymers with a good degree of control, that is, controlled molecular weights and relatively narrow polydispersities ($1.09 < M_w/M_n < 1.77$), provided moderate substrate-to-initiator ratios are used.
(© Wiley-VCH Verlag GmbH & Co. KGaA, 69451 Weinheim, Germany, 2007)

## Introduction

Metallocene-type lanthanide borohydride complexes have been known for three decades;[1] nevertheless, this class of compounds still attracts considerable attention because of their structural diversity and high catalytic activity.[2] Monoanionic borohydride groups can perform both μ-bridging and terminal coordination modes that result in formation of dimeric[3,4] or monomeric organolanthanide complexes.[5–7] Depending on the central atom size and its coordination environment, borohydride anions can act in monomeric complexes as bi-[1,3,5,7,8] and tridentate[1,4,9,10] ligands. For dimeric complexes $\mu^3$:$\mu^2$-bridging coordination has been described.[4,11] A renewed interest in lanthanide borohydride complexes arose from communications on their catalytic activity in lactone,[12] lactide,[13] and methyl methacrylate[14] polymerizations. Also, some lanthanide sandwich and half-sandwich borohydrides have been used as precatalysts in two-component systems for ethylene,[9] styrene,[10a,10b] and isoprene[9,10a] polymerizations.

The stability, structures and reactivity of organic derivatives of lanthanides are known to be mainly determined by the electropositivity, Lewis acidity, and large ionic radii of these elements. These factors render organolanthanides highly sensitive to steric saturation of the metal coordination sphere and, therefore, design of the environment about the metal center is crucial. On the other hand, investigation of the influence of the ancillary ligation on the reactivity of Ln–C and Ln–H bonds may be rewarding, as it may serve as a useful tool for modification of catalytic activity of lanthanide hydrocarbyl and hydrido complexes. To date, lanthanide borohydride complexes are mainly presented by sandwich- and half-sandwich-type derivatives,[2] while compounds supported by non-cyclopentadienyl ligands still remain virtually unexplored. The yttrium borohydride complex $[Ph(NSiMe_3)_2]_2Y(BH_4)(THF)$ supported by amidinate ligands was reported by Teuben and co-workers.[15] Recently, synthesis of lanthanide borohydrides containing aryl oxide,[16] polydentate diamino-bis(phenoxide),[13] and diamide–diamine[14] ligands was described. In our continuing research we have shown that bulky guanidinate ligands provide a useful coordination environment, which allows the synthesis of isolable lanthanide hydrocarbyl[17,18] and hydrido[19,20] species. That is why we employed the guanidinate ligands for preparing lanthanide mono-[21a] and bis(borohydride)[21b] complexes. Later, Yuan and co-workers synthesized the mono(guanidinate) lanthanide borohydride complexes $[(Me_3Si)_2NC(N\text{-}Cy)_2]Ln(BH_4)_2(THF)_2$ (Ln = Er, Yb).[22] Herein we report on the synthesis, structure, and

[a] G.A. Razuvaev Institute of Organometallic Chemistry of Russian Academy of Sciences,
Tropinina 49, 603950 Nizhny Novgorod GSP-445, Russia
Fax: +7-8312-127-497
E-mail: trif@iomc.ras.ru
[b] Organometallics and Catalysis, UMR 6226, Institute of Chemistry, University of Rennes 1,
35042 Rennes Cedex, France
E-mail: jcarpent@univ-rennes1.fr
Supporting information for this article is available on the WWW under http://www.eurjic.org or from the author.

 © 2007 Wiley-VCH Verlag GmbH & Co. KGaA, Weinheim 

catalytic activity in lactide polymerization of heterodimetallic bis(guanidinate) borohydride complexes $\{(Me_3Si)_2NC(N\text{-}Cy)_2\}_2Ln(BH_4)_2Li(THF)_2$ (Ln = Nd, Sm, Yb).

## Results and Discussion

### Synthesis and Characterization of Lanthanide Bis(guanidinate) Borohydrides

Initially the metathesis reactions of lanthanide bis(guanidinate)chloride complexes $[\{(Me_3Si)_2NC(N\text{-}Cy)_2\}_2LnCl]_2$ (Ln = Nd, Sm) with $NaBH_4$ were investigated as a synthetic route to the related borohydrides. However, this method was found to be inefficient as the prolonged heating (48 h) of equimolar amounts of the starting reagents in THF at 65° did not allow preparation of the borohydride complexes in good yields. Increasing the amount of $NaBH_4$ (to a 1.5-fold molar excess) did not result in a higher product yield and considerable amounts (about 15–20%) of the starting chloride complexes $[\{(Me_3Si)_2NC(N\text{-}Cy)_2\}_2LnCl]_2$ were recovered in the reaction mixture. This hampered isolation and purification of the borohydride complexes. Moreover, the reaction of $[\{(Me_3Si)_2NC(N\text{-}iPr)_2\}_2SmCl]_2$ with $NaBH_4$ was found to occur with redistribution of guanidinate ligands and formation of the bis(borohydride) derivative $\{(Me_3Si)_2NC(N\text{-}iPr)_2\}Sm(BH_4)_2(DME)$.[21a] During the past decade, several reports[10–14,16] on the successful conversions of lanthanide tris(borohydrides) $Ln(BH_4)_3(THF)_n$[23–25] into new derivatives by reactions with anionic reagents have appeared. This prompted us to use $Ln(BH_4)_3(THF)_n$ complexes as starting reagents for preparation of related bis(guanidinate) borohydrides.

The reactions of $Ln(BH_4)_3(THF)_2$ (Ln = Nd, Sm, Yb) with a twofold molar excess of the lithium guanidinate $[(Me_3Si)_2NC(N\text{-}Cy)_2]Li$, obtained in situ from the amide $(Me_3Si)_2NLi(Et_2O)$ and 1,3-dicyclohexylcarbodiimide, were carried out in toluene at 65 °C (Scheme 1).

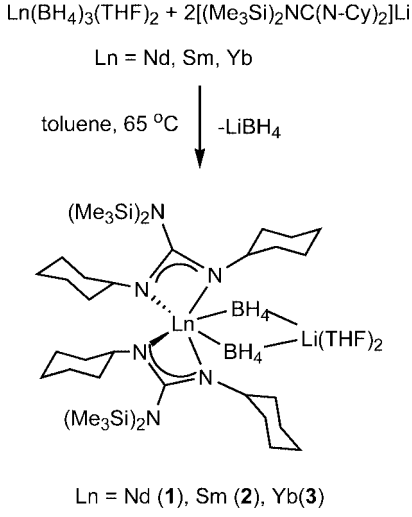


Scheme 1.

Filtration of the reaction mixture, evaporation of toluene, subsequent recrystallization of the solid residue from hexane, and drying in vacuo at room temperature afforded complexes $[(Me_3Si)_2NC(N\text{-}Cy)_2]_2Ln(\mu\text{-}BH_4)_2Li(THF)_2$ [Ln = Nd (**1**), Sm (**2**), Yb (**3**)] in 66, 64, and 68% yield, respectively. Complex **1** was isolated as blue, **2** yellow and **3** orange crystalline solids. Complexes **1**–**3** are highly air- and moisture-sensitive. Nevertheless, in an inert atmosphere, they can be stored for weeks without decomposition at room temperature. They are readily soluble in hydrocarbon solvents, which hampers their isolation by recrystallization and decreases the yields. The IR spectra of complexes **1**–**3** show, in the region 2000–2500 $cm^{-1}$, four strong absorptions diagnostic of $\mu^3$- and $\mu^2$-bridging borohydride ligands.[4,5] The $^1H$ and $^{13}C$ NMR spectra of the slightly paramagnetic complex **2** in [D$_6$]benzene at 20 °C show the expected sets of resonances for the guanidinate ligand and the coordinated THF. The borohydride group appears in the $^1H$ NMR spectrum as a broad singlet at $\delta$ = –1.34 ppm. The $^7Li$ and $^{11}B$ NMR spectra contain sole singlets at $\delta$ = 0.03 and 49.04 ppm, respectively.

Crystals suitable for single-crystal X-ray diffraction studies of **1**–**3** were obtained from hexane solutions by slow evaporation of the solvent at room temperature and were isolated as the hexane solvates $[(Me_3Si)_2NC(N\text{-}Cy)_2]_2Ln(\mu\text{-}BH_4)_2Li(THF)_2\cdot(C_6H_{14})_{0.5}$. The X-ray crystal structure investigations revealed that complexes **1**–**3** have similar structures. The molecular structure of **3** is depicted in Figure 1; the crystal and structural refinement data, and selected bond lengths and angles for **1**–**3** are listed in Tables 1 and 2, respectively. The molecular structure (Figure 1) shows that compounds **1**–**3** are heterodimetallic complexes containing one residual $LiBH_4$ per $[(Me_3Si)_2NC(N\text{-}Cy)_2]_2Ln(BH_4)$ unit in which the lanthanide and the lithium atoms are connected by two μ-bridging $BH_4$ groups. The coordination sphere of the lanthanide atoms in complexes **1**–**3** is set up by four nitrogen atoms of two guanidinate ligands and by two borohydride anions. The lithium atom is further coordinated by two THF molecules.

Despite the fact that both borohydride groups in complexes **1**–**3** are μ-bridging, their coordination modes are different: one group is tridentate with respect to the lanthanide atom and bidentate with respect to the lithium, while the second one is $\mu\text{-}\eta^2\text{:}\eta^2$-bridging in complexes **1** and **2**, but $\mu\text{-}\eta^2\text{:}\eta^1$-bridging in complex **3** (Figure 2).

The Ln–H and Li–H distances fall in the ranges 2.42(2)–2.56(2) and 1.89(2)–2.29(2) Å in complex **1**, 2.36(2)–2.53(2) and 1.88(2)–2.30(2) Å in **2**, and 2.29(2)–2.47(2) and 1.92(2)–2.13(2) Å in **3**, respectively. It should be noted that the interatomic Li(1)···H(2A) distance in **3** [2.91(2) Å] is noticeably longer than the other Li–H distances in **1**–**3** [1.89(2)–2.29(2) Å]. Obviously, the difference of the coordination modes of borohydride groups in complex **3** is caused by steric factors, which is consistent with the smallest ionic radius of ytterbium in the series of the prepared lanthanide compounds.[26] The difference in the coordination mode of the borohydride moieties to the lanthanide atom does not strongly affect the Ln–B distances: in all three complexes

 © 2007 Wiley-VCH Verlag GmbH & Co. KGaA, Weinheim 

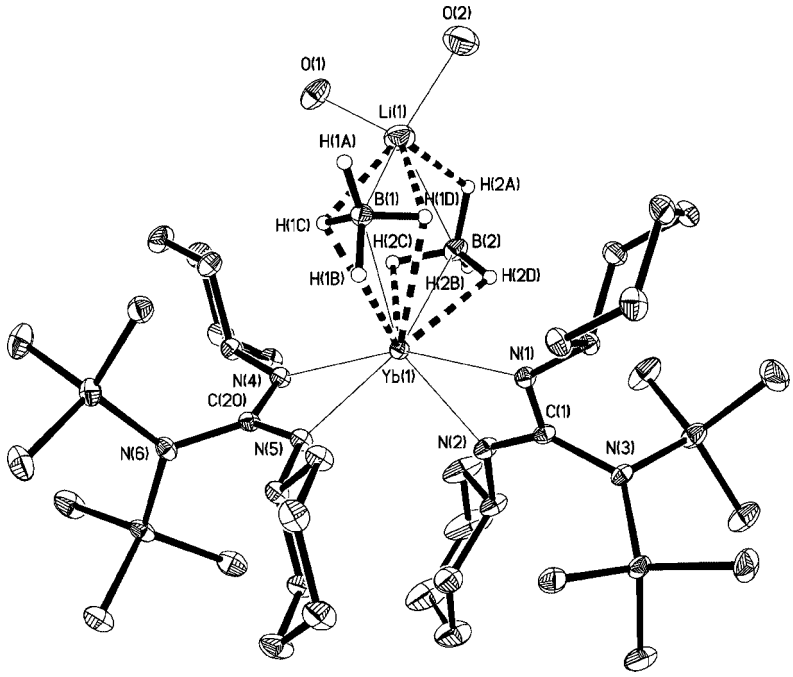


Figure 1. ORTEP diagram (30% probability thermal ellipsoids) of $[(Me_3Si)_2NC(N\text{-}Cy)_2]_2Yb(\mu\text{-}BH_4)_2Li(THF)_2$ (**3**). Hydrogen atoms of the guanidinate ligands and THF methylene groups are omitted.

Table 1. Crystallographic data and structure refinement details for **1**–**3**.

| | **1** | **2** | **3** |
|---|---|---|---|
| Empirical formula | $C_{49}H_{111}B_2LiN_6NdO_2Si_4$ | $C_{49}H_{111}B_2LiN_6O_2Si_4Sm$ | $C_{49}H_{111}B_2LiN_6O_2Si_4Yb$ |
| Formula mass | 1101.6 | 1107.7 | 1130.4 |
| $T$ [K] | 100(2) | 100(2) | 100(2) |
| $\lambda$ [Å] | 0.71073 | 0.71073 | 0.71073 |
| Crystal system | triclinic | triclinic | triclinic |
| Space group | $P\bar{1}$ | $P\bar{1}$ | $P\bar{1}$ |
| $a$ [Å] | 13.7938(6) | 13.7979(8) | 13.8325(5) |
| $b$ [Å] | 15.0978(7) | 15.0630(9) | 14.9469(6) |
| $c$ [Å] | 17.2382(7) | 17.215(1) | 17.1896(7) |
| $\alpha$ [°] | 86.854(1) | 86.906(1) | 81.886(1) |
| $\beta$ [°] | 77.232(1) | 77.355(1) | 78.015(1) |
| $\gamma$ [°] | 63.041(1) | 62.918(1) | 62.505(1) |
| $V$ [Å$^3$] | 3116.48(8) | 3104.1(3) | 3079.7(2) |
| $Z$ | 2 | 2 | 2 |
| $D_{calcd}$ [g/cm] | 1.179 | 1.185 | 1.219 |
| Absorption coefficient [mm$^{-1}$] | 0.952 | 1.061 | 1.635 |
| $F$(000) | 1184 | 1188 | 1204 |
| Crystal size [mm] | $0.37 \times 0.24 \times 0.22$ | $0.31 \times 0.17 \times 0.15$ | $0.36 \times 0.30 \times 0.27$ |
| $\theta$ range for data collection [°] | 1.70–29.30 | 1.70–29.00 | 1.70–29.18 |
| Index ranges | $-18 \le h \le 18$ | $-18 \le h \le 18$ | $-18 \le h \le 18$ |
| | $-20 \le k \le 20$ | $-20 \le k \le 20$ | $-20 \le k \le 20$ |
| | $-23 \le l \le 23$ | $-23 \le l \le 22$ | $-23 \le l \le 23$ |
| Reflections collected | 33266 | 32642 | 32805 |
| Independent reflections | 16392 ($R_{int}$ = 0.0168) | 16107 ($R_{int}$ = 0.0227) | 16163 ($R_{int}$ = 0.0189) |
| Completeness to $\theta$ | 96.6 | 99.9 | 97.4 |
| Data/restraints/parameters | 16392/61/1024 | 25718/108/1378 | 16107/55/1034 |
| Goodness-of-fit on $F^2$ | 1.068 | 1.259 | 1.044 |
| Final $R$ indices [$I > 2\sigma(I)$] | $R_1$ = 0.0263, $wR_2$ = 0.0640 | $R_1$ = 0.0664, $wR_2$ = 0.1350 | $R_1$ = 0.0287, $wR_2$ = 0.0648 |
| $R$ indices (all data) | $R_1$ = 0.0309, $wR_2$ = 0.0660 | $R_1$ = 0.0377, $wR_2$ = 0.0685 | $R_1$ = 0.0307, $wR_2$ = 0.0698 |
| Largest diff. peak and hole [e/Å$^3$] | 1.421/–0.379 | 1.308/–0.378 | 1.861/–0.752 |

one distance is substantially longer than the second one (Table 2). The average Ln–N bond lengths in complexes **1**–**3** [**1**, 2.4483(8); **2**, 2.4248(10); **3**, 2.3315(11) Å] are comparable to those previously reported for related bis(guanidinate) derivatives[21,27–29] and their values decrease in the series Nd > Sm > Yb, reflecting the lanthanide contraction.[26] The Ln–B and Ln–Li distances in complexes **1**–**3** also correspond to this tendency and diminish from Nd to

 © 2007 Wiley-VCH Verlag GmbH & Co. KGaA, Weinheim 

Table 2. Selected bond lengths [Å] and angles [°] for complexes **1**–**3**.

| | **1** | **2** | **3** |
|---|---|---|---|
| Bond lengths [Å] | | | |
| Ln–N(1) | 2.4812(8) | 2.4612(10) | 2.3528(11) |
| Ln–N(2) | 2.4158(10) | 2.3852(12) | 2.3044(11) |
| Ln–N(4) | 2.4284(8) | 2.4025(10) | 2.3454(12) |
| Ln–N(5) | 2.4680(8) | 2.4505(9) | 2.3235(13) |
| Li–B(1) | 2.454(3) | 2.450(3) | 2.428(4) |
| Li–B(2) | 2.504(3) | 2.498(3) | 2.507(3) |
| Ln–Li | 3.663(3) | 3.643(3) | 3.595(3) |
| Ln–H | 2.42(2)–2.56(2) | 2.36(2)–2.53(2) | 2.29(2)–2.47(2) |
| Li–H | 1.89(2)–2.29(2) | 1.88(2)–2.30(2) | 1.92(2)–2.13(2) |
| N(1)–C(1) | 1.3344(13) | 1.3311(16) | 1.3334(16) |
| N(2)–C(1) | 1.3296(12) | 1.3324(14) | 1.3298(18) |
| N(4)–C(20) | 1.3275(13) | 1.3311(15) | 1.3341(19) |
| N(5)–C(20) | 1.3320(14) | 1.3310(17) | 1.3274(16) |
| Distances Ln–B [Å] | | | |
| Ln–B(1) | 2.7390(13) | 2.7019(15) | 2.6193(16) |
| Ln–B(2) | 2.9251(14) | 2.8937(17) | 2.7935(19) |
| Bond angles [°] | | | |
| N(1)–Ln–N(2) | 54.53(3) | 55.02(3) | 57.33(4) |
| N(4)–Ln–N(5) | 54.51(3) | 55.04(4) | 57.27(4) |
| B(1)–Ln–B(2) | 84.49(4) | 84.83(5) | 86.07(5) |
| B(1)–Li–B(2) | 100.44(10) | 99.52(12) | 96.98(12) |

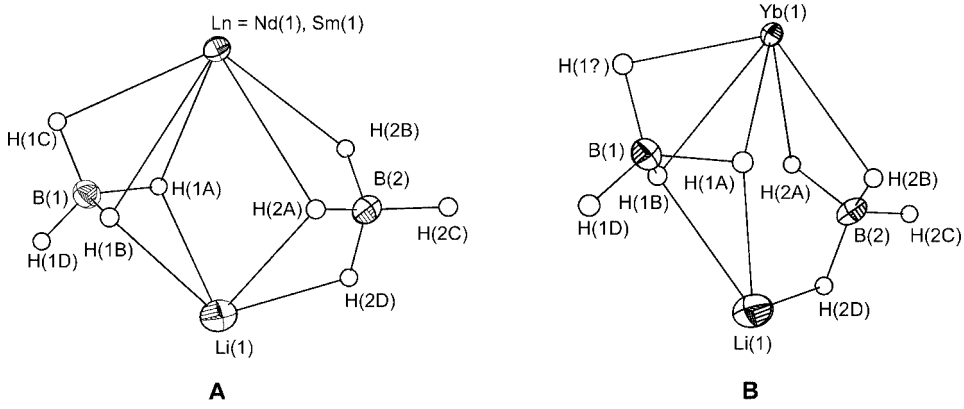


Figure 2. The coordination modes of borohydride groups in complexes $[(Me_3Si)_2NC(N\text{-}Cy)_2]_2Ln(\mu\text{-}BH_4)_2Li(THF)_2$ (A, **1**, **2**; B, **3**).

Yb. The Ln–B distances for bridging borohydride groups in complexes **1**–**3** are expectedly longer than those in complexes with terminal $BH_4$ groups[6,8,10,21] and comparable to the values reported for related dimeric compounds.[11,14] The N–C distances in the guanidinate ligands of **1**–**3** differ only slightly between each other (Table 2), which reflects the electron delocalization within the anionic NCN units. Shortening of the Ln–N, Ln–B, and Ln···Li distances in complexes **1**–**3** should lead to an increase of nonvalent interactions in the coordination sphere of the Ln atoms. Calculations[30] of the steric saturation degree about the Ln atoms have shown that the total metal atom shielding increases in the series of complexes **1** [86.6(2)%], **2** [87.8(2)%], and **3** [91.3(2)%] and reflects the steric crowding in the coordination sphere of the metal centers. The value of the dihedral angle between the N(1)C(1)N(2) and N(4)C(20)N(5) planes in **3** [78.1(1)°] is noticeably smaller than the analogous parameters in complexes **1** [79.7(1)°] and **2** [79.7(1)°], thus providing evidence for the strongest nonvalent interactions in the coordination sphere of the Yb atom.

### Ring-Opening Polymerization of *rac*-Lactide and (*S*,*S*)-Lactide

There is considerable interest in the controlled ring-opening polymerization (ROP) of lactides (LAs) by well-defined metal initiators because of the biodegradable and biocompatible nature of polylactides (PLAs) and their potential commercial applications.[31–34] Bonnet, Mountford et al. have studied the ROP of racemic (*S*,*S*/*R*,*R*)- and (*S*,*S*)-lactide with monoborohydride rare earth complexes (Y, Sm, Nd) supported by diamino-bis(phenolate) ligands.[13] These systems feature moderate activity and enable the formation of heterotactic-enriched (up to 87% $P_r$) or isotactic PLAs, with relatively narrow molecular-weight distributions ($M_w/M_n$ = 1.3–1.7), though the molecular weights were lower than expected, because of chain transfer reactions. Arnold and co-workers have investigated the ROP of lactide with monoguanidinate–lanthanum complexes having two reactive phenolate ligands.[35] The PLAs obtained had relatively broad molecular-weight distributions ($M_w/M_n$ = 1.5–2.0)

 © 2007 Wiley-VCH Verlag GmbH & Co. KGaA, Weinheim 

and no control over the stereochemistry of the polymer was observed. Interestingly, the molecular weights increased linearly with a monomer-to-metal ratio up to 500, but dramatically decreased for higher [LA]/[La] ratios, an observation indicative of a high degree of chain transfer, ascribed to the presence of two phenoxide groups per metal center.

Complexes **1**–**3** have been evaluated in the ROP of *rac*- and (*S*,*S*)-lactide (Scheme 2). A blank experiment using $LiBH_4$ showed this compound is not active for the ROP of *rac*-lactide under the conditions used. This observation is in line with previous observations in the ROP of cyclic esters (ε-caprolactone) and carbonates (TMC) (S. Guillaume, personal communication), and discards the possibility that ROP is initiated by $LiBH_4$ arising from dissociation of complexes **1**–**3**.

Representative results are summarized in Table 3. Complexes **1**–**3** are moderately active under mild conditions, allowing conversion of 100–400 equiv. of lactide in 10–1000 min at room temperature in either toluene or THF solutions at [LA] = 0.5 mol/L. Kinetic monitoring revealed, however, that activities of the complexes are dramatically affected by the nature of the metal center and polymerization solvent. With the three complexes investigated, the reactions proceeded much faster in an apolar, noncoordinating solvent such as toluene than in THF. It is assumed that the latter solvent, because of its high affinity for oxophilic metals such as lanthanides, competes with the lactide monomer in the coordination onto the metal center, thus accounting for the longer completion times. A similar detrimental effect of THF on the rate of ROP reactions promoted by group 3 metal complexes is often observed.[36] Nevertheless, it is noteworthy that Bonnet, Mountford et al. have observed an opposite trend for the ROP of lactides with diamino-bis(phenolate)-lanthanide borohydride complexes; that is, polymerization rates are higher in THF than in toluene.[13] For both series of reactions carried out in toluene and in THF with complexes **1**–**3**, the observed decreasing order of activity was Nd >> Yb > Sm. There is, therefore, no direct correlation of the polymerization activity with ionic radii of the lanthanide centers, and this observation rather points out that more subtle parameters should be taken into account.

All the PLAs produced from *rac*-lactide with the initiators **1**–**3** show atactic microstructures, as determined by NMR analysis.[37–39] Contrary to our previous observations with [amino-ether-bis(phenolate)]-lanthanide amido systems,[13,37] decreasing the temperature down to –20 °C and changing the solvent (toluene vs. THF) resulted in no en-

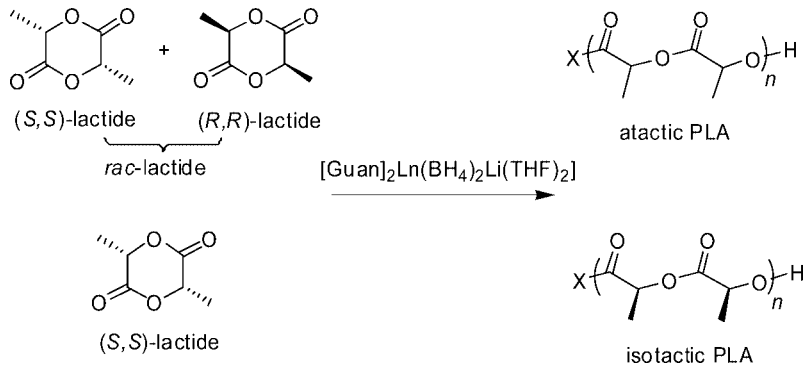


Scheme 2.

Table 3. Polymerization of *rac*- and (*S*,*S*)-lactide with complexes **1**–**3**.[a]

| Entry | M | Complex | [M]/[Ln] | Solvent | Time[b] [min] | Conv.[c] [mol-%] | $M_{n,th}$[d] [g/mol] | $M_{n,exp}$[e] [g/mol] | $M_w/M_n$[e] |
|---|---|---|---|---|---|---|---|---|---|
| 1 | *rac*-LA | **1** | 100 | toluene | 17 | >98 | 14100 | 16500 | 1.98 |
| 2 | *rac*-LA | **1** | 200 | toluene | 10 | 62 | 17900 | 20800 | 1.68 |
| 3 | *rac*-LA | **1** | 200 | toluene | 30 | >98 | 25900 | 26300 | 1.51 |
| 4 | *rac*-LA | **1** | 400 | toluene | 60 | >98 | 51800 | 52000 | 1.09 |
| 5 | *rac*-LA | **1** | 100 | THF | 60 | 97 | 8400 | 6500 | 2.16 |
| 6 | (*S*,*S*)-LA | **1** | 200 | THF | 20 | 30 | 8600 | 6000 | 1.44 |
| 7 | (*S*,*S*)-LA | **1** | 200 | THF | 60 | 98 | 28200 | 17300 | 1.63 |
| 8 | *rac*-LA | **2** | 100 | toluene | 300 | 95 | 13700 | 9100 | 1.50 |
| 9 | *rac*-LA | **2** | 200 | toluene | 480 | 96 | 27600 | 23500 | 1.16 |
| 10 | *rac*-LA | **2** | 400 | toluene | 1000 | 95 | 54700 | 20100 | 2.73 |
| 11 | (*S*,*S*)-LA | **2** | 200 | THF | 60 | 12 | 3400 | 2200 | 1.56 |
| 12 | *rac*-LA | **2** | 200 | THF | 1000 | 98 | 28200 | 9400 | 2.99 |
| 13 | *rac*-LA | **3** | 100 | toluene | 150 | 95 | 13700 | 11100 | 1.24 |
| 14 | *rac*-LA | **3** | 200 | toluene | 270 | 95 | 27400 | 15500 | 1.77 |
| 15 | *rac*-LA | **3** | 400 | toluene | 1000 | 94 | 54100 | 25000 | 2.17 |

[a] General conditions: [LA] = 0.5 mol/L, $T$ = 20 °C. [b] Reaction time was not necessarily optimized. [c] Conversion of monomer M as determined by $^1$H NMR spectroscopy. [d] $M_n$ value calculated assuming one polymer chain per metal center, from the relation: 144 × conv × [M]/[Ln]. [e] Experimental (corrected; see Exp. Sect.) $M_n$ and $M_w/M_n$ values determined by GPC in THF vs. polystyrene standards.

 © 2007 Wiley-VCH Verlag GmbH & Co. KGaA, Weinheim 

hancement of stereoselectivity. Polymerization of (*S*,*S*)-lactide by **2** (entry 11) or **1** resulted in pure isotactic PLA; the decoupled $^1$H NMR spectrum of the polymer showed one sharp resonance for the methine region. This observation supports the lack of base-promoted epimerization of lactide or PLA and argues against an anionic polymerization mechanism being operative.[40,41]

Experiments aimed at investigating the degree of control of polymerizations were carried out. All the PLAs obtained with borohydride complexes **1**–**3** showed monomodal GPC traces with polydispersity values in the range $M_w/M_n$ = 1.09–2.99. In general, quite narrow molecular-weight distributions ($1.09 < M_w/M_n < 1.50$) were observed for polymerizations carried out in toluene and for monomer-to-metal ratios ≤200, indicative of a single-site character under these conditions. For the three initiators, the number-average molecular mass ($M_n$) values increase monotonously, though not linearly, with the monomer-to-metal ratio. An important issue with complexes **1**–**3** is to assess if they act as mono- or di-initiators; that is, if only one or both borohydride groups initiate a polymer chain. The corrected experimental number-average molecular mass ($M_n$) values of PLAs produced with **1** are in most cases close to the theoretical ones, calculated on the assumption that a single $HBH_3$ group initiates the polymerization, that is a single PLA chain is produced per metal center (entries 1–4). For PLAs produced by **2** and **3**, the experimental $M_n$ values approximately matched the calculated ones on the latter principle, but only if the monomer-to-metal ratio was low. For [LA]/[Sm] = 400 and [LA]/[Yb] > 200, the molecular weight distributions were large, which hampers meaningful comparisons of $M_n$ values. Thus, system **1** features overall a better control of polymerizations than complexes **2** and **3** do. This observation corroborates the aforementioned difference in activity between **1**, and **2** and **3**, and suggests that the former and latter complexes may have different initiation processes.

The $^1$H NMR spectra in $CDCl_3$ of relatively low-molecular-weight samples of PLA (e.g., entry 6) all show the quartet characteristic of the C*H*(Me)OH terminal group at $\delta$ = 4.33 ppm. The latter group is formed after hydrolysis of the metal–alkoxide bond, an observation that is indicative of a classical coordination/insertion mechanism with an initial ring-opening through acyl–oxygen bond cleavage.[42–45] It has been recently reported by Guillaume and co-workers that, in the ROP of ε-caprolactone with lanthanide borohydride complexes, the [$HBH_3$] functionality acts as both an initiating group and a reducing agent, yielding α,ω-telechelic poly(ε-caprolactone) diols by reduction of the aldehyde formed after the insertion of the first monomer into the metal–hydride bond.[12,46,47] A similar result was asserted about the ROP of *rac*- and (*S*,*S*)-lactide with diamino-bis(phenolate)-lanthanide borohydride initiators, yielding α,ω-telechelic PLA diols, however without supporting this statement with experimental data.[13] In our case, the presence of a second alcohol function at the other extremity of the polymer chain could not be established unambiguously; additional resonances were observed, which include a doublet of doublet at $\delta$ = 5.50 ppm and two doublets/quartets at $\delta$ = 4.15 and 4.45 ppm, which could correspond to C$H_2$OH end-groups; but their lower than expected intensity and diversity suggest incomplete and/or multiple processes (see Supporting Information; see footnote on the first page of this article).

## Conclusions

Bulky guanidinate ligands provide a suitable coordination environment that allows synthesis of isolable monomeric borohydride derivatives $[(Me_3Si)_2NC(N\text{-}Cy)_2]_2Ln(\mu\text{-}BH_4)_2Li(THF)_2$ (Ln = Nd, Sm, Yb) in reasonable yields. The complexes, especially neodymium complex **1**, act as monoinitiators for the ring-opening polymerization of racemic lactide, providing atactic polymers with a certain degree of control, that is, controlled molecular weights and relatively narrow polydispersities, provided moderate substrate-to-initiator ratios are used.

## Experimental Section

**General Conditions:** All experiments were performed in evacuated tubes, using standard Schlenk techniques, with rigorous exclusion of traces of moisture and air. After drying over KOH, THF was purified by distillation from sodium/benzophenone ketyl, and hexane and toluene were dried by distillation from sodium/triglyme and benzophenone ketyl prior to use. [$D_6$]benzene was dried with sodium and condensed in vacuo into the NMR tubes prior to use. *N*,*N*′-Dicyclohexylcarbodiimide was purchased from Acros. Anhydrous $LnCl_3$,[48] and $(Me_3Si)_2NLi(Et_2O)$[49] were prepared according to literature procedures. All other commercially available chemicals were used after the appropriate purification.

**Instruments and Measurements:** NMR spectra were recorded with a Bruker DPX 200 spectrometer ($^1$H, 200 MHz; $^{13}$C, 50 MHz; $^{11}$B, 64.2 MHz; $^7$Li, 77.7 MHz). Chemical shifts for $^1$H and $^{13}$C spectra were referenced internally using the residual solvent resonances and are reported relative to TMS. IR spectra were recorded as Nujol mulls with a Specord M80 instrument. Lanthanide metal analysis was carried out by complexometric titration and the C,H elemental analysis by the microanalytical laboratory of IOMC. Size exclusion chromatography (SEC) of PLAs was performed in THF at 20 °C using a Waters SIS HPLC pump, a Waters 410 refractometer, a DAD-UV detector, and Waters styragel columns (HR2, HR3, HR4, HR5E) or PL-GEL Mixte B and 100A columns. The number average molecular masses ($M_n$) and polydispersity index ($M_w/M_n$) of the resultant polymers were calculated with reference to a polystyrene calibration. $M_n$ values were corrected with a Mark-Houwink factor of 0.58 to account for the difference in hydrodynamic volumes between polystyrene and polylactide (PLA).[50,51] The microstructure of PLAs was measured by homodecoupling $^1$H NMR spectroscopy at 20 °C in $CDCl_3$ on a Bruker AC-500 spectrometer.[37]

**Synthesis of $[(Me_3Si)_2NC(N\text{-}Cy)_2]_2Nd(\mu\text{-}BH_4)_2Li(THF)_2$ (1):** CyN=C=NCy (0.52 g, 2.52 mmol) was added to a solution of $(Me_3Si)_2NLi(Et_2O)$ (0.61 g, 2.52 mmol) in toluene (30 mL) at 20 °C and after 45 min stirring $Nd(BH_4)_3(THF)_2$ (0.43 g, 1.26 mmol) was added. The reaction mixture was stirred and heated at 65 °C for a further 12 h. The reaction mixture was filtered off and from the clear solution the solvent was evaporated in vacuo. The remaining

 © 2007 Wiley-VCH Verlag GmbH & Co. KGaA, Weinheim 

solid was extracted with hexane (2 × 20 mL). After filtration of the hexane extracts, the resulting solution was slowly concentrated under vacuum at room temperature. The blue crystalline solid formed overnight was washed with cold hexane and dried in vacuo at room temperature for 40 min, yielding **1** (0.88 g, 66%) as a blue crystalline solid. $C_{46}H_{104}B_2LiN_6NdO_2Si_4$ (1057.7): calcd. C 52.23, H 9.83, Nd 13.63; found C 52.00, H 9.41, Nd 13.23. IR (Nujol, KBr): $\tilde{\nu}$ = 2265 (m), 2408 (s), 2308 (s), 2242 (s), 2220 (s), 1638 (s), 1538 (s), 1347 (s), 1300 (s), 1249 (s), 1175 (s), 1132 (s), 1079 (s), 948 (s), 834 (s), 756 (m) $cm^{-1}$.

**Synthesis of $[(Me_3Si)_2NC(N\text{-}Cy)_2]_2Sm(\mu\text{-}BH_4)_2Li(THF)_2$ (2):** Complex **2** was synthesized following the standard procedure described for **1** starting from $(Me_3Si)_2NLi(Et_2O)$ (0.58 g, 2.42 mmol), CyN=C=NCy (0.50 g, 2.42 mmol), and $Sm(BH_4)_3(THF)_2$ (0.40 g, 1.21 mmol) in toluene (30 mL). Complex **2** was isolated as a yellow crystalline solid (0.83 g, 64%). $C_{46}H_{104}B_2LiN_6O_2Si_4Sm$ (1063.9): calcd. C 51.93, H 9.77, Sm 14.13; found C 51.55, H 9.34, Sm 14.26. $^1H$ NMR (200 MHz, [D$_6$]benzene ): $\delta$ = –1.34 (br. s, 8 H, B$H_4$), 0.28, 0.35 [both s, together 36 H, Si(C$H_3$)$_3$], 1.32–1.94 (br. m, 48 H, C$H_2$ Cy, β-C$H_2$, THF), 2.83 (br. m, 4 H, C$H$ Cy), 3.56 (br. s, 8 H, α-C$H_2$, THF) ppm. $^7Li$ NMR (77.7 MHz, [D$_6$]benzene ): $\delta$ = 0.03 ppm. $^{11}B$ NMR (64.2 MHz, [D$_6$]benzene): $\delta$ = 49.04 ppm. $^{13}C\{^1H\}$ NMR (50 MHz, [D$_6$]benzene): $\delta$ = 4.2 [(NSi$CH_3$)$_2$], 25.4 (β-$CH_2$, THF), 22.0, 25.7, 26.3, 31.9, 36.7 ($CH_2$, Cy), 53.3 ($CH$, Cy), 68.3 (α-$CH_2$, THF), 208.6 ($CN_3$) ppm. IR (Nujol, KBr): $\tilde{\nu}$ = 2658 (m), 2419 (s), 2396 (s), 2244 (s), 2204 (s), 1638 (s), 1600 (m), 1405 (s), 1355 (s), 1300 (s), 1187 (m), 1175 (m), 1136 (m), 1071 (m), 1057 (s), 1004 (s), 943 (s), 841 (s), 676 (m) $cm^{-1}$.

**Synthesis of $[(Me_3Si)_2NC(N\text{-}Cy)_2]_2Yb(\mu\text{-}BH_4)_2Li(THF)_2$ (3):** Complex **3** was synthesized following the standard procedure described for **1** starting from $(Me_3Si)_2NLi(Et_2O)$ (0.89 g, 3.73 mmol), CyN=C=NCy (0.77 g, 3.73 mmol), and $Yb(BH_4)_3(THF)_2$ (0.67 g, 1.86 mmol) in toluene (30 mL). Complex **3** was isolated as an orange crystalline solid (1.37 g, 68%). $C_{46}H_{104}B_2LiN_6O_2Si_4Yb$ (1086.5): calcd. C 50.85, H 9.57, Yb 15.92; found C 50.39, H 9.21, Yb 16.06. IR (Nujol, KBr): $\tilde{\nu}$ = 2661 (m), 2431 (s), 2296 (s), 2246 (s), 2200 (s), 1634 (s), 1600 (m), 1405 (s), 1358 (s), 1304 (s), 1249 (s), 1190 (s), 1136 (m), 1073 (m), 1050 (s), 1002 (s), 944 (s), 842 (s), 678 (m) $cm^{-1}$.

**General Procedure for Lactide Polymerization:** In the glovebox, a Schlenk flask was charged with a solution of the metal initiator (typically 0.019 mmol, about 10 mg) in toluene (0.2 mL) or THF (0.2 mL). A solution of the monomer [*rac*-LA, (*S*,*S*)-LA; previously recrystallized twice from dry toluene and then sublimed under vacuum at 50 °C] was added rapidly to this solution in the appropriate ratio in toluene or THF (3.0 mL). The mixture was immediately stirred with a magnetic stir bar at room temperature. Aliquots were periodically removed with a pipette for monitoring the monomer conversion by $^1H$ NMR spectroscopy. After completion or the desired time, the reaction was quenched with acidic methanol (0.5 mL of a 1.2 M HCl solution), and the polymer was precipitated with excess methanol (100 mL). The polymer was then dried under vacuum to constant weight.

**X-ray Crystallographic Study:** The crystal data and details of data collection are given in Table 1. X-ray data were collected on a SMART APEX diffractometer (graphite-monochromated Mo-$K_\alpha$ radiation, $\lambda$ = 0.71073 Å, $\phi$-$\omega$-scan technique) at –100 °C. The intensity data were integrated in the SAINT program.[52] SADABS[53] was used to perform area-detector scaling and absorption corrections. The structures were solved by direct methods and were refined on $F^2$ using all reflections with SHELXTL.[54] All non-hydrogen atoms were refined anisotropically. The hydrogen atoms in **1** and **2** were found from the Fourier syntheses of electron density except the H atoms of THF ligands and solvate hexane molecules. The H atoms of $BH_4$ groups in **3** were found from the Fourier syntheses of electron density whereas the remaining hydrogen atoms were placed in calculated positions. The H atoms in **1**–**3**, found from the differential syntheses of electron density, were refined isotropically, whereas all other hydrogen atoms were refined in the "riding model".

CCDC-634981 (for **1**), -634982 (for **2**), and -634983 (for **3**) contain the supplementary crystallographic data for this paper. These data can be obtained free of charge from The Cambridge Crystallographic Data Centre via www.ccdc.cam.ac.uk/data_request/cif.

**Supporting Information** (see also the footnote on the first page of this article): Details of the $^1H$ NMR spectrum and GPC trace of a PLA sample.

## Acknowledgments

This work was supported by the Russian Foundation for Basic Research (Grant Nos. 05-03-32390, 06-03-32728), Program of the Presidium of the Russian Academy of Science (RAS), and RAS Chemistry and Material Science Division. A. T. thanks the Russian Foundation for science support.

[1] T. J. Marks, G. W. Grynkewich, *Inorg. Chem.* **1976**, *15*, 1302–1307.
[2] M. Ephritikhine, *Chem. Rev.* **1997**, *97*, 2193–2242.
[3] Y. K. Gun'ko, B. M. Bulychev, G. L. Soloveichik, V. K. Belsky, *J. Organomet. Chem.* **1992**, *424*, 289–300.
[4] E. B. Lobkovsky, Y. K. Gun'ko, B. M. Bulychev, V. K. Belsky, G. L. Soloveichik, M. Yu. Antipin, *J. Organomet. Chem.* **1991**, *406*, 343–352.
[5] M. F. Lappert, A. Singh, J. L. Atwood, W. E. Hunter, *J. Chem. Soc., Chem. Commun.* **1983**, 206–207.
[6] A. V. Khvostov, V. V. Nesterov, B. M. Bulychev, A. I. Sizov, M. Yu. Antipin, *J. Organomet. Chem.* **1999**, *583*, 222–225.
[7] D. Deng, X. Zheng, C. Qian, J. Sun, L. Chang, *J. Organomet. Chem.* **1994**, *466*, 95–100.
[8] H. Schumann, M. R. Keitsch, J. Demtschuk, S. Mühle, *Z. Anorg. Allg. Chem.* **1998**, *624*, 1811–1818.
[9] M. Visseaux, T. Chenal, P. Roussel, A. Mortreux, *J. Organomet. Chem.* **2006**, *691*, 86–92.
[10] a) D. Barbier-Baudry, O. Blacque, A. Hafid, A. Nyassi, H. Sitzmann, M. Visseaux, *Eur. J. Inorg. Chem.* **2000**, 2333–2336; b) P. Zink, M. Visseaux, A. Mortreux, *Z. Anorg. Allg. Chem.* **2006**, *632*, 1943–1944.
[11] S. M. Cendrowski-Guillaume, M. Nierlich, M. Lance, M. Ephritikhine, *Organometallics* **1998**, *17*, 786–788.
[12] I. Palard, A. Soum, S. M. Guillaume, *Chem. Eur. J.* **2004**, *10*, 4054–4062.
[13] F. Bonnet, A. R. Cowley, P. Mountford, *Inorg. Chem.* **2005**, *44*, 9046–9055.
[14] F. Bonnet, A. C. Hilier, A. Collins, S. R. Dubberley, P. Mountford, *Dalton Trans.* **2005**, 421–423.
[15] R. Duchateau, C. T. van Wee, A. Meetsma, P. Th. Van Duijnen, J. H. Teuben, *Organometallics* **1996**, *15*, 2279–2290.
[16] F. Yuan, J. Yang, L. Xiong, *J. Organomet. Chem.* **2006**, *691*, 2534–2539.
[17] A. A. Trifonov, D. M. Lyubov, G. K. Fukin, E. V. Baranov, Yu. A. Kurskii, *Organometallics* **2006**, *25*, 3935–3942.
[18] A. A. Trifonov, D. M. Lyubov, E. A. Fedorova, G. K. Fukin, H. Schumann, S. Mühle, M. Hummert, M. N. Bochkarev, *Eur. J. Inorg. Chem.* **2006**, 747–756.
[19] A. A. Trifonov, E. A. Fedorova, G. K. Fukin, M. N. Bochkarev, *Eur. J. Inorg. Chem.* **2004**, 4396–4401.

 © 2007 Wiley-VCH Verlag GmbH & Co. KGaA, Weinheim 

[20] A. A. Trifonov, G. G. Skvortsov, D. M. Lyubov, N. A. Skorodumova, G. K. Fukin, E. V. Baranov, V. N. Glushakova, *Chem. Eur. J.* **2006**, *12*, 5320–5327.
[21] a) A. A. Trifonov, G. G. Skvortsov, D. M. Lyubov, G. K. Fukin, E. A. Fedorova, M. N. Bochkarev, *Russ. Chem. Bull.* **2005**, *54*, 2511–2518; b) G. G. Skvortsov, M. V. Yakovenko, G. K. Fukin, E. V. Baranov, Yu. A. Kurskii, A. A. Trifonov, *Russ. Chem. Bull.* accepted for publication.
[22] F. Yuan, Y. Zhu, L. Xiong, *J. Organomet. Chem.* **2006**, *691*, 3377–3382.
[23] U. Mirsaidov, A. Kurbonbekov, T. Rotenberg, K. Dzhuraev, *Neorg. Mater.* **1978**, *14*, 1340–1343.
[24] U. Mirsaidov, A. Rakhimova, T. Dymova, *Neorg. Mater.* **1979**, *15*, 1248–1251.
[25] U. Mirsaidov, I. Shaimuradov, M. Khikmatov, *Zh. Neorg. Khim.* **1986**, *31*, 753–755.
[26] R. D. Schannon, *Acta Crystallogr., Sect. A: Found. Crystallogr.* **1976**, *32*, 751–767.
[27] Y. Yao, Y. Luo, J. Chen, Z. Zhang, Y. Zhang, Q. Shen, *J. Organomet. Chem.* **2003**, *679*, 229–237.
[28] Y. Luo, Y. Yao, Q. Shen, K. Yu, L. Weng, *Eur. J. Inorg. Chem.* **2003**, 318–323.
[29] M. Deng, Y. Yao, Y. Zhang, Q. Shen, *Chem. Commun.* **2004**, 2742–2743.
[30] I. A. Guzei, M. Wendt, *Dalton Trans.* **2006**, 3991–3999.
[31] C. K. Ha, J. A. Gardella Jr, *Chem. Rev.* **2005**, *105*, 4205–4232.
[32] O. D. Cabaret, B.-M. Vaca, D. Bourissou, *Chem. Rev.* **2004**, *104*, 6147–6176.
[33] R. E. Drumright, P. R. Gruber, D. E. Henton, *Adv. Mater.* **2000**, *12*, 1841–1846.
[34] M. H. Chisholm, Z. Zhou, *J. Mater. Chem.* **2004**, *14*, 3081–3092.
[35] G. R. Giesbrecht, G. D. Whitener, J. Arnold, *J. Chem. Soc., Dalton Trans.* **2001**, 923–927.
[36] See for example: A. Amgoune, C. M. Thomas, S. Ilinca, T. Roisnel, J.-F. Carpentier, *Angew. Chem. Int. Ed.* **2006**, *45*, 2782–2784 and references cited therein.
[37] A. Amgoune, C. M. Thomas, T. Roisnel, J.-F. Carpentier, *Chem. Eur. J.* **2006**, *12*, 169–179.
[38] K. A. M. Thakur, R. T. Kean, E. S. Hall, J. J. Kolstad, T. A. Lindgren, M. A. Doscotch, J. I. Siepmann, E. J. Munson, *Macromolecules* **1997**, *30*, 2422–2428.
[39] J. E. Kasperczyk, *Macromolecules* **1995**, *28*, 3937–3939.
[40] B. M. Chamberlain, Y. Sun, J. R. Hagadorn, E. W. Hemmesch, V. G. Young Jr, M. Pink, M. A. Hillmyer, W. B. Tolman, *Macromolecules* **1999**, *32*, 2400–2402.
[41] M. H. Chisholm, N. W. Eilerts, *Chem. Commun.* **1996**, 853–854.
[42] H. R. Kricheldorf, M. Berl, N. Scharnagi, *Macromolecules* **1988**, *21*, 286–293.
[43] P. Dubois, C. Jacobs, R. Jérôme, P. Teyssié, *Macromolecules* **1991**, *24*, 2266–2270.
[44] M. Lahcini, P. M. Castro, M. Kalmi, M. Leskelä, T. Repo, *Organometallics* **2004**, *23*, 4547–4549.
[45] M. Kalmi, M. Lahcini, P. M. Castro, O. Lehtonen, A. Belfkira, M. Leskelä, T. Repo, *J. Polym. Sci., Part A: Polym. Chem.* **2004**, *42*, 1901–1911.
[46] S. M. Guillaume, M. Schappacher, A. Soum, *Macromolecules* **2003**, *36*, 54–60.
[47] I. Palard, A. Soum, S. M. Guillaume, *Macromolecules* **2005**, *38*, 6888–6894.
[48] M. D. Taylor, C. P. Carter, *J. Inorg. Nucl. Chem.* **1962**, *24*, 387–393.
[49] L. E. Manzer, *Inorg. Chem.* **1978**, *17*, 1552–1558.
[50] I. Barakat, P. Dubois, R. Jerome, P. Teyssie, *J. Polym. Sci., Part A: Polym. Chem.* **1993**, *31*, 505–514.
[51] H. Ma, J. Okuda, *Macromolecules* **2005**, *38*, 2665–2673.
[52] Bruker, SAINTPlus Data Reduction and Correction Program v.6.02a, *Bruker AXS*, Madison, WI, USA, **2000**.
[53] G. M. Sheldrick, SADABS v.2.01, *Bruker/Siemens Area Detector Absorption Correction Program*, Bruker AXS, Madison, WI, USA, **1998**.
[54] G. M. Sheldrick, SHELXTL v.6.12, Structure Determination Software Suite, Bruker AXS, Madison, WI, USA, **2000**

Received: January 30, 2007
Published Online: May 22, 2007

 © 2007 Wiley-VCH Verlag GmbH & Co. KGaA, Weinheim 

DOI: 10.1002/ejic.200700148

# (Phthalocyaninato)copper(II) Complexes Fused with Different Numbers of 15-Crown-5 Moieties – Synthesis, Spectroscopy, Supramolecular Structures, and the Effects of Substituent Number and Molecular Symmetry

**Ning Sheng,[a] Yuexing Zhang,[a] Hui Xu,[a] Meng Bao,[b] Xuan Sun,*[a] and Jianzhuang Jiang*[a]**

**Keywords:** Phthalocyanines / Crown ether / Supramolecular chemistry / Molecular symmetry

Symmetrical (phthalocyaninato)copper(II) complexes Cu(Pc′) [Pc′ = Pc(15C5), Pc(opp-15C5)$_2$, Pc(adj-15C5)$_2$, Pc(15C5)$_3$; Pc = unsubstituted phthalocyaninate, Pc(15C5) = 2,3-(15-crown-5)phthalocyaninate, Pc(opp-15C5)$_2$ = 2,3,16,17-bis(15-crown-5)phthalocyaninate, Pc(adj-15C5)$_2$ = 2,3,9,10-bis(15-crown-5)phthalocyaninate, Pc(15C5)$_3$ = 2,3,9,10,16,17-tris(15-crown-5)phthalocyaninate] (**2**–**5**) have been prepared by the reaction of corresponding heteroleptic bis(phthalocyaninato)europium complexes Eu(Pc)(Pc′) [Pc′ = Pc(15C5), Pc(opp-15C5)$_2$, Pc(adj-15C5)$_2$, Pc(15C5)$_3$, Pc(15C5)$_4$; Pc = unsubstituted phthalocyaninate] with Cu(OAc)$_2$ in dry dmf at 100 °C. For the purpose of comparative studies, the symmetrical counterparts CuPc (**1**) and CuPc(15C5)$_4$ [Pc(15C5)$_4$ = 2,3,9,10,16,17,24,25-tetrakis(15-crown-5)phthalocyaninate] (**7**) have also been prepared. These monomeric complexes have been characterized by spectroscopic methods in addition to elemental analysis. Having a series of closely related phthalocyanines with a different number and/or disposition of 15-crown-5 groups at the peripheral positions, the effects of 15-crown-5 substituent number and molecular symmetry on the electronic absorption spectra, infra-red (IR) spectra, and supramolecular structure formation induced by $K^+$ ions have been investigated. Systematic studies on the formation of dimeric supramolecular structures of the series of monomers **2**–**6** reveal and confirm the previously proposed two-step three-stage process of $K^+$-induced dimerization of phthalocyanines with three or four 15-crown-5 moieties.

(© Wiley-VCH Verlag GmbH & Co. KGaA, 69451 Weinheim, Germany, 2007)

## Introduction

The design and preparation of supramolecular structures have attracted significant research interest due to their great potential applications in materials science and molecular electronics. Phthalocyanines have been an important class of molecular materials since their first synthesis early in the last century.[1] Crown ethers have also found wide application in molecular electronic devices due to their remarkable recognition and metal-binding properties.[2] The combination of these two functional subunits for the purpose of constructing novel supramolecular structures with novel multi-functional properties has stimulated wide research interest since the 1980s.[3]

The first trial in this direction was the preparation of CuPc(15C5)$_4$ in 1986 by three independent research groups.[3] Subsequently, these crown ether substituted metal-free or metallo-phthalocyanines have been studied for their dimerization in a two-step three-stage process in the presence of potassium ions in a mixed solvent of chloroform and methanol.[4] Since then, significant efforts have been put into adding different numbers of 15-crown-5 voids onto the phthalocyanine skeleton through asymmetric σ-bonded substitution of the peripheral protons. However, most probably because of the absence of a suitable effective separation method for the mono-, bis-, tris-, and tetrakis(15-crown-5)-substituted phthalocyanine compounds, which each have a high and similar polarity, only a few tris(15-crown-5)-substituted phthalocyanine analogues have been isolated.[5] The main target of the present work is to introduce different numbers of 15-crown-5 groups, from one to four, at different peripheral positions of the phthalocyanine ligand of (phthalocyaninato)copper complexes, and then systematically study their spectroscopic and dimeric supramolecular structure formation characteristics.

It is worth pointing out that the effects of lowering the molecular symmetry of phthalocyanine molecules on the spectra have not yet been fully exploited. Most of the studies so far have focused on the spectral properties of phthalocyanine analogues with reduced molecular symmetry because of their lower π-system symmetry than $D_{4h}$,[6] which are obviously significantly affected by the change in the size of the π-system.

[a] Department of Chemistry, Shandong University, Jinan 250100, China
Fax: +86-531-856-5211
E-mail: jzjiang@sdu.edu.cn
[b] Department of Chemistry, Jinan University, Jinan 250100, China

Supporting information for this article is available on the WWW under http://www.eurjic.org/ or from the authors.

 © 2007 Wiley-VCH Verlag GmbH & Co. KGaA, Weinheim 

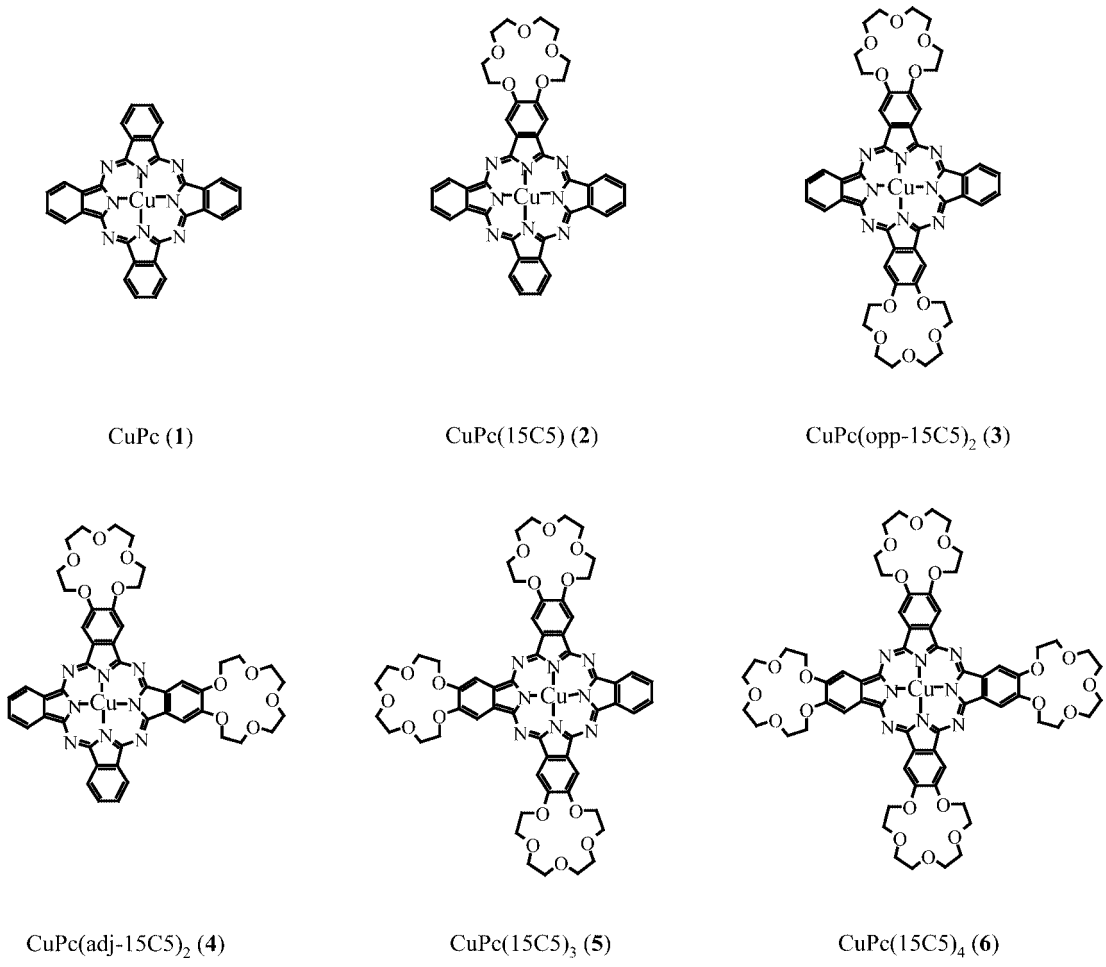


Figure 1. Schematic molecular structures of (phthalocyaninato)copper complexes fused with different numbers of 15-crown-5 moieties.

In this paper, we report the synthesis of a series of unsymmetrical (phthalocyaninato)copper(II) complexes, namely CuPc(15C5) (**2**), CuPc(opp-15C5)$_2$ (**3**), CuPc(adj-15C5)$_2$ (**4**), and CuPc(15C5)$_3$ (**5**) as well as symmetrical CuPc (**1**) and CuPc(15C5)$_4$ (**6**) with zero, one, two, three, and four 15-crown-5 voids attached at different positions of the phthalocyanine ring (Figure 1). Their spectroscopic properties have also been comparatively studied, trying to reveal the effects of lowering the molecular symmetry of phthalocyanines. It is worth mentioning that in spite of the very recent efforts on the heteroleptic bis(phthalocyaninato)europium complexes Eu(Pc)(Pc′) [Pc′ = Pc(15C5), Pc(opp-15C5)$_2$, Pc(adj-15C5)$_2$, Pc(15C5)$_3$, Pc(15C5)$_4$],[7] these effects could not be clearly revealed due to the attenuation and/or covering of such effects by strong π-π interactions in the double-decker molecules, which predominantly control their spectral properties.

## Results and Discussion

### Synthesis

Two synthetic pathways have been reported so far to prepare unsymmetrical monomeric phthalocyanine analogues. The first method involves a mixed cyclization of two phthalonitrile (or isoindole) precursors in the presence of a metal salt or organic base.[8] As can easily be expected, the separation of a series of closely related and isomeric phthalocyanines obtained in this way has been a great challenge for chemists. As a result, except for the two whole series of phthalocyanine analogues, whose π-system itself has a lower symmetry than $D_{4h}$, reported by Kenny and Tian,[6a,9] respectively, from the reaction between a tetraazaporphyrin precursor and a phthalocyanine precursor and between a phthalocyanine precursor and a naphthalocyanine precursor, unsymmetrical phthalocyanine derivatives whose π-system itself still maintains the $D_{4h}$ symmetry prepared and isolated with this method as a whole series are still very rare, limited to MPc[(R)$_n$(OCH$_2$CH$_2$OCH$_2$CH$_2$OCH$_2$CH$_2$OCH$_3$)$_{8-n}$] (M = 2H), to the best of our knowledge.[10] The second pathway involves the ring-expansion reaction of subphthalocyanine. Treatment of a new dinitrile in the isoindole form with a subphthalocyanine led to the formation of phthalocyanine analogues with a 3:1 ratio of the two dinitriles. This method, again, is not practical for the present case. In this work, we employed a novel methodology using heteroleptic bis(phthalocyaninato) rare earth complexes Eu(Pc)(Pc′) [Pc′ = Pc(15C5), Pc(opp-15C5)$_2$, Pc(adj-

 © 2007 Wiley-VCH Verlag GmbH & Co. KGaA, Weinheim 

Table 1. Analytical and mass spectrometric data for (phthalocyaninato)copper complexes **2**–**7**.[a]

| Compound | $[M]^+$ ($m/z$)[b] | Analysis | | |
|---|---|---|---|---|
| | | C | H | N |
| CuPc(15C5) (**2**) | 765.3 (765.2) | [c] | [c] | [c] |
| CuPc(opp-15C5)$_2$·2CH$_3$OH (**3**) | 955.4 (955.2) | 58.48 (58.85) | 5.11 (5.14) | 10.38 (10.98) |
| CuPc(adj-15C5)$_2$·2CH$_3$OH (**4**) | 955.5 (955.2) | 58.84 (58.85) | 5.22 (5.14) | 10.29 (10.98) |
| CuPc(15C5)$_3$·2CHCl$_3$ (**5**) | 1145.7 (1145.3) | 50.71 (50.28) | 4.15 (4.30) | 8.20 (8.20) |

[a] Calculated values given in parentheses. [b] By MALDI-TOF mass spectrometry. [c] Satisfactory elemental analysis data is not obtained for this compound.

15C5)$_2$, Pc(15C5)$_3$, Pc(15C5)$_4$] as the starting material. Reaction with a large excess of copper acetate in dry dmf at 100 °C for 1.5 h provides two different kinds of (phthalocyaninato)copper compounds Cu(Pc) and CuPc(15C5)$_n$ ($n$ = 1–4) (**2**–**6**) in relatively good yields. Fortunately, all the 15-crown-5-substituted (phthalocyaninato)copper complexes **3**–**6**, except for **2**, could be relatively easily separated and purified from its unsubstituted analogue CuPc (**1**) by simple filtration followed by general neutral alumina column chromatography, due to the presence of 15-crown-5 moieties on the phthalocyanine ring of compounds **3**–**6**. It is worth noting that the symmetrical compound CuPc(15C5)$_4$ (**6**) together with CuPc (**1**) was actually obtained from the simple tetramerization of 4,5-dicyanobenzo-15-crown-5 or unsubstituted dicyanobenzene, in the presence of copper acetate.

Because of the low solubility of CuPc(15C5) (**2**), similar to that of CuPc, complex **2** could not be isolated from the reaction between Eu(Pc)[Pc(15C5)] and Cu(OAc)$_2$. This compound, however, was actually prepared by the reaction between Cu(OAc)$_2$ and metal-free H$_2$Pc(15C5), the latter of which was prepared and separated from mixed ring tetramerization of dicyanobenzene and 4,5-dicyanobenzo-15-crown-5.

All the newly prepared (phthalocyaninto)copper(II) complexes **2**–**5** gave satisfactory elemental analysis results as given in Table 1. They were further characterized by spectroscopic methods. The MALDI-TOF spectra of all these compounds showed the molecular ion $[M]^+$ signals with correct isotopic pattern (Table 1).

### Electronic Absorption Spectra

The electronic absorption spectra of the series of (phthalocyaninato)copper complexes **1**–**6** were recorded in CHCl$_3$ and the data are summarized in Table 2. Figure 2 compares the UV/Vis spectra in the range of 300–900 nm of the whole series of compounds. All the absorption spectra show a typical broad Soret band at 340–343 nm, involving a couple of electronic transitions dealing with the third occupied HOMO and the first LUMO. The Q bands for these compounds are observed in the range of 666–677 nm, with two vibrational shoulders at 602–611 and 637–648 nm. In addition, a weak band at 411–435 nm is also observed. Except for the Soret band, both the absorption positions of the Q band and the weak band at 411–435 nm show dependence on the number of 15-crown-5 substituents. The Q band shifts gradually and slightly to the red and the weak band at 411–435 nm to the blue upon an increase in the number of 15-crown-5 substituents. Apart from the absorption position, the appearance of the electronic spectra is also sensitive to the number of 15-crown-5 substituents. For example, the weak band in the range of 411–435 nm for 15-crown-5-containing (phthalocyaninato)copper complexes **2**–**6**, which is absent in the unsubstituted CuPc (**1**), gradually increases in intensity and moves to the higher energy side coinciding with the increase in the number of 15-crown-5 groups from **2** to **6**. This result clearly reveals the origin of this absorption which is associated with the 15-crown-5 substituents. In combination with the fact that a similar band was observed for all the 15-crown-5-substituted monomeric phthalocyanines[3] and even the alkoxy-substituted phthalocyanine derivatives,[11] this absorption can be attributed to the n→π* transitions arising from the oxygen lone pairs of electrons. This assignment is further confirmed by our recent calculation results on the electronic absorption spectra of nonperipherally tetraalkoxy-substituted (phthalocyaninato)lead complexes.[12] It is also noteworthy that for the isomeric complexes **3** and **4**, a very slight shift is still observed for some of the absorption bands, indicating that the electronic absorption properties are also more or less dependent on the substituent positions.

Table 2. Electronic absorption data for (phthalocyaninato)copper complexes **1**–**6** in CHCl$_3$.

| Compound | $\lambda_{max}$ [nm] (log ε) | | | | |
|---|---|---|---|---|---|
| 1 | 343 (4.50) | | 602 (4.22) | 637 (4.19) | 666 (5.02) |
| 2 | 341 (4.55) | 435 (3.62) | 608 (4.24) | 644 (4.26) | 673 (4.87) |
| 3 | 340 (4.58) | 423 (3.75) | 610 (4.29) | 646 (4.28) | 675 (4.88) |
| 4 | 340 (4.48) | 424 (3.75) | 609 (4.17) | 646 (4.17) | 674 (4.77) |
| 5 | 341 (4.61) | 414 (4.01) | 611 (4.35) | 647 (4.38) | 676 (4.95) |
| 6 | 341 (4.53) | 411 (4.09) | 611 (4.26) | 648 (4.28) | 677 (4.93) |

As shown in Figure 2, except for the weak n→π* transition band at ca. 420 nm, all the unsymmetrical (phthalocyaninato)copper(II) complexes **2**–**5** display very similar absorption features, which also resemble their symmetrical counterparts **1** and **6**. This observation reveals that the effect of lowering the molecular symmetry of phthalocyanines only through asymmetric σ-bonded substitution of the peripheral protons is too small to be reflected in their electronic absorption spectra. Phthalocyanines with diminished molecular symmetry through asymmetric σ-bonded substitution of the nonperipheral protons are expected to provide more information in this regard.

 © 2007 Wiley-VCH Verlag GmbH & Co. KGaA, Weinheim 

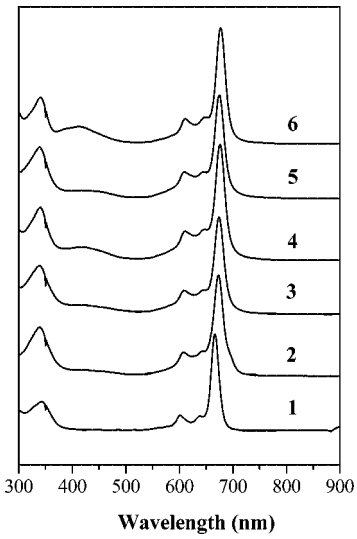


Figure 2. The electronic absorption spectra of CuPc (**1**), CuPc(15C5) (**2**), CuPc(opp-15C5)$_2$ (**3**), CuPc(adj-15C5)$_2$ (**4**), CuPc(15C5)$_3$ (**5**), and CuPc(15C5)$_4$ (**6**) in $CHCl_3$.

## IR Spectra

Because of the interest in the sandwich-type (tetrapyrrole)metal complexes related to their potential applications in molecular electronics and magnetism, we have focused our attention on the synthesis and structures of a series of (na)phthalocyaninato and/or porphyrinato rare earth complexes in the past decade.[13–16] IR spectroscopic characteristics of (na)phthalocyanine in these sandwich-type complexes have also been systematically studied for the purpose of investigating the intrinsic properties of these phthalocyanine compounds.[17–19] However, except for the early efforts paid to the metal-free and metalo-phthalocyanines without peripheral substituents and the recent work on the calculated spectra of several phthalocyanine compounds employing the DFT method, systematic investigation of the IR spectroscopy of monomeric phthalocyanine compounds seems not to have been conducted to date. Our compounds in the present work are therefore expected to give representative data for the series of peripherally substituted (phthalocyaninato)metal complexes.

As clearly shown in Figure S1 and Table S1 (Supporting Information), the presence of one, two, three, and four 15-crown-5 moieties on the peripheral positions of the phthalocyanine ring in the molecules of compounds **2**, **3** and **4**, **5**, and **6** increases the number of IR-active modes. The common absorptions for the 15-crown-5-substituted complexes **2**–**6** observed at 2954–2958, 2921–2924, 2871–2872, 2851–2856, 1280–1287, and 1045–1047 $cm^{-1}$, which are absent in the spectrum of unsubstituted CuPc (**1**), are attributed to the asymmetric and symmetric C–H stretching vibrations and C–O–C stretching vibrations of the 15-crown-5 groups, respectively. Nevertheless, the intensity of all these absorptions has been found to increase along with the number of 15-crown-5 moieties from **2** to **6**.

It is also worth noting that despite of several additional peaks observed for CuPc(15C5)$_4$ (**6**) compared with CuPc (**1**), the characteristic pattern of the IR spectrum of CuPc(15C5)$_4$ (**6**) still remains simple, somewhat simpler than those of **2**–**5**, revealing the relatively higher molecular symmetry of the former compound. The static molecular geometry of CuPc (**1**) and CuPc(15C5)$_4$ (**6**) suggests a $D_{4h}$ point group for their molecule, while **2**, **3**, **4**, and **5**, have a $C_{2v}$, $D_{2h}$, $C_{2v}$, and $C_{2v}$ point group, respectively. This is clearly revealed by the larger number of vibrational modes observed in the IR spectra of **2**–**5** compared with those of either CuPc (**1**) or CuPc(15C5)$_4$ (**6**) (Figure S1 and Table S1; Supporting Information). The difference in the characteristic pattern of IR spectra between the isomers **3** and **4** is clearly due to their different molecular symmetry.

## Formation of Dimeric Phthalocyanine Supramolecular Structures

The $K^+$-induced cofacial dimer formation of monomeric phthalocyanine derivatives substituted with three or four 15-crown-5 voids, in particular CuPc(15C5)$_4$, has been well studied by Kobayashi and co-workers.[4a,5] On the basis of corresponding results, a two-step three-stage process was proposed for cofacial dimer formation of monomeric phthalocyanine derivatives. In the present study, the formation process of $K^+$-induced dimeric supramolecular structures of 15-crown-5-substituted (phthalocyaninato)metal complexes, *in a two-step three-stage process*, has been clearly revealed and confirmed by studying the formation processes of (phthalocyaninato)copper complexes in $CHCl_3$ mixed with a trace amount of MeOH due to the availability of the series of mono-, bis-, tris-, and tetrakis(15-crown-5)-substituted (phthalocyaninato)copper complexes, in particular CuPc(15C5) (**2**), CuPc(adj-15C5)$_2$ (**4**), CuPc(15C5)$_3$ (**5**), and CuPc(15C5)$_4$ (**6**).

Figure 3 compares the systematic changes in absorption spectra of CuPc(15C5) (**2**), CuPc(adj-15C5)$_2$ (**4**), CuPc(15C5)$_3$ (**5**), and CuPc(15C5)$_4$ (**6**) in $CHCl_3$ upon titration with KOAc in $CHCl_3$/MeOH (9:1, v/v) and the final spectra obtained when [$CH_3COOK$]/[compound] = 3.0 for all these compounds are listed in Figure S2 (Supporting Information). It can be seen that after adding $K^+$ ions, the intense Q-band at 673 nm for **2** does not take a blue shift but gradually attenuates in intensity. Moreover, no new peak appears in this Q-band region. These results indicate the formation of linear (or noncofacial) dimeric supramolecular structure [CuPc(15C5)]$(K^+)_1$[CuPc(15C5)][(**2**)$(K^+)_1$-(**2**)]. This is also true for the formation of linear (or noncofacial) dimeric supramolecular structure [CuPc(adj-15C5)$_2$]-$(K^+)_2$[CuPc(adj-15C5)$_2$] [(**4**)$(K^+)_2$(**4**)] when $K^+$ ions are added to a solution of the (phthalocyaninato)copper compound with two 15-crown-5 moieties at the adjacent peripheral positions according to the experimental results shown in Figure 3 and Figure S2 (Supporting Information).

However, significant change in the electronic absorption spectrum takes place after $K^+$ ions are added to the solution of compound **5**, see Figure 3 and Figure S2 (Supporting Information). Along with the decrease of the Q-band

 © 2007 Wiley-VCH Verlag GmbH & Co. KGaA, Weinheim 

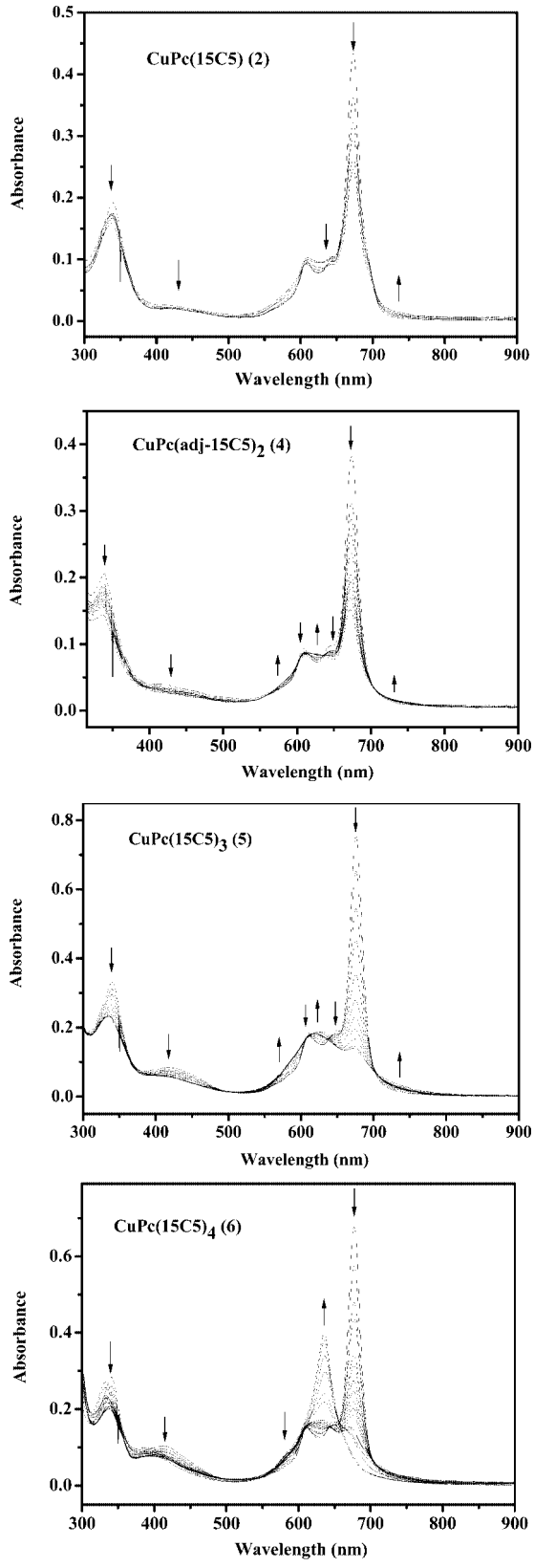


Figure 3. Changes in absorption spectra of CuPc(15C5) (**2**), CuPc(adj-15C5)$_2$ (**4**), CuPc(15C5)$_3$ (**5**), and CuPc(15C5)$_4$ (**6**) in $CHCl_3$ upon titration with KOAc in $CHCl_3$/MeOH (9:1, v/v). Arrows indicate the direction of the spectral changes. The final spectra were obtained when [$CH_3COOK$]/[compound] = 3.0 (for **2**, **4**–**6**).

of **5** at 676 nm, a new band appears at 624 nm due to the formation of cofacial dimeric supramolecule [CuPc(15C5)$_3$]($K^+$)$_3$[CuPc(15C5)$_3$] [(**5**)($K^+$)$_3$(**5**)]. This is in line with the results found during the formation of $K^+$-induced cofacial dimerization of phthalocyanine analogues with three 15-crown-5 voids.[4a,5] It is worth noting that the Soret band at 341 nm for **5** also shifts to the shorter wavelength (335 nm) with addition of $K^+$. In line with the previous reports,[4a,5] cofacial dimeric supramolecular structure [CuPc(15C5)$_4$]($K^+$)$_4$[CuPc(15C5)$_4$] [(**6**)($K^+$)$_4$(**6**)] is formed with addition of $K^+$.

It is noteworthy that a similar result to that of **5** was observed for compound **3** (Figures S2 and S3; Supporting Information). When no changes occur anymore upon addition of excess $K^+$ ions, the electronic absorption spectrum can be ascribed to the cofacial dimeric supramolecular structure [CuPc(opp-15C5)$_2$]($K^+$)$_2$[CuPc(opp-15C5)$_2$] [(**3**)($K^+$)$_2$(**3**)].

As a result, it has been found that $K^+$-induced cofacial dimerization of phthalocyanines with three or four 15-crown-5 voids, for instance compound **5** or **6**, should proceed in the following manner: two monomeric 15-crown-5-substituted phthalocyanine molecules combine with the first $K^+$ cation to form a linear dimer, which then combines with the second $K^+$ cation to form a linear or cofacial dimer, and finally transforms into a stable cofacial dimer when the third and/or fourth $K^+$ cation(s) are combined. In other words, $K^+$-induced cofacial dimerization of phthalocyanines with three or four 15-crown-5 voids should proceed according to the following three stages:[4a,5] (1) The first involves the formation of a linear (or noncofacial) dimer at a [$K^+$]/[MPc(15C5)$_4$] value of 0–0.5; (2) the second in the region of $0.5 \leq [K^+]/[MPc(15C5)_4] \leq 1.5$ involves the transition from the linear (or noncofacial) dimer to the cofacial dimer when the second and third $K^+$ cations are combined; (3) the third involves the complete formation of a cofacial dimer at $[K^+]/[MPc(15C5)_4] \geq 1.5$.

In addition, to monitor the cofacial supramolecular formation for compounds **5** and **3**, the changes in absorption of the so-called monomer band (at 676 nm) and the dimer band (at 592 nm) for **5** (Tables 2 and 3), and monomer band (at 675 nm) and the dimer band (at 593 nm) for **3**, were recorded as a function of [$K^+$]/[**5**] and [$K^+$]/[**3**], respectively. As shown in Figure 4 and Figure S4 (Supporting Information), the concomitant change of the two characteristic bands indicates that upon addition of $K^+$ ions, monomer **5** or **3** is converted exclusively to the dimeric supramolecular

Table 3. Electronic absorption data for the supramolecular dimers (SD) formed from the 15-crown-5-substituted (phthalocyaninato)-copper complexes **2**–**6** in $CHCl_3$ upon titration with KOAc in $CHCl_3$/MeOH (9:1, v/v).

| Compound | $\lambda_{max}$ [nm] (log ε) | | | | |
|---|---|---|---|---|---|
| SD2 | 338 (4.45) | | 610 (4.19) | 643 (4.20) | 673 (4.61) |
| SD3 | 333 (4.45) | | 615 (4.31) | | 673 (4.22) |
| SD4 | 335 (4.37) | | 623 (4.18) | | 672 (4.36) |
| SD5 | 335 (4.44) | | 624 (4.33) | | 671 (4.22) |
| SD6 | 334 (4.41) | 389 (3.98) | 637 (4.53) | | |

 © 2007 Wiley-VCH Verlag GmbH & Co. KGaA, Weinheim 

structure. The formation process is similar to that of $MPc(15C5)_4$ (M = $H_2$, Zn, Co, Ni, Cu) in $CHCl_3$. However, probably due to the low solubility of these compounds including complexes **4** and **2**, about a threefold amount of $K^+$ ions (i.e. $[K^+]/[\mathbf{5}$ or $\mathbf{3}] \approx 3$) is required to reach a steady state (Figure 4 and Figure S4; Supporting Information), instead of the value of 2 observed for other reported monomeric phthalocyanine counterparts.[4a,5]

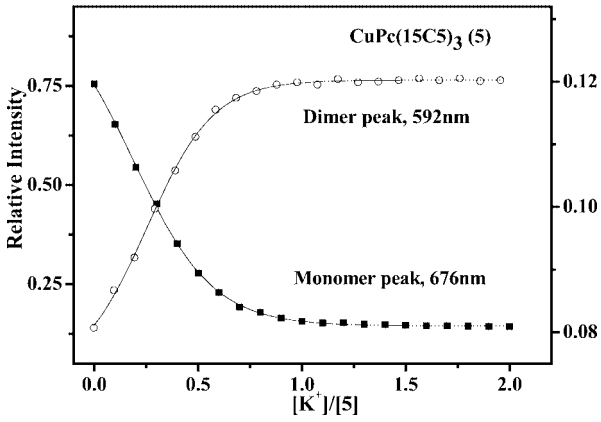


Figure 4. Variation of the absorbance 676 and 592 nm during titration of **5** in $CHCl_3$ with KOAc in $CHCl_3$/MeOH (9:1). The curve going up with $[K^+]$ represents the change at the dimer peak and should be referred to the right-hand axis, while that going down is the change at the monomer peak and should be referred to the left-hand axis.

Equation (1) shows the equilibrium between monomer **5** or **3** (upon addition of $K^+$ ions) and the corresponding dimer. According to the method described by West and Pearce,[20] the monomer and dimer concentrations could be calculated from the spectral changes during titration, and their relationship be depicted as shown in Figure 5 and Figure S5 (Supporting Information) for the present systems. The region with a slope of ca. 2.0 indicates the dimerization occurs in this region. For these present systems, this includes the data point of $[K^+]/[\mathbf{5}$ or $\mathbf{3}] = 0.5$. When $[K^+]/[\mathbf{5}$ or $\mathbf{3}] > 3$, the slope of the plot approaches zero.

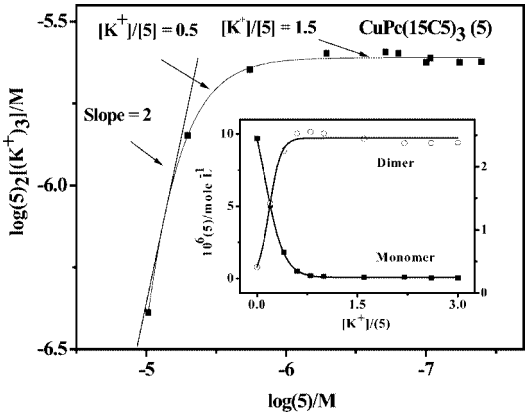


Figure 5. Plots of log[**5**] vs. log[(**5**)$(K^+)_3$(**5**)] for $CuPc(15C5)_3$ (**5**) in $CHCl_3$/MeOH. The inset shows the dependence of monomer and dimer concentrations on $[K^+]/[\mathbf{5}]$.

$$n\ K^+ + 2\ CuPc(15C5)_n \overset{K}{\leftrightarrow} dimer{\cdot}K^+_n \quad (1)$$

It is worth pointing out that for all the crown ether substituted (phthalocyaninato)copper compounds, namely CuPc(15C5) (**2**), $CuPc(opp\text{-}15C5)_2$ (**3**), $CuPc(adj\text{-}15C5)_2$ (**4**), $CuPc(15C5)_3$ (**5**), and $CuPc(15C5)_4$ (**6**), when two $CuPc(15C5)_n$ units bind one $K^+$ cation and start to form the dimer in the first stage, the monomer–dimer conversion proceeds with a very high formation constant, $K = 3.0 \times 10^{10}$ to $7.0 \times 10^{10}$ L$^2$ mol$^{-2}$ with $n = 1$ for Equation (1).[4a]

## Conclusions

We have prepared a series of unsymmetrical (phthalocyaninato)copper(II) complexes **2**–**5**, containing different numbers and positions of 15-crown-5 substituents, from the reaction of corresponding heteroleptic bis(phthalocyaninato)europium complexes Eu(Pc)(Pc′) with $Cu(OAc)_2{\cdot}nH_2O$. It has been found that all the unsymmetrical compounds **2**–**5** and the symmetrical analogues **1** and **6** display very similar absorption features, indicating that the electronic absorption spectra of these compounds are not sensitive enough to show the change in the molecular symmetry due to unsymmetrical substitution of 15-crown-5 moieties, which however can be clearly reflected by their IR spectra. Systematic studies over the formation of dimeric supramolecular structures of the series of monomers **2**–**6** clearly reveal and confirm the previously proposed two-step three-stage process of phthalocyanines with three or four 15-crown-5 moieties in $CHCl_3$ with trace amounts of MeOH in the presence of $K^+$.

## Experimental Section

**General Remarks:** 1,8-Diazabicyclo[5.4.0]undec-7-ene (dbu) and dicyanobenzene were purchased from Aldrich. *n*-Pentanol and *N*,*N*-dimethylformamide (dmf) were freshly distilled from Na and $CaH_2$, respectively, under nitrogen. Column chromatography was carried out on neutral alumina (SCRC, 200–300 mesh) with the indicated eluents. All other reagents and solvents were used as received. 4,5-Dicyanobenzo-15-crown-5,[4,21] Eu(Pc)(Pc′) [Pc′ = Pc(15C5), $Pc(opp\text{-}15C5)_2$, $Pc(adj\text{-}15C5)_2$, $Pc(15C5)_3$, $Pc(15C5)_4$],[7] CuPc (**1**),[22] and $CuPc(15C5)_4$ (**6**)[4] were prepared according to published procedures. $^1$H NMR spectra were recorded with a Bruker DPX 300 spectrometer (300 MHz) in [$D_6$]dmso. Spectra were referenced internally by using the residual solvent resonance ($\delta$ = 2.49 for [$D_6$]-dmso) relative to $SiMe_4$. Electronic absorption spectra were recorded with a Hitachi U-4100 spectrophotometer. MALDI-TOF mass spectra were measured with a Bruker BIFLEX III ultra-high resolution mass spectrometer with α-cyano-4-hydroxycinnamic acid as matrix. Elemental analyses were performed by the Institute of Chemistry, Chinese Academy of Sciences.

**Preparation of $H_2Pc(15C5)$:** According to a literature method,[23] a mixture of dicyanobenzene (76.8 mg, 0.60 mmol), 4,5-dicya-

 © 2007 Wiley-VCH Verlag GmbH & Co. KGaA, Weinheim 

nobenzo-15-crown-5 (31.8 mg, 0.10 mmol), and an excess amount of lithium (2.8 mg, 0.40 mmol) in *n*-pentanol (3 mL) was heated to reflux under nitrogen for 2 h. After cooling to room temperature, the resulting green solution was poured into methanol (100 mL) containing a few drops of concentrated HCl. The precipitate was collected by filtration and chromatographed on an alumina column using $CHCl_3$/MeOH (99:1) as the eluent. After eluting the first band containing unsubstituted metal-free $H_2Pc$, the second green band containing the target compound $H_2Pc(15C5)$ was developed which was collected and the solvent removed in a rotary evaporator. Repeated chromatography followed by recrystallization from $CHCl_3$ and MeOH gave pure $H_2Pc(15C5)$ as a blue powder (12 mg, 16%). MS: calcd. for $C_{40}H_{32}N_8O_5$ $[M]^+$ 704.2; found for $H_2Pc(15C5)$ 704.8.

**Preparation of CuPc(15C5) (2):** A mixture of $H_2Pc(15C5)$ (12 mg, 0.017 mmol) and $Cu(OAc)_2$ (15 mg, 0.08 mmol) in dry dmf (3 mL) was heated to 100 °C for 1.5 h under a slow stream of nitrogen. After cooling to room temperature, MeOH (30 mL) was poured into the resulting blue solution. The precipitate was collected by filtration and chromatographed on an alumina column using $CH_2Cl_2$/MeOH (99.5:0.5) as the eluent. The blue band containing the target compound CuPc(15C5) was then collected. Repeated chromatography followed by recrystallization from $CH_2Cl_2$ and MeOH gave pure CuPc(15C5) as a blue powder (8 mg, 60%). It is worth noting that a satisfactory elemental analysis result could not be obtained for this compound even after repeated purification by column chromatography and recrystallization due to its limited solubility in common organic solvent.

**Preparation of CuPc(opp-15C5)$_2$ (3), CuPc(adj-15C5)$_2$ (4), and CuPc(15C5)$_3$ (5):** A mixture of Eu(Pc)(Pc′) [Pc′ = $Pc(opp\text{-}15C5)_2$, $Pc(adj\text{-}15C5)_2$, $Pc(15C5)_3$] (20 mg) and a large excess amount of $Cu(OAc)_2$ (15 mg, 0.08 mmol) in dry dmf (3 mL) was heated to 100 °C for 1.5 h under a slow stream of nitrogen. After cooling to room temperature, MeOH (30 mL) was poured into the resulting blue solution. The precipitate collected by filtration was then dissolved in $CHCl_3$. After removing the undissolved CuPc by filtration, the resulting product was then chromatographed on an alumina column using $CH_2Cl_2$/MeOH (98.5:1.5 for **3** and **4**, 98:2 for **5**) as the eluent. The blue band containing the target compound $CuPc(15C5)_n$ ($n$ = 2–4) (**3**–**5**) was then collected. Repeated chromatography followed by recrystallization from $CHCl_3$ and MeOH gave pure $CuPc(15C5)_n$ as green powders. Yield: $CuPc(opp\text{-}15C5)_2$ (**3**) (8 mg, 56%), $CuPc(adj\text{-}15C5)_2$ (**4**) (7 mg, 53%), and $CuPc(15C5)_3$ (**5**) (10 mg, 61%).

**Supporting Information** (see footnote on the first page of this article)(see also the footnote on the first page of this article): IR spectra of (phthalocyaninato)copper complexes **1**–**6** in the region of 400–1800 $cm^{-1}$. UV/Vis absorption spectra of monomers **2**–**5** and corresponding dimers in $CHCl_3$ and in $CHCl_3$/MeOH (9:1, v/v), respectively; changes in absorption spectrum of $CuPc(opp\text{-}15C5)_2$ (**3**) in $CHCl_3$ upon titration with KOAc in $CHCl_3$/MeOH (9:1, v/v); variation of the absorbance at 675 and 593 nm during titration of **3** in $CHCl_3$ with KOAc in $CHCl_3$/MeOH (9:1); plots of log[**3**] vs. log[(**3**)$(K^+)_2$(**3**)] for $CuPc(opp\text{-}15C5)_2$ (**3**) in $CHCl_3$/MeOH; characteristic IR bands ($cm^{-1}$) of (phthalocyaninato)copper complexes **1**–**6** with 2 $cm^{-1}$ resolution.

## Acknowledgments

Financial support from the Natural Science Foundation of China (grant nos. 20325105, 20431010), National Ministry of Science and Technology of China (grant no. 2001CB6105-07), Ministry of Education of China, Shandong University, and The Chinese University of Hong Kong is gratefully acknowledged.

[1] a) A. B. P. Lever, C. C. Leznoff, *Phthalocyanine: Properties and Applications*, VCH, New York, **1989**, vol. 1, **1993**, vols. 2 and 3, **1996**, vol. 4; b) N. B. McKeown, *Phthalocyanine Materials: Synthesis, Structure and Function*, Cambridge University Press, New York, **1998**; c) K. M. Kadish, M. K. Smith, R. Guilard, *The Porphyrin Handbook*, Academic Press, San Diego, **2000–2003**, vols. 1–20.

[2] a) C. J. Pederson, *J. Am. Chem. Soc.* **1967**, *89*, 2495–2496; b) C. Liu, D. Walter, D. Neuhauser, R. Baer, *J. Am. Chem. Soc.* **2003**, *125*, 13936–13937 and references cited therein.

[3] a) A. R. Koray, V. Ahsen, O. Bekaroglu, *J. Chem. Soc., Chem. Commun.* **1986**, 932–933; b) N. Kobayashi, Y. Nishiyama, *J. Chem. Soc., Chem. Commun.* **1986**, 1462–1463; c) R. Hendriks, O. E. Sielecken, W. Drenth, R. J. M. Nolte, *J. Chem. Soc., Chem. Commun.* **1986**, 1464–1465.

[4] a) N. Kobayashi, A. B. P. Lever, *J. Am. Chem. Soc.* **1987**, *109*, 7433–7441; b) O. E. Sielecken, M. M. van Tilborg, M. F. M. Roks, R. Hendriks, W. Drenth, R. J. M. Nolte, *J. Am. Chem. Soc.* **1987**, *109*, 4261–4265.

[5] N. Kobayashi, M. Togashi, T. Osa, K. Ishii, S. Yamauchi, H. Hino, *J. Am. Chem. Soc.* **1996**, *118*, 1073–1085.

[6] a) M. Aoudia, G. Cheng, V. O. Kennedy, M. E. Keny, M. A. J. Rodgers, *J. Am. Chem. Soc.* **1997**, *119*, 6029–6039; b) J. Mack, N. Kobayashi, K. Ishii, M. J. Stillman, *Inorg. Chem.* **2002**, *41*, 5350–5363.

[7] N. Sheng, R. Li, C.-F. Choi, W. Su, D. K. P. Ng, X. Cui, K. Yoshida, N. Kobayashi, J. Jiang, *Inorg. Chem.* **2006**, *45*, 3794–3802.

[8] N. Kobayashi in *The Porphyrin Handbook* (Eds.: K. M. Kadish, K. M. Smith, R. Guilard), Academic Press, San Diego, **2003**, vol. 15, chapter 100, pp. 161–262.

[9] Q. Luo, B. Chen, M. Wang, H. Tian, *Adv. Funct. Mater.* **2003**, *13*, 233–239.

[10] G. J. Clarkson, N. B. McKeown, K. E. Treacher, *J. Chem. Soc., Perkin Trans. 1* **1995**, *14*, 1817–1823.

[11] W.-F. Law, R. C. W. Liu, J. Jiang, D. K. P. Ng, *Inorg. Chim. Acta* **1997**, *256*, 147–150.

[12] Y. Zhang, X. Zhang, Z. Liu, Y. Bian, J. Jiang, *J. Phys. Chem. A* **2005**, *109*, 6363–6370.

[13] a) J. Jiang, K. Kasuga, D. P. Arnold in *Supramolecular Photosensitive and Electroactive Materials* (Ed.: H. S. Nalwa), Academic Press, New York, **2001**, chapter 2, pp. 113–210; b) D. K. P. Ng, J. Jiang, *Chem. Soc. Rev.* **1997**, *26*, 433–442; c) J. Jiang, W. Liu, D. P. Arnold, *J. Porphyrins Phthalocyanines* **2003**, *7*, 459–473.

[14] a) T. Ye, T. Takami, R. Wang, J. Jiang, P. S. Weiss, *J. Am. Chem. Soc.* **2006**, *128*, 10984–10985; b) Y. Chen, W. Su, M. Bai, J. Jiang, X. Li, Y. Liu, L. Wang, S. Wang, *J. Am. Chem. Soc.* **2005**, *127*, 15700–15701; c) Y. Bian, J. Jiang, Y. Tao, M. T. M. Choi, R. Li, A. C. H. Ng, P. Zhu, N. Pan, X. Sun, D. P. Arnold, Z. Zhou, H.-W. Li, T. C. W. Mak, D. K. P. Ng, *J. Am. Chem. Soc.* **2003**, *125*, 12257–12267.

[15] a) R. Wang, R. Li, Y. Li, X. Zhang, P. Zhu, P.-C. Lo, D. K. P. Ng, N. Pan, C. Ma, N. Kobayashi, J. Jiang, *Chem. Eur. J.* **2006**, *12*, 1475–1485; b) R. Wang, R. Li, Y. Bian, C.-F. Choi, D. K. P. Ng, J. Dou, D. Wang, P. Zhu, C. Ma, R. D. Hartnell, D. P. Arnold, J. Jiang, *Chem. Eur. J.* **2005**, *11*, 7351–7357; c) P. Zhu, N. Pan, R. Li, J. Dou, Y. Zhang, D. Y. Y. Cheng, D. Wang, D. K. P. Ng, J. Jiang, *Chem. Eur. J.* **2005**, *11*, 1425–1432; d) J. Jiang, Y. Bian, F. Furuya, W. Liu, M. T. M. Choi, H. W. Li, N. Kobayashi, Q. Yang, T. C. W. Mak, D. K. P. Ng, *Chem. Eur. J.* **2001**, *7*, 5059–5069.

[16] a) R. Wang, Y. Li, R. Li, D. Y. Y. Cheng, P. Zhu, D. K. P. Ng, M. Bao, X. Cui, J. Jiang, *Inorg. Chem.* **2005**, *44*, 2114–2120; b) H. Zhang, R. Wang, P. Zhu, J. Han, F. Lu, C.-H. Lee, D. K. P. Ng, X. Cui, C. Ma, J. Jiang, *Inorg. Chem.* **2004**, *43*, 4740–4742;

 © 2007 Wiley-VCH Verlag GmbH & Co. KGaA, Weinheim 

c) Y. Bian, R. Wang, J. Jiang, C.-H. Lee, J. Wang, D. K. P. Ng, *Chem. Commun.* **2003**, 1194–1195.
[17] J. Jiang, M. Bao, L. Rintoul, D. P. Arnold, *Coord. Chem. Rev.* **2006**, *250*, 424–448.
[18] W. Su, M. Bao, J. Jiang, *Vibrat. Spectrosc.* **2005**, *39*, 186–190.
[19] F. Lu, L. Rintoul, X. Sun, D. P. Arnold, X. Zhang, J. Jiang, *J. Raman Spectrosc.* **2004**, *35*, 860–868.
[20] S. Pearce, W. P. West, *J. Phys. Chem.* **1965**, *69*, 1894–1903.
[21] V. Ahsen, E. Yilmazer, M. Ertas, O. Bekaroglu, *J. Chem. Soc., Dalton Trans.* **1988**, 401–406.
[22] C. E. Dent, R. P. Linstead, *J. Chem. Soc.* **1934**, 1027–1031.
[23] R. Li, X. Zhang, P. Zhu, D. K. P. Ng, N. Kobayashi, J. Jiang, *Inorg. Chem.* **2006**, *45*, 2327–2334.

Received: February 1, 2007
Published Online: May 23, 2007

 © 2007 Wiley-VCH Verlag GmbH & Co. KGaA, Weinheim 

DOI: 10.1002/ejic.200700222

# Pentadentate Ligands for the 1:1 Coordination of Lanthanide(III) Salts

**Markus Albrecht,*[a] Sebastian Mirtschin,[a] Olga Osetska,[a] Sabrina Dehn,[a] Dieter Enders,[a] Roland Fröhlich,[b] Tanja Pape,[c] and Ekkehardt F. Hahn[c]**

*Dedicated to Professor Dr. H.-J. Gais on the occasion of his 65th birthday*

**Keywords:** Hydrazone / Lanthanides / Coordination compounds / Chelating ligands / Helical compounds

Three hydrazone type ligands, namely **2**-H, **3**, and **4**, which were designed to form 1:1 complexes with lanthanoid(III) ions, are presented. Although the tetradentate ligand **2**$^-$ leads to an interesting complex [(**2**)(**2**-H)$YCl_2$] with yttrium(III), a more general principle for the coordination of the metal ions by hydrazone-type ligands can be found with ligand **3**, where 1:1 complexes are obtained with an effective coordination of the metal salts by the ligand. The stable dimer [{(**3**)$Nd(CF_3SO_3)$}$_2$(μ-$CF_3SO_3$)$_3$]$CF_3SO_3$ was characterized by X-ray structure determination. Depending on the size of the metal ion, additional co-ligands can also be bound to the metal centers. This is observed in the molecular structures of [(**3**)$Pr(NO_3)_2(MeOH)_2$]$(NO_3)$, [(**3**)$NdCl_2$(MeOH)(EtOH)]Cl, [(**3**)$ErCl_2$(MeOH)]Cl, and [(**3**)$LuCl_2$]Cl. The solid-state molecular structures of **4** and **4**·HCl show the helicating ability of this ligand upon metal coordination. The corresponding lanthanide complexes of **4** are characterized by standard techniques such as NMR and CD spectroscopy and mass spectrometry.

(© Wiley-VCH Verlag GmbH & Co. KGaA, 69451 Weinheim, Germany, 2007)

## Introduction

Lanthanide chemistry has become more and more important in recent years due to the special properties of these metal ions. Their use in lighting devices, their magnetic properties, their unique redox chemistry, and their application in catalysis and diagnostics make them an attractive target of current research,[1] with the main focus being on solid-phase materials and organometallic chemistry.[2] Coordination chemistry is mainly based on the development of new imaging agents and sensors.[3] However, this field offers an easy entry to prepare stable, well-defined molecular species and to introduce special properties with the ligand.

Coordination compounds of the lanthanides are frequently used as catalysts, as impressively demonstrated by the work of Shibasaki,[4] Kobayashi,[5] and others,[6] although often the catalytically active complexes are not isolated but are only generated in solution.

Herein we present a general study of the preparation of a series of lanthanide(III) complexes with pentadentate ligands in order to obtain Lewis acidic compounds. The introduction of chirality at the ligands offers the opportunity to prepare enantiomerically pure complexes with ligands wrapping around the metal in a helical fashion.[7]

[a] Institut für Organische Chemie, RWTH Aachen
Landoltweg 1, 52074 Aachen, Germany
E-mail: markus.albrecht@oc.rwth-aachen.de
[b] Organisch-Chemisches Institut, Universität Münster
Corrensstrasse 40, 48149 Münster, Germany
[c] Institut für Anorganische und Analytische Chemie, Universität Münster
Corrensstrasse 36, 48149 Münster, Germany

## Results and Discussion

### Studies with 8-Hydroxyquinoline Derivatives

We recently described the formation and molecular structures of a series of lanthanide(III) complexes with the semicarbazone ligand **1**-H.[8,9] In order to get enantiomerically pure coordination compounds the semicarbazone moiety is now substituted by the SAMP hydrazone to give ligand **2**-H, which can be prepared in a simple condensation reaction of SAMP[10] with 8-hydroxyquinoline 2-carbaldehyde in 94% yield (Scheme 1).[11]

Compound **2**-H is a tetradentate ligand like **1**-H with the difference that the strongly donating carbonyl unit is substituted by a more weakly donating ether moiety and that the chelating N,O unit in the side chain is elongated by one atom. In addition, the chiral information at the hydrazone leads to a helical twisting in **2**-H, while **1**-H usually adopts a planar conformation.

Treatment of **2**-H with a series of lanthanide(III) salts under different conditions did not lead to well-defined complexes, and only the reaction of **2**-H with $YCl_3$ in methanol in the presence of potassium carbonate gave a red powder, which exhibits in its $^1$H NMR spectrum two different sets

 © 2007 Wiley-VCH Verlag GmbH & Co. KGaA, Weinheim 

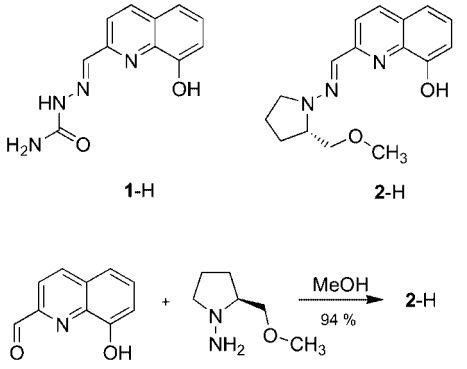


Scheme 1. Semicarbazone ligands **1**-H and **2**-H.

of signals for two unsymmetrically bound $\mathbf{2}^-$ ligands. The ESI mass spectrum reveals the peak of $[(\mathbf{2})_2Y]^+$ at *m*/*z* 657.

X-ray quality crystals were obtained from a $CH_3CN/CHCl_3$ solution of the complex. The X-ray diffraction analysis shows that the two ligands are coordinated in different ways, with one binding in a tetradentate and the other a monodentate fashion. The latter binds to the metal through the phenolate oxygen atom and is additionally fixed by hydrogen bonding of the protonated quinoline to the phenolate of the tetracoordinate ligand. This bridging hydrogen atom can be observed by $^1H$ NMR spectroscopy at $\delta = 15.80$ ppm in $CDCl_3$ solution. In addition, two chloride atoms bind to yttrium(III) in mutually *trans* position. The molecular structure of $[(\mathbf{2})(\mathbf{2}\text{-H})YCl_2]$ is shown in Figure 1.

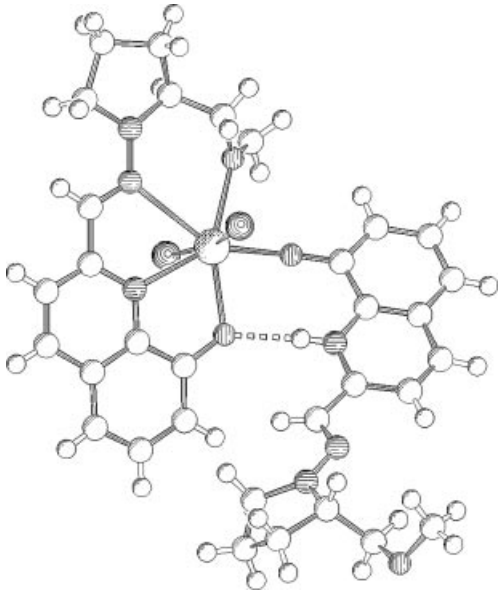

Figure 1. Molecular structure of $[(\mathbf{2})(\mathbf{2}\text{-H})YCl_2]$ as found in the crystal.

Based on those preliminary results, which show that ligand **2**-H is not ideal for the effective coordination of lanthanide(III) ions, the new pentadentate ligands **3** and **4** were developed.[12] Compound **4** (Figure 2) is a helicating ligand[13] with the potential to wrap around a single lanthanide(III) center to form a single-stranded helix.[14]

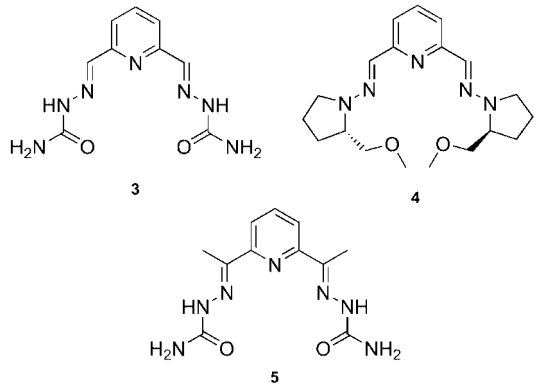


Figure 2. Pentadentate ligands **3**–**5**.

While we were investigating the coordination chemistry of ligands **3** and **4**, a publication by Palenik on the lanthanide(III) coordination chemistry of the related ligand **5** appeared concerning various lanthanide(III) coordination compounds $[(\mathbf{5})LnX_n]$. As expected, **5** provides a planar pentacoordinate platform.[15a]

## Preparation of Ligands 3 and 4 and the Solid-State Structures of 4 and 4·HCl

Ligands **3** and **4** were synthesized by a simple imine-type condensation of the easy to prepare 2,6-pyridinedicarbaldehyde with either semicarbazide hydrochloride or SAMP [(*S*)-1-amino-2-(methoxymethyl)pyrrolidine] in methanol. Ligand **3** was obtained in 72% yield as its bis-HCl adduct, while **4** was isolated as the unprotonated species in 78% yield. Both compounds were characterized by standard procedures.

We were able to obtain X-ray quality crystals of the chiral compound **4** as well as of its mono-HCl adduct **4**·HCl (Figure 3). In both compounds the external imine bonds show an *s-trans* conformation at the pyridine nitrogen. The methoxymethyl substituents at the pyrrolidine units are located at the "back side" of the molecules. One of the substituents is placed above the plane of the molecule while the other is pointing downwards, which means that the symmetry of the molecule is close to $C_2$.

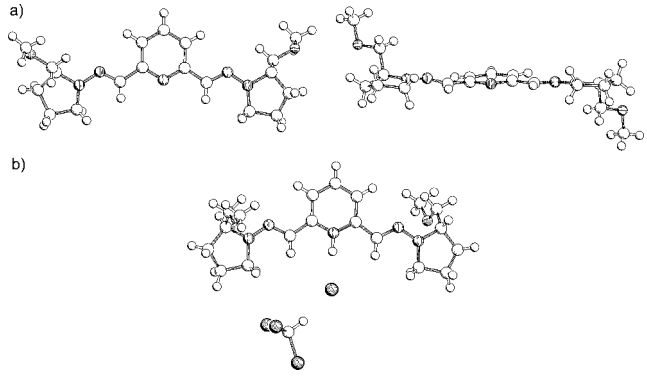


Figure 3. Molecular structures of compounds **4**; a) top and side view, b) **4**·HCl.

 © 2007 Wiley-VCH Verlag GmbH & Co. KGaA, Weinheim 

The conformations of **4** in its free as well as in its protonated form are very similar. However, the additional proton of **4**·HCl is located at the pyridine nitrogen atom with the chloride atom in close contact with this positively charged unit. In addition, one molecule of chloroform co-crystallizes with its hydrogen atom pointing towards the halide anion.

In order to form coordination compounds ligand **4** has to undergo a conformational change of the $C_{pyridine}$–$C_{imine}$ bonds involving a 180° rotation. This provides a pocket that is ideal for metal binding in a tri- or pentadentate fashion.

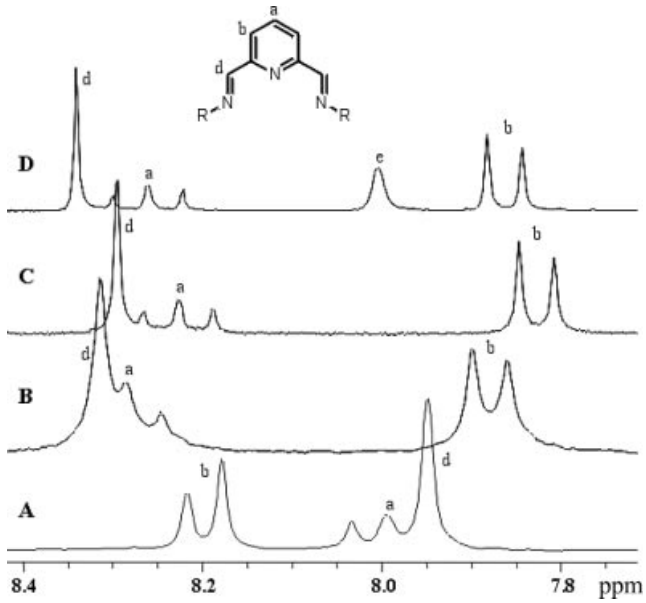


Figure 4. Portions of the $^1$H NMR spectra of **3** in [$D_6$]DMSO (A) and [(**3**)La][$CF_3SO_3$]$_3$ (B), [(**3**)La][Cl]$_3$ (C), and [(**3**)Lu][$NO_3$]$_3$ (D) in [$D_4$]MeOH. The assignment of ligand signals is presented in the inset (e = $NH_{hydrazone}$).

### Coordination Chemistry of Ligand 3 with Lanthanide(III) Ions

Complexes of ligand **3** with lanthanides were prepared by addition of lanthanide(III) salts to a suspension of **3** in either methanol or acetonitrile. Characterization of the complexes was done by mass spectrometry and, where possible, by elemental analysis. Coordination compounds of the diamagnetic meta ions yttrium(III), lanthanum(III), and lutetium(III) were also characterized by NMR spectroscopy (Table 1).

Table 1 lists some results of mass spectrometric investigations of the coordination compounds of ligand **3** with lanthanides. In all cases 1:1 complexes between the ligands and the metals are observed, although with neodymium(III) triflate a dimeric 2:2 species is found in addition to the monomer. In some cases displacement of the anion by hydroxide or methoxide from the solvent matrix occurs.

Representative portions of the $^1$H NMR spectra of complexes of **3** with diamagnetic lanthanum(III) and lutetium(III) ions in [$D_4$]MeOH are depicted in Figure 4. Unfortunately, the free ligand **3** is not soluble in this solvent therefore the spectrum of the ligand was recorded in [$D_6$]-DMSO.

Due to the different solvents the spectra of the ligand and the complexes cannot be compared directly. However, a remarkable shift difference can be detected for the hydrazone CH=N proton. Thus, in the ligand (in [$D_6$]DMSO) its resonance is observed at $\delta$ = 7.95 ppm while in the complexes (in $CD_3OD$) shifts of $\delta$ = 8.32 [La($CF_3SO_3$)], 8.30 (LaCl), and 8.38 ppm [Lu($NO_3$)] are found. In addition, significant low-field shifts are observed for the proton in the 4-position and high-field shifts for the protons in the 3- and 5-positions of the pyridine ring of **3**. The shift differences between coordinated and free ligands are due to the conformational changes that occur in **3** upon coordination to the metal, and the differences in the NMR spectra of complexes with different anions indicate that at least some of the anions are still coordinated to the metals in solution.

We were able to obtain X-ray quality crystals of several coordination compounds of ligand **3** with different lanthanide salts and the complexes of the larger lanthanides $Pr^{III}$ and $Nd^{III}$ as well as of the smaller lanthanides $Er^{III}$ and $Lu^{III}$ were structurally characterized (Table 2).

Table 1. Representative results of mass spectrometric investigations of the lanthanide(III) complexes of ligand **3** (anion: triflate, chloride, nitrate).

| Ln | [(**3**)Ln($F_3CSO_3$)$_3$] | [(**3**)Ln$Cl_3$] | [(**3**)Ln($NO_3$)$_3$] |
|---|---|---|---|
| Y | _[d] | 407 [(**3**)$YCl_2$]$^+$<br>400 [(**3**)Y($OCH_3$)$_2$]$^+$[c] | 462 [(**3**)Y($NO_3$)$_2$]$^+$ [c] |
| La | 686 [(**3**)La($F_3CSO_3$)$_2$]$^+$[a] | 458 [(**3**)$LaCl_2$]$^+$[c] | 209.5 [(**3**)La($CH_3O$)]$^{2+}$[c] |
| Pr | 688 [(**3**)Pr($F_3CSO_3$)$_2$]$^+$[b] | _[d] | 451.5 [(**3**)Pr($NO_3$) – H]$^{2+}$ [c] |
| Nd | 1531 [(**3**)$_2$Nd$_2$($F_3CSO_3$)$_5$]$^+$<br>691 [(**3**)Nd($F_3CSO_3$)$_2$]$^+$[c] | 269.5 [(**3**)NdCl($CH_3OH$)$_3$($H_2O$)]$^{2+}$<br>254 [(**3**)NdCl($CH_3OH$)$_2$($H_2O$)]$^{2+}$[c] | _[d] |
| Sm | 699 [(**3**)Sm($F_3CSO_3$)$_2$]$^+$[b] | _[d] | 209.5 [(**3**)Sm(OH)]$^{2+}$ [b] |
| Er | 715 [(**3**)Er($F_3CSO_3$)$_2$]$^+$[c] | 451 [(**3**)ErCl – H]$^+$[b] | _[d] |
| Lu | 722 [(**3**)Lu($F_3CSO_3$)$_2$]$^+$[a] | 458 [(**3**)LuCl – H]$^+$[b] | 229.5 [(**3**)Lu($H_2O$)(OH)]$^{2+}$[c] |

[a] MALDI-TOF. [b] LDI-TOF. [c] ESI. [d] Not prepared.

 © 2007 Wiley-VCH Verlag GmbH & Co. KGaA, Weinheim 

Table 2. Selected bond lengths [Å] and angles [°] of lanthanide(III) complexes of ligand **3** with different co-ligands (anions: triflate, chloride; methanol). OTf = triflate.

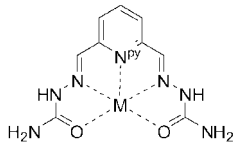


| | [(**3**)Pr(NO$_3$)$_2$ (MeOH)$_2$]$^+$ | | [{(**3**)Nd(CF$_3$SO$_3$)}$_2$ (μ-CF$_3$SO$_3$)$_3$]$^+$ | | [(**3**)NdCl$_2$ (MeOH)(EtOH)]$^+$ | [(**3**)ErCl$_2$ (MeOH)]$^+$ |
|---|---|---|---|---|---|---|
| N$^{py}$–M | 2.740 | 2.619 | 2.633 | 2.785 | 2.500 | 2.426 |
| N–M | 2.712/2.684 | 2.623/2.621 | 2.628/2.624 | 2.704/2.708 | 2.481/2.480 | 2.414 |
| O–M | 2.531/2.549 | 2.403/2.407 | 2.412/2.387 | 2.474/2.413 | 2.336/2.283 | 2.264 |
| Cl–M | | | | 2.774/2.779 | 2.657/2.628 | 2.560 |
| O$^{OTf}$–M | 2.625/2.637 | | | | 2.430 | |
| O$^{OTf}$–M (bridging) | | 2.549/2.502 2.474 | 2.462/2.459/2.484 | | | |
| O$^{OTf}$–M (terminal) | | 2.411 | 2.437 | | | |
| N$^{py}$–M–N | 58.54/58.96 | 60.58/60.30 | 59.65/60.25 | 57.68/57.98 | 63.32/63.41 | 64.54 |
| N–M–O | 59.52/59.98 | 61.80/61.35 | 61.58/61.67 | 59.54/60.10 | 63.98/6439 | 66.58 |
| Cl–M–Cl | | | | 143.33 | 150.91 | 177.14 |
| N$^{py}$–M–O$^{ROR'}$ | 141.31/142.37 | | | 141.24 (MeOH) 145.73 (Et$_2$O) | 141.18 | |
| O$^{MeOH}$–M–O$^{ROR'}$ | 75.64 | | | 72.88 | | |

### *[(3)Pr(NO$_3$)$_2$(CH$_3$OH)$_2$]NO$_3$·CH$_3$OH*

X-ray quality crystals of the complex of **3** with praseodymium(III) nitrate were obtained from methanol solution. Two different views of the molecular structure of the cation [(**3**)Pr(NO$_3$)$_2$(CH$_3$OH)$_2$]$^+$ are presented in Figure 5 and selected bond lengths and angles are listed in Table 2. Compound **3** acts as a pentadentate ligand that coordinates to the praseodymium ion through the pyridine and two "imine" nitrogen atoms of the semicarbazone as well as through the two carbonyl oxygen atoms. The coordinated ligand is not planar but possesses a slight helical twisting. In addition, two bidentate nitrate anions binding to the metal above and below the plane of the "(**3**)Pr" platform. The third nitrate anion does not coordinate to the metal center. This leaves additional sites in the front of the complex, where two molecules of methanol are coordinated to the metal. The coordination number for Pr$^{III}$ is therefore eleven. The coordination of two nitrate anions to the metal center presents a remarkable difference to the structures obtained by Palenik et al. for their complexes of ligand **5**,[15b] where only one nitrate as well as numerous water molecules bind to the metals.

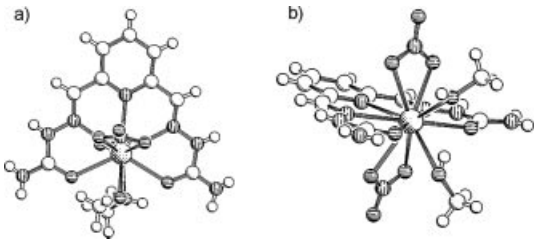


Figure 5. Top (a) and side view (b) of the cation [(**3**)Pr(NO$_3$)$_2$(CH$_3$OH)$_2$]$^+$ as observed in the solid state.

### *[{(3)Nd(CF$_3$SO$_3$)}$_2$(μ-CF$_3$SO$_3$)$_3$]CF$_3$SO$_3$·2CH$_3$CN·(CH$_3$CH$_2$)$_2$O*

Crystals of neodymium(III) triflate were obtained from acetonitrile/diethyl ether solution. The molecular structure of the cation [{(**3**)Nd(CF$_3$SO$_3$)}$_2$(μ-CF$_3$SO$_3$)$_3$]$^+$ in the crystal is depicted in Figure 6 and representative bond length and angles are listed in Table 2.

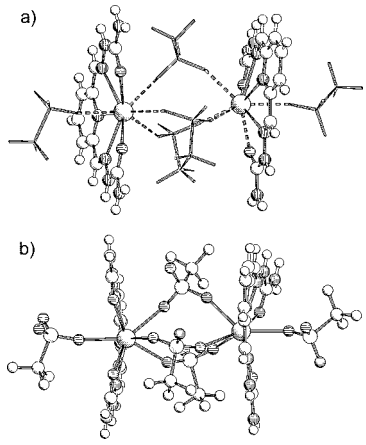


Figure 6. Two different views of the cation [{(**3**)Nd(CF$_3$SO$_3$)}$_2$(μ-CF$_3$SO$_3$)$_3$]$^+$ as observed in the solid state. The triflate anions in a) are indicated by lines.

 © 2007 Wiley-VCH Verlag GmbH & Co. KGaA, Weinheim 

The cation $[\{(\mathbf{3})Nd(CF_3SO_3)\}_2(\mu\text{-}CF_3SO_3)_3]^+$ adopts a dimeric structure with two "(**3**)Nd(OTf)" moieties connected by three bridging triflate anions. The bridging triflates each coordinate through two different oxygen atoms to the different metals, while the terminal triflates act only as monodentate ligands. The two ligands **3** are orientated in an *anti* fashion within a planar arrangement. However, the steric bulk of the three bridging anions forces the metal ions out of the plane of the pentacoordinate ligands. The remaining triflate anion does not interact with the metal center but is incorporated within the crystal lattice. This dimer possesses an unusual stability as positive-ion ESI mass spectrometry showed its presence even in methanol solution. The corresponding peak of the dimer $[(\mathbf{3})_2Nd_2(F_3CSO_3)_5]^+$ is detected at *m*/*z* 1531 along with the monomer $[(\mathbf{3})Nd(F_3CSO_3)_2]^+$ at *m*/*z* 691.

### *[(3)NdCl$_2$(CH$_3$OH){(CH$_3$CH$_2$)$_2$O}]Cl*

The complex of neodymium(III) chloride with **3** was crystallized from methanol/ethanol solution. Figure 7 presents the solid-state structure of $[(\mathbf{3})NdCl_2(CH_3OH)\{(CH_3CH_2)_2O\}]^+$.

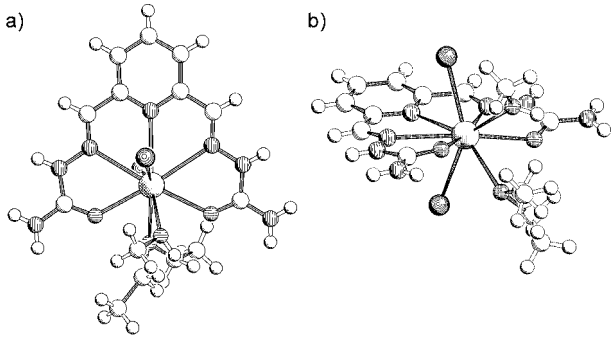


Figure 7. Two different views of the cation $[(\mathbf{3})NdCl_2(CH_3OH)\{(CH_3CH_2)_2O\}]^+$ as observed in the solid state.

Ligand **3** coordinates to the metal center in an almost planar fashion with the chloride atoms sitting above and below the plane of the ligand. In addition, one methanol molecule and one molecule of diethyl ether coordinate at the front of the complex. Due to the high coordination number and the steric bulk of the co-ligands, the Nd–N bonds are longer than those in the dimer $[\{(\mathbf{3})Nd(CF_3SO_3)\}_2(\mu\text{-}CF_3SO_3)_3]^+$ (see Table 2).

### *[(3)ErCl$_2$(CH$_3$OH)]Cl*

Crystals of the erbium complex of ligand **3** were obtained from methanol. Figure 8 (a) shows a top view of the structure of the cation $[(\mathbf{3})ErCl_2(CH_3OH)]^+$ where the almost planar coordination of the ligand is clear. However, the side view (Figure 8 b) reveals a slight helical twisting. This is caused by an asymmetric coordination of further ligands; one chloride anion from the top and chloride and methanol from the bottom. The steric bulk of the methanol forces the ligand to deviate from planarity and additionally leads to a nonplanar Cl–Er–Cl arrangement with an angle of 150.92°. In the crystal, the third chloride ion is found close to the NH units of the semicarbazones.

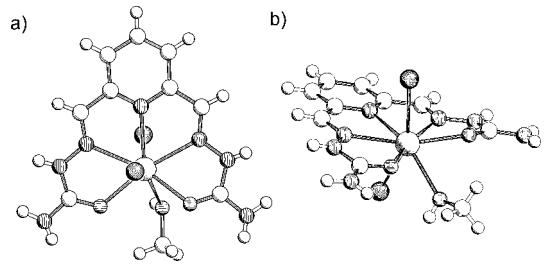


Figure 8. Two different views of the cation $[(\mathbf{3})ErCl_2(CH_3OH)]^+$ as observed in the solid state.

### *[(3)LuCl$_2$]Cl*

X-ray quality crystals of $[(\mathbf{3})LuCl_2]Cl$ were obtained by diffusion of diethyl ether into a solution of the complex in acetonitrile/methanol. The solid-state structure of the cation $[(\mathbf{3})LuCl_2]^+$ is shown in Figure 9.

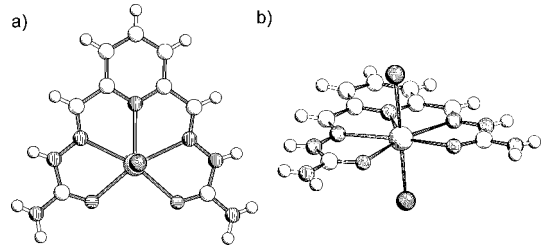


Figure 9. Two different views of the cation $[(\mathbf{3})LuCl_2]^+$ as observed in the solid state.

In principle it is related to the corresponding cation $[(\mathbf{3})ErCl_2(CH_3OH)]^+$ described above. Due to the smaller size of lutetium(III) than erbium(III), however, a lower coordination number of seven is adopted, which means that no methanol is bound to the metal in the lutetium complex. This results in some structural differences between $[(\mathbf{3})LuCl_2]^+$ and $[(\mathbf{3})ErCl_2(CH_3OH)]^+$. Thus, the chloride atoms are now bound in a more symmetric fashion leading to a nearly planar Cl–Lu–Cl arrangement of 177.14°. Consequently, the ligand adopts a close to planar geometry with no significant helical distortion.

The results of the above X-ray structural investigations show that ligand **3** acts as a pentadentate ligand for the complexation of lanthanide(III) ions. Due to the different sizes of the different metal ions, varying numbers of co-ligands are bound to the metal centers. In order to adjust to the different metals, the ligand has to adopt a more open (for larger ions) or a more closed (for smaller ions) tweezer-type arrangement. This is demonstrated by a decrease of the distance between the two terminal $NH_2$ groups of **3** depending on the size of the metals. This N–N distance is 8.998 Å for Pr, 8.783 Å for the Nd monomer, 8.134/8.230 Å for the Nd dimer, 7.983 Å for Er, and 7.842 Å for Lu.

 © 2007 Wiley-VCH Verlag GmbH & Co. KGaA, Weinheim 

Following the series of structures with chloride anions, it is clear that the $[(\mathbf{3})MCl_2]^+$ cation is only observed for the small lutetium(III) ion, whereas for the larger erbium(III) ion the metal center is not coordinatively saturated and an additional solvent molecule is bound in the front of the complex. The still larger neodymium(III) ion even provides space for two such solvent molecules, which means that the complexes of the larger cations would be the best candidates to test their ability to act as Lewis acid catalysts.

### Coordination Chemistry of the Chiral Ligand 4 with Lanthanide(III) Ions

Coordination compounds of lanthanides with the chiral ligand **4** were synthesized in analogy to the preparation of complexes with the semicarbazone ligand **3**. Thus, the corresponding lanthanide(III) salt in methanol or acetonitrile was added to a solution of the ligand **4** in methanol or acetonitrile. The mixture was stirred for 16–72 h and the solvent was then removed in vacuo to yield orange-yellow to red compounds (Scheme 2).

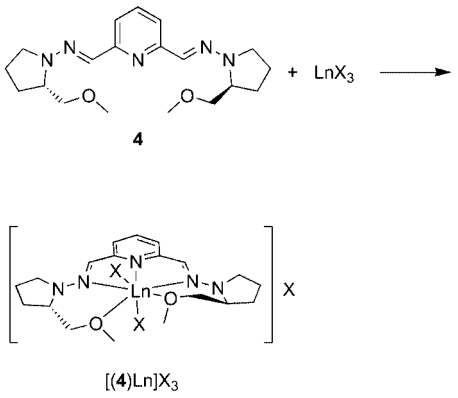


Scheme 2. Formation of lanthanide(III) complexes of ligand **4**. The coordination at the metal is proposed based on the described results obtained with ligand **3** and the NMR spectroscopic and mass spectrometric observations. Ln = La, Pr, Nd, Sm, Er, Yb, Lu, and Y; X = Cl, $NO_3$, and triflate.

We could not obtain X-ray quality crystals of the complexes with ligand **4**, although we were able to characterize them by NMR spectroscopy, mass spectrometry, and, in several cases, by elemental analysis. The $^1$H NMR spectrum of ligand **4** (A) is compared with the corresponding spectra of representative complexes in Figure 10. The spectra of the diamagnetic lutetium (B) and the paramagnetic ytterbium complex (C) are shown, the latter of which reveals a nicely resolved NMR spectrum with some line broadening due to the presence of the paramagnetic metal ion.

Similarly to the coordination compounds with ligand **3**, complexes of **4** exhibit a low-field shift for the proton in the 4-position of the pyridine and a high-field shift for those in the 3- and 5-positions relative to the signals of free ligand (in $[D_3]$acetonitrile). However, in contrast to complexes of **3**, the signal for the CH=N "imine" proton is observed at higher field. This is probably due to the different nature of the two hydrazone-type substituents of **3** and **4**, which leads to different electronic influences on the CH=N proton upon metal coordination. In addition, ligand **4** adopts a helical conformation upon complexation while **3** is more or less planar.

A strong influence of the anions on the NMR spectra is found for these complexes, as shown in Figure 11 for the $^1$H NMR spectrum of the lutetium(III) complexes of **4** in $[D_3]$acetonitrile. The "imine" proton only shifts to higher field if anions are present that coordinate in a bidentate fashion [triflate (A) or nitrate (C)]. In the presence of chloride a shift of this ligand signal to lower field occurs upon complexation to lutetium (B). The differences in the chemical shifts of the imine, 3- and 5-pyridine protons, and of the proton in the 4-position show that the anions are still coordinated to the lutetium in solution.

As representative examples of the mass spectrometric investigations, the molar peaks, including the isotopic patterns, of the cations $[(\mathbf{4})ErX_2]^+$ (X = triflate, chloride, nitrate) are presented in Figure 12. The depicted spectra were obtained by using the positive-ion LDI-TOF technique. The observed patterns correspond to the calculated ones. Similar spectra are observed for most of the prepared coor-

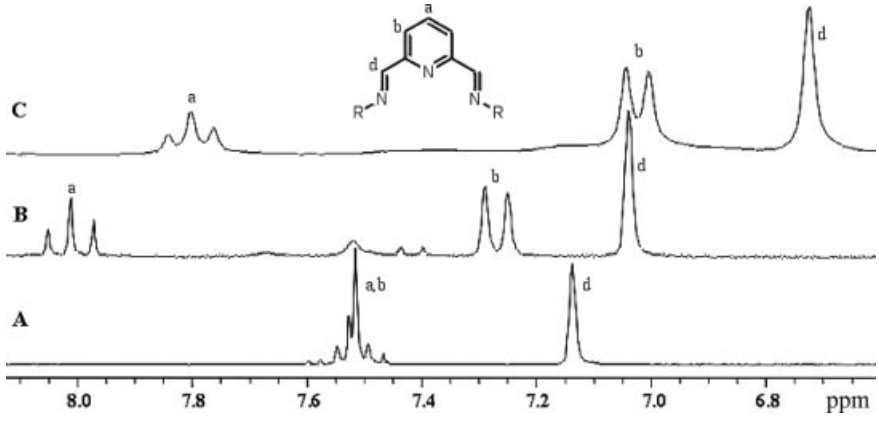


Figure 10. Portions of the $^1$H NMR spectra of **4** (A), $[(\mathbf{4})Lu][F_3CSO_3]_3$ (B), and $[(\mathbf{4})Yb][F_3CSO_3]_3$ (C) in $[D_3]$acetonitrile. The assignment of the protons to the pyridine and the imine moiety is indicated.

 © 2007 Wiley-VCH Verlag GmbH & Co. KGaA, Weinheim 

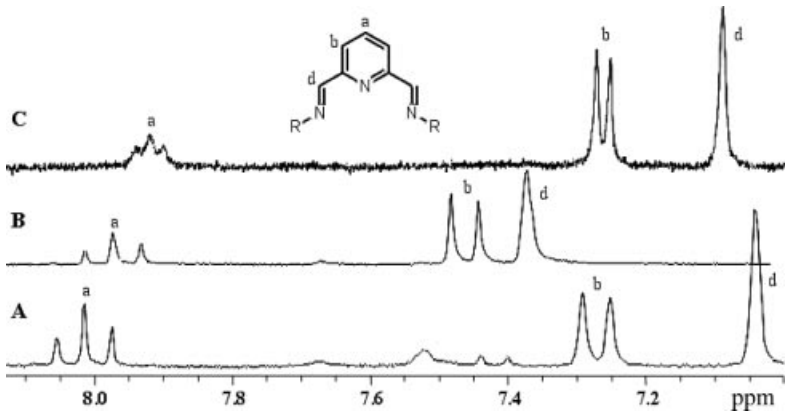


Figure 11. Portions of the $^1$H NMR spectra of [(**4**)Lu][$F_3CSO_3$]$_3$ (A), [(**4**)Lu][Cl]$_3$ (B), and [(**4**)Lu][$NO_3$]$_3$ (C) in [$D_3$]acetonitrile. The assignment of the protons to the pyridine and imine moieties is indicated.

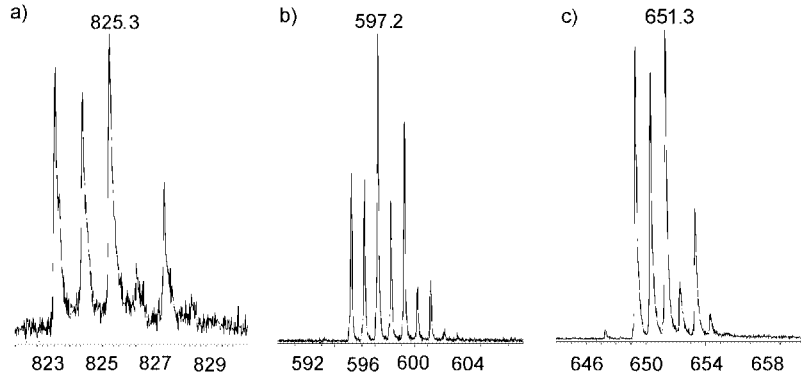


Figure 12. Part of the positive-ion LDI-TOF mass spectra of the cationic complexes [(**4**)Er($F_3CSO_3$)$_2$]$^+$ (a), [(**4**)Er(Cl)$_2$]$^+$ (b), and [(**4**)Er($NO_3$)$_2$]$^+$ (c). The observed isotopic patterns correspond to the calculated ones.

dination compounds (see Table 3), which shows that stable 1:1 complexes are formed between ligand **4** and lanthanide(III) ions.

Table 3. Representative results of mass spectrometric investigations of the lanthanide(III) complexes of ligand **4** (anions: triflate, chloride, nitrate). Measurements were performed with either the positive-ion ESI or LDI-TOF technique. n.d. = not determined.

| Ln | [(**4**)Ln($F_3CSO_3$)$_3$] | [(**4**)LnCl$_3$] | [(**4**)Ln($NO_3$)$_3$] |
|---|---|---|---|
| Y | –[a] | n.d. | 572 [(**4**)Y($NO_3$)$_2$]$^+$ |
| La | 796 [(**4**)La($F_3CSO_3$)$_2$]$^+$ | 568 [(**4**)LaCl$_2$]$^+$ | –[a] |
| Pr | 798 [(**4**)Pr($F_3CSO_3$)$_2$]$^+$ | –[a] | –[a] |
| Nd | 801 [(**4**)Nd($F_3CSO_3$)$_2$]$^+$ | n.d. | –[a] |
| Sm | 809 [(**4**)Sm($F_3CSO_3$)$_2$]$^+$ | 583 [(**4**)SmCl$_2$]$^+$ | 635 [(**4**)Sm($NO_3$)$_2$]$^+$ |
| Er | 825 [(**4**)Er($F_3CSO_3$)$_2$]$^+$ | 597 [(**4**)ErCl$_2$]$^+$ | 651 [(**4**)Er($NO_3$)$_2$]$^+$ |
| Yb | 831 [(**4**)Yb($F_3CSO_3$)$_2$]$^+$ | –[a] | –[a] |
| Lu | 832 [(**4**)Lu($F_3CSO_3$)$_2$]$^+$ | 604 [(**4**)LuCl$_2$]$^+$ | 658 [(**4**)Lu($NO_3$)$_2$]$^+$ |

[a] Not prepared.

We also performed CD spectroscopic studies with ligand **4** and selected complexes of this ligand with lanthanides. The spectra of the complexes in dichloromethane reveal essentially the same features and therefore only the spectrum of [(**4**)Er(Cl)$_3$] is described as a representative example. Very similar UV spectra are observed for ligand **4** and [(**4**)Er-

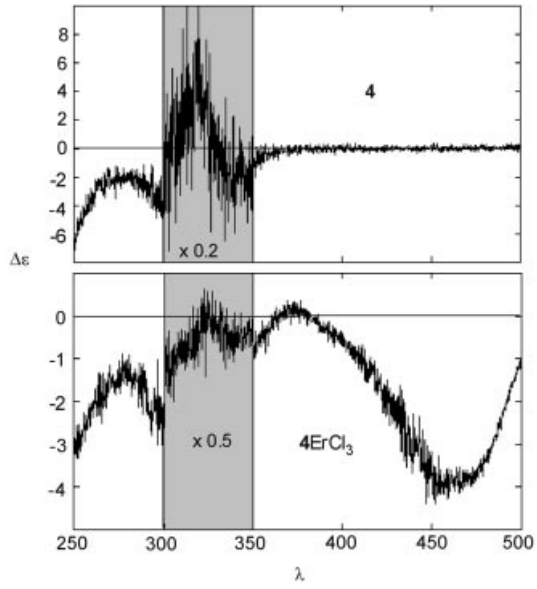


Figure 13. CD spectra of **4** (top) and [(**4**)Er(Cl)$_3$] (bottom) in dichloromethane. Note that measurement of the spectrum between 300 and 350 nm (grey) was problematic due to the high optical density of the sample in this region. The measurements in this region therefore had to be performed at lower concentrations.

 © 2007 Wiley-VCH Verlag GmbH & Co. KGaA, Weinheim 

$(Cl)_3$], both of which show an intense transition at 320 nm. CD spectra proved difficult to record in the region of this band due to the high optical density of the sample (Figure 13).

The most intriguing difference between the CD spectra of **4** and [(**4**)$ErCl_3$] is the presence of a strong band with a negative Cotton effect at 400–500 nm. This becomes dominant in the CD spectrum due to the chirality that is induced around the metal center.

## Conclusions

We have presented a structural work on the coordination chemistry of the pentadentate bis-semicarbazone pyridine ligand **3**. The ligand provides a planar coordination platform and effectively binds lanthanide(III) salts (chlorides, nitrates, or triflates). Small lanthanide(III) ions preferably form cationic complexes $[(\mathbf{3})LnX_2]^+$. One or more additional co-ligands, which are often are not the remaining third counteranions but solvent molecules, bind to the metal center in the case of the bigger ions. This latter finding gives some hint as to how complexes related to those of ligand **4** should be designed to obtain effective Lewis acid catalysts: (i) a pentadentate ligand must exhibit poorer donor ability than **3** in order to enhance Lewis acidity, (ii) the "side arms" of the ligand have to be more labile coordinating units, and (iii) chirality should be introduced.

Following those three requirements we prepared the helicating ligand **4** and showed that it can form 1:1 complexes with lanthanide(III) salts. Further studies will be directed towards the use of complexes of **4** with lanthanides as Lewis acid catalysts.

## Experimental Section

**General:** NMR spectra were recorded with a Bruker AC 200, AMX 400, or a Varian Inova 400 or Mercury 300 spectrometer. FT-IR spectra were recorded by the diffuse reflection technique (KBr) with a Bruker Vector 22 or Perkin–Elmer PE-1760 FT spectrometer. Mass spectra were recorded with a Finnigan MAT MS 90, LCQ Deca XP Plus, Bruker Reflex IV, or Micromass Quattro LC-Z mass spectrometer. Elemental analyses were obtained with a Heraeus CHN-O-Rapid analyzer or a Vario EL III CHNS. Melting points: Büchi B-540 (uncorrected). Lanthanide chlorides, triflates, and nitrates were prepared as described before.[16]

**X-ray Crystallography:** Data sets were collected with Nonius KappaCCD and Bruker APEX CCD diffractometers, both equipped with rotating anode generators. Programs used: data collection: COLLECT (Nonius B.V., 1998) and SMART (Bruker AXS, 2000); data reduction: Denzo-SMN[17] and SAINT (BrukerAXS, 2000); absorption correction: SORTAV,[18] Denzo,[19] and SADABS (Bruker AXS, 2000); structure solution: SHELXS-97;[20] structure refinement: SHELXL-97 (G. M. Sheldrick, University of Göttingen, 1997); graphics: SCHAKAL (E. Keller, University of Freiburg, 1997).

CCDC-631745 to -631752 contain the supplementary crystallographic data for this paper. These data can be obtained free of charge from The Cambridge Crystallographic Data Centre via www.ccdc.cam.ac.uk/data_request/cif.

**2-H:** A mixture of 8-hydroxyquinoline-2-carbaldehyde (1 equiv., 0.052 g, 0.3 mmol) and SAMP (1.1 equiv., 0.043 g, 0.33 mmol) in methanol was stirred overnight at room temp. The solvent was then distilled off and the crude residue was washed with diethyl ether and dried in vacuo. The product was obtained in 94% yield (0.08 g, 0.28 mmol) as a yellow oil. $^1$H NMR (300 MHz, $CDCl_3$): $\delta$ = 7.98 (m, 2 H), 7.33 (d, $J$ = 7.4 Hz, 1 H), 7.30 (d, $J$ = 7.4 Hz, 1 H), 7.23 (dd, $J$ = 8.2, 1.5 Hz, 1 H), 7.11 (dd, $J$ = 7.4, 1.5 Hz, 1 H), 3.83 (m, 1 H), 3.68 (dd, $J$ = 9.4, 3.7 Hz, 1 H), 3.55 (dd, $J$ = 9.4, 6.7 Hz, 1 H), 3.46 (m, 1 H), 3.40 (s, 3 H), 3.21 (m, 1 H), 2.00 (m, 4 H) ppm. $^{13}$C NMR ($CDCl_3$): $\delta$ = 154.62 (C), 151.80 (C), 137.70 (C), 135.49 (CH), 130.89 (CH), 127.27 (C), 126.40 (CH), 117.97 (CH), 117.74 (CH), 109.98 (CH), 74.33 ($CH_2$), 62.89 (CH), 59.34 ($CH_3$), 48.36 ($CH_2$), 26.99 ($CH_2$), 22.29 ($CH_2$) ppm. Positive-ion ESI MS: $m/z$ 286.2 $[M + H]^+$.

**[(2)(2-H)$YCl_2$]:** The ligand **2**-H (2 equiv., 0.04 g, 0.14 mmol) and $YCl_3$ (1 equiv., 0.021 g, 0.07 mmol) were stirred overnight in MeOH (10 mL) in the presence of $K_2CO_3$ as a base (1.9 equiv., 0.01 g, 0.072 mmol) at room temp. The solvent was then removed and the residue dried in vacuo. Extraction with $CH_2Cl_2$ gave a red powder in quantitative yield (0.053 g, 0.07 mmol). $^1$H NMR (300 MHz, $CDCl_3$): $\delta$ = 15.80 (br., 1 H), 8.18 (d, $J$ = 8.4 Hz, 1 H), 8.09 (d, $J$ = 8.4 Hz, 1 H), 7.55 (m, 1 H), 7.63 (d, $J$ = 7.9 Hz, 1 H), 7.4–7.2 (m, 6 H), 6.92 (d, $J$ = 8.2 Hz, 1 H), 6.69 (d, $J$ = 7.4 Hz, 1 H), 5.23 (d, $J$ = 9.1 Hz, 1 H), 4.94 (d, $J$ = 6.2 Hz, 1 H), 4.06 (m, 1 H), 3.99 (s, 2 H), 3.85 (m, 2 H), 3.70 (s, 3 H), 3.56 (m, 3 H), 3.41 (s, 3 H), 2.31 (m, 1 H), 2.03 (m, 6 H), 1.71 (m, 2 H), 1.61 (m, 2 H) ppm. Positive-ion ESI MS: $m/z$ 657.4 $[M - HCl - Cl]^+$. IR (KBr): $\tilde{\nu}$ = 3851, 3745, 3406, 2929, 2873, 2361, 2338, 1629, 1586, 1527, 1456, 1389, 1323, 1235, 1099, 848, 744, 677, 598 $cm^{-1}$. $C_{32}H_{37}Cl_2N_6O_4Y{\cdot}H_2O{\cdot}CH_3OH$: calcd. C 50.84, H 5.56, N 10.78; found C 51.06, H 5.45, N 11.01.

X-ray quality crystals of [(**2**)(**2**-H)$YCl_2$] were obtained by slow evaporation of a concentrated $CH_3CN/CHCl_3$ solution. X-ray crystal structure analysis for [(**2**)(**2**-H)$YCl_2$]: formula $C_{32}H_{37}Cl_2N_6O_4Y$, $M$ = 729.49, orange crystal $0.10 \times 0.06 \times 0.05$ $mm^3$, $a$ = 15.660(1), $b$ = 12.582(1), $c$ = 17.051(1) Å, $\beta$ = 104.64(1)°, $V$ = 3250.6(4) $Å^3$, $\rho_{calc}$ = 1.491 $g cm^{-3}$, $\mu$ = 2.005 $mm^{-1}$, empirical absorption correction ($0.825 \leq T \leq 0.906$), $Z$ = 4, monoclinic, space group $P2_1$ (no. 4), $\lambda$ = 0.71073 Å, $T$ = 198 K, $\omega$ and $\phi$ scans, 12952 reflections collected ($\pm h$, $\pm k$, $\pm l$), $[(\sin\theta)/\lambda]$ = 0.54 $Å^{-1}$, 7864 independent ($R_{int}$ = 0.081) and 5566 observed reflections [$I \geq 2\sigma(I)$], 815 refined parameters, $R$ = 0.066, $wR_2$ = 0.113, Flack parameter –0.004(11), max. residual electron density 0.43 (–0.45) e $Å^{-3}$. The hydrogen atom at nitrogen was found from difference Fourier calculations. The others were calculated and refined as riding on their parent atoms. Due to crystal size the analysis is of limited accuracy.

**2,2′-[Pyridine-2,6-diylbis(methan-1-yl-1-ylidene)]bis(hydrazinecarboxamide) (3):** Semicarbazone hydrochloride (670 mg, 6.0 mmol) was dissolved in 40 mL of methanol and pyridine-2,5-dicarbaldehyde (400 mg, 2.9 mmol) in 15 mL of methanol was added. The yellow precipitate that formed over 70 h was collected, washed with cold methanol, and dried in vacuo to give a yellow solid. Yield: 666 mg (2.1 mmol, 72%). M.p. 214.8 °C (dec.). $^1$H NMR (400 MHz, [D$_6$]DMSO): $\delta$ = 10.88 (s, 2 H), 8.23 (d, $J$ = 7.9 Hz, 2 H, b), 8.04 (t, $J$ = 7.9 Hz, 1 H), 7.99 (s, 2 H), 6.76 (br. s, 2 H) ppm. $^{13}$C NMR (50 MHz, [D$_6$]DMSO): $\delta$ = 156.2, 151.2, 139.3, 136.1, 120.1 ppm. IR (KBr): $\tilde{\nu}$ = 3779, 3705, 3632, 3411, 2974, 2381, 2275, 1815, 1717, 1587, 1513, 1430, 1343, 1294, 1229, 1178, 1074, 933, 817, 725, 634, 559, 486 $cm^{-1}$. MS (pos. MALDI-TOF, DHB): $m/z$ 272.0 (26) $[M + Na]^+$, 250.0 (100) $[M + H]^+$. $C_9H_{11}N_7O_2{\cdot}2HCl{\cdot}H_2O$: calcd. C 31.78, H 4.44, N 28.82; found C 31.70, H 4.60, N 27.96.

 © 2007 Wiley-VCH Verlag GmbH & Co. KGaA, Weinheim 

**(2*S*,2′*S*)-*N*,*N*′-[Pyridine-2,6-diylbis(methan-1-yl-1-ylidene)]bis[2-(methoxymethyl)pyrrolidin-1-amine] (4):** Pyridine-2,6-dicarbaldehyde (1.00 g, 7.4 mmol) in 10 mL of methanol was slowly added to a solution of SAMP (2.00 g, 15.4 mmol) in 4 mL of methanol and, after stirring overnight, the solvent was removed in vacuo. The crude product was recrystallized from hot pentane by cooling to 6 °C. Yield: 2.07 g (5.8 mmol, 78%) of a colorless solid. M.p. 77.8 °C. $^1$H NMR (400 MHz, $CD_3CN$): $\delta$ = 7.54 (t, $J$ = 6.0 Hz, 1 H), 7.51 (d, $J$ = 6.0 Hz, 2 H), 7.14 (s, 2 H), 3.69 (quint, $J$ = 4.0 Hz, 2 H), 3.60 (dd, $J$ = 7.6, 4.0 Hz, 2 H), 3.47 (dd, $J$ = 9.6, 6.9 Hz, 2 H), 3.41 (dt, $J$ = 6.9, 4.0 Hz, 2 H), 3.33 (s, 6 H), 3.13 (dt, $J$ = 9.6, 7.6 Hz, 2 H), 2.08–1.77 (m, 8 H) ppm. $^{13}$C NMR (100 MHz, $CD_3CN$): $\delta$ = 156.9, 137.1, 132.2, 116.2, 75.3, 63.9, 59.4, 49.4, 27.8, 23.0 ppm. IR (KBr): $\tilde{\nu}$ = 3851, 3745, 3678, 3621, 2361, 1836, 1649, 1547, 1459, 1107, 669 cm$^{-1}$. MS (EI-DIP, 70 eV): *m*/*z* (%) 359.1 (66) [M$^+$], 314.1 (45), 246 (100), 219 (59), 201 (47). $C_{19}H_{29}N_5O_2$: calcd. C 63.48, H 8.13, N 19.48; found C 63.21, H 8.00, N 19.08.

**X-ray Crystal Structure Analysis for 4:** $C_{19}H_{27}N_5O_2$, $M$ = 357.46, colorless crystal 0.49 × 0.28 × 0.17 mm$^3$, $a$ = 7.8706(15), $b$ = 12.524(2), $c$ = 20.475(4) Å, $V$ = 2018.2(7) Å$^3$, $\rho_{calc}$ = 1.176 g cm$^{-3}$, $\mu$ = 0.079 mm$^{-1}$, empirical absorption correction (0.962 ≤ $T$ ≤ 0.987), $Z$ = 4, orthorhombic, space group $P2_12_12_1$ (no. 19), $\lambda$ = 0.71073 Å, $T$ = 233 K, $\omega$ and $\phi$ scans, 16268 reflections collected ($\pm h$, $\pm k$, $\pm l$), [(sin$\theta$)/$\lambda$] = 0.60 Å$^{-1}$, 3549 independent ($R_{int}$ = 0.038) and 2835 observed reflections [$I \geq 2\sigma(I)$], 237 refined parameters, $R$ = 0.065, $wR_2$ = 0.185, Flack parameter 3(3), max. residual electron density 0.38 (–0.20) e Å$^{-3}$; hydrogen atoms were calculated and refined as riding.

**X-ray Crystal Structure Analysis for 4·HCl·CHCl$_3$:** $C_{20}H_{31}Cl_4N_5O_2$, $M$ = 515.30, colorless crystal 0.22 × 0.20 × 0.15 mm$^3$, $a$ = 5.601(1), $b$ = 17.230(1), $c$ = 13.217(4) Å, $\beta$ = 93.41(1)°, $V$ = 1273.3(3) Å$^3$, $\rho_{calc}$ = 1.344 g cm$^{-3}$, $\mu$ = 0.491 mm$^{-1}$, empirical absorption correction (0.902 ≤ $T$ ≤ 0.930), $Z$ = 4, monoclinic, space group $P2_1$ (no. 4), $\lambda$ = 0.71073 Å, $T$ = 198 K, $\omega$ and $\phi$ scans, 10536 reflections collected ($\pm h$, $\pm k$, $\pm l$), [(sin$\theta$)/$\lambda$] = 0.66 Å$^{-1}$, 5622 independent ($R_{int}$ = 0.051) and 4225 observed reflections [$I \geq 2\sigma(I)$], 286 refined parameters, $R$ = 0.045, $wR_2$ = 0.109, Flack parameter 0.02(5), max. residual electron density 0.38 (–0.20) e Å$^{-3}$. The hydrogen atom at nitrogen was observed in the difference Fourier calculations; the others were calculated and refined as riding.

**General Procedure for the Preparation of Metal Complexes:** A solution of the lanthanoid(III) salt (approx. 0.1 mmol) in methanol or acetonitrile was added to the ligand (**3** or **4**) in either methanol, acetonitrile, or nitromethane and the mixture was stirred overnight. The solvent was then removed in vacuo and the residue dried in vacuo. In the case of complexations with ligand **3** in acetonitrile, the mixture was filtered prior to work up.

**[(3)YCl$_3$]:** The reaction was performed in methanol. Yield: 70.7 mg (0.12 mmol, quant.), colorless solid. $^1$H NMR (200 MHz, $CD_3OD$): $\delta$ = 8.30 (t, $J$ = 8.0 Hz, 1 H), 8.27 (s, 2 H), 7.88 (d, $J$ = 8.0 Hz, 2 H) ppm. IR (KBr): $\tilde{\nu}$ = 3381, 3220, 1670, 1543, 1388, 1175 cm$^{-1}$. MS (pos. ESI, $CH_3OH$): *m*/*z* 407.9 (18) [(**3**)YCl$_2$]$^+$, 399.7 (100) [(**3**)Y(CH$_3$O)$_2$]$^+$. $C_9H_{11}Cl_3N_7O_2Y\cdot 7H_2O$: calcd. C 18.94, H 4.42, N 17.18; found C 18.49, H 3.82, N 16.63.

**[(3)Y(NO$_3$)$_3$]:** This complex was prepared in acetonitrile. Yield: 75.4 mg (0.12 mmol, quant.), pale-yellow solid. $^1$H NMR (200 MHz, $CD_3OD$): $\delta$ = 8.31 (t, $J$ = 7.9 Hz, 1 H), 8.29 (s, 2 H), 7.90 (d, $J$ = 7.9 Hz, 2 H) ppm. IR (KBr): $\tilde{\nu}$ = 3422, 1670, 1559, 1386, 1167 cm$^{-1}$. MS (pos. ESI, $CH_3OH$): *m*/*z* 462.0 (10) [(**3**)Y(NO$_3$)$_2$]$^+$, 209.5 (79) [(**3**)Y(CH$_3$OH)(OH)]$^{2+}$, 200.5 (100) [(**3**)Y(CH$_3$O)]$^{2+}$, 193.5 (95) [(**3**)Y(OH)]$^{2+}$. $C_9H_{11}N_{10}O_{11}Y\cdot CH_3OH\cdot 4H_2O$: calcd. C 19.12, H 3.69, N 22.29; found C 18.89, H 3.65, N 21.23.

**[(3)La(CF$_3$SO$_3$)$_3$]:** This complex was prepared in acetonitrile. Yield: 59.5 mg (0.07 mmol, 59%) colorless solid. $^1$H NMR (200 MHz, $CD_3OD$): $\delta$ = 8.32 (s, 2 H), 8.28 (t, $J$ = 7.9 Hz, 1 H), 7.87 (d, $J$ = 7.9 Hz, 2 H) ppm. IR (KBr): $\tilde{\nu}$ = 3422, 1684, 1559, 1409, 1255, 1168, 1037, 643 cm$^{-1}$. MS (pos. MALDI-TOF, DCTB): *m*/*z* 686.0 (100) [(**3**)La(CF$_3$SO$_3$)$_2$]$^+$, 536.1 (58) [(**3**)La(CF$_3$SO$_3$) – H]$^+$.

**[(3)La(Cl)$_3$]:** This complex was prepared in methanol. Yield: 46.4 mg (0.09 mmol, 78%), colorless solid. $^1$H NMR (200 MHz, $CD_3OD$): $\delta$ = 8.30 (s, 2 H), 8.23 (t, $J$ = 7.7 Hz, 1 H), 7.83 (d, $J$ = 7.7 Hz, 2 H) ppm. IR (KBr): $\tilde{\nu}$ = 3448, 1670, 1559, 1406, 1168 cm$^{-1}$. MS (pos. ESI, $CH_3OH$): *m*/*z* 457.7 (75) [(**3**)La(Cl)$_2$]$^+$, 421.9 (80) [(**3**)La(Cl) – H]$^+$, 417.8 (100) [(**3**)La(MeO) – H]$^+$.

**[(3)La(NO$_3$)$_3$]:** This reaction was performed in acetonitrile. Yield: 68.9 mg (0.12 mmol, quant.), colorless solid. $^1$H NMR (200 MHz, $CD_3OD$): $\delta$ = 8.34 (s, 2 H), 8.26 (t, $J$ = 7.7 Hz, 1 H), 8.00 (br. s, 2 H), 7.86 (d, $J$ = 7.7 Hz, 2 H) ppm. IR (KBr): $\tilde{\nu}$ = 3394, 1676, 1551, 1396, 1166 cm$^{-1}$. MS (pos. ESI, $CH_3OH$): *m*/*z* 218.5 (89) [(**3**)-La(CH$_3$OH)(OH)]$^{2+}$, 209.5 (100) [(**3**)La(CH$_3$O)]$^{2+}$.

**[(3)Pr(CF$_3$SO$_3$)$_3$]:** This complex was prepared in methanol. Yield: 66.7 mg (0.08 mmol, 66%), colorless solid. IR (KBr): $\tilde{\nu}$ = 3432, 3318, 3226, 1684, 1625, 1559, 1255, 1169, 1029, 633 cm$^{-1}$. MS (pos. LDI-TOF): *m*/*z* 688 [(**3**)Pr(CF$_3$SO$_3$)$_2$]$^+$.

**[(3)Pr(NO$_3$)$_3$]:** This complex was prepared in acetonitrile. Yield: 32.4 mg (0.05 mmol, 43%), pale-yellow solid. IR (KBr): $\tilde{\nu}$ = 3453, 3373, 1672, 1559, 1464, 1385, 1320, 1171, 1041 cm$^{-1}$. MS (pos. ESI, $CH_3OH$): *m*/*z* 451.5 (65) [**3**Pr(NO$_3$) – H]$^{2+}$. $C_9H_{11}N_{10}O_{11}Pr\cdot 5H_2O$: calcd. C 16.23, H 3.18, N 21.02; found C 15.86, H 2.58, N 20.40.

**X-ray Crystal Structure Analysis for [(3)Pr(NO$_3$)$_3$]·MeOH:** $C_{12}H_{23}N_{10}O_{14}Pr$, $M$ = 672.31, yellow crystal 0.30 × 0.30 × 0.15 mm$^3$, $a$ = 8.175(1), $b$ = 11.971(1), $c$ = 13.054(4) Å, $\alpha$ = 90.35(1)°, $\beta$ = 103.78(1)°, $\gamma$ = 101.02(1)°, $V$ = 1216.1(2) Å$^3$, $\rho_{calc}$ = 1.836 g cm$^{-3}$, $\mu$ = 2.089 mm$^{-1}$, empirical absorption correction (0.573 ≤ $T$ ≤ 0.745), $Z$ = 2, triclinic, space group $P\bar{1}$ (no. 2), $\lambda$ = 0.71073 Å, $T$ = 223 K, $\omega$ and $\phi$ scans, 13426 reflections collected ($\pm h$, $\pm k$, $\pm l$), [(sin$\theta$)/$\lambda$] = 0.66 Å$^{-1}$, 5743 independent ($R_{int}$ = 0.041) and 5311 observed reflections [$I \geq 2\sigma(I)$], 358 refined parameters, $R$ = 0.031, $wR_2$ = 0.084, max. residual electron density 0.38 (–0.20) e Å$^{-3}$. The hydrogen atoms at nitrogens were obtained from the difference Fourier calculations; the others were calculated and refined as riding.

**[(3)Nd(CF$_3$SO$_3$)$_3$]:** This complex was prepared in acetonitrile. Yield: 88.2 mg (0.10 mmol, 88%), colorless solid. IR (KBr): $\tilde{\nu}$ = 3448, 1654, 1559, 1406, 1256, 1169, 682, 639 cm$^{-1}$. MS (pos. ESI, $CH_3OH$): *m*/*z* 1530.9 (8) [{(**3**)Pr}$_2$(CF$_3$SO$_3$)$_5$]$^+$, 691.0 (84) [(**3**)-Pr(CF$_3$SO$_3$)$_2$]$^+$, 539.1 (69).

**X-ray Crystal Structure Analysis for [{(3)Nd(CF$_3$SO$_3$)}$_2$(μ-CF$_3$SO$_3$)$_3$]CF$_3$SO$_3$·2CH$_3$CN·Et$_2$O:** $C_{32.4}H_{37}N_{17}Nd_2O_{22.6}PS_6$, $M$ = 1849.03, colorless crystal 0.16 × 0.12 × 0.10 mm$^3$, $a$ = 18.296(3), $b$ = 19.739(4), $c$ = 18.033(3) Å, $\beta$ = 90.275(4)°, $V$ = 6512(2) Å$^3$, $\rho_{calc}$ = 1.886 g cm$^{-3}$, $\mu$ = 1.903 mm$^{-1}$, empirical absorption correction (0.751 ≤ $T$ ≤ 0.833), $Z$ = 4, monoclinic, space group $P2_1/c$ (no. 14), $\lambda$ = 0.71073 Å, $T$ = 153 K, $\omega$ and $\phi$ scans, 62688 reflections collected ($\pm h$, $\pm k$, $\pm l$), [(sin$\theta$)/$\lambda$] = 0.65 Å$^{-1}$, 14981 independent ($R_{int}$ = 0.070) and 11053 observed reflections [$I \geq 2\sigma(I)$], 358 refined parameters, $R$ = 0.052, $wR_2$ = 0.120, max. residual electron density 1.51 (–1.09) e Å$^{-3}$. The hydrogen atoms at nitrogens were obtained from the difference Fourier calculations; the others were calculated and refined as riding.

 © 2007 Wiley-VCH Verlag GmbH & Co. KGaA, Weinheim 

**[(3)Nd(Cl)$_3$]:** This complex was prepared in methanol. Yield: 68.6 mg (0.12 mmol, quant.), pale-yellow solid. IR (KBr): $\tilde{\nu}$ = 3448, 1654, 1636, 1559, 1400, 1341, 1168 cm$^{-1}$. MS (pos. ESI, $CH_3OH$): *m*/*z* 269.5 (22) [(**3**)NdCl($CH_3OH$)$_3$($H_2O$)]$^{2+}$, 253.9 (100) [(**3**)-NdCl($CH_3OH$)$_2$($H_2O$)]$^{2+}$. $C_9H_{11}Cl_3N_7ONd_2{\cdot}4H_2O$: calcd. C 18.90, H 3.35, N 17.14; found C 19.35, H 3.41, N 17.30.

**X-ray Crystal Structure Analysis for [(3)NdCl$_2$($CH_3OH$)($Et_2O$)]Cl:** $C_{14}H_{27}N_7O_5Cl_3Nd$, *M* = 624.02, colorless crystal 0.20 × 0.10 × 0.02 mm$^3$, *a* = 7.7520(16), *b* = 27.659(6), *c* = 10.055(2) Å, $\beta$ = 95.335(4)°, *V* = 2146.6(8) Å$^3$, $\rho_{calc}$ = 1.931 g cm$^{-3}$, $\mu$ = 2.835 mm$^{-1}$, empirical absorption correction (0.601 ≤ *T* ≤ 0.946), *Z* = 4, monoclinic, space group $P2_1/c$ (no. 14), $\lambda$ = 0.71073 Å, *T* = 153 K, $\omega$ and $\phi$ scans, 16991 reflections collected ($\pm h$, $\pm k$, $\pm l$), [(sin$\theta$)/$\lambda$] = 0.59 Å$^{-1}$, 3769 independent ($R_{int}$ = 0.057) and 3043 observed reflections [$I \geq 2\sigma(I)$], 255 refined parameters, *R* = 0.046, $wR_2$ = 0.105, max. residual electron density 1.53 (–1.12) e Å$^{-3}$. The hydrogen atoms at nitrogens were obtained from the difference Fourier calculations; the others were calculated and refined as riding.

**[(3)Sm($CF_3SO_3$)$_3$]:** This complex was prepared in acetonitrile. Yield: 76.7 mg (0.09 mmol, 75%), colorless solid. IR (KBr): $\tilde{\nu}$ = 3463, 1685, 1654, 1559, 1395, 1256, 1229, 1171, 637 cm$^{-1}$. MS (pos. LDI-TOF): *m*/*z* 699 [(**3**)Sm($CF_3SO_3$)$_2$]$^+$. $C_{12}H_{11}F_9N_7O_{11}S_3Sm{\cdot}CH_3OH{\cdot}9H_2O$: calcd. C 15.00, H 3.20, N 9.42; found C 14.70, H 3.05, N 9.43.

**[(3)Sm($NO_3$)$_3$]:** This complex was prepared in acetonitrile. Yield: 32.7 mg (0.05 mmol, 39%), pale-yellow solid. IR (KBr): $\tilde{\nu}$ = 3453, 3365, 1675, 1559, 1491, 1405, 1385, 1301, 1165 cm$^{-1}$. MS (pos. LDI-TOF): *m*/*z* 209 [(**3**)Sm(OH)]$^{2+}$. $C_9H_{11}N_{10}O_{11}Sm{\cdot}CH_3CN{\cdot}3H_2O$: calcd. C 19.41, H 2.96, N 22.63; found C 19.51, H 2.53, N 22.10.

**[(3)Er($CF_3SO_3$)$_3$]:** This complex was prepared in acetonitrile. Yield: 65.5 mg (0.08 mmol, 63%), colorless solid. IR (KBr): $\tilde{\nu}$ = 3449, 1701, 1654, 1256, 1174, 1031, 641 cm$^{-1}$. MS (pos. ESI, $CH_3OH$): *m*/*z* 714.9 (12) [(**3**)Er($CF_3SO_3$)$_2$]$^+$, 223.1 (100) [(**3**)Er($CH_3O$)]$^{2+}$. $C_{12}H_{11}ErF_9N_7O_{11}S_3{\cdot}8H_2O$: calcd. C 14.30, H 2.70, N 9.73; found C 14.53, H 2.84, N 9.31.

**[(3)Er(Cl)$_3$]:** This complex was prepared in methanol. Yield: 60.1 mg (0.09 mmol, 78%), colorless solid. IR (KBr): $\tilde{\nu}$ = 3448, 1664, 1637, 1396, 1174 cm$^{-1}$. MS (pos. LDI-TOF): *m*/*z* 451 [(**3**)-ErCl – H]$^+$.

**X-ray Crystal Structure Analysis for [(3)ErCl$_2$($CH_3OH$)]Cl:** $C_{10}H_{15}N_7O_3Cl_3Er$, *M* = 554.90, pale-yellow crystal 0.20 × 0.15 × 0.10 mm$^3$, *a* = 12.004(1), *b* = 13.769(1), *c* = 21.713(1) Å, *V* = 3588.8(4) Å$^3$, $\rho_{calc}$ = 2.054 g cm$^{-3}$, $\mu$ = 5.148 mm$^{-1}$, empirical absorption correction (0.426 ≤ *T* ≤ 0.627), *Z* = 8, orthorhombic, space group *Pbca* (no. 61), $\lambda$ = 0.71073 Å, *T* = 223 K, $\omega$ and $\phi$ scans, 21485 reflections collected ($\pm h$, $\pm k$, $\pm l$), [(sin$\theta$)/$\lambda$] = 0.67 Å$^{-1}$, 4329 independent ($R_{int}$ = 0.033) and 3535 observed reflections [$I \geq 2\sigma(I)$], 239 refined parameters, *R* = 0.028, $wR_2$ = 0.072, max. residual electron density 1.35 (–1.28) e Å$^{-3}$. The hydrogen atoms at nitrogens were obtained from the difference Fourier calculations; the others were calculated and refined as riding.

**[(3)Lu($CF_3SO_3$)$_3$]:** This complex was prepared in acetonitrile. Yield: 104.5 mg (0.12 mmol, quant.), colorless solid. $^1$H NMR (200 MHz, $CD_3OD$): $\delta$ = 8.36 (t, *J* = 7.9 Hz, 1 H), 8.31 (s, 2 H), 7.95 (d, *J* = 7.9 Hz, 2 H) ppm. IR (KBr): $\tilde{\nu}$ = 3443, 1656, 1540, 1399, 1276, 1252, 1174, 1034, 646 cm$^{-1}$. MS (pos. MALDI-TOF, DCTB): *m*/*z* [(**3**)Lu($CF_3SO_3$)$_2$]$^+$.

**[(3)Lu(Cl)$_3$]:** This complex was prepared in methanol. Yield: 68.3 mg (0.11 mmol, 93%), pale-yellow solid. $^1$H NMR (200 MHz, $CD_3OD$): $\delta$ = 8.40 (s, 2 H), 8.35 (t, *J* = 7.8 Hz, 1 H), 7.95 (d, *J* = 7.8 Hz, 2 H) ppm. IR (KBr): $\tilde{\nu}$ = 3448, 3170, 1670, 1648, 1600, 1541, 1396, 1177 cm$^{-1}$. MS (pos. LDI-TOF): *m*/*z* 458 [(**3**)LuCl – H]$^+$. $C_9H_{11}Cl_3LuN_7O_2{\cdot}5H_2O$: calcd. C 17.42, H 3.41, N 15.80; found C 17.73, H 3.38, N 15.26.

**X-ray Crystal Structure Analysis for [(3)LuCl$_2$]Cl:** $C_{18}H_{22}Cl_6Lu_2N_{14}O_4$, *M* = 1061.14, pale-yellow crystal 0.18 × 0.09 × 0.07 mm$^3$, *a* = 11.126(3), *b* = 10.348(3), *c* = 13.655(3) Å, $\beta$ = 101.281(4)°, *V* = 1541.7(6) Å$^3$, $\rho_{calc}$ = 2.286 g cm$^{-3}$, $\mu$ = 6.939 mm$^{-1}$, empirical absorption correction (0.368 ≤ *T* ≤ 0.642), *Z* = 2, monoclinic, space group *C*2/*c* (no. 15), $\lambda$ = 0.71073 Å, *T* = 153 K, $\omega$ and $\phi$ scans, 8687 reflections collected ($\pm h$, $\pm k$, $\pm l$), [(sin$\theta$)/$\lambda$] = 0.71 Å$^{-1}$, 2263 independent ($R_{int}$ = 0.040) and 2133 observed reflections [$I \geq 2\sigma(I)$], 111 refined parameters, *R* = 0.030, $wR_2$ = 0.064, max. residual electron density 1.47 (–1.42) e Å$^{-3}$. The hydrogen atoms at nitrogens were obtained from the difference Fourier calculations; the others were calculated and refined as riding.

**[(3)Lu($NO_3$)$_3$]:** This complex was prepared in acetonitrile. Yield: 96.0 mg (0.12 mmol, quant.), colorless solid. $^1$H NMR (200 MHz, $CD_3OD$): $\delta$ = 8.38 (s, 2 H), 8.33 (t, *J* = 7.8 Hz, 1 H), 7.94 (d, *J* = 7.8 Hz, 2 H) ppm. IR (KBr): $\tilde{\nu}$ = 3406, 1670, 1546, 1384, 1172 cm$^{-1}$. MS (pos. ESI, $CH_3OH$): *m*/*z* (%) 236.5 (70) [(**3**)Lu($CH_3OH$)-(OH)]$^{2+}$, 229.5 (100) [(**3**)Lu($H_2O$)(OH)]$^{2+}$. $C_9H_{11}LuN_{10}O_{11}{\cdot}2CH_3CN{\cdot}6H_2O$: calcd. C 19.51, H 3.65, N 21.00; found C 19.53, H 3.51, N 20.55.

**[(4)Y(Cl)$_3$]:** This complex was prepared in methanol. Yield: 72.9 mg (0.11 mmol, quant.), yellow solid. $^1$H NMR (200 MHz, $CD_3OH$): $\delta$ = 8.06 (t, *J* = 7.9 Hz, 1 H), 7.52 (d, *J* = 7.9 Hz, 2 H), 7.20 (s, 2 H), 4.02 (br. m, 2 H), 3.70 (d, *J* = 5.2 Hz, 4 H), 3.60–3.30 (m, 4 H), 3.42 (s, 6 H), 2.31–1.95 (m, 8 H) ppm. $^{13}$C NMR (50 MHz, $CDCl_3$): $\delta$ = 149.9, 141.5, 112.0, 114.7, 74.1, 63.5, 59.6, 48.9, 27.1, 22.3 ppm. IR (KBr): $\tilde{\nu}$ = 3448, 1617, 1540, 1341, 1276, 1154, 669 cm$^{-1}$. $C_{19}H_{29}Cl_3N_5O_2Y{\cdot}6H_2O$: calcd. C 34.43, H 6.23, N 10.57; found C 34.38, H 6.41, N 10.33.

**[(4)Y($NO_3$)$_3$]:** This complex was prepared in methanol. Yield: 78.7 mg (0.11 mmol, quant.), orange/green solid. $^1$H NMR (200 MHz, $CD_3CN$): $\delta$ = 8.00 (t, *J* = 8.1 Hz, 1 H), 7.27 (d, *J* = 8.1 Hz, 2 H), 7.03 (s, 2 H), 3.94 (br. m, 2 H), 3.62 (d, *J* = 5.1 Hz, 4 H), 3.52–3.26 (m, 4 H), 3.32 (s, 6 H), 2.23–1.85 (m, 8 H) ppm. $^{13}$C NMR (50 MHz, $CD_3CN$): $\delta$ = 148.7, 146.3, 119.1, 118.0, 74.2, 64.6, 59.5, 49.9, 27.5, 22.8 ppm. MS (pos. ESI, $CH_3CN$): *m*/*z* (%) 572.3 (15) [(**3**)Y($NO_3$)$_2$]$^+$. MS (pos. LDI-TOF): *m*/*z* 572 [(**3**)Y-($NO_3$)$_2$]$^+$. $C_{19}H_{29}N_8O_{11}Y{\cdot}2CH_3OH{\cdot}H_2O$: calcd. C 34.20, H 5.31, N 15.95; found C 34.60, H 5.11, N 16.05.

**[(4)La($CF_3SO_3$)$_3$]:** This complex was prepared in acetonitrile. Yield: 56.7 mg (0.06 mmol, 54%), orange solid. $^1$H NMR (200 MHz, $CDCl_3$): $\delta$ = 7.78 (t, *J* = 7.9 Hz, 1 H), 7.52 (d, *J* = 7.9 Hz, 2 H), 7.19 (s, 2 H), 3.68–3.20 (m, 16 H), 2.27–1.88 (m, 8 H) ppm. IR (KBr): $\tilde{\nu}$ = 3445, 1617, 1560, 1275, 1255, 1161, 1032, 756, 639 cm$^{-1}$. MS (pos. ESI, $CH_3CN$): *m*/*z* (%) 796.1 (4) [(**4**)La($CF_3SO_3$)$_2$]$^+$, 360.3 (100) [(**4**)LaH($CF_3SO_3$)$_3$]$^+$.

**[(4)La(Cl)$_3$]:** This complex was prepared in methanol. Yield: 73.4 mg (0.11 mmol, 99%), orange solid. $^1$H NMR (200 MHz, $CDCl_3$): $\delta$ = 7.81 (s, 2 H), 7.79–7.49 (m, 3 H), b), 3.90 (br. m, 2 H), 3.70 (d, *J* = 5.2 Hz, 4 H), 3.67–3.31 (m, 4 H), 3.37 (s, 6 H), 2.21–1.88 (m, 8 H) ppm. IR (KBr): $\tilde{\nu}$ = 3400, 2929, 1610, 1539, 1274, 1152, 1116, 728 cm$^{-1}$. MS (pos. LDI-TOF): *m*/*z* 568 [(**4**)-La(Cl)$_2$]$^+$. $C_{19}H_{29}Cl_3LaN_5O_2{\cdot}4H_2O$: calcd. C 33.72, H 5.51, N 10.35; found C 34.18, H 5.50, N 10.33.

 © 2007 Wiley-VCH Verlag GmbH & Co. KGaA, Weinheim 

**[(4)Pr(CF$_3$SO$_3$)$_3$]:** This complex was prepared in methanol. Yield: 104.2 mg (0.11 mmol, quant.), orange solid. IR (KBr): $\tilde{\nu}$ = 2933, 2883, 1617, 1540, 1450, 1350, 1276, 1198, 1162, 1032, 839, 757, 640 cm$^{-1}$. MS (pos. ESI, $CH_3CN$): *m/z* (%) 798.1 (6) [(**4**)Pr(CF$_3$SO$_3$)$_2$]$^+$, 360.3 (100) [(**4**)PrH(CF$_3$SO$_3$)$_3$]$^+$.

**[(4)Nd(CF$_3$SO$_3$)$_3$]:** This complex was prepared in methanol. Yield: 104.5 mg (0.11 mmol, quant.), orange solid. IR (KBr): $\tilde{\nu}$ = 3448, 1663, 1559, 1256, 1235, 1169, 1031, 754, 639 cm$^{-1}$. MS (pos. ESI, $CH_3CN$): *m/z* (%) 801.1 (4) [(**4**)Nd(CF$_3$SO$_3$)$_2$]$^+$.

**[(4)Nd(Cl)$_3$]**: This complex was prepared in methanol. Yield: 54.5 mg (0.08 mmol, 73%), orange-red solid. $^1$H NMR (200 MHz, $CDCl_3$): $\delta$ = 7.81 (s, 2 H), 7.87–7.51 (m, 3 H), b), 3.90 (br. m, 2 H), 3.70–3.25 (m, 8 H), 3.36 (s, 6 H), 2.21–1.86 (m, 8 H) ppm. IR (KBr): $\tilde{\nu}$ = 3448, 2885, 1635, 1608, 1544, 1453, 1360, 1325, 1281, 1155, 1117, 749 cm$^{-1}$. $C_{19}H_{29}Cl_3N_5NdO_2{\cdot}CH_3OH{\cdot}2H_2O$: calcd. C 35.42, H 5.50, N 10.33; found C 35.98, H 5.68, N 10.91.

**[(4)Sm(CF$_3$SO$_3$)$_3$]:** This complex was prepared in acetonitrile. Yield: 105.4 mg (0.11 mmol, quant.), orange solid. IR (KBr): $\tilde{\nu}$ = 2936, 2894, 1617, 1535, 1445, 1415, 1344, 1273, 1256, 1162, 1032, 749, 640 cm$^{-1}$. MS (pos. ESI, $CH_3CN$): *m/z* (%) 809.1 (2) [(**4**)Sm(CF$_3$SO$_3$)$_2$]$^+$.

**[(4)Sm(Cl)$_3$]:** This complex was prepared in methanol. Yield: 70.0 mg (0.11 mmol, quant.), orange solid. IR (KBr): $\tilde{\nu}$ = 3448, 1617, 1540, 1340, 1288, 1271, 1155 cm$^{-1}$. MS (pos. LDI-TOF): *m/z* 583 [(**4**)SmCl$_2$]$^+$. $C_{19}H_{29}Cl_3N_5O_2Sm{\cdot}H_2O$: calcd. C 33.16, H 5.42, N 10.18; found C 33.15, H 5.14, N 10.05.

**[(4)Sm(NO$_3$)$_3$]:** This complex was prepared in acetonitrile. Yield: 66.9 mg (0.10 mmol, 87%), orange solid. $^1$H NMR (200 MHz, $CD_3CN$): $\delta$ = 8.01 (t, *J* = 7.8 Hz, 1 H), 7.27 (d, *J* = 7.8 Hz, 2 H), 7.04 (s, 2 H), 3.94 (br. m, 2 H), 3.62 (d, *J* = 4.8 Hz, 4 H), 3.47–3.26 (m, 4 H), 3.32 (s, 6 H), 2.23–1.84 (m, 8 H) ppm. IR (KBr): $\tilde{\nu}$ = 3443, 1617, 1540, 1384, 1288, 1271, 1155 cm$^{-1}$. MS (pos. LDI-TOF): *m/z* 635 [(**4**)Sm(NO$_3$)$_2$]$^+$.

**[(4)Er(CF$_3$SO$_3$)$_3$]:** This complex was prepared in acetonitrile. Yield: 107.2 mg (0.11 mmol, quant.), orange solid. IR (KBr): $\tilde{\nu}$ = 3446, 1617, 1559, 1273, 1261, 1160, 1033, 755, 640 cm$^{-1}$. MS (pos. ESI, CH3CN): *m/z* (%) 825.1 (3) [(**4**)Er(CF$_3$SO$_3$)$_2$]$^+$. MS (pos. LDI-TOF): *m/z* 825 [(**4**)Er(CF$_3$SO$_3$)$_2$]$^+$).

**[(4)Er(Cl)$_3$]:** This complex was prepared in methanol. Yield: 79.0 mg (0.11 mmol, quant.), orange solid. $^1$H NMR (200 MHz, $CD_3OD$): $\delta$ = 8.07 (t, *J* = 7.9 Hz, 1 H), 7.52 (d, *J* = 7.9 Hz, 2 H), 7.20 (s, 2 H), 4.00 (br. m, 2 H), 3.67 (d, *J* = 4.7 Hz, 4 H), 3.60–3.20 (m, 4 H), 3.40 (s, 6 H), 2.32–1.89 (m, 8 H) ppm. IR (KBr): $\tilde{\nu}$ = 3443, 1617, 1534, 1340, 1288, 1156 cm$^{-1}$. MS (pos. LDI-TOF): *m/z* 597 [(**4**)ErCl$_2$]$^+$. $C_{19}H_{29}Cl_3ErN_5O_2{\cdot}CH_3OH{\cdot}3H_2O$: calcd. C 33.40, H 5.47, N 9.74; found C 33.48, H 5.58, N 10.21.

**[(4)Er(NO$_3$)$_3$]:** This complex was prepared in acetonitrile. Yield: 75.7 mg (0.10 mmol, 94%), yellow solid. $^1$H NMR (200 MHz, $CD_3OD$): $\delta$ = 7.74 (br. t, *J* = 7.6 Hz, 1 H), 7.54 (br. d, *J* = 7.6 Hz, 2 H), 7.16 (br. s, 2 H), 3.92–3.13 (br. m, 10 H), 3.40 (br. s, 6 H), 2.24–1.86 (br. m, 8 H) ppm. IR (KBr): $\tilde{\nu}$ = 3443, 1617, 1540, 1384, 1288, 1270, 1155 cm$^{-1}$. MS (pos. LDI-TOF): *m/z* 651 [(**4**)Er(NO$_3$)$_2$]$^+$. $C_{19}H_{29}ErN_8O_{11}{\cdot}H_2O$: calcd. C 29.08, H 4.75, N 14.28; found C 29.59, H 4.18, N 15.21.

**[(4)Yb(CF$_3$SO$_3$)$_3$]:** This complex was prepared in acetonitrile. Yield: 107.8 mg (0.11 mmol, quant.), orange solid. $^1$H NMR (200 MHz, $CD_3CN$): $\delta$ = 7.80 (t, *J* = 7.9 Hz, 1 H), 7.02 (d, *J* = 7.9 Hz, 2 H), 6.72 (s, 2 H), 3.69 (br. m, 2 H), 3.38 (br. d, *J* = 5.1 Hz, 4 H), 3.13 (br. s, 6 H), 2.88 (m, 4 H), 2.05–1.62 (m, 8 H) ppm. $^{13}$C NMR (50 MHz, $CD_3CN$): $\delta$ = 147.1, 144.7, 121.7, 117.4, 116.2, 72.5, 62.9, 57.9, 46.3, 25.9, 21.2 ppm. IR (KBr): $\tilde{\nu}$ = 3446, 1624, 1540, 1275, 1261, 1162, 1032, 756, 641 cm$^{-1}$. MS (pos. ESI, $CH_3CN$): *m/z* (%) 831.1 (1) [(**4**)Yb(CF$_3$SO$_3$)$_2$]$^+$ ppm. MS (pos. LDI-TOF): *m/z* 831 [(**4**)Yb(CF$_3$SO$_3$)$_2$]$^+$.

**[(4)Lu(CF$_3$SO$_3$)$_3$]:** This complex was prepared in acetonitrile. Yield: 106.9 mg (0.11 mmol, quant.), orange solid. $^1$H NMR (200 MHz, $CD_3CN$): $\delta$ = 8.02 (t, *J* = 7.9 Hz, 1 H), 7.27 (d, *J* = 7.9 Hz, 2 H), 7.04 (s, 2 H), 4.08–3.22 (m, 16 H), 2.25–1.84 (m, 8 H) ppm. IR (KBr): $\tilde{\nu}$ = 3447, 2993, 2881, 1617, 1544, 1450, 1347, 1276, 1198, 1161, 1032, 756, 640 cm$^{-1}$. MS (pos. ESI, CH3CN): *m/z* (%) 832.1 (4) [(**4**)Lu(CF$_3$SO$_3$)$_2$]$^+$.

**[(4)Lu(Cl)$_3$]:** This complex was prepared in methanol/acetonitrile. Yield: 76.2 mg (0.11 mmol, quant.), orange solid. $^1$H NMR (200 MHz, $CD_3CN$): $\delta$ = 7.96 (t, *J* = 8.1 Hz, 1 H), 7.44 (d, *J* = 8.1 Hz, 2 H), 7.35 (s, 2 H), 3.92 (br. m, 2 H), 3.61 (d, *J* = 4.8 Hz, 4 H), 3.49–3.23 (m, 4 H), 3.32 (s, 6 H), 2.21–1.82 (m, 8 H) ppm. IR (KBr): $\tilde{\nu}$ = 3448, 1617, 1540, 1340, 1287, 1154 cm$^{-1}$. MS (pos. LDI-TOF): *m/z* 604 [(**4**)LuCl$_2$]$^+$. $C_{19}H_{29}Cl_3LuN_5O_2{\cdot}3H_2O$: calcd. C 32.84, H 5.08, N 10.08; found C 32.77, H 5.15, N 9.99.

**[(4)Lu(NO$_3$)$_3$]:** This complex was prepared in acetonitrile. Yield: 77.7 mg (0.10 mmol, 94%), yellow solid. $^1$H NMR (200 MHz, $CD_3CN$): $\delta$ = 7.92 (br. t, *J* = 8.0 Hz, 1 H), 7.26 (d, *J* = 7.6 Hz, 2 H), 7.09 (s, 2 H), 3.92 (br. m, 2 H), 3.60 (br. d, *J* = 4.7 Hz, 4 H), 3.42 (dt, *J* = 8.0, 6.7 Hz, 4 H), 3.34 (s, 6 H), 2.36–1.75 (hidden under solvent peak, 8 H) ppm. MS (pos. LDI-TOF): *m/z* 658 [(**4**)Lu(NO$_3$)$_2$]$^+$.

## Acknowledgments

This work was supported by the Deutsche Forschungsgemeinschaft (DFG) (Schwerpunktprogramm 1166 "Lanthanoidspezifische Funktionalität in Molekül und Material", Graduiertenkolleg 440 "Methoden der asymmetrischen Synthese") and the NRW Graduate School of Chemistry (Münster). Prof. Dr. G. Raabe's help with the CD spectra is gratefully acknowledged.

[1] a) J.-C. G. Bünzli, G. R. Choppin, *Lanthanide Probes in Life, Chemical, and Earth Sciences*, Elsevier, Amsterdam, **1989**; b) V. Alexander, *Chem. Rev.* **1995**, *95*, 273; c) D. Parker, J. A. G. Williams, *J. Chem. Soc., Dalton Trans.* **1996**, 3613.
[2] R. Anwander, *Top. Curr. Chem.* **1996**, *179*, 33.
[3] See special issue of Chemical Reviews on Frontiers in Lanthanide Chemistry (Ed.: H. B. Kagan), *Chem. Rev.* **2002**, *102*, issue 6.
[4] M. Shibasaki, H. Sasai, T. Arai, *Angew. Chem.* **1997**, *109*, 1290; *Angew. Chem. Int. Ed.* **1997**, *36*, 1236.
[5] a) S. Kobayashi, H. Ishitani, *J. Am. Chem. Soc.* **1994**, *116*, 4083; b) S. Kobayashi, H. Ishitani, *J. Chem. Soc., Chem. Commun.* **1995**, 1379.
[6] K. Mikami, M. Terada, H. Matsuzawa, *Angew. Chem.* **2002**, *114*, 3704; *Angew. Chem. Int. Ed.* **2002**, *41*, 3554.
[7] For reviews on lanthanide helicates see: a) C. Piguet, J.-C. G. Bünzli, *Chem. Soc. Rev.* **1999**, *28*, 347; b) J.-C. G. Bünzli, C. Piguet, *Chem. Soc. Rev.* **2005**, *34*, 1048.
[8] M. Albrecht, O. Osetska, R. Fröhlich, *Dalton Trans.* **2005**, 3757.
[9] a) A. Jagst, A. Sanchez, E. M. Vazquez-Lopez, U. Abram, *Inorg. Chem.* **2005**, *44*, 5738–5744; b) C. A. Brown, W. Kaminsky, K. A. Claborn, K. I. Goldberg, D. X. West, *J. Braz. Chem. Soc.* **2002**, *13*, 10–18.
[10] a) D. Enders, H. Eichenauer, *Chem. Ber.* **1979**, *112*, 2933; b) D. Enders, P. Fey, H. Kipphardt, *Org. Synth.* **1987**, *65*, 173.
[11] For related pyridine SAMP hydrazones see: a) J. Ehlers, H. tom Dieck, *Z. Anorg. Allg. Chem.* **1988**, *560*, 80; b) T. Mino,

 © 2007 Wiley-VCH Verlag GmbH & Co. KGaA, Weinheim 

W. Imiya, M. Yamashita, *Synlett* **1997**, 583; c) T. Mino, Y. Shirae, T. Yajima, M. Sakamoto, T. Fujita, *Heterocycles* **2006**, *68*, 1233. d) For semicarbazone type ligands see, for example: R. Pedrido, M. J. Romero, M. R. Bermejo, A. M. Gonzalez-Noya, M. Maneiro, M. J. Rodriguez, G. Zaragoza, *Dalton Trans.* **2006**, 5304.
[12] G. Queguiner, P. Pastour, *Bull. Soc. Chim. Fr.* **1969**, *10*, 3659.
[13] E. C. Constable, *Tetrahedron* **1992**, *48*, 10013.
[14] For related complexes with d- and f-metals see, for example: a) T. Le Borgne, J.-M. Benech, S. Floquet, G. Bernardinelli, C. Aliprandini, P. Bettens, C. Piguet, *Dalton Trans.* **2003**, 3856; b) C. Quian, L. Wang, *Tetrahedron Lett.* **2000**, *41*, 2203; c) J. F. Folmer-Andersen, V. M. Lynch, E. V. Anslyn, *Chem. Eur. J.* **2005**, *11*, 5319.
[15] a) R. C. Palenik, K. A. Abboud, S. P. Summers, L. L. Reitfort, G. J. Palenik, *Inorg. Chim. Acta* **2006**, *359*, 4645. See also: b) J. E. Thomas, R. C. Palenik, G. J. Palenik, *Inorg. Chim. Acta* **1979**, *37*, L459; c) J. E. Thomas, G. J. Palenik, *Inorg. Chim. Acta* **1980**, *38*, L303.
[16] a) F. E. Hahn, J. Mohr, *Chem. Ber.* **1990**, *123*, 481; b) J. F. Desreux, in *Lanthanide Probes in Life, Chemical, and Earth Sciences* (Eds.: J.-C. G. Bünzli, G. R. Choppin), Elsevier, Amsterdam, **1989**, p. 43.
[17] Z. Otwinowski, W. Minor, *Methods Enzymol.* **1997**, *276*, 307.
[18] a) R. H. Blessing, *Acta Crystallogr., Sect. A* **1995**, *51*, 33; b) R. H. Blessing, *J. Appl. Crystallogr.* **1997**, *30*, 421.
[19] Z. Otwinowski, D. Borek, W. Majewski, W. Minor, *Acta Crystallogr., Sect. A* **2003**, *59*, 228.
[20] G. M. Sheldrick, *Acta Crystallogr., Sect. A* **1990**, *46*, 467.

Received: January 8, 2007
Published Online: May 22, 2007

 © 2007 Wiley-VCH Verlag GmbH & Co. KGaA, Weinheim

**The EUChemSoc Societies have taken the significant step into the future by merging their traditional journals, to form two leading chemistry journals, the *European Journal of Inorganic Chemistry* and the *European Journal of Organic Chemistry.* Three further EUChemSoc Societies (Austria, Czech Republic and Sweden) are Associates of the two journals.**

## COVER PICTURE

**The cover picture shows** how aminoguanidine may behave as either a monodentate or bidentate ligand in square-planar complexes of platinum or palladium. In each case, the coordinating ligands can participate in extensive hydrogen-bonding networks. Details are discussed in the article by D. J. Aitken, J. Kozelka et al. on p. 3327ff.

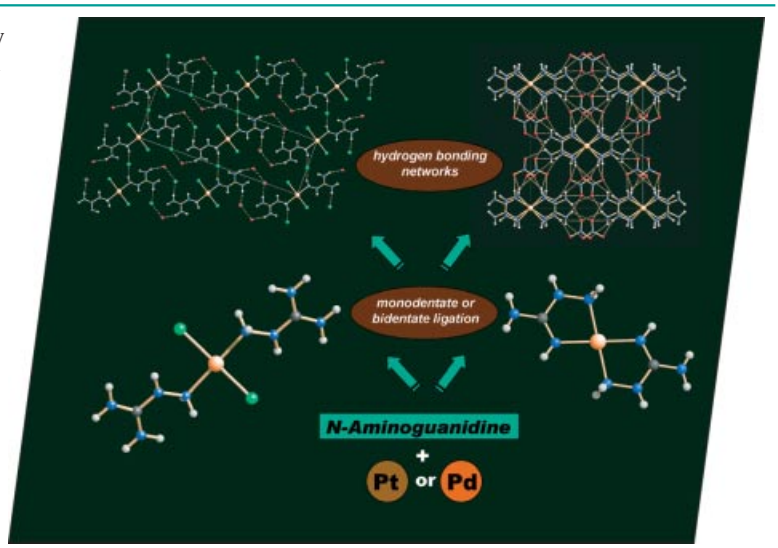


 © 2007 Wiley-VCH Verlag GmbH & Co. KGaA, Weinheim 

# CONTENTS

## MICROREVIEW

### Oxovanadium Calixarenes

**C. Limberg* ..... 3303–3314**

Calixarene-Based Oxovanadium Complexes as Molecular Models for Catalytically Active Surface Species and Homogeneous Catalysts

**Keywords:** Vanadium / Oxo complexes / Models / Calixarenes / Catalysis

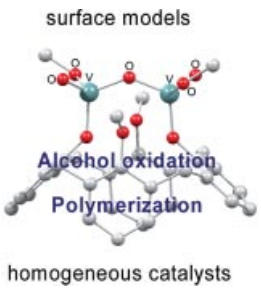


Oxovanadium calixarene complexes can be regarded as models for active surface species on vanadium oxide based heterogeneous catalysts, and their investigation thus contributes to a more comprehensive understanding of the effective mechanisms. In addition, they are interesting as homogeneous catalysts, for instance for aerobic alcohol oxidation and olefin polymerization.

## SHORT COMMUNICATIONS

### Supramolecular Helical Assemblies

**X.-F. Shan, L.-Z. Wu,* X.-Y. Liu, L.-P. Zhang, C.-H. Tung ..... 3315–3319**

C–H···$Ni^{II}$ Interaction-Driven Homochiral *M* and *P* Helices of Neutral (*R,R*)- and (*S,S*)-Bis(pyrrol-2-ylmethyleneamino)-cyclohexane $Ni^{II}$ Complexes

**Keywords:** Nickel(II) complexes / C–H···$Ni^{II}$ interactions / Helical structures

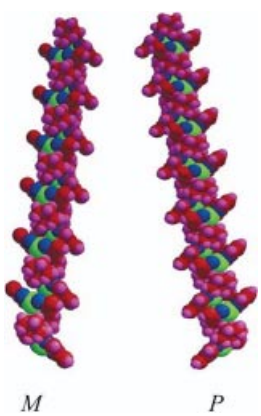


Reaction of (*R,R*)- and (*S,S*)-bis(pyrrol-2-ylmethyleneamino)cyclohexane with $Ni^{II}(OAc)_2 \cdot 4H_2O$ afforded enantiomeric nickel(II) Schiff-base complexes. Rare C–H···$Ni^{II}$ interactions were found to be responsible for the facile formation of the homochiral *M* and *P* helices of the neutral, chiral, mononuclear complexes in crystal lattices.

### Heterodimetallic Dinuclear Complexes

**C. A. Vock, R. Scopelliti, P. J. Dyson* ..... 3320–3322**

Synthesis and Crystallographic Characterisation of the Heterodimetallic Complex [(Dibenzo-18-crown-6)K($\mu$-Cl)$_3$Ru($\eta^6$-*p*-cymene)]

**Keywords:** Heterometallic complexes / Bridging ligands / Ruthenium / Crown compounds / X-ray crystallography

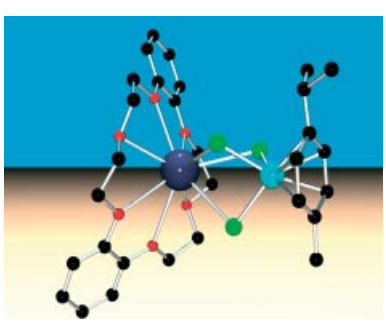

The first example of a triple-chlorido-bridged heterodimetallic dinuclear complex comprising an ($\eta^6$-arene)$Ru^{II}$ fragment and a Group 1 metal crown ether fragment is presented. The solid-state structure was determined by X-ray crystallography. NMR investigations indicate the presence of a dynamic equilibrium in solution.

### Carbon Dioxide Fixation

**J. Meléndez, M. North,* R. Pasquale ..... 3323–3326**

Synthesis of Cyclic Carbonates from Atmospheric Pressure Carbon Dioxide Using Exceptionally Active Aluminium(salen) Complexes as Catalysts

**Keywords:** Carbon dioxide fixation / Aluminium / Schiff bases / Epoxides / Catalysis

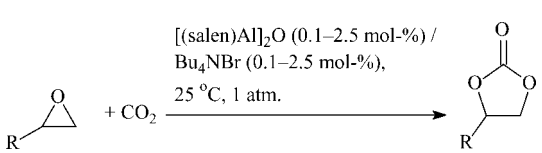


Dimetallic aluminium(salen) complexes show exceptionally high catalytic activity for the synthesis of cyclic carbonates from terminal epoxides at ambient temperature and pressure. The process has the potential to contribute towards decreasing atmospheric carbon dioxide emissions from the burning of fossil fuels.

 © 2007 Wiley-VCH Verlag GmbH & Co. KGaA, Weinheim 

# FULL PAPERS

## Aminoguanidine Coordination Modes

Aminoguanidine forms monodentate and bidentate complexes with $Pt^{II}$ and $Pd^{II}$. A series of N4-bound monodentate and N1,N4-bound chelate complexes was synthesized and characterized by solution NMR and by X-ray crystallography. In the solid state, hydrogen-bonding networks were observed; all four nitrogens of the Amgu ligand are able to behave as hydrogen atom donors.

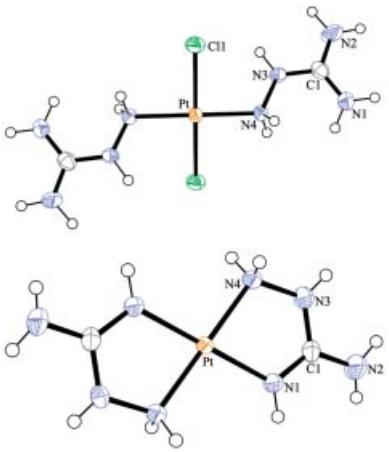


**D. J. Aitken,* A. Albinati, A. Gautier, H.-P. Husson, G. Morgant, D. Nguyen-Huy, J. Kozelka,* P. Lemoine, S. Ongeri, S. Rizzato, B. Viossat ..... 3327–3334**

Platinum(II) and Palladium(II) Complexes with *N*-Aminoguanidine

**Keywords:** Platinum / Palladium / N ligands / Coordination modes

## Gas-Phase Fragmentation

Electrospray ionization is used for the investigation vanadium(V) complexes of maleic and succinic acid. The fragmentation patterns of the mass-selected ions inter alia reveal a hitherto unrecognized connection between succinato and maleato complexes, which may be relevant in the context of vanadium-oxide-mediated formation of maleic acid upon partial oxidation of $C_4$-hydrocarbons.

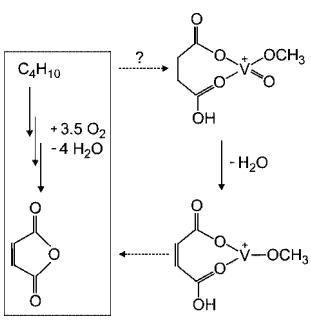


**M. Kaczorowska, H. Schwarz, D. Schröder* ..... 3335–3341**

Gas-Phase Fragmentation Behavior of Vanadium(V) Complexes Containing One Molecule of a $C_4$-Dicarboxylic Acid

**Keywords:** Carboxylato complexes / Vanadium / Electrospray ionization / Maleic anhydride / Mass spectrometry

## Hybrid Nanocomposites

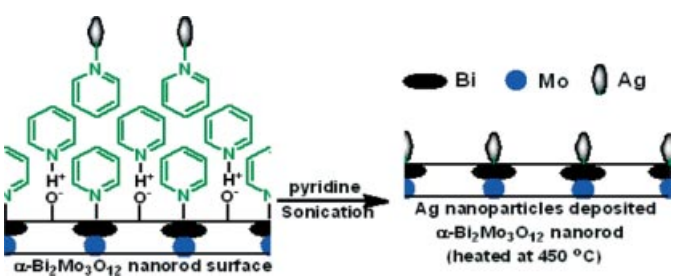


Silver nanoparticles with an average size of about 10 nm were uniformly deposited on the surface of $\alpha$-$Bi_2Mo_3O_{12}$ nanorods by using power ultrasound. Pyridine as a medium assisted the deposition process of the Ag nanoparticles, whereas Bi was observed to be the preferred binding site on the surface of the nanorods.

**A. V. Ghule, K. Ghule, S.-H. Tzing, Y.-C. Ling* ..... 3342–3349**

Synthesis and Characterization of Silver-Nanoparticle-Deposited $\alpha$-$Bi_2Mo_3O_{12}$ Nanorods

**Keywords:** Nanoparticles / Ultrasound / Deposition / Nanorods / Surface analysis / Electron microscopy

## Magnetic Perovskites

Oxygen-deficient manganites, with the same composition but different oxidation states of Mn, were stabilized through a reversible topotactic process using different pathways. Dramatic changes in the magnetic behaviour were observed due to the stabilization of different Mn oxidation states.

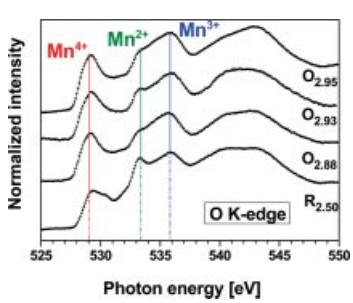


**J. M. Alonso, R. Cortés-Gil, L. Ruiz-González, J. M. González-Calbet,* A. Hernando, M. Vallet-Regí, M. E. Dávila, M. C. Asensio ..... 3350–3355**

Influence of the Synthetic Pathway on the Properties of Oxygen-Deficient Manganese-Related Perovskites

**Keywords:** Mixed-valent compounds / Perovskite phases / Magnetic properties / X-ray absorption near-edge spectroscopy (XANES) / Topotactic reaction

 © 2007 Wiley-VCH Verlag GmbH & Co. KGaA, Weinheim 

# CONTENTS


## Metal Nanoparticles

**S. H. Toma, J. A. Bonacin, K. Araki, H. E. Toma* ..... 3356–3364**

Controlled Stabilization and Flocculation of Gold Nanoparticles by Means of 2-Pyrazin-2-ylethanethiol and Pentacyanidoferrate(II) Complexes

**Keywords:** Aggregation / Colloids / Semiempirical calculations / Raman spectroscopy / UV/Vis spectroscopy / Charge transfer

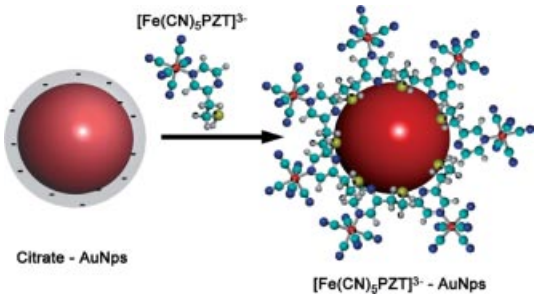


Coordination of pentacyanidoferrates and 2-pyrazin-2-ylethanethiol exerts a strong influence on the flocculation of gold nanoparticles, giving rise to contrasting SERS effects.

## Heterodimetallic Bisporphyrins

**F.-L. Jiang, W.-K. Wong,* X.-J. Zhu, G.-J. Zhou, W.-Y. Wong, P.-L. Wu, H.-L. Tam, K.-W. Cheah, C. Ye, Y. Liu* ..... 3365–3374**

Synthesis, Characterization, and Photophysical Properties of Some Heterodimetallic Bisporphyrins of Ytterbium and Transition Metals – Enhancement and Lifetime Extension of $Yb^{3+}$ Emission by Transition-Metal Porphyrin Sensitization

**Keywords:** Lanthanides / Optical limiting / Photoluminescence / Porphyrins / Transition metals

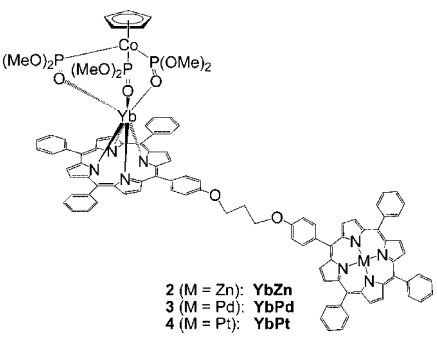


A series of heterodimetallic bisporphyrins of ytterbium and transition metals (**YbZn**, **YbPd**, and **YbPt**) have been synthesized and fully characterized. Their near-infrared photophysical studies show that the transition-metal porphyrinate unit enhances the $Yb^{III}$ emission and the $Yb^{III}$ lifetimes of **YbPd** and **YbPt** are extended because of sensitization of the $^3$Pd(TPP)* and $^3$Pt(TPP)* cores, respectively. The two-photon absorption and optical limiting properties of these mixed-metal complexes have also been investigated.

## Ramsdellites for Lithium Batteries

**A. Kuhn, P. Díaz-Carrasco, M. E. Arroyo y de Dompablo,* F. García-Alvarado* ..... 3375–3384**

On the Synthesis of Ramsdellite $LiTiMO_4$ (M = Ti, V, Cr, Mn, Fe): An Experimental and Computational Study of the Spinel–Ramsdellite Transformation

**Keywords:** Titanates / Phase transitions / Ab initio calculations / Solid-state reactions / Electrochemistry

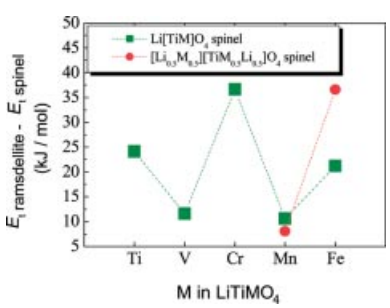


The $LiTiMO_4$ (spinel) ↔ $LiTiMO_4$ (ramsdellite) transformation is investigated by a combination of computational and experimental techniques for M = Ti, V, Cr, Mn, and Fe in order to understand the characteristics of this transformation.

## [NiFe] Hydrogenase Model Complex

**F. Lauderbach, R. Prakash,* A. W. Götz,* M. Munoz, F. W. Heinemann, U. Nickel, B. A. Hess, D. Sellmann ..... 3385–3393**

Alternative Synthesis, Density Functional Calculations and Proton Reactivity Study of a Trinuclear [NiFe] Hydrogenase Model Compound

**Keywords:** Constant potential coulometry / Density functional calculations / Iron / Nickel / NiFe hydrogenases / S ligands

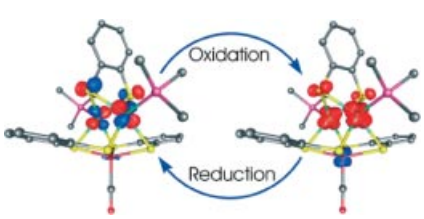


Reversible oxidation of a trinuclear [NiFe] hydrogenase model compound (see picture) can be employed electrochemically for the reduction of protons to dihydrogen at a mild reduction potential. Density functional theory calculations give an insight into the redox process. The trinuclear compound can be synthesized from simple metal salts without use of any precursor complexes.


 © 2007 Wiley-VCH Verlag GmbH & Co. KGaA, Weinheim 

## Ligand Effects

The effect of the co-ligand (X) on the $^2H$ NMR chemical shift difference ($\Delta\delta$) for *trans*-$[CrX_2([D_4]3,2,3\text{-tet})]^{n+}$ and *cis*-α-$[CrX_2([D_4]trien)]^{n+}$ is found to correlate well with the reported $e_\sigma(X)$ values of these co-ligands, thereby demonstrating the first example of the co-ligand effect or a mutual influence of ligands associated with variation of the Cr−N and Cr−X bonds in *cis*- and *trans*-$[CrX_2N_4]$-type complexes.

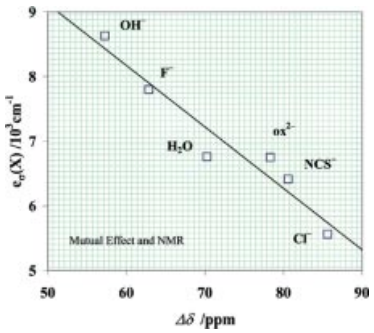


**Y. Yamaguchi-Terasaki, T. Fujihara, S. Kaizaki* ..... 3394−3399**

Mutual Influences of Ligands as Revealed by $^2H$ NMR Shifts and the Angular Overlap Model Parameters: *trans*- and *cis*-$[CrX_2(N)_4]$-Type Complexes with Aliphatic Amine Ligands

**Keywords:** Chromium complexes / Ligand effects / N ligands / NMR spectroscopy / Angular overlap model parameters

## Ligand Effects

The dependence of the $^2H$ NMR shifts of *cis*-$[CrX_2([D_4]bpy)_2]^{n+}$ and *fac*-$[CrX_3([D_{12}]tpa)]^{n+}$ on the co-ligands X allows the ordering of the AOM parameter for monodentate and/or didentate ligands, from which the ranking of the two-dimensional spectrochemical series for $Cl^-$ and $Br^-$ is found to differ from that in the aliphatic amine complexes. This change is explained in terms of the hard/soft acid/base (HSAB) concept.

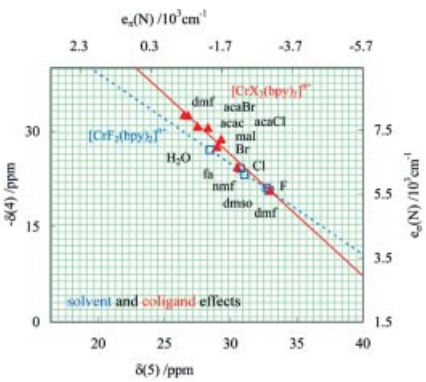


**Y. Terasaki, T. Fujihara, S. Kaizaki* ..... 3400−3404**

Mutual Influences of Ligands as Revealed by the $^2H$ NMR Chemical Shifts and the Angular Overlap Model Parameters: *cis*-$[CrX_2(N)_4]$ and *fac*-$[CrX_3(N)_3]$-Type Complexes with Aromatic Amines

**Keywords:** Chromium complexes / Ligand effects / N ligands / NMR spectroscopy / Angular overlap model parameters

## Molecular Magnetism

A new lanthanide citrate $[Dy(citrate)(H_2O)]_n$ (**1**) was hydrothermally synthesized and structurally characterized. The structure of **1** exhibits a 2D layer structure. The photoluminescence spectrum shows blue luminescence in the solid state at room temperature. Owing to the special frustration structure, unusual magnetic relaxation was found in compound **1**.

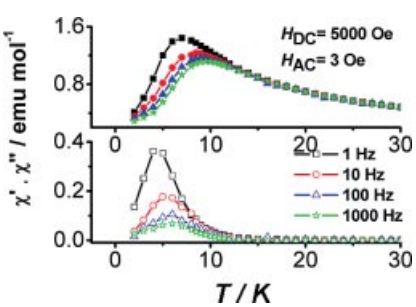


**F.-Y. Li, L. Xu,* G.-G. Gao, L.-H. Fan, B. Bi ..... 3405−3409**

Unusual Magnetic Behavior of a 2D Citrate-Bridged Dysprosium(III) Coordination Polymer

**Keywords:** Lanthanides / Coordination chemistry / Magnetic properties / Hydrothermal synthesis

## Lanthanide−Organic Frameworks

Three novel LnOFs $[Ln(pza)(OH)(H_2O)]_n$ (Ln = Y, Er and Yb) with helical chains and 2D $(4^3)_2(4^6,6^6,8^3)$ topology were obtained by hydrothermal synthesis. The upconversion properties resulting from two-photon excitation of Y: Er, Yb codoped coordination polymer and the magnetic properties of the Er and Yb complexes are investigated.

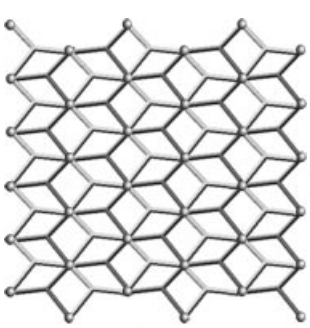

**D. Weng, X. Zheng,* X. Chen, L. Li, L. Jin* ..... 3410−3415**

Synthesis, Upconversion Luminescence and Magnetic Properties of New Lanthanide−Organic Frameworks with $(4^3)_2(4^6,6^6,8^3)$ Topology

**Keywords:** Lanthanide−organic frameworks / Codoped coordination polymers / Upconversion properties / Magnetic properties

 © 2007 Wiley-VCH Verlag GmbH & Co. KGaA, Weinheim 

# CONTENTS

## Organotin Complexes

**H. Braunschweig,* H. Bera, B. Geibel, R. Dörfler, D. Götz, F. Seeler, T. Kupfer, K. Radacki ..... 3416–3424**

Synthesis of Half-Sandwich Tungsten Chlorogermyl and Chlorostannyl Complexes

**Keywords:** Half-sandwich complexes / Tungsten complexes / Germanes / Stannanes / Stannylcyclopentadienes

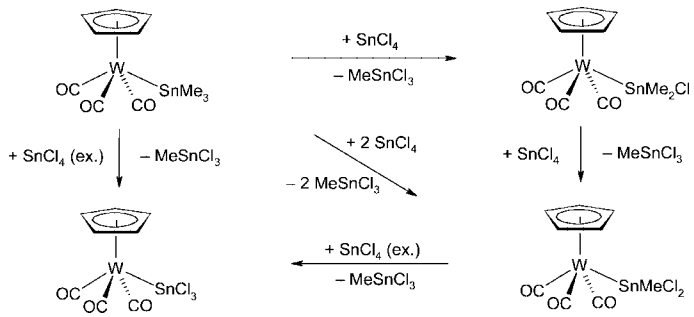


A chlorination system is established, which enables a controlled and successive chlorination of a trimethylstannyl tungsten complex to the trichlorostannyl derivative via the isolable mono- and double-chlorinated compounds by use of $SnCl_4$. In addition, we proved that alkali salt elimination has to be regarded as a straightforward route to synthesize a range of diorgano chlorogermyl and chlorostannyl tungsten complexes of the general formula $[(\eta^5\text{-}C_5R'_5)L(OC)_2W(ER_2Cl)]$ (R′ = H, Me; L = CO, $PPh_3$; E = Ge, Sn; R = Me, Bu).

## Nitrosyl Complexes

**S. Maji, C. Chatterjee, S. M. Mobin, G. K. Lahiri* ..... 3425–3434**

Synthesis and Spectro-electrochemical Aspects of $[Ru^{II}(trpy)(pdt)(X)]^{n+}$ (trpy = 2,2′:6′,2″-Terpyridine, pdt = 5,6-Diphenyl-3-pyridyl-*as*-triazine, X = $Cl^-$, $CH_3CN$, $NO_2^-$, $NO^+$, $NO^{\cdot}$) – Electrophilicity of $\{Ru^{II}\text{–}NO^+\}$ and Photolability of $\{Ru^{II}\text{–}NO^{\cdot}\}$

**Keywords:** Ruthenium / Nitrosyl complex / Spectroscopy / Electrochemistry / Reactivity

Moderately electrophilic nitrosyl ($\nu NO^+$ = 1944 $cm^{-1}$) in $\mathbf{4}^{3+}$ transforms to the corresponding nitro species in $CH_3CN$ under alkaline conditions with a pseudo-first-order rate constant ($k$/s) of $4.13 \times 10^{-4}$ at 298 K and on exposure of light $\mathbf{4}^{2+}$ undergoes slow photocleavage of the $Ru^{II}\text{–}NO\cdot$ bond in $CH_3CN$ with a $k_{NO}$ of $4.4 \times 10^{-3}$ $min^{-1}$ ($t_{1/2} \approx 157$ min).

**If not otherwise indicated in the article, papers in issue 20 were published online on July 4, 2007**

 © 2007 Wiley-VCH Verlag GmbH & Co. KGaA, Weinheim

**The EUChemSoc Societies have taken the significant step into the future by merging their traditional journals, to form two leading chemistry journals, the *European Journal of Inorganic Chemistry* and the *European Journal of Organic Chemistry.* Three further EUChemSoc Societies (Austria, Czech Republic and Sweden) are Associates of the two journals.**

## COVER PICTURE

**The cover picture shows** how aminoguanidine may behave as either a monodentate or bidentate ligand in square-planar complexes of platinum or palladium. In each case, the coordinating ligands can participate in extensive hydrogen-bonding networks. Details are discussed in the article by D. J. Aitken, J. Kozelka et al. on p. 3327ff.

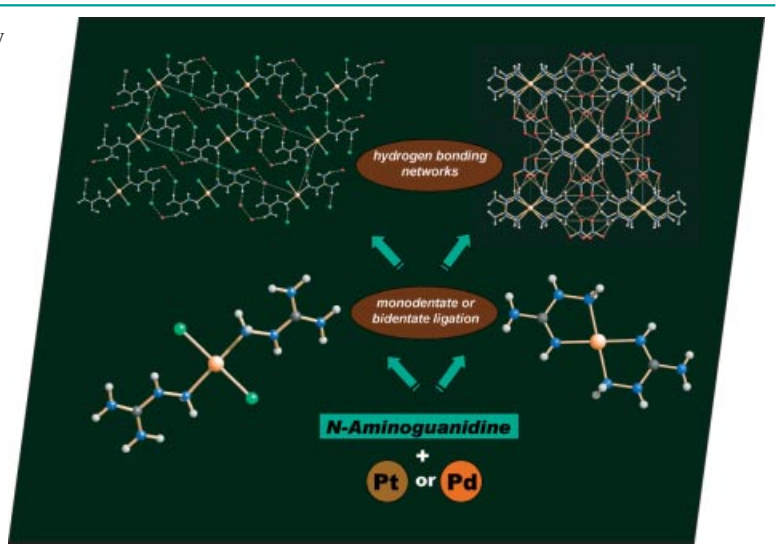


 © 2007 Wiley-VCH Verlag GmbH & Co. KGaA, Weinheim 

# SPOTLIGHTS …

## *Hollow Spheres*

H. Xu, W. Wei, C. Zhang, S. Ding, X. Qu, J. Liu, Y. Lu, Z. Yang*

**Low-Temperature Facile Template Synthesis of Crystalline Inorganic Composite Hollow Spheres**

*Chem. Asian J.*
DOI: **10.1002/asia.200700017**

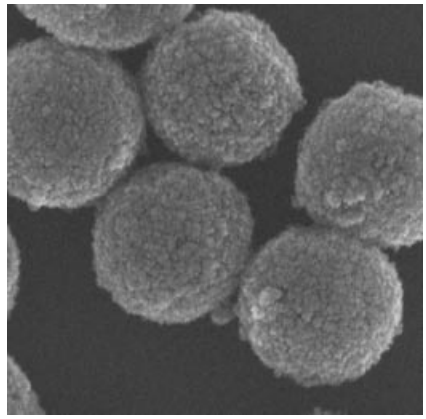

**Nothing in it!** Composite hollow spheres of $TiO_2$ (shown), $BaTiO_3$, and $SrTiO_3$ with varied crystalline phases and compositions can be synthesized under mild conditions. The sulfonated polystyrene gel templates used ensure that the crystalline hollow spheres grow without damage to their shells.

## *FRET Sensors*

J. L. Vinkenborg, T. H. Evers, S. W. A. Reulen, E. W. Meijer, M. Merkx*

**Enhanced Sensitivity of FRET-Based Protease Sensors by Redesign of the GFP Dimerization Interface**

*ChemBioChem*
DOI: **10.1002/cbic.200700109**

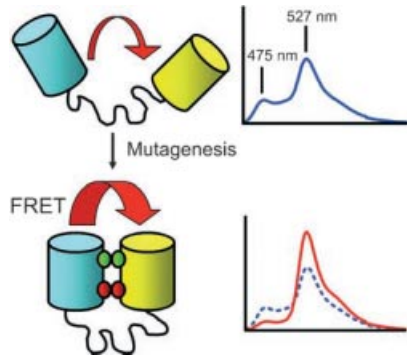


**Close encounters**. Sensor proteins based on fluorescence resonance energy transfer (FRET) often display a modest change in emission ratio upon activation. Here, we show that promoting intramolecular interactions between donor and acceptor fluorescent domains is an attractive new strategy for increasing the ratiometric change in FRET-based protease sensors.

## *Franck–Condon Analysis*

R. Brause, M. Santa, M. Schmitt,* K. Kleinermanns*

**Determination of the Geometry Change of the Phenol Dimer upon Electronic Excitation**

*ChemPhysChem*
DOI: **10.1002/cphc.200700127**

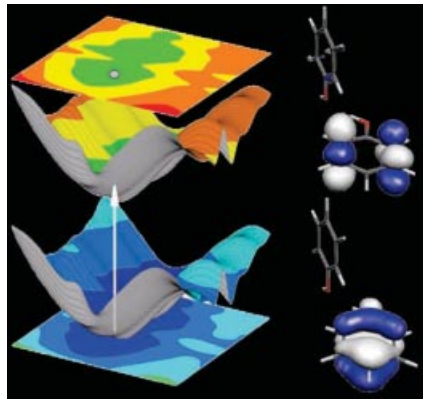

**Analysing phenol:** The structural changes of phenol upon electronic excitation are quantified experimentally and theoretically. A Franck–Condon analysis of the fluorescence emission spectra confirms the local nature of the excitation.

## *Cheminformatics*

A. Bender,* J. Scheiber, M. Glick, J. W. Davies, K. Azzaoui, J. Hamon, L. Urban, S. Whitebread, J. L. Jenkins

**Analysis of Pharmacology Data and the Prediction of Adverse Drug Reactions and Off-Target Effects from Chemical Structure**

*ChemMedChem*
DOI: **10.1002/cmdc.200700026**

**Preclinical Safety Pharmacology** attempts to anticipate adverse drug reactions (ADRs) during early phases of drug discovery by testing compounds in simple, in vitro binding assays. In this paper we describe the successful application of cheminformatics methods to predict adverse side effects of drugs to accelerate drug discovery and decrease late stage attrition in drug discovery projects.

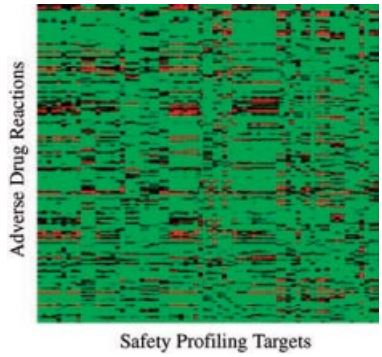


 © 2007 Wiley-VCH Verlag GmbH & Co. KGaA, Weinheim 

# … ON OUR SISTER JOURNALS

EurJIC European Journal of Inorganic Chemistry

## *Iron Complexes*

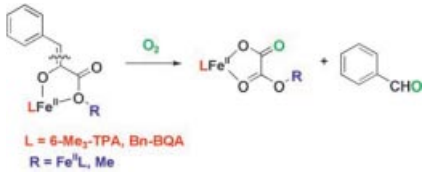


**Unusual cleavage**: A series of mononuclear or dinuclear $Fe^{II}$–phenylpyruvate enolate complexes that contain tetradentate tris(6-methyl-2-pyridylmethyl)amine (6-$Me_3$-TPA) or tridentate benzyl bis(2-quinolinylmethyl)amine (Bn-BQA) ligands are reported. The phenylpyruvate complexes react with dioxygen to undergo oxidative C2–C3 bond cleavage of phenylpyruvate (see scheme).

T. K. Paine, J. England, L. Que, Jr.*

**Iron-Catalyzed C2–C3 Bond Cleavage of Phenylpyruvate with $O_2$: Insight into Aliphatic C–C Bond Cleaving Dioxygenases**

*Chem. Eur. J.*
DOI: **10.1002/chem.200601844**

## *Affinity Separation*

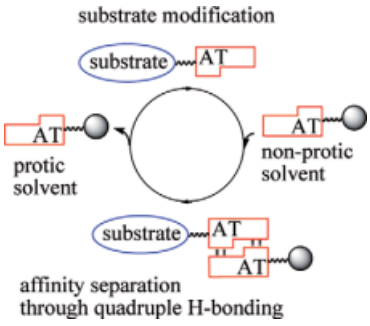


A new workup and purification method based on quadruple hydrogen-bonding interactions is reported. Substrates with a hydrogen-bonding affinity tag were conveniently separated from a reaction mixture and purified using a resin with self-complementary affinity tags. Ugi reaction products and substitution products were successfully purified by this affinity separation protocol.

B. W. T. Gruijters, J. M. M. Verkade, F. L. van Delft, R. P. Sijbesma, P. H. H. Hermkens, F. P. J. T. Rutjes*

**A Novel Purification Method in Organic Synthesis Using Hydrogen Bonding**

*Eur. J. Org. Chem.*
DOI: **10.1002/ejoc.200700242**

## *Imaging Agents*

**Contrasting images**: A new $T_1$ contrast agent for magnetic resonance imaging (MRI) based on MnO nanoparticles reveals a bright signal enhancement and fine anatomic structures in the $T_1$-weighted MR image of a mouse brain (see picture; left MRI, right MnO-enhanced MRI (MONEMRI)). Furthermore, MnO nanoparticles conjugated with a tumor-specific antibody were used for selectively imaging breast cancer cells in a metastatic brain tumor.

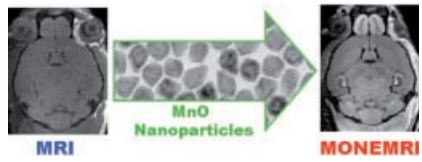


H. B. Na, J. H. Lee,* K. An, Y. I. Park, M. Park, I. S. Lee, D.-H. Nam, S. T. Kim, S.-H. Kim, S.-W. Kim, K.-H. Lim, K.-S. Kim, S.-O. Kim, T. Hyeon*

**Development of a $T_1$ Contrast Agent for Magnetic Resonance Imaging Using MnO Nanoparticles**

*Angew. Chem. Int. Ed.*
DOI: **10.1002/anie.200604775**

On these pages, we feature a selection of the excellent work that has recently been published in our sister journals. If you are reading these pages on a computer, click on any of the items to read the full article. Otherwise please see the DOIs for easy online access through Wiley InterScience.

 © 2007 Wiley-VCH Verlag GmbH & Co. KGaA, Weinheim 

DOI: 10.1002/ejic.200700413

# Calixarene-Based Oxovanadium Complexes as Molecular Models for Catalytically Active Surface Species and Homogeneous Catalysts

**Christian Limberg*[a]**

**Keywords:** Vanadium / Oxo complexes / Models / Calixarenes / Catalysis

There are several reasons that make the combination of calixarenes with oxovanadium moieties attractive. Calixarenes are capable of simulating the surfaces of oxide bulk materials and supports, and on the other hand, supported vanadium oxides are an important class of heterogeneous catalysts, whose reactivity is still discussed controversially with respect to the effective mechanisms. Oxovanadium calixarene complexes can thus represent molecular models whose investigation in the homogeneous phase can shed some light into surface processes. This review describes the recent achievements in the synthesis of oxovanadium calixarene, thiacalixarene, and oxacalixarene complexes and the investigation of their reactivity. It has been shown that they represent active catalysts for the oxidation of alcohols and the polymerization/copolymerization of olefins.

(© Wiley-VCH Verlag GmbH & Co. KGaA, 69451 Weinheim, Germany, 2007)

## 1. Introduction

Heterogeneous catalysts play an important role in the chemical and pharmaceutical industry where 90% of all compounds produced require at least one *catalytic* step during their synthesis.[1] While in comparison to homogeneous catalysts the employment of heterogeneous catalysts has certain advantages with respect to product separation, stability (for instance at higher temperatures), and technical issues,[1] the unequivocal identification of their surface constitution and active sites poses problems. These properties are best studied by a combination of physical and chemical methods such as IR, Raman, Mössbauer, and solid-state NMR spectroscopy as well as EXAFS, XANES, and XPS.[2] However, these techniques involve bulk measurements, and their sensitivity is often inadequate for obtaining accurate data from the various sites that are present on the surface in low concentration.[3] Furthermore, even if the active sites are known, the clarification of mechanistic questions is far more difficult for heterogeneous catalysts than for homogeneous catalysts, as in situ studies on surfaces under catalytic conditions require methods far from routine. Naturally, the results of such investigations as well as hypotheses derived from kinetic investigations and isotopic enrichment studies provide a stimulus for the synthesis of molecular models: these can be investigated in the homogeneous phase and may serve to support or defeat mechanistic proposals, thus offering hope that heterogeneous catalysts can be designed rationally. In addition, such models can in turn prove themselves as novel homogeneous catalysts, independently of the heterogeneous process that led to their synthesis.

One important class of heterogeneous catalysts consists of metal oxides on inert supports which are employed, for instance, to mediate oxidations with $O_2$ as well as other processes like polymerizations.[4] The construction of molecular models for oxometal (the terms "oxo" and "chloro" are used as ligand names throughout this Microreview as in the original articles) surface sites requires ligands that are capable of mimicking the oxide environments surrounding oxometal moieties on oxide supports or in bulk materials,

[a] Humboldt-Universität zu Berlin, Institut für Chemie, Brook-Taylor-Str. 2, 12489 Berlin
E-mail: christian.limberg@chemie.hu-berlin.de

*Christian Limberg was born in 1965 in Essen and studied chemistry from 1985 to 1990 in Bochum. He earned his doctorate with Professor A. Haas in 1992 and concluded his postdoctoral work together with Professor A. J. Downs at Oxford University with a further Ph. D. thesis and Inauguration (D. Phil.). In 1995 he then joined the research group of Professor G. Huttner in Heidelberg to start his Habilitation work, which was finished in 1999. Having received a Heisenberg scholarship, he stayed in Heidelberg until 2001, when he moved to the TU Munich to lead the Inorganic Chemistry chair on behalf of Professor Herrmann. In 2002 he accepted an offer to become full professor at the Humboldt-University of Berlin, where he is currently Dean of the Faculty I for Mathematics and Natural Sciences. The author of this contribution is mainly concerned with oxometal complexes and their reactivity under synthetic and mechanistic viewpoints. He received the ADUC prize for Habilitanden and was further awarded a Karl-Winnacker-Stipendium, the academy prize of the Academy of Science in Göttingen, as well as the Carl-Duisberg-Gedächtnispreis of the GDCh.*

 © 2007 Wiley-VCH Verlag GmbH & Co. KGaA, Weinheim 

and in this context in particular, two ligand systems have established themselves: silsesquioxanes[3,5a–5d] and calixarenes.[5e,5f] This review focuses on the most recent research concerning oxovanadium calixarene complexes that were synthesized in order to model supported vanadium catalysts, finding applications for instance in the oxidative dehydrogenation (ODH)[6] of light alkanes and methanol. Various surface species have been found to be active during the heterogeneous processes in one way or the other, and hence these structural motifs represent an inspiration for attempts to mimic them in molecular compounds.

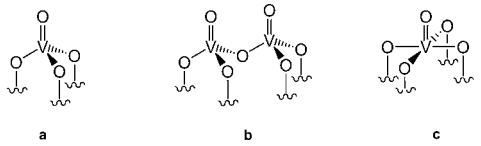


On the other hand, silica-supported vanadium materials have proved to be efficient as heterogeneous catalysts for olefin polymerization,[7a–7d] and oxovanadium complexes with multipodal ligands were shown to catalyze such polymerizations homogeneously.[7e] It follows that oxovanadium calixarene complexes were also investigated in this respect.

The results of studies on both aspects are discussed below.

## 2. Synthesis of Oxovanadium Calixarene Complexes and Their Properties

### 2.1. Complexes with "Classical" Calixarene Ligands

In addition to silsesquioxane ligands, calixarene ligands such as $H_4$**C**, $H_6$**C**′, and $H_8$**C**′′ have recommended themselves for the simulation of oxide surfaces in recent years.[5e,5f] While $H_4$**C** yields a tetrapodal ligand after deprotonation, $H_3$**C**$^{\mathbf{R}}$ (a derivative of $H_4$**C** where one of the phenolic protons is replaced by an alkyl group R) leads to a tripodal ligand. Employing $H_4$**C** and $H_3$**C**$^{\mathbf{R}}$ thus enables modelling the embedding of a transition metal ion in the midst of three and four oxygen atoms of an oxide surface (for instance a support), respectively. On the other hand, ligands like [**C**′]$^{6-}$ or a calix[8]arene with eight phenolate units ([**C**′′]$^{8-}$) provide more extended platforms of oxygen atoms, where polynuclear moieties can arrange themselves, too.

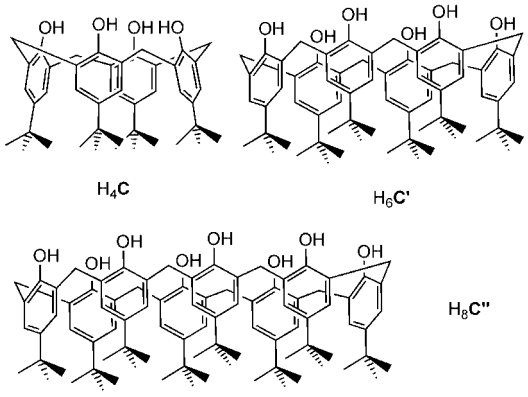


Until recently, oxovanadium complexes of calix[4]arenes (**C**$^{4-}$) were not known, and the literature on the coordination of oxovanadium units by other calixarene-based ligands was scarce, too: one complex with a ligand derived from $H_4$**C** by monomethylation of a phenolic function, **C**$^{\mathbf{Me}}$**V**$^{\mathbf{V}}$=O (**1**), (see Scheme 1) had been reported[8] as well as a few others containing calix[3]-, calix[6]-, and calix[8]arene ligands, which, however, were either not characterized structurally or contained vanadium centers that were not exclusively ligated by O donor atoms.[9,8]

Whereas these examples all involve $V^V$, naturally, there is also interest in reduced complexes that could model reduced species formed after oxidation reactions on surfaces, and in this context $V^{IV}$ and $V^{III}$ are important. The chemistry of a vanadium(III) center complexed by calix[4]arene has been investigated by C. Floriani et al.[8] Metalation of $H_3$**C**$^{\mathbf{Me}}$ with [$VMes_3$·thf] led to the collapse of the coordinatively unsaturated $V^{III}$-$d^2$ fragment **C**$^{\mathbf{Me}}$**V**$^{\mathbf{III}}$ to the dimer [{μ-**C**$^{\mathbf{Me}}$}V]$_2$ (**2**). In addition to reactions with *t*BuNC, PhCN, pyridine, and 4,4′-bipyridine, the one-electron oxidation with $I_2$, which led to the $V^{IV}$ complex [{μ-**C**}V]$_2$ (**3**), was investigated. A two-electron oxidation of the $V^{III}$-$d^2$ system to the oxovanadium(V) derivative **C**$^{\mathbf{Me}}$**V**$^{\mathbf{V}}$=O (**1**), has been achieved by using styrene oxide. Very recently, Redshaw et al.[10] published synthetic methods that lead to a complex **3**$^{\mathbf{AN}}$, which is closely related to **3**: **3**$^{\mathbf{AN}}$ differs from **3** (Scheme 1) in that it additionally contains two metal-bound acetonitrile molecules within the two calyx cavities, which results in pseudo-octahedral coordination spheres for the vanadium atoms, and it can be obtained by starting from $H_4$**C** upon treatment with [V(N*p*-tolyl)-

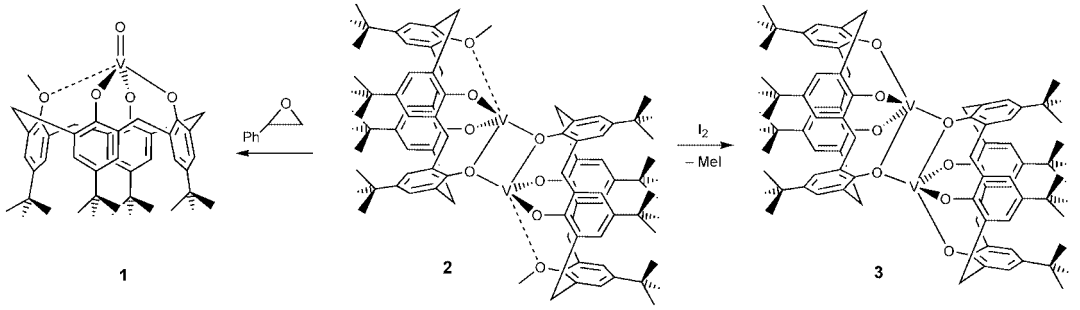


Scheme 1.

 © 2007 Wiley-VCH Verlag GmbH & Co. KGaA, Weinheim 

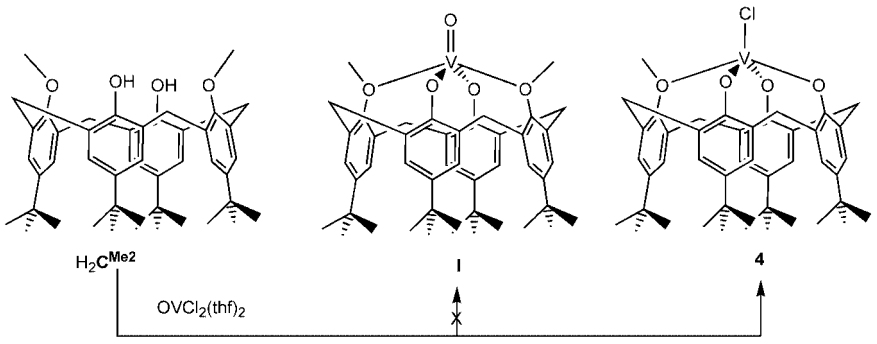


Scheme 2.

($O$*n*Pr)$_3$] or [$VCl_3$(thf)$_3$] followed by recrystallization from acetonitrile. Moreover, it was found that **1** is also accessible by the use of $H_3\mathbf{C}^{\mathbf{Me}}$ and [VO($O$*n*Pr)$_3$].[10]

We set out to investigate the chemistry of $V^{IV}$ on an oxo surface modeled by calixarene ligands in order to study possible reoxidation reactions. Accordingly, we treated [$VOCl_2$(thf)$_2$] with dimethylated $H_4\mathbf{C}$ and $H_2\mathbf{C}^{\mathbf{Me2}}$, in order to synthesize a complex **I** as depicted in Scheme 2. A pure product was obtained in good yield, whose characterization, however, showed that the expected complex **I** had not been formed, but a compound that had been previously suggested by Floriani et al.[11] as the product of the reaction between the complex $\mathbf{C}^{\mathbf{Me2}}\mathbf{V}^{\mathbf{III}}$-Cl and iodine on the basis of an elemental analysis and decomposition studies: $\mathbf{C}^{\mathbf{Me}}\mathbf{V}^{\mathbf{IV}}$-Cl (**4**).[12] The preparation of **4** by the route shown in Scheme 2 allowed its full characterization, and its crystal structure could be determined, too (very recently it has also been identified as the product of the reaction between $H_3\mathbf{C}^{\mathbf{Me}}$ and [RN=$VCl_3$]).[13] Compound **4** was found to be sensitive to both water and $O_2$.

Hydrolysis leads to $H_3\mathbf{C}^{\mathbf{Me}}$ as well as unidentified oxovanadium halides. The reaction with oxygen astonishingly leads to **1**, which crystallizes isotypically with **4**, so that both compounds can be present side by side (cocrystallized) within the same crystal. Naturally, the question arose as to how **1** is formed from **4** and dioxygen. Most likely, the initiating step consists of an end-on addition of $O_2$ to the Lewis acidic $V^{IV}$ center to form a $V^{IV}Cl(\eta^1\text{-}O{=}O)$ unit. Subsequently, an electron can be expected to flow from the vanadium center to the oxygen ligand so that a vanadium(V)superoxide moiety is produced (Scheme 3).

The next step should represent a reaction with a second molecule of **4** to give a peroxide unit. To generate **1**, the O–O bond then has to be cleaved homolytically, but since the V centers are already in their highest oxidation states, a V=O bond can only form if an additional electron is provided, and at the same time the chloride ligands have to leave the molecule. How these subsequent steps proceed remains unclear; they result in chloride and organic decomposition products. This type of reactivity is not restricted to **4**: replacement of chloride by triphenylsiloxide followed by exposure to $O_2$ leads to the same results.[12]

We next turned our attention to the synthesis and reactivity of oxovanadium(V) complexes. Would a complex like

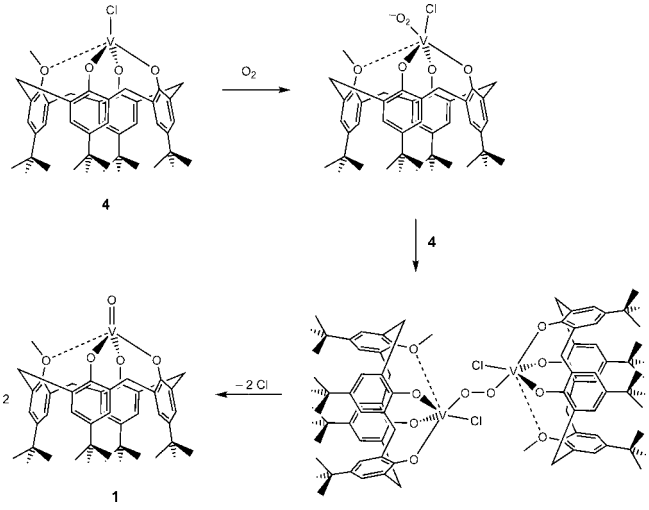


Scheme 3.

**1** behave as a functional model for oxovanadium sites on surfaces, that is, would it show any oxidation chemistry? How would an additional charge alter the situation, and would polynuclear species behave differently? In order to address these questions, systematic studies on the preparation of calixarene oxovanadium complexes with varying nuclearity and charge were performed. This was followed by an investigation of their reactivity and potential as structural or functional models for active sites on surfaces.[14,15]

In order to obtain a complex containing an $O{=}V^{3+}$ unit embedded in a tetragonal oxo coordination environment, tetrabutylammonium metavanadate was treated with $H_4\mathbf{C}$ in the presence of $NEt_3$, and indeed the envisioned complex, $NBu_4[\mathbf{C}V{=}O]$ ($^{\mathbf{NBu4}}\mathbf{5}$) (Scheme 4) formed in good yields.[14] Alternatively, the complex anion **5** can be synthesized starting from the lithium salt $Li_4\mathbf{C}$ that can be obtained by treatment of $H_4\mathbf{C}$ with lithium naphthalenide: The corresponding reaction with tetraphenylphosphonium dichlorodioxovanadate $PPh_4[VO_2Cl_2]$ leads to the elimination of LiCl (and apparently also $Li_2O$), yielding $PPh_4[\mathbf{C}V{=}O]$ ($^{\mathbf{PPh4}}\mathbf{5}$) (Scheme 4).[14]

According to a crystal structure analysis, the V=O group in **5** is surrounded symmetrically by an $O_4$ donor set as expected, and **5** therefore represents the first model for such a situation on an oxide support.

 © 2007 Wiley-VCH Verlag GmbH & Co. KGaA, Weinheim 

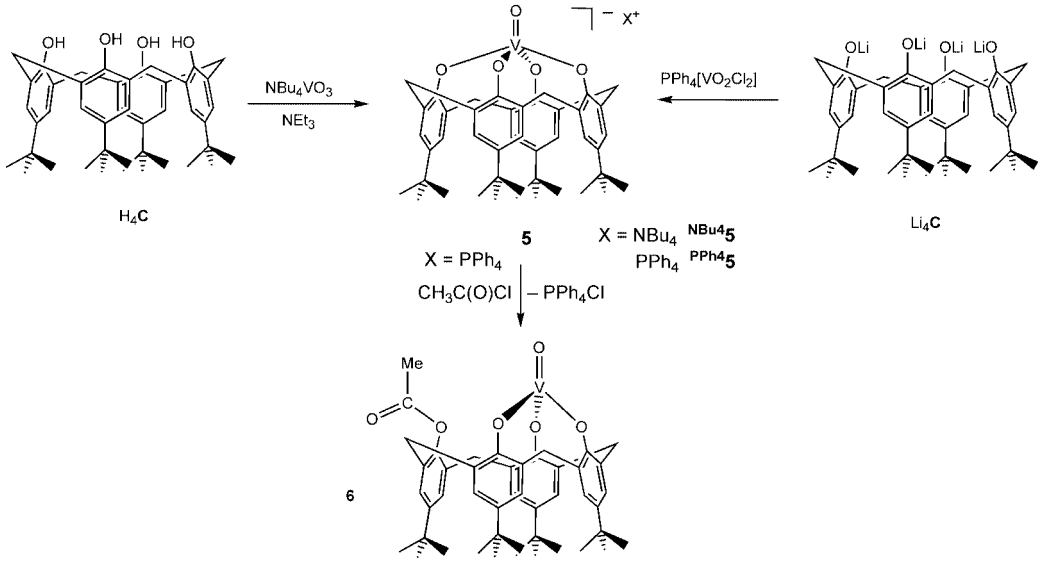


Scheme 4.

For comparative reactivity studies it seemed desirable to also investigate a neutral calixarene oxovanadium(V) complex. As mentioned, there is one complex known, **1**, which, however, is difficult to isolate in larger quantities and in a pure state free from $V^{IV}$ impurities by the reactions shown in Scheme 1 and Scheme 3. Hence, we contemplated the synthesis of a more easily accessible derivative. Indeed, starting from $^{PPh4}$**5** such a neutral complex can be obtained in a clean and facile synthesis: addition of $CH_3C(O)Cl$ leads to the precipitation of $PPh_4Cl$ and formation of $\mathbf{C}^{OAc}V^{V}$=O (**6**) (see Scheme 4).[14]

Whereas the coordination geometry around V in **1** – due to the fact that the methoxy group binds at a longer distance to V, too (compare Scheme 1) – has to be described most appropriately as distorted trigonal bipyramidal, the vanadium center in **6** is coordinated tetrahedrally; there is no interaction with the O atom of the acetyl unit, and **6** can thus be regarded as a model for a species **a**.

We next turned our attention to the synthesis of compounds containing two oxovanadium units to also allow a comparison of the reactivities of dinuclear and mononuclear complexes. Accordingly, higher calixarenes were employed as starting materials, as these offer room for more than one vanadium center. First of all, $H_8$**C**′′ was chosen to be treated with $PPh_4[VO_2Cl_2]$ in the presence of $Et_3N$ as a base. The resulting product was fully characterized, and a single-crystal X-ray analysis revealed the structure (Scheme 5) and constitution of $PPh_4[HC''V_2O_2]$ (**7**).[14]

It turned out that a salt containing the anion of **7** in combination with a different cation had been reported before by Pedersen and co-workers[16] as the product of the conversion of $VO(OiPr)_3$ with $H_8$**C**′′ in the presence of (*R*)-(+)-1-(1-naphthyl)ethylamine. A single-crystal X-ray diffraction study had not been performed, but the constitution was suggested correctly on the basis of a structure determination for a similar titanium complex. The formation of **7** must have proceeded by reaction of OH functions with V–

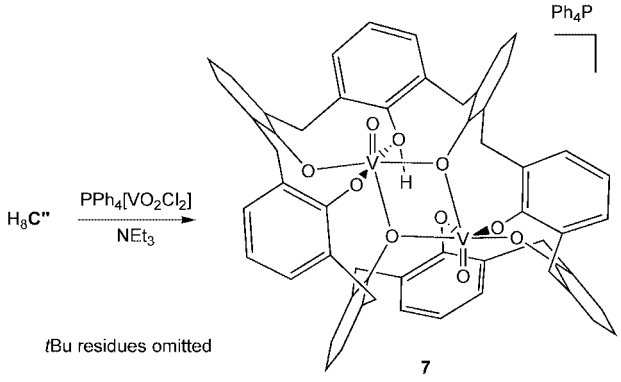


Scheme 5.

Cl and V=O groups under elimination of HCl and water, so that two – at first independent – $O=V^{3+}$ units are initially coordinated by four aryloxo ligands each, as in **5**. However, two facts prohibit a description of **7** as a dinuclear version of **5**: First of all, one of the phenol functions in $H_8$**C**′′ is *not* deprotonated (i.e. a coordinated alcohol function results), so that **7** contains only a monoanion, and secondly, the arene band folds in a way that allows two of the phenoxy functions to adopt a bridging binding mode, such that the two vanadium atoms are located in pseudo-octahedral environments.

Having accessed a dinuclear, singly charged oxovanadium complex, we also pursued the synthesis of a corresponding neutral complex, ideally containing V–O–V units. Heating a mixture of $H_2\mathbf{C}^{Me2}$ with $[VO(OCH_3)_3]$ in acetonitrile solution at reflux led to such a compound, [$\mathbf{C}^{Me2}$-[O=V(OMe)]$_2$μ-O] (**8a**), which also represents the first dinuclear calix[4]arene complex in general (see Scheme 6).[14]

The two phenoxy functions in $\mathbf{C}^{Me2}$ bind two V=O units that are connected by a bridging oxo ligand. The residual coordination sphere is completed for each V center by

 © 2007 Wiley-VCH Verlag GmbH & Co. KGaA, Weinheim 

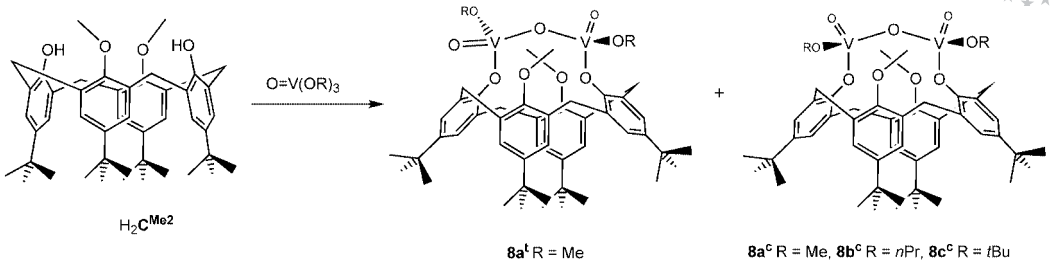


Scheme 6.

methoxy ligands, which can either be located *cis* or *trans* to each other (a mixture of isomers is obtained), i.e. the geometries around the V atoms can be assigned as tetrahedral. At the same time and independently, Redshaw and co-workers reported the analogous syntheses of the corresponding *n*-propyl and *tert*-butyl derivatives **8b**$^{c}$ and **8c**$^{c}$.[10] The origin of the μ-O bridge is still unclear. Whereas in alkoxide chemistry there is sufficient precedence for the formation of oxo ligands by ether elimination, Redshaw and co-workers contemplated a fortuitous hydrolysis reaction of the vanadyl esters prior to the reaction with $H_2C^{Me2}$. Envisioning that a more rational route might involve the initial formation of a chloro alkoxide complex of the form $[VOCl(OtBu)_2]$ to which an oxo bridge could be introduced by reaction with $(Me_3Si)_2O$ before the addition to $H_2C^{Me2}$, a corresponding investigation was carried out: After reaction of $[VOCl_3]$ with a twofold excess of LiO*t*Bu, first $(Me_3Si)_2O$ and then $H_2C^{Me2}$ were added to the resulting mixture in order to obtain **8c**$^{c}$. However, $[\{C^{Me2}V(OtBu)(O)\}_2Li_4O_4]$ (**9**) was isolated instead, where a $Li_4O_4$ cubane-type core is trapped between two oxovanadium calix[4]arene units (Scheme 7).[10]

With the aim of preparing a different type of dinuclear oxovanadium calix[4]arene complex, a special type of ligand was employed where two calix[4]arene units are linked by two lutidene moieties. Reaction with $[VOCl_3]$ in refluxing toluene led to the loss of one of these linkers and to the formation of the bimetallic complex **10** (Scheme 8). As in the mononuclear "version" **1**, each vanadium atom here adopts a trigonal bipyramidal geometry, for which both vanadyl groups are oriented in the same direction with respect to the lutidene bridge.[10]

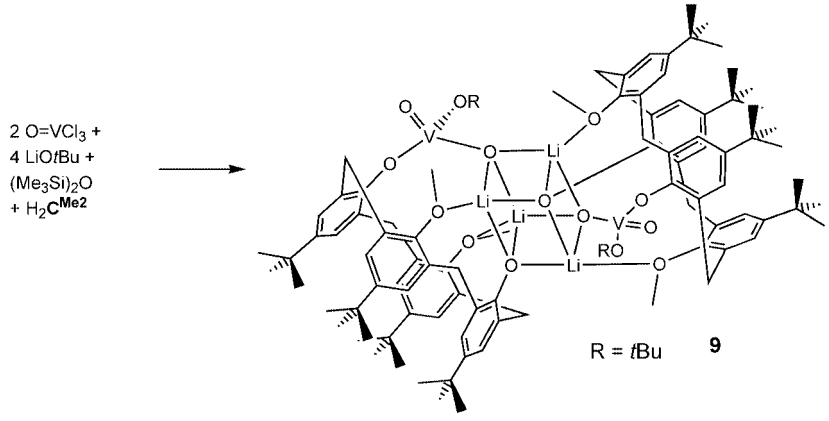


Scheme 7.

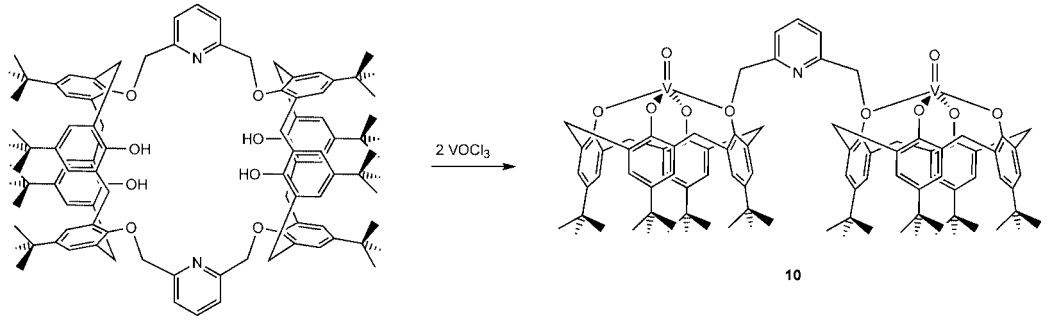


Scheme 8.

 © 2007 Wiley-VCH Verlag GmbH & Co. KGaA, Weinheim 

### 2.2. Complexes with Thiacalixarene Ligands

Compared with that of the related *p-tert*-butylcalix[4]-arene, the chemistry of thiacalixarenes is still in its infancy, as the synthesis of thiacalixarenes and their sulfinyl and sulfonyl derivatives has been known only since the late 1990's.[17] Recent publications provide evidence that the thioether units can take part in metal ion coordination, which leads to a stronger interaction with transition metals relative to calixarenes.[18] As such interactions can be anticipated to lead to significant chemical differences, it seemed interesting to also prepare oxovanadium thiacalix[4]arene complexes in order to compare their reactivities with those of the corresponding complexes based on the "classical" calixarenes. First, a reaction of *p-tert*-butyltetrathiacalix[4]-arene ($H_4$**TC**) with $Ph_4P[VO_2Cl_2]$ was carried out in the absence of an external base; this led to $PPh_4[(H_2$**TC**$)VOCl_2]$ (**11**), as demonstrated by single-crystal X-ray crystallography, elemental analysis, and IR and NMR spectroscopy (Scheme 9).[15]

In **11** a vanadyl unit is positioned somewhat above the plane defined by the O atoms belonging to the two calixarene phenolate functions and the two terminal chloride ligands. The coordination sphere of V is completed by one of the thioether functions belonging to the ligand: The distance to the closest S atom is significantly shorter than the sum of the van der Waals radii of vanadium and sulfur, indicating a coordinative interaction.

The formation of **11** must have proceeded by addition of two OH functions to one of the V=O groups belonging to the starting material with elimination of water. Accordingly, in the absence of an external base, the protons of $H_4$**TC** are acidic enough to attack one of the nucleophilic oxygen atoms of $[VO_2Cl_2]^-$, as in the case of the "normal" calixarenes. However, they are not acidic enough to further induce intramolecular HCl elimination: the anion of **11** formally still contains two equivalents of HCl, whose elimination would lead to the thia analog of **5**. The fact that such a complex is not formed spontaneously may to some extent be a result of the coordinative support of the sulfur atom at the vanadium center. On the other hand, the formation of **5** – as mentioned before – required the addition of a base at least as strong as $NEt_3$. Therefore, the reaction in Scheme 9 was repeated in the presence of $NEt_3$, which led to the precipitation of a red solid. After purification and crystallization, this solid was identified as $(PPh_4)_2$-$[H_2$**TC**$V(O)(\mu\text{-}O)]_2$ (**12**) with the aid of X-ray crystal structure determination, elemental analysis, and IR and NMR spectroscopy (Scheme 10).[15]

In the molecular structure of the anion of **12**, two O=V groups are linked by two bridging oxo ligands in a way that positions the terminal O ligands in an *anti* fashion, and a noncrystallographic mirror plane runs through them. Furthermore, each vanadium center coordinates a calixarene ligand in a cone conformation through two phenolate

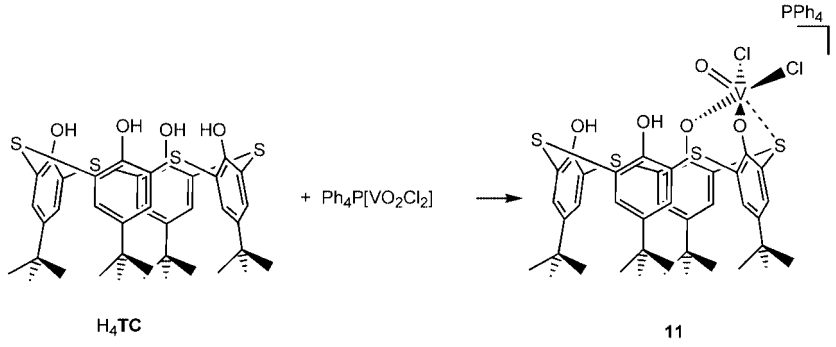


Scheme 9.

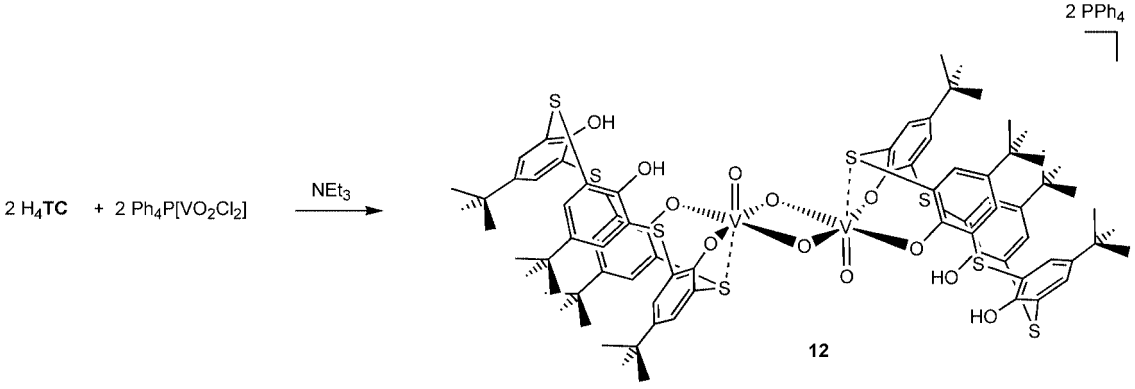


Scheme 10.

 © 2007 Wiley-VCH Verlag GmbH & Co. KGaA, Weinheim 

functions and again also through interaction with a thioether function.

### 2.3. Complexes with Oxacalixarene Ligands

In 1997, Hampton et al. treated lithiated *p*-methylhexahomotrioxacalix[3]arene, $H_3OC^{p\text{-}Me}$, with [$VOCl_3$], in order to prepare linear chain polymers, and obtained a compound of the expected stoichiometry, [$OC^{p\text{-}Me}V{=}O$] (**13**).[9b] On the basis of spectroscopic data obtained for solutions of **13**, a structure in which the vanadyl group is positioned within the calyx (Scheme 11) was proposed, even though the corresponding "oxo-out" structure could not be ruled out. A fibrous solid precipitated from such solutions after several days, and the spectroscopic data obtained for this solid indicated that an asymmetric μ-oxo-bridged linear chain polymer had formed. Unfortunately, single crystals suitable for an X-ray diffraction study could not be grown for any of the forms of **13**.

Recently, the *p-tert*-butyl derivative of **13** was prepared by treating the corresponding calix[3]arene $H_3OC^{p\text{-}Bu}$ with [$VO(OnPr)_3$] or by treating $Li_3OC^{p\text{-}Bu}$ with [$VOCl_3$].[10] A single-crystal X-ray analysis showed that the resulting complex **14a** (Scheme 11) is monomeric with a trigonal pyramidal coordination of the vanadium atom. In the solid state, there are only very weak intermolecular interactions between the vanadium center of one molecule and a phenoxy function of another molecule. This gives rise to a pair of molecules that lie face to face over an inversion center, which contrasts the identification of a polymeric structure for **13**. Interestingly, the reaction of [$VMes_3$·thf] with $H_3OC^{p\text{-}Bu}$ followed by treatment with $O_2$ provided a complex that could be identified as a discretely monomeric molecule **14b** by means of X-ray diffraction after crystallization of the compound.[10]

## 3. Catalytic Activity

### 3.1. Evaluation of the Potential of the Compounds as Functional Models for ODH

As outlined in the introduction, the most prominent conversions that can be carried out by using vanadia on oxide supports as heterogeneous catalysts are the ODH of methanol and alkanes. Naturally, molecular models such as those described here will prove to be unreactive in contact with alkanes, as the rate-determining step of ODH is the first C–H bond cleavage, which has a large activation barrier (which means that heterogeneous catalysis at elevated temperatures is required for the reaction to take place). However, methanol and higher alcohols are less inert as substrates, so that their reactions can also be investigated with molecular compounds in the liquid phase. Any information derived from such studies might contribute to a

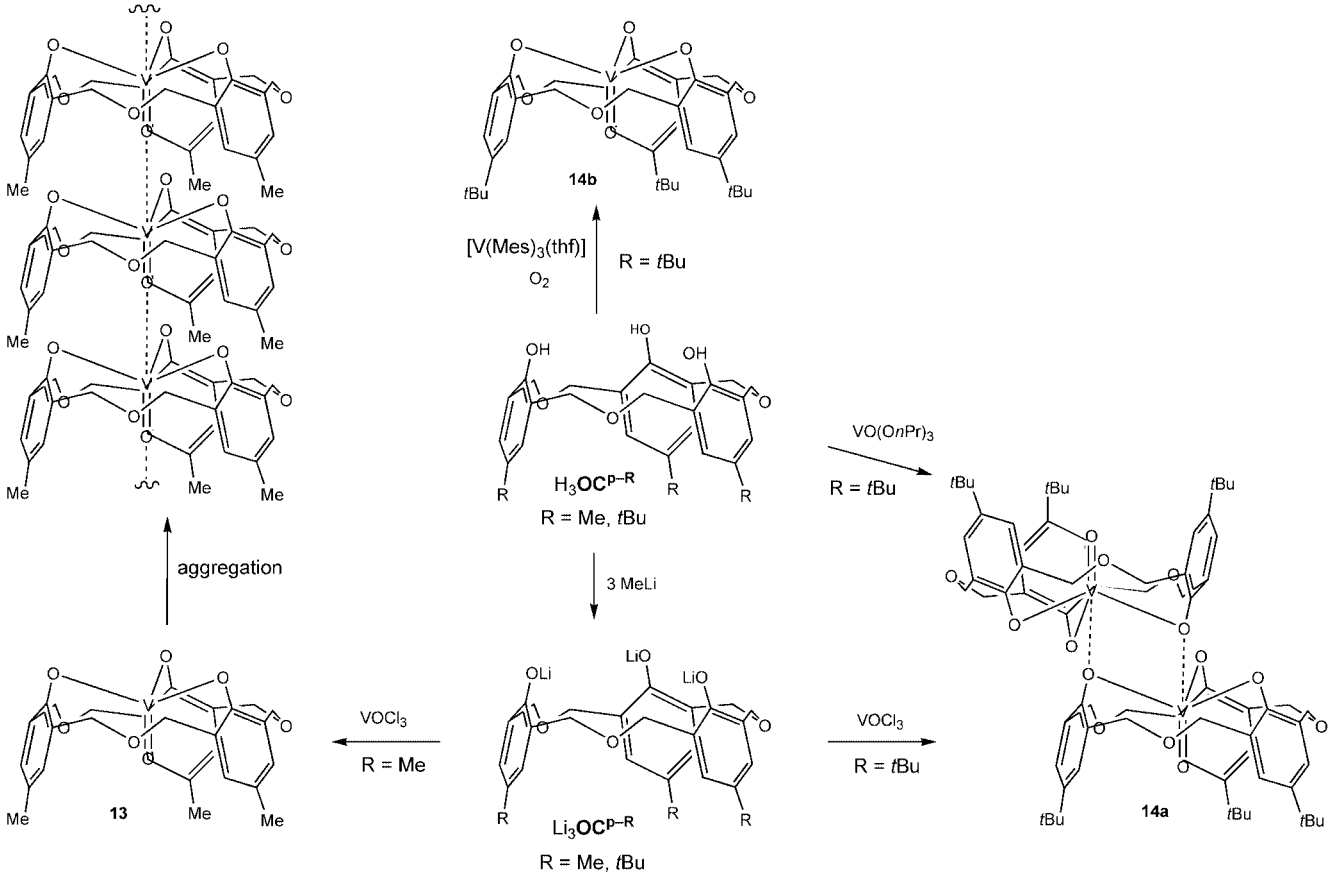


Scheme 11.

 © 2007 Wiley-VCH Verlag GmbH & Co. KGaA, Weinheim 

more comprehensive understanding of methanol oxidation at vanadia catalysts, and they might as well provide ideas for the (probably) more complex ODH of alkanes.

In order to test the compounds described above for reactivity in relation to ODH and to establish their suitability as models, we therefore decided to investigate the oxidation of a palette of various alcohols to the corresponding carbonyl compounds with $O_2$ as the reagent.[14,15] Of course there are numerous methods to oxidize alcohols with organic or inorganic reagents,[19] which, however, are often stoichiometric and/or lead to toxic waste products. Hence, at present, the performance of catalytic oxidations with $O_2$ is still an attractive topic, and a lot of research has been devoted to it in the past.[19] Certainly, the background of the study presented here – as mentioned – was an inquiry as to whether oxovanadium calixarene and thiacalixarene complexes could represent not only structural but also functional models for the heterogeneously catalyzed ODH, and we did not have the aim of finding an improved catalyst for the aerobic oxidation of alcohols. Nevertheless, the latter aspect was borne in mind as a potential, beneficial part of the investigation.

As we consider the $V^V$ compounds **5**–**8**, **11**, and **12** as functional models, they are expected to contain functional moieties already, i.e. the first step of a possible catalytic cycle should consist of a reaction with the chosen alcohol (vide infra). After a potential oxidation reaction, $O_2$ could serve to regenerate the active species. As a reference, a system was chosen that has been recently shown to efficiently catalyze the aerobic oxidation of 1-phenyl-1-propargyl alcohol,[20] $OV(acac)_2$. This system probably belongs to the category of complexes that activate $O_2$ first. Figure 1 combines the list of alcohols chosen and the complexes tested with the turnover frequencies (TOFs) measured at 80 °C in the presence of molecular sieves to remove the water generated during the ODH.

For none of the nonactivated aliphatic alcohols was any activity observed by employing the catalysts depicted. When focusing on the complexes with the classical calixarene ligands first, the following picture emerged on employment of 1-phenyl-1-propargylic alcohol and fluorenol: the mononuclear complexes **5** and **6** only led to low conversions. However, the dinuclear complexes and the reference system led to much higher TOFs between 7.7 and 43 $h^{-1}$. With a TOF of 43 $h^{-1}$, the activity of **7** for the oxidation of fluorenol was even almost twice as high as that of $OV(acac)_2$.[14]

Subsequent studies even showed that the singly charged mononuclear complex **5** is completely inert under various conditions also towards other substrates, whereas the two dinuclear complexes were also capable of oxidizing a nonfunctionalized hydrocarbon such as 9,10-dihydroanthracene, although the TOFs are much lower in than those for the alcohol oxidations. The oxidation products were identified as 10.0% (1.0%) anthracene, 13.0% (1.5%) 10*H*-anthracene-9-one, and 7% (1.5%) 9,10-dihydroanthracene-

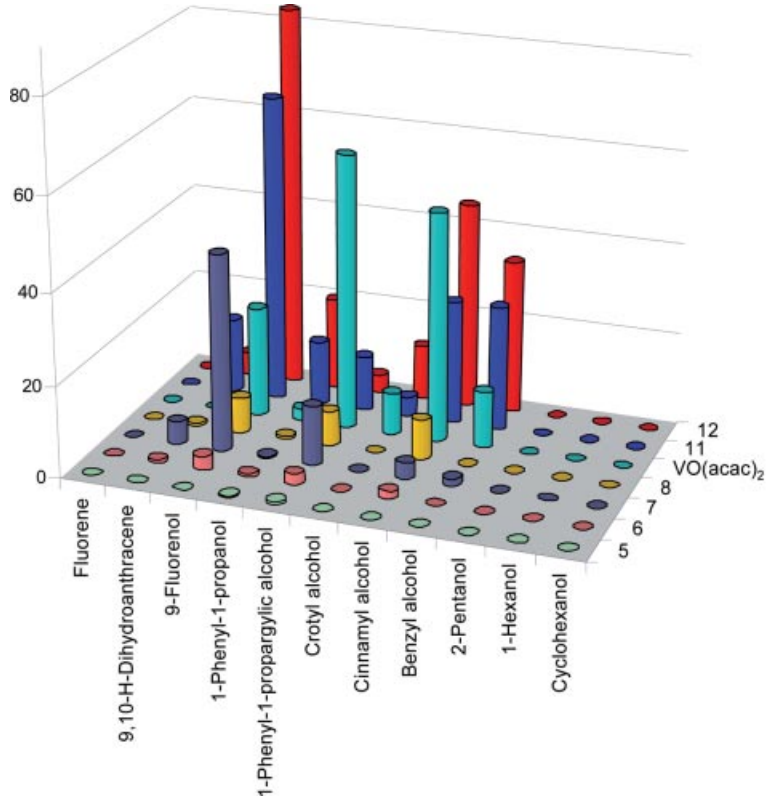


Figure 1. Substrate oxidation with $O_2$ catalyzed by complexes **5**–**8**, **11**, and **12**. The numbers refer to TOFs ($h^{-1}$), calculated per V center present.[15]

 © 2007 Wiley-VCH Verlag GmbH & Co. KGaA, Weinheim 

9,10-diol (the percentage values specify the yield of oxidation product obtained by employing **7** (**8**) [1 mol-%] within 3 h with respect to the alcohol employed).

Turning our attention now to the thiacalixarene complexes, it can be noted that **11** and **12** are significantly more active than **5**–**8**,[15] and **12** catalyzes the oxidation of benzyl alcohol (33.6 $h^{-1}$) and crotyl alcohol (12.0 $h^{-1}$) even more efficiently than the reference system. The outstanding behavior of **12** fits the observation that dinuclear complexes are more active than the corresponding mononuclear ones, as was already evident during the investigation of the classical calixarenes.[14] In fact, **12** is more active than **11** for all alcohols except for one: 1-phenyl-1-propargyl alcohol. At the same time, this is the only case where **11** and **12** are less active than **7** and **8**, so that something seems to be special about the reactivity of this alcohol in combination with the thiacalixarene complexes. In contrast, the TOF observed for the oxidation of fluorenol catalyzed by **12** (83.4 $h^{-1}$) is twice as high as that observed for **7** (43.0 $h^{-1}$), and **11** is also very active (67.0 $h^{-1}$), whereas the two mononuclear calixarene complexes **5** and **6** – as mentioned previously – show hardly any activity. With reference to 9,10-dihydroanthracene, it becomes evident that, of all complexes investigated, **11** performs best (13.0 $h^{-1}$), whereas **12** is three times more active than **8** but only half as active as **7**. With fluorene, whose C–H bonds are somewhat (ca. 23 kJ/mol) stronger, as the substrate, none of the compounds employed showed any activity.

Having identified **11** and **12** as the most active catalysts, we subjected them to studies concerning mechanistic questions. Hence, the effects of the individual reagents and reaction conditions were analyzed, and it was found that heating dissolved **11** to 80 °C in the absence of alcohol and $O_2$ leads to the thia analog of **5**, $PPh_4$[(**TC**)V=O] (**15**) (Scheme 12).

This indicates that, whenever **11** is employed as a catalyst for conversions at 80 °C, **15** will be the active species being generated from **11** in situ by a double intramolecular HCl elimination. Compound **15** then reacts with convertible alcohols, as indicated by a further color change, and most likely this leads to the carbonyl compounds. $O_2$ is then needed to reoxidize the V center, which apparently yields **15** again. So far we were not able to identify any of the intermediates occurring in the catalytic cycle involving **15** in contact with alcohols. However, we were more successful in the case of **12**: Treating **12** with two equivalents of fluorenol at 80 °C in the absence of $O_2$ led to a light green solution from which $(PPh_4)_2$[{$H_2$**TC**V(O)}$_2$(μ-OH)(μ-$OC_{13}H_9$)] (**16**) could be isolated in good yields.[15] Compound **16** can be derived from **12** by formally replacing one of the two divalent μ-O ligands in **12** by one μ-OH and one μ-fluorenolate ligand, and in consequence both vanadium atoms are then in the oxidation state +IV. How is **16** formed? Scheme 13 shows a possible catalytic cycle involving **16**.

It is not clear whether a prebinding of the alcohol is necessary for the oxidation step, but if this were the case, it most likely occurs at one of the V centers through a replacement of the weakly bound, "soft" thioether donor belonging to the calixarene ligand as shown in Scheme 13. The next steps might consist of a dehydrogenation (possibly in the form of two consecutive H atom abstractions) leading to fluorenone and a complex with two hydroxo bridges. To get from there to **16** a replacement of one of the two hydroxo bridges by an alcoholate ligand with elimination of water has to occur, a step that should be sufficiently fast at 80 °C, especially in the presence of molecular sieves that constantly remove the water out of the equilibrium. By the mechanism in Scheme 13, one equivalent of fluorenone should be formed simultaneously with **16**, and indeed this could be detected. $O_2$ can then oxidize **16** to give a second equivalent of fluorenone and the starting material **12**, and this was independently shown to proceed already at room temp.; the process involves four electrons and two protons, which, in combination with $O_2$, lead to one equivalent of water and the $O^{2-}$ ligand necessary to regenerate **12**.

Hence, this catalytic cycle for the oxidation of fluorenol with $O_2$ mediated by **12** is plausible, and it additionally even seems to be conferrable to the oxidations of other alcohols: After analogous treatment of **12** with benzyl alcohol, **17**, the derivative corresponding to **16**, (Scheme 13) was isolated. It is interesting to note that oxidation chemistry preferably takes place at the bridging oxo functions and not at the terminal oxo ligands present. This in turn means that the conclusion drawn for the functioning of **12** can not be valid as such for the other calixarene-based catalysts (**5**–**8** and **11**/**15**), since each of those has its individual features

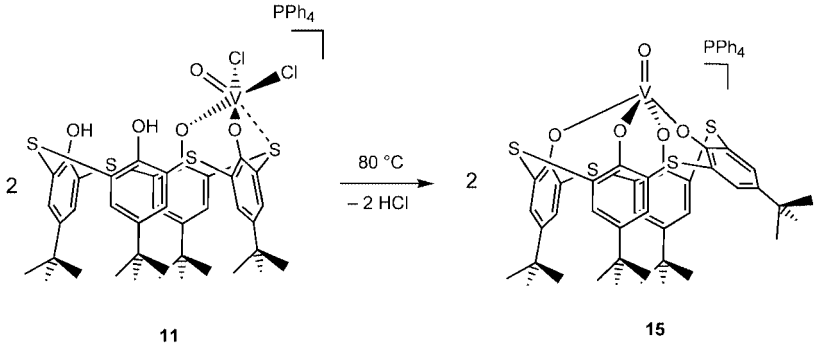


11 15

Scheme 12.

 © 2007 Wiley-VCH Verlag GmbH & Co. KGaA, Weinheim 

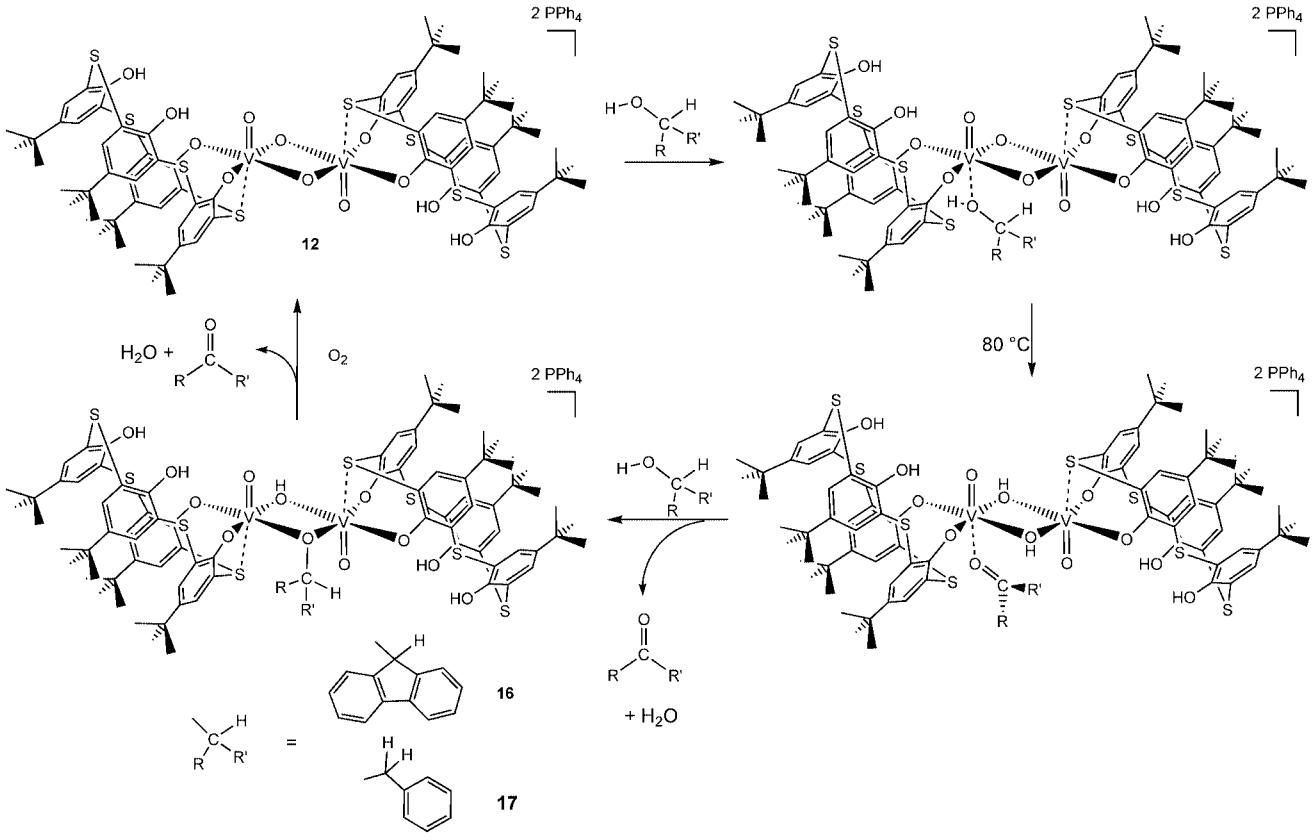


Scheme 13.

and none of them contains a bis(μ-oxo) unit. However, the mechanism in Scheme 13 exemplifies why it might be advantageous for a catalyst to contain two V centers, putting across the observation that dinuclear catalysts are more effective: all oxidation equivalents of $O_2$ are consumed within one cycle, and the vanadium centers only have to switch oxidation states between +V and +IV, whereas the functioning of mononuclear catalysts requires a change between +V and +III. This finding could, in principle, apply to the ODH of alcohols by surface sites, too, i.e. dinuclear sites containing bridging oxo functions should be more active than mononuclear ones. It will be interesting to follow up this working hypothesis in the future.

### 3.2. Olefin Polymerization

With the background described above in the Introduction, a number of the above-mentioned compounds were screened as potential catalysts for the polymerization of ethylene and for ethylene/propylene copolymerization in the presence of a number of organoaluminum cocatalysts as for instance MAO, and dimethylaluminum chloride (DMAC); the effect of the presence of the reactivating substance ethyl trichloroacetate (ETA) was tested, too.[10]

Among the oxovanadium calixarene compounds tested as catalysts, **1**, **3**$^{AN}$, **8b**$^{c}$, **9**, **10**, and **14**, **14** in combination with DMAC/ETA displayed the highest activity for ethylene polymerization [up to 130,000 g mmol$^{-1}$ h$^{-1}$ bar$^{-1}$ at 80 °C, yielding ultra-high-molecular-weight (>5,500,000) linear polyethylene], and ethylene/propylene copolymerization (up to 10,000 g mmol$^{-1}$ h$^{-1}$ bar$^{-1}$ at 25 °C) with about 14.5 mol-% propylene incorporation. These activities are amongst the highest reported to date for nonmetallocene systems.[21] An additional advantageous property of **14** is its stability to prolonged exposure to air. If other organoaluminum cocatalysts are employed such as MAO, much poorer catalytic activities are observed. In comparison to the oxacalix[3]arene complex **14** calix[4]arene-based procatalysts are at best an order of magnitude less active. Hence, the variation from oxa(-$CH_2OCH_2$-)- to methylene (-$CH_2$-)-bridged calixarenes as ancillary ligands leads to clear differences in catalytic performance for α-olefin polymerization systems. Although the nature of the active species formed upon addition of excess DMAC remains uncertain, the reasons are thought to be both steric and electronic in nature and relate to the ease with which the macrocycle can be disconnected from the vanadium center.[10] The shape and size of the oxacalix[3]arene ligand (and associated cavity) is very different from that of the calix[4]arene ligand, and this clearly leads, for instance, to different binding modes (exo vs. endo) for the V=O group: in oxacalixarene complexes this unit is located in the cavity, and this renders the vanadium somewhat exposed, whereas in vanadyl calix[4]arene complexes an exo orientation is observed. The depths of each type of cavity are also very different.[10]

 © 2007 Wiley-VCH Verlag GmbH & Co. KGaA, Weinheim 

Among the vanadyl calix[4]arene complexes investigated, those containing two vanadium centers (**8b**$^{c}$ and **10**) exhibit the highest activities, which may be the result of cooperative effects between the vanadium centers upon formation of the active species.

## 4. Conclusions and Outlook

Taken together, all the findings described in 3.1. may have implications on the discussion of which kind of species are active in oxidative dehydrogenation with vanadia catalysts, as they suggest an increase of activity through the cooperative behavior of two metal centers. However, a larger number of complexes has to be synthesized, and more detailed mechanistic investigations have to be performed to support this hypothesis.

With regard to the mechanism suggested for catalyst **12**, it seems interesting to investigate the kind of reactivity that forms the basis for the activity of mononuclear complexes: the identity of the products generated after addition of the alcohols to **15** at 80 °C or the other mononuclear complexes remains unclear, as we were so far not able to identify any of these potential intermediates. A further question concerns the reasons for the better performance of the thiacalixarene complexes relative to **5**–**8**. A striking result is the high activity observed for **15** (which is identical with the one ascribed to **11**), whereas the calixarene analog **5** is absolutely inert. The rate-determining step (probably the alcohol conversion) seems to be accelerated by the interaction of the thioether functions with the vanadium centers. More detailed and extensive studies might provide some insight in the future.

Interestingly, the results of the investigations concerning the catalytic activity for olefin polymerization (section 3.2) seem to suggest the same general trends as in the alcohol oxidation: the heterocalixarenes (here oxacalixarenes) are more active, and dinuclear complexes display higher activities than mononuclear compounds. It will be interesting to examine the reasons in the future and to investigate other open questions concerning the exact role played by DMAC, which is still far from clear. Success in the identification of the active species in these vanadium-based systems would be a major step forward in the current understanding and provide information vital to the future design of new vanadium-based catalytic systems.

## Acknowledgments

I am grateful to the Collaborative Research Center 546 of the Deutsche Forschungsgemeinschaft, the Fonds der Chemischen Industrie, the Bundesministerium für Bildung, Wissenschaft und Technologie, and the Dr. Otto Röhm Gedächtnisstiftung for financial support.

[1] R. A. van Santen, M. Neurock, *Molecular Heterogeneous Catalysis*, Wiley-VCH, Weinheim, **2006**; J. M. Thomas, W. J. Thomas, *Principles and Practice of Heterogeneous Catalysis*, VCH, Weinheim, **2005**.

[2] X. S. Zhao, G. Q. Lu, A. K. Whittaker, G. J. Millar, H. Y. Zhu, *J. Phys. Chem. B* **1997**, *101*, 6525–6531; B. A. Morrow, I. D. Gay in *Adsorption on Silica Surfaces* (Ed.: E. Papirer), Marcel Dekker, New York, **2000**, 9–33.

[3] T. W. Dijkstra, R. Duchateau, R. A. van Santen, A. Meetsma, G. P. A. Yap, *J. Am. Chem. Soc.* **2002**, *124*, 9856.

[4] a) G. Golodets, *Heterogeneous Catalytic Reactions Involving Molecular Oxygen*, Elsevier, New York, **1983**; b) F. J. Karol, C. Wu, W. T. Reichle, N. J. J. Maraschin, *J. Catal.* **1979**, *60*, 68; H. Sinn, W. Kaminsky, *Adv. Organomet. Chem.* **1980**, *18*, 99; J. H. Lunsford, S.-L. Fu, D. L. Myers, *J. Catal.* **1988**, *111*, 231; M. P. McDaniel, *Adv. Catal.* **1985**, *33*, 47; c) G. Fink, B. Steinmetz, J. Zechlin, C. Przybyla, B. Tesche, *Chem. Rev.* **2000**, *100*, 1377–1390; d) G. G. Hlatky, *Chem. Rev.* **2000**, *100*, 1347 and the references cited therein; C. Merckle, J. Blümel, *Chem. Mater.* **2001**, *13*, 3617 and the references cited therein.

[5] a) R. Duchateau, *Chem. Rev.* **2002**, *102*, 3525 b) V. Lorenz, F. T. Edelmann, *Z. Anorg. Allg. Chem.* **2004**, *630*, 1147; c) C. Copéret, M. Chabanas, R. P. Saint-Arroman, J.-M. Basset, *Angew. Chem.* **2003**, *115*, 164; d) F. J. Feher, T. A. Budzichowski, *Polyhedron* **1995**, *14*, 3239; e) U. Radius, *Z. Anorg. Allg. Chem.* **2004**, *630*, 957; f) C. Floriani, *Chem. Eur. J.* **1999**, *5*, 19.

[6] a) A. Comite, A. Sorrentino, G. Capannelli, M. Di Serio, R. Tesser, E. Santacesaria, *J. Mol. Catal.* **2003**, *A 198*, 151; b) R. Zhou, Y. Cao, S. Yan, J. Deng, Y. Liao, B. Hong, *Catal. Lett.* **2001**, *75*, 107; c) T. Blasco, A. Galli, J. M. Lopez Nieto, F. Trifido, *J. Catal.* **1997**, *169*, 203; d) M. A. Chaar, D. Patel, H. H. Kung, *J. Catal.* **1988**, *109*, 463; e) A. Corma, J. M. Lopez Nieto, N. Paredes, *J. Catal.* **1993**, *144*, 425; f) F. D. Hardcastle, I. E. Wachs, *J. Mol. Catal.* **1988**, *46*, 173; g) G. Deo, I. E. Wachs, J. Haber, *Crit. Rev. Surf. Chem.* **1994**, *4*, 141; h) I. E. Wachs, B. M. Weckhuysen, *Appl. Catal., A* **1997**, *157*, 67; i) J. G. Eon, R. Olier, J. C. Volta, *J. Catal.* **1994**, *145*, 318; j) T. Balsco, J. M. Lopez Nieto, *Appl. Catal. A* **1997**, *157*, 117; k) A. Khodakov, B. Olthof, A. T. Bell, E. Iglesia, *J. Catal.* **1999**, *181*, 205; l) A. Khodakov, J. Yang, S. Su, E. Iglesia, A. T. Bell, *J. Catal.* **1998**, *177*, 343; m) E. V. Kondratenko, M. Baerns, *Appl. Catal. A* **2001**, *222*, 133; n) M. D. Argyle, K. D. Chen, A. T. Bell, E. Iglesia, *J. Catal.* **2002**, *208*, 139; o) L. Owens, H. H. Kung, *J. Catal.* **1993**, *144*, 202; p) O. R. Evans, A. T. Bell, T. D. Tilley, *J. Catal.* **2004**, *226*, 292.

[7] Low-valent V species on supports: a) F. J. Karol, K. J. Cann, B. E. Wagner in *Transition Metals and Organometallics as Catalysts for Olefin Polymerization* (Eds.: W. Kaminsky, H. Sinn), Springer-Verlag, New York, **1988**, pp 149–61 and the references cited therein; b) D. Damyanov, M. Velikova, *Eur. Polym. J.* **1979**, *15*, 1075–1078; c) W. E. Smith, R. G. Zelmer, *J. Polym. Sci., PI. A* **1963**, *I*, 2587–2600; d) The presence of high-valent species suggested by F. J. Feher, R. L. Blanski, *J. Am. Chem. Soc.* **1992**, *114*, 5886; also see refs.[1–6] therein; e) homogeneous catalysts: C. Redshaw, M. A. Rowan, D. M. Homden, S. H. Dale, M. R. J. Elsegood, S. Matsui, S. Matsuura, *Chem. Commun.* **2006**, 3329.

[8] B. Castellano, E. Solari, C. Floriani, R. Scopelliti, N. Re, *Inorg. Chem.* **1999**, *38*, 3406.

[9] a) V. C. Gibson, C. Redshaw, M. R. J. Elsegood, *J. Chem. Soc. Dalton Trans.* **2001**, 767; b) P. D. Hampton, C. E. Daitch, T. M. Alam, E. A. Pruss, *Inorg. Chem.* **1997**, *36*, 2879; see also ref.[16a].

[10] C. Redshaw, M. A. Rowan, L. Warford, D. M. Homden, A. Arbaoui, M. R. J. Elsegood, S. H. Dale, T. Yamato, C. P. Casas, S. Matsui, S. Matsuura, *Chem. Eur. J.* **2007**, *13*, 1090–1107.

[11] B. Castellano, E. Solari, C. Floriani, N. Re, A. Chiesi-Villa, C. Rizzoli, *Organometallics* **1998**, *17*, 2328.

[12] E. Hoppe, C. Limberg, B. Ziemer, C. Mügge, *J. Mol. Cat. A* **2006**, *251*, 34.

 © 2007 Wiley-VCH Verlag GmbH & Co. KGaA, Weinheim 

[13] S. Durr, B. Bechlars, U. Radius, *Inorg. Chim. Acta* **2006**, *359*, 4215–4226.
[14] E. Hoppe, C. Limberg, B. Ziemer, *Inorg. Chem.* **2006**, *45*, 8308.
[15] E. Hoppe, C. Limberg, *Chem. Eur. J.*, DOI: 10.1002/chem.200700354.
[16] a) G. E. Hofmeister, F. E. Hahn, S. F. Pedersen, *J. Am. Chem. Soc.* **1989**, *111*, 2318; b) G. E. Hofmeister, E. Alvarado, J. A. Leary, D. I. Yoon, S. F. Pedersen, *J. Am. Chem. Soc.* **1990**, *112*, 8843.
[17] a) H. Kumagai, M. Hasegawa, S. Miyanari, Y. Sugawa, Y. Sato, T. Hori, S. Ueda, H. Kamiyama, S. Miyano, *Tetrahedron Lett.* **1997**, *38*, 3971; b) N. Morohashi, F. Narumi, N. Iki, T. Hattori, S. Miyano, *Chem. Rev.* **2006**, *106*, 5291; c) J. Zeller, U. Radius, *Inorg. Chem.* **2006**, *45*, 9487; d) N. Iki, C. Kabuto, T. Fukushima, H. Kumagai, H. Takeya, S. Miyanari, T. Miyashi, S. Miyano, *Tetrahedron* **2000**, *56*, 1437; e) N. Iki, N. Morohashi, T. Suzuki, S. Ogawa, M. Aono, C. Kabuto, H. Kumagai, H. Takeya, S. Miyanari, S. Miyano, *Tetrahedron Lett.* **2000**, *41*, 2587; f) N. Morohashi, N. Iki, A. Sugawara, S. Miyano, *Tetrahedron* **2001**, *57*, 5557; g) N. Kon, N. Iki, S. Miyano, *Tetrahedron Lett.* **2002**, *43*, 2231; h) N. Kon, N. Iki, Y. Yamane, S. Shirasaki, S. Miyano, *Tetrahedron Lett.* **2004**, *45*, 207.
[18] a) T. Kajiwara, S. Yokozawa, T. Ito, N. Iki, N. Morohashi, S. Miyano, *Chem. Lett.* **2001**, 6; b) A. Bilyk, A. K. Hall, J. M. Harrowfield, M. W. Hosseini, G. Mislin, B. W. Skelton, C. Taylor, A. H. White, *Eur. J. Inorg. Chem.* **2000**, 823; c) T. Kajiwara, S. Yokozawa, T. Ito, N. Iki, N. Morohashi, S. Miyano, *Angew. Chem. Int. Ed.* **2002**, *41*, 2076; d) K. Hirata, T. Suzuki, A. Noya, I. Takei, M. Hidai, *Chem. Commun.* **2005**, 3718; e) Z. Asfari, A. Bilyk, J. W. C. Dunlop, A. K. Hall, J. M. Harrowfield, M. W. Hosseini, B. W. Skelton, A. H. White, *Angew. Chem. Int. Ed.* **2001**, *40*, 721; f) A. Bilyk, A. K. Hall, J. M. Harrowfield, M. W. Hosseini, B. W. Skelton, A. H. White, *Aust. J. Chem.* **2000**, *53*, 895.
[19] I. W. C. E. Arends, R. A. Sheldon in *Modern Oxidation Methods* (Ed.: J.-E. Bäckvall), Wiley-VCH, Weinheim, **2004**, pp. 83.
[20] Y. Maeda, N. Kakiuchi, S. Matsumura, T. Nishimura, T. Kawamura, S. Uemura, *J. Org. Chem.* **2002**, *67*, 6718.
[21] a) G. J. P. Britovsek, V. C. Gibson, D. F. Wass, *Angew. Chem.* **1999**, *111*, 448; *Angew. Chem. Int. Ed.* **1999**, *38*, 428; b) V. C. Gibson, S. K. Spitzmesser, *Chem. Rev.* **2003**, *103*, 283; c) V. C. Gibson, E. L. Marshall in *Comprehensive Coordination Chemistry II, Vol. 9* (Eds.: J. A. McCleverty, T. J. Meyer, M. D. Ward), Elsevier, **2004**.

Received: April 16, 2007
Published Online: June 29, 2007

 © 2007 Wiley-VCH Verlag GmbH & Co. KGaA, Weinheim 

DOI: 10.1002/ejic.200700352

# C–H···Ni$^{II}$ Interaction-Driven Homochiral *M* and *P* Helices of Neutral (*R*,*R*)- and (*S*,*S*)-Bis(pyrrol-2-ylmethyleneamino)cyclohexane Ni$^{II}$ Complexes

**Xu-Feng Shan,[a] Li-Zhu Wu,*[a] Xian-Yu Liu,[a] Li-Ping Zhang,[a] and Chen-Ho Tung[a]**

**Keywords:** Nickel(II) complexes / C–H···Ni$^{II}$ interactions / Helical structures

Reaction of (*R*,*R*)- and (*S*,*S*)-bis(pyrrol-2-ylmethyleneamino)-cyclohexane with Ni$^{II}$(OAc)$_2$·4H$_2$O afforded enantiomeric nickel(II) Schiff-base complexes (*R*,*R*)-**1** and (*S*,*S*)-**1**, respectively. Rare C–H···Ni$^{II}$ interactions were found to be responsible for the facile formation of homochiral *M* and *P* helices of the neutral, chiral, mononuclear complexes in crystal lattices. (© Wiley-VCH Verlag GmbH & Co. KGaA, 69451 Weinheim, Germany, 2007)

## Introduction

Inspired by biology and driven by applications in material science, chemists have made tremendous efforts in building helical arrays that play important roles across the whole spectrum of science and technology.[1–2] A large number of supramolecular helical architectures of coordination compounds have been constructed over the years.[2–6] It is known that the size and structure of the helix can be altered by subtle manipulation of the intermolecular interactions, such as hydrogen bonding, π–π stacking, and electrostatic and van der Waals forces.[1–6] Although C–H···M (M: metal) interaction was initially postulated in the literature,[7] its significance in self-assembling processes has not been realized until recently.[8] Ma and coworkers[8a] described in 2004 that the weak intermolecular C–H···Cu hydrogen bond plays a crucial role in constructing the network polymer of bis(pyrrol-2-ylmethyleneamine) ligands with Cu$^{II}$. Earlier work by Alyea et al.[8b] revealed that pairs of *cis*-[PdCl$_2$(TPA)$_2$] (TPA = 1,3,5-triaza-7-phosphaadamantane) molecules are linked about inversion centers by intermolecular C–H···Pd hydrogen interactions, where water molecules link these dimers via O–H···N hydrogen bonds to form infinite chains that extends in the *c* direction in the crystal lattice.

In this communication, we report homochiral supramolecular left-handed (*M*) and right-handed (*P*) helices, which are derived from chiral neutral mononuclear (*R*,*R*)- and (*S*,*S*)-bis(pyrrol-2-ylmethyleneamino)cyclohexane nickel(II) complexes, (*R*,*R*)-**1** and (*S*,*S*)-**1**, respectively. The use of pyrrol-2-yl Schiff base avoids counterion coordination,[3c,8a] and thereby achieves exclusive coordination of the tetradentate ligand to nickel(II) center. X-ray crystal structural analysis reveals that (*R*,*R*)-**1** and (*S*,*S*)-**1** self-assemble via the intermolecular C–H···Ni$^{II}$ interaction and the chirality of mononuclear nickel(II) complexes of (*R*,*R*)-**1** and (*S*,*S*)-**1** extends over the whole supramolecular structure. Although the chiral Schiff complexes are known to construct supramolecular helical structures,[3–7] to the best of our knowledge, the homochiral helix solely driven by the rare C–H···M interaction in neutral mononuclear metal complex has not yet been reported.

## Results and Discussion

The optically pure ligands of (*R*,*R*)- and (*S*,*S*)-bis(pyrrol-2-ylmethyleneamino)cyclohexane were prepared by condensation of (*R*,*R*)-1,2-diaminocyclohexane mono-(+)-tartrate salt and (*S*,*S*)-1,2-diaminocyclohexane with 2-pyrrolealdehyde, respectively.[9] Under the base conditions, the two enantiomeric ligands were further reacted with Ni$^{II}$(OAc)$_2$·4H$_2$O at room temperature to afford neutral mononuclear complexes (*R*,*R*)-**1** and (*S*,*S*)-**1** with yields of 93 and 92%, respectively (Scheme 1). For comparison, racemic complex **1**[9b] was also synthesized.

Figure 1 shows the UV/Vis absorption and circular dichromism (CD) spectra of neutral complexes (*R*,*R*)-**1** and (*S*,*S*)-**1**. It was noted that the optically pure enantiomers of (*R*,*R*)-**1** {$[\alpha]_D^{20}$ = –3832 (*c* = 0.0033, $CH_2Cl_2$)} and (*S*,*S*)-**1** {$[\alpha]_D^{20}$ = +3833 (*c* = 0.0032, $CH_2Cl_2$)} show near mirror image behaviors in the circular dichroism (CD) spectra, while the absorption spectra are not distinguishable from each other. Correlated with the observed CD spectra, the absolute configuration of (*R*,*R*)-**1** and (*S*,*S*)-**1** can be subsequently assigned to Δ and Λ, respectively, in terms of the definition of IUPAC nomenclature[10a] and the reference method.[10b–10c]

[a] Laboratory of Organic Optoelectronic Functional Materials and Molecular Engineering, Technical Institute of Physics and Chemistry & Graduate University, The Chinese Academy of Sciences,
Beijing, 100080 P. R. China
Fax: +86-10-82543580
E-mail: lzwu@mail.ipc.ac.cn

 © 2007 Wiley-VCH Verlag GmbH & Co. KGaA, Weinheim 

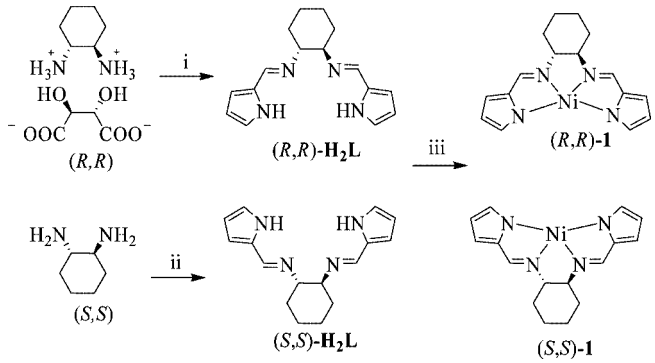


Scheme 1. Synthesis of (*R*,*R*)-**1** and (*S*,*S*)-**1** complexes. Reaction conditions: i) $K_2CO_3$, 2-pyrrolealdehyde, 80 °C, 4 h, water/ethanol (2:1); ii) 2-pyrrolealdehyde, reflux, 12 h, ethanol; iii) $Ni^{II}(OAc)_2 \cdot 4H_2O$, KOH, r.t., 2 h, methanol.

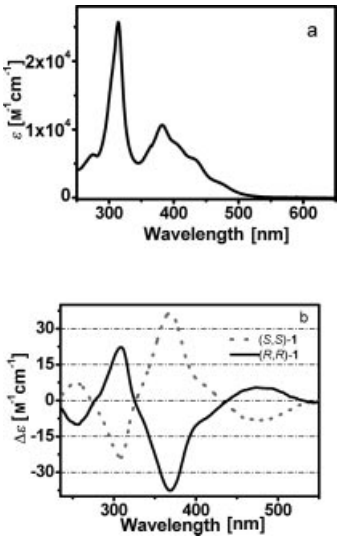


Figure 1. The absorption spectrum (a) and circular dichroism spectrum (b) of (*R*,*R*)-**1** ($4.43 \times 10^{-5}$ M) and (*S*,*S*)-**1** ($3.68 \times 10^{-5}$ M) in acetonitrile solution at room temperature.

Single crystals of (*R*,*R*)-**1**, (*S*,*S*)-**1**, and **1** were obtained by slow evaporation of a $CH_2Cl_2$/methanol solution. Red single crystals of these three complexes as needles were used for data collection with the use of a Bruker Smart 1000 X-ray diffractometer with Mo-$K_\alpha$ radiation. The crystals of (*R*,*R*)-**1** and (*S*,*S*)-**1** belong to the monoclinic crystal system and $P2_1$ space group, while **1** is the monoclinic crystal system and $P2_1/c$ space group. The crystallographic data for (*R*,*R*)-**1** and (*S*,*S*)-**1**, as well as **1** were listed in Table 2. Figure 2 shows the two neutral mononuclear (*R*,*R*)-**1** and (*S*,*S*)-**1** complexes. Each $Ni^{II}$ center is four-coordinate to four N atoms from pyrrol-2-yl-cyclohexenediamine Schiff-base unit. The length of the $Ni^{II}$–N bond is in the range of 1.844–1.890 Å. The dative $Ni^{II}$–N(imine) bond lengths (1.844–1.867 Å) are comparable to those of other similar $Ni^{II}$–N bonds (1.843–1.895 Å) in the literature,[9b] but are shorter than those of the $Ni^{II}$–N(pyrrole) (1.877–1.890 Å). The conformation of *trans*-1,2-cyclohexyldiamine leads to a twisted conformation, where the cyclohexyl ring is in a stable chair conformation and the two pyrrol-2-yl units of same ligand adopt a *cis* conformation with dihedral angles of 18° (Ni1–N1–N2 and Ni1–N4–N3) in (*R*,*R*)-**1** and 18.3° (Ni1–N1–N2 and Ni1–N4–N3) in (*S*,*S*)-**1**, respectively. The dihedral angles in (*R*,*R*)-**1** and (*S*,*S*)-**1** implied that the $Ni^{II}$ center has a small deviation from the square-planar coordination geometry. Evidently, the configuration of (*R*,*R*)-**1** and (*S*,*S*)-**1** can be definitely evaluated as Δ and Λ with respect to the $C_2$-axis, which is consistent with their assignments on the basis of CD spectra.

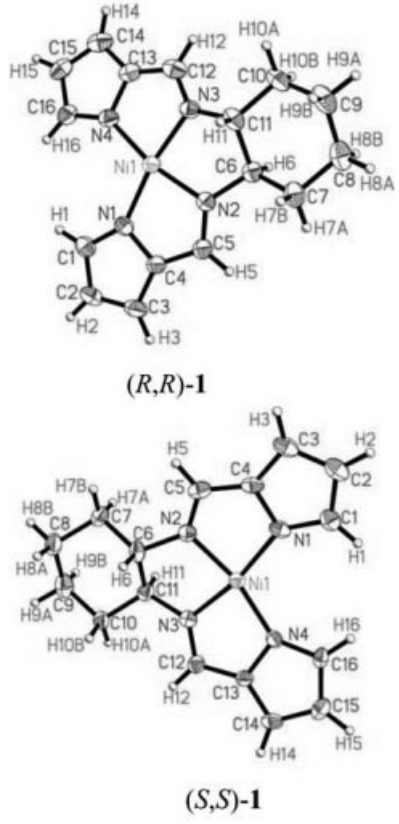


Figure 2. Crystal structures of (*R*,*R*)-**1** and (*S*,*S*)-**1** with atom numbering.

A noticeable feature of (*R*,*R*)-**1** and (*S*,*S*)-**1** lies in the weak intermolecular C–H···$Ni^{II}$ interactions in the molecular packing (Figure 3). As in the case of (*R*,*R*)-**1**, each ligand uses its hydrogen atoms to bind the nickel(II) center of the others. Because the two pyrrol-2-yldiamine units of the same ligand adopt a *cis* conformation and the C–N-(imine) bonds in the rigid *trans*-1,2-cyclohexyl moiety are arranged reciprocally, the unit cell contains three different intermolecular C–H···$Ni^{II}$ interactions in the crystal of (*R*,*R*)-**1**. As sketched in Figure 3, each molecule of (*R*,*R*)-**1** is stacking with two adjacent molecules via the intermolecular C–H···$Ni^{II}$ interactions. Table 1gives the structural parameters related to the C–H···$Ni^{II}$ interactions in (*R*,*R*)-**1** and (*S*,*S*)-**1**. The $Ni^{II}$···H distance is similar to that recently observed by Pal. et al., who demonstrated the presence of intramolecular apical C–H···$Ni^{II}$ interactions in square-planar nickel(II) complexes with dianionic tridentate ligands and 2-phenylimidazole.[11] The intermolecular contacts of 3.002 Å at C43A–H43A···Ni1A, 3.025 Å at

 © 2007 Wiley-VCH Verlag GmbH & Co. KGaA, Weinheim 

C6A–H6A···Ni3A, and 3.127 Å at C7A–H7BA···Ni3B with the C–H···Ni$^{II}$ angle of 141.1°, 166.9°, and 141.5°, respectively, lead to the formation of helical assemblies with different pitches in the helix. Two sets, four complex fragments form one helix with a screw-pitch of 17.242 Å. The intermolecular metal···metal contacts are found to be 5.989 Å (Ni3A–Ni1A) and 8.621 Å (Ni1A–Ni3B), respectively. Obviously, the turn required to generate a perfect periodic self-assembly of (*R*,*R*)-**1** in a helical fashion is induced by the chirality of the building block coupled with the weak intermolecular C–H···Ni$^{II}$ interactions. An *M* handedness can be clearly assigned to complexes (*R*,*R*)-**1** when viewed along the *b* axis. At the molecular level, this local chirality translates throughout the crystal into the formation of only left-handed (*M*) helix at the supramolecular level. The path of the helix can be easily traced by following the C–H···Ni$^{II}$ interactions counterclockwise around the screw axis of the helix. A similar self-assembly pattern exists in the crystal packing of (*S*,*S*)-**1**. The only difference is the opposite direction presented in which the intermolecular C–H···Ni$^{II}$ interactions show a clockwise turn around the screw axis to give a right-handed (*P*) helix. A comparison of the two space-filling models evidences the near mirror image behavior of the (*R*,*R*)-**1** and (*S*,*S*)-**1** helices (Figure 3), indicating they are enantiomeric from a supramolecular point of view.

To provide more evidence for the unique intermolecular C–H···Ni$^{II}$ interaction, the self-assembly manner presented in racemic complex **1** was also investigated. Apparently, the situation is quite different from that in (*R*,*R*)-**1** and (*S*,*S*)-**1**. Two molecules of (*R*,*R*)-**1** and (*S*,*S*)-**1** interact with each other in one unit cell via intermolecular C–H···Ni$^{II}$ interactions (Figure 4). However, one H atom from the pyrrole

Table 1. Parameters for C–H···Ni$^{II}$ intermolecular interactions in three Ni$^{II}$ complexes.

| Complex | C–H···Ni$^{II}$ | *d*[a] [Å] | *d*[b] [Å] | *D*[c] [Å] | *θ*[d] [°] |
|---|---|---|---|---|---|
| (*R*,*R*)-**1** | C43A–H43A···Ni1A | 0.98 | 3.002 | 3.817 | 141.1 |
| | C7A–H7BA···Ni3B | 0.97 | 3.025 | 3.976 | 166.9 |
| | C6A–H6A···Ni3A | 0.98 | 3.127 | 3.942 | 141.5 |
| (*S*,*S*)-**1** | C22B–H22B···Ni3B | 1.00 | 3.140 | 3.952 | 139.3 |
| | C23B–H23C···Ni3A | 0.99 | 2.983 | 3.945 | 164.2 |
| | C38A–H38A···Ni2A | 1.00 | 2.978 | 3.792 | 139.2 |
| **1** | C14D–H14D···Ni1I | 0.95 | 3.154 | 3.954 | 156.4 |
| | C11D–H11D···Ni1B | 1.00 | 2.884 | 3.721 | 141.8 |
| | C14I–H14I···Ni1E | 0.95 | 3.154 | 3.954 | 156.4 |
| | C11B–H11B···Ni1D | 1.00 | 2.884 | 3.721 | 141.8 |

[a] For C–H distance. [b] For H···Ni$^{II}$ distance. [c] For C–Ni$^{II}$ distance. [d] C–H···Ni$^{II}$ angle.

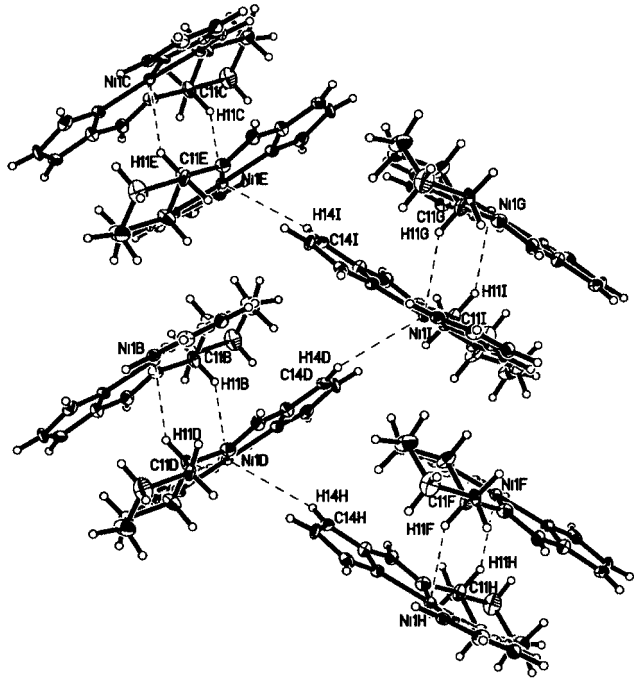


Figure 4. Crystal packing diagram of racemic **1** with atom numbering.

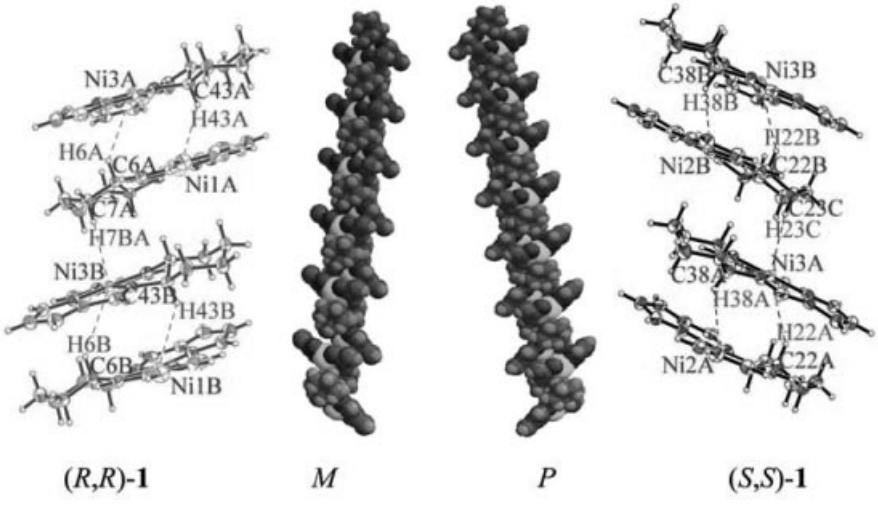


Figure 3. Crystal packing diagram of (*R*,*R*)-**1** and (*S*,*S*)-**1** (carbon and hydrogen atoms at pyrrole cycles were omitted for clarity in space-filling view).

 © 2007 Wiley-VCH Verlag GmbH & Co. KGaA, Weinheim 

ring rather than from the 1,2-cyclohexyl unit in one molecule is bound to the Ni center of the other. Since the intermolecular C–H···$Ni^{II}$ distance of 2.884 Å at C11D–H11D···Ni1B and 2.884 Å at C11B–H11B···Ni1D in complex **1** are appreciably shorter than those of either (*R*,*R*)-**1** or (*S*,*S*)-**1**, homochiral *M* and *P* helices were not observed in the crystal packing of **1**. Alternatively, the racemic unit cell of complex **1** is assembled to display a picture that is far from that observed for the (*R*,*R*)-**1** and (*S*,*S*)-**1** helices.

## Conclusions

We demonstrated that the rare C–H···$Ni^{II}$ interaction is responsible for controlling self-assembly of neutral, chiral, mononuclear complexes of (*R*,*R*)-**1** and (*S*,*S*)-**1**, leading to the formation of *M* and *P* helices of (*R*,*R*)-**1** and (*S*,*S*)-**1** in crystal lattices. Extending the scope of the intriguing complexes and exploring their applications are ongoing in our laboratory.

## Experimental Section

All synthetic regents were of analytical grade and used as received. The solvents used for spectroscopic measurements were purified according to the literature method.[12] Melting points were determined with a Yanaco MP-500 micro-melting point apparatus. NMR spectra were recorded with a Bruker Avance dpx 400 MHz instrument using TMS as an internal standard. Mass spectra were obtained with Bruker APEX II spectrometers. Elemental analyses were performed with a FLASH EA1112 elemental analyzer. The UV/Vis absorption spectra of these compounds were recorded using a Shimadzu 1601 spectrophotometer. The circular dichroism (CD) spectra were measured with a JASCO J-810 spectropolarimeter. The values of specific rotation were measured with a Perkin–Elmer 341LC polarimeter.

**(*R*,*R*)-Bis(pyrrol-2-ylmethyleneamino)cyclohexane [(*R*,*R*)-$H_2$L]:** A 100-mL two-necked flask equipped with a magnetic stirrer, a reflux condenser, and an addition funnel was charged with (*R*,*R*)-1,2-diaminocyclohexane mono-(+)-tartrate salt (2.64 g), $K_2CO_3$ (2.79 g) and distilled water/ethanol (2:1, 60 mL). The mixture was heated to 80°C, and then 2-formylpyrrole (1.9 g) in ethanol (10 mL) was added slowly over 20 min. The yellow solution was heated at reflux for 2 h before distilled water (20 mL) was added. The solution was placed in an ice bath for 4 h to afford a white solid, which was collected by vacuum filtration, washed with water, and dried under vacuum. The product was further recrystallized from ethanol to give optically pure (*R*,*R*)-**$H_2$L**. Yield: 2.2 g, 78%. M.p. 204 °C (dec.). $[\alpha]_D^{20}$ = –1041 (*c* = 0.0023, $CH_3OH$). $^1$H NMR (400 MHz, $CDCl_3$, 25 °C): $\delta$ = 1.36–1.79 (m, 8 H), 3.01–3.05 (m, 2 H), 6.17 (dd, *J* = 2.5, 2.7 Hz, 2 H), 6.36 (d, *J* = 2.5 Hz, 2 H); 6.81 (s, 2 H), 7.77 (s, 2 H) ppm. $^{13}$C NMR (100 MHz, $CDCl_3$): $\delta$ = 24.92, 34.34, 72.87, 109.69, 114.55, 122.01, 130.66, 152.32 ppm. MS (EI): *m*/*z* = 268. $C_{16}H_{20}N_4 \cdot H_2O$ (286.4): calcd. C 67.11, H 7.74, N 19.56; found C 66.96, H 7.75, N 19.40.

**(*S*,*S*)-Bis(pyrrol-2-ylmethyleneamino)cyclohexane [(*S*,*S*)-$H_2$L]:** 2-Formylpyrrole (6 mmol) and (*S*,*S*)-1,2-diaminocyclohexane (3 mmol) were dissolved in ethanol (35 mL). The yellow solution was heated at reflux for 12 h under an atmosphere of argon. The solvent was removed by evaporation. The residue was further recrystallized from 95% ethanol to give optically pure (*S*,*S*)-**$H_2$L**. Yield: 0.58 g, 68%. M.p. 206 °C (dec.). $[\alpha]_D^{20}$ = +1040 (*c* = 0.0021, $CH_3OH$). $^1$H NMR (400 MHz, $CDCl_3$, 25 °C): $\delta$ = 1.36–1.79 (m, 8 H), 3.01–3.05 (m, 2 H), 6.17 (dd, *J* = 2.5, 2.7 Hz, 2 H), 6.36 (d, *J* = 2.5 Hz, 2 H); 6.81 (s, 2 H), 7.77 (s, 2 H) ppm. $^{13}$C NMR (100 MHz, $CDCl_3$): $\delta$ = 24.93, 34.33, 72.88, 109.68, 114.57, 122.02, 130.66, 152.30 ppm. MS (EI): *m*/*z* = 268. $C_{16}H_{20}N_4 \cdot H_2O$ (286.4): calcd. C 67.11, H 7.74, N 19.56; found C 66.98, H 7.73, N 19.42.

**(*R*,*R*)-Bis(pyrrol-2-ylmethyleneamino)cyclohexane Nickel(II) Complex [(*R*,*R*)-1]:** A mixture of optically pure (*R*,*R*)-**$H_2$L** (1 mmol) and $Ni^{II}(OAc)_2 \cdot 4H_2O$ (1.1 mmol) in methanol (30 mL) was stirred for 10 min at r.t. With the addition of KOH (2 mmol) in methanol (10 mL), the mixture was stirred for another 2 h accompanying the formation of a precipitate, which was collected by suction filtration followed by washing with distilled water and methanol. Recrystallization from dichloromethane/methanol produced the expected red crystals. Yield: 301 mg, 93%. M.p. 272 °C (dec.). $[\alpha]_D^{20}$ = –3832 (*c* = 0.0033, $CH_2Cl_2$). $^1$H NMR (400 MHz, $CDCl_3$, 25°C): $\delta$ = 1.27–1.29 (m, 4 H, $CH_2$), 1.80–1.81 (br. s, 2 H, $CH_2$), 2.19–2.20 (br. s, 2 H, $CH_2$), 3.41–3.42 (br. s, 2 H, CH), 6.12 (dd, *J* = 3.6, 3.4 Hz, 2 H, pyrrole-βH), 6.58 (d, *J* = 3.6 Hz, 2 H, pyrrole-γH), 6.80 (s, 2 H, pyrrole-αH), 7.17 (s, 2 H, imine-H) ppm. $^{13}$C NMR (100 MHz, $CDCl_3$): $\delta$ = 24.1, 28.0, 70.4, 111.3, 116.3, 136.0, 142.9, 154.0 ppm. HRMS (FAB): calcd. for $C_{16}H_{18}N_4Ni$ $[M + H]^+$ 324.0878; found 324.0877. $C_{16}H_{18}N_4Ni$ (324.1): calcd. C 59.12, H 5.58, N 17.24; found C 58.94, H 5.58, N 17.28.

**(*S*,*S*)-Bis(pyrrol-2-ylmethyleneamino)cyclohexane Nickel(II) Complex [(*S*,*S*)-1]:** The synthetic procedure was similar to that of (*R*,*R*)-**1** except for optically pure (*S*,*S*)-**$H_2$L** was used. Yield: 298 mg, 92%. M.p. 268 °C (dec.). $[\alpha]_D^{20}$ = +3833 (*c* = 0.0032, $CH_2Cl_2$). $^1$H NMR (400 MHz, $CDCl_3$, 25°C): $\delta$ = 1.27–1.29 (m, 4 H, $CH_2$); 1.80–1.81 (br. s, 2 H, $CH_2$), 2.19–2.20 (br. s, 2 H, $CH_2$), 3.41–3.42 (br. s, 2 H, CH), 6.12 (dd, *J* = 3.6, 3.5 Hz, 2 H, pyrrole-βH), 6.57 (d, *J* = 3.6 Hz, 2 H, pyrrole-γH), 6.80 (s, 2 H, pyrrole-αH), 7.17 (s, 2 H, imine-H) ppm. $^{13}$C NMR (100 MHz, $CDCl_3$): $\delta$ = 24.1, 27.9, 70.5, 111.3, 116.2, 135.6, 143.0, 154.2 ppm. HRMS (FAB): calcd. for $C_{16}H_{18}N_4Ni$ $[M + H]^+$ 324.0878; found 324.0870. $C_{16}H_{18}N_4Ni$ (324.1): calcd. C 59.12, H 5.58, N 17.24; found C 58.94, H 5.48, N 17.30.

**X-ray Crystallographic Studies:** Crystals suitable for X-ray analysis were obtained by slow evaporation of a saturated solution of dichloromethane/methanol. Accurate unit cell parameters were determined by least-squares fit of 2$\theta$ values, measured for 200 strong reflections, and intensity data sets were measured with a Bruker Smart 1000 CCD diffractometer with Mo-$K_\alpha$ radiation ($\lambda$ = 0.71073 Å) at 294 K. The intensities were corrected for Lorentz and polarization effects. All structures were analyzed by direct methods. The non-hydrogen atoms were located in successive difference Fourier synthesis. The final refinement was performed by full-matrix least-squares methods with anisotropic thermal parameters for non-hydrogen atoms on $F^2$ (SHELXL-97).[13] The hydrogen atoms were added theoretically and treated as riding on the concerted atoms. Crystallographic data and experimental details for structure analyses are summarized in Table 2. CCDC-638806, -638807, and -638808 [for (*R*,*R*)-**1**, (*S*,*S*)-**1**, and **1**, respectively] contain the supplementary crystallographic data for this paper. These data can be obtained free of charge from The Cambridge Crystallographic Data Centre via www.ccdc.cam.ac.uk/data_request/cif.

 © 2007 Wiley-VCH Verlag GmbH & Co. KGaA, Weinheim 

Table 2. Crystallographic data and structure refinement summary for (*R*,*R*)-**1**, (*S*,*S*)-**1**, and **1**.

| Compound | (*R*,*R*)-**1** | (*S*,*S*)-**1** | **1** |
|---|---|---|---|
| Empirical formula | $C_{16}H_{18}N_4Ni$ | $C_{16}H_{18}N_4Ni$ | $C_{16}H_{18}N_4Ni$ |
| Formula weight | 325.05 | 325.05 | 325.05 |
| Crystal system | monoclinic | monoclinic | monoclinic |
| Space group | $P2_1$ | $P2_1$ | $P2_1/c$ |
| *a* [Å] | 17.458(2) | 17.2362(17) | 21.3123(18) |
| *b* [Å] | 8.6212(10) | 8.5702(8) | 8.7642(8) |
| *c* [Å] | 21.366(3) | 21.305(3) | 16.9496(12) |
| *α* [°] | 90 | 90 | 90 |
| *β* [°] | 111.681(2) | 111.733(6) | 111.633(7) |
| *γ* [°] | 90 | 90 | 90 |
| Volume [Å$^3$] | 2988.2(6) | 2923.5(5) | 2942.9(4) |
| *Z*, Calculated density [g cm$^{-3}$] | 8, 1.445 | 8, 1.477 | 8, 1.467 |
| Absorption coefficient [mm$^{-1}$] | 1.297 | 1.325 | 1.317 |
| F (000) | 1360 | 1360 | 1360 |
| Crystal size [mm] | 0.22 × 0.18 × 0.10 | 0.18 × 0.14 × 0.10 | 0.20 × 0.14 × 0.12 |
| *θ* Range for data collection [°] | 1.03 to 26.47 | 1.03 to 27.79 | 2.40 to 25.00 |
| Limiting indices | $-19 \le h \le 21$<br>$-8 \le k \le 10$<br>$-26 \le l \le 24$ | $-22 \le h \le 21$<br>$-11 \le k \le 11$<br>$-27 \le l \le 27$ | $-25 \le h \le 25$<br>$-10 \le k \le 10$<br>$-20 \le l \le 20$ |
| Reflections collected/unique | 17099/10244<br>[*R*(int) = 0.0323] | 27420/13723<br>[*R*(int) = 0.0425] | 21327/5170<br>[*R*(int) = 0.1324] |
| Completeness to *θ* | 99.9% | 99.6% | 99.7% |
| Data/restraints/parameters | 10244/1/758 | 13723/1/759 | 5170/0/380 |
| Goodness-of-fit on $F^2$ | 1.016 | 0.990 | 0.912 |
| Final *R* indices [$I > 2\sigma(I)$] | *R*1 = 0.0379,<br>*wR*2 = 0.0833 | *R*1 = 0.0404,<br>*wR*2 = 0.0810 | *R*1 = 0.0807,<br>*wR*2 = 0.1200 |
| Absolute structure parameter | –0.050(17) | 0.024(12) | – |
| Extinction coefficient | 0.0044(2) | 0.00194(17) | 0.033(2) |
| Largest diff. peak/hole [e Å$^{-3}$] | 0.286/–0.424 | 0.567/–0.400 | 1.149/–1.361 |

## Acknowledgments

We are grateful for financial support from the National Science Foundation of China (Nos. 20333080, 20332040, 20472091, 50473048, 20472092, and 20403025), the Ministry of Science and Technology of China (Grant Nos. 2003CB716802, 2004CB719903, 2006CB806105, and G2007CB808004), and the Bureau for Basic Research of the Chinese Academy of Sciences.

[1] a) J. M. Lehn, *Supramolecular Chemistry Concepts and Perspectives*, VCH, Weinheim, Germany, **1995**; b) M. Fujita, *Comprehensive Supramolecular Chemistry*, Pergamon, Oxford, **1996**.

[2] a) C. Piguet, G. Bernardinelli, G. Hopfgartner, *Chem. Rev.* **1997**, *97*, 2005–2062; b) U. Knof, A. von Zelewsky, *Angew. Chem. Int. Ed.* **1999**, *38*, 302–322; c) T. Mizutani, S. Yagi, T. Morinaga, T. Nomura, T. Takagishi, S. Kitagawa, H. Ogoshi, *J. Am. Chem. Soc.* **1999**, *121*, 754–759.

[3] a) G. C. Stein, G. van Koten, K. Vrieze, C. Brevard, A. L. Spek, *J. Am. Chem. Soc.* **1984**, *106*, 4486–4492; b) V. Amendola, L. Fabbrizzi, C. Mangano, P. Pallavicini, E. Roboli, M. Zema, *Inorg. Chem.* **2000**, *39*, 5803–5806; c) Z. K. Wu, Q. Q. Chen, S. X. Xiong, B. Xin, Z. W. Zhao, L. J. Jiang, J. S. Ma, *Angew. Chem. Int. Ed.* **2003**, *42*, 3271–3274.

[4] a) T. E. Wood, N. D. Dalgleish, E. D. Power, A. Thompson, X. M. Chen, Y. Okamoto, *J. Am. Chem. Soc.* **2005**, *127*, 5740–5741; b) T. E. Wood, A. C. Ross, N. D. Dalgleish, E. D. Power, A. Thompson, X. M. Chen, Y. Okamoto, *J. Org. Chem.* **2005**, *70*, 9967–9974; c) A. Al-Sheikh-Ali, K. S. Cameron, T. S. Cameron, K. N. Robertson, A. Thompson, *Org. Lett.* **2005**, *7*, 4773–4775.

[5] a) A. V. Wiznycia, H. Desper, C. J. Levy, *Chem. Commun.* **2005**, 4693–4695; b) A. V. Wiznycia, H. Desper, C. J. Levy, *Inorg. Chem.* **2006**, *45*, 10034–10036.

[6] a) M. Prabhakar, P. S. Zacharias, S. K. Das, *Inorg. Chem.* **2005**, *44*, 2585–2587; b) C. P. Pradeep, P. S. Zacharias, S. K. Das, *Eur. J. Inorg. Chem.* **2005**, 3405–3408; c) H. R. Wen, C. F. Wang, Y. Z. Li, J. L. Zuo, Y. Song, X. Z. You, *Inorg. Chem.* **2006**, *45*, 7032–7034.

[7] a) D. Braga, F. Grepioni, E. Tedesco, *Organometallics* **1997**, *16*, 1846–1856; b) L. Brammer, *Dalton Trans.* **2003**, 3145–3157; c) M. J. Calhorda, *Chem. Commun.* **2000**, 801–809.

[8] a) L. Y. Yang, Q. Q. Chen, Y. Li, S. X. Xiong, G. P. Li, J. S. Ma, *Eur. J. Inorg. Chem.* **2004**, 1478–1487; b) E. C. Alyea, G. Ferguson, S. Kannan, *Chem. Commun.* **1998**, 345–346.

[9] a) J. F. Larrow, E. N. Jacobsen, Y. Gao, Y. Hong, X. Nie, C. M. Zepp, *J. Org. Chem.* **1994**, *59*, 1939–1945; b) A. Bacchi, M. Carcelli, L. Gabba, S. Ianelli, P. Pelagatti, G. Pelizzi, D. Rogolino, *Inorg. Chim. Acta* **2003**, *342*, 229–235.

[10] a) J. Fujita, Y. Shimura in *Spectroscopy and Structure of Metal Chelate Compounds* (Eds: K. Nakamoto, P. J. McCarthy), John Wiley and Sons, New York, N. Y., **1968**, ch. 5, and references cited therein; b) R. S. Downing, F. L. Urbach, *J. Am. Chem. Soc.* **1970**, *92*, 5861–5865; c) F. Wang, H. Zhang, Li Li, H. Q. Hao, X. Y. Wang, J. G. Chen, *Tetrahedron: Asymmetry* **2006**, *17*, 2059–2063.

[11] A. Mukhopadhyay, S. Pal, *Eur. J. Inorg. Chem.* **2006**, 4879–4887.

[12] W. L. F Armarego, C. L. L. Chai, *Purification of Laboratory Chemicals*, 5th ed., Elsevier Science, Butterworth-Heinemann Press, **2003**.

[13] G. M. Sheldrick, *SHELXL-97, Programs for Crystal Structure Solution and Refinement*, University of Göttingen, Germany, **1997**.

Received: March 29, 2007
Published Online: June 19, 2007

 © 2007 Wiley-VCH Verlag GmbH & Co. KGaA, Weinheim 

DOI: 10.1002/ejic.200700430

# Synthesis and Crystallographic Characterisation of the Heterodimetallic Complex [(Dibenzo-18-crown-6)K(μ-Cl)$_3$Ru(η$^6$-*p*-cymene)]

**Carsten A. Vock,[a] Rosario Scopelliti,[a] and Paul J. Dyson*[a]**

**Keywords:** Heterometallic complexes / Bridging ligands / Ruthenium / Crown compounds / X-ray crystallography

The triple-chlorido-bridged heterodimetallic dinuclear complex [(dibenzo-18-crown-6)K(μ-Cl)$_3$Ru(η$^6$-*p*-cymene)] containing an (η$^6$-arene)Ru$^{II}$ fragment and a Group 1 metal crown ether fragment was synthesized and characterized by spectroscopy and X-ray crystallography. The solid-state structure clearly reveals the presence of the triple-chlorido-bridged dinuclear complex, whereas NMR investigations in different deuteriated solvents reveal the presence of an essentially 1:1 mixture of **1** and starting materials, indicating the presence of a dynamic equilibrium.
(© Wiley-VCH Verlag GmbH & Co. KGaA, 69451 Weinheim, Germany, 2007)

## Introduction

Dinuclear homometallic cationic ruthenium(II) complexes of the general type [(η$^6$-arene)Ru(μ-Cl$_3$)(η$^6$-arene)]$^+$ were first described in the early 1970s by Bennett and Smith.[1] Subsequently, these compounds were explored in more detail by Stephenson et al.,[2] with an emphasis on synthetic and electrochemical aspects. A series of crystallographic analyses[3] in combination with theoretical investigations,[4] have also been reported, and applications in hydrogen transfer reactions were reported.[5]

In recent years, dimetallic complexes involving the (η$^6$-arene)Ru$^{II}$ fragment and another transition metal fragment have been widely explored, and impressive applications in catalysis have been observed. For example, the metathesis catalysts Ru(=CHR)Cl$_2$(PCy$_3$)$_2$ (R = CHCPh$_2$ or Ph), react quantitatively with the bridged dimers [M(η$^6$-*p*-cymene)Cl$_2$]$_2$ (M = Ru or Os) to form dimetallic complexes in which the two metal centres are bridged by two chlorido ligands;[6] the resulting dimetallic complexes were found to have higher activities than the mononuclear complexes. Moreover, dimetallic complexes, in which two metal fragments are connected by three halogenido bridges also exhibit interesting properties. Their potential as precursors in catalytic reactions has been demonstrated in Oppenauer-type oxidation reactions of alcohols[7] and for atom-transfer radical reactions.[8] The dimetallic precursors are composed of two transition metal fragments; prominent examples for metal combinations in these heterodimetallic complexes are Ru–Rh[7] and Ru–Ir.[7c,9] However, to the best of our knowledge, halogenido-bridged dimetallic complexes, in which one metal fragment is ruthenium and the other is a main group metal, have not been reported. Herein, we describe the synthesis and characterisation of the first triple-chlorido-bridged Ru$^{II}$–alkali metal heterodimetallic dinuclear complex (Scheme 1).

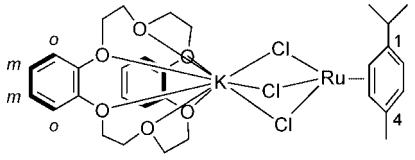


**1**

Scheme 1. [(Dibenzo-18-crown-6)K(μ -Cl)$_3$Ru(η$^6$-*p*-cymene)] (**1**) including NMR numbering scheme.

## Results and Discussion

Treatment of [Ru(η$^6$-*p*-cymene)Cl$_2$]$_2$ with a slight excess of [(dibenzo-18-crown-6)K][Cl] (freshly prepared from dibenzo-18-crown-6 and KCl in MeOH/H$_2$O) in CH$_2$Cl$_2$ at room temperature and subsequent precipitation by addition of ethyl acetate and slow evaporation of CH$_2$Cl$_2$ in vacuo afforded [(dibenzo-18-crown-6)K(μ-Cl)$_3$Ru(η$^6$-*p*-cymene)]·EtOAc (**1**·EtOAc) in moderate yield as orange-brown solid. NMR studies in CD$_2$Cl$_2$ revealed the presence of a mixture of essentially equal amounts of a new species and starting material [Ru(η$^6$-*p*-cymene)Cl$_2$]$_2$, indicating a dynamic equilibrium in solution, as recently described for the salt [Ph$_4$P][Ru(η$^6$-*p*-cymene)Cl$_3$].[10] However, for the system described herein, the equilibrium is not strongly dependent on the solvent, since measurements in CDCl$_3$ and C$_6$D$_6$ lead only to marginal changes in the starting material/product ratio. In comparison, for [Ph$_4$P][Ru(η$^6$-*p*-cymene)Cl$_3$],[10] changing the solvent from CD$_2$Cl$_2$ to CDCl$_3$ led to an al-

[a] Institut des Sciences et Ingénierie Chimiques, Ecole Polytechnique Fédérale de Lausanne (EPFL),
1015 Lausanne, Switzerland
Fax: +41-21-693-98-85
E-mail: paul.dyson@epfl.ch

 © 2007 Wiley-VCH Verlag GmbH & Co. KGaA, Weinheim 

most complete shift of the equilibrium towards the starting material.

Crystallization by layering a $CH_2Cl_2$ solution of the obtained material with ethyl acetate and storage at 4 °C for several days yielded orange crystals of **1**·EtOAc that were suitable for X-ray analysis. An ORTEP plot of the structure is depicted in Figure 1. Crystal data and data of the structure refinement are presented in Table 1. Compound **1** crystallizes as discrete molecules in space group $P2_1/n$. The coordination around the Ru$^{II}$ centre is defined by an η$^6$-*p*-cymene ligand [Ru–centroid 1.653(3) Å] and by three chlorido bridges [Ru–Cl$_{av}$, 2.437(2) Å]. The potassium ion lies in the middle of the crown ether and is displaced by 1.216 Å towards the chlorido ligands and the Ru ion [Ru···K, 4.066(2) Å]. The potassium ion completes its ninefold coordination with the three bridging chlorido ligands [K–Cl$_{av}$, 3.232(2) Å], these distances being slightly longer than those found in solid KCl [3.146 Å].[11] The K–O distances within the crown ether show a wide range of values [2.938(4)–3.127(4) Å] and, compared to those found in a similar molecule,[12] clearly bear out the reduced flexibility of this ligand with respect to the classical 18-crown-6. The solvent molecule lies in the large cavity formed by the crown ether, and it shows short K···C interactions [3.555(8) Å; K···H$_{Me}$, 3.07 Å]. Some weak CH···O hydrogen bonds are observed between the complex and the ethyl acetate of a neighbouring asymmetric unit.

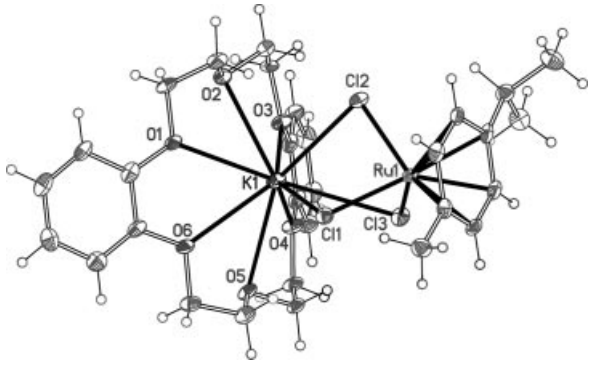


Figure 1. ORTEP representation of **1**·EtOAc; EtOAc solvent has been omitted for clarity; thermal ellipsoids are drawn at the 50% probability level. Selected bond lengths [Å] and angles [°]: Ru1–Cl1 2.4334(15), Ru1–Cl2 2.4302(14), Ru1–Cl3 2.4460(14), K1–Cl1 3.2350(19), K1–Cl2 3.2268(18), K1–Cl3 3.2342(18), K1–O1 3.099(4), K1–O2 2.952(4), K1–O3 2.952(4), K1–O4 2.938(4), K1–O5 2.943(4), K1–O6 3.127(4); Cl2–Ru1–Cl1 86.40(5), Cl1–Ru1–Cl3 87.11(5), Cl2–Ru1–Cl3 87.51(5), O2–K1–O1 101.41(10), O1–K1–O6 49.52(9), O1–K1–Cl2 97.70(8), O1–K1–Cl3 150.38(8).

(Arene)ruthenium(II) compounds are playing an increasingly important role in organometallic chemistry,[13] and as far as we are aware the structural motif of the (arene)ruthenium(II) compound described herein is unique. The structure demonstrates that under certain conditions Group 1 metal ions can interact with the (arene)ruthenium(II) unit. The implications of such an observation are potentially far-reaching as the Noyori-type transfer hydrogenation catalysts based on the (arene)ruthenium(II) unit are activated in the presence of KOH.[14] It has previously been shown that attaching a crown ether to the arene ring in these catalysts influences the rate of the reaction depending on the nature of the ion, viz. $Na^+$, $K^+$ or $Cs^+$.[15] (Arene)ruthenium(II) compounds have also been immobilised in materials which contain Group 1 ions, such as clays,[16] and again, interactions between the two units could be present. (Arene)ruthenium(II) complexes are also being increasingly evaluated in medicinal applications,[17] and again, in a physiological environment interactions with ions such as $Na^+$ or $K^+$ could prove to be important, activating the compounds towards reaction with biomolecular targets.

Table 1. Crystallographic parameters for **1**·EtOAc.

| | **1**·EtOAc |
|---|---|
| Empirical formula | $C_{34}H_{46}Cl_3KO_8Ru$ |
| Formula mass | 829.23 |
| Colour and shape of crystal | orange, long needle |
| Temperature | 100(2) K |
| Wavelength | 0.71073 Å |
| Crystal system | monoclinic |
| Space group | $P2_1/n$ |
| Unit cell dimensions | $a$ = 15.129(4) Å, $\alpha$ = 90°<br>$b$ = 17.702(6) Å, $\beta$ = 118.573(16)°<br>$c$ = 15.667(4) Å, $\gamma$ = 90° |
| Volume | 3684.8(17) Å$^3$ |
| Z | 4 |
| Density (calculated) | 1.495 Mg/m$^3$ |
| Absorption coefficient | 0.804 mm$^{-1}$ |
| $F$(000) | 1712 |
| Crystal size | 0.83 × 0.34 × 0.30 mm |
| $\theta$ range for data collection | 3.29–25.03° |
| Index ranges | $-17 \le h \le 17$<br>$-21 \le k \le 21$<br>$-18 \le l \le 18$ |
| Reflections collected | 47956 |
| Independent reflections | 6412 [$R$(int) = 0.1301] |
| Completeness to $\theta$ = 25.03° | 98.8% |
| Absorption correction | semiempirical from equivalents (SADABS) |
| Max./min. transmission | 1.0000/0.5927 |
| Refinement method | full-matrix least squares on $F^2$ |
| Data/restraints/parameters | 6412/0/424 |
| Goodness-of-fit on $F^2$ | 1.109 |
| Final $R$ indices [$I > 2\sigma(I)$] | $R_1$ = 0.0499, $wR_2$ = 0.1082 |
| $R$ indices (all data) | $R_1$ = 0.0819, $wR_2$ = 0.1295 |
| Largest difference peak/hole | 1.220/–1.056 e·Å$^{-3}$ |

## Experimental Section

**Synthesis and Spectroscopic Characterization:** [RuCl$_2$(η$^6$-*p*-cymene)]$_2$ was synthesized according to a literature protocol.[18] All other reagents and solvents were obtained from commercial sources and used without further purification. $^1$H and $^{13}$C NMR spectra were recorded with a Bruker 400 MHz spectrometer at room temperature in $CD_2Cl_2$. NMR spectra were referenced to internal solvents as follows: $\delta(CH_2Cl_2, {}^1H)$ = 5.35 and $\delta(CD_2Cl_2, {}^{13}C)$ = 53.45. Elemental analyses were conducted at the EPFL.

**Synthesis of [(Dibenzo-18-crown-6)K(μ-Cl)$_3$Ru(η$^6$-*p*-cymene)]·EtOAc (1·EtOAc):** To a solution of KCl (49.0 mg, 0.657 mmol, 2.12 equiv.) in $H_2O$ (1 mL) and MeOH (10 mL), dibenzo-18-crown-6 (237 mg, 0.658 mmol, 2.12 equiv.) was added, and the resulting mixture was stirred at room temperature for 75 min. The solvent was removed in vacuo. The white solid residue was dissolved in

 © 2007 Wiley-VCH Verlag GmbH & Co. KGaA, Weinheim 

$CH_2Cl_2$ (10 mL), [Ru($\eta^6$-*p*-cymene)$Cl_2$]$_2$ (190 mg, 0.310 mmol) was added, and the mixture was stirred at room temperature for 1 h. The solution was filtered, and the residue was washed with $CH_2Cl_2$ (2 × 5 mL). EtOAc (30 mL) was added to the combined filtrates, and $CH_2Cl_2$ was removed in vacuo. After standing at room temperature overnight, the formed voluminous precipitate was filtered, washed with EtOAc (2 × 10 mL) and dried in vacuo, affording **1** as an orange-brown solid (271 mg, 0.327 mmol, 53%). Crystals of the solvated compound **1**·EtOAc suitable for X-ray analysis were obtained by layering a $CH_2Cl_2$ solution of the obtained product with EtOAc and storing at 4 °C for several days. $^1$H NMR (400 MHz, $CD_2Cl_2$): $\delta$ = 1.29 [d, $J$ = 7.0 Hz, 6 H, 1-CH(C$H_3$)$_2$], 2.14 (s, 3 H, 4-C$H_3$), 2.99 [sept, $J$ = 7.0 Hz, 1 H, 1-C$H$(CH$_3$)$_2$], 4.05 (br. t, $J$ = 4.2 Hz, 8 H, 4 × OC$H_2$CH$_2$OC$_6$H$_4$ of dibenzo-18-crown-6), 4.17 (br. t, $J$ = 4.2 Hz, 8 H, 4 × OCH$_2$C$H_2$OC$_6$H$_4$ of dibenzo-18-crown-6), 5.12 (d, $J$ = 5.8 Hz, 2 H, 2-H, 6-H), 5.35–5.37 (m, 2 H, 3-H, 5-H), 6.91 (m$_c$, 8 H, 2 × OC$_6$$H_4$O). $^{13}$C NMR (101 MHz, $CD_2Cl_2$): $\delta$ = 18.47 (4-*C*H$_3$), 21.98 [1-CH(*C*H$_3$)$_2$], 30.76 [1-*C*H(CH$_3$)$_2$], 67.26 (4 × O*C*H$_2$CH$_2$OC$_6$H$_4$ of dibenzo-18-crown-6), 69.05 (4 × OCH$_2$-*C*H$_2$OC$_6$H$_4$ of dibenzo-18-crown-6), 79.17 (C-2, C-6), 81.84 (C-3, C-5), 96.30 (C-4), 100.9 (C-1), 111.7 (4 × *ortho*-C of dibenzo-18-crown-6), 120.9 (4 × *meta*-C of dibenzo-18-crown-6), 147.8 (4 × *C*O of dibenzo-18-crown-6). $C_{30}H_{38}Cl_3KO_6Ru$·1.5 EtOAc (873.30): calcd. C 49.51, H 5.77; found C 49.87, H 5.43.

**Crystallography:** Diffraction data for **1** were measured with a Bruker-Nonius kappa diffractometer equipped with an APEX II CCD using Mo-$K_\alpha$ radiation. Data were reduced by EvalCCD[19] and then corrected for absorption by a semiempirical method.[20] The structure was solved by direct methods,[21] and refined using full-matrix least squares on $F^2$ with all non-H atoms anisotropically defined. Hydrogen atoms were placed in calculated positions using the "riding model". Structure solution, refinement, geometrical calculations and geometrical representations were carried out with SHELXTL.[22] CCDC-643569 contains the supplementary crystallographic data for this paper. These data can be obtained free of charge from The Cambridge Crystallographic Data Centre via www.ccdc.cam.ac.uk/data_request/cif.

## Acknowledgments

We thank the EPFL for financial support. A postdoc stipend provided by the German Academic Exchange Service (DAAD) and the Swiss National Science Foundation to C. A. V. is gratefully acknowledged. We thank Dr. Frank W. Heinemann (University of Erlangen-Nürnberg, Germany) for kind literature support.

[1] M. A. Bennett, A. K. Smith, *J. Chem. Soc. Dalton Trans.* **1974**, 233–241.
[2] a) T. Arthur, T. A. Stephenson, *J. Organomet. Chem.* **1981**, *208*, 369–387; b) T. Arthur, T. A. Stephenson, *J. Organomet. Chem.* **1979**, *168*, C39–C41; c) D. R. Robertson, T. A. Stephenson, T. Arthur, *J. Organomet. Chem.* **1978**, *162*, 121–136; d) G. A. Heath, G. Hefter, D. R. Robertson, W. J. Sime, T. A. Stephenson, *J. Organomet. Chem.* **1978**, *152*, C1–C4; e) D. R. Robertson, T. A. Stephenson, *J. Organomet. Chem.* **1976**, *116*, C29–C30.
[3] For example, see: a) D. S. Pandey, A. N. Sahay, O. M. Sisodia, N. K. Jha, P. Sharma, H. E. Claus, A. Cabrera, *J. Organomet. Chem.* **1999**, *592*, 278–282; b) F. B. McCormick, W. B. Gleason, *Acta Crystallogr., Sect. C* **1993**, *49*, 1493–1496; c) D. A. Tocher, M. D. Walkinshaw, *Acta Crystallogr., Sect. B* **1982**, *38*, 3083–3085.
[4] F. Grepioni, D. Braga, P. J. Dyson, B. F. G. Johnson, F. M. Sanderson, M. J. Calhorda, L. F. Veiros, *Organometallics* **1995**, *14*, 121–130.
[5] A. Rojas, M. Scotti, M. Valderrama, *Bol. Soc. Chil. Quim.* **1988**, *33*, 103–105.
[6] E. L. Dias, R. H. Grubbs, *Organometallics* **1998**, *17*, 2758–2767.
[7] a) S. Gauthier, K. Severin, *Chimia* **2005**, *59*, 111–112; b) S. Gauthier, R. Scopelliti, K. Severin, *Organometallics* **2004**, *23*, 3769–3771; c) A. C. da Silva, H. Piotrowski, P. Mayer, K. Polborn, K. Severin, *Eur. J. Inorg. Chem.* **2001**, 685–691.
[8] a) L. Quebatte, E. Solari, R. Scopelliti, K. Severin, *Organometallics* **2005**, *24*, 1404–1406; b) L. Quebatte, M. Haas, E. Solari, R. Scopelliti, Q. T. Nguyen, K. Severin, *Angew. Chem. Int. Ed.* **2005**, *44*, 1084–1088; c) B. De Clerq, F. Verpoort, *Tetrahedron Lett.* **2002**, *43*, 4687–4690.
[9] A. R. Al-Ohaly, J. F. Nixon, *Inorg. Chim. Acta* **1985**, *103*, 83–93.
[10] C. A. Vock, P. J. Dyson, *Z. Allg. Anorg. Chem.* **2007**, *633*, 640–642.
[11] Landolt-Börnstein, Numerical Data and Functional Relationships in Science and Technology, vols. II/6, II/21, III/7a, Springer, Berlin, **1974**, **1992**, **1973**.
[12] F. W. Heinemann, M. Gerisch, D. Steinborn, *Z. Kristallogr.* **1997**, *212*, 462–464.
[13] a) G. Süss-Fink, B. Therrien, *Organometallics* **2007**, *26*, 766–774; b) M. A. Bennett, *Coord. Chem. Rev.* **1997**, *166*, 225–254; c) W. H. Ang, P. J. Dyson, *Eur. J. Inorg. Chem.* **2006**, 4003–4018.
[14] R. Noyori, S. Hashiguchi, *Acc. Chem. Res.* **1997**, *30*, 97–102.
[15] T. J. Geldbach, M. R. H. Brown, R. Scopelliti, P. J. Dyson, *J. Organomet. Chem.* **2005**, *690*, 5055–5065.
[16] For example, see: a) G. Süss-Fink, B. Mollwitz, B. Therrien, M. Dadras, G. Laurenczy, A. Meister, G. Meister, *J. Cluster Sci.* **2007**, *18*, 87–95; b) A. Meister, G. Meister, G. Süss-Fink, *J. Mol. Catal.* **1994**, *92*, 123–126.
[17] For example, see: a) A. Dorcier, P. J. Dyson, C. Gossens, U. Rothlisberger, R. Scopelliti, I. Tavernelli, *Organometallics* **2005**, *24*, 2114–2123; b) C. Scolaro, A. Bergamo, L. Brescacin, R. Delfino, M. Cocchietto, G. Laurenczy, T. J. Geldbach, G. Sava, P. J. Dyson, *J. Med. Chem.* **2005**, *48*, 4161–4171; c) C. Scolaro, T. J. Geldbach, S. Rochat, A. Dorcier, C. Gossens, A. Bergamo, M. Cocchietto, I. Tavernelli, G. Sava, U. Rothlisberger, P. J. Dyson, *Organometallics* **2006**, *25*, 756–765; d) C. A. Vock, C. Scolaro, A. D. Phillips, R. Scopelliti, G. Sava, P. J. Dyson, *J. Med. Chem.* **2006**, *49*, 5552–5561.
[18] ($\eta^6$-Hexamethylbenzene)ruthenium complexes: M. A. Bennett, T.-N. Huang, T. W. Matheson, A. K. Smith, *Inorg. Synth.* **1982**, *21*, 74–78.
[19] A. J. M. Duisenberg, L. M. J. Kroon-Batenburg, A. M. M. Schreurs, *J. Appl. Crystallogr.* **2003**, *36*, 220–229.
[20] R. H. Blessing, *Acta Crystallogr., Sect. A* **1995**, *51*, 33–38.
[21] G. M. Sheldrick, *Acta Crystallogr., Sect. A* **1990**, *46*, 467–473.
[22] *SHELXTL*, Version 6.1.4, Bruker AXS, Inc., Madison, WI, **2003**.

Received: April 19, 2007
Published Online: June 19, 2007

 © 2007 Wiley-VCH Verlag GmbH & Co. KGaA, Weinheim 

DOI: 10.1002/ejic.200700521

# Synthesis of Cyclic Carbonates from Atmospheric Pressure Carbon Dioxide Using Exceptionally Active Aluminium(salen) Complexes as Catalysts

**Jaisiel Meléndez,[a] Michael North,*[a] and Riccardo Pasquale[a]**

**Keywords:** Carbon dioxide fixation / Aluminium / Schiff bases / Epoxides / Catalysis

Dimetallic aluminium(salen) complexes show exceptionally high catalytic activity for the synthesis of cyclic carbonates from terminal epoxides at ambient temperature and pressure. The process has the potential to contribute towards decreasing atmospheric carbon dioxide emissions from the burning of fossil fuels.
(© Wiley-VCH Verlag GmbH & Co. KGaA, 69451 Weinheim, Germany, 2007)

## Introduction

One of the main scientific challenges facing the human race in the 21st century is controlling global warming due to increasing levels of atmospheric carbon dioxide.[1] In the long term, it may be possible to move entirely to renewable, or non-carbon-based fuels; however, for the foreseeable future, annual consumption of fossil fuels is predicted to continue to increase markedly with a corresponding rise in atmospheric carbon dioxide levels.[2] The only solution currently being considered to this problem is "carbon capture and storage" which involves concentrating and compressing carbon dioxide and then storing it in disused oil/gas wells or under the ocean.[3] However, it is far from certain that long-term containment is feasible given the volatile nature of carbon dioxide.

An alternative solution to the problem would be to convert the carbon dioxide at source (taking advantage of the relatively high concentration of carbon dioxide in for example the exhaust stream of a fossil fuel power station) into a chemical for which there is a significant commercial demand.[1,3,4] In order to be feasible, any such procedure would have to occur at atmospheric pressure and near ambient temperature; otherwise the energy required to operate the process will generate more carbon dioxide than is remediated. Unfortunately, the low chemical reactivity of carbon dioxide severely restricts the range of chemical reactions which might be feasible.

One unusually facile reaction of carbon dioxide is its insertion into epoxides to generate cyclic carbonates or a polycarbonate[5–7] as shown in Scheme 1. Ethylene, propylene and butylene carbonates are manufactured commercially and it has been estimated that cyclic carbonates and products derived from them could reduce atmospheric carbon dioxide emissions by up to 120 million tons per year if the economics of the process could be improved.[3] The epoxide co-reactants required for the chemistry shown in Scheme 1 are readily available by the catalytic epoxidation of alkenes, a process which can be achieved using hydrogen peroxide as a green oxidant,[8] and the alkenes can be obtained from waste plastics or biological sources. A large number of homogeneous and heterogeneous catalysts have been reported to induce the reaction between epoxides and carbon dioxide.[7,9] However, almost all of these require elevated reaction temperatures and/or high pressures of carbon dioxide; often the reaction is conducted in supercritical carbon dioxide.

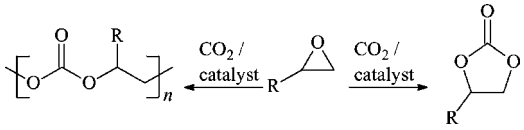


Scheme 1. Synthesis of polymeric or cyclic carbonates from $CO_2$ and epoxides.

Notable amongst the catalysts which have been employed to synthesise cyclic carbonates are metal(salen) complexes[6,10] derived from aluminium,[11] nickel,[11a] copper,[11a,12] zinc,[11a,12] magnesium,[11a] cobalt,[11a,12–14] chromium,[11a,15] or tin.[16] In previous work from our group,[17] we have demonstrated that dimetallic salen complexes display much higher catalytic activity than their monometallic counterparts in asymmetric cyanohydrin synthesis because the two metal ions can each activate one of the two components of the reaction. Polycarbonate and cyclic carbonate synthesis using chromium(salen) complexes are known to be bimolecular,[15] therefore, we reasoned that a suitable dimetallic salen complex might display significantly improved catalytic activity in the reaction between carbon dioxide and epoxides. Here we report the successful accomplish-

[a] School of Natural Sciences, Newcastle University, Bedson Building, Newcastle upon Tyne, NE1 7RU, UK
Fax: +44-870-131-3783
E-mail: michael.north@ncl.ac.uk
Supporting information for this article is available on the WWW under http://www.eurjic.org or from the author.

 © 2007 Wiley-VCH Verlag GmbH & Co. KGaA, Weinheim 

ment of this concept through the development of a dimetallic aluminium(salen) complex which will catalyse the insertion of carbon dioxide into epoxides at atmospheric pressure and ambient temperature.

## Results and Discussion

We selected aluminium as the metal of choice due to its low environmental impact and previous use in cyclic carbonate synthesis, albeit at elevated pressures of carbon dioxide (at least 6 atm).[11] Thus, treatment of a salen ligand with aluminium triethoxide in toluene gave complexes **1a**–**h** as yellow or orange solids in 33–63% yields as shown in Scheme 2. The μ-O atom in complexes **1a**–**h** could be derived from adventitious moisture, by decomposition of ethanol formed during the reaction, and/or from the ethoxy group. Complexes **1a** and **1c** have previously been prepared by a different route[18,19] and used to catalyse asymmetric Michael additions.[19] The X-ray structure of complexes **1c**[20] and **1d**[21] have previously been reported, and the mass spectra of compounds **1a**–**h** confirmed their dimetallic structures (see Supporting Information).

Complexes **1a**–**h** were tested for their ability to catalyse the formation of carbonate **3a** from racemic styrene oxide (**2a**) and carbon dioxide under solvent-free conditions as shown in Scheme 3, and the results are summarised in Table 1. In the absence of a co-catalyst, no reaction occurred, even at 5 atm pressure and elevated temperature (Table 1, Entries 1 and 2). This is in line with previous work using aluminium(salen)-derived catalysts where reaction only occurred in the presence of a tetrabutylammonium halide,[11a–11d] DMAP[11e,11f] or *N*-methylimidazole[11e] co-catalyst. The combination of complex **1a** and tetrabutylammonium bromide was found to display extremely high catalytic activity (Table 1, Entries 4–11). This combination of catalysts displayed unprecedented catalytic activity at 1 atm carbon dioxide pressure and room temperature. Tetrabutylammonium chloride and iodide were also investigated as co-catalysts, but were found to be less effective than the use of tetrabutylammonium bromide. The only previous reports of synthetic studies[11c,13c] on the preparation of cyclic carbonates at ambient temperature required carbon dioxide pressures of 6–15 atm[14,22] or reaction times of up to 7 d.[23] That the observed catalysis was not due solely to the tetrabutylammonium bromide co-catalyst was demonstrated by a reaction run in the absence of an aluminium(salen) complex (Table 1, Entry 3). Although use of just 1.0 mol-% of catalyst **1a** gave a good conversion after 24 h (Table 1, Entry 10), use of 2.5 mol-% was adopted as standard in subsequent studies as this allowed good conversions (62% with 57% isolated yield) to be achieved after just 3 h (Table 1, Entry 8).

Attempts to increase the reactivity of the catalyst by varying the substituents on the aromatic rings or the diamine of the salen ligand were not successful as none of catalysts **1b**–**h** were significantly more active than complex **1a** (Table 1, Entries 12–18). The trend in reactivity appears

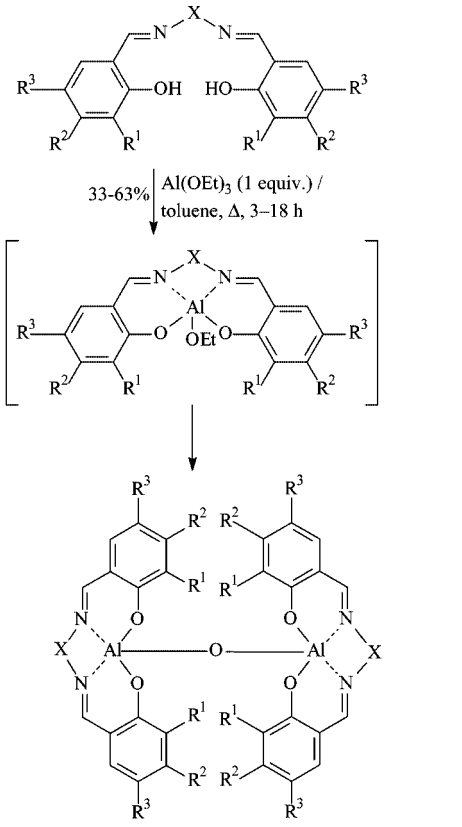


**1a**: X = (1*R*,2*R*)-cyclohexyl; $R^1 = R^3 = t$Bu; $R^2$ = H
**1b**: X = (1*R*,2*R*)-cyclohexyl; $R^1 = t$Bu; $R^2$ = H; $R^3 = NO_2$
**1c**: X = $(CH_2)_2$; $R^1 = R^3 = t$Bu; $R^2$ = H
**1d**: X = 1,2-$C_6H_4$; $R^1 = R^3 = t$Bu; $R^2$ = H
**1e**: X = (1*R*,2*R*)-cyclohexyl; $R^1 = R^3$ = H; $R^2$ = OMe
**1f**: X = (1*R*,2*R*)-cyclohexyl; $R^1 = R^2 = R^3$ = H
**1g**: X = (1*R*,2*R*)-cyclohexyl; $R^1 = t$Bu; $R^2 = R^3$ = H
**1h**: X = (1*R*,2*R*)-cyclohexyl; $R^1 = t$Bu; $R^2$ = H; $R^3$ = OMe

Scheme 2. Synthesis of catalysts **1a**–**h**.

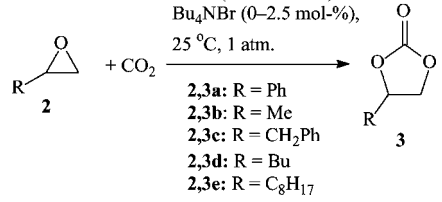


Scheme 3. Synthesis of cyclic carbonates **3** using complexes **1a**–**h**.

to be related to the solubility of the catalyst in styrene oxide rather than to any steric or electronic factors, as the highest catalytic activity was observed with the most hydrophobic complexes, and complexes **1d** and **1f** which gave the lowest conversions (Table 1, Entries 14 and 16) did not fully dissolve during the reaction.

Cyclic carbonates derived from other monosubstituted epoxides could also be obtained from the combination of complex **1a** and tetrabutylammonium bromide (Scheme 3), as detailed in Table 2. Propylene oxide was a particularly reactive substrate, and only 1 mol-% of catalyst was necessary to convert it into propylene carbonate in good yield,

 © 2007 Wiley-VCH Verlag GmbH & Co. KGaA, Weinheim 

Table 1. Synthesis of carbonate **3a** catalysed by complexes **1a**–**h**.

| Entry | Catalyst [mol-%] | Co-catalyst [mol-%] | $CO_2$ pressure [atm] | Temp. [°C] | Time [h] | Conversion[a] [%] |
|---|---|---|---|---|---|---|
| 1 | **1a** (1.0) | | 1 | 25 | 3 | 0 |
| 2 | **1a** (1.0) | | 5 | 50 | 24 | 0 |
| 3 | | $Bu_4NBr$ (1.0) | 1 | 25 | 3 | 4 |
| 4 | **1a** (0.1) | $Bu_4NBr$ (0.1) | 1 | 25 | 3 | 5 |
| 5 | **1a** (1.0) | $Bu_4NBr$ (1.0) | 1 | 25 | 3 | 38 |
| 6 | **1a** (1.0) | $Bu_4NBr$ (2.5) | 1 | 25 | 3 | 56 |
| 7 | **1a** (2.5) | $Bu_4NBr$ (1.0) | 1 | 25 | 3 | 51 |
| 8 | **1a** (2.5) | $Bu_4NBr$ (2.5) | 1 | 25 | 3 | 62 |
| 9 | **1a** (0.1) | $Bu_4NBr$ (0.1) | 1 | 25 | 24 | 27 |
| 10 | **1a** (1.0) | $Bu_4NBr$ (1.0) | 1 | 25 | 24 | 86 |
| 11 | **1a** (2.5) | $Bu_4NBr$ (2.5) | 1 | 25 | 24 | 98 |
| 12 | **1b** (2.5) | $Bu_4NBr$ (2.5) | 1 | 25 | 3 | 50 |
| 13 | **1c** (2.5) | $Bu_4NBr$ (2.5) | 1 | 25 | 3 | 52 |
| 14 | **1d** (2.5) | $Bu_4NBr$ (2.5) | 1 | 25 | 3 | 33 |
| 15 | **1e** (2.5) | $Bu_4NBr$ (2.5) | 1 | 25 | 3 | 41 |
| 16 | **1f** (2.5) | $Bu_4NBr$ (2.5) | 1 | 25 | 3 | 28 |
| 17 | **1g** (2.5) | $Bu_4NBr$ (2.5) | 1 | 25 | 3 | 51 |
| 18 | **1h** (2.5) | $Bu_4NBr$ (2.5) | 1 | 25 | 3 | 64 |

[a] Conversions are based on $^1H$ NMR analysis of the reaction mixture.

even at 0 °C (Table 2; Entries 1–3). The other monosubstituted epoxides studied were converted into the corresponding carbonates in good to high yield using the standard conditions developed above (Table 2, Entries 4–7), but use of lower amounts of catalyst/co-catalyst seriously reduced the yields in these cases. Disubstituted epoxides were much less reactive with *trans*-stilbene oxide giving just 8% of the corresponding cyclic carbonate after a reaction time of 48 h, whilst cyclohexene oxide and 2-phenylpropylene oxide failed to give any cyclic carbonate under these conditions. No polycarbonate was detected in any reaction catalysed by complexes **1a**–**h** with any of substrates **2a**–**e**, indicating that these complexes display a high selectivity for cyclic carbonate rather than polycarbonate formation.

Table 2. Synthesis of carbonates **3b**–**e** using catalyst **1a**.

| Entry[a] | Epoxide | **1a**/$Bu_4NBr$ [mol-%] | Time [h] | Yield [%][c] |
|---|---|---|---|---|
| 1[b] | **2b** (R = Me) | 2.5 + 2.5 | 3 | 77 |
| 2[b] | **2b** (R = Me) | 1 + 1 | 3 | 40 |
| 3[b] | **2b** (R = Me) | 1 + 1 | 24 | 63 |
| 4 | **2c** (R = $CH_2Ph$) | 2.5 + 2.5 | 3 | 44 |
| 5 | **2c** (R = $CH_2Ph$) | 2.5 + 2.5 | 24 | 99 |
| 6 | **2d** (R = Bu) | 2.5 + 2.5 | 3 | 87 |
| 7 | **2e** (R = $C_8H_{17}$) | 2.5 + 2.5 | 3 | 64 |

[a] All reactions were conducted in the absence of solvent at 1 atm pressure of carbon dioxide and at 25 °C, unless otherwise stated. [b] Reaction at 0 °C. [c] Yield of isolated product obtained after chromatographic purification. Conversions (based on $^1H$ NMR analysis of the reaction mixture) are also given in the Supporting Information.

The exceptional catalytic activity of the catalysts **1a**–**h** is consistent with a mechanism in which both aluminium ions of the complex play a role in activating the components of the reaction as shown in Scheme 4. Thus, ring-opening of the epoxide by bromide results in an aluminium-bound alkoxide. Coordination of carbon dioxide to the second aluminium ion, followed by intramolecular transfer of the alkoxide onto the coordinated carbon dioxide gives an aluminium carbonate which can cyclize to form the cyclic carbonate product and regenerate both catalysts. Work is currently underway to study the kinetics of this process and to detect reaction intermediates to confirm this mechanistic hypothesis.

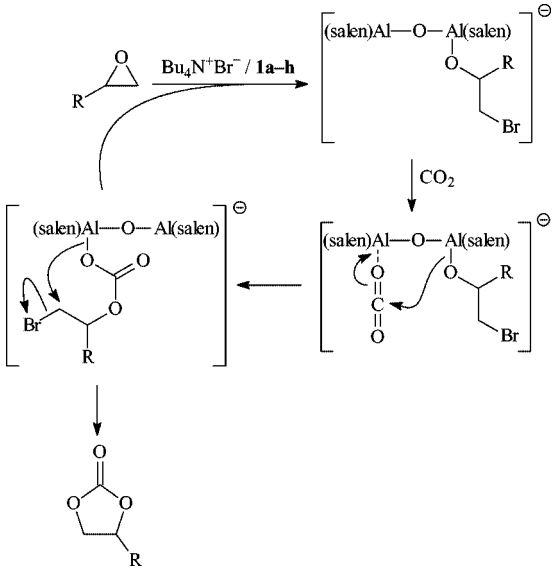


Scheme 4. Possible mechanism to explain the catalytic activity of complexes **1a**–**h**.

## Conclusions

The dimetallic aluminium(salen) complexes **1a**–**h** display exceptionally high catalytic activity for the conversion of terminal epoxides into cyclic carbonates at room temperature and 1 atm pressure.

 © 2007 Wiley-VCH Verlag GmbH & Co. KGaA, Weinheim 

## Experimental Section

Experimental details for the synthesis of catalysts **1a**–**h** and cyclic carbonates **3a**–**e** are given in the Supporting Information.

**Supporting Information** (see footnote on the first page of this article): Full experimental details and characterising data for the synthesis of catalysts **1a**–**h** and cyclic carbonates **3a**–**e**.

## Acknowledgments

The authors thank Newcastle University for a studentship (to R. P.), the Engineering and Physical Sciences Research Council (EPSRC) for funding and the EPSRC national mass spectrometry service at the University of Wales, Swansea for recording mass spectra.

[1] For a detailed analysis of this issue from a chemical catalysis perspective, see: H. Arakawa, M. Aresta, J. N. Armor, M. A. Barteau, E. J. Beckman, A. T. Bell, J. E. Bercaw, C. Creutz, E. Dinjus, D. A. Dixon, K. Domen, D. L. DuBois, J. Eckert, E. Fujita, D. H. Gibson, W. A. Goddard, D. W. Goodman, J. Keller, G. J. Kubas, H. H. Kung, J. E. Lyons, L. E. Manzer, T. J. Marks, K. Morokuma, K. M. Nicholas, R. Periana, L. Que, J. Rostrup-Nielson, W. M. H. Sachtler, L. D. Schmidt, A. Sen, G. A. Somorjai, P. C. Stair, B. R. Stults, W. Tumas, *Chem. Rev.* **2001**, *101*, 953–996.

[2] a) X. Xiaoding, J. A. Moulijin, *Energy Fuels* **1996**, *10*, 305–325; b) M. Pervaiz, M. M. Sain, *Resour., Conserv. Recycl.* **2003**, *39*, 325–340 and references cited therein.

[3] M. Aresta, A. Dibenedetto, *Catal. Today* **2004**, *98*, 455–462.

[4] For reviews of the potential utilisation of atmospheric carbon dioxide, see: a) A. Baiker, *Appl. Organomet. Chem.* **2000**, *14*, 751–762; b) I. Omae, *Catal. Today* **2006**, *115*, 33–52; c) R. Zevenhoven, S. Eloneva, S. Teir, *Catal. Today* **2006**, *115*, 73–79.

[5] For a review of polycarbonate synthesis, see: G. W. Coates, D. R. Moore, *Angew. Chem. Int. Ed.* **2004**, *43*, 6618–6639.

[6] For a review of the use of metal(salen) complexes in the synthesis of polycarbonates, see: D. J. Darensbourg, R. M. Mackiewicz, A. L. Phelps, D. R. Billodeaux, *Acc. Chem. Res.* **2004**, *37*, 836–884.

[7] For a review of the reaction between epoxides and $CO_2$, see: D. J. Darensbourg, M. W. Holtcamp, *Coord. Chem. Rev.* **1996**, *153*, 155–174.

[8] For leading references, see: a) R. I. Kureshy, S. Singh, N. H. Khan, S. H. R. Abdi, I. Ahmed, A. Bhatt, R. V. Jasra, *Catal. Lett.* **2006**, *107*, 127–130; b) K. Matsumoto, Y. Sawada, T. Katsuki, *Synlett* **2006**, 3545–3547; c) H. Shitama, T. Katsuki, *Tetrahedron Lett.* **2006**, *47*, 3203–3207.

[9] For reviews of cyclic carbonate synthesis, see: a) M. Yoshida, M. Ihara, *Chem. Eur. J.* **2004**, *10*, 2886–2893; b) J. Sun, S. Fujita, M. Arai, *J. Organomet. Chem.* **2005**, *690*, 3490–3497.

[10] Unmetallated salen ligands will also catalyse this reaction, but only at high pressures (>30 atm) and high temperatures (>100 °C): Y. M. Shen, W. L. Duan, M. Shi, *Eur. J. Org. Chem.* **2004**, 3080–3089.

[11] a) X.-B. Lu, X.-J. Feng, R. He, *Appl. Catal. A* **2002**, *234*, 25–34; b) X.-B. Lu, R. He, C.-X. Bai, *J. Mol. Catal. A* **2002**, *186*, 1–11; c) X.-B. Lu, Y.-J. Zhang, B. Liang, X. Li, H. Wang, *J. Mol. Catal. A* **2004**, *210*, 31–34; d) X.-B. Lu, Y.-J. Zhang, K. Jin, L.-M. Luo, H. Wang, *J. Catal.* **2004**, *227*, 537–541; e) M. Alvaro, C. Baleizao, E. Carbonell, M. El Ghoul, H. García, B. Gigante, *Tetrahedron* **2005**, *61*, 12131–12139; f) G. A. Luinstra, G. R. Haas, F. Molnar, V. Bernhart, R. Eberhardt, B. Rieger, *Chem. Eur. J.* **2005**, *11*, 6298–6314.

[12] Y.-M. Shen, W.-L. Duan, M. Shi, *J. Org. Chem.* **2003**, *68*, 1559–1562.

[13] a) X.-B. Lu, J.-H. Xiu, R. He, K. Jin, L.-M. Luo, X.-J. Feng, *Appl. Catal. A* **2004**, *275*, 73–78; b) R. L. Paddock, S. T. Nguyen, *Chem. Commun.* **2004**, 1622–1623; c) X.-B. Lu, B. Liang, Y.-J. Zhang, Y.-Z. Tian, Y.-M. Wang, C.-X. Bai, H. Wang, R. Zhang, *J. Am. Chem. Soc.* **2004**, *126*, 3732–3733; d) X.-B. Lu, Y. Wang, *Angew. Chem. Int. Ed.* **2004**, *43*, 3574–3577.

[14] For the kinetic resolution of propylene oxide using Co(salen) complexes, see: A. Berkessel, M. Brandenburg, *Org. Lett.* **2006**, *8*, 4401–4404.

[15] a) R. L. Paddock, S. T. Nguyen, *J. Am. Chem. Soc.* **2001**, *123*, 11498–11499; b) D. J. Darensbourg, J. C. Yarbrough, C. Ortiz, C. C. Fang, *J. Am. Chem. Soc.* **2003**, *125*, 7586–7591; c) M. Alvaro, C. Baleizao, D. Das, E. Carbonell, H. García, *J. Catal.* **2004**, *228*, 254–258.

[16] H. Jing, S. K. Edulji, J. M. Gibbs, C. L. Stern, H. Zhou, S. T. Nguyen, *Inorg. Chem.* **2004**, *43*, 4315–4327.

[17] For a review of this work, see: T. R. J. Achard, L. A. Clutterbuck, M. North, *Synlett* **2005**, 1828–1847.

[18] S. J. Dzugan, V. L. Goedken, *Inorg. Chem.* **1986**, *25*, 2858–2864.

[19] For a leading reference, see: E. P. Balskus, E. N. Jacobsen, *J. Am. Chem. Soc.* **2006**, *128*, 6810–6812.

[20] D. Rutherford, D. A. Atwood, *Organometallics* **1996**, *15*, 4417–4422.

[21] Y. Wang, S. Bhandari, S. Parkin, D. A. Atwood, *J. Organomet. Chem.* **2004**, *689*, 759–765.

[22] For mechanistic studies on the reaction between propylene oxide and carbon dioxide at room temperature and 1 atm pressure with long reaction times, see: a) K. Kasuga, S. Nagao, T. Fukumoto, M. Handa, *Polyhedron* **1996**, *15*, 69–72; b) H. Sugimoto, T. Kimura, S. Inoue, *J. Am. Chem. Soc.* **1999**, *121*, 2325–2326.

[23] a) M. Ratzenhofer, H. Kisch, *Angew. Chem. Int. Ed. Engl.* **1980**, *19*, 317–318; b) H. Kisch, R. Millini, I.-J. Wang, *Chem. Ber.* **1986**, *119*, 1090–1094.

Received: May 16, 2007
Published Online: June 21, 2007

 © 2007 Wiley-VCH Verlag GmbH & Co. KGaA, Weinheim 

DOI: 10.1002/ejic.200600998

# Platinum(II) and Palladium(II) Complexes with *N*-Aminoguanidine

David J. Aitken,*[a] Alberto Albinati,[b] Arnaud Gautier,[a] Henri-Philippe Husson,[c] Georges Morgant,[d] Dung Nguyen-Huy,[d] Jiří Kozelka,*[e] Pascale Lemoine,[f] Sandrine Ongeri,[c] Silvia Rizzato,[b] and Bernard Viossat[f]

**Keywords:** Platinum / Palladium / N ligands / Coordination modes

*N*-Aminoguanidine (Amgu) was examined for its behaviour as a ligand for platinum(II) and palladium(II). Protonated $AmguH^+$ can coordinate platinum as a monodentate ligand bound via the N4 amino group. Deprotonated, electrically neutral Amgu forms chelate complexes with both $Pt^{II}$ and $Pd^{II}$; in these complexes Amgu is coordinated to the metal by the N4 amino group and the deprotonated N1 imino group, forming a five-membered ring. $K[PtCl_3(dmso)]$ reacted with Amgu·HCl to yield a chelate complex with N1 bound *trans* to S, suggesting that an exchange between the N1 and N4 binding sites followed the primary nucleophilic attack of N4 on platinum. Whereas reactions between $K_2PdCl_4$ and Amgu·HCl were rapid and straightforward, $K_2PtCl_4$ was easily reduced to metallic platinum by Amgu·HCl, especially in stoichiometric conditions. Solution NMR and X-ray crystallographic characterization is presented for five new complexes: *trans*-$[PtCl_2(AmguH\text{-}N4)_2]Cl_2\cdot 2^1/_2H_2O$ (**3**), *trans*-$[Pt(Amgu\text{-}N1,N4)_2](NO_3)_2$ (**4**), $[PtCl(Amgu\text{-}N1,N4)(dmso)]Cl\cdot 2H_2O$ (**5**), $[PdCl_2(AmguH\text{-}N1,N4)]$ (**6**), and *trans*-$[Pd(Amgu\text{-}N1,N4)_2]Cl_2$ (**7**).

(© Wiley-VCH Verlag GmbH & Co. KGaA, 69451 Weinheim, Germany, 2007)

## Introduction

Cisplatin (*cis*-$[PtCl_2(NH_3)_2]$; cisplatyl®; platinol®; Figure 1) is one of the most successful drugs used currently in cancer chemotherapy.[1,2] Despite numerous efforts to synthesize analogues which would cause less severe side effects, have improved activity profiles, and/or allow the resistance to cisplatin to be circumvented, only three cisplatin analogues have been admitted for clinical use to date, carboplatin,[3] oxaliplatin,[4] and nedaplatin,[5] although none of them has brought about a real breakthrough in cancer chemotherapy. The particular features of the parent drug cisplatin, which distinguish it from its analogues, are its unique hydrogen-bonding capacity and its small size.[6] In this respect, aminoguanidine (Amgu; Figure 1) is an interesting potential bidentate ligand for replacement of the two $NH_3$ ligands, since it is only slightly bulkier and has six N–H bonds oriented in a manner different to those of cisplatin, thus offering a different pattern of strong hydrogen bonds. Amgu is in fact a molecule of considerable biological importance in its own right,[7–9] and its structure has been incorporated into a wide variety of organic compounds displaying diverse pharmacological activities.[10–15] Amgu is a

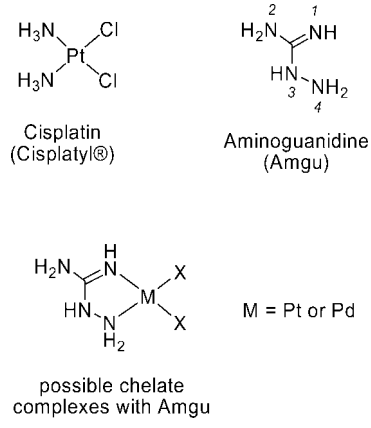


Figure 1. Structural formulae of cisplatin, aminoguanidine, and possible chelates of $Pt^{II}$ or $Pd^{II}$ analogous to cisplatin.

[a] Laboratoire SEESIB, UMR 6504 – CNRS, Département de Chimie, Université Blaise Pascal – Clermont-Ferrand II, 24 avenue des Landais, 63177 Aubière cedex, France
Fax: +33-4-73407717
E-mail: David.Aitken@univ-bpclermont.fr
[b] Dipartimento di Chimica Strutturale e Stereochimica Inorganica, Università di Milano, Via G. Venezian 21, 20133 Milano, Italy
[c] Laboratoire de Chimie Thérapeutique, UMR 8638 – CNRS, Faculté des Sciences Pharmaceutiques et Biologiques, Université René Descartes – Paris V, 4 avenue de l'Observatoire, 75270 Paris cedex 06, France
[d] Laboratoire de Cristallochimie Bioinorganique, Faculté de Pharmacie, Université de Paris-Sud, Rue Jean Baptiste Clément, 92296 Châtenay-Malabry cedex, France
[e] Laboratoire de Chimie et Biochimie Pharmacologiques et Toxicologiques, UMR 8601 – CNRS, Université René Descartes – Paris V, 45 rue des Saints-Pères, 75270 Paris cedex 06, France
Fax: +33-1-42868387
E-mail: jiri.kozelka@univ-paris5.fr
[f] Laboratoire de Cristallographie et RMN Biologiques, UMR 8015 – CNRS, Faculté des Sciences Pharmaceutiques et Biologiques, Université René Descartes – Paris V, 4 avenue de l'Observatoire, 75270 Paris cedex 06, France

 © 2007 Wiley-VCH Verlag GmbH & Co. KGaA, Weinheim 

dibasic compound, which is unstable in the free state; the guanidinium centre has the higher proton affinity (protonation on N1) but a dicationic species (second protonation on N4) is also known.[16–18]

The coordination chemistry of Amgu has been described for a few transition metals. In one of the earliest studies, Thiele[19] described a complex salt of copper with the formula $[(CN_4H_5)_2Cu](HNO_3)_2$, which was later confirmed as the double chelate $[Cu(Amgu)_2](NO_3)_2$.[20,21] Similar square-planar chelate structures have been attributed to complexes of nickel(II).[21,22] Dirhodium(II) tetracarboxylate complexes of general formula $Rh_2(RCOO)_4(Amgu)(H_2O)$ where R = H, $CH_3$ or $C_2H_5$ have been described, in which the presence of a C=N→Rh bond was deduced; no evidence for the coordination of a second nitrogen function was found, although a bridging role for the Amgu ligand was not entirely ruled out.[23] In 1985, the preparation of a platinum(II) complex of Amgu having promising biological activity was reported in a patent.[24] Presumably on the basis of analogy with other diamino ligands, it was assumed that a chelate structure was obtained; no characterisation of the material was described, however.

In order to gain insight into the behaviour of Amgu as a ligand for $Pt^{II}$, particularly with a view to establishing a basis for new antitumour candidates, we undertook an investigation of the synthesis of several $Pt^{II}$-aminoguanidine complexes, and also of related $Pd^{II}$ complexes for comparison.

## Results and Discussion

### Platinum Complexes

In our first experiments, we reacted equimolar amounts of Amgu·HCl and $K_2PtCl_4$ in aqueous solution at ambient temperature for 15 h, according to the patent procedure.[24] In contrast to the literature report, no solid product appeared during this time; instead, small amounts of a black deposit (presumably reduced platinum) appeared on the walls of the reaction vessel. The remaining solution was evaporated and the residue was examined by NMR spectroscopy. Integration of $^1H$ NMR signals of a $[D_7]$dmf solution showed the presence of seven protons, which suggested that the Amgu ligand was protonated. The $^{195}Pt$ NMR spectrum showed one major signal at $\delta$ = –1997 ppm, corresponding to an $NCl_3$ ligand set for square planar platinum(II) species.[25] Minor peaks at $\delta$ = –1631, –2128 and –2218 ppm correspond to $Cl_4$ and two $N_2Cl_2$ ligand sets, respectively. We suspect that one of the latter two constituents was the anticipated chelate structure **2**, but the major species appeared to be a monodentate zwitterionic compound **1** (Scheme 1). N4 is the only nitrogen of Amgu having a lone-pair available to coordinate platinum when N1 of the guanidinium centre is protonated.

Attempts to adapt the reaction conditions in order to obtain chelate **2** met with failure. Neutralization of an aqueous Amgu·HCl solution with one equivalent of KOH immediately prior to addition of one equivalent of $K_2PtCl_4$ simply increased the production of the black deposit. Treatment of an aqueous Amgu·HCl solution with $AgNO_3$ immediately produced a white precipitate of AgCl which was removed by filtration, leaving a solution of Amgu·$HNO_3$. Addition of $K_2PtCl_4$ to Amgu·$HNO_3$ solution (or to Amgu·$HNO_3$ solution + one equivalent of KOH) produced an intractable solution containing the usual black deposit. Treating $K_2PtCl_4$ with two or four equivalents of $AgNO_3$ to replace chloride ions followed by addition of one equivalent of Amgu·$HNO_3$ solution (with or without one equivalent of KOH) gave similar results.

These unsuccessful attempts to isolate a single-chelate ligand complex such as **2** prompted us to investigate the possibility of forming a bis-chelate. In an initial effort, treatment of $K_2PtCl_4$ with two equivalents of Amgu·HCl lead once again to extensive black deposit formation over a 15 h reaction period. However, when an aqueous solution of $K_2PtCl_4$ was treated with 5 equiv. of Amgu·HCl and the solvent was evaporated under reduced pressure over a period of several hours, a yellow crystalline product was formed. Its NMR spectroscopic data in $[D_7]$dmf solution (8 identical N1 and N2 guanidinium protons at $\delta$ = 8.27 and a single $^{195}Pt$ signal at $\delta$ = –2277) and microanalytical data were consistent with the formula *trans*-$[PtCl_2(AmguH\text{-}N4)_2]Cl_2$ (**3**) (Scheme 1); the structure was confirmed by X-ray crystallographic analysis (Figure 2).

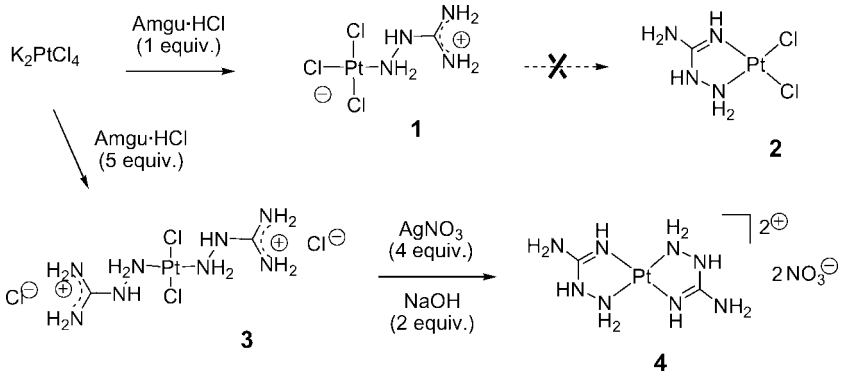


Scheme 1.

 © 2007 Wiley-VCH Verlag GmbH & Co. KGaA, Weinheim 

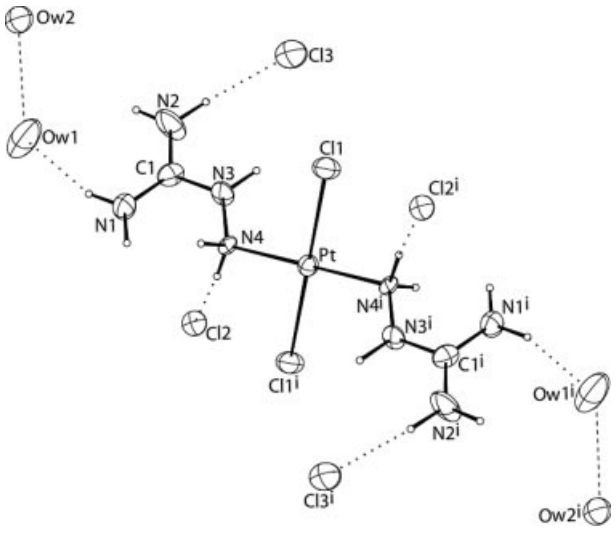


Figure 2. CAMERON plot (50% thermal probability ellipsoids) of the crystal structure of **3**. Selected bond lengths [Å] and angles [°]: Pt–Cl1 2.295(3), Pt–N4 2.064(7), C1–N1 1.295(13), C1–N2 1.283(13), C1–N3 1.350(13), N4–N3 1.389(11), Cl1–Pt–N4 90.8(2), Cl1–Pt–N4i 89.2(2), N1–C1–N2 121.9(10), N1–C1–N3 121.6(9), N2–C1–N3 116.4(10).

In the crystal, the structure is centrosymmetric, so that only half of the molecule is independent, with two Amgu molecules acting as monodentate ligands, coordinating to platinum through the hydrazine-type nitrogen N4, whose geometry and hydrogen atom count clearly indicate $sp^3$ hybridization. Two chlorine atoms complete the inner ligand sphere with a *trans*-geometry, and two chloride ions and 2.5 water molecules per unit cell are located in the crystal. The Pt atom lies on a centre of symmetry. The N1 and N2 atoms of Amgu each bear two hydrogens; one of the N1 hydrogens participates in a hydrogen bond with a water molecule. Hydrogen bonds with chloride counterions are also observed for one hydrogen on each atom N2 and N4. Distances and angles at the platinum centre have usual values, while distances and angles of the Amgu moiety are comparable to those observed for uncomplexed Amgu cations in the solid state.[16,26–28] Distances C1–N1, C1–N2 and C1–N3 have approximately equal values, as should be expected for a delocalized guanidinium system. The Amgu ligand is approximately planar (maximum deviation from the least-squares-plane defined by the atoms C1, N1, N2, N3, and N4 is 0.039(2) Å for N3), confirming that nitrogen N3 is $sp^2$ hybridized. On the other hand, the overall structure of **3** is not planar; the angle between the platinum coordination plane and the mean ligand plane (N1–C1–N2–N3–N4) is 147.4°.

In an effort to make the Amgu ligands of complex **3** behave as chelates, a sample of **3** was treated with 4 equiv. of silver nitrate to precipitate all halide, then with 2 equiv. of base. This induced the slow appearance of colourless crystals, which were identified as *trans*-$[Pt(Amgu)_2](NO_3)_2$ (**4**; Scheme 1) by X-ray diffraction analysis, as shown in Figure 3.

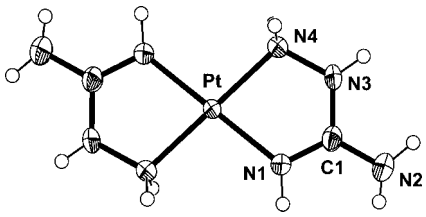


Figure 3. ORTEP plot (50% thermal probability ellipsoids) of the crystal structure of **4**; nitrate counterions are omitted. Selected bond lengths [Å] and angles [°]: Pt–N1 1.996(6), Pt–N4 2.031(6), N1–C1 1.305(10), C1–N2 1.331(10), C1–N3 1.348(10), N4–N3 1.434(9), N1–Pt–N4 80.0(2), C1–N1–Pt 116.2(5), N1–C1–N2 125.8(8), N1–C1–N3 117.0(6), C1–N3–N4 116.6(5), N3–N4–Pt 110.1(4), N2–C1–N3 116.8(7).

The structure consists of centrosymmetric square planar $[Pt(Amgu)_2]^{2+}$ cations and nitrate counterions; the Pt atom lies on a centre of symmetry. The coordination sphere of the Pt atom is formed by two *trans*-oriented bidentate Amgu ligands coordinated through the terminal hydrazine N4 atom and the imine N1 atom, each of which forms a planar five-membered chelate ring with the metal centre (maximum deviation from the $PtN_4$ least-squares plane: 0.04 Å). The small bite angle of Amgu constrains the endocyclic N1–Pt–N4 angle to 80.0(2)° which is slightly less than the angle of 83.1(1)° found for the bis(ethylenediamine) complex $[Pt(en)_2]^{2+}$.[29] The Amgu moiety of **4** is nearly planar (torsion angle N2–C1–N3–N4 4.6°). Distances C1–N1, C1–N2 and C1–N3 are again of approximately equal values, and are comparable with those for protonated uncomplexed ligand.[16,26–28] There is no localised double bond, and the positions of the H atoms and the planarity of the ligand suggest an $sp^2$ hybridisation for all atoms except N4, which remains $sp^3$-hybridised.

The packing of the Pt units gives rise to infinite stacks of square-planar complexes (correlated by a *c* glide plane) with a Pt–Pt separation of 3.332(1) Å. The molecular packing is stabilized by hydrogen-bonding interactions between the cationic complex and the oxygen atoms of nitrate (N–O in the range 2.90–3.28 Å), generating a complex supramolecular three-dimensional network in which all the nitrate oxygens and the N-bonded hydrogens of the ligands are involved (Figure 4). This network demonstrates the hydrogen-bond forming potential of platinum-chelated Amgu.

The unsuccessful attempts to prepare a mono-Amgu complex from $K_2PtCl_4$ prompted us to investigate alternative platinum(II) starting materials. We have previously found $K[PtCl_3(dmso)]$[30] to be more convenient than $K_2PtCl_4$ for the formation of binuclear platinum(II) complexes with rigid diamine ligands.[31,32] Furthermore, $K[PtCl_3(dmso)]$ successfully provided a chelate complex with Gly-His where reaction of this ligand with $K_2PtCl_4$ failed.[33] In the event, when a slight molar excess of Amgu·HCl was added to a solution of $K[PtCl_3(dmso)]$ in water, a solid product began forming after only 90 min. A satisfactory 73% yield of a single chelate complex was obtained; its composition was suggested as [PtCl(Amgu)(dmso)]Cl (**5**) from analytical and spectro-

 © 2007 Wiley-VCH Verlag GmbH & Co. KGaA, Weinheim 

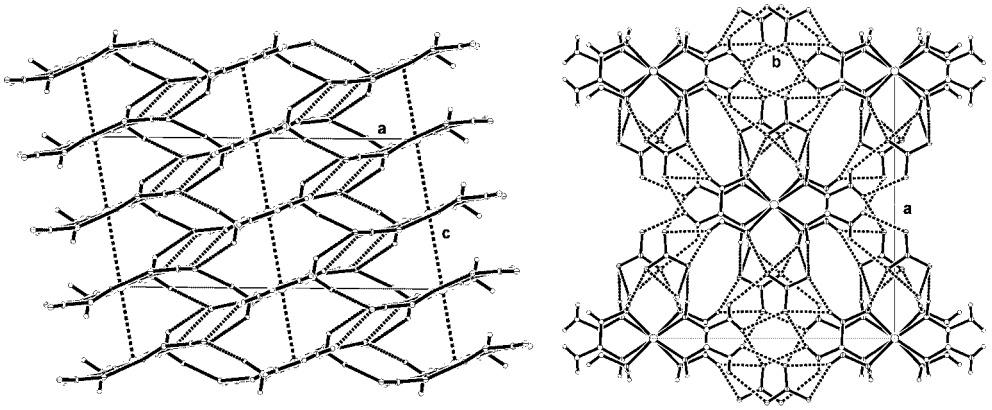


Figure 4. Views along the b (left) and c (right) crystallographic axes of the molecular packing of **4**. The selection criteria for hydrogen bonds (depicted as thin dotted lines) were: $d$(N···O) < R(N) + R(O) + 0.50, $d$(H···O) < R(H) + R(O) –0.12, N–H···O > 100.0°.

scopic data (in particular $^1$H NMR signal integrations and a single $^{195}$Pt NMR signal at $\delta$ = –3134 ppm) and was confirmed by X-ray diffraction (Figure 5).

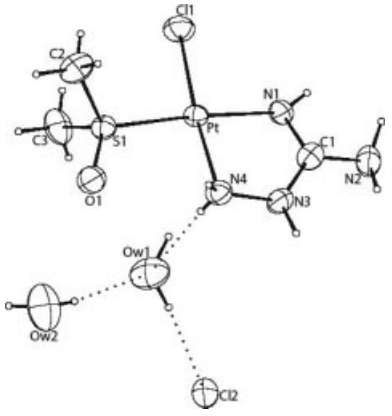


Figure 5. CAMERON plot (50% thermal probability ellipsoids) of the crystal structure of **5**. Selected bond lengths [Å] and angles [°]: Pt–Cl1 2.298(1), Pt–S1 2.208(1), Pt–N1 1.990(4), Pt–N4 2.034(4), C1–N1 1.312(6), C1–N2 1.340(6), C1–N3 1.338(7), N3–N4 1.443(6), N1–Pt–N4 80.6(2), Pt–N1–C1 115.2(3), N1–C1–N2 124.5(5), N1–C1–N3 117.4(4). N2–C1–N3 118.0(5), C1–N3–N4 117.0(4), N3–N4–Pt 109.1(3), Cl1–Pt–N1 93.9(1), Cl1–Pt–S1 92.81(6), S1–Pt–N4 92.8(1).

Distances and angles at the platinum centre have typical values. Comparison of the Pt–N1 and Pt–N4 bond lengths for **4** with those observed for **5** reveals no indication for any significahe least-squares-plane of 0.050(2) Å for N4. The crystal packing of this complex involves several hydrogen bonds, in particular N4–H4B···Ow1 [2.996(7) Å, 167°].

When $[PtCl_3(dmso)]^-$ reacts with $AmguH^+$, the first nucleophilic substitution is expected to occur *trans* to the dmso ligand,[30,34] yielding *trans*-$[PtCl_2$(AmguH-*N4*)-(dmso)$]^+$. Deprotonation (aided by the acidifying effect that N4-coordination to platinum is expected to exert on the N3 imonium group) and chelation would produce the isomer of $[PtCl$(Amgu-*N1*,*N4*)(dmso)$]^+$ with N4 bound *trans* to dmso. The fact that in crystals of complex **5** the N4 atom is coordinated *trans* to $Cl^-$ suggests that a rearrangement has occurred following the first N4 attack, producing the thermodynamically more stable isomer (Scheme 2).

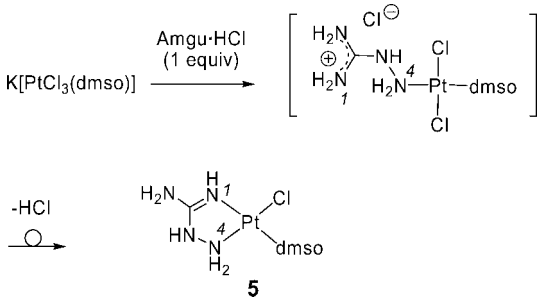


Scheme 2.

## Palladium Complexes

The stoichiometric reaction between $K_2PdCl_4$ and Amgu·HCl proceeded smoothly, in contrast to that with $K_2PtCl_4$, yielding $[PdCl_2$(AmguH-*N1*,*N4*)] (**6**), without any sign of reduction of $Pd^{II}$ (Scheme 3). This difference can be attributed to the standard oxidation potentials for the $M^0$/$M^{II}$ couples which are more negative for platinum than for palladium[35] and to the $10^3$ times faster substitution reaction rates of $Pd^{II}$ compared to $Pt^{II}$.[36] The structure of **6** (Figure 6), indicated by solution state NMR spectroscopic data, was confirmed by X-ray crystallographic analysis. The

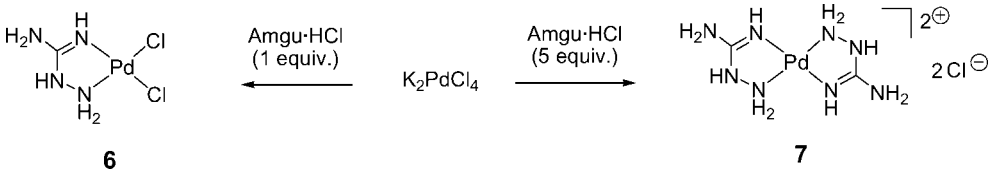


Scheme 3.

 © 2007 Wiley-VCH Verlag GmbH & Co. KGaA, Weinheim 

square planar palladium(II) centre presents usual bond lengths and angles, while the chelating ligand, coordinated through N1 and N4, is virtually planar (torsion angle N1–C1–N3–N4 2°). It is noteworthy that there was no need to liberate the Amgu ligand in its free base form in order to obtain complex **6**; indeed, repeating the reaction in the presence of 1 equiv. of NaOH led to a lower isolated yield (72%) of compound **6**.

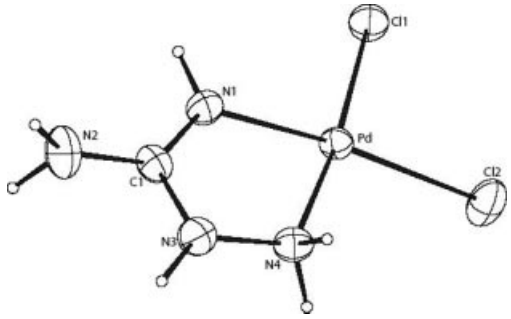


Figure 6. CAMERON plot (50% thermal probability ellipsoids) of the crystal structure of **6**; selected bond lengths [Å] and angles [°]: Pd–Cl1 2.303(2), Pd–Cl2 2.322(2), Pd–N1 1.968(6), Pd–N4 2.019(5), C1–N1 1.307(8), C1–N2 1.339(9), C1–N3 1.347(9), N3–N4 1.407(8), Cl1–Pd–Cl2 93.86(6), Cl1–Pd–N1 92.7(2), Cl2–Pd–N4 92.5(2), N1–Pd–N4 81.0(2), N1–C1–N2 123.7(7), N1–C1–N3 117.9(6), N3–C1–N2 118.3(6).

Treatment of $K_2PdCl_4$ with 5 equiv. of Amgu·HCl in aqueous solution followed by evaporation of the solvent over a period of several hours gave a good yield of *trans*-[Pd(Amgu-*N1*,*N4*)$_2$]Cl$_2$ (**7**) (Scheme 3). Once again, the prerequisite loss of one proton for coordination of N1 proceeded even in the acidic solution; the final pH of the reaction mixture was 1.5. The bis-chelate structure of **7** was confirmed by X-ray crystallographic analysis (Figure 7). The planar palladium(II) centre is centrosymmetric, bearing two Amgu ligands chelated through N1 and N4 in a *trans* fashion. The ligand is again almost planar (torsion angle N1–C1–N3–N4 5°) and the overall structure of the metal complex is very similar to that of **4**. Two chloride ions are located in the crystal packing and are involved in two hydrogen bonds with the complex.

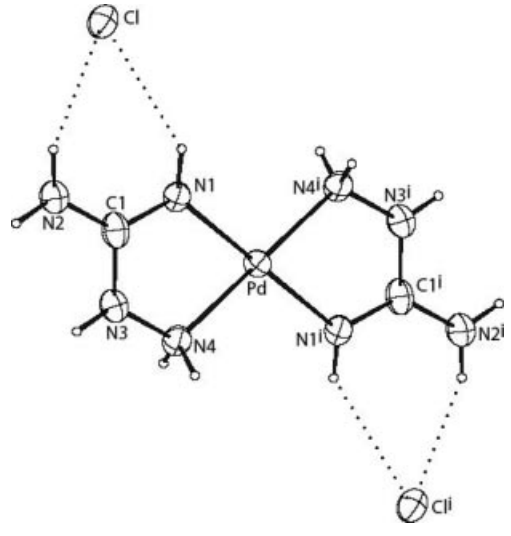


Figure 7. CAMERON plot (50% thermal probability ellipsoids) of the crystal structure of **7**. Selected bond lengths [Å] and angles [°]: Pd–N1 1.977(7), Pd–N4 2.029(7), C1–N1 1.303(11), C1–N2 1.341(12), C1–N3 1.358(11), N3–N4 1.401(9), H1···Cl 3.436(8), H21···Cl 3.288(9), N1–Pd–N4 80.6(3), Pd–N1–C1 115.2(6), N1–C1–N3 117.2(8), N2–C1–N3 116.8(9). N1–C1–N2 125.9(9), C1–N3–N4 116.9(7), N3–N4–Pd 109.7(5), N1–H1···Cl 142, N2–H21···Cl 151.

## Conclusions

*N*-Aminoguanidine has been shown to be a chelator of platinum(II) and palladium(II), coordinating the metal through the hydrazine-type amino N4 group and the imino groupN1. Reaction between K[PtCl$_3$(dmso)] and Amgu·HCl yielded the mono-chelate [PtCl(Amgu-*N1*,*N4*)(dmso)]$^+$ (**5**) in which the N4 atom of Amgu is bound *trans* to Cl$^-$, whereas the initial coordination is expected to place N4 *trans* to dmso. Thus, the activation barrier for breakage of the Pt–N4 bond *trans* to Pt–S does not seem to be high, and the thermodynamically more stable isomer is obtained. For the Pd$^{II}$ complexes, kinetic lability and formation of the thermodynamically more stable isomers was expected in any case.

Amgu is also a reducing agent, and in some cases reactions with Pt$^{II}$ complexes led to reduction to Pt$^0$, whereas the analogous Pd$^{II}$ complex underwent a clean ligand-substitution reaction under the same conditions. K[PtCl$_3$(dmso)] proved to be a starting material less susceptible to reduction by Amgu than $K_2PtCl_4$. Protonated AmguH$^+$ has a single coordination site, the hydrazine-type amino group N4, and we have characterized one platinum complex with two AmguH$^+$ ligands bound in a *trans*-configuration (complex **3**).

The solid-state structures of the compounds studied here show a variety of hydrogen bonding networks. All four nitrogens of the Amgu ligand are able to behave as hydrogen atom donors, suggesting that platinum complexes of this ligand may warrant further investigation for their interactions with DNA. Hydrogen bonding between platinum spectator ligands and DNA are thought to play a role in stabilizing particular conformers in guanine···guanine crosslinks[37] and it has been hypothesized that they may be important for antitumour activity.[38,39]

## Experimental Section

**General Remarks:** Melting points were determined on a Thermovar apparatus and are uncorrected. Electrospray mass spectra were obtained using a Thomson quadrupole instrument equipped with an Analytica atmospheric pressure source. IR spectra were recorded from samples dispersed as nujol mulls between KBr plates on a Perkin–Elmer 1600 Fourier Transform instrument. NMR spectra were recorded on a Bruker AC-300 instrument ($^1$H: 300.13 MHz; $^{13}$C{$^1$H}: 75.43 MHz) and a Bruker ARX-250 instrument ($^{195}$Pt: 53.63 MHz) using standard pulse sequences. Chemical shifts ($\delta$) are given in ppm and are quoted relative to TMS or $Na_2PtCl_6$. Elemental analyses were carried out by Laboratoire de Microanalyse, Insti-

 © 2007 Wiley-VCH Verlag GmbH & Co. KGaA, Weinheim 

tut de Chimie des Substances Naturelles du CNRS, Gif-sur-Yvette, France. Water was doubly distilled and organic solvents were purified by standard procedures before use. Aminoguanidine hydrochloride, potassium tetrachloroplatinate and potassium tetrachloropalladate were obtained commercially and used without further purification. The salt $K[PtCl_3(dmso)]$ was prepared via the literature procedure.[30]

**$K[PtCl_3(AmguH)]$ (1):** Amgu·HCl (55 mg, 0.5 mmol) was added to a solution of $K_2PtCl_4$ (207 mg, 0.5 mmol) in water (1 mL), and the mixture was stirred at room temp. for 12 h. A dark deposit was removed by filtration and the filtrate was evaporated to leave an amorphous brown residue (220 mg). This sample showed: $^1$H NMR ([D$_7$]dmf): $\delta$ = 7.44 (s, 2 H), 7.95 (s, 2 H), 8.45 (s, 1 H), 8.99 (s, 2 H) ppm. $^{13}C\{^1H\}$ NMR ([D$_7$]dmf): $\delta$ = 157.9 ppm. $^{195}$Pt NMR ([D$_7$]dmf): $\delta$ = –1631 (minor), –1997 (major), –2128 (minor), –2218 (minor) ppm.

***trans*-$[PtCl_2(AmguH\text{-}N4)_2]Cl_2\cdot 2^1/_2H_2O$ (3):** Amgu·HCl (220 mg, 2.0 mmol) was added to a solution of $K_2PtCl_4$ (166 mg, 0.4 mmol) in water (2 mL). The mixture was stirred at room temp. for 15 min, during which time the pH dropped to 2.7, and was then placed in a vacuum desiccator (10 Torr) in the presence of active silica gel and left at room temp. for 15 h. The slow evaporation of water left yellow crystals which were washed successively with water, ethanol, ether, then dried under vacuum (0.5 Torr) to give a first crop of compound **3** (39 mg). The combined washings were evaporated to leave more yellow crystals which were washed with water, ethanol and ether, as before, to give a second crop of compound **3** (62 mg). Combined yield: 52%. M.p. 140 °C. ESMS: $m/z$ = 208 $[M]^{2+}$. IR: $\tilde{\nu}$ = 3379 (NH), 3329 (NH), 3134 (NH), 1674 (C=N), 1607 (NH) cm$^{-1}$. $^1$H NMR ([D$_7$]dmf): $\delta$ = 8.27 (s, 8 H), 8.54 (s, 4 H), 9.31 (s, 2 H) ppm. $^{13}C\{^1H\}$ NMR ([D$_7$]dmf): $\delta$ = 158.7 ppm. $^{195}$Pt NMR ([D$_7$]dmf): $\delta$ = –2277 ppm. $C_2H_{14}Cl_4N_8Pt\cdot 2^1/_2H_2O$ (532.2): calcd. C 4.51, H 3.60, N 21.06, Cl 26.64; found C 4.86, H 3.31, N 20.66, Cl 26.66.

***trans*-$[Pt(Amgu\text{-}N1,N4)_2](NO_3)_2$ (4):** Complex **3** (15 mg; 0.029 mmol) and 4 equiv. $AgNO_3$ (19.7 mg) in 0.5 mL $D_2O$ were stirred at ambient temperature for 3 d. The precipitate was filtered off, the filtrate was treated with 6 μL of 1 N NaOH (ca. 2 equiv.), and the solution placed in an NMR tube. A $^{195}$Pt NMR spectrum recorded overnight did not show any peaks but it the tube colorless crystals appeared. The crystals were identified as $[Pt(Amgu)_2](NO_3)_2$ by means of a structure analysis using X-ray diffractometry.

**$PtCl(Amgu\text{-}N1,N4)(dmso)]Cl\cdot 2H_2O$ (5):** Amgu·HCl (46 mg, 0.42 mmol) was added to a solution of $K[PtCl_3(dmso)]$ (160 mg, 0.38 mmol) in water (1.2 mL). The mixture was stirred at room temp. for 90 min, during which time few crystals started to precipitate. The mixture was then placed in a vacuum desiccator (10 Torr) over $CaCl_2$ and left until one third of the volume remained. The solid residue was filtered, washed with water, then dried under vacuum (0.5 Torr). Compound **5** was thus obtained as yellow-white crystals. Yield: 117 mg, 73%. M.p. 192 °C (dec.). ESMS: $m/z$ = 383 [M – Cl]. IR: $\tilde{\nu}$ = 1635 (C=N), 1553 (NH), 1126 (S=O), 1023 (S=O) cm$^{-1}$. $^1$H NMR ([D$_7$]dmf): $\delta$ = 3.62 (s, 6 H), 6.68 (s, 1 H), 7.16 (s, 2 H), 9.38 (s, 2 H), 10.00 (s, 2 H) ppm. $^{13}C\{^1H\}$ NMR ([D$_7$]dmf): $\delta$ = 43.3, 167.8 ppm. $^{195}$Pt NMR ([D$_7$]dmf): $\delta$ = –3134 ppm. $C_3H_{12}Cl_2N_4OPtS\cdot 2H_2O$: calcd. C 7.93, H 3.55, N 12.33, S 7.06; found C 7.62, H 3.29, N 11.89, S 7.48.

**$[PdCl_2(AmguH\text{-}N1,N4)]$ (6):** Amgu·HCl (55 mg, 0.5 mmol) was added to a solution of $K_2PdCl_4$ (163 mg, 0.5 mmol) in water (2.5 mL). The mixture was stirred at room temp. for 15 min, during which time a precipitate formed. This solid was isolated by filtration and washed with ethanol then ether, and dried under vacuum (0.5 Torr). Compound **6** was thus obtained as brownish-red crystals. Yield: 102 mg, 82%. M.p. 188–190 °C (dec.). IR: $\tilde{\nu}$ = 3423 (NH), 3338 (NH), 3186 (NH), 3106 (NH), 1620 (C=N), 1580 (NH) cm$^{-1}$. $^1$H NMR ([D$_7$]dmf): $\delta$ = 5.06 (s, 1 H), 6.44 (s, 2 H), 7.77 (s, 2 H), 8.59 (s, 1 H) ppm. $^{13}C\{^1H\}$ NMR ([D$_7$]dmf): $\delta$ = 166.1 ppm. $CH_6Cl_2N_4Pd$ (251.4): calcd. C 4.78, H 2.41, N 22.28, Cl 28.20; found C 4.51, H 2.51, N 22.32, Cl 28.16.

***trans*-$[Pd(Amgu\text{-}N1,N4)_2]Cl_2$ (7):** Amgu·HCl (276 mg, 2.5 mmol) was added to a solution of $K_2PdCl_4$ (163 mg, 0.5 mmol) in water (2.5 mL). The mixture was stirred at room temp. for 15 min, during which time the pH dropped to 1.5 and a precipitate formed. The mixture was then placed in a vacuum desiccator (10 Torr) in the presence of active silica gel and left at room temp. for 5 h. The solid residue was washed with a methanol/water mixture (9:1), then dried under vacuum (0.5 Torr). Compound **7** was thus obtained as yellow crystals. Yield: 146 mg, 89%. M.p. 200 °C (dec.). ESMS: $m/z$ = 127 $[M]^{2+}$. IR: $\tilde{\nu}$ = 3392 (NH), 3332 (NH), 3106 (NH), 1639 (C=N), 1560 (NH) cm$^{-1}$. $^1$H NMR ([D$_6$]dmso): $\delta$ = 5.20 (s, 2 H), 6.51 (s, 4 H), 7.93 (s, 4 H), 8.66 (s, 2 H) ppm. $^{13}C\{^1H\}$ NMR ([D$_6$]-dmso): $\delta$ = 165.5 ppm. $C_2H_{12}Cl_2N_8Pd$ (325.5): calcd. C 7.38, H 3.72, N 34.43, Cl 21.78; found C 7.89, H 3.38, N 33.82, Cl 22.86.

**X-ray Crystallographic Studies:** For compounds **3**, **5**, **6** and **7**, diffraction intensity data were collected at $T$ = 292 K using CAD4 Express Enraf–Nonius software[40] with a CAD4 diffractometer equipped with a graphite monochromator [Mo-$K_\alpha$ radiation ($\lambda$ = 0.7107 Å)], and data reduction using RC93.[41] All data were corrected for Lorentz-polarisation effects and empirical absorption correction using DIFABS[42] was applied. The structure was solved by direct methods using SIR-92[43] and refined by least-squares methods on $F$ using CRYSTALS,[44] except in the case of compound **5**, for which the structure was refined by least-squares methods on $F^2$ using SHELXL-97[45] incorporated in the WinGX package.[46] Hydrogen atoms were placed geometrically after each cycle with isotropic parameters constrained to be 1.2 times the $U_{eq}$ of the carrier atoms. Molecules were drawn using CAMERON.[47]

For compound **4**, despite the screening of a large number of crystals, we were unable to find crystals for which the conventional auto-indexing routine of the SMART programme[48] could find a plausible unit cell. Nonetheless, data collection was performed at $T$ = 293 K on a SMART-CCD Bruker diffractometer [Mo-$K_\alpha$ radiation ($\lambda$ = 0.7107 Å)] using the $\omega$-scan method, in the range $2° < \theta < 25°$. Many reflections showed a splitting typical of twin crystals; therefore a twin analysis with the program GEMINI[49] was attempted using about 800 of the collected reflections. This analysis revealed a multiple twinning with at least two different crystal components. It was possible to obtain a substantial number of pure reflections, from the larger of the two identified domains, which allowed the resolution of the structure by traditional Patterson methods. Data from the second component were also integrated, but due to the much worse internal agreement, were neglected. The space group was determined from the systematic absences, while the cell constants were refined with the data reduction software SAINT.[50] The collected intensities were corrected for Lorentz and polarization factors and empirically for absorption using the SADABS program.[51] The structure was refined by full-matrix least-squares on $F^2$ using SHELX-97[52] using anisotropic thermal parameters for all atoms except hydrogens. The hydrogen atoms were located, during the last stage of refinement, in the difference Fourier maps. The molecule was drawn using ORTEP.[53] The search for hydrogen bonds in the packing was carried out using PLATON.[54]

Crystal data, data collection parameters and convergence results are listed in Table 1.

 © 2007 Wiley-VCH Verlag GmbH & Co. KGaA, Weinheim 

Table 1. Crystal data and structure refinement for **3**, **4**, **5**, **6** and **7**.

| | **3** | **4** | **5** | **6** | **7** |
|---|---|---|---|---|---|
| Empirical formula | $C_2H_{14}Cl_4N_8Pt{\cdot}2^1/_2H_2O$ | $C_2H_{12}N_{10}O_6Pt$ | $C_3H_{12}Cl_2N_4OPtS{\cdot}2H_2O$ | $CH_6Cl_2N_4Pd$ | $C_2H_{12}Cl_2N_8Pd$ |
| $M_w$ | 532.2 | 467.3 | 454.3 | 251.4 | 325.5 |
| Crystal system | monoclinic | monoclinic | monoclinic | monoclinic | monoclinic |
| Space group | *I*2/*a* | *C*2/*c* | $P2_1/n$ | $P2_1/n$ | $P2_1/n$ |
| *a* [Å] | 7.316(1) | 14.154(3) | 8.520(4) | 5.866(1) | 5.991(2) |
| *b* [Å] | 24.659(1) | 12.633(2) | 8.950(6) | 11.644(2) | 10.939(3) |
| *c* [Å] | 8.494(1) | 6.664(1) | 16.586(8) | 9.401(2) | 7.786(2) |
| $\alpha$ [°] | 90 | 90 | 90 | 90 | 90 |
| $\beta$ [°] | 96.87(1) | 100.40(1) | 90.45(1) | 90.45(2) | 102.24(2) |
| $\gamma$ [°] | 90 | 90 | 90 | 90 | 90 |
| *V* [Å$^3$] | 1521.3(6) | 1172.0(4) | 1265(1) | 642.0(2) | 498.7(3) |
| *Z* | 4 | 4 | 4 | 4 | 2 |
| $\rho_{calcd.}$ [g·cm$^{-3}$] | 2.33 | 2.65 | 2.39 | 2.60 | 2.17 |
| *F*(000) | 992 | 880 | 856 | 480 | 320 |
| $\mu$ [mm$^{-1}$] | 9.93 | 12.02 | 11.67 | 3.62 | 2.37 |
| $\theta$ range [°] | 2.55–27.96 | 2–25 | 2.46–29.98 | 2.79–27.96 | 3.26–27.96 |
| Measured reflections | 4026 | 4707 | 7328 | 1768 | 1376 |
| Independent reflections | 1837 | 1027 | 3672 | 1550 | 1205 |
| Observed reflections | 1082 | 762 | 2866 | 997 | 697 |
| Selection criterion | $I > 3\sigma(I)$ | $I \geq 4\sigma(I)$ | $I > 2\sigma(I)$ | $I > 3\sigma(I)$ | $I > 2\sigma(I)$ |
| $R_1$ | 0.037 | 0.0313 | 0.030 | 0.030 | 0.043 |
| $wR_2$ | 0.040 | 0.0741 | 0.071 | 0.076 | 0.045 |
| GOF | 0.91 | 1.06 | 1.02 | 0.97 | 0.96 |
| Residual electron density [e·Å$^{-3}$] | –2.16/1.03 | –0.94/5.07 | –1.38/1.74 | –0.69/0.63 | –1.33/0.84 |

CCDC-279695 (for **3**), -623191 (for **4**), -296006 (for **5**), -279568 (for **6**), and -279569 (for **7**) contain the supplementary crystallographic data for this paper. These data can be obtained free of charge from The Cambridge Crystallographic Data Centre via www.ccdc.cam.ac.uk/data_request/cif.

## Acknowledgments

Parts of this work were supported by a grant from the Rectorat des Universités de Paris (to S. O.) and by funding from the Région d'Auvergne. We are grateful to F. Libot (Université Paris-V) for recording the electrospray mass spectra.

[1] E. Wong, C. M. Giandomenico, *Chem. Rev.* **1999**, *99*, 2451–2466.
[2] P. J. O. Dwyer, J. P. Stevenson, S. W. Johnson, in *Cisplatin: Chemistry and Biochemistry of a Leading Anticancer Drug* (Ed.: B. Lippert), Wiley-VCH, Weinheim, **1999**, pp. 29–69.
[3] R. Canetta, K. Bragman, L. Smaldone, M. Rosenzweig, *Cancer Treat. Rev.* **1988**, *15 Suppl. B*.
[4] E. Raymond, S. Faivre, S. Chaney, J. Woynarowski, E. Cvitkovic, *Mol. Cancer Ther.* **2002**, *1*, 227–235.
[5] L. R. Kelland, in *Cisplatin: Chemistry and Biochemistry of a Leading Anticancer Drug* (Ed.: B. Lippert), Wiley-VCH, Weinheim, **1999**, pp. 497–521.
[6] S. T. Sullivan, A. Ciccarese, F. P. Fanizzi, L. G. Marzilli, *J. Am. Chem. Soc.* **2001**, *123*, 9345–9355.
[7] B.-O. Nilsson, *Inflammation Res.* **1999**, *48*, 509–515.
[8] E. Abdel-Rahman, W. K. Bolton, *Exp. Opin. Invest. Drugs* **2002**, *11*, 565–574.
[9] P. J. Thornalley, *Arch. Biochem. Biophys.* **2003**, *419*, 31–40.
[10] B. S. Pitzele, A. E. Moormann, G. W. Gullikson, D. Albin, R. G. Bianchi, P. Palicharla, E. L. Sanguinetti, D. E. Walters, *J. Med. Chem.* **1988**, *31*, 138–144.
[11] V. A. Vaillancourt, S. D. Larsen, S. P. Tanis, J. E. Burr, M. A. Connell, M. M. Cudahy, B. R. Evans, P. V. Fisher, P. D. May, M. D. Meglasson, D. D. Robinson, F. C. Stevens, J. A. Tucker, T. J. Vidmar, J. H. Yu, *J. Med. Chem.* **2001**, *44*, 1231–1248.
[12] K.-H. Buchheit, R. Gamse, R. Giger, D. Hoyer, F. Klein, E. Klöppner, H.-J. Pfannkuche, H. Mattes, *J. Med. Chem.* **1995**, *38*, 2331–2338.
[13] A. Balsamo, D. Gentili, M. Macchia, E. Martinotti, A. Rossello, R. Scatizzi, *Eur. J. Med. Chem.* **1996**, *31*, 713–716.
[14] H. U. Bryant, D. L. Nelson, D. Button, H. W. Cole, M. B. Baez, V. L. Lucaites, D. B. Wainscott, C. Whitesitt, J. Reel, R. Simon, G. A. Koppel, *Life Sci.* **1996**, *59*, 1259–1268.
[15] G. J. Durant, G. M. Smith, R. G. W. Spickett, S. H. B. Wright, *J. Med. Chem.* **1966**, *9*, 22–27.
[16] M. Koskinen, I. Mutikainen, H. Elo, *Z. Naturforsch., Teil B* **1994**, *49*, 556–560.
[17] I. Mutikainen, M. Koskinen, H. Elo, *Pharmazie* **1994**, *49*, 739–742.
[18] M. Bujak, P. Osadczuk, J. Zaleski, *Acta Crystallogr., Sect. C* **2001**, *57*, 388–391.
[19] J. Thiele, *Justus Liebigs Ann. Chem.* **1892**, *270*, 1–63.
[20] E. Lieber, G. B. L. Smith, *Chem. Rev.* **1939**, *25*, 213–271.
[21] V. V. Boldyrev, R. K. Tukhtaev, A. I. Gavrilov, S. V. Larionov, Z. A. Savel'eva, L. G. Lavrenova, *Russ. J. Inorg. Chem.* **1998**, *43*, 302–305.
[22] S. V. Zubkov, I. I. Seifullina, S. V. Fel'dman, *Russ. J. Coord. Chem.* **1996**, *22*, 181–184.
[23] T. A. Vetera, V. N. Shafranskii, *Russ. J. Gen. Chem.* **1979**, *49*, 428–433.
[24] J. J. Hlavka, P. Bitha, Y.-i. Lin, *Platinum complexes of antitumor agents*, US Patent 4544759, **1985**; *Chem. Abstr.* **1986**, *104*, 149174h.
[25] P. S. Pregosin, *Annu. Rep. NMR Spectrosc.* **1986**, *17*, 285–349.
[26] J. T. Koskinen, M. Koskinen, I. Mutikainen, B. Mannfors, H. Elo, *Z. Naturforsch., Teil B* **1996**, *51*, 1771–1778.
[27] M. Koskinen, I. Mutikainen, P. Tilus, E. Pelttari, M. Korvela, H. Elo, *Monatsh. Chem.* **1997**, *128*, 767–775.
[28] R. L. Davidovich, V. B. Logvinova, V. V. Tkachev, L. O. Atovmyan, *Russ. J. Coord. Chem.* **1995**, *21*, 783–787.
[29] S. Sato, M. Haruku, S. Kurita, *Acta Crystallogr., Sect. C* **1990**, *46*, 1107–1108.
[30] Yu. N. Kukushkin, Yu. E. Vyaz'menskii, L. I. Zorina, *Russ. J. Inorg. Chem.* **1968**, *13*, 1573–1576.

 © 2007 Wiley-VCH Verlag GmbH & Co. KGaA, Weinheim 

[31] D. J. Aitken, H.-P. Husson, D. Nguyen-Huy, S. Ongeri, F. Vergne, B. Viossat, *Inorg. Chem. Commun.* **1998**, *1*, 314–316.
[32] S. Ongeri, D. J. Aitken, H.-P. Husson, J. Kozelka, B. Viossat, *Inorg. Chem.* **2000**, *39*, 6131–6133.
[33] D. Shi, T. W. Hambley, H. C. Freeman, *J. Inorg. Biochem.* **1999**, *73*, 173–186.
[34] Yu. N. Kukushkin, Yu. E. Vyaz'menskii, *Russ. J. Inorg. Chem.* **1970**, *15*, 1713–1716.
[35] F. R. Hartley, *The Chemistry of Platinum and Palladium*, Applied Science Publishers Ltd., London, **1973**, p.12.
[36] L. D. Pettit, M. Bezer, *Coord. Chem. Rev.* **1985**, *61*, 97–114.
[37] D. Over, G. Bertho, M.-A. Elizondo-Riojas, J. Kozelka, *J. Biol. Inorg. Chem.* **2006**, *11*, 139–152.
[38] S. E. Sherman, D. Gibson, A. H. J. Wang, S. J. Lippard, *J. Am. Chem. Soc.* **1988**, *110*, 7368–7381.
[39] J. Reedijk, *Chem. Commun.* **1996**, 801–806.
[40] Enraf–Nonius, CAD Express Software, Enraf–Nonius, Delft, The Netherlands, **1994**.
[41] D. J. Watkin, C. K. Prout, P. M. De Q. Lilley, *RC93*. Chemical Crystallography Laboratory, Oxford, UK, **1994**.
[42] N. Walker, D. Stuart, *Acta Crystallogr., Sect. A* **1983**, *39*, 158–166.
[43] A. Altomare, G. Cascarano, C. Giacovazzo, A. Guagliardi, M. C. Burla, G. Polidori, M. Camalli, *J. Appl. Crystallogr.* **1994**, *27*, 435–436.
[44] D. J. Watkin, C. K. Prout, J. R. Carruthers, P. W. Betteridge, R. I. Cooper, *CRYSTALS. Issue 11*, Chemical Crystallography Laboratory, Oxford, UK, **2001**.
[45] G. M. Sheldrick, *SHELXL-97 Program for crystal structure refinement*, University of Göttingen, Göttingen, Germany, **1997**.
[46] Anon, *J. Appl. Crystallogr.* **1999**, *32*, 837–838.
[47] D. J. Watkin, C. K. Prout, L. J. Pearce, *CAMERON*, Chemical Crystallography Laboratory, Oxford, UK, **1996**.
[48] *SMART*, Siemens Analytical X-ray Instruments Inc., Madison, Wisconsin, USA, **1993**.
[49] R. Sparks, *GEMINI*, Version 1.02. Bruker AXS Inc., Madison, Wisconsin, USA, **2000**.
[50] *SAINT*, Integration Software, Bruker AXS Inc., Madison, Wisconsin, USA, **1995**.
[51] G. M. Sheldrick, *SADABS Program for Absorption Correction*, University of Gottingen, Göttingen, Germany, **1996**.
[52] G. M. Sheldrick, *SHELX-97 Structure Solution and Refinement Package*, University of Göttingen, Göttingen, Germany, **1997**.
[53] L. J. Farrugia, *J. Appl. Crystallogr.* **1997**, *30*, 565.
[54] A. L. Spek, *PLATON A Multipurpose Crystallographic Tool*, Utrecht University, Utrecht, The Netherlands, **1998**.

Received: October 23, 2006
Published Online: February 26, 2007

 © 2007 Wiley-VCH Verlag GmbH & Co. KGaA, Weinheim 

DOI: 10.1002/ejic.200601171

# Gas-Phase Fragmentation Behavior of Vanadium(V) Complexes Containing One Molecule of a $C_4$-Dicarboxylic Acid

**Malgorzata Kaczorowska,[a] Helmut Schwarz,[a] and Detlef Schröder*[b]**

**Keywords:** Carboxylato complexes / Vanadium / Electrospray ionization / Maleic anhydride / Mass spectrometry

Complexes of vanadium(V) with $C_4$-dicarboxylic acids, i.e. maleic, fumaric, and succinic acid, are investigated by means of electrospray ionization (ESI) mass spectrometry. Under soft conditions of ionization, ESI of a diluted solution of $OV(OC_2H_5)_3$ in methanol gives rise to complexes, which are best described by the general formula $[(XCOO)_2VO(C,H_4,O)]^+$ (X = CH, $CH_2$), where the solvent employed delivers the $(C,H_4,O)$ unit, whose components are either attached to vanadium as an intact methanol ligand or are distributed over the other atoms. In the complexes containing maleic or succinic acid, the acids appear to act as chelating ligands with coordination of the vanadium center by two oxygen atoms from two different carboxylic groups. In contrast, the *trans*-configuration in fumaric acid prevents the formation of similar chelate complexes. The fragmentation reactions of the complexes are studied by collision-induced dissociation and labeling experiments. For the vanadium(V) complex derived from maleic acid, a preferential elimination of $CO_2$ is observed, followed by combined losses of $CO_2$, CO, and $C_2H_2$ or alternatively an intact $C_4H_2O_3$ unit, which most likely corresponds to maleic anhydride. Instead, evaporation of water followed by loss of carbon monoxide predominates for the corresponding $V^V$ cation generated in the presence of succinic acid. Due to the fact that the loss of water involves the central methylene groups of succinic acid, a connection to the vanadium-oxide-mediated formation of maleic acid upon partial oxidation of $C_4$-hydrocarbons is proposed.

(© Wiley-VCH Verlag GmbH & Co. KGaA, 69451 Weinheim, Germany, 2007)

## Introduction

Transition metals and their oxides play important roles as catalysts exhibiting high selectivities and activities in many processes[1] and therefore are widely used in chemical and petrochemical industries since more than a century. Among the transition-metal oxides, a particularly important class of catalysts are vanadium oxides, which are employed in several selective oxidations and also act as an important support material in numerous technical applications.[2–7]

One of the most complex selective oxidation reactions is the conversion of *n*-butane to maleic anhydride on the surface of vanadyl-pyrophosphate oxide (VPO).[8–10] In this reaction, eight hydrogen atoms are abstracted from the reactant and three oxygen atoms are added to eventually afford maleic anhydride as a product.[11] Although the reaction has been extensively studied during recent years, the mechanistic knowledge is still limited, mainly because of the complexity of the oxidation as well as the fact that none of the potential reaction intermediates, such as butenes or furane, have been observed among the reaction products under standard industrial conditions.[12] Based on studies of reaction kinetics[13,14] and on the observation of intermediates under non-standard conditions,[13,15] the oxidation of *n*-butane to maleic anhydride has been proposed to proceed via two independent pathways.[16] The first is referred to as the olefinic route, which involves a consecutive conversion of *n*-butane to butene and then to butadiene, followed by oxygenation of butadiene to form furane and the subsequent conversion of furane into maleic anhydride.[9] For the olefinic route, the intermediate products were proposed to easily desorb from the oxidic surface of the catalyst. In contrast, on the basis of kinetic data Zhang-Lin et al.[13,14] concluded that the main pathway for the formation of maleic anhydride from *n*-butane proceeds via metal-alkoxide species as key intermediates, which are able to maintain σ-bonds between the organic components and vanadium species present on the catalyst ("alkoxide route"). In this reaction sequence, the intermediate products do not leave the surface until completion of the reaction.[17] Despite numerous studies aimed at gaining insight into the mechanisms, it is still not settled which route is preferred. Further, based on isotopic labeling studies, Chen and Munson[18] presented direct evidence that the conversion of *n*-butane into maleic anhydride on VPO catalysts proceeds via two different mechanistic scenarios. Supported by NMR spectroscopic data, they suggested that both routes may occur simulta-

[a] Institut für Chemie der Technischen Universität Berlin, Strasse des 17. Juni 135, 10623 Berlin, Germany
[b] Institute of Organic Chemistry and Biochemistry, Academy of Sciences of the Czech Republic, Flemingovo nám. 2, 16610 Prague 6, Czech Republic
Fax: +420-220-183-117
E-mail: detlef.schroeder@uochb.cas.cz

 © 2007 Wiley-VCH Verlag GmbH & Co. KGaA, Weinheim 

neously to produce maleic acid, before conversion to the final product maleic anhydride is achieved. Using $^{13}C$ NMR, Chen and Munson recently proposed a single-site organometallic mechanism for the selective oxidation of *n*-butane on VPO catalysts.[19] According to their conclusions, activated butane forms a chelating configuration on the surface of the catalyst by coordination of C(1) and C(4) of butane to vanadium species. The chelating configuration is kept during the reaction sequence until maleic anhydride is formed. The reaction model proposed by Chen and Munson can also account for a number of other previous observations, such as the formation of ethylene as a side product, for example. Control of the formation of side products during the production of maleic anhydride is a non-trivial problem. Various species are formed in different processes and both the presence and ratios of side products and intermediates depend on many factors, for example, the ratio of V/P in the VPO catalysts and the presence of gaseous oxygen.[18] In particular, the formation of maleic anhydride is further associated with partial combustion leading to the formation of carbon oxides. In fact, the variety of intermediates and side products conceivable during the formation of maleic anhydride and their possible reactions with surface species render the complete understanding of the catalytic process rather difficult.

Information about mechanistic aspects in heterogeneous catalysis has been derived mainly from in-situ characterization of the catalysts and from observations of related processes which occur in solution or at liquid-solid or gas-solid interfaces. Recently, gas-phase studies of mass-selected cluster ions have been introduced as a complementary method for gaining information about the elementary steps of such reactions.[20–22]

In this respect, vanadium(V) complexes are of interest because they may be formed as transients in alkane oxidation on vanadium oxides in general and in particular because they have been shown to be involved in the oxidation of *n*-butane to maleic anhydride.[9,23] While most previous gas-phase studies on this topic have addressed the oxidation of hydrocarbons by gaseous vanadium-oxide ions,[21,24–29] here, we approach the problem from the side of the putative products. Accordingly, we investigate the generation and the behavior of vanadium(V) complexes containing one molecule of either maleic acid, fumaric acid, or succinic acid, which contain the $C_4$ skeleton of *n*-butane. The investigation of the dissociation behavior of these complexes may in turn add to the understanding of the processes which occur during the production of maleic anhydride. The ions of interest were produced using electrospray ionization (ESI) mass spectrometry,[30] a technique which permits transfer of ionic complexes into the gas phase directly from solution, with a variable degree of desolvation or fragmentation. Accordingly, ESI has been used for the analysis of inorganic and organometallic systems,[31–33] also including vanadium-oxide clusters.[9,25,26,28,30]

## Results

Electrospray ionization of $OV(OC_2H_5)_3$ dissolved in methanol together with a small amount of maleic acid or succinic acid inter alia leads to the formation of vanadium(V) complexes which formally include a $VO^+$ unit originating from the metal precursor, one (doubly deprotonated) unit of the diacid, and one solvent molecule, i.e. formally corresponding to $[(XCOO)_2VO(C,H_4,O)]^+$ with X = CH or $CH_2$ and the $(C,H_4,O)$ unit stemming from the solvent. The precise connectivity of the complexes is unknown, however; specifically, it is not certain, how the $(C,H_4,O)$ unit is distributed over the rest of the molecule. The first task is accordingly to investigate the types of ionic complexes formed. Given the components of the solutions used in ESI, structures **1**–**5** appear plausible for the case of maleic acid (Scheme 1); note that in addition to structures **1**–**5**, various related arrangements are conceivable (e.g. interchange of coordination from the carbonyl to the ester oxygen atoms).

Before addressing the ion structures, we note that the abundances of the $[(XCOO)_2VO(C,H_4,O)]^+$ complexes strongly depend on the concentrations of $OV(OC_2H_5)_3$ as well as the acids. If the concentration of acid is too high, the positive ion mass spectra are dominated by proton-bound oligomers of the acid itself, such as $[((CHCOOH)_2)_2H]^+$ ($m/z$ = 233) and $[((CHCOOH)_2)_3H]^+$ ($m/z$ = 349) in the case of maleic acid (X = CH). Vice versa, the yields of the desired mononuclear carboxylato-vanadium(V) complexes are also poor when the concentration of triethoxovanadate(V) is too large, due to the formation of polynuclear metal complexes.

### Complexes of Vanadium(V) with Maleic Acid

Under soft ionization conditions, ESI of a triethoxovanadate(V) solution in methanol with a trace of maleic acid provides an abundant signal at $m/z$ = 213 which can be attributed to the above mentioned $[(XCOO)_2VO(C,H_4,O)]^+$ species. According to the structural proposals shown in Scheme 1, the vanadium(V) center is connected with maleic acid through oxygen atoms from both carboxy groups,

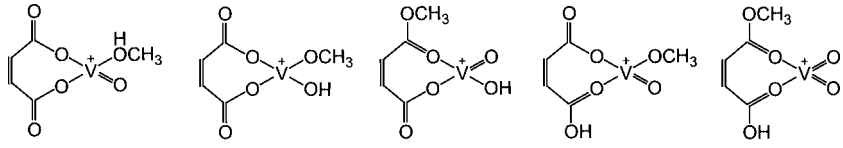


Scheme 1.

 © 2007 Wiley-VCH Verlag GmbH & Co. KGaA, Weinheim 

Table 1. Neutral losses (given as mass differences, $\Delta m$) observed upon CID of the mass-selected cations with $m/z$ = 213 and 217 generated by ESI of $OV(OC_2H_5)_3$ and maleic acid in $CH_3OH$ and $CD_3OD$, respectively. Data are given relative to the base peak (100) of the CID products at $E_{lab}$ = 5 eV.

| $\Delta m$ | –18 | –20 | –30 | –32 | –36 | –44 | –58 | –62 | –74 | –76 | –98 | –114 | –117 | –128 | –130 |
|---|---|---|---|---|---|---|---|---|---|---|---|---|---|---|---|
| $m/z$ 213 | 20 | | 5 | 13 | | 100 | 11 | | 19 | | 50 | 2 | | 6 | |
| $m/z$ 217 | | 9 | | 4 | 10 | 100 | | 15 | | 20 | 60 | | 5 | | 3 |

thereby forming a chelating configuration. The coordination shell is filled by an oxo- and a methanol ligand in the case of structure **1**, a hydroxy- and a methoxy group in structure **2**, an oxo- and a hydroxo group with the methyl group forming an ester with one carboxy unit, i.e. a complex of the singly deprotonated monomethyl ester of maleic acid with a $V(O)(OH)^+$ unit (structure **3**), the reverse arrangement of H and $CH_3$ in structure **4**, and finally H and $CH_3$ are both connected with oxygen atoms of the acid with two oxo ligands at vanadium, structure **5**. In all structures considered, the vanadium is coordinated by four oxygen atoms, and thus **1**–**5** only differ by the location of the hydrogen atom and the methyl group of the $(C,H_4,O)$ unit.

The CID spectrum of the mass-selected ion with $m/z$ = 213 produced upon ESI of a methanolic solution of triethoxovanadate(V) and maleic acid is dominated by the expulsion of neutral $CO_2$ ($\Delta m$ = –44, Table 1). The next intense signal, corresponding to $\Delta m$ = –98, can be assigned to a combined loss of $CO_2$, CO, and $C_2H_2$, suggesting a complete disintegration of the maleic acid attached as a ligand. Alternatively, this dissociation may involve the elimination of maleic anhydride as an intact $C_4H_2O_3$ entity. The latter conjecture is supported by the formation of protonated maleic anhydride (**6**) upon dissociation of the ion with $m/z$ = 213 ($\Delta m$ = –114, Scheme 2). As a result of the formal loss of neutral $C_4H_2O_3$, the cationic fragment ion $[OV(OH)(OCH_3)]^+$ is proposed to be formed (structure **8** in Scheme 2). This ion undergoes subsequent isomerization via hydrogen migration from the methoxo ligand to the oxo group (**8** → **9**) followed by elimination of $CH_2O$ (thus, $\Delta m$ = –128 in total) to yield the dihydroxo vanadium-cation $V(OH)_2^+$, which can then expel water to finally afford the diatomic cation $VO^+$.[34] Minor dissociation pathways correspond to the expulsions of water ($\Delta m$ = –18), formaldehyde ($\Delta m$ = –30), methanol ($\Delta m$ = –32), and the combined losses of methanol and acetylene ($\Delta m$ = –58).

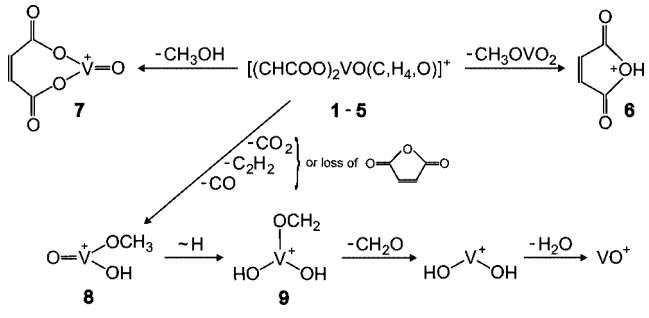


Scheme 2.

If deuterated methanol is used as a solvent, the mass of the precursor ion shifts to $m/z$ = 217, and CID of this species shows a similar fragmentation pattern. The most notable shifts of the mass differences upon ion fragmentation are those expected for the reactions in which neutral methanol or its fragments, such as formaldehyde, are lost. In contrast, the mass difference $\Delta m$ = –98 remains unchanged, consistent with the suggested formation of maleic anhydride without participation of the $(C,H_4,O)$ unit.

With regard to the ion structures **1**–**5**, there are a few, indirect arguments in favor of the presence of isomers **2** and/or **4**. (i) For a methoxo ligand directly attached to a metal core, such as in structures **2** and **4**, there is ample evidence of prevailing redox reactions via β-hydrogen migrations which then provide neutral formaldehyde as a fragment ($\Delta m$ = –30),[35–37] even including cationic catecholatovandadium(V) methoxides closely related to structure **2**.[38] Further, the loss of methanol ($\Delta m$ = –32) can easily occur from **2** and **4** after hydrogen migration to form isomer **1** followed by dissociation. (ii) While consideration of structures **2** and/or **4** provide an explanation for the minor losses of formaldehyde and methanol, respectively, the prevailing decarboxylation upon CID implies the presence of a carboxylato group from which $CO_2$ can be lost easily, which can occur for isomers **1**–**4** bearing carboxylato ligands.[39–42] (iii) Structurally indicative are the competing losses of neutral $CH_3OVO_2$ and neutral $C_4H_2O_3$, which only differ by the location of the proton in the ionic product. Assuming the smallest amount of rearrangement prior to fragmentation, this is consistent with the presence of structures **1**, **2**, and **4**; in case of structure **4**, the loss of neutral methoxovanadium dioxide $CH_3OVO_2$ ($\Delta m$ = –114) to afford protonated maleic anhydride can proceed from without any further hydrogen migrations prior to dissociation. (iv) Structures **3** and **5** derived from the monomethylester of maleic acid appear less likely, because the CID spectrum of the ion with $m/z$ = 213 independently prepared from a solution of $OV(OC_2H_5)_3$ and the monomethyl ester in methanol is dominated by loss of methanol and, in particular, decarboxylation is only a very minor process. (v) Last but not least, structure **1** with a presumably loosely bound methanol unit appears less likely because predominating loss of $CH_3OH$ would be expected upon CID, which is not the case in the experiment. As a general note of caution we add, however, that the assignment of the ion structure is further complicated by the fact that proton migrations may allow for a facile interconversion between the various isomers. Strictly speaking, no unambiguously distinction between isomers **1**–**5** can be made based on the CID experiments, and par-

 © 2007 Wiley-VCH Verlag GmbH & Co. KGaA, Weinheim 

ticularly the presence of a mixture of ion structures cannot be ruled out. Nevertheless, the CID data reported in Table 1 can be explained by the mechanism depicted in Scheme 2, which is also fully consistent with the labeling data. Further, the loss of methanol is suggested to afford the oxo complex **7**, whose CID spectrum has been recorded independently and is dominated by an expulsion of CO ($\Delta m$ = –28) with minor pathways corresponding to losses of $CO_2$ ($\Delta m$ = –44), two molecules of CO ($\Delta m$ = –56), and maleic anhydride (or $CO_2$, CO, and $C_2H_2$, both $\Delta m$ = –98) to afford bare $VO_2^+$.

Notably, a mixture of $OV(OC_2H_5)_3$ and fumaric acid does not form a corresponding ion with $m/z$ = 213 under ESI conditions, no matter which concentrations of the precursors were used. Specifically, the ESI solutions were prepared by mixing of 0.5 mL of methanolic triethoxovanadate solution (0.5 μL triethoxovanadate in 10 mL methanol) with 0.5 mL of a solution of fumaric acid in methanol (different concentrations from 0.05 to 1 g of fumaric acid in 10 mL methanol were applied). As the same mixing ratios were used successfully in the cases of maleic and succinic acid, we conclude that the *trans*-configuration of fumaric acid prevents the formation of chelate rings with the cationic vanadium core.

### Complexes of Vanadium(V) with Succinic Acid

Similar to the case of maleic acid, ESI of a dilute methanolic solution of succinic acid and triethoxovanadate(V) affords a monocationic complex with $m/z$ = 215, which, by analogy, we attribute to one of the vanadium(V) species **10**–**14** shown in Scheme 3; again, a more definitive assignment cannot be made on the basis of the CID spectra.

The CID spectrum of the mass-selected complex with $m/z$ = 215 (Table 2) is dominated by eliminations of water ($\Delta m$ = –18), methanol ($\Delta m$ = –32), as well as a combined loss of CO and $H_2O$ ($\Delta m$ = –46). Minor dissociation pathways correspond to combined eliminations of $CO_2$ and $H_2O$ ($\Delta m$ = –62), $CO_2$, $H_2O$, and CO ($\Delta m$ = –90), as well as $CO_2$, CO, and $C_2H_4$ ($\Delta m$ = –100); again, the latter fragmentation can also be due to the loss of an intact unit, i.e. succinic anhydride in this case. As a result of these minor dissociation processes, the cation $[OV(OH)(OCH_3)]^+$ is formed which already was observed in the case of the complex with maleic acid (structure **8** in Scheme 2) and which undergoes a subsequent loss of $CH_2O$ (thus, $\Delta m$ = –130 in total). Also similar to the complex derived from maleic acid, an expulsion of $CH_3OVO_2$ concomitant with formation of protonated succinic anhydride is observed as a minor channel ($\Delta m$ = –114).

Table 2. Neutral losses (gives as mass differences, $\Delta m$) observed upon of CID of the mass-selected cations [**A** = $(CH_2COO)_2VO(C,H_4,O)]^+$, **B** = $[(CD_2COO)_2VO(C,H_4,O)]^+$, and **C** = $[(CH_2COO)_2VO(C,D_4,O)]^+$ generated by ESI of $OV(OC_2H_5)_3$ and succinic acid in methanol using either unlabeled reagents or [2,2,3,3-$D_4$]-succinic acid and $CD_3OD$, respectively. Data are given relative to the base peak (100) of the CID products at $E_{lab}$ = 5 eV.

| $\Delta m$ | A | B | C |
|---|---|---|---|
| –18 | 100 | | 50 |
| –19 | | 46 | 38 |
| –20 | | 62 | |
| –30 | 6 | | |
| –32 | 57 | 8 | |
| –36 | | | 5 |
| –46 | 43 | | 100 |
| –47 | | 69 | 82 |
| –48 | | 100 | |
| –62 | 12 | | 21 |
| –63 | | 23 | 5 |
| –64 | | 31 | |
| –90 | 14 | | 25 |
| –92 | | 9 | |
| –100 | 14 | | 38 |
| –101 | | 33 | |
| –103 | | 31 | |
| –104 | | 15 | |
| –114 | 7 | 4 | |
| –117 | | | 17 |
| –120 | 1 | | 8 |
| –122 | | 8 | |
| –130 | 7 | | |
| –132 | | | 5 |
| –133 | | 4 | 3 |
| –134 | | | 2 |
| –160 | 28 | | |
| –161 | | 23 | |
| –162 | | 15 | |
| –163 | | | 27 |
| –164 | | | 17 |

The experimentally observed mass difference $\Delta m$ = –46 can be assigned to the expulsion of CO and $H_2O$, but it may also correspond to the loss of an ethanol molecule formed from the triethoxovanadate precursor. Hence, an additional labeling experiment was performed using $(CD_2COOH)_2$ as the acidic component. From methanolic solution of a mixture of triethoxovanadate(V) and $(CD_2COOH)_2$, the corresponding cation $[(CD_2COO)_2VO(C,H_4,O)]^+$, $m/z$ = 219, is generated under soft ESI condi-

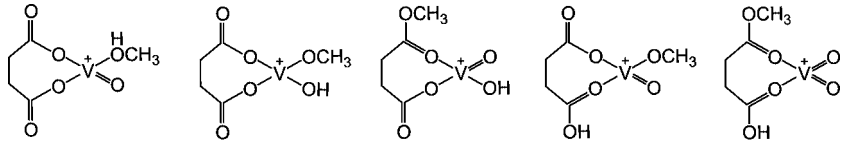


Scheme 3.

 © 2007 Wiley-VCH Verlag GmbH & Co. KGaA, Weinheim 

tions. The CID spectrum of mass-selected $m/z$ = 219 shows a mass difference of $\Delta m$ = –48 as the base peak (Table 2), which can thus be only assigned to a combined expulsion of CO and $D_2O$. The mass difference of $\Delta m$ = –47 is accordingly attributed to a combined elimination of CO and HDO. The CID spectrum of $[(CD_2COO)_2VO(C,H_4,O)]^+$ is further characterized by expulsions of HDO ($\Delta m$ = –19), $D_2O$ ($\Delta m$ = –20), methanol ($\Delta m$ = –32), respectively, as well as the combined losses of $CO_2$ and $D_2O$ ($\Delta m$ = –64), $CO_2$ and HDO ($\Delta m$ = –63), $CO_2$, CO, and $C_2HD_3$ ($\Delta m$ = –103), as well as $CO_2$, CO, and $C_2D_4$ ($\Delta m$ = –104). Once more, the combined losses of carbon oxides and ethylene may also be assigned to the expulsion of an intact acid anhydride. In addition to the expulsions of $H_2O$ ($\Delta m$ = –18) and HDO ($\Delta m$ = –19), the CID spectra of the mass-selected ion $[(CH_2COO)_2VO(C,D_4,O)]^+$ generated from $CD_3OD$ solution reveal preferential combined eliminations of CO and $H_2O$ ($\Delta m$ = –46) as well as CO and HDO ($\Delta m$ = –47).

In comparison, the fragmentations of the complexes derived from maleic and succinic acid are closely related to each other. In both cases, the CID spectra are characterized by the eliminations of identical or very similar neutral fragments. In fact, the mechanism proposed in Scheme 2 can describe the dissociation reactions observed in both cases. The main difference is that for the complex derived from maleic acid the major fragmentations are associated with an expulsion of $CO_2$ ($\Delta m$ = –44) and the elimination of $C_4H_2O_3$ ($\Delta m$ = –98), whereas for the complex generated using succinic acid the most abundant fragmentations correspond to the elimination of water ($\Delta m$ = –18) and the combined loss of $H_2O$ and CO ($\Delta m$ = –46). We note in passing that the pronounced loss of water from the complexes derived from succinic acid might be associated to contributions of enol forms as reaction intermediates, e.g. structure **15** (Scheme 4).

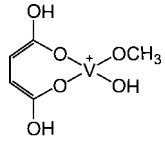


**15**

Scheme 4.

### Complexes of Vanadium (V) with Acetic Acid

ESI of triethoxovanadate dissolved in methanol with up to 20% of acetic acid leads to the formation of various complexes containing vanadium as well as acetic acid. For comparison with the complexes derived from the diacids discussed above, we focus on the vanadium(V) complex containing a vanadyl cation, two (deprotonated) molecules of acetic acid, and one methanol unit, i.e. formally $[(CH_3COO)_2V(O)(C,H_4,O)]^+$ ($m/z$ = 217). Upon CID of the mass-selected complex with $m/z$ = 217, the main process corresponds to the expulsion of neutral acetic acid ($\Delta m$ = –60). Minor dissociation pathways are associated with the expulsion of water ($\Delta m$ = –18), methanol ($\Delta m$ = –32), and a combined loss of water and acetic acid ($\Delta m$ = –78). Like for all vanadium(V) complexes studied here, the formation of $VO^+$ ($\Delta m$ = –150) as a terminal fragment is observed at larger collision energies.[43] In marked contrast to the complexes derived from maleic and succinic acid, however, no losses of carbon oxides are observed. Hence, consistent with the results obtained in the case of fumaric acid, the ability of maleic as well as succinic acid to form a chelating coordination to the vanadium center gives rise to a unique reactivity pattern. The fact that we can observe the complex with acetic acid, while the corresponding experiments with fumaric acid were not successful may be attributed to the experimental circumstances. Thus, due to the reasonable volatility of acetic acid, larger quantities of this compound can be added to the solution used in ESI and also gas-phase reactions occurring during the spray process may enhance formation of loosely bound ion/molecule complexes,[44] e.g. the tautomeric structure $[(CH_3COOH)(CH_3COO)V(O)(OCH_3)]^+$ with an intact acetic acid ligand.

### Mechanistic Implications

Most of the results reported here follow general expectations. Thus, among the major dissociation pathways for the $V^V$ cations derived from maleic as well as succinic acid are routes leading to the formation of carbon oxides. Similar decarbonylations as well as decarboxylations of carboxylic acids are known ever since the beginning of organic chemistry, e.g. the Kolbe synthesis. Further, the apparent losses of the maleic and succinic anhydride as intact neutral fragments from the respective complexes is consistent with the way of ion generation, but does not provide further insight with regard to the production of maleic anhydride from butane.

Nevertheless, there is one specific aspect in the fragmentation patterns of the ion derived from succinic acid which deserves particular attention with respect to oxidation catalysis. Specifically, loss of water is found as the most abundant process upon low-energy CID of complex $[(CH_2COO)_2VO(C,H_4,O)]^+$. Deuterium labeling in both ions, $[(CD_2COO)_2VO(C,H_4,O)]^+$ and $[(CH_2COO)_2VO(C,D_4,O)]^+$, demonstrates that the majority of the neutral water molecules lost incorporate H(D) atoms from the methylene groups of succinic acid, in that loss of $D_2O$ ($\Delta m$ = –20) prevails for $[(CD_2COO)_2VO(C,H_4,O)]^+$, whereas expulsion of $H_2O$ ($\Delta m$ = –18) predominates in the case of $[(CH_2COO)_2VO(C,D_4,O)]^+$ (Table 2). This finding implies that the central C–C bond undergoes dehydrogenation, thereby suggesting a possible connection from succinic to maleic acid in vanadium-mediated oxidations of hydrocarbons; an example for an illustration of this perspective is shown in Scheme 5 for the isomer **13** proposed to be involved for the ion formed upon ESI of the solution contained succinic acid, whose dehydration would lead from the $V^V$ species **13** to the $V^{III}$ complex **16**.

 © 2007 Wiley-VCH Verlag GmbH & Co. KGaA, Weinheim 

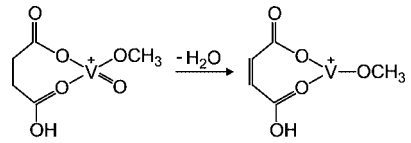


13 16

Scheme 5.

In a more general perspective of the butane oxidation to maleic anhydride, the obvious importance of chelating coordination by maleic as well as succinic acid supports the formation of surface-bound intermediates in the course of the oxidation reaction. Thus, the suggested alkoxide route or related pathways, which involve the formation of reaction intermediates covalently bound to vanadium surface species, find some analogy in the gas-phase chemistry of these systems.

## Conclusions

Electrospray ionization mass spectrometry is applied for the generation of dicarboxylato-vanadium(V) complexes derived from maleic and succinic acid, respectively. The results suggest that acids which are capable of forming a chelate ligand bring about an efficient coordination with a vanadium(V) center under ESI conditions. Upon collision-induced dissociation of the $V^V$ complexes, the expulsion of $CO_2$ is favored for the complexes derived from maleic acid, whereas a combined evaporation of $H_2O$ and CO is preferred for the corresponding complexes formed from succinic acid. Interestingly, the dehydration observed in the latter case provides a connection between succinic and maleic acid, which has not been considered so far in mechanistic considerations regarding the partial oxidation of $C_4$ hydrocarbons to maleic anhydride on vanadia-based catalysts.

## Experimental Section

The experiments were performed using a VG BIO-Q mass spectrometer of QHQ configuration (Q: quadrupole, H: hexapole) equipped with an electrospray ionization source.[45] The vanadium(V) complexes of interest were generated by ESI of dilute solutions of $OV(OC_2H_5)_3$ and the appropriate acids in methanol (or $CD_3OD$). The solutions were introduced into the ESI source via a silica capillary using a syringe pump at a flow rate of 5 μL/min and a source temperature of 80 °C with nitrogen as nebulizing and drying gas. All data were collected and averaged over at least 20 scans. Collision-induced dissociation experiments were performed with Q1 mass-selected ions using xenon as a collision gas in the hexapole at a pressure of ca. $2 \times 10^{-4}$ mbar and collision energies from $E_{lab}$ = 0–30 eV, while analyzing the ionic products by scanning Q2.

Although many different cations of rather broad stoichiometric compositions are formed from the solutions studied by ESI, we were interested only in complexes containing a single vanadium(V) and one molecule of the corresponding diacid. The number of ligands of the solvated cations is crucially dependent on the cone voltage of the ESI source.[45–48] All vanadium(V) complexes presented here are formed under comparably soft conditions of ionization, i.e. at cone voltages between 20 and 40 V, where multiply ligated ions predominate; at cone voltages above 80 V, diatomic $VO^+$ prevails for all mixtures studied.[43]

## Acknowledgments

Financial support by the Deutsche Forschungsgemeinschaft (DFG, SFB 546) and the Fonds der Chemischen Industrie (FCI) is appreciated. Further, we are grateful to the reviewers for valuable comments.

[1] K. Liu, A. Wagner, *The chemical dynamics and kinetics of small radicals*, parts I and II, World Scientific, Singapore, **1995**.
[2] J. R. Anderson, M. Boudart, *Catalysis: Science and Technology*, Springer-Verlag, Berlin, **1984**.
[3] T. Hirao, *Chem. Rev.* **1997**, *97*, 2707.
[4] B. Grzybowska-Swierkosz, F. Trifiro, J. C. Vedrine, *J. Appl. Catal.* **1997**, *96*, 442.
[5] R. Ramirez, B. Casal, L. Utrera, E. Ruiz-Hitzky, *J. Phys. Chem.* **1990**, *94*, 8960.
[6] S. Y. Chen, D. Willcox, *Ind. Eng. Chem. Res.* **1993**, *32*, 584.
[7] B. M. Weckhuysen, D. E. Keller, *Catal. Today* **2003**, *78*, 25.
[8] P. L. Gai, K. Kourtakis, *Science* **1995**, *267*, 661.
[9] G. W. Coulston, S. R. Bare, H. Kung, K. Birkeland, G. K. Bethke, R. Harlow, N. Herron, P. L. Lee, *Science* **1997**, *275*, 191.
[10] G. Centi, F. Trifiro, J. R. Ebner, V. M. Franchetti, *Chem. Rev.* **1988**, *88*, 55.
[11] G. Centi, *Catal. Today* **1993**, *16*, 5.
[12] G. Centi, G. Fornassari, F. Trifiro, *Ind. Eng. Chem. Prod. Res. Dev.* **1985**, *24*, 32.
[13] Y. Zhang-Lin, M. Forissier, R. P. Sneeden, J. C. Vedrine, J. C. Volta, *J. Catal.* **1994**, *145*, 256.
[14] Y. Zhang-Lin, M. Forissier, R. P. Sneeden, J. C. Vedrine, J. C. Volta, *J. Catal.* **1994**, *145*, 267.
[15] F. Cavani, F. Trifirio, *Catalysis* **1994**, *11*, 246.
[16] See also: a) B. Schiott, K. A. Jorgensen, R. Hoffmann, *J. Phys. Chem.* **1991**, *95*, 2297; b) J. M. L. Nieto, P. Concepcion, A. Dejoz, H. Knozinger, F. Melo, M. I. Vazquez, *J. Catal.* **2000**, *189*, 147; c) D. J. Thompson, M. O. Fanning, B. K. Hodnett, *J. Mol. Catal. A* **2003**, *206*, 435.
[17] A. Aguero, R. P. Sneeden, J. C. Volta, in *Heterogeneous Catalysis and Fine Chemicals. Studies in Surface Science and Catalysis* (Ed.: M. Guisnet), vol. 41, Elsevier, Amsterdam, **1988**, p. 353.
[18] B. Chen, E. J. Munson, *J. Am. Chem. Soc.* **1999**, *121*, 11024.
[19] B. Chen, E. J. Munson, *J. Am. Chem. Soc.* **2002**, *124*, 1638.
[20] M. Aschi, M. Brönstrup, M. Diefenbach, J. N. Harvey, D. Schröder, H. Schwarz, *Angew. Chem.* **1998**, *110*, 858; *Angew. Chem. Int. Ed. Engl.* **1998**, *37*, 829.
[21] R. C. Bell, K. A. Zemski, A. W. Castleman, *J. Cluster Sci.* **1999**, *10*, 509.
[22] Review: D. K. Bohme, H. Schwarz, *Angew. Chem.* **2005**, *117*, 2388; *Angew. Chem. Int. Ed.* **2005**, *44*, 2336.
[23] B. Kubias, U. Rodemerck, H. W. Zanthoff, M. Meisel, *Catal. Today* **1996**, *32*, 243.
[24] R. C. Bell, A. W. Castleman, *J. Phys. Chem. A* **2002**, *106*, 9893.
[25] D. Schröder, M. Engeser, M. Brönstrup, C. Daniel, J. Spandl, H. Hartl, *Int. J. Mass Spectrom.* **2003**, *228*, 743.
[26] S. Feyel, D. Schröder, H. Schwarz, *J. Phys. Chem. A* **2006**, *110*, 2647.
[27] N. A. Moore, R. Mitric, D. R. Justes, V. Bonacic-Koutecky, A. W. Castleman, *J. Phys. Chem. B* **2006**, *110*, 3015.
[28] S. Feyel, D. Schröder, X. Rozanska, J. Sauer, H. Schwarz, *Angew. Chem.* **2006**, *118*, 4793; *Angew. Chem. Int. Ed.* **2006**, *45*, 4677.
[29] S. Feyel, J. Döbler, D. Schröder, J. Sauer, H. Schwarz, *Angew. Chem.* **2006**, *118*, 4797; *Angew. Chem. Int. Ed.* **2006**, *45*, 4681.
[30] M. Yamashita, J. B. Fenn, *J. Phys. Chem.* **1984**, *88*, 4451.

 © 2007 Wiley-VCH Verlag GmbH & Co. KGaA, Weinheim 

[31] P. Chen, *Angew. Chem.* **2003**, *115*, 2938; *Angew. Chem. Int. Ed.* **2003**, *42*, 2832.
[32] L. A. Hammad, G. Gerdes, P. Chen, *Organometallics* **2005**, *24*, 1907.
[33] For a recent review, see: M. Y. Combariza, A. M. Fahey, A. Milshteyn, R. W. Vachet, *Int. J. Mass Spectrom.* **2005**, *244*, 109.
[34] G. K. Koyanagi, D. K. Bohme, I. Kretzschmar, D. Schröder, H. Schwarz, *J. Phys. Chem. A* **2001**, *105*, 4259.
[35] D. Schröder, H. Schwarz, *Angew. Chem.* **1990**, *102*, 925; *Angew. Chem. Int. Ed. Engl.* **1990**, *29*, 910.
[36] A. Fiedler, D. Schröder, H. Schwarz, B. L. Tjelta, P. B. Armentrout, *J. Am. Chem. Soc.* **1996**, *118*, 5047.
[37] D. Schröder, H. Schwarz, S. Polarz, M. Driess, *Phys. Chem. Chem. Phys.* **2005**, *7*, 1049.
[38] M. Kaczorowska, D. Schröder, H. Schwarz, *Eur. J. Inorg. Chem.* **2005**, 2919.
[39] D. Schröder, H. Schwarz, *Organometallics* **1992**, *11*, 2296.
[40] T. Waters, R. A. J. O'Hair, A. G. Wedd, *Int. J. Mass Spectrom.* **2003**, *228*, 599.
[41] R. A. J. O'Hair, A. K. Vrkic, P. F. James, *J. Am. Chem. Soc.* **2004**, *126*, 12173.
[42] D. Schröder, H. Schwarz, N. Aliaga-Alcalde, F. Neese, *Eur. J. Inorg. Chem.* **2007**, *219*, 729.
[43] D. Schröder, M. Engeser, H. Schwarz, E. C. E. Rosenthal, J. Döbler, J. Sauer, *Inorg. Chem.* **2006**, *45*, 6235.
[44] J. Roithová, J. Hrušak, D. Schröder, H. Schwarz, *Inorg. Chim. Acta* **2005**, *358*, 4287.
[45] D. Schröder, T. Weiske, H. Schwarz, *Int. J. Mass Spectrom.* **2002**, *213–221*, 816.
[46] N. Tsierkezos, D. Schröder, H. Schwarz, *J. Phys. Chem. A* **2003**, *107*, 9575.
[47] M. C. Holthausen, D. Schröder, H. Schwarz, *J. Phys. Chem. B* **2004**, *108*, 14407.
[48] M. Schlangen, D. Schröder, H. Schwarz, *Angew. Chem.* **2007**, *119*, 1667; *Angew. Chem. Int. Ed.* **2007**, *46*, 1641.

Received: December 11, 2006
Published Online: June 1, 2007

 © 2007 Wiley-VCH Verlag GmbH & Co. KGaA, Weinheim 

DOI: 10.1002/ejic.200700181

# Synthesis and Characterization of Silver-Nanoparticle-Deposited α-$Bi_2Mo_3O_{12}$ Nanorods

**Anil Vithal Ghule,[a] Kalyani Ghule,[a] Shin-Hwa Tzing,[a] and Yong-Chien Ling*[a]**

**Keywords:** Nanoparticles / Ultrasound / Deposition / Nanorods / Surface analysis / Electron microscopy

Silver (Ag) nanoparticles with an average size of ca. 10 nm were uniformly deposited on the surface of α-$Bi_2Mo_3O_{12}$ nanorods by using an ultrasound sonication method. Ultrasonic irradiation of preformed α-$Bi_2Mo_3O_{12}$ spherical nanoparticles (ca. 200 nm) in pyridine resulted in α-$Bi_2Mo_3O_{12}$ nanorods (ca. 100 nm diameter). Further, sonication of the mixture of α-$Bi_2Mo_3O_{12}$ nanorods and $Ag_2O$ in pyridine yielded a nanocomposite of α-$Bi_2Mo_3O_{12}$ nanorods with deposited Ag nanoparticles and pyridine. Calcination of the nanocomposite at 450 °C afforded pyridine-free α-$Bi_2Mo_3O_{12}$ nanorods with deposited Ag nanoparticles. A plausible mechanism is proposed. The crystallized Ag nanoparticles are uniformly deposited on the surface, with bismuth (Bi) as the preferential binding site, as revealed by time-of-flight secondary ion mass spectrometry (TOF-SIMS). Structural, compositional and morphological characterization of the products is carried out by using transmission electron microscopy, energy-dispersive X-ray analysis, scanning electron microscopy, thermogravimetric analysis, X-ray diffraction, X-ray photoelectron spectroscopy and TOF-SIMS.
(© Wiley-VCH Verlag GmbH & Co. KGaA, 69451 Weinheim, Germany, 2007)

## Introduction

Since last decade, the science and technology of nanomaterials has created immense interest in their potential technological applications. This has inspired the synthesis of nanomaterials of various shapes and sizes including nanoparticles, nanotubes, nanorods, nanoribbons, nanowires, nanospheres, nanocrystals, nanoflasks and so on, composed of metals, metal oxides, organic, inorganic and bioinorganic compounds, and their hybrid composites.[1] The category of hybrid nanocomposites in general has broadened significantly to encompass a large variety of systems and is a fast-growing area of research. Layered inorganic compounds have been studied for a considerable time as candidates for the generation of nanohybrids. This area is enjoying a resurgence of interest and activity as a result of the exceptional properties that can be realized from these nanocomposites. Because inorganic layered materials exist in great variety with a well-defined ordered intralamellar space, they serve as hosts accessible to guest species and yield interesting hybrid nanocomposites. Significant efforts are focused on the ability to obtain control of the nanoscale structures by judiciously engineering the host–guest interactions through innovative synthetic approaches. This has enabled the synthesis of nanocomposites with a broad range of properties. The properties of nanocomposites depend not only on the properties of their individual parents, but also on their morphology and interfacial characteristics. As the remarkable properties of conventional composites are mainly due to interface interactions, any system that is subjected to critical analysis is of interest. Although selected classes of these composites may be amenable to direct structural characterization by standard crystallographic methods, an important issue in this area is the limited availability of structural and morphological details. Furthermore, nanocomposites also offer the possibility to combine diverse properties, which is impossible within a single material; thus, they promise new applications in many fields.

Bismuth, molybdenum and their oxides have been explored with great interest for technological applications.[2] However, very little attention was focused on binary oxides, despite their wide applicability. Bismuth molybdates (α-$Bi_2Mo_3O_{12}$, β-$Bi_2Mo_2O_9$ and γ-$Bi_2MoO_6$) are popular and widely explored catalysts of commercial importance.[3] Furthermore, bismuth–molybdenum-based oxides have also found applications as pure oxide ionic conductors,[4] as optical[5] and acousto–optical materials,[6] as photoconductors in thin films,[7] and as gas sensors in breath-analyzer devices.[8] Modification of the surface properties plays an important role in the behaviour of these compounds; thus, increased effort has been made to modify their surfaces to create new classes of compounds with different properties.[9]

Ag dispersed on metal oxides is gaining popularity as a catalyst.[10] Moreover, Ag has low hardness and wear resistance, and thus it is often alloyed with other metals to improve its properties.[11] For example, Ag–Bi alloys have gained importance as they find applications in electronics, lead-free soldering, radiotechnics and in the production of

[a] Department of Chemistry, National Tsing Hua University, Hsinchu, Taiwan 30013
Fax: +886-3-5711082
E-mail: ycling@mx.nthu.edu.tw

 InterScience © 2007 Wiley-VCH Verlag GmbH & Co. KGaA, Weinheim 

coatings exposed to severe conditions, for example, friction under high pressure.[12] The use of Ag films as a buffer layer for the preparation of Bi-2212 tapes on Ni, Ni–Cr, stainless steel and Hastelloy substrates has also been exploited with great interest.[13] Thus, by banking on the information that Ag has a good interaction with Bi, Ag was selected for deposition on α-$Bi_2Mo_3O_{12}$ nanorods in this work. It was also of interest to investigate the mode of interaction and preferred binding site of Ag on the surface of the α-$Bi_2Mo_3O_{12}$ nanorods, which would provide useful information for the design of novel composite materials with improved properties.

Various methods, including wet chemistry techniques, colloid reduction chemical routes, inverse micelle and surfactant utilization, electrochemical and electroless plating, sol-gel and spray pyrolysis etc., have been employed to modify or coat the substrates with noble metals, and complicated apparatus are usually required. In contrast, sonochemistry is a simple alternative technique, which has been exploited extensively to coat nanoparticles and prepare a variety of metal nanoparticles and oxide nanorods.[14,15] Herein, we use a simple ultrasound method[16,17] to deposit Ag nanoparticles on the surface of α-$Bi_2Mo_3O_{12}$ nanorods. To the best of our knowledge, this is the first report of this procedure.

## Results and Discussion

Sonochemistry is gaining importance for its simplicity in the synthesis of nanomaterials and coating nanoparticles on substrates.[18] Power ultrasound effecting chemical changes by cavitation phenomena that involves the formation, growth and implosive collapse of bubbles in liquid, is exploited in this technique.[17] Synthesis of metal nanoparticles by using ultrasound techniques is well reported.[14] Furthermore, sonication of the precursor nanoparticles in the presence of an inorganic support such as α-$Bi_2Mo_3O_{12}$ nanorods provides a means of trapping the nanoparticles by chemical affinity to produce heterogeneous catalysts. Herein it is exploited to deposit Ag nanoparticles on the surface of α-$Bi_2Mo_3O_{12}$ nanorods by using pyridine as a medium.

The motivation for the use of pyridine in this work comes from the extensive studies conducted on pyridine intercalation with bismuth molybdate as substrates, where mostly hydrated forms were used as starting material.[19–21] The use of the hydrated form of bismuth molybdate adds to the controversy and thus the anhydrous form is used in this work, the details of which are discussed elsewhere.[16,22] Moreover, no change in the composition of the substrates was reported or observed by us with the use of pyridine.[16,22] In contrast, sonication of α-$Bi_2Mo_3O_{12}$ in water and $NH_4OH$ (pH of 8) results in the formation of $MoO_3$ nanorods and nanoribbons instead of the formation of α-$Bi_2Mo_3O_{12}$ nanorods. This is confirmed by transmission electron microscopy (TEM) images, energy dispersive X-ray analysis (EDS) spectra and selected area electron diffraction (SAED) patterns (data not shown).[16] This supports the importance of pyridine in α-$Bi_2Mo_3O_{12}$ nanorod formation. Furthermore, it was observed that the intercalation and adsorption of pyridine on the surface of α-$Bi_2Mo_3O_{12}$ nanorods helps to retain its phase without degradation to form mixed phases.[16] Extensive reports on the adsorption of pyridine on metal surfaces also exist,[23] which provides active sites for chemical manipulation of the surfaces. This N-containing aromatic compound has generated particular interest because of its useful physical and chemical properties that are derived from the lone pair of electrons on the N atom. Pyridine molecules are adsorbed on the surface predominantly through metal–N dative bonding and to oxygen as pyridinium or pyridinium oxide.[16,24] The pyridine molecules orient themselves perpendicular to the surface and parallel to each other.

### Electron Microscopy

Scanning electron microscopy (SEM) and TEM are used for morphological characterization of Ag-nanoparticle-deposited α-$Bi_2Mo_3O_{12}$ nanorods and also to investigate the nature of the adherence of the particles to the surface. The SEM and TEM micrographs of Ag nanoparticles that are deposited on α-$Bi_2Mo_3O_{12}$ nanorods obtained after sonication for 60 min are shown in Figure 1a and b, respectively. The Ag nanoparticles, which are about 10 nm in size, deposit uniformly on the surface of α-$Bi_2Mo_3O_{12}$ nanorods as shown in Figure 1b. The inset of Figure 1b shows a TEM image of Ag nanoparticles (ca. 10 nm size) obtained on sonication of $Ag_2O$ in pyridine for 60 min. Figure 1c shows a high-resolution TEM micrograph of a Ag nanoparticle. Crystallinity of the Ag nanoparticles is confirmed by the lattice fringes and lattice spacing, which are characteristic of Ag. The lattice spacing is noted to be 0.235 nm for the (111) plane and is in agreement with earlier reports.[25] To further confirm the crystallinity of the Ag nanoparticles, SAED patterns and EDS spectra were also recorded. The SAED pattern of a single Ag nanoparticle is shown in the inset of Figure 1c. It shows diffused rings with *d* spacing 0.235 [111], 0.144 [220], 0.118 [222] and 0.091 [420], which is characteristic of FCC silver metal and in agreement with the International Center for Diffraction Data file #03-0931. For better comparison, EDS spectra from (i) α-$Bi_2Mo_3O_{12}$ nanorods, (ii) α-$Bi_2Mo_3O_{12}$ nanorods coated with Ag nanoparticles and (iii) a single Ag nanoparticle are recorded as shown in Figure 1d. The presence of silver, bismuth, molybdenum, oxygen and copper is confirmed from the α-$Bi_2Mo_3O_{12}$ nanorods that contain deposited Ag nanoparticles [Figure 1d, spectrum (ii)], whereas the EDS spectrum procured from a single Ag nanoparticle shows the exclusive presence of Ag [Figure 1d, spectrum (iii)].

Experiments with an increased sonication time (90 and 120 min) were also conducted and showed aggregation of Ag nanoparticles possibly because of forced excess collapse of Ag nanoparticles with increased sonication time. The representative TEM micrograph of Ag nanoparticles aggre-

 © 2007 Wiley-VCH Verlag GmbH & Co. KGaA, Weinheim 

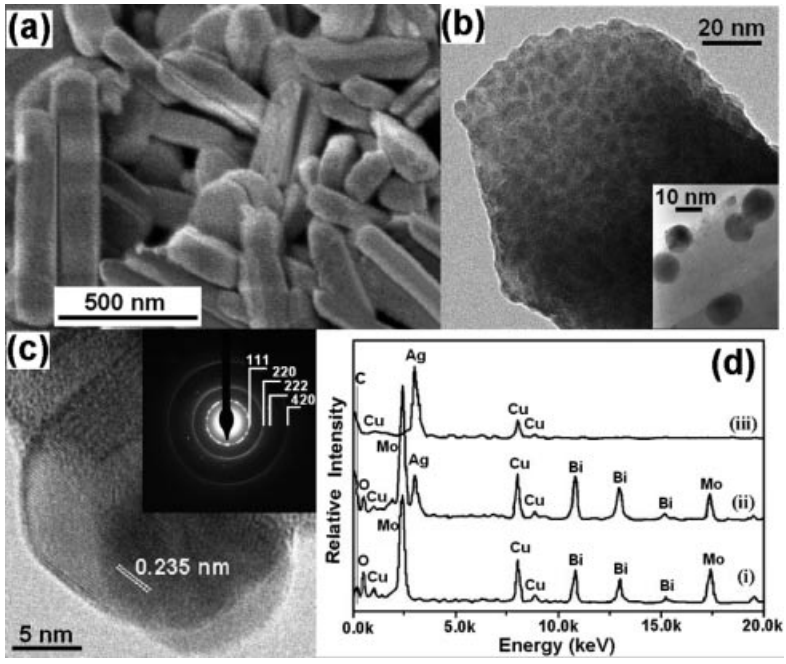


Figure 1. (a) SEM and (b) TEM micrographs of α-$Bi_2Mo_3O_{12}$ nanorods with deposited Ag nanoparticles obtained after sonication for 60 min. Inset shows Ag nanoparticles (ca. 10 nm) obtained from sonication of $Ag_2O$ in pyridine for 60 min. (c) HRTEM image of a single Ag nanoparticle, indicating the size of ca. 10 nm and showing lattice fringes characteristic of metallic Ag. The inset is the characteristic SAED pattern obtained from the Ag nanoparticle. (d) Representative energy-dispersive X-ray analysis spectra (EDS) of (i) α-$Bi_2Mo_3O_{12}$ nanorods, (ii) α-$Bi_2Mo_3O_{12}$ nanorods with deposited Ag nanoparticles showing the presence of Bi, Mo, Ag and O and (iii) a single Ag nanoparticle.

gated on α-$Bi_2Mo_3O_{12}$ nanorods obtained after sonication for 120 min is shown in Figure 2a. When the amount of $Ag_2O$ is varied (200 and 300 mg) with the use of the same amount of α-$Bi_2Mo_3O_{12}$ nanorods (2 g) and a sonication time of 60 min, the number of deposited Ag nanoparticles increased. Figure 2b shows a representative TEM micrograph of one end (tip) of Ag nanoparticles deposited α-$Bi_2Mo_3O_{12}$ nanorods obtained from the use of 300 mg of $Ag_2O$ and a sonication time of 60 min. The Ag nanoparticles appear to be localized in close vicinity with minimal aggregation; however, the particle size is observed to be same (ca. 10 nm) unlike that observed after an increased sonication time (Figure 2a). It appears that subsequently deposited Ag nanoparticles are directed to the voids of the previously deposited nanoparticles (inset in Figure 2b) as a result of pyridine being adsorbed on the surface. It is also observed that the number of free Ag nanoparticles in the product increases with increased amounts of $Ag_2O$. Figure 2c shows a TEM image of randomly deposited $Ag_2O$ nanoparticles on the surface of α-$Bi_2Mo_3O_{12}$ nanorods obtained from vigorous stirring of the mixture of $Ag_2O$ and α-$Bi_2Mo_3O_{12}$ nanorods at 40 °C for 60 min. The size of the deposited and free nanoparticles in the product is larger and the particles are confirmed to be of $Ag_2O$. The XRD pattern obtained from the product shows characteristic peaks at $2\theta$ = 32.85°, 38.10°, 55.01° and 65.57°, which can be indexed to [111], [200], [220] and [311] reflection lines, respectively, of $Ag_2O$ particles (JCPDS 75-1532). Additionally, chains of large $Ag_2O$ particles are also observed in the

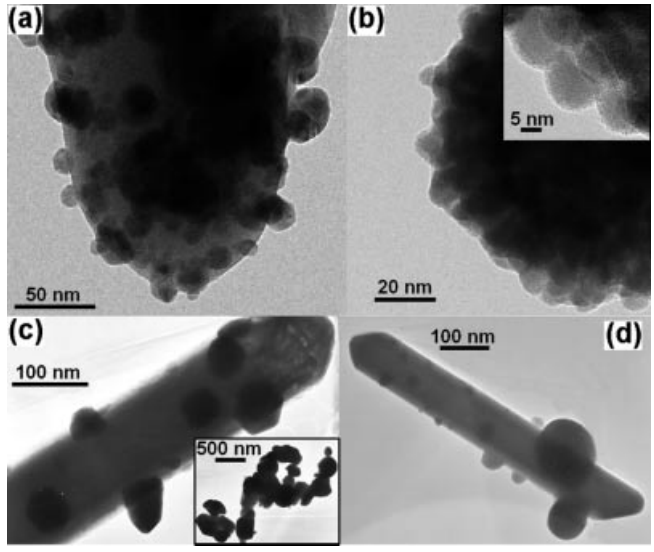


Figure 2. (a) Aggregation and growth of Ag nanoparticles with increased sonication time (120 min; after calcination to 450 °C). (b) TEM micrograph of the tip of a α-$Bi_2Mo_3O_{12}$ nanorod with deposited Ag nanoparticles, showing the nature of deposition and morphology of deposited Ag nanoparticles when 300 mg of $Ag_2O$ was used. Inset shows an HRTEM image. (c) TEM image of randomly deposited $Ag_2O$ nanoparticles on α-$Bi_2Mo_3O_{12}$ nanorods obtained after stirring the mixture of $Ag_2O$ and α-$Bi_2Mo_3O_{12}$ nanorods in pyridine at 40 °C. Inset shows TEM image of a chain of large $Ag_2O$ nanoparticles observed in the product. (d) Representative TEM micrograph of a nanorod obtained on heating the homogenized mixture of $Ag_2O$ and α-$Bi_2Mo_3O_{12}$ nanorods at a controlled rate of 5 °C $min^{-1}$.

 © 2007 Wiley-VCH Verlag GmbH & Co. KGaA, Weinheim 

product, as shown in the inset in Figure 2c. These might be due to the fusion of free $Ag_2O$ particles during the calcination process. In contrast, when a homogenized mixture of $Ag_2O$ and α-$Bi_2Mo_3O_{12}$ nanorods is heated to 450 °C in the absence of pyridine and at a controlled heating rate of 5 °C min$^{-1}$, very few $Ag_2O$ particles of varying size are seen bound to the surface of the nanorods, as shown in Figure 2d. Furthermore, the XRD pattern (Figure 4e) obtained from the product shows a change in composition and the pattern is observed to be in good agreement with that of $AgBi(MoO_4)_2$ (JCPDS 32-0999).

### Thermal Analysis

TG-DTG thermograms recorded in the temperature range from 30 to 500 °C with a heating rate of 5 °C min$^{-1}$ in a flow of air at 20 mL min$^{-1}$ using pyridine-intercalated α-$Bi_2Mo_3O_{12}$ nanorods are shown in Figure 3a and 3a′and those of α-$Bi_2Mo_3O_{12}$ nanorods with deposited Ag nanoparticles are shown in Figure 3b and b′. The TG thermogram (Figure 3a) recorded from pyridine-intercalated α-$Bi_2Mo_3O_{12}$ nanorods shows a weight loss of 5% and can be attributed to the loss of pyridine. The respective DTG thermogram (Figure 3a′), which is derivative of the TG thermogram, shows dips at 187, 245 and 314 °C, which indicates that the weight loss takes place in three steps. The deintercalation process extends up to 400 °C and no further weight loss is observed at higher temperatures. The TG thermogram (Figure 3b) recorded from α-$Bi_2Mo_3O_{12}$ nanorods with deposited Ag nanoparticles shows a weight loss of 8.8% due to loss of pyridine. The desorption and deintercalation process extends up to 450 °C, slightly higher than that observed in the earlier thermogram, which might be due to the deposited silver nanoparticles. Moreover, the observed weight loss is also higher and can be attributed to the loss of pyridine adsorbed on Ag nanoparticles in addition to loss of pyridine intercalated in α-$Bi_2Mo_3O_{12}$ nanorods. The respective DTG thermogram (Figure 3b′) shows a sharp dip at 90.1 °C and can be attributed to desorption of pyridine adsorbed on Ag nanoparticles. The two broad dips at 209 and 314 °C might be due to slow elongated deintercalation of pyridine from the product because of the deposited Ag nanoparticles on the surface.

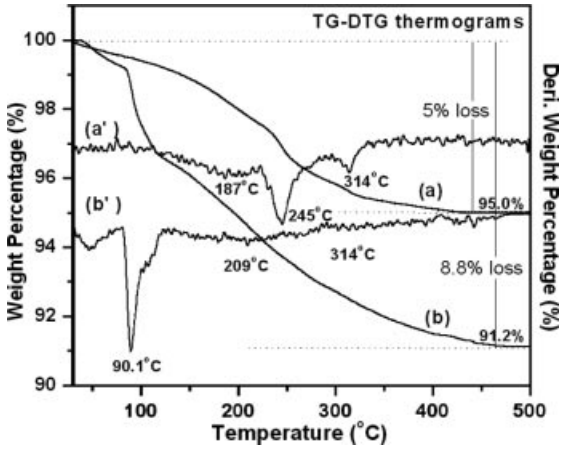


Figure 3. (a) TG thermogram obtained from pyridine-intercalated α-$Bi_2Mo_3O_{12}$ nanorods and (a′) its DTG thermogram. (b) TG thermogram obtained from α-$Bi_2Mo_3O_{12}$ nanorods with deposited Ag nanoparticles obtained after sonication for 60 min with 100 mg $Ag_2O$ and (b′) its DTG thermogram.

### X-ray Diffraction

The XRD patterns of the product and intermediates are shown in Figure 4. Representative XRD patterns of $Bi_2Mo_3O_{12}\cdot 5H_2O$ shown in Figure 4a can be indexed to a monoclinic cell with lattice parameters of $a$ = 6.334, $b$ = 11.593, $c$ = 5.777 Å and $\beta$ = 113.166° (JCPDS 41-0361), even though the formula is given to be $Bi_2Mo_3O_{12}\cdot 4.75H_2O$. The XRD pattern is also observed to be in close agreement with that reported by Barnes et al.,[21] even though they claimed the correct formula to be $BiMo_2O_7OH\cdot 2H_2O$. However, our EDS analysis is in accordance with the expected Bi/Mo ratio of 2:3 and also the TG analysis shows weight loss corresponding to five molecules of water.[26] The XRD pattern obtained from spherical nanoparticles of α-$Bi_2Mo_3O_{12}$ phase as shown in Figure 4b is in close agreement with that reported by Li and Cheng[27] and in a literature report (JCPDS 70-1396). The crystal structure of α-$Bi_2Mo_3O_{12}$ phase (scheelite structure) is reported to be monoclinic, trigonal-bipyramidal or distorted tetrahedral with space group $P2_1/c$ and cell parameters $a$ = 7.685, $b$ = 11.491 and $c$ = 11.929 Å and characteristic edge $\beta$ = 115.40°. The XRD pattern of pyridine-intercalated α-$Bi_2Mo_3O_{12}$ nanorods is shown in Figure 4c. It exhibits some similarities with that of pure α-$Bi_2Mo_3O_{12}$ phase (Figure 4b) owing to the use of α-$Bi_2Mo_3O_{12}$ as the starting material for pyridine intercalation. The peaks observed at lower $2\theta$ values are indicative of an increased interlayer region due to pyridine intercalation similar to that reported earlier.[19,21] The peaks appear to be broad, probably because of the reduced particle size and intercalation of pyridine. To the best of our knowledge, the reference database file (JCPDS) does not exist, as most of the researchers used the hydrated form of $Bi_2Mo_3O_{12}$ for pyridine intercalation studies, as discussed in an earlier report.[16] The XRD pattern of α-$Bi_2Mo_3O_{12}$ nanorods with deposited Ag nanoparticles (Figure 4d) is different from its counterpart in the sense that it shows characteristic peaks at $2\theta$ = 38.04°, 44.22° and 64.36° that could be indexed to [111], [200] and [220] reflection lines, respectively, of FCC Ag particle (JCPDS 04-0783). Traces of less intense peaks indicative of cubic $Ag_2O$ (JCPDS 75-1532) are also observed and can be attributed to the surface oxidation of Ag nanoparticles. The XRD pattern obtained from slow controlled heating of a homogenized mixture of α-$Bi_2Mo_3O_{12}$ nanorods and $Ag_2O$ is shown in Figure 4e. The pattern is in good agreement with that reported for $AgBi(MoO_4)_2$ (JCPDS 32-0999) and different from that observed for α-$Bi_2Mo_3O_{12}$ nanorods with deposited Ag nanoparticles. This indicates a change in composition during solid-state reaction as a result of diffusion of Ag atoms, which

 © 2007 Wiley-VCH Verlag GmbH & Co. KGaA, Weinheim 

alter the composition during the heating process. It is interesting to note that the α-$Bi_2Mo_3O_{12}$ nanorods with deposited Ag nanoparticles (Figure 4d) do not show diffusion of Ag or change in composition. This might be due to intercalated pyridine preventing the diffusion of Ag, as diffusion and deintercalation processes are expected to occur at the same time during heating.

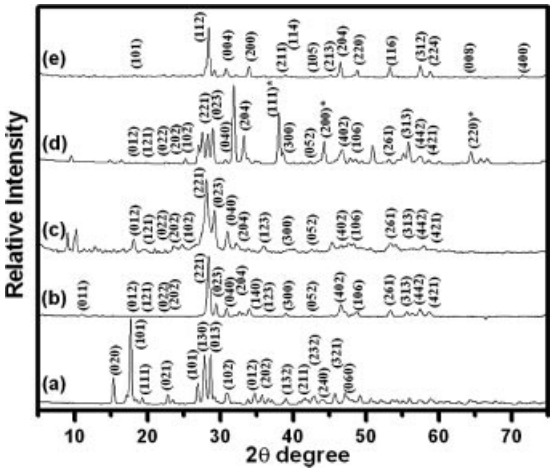


Figure 4. XRD spectra of (a) $Bi_2Mo_3O_{12}·5H_2O$, (b) α-$Bi_2Mo_3O_{12}$, (c) pyridine-intercalated α-$Bi_2Mo_3O_{12}$ nanorods, (d) α-$Bi_2Mo_3O_{12}$ nanorods with deposited Ag nanoparticles obtained after sonication for 60 min with 100 mg $Ag_2O$ and (e) product obtained from heating the homogenized mixture of $Ag_2O$ and α-$Bi_2Mo_3O_{12}$ nanorods.

### X-ray Photoelectron Spectroscopy

An XPS surface scan spectrum of α-$Bi_2Mo_3O_{12}$ nanorods with deposited Ag nanoparticles is shown in Figure 5. It shows characteristic peaks for $Mo3d_{5/2}$ (233 eV), $Mo3d_{3/2}$ (235.8 eV), $Bi4f_{7/2}$ (160 eV) and $Bi4f_{5/2}$ (165 eV). XPS analysis did not detect any modification in the atomic ratio or Mo oxidation state of the Ag-nanoparticle-deposited α-$Bi_2Mo_3O_{12}$ nanorods compared to those of α-$Bi_2Mo_3O_{12}$. However, a considerable shift in the $Bi4f_{5/2}$ peak is observed, probably because of the change in oxidation state of Bi. It is well known that there is a strong interaction between Bi and Ag, and thus, it is expected that the deposited Ag nanoparticles would prefer Bi sites rather than Mo for binding on the surface. Reports on the presence of stable Ag–Bi alloys support our speculation.[12,13] To further confirm this possibility, TOF-SIMS analysis and TOF-SIMS imaging were also conducted.

### TOF-SIMS

Figure 6 shows a positive TOF-SIMS spectrum of α-$Bi_2Mo_3O_{12}$ nanorods with deposited Ag nanoparticles. A typical TOF-SIMS spectrum in positive-ion mode shows the presence of characteristic ions of $^{98}Mo^+$ ($m/z$ = 98), $MoO^+$ ($m/z$ = 114), $^{209}Bi^+$ ($m/z$ = 209), $^{107}Ag^+$ ($m/z$ = 107) and $^{109}Ag^+$ ($m/z$ = 109) supporting the deposition of Ag nanoparticles on the surface of α-$Bi_2Mo_3O_{12}$ phase nanorods. Additionally, ions corresponding to $Na^+$ and $K^+$ as trace impurities were also observed. The absence of ions corresponding to pyridine indicates the complete removal of pyridine on heating at 450 °C. The high-intensity peaks $^{107}Ag^+$ and $^{109}Ag^+$ confirm the major composition of Ag nanoparticles deposited on the surface of α-$Bi_2Mo_3O_{12}$ nanorods. No more information with regards to the site or nature of binding of the Ag nanoparticles could be extracted and thus TOF-SIMS imaging is also performed.

To investigate the dispersion and binding site of Ag nanoparticles on the surface of α-$Bi_2Mo_3O_{12}$ nanorods, secondary-ion images characteristic of Bi, Mo and Ag were obtained. Figure 7 shows secondary-ion images of individual elemental components (a) $^{209}Bi^+$, (b) $^{98}Mo^+$, (c) $^{107}Ag^+$ and (d) $^{109}Ag^+$ obtained from Ag-nanoparticle-deposited α-$Bi_2Mo_3O_{12}$ nanorods that were sonicated for 60 min. The two-component total-ion images of $^{209}Bi^+$ and $^{107}Ag^+$ (Figure 7e), and $^{98}Mo^+$ and $^{109}Ag^+$ (Figure 7f) were also recorded for comparison. The bright spots in the image indicate the presence of characteristic metal species. Homogen-

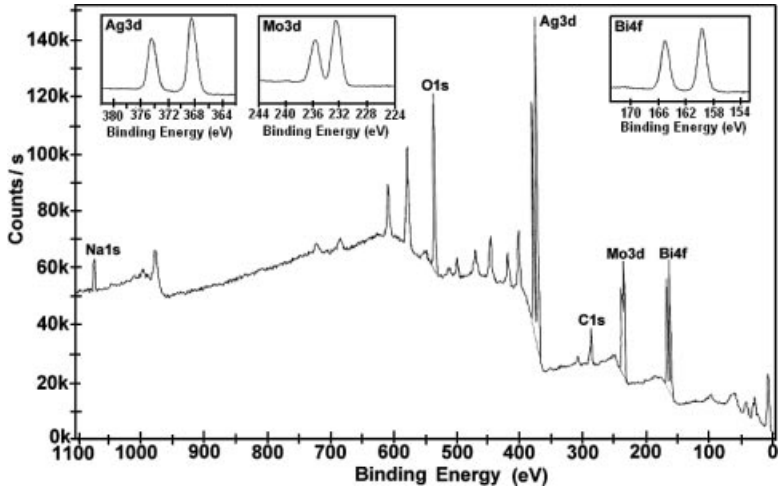


Figure 5. XPS spectrum measured on α-$Bi_2Mo_3O_{12}$ nanorods with deposited Ag nanoparticles.

 © 2007 Wiley-VCH Verlag GmbH & Co. KGaA, Weinheim 

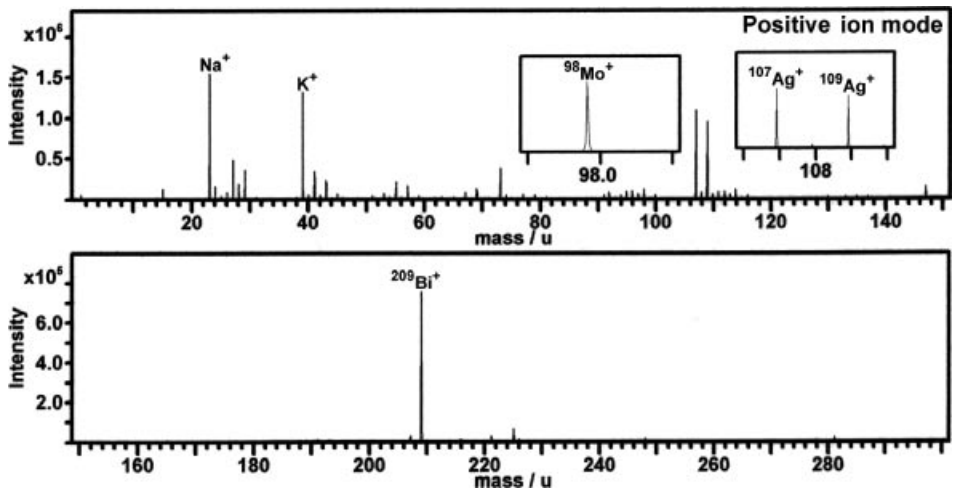


Figure 6. TOF-SIMS spectra of α-$Bi_2Mo_3O_{12}$ nanorods with deposited Ag nanoparticles in positive-ion detection mode.

eous distribution of Bi and Mo is observed (Figure 7a and b). However, the ion images of $^{107}Ag^+$ and $^{109}Ag^+$ show significant overlap with $^{209}Bi^+$, as depicted from the bright spots in the pattern of Figure 7a, b, d and e. In other words, the image pattern characteristic of Bi and that of Ag are similar. This supports our speculation that Bi might be the preferred site for deposition of Ag nanoparticles on the surface of α-$Bi_2Mo_3O_{12}$ nanorods. The fact that the Ag nanoparticles are dispersed on the surface suggests that Bi is localized on the α-$Bi_2Mo_3O_{12}$ nanorods, maintaining the compositional structure of the nanorods.

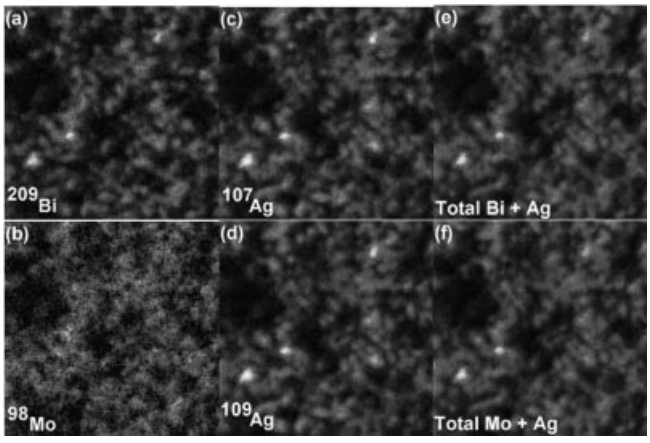


Figure 7. TOF-SIMS images of characteristic elements: (a) $^{209}Bi^+$, (b) $^{98}Mo^+$, (c) $^{107}Ag^+$ and (d) $^{109}Ag^+$ from α-$Bi_2Mo_3O_{12}$ nanorods with deposited Ag nanoparticles. Two-component total-ion images of (e) $^{209}Bi^+$ and $^{107}Ag^+$ and (f) $^{98}Mo^+$ and $^{109}Ag^+$.

## Proposed Mechanism

Sonication of $Ag_2O$ in pyridine results in the formation of Ag nanoparticles of about 10 nm (inset in Figure 1b) and subsequently pyridine is adsorbed on the surface. Similarly, synthesis and crystal growth of uniform Ag nanoplates and ring-like gold nanocrystals in *N*,*N*-dimethylformamide solution were reported by using the sonochemical route.[28] The pyridine-adsorbed Ag nanoparticles eventually align in the vicinity of pyridine-adsorbed α-$Bi_2Mo_3O_{12}$ nanorods through π stacking interactions of surface-adsorbed pyridine. The adsorption and intercalation of pyridine is confirmed by thermogravimetric analysis. Further, with the implosive collapse of bubbles in the liquid due to ultrasonic irradiation, the Ag nanoparticles deposit on the surface of the α-$Bi_2Mo_3O_{12}$ nanorods and form a Ag-nanoparticle-deposited α-$Bi_2Mo_3O_{12}$ nanorod and pyridine nanocomposite. The uniform deposition of Ag nanoparticles on the surface might be due to the presence of adsorbed pyridine on the Ag nanoparticles, which would prevent aggregation.

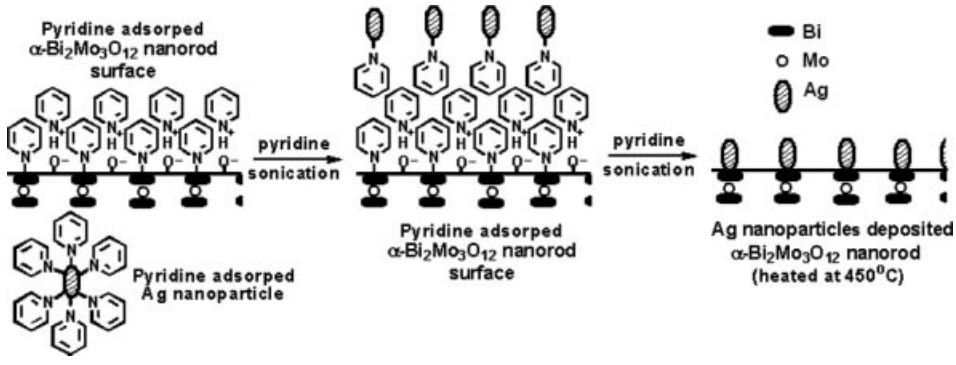


Figure 8. Schematic diagram for the proposed mechanism producing α-$Bi_2Mo_3O_{12}$ nanorods with deposited Ag nanoparticles.

 © 2007 Wiley-VCH Verlag GmbH & Co. KGaA, Weinheim 

With the use of increased amounts of $Ag_2O$, the deposition of Ag nanoparticles was found to increase; the particles were localized in close vicinity to each other on the surface of the α-$Bi_2Mo_3O_{12}$ nanorods, with less aggregation, and the particles maintained their size. The particles seem to deposit in the voids of the Ag nanoparticles instead of collapsing on the previously deposited Ag nanoparticles, probably because of surface-adsorbed pyridine. However, it was observed that an increased sonication time forces the collapse of the Ag nanoparticles and the formation of aggregates of Ag nanoparticles on the surface. Further, calcination of the nanocomposite at 450 °C results in pyridine-free, Ag-nanoparticle-deposited α-$Bi_2Mo_3O_{12}$ nanorods. A schematic diagram of the proposed mechanism is shown in Figure 8.

## Conclusions

Silver nanoparticles are uniformly deposited on the surface of α-$Bi_2Mo_3O_{12}$ nanorods by using a simple ultrasonication method. The Ag nanoparticles disperse well in pyridine and bind to the surface of nanorods under the influence of the liquid bubbles generated by ultrasound in the pyridine medium, forming a nanocomposite of α-$Bi_2Mo_3O_{12}$ nanorods with deposited Ag nanoparticles, and pyridine. Adsorption and intercalation of pyridine prevents aggregation and diffusion of Ag nanoparticles. By heating the sample at 450 °C, the formation of a pyridine-free nanocomposite with deposited crystalline Ag nanoparticles is observed. Thorough characterization using TEM, SAED, EDS, XRD, XPS and TOF-SIMS was carried out to confirm the presence of crystalline Ag nanoparticles. Additionally, the use of TOF-SIMS imaging could provide information with regards to the possible binding site of the Ag nanoparticles on the surface of the α-$Bi_2Mo_3O_{12}$ nanorods. These Ag-nanoparticle-deposited α-$Bi_2Mo_3O_{12}$ nanorods might find applications in catalysis.

## Experimental Section

$Bi_2O_3$ (Aldrich, 99%), $Na_2MoO_4{\cdot}2H_2O$ (Riedel-de Haën, 99%), $Ag_2O$ (Showa, 98%) and pyridine (Fluka, >99%) were purchased and used without further purification.

Large spherical nanoparticles of α-$Bi_2Mo_3O_{12}$ (ca. 200 nm size) were prepared as discussed in our earlier report.[16,26] The resultant α-$Bi_2Mo_3O_{12}$ product (2 g in each experiment) was further treated with an excess of pyridine (10 mL), and sonicated at 30–40 °C by using a fixed power sonicator (L&R Ultrasonics, Quantrex 140, 150 W, 45 kHz) under a nitrogen atmosphere for 60 min to produce α-$Bi_2Mo_3O_{12}$ nanorods (ca. 100 nm diameter). The excess pyridine was vacuum evaporated, followed by an acetone wash and dried at 60 °C. Compositional and morphological characterization of nanorods was performed thereafter. Thermal treatment (calcination) of the nanocomposite at 450 °C removed the residual pyridine and afforded pyridine-free nanorods of α-$Bi_2Mo_3O_{12}$. The morphological features of the nanorods thus obtained did not vary from those of the intercalated product, similar to those observed in our earlier report.[16] The deposition of Ag nanoparticles on the surface of α-$Bi_2Mo_3O_{12}$ nanorods was conducted by sonicating the mixture of $Ag_2O$ (100 mg) and α-$Bi_2Mo_3O_{12}$ nanorods (2 g) in the presence of pyridine for 60 min. Alternatively, the same results were obtained when α-$Bi_2Mo_3O_{12}$ nanorods formed after sonication in pyridine (from α-$Bi_2Mo_3O_{12}$ nanoparticles) were subsequently treated with $Ag_2O$ (100 mg) and further sonicated for 60 min. The $Ag_2O$ used was free of trace amounts of elemental silver. Experiments with an increased sonication time (60, 90 and 120 min) and the use of different amounts of $Ag_2O$ (100, 200 and 300 mg) were also conducted. Prior to characterization, the final product was washed, dried and calcinated by using the same protocol as mentioned earlier. Furthermore, to prove the effect of ultrasound in uniform deposition of Ag nanoparticles on α-$Bi_2Mo_3O_{12}$ nanorods, a contrast experiment involving controlled heating (5 °C min$^{-1}$) of a homogenized mixture of pyridine-free α-$Bi_2Mo_3O_{12}$ nanorods (2 g) and $Ag_2O$ (100 mg) was conducted. The mixture was heated to 450 °C and cooled naturally. An additional experiment involving vigorous stirring of a mixture of α-$Bi_2Mo_3O_{12}$ nanorods (2 g) and $Ag_2O$ (100 mg) in pyridine (10 mL) at 40 °C for 60 min in nitrogen was also conducted.

A thermogravimetric analyzer (Perkin–Elmer TGA6) was used to record the thermograms in the temperature range 30–500 °C with a heating rate of 5 °C min$^{-1}$ in a flow of air at 20 mL min$^{-1}$. Morphological characterization was performed using a transmission electron microscope (TEM) (Philips, Tecnai 20) working at 200 kV accelerating voltage. A drop of sample suspension, which had been previously dispersed in methanol by ultrasonication, was placed on the Cu microgrid coated with lacey carbon film and dried before microscopy study. Elemental composition was obtained by energy-dispersive X-ray analysis (EDS) (Philips, Tecnai 20). Scanning electron microscope (SEM) (Hitachi-S4700, Noran Instruments) was also employed. The samples in powder form were dispersed on the carbon tape mounted on the sample holder and an epitaxial thin film of platinum was coated (plasma coating technique) on the sample surface to avoid surface charging problems. The X-ray diffraction (XRD) patterns were obtained using Material Analysis and Characterization (MAC) advanced powder X-ray diffractometer (using Cu-$K_\alpha$ = 1.54056 Å radiation) and scanning in the $2\theta$ range between 5° and 100° at a rate of 0.25° min$^{-1}$. An X-ray photoelectron spectrometer (Thermo VG Scientific) with monochromatized Al-$K_\alpha$ X-ray (1486.6 eV) source and a spherical capacitor analyzer with multichannel detector was used for surface composition study. The samples were pressed into pellets and mounted on a standard sample holder using conductive carbon tape. The vacuum in the analysis chamber was maintained at $10^{-9}$ Torr. A total of 10–30 scans were collected from the spot size of 400 μm, with an energy step of 1 eV and pass energy of 100 eV. A detailed surface composition of metal deposits was obtained by analysis of Ag3d, Mo3d, Bi4f, O1s and C1s peaks.

TOF-SIMS (ION-TOF; Munich, Germany) measurements in positive-ion mode were performed for the analysis of α-$Bi_2Mo_3O_{12}$ nanorods and Ag-nanoparticle-deposited α-$Bi_2Mo_3O_{12}$ nanorods. The samples were pressed onto the carbon tape supported on a clean Si wafer. Excess particles were removed by blowing with compressed air such that the layer thickness was minimal, but large enough to prevent exposure of the carbon tape. The primary-ion source was a pulsed $^{69}Ga^+$ source (pulsing current 2.5 pA, and a pulse width of 30 ns) operated at 15 keV with postacceleration of 10 kV. An analysis area of 100 × 100 μm, data acquisition time of 200 s and charge compensation by applying low-energy electrons (ca. 30 eV) from a pulsed flood gun were used for the measurements. The pressure of the main chamber was kept between $10^{-8}$ and $10^{-9}$ Torr. The best resolution obtained was $m/\Delta m$ = 8000.

 © 2007 Wiley-VCH Verlag GmbH & Co. KGaA, Weinheim 

Calibration of the mass spectra was based on peaks such as $H^+$ (1.007 *m*/*z*), $CH_3^+$ (15.024 *m*/*z*), $C_2H_5^+$ (29.044 *m*/*z*), $Mo^+$ (97.908 *m*/*z*), $^{107}Ag^+$ (106.907 *m*/*z*), $^{109}Ag^+$ (108.906 *m*/*z*) and $Bi^+$ (208.983 *m*/*z*), and the peak areas were normalized to the most intense peak in the spectrum. The generated data were processed using inbuilt IonSpec and Ionimage software.

## Acknowledgments

Financial support by National Science Council (NSC94-2218-E-007-052) and National Tsing Hua University is gratefully acknowledged.

[1] a) G. R. Patzke, F. Krumeich, R. Nesper, *Angew. Chem. Int. Ed.* **2002**, *41*, 2446–2461; b) Y. Xia, P. Yang, Y. Sun, Y. Wu, B. Mayers, B. Gates, Y. Yin, F. Kim, H. Yan, *Adv. Mater.* **2003**, *15*, 353–389; c) M. Alexandre, P. Dubois, *Mater. Sci. Eng.* **2000**, *28*, 1–63.

[2] a) T. E. Crumpton, C. Greaves, *J. Mater. Chem.* **2004**, *14*, 2433–2437; b) Z. Ban, J. He, G. Vladimir, W. Wang, C. J. O'Connor, *J. Mater. Chem.* **2005**, *15*, 1244–1247; c) P. Christian, P. O'Brien, *J. Mater. Chem.* **2005**, *15*, 3021–3025; d) M. H. Tran, H. Ohkita, T. Mizushima, N. Kakuta, *Appl. Catal. A* **2005**, *287*, 129–134; e) K. A. Gesheva, T. Ivanova, F. Hamelmann, *J. Optoelectronics Adv. Mater.* **2005**, *7*, 1243–1252.

[3] a) A. M. Beale, G. Sankar, *Chem. Mater.* **2003**, *15*, 146–153; b) E. Godard, E. M. Gaigneaux, P. Ruiz, B. Delmon, *Catal. Today* **2000**, *61*, 279–285; c) N. Arora, G. Deo, I. E. Wachs, A. M. Hirt, *J. Catal.* **1996**, *159*, 1–13.

[4] a) R. N. Vannier, F. Abraham, G. Nowogrocki, G. Mairesse, *J. Solid State Chem.* **1999**, *142*, 294–304; b) L. Boon, R. Metselaar, *Eur. J. Solid State Inorg. Chem.* **1990**, *27*, 381–389.

[5] V. Marinova, M. Veleva, *Opt. Mater.* **2002**, *19*, 329–333.

[6] K. Y. Kang, P. H. Her, M. S. Jang, H. K. Kim, H. L. Park, D. Finotello, M. H. W. Chan, *Solid State Commun.* **1988**, *67*, 723–724.

[7] T. Sekiya, A. Tsuzuki, Y. Torii, *Mater. Res. Bull.* **1985**, *21*, 601–608.

[8] N. Hykaway, W. M. Sears, R. F. Frindt, S. R. Morrison, *Sens. Actuators* **1988**, *15*, 105–118.

[9] a) J. H. Fendler, *Nanoparticles and Nanostructured Films: Preparation, Characterization and Applications*, John Wiley & Sons, New York, **1998**; b) J. Jose, M. A. Khadar, *Acta Mater.* **2001**, *49*, 729–735; c) L. Kutsenko, D. Fuks, A. Kiv, L. Burlaka, M. Talianker, O. Monteiro, I. Brown, *Acta Mater.* **2004**, *52*, 4329–4335.

[10] a) Y. Shiraishi, N. Toshima, *J. Mol. Catal. A: Chem.* **1999**, *141*, 187–192; b) J. G. Serafin, A. C. Liu, S. R. Seyedmonir, *J. Mol. Catal. A: Chem.* **1998**, *131*, 157–168; c) S. Imamura, M. Ikebata, T. Ito, T. Ogita, *Ind. Eng. Chem. Res.* **1991**, *30*, 217–221.

[11] a) B. M. Luce, D. G. Foulke, *Modern Electroplating*, 3rd ed., John Wiley and Sons, New York, **1974**; b) K. Chatterjee, J. M. Howe, W. C. Johnson, M. Murayama, *Acta Mater.* **2004**, *52*, 2923–2935; c) S. V. Divinski, F. Hisker, Y. S. Kang, J. S. Lee, C. Herzig, *Acta Mater.* **2004**, *52*, 631–645; d) I. Krastev, T. Valkova, A. Zielonka, *J. Appl. Electrochem.* **2003**, *33*, 1199–1204.

[12] I. Krastev, T. Valkova, A. Zielonka, *J. Appl. Electrochem.* **2004**, *34*, 79–85.

[13] R. Regnier, C. Bifulco-Michon, F. Legendre, S. Poissonnet, G. Giunchi, *Physica C* **2002**, *372–376*, 923–926.

[14] Q. Li, H. Li, V. G. Pol, I. Bruckental, Y. Koltypin, J. Calderon-Moreno, I. Nowik, A. Gedanken, *New J. Chem.* **2003**, *27*, 1194–1199.

[15] a) V. G. Pol, A. Gedanken, J. Calderon-Moreno, *Chem. Mater.* **2003**, *15*, 1111–1118; b) V. G. Pol, O. Palchik, A. Gedanken, I. Felner, *J. Phys. Chem. B* **2002**, *106*, 9737–9743; c) V. G. Pol, M. Motiei, A. Gedanken, J. Calderon-Moreno, Y. Mastai, *Chem. Mater.* **2003**, *15*, 1378–1384.

[16] A. V. Ghule, K. A. Ghule, S. H. Tzing, J. Y. Chang, H. Chang, Y. C. Ling, *Chem. Phys. Lett.* **2004**, *383*, 208–213.

[17] K. S. Suslick (Ed.), *Ultrasound: Its Chemical, Physical and Biological Effects*, VCH, Weinheim, Germany, **1988**.

[18] Y. Socol, O. Abramson, A. Gedanken, Y. Meshorer, L. Berenstein, A. Zaban, *Langmuir* **2002**, *18*, 4736–4740.

[19] Y. Murakami, H. Imai, *J. Mater. Sci. Lett.* **1990**, *10*, 107–108.

[20] S. Yinjie, Z. Aimin, *J. Radioanal. Nucl. Chem.* **1998**, *231*, 17–20.

[21] N. Barnes, S. J. Kitchin, J. A. Hriljac, *Inorg. Chem.* **1999**, *38*, 6317–6319.

[22] A. V. Ghule, C. Y. Chen, F. D. Mei, Y. C. Ling, *Appl. Surf. Sci.* **2004**, *231–2*, 840–844.

[23] a) Y. E. Cho, J. Y. Maeng, S. Kim, *J. Am. Chem. Soc.* **2003**, *125*, 7514–7515; b) E. Lust, A. Janes, P. Miidla, K. Lust, *J. Electroanal. Chem.* **1997**, *425*, 25–37; c) D. Y. Wu, M. Hayashi, Y. J. Shiu, K. K. Liang, C. H. Chang, Y. L. Yeh, S. H. Lin, *J. Phys. Chem. A* **2003**, *107*, 9658–9667.

[24] M. I. Zaki, M. A. Hasan, F. A. Al-Sagheer, L. Pasupulety, *Colloids Surf., A* **2001**, *190*, 261–274.

[25] a) H. N. Kwok, H. Liu, R. M. Penner, *Langmuir* **2000**, *16*, 4016–4023; b) R. M. Stiger, S. Gorer, B. Craft, R. M. Renner, *Langmuir* **1999**, *15*, 790–798.

[26] A. V. Ghule, S. H. Tzing, J. Y. Chang, K. A. Ghule, H. Chang, Y. C. Ling, *Eur. J. Inorg. Chem.* **2004**, 1753–1762.

[27] K. T. Li, W. D. Cheng, *Appl. Catal., A* **1996**, *142*, 315–326.

[28] L. P. Jiang, S. Xu, J. M. Zhu, J. R. Zhang, J. J. Zhu, H. Y. Chen, *Inorg. Chem.* **2004**, *43*, 5877–5883.

Received: February 7, 2007
Published Online: May 30, 2007

 © 2007 Wiley-VCH Verlag GmbH & Co. KGaA, Weinheim 

DOI: 10.1002/ejic.200700108

# Influence of the Synthetic Pathway on the Properties of Oxygen-Deficient Manganese-Related Perovskites

José M. Alonso,[a,b] Raquel Cortés-Gil,[a,c] Luisa Ruiz-González,[c] José M. González-Calbet,*,[a,c] Antonio Hernando,[a,d] María Vallet-Regí,[a,e] María E. Dávila,[b] and María C. Asensio[b,f]

**Keywords:** Mixed-valent compounds / Perovskite phases / Magnetic properties / X-ray absorption near-edge spectroscopy (XANES) / Topotactic reaction

Thermogravimetry, X-ray and electron diffraction and high resolution electron microscopy show that the reduction process from perovskite $La_{0.5}Ca_{0.5}MnO_3$ to brownmillerite $La_{0.5}Ca_{0.5}MnO_{2.5}$ is a reversible topotactic process. Two series of monophasic $La_{0.5}Ca_{0.5}MnO_{3-\delta}$ oxygen-deficient perovskites were stabilized in the $0 \leq \delta \leq 0.12$ range, either from reduction of $La_{0.5}Ca_{0.5}MnO_3$ or oxidation of $La_{0.5}Ca_{0.5}MnO_{2.5}$. Soft X-ray absorption spectroscopy shows that Mn oxidation states differ as a function of the synthetic pathway. Temperature dependence of the magnetization as a function of anionic vacancies concentration at constant doping level are reported together with the evolution of high-resolution O K-edge and Mn L-edge spectra. Our results show dramatic changes in the magnetic behaviour due to the stabilization of different Mn oxidation states.

(© Wiley-VCH Verlag GmbH & Co. KGaA, 69451 Weinheim, Germany, 2007)

## Introduction

The influence of cationic substitution and anionic vacancies on the magnetic and conducting properties of transition-metal oxides is a subject of high scientific and technological interest. The main objective of most of these studies is to get a precise understanding of the nominal composition, microstructure and electronic properties of intriguing and complex materials, as in the case of manganese-related perovskites. These materials exhibit a wide range of unusual magnetic properties, which can be modified by changing the doping level due to the long-established ability of the manganese ion to develop several oxidation states. This essential property could be directly related to the number of unpaired electrons in the 3d orbitals, as well as to the magnetic moment associated with each of the Mn ions present in the compound.

Particularly interesting in the $La_{1-x}Ca_xMnO_3$ system is the $La_{0.5}Ca_{0.5}MnO_3$ material, which shows a remarkable coexistence of ferromagnetism and charge ordered (CO) phase.[1–4] At this state, the 1:1 arrangement of octahedrally coordinated $Mn^{3+}$ and $Mn^{4+}$ leads to charge and orbital order at low temperature. However, some authors disagree with this general description.[5–8]

From a magnetic point of view, CO represents the limit between ferromagnetic (FM) metallic (M) and antiferromagnetic (AF) insulator (I) behaviour.[9,10] The shift towards one behaviour or the other is obtained by varying the $Mn^{4+}/Mn^{3+}$ ratio. Thus, when such a ratio verifies $0.20 < Mn^{4+}/Mn^{3+} < 1$, the system is FM-M, whereas values of $Mn^{4+}/Mn^{3+} \geq 1$ give rise to an AF-I system. To modify the concentration of doped holes ($Mn^{4+}$ ions), it suffices to change the $x$ value. However, introducing anionic vacancies can also modify this ratio. Actually, for a small concentration of anionic vacancies, the FM fraction in $La_{0.5}Ca_{0.5}MnO_{3-\delta}$ increases as the CO fraction decreases; this effect yields a net FM behaviour, related in turn to the decrease in the $Mn^{4+}/Mn^{3+}$ ratio.[11,12] Despite experimental effort, a clear relationship between the CO state in $La_{0.5}Ca_{0.5}MnO_{3-\delta}$ and the valence d-configuration of the Mn ions is still missing.

In a previous paper,[13] it was shown that the reduction process of $La_{0.5}Ca_{0.5}Mn^{4+}{}_{0.5}Mn^{3+}{}_{0.5}O_{3-\delta}$ down to an oxy-

[a] Instituto de Magnetismo Aplicado (UCM-CSIC-ADIF), Las Rozas, P. O. Box 155, 28230 Madrid, Spain
Fax: +34-91-300-71-76
E-mail: josea@adif.es
[b] Instituto de Ciencia de Materiales (CSIC), 28049 Cantoblanco, Madrid, Spain
[c] Dpto. Química Inorgánica, Facultad de Químicas, Universidad Complutense, 28040 Madrid, Spain
Fax: +34-91-394-43-52
E-mail: jgcalbet@quim.ucm.es
[d] Dpto. Física de Materiales, Facultad de Físicas, Universidad Complutense, 28040 Madrid, Spain
[e] Dpto. Química Inorgánica y Bioinorgánica, Facultad de Farmacia, Universidad Complutense, 28040 Madrid, Spain
Fax: +34-91-394-17-86
E-mail: vallet@farm.ucm.es
[f] Synchroton SOLEIL, B. P. 48, 91192 Gif sur Yvette Cedex, France

 © 2007 Wiley-VCH Verlag GmbH & Co. KGaA, Weinheim 

gen deficiency $\delta = 0.5$ gave rise to a new oxide with the composition $La_{0.5}Ca_{0.5}MnO_{2.5}$, isostructural to $Sr_2Fe_2O_5$.[14] This reduction process is a topotactic one since the perovskite framework is kept as the oxygen content decreases, that is, the reduction pathway involves ordering of the anionic vacancies through the tetrahedra formation leading to the basic sequence ···OT··· (O = octahedron and T = tetrahedron) of the brownmillerite structure. Different topotactic processes have been already described for other Mn-related perovskite oxides. A well-known example is the case of $CaMnO_3$ which is transformed into $CaMnO_{2.5}$ through the formation of squared pyramids.[15] Another example is the reduction process of $LaMnO_3$ to $LaMnO_{2.75}$ which involves tetrahedra formation.[16] Moreover in $La_{0.5}Ca_{0.5}MnO_{2.5}$, Mn shows an average oxidation state of 2.5 which, according to the structural data,[13] could fit to contents of 75% of $Mn^{2+}$ and 25% of $Mn^{4+}$. Taking this into account, the reduction process $La_{0.5}Ca_{0.5}Mn^{4+}_{0.5}Mn^{3+}_{0.5}O_3 \rightarrow La_{0.5}Ca_{0.5}Mn^{4+}_{0.25}Mn^{2+}_{0.75}O_{2.5}$ obviously involves the coexistence of $Mn^{4+}$, $Mn^{3+}$ and $Mn^{2+}$ for certain oxygen contents. Although rather unusual, the coexistence of a single metallic cation in three different oxidation states within a mixed oxide has been suggested by some authors in $Ln_{1-x}A_xMnO_3$ systems, as a consequence of the $Mn^{3+}$ disproportion.[17] Moreover, such behaviour was previously observed in the oxygen-deficient perovskite $CaLaMgMnO_{6-\delta}$[18] and also in the solid solution goethite-groutite $\alpha$-$Mn_xFe_{1-x}OOH$.[19] In order to confirm this assertion for $La_{0.5}Ca_{0.5}MnO_{2.5}$, which is basic to understanding the magnetic behaviour, further experimental evidence of the manganese oxidation state is clearly needed.

In this sense, it is well known that one of the most useful tools in the study of the atom-resolved unoccupied electronic structure of multi-element compounds is X-ray absorption fine structure spectroscopy. By tuning the photon energy to the threshold of a specific element, the shape of the absorption spectrum by its X-ray absorption near-edge spectroscopy (XANES) gives the electronic structure projected onto this particular site. This projection is usually strongly influenced by the hybridization between the states of different atoms, for complex multicomponent compounds. Because of the site- and symmetry-selective character of XANES, a simultaneous Mn L-edge and O K-edge study can give information about the manganese oxidation state and slight structural changes induced by cationic doping and anionic vacancies. This XANES ability has been previously illustrated by numerous studies on doped manganites.[20–23]

In this work, the Mn oxidation states and the magnetic properties of several $La_{0.5}Ca_{0.5}MnO_{3-\delta}$ materials as a function of the synthetic pathway were studied. In this sense, we prepared samples with the same oxygen content through two different methods: (i) reduction of $La_{0.5}Ca_{0.5}MnO_3$ and (ii) oxidation of $La_{0.5}Ca_{0.5}MnO_{2.5}$. The evolution of high-resolution O K-edge and Mn L-edge X-ray absorption spectroscopy as a function of anionic vacancies concentration at constant doping level is reported.

## Results and Discussion

The powder XRD pattern corresponding to the $La_{0.5}Ca_{0.5}MnO_3$ ($A_{3.00}$) sample is in agreement with a perovskite-like orthorhombic structure[1] [$a$ = 0.5407(2), $b$ = 0.7629(2) and $c$ = 0.5401(2) nm] with space group (SG) *Pnma*. A different situation is observed for the reduced sample, $La_{0.5}Ca_{0.5}MnO_{2.5}$ ($R_{2.50}$), which can be indexed on the basis of a brownmillerite unit cell[14] with parameters $a$ = 0.5361(3), $b$ = 1.6463(9) and $c$ = 0.5340(3) nm (SG *Ibm*2) as a consequence of ordering of anionic vacancies. This structure can be described as an alternating sequence of octahedral and tetrahedral layers along the $b$ direction of the perovskite subcell (Figure 1). The SAED and HREM study is in agreement with this model. Figure 2 shows a SAED pattern and its corresponding HREM image along [10$\bar{1}$] zone axis. An image calculation was performed taking into account the given unit cell and the atomic parameters characteristic of the brownmillerite structure.[13] A good agreement between experimental and calculated image (Figure 2, c) is observed. The charge balance in $La_{0.5}Ca_{0.5}MnO_{2.5}$ corresponds to a Mn average oxidation state of 2.50, which would fit to 50% of $Mn^{3+}$ and 50% of $Mn^{2+}$. This is an unexpected situation since it would involve a smaller $b$ parameter than the experimental one.[13] Considering the ionic radius[24] and the oxygen content, a more plausible situation would be 75% of $Mn^{2+}$ and 25% of $Mn^{4+}$, although obviously an experimental measurement of the oxidation states is required.

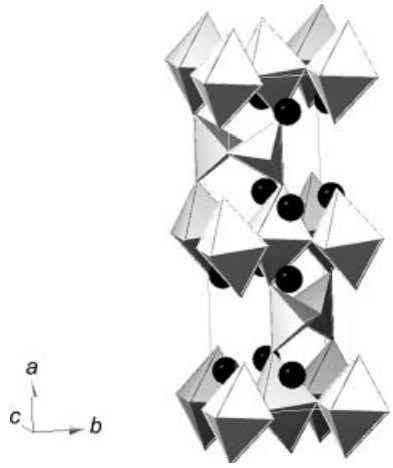


Figure 1. Brownmillerite structural model showing the alternating sequence of octahedral and tetrahedral layers along the $b$ direction.

In order to determine the oxidation state of Mn in these materials, a detailed XANES study was performed. XANES spectra were treated quantitatively by using a factorial analysis taking into account the reference compounds spectra. This method was based on the modelling of the experimental spectra by means of a linear combination of reference spectra. The first step was to analyse well-defined patterns for the different oxidation states that Mn can adopt. In this sense, three different manganese compounds, $MnO_2$, $LaMnO_3$ and $MnCO_3$, exhibiting the three characteristic oxidation states $Mn^{4+}$, $Mn^{3+}$ and $Mn^{2+}$, respec-

 © 2007 Wiley-VCH Verlag GmbH & Co. KGaA, Weinheim 

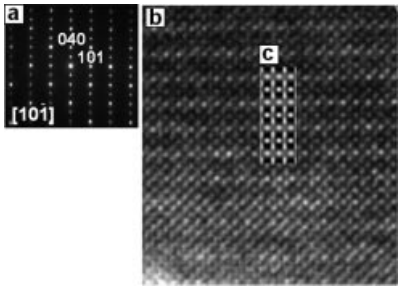


Figure 2. (a) SAED diffraction pattern along [10$\bar{1}$] zone axis; (b) HREM image; (c) calculated image taking into account the brownmillerite atomic positions.

tively, were used. Note that a perovskite-related compound $LaMnO_3$ was chosen as $Mn^{3+}$ standard, while an oxide and a carbonate were selected for $Mn^{4+}$ and $Mn^{2+}$, respectively. This was done because manganese perovskite-related phases only containing $Mn^{4+}$ or $Mn^{2+}$ have not been stabilized in the $La_{1-x}Ca_xMnO_3$ system. In fact, $CaMnO_3$ is always slightly deficient ($CaMnO_{3-\delta}$), leading to a small fraction of $Mn^{3+}$. In this sense, $MnO_2$ was used for $Mn^{4+}$. However, MnO was not used as the standard for $Mn^{2+}$ because $Mn_3O_4$ impurities were detected by magnetic measurements, and thus $MnCO_3$ was considered more appropriate. In addition, we compared these data with already published standards of $Mn^{4+}$[25] and $Mn^{2+}$.[26]

The spectra in Figure 3 (a–c) show the Mn L-edge of the three different manganese compounds. For $MnO_2$ and $LaMnO_3$, the Mn L-edge spectra (Figure 3, parts a and b, respectively) present two main maxima, at 643 and 653 eV, which are accompanied by fine modulation. In fact, the first maximum of the $MnO_2$ spectrum shows a shoulder around 640 eV. Similar features are observed for the Mn L-edge spectrum of $LaMnO_3$. For $Mn^{2+}$, the main feature is a well-defined maximum at 641.2 eV accompanied by two small peaks at 640.5 and 642.7 eV. More pronounced differences are observed in the O K-edge spectra in the 528–538 eV range (Figure 4). Actually, $Mn^{4+}$ shows two peaks: a more intense peak located at 529 eV and a second peak at 531.8 eV. For $Mn^{3+}$, the spectrum shows two broad maxima accompanied by fine modulation, whereas the $Mn^{2+}$ shows only a peak located at 533.5 eV. Once the characteristic energies of $Mn^{4+}$, $Mn^{3+}$ and $Mn^{2+}$ have been established, the XANES spectra of the manganese materials can be more easily interpreted. Parts d and e in Figure 3 show the Mn L-edge XANES spectra of $A_{3.00}$ and $R_{2.50}$ samples, respectively. For $A_{3.00}$, two main peaks and a shoulder (around 641 eV) appear, as observed in $MnO_2$ and $LaMnO_3$, suggesting the presence of both $Mn^{3+}$ and $Mn^{4+}$. $R_{2.50}$ exhibits similar features but the shoulder is transformed into a clear peak around 641 eV, which could be related to the presence of $Mn^{2+}$. In order to get more reliable information, the O K-edge spectra were studied (Figure 4, d and e). For $A_{3.00}$, the spectrum shows a profile characteristic of the coexistence of $Mn^{3+}$ and $Mn^{4+}$, in agreement with the O K-edge of the reference materials. The spectrum corresponding to $R_{2.50}$ (Figure 4, e) shows a clear peak at around 533 eV which, in agreement with the O K-edge of the reference, is related to $Mn^{2+}$. Moreover, two more peaks appear at 529 and 536 eV indicating the presence of $Mn^{4+}$ and $Mn^{3+}$, respectively. The data set of O K-edge and Mn L-edge of $A_{3.00}$ and $R_{2.50}$ XANES spectra were quantitatively treated, taking into account the reference compounds spectra, as depicted in Table 1. The ensemble of these results shows the coexistence of $Mn^{2+}$, $Mn^{3+}$ and $Mn^{4+}$ in $La_{0.5}Ca_{0.5}MnO_{2.5}$, obtained through the topotactic reduction process $A_{3.00} \rightarrow R_{2.50}$.

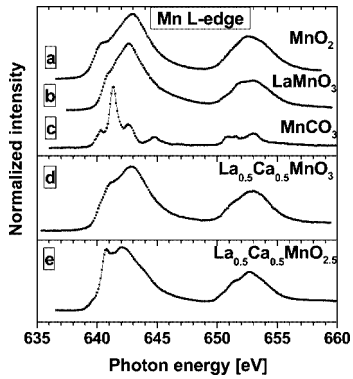


Figure 3. Mn L-edge XANES spectra of manganese reference compounds (a) $MnO_2$; (b) $LaMnO_3$; (c) $MnCO_3$ and samples (d) $La_{0.5}Ca_{0.5}MnO_3$; (e) $La_{0.5}Ca_{0.5}MnO_{2.5}$.

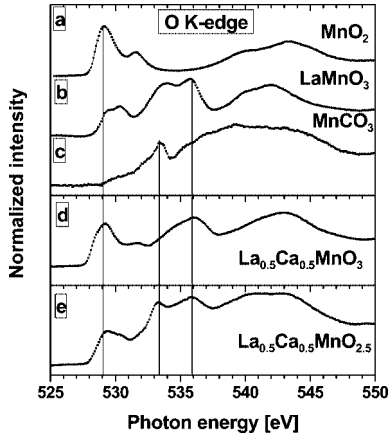


Figure 4. O K-edge XANES spectra of manganese reference compounds (a) $MnO_2$; (b) $LaMnO_3$; (c) $MnCO_3$ and samples (d) $La_{0.5}Ca_{0.5}MnO_3$; (e) $La_{0.5}Ca_{0.5}MnO_{2.5}$.

Table 1. Mn oxidation state of $A_{3.00}$ and $R_{2.50}$ samples as determined by XANES.

| Sample | % $Mn^{4+}$ | % $Mn^{3+}$ | % $Mn^{2+}$ |
|---|---|---|---|
| $A_{3.00}$ | 50.00 | 50.00 | 0 |
| $R_{2.50}$ | 12.50 | 25.00 | 62.50 |

The oxidation process $R_{2.50} \rightarrow A_{3.00}$ is again a topotactic one involving the transformation of brownmillerite to perovskite.[27] At this point, in order to ascertain whether or not samples with the same composition comprise the same oxidation states, the oxidation mechanism was studied, since different pathways would involve different oxidation states and properties.

 © 2007 Wiley-VCH Verlag GmbH & Co. KGaA, Weinheim 

The influence of the anionic vacancies concentration in the crystalline structure and magnetotransport properties of samples obtained by reduction of the $La_{0.5}Ca_{0.5}MnO_3$ material has already been studied by several authors.[11–13] It has been shown that for a small concentration of anionic vacancies the CO state disappears whereas the ferromagnetic character is preserved. In particular, according to Trukhanov et al.,[12] the anionic vacancies originated in the reduction process are randomly distributed and the orthorhombic symmetry of the starting material remains up to $\delta$ = 0.25 ppm. However, when samples are obtained by oxidation of $R_{2.50}$, monophasic materials are only obtained, under the synthetic conditions described in ref.,[25] for $\delta <$ 0.15. For this reason, the comparative study of $R_y$ and $O_y$ materials was limited to the $0 \leq \delta \leq 0.12$ range.

All $R_y$ and $O_y$ materials show very similar X-ray diffraction patterns, which can be indexed on the basis of an orthorhombic symmetry and space group *Pnma*. All samples were characterized by SAED and HREM. Electron diffraction patterns did not show superstructure spots, suggesting that anionic vacancies in both $R_y$ and $O_y$ samples are randomly distributed in the $0 \leq \delta \leq 0.12$ range.

As in the starting materials, a detailed XANES study was performed. Figure 5 (a) shows the Mn L-edge XANES spectra of $R_y$ samples. Taking into account the described reference patterns, spectra peaks suggest the presence of $Mn^{3+}$ and $Mn^{4+}$. The spectra corresponding to the O K-edge (Figure 5, b) show maxima around 529 and 536 eV characteristic of $Mn^{3+}$ and $Mn^{4+}$, respectively. Therefore, the reduction pathway $A_{3.00} \rightarrow R_{2.88}$ only involves the coexistence of both $Mn^{4+}$ and $Mn^{3+}$. Figure 6 (a and b) show the Mn L-edge and O K-edge characteristics, respectively, of the oxidized samples. The presence of $Mn^{3+}$ and $Mn^{4+}$ is observed in Mn L-edge while an additional peak around 533 eV, suggesting $Mn^{2+}$, appears at the O K-edge. The quantification led to the results shown in Table 2, which confirm the presence of $Mn^{3+}$ and $Mn^{4+}$ in the R series while the three oxidation states $Mn^{2+}$, $Mn^{3+}$ and $Mn^{4+}$ coexist in the O series of samples. This table summarizes the fact that both topotactic reactions, $A_{3.00} \rightarrow R_{2.50}$ and $R_{2.50} \rightarrow A_{3.00}$, in the $0 \leq \delta \leq 0.12$ compositional range, occur through different pathways, that is, comprising different oxidation states. It is then clear that materials exhibiting the same composition but different electronic environment for Mn ions were stabilized. This should influence the properties, producing dramatic effects on the magnetic behaviour of these manganites.

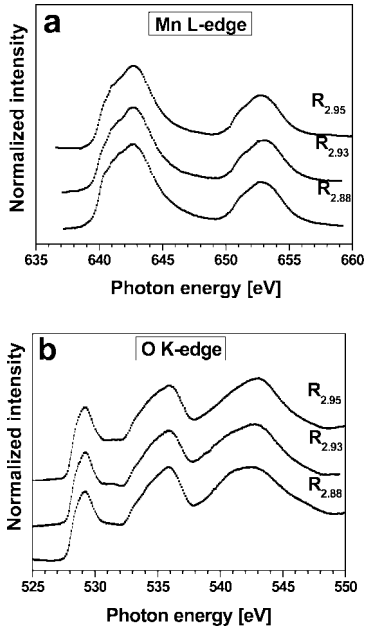


Figure 5. XANES spectra of $R_y$ samples (a) Mn L-edge and (b) O K-edge.

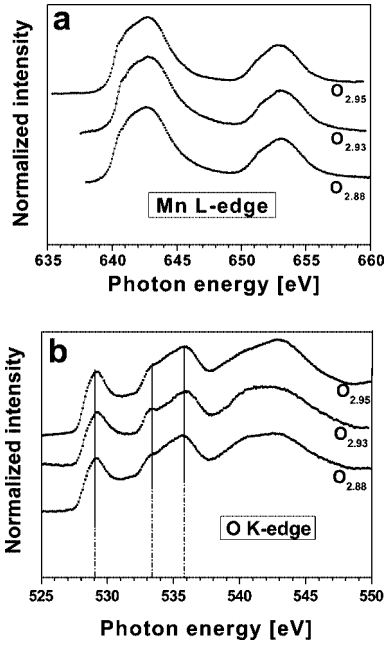


Figure 6. XANES spectra of $O_y$ samples (a) Mn L-edge and (b) O K-edge.

Table 2. Mn oxidation state of $R_y$ and $O_y$ samples as determined by XANES.

| Sample $y$ | $R_y$ % Mn (XANES) | | | $O_y$ % Mn (XANES) | | |
|---|---|---|---|---|---|---|
| | $Mn^{4+}$ | $Mn^{3+}$ | $Mn^{2+}$ | $Mn^{4+}$ | $Mn^{3+}$ | $Mn^{2+}$ |
| 2.95 | 40.00 | 60.00 | 0.00 | 40.00 | 55.00 | 5.00 |
| 2.93 | 38.00 | 62.00 | 0.00 | 39.00 | 54.00 | 7.00 |
| 2.88 | 30.00 | 70.00 | 0.00 | 32.00 | 56.00 | 12.00 |

Figure 7 shows the temperature dependence of magnetization for $A_{3.00}$ and $R_y$ samples. In agreement with previous results,[1,2,13] the fully oxidized $A_{3.00}$ sample shows a first transition from paramagnetic (PM) to almost FM at $T_C \approx 250$ K and a second transition at lower temperature to an AF state associated with CO of the charge carriers ($T_{CO} \approx 190$ K). At low temperature, a magnetization value of 0.25 $\mu_B$/u.f. is still obtained since a 10% FM phase is observed despite the material being chemically homogeneous.[3,28] The reduction process of $A_{3.00}$ material involves the transformation of octahedra into square pyramids, inducing a rapid increase in the magnetization at low tem-

 © 2007 Wiley-VCH Verlag GmbH & Co. KGaA, Weinheim 

perature: 0.69 $\mu_B$/u.f at 80 K for $R_{2.95}$. This fact is due to a partial breaking of the CO state which leads to a rapid increase in the FM fraction. A higher anionic vacancies concentration leads to a decrease in the magnetization for $R_{2.93}$ and $R_{2.88}$ samples. Similar behaviour was reported by Trukhanov et al.[12] where a maximum magnetization value was obtained for $y = 2.96$ and a minimum value for $y = 2.80$. This fact suggests that a high concentration of the anionic vacancies breaks the FM ordering due to a decrease in the $Mn^{4+}/Mn^{3+}$ ratio and so allows the possibility of double exchange. In fact, when anionic vacancies content is increased to $\delta = 0.50$, the ferromagnetic interactions disappear as can be observed in the variation of the magnetization curve versus applied magnetic field (Figure 8).

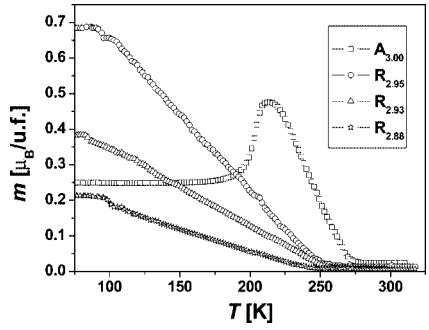


Figure 7. Magnetization vs. temperature corresponding to $R_y$ samples.

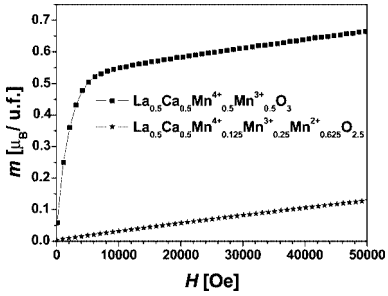


Figure 8. Magnetization vs. applied magnetic field at 5 K.

The magnetic behaviour of $O_y$ materials (Figure 9) is different from that shown by $R_y$ samples despite both composition and structure being identical. These oxidized samples show a first PM-FM transition: the magnetization value being higher for the $O_{2.95}$ sample. At 205 K, this sample shows again, although less markedly, the FM-AF transition associated with the CO observed in $A_{3.00}$. In fact, from 150 K, the magnetization corresponding to $O_{2.95}$ is lower than that observed for $O_{2.93}$, probably due to the presence of a higher number of AF regions in CO state, as a consequence of the lower $Mn^{2+}$ content. The lowest oxygen-content sample, $O_{2.88}$, shows the highest 0.64 $\mu_B$/u.f. magnetization value, which could be related to the absence of CO region in this composition. From the structural point of view,[29] the oxidation process leads to isolated rows of tetrahedrally coordinated $Mn^{2+}$, randomly distributed in an octahedrally coordinated $Mn^{3+}$–$Mn^{4+}$ matrix, which accounts for the double exchange and, as a consequence, for FM behaviour. This situation is different from the one observed in the reduced sample of the same composition and can be explained taking into account structural considerations as well as the corresponding oxidation states. In this sense, for $O_{2.88}$ the FM ordering is locally broken due to the anionic vacancies concentrated around $Mn^{2+}$, whereas for $R_{2.88}$ it is associated with the vacancies around $Mn^{3+}$. In this last case, the number of Mn ions accompanied by a vacant is double than that in $O_{2.88}$ and, therefore, is also twice the number of positions where the double exchange is broken, leading to a lower magnetization value.

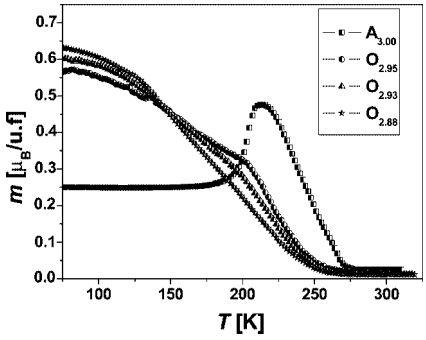


Figure 9. Magnetization vs. temperature corresponding to $O_y$ samples.

## Conclusions

The described results clearly show that the synthetic conditions play an important role in the stabilization of Mn oxidation state in perovskite-related materials. Numerous papers[11–13] have been devoted to studying the influence of an oxygen content change on the magnetic properties of these manganites. Up to now, it has been considered that the introduction of anionic vacancies only affects the $Mn^{4+}/Mn^{3+}$ ratio. We have shown that, as a function of the synthetic pathway, $Mn^{2+}$ can also be stabilized, leading to materials with Mn in three oxidation states.

## Experimental Section

Two materials with the composition $La_{0.5}Ca_{0.5}MnO_3$ ($A_{3.00}$) and $La_{0.5}Ca_{0.5}MnO_{2.5}$ ($R_{2.50}$) were initially prepared. The starting material, $A_{3.00}$, was prepared by solid-state reaction of stoichiometric amounts of $La_2O_3$, $CaCO_3$ and $MnO_2$ at 1400 °C in air for 110 h. $La_{0.5}Ca_{0.5}MnO_{2.5}$ was obtained under controlled reduction of the $La_{0.5}Ca_{0.5}MnO_3$ sample. The reduction process was performed in a CAHN D-200 electrobalance, equipped with a furnace and a two-channel register, by heating the starting material at 630 °C under $H_2$ (200 mbar) and He (300 mbar) at 6 °C min$^{-1}$. Once a desired weight loss was attained, the sample was annealed at 630 °C, under He, for 24 h to facilitate a more homogeneous distribution of anionic vacancies. The oxygen content can be determined within $\pm 10^{-3}$ for a sample of total mass about 100 mg. Oxygen content

 © 2007 Wiley-VCH Verlag GmbH & Co. KGaA, Weinheim 

(as determined in this reduction process) and cationic composition of both materials (as determined by atomic absorption, plasma source emission spectroscopy and electron probe microanalysis) are in agreement with the nominal composition.

On the other hand, two series of samples $La_{0.5}Ca_{0.5}MnO_{3-\delta}$ were prepared by two different synthetic routes: (i) samples $R_y$, obtained by reduction of $La_{0.5}Ca_{0.5}MnO_3$ and (ii) samples $O_y$, after oxidation of $La_{0.5}Ca_{0.5}MnO_{2.5}$ until reaching, in both cases, the desired oxygen content $y$ ($y = 3 - \delta$). Reduced $R_{2.95}$, $R_{2.93}$ and $R_{2.88}$ samples were obtained from $A_{3.00}$ under $H_2$ (200 mbar) and He (300 mbar) around 450 °C, whereas oxidized $O_{2.95}$, $O_{2.93}$ and $O_{2.88}$ materials were obtained from $R_{2.50}$ under $O_2$ (100 mbar) and He (400 mbar) around 170 °C. Both series were synthesized in an electrobalance allowing rigorous control of the oxygen content.

Powder X-ray diffraction (XRD) was performed by using a Philips X'Pert diffractometer with Cu-$K_\alpha$ radiation. Selected area electron diffraction (SAED) was performed by using a JEOL 2000FX electron microscope fitted with a double tilting goniometer stage (±45°), and high resolution electron microscopy (HREM) was carried out with a JEOL 3000FEG electron microscope fitted with an Oxford LINK EDS analyser. The sample was ultrasonically dispersed in 1-butanol and then transferred to holey carbon-coated copper grids. Magnetic properties were obtained using a LDJ vibrating sample and Quantum Design SQUID magnetometers in the temperature range 5 to 350 K under applied fields up to 5 T. Magnetic measurements versus temperature (5–350 K) were performed under field cool conditions in a 1000 Oe applied magnetic field. Magnetization measurements versus magnetic field (0–5 T) were carried out at 5 K.

Both Mn L-edge and O K-edge XANES measurements were performed using the PGM monochromator of the SU8 undulator-beamline at LURE. The spectra were collected in the total electron yield mode measuring the sample current. The energy resolution at the O K-edge and Mn L-edge X-ray absorption edge, around 530 and 643 eV was better than 0.5 and 0.6 eV, respectively. The surface sensibility of the XANES total yield technique was evaluated for these particular samples, recording the same absorption spectra by using the photoelectron effect. In this case, the detector was the photoelectron current recorded at the analyser. As the excited electrons should leave the solid to be collected at the vacuum, this recording mode is particularly sensible to the surface. A close comparison of XANES spectra recorded by both methods, evidences that surface effects can be ignored. The base pressure in the experimental chamber was in the low $10^{-10}$ mbar range. The samples were scraped in situ with a diamond file to remove surface contamination. Before every experiment, the samples were refreshed in order to avoid the formation of any stable carbonate. High level of sample cleanliness was guaranteed by synchrotron radiation core level photoemission continuous checking throughout the experiment. In particular, the evolution of the shape and intensity of the O K-edge and C K-edge core levels were monitored before and after the absorption measurements. As the valence band states near the Fermi level have shown to be very sensitive to external agents and spurious contamination, this kinetic energy range was monitored for all investigated samples.

## Acknowledgments

Financial support through the Ministerio de Educación y Ciencia (MEC), Spain MAT2004-01248 is acknowledged.

[1] C. H. Chen, S.-W. Cheong, *Phys. Rev. Lett.* **1996**, *76*, 4042–4045.
[2] P. G. Radaelli, D. E. Cox, M. Marezio, S.-W. Cheong, *Phys. Rev. B* **1997**, *55*, 3015–3023.
[3] G. Xiao, E. J. McNiff Jr, G. Q. Gong, A. Gupta, C. L. Canedy, J. Z. Sun, *Phys. Rev. B* **1996**, *54*, 6073–6076.
[4] S. Mori, C. H. Chen, S.-W. Cheong, *Phys. Rev. Lett.* **1998**, *81*, 3972–3975.
[5] J. Herrero-Martín, J. García, G. Subías, J. Blasco, M. C. Sánchez, *Phys. Rev. B* **2004**, *70*, 024408.
[6] L. Brey, *Phys. Rev. Lett.* **2004**, *92*, 127202.
[7] M. Coey, *Nature* **2004**, *430*, 155–157.
[8] G. C. Milward, M. J. Calderon, P. B. Littlewood, *Nature* **2005**, *433*, 607–610.
[9] P. Schiffer, A. P. Ramirez, W. Bao, S.-W. Cheong, *Phys. Rev. Lett.* **1995**, *75*, 3348–3351.
[10] C.-W. Cheong, H. Y. Hwang, "Ferromagnetism vs. Charge/Orbital Ordering in Mixed-Valent Manganites" in *Advances in Condensed Matter Science*, vol. 2: *Colossal Magnetoresistance Oxides* (Ed.: Y. Tokura), Gordon & Breach Science Publishers, London, **2000**.
[11] W. Schuddinck, G. Van Tendeloo, C. Martin, M. Hervieu, B. Raveau, *J. Alloys Compd.* **2002**, *333*, 13–20.
[12] S. V. Trukhanov, N. V. Kasper, I. O. Troyanchuk, M. Tovar, H. Szymczak, K. Bärner, *J. Solid State Chem.* **2002**, *169*, 85–95.
[13] J. M. González-Calbet, E. Herrero, N. Rangavittal, J. M. Alonso, J. L. Martinez, M. Vallet-Regí, *J. Solid State Chem.* **1999**, *148*, 158–168.
[14] M. Von Harder, Hk. Müller-Buschbaum, *Z. Anorg. Allg. Chem.* **1980**, *464*, 169–175.
[15] A. Reller, J. M. Thomas, D. A. Jefferson, M. K. Uppal, *Proc. R. Soc. Lond. A* **1984**, *394*, 223–241.
[16] M. L. Ruiz-González, R. Cortés-Gil, J. M. Alonso, A. Hernando, M. Vallet-Regí, J. M. González-Calbet, *Chem. Mater.* **2006**, *18*, 5756–5763.
[17] J. A. M. van Roosmalen, E. H. P. Cordfunke, *J. Solid State Chem.* **1994**, *110*, 109–112.
[18] J.-H. Choy, S.-T. Hong, N.-G. Park, S.-H. Byeon, G. Demazeau, *Bull. Korean. Chem. Soc.* **1995**, *16*, 105–110.
[19] A. C. Scheinost, H. S. Darrell, G. Schulze, U. Gasser, D. L. Sparks, *Am. Miner* **2001**, *86*, 139–146.
[20] F. Bridges, C. H. Booth, G. H. Kwei, J. J. Neumeier, G. A. Sawatzky, *Phys. Rev. B* **2000**, *61*, R9237–R9240.
[21] J. C. Fuggle, J. E. Inglesfield, *Unoccupied Electronic States*, Springer, Berlin, **1982**.
[22] M. Abbate, F. M. F. de Groot, J. C. Fuggle, A. Fujimori, Y. Tokura, Y. Fujushima, O. Strebel, M. Domke, G. Kaindl, J. van Elp, B. T. Thole, G. A. Sawatzky, M. Sacchi, N. Tsuda, *Phys. Rev. B* **1991**, *44*, 5419–5422.
[23] M. Abbate, F. M. F. de Groot, J. C. Fuggle, A. Fujimori, O. Strebel, F. Lopéz, M. Domke, G. Kaindl, G. A. Sawatzky, M. Takano, Y. Takeda, H. Eisaki, S. Uchida, *Phys. Rev. B* **1992**, *46*, 4511–4519.
[24] R. D. Shannon, *Acta Crystallogr., Sect. A* **1976**, *32*, 751–767.
[25] M. Abbate, D. Z. N. Cruz, G. Zampieri, J. Briatico, M. T. Causa, M. Tovar, A. Caneiro, B. Alascio, E. Morikawa, *Solid State Commun.* **1997**, *103*, 9–13.
[26] B. Gilbert, B. H. Frazer, A. Belz, P. G. Conrad, K. H. Nealson, D. Haskel, J. C. Lang, G. Srajer, G. De Stasio, *J. Phys. Chem. A* **2003**, *107*, 2839–2847.
[27] M. Vallet-Regí, E. Herrero, J. Alonso, A. Hernando, J. M. González-Calbet, *Solid State Ionics* **2001**, *141–142*, 427–432.
[28] R. S. Freitas, L. Ghivelder, P. Levy, F. Parisi, *Phys. Rev. B* **2002**, *65*, 104403.
[29] S. Komornicki, J. C. Grenier, M. Pouchard, P. Hagenmuller, *Nuovo J. Chim.* **1981**, *5*, 161–168.

Received: January 26, 2007
Published Online: June 1, 2007

 © 2007 Wiley-VCH Verlag GmbH & Co. KGaA, Weinheim 

DOI: 10.1002/ejic.200700151

# Controlled Stabilization and Flocculation of Gold Nanoparticles by Means of 2-Pyrazin-2-ylethanethiol and Pentacyanidoferrate(II) Complexes

**Sergio H. Toma,[a] Juliano A. Bonacin,[a] Koiti Araki,[a] and Henrique E. Toma*[a]**

**Keywords:** Aggregation / Colloids / Semi-empirical calculations / Raman spectroscopy / UV/Vis spectroscopy / Charge transfer

2-Pyrazin-2-ylethanethiol (PZT) interacts with gold nanoparticles (AuNps) and pentacyanidoferrates, providing a suitable bridging ligand for the exploitation of the coordination chemistry involved in the stabilization of the colloidal solutions and in the controlled formation of aggregates in the presence of dimethyl sulfoxide. The electronic and vibrational spectra of the molecules have been investigated and discussed based on DFT and ZINDO/S theoretical calculations. The PZT-modified AuNps exhibit strong SERS, coherent with the electromagnetic enhancement mechanism. In contrast, the charge-transfer mechanism seems to predominate in the Raman spectra of the $[Fe(CN)_5PZT]^{3-}$-modified gold nanoparticles.

(© Wiley-VCH Verlag GmbH & Co. KGaA, 69451 Weinheim, Germany, 2007)

## Introduction

Gold nanoparticles (AuNps) exhibit interesting properties associated with the surface plasmons, allowing a wide range of applications in chemistry, biology, and nanotechnology.[1–4] Most applications require their stabilization as a colloidal solution by means of surface modification with electrically charged species, such as citrate ions, or by using long-chain alkane thiols and detergents.[1–3,5,6] Another method is based on the coordination chemistry analogy between the gold nanoparticles and the transition-metal complexes. According to this approach, the stabilization of the gold nanoparticles can be conveniently performed by means of multifunctional bridging ligands, such as those containing thiol groups, capable of simultaneously binding transition-metal ions and the gold surface atoms.[7] The attractive point of this approach is the possibility of exploiting the controlled charge stabilization promoted by the metal complexes, while incorporating their characteristics and properties into the modified nanoparticles.

Pentacyanidoferrate(II) ions are unique candidates for this purpose, because of their high ionic charges, and suitable kinetic and thermodynamic behavior. Such species have been extensively used to probe the binding affinity of specific donor atoms towards iron ions.[8] This is justified, since the cyanido ligands in the $[Fe(CN)_5]^{3-}$ group are substitution-inert, leaving only one coordinating site for interacting with a specific donor atom of a multifunctional ligand (L).[8,9] On the other hand, the chemical properties of the products, $[Fe(CN)_5L]^{3-}$, are strongly dependent on the nature of L. For instance, pentacyanidoferrate(II) ions show a high affinity for N-heterocycles, amino acids and S-containing ligands, such as sulfoxides, thioethers, and thioamides.[8–16] Interestingly, the affinity of the pentacyanidoferrate(II) ions for thiol groups is relatively small,[7] in contrast to their high affinity for strong π-acceptor ligands, such as pyrazine.[8] Therefore, by using the 2-pyrazin-2-ylethanethiol (PZT) ligand, a preferential binding of the $[Fe(CN)_5]^{3-}$ complex to the pyrazine moiety is expected, leaving the SH group available for interaction with the gold nanoparticles, as illustrated in Figure 1.

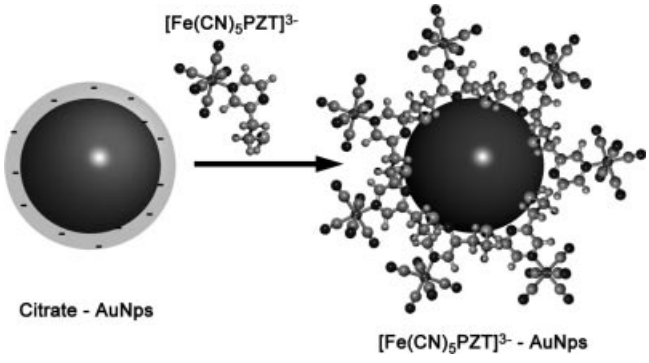


Figure 1. Representation of a gold nanoparticle stabilized with $[Fe(CN)_5PZT]^{3-}$ complexes.

In the presence of dimethyl sulfoxide (dmso) in excess, the pentacyanidoferrate(II) complexes undergo complete ligand exchange, yielding the very stable, colorless $[Fe(CN)_5(dmso)]^{3-}$ complex.[10] In this way, the electrostatic stabilization of the pentacyanidoferrate(II)-modified gold nanoparticles can be removed in the presence of dmso, providing an interesting way of controlling the flocculation of the gold nanoparticles. Because of the many interesting aspects in-

[a] Instituto de Química, Universidade de São Paulo, Caixa Postal 26077, CEP 05513-970 São Paulo, SP, Brazil

 InterScience © 2007 Wiley-VCH Verlag GmbH & Co. KGaA, Weinheim 

volved, we carried out a detailed investigation of this system, focusing especially on the coordination chemistry of pentacyanidoferrates and on the flocculation behavior of the gold nanoparticles, including their characterization based on surface-enhanced Raman scattering (SERS).

## Results and Discussion

The electronic configuration of the $[Fe(CN)_5PZT]^{3-}$ complex is typically low-spin, as a consequence of the strong ligand-field strength of the cyanido ligands. The UV/Vis spectrum exhibits two characteristic strong absorption bands at $\lambda_{max}$ = 266 and 461 nm (log $\varepsilon$ = 3.68), ascribed to PZT intraligand π-π* transition, and to metal-to-ligand charge transfer transition, i.e., $d\pi(Fe^{II})\rightarrow p\pi^*(PZT)$, respectively, by analogy with the literature.[8]

The $^1H$ NMR spectrum of the pentacyanidoferrate(II) complex in $^2H_2O$ exhibits the characteristic downfield shift of the signals of the adjacent aromatic protons (*α*) of the N-heterocycles coordinated to the $Fe(CN)_5^{3-}$ moiety, changing from δ = 8.41 to 9.03 ppm for $H^{2'}$ and from δ = 8.41 to 8.93 ppm for the $H^2$ signal in respect of the free ligand. This behavior follows the spectroscopic trends for monomeric pentacyanidoferrate(II) complexes, as shown in Figure 2, in which the downfield shift increases from 4-methylpyridine ($\Delta\delta^1H$ = 0.40 ppm) ≈ pyridine ($\Delta\delta^1H$ = 0.33 ppm) < isonicotinamide ($\Delta\delta^1H$ = 0.40 ppm) < pyrazine ($\Delta\delta^1H$ = 0.50 ppm) < *N*-methylpyrazinium ion ($\Delta\delta^1H$ = 0.80 ppm). For the PZT α-proton signals, downfield shifts of $\Delta\delta^1H^{2'}$ = 0.62 ppm and $\Delta\delta^1H^2$ = 0.52 ppm were observed, which are close to that expected from the spectrochemical series ($E_{TE}$ = 21.7 kK). The PZT β-aromatic proton signal underwent an upfield shift from δ = 8.34 to 8.14 ppm.

The observed behavior of the aromatic protons in pentacyanidoferrate(II) N-heterocyclic complexes involves main contributions from the $d\pi\rightarrow p\pi$ back-bonding to the heterocyclic ligand and the opposing inductive effect, whereas for the α-protons the magnetic anisotropy due to the electron looping at the CN axis bond is most relevant.[17] Curiously, the thiol proton signal exhibits a pronounced change in the chemical shift with respect to that of the free PZT ligand, i.e., from δ = 1.43 ($^2H_2O$) or 1.46 ($C^2HCl_3$) to 3.33 ppm in the pentacyanidoferrate(II) complex. This effect can be ascribed to the magnetic anisotropy of the cyanido ligands, producing a deshielding effect on the nuclei located perpendicular to this triple bond. As the thiol proton lies in a deshielding region, a large downfield shift is observed. Another evidence of the magnetic anisotropy of the cyanido ligands is reflected in the shape of the thiol proton peak. In fact, in $^2H_2O$, the S–H signal of the free PZT ligand appears as a broad coalescent peak at $\delta$ = 1.43 ppm. After coordination to the pentacyanidoferrate(II) complex, this peak became rather narrow, at $\delta$ = 3.33 ppm, exhibiting a strong spin-decoupling effect, removing the triplet feature observed in aprotic solvents.

Cyclic voltammetry (CV) and differential pulse voltammetry (DPV) for $[Fe(CN)_5PZT]^{3-}$ exhibited only a single redox process at 0.55 V (SHE), $E_{pa} - E_{pc}$ = 60 mV, showing no evidence of formation of dinuclear or any other species in solution. The $E_{1/2}$ is in good agreement with the analogous $[Fe(CN)_5pz]^{3-}$ (pz = pyrazine) species (0.55 V vs. SCE).[8]

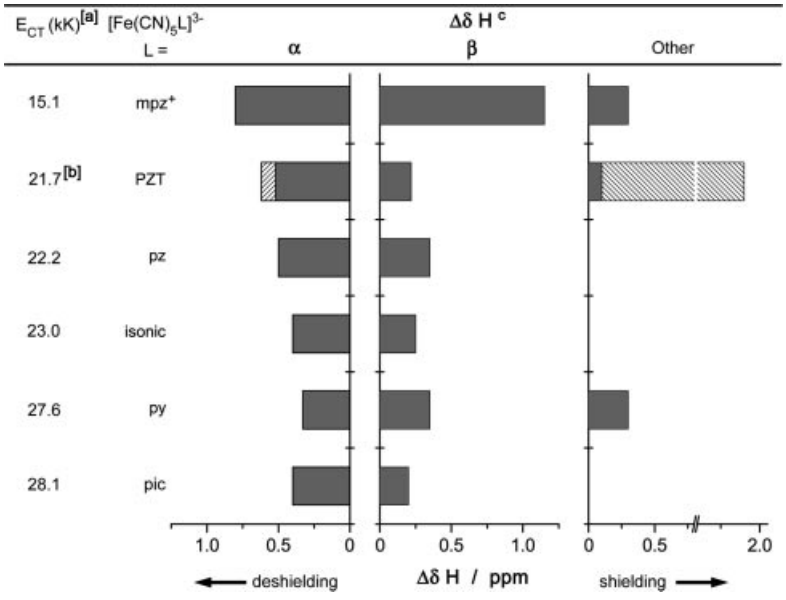


Figure 2. $\Delta\delta(^1H)$ for the protons α, β and others in pentacyanidoferrate(II) complexes of aromatic N-heterocycles, L. [a] Energy of metal-to-ligand charge transfer from ref.[17] and this work. [b] $\Delta\delta(^1H)$ for the α, β and other protons in $^2H_2O$. Striped bars correspond to $H^{2'}$ (*α*) and S–H signals (other). $mpz^+$ = *N*-methylpyrazinium ligand; PZT = 2-pyrazin-2-ylethanethiol; pz = pyrazine; isonic = isonicotinamide; py = pyridine; pic = 4-methylpyridine.

 © 2007 Wiley-VCH Verlag GmbH & Co. KGaA, Weinheim 

### Solvatochromic Behavior

Cyanidoiron complexes exhibit strong solvent effects influencing their chemical reactivity and solvatochromic behavior.[18–22] Such solvent effects arise from specific donor–acceptor interactions of the solvent molecules with the available nonbonding electron pairs of the cyanido ligands. For this reason, the observed solvatochromism is best correlated with the acceptor number[23] (AN) of the solvents. In Figure 3 the normalized spectra of $[Fe(CN)_5PZT]^{3-}$ in the different solvents are shown.

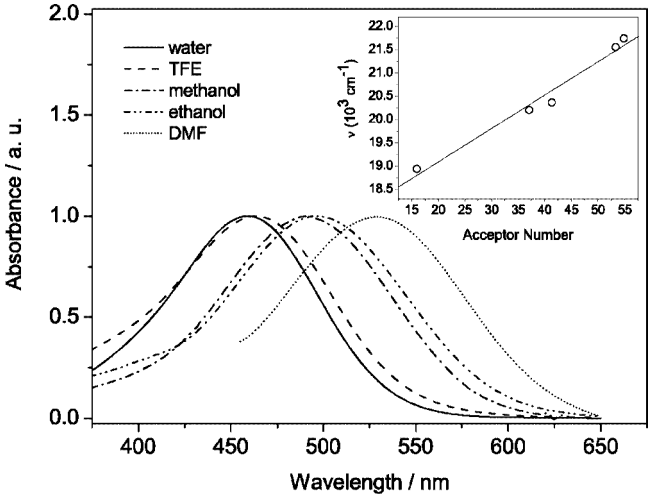


Figure 3. Normalized spectra of the $[Fe(CN)_5PZT]^{3-}$ complex in several solvents, as a function of the acceptor number: (——) water (AN = 54.8), (– – –) trifluoroethanol (TFE) (AN = 53.3), (– · – · –) methanol (AN = 41.3), (– ·· – ·· –) ethanol (AN = 37.1), (···) DMF (AN = 16.0). Inset: Correlation between the MLCT band energies of the $[Fe(CN)_5PZT]^{3-}$ complex and the AN parameter of the solvents (water, trifluoroethanol, methanol, ethanol, DMF).

As expected, the energy of the charge-transfer band shows a strong dependence with the solvent acceptor number.[20–22] Solvents displaying high AN values are able to interact with the nitrogen electron pair on the cyanido ligands, removing part of σ-electron density, while increasing the dπ→pπ* back-bonding contribution. This leads to the stabilization of the occupied metal dπ orbitals, thus increasing the energies of the MLCT bands, as expressed by the equation:[20]

$$\nu_s = \nu_0 + a(AN)$$

where $\nu_s$ is the experimental wavenumber and $\nu_0$ corresponds to the extrapolated value at AN = 0 (Figure 3, inset). The parameter $a$ measures the sensitivity of the charge-transfer band to the solvent acceptor properties. For the $[Fe(CN)_5PZT]^{3-}$ complex, $\nu_0$ = 17660 cm$^{-1}$, and $a$ = 72 cm$^{-1}$.

### Theoretical Simulation of the Electronic Spectrum

The DFT-optimized geometry for the $[Fe(CN)_5PZT]^{3-}$ ion is consistent with an octahedral configuration, with four equatorial Fe–C and C≡N bonds of 1.982 and 1.178 Å, respectively. The corresponding axial bond lengths were 1.970 and 1.176 Å, respectively, reflecting the *trans*-influence of the dπ→pπ* interactions from the Fe–PZT moiety. On the basis of the DFT-optimized geometry, ZINDO/S calculations were carried out, simulating the electronic spectrum of the $[Fe(CN)_5PZT]^{3-}$ ion, with the MLCT band at 17827 cm$^{-1}$ displaying an oscillator strength of 0.496. This theoretical value refers to a vacuum calculation, and differs significantly from the experimental value of 21700 cm$^{-1}$ in aqueous solution, coinciding, however, with the extrapolated value at AN = 0 ($\nu_0$ = 17660 cm$^{-1}$).[20] This observation is quite relevant, justifying a careful investigation of the solvatochromic effects, prior to the theoretical simulation of the electronic spectra.

According to the theoretical calculations, the observed MLCT transition involves the HOMO→LUMO (MOs 52→53) excitation. The composition of the HOMO and LUMO levels is shown in Table 1. The HOMO level (MO-52) is mainly composed of the metal dπ orbitals (68%), as illustrated in Figure 4, while the LUMO (MO-53) has the largest contribution from the PZT π* orbitals (Figure 4, B).

Table 1. MOs' percent composition obtained from ZINDO/S calculations.

| | HOMO | LUMO |
|---|---|---|
| MO | 52 | 53 |
| Energy [eV] | 1.8834 | 7.1168 |
| % Fe | 68.36[a] | 13.45[b] |
| % CN | 14.56 | 28.55 |
| % PZT | 17.08 | 58.00 |

[a] d($xz$): 39.25%, d($yz$): 29.06%, d($xy$): 0.02%, d($z^2$): 0.02%, d($x^2$–$y^2$): 0.01%. [b] d($xz$): 7.64%, d($yz$): 5.80%, d($xy$): 0.01%, d($z^2$): 0.00%, d($x^2$–$y^2$): 0.00%.

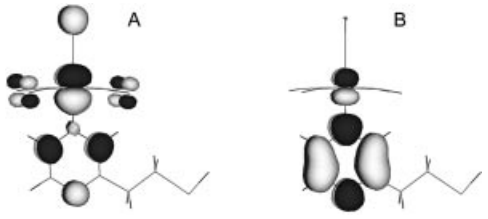


Figure 4. Plots of the frontier orbitals of the $[Fe(CN)_5PZT]^{3-}$ (A) HOMO and (B) LUMO.

### Vibrational Study of PZT and $[Fe(CN)_5PZT]^{3-}$

In Figure 5 is shown the FT-IR spectra of the PZT ligand and its corresponding pentacyanidoferrate(II) complex. The IR spectrum of PZT exhibits the characteristic high-energy frequencies associated with the C–H stretching modes of the $–CH_2–CH_2–$ group, and a broad band at 2540 cm$^{-1}$ related to the S–H stretching vibration. In the pentacyanidoferrate(II) complex, the FT-IR spectrum presents two characteristic bands at ca. 2050 and 570 cm$^{-1}$ associated with the vibrational modes of the C≡N and Fe–CN bonds. The S–H stretching mode can also be detected in the FTIR spectra, shifting from 2540 to 2470 cm$^{-1}$ upon the N-coordination to the pentacyanidoferrate complex,

 © 2007 Wiley-VCH Verlag GmbH & Co. KGaA, Weinheim 

corroborating the observed influence on the S–H group in the NMR spectrum.

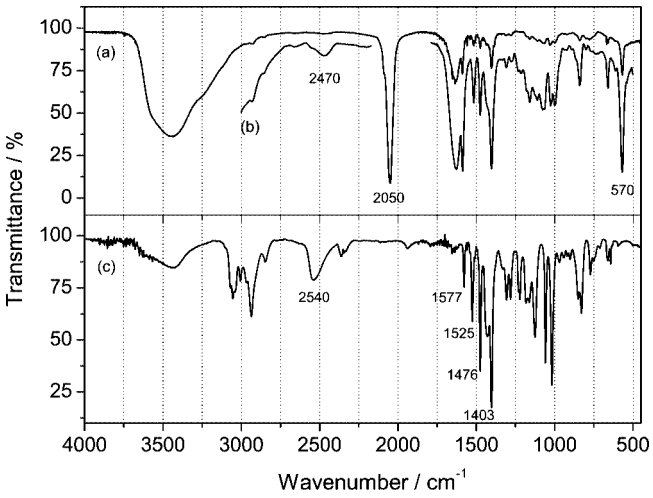


Figure 5. IR spectra of $Na_3[Fe(CN)_5PZT]\cdot 3H_2O$ in KBr pellets: (a) diluted and (b) three times more concentrated, (c) IR spectrum of pure liquid PZT.

The Raman spectrum of the PZT ligand is dominated by two intense bands at 1058 and 1018 $cm^{-1}$ ascribed to the vibrational modes of the $–CH_2–CH_2–$ and pyrazine moieties, respectively.

The complete assignment of the PZT and $Na_3[Fe(CN)_5$-PZT]$\cdot 3H_2O$ vibrational frequencies was carried out based on the theoretical calculations, as shown in Tables 2 and 3.

### Interaction of Gold Nanoparticles with PZT

The colloidal solutions of citrate-stabilized gold nanoparticles (average size 20 nm) exhibit a characteristic red-wine color ascribed to the optical interaction with the surface plasmons, as accounted for by the Mie theory.[24] The spectral variation of the gold nanoparticles in the presence of PZT ($1 \times 10^{-5}$ mol $dm^{-3}$) can be seen in Figure 6. After the addition of PZT to the gold nanoparticles solution, the intensity of the plasmon absorption band at 520 nm decreases in parallel with the rise of a new band above 600 nm. As this band becomes more intense, there is a bathochromic shift to 660 nm. Such optical changes can be

Table 2. Assignment of calculated wavenumber [$cm^{-1}$] to experimental bands in the FT-IR and Raman of PZT.

| Mode | Experimental | | Calculated | Assignment |
|---|---|---|---|---|
| | FT-IR | Raman | frequencies | |
| 45 | 3069 (w) | – | 3175 | ν C–$H_{pz}$ |
| 44 | 3054 (w) | – | 3170 | ν C–$H_{pz}$ |
| 43 | 3007 (m) | – | 3143 | ν C–$H_{pz}$ |
| 42 | 2968 (w) | – | 3098 | $\nu_{as}$ C–$H^2$ |
| 41 | 2937 (m) | – | 3051 | $\nu_s$ C–$H^2$; $\nu_{as}$ C–$H^2$ |
| 40 | | – | 3042 | $\nu_{as}$ C–$H^2$; $\nu_s$ C–$H^2$ |
| 39 | 2847 (w) | – | 3020 | $\nu_s$ C–$H^2$; $\nu_{as}$ C–$H^2$ |
| 38 | 2540 (w) | – | 2678 | ν S–H |
| 37 | 1577 (m) | 1577 (m) | 1609 | ν ring; δ C–$H^2$ |
| 36 | | | 1581 | ν ring; ω C–$H^2$ |
| 35 | 1525 (m) | 1525 (w) | 1511 | δ C–$H_2$ |
| 34 | 1475 (s) | – | 1504 | δ C–$H_{pz}$; ν C–$C_{pz–eth}$ |
| 33 | 1428 (s) | 1428 (w) | 1490 | δ C–$H^2$ |
| 32 | 1403 (vs) | 1403 (sh) | 1425 | δ C–$H_{pz}$; ω C–$H_2$; ν C–$N_{pz}$ |
| 31 | 1331 (w) | 1331 (vw) | 1370 | ω C–$H^2$; δ C–$H_{pz}$ |
| 30 | 1307 (m) | 1307 (vw) | 1315 | δ C–$H_{pz}$; ω C–$H^2$ |
| 29 | 1282 (m) | 1275 (vw) | 1288 | τ C–$H^2$ |
| 28 | | 1248 (vw) | 1265 | ω C–$H^2$; δ C–$H_{pz}$; ν C–$C_{pz–eth}$ |
| 27 | 1231 (m) | 1231 (vw) | 1251 | ω C–$H^2$; δ C–$H_{pz}$ |
| 26 | 1223 (m) | | 1205 | ω C–$H^2$; δ S–H |
| 25 | 1183 (m) | 1183 (vw) | 1188 | δ C–$H_{pz}$; ω C–$H^2$; δ S–H |
| 24 | 1163 (m) | 1163 (vw) | 1150 | τ C–$H^2$ |
| 23 | 1125 (s) | 1058 (s) | 1091 | ν C–$C_{eth}$; δ C–$H_{pz}$; δ S–H |
| 22 | 1058 (s) | | 1070 | |
| 21 | 1018 (s) | 1018 (s) | 1029 | ν ring |
| 20 | 969 (vw) | 969 (vw) | 996 | π ring; τ C–$H_2$; ρ C–$H^2$ |
| 19 | 940 (vw) | – | 982 | τ C–$H^2$; π ring; ρ C–$H^2$ |
| 18 | 920 (vw) | – | 944 | π ring; τ C–$H_2$; ρ C–$H^2$ |
| 17 | 840 (m) | 873 (w) | 908 | δ S–H; ω C–$H^2$; ν ring |
| 16 | 830 (m) | 830 (m) | 848 | π ring; ρ C–$H^2$ |
| 15 | | | 830 | δ ring; ν C–$C_{eth}$; δ S–H |
| 14 | 771 (w) | 774 (w) | 780 | π ring; ρ C–$H_2$; τ C–$H^2$ |
| 13 | 750 (w) | 738 (m) | 760 | ν S–C; δ ring |
| 12 | 661 (w) | 660 (m) | 690 | ρ C–$H_2$; π ring |
| 11 | 643 (w) | 632 (m) | 650 | δ ring; ν C–$C_{pz–eth}$; ν S–C |
| 10 | – | 589 (vw) | 588 | δ ring; ν C–$C_{pz–eth}$; ν S–C |
| 9 | – | 500 (w) | 465 | π ring; τ C–$H^2$; ρ C–$H^2$ |

 © 2007 Wiley-VCH Verlag GmbH & Co. KGaA, Weinheim 

Table 3. Assignment of calculated wavenumber [$cm^{-1}$] to experimental bands in the FT-IR and Raman of $Na_3[Fe(CN)_5PZT]$.

| Mode | Experiment | | Calculated | Assignment |
|---|---|---|---|---|
| | FT-IR | Raman | frequencies | |
| 71 | 2470 (m) | – | 2649 | ν S–H |
| 70 | | – | 2189 | ν C≡N |
| 69 | | – | 2181 | ν C≡N |
| 68 | 2050 (vs) | – | 2176 | ν C≡N |
| 67 | | – | 2169 | ν C≡N |
| 66 | | – | 2167 | ν C≡N |
| 65 | 1590 (s) | 1590 (s) | 1620 | ν ring; δ $C–H^2_{eth}$ |
| 64 | 1516 (m) | – | 1505 | δ $C–H^2_{eth}$ |
| 63 | 1476 (m) | – | 1497 | δ $C–H_{pz}$; δ $C–H^2_{eth}$ |
| 62 | | – | 1492 | δ $C–H^2_{eth}$; δ $C–H_{pz}$ |
| 61 | 1430 (sh) | – | 1481 | δ $C–H^2_{eth}$; δ $C–H_{pz}$ |
| 60 | 1403 (s) | – | 1439 | δ $C–H_{pz}$; ω $CH_{2eth}$; ν $C–N_{pz}$ |
| 59 | | – | 1373 | ω $C–H^2_{eth}$; δ $C–H_{pz}$ |
| 58 | 1308 (vw) | 1308 (vw) | 1320 | ω $C–H^2_{eth}$; τ $C–H^2_{eth}$; δ $C–H_{pz}$ |
| 57 | | | 1312 | τ $C–H^2_{eth}$; τ $C–H^2_{eth}$; δ $C–H_{pz}$ |
| 56 | 1277 (vw) | – | 1290 | ω $C–H^2_{eth}$; δ $C–H_{pz}$ |
| 55 | 1233 (vw) | 1241 (vw) | 1268 | δ $C–H_{pz}$; ω $C–H^2_{eth}$ |
| 54 | 1214 (vw) | – | 1225 | ω $C–H^2_{eth}$; δ $C–H_{pz}$ |
| 53 | 1179 (sh) | 1179 (sh) | 1177 | τ $C–H^2_{eth}$; δ $C–H_{pz}$ |
| 52 | 1159 (m) | 1159 (m) | 1159 | δ $C–H_{pz}$; τ $C–H^2_{eth}$; |
| 51 | 1110 (m) | 1076 (m) | 1081 | ν $C–C_{pz–eth}$; δ $C–H_{pz}$; δ S–H |
| 50 | 1076 (m) | | 1079 | δ$C–H_{pz}$; ν $C–C_{pz–eth}$; δ S–H |
| 49 | 1026 (w) | 1034 (m) | 1033 | τ $C–H^2_{eth}$; ring breathing |
| 48 | 998 (w) | – | 1030 | ring breathing; τ $C–H^2_{eth}$ |
| 47 | 970 (sh) | – | 936 | π ring; τ $C–H^2_{eth}$ |
| 46 | | | 916 | ν $C–C_{eth}$; δ S–H; ring breathing |
| 45 | 867 (sh) | 867 (vw) | 869 | π ring; ρ $C–H^2_{eth}$ |
| 44 | 841 (w) | 841 (w) | 850 | δ ring; δ S–H; ν $C–C_{eth}$ |
| 43 | 800 (vw) | 800 (vw) | 832 | π ring (54.9) + ρ $C^8H_2$ (28.0) + ρ $C^7–H^2$ (14.2) |
| 42 | | | 807 | ρ $C–H^2_{eth}$; π ring |
| 41 | 659 (w) | 659 (s) | 724 | π ring; ν S–C; ρ $C–H^2_{eth}$ |
| 40 | | | 720 | π ring; ν S–C; ρ $C–H^2_{eth}$ |
| 39 | | | 678 | δ ring; ν S–C |
| 38 | 612 (vw) | 612 (w) | 591 | δ ring; ω $C–H^2_{eth}$; ν S–C |
| 37 | | | 577 | π ring; ρ $C–H^2_{eth}$; π Fe–C (17.4) |
| 36 | | | 534 | π Fe–C; π ring |
| 35 | 570 (s) | 570 (s) | 526 | π Fe–C; π ring; δ S–C |
| 34 | | | 505 | π Fe–C; π ring; ρ $C–H^2_{eth}$ |
| 33 | | | 463 | π Fe–C; π ring |
| 32 | | 500 (w) | 460 | π Fe–C; π ring; ρ $C–H^2_{eth}$ |

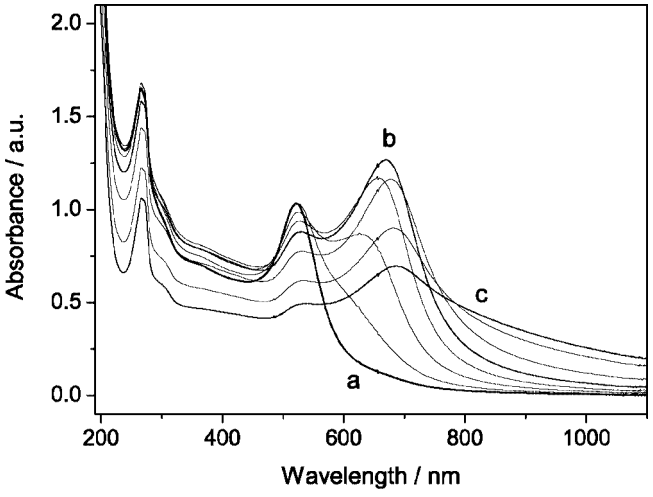


Figure 6. Changes of the UV/Vis spectra of AuNps upon addition of the PZT ($1 \times 10^{-5}$ mol dm$^{-3}$) ligand as a function of time: (a) starting solution ($t$ = 0 min), (b) flocculation ($t$ = 42 min), (c) precipitation ($t$ = 90 min).

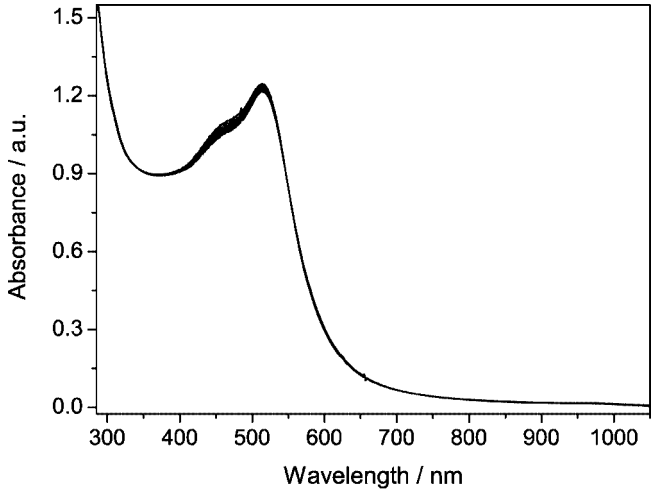


Figure 7. Successive UV/Vis spectra of AuNps showing only a very small decrease of intensity, after adding $1 \times 10^{-5}$ mol dm$^{-3}$ $[Fe(CN)_5PZT]^{3-}$ ($t$ = 120 min).

 © 2007 Wiley-VCH Verlag GmbH & Co. KGaA, Weinheim 

ascribed to the aggregation of the gold nanoparticles, arising from the mutual interference of the plasmon levels in neighboring nanoparticles.[1] The intensity of the 660 nm band reaches a maximum, after which there is a gradual decay and shift to about 700 nm, due to the precipitation process.

A contrasting behavior is observed for the $[Fe(CN)_5PZT]^{3-}$-modified AuNps. In Figure 7 the spectra of the AuNps upon addition of $[Fe(CN)_5PZT]^{3-}$ ($1 \times 10^{-5}$ mol dm$^{-3}$) is shown. The characteristic MLCT band at 460 nm for the $[Fe(CN)_5PZT]^{3-}$ complex can be observed as a shoulder of the plasmon resonance band at 520 nm, exhibiting only a small decrease in intensity after the binding and replacement of the citrate shell of the gold nanoparticles. In this case, a stable colloidal solution is obtained, which can be stored for many days, under argon, without any evidence of the plasmon coupling band above 600 nm, associated with flocculation.

### SERS Effect on PZT-AuNps and $Na_3[Fe(CN)_5PZT]$-AuNps

Because of the expected occurrence of SERS, the aggregated PZT-AuNps in aqueous media were also studied by Raman spectroscopy. Typical spectra can be seen in Figure 8, in comparison with the normal Raman spectra of the PZT ligand (pure form).

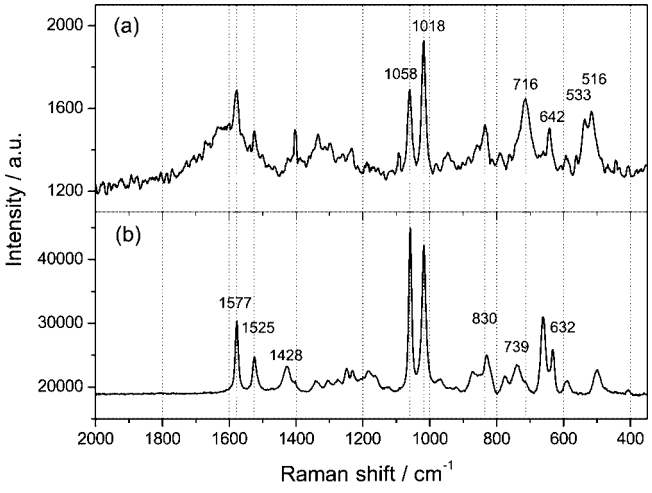


Figure 8. SERS spectrum of the PZT-AuNps ([PZT] = $1 \times 10^{-5}$ mol dm$^{-3}$) (a) and Raman spectrum of the PZT in pure liquid form (b).

Considering the very low concentrations ([PZT] = $10^{-5}$ mol dm$^{-3}$) employed in the measurements, the strong (SERS) intensification of the PZT vibrational peaks becomes quite evident in Figure 8. It is known that the SERS effect can involve either electromagnetic (EM)[25] or charge transfer (CT)[26] mechanisms. In the EM model, the Raman enhancement is attributed to the excitation of the surface plasmon polaritons by the exciting wavelength, as described by the Mie formalism.[24] This mechanism is typically observed in the case of plasmon resonance involving physically adsorbed molecules.[27] Usually, SERS of particles smaller than the exciting wavelength are a function of the radius and refractive index, and the maximum enhancement is observed when the molecules are as close as possible to the surface and the incident and scattered waves are perpendicular to the scattering plane.

In the case of chemically adsorbed molecules, a charge-transfer mechanism becomes plausible. Generally, it involves the transfer of an electron from the Fermi level of the metal atom to an unoccupied molecular orbital of the adsorbate or vice versa, but the evidence of this particular type of excitation has been mainly obtained from electrochemical experiments. It should be noted that SERS can be observed even for chemically adsorbed molecules without charge-transfer resonance.[27] When charge-transfer resonance and surface-enhanced resonance Raman scattering are involved, the mechanism is referred to as SERRS (Surface Enhanced Resonance Raman Scattering). One of the first reports on the SERRS mechanism dealt with the $[\{Fe(CN)_5\}_2(\mu\text{-bipy})]^{6-}$ complex adsorbed on a silver electrode.[28] Although a direct spectroscopic evidence has not been obtained in this case, it is important to notice that outer-sphere charge-transfer excitation in pentacyanidoferrate(II) complexes have already been reported in the literature,[29,30] as well as in $TiO_2$ films containing anchored $[Fe(CN)_5L]^{n-}$ species.[31]

In the case of the PZT-AuNps, the aggregation phenomenon in aqueous solution leads to the selective enhancement of the vibrational modes associated with the PZT ligand, involving both the pyrazine ring and thioalkane moieties. It is interesting to note that the relative intensity of the peaks at 1058 and 1018 cm$^{-1}$ associated with ethanethiol and pyrazine vibrational modes, respectively, is inverted in relation to the normal Raman spectrum of the PZT species. The peaks at ca. 738 and 500 cm$^{-1}$, ascribed to C–S stretching and–$CH_2$–$CH_2$– vibrational modes undergo strong enhancement, shifting to 716 and 516 cm$^{-1}$, respectively. This is in agreement with the electromagnetic mechanism, since such groups are in close proximity to the gold surface due to the thiol binding.

The Raman spectrum of the pentacyanidoiron-stabilized AuNps shows a strong enhancement of the vibrational modes, exhibiting a rather contrasting profile in relation to the normal spectrum of the isolated complex, as can be observed in Figure 9.

The 659 cm$^{-1}$ peak ascribed to the C–S stretching mode exhibits the greatest enhancement, shifting to 700 cm$^{-1}$. The original peaks at 1590, 1159, 1076, and 1034 cm$^{-1}$ in the normal spectra practically vanish and some new peaks arise in this region. This result suggests a different origin for the SERS effect in the $[Fe(CN)_5PZT]^{3-}$-stabilized AuNps, in comparison with the PZT-AuNps aggregates. The enhancement of the new bands seems to be associated with the electronic character of the excited state, and the occurrence of a charge-transfer mechanism can be plausible in this case. The puzzling point, however, is that there is no plasmon coupling band above 600 nm, as in the case of the PZT-AuNps. Presumably, an interfacial charge-transfer excitation is involved, as in the preceding example involving

 © 2007 Wiley-VCH Verlag GmbH & Co. KGaA, Weinheim 

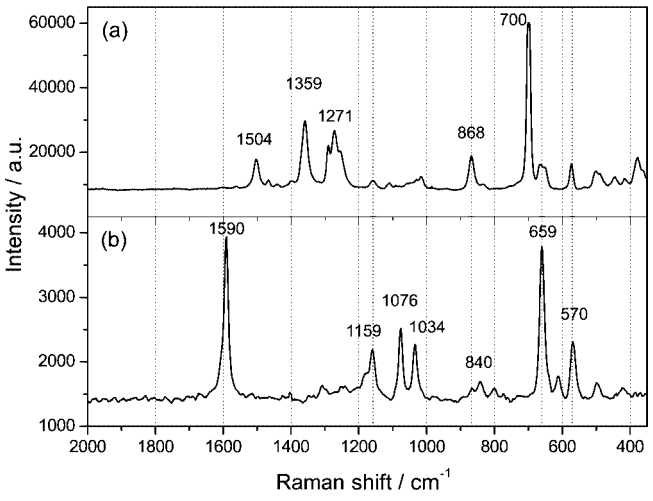


Figure 9. SERS spectrum of the complex $Na_3[Fe(CN)_5PZT]$ at $10^{-5}$ mol dm$^{-3}$ stabilizing AuNps (a) and Raman spectrum of the iron complex at 1 mol dm$^{-3}$ in aqueous solution (b).

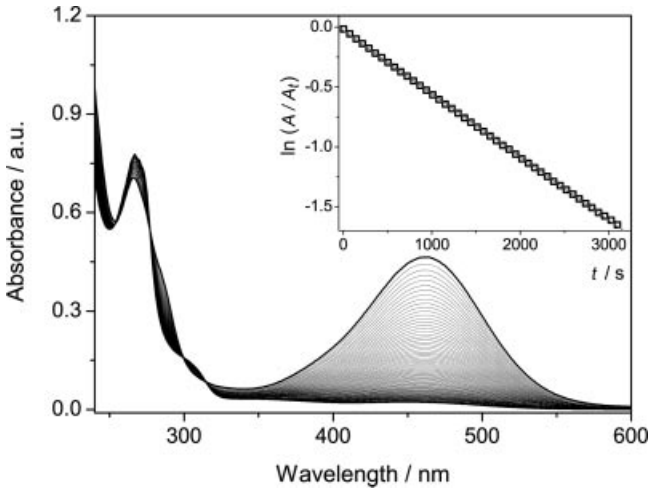


Figure 10. UV/Vis spectra of $1 \times 10^{-4}$ mol dm$^{-3}$ $[Fe(CN)_5PZT]^{3-}$ in the presence of 0.5 mol dm$^{-3}$ dmso. Inset: first-order kinetic plot, where $k_{obs} = 5.2 \times 10^{-4}$ s$^{-1}$ with 99.9% correlation.

cyanidoiron complexes, from the literature.[28] In addition, it has been shown that many chromophore-functionalized gold nanoparticles[32] undergo complete quenching of emission, from such interfacial charge transfer effects. At the present time, the SERS phenomenon and their many variations are not yet completely understood,[27] and the unusual behavior of the $[Fe(CN)_5PZT]^{3-}$-stabilized AuNps will be subject of a future, detailed investigation.

### Dissociation Kinetics of $[Fe(CN)_5PZT]^{3-}$ and Controlled Aggregation of the Modified Gold Nanoparticles

The dissociation kinetics of the $[Fe(CN)_5PZT]^{3-}$ complex was studied in the presence of a large excess of dimethyl sulfoxide as the attacking ligand. The resulting $[Fe(CN)_5dmso]^{3-}$ complex is quite stable, and does not absorb in the visible region.[10] Therefore, the dissociation reaction can be conveniently monitored by the disappearance of the MLCT band at 461 nm.

The substitution kinetics of the PZT ligand by dmso, in large excess (0.5 mol dm$^{-3}$), proceeded according to first-order kinetics, as shown in Figure 10 (inset). It should be noted that ligand substitution in aromatic N-heterocycle pentacyanidoferrates(II) complexes occurs by a dissociative mechanism,[8–13] as expressed by the equations:

$$[Fe(CN)_5pzt]^{3-} \underset{k_{-PZT}}{\overset{k_{PZT}}{\rightleftharpoons}} [Fe(CN)_5]^{3-} + pzt$$

$$[Fe(CN)_5]^{3-} + H_2O \underset{k_1}{\overset{k_{-1}}{\rightleftharpoons}} [Fe(CN)_5H_2O]^{3-}$$

$$[Fe(CN)_5]^{3-} + dmso \xrightarrow{k_{dmso}} [Fe(CN)_5dmso]^{3-}$$

$$k_{obs} = \frac{k_{-PZT}\, k_{dmso}\, [dmso]}{k_{PZT}\, [PZT] + k_{dmso}[dmso]}$$

As previously shown,[8] under pseudo-first-order conditions, and assuming steady-state hypothesis for the $[Fe(CN)_5]^{3-}$ intermediate, the observed rate constants are given by:

In the presence of a large excess of dmso, $k_{dmso}[dmso] >> k_{PZT}[PZT]$, and the observed rate constant coincides with the limiting dissociation rate constant for the $[Fe(CN)_5PZT]^{3-}$ complex, i.e., $k_{obs} = k_{-PZT}$.

The same pattern was also observed (Figure 11) for the $[Fe(CN)_5PZT]^{3-}$-stabilized gold nanoparticles in the presence of dmso (0.5 mol dm$^{-3}$). As observed for the free complex, the reaction with dmso leads to an exponential decrease of the MLCT band at ca. 460 nm (Figure 11, inset), with a kinetic dissociation constant of $6.2 \times 10^{-4}$ s$^{-1}$. This value is comparable to $5.2 \times 10^{-4}$ s$^{-1}$ obtained for the free complex.

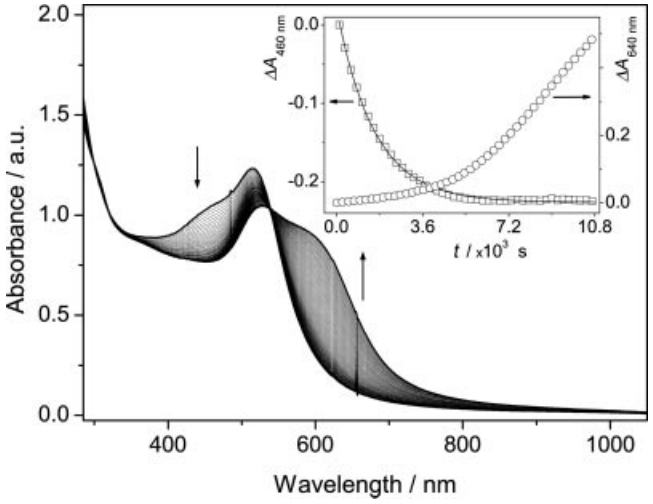


Figure 11. UV/Vis spectra and dissociation kinetics of the $[Fe(CN)_5PZT]^{3-}$-stabilized gold nanoparticles after addition of 0.5 mol dm$^{-3}$ dmso. Inset: Decrease of absorbance at 460 (□, left) and 640 nm (○, right). The solid line is a pseudo-first-order behavior fit at 460 nm, where $k_{obs} = 6.2 \times 10^{-4}$ s$^{-1}$ with 99.8% of correlation.

It should be noted that the dissociation of the pentacyanidoferrate(II) complex from the AuNps surface removes the electrostatic stabilization of the nanoparticles. Therefore, as

 © 2007 Wiley-VCH Verlag GmbH & Co. KGaA, Weinheim 

Table 4. Kinetic and thermodynamic data for $[Fe(CN)_5L]^{2-/3-}$ complexes.[a]

| Ligand | $E_{CT}$ $10^3$ cm$^{-1}$ | Donor group | $k_d^{II}$ $\times10^{-4}$ s$^{-1}$ | $k_f^{II}$ $\times10^{2}$ mol$^{-1}$ s$^{-1}$ | $K_f^{II}$ $\times10^{5}$ dm$^3$ mol$^{-1}$ | $K_f^{III}$ dm$^3$ mol$^{-1}$ | $E°_L$[b] | Ref. |
|---|---|---|---|---|---|---|---|---|
| dmso | – | S=O | 0.75 | 2.4 | 49 | $3.7\times10^{-2}$ | 850 | [10–12] |
| Methylpyrazinium | 15.1 | C=N | 2.8 | 5.5 | 20 | $4.7\times10^{-1}$ | 780 | [10,33] |
| Pyrazine | 22.2 | C=N | 4.2 | 3.80 | 9.0 | $1.7\times10^{3}$ | 550 | [8,11,12,15,16] |
| PZT | 21.7 | C=N | 5.2 | 3.8[c] | 7.3[c] | $1.4\times10^{3}$[c] | 550 | – |
| AuNps-PZT | 21.7 | C=N | 6.4 | – | – | – | – | – |
| Isonicotinamide | 23.0 | C=N | 7.3 | 2.95 | 8.2 | 5.2 x10$^3$ | 500 | [8,11,12,15,16] |
| 4-Mercaptopyridine | 24.7 | C=N | 11.0 | 2.9 | 2.6 | $3.4\times10^{4}$ | 442 | [7] |
| Pyridine | 27.6 | C=N | 11.0 | 3.65 | 4.6 | $9.4\times10^{3}$ | 470 | [8,11,12,15,16] |

[a] The complexes are listed in decreasing order of reduction potential. [b] In mV (SHE). [c] Estimated values based on assumed value of the pyrazine: $k_f^{II}$ = 380 mol$^{-1}$ s$^{-1}$.

expected, the ligand-substitution reaction is followed by the flocculation of the resulting PZT-AuNps, leading to an increase of the absorbance at 640 nm, i.e.:

$[Fe(CN)_5PZT]$-AuNps + dmso → $[Fe(CN)_5dmso]^{3-}$ + PZT-AuNps

PZT-AuNps → flocculation

From the kinetics and electrochemical parameters obtained in this work, it is possible to estimate the equilibrium constants for $[Fe(CN)_5PZT]^{3-}$ and to compare with related systems, as shown in Table 4. The results are rather consistent, indicating that the characteristic properties of the pentacyanidoferrate(II) complexes are preserved after their binding to the gold nanoparticles.

## Conclusions

Gold nanoparticles and pentacyanidoferrates can be successfully combined by means of a suitable bridging ligand such as 2-pyrazin-2-ylethanethiol, allowing the exploitation of the coordination chemistry involved, especially, the stabilization of the colloidal solutions and the controlled formation of aggregates in the presence of a strong ligand, such as dimethyl sulfoxide. The modified gold nanoparticles exhibit a strong SERS effect. The results are coherent with the enhancement by the electromagnetic mechanism for the PZT-modified gold nanoparticles, while the charge-transfer mechanism seems to predominate in the case of the $[Fe(CN)_5PZT]^{3-}$-modified gold nanoparticles. The reported strategy, based on a typical coordination chemistry approach, can be extended to the generation of functional, self-assembled nanoparticle films, of great relevance in molecular devices.

## Experimental Section

**Materials:** All solvents and reactants used in this work were of analytical grade and used as supplied. $HAuCl_4{\cdot}3H_2O$, trisodium citrate hydrate, and 2-pyrazin-2-ylethanethiol (PZT), were purchased from Aldrich. $Na_3[Fe(CN)_5NH_3]{\cdot}3H_2O$ was prepared from sodium nitroprusside, $Na_3[Fe(CN)_5NO]{\cdot}2H_2O$ (Carlos Erba), according to the usual procedure.[34] All aqueous solutions were prepared using MilliQ water (18.2 MΩ cm). Citrate-stabilized gold nanoparticles (AuNps) were prepared according to the Turkevitch[35] method as described previously.[7] The concentration of gold nanoparticles suspension used in the experiments was calculated as $10^{-9}$ mol dm$^{-3}$, assuming a total conversion of $AuCl_4^-$ ions into colloidal nanoparticles of 20 nm average size, as previously measured by MEV and STM on HOPG substrate. The calculated area per particle was $1.26\times10^{-15}$ m$^2$, yielding a total surface area of 0.756 m$^2$ dm$^{-3}$. $Na_3[Fe(CN)_5PZT]{\cdot}3H_2O$ was prepared by adapting the procedures described by Toma et al.[8–14] $Na_3[Fe(CN)_5NH_3]{\cdot}3H_2O$ (0.326 g or 1.0 mmol) was mixed with a tenfold excess of 2-pyrazin-2-ylethanethiol (1.40 g or 10.0 mmol) in 10 mL of water, and the mixture magnetically stirred at room temperature under argon for 30 min. The product precipitated by addition of ethanol, and was collected on a glass filter, washed with cold ethanol and dried under vacuum. Yield: 84%. $Na_3[Fe(CN)_5PZT]{\cdot}3H_2O$: $C_{11}H_{14}FeN_7Na_3SO_3$ (449.15): calcd. C 30.4, H 3.24, N 19.3; found C 30.3, H 3.35, N 19.3. $^1$H NMR (300 MHz, $^2H_2O$): $\delta$ = 9.03 (s, 1 H, H$^{2'}$), 8.93 (m, 1 H, H$^2$), 8.13 (m, 1 H, H$^3$), 3.06 (m, 2 H, H$^5$), 2.90 (m, 2 H, H$^6$), 3.33 (s, 1 H, SH) ppm. For comparison purposes: PZT: $^1$H NMR (300 MHz, $^2H_2O$): $\delta$ = 8.41 (m, 2 H, H$^2$ and H$^{2'}$), 8.35 (m, 1 H, H$^3$), 2.99 (t, $J$ = 6.9 Hz, 2 H, H$^5$), (t, $J$ = 6.9 Hz, 2 H, H$^6$), 1.43 (shoulder, SH) ppm. PZT: $^1$H NMR (300 MHz, $C^2HCl_3$): $\delta$ = 8.535 (m, $J'$ = 2.7 Hz, $J''$ = 1.5 Hz, 1 H, H$^2$), (d, $J$ = 1.5 Hz, 1 H, H$^{2'}$), (d, $J$ = 2.7 Hz, 1 H, H$^3$), 3.132 (t, $J$ = 6.9 Hz, 2 H, H$^5$), 2.978 (m, $J'$ = 6.9 Hz, $J''$ = 1 Hz, 2 H, H$^6$), 1.46 (t, $J$ = 8.2 Hz, 1 H, SH) ppm. CV for $Na_3[Fe(CN)_5PZT]{\cdot}3H_2O$: $E_{1/2}$ = +0.55 V (SCE). For comparison purposes: $[Fe(CN)_5pz]^{3-}$ (where pz = pyrazine): $E_{1/2}$ = +0.55 V (SCE).[8]

**Physical Measurements:** NMR spectra were recorded with a Varian 300 MHz (INOVA 1) spectrometer using $1\times10^{-2}$ mol dm$^{-3}$ solutions. All peaks were related to tetramethylsilane (TMS). Cyclic and differential pulse voltammetry measurements were carried out with an Autolab PGSTAT 30 potentiostat/galvanostat with a conventional three-electrode cell constituted by a carbon glass disk working electrode (0.196 cm$^2$), a coiled platinum wire as the counter electrode, and an Ag/AgCl (KCl 0.1 mol dm$^{-3}$) reference electrode. The electrolyte employed was 0.1 mol dm$^{-3}$ KCl in water containing 1 mmol dm$^{-3}$ of the iron complex. UV/Vis spectra and kinetics experiments were recorded with a Hewlett Packard model HP-8453 diode-array spectrophotometer with a thermostatted cell holder. FT-IR spectra were recorded with a Shimadzu model FTIR 8300 spectrophotometer. Raman measurements were performed using an InPhotote portable instrument equipped with Raman probe optical fiber and a 300-mW (785 nm) diode laser (resolution of 6 cm$^{-1}$ and 350–2000 cm$^{-1}$ spectral range). Typically, an accumulation time of 120 s was employed to obtain the Raman spectra. For the free PZT and $Na_3[Fe(CN)_5PZT]{\cdot}3H_2O$ complex, the Raman spectra were recorded from pure sample and 1 mol dm$^{-3}$ aqueous solution, respectively. SERS measurements were performed using $1\times10^{-5}$ mol dm$^{-3}$ aqueous solutions. The dissoci-

 © 2007 Wiley-VCH Verlag GmbH & Co. KGaA, Weinheim 

ation kinetics of $[Fe(CN)_5PZT]^{3-}$ were studied in the presence of a large excess of dimethyl sulfoxide (dmso), at $25.0 \pm 0.1$ °C and 0.1 mol dm$^{-3}$ LiCl. The disappearance of the MLCT band of the $[Fe(CN)_5PZT]^{3-}$ species at 461 nm, was monitored under pseudo-first-order conditions, and the observed rate constants, $k_{obs}$, were obtained by linear fitting of $\ln(A_\infty/A_t)$ vs. time. For the evaluation of the dissociation kinetic constants of the gold nanoparticles stabilized with the iron complex, the changes of optical density at 460 nm were plotted vs. time, yielding a single exponential curve. The kinetic constant was obtained by a simplex fitting of this curve, according to the equation $y = y_0 + A\exp(-kt)$.

**Theoretical Calculations:** The DFT method was employed for geometry optimization, using GAMESS[36] software running on a PC cluster. Becke's three-parameter hybrid functional[37] with the LYP correlation functional[38] (B3LYP) was employed with a 6-31G(d,p) basis set for all atoms. Semi-empirical calculations were performed using the HYPERCHEM software package.[39] Theoretical calculations of the electronic spectrum were carried out using ZINDO/S,[40] employing a convergence criterion of $10^{-7}$ kcal mol$^{-1}$ for SCF and single CI excitations, using an active space of 40 frontier molecular orbitals (20 highest occupied and 20 lowest unoccupied MOs). The harmonic vibrational frequencies and intensities were calculated at this same level of theory, based on the analytical evaluation of second derivatives of energy as a function of atomic coordinates. Raman intensities were simulated by the numerical differentiation procedure of Komornicki and others,[41,42] applying an intensity of $2 \times 10^{-3}$ a.u. for the electric field.

## Acknowledgments

The authors gratefully acknowledge the financial support from Fundacao de Amparo a Pesquisa do Estado de Sao Paulo (FAPESP), Conselho Nacional de Desinvolvimento Cientifico e Tecnologico (CNPq), and Instituto do Milenio de Materiais Complexos (IM2C). S. H. T. thanks the Centro Brasileiro-Argentino de Nanotecnologia and Professors D. Zanchet, E. J. Calvo, M. Brust, and D. J. Schiffrin, for their precious lectures at the "Escuela de Nanopartículas" in Buenos Ayres.

[1] M. C. Daniel, D. Astruc, *Chem. Rev.* **2004**, *104*, 293–346.
[2] Y. Yang, S. Matsubara, M. Nogami, J. Shi, W. Huang, *Nanotechnology* **2006**, *17*, 2821–2827.
[3] E. Katz, I. Willner, *Angew. Chem. Int. Ed.* **2004**, *43*, 6042–6108.
[4] K. G. Thomas, P. V. Kamat, *Acc. Chem. Res.* **2003**, *36*, 888–898.
[5] A. J. Viudez, R. Madueno, T. Pineda, M. Blazquez, *J. Phys. Chem. B* **2006**, *110*, 17840–17847.
[6] H.-L. Zhang, D. S. Evans, J. R. Henderson, R. E. Miles, T. Shen, *J. Phys. Chem. B* **2003**, *107*, 6087–6095.
[7] F. S. Nunes, L. S. Bonifacio, K. Araki, H. E. Toma, *Inorg. Chem.* **2006**, *45*, 94–101.
[8] H. E. Toma, J. M. Malin, *Inorg. Chem.* **1973**, *12*, 1039–1045.
[9] H. E. Toma, J. M. Malin, *Inorg. Chem.* **1973**, *12*, 2080–2084.
[10] H. E. Toma, J. M. Malin, E. Giesbrecht, *Inorg. Chem.* **1973**, *12*, 2084–2089.
[11] H. E. Toma, J. M. Martins, E. Giesbrecht, *J. Chem. Soc. Dalton Trans.* **1978**, 1610–1617.
[12] H. E. Toma, A. A. Batista, H. B. Gray, *J. Am. Chem. Soc.* **1982**, *104*, 7509–7515.
[13] H. E. Toma, A. L. Coelho, H. M. Malin, *Inorg. Chem.* **1983**, *22*, 2703–2707.
[14] H. E. Toma, M. S. Takasugi, *Polyhedron* **1982**, *1*, 429–436.
[15] S. S. S. Borges, A. L. Coelho, I. S. Moreira, M. A. B. Araújo, *Polyhedron* **1994**, *13*, 1015–1022.
[16] L. M. Baraldo, P. F. Forlano, A. R. Parise, L. D. Slep, J. A. Olabe, *Coord. Chem. Rev.* **2001**, *219*, 881–921.
[17] J. M. Malin, C. F. Schmidt, H. E. Toma, *Inorg. Chem.* **1975**, *14*, 2924–2928.
[18] J. Burges, *Spectrochim. Acta, Part A* **1970**, *26*, 1369–1374.
[19] J. Burges, *Spectrochim. Acta, Part A* **1970**, *26*, 1957–1962.
[20] H. E. Toma, M. S. Takasugi, *J. Solution Chem.* **1983**, *12*, 547–561.
[21] H. E. Toma, M. S. Takasugi, *Polyhedron* **1989**, *8*, 941–945.
[22] H. E. Toma, M. S. Takasugi, *J. Solution Chem.* **1989**, *18*, 575–583.
[23] U. Mayer, *Pure Appl. Chem.* **1979**, *51*, 1697–1712.
[24] G. Mie, *Ann. Phys.* **1908**, *25*, 377.
[25] M. Moskovits, *Rev. Mod. Phys.* **1985**, *57*, 783–826.
[26] A. Otto, I. Mrozek, H. Grabhorn, W. Akemann, *J. Phys.: Condens. Matter* **1992**, *4*, 1143–1212.
[27] R. Aroca, *Surface-Enhanced Vibrational Spectroscopy*, John Wiley & Sons, Chichester, England, **2006**.
[28] J. C. Rubim, P. Corio, M. C. C. Ribeiro, M. Matz, *J. Phys. Chem.* **1995**, *99*, 15765–15774.
[29] H. E. Toma, *J. Chem. Soc. Dalton Trans.* **1980**, 471–475.
[30] H. E. Toma, *Can. J. Chem.* **1979**, *57*, 2079–2084.
[31] K. Szacilowski, W. Macyk, M. Hebda, G. Stochel, *Chemphyschem* **2006**, *7*, 2384–2391.
[32] K. G. Thomas, P. V. Kamat, *Acc. Chem. Res.* **2003**, *36*, 888–898.
[33] H. E. Toma, C. Creutz, *Inorg. Chem.* **1977**, *76*, 545–550.
[34] G. Brauer, *Handbook of Preparative Inorganic Chemistry*, 2nd ed., Academic Press, New York, **1965**, vol. 2, p. 1511.
[35] J. Turkevitch, P. C. Stevenson, J. Hilier, *Discuss. Faraday Soc.* **1951**, *11*, 55.
[36] M. W. Schmidt, K. K. Baldridge, J. A. Boatz, S. T. Elbert, M. S. Gordon, J. J. Jensen, S. Koseki, N. Matsunaga, K. A. Nguyen, S. Su, T. L. Windus, M. Dupuis, J. A. Montgomery, *J. Comput. Chem.* **1993**, *14*, 1347–1363.
[37] A. D. Becke, *J. Chem. Phys.* **1993**, *98*, 5648.
[38] C. Lee, W. Yang, R. G. Parr, *Phys. Rev. B* **1988**, *37*, 785.
[39] Hypercube Inc., Gainesville, FL, USA, **2002**.
[40] a) M. C. Zerner, G. H. Loew, R. F. Kirchner, U. T. Mueller-Westerhoff, *J. Am. Chem. Soc.* **1980**, *102*, 589; b) J. E. Ridley, M. C. Zerner, *Theor. Chim. Acta* **1976**, *42*, 223; c) J. E. Ridley, M. C. Zerner, *Theor. Chim. Acta* **1973**, *32*, 111; d) A. D. Bacon, M. C. Zerner, *Theor. Chim. Acta* **1979**, *53*, 21.
[41] A. Komornicki, J. W. McIver, *J. Chem. Phys.* **1979**, *70*, 2014.
[42] G. B. Bacskay, S. Saebo, P. R. Taylor, *Chem. Phys.* **1984**, *90*, 215.

Received: February 1, 2007
Published Online: June 14, 2007

 © 2007 Wiley-VCH Verlag GmbH & Co. KGaA, Weinheim 

DOI: 10.1002/ejic.200700153

# Synthesis, Characterization, and Photophysical Properties of Some Heterodimetallic Bisporphyrins of Ytterbium and Transition Metals – Enhancement and Lifetime Extension of $Yb^{3+}$ Emission by Transition-Metal Porphyrin Sensitization

**Feng-Lei Jiang,[a,b] Wai-Kwok Wong,*[b,c] Xun-Jin Zhu,[b] Gui-Jiang Zhou,[b] Wai-Yeung Wong,[b,c] Po-Lam Wu,[c,d] Hoi-Lam Tam,[c,d] Kok-Wai Cheah,[c,d] Cheng Ye,[e] and Yi Liu*[a]**

**Keywords:** Lanthanides / Optical limiting / Photoluminescence / Porphyrins / Transition metals

A series of d-f heterodimetallic bisporphyrin complexes (**YbZn**, **YbPd**, and **YbPt**), in which a $Yb^{III}$ porphyrinate moiety is linked to a transition-metal porphyrinate moiety by a flexible three-carbon chain, were synthesized. They were fully characterized by high-resolution mass spectrometry, $^1H$ and $^{31}P$ NMR spectroscopy, electronic absorption, and fluorescence methods. Variable-temperature near-infrared photoluminescence studies showed that the transition-metal porphyrinate moiety would enhance the ytterbium(III) emission centered at about 998 nm and extend its emission lifetime. **YbPd** and **YbPt** showed large two-photon absorption cross-section values because of the interaction between the porphyrin units, which caused a loss of centrosymmetry. Optical limiting investigation demonstrated that [Yb(TPP)($L_{OMe}$)] and **YbPt** have comparable performance to $C_{60}$ by virtue of their heavy-metal effect. Our results indicate that these bisporphyrin dimetallic complexes will find valuable applications in the field of nonlinear optics.
(© Wiley-VCH Verlag GmbH & Co. KGaA, 69451 Weinheim, Germany, 2007)

## Introduction

In the late 1970s, bisporphyrins with four linkages each on the *meso* position[1a] and β position[1b] were reported. Later on, bisporphyrins and their metal complexes were synthesized to study the photoinduced energy transfer from porphyrin to $O_2$.[2] Bisporphyrins are basically divided into two classes by virtue of their conformations: cofacial (mostly linked on the *ortho* position of the *meso*-phenyl group of porphyrin macrocycles) and linear (mostly linked on the *para* position of the *meso*-phenyl group of porphyrin macrocycles). Other than the linkage at the *meso*-phenyl group, there are bisporphyrins with linkages at the β position of the pyrrole unit as well.[3] Bisporphyrins with various kinds of linkages and different central metal ions have attracted much attention because of their potential application in host–guest chemistry,[4] chemical sensing,[5] supramolecular chirogenesis,[6] catalytic photooxidation,[7] molecular switches,[8] photoinduced energy transfer,[9] two-photon absorption,[10] etc. Linear bisporphyrins were mainly investigated on the energy transfer from one porphyrin unit to the other one by varying the rigid linkages, such as the phenylene and alkyne units.[11]

Trivalent lanthanide ions continue to attract considerable interest because of their unique optical properties such as line-like emission bands and relatively long luminescence lifetimes.[12] However, while it was recently reported that $Sm^{2+}$ complexes can be directly excited because the transitions are allowed,[13a] it is generally difficult to excite lanthanide ions directly because of the forbidden nature of their electronic transitions.[13] In order to overcome this problem, lanthanide ions are usually excited by the energy transferred from organic chromophores, which can encapsulate the lanthanide ions. Porphyrin can act as an antenna for photoluminescence (PL) in light of its highly conjugated system, which absorbs strongly in the UV/Vis region. Ytterbium(III) complexes, which emit in the near-infrared (NIR) region centered at about 998 nm, where biological tissues and fluids are relatively transparent, are promising probes

[a] College of Chemistry and Molecular Sciences, Wuhan University,
430072 Wuhan, P. R. China
Fax: +86-27-68754067
E-mail: prof.liuyi@263.net
[b] Department of Chemistry, Hong Kong Baptist University,
Waterloo Road, Hong Kong, P. R. China
Fax: +852-3411-7348
E-mail: wkwong@hkbu.edu.hk
[c] Centre for Advanced Luminescence Materials, Hong Kong Baptist University,
Waterloo Road, Hong Kong, P. R. China
[d] Department of Physics, Hong Kong Baptist University,
Waterloo Road, Hong Kong, P. R. China
[e] Center for Molecular Science, Institute of Chemistry, Chinese Academy of Sciences,
10080 Beijing, P. R. China
Supporting information for this article is available on the WWW under http://www.eurjic.org or from the author.

 © 2007 Wiley-VCH Verlag GmbH & Co. KGaA, Weinheim 

for fluoroimmunoassays. We have shown that porphyrinato ligands could act as antennae and sensitize NIR emission of $Nd^{3+}$, $Er^{3+}$, and $Yb^{3+}$ ions.[14] Recently, there has been considerable interest in extending the lifetimes of $Nd^{III}$, $Er^{III}$, and $Yb^{III}$. Transition-metal ions with long lifetimes, such as $Cr^{III}$, $Ru^{II}$, and $Pt^{II}$, were inserted into d-f heterodimetallic complexes and found to serve as sensitizers for lanthanide ions.[15–17] The best result of lifetime extension was observed for the CrLn (Ln = Nd, Yb) complex,[15] which showed that $Cr^{III}\rightarrow Ln^{III}$ intramolecular energy transfer could extend the lifetimes of lanthanide ions from the microsecond to millisecond timescale at 10 K. However, the

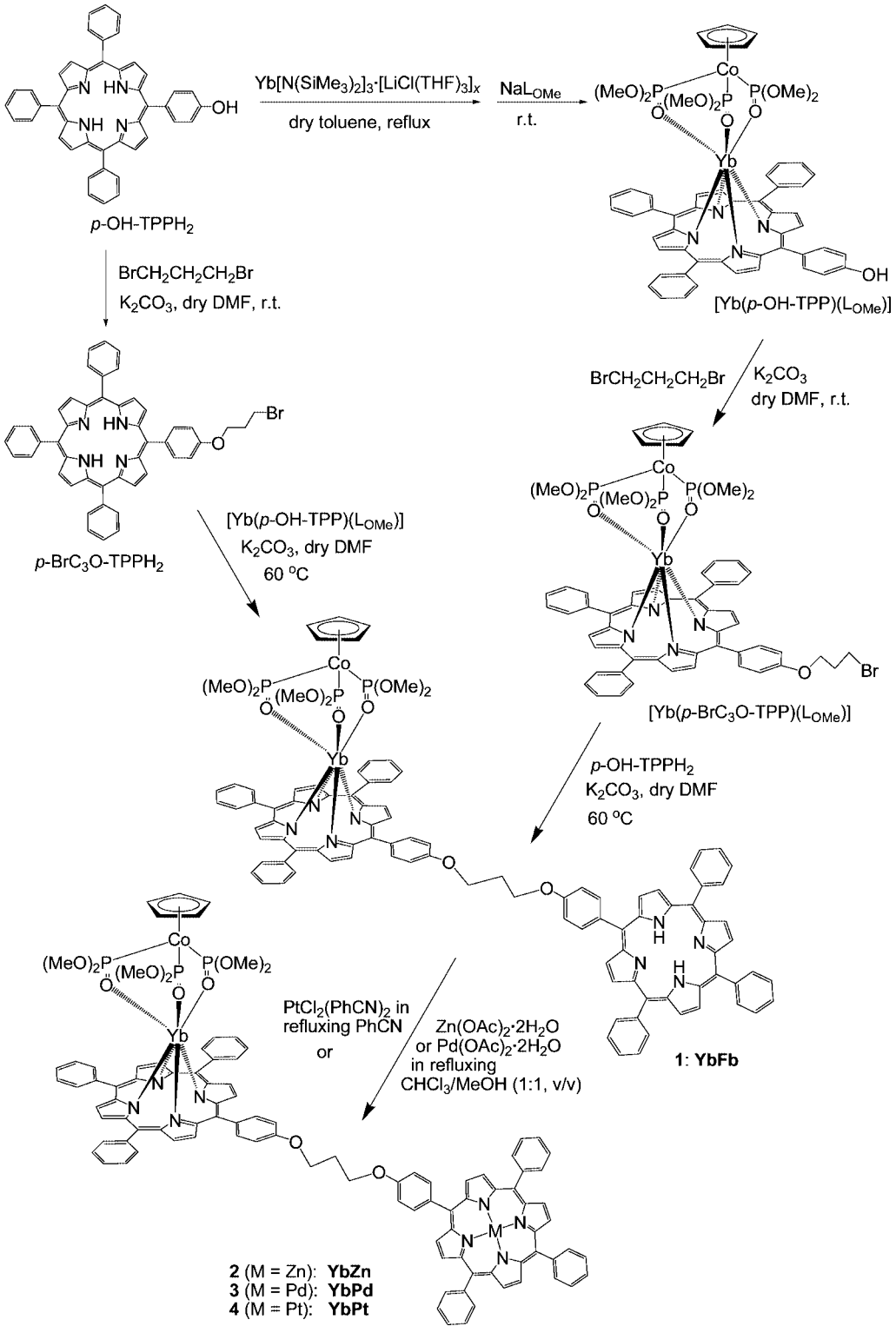


Scheme 1. Preparation of the dyads **YbFb**, **YbZn**, **YbPd**, and **YbPt**.

 © 2007 Wiley-VCH Verlag GmbH & Co. KGaA, Weinheim 

ligands only absorbed light in the high-energy region at 247 and 334 nm. To this end, we want to develop a strategy to extend the lanthanide lifetime by using sensitizers that absorb strongly in the UV/Vis region, such as metalloporphyrins of transition metals. To the best of our knowledge, there is no report in the literature on the synthesis of bisporphyrin complexes containing a lanthanide and a d-block transition metal. Herein, we report the synthesis, and photophysical and optical limiting properties of several bisporphyrin complexes, in which a $Yb^{III}$ porphyrinate moiety is linked to a transition-metal porphyrinate moiety by a flexible three-carbon chain.

## Results and Discussion

### Synthesis

Ytterbium(III) bisporphyrinate complexes **YbFb** (**1**), **YbZn** (**2**), **YbPd** (**3**), and **YbPt** (**4**) were prepared as shown in Scheme 1. When 5-(*p*-hydroxyphenyl)-10,15,20-triphenylporphyrin (*p*-OH-$TPPH_2$) was treated with excess $Yb[N(SiMe_3)_2]_3{\cdot}[LiCl(THF)_3]_x$ under nitrogen in refluxing toluene for 12 h followed by the addition of excess $Na\{(\eta^5\text{-}C_5H_5)Co[P(=O)(OMe)_2]_3\}$ ($NaL_{OMe}$) to the reaction mixture at room temperature (room temp.), workup gave purple air-stable crystals of [Yb(*p*-OH-TPP)($L_{OMe}$)] in 84% yield. The complex [Yb(*p*-OH-TPP)($L_{OMe}$)] was quite stable towards moisture and could be purified by column chromatography on silica gel. In the presence of $K_2CO_3$, reaction of *p*-OH-$TPPH_2$ with excess 1,3-dibromopropane in dry DMF under nitrogen at room temp. overnight gave 5-[*p*-(3-bromopropoxy)phenyl]-10,15,20-triphenylporphyrin (*p*-$BrC_3O$-$TPPH_2$) in 94% yield. The interaction of [Yb(*p*-OH-TPP)($L_{OMe}$)] with *p*-$BrC_3O$-$TPPH_2$, in the presence of $K_2CO_3$ in dry DMF at 60 °C overnight, gave the porphyrin complex **YbFb** (**1**), in which a porphyrin free base is appended to the $Yb^{III}$ porphyrinate complex by a flexible linkage, $-OCH_2CH_2CH_2O-$, in 58% yield. **YbFb** could also be prepared by the reaction of *p*-OH-$H_2$TPP with [Yb(*p*-$BrC_3O$-TPP)($L_{OMe}$)], which was synthesized by the reaction of [Yb(*p*-OH-TPP)($L_{OMe}$)] with 1,3-dibromopropane in the presence of $K_2CO_3$. All the above porphyrin free bases and Yb porphyrinate complexes were fully characterized by $^1H$ and $^{31}P$ (if applicable) NMR, MS, and UV/Vis spectroscopy. The solid-state structure of [Yb(*p*-$BrC_3O$-TPP)($L_{OMe}$)] (Figure 1), ascertained by X-ray crystallography, is very similar to that of [Yb(TMPP)($L_{OEt}$)].[14c] Crystal structure analysis revealed that the Yb ion is seven-coordinate, surrounded by four N atoms of the porphyrinate dianion and three O atoms of the three phosphito groups. The Yb–N and Yb–O distances are in the ranges 2.343(6)–2.367(5) and 2.260(7)–2.281(7) Å, respectively. The bond lengths and bond angles are almost the same as those in [Yb(TMPP)($L_{OEt}$)].[14c]

When **YbFb** was treated with $M(OAc)_2{\cdot}2H_2O$ (M = Zn, Pd) in a refluxing $CHCl_3$/MeOH (1:1, v/v) mixture for 24 h, **YbZn** (**2**) and **YbPd** (**3**) were obtained in 83% and 88% yields, respectively; and with $PtCl_2(PhCN)_2$ in refluxing PhCN, **YbPt** (**4**) was obtained in 60% yield. Complexes **1**–**4** are thermally and air-stable and can be purified by column chromatography. The four bisporphyrins were fully characterized by mass spectrometry, $^1H$ and $^{31}P$ (if applicable) NMR, and UV/Vis spectroscopy. The MALDI-TOF mass spectra of complexes **1**–**4** exhibit the $[M + 1]^+$ peaks at *m*/*z* = 1924.4353, 1988.3409, 2028.3187, and 2117.3801, respectively, which deviate less than 5 ppm from the theoretical values of 1924.4363, 1988.3490, 2028.3251, and 2117.3859, respectively, and their isotopic distribution patterns match

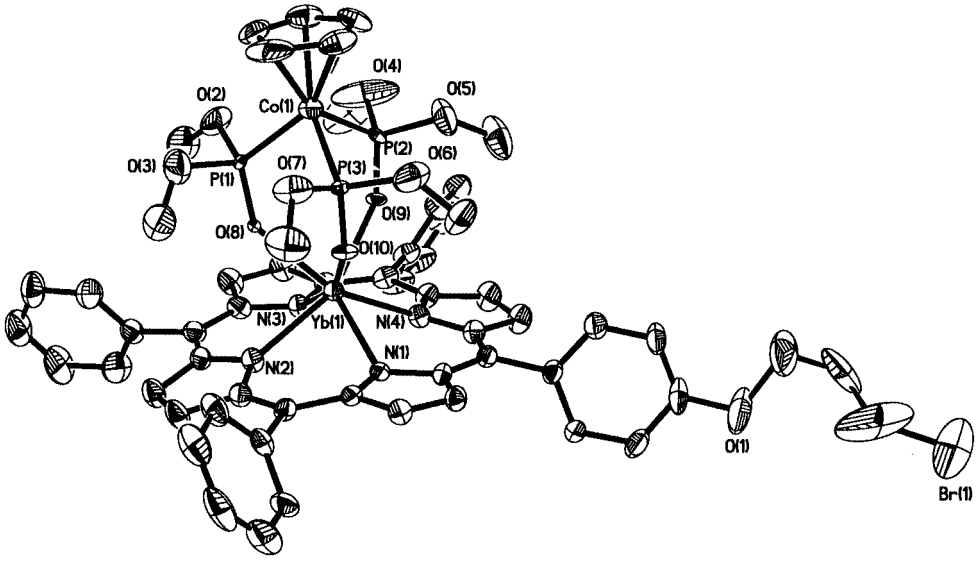


Figure 1. Perspective drawing of [Yb(*p*-$BrC_3O$-TPP)($L_{OMe}$)]. Hydrogen atoms were omitted for clarity. Selected bond lengths [Å] and bond angles [°]: N(1)–Yb(1) 2.367(5), N(2)–Yb(1) 2.350(6), N(3)–Yb(1) 2.343(6), N(4)–Yb(1) 2.350(5), O(8)–Yb(1) 2.260(7), O(9)–Yb(1) 2.280(7), O(10)–Yb(1) 2.281(7); O(8)–Yb(1)–O(9) 76.4(3), O(8)–Yb(1)–O(10) 78.9(3), O(9)–Yb(1)–O(10) 80.7(3), N(3)–Yb(1)–N(2) 77.99(19), N(3)–Yb(1)–N(4) 75.51(19), N(2)–Yb(1)–N(4) 122.5(2), N(3)–Yb(1)–N(1) 121.9(2), N(2)–Yb(1)–N(1) 76.17(18), N(4)–Yb(1)–N(1) 76.23(17).

 © 2007 Wiley-VCH Verlag GmbH & Co. KGaA, Weinheim 

the theoretical distribution. The $^1$H NMR spectrum (in $CDCl_3$) of **1** shows a singlet at $\delta$ = –2.64 ppm for the inner NH groups of the porphyrin free base moiety. This peak is absent in the $^1$H NMR spectra of dyads **2**–**4**, which indicates that the transition metals are coordinated to the four nitrogen atoms of the appended porphyrin free base. The $^1$H NMR spectra of the four dyads exhibit single peaks at $\delta$ = –4.52 ppm for the five cyclopentadienyl protons, quartets at $\delta \approx$ 3.34 ppm for the –$OCH_2CH_2CH_2O$– protons, and two triplets at $\delta \approx$ 5.20 and 5.64 ppm for the –$OCH_2CH_2CH_2O$– protons. The $^{31}P\{^1H\}$ NMR spectra (vs. 85% $H_3PO_4$) of **1**–**4** show single peaks at $\delta$ = 69.2, 69.2, 69.2, and 69.0 ppm, respectively, for the phosphito groups of the anionic $L_{OMe}^-$ ligand.

## Photophysical Properties

The photophysical properties of the four dyads **1**–**4** have been examined and the data are summarized in Table 1. The absorption spectrum of each of the four dyads **1**–**4** is the sum of the absorption spectra of the two separate porphyrinate moieties, [Yb(TPP)($L_{OMe}$)] and [M(TPP)] (M = $H_2$, Zn, Pd or Pt). Figure 2 shows the absorption spectra of [Yb(TPP)($L_{OMe}$)], [Pt(TPP)], and **4** (**YbPt**) in toluene at room temp. The room-temperature solution electronic absorption, excitation, and emission spectra of **1**–**4** in the UV/Vis region are characteristic of intraligand transitions of normal porphyrinate complexes. The absorption bands (Soret and Q bands) and emission peaks in the visible region are typical of the intraligand $\pi \rightarrow \pi^*$ transitions of the porphyrinato ligand. The visible emissions, which have a decay time ($\tau$) of about 3.79–9.17 ns and quantum yields ($\Phi_{em}$) of $(1.1–9.1) \times 10^{-2}$, can be assigned to the $S_1 \rightarrow S_0$ ligand-centered singlet ($^1$LC) fluorescence. The photoluminescence intensity of the four dyads strongly increases at 77 K and other than for **YbFb**, which exhibits no bathochromicity, the emission peaks of the dyads are redshifted by about 10 nm as compared with their emission bands at room temp. Lifetime measurements at 77 K showed that unlike dyads **YbFb** and **YbZn**, which exhibit only $^1$LC fluorescence at 652 ($\tau$ = 12.96 ns) and 611 ($\tau$ = 3.88 ns) nm, respectively, dyads **YbPd** and **YbPt** also exhibit phosphorescence at 693 ($\tau$ = 950 μs) and 660 ($\tau$ = 100 μs) nm, which almost coincides with the ligand-centered triplet ($^3$LC) emission of [Pd(TPP)] and [Pt(TPP)] complexes, respectively, and could be assigned to the $^3$LC emission of the [M(TPP)] moiety of the dyads. Figure 3 shows the solution excitation and emission spectra of dyad **YbPd** and the [Pd(TPP)] complex in the visible region at both room temp. and 77 K. The lowest $^3$LC state of the [Yb(TPP)($L_{OMe}$)] moiety of the dyads can be identified by measuring the emission spectrum and decay time of the [Gd(TPP)($L_{OMe}$)] complex.[18–21] This is possible because the metal-centered (MC) electronic levels of $Gd^{3+}$ are known to be located at 31000 $cm^{-1}$, typically well above the LC electronic levels of the aromatic ligands.[22] Therefore, ligand-to-metal energy transfer and the consequent MC luminescence cannot be observed. The time-resolved spectrum of the [Gd(TPP)($L_{OMe}$)] complex at 77 K shows that the LC long-lived phosphorescence is detected at 792 nm ($\tau$ = 136 μs).[23]

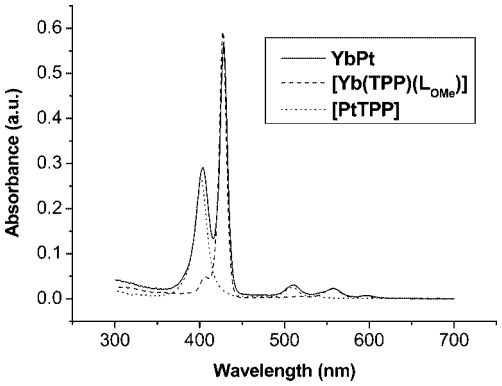


Figure 2. Absorption spectra of **YbPt**, [Yb(TPP)($L_{OMe}$)], and [Pt(TPP)].

Table 1. Photophysical data of **YbFb**, **YbZn**, **YbPd**, and **YbPt** in toluene.[a]

| Compound | Absorption $\lambda_{max}$ (log $\varepsilon$) [nm ($dm^3 mol^{-1} cm^{-1}$)] | Excitation $\lambda_{exc}$ [nm] | Emission at 298 K $\lambda_{em}$ [nm] ($\tau$, $\Phi_{em} \times 10^2$)[b–d] | Emission at 77 K $\lambda_{em}$ [nm] ($\tau$) |
|---|---|---|---|---|
| **YbFb** | 428 (5.86), 517 (4.34), 556 (4.48) 595 (4.06), 646 (3.71) | 419 | 652 (9.02 ns, 9.1), 717 998 (30 μs) | 652 (12.96 ns), 717 998 (30 μs) |
| **YbZn** | 427 (5.95), 557 (4.61), 595 (4.12) | 422 | 601, 651 (3.79 ns, 1.1) 998 (30 μs) | 611 (3.88 ns), 670 998 (30 μs) |
| **YbPd** | 428 (5.81), 524 (4.51), 557 (4.43) 596 (3.92) | 420 | 654 (9.17 ns, 1.6), 721 998 (40 μs) | 648, 693 (950 μs), 772 998 (40 μs) |
| **YbPt** | 403 (5.46), 428 (5.75), 511 (4.49) 558 (4.36), 596 (3.88) | 420 | 652 (8.72 ns, 2.0), 716 998 (30 μs) | 660 (100 μs), 726 998 (70 μs) |
| [Yb(TPP)($L_{OMe}$)] | 428 (5.79), 558 (4.40), 597 (3.85) | 419 | 652 (6.93 ns), 718 998 (30 μs) | 652 (9.15 ns), 718 998 (30 μs) |
| [Gd(TPP)($L_{OMe}$)] | 428 (5.86), 559 (4.35), 597 (3.76) | 420 | 656 (9.92 ns), 720 | 650 (12.71 ns), 792 (136 μs) |
| [Pd(TPP)] | 416, 524 | 420 | 610, 652, 715 | 698 (1340 μs) |
| [Pt(TPP)] | 402, 509, 540 | 403 | 662 | 660 (120 μs) |

[a] Measurements were carried out at a concentration of $1 \times 10^{-6}$ M in toluene. [b] The quantum yield standard used in this study was tetraphenylporphyrin ($H_2$TPP) in anhydrous benzene in air ($\Phi_F$ = 0.11 at 298 K). Quantum yields were calculated using standard methods. [c] Near-infrared (NIR) photoluminescence measurements were carried out in toluene at a concentration of $1 \times 10^{-6}$ M excited at 514 nm. [d] The wavelength of the laser for lifetime measurement was 337 nm.

 © 2007 Wiley-VCH Verlag GmbH & Co. KGaA, Weinheim 

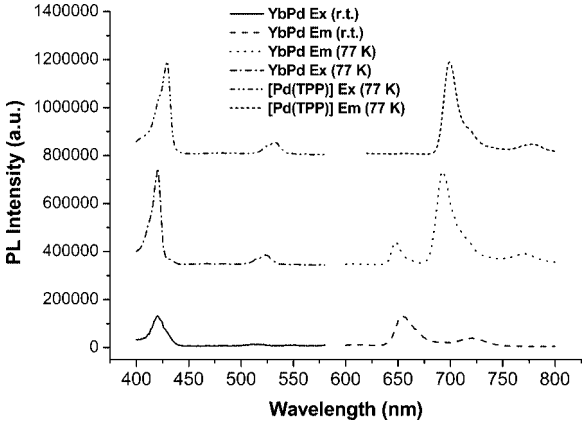


Figure 3. Excitation and emission spectra of **YbPd** and [Pd(TPP)] at 77 K and room temperature.

Other than the visible emission, dyads **1**–**4** also exhibit $Yb^{3+}$ ion emission in the NIR region. The emissions at 998 nm can be assigned to the $^2F_{5/2}\rightarrow{}^2F_{7/2}$ transition of $Yb^{3+}$. These NIR emissions are very similar to those reported for $Yb^{III}$ monoporphyrinate complexes, and the lifetime values are in good agreement with the literature values.[24,25] The $Yb^{3+}$ luminescence lifetimes at room temp. lie within 30–40 μs for the four dyads and are much longer than the lifetime of the porphyrinate emission. Figure 4 shows the visible and NIR emission and the excitation spectra of **YbPd** in toluene. The excitation spectrum of **YbPd** monitored at 998 nm is identical to that monitored at 654 nm, and its excitation bands at 526, 560, and 602 nm almost coincide with its visible absorption bands at 524, 557, and 596 nm. This clearly shows that both the visible and NIR emissions originate from the $\pi\rightarrow\pi^*$ transitions of the porphyrinate antenna, and excitation of porphyrin is the photophysical pathway leading to the observable NIR luminescence. A comparison of the NIR luminescence intensity of the dyads with that of the [Yb(TPP)($L_{OMe}$)] complex at room temp. shows that the relative intensity increases in the order of [Yb(TPP)($L_{OMe}$)] (1.0) < **YbZn** (1.8) < **YbPd** (4.0) < **YbPt** (5.0) (Figure 5). This suggests that

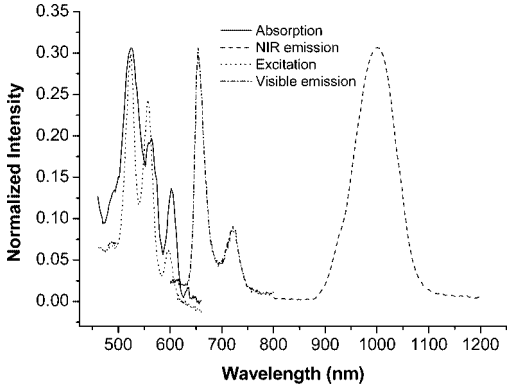


Figure 4. Room-temperature absorption, NIR emission (excited at 514 nm) and excitation (monitored at 998 nm) spectra of **YbPd** in toluene.

the [M(TPP)] (M = Zn, Pd and Pt) moiety, which contributes to the enhancement of NIR emission, transfers its energy to the $Yb^{3+}$ ion. Fluorescence studies at room temp. further support the above donor-acceptor-based hypothesis. The visible fluorescence intensity of the **YbPd** dyad is much weaker than that of the [Pd(TPP)] complex (Figure 6). This indicates that the [Pd(TPP)] moiety (donor) of the **YbPd** dyad is quenched by the [Yb(TPP)($L_{OMe}$)] moiety, probably by the transfer of the $^1$LC energy to the $Yb^{3+}$ ion center (acceptor).

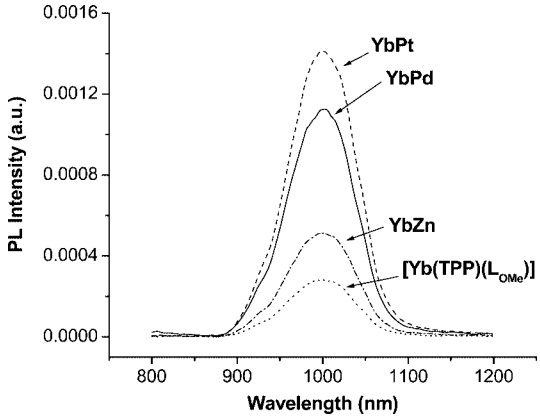


Figure 5. Near-infrared photoluminescence spectra excited at 514 nm at the same concentration in toluene.

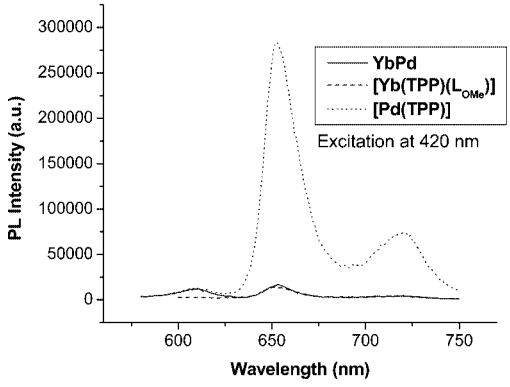


Figure 6. Emission spectra of **YbPd**, [Yb(TPP)($L_{OMe}$)], and [Pd(TPP)] at the same concentration at room temperature.

Optical absorption of the $^1$M(TPP) unit leads to an $S_0\rightarrow S_1$ transition to the singlet excited state $^1$M(TPP)*, followed by a fluorescent emission or intersystem crossing to the triplet excited state $^3$M(TPP)*, which results in the phosphorescent emission and nonradiative deactivation with rate constants $k_r$ and $k_{nr}$, respectively. The energy of the $^3$M(TPP)* excited state can be transferred to $(Yb^{3+})$* with rate constant $k_{ET}$ so that the $Yb^{III}$ NIR emission is enhanced and the lifetime extended (Figure 7). At 77 K, the $Yb^{3+}$ luminescence lifetime of dyads **YbFb** and **YbZn** remains unchanged (30 μs) and is the same as that of [Yb(TPP)($L_{OMe}$)], whereas that of **YbPd** and **YbPt** is extended from 30 to 40 and 70 μs, respectively. This may be

 © 2007 Wiley-VCH Verlag GmbH & Co. KGaA, Weinheim 

due to the presence of a very intense, long-lived $^3$M(TPP)* state in **YbPd** ($\lambda$ = 693 nm, $\tau$ = 950 μs) and **YbPt** ($\lambda$ = 660 nm, $\tau$ = 100 μs), which sensitizes and prolongs the lifetime of the $Yb^{3+}$ luminescence. Such a long-lived $^3$M(TPP)* state is absent in **YbFb** and **YbZn**. The better extension of the $Yb^{III}$ lifetime of **YbPt** than **YbPd** clearly shows that the efficiency of energy transfer by the triplet excited state is better in the former than in the latter.

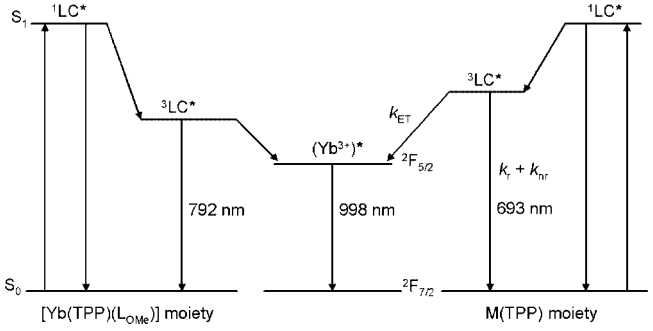


Figure 7. Scheme for the energy transfer from the transition-metal porphyrin unit {[Pd(TPP)] for example} to the Yb porphyrin unit (LC = ligand center). $k_{ET}$ is the rate constant for energy transfer; $k_r$ is the rate constant for radiative deactivation; $k_{nr}$ is the rate constant for nonradiative deactivation. $k_r + k_{nr} = \tau_0^{-1}$ and $k_r + k_{nr} + k_{ET} = \tau^{-1}$.

$H_2$TPP and [Zn(TPP)] are strongly fluorescent while [Pd(TPP)] and [Pt(TPP)] are strongly phosphorescent.[26] Brookfield et al.[27] investigated the energy transfer in Zn-metal-free porphyrin dimers and found that the Zn porphyrin unit transfers singlet-state excitation energy to the free-base porphyrin unit. For the bisporphyrins here, dipole–dipole energy transfer is the dominant mechanism. Here, the $Yb^{III}$ ion is sensitized by two species: one is the porphyrin chromophore, which is coordinated to it; the other is the triplet excited state of the transition-metal porphyrinate unit, which enhances its NIR luminescence. Because the lifetimes of **YbPd** at 693 nm and **YbPt** at 660 nm at 77 K are mainly contributed by the triplet excited state $^3$M(TPP)* lifetimes of the [Pd(TPP)] and [Pt(TPP)] moiety, respectively, the rate constants for the energy transfer from the [M(TPP)] chromophores to the $Yb^{3+}$ ion, $k_{ET}$, can be calculated from Equation (1), where $\tau$ and $\tau_0$ are the lifetimes of the donor-acceptor dyad (**YbPd** and **YbPt**) and the donor chromophore [M(TPP)] (M = Pd and Pt), respectively.

$$k_{ET} = \left(\frac{1}{\tau} - \frac{1}{\tau_0}\right) \quad (1)$$

As a result, $k_{ET}$ for **YbPd** and **YbPt** is 306 and 1667 $s^{-1}$, respectively. Comparing the $k_{ET}$ values, triplet excited state energy transfer of **YbPt** is much faster than that of **YbPd**.

## Two-Photon Absorption

Porphyrin derivatives have attracted increasing attention because of their two-photon absorption (TPA) properties, which could be applied in many research fields, such as 3D microfabrication,[28] photodynamic therapy[29] and optical limiting.[30] The TPA efficacy, which is evaluated by the TPA cross-section value, $\sigma^{(2)}$, is defined as the excitation obtained by the simultaneous absorption of two photons at a longer wavelength followed by the emission at a shorter wavelength (Figure 8). Because of the low quantum yield of porphyrin, the nonlinear transmittance method was used to determine $\sigma^{(2)}$. In this paper, $\sigma^{(2)}$ was measured at 800 nm with 100-fs pulses by an open-aperture *Z*-scan method. Porphyrin is supposed to be excited to the singlet excited state by simultaneously absorbing two photons at 800 nm. It can then emit photons at 650 nm or relax to the triplet excited state through intersystem crossing; thereafter energy could

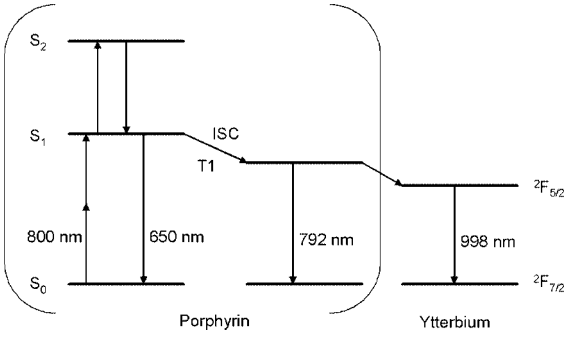


Figure 8. Scheme for the two-photon absorption of Yb porphyrinate complexes.

Table 2. TPA cross-section $\sigma^{(2)}$ (GM) values.[a]

| Compound | Concentration [mol $L^{-1}$] | $\beta$ [cm $GW^{-1}$] | Cross section $\sigma$[b] [GM] |
|---|---|---|---|
| YbFb | $2.5 \times 10^{-4}$ | 0.00061 | 101 |
| YbZn | $2.5 \times 10^{-4}$ | too weak | too weak |
| YbPd | $2.5 \times 10^{-4}$ | 0.00088 | 145 |
| YbPt | $2.5 \times 10^{-4}$ | 0.00147 | 247 |
| [Yb(TPP)($L_{OMe}$)] | $2.5 \times 10^{-4}$ | too weak | too weak |
| $H_2$TPP | $1 \times 10^{-3}$ | 0.00068 | 28 |
| [Zn(TPP)] | $1 \times 10^{-3}$ | 0.00036 | 15 |
| [Pd(TPP)] | $1 \times 10^{-3}$ | 0.00060 | 25 |
| [Pt(TPP)] | $1 \times 10^{-3}$ | 0.00067 | 28 |

[a] The TPA measurements were carried out at an excitation wavelength of 800 nm. [b] 1 GM = $10^{-50}$ $cm^4 \cdot s$ $photon^{-1}$.

 © 2007 Wiley-VCH Verlag GmbH & Co. KGaA, Weinheim 

be transferred to the $Yb^{III}$ ion, which emits at 998 nm. While the $\sigma^{(2)}$ value is wavelength-dependent, it is 28 GM for $H_2TPP$ at 800 nm in this work (cf. the reported value of 15 GM at 780 nm).[31] [Yb(TPP)($L_{OMe}$)] has a very low $\sigma^{(2)}$ value, whereas the dyads **YbFb**, **YbPd**, and **YbPt** have four to eight times larger $\sigma^{(2)}$ values than the corresponding transition-metal porphyrin [M(TPP)] monomers (Table 2).

### Optical Limiting Properties

Optical limiters are typically those dyes with nonlinear optical properties in which the light transmittance will decrease sharply under high light flux so that they can protect sensors from high optical power. Optical limiting (OL) effect can be explained by a mechanism known as reverse saturable absorption (RSA)[32] (see Supporting Information). Until now, indium tetra-*tert*-butylphthalocyanine chloride (InClPc) has been considered to be one of the best optical limiters.[33] Among many different kinds of OL materials, porphyrins continue to attract considerable attention because the structure-property relationships can be investigated easily through structural modification by changing the central metal center, ligand substituents etc. In general, porphyrins exhibit strong excited-state absorptions and long-lived triplet excited states.[30] In addition, they allow high transmission in the visible region because their ground-state absorptions are mainly confined to a few narrow regions (Soret and Q bands). Recently, the optical limiting properties of metalloporphyrins have been examined.[34] Herein, we studied the OL effect of our porphyrin dyads with the *Z*-scan technique[35] at 532 nm. The transmittances for **YbPd**, **YbZn**, **YbPt**, and [Yb(TPP)($L_{OMe}$)] decrease to 55%, 54%, 44%, and 40%, respectively, of their original linear transmission (Figure 9). The OL performance of [Yb(TPP)($L_{OMe}$)] and **4** is comparable to the benchmark material $C_{60}$.

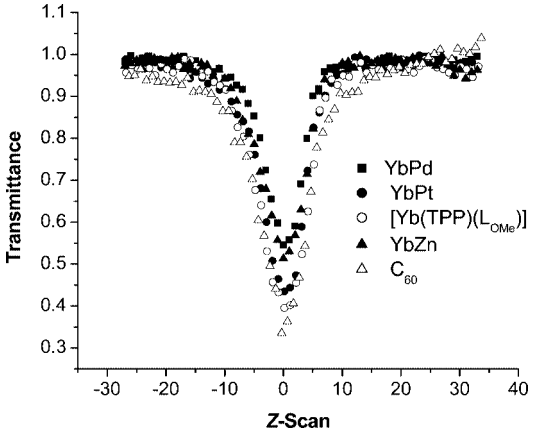


Figure 9. Open-aperture *Z*-scans at 532 nm for optical limiting measurements at a linear transmittance of 85%.

## Conclusions

We have prepared and characterized a series of d-f heterodimetallic bisporphyrin complexes, in which a $Yb^{III}$ porphyrinate moiety was linked to a transition-metal porphyrinate moiety by a flexible three-carbon chain. Upon excitation at 514 nm, the four dyads gave NIR emission centered at 998 nm, with the emission intensity increasing in the order of **YbZn** < **YbPd** < **YbPt**. Photophysical studies showed that the transition-metal porphyrinate moiety sensitized NIR emission and enhanced the $Yb^{III}$ emission intensity and lifetime. Two-photon absorption (TPA) measurements at 800 nm showed that, except for **YbZn**, the bisporphyrins had much larger TPA cross-section values, $\sigma^{(2)}$, than those of [Yb(TPP)($L_{OMe}$)] and [M(TPP)] (M = $H_2$, Zn, Pd, and Pt) complexes. The optical limiting (OP) measurements at 532 nm showed that the OL property was enhanced in the order of **YbPd** < **YbZn** < **YbPt** < [Yb(TPP)($L_{OMe}$)], and the OL performance of [Yb(TPP)($L_{OMe}$)] and **YbPt** is comparable to that of $C_{60}$.

## Experimental Section

**General:** All reactions were carried out in dry nitrogen. Solvents were dried by standard procedures, distilled, and deaerated prior to use. All chemicals used were obtained from Aldrich Chemical Company. $PtCl_2(PhCN)_2$,[36] $Yb[N(SiMe_3)_2]_3$·[$LiCl(THF)_3$]$_x$,[14d] and [Yb(TPP)($L_{OMe}$)][14c] were prepared according to literature methods. Electronic absorption spectra in the UV/Vis region were recorded with a Varian Cary 100 UV/Vis spectrophotometer, steady-state visible fluorescence and PL excitation spectra were recorded with a Photon Technology International (PTI) Alphascan spectrofluorimeter, and visible decay spectra with a pico-$N_2$ laser system (PTI TimeMaster) using $\lambda_{exc}$ = 337 nm. NIR emission was detected by a liquid-nitrogen-cooled InSb IR detector (EG & G) with a preamplifier and recorded by a lock-in amplifier system as the third harmonics. Quantum yields of the visible emissions were computed according to the literature method[37] using tetraphenylporphyrin ($H_2TPP$) as the reference standard ($\Phi$ = 0.11 at 419 nm in benzene in air). NMR spectra were recorded with a Varian Unity Inova 400 MHz spectrometer. $^1H$ NMR chemical shifts were referenced to internal deuteriated chloroform and then recalculated to TMS ($\delta$ = 0.00 ppm) and those from the $^{31}P\{^1H\}$ NMR spectra to external 85% $H_3PO_4$. High- and low-resolution mass spectra, reported as *m*/*z*, were obtained with an Autoflex Bruker MALDI-TOF system and a Finnigan MAT SSQ710 mass spectrometer, respectively. Elemental analyses carried out at the Department of Chemistry, Shanxi University, P. R. China.

**Two-Photon Absorption Measurement:** The two-photon absorption spectra were measured at 800 nm by using the open-aperture *Z*-scan method with 100-fs pulses with a peak power of 276 GW cm$^{-2}$ from an optical parametric amplifier operating at a 1-kHz repetition rate generated from a Ti:sapphire regenerative amplifier system. The laser beam was split into two parts by a beam splitter. One was monitored by a photodiode (D1) as the incident intensity reference, and the other (D2) was detected for the transmitted intensity. After passing through a lens with *f* = 20 cm, the laser beam was focused and passed through a quartz cell. The position of the sample cell was moved along the laser-beam direction (*z* axis) by a computer-controlled translatable table, so the local power density within the sample cell would be changed under the constant incident intensity laser power level. Finally, the transmitted intensity from the sample cell was detected by the photodiode (D2). The photodiode (D2) was connected to the computer, so each transmitted intensity would be taken over 100 times iteration by the

 © 2007 Wiley-VCH Verlag GmbH & Co. KGaA, Weinheim 

computer. Assuming a Gaussian beam profile, the nonlinear absorption coefficient $\beta$ can be obtained by curve fitting to the observed open-aperture traces with Equation (2), where $\alpha_0$ is the linear absorption coefficient, $l$ is the sample length, and $z_0$ is the diffraction length of the incident beam.

$$T(z) = 1 - \frac{\beta I_0 (1 - e^{-\alpha_0 l})}{2a_0(1 + (z/z_0)^2)} \quad (2)$$

After obtaining the nonlinear absorption coefficient $\beta$, the TPA cross-section $\sigma^{(2)}$ of one solute molecule (in units of 1 GM = $10^{-50}$ cm$^4$ s photon$^{-1}$) can be determined by using Equation (3), where $N_A$ is the Avogadro constant, $d$ is the concentration of the TPA compound in solution, $h$ is the Planck constant, and $v$ is the frequency of the incident laser beam.

$$\sigma^{(2)} = \frac{1000\beta h v}{N_A d} \quad (3)$$

**Optical Limiting Measurement:** The investigation of optical limiting properties was performed with a Q-switched Nd:YAG laser at the repetition of 10 Hz. The arrangement of the system is shown in the Supporting Information. The laser was frequency-doubled with an output wavelength of 532 nm with 10-ns pulse width for Gaussian mode by a frequency double crystal (FDC). Then the laser beam was split into two beams by a beam splitter (BS). One was used as the reference beam, which was received by a detector ($D_1$), and the other was for the sample measurement and was focused with a lens ($L_1$, $f$ = 20 cm). After transmitting the light beam through the sample (S), it entered another detector ($D_2$). The sample to be measured was moved along a rail to change the incidence irradiance on it. The incident and transmitted energies were detected simultaneously by the two detectors $D_1$ and $D_2$ (LPE-1A) individually. The solution samples were measured in a 1-mm quartz cell.

**Preparation of Porphyrin Free Bases**

**5-(*p*-Hydroxyphenyl)-10,15,20-triphenylporphyrin (*p*-OH-TPPH$_2$):** This compound was prepared according to a modified literature method.[14b] A solution of benzaldehyde (18.29 mL, 180 mmol) and *p*-hydroxybenzaldehyde (7.32 g, 60 mmol) in propionic acid (700 mL) was heated to 130 °C. Then freshly distilled pyrrole (16.65 mL, 240 mmol) in propionic acid (50 mL) was added slowly to the solution over a period of 0.5 h. The reaction mixture was heated to reflux for another 0.5 h and then cooled to room temp. Then the volume of the reaction mixture was reduced to about half of its original volume under reduced pressure, and methanol (300 mL) was added to the concentrated solution. The resultant solution was kept in a refrigerator overnight. Filtration gave about 4.5 g of crude product, which was redissolved in a minimum amount of chloroform and chromatographed on a silica gel column with dichloromethane as eluent. The second band gave the desired *p*-OH-TPPH$_2$. Yield: 1.9 g (5%). FAB-MS: 631 [M + H]$^+$. $^1$H NMR ($CDCl_3$): $\delta$ = –2.78 (s, 2 H), 4.14 (s, 1 H), 7.19 (m, 2 H), 7.74 (m, 9 H), 8.05 (m, 2 H), 8.21 (m, 6 H), 8.85 (m, 8 H) ppm. UV/Vis (toluene): $\lambda_{max}$ (log $\varepsilon$) = 419 (5.48), 515 (4.20), 550 (3.88), 592 (3.64), 651 (3.71 dm$^3$ mol$^{-1}$ cm$^{-1}$) nm.

**5-[*p*-(3-Bromopropoxy)phenyl]-10,15,20-triphenylporphyrin (*p*-BrC$_3$O-TPPH$_2$):** This compound was prepared according to a modified literature method.[14b] 1,3-Dibromopropane (2 mL, 800 μL, 7.9 mmol) was added to a suspension of *p*-OH-TPPH$_2$ (0.50 g, 0.8 mmol) and anhydrous $K_2CO_3$ in dry DMF (20 mL). The mixture was stirred at room temp., and the progress of the reaction was monitored by TLC. After 24 h, dichloromethane (20 mL) was added to the reaction mixture, which was then washed with water (6 × 20 mL) until all of the DMF and potassium carbonate were removed. The organic phase was dried with sodium sulfate, filtered and the solvents were evaporated to dryness in vacuo. The residue was redissolved in a chloroform/hexane mixture (1:1, v/v) and chromatographed on a silica gel column using chloroform/hexane (5:1, v/v) as eluent. The first band gave the product *p*-BrC$_3$O-TPPH$_2$. Yield: 560 mg (94%). FAB-MS: 752 [M + H]$^+$. $^1$H NMR ($CDCl_3$): $\delta$ = –2.77 (s, 2 H), 2.50 (m, 2 H), 3.77 (q, 2 H), 4.38 (q, 2 H), 7.28 (m, 2 H), 7.74 (m, 9 H), 8.12 (m, 2 H), 8.21 (m, 6 H), 8.86 (m, 8 H) ppm. UV/Vis (toluene): $\lambda_{max}$ (log $\varepsilon$) = 420 (5.43), 515 (4.07), 550 (3.74), 594 (3.50), 650 (3.44 dm$^3$ mol$^{-1}$ cm$^{-1}$) nm.

**Preparation of Yb Porphyrinate Complexes**

**[Yb(*p*-OH-TPP)(L$_{OMe}$)]:** This compound was prepared according to a modification of the literature method.[14c] After *p*-OH-TPPH$_2$ (518 mg, 0.82 mmol) had been treated with excess Yb[N(SiMe$_3$)$_2$]$_3$·[LiCl(THF)$_3$]$_x$ (0.16 mol L$^{-1}$, 10 mL) under nitrogen in refluxing toluene for 12 h, the mixture was cooled down to room temp., followed by the addition of excess NaL$_{OMe}$. The reaction mixture was concentrated under reduced pressure to remove toluene and purified by column chromatography on silica to give purple crystals of [Yb(*p*-OH-TPP)(L$_{OMe}$)] after recrystallization. Yield: 863 mg (84%). MALDI-TOF MS: calcd. for [M$^+$] 1253.1549, found 1253.1516. $^1$H NMR ($CDCl_3$): $\delta$ = –4.62 (s, 5 H), 6.98 (s, 18 H), 8.13 (s, 1 H), 8.57–8.76 (br., 8 H), 9.36–9.42 (br., 3 H), 9.93 (br., 1 H), 10.56 (br., 3 H), 15.29 (br., 8 H), 16.56 (br., 1 H), 16.85 (br., 3 H) ppm. $^{31}$P{$^1$H} NMR ($CDCl_3$): $\delta$ = 69.2 ppm. UV/Vis (toluene): $\lambda_{max}$ (log $\varepsilon$) = 429 (5.80), 558 (4.37), 599 (3.82 dm$^3$ mol$^{-1}$ cm$^{-1}$) nm.

**[Yb(*p*-BrC$_3$O-TPP)(L$_{OMe}$)]:** [Yb(*p*-OH-TPP)(L$_{OMe}$)] (100 mg, 0.08 mmol) was stirred in dry DMF (10 mL) in the presence of anhydrous potassium carbonate (300 mg) for 20 min, followed by addition of 10 equiv. of 1,3-dibromopropane. The reaction mixture was stirred overnight, and dichloromethane (20 mL) was then added. The mixture was washed with deionized water (3 × 20 mL) until all the DMF was washed away. The solution was dried with anhydrous sodium sulfate, and the residue upon concentration was purified by column chromatography on silica with dichloromethane as eluent. The first band gave [Yb(*p*-BrC$_3$O-TPP)(L$_{OMe}$)]. Yield: 90 mg (82%). MALDI-TOF MS: calcd. for [M + H]$^+$ 1374.1178, found 1374.1234. $^1$H NMR ($CDCl_3$): $\delta$ = –4.54 (s, 5 H), 3.25 (q, 2 H), 4.53 (t, 2 H), 5.38 (t, 2 H), 6.62 (s, 18 H), 8.38 (br., 1 H), 8.90–9.02 (br., 7 H), 9.64 (m, 3 H), 10.24 (br., 1 H), 10.80 (br., 3 H), 15.62 (br., 8 H), 16.87–17.18 (br., 4 H) ppm. $^{31}$P{$^1$H} NMR ($CDCl_3$): $\delta$ = 68.2 ppm. UV/Vis (toluene): $\lambda_{max}$ (log $\varepsilon$) = 429 (5.68), 558 (4.26), 598 (3.77 dm$^3$ mol$^{-1}$ cm$^{-1}$) nm.

**Preparation of Yb Bisporphyrin Complexes**

**YbFb:** *p*-BrC$_3$O-TPPH$_2$ (200 mg, 0.27 mmol) was added to a suspension of [Yb(*p*-OH-TPP)(L$_{OMe}$)] (358 mg, 0.29 mmol) in dry DMF (10 mL) in the presence of anhydrous potassium carbonate. The resultant mixture was stirred at 60 °C overnight and cooled to room temp. Dichloromethane (10 mL) was added to the reaction mixture, which was then washed with water (6 × 10 mL) until all of the DMF and potassium carbonate was removed. The organic phase was dried with sodium sulfate, filtered, and the solvents were evaporated to dryness in vacuo. The residue was redissolved in chloroform/hexane (1:1, v/v) and chromatographed on a silica gel column using chloroform/hexane (5:1, v/v) as eluent to give **YbFb** from the first band. Yield: 318 mg (58%). MALDI-TOF MS: calcd. for [M + H]$^+$ 1924.4363, found 1924.4353. IR (KBr): $\tilde{\nu}$ = 3446 (s),

 © 2007 Wiley-VCH Verlag GmbH & Co. KGaA, Weinheim 

2939 (w), 1701 (w), 1652 (w), 1600 (w), 1511 (m), 1472 (m), 1438 (w), 1240 (m), 1175 (m), 1141 (s), 1035 (m), 1007 (m), 799 (s), 775 (m), 727 (s), 702 (m), 620 (w), 587 (m) $cm^{-1}$. $^1H$ NMR ($CDCl_3$): $\delta$ = –4.52 (s, 5 H), –2.64 (s, 2 H), 3.34 (q, 2 H), 5.20 (t, 2 H), 5.64 (t, 2 H), 6.34 (s, 18 H), 7.20–7.83 (m, 11 H), 8.24–8.30 (m, 6 H), 8.47 (d, 2 H), 8.65–8.73 (br., 8 H), 8.89 (s, 4 H), 9.00 (d, 2 H), 9.19 (d, 2 H), 9.36 (br., 3 H), 10.15 (br., 1 H), 10.52 (br., 3 H), 15.22 (br., 8 H), 16.60–16.78 (br., 4 H) ppm. $^{31}P\{^1H\}$ NMR ($CDCl_3$): $\delta$ = 69.2 ppm. **YbFb** could also be prepared by the reaction of [Yb(*p*-$BrC_3O$-TPP)($L_{OMe}$)] with *p*-OH-$TPPH_2$. [Yb(*p*-$BrC_3O$-TPP)($L_{OMe}$)] (100 mg, 0.073 mmol) was added to a suspension of *p*-OH-$TPPH_2$ (70 mg, 0.11 mmol) in dry DMF (10 mL) in the presence of anhydrous potassium carbonate (300 mg). Then the resultant mixture was stirred at 60 °C overnight and cooled to room temp. Dichloromethane (10 mL) was added to the reaction mixture, which was then washed with water (6 × 10 mL) until all of the DMF and potassium carbonate were removed. The organic phase was dried with sodium sulfate, filtered, and the solvents were evaporated to dryness in vacuo. The residue was redissolved in chloroform/hexane (1:1, v/v) and chromatographed on a silica gel column using chloroform/hexane (5:1, v/v) as eluent to give **YbFb** from the first band. Yield: 84 mg (60%). $C_{102}H_{85}CoN_8O_{11}P_3Yb{\cdot}CHCl_3{\cdot}1.5C_7H_8{\cdot}2H_2O$ (2217.32): calcd. C 61.48, H 4.64, N 5.05; found C 61.55, H 4.59, N 4.96.

**YbZn and YbPd: YbFb** (100 mg, 0.052 mmol) was treated with $Zn(OAc)_2$ hydrate (300 mg, 1.37 mmol) or $Pd(OAc)_2$ hydrate (550 mg, 2.45 mmol) in a refluxing solution mixture of chloroform/methanol (1:1, v/v) (20 mL) for 24 h. Then chloroform and methanol were removed in a rotary evaporator. The resulting solid was dissolved in chloroform and chromatographed on a silica gel column using chloroform/hexane (5:1, v/v) as eluent. The second band gave **YbZn** (86 mg, 83%) or **YbPd** (93 mg, 88%) in good yields. **YbZn:** MALDI-TOF MS: calcd. for $[M + H]^+$ 1988.3490, found 1988.3409. IR (KBr): $\tilde{\nu}$ = 3449 (s), 2939 (w), 1711 (s), 1600 (w), 1513 (m), 1480 (m), 1436 (w), 1359 (m), 1333 (w), 1225 (m), 1174 (w), 1140 (s), 1097 (w), 1064 (w), 1034 (m), 997 (s), 837 (w), 797 (m), 752 (m), 725 (m), 702 (m), 654 (w), 620 (w), 588 (w), 531 (w) $cm^{-1}$. $^1H$ NMR ($CDCl_3$): $\delta$ = –4.54 (s, 5 H), 3.34 (q, 2 H), 5.21 (t, 3 H), 5.62 (t, 3 H), 6.33 (s, 18 H), 7.76–7.83 (m, 11 H), 8.24–8.31 (m, 6 H), 8.48 (d, 2 H), 8.65–8.73 (br., 8 H), 8.98 (s, 4 H), 9.11 (d, 2 H), 9.30 (d, 2 H), 8.34–8.39 (br., 3 H), 10.13 (br., 1 H), 10.51 (br., 3 H), 15.23 (br., 8 H), 16.78 (br., 4 H) ppm. $^{31}P\{^1H\}$ NMR ($CDCl_3$): $\delta$ = 69.2 ppm. $C_{102}H_{83}CoN_8O_{11}P_3YbZn{\cdot}CHCl_3{\cdot}1.5C_7H_8{\cdot}H_2O$ (2262.68): calcd. C 60.25, H 4.36, N 4.95; found C 60.30, H 4.41, N 4.93. **YbPd:** MALDI-TOF MS: calcd. for $[M + H]^+$ 2028.3251, found 2028.3187. IR (KBr): $\tilde{\nu}$ = 3445 (s), 2939 (w), 1710 (s), 1599 (m), 1510 (m), 1474 (m), 1440 (m), 1354 (m), 1238 (m), 1140 (s), 1009 (s), 798 (m), 752 (m), 725 (m), 704 (m), 587 (m) $cm^{-1}$. $^1H$ NMR ($CDCl_3$): $\delta$ = –4.54 (s, 5 H), 3.30 (q, 2 H), 5.14 (t, 2 H), 5.60 (t, 2 H), 6.34 (s, 18 H), 7.77 (m, 11 H), 8.23 (m, 6 H), 8.40 (d, 2 H), 8.73 (br., 8 H), 8.87 (s, 4 H), 8.97 (d, 2 H), 9.15 (d, 2 H), 9.37 (br., 3 H), 10.12 (br., 1 H), 10.52 (br., 3 H), 15.24 (br., 8 H), 16.79 (br., 4 H) ppm. $^{31}P\{^1H\}$ NMR ($CDCl_3$): $\delta$ = 69.2 ppm. $C_{102}H_{83}CoN_8O_{11}P_3PdYb{\cdot}CHCl_3{\cdot}C_7H_8{\cdot}H_2O$ (2257.64): calcd. C 58.52, H 4.20, N 4.96; found C 58.51, H 4.18, N 4.88.

**YbPt:** After **YbFb** (100 mg, 0.052 mmol) had been treated with $PtCl_2(PhCN)_2$ (125 mg, 0.26 mmol) in refluxing benzonitrile (5 mL) for 24 h, the solvent was removed under reduced pressure. The resulting solid was dissolved in a minimum amount of dichloromethane and chromatographed on a silica gel column using dichloromethane as eluent. The second band gave **YbPt** in 60% yield (66 mg). MALDI-TOF MS: calcd. for $[M + H]^+$ 2117.3859, found 2117.3801. IR (KBr): $\tilde{\nu}$ = 3434 (s), 2925 (m), 1602 (m), 1510 (w), 1444 (w), 1359 (w), 1325 (w), 1240 (m), 1175 (m), 1142 (s), 1014 (s), 796 (m), 753 (m), 726 (m), 704 (m), 588 (m) $cm^{-1}$. $^1H$ NMR ($CDCl_3$): $\delta$ = –4.53 (s, 5 H), 3.36 (q, 2 H), 5.22 (t, 2 H), 5.67 (t, 2 H), 6.35 (s, 18 H), 7.74–7.82 (m, 11 H), 8.21 (m, 6 H), 8.41 (d, 2 H), 8.55–8.75 (br., 8 H), 8.80 (s, 4 H), 8.91 (d, 2 H), 9.10 (d, 2 H), 9.38 (br., 3 H), 10.14 (br., 1 H), 10.52 (br., 3 H), 15.25 (br., 8 H), 16.81 (br., 4 H) ppm. $^{31}P\{^1H\}$ NMR ($CDCl_3$): $\delta$ = 69.0 ppm. $C_{102}H_{83}CoN_8O_{11}P_3PtYb{\cdot}CHCl_3{\cdot}1.5C_7H_8$ (2374.36): calcd. C 57.41, H 4.08, N 4.72; found C 57.57, H 4.02, N 5.08.

**X-ray Crystallography:** Pertinent crystallographic data and other experimental details are summarized in Table 3. Crystals of [Yb(*p*-$BrC_3O$-TPP)($L_{OMe}$)]·$2CHCl_3$ suitable for X-ray diffraction studies were grown by slow concentration of a chloroform/methanol solution of the complex in air. The crystals were wrapped in epoxy glue to prevent them from losing solvent, and mounted on a thin glass fiber. Intensity data were collected at 293 K with a Bruker Axs SMART 100 CCD area-detector diffractometer using graphite-monochromated Mo-$K_\alpha$ radiation ($\lambda$ = 0.71073 Å). The collected frames were processed with the software SAINT,[38] and an absorption correction was applied (SADABS)[39] to the collected reflections. The space group of the crystal was determined from the systematic absences and Laue symmetry checks and confirmed by successful refinement of the structure. The structure was solved by direct methods (SHELXTL)[40] and refined against $F^2$ by full-matrix least-squares analyses. All non-hydrogen atoms were refined anisotropically. Hydrogen atoms were generated in their idealized positions and allowed to ride on their respective parent carbon atoms. CCDC-635196 contains the supplementary crystallographic data for this paper. These data can be obtained free of charge from The Cambridge Crystallographic Data Centre via www.ccdc.cam.ac.uk/data_request/cif.

Table 3. Crystallographic data for [Yb(*p*-$BrC_3O$-TPP)($L_{OMe}$)]·$2CHCl_3$.

| | |
|---|---|
| Empirical formula | $C_{60}H_{58}BrCl_6CoN_4O_{10}P_3Yb$ |
| Formula mass | 1612.59 |
| Color and habit | purple block |
| Crystal size [mm] | 0.30 × 0.25 × 0.21 |
| Crystal system | monoclinic |
| Space group | $P2_1/c$ |
| $a$ [Å] | 13.2139(6) |
| $b$ [Å] | 43.627(2) |
| $c$ [Å] | 12.3255(6) |
| $\alpha$ [°] | 90 |
| $\beta$ [°] | 109.3310(10) |
| $\gamma$ [°] | 90 |
| $V$ [Å$^3$] | 6704.9(6) |
| $Z$ | 4 |
| $D_{calcd.}$ [g cm$^{-3}$] | 1.598 |
| Absorption coefficient [mm$^{-1}$] | 2.597 |
| $F(000)$ | 3220 |
| $\theta$ range [°] | 1.87–25.00 |
| Reflections collected | 32118 |
| Independent reflections | 11531 ($R_{int}$ = 0.0429) |
| Observed reflections [$I > 2.0\sigma(I)$] | 8698 |
| Goodness of fit on $F^2$ | 1.098 |
| Final $R$ indices [$I > 2\sigma(I)$] | $R_1$ = 0.0785, $wR_2$ = 0.1807 |
| $R$ indices (all data) | $R_1$ = 0.1063, $wR_2$ = 0.1955 |

**Supporting Information** (see footnote on the first page of this article): $^1H$ NMR and COSY spectra of [Yb(TPP)($L_{OMe}$)], the optical limiting (OL) mechanism and experimental setup for OL.

 © 2007 Wiley-VCH Verlag GmbH & Co. KGaA, Weinheim 

## Acknowledgments

We thank the Hong Kong Baptist University (Grant FRG/03-04/II-05), the Hong Kong Research Grants Council (Grant HKBU 2023/04P), the National Natural Science Foundation of China (30570015), and the Science Fund for Creative Research Group (No. 20621502 NSFC) for financial support.

[1] a) N. E. Kagan, D. Mauzerall, R. B. Merrifield, *J. Am. Chem. Soc.* **1977**, *99*, 5484–5486; b) I. Kunihiro, *Chem. Lett.* **1977**, *6*, 641–644.
[2] a) P. Maillard, P. Krausz, C. Giannotti, *J. Organomet. Chem.* **1980**, *197*, 285–290; b) P. Maillard, S. Gaspard, P. Krausz, C. Giannotti, *J. Organomet. Chem.* **1981**, *212*, 185–191.
[3] L. Jiao, B. H. Courtney, F. R. Fronczek, K. M. Smith, *Tetrahedron Lett.* **2006**, *47*, 501–504.
[4] a) K. Wada, T. Mizutani, H. Matsuoka, S. Kitagawa, *Chem. Eur. J.* **2003**, *9*, 2368–2380; b) T. Mizutani, K. Wada, S. Kitagawa, *Chem. Commun.* **2002**, 1626–1627; c) T. Mizutani, K. Wada, S. Kitagawa, *J. Am. Chem. Soc.* **2001**, *123*, 6459–6460.
[5] X.-B. Zhang, C.-C. Guo, Z.-Z. Li, G.-L. Shen, R.-Q. Yu, *Anal. Chem.* **2002**, *74*, 821–825.
[6] V. V. Borovkov, G. A. Hembury, Y. Inoue, *Acc. Chem. Res.* **2004**, *37*, 449–459.
[7] a) B. J. Pistorio, C. J. Chang, D. G. Nocera, *J. Am. Chem. Soc.* **2002**, *124*, 7884–7885; b) J. Rosenthal, B. J. Pistorio, L. L. Chng, D. G. Nocera, *J. Org. Chem.* **2005**, *70*, 1885–1888.
[8] a) G. Pognon, C. Boudon, K. J. Schenk, M. Bonin, B. Bach, J. Weiss, *J. Am. Chem. Soc.* **2006**, *128*, 3488–3489; b) Y. Tomohiro, A. Satake, Y. Kobuke, *J. Org. Chem.* **2001**, *66*, 8442–8446.
[9] S. Faure, C. Stern, R. Guilard, P. D. Harvey, *J. Am. Chem. Soc.* **2004**, *126*, 1253–1261.
[10] K. Ogawa, A. Ohashi, Y. Kobuke, K. Kamada, K. Ohta, *J. Am. Chem. Soc.* **2003**, *125*, 13356–13357.
[11] a) I. V. Sazanovich, A. Balakumar, K. Muthukumaran, E. Hindin, C. Kirmaier, J. R. Diers, J. S. Lindsey, D. F. Bocian, D. Holten, *Inorg. Chem.* **2003**, *42*, 6616–6628; b) M. Speckbacher, L. Yu, J. S. Lindsey, *Inorg. Chem.* **2003**, *42*, 4322–4337; c) W. J. Youngblood, D. T. Gryko, R. K. Lammi, D. F. Bocian, D. Holten, J. S. Lindsey, *J. Org. Chem.* **2002**, *67*, 2111–2117; d) S. Prathapan, S. I. Yang, J. Seth, M. A. Miller, D. F. Bocian, D. Holten, J. S. Lindsey, *J. Phys. Chem. B* **2001**, *105*, 8237–8248; e) S. I. Yang, S. Prathapan, M. A. Miller, J. Seth, D. F. Bocian, J. S. Lindsey, D. Holten, *J. Phys. Chem. B* **2001**, *105*, 8249–8258.
[12] W. D. Horrocks Jr, M. Albin in *Progress in Inorganic Chemistry* (Ed.: S. J. Lippard), John Wiley & Sons, New York, **1984**, vol. 31, pp. 1–104.
[13] a) J. A. Teprovich Jr, E. Prasad, R. A. Flowers, *Angew. Chem.* **2007**, *119*, 1163–1166; *Angew. Chem. Int. Ed.* **2007**, *46*, 1145–1148; b) K. A. Gschneider Jr, L. Eyring, *Handbook on the Physics and Chemistry of Rare Earths*, North-Holland, Amsterdam, **1979**, vol. 15; c) P. Dorenbos, *J. Phys.: Condens. Matter* **2003**, *15*, 575–594.
[14] a) H. He, X. Zhu, A. Hou, J. Guo, W. K. Wong, W. Y. Wong, K. F. Li, K. W. Cheah, *Dalton Trans.* **2004**, 4064–4073; b) H. S. He, Z. X. Zhao, W. K. Wong, K. F. Li, J. X. Meng, K. W. Cheah, *Dalton Trans.* **2003**, 980–986; c) W. K. Wong, A. Hou, J. Guo, H. He, L. Zhang, W. Y. Wong, K. F. Li, K. W. Cheah, F. Xue, T. C. W. Mak, *J. Chem. Soc. Dalton Trans.* **2001**, 3092–3098; d) W. K. Wong, L. L. Zhang, W. T. Wong, F. Xue, T. C. W. Mak, *J. Chem. Soc. Dalton Trans.* **1999**, 615–622.
[15] D. Imbert, M. Cantuel, J.-C. G. Bünzli, G. Bernardinelli, C. Piguet, *J. Am. Chem. Soc.* **2003**, *125*, 15698–15699.
[16] N. M. Shavaleev, L. P. Moorcraft, S. J. A. Pope, Z. R. Bell, S. Faulkner, M. D. Ward, *Chem. Commun.* **2003**, 1134–1135.
[17] S. I. Klink, H. Keizer, F. C. J. M. van Veggel, *Angew. Chem.* **2000**, *112*, 4489–4491; *Angew. Chem. Int. Ed.* **2000**, *39*, 4319–4321.
[18] S. I. Klink, L. Grave, D. N. Reinhoudt, F. C. J. M. van Veggel, M. H. Werts, F. A. J. Geurts, J. W. Hofstraat, *J. Phys. Chem. A* **2000**, *104*, 5457.
[19] Z. R. Reeves, K. L. V. Mann, J. C. Jeffery, J. A. McCleverty, M. D. Ward, F. Barigelletti, N. Armaroli, *J. Chem. Soc. Dalton Trans.* **1999**, 349–356.
[20] Y. Kawamura, Y. Wada, S. Yanagida, *Jpn. J. Appl. Phys.* **2001**, *40*, 350–356.
[21] G. F. De Sá, O. L. Malta, C. de Mello Donegai, A. M. Simas, R. L. Longo, P. A. Santa-Cruz, E. F. da Silva Jr, *Coord. Chem. Rev.* **2000**, *196*, 165–195.
[22] R. Reisfeld, C. K. Jorgensen, *Lasers and Excited States of Rare Earths*, Springer, Berlin, **1977**.
[23] X. Zhu, PhD Thesis, Hong Kong Baptist University, **2006**.
[24] M. H. V. Werts, J. W. Hofstraat, F. A. J. Geurts, J. W. Verhoeven, *Chem. Phys. Lett.* **1997**, *276*, 196–201.
[25] a) H.-S. He, J.-P. Guo, Z.-X. Zhao, W. K. Wong, W. Y. Wong, W. K. Lo, K. F. Li, L. Luo, K. W. Cheah, *Eur. J. Inorg. Chem.* **2004**, 837–845; b) W. K. Wong, H. Liang, W. Y. Wong, Z. Cai, K. F. Li, K. W. Cheah, *New J. Chem.* **2002**, *26*, 275–278; c) W. K. Wong, A. Hou, J. Guo, H. He, L. Zhang, W. Y. Wong, K. F. Li, K. W. Cheah, F. Xue, T. C. W. Mak, *J. Chem. Soc. Dalton Trans.* **2001**, 3092–3098.
[26] S. Faure, C. Stern, E. Espinosa, J. Douville, R. Guilard, P. D. Harvey, *Chem. Eur. J.* **2005**, *11*, 3469–3481.
[27] R. L. Brookfield, H. Ellul, A. Harriman, G. Porter, *J. Chem. Soc. Faraday Trans. 2* **1986**, *82*, 219–233.
[28] S. Kawata, H.-B. Sun, T. Tanaka, K. Takada, *Nature* **2001**, *412*, 697–698.
[29] A. Karotki, M. Khurana, J. R. Lepock, B. C. Wilson, *Photochem. Photobiol.* **2006**, *82*, 443–452.
[30] M. Calvete, G. Y. Yang, M. Hanack, *Synth. Met.* **2004**, *141*, 231–243.
[31] M. Drobizhev, A. Karotki, M. Kruk, A. Rebane, *Chem. Phys. Lett.* **2002**, *355*, 175–182.
[32] D. G. Mclean, R. L. Sutherland, M. C. Brant, D. M. Brandelik, *Opt. Lett.* **1993**, *18*, 858–860.
[33] a) J. W. Perry, K. Mansour, I.-Y. S. Lee, X.-L. Wu, P. V. Bedworth, C.-T. Chen, D. Ng, S. Marder, P. Miles, *Science* **1996**, *273*, 1533–1536; b) J. W. Perry, K. Mansour, S. R. Marder, K. J. Perry, D. Alvarez Jr, I. Choong, *Opt. Lett.* **1994**, *19*, 625–627.
[34] a) X. Zhong, Y. Feng, S.-L. Ong, J. Hu, W.-J. Ng, Z. Wang, *Chem. Commun.* **2003**, 1882–1883; b) A. Krivokapic, H. L. Anderson, G. Bourhill, R. Ives, S. Clark, K. J. McEwan, *Adv. Mater.* **2001**, *13*, 652–656; c) G. Y. Yang, S. G. Ang, L. L. Chng, Y. W. Lee, E. W.-P. Lau, K. S. Lai, H. G. Ang, *Chem. Eur. J.* **2003**, *9*, 900–904; d) S. Vagin, M. Barthel, D. Dini, M. Hanack, *Inorg. Chem.* **2003**, *42*, 2683–2694; e) R. B. Martin, H. Li, L. Gu, S. Kumar, C. M. Sanders, Y.-P. Sun, *Opt. Mater.* **2005**, *27*, 1340–1345; f) S. Fu, G. Zhou, X. Zhu, C. Ye, W. K. Wong, Z. Li, *Chem. Lett.* **2006**, *35*, 802–803.
[35] M. Sheik-Bahae, A. A. Said, E. W. Van Stryland, *Opt. Lett.* **1989**, *14*, 955–957.
[36] R. J. Angelici, *Reagents for Transition Metal Complex and Organometallic Syntheses*, vol. 28 (Inorganic Syntheses), 1st ed., John Wiley & Sons, New York, **1990**.
[37] C. A. Parker, W. T. Rees, *Analyst (London)* **1960**, *85*, 587–600.
[38] *SAINT, Reference manual*, Siemens Energy and Automation, Madison, WI, **1994–1996**.
[39] G. M. Sheldrick, *SADABS, Empirical Absorption Correction Program,* University of Göttingen, Germany, **1997**.
[40] G. M. Sheldrick, *SHELXTL™, Reference manual*, version 5.1, Siemens, Madison, WI, **1997**.

Received: March 19, 2007
Published Online: June 5, 2007

 © 2007 Wiley-VCH Verlag GmbH & Co. KGaA, Weinheim 

DOI: 10.1002/ejic.200600993

# On the Synthesis of Ramsdellite $LiTiMO_4$ (M = Ti, V, Cr, Mn, Fe): An Experimental and Computational Study of the Spinel–Ramsdellite Transformation

**Alois Kuhn,[a] Pilar Díaz-Carrasco,[a] María Elena Arroyo y de Dompablo,*[b] and Flaviano García-Alvarado*[a]**

**Keywords:** Titanates / Phase transitions / Ab initio calculations / Solid-state reactions / Electrochemistry

The $LiTiMO_4$ (spinel) ↔ $LiTiMO_4$ (ramsdellite) transformation has been investigated by combining computational and experimental techniques, for M = Ti, V, Cr, Mn, and Fe, in order to understand the characteristics of this transformation and the influence of the metal M on the relative stability of the ramsdellite polymorph. The calculations predict that all the aforementioned $LiTiMO_4$ spinels are thermodynamically stable with respect to the ramsdellite polymorph, with the calculated enthalpy variation of the transformation being less than 40 $kJ\,mol^{-1}$. In the case of normal spinels $[Li]_t[TiM]_oO_4$ we estimated a transformation temperature in the range 900–1600 °C, whereas the polymorphic transformation for inverse spinels $[Li_{0.5}M_{0.5}]_t[TiM_{0.5}Li_{0.5}]_oO_4$ is accompanied by a lower entropy gain, hence a much higher temperature would be needed to overcome the enthalpy of the transformation. The transformation is thus entropically controlled. Accordingly, experimental results show that normal $[Li]_t[TiM]_oO_4$ spinels (M = Ti, V, Cr) readily transform into ramsdellites at temperatures between 900 and 1400 °C, whereas this transition is hindered for spinels $LiTiMO_4$ (M = Fe, Mn), which possess a high degree of inversion. Based on a possible mechanism for the transformation, we infer that the impossibility of transforming the Mn and Fe inverse-spinels into their ramsdellite forms is also due to the high energy barriers that must be overcome during the transformation. The obtained $LiTiMO_4$ (M = Ti, V, and Cr) ramsdellites, which contain $Ti^{IV}$ and $M^{III}$, display a twofold electrochemical application, namely that one lithium ion per formula unit can be inserted into these compounds at about 1.4 V vs. Li (reduction of $Ti^{IV}$ to $Ti^{III}$). The oxidation of $M^{III}$ ions to $M^{IV}$ enables lithium deinsertion from $LiTiMO_4$ (M = Ti, V, and Cr) at potentials of 1.9 V (M = Ti), 3.1 V (M = V), and 4.2 (M = Cr) vs. Li.
(© Wiley-VCH Verlag GmbH & Co. KGaA, 69451 Weinheim, Germany, 2007)

## Introduction

Electrode materials for rechargeable lithium batteries are based on transition metal inorganic frameworks that can reversibly intercalate large amounts of lithium ions. The application of such materials as positive or negative electrodes depends on the potential at which lithium ions are intercalated − potentials above 3 V and below 1 V vs. Li are desirable for the positive and the negative electrode, respectively. In terms of lithium battery applications, titanates with the ramsdellite structure are of considerable interest because this structure enables fast and reversible insertion of a good quantity of lithium ions. A schematic representation of the ramsdellite structure is depicted in part a of Figure 1. It is built up by $[TiO]_6$ octahedra that form double edge-sharing chains running along [001]. These chains are interconnected through corners in the *ab* plane. Lithium ions partially occupy some crystallographic sites located in the $1 \times 2$ tunnels running parallel to the *c* axis.[1,2] The presence of unoccupied Li sites in these channels in ramsdellite $Li_2Ti_3O_7$ allows for a further lithium uptake of up to 2.24 Li ions, which means that $Li_2Ti_3O_7$ would deliver a specific capacity of 240 $Ah\,kg^{-1}$ as an electrode in a lithium cell.[3] The high temperature polymorph of spinel $LiTi_2O_4$ also presents the ramsdellite structural type. Hereafter the spinel polymorph will be denoted as $LiTi_2O_4$(S) while the ramsdellite polymorph will be denoted as $LiTi_2O_4$(R). The latter has recently been proposed as a new electrode material for lithium batteries.[4–6] $LiTi_2O_4$(R) is nominally formulated as $LiTi^{3+}Ti^{4+}O_4$, therefore lithium intercalation into this material proceeds only up to a maximum of one Li per formula unit (specific capacity of 160 $Ah\,kg^{-1}$), in other words complete reduction of the $Ti^{4+}$ ions. The reversible reduction of $Ti^{4+}$ ions in both $Li_2Ti_3O_7$ and $LiTi_2O_4$ occurs at 1.4 V vs. the lithium electrode.

The presence of $Ti^{3+}$, which can be oxidised, in $LiTi_2O_4$(R) permits the deintercalation of a maximum of one Li per formula unit. Indeed, the extraction of lithium from

[a] Departamento de Química, Universidad San Pablo – CEU, 28668 Boadilla del Monte, Madrid, Spain
E-mail: flaga@ceu.es
[b] Departamento de Química Inorgánica, Universidad Complutense de Madrid, 28040 Madrid, Spain
E-mail: e.arroyo@quim.ucm.es

 © 2007 Wiley-VCH Verlag GmbH & Co. KGaA, Weinheim 

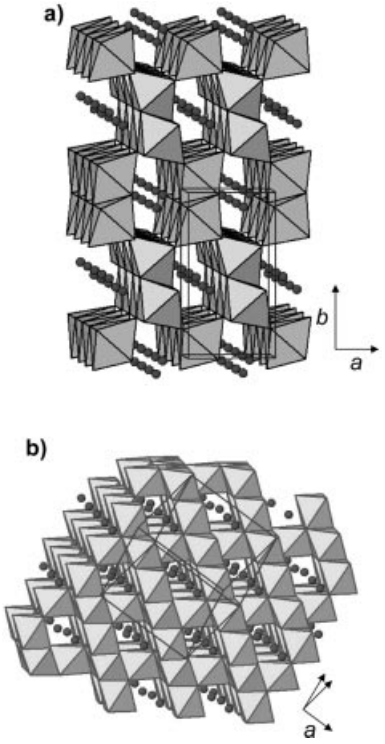


Figure 1. Schematic representation of a) the ramsdellite structure of $Li_2Ti_3O_7$ and b) the spinel structure of $LiTi_2O_4$. In both cases circles correspond to lithium ions and octahedra represent $TiO_6$ coordination.

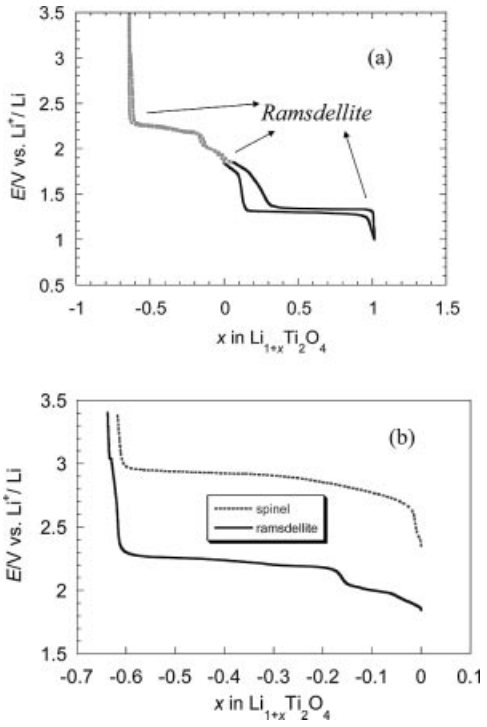


Figure 2. (a) Voltage vs. composition curve of a $LiTi_2O_4$ (ramsdellite)//Li cell started on discharge (continuous line) and started on charge (dashed line). (b) Voltage vs. composition curve of a $LiTi_2O_4$//Li cell started on charge showing the behavior of the two different polymorphs [ramsdellite (continuous line) and spinel (dashed line)].

$LiTi_2O_4$ at room temperature by both chemical and electrochemical methods has been reported as a route to the ramsdellite polymorph of $TiO_2$.[4,7] Thus, the coexistence of $Ti^{3+}$ and $Ti^{4+}$ in $LiTi_2O_4$ allows for the deinsertion of one lithium ion (oxidation of $Ti^{3+}$) and the insertion of one lithium ion (reduction of $Ti^{4+}$). Figure 2 (a) shows a typical voltage composition plot obtained when a Li//$LiTi_2O_4$(R) cell is cycled between either 1.8 and 1 V (continuous line) or 1.8 and 3.5 V (dashed line), which correspond to the intercalation of lithium into $LiTi_2O_4$(R) and de-intercalation of lithium from $LiTi_2O_4$(R), respectively. Both processes are reversible. The flat intercalation and de-intercalation regions are characteristic of two-phase domains, as indicated in previous works[4,5] and confirmed by in situ XRD studies using synchrotron radiation.[8] At the end of the intercalation (1 V) and de-intercalation curves (3.5 V), two different ramsdellites with formulae $Li_2Ti_2O_4$ and $TiO_2$, respectively, exist. In other words, the intermediate $Li_xTi_2O_4$ composition located at the plateaux actually corresponds to mixtures of the two ramsdellite extremes ($x$ = 0, 1, or 2) in different ratios.

The main advantage of ramsdellites as an electrode material for rechargeable lithium batteries is the high reversibility of the intercalation process. It has been demonstrated that electrochemically inserted $Li_{2+x}Ti_3O_7$ compounds retain the ramsdellite framework for large amounts of lithium ($x \approx 2.24$). The small changes in the basic ramsdellite cell parameters during the intercalation process, also known as zero-strain behavior, are likely to be the origin of the good capacity retention with cycling.[3] The formation of $Li_2Ti_2O_4$(R)/$TiO_2$(R) upon reduction/oxidation of $LiTi_2O_4$ is also accompanied by very small volume changes. Bearing in mind the good reversibility and high capacity of ramsdellites, we have been working on the synthesis and characterization of novel $LiTi_{2-y}M_yO_4$ ramsdellites obtained by substitution of the trivalent Ti by other ions. The oxidation of $Ti^{3+}$ in $LiTi_2O_4$ occurs at about 1.9 V and it is therefore desirable to increase this potential to the 3–4 V range, as the $V^{3+}/V^{4+}$, $Fe^{3+}/Fe^{4+}$, $Mn^{3+}/Mn^{4+}$, and $Cr^{3+}/Cr^{4+}$ redox couples are known to be operative at such high voltages vs. Li.

Although $LiTi_2O_4$ can be prepared in the ramsdellite structure, its stable form at room temperature is spinel-like. Transformation of $LiTi_2O_4$(S) into $LiTi_2O_4$(R) occurs at 925 °C.[9,10] On the other hand, spinels with the formula $LiTiMO_4$ (M = Ti, V, Cr, Mn, and Fe) are known to exist. With the aim of preparing the novel ramsdellites $LiTiMO_4$ (M = V, Cr, Mn, and Fe), in this work we will try to induce the spinel–ramsdellite phase transformation by thermal treatment in a reaction that can be written as:

$$LiTiMO_4(S) \leftrightarrow LiTiMO_4(R) \quad (1)$$

The relative thermodynamic stability of polymorphs can be explored by first-principles methods, a good example of which is the investigation of Reed et al.[11] dealing with the stability of layered $Li_{0.5}MO_2$ with respect to its transformation into spinel $LiM_2O_4$ (M is a transition metal). In this

 © 2007 Wiley-VCH Verlag GmbH & Co. KGaA, Weinheim 

work we have performed a computational study on the stability of ramsdellite with respect to the spinel form to assess whether the transformation of spinel $LiTiMO_4$ (M = V, Cr, Mn and Fe) to ramsdellite is feasible from a thermodynamic point of view. Based on these predictions we have attempted to synthesize the new ramsdellites $LiTiMO_4$ (M = V, Cr, Mn and Fe) starting from the spinel-like polymorphs. A preliminary structural characterization is also presented for those ramsdellites that have been obtained. Finally, although full electrochemical studies of individual ramsdellites are described elsewhere,[12–14] the general electrochemical behavior of the novel ramsdellites is also included here for completeness.

## Results and Discussion

### Computational Analysis of the $LiTiMO_4$(S) ↔ $LiTiMO_4$(R) Transformation

Computing the energy of a periodic electronic structure requires a cation-ordering scheme to be imposed on the simulated unit cell. The unit cell of $LiTiMO_4$(S) contains eight formula units and shows cubic symmetry (space group *Fd3m*) with a lattice parameter *a* of about 8.2 Å. In this cell we have imposed the simplest order in which Ti and M atoms alternate in the octahedral sites of the spinel along two main crystallographic directions. By doing so, the *Fd3m* symmetry is broken and the new cell must be redefined in the *Imma* space group. The lattice parameters of the ordered structure are $a = a_o/\sqrt{2}$, $b = a_o/\sqrt{2}$, and $c = a_o$, where $a_o$ denotes the lattice parameter of the cubic spinel ($a_o \approx 8.2$ Å). Hence, the unit cell of the ordered spinel (space group *Imma*) is related to that of the cubic spinel (space group *Fd3m*) by a 45° rotation around the *c* axis. In the case of the ramsdellite compounds, M and Ti ions alternate along the [010] direction in the ordered cell used for the calculations in such a way that chains of either M or Ti edge-sharing octahedra run parallel to the [001] axis.

Tables 1 and 2 list the optimized values of the lattice parameters for spinel and ramsdellite $LiTiMO_4$ (M = Ti, V, Cr, Mn and Fe) obtained in this ab initio study. It should be noted that all the transition metal ions occupy octahedral sites in the computed spinel cell. However, experimental results indicate that in the case of M = Cr, Mn and Fe some transition metal ions are located in the tetrahedral sites.[15–18] Note that in the first part of this computational study we have not considered the degree of inversion. In view of the data in Tables 1 and 2, it can be concluded that, generally speaking, the calculation method allows a correct prediction of the cell parameters, with differences of around 2–4% that are typical for state-of-the-art approximations to density functional theory in transition metal oxides. It is well documented that the generalized gradient approximation (GGA) method has a tendency to overestimate the equilibrium volume.

Table 1. Calculated and experimental lattice parameters of spinels $LiTiMO_4$ (M = Ti, V, Cr, Mn, and Fe). The parameters are given for a cell of *Imma* symmetry (four $LiTiMO_4$ formula units per cell) that was used for the calculations (see text). Experimental data are given in parentheses.

| | *a* [Å] | *b* [Å] | *c* [Å] | *V* [Å$^3$] | Err[a] [%] | Ref. |
|---|---|---|---|---|---|---|
| $LiTi_2O_4$ | 5.967 | 5.967 | 8.439 | 300.50 | | |
| | (5.9430) | (5.9430) | (8.405) | (296.85) | 1.23 | [10] |
| $LiTiVO_4$ | 5.978 | 5.846 | 8.416 | 294.12 | | |
| | (5.8237) | (5.8237) | (8.236) | (279.33) | 5.29 | [19] |
| $LiTiCrO_4$ | 5.933 | 5.948 | 8.333 | 294.07 | | |
| | (5.867) | (5.867) | (8.297) | (285.58) | 2.97 | [19] |
| | (5.882) | (5.882) | (8.318) | (287.76) | 2.19 | [20] |
| | (5.875) | (5.875) | (8.308) | (286.72) | 2.56 | [21] |
| $LiTiMnO_4$ | 6.013 | 6.072 | 8.208 | 299.68 | | |
| | (5.919) | (5.919) | (8.371) | (293.29) | 2.17 | [16] |
| | (5.893) | (5.893) | (8.334) | (289.42) | 3.55 | [18] |
| $LiTiFeO_4$ | 5.981 | 5.981 | 8.448 | 302.20 | | |
| | (5.910) | (5.910) | (8.358) | (291.93) | 3.52 | [22] |
| | (5.913) | (5.913) | (8.362) | (292.36) | 3.36 | [17] |

[a] Error between calculated and experimental data.

In the last year first-principles calculations have been widely use to accurately predict the lithium intercalation voltage of a large variety of electrode materials (see, for instance, refs.[23–25]). The average lithium de-intercalation voltages of $LiTi_2O_4$ for both ramsdellite and spinel structural types have also been computed in this work as some of them are known experimentally and their comparison may be a convenient way of validating the calculations. Since the insertion reaction is written as Equation (2) the open-circuit average voltage for the lithium insertion pro-

Table 2. Calculated and experimental lattice parameters of ramsdellites $LiTiMO_4$ (M = Ti, V, Cr, Mn and Fe) with two $LiTiMO_4$ formula units per cell. Experimental data are given in parentheses.

| Compound | *a* [Å] | *b* [Å] | *c* [Å] | *V* [Å$^3$] | Err[a] [%] | Ref. |
|---|---|---|---|---|---|---|
| $LiTi_2O_4$ | 5.071 | 9.745 | 2.961 | 146.319 | | |
| | (5.0342) | (9.6201) | (2.9481) | (142.781) | 2.48 | [10] |
| $LiTiVO_4$ | 5.043 | 9.649 | 2.962 | 144.16 | | |
| | (5.0090) | (9.5570) | (2.9424) | (140.857) | 2.34 | this work |
| $LiTiCrO_4$ | 4.978 | 9.597 | 2.952 | 141.03 | | |
| | (4.9818) | (9.503) | (2.9263) | (138.541) | 1.79 | this work |
| $LiTiMnO_4$ | 5.051 | 9.876 | 2.949 | 147.10 | – | this work |
| $LiTiFeO_4$ | 5.074 | 9.807 | 2.995 | 149.04 | – | this work |

[a] Error between calculated and experimental data.

 © 2007 Wiley-VCH Verlag GmbH & Co. KGaA, Weinheim 

cess can be obtained as explained by Aydinol et al.[24] from a total energy difference expression [see Equation (3); $E_{total}$ refers to the total energy per formula unit] if entropy and volumetric effects are ignored.

$$Ti_2O_4 + Li \leftrightarrow LiTi_2O_4 \quad (2)$$

$$V_a = E_{total(Ti_2O_4)} + E_{total(Li)} - E_{total(LiTi_2O_4)} \quad (3)$$

Calculations predict an average lithium insertion voltage of 1.86 V for $TiO_2$(R), which is about 0.3 V below the experimental results presented in Figure 2 (b). Such voltage underestimations are usually reported in the literature for transition metal oxides in the GGA implementation (see, for instance, refs.[24,26]). Regarding the spinel, the calculated potential is 3 V, which is in good agreement with the experimental data (see Figure 2, b).

The relative thermodynamic stability of both spinel and ramsdellite $LiMTiO_4$ can be inferred from the difference between their calculated total energies. The results obtained for M = Ti, V, Cr, Mn, and Fe are summarized in Figure 3 for normal (squares) and inverse spinels (circles). The spinel structure is energetically more stable than the ramsdellite form in all cases. To produce a phase transformation between the polymorphs the free-energy variation of Equation (1) should be zero:

$$\Delta G_r = \Delta E_r + P\Delta V_r - T\Delta S_r \quad (4)$$

In this equation $E_r$ is the reaction energy, whose calculated values are given in Figure 3, and the term $P\Delta V_r$ can be obtained from the calculated volume data summarized in Tables 1 and 2. At ambient pressure the $P\Delta V_r$ term has a small value of the order of $10^{-4}$ kJ mol$^{-1}$, and is therefore negligible compared to the energy of the reaction ($E_r$ is of the order of $10^1$ kJ mol$^{-1}$). Obviously, the transformation is an endothermic reaction ($\Delta H_r = \Delta E_r + P\Delta V_r$, $\Delta H_r \approx \Delta E_r$). Even if the polymorphic transformation has a positive reaction enthalpy, it might occur if a large positive entropy accompanies the transformation reaction. In this case, the transformation would become favorable at high temperature ($\Delta H_r = T\Delta S_r$). This is indeed found experimentally in the case of M = Ti, since it is well known that the spinel is the low-temperature polymorph and that the transformation to ramsdellite requires heating at 925 °C and final quenching to room temperature. Computational results indicate that the enthalpy of transformation between spinel and ramsdellite $LiTi_2O_4$ is about 24.14 kJ mol$^{-1}$. The free-energy difference between polymorphs at the transition temperature is zero, therefore the enthalpy variation of the reaction is equal to the $T\Delta S_r$ term. First-principles investigations do not provide information about the entropy term, which makes it impossible to predict the transition temperature. However, the entropy term can be approximated for the $LiTi_2O_4$(S)–$LiTi_2O_4$(R) transformation, which occurs at a temperature of 925 °C. Thus, taking into account the calculated value of the enthalpy (24.14 kJ mol$^{-1}$), the entropy value for this transformation is 20.13 J mol$^{-1}$ K$^{-1}$. To estimate the temperature needed for the remaining $LiMTiO_4$ spinels we can assume that the entropy variation between the normal spinel and the ramsdellite forms is similar for any M.

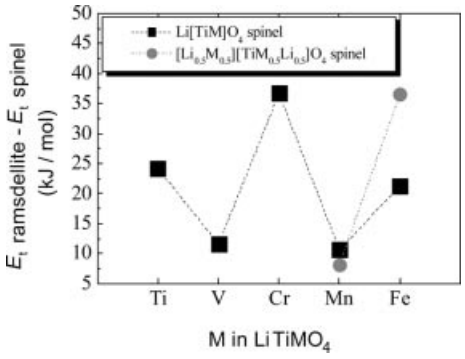


Figure 3. Calculated total energy difference between the ramsdellite and spinel polymorphs for $LiTiMO_4$ (M = Ti, V, Cr, Mn, and Fe). Two configurations, namely the normal cationic distribution $[Li]_t[TiM]_oO_4$ (squares) and the inverse $[Li_{0.5}M_{0.5}]_t[TiM_{0.5}Li_{0.5}]_oO_4$ configuration (circles), were computed for the spinel structure.

The energy difference between the Fe-substituted ramsdellite and the normal spinel (21 kJ mol$^{-1}$) is close to that of the $LiTi_2O_4$ system, therefore calculations suggest that $LiTiFeO_4$(R) could be stabilized by similar thermal treatment (considering $\Delta S$ to be 0.02 kJ mol$^{-1}$ K$^{-1}$). In light of this entropy value, the phase transformation for M = V and Mn would occur at lower temperatures, at around 300 °C. The spinel-ramsdellite transformation in the Cr system seems to be the most unfavorable since it presents the largest energy difference (36.6 kJ mol$^{-1}$). This suggests that the transformation would occur at higher temperatures, around 1550 °C.

So far we have discussed the results considering the normal spinel structure $Li_2(Ti_2M_2)_oO_8$, where all the M ions occupy octahedral sites. However, neutron diffraction measurements have shown that Li and Ti ions show a partial inverted distribution in $LiMnTiO_4$ over the tetrahedral and octahedral sites, although a more recent study has suggested that the Mn ion is disordered between these sites.[18] The same situation occurs in $LiFeTiO_4$ with Li and Fe ions.[17,22] The corresponding formulae – $[Li_{0.66}Ti_{0.34}]_{8a}[Li_{0.34}MnTi_{0.66}]_{16d}O_4$ and $[Li_{0.47}Fe_{0.53}]_{8a}[Li_{0.53}Fe_{0.47}Ti]_{16d}O_4$ – suggest inversion degrees of 34% and 53%, respectively. To account for this degree of inversion, in a second stage we have computed the total energy of the spinels $[Li_{0.5}M_{0.5}]_t[Ti_1M_{0.5}Li_{0.5}]_oO_4$ (M = Fe and Mn). In the case of Fe the inverse spinel is 15.8 kJ mol$^{-1}$ more stable than the normal spinel, hence the energy difference between ramsdellite and spinel forms increases by the same amount to 36.5 kJ mol$^{-1}$, which is the same energy difference found in the Cr system (see Figure 3). The enthalpic stabilization of the inverse spinel with respect to the normal configuration is rooted in the tetrahedral-site preference of $Fe^{3+}$ (although small). In addition, the configurational entropy also

 © 2007 Wiley-VCH Verlag GmbH & Co. KGaA, Weinheim 

minimizes the free energy of the inverse spinel with respect to the normal spinel. Navrotsky et al.,[27] amongst others, have reported that the configurational entropy in spinels depends on the degree of inversion, and is 11.3 and 14.6 $J\,mol^{-1}\,K^{-1}$ larger for the inverse spinels $B(AB)O_4$ and $A_{0.5}B_{0.5}(A_{0.5}B_{1.5})O_4$, respectively, than for the normal spinel $A(B_2)O_4$. Hence, the inverse spinel↔ramsdellite transformation is accompanied by a lower entropy gain than the normal spinel↔ramsdellite transformation. The entropy of the inverse-spinel↔ramsdellite transformation can be roughly approximated as follows:

$LiTiMO_4$ (normal spinel) ↔ $LiTiMO_4$ (ramsdellite)
$\Delta S \approx 0.02\ kJ\,mol^{-1}\,K^{-1}$

$LiTiMO_4$ (normal spinel) ↔ $[Li_{0.5}M_{0.5}]_t[TiM_{0.5}Li_{0.5}]_oO_4$ (inverse spinel)
$\Delta S \approx 0.015\ kJ\,mol^{-1}\,K^{-1}$[27]

$[Li_{0.5}M_{0.5}]_t[TiM_{0.5}Li_{0.5}]_oO_4$ (inverse spinel) ↔ $LiTiMO_4$ (ramsdellite)
$\Delta S \approx 0.005\ kJ\,mol^{-1}\,K^{-1}$

The estimated entropy variation of the inverse spinel–ramsdellite transformation is 0.005 $kJ\,mol^{-1}\,K^{-1}$, while the calculated enthalpy for the Fe system is 36.5 $kJ\,mol^{-1}$ (Figure 3). With these data, the transformation would occur at about 7000 °C, which is significantly higher than the value of 900 °C estimated for the normal spinel–ramsdellite transformation. These results therefore suggest that the spinel↔ramsdellite transformation is entropically controlled.

The Mn inverse spinel is calculated to be 3 $kJ\,mol^{-1}$ *less* stable than its normal configuration. This apparent disagreement with experiment does not come as a surprise, however, as $Mn^{3+}$ has a large octahedral-site preference and the inverse $Mn^{3+}$ spinels are not enthalpically stabilized. Considering entropic factors, the disorder of cations in the octahedral/tetrahedral sites in the inverse spinels supposes a gain of mixing entropy which, together with the gain of configurational entropy mentioned above, allows to overcome the small energy of 3 $kJ\,mol^{-1}$ at high temperature (DFT refers to zero Kelvin). Therefore the inability of DFT to accurately predict the inversion in Mn spinels is likely rooted in the fact that these spinels are stabilized by entropic factors (configurational and mixing entropy), which cannot be taken into account by first-principles methods. Furthermore, the possibility of valence changes when $Mn^{3+}$ migrates to tetrahedral sites[11,28] also complicates the picture. Concerning the temperature of the $[Li_{0.5}Mn_{0.5}]_t$-$[TiMn_{0.5}Li_{0.5}]_oO_4$ inverse spinel↔ramsdellite transformation, the estimated entropy of 0.005 $kJ\,mol^{-1}\,K^{-1}$ suggests that a temperature of 1327 °C will be needed to produce such a transformation.

As this works aims to prepare novel ramsdellites $LiM^{III}Ti^{IV}O_4$, it is important to determine the oxidation state of M and Ti in the fully relaxed structures of the calculated $LiTiMO_4$ ramsdellites. An approximate oxidation state for Ti and M in the studied compounds can be obtained by integrating the net electron spin density over a radius sphere around each transition metal ion.[11,29] Some of the results are shown in Figure 4 for $LiTi_2O_4$(R) and the substituted ramsdellites with Cr and Mn. The net spin density increases steeply when integrated through the *d*-states of the metal ion up to 1 Å, then a plateau is observed because the charge density of the oxygen ions does not contribute to the spin density. The net spin around Ti ions in $LiTi_2O_4$(R) suggests that the oxidation state of both titanium ions is +3.5, in agreement with the metallic behavior reported previously.[7,30] On the contrary, titanium is present in the substituted ramsdellites $LiTiCrO_4$ and $LiTiMnO_4$ as a diamagnetic tetravalent ion ($Ti^{4+}$), while both Cr and Mn are in the trivalent state, with three ($t_{2g}^3$) and four ($t_{2g}^3\ e_g^1$) unpaired electrons, respectively. Similar results are obtained for the $LiTiVO_4$ and $LiTiFeO_4$ spinels.

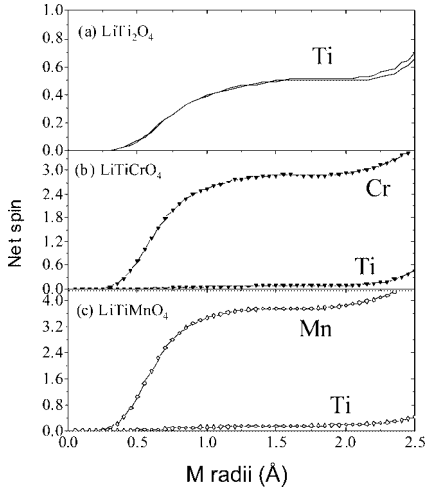


Figure 4. Integral of the net spin density for the calculated $LiTiMO_4$ ramsdellites with M = Ti (a), Cr (b), and Mn (c).

## Experimental Study of the $LiTiMO_4$(S) ↔ $LiTiMO_4$(R) Transformation

The computational data suggest that the normal spinel↔ramsdellite transformation could be achieved at temperatures below 1600 °C, whereas the inverse spinel↔ramsdellite transformation is entropically hindered. We therefore attempted to induce the spinel↔ramsdellite transformation for the $LiTiMO_4$ spinels (M = V, Cr, Mn and Fe) as described in the Methodology section. For comparison purposes we also carried out the transformation of $LiTi_2O_4$.

Transformation of $LiTi_2O_4$ was achieved at 950 °C, in agreement with previously reported results.[9,10] A slightly higher temperature (1050 °C) was required for $LiTiVO_4$ since mixtures of spinel and ramsdellite are obtained at lower temperature. The corresponding X-ray diffraction pattern and Rietveld refinement of the new ramsdellite with composition $LiTiVO_4$ are shown in Figure 5 ($R_{wp}$ = 0.062; $R_p$ = 0.048; $R_B$ = 0.088, $\chi^2$ = 1.38). The cell parameters are given in Table 2. The structural model is that corresponding to $LiTi_2O_4$(R) with Ti and V disordered in the octahedral positions. The light lithium ions could not be located from the X-ray data, therefore they were modeled as occupying

 © 2007 Wiley-VCH Verlag GmbH & Co. KGaA, Weinheim 

the same position as in $LiTi_2O_4$. The lithium parameters were therefore held constant at the start of the refinement, assuming an ideal occupancy of 0.5.

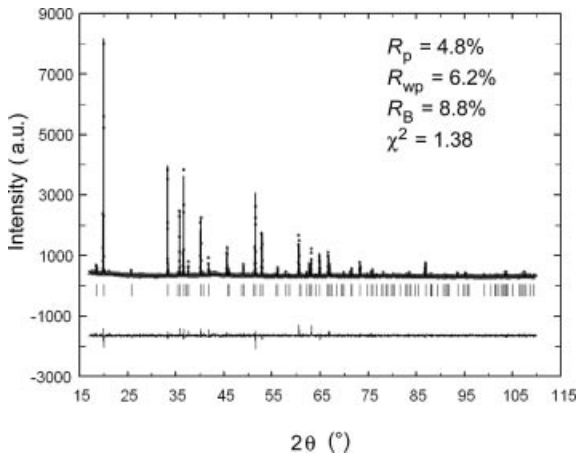


Figure 5. Rietveld refinement plot (experimental, calculated, and difference curve) for ramsdellite $LiTiVO_4$ in the space group *Pbnm* and with $a$ = 5.0090(8), $b$ = 9.5570(1), $c$ = 2.94242(3) Å.

The computational data indicate that the enthalpy of the transformation reaction is lower for V than for Ti. As discussed above, assuming that the entropy change is similar, the transformation temperature should be lower for V than for Ti, which is not what we found experimentally. We note that kinetics may be the origin of this mismatch between estimated and experimental transition temperatures.

The transformation from spinel to ramsdellite for the Cr system occurs over a rather wide temperature range. Transformation begins at around 900 °C but is not complete until about 1250 °C. The evolution of the ratio of each polymorph with temperature was followed by means of high temperature X-ray diffraction. The results are shown in Figure 6. It can be seen that the spinel continuously transforms to ramsdellite following the typical behavior of a two-phase transformation, and a new pure ramsdellite phase is obtained at 1250 °C. The corresponding XRD pattern is similar to that shown in Figure 5 and Rietveld refinement was performed using the same structural model as above ($R_{wp}$ = 0.183; $R_p$ = 0.138; $R_B$ = 0.079, $\chi^2$ = 3.9). The lattice parameters of this new ramsdellite are also given in Table 2. The difference in the temperature needed to obtain $LiTi_2O_4$(R) and $LiTiCrO_4$(R) seems to be related, at least partially, to the larger energy difference calculated between spinel and ramsdellite for $LiTiCrO_4$ in comparison to $LiTi_2O_4$ (see above).

A quite different behavior was found for the Mn and Fe cases. Treatment at temperatures ranging from 925 to 1400 °C produced either no transformation or mixtures of several phases without any evidence of a ramsdellite phase. It therefore seems that the high-temperature polymorph cannot be stabilized for these two cases. This is obviously expected from the computational results, which indicate that the inverse spinel↔ramsdellite transformation is entropically hindered.

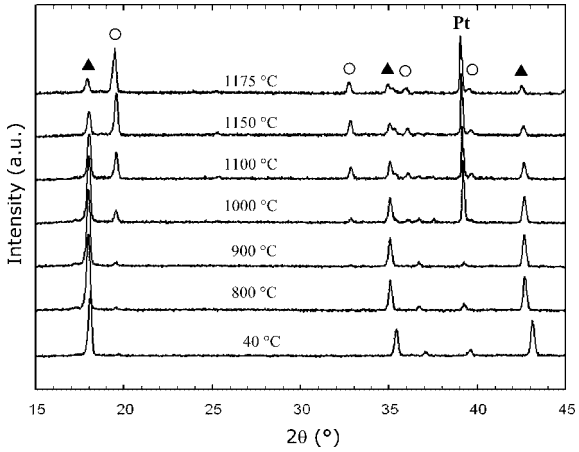


Figure 6. Temperature-resolved in situ X-ray diagrams of the spinel to ramsdellite transition of $LiTiCrO_4$ between 40 and 1175 °C. ▲ spinel reflections, ○ ramsdellite reflections.

We will now consider the possible mechanism for the spinel–ramsdellite transformation. A mechanism for this transformation can be proposed based on the model proposed by Thackeray and co-workers for the process occurring in ramsdellite-like γ-$MnO_2$.[31,32] A schematic representation is depicted in Figure 7 and can be described in two stages, as follows. The spinel structure initially responds (Figure 7, a) with a cooperative displacement of one quarter of the titanium ions (see arrows on filled octahedra) and half of the lithium ions (see arrows on filled circles). Displacement of the metals is followed by a shear operation of the spinel blocks perpendicular to the (111) spinel direction (dashed arrows in Figure 7, a). A second shear operation in the same direction (dashed arrows in Figure 7, b) produces the hexagonal packed $(Ti_2)O_4$ framework of $LiTi_2O_4$(R) that is shown in Figure 7 (c). It is evident that a relatively high energy is needed to displace the titanium ions from the octahedral sites of the spinel structure to interstitial octahedral sites. The use of high temperatures assists the diffusion of the titanium and lithium cations and rearrangement of the oxygen ions from cubic close packing in the spinel structure to hexagonal packing in the ramsdellite structure. This structural transformation does not, in principle, affect either the tetrahedral coordination of Li or the octahedral coordination of Ti, but it does affect the structural connection between the polyhedra. Thus, while Li ions in the spinel structure are located in the vicinity of titanium ions in vertex-shared octahedra, in the ramsdellite structure the Li ions are located in the vicinity of titanium ions that reside in neighboring face-sharing octahedra. This produces an increase in the electrostatic interaction between face-sharing Li and Ti polyhedra, which means that the phase transformation should be favored for spinels with a normal cationic distribution (the normal spinel structure), whereas an inversion of the cationic distribution, especially of highly charged transition metals in the tetrahedral sites, will destabilize the ramsdellite structure due to electrostatic repulsion

 © 2007 Wiley-VCH Verlag GmbH & Co. KGaA, Weinheim 

between metal ions in face-sharing polyhedra. Thus, kinetic factors might also hinder the inverse spinel↔ramsdellite transformation.

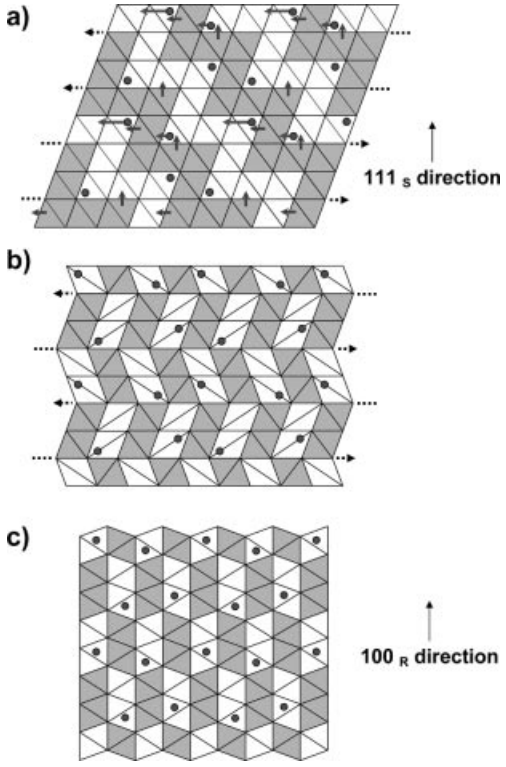


Figure 7. Proposed schematic representation for the spinel $LiTiMO_4$ to ramsdellite $LiTiMO_4$ transformation based on refs.[31,32] Filled octahedra: $(M,Ti)O_6$; small circles: $Li^+$ ions.

In agreement with this $LiTi_2O_4$(S) and $LiTiVO_4$(S),[19] which are normal spinels, transform readily into the corresponding ramsdellites. $LiTiCrO_4$(S) has been reported by several authors to adopt a normal spinel structure (space group *Fd3m*) with all Li ions at the (tetrahedral) 8a site and a random distribution of Ti and Cr over the (octahedral) 16d site, corresponding to the formulation $[Li]_t[Ti,Cr]_oO_4$,[20,33–36] although a slight inversion (12%) in cationic site distribution regarding Li and Ti has been found by neutron diffraction experiments.[15] This, in addition to the higher enthalpy calculated for the transformation, would account for a more hindered phase transition and mean that the full transformation requires a much higher temperature than in the case of Ti or V. The situation is different for Mn and Fe, however, which present an important degree of inversion, with the proposed cationic distributions being $[Li_{0.66}Ti_{0.34}]_{8a}[Li_{0.34}MnTi_{0.66}]_{16d}O_4$[16,18] and $[Li_{0.47}Fe_{0.53}]_{8a}[Li_{0.53}Fe_{0.47}Ti]_{16d}$.[17,22] We have already discussed that the spinel↔ramsdellite transformation is entropically controlled therefore, in view of the proposed mechanism, the phase transition for the Mn and Fe systems will also be impeded due to enhanced electrostatic repulsions between higher valent cations in neighboring face-sharing polyhedra. The transformation into ramsdellite in these cases must therefore be linked to a more reconstructive mechanism in which all lithium ions would remain in the tetrahedral position and all higher valent transition metals would occupy the octahedral position.

### Electrochemistry of the Novel $LiTiVO_4$ and $LiTiCrO_4$ Ramsdellites

The electrochemical behavior of $LiTiVO_4$(R) and $LiTiCrO_4$(R) can be fully interpreted assuming the replacement of $Ti^{3+}$ in $LiTi_2O_4$ by $V^{3+}$ and $Cr^{3+}$, respectively. Such a hypothesis is in good agreement with the computational results, and has been confirmed by magnetic susceptibility measurements, as reported elsewhere.[13,14,30]

As expected, no significant differences were found for the three ramsdellites $LiTiMO_4$ (M = Ti, V, and Cr) regarding intercalation of lithium (reduction). The same voltage profile is observed down to 1 V, with the plateau characteristic of reduction of $Ti^{4+}$ to $Ti^{3+}$ at about 1.4 V (see part a in Figure 2, continuous line). This result can be explained in terms of the occurrence of the same reaction in all three cases, namely

$$LiTi^{4+}M^{3+}O_4(R) + xLi \rightarrow Li_{1+x}\ Ti^{4+}{}_{1-x}Ti^{3+}{}_x\ M^{3+}{}_xO_4(R);\ x < 1 \quad (5)$$

Figure 8 shows the first charge of a Li//$LiTiMO_4$(R) cell for M = Ti, V, and Cr. Any differences in polarization and quantity of lithium extracted are mainly due to the different electrical conductivity that is expected for the different ramsdellites. The oxidative reaction can be written as

$$LiTi^{4+}M^{3+}O_4(R) \rightarrow Li_{1-x}Ti^{4+}M^{3+}{}_{1-x}M^{4+}{}_xO_4(R) + xLi;\ x < 1 \quad (6)$$

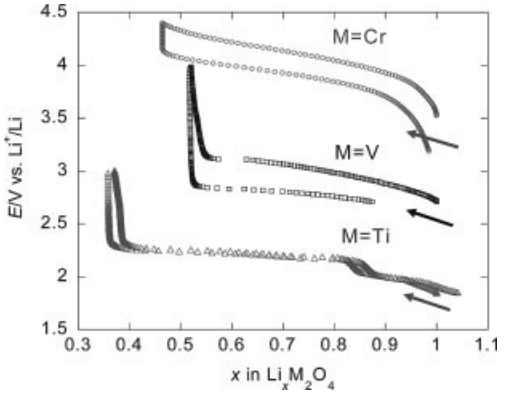


Figure 8. Typical voltage composition plot obtained from galvanostatic experiments (0.1 $mA\,cm^{-2}$) on cells $LiTiMO_4$//Li. Data were recorded by starting the cells first on oxidation followed by reduction down to the initial open circuit voltage.

For M = Ti this process occurs at an average voltage of 1.9 V, as reported previously.[4,5,8] When $Ti^{3+}$ is replaced by $V^{3+}$ the average oxidation voltage increases to 3.1 V, which is characteristic of $V^{III}$ oxidation. The oxidation voltage for $LiTiCrO_4$(R) is shifted to an average voltage of 4.2 V, which is in agreement with the value observed for the $Cr^{4+}/Cr^{3+}$ redox couple in related systems.[37,38] Since the average oxidative voltage of $LiTi_2O_4$ has increased by more than 1 and 2 V for $LiTiVO_4$ and $LiTiCrO_4$, respectively, the electro-

 © 2007 Wiley-VCH Verlag GmbH & Co. KGaA, Weinheim 

chemical performance of a lithium cell made from either $LiTiVO_4$(R) or $LiTiCrO_4$(R) as the positive electrode is much better. The maximum quantity of lithium that can be de-intercalated is expected to be constant as it is limited by the content of lithium and $M^{3+}$ (one ion per formula unit), therefore the maximum theoretical capacity of $LiTiVO_4$(R) or $LiTiCrO_4$(R) is around 160 $mAh\,g^{-1}$, as in $LiTi_2O_4$. However, the higher oxidation voltage of $LiTiVO_4$ and $LiTiCrO_4$ results in a significant increase of the specific energy delivered by the electrode material of 50% and 100%, respectively.

To sum up the electrochemical performance, it is interesting to note that the new ramsdellites described herein present two different processes at very different voltages that correspond to the oxidation of $V^{3+}$ and $Cr^{3+}$ at high voltage and the reduction of $Ti^{4+}$ at low voltage. The application of these materials in lithium batteries as high voltage cathodes might make use of the former process, while if a low voltage anode material is desired the low voltage process could be used. More detailed studies on performances, mainly regarding cyclability, will be published elsewhere,[13,14] while the influence of the $Ti^{3+}/M^{3+}$ ratio on performance is now under investigation.

## Conclusions

As part of our search for novel materials with potential interest as electrodes in lithium batteries, we have reported the preparation of novel $LiTiMO_4$ ramsdellites by inducing a temperature-driven transformation in the corresponding spinel-like forms and have combined computational and experimental techniques to study this $LiTiMO_4$ (spinel) ↔ $LiTiMO_4$ (ramsdellite) transformation.

The computational study performed on the compounds $LiTiMO_4$ (M = Ti, V, Cr, Mn, and Fe) indicates that the spinel form is enthalpically more stable than the corresponding ramsdellite. However, in agreement with the order of the total energy differences (below 40 $kJ\,mol^{-1}$ per formula unit), the spinels can be transformed into their corresponding ramsdellites by thermal treatment. While it is possible to compute the enthalpy of the transformation, it is impossible to predict the temperature at which it will occur. The reasons for these limitations are: (i) first-principle methods refer to zero Kelvin, (ii) calculations are performed for perfectly ordered structures while, experimentally, M and Ti ions randomly occupy the octahedral sites of the ramsdellite/spinel structure. Hence no information about the entropy that accompanies the transformation can be obtained from first principles. The entropy of the transformation has been approximated here from values of temperatures and entropies available in the literature. The estimated temperatures for the $LiTiMO_4$(S) ↔ $LiTiMO_4$(R) transformation are lower than 1600 °C for all the metals studied, hence this transformation is feasible from a thermodynamic point of view. Since the experimental findings showed that the transition metal ions can move to the tetrahedral sites, in a second step we have estimated the temperature of the $LiTiMO_4$(inverse spinel) ↔ $LiTiMO_4$(R) transformation. Our data support that this transformation is entropically hindered.

Experimental results have shown that thermal treatment of spinels $LiTiMO_4$ induces a phase transformation to the ramsdellite-like polymorph for M = Ti, V, and Cr. Indeed, the new ramsdellites $LiTiMO_4$ (M = V and Cr) have been isolated and characterized. Such a transformation could not be detected in the explored temperature range ($T \leq$ 1400 °C) for Fe- and Mn-containing spinels. Therefore the experimental results corroborate that the degree of inversion of the spinel has an influence on the transformation: the transformation only occurs if the starting spinel has a normal cationic distribution while it does not for the inverse spinel. The former situation is found for M = Ti and V, and even for Cr with only a slight degree of inversion, whereas the second situation is found for M = Mn and Fe. We have proposed a mechanism for the transformation in which strong cationic repulsions exist along the transformation pathway in the case of inverse spinels. Thus, in light of the experimental and computational results we can conclude that the impossibility of transforming the Mn and Fe inverse-spinel into their ramsdellite forms is due to at least two reasons, firstly that the transformation is entropically hindered and secondly that there are kinetic limitations due the high energetic barriers that should be overcome during the transformation. At present we cannot say whether the entropy or the kinetic impediment is the main limiting factor of this transformation.

The substituted $LiTiMO_4$ (M = Ti, V and Cr) compounds contain $Ti^{4+}$ and $M^{3+}$, both of which are ions that are electrochemically active in a lithium cell on reduction ($Ti^{4+}/Ti^{3+}$ couple) or oxidation ($M^{3+}/M^{4+}$ couple). In all the prepared $LiTiMO_4$ ramsdellites the reduction of $Ti^{4+}$ occurs at a similar voltage (1.4 V vs. lithium electrode) and develops the same capacity (160 $Ah\,kg^{-1}$). On the other hand, the measured oxidation potentials of the $M^{3+}$ ions in $LiTiMO_4$ range from around 2 V for $LiTi_2O_4$, to about 3 V for $LiTiVO_4$ and 4 V for $LiTiCrO_4$, with the two latter cases being particularly interesting. The high voltage observed when $LiTiMO_4$(R) (M = V, Cr) are oxidized may allow further development of new high-energy positive-electrode materials for rechargeable lithium batteries.

Taking into account the promising electrochemical performances of $LiTiMO_4$(R), the possible relationship between the transformation of the spinels and the inversion factor may be considered as a guide in the search for new electrode materials for rechargeable lithium batteries based on the ramsdellite structure.

## Methodology

### Computational

The total energy of $LiTiMO_4$ (M = Ti, V, Cr, Mn and Fe) was calculated using the Vienna ab initio Simulation Package (VASP).[39] The exchange-correlation energy was approximated in the generalized gradient approximation (GGA), using ultra-soft

 © 2007 Wiley-VCH Verlag GmbH & Co. KGaA, Weinheim 

pseudopotentials. A plane-wave basis set with a kinetic energy cutoff of 500 eV was used. The reciprocal space sampling was done with *k*-point grids of $4\times4\times4$. Relaxation was allowed and the final energies of the optimized geometries were recalculated so as to correct for changes in basis during relaxation. All the calculations are spin-polarized. Calculations were initialized considering a ferromagnetic ordering of ions for normal spinels $Li(TiM)_oO_4$ and ramsdellites. In the case of inverse spinels $[Li_{0.5}M_{0.5}]_t$-$[TiM_{0.5}Li_{0.5}]_oO_4$ antiferromagnetic interactions between ions in the tetrahedral and octahedral sites were considered.

**Experimental**

The synthesis of ramsdellite $LiTiMO_4$ (M = Ti, V, Cr, Mn, and Fe) was attempted by heating the corresponding spinel-like compounds in the hope of achieving the polymorphic transformation. Different temperatures above 900 °C were used until either full transformation to ramsdellite or decomposition of the corresponding spinel was detected. The spinels were prepared by a ceramic procedure. Thus, in order to minimize loss of lithium oxide, a mixture of $Li_2CO_3$ and $TiO_2$ in a 1:1 ratio was fired at 700 °C for 24 h to produce $Li_2TiO_3$. The carbonate-free product was mixed with stoichiometric amounts of $TiO_2$ and $M_2O_3$ (M = Cr, Mn, or Fe) and heated at different temperatures. For M = Ti and V, handling and mixing of the air-sensitive reagents $V_2O_3$ and $Ti_2O_3$ was done under argon in a dry glove box (water content < 1 ppm). Mixtures were pressed, wrapped in copper foil, and placed into a quartz ampoule, which was vacuum-sealed and fired. In all cases a typical treatment consisted of heating for 24 h followed by quenching to room temperature.

A preliminary structural characterization was made by means of powder X-ray diffraction with a Bruker D8 high-resolution X-ray powder diffractometer using monochromatic Cu-$K_{\alpha1}$ ($\lambda$ = 1.5406 Å) radiation produced with a germanium primary monochromator. The diffractometer was equipped with an MBraun PSD-50M position sensitive detector (PSD). For the case of samples containing either trivalent V or Ti the XRD patterns were collected in transmission mode using glass capillaries of 0.5-mm diameter, which were filled inside a glove box. Diffraction patterns were analyzed using the FullProf program.[40] X-ray diffraction experiments at high temperature were performed in the case of $LiTiCrO_4$ with a Siemens D5000 diffractometer working in reflection mode (Cu-$K_{\alpha1}$ radiation) equipped with a Bühler HDKS1 high-temperature chamber. Diffraction patterns at temperatures ranging from 800 to 1200 °C were collected in a selected $2\theta$ range (15–45°).

Electrochemical experiments were performed in Swagelok cells with the following configuration: Li|$LiPF_6$ (1 M) in EC (ethylene carbonate) + DMC (dimethyl carbonate) (2:1) host material + carbon black + binder. Positive electrodes were fabricated as pellets 8 mm in diameter from a mixture consisting of 75–85% (w/w) $LiTiMO_4$ (M = Ti, Cr, V), 20–10% (w/w) carbon black, and 5% (w/w) Kynarflex® (kindly provided by Elf-Atochem). A disk of lithium metal was used as the negative and reference electrode. Commercial Selectipur LP31® (Merck) electrolyte solution for lithium batteries was used. Cells were cycled under galvanostatic conditions at a current density of 0.1 $mA\,cm^{-2}$.

## Acknowledgments

Financial support for this research was provided by the Ministerio de Educación y Ciencia (MAT2004-03070-C05-01 and the Ramon y Cajal Program) and the Comunidad de Madrid (S-0505/PPQ/0358). MEAD is grateful to CIEMAT Supercomputing Centre for access to the jen50 SGI. The authors also thank Dr. Martín-Gil for help in the Experimental Section of vanadium and chromium systems and Dr. E. Moran for valuable comments and discussions. The authors are also grateful to the Universidad San Pablo, Madrid for continuous financial support.

[1] B. Morosin, J. C. Mikkelsen, *Acta Crystallogr., Sect. B* **1979**, *35*, 798–800.
[2] I. Abrahams, P. G. Bruce, W. I. F. David, A. R. West, *J. Solid State Chem.* **1989**, *78*, 170–177.
[3] M. E. Arroyo y de Dompablo, A. Varez, F. Garcia-Alvarado, *J. Solid State Chem.* **2000**, *153*, 132–139.
[4] A. Kuhn, R. Amandi, F. Garcia-Alvarado, *J. Power Sources* **2001**, *92*, 221–227.
[5] R. K. B. Gover, J. R. Tolchard, H. Tukamoto, T. Murai, J. T. S. Irvine, *J. Electrochem. Soc.* **1999**, *146*, 4348–4353.
[6] M. Arroyo y de Dompablo, E. Moran, A. Varez, F. Garcia-Alvarado, *Mater. Res. Bull.* **1997**, *32*, 993–1001.
[7] J. Akimoto, Y. Gotoh, Y. Oosawa, N. Nonose, T. Kumagai, K. Aoki, H. Takei, *J. Solid State Chem.* **1994**, *113*, 27–36.
[8] A. Kuhn, C. Baethz, F. García-Alvarado, *J. Power Sources* **2007**, in press.
[9] K. Petrov, I. Tsolovski, *Phys. Status Solidi A* **1980**, *58*, K85–K88.
[10] R. K. B. Gover, J. T. S. Irvine, A. A. Finch, *J. Solid State Chem.* **1997**, *132*, 382–388.
[11] J. Reed, G. Ceder, *Chem. Rev.* **2004**, *104*, 4513–4533.
[12] F. Garcia-Alvarado, M. Martin-Gil, A. Kuhn, in *Synthesis and Electrochemical Behavior of Ramsdellite LiCrTiO4*, *Materials Research Society Symposium Proceedings Vol. 756* (Eds.: P. Knauth, J. M. Tarascon, E. Traversa, H. L. Tuller), **2003**, pp. 255–260.
[13] A. Kuhn, M. Martín-Gil, F. García-Alvarado, *Chem. Mater.* **2007**, submitted.
[14] A. Kuhn, M. Martín-Gil, F. García-Alvarado, *Z. Anorg. Allg. Chem.* **2007**, submitted.
[15] M. A. Arillo, M. L. Lopez, M. T. Fernandez, M. L. Veiga, C. Pico, *J. Solid State Chem.* **1996**, *125*, 211–215.
[16] M. A. Arillo, G. Cuello, M. L. Lopez, P. Martin, C. Pico, M. L. Veiga, *Solid State Sci.* **2005**, *7*, 25–32.
[17] M. A. Arillo, M. L. Lopez, E. Perez-Cappe, C. Pico, M. L. Veiga, *Solid State Ionics* **1998**, *107*, 307–312.
[18] N. Krins, F. Hatert, K. Traina, L. Dusoulier, I. Molenberg, J. F. Fagnard, P. Vanderbemden, A. Rulmont, R. Cloots, B. Vertruyen, *Solid State Ionics* **2006**, *177*, 1033–1040.
[19] J. Barker, M. Y. Saidi, J. L. Swoyer, *Solid State Ionics* **2004**, *167*, 413–418.
[20] T. Ohzuku, K. Tatsumi, N. Matoba, K. Sawai, *J. Electrochem. Soc.* **2000**, *147*, 3592–3597.
[21] Y. K. Sun, D. J. Jung, Y. S. Lee, K. S. Nahm, *J. Power Sources* **2004**, *125*, 242–245.
[22] A. D. Robertson, H. Tukamoto, J. T. S. Irvine, *J. Electrochem. Soc.* **1999**, *146*, 3958–3962.
[23] F. Zhou, M. Cococcioni, C. A. Marianetti, D. Morgan, G. Ceder, *Phys. Rev. B* **2004**, *15*, 235121-1–235121-8.
[24] M. K. Aydinol, A. F. Kohan, G. Ceder, K. Cho, J. Joannopoulos, *Phys. Rev. B* **1997**, *56*, 1354–1365.
[25] M. E. Arroyo-de Dompablo, M. Armand, J. M. Tarascon, U. Amador, *Electrochem. Commun.* **2006**, *8*, 1292–1298.
[26] M. E. Arroyo y de Dompablo, A. Van der Ven, G. Ceder, *Phys. Rev. B* **2002**, *66*, 064112-1–064112-9.
[27] A. Navrotsky, J. O. Kleppa, *J. Inorg. Nucl. Chem.* **1967**, *29*, 2701.
[28] M. E. Arroyo y de Dompablo, J. Morales, *J. Electrochem. Soc.* **2006**, *153*, 2098–2102.
[29] M. E. Arroyo y de Dompablo, C. Marianetti, A. Van der Ven, G. Ceder, *Phys. Rev. B* **2001**, *63*, 144107-1–144107-9.

 © 2007 Wiley-VCH Verlag GmbH & Co. KGaA, Weinheim 

[30] M. Martín-Gil, *Nuevos Electrodos Para Baterías Recargables de Litio*, Ph.D. thesis, Universidad San Pablo CEU, Madrid, **2006**.
[31] M. M. Thackeray, R. H. Rossouw, R. J. Gummow, D. C. Liles, K. Pearce, A. de Kock, W. I. F. David, S. Hull, *Electrochim. Acta* **1993**, *38*, 1259–1267.
[32] M. M. Thackeray, *Prog. Solid State Chem.* **1997**, *25*, 1–71.
[33] P. M. Lambert, P. P. Edwards, M. R. Harrison, *J. Solid State Chem.* **1990**, *89*, 345–360.
[34] E. Kordes, E. Rottig, *Z. Anorg. Chem.* **1951**, *264*, 34–47.
[35] G. Blasse, *Z. Anorg. Allg. Chem.* **1964**, *331*, 44–50.
[36] G. Blasse, *J. Inorg. Nucl. Chem.* **1964**, *26*, 1473–1474.
[37] H. Kawai, M. Nagata, H. Tukamoto, A. R. West, *J. Power Sources* **1999**, *82*, 67–72.
[38] A. Kajiyama, K. Takada, K. Arihara, T. Inada, H. Sasaki, S. Kondo, M. Watanabe, *J. Electrochem. Soc.* **2003**, *150*, A157–A160.
[39] J. F. G. Kresse, *Comput. Mat. Sci.* **1996**, *15*, 6.
[40] J. Rodriguez-Carvajal, *Physica B* **1993**, *192*, 55–69.

Received: October 21, 2006
Published Online: May 25, 2007

 © 2007 Wiley-VCH Verlag GmbH & Co. KGaA, Weinheim 

DOI: 10.1002/ejic.200601077

# Alternative Synthesis, Density Functional Calculations and Proton Reactivity Study of a Trinuclear [NiFe] Hydrogenase Model Compound

**Frank Lauderbach,[a] Raju Prakash,*[a][‡] Andreas W. Götz,*[b][‡‡] Marcela Munoz,[b] Frank W. Heinemann,[a] Ulrich Nickel,[b] Bernd A. Hess,[c][†] and Dieter Sellmann[a][†]**

**Keywords:** Constant potential coulometry / Density functional calculations / Iron / Nickel / NiFe hydrogenases / S ligands

The trinuclear complex [('$S_2$')\{Ni($PMe_3$)\}$_2$Fe(CO)('$S_2$')$_2$] (**1**) {'$S_2$'$^{2-}$ = 1,2-benzenedithiolate(2–)} has been reported as a structural as well as functional model for [NiFe] hydrogenases since it contains key structural features of the [NiFe] hydrogenase active site, and is oxidized by protons to give [**1**]$^+$ and $H_2$. Complex **1** formed as an unexpected product from the reaction of [Fe(CO)$_2$('$S_3$')]$_2$ {'$S_3$'$^{2-}$ = bis(2-mercaptophenyl) sulfide(2–)} and [Ni($PMe_3$)$_2$('$S_2$')]. Both the iron and nickel centers of **1** are chelated by '$S_2$' donors, but not with any '$S_3$' ligand. In order to understand this reaction, the new precursor [Fe(CO)$_2$($^{si}S_3$)]$_2$ (**2**) {$^{si}S_3^{2-}$ = bis(2-mercapto-3-trimethylsilylphenyl) sulfide(2–)} was synthesized. Compound **2** readily loses its CO ligand to give [Fe(CO)($^{si}S_3$)]$_2$ (**3**), which consists of two 16 valence electron fragments and could be isolated in the solid state. Conversion of **3** to **2** is feasible with gentle bubbling of CO gas for about 2 min. Treatment of **2** with [Ni($PMe_3$)$_2$('$S_2$')] resulted exclusively in the formation of complex **1**, which confirms that all three '$S_2$' ligands in **1** originate from [Ni($PMe_3$)$_2$('$S_2$')]. Therefore, an alternative synthesis of **1**, which does not involve any '$S_3$' ligand, has been developed. Density functional theory (DFT) calculations suggest that the oxidation states of the metal centers are $Fe^{II}$ and $Ni^{II}$ and do not change upon oxidation of **1** to [**1**]$^+$. The unpaired electron in [**1**]$^+$ is located to a large extent on the nickel atoms and the adjacent thiolate donor functions. The charge, however, is distributed over the whole cluster, main parts residing on the '$S_2$' ligands. Preliminary constant potential coulometric measurements indicate that **1** mediates the reduction of protons to dihydrogen at a mild potential (–0.48 V vs. NHE). Based upon these experimental and theoretical results, plausible mechanisms for this reduction are briefly discussed.
(© Wiley-VCH Verlag GmbH & Co. KGaA, 69451 Weinheim, Germany, 2007)

## Introduction

Hydrogenases comprise a fundamental group of bacterial enzymes that catalyze the reversible interconversion of protons and molecular hydrogen. Thus, they play a key role in molecular bioenergetics.[1] In recent years, interest in hydrogenases has intensified due to their environmental and industrial potential in the context of the development of a pollution-free and sustainable hydrogen economy.[2] Hydrogenases can be divided into two main groups based on the type of metal containing active sites, namely, [NiFe][3] and [Fe]-only[4] hydrogenases. [NiFe] hydrogenases represent the major class among hydrogenases, consisting of a dinuclear nickel–iron active site (Figure 1).

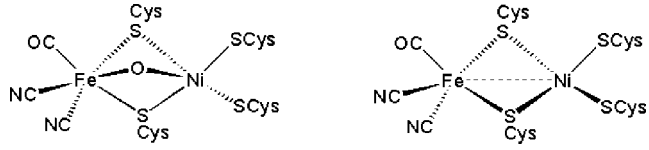


Figure 1. Schematic structures of the active sites of [NiFe] hydrogenases. Left: oxidized form from *D. gigas.*[3a,3b] Right: Reduced form from *D. vulgaris* Miyazaki.[3d]

Numerous spectroscopic,[5] structural,[3,6] and theoretical[7] studies on various enzymes have provided further insight into the structure and function of the active sites of [NiFe] hydrogenases. Despite these efforts, the exact nature of the catalytic cycle and the exact oxidation state of nickel during the catalytic cycle remain uncertain. This has prompted the synthesis of a number of low-molecular weight di- and oligonuclear heterometallic complex analogues to the active site of the [NiFe] enzymes.[8,9] Studies on such compounds can lead to a better understanding of the properties of the active site and can shed light on the catalytic reaction that takes place in the enzyme. The advantage of such models is that they are low-molecular

[a] Institut für Anorganische Chemie der Universität Erlangen-Nürnberg,
Egerlandstrasse 1, 91058 Erlangen, Germany
Fax: +49-9131-852-1165
E-mail: raju.prakash@chemie.uni-erlangen.de
[b] Institut für Physikalische und Theoretische Chemie der Universität Erlangen-Nürnberg,
Egerlandstrasse 3, 91058 Erlangen, Germany
[c] Lehrstuhl für Theoretische Chemie der Universität Bonn,
Wegelerstrasse 12, 53115 Bonn, Germany
[‡] Present address: Institut für Organische Chemie der Universität Erlangen-Nürnberg, Henkestrasse 42, 91054 Erlangen, Germany.
[‡‡] Present address: Department of Theoretical Chemistry, Faculty of Sciences, Vrije Universiteit Amsterdam, De Boelelaan 1083, 1081 HV Amsterdam, The Netherlands;
E-mail: agoetz@few.vu.nl
[†] Deceased.

 © 2007 Wiley-VCH Verlag GmbH & Co. KGaA, Weinheim 

weight compounds and therefore are often more easily isolated and examined by various physicochemical methods than the macromolecular enzyme itself. In addition, electronic and steric modifications can be generated by adjusting the ligand environment.

Recently, two [NiFe] model complexes $[Fe(CO)_2(CN)_2(\mu\text{-}SCH_2CH_2CH_2S)Ni(S_2CNR_2)]$ [R = Et and -$(CH_2)_5$-] were synthesized which up to now resemble the structural features of hydrogenases most closely.[10] However, in practice, none of the reported sulfur-bridged [NiFe] model complexes shows any hydrogenase-like reactivity.

We have previously reported on the sulfur-bridged trinuclear complex [('$S_2$')\{$Ni(PMe_3)$\}$_2$Fe(CO)('$S_2$')$_2$] (**1**) {'$S_2$'$^{2-}$ = 1,2-benzenedithiolate(2–)}, which stoichiometrically reduces protons to dihydrogen and in turn gets oxidized to [('$S_2$')\{$Ni(PMe_3)$\}$_2$Fe(CO)('$S_2$')$_2$]$^+$ ([**1**]$^+$).[11] The reversible conversion of **1**/[**1**]$^+$ was also achieved with ferrocenium salt and $NBu_4BH_4$, respectively. Moreover, the structural parameters (bond lengths and angles) of **1** and [**1**]$^+$ are nearly identical. This structural rigidity during the redox reaction indicates a low reorganization barrier and therefore favors a rapid electron transfer.[12] This result is insofar highly interesting as many oxidoreductases undergo redox reactions which are accompanied only by marginal structural changes. These intriguing facts inspired us to investigate the properties of **1** in greater detail. Herein, we describe the exact formation pathway and a novel straightforward synthetic route of **1**. Density functional Theory (DFT) calculations reveal important insights into the oxidation reaction of **1** to [**1**]$^+$. In addition, we report preliminary coulometric studies which employed **1** as an electrocatalyst for the reduction of protons to dihydrogen at a low reduction potential.

## Results and Discussion

### Synthesis

It has already been reported that the trinuclear NiFe complex **1** formed by the reaction of [Fe(CO)$_2$('$S_3$')]$_2$ {'$S_3$'$^{2-}$ = bis(2-mercaptophenyl) sulfide(2–)} with [$Ni(PMe_3)_2$('$S_2$')] according to Scheme 1.[11] In this reaction compound **1** was the only isolated product with 18% yield (it is not possible to give the exact stoichiometry for Scheme 1, however, the given numbers denote only the ratio of the initial reactants used). Both the iron as well as the nickel coordination centers of **1** are chelated by '$S_2$' donors, but surprisingly not with any '$S_3$' ligand. Therefore, it is interesting to know how **1** can be formed from the reactants in which the Fe center is not bearing any '$S_3$' ligand. We can think about two possible pathways for the formation of **1**: in the first route, an initial reductive cleavage of the '$S_3$' ligand at the iron center to an '$S_2$' ligand and subsequent reaction of this intermediate species with [$Ni(PMe_3)_2$('$S_2$')] to form **1**; in the second route, a ligand exchange type of reaction in which all '$S_2$' ligands originate from the reactant [$Ni(PMe_3)_2$('$S_2$')]. If **1** would be formed via the reductive cleavage pathway, the use of a derivatized '$S_3$' ligand in the dinuclear iron precursor complex should result in a new trinuclear NiFe complex containing at least one derivatized '$S_2$' ligand. Conversely if the reaction proceeded via a ligand-exchange pathway, the use of a derivatized '$S_3$' ligand in the dinuclear iron precursor complex should result in exclusively the trinuclear complex **1**. Herein we have chosen the twofold silylated derivative of the '$S_3$' ligand, $^{si}S_3$–$H_2$ {$^{si}S_3^{2-}$ = bis(2-mercapto-3-trimethylsilylphenyl) sulfide(2–)}, for the synthesis of the derivative of the [Fe(CO)$_2$('$S_3$')]$_2$ precursor. Since the $SiMe_3$ group is a good NMR probe, it enables the detection of the reaction pathway of the formation of **1**.

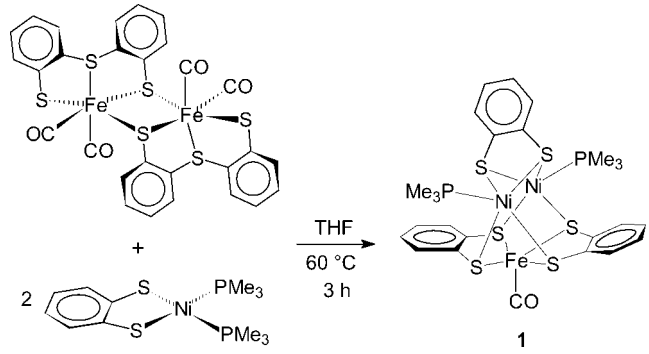


Scheme 1. Synthesis of complex **1**.

The silylated precursor complex [Fe(CO)$_2$($^{si}S_3$)]$_2$ (**2**) was prepared similarly to the synthesis of the unsubstituted parent compound as reported in the literature,[13] except that the reaction was performed under CO atmosphere. Addition of the ligand $^{si}S_3$–$H_2$ to [Fe(bda)(CO)$_3$] (bda = benzylideneacetone) in THF led to a dark green solution and gas evolution. Keeping this solution at –20 °C for two weeks, brown crystals suitable for X-ray structure analysis were obtained. The molecular structure of **2** is shown in Figure 2 and selected bond lengths and bond angles are given in Table 1. The structural parameters of the silylated centrosymmetric compound **2** differ only marginally from the parent compound [Fe(CO)$_2$('$S_3$')]$_2$.[13] Complex **2** consists of two distorted octahedral fragments that are linked by an edge. Within these fragments, the thiolate donors are *cis* to each other. One CO is coordinated *trans* to a bridging thiolate S atom, whereas the other CO is in *trans* position to the thioether S donor. The distances around Fe, including Fe–CO bonds, are in the range usually found for diamagnetic octahedral thiolate-thioether complexes.[12] The Fe–thiolate bond lengths are longer than the Fe–thioether bond lengths. The Fe–Fe distance of 341.51(6) pm indicates that there is no metal–metal interaction.

Compound **2** is diamagnetic and sparingly soluble in most common solvents. However, it is better soluble than the unsubstituted derivative. It is stable in CO saturated solvents for about two weeks. On prolonged standing, it gradually decomposes to form a stable five-coordinate dinuclear species [Fe(CO)($^{si}S_3$)]$_2$ (**3**).

The molecular structure of **3** is depicted in Figure 3 and selected bond lengths and angles are given in Table 1. The molecule can be described as two edge-linked distorted trigonal bipyramids. It contains two 16 valence electron frag-

 © 2007 Wiley-VCH Verlag GmbH & Co. KGaA, Weinheim 

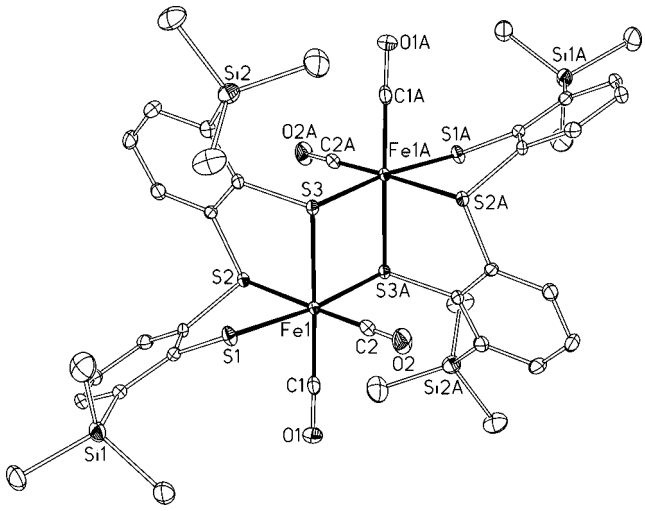


Figure 2. Molecular structure of **2** (50% thermal ellipsoids, H atoms and solvent molecules omitted).

Table 1. Selected bond lengths [pm] and angles [°] of **2** and **3**.

| | **2** | **3** |
|---|---|---|
| Fe1–Fe1A[a] | 341.51(6) | 271.95(6) |
| Fe1–S1 | 230.55(6) | 220.5(1) |
| Fe1–S2 | 227.91(6) | 226.7(2) |
| Fe1–S3 | 229.64(6) | 221.6(2) |
| Fe1–S3A[b] | 233.65(6) | 229.0(1) |
| Fe1–C1 | 179.5(2) | 178.0(4) |
| Fe1–C2 | 178.1(2) | – |
| C1–O1 | 114.3(3) | 114.1(4) |
| Fe1–S3–Fe1A[a] | 94.97(2) | 74.29(3) |
| S1–Fe1–S2 | 85.49(2) | 88.06(4) |
| S2–Fe1–S3 | 87.92(2) | 89.32(4) |

[a] Fe1A in **2** = Fe2 in **3**. [b] S3A in **2** = S6 in **3**.

ments that are linked by thiolate bridges. The CO ligands and thioether donors are in axial positions with the two thiolate donors and iron atoms lying in the base plane. Due to the loss of a CO group the Fe–Fe distance in **3** [271.95(6) pm] decreases by 70 pm compared to that of **2** [341.51(6) pm].

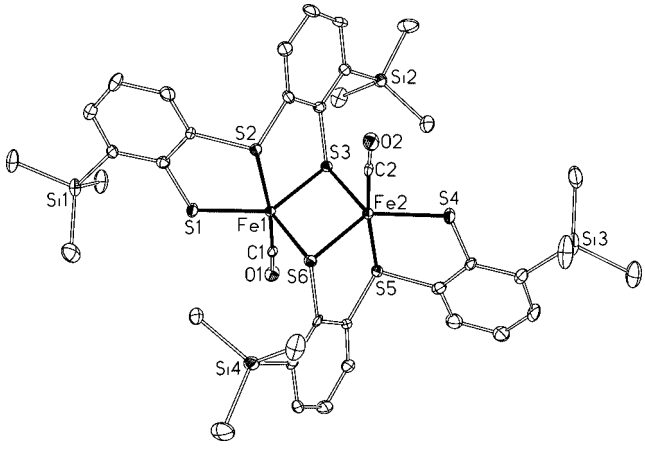


Figure 3. Molecular structure of **3** (50% thermal ellipsoids, H atoms and solvent molecules omitted).

When a solution of **3** in THF is either stirred under an atmosphere of CO for about 30 min or by bubbling of CO gas for about 2 min, compound **2** is formed again. The IR spectroscopic monitoring of the reaction confirmed that the ν(CO) band of **3** at 1975 $cm^{-1}$ vanished and two bands at 2032 $cm^{-1}$ and 1993 $cm^{-1}$ appeared which correspond to the ν(CO) bands of **2**.

In analogy to the synthesis of **1**, complex **2** was treated with $[Ni(PMe_3)_2(‘S_2’)]$ in THF at 60 °C for about 4 h. During the course of the reaction, the green suspension turned into a dark-red solution. The IR spectrum of the solution showed a ν(CO) band at 1916 $cm^{-1}$. Treatment of the solution with methanol resulted in a black-grey microcrystalline material. The $^1H$ and $^{13}C$ NMR spectra of the isolated material (see Experimental Section) showed signals identical to those obtained for **1**. It did not show any signals for $SiMe_3$ groups, indicating the unique formation of **1**. An X-ray structure determination of a single crystal obtained from this material further corroborated this result. Thus, the formation of complex **1** via the ligand exchange type of reaction has unambiguously been proven.

Based upon this encouraging result we devised an alternative way of synthesizing **1** without using the ‘$S_3$’ ligand (Scheme 2). Treatment of $FeCl_2·4H_2O$ with two equivalents of deprotonated ‘$S_2$’$^{2-}$ in THF led to a red solution of $[Fe(‘S_2’)_2]^{2-}$ which was subsequently treated with $PMe_3$ and $Ni(BF_4)_2·6H_2O$. After addition of one more equivalent of ‘$S_2$’$^{2-}$ a slurry formed. Upon diffusion of CO gas into the slurry, a dark red solution formed gradually. The IR spectrum of the solution exhibited a ν(CO) band at 1916 $cm^{-1}$. Further work-up of the mixture afforded complex **1** in an isolable yield of 18%. It is noteworthy that a strict order of addition of the reactants is necessary for the formation of **1** in this one-pot synthesis.

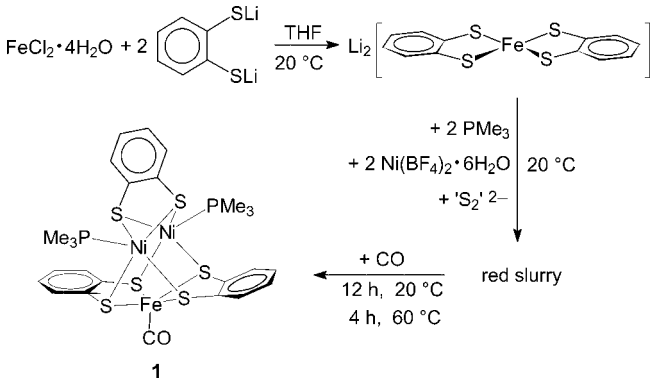


Scheme 2. Alternative synthesis of complex **1**.

## DFT Calculations

Complex **1** readily reacts with protons to give dihydrogen and $[\mathbf{1}]^+$. When the solution of $[\mathbf{1}]^+$ is treated with hydride, the reduced complex **1** is formed again. Both complex **1** and its oxidation product $[\mathbf{1}]^+$ were characterized by single-crystal X-ray structure analysis.[11] In order to gain insight

 © 2007 Wiley-VCH Verlag GmbH & Co. KGaA, Weinheim 

Table 2. Comparison of selected bond lengths [pm] and angles [°] obtained experimentally and calculated theoretically for **1** and $[\mathbf{1}]^+$ along with the structural changes **Δ** upon oxidation. The average of experimental values which are symmetry-equivalent in the calculations is given.

| | **[1]** | | $[\mathbf{1}]^+$ | | **Δ** | |
|---|---|---|---|---|---|---|
| | Calcd. | Exp. | Calcd. | Exp. | Calcd. | Exp. |
| Fe1–S1/S2 | 223.6 | 221.9(1) | 222.6 | 220.1(2) | –1.0 | –1.8 |
| Fe1–C1 | 173.6 | 173.8(5) | 175.4 | 174.4(8) | +1.8 | + 0.6 |
| Fe1–Ni1/Ni2 | 260.5 | 259.6(1) | 259.7 | 258.3(2) | –0.8 | –1.3 |
| Ni1–Ni2 | 241.5 | 240.5(1) | 246.0 | 243.1(2) | +4.5 | +2.6 |
| Ni1/Ni2–S2/S1 | 241.1 | 237.0(1) | 237.6 | 232.6(2) | –3.5 | –4.4 |
| Ni1/Ni2–P1 | 221.2 | 220.3(2) | 224.1 | 221.3(2) | +2.9 | +1.0 |
| Ni1/Ni2–S5 | 234.4 | 231.4(1) | 232.7 | 229.2(2) | –1.7 | –2.2 |
| S1–Fe1–S2 | 90.26 | 90.00(4) | 90.66 | 91.37(8) | +0.40 | +1.37 |
| S1–Fe1–S1A | 84.76 | 84.01(5) | 84.17 | 83.33(8) | –0.59 | –0.68 |
| S1–Fe1–S2A | 155.96 | 154.24(5) | 155.51 | 154.17(9) | –0.45 | –0.07 |
| Ni2–Fe1–Ni1 | 55.23 | 55.18(3) | 56.54 | 56.14(3) | +1.31 | +0.96 |
| Ni2/Ni1–Ni1/Ni2–Fe1 | 62.39 | 62.41(3) | 61.73 | 61.93(4) | –0.66 | –0.48 |

into this redox process and to determine the details of the electronic structure, DFT calculations were carried out on cluster **1** and its cation $[\mathbf{1}]^+$. The symmetry has been constrained to $C_{2v}$ for both the neutral and the oxidized cluster in all calculations. Therefore, one of the $PMe_3$ groups had to be rotated around the P–Ni bond as compared to the X-ray structures. Test calculations without symmetry constraints showed that the structures with $C_{2v}$ symmetry are indeed lower in energy, thus legitimating this procedure.

As illustrated in Table 2, the theoretical structure determination (geometry optimization) yielded bond lengths and bond angles in very good agreement with the X-ray structure determination. For clarity, the molecular structure of **1** is depicted in Figure 4.

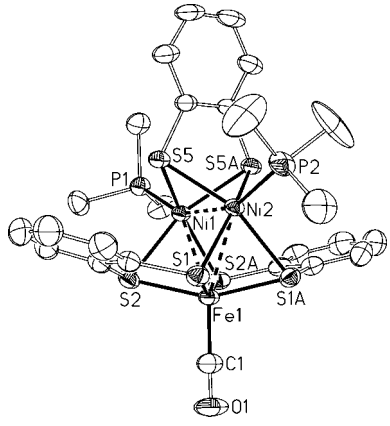


Figure 4. Molecular structure of **1** (50% thermal ellipsoids, H atoms and solvent molecules omitted, dashed lines represent the metal–metal distances).[11]

Differences in experimental bond lengths and bond angles, which are symmetry-equivalent in the DFT calculations, can be attributed to packing effects in the crystals. Therefore the data from the calculations were compared to the average value of these experimental bond lengths and angles. The plane defined by the '$S_2$' ligand coordinating to the nickel atoms (denoted as '$S_2^{Ni}$' in the following) and the axis of the CO ligand are slightly tilted in the experimental structures, while the calculations find a coplanar arrangement. However, it was found that the normal modes describing this movement are very low in both redox states of the cluster (around 50 $cm^{-1}$). Thus, such a distortion should be facile if a small force is exerted on the cluster due to the crystal environment. No significant change of the structural parameters upon oxidation of the cluster **1** is observed both for the experimental and the calculated structures. However, the trend of the changes of the structural parameters upon oxidation, e.g. slight elongation of the Ni1–Ni2 distance and shortening of the Ni1/Ni2–S2/S1 distance, is in general well reproduced by the calculations.

The calculation of the harmonic forcefield results in a frequency of 1955 $cm^{-1}$ (exp. 1910 $cm^{-1}$ in KBr/1916 $cm^{-1}$ in $CH_2Cl_2$) for the ν(CO) band in **1**, and 1998 $cm^{-1}$ (exp. 1952 $cm^{-1}$ in KBr/1976 $cm^{-1}$ in $CH_2Cl_2$) in $[\mathbf{1}]^+$. The experimentally observed blue-shift (42 $cm^{-1}$ in KBr/60 $cm^{-1}$ in $CH_2Cl_2$) upon oxidation is thus confirmed. The Kohn–Sham molecular orbitals were used for analyzing the electronic structure of our complexes. A stability analysis[14] of the restricted Hartree–Fock wavefunction of **1** showed that it is stable with respect to singlet and triplet instabilities. The $S^2$ value of 0.787 ($S^2$ = 0.75 for a doublet without spin contamination) in the unrestricted Hartree–Fock wave function of $[\mathbf{1}]^+$ does not indicate substantial multi-reference character for both compounds which would render such an analysis questionable. The results of several types of population analyses are summarized in Table 3. Note that the assignment of a charge to an atom within a polyatomic molecule cannot be carried out unambiguously. Different kinds of population analyses therefore will give different answers. It should be mentioned that the Mulliken population analysis[15] in particular is strongly dependent on the basis set and doubtful for an extended basis set, as far as absolute values of charges are concerned. Therefore, the common features of a Mulliken analysis, a natural population analysis (NPA),[16] and of a charge analysis based on generalized atomic polar tensors[17] are extracted. The latter is dependent on the basis set only implicitly by the way of the general quantum-mechanical description.

 © 2007 Wiley-VCH Verlag GmbH & Co. KGaA, Weinheim 

Table 3. Partial charges and d orbital occupations as calculated by various types of analysis of the density obtained in the DFT calculations. '$S_2^{Fe}$' denotes the '$S_2$' ligands coordinating to the iron atom, '$S_2^{Ni}$' the '$S_2$' ligand coordinating to the nickel atoms.

| | **1** | $[\mathbf{1}]^+$ α+β | α-β |
|---|---|---|---|
| Mulliken population analysis | | | |
| Fe | –0.545 | –0.569 | –0.116 |
| Ni | 0.010 | –0.030 | 0.315 |
| S1/S2 | –0.015 | 0.053 | 0.040 |
| '$S_2^{Fe}$' | 0.008 | 0.276 | 0.100 |
| S5 | –0.009 | 0.027 | 0.109 |
| '$S_2^{Ni}$' | –0.223 | 0.026 | 0.301 |
| $PMe_3$ | 0.302 | 0.425 | –0.010 |
| CO | 0.129 | 0.201 | 0.003 |
| *d*(Fe) | 6.925 | 6.925 | –0.104 |
| *d*(Ni) | 8.705 | 8.662 | 0.329 |
| Natural Population Analysis | | | |
| Fe | –0.129 | –0.135 | –0.099 |
| Ni | 0.562 | 0.593 | 0.305 |
| S1/S2 | –0.012 | 0.046 | 0.042 |
| '$S_2^{Fe}$' | –0.407 | –0.168 | 0.104 |
| S5 | –0.115 | –0.080 | 0.113 |
| '$S_2^{Ni}$' | –0.727 | –0.489 | 0.302 |
| $PMe_3$ | 0.254 | 0.339 | –0.009 |
| CO | 0.038 | 0.096 | –0.004 |
| *d*(Fe) | 7.626 | 7.621 | –0.096 |
| *d*(Ni) | 8.964 | 8.909 | 0.317 |
| Charges from generalized atomic polar tensors | | | |
| Fe | –0.679 | –0.672 | – |
| Ni | –0.145 | –0.021 | – |
| S1/S2 | –0.076 | 0.008 | – |
| '$S_2^{Fe}$' | –0.171 | 0.082 | – |
| S5 | –0.019 | –0.015 | – |
| '$S_2^{Ni}$' | –0.041 | 0.048 | – |
| $PMe_3$ | 0.443 | 0.486 | – |
| CO | 0.435 | 0.539 | – |

The oxidation states of iron and nickel (represented by their d occupations) do not change upon oxidation of **1** to $[\mathbf{1}]^+$. They are compatible with the formulation of $Fe^{II}$ and $Ni^{II}$. This is consistent with the observation that only very small structural changes take place when **1** is oxidized to its cation. For example, the iron atom lies 4.95(1) pm above the plane defined by the atoms S1, S2, S1A and S2A in the crystal structure of **1**. Its distance from the plane defined by the atoms S1, S2, S3 and S4 in the crystal structure of $[\mathbf{1}]^+$ is with 4.98(2) pm almost identical, indicating that the iron center is not affected by the oxidation. The computed values for these distances in **1** and $[\mathbf{1}]^+$ coincide with the experimental data. No significant differences of the partial charges on any particular atoms are observed upon oxidation of the cluster. This means that the positive charge in $[\mathbf{1}]^+$ cannot be assigned to individual atoms but is distributed over the whole cluster. What at first seems surprising is the fact that no charge ends up on the metal centers. However, this is in line with the negligible changes in the d level occupation. On the other hand the partial charges on all ligands are increased upon oxidation. Thus, main parts of the positive charge in $[\mathbf{1}]^+$ are residing on the '$S_2$' ligands.

The picture is very different for the spin polarization. As opposed to the positive charge, the unpaired electron is confined to a more restricted region of the molecule. A small negative spin polarization arises at the iron atom, but the main part of the spin polarization is located on the $Ni_2$'$S_2^{Ni}$' fragment of the cluster. About two thirds of the magnetic moment are located on the nickel d orbitals and about one third on the '$S_2^{Ni}$' ligand. Approximately two thirds of the spin polarization on the '$S_2^{Ni}$' ligand are located on the thiolate donor functions. This data can be very nicely visualized by an analysis of the molecular orbitals. Upon oxidation an electron is removed from the HOMO of **1** which has essentially the same form as the SOMO in $[\mathbf{1}]^+$ and is mainly formed from d orbitals on the nickel atoms and p orbitals on the adjacent sulfur atoms (Figure 5). The localization of the unpaired electron at these atoms with a small contribution at the iron atom can be clearly seen from a plot of the spin density of $[\mathbf{1}]^+$ (Figure 6). These findings are consistent with EPR measurements, which have been reported in ref.[11]

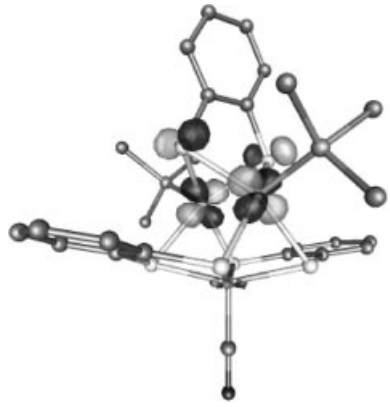

Figure 5. Plot of the highest occupied molecular orbital (HOMO) of **1** (H atoms omitted).

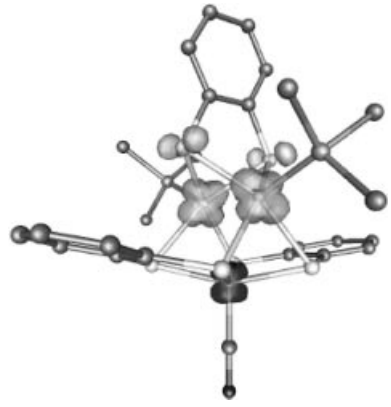

Figure 6. Plot of the spin density in $[\mathbf{1}]^+$ (H atoms omitted).

At first this localization of the spin density on the nickel atoms and the adjacent sulfur atoms seems to be contradictory to the above described delocalization of the positive charge in $[\mathbf{1}]^+$. Things become clear, however, if we imagine the oxidation as a two-step procedure. In the first step an electron is removed from the HOMO, which leaves an *unpaired* electron in an orbital located mainly at the nickel and adjacent sulfur atoms. At the same time the electronic

 © 2007 Wiley-VCH Verlag GmbH & Co. KGaA, Weinheim 

structure of the complex cation relaxes and a substantial donation of *paired* electrons from the '$S_2$' ligands takes place to compensate for the lack of electrons on the metal centers. Thus, the '$S_2$' ligands serve as a kind of electron density reservoir, which prevent the buildup of positive charge on the nickel atoms upon removal of one electron.

### Constant Potential Coulometry

The cyclic voltammogram of **1** (given in ref.[11]) exhibits three quasi-reversible one-electron waves at –1.071, –0.095, and 0.844 V relative to NHE, which are assigned to the redox couples $\mathbf{1}^{0/-}$, $\mathbf{1}^{0/+}$, and $\mathbf{1}^{+/2+}$, respectively.[11] The potential of the second wave lies within the range which has been observed for several [NiFe] hydrogenase redox reactions.[3c,5d] In addition, the small difference in the X-ray structure parameters of **1** and $[\mathbf{1}]^+$ suggests that the electron transfer should be quite fast as a result of a low reorganization barrier. This exciting result prompted us to check the ability of **1** in catalyzing the reduction of $H^+$ to $H_2$ by constant potential coulometry. A solution of 3.2 mmol of $HBF_4$ in $CH_2Cl_2$ was electrolyzed in the presence of 0.1 mmol of **1** by a platinum electrode at –0.48 V relative to NHE for 2 h. Interestingly, the number of coulombs increases with time (Figure 7). $H_2$ gas evolution was observed during the electrolysis. Samples of the gas phase were taken at 0, 1 and 2 h of electrolysis, and the amount of the formation of $H_2$ was estimated by gas chromatography. After the end of 1 and 2 h of electrolysis $0.09 \pm 0.004$ and $0.15 \pm 0.004$ mmol of $H_2$ was detected, respectively. When the electrolysis was performed under identical conditions but in the absence of the complex, the number of coulombs did not increase with time and no $H_2$ formation was observed. The IR spectrum of the electrolyzed solution exhibited the CO band at 1917 $cm^{-1}$, which confirmed that the CO molecule did not dissociate during electrolysis. These results suggest that complex **1** is capable of mediating the reaction. But, the amount of charge transferred is nearly twice as high as the corresponding amount of $H_2$ produced, which indicates that some side reaction takes place. Nevertheless, **1** seems to be the first [NiFe] complex that mediates the reduction of protons to $H_2$ at a very mild reduction potential. Efforts are needed to optimize the coulometric experimental conditions.

The exact site of **1** where the proton initially interacts and is reduced to $H_2$ is not yet been understood. The reaction may either be preceded via an initial formation of a protonated thiolate species or via a $Ni^{III}$–H like intermediate.[18] According to the DFT studies on **1** and $[\mathbf{1}]^+$, an initial formation of a protonated thiolate species (at the nickel centers) is fairly reasonable, because the HOMO has also a large amplitude on the thiolate donor atoms adjacent to the nickel atoms. Furthermore, a considerable part of the spin density of the oxidized cluster is located on these atoms.

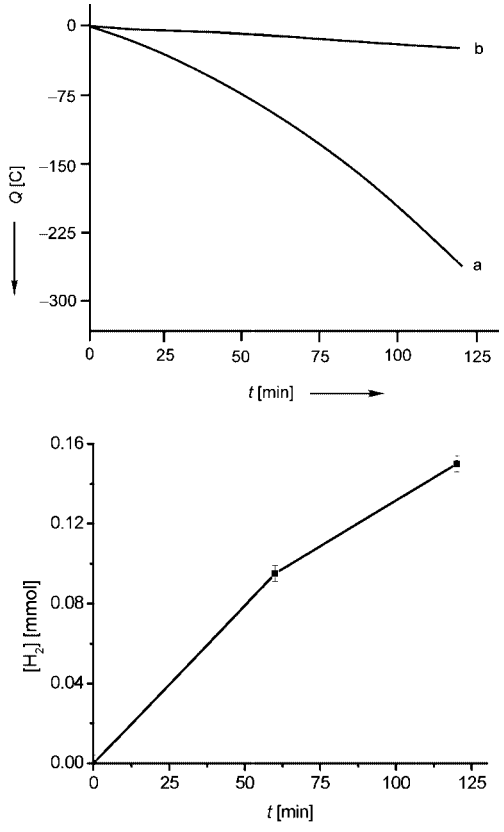


Figure 7. Top: plot of number of coulombs vs. electrolysis time in the presence (a) and in the absence (b) of complex **1**. Bottom: plot of mmols of $H_2$ produced per mmol of **1** vs. electrolysis time.

## Conclusions

The formation of **1** from the reaction between $[Fe(CO)_2('S_3')]_2$ and $[Ni(PMe_3)_2('S_2')]$ was not understood up to now. Through the synthesis of a silylated precursor $[Fe(CO)_2(^{si}S_3)]_2$ (**2**), an earlier observation of the formation of **1** from $[Fe(CO)_2('S_3')]_2$ and $[Ni(PMe_3)_2('S_2')]$ is now understood to be a ligand exchange process. Based on this result, an alternative route for the synthesis of **1** in a one-pot reaction has been developed. The reported trinuclear [NiFe] complex **1** readily reduces protons to $H_2$ and in turn undergoes oxidation to form $[\mathbf{1}]^+$. DFT calculations suggest that the oxidation states of the metal centers are $Fe^{II}$ and $Ni^{II}$ and do not change upon oxidation of **1** to $[\mathbf{1}]^+$. The unpaired electron in $[\mathbf{1}]^+$ is located to a large extent on the nickel atoms and the adjacent thiolate donor functions. The charge, however, is distributed over the whole cluster and main parts reside on the '$S_2$' ligands. These results are compatible with the protonation of a thiolate group as a first step of the reduction mechanism. Preliminary constant potential coulometric results indicate that the trinuclear model complex has catalytic activity for proton reduction under mild potential.

## Experimental Section

**General:** Unless noted otherwise, all manipulations were carried out in absolute solvents under exclusion of air using standard Schlenk techniques. IR spectra of solutions were recorded in $CaF_2$

 © 2007 Wiley-VCH Verlag GmbH & Co. KGaA, Weinheim 

cuvettes with compensation of the solvent bands, and solids were measured as KBr pellets. NMR spectra were recorded at room temperature and chemical shifts are quoted in $\delta$ scale (downfield shifts positive) with the residual signals of the deuterated solvent used as an internal reference. Mass spectra were measured in the field desorption (FD) or fast atom bombardment (FAB) mode. Physical measurements were carried out with the following instruments: IR: Perkin–Elmer 983, Perkin–Elmer 1600 FTIR, and Perkin–Elmer 16PC FTIR; NMR: JEOL FT-JNM-GX 270, Lambda LA 400. MS: JEOL MSTATION 700. Constant Potential Coulometry: Experiments were performed on Autolab Potentiostat/Galvanostat equipped with a personal computer. A coulometric cell assembly consisting of a Pt-gauge working electrode, a platinum wire counter electrode, and a 1 M SCE reference electrode was used. The reference and counter electrodes were separated from the experimental solution by a glass frit. This closed cell assembly (total cell volume of 310 mL) provides with a probe for sampling. This was fitted with a rubber septum and the gas samples were taken before, during, and at the end of the electrolysis. The amount of $H_2$ gas produced during electrolysis was detected by gas chromatography. The compounds 1,2-Benzenedithiol ('$S_2$'–$H_2$),[19] [Fe(bda)$(CO)_3$],[20] $PMe_3$,[21] bis(2-mercapto-3-trimethylsilylphenyl) sulfide(2–) ($^{si}S_3$–$H_2$),[22] and $(NMe_4)_2$[Fe$(CO)_2$('$S_2$')$_2$][13] were prepared according the literature methods.

**[Fe$(CO)_2$($^{si}S_3$)]$_2$ (2):** All manipulations were carried out under CO atmosphere. To a solution of [Fe(bda)$(CO)_3$] (716 mg, 2.503 mmol) in THF (5 mL) a solution of $^{si}S_3$–$H_2$ (974 mg, 2.473 mmol) in THF (5 mL) was added. A gas evolution was observed and the solution color changed to dark-green. This solution was kept at 20 °C. The black green microcrystal that formed after 15 d, were separated from the mother liquor and dried with a stream of CO. Yield: 250 mg (17.5%); $C_{40}H_{48}Fe_2O_4S_6Si_4$·2THF (1153.46): calcd. C 49.98, H 5.59, S 16.68; found C 50.43, H 5.93, S 16.67. IR (KBr): $\tilde{\nu}$ = 2029, 1988 (CO) cm$^{-1}$. Due to the lability of **2** in solution, NMR spectra that were readily analyzed could not be obtained.

**[('$S_2$')$_2$Ni$(PMe_3)$}$_2$Fe(CO)('$S_2$')$_2$] (1) Starting from 2:** A THF suspension (30 mL) of a mixture of **2** (630 mg, 0.624 mmol) and [Ni$(PMe_3)_2$('$S_2$')] (436 mg, 1.220 mmol) was stirred at 60 °C for 4 h. During the course of time, the suspension changed to a clear dark-red solution. This was filtered, and treated with MeOH (240 mL). Black-grey microcrystals precipitated, were removed after 24 h, washed with MeOH (15 mL) and dried in vacuo. Yield: 90 mg (19%). IR (KBr): $\tilde{\nu}$ = 1910 (CO) cm$^{-1}$. IR ($CH_2Cl_2$): $\tilde{\nu}$ = 1916 (CO) cm$^{-1}$. $^1$H NMR (269.6 MHz, $CD_2Cl_2$): $\delta$ = 7.33 (m, 4 H, $C_6H_4$), 6.81 (m, 4 H, $C_6H_4$), 6.67 (m, 2 H, $C_6H_4$), 6.33 (m, 2 H, $C_6H_4$), 1.97 (s, 18 H, $PC_3H_9$) ppm. $^{13}$C{$^1$H} NMR (100.4 MHz, $CD_2Cl_2$): $\delta$ = 207.3 (CO), 146.7, 131.0, 130.3, 125.2, 123.4, ($C_6H_4$), 18.2 ($PMe_3$) ppm. $^{31}$P{$^1$H} NMR (161.7 MHz, $CD_2Cl_2$): $\delta$ = 214.6 ($PMe_3$) ppm. $C_{25}H_{30}FeNi_2OP_2S_6$ (744.09): calcd. C 38.79, H 3.91, S 24.85; found C 38.54, H 3.82, S 24.80.

**Alternative Synthesis of 1:** To a suspension of $FeCl_2$·$4H_2O$ (200 mg, 1.001 mmol) in THF (10 mL) a solution of '$S_2$'–$H_2$ (0.23 mL, 2.001 mmol) and BuLi (2.5 M in *n*-hexane, 1.61 mL, 4.025 mmol) in THF (10 mL) was added. The resulting red solution was treated with $PMe_3$ (0.21 mL, 2.04 mmol) and then with a solution of $Ni(BF_4)_2$·$6H_2O$ (684 mg, 2.001 mmol) in THF (15 mL). To this mixture again a solution of '$S_2$'–$H_2$ (0.12 mL, 1.046 mmol) and BuLi (2.5 M in *n*-hexane, 0.81 mL, 2.025 mmol) in THF (10 mL) was added. A slurry was formed, to this, additional THF (75 mL) was added. Then the Schlenk tube was fitted with a septum. CO gas (60 mL, 2.68 mmol) was allowed to diffuse slowly into the mixture, and the solution was stirred vigorously at 20 °C for 15 h. During the course, the suspension was changed to a clear solution, which was stirred again at 60 °C for 4 h. Half of the solvent was evaporated, the solution was filtered and MeOH (140 mL) was added. Black-grey microcrystals formed, were filtered, washed with MeOH (25 mL) and dried in vacuo. Yield: 140 mg (18%). Characterization: similar as above.

**Density Functional Theory (DFT) Calculations:** The DFT modules of the program package Turbomole[23] were used and the BP86 exchange-correlation functional[24] with a triple-zeta valence-polarized Gaussian basis set[25] was employed for all calculations. The resolution of identity (RI) technique[26] was employed to accelerate the calculations. The natural population analysis (NPA) [16] was done with Gaussian98[27] employing the Kohn–Sham molecular orbitals obtained from the Turbomole calculations. The program gOpenmol[28] was used for the visualizations (Figure 5 and Figure 6). All structures were fully optimized and characterized as true minima on the potential energy hypersurface by means of a vibrational analysis. Accurately converged SCF results (a termination threshold of at least $10^{-8}$ a.u. for the total energy) were used to guarantee satisfactory accuracy in the force constant calculations. The force constants were obtained as numerical first derivatives of the analytical energy gradients as implemented in the parallel PVM code SNF.[29]

**Constant Potential Coulometry:** In a typical experiment, a coulometric cell (320 mL capacity) containing a solution of **1** (80 mg, 0.103 mmol) in $CH_2Cl_2$ (100 mL), $HBF_4$ (54% solution in $Et_2O$, 5 mL, 3.2 mmol) and $NBu_4PF_6$ (3.874 g, 10 mmol) was electrolyzed at –0.15 V vs. 0.1 M SCE for 2 h (25 μL gas samples were taken from the cell at every hour intervals) and the formation of $H_2$ gas was analyzed by GC (TC detector, retention time: 0.733 s). An identical experiment without **1** was also performed.

**X-Ray Structure Determination of [Fe$(CO)_2$($^{si}S_3$)]$_2$·2THF (2·2THF) and [Fe(CO)($^{si}S_3$)]$_2$·3THF (3·3THF):** Suitable single crystals were embedded in protective perfluoro polyether oil. Data were collected at 100 K on a Bruker–Nonius KappaCCD diffractometer using Mo-$K_\alpha$ radiation ($\lambda$ = 71.073 pm), and a graphite monochromator. A numerical absorption correction was applied.[30] for **2**·2THF, while for **3**·3THF a semiempirical absorption correction based on multiple scans was performed (SADABS).[31] The structures were solved by direct methods; full-matrix least-squares refinement was carried out on $F^2$ using SHELXTL NT 6.12.[32] All non-hydrogen atoms were refined anisotropically. All hydrogen atoms were geometrically positioned; their isotropic displacement parameters were tied to those of their corresponding carrier atoms by a factor of 1.2 or 1.5. In the case of **3**·3THF there is pseudosymmetry which emulates a *Pccn* unit cell, but is not fully supported by the diffraction pattern which is consistent with the correct space group $P2_12_12$. The Flack parameter of approx. 0.5 suggests a centrosymmetric space group, though. A solution of the structure in *Pccn* is possible, but the subsequent refinement results in a dramatical increase of all *R*-values and estimated standard deviations. Therefore, the presence of an inversion twin is the best explanation and consistent with the experimental data. One of the three THF solvent molecules present in the asymmetric unit is disordered on two different crystallographic twofold axes. This disordered solvent molecule has been refined using constraints and no hydrogen atoms have been introduced for it. Selected crystallographic data are summarized in Table 4.

CCDC-608118 and -608119 contain the supplementary crystallographic data for this paper. These data can be obtained free of charge from The Cambridge Crystallographic Data Centre via www.ccdc.cam.ac.uk/data_request/cif.

 © 2007 Wiley-VCH Verlag GmbH & Co. KGaA, Weinheim 

Table 4. Selected crystallographic data for **2**·2THF and **3**·3THF.

| Compound | **2**·2THF | **3**·3THF |
|---|---|---|
| Formula | $C_{48}H_{64}Fe_2O_6S_6Si_4$ | $C_{50}H_{72}Fe_2O_5S_6Si_4$ |
| $M_r$ [g mol$^{-1}$] | 1153.41 | 1169.50 |
| Crystal system | triclinic | orthorhombic |
| Space group | $P\bar{1}$ | $P2_12_12$ |
| $a$ [pm] | 971.05(5) | 2117.5(3) |
| $b$ [pm] | 1155.9(1) | 27.526(4) |
| $c$ [pm] | 1358.4(2) | 982.7(1) |
| $\alpha$ [°] | 103.238(7) | 90 |
| $\beta$ [°] | 99.060(5) | 90 |
| $\gamma$ [°] | 103.119(6) | 90 |
| $V$ [nm$^3$] | 1.4097(3) | 5.7278(13) |
| $Z$ | 1 | 4 |
| $\rho_{calcd}$[g cm$^{-3}$] | 1.359 | 1.356 |
| $\mu$[mm$^{-1}$] | 0.865 | 0.852 |
| Crystal size [mm$^3$] | $0.35 \times 0.32 \times 0.14$ | $0.32 \times 0.23 \times 0.08$ |
| $T_{min.}/T_{max.}$ | 0.764/0.898 | 0.756/0.934 |
| Measured reflections | 34052 | 39756 |
| Independent reflections | 6715 | 13148 |
| Observed reflections[a] | 5335 | 9953 |
| Refined parameters | 304 | 635 |
| Largest diff. peak and hole [e nm$^{-3}$] | 585/–640 | 438/–420 |
| $R1$[a]; $wR_2$[b] (%) | 3.58; 8.76 | 4.47; 8.60 |

[a] [$I > 2\sigma(I)$]. [b] All data.

## Acknowledgments

We gratefully acknowledge the financial support provided by the Deutsche Forschungsgemeinschaft (DFG), Sonderforschungsbereich (SFB-583) and the Fonds der Chemischen Industrie.

[1] a) P. M. Vignais, B. Billoud, J. Meyer, *FEMS Microbiol. Rev.* **2001**, *25*, 455–501; b) R. K. Thauer, A. R. Klein, G. C. Hartmann, *Chem. Rev.* **1996**, *96*, 3031–3042; c) S. P. J. Albracht, *Biochim. Biophys. Acta* **1994**, *1188*, 167–204; d) T. Lissolo, S. Pulvin, D. Thomas, *J. Biol. Chem.* **1984**, *259*, 11725–11729; e) M. W. W. Adams, L. E. Mortenson, J.-S. Chen, *Biochim. Biophys. Acta* **1980**, *594*, 105–176.

[2] V. Artero, M. Fontecave, *Coord. Chem. Rev.* **2005**, *249*, 1518–1554.

[3] a) A. Volbeda, M. H. Charon, C. Piras, E. C. Hatchikian, M. Frey, J. C. Fontecilla-Camps, *Nature* **1995**, *373*, 580–587; b) A. Volbeda, E. Garcin, A. L. de Lacey, V. M. Fernandes, E. C. Hatchikian, M. Frey, J. C. Fontecilla-Camps, *J. Am. Chem. Soc.* **1996**, *118*, 12989–12996; c) M. Frey, *Struct. Bonding (Berlin)* **1998**, *90*, 97–126; d) Y. Higuchi, H. Ogata, K. Miki, N. Yasuoka, T. Yagi, *Structure* **1999**, *7*, 549–556.

[4] a) J. W. Peters, W. N. Lanzilotta, B. J. Lemon, L. C. Seefeldt, *Science* **1998**, *282*, 1853–1858; b) Y. Nicolet, C. Piras, P. Legrand, C. E. Hatchikian, J. C. Fontecilla-Camps, *Structure* **1999**, *7*, 13–23.

[5] a) Z. J. Gu, J. Dong, C. B. Allan, S. B. Choudhury, R. Franco, J. J. G. Moura, I. Moura, J. LeGall, A. E. Przybyla, W. Roseboom, S. P. J. Albracht, M. J. Axley, R. A. Scott, M. J. Maroney, *J. Am. Chem. Soc.* **1996**, *118*, 11155–11165; b) A. L. de Lacey, E. C. Hatchikian, A. Volbeda, M. Frey, J. C. Fontecilla-Camps, V. M. Fernandez, *J. Am. Chem. Soc.* **1997**, *119*, 7181–7189; c) Y. Montet, P. Amara, A. Volbeda, X. Vernede, E. C. Hatchikian, M. J. Field, M. Frey, J. C. Fontecilla-Camps, *Nat. Struct. Biol.* **1997**, *4*, 523–526; d) A. K. Jones, S. E. Lamle, H. R. Pershad, K. A. Vincent, A. P. J. Albracht, F. A. Amstrong, *J. Am. Chem. Soc.* **2003**, *125*, 8505–8524; e) M. Brecht, M. van Gastel, T. Buhrke, B. Friedrich, W. Lubitz, *J. Am. Chem. Soc.* **2003**, *125*, 13075–13083.

[6] a) *The Bioinorganic Chemistry of Nickel* (Ed.: J. R. Lancaster Jr), VCH, Weinheim, **1988**; b) J. C. Fontecilla-Camps, *Struct. Bond.* **1998**, *91*, 1–29; c) M. Frey, *Struct. Bonding (Berlin)* **1998**, *90*, 97–126; d) R. Cammack, *Nature* **1999**, *397*, 214–215; e) M. W. W. Adams, E. I. Stiefel, *Science* **1998**, *282*, 1842–1843; f) M. J. Maroney, G. Davidson, C. B. Allan, J. Figlar, *Struct. Bonding (Berlin)* **1998**, *92*, 2–65.

[7] a) S. Foerster, M. Stein, M. Brecht, H. Ogata, Y. Higutchi, W. Lubitz, *J. Am. Chem. Soc.* **2003**, *125*, 83–93; b) H.-J. Fan, M. B. Hall, *J. Am. Chem. Soc.* **2002**, *124*, 394–395, and references cited therein; c) P. E. M. Siegbahn, M. R. A. Blomberg, M. Wirstam née Pavlov, R. H. Crabtree, *J. Biol. Inorg. Chem.* **2001**, *6*, 460–466, and references therein.

[8] a) M. Y. Darensbourg, E. J. Lyon, J. J. Smee, *Coord. Chem. Rev.* **2000**, 553–561; b) A. C. Marr, D. J. E. Spencer, M. Schröder, *Coord. Chem. Rev.* **2001**, *219*, 1055–1074; c) D. J. Evans, C. J. Pickett, *Chem. Soc. Rev.* **2003**, *32*, 268–275; d) E. Bouwman, J. Reedijk, *Coord. Chem. Rev.* **2005**, *249*, 1555–1581.

[9] a) S. Ciurli, S.-B. Yu, R. H. Holm, K. K. P. Srivastava, E. Munck, *J. Am. Chem. Soc.* **1990**, *112*, 8169–8171; b) W. Saak, S. Pohl, *Angew. Chem.* **1991**, *103*, 869–870; *Angew. Chem. Int. Ed. Engl.* **1991**, *30*, 881–883; c) J. Zhou, M. J. Scott, Z. Hu, G. Peng, E. Munck, R. H. Holm, *J. Am. Chem. Soc.* **1992**, *114*, 10843–10854; d) C. Junghams, W. Saak, S. Pohl, *J. Chem. Soc. Chem. Commun.* **1994**, 2327–2328; e) R. L. Holliday, L. C. Roof, B. Hargus, D. M. Smith, P. T. Wood, W. T. Pennington, J. W. Kolis, *Inorg. Chem.* **1995**, *34*, 4392–4401; f) C. H. Lai, J. H. Reibenspies, M. Y. Darensbourg, *Angew. Chem.* **1996**, *108*, 2551–2554; *Angew. Chem. Int. Ed. Engl.* **1996**, *35*, 2390–2393; g) F. Osterloh, W. Saak, S. Pohl, *J. Am. Chem. Soc.* **1997**, *119*, 5648–5656; h) E. Bouwman, R. K. Henderson, A. L. Spek, J. Reedijk, *Eur. J. Inorg. Chem.* **1999**, *4*, 217–219; i) S. C. Davies, D. J. Evans, D. L. Hughes, S. Longhurst, J. R. Sanders, *Chem. Commun.* **1999**, 1935–1936; j) T. Glaser, T. Beissel, E. Bill, T. Weyhermüller, V. Schünemann, W. Meyer-Klaucke, A. X. Trautwein, K. Wieghardt, *J. Am. Chem. Soc.* **1999**, *121*, 2193–2208; k) G. Steinfeld, B. Kersting, *Chem. Commun.* **2000**, 205–206; l) M. Razavet, S. C. Davis, D. L. Hughes, C. J. Pickett, *Chem. Commun.* **2001**, 847–848; m) M.-C. Chalbot, A. M. Mills, A. L. Spek, G. J. Long, E. Bouwman, *Eur. J. Inorg. Chem.* **2003**, 453–457; n) M. C. Smith, J. E. Barclay, S. P. Cramer, S. C. Davies, W.-W. Gu, D. L. Hughes, S. Longhurst, D. J. Evans, *J. Chem. Soc. Dalton Trans.* **2002**, 2641–3647; o) D. Sellmann, F. Geipel, F. Lauderbach, F. W. Heinemann, *Angew.*

 © 2007 Wiley-VCH Verlag GmbH & Co. KGaA, Weinheim 

*Chem.* **2002**, *114*, 654–656; *Angew. Chem. Int. Ed.* **2002**, *41*, 632–634; p) M. C. Smith, J. E. Barclay, S. C. Davies, D. L. Hughes, D. J. Evans, *Dalton Trans.* **2003**, 4147–4151; q) D. Sellmann, R. Prakash, F. W. Heinemann, M. Moll, M. Klimowicz, *Angew. Chem.* **2004**, *116*, 1913–1916; *Angew. Chem. Int. Ed.* **2004**, *43*, 1877–1880; r) P. A. Stenson, A. Martin-Becerra, C. Wilson, A. J. Blake, J. McMaster, M. Schröder, *Chem. Commun.* **2006**, 317–319.

[10] Z. Li, Y. Ohki, K. Tatsumi, *J. Am. Chem. Soc.* **2005**, *127*, 8950–8951.

[11] D. Sellmann, F. Lauderbach, F. Geipel, F. W. Heinemann, M. Moll, *Angew. Chem.* **2004**, *116*, 3203–3206; *Angew. Chem. Int. Ed.* **2004**, *43*, 3141–3144.

[12] D. Sellmann, J. Sutter, *Prog. Inorg. Chem.* **2003**, *52*, 585–681.

[13] D. Sellmann, F. Geipel, F. Lauderbach, F. W. Heinemann, *Chem. Eur. J.* **2002**, *8*, 958–966.

[14] R. Bauernschmitt, R. Ahlrichs, *J. Chem. Phys.* **1996**, *104*, 9047–9052.

[15] a) R. S. Mulliken, *J. Chem. Phys.* **1955**, *23*, 1833–1840; b) R. S. Mulliken, *J. Chem. Phys.* **1955**, *23*, 1841–1846.

[16] A. E. Reed, R. B. Weinstock, F. Weinhold, *J. Chem. Phys.* **1985**, *83*, 735–746.

[17] J. Cioslowski, *J. Am. Chem. Soc.* **1989**, *111*, 8333–8336.

[18] V. Grass, D. Lexa, J.-M. Savéant, *J. Am. Chem. Soc.* **1997**, *119*, 7526–7532.

[19] J. Degani, R. Fochi, *Synthesis* **1976**, *7*, 471–472.

[20] A. J. P. Domingos, J. A. S. Howell, B. F. G. Johnson, J. Lewis, *Inorg. Synth.* **1990**, *28*, 52–55.

[21] W. Wolfsberger, H. Schmidbaur, *Synth. React., Inorg. Met.-Org. Chem.* **1974**, *4*, 149–156.

[22] D. Sellmann, R. Prakash, F. Geipel, F. W. Heinemann, *Eur. J. Inorg. Chem.* **2002**, 2138–2146.

[23] a) R. Ahlrichs, M. Bär, M. Häser, H. Horn, C. Kölmel, *Chem. Phys. Lett.* **1989**, *162*, 165–169; b) O. Treutler, R. Ahlrichs, *J. Chem. Phys.* **1995**, *102*, 346–354.

[24] a) A. D. Becke, *Phys. Rev. A* **1988**, *38*, 3098–3100; b) J. P. Perdew, *Phys. Rev. B* **1986**, *33*, 8822–8824; c) S. H. Vosko, L. Wilk, M. Nusair, *Can. J. Phys.* **1980**, *58*, 1200–1211.

[25] A. Schäfer, C. Huber, R. Ahlrichs, *J. Chem. Phys.* **1994**, *100*, 5829–5835.

[26] K. Eichkorn, F. Weigend, O. Treutler, R. Ahlrichs, *Theor. Chem. Acc.* **1997**, *97*, 119–124.

[27] *Gaussian 98*, Revision A.11.3, M. J. Frisch, G. W. Trucks, H. B. Schlegel, G. E. Scuseria, M. A. Robb, J. R. Cheeseman, V. G. Zakrzewski, J. A. Montgomery Jr, R. E. Stratmann, J. C. Burant, S. Dapprich, J. Millam, A. D. Daniels, K. N. Kudin, M. C. Strain, O. Farkas, J. Tomasi, V. Barone, M. Cossi, R. Cammi, B. Mennucci, C. Pomelli, C. Adamo, S. Clifford, J. Ochterski, G. A. Petersson, P. Y. Ayala, Q. Cui, K. Morokuma, N. Rega, P. Salvador, J. J. Dannenberg, D. K. Malick, A. D. Rabuck, K. Raghavachari, J. B. Foresman, J. Cioslowski, J. V. Ortiz, A. G. Baboul, B. B. Stefanov, G. Liu, A. Liashenko, P. Piskorz, I. Komaromi, R. Gomperts, R. L. Martin, D. J. Fox, T. Keith, M. A. Al-Laham, C. Y. Peng, A. Nanayakkara, M. Challacombe, P. M. W. Gill, B. Johnson, W. Chen, M. W. Wong, J. L. Andres, C. Gonzalez, M. Head-Gordon, E. S. Replogle, J. A. Pople, Gaussian, Inc., Pittsburgh PA, **2002**.

[28] a) L. Laaksonen, *J. Mol. Graphics Modell.* **1992**, *10*, 33–34; b) D. L. Bergman, L. Laaksonen, A. Laaksonen, *J. Mol. Graphics Modell.* **1997**, *15*, 301–306.

[29] a) C. Kind, M. Reiher, J. Neugebauer, B. A. Hess, *SNF,* Universität Erlangen-Nürnberg, **1999–2000**; b) J. Neugebauer, M. Reiher, C. Kind, B. A. Hess, *J. Comput. Chem.* **2002**, *23*, 895–910.

[30] P. Coppens, *Crystallographic Computing (Copenhagen).* **1970**, 225–270.

[31] *SADABS* 2.06, Bruker AXS, Inc., Madison, WI, **2002**.

[32] *SHELXTL* NT 6.12, Bruker AXS, Inc., Madison, WI, **2002**.

Received: November 16, 2006
Published Online: May 29, 2007

 © 2007 Wiley-VCH Verlag GmbH & Co. KGaA, Weinheim 

DOI: 10.1002/ejic.200601092

# Mutual Influences of Ligands as Revealed by $^2$H NMR Shifts and the Angular Overlap Model Parameters: *trans*- and *cis*-[$CrX_2(N)_4$]-Type Complexes with Aliphatic Amine Ligands[‡]

**Yukiko Yamaguchi-Terasaki,[a] Takashi Fujihara,[b] and Sumio Kaizaki*[c]**

**Keywords:** Chromium complexes / Ligand effects / N ligands / NMR spectroscopy / Angular overlap model parameters

We have previously reported the relationship between $^2$H NMR chemical shift differences ($\Delta\delta$) and the angular overlap model (AOM) parameter $e_\sigma$(F), which represents the σ antibonding interaction energy obtained from the solvatochromism, for *trans*-[$CrF_2$([$D_4$]-3,2,3-tet)]$^{n+}$ {[$D_4$]3,2,3-tet = 1,10-diamino-4,7-diazadecane [$NH_2(CH_2)_3NH(CD_2)_2NH(CH_2)_3NH_2$]} and *cis*-α-[$CrF_2$([$D_4$]trien)]$^{n+}$ {[$D_4$]trien = triethylenetetraamine [$NH_2(CH_2)_2NH(CD_2)_2NH(CH_2)_2NH_2$]}. In analogy to these relations, the co-ligand effect on the $\Delta\delta$ values for *cis*-α-[$CrX_2$([$D_4$]trien)]$^{n+}$ and *trans*-[$CrX_2$([$D_4$]3,2,3-tet)]$^{n+}$ is found to be well correlated with the reported $e_\sigma$(X) values for the co-ligands X. This is the first example of the co-ligand effect, or a mutual influence of ligands, associated with variation of the Cr–N and Cr–X bonds in *cis*- and *trans*-[$CrX_2N_4$]-type complexes. This $\Delta\delta$ vs. $e_\sigma$(X) correlation offers an indirect method for estimating the $e_\sigma$(X) values for didentate $X_2$ as well as monodentate X ligands from the $^2$H NMR chemical shifts and ranking them in the two-dimensional spectrochemical series. Plots of $\Delta\delta$ vs. $e_\sigma$(FX) for *trans*-[CrF(X)-([$D_4$]3,2,3-tet)]$^{n+}$ do not necessarily lie on the $\Delta\delta$ vs. $e_\sigma$(X) correlation line for the F(X) complexes with averaged $e_\sigma$(FX) = 1/2[$e_\sigma$(X) + $e_\sigma$(F)] values − $e_\sigma$[F(CN)] is close to $e_\sigma$(F), for example − thereby demonstrating a mutual influence between the $CN^-$ and $F^-$ ligands in the *trans* positions through a push-pull action or π donor–acceptor interaction.

(© Wiley-VCH Verlag GmbH & Co. KGaA, 69451 Weinheim, Germany, 2007)

## Introduction

The mutual influence between ligands is one of the fundamental subjects in coordination chemistry since it governs the relative changes in properties upon replacement of one ligand by another.[1] General regularities in mutual influences for SP-4 platinum(II) complexes have been established, such as the *trans* influence, but for OC-6 mixed-ligand complexes they are limited to some *trans*-[$MX_2N_4$]-type complexes where negative correlations have been found between the axial M–X and the basal M–N bond lengths both theoretically and experimentally by X-ray analysis and UV/Vis spectroscopy.[1–5] For example, Bertini et al.[2] and Lever et al.[3] have established negative linear correlations between Ni–N bond lengths and 10 Dq(N) or angular overlap model (AOM) parameter $e_\sigma$(N) values, which represent the σ antibonding energy parameter, for some *trans*-[$NiX_2N_4$] complexes, while Busch et al. have shown that the axial ligand field parameter [10 $Dq^z$(X)] decreases as the basal (in-plane) ligand field parameter [10 $Dq^{xy}$(N)] increases, which they termed the "electronic *cis* effect".[4] Ito et al. have studied this phenomenon extensively using the X-ray structural parameters of a series of $Co^{III}$, $Ni^{II}$, and $Zn^{II}$ macrocyclic tetraamine complexes[5] and a theoretical examination of the relationship between the softness of metal ions in terms of ab initio MO calculations.[6] They found that the lengthening of the average basal M–N bonds on going from smaller to larger macrocyclic tetraamine rings is associated systematically with a shortening of the axial M–NCS or M–Cl bonds and an increase of the overlap population of M–NCS or M–Cl.[6] We have also demonstrated an analogous bond-length variation from solvatochromism and solvent-dependent NMR spectroscopy for the aliphatic amine difluoridochromium(III) complexes *trans*-[$CrF_2$([$D_4$]3,2,3-tet)] {[$D_4$]3,2,3-tet = 1,10-diamino-4,7-diazadecane [$NH_2(CH_2)_3NH(CD_2)_2NH(CH_2)_3NH_2$]} and *cis*-α-[$CrF_2$([$D_4$]trien)]$^+$ {[$D_4$]trien = triethylenetetraamine [$NH_2(CH_2)_2NH(CD_2)_2NH(CH_2)_2NH_2$]}, or their aromatic amine analogs, as well as the amino polycarboxylato $Cr^{III}$ or $Co^{III}$ complexes in terms of the AOM parametrization.[7–11] We also found a negative correlation between the $^2$H NMR shift differences, $\Delta\delta$, and the σ donor AOM parameters $e_\sigma$(X) and $e_\sigma$(N) of the ligands X and N, which manifests itself as an electronic *cis* effect, or a mutual influ-

[‡] Part 1 of the Series "Mutual Influences of Ligands as Revealed by $^2$H NMR Shifts and the Angular Overlap Model Parameters". Part 2: Ref.[25]

[a] Toyama National College of Maritime Technology, Imizu, Toyama 933-0293, Japan
[b] Department of Chemistry, Faculty of Science, Saitama University, Shimo-Okubo 255, Sakuraku, Saitama 338-8570, Japan
[c] Department of Chemistry, Graduate School of Science, Osaka University, Toyonaka, Osaka 560-0043, Japan
kaizaki@chem.sci.osaka-u.ac.jp

 © 2007 Wiley-VCH Verlag GmbH & Co. KGaA, Weinheim 

ence of ligands, for *trans*-[$CrX_2$([$D_4$]3,2,3-tet)].[7] Such a $\Delta\delta$ vs. $e_\sigma$(X) correlation should also be present in *cis*-α-[$CrX_2$([$D_4$]trien)]$^+$ in view of the solvatochromism and solvent-dependent NMR behavior of the corresponding fluorido complex, although no mutual influence has ever been found for *cis*-[$CrX_2N_4$]-type complexes on the basis of X-ray structural data or spectroscopic methods. This could provide a convenient and indirect means of estimating the AOM parameter values for didentate as well as monodentate ligands or for ranking them in the two-dimensional spectrochemical series.[12,13] Furthermore, it may offer the possibility of clarifying numerical ambiguities[14,15] in the AOM parameter values and allow the elucidation of chemical properties in the ground or excited states relevant to the thermodynamics or kinetics of thermal or photochemical reactions.[15] Another mutual influence or compensation due to the π donor–acceptor interaction of X–M–Y systems in a *trans* disposition has been theoretically claimed by Burdett,[16] although no such example has been reported so far. Such a mutual influence is expected to be found by examining the solvent-dependent $^2$H NMR spectra of *trans*-[CrF(CN)([$D_4$]3,2,3-tet)]$^+$.

Herein we will explore the mutual influence of ligands by studying the correlation of the $^2$H NMR shifts and AOM parameters of the X co-ligands in *cis*-α-[$CrX_2$([$D_4$]trien)]$^{n+}$ and *trans*-[CrF(X)([$D_4$]3,2,3-tet)]$^{n+}$ and redefining the solvatochromism and $^2$H NMR spectra of *trans*-[Cr(F or X)$_2$-([$D_4$]3,2,3-tet)]$^{n+}$.

## Results and Discussion

### $^2$H NMR Chemical Shifts and AOM Parametrization for *trans*-[$CrX_2$([$D_4$]3,2,3-tet)]$^{n+}$

One of the main aims of this paper concerns the *cis* effect, or the mutual influence of ligands in low symmetry, of *cis*-α-[$CrX_2$([$D_4$]trien)]$^+$ complexes by examining their $^2$H NMR chemical shifts and AOM parametrization. Prior to this, however, the $^2$H NMR spectra of high-symmetry *trans*-[$CrF_2$(3,2,3-tet)]$^+$ and *trans*-[$CrX_2$(3,2,3-tet)]$^+$ will be reviewed and re-examined.

As shown in Figure 1, two well-separated $^2$H NMR signals are observed due to paramagnetic isotropic contact shifts for inequivalent (axial and equatorial) deuterons in the ethylene backbone of *trans*-[$CrF_2$(3,2,3-tet)]$^+$ (inset of Figure 1) in water. The $^2$H NMR chemical shift differences ($\Delta\delta$) are well correlated with each of the $^4B_2$ and $^4A_2$ tetragonal splitting components in the ligand-field d–d transition region as well as the solvent acceptor number ($A_N$) according to the equation $\Delta\delta = 0.409\,A_N + 66.3$ [correlation coefficient ($r$) = 0.99]. This correlation of $\Delta\delta$ with $A_N$ has been interpreted by a Karplus-like or $\cos^2\theta$ relation for the paramagnetic contact shifts of $Cr^{III}$ complexes according to the following equation:[7] $\Delta\delta = -(3^{1/2}/2)(C{\cdot}A)\sin2\phi$, where $C$ is a constant that varies reciprocally with absolute temperature, $A$ is the hyperfine constant for the spin density of deuterons, and φ is the torsion angle of the Cr–N–C–C chain of the ethylene backbone in 3,2,3-tet. Since a plot of $\Delta\delta$ vs. inverse temperature ($1/T$) gives a constant value, $\Delta\delta$ is proportional to the spin density of the deuterons concerned, although, in view of the temperature-independent nature of sin2φ, there is no conformational change in 3,2,3-tet. In other words the increase of $\Delta\delta$ reflects the increase of the deuteron spin density of C–D or the Cr–N σ-bond interaction energy [$e_\sigma$(N)], which is followed by a decrease in the Cr–F σ-bond interaction energy [$e_\sigma$(F)], associated with an attack of the stronger electron-acceptor solvents on the fluorido ligands.[7] Evaluation of $e_\sigma$(N) and $e_\sigma$(F) values obtained from the tetragonal components of the UV/Vis ligand-field bands was revised by using the appropriate Racah parameter $B$ and involving the configurational interaction between the $^4A_2$ ($^4T_1{}^a$) and $^4A_2$ ($^4T_1{}^b$) states.[7] The revised correlations between the AOM parameters and the NMR shift difference $\Delta\delta$ are $e_\sigma(N_c) = 0.013\,\Delta\delta + 6.02$, where $N_c$ is the amine nitrogen *cis* to the fluorido ligands, and $e_\sigma(F) = -0.048\,\Delta\delta + 11.0$.[17]

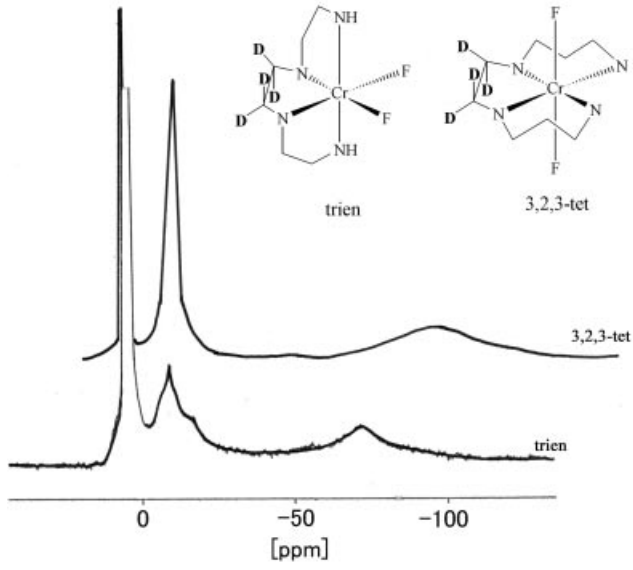


Figure 1. $^2$H NMR spectra of *trans*-[$CrF_2$([$D_4$]3,2,3-tet)]$^+$ and *cis*-α-[$CrF_2$([$D_4$]trien)]$^+$ in dmf at 26 °C. The inset shows the structures of the 3,2,3-tet and trien complexes.

In an analogous manner to the difluorido complex, we also examined whether there is a linear correlation between $\Delta\delta$ and $e_\sigma$(N) or $e_\sigma$(X) for *trans*-[$CrX_2$([$D_4$]3,2,3-tet)]$^{n+}$ complexes. The $^2$H NMR spectrum of *trans*-[$CrF_2$([$D_4$]-3,2,3-tet)]$^+$ in dmf at 26 °C is shown in Figure 1 and Table 1 gives the shift differences ($\Delta\delta$) together with the AOM parameter values for the $X_2$ complexes. We re-examined the previously reported relationship between $^2$H NMR $\Delta\delta$ and $e_\sigma$(X) values by replacing the appropriate $e_\sigma$(X) values for $F^-$, $H_2O$, $NH_3$, and $Br^-$ (Table 1). This gave a slightly better correlation ($r$ = 0.97) for plots of $\Delta\delta$ vs. $e_\sigma$(X) values (Table 1) than obtained previously ($r$ = 0.95),[7] as summarized in Table 1 and shown in Figure 2. However, this should not be over-estimated in view of the ranges of estimated $e_\sigma$(X) values for some ligands, which depend on the complexes used or the estimation methods.[15] Furthermore, $\Delta\delta$ is also correlated with the $e_\sigma$(N) values obtained from

 © 2007 Wiley-VCH Verlag GmbH & Co. KGaA, Weinheim 

the $^4B_2(^4T_1)$ component [$E = 3e_\sigma(N)$] observed for some $[CrX_2(3,2,3\text{-tet})]^{n+}$ complexes, as reported previously,[7] where the least-squares calculation for the correlation was incorrectly made. In fact, the $e_\sigma(X)$ values decrease and the $e_\sigma(N)$ ones increase with increasing $\Delta\delta$, as shown in Figure 2, which leads to Equations (1) and (2) (in units of $10^3$ cm$^{-1}$).

Table 1. AOM parameter values and $^2$H NMR chemical shift differences for *trans*-$[CrX_2(3,2,3\text{-tet})]^{n+}$ in $H_2O$.

| $X_2$ | $\Delta\delta$ [ppm] | $e_\sigma(N)$[a] | $e_\sigma(X)$[a] | Ref. |
|---|---|---|---|---|
| $OH^-$ | 73.3 | 6.80 | 8.63 | [19] |
| $F^-$ | 87.9 | 7.23 | 7.80 | [18] |
| $CN^-$ | 89.7 | | 7.50 | [21] |
| $NH_3$ | 101.9 | | 6.97 | [19] |
| $NCS^-$ | 103.7 | | 6.41 | [20] |
| $H_2O$ | 97.5 | 7.52 | 6.76 | [13] |
| $Cl^-$ | 109.0 | 7.40 | 5.56 | [19] |
| $Br^-$ | 113.7 | 7.68 | 5.34 | [19] |

[a] Calculated from Equations (1–3), see text.

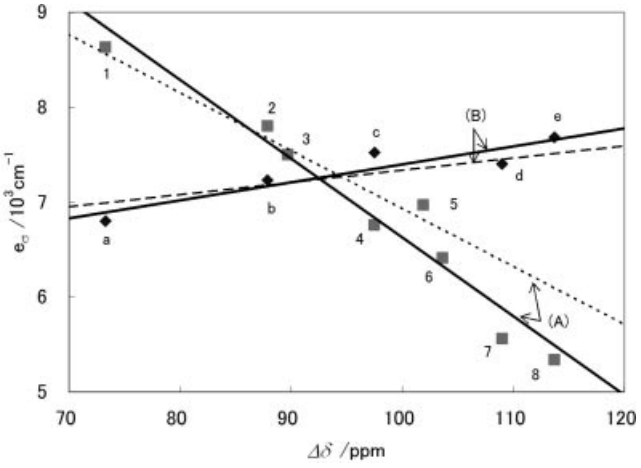


Figure 2. Plots of the AOM parameter values $e_\sigma(X)$ vs. the $^2$H NMR shift difference ($\Delta\delta$) in $H_2O$ for *trans*-$[Cr(X)_2(3,2,3\text{-tet})]^{n+}$ (——). (A): 1–8: $e_\sigma(X)$ values taken from the literature (see text and Table 1); (B) a–d: $e_\sigma(N)$ values obtained from the aqueous absorption data ($^4B_2$ component). 1/a: $(OH)_2$; 2/b: $F_2$; 3: $(CN)_2$; 4: $(NH_3)_2$; 5: $(H_2O)_2$; 6: $(NCS)_2$; 7/c: $Cl_2$; 8/d: $Br_2$. The solid lines are least-squares fits. The dotted lines in (A) and (B) are calculated from $e_\sigma(N_c) = 0.013\Delta\delta + 6.02$ (6) and the solid lines from $e_\sigma(F) = -0.048\Delta\delta + 11.0$ (7) for the difluorido complex [see Equations (f) and (g) in ref.[17]].

$$e_\sigma(X) = -0.083\,\Delta\delta + 14.9 \quad (r = 0.97) \tag{1}$$

$$e_\sigma(N) = 0.019\,\Delta\delta + 5.50 \quad (r = 0.92) \tag{2}$$

Combining these two equations leads to Equation (3).

$$e_\sigma(X) = -4.37\,e_\sigma(N) + 38.9 \tag{3}$$

The slope and intercept of Equation (3) are similar to those of the revised equation $e_\sigma(F) = -3.67\,e_\sigma(N) + 33.1$ (8) [see also caption of Figure 2 and Equation (h) in ref.[17]] for the difluorido complex discussed in ref.[17] It is possible that the change of $e_\sigma(F)$ or $e_\sigma(X)$ can vary 3–4 times as much as $e_\sigma(N)$ since the Cr–F or Cr–X bond is influenced by four *cis*(basal N) ligands, in analogy to the ligand effect reported by Burdett et al.[16] and Timney.[23] The $e_\sigma(X)$ vs. $e_\sigma(N)$ correlation for the $X_2$ complexes is parallel to the $e_\sigma(F)$ vs. $e_\sigma(N)$ correlation for the difluorido complex.[7] This means that a mutual influence between the axial X ligands and the basal amine ligands occurs through the σ-bond interactions in a compensatory way according to the electronic *cis* effect as a result of a cooperative charge redistribution due to the electroneutrality principle through the σ bonds. This σ bond pathway gives more definite and clearer physical meaning to the negative correlation between the axial-basal bond length than the ligand-field parameter 10 Dq (Δ) values consisting of $e_\sigma$ and $e_\pi$ [10 Dq (Δ) = $3e_\sigma - 4e_\pi$] for which correlations between the axial and basal ligands have been claimed for several tetragonal $[MX_2Y_4]$-type complexes.[2–6] The change of $e_\sigma(N)$ associated with the variation of $e_\sigma(X)$ indicates the invalidity of transferring the AOM parameters from one complex to another.

The $e_\sigma[F(X)]$ values for the heteroligand complexes *trans*-$[CrF(X)(3,2,3\text{-tet})]^{n+}$ (X = $NH_3$, $CN^-$, $Cl^-$, $Br^-$) were estimated from the observed $^2$H NMR shift difference ($\Delta\delta$) according to Equation (3). These $e_\sigma(FX)$ values were compared with the average $e_\sigma(FX)$ value $[e_\sigma(F) + e_\sigma(X)]/2$ obtained by assuming holohedralized symmetry, as shown in Table 2. The estimated $e_\sigma(FX)$ values calculated from the $\Delta\delta$ values deviate from the average values by 1.6–9.7%, although the increasing order is not necessarily in line with the predicted one given in Table 2.

Table 2. AOM parameter values and $^2$H NMR chemical shift differences for *trans*-$[CrF(X)(3,2,3\text{-tet})]^{n+}$ in $H_2O$.

| X | $\Delta\delta$ [ppm] | $e_\sigma(FX)$ (est.) [$10^3$ cm$^{-1}$] | $e_\sigma(FX)$ (av.) [$10^3$ cm$^{-1}$] | Error $[e_\sigma(est.) - e_\sigma(av.)]/e_\sigma(av.)$ |
|---|---|---|---|---|
| CN | 86.2 | 7.78 | 7.65 | 0.016 |
| Cl | 93.2 | 7.19 | 6.68 | 0.077 |
| Br | 93.0 | 7.20 | 6.57 | 0.097 |
| $NH_3$ | 98.2 | 6.77 | 7.39 | –0.083 |
| OH | 72.7 | 8.89 | 8.22 | 0.082 |
| $H_2O$ | 95.7 | 6.98 | 7.70 | –0.092 |

The solvent-dependent $^2$H NMR shift behavior for the FX complexes demonstrates a fairly linear correlation of the $\Delta\delta$ values with $A_N$, as shown in Figure 3. Moreover, the least-squares lines for the plots of $\Delta\delta$ vs. $A_N$ lie roughly between those of the $F_2$ and $X_2$ complexes, except for the F(CN) complex (see below). This fact indicates the additivity of the σ interaction as well as the selective solvation, which affects the energies of the d orbitals that point towards the axial ligands in the FX complexes in the same way as in the $F_2$ complex.

For the F(CN) complex, the solvent-dependent NMR shift differences ($\Delta\delta$) tend to deviate from the average values with decreasing solvent acceptor number ($A_N$) and lie closer to those for the $F_2$ complex than the average of the $F_2$ and $(CN)_2$ complexes, as shown in Figure 3. This may be due to a mutual influence through the push-pull action[24] or an additional *trans* influence between the π-donor $F^-$ and π-acceptor $CN^-$ ligands similar to that found for the aromatic amine complexes.[8,25] The larger the σ donor or $e_\sigma(F)$ and

 © 2007 Wiley-VCH Verlag GmbH & Co. KGaA, Weinheim 

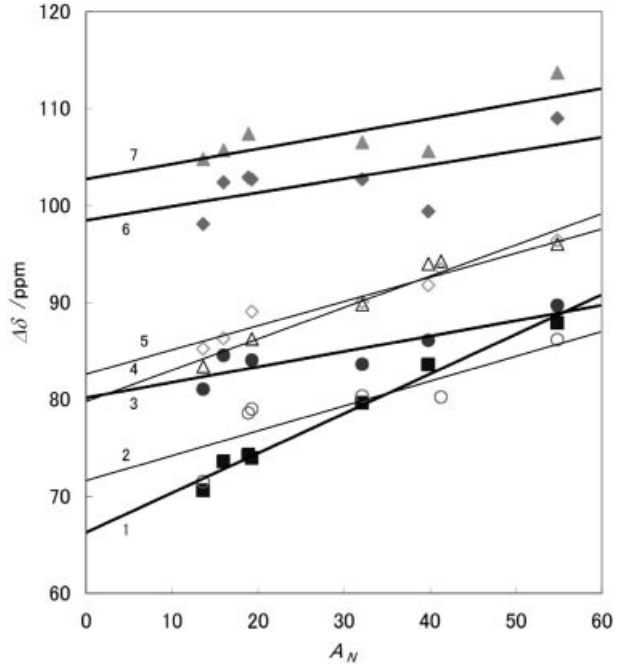


Figure 3. Plots of the $^2$H NMR shift differences ($\Delta\delta$) vs. the acceptor numbers $A_N$ for *trans*-[$CrX_2$(3,2,3-tet)]$^+$. 1: $F_2$; 2: F(CN); 3: $(CN)_2$; 4: F(Cl); 5: F(Br); 6: $Cl_2$; 7: $Br_2$.

the larger the π donor or $|e_\pi(F)|$, then the larger the π acceptor or $e_\pi(CN)$ becomes by the push-pull action, which leads to a smaller $e_\sigma(CN)$ due to the relationship $\Delta = 3e_\sigma(CN) - 4e_\pi(CN)$. The $e_\sigma(F)$ and $e_\sigma(CN)$ values in the F(CN) complex are larger and smaller by $\delta e_\sigma(F)$ and $\delta e_\sigma(CN)$, respectively, than those in the $F_2$ and $(CN)_2$ complexes. The additional parts $\delta e_\sigma(F)$ and $\delta e_\sigma(CN)$ may also be elucidated on the basis of the AOM approach including the quartic terms of Burdett et al.,[16] which gives $\delta e_\sigma(F) \propto e_\sigma(F)[e_\sigma(F) - e_\sigma(CN)]$ and $\delta e_\sigma(CN) \propto e_\sigma(CN)[e_\sigma(CN) - e_\sigma(F)]$. As $e_\sigma(F)$ is larger than $e_\sigma(CN)$, and since the difference $e_\sigma(F) - e_\sigma(CN)$ increases for the $F_2$ and $(CN)_2$ complexes with decreasing $A_N$, $e_\sigma$[F(CN)] is predicted to become closer to that of $e_\sigma(F)$,[26] as found for the solvent-dependent $^2$H NMR spectra (Figure 3). This mutual influence between $F^-$ and $CN^-$ is in accordance with the interpretation for the unusual photochemical reactivity of *trans*-[CrF(CN)$(NH_3)_4$]$^+$.[27] It follows, however, that the additive ligand-field or holohedralized symmetry assumption[13] may not always be confirmed for the F(CN) complex.

### $^2$H NMR Chemical Shifts and AOM Parametrization for *cis*-α-[$CrX_2$([$D_4$]trien)]$^{n+}$

Two well-separated $^2$H NMR signals are observed for *cis*-α-[$CrX_2$([$D_4$]trien)]$^{n+}$, similarly to the *trans*-3,2,3-tet complexes (Figure 1). The chemical shift difference ($\Delta\delta$) values are summarized in Table 3. A plot of $\Delta\delta$ vs. $e_\sigma(X)$ gives a fairly linear correlation for the reported $e_\sigma(X)$ values of the monodentate ligands together with that of the didentate dianionic oxalato ligand (Table 3 and Figure 4). This correlation gives Equation (4).

Table 3. AOM parameter values and $^2$H NMR chemical shift differences for *cis*-α-[$CrX_2$([$D_4$]trien)]$^{n+}$.

| $X_2$ | $\Delta\delta$ [ppm] | $e_\sigma(X)$ [$10^3$ cm$^{-1}$][a] |
|---|---|---|
| $F_2$ | 62.9 | 7.80[18] |
| $Cl_2$ | 85.6 | 5.56[19] |
| $(NCS)_2$ | 80.6 | 6.41[20] |
| $(OH)_2$ | 57.3 | 8.63[19] |
| $(H_2O)_2$ | 70.3 | 6.76[13] |
| ox | 78.3 | 6.75[28] |

[a] Calculated from Equation (4).

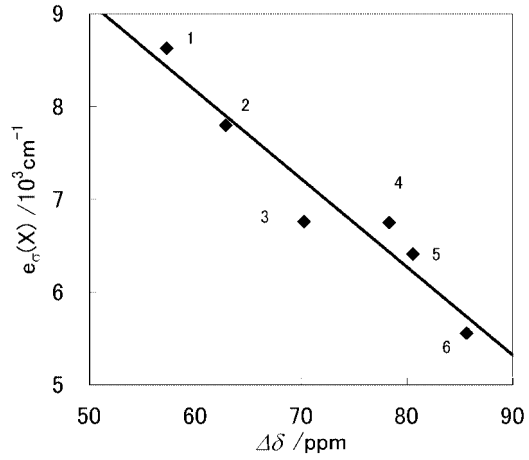


Figure 4. Plots of the AOM parameter values vs. the $^2$H NMR shift difference ($\Delta\delta$) for *cis*-α-[$CrX_2$(trien)]$^{n+}$ in water. 1: $OH^-$; 2: $F^-$; 3: $H_2O$, 4: oxalato$^{2-}$; 5: $NCS^-$; 6: $Cl^-$.

$$e_\sigma(X) = -0.095\Delta\delta + 13.90 \ (r = 0.96) \quad (4)$$

The slope and intercept of this equation are not very different from those of Equation (1) for the *trans*-[$CrX_2$(3,2,3-tet)]$^+$ complexes, which suggests that the variation of $\Delta\delta$ with $e_\sigma(X)$ for the *cis* complexes has the same cause as for the *trans* complexes.

Equation (4) could therefore be used to provide $e_\sigma(X)$ values for didentate and monodentate ligands from the $^2$H NMR shift difference for the deuterated trien complexes. The $e_\sigma$ value for the acac complex [$e_\sigma$(acac)], for example, was estimated from its $\Delta\delta$ value to be 6770 cm$^{-1}$ which is smaller than that (7400–7700 cm$^{-1}$) obtained spectroscopically and by AOM calculations for [Cr(acac)$_3$].[28a] This may be due to the different number of acac ligands in the tris(acac) and mono(acac) complexes as the spin-forbidden transition energy of [Cr(acac)$(en)_2$]$^{2+}$[29] is larger than that of [Cr(acac)$_2$(en)]$^+$[29] and [Cr(acac)$_3$][30] – the mono(acac) complex is less covalent than the tris- and bis(acac) complexes.

## Conclusions

The mutual influence of ligands for both *trans*- and *cis*-[$CrX_2(N)_4$] complexes of aliphatic amines behaves in a fundamentally similar manner to the solvent-dependence of the

 © 2007 Wiley-VCH Verlag GmbH & Co. KGaA, Weinheim 

AOM parameter $e_\sigma$(F) and the $^2$H NMR chemical-shift difference $\Delta\delta$ in *trans*- and *cis*-[$CrF_2(N)_4$]-type complexes. In view of this significant correlation, the $\Delta\delta$ values are an indicator of the relative strength of the Cr–N and Cr–X σ-bonds: the smaller the $e_\sigma$(N), the larger the $e_\sigma$(X). This suggests that the transferability assumption from one complex to another[13] is invalid for both $e_\sigma$(X) and $e_\sigma$(N).

In general, the AOM parameters have been evaluated by a conventional procedure that involves fitting the absorption bands in the spin-allowed ligand-field d–d transitions to the calculated energy levels by varying the AOM parameter values,[13,18–22] which requires the correct assignment of the well-resolved ligand-field band components. However, the spin-allowed ligand-field bands of most *trans*- and *cis*-[$CrX_2N_4$]-type complexes exhibit poorly defined or no splitting into degenerate or nondegenerate components, except for a limited number of complexes such as *trans*-difluorido tetraamine complexes. Thus, the positions of the absorption bands have to be resolved into their Gaussian components by curve deconvolution techniques for most complexes. This often produces uncertainties in the AOM parameter estimations. The present procedure for estimating the AOM parameters overcomes this major disadvantage of the conventional direct method even though preparation of the deuterated ligands is a tedious process. In addition, this method can be applied to complexes whose ligand-field bands cannot be observed due to overlapping with intraligand transitions of spectroscopically nontransparent ligands or with MLCT bands in the ligand-field band region, as found for complexes of the nitroxide radical.[31]

Once the $e_\sigma$(X) values have been obtained from Equations (1) or (4), the Cr–X π-bond interaction or $e_\pi$(X) parameter values can be estimated from the relation of the available ligand-field parameter $\Delta(X) = 10\,Dq(X) = 3e_\sigma(X) - 4e_\pi(X)$ by substituting the appropriate $e_\sigma$(X) values. Both $e_\sigma$(X) and $e_\pi$(X) for the ligands can then be positioned in the two-dimensional spectrochemical series, which is distinguished from the traditional spectrochemical series by the straightforward reflection of the ground-state electronic properties. Thus, the present complexes *trans*-[$CrX_2$([$D_4$]3,2,3-tet)]$^{n+}$ and *cis*-α-[$CrX_2$([$D_4$]trien)]$^{n+}$ can be used as reference complexes for ranking the two-dimensional spectrochemical series.

The additive nature of the ligand field for *trans*-[CrF(X)(3,2,3-tet)]$^{n+}$, is mostly validated for the FCl and FBr complexes but not for the F(CN) complex, which demonstrates a mutual influence between F and CN through a push-pull action or a donor–acceptor π mutual compensation.

## Experimental Section

### Preparation of the 3,2,3-tet Complexes

***trans*-[CrF($H_2O$)(3,2,3-tet)]($ClO_4$)$_2$:** *trans*-[$CrF_2$(3,2,3-tet)]($ClO_4$)[7] (1.0 g) was stirred with 5 mL of perchloric acid (70%) at 30 °C overnight.[32] The resultant orange crystals were filtered, then washed with acetone and diethyl ether and dried in air. Yield: 52.7%. $C_8H_{24}Cl_2CrFN_4O_9$ (462.20): calcd. C 20.79, H 5.23, N 12.12; found C 20.85, H 5.30, N 12.06.

***trans*-[CrF(X)(3,2,3-tet)]$ClO_4$ (X = Cl, Br):** A mixture of *trans*-[CrF($H_2O$)(3,2,3-tet)]($ClO_4$)$_2$ (0.5 g) and an excess of $NH_4X$ (X = Cl, Br; 0.5 g) was refluxed in methanol at 70 °C for 45 min. The color of the solution turned from orange to red and powdery complexes were obtained after filtration and drying. Yields for the Cl and Br complexes were about 70%. $C_8H_{22}Cl_2CrFN_4O_4$ (380.18): calcd. C 25.27, H 5.83, N 14.74; found C 25.39, H 5.94, N 14.64. $C_8H_{22}BrClCrFN_4O_4$ (424.64): calcd. C 22.63, H 5.22, N 13.19; found. C 22.71, H 5.30, N 13.13.

***trans*-[CrF($NH_3$)(3,2,3-tet)]($ClO_4$)$_2$:** *trans*-[CrBr(F)(3,2,3-tet)]$ClO_4$ was treated with an excess of liquid ammonia in a pressure tube at 0 °C for 2 h. The ammonia was then evaporated at atmospheric pressure at room temperature to give an orange powder. This was recrystallized by adding sodium perchlorate to the aqueous solution. Yield was about 60%. $C_8H_{25}Cl_2CrFN_5O_8$ (461.21): calcd. C 20.83, H 5.46, N 15.19; found C 21.21, H 5.56, N 15.29.

***trans*-[CrF(CN)(3,2,3-tet)]$BPh_4$·0.46$NaBPh_4$·3$H_2O$:** *trans*-[CrF($H_2O$)(3,2,3-tet)]($ClO_4$)$_2$ (0.76 g) was dissolved in 10 mL of DMSO. Sodium cyanide (0.1 g) was added to this solution and the mixture was heated to 140 °C. The solution was then cooled to room temperature and the desired complex was eluted on a column of Sephadex C-25 using 0.1 M sodium bromide solution as the eluent. A small amount of the starting complex remained on the top of the column. The first eluate was collected by filtration and was desalted by condensation a few times. The desired complex precipitated upon addition of sodium tetraphenylborate to the aqueous solution. $C_{44.02}H_{57.2}B_{1.46}CrFN_5Na_{0.46}O_3$ (801.99): calcd. for C 65.96, H 7.19, N 8.73; found C 65.25, H 7.23, N 8.85.

### Preparation of the [$D_4$]3,2,3-tet Complexes

Deuterated [$D_4$]3,2,3-tet was prepared by a previously reported method.[7] The [$D_4$]3,2,3-tet complexes were prepared by the same methods as the corresponding 3,2,3-tet complexes.

### Preparation of the trien Complexes

***cis*-α-[$CrF_2$(trien)]$ClO_4$:** This complex was prepared by a literature method.[33]

*cis*-α-[$CrCl_2$(trien)]Cl, *cis*-α-[$Cr(NCS)_2$(trien)]Cl, and *cis*-α-[Cr(ox)(trien)]$ClO_4$ were also prepared by literature methods.[34]

***cis*-α-[Cr(acac)(trien)]($PF_6$)$_2$:** Acetylacetone (1.0 g) was added to 100 mL of an aqueous solution of *cis*-α-[$CrCl_2$(trien)]Cl (3.3 g). The solution was then neutralized with 1 M NaOH solution, and the mixture was heated in a water bath for 60 min. The color of the solution changed from violet to red. The desired complex was separated by column chromatography on SP-Sephadex $Na^+$ with 0.2 M sodium chloride solution as eluent. The sodium chloride in the eluate was removed by condensation. The $PF_6$ salt was obtained by adding $NaPF_6$ to the aqueous solution. $C_{11}H_{25}CrF_{12}N_4O_2P_2$ (587.27): calcd. C 22.50, H 4.29, N 9.54; found C 22.48, H 4.31, N 9.52.

**Deuteriation of [$D_4$]trien and Its Complexes:** Deuteriated triethylenetetraamine ([$D_4$]trien = $NH_2CH_2CH_2NHCD_2CD_2NHCH_2CH_2NH_2$) was prepared by a previously reported method.[8] The product was used without purification. The [$D_4$]trien complexes were prepared by the same methods as the trien complexes.

**Measurements:** UV/Vis spectra in solution were measured with a Shimazu UV-2100 and/or a Hitachi UV-330 spectrophotometer. $^2$H NMR spectra were measured with a Jeol JMN GX-400 and/or a JEOL JMN GSX-270 spectrometer at 26 °C for products in 2 mM

 © 2007 Wiley-VCH Verlag GmbH & Co. KGaA, Weinheim 

dmf solution. External standards of $CDCl_3$ and $(CH_3)_3SiCD_2CD_2CO_2Na$ (TSP) were assigned chemical shifts of $\delta = 7.24$ and 0.589 ppm, respectively. The solvents used for the measurements were of spectro or reagent grade. The abbreviations for the solvents (in parentheses) and their $A_N$ values (in square brackets), as found in ref.[7–11], are as follows: *N*,*N*-dimethylacetamide (dma) [13.6], *N*,*N*-dimethylformamide (dmf) [16.0], acetonitrile (an) [18.9], dimethyl sulfoxide (dmso) [19.3], chloroform [23.1], *N*-methylformamide (nmf) [32.1], formamide (fm) [39.8], methanol [41.3], water [54.8].


[1] J. Gažo, B. Boča, E. Jna, M. Kabešová, Ľ. Macášková, J. Šima, P. Pelikán, E. Valach, *Coord. Chem. Rev.* **1982**, *43*, 87–131.

[2] I. Bertini, D. Gatteschi, A. Scozzafava, *Inorg. Chem.* **1976**, *15*, 203–207.

[3] A. B. P. Lever, I. M. Walker, P. J. McCarthy, K. B. Mertes, A. Jircitano, R. Sheldon, *Inorg. Chem.* **1983**, *22*, 2252–2258.

[4] L. Y. Martin, C. R. Sperati, D. H. Bush, *J. Am. Chem. Soc.* **1977**, *99*, 2968–2981.

[5] T. Ito, M. Kato, H. Ito, *Bull. Chem. Soc. Jpn.* **1984**, *57*, 1556–1561.

[6] T. Ito, M. Kato, H. Ito, *Bull. Chem. Soc. Jpn.* **1984**, *57*, 2641–2649.

[7] S. Kaizaki, H. Takemoto, *Inorg. Chem.* **1990**, *29*, 4960–4964.

[8] Y. Terasaki, S. Kaizaki, *J. Chem. Soc. Dalton Trans.* **1995**, 2837–2841.

[9] Y. Terasaki, T. Fujihara, T. Schönherr, S. Kaizaki, *Inorg. Chim. Acta* **1999**, *295*, 84–90.

[10] S. Kaizaki, N. Koine, N. Sakagami, *Bull. Chem. Soc. Jpn.* **1991**, *64*, 2058–2064.

[11] S. Kaizaki, *Trends Inorg. Chem.* **1999**, *6*, 105–136.

[12] D. S. McClure, *Advances in the Chemistry of Coordination Compounds* (Ed.: S. Kirshner), Macmillan, New York, NY, **1961**, pp. 498–508.

[13] J. Glerup, O. Mønsted, C. E. Schäffer, *Inorg. Chem.* **1976**, *15*, 1399–1407.

[14] C. Anthon, J. Bendix, C. E. Schäffer, *Inorg. Chem.* **2004**, *43*, 7882–7886.

[15] L. G. Vanquickenborne, A. Ceulemans, *Coord. Chem. Rev.* **1983**, *48*, 157–202.

[16] a) J. K. Burdett, T. A. Alright, *Inorg. Chem.* **1979**, *18*, 2112–2120; b) J. K. Burdett, *Molecular Shapes*, John Wiley & Sons, New York, **1980**, 218.

[17] In ref.[7] the correlation coefficients with the solvatochromism were recalculated by using the newly re-measured UV/Vis spectroscopic data. They are $E(^4B_2) = 0.016A_N + 20.7$ (a) and $E(^4A_2) = -0.034A_N + 30.3$ (b), $\Delta\delta = 0.409A_N + 66.34$ (c). These lead to the following relations: $e_\sigma(N) = E(^4B_2)/3 = 0.0054A_N + 6.90$ (d) and $e_\sigma(F) = -0.020A_N + 7.80$ (e). Equation (e) is obtained by including the configurational interaction between $^4A_2(^4T_2{}^a)$ and $^4A_2(^4T_2{}^b)$ with more appropriate Racah parameter B (650 $cm^{-1}$) than the previous one (460 $cm^{-1}$) by using the observed relation $e_\sigma(N) = E(^4B_2)/3$. Accordingly, Eqs. (c)–(e) give $e_\sigma(N_c) = 0.013\Delta\delta + 6.02$ (f) and $e_\sigma(F) = -0.048\Delta\delta + 11.0$ (g), and Eqs. (f) and (g) give $e_\sigma(F) = -3.67e_\sigma(N_c) + 33.1$ (h). These revisions do not materially alter the discussion.

[18] L. Dubicki, M. A. Hitchman, P. Day, *Inorg. Chem.* **1970**, *9*, 188–190.

[19] M. Keeton, B. F-C. Chou, A. B. P. Lever, *Can. J. Chem.* **1971**, *49*, 192–198; Errantum, *Can. J. Chem.* **1973**, *51*, 3690.

[20] W. Fee, J. N. MacB. Harrowfield, *Aust. J. Chem.* **1970**, *23*, 1049–1052.

[21] a) A. Urushiyama, M. Itoh, T. Schonherr, *Bull. Chem. Soc. Jpn.* **1995**, *68*, 594–603; b) T. Schönherr, M. Itoh, A. Urushiyama, *Bull. Chem. Soc. Jpn.* **1995**, *68*, 2271–2279; c) B. Schatschneider, J. R. Perumareddi, *Inorg. Chim. Acta* **2005**, *358*, 4571–4574.

[22] a) D. W. Smith, *Struct. Bonding* **1978**, 87–117; b) A. Bencini, C. Benelli, D. Gatteschi, *Coord. Chem. Rev.* **1984**, *60*, 131–169; c) P. Hoggard, *Structure Bonding* **2003**, *106*, 37–57.

[23] J. A. Timney, *Inorg. Chem.* **1979**, *18*, 2502–2506.

[24] P. Riccieri, E. Zinato, A. Damiani, *Inorg. Chem.* **1988**, *27*, 3755–3760.

[25] Y. Terasaki, T. Fujihara, S. Kaizaki, *Eur. J. Inorg. Chem.* **2007**, 3400–3404, following paper.

[26] $e_\sigma(FX) = 1/2[e_\sigma(F) + \delta e_\sigma(F) + e_\sigma(X) + \delta e_\sigma(CN)] \propto 1/2\{e_\sigma(F) + e_\sigma(F)[e_\sigma(F) - e_\sigma(CN)] + e_\sigma(CN) + e_\sigma(CN)[e_\sigma(CN) - e_\sigma(F)]\} = 1/2\{e_\sigma(F) + e_\sigma(CN) + [e_\sigma(F) - e_\sigma(CN)]^2\}$.

[27] P. Riccieri, E. Zinato, A. Damiani, *Inorg. Chem.* **1987**, *26*, 2667–2674.

[28] a) M. A. Atanasov, T. Schönherr, H.-H. Schmidtke, *Theor. Chim. Acta* **1987**, *71*, 59–73; b) T. Schönherr, J. Degen, *Z. Naturforsch., Teil A* **1990**, *45*, 161–168.

[29] P. X. Armendarez, L. S. Forster, *J. Chem. Phys.* **1964**, *40*, 273–277.

[30] S. Kaizaki, J. Hidaka, Y. Shimura, *Inorg. Chem.* **1973**, *12*, 142–150.

[31] S. Kaizaki, *Bull. Chem. Soc. Jpn.* **2003**, *76*, 673–688; S. Kaizaki, *Coord. Chem. Rev.* **2006**, *250*, 1804–1818.

[32] J. W. Vaughn, O. J. Stvan, V. E. Magnuson, *Inorg. Chem.* **1968**, *7*, 736.

[33] J. Glerup, J. Josephsen, E. Michelsen, E. Pedersen, C. E. Schäffer, *Acta Chem. Scand.* **1970**, *24*, 247–254.

[34] D. A. House, C. S. Garner, *J. Am. Chem. Soc.* **1966**, *88*, 2156–2162.


Received: November 21, 2006
Published Online: June 14, 2007

 © 2007 Wiley-VCH Verlag GmbH & Co. KGaA, Weinheim 

DOI: 10.1002/ejic.200601093

# Mutual Influences of Ligands as Revealed by the $^2$H NMR Chemical Shifts and the Angular Overlap Model Parameters: *cis*-$[CrX_2(N)_4]$ and *fac*-$[CrX_3(N)_3]$-Type Complexes with Aromatic Amines[‡]

**Yukiko Terasaki,[a] Takashi Fujihara,[b] and Sumio Kaizaki*[c]**

**Keywords:** Chromium complexes / Ligand effects / N ligands / NMR spectroscopy / Angular overlap model parameters

A mutual influence of ligands through a π donor–acceptor interaction is found by examining how the X co-ligands of the aromatic amine complexes *cis*-$[CrX_2([D_4]bpy)_2]^{n+}$ (bpy = 2,2′-bipyridine) and *fac*-$[CrX_3([D_{12}]tpa)]^{n+}$ [tpa = tris(2-pyridyl)amine] affect the $^2$H NMR chemical shifts in connection with the Angular Overlap Model (AOM) parameterization in an analogous manner to our previous study on the solvatochromism and solvent-dependent $^2$H NMR spectra of *cis*-$[CrF_2([D_4]bpy)_2]^+$ and *fac*-$[CrF_3([D_{12}]tpa)]$. The ranking of the AOM parameter for monodentate and/or didentate ligands can be obtained from this co-ligand effect only from the $^2$H NMR shifts. The postulated relative order in the two-dimensional spectrochemical series is $Cl^- > Br^-$ > O or N donors ($mal^{2-} > acac^-$ or $H_2O$ > dmf > $NCS^-$) for the aromatic amine complexes, which contrasts with the order O or N donors > $Cl^- > Br^-$ for the aliphatic amine complexes(see the preceding paper in this issue). This fact suggests that the Cr–Cl and Cr–Br σ bonds are stronger in the soft acidic aromatic amine complexes than those in the hard acidic aliphatic amine complexes. This means they have a higher affinity for soft basic $Cl^-$ and $Br^-$ ligands and can be explained in terms of the hard/soft acid/base (HSAB) concept.
(© Wiley-VCH Verlag GmbH & Co. KGaA, 69451 Weinheim, Germany, 2007)

## Introduction

In the preceding paper in this issue[1] we found a linear correlation between the Angular Overlap Model (AOM) parameter $e_\sigma(X)$ for the X co-ligands and the $^2$H NMR chemical shift differences ($\Delta\delta$) for the aliphatic amine complexes *trans*-$[CrX_2([D_4]3,2,3\text{-tet})]^{n+}$ {[D$_4$]3,2,3-tet = 1,10-diamino-4,7-diazadecane $[NH_2(CH_2)_3NH(CD_2)_2NH(CH_2)_3NH_2]$}, and *cis*-$[CrX_2([D_4]trien)]^{n+}$ {[D$_4$]trien = triethylenetetramine $[NH_2(CH_2)_2NH(CD_2)_2NH(CH_2)_2NH_2]$}, which demonstrates a mutual influence between the amine and X ligands. This is based on the fact that the $e_\sigma(X)$ vs. $\Delta\delta$ relation is parallel to the $e_\sigma(F)$ vs. $\Delta\delta$ relation, with a variation of the solvent acceptor number ($A_N$), in the *trans*- and *cis*-$[CrF_2(N)_4]$ complexes. As a result, we devised a more convenient method for estimating the AOM parameter values, even for didentate ligands, which allows them to be positioned in the two-dimensional spectrochemical series. On the other hand, the solvatochromism and solvent-dependent $^2$H NMR spectra of the aromatic amine complexes *cis*-$[CrF_2([D_4]bpy)_2]^+$ (bpy = 2,2′-bipyridine)[2] and *fac*-$[CrF_3([D_{12}]tpa)_3]$ [tpa = tris(2-pyridyl)amine][3] have revealed more direct and clearer evidence for a mutual F–Cr–N(aromatic amine) influence due to the strong Cr–N π acceptor and Cr–F π donor properties in terms of the AOM parametrization, as has been found for the NC–Cr–F bond in *trans*-$[CrF(CN)(3,2,3\text{-tet})]^+$.[1] In an analogous manner to this solvent-dependent spectroscopic behavior for the fluorido aromatic amine complexes as well as the co-ligand effect for *trans*- and *cis*-$[CrX_2(N)_4]$ complexes with aliphatic amines (see ref.[1]), the mutual influence between X ligands and the aromatic amine in *cis*-$[CrX_2([D_4]bpy)_2]^{n+}$ and *fac*-$[CrX_3([D_{12}]tpa)_3]$ is expected to be revealed by examining the $^2$H NMR chemical shifts in terms of the AOM parameterization.

In this paper, the $^2$H NMR chemical shifts of *cis*-$[CrX_2([D_4]bpy)_2]^{n+}$ and *fac*-$[CrX_3([D_{12}]tpa)]^{n+}$ will be explored in terms of the AOM parameterization of the X co-ligands. This could provide a qualitative ranking of the two-dimensional spectrochemical series[4] for the AOM parameters of the co-ligand X in the aromatic amine complexes, which would shed light on how the coordination bond properties differ from each upon replacing the co-ligands and also how they differ from those in the aliphatic amine complexes.

[‡] Mutual Influences of Ligands as Revealed by $^2$H NMR Shifts and the Angular Overlap Model Parameters, 2. Part 1: Ref.[1]

[a] Toyama National College of Maritime Technology, Imizu, Toyama 933-0293, Japan,
[b] Department of Chemistry, Faculty of Science, Saitama University, Sakuraku, Saitama, 338-8570, Japan
[c] Department of Chemistry, Graduate School of Science, Osaka University, Toyonaka, Osaka 560-0043, Japan
E-mail: kaizaki@chem.sci.osaka-u.ac.jp

 © 2007 Wiley-VCH Verlag GmbH & Co. KGaA, Weinheim 

## Results and Discussion

### 2,2′-Bipyridine(bpy) Complexes {*cis*-[Cr($F_2$ or $X_2$)(bpy)$_2$]$^+$}

Of the four $^2$H NMR signals of *cis*-[$CrF_2$([$D_4$]bpy)$_2$]$^+$ shown in Figure 1, the signal at around $\delta$ = –25 ppm for the deuteron at the 4 (*para*)-position and that at around $\delta$ = 30 ppm for the deuteron at the 5 (*meta*)-position of the pyridyl ring of bpy *trans* to F increase and decrease in absolute shift values, respectively, upon increasing the solvent acceptor number ($A_N$), as reported previously.[2] This change is also correlated to the AOM parameter $e_\sigma(N_t)$ ($N_t$ denotes the nitrogen of the pyridyl ring *trans* to F) in terms of the ligand-field band analysis on the basis of a fairly large $A_N$-dependence of the first ligand-field ($^4A_{2g}$-$^4T_{2g}$) band.[2] In other words, the $e_\sigma(N_t)$ and $e_\pi(N_t)$ values change with variation of $A_N$, as shown by the right ordinate and upper abscissa, respectively, in Figure 2,[2] which suggests that the solvent-dependent behavior of the chemical shifts of $\delta$(4) and $\delta$(5) reflects the variation of the Cr–N σ- and π-bond properties, respectively, in the bpy complex: the larger the acceptor number $A_N$, the smaller the $e_\sigma$(F) and $e_\pi$(F) values or the weaker the Cr–F σ and π bonds, and also the larger the $e_\sigma(N_t)$ value or the stronger the Cr–$N_t$ σ bond, the smaller the $|e_\pi(N_t)|$ value or the stronger the Cr–$N_t$ π acceptor bond. This relationship demonstrates the mutual compensation between Cr–N and Cr–F σ and π bonds. The mutual compensation of $e_\pi(N_t)$ and $e_\pi$(F) in *cis*-[$CrF_2$-(bpy)$_2$]$^+$ is confirmed by the solvatochromic shift behavior from the $^2E(^2E_g)$ to $^2E(^2T_{1g})$ emitter in a mixture of dmf and water in solvents with smaller $A_N$ with increasing dmf fraction,[5] as also observed for *trans*-[$CrF_2$(py)$_4$]$^+$.[2] The $^2E(^2T_{1g})$ emitter, or the lowest excited $^2E(^2T_{1g})$ state, results from a lowering, by $\Delta(t_{2g})^2/[E(^2t_{2g}) - E(^2T_{1g})]$, of the large configurational interaction between the $^2E(^2T_{1g})$ and $^2E(^2T_{2g})$ states due to an increase in [$\Delta(t_{2g}) = e_\pi$(F) + $|e_\pi(N_t)|$] caused by the push-pull action between the Cr–F and Cr–N bonds in solvents with smaller $A_N$. This mutual influence is also supported by the Cr–F and Cr–N bond lengths in *cis*-[$CrF_2$(bpy)$_2$]$ClO_4$, where our recent X-ray analysis revealed that the Cr–N bonds *trans* to F [Cr–N2 2.0680(13), Cr–N3 2.0842(14) Å] are significantly longer than those *trans* to another bpy nitrogen atom [Cr–N1 2.0480(14), Cr–N4 2.0511(14) Å].[6]

The four $^2$H NMR signals observed for the 4-,5- and 4′-,5′-deuterons in the *cis*-[$CrX_2$([$D_4$]bpy)$_2$]$^{n+}$ complexes are assigned to two inequivalent deuterons of the pyridyl rings *trans* [$\delta$(4) and $\delta$(5)] and *cis* [$\delta$(4′) and $\delta$(5′)] to the X ligand in analogy to those for the corresponding difluorido complex [$\delta(4) > \delta(4')$ and $\delta(5) > \delta(5')$], as shown in Figure 1. The NMR spectroscopic data are summarized in Table 1.

A plot of $\delta$(4) vs. $\delta$(5) gives the following well-defined linear correlation for the X complexes in water: $-\delta(4) = -1.91\delta(5) + 83.7$ ($r$ = 0.98).

This correlation is similar to that for *cis*-[$CrF_2$([$D_4$]-bpy)$_2$]$^+$ [$-\delta(4) = -1.45\delta(5) + 68.65$ ($r$ = 0.99)], as shown in Figure 2. Since there is no direct method for correlating the ligand-field band with the $^2$H NMR chemical shift for *cis*-

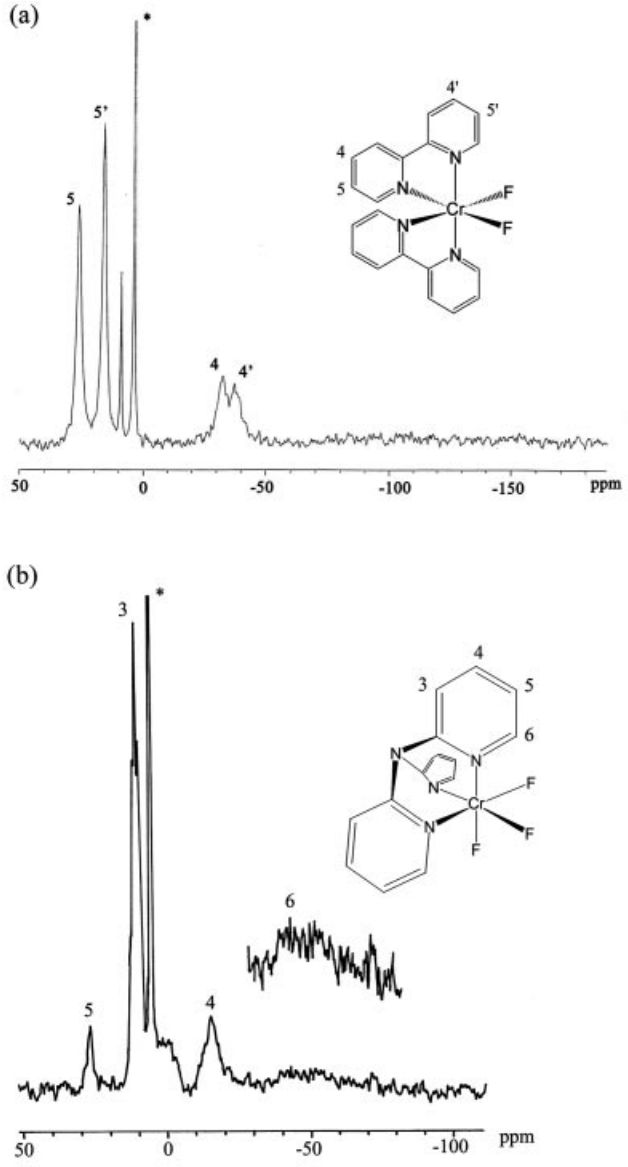


Figure 1. $^2$H NMR spectra of [$CrF_2$([$D_4$]bpy)$_2$]$^+$ in formamide (a) and [$CrF_3$([$D_{12}$]tpa)] in dmf (b). The insets show the structures with the positions of the deuterons used for assignment of the NMR signals labeled. The asterisks indicate solvent signals.

[$CrX_2$(bpy)$_2$]$^{n+}$ complexes, however, the scales for the $e_\sigma(N_t)$ and $e_\pi(N_t)$ values in Figure 2 are not necessarily useful for estimating the AOM parameters. Assuming that the variation of $e_\sigma$(X) results in change in the $e_\sigma$(N) values similar to that found for the aliphatic amine complexes,[1] the increase in $\delta$(4) and the decrease in $\delta$(5) should be associated with the increase in $e_\sigma(N_t)$ and the decrease in $e_\pi(N_t)$, respectively, as a result of the decrease in $e_\sigma$(X) in a manner analogous to that for *cis*-[$CrF_2$([$D_4$]bpy)$_2$]$^+$. The co-ligand dependence of the $^2$H NMR chemical shifts for the bpy complexes shows that $\delta$(4) or $e_\sigma(N_t)$ increase in the order $F^- < Cl^- < Br^- < mal^{2-} < acac^- <$ dmf in dmf and $Cl^- < Br^- < F^- < mal^{2-} < acac^-$ < dmf in $H_2O$, thereby reflecting the increasing order of the Cr–N σ-bond interaction energy or $e_\sigma(N_t)$. Likewise, the decreasing order of $\delta$(4) corre-

 © 2007 Wiley-VCH Verlag GmbH & Co. KGaA, Weinheim 

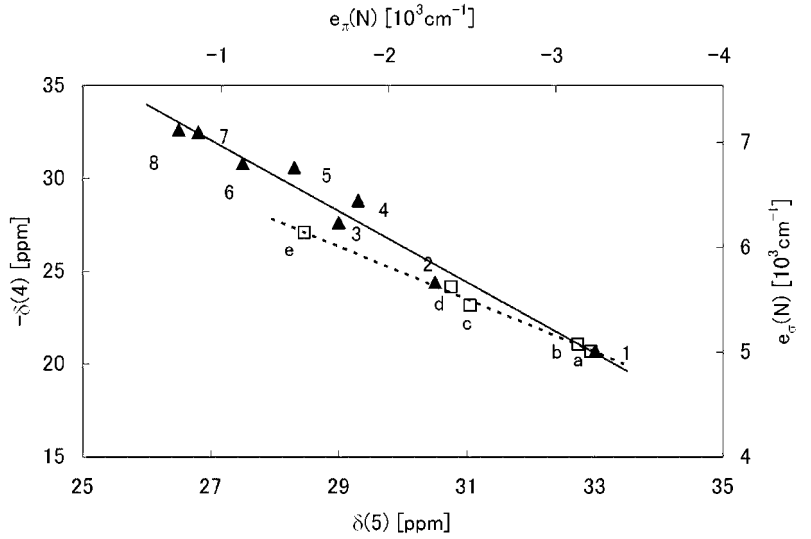


Figure 2. Plots of the $^2$H NMR chemical shifts of the deuterons in the 4- and 5-positions of *cis*-$[CrF_2([D_4]bpy)_2]^+$ (□) in dmf (a), dmso (b), nmf (c), fa (d), and water (e) and for *cis*-$[CrX_2([D_4]bpy)_2]^{n+}$ (▲) [X = F (1), Cl (2), Br (3), mal (4), acac (5), acaCl (6), acaBr (7), and dmf (8)]. The lines shown are the least-squares fit. The right ordinate and upper abscissa show the $e_\sigma(N_t)$ and $e_\pi(N_t)$ values, respectively, for *cis*-$[CrF_2(bpy)_2]^+$.

Table 1. $^2$H NMR chemical shifts (δ values, ppm) of *cis*-$[CrX_2([D_4]bpy)_2]^{n+}$.

| $X_2$ | Chemical shift[a] | |
|---|---|---|
| | $-\delta(4)$ | $\delta(5)$ |
| $F_2$ | 20.7 | 33.0 |
| $Cl_2$ | 24.4 | 30.5 |
| $Br_2$ | 27.6 | 29.0 |
| acac | 30.6 | 28.3 |
| $(dmf)_2$ | 32.6 | 26.5 |
| mal | 28.8 | 29.3 |
| acaCl | 30.8 | 27.5 |
| acaBr | 32.5 | 26.8 |

[a] $-\delta(4) = -1.91\delta(5) + 83.7$ ($r = 0.98$).

sponds to that of $e_\sigma$(X), namely $F^- > Cl^- > Br^- > mal^{2-} > acac^- >$ dmf in dmf and $Cl^- > Br^- > F^- > mal^{2-} > acac^- >$ dmf in water. This order is similar to the rank of the two-dimensional spectrochemical series for $e_\sigma$(X),[1,4,9–11] excluding $Cl^-$ and $Br^-$, rather than the rank for $e_\pi$(X), in other words the Cr–X σ-bond properties or $e_\sigma$(X) are correlated directly with the variation of $e_\sigma(N_t)$ and $e_\pi(N_t)$. Thus, the $^2$H NMR chemical shifts provide a method for evaluating the rank of the AOM parameter $e_\sigma$(X) in the two-dimensional spectrochemical series.

Like the aliphatic amine complex *cis*-α-$[CrX_2([D_4]-trien)]^{n+}$, the bpy complexes are able to provide some information about the as-yet unknown ranking of the AOM parameters even for the didentate ligands. Thus, the $^2$H NMR spectroscopic data of *cis*-$[Cr([D_4]bpy)_2(acaX)]^{2+}$ complexes (X = Cl, Br) containing didentate ligands were examined by plotting $\delta(4)$ vs. $\delta(5)$. As compared with the $-\delta(4)$ or $e_\sigma$(N) values for the acetylacetonate analogues, the Cr–O(acaX) σ bond is a little weaker than the Cr–O(acac) σ bond, although the covalency in Cr–O(acaX) is estimated to be larger than that in Cr–O(acac), as inferred from the nephelauxetic effect estimated from the lowest ligand-field doublet ($^2E_g$) position by the emission for $[Cr(acaX)_3]$[7] and circular dichroism for (+)-$[Cr(acaX)_2(en)]^+$.[8] This may result from a difference in co-ligands between bpy and acac or en (ethylenediamine) and/or in the number of acac ligands as found in the aliphatic amine (acac) complexes.[1]

It should be noted that the rank of $e_\sigma$(X) in the two-dimensional spectrochemical series for the bpy complexes is $F^- > Cl^- > Br^-$ > oxygen donors ($mal^{2-} > acac^-$ > dmf) in dmf and $Cl^- > Br^-$ > oxygen donors ($mal^{2-} > acac^-$ > dmf) > $F^-$ in water, as suggested from the order of $-\delta(4)$. This is contrast to the order of the AOM parameters ($OH^- > F^- > CN^- > NH_3 > NCS^- > H_2O > Cl^- > Br^-$) of 3,2,3-tet and trien complexes.[1,4,9–11] This difference will be discussed in connection with the case of the tpa complexes.

### Tris(2-pyridyl)amine (tpa) Complexes

As shown in Figure 1, *fac*-$[CrF_3([D_{12}]tpa)]$ exhibits four $^2$H NMR signals. A pair of signals at the 4 (*para*)- and 3 (*meta*)-positions is found to demonstrate a linear correlation with variation of $A_N$, as shown in Figure 3 and represented by $-\delta(4) = -4.00\delta(3) + 63.6$ ($r = 0.90$). Such a solvent-dependent NMR behavior is related to the significant solvatochromism observed: the AOM parameters $e_\sigma$(N) and $e_\pi$(N) associated with variation of the Cr–F σ-donor interaction, or $e_\sigma$(F), are evaluated by considering a large trigonal splitting due to the unusual anisotropic π interaction in the ligand-field ($^4T_2$–$^4A_2$) transition.[3]

In analogy to this correlation, *fac*-$[CrX_3([D_{12}]tpa)]$ complexes exhibit a linear relation between the $^2$H NMR chemical shifts of the deuterons at positions 4 ($\delta \approx -20$ ppm) and 5 ($\delta \approx 20$ ppm) with change of X, as shown in Figure 3; the NMR spectroscopic data are summarized in Table 2. In the case of the $X_3$ complexes, $\delta(4)$ is linearly correlated with $\delta(5)$ but not with $\delta(3)$, which gives $-\delta(4) = -2.05\delta(5) + 66.1$

 © 2007 Wiley-VCH Verlag GmbH & Co. KGaA, Weinheim 

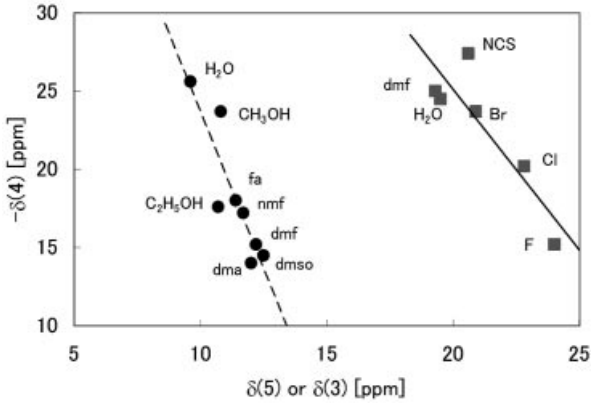


Figure 3. Plots of the $^2$H NMR chemical shifts for the deuterons in the 4- and 3-positions of *fac*-[$CrF_3$([$D_{12}$]tpa)] (●) and the deuterons in the 4- and 5-positions of *fac*-[$CrX_3$([$D_{12}$]tpa)]$^{n+}$ (■). The lines shown are the least-squares fit.

($r$ = 0.88). Although the reason for the discrepancy between $\delta$(3) and $\delta$(5) on going from the F complex to the X complexes is not clear so far, the same situation is encountered, in an electronic sense, for *fac*-[$CrX_3$([$D_{12}$]tpa)]$^{n+}$ as for the fluorido complex, since both 3- and 5-$^2$H of the pyridyl groups in tpa are located at the *meta* position, which makes it likely that the relation between $\delta$(3) and $\delta$(5) in Figure 3 reflects a similar co-ligand dependence on the $e_\sigma$(N) and $e_\pi$(N) values to that found for the bpy complexes (vide supra). This parallel correlation between the F and X complexes means that the variation of $e_\sigma$(X) must be associated with a change of $e_\sigma$(N) and $e_\pi$(N) values. Thus, the variation of $\delta$(4) with change of X ligands corresponds to the changes of the Cr–N σ-bond properties, or $e_\sigma$(N), for *fac*-[$CrX_3$(tpa)]$^{n+}$; the $e_\sigma$(N) values increase in the order $F^- < Cl^- < Br^- < H_2O <$ dmf $< NCS^-$ in dmf. On the other hand, the Cr–X σ-bond properties, or $e_\sigma$(X), decrease in the reverse order ($F^- > Cl^- > Br^- > H_2O >$ dmf $> NCS^-$ in dmf). This order is similar to that for the aliphatic amine complexes except that the $e_\sigma$(Cl) and $e_\sigma$(Br) values are larger than those of the $NCS^-$ and O-donor ligands as well as those for the bpy complexes (see above), thereby corresponding to the ranking in the two-dimensional spectrochemical series.

Table 2. $^2$H NMR chemical shifts (δ values, ppm) for *fac*-[$CrX_3$([$D_{12}$]tpa)]$^{n+}$ in dmf.

| X | Chemical shifts[a] | |
|---|---|---|
| | $\delta$(4) | $\delta$(5) |
| F | –15.2 | 24.0 |
| Cl | –20.2 | 22.8 |
| Br | –23.7 | 20.9 |
| dmf | –25.0 | 19.3 |
| $H_2O$ | –24.5 | 19.5 |
| NCS | –27.4 | 20.6 |

[a] $-\delta(4) = -2.05\delta(5) + 66.1$ ($r$ = 0.88).

The difference in ranking of $e_\sigma$(Cl) and $e_\sigma$(Br) in the two-dimensional spectrochemical series between the aliphatic and aromatic amine complexes can be explained as follows. This difference in Cr–X σ bond is related to the symbiosis[12] in terms of the hard/soft acid/base (HSAB) principle.[13] Since the coordination site at {Cr(bpy)$_2$} or {Cr(tpa)} becomes a softer acid due to the π donor–accepter cooperative interaction through the dπ orbital,[13c] the $Cl^-$ and $Br^-$ ligands, which are soft bases, are more favored in the aromatic amine complexes than in the aliphatic amine complexes. The present result may provide a clue to explaining the confusing experimental results whereby the much greater robustness of the Cr–Cl bond towards acid hydrolysis for aromatic amine complexes than for the corresponding aliphatic amine complexes is not necessarily accompanied by an increased thermodynamic stability of $[CrCl_2(bpy)_2]^+$, which is not very different from that of the corresponding ethylenediamine complex.[14–16]

## Conclusions

We have demonstrated that there are significant correlations between the $^2$H NMR chemical shifts $\delta$(4) and $\delta$(5) of the pyridyl deuterons of *cis*-[$CrX_2$([$D_4$]bpy)$_2$]$^{n+}$ and *fac*-[$CrX_3$([$D_{12}$]tpa)]$^{n+}$. These correlations reflect the variation of the AOM parameters with change of the X co-ligands in an analogous manner to the solvent-dependency of the $^2$H NMR chemical shifts of the fluorido complexes *cis*-$[CrF_2([D_4]bpy)_2]^+$ and *fac*-[$CrF_3$([$D_{12}$]tpa)], and is an indicator of the relative strength of $e_\sigma$(X) for certain didentate as well as monodentate X ligands. The ranking of $e_\sigma$(X) of both the bpy and tpa complexes in the two-dimensional spectrochemical series is different from that for complexes of the aliphatic amines 3,2,3-tet and trien, and this difference has been explained on the basis of the bond nature or a symbiosis in terms of the HSAB principle, which may provide a clue to explaining the robustness of the chlorido and bromido aromatic amine complexes.

## Experimental Section

**Preparation:** *cis*-[$CrF_2$(bpy)$_2$]$ClO_4$,[17] *cis*-[$CrCl_2$(bpy)$_2$]$ClO_4$,[16] and *cis*-[$CrBr_2$(bpy)$_2$]$ClO_4$[16] were prepared by literature methods.

***cis*-[Cr(mal)(bpy)$_2$]$ClO_4$:** This complex was obtained from the reaction of an equimolar mixture of *cis*-[$CrCl_2$(bpy)$_2$]$ClO_4$ and sodium malonate in water. The yield was about 50%. $C_{23}H_{18}ClCrN_4O_8$ (565.86): calcd. C 48.82, H 3.21, N 9.90; found C 48.81, H 3.23, N 9.88.

***cis*-[Cr(acac)(bpy)$_2$](ClO$_4$)$_2$:** *cis*-[Cr(OTf)$_2$(bpy)$_2$](OTf) [OTf = trifluoromethanesulfonate ($CF_3SO_3^-$)] was obtained by treating *cis*-[$CrCl_2$(bpy)$_2$]Cl with HOTf according to the method described for *cis*-[Cr(OTf)$_2$(en)$_2$]Cl.[18] This OTf complex was dissolved in methanol together with an equimolar amount of acetylacetone and urea and the solution was refluxed for 1.5 h at 70 °C in a water bath. After cooling, the solvent was removed on a rotary evaporator under reduced pressure. The solution was chromatographed on a SP-Sephadex $Na^+$ column with 0.2 M sodium chloride solution as eluent. The first orange eluate was desalted by concentration. An orange precipitate was obtained by adding sodium perchlorate to the solution. The precipitate was filtered off, washed with ethanol and diethyl ether and air-dried. The precipitate was recrystallized from acetone by adding ethanol. The crystals were washed with

 © 2007 Wiley-VCH Verlag GmbH & Co. KGaA, Weinheim 

ethanol and diethyl ether and air-dried. The yield was about 9%. $C_{25}H_{23}Cl_2CrN_4O_{10}$ (662.37): calcd. C 45.33, H 3.50, N 8.46; found C 44.89, H 3.45, N 8.52.

***cis*-[Cr(acaCl)(bpy)$_2$](ClO$_4$)$_2$·0.75H$_2$O and *cis*-[Cr(acaBr)(bpy)$_2$](ClO$_4$)$_2$·0.75H$_2$O:** These complexes were prepared by treating $[Cr(acac)(bpy)_2](ClO_4)_2$ with an equimolar amount of the corresponding *N*-halosuccinimide according to the method reported for the 3-haloacetylacetonato complexes $[Cr(acaX)(en)_2]Cl_2$.[19] The yields for the acaCl and acaBr complexes were about 15 and 22%, respectively. $C_{25}H_{23.5}Cl_3CrN_4O_{10.75}$ (710.33): calcd. C 42.27, H 3.34, N 7.89; found C 41.50, H 3.44, N 8.10. $C_{25}H_{23.5}BrCl_2CrN_4O_{10.75}$ (754.78): calcd. C 39.78, H 3.14, N 7.42; found C 38.76, H 2.99, N 7.35.

***fac*-[CrF$_3$(tpa)] and *fac*-[Cr(H$_2$O)$_3$(tpa)](OTf)$_3$:** These complexes were synthesized by the previously reported method.[2,20]

***fac*-[Cr(NCS)$_3$(tpa)]:** A 1:3 mixture of $[Cr(H_2O)_3(tpa)](OTf)_3$ and sodium thiocyanate was refluxed in ethanol for 50 min. After cooling, the red precipitate was filtered off and washed with ethanol, water, and diethyl ether. The yield was about 73%. $C_{18}H_{12}CrN_7S_3$ (474.53): calcd. C 45.56, H 2.55, N 20.66; found C 45.60, H 2.61, N 20.41.

***fac*-[Cr(dmf)$_3$(tpa)] (OTf)$_3$:** This complex was obtained by leaving *fac*-$[Cr(OTf)_3(tpa)]$ to stand overnight in dmf. The color of the solution changed from violet to pink. Diethyl ether was added to this reaction solution to give an oily residue. The supernatant fluid was then decanted off and the residual oil was treated with diethyl ether to give a pink precipitate, which was filtered off, washed with diethyl ether, and air-dried. The yield was about 88%. $C_{27}H_{33}CrF_9N_7O_{12}S_3$ (966.77): calcd. C 33.54, H 3.44, N 10.14; found. C 33.19, H 3.33, N 10.16.

The deuterated bpy and tpa ligands were obtained by a previously reported method.[2,3] The deuterated bpy and tpa complexes were prepared according to the above methods for the corresponding bpy and tpa complexes.

**Measurements:** The $^2$H NMR spectra were recorded with Jeol JMN GX-400 and/or GSX270 spectrometers at 26 °C for 2 mM solutions. External standards of $CDCl_3$ and $(CH_3)_3SiCD_2CD_2CO_2Na$ (TSP) were assigned chemical shifts of $\delta$ = 7.24 and 0.589 ppm, respectively.


[1] Y. Terasaki, T. Fujihara, S. Kaizaki, *Eur. J. Inorg. Chem.* **2007**, 3394–3399, preceding paper.
[2] Y. Terasaki, S. Kaizaki, *J. Chem. Soc. Dalton Trans.* **1995**, 2837–2841.
[3] Y. Terasaki, T. Fujihara, T. Schönherr, S. Kaizaki, *Inorg. Chim. Acta* **1999**, *295*, 84–90.
[4] a) J. Glerup, O. Mønsted, C. E. Schäffer, *Inorg. Chem.* **1976**, *15*, 1399–1407; b) J. Glerup, O. Mønsted, C. E. Schäffer, *Inorg. Chem.* **1980**, *19*, 2855–2857.
[5] A. M. Ghaith, L. S. Forster, J. V. Rund, *Inorg. Chem.* **1987**, *26*, 2493–2498.
[6] Y. Terasaki, T. Fujihara, A. Nagasawa, S. Kaizaki, *Acta Crystallogr., Sect. E* **2007**, *63*, m593–m595.
[7] P. X. Armendarez, L. S. Forster, *J. Chem. Phys.* **1964**, *40*, 273–277.
[8] S. Kaizaki, J. Hidaka, Y. Shimura, *Inorg. Chem.* **1973**, *12*, 142–150.
[9] a) M. Keeton, B. F.-C. Chou, A. B. O. Lever, *Can. J. Chem.* **1971**, *49*, 192–198; Erratum: *Can. J. Chem.* **1973**, *51*, 3690; b) J. Glerup, J. Josephsen, K. Michelsen, E. Pedersen, C. E. Schäffer, *Acta Chem. Scand.* **1970**, *24*, 247–254; c) W. Fee, J. N. MacB. Harrowfield, *Aust. J. Chem.* **1970**, *23*, 1049–1052.
[10] a) T. Schönherr, *Top. Curr. Chem.* **1997**, *191*, 88–152; b) T. Schönherr, M. Atanasov, A. Hauser, *Inorg. Chem.* **1996**, *35*, 2077–2084; c) T. Schönherr, J. Degen, *Z. Naturforsch., Teil A* **1990**, *45*, 161–168.
[11] a) D. W. Smith, *Struct. Bonding (Berlin)* **1978**, 87–117; b) A. Bencini, C. Benelli, D. Gatteschi, *Coord. Chem. Rev.* **1984**, *60*, 131–169; c) P. Hoggard, *Struct. Bonding (Berlin)* **2003**, *106*, 37–57.
[12] C. K. Jørgensen, *Inorg. Chem.* **1964**, *3*, 1201–1202.
[13] a) R. G. Pearson, *Science* **1966**, *151*, 1721–1727; b) R. G. Pearson, *J. Chem. Educ.* **1968**, *45*, 581–587; c) R. G. Pearson, *J. Chem. Educ.* **1968**, *45*, 643–648.
[14] J. Josephsen, C. E. Schäffer, *J. Chem. Soc. C* **1970**, 61.
[15] N. Y. Ng, C. S. Garner, *Inorg. Chim. Acta* **1971**, *5*, 365–371.
[16] M. P. Hanckok, J. Josephsen, C. E. Schäffer, *Acta Chim. Scand., Sect. A* **1976**, *30*, 79–97.
[17] J. Glerup, J. Josephsen, E. Michelsen, E. Pedersen, C. E. Schäffer, *Acta Chem. Scand.* **1970**, *24*, 247–254.
[18] G. A. Lawrence, A. M. Sargeson, *Inorg. Synth.* **1986**, *24*, 250–252.
[19] S. Kaizaki, J. Hidaka, Y. Shimura, *Inorg. Chem.* **1973**, *12*, 135–142.
[20] Y. Terasaki, T. Fujihara, S. Kaizaki, *Acta Crystallogr., Sect. E* **2004**, *60*, m854–m856.


Received: November 21, 2006
Published Online: June 14, 2007

 © 2007 Wiley-VCH Verlag GmbH & Co. KGaA, Weinheim 

DOI: 10.1002/ejic.200601113

# Unusual Magnetic Behavior of a 2D Citrate-Bridged Dysprosium(III) Coordination Polymer

**Feng-Yan Li,[a] Lin Xu,*[a] Guang-Gang Gao,[a] Li-Hua Fan,[a] and Bo Bi[a]**

**Keywords:** Lanthanides / Coordination chemistry / Magnetic properties / Hydrothermal synthesis

A new lanthanide citrate coordination polymer [Dy(citrate)-$(H_2O)]_n$ (**1**) was hydrothermally synthesized and structurally characterized by elemental analyses, single-crystal X-ray diffraction, IR spectroscopy, thermogravimetric analysis, photoluminescence spectrum, and magnetic measurements. The structure of **1** exhibits a 2D layer structure, in which the $Dy_2O_2$ dimer serves as the building block. The photoluminescence spectrum shows blue luminescence in the solid state at room temperature. Owing to the special frustration structure, unusual magnetic relaxation was found in compound **1**.
(© Wiley-VCH Verlag GmbH & Co. KGaA, 69451 Weinheim, Germany, 2007)

## Introduction

The current interest in the synthesis of new metal–organic coordination polymers continues to expand in virtue of not only their intriguing variety of architectures, but also their potential applications in many fields, such as catalysis, material science, medicine, and magnetochemistry,[1–4] which may originate either from the metal centers and/or the organic components. Recently, polycarboxylates have been widely used to produce high-nuclearity magnetic clusters.[5–8] Particularly attractive interest is the construction of lanthanide carboxylates, owing to the wide variety of structures and their unique f–f electronic transitions.

Citric acid, a hydroxy tricarboxylic acid, is well known on account of its important role in biosystems. Moreover, it was found to be a versatile ligand in coordination chemistry by virtue of its conformational flexibility, its ability to deprotonate completely or partially, and its diversity in complexing behavior. A large number of metal–citrate compounds have been structurally characterized.[5–11] However, most of the work in this area has focused on the assembly of the d-block metals. By contrast, less work has been done to date on the lanthanide–citrate systems.[12] Additionally, the reported work of the lanthanide–citrates mostly concentrates on their luminescent properties, whereas the rich magnetic properties of lanthanide–citrate have been neglected. To the best of our knowledge, there has been only one reported lanthanide–citrate polymer that was studied with its magnetic properties, in which ferromagnetic exchange interactions were found between the neighboring magnetic centers.[12d] Hence, the citrate ligand could act as an efficient magnetic coupler owing to its diverse bridging modes.

It is well known that in the f-block the Dy compounds generally exhibit novel magnetic properties as well as the Gd, Tb, Ho, and Er complexes. In the Dy cluster compounds reported in the literature, most of them display frequency-dependent, out-of-phase AC signals, magnetization hysteresis loops, or quantum tunneling behavior, such as the triangular dysprosium compound $[Dy_3(\mu_3\text{-}OH)_2L_3Cl_2(H_2O)_4]$ $[Dy_3(\mu_3\text{-}OH)_2L_3Cl(H_2O)_5]Cl_5\cdot 19H_2O$ (HL = *o*-vanillin),[13a] and the dysprosium–manganese cluster $[Dy_6Mn_6(Hshi)_2(shi)_{10}(CH_3OH)_{10}(H_2O)_2]\cdot 9CH_3OH\cdot 8H_2O$ ($H_3$shi = salicylhydroxamic acid).[13b] Also, in the complex $[Mn_{11}Dy_4O_8(OH)_6(OMe)_2(O_2CPh)_{16}(NO_3)_5(H_2O)_3]\cdot$ 15MeCN, magnetization hysteresis loops and quantum tunneling behavior have been observed.[13c] Noting that dysprosium(III) shows manifold magnetic behavior and the aforementioned features of the citrate, we decided to explore the assembly of the Dy–citrate polymer and investigate its magnetic properties, aiming to obtain new compounds with novel magnetic properties.

In this paper, by using hydrothermal synthesis, which has become a convenient technique for the preparation of a wide range of organic–inorganic hybrid materials, we successfully prepared a lanthanide citrate complex: [Dy-(citrate)$(H_2O)]_n$, which exhibits a 2D layer structure, in which the $Dy_2O_2$ dimer serves as the building block. Weak antiferromagnetic interactions were found between the Dy ions in the layer. With an applied magnetic field, unusual magnetic relaxation was observed owing to the frustration structure.

[a] Key Laboratory of Polyoxometalates, Science of Ministry of Education, College of Chemistry, Northeast Normal University,
Changchun, 130024 P. R. China
E-mail: linxu@nenu.edu.cn
Supporting information for this article is available on the WWW under http://www.eurjic.org or from the author.

 © 2007 Wiley-VCH Verlag GmbH & Co. KGaA, Weinheim 

## Results and Discussion

### Description of the Crystal Structure

Single-crystal X-ray analysis revealed that complex **1** crystallizes in the monoclinic space group *C*2/*c*. In compound **1**, there is one crystallographically independent $Dy^{III}$ ion. The Dy ion has a nine-coordinate environment, seven of which are occupied by seven carboxylate oxygen atoms from four citrate ions, and the other two sites are occupied by one hydroxy oxygen of the citrate ion and one water molecule oxygen. The O4 and O8 atoms from one β-carboxylate are bonded in a chelated mode. Also, the ligand has a tridentate coordination mode and binds through one *α*-carboxylate (O3), one β-carboxylate (O7), and the *α*-hydroxy (O1) oxygen atoms (see Figure 1). The adjacent $Dy^{III}$ ions are edge-shared through O(7) and O($7^{\#2}$), resulting in the formation of a $Dy_2O_2$ dimer (see Figure S1); the dinuclear $Dy_2O_2$ units are firstly linked by the central carboxylate of the citrate to form a ladder chain, and then the ladder chains are additionally bridged into a 2D layer structure by the terminal carboxylate of the citrate (see Figure 2). The adjacent layers are parallel and stack along the *c* axis without interpenetration, leading to a 3D framework by the H-bond interactions. (Figures S2 and S3).

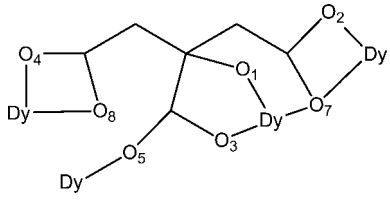


Figure 1. Structure of compound **1**.

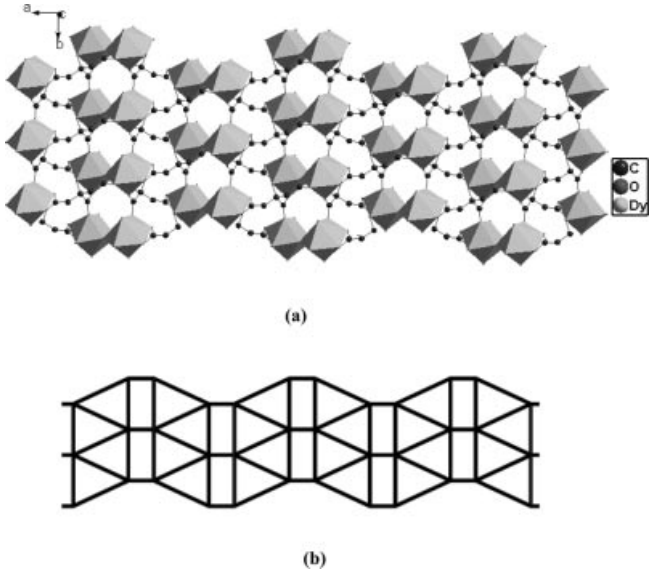


Figure 2. (a) 2D layer structure of compound **1** (viewed along the *c* axis). (b) A schematic illustration of the 2D layer structure.

Among the reported Ln–citrate series, $[Ln(Hcit)(H_2O)]_n$, Ln = La,[12a] Nd,[12b] the chains are bound together by covalent bonds with the citrate ligands, leading to 3D structures. When Ln = Gd, Nd,[12d] and with a relatively low temperature (100 °C) hydrothermal reaction, 1D chain structures are obtained. Whereas when Ln = Dy (this work), Eu, and Tb,[12c] 2D structure coordination polymers are formed. The versatile structures owe to the high coordination number of lanthanide ions and the flexible coordination geometry of citrate ligands.

In compound **1**, each $Dy^{III}$ is coordinated to three symmetry-related citrate ligands whereas each citrate ion is coordinated to four $Dy^{III}$ ions. The Dy–O bond lengths are in the range 2.321(2)–2.608(3) Å with an average of 2.423 Å and the closest distance between two neighboring Dy ions [bridged by $\mu_2$-O(7)] is 4.104 Å (see Figure S1), which is shorter than that in $[Eu(citrate)(H_2O)]_n$[12c] (Eu–Eu: 4.162 Å) and $[Gd(Hcit)(H_2O)_2{\cdot}H_2O]$[12d] (Gd–Gd: 4.321 Å). Within the *ab* plane, square and triangle grids arrange alternately with Dy–Dy separations of 4.104, 6.076, and 6.619 Å (see Figure S4), which can be viewed as geometrically frustration system. Considering that the frustration structure will influence the orientation of the electron spin, we are interested with the magnetic behavior of compound **1**, and the magnetic study of compound **1** was carried out.

### Magnetic Properties

Magnetic measurements were performed on a crystalline sample confined within a gelatin capsule under a field of 1 kOe in the temperature range 2–300 K. A plot of $\chi_m T$ vs. *T* is shown in Figure S5. The $\chi_m T$ value at room temperature is ca. 14.55 emu K mol$^{-1}$ [closed to the expected value for one $Dy^{3+}$ ($S$ = 5/2, $L$ = 5, $^6H_{15/2}$) of 14.18 emu K mol$^{-1}$], which decreases smoothly with decreasing temperature, reaching a minimum value of 13.45 emu K mol$^{-1}$ at 12 K. With a further decrease in the temperature, $\chi_m T$ increases sharply, reaching a maximum value of 14.98 emu K mol$^{-1}$at 2.0 K. The thermal variation of $\chi_m T$ mainly depends on the populations of the Stark levels and on the possible antiferromagnetic or ferromagnetic interactions between the two $Dy^{III}$ ions. It is well known that by interelectronic repulsion and spin-orbit coupling, the $4f^n$ configuration of a $Ln^{III}$ ion is split into $^{2S+1}L_J$ states. The crystal-field perturbation further leads to the splitting into Stark components. At room temperature, all the Stark levels of the 16-fold degenerate $^6H_{15/2}$ ground states are populated. While the temperature decreases, a gradual depopulation of these levels takes place.[14a] Therefore, in order to elucidate the magnetic properties, the field dependence of the $\chi_m T$ product of **1** (Figure S6) was also measured in the range 2–30 K except for the data of thermal dependence at 1 kOe of the $\chi_m T$ product (Figure S5). When the field is less and equal to 10 kOe, the $\chi_m T$ value slightly increases below 5 K, suggesting the occurrence of a weak ferromagnetic interaction arising from $Dy_2O_2$ dimers (Figure S1). When the magnetic field is stronger than 20 kOe the $\chi_m T$ value decreases, which results from the field saturation effect. Because of the presence of the large unquenched orbital angular momentum and spin-orbit coupling, no satisfactory result of the fit is

 © 2007 Wiley-VCH Verlag GmbH & Co. KGaA, Weinheim 

obtained by introducing exchange interactions through a simple dimer law deduced from the isotropic spin Hamiltonian.

To investigate the magnetic properties in detail, the field dependence of the magnetization (0–50 kOe) for compound **1** was measured at 2, 5, 10, and 20 K (Figure 3). The magnetization at 2 and 5 K increases very rapidly in low field and reaches the saturation value of ca. 5.5 $N\beta$ at 50 kOe, whereas the magnetization at 10 and 20 K increases slowly as the magnetic field increases. Interestingly, a small hysteresis loop is observed at 2 K with a coercive field ($H_c$) of 10 Oe and remnant magnetization ($M_r$) of 94 Oe emu $mol^{-1}$ (Figure 4), which is an intrinsic behavior, because a single-crystal sample was used in the measurements.

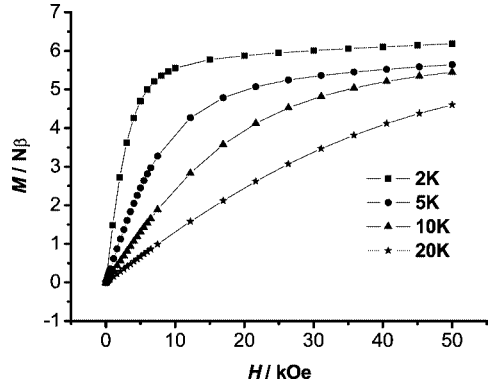


Figure 3. Magnetization vs. applied magnetic field plots at 2, 5, 10, and 20 K of complex **1**.

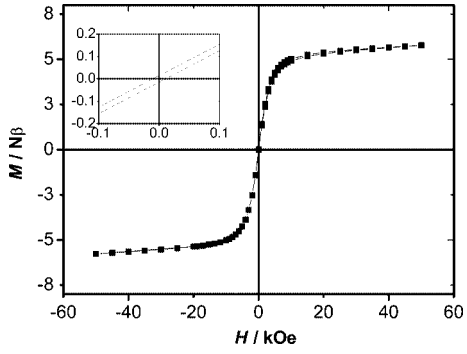


Figure 4. Hysteresis loop at 2 K for **1**. Inset: expansion showing the very small coercivity (left top).

The above unusual magnetic properties drive us to find sufficient reason for explanation. The temperature dependence of the alternating current magnetic susceptibility for compound **1** was thus measured in zero-dc field in the range of 2–20 K at different frequencies (1–1000 Hz) as shown in Figure 5. However, no frequency-dependent cusp was observed for either the in-phase component $\chi'_m$ or the out-of-phase component $\chi''_m$ at zero field, probably owing to weak coupling between Dy ions in **1** considering the long Dy···Dy separation. When a dc field (5 kOe) was applied, two peaks ($T_p$) appeared for both $\chi'_m$ and $\chi''_m$, respectively (Figure 6), indicating a field-dependent magnetic behavior for compound **1**. Moreover, $\chi'_m$ and $\chi''_m$ are strongly frequency-dependent with a larger $\Phi$ value of 0.16 {$\Phi = (\Delta T_p/T_p)/[\Delta(\log f)]$} than that for normal spin glass (<0.1),[14b] displaying an unusual glass-like behavior. Such a result should be attributed to the geometrical frustration for Dy ions in compound **1**, because the 2D connection of the Dy ions in compound **1** appeared in the pattern of the alternately arrayed square and triangle grids (Figure 2b), which is similar to the Shastry–Sutherland lattice in compound $DyB_4$. The Shastry–Sutherland lattice was demonstrated to cause geometrical frustration in some magnetic systems.[15] Without the applied DC magnetic field, the magnetic interactions between the Dy ions in compound **1** are rather weak owing to the long Dy···Dy separations, which leads to the frustration unobserved. When the introduction of a DC field, the antiferromagnetic interaction between Dy ions could be enhanced and became dominant, leading to the unusual field-dependent magnetic relaxation behavior in compound **1**. Similar phenomenon was reported by Gao and co-workers.[16]

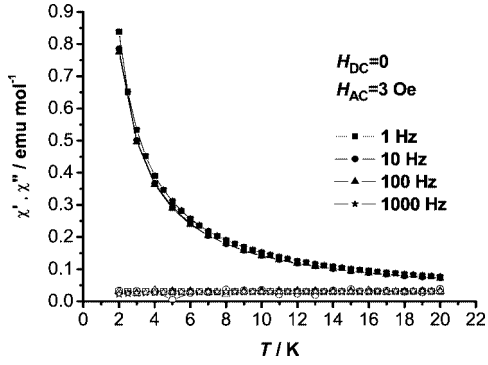


Figure 5. Temperature dependence of the real (top) and imaginary (bottom) components of the ac susceptibility in a zero applied static field with an oscillating field of 3 Oe at a frequency of 1–1000 Hz. The filled symbols are for the in-phase component $\chi'_m$, the open symbols are for the out-of-phase component $\chi''_m$.

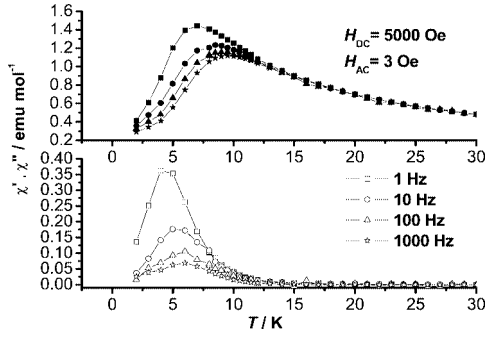


Figure 6. Frequency dependence of the AC susceptibility at 5 kOe applied static field with an oscillating field of 3 Oe at a frequency of 1–1000 Hz. The lines are guides.

### IR Spectrum, Thermogravimetric Analysis (TGA), and Photoluminescence Properties

Strong characteristic absorptions around 1610, 1560, 1430, and 1380 $cm^{-1}$ in the IR spectrum are observed for the carboxyl groups in compound **1**. No signal appears in

 © 2007 Wiley-VCH Verlag GmbH & Co. KGaA, Weinheim 

the region 1690 and 1730 $cm^{-1}$, indicating the complete deprotonation of the carboxyl groups in the complex. The TGA performed on **1** (as shown in Figure S7), shows that compound **1** is stable up to 250 °C, and the first weight loss in the range of 250–350 °C corresponds to the loss of coordinated water. The complete decomposition of **1** occurs at above 650 °C. The residual mass at 650 °C (55% approximately) corresponds to the formation of $Dy_2O_3$.

The photoluminescence spectrum of complex **1** is shown in Figure 7, which is blue luminescent in the solid state with typical $Dy^{3+}$ emissions at 479, 570, and 620 nm that are ascribed to the characteristic emission $^4F_{9/2} \rightarrow {}^6H_J$ transitions of the $Dy^{3+}$ ion ($J$ = 15/2, 13/2, and 11/2). The strongest emission band is located at 479 nm ($^4F_{9/2} \rightarrow {}^6H_{15/2}$), suggesting the citric acid ligand is suitable for the sensitization of blue luminescence for $Dy^{3+}$.

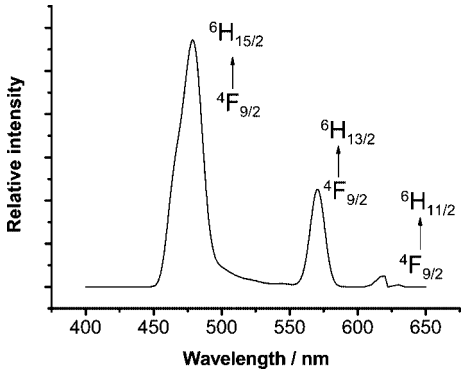


Figure 7. Emission spectra of compound **1** in the solid state at room temperature (excitation at 325 nm).

## Conclusions

A new lanthanide 2D coordination polymer, in which the citrate bridges the $Dy_2O_2$ dimer into a 2D layer, was successfully produced by a hydrothermal reaction. The coordination polymer of dysprosium exhibits interesting magnetic properties in that the geometrical frustration resulting from the structure of the alternately arrayed square and triangle grids in compound **1** causes an unusual magnetic relaxation behavior, providing valuable information for exploring molecular magnetic materials with lanthanides.

## Experimental Section

**Materials and Methods:** All purchased chemicals were of reagent grade and used without further purification. Elemental analyses (C, H, and N) were performed with a Perkin–Elmer 2400 Elemental Analyzer. Dy was determined by a Leaman inductively coupled plasma (ICP) spectrometer. The IR spectra were obtained in the range 400–4000 $cm^{-1}$ with an Alpha Centaure FTIR spectrophotometer by using KBr pellets. Thermogravimetric analysis was performed with a Perkin–Elmer TGA7 instrument in flowing $N_2$ with a heating rate of 5 °C $min^{-1}$. The magnetic susceptibility measurements for **1** were carried out on polycrystalline samples by using a Quantum Design MPMS-XL-5 SQUID magnetometer in the temperature range 2–300 K and magnetic field up to 5 T. Diamagnetic corrections were estimated from Pascal's constants.

**Synthesis:** The title compound was hydrothermally synthesized [Equation (1)] under autogenous pressure. A mixture of $Dy_2O_3$ (0.1 g, 0.27 mmol), citric acid (0.192 g, 1.0 mmol), and water (10 mL) was simply stirred and then sealed in a 15-mL Teflon-lined autoclave, which was heated to 170 °C for 2 d. After slow cooling to room temperature at a rate of 10 °C $h^{-1}$, colorless block crystals of compound **1** were separated in pure phase (80% yield based on Dy). $C_6H_7DyO_8$ (369.59): calcd. C 19.49, H 1.89, Dy 43.98; found C 19.47, H 1.88, Dy 43.99. Compound **1** is insoluble in common organic solvent and water.

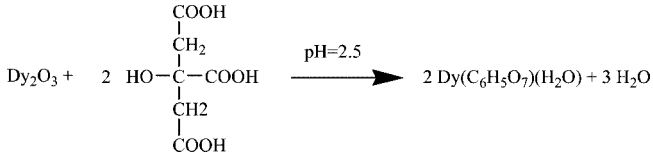


(1)

**X-ray Crystallography:** Crystal data for **1**: monoclinic, space group $C2/c$; $a$ = 19.145(4), $b$ = 6.076(12), $c$ = 15.577(3) Å; $\beta$ = 103.35(3)°; $V$ = 1762.9(6) $Å^3$; $T$ = 298 K; $Z$ = 8; $\mu$ = 8.5 $mm^{-1}$; 8178 reflections measured, 2013 unique ($R_{int}$ = 0.0269) which were used in all calculations. The structure was solved by direct methods by using the program SHELXS-97 and refined by full-matrix least-squares methods on $F^2$ with the use of the SHELXL-97 program package. Structure solution and refinement based on 2013 independent reflections with $I > 2\sigma(I)$ and 136 parameters gave $R_1(wR_2)$ = 0.0192 (0.0507). The structure of compound **1** was determined by single-crystal X-ray diffraction. A single colorless crystal with approximate dimensions of 0.2 × 0.1 × 0.1 mm was mounted to the end of a glass fiber capillary. Data were collected with a Rigaku R-AXIS RAPID IP diffractometer at 293 K by using graphite-monochromated Mo-$K_\alpha$ radiation ($\lambda$ = 0.71073 Å) and oscillation scans technique in the range of $3.05 < \theta < 27.47°$. A summary of the crystal data and structure refinement for compound **1** is provided in Table 1. Selected bond lengths and bond angles of **1** are listed in

Table 1. Crystal data and structure refinement of compound **1**.

| | |
|---|---|
| Molecular formula | $C_6H_7DyO_8$ |
| Formula weight | 369.59 |
| $T$ / K | 293(2) |
| $\lambda$ / Å | 0.71073 |
| Space group | $C2/c$ |
| Crystal system | monoclinic |
| $a$ / Å | 19.145(4) |
| $b$ / Å | 6.0758(12) |
| $c$ / Å | 15.577(3) |
| $\beta$ / ° | 103.35(3) |
| $V$ / $Å^3$ | 1762.9(6) |
| $Z$, $\rho_c$ / g $cm^{-3}$ | 8, 2.762 |
| $\mu$ / $mm^{-1}$ | 8.500 |
| $F$(000) | 1360 |
| Reflections collected | 8178 |
| Indenpant reflections | 2013 ($R_{int}$ = 0.0269) |
| Data/restraints/parameters | 2013/0/136 |
| Goodness-of-fit on $F_2$ | 1.282 |
| Final $R$ indices $[I > 2\sigma(I)]$[a] | $R_1$ = 0.0192, $wR_2$ = 0.0507 |
| $R$ indices (all data)[a] | $R_1$ = 0.0207, $wR_2$ = 0.0511 |

[a] $R_1 = \Sigma||F_o| - |F_c||/\Sigma|F_o|$; $wR_2 = \Sigma[w(F_o^2 - F_c^2)^2]/\Sigma[w(F_o^2)^2]^{1/2}$.

 © 2007 Wiley-VCH Verlag GmbH & Co. KGaA, Weinheim 

Table 2. CCDC-602711 contains the supplementary crystallographic data for this paper. These data can be obtained free of charge from The Cambridge Crystallographic Data Centre via www.ccdc.cam.ac.uk/data_request/cif.

Table 2. Selected bond lengths [Å] and bond angles [°].

| | |
|---|---|
| Dy(1)–O(3) | 2.321(2) |
| Dy(1)–O(6) | 2.322(3) |
| Dy(1)–O(5) | 2.354(2) |
| Dy(1)–O(7)#1[a] | 2.369(2) |
| Dy(1)–O(8) | 2.425(3) |
| Dy(1)–O(4) | 2.449(3) |
| Dy(1)–O(7) | 2.474(3) |
| Dy(1)–O(1) | 2.489(3) |
| Dy(1)–O(2) | 2.608(3) |
| O(3)–Dy(1)–O(5) | 138.48(9) |
| O(3)–Dy(1)–O(6) | 143.86(10) |
| O(3)–Dy(1)–O(7)#1[a] | 76.55(10) |
| O(3)–Dy(1)–O(1) | 65.86(9) |

[a] Symmetry transformations used to generate equivalent atoms: #1 –x, y, $–z + 1/2$.

**Supporting Information** (see footnote on the first page of this article): Figures of the structure of **1** and magnetic data of **1**.

## Acknowledgments

The authors are thankful for the financial support of the National Natural Science Foundation of China (Grant No. 20371010; 20671017) and the Specialized Research Fund for the Doctoral Program of Higher Education.

[1] a) For recent reviews, see: P. J. Hagrman, D. Hagrman, J. Zubieta, *Angew. Chem. Int. Ed.* **1999**, *111*, 2798–2848; b) O. M. Yahgi, M. O'Keeffe, N. W. Ockwig, H. K. Chae, M. Eddaoudi, J. Kim, *Nature* **2003**, *423*, 705–714; c) C. N. R. Rao, S. Natarajan, R. Vaidhyanathan, *Angew. Chem. Int. Ed.* **2004**, *43*, 1466–1496; d) D. Maspoch, D. Ruiz-Molina, J. Veciana, *J. Mater. Chem.* **2004**, *14*, 2713–2723; e) C. Janiak, *Dalton Trans.* **2003**, 2781–2804.

[2] a) For examples, see: S. Golhen, L. Quahab, D. Drandjean, P. Molinie, *Inorg. Chem.* **1998**, *37*, 1499; b) Q. Ye, Y. H. Li, Y. M. Song, X. F. Huang, R. G. Xiong, Z. Xue, *Inorg. Chem.* **2005**, *44*, 3618–3622; c) S. Hermes, M. K. Schröter, R. Schmid, L. Khodeir, M. Muhler, A. Tissler, R. W. Fischer, R. A. Fischer, *Angew. Chem. Int. Ed.* **2005**, *44*, 6237–6241; d) J. P. Costes, F. Dahan, F. Nicodeme, *Inorg. Chem.* **2001**, *40*, 5285–5287; e) S. S. Kaye, J. R. Long, *J. Am. Chem. Soc.* **2005**, *127*, 6506–6507; f) L. Pan, H. Liu, X. Lei, X. Huang, D. H. Olson, N. J. Turro, J. Li, *Angew. Chem. Int. Ed.* **2003**, *42*, 542–546; g) B. Q. Ma, H. L. Sun, S. Gao, *Chem. Commun.* **2003**, 2164–2165.

[3] a) H. Ohno, *Science* **2001**, *291*, 840–841; b) S. A. Wolf, D. D. Awschalom, R. A. Buhrman, J. M. Daughton, S. Molnar, M. L. Roukes, A. Y. Chtchelkanova, D. M. Treger, *Science* **2001**, *294*, 1488–1495; c) J. J. Attema, G. A. de Wijs, G. R. Blake, R. A. de Groot, *J. Am. Chem. Soc.* **2005**, *127*, 16325–16328.

[4] a) R. Sessoli, H. L. Tsai, A. R. Schake, S. Sheyi, J. B. Vincent, K. Folting, D. Gatteschi, G. Christou, D. N. Hendrickson, *J. Am. Chem. Soc.* **1993**, *115*, 1804–1816; b) A. Caneschi, D. Gatteschi, R. Sessoli, A.-L. Barra, L. C. Brunel, M. Guillot, *J. Am. Chem. Soc.* **1991**, *113*, 5873–5874; c) R. Sessoli, D. Gatteschi, A. Caneschi, M. A. Novak, *Nature* **1993**, *365*, 141–143.

[5] a) M. Murrie, H. Stoeckli-Evans, H. U. Güdel, *Angew. Chem. Int. Ed.* **2001**, *40*, 1957–1960; b) M. Murrie, D. Biner, H. Stoeckli-Evans, H. U. Güdel, *Chem. Commun.* **2003**, 230–231; c) S. T. Ochsenbein, M. Murrie, E. Rusanov, H. Stoeckli-Evans, C. Sekine, H. U. Güdel, *Inorg. Chem.* **2002**, *41*, 5133–5140; d) M. Murrie, S. J. Teat, H. Stoeckli-Evans, H. U. Güdel, *Angew. Chem. Int. Ed.* **2003**, *42*, 4653–4656.

[6] S. C. Xiang, X. T. Wu, J. J. Zhang, R. B. Fu, S. M. Hu, X. D. Zhang, *J. Am. Chem. Soc.* **2005**, *127*, 16352–16353.

[7] A. Bino, I. Shweky, S. Cohen, E. R. Bauminger, S. J. Lippard, *Inorg. Chem.* **1998**, *37*, 5168–5172.

[8] I. Gautier-Luneau, C. Fouquard, C. Merle, J. L. Pierre, D. Luneau, *J. Chem. Soc. Dalton Trans.* **2001**, 2127–2131.

[9] Z. H. Zhou, Y. F. Deng, Z. X. Cao, R. H. Zhang, Y. L. Chow, *Inorg. Chem.* **2005**, *44*, 6912–6914.

[10] Z. H. Zhou, Y. F. Deng, H. L. Wan, *Cryst. Growth Des.* **2005**, *5*, 1109–1117.

[11] N. Kotsakis, C. P. Raptopoulou, V. Tangoulis, A. Terzis, J. Giapintzakis, T. Jakusch, T. Kiss, A. Salifoglou, *Inorg. Chem.* **2003**, *42*, 22–31.

[12] a) R. Baggio, M. Perec, *Inorg. Chem.* **2004**, *43*, 6965–6968; b) Y. Q. Yuan, Y. Q. Xu, M. Y. Wu, M. C. Hong, *Acta Crystallogr., Sect. E* **2005**, *61*, m108–m109; c) S. G. Liu, W. Liu, J. L. Zuo, Y. Z. Li, X. Z. You, *Inorg. Chem. Commun.* **2005**, *8*, 328–330; d) R. Baggio, R. Calvo, M. T. Garland, O. Peña, M. Perec, A. Rizzi, *Inorg. Chem.* **2005**, *44*, 8979–8987.

[13] a) J. Tang, I. Hewitt, N. T. Madhu, G. Chastanet, W. Wernsdorfer, C. E. Anson, C. Benelli, R. Sessoli, A. K. Powell, *Angew. Chem. Int. Ed.* **2006**, *45*, 1729–1733; b) C. M. Zaleski, E. C. Depperman, J. W. Kampf, M. L. Kirk, V. L. Pecoraro, *Angew. Chem. Int. Ed.* **2004**, *43*, 3912–3914; c) A. Mishra, W. Wernsdorfer, K. A. Abboud, G. Christou, *J. Am. Chem. Soc.* **2004**, *126*, 15648–15649.

[14] a) H. W. Hou, G. Li, L. K. Li, Y. Zhu, X. R. Meng, Y. T. Fan, *Inorg. Chem.* **2003**, *42*, 428–435; b) J. A. Mydosh, *Spin Glasses: An Experimental Introduction*, Taylor and Francis, London, **1993**.

[15] O. Daisuke, M. Takeshi, N. Hironori, M. Youichi, *J. Phys. Soc. Jpn.* **2005**, *74*, 2434–2437.

[16] a) S. Gao, G. Su, T. Yi, B. Q. Ma, *Phys. Rev. B* **2001**, *63*, 054431; b) B. Q. Ma, S. Gao, G. Su, G. X. Xu, *Angew. Chem. Int. Ed.* **2001**, *40*, 434–437; c) Q. D. Liu, J. R. Li, S. Gao, B. Q. Ma, Q. Z. Zhou, K. B. Yu, H. Liu, *Chem. Commun.* **2000**, 1685–1686; d) Y. Z. Zhang, G. P. Duan, O. Sato, S. Gao, *Dalton Trans.* **2006**, 2625–2634.

Received: November 25, 2006
Published Online: June 5, 2007

 © 2007 Wiley-VCH Verlag GmbH & Co. KGaA, Weinheim 

DOI: 10.1002/ejic.200700140

# Synthesis, Upconversion Luminescence and Magnetic Properties of New Lanthanide–Organic Frameworks with $(4^3)_2(4^6,6^6,8^3)$ Topology

**Danfeng Weng,[a] Xiangjun Zheng,*[a] Xiaobo Chen,[b] Licun Li,[c] and Linpei Jin*[a]**

**Keywords:** Lanthanide–organic frameworks / Codoped coordination polymers / Upconversion properties / Magnetic properties

The synthesis and crystal structures of three new lanthanide–organic frameworks $[Ln(pza)(OH)(H_2O)]_n$ (Ln = Y(**1**), Er(**2**), Yb(**3**); $H_2$pza = 2,3-pyrazinedicarboxylic acid) with helical chains and novel 2D $(4^3)_2(4^6,6^6,8^3)$ topology are reported. The topology is obtained by simplifying the dinuclear metal core as a six-connected node and the ligand as a three-connected linker. The upconversion property measurement gives green and red emissions coming from two-photon excitation of Y: Er, Yb codoped coordination polymer and arising from $Er^{III}$ transitions of $^4S_{3/2}/^2H_{11/2}\rightarrow{}^4I_{15/2}$ and $^4F_{9/2}\rightarrow{}^4I_{15/2}$. The magnetic properties of complexes **2** and **3** are also studied.

(© Wiley-VCH Verlag GmbH & Co. KGaA, 69451 Weinheim, Germany, 2007)

## Introduction

The synthesis of metal–organic frameworks (MOFs) is an area of chemistry that has undergone a dramatic advance over recent years. Concerted efforts have been focused on exploiting the synthetic strategies at a level of framework design, with an impetus for illumination of structure–property relationships and an aim at certain properties and possible applications.[1] Various intriguing architectures and novel topologies have been reported,[2] among which the helical coordination polymers attracted special interests.[1f,1g,2d–g] These new materials with exploitable properties like microporosity,[3] chirality,[4] nonlinear optics,[2a,5] magnetism,[4d,6] etc. broaden the potential applications in gas storage and separation, catalysis, information storage and so on. Meanwhile, the multifunctional properties and potential applications of MOFs have gradually received more and more attention.[7] As for lanthanide–organic frameworks, complexes of $Eu^{III}$ and $Tb^{III}$, which show luminescence in the visible region, are the most frequently employed, and their luminescence properties are extensively investigated.[8] To date, lanthanide upconversion phosphors which emit higher-energy photons when excited by lower-energy photons have attracted a great deal of interest, while the upconversion of lanthanide coordination polymers is less studied.[9] Recently, we have synthesized three new lanthanide–organic frameworks $[Ln(pza)(OH)(H_2O)]_n$ (Ln = Y(**1**), Er(**2**), Yb(**3**); $H_2$pza = 2,3-pyrazinedicarboxylic acid), which possess a novel $(4^3)_2(4^6,6^6,8^3)$ topology and multifunctional properties. The magnetic properties of complexes **2** and **3** and the upconversion properties of the codoped lanthanide (Y: Er, Yb) coordination polymers are investigated.

## Results and Discussion

### Structural Description

An X-ray diffraction study reveals that compound **1** adopts a layered, two-dimensional structure consisting of centrosymmetric $Y_2(\mu_2\text{-OH})_2$ units in which two $\mu_2$-OH groups bridge two Y atoms with a Y···Y distance of 3.636 Å. The seven-coordinate environment around each Y centre is completed by two O atoms of two hydroxy groups, two O atoms from two pza ligands, one O atom and one N atom of a chelating pza ligand, and one O atom from one water molecule (see Figure 1). The pza ligand adopts a

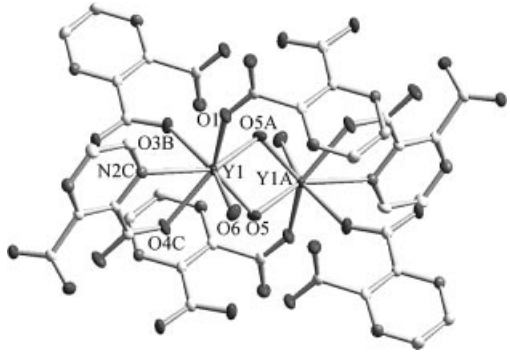


Figure 1. View of the dinuclear unit in complex **1** with ellipsoids drawn at the 50% probability level. All hydrogen atoms are omitted for clarity.

[a] Department of Chemistry, Beijing Normal University, Beijing 100875, P. R. China
Fax: +86-10-58802075
E-mail: lpjin@bnu.edu.cn
[b] Analytical and Testing Center, Beijing Normal University, Beijing 100875, P. R. China
[c] Department of Chemistry, Nankai University, Tianjin 300071, P. R. China

 © 2007 Wiley-VCH Verlag GmbH & Co. KGaA, Weinheim 

tetradentate coordination mode (Scheme 1). Selected bond lengths and bond angles of **1** are listed in Table 1.

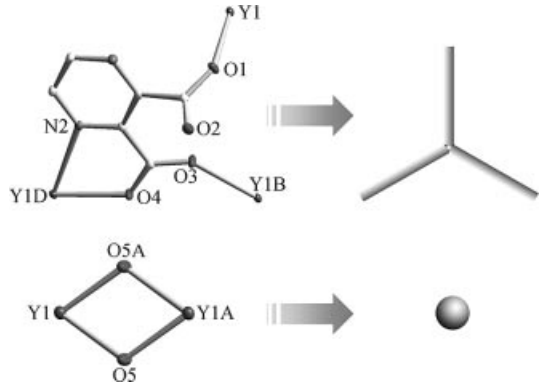


Scheme 1. Coordination mode of the pza ligand and topological simplification of the metal dinuclear unit and ligand.

The dinuclear $Y_2(\mu_2\text{-}OH)_2$ clusters bridged by pza ligands give rise to a neutral 2D grid extended in the (100) plane. Suitable nodes should be defined in order to analyze the network. In this complex, every $Y_2(\mu_2\text{-}OH)_2$ core is connected through six carboxylate groups from six pza ligands, in which there are two chelating N and O atom linkages simplified as monodentate linkers. Thus, the $Y_2(\mu_2\text{-}OH)_2$ core can be regarded as a six-connected node. And the pza ligand can be considered as a three-connected linker as shown in Scheme 1.

When viewed along the *b* axis, outer layers consisting of pza ligands and the dinuclear metal core layer that is embedded inside can be observed. Taking one surface of the pza ligand layer and the metal layer into consideration, the structure can be best described as a 2D network with a $(6^3)$ topology (see Figure 2a). Further investigation of the whole 2D grid implies that two $(6^3)$ topological structures arranged alternately are interweaved by metal nodes. There are six four-membered rings, six six-membered rings and three eight-membered rings around the six-connected metal node, while the three-connected linker is surrounded by three four-membered rings. Because the six-connected nodes and three-connected linkers are arranged in a ratio of $Y_2(OH)_2$/pza = 1:2, the short Schläfli symbol of the topology can be expressed as $(4^3)_2(4^6,6^6,8^3)$ (Figure 2b). The topological study for complex **1** was performed with TOPOS.[10] Furthermore, a supramolecular 3D framework can be built up from the 2D lanthanide–organic framework via hydrogen bonds [O6···N1E, 2.960(4) Å] and the π–π stacking of pyrazine rings with a calculated face-to-face distance of 3.261 Å (Figure 2a).

Another interesting feature of complex **1** is its single-helical chains (Figure 2c). The Y atoms are linked into an extended chain through the O5 atom from $\mu_2$-OH and O1-, O3- carboxylate groups of the pza ligands. The repeating unit can be described as $(–Y1–O1–pza–O3–Y1B–O5B–)_n$, and the pitch of the helix running along the *b* axis is the same as its length (6.125 Å). It is worth noting that the chi-

Table 1. Selected bond lengths and bond angles of complexes **1**, **2** and **3** /Å [°].

| Complex **1**[a] | | Complex **2**[b] | | Complex **3**[b] | |
|---|---|---|---|---|---|
| Y1–O5 | 2.193(2) | Er1–O5 | 2.180(3) | Yb1–O5 | 2.174(5) |
| Y1–O5#1 | 2.221(2) | Er1–O5#1 | 2.226(3) | Yb1–O5#1 | 2.196(5) |
| Y1–O1 | 2.268(2) | Er1–O4#2 | 2.266(4) | Yb1–O4#2 | 2.258(6) |
| Y1–O3#2 | 2.306(2) | Er1–O1 | 2.292(4) | Yb1–O1 | 2.283(6) |
| Y1–O4#3 | 2.325(2) | Er1–O2#3 | 2.312(3) | Yb1–O2#3 | 2.285(5) |
| Y1–O6 | 2.338(2) | Er1–O6 | 2.324(4) | Yb1–O6 | 2.313(5) |
| Y1–N2#3 | 2.586(2) | Er1–N2#3 | 2.566(4) | Yb1–N2#3 | 2.548(7) |
| O5–Y1–O5#1 | 69.0(1) | O5–Er1–O5#1 | 69.3(1) | O5–Yb1–O5#1 | 69.0(2) |
| O5–Y1–O1 | 133.5(1) | O5–Er1–O4#2 | 134.2(1) | O5–Yb1–O4#2 | 133.6(2) |
| O5#1–Y1–O1 | 82.2(1) | O5#1–Er1–O4#2 | 82.3(1) | O5#1–Yb1–O4#2 | 82.4(2) |
| O5–Y1–O3#2 | 117.9(1) | O5–Er1–O1 | 118.0(1) | O5–Yb1–O1 | 119.0(2) |
| O5#1–Y1–O3#2 | 79.4(1) | O5#1–Er1–O1 | 79.3(1) | O5#1–Yb1–O1 | 79.2(2) |
| O1–Y1–O3#2 | 90.3(1) | O4#2–Er1–O1 | 89.6(1) | O4#2–Yb1–O1 | 88.8(2) |
| O5–Y1–O4#3 | 78.0(1) | O5–Er1–O2#3 | 77.4(1) | O5–Yb1–O2#3 | 77.8(2) |
| O5#1–Y1–O4#3 | 133.3(1) | O5#1–Er1–O2#3 | 132.9(1) | O5#1–Yb1–O2#3 | 132.3(2) |
| O1–Y1–O4#3 | 143.2(1) | O4#2–Er1–O2#3 | 143.5(1) | O4#2–Yb1–O2#3 | 143.7(2) |
| O3#2–Y1–O4#3 | 88.3(1) | O1–Er1–O2#3 | 88.4(1) | O1–Yb1–O2#3 | 88.4(2) |
| O5–Y1–O6 | 82.5(1) | O5–Er1–O6 | 82.3(1) | O5–Yb1–O6 | 82.4(2) |
| O5#1–Y1–O6 | 120.1(1) | O5#1–Er1–O6 | 119.6(1) | O5#1–Yb1–O6 | 120.9(2) |
| O1–Y1–O6 | 81.4(1) | O4#2–Er1–O6 | 81.6(1) | O4#2–Yb1–O6 | 82.0(2) |
| O3#2–Y1–O6 | 157.1(1) | O1–Er1–O6 | 157.4(1) | O1–Yb1–O6 | 156.2(2) |
| O4#3–Y1–O6 | 85.8(1) | O2#3–Er1–O6 | 86.5(1) | O2#3–Yb1–O6 | 86.1(2) |
| O5–Y1–N2#3 | 138.9(1) | O5–Er1–N2#3 | 138.8(1) | O5–Yb1–N2#3 | 139.3(2) |
| O5#1–Y1–N2#3 | 151.3(1) | O5#1–Er1–N2#3 | 151.2(1) | O5#1–Yb1–N2#3 | 151.1(2) |
| O1–Y1–N2#3 | 78.7(1) | O4#2–Er1–N2#3 | 78.2(1) | O4#2–Yb1–N2#3 | 78.0(2) |
| O3#2–Y1–N2#3 | 79.4(1) | O1–Er1–N2#3 | 79.6(1) | O1–Yb1–N2#3 | 79.3(2) |
| O4#3–Y1–N2#3 | 64.9(1) | O2#3–Er1–N2#3 | 65.6(1) | O2#3–Yb1–N2#3 | 65.9(2) |
| O6–Y1–N2#3 | 78.0(1) | O6–Er1–N2#3 | 78.3(1) | O6–Yb1–N2#3 | 77.3(2) |

[a] Symmetry operations: #1 $–x + 2, –y + 2, –z$; #2 $–x + 2, –y + 1, –z$; #3 $x + 1/2, –y + 3/2, z + 1/2$. [b] Symmetry operations: #1 $–x + 1/2, –y + 5/2, –z + 1$; #2 $–x + 1/2, –y + 3/2, –z + 1$; #3 $–x + 1/2, y + 1/2, –z + 1/2$.

 © 2007 Wiley-VCH Verlag GmbH & Co. KGaA, Weinheim 

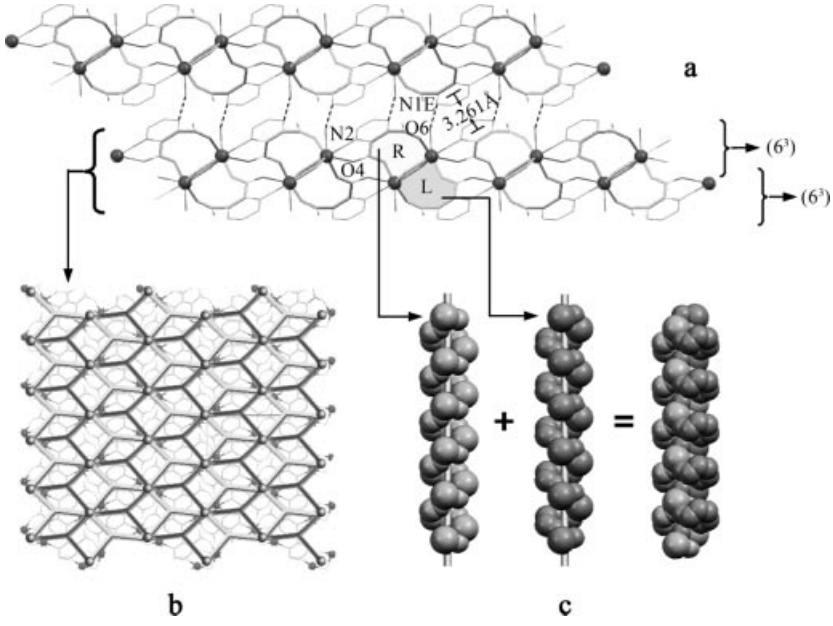


Figure 2. (a) 2D crystal packing diagram along the *b* axis for complex **1** showing interlayer interactions (hydrogen bonds indicated by dashed lines and π–π interactions by arrows and helical chains. (b) Topological representation of complex **1** down the *c* axis. (c) Space-filling model showing the helices constituted from two homochiral chains.

rality of the helices is in the RLLR mode in one layer as shown in Figure 2a. The same chiral helices are linked together through the remaining N2 and O4 atoms of the pza ligands, while two helical chains with opposite chirality are united directly at the metal nodes. This phenomenon may indicate that the twisted conformation of the ligand can effectively transfer the chiral information between the helices. However, packing these helical chains into a chiral solid still remains a challenge, which requires a deeper understanding of the role that the ligand has in the delivery of chirality and the crystal packing.

Table 2. Crystallographic data of **1**, **2** and **3**.

| | **1** | **2** | **3** |
|---|---|---|---|
| Empirical formula | $C_6H_5N_2O_6Y$ | $C_6H_5N_2O_6Er$ | $C_6H_5N_2O_6Yb$ |
| $F_w$ | 290.03 | 368.39 | 374.16 |
| $T$ /K | 294(2) | 294(2) | 294(2) |
| Wavelength /Å | 0.71073 | 0.71073 | 0.71073 |
| Crystal system | Monoclinic | Monoclinic | Monoclinic |
| Space group | *C*2/*c* | *C*2/*c* | *C*2/*c* |
| *a* /Å | 22.593(9) | 22.514(5) | 22.522(4) |
| *b* /Å | 6.1250(19) | 6.0984(12) | 6.1128(12) |
| *c* /Å | 17.960(7) | 15.048(3) | 14.998(3) |
| *α* /° | 90 | 90 | 90 |
| *β* /° | 138.199(5) | 127.760(3) | 127.473(2) |
| *γ* /° | 90 | 90 | 90 |
| $V$ /Å$^3$ | 1656.6(1) | 1633.5(6) | 1638.7(5) |
| $Z$ | 8 | 8 | 8 |
| $D_c$ /g cm$^{-3}$ | 2.326 | 3.004 | 3.033 |
| $\mu$ /mm$^{-1}$ | 7.054 | 10.288 | 11.427 |
| Reflections collected, unique, Rint | 6121, 1963, 0.0443 | 5773, 1864, 0.0374 | 3851, 1424, 0.0657 |
| $R$ indices [$I>2\sigma(I)$] | $R_1$ = 0.0302, $wR_2$ = 0.0670 | $R_1$ = 0.0284, $wR_2$ = 0.0491 | $R_1$ = 0.0319, $wR_2$ = 0.0677 |
| $R$ indices (all data) | $R_1$ = 0.0403, $wR_2$ = 0.0702 | $R_1$ = 0.0358, $wR_2$ = 0.0517 | $R_1$ = 0.0470, $wR_2$ = 0.0769 |

Complexes **2** and **3** are isomorphous, and their structures are similar to complex **1** (see Table 1 and Table 2), except that complex **1** has a nearly 3-Å larger *c* value and a 10° larger *β* value than those of complexes **2** and **3**.

## Upconversion Properties

In Figure 3 we can see a green emission band in the range 520–550 nm and a weaker red emission at 650–660 nm, which correspond to the transitions $^4S_{3/2}/^2H_{11/2}\rightarrow{}^4I_{15/2}$ and $^4F_{9/2}\rightarrow{}^4I_{15/2}$ respectively, for the codoped complex [(Y: Er, Yb)(pza)(OH)($H_2O$)]$_n$ upon excitation at 975 nm.

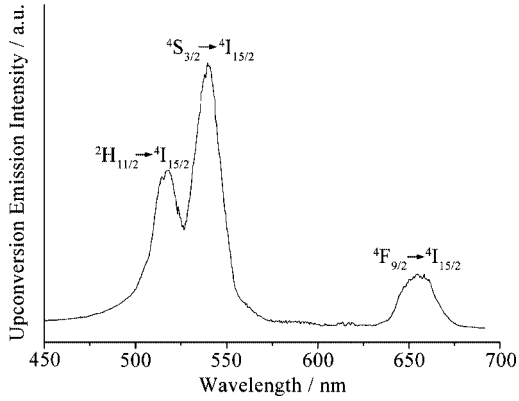


Figure 3. Upconversion emission for the Er$^{III}$ ion in the Y: Er, Yb codoped coordination polymer.

Figure 4 shows the energy levels and upconversion mechanism in the Y: Er, Yb codoped coordination polymer. The Yb$^{III}$ ion was excited by a 975 nm photon from the $^2F_{7/2}$ level to the excited $^2F_{5/2}$ state first. Then the energy was transferred from Yb$^{III}$ to Er$^{III}$ to pump the Er$^{III}$ ion

 © 2007 Wiley-VCH Verlag GmbH & Co. KGaA, Weinheim 

from the $^4I_{15/2}$ state to the $^4I_{11/2}$ state. The $Er^{III}$ ion, populated at the $^4I_{11/2}$ level, may transit to the $^4F_{7/2}$ state by a second-photon promotion. The $^4S_{3/2}$ and $^2H_{11/2}$ states can be populated by nonradiative relaxations from the $^4F_{7/2}$ state in the form of thermal vibration carried by phonons of ca. 2100 $cm^{-1}$ (1620 $cm^{-1}$ + 476 $cm^{-1}$ in the IR spectrum) and 1400 $cm^{-1}$ (1398 $cm^{-1}$ in IR spectrum), respectively. The $Er^{III}$ ions in the $^4S_{3/2}$ and $^2H_{11/2}$ states emit in the green range (518 and 540 nm) when going back to the ground state $^4I_{15/2}$.

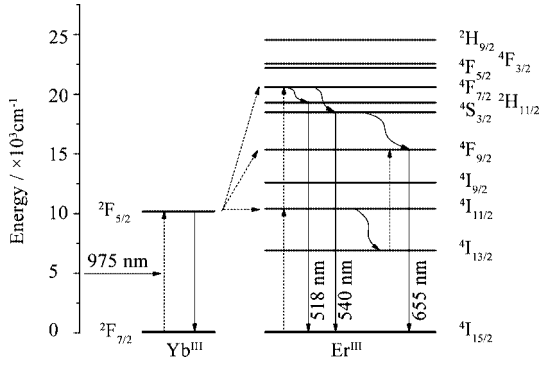


Figure 4. Energy-level diagram for the upconversion mechanism of the Y: Er, Yb codoped coordination polymer with excitation at 975 nm.

The red emission centred at 650 nm is generated by the $^4F_{9/2}$ to $^4I_{15/2}$ transition. There exist two possible routes for this process. The $^4F_{9/2}$ level can be reached by the nonradiative decay from the upper level, $^4S_{3/2}$.[11] However, the green emission ($^4S_{3/2}\rightarrow{}^4I_{15/2}$) was the strongest peak in our system, so this is not the main channel to the $^4F_{9/2}$ level. In the second possible route, $Er^{III}$ ions in the $^4I_{11/2}$ state lose their energy in going to the $^4I_{13/2}$ level with some nonradiative decay involved. There is an energy gap of ca. 3500 $cm^{-1}$ between the two states. The high-energy vibrations from the O–H group make the relaxation ($^4I_{11/2}\rightarrow{}^4I_{13/2}$) much more probable in this system. Then, a second photon energy (975 nm) pumps the $Er^{III}$ from the $^4I_{13/2}$ to the $^4F_{9/2}$ level, and thus the red emission is obtained (see Figure 4).

### Magnetic Properties

We investigated the magnetic properties of complexes **2** and **3** in the solid state at 2 kOe within the temperature range 2–300 K (Figure 5). For **2**, the observed value of $\chi_M T$ per [Er] unit is 12.22 $cm^3\,K\,mol^{-1}$ at room temperature (Figure 5a), which is slightly higher than the value expected for a free $Er^{III}$ ion (11.48 $cm^3\,K\,mol^{-1}$).[12] Upon cooling, the value of $\chi_M T$ increases up to a maximum of 13.90 $cm^3\,K\,mol^{-1}$ at ca. 45 K and then abruptly decreases to reach 4.51 $cm^3\,K\,mol^{-1}$ at 2 K. The plot of $\chi_M^{-1}$ vs. $T$ over the temperature range 50–300 K obeys the Curie–Weiss law [$\chi = C/(T - \theta)$] with $C$ = 1.20 $cm^3\,K\,mol^{-1}$ and $\theta$ = 1.00 K. All of these results indicate that there is a ferromagnetic coupling between the $Er^{III}$ ions. For **3**, the observed value of $\chi_M T$ per [Yb] unit is 2.47 $cm^3\,K\,mol^{-1}$ at room temperature (Figure 5b), which is close to the calculated value (2.57 $cm^3\,K\,mol^{-1}$) for a free $Yb^{III}$ ion.[12] The value of $\chi_M T$ decreases slowly as the temperature decreases, to reach a value of 1.91 emu K $mol^{-1}$ at 2 K. The plot of $\chi_M^{-1}$ vs. $T$ over the temperature range 50–300 K obeys the Curie–Weiss law with $C$ = 2.60 $cm^3\,K\,mol^{-1}$, $\theta$ = –17.13 K. The decrease in $\chi_M T$ and the negative value of $\theta$ are due primarily to the depopulation of the Stark levels of the $Yb^{III}$ ion together with the possible weak antiferromagnetic coupling between the $Yb^{III}$ ions, considering a possible interaction path through hydroxy bridges with a Yb···Yb distance of 3.601 Å.

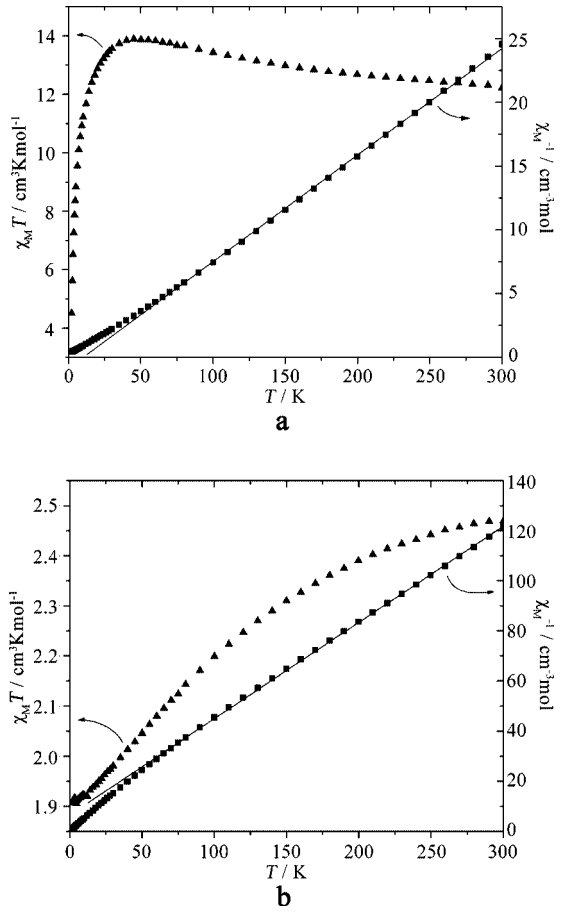


Figure 5. Plots of the temperature dependences of $\chi_M^{-1}$ (■) and $\chi_M T$ (▲) for complexes **2** (a) and **3** (b).

## Conclusions

Three new lanthanide–organic frameworks with unusual $(4^3)_2(4^6,6^6,8^3)$ topology were synthesized under hydrothermal conditions. The arrangement of the helices in one layer in **1**–**3** shows that the twisted conformation of the ligand can effectively transfer the chiral information between the helices. The codoped coordination polymer [(Y: Er, Yb)(pza)(OH)($H_2O$)]$_n$ emits green and red fluorescence by two-photon excitation. In addition, complex **2** shows a ferromagnetic coupling between the $Er^{III}$ ions.

 © 2007 Wiley-VCH Verlag GmbH & Co. KGaA, Weinheim 

## Experimental Section

**General:** All reagents were commercially available and were used without further purification. Elemental analyses of C, H and N were performed with an Elementar Vario EL analyzer. The IR spectra were recorded with a Nicolet Avatar 360 FTIR spectrometer by using the KBr pellet technique. The inductively coupled plasma (ICP) analysis was performed with a JY ULTIMA spectrometer. The upconversion luminescence spectra were measured by using a fluorescence spectrophotometer with a double-grating monochromator (JY-ISA, Fluorolog-Tau-3). A 975 nm continuous diode laser was used as the pump source. The direction of observation of the fluorescence was perpendicular to the direction of propagation of the pumping laser. Only the fluorescence emitted from the front surface of the samples was collected. The experimental conditions were held unchanged so as to ensure that the measurements for all the samples were comparable. The magnetic susceptibilities were obtained on crystalline samples with a Quantum Design MPMS XL-7 SQUID magnetometer. The experimental susceptibilities were corrected for contributions from the sample holder and the diamagnetism estimated from Pascal's constants.

**$[Y(pza)(OH)(H_2O)]_n$ (1):** The mixture of $YCl_3{\cdot}6H_2O$ (0.030 g, 0.1 mmol), 2,3-pyrazinedicarboxylic acid (0.017 g, 0.1 mmol), $H_2O$ (5 mL) and aqueous NaOH (0.3 mL, 0.65 mol $L^{-1}$) was sealed in a 25-mL stainless steel reactor with a Teflon liner and heated at 190 °C for 72 h. Colourless plate-like crystals of **1** were obtained and washed with water. Yield: 0.020 g (68.96%). $C_6H_5N_2O_6Y$ (290.03): calcd. C 24.85, H 1.74, N 9.66; found C 24.70, H 1.97, N 9.54. IR (KBr): $\tilde{\nu}$ = 3405 (s), 1643 (vs), 1620 (vs), 1566 (m), 1448 (s), 1398 (s), 1360 (s), 1119 (m), 847 (m), 475 (m), 439 (m), 408 (m) $cm^{-1}$.

**$[Er(pza)(OH)(H_2O)]_n$ (2):** This compound was prepared by following the procedure for **1** but using $ErCl_3{\cdot}6H_2O$ instead of $YCl_3{\cdot}6H_2O$. Pink plate-like crystals of **2** were obtained. Yield: 0.019 g (51.58%). $C_6H_5ErN_2O_6$ (368.39): calcd. C 19.56, H 1.37, N 7.60; found C 19.53, H 1.59, N 7.61. IR (KBr): $\tilde{\nu}$ = 3399 (s), 1643 (vs), 1619 (vs), 1567 (m), 1448 (s), 1396 (s), 1363 (s), 1119 (m), 847 (m), 473 (m), 439 (m), 406 (m) $cm^{-1}$.

**$[Yb(pza)(OH)(H_2O)]_n$ (3):** This compound was prepared by following the procedure for **1** but using $Yb(NO_3)_3{\cdot}6H_2O$ instead of $YCl_3{\cdot}6H_2O$. Colourless plate-like crystals of **3** were obtained. Yield: 0.022 g (58.80%). $C_6H_5N_2O_6Yb$ (374.16): calcd. C 19.26, H 1.35, N 7.49; found C 19.17, H 1.35, N 7.34. IR (KBr): $\tilde{\nu}$ = 3406 (s), 1645 (vs), 1620 (vs), 1568 (m), 1450 (s), 1399 (s), 1363 (s), 1120 (m), 848 (m), 477 (m), 443 (m), 401 (m) $cm^{-1}$.

**$[(Y: Er, Yb)(pza)(OH)(H_2O)]_n$:** The codoped compounds were prepared by following the procedure for **1** but using $YCl_3{\cdot}6H_2O$, $ErCl_3{\cdot}6H_2O$ and $Yb(NO_3)_3{\cdot}6H_2O$ (for example, molar ratio: 92.0:4.0:4.0%) instead of 100% $YCl_3{\cdot}6H_2O$. Colourless plate-like crystals were obtained. Yield: 0.018 g (70.17%). $C_6H_5N_2O_6$(Y: Er, Yb) (296.53): calcd. C 24.30, H 1.82, N 9.45; found C 24.42, H 1.93, N9.33. IR (KBr): $\tilde{\nu}$ = 3404 (s), 1646 (vs), 1620 (vs), 1567 (m), 1449 (s), 1398 (s), 1363 (s), 1119 (m), 848 (m), 476 (m), 440 (m), 408 (m) $cm^{-1}$. ICP analysis showed that the molar ratio of Y/Er/Yb was 90.9:4.5:4.6 (%) in the product.

**X-ray Structure Determination:** Intensity data for **1**, **2** and **3** were collected at 294 K with a Bruker SMART 1000 CCD area detector diffractometer, using graphite-monochromated Mo-$K_\alpha$ radiation ($\lambda$ = 0.71073 Å) in $\phi$ and $\omega$ scan modes, $\theta$ ranges 2.7° to 27.9° for **1**, 2.29° to 27.51° for **2**, 2.28° to 26.34° for **3**. Semiempirical absorption corrections were applied by using the SADABS program.[13] The structures were solved by direct methods[14] and refined by full-matrix least-squares on $F^2$ by using the programs SHELXS 97 and SHELXL 97, respectively.[14,15] All non-hydrogen atoms were refined anisotropically. The hydrogen atoms attached to the bridging hydroxy and the coordinated water molecules of **1**, **2** and **3** were located from the difference Fourier map. The other hydrogen atoms were generated geometrically and treated by a mixture of independent and constrained refinements. Details of crystallographic data of **1**, **2** and **3** are summarized in Table 2. CCDC 635120–635122 contain the supplementary crystallographic data for this paper. These data can be obtained free of charge from the Cambridge Crystallographic Data Centre via www.ccdc.cam.ac.uk/datarequest/cif.

## Acknowledgments

We acknowledge the support from the National Natural Science Foundation of China (20331010, 20501003) and thank Prof. V. A. Blatov for help with the solution of the structure.

[1] a) U. Mueller, M. Schubert, F. Teich, H. Puetter, K. Schierle-Arndt, J. Pastré, *J. Mater. Chem.* **2006**, *16*, 626–636; b) C. J. Kepert, *Chem. Commun.* **2006**, 695–700; c) S. Kitagawa, S. I. Noro, T. Nakamura, *Chem. Commun.* **2006**, 701–707; d) N. R. Champness, *Dalton Trans.* **2006**, 877–880; e) J. D. Wuest, *Chem. Commun.* **2005**, 5830–5837; f) D. Bradshaw, J. B. Claridge, E. J. Cussen, T. J. Prior, M. J. Rosseinsky, *Acc. Chem. Res.* **2005**, *38*, 273–282; g) B. Kesanli, W. B. Lin, *Coord. Chem. Rev.* **2003**, *246*, 305–326.

[2] a) H. L. Sun, B. Q. Ma, S. Gao, S. R. Batten, *Cryst. Growth Des.* **2006**, *6*, 1261–1263; b) J. F. Eubank, R. D. Walsh, P. Poddar, H. Srikanth, R. W. Larsen, M. Eddaoudi, *Cryst. Growth Des.* **2006**, *6*, 1453–1457; c) B. Gómez-Lor, E. Gutiérrez-Puebla, M. Iglesias, M. A. Monge, C. Ruiz-Valero, N. Snejko, *Chem. Mater.* **2005**, *17*, 2568–2573; d) L. Chen, X. H. Bu, *Inorg. Chem.* **2006**, *45*, 4654–4660; e) S. Q. Zang, Y. Su, Y. Z. Li, Z. P. Ni, H. Z. Zhu, Q. J. Meng, *Inorg. Chem.* **2006**, *45*, 3855–3857; f) Y. Q. Sun, J. Zhang, Y. M. Chen, G. Y. Yang, *Angew. Chem. Int. Ed.* **2005**, *44*, 5814–5817; g) L. Han, M. C. Hong, *Inorg. Chem. Commun.* **2005**, *8*, 406–419; h) B. Zhai, L. Yi, H. S. Wang, B. Zhao, P. Cheng, D. Z. Liao, S. P. Yan, *Inorg. Chem.* **2006**, *45*, 8471–8473.

[3] a) X. B. Zhao, B. Xiao, A. J. Fletcher, K. M. Thomas, D. Bradshaw, M. J. Rosseinsky, *Science* **2004**, *306*, 1012–1015; b) S. Kitagawa, R. Kitaura, S. I. Noro, *Angew. Chem. Int. Ed.* **2004**, *43*, 2334–2375; c) G. Férey, C. Mellot-Draznieks, C. Serre, F. Millange, *Acc. Chem. Res.* **2005**, *38*, 217–225; d) J. L. C. Rowsell, O. M. Yaghi, *Angew. Chem. Int. Ed.* **2005**, *44*, 4670–4679; e) M. Latroche, S. Surblé, C. Serre, C. Mellot-Draznieks, P. L. Llewellyn, J. H. Lee, J. S. Chang, S. H. Jhung, G. Férey, *Angew. Chem. Int. Ed.* **2006**, *45*, 8227–8231; f) S. M. Humphrey, J. S. Chang, S. H. Jhung, J. W. Yoon, P. T. Wood, *Angew. Chem. Int. Ed.* **2007**, *46*, 272–275.

[4] a) T. Ezuhara, K. Endo, Y. Aoyama, *J. Am. Chem. Soc.* **1999**, *121*, 3279–3283; b) Y. Xu, L. Han, Z. Z. Lin, C. P. Liu, D. Q. Yuan, Y. F. Zhou, M. C. Hong, *Eur. J. Inorg. Chem.* **2004**, 4457–4462; c) P. A. Maggard, C. L. Stern, K. R. Poeppelmeier, *J. Am. Chem. Soc.* **2001**, *123*, 7742–7743; d) M. H. Zeng, B. Wang, X. Y. Wang, W. X. Zhang, X. M. Chen, S. Gao, *Inorg. Chem.* **2006**, *45*, 7069–7076; e) C. D. Wu, A. G. Hu, L. Zhang, W. B. Lin, *J. Am. Chem. Soc.* **2005**, *127*, 8940–8941.

[5] a) J. Wu, Y. L. Song, E. P. Zhang, H. W. Hou, Y. T. Fan, Y. Zhu, *Chem. Eur. J.* **2006**, *12*, 5823–5831; b) K. Liang, H. G. Zheng, Y. L. Song, M. F. Lappert, Y. Z. Li, X. Q. Xin, Z. X. Huang, J. T. Chen, S. F. Lu, *Angew. Chem. Int. Ed.* **2004**, *43*, 5776–5779.

[6] a) T. Glaser, M. Heidemeier, T. Weyhermüller, R. D. Hoffmann, H. Rupp, P. Müller, *Angew. Chem. Int. Ed.* **2006**,

 © 2007 Wiley-VCH Verlag GmbH & Co. KGaA, Weinheim 

*45*, 6033–6037; b) U. García-Couceiro, O. Castillo, A. Luque, J. P. García-Terán, G. Beobide, P. Román, *Cryst. Growth Des.* **2006**, *6*, 1839–1847; c) X. T. Liu, X. Y. Wang, W. X. Zhang, P. Cui, S. Gao, *Adv. Mater.* **2006**, *18*, 2852–2856; d) Y. Z. Zhang, Z. M. Wang, S. Gao, *Inorg. Chem.* **2006**, *45*, 5447–5454; e) Y. Z. Zheng, M. L. Tong, W. X. Zhang, X. M. Chen, *Angew. Chem. Int. Ed.* **2006**, *45*, 6310–6314.

[7] a) D. Bradshaw, T. J. Prior, E. J. Cussen, J. B. Claridge, M. J. Rosseinsky, *J. Am. Chem. Soc.* **2004**, *126*, 6106–6114; b) W. Gerhardt, M. Črne, M. Weck, *Chem. Eur. J.* **2004**, *10*, 6212–6221; c) Q. R. Fang, G. S. Zhu, M. Xue, J. Y. Sun, F. X. Sun, S. L. Qiu, *Inorg. Chem.* **2006**, *45*, 3582–3587.

[8] a) A. de Bettencourt-Dias, *Inorg. Chem.* **2005**, *44*, 2734–2741; b) P. Lenaerts, K. Driesen, R. V. Deun, K. Binnemans, *Chem. Mater.* **2005**, *17*, 2148–2154; c) Z. H. Zhang, Y. Song, T. A. Okamura, Y. Hasegawa, W. Y. Sun, N. Ueyama, *Inorg. Chem.* **2006**, *45*, 2896–2902; d) A. Nag, P. J. Schmidt, W. Schnick, *Chem. Mater.* **2006**, *18*, 5738–5745; e) H. T. Zhang, Y. Song, Y. X. Li, J. L. Zuo, S. Gao, X. Z. You, *Eur. J. Inorg. Chem.* **2005**, 766–772.

[9] a) L. Luo, W. P. W. Lai, L. K. Wong, W. T. Wong, K. F. Li, K. W. Cheah, *Chem. Phys. Lett.* **2004**, *398*, 372–376; b) K. L. Wong, W. M. Kwok, W. T. Wong, D. L. Phillips, K. W. Cheah, *Angew. Chem. Int. Ed.* **2004**, *43*, 4659–4662; c) J. Yang, Q. Yue, G. D. Li, J. J. Gao, G. H. Li, J. S. Chen, *Inorg. Chem.* **2006**, *45*, 2857–2865; d) D. F. Weng, X. J. Zheng, L. P. Jin, *Eur. J. Inorg. Chem.* **2006**, 4184–4190.

[10] a) V. A. Blatov, A. P. Shevchenko, V. N. Serezhkin, *J. Appl. Crystallogr.* **2000**, *33*, 1193–1193; b) V. A. Blatov, L. Carlucci, G. Ciani, D. M. Proserpio, *CrystEngComm* **2004**, *6*, 377–395.

[11] G. S. Yi, B. Q. Sun, F. Z. Yang, D. P. Chen, Y. X. Zhou, J. Cheng, *Chem. Mater.* **2002**, *14*, 2910–2914.

[12] O. Kahn in *Molecular Magnetism*, VCH Publishers, New York, **1993**.

[13] G. M. Sheldrick, *SADABS*, Program for Empirical Absorption Correction of Area Detector Data, University of Göttingen, Göttingen, Germanny, **1997**.

[14] G. M. Sheldrick, *SHELXS 97*, Program for Crystal Structure Solution, University of Göttingen, Göttingen, Germanny, **1997**.

[15] G. M. Sheldrick, *SHELXL 97*, Program for Crystal Structure Refinement, University of Göttingen, Göttingen, Germanny, **1997**.

Received: January 31, 2007
Published Online: June 1, 2007

 © 2007 Wiley-VCH Verlag GmbH & Co. KGaA, Weinheim 

DOI: 10.1002/ejic.200700292

# Synthesis of Half-Sandwich Tungsten Chlorogermyl and Chlorostannyl Complexes

**Holger Braunschweig,*[a] Holger Bera,[a] Barbara Geibel,[a] Rainer Dörfler,[a] Daniel Götz,[a] Fabian Seeler,[a] Thomas Kupfer,[a] and Krzysztof Radacki[a]**

**Keywords:** Half-sandwich complexes / Tungsten complexes / Germanes / Stannanes / Stannylcyclopentadienes

The reaction of the dichlorogermane $Me_2GeCl_2$ and stannanes $R_2SnCl_2$ (R = Me, Bu) with the alkali tungsten salts $M[(\eta^5\text{-}C_5R'_5)L(OC)_2W]$ (L = CO, $PPh_3$; M = Li, Na; R′ = H, Me) yields via alkali salt elimination a range of novel chlorostannyl- and chlorogermyl-functionalized tungsten complexes of the general formula $[(\eta^5\text{-}C_5R'_5)L(OC)_2W(ER_2Cl)]$ (R′ = H, Me; L = CO, $PPh_3$; E = Ge, Sn; R = Me, Bu) (**3a–e**). The use of the phosphane-substituted tungsten anion $Na[(\eta^5\text{-}C_5Me_5)(Ph_3P)(OC)_2W]$ (**1c**) and $Me_2SnCl_2$ leads to a mixture consisting of the mono- (**3e**) as well as the di-substituted stannyl compound $[\{(\eta^5\text{-}C_5H_5)(Ph_3P)(OC)_2W\}_2(SnMe_2)]$ (**4**). Access to **3a** is also given by reaction of $ClMe_2Sn\text{–}C_5H_5$ (**5**) with $[(MeCN)_3W(CO)_3]$ which includes chemoselective tin shift from the cyclopentadiene to the tungsten atom. In addition, a successive chlorination of $[(\eta^5\text{-}C_5H_5)(OC)_3W(SnMe_3)]$ (**6**) via $[(\eta^5\text{-}C_5H_5)(OC)_3W(SnMe_2Cl)]$ (**3a**) and $[(\eta^5\text{-}C_5H_5)(OC)_3W(SnMeCl_2)]$ (**7**) to $[(\eta^5\text{-}C_5H_5)(OC)_3W(SnCl_3)]$ (**8**) is presented. All new compounds have been fully characterized by elemental analyses and in solution by IR and multinuclear NMR spectroscopy. The crystal structures of complexes **3b–d** and **8** were presented and discussed, showing bond lengths of 2.6272(4) Å for Ge–W, 2.7959(5) (**3b**), 2.7866(3) (**3d**) and 2.7244(3) (**8**) Å for the Sn–W bonds.

(© Wiley-VCH Verlag GmbH & Co. KGaA, 69451 Weinheim, Germany, 2007)

## Introduction

The first germanium and tin complexes of molybdenum and tungsten have been prepared in the 1960's[1] and since that time [M]–$SnR_3$ bonds are ubiquitous up to the present day.[2] The chemistry of such complexes has been the object of extensive studies due to their potential in many catalytic and stoichiomtric processes.[3] Two important reactions of transition-metal stannyl complexes [M]–$SnR_3$ (R = organic group) are the chlorination with hydrogen halides[4] and the stanna-tropic shift from the transition-metal to the cyclopentadienyl ligand in half-sandwich complexes, induced by a strong base.[5] Despite this fact, the amount of complexes owing a chlorogermyl or chlorostannyl moiety, which allow further functionalization and reaction chemistry, is fairly limited – in particular in the case of germanium, and only little work has been carried out concerning investigations of the Cl–Sn unit of a transition metal. One of them – the most recent work – deals with chloride displacement by nucleophilic sulfur or oxygen groups with the latter (pyridinedicarboxylic acid) leading to an iron complex with fivefold-coordinated tin[6] (Figure 1). Another investigation topic is the Lewis basicity of the $Cl_3Sn$ group. In this context, some interesting molybdenum and tungsten *ansa* complexes were built up showing an intramolecular Lewis acid–base interaction of a cyclopentadienyl-bound donor group (with N and O as donor atoms) and the transition-metal bound $Cl_3Sn$ moiety giving a sixfold-coordinated tin centre[7] (Figure 1).

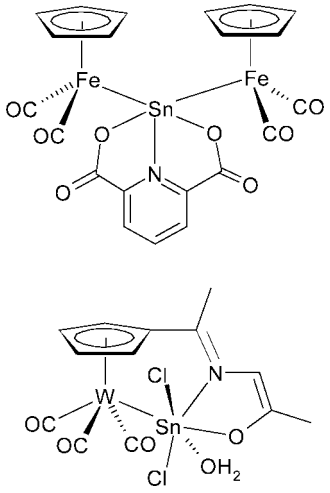


Figure 1. Iron and tungsten half-sandwich complexes with fivefold- and sixfold-coordinated tin atoms.

Nevertheless, with regard to the facile chemistry of $R_3ECl$ (E = Ge, Sn) which includes a wide variety of reactions with alkali metals, organolithium compounds, hydroxides, sulfides, Lewis bases, amides, alkoxides, etc., it seems self-evident that much of it can be yet transferred to chlorogermyl and chlorostannyl transition-metal complexes.

[a] Institut für Anorganische Chemie, Universität Würzburg, Am Hubland, 97074, Würzburg, Germany

 © 2007 Wiley-VCH Verlag GmbH & Co. KGaA, Weinheim 

In an extension of our work on the reactivity of boryl-, borylene-,[8] or diborane(4)yl[9] moieties linked to half-sandwich metal fragments (e.g. compound $[(\eta^5\text{-}C_5Me_5)(OC)_2Fe\text{–}(BX_2\leftarrow py)]$ (X = Cl, Br; py = pyridine),[8f] $[(\eta^5\text{-}C_5H_5)(R_3P)(OC)_2W\text{–}\{B(NMe_2)\text{–}B(NMe_2)Cl\}]$ (R = Me, Ph)[9a] in Figure 2) which included the addition of Lewis bases to $BCl_2$ ligands[8f,8i] analogous to $Cl_3Sn$ complexes, we became interested in some aspects of the chemistry of corresponding halogermyl and stannyl complexes.

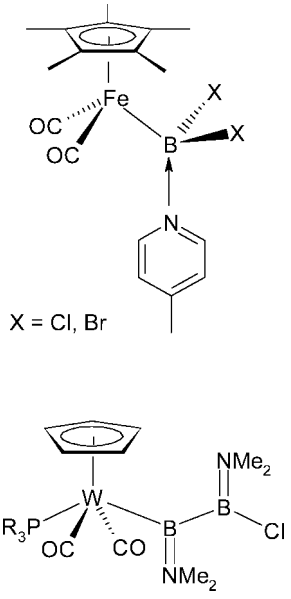


Figure 2. Methylpyridine Lewis base adduct of a $X_2B$-substituted iron complex and phosphane-substituted diborane(4)yl tungsten half-sandwich complex.

In this paper we report on the synthesis, spectroscopic and structural characterisation of the novel chlorodiorgano germyl and stannyl complexes of tungsten. The synthetic method chosen is straightforward and widely variable and so should give access to a range of analogue complexes. Additionally, we have developed three convenient and new methods for a facile preparation of **3a**, and established a chlorination chemistry which allows the facile synthesis of tungsten complexes with mono, di- and trichlorinated stannyl ligands.

## Results and Discussion

The complexes of the general formula $[(\eta^5\text{-}C_5R'_5)L(OC)_2W(ER_2Cl)]$ (R′ = H, Me; L = CO, $PPh_3$; E = Ge, Sn; R = Me, Bu) (**3a**–**e**) are obtained from the corresponding dichlorogermanes and stannanes $R_2ECl_2$ (E = Ge, Sn; R = Me, Bu) (**2a**–**c**) with the alkali tungsten salts $M[(\eta^5\text{-}C_5R'_5)L(OC)_2W]$ (L = CO, $PPh_3$; M = Li, Na; R′ = H, Me) (**1a**–**c**) after 16–22 h reaction time at ambient temperature in diethyl ether, according to Equation (1). The new compounds are isolated as yellow and dark yellow (**3e** and **3a**,**b**), ochre (**3d**) and brown (**3c**) powders in yields between 70% (**3b**) and 85% (**3d**). These results demonstrate that the synthetic method chosen is straightforward and widely variable and hence should give access to a range of analogue complexes. **3a**–**e** show moderate solubility in pentane or hexane and dissolve readily in diethyl ether and aromatic solvents. They can be stored under argon atmosphere at –30 °C for several months without signs of decomposition. **3d** can be even stored at ambient temperature.

The reaction of the triphenylphosphane-substituted tungsten anion **1c** with dichlorodimethylstannane (**2b**) does not give exclusively **3e**. Instead, a product mixture of **3e** and the dinuclear complex **4** is obtained (Figure 3). The ratio of **3e** and **4** is determined by integration of the $^1H$ NMR spec-

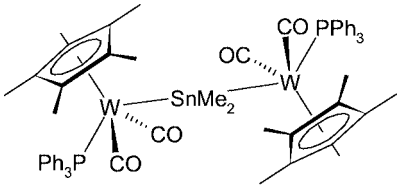


**4**

Figure 3. Disubstituted dimethylstannane *trans*-**4**.

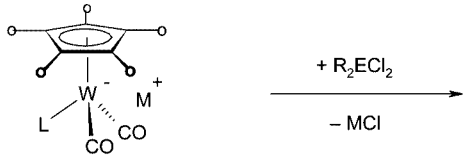


(1)

| 1 | a | b | c |
|---|---|---|---|
| o- | H | Me | Me |
| L | CO | CO | $PPh_3$ |
| M | Li | Li | Na |

| 2 | a | b | c |
|---|---|---|---|
| R | Me | Me | Bu |
| E | Ge | Sn | Sn |

| 3 | a | b | c | d | e |
|---|---|---|---|---|---|
| o- | H | H | Me | Me | Me |
| L | CO | CO | CO | CO | $PPh_3$ |
| R | Me | Bu | Me | Me | Me |
| E | Sn | Sn | Ge | Sn | Sn |

 © 2007 Wiley-VCH Verlag GmbH & Co. KGaA, Weinheim 

trum and amounts to 2:1. The formation of **3e** and **4** proceeds stereospecifically and only the *trans*-products are observed, which is consistent with the synthesis of the parent $[(\eta^5\text{-}C_5H_5)(Ph_3P)(OC)_2W(SnMe_3)]$.[10] Due to the different solubility in hexane both compounds can be easily separated from each other. This reaction demonstrates the higher nucleophilic character of the phosphane-substituted tungsten anion **1c** in comparison to the tricarbonyl derivative (**1b**) in spite of its higher steric demands.

All new complexes were characterised in solution by IR and multinuclear NMR spectroscopy. The complexes **3a**,**c**–**e** show singlets for the dimethyl groups attached to the germanium and tin atom in the $^1$H NMR spectra between 0.87 (**3a**) and 1.17 (**3c**) ppm, characteristic for an element nucleus being deshielded with respect to those of the starting dichlorogermane and stannanes. These values are in good agreement to the corresponding signal found for $[\{H_2C(O)\text{-}C(\eta^5\text{-}C_5H_4)\}(OC)_3W(SnMe_2Cl)]_2$ ($\delta$ = 0.95 ppm).[11] The signals of the Sn-bound methyl moieties are accompanied by $^{117/119}$Sn satellites showing $^2J_{HCSn}$ coupling constants of 45.3, 47.3 (**3a**), 42.5, 44.4 (**3d**) and 40.2, 41.8 (**3e**) Hz, thus reflecting the increasing electron density of the tungsten fragments in this row. The $^{119}$Sn NMR resonances of **3a**,**d**,**e** are detected in close proximity at 227.0 (**3a**), 233.0 (**3d**) and 233.8 (**3e**) ppm, whereas the one of the butyl derivative **3b** differs significantly and appears at $\delta$ = 26.7 ppm due to the electron-releasing effect of the butyl groups. Only in two cases the $^1J_{SnW}$ coupling was observed amounting to 162.8 (**3b**) and 347.0 Hz (**3d**). Due to the fact that in the case of **3e** and **4** the *trans*-product is exclusively formed, in the $^{31}$P NMR spectra appears in each case one resonance at 38.61 (**3e**) and 44.50 ppm (**4**), accompanied by $^{183}$W [$^1J_{WP}$ = 293.6 Hz (**3e**), 267.3 Hz (**4**)] and $^{117/119}$Sn satellites [$^2J_{SnWP}$ = 123.9 and 128.8 Hz (**3e**), 125.4 and 130.8 Hz (**4**)]. As expected, **3a**,**c**,**d** show three CO-stretching frequencies ($A_{(1)}'$, $A''$ and $A_{(2)}'$) each in the IR spectra between 1901 and 2010 cm$^{-1}$, as expected for such tungsten complexes.[11] Surprisingly, the butyl derivative **3b** shows only two bands (1999 and 1981 cm$^{-1}$), one of which, however, is thus possibly indicating an overlap of two bands. In contrast, the observed number of two CO-stretching frequencies for **3e** and **4** is in agreement with phosphane-substituted tungsten stannyl complexes, as loss of a carbonyl group usually decreases the number of absorption bands from 3 to 2. As expected, the carbonyl stretching frequencies decrease in comparison to **3a**,**c**,**d** and are found for **3e** and **4** at 1904, 1835 and 1901, 1832 cm$^{-1}$, respectively which lie very close to those of $[(\eta^5\text{-}C_5H_5)(Ph_3P)(OC)_2W(SnMe_3)]$.[10]

*X-ray diffraction analyses.* The molecular structures of $[(\eta^5\text{-}C_5H_5)(OC)_3W(SnBu_2Cl)]$ (**3b**), $[(\eta^5\text{-}C_5Me_5)(OC)_3W(GeMe_2Cl)]$ (**3c**) and $[(\eta^5\text{-}C_5Me_5)(OC)_3W(SnMe_2Cl)]$ (**3d**) have been confirmed by X-ray diffraction studies and are presented in Figure 4, Figure 5, and Figure 6. Selected bond lengths and angles are listed below each Figure and crystal data and refinement parameters in Table 2 in the experimental section. In all cases, crystals, suitable for X-ray analysis, are obtained upon slow evaporation of saturated benzene solutions at room temperature. The compounds crystallize in triclinic (**3b**) and monoclinic (**3c**,**d**) crystal systems with space groups $P\bar{1}$ (**3b**), $P2_1/c$ (**3c**) and $C2/c$ (**3d**), respectively.

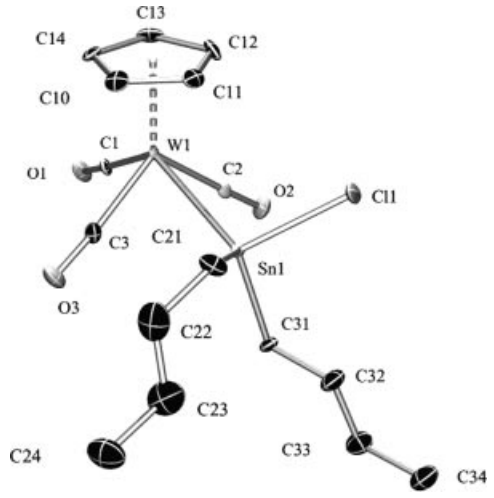


Figure 4. Molecular structure of $[(\eta^5\text{-}C_5H_5)(OC)_3W(SnBu_2Cl)]$ (**3b**) in the solid state with the atom-numbering scheme. Displacement ellipsoids are drawn at the 50% probability level and the hydrogen atoms have been omitted for clarity. Selected bond lengths [Å] and angles [°]: W1–C1 1.983(7), W1–C3 1.984(8), W1–C2 1.985(7), W1–Sn1 2.7959(5), Sn1–C31 2.156(7), Sn1–C21 2.168(8), Sn1–Cl1 2.4203(18), C31–Sn1–C21 114.6(3), C31–Sn1–Cl1 99.1(2), C21–Sn1–Cl1 99.6(2), C31–Sn1–W1 120.56(19), C21–Sn1–W1 114.1(2), Cl1–Sn1–W1 104.34(5).

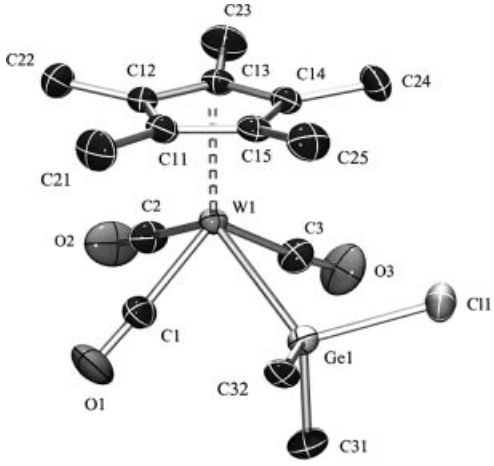


Figure 5. Molecular structure of $[(\eta^5\text{-}C_5Me_5)(OC)_3W(GeMe_2Cl)]$ (**3c**) in the solid state with the atom-numbering scheme. Displacement ellipsoids are drawn at the 50% probability level and the hydrogen atoms have been omitted for clarity. Selected bond lengths [Å] and angles [°]: W1–C1 1.971(4), W1–C2 1.982(4), W1–C3 1.982(4), W1–Ge1 2.6272(4), Ge1–C31 1.948(4), Ge1–C32 2.008(3), Ge1–Cl1 2.2428(10), C1–W1–Ge1 70.04(11), C2–W1–Ge1 123.98(11), C3–W1–Ge1 72.07(12), C31–Ge1–C32 106.44(17), C31–Ge1–Cl1 101.62(13), C32–Ge1–Cl1 101.97(10), C31–Ge1–W1 117.55(13), Cl1–Ge1–W1 109.74(3).

The coordination sphere around each tungsten atom can be considered as a pseudo square-pyramid, with the three carbonyl ligands [mean W–C 1.984 (**3b**), 1.978 (**3c**) and 1.978 Å (**3d**)] and the germyl or rather stannyl group forming the base, while the aromatic ring systems occupie the

 © 2007 Wiley-VCH Verlag GmbH & Co. KGaA, Weinheim 

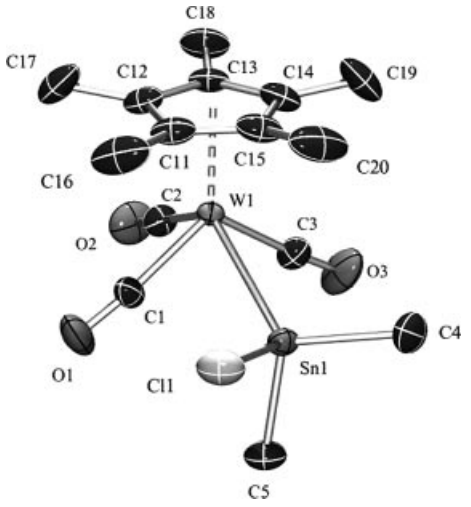


Figure 6. Molecular structure of [($\eta^5$-$C_5Me_5$)$(OC)_3$W($SnMe_2$Cl)] (**3d**) in the solid state with the atom-numbering scheme. Displacement ellipsoids are drawn at the 50% probability level and the hydrogen atoms have been omitted for clarity. Selected bond lengths [Å] and angles [°]: W1–C3 1.976(4), W1–C1 1.977(3), W1–C2 1.982(4), W1–Sn1 2.7866(3), Sn1–C5 2.146(4), Sn1–C4 2.157(4), Sn1–Cl1 2.4215(10), C5–Sn1–C4 107.61(16), C5–Sn1–Cl1 99.75(12), C4–Sn1–Cl1 100.48(13), Cl1–Sn1–W1 108.97(3), C5–Sn1–W1 118.56(11), C4–Sn1–W1 118.31(12).

apical position ("four-legged piano stool" complex). In the case of **3c**,**d**, the five methyl groups are slightly bent out of the plane of the cyclopentadienyl ligand [mean 6.7° (**3c**) and 6.5° (**3d**)]. All these structural parameters lie in the range reported in literature for comparable compounds.[7,11,12] The base-forming angles lie all between 70 and 75°. The determined W–Ge distance amounts to 2.6272(4) Å, which is about 0.1 Å shorter than the values in the $PMe_3$-substituted trichlorogermanium complexes *cis*- and *trans*-[($\eta^5$-$C_5Me_5$)$(Me_3P)(OC)_2$W($GeCl_3$)] [2.559(5) (*cis*) and 2.5159(14) Å (*trans*)].[12a] This finding supports the observation that increased electron density at a central transition metal atom – evoked by the introduction of a phosphane ligand – strengthens the transition metal–element bond. The determined Ge–C bond lengths are 1.948(4) (Ge1–C31) and 2.008(3) (Ge1–C32) Å. For the germanium–chlorine bond a length of 2.2428(10) Å is found, which is only slightly longer than the corresponding bonds in the $Cl_3Ge$ derivative [mean 2.206 (*cis*) and 2.199 Å (*trans*)].[12a] The tetrahedral coordination geometry of the germanium atom is strongly distorted indicated by angles in the range from 101.62(13) (C31–Ge1–Cl1) to 117.55(13)° (C31–Ge1–W1). Only Cl1–Ge1–W1 shows an almost ideal tetrahedron angle [109.74(3)°].

The determined W–Sn bond lengths are 2.7959(5) (**3b**) and 2.7866(3) Å (**3d**), thus being in the range of tin-substituted tricarbonyl tungsten complexes.[7,11] The Sn–C bonds of **3b** are slightly longer [2.168(8) (Sn1–C21) and 2.156(7) Å (Sn1–C31)] than those of **3d** [2.146(4) (Sn1–C5) and 2.157(4) Å (Sn1–C4)]. For the tin–chlorine bonds, distances of 2.4203(18) (**3b**) and 2.4215(10) Å (**3d**) are found, which is very similar to those in tungsten complexes with sixfold-coordinated tin atoms, e.g. 2.404(1) and 2.459(2) Å in the tungsten complex in Figure 1.[7] As expected, the tetrahedral coordination geometry of the tin atoms of **3b**,**d** is significantly distorted almost to the same extent as already mentioned for the Ge analogue and thus, angles between 99.1(2) (C31–Sn1–Cl1) and 120.56(19) (C31–Sn1–W1) (**3b**) or rather 99.75(12) (C5–Sn1–Cl1) and 118.56(11) Å (C5–Sn1–W1) (**3d**) were found. Interestingly, in both compounds the W–Sn–C angles are widened whereas the C–Sn–Cl angles are more acute in comparison to the ideal tetrahedron angle. This characteristic could also be observed in the Ge compound and was found in diorganostannyl molybdenum complexes, too.[11,13] In **3b**, there is an interaction of one carbonyl oxygen (O1) with a hydrogen atom of the second molecule of the same cell (H51A) which can be classified as moderate hydrogen bond according to the value of 2.508 Å (O1···H51A).

*Alternative syntheses of **3a** and chlorination reactions.* Even though the following compounds were already mentioned in literature, not all of them have been isolated and their characterisation has not been carried out to full extent. For example, up to now, it was only possible to obtain the di-chlorinated complex **7** together with **3a** as an inseparable mixture by treatment of **6** with hydrogen chloride.[4] Therefore, we developed new and convenient syntheses for these chlorostannyl compounds, isolated them and completed their characterization.

One alternative route leading to **3a** proceeds via the chlorodimethylstannyl-cyclopentadiene **5** which is literature-known,[14] but was here synthesized in a more convenient way. The alkali salt elimination of sodium cyclopentadienide and dichlorodimethylstannane yields after 18 h stirring at ambient temperature **5** according to Scheme 1. **5** is obtained as a yellow oil in 84% and can be stored at –30 °C under Ar atmosphere over a period of months. Due to the fast stannatropic shift of the $ClMe_2Sn$ group with respect to the NMR time-scale, a singlet at $\delta$ = 5.99 ppm is observed for the cyclopentadiene protons at ambient temperature. This chemical shift agrees very well with the literature data ($\delta$ = 6.02 ppm[14a]) and the signal shows the expected

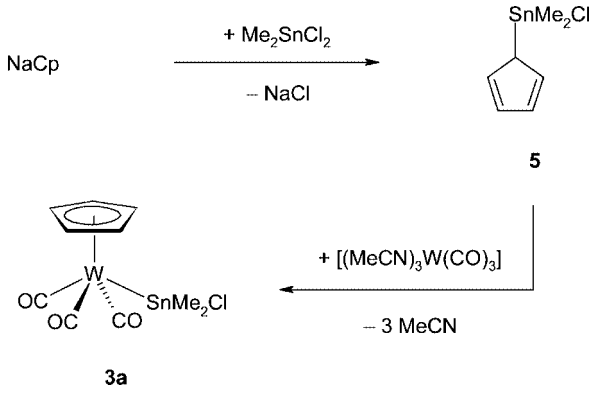


Scheme 1. Alternative synthesis of **3a** via the chlorostannyl-functionalized cyclopentadiene **5** which is obtained from alkali salt elimination of sodium cyclopentadienyl and dichlorodimethyl stannane.

 © 2007 Wiley-VCH Verlag GmbH & Co. KGaA, Weinheim 

tin satellites with coupling constants of 29.0 and 30.0 Hz. In the $^{119}$Sn NMR spectrum a singlet is observed at $\delta$ = 101.45 ppm.[14b]

In the last step, **5** is treated with $[(MeCN)_3W(CO)_3]$ in refluxing THF over a period of 18 h, leading to **3a** in 90% yield (Scheme 1). **3a** is obtained as an analytically pure yellow solid. The reaction proceeds chemoselectively and only the chlorostannyl group shifts to the tungsten centre – no complex tungsten hydride is observed as by-product. This insertion of a coordinatively unsaturated transition-metal fragment (W) into a Sn–C bond which is accompanied by oxidation of the W centre has precedence but only for trimethylgermanium- and -tin-functionalized cyclopentadienes.[15] In contrast, in $Me_3Si$-substituted cyclopentadienes the Si–C unit tends to remain intact due to a stronger and less polar bond.[15a]

Besides, we developed not only a selective synthesis of **7**, but also a controlled, successive chlorination of the trimethylstannyl tungsten complex **6** to the trichlorostannyl derivative **8** (Scheme 2) via isolable intermediates.

The first Me/Cl exchange is achieved by use of exactly one equivalent of $SnCl_4$ at ambient temperature, leading after two hours exclusively to **3a**. After work up, **3a** can be obtained analytically pure in 92% yield. The second chlorination is realized with a further equivalent of $SnCl_4$ at ambient temperature, too. The reaction is finished after two hours and yields **7** in 88%. The di-chlorination product **7** can also be obtained directly from **6** if an excess of $SnCl_4$ is employed. **7** is characterized by a high stability even towards concentrated hydrochloric acid. For the tin-bound methyl group a singlet at $\delta$ = 1.11 ppm is observed, showing the expected $^{117/119}$Sn satellites of 45.2 and 46.2 Hz, respectively. The $^{119}$Sn signal is detected at $\delta$ = 198.9 ppm. An excess of $SnCl_4$ in refluxing chloroform gives access to the trichlorostannyl complex **8**, when the mixture is heated over a period of six days. **8** can be obtained in 60% as a yellow powder, which can be also exposed to air for a prolonged period without decomposition. The detected $^1$H NMR chemical shift at 5.77 for the Cp is in accordance with literature ($\delta$ = 5.6 ppm) as well as the IR data.[16] The $^{119}$Sn NMR resonance was detected at $\delta$ = –89.4 ppm, which is about 115 ppm shifted to higher field in comparison to the Mo analogue $[(\eta^5\text{-}C_5H_5)(OC)_3Mo(SnCl_3)]$ ($\delta$ = 26 ppm).[6] Due to the fact that only IR data of **7** are published[16] (except for $^1$H NMR of **8**,[16b]), we characterized **7** and **8** by $^1$H, $^{13}$C and $^{119}$Sn NMR as well as elemental and melting point analysis. Some of these data are listed in Table 1.

Table 1. NMR spectroscopic features depending on the chlorination degree of the W-bound tin atom.[a]

| | $[WpSnMe_3]$ (**6**) | $[WpSnMe_2Cl]$ (**3a**) | $[WpSnMeCl_2]$ (**7**) | $[WpSnCl_3]$ (**8**) |
|---|---|---|---|---|
| $^1$H(MeSn) | 0.51 | 0.87 | 1.11 | – |
| $^{119}$Sn | 42.3[b] | 227.0 | 198.9[c] | –89.4 |
| $^2J_{HCSn}$ | 48.4, 46.4 | 47.3, 45.3 | 46.2, 45.2 | – |

[a] NMR spectroscopic data in ppm (in $C_6D_6$, except **8**: $CDCl_3$), coupling constants in Hz. For a more detailed discussion of the IR data and bonding energies see ref.[16a]. Wp ≡ $(\eta^5\text{-}C_5H_5)(OC)_3W$. [b] $^1J_{SnW}$ = 150.5 Hz. [c] $^1J_{SnW}$ = 596.8 Hz.

For better comparison of the compounds of **6**, **3a**, **7** and **8**, we determined the $^1$H and $^{119}$Sn NMR chemical shifts and the coupling constants $^2J_{HCSn}$ of the Sn-attached methyl groups (Table 1). The trends of the $^1$H NMR chemical shifts in the row $[(\eta^5\text{-}C_5H_5)(OC)_3W(SnMe_3)]$ (**6**), $[(\eta^5\text{-}C_5H_5)(OC)_3W(SnMe_2Cl)]$ (**3a**), $[(\eta^5\text{-}C_5H_5)(OC)_3W(SnMeCl_2)]$ (**7**) and $[(\eta^5\text{-}C_5H_5)(OC)_3W(SnCl_3)]$ (**8**) are very regular and behave as expected – the more electronegative chlorine atoms are bound at the tin atom the higher is the detected chemical shift value. Parallel, the $^2J_{HCSn}$ coupling constants (MeSn) decrease continuously. In contrast to

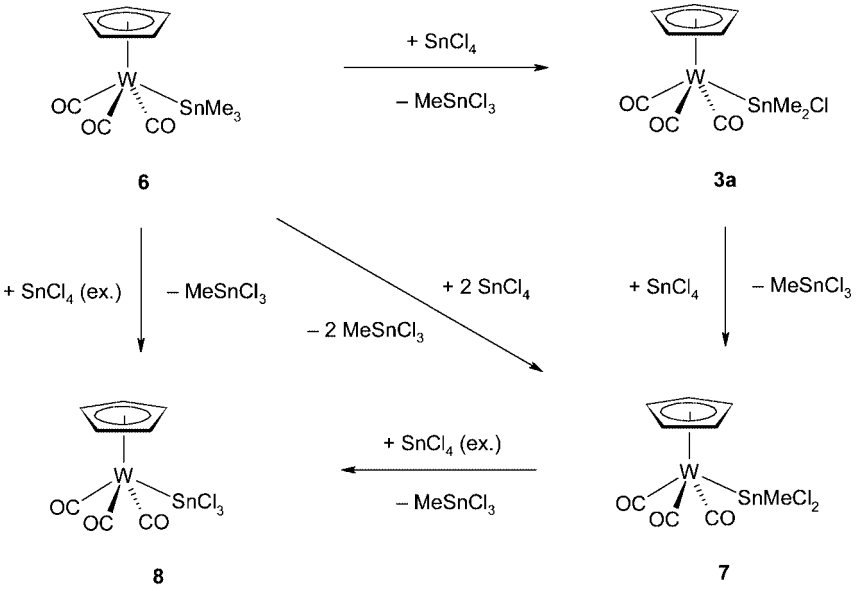


Scheme 2. Stepwise chlorination of **6** via mono- and dichlorinated stannyl tungsten complexes **3a** and **7** leading to the trichlorostannyl complex **8** and direct synthesis of **7** and **8**.

 © 2007 Wiley-VCH Verlag GmbH & Co. KGaA, Weinheim 

these findings, the $^{119}$Sn NMR shifts display no regular trend, and after the first Me/Cl substitution a maximum shift value of 227.0 ppm is observed. Further chlorine substitution leads to a decrease of the $^{119}$Sn chemical shift up to –89.4 ppm for **8**. Apparently, two effects are responsible for this feature namely the electronegative character of chlorine as well as the π-back bonding of the *p*-lone pairs of the chlorine. The latter effect increases with a growing number of chlorine atoms due to the fact that the Lewis acid character of the tin atom is increasing at the same time.

*X-ray diffraction analysis.* The molecular structure of $[(\eta^5\text{-}C_5H_5)(OC)_3W(SnCl_3)]$ (**8**) has been confirmed by X-ray diffraction study and is depicted in Figure 7. Selected bond lengths and angles are listed below the Figure and crystal data and refinement parameters in Table 2 in the experimental section. Suitable crystals are obtained upon slow evaporation of saturated $CDCl_3$ solution at room temperature. **8** crystallizes in a triclinic crystal system with space group $P\bar{1}$.

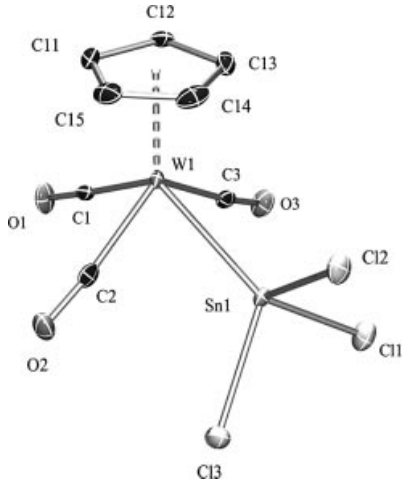


Figure 7. Molecular structure of $[(\eta^5\text{-}C_5H_5)(OC)_3W(SnCl_3)]$ (**8**) in the solid state with the atom-numbering scheme. Displacement ellipsoids are drawn at the 50% probability level and the hydrogen atoms have been omitted for clarity. Selected bond lengths [Å] and angles [°]: W1–C1 1.998(5), W1–C2 2.011(5), W1–C3 2.001(4), W1–Sn1 2.7244(3), Sn1–Cl1 2.3450(11), Sn1–Cl3 2.3616(11), Sn1–Cl2 2.3681(11), C1–W1–Sn1 126.42(12), C3–W1–Sn1 75.08(12), C2–W1–Sn1 76.17(12), Cl1–Sn1–Cl3 96.41(4), Cl1–Sn1–Cl2 98.94(4), Cl3–Sn1–Cl2 99.45(4), Cl1–Sn1–W1 121.81(3), Cl3–Sn1–W1 119.57(3), Cl2–Sn1–W1 116.14(3).

**8** shows the typical piano-stool arrangement as expected for a half-sandwich compound. The geometrical features of **8** in the solid state are very similar to that found for the Mo analogue $[(\eta^5\text{-}C_5H_5)(OC)_3Mo(SnCl_3)]$:[6] the tetrahedral coordination geometry of the tin atom is strongly distorted and resemble a trigonal pyramid also found for the Mo compound. All Cl–Sn–Cl angles are acute (mean: 98.27°) whereas the Cl–Sn–W angles are more obtuse showing values between 116.14(3) (Cl2–Sn1–W1) and 121.81(3)° (Cl1–Sn1–W1). Not only the Sn–Cl distances (mean: 2.358 Å) are similar to those of the Mo complex, but also the transition-metal–tin distances, which amount to 2.7244(3) Å in the tungsten and 2.7223(4) in the molybdenum case. Additionally, we found a short distance of 2.925 Å between the chlorine atom Cl2 and the proton bound to C14, which can be classified as a weak, intramolecular hydrogen bond interaction.

It is known that organotin halides tend to build up associated arrangements with formation of σ-donor bridges in the solid state. It is interesting that **8** shows not such a intermolecular association behaviour. Presumably, this finding is caused by the transition-metal fragment but it remains open whether steric or electronic effects are responsible.

## Conclusions

We were able to show that the alkali salt elimination has to be regarded as a straightforward route to synthesize chlorogermyl and chlorostannyl tungsten complexes and allows the variation of the organo groups being attached to the element as well as the transition-metal fragment itself. The chlorination degree of the transition-metal bound tin atom can be varied successively and selectively by use of $SnCl_4$. Thus, the work reported in this paper opens the door to a range of chlorogermyl and chlorostannyl tungsten complexes which enables further investigations of the chemical behaviour, e.g. with respect to alkali metals, organolithium compounds, hydroxides, sulfides, Lewis bases, amides or alkoxides.

## Experimental Section

All manipulations were conducted either under an atmosphere of dry argon or in vacuo using standard Schlenk line or glovebox techniques. Solvents (benzene and pentane) were purified by distillation from appropriate drying agents (sodium and sodium wire) under dry argon, immediately prior to use. $C_6D_6$ was degassed by three freeze-pump-thaw cycles and stored over molecular sieves. IR spectra were recorded as $CH_2Cl_2$ solutions between KBr plates on a Bruker Vector 22 FT-IR spectrometer. $^1$H, $^{31}$P{$^1$H} and $^{119}$Sn{$^1$H} NMR spectra were acquired on a Bruker Avance 200 NMR spectrometer at 200.1, 121.5 and 111.9 or 186.5 MHz, respectively and referenced to external TMS or $SnMe_4$ ($^{119}$Sn). $^{13}$C{$^1$H} NMR spectra were recorded on a Bruker AMX 400 NMR spectrometer at 125.8 MHz and referenced to the solvent. Microanalyses for C, H and N were performed by Mrs. L. Michels (University of Würzburg) on a Vario Micro instrument (Elementar Analysensysteme). Starting materials were prepared according to literature procedures: $Li[W(\eta^5\text{-}C_5H_5)(CO)_3]$[17] (**1a**), $[(\eta^5\text{-}C_5Me_5)(OC)_3WCl]$,[18] $[(\eta^5\text{-}C_5H_5)(OC)_3WSnMe_3]$[1b] (**6**) and $[(MeCN)_3W(CO)_3]$.[19] The reagents $Me_2GeCl_2$ (**2a**), $Me_2SnCl_2$ (**2b**), $SnCl_4$ and $Bu_2SnCl_2$ (**2c**) were purchased from commercial sources and not further purified prior use.

### Preparation of Starting Material

#### 1. $Li[W(\eta^5\text{-}C_5Me_5)(CO)_3]$ (1b)

#### Lithium Tricarbonyl(pentamethylcyclopentadienyl)tungstate

A solution of 1.80 g (4.45 mmol) of $(\eta^5\text{-}C_5Me_5)(OC)_3WH$ in 15 mL $Et_2O$ was treated with 2.09 mL (5.35 mmol) of BuLi (2.5 M) at 0 °C. The color of the solution changed from yellow to brown and after 15 min **1b** started to precipitate. The mixture was stirred for 1.5 h at ambient temperature. After reaction the precipitate consisting of

 © 2007 Wiley-VCH Verlag GmbH & Co. KGaA, Weinheim 

**1b** was filtered off, washed twice with 10 mL of hexane and finally dried in vacuo. Yield 1.64 g (4.01 mmol; 90%). Pale brown, pyrophoric powder. Elemental analysis was not carried out due to the pyrophoric behaviour of **1b**.

**2. [(η$^5$-$C_5Me_5$)($Ph_3P$)$(OC)_2$WCl] (9)**

**Dicarbonyl(chloro)(η$^5$-pentamethylcyclopentadienyl)(triphenylphosphanyl)tungsten(II)**

A solution of 3.20 g (7.30 mmol) of [(η$^5$-$C_5Me_5$)$(OC)_3$WCl] and 1.91 g (7.30 mmol) $PPh_3$ in 10 mL benzene in was irradiated with UV light for 5 d. The solvent was removed in vacuo, the crude residue washed with 20 mL hexane and the product dried in vacuo. Yield 4.11 g (6.11 mmol, 84%). Orange powder. $^1$H NMR (300.4 MHz, $C_6D_6$): $\delta$ = 7.62–7.52 (m, 6 H, Ph), 7.08–6.98 (m, 9 H, Ph), 1.65 (s, 15 H, $C_5Me_5$) ppm. $^{13}$C{$^1$H} NMR (75.5 MHz, $C_6D_6$): $\delta$ = 250.75 (d, $^2J_{CWP}$ = 18.5 Hz, *cis*-CO), 237.99 (d, $^2J_{CWP}$ = 7.3 Hz, *trans*-CO), 135.85 (d, $^1J_{CP}$ = 47.4 Hz, *ipso*-$C_6H_5$), 132.28 (d, $^3J_{CCCP}$ = 10.1 Hz, *meta*-$C_6H_5$), 130.95 (d, $^4J_{CCCCP}$ = 2.4 Hz, *para*-$C_6H_5$), 128.69 (d, $^2J_{CCP}$ = 9.0 Hz, *ortho*-$C_6H_5$), 112.80 (d, $^2J_{CWP}$ = 1.2 Hz, $H_3CC_5$), 11.00 (s, $H_3CC_5$) ppm. $^{31}$P{$^1$H} NMR (121.5 MHz, $C_6D_6$): $\delta$ = 26.57 (s, $^1J_{PW}$ = 274.6 Hz) ppm. IR ($Et_2O$): $\tilde{\nu}$(C=O) = 1947 (vs), 1870 (m) cm$^{-1}$. $C_{30}H_{30}ClO_2PW$ (672.82): calcd. C 53.55, H 4.49; found C 53.68, H 4.66.

**3. Na[W(η$^5$-$C_5Me_5$)$(CO)_2(PPh_3)$] (1c)**

**Sodium Dicarbonyl(η$^5$-pentamethylcyclopentadienyl)(triphenylphosphanyl)tungstate**

Na amalgam was prepared by dissolving 0.28 g (12.22 mmol) sodium in 50 g mercury. 35 mL THF were added and then 4.11 g (6.10 mmol) of [(η$^5$-$C_5Me_5$)$(Ph_3P)(OC)_2$WCl] (**9**). The reaction mixture was stirred for 18 h at ambient temperature. The suspension was separated from the sodium amalgam and the solvents evaporated to dryness. The crude solid was washed with three 10 mL portions of hexane and dried in vacuo. Yield 3.75 g (5.67 mmol, 93%). Yellow-green, pyrophoric powder. $^1$H NMR (300.4 MHz, [D$_8$]THF): $\delta$ = 7.84–7.82 (m, 6 H, Ph), 7.13–7.02 (m, 9 H, Ph), 1.89 (s, $^4J_{HCCWP}$ = 29.4 Hz, 5 H, Cp) ppm. $^{31}$P{$^1$H} NMR (121.5 MHz, $C_6D_6$): $\delta$ = 31.44 (s, $^1J_{PW}$ = 278.9 Hz) ppm. IR (THF): $\tilde{\nu}$(C=O) = 1780 (s), 1729 (s) cm$^{-1}$. $C_{30}H_{30}NaO_2PW$ (660.36). Elemental analysis was not carried out due to the pyrophoric behaviour of **1c**.

**Preparation of Germyl and Stannyl Tungsten Complexes**

**1. [(η$^5$-$C_5H_5$)$(OC)_3$W($SnMe_2$Cl)] (3a)**

**Tricarbonyl(chlorodimethylstannyl)(η$^5$-cyclopentadienyl)tungsten(II)**

To a suspension of 635 mg (1.87 mmol) of Li[W($C_5H_5$)$(CO)_3$] (**1a**) in 10 mL diethyl ether were added 411 mg (1.87 mmol) of $Me_2SnCl_2$ and the mixture was stirred at ambient temperature overnight. The solvent was removed in vacuo and the residue was extracted with of hexane (3 × 10 mL). The combined extracts were filtered through celite and the filtrate was evaporated to dryness. Yield 793 mg (1.53 mol, 72%). Dark yellow powder. M.p. 91 °C. $^1$H NMR (300 MHz, $C_6D_6$): $\delta$ = 4.52 (s, 5 H, Cp), 0.87 (s, $^2J_{HCSn}$ = 47.3, 45.3 Hz, 6 H, $SnMe_2$) ppm. $^{13}$C{$^1$H} NMR (75.5 MHz, $C_6D_6$): $\delta$ = 89.04 (s, Cp), 2.99 (s, $SnMe_2$) ppm. $^{119}$Sn{$^1$H} NMR (111.9 MHz, $C_6D_6$): $\delta$ = 227 (s) ppm. IR (hexane): $\tilde{\nu}$(C=O) = 2010 (m), 1940 (m), 1911 (m) cm$^{-1}$. $C_{10}H_{11}ClO_3SnW$ (517.20): calcd. C 23.22, H 2.14; found C 23.44, H 2.24.

**2. [(η$^5$-$C_5H_5$)$(OC)_3$W($SnBu_2$Cl)] (3b)**

**(Dibutylchlorostannyl)(tricarbonyl)(η$^5$-cyclopentadienyl)tungsten(II)**

Similar to paragraph **1.** above, from 570 mg (1.68 mmol) of Li[W($C_5H_5$)$(CO)_3$] (**1a**) and 380 mg (1.25 mmol) of $Bu_2SnCl_2$ in 10 mL diethyl ether. The mixture was stirred at ambient temperature overnight. The ether was removed under reduced pressure and the oily residue was extracted with pentane (3 × 10 mL). The combined extracts were filtered through celite and the filtrate was evaporated to dryness. The sticky residue was washed with ice-cold pentane (3 × 2 mL) and was dried in vacuo. Yield 526 mg (0.88 mol, 70%). Dark yellow powder. M.p. 74 °C. $^1$H NMR (300 MHz, $C_6D_6$): $\delta$ = 4.82 (s, 5 H, Cp), 1.91–1.73 (m, 8 H, $CH_2$-$CH_2$), 1.55–1.52 (m, 4 H, $SnCH_2$), 1.05 (t, 6 H, $CH_3$) ppm. $^{13}$C{$^1$H} NMR (75.5 MHz, $C_6D_6$): $\delta$ = 88.43 (s, Cp), 31.64 (s, $CH_2$), 27.40 (s, $CH_2$), 19.24 (s, $CH_2$), 13.69 (s, $CH_3$) ppm. $^{119}$Sn{$^1$H} NMR (111.9 MHz, $C_6D_6$): $\delta$ = 26.7 (s, $^1J_{SnW}$ = 162.8 Hz) ppm. IR (hexane): $\tilde{\nu}$(C=O) = 1999 (m), 1981 (m) cm$^{-1}$. $C_{16}H_{23}ClO_3SnW$ (601.35): calcd. C 31.96, H 3.86; found C 32.29, H 3.99.

**3. [(η$^5$-$C_5Me_5$)$(OC)_3$W($GeMe_2$Cl)] (3c)**

**Tricarbonyl(chlorodimethylgermyl)(η$^5$-pentamethylcyclopentadienyl)tungsten(II)**

0.52 g (1.27 mmol) of Li[W(η$^5$-$C_5Me_5$)$(CO)_3$] (**1b**) were suspended in 10 mL $Et_2O$ and treated with 0.18 mL (1.27 mmol, 0.22 g) of $Me_2GeCl_2$. The reaction mixture was stirred for 22 h at ambient temperature. After reaction LiCl was filtered off by use of a celite pad. The filtrate was evaporated to dryness giving a dark brown residue which was washed with 3 mL hexane at –40 °C and dried in vacuo. Yield 0.56 g (81%). Brown solid, m.p. 62 °C. $^1$H NMR (200.1 MHz, $C_6D_6$): $\delta$ = 1.71 [s, 15 H, $C_5(CH_3)_5$], 1.17 [s, 6 H, $Ge(CH_3)_2$] ppm. $^{13}$C{$^1$H} NMR (75.5 MHz, $C_6D_6$): $\delta$ = 217.95 (s, CO-*trans*), 202.29 (s, CO-*cis*), 102.52 (s, $C_5Me_5$), 28.67 [s, Ge-($CH_3$)$_2$], 9.00 [s, $C_5(CH_3)_5$] ppm. IR (hexane): $\tilde{\nu}$(C=O) = 2003 (s), 1931 (s), 1907 (s) cm$^{-1}$. $C_{15}H_{21}ClGeO_3W$ (541.23): calcd. C 33.29, H 3.91; found C 32.62, H 3.81.

**4. [(η$^5$-$C_5Me_5$)$(OC)_3$W($SnMe_2$Cl)] (3d)**

**Tricarbonyl(chlorodimethylstannyl)(η$^5$-pentamethylcyclopentadienyl)tungsten(II)**

To a suspension of 0.66 g (1.16) of Li[W(η$^5$-$C_5Me_5$)$(OC)_3$] (**1b**) in 20 mL $Et_2O$ were added 0.36 g (1.64 mmol) of $Me_2SnCl_2$ and the reaction mixture stirred for 17 h at ambient temperature. After reaction LiCl was filtered off over celite and the filtrate evaporated to dryness. The crude brown product was washed with 5 mL of hexane at –40 °C and dried in vacuo. Yield 0.80 g (85%). Ochre solid, m.p. 122 °C. $^1$H NMR (200.1 MHz, $C_6D_6$): $\delta$ = 1.70 (s, 15 H, $C_5Me_5$), 0.91 [s, $^2J_{HCSn}$ = 42.5 and 44.4 Hz, 6 H, $(H_3C)_2Sn$] ppm. $^{13}$C{$^1$H} NMR (125.8 MHz, $C_6D_6$): $\delta$ = 220.89 (s, CO-*trans*), 217.87 (s, CO-*cis*), 103.70 (s, $C_5Me_5$), 10.71 [s, $C_5(CH_3)_5$], 2.48 [s, $^1J_{CSn}$ = 245.5 and 259.9 Hz, $Sn(CH_3)_2$] ppm. $^{119}$Sn NMR (186.5 MHz, $C_6D_6$): $\delta$ = 233.04 [s, $^1J_{WSn}$ = 347.0 Hz] ppm. IR (hexane): $\tilde{\nu}$(C=O) = 1901 (s), 1927 (s), 1997 (s) cm$^{-1}$. $C_{15}H_{21}ClO_3SnW$ (587.33): calcd. C 30.67, H 3.60; found C 30.34, H 3.67.

**5. [(η$^5$-$C_5Me_5$)$(OC)_2(Ph_3P)$W($SnMe_2$Cl)] (3e) and {[(η$^5$-$C_5Me_5$)-$(OC)_2(Ph_3P)$W]$_2$($SnMe_2$)} (4)**

**Dicarbonyl(trimethylstannyl)(η$^5$-pentamethylcyclopentadienyl)(triphenylphosphanyl)tungsten(II)**

600 mg (0.83 mmol) of Na[W(η$^5$-$C_5Me_5$)$(OC)_2(PPh_3)$] (**1c**) were suspended in 20 mL $Et_2O$ and treated with 183 mg (0.83 mmol) of $Me_2SnCl_2$. The reaction mixture was stirred for 16 h at ambient temperature and NaCl filtered through by use of a celite pad. The filtrate was evaporated to dryness and the residue consisting of **3e** and **4** extracted with 25 mL of hexane. **3e** dissolves readily in hexane whereas **4** remains as an yellow solid which was dried in vacuo. The combined hexane extracts were concentrated and crystallized at –30 °C. The hexane phase was separated and the solid dried in

 © 2007 Wiley-VCH Verlag GmbH & Co. KGaA, Weinheim 

vacuo. **3e**: Yield 340 mg (0.42 mmol, 51%). Yellow solid, m.p. 87 °C. $^1$H NMR (200.13 MHz, $C_6D_6$): $\delta$ = 7.68–7.43 (m, 6 H, Ph), 7.09–6.93 (m, 9 H, Ph), 1.68 (s, 15 H, $Me_5C_5$), 1.05 [s, $^2J_{HCSn}$ = 40.2 and 41.8 Hz, 6 H, MeSn] ppm. $^{13}$C{$^1$H} NMR (75.5 MHz, $C_6D_6$): $\delta$ = 230.06 [d, $^2J_{CP}$ = 132.3 Hz, CO], 134.54 [d, $^1J_{CP}$ = 46.6 Hz, *ipso*-$C_6H_5$], 134.29 [d, $^1J_{CP}$ = 10.0 Hz, *meta*-$C_6H_5$], 130.53 [d, $^3J_{CCCP}$ = 2.4 Hz, *para*-$C_6H_5$], 128.56 [d, $^2J_{CCP}$ = 9.9 Hz, *ortho*-$C_6H_5$], 101.16 [s, $^1J_{CW}$ = 5.4 Hz, $C_5Me_5$], 11.25 (s, $C_5Me_5$), 2.88 (s, $CH_3Sn$) ppm. $^{31}$P{$^1$H} NMR (121.5 MHz, $C_6D_6$): $\delta$ = 38.61 [s, $^1J_{PW}$ = 293.6, $^2J_{PWSn}$ = 128.8 und 123.9 Hz] ppm. $^{119}$Sn{$^1$H} NMR (300.13 MHz, $C_6D_6$): $\delta$ = 233.80 [d, $^2J_{SnWP}$ = 132.1 Hz] ppm. IR ($Et_2O$): $\tilde{\nu}$(C=O) = 1904 (vs), 1835 (vs) cm$^{-1}$. $C_{32}H_{36}ClO_2PSnW$ (821.60): calcd. C 46.78, H 4.42; found C 46.67, H 4.25.

**4**: Yield 138 mg (0.11 mmol, 13%). Yellow solid, m.p. 123 °C. $^1$H NMR (300.4 MHz, $C_6D_6$): $\delta$ = 7.68–7.43 (m, 6 H, Ph), 7.09–6.93 (m, 9 H, Ph), 1.78 (s, 30 H, $Me_5C_5$), 0.91 [d, $^4J_{HCSnWP}$ = 1.2, $^2J_{HCSn}$ = 44.0 and 48.0 Hz, 6 H, $H_3CSn$] ppm. $^{31}$P{$^1$H} NMR (121.5 MHz, $C_6D_6$): $\delta$ = 44.50 [s, $^1J_{PW}$ = 267.3, $^2J_{PWSn}$ = 130.8 und 125.4 Hz] ppm. IR ($Et_2O$): $\tilde{\nu}$(C=O) = 1901 (vs), 1832 (vs) cm$^{-1}$. $C_{52}H_{46}O_4P_2SnW_2$ (1283.26): calcd. C 48.67, H 3.61; found C 48.47, H 4.05.

### 6. $C_5H_5SnMe_2Cl$ (5)

**(Chlorodimethylstannyl)cyclopentadiene**

A suspension of 418 mg (4.75 mmol) of NaCp and 15 mL $Et_2O$ was treated with 1.04 g (4.75 mmol) of $Me_2SnCl_2$. The mixture was stirred for 18 h at ambient temperature and NaCl was removed by filtration through a celite pad. The filtrate was evaporated under reduced pressure (70 mbar) at ambient temperature. Yield 1.00 g (4.01 mmol, 84%). Yellow oil. $^1$H NMR (200.1 MHz, $C_6D_6$): $\delta$ = 5.99 (s, $^3J_{HCCSn}$ = 30.0 and 29.0 Hz, 5 H, $C_5H_5$), 0.03 [s, $^2J_{HCSn}$ = 59.2 and 56.8 Hz, 6 H, $(H_3C)_2Sn$] ppm. $^{13}$C{$^1$H} NMR (125.8 MHz, $C_6D_6$): $\delta$ = 114.91 (s, $^1J_{CSn}$ = 96.8 Hz, $C_5H_5Sn$), –2.96 [s, $(H_3C)_2Sn$] ppm. $^{119}$Sn NMR (186.5 MHz, $C_6D_6$): $\delta$ = 101.45 (s) ppm. $C_7H_{11}ClSn$ (249.32): calcd. C 33.72, H 4.45; found C 33.34, H 4.67.

### 7. $[(\eta^5\text{-}C_5H_5)(OC)_3W(SnMe_2Cl)]$ (3a) by Reaction of 5 with $[(MeCN)_3W(CO)_3]$

A suspension of 450 mg (1.80 mmol) of $C_5H_5SnMe_2Cl$ (**5**), 704 mg (1.80 mmol) of $[(MeCN)_3W(CO)_3]$ and 10 mL THF was refluxed over the period of 18 h. After cooling to room temperature, all volatiles were removed in vacuo and the residue was extracted with hexane (3 × 10 mL). The hexane extracts were combined and filtered through a celite pad. The filtrate was concentrated and stored at –70 °C over the period of one week. The hexane phase was removed and the solid dried in vacuo. Yield 837 mg (1.62 mmol, 90%). Yellow solid.

### 8. $[(\eta^5\text{-}C_5H_5)(OC)_3W(SnMe_2Cl)]$ (3a) by Reaction of 6 with $SnCl_4$

A solution of 270 mg (0.54 mmol) of $[(\eta^5\text{-}C_5H_5)(OC)_3W(SnMe_3)]$ (**6**) in 5 mL benzene was treated with 142 mg (0.54 mmol) of $SnCl_4$ and the mixture was stirred at ambient temperature for 2 h. All volatiles were removed in vacuo and the residue was extracted with hexane (3 × 19 mL). The combined extracts were filtered through celite and the filtrate was evaporated to dryness. Yield 258 mg (0.50 mmol, 92%). Dark yellow powder.

### 9. $[(\eta^5\text{-}C_5H_5)(OC)_3W(SnMeCl_2)]$ (7) by Reaction of 3a with $SnCl_4$

**Tricarbonyl(dichloromethylstannyl)($\eta^5$-cyclopentadienyl)tungsten(II)**

A solution of 258 mg (0.50 mmol) of $[(\eta^5\text{-}C_5H_5)(OC)_3W\text{-}(SnMe_2Cl)]$ (**3a**) in 5 mL diethyl ether was treated slowly with 131 mg (0.50 mmol) of $SnCl_4$ at 0 °C and the mixture was stirred at ambient temperature for 2 h. All volatiles were removed in vacuo and the residue was extracted with $Et_2O$ (2 × 10 mL). The combined extracts were filtered through celite and the filtrate was evaporated to dryness. Yield 237 mg (0.44 mmol, 88%). Yellow powder. M.p. 189 °C. $^1$H NMR (300 MHz, $C_6D_6$): $\delta$ = 4.49 (s, 5 H, Cp), 1.11 (s, $^2J_{HCSn}$ = 46.2, 45.2 Hz, 3 H, $SnMe_2$) ppm. $^{13}$C{$^1$H} NMR

Table 2. Crystal data and refinement parameters for the compounds **3b**–**d** and **8**.

| Compound | **3b** | **3c** | **3d** | **8** |
|---|---|---|---|---|
| Empirical formula | $C_{16}H_{23}ClO_3SnW$ | $C_{15}H_{21}ClGeO_3W$ | $C_{15}H_{21}ClO_3SnW$ | $C_8H_5Cl_3O_3SnW$ |
| Formula weight (g mol$^{-1}$) | 601.33 | 541.21 | 587.31 | 558.01 |
| Temperature [K] | 100(2) | 193(2) | 173(2) | 97(2) |
| Radiation, $\lambda$ [Å] | 0.71073 (Mo-$K_\alpha$) | | | |
| Crystal system | triclinic | monoclinic | monoclinic | triclinic |
| Space group | $P\bar{1}$ | $P2_1/c$ | $C2/c$ | $P\bar{1}$ |
| Unit cell dimensions | | | | |
| $a$ [Å] | 7.8200(6) | 8.2325(5) | 30.036(3) | 7.7851(3) |
| $b$ [Å] | 11.4910(9) | 25.4316(15) | 8.3148(7) | 8.2946(3) |
| $c$ [Å] | 21.0814(16) | 9.4108(6) | 17.7603(15) | 11.1925(4) |
| $\alpha$ [°] | 79.768(3) | 90.00 | 90.00 | 93.7950(10) |
| $\beta$ [°] | 89.533(3) | 111.8140(10) | 122.8430(10) | 108.7020(10) |
| $\gamma$ [°] | 89.927(3) | 90.00 | 90.00 | 108.2510(10) |
| Volume [Å$^3$] | 1864.2(2) | 1829.21(19) | 3726.6(5) | 638.90(4) |
| $Z$ | 4 | 4 | 8 | 2 |
| Calculated density (g cm$^{-3}$) | 2.143 | 1.965 | 2.094 | 2.901 |
| Absorbtion coefficient [mm$^{-1}$] | 7.657 | 8.078 | 7.658 | 11.563 |
| $F$(000) | 1136 | 1032 | 2208 | 504 |
| Theta range for collection | 0.98 to 31.95° | 2.46 to 26.08° | 2.30 to 26.39° | 1.95 to 26.08° |
| Reflections collected | 88054 | 3624 | 24318 | 15287 |
| Independent reflections | 11465 | 3481 | 6061 | 2513 |
| Refinement method | Full-matrix last-squares on $F^2$ | | | |
| Data/parameters | 11465 –397/6 | 3624/190 | 3826/190 | 2513/145 |
| Goodness-of-fit on $F^2$ | 1.138 | 1.170 | 1.096 | 1.088 |
| Final $R$ indices [$I > 2\sigma(I)$] | $R_1$ = 0.0497, $wR_2$ = 0.1287 | $R_1$ = 0.0205, $wR_2$ = 0.0509 | $R_1$ = 0.0198, $wR_2$ = 0.0462 | $R_1$ = 0.0234, $wR_2$ = 0.0605 |
| R Indices (all data) | $R_1$ = 0.0532, $wR_2$ = 0.1342 | $R_1$ = 0.0217, $wR_2$ = 0.0514 | $R_1$ = 0.0215, $wR_2$ = 0.0469 | $R_1$ = 0.0238, $wR_2$ = 0.0608 |

 © 2007 Wiley-VCH Verlag GmbH & Co. KGaA, Weinheim 

(75.5 MHz, $C_6D_6$): $\delta$ = 215.16 (s, *trans*-CO), 211.89 (s, $^1J_{CW}$ = 144.6 Hz, *cis*-CO), 89.91 (s, $^1J_{CW}$ = 4.9 Hz, Cp), 11.46 (s, $^1J_{CSn}$ = 7.7 Hz, MeSn) ppm. $^{119}Sn\{^1H\}$ NMR (111.9 MHz, $C_6D_6$): $\delta$ = 198.88 (s, $^1J_{WSn}$ = 596.8 Hz) ppm. $C_9H_8Cl_2O_3SnW$ (537.61): calcd. C 20.11, H 1.50; found C 20.03, H 1.80.

**10. [($\eta^5$-$C_5H_5$)(OC)$_3$W(SnMeCl$_2$)] (7) by Reaction of 6 with 2 Equiv. of $SnCl_4$**

Analogously to paragraph 9., from 320 mg (0.64 mmol) of [($\eta^5$-$C_5H_5$)(OC)$_3$W(SnMe$_3$)] (**6**) and 335 mg (1.28 mmol) of $SnCl_4$ in 10 mL diethyl ether over the period of 4 h. Yield 242 mg (0.45 mol, 90%). Yellow powder.

**11. [($\eta^5$-$C_5H_5$)(OC)$_3$W(SnCl$_3$)] (8) by Reaction of 7 with $SnCl_4$ (ex.)**

**Tricarbonyl(trichlorostannyl)($\eta^5$-cyclopentadienyl)tungsten(II)**

To a suspension of 266 mg (0.49 mmol) of [($\eta^5$-$C_5H_5$)(OC)$_3$W(SnMeCl$_2$)] (**7**) in 10 mL chloroform were added 1.28 mg (4.90 mmol) of $SnCl_4$ and the mixture was heated and stirred under reflux over the period of 6 d. All insoluble material was filtered off and the solvent and unreacted $SnCl_4$ were removed in vacuo. The residue was washed with hexane (3 × 10 mL) and the solvents evaporated to dryness. Yield 164 mg (0.29 mol, 60%). Yellow powder. M.p. 91 °C. $^1H$ NMR (300 MHz, $CDCl_3$): $\delta$ = 5.77 (s, $^3J_{HCWSn}$ = 3.4 Hz, 5 H, Cp) ppm. $^{13}C\{^1H\}$ NMR (75.5 MHz, $CDCl_3$): $\delta$ = 89.17 (s, Cp) ppm. $^{119}Sn\{^1H\}$ NMR (111.9 MHz, $CDCl_3$): $\delta$ = –89.4 (s) ppm. $C_8H_5Cl_3O_3SnW$ (558.03): calcd. C 17.22, H 0.90; found C 17.44, H 1.24.

**12. [($\eta^5$-$C_5H_5$)(OC)$_3$W(SnCl$_3$)] (8) by Reaction of 6 with $SnCl_4$ (ex.)**

**Tricarbonyl(trichlorostannyl)($\eta^5$-cyclopentadienyl)tungsten(II)**

Analogously to paragraph 11., from 326 mg (0.60 mmol) of [($\eta^5$-$C_5H_5$)(OC)$_3$W(SnMe$_3$)] (**6**) and 1.28 mg (4.90 mmol) of $SnCl_4$ in 15 mL chloroform over the period of 6 d. Yield 148 mg (0.26 mol, 55%). Yellow powder.

**Crystal Structure Determination:** The crystal data of **3b**–**d** and **8** (Table 2) were collected with a Bruker Apex2 diffractometer with a CCD area detector and multi-layer mirror monochromated Mo-$K_\alpha$ radiation. The structures were solved by direct methods, refined with the Shelx software package (G. Sheldrick, University of Göttingen, 1997) and expanded using Fourier techniques. All non-hydrogen atoms were refined anisotropically. Hydrogen atoms were assigned idealized position and were included in structure factor calculations.

CCDC-644418 (for **3b**), -636078 (for **3c**), -636079 (for **3d**) and -640077 (for **8**) contain the supplementary crystallographic data for this paper. These data can be obtained free of charge from The Cambridge Crystallographic Data Centre via www.ccdc.cam.ac.uk/data_request/cif.

## Acknowledgments

We thank Deutsche Forschungsgemeinschaft (DFG) and Fonds der Chemischen Industrie (FCI) for financial support.

[1] a) D. J. Cardin, S. A. Keppie, M. F. Lappert, *Inorg. Nucl. Chem. Lett.* **1968**, *4*, 365; b) H. R. H. Patil, W. A. G. Graham, *Inorg. Chem.* **1966**, *5*, 1401; c) F. Bonati, G. Wilkinson, *J. Chem. Soc.* **1964**, 179.

[2] M. S. Holt, W. L. Wilson, J. H. Nelson, *Chem. Rev.* **1989**, *89*, 11.

[3] a) T. Szymanska-Buzar, T. Gtowiak, *Polyhedron* **1998**, *17*, 3419; b) L. Benczene, G. Szalai, T. L. Overton, *Inorg. Chim. Acta* **1997**, *254*, 5; c) T. Szymanska-Buzar, T. Gtowiak, *J. Organomet. Chem.* **1995**, *489*, 207; d) P. K. Baker, *Adv. Organomet. Chem.* **1996**, *40*, 45.

[4] R. E. J. Bichler, H. C. Clark Hunter, A. T. Rake, *J. Organomet. Chem.* **1974**, *69*, 367.

[5] a) J. Cervantes, St. P. Vincenti, R. N. Kapoor, K. H. Pannell, *Organometallics* **1989**, *8*, 744; b) W. K. Dean, W. A. G. Graham, *Inorg. Chem.* **1977**, *16*, 1061.

[6] J. L. Neto, G. M. Lima, A. O. Porto, J. D. Ardisson, A. C. Doriguetto, J. Ellena, *J. Mol. Struct.* **2006**, *782*, 110.

[7] L.-F. Tang, X.-M. Zhao, Z.-H. Zou, H.-B. Song, Y.-P. Zhai, *J. Organomet. Chem.* **2005**, *690*, 4142.

[8] For reviews seea) H. Braunschweig, C. Kollann, D. Rais, *Angew. Chem.* **2006**, *118*, 5380; *Angew. Chem. Int. Ed.* **2006**, *45*, 5254; b) H. Braunschweig, *Adv. Organomet. Chem.* **2004**, *51*, 163; c) H. Braunschweig, M. Colling, *Eur. J. Inorg. Chem.* **2003**, 393; d) H. Braunschweig, M. Colling, *Coord. Chem. Rev.* **2001**, *223*, 1; e) H. Braunschweig, *Angew. Chem.* **1998**, *110*, 1882; *Angew. Chem. Int. Ed.* **1998**, *37*, 1786. For selected examples on the reactivity of metal bound boron halides see:; f) H. Braunschweig, K. Radacki, F. Seeler, G. R. Whittell, *Organometallics* **2006**, *25*, 4605; g) H. Braunschweig, K. Radacki, D. Rais, D. Scheschkewitz, *Angew. Chem.* **2005**, *117*, 5796; *Angew. Chem. Int. Ed.* **2005**, *44*, 5651; h) H. Braunschweig, K. Radacki, D. Rais, F. Seeler, K. Uttinger, *J. Am. Chem. Soc.* **2005**, *127*, 1386; i) H. Braunschweig, K. Radacki, D. Rais, G. R. Whittell, *Angew. Chem.* **2005**, *117*, 1217; *Angew. Chem. Int. Ed.* **2005**, *44*, 1192; j) H. Braunschweig, M. Müller, *Chem. Ber./Recueil* **1997**, *130*, 1295.

[9] a) H. Braunschweig, H. Bera, D. Götz, K. Radacki, *Z. Naturforsch., Teil B* **2006**, *61*, 29; b) H. Braunschweig, M. Koster, K. W. Klinkhammer, *Angew. Chem.* **1999**, *111*, 2368; *Angew. Chem. Int. Ed.* **1999**, *38*, 2229; c) H. Braunschweig, M. Koster, R. Wang, *Inorg. Chem.* **1999**, *38*, 415; d) H. Braunschweig, B. Ganter, M. Koster, T. Wagner, *Chem. Ber.* **1996**, *129*, 1099.

[10] T. A. George, C. D. Turnipsed, *Inorg. Chem.* **1973**, *12*, 394.

[11] L.-F. Tang, J.-F. Chai, Zh.-H. Hong, W.-L. Jia, J.-T. Wang, *Polyhedron* **2001**, *20*, 403.

[12] a) A. C. Filippou, J. G. Winter, M. Feist, G. Kociok-Köhn, I. Hinz, *Polyhedron* **1998**, *17*, 1103; b) A. C. Filippou, J. G. Winter, M. Feist, G. Kociok-Köhn, C. Troll, I. Hinz, *Organometallics* **1999**, *18*, 2649.

[13] J.-T. Wang, H.-Y. He, Y.-M. Xu, J. Sun, X.-F. Kong, *Heteroat. Chem.* **1998**, *9*, 169.

[14] a) K. D. Bos, E. J. Bulten, J. G. Noltes, *J. Organomet. Chem.* **1974**, *67*, C13; b) V. N. Torocheshnikov, A. P. Tupciauskas, Y. A. Ustynyuk, *J. Organomet. Chem.* **1974**, *81*, 351.

[15] a) S. A. Keppie, M. F. Lappert, *J. Chem. Soc. A* **1971**, 3216; b) E. W. Abel, S. A. Keppie, M. F. Lappert, *J. Organomet. Chem.* **1970**, *22*, C31; c) S. A. Keppie, M. F. Lappert, *J. Organomet. Chem.* **1969**, *19*, P5.

[16] a) H. Willemen, L. F. Wuyts, D. F. Van der Vondel, G. P. Van der Kelen, *J. Electron Spectrosc. Relat. Phenom.* **1977**, *11*, 245; b) F. Bonati, S. Cenini, R. Ugo, *J. Chem. Soc. A* **1967**, 932.

[17] W. Baumann, W. Malisch, *J. Organomet. Chem.* **1986**, *303*, C33.

[18] Th. Straub, M. Haukka, M. Brunner, A. M. P. Koskinen, T. A. Pakkanen, *J. Organomet. Chem.* **2005**, *690*, 674–677.

[19] F. Edelmann, P. Behrens, S. Behrens, U. Behrens, *J. Organomet. Chem.* **1986**, *310*, 333.

Received: March 15, 2007
Published Online: June 6, 2007

 © 2007 Wiley-VCH Verlag GmbH & Co. KGaA, Weinheim 

DOI: 10.1002/ejic.200700143

# Synthesis and Spectro-electrochemical Aspects of $[Ru^{II}(trpy)(pdt)(X)]^{n+}$ (trpy = 2,2′:6′,2′′-Terpyridine, pdt = 5,6-Diphenyl-3-pyridyl-*as*-triazine, X = $Cl^-$, $CH_3CN$, $NO_2^-$, $NO^+$, $NO^·$) – Electrophilicity of $\{Ru^{II}–NO^+\}$ and Photolability of $\{Ru^{II}–NO^·\}$

**Somnath Maji,[a] Chandrani Chatterjee,[a] Shaikh M. Mobin,[a] and Goutam Kumar Lahiri*[a]**

**Keywords:** Ruthenium / Nitrosyl complexes / Spectroscopy / Electrochemistry / Reactivity

Nitrosylruthenium derivatives having $NO^+$ and $NO^·$ states have been synthesized in a stepwise manner starting from $[Ru^{II}(trpy)(pdt)(Cl)](ClO_4)$ $\{[\mathbf{1}](ClO_4)\}$ → $[Ru^{II}(trpy)(pdt)(CH_3CN)](ClO_4)_2$ $\{[\mathbf{2}](ClO_4)_2\}$ → $[Ru^{II}(trpy)(pdt)(NO_2)](ClO_4)$ $\{[\mathbf{3}](ClO_4)\}$ → $[Ru^{II}(trpy)(pdt)(NO^+)](ClO_4)_3$ $\{[\mathbf{4}](ClO_4)_3\}$ → $[Ru^{II}(trpy)(pdt)(NO^·)](ClO_4)_2$ $\{[\mathbf{4}](ClO_4)_2\}$ [trpy = 2,2′:6′,2′′-terpyridine, pdt = 5,6-diphenyl-3-pyridyl-*as*-triazine]. The molecular identity of $[\mathbf{1}](ClO_4)$ and $[\mathbf{2}](ClO_4)_2$ and the subsequent stereoretentive transformation of $[\mathbf{1}](ClO_4)$ → $[\mathbf{2}](ClO_4)_2$ have been authenticated by single-crystal X-ray structures. Electrochemical and spectral features are investigated as a function of the monodentate ligands ($Cl^-$, $CH_3CN$, $NO_2^-$, $NO^+$, $NO^·$). The kinetic and thermodynamic aspects of the reaction of the moderately strong electrophilic $\{Ru^{II}–NO^+\}$ center [$\nu$(NO): 1944 $cm^{-1}$] in $[\mathbf{4}]^{3+}$ with a nucleophile such as $OH^-$ have been studied. The nitrosyl species $[Ru^{II}(trpy)(pdt)(NO^+)]^{3+}$ ($[\mathbf{4}]^{3+}$) can be selectively reduced to $[Ru^{II}(trpy)(pdt)(NO^·)]^{2+}$ ($[\mathbf{4}]^{2+}$) electrochemically as well as chemically by hydrazine hydrate. On exposure to light an acetonitrile solution of $[Ru^{II}(trpy)(pdt)(NO^·)]^{2+}$ ($[\mathbf{4}]^{2+}$) undergoes slow photocleavage of the $Ru^{II}–NO$ bond over a period of 4 h, resulting in the corresponding solvated species $[Ru^{II}(trpy)(pdt)(CH_3CN)]^{2+}$ ($[\mathbf{2}]^{2+}$). The rate of photolability of the $Ru^{II}–NO$ bond in $[\mathbf{4}]^{2+}$ has been monitored spectrophotometrically.
(© Wiley-VCH Verlag GmbH & Co. KGaA, 69451 Weinheim, Germany, 2007)

## Introduction

The biological[1] and environmental[2] relevance of the nitrosyl molecule has led to a resurgence of interest in the metal–NO interaction. This is primarily due to fundamental issues such as (i) bonding and redox features,[3] (ii) reactivity profile of metal-bound NO function with a variety of nucleophiles,[4] (iii) uses of nitrosylmetal derivatives as antitumor and antiseptic agents,[5] and (iv) photolytic cleavage of the M–NO bond and subsequent transfer of photoreleased "NO" to the biological targets such as myoglobin (Mb) or cytochrome c oxidase.[6]

The stability of possible redox states of the nitrosyl molecule, $NO^+$, $NO^·$, and $NO^-$, in the complex framework of (AL)M–NO depends on a variety of factors, including the nature of the metal ions and the ancillary ligands (AL). For example, in reduced vitamin $B_{12}$, the cobalt center formally binds with the NO in the form of $Co^{III}–NO^-$,[7] while in metmyoglobin the iron center binds with the NO formally as $Fe^{II}–NO^+$.[8] Similarly, electrophilicity of the coordinated NO center in $\{(AL)(trpy)Ru^{II}–NO\}$ (trpy = 2,2′:6′,2′′-terpyridine) can also be nicely tuned primarily depending on the electronic aspects of AL. Thus, the $\nu_{NO^+}$ frequency as well as the $E°(NO^+/NO^·)$ values systematically vary with AL = 2-phenylpyridine (pp),[9] acetylacetone (acac),[10] *N*-methyl-2-(2-pyridyl)benzimidazole (pNMebi),[11] (2-pyridyl)benzimidazole (pbi),[11] 2,2′-dipyridylamine (dpa),[12] bis(2-pyridyl) ketone (dpk),[13] 2,2′-bipyridine (bpy),[14] 2-(2-pyridyl)benzoxazole (pbo),[11] and 2-(phenylazo)pyridine (pap),[15] as shown in Table 1.

The observed distinct role of AL in the complex framework of $\{(AL)(trpy)Ru^{II}–NO^+\}$ (Table 1) has initiated the selective introduction of 5,6-diphenyl-3-pyridyl-*as*-triazine (pdt) as AL to explore its specific effect towards the stability of coordinated NO in accessible redox states. The ligand pdt has been of interest in the field of coordination chemistry as well as organometallic chemistry since early 1964.[16] However, only a limited number of ruthenium complexes of pdt and its derivatives have been reported so far from different perspectives.[17]

The present article thus describes the stepwise synthetic aspects of the nitrosyl complexes starting from $[Ru^{II}(trpy)(pdt)(Cl)](ClO_4)$ $\{[\mathbf{1}](ClO_4)\}$ → $[Ru^{II}(trpy)(pdt)(CH_3CN)](ClO_4)_2$ $\{[\mathbf{2}](ClO_4)_2\}$ → $[Ru^{II}(trpy)(pdt)(NO_2)](ClO_4)$ $\{[\mathbf{3}](ClO_4)\}$ → $[Ru^{II}(trpy)(pdt)(NO^+)](ClO_4)_3$

[a] Department of Chemistry, Indian Institute of Technology-Bombay,
Powai, Mumbai 400076, India
E-mail: lahiri@chem.iitb.ac.in
Supporting information for this article is available on the WWW under http://www.eurjic.org or from the author.

 © 2007 Wiley-VCH Verlag GmbH & Co. KGaA, Weinheim 

Table 1. $\nu(NO^+)$ frequencies and reduction potentials of $\{Ru^{II}(NO^+)\} \rightarrow \{Ru^{II}(NO^{\cdot})\}$ in $[Ru^{II}(trpy)(AL)(NO^+)]^{n+}$.

Ancillary ligands (AL)

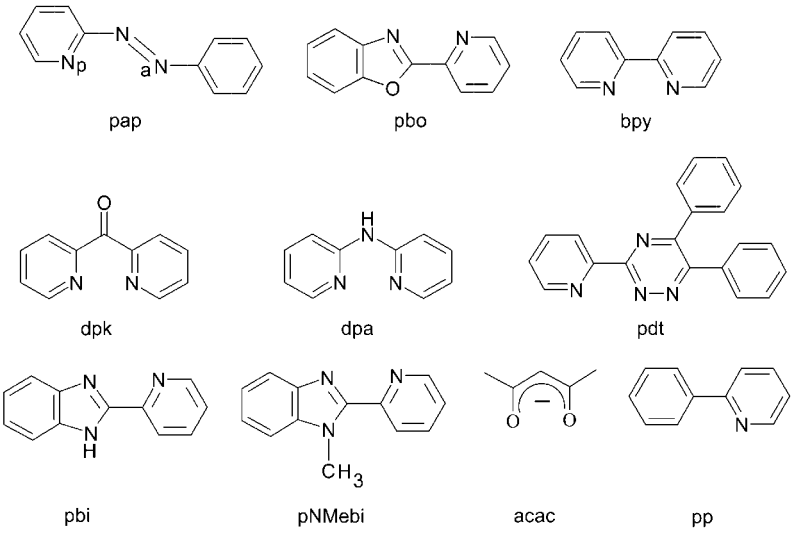


| Ancillary ligand (AL) | $\nu(NO^+)/cm^{-1}$[a] | $E°_{298}/V$[b] | Ref. |
|---|---|---|---|
| pap | 1960 | 0.72 | [15] |
| pbo | 1957 | 0.45 | [11] |
| bpy | 1952 | 0.45 | [14] |
| dpk | 1949 | 0.36 | [13] |
| dpa | 1945 | 0.34 | [12] |
| pdt | 1944 | 0.40 | this work |
| pbi | 1940 | 0.33 | [11] |
| pNMebi | 1932 | 0.31 | [11] |
| acac | 1914 | 0.02 | [10] |
| pp | 1858 | –0.28 | [9] |

[a] In KBr disk. [b] $CH_3CN$/0.1 M $Et_4NClO_4$/SCE.

$\{[\mathbf{4}](ClO_4)_3\} \rightarrow [Ru^{II}(trpy)(pdt)(NO^{\cdot})]^{2+}$ $\{[\mathbf{4}](ClO_4)_2\}$. Crystal structures of $[\mathbf{1}](ClO_4)$ and $[\mathbf{2}](ClO_4)_2$ and spectroelectrochemical features of all four complexes are reported. The reactivity of the ruthenium-bound electrophilic $NO^+$ in $[\mathbf{4}](ClO_4)_3$ in the presence of a nucleophile such as $OH^-$ and the aspects of photolytic cleavage of the $Ru^{II}$–$NO^{\cdot}$ bond in $[\mathbf{4}]^{2+}$ are also investigated.

## Results and Discussion

### Synthesis and Characterization

The precursor chlorido complex $[Ru^{II}(trpy)(pdt)(Cl)]^+$ $[\mathbf{1}]^+$ [trpy = 2,2′:6′,2′′-terpyridine, pdt = 5,6-diphenyl-3-pyridyl-*as*-triazine] has been synthesized from $[Ru(trpy)Cl_3]$ and pdt in the presence of excess $Et_3N$ and LiCl in refluxing EtOH. The crude product was subsequently purified by column chromatography on alumina. The product was isolated as its perchlorate salt $[\mathbf{1}](ClO_4)$. The solvated species $[\mathbf{2}](ClO_4)_2$ and the nitro derivative $[\mathbf{3}](ClO_4)$ were prepared from $[\mathbf{1}](ClO_4)$ and $[\mathbf{2}](ClO_4)_2$, respectively, as shown in Scheme 1. The desired nitroso complex $[Ru^{II}(trpy)(pdt)(NO^+)](ClO_4)_3$ $\{[\mathbf{4}](ClO_4)_3\}$ was prepared from the nitro derivative $[\mathbf{3}](ClO_4)$ by using concentrated nitric acid followed by concentrated perchloric acid at 273 K (Scheme 1).

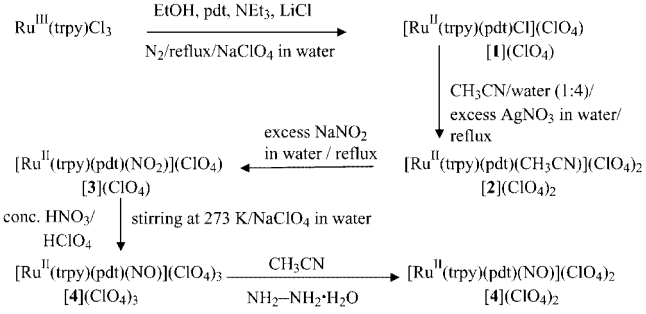


Scheme 1.

The direct synthesis of $[\mathbf{4}](ClO_4)_3$ either from the chlorido $\{[\mathbf{1}](ClO_4)\}$ or solvated $\{[\mathbf{2}](ClO_4)_2\}$ derivative using NO gas or $NOBF_4$ was not successful. Therefore, the stepwise synthetic route as shown in Scheme 1 was followed.

The diamagnetic complexes $[\mathbf{1}](ClO_4)$, $[\mathbf{2}](ClO_4)_2$, $[\mathbf{3}](ClO_4)$, and $[\mathbf{4}](ClO_4)_3$ exhibit expected molar conductivities and microanalytical data (see Experimental Section).

 © 2007 Wiley-VCH Verlag GmbH & Co. KGaA, Weinheim 

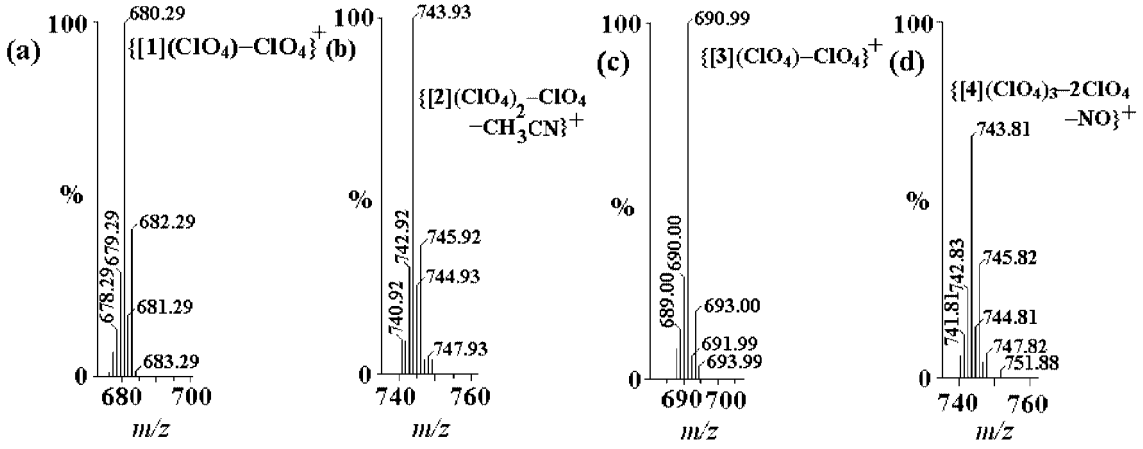


Figure 1. ESI mass spectra of (a) [**1**]($ClO_4$), (b) [**2**]($ClO_4$)$_2$, (c) [**3**]($ClO_4$), and (d) [**4**]($ClO_4$)$_3$ in $CH_3CN$.

The positive-ion electrospray mass spectra of [**1**]($ClO_4$), and [**3**]($ClO_4$) show molecular ion peaks centered at *m*/*z* = 680.29 and 690.99, respectively, corresponding to [**1**]$^+$ (calculated molecular mass: 680.09) and [**3**]$^+$ (calculated molecular mass: 690.11). Molecular ion peaks for [**2**]($ClO_4$)$_2$ and [**4**]($ClO_4$)$_3$ appear at *m*/*z* = 743.93 and 743.81 corresponding to {[**2**]($ClO_4$)$_2$ – $ClO_4$ – $CH_3CN$}$^+$ (calculated molecular mass: 744.07) and {[**4**]($ClO_4$)$_3$ – 2 $ClO_4$ – NO}$^+$ (calculated molecular mass: 744.15), respectively (Figure 1).

Orientation of the pyridyl or triazine ring of the unsymmetric pdt with respect to the monodentate ligand (X = $Cl^-$ or $CH_3CN$ or $NO_2^-$ or NO) in the complex frameworks gives rise to two possible isomeric structures, **A** and **B**.

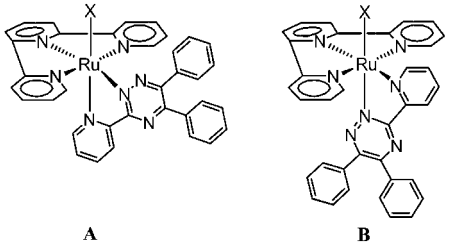


However, in practice, only one of the structural forms (**A** or **B**) has been systematically isolated by column chromatography for all the complexes. The preferential crystallization of isomer **A** where the pyridyl nitrogen atom is *trans* to "X" has been established by crystal structure analyses of [**1**]($ClO_4$) and [**2**]($ClO_4$)$_2$.

### Crystal Structures of [1]($ClO_4$) and [2]($ClO_4$)$_2$·3$H_2O$

The crystal structures of [**1**]($ClO_4$) and [**2**]($ClO_4$)$_2$·3$H_2O$ are shown in Figures 2 and 3, respectively. Selected crystallographic and structural parameters are listed in Tables 2 and 4, respectively.

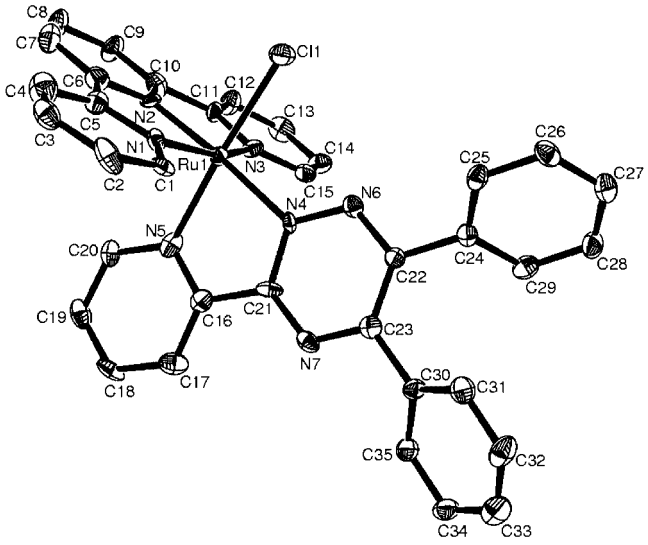


Figure 2. Crystal structure of the cation of [**1**]($ClO_4$).

The trpy ligand in the complexes is coordinated to the ruthenium ion in the expected meridional fashion with the bidentate pdt ligand in *cis* position. The intraligand *trans* angles, N1–Ru–N3 of 159.1(2) and 158.5(2)°, in [**1**]($ClO_4$) and [**2**]($ClO_4$)$_2$, respectively, reflect the usual geometrical constraints due to the meridional binding mode of tridentate trpy.[18] The other two interligand *trans* angles, N2–Ru–N4 and N5–Ru–X, remain close to 180° for both the complexes. As in other Ru–trpy derivatives,[18,19] the central $Ru^{II}$–N2(trpy) bonds {1.954(6) and 1.977(5) Å in [**1**]($ClO_4$) and [**2**]($ClO_4$)$_2$, respectively} are significantly shorter than the corresponding terminal $Ru^{II}$–N(trpy) distances, Ru–N1 [2.058(6) and 2.078(5) Å] and $Ru^{II}$–N3 [2.057(6) and 2.073(5) Å]. The pdt ligand forms a five-membered chelate ring to the metal ion through pyridyl and triazine nitrogen atoms. The coordinated pdt ligand is slightly nonplanar; the dihedral angles between the chelated pyridine and triazine

 © 2007 Wiley-VCH Verlag GmbH & Co. KGaA, Weinheim 

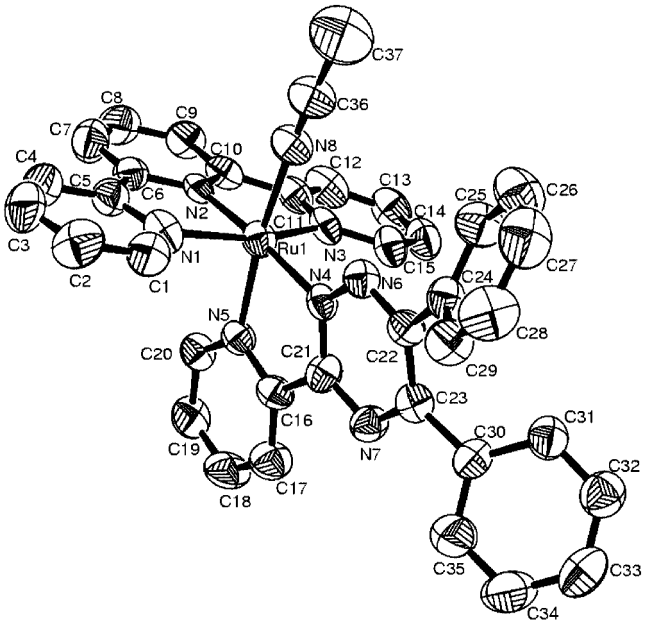


Figure 3. Crystal structure of the cation of [**2**]$(ClO_4)_2$. Water molecules of crystallization have been removed for clarity.

Table 2. Selected bond lengths [Å] and bond angles [°] for [**1**]$(ClO_4)$ and [**2**]$(ClO_4)_2 \cdot 3H_2O$.

| | [**1**]$(ClO_4)$ (X = Cl) | [**2**]$(ClO_4)_2$ (X = $CH_3CN$) |
|---|---|---|
| Ru–X | 2.392(2) | 2.037(5) |
| Ru–N(1) | 2.058(6) | 2.078(5) |
| Ru–N(2) | 1.954(6) | 1.977(5) |
| Ru–N(3) | 2.057(6) | 2.073(5) |
| Ru–N(4) | 2.042(6) | 2.035(5) |
| Ru–N(5) | 2.034(6) | 2.047(4) |
| N(4)–N(6) | 1.340(9) | 1.355(6) |
| N(4)–C(21) | 1.367(10) | 1.348(7) |
| C(16)–C(21) | 1.462(13) | 1.471(9) |
| N(5)–C(16) | 1.349(9) | 1.347(7) |
| N(5)–C(20) | 1.371(10) | 1.356(7) |
| C(36)–N(8) | – | 1.121(7) |
| N(1)–Ru–N(2) | 79.7(2) | 79.2(2) |
| N(1)–Ru–N(3) | 159.1(2) | 158.5(2) |
| N(1)–Ru–N(4) | 100.6(2) | 100.8(2) |
| N(1)–Ru–N(5) | 87.0(2) | 94.84(19) |
| N(2)–Ru–N(3) | 79.4(2) | 79.3(2) |
| N(2)–Ru–N(4) | 175.5(3) | 175.24(17) |
| N(2)–Ru–N(5) | 96.9(2) | 96.7(2) |
| N(3)–Ru–N(4) | 100.3(2) | 100.7(2) |
| N(3)–Ru–N(5) | 96.6(2) | 88.00(18) |
| N(4)–Ru–N(5) | 78.6(2) | 78.6(2) |
| N(1)–Ru–X | 91.66(17) | 87.4(2) |
| N(2)–Ru–X | 87.91(18) | 92.11(19) |
| N(3)–Ru–X | 86.48(17) | 93.00(19) |
| N(4)–Ru–X | 96.55(17) | 92.6(2) |
| N(5)–Ru–X | 174.68(18) | 171.2(2) |
| N(6)–N(4)–C(21) | 119.2(6) | 118.1(5) |
| N(4)–C(21)–C(16) | 114.8(6) | 114.6(6) |
| C(21)–C(16)–N(5) | 114.0(7) | 114.1(5) |
| C(16)–N(5)–C(20) | 116.1(7) | 116.8(5) |
| N(8)–C(36)–C(37) | – | 177.8(9) |

rings in [**1**]$(ClO_4)$ and [**2**]$(ClO_4)_2$ are 2.80(0.17) and 4.81(0.15)°, respectively. The dihedral angles between the pendant phenyl rings linked to the triazine ring are 52.13(0.26), 49.12(0.30) and 44.84(0.21), 55.09(0.25)° in [**1**]$(ClO_4)$ and [**2**]$(ClO_4)_2$, respectively. The $Ru^{II}$–Cl and $Ru^{II}$–N(pdt/trpy) bond lengths and the associated angles are in good agreement with the reported data on related molecules.[17a,18,19] The coordinated acetonitrile molecule in [**2**]$(ClO_4)_2$ is in its usual nearly linear mode with an N8–C36–C37 angle of 177.8(9)°.[13] The packing diagram of [**2**]$(ClO_4)_2 \cdot 3H_2O$ is shown in Figure S1 (Supporting Information).

### $^1$H NMR, IR, UV/Vis and Emission Spectral Aspects

The $^1$H NMR spectra of [**1**]$(ClO_4)$, [**2**]$(ClO_4)_2$, [**3**]$(ClO_4)$, and [**4**]$(ClO_4)_3$ in $(CD_3)_2SO$ are shown in Figure S2 (Supporting Information and Experimental Section). The complexes display 25 severely overlapping signals in the aromatic region between δ = 7.0 and 9.0 ppm. This matches well with the calculated number of aromatic signals, 11 and 14 resonances from the trpy and pdt ligands, respectively.

The $ClO_4^-$ vibrations are observed at 1096/623, 1089/625, 1097/623, and 1087/626 $cm^{-1}$ for [**1**]$(ClO_4)$, [**2**]$(ClO_4)_2$, [**3**]$(ClO_4)$, and [**4**]$(ClO_4)_3$, respectively. $Ru^{II}$–$NO_2$ stretching frequencies of [**3**]$(ClO_4)$ fall at 1366 $cm^{-1}$ (asym.) and 1276 $cm^{-1}$ (sym.). The $\nu_{NO^+}$ stretching frequency of 1944 $cm^{-1}$ for [**4**]$(ClO_4)_3$ (Figure 4) is comparable to that reported for analogous complexes with AL = pbi, dpa or dpk (Table 1). However, it is much lower than that reported for AL = strongly π-acidic pap, pbo or bpy and much higher with respect to AL = strongly σ-donating pp, acac or pNMebi (Table 1). Thus, the observed reasonably high $\nu_{NO}$ stretching frequency of [**4**]$(ClO_4)_3$ is suggestive of its moderate electrophilic character.

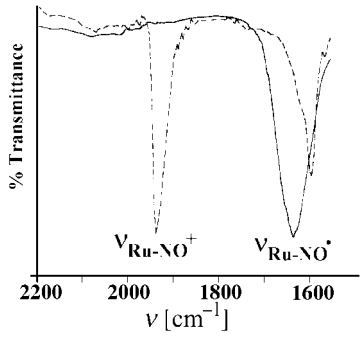


Figure 4. IR spectra (KBr disk) of (a) [**4**]$(ClO_4)_3$ (------) and (b) [**4**]$(ClO_4)_2$ (—) in the region of 2200–1600 $cm^{-1}$.

The complexes exhibit multiple transitions in the UV/Vis region in $CH_3CN$ (Figure 5, Table 3). Intense ligand-based transitions (π → π* and n → π*) are observed in the UV region. The ruthenium(II)-based moderately intense metal-to-ligand charge-transfer (MLCT) transitions appear near 500 nm. The Gaussian analysis of the visible region of the spectra reveals the presence of two close bands in each of $[\mathbf{1}]^+$, $[\mathbf{2}]^{2+}$, and $[\mathbf{3}]^+$ (Table 3 and inset of Figure 5).

These are tentatively assigned to dπ($Ru^{II}$) → π*(pdt)- and dπ($Ru^{II}$) → π*(trpy)-based transitions.[13,17] The MLCT band energy in acetonitrile solution follows the or-

 © 2007 Wiley-VCH Verlag GmbH & Co. KGaA, Weinheim 

Table 3. Redox potentials[a,b] and electronic spectroscopic data.

| Compound | Couple | | | | λ/nm |
|---|---|---|---|---|---|
| | I | II | III | IV | (ε/M$^{-1}$ cm$^{-1}$)[d] |
| [**1**]$ClO_4$ | 0.89(90) | –1.07(120) | –1.54(190) | – | 520 (15073), [522 (4668), 506 (13100)[e]], 312 (38078), 279 (38762), 236 (33057), 204 (65481) |
| [**2**]$(ClO_4)_2$ | 1.33(80) | –1.04(100) | –1.50(90) | – | 470 (13942), [471 (6518), 448 (9499)[e]], 327 (23247),[f] 297 (38484), 202 (67952) |
| [**3**]$ClO_4$ | 1.09(90) | –1.05(80) | –1.54(110) | – | 482 (11273), [479 (6952), 465 (4192)[e]], 297 (31685), 205(63910) |
| [**4**]$(ClO_4)_3$ | 0.40(110) | –0.33[c] | –0.90(50) | –1.11(120) | 467 (15528), [470 (4728), 451 (10036)[e]], 335 (27408),[f] 300 (40440), 207 (70624) |
| [**4**]$(ClO_4)_2$ | | | | | 494 (15536), [505 (5350), 484 (13214)[e]], 307 (37634), 281 (36672), 272 (36284) |

[a] Potentials $E°_{298}$/V ($\Delta E$/mV) vs. SCE. [b] In $CH_3CN$/0.1 M $Et_4NClO_4$. [c] $E_{pc}$ is considered due to the irreversible nature of the wave. [d] In acetonitrile. [e] Bands obtained by Gaussian analysis of the lowest energy transition. [f] Shoulder.

der $Cl^-$ (520 nm) < $NO_2^-$ (482 nm) < $CH_3CN$ (470 nm) < $NO^+$ (467 nm) depending on the relative stabilization of the dπ($Ru^{II}$) level.[20] The tripositive charge as well as pronounced π-acceptor characteristics of $NO^+$ in [**4**]$^{3+}$ are indeed reflected in the relatively higher MLCT band energy and the corresponding redox processes (see later). The 15-nm (666 cm$^{-1}$) blueshift in the MLCT band energy while moving from $Ru^{II}$–$NO_2^-$ [**3**]$(ClO_4)$ (482 nm) to $Ru^{II}$–$NO^+$ [**4**]$(ClO_4)_3$ (467 nm) is much less than that observed for analogous complexes having π-acidic ancillary ligands (dpk, bpy, pap).[13–15] This implies relatively weaker d$\pi Ru^{II}$ → π*($NO^+$) backbonding in [**4**]$(ClO_4)_3$, as is also been evidenced in the $\nu(NO^+)$ stretching frequency (Table 1).

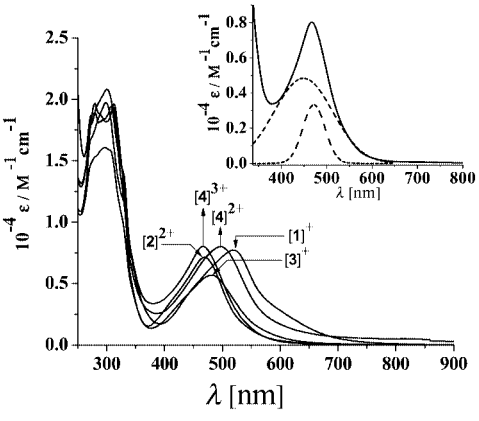


Figure 5. Electronic spectra in acetonitrile of [**1**]$^+$, [**2**]$^{2+}$, [**3**]$^+$, [**4**]$^{3+}$, and [**4**]$^{2+}$. Inset shows the Gaussian analysis (------) of the experimental spectrum (—) of [**2**]$^{2+}$ in the visible region.

Though excitations of [**1**]$^+$, [**3**]$^+$, and [**4**]$^{3+}$ at the lowest energy MLCT bands failed to show emissions even in EtOH/MeOH (4:1) glass (77 K), [**2**]$^{2+}$ exhibits weak emission at 640 nm (Figure S3, Supporting Information). The quantum yield, $\&\pi\eta\iota;$ = 0.026, was calculated with reference to $Ru(bpy)_3^{2+}$ ($\&\pi\eta\iota;$ = 0.34).[21] The observed emission of [**2**]$^{2+}$ can be attributed to the triplet MLCT state.[22]

### Rates and Equilibrium Constant for the Conversion of [$Ru^{II}$(trpy)(pdt)($NO^+$)]$^{3+}$ [**4**]$^{3+}$ → [$Ru^{II}$(trpy)(pdt)($NO_2$)]$^+$ [**3**]$^+$

Unlike earlier reported analogous nitrosyl complexes,[11–13,15] [**4**]$^{3+}$ is found to be quite stable both in the solid state as well as in $CH_3CN$ or even in poorly soluble water medium, in spite of the reasonably high $\nu(NO^+)$ stretching frequency of 1944 cm$^{-1}$. However, in the presence of a strong nucleophile such as $OH^-$, it undergoes slow transformation to the corresponding nitro derivative ([**3**]$^+$) [Equation (1)] (Figure 6). On the other hand, for the aforesaid analogous complexes, a weak nucleophile such as $H_2O$ was found to be effective to perform the reaction stated in Equation (1).

$$\underset{[\mathbf{4}]^{3+}}{[Ru^{II}(trpy)(pdt)(NO^-)]^{3+}} + OH^- \rightarrow \underset{[\mathbf{3}]^{+}}{[Ru^{II}(trpy)(pdt)(NO_2)]^{+}} + H^+ \quad (1)$$

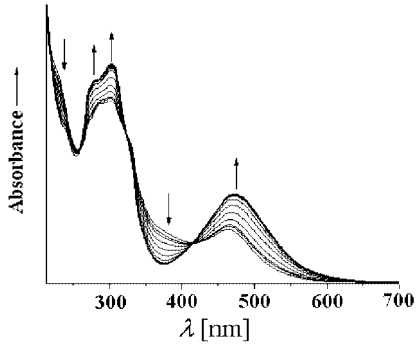


Figure 6. Time evolution of the electronic spectra (5-min time interval) of a changing solution of [$Ru^{II}$(trpy)(pdt)($NO^+$)]$^{3+}$ ($0.4 \times 10^{-4}$ M) + $OH^-$ ($0.1 \times 10^{-2}$ M) → [$Ru^{II}$(trpy)(pdt)($NO_2$)]$^+$ + $H^+$ in $CH_3CN$ at 318 K. Arrows indicate increase or decrease in absorbances with the progression of the reaction.

The rate of conversion of the nitroso derivative ([**4**]$^{3+}$, $0.4 \times 10^{-4}$ M) to the nitro counterpart ([**3**]$^+$) was monitored spectrophotometrically in the temperature range of 298–

 © 2007 Wiley-VCH Verlag GmbH & Co. KGaA, Weinheim 

318 K in $CH_3CN$ solvent using a calculated optimum concentration of aqueous NaOH solution ($0.1 \times 10^{-2}$ M). $CH_3CN$ was chosen as a solvent because of the poor solubility of $[4]^{3+}$ in $H_2O$ and thus the transformation process was monitored without any pH control. The well-defined isosbestic points (Figure 6) imply the involvement of nitrosyl and nitro species as the primary components in the conversion process. The pseudo-first-order rate constant ($k$/s), activation parameters ($\Delta H^{\#}/\Delta S^{\#}$), and equilibrium constant ($K$) values are calculated to be: $4.13 \times 10^{-4}$ (298 K), $7.30 \times 10^{-4}$ (308 K), $1.29 \times 10^{-3}$ (318 K); 42.26 kJ mol$^{-1}$/–110.48 J K$^{-1}$ mol$^{-1}$; 6.6, respectively. The observed appreciably large negative $\Delta S^{\#}$ value confirms that the nucleophilic attack of the electrophilic $NO^+$ site in $[4]^{3+}$ by $OH^-$ occurs through an associatively activated process. The equilibrium constant value of 6.6 indicates the presence of an appreciable concentration of the initial nitrosyl species $[Ru^{II}(trpy)(pdt)(NO^+)]^{3+}$ ($[4]^{3+}$) in the equilibrated situation even under strongly alkaline condition.

### Redox and Spectroelectrochemical Aspects

The $Ru^{III}/Ru^{II}$ potentials of $[1]^+$, $[2]^{2+}$, and $[3]^+$ (couple I, Figure 7a–c; Table 3) vary depending on the electron-donating/-withdrawing nature of the monodentate ligand (X) as well as the electrostatic factor because of the overall charge of the complex moieties. They follow the expected trend of X = $Cl^-$ (0.89) < $NO_2^-$ (1.09) << $CH_3CN$ (1.33 vs. SCE). The potentials are comparable to those of the corresponding $[Ru^{II}(trpy)(AL)(X)]^{n+}$, where AL = dpk,[13] having a π-conjugated electron-withdrawing C=O function (X = $Cl^-$, 0.88; $NO_2^-$, 1.02 V; $CH_3CN$, 1.37 V vs. SCE). However, the potentials are much higher than those of the analogous AL = dpa[12] derivatives incorporating a π-donor amine group (X = $Cl^-$, 0.64; $NO_2^-$, 0.88 vs. SCE). The two ligand-based reductions are observed in the range of –1.0 to –1.5 V (couples II and III, Figure 7a–c, Table 3). The first reduction wave near –1.0 V appears to be less than that typical for the trpy-based reductions (–1.30 and –1.80 V) observed in numerous Ru–trpy complexes.[18–20,23] On the other hand, the free pdt ligand reduces reversibly, $E°_{298}$/V ($\Delta E$/mV) at –1.49 (120) versus SCE in $CH_3CN$ (Figure 7e). Thus, couples II and III are assigned as the reduction processes involving pdt and trpy ligands, respectively.

The nitrosyl complex $[4]^{3+}$ exhibits four successive reduction processes (couples I–IV, Figure 7d, Table 3). The effects of neutrality as well as low basicity of both the pdt and trpy ligands and the highly charged feature of $[4]^{3+}$ facilitate the reversible reduction at the rather positive potential of 0.40 V versus SCE in $CH_3CN$ (couple 1, Figure 7d). The same effect has also been extended even for the second one-electron reduction of $[4]^{3+}$ (couple II, Figure 7d) at a reasonably less negative potential of –0.33 V, though irreversible at the cyclic voltammetric timescale. The potentials of couples I and II are much more positive relative to the reductions involving the coordinated pdt and trpy ligands, –0.90 and –1.11 V (couples III and IV, Figure 7d).

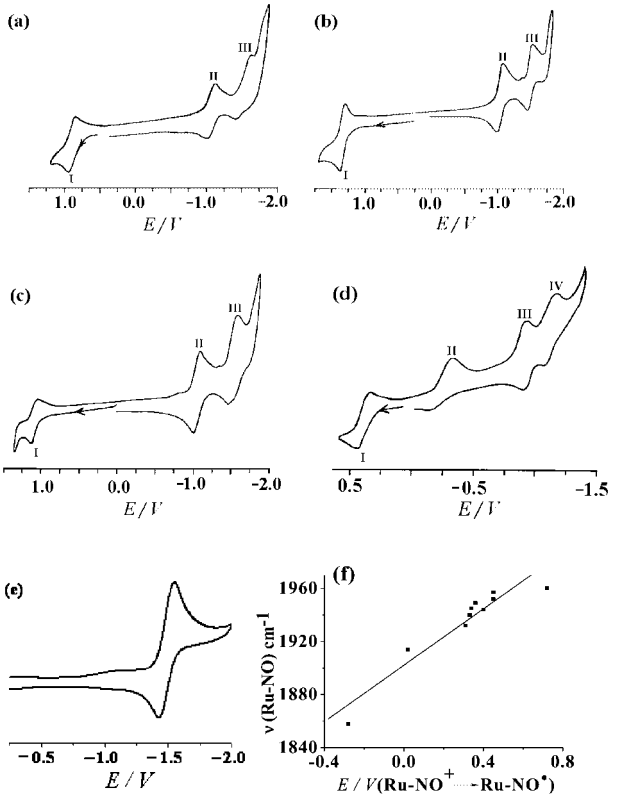


Figure 7. Cyclic voltammograms of (a) $[1]^+$, (b) $[2]^{2+}$, (c) $[3]^+$, (d) $[4]^{3+}$, (e) free ligand, pdt in $CH_3CN$ (scan rate: 50 mV s$^{-1}$), and (f) least-squares plot of $E$/V ($Ru^{II}$–$NO^+$–$Ru^{II}$–$NO^{\cdot}$) vs. $\nu(Ru^{II}–NO^+)$ frequency of $[Ru^{II}(trpy)(AL)(NO^+)]^{3+}$ complexes where AL = pap, bpy, pbo, pdt, dpk, dpa, pbi, pNMebi, acac, and pp as listed in Table 1.

Therefore, couples I and II are logically considered as the expected successive reductions of the redox facile coordinated $NO^+$, that is, $\{Ru^{II}–NO^+\} \rightarrow \{Ru^{II}–NO^{\cdot}\}$ and $\{Ru^{II}–NO^{\cdot}\} \rightarrow \{Ru^{II}–NO^-\}$, respectively. The difference in potential of 0.73 V (couple II/couple I) between the successive NO-centered reductions leads to a large comproportionation constant ($K_c$) value of $10^{12.4}$ ($RT\ln K_c = \Delta E/0.059$)[24] for the intermediate $\{Ru^{II}–NO^{\cdot}\}$ radical species $[4]^{2+}$. The $Ru^{II}–NO^+ \rightarrow Ru^{II}–NO^{\cdot}$ reduction potentials and the corresponding $\nu(NO^+)$ values for the analogous $[Ru^{II}(trpy)(AL)(NO^+)]^{3+}$ complexes with AL = pap,[15] bpy,[14] pbo,[11] dpk,[13] dpa,[12] pbi,[11] pNMebi,[11] acac,[10] and pp[9] (Table 1) follow a general trend. Consequently, the plot of $E_{1/2}$ of the $Ru^{II}–NO^+/Ru^{II}–NO^{\cdot}$ couple versus the $\nu(NO^+)$ frequency for the known $[Ru^{II}(trpy)(AL)(NO^+)]^{3+}$ derivatives yields a reasonably linear relationship (Figure 7f).

Nitrosyl species $[4]^{3+}$ can be quantitatively reduced to $[4]^{2+}$ either coulometrically or by using hydrazine hydrate as a chemical reducing agent. The relevant microanalytical, conductivity, and mass spectrometric data are given in the Experimental Section. On reduction of $[4]^{3+}$ to $[4]^{2+}$, the $\nu(NO)$ frequency is shifted from 1944 to 1633 cm$^{-1}$ (Figure 4) The large $\Delta\nu$ value of 311 cm$^{-1}$ on moving from $[4]^{3+}$ to $[4]^{2+}$ confirms[25] the reduction of coordinated $NO^+$ to

 © 2007 Wiley-VCH Verlag GmbH & Co. KGaA, Weinheim 

$NO^{\cdot}$. Consequently, the reduced species $[\mathbf{4}]^{2+}$ exhibits a radical-type EPR spectrum ($g$ = 2.003) with partially resolved nitrogen hyperfine splittings.[11–13,26] On reduction to the nitrosyl radical complex $[\mathbf{4}]^{2+}$, the visible-energy charge-transfer band has been reasonably redshifted from 467 to 494 nm (Figure 5). Moreover, two distinct bands involving the singly occupied MO appear at 307 and 281 nm[13] (Figure 5, Table 3). However, the second reduced species $[\mathbf{4}]^{+}$ with the $NO^{-}$ state was found to be unstable even on the coulometric timescale at 298 K.

### Photocleavage of the $Ru^{II}$–NO Bond in $[Ru^{II}(trpy)(pdt)(NO^{\cdot})]^{2+}$ ($[\mathbf{4}]^{2+}$)

Though $[\mathbf{4}]^{2+}$ is quite stable in $CH_3CN$ under ambient light conditions, exposure of an acetonitrile solution of $[\mathbf{4}]^{2+}$ to light (Xenon 350 W lamp) for a period of about 4 h results in quantitative transformation to the solvated species $[\mathbf{2}]^{2+}$ by the selective cleavage of the $Ru^{II}$–$NO^{\cdot}$ bond. The slow but steady progression of photocleavage of the $Ru^{II}$–$NO^{\cdot}$ bond of $[\mathbf{4}]^{2+}$ was monitored spectrophotometrically in $CH_3CN$ (Figure 8) and the presence of isosbesticities suggests the clean conversion of $[Ru^{II}(trpy)(pdt)(NO^{\cdot})]^{2+}$ ($[\mathbf{4}]^{2+}$) to $[Ru^{II}(trpy)(pdt)(CH_3CN)]^{2+}$ ($[\mathbf{2}]^{2+}$). The rate of first-order photolytic release of NO ($k_{NO}$) has been determined to be $4.4\times10^{-3}$ $min^{-1}$ ($t_{1/2}\approx157$ min). This sort of photolytic cleavage of the M–NO bond maintaining the overall integrity of the rest of the molecule is known to have biological relevance.[6] However, because of the insolubility of $[\mathbf{4}]^{2+}$ in aqueous medium, it has not been possible so far to explore the feasibility of transferring the photoliberated NO to biomolecules such as myoglobin or cytochrome c oxidase. Thus, further work in the direction of developing newer classes of water-soluble nitrosyl derivatives is in progress.

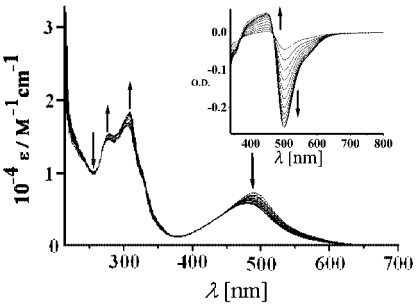


Figure 8. Time evolution of the electronic spectra (20-min time interval) of a changing solution of $[Ru^{II}(trpy)(pdt)(NO^{\cdot})]^{2+}$ ($\mathbf{4}^{2+}$, $0.4\times10^{-4}$ M) in $CH_3CN$ exposed to light (Xe lamp 350 W). Arrows indicate increase or decrease in absorbances with the progression of the reaction. The inset shows the difference spectra of $\mathbf{4}^{2+}$ exposed to light (Xe lamp 350 W) at different time intervals with respect to unexposed $[\mathbf{4}]^{2+}$ in acetonitrile as the reference solution.

## Conclusions

The present work demonstrates the substitutional and electron-transfer aspects of a series of four compounds based on the framework of $[Ru^{II}(trpy)(pdt)X]^{n+}$ {X = $Cl^{-}$ ($[\mathbf{1}]^{+}$), $CH_3CN$ ($[\mathbf{2}]^{2+}$), $NO_2^{-}$ ($[\mathbf{3}]^{+}$), $NO^{+}$ ($[\mathbf{4}]^{3+}$)}. The nitrosyl function in $[\mathbf{4}]^{3+}$ undergoes facile two-step one-electron reductions: $\{Ru^{II}–NO^{+}\}$ to $\{Ru^{II}–NO^{\cdot}\}$ to $\{Ru^{II}–NO^{-}\}$. Unlike earlier reported analogous complexes $\{[Ru^{II}(trpy)(AL)(NO^{+})]^{n+}\}$ with AL = pap, pbo, bpy, dpk, dpa, pbi, pNMebi, $[\mathbf{4}]^{3+}$ is found to be sufficiently stable both in the solid and solution ($CH_3CN$ or poorly in water medium) states in spite of the moderately strong electrophilic character of the nitrosyl function [$\nu(Ru^{II}–NO^{+})$ = 1944 $cm^{-1}$]. $[\mathbf{4}]^{3+}$ transforms slowly and partially to the corresponding nitro derivative $[\mathbf{3}]^{+}$ only in the presence a of strongly alkaline medium. The $NO^{+}$ function in $[Ru^{II}(trpy)(pdt)(NO^{+})]^{3+}$ ($[\mathbf{4}]^{3+}$) can be quantitatively reduced to the corresponding $NO^{\cdot}$ state in $[Ru^{II}(trpy)(pdt)(NO^{\cdot})]^{2+}$ ($[\mathbf{4}]^{2+}$) either electrochemically or chemically by using hydrazine hydrate. Though $[\mathbf{4}]^{2+}$ is stable under ambient light conditions, the exposure of an acetonitrile solution of $[\mathbf{4}]^{2+}$ to light (Xenon 350 W lamp) for a period of 4 h results in the solvated species $[\mathbf{2}]^{2+}$ by the slow photorelease of NO with $k_{NO}$ of $4.4\times10^{-3}$ $min^{-1}$ ($t_{1/2}\approx157$ min).

## Experimental Section

**Materials and Instrumentation:** The precursor complexes $Ru^{III}(trpy)Cl_3$[27] and 5,6-diphenyl-3-pyridyl-*as*-triazine (pdt)[28] were prepared according to reported procedures. 2,2′:6′,2″-Terpyridine, 2-cyanopyridine, and silver nitrate were purchased from Aldrich. Other chemicals and solvents were reagent-grade and used as received. For spectroscopic studies, HPLC-grade solvents were used. Solution electrical conductivity was checked using a Systronic conductivity bridge 305. Infrared spectra were taken with a Nicolet spectrophotometer with samples prepared as KBr pellets. $^1H$ NMR spectra were recorded with a 300-MHz Varian FT spectrometer with $(CD_3)_2SO$ used as solvent. Cyclic voltammetric and coulometric measurements were carried out using a PAR model 273A electrochemistry system. A platinum wire working electrode, a platinum wire auxiliary electrode, and a saturated calomel reference electrode (SCE) were used in a standard three-electrode configuration. Tetraethylammonium perchlorate (TEAP) was used as the supporting electrolyte and the solution concentration was about $10^{-3}$ M; the scan rate used was 50 mV $s^{-1}$. A platinum gauze working electrode was used in the coulometric experiments. All electrochemical experiments were carried out under dinitrogen. UV/Vis spectral studies were performed with a Perkin–Elmer Lambda 950 spectrophotometer. The elemental analyses were carried out with a Perkin–Elmer 240C elemental analyzer. Electrospray mass spectra were recorded with a Micromass Q-ToF mass spectrometer. Steady-state emission experiments were performed using a Perkin–Elmer LS 55 luminescence spectrometer fitted with a cryostat.

**Synthesis of $[Ru^{II}(trpy)(pdt)(Cl)]ClO_4$ {[1](ClO$_4$)}:** $[Ru^{III}(trpy)Cl_3]$ (100 mg, 0.23 mmol) was dissolved in ethanol (20 mL) and 5,6-diphenyl-3-pyridyl-*as*-triazine (pdt) (41.8 mg, 0.227 mmol), excess LiCl (54 mg, 1.3 mmol), and $NEt_3$ (0.4 mL) were added to it. The mixture was heated at reflux under dinitrogen for 5 h. The initial dark brown solution gradually changed to deep purple. The dry mass thus obtained on removal of solvent under reduced pressure was dissolved in a minimum volume of acetonitrile, and excess saturated aqueous solution of $NaClO_4$ was added to it. The resulted solid precipitate was filtered off and washed thoroughly with cold water. The product was dried in vacuo over $P_4O_{10}$. It was then

 © 2007 Wiley-VCH Verlag GmbH & Co. KGaA, Weinheim 

purified on a neutral alumina column. The complex [**1**]($ClO_4$) was eluted with $CH_2Cl_2$/$CH_3CN$ (3:1). Evaporation of the solvents under reduced pressure afforded pure complex [**1**]($ClO_4$). Yield: 113.2 mg (64%). $C_{35}H_{25}Cl_2N_7O_4Ru$ (779.04): calcd. C 53.91, H 3.23, N 12.58; found C 54.27, H 3.08, N 12.27. Molar conductivity in acetonitrile: $\Lambda_M$ = 127 $\Omega^{-1}$ cm$^2$ M$^{-1}$. $^1$H NMR [300 MHz, $(CD_3)_2SO$, 298 K]: $\delta$ = 8.87 (d, $J$ = 8.1 Hz, 1 H), 8.75 (d, $J$ = 8.1 Hz, 2 H), 8.65 (d, $J$ = 8.1 Hz, 1 H), 8.45 (d, $J$ = 8.1 Hz, 1 H), 8.27 (m, 2 H), 8.03 (t, $J$ = 8.1, 6.9 Hz, 3 H), 7.77 (d, $J$ = 4.8 Hz, 2 H), 7.59 (m, 3 H), 7.42 (m, 7 H), 7.23 (t, $J$ = 7.8, 7.5 Hz, 1 H), 7.05 (1 H), 6.94 (d, $J$ = 7.2 Hz, 1 H) ppm.

**Synthesis of [Ru$^{II}$(trpy)(pdt)($CH_3CN$)]($ClO_4$)$_2$ {[2]($ClO_4$)$_2$}:** The chlorido complex [**1**]($ClO_4$) (100 mg, 0.128 mmol) was dissolved in $CH_3CN$ (5 mL), water (20 mL) was added and then the mixture was heated at reflux for 10 min. An excess of $AgNO_3$ (217 mg, 1.28 mmol) was added to the above hot solution and the heating was continued for a further 2 h. The solution was then cooled and the precipitated AgCl was separated by filtration through a sintered glass crucible (G-4). On concentration of the filtrate, the desired solid complex [**2**]($ClO_4$)$_2$ separated. It was filtered and washed with ice-cold water and subsequently dried in vacuo over $P_4O_{10}$. Yield: 90.8 mg (80%). $C_{37}H_{28}Cl_2N_8O_8Ru$ (884.04): calcd. C 50.22, H 3.19, N 12.67; found C 49.99, H 3.13, N 12.45. Molar conductivity ($CH_3CN$): $\Lambda_M$ = 270 $\Omega^{-1}$ cm$^2$ M$^{-1}$. $^1$H NMR [300 MHz, $(CD_3)_2SO$, 298 K]: $\delta$ = 8.99 (d, $J$ = 8.1 Hz, 2 H), 8.83 (t, $J$ = 6.6, 7.8 Hz, 3 H), 8.72 (d, $J$ = 7.8 Hz, 1 H), 8.55 (t, $J$ = 7.8, 8.1 Hz, 1 H), 8.27 (d, $J$ = 4.8 Hz, 1 H), 8.16 (t, $J$ = 7.5, 7.8 Hz, 2 H), 8.07 (t, $J$ = 7.5, 6.6 Hz, 1 H), 7.91 (m, 2 H), 7.79 (d, $J$ = 2.1 Hz,1 H), 7.53 (m, 9 H), 7.25 (t, $J$ = 8.1, 7.5 Hz, 1 H), 6.92 (d, $J$ = 7.2 Hz, 1 H) ppm.

**Synthesis of [Ru$^{II}$(trpy)(pdt)($NO_2$)]($ClO_4$) [3]($ClO_4$):** The complex [**2**]($ClO_4$)$_2$ (100 mg, 0.116 mmol) was dissolved in $CH_3CN$ (5 mL) and then water (20 mL) was added followed by an excess of $NaNO_2$ (200 mg, 2.90 mmol). The mixture was heated at reflux for 2.5 h. The deep red solution of [**2**]($ClO_4$)$_2$ changed to deep orange during the course of the reaction. The pure crystalline nitro complex precipitated when the hot solution cooled to room temperature. The solid [**3**]($ClO_4$) thus obtained was filtered off, washed with ice-cold water, and dried in vacuo over $P_4O_{10}$. Yield: 73.3 mg (82%). $C_{35}H_{25}ClN_8O_6Ru$ (790.06): calcd. C 53.20, H 3.19, N 14.18; found C 53.37, H 3.26, N 13.94. Molar conductivity in acetonitrile: $\Lambda_M$ = 120 $\Omega^{-1}$ cm$^2$ M$^{-1}$. $^1$H NMR [300 MHz, $(CD_3)_2SO$, 298 K]: $\delta$ = 8.99 (d, $J$ = 8.1 Hz, 1 H), 8.85 (m, 2 H), 8.75 (m, 2 H), 8.27 (d, $J$ = 5.1 Hz,1 H), 8.17 (t, $J$ = 6.3, 8.7 Hz, 1 H), 8.05 (m, 2 H), 7.90 (m, 2 H), 7.75 (m, 2 H), 7.49 (m, 10 H), 7.24 (t, $J$ = 7.5, 7.8 Hz, 1 H), 6.95 (d, $J$ = 7.5 Hz, 1 H) ppm.

**Synthesis of [Ru$^{II}$(trpy)(pdt)($NO^+$)]($ClO_4$)$_3$ {[4]($ClO_4$)$_3$}:** Dropwise addition of concentrated $HNO_3$ (2 mL) to the powdered nitro complex [**3**]($ClO_4$) (100 mg, 0.126 mmol) at 273 K whilst stirring resulted in a pasty mass. The pasty mass thus formed was added to ice-cold concentrated $HClO_4$ (6 mL) dropwise with continuous stirring using a glass rod. On further addition of saturated aqueous $NaClO_4$ solution, a yellow solid product formed. The precipitate was filtered off immediately, washed with a little ice-cold water and then dried in vacuo over $P_4O_{10}$. Yield: 98.3 mg (80%). $C_{35}H_{25}Cl_3N_8O_{13}Ru$ (971.96): calcd. C 43.20, H 2.59, N 11.52; found C 43.02, H 2.46, N 11.74. Molar conductivity ($CH_3CN$): $\Lambda_M$ = 310 $\Omega^{-1}$ cm$^2$ M$^{-1}$. $^1$H NMR [300 MHz, $(CD_3)_2SO$, 298 K]: $\delta$ = 9.20 (m, 1 H), 9.08 (d, $J$ = 3.9 Hz, 1 H), 8.96 (m, 1 H), 8.83 (t, $J$ = 7.5, 7.8 Hz, 1 H), 8.57 (m, 3 H), 8.27 (d, $J$ = 5.1 Hz, 1 H), 8.19 (m, 2 H), 8.05 (m, 1 H), 7.88 (m, 3 H), 7.51 (m, 9 H), 6.97 (t, $J$ = 7.1, 6.9 Hz, 1 H), 6.85 (d, $J$ = 7.5 Hz, 1 H) ppm.

**Synthesis of [Ru$^{II}$(trpy)(pdt)($NO^-$)]($ClO_4$)$_2$ {[4]($ClO_4$)$_2$}:** The nitroso complex [**4**]($ClO_4$)$_3$ (100 mg, 0.102 mmol) was dissolved in 5 mL of $CH_3CN$ and excess hydrazine hydrate was added whilst stirring over a period of 5 min. The stirring was continued for a further 1 h. The initial yellow solution of [**4**]($ClO_4$)$_3$ changed to red-brown. The solvent was then removed under reduced pressure and the solid mass thus obtained was washed with a little ice-cold water and then dried in vacuo over $P_4O_{10}$. Yield: 67.4 mg (75%). $C_{35}H_{25}Cl_2N_8O_9Ru$ (873.02): calcd. C 48.11, H 2.89, N 12.83; found C 47.92, H 2.86, N 12.98. Molar conductivity ($CH_3CN$): $\Lambda_M$ = 225 $\Omega^{-1}$ cm$^{-2}$ M$^{-1}$. Magnetic moment (298 K): $\mu_B$ = 1.87. MS: $m/z$ = calcd. for {[**4**]($ClO_4$)$_2$ – $ClO_4$ – NO} 744.15, found 744.31.

***CAUTION!*** *Perchlorate salts of metal complexes with organic ligands are potentially explosive. Heating of dried samples must be avoided and handling of small amounts has to proceed with great caution, using protection.*

**Kinetic Experiments:** For the determination of $k$ of the conversion process of [Ru$^{II}$(trpy)(pdt)($NO^+$)]$^{3+}$ ([**4**]$^{3+}$) → [Ru$^{II}$(trpy)(pdt)-($NO_2$)]$^+$ ([**3**]$^+$) in acetonitrile in the presence of aqueous sodium hydroxide solution, the increase in absorbance ($A_t$) at 482 nm corresponding to $\lambda_{max}$ of the nitro complex was recorded as a function of time ($t$). $A\alpha$ was measured when the intensity changes leveled off. Values of pseudo-first-order rate constants, $k$, were obtained from the slopes of linear least-squares plots of $-\ln(A\alpha - A_t)$ against $t$. The activation parameters $\Delta H^{\#}$ and $\Delta S^{\#}$ were determined from the Eyring plot.[29] The first-order rate constant for the photo release of NO from [**4**]$^{2+}$ was determined from the single-exponential fitting of the plot of Δ(OD) against time, where Δ(OD) is the differential absorbance at 494 nm of [**4**]$^{2+}$ in acetonitrile, exposed to light, with respect to unexposed [**4**]$^{2+}$ in acetonitrile as the reference solution.

**X-ray Crystallography:** Single crystals of [**1**]($ClO_4$) or [**2**]($ClO_4$)$_2$ were grown by slow diffusion of an acetonitrile solution of the complex into toluene, followed by slow concentration. X-ray data were collected using an Oxford Xcalibur-S CCD single-crystal X-ray diffractometer using Mo-$K_\alpha$ radiation. Crystal data and data collection parameters are listed in Table 4. The structures were solved and refined by full-matrix least squares on $F^2$ using SHELX-97 (SHELXTL).[30] Absorption corrections for [**1**]($ClO_4$) and [**2**]-($ClO_4$)$_2$ were performed by multiscan. All the data were corrected

Table 4. Crystallographic data for [**1**]($ClO_4$) and [**2**]($ClO_4$)$_2$·3$H_2O$.

| | [**1**]($ClO_4$) | [**2**]($ClO_4$)$_2$ |
|---|---|---|
| Empirical formula | $C_{35}H_{25}Cl_2N_7O_4Ru$ | $C_{37}H_{28}Cl_2N_8O_{11}Ru$ |
| Formula mass | 779.59 | 932.64 |
| Crystal symmetry | monoclinic | monoclinic |
| Space group | $P21$ | $P21/a$ |
| $a$/Å | 8.485(3) | 19.612(5) |
| $b$/Å | 14.4596(8) | 8.6085(10) |
| $c$/Å | 13.368(3) | 25.267(6) |
| $\alpha$/° | 90.0 | 90.0 |
| $\beta$/° | 102.89(3) | 108.21(2) |
| $\gamma$/° | 90.0 | 90.0 |
| $V$/Å$^3$ | 1598.7(7) | 4052.2(14) |
| $Z$ | 2 | 4 |
| $\mu$/mm$^{-1}$ | 0.711 | 0.588 |
| $T$/K | 100(2) | 293(2) |
| $D_{calcd}$/g cm$^{-3}$ | 1.602 | 1.529 |
| $F$ (000) | 788 | 1888 |
| 2$\theta$ range/° | 5.92–50.0 | 6.32–57.20 |
| $e$ data ($R_{int}$) | 5164 (0.0438) | 8003 (0.0605) |
| $R_1$, $wR_2$ [$I > 2\sigma(I)$] | 0.0505, 0.1152 | 0.0687, 0.1426 |
| $R_1$, $wR_2$ (all data) | 0.0629, 0.1193 | 0.1657, 0.1670 |
| Gof | 1.042 | 0.885 |
| Largest diff. peak/hole/e Å$^{-3}$ | 2.354/–0.486 | 0.607/–0.596 |

 © 2007 Wiley-VCH Verlag GmbH & Co. KGaA, Weinheim 

for Lorentz and polarization effects, and the non-hydrogen atoms were refined anisotropically. Hydrogen atoms were included in the refinement process as per the riding model. X-ray analysis revealed the presence of three water molecules as solvent of crystallization in [**2**]$(ClO_4)_2$. CCDC-635850 {for [**1**]$(ClO_4)$} and -635851 {for [**2**]$(ClO_4)_2$} contain the supplementary crystallographic data for this paper. These data can be obtained free of charge from The Cambridge Crystallographic Data Centre via www.ccdc.cam.ac.uk/data_request/cif.

**Supporting Information** (see footnote on the first page of this article): Packing diagram of [**2**]$(ClO_4)_2 \cdot 3H_2O$ along the *b* axis (Figure S1), $^1$H NMR spectra of (a) [**1**]$^+$, (b) [**2**]$^{2+}$, (c) [**3**]$^+$, and (d) [**4**]$^{3+}$ in $(CD_3)_2SO$ (Figure S2), and emission spectrum of [**2**]$^{2+}$ in EtOH/MeOH (4:1) glass at 77 K (Figure S3).

## Acknowledgments

Financial support received from the Department of Science and Technology and Council of Scientific and Industrial Research, New Delhi, India is gratefully acknowledged. X-ray structural studies for [**1**]$(ClO_4)$ and [**2**]$(ClO_4)_2$ were carried out at the National Single Crystal Diffractometer Facility, Indian Institute of Technology, Bombay. Special acknowledgment is made to the Sophisticated Analytical Instrument Facility (SAIF) for providing the NMR and EPR facilities.

[1] a) J. B. Howard, D. C. Rees, *Chem. Rev.* **1996**, *96*, 2965; b) B. K. Burgees, D. J. Lowe, *Chem. Rev.* **1996**, *96*, 2983; c) R. R. Eady, *Chem. Rev.* **1996**, *96*, 3013; d) J. S. Stamler, D. J. Singel, J. Loscalzo, *Science* **1992**, *258*, 1898; e) E. Culotta Jr, D. E. Koshland, *Science* **1992**, *258*, 1862; f) S. Pfeiffer, B. Mayer, B. Hemmens, *Angew. Chem. Int. Ed.* **1999**, *38*, 1714; g) G. B. Richter-Addo, P. Legzdins, J. Burstyn, *Chem. Rev.* **2002**, *102*, 857; h) S. Moncada, R. M. J. Palmer, E. A. Higgs, *Pharmacol. Rev.* **1991**, *43*, 109; i) G. B. Ritcher-Addo, P. Legzdins in *Metal Nitrosyls*, Oxford University Press, New York, **1992**; j) W. R. Scheidt, M. K. Ellison, *Acc. Chem. Res.* **1999**, *32*, 350; k) K. Karidi, A. Garoufis, A. Tsipis, N. Hadjiliadis, H. D. Dulk, J. Reedijk, *Dalton Trans.* **2005**, 1176; l) N. Bettache, T. Carter, J. E. T. Corrie, D. Ogden, D. R. Trentham in *Methods in Enzymology* (Ed.: L. Packer), Academic Press, San Diego, CA, **1996**, vol. 268, p. 266; m) D. R. Lang, J. A. Davis, L. G. F. Lopes, A. A. Ferro, L. C. G. Vasconcellos, D. W. Franco, E. Tfouni, A. Wieraszko, M. J. Clarke, *Inorg. Chem.* **2000**, *39*, 2294; n) P. C. Ford, J. Bourassa, K. Miranda, B. Lee, I. Lorkovic, S. Boggs, S. Kudo, L. Laverman, *Coord. Chem. Rev.* **1998**, *171*, 185; o) E. Tfouni, M. Krieger, B. R. McGarvey, D. W. Franco, *Coord. Chem. Rev.* **2003**, *236*, 57; p) A. Franke, N. Hessenauer-Ilicheva, D. Meyer, G. Stochel, W. D. Woggon, R. van Eldik, *J. Am. Chem. Soc.* **2006**, *128*, 13611; q) R. K. Afshar, A. A. Eroy-Reveles, M. M. Olmstead, P. K. Mascharak, *Inorg. Chem.* **2006**, *45*, 10347.

[2] a) K. K. Pandey, *Coord. Chem. Rev.* **1983**, *51*, 69; b) V. Zang, R. van Eldik, *Inorg. Chem.* **1990**, *29*, 4462; c) E. K. Pham, S. G. Chang, *Nature* **1994**, *369*, 139.

[3] a) M. Videla, J. S. Jacinto, R. Baggio, M. T. Garland, P. Singh, W. Kaim, L. D. Slep, J. A. Olabe, *Inorg. Chem.* **2006**, *45*, 8608; b) P. Singh, B. Sarkar, M. Sieger, M. Niemeyer, J. Fiedler, S. Zalis, W. Kaim, *Inorg. Chem.* **2006**, *45*, 4602; c) M. Sieger, B. Sarkar, S. Zalis, J. Fiedler, N. Escola, F. Doctorovich, J. A. Olabe, W. Kaim, *Dalton Trans.* **2004**, 1797.

[4] a) J. A. McCleverty, *Chem. Rev.* **1979**, *79*, 53; b) A. Das, C. J. Jones, J. A. McCleverty, *Polyhedron* **1993**, *12*, 327; c) M. H. Thiemens, W. C. Trogler, *Science* **1991**, *251*, 932; d) M. Feelisch, J. S. Stamler (Eds.), *Methods in Nitric Oxide Research*, Wiley, Chichester, England, **1996**; e) J. H. Enemark, R. D. Feltman, *Coord. Chem. Rev.* **1974**, *13*, 339; f) F. Bottomley in *Reactions of Coordinated Ligands* (Ed.: P. S. Braterman), Plenum, New York, **1985**, vol. 2, p. 115; g) P. C. Ford, I. M. Lorkovic, *Chem. Rev.* **2002**, *102*, 993; h) F. Bottomley, *Acc. Chem. Res.* **1978**, *11*, 158; i) F. Roncaroli, M. E. Ruggiero, D. W. Franco, G. L. Estiu, J. A. Olabe, *Inorg. Chem.* **2002**, *41*, 5760.

[5] a) S. P. Fricker, E. Slade, N. A. Powell, O. J. Vaughn, G. R. Henderson, S. A. Murrer, I. C. Megson, S. K. Bisland, F. W. Flitney, *Br. J. Pharmacol.* **1997**, *122*, 1441; b) N. Bettache, T. Carter, J. E. T. Corrie, D. Ogden, D. R. Trentham in *Methods in Enzymology* (Ed.: L. Packer), Academic Press, San Diego, CA, **1996**, Vol. 268, p. 266; c) N. Davies, M. T. Wilson, E. Slade, S. P. Fricker, B. A. Murrer, N. A. Powell, G. R. Henderson, *Chem. Commun.* **1997**, 47; d) Y. Chen, R. E. Shepherd, *J. Inorg. Biochem.* **1997**, *68*, 183; e) J. M. Slocik, M. S. Ward, R. E. Shepherd, *Inorg. Chim. Acta* **2001**, *317*, 290; f) L. G. F. Lopes, A. Wieraszko, Y. El-Sherif, M. J. Clarke, *Inorg. Chim. Acta* **2001**, *312*, 15; g) C. W. B. Bezerra, S. C. Silva, M. T. P. Gambardella, R. H. A. Santos, L. M. A. Plicas, E. Tfouni, D. W. Franco, *Inorg. Chem.* **1999**, *38*, 5660; h) J. W.-S. Hui, W.-T. Wong, *Coord. Chem. Rev.* **1998**, *172*, 389; i) S.-M. Lee, W.-T. Wong, *Coord. Chem. Rev.* **1997**, *164*, 415.

[6] a) A. K. Patra, P. K. Mascharak, *Inorg. Chem.* **2003**, *42*, 7363; b) B. O. Fernandez, I. M. Lorkovic, P. C. Ford, *Inorg. Chem.* **2004**, *43*, 5393.

[7] M. Wolak, G. Stochel, A. Zahl, T. Schneppensieper, R. van Eldik, *J. Am. Chem. Soc.* **2001**, *123*, 9780.

[8] L. E. Laverman, A. Wanat, J. Oszajca, G. Stochel, P. C. Ford, R. van Eldik, *J. Am. Chem. Soc.* **2001**, *123*, 285.

[9] H. Hadadzadeh, M. C. DeRosa, G. P. A. Yap, A. R. Rezvani, R. J. Crutchley, *Inorg. Chem.* **2002**, *41*, 6521.

[10] A. Dovletoglou, S. A. Adeyemi, T. J. Meyer, *Inorg. Chem.* **1996**, *35*, 4120.

[11] N. Chanda, D. Paul, S. Kar, S. M. Mobin, A. Datta, V. G. Puranik, K. K. Rao, G. K. Lahiri, *Inorg. Chem.* **2005**, *44*, 3499.

[12] N. Chanda, S. M. Mobin, V. G. Puranik, A. Datta, M. Niemeyer, G. K. Lahiri, *Inorg. Chem.* **2004**, *43*, 1056.

[13] S. Sarkar, B. Sarkar, N. Chanda, S. Kar, S. M. Mobin, J. Feidler, W. Kaim, G. K. Lahiri, *Inorg. Chem.* **2005**, *44*, 6092.

[14] D. W. Pipes, T. J. Meyer, *Inorg. Chem.* **1984**, *23*, 2466.

[15] B. Mondal, H. Paul, V. G. Puranik, G. K. Lahiri, *J. Chem. Soc., Dalton Trans.* **2001**, 481.

[16] a) A. A. Soudi, F. Marandi, A. Morsali, R. Kempe, I. Hortle, *J. Coord. Chem.* **2005**, *58*, 1631; b) W. Xiang-Li, *J. Inorg. Biochem.* **2004**, *98*, 1143; c) M. Koerner, P. A. Tregloan, R. van Eldik, *Dalton Trans.* **2003**, 2710; d) S. Das, B. K. Panda, *Polyhedron* **2006**, *25*, 2289; e) C. W. Jiang, *Eur. J. Inorg. Chem.* **2004**, *11*, 2217; f) R. Hege, J. G. Haasnoot, J. Reedijk, *Inorg. Chim. Acta* **1990**, *172*, 19.

[17] a) H. Deng, J. Li, K. C. Zheng, Y. Yang, H. Chao, L. N. Li, *Inorg. Chim. Acta* **2005**, *358*, 3430; b) C. W. Jiang, *Inorg. Chim. Acta* **2005**, *358*, 1231; c) C. W. Jiang, *Inorg. Chim. Acta* **2004**, *357*, 3403; d) C. W. Jiang, *J. Inorg. Biochem.* **2004**, *98*, 497; e) C. W. Jiang, H. Chao, X. L. Hong, H. Li, W. J. Mei, L. N. Ji, *Inorg. Chem. Commun.* **2003**, *6*, 773; f) H. Chao, G. Yang, G. Q. Xue, H. Li, H. Zang, I. D. Williams, L. N. Ji, X. M. Chen, X. Y. Li, *J. Chem. Soc., Dalton Trans.* **2001**, 1326; g) X. L. Hong, H. Chao, J. H. Yao, H. Li, L. N. Ji, *Polyhedron* **2004**, *23*, 815.

[18] a) B. Mondal, V. G. Puranik, G. K. Lahiri, *Inorg. Chem.* **2002**, *41*, 5831; b) N. Chanda, B. Mondal, V. G. Puranik, G. K. Lahiri, *Polyhedron* **2002**, *21*, 2033; c) V. J. Catalano, R. A. Heck, A. Ohman, M. G. Hill, *Polyhedron* **2000**, *19*, 1049; d) V. J. Catalano, R. A. Heck, C. E. Immoos, A. Ohman, M. G. Hill, *Inorg. Chem.* **1998**, *37*, 2150.

[19] S. Patra, B. Sarkar, S. Ghumaan, M. P. Patil, S. M. Mobin, R. B. Sunoj, W. Kaim, G. K. Lahiri, *Dalton Trans.* **2005**, 1188.

[20] B. Mondal, M. G. Walawalkar, G. K. Lahiri, *J. Chem. Soc., Dalton Trans.* **2000**, 4209.

 © 2007 Wiley-VCH Verlag GmbH & Co. KGaA, Weinheim 

[21] a) R. Alsfasser, R. van Eldik, *Inorg. Chem.* **1996**, *35*, 628; b) P. Chen, R. Duesing, D. K. Graff, T. J. Meyer, *J. Phys. Chem.* **1991**, *95*, 5850.
[22] a) S. Kar, N. Chanda, S. M. Mobin, A. Datta, F. A. Urbanos, V. G. Puranik, R. Jimenez-Aparicio, G. K. Lahiri, *Inorg. Chem.* **2004**, *43*, 4911; b) B. Sarkar, R. H. Laye, B. Mondal, S. Chakraborty, R. L. Paul, J. C. Jeffery, V. G. Puranik, M. D. Ward, G. K. Lahiri, *J. Chem. Soc., Dalton Trans.* **2002**, 2097; c) A. Juris, V. Balzani, F. Barigelletti, S. Campagna, P. Belser, A. Von Zelewsky, *Coord. Chem. Rev.* **1988**, *84*, 85.
[23] a) T. B. Hedda, H. L. Bozec, *Inorg. Chim. Acta* **1993**, *204*, 103; b) G. B. Deacon, J. M. Patrick, B. W. Skelton, N. C. Thomas, A. H. White, *Aust. J. Chem.* **1984**, *37*, 929.
[24] C. Creutz, *Prog. Inorg. Chem.* **1983**, *30*, 1.
[25] M. Wanner, T. Scheiring, W. Kaim, L. D. Slep, L. M. Baraldo, J. A. Olabe, S. Zalis, E. J. Baerends, *Inorg. Chem.* **2001**, *40*, 5704.
[26] a) V. R. de Souza, A. M. da Costa Ferreira, H. E. Toma, *Dalton Trans.* **2003**, 458; b) B. R. McGarvey, A. A. Ferro, E. Tfouni, C. W. D. Bezerra, I. A. Bagatin, D. W. Franco, *Inorg. Chem.* **2000**, *39*, 3577; c) R. W. Callahan, T. J. Meyer, *Inorg. Chem.* **1977**, *16*, 574; d) P. Diversi, M. Fontani, M. Fuligni, F. Laschi, F. Marchetti, S. Matteoni, C. Pinzino, P. Zanello, *J. Organomet. Chem.* **2003**, *675*, 21.
[27] M. T. Indelli, C. A. Bignozzi, F. Scandola, J.-P. Collin, *Inorg. Chem.* **1998**, *37*, 6084.
[28] F. H. Case, *J. Org. Chem.* **1965**, *30*, 931.
[29] R. G. Wilkins, *The Study of Kinetics and Mechanism of Reaction of Transition Metal Complexes*, Allyn and Bacon, Boston, MA, **1974**.
[30] G. M. Sheldrick, *Program for Crystal Structure Solution and Refinement*, Universität Göttingen, Göttingen, Germany, **1997**.
Received: January 31, 2007
Published Online: May 25, 2007

 © 2007 Wiley-VCH Verlag GmbH & Co. KGaA, Weinheim

**The EUChemSoc Societies have taken the significant step into the future by merging their traditional journals, to form two leading chemistry journals, the *European Journal of Inorganic Chemistry* and the *European Journal of Organic Chemistry*. Three further EUChemSoc Societies (Austria, Czech Republic and Sweden) are Associates of the two journals.**

## COVER PICTURE

**The cover picture shows** the structure and the $^{13}C$ NMR spectrum of $[Ir_6(CO)_{15}]^{2-}$ at 173 K. It features an unprecedented $\mu_2$-bridging carbonyl low frequency shift; the resonances of the terminal $\mu_1$-carbonyl groups are placed at higher frequencies. This unusual trend has been explained by combined use of DFT calculations and solid-state NMR parameters, such us chemical shift tensors and shielding anisotropies. The scalar and *S*pin-*O*rbit (SO) relativistic two-component *Z*ero-*O*rder *R*egular *A*pproximation (ZORA) methods have been employed in the geometry optimization and NMR chemical shift calculations, respectively. The large SO contribution (26.6 ppm) to the $^{13}C$ chemical shifts of the $\mu_2$-bridging CO groups accounts for the position of the experimentally observed resonance. This work outlines the importance of the SO evaluation in cases of atoms connected to heavy metal atoms. Details are discussed in the article by L. Garlaschelli, R. Gobetto et al. on p. 3487ff.

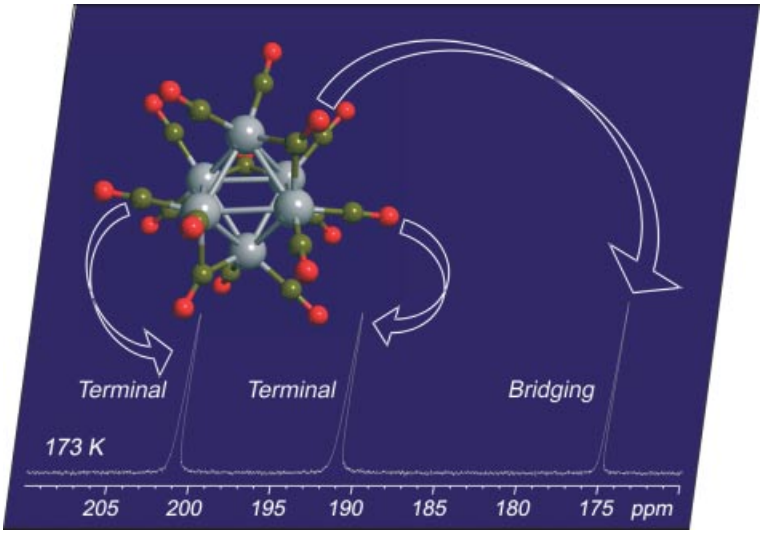


 © 2007 Wiley-VCH Verlag GmbH & Co. KGaA, Weinheim 

# CONTENTS

## MICROREVIEW


### Chirality Transfer

**C. He, Y. G. Zhao, D. Guo,* Z. H. Lin, C. Y. Duan* ..... 3451–3463**

Chirality Transfer through Helical Motifs in Coordination Compounds

**Keywords:** Helical structures / Chirality / Building intermediates / Conformational chirality

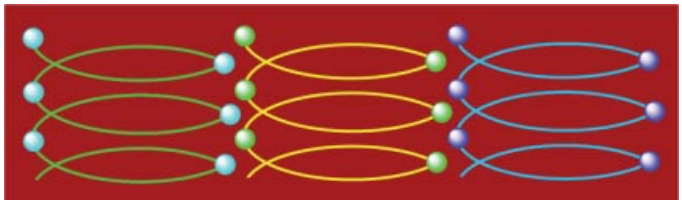

This microreview describes the design of helicates and the structural features that are necessary for chirality transfer. The extension of chirality from one-dimensional to three-dimensional chiral polymers in complicated chiral architectures is also described.


## SHORT COMMUNICATIONS


### Luminescent Lanthanide Complexes

**G. S. Kottas, M. Mehlstäubl, R. Fröhlich, L. De Cola* ..... 3465–3468**

Highly Luminescent, Neutral, Nine-Coordinate Lanthanide(III) Complexes

**Keywords:** Lanthanides / Luminescence / Sensitizers / Energy transfer / Carboxylate ligands

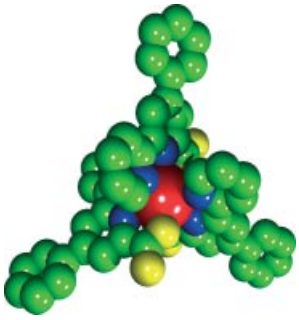

A simple approach to synthesize small and neutral, but highly luminescent lanthanide complexes has been used.

### Bridging Antimony Ligands

**D. Fenske,* A. Rothenberger, S. Wieber ..... 3469–3471**

Synthesis and Characterization of a Gold Complex Containing $[SbPh]^{2-}$ and $[SbPh_2]^-$ Anions as Bridging Ligands

**Keywords:** Bridging ligands / Aurophilicity / Antimony / Gold / Group 15 ligands

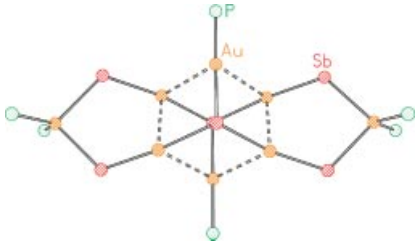


The synthesis and structural characterization of the gold antimony complex $[Au_8(SbPh)_2(SbPh_2)_4(PEt_3)_6]$ is reported. The $Au^I$ ions show weak aurophilic interactions and are bridged by $[SbPh]^{2-}$ and $[SbPh_2]^-$ anions.

### Coordinative Unsaturation

**D. Petrovic, T. Glöge, T. Bannenberg, C. G. Hrib, S. Randoll, P. G. Jones, M. Tamm* ..... 3472–3475**

Synthesis and Reactivity of 16-Electron Pentamethylcyclopentadienyl–Ruthenium(II) Complexes with Bis(imidazolin-2-imine) Ligands

**Keywords:** Ruthenium / Cyclopentadienyl ligands / N ligands / 16-electron complexes / Coordinative unsaturation

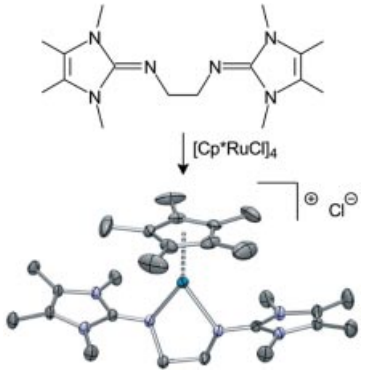


The syntheses of stable 16-electron ruthenium half-sandwich complexes bearing bis(imidazolin-2-imine) ligands are presented and their stabilities are ascribed to the strong π-electron releasing capability of the imine ligand on the basis of experimental results and DFT calculations.


 © 2007 Wiley-VCH Verlag GmbH & Co. KGaA, Weinheim 

# FULL PAPERS

## Unprecedented $\mu_2$-CO Shift

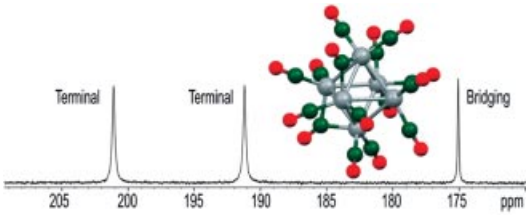


Terminal or bridging CO peak in Ir cluster? The unusual chemical shift of the bridging carbonyl ligands in $[Ir_6(CO)_{15}]^{2-}$ is explained by a combined use of solid-state NMR parameters and DFT calculations.

**M. R. Chierotti, L. Garlaschelli,* R. Gobetto,* C. Nervi, G. Peli, A. Sironi, R. Della Pergola ..... 3477–3483**

An Unusual Carbonyl Chemical Shift in a Carbonylhexairidium Cluster: A Combined Solid-State NMR and DFT Approach

**Keywords:** NMR spectroscopy / DFT calculations / Carbonyl cluster / Iridium / Chemical shift tensors / Shielding anisotropy

## DNA Cleavage

DNA binding and cleavage reactions in the presence of copper(II) terpyridine complexes were investigated, and the effect of the substituent on the terpyridine ring was explained by computational studies.

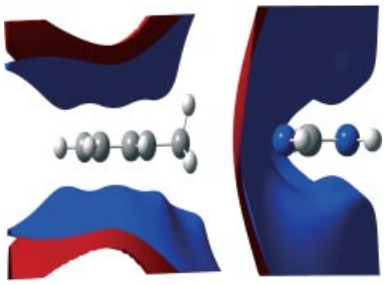

**V. Uma, M. Elango, B. U. Nair* ..... 3484–3490**

Copper(II) Terpyridine Complexes: Effect of Substituent on DNA Binding and Nuclease Activity

**Keywords:** Copper / Tridentate ligands / DNA binding / Nuclease activity

## Phosphorus Heterocycles

[2+3] Cycloaddition of phosphaalkynes with trimethylsilyldiazomethane derivatives proceeds in spite of the presence of a bulky Mes* (= 2,4,6-$t$Bu$_3$C$_6$H$_2$) group which exceedingly stabilizes the C≡P moiety. The corresponding [2+3] adducts, 1,2,4-diazaphospholes, show dimer or trimer structure connected by hydrogen bonds. The first observed trimer structure of 1,2,4-diazaphosphole includes effects of the bulky aryl group enhancing the molecular aggregation by the CH–π interaction.

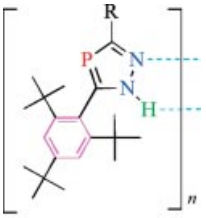


$n$ = 2 (R = SiMe$_3$)
3 (R = H)

**S. Ito,* H. Miyake, M. Yoshifuji* ..... 4911–3496**

1,3-Dipolarophile Character of an Extremely Bulky Phosphaalkyne Mes*C≡P (Mes* = 2,4,6-$t$Bu$_3$C$_6$H$_2$) Leading to the Formation of 1,2,4-Diazaphospholes with Unique Hydrogen Bonding Properties

**Keywords:** Heterocycles / Phosphaalkynes / Cycloaddition / Hydrogen bonds / DFT calculations / X-ray crystallography

## Carbonylation on Metal Surfaces

The reductive carbonylation of ruthenium and osmium halides in the presence of cobalt and iron surfaces has been used for synthesis of mixed-metal complexes. Linear, dimetallic, chlorido-bridged, trinuclear complexes $[M_2Cl_2(\mu\text{-}Cl)_4(CO)_6M'(L)_2]$ (M = Ru, Os; M′ = Fe, Co; L = $CH_3CH_2OH$, $H_2O$) were obtained through the interaction between reducing $RuCl_3$ or $OsCl_3$ and the oxidizing solid metal surface.

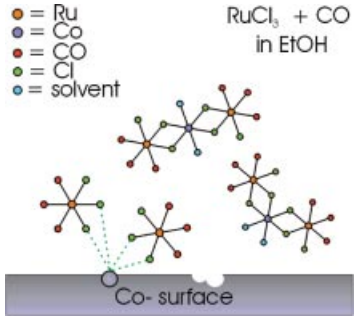


**M. Jakonen, P. Hirva, T. Nivajärvi, M. Kallinen, M. Haukka* .... 3497–3588**

Surface-Assisted Synthesis and Behavior of Dimetallic Mixed-Metal Complexes $[M_2Cl_2(\mu\text{-}Cl)_4(CO)_6M'(L)_2]$ (M = Ru, Os; M′ = Fe, Co; L = $CH_3CH_2OH$, $H_2O$)

**Keywords:** Ruthenium / Osmium / Cobalt / Iron / Synthesis design

 © 2007 Wiley-VCH Verlag GmbH & Co. KGaA, Weinheim 

# CONTENTS

## Chromium Complexes

**F. A. Cotton, Z. Li, C. A. Murillo* ..... 3509–3513**

Precursors for Assembly of Supramolecules Containing Quadruply Bonded $Cr_2^{4+}$ Units: Systematic Preparation of $Cr_2$(formamidinate)$_n$(acetate)$_{4-n}$ ($n$ = 2–4)

**Keywords:** Metal–metal bonds / Supramolecular chemistry / Chromium / Corner piece precursors

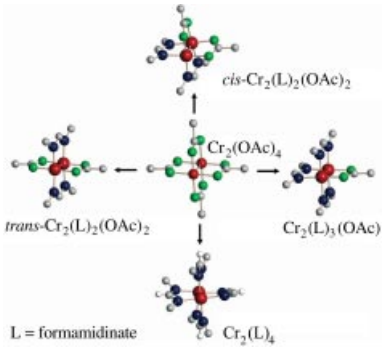


Quadruply bonded dichromium complexes with a mixed set of ligands having different labilities, $Cr_2$(formamidinate)$_n$(acetate)$_{4-n}$ ($n$ = 2–4), were synthesized to serve as corner-piece precursors for assembly of large molecules by selective substitution of the labile acetate groups by polydentate dianions.

## Mixed-Valence Compounds

**B. M. Casari,* V. Langer ..... 3514–3518**

New Open-Framework Mixed-Valence Chromium(III) Cerium(III)/(IV) Sulfate: $CrCe^{III}_7Ce^{IV}_6(HSO_4)_6(SO_4)_{21}\cdot 75H_2O$

**Keywords:** Mixed-valent compounds / Lanthanides / Cerium sulfate / X-ray diffraction

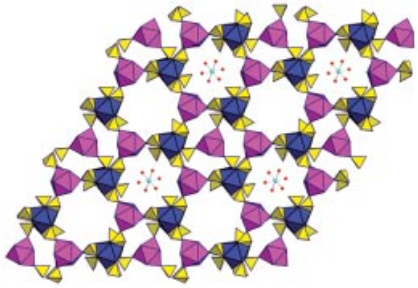

The cerium atoms, interlinked by sulfate groups, extend to form layers held together by hydrogen-bonding contacts. Perpendicular to these layers there are 10 Å wide channels.

## Cofacial Bismetallophthalocyanine

**M. Özer, A. Altındal, A. R. Özkaya, B. Salih, M. Bulut, Ö. Bekaroğlu* ..... 3519–3526**

Synthesis, Characterization, and Electrochemical and Electrical Properties of Novel Pentaerythritol-Bridged Cofacial Bismetallophthalocyanines and Their Water-Soluble Derivatives

**Keywords:** Phthalocyanines / Cofacial configuration / Synthesis / Cyclic voltammetry / Thermopower

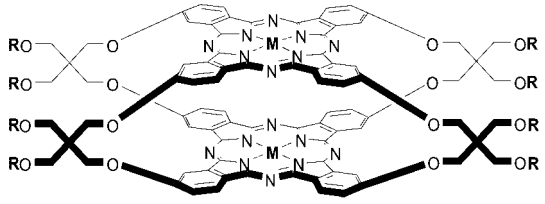


Novel cofacial bismetallophthalocyanines were synthesized at 300 °C. The resulting Pcs accommodating four pentaerythritol monoacetal side groups were hydrogenated. The target water-soluble cofacial bismetallophthalocyanines were obtained by heating suspensions of the compounds bearing the eight OH side groups in aqueous KOH.

## Wanzlick Carbenes

**M. K. Denk,* A. Hezarkhani, F.-L. Zheng ..... 3527–3534**

Steric and Electronic Effects in the Dimerization of Wanzlick Carbenes: The Alkyl Effect

**Keywords:** Carbenes / Thiourea / Thermochemistry / Dimerization / Enetetramine / Steric hindrance / DFT calculations / Steric effects / Electronic effects

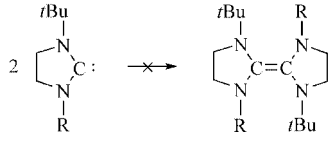


| | $\Delta G^\circ$ [kcal] |
|---|---|
| R = Me | –0.9 |
| R = Et | +2.1 |
| R = *i*Pr | +4.5 |
| R = *t*Bu | +25.5 |

The study of Wanzlick carbenes with mixed *N*-alkyl substitution reveals the relative importance of electronic and steric effects preventing dimerization to the respective enetetramines.

 © 2007 Wiley-VCH Verlag GmbH & Co. KGaA, Weinheim 

## Sulfur Imides

The structure of (*Z*)-$CF_3CF_2N{=}SCl_2$ is determined by X-ray diffraction analysis at low temperature. The central sulfur(+IV)−imide bond is well described by the NBO analysis model as a semipolar $S^+{-}N^-$ bond with strong hyperconjugative interactions.

**N. L. Robles, R. M. S. Álvarez, E. H. Cutin, C. O. Della Védova,* M. F. Erben, R. Boese, H. Willner, R. Mews ..... 3535−3542**

Anomeric Interactions in Pentafluoroethylimidosulfurous Dichloride, $CF_3CF_2N{=}SCl_2$: Structural, Conformational and Configurational Properties in the Gaseous and Condensed Phases

**Keywords:** Imides / Conformation analysis / Structural analysis / Hyperconjugation / Sulfur

## Multidentate Ligands

The general stereochemical features of cobalt thiodiacetate and oxydiacetate complexes are illustrated on the basis of the available structural data and some new crystal structures presented in this paper (red dots).

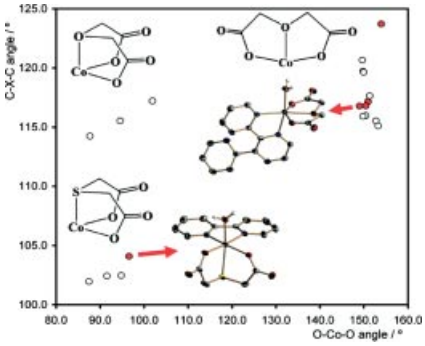


**A. Grirrane, A. Pastor, E. Álvarez, C. Mealli, A. Ienco, P. Rosa, A. Galindo* ..... 3543−3552**

Thiodiacetate and Oxydiacetate Cobalt Complexes: Synthesis, Structure and Stereochemical Features

**Keywords:** Cobalt / Thiodiacetate / Oxydiacetate / Tridentate Ligands / Coordination modes

## Alkynylplatinum Complexes

The platinum complexes *cis*-[{$Pt(PPh_2C{\equiv}CR)_2(\mu\text{-}\eta^1{:}\eta^2\text{-}C^\alpha,C^\beta\text{-}C{\equiv}CC_6H_4C{\equiv}CPh)_2$}-$Pt(C_6F_5)_2$] (**4**, **5**) and [{$Pt(\mu\text{-}\eta^1{:}\eta^2\text{-}C^\alpha,C^\beta\text{-}C{\equiv}CC_6H_4C{\equiv}CPh)_2(\mu\text{-}1\kappa P{:}2\eta^2\text{-}C^\alpha,C^\beta\text{-}PPh_2C{\equiv}CR)_2$}$\{Pt(C_6F_5)_2\}_2$] (**6**, **7**) stabilized by double ethynyltolan or mixed ethynyltolan/(arylalkynyl)phosphane bridging systems, respectively, have been synthesised from *cis*-[$Pt(C{\equiv}CC_6H_4C{\equiv}CPh)_2(PPh_2C{\equiv}CR)_2$] by treatment with *cis*-[$Pt(C_6F_5)_2(thf)_2$].

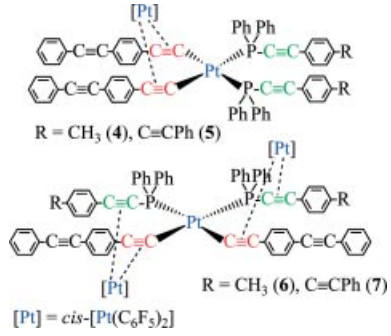


**A. García, E. Lalinde,* M. T. Moreno ..... 3553−3560**

Ethynyltolan Platinum Complexes with (Arylalkynyl)phosphane Ligands

**Keywords:** Alkyne ligands / Phosphane ligands / Platinum / X-ray diffraction

## InCp* Coordination Chemistry

Reaction of the hexanuclear carbonyl rhodium cluster $Rh_6(CO)_{15}(NCMe)$ with InCp* complex under mild conditions results in the formation of $Rh_6(CO)_{16-x}(InCp^*)_x$, $x = 1-2$ clusters.

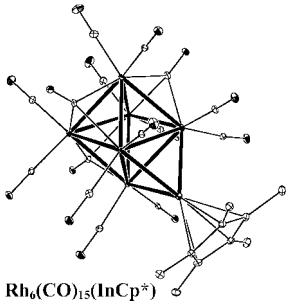


**E. V. Grachova,* G. Linti ..... 3561−3564**

Reactivity of InCp* Towards Transition Metal Carbonyl Clusters: Synthesis and Structural Characterization of the $Rh_6(CO)_{16-x}(InCp^*)_x$ Mixed-Metal Cluster Compounds, $x = 1-2$

**Keywords:** Rhodium / Indium / Cluster compounds

 © 2007 Wiley-VCH Verlag GmbH & Co. KGaA, Weinheim 

# CONTENTS

## $H_2$ Elimination Reactions

**O. Ciobanu, H.-J. Himmel* .... 3565–3572**

Repeated Dihydrogen Elimination from Boranes and Gallanes Stabilized by Guanidine-Type Bases: A Quantum Chemical Study Motivated by Recent Experimental Results

**Keywords:** Hydrides / Group 13 elements / Quantum chemical calculations / Hydrogen storage

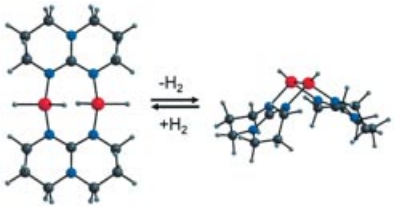


The thermodynamic properties of repeated $H_2$ eliminations from guanidine-stabilized group 13 element hydrides are analysed on the basis of quantum chemical calculations. Some of these reactions might be interesting for hydrogen storage and/or olefin hydrogenation.

## Oxotitanium Phthalocyanines

**D. Atilla, M. Durmuş, Ö. Yılmaz, A. G. Gürek, V. Ahsen, T. Nyokong* ..... 3573–3581**

Synthesis, Photophysical and Photochemical Properties of Poly(oxyethylene)-Substituted Phthalocyaninato Oxotitanium(IV) Complexes

**Keywords:** Phthalocyanine / Titanium / Quantum yields / Singlet oxygen / Fluorescence

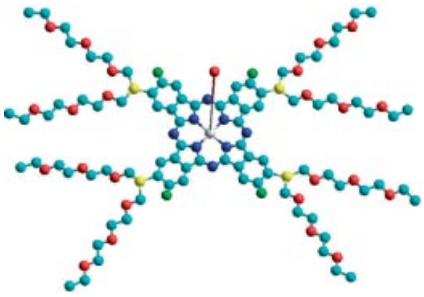

The synthesis, photophysical and photochemical properties of tetra- and chlorotetrapoly(oxyethylene)-substituted oxotitanium(IV) phthalocyanines are reported for the first time. The complexes show high singlet oxygen quantum yields, which make them useful for PDT applications.

## Vanadium Organophosphonates

**N. H. Thong, J. K. Jabor, R. Stößer, M. Meisel,* B. Ziemer ..... 3582–3593**

Localization and Delocalization of Spin Density in Mixed-Valence ($V^{IV}/V^{V}$) $[(V_2O_3)_2(PhPO_3)_4\subset F]^{-n}$ ($n$ = 1, 2): Theoretical and Experimental Studies

**Keywords:** Adsorption / DFT calculation / ESR / Hyperfine structure / Vanadium / Cage compounds

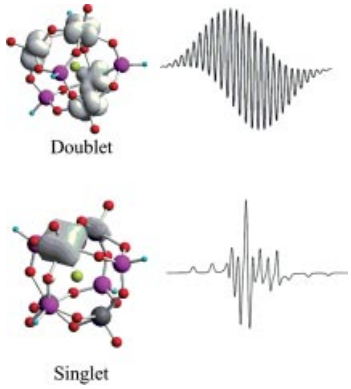


DFT calculations were carried out to determine the energies and spin-density distribution for the cage $[(V_2O_3)_2(PhPO_3)_4\subset F]^{-n}$ structures with the symmetries $D_{2d}$, $C_{2v}$, and $C_s$. The calculated hyperfine coupling constants are in a good agreement with those determined by ESR spectroscopy. A proposal is given for the localization/delocalization of spin density based on thermally driven fluctuations of the cage geometry or alternatively by hopping of the unpaired electron inside the cage.

**If not otherwise indicated in the article, papers in issue 21 were published online on July 9, 2007**

 © 2007 Wiley-VCH Verlag GmbH & Co. KGaA, Weinheim

**The EUChemSoc Societies have taken the significant step into the future by merging their traditional journals, to form two leading chemistry journals, the *European Journal of Inorganic Chemistry* and the *European Journal of Organic Chemistry*. Three further EUChemSoc Societies (Austria, Czech Republic and Sweden) are Associates of the two journals.**

## COVER PICTURE

**The cover picture shows** the structure and the $^{13}C$ NMR spectrum of $[Ir_6(CO)_{15}]^{2-}$ at 173 K. It features an unprecedented $\mu_2$-bridging carbonyl low frequency shift; the resonances of the terminal $\mu_1$-carbonyl groups are placed at higher frequencies. This unusual trend has been explained by combined use of DFT calculations and solid-state NMR parameters, such us chemical shift tensors and shielding anisotropies. The scalar and *S*pin-*O*rbit (SO) relativistic two-component *Z*ero-*O*rder *R*egular *A*pproximation (ZORA) methods have been employed in the geometry optimization and NMR chemical shift calculations, respectively. The large SO contribution (26.6 ppm) to the $^{13}C$ chemical shifts of the $\mu_2$-bridging CO groups accounts for the position of the experimentally observed resonance. This work outlines the importance of the SO evaluation in cases of atoms connected to heavy metal atoms. Details are discussed in the article by L. Garlaschelli, R. Gobetto et al. on p. 3487ff.

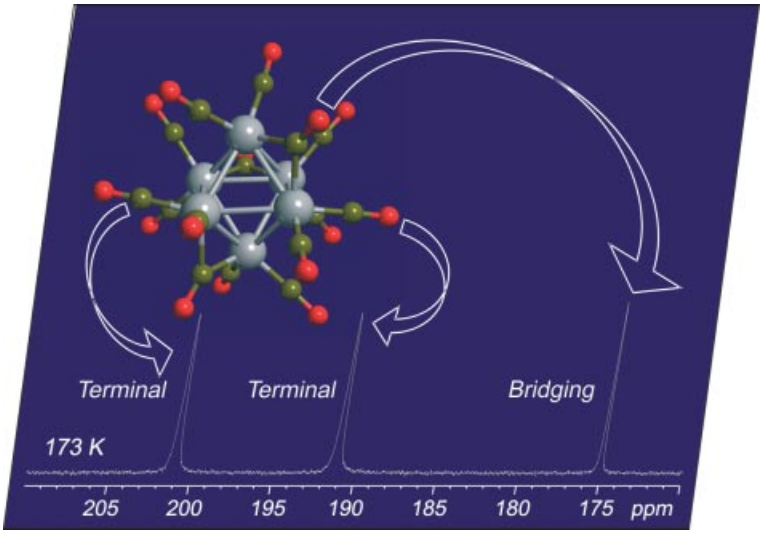


 © 2007 Wiley-VCH Verlag GmbH & Co. KGaA, Weinheim 

# SPOTLIGHTS …

## *Phosphaalkenes*

M. Song, B. Donnadieu,
M. Soleilhavoup, G. Bertrand*

**Synthesis of Phosphaformamidines and Phosphaformamidinates**

*Chem. Asian J.*
DOI: **10.1002/asia.200700103**

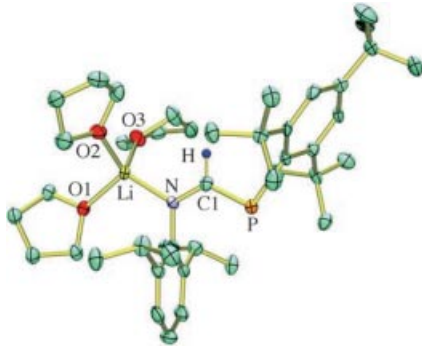


**Forming a formation**: Phosphaformamidines and -formamidinates can be readily prepared by reaction of *N*-arylformimidates with lithium phosphanides. These compounds were previously inaccessible by methods for the preparation of phosphaamidines and -amidinates. They have the potential to be precursors of P,N-heterocyclic carbenes, which are as yet unknown.

## *Chemical Chaperones*

K. Stankunas, J. H. Bayle,
J. J. Havranek, T. J. Wandless,
D. Baker, G. R. Crabtree,
J. E. Gestwicki*

**Rescue of Degradation-Prone Mutants of the FK506-Rapamycin Binding (FRB) Protein with Chemical Ligands**

*ChemBioChem*
DOI: **10.1002/cbic.200700087**

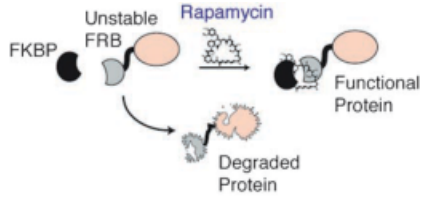


**Chemical chaperones**. Single point mutations in the ligand-binding pocket of the FK506-rapamycin binding (FRB) protein were found to severely damage its folding and stability. However, addition of a chemical ligand, rapamycin, stabilized the mutants and protected them from degradation in cells or thermal denaturation in vitro.

## *Time-Resolved Spectroscopy*

E. Fron, G. Schweitzer, J. Jacob,
A. Van Vooren, D. Beljonne,
K. Müllen, J. Hofkens,
M. Van der Auweraer,
F. C. De Schryver*

**Singlet–Singlet Annihilation Leading to a Charge-Transfer Intermediate in Chromophore-End-Capped Pentaphenylenes**

*ChemPhysChem*
DOI: **10.1002/cphc.200700136**

**Higher excited states**: A singlet–singlet annihilation mechanism was found to promote one chromophore into a higher excited state, thus allowing observation of an ultrashort-living intermediate charge-transfer (CT) state in the $S_n$–$S_1$ deactivation pathway (see picture).

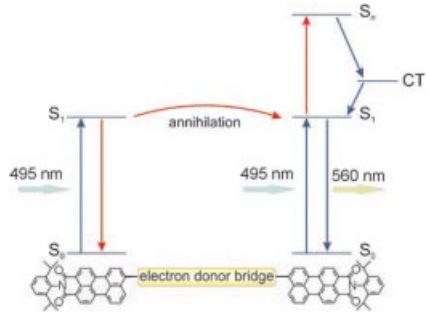


## *Drug Lead Optimization*

M. Morgenthaler, E. Schweizer,
A. Hoffmann-Röder, F. Benini,
R. E. Martin, G. Jaeschke, B. Wagner,
H. Fischer, S. Bendels, D. Zimmerli,
J. Schneider, F. Diederich,*
M. Kansy,* K. Müller*

**Predicting and Tuning Physicochemical Properties in Lead Optimization: Amine Basicities**

*ChemMedChem*
DOI: **10.1002/cmdc.200700059**

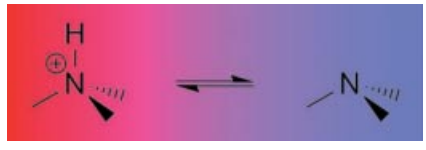


**Predicting and tuning** amine basicity is one of the crucial factors determining physicochemical properties of leads in drug-discovery research. We present simple-to-use rules for p$K_a$ prediction based on extensive database mining and several case studies from our medicinal chemistry programs over the last years. Stereochemical and conformational factors influencing amine basicity are discussed, and the emergent computational approaches to p$K_a$ predictions are briefly surveyed.


© 2007 Wiley-VCH Verlag GmbH & Co. KGaA, Weinheim

# … ON OUR SISTER JOURNALS

EurJIC European Journal of Inorganic Chemistry

**High nuclearity, but low oxidation states**: A family of high-nuclearity vanadium(III/IV/V) clusters (an example of which is shown here; green: vanadium; red: oxygen; grey: carbon) are reported, analogous to the polyoxo(alkoxo)vanadates but in uniquely low oxidation states.

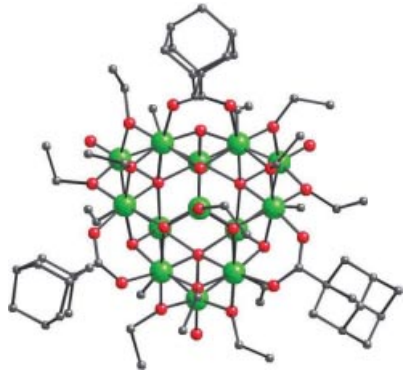

## *Polyoxometalates*

I. S. Tidmarsh, R. H. Laye,*
P. R. Brearley, M. Shanmugam,
E. C. Sañudo, L. Sorace, A. Caneschi,
E. J. L. McInnes*

**Highly Reduced, Polyoxo(alkoxo)vanadium(III/IV) Clusters**

*Chem. Eur. J.*
DOI: **10.1002/chem.200700247**

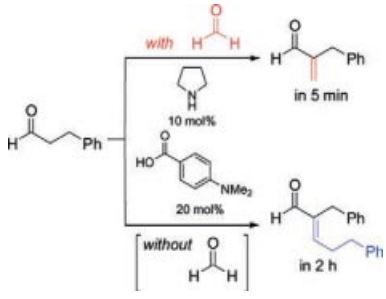


An efficient secondary amine catalyst/acid co-catalyst combination has been identified, allowing the preparation of α-substituted acroleins and α,β-unsaturated aldehydes in a matter of minutes.

## *Amine Catalysis*

A. Erkkilä, P. M. Pihko*

**Rapid Organocatalytic Aldehyde-Aldehyde Condensation Reactions**

*Eur. J. Org. Chem.*
DOI: **10.1002/ejoc.200700292**

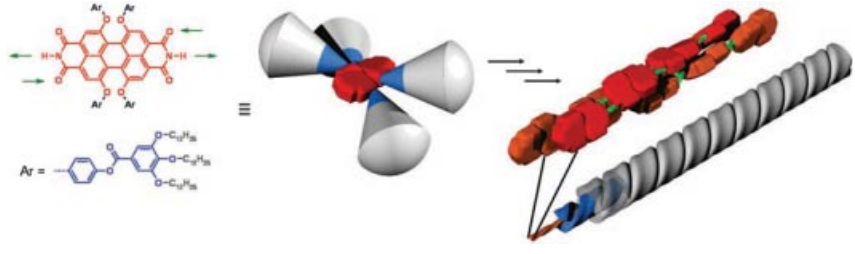


**Luminous nanorods**: The self-assembly of core-twisted perylene bisimide fluorophores (see structures) in nonpolar organic solvents is directed by hydrogen-bonding interactions. This supermolecular concept resulted in one-dimensional J-aggregates with a fluorescence quantum yield of near unity.

## *Self-Assembly Processes*

T. E. Kaiser, H. Wang,
V. Stepanenko, F. Würthner*

**Supramolecular Construction of Fluorescent J-Aggregates Based on Hydrogen-Bonded Perylene Dyes**

*Angew. Chem. Int. Ed.*
DOI: **10.1002/anie.200701139**

On these pages, we feature a selection of the excellent work that has recently been published in our sister journals. If you are reading these pages on a computer, click on any of the items to read the full article. Otherwise please see the DOIs for easy online access through Wiley InterScience.

 © 2007 Wiley-VCH Verlag GmbH & Co. KGaA, Weinheim 

DOI: 10.1002/ejic.200700360

# Chirality Transfer through Helical Motifs in Coordination Compounds

Cheng He,[a] Yonggang Zhao,[a] Dong Guo,*[b] Zhihua Lin,[a] and Chunying Duan*[a]

**Keywords:** Helical structures / Chirality / Building intermediates / Conformational chirality

Helicates obtained by self-assembly have initiated a revolution from classical coordination chemistry to extensive supramolecular concepts. The design of helicates will be described, and the structural features that are necessary for chirality transfer, as well as the extension of chirality from one-dimensional to three-dimensional chiral polymers in complicated chiral architectures will also be addressed. Chiral assembly by using achiral components has been given considerable attention in this review paper. The understanding of the essential processes and mechanisms in the chiral assembly on the basis of helicate supramolecular structures is a fundamental study in a variety of disciplines ranging from biology to materials science.

(© Wiley-VCH Verlag GmbH & Co. KGaA, 69451 Weinheim, Germany, 2007)

## 1. Introduction

The term helicate was introduced by Lehn in 1987 to describe a discrete metal-based helix comprising one or more covalent organic strands wrapped and coordinated to a series of ions defining the helical axis.[1] Such kinds of complexes have elegantly illustrated how the specific formation of architecturally complicated assemblies are directed by the interplay between relatively simple parameters such as the stereoelectronic preference of the metals and the position of the binding sites of the helicands (helicating ligands). Previously, the chemistry of helicates was reviewed thoroughly with a focus on the description of the topologies and conformations of the helical structures, as well as an investigation into the design of special helicates.[2,3]

Chirality is the intrinsic character of helicates. It can be right-handed (plus, *P*) or left-handed (minus, *M*), depending on whether the rotation is clockwise or anticlockwise when a helicate is considered to wind from the eye of the viewer towards a distant point from the viewer. If we neglect the helical domain produced by the spacers between the binding units, the chirality of a helicate would be deduced from the absolute configurations of the metal centers (Figure 1). Clearly, chiral helicates will be created only when the metal ions in the helical axis display the same absolute configuration. Because they are constructed from achiral components, the helical molecular assemblies in the crystalline phase have two possibilities: either the crystals are composed of both *P* and *M* helices (centric space group) to afford an internal racemate or by a spontaneous resolution process where each crystal is enantiomerically pure (*P* or *M* helicity, chiral space group), but the mixture of crystals is racemic, as a so-called conglomerate.[4] A much more interesting case for the latter is homochiral crystallization, by which all the crystals obtained in one crystallization have the same chirality. Usually, the interhelicate interactions associated with donor (or acceptor) groups hosted on the chiral helicates should be always directional and homochiral. If such kinds of interactions are substantially strong, the chiralities of the metal centers could be extended into high-dimensional frameworks to achieve the complicated chiral species. Whereas a large number of chiral superstructures were developed through the covalent arrangements of chiral building blocks at the molecular level by using the "bottom-up" strategy,[5] the chiral assembly from achiral components on the basis of helical motifs is of current interest in both supramolecular chemistry and materials science as one of the most attractive and evocative strategies. This microreview will focus on the current research developments in the structural features and the design of helicates modulating the transfer of chirality between metal ions, and chirality extension in the formation of high-dimensional chiral polymers.

[a] State Key Laboratory of Fine Chemicals, Dalian University of Technology,
Dalian 116012, China
E-mail: cyduan@dlut.edu.cn
[b] School of Materials Science and Engineering, Wuhan Institute of Technology,
Wuhan 430073, China
E-mail: dn_guo@yahoo.com

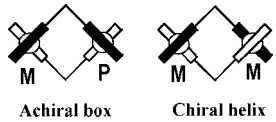


Figure 1. Helical and chiral properties of double-stranded dinuclear helicate with $C_2$ symmetrical ligand strands.

 © 2007 Wiley-VCH Verlag GmbH & Co. KGaA, Weinheim 

## 2. Discrete Oligonuclear Helicates – Local Chiral Translation in Helicates

Oligonuclear helicates, especially dinuclear helicates, are one kind of classical helicates that have been investigated most extensively. Proverbially, single-, double-, and triple-stranded helicates possess one, two, and three coordinated strands wrapped around the metal ions, respectively. The ligands are obviously partitioned into two or more distinct multidentate (commonly bidentate) binding sites with a spacer linking them together. For a dinuclear double helical architecture, it is postulated that the chosen spacer should have enough rigidity to sterically prevent the two binding sites from coordinating to one single metal center, and in the mean time it should also have enough flexibility to permit it to wrap around the metal–metal axis.[2,3,6] However, investigations on the construction of helicates by using ligands $L^1-L^4$ (Figure 2)[7–10] showed that each ligand spans both metal ions but does not wrap over (from one side to the other) the metal–metal axis (Figure 3). Despite the fact that both the rigidity of the ligands and the close proximity of the two metal centers seem to be unfavorable for the formation of helicates, the absolute configurations of the two metal centers in each molecule are identical. Further structural studies of double and triple helicates with two pyridylimine units linked by a single –N–N– confirm that

*Dr. Cheng He was born in 1973. He completed his Ph.D. in 2000 under the supervision of Profs. Chunying Duan and Qingjin Meng at Nanjing University, China. After postdoctoral studies at Peking University and the Pohang University of Technology, he was awarded the Alexander von Humboldt fellowship and then worked with Prof. Herbert W. Roesky as a postdoctoral researcher at Goettingen University. Since 2006 he has been an Associate Professor at the Dalian University of Technology. His research interests are in the area of coordination chemistry.*

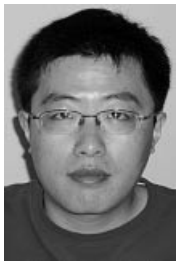

*Yonggang Zhao completed his B.S. in Polymer Materials Science in 1996 at Nanjing University, China. Five years later, he returned to Nanjing University and joined Prof. Chunying Duan's group. After finishing his Ph.D. in 2006, he moved to the Dalian University of Technology as a postdoctoral fellow. Currently, his research focuses on molecular assembly and modulation in the metal-directed self-assembly of functional molecules.*

*Dong Guo was born in 1973. He completed his Ph.D. in 2003 under the supervision of Profs. Chunying Duan and Qingjin Meng at Nanjing University, China. He then worked with Prof. James K. McCusker as a postdoctoral researcher at Michigan State University. His main research interests are in the areas of inorganic and materials chemistry.*

*Zhihua Lin completed her undergraduate studies in chemistry at Fuzhou University, Fuzhou, China, in 2000. She completed her Ph.D. in 2006 under the supervision of Prof. Chunying Duan and Dr. Zhiping Bai at Nanjing University. She then moved to the Dalian University of Technology as a postdoctoral fellow. Her current research interests are focused on the self-assembly and host–guest chemistry of cage compounds.*

*Prof Chunying Duan was born in 1967, China. He completed his Ph.D. in 1992 under the supervision of Prof. Xiaozeng You and Yuansheng Jiang at Nanjing University. He then started his academic career in the Department of Chemistry at Nanjing University. Since 2006, he has worked at the DaLian University of Technology. His research interests cover aspects of coordination chemistry, supramolecular chemistry, molecular sensors, and chiral materials.*

 © 2007 Wiley-VCH Verlag GmbH & Co. KGaA, Weinheim 

the nonplanar bridging mode might be essential for such kinds of ligands to encode metal ions in the formation of helicates.[11] From a mechanistic viewpoint, upon coordination, the rotating freedom of the –N–N– bonds on the ligands is restrained, and the ligands can be locked in an atropisomerically chiral conformation. At the same time, the strong and directional bonding interactions could transmit the original chirality of one metal center to another, leading to the formation of the helical species. Reasonably, it suggests that in both double and triple helicates, there is not any necessary relationship between their formation and the rigidity/flexibility of the spacers in ligands. In other words, the chirality translation between the metal centers only occurs when the bridging modes of the ligands exhibit atropisomeric chiralities in the formation of a helicate.

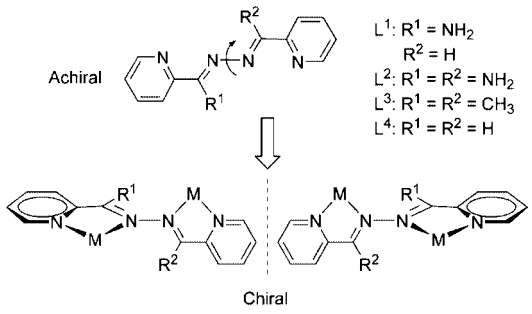


Figure 2. Diazine ligands and generation of conformational chirality.[9]

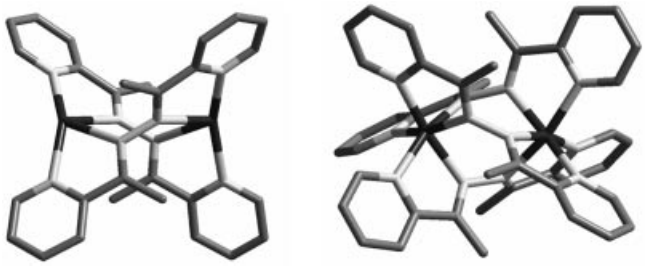

Figure 3. Structures of helicates $Ag_2L^3_2$ (left) and $Co_2L^3_3$ (right). The rigid ligands are twisted but not wrap over the metal centers.[10]

This type of chirality translation through atropisomeric chiral bridging modes of the ligands could also be observed directly in the formation of helicates that are based on biphenyl ligands (Figure 4).[12,13] For example, ligand $L^5$ in solution is achiral due to the free rotation about the two phenyl groups.[12] In the solid state, however, this ligand shows atropisomeric chirality due to the constraint of the rotation around the C–C bond as described as a monohelix. Upon coordination to the metal centers as a bridge, such a special conformation of the ligand induces the formation of helical species with the metal centers being homochiral, even in the case where the two metal centers are bridged by one ligand. Similar atropisomeric chiralities of ligands were observed in several other dinuclear monohelicates of which

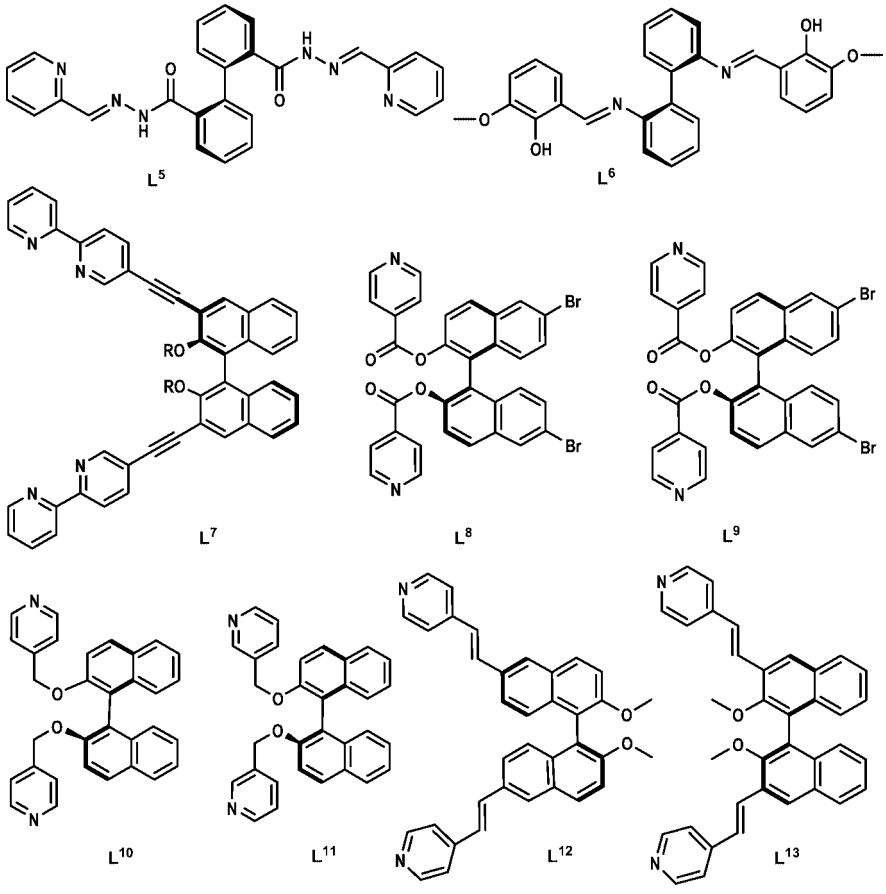


Figure 4. Ligands exhibiting an atropisomerically chiral bridging mode.[12,13,15–18]

 © 2007 Wiley-VCH Verlag GmbH & Co. KGaA, Weinheim 

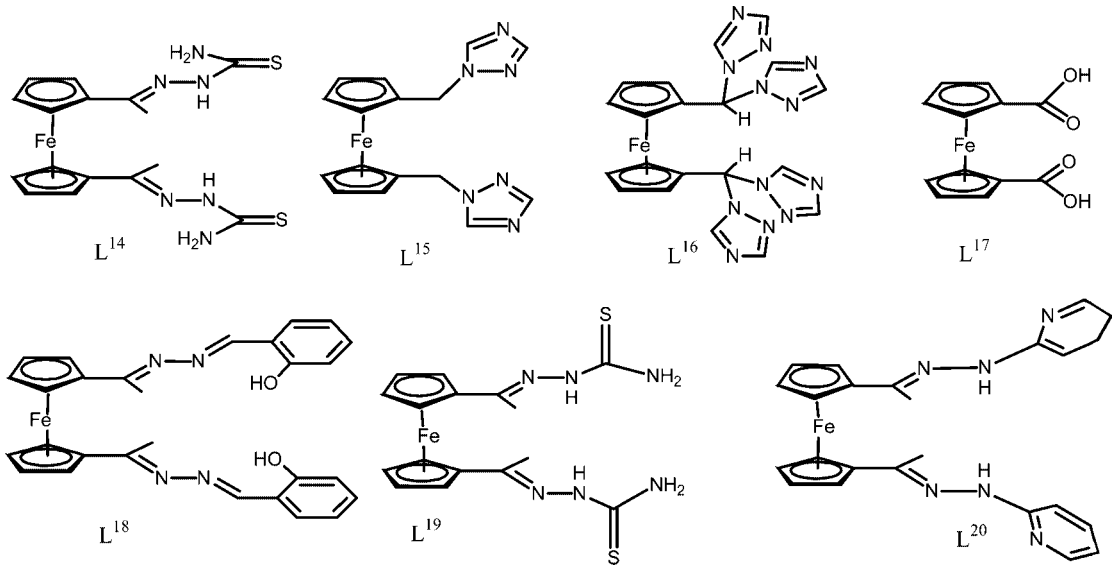


Figure 5. Ferrocene-containing ligands exhibiting a conformationally chiral bridging mode.[19,20,29,30,32]

the chiralities are determined by the helicands themselves rather than the metal centers.[14]

Another evidence to support the above hypothesis comes from the assembly of enantiopure double helicates derived from conformationally chiral ligand $L^7$. Generally, enantiomerically pure chiral ligands only introduce a second source of chirality into the helicates, forming diastereomers according to the screw turn and the arrangement of the ligands. However, in the resulting triple helicate $Zn_2L^7{}_3$, the configurations of the stereogenic metal centers are completely controlled by the atropisomeric chiral configuration of the binaphthyl groups, and the discrete dinuclear complex adopts an overall $D_3$ symmetric *P* configuration with both of the two octahedral metal centers exhibiting the Δ configuration.[15] In fact, a lot of homochiral discrete polynuclear complexes and infinite coordination polymers were constructed by introducing the binaphthyl group as the stereogenic resource of conformational chirality (Figure 4).[16–18]

Two-armed, multidentate, ferrocene-containing compounds are another sort of ligands that could efficiently translate chirality from one transition metal center to the others (Figure 5).[19,20] Generally, the 1,1′-substituted ferrocene derivatives exhibit a planar chirality. When they act as bridging ligands to coordinate to metal centers in the formation of the helicates, atropisomeric chirality of the ligand is generated and replicated with the bridged metal centers being homochiral (Figure 6).

In terms of the structural requirements of bridging ligands for chirality translation between metal centers, the principle obtained from the dinuclear species − *that the chirality transformation between the metal centers occurs only when the bridging mode of the ligands exhibit conformational chiralities* − should be valid to explain the formation of some complicated helicates besides the dinuclear helicates.[21] For example, in the trinuclear $Cu^I$ complex derived from ligand $L^3$ and a variety of other circular helicates,[22–24] the nonplanar bridging modes of these ligands

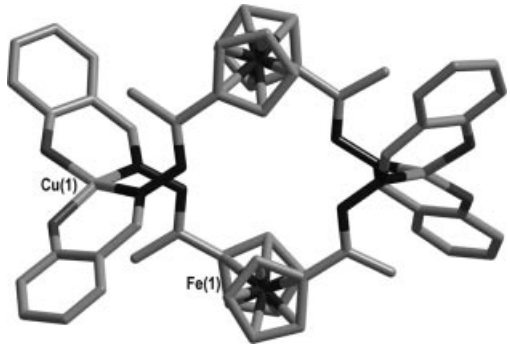


Figure 6. Molecular structure of the copper–ferrocene helicate $Cu_2L^{18}{}_2$.[20]

are likely to facilitate the chirality transfer, which results in homochiral metal centers. Whereas in the metallocycles derived from the ligands containing carboxhydrazone units, the planar bridging conformation causes the formation of achiral species, despite the presence of a similar –N–N– bond within the backbone of the ligands.[25]

Recent developments in the design and assembly of helical species have spanned to the construction of supramolecular architectures by hydrogen bonding and coordination bonding. As shown in Figure 7, two ligands $L^{21}$ coordinate

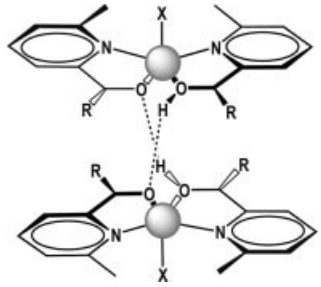

Figure 7. Hydrogen-bond-linked dinuclear helicates $Co_2L^{21a}{}_2X_2$, $L^{21a}$,R = H; $L^{21b}$, R = $CH_3$, X = Cl, Br, $NO_3$.[26,27]

 © 2007 Wiley-VCH Verlag GmbH & Co. KGaA, Weinheim 

to a cobalt(II) atom in a bis(bidentate) fashion by the pyridyl and alcohol donor groups.[26] Two chelating units are twisted through the O–H···O hydrogen bond, achieving a new conformational chirality, which is transmitted from one cobalt center to another by hydrogen bonds between the alcohol oxygen atoms. Interestingly, when the alcohol carbon atom is stereogenic, the chirality at this point could control the absolute configurations of the metal centers and the helicity sense of the overall structure.

## 3. Aggregation of Oligonuclear Helicates – Chirality Translation in Supramolecular Assemblies

Whereas the basic requirements for the design of a discrete helicate from achiral components have been well-established, the design and control of the formation of homochiral superstructures that are based on helical units still remain a substantial challenge. Assembling small molecular units into complicated aggregations in a controlled fashion is one target of sophisticated supramolecular chemistry.[27] Especially, the assembly of helical units into a homochiral array is of great interest in this case.

Investigation into the superstructures assembled from helicate building blocks reveals that the functional groups attached to the ligands of helicates are able to carry weak interactions to favor the extension of the homochiralities. In principle, if the interactions between helicates are substantially strong and directional without mirror symmetric elements, the local or whole homochiral assembly might be achieved.[28] As shown in Figure 8, the twisted bridging mode of diacetylferrocene thiosemicarbazone $L^{19}$ leads to dinuclear complexes that crystallize in a helical fashion.[29] The imino nitrogen atoms of the thiosemicarbazone moieties attached in the double helicates act as H-bond acceptors paired up with the corresponding amino nitrogen atoms of the thiosemicarbazone group on a parallel neighboring helix through hydrogen bonds. Only the helicates with the same chirality can be connected to each other into an infinite chain such that all the zinc ions in the infinite chiral chain have the same chirality. It is likely that the chirality of the helicates is translated through the discriminative bridges. The same structure is also found in an analogous $Co^{II}$ compound.[30] Weak additional coordination interactions could also be utilized to construct helical chains.[31] In the ferrocene-containing double helicate $CuL^{20}{}_2Cl_2$, the copper center is coordinated by two pyridylimine groups with the fifth coordination site occupied by a chloride ion.[32] In the crystal, a chloride anion bridges two homochiral double helicates featuring a one-dimensional polymer. Each chain exhibits a crystallographic $2_1$ helix with the double helicates in the chain being a single enantiomer.

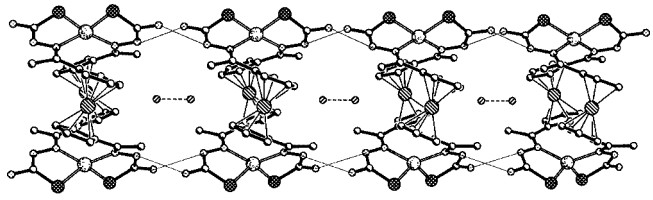

Figure 8. The hydrogen-bonding one-dimensional tube from ferrocenyl-based $Zn_2L^{19}{}_2$ dinuclear helicate with water molecules included.[29]

By introducing multiaromatic rings into the dinuclear helicates, homochiral assemblies and even 3D homochiral conglomerates could be obtained through π–π stacking interactions. Reaction of potentially atropisomeric chiral ligands $L^{22}$ and $L^{23}$ with $Ag^{I}$ generate the silver double helicates $[Ag_2L^{22}{}_2]^{2+}$ and $[Ag_2L^{23}{}_2]^{2+}$, respectively.[33] The symmetry-related helicates are connected together through face-to-face stacking interactions between the pyridine and benzene rings to form an infinite chain around a $3_2$ screw axis (Figure 9). Owing to the twofold symmetry of the dinuclear helicates, these screws align in parallel and maintain the helical chirality, featuring a homochiral 3D structure with the spontaneous resolution occurring. On the basis of solid CD measurements of the 20 crystals of the latter upon crystallization (Figure 10), the *ee* value of 60% clearly reveals the appearance of a chiral selectivity in the bulk crystals. From

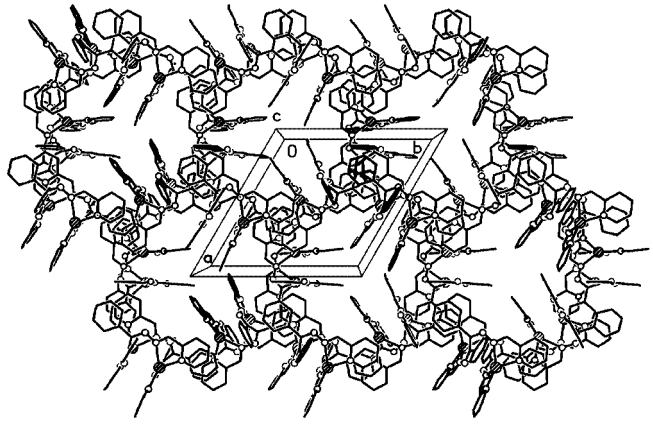


Figure 9. Infinite helical chain for $Ag_2L^{23}{}_2$ with *P* helicate through π–π stacking interactions and the 3D network stabilized by the homochiral interactions.[33]

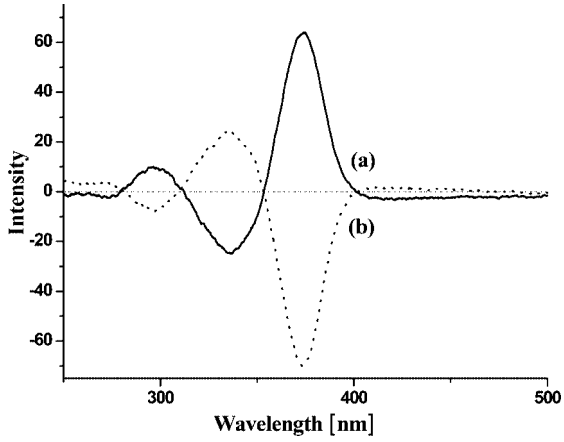


Figure 10. Solid-state CD spectra exhibiting the significant Cotton effect of the crystals of compound $Ag_2L^{23}{}_2$ consisting of *P* (a) and *M* (b) configurations of helicates.[33]

 © 2007 Wiley-VCH Verlag GmbH & Co. KGaA, Weinheim 

further investigations of the crystals in 50 independent crystallizations, it was found that the intensities of the CD signals show a bimodal probability distribution. Such an occurrence of bulk crystal chirality, namely spontaneous resolution, accidentally through a chiral autocatalytic resolution process in the absence of molecular chirality is much more haphazard.

High-dimensional homochiral structures could also be assembled by the helical fragments and adducts as initial components. Chen et al. reported a 2D network built from hydrogen bonds between the connecting water clusters and the helicates.[34] The initial fragment for the assembly is a binuclear $Cd^{II}$ helicate with two spiral-like *N*,*N*′-bis(picolinamide)azine ligands ($L^2$) coordinated to the two $Cd^{II}$ centers. The chiral binuclear helicates are assembled into homochiral layers by water tapes. However, owing to the lack of strong interlayer chiral interactions, the layers are alternatively stacked in a heterochiral fashion to yield the final racemic crystal. Hahn and coworkers reported a triple-stranded helical complex $Na(PNP)_3[Ti_2(L^{25})_3]$ [PNP = bis(triphenylphosphoranylidene)ammonium], where the $Na^+$ ions act as bridges between the $[Ti_2(L^{25})_3]^{4-}$ helicates, leading to the infinite homochiral chains in the crystal lattice.[35] Both metal centers of $[Ti_2(L^{25})_3]^{4-}$ in the crystal are formed with the same configuration, but crystallization in the $P\bar{1}$ acentric space group indicates that the opposite enantiomer must have also formed.

Another interesting example of the aggregation of helical species was reported by Matsumoto et al. He described a fascinating model for the assembly of the homochiral structure.[36,37] The initial building block is a mononuclear $CuL^{26}$ complex containing two imidazole groups. This species could be described as a mononuclear helicate with either Δ (clockwise) or Λ (anticlockwise) enantiomorph (Figure 11) owing to the spiral arrangement of the ligands around the copper(II) ion. In the presence of an equimolar ratio of base, one of the two imidazole groups loses a proton and functions as a hydrogen-bond acceptor to connect with the neighboring protonated imidazole as a donor. For this to occur, the hydrogen bond between the imidazole group and the deprotonated imidazolate group in the two neighboring molecules is asymmetric, and the helicates are linked into a one-dimensional helical chain with the chirality of the initial unit being translated from one to the other, and then extending to the whole helical chain.[36] Similarly, the cobalt(III) complex with achiral tripodal-type ligands consisting of three imidazole groups induces the chiralities of the *C* and *A* enantiomers,[37] The hemideprotonated species $[Co(H_{1.5}L^{27})]^{1.5+}$ functions as a self-complementary chiral building block, generating equal numbers of protonated and deprotonated molecules by an acid–base reaction to form an extended 2D homochiral layer consisting of hexanuclear structures with trigonal void units (Figure 12).

To further develop such a synthetic strategy, an interesting mononuclear helicate $Mn^{II}$ compound was synthesized.[38] The thiosemicarbazone metal complex $MnL^{28}{}_2$ adopts either a Δ or a Λ enantiomorph, depending on the arrangement of the two thiosemicarbazone ligands in which

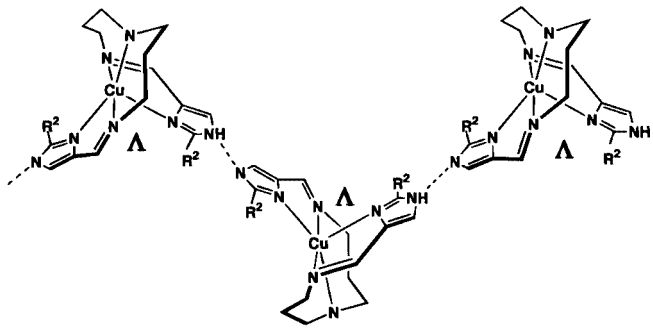


Figure 11. 1D helical chain formed from hydrogen bonds between the imidazole and imidazolate groups of adjacent mononuclear $CuL^{26}$ units ($R^2$ = Me).[36]

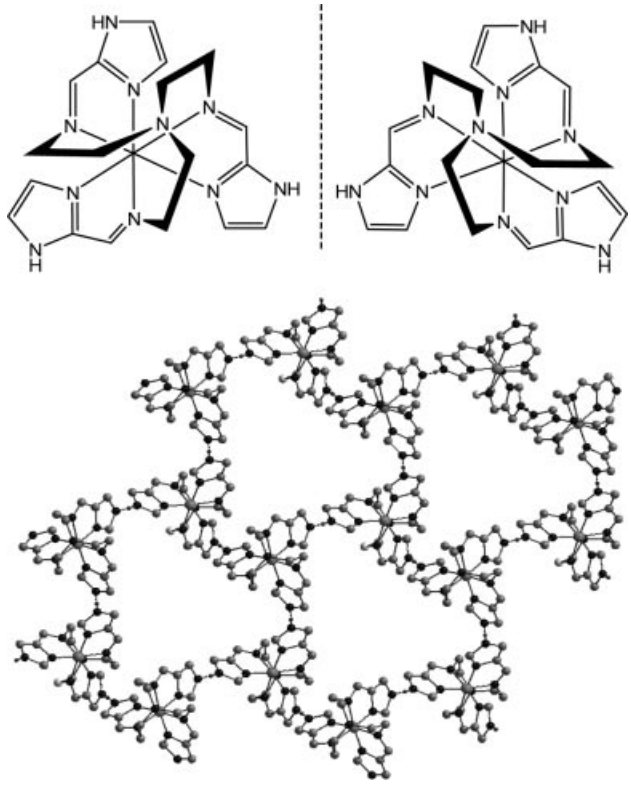

Figure 12. Structures of *C* (clockwise) and *A* (anticlockwise) mononuclear $CoL^{27}$ enantiomers (top), and the top view of the 2D homochiral sheet in which the same enantiomers are linked by the intermolecular imidazole–imidazolate hydrogen bonds (bottom).[37]

the amine groups act as the proton donors and the pyrazine groups as acceptors. The neutral complex functions as chiral building blocks to be assembled into 2D layers through the pyrazine–amino hydrogen bonds (Figure 13). The head-to-tail fashion suggests that the hydrogen bonds that link the neighboring mononuclear units are chirally discriminative and maintains the metal coordinative spheres to exhibit the same absolute configuration. The chirality is then preserved and extended into the whole 2D sheet. Furthermore, the homochiral layers develop parallel to the *ab* plane and stack along the *c* direction through π–π interactions between the neighboring delocalization skeletons of the ligands. Adjacent sheets are related by $4_1$ screw axes and

 © 2007 Wiley-VCH Verlag GmbH & Co. KGaA, Weinheim 

stack in an ABAB fashion (A and B represent layers with different orientations but with the same chirality, respectively), resulting in a homochiral porous 3D network.

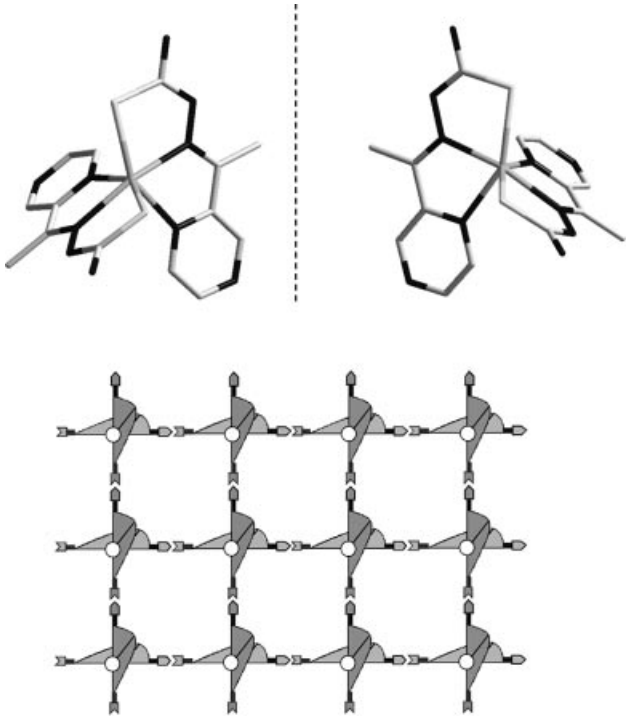

Figure 13. Structures of the Δ and Λ mononuclear Mn helicate enantiomorphs (top), and the carton scheme of the hydrogen bonding homochiral discriminating $MnL^{28}_2$ (bottom).[38]

## 4. One-Dimensional Helical Coordination Polymers – Precursors of Chiral Crystals

One-dimensional helicates are intermediates between the discrete molecular helicates and the solid-state helicity (chiral crystals) in the homochiral aggregations from achiral building blocks. Obviously, the construction of chiral solids from one-dimensional metallohelical chains would be more efficient than that from the oligohelicates. As mentioned above, the simple way to ensure the chirality extension within the infinite chain is to use the ligands as bridges that exhibit atropisomeric chirality. For example, assembling silver(I) or copper(I)[22] with helicand $L^4$ facilitates an infinite monohelicate with each metal atom bound to two bis(bidentate) ligands in a distorted tetrahedral geometry, and the ligands chelate and bridge the two metal centers by turns.[10a] Thus, the obstacle that limits the possibility to obtain a chiral solid from one-dimensional helicates hinges on how the chirality of the building fragments can be extended by chiral discriminative interactions.

An interesting example reported by Aoyama et al.[39] is chiral adduct $L^{29}{\cdot}Cd(NO_3)_2{\cdot}H_2O{\cdot}EtOH$, which was prepared from achiral 5-(9-anthracenyl)pyrimidine ($L^{29}$) but crystallizes in a chiral space group $P2_1$. The chirality of this compound arises from the twist of the two pyrimidine rings in a helical array of the pyrimidine/$Cd^{2+}$ coordination polymer, in which the anthracene substituents are arranged in $C_2$ chirality across the chain (Figure 14). The helices are stabilized by intrastrand water–nitrate and ethanol–nitrate hydrogen bonds. The ligand has one extra free proton, which is used to connect the neighboring helix chains with the *same* chirality (helicity) by interstrand water–nitrate hydrogen bonds. Thus, the chirality translation through H-bonds occurs inside the layer and then is preserved on both sides of the resulting sheet across the helices. The sheets are then assembled through herringbone-type packing of the anthracene moieties into the actual 3D structure. Crystals of this adduct exhibit significant CD signals that are consistent with the absolute helicity *P* or *M* with a positive or negative Cotton effect, respectively. All the crystals recovered from one operation of crystallization show the same CD sign with the same chirality (helicity). It is reasonable that the chirality of the crystals is essentially governed by the chirality that happened to the first-separating nucleus serving as the seed for the subsequent crystal growth.

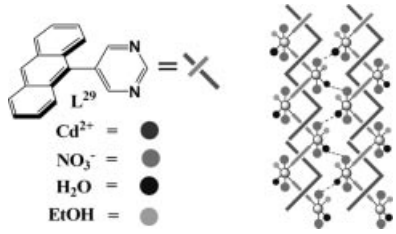


Figure 14. Crystal structure of $L^{29}{\cdot}Cd(NO_3)_2{\cdot}H_2O{\cdot}EtOH$: front view of two neighboring helices hydrogen bonded to form a sheet and its schematic explanations.[39]

Because the direction of the interhelicate donor–acceptor interactions between the chiral helicates is controlled by spatial affects and intrinsic characters of the interactions themselves, these interactions are likely to be characteristically chiral and run through inheriting the original chirality of the helicates they linked. Thus, the strategy to connect helical chains in a homochiral fashion rests on the potential chiral interactions, despite that some of these interactions are quite weak. As shown in Figure 15, a helical chain is also formed through the coordination of potential atropisomeric chiral ligand $L^{30}$ to the $Zn^{II}$ ions. Neighboring chains are bonded together through π–π interactions between the phenyl groups and the cyclopentadienone units.[40] These supramolecular interactions of exclusively achiral building blocks contribute to the helical chirality of the coordination polymers that arise from spontaneous chiral resolution. The bunches of needle crystals show pronounced (and partially opposite) Cotton effects in their CD spectra, suggesting that one kind of enantiomer is in local excess and even dominant.

C–H···X interactions also have the potential to act as directional interactions in the formation of helical chains and the homochiral aggregation of helicates.[41] With the use of an achiral α,α,′-bis(pyrazolyl)-*m*-xylene ligand ($L^{31}$), Mukherjee and coworkers identified two different handed solids of $Zn^{II}$ coordination polymers.[42] As shown in Figure 16, the chiral pseudotetrahedral coordination environ-

 © 2007 Wiley-VCH Verlag GmbH & Co. KGaA, Weinheim 

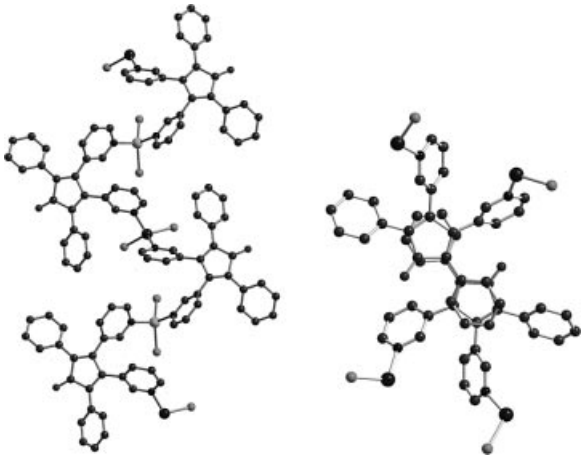

Figure 15. Multiaromatic ring ligand $L^{30}$ (left) and π–π interactions leading to homochiral interactions between helical chains $(ZnCl_2L^{30})_\infty$.[40]

ment around the Zn centers and the twisted conformation of the bidentate ligands bring about the formation of helical chains with the positions of the chlorine atoms fixed. The adjacent parallel helices are held together along the *b* axis primarily by directional C–H···Cl interactions and secondarily by weak π–π interactions between the phenyl rings, leading to the formation of the homochiral 2D sheet. The sheets are again stitched together through the chiral intermolecular C–H···Cl interactions to generate the chiral channels.

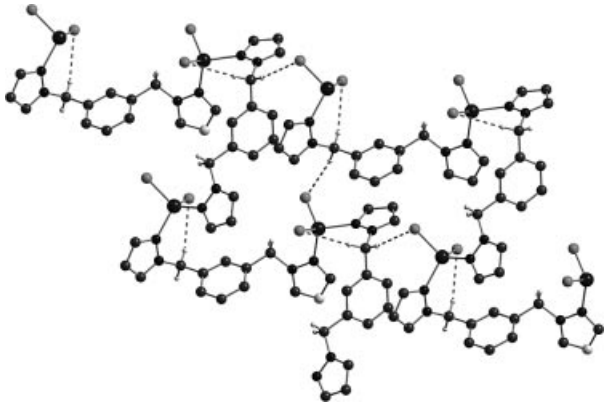

Figure 16. View of the 2D helical sheet $(L^{31}ZnCl_2)_\infty$ formed through C–H···Cl interactions.[42]

The N-positional isomer 2-pyridinyl-3-pyridinylmethanone ($L^{32}$) is another simple ligand that was investigated in terms of chirality transfer.[43,44] Reaction of ligand $L^{32}$ with $Ag(CF_3SO_3)$ in different solvents lead to the generation of a pair of different helical conformational polymorphs. In the racemic crystal A, the ligand winds latitudinally around the helical axis of $2_1$. In the chiral crystal B, the ligand spans longitudinally around a $4_1$helical axis (Figure 17). Spontaneous resolution occurs in the assembly from the helical chains to a homochiral conglomerate $\{[AgL^{32}](CF_3SO_3)\}_\infty$. It seems that the rotation of the pyridyl rings causes the presence of atropisomeric chirality, and the metal centers are bridged to form the homochiral helical chains directly.[44]

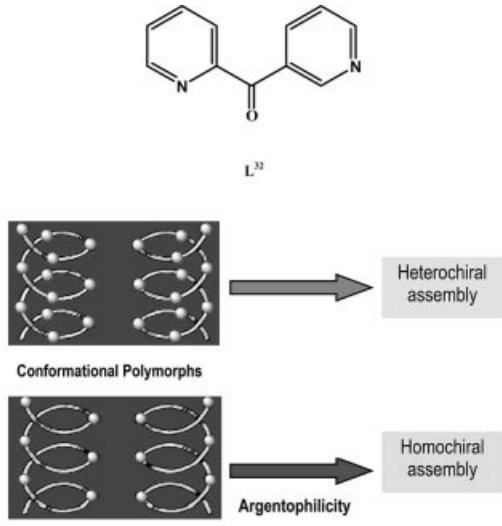


Figure 17. Two kinds of bridging conformations of $L^{32}$ in its coordination complexes. Heterochiral (A, top) and homochiral (B, bottom) assembly of different conformational polymorphs $AgL^{32}$ helical chains by argentophilic interactions.[43,44]

## 5. Homochiral Frameworks – From Achiral Components to Chiral Crystals

Chiral coordination polymers, which possess chiral functionalities such as enantioselective absorption and catalysis, are of great interest. The generation of chiral coordination polymers from achiral ligands without any chiral auxiliary through spontaneous resolution not only provides an easy method for the preparation of chiral functional materials, but also helps the understanding of the chirality origin of life.

Discovered as early as 1846 by Louis Pasteur, spontaneous resolution is still a relatively scarce phenomenon and cannot be predicted a priori because the laws of physics determining the processes are not yet fully understood. The formation of three-dimensional crystal conglomerates is not very frequent (and is even less predictable), reflecting the tremendous preference (more than 90%) for compounds to crystallize in centrosymmetric space groups. However, if there are substantially strong, selective, and directional enough interactions, such as coordination bonds, between neighboring chiral units, the chirality would be able to extend to higher dimensionality, and hence spontaneous resolution would be more likely to occur. Usually, in the preparation of homochiral coordination polymers by spontaneous resolution, two steps are achieved: the generation of the chiral units from the achiral components, and the chirally discriminative interactions may arise from additional intermolecular interactions. Of course, it is quite difficult to isolate the chiral units, always helical chains, from the well-connected network in some case.

 © 2007 Wiley-VCH Verlag GmbH & Co. KGaA, Weinheim 

One simple way to construct a homochiral 3D framework is to use the ligands that not only have an atropisomerically chiral bridging mode but also several additional chelating units – some chelators attribute to the formation of helical units, and the others contribute to the extension of the chirality to the whole crystal. Ligand $L^{24}$, *N*,*N*′-bis[1-(pyrazine-2-yl)ethylidene]benzil dihydrazone (Figure 18), falls well into the category of conformational chiral bridging models.[45] As shown in Figure 19, its silver complex comprises a chiral infinite $4_1$ monohelical chain through the two pyrazine–imine bidentate chelating sites. Each ligand adopts a twisted chiral conformation and spans two silver ions to transmit the chirality from one silver center to the other. The metal centers with the same chirality are coordinated by the coupled ligands, leading to the replication of the conformational chirality from one ligand to the other. Such a helical fashion provides an opportunity to modulate the positions and the directions of the additional groups associated with the pyrazine nitrogen atom for interhelicate coordination bonding. Two pyrazine nitrogen atoms from different helical chains coordinate to one silver atom Ag(2) and connect the helical chains together to form a three-dimensional helical network, in which all the fourfold helices are homochiral. Therefore, it is revealed that the chirality of the silver(I) is transmitted through the discriminative helical linkage, or alternatively, the chirality of the helical chain is transmitted through the discriminative bridged units. However, owing to the presence of large voids, the second network with the opposite chirality interpenetrates the former one. The two enantiomeric frames are centrosymmetrically relative, forming a three-dimensional enmeshed "racemate".

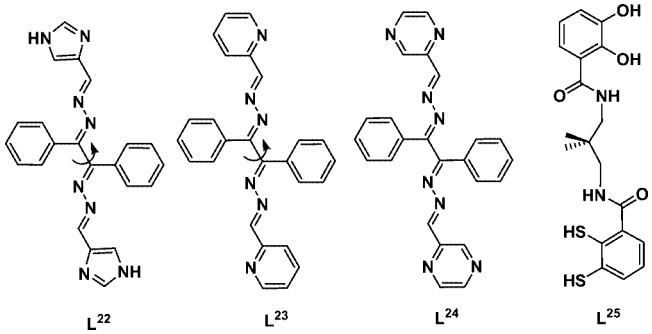


Figure 18. Benzil-based and -related ligands exhibiting a conformationally chiral bridging mode.[33,35,45]

Multicarboxylates with two or more carboxylates connected to aromatic rings are another kind of ligand for the construction of high-dimensional frameworks (Figure 20).[46–50] These species with conformationally chiral coordination modes were also used for homochiral assembly in which the versatile coordination modes of the carboxylate donors make the networks quite complicated.[51] Ligands containing biphenyl groups with more than two carboxylate groups might induce all the metal centers in the network to exhibit the same absolute configuration. 2,2′,3,3′-Oxydiphthalic acid ($L^{33}$) is one such ligand, which was used to build various homochiral 3D features based on

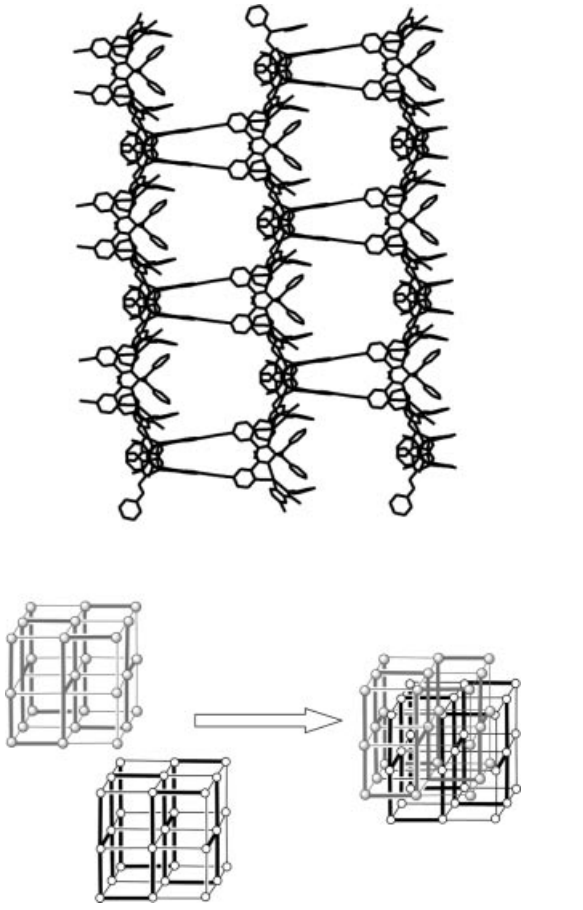

Figure 19. A view of the double interpenetrating nets of $AgL^{24}$ enantiomeric forms of the chiral 3D networks.[45]

helical chains with a suitably bridged bipyridine coligand.[52,53] For example, in the $Zn^{II}$ complex,[52] two kinds of Zn ions are bridged by 2,3- and 2′,3′-carboxylate groups, respectively, to form two similar helical chains from which the chiral puckered herringbones are formed by aligning these helices in parallel (Figure 21). Adjacent layers are interrelated by the $2_1$-screw axis and stack in a slipped *AAA*

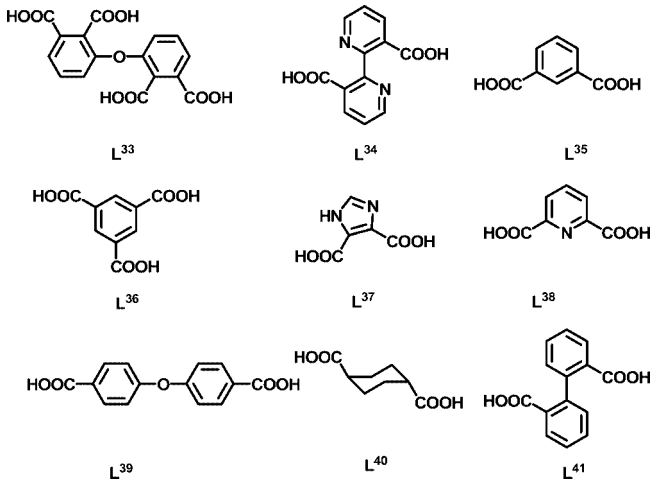


Figure 20. Symmetrical multicarboxylate ligands.[46–50,52,53]

 © 2007 Wiley-VCH Verlag GmbH & Co. KGaA, Weinheim 

fashion through hydrogen bonds, resulting in a 3D homochiral network. The Cd complex also has two kinds of homochiral helices and chiral 2D sheets, and different from that of the $Zn^{II}$ complex, the chiral layers are parallel and stack through interlayer interactions of coordination bonds (Cd–O) to give a 3D chiral network.

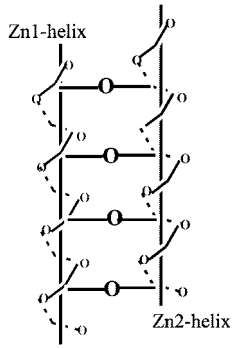


Figure 21. Zn(bpy)$L^{33}$ complexes with homochiral 3D structure assembled from helical chain building units.[52]

Of course, the additional coordinated sites might come from short auxiliary ligands, so that the direction of these interactions could be controlled by the spatial affects of the chiral building units.[54,55] Yan et al. used the simple bis(didentate) pyridylimine ligand containing a –N–N– bond to build a 2D manganese–azido framework.[9] The chirality of the structure unit is induced by the twisted chiral conformation of the coordinated diazine ligands (Figure 2). The constraint of the diazine ligands in the twisted chiral conformation imparts chirality to the triple linkage that consists of two end-on azido bridges plus a –N–N– bridge. This chiral linkage equipped with two chelate sites is chirally discriminative and requires that the two metal coordination spheres have the same absolute configuration. The chirality is preserved when the dimers are interlinked into the 2D network by the homochiral interdimer interactions that arise from the unique bridging topology of the single EE azido bridges. As a result, two kinds of crystals are obtained in the same batch by evaporating the solution of this compound and separating the crystals manually. In both crystals, the homochiral layers extend parallel to the *ab* plane and stack along the *c* direction. In one of these two kinds of crystals, adjacent layers are related by $3_1$ screw axes and stack in an *ABCABC* fashion (*A*, *B*, and *C* represent layers with different orientations but with the same chirality), resulting in a homochiral crystal.

Poeppelmeier et al. reported another interesting complex Zn(pyrazine)($H_2O$) ($MoO_2F_4$),[56] where the *cis*-$MoO_2F_4^{2-}$ anions in the complex are ordered and coordinated to *trans*-$[Zn(pyrazine)_2(H_2O)_2]^{2+}$ cations in an alternating fashion, forming a $3_1$ inorganic helical chain. It is found that when the large organic cations associated with the coordinated donors pack orderly in the solid, the negatively charged $MoO_2F_4^{2-}$ anions are fixed in a special arrangement to fit the helical formation with the two bridged fluoride sites positioned oppositely to the *cis* O atoms. Considering more than six helices interleaved through the Zn–pyrazine–Zn bridges, it is likely that the presence of a short enough linear pyrizine bridging ligand could give rise to the helices packing without introducing any inversion center among them. As illustrated in Figure 22, helices with the same handedness share identical spatial and translational orientations along the Zn–N bridges. When two helices with opposite handedness are bonded together, there are no matching sites for any other helices of either handedness.

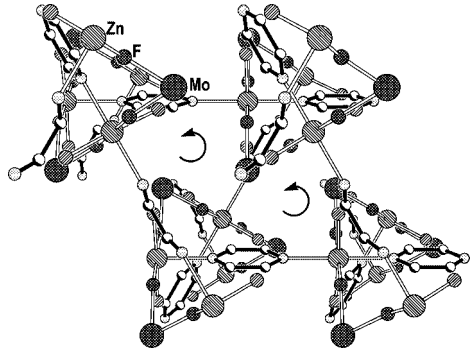


Figure 22. Helix with possible interaction packs with other helices that have the same handedness in compound Zn(pyrazine)($H_2O$)-($MoO_2F_4$).[56]

Another way to construct homochiral 3D frameworks is by using the unsymmetrical ligands as effective connectors to form the polymeric chiral helicates (Figure 23).[57] Lin and his coworkers pointed out that the steric interactions in *cis*-pyridylethenylbenzoate ($L^{42}$) would cause the pyridyl and phenyl groups to be significantly deviated from coplanarity.[58] Such a "skewing" of coordination sites of $L^{42}$ should favor the formation of a helical structure. Hong and coworkers used 4-sulfanylmethyl-4′-phenyl carboxylate pyridine ($L^{43}$)[59] to construct a homochiral $Zn^{II}$ coordination network. As shown in Figure 24, each zinc(II) atom is located in a distorted tetrahedral environment. The chirality transmitting model could be described as that in the former example, in which two kinds of homochiral helices are alternatively assembled along the crystallographic *b* axis. One type of helix is formed by hydroxy-bridging $Zn^{II}$ atoms, and the other is constructed by $L^{43}$-bridging $Zn^{II}$ centers. These distinct homochiral helices are arranged orderly with the zinc(II) atoms acting as hinges, and the novel two-dimensional layers in the *bc* plane stack along the crystallographic *a* axis in an interlocking fashion. The chirality of the [Zn–spcp] helicate should also arise from the $sp^3$ configurations of the C and S atoms in the $–CH_2S–$ spacer, which forces the ligand to be nonlinear and results in the formation of the twisty helical conformation. Because the compound crystallizes in an asymmetric space group $P2_1$, only one kind of tubular helix is involved in the crystal structure.

Another interesting ligand is 2,5-pyridinedicarboxylate $L^{45}$. Its unsymmetricial coordinated mode and the short separation could force the helices to pack together without the introduction of any inversion center.[60] Hong et al. illustrated the dimensional extension of chirality in the helicates based on $\{[NH_2(CH_3)_2]Fe^{III}(L^{45})_2\}_n$. In this complex, the $Fe^{III}$ coordinates to $L^{45}$ in a *cis* mode, forming $2_1$ helical

 © 2007 Wiley-VCH Verlag GmbH & Co. KGaA, Weinheim 

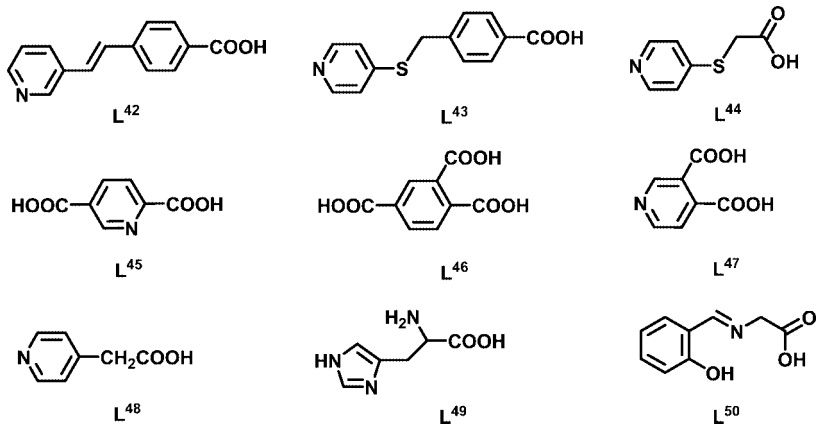


Figure 23. Unsymmetrical ligands.[57–61]

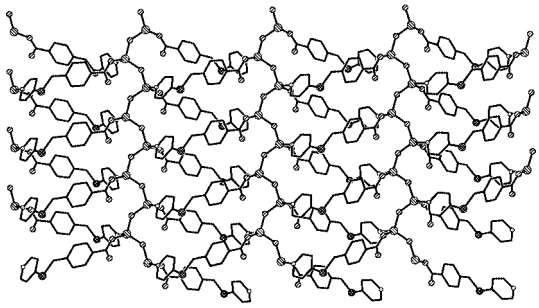

Figure 24. A view of the two types of homochiral helices in the $ZnL^{43}$ complex.[59]

chains that are arranged parallel or perpendicular to each other with the metal atoms as the connective nodes. This kind of interaction of the helical chains is directional enough to force the 3D network to be homochiral (space group $P4_32_12$), namely the overall structure being chiral. Qiu et al. synthesized the compound $Co(L^{45})(H_2O)_2{\cdot}H_2O$, which crystallized in a space group $P2_12_12_1$.[61] In this compound, there are two types of twofold screw axes along the crystallographic *b* axis, and the helices are interconnected to each other through the cobalt centers to produce an interesting two-dimensional layered structure (Figure 25). Furthermore, the interlayer hydrogen bonds corresponding to the homochiral sheets are directional and strong enough to further pack the 2D undulating layers into a 3D homochiral supramolecular framework. It is notable that the resulting crystals are not racemic as verified by the observation of strong signals in the vibrational circular dichroism (VCD) spectra. The enantiomeric excess might be ascribable to the initial crystals formed as seeds for the handedness of the bulk product, in which the particular handedness of the bulk sample is dependent on what random handedness was formed in the initial crystals.

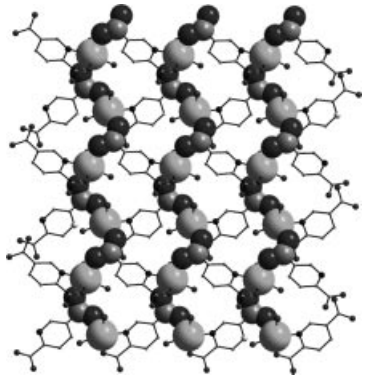

Figure 25. The 2D structure including the right-handed helical chains of –C–O–Co– (the space-filling view) and the left-handed helical chains of –PDC–Co– (the cylindrical view).

## 6. Conclusions

The rational design and construction of chiral materials from achiral sources requires fundamental understanding of the chirality origination and translation. Helicates obtained by self-assembly possess fascinating structures and could act as excellent model systems for studying the extended supramolecular chirality developed from the conformational chirality in classical coordination complexes. In these processes, the coordination bond has become a very useful tool for the construction of large, well-organized, chiral architectures and further chiral aggregations, in the presence of various noncovalent interactions, such as hydrogen bonding, π–π stacking interactions, and van der Waals interactions. Though the structural control and molecular programming in the chiral assembly by using helicates as building intermediates with conformational chiral bridging modes have been significantly explored and improved, the use of achiral ligands to provide self-organized chiral supramolecular species through spontaneous resolution is still in its infancy. The construction and chiral aggregation of helicates will probably suffer from the competition of other fascinating metal-containing achiral assemblies, but they will keep a dominant place if their promising potential applications as molecular and supramolecular functional devices are confirmed and developed. We have no doubt that academic and aesthetic interests will lead to further development in the formation and aggregation of new chiral crystals with helical features. We do think that the enormous potential applications of helical complexes will make it become a considerably attractive field in the near future.

 © 2007 Wiley-VCH Verlag GmbH & Co. KGaA, Weinheim 

## Acknowledgments

Financial support from the National Natural Science Foundation of China is gratefully acknowledged.

[1] J. M. Lehn, A. Rigault, J. Siegel, J. Harrowfield, B. Chevrier, D. Moras, *Proc. Natl. Acad. Sci. USA* **1987**, *84*, 2565–2569.
[2] C. Piguet, G. Bernardinelli, G. Hopfgartner, *Chem. Rev.* **1997**, *97*, 2005–2062.
[3] M. Albrecht, *Chem. Rev.* **2001**, *101*, 3457–3498.
[4] L. Pérez-García, D. B. Amabilino, *Chem. Soc. Rev.* **2002**, *31*, 342–456.
[5] a) L. J. Prins, J. Huskens, F. de Jong, P. Timmerman, D. N. Reinhoudt, *Nature* **1999**, *398*, 498–502; b) L. J. Prins, F. de Jong, P. Timmerman, D. N. Reinhoudt, *Nature* **2000**, *408*, 181–184; c) J. H. K. K. Hirschberg, L. Brunsveld, A. Ramzi, J. A. J. M. Vekemans, R. P. Sijbesma, E. W. Meijer, *Nature* **2000**, *407*, 167–170.
[6] M. Albrecht, *Chem. Eur. J.* **2000**, *6*, 3485–3489.
[7] a) Z. Xu, L. K. Thompson, D. O. Miller, H. J. Clase, J. A. K. Howard, A. E. Goeta, *Inorg. Chem.* **1998**, *37*, 3620–3627; b) Z. Xu, L. K. Thompson, C. J. Matthews, D. O. Miller, A. E. Goeta, C. Wilson, J. A. K. Howard, M. Ohba, H. Ōkawa, *J. Chem. Soc. Dalton Trans.* **2000**, 69–77; c) Z. Xu, S. White, L. K. Thompson, D. O. Miller, M. Ohba, H. Ōkawa, C. Wilson, J. A. K. Howard, *J. Chem. Soc. Dalton Trans.* **2000**, 1751–1757; d) Z. Xu, L. K. Thompson, D. A. Black, C. Ralph, D. O. Miller, M. A. Leech, J. A. K. Howard, *J. Chem. Soc. Dalton Trans.* **2001**, 2042–2048.
[8] a) J. Hamblin, A. Jackson, N. W. Alcock, M. J. Hannon, *J. Chem. Soc. Dalton Trans.* **2002**, 1635–1641; b) F. Tuna, G. Clarkson, N. W. Alcock, M. J. Hannon, *Dalton Trans.* **2003**, 2149–2155.
[9] a) E. Q. Gao, S. Q. Bai, Z. M. Wang, C. H. Yan, *J. Am. Chem. Soc.* **2003**, *125*, 4984–4985; b) E. Q. Gao, Y. F. Yue, S. Q. Bai, Z. He, C. H. Yan, *J. Am. Chem. Soc.* **2004**, *126*, 1419–1429.
[10] a) D. Guo, C. He, C. Y. Duan, C. Q. Qian, Q. J. Meng, *New J. Chem.* **2002**, *26*, 796–802; b) D. Guo, K. L. Pang, C. Y. Duan, C. He, Q. J. Meng, *Inorg. Chem.* **2002**, *41*, 5978–5985.
[11] a) H. Mo, D. Guo, C. Y. Duan, Y. T. Li, Q. J. Meng, *J. Chem. Soc. Dalton Trans.* **2002**, 3422–3424; b) H. Mo, C. J. Fang, C. Y. Duan, Y. T. Li, Q. J. Meng, *Dalton Trans.* **2003**, 1229–1234; c) S. G. Sreerama, S. Pal, *Inorg. Chem.* **2005**, *44*, 6299–6307.
[12] D. Y. Wu, L. X. Xie, C. L. Zhang, C. Y. Duan, Y. G. Zhao, Z. J. Guo, *Dalton Trans.* **2006**, 3528–3533.
[13] D. Cunningham, K. Gilligan, M. Hannon, C. Kelly, P. McArdle, A. O'Malley, *Organometallics* **2004**, *23*, 984–994.
[14] a) P. K. K. Ho, K. K. Cheung, S. M. Peng, C. M. Che, *J. Chem. Soc. Dalton Trans.* **1996**, 1411–1417; b) C. J. Cathey, E. C. Constable, M. J. Hannon, D. A. Tohcer, M. D. Ward, *J. Chem. Soc. Chem. Commun.* **1990**, 621–622.
[15] A. Lützen, M. Hapke, J. Griep-Raming, D. Haase, W. Saak, *Angew. Chem. Int. Ed.* **2002**, *41*, 2086–2089.
[16] a) H. C. Aspinall, J. F. Bickley, J. L. M. Dwyer, N. Greeves, A. Steiner, *Angew. Chem. Int. Ed.* **2000**, *39*, 2858–2861; b) M. Capó, J. M. Saá, A. Alvarez**,** *Chem. Commun.* **2002**, 1982–1983; c) A. Orita, T. Nakano, D. L. An, K. Tanikawa, K. Wakamatsu, J. Otera, *J. Am. Chem. Soc.* **2004**, *126*, 10389–10396; d) A. Jouaiti, M. W. Hosseini, N. Kyritsakas, P. Grosshans, J. M. Planeix, *Chem. Commun.* **2006**, 3078–3080.
[17] a) R. H. Wang, L. J. Xu, X. S. Li, Y. M. Li, Q. Shi, Z. Y. Zhou, M. C. Hong, A. S. C. Chan, *Eur. J. Inorg. Chem.* **2004**, 1595–1599; b) R. H. Wang, L. J. Xu, J. X. Ji, Q. Shi, Y. M. Li, Z. Y. Zhou, M. C. Hong, A. S. C. Chan, *Eur. J. Inorg. Chem.* **2005**, 751–758.
[18] a) Y. Cui, S. J. Lee, W. Lin, *J. Am. Chem. Soc.* **2003**, *125*, 6014–6015; b) C. D. Wu, H. L. Ngo, W. Lin, *Chem. Commun.* **2004**, 1588–1589 ; c) Y. Cui, H. L. Ngo, W. Lin, *Chem. Commun.* **2003**, 1388–1389.
[19] a) Y. Gao, B. Twamley, J. M. Shreeve, *Organometallics* **2006**, *25*, 3364–3369; b) D. L. Reger, K. J. Brown, J. R. Gardinier, M. D. Smith, *Organometallics* **2003**, *22*, 4973–4983; c) G. Li, Z. F. Li, H. W. Hou, X. R. Meng, Y. T. Fan, W. H. Chen, *J. Mol. Struct.* **2004**, *694*, 179–183.
[20] C. J. Fang, C. Y. Duan, H. Mo, C. He, Q. J. Meng, Y. J. Liu, Y. H. Mei, Z. M. Wang, *Organometallics* **2001**, *20*, 2525–2532.
[21] a) M. Greenwald, D. Wessely, I. Goldberg, Y. Cohen, *New J. Chem.* **1999**, *23*, 337–344; b) P. N. W. Baxter, J. M. Lehn, G. Baum, D. Fenske, *Chem. Eur. J.* **2000**, *6*, 4510–4517; c) C. R. Rice, C. J. Baylies, H. J. Clayton, J. C. Jeffery, R. L. Paul, M. D. Ward, *Inorg. Chim. Acta* **2003**, *351*, 207–216; d) C. J. Matthews, S. T. Onions, G. Morata, L. J. Davis, S. L. Heath, D. J. Price, *Angew. Chem. Int. Ed.* **2003**, *42*, 3166–3169; e) B. Conerney, P. Jensen, P. E. Kruger, C. MacGloinn, *Chem. Commun.* **2003**, 1274–1275.
[22] F. Tuna, J. Hamblin, A. Jackson, G. Clarkson, N. W. Alcock, M. J. Hannon, *Dalton Trans.* **2003**, 2141–2148.
[23] a) P. N. W. Baxter, R. G. Khoury, J. M. Lehn, G. Baum, D. Fenske, *Chem. Eur. J.* **2000**, *6*, 4140–4148; b) O. Mamula, F. J. Monlien, A. Porquet, G. Hopfgartner, A. E. Merbach, A. V. Zelewsky, *Chem. Eur. J.* **2001**, *7*, 533–539; c) M. R. A. Al-Mandhary, P. J. Steel, *Inorg. Chem. Commun.* **2002**, *5*, 954–957; d) L. J. Childs, M. Pascu, A. J. Clarke, N. W. Alcock, M. J. Hannon, *Chem. Eur. J.* **2004**, *10*, 4291–4300; e) S. P. Argent, H. Adams, T. Riis-Johannessen, J. C. Jeffery, L. P. Harding, O. Mamula, M. D. Ward, *Inorg. Chem.* **2006**, *45*, 3905–3919.
[24] D. Guo, C. Y. Duan, C. J. Fang, Q. J. Meng, *J. Chem. Soc. Dalton Trans.* **2002**, 834–836.
[25] a) S. X. Liu, S. Lin, B. Z. Lin, C. C. Lin, J. Q. Huang, *Angew. Chem. Int. Ed.* **2001**, *40*, 1084–1087; b) S. Lin, S. X. Liu, J. Q. Huang, C. C. Lin, *J. Chem. Soc. Dalton Trans.* **2002**, 1595–1601; c) S. Lin, S. X. Liu, Z. Chen, B. Z. Lin, S. Gao, *Inorg. Chem.* **2004**, *43*, 2222–2224; d) R. P. John, K. Lee, B. J. Kim, B. J. Suh, H. Rhee, M. S. Lah, *Inorg. Chem.* **2005**, *44*, 7109–7121; e) Y. Bai, D. B. Dang, C. Y. Duan, Y. Song, Q. J. Meng, *Inorg. Chem.* **2005**, *44*, 5972–5974.
[26] a) S. G. Telfer, T. Sato, R. Kuroda, *Angew. Chem. Int. Ed.* **2004**, *43*, 581–584; b) S. G. Telfer, R. Kuroda, *Chem. Eur. J.* **2005**, *11*, 57–68.
[27] a) A. J. Blake, N. R. Champness, P. Hubberstey, W. S. Li, M. A. Withersby, M. Schröeder, *Coord. Chem. Rev.* **1999**, *183*, 117–138; b) A. M. Beatty, *Coord. Chem. Rev.* **2003**, *246*, 131–143; c) M. A. Mateos-Timoneda, M. Crego-Calama, D. N. Reinhoudt, *Chem. Soc. Rev.* **2004**, *33*, 363–372; d) H. M. Keizer, R. P. Sijbesma, *Chem. Soc. Rev.* **2005**, *34*, 226–234.
[28] a) K. K. Rajak, S. Mondal, S. P. Rath, *Polyhedron* **2000**, *19*, 931–936; b) D. G. Lonnon, S. B. Colbran, D. C. Craig, *Eur. J. Inorg. Chem.* **2006**, 1190–1197.
[29] C. J. Fang, C. Y. Duan, C. He, Q. J. Meng, *Chem. Commun.* **2000**, 1187–1188.
[30] M. X. Li, Y. Bai, B. G. Zhang, C. Y. Duan, J. Xu, Q. J. Meng, *Inorg. Chem.* **2005**, *44*, 5459–5466.
[31] a) A. J. Blake, N. R. Champness, A. N. Khlobystov, S. Parsons, M. Schröeder, *Angew. Chem. Int. Ed.* **2000**, *39*, 2317–2320; b) A. N. Khlobystov, M. T. Brett, A. J. Blake, N. R. Champness, P. M. W. Gill, D. P. O'Neill, S. J. Teat, C. Wilson, M. Schröeder, *J. Am. Chem. Soc.* **2003**, *125*, 6753–6761; c) N. Niklas, F. Hampel, R. Alsfasser, *Chem. Commun.* **2003**, 1586–1587; d) M. Seitz, A. Kaiser, S. Stempfhuber, M. Zabel, O. Reiser, *J. Am. Chem. Soc.* **2004**, *126*, 11426–11427.
[32] C. J. Fang, C. Y. Duan, D. Guo, C. He, Q. J. Meng, Z. M. Wang, C. H. Yan, *Chem. Commun.* **2001**, 2540–2541.
[33] Q. Z. Sun, Y. Bai, G. J. He, C. Y. Duan, Z. H. Lin, Q. J. Meng, *Chem. Commun.* **2006**, 2777–2779.
[34] B. H. Ye, A. P. Sun, T. F. Wu, Y. Q. Weng, X. M. Chen, *Eur. J. Inorg. Chem.* **2005**, 1230–1234.

 © 2007 Wiley-VCH Verlag GmbH & Co. KGaA, Weinheim 

[35] F. E. Hahn, C. S. Isfort, T. Pape, *Angew. Chem. Int. Ed.* **2004**, *43*, 4807–4810.
[36] Y. Shii, Y. Motoda, T. Matsuo, F. Kai, T. Nakashima, J. P. Tuchagues, N. Matsumoto, *Inorg. Chem.* **1999**, *38*, 3513–3522.
[37] I. Katsuki, Y. Motoda, Y. Sunatsuki, N. Matsumoto, T. Nakashima, M. Kojima, *J. Am. Chem. Soc.* **2002**, *124*, 629–640.
[38] M. X. Li, Q. Z. Sun, Y. Bai, C. Y. Duan, B. G. Zhang, Q. J. Meng, *Dalton Trans.* **2006**, 2572–2578.
[39] T. Ezuhara, K. Endo, Y. Aoyama, *J. Am. Chem. Soc.* **1999**, *121*, 3279–3283.
[40] U. Siemeling, I. Scheppelmann, B. Neumann, A. Stammler, H. G. Stammler, J. Frelek, *Chem. Commun.* **2003**, 2236–2237.
[41] a) S. K. Singh, M. Chandra, D. S. Pandey, M. C. Puerta, P. Valerga, *J. Organomet. Chem.* **2004**, *689*, 3612–3620; b) V. Balamurugan, M. S. Hundal, R. Mukherjee, *Chem. Eur. J.* **2004**, *10*, 1683–1690; c) A. Singh, S. K. Singh, M. Trivedi, D. S. Pandey, *J. Organomet. Chem.* **2005**, *690*, 4243–4251 ; d) X. J. Zhang, Y. P. Tian, F. Jin, J. Y. Wu, Y. Xie, X. T. Tao, M. H. Jiang, *Cryst. Growth Des.* **2005**, *5*, 565–570.
[42] V. Balamurugan, R. Mukherjee, *CrystEngComm* **2005**, *7*, 337–341.
[43] X. D. Chen, T. C. W. Mak, *Dalton Trans.* **2005**, 3646–3652.
[44] X. D. Chen, M. Du, T. C. W. Mak, *Chem. Commun.* **2005**, 4417–4419.
[45] Y. Bai, C. Y. Duan, P. Cai, D. B. Dang, Q. J. Meng, *Dalton Trans.* **2005**, 2678–2680.
[46] R. H. Wang, Y. F. Zhou, Y. Q. Sun, D. Q. Yuan, L. Han, B. Y. Lou, B. L. Wu, M. C. Hong, *Cryst. Growth Des.* **2005**, *5*, 251–256.
[47] Y. F. Zhou, F. L. Jiang, Y. Xu, R. Cao, M. C. Hong, *J. Mol. Struct.* **2004**, *691*, 191–195.
[48] a) C. J. Kepert, T. J. Prior, M. J. Rosseinsky, *J. Am. Chem. Soc.* **2000**, *122*, 5158–5168; b) T. J. Prior, M. J. Rosseinsky, *Inorg. Chem.* **2003**, *42*, 1564–1575.
[49] Y. Q. Sun, J. Zhang, Y. M. Chen, G. Y. Yang, *Angew. Chem. Int. Ed.* **2005**, *44*, 5814–5817.
[50] L. Y. Duan, Y. G. Li, F. C. Liu, E. B. Wang, X. L. Wang, C. W. Hu, L. Xu, *J. Mol. Struct.* **2004**, *689*, 269–274.
[51] a) Y. Cui, O. R. Evans, H. L. Ngo, P. S. White, W. Lin, *Angew. Chem. Int. Ed.* **2002**, *41*, 1159–1162 ; b) Y. Cui, H. L. Ngo, P. S. White, W. Lin, *Inorg. Chem.* **2003**, *42*, 652–654.
[52] S. Q. Zang, Y. Su, Y. Z. Li, Z. P. Ni, Q. J. Meng, *Inorg. Chem.* **2006**, *45*, 174–180.
[53] S. Q. Zang, Y. Su, Y. Z. Li, H. Z. Zhu, Q. J. Meng, *Inorg. Chem.* **2006**, *45*, 2972–2978.
[54] L. Han, M. C. Hong, *Inorg. Chem. Commun.* **2005**, *8*, 406–419.
[55] a) X. H. Bu, W. Chen, M. Du, K. Biradha, W. Z. Wang, R. H. Zhang, *Inorg. Chem.* **2002**, *41*, 437–439; b) D. Moon, J. Song, B. J. Kim, B. J. Suh, M. S. Lah, *Inorg. Chem.* **2004**, *43*, 8230–8232; c) H. Y. An, E. B. Wang, D. R. Xiao, Y. G. Li, Z. M. Su, L. Xu, *Angew. Chem. Int. Ed.* **2006**, *45*, 904–908.
[56] P. A. Maggard, C. L. Stern, K. R. Poeppelmeier, *J. Am. Chem. Soc.* **2001**, *123*, 7742–7743.
[57] a) K. Nomiya, S. Takahashi, R. Noguchi, S. Nemoto, T. Takayama, M. Oda, *Inorg. Chem.* **2000**, *39*, 3301–3311; b) A. Erxleben, *Inorg. Chem.* **2001**, *40*, 2928–2931; c) M. Kondo, M. Miyazawa, Y. Irie, R. Shinagawa, T. Horiba, A. Nakamura, T. Naito, K. Maeda, S. Utsuno, F. Uchidac, *Chem. Commun.* **2002**, 2156–2157; d) X. L. Wang, C. Qin, E. B. Wang, Y. G. Li, N. Hao, C. W. Hu, L. Xu, *Inorg. Chem.* **2004**, *43*, 1850–1856; e) C. Qin, X.-L. Wang, Y.-G. Li, E.-B. Wang, Z.-M. Su, L. Xua, R. Clerac, *Dalton Trans.* **2005**, 2609–2614; f) X. Li, R. Cao, Y. Q. Sun, Q. Shi, D. Q. Yuan, D. F. Sun, W. H. Bi, M. C. Hong, *Cryst. Growth Des.* **2004**, *4*, 255–261.
[58] O. R. Evans, Z. Y. Wang, W. Lin, *Chem. Commun.* **1999**, 1903–1904.
[59] L. Han, M. C. Hong, R. H. Wang, J. H. Luo, Z. Z. Lin, D. Q. Yuan, *Chem. Commun.* **2003**, 2580–2581.
[60] Y. Xu, L. Han, Z. Z. Lin, C. P. Liu, D. Q. Yuan, Y. F. Zhou, M. C. Hong, *Eur. J. Inorg. Chem.* **2004**, 4457–4462.
[61] G. Tian, G. S. Zhu, X. Y. Yang, Q. R. Fang, M. Xue, J. Y. Sun, Y. Wei, S. L. Qiu, *Chem. Commun.* **2005**, 1396–1398.

Received: April 1, 2007
Published Online: June 29, 2007

 © 2007 Wiley-VCH Verlag GmbH & Co. KGaA, Weinheim 

DOI: 10.1002/ejic.200700514

# Highly Luminescent, Neutral, Nine-Coordinate Lanthanide(III) Complexes

Gregg S. Kottas,[a] Marita Mehlstäubl,[a] Roland Fröhlich,[b] and Luisa De Cola*[a]

**Keywords:** Lanthanides / Luminescence / Sensitizers / Energy transfer / Carboxylate ligands

Using a simple ligand design, we have prepared neutral, nine-coordinate lanthanide complexes that exclude water from the inner coordination sphere, thus leading to high emission quantum yields and long excited-state lifetimes. The complexes form in high synthetic yields (49–87 %) by simply mixing the ligand and the lanthanide. Visible luminescence from $Eu^{III}$ ($\Phi$ = 60 %, $\tau$ = 2.2 ms) and $Tb^{III}$ ($\Phi$ = 7 %, $\tau$ = 0.2 ms) and near-infrared luminescence from $Yb^{III}$ ($\Phi$ = 0.7 %), $Nd^{III}$ and $Er^{III}$ were observed in acetonitrile and $CH_2Cl_2$ at room temperature. In addition, the $Gd^{III}$ complex was prepared to gain information about the triplet state of the ligand.
(© Wiley-VCH Verlag GmbH & Co. KGaA, 69451 Weinheim, Germany, 2007)

## Introduction

Lanthanide (Ln) complexes[1] that emit in the visible region of the electromagnetic spectrum (Tb, Eu) are important in light-emitting diodes (LEDs),[2] and near-infrared (NIR) emitting $Ln^{III}$ complexes (Yb, Nd, Er) have potential applications in fiber-optic technologies[3] and biomedical imaging.[4] Because $Ln^{III}$ salts have intrinsically low extinction coefficients ($\varepsilon \approx 1–10\ M^{-1}cm^{-1}$),[5] direct excitation is difficult without high intensity sources. The low absorption coefficients are due to intra-4f transitions, which are parity-forbidden. Therefore, it is common to indirectly excite lanthanide ions through an antenna chromophore – a molecule with a high absorption cross section that can readily transfer its energy to the lanthanide ion.[5,6] The advantages of lanthanide luminescence are their narrow emission bands, large Stokes' shifts and long lifetimes (μs to ms). Because the 4f orbitals are shielded by the outer 5s and 5p orbitals, these properties are mostly insensitive to chemical environment. Ln complex emission quantum yields and excited-state lifetimes decrease dramatically upon coordination of solvents (especially water) through vibronic coupling[6c] – a problem compounded for NIR-emitting Ln complexes due to the energy gap law.[7] In addition, lanthanide ions have coordination numbers between 6 and 12, although for bulky ligands it is effectively 8–10,[8] making full coordination somewhat difficult (remaining coordination sites are usually occupied by available solvent). Many lanthanide complexes reported in the literature are charged, rendering them unusable for many applications that require evaporation, such as in the fabrication of small-molecule light-emitting diodes (SMOLEDS).[2,9]

Here we report neutral, nine-coordinate lanthanide complexes with a simple tridentate ligand, which display high emission quantum yields due to the exclusion of solvent molecules from the first coordination sphere.

## Results and Discussion

The syntheses of the complexes are shown in Scheme 1. Dropwise addition of the corresponding $Ln^{III}$ salt, dissolved in water, to a mixture of readily available precursor **1** in EtOH/$H_2O$ at 0 °C gave sparingly soluble complexes **2a**–**2g** in 49–87 % yield (see Supporting Information). After filtration of the resulting precipitated solid, the complexes were crystallized by slow evaporation of $CH_2Cl_2$ from a $CH_2Cl_2$/MeOH solution. All compounds were characterized by elemental analysis and mass spectrometry, and the diamagnetic lanthanum complex **2g** was also characterized by NMR spectroscopy (Figures S4 and S5).

To the best of our knowledge, the only report of similar systems is that of Comby et al.,[10] but these authors investigated the complexation of the ligand **3** with $Ln^{III}$ ions in situ, without isolation of the products (Scheme 1). Ziessel and co-workers have developed a number of macrocyclic ligands based on the bipyridine carboxylate architecture.[11] Multinuclear complexes using a tridentate ligand containing a bipyridine moiety and a carboxylate group have recently been reported by Mamula and co-workers[12] and nonalanthanide cluster based on a derivative of **3** by Comby et al.[13]

The Eu and La complexes **2b** and **2g** formed crystals suitable for X-ray diffraction, and the resulting molecular structure of **2b** is shown in Figure 1 (**2g** is shown in Figure S1).

[a] Westfälische Wilhelms-Universität Münster, Department of Physics,
Mendelstrasse 7, 48149 Münster, Germany
Fax: +49-251-980-2834
E-mail: decola@uni-muenster.de
[b] Westfälische Wilhelms-Universität Münster, Organisch-Chemisches Institut,
Corrensstrasse 40, 48149 Münster, Germany
Supporting information for this article is available on the WWW under http://www.eurjic.org or from the author.

 © 2007 Wiley-VCH Verlag GmbH & Co. KGaA, Weinheim 

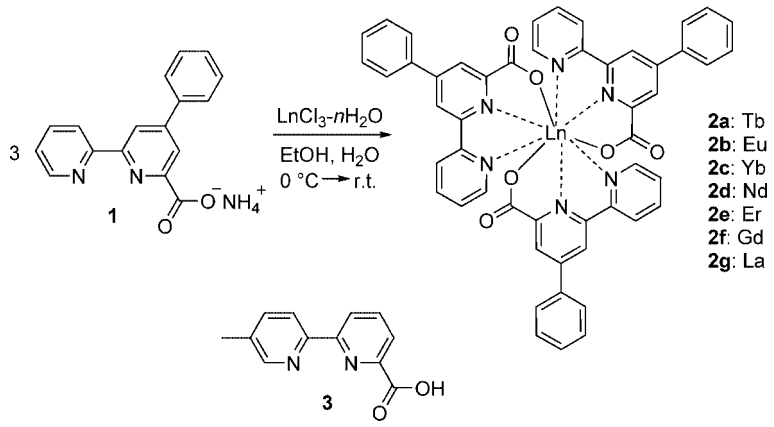


Scheme 1. Synthesis of the lanthanide complexes **2a**–**2g** and previously studied ligand **3**.[10]

The unit cell of **2b** contains one molecule each of MeOH and $CH_2Cl_2$ and that of **2g** contains three molecules of MeOH that are *not coordinated* to the Ln ions (i.e., the ligands fully saturate the inner coordination sphere of the Ln ions).

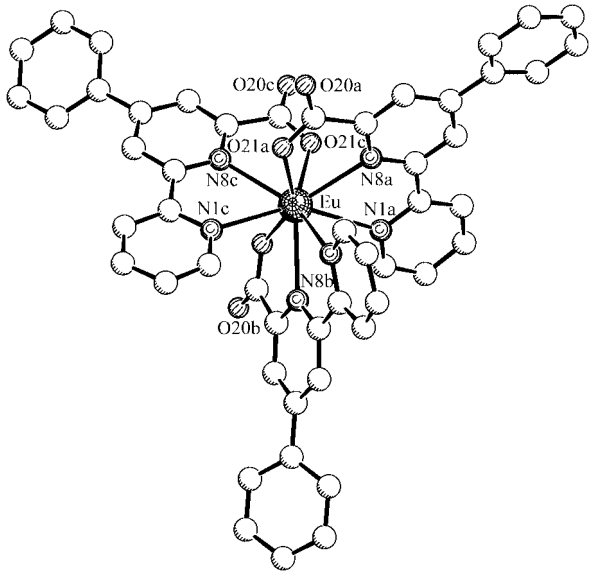


Figure 1. Molecular structure of complex **2b**. The hydrogen atoms and solvent molecules are omitted for clarity.

In **2g**, two La–O bonds have nearly the same length (2.44 Å), while the third is slightly longer (2.47 Å). In addition, the La–N distances range from 2.64 to 2.81 Å, where the longest La–O distance corresponds to the carbonyl group on the pyridine ring containing the longest La–N distance, indicating that there is steric hindrance around the La ion causing one ligand to be slightly crowded out. In **2b**, all distances are slightly shorter, but the same pattern exists: Eu–N distances range from 2.54–2.65 Å for two ligands, while the third has the longest Eu–N bond at 2.72 Å. Likewise, this third ligand has a slightly longer Eu–O distance (2.37 Å) than the other two (2.36 and 2.35 Å). In all cases, the pyridine ring containing the carbonyl group has the shorter of the two Ln–N distances. A table of selected crystal properties is given in the Supporting Information (Table S1).

It should be noted that different isomers of the complexes are possible, based on whether the carboxylate groups are up or down [up-up-up (*fac*) or up-up-down (*mer*)].[14] In the molecular structures isolated, the up-up-down (*mer*) isomer was exclusively observed. However, isomerization in solution is likely as indicated by the broad signals in the NMR spectrum of lanthanum complex **2g** (Figures S4 and S5) and the excited-state lifetime of terbium complex **2a**.[15] We attempted variable-temperature NMR experiments in order to observe the isomerization, but solubility problems prevented us from obtaining reliable measurements.

The complexes do not show absorption bands at energies lower than 340 nm, as can be expected for a simple ligand structure, and the bands can be assigned to π-π* transitions in the ligand with the highest energy transitions localized on the bipyridine units and the shoulder at 320 nm on the carboxylate moieties. Molar extinction coefficient values for the peak maximum at 276 nm are ca. 70000 $M^{-1}cm^{-1}$, and all the complexes show the same features (Figure S2).[16] The transitions in the absorption spectrum of ligand **1** (not shown) are slightly blueshifted vs. those in the complexes, but the features are similar.

The terbium (**2a**) and europium (**2b**) complexes emit brightly at room temperature in acetonitrile and $CH_2Cl_2$ solutions, showing the typical narrow spectra of $Ln^{III}$ cations (Figure 2). For **2a**, excitation of the antenna at 315 nm leads to the characteristic green emission from $Tb^{3+}$ arising from $^5D_4 \rightarrow {}^7F_j$ transitions, with the most intense band at 545 nm corresponding to the $^5D_4 \rightarrow {}^7F_5$ transition. Likewise, for **2b**, excitation of the ligand at 315 nm populates the $Eu^{3+}$ excited state, leading to $^5D_0 \rightarrow {}^7F_j$ transitions, with the most intense at 617 nm ($^5D_0 \rightarrow {}^7F_2$). The nondegenerate $^7F_0$ (579 nm) level is not split, giving evidence that complex **2b** exists as a single (time-averaged) luminescent species in solution.[7b] Due to the exclusion of solvent from the inner coordination sphere of the lanthanide, relatively long excited-state lifetimes (0.2 ms for **2a** and 2.2 ms for **2b**) and high emission quantum yields (7% for **2a**[17] and 60% for **2b**[18]) were found. This is in contrast to the estimated values found by Comby et al.[10] for ligand **3** (7% for $Eu^{III}$

 © 2007 Wiley-VCH Verlag GmbH & Co. KGaA, Weinheim 

complexes and 55% for the $Tb^{III}$ derivatives), but this can be explained by the relative ordering of the energy levels (vide infra).

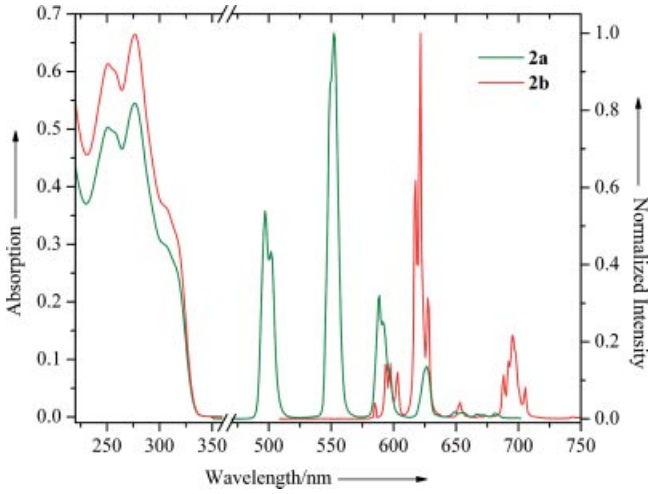


Figure 2. Absorption and normalized emission spectra of complexes **2a** ($1 \times 10^{-5}$ M) and **2b** ($0.8 \times 10^{-5}$ M) in aerated $CH_3CN$ at room temperature ($\lambda_{exc.}$ = 315 nm).

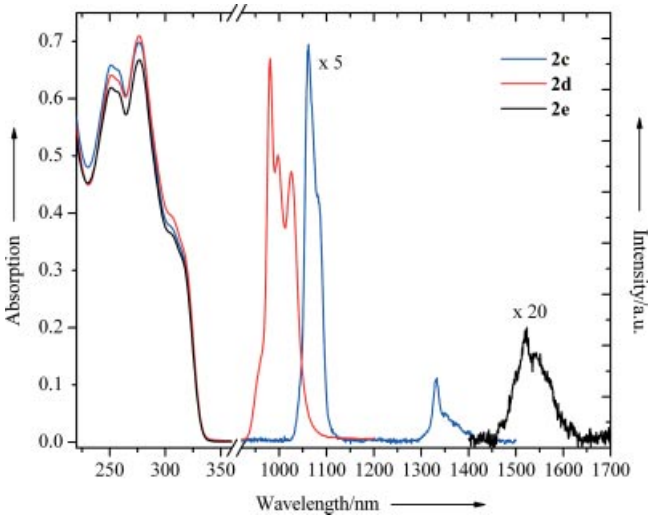


Figure 3. Absorption and emission spectra of complexes **2c**–**2e** in aerated $CH_3CN$ ($1 \times 10^{-5}$ M) at room temperature. The emission spectra were recorded for samples having the same absorption at the excitation wavelength (315 nm) and identical conditions for emission and scaled [**2c** (1×), **2d** (5×), and **2e** (20×)].

The infrared emitters were likewise measured and found to give intense emission in the NIR region. Figure 3 shows the absorption and normalized emission spectra of complexes **2c**–**2e**, where the spectra shown are recorded for samples with identical absorbance values at the excitation wavelength and constant bandpass for emission. Excitation of **2c** at 315 nm led to infrared emission with a maximum at 980 nm, corresponding to the $^2F_{5/2} \rightarrow {}^2F_{7/2}$ transition for $Yb^{3+}$. The quantum yield of **2c** was found to be 0.7%,[19] which is quite remarkable for NIR emitters when taking into consideration the energy gap law.[7] Complex **2d** has two emission peaks at 1060 nm ($^4F_{3/2} \rightarrow {}^4I_{11/2}$) and 1333 nm ($^4F_{3/2} \rightarrow {}^4I_{9/2}$) typical of $Nd^{III}$ complexes.[20] Complex **2e** shows the typical broad emission of $Er^{III}$ complexes, with a maximum at 1523 nm corresponding to the $^4I_{13/2} \rightarrow {}^4I_{15/2}$ transition. The spectra shown in Figure 3 are scaled due to the relatively low luminescence of **2d** and **2e** compared to $Yb^{III}$ complex **2c**, showing the dramatic effect of the energy gap law on the emission properties of the complexes.

All complexes showed identical photophysical properties in acetonitrile and $CH_2Cl_2$ solutions.[15,21] In addition to the emitting lanthanides, gadolinium complex **2f** was prepared to ascertain the level of the ligand triplet state ($^3\pi$-$\pi^*$). Because the excited state of $Gd^{III}$ ($^6P_{7/2}$) lies at 32150 $cm^{-1}$ (≈ 311 nm),[7] it is very difficult to populate it through organic excited ligand triplet states. Therefore, $Gd^{III}$ complexes offer the possibility to probe the ligand excited-state properties in systems nearly identical to the luminescent lanthanide complexes, including the enhanced intersystem crossing offered by the heavy gadolinium ion itself.

At room temperature, gadolinium complex **2f** shows a broad emission with a maximum at 350 nm (not shown), which corresponds to fluorescence of the ligand. Upon cooling to 77 K, a small amount of residual singlet emission is observed, but the emission spectrum is dominated by the phosphorescent triplet emission from the ligand (Figure S3). When a delay of 100 μs after the excitation pulse was applied, the singlet emission disappeared. The $^3\pi$-$\pi$ state of the ligand was determined to be 22700 $cm^{-1}$ (2.82 eV) from the 0-0 transition in the phosphorescence spectrum (440 nm) at 77 K. At room temperature, **2f** has a fluorescence lifetime <1 ns, while at 77 K, the lifetime of the phosphorescent triplet state is 5.4 ms.

The emitting levels of $Eu^{III}$ ($^5D_0$) and $Tb^{III}$ ($^5D_4$) lie at 17500 $cm^{-1}$ and 20430 $cm^{-1}$, respectively, and therefore below the triplet state of the ligand (22700 $cm^{-1}$). However, the $^3\pi$-$\pi$ state of the ligand should be sufficiently higher than the emitting level of the lanthanides such that energy transfer is fast and irreversible (i.e., no back energy transfer can occur). Experimental results have previously shown that triplet states of the ligand should be between 2000 $cm^{-1}$[6b] and 3500 $cm^{-1}$[22] above the emitting state of the $Ln^{III}$ ion ($\Delta E$). In the systems reported here, $\Delta E$ is 2270 $cm^{-1}$ for **2a** and 5200 $cm^{-1}$ for **2b**. Although the emission quantum yield of **2a** is still relatively high (5%), it is clear that the $^3\pi$-$\pi$ state of the ligand and the $^5D_4$ state on $Tb^{III}$ are not well matched. Although the $^5D_0$ state of $Eu^{III}$ and the triplet state of the ligand have a high $\Delta E$ value, an emission quantum yield of 60% is obtained. This indicates that $\Delta E$ of 2000 $cm^{-1}$ may allow, for these complexes at room temperature, back energy transfer into the triplet manifold of the ligand in complex **2a**. For the related complexes based on ligand **3**,[10] the quantum yields for the $Eu^{III}$ and $Tb^{III}$ complexes are reversed. Ligand **3** lacks a phenyl ring on the bipyridine ligand and the increased conjugation offered in the ligand reported here would serve to lower the triplet state and improve the energy match between the ligand and the $Eu^{III}$ emitting state. Conversely, ligand **3**, with its higher triplet state, would favor energy matching the $Tb^{III}$ emitting

 © 2007 Wiley-VCH Verlag GmbH & Co. KGaA, Weinheim 

state, which shows the higher emission quantum yield in the previous study.

The gap between the ligand state in **2c** and that of the $Yb^{III}$ $^2F_{5/2}$ state is quite high (ca. 12000 $cm^{-1}$), but still leads to a relatively high emission quantum yield (0.7%). Presumably, this can be increased by better energy matching of the $^3\pi$-$\pi$ state of the ligand and the $^2F_{5/2}$ level of $Yb^{III}$ (i.e., lowering the triplet level of the ligand by redshifting the absorption), although other processes may play a role.[23]

## Conclusions

We have synthesized a series of neutral lanthanide (Ln) complexes based on simple ligand structures that effectively serve as antennae for energy transfer to the $Ln^{III}$ ion, giving the typical narrow emission spectra, large Stokes' shifts and long luminescence lifetimes typical of $Ln^{III}$ ions. In addition, the red- and near-infrared-emitting complexes have high emission quantum yields, which is likely due to the exclusion of vibronically deactivating solvent molecules from the inner coordination sphere of the complex. Another advantage of the present complexes is their neutrality, making them amenable to applications where charged lanthanide complexes are not, such as in the fabrication of SMOLEDs. We are currently investigating the volatility of the complexes.

Furthermore, functionalization of the ligand allows for the synthesis of more soluble derivatives in solvents of different polarity. Finally, more highly conjugated systems will shift the absorption into the visible region, potentially making the complexes more suitable for biological imaging, where ultraviolet excitation light can cause severe damage to biological tissue. The aforementioned derivatives will be presented in a forthcoming full paper.

**Supporting Information** (see footnote on the first page of this article): Synthetic, photophysical and X-ray methods, characterization data for the products, absorption spectra of all complexes, emission spectra of complex **2f**, crystal structure of **2g**, and NMR spectra of **1** and **2g**.

## Acknowledgments

We would like to thank the Dutch Ministry of Economic Affairs (SENTER) (TSGE3140) and Deutsche Forschungsgemeinschaft (SFB 656) for support of this work.

[1] V. S. Sastri, J.-C. G. Bünzli, V. R. Rao, G. V. S. Rayudu, J. R. Perumareddi, *Modern Aspects of Rare Earths and Complexes*, Elsevier, Amsterdam, **2003**.
[2] J. Kido, Y. Okamoto, *Chem. Rev.* **2002**, *102*, 2357–2368.
[3] K. Kuriki, Y. Koike, Y. Okamoto, *Chem. Rev.* **2002**, *102*, 2347–2356 and references cited therein.
[4] a) S. Pandya, J. Yu, D. Parker, *Dalton Trans.* **2006**, 2757–2766; b) S. Faulkner, S. J. A. Pope, B. P. Burton-Pye, *Appl. Spectrosc. Rev.* **2005**, *40*, 1–31; c) D. Parker, *Chem. Soc. Rev.* **2004**, *33*, 156–165; d) P. Caravan, J. J. Ellison, T. J. McMurry, R. B. Lauffer, *Chem. Rev.* **1999**, *99*, 2293–2352; e) S. Aime, M. Botta, M. Fasano, E. Terreno, *Chem. Soc. Rev.* **1998**, *27*, 19–29; f) M. H. V. Werts, R. H. Woudenberg, P. G. Emmerink, R. v. Gassel, J. W. Hofstraat, J. W. Verhoeven, *Angew. Chem. Int. Ed.* **2000**, *39*, 4542–4544.
[5] a) M. Sabbatini, M. Guardigli, J.-M. Lehn, *Coord. Chem. Rev* **1993**, *123*, 201–228 and references cited therein; b) J.-C. G. Bünzli, C. Piguet, *Chem. Soc. Rev.* **2005**, *34*, 1048–1077.
[6] a) S. I. Weissman, *J. Chem. Phys.* **1942**, *10*, 214–217; b) S. Sato, M. Wada, *Bull. Chem. Soc. Jpn.* **1970**, *43*, 1955–1962; c) W. D. Horrocks Jr, D. R. Sudnick, *Acc. Chem. Res.* **1981**, *14*, 384–392.
[7] a) G. Stein, E. Würzberg, *J. Chem. Phys.* **1975**, *62*, 208–213; b) S. I. Klink, L. Grave, D. M. Reinhoudt, F. C. J. M. van Veggel, M. H. V. Werts, F. A. J. Geurts, J. W. Hofstraat, *J. Phys. Chem. A* **2000**, *104*, 5457–5468.
[8] J.-C. G. Bunzli, *Acc. Chem. Res.* **2006**, *39*, 53–61.
[9] a) R. J. Curry, W. P. Gillin, *Curr. Opin. Solid State Mater. Sci.* **2001**, *5*, 481–486; b) E. Holder, B. M. W. Langeveld, U. S. Schubert, *Adv. Mater.* **2005**, *17*, 1109–1121.
[10] S. Comby, D. Imbert, A.-S. Chauvin, J.-C. G. Bünzli, L. J. Charbonnière, R. F. Ziessel, *Inorg. Chem.* **2004**, *43*, 7369–7379.
[11] See, for example: a) L. J. Charbonnière, N. Hildebrandt, R. F. Ziessel, H.-G. Löhmannsröben, *J. Am. Chem. Soc.* **2006**, *128*, 12800–12809; b) L. J. Charbonnière, R. Schurhammer, S. Mameri, G. Wipff, R. F. Ziessel, *Inorg. Chem.* **2005**, *44*, 7151–7160; c) N. Weibel, L. J. Charbonnière, M. Guargigli, A. Roda, R. F. Ziessel, *J. Am. Chem. Soc.* **2004**, *126*, 4888–4896; d) L. J. Charbonnière, R. F. Ziessel, M. Montalti, L. Prodi, N. Zaccheroni, C. Boehme, G. Wipff, *J. Am. Chem. Soc.* **2002**, *124*, 7779–7788 and references cited therein.
[12] a) O. Mamula, M. Lama, H. Stoeckli-Evans, S. Shova, *Angew. Chem. Int. Ed.* **2006**, *45*, 4940–4944; b) O. Mamula, M. Lama, S. G. Telfer, A. Nakamura, R. Kuroda, H. Stoeckli-Evans, R. Scopelitti, *Angew. Chem. Int. Ed.* **2005**, *44*, 2527–2531; c) M. Lama, O. Mamula, G. S. Kottas, F. Rizzo, L. De Cola, A. Nakamura, R. Kuroda, H. Stoeckli-Evans, *Eur. J. Org. Chem.*, in press.
[13] S. Comby, R. Scopelliti, D. Imbert, L. Charbonnière, R. Ziessel, J.-C. Bünzli, *Inorg. Chem.* **2006**, *45*, 3158–3160.
[14] T. Le Borgne, P. Altmann, N. André, J.-C. G. Bünzli, G. Bernardinelli, P.-Y. Morgantini, J. Weber, C. Piguet, *Dalton Trans.* **2004**, 723–733.
[15] Terbium complex **2a** has a much longer excited state lifetime (1.6 ms) in $CH_2Cl_2$ (vs. 0.2 ms in acetonitrile). We have no concrete explanation for this dramatic change, but experiments are currently underway to understand it. One possible explanation is an isomerization in solution leading to different isomers with different properties, as discussed in the text.
[16] Due to the low solubility of the complexes, we do not feel confident quoting exact molar absorptivity values.
[17] Measured vs. quinine bisulfate in 1 N $H_2SO_4$ ($\Phi$ = 0.546).
[18] Measured vs. rhodamine 101 in ethanol ($\Phi$ = 1.0).
[19] Measured vs. $Yb(TTA)_3$ in toluene ($\Phi$ = 0.0035; TTA = thenoyltrifluoroacetylacetonat e). See: S. B. Meshkova, Z. M. Topilova, D. V. Bolshov, S. V. Beltyukova, M. P. Tsvirko, V. Y. Venchikov, *Acta Phys. Pol. A* **1999**, *95*, 983.
[20] Due to the effective range of our NIR photomultiplier tube, we could not observe the band at ca. 880 nm ($^4F_{3/2} \rightarrow {}^4I_{13/2}$).
[21] For the absorption spectra in $CH_2Cl_2$, see Figure S3.
[22] F. J. Steemers, W. Verboom, D. M. Reinhoudt, E. B. Van der Tol, J. W. Verhoeven, *J. Am. Chem. Soc.* **1995**, *117*, 9408–9414.
[23] a) P. J. Breen, E. K. Hild, W. D. Horrocks Jr, *Biochemistry* **1985**, *24*, 4991–4997; b) W. D. Horrocks Jr, J. P. Bolender, W. D. Smith, R. M. Supkowski, *J. Am. Chem. Soc.* **1997**, *119*, 5972–5973.

Received: May 14, 2007
Published Online: June 25, 2007

 © 2007 Wiley-VCH Verlag GmbH & Co. KGaA, Weinheim 

DOI: 10.1002/ejic.200700541

# Synthesis and Characterization of a Gold Complex Containing $[SbPh]^{2-}$ and $[SbPh_2]^-$ Anions as Bridging Ligands

**Dieter Fenske,*[a,b] Alexander Rothenberger,[a,b] and Stephan Wieber[a,b]**

**Keywords:** Bridging ligands / Aurophilicity / Antimony / Gold / Group 15 ligands

The synthesis and structural characterization of the gold antimony complex $[Au_8(SbPh)_2(SbPh_2)_4(PEt_3)_6]$ (**1**) is reported. Complex **1** can be obtained by the reaction of $[AuCl(PEt_3)]$ with a mixture of $PhSb(SiMe_3)_2$ and $Ph_2(SbSiMe_3)$ in presence of the bidentate phosphane ligand dppm [dppm = bis(diphenylphosphanyl)methane]. Complex **1** consists of a distorted heterocubic central $[Au_6Sb_2]$ unit connected to two annulated five-membered rings on two opposite edges. The $Au^I$ ions show weak aurophilic interactions and are bridged by $[SbPh]^{2-}$ and $[SbPh_2]^-$ anions. Despite the high oxidation potential of $Au^I$, the reaction mixtures and crystals are surprisingly stable.
(© Wiley-VCH Verlag GmbH & Co. KGaA, 69451 Weinheim, Germany, 2007)

## Introduction

Gold complexes have been the subject of interest over a long period of time and some of the latest investigations focus on the catalytic and pharmaceutical aspects of gold compounds.[1–5] There has also been great interest in the chemistry of gold phosphane complexes and gold chalcogenide clusters.[6–12] However, gold complexes containing heavier group 15 elements are scarce. Recently, Au–As cluster complexes[13,14] were obtained by the synthesis of silylated arsines with $Au^I$ phosphane complexes and a few $Au^I$ complexes with tertiary ligands of the type $ER_3$ (E = Sb, Bi; R = organic group) are known for antimony,[15–17] but none for bismuth.[18] Only recently, the first $Au^I$ and $Cu^I$ complexes $[Au(C_6F_5)_2][Bi\{C_6H_4(2\text{-}CH_2NMe_2)\}_2]$ and $[(PMe_3)_2CuBi(SiMe_3)_2]$ with a M···Bi interaction (M = Cu, Bi) were reported.[19,20] In contrast, there are several copper and silver antimony clusters.[21–24] The copper antimony clusters, for example $[Cu_{20}Sb_{10}(PCy_3)_8]$, $[Cu_{45}Sb_{16}(PEt_2Me)_{16}]$ and $[Cu_{28}Sb_{12}(PEt_3)_{12}\{Sb(SiMe_3)_2\}_2]$ can be obtained by reactions of $Cu^I$ salts with $Sb(SiMe_3)_3$ in the presence of tertiary phosphanes. The concept of oxidation numbers and localised $Cu^I$ and $Cu^{II}$ centres cannot be applied to these CuSb clusters and they are described as molecular alloys. For silver, molecular alloys were not found. Instead reactions between silver nitrate and $PhSb(SiMe_3)_2$ yielded the silver antimony complexes $[Ag_4(Sb_4Ph_4)_2(PiPr_3)_4]$ and $[Ag_4(Sb_6Ph_6)_2(PnBu_3)_4]$ where oxidation of the antimony precursors to anions with Sb–Sb bonds took place.[24]

[a] Institut für Anorganische Chemie, Universität Karlsruhe, Geb. 30.45,
Engesserstr. 15a, 76131 Karlsruhe, Germany
E-mail: dieter.fenske@chemie.uni-karlsruhe.de
[b] Institut für Nanotechnologie, Forschungszentrum Karlsruhe GmbH,
P. O. Box 3640, 76021 Karlsruhe, Germany

## Results and Discussion

Here we report the synthesis of the 12-membered Au–Sb ring $[Au_8(SbPh)_2(SbPh_2)_4(PEt_3)_6]$ (**1**)·$16CH_2Cl_2$ by the reaction of $[AuCl(PEt_3)]$ with a mixture of $PhSb(SiMe_3)_2$ and $Ph_2(SbSiMe_3)$ in presence of the bidentate phosphane ligand dppm [dppm = bis(diphenylphosphanyl)methane] (Scheme 1).

$$[AuCl(PEt_3)] + PhSb(SiMe_3)_2/Ph_2Sb(SiMe_3) \xrightarrow{dppm} [Au_8(SbPh)_2(SbPh_2)_4(PEt_3)_6] \quad (1)$$

Scheme 1. Synthesis of $[Au_8(SbPh)_2(SbPh_2)_4(PEt_3)_6]$ (**1**).

Complex **1** crystallizes from $CH_2Cl_2$ as yellow blocks in the triclinic space group $P\bar{1}$ (Figure 1) with one molecule in the unit cell and 16 $CH_2Cl_2$ molecules per unit cell.

The molecular structure of **1** can be described as a 12-membered Au–Sb ring or a distorted heterocubic central $[Au_6Sb_2]$ unit connected to two annulated five-membered rings on two opposite edges. Two gold atoms (Au1, Au1A) are coordinated to a phosphorus atom of triethylphosphane [Au1–P1 2.277(5) Å], whereas the other four gold atoms belong to the nonplanar five-membered rings formed with another four Sb atoms of the $[SbPh_2]^-$ ligands and two further gold atoms [Au4, Au4A]. The bridging angle of the $[SbPh_2]^-$ ligand is about 120° [Au3–Sb3–Au4 118.87(5)°]. Within the peripheral rings the Au4,4A atoms are surrounded by two phosphorus atoms of the phosphane groups and the two antimony atoms of the $[SbPh_2]^-$ ligands in a distorted tetrahedral fashion [P3–Au4–Sb2 108.89(12)°]. Noteworthy structural features are the acute Sb–Au–Sb angle of almost 90° [Sb3–Au4–Sb2 90.50(5)°] and the large P–Au–P angle [P2–Au4–P3 125.25(18)°], which may be the result of steric repulsion of the bulky phosphane ligands. This situation is also reflected in the slightly longer Au–P distance [Au4–P3 2.358(5) Å] relative

 © 2007 Wiley-VCH Verlag GmbH & Co. KGaA, Weinheim InterScience 

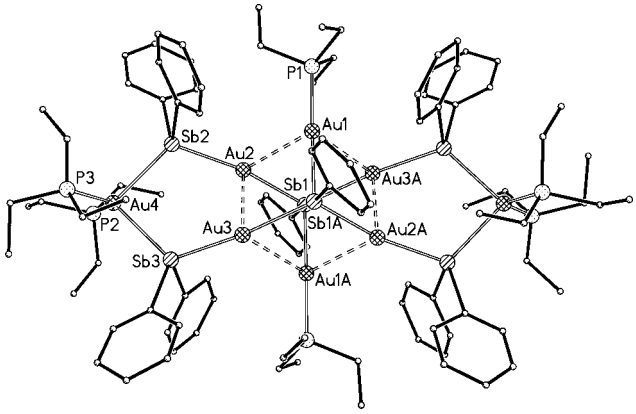


Figure 1. Molecular structure of $[Au_8(SbPh)_2(SbPh_2)_4(PEt_3)_6]$ (**1**) in the solid state [symmetry operation (A) $-x + 1, -y + 1, -z + 1$]. Selected distances [Å] and angles [°]: Au1–Au2 3.0100(10), Au2–Au3 3.0412(17), Au2–Sb2 2.5774(15), Au2–Sb1 2.5883(15), Au3–Sb3 2.5803(12), Au4–Sb3 2.7298(16), Au4–Sb2 2.7350(15), Au1–P1 2.277(5), Au4–P2 2.351(4), Au4–P3 2.358(5), P1–Au1–Sb1A 169.80(11), P1–Au1–Au2 103.92(10), Sb1A–Au1–Au2 83.32(4), P1–Au1–Au3A 102.17(12), Sb1A–Au1–Au3A 84.74(4), Au2–Au1–Au3A 90.48(3), Sb2–Au2–Sb1 167.51(4), Sb2–Au2–Au1 115.45(4), Sb1–Au2–Au1 77.03(3), Sb2–Au2–Au3 93.16(4), Sb1–Au2–Au3 87.47(4), Au1–Au2–Au3 85.21(4), Sb3–Au3–Sb1A 173.68(4), Sb3–Au3–Au2 91.50(4), Sb1A–Au3–Au2 82.56(4), Sb3–Au3–Au1 107.37(4), Sb1A–Au3–Au1A 73.98(3), Au2–Au3–Au1A 81.44(4), P2–Au4–P3 125.25(18), P2–Au4–Sb3 111.05(13), P3–Au4–Sb3 108.74(16), P2–Au4–Sb2 106.81(12), P3–Au4–Sb2 108.89(12), Sb3–Au4–Sb2 90.50(5), Au1A–Sb1–Au2 103.43(5), Au1A–Sb1–Au3A 104.75(5), Au2–Sb1–Au3A 116.13(5), Au2–Sb2–Au4 115.41(5), Au3–Sb3–Au4 118.87(5).

to Au1–P1 with 2.277(5) Å. The same applies to the Au4,4a–Sb bond length, which is the largest observed in **1** [Au4–Sb2 2.7350(15) Å]. Au–Sb bond lengths within the central heterocubic unit are about 0.15 Å shorter [Au2–Sb2 2.5774(15) Å; Sb1–Au3A 2.5903(13) Å]. Au–Sb distances in $Au^I$ stibane complexes are between 2.605 and 2.65 Å.[15–17] If one considers the estimated van der Waals radii of gold (3.6 Å), aurophilic interactions could be expected in compound **1** with Au–Au distances of 3.0100(10) [Au1–Au2] to 3.1773(14) Å [Au3–Au1A].[25] Similar distances are known for other gold compounds, for example the Au–As cluster complexes $[Au_{19}(As\textit{n}Pr)_8(dppe)_6]Cl_3$, $[Au_{10}(As\textit{n}Pr)_4(dppe)_4]Cl_2$ and $[Au_{10}(AsPh)_4(PhAsSiMe_3)_2(P\textit{n}Pr_3)_6]$ or the Au–Se clusters $[Au_{10}Se_4(dpppe)_4]Br_2$ and $[Au_{18}Se_8(dppe)_6]Br_2$ [dppe, dpppe = 1,2-bis(diphenylphosphanyl)ethane or -pentane].[11,13] Aurophilic interactions discussed in the literature for mononuclear gold complexes with Au–Au distances of about 3.05 Å are indicated in **1** by dashed-open bonds (Figure 1).[26] These are longer than Au–Au distances in $Au_2$(g) (2.472 Å) or the Au–Au distance in cubic close packed gold (2.884 Å).[25]

Contrary to copper or silver complexes with stibido ligands, the $Au^I$ ions in **1** adopt a linear coordination with the Sb anions. Despite the high oxidation potential of $Au^I$, the reaction mixture and crystals are surprisingly stable, which is also in marked contrast to the silver antimony cluster complexes that decompose at –40 °C.[24] The added phosphane dppm is not found in the solid-state structure of **1**, but it plays an important role in the reaction. If there is no additional phosphane in the mixture, the reaction turns green immediately, indicating a different reaction pathway that is currently being investigated. However, Au–Sb cluster **1** can also be obtained by the reaction with $PPh_3$ as a stabilizing ligand.

## Conclusions

Despite the high oxidation potential of $Au^I$, the first Au–Sb cluster was described; it was found to exhibit linear coordination of the gold centres to the antimony anions with weak additional aurophilic interactions. The Au–Sb system is surprisingly stable relative to previously described Ag–Sb complexes. With the consideration that gold tends to form Au–Au interactions, further investigations will focus on the synthesis of linked Au–Sb complexes, which may result in novel mixed-metal wires or wires consisting of linked molecular Au–Sb alloys.

## Experimental Section

**General Remarks:** All operations were carried out under an atmosphere of purified nitrogen. $CH_2Cl_2$ was refluxed over $P_2O_5$ and freshly distilled prior to use. The dppm ligand was purchased from Sigma–Aldrich. $[AuCl(PEt_3)]$, $PhSbSiMe_3$ and $Ph_2SbSiMe_3$ were prepared according to published procedures.[27,28] The UV/Vis spectrum was recorded in KBr pellets with a Perkin–Elmer Lambda 900 spectrophotometer. Fourier-transform infrared spectroscopy on KBr pellets was performed with a Bruker IFS 28 FTIR instrument.

**1:** $[AuCl(PEt_3)]$ (0.08 g, 0.228 mmol) was dissolved in $CH_2Cl_2$ (8 mL) and dppm (0.18 g, 0.456 mmol) was then added. The clear, colourless solution was cooled to –78 °C and $PhSbSiMe_3$/$Ph_2SbSiMe$ (1:1.25, 0.03 mL) was added. The yellow reaction mixture was stored at –78 °C overnight, and then it was warmed up to –40 °C and stored over a period of one week. After one week at –40 °C, yellow crystals of **1** could be isolated for crystallographic measurements. UV/Vis (KBr): $\lambda$ = 575 (absorption edge) nm. IR (KBr): $\tilde{\nu}$ = 1584.90 (vw), 1571.11 (m), 1474.54 (m), 1428.29 (s), 1377.15 (vw), 1299.70 (vw), 1260.71 (w), 1180.79 (vw), 1155.11 (vw), 1092.43 (m), 1064.44 (w), 1026.97 (m), 1017.86 (m), 996.89 (w), 802.43 (w), 764.14 (w), 741.80 (m), 727.38 (s), 692.96 (vs), 522.49 (m), 506.21 (m), 458.04 (m), 450.2 (m) $cm^{-1}$.

**X-Ray Crystallographic Study:** Crystallographic data for the compounds were collected with a STOE IPDS II diffractometer by using graphite-monochromatic Mo-$K_\alpha$ radiation ($\lambda$ = 0.71073 Å). The structures were solved by direct methods and refined by full-matrix least-squares on $F^2$ (all data) using the SHELXTL software package.[29] Hydrogen atoms were placed in calculated positions, non-hydrogen atoms were assigned anisotropic thermal parameters. Disordered components were refined with isotropic thermal parameters. **1**: $C_{104}H_{156}Au_8Cl_{16}P_6Sb_6$: $M_r$ = 4465.54; triclinic, space group $P\bar{1}$, $Z$ = 1; $a$ = 14.270(3), $b$ = 15.365(3), $c$ = 18.851(4) Å; $\alpha$ = 105.47(3), $\beta$ = 90.78(3), $\gamma$ = 113.47(3)°; $V$ = 3620.0(13) $Å^3$; $T$ = 150(2) K; $F(000)$ = 2080; $\rho_{calcd.}$ = 2.048 $g\,cm^{-3}$; reflections measured 22500, of which 13237 were independent ($R_{int}$ = 0.0899); 603 parameters; $wR_2$ = 0.2473 (all data); $R_1$ = 0.0883 [$I > 2\sigma(I)$]; Largest diff. peak and hole 5.289/–3.575 $e\,Å^{-3}$.

 © 2007 Wiley-VCH Verlag GmbH & Co. KGaA, Weinheim 

CCDC-647732 contains the supplementary crystallographic data for this paper. These data can be obtained free of charge from The Cambridge Crystallographic Data Centre via www.ccdc.cam.ac.uk/data_request/cif.

## Acknowledgments

We gratefully acknowledge the DFG Center for Functional Nanostructures, the Forschungszentrum Karlsruhe and the Fonds der Chemischen Industrie for financial support.

[1] D. J. Gorin, F. D. Toste, *Nature* **2007**, *446*, 395–403.
[2] A. S. K. Hashmi, G. J. Hutchings, *Angew. Chem.* **2006**, *118*, 8064–8105; *Angew. Chem. Int. Ed.* **2006**, *45*, 7896–7936 and references cited therein.
[3] S. S. Gunatilleke, A. M. Barrios, *J. Med. Chem.* **2006**, *49*, 3933–3937.
[4] R. V. Parish, S. M. Cottrill, *Gold Bull.* **1987**, *20*, 3–12 and references cited therein.
[5] P. Pyykkö, *Angew. Chem.* **2004**, *116*, 4512–4557; *Angew. Chem. Int. Ed.* **2004**, *43*, 4412–4456.
[6] V. G. Albano, P. L. Bellon, M. Manassero, M. Sansoni, *J. Chem. Soc. C* **1970**, 1210–1211.
[7] C. E. Briant, K. P. Hall, D. M. P. Mingos, A. C. Wheeler, *J. Chem. Soc. Dalton Trans.* **1986**, 687–692.
[8] H. Schmidbaur, F. Scherbaum, B. Huber, G. Müller, *Angew. Chem.* **1988**, *100*, 441–443; *Angew. Chem. Int. Ed. Engl.* **1988**, *27*, 419–421.
[9] H. Schmidbaur, G. Weidenhiller, O. Steigelmann, *Angew. Chem.* **1991**, *103*, 442–444; *Angew. Chem. Int. Ed. Engl.* **1991**, *30*, 433–435.
[10] J. Phete, C. Maichle-Mössmer, J. Strähle, *Z. Anorg. Allg. Chem.* **1998**, *624*, 1207–1210.
[11] D. Fenske, T. Langetepe, M. M. Kappes, O. Hampe, P. Weis, *Angew. Chem.* **2000**, *112*, 1925–1928; *Angew. Chem. Int. Ed.* **2000**, *39*, 1857–1860.
[12] S. Lebedkin, T. Langetepe, P. Sevillano, D. Fenske, M. M. Kappes, *J. Phys. Chem. B* **2002**, *106*, 9019–9026.
[13] P. Sevillano, O. Fuhr, M. Kattannek, P. Nava, O. Hampe, S. Lebedkin, R. Ahlrichs, D. Fenske, M. M. Kappes, *Angew. Chem.* **2006**, *118*, 3785–3791; *Angew. Chem. Int. Ed.* **2006**, *45*, 3702–3708.
[14] D. Fenske, F. Simon, *Z. Anorg. Allg. Chem.* **1996**, *622*, 45–52.
[15] J. Vicente, A. Arcas, P. G. Jones, J. Lautner, *J. Chem. Soc. Dalton Trans.* **1990**, 451–456.
[16] V. R. Bojan, E. J. Fernandez, A. Laguna, J. M. Lopez-de-Luzuriaga, M. Monge, M. E. Olmos, C. Silvestru, *J. Am. Chem. Soc.* **2005**, *127*, 11564–11565.
[17] N. R. Champness, W. Levason, *Coord. Chem. Rev.* **1994**, *133*, 115–217.
[18] O. Schuster, A. Schier, H. Schmidbaur, *Organometallics* **2003**, *22*, 4079–4083.
[19] E. J. Fernandez, A. Laguna, J. M. Lopez-de-Luzuriaga, M. Monge, M. Nema, M. E. Olmos, J. Perez, C. Silvestru, *Chem. Commun.* **2007**, 571–573.
[20] D. Fenske, A. Rothenberger, S. Wieber, *Z. Anorg. Allg. Chem.* **2003**, *629*, 929–930.
[21] R. Ahlrichs, D. Fenske, M. McPartlin, A. Rothenberger, C. Schrodt, S. Wieber, *Angew. Chem.* **2005**, *117*, 4002–4005; *Angew. Chem. Int. Ed.* **2005**, *44*, 3932–3936.
[22] R. Ahlrichs, C. E. Anson, R. Clerac, D. Fenske, A. Rothenberger, M. Sierka, S. Wieber, *Eur. J. Inorg. Chem.* **2004**, 2933–2936.
[23] R. Ahlrichs, D. Fenske, A. Rothenberger, C. Schrodt, S. Wieber, *Eur. J. Inorg. Chem.* **2006**, 1127–1129.
[24] D. Fenske, A. Rothenberger, S. Wieber, *Eur. J. Inorg. Chem.* **2007**, 648–651.
[25] D. M. P. Mingos, *J. Chem. Soc. Dalton Trans.* **1996**, 561–566.
[26] H. Schmidbaur, *Chem. Soc. Rev.* **1995**, *24*, 391–400.
[27] C. A. McAuliffe, R. V. Parish, P. D. Randall, *J. Chem. Soc. Dalton Trans.* **1979**, 1730–1735.
[28] M. Ates, H. J. Breunig, S. Gülec, *Phosphorus, Sulfur Silicon Relat. Elem.* **1989**, *44*, 129–133.
[29] G. M. Sheldrick, *SHELXTL-97*, University of Göttingen, **1997**.

Received: May 23, 2007
Published Online: June 29, 2007

 © 2007 Wiley-VCH Verlag GmbH & Co. KGaA, Weinheim 

DOI: 10.1002/ejic.200700569

# Synthesis and Reactivity of 16-Electron Pentamethylcyclopentadienyl–Ruthenium(II) Complexes with Bis(imidazolin-2-imine) Ligands

**Dejan Petrovic,[a] Thomas Glöge,[a] Thomas Bannenberg,[a] Cristian G. Hrib,[a] Sören Randoll,[a] Peter G. Jones,[a] and Matthias Tamm*[a]**

**Keywords:** Ruthenium / Cyclopentadienyl ligands / N ligands / 16-electron complexes / Coordinative unsaturation

The 1,2-bis(imidazolin-2-imino)ethane ligands $BL^{Me}$ and $BL^{iPr}$ were prepared, in which the ability of the imidazolium moiety to effectively stabilize a positive charge leads to highly basic ligands with a strong electron-donating capacity. This feature is illustrated by the isolation of very stable half-sandwich 16-electron ruthenium complexes of the type $[(\eta^5\text{-}C_5Me_5)Ru(BL^R)]^+$ (**1**, R = Me; **2**, R = *i*Pr), which even resist coordination of the chloride counterion. Their inertness towards hard, π-basic ligands does not prevent these complexes from displaying high reactivity towards soft σ-donor/π-acceptor ligands such as CO and isocyanides, and the complexes $[\mathbf{1}\cdot CO]CF_3SO_3$ and $[\mathbf{1}\cdot CNXy]CF_3SO_3$ (XyNC = 2,6-dimethylphenyl isocyanide) can be isolated. These complexes exhibit CO and CN stretching vibrations at 1886 and 1991 $cm^{-1}$, respectively, which reveals the electron richness and strong π-electron releasing capability of the ruthenium–imine moiety.

(© Wiley-VCH Verlag GmbH & Co. KGaA, 69451 Weinheim, Germany, 2007)

## Introduction

Coordinatively unsaturated organometallic complexes play a fundamental role as intermediates in homogeneous transition-metal-catalyzed reactions, and their occurrence is rationalized by the 16- and 18-electron rule proposed by Tolman.[1] Numerous examples have been prepared to date, and their electronic and magnetic properties have been studied.[2] Various factors can be responsible for the stabilization of these species, amongst which the introduction of π-donor ligands such as alkoxides, alkylthiolates, amides, or halides can be successfully employed for the creation of π-stabilized unsaturation.[2,3] Accordingly, the stabilization of 16-electron half-sandwich ruthenium complexes of the type $[(\eta^5\text{-}C_5Me_5)Ru(PR_3)X]$ (X = OR, NHR, Cl, Br, I) can be achieved by electron donation from the heteroatomic anionic ligand.[4] Similarly, ligand π-coordination has been suggested to exist in highly reactive ruthenium–amidinate complexes such as $[(\eta^5\text{-}C_5Me_5)Ru\{i\text{PrNC(Me)N}i\text{Pr}\}]$.[5] In contrast, the cationic 16-electron tmeda complex $[(\eta^5\text{-}C_5Me_5)Ru(Me_2NCH_2CH_2NMe_2)]^+$ can be isolated despite the lack of nitrogen-to-metal π-donation. This complex, however, can only be stabilized by the use of the noncoordinating $[B\{3,5\text{-}C_6H_3(CF_3)_2\}_4]^-$ ($BAr'_4$) counteranion.[6] The same holds true for the rare 16-electron phosphane complexes $[(\eta^5\text{-}C_5Me_5)Ru(PP)]BAr'_4$ [PP = $(PEt_3)_2$, $i\text{Pr}_2\text{PCH}_2\text{CH}_2\text{P}i\text{Pr}_2$].[7]

## Results and Discussion

We present herein the neutral 1,2-bis(imidazolin-2-imino)ethane ligands $BL^{Me}$ and $BL^{iPr}$ and their ability to form 16-electron half-sandwich ruthenium complexes of unprecedented stability. $BL^R$ (R = Me, *i*Pr) are obtained in high yield as air-stable off-white solids from the reaction of the readily available imidazolin-2-imines[8] $Imine^{Me}$ and $Imine^{iPr}$ with 1,2-ethyleneditosylate followed by deprotonation with KO*t*Bu.[9,10] The reaction of $BL^{Me}$ and $BL^{iPr}$ with $[(\eta^5\text{-}C_5Me_5)RuCl]_4$[11] in thf affords the violet-colored complexes $[(\eta^5\text{-}C_5Me_5)Ru(BL^{Me})]Cl$, [**1**]Cl, and $[(\eta^5\text{-}C_5Me_5)Ru(BL^{iPr})]Cl$, [**2**]Cl, in which the chloride counteranions can be easily exchanged for the triflate anion (Scheme 1). Crystals of [**1**]OTf·thf suitable for X-ray diffraction analysis could be obtained from a thf/hexane solution. The unit cell is composed of noninteracting cations **1** and triflate anions, and the shortest Ru–O and Ru–F distances are 5.65 and 6.87 Å, respectively. Any interaction between the cations and the thf solvent molecules can also be excluded as the shortest $Ru\text{–}O_{thf}$ separation is 5.97 Å. In addition, there is no indication of any agostic interaction between the ruthenium center and the C–H bonds of the diimine ligand. The cationic half-sandwich complex exhibits a two-legged piano stool geometry with the $\eta^5\text{-}C_5Me_5$ and the $\eta^2$-diimine ligands adopting a pseudotrigonal planar coordination sphere around the ruthenium atom (Figure 1). The Ct–Ru–N1–N2 dihedral angle (Ct = centroid of the Cp

[a] Institut für Anorganische und Analytische Chemie, Technische Universität Carolo-Wilhelmina
Hagenring 30, 38106 Braunschweig, Germany
Fax: +49-251-391-5309
E-mail: m.tamm@tu-bs.de

Supporting information for this article is available on the WWW under http://www.eurjic.org or from the author.

 © 2007 Wiley-VCH Verlag GmbH & Co. KGaA, Weinheim 

ring) is 179.6°, and the sum of the N1–Ru–N2 angle [76.71(6)°] and the two Ct–Ru–N angles is 360.0°. Accordingly, cation **1** can be regarded as being almost perfectly $C_{2v}$-symmetric.

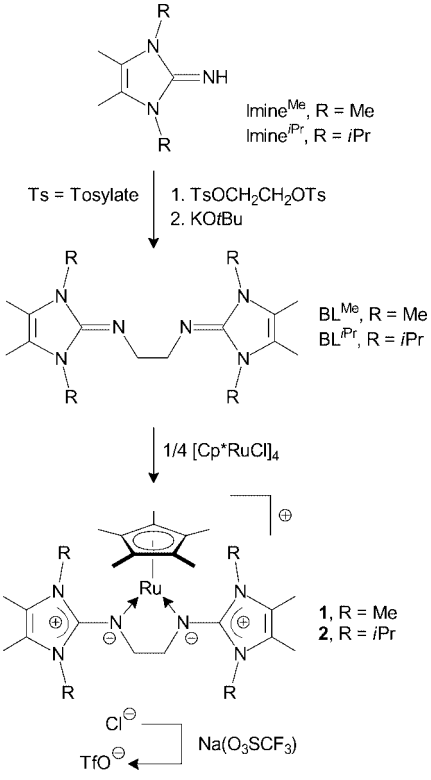


Scheme 1.

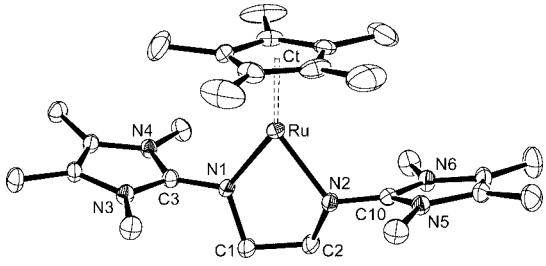


Figure 1. ORTEP diagram of the cation in [**1**]OTf with thermal displacement parameters drawn at 50% probability.[18] The Cp* ligand is disordered over two positions; only one position is shown. Selected bond lengths [Å] and angles [°]: Ru–N1 2.060(2), Ru–N2 2.073(2), Ru–C(Cp*) 2.103(4)–2.194(4), N1–C3 1.349(2), N2–C10 1.345(2); N1–Ru–N2 76.71(6).

The Ru–N distances of 2.060(2) and 2.073(2) Å are significantly shorter than those in the related complex [($\eta^5$-$C_5Me_5$)Ru(tmeda)]BAr′$_4$ [2.183(7), 2.180(6) Å],[6a] and they fall in the same range as the Ru–N bond length observed for the amidinate complex [($\eta^5$-$C_5Me_5$)Ru{iPrNC(Me)-NiPr}] [2.073(3) Å].[5a] Even shorter Ru–N distances are found in neutral bimetallic Cp*Ru complexes containing a highly π-basic diamide ligand.[12] The short Ru–N bonds in **1** are in agreement with a strong electron-releasing capability of the BL$^{Me}$ ligand, which is implied by the ylidic resonance structure shown in Scheme 1. Charge separation in coordinated BL$^{Me}$ can be also clearly deduced from the observation of perpendicularly oriented imidazole moieties with respect to the Ru–N–N coordination plane (dihedral angles = 86.0 and 82.6°). This orientation rules out the possibility of π-interaction between the exocyclic nitrogen atoms and the imidazole rings, leading to elongated C–N distances [N1–C3 = 1.349(2) Å and N2–C10 = 1.345(2) Å], much longer than expected for a N–C($sp^2$) double bond (1.28 Å) and almost in the range of a N–C($sp^2$) single bond (1.38 Å).[13]

The molecular structure of cation **2** in [**2**]OTf·thf, which displays crystallographic mirror symmetry, is shown in Figure 2. Inspection of the crystal packing reveals the absence of any relevant intermolecular contact between the cation and the triflate and the thf molecules. In comparison to **1**, however, the coordination sphere around the ruthenium atom is slightly distorted from a pseudotrigonal planar arrangement. The Ct–Ru–N1–N1a dihedral angle is 168.0°, and the sum of the N1–Ru–N1a angle [77.56(9)°] and the Ct–Ru–N angles is 358.8°. This distortion is associated with a slippage of the $NCH_2CH_2N$ moiety of the diimine ligand to one side of the molecule, opening the opposite side of the ruthenium coordination sphere for two intramolecular C7–H7···Ru contacts of 2.88 Å. This rather long distance excludes the presence of a strong agostic interaction,[7,14] but could imply intramolecular hydrogen bonds of the X–H···M type.[15,16] The Ru–N/N1a bond length in **2** is 2.076(2) Å, which is slightly longer than the corresponding distances found in **1**.

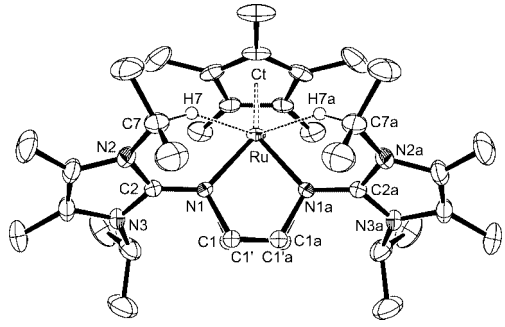


Figure 2. ORTEP diagram of the cation in [**2**]OTf with thermal displacement parameters drawn at 50% probability.[18] The ethylene bridge is disordered. Selected bond lengths [Å] and angles [°]: Ru–N1 2.076(2), Ru–C(Cp*) 2.120(2)–2.156(2), N1–C2 1.340(2); N1–Ru–N1a 77.50(8).

In agreement with the presence of 16-electron species in the solid state, the cations in [**1**]OTf and [**2**]OTf also exhibit $C_{2v}$ symmetry in solution according to their $^1$H and $^{13}$C NMR spectra in [$D_6$]acetone. For instance, the $^1$H NMR spectrum of [**1**]OTf shows one singlet for the $NCH_2CH_2N$ moiety together with three singlets for the three different types of methyl groups. In contrast, two doublets are observed in the $^1$H NMR spectrum of [**2**]OTf for the diastereotopic isopropyl methyl groups, indicating a hindered rotation of the imidazoline moieties around the N1–C2 axis at r.t. on the NMR timescale. Furthermore, the nature of the counterion does not have any impact on the chemical

 © 2007 Wiley-VCH Verlag GmbH & Co. KGaA, Weinheim 

shifts, and the $^1H$ and $^{13}C$ NMR spectra recorded for [**1**]Cl and [**2**]Cl are identical with those observed for the corresponding triflates. Low-temperature NMR spectroscopic studies of the chloride complexes in [$D_6$]acetone solution do not reveal any significant changes, suggesting negligible ruthenium–chloride interaction or a rapid dynamic behavior even at –90 °C (see NMR spectra in the Supporting Information). Low solubility impeded NMR measurements in less polar solvents such as [$D_8$]toluene. Ultimately, the solid-state structure of [**2**]Cl·0.75thf shows an asymmetric unit, which is composed of four independent cations **2**, four chloride anions, and three thf molecules (Figure 3). The shortest Ru–Cl distance is 5.89 Å, excluding any interaction and providing final proof of the stability of these unsaturated 16-electron complexes. The geometries at the ruthenium centers and the Ru–N distances are very similar to the parameters observed in [**2**]OTf·thf with the exception of Ru···H interactions, which were not observed.

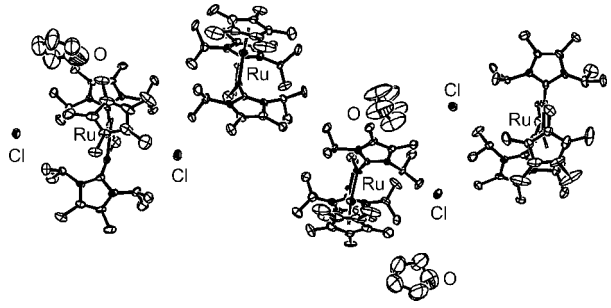


Figure 3. ORTEP diagram of the asymmetric unit of [**2**]Cl·0.75thf with thermal displacement parameters drawn at 50% probability.[18,19]

It should be noted that dynamic behavior in solution was reported for the related complex [($\eta^5$-$C_5Me_5$)RuCl(tmeda)], for which the solid-state structure shows that the chloride atom is attached to the ruthenium center with an unusually long Ru–Cl distance of 2.5116(9) Å.[17] To compare this complex, which contains a hard σ-donor diamine ligand, with our Cp*Ru–diimine complexes, we performed DFT (density functional theory) calculations to determine their heterolytic gas phase Ru–Cl bond dissociation enthalpies.[18] For [**1**]Cl and [**2**]Cl, the enthalpies required to split the chloride ion from the corresponding complex cations are 295.0 and 294.4 kJ/mol, respectively, whereas for the tmeda complex, a significantly higher value of 413.8 kJ/mol was obtained, indicating a much stronger Ru–Cl interaction. These results suggest that the large difference of almost 120 kJ/mol between the gas phase dissociation enthalpies accounts for the observed strong dissociation of the Cp*Ru–diimine complexes in solution, where anion and cation solvation supports straightforward heterolytic Ru–Cl bond cleavage.

On the basis of structural and theoretical results, it can be assumed that the unusual stability of cationic complexes **1** and **2** stems from the strong π-electron releasing capability of the diimine ligands $BL^{Me}$ and $BL^{iPr}$. Indeed, cyclic voltammetric studies on [**1**]OTf and [**2**]OTf in acetonitrile afford very negative redox potentials of $E°$ = –588 mV and $E°$ = –569 mV versus the ferrocene/ferrocenium couple.[20] These potentials are much lower than usually observed for a reversible one-electron $Ru^{II}/Ru^{III}$ oxidation process in cyclopentadienyl–ruthenium complexes.[21] In contrast, it is not surprising that the values reported for *neutral* 16-electron Cp*Ru–amidinate complexes obviously fall in an even more negative range.[5d] The reactivity of [**1**]OTf towards carbon monoxide and 2,6-dimethylphenyl isocyanide (XyNC) gives further evidence for the electron richness of the metal center. Treatment of thf solutions of [**1**]OTf with CO gas or 1 equiv. of XyNC at ambient temperature yields the complexes [**1**·CO]OTf and [**1**·CNXy]OTf as a yellow or red crystalline solid, respectively. In the IR spectra, the CO and CN stretching vibrations are at 1886 and 1991 $cm^{-1}$, which is strongly shifted to lower wavenumbers in comparison to the free, uncoordinated ligands. In general, significantly higher values were reported for other cationic complexes of the type [Cp*Ru(N∩N)CO]$^+$, for examle $\tilde{\nu}_{CO}$ = 1959 and 1963 $cm^{-1}$ for N∩N = RN=CH–CH=NR (R = *i*Pr, Mes),[22] $\tilde{\nu}_{CO}$ = 1963 $cm^{-1}$ for N∩N = bipy,[23] $\tilde{\nu}_{CO}$ = 1948 $cm^{-1}$ for N∩N = phenanthroline,[24] and $\tilde{\nu}_{CO}$ = 1931 $cm^{-1}$ for N∩N = $Me_2NCH_2CH_2NH_2$.[25] Remarkably, the CO stretching frequency in [**1**·CO]OTf is even slightly lower than the values reported for the amidinate complexes [($\eta^5$-$C_5Me_5$)Ru{*i*PrNC(Me)N*i*Pr}CO] ($\tilde{\nu}_{CO}$ = 1901 $cm^{-1}$) and [($\eta^5$-$C_5Me_5$)Ru{*t*BuNC(Ph)N*t*Bu}CO] ($\tilde{\nu}_{CO}$ = 1888 $cm^{-1}$).[5a]

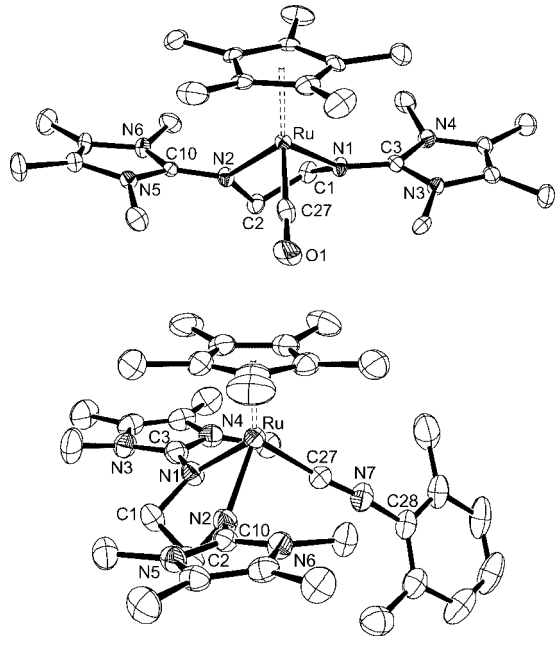


Figure 4. ORTEP diagram of the cations in [**1**·CO]OTf (top) and [**1**·CNXy]OTf (bottom) with thermal displacement parameters drawn at 50% probability.[18] Selected bond lengths [Å] and angles [°] in [**1**·CO]$^+$/[**1**·CNXy]$^+$: Ru–N1 2.165(3)/2.185(3), Ru–N2 2.145(3)/2.153(2), Ru–C27 1.831(4)/1.907(3), Ru–C(Cp*) 2.192(3)–2.272(4)/2.194(3)–2.233(3), N1–C3 1.323(4)/1.331(4), N2–C10 1.319(5)/1.335(4), C27–O1 1.162(5), C27–N7 1.179(4); N1–Ru–N2 77.38(12)/77.94(9), Ru–C27–O1 172.0(4), Ru–C27–N7 175.6(3), C27–N7–C28 174.8(4).

 © 2007 Wiley-VCH Verlag GmbH & Co. KGaA, Weinheim 

The molecular structures of the cations in [**1**·CO]OTf and [**1**·CNXy]OTf are shown in Figure 4. Both complexes exhibit a three-legged piano stool geometry with elongated Ru–N bonds in comparison to the structure of **1**. The ruthenium–carbon bonds are short [Ru–CO 1.831(4) Å, Ru–CN 1.907(3) Å], confirming strong metal-to-ligand π-back-donation. For instance, the Ru–C distance in [**1**·CO]OTf is significantly shorter than the distances observed for related cationic complexes of the type $[Cp^*Ru(N^{\frown}N)CO]^+$,[26] and it falls in the same range as the bond length observed for the neutral amidinate complex $[(\eta^5\text{-}C_5Me_5)Ru\{t\text{BuNC(Ph)-N}t\text{Bu}\}CO]$.[5a]

## Conclusions

In this contribution, we have presented 16-electron ruthenium half-sandwich complexes of unusual stability, which can be ascribed to the strong π-basic nature of the novel bis(imidazolin-2-imine) ligands $BL^{Me}$ and $BL^{iPr}$, leading to a weak propensity of the Ru atom to coordinate other π-basic ligands such as chloride. In contrast, strong binding of σ-donor/π-acceptor ligands such as CO or isocyanides can be observed. This behavior makes these highly stabilized, yet reactive 16-electron complexes suitable systems for the activation of small molecules such as $N_2$ and $H_2$ and promising candidates for catalytic applications. These investigations are currently in progress in our laboratory.

**Supporting Information** (see footnote on the first page of this article): Preparation of the compounds, selected NMR spectra, cyclic voltammetric traces, crystal data, computational details, presentations of the calculated molecular structures together with Cartesian coordinates of their atomic positions.

## Acknowledgments

This work is supported by the Deutsche Forschungsgemeinschaft (DFG) through grant number Ta 189/6–1.

[1] C. A. Tolman, *Chem. Soc. Rev.* **1972**, *1*, 337–353.
[2] a) R. Poli, *Chem. Rev.* **1996**, *96*, 2135–2204; b) R. Poli, *J. Organomet. Chem.* **2004**, *689*, 4291–4304.
[3] K. G. Caulton, *New J. Chem.* **1994**, *18*, 25–41.
[4] T. J. Johnson, K. Folting, W. E. Streib, J. D. Martin, J. C. Huffman, S. A. Jackson, O. Eisenstein, K. G. Caulton, *Inorg. Chem.* **1995**, *34*, 488–499.
[5] a) Y. Yamaguchi, H. Nagashima, *Organometallics* **2000**, *19*, 725–727; b) H. Kondo, Y. Yamaguchi, H. Nagashima, *Chem. Commun.* **2000**, 1075–1076; c) H. Kondo, Y. Yamaguchi, H. Nagashima, *J. Am. Chem. Soc.* **2001**, *123*, 500–501; d) H. Kondo, A. Kageyama, Y. Yamaguchi, M.-a. Haga, K. Kirchner, H. Nagashima, *Bull. Chem. Soc. Jpn.* **2001**, *74*, 1927–1937; e) J.-i. Terasawa, H. Kondo, T. Matsumoto, K. Kirchner, Y. Motoyama, H. Nagashima, *Organometallics* **2005**, *24*, 2713–2721.
[6] a) C. Gemel, K. Mereiter, R. Schmid, K. Kirchner, *Organometallics* **1997**, *16*, 5601–5603; b) C. Gemel, V. N. Sapunov, K. Mereiter, M. Ferencic, R. Schmid, K. Kirchner, *Inorg. Chim. Acta* **1999**, *286*, 114–120; c) C. Gemel, J. C. Huffman, K. G. Caulton, K. Mauthner, K. Kirchner, *J. Organomet. Chem.* **2000**, *593–594*, 342–353; d) C. Gemel, A. LaPensée, K. Mauthner, K. Mereiter, R. Schmid, K. Kirchner, *Monatsh. Chem.* **1997**, *128*, 1189–1199.
[7] a) M. Jiménez-Tenorio, K. Mereiter, M. C. Puerta, P. Valerga, *J. Am. Chem. Soc.* **2000**, *122*, 11230–11231; b) H. Aneetha, M. Jiménez-Tenorio, M. C. Puerta, P. Valerga, V. N. Sapunov, R. Schmid, K. Kirchner, K. Mereiter, *Organometallics* **2002**, *21*, 5334–5346.
[8] M. Tamm, D. Petrovic, S. Randoll, S. Beer, T. Bannenberg, P. G. Jones, J. Grunenberg, *Org. Biomol. Chem.* **2007**, *5*, 523–530.
[9] For the synthesis of a related bidentate ligand with 1,3-dimethylimidazolin-2-imino groups, see: N. Kuhn, M. Grathwohl, M. Steinmann, G. Henkel, *Z. Naturforsch., Teil B* **1998**, *53*, 997–1003.
[10] For the synthesis of a related tridentate pincer-type ligand with 1,3-di-*tert*-butylimidazolin-2-imino groups, see: D. Petrovic, T. Bannenberg, S. Randoll, P. G. Jones, M. Tamm, *Dalton Trans.* **2007**, DOI: 10.1039/b703183a.
[11] P. J. Fagan, M. D. Ward, J. C. Calabrese, *J. Am. Chem. Soc.* **1989**, *111*, 1698–1719.
[12] S. Takemoto, S. Oshio, T. Shiromoto, H. Matsuzaka, *Organometallics* **2005**, *24*, 801–804.
[13] J. March, *Advanced Organic Chemistry*, 4th ed., John Wiley & Sons, Inc., New York, **1992**, p. 21.
[14] a) Y. Takahashi, S. Hikichi, M. Akita, Y. Moro-oka, *Organometallics* **1999**, *18*, 2571–2573; b) Q. Major, A. J. Lough, D. G. Gusev, *Organometallics* **2005**, *24*, 2492–2501.
[15] a) M. J. Calhorda, *Chem. Commun.* **2000**, 801–809; b) L. Brammer, D. Zhao, F. T. Ladipo, J. Braddock-Wilking, *Acta Crystallogr., Sect. B* **1995**, *51*, 632–640.
[16] G. R. Desiraju, T. Steiner, *The Weak Hydrogen Bond*, Oxford University Press, New York, **1999**.
[17] M. H. Wang, U. Englert, U. Koelle, *J. Organomet. Chem.* **1993**, *453*, 127–131.
[18] Details of the electronic structure calculations and of the X-ray crystal structure determinations and presentations of the calculated molecular structures can be found in the Supporting Information. CCDC-646821 to -646825 contain the supplementary crystallographic data for this paper. These data can be obtained free of charge from The Cambridge Crystallographic Data Centre via www.ccdc.cam.ac.uk/data_request/cif.
[19] The crystal of [**2**]Cl was not of high quality. The structure is noncentrosymmetric and contains four independent formula units, but a variety of programs failed to indicate any higher symmetry. All ethylene bridges fail to refine satisfactorily, which may indicate disorder problems. We are attempting to obtain a more reliable dataset, but the current data definitely establish that there is no coordination of chloride to ruthenium.
[20] The potentials were measured at a scan rate of 100 mV/s against a Ag/AgCl reference electrode (3 M KCl). The ferrocene/ferrocenium couple displays a reversible cyclic voltammetric trace with a redox potential $E° = +476$ mV under these conditions; the values given in the text are referenced to $E°(Fc/Fc^+) = 0$ mV.
[21] a) U. Koelle, J. Kossakowski, *Inorg. Chim. Acta* **1989**, *164*, 23; b) B. de Klerk-Engels, F. Hartl, K. Vrieze, *Inorg. Chim. Acta* **1997**, *254*, 239–250.
[22] M. D. Mbaye, B. Demerseman, J.-L. Renaud, C. Bruneau, *J. Organomet. Chem.* **2005**, *690*, 2149–2158.
[23] G. G. A. Balavoine, T. Boyer, C. Livage, *Organometallics* **1992**, *11*, 456–459.
[24] M. O. Albers, D. C. Liles, D. J. Robinson, E. Singleton, *Organometallics* **1987**, *6*, 2179–2189.
[25] M. Ito, M. Hirakawa, A. Osaku, T. Ikariya, *Organometallics* **2003**, *22*, 4190–4192.
[26] a) H. Brunner, J. Klankermayer, M. Zabel, *Organometallics* **2002**, *21*, 5746–5756; b) C. M. Standfest-Hauser, K. Mereiter, R. Schmid, K. Kirchner, *Eur. J. Inorg. Chem.* **2003**, 1883–1892.

Received: June 1, 2007
Published Online: June 29, 2007

 © 2007 Wiley-VCH Verlag GmbH & Co. KGaA, Weinheim 

DOI: 10.1002/ejic.200601040

# An Unusual Carbonyl Chemical Shift in a Carbonylhexairidium Cluster: A Combined Solid-State NMR and DFT Approach

**Michele R. Chierotti,[a] Luigi Garlaschelli,*[b] Roberto Gobetto,*[a] Carlo Nervi,[a] Giulia Peli,[b] Annalisa Sironi,[b] and Roberto Della Pergola[c]**

**Keywords:** NMR spectroscopy / DFT calculations / Carbonyl cluster / Iridium / Chemical shift tensors / Shielding anisotropy

The $^{13}C$ NMR spectrum of $TMBA_2[Ir_6(CO)_{15}]$ [TMBA = $(CH_3)_3N(CH_2C_6H_5)$] shows, at low temperatures, an unprecedented $\mu_2$-bridging carbonyl low-frequency shift, with the resonances of the terminal $\mu_1$-carbonyl ligands placed at higher frequencies. The chemical shift tensors and the shielding anisotropies of the carbonyl ligands, obtained from solid-state NMR analysis, allow us to determine the nature of the M–CO interaction. The results have been compared with the $^{13}C$ MAS data of $Ir_6(CO)_{16}$ where $\mu_3$-CO ligands are present. Further evidence for the assignment and for the peculiar chemical shift value of bridging carbonyl ligands in $TMBA_2[Ir_6(CO)_{15}]$ has been obtained by the DFT calculation of the NMR parameters. The scalar and spin-orbit (SO) relativistic two-component zero-order regular approximation (ZORA) methods were employed in the geometry optimization and NMR chemical shift calculations, respectively. The large SO contribution ($\delta$ = 26.6 ppm) to the $\mu_2$-bridging CO ligand $^{13}C$ chemical shifts accounts for the position of the experimentally observed resonance.

(© Wiley-VCH Verlag GmbH & Co. KGaA, 69451 Weinheim, Germany, 2007)

## Introduction

Medium- to high-nuclearity carbonylmetal clusters may present terminal, double-bridging ($\mu_2$) and triple-bridging ($\mu_3$) CO ligands. Thanks to the different M–CO bonding order, it is possible to discriminate the three kinds of ligands by means of spectroscopic techniques such as IR and $^{13}C$ NMR spectroscopy. Increasing the back-bonding in the coordination between metal atom and carbon monoxide ligand results in a higher frequency shift of the CO resonances. Indeed, in most cases CO chemical shifts follow the series:[1] $\delta(M–CO) < \delta(M_2–\mu_2\text{-}CO) < \delta(M_3–\mu_3\text{-}CO)$.

Also within subgroups there is a progressive low-frequency shift as the atomic number increases, for example:[1] $\delta(Co–CO) > \delta(Rh–CO) > \delta(Ir–CO)$.

Stereochemical nonrigidity both in solution and in the solid state is a common feature of carbonylmetal clusters and is well documented in several papers.[2] In many cases, however, solution structures were fully consistent with solid-state X-ray structural determination.

Most carbonyliridium clusters present a complete CO fluxionality at room temperature that yields magnetically equivalent ligands; usually the low-temperature spectrum shows signals between $\delta$ = 160 and 180 ppm for terminal CO ligands, between $\delta$ = 180 and 210 ppm for the edge-bridging ones and between $\delta$ = 220 and 260 ppm for the $\mu_3$-CO ligands.[1]

In this paper we report the NMR characterization of two carbonyliridium clusters, namely $[Ir_6(CO)_{15}]^{2-}$ and $Ir_6(CO)_{16}$. Both compounds have been previously synthesized in 1970 by Malatesta and co-workers,[3] but only in the middle of the 1980s did we manage to determine the cluster's structures. $[Ir_6(CO)_{15}]^{2-}$ shows 12 terminal and three edge-bridging CO ligands,[4] while $Ir_6(CO)_{16}$ has been isolated in two different isomeric forms: a red and a black isomer, the latter being quite unstable.[5]

Our aim is to elucidate and compare the particular spectroscopic properties of the $[Ir_6(CO)_{15}]^{2-}$ and $Ir_6(CO)_{16}$ complexes, using a combined experimental-theoretical approach, employing solid-state NMR and DFT calculations of $^{13}C$ NMR chemical shifts. Within this paper the discussion of only the red isomer of $Ir_6(CO)_{16}$ has been taken into account.

## Results and Discussion

### Spectroscopic Results

The compound $Ir_6(CO)_{16}$ is isostructural with $Rh_6(CO)_{16}$, with four face-bridging and 12 terminal carbonyl

[a] Dipartimento di Chimica Inorganica, Chimica Fisica, Chimica dei Materiali, Università degli Studi di Torino,
Via P. Giuria 7, 10125 Torino, Italy
E-Mail: roberto.gobetto@unito.it
[b] Dipartimento di Chimica Inorganica, Metallorganica e Analitica, Università degli Studi di Milano,
Via G. Venezian 21, 20133 Milano, Italy
[c] Dipartimento di Scienze dell'Ambiente e del Territorio dell'Università di Milano-Bicocca,
Piazza della Scienza 1, 20126 Milano, Italy

 © 2007 Wiley-VCH Verlag GmbH & Co. KGaA, Weinheim 

ligands.[5] However, in solution they show very different behaviors. Indeed, $Rh_6(CO)_{16}$ possesses an $O_h$ symmetry and its spectrum, reported by Heaton et al.,[6] is characterized by two resonances, in a 3:1 ratio, at $\delta$ = 180.1 and at 231.5 ppm attributed to the terminal and bridging ($\mu_3$) carbonyl ligands, respectively. On the contrary, the $^{13}C$ NMR solution spectrum of $Ir_6(^{13}CO)_{16}$ in $CD_2Cl_2$ displays a single peak at $\delta$ = 177.60 ppm clearly indicating the presence of chemical exchange among the carbonyl ligands. Even though we used a $^{13}C$-enriched sample, the low solubility of the cluster did not allow us to perform variable-temperature (VT) experiments.

In the solid state $Ir_6(CO)_{16}$ possesses a simple $C_2$ symmetry. Hence, for this reason we expect two distinct signals for the bridging carbonyl ligands and six overlapped peaks for the 12 terminal ligands as already observed for $Rh_6(CO)_{16}$. Indeed, the carbonyl isotropic region of the solid-state spectrum (Figure 1) is characterized by three peaks at $\delta$ = 168.8, 203.9, and 209.2 ppm assigned to the terminal and to the two pairs of equal $\mu_3$-CO ligands, respectively. Because of the overlapping of the signals, instead of six resonances for 12 terminal carbonyl ligands only a single broad asymmetric peak with a shoulder at $\delta \approx$ 166.8 ppm is observed, as has already been seen for the isostructural $Rh_6(CO)_{16}$.[6]

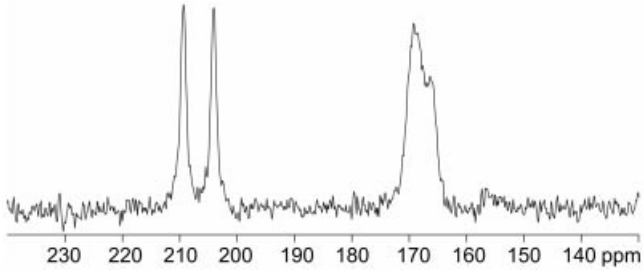


Figure 1. Isotropic region of the solid-state $^{13}C$ MAS NMR spectrum of $Ir_6(^{13}CO)_{16}$ recorded at 68.7 MHz, 25 °C, and at a spinning speed of 5.9 kHz.

We also performed an analysis of the chemical shift tensors $\delta_{11}$, $\delta_{22}$, $\delta_{33}$, where $\delta_{11} \geq \delta_{22} \geq \delta_{33}$, and of the shielding anisotropy (CSA) of the different carbonyl signals, defined as $\Delta\sigma = \sigma_{33} - (\sigma_{11} + \sigma_{22})/2$ with $\sigma_{11} \leq \sigma_{22} \leq \sigma_{33}$. By recording a spectrum at a low spinning speed (about 3.8 kHz) (Figure 2) it has been possible to calculate the chemical shift tensors by means of the Herzfeld–Berger method.[7] The obtained tensor values, as well as the shielding anisotropy $\Delta\sigma$, are reported in Table 1. Unfortunately, for the $\mu_3$-carbonyl moieties the analysis is slightly approximated due to the small amount of overlapping between the resonances. The terminal CO ligands show a shielding anisotropy value ($\Delta\sigma$ = 385.9 ppm) with pseudo-axial symmetry similar to that observed for the terminal carbonyl ligand of many other organometallic compounds such us $Rh_6(CO)_{16}$, $Os_3(CO)_{12}$, etc., (about 400 ppm).[8] On the other hand, as expected, the bridging ($\mu_3$) carbonyl ligands give rise to a smaller anisotropy of 114.6 ppm. It is worth noting that the chemical shift tensor of the bridging CO sites is axially symmetric due to the threefold rotational symmetry about the C–O axis.

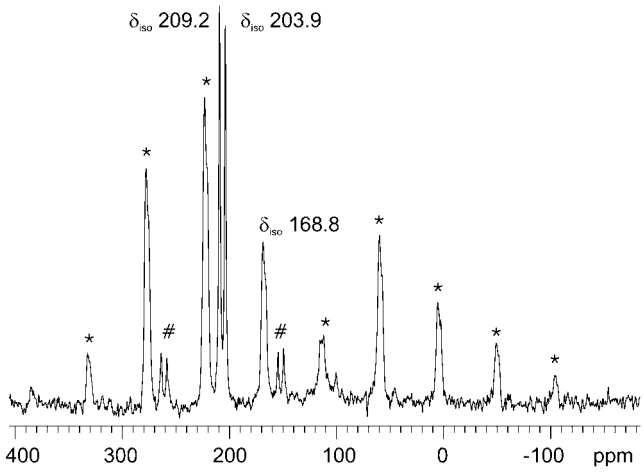


Figure 2. Solid-state $^{13}C$ MAS NMR spectrum of $Ir_6(^{13}CO)_{16}$ recorded at 68.7 MHz, 25 °C, and at a spinning speed of 3.8 kHz. Spinning sidebands marked with * are associated with the peak at $\delta$ = 168.8 ppm, while those marked with # are related to the peaks at $\delta$ = 209.2 and 203.9 ppm.

Table 1. $^{13}C$ chemical shift tensors, shielding anisotropy, and integral values for compound $Ir_6(CO)_{16}$. The shielding anisotropy is defined as $\Delta\sigma = \sigma_{33} - (\sigma_{11} + \sigma_{22})/2$ with $\sigma_{11} \leq \sigma_{22} \leq \sigma_{33}$ and $\delta_{ii} = -\sigma_{ii}$.

| $\delta_{iso}$ [ppm] | $\delta_{11}$ [ppm] | $\delta_{22}$ [ppm] | $\delta_{33}$ [ppm] | $\Delta\sigma$ [ppm] | Integral value |
|---|---|---|---|---|---|
| 168.8 | 352.7 | 241.9 | –88.6 | 385.9 | 12 |
| 203.9 | 244.8[a] | 244.8[a] | 130.3[a] | 114.6[a] | 4 |
| 209.2 | | | | | |

[a] The spinning sideband analysis was performed by considering a single peak, due to high-resonance overlapping. All these resonances are associated to bridging ligands and then a similar anisotropy is expected.

The structure of $[Ir_6(CO)_{15}]^{2-}$ has been previously reported by Demartin et al.[9] Briefly, it consists of a regular octahedron of stereochemically equivalent iridium atoms connected to 12 terminal and three symmetrically edge-bridging ($\mu_2$) carbonyl ligands. The 12 terminal CO ligands can be divided into two sets, six of them being in an axial and six in an equatorial configuration.

The VT $^{13}C$ NMR experiments of a $^{13}CO$-enriched sample of $TMBA_2[Ir_6(^{13}CO)_{15}]$ dissolved in $[D_8]THF$ are reported in Figure 3. In the range 173–298 K the NMR spectroscopic data clearly show the presence of one or more fluxional processes involving the carbonyl resonances. At room temperature the spectrum is characterized by a single peak at $\delta$ = 191.9 ppm. By decreasing the temperature, the signal broadens and the coalescence temperature is reached at 213 K. By further decreasing the temperature, it is possible to freeze the fluxionality, and three signals appear at $\delta$ = 201.1, 191.2, and 175.2 ppm with relative intensities of 6:6:3, respectively. A careful inspection of the VT spectra reveals that the resonance centered at $\delta$ = 201.1 ppm in the

 © 2007 Wiley-VCH Verlag GmbH & Co. KGaA, Weinheim 

temperature range 203–183 K is sharper than the other two resonances; thus, at least two different processes involving the carbonyl ligands determine the fluxional behavior of $TMBA_2[Ir_6(^{13}CO)_{15}]$. The presence of three resonances in the low-temperature limiting spectrum (173 K) agrees with the X-ray structure in which three different types of carbonyl ligands are present (two sets of six terminal CO ligands and one set of three $\mu_2$-CO ligands).

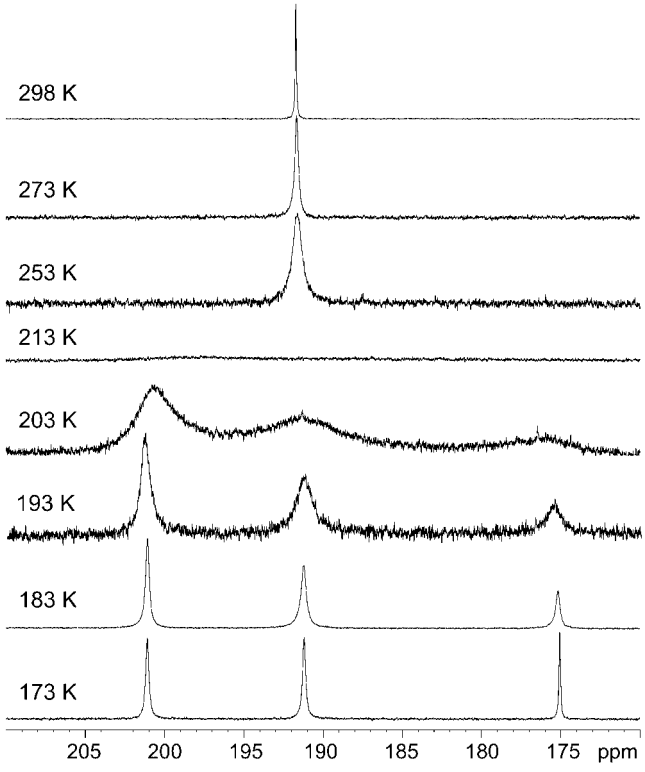


Figure 3. Solution VT $^{13}C$ NMR spectra of $TMBA_2[Ir_6(^{13}CO)_{15}]$ recorded at 151 MHz in the temperature range 173–298 K.

One would expect the bridging carbonyl signals to fall at a higher frequency with respect to the terminal ones, in this case we need to assume an unprecedented low-frequency value for the bridging CO resonance ($\delta$ = 175.2 ppm), and a quite high chemical shift value for the two sets of terminal carbonyl ligands. These results, never reported before, prompted us to find experimental evidence for our assignment. Solid-state NMR is often used as a bridge technique between the solid structure obtained by single crystal X-ray determination and solution NMR spectroscopic data. For this reason we decided to undertake a solid-state NMR investigation of the molecule in order to find NMR parameters corroborating our assignment.

The whole $^{13}C$ MAS spectrum of $TMBA_2[Ir_6(^{13}CO)_{15}]$ is reported in Figure 4. In the carbonyl isotropic region (Figure 5) it is possible to observe 11 isotropic resonances, at $\delta$ = 179.0, 181.5, 184.2, 187.1, 189.5 (sh), 190.5, 193.8, 196.1, 198.3, 202.3, and 205.3 ppm. It is worth noting that the intensities of the signals are quite different and in particular higher integration values are associated with the signals that fall at $\delta$ = 179.0, 184.2, and 196.1 ppm. It is well known that the intensities of the isotropic peaks in solid-state NMR spectra cannot be directly compared without considering the different spinning sideband patterns associated with each resonance (see Figure 4). By careful integration of the isotropic and anisotropic part of the spectrum, we can conclude that all the peaks have the same cumulative intensity except the signals at $\delta$ = 179.0, 196.1, and 205.3 ppm where the relative intensities are 2:3:2 with respect to the other resonances. Thus, the number and the intensities of the peaks are in agreement with the presence of 15 carbonyl ligands.

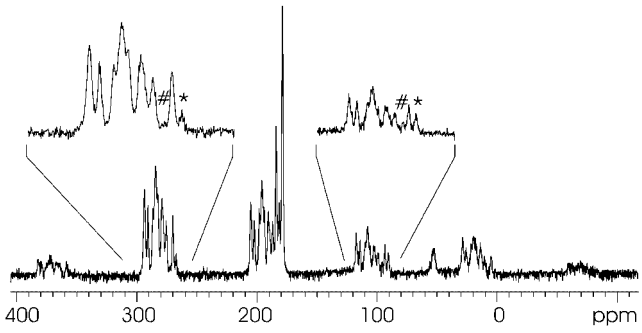


Figure 4. Solid-state $^{13}C$ MAS NMR spectrum of $TMBA_2[Ir_6(^{13}CO)_{15}]$ recorded at 68.7 MHz, 25 °C, and at a spinning speed of 5.9 kHz. Spinning sidebands marked with * are associated with the peak at $\delta$ = 179.0 ppm, while those marked with # are related to the peak at $\delta$ = 184.2 ppm.

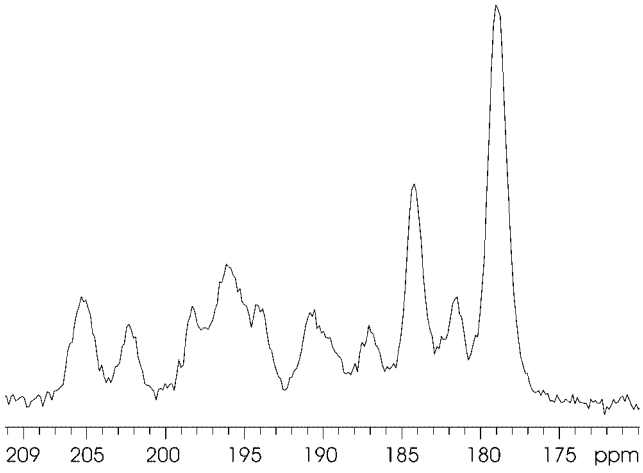


Figure 5. Isotropic region of the solid-state $^{13}C$ MAS NMR spectrum of $TMBA_2[Ir_6(^{13}CO)_{15}]$ recorded at 68.7 MHz, 25 °C, and at a spinning speed of 5.9 kHz.

The chemical shift tensors ($\delta_{11}$, $\delta_{22}$, and $\delta_{33}$) and the shielding anisotropies ($\Delta\sigma$) associated with the different carbonyl signals (see Table 2) afford further information.

From an accurate spectrum analysis it is possible to observe that the spinning sideband manifolds of the peaks centered at $\delta$ = 179.0 and 184.2 ppm are much narrower with respect to the spinning sideband envelopes associated with all other resonances. In particular, the intensities of the first group of the spinning sidebands related to the isotropic peak at $\delta$ = 179.0 ppm (marked with * in Figure 4) drastically decrease as well as those associated with the res-

 © 2007 Wiley-VCH Verlag GmbH & Co. KGaA, Weinheim 

Table 2. $^{13}C$ chemical shift tensors, shielding anisotropy, and integral values for compound $TMBA_2[Ir_6(CO)_{15}]$. The shielding anisotropy is defined as $\Delta\sigma = \sigma_{33} - (\sigma_{11} + \sigma_{22})/2$ with $\sigma_{11} \leq \sigma_{22} \leq \sigma_{33}$ and $\delta_{ii} = -\sigma_{ii}$.

| $\delta_{iso}$ [ppm] | $\delta_{11}$ [ppm] | $\delta_{22}$ [ppm] | $\delta_{33}$ [ppm] | $\Delta\sigma$ [ppm] | Integral value |
|---|---|---|---|---|---|
| 178.9 | 265.1 | 165.6 | 105.9 | 109.4 | 2 |
| 181.5 | 303.1 | 303.1 | –61.8 | 364.9 | 1 |
| 184.2 | 263.5 | 172.6 | 116.5 | 101.6 | 1 |
| 187.1 | 359.9 | 292.4 | –90.8 | 417.0 | 1 |
| 189.5(sh)[a] | 364.9[a] | 292.5[a] | –87.3[a] | 416.0[a] | 2 |
| 190.5 | | | | | |
| 193.8[a] | | | | | |
| 196.1 | 358.9[a] | 310.7[a] | –81.4[a] | 416.2[a] | 5 |
| 198.3 | | | | | |
| 202.3 | 375.1 | 290.8 | –58.9 | 391.9 | 1 |
| 205.3 | 389.6 | 296.3 | –69.9 | 412.8 | 2 |

[a] The spinning sideband analysis was performed by considering a single peak, due to high-resonance overlapping. All these resonances are associated to terminal ligands and then a similar anisotropy is expected.

onance at $\delta$ = 184.2 ppm (marked with # in Figure 4). Furthermore, we decided to perform the Herzfeld–Berger analysis on the spinning sideband patterns to assert whether terminal and bridging carbonyl ligands give rise to different chemical shift tensor values. The computer simulation of the experimental spinning sideband patterns gave us the tensor and anisotropy values reported in Table 2. By comparing the shielding anisotropies, we can observe that those related to the resonances at $\delta$ = 179.0 and 184.2 ppm ($\Delta\sigma$ = 109.4 and 101.6 ppm, respectively) are about 298 ppm lower than the average anisotropy value of the other signals ($\Delta\sigma$ = 404 ppm); since it is well known that the terminal carbonyl ligands have a CSA value of the order of 400 ppm, whereas bridging carbonyl ligands show smaller values,[10,11] we can assert that the resonances at $\delta$ = 179.0 and 184.2 ppm are associated with the bridging CO ligands.

The counter-intuitive shifts of the bridging carbonyl ligands to lower frequencies with respect to the terminal ones prompted us to try to rationalize by quantum mechanical calculations the observed spectroscopic data and to take advantage of DFT calculations for a full understanding of the system.

## Computational Results

The geometry of $[Ir_6(CO)_{15}]^{2-}$ has been fully optimized by means of the Jaguar program at the B3LYP/LACV3P**++ level, which resulted in a molecular geometry very close to $D_3$ symmetry, even if no symmetry constrains have been imposed. The geometry (Figure 6) shows three types of carbonyl ligands: two groups of terminal ligands each composed of six carbonyl ligands and a single group of three $\mu_2$-bridging carbonyl ligands. The first type of terminal carbonyl ligands points in between the other two $\mu_1$-carbonyl ligands placed on the adjacent Ir atom (t1 in Figure 6), whereas the other group of six terminal carbonyl ligands (type t2, not labelled in Figure 6) are pointing towards each other. The $^{13}C$ NMR chemical shifts calculated at this level by the GIAO method employed by Jaguar are intuitively in agreement with the common chemical experience that predicts bridging CO ligands as being less shielded than terminal ones, but do not correlate with the experimental data, resulting in a complete reversal of the order of the assignment of the resonances (Table 3). Methods that can calculate chemical shifts of main group elements are routinely implemented in most standard quantum chemical packages, but the calculation of NMR shielding constants is particularly challenging in $[Ir_6(CO)_{15}]^{2-}$ because relativistic effects are important even for lighter elements if these elements are bound to heavier metals.[12,13] In these atoms the spin-orbit (SO) coupling induces a non-negligible effect. The calculation of NMR parameters, that take into account the SO coupling, has shown an improved agreement with experimentally determined parameters over previous scalar-relativistic calculations for iodo compounds,[14] mercury halides,[13] and for the $^{13}C$ NMR shifts of 5d transition metal carbonyl complexes.[15] This prompted us to investigate the SO contributions taking advantage of the ADF package.

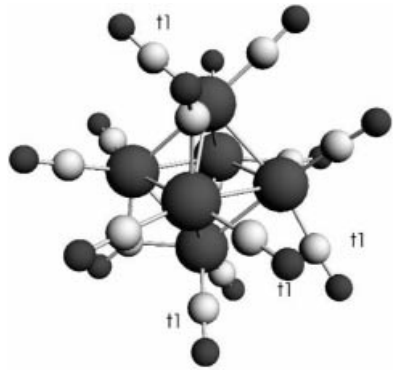


Figure 6. Optimized structure of $[Ir_6(CO)_{15}]^{2-}$, with labels on axial and equatorial terminal carbonyl ligands.

Table 3. Experimental (solution) and calculated[a] $^{13}C$ NMR parameters (ppm) of $[Ir_6(CO)_{15}]^{2-}$. Paramagnetic ($\sigma^{para}$), diamagnetic ($\sigma^{dia}$), and relativistic spin-orbit ($\sigma^{SO}$) contributions to the values of the absolute isotropic shieldings.

| | Exp. | GIAO Jaguar B3LYP/LACV3P**++ | GIAO ADF spin-orbit (and scalar) BP-ZORA/TZ2P | | | |
|---|---|---|---|---|---|---|
| | | $\delta^{iso}$ | $\delta^{iso}$ | $\sigma^{para}$ | $\sigma^{dia}$ | $\sigma^{SO}$ |
| $\mu_2$-CO | 175.2 | 228.4 | 187.7 (212.4) | –274.3 (–272.6) | 242.7 (242.8) | 26.6 |
| $\mu_1$-CO t1 | 191.2 | 211.1 | 198.2 (199.8) | –274.1 (–273.6) | 256.4 (256.4) | 2.3 |
| $\mu_1$-CO t2 | 201.1 | 211.1 | 203.0 (199.2) | –274.0 (–273.7) | 257.1 (257.1) | –3.4 |

[a] The values are the mean of 3 ($\mu_2$) or 6 ($\mu_1$ t1 and $\mu_1$ t2) carbonyl ligands that are nonequivalent because we do not impose the symmetry during calculations. Standard deviations are typically 0.1 ppm and in any case below 0.3 ppm.

 © 2007 Wiley-VCH Verlag GmbH & Co. KGaA, Weinheim 

The geometry optimized using the ADF program with the BP-ZORA/TZ2P method is almost identical to that obtained by Jaguar at the B3LYP/LACV3P**++ level. The results of the ZORA spin-orbit (SO) coupling method reproduce the spectroscopic data of the carbon atoms (Tables 3 and 4). A close inspection of the contributions to the values of the absolute isotropic shielding reveals that the paramagnetic part ($\sigma^{para}$) has almost the same contribution for all three types of carbonyl ligands. The lower contribution of the diamagnetic part ($\sigma^{dia}$) for the bridging $\mu_2$-CO ligands moves the calculated $^{13}C$ chemical shift to higher values, but a much stronger correction of 26.6 ppm with the opposite sign comes from the relativistic spin-orbit part of the shielding ($\sigma^{SO}$). In the case of $[Ir_6(CO)_{15}]^{2-}$, $\sigma^{SO}$ accounts for almost all the observed trend in the chemical shifts. The calculation of $^{13}C$ NMR parameters performed with the scalar BP-ZORA/TZ2P method does not differ substantially from those obtained previously by the Jaguar method (Table 3), pointing out the importance of the SO contribution. This appears to be a case in which the combination of spin-orbit coupling and magnetic field mixes spin triplet states into the ground state, inducing a spin density that then interacts with the nuclei of the carbonylmetal via the Fermi-contact term, as already outlined in the literature.[14,15]

Table 4. Calculated chemical shift tensors ($\delta_{11}$, $\delta_{22}$, $\delta_{33}$) and shielding anisotropy ($\Delta\sigma$) for $[Ir_6(CO)_{15}]^{2-}$ with ADF at spin-orbit BP-ZORA/TZ2P level.

| $\delta_{iso}$ [ppm] | $\delta_{11}$ [ppm] | $\delta_{22}$ [ppm] | $\delta_{33}$ [ppm] | $\Delta\sigma$ [ppm] | Integral value |
|---|---|---|---|---|---|
| 187.7 | 247.9 | 209.2 | 106.0 | 122.6 | 3 |
| 198.2 | 334.0 | 317.6 | –57.2 | 383.0 | 6 |
| 203.0 | 345.9 | 329.3 | –66.4 | 404.0 | 6 |

## Conclusions

In this paper we have finally solved the NMR assignment of the CO resonances of $TMBA_2[Ir_6(^{13}CO)_{15}]$ by using a complementary solid-state NMR and computational approach. VT solution NMR studies on a $^{13}C$-enriched sample of $TMBA_2[Ir_6(^{13}CO)_{15}]$ have shown a fluxionality in the behavior of the CO ligands around the metal cluster. Three sets of carbonyl ligands (two terminal and one bridging) have been found in the cluster giving rise to three peaks in the $^{13}C$ NMR solution spectrum at low temperatures. An unusually low-frequency chemical shift for the bridging carbonyl ligand has been observed at 173 K when the CO ligands are almost frozen. Solid-state NMR spinning sideband analysis has given further proof to the right assignment of the bridging carbonyl resonance. Indeed, their signals are associated with a much lower $\Delta\sigma$ than the terminal ligands. This confirms the reliability of solid-state NMR spectroscopy as a bridging technique between crystal structure analysis and solution NMR spectroscopy.

Moreover, we demonstrate by means of ADF with the BP-ZORA/TZ2P method that the low-frequency shift in the bridging carbonyl chemical shift has a significant relativistic spin-orbit contribution that cannot be neglected in a proper assignment of the $^{13}C$ resonances. Therefore, care should also be taken in the evaluation of NMR parameters for lighter elements, in particular when they are bonded to third-row transition metal atoms. The spin-orbit two-component relativistic protocol has been successfully adopted in DFT calculations to evaluate the NMR shielding constants of carbon atoms directly bonded to Ir nuclei. A satisfactory agreement between the calculated and experimental NMR spectroscopic data has been obtained.

## Experimental Section

### General

All operations were carried out under $N_2$ using Schlenk tube techniques. Tetrahydrofuran was distilled from Na/naphthalene; all other analytical-grade solvents were degassed and stored under $N_2$. $[Ir(CO)_4]^-$,[16] $[Ir_4(CO)_{12}]$,[17] $[Ir_6(CO)_{15}]^{2-}$,[18] and $[Ir_6(CO)_{16}]$[19] were prepared according to the published methods; IR spectra were recorded with a Bruker Vector 22 FT-IR spectrophotometer, using 0.1 mm $CaF_2$ cells previously purged with $N_2$.

### Sample Preparation

It has been proved that $[Ir_6(CO)_{15}]^{2-}$ and the closely related neutral cluster $Ir_6(CO)_{16}$ do not exchange their coordinated CO ligands with gaseous $^{13}CO$ and hence they cannot be conveniently enriched for $^{13}C$ NMR studies. Therefore, in order to obtain a $^{13}CO$ enriched sample of both clusters, we had to follow particular synthetic routes, shown in Scheme 1.

$Ir_4(CO)_{12}$ is the key compound for the preparation of the two hexanuclear clusters. However, its direct $^{13}CO$ enrichment is impossible owing to its insolubility in all common organic solvents; therefore, a suitable precursor is necessary which can directly exchange with $^{13}CO$ on the one hand, and on the other hand can be easily transformed back into $Ir_4(CO)_{12}$. This compound is $[Ir_4(CO)_{11}(COOMe)]^-$; in fact it can be obtained by treatment of the parent cluster with sodium methoxide in methanol, it gives a fast exchange with $^{13}CO$ at room temperature and, as already reported,[20] can regenerate $Ir_4(CO)_{12}$ by simple acidification with acetic acid.

The $^{13}CO$-enriched samples of $[Ir_4(CO)_{11}(COOMe)]^-$ (ca. 30%) were obtained by direct exchange at room temperature with the 99% $^{13}CO$ standard, commercially available from Cambridge Isotope Laboratories, by using standard vacuum-line techniques.

The $^{13}C$-enriched tetranuclear cluster then reacts with 2 equiv. of $[Ir(CO)_4]^-$ in refluxing THF to give $^{13}C$-enriched $[Ir_6(CO)_{15}]^{2-}$, which can be isolated as a brown reddish powder by precipitation with an aqueous solution of $[(CH_3)_3N(CH_2C_6H_5)]Cl$ or converted into $Ir_6(^{13}CO)_{16}$ by acidification under $^{13}CO$ (0.051 g, 0.032 mmol, 30% yield).

In a typical preparation, $Ir_4(CO)_{12}$ (1.500 g, 1.359 mmol) was suspended in 60 mL of dry methanol in a 250-mL Schlenk flask and stirred under $^{12}CO$ at room temperature; 10.6 mL of a 0.9 M solution of $NaOCH_3$ in dry methanol (molar ratio $Ir_4(CO)_{12}/NaOCH_3$ = 1:7) was added dropwise to the light yellow suspension; after about 5 h, a clear orange-yellow solution was obtained, due to the formation of the $[Ir_4(CO)_{11}(COOCH_3)]^-$ derivative. After removing the $^{12}CO$ in vacuo, the solution was stirred under $^{13}CO$ (90% v/v) at room temperature for about 4 h. Then an excess of glacial $CH_3COOH$ was added to the solution causing the immediate pre-

 © 2007 Wiley-VCH Verlag GmbH & Co. KGaA, Weinheim 

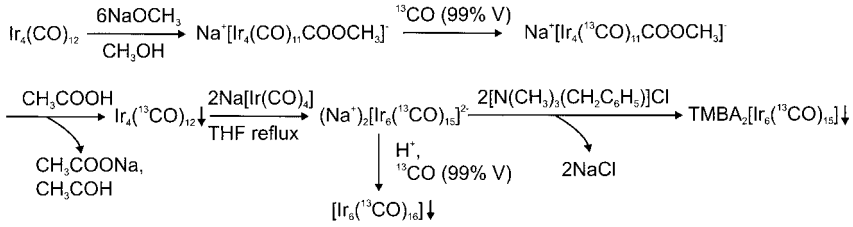


Scheme 1.

cipitation of the light yellow $Ir_4(^{13}CO)_{12}$; the product was filtered, washed several times with water and finally with methanol before being dried in vacuo (1.425 g, 1.291 mmol, 95% yield).

Sodium was added to a suspension of $Ir_4(^{13}CO)_{12}$ (0.429 g, 0.386 mmol) in dry THF (30 mL) and the mixture was vigorously stirred under CO for about 24 h. The FT-IR spectrum of the decanted light yellow liquid showed a typical band of $[Ir(CO)_4]^-$ at 1894 $cm^{-1}$; the brown mixture was filtered and solid $Ir_4(^{13}CO)_{12}$ (0.437 g, 0.396 mmol) was added to the filtrate. The yellow suspension was heated at the reflux temperature under $N_2$ for about 24 h; the FT-IR spectrum of the obtained dark red-brown solution showed an intense band at 1984 $cm^{-1}$, characteristic of the $[Ir_6(^{13}CO)_{15}]^{2-}$ dianion. A solution of $[(CH_3)_3N(CH_2C_6H_5)]Cl$ (0.222 g, 1.193 mmol) in water (60 mL) was then added dropwise to the cluster solution; after removing THF in vacuo, the brown reddish precipitate was collected by filtration, washed with water and finally dried (0.472 g, 0.252 mmol, 64% yield).

### NMR Characterization of $Ir_6(^{13}CO)_{16}$ and $TMBA_2[Ir_6(^{13}CO)_{15}]$

**Solution NMR Measurements:** Solution spectra were recorded with a Bruker Avance 600 spectrometer operating at 150.1 MHz for the $^{13}C$ nucleus. For the VT experiments the compound $TMBA_2[Ir_6(^{13}CO)_{15}]$ was dissolved in $[D_8]$THF and the temperature was varied between 173 and 298 K.

**Solid-State NMR Measurements:** Solid-state data were collected with a Jeol GSX 270 spectrometer equipped with a Doty probe operating at 67.8 MHz for $^{13}C$ and 270 MHz for $^1H$. A standard 90° pulse sequence was used with a pulse duration of 2.5 μs corresponding to a 60° pulse. The recycle delay was 250 s to allow the complete recovery of the magnetization after the pulse; 600–2000 transients were sufficient to obtain a good signal/noise ratio. The spectra were recorded at room temperature at different spinning speeds. Cylindrical 5-mm (o.d.) zirconia rotors with sample volumes of 120 μL were employed. For the sample the magic angle was carefully adjusted from the $^{79}Br$ spectrum of KBr by minimizing the line width of the spinning sideband satellite transitions.

The principal components of the chemical shift tensors were extracted by computer simulation of the spinning sideband patterns obtained at low speed using the HBA program[21] based on the algorithm developed by Herzfeld and Berger.[7] The errors in the evaluation of the chemical shift tensors are less than 4 ppm as evaluated by repetition of the calculation at different spinning speeds. The $^{13}C$ principal tensor components are reported according to the standard convention[10] where $\delta_{11} \geq \delta_{22} \geq \delta_{33}$ and the shielding anisotropy is defined as $\Delta\sigma = \sigma_{33} - (\sigma_{11}+\sigma_{22})/2$ with $\sigma_{11} \leq \sigma_{22} \leq \sigma_{33}$ and $\delta_{ii} = -\sigma_{ii}$.

### Computational Details

The initial geometry of $[Ir_6(CO)_{15}]^{2-}$ was taken from the literature.[9] Calculations were performed either with Jaguar[22] or with ADF2005.1.[23] In Jaguar we adopted the DFT method based on Becke's three-parameter hybrid functional and Lee–Yang–Parr's gradient-corrected correlation functional (B3LYP), with a triple-ζ basis set LACV3P**++,[24] which also includes the outermost core orbitals and effective core potentials (ECPs). The NMR properties were calculated by the GIAO method used by Jaguar.[25] In the geometry optimization carried out with ADF we used the scalar relativistic two-component zero-order regular approximation (ZORA) method,[26] which requires a specially optimized basis set.[27] The default ZORA doubly polarized triple-ζ (TZ2P) basis set was used. The inner shells were represented by the frozen core approximation (1s for C, O and 1s–4d for Ir were kept frozen). We adopted the generalized gradient approximation (CGA) with Becke (exchange) and Perdew (correlation) gradient corrections (BP). The calculations of the NMR parameters were performed by the ADF NMR property module by means of the scalar and the spin-orbit ZORA methods.[28] In the SO coupling method, which takes into account the interactions between the electron magnetic moments and the magnetic field generated by their own orbital motion, the U1K BEST option was used.[23] The absolute isotropic constant shielding values ($\sigma$) for $^{13}C$ of TMS, used as a reference, were calculated from the optimized structures of TMS with Jaguar ($\sigma^{ref}$ = 184.02 ppm) and with ADF [$\sigma^{ref}$(SO) = 182.71 ppm, $\sigma^{ref}$(scalar) = 182.61 ppm], with the methods and basis sets described above. The $^{13}C$ chemical shift values of the carbonyl ligands were therefore calculated as $\delta = \sigma^{ref} - \sigma^{calcd}$.


[1] B. E. Mann, B. F. Taylor, *$^{13}C$ NMR Data for Organometallic Compounds* (Eds.: P. M. Maitlis, F. G. A. Stone, R. West), Academic Press, London, **1981**, and references cited therein.
[2] a) M. J. McGlinchey, *Can. J. Chem.* **2001**, *79*, 1295–1309; b) L. J. Farrugia, A. L. Gillon, D. Braga, F. Grepioni, *Organometallics* **1999**, *18*, 5022–5033.
[3] L. Malatesta, G. Caglio, M. Angoletta, *J. Chem. Soc. C* **1970**, 532–533.
[4] L. Garlaschelli, M. C. Malatesta, S. Martinengo, F. Demartin, M. Manassero, M. Sansoni, *J. Chem. Soc., Dalton Trans.* **1986**, 777–782.
[5] L. Garlaschelli, S. Martinengo, P. L. Bellon, F. Demartin, M. Manassero, M. Y. Chiang, C. Y. Wei, R. Bau, *J. Am. Chem. Soc.* **1984**, *106*, 6664–6667.
[6] B. T. Heaton, A. D. C. Towl, P. Chini, A. Fumagalli, D. J. A. McCaffrey, S. Martinengo, *J. Chem. Soc., Chem. Commun.* **1975**, 523–524.
[7] J. Herzfeld, A. E. Berger, *J. Chem. Phys.* **1980**, *73*, 6021–6030.
[8] T. H. Walter, L. Reven, E. Oldfield, *J. Phys. Chem.* **1989**, *93*, 1320–1326.
[9] F. Demartin, M. Manassero, M. Sansoni, L. Garlaschelli, S. Martinengo, F. Canziani, *J. Chem. Soc., Chem. Commun.* **1980**, 903–904.
[10] G. E. Hawkes, K. D. Sales, S. Aime, R. Gobetto, L.-Y. Lian, *Inorg. Chem.* **1991**, *30*, 1489–1493.
[11] a) E. Oldfield, L. Reven, *Inorg. Chem.* **1992**, *31*, 243–252; b) S. Aime, W. Dastrù, R. Gobetto, G. E. Hawkes, in *Advanced Application of NMR to Organometallic Chemistry* (Eds.: M. Gielen, R. Willem, B. Wrackmeyer), Wiley, Chichester, **1996**.
[12] T. Ziegler, J. Autschbach, *Chem. Rev.* **2005**, *105*, 2695–2722.


 © 2007 Wiley-VCH Verlag GmbH & Co. KGaA, Weinheim 

[13] M. Kaupp, M. Bühl, V. G. Malkin, *Calculation of NMR and EPR Parameters. Theory and Applications*, Wiley-VCH, Weinheim, **2004**.
[14] M. Kaupp, O. L. Malkina, V. G. Malkin, P. Pyykkö, *Chem. Eur. J.* **1998**, *4*, 118–126.
[15] S. K. Wolff, T. Ziegler, *J. Chem. Phys.* **1998**, *109*, 895–905.
[16] L. Garlaschelli, R. Della Pergola, S. Martinengo, *Inorg. Synth.* **1990**, *28*, 211–215.
[17] F. P. Pruchnik, K. Wajda-Hermanowicz, M. Koralewicz, *J. Organomet. Chem.* **1990**, *384*, 381–383.
[18] M. Angoletta, L. Malatesta, G. Caglio, *J. Organomet. Chem.* **1975**, *94*, 99–106.
[19] R. E. Stevens, P. C. C. Liu, W. L. Gladfelter, *J. Organomet. Chem.* **1985**, *287*, 133–143.
[20] L. Garlaschelli, S. Martinengo, P. Chini, F. Canziani, R. Bau, *J. Organomet. Chem.* **1981**, *213*, 379–388.
[21] K. Eichele, R. E. Wasylishen, *HBA 1.5*, Dalhousie University, Halifax, Nova Scotia.
[22] *Jaguar*, version 6.5, Schrödinger LLC, New York, NY, **2005**.
[23] a) G. te Velde, F. M. Bickelhaupt, S. J. A. van Gisbergen, C. Fonseca Guerra, E. J. Baerends, J. G. Snijders, T. Ziegler, *J. Comput. Chem.* **2001**, *22*, 931–967; b) C. Fonseca Guerra, J. G. Snijders, G. te Velde, E. J. Baerends, *Theor. Chem. Acc.* **1998**, *99*, 391–403; c) ADF2005.01, SCM, Theoretical Chemistry, Vrije Universiteit, Amsterdam, The Netherlands, http://www.scm.com.
[24] The basis set LACVP has been developed at the Los Alamos National Laboratories (see: P. J. Hay, W. R. Wadt, *J. Chem. Phys.* **1985**, *82*, 270–283, 284–298, 299–310). The LACV3P basis set is a triple-zeta contraction of the LACVP basis set developed and tested at Schrödinger, Inc. Lighter elements (i.e. C and O in this case) employ the 6-311G basis set.
[25] Y. Cao, M. D. Beachy, D. A. Braden, L. A. Morrill, M. N. Ringnalda, R. A. Friesner, *J. Chem. Phys.* **2005**, *122*, art. no. 224116.
[26] F. Jansen, *Introduction to Computational Chemistry*, Wiley, Chichester, **1999**.
[27] a) E. van Lenthe, E. J. Baerends, J. G. Snijders, *J. Chem. Phys.* **1993**, *99*, 4597–4610; b) E. van Lenthe, E. J. Baerends, J. G. Snijders, *J. Chem. Phys.* **1994**, *101*, 9783–9792; c) E. van Lenthe, A. E. Ehlers, E. J. Baerends, *J. Chem. Phys.* **1999**, *110*, 8943–8953.
[28] a) G. Schreckenbach, T. Ziegler, *J. Phys. Chem.* **1995**, *99*, 606–611; b) G. Schreckenbach, T. Ziegler, *Int. J. Quantum Chem.* **1997**, *61*, 899–918; c) S. K. Wolff, T. Ziegler, E. van Lenthe, E. J. Baerends, *J. Chem. Phys.* **1999**, *110*, 7689–7698; d) J. Autschbach, T. Ziegler, *J. Chem. Phys.* **2000**, *113*, 936–947; e) J. Autschbach, T. Ziegler, *J. Chem. Phys.* **2000**, *113*, 9410–9418.
Received: November 6, 2006
Published Online: March 28, 2007

 © 2007 Wiley-VCH Verlag GmbH & Co. KGaA, Weinheim 

DOI: 10.1002/ejic.200700053

# Copper(II) Terpyridine Complexes: Effect of Substituent on DNA Binding and Nuclease Activity

Varadarajan Uma,[a] Munusamy Elango,[a] and Balachandran Unni Nair*[a]

**Keywords:** Copper / Tridentate ligands / DNA binding / Nuclease activity

Mononuclear copper(II) terpyridine complexes, [Cu(ttpy)Cl]Cl (**1**) and [Cu(itpy)Cl]Cl (**2**) (ttpy = tolylterpyridine and itpy = imidazolylterpyridine) were synthesized and characterized. The interaction of the complexes with DNA was studied by electronic and CD spectroscopy, viscosity and gel electrophoresis. Absorption titrations, viscosity and CD experiments reveal an intercalative mode of DNA binding for these complexes. The binding constant values for **1** and **2** are $(5.6 \pm 0.2) \times 10^4$ and $(1.4 \pm 0.2) \times 10^4$ $M^{-1}$, respectively, and suggest moderate binding of these complexes to DNA. From computational studies, it was found that the aromatic π cloud is more uniformly distributed in the case of tolylterpyridine (complex **1**), which possibly leads to better stacking interactions with the DNA bases and hence a higher binding constant value for complex **1**. From the gel electrophoresis experiments, it is inferred that both complex **1** and **2** cleave plasmid DNA in the presence of ascorbic acid and the cleavage efficiency of complex **1** is greater than that of complex **2**.

(© Wiley-VCH Verlag GmbH & Co. KGaA, 69451 Weinheim, Germany, 2007)

## Introduction

Small molecules that bind and cleave double-stranded DNA under physiological conditions have found wide applications in the field of medicine, molecular biology and biotechnology.[1–5] Transition-metal complexes characterized by high stability, structural versatility and unique spectroscopic and redox properties are exploited largely in many of these efforts. These metal complexes are capable of binding to DNA by a multitude of interactions and cleave DNA by virtue of their intrinsic chemical, electrochemical and photochemical reactivities.[6–10] In the majority of the complexes studied, the metal ion usually serves as the redox centre and the ligand is responsible for DNA recognition. The modes of recognition are primarily based upon intercalation, groove-binding, hydrogen bonding and electrostatic interactions.

Since the success of platinum complexes as anticancer drugs, studies on the interaction of transition-metal complexes with nucleic acids has been a topic of interest in biochemical and coordination chemical research.[11] Ruthenium(II) polypyridyl complexes have attracted comprehensive attention due to their significance in the development of new therapeutic agents and novel nucleic acid structural probes.[12–14] A number of dinuclear iron complexes are known to exhibit hydrolytic cleavage of duplex DNA.[15–16] Nickel(II) and cobalt(II) macrocyclic complexes have been investigated as potential site-specific DNA modification agents.[17–18] The other metal that has been most widely used in these studies is copper; complexes of copper with different types of ligands have been tested as potential chemical nucleases.[19–22] Among them, 1,10-phenanthroline and its derivatives have attracted great attention due to their high nucleolytic efficiency.[23–26] Studies by Sigman and coworkers have shown that bis(1,10-phenanthroline)copper(I) complex efficiently cleaves DNA through the formation of a sugar hydrogen abstracting active oxygen species.[27–28] They have also been broadly used as foot printing agents of both proteins and DNA,[29] probes of the dimensions of the minor groove of duplex structures,[30] and identifiers of transcription starting sites.[31]

Our laboratory has been focusing on DNA interaction studies of bis-chelated copper(II) complexes with various tridendate terpyridine ligand systems.[32,33] The present work stems from our interest to explore the DNA binding properties and nuclease activity of 1:1 copper(II) complex with these ligand systems and to examine whether they exhibit a significant change in the binding properties as compared to the bis-chelated complexes. In this paper, we report the synthesis and DNA interaction and cleavage studies of copper(II) complexes with two terpyridine derivatives, namely tolyl terpyridine (ttpy), and imidazolyl terpyridine (itpy) ligands, the structures of which are shown in Figure 1. The DNA interaction has been investigated using a host of physical methods like electronic absorption spectroscopy, viscosity measurements, electrochemical methods and circular dichroic studies and the cleavage reactions have been assayed using agarose gel electrophoresis.

[a] Chemical Laboratory, Central Leather Research Institute, Adyar, Chennai, 600020 Tamil Nadu, India
Fax: +91-44-2491-1589
E-mail: bunair@clri.info

 © 2007 Wiley-VCH Verlag GmbH & Co. KGaA, Weinheim 

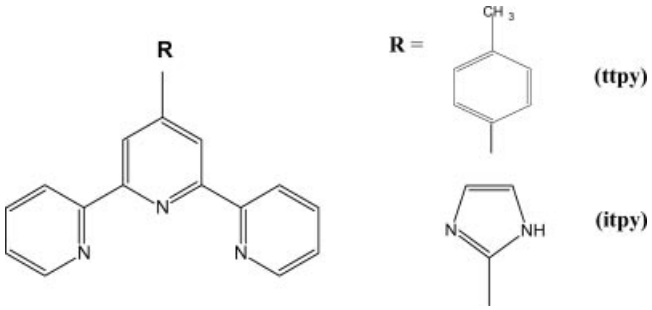


Figure 1. The structures of the ttpy and itpy ligands.

## Results and Discussion

### Synthesis and Spectral Properties

Complexes **1** and **2** could be obtained in good yields and sufficiently pure forms by mixing hot methanolic solutions of copper chloride and the respective terpyridine ligands in equimolar quantities. The authenticity of the complexes was ascertained from mass spectral analysis. The ESI mass spectra of the complexes show base peaks assignable to the parent ion $[Cu{\cdot}L{\cdot}Cl]^+$, where L corresponds to ttpy and itpy for complexes **1** and **2**, respectively.

The electronic spectra of the complexes exhibit intense intraligand bands in the region 280–350 nm and a broad ligand field band in the region 550–800 nm (Table 1). The absorptions in the UV region show a shift to higher wavelengths relative to the unsubstituted terpy complex (228 and 324 nm). This shift is due to the lowering of the LUMO (π*) energy in the ttpy ligand owing to a more extended conjugation relative to the terpy ligand. In the case of copper(II) complexes, three d–d transitions are possible: $d_{xz},d_{yz}\rightarrow d_{x^2-y^2}$, $d_{z^2}\rightarrow d_{x^2-y^2}$, $d_{xy}\rightarrow d_{x^2-y^2}$. However, only a single broad band is observed for both the copper(II) complexes, which indicates the total sum of all the above transitions. The broadness associated with the d–d bands is generally taken as an indication of the geometrical distortion of the complex from perfect planar symmetry.

Table 1. Electronic and EPR (taken at 77 K) spectral parameters for complexes **1** and **2**.

| Complex | Electronic spectra[a] $\lambda$ [nm] ($\varepsilon$, $M^{-1}cm^{-1}$) | $g$ values | $A$ values |
|---|---|---|---|
| Complex **1** | 287 (18,050)<br>318 sh (11,800)<br>690 br (160) | $g_\parallel = 2.36$<br>$g_\perp = 2.06$ | $A_\parallel = 161$ G |
| Complex **2** | 288 (17,765)<br>338 (22,995<br>350 sh (23,595)<br>710 br (153) | $g_\parallel = 2.39$<br>$g_\perp = 2.08$ | $A_\parallel = 165$ G |

[a] br = broad, sh = shoulder.

EPR spectra of complexes **1** and **2** (frozen solutions at 77 K) in DMSO reveal an axial nature with four well-resolved peaks of low intensity in the low-field region and one intense peak in the high-field region. No band corresponding to $M_s = \pm 2$ was observed in the spectra, ruling out any copper–copper interaction. Figure 2 shows the EPR spectrum of complex **1** and the EPR parameters are provided in Table 1. From the observed values for both complex **1** and **2**, it is clear that $g_\parallel > g_\perp$, which indicates that the unpaired electron predominantly lies in the $d_{x^2-y^2}$ orbital.[34] The ratio of $g_\parallel/A_\parallel$ may be considered as a diagnostic parameter of the stereochemistry of the complex, and the range reported for square-planar complexes is 105–135 G.[35] In the present case, this value is higher than 135 G, indicating a considerable tetrahedral distortion around the copper site that could be due to the rigidity of the terpy moiety and the geometrical constraint it imposes on the central metal ion.

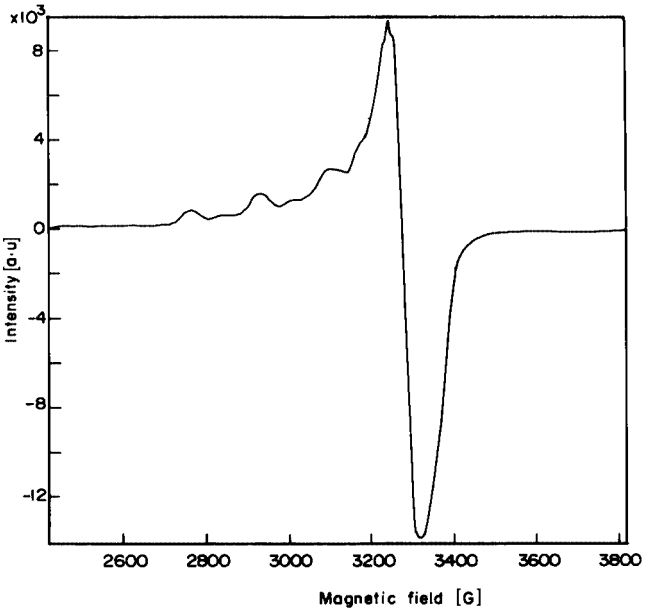


Figure 2. EPR spectrum of a frozen solution of complex **1** at 77 K in DMSO (microwave frequency = 9.5 GHz, power = 3 mW, modulation frequency = 100 kHz, modulation amplitude = 3 G).

Cyclic voltammetric studies to establish the redox behaviour of the copper(II) complexes reveal a non-Nernstian, almost irreversible redox process involving the $Cu^{II}/Cu^{I}$ couple near –0.2 V for both of the complexes (values provided in Table 2). The anodic to cathodic peak current ratio of around 0.2 for both the complexes suggests poor reversibility of the electron transfer process. Figure 3 depicts the cyclic voltammograms of complexes **1** and **2**. The $Cu^{II}/Cu^{I}$ redox potential of complex **1** is slightly more negative relative to **2**, which indicates that the +1 oxidation state is more stabilized in complex **2** than it is in complex **1**.

Table 2. Electrochemical behaviour of complexes **1** and **2**.[a]

| Complexes | $E_{1/2}$ [V] CV | $E_{1/2}$ [V] DPV | $\Delta E_p$ [mV] | $i_{pa}/i_{pc}$ |
|---|---|---|---|---|
| **1** | –0.257 | –0.248 | 101 | 0.25 |
| **2** | –0.223 | –0.224 | 109 | 0.20 |

[a] Reference electrode: SCE; supporting electrolyte: TBAP.

 © 2007 Wiley-VCH Verlag GmbH & Co. KGaA, Weinheim 

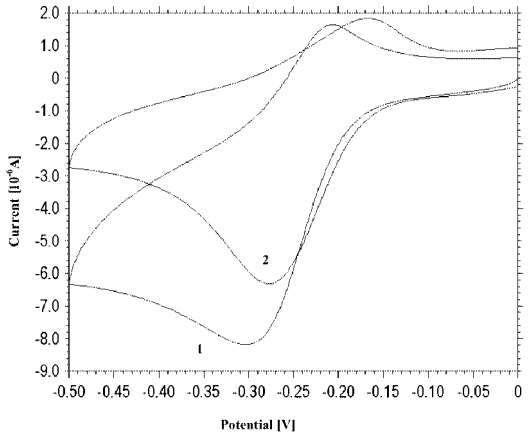


Figure 3. Cyclic voltammograms of complexes **1** and **2** (0.2 mM); scan rate 50 mV s$^{-1}$; supporting electrolyte, TBAP (100 mM), reference electrode SCE.

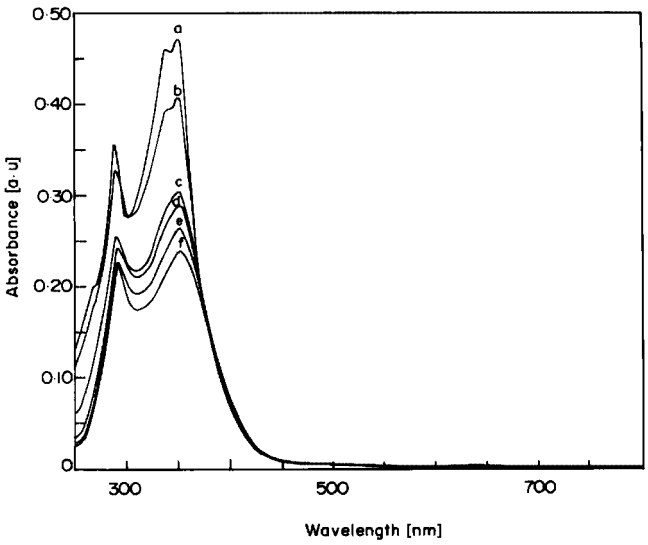


Figure 4. Absorption spectra of complex **2** (20 μM) in the absence (a) and presence (b–f) of increasing concentrations of CT DNA (40–120 μM).

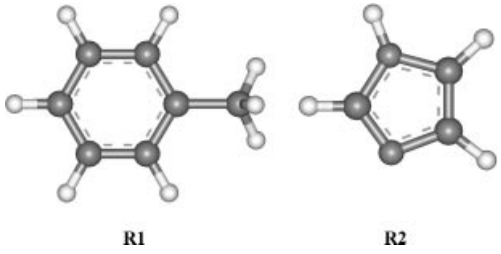


Figure 5. Optimized molecular structures of **R1** (toluene) and **R2** (imidazole) obtained at the B3LYP/6-31G* level of calculation (grey spheres represent carbon atoms; black spheres represent nitrogen atoms).

### Absorption Titration Experiments

The interaction of the metal complex with DNA causes significant changes in the ligand-centred spectral transitions of the complex and these changes are monitored to calculate the binding constant. In the presence of increasing concentrations of DNA, both **1** and **2** were found to exhibit hypochromism with an almost negligible shift in the absorption maxima. This decrease in the intensity of the spectral band is typical of an intercalative mode of binding wherein the interacting molecule is sandwiched between the DNA base pairs.[36,37] The planarity and extended aromaticity of the terpyridine ligand systems bring about the stacking of the molecule between the DNA bases. The spectral changes on interaction of complex **2** with DNA are shown in Figure 4. The binding constant $K_b$ was estimated to be $(5.6 \pm 0.2) \times 10^4$ and $(1.4 \pm 0.2) \times 10^4$ M$^{-1}$ for complexes **1** and **2**, respectively. The binding constant values for these complexes are of the same order of magnitude as those observed for the corresponding bis-chelate systems reported in our earlier publications.[32] Also, the mode of binding remains intercalative in both cases. This suggests that the major factor influencing the mode and extent of binding could be the large size of the ligand system. The planar terpyridine ring appears to dictate the binding characteristics irrespective of the geometry of the complex (four or six coordinate).

To further explore the influence of substituents on the binding constant values, computational studies were carried out for complexes **1** and **2**. As seen from Figure 1, complexes **1** and **2** differ only in their substituents (R group). Therefore, calculations were carried out by considering only the tolyl and imidazolyl groups (**R1** and **R2**, respectively) as representative of **1** and **2**. Hydrogen atoms were added in the R groups to satisfy the valency (optimized molecular structures shown in Figure 5).

The structures were optimized at the B3LYP/6-31G* level of theory by using the Gaussian 98W suite of programs.[38] Density functional theory (DFT) based descriptors such as chemical hardness ($\eta$) and electrophilicity ($\omega$) were calculated for **R1** and **R2**[39] and the results are presented in Table 3. Nucleus independent chemical shift (NICS) criteria proposed by Schleyer[40] is also calculated at the centre of the rings. All the three parameters, namely, $\eta$, $\omega$ and NICS are measures of reactivity and stability. From the table, it is observed that **R1** is less hard and more reactive than **R2**. This is also implied in the values of $\omega$; the $\omega$ value of **R1** is higher than that of **R2**, indicating the higher reactivity of **R1**. NICS values indicate the degree of aromaticity: the more negative the NICS value, the more aromatic the system and higher the stability. From Table 3, we observe that the NICS value of **R2** is greater than that of **R1**, indicating the higher reactivity and lesser stability of **R1**. Thus, the tolyl-substituted molecule, complex **1**, binds to DNA more strongly [$(5.6 \pm 0.2) \times 10^4$ M$^{-1}$]

Table 3. Chemical hardness ($\eta$), electrophilicity ($\omega$) and nucleus independent chemical shift [NICS(0)] values of R1 and R2 calculated by using the B3LYP/6-31G* level of theory.

| Species | $\eta$ [eV] | $\omega$ [eV] | NICS(0) [ppm] |
|---|---|---|---|
| Toluene | 3.27 | 1.49 | –9.6 |
| Imidazole | 3.51 | 0.97 | –14.4 |

 © 2007 Wiley-VCH Verlag GmbH & Co. KGaA, Weinheim 

relative to the imidazole substituted molecule, complex **2** [$(1.4 \pm 0.2) \times 10^4$ M$^{-1}$].

In addition to this, the molecular electrostatic potential map of **R1** and **R2** was calculated at the B3LYP/6-31G* level of theory and is presented in Figure 6. The Gaussview package was used for viewing the map.[41] In the case of **R2**, the π cloud is substantially influenced by the electronegative nitrogen atom of the imidazole ring, but in **R1**, the aromatic π cloud is uniformly distributed above and below the molecular plane, which could bring about favourable stacking interactions with the DNA bases during intercalation (Figure 6). Hence, intercalation in this case would be comparatively more favourable than it is in **R2**. Thus, computational studies clearly show that the tolyl substituent makes complex **1** a better intercalator relative to imidazolyl-substituted complex **2**.

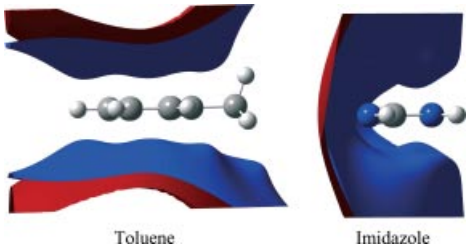


Figure 6. Total electron density map of **R1** and **R2** obtained at 0.003 au surface.

## Viscosity Experiments

Measurement of DNA viscosity is regarded as the least ambiguous and the most critical test of the binding mode of DNA in solution and affords stronger arguments for an intercalative DNA binding mode. The viscosity of DNA is enhanced in a complete or partial intercalative mode of binding where an increase in the length of the polynucleotide occurs as a result of the destacking of the base pairs.[42] A partial nonclassical mode of binding could bend or kink the DNA helix, reduce its effective length and thereby its viscosity. The effect of increasing concentrations of complexes **1** and **2** on the specific relative viscosity of DNA is shown in Figure 7. The relative viscosity of DNA increases steadily with an increase in the concentration of the complex and this result parallels the pronounced absorbance hypochromism that was observed for the complexes and further confirms their intercalative mode of binding. However, the increase in viscosity is less than that observed for proven intercalators.[43] Among the two, the increase in the relative viscosity is more pronounced for complex **1** than for **2**, which parallels the trend in DNA binding studies.

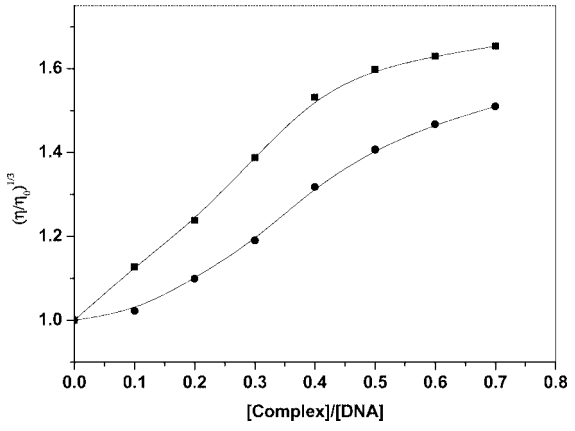


Figure 7. Effect of increasing concentration of complexes **1** (square) and **2** (circle) on the relative viscosity of CT DNA (200 μM).

## Circular Dichroism

Circular dichroic spectral techniques may give us useful information on how the conformation of the DNA chain is influenced by the bound complex. The CD spectrum of CT DNA consists of a positive band at 275 nm that can be due to base stacking and a negative band at 245 nm that can be due to helicity and it is also characteristic of DNA in a right-handed B form.[44] Thus, simple groove binding and electrostatic interaction of small molecules with DNA show less or no perturbations on the base stacking and helicity bands, whereas intercalation enhances the intensities of both the bands stabilizing the right-handed B conformation of CT DNA as observed for classical intercalators.[45] The CD spectrum of CT DNA was monitored in the presence of increasing amounts of complexes **1** and **2**; the changes observed in the case of complex **2** are shown in Figure 8. The positive band showed an enhancement in the molar ellipticity with a slight redshift of the band maxima whereas the negative band showed a decrease in the intensity when the complex concentration was progressively increased. Similar changes were observed in the CD spectrum of DNA in the case of complex **2**. These observations are supportive of the intercalative mode of binding of these complexes, where in the stacking of the complex molecules between the base pairs of DNA leads to an enhancement in the positive band and the partial unwinding of the helix is reflected in the decreased intensity of the negative band. It is also evi-

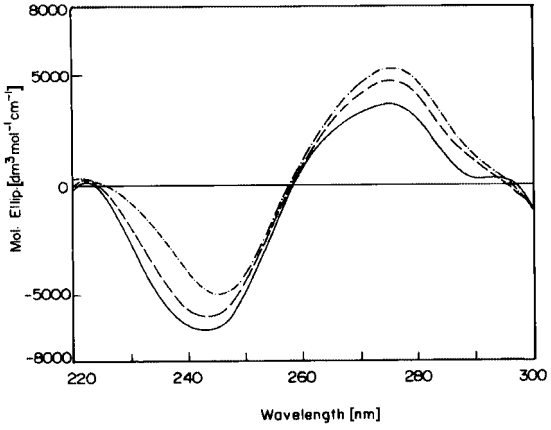


Figure 8. CD spectra of CT DNA (200 μM) in the absence (– – –) and presence of 20 (·-·-·-·-·-) and 40 μM (- - - - - - - -) of complex **1**.

 © 2007 Wiley-VCH Verlag GmbH & Co. KGaA, Weinheim 

dent from the CD spectra that binding of the complex does not lead to any significant change in the conformation of CT DNA.

### Gel Electrophoresis Studies

To determine the ability of the present copper complexes to serve as metallonucleases, DNA cleavage studies were performed on plasmid pBR322 DNA and the results were monitored by gel electrophoresis. The naturally occurring super coiled form (Form I), when nicked, gives rise to an open circular relaxed form (Form II). This upon further cleavage results in the linear form (Form III). When subjected to gel electrophoresis, Form I shows a relatively faster migration than Forms II and III. Form II migrates very slowly owing to its relaxed structure whereas the linear form shows a migration in between Form I and Form II. Figure 9 shows the electrophoretic pattern of plasmid DNA treated with complexes **1** and **2**. Control experiments suggest that untreated DNA and DNA incubated with either complex or ascorbic acid alone does not show any significant DNA cleavage (Figure 9, lanes 1–3) but in the presence of ascorbic acid, the complexes were found to exhibit nuclease activity. In the presence of 25 μM of complex **1** and 75 μM of ascorbic acid, slight cleavage of plasmid DNA occurs as is evident from lane 4 (Figure 9) whereas there is hardly any cleavage in lane 5 (Figure 9), which represents the same concentration of the complex and reductant for **2**. On increasing the concentration of the complex to 50 μM while maintaining the concentration of the reducing agent at 75 μM, the cleavage was found to be much more efficient, as is evident from the increase in Form II (Figure 9, lanes 6 and 7). A further increase in the concentration of the complex to 75 μM and ascorbic acid to 150 μM leads to complete conversion of the supercoiled form to Form II and III (Figure 9, lanes 8 and 9). From Table 4 it is clear that complex **1** exhibits better nuclease activity than **2**.

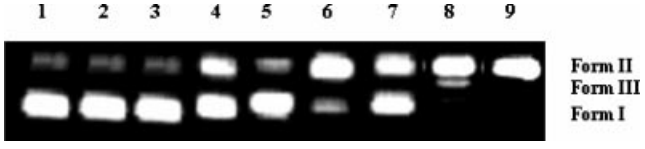


Figure 9. Cleavage of pBR322 DNA by complexes **1** and **2** in the presence of ascorbic acid. DNA (250 ng) was incubated with **1** and **2** for 60 min. in Tris buffer (pH 7.5). Lane 1, DNA control; lane 2, DNA + **1** (75 μM) alone; lane 3, DNA + ascorbic acid (150 μM); lane 4, DNA + **1** (25 μM) + ascorbic acid (75 μM); lane 5, DNA + **2** (25 μM) + ascorbic acid (75 μM); lane 6, DNA + **1** (50 μM) + ascorbic acid (75 μM); lane 7, DNA + **2** (50 μM) + ascorbic acid (75 μM); lane 8, DNA + **1** (75 μM) + ascorbic acid (150 μM); lane 9, DNA + **2** (75 μM) + ascorbic acid (150 μM).

To quantify the nuclease activity of the complexes, rate constants were determined for both complex **1** and **2** by further studying the extent of DNA cleavage in a time dependent manner. The complex concentration was maintained at 75 μM for both **1** and **2** as maximum DNA damage occurs at this particular concentration. The results of gel

Table 4. Extent of DNA cleavage by complexes **1** and **2**.

| Complexes | Concentration of Complex [μM] | %SC | %NC | %L[a] |
|---|---|---|---|---|
| **1** | 25 | 65 | 35 | |
| | 50 | 14 | 86 | |
| | 75 | | 85 | 15 |
| **2** | 25 | 89 | 11 | |
| | 50 | 53 | 47 | |
| | 75 | 2 | 98 | |

[a] SC = supercoiled; NC = nicked circular; L = linear.

electrophoresis were subjected to densitometric quantification and the kinetic parameters were analyzed by assuming a simple pseudofirst-order process for conversion of Form I to Form II. The rate constants determined from the plot of ln(%SC DNA) versus time (shown in Figure 10) were found to be $4.32 \times 10^{-4}$ $s^{-1}$ for complex **1** and $3.14 \times 10^{-4}$ $s^{-1}$ for complex **2**. The higher $k$ value for **1** is clearly indicative of a better nuclease activity of **1** relative to **2**.

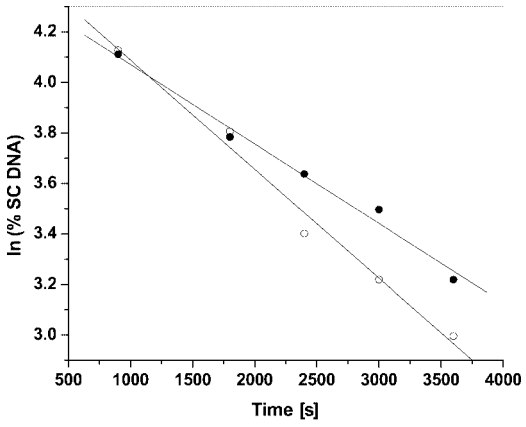


Figure 10. Plot of ln(%SC DNA) versus time for a complex concentration of 75 μM; complex **1** (○), Complex **2** (●).

To explain the cleavage efficiency of **1** being greater than **2** it is essential to look at the probable mechanistic pathway for this process. Because the complexes exhibit nuclease activity only in the presence of ascorbic acid, it is clear that the copper(II) complex in both cases is first reduced to a copper(I) complex, which then reacts with molecular oxygen to produce reactive oxygen species (ROS). A species with a more negative redox potential is always a better reducing agent and would reduce molecular oxygen much more readily thereby causing efficient DNA cleavage. In the present case, because complex **1** has a more negative redox potential than **2**, the former is a better DNA cleaving agent than the latter. Similar observations were also reported by other research groups.[46,47] Moreover, the higher binding affinity of complex **1** towards DNA relative to **2**, could also possibly be another reason for the higher cleavage efficiency of complex **1**. Further studies are under progress to investigate the DNA cleavage in detail.

 © 2007 Wiley-VCH Verlag GmbH & Co. KGaA, Weinheim 

## Conclusions

The present communication reports the synthesis and characterization of two four-coordinate copper(II) complexes with tridentate terpyridine ligands. On the basis of electronic and EPR spectral studies, the complexes are suggested to have a four-coordinate geometry with considerable tetrahedral distortion in the square plane. The complexes are found to adopt an intercalative mode of binding with moderate binding strengths. The influence of the substituents of the terpyridine ligand was discussed on the basis of computational studies. The tolyl substituent in complex **1** is less hard and more reactive relative to the imidazolyl substituent of complex **2**. Also, the aromatic π cloud almost uniformly lies above and below the molecular plane in complex **1**, which leads to its better intercalative binding with DNA. They exhibit efficient nuclease activity in the presence of ascorbic acid and the differences in their cleavage efficiencies were explained on the basis of spectral and electrochemical results.

## Experimental Section

**General:** 2-Acetyl pyridine, tolualdehyde, *p*-bromobenzaldehyde and imidazole 2-carboxaldehyde were obtained from Sigma Aldrich, USA and used as received. Tris(hydroxymethyl) methylamine (Tris) was obtained from SRL Chemicals. Calf Thymus DNA (CT DNA) was obtained from Fluka Chemicals. All chemicals and reagents used were of analytical grade received from Ranbaxy, Mumbai. Stock solution of DNA was prepared by stirring a sample dissolved in 10 mM (Tris) buffer, (pH 7.2) at 4 °C. The solution was dialyzed exhaustively against the Tris buffer for 48 h and filtered through a membrane filter obtained from Sartorius (45 μM). The filtered DNA solution in the buffer gave a UV absorbance ratio ($A_{260}/A_{280}$) of about 1.8, indicating DNA was sufficiently free from protein.[48] The concentration of DNA was determined by using an extinction coefficient of 6600 $M^{-1}cm^{-1}$ at 260 nm.[49]

**[Cu(ttpy)Cl]Cl (1):** The complex was prepared in good yield from the reaction of $CuCl_2{\cdot}2H_2O$ in methanol with tolyl terpyridine ligand, which was prepared by a procedure reported in the literature.[50] The ligand (0.323 g, 1 mmol) and $CuCl_2{\cdot}2H_2O$ (0.170 g, 1 mmol) were dissolved in methanol individually and the solutions were warmed. The hot solution of the ligand was added slowly with constant stirring to copper chloride when the colour changed to intense green. The solution was cooled to room temperature and the green precipitate of the copper–ttpy complex separated out and was filtered and dried. IR [KBr disc]: $\tilde{\nu}$ = 3069, 1619, 1451, 1098 $cm^{-1}$. MS (ESI): *m*/*z* = 421 $[M - L{\cdot}Cl]^+$. $C_{22}H_{17}Cl_2CuN_3$ (456.5): calcd. C 57.83, H 3.72, N 9.20, Cu 13.91; found: C 57.78, H 3.69, N 9.25, Cu 13.93. The complex is soluble in DMSO and partially soluble in methanol.

**[Cu(itpy)Cl]Cl (2):** The complex was prepared by a similar procedure to that of complex **1**, by taking $CuCl_2{\cdot}2H_2O$ (0.170 g) and itpy (0.299 g) in the mole ratio 1:1; the ligand was prepared by a similar procedure as that of ttpy. IR (KBr disc): $\tilde{\nu}$ = 3068, 1616, 1450, 794 $cm^{-1}$. MS (ESI): *m*/*z* = 397 $[M - L{\cdot}Cl]^+$. $C_{18}H_{13}Cl_2CuN_5$ (432.5): calcd. C 49.94, H 3.00, N 16.18, Cu 14.68; found C 49.87, H 2.94, N 16.09, Cu 14.60. The solubility of the complex is similar to that of **1**.

**Physical Measurements:** ESI mass spectra were recorded with a Finnigan LCQ Advantage mass spectrometer equipped with an electron spray source. Infrared spectra were recorded for the complexes and the ligand by using a Perkin–Elmer RX-1 FTIR spectrometer and the samples were prepared by KBr mull sampling technique. Electronic spectra were recorded with a Perkin–Elmer Lamda35 double beam spectrophotometer. Circular dichroic spectra were recorded with a J-715 spectropolarimeter (Jasco) at 25 °C with a 0.1-cm pathlength cuvette. Cyclic voltammetry was performed on CH-Instruments, electrochemical analyzer, CH-620 B. X-band electron paramagnetic resonance (EPR) spectra at room temperature and liquid nitrogen temperature were recorded with a Bruker EMX 6/1 spectrometer and the field calibration was done by using diphenylpicrylhydrazyl (DPPH).

**DNA Binding and Cleavage Studies – Absorption Titration Experiments:** The electronic spectra of complexes **1** and **2** were monitored in the absence and presence of DNA in the UV region. Absorption titration experiments were conducted by maintaining the metal ion concentration constant (20 μM) and varying the concentration of DNA (0–150 μM). In the reference cell, a DNA blank was placed so as to cancel any absorbance due to DNA at the measured wavelength. From the absorption titration data the binding constant ($K_b$) was determined by using the following equation.

$$[DNA]/(\varepsilon_a - \varepsilon_f) = [DNA]/(\varepsilon_b - \varepsilon_f) + 1/K_b(\varepsilon_b - \varepsilon_f)$$

where $\varepsilon_a$, $\varepsilon_f$ and $\varepsilon_b$ corresponds to $A_{obs}$/[Cu], the extinction coefficient for the free copper complex and the extinction coefficient for the complex in the bound form, respectively. A plot of $[DNA]/(\varepsilon_a - \varepsilon_f)$ versus [DNA] gives $K_b$ as the ratio of the slope to the intercept. Density functional theory calculations were performed to explore the reactivity, stability and electron density parameters of the terpyridine substituents. From the theoretical investigation, the influence of substituent on the magnitude of binding constant is explained.

Viscometric experiments were carried out by using an Ostwald-type viscometer of 2 mL capacity, thermostatted in a water bath maintained at 25 °C. The flow rates for the buffer (10 mM), DNA (200 μM) and DNA in the presence of copper(II) complex at various concentrations (20–140 μM) were measured with a manually operated timer at least three times to agree within 0.2 s. The relative viscosity was calculated according to the relation, $\eta = (t - t_0)/t_0$ where $t_0$ is the flow time of the buffer and $t$ is the observed flow time for DNA, in the presence and absence of the complex. A plot of $(\eta/\eta_0)^{1/3}$ versus $1/R$ ($R$ = [DNA]/[Complex]) was constructed from viscosity measurements.[51]

Voltammetric experiments were carried out by using a standard three-electrode system comprising glassy carbon working electrode with 3 mm diameter, platinum auxillary electrode and saturated calomel reference electrode (SCE). The samples were prepared in DMSO, and the solutions were deoxygenated by purging nitrogen gas for 10 min. prior to the measurements. The experiments were carried out with a complex concentration of $0.2 \times 10^{-3}$ M by using tetrabutylammonium perchlorate (TBAP) as the supporting electrolyte.

Circular dichroic spectrum of DNA in the absence and presence of complexes was recorded with a J-715 spectropolarimeter (Jasco) at 25 °C with a 0.1-cm pathlength cuvette. The spectra were recorded for 200 μM of DNA in the absence and presence of 5–40 μM of the copper(II) complex in the region 220–300 nm.

Cleavage of plasmid DNA was monitored by using agarose gel electrophoresis. Supercoiled pBR322 DNA (180 ng) in tris(hydroxymethyl)methylamine (Tris) buffer was treated with copper(II) complex (25–75 μM) and ascorbic acid (75–150 μM). The samples were incubated for 60 min at 35 °C. A second set of experiments was performed by maintaining the complex concentration at 75 μM and

 © 2007 Wiley-VCH Verlag GmbH & Co. KGaA, Weinheim 

ascorbic acid at 150 μM and varying the incubation time from 0–60 min. The agarose gel (0.8%) containing 0.5 μg of ethidium bromide was prepared and the electrophoresis of the DNA cleavage products was performed on it. The gels were run at 100 V for 1 h in Tris(boric acid) ethylenediaminetetraacetic acid (TBE) buffer and the bands were identified by placing the stained gel under an illuminated UV lamp. The fragments identified were photographed by using a gel documentation system.

## Acknowledgments

V. U. thanks University Grants Commission for a teacher fellowship.

[1] D. S. Sigman, *Acc. Chem. Res.* **1986**, *19*, 180–186.
[2] P. B. Dervan, *Science* **1986**, *232*, 464–471.
[3] R. E. Hillman, P. J. Dandliker, J. K. Barton, *Angew. Chem. Int. Ed. Engl.* **1997**, *36*, 2714–2730.
[4] B. Meunier, *Chem. Rev.* **1992**, *92*, 1411–1456.
[5] J. K. Barton, *Science* **1986**, *233*, 727–734.
[6] B. Norden, P. Lincoln, B. Akerman, E. Tuite in *Metal Ions in Biological Systems: Probing of Nucleic Acids by Metal Ion Complexes of Small Molecules* (Eds.: A. Sigel, H. Sigel), Marcel Dekker, New York, **1996**, vol. 33, pp. 177.
[7] N. J. Turro, J. K. Barton, D. A. Tamalia, *Acc. Chem. Res.* **1991**, *24*, 332–340.
[8] K. W. Jennette, S. J. Lippard, G. A. Vassiliades, W. R. Bauer, *Proc. Natl. Acad. Sci. USA* **1974**, *71*, 3839–3843.
[9] C. Tu, Y. Shao, N. Gan, O. Xu, Z. Guo, *Inorg. Chem.* **2004**, *43*, 4761–4766.
[10] C. J. Burrows, S. E. Rokita in *Metal ions in Biological Systems* (Eds.: A. Sigel, H. Sigel), Marcel Dekker, New York, **1996**, vol. 33, pp. 537–560.
[11] a) K. R. Barnes, S. J. Lippard in *Metal ions in Biological Systems*, **2004**, vol 42, pp. 143–177; b) B. Rosenberg in *Nucleic Acid–Metal Ion Interactions* (Ed.: T. G. Spiro), John Wiley & Sons, New York, **1980**, vol. 1, pp. 1–29.
[12] V. G. Vaidyanathan, B. U. Nair, *Dalton Trans.* **2005**, 2842–2848.
[13] D. B. Hall, R. E. Holmlin, J. K. Barton, *Nature* **1996**, *382*, 731–734.
[14] a) J. P. Rehmann, J. K. Barton, *Biochemistry* **1990**, *29*, 1701–1709; b) T. Urathamkul, J. L. Beck, M. M. Sheil, J. R. Aldrich-Wright, S. F. Ralph, *Dalton Trans.* **2004**, 2683–2690.
[15] P. J. M. W. L. Birker, A. J. Schierbeek, G. C. Verschoor, J. Reedijk, *J. Chem. Soc. Chem. Commun.* **1981**, 1124–1125.
[16] S. Routier, H. Vezin, E. Lamour, J. L. Bernier, J. P. Catteau, C. Bailly, *Nucleic Acids Res.* **1999**, *27*, 4160–4166.
[17] J. G. Muller, X. Chen, A. C. Dadiz, S. E. Rokita, C. J. Burrows, *Pure Appl. Chem.* **1993**, *65*, 545–550.
[18] V. G. Vaidyanathan, B. U. Nair, *J. Inorg. Biochem.* **2003**, *94*, 121–126.
[19] D. S. Sigman, D. R. Graham, V. D'Aurora, A. M. Stern, *J. Biol. Chem.* **1979**, *254*, 12265–12268.
[20] O. Zelenko, J. Gallagher, D. S. Sigman, *Angew. Chem. Int. Ed. Engl.* **1997**, *36*, 2776–2778.
[21] T. B. Thederahn, M. D. Kuwabara, T. A. Larsen, D. S. Sigman, *J. Am. Chem. Soc.* **1989**, *111*, 4941–4946.
[22] V. G. Vaidyanathan, B. U. Nair, *J. Inorg. Biochem.* **2003**, *93*, 271–276.
[23] S. A. Ross, M. Pitie, B. Meunier, *Eur. J. Inorg. Chem.* **1999**, 557–563.
[24] J.-Z. Wu, H. Li, J.-G. Zhang, J.-H. Xu, *Inorg. Chem. Commun.* **2002**, *5*, 71–76.
[25] K. J. Humphreys, A. E. Johnson, K. D. Karlin, S. E. Rokita, *J. Biol. Inorg. Chem.* **2002**, *7*, 835–842.
[26] T. Gupta, S. Dhar, M. Nethaji, A. R. Chakravarty, *Dalton Trans.* **2004**, 1896–1900.
[27] D. S. Sigman, A. Mazumder, D. M. Perrin, *Chem. Rev.* **1993**, *93*, 2295–2316.
[28] S. Oikawa, S. Kawanishi, *Biochemistry* **1996**, *35*, 4584–4590.
[29] M. D. Kuwabara, C. Yoon, T. E. Goyne, T. Thederahn, D. S. Sigman, *Biochemistry* **1986**, *25*, 7401–7408.
[30] J. A. Cowan, *Curr. Opin. Chem. Biol.* **2001**, *5*, 634–642.
[31] T. B. Thederahn, A. Spassky, M. D. Kuwabara, D. S. Sigman, *Biochem. Biophys. Res. Commun.* **1990**, *168*, 756–762.
[32] V. Uma, V. G. Vaidyanathan, B. U. Nair, *Bull. Chem. Soc. Jpn.* **2005**, *78*, 845–850.
[33] V. Uma, M. Kanthimathi, T. Weyhermuller, B. U. Nair, *J. Inorg. Biochem.* **2005**, *99*, 2299–2307.
[34] A. W. Addison, "Copper Coordination Chemistry" in *Biochemical and Inorganic Perspectives* (Eds.: K. D. Karlin, J. Zubieta), Adenine, Guilderland, New York, **1983**, p. 109.
[35] J. Peisach, W. E. Blumberg, *Arch. Biochem. Biophys.* **1974**, *165*, 691–708.
[36] P. Uma Maheswari, M. Palaniandavar, *J. Inorg. Biochem.* **2004**, *98*, 219–230.
[37] J. K. Barton, A. T. Danishefsky, J. M. Golberg, *J. Am. Chem. Soc.* **1984**, *106*, 2172–2176.
[38] M. J. Frisch, *Gaussian 98*, revision A.7, Gaussian, Inc., Pittsburgh, PA, **1998**.
[39] P. Geerlings, F. De Proft, W. Langenaeker, *Chem. Rev.* **2003**, *103*, 1793–1874.
[40] P. v. R. Schleyer, C. Maerker, A. Dransfeld, H. Jiao, N. J. R. v. E. Hommes, *J. Am. Chem. Soc.* **1996**, *118*, 6317–6318.
[41] *GaussianView 3.0*; Gaussian Inc., Pittsburgh, PA, **2003**.
[42] G. Yang, J. Z. Wu, L. Wang, L. N. Ji, X. Tian, *J. Inorg. Biochem.* **1997**, *66*, 141–144.
[43] M. J. Waring, *J. Mol. Biol.* **1965**, *13*, 269–282.
[44] V. I. Ivanov, L. E. Minchenkova, A. K. Schyolkina, A. I. Poletayev, *Biopolymers* **1973**, *12*, 89–110.
[45] J. G. Collins, T. P. Shields, J. K. Barton, *J. Am. Chem. Soc.* **1994**, *116*, 9840–9846.
[46] C. Liu, J. Zhou, Q. Li, L. Wang, Z. Liao, H. Xu, *J. Inorg. Biochem.* **1999**, *75*, 233–240.
[47] A. Raja, V. Rajendiran, P. Uma Maheswari, R. Balamurugan, C. A. Kilner, M. A. Halcrow, M. Palaniandavar, *J. Inorg. Biochem.* **2005**, *99*, 1717–1732.
[48] J. Marmur, *J. Mol. Biol.* **1961**, *3*, 208–218.
[49] R. E. Reichmann, S. A. Rice, C. A. Thomas, P. J. Doty, *J. Am. Chem. Soc.* **1954**, *76*, 3047–3053.
[50] G. W. V. Cave, C. L. Raston, *J. Chem. Soc., Perkin Trans. 1* **2001**, 3258–3264.
[51] G. Cohen, H. Eisenberg, *Biopolymers* **1969**, *8*, 45–55.

Received: January 17, 2007
Published Online: June 8, 2007

 © 2007 Wiley-VCH Verlag GmbH & Co. KGaA, Weinheim 

DOI: 10.1002/ejic.200700180

# 1,3-Dipolarophile Character of an Extremely Bulky Phosphaalkyne Mes*C≡P (Mes* = 2,4,6-*t*Bu$_3$C$_6$H$_2$) Leading to the Formation of 1,2,4-Diazaphospholes with Unique Hydrogen Bonding Properties

**Shigekazu Ito,*[a] Hideaki Miyake,[a] and Masaaki Yoshifuji*[a][‡]**

**Keywords:** Heterocycles / Phosphaalkynes / Cycloaddition / Hydrogen bonds / DFT calculations / X-ray crystallography

2-(2,4,6-Tri-*tert*-butylphenyl)-1-phosphaethyne was allowed to react with trimethylsilyldiazomethane derivatives to afford the corresponding 1,2,4-diazaphospholes via [2+3] cycloaddition followed by H/SiMe$_3$ migration, in spite of the steric encumbrance of the substrates. The aromatic character of 1,2,4-diazaphosphole is indicated by the NMR spectroscopic data and the X-ray structure analysis as well as by theoretical calculation to confirm the planar delocalized ring skeleton. The crystal structure of the obtained 1,2,4-diazaphospholes showed remarkable hydrogen bonding character in relation to molecular aggregation due to the presence of bulky aryl groups.
(© Wiley-VCH Verlag GmbH & Co. KGaA, 69451 Weinheim, Germany, 2007)

## Introduction

Phosphaalkynes [R–C≡P] are only stable if protected by bulky substituents such as the *tert*-butyl or 2,4,6-tri-*tert*-butylphenyl (Mes*) group. Cycloaddition reactions of such phosphaalkynes have extensively been developed to provide a number of P-heterocyclic compounds which have widely been utilized especially in coordination and organometallic chemistry.[1] Throughout the investigation of phosphaalkynes, *tert*-butylphosphaacetylene [*t*BuC≡P] has played a principal role in the synthesis of P-heterocyclic compounds because of its moderate stability and desirable reactivity,[1,2] and a number of [2+1], [2+2], [2+3], and [2+4] cycloadditions have been observed so far. On the contrary, a phosphaalkyne bearing an extremely bulky Mes* group (**1**, [Mes*C≡P])[3] showed considerably low reactivity in comparison with *t*BuC≡P. Whereas *t*BuC≡P reacts with a diene to afford the corresponding [2+4] adduct,[1] compound **1** gave no six-membered ring compound as a result of Diels–Alder cycloaddition.[4] In addition to the low reactivity and high stability of **1**, the presence of the Mes* group often causes unusual reactions. In the [2+1] cycloaddition with compound **1**, expulsion of the P atom from the initially formed three-membered phosphirene intermediate leads to the formation of the corresponding acetylene derivative **2**,[5,6] probably because of the congestion around the phosphorus, whereas *t*BuC≡P reacts with a carbene (or its heavier congener) to afford the corresponding three-membered phosphirene.[1] Although the presence of bulky substituents in **1** induces such unexpected conversion as to give **3**[6] and **4**[7] in an attempted synthesis of P-heterocyclic compounds, we have utilized **1** for investigations of unique P-heterocyclic diradicals **5**[8] and a monoradical **6**,[8e] which shows the advantage of the introduced Mes* group (Figure 1). Thus, these individual properties of the bulky phosphaalkyne **1** prompted us to explore its unique character, leading to novel findings in the chemistry of P-heterocycles.

In this paper we describe [2+3] additions of compound **1** and trimethylsilyldiazomethane derivatives as dipolar CN$_2$ reagents to demonstrate the ordinary reaction mode of phosphaalkynes[1] leading to important results on novel extremely bulky 1,2,4-diazaphospholes. In these reactions, diazoalkanes overcome the shielding effect of the Mes* group, leading to regioselective cycloaddition for 1,2,4-diazaphospholes, and the formal control of silyl and hydrogen migrations has been accomplished by employing neutral and lithiated trimethylsilyldiazomethanes.[9] Structures of the newly synthesized 1,2,4-diazaphospholes, one of which carries substantial aromatic character,[1,10,11] are discussed in terms of hydrogen-bonding control of molecular aggregation in the presence of the Mes* group. Several 1,2,4-diazaphosphole nucleosides **7** are known, and even the X-ray structures have been reported for **7A** and **7C**. Furthermore, thiocarboxamide **7C** shows antitumor activity against L1210 in vivo,[12] and therefore the newly obtained 1,2,4-diazaphospholes might be available for drug design (Figure 2).

[a] Department of Chemistry, Graduate School of Science, Tohoku University,
Aoba, Sendai 980-8578, Japan
Fax: +81-22-795-6562
E-mail: shigeito@mail.tains.tohoku.ac.jp
[‡] Present address: Department of Chemistry, The University of Alabama,
Tuscaloosa, Alabama 35487-0336, USA
Fax: +1-205-348-4704
E-mail: myoshifuji@bama.ua.edu
Supporting information for this article is available on the WWW under http://www.eurjic.org or from the author.

 © 2007 Wiley-VCH Verlag GmbH & Co. KGaA, Weinheim 

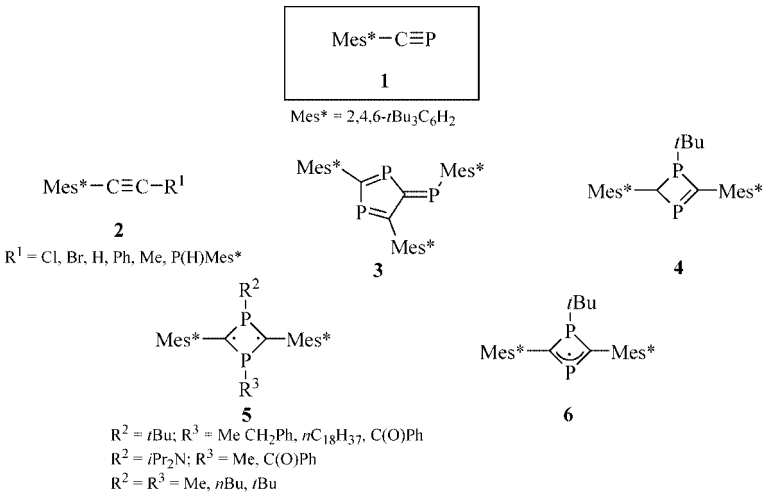


Figure 1. Selected products from phosphaalkyne **1**.

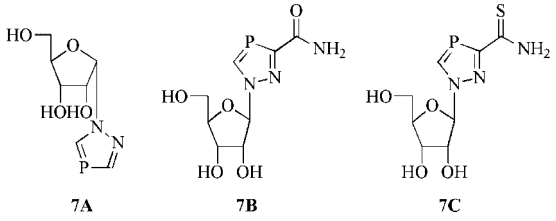


Figure 2. 1,2,4-Diazaphosphole nucleosides **7**.

## Results and Discussion

### 1,3-Dipolar Cycloaddition of Mes*C≡P (1) with $Me_3Si(CN_2)H$

Phosphaalkyne **1**, prepared according to our previous reports,[8a,8b] was allowed to react with trimethylsilyldiazomethane in a similar manner to the reported procedures,[13] and 1-trimethylsilyl-1,2,4-diazaphosphole **9** was formed through intermediate **8** almost quantitatively after the solvent was removed (Scheme 1). $^1H$ and $^{13}C$ NMR spectroscopic data of **9** confirm the presence of $NSiMe_3$ and =*C*H groups as well as a 1*H*-1,2,4-diazaphosphole structure. The migration of the silyl group has been observed in previous studies.[13,14] Actually, the total energy of theoretically optimized structures for model compounds **8x**, **9x**, and **9xx** suggested facile conversion from **8** to **9** as well as the migratory aptitude of the silyl group (Figure 3).[15–17] In the $^{13}C$ NMR spectroscopic data of **9**, the H-substituted carbon atom C($sp^2$)-3 has a slightly smaller $^1J_{PC}$ constant ($^1J_{PC}$ = 53.7 Hz, *C*H) than the C-5 ($^1J_{PC}$ = 59.7 Hz, *C*Mes*), which might represent a 5-substituted 1*H*-1,2,4-diazaphosphole.[18–20] The exclusive formation of **9** without a 1,2,3-diazaphosphole isomer indicates that regioselective [2+3] cycloaddition of **1** with the $CN_2$ moiety proceeds under kinetic control by the bulky Mes* group[21] followed by subsequent silyl group migration[13,14,16] to gain higher aromatic stabilization. The N–Si bond in **9** is sensitive to alcohol and moisture, and desilylation took place to afford **10** by addition of ethanol (Scheme 1).[13,22] In the $^1H$ NMR spectrum, the *o-tert*-butyl groups in both **9** and **10** showed a shift to a higher field, because of the aromatic character of the 1,2,4-diazaphosphole ring. A more detailed discussion about structures in relation to aggregation in solution is in progress.

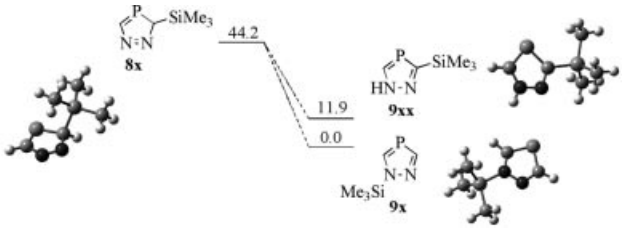


Figure 3. Energy profile (kcal mol$^{-1}$) for the optimized structures **8x**, **9x**, and **9xx** at the B3LYP/6-31+G(d) level.

### Molecular and Crystal Structure of a Bulky 1,2,4-Diazaphosphole 10

The structure of **10** was confirmed by X-ray crystallography. Figure 4a shows one of the three independent molecules of **10** (molecule A) in the unit cell. Table 1 shows se-

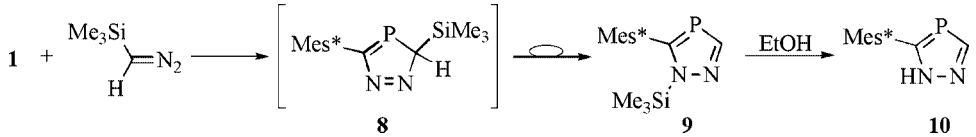


Scheme 1. Reaction of **1** with trimethylsilyldiazomethane.

 © 2007 Wiley-VCH Verlag GmbH & Co. KGaA, Weinheim 

lected bond lengths and angles of **10**, indicating that the parameters are similar to the previously reported 1,2,4-diazaphospholes.[12,23–25] The parameters indicate a relatively large contribution of a 5-substituted 1*H*-1,2,4-diazaphosphole structure: the P1–C1 bonds are longer than the P1–C2 distances, and correspondingly the N1–C1 lengths are shorter than the N2–C2 values. Such bonding properties are almost equal to the previously analyzed structures of nonsubstituted or 3,5-disubstituted 1,2,4-diazaphospholes.[23] The diazaphosphole ring is almost planar [$\Theta$(P–C1–N1–N2) = 0.3–0.7°, $\Theta$(P–C2–N1–N2) = 0.6–1.0°], and the Mes* ring is perpendicular to the five-membered ring (dihedral angle: 89.8–90.0°) in order to reduce the steric congestion. As displayed in Figure 4b, three molecules (A, B, and C) form a trimer structure connected by three N–H···N hydrogen bonds (H···N 1.945–1.971 Å; N···N 2.861–2.867 Å). Such a trimer structure of 1,2,4-diazaphospholes has never been reported so far, whereas pyrazoles, a carbon congener of diazaphospholes, show several aggregation modes.[26] The trimer seems to be additionally stabilized by C–H···$\pi_{Mes*}$ interactions, with H···$\pi_{Mes*}$ distances of 2.763, 2.788, and 2.804 Å.[26] Therefore, the first characterized trimer structure[27] of 1,2,4-diazaphosphole **10** in the crystalline state reflects the effect of the Mes* group in determining the position of the atoms as a result of CH–π interaction.[28]

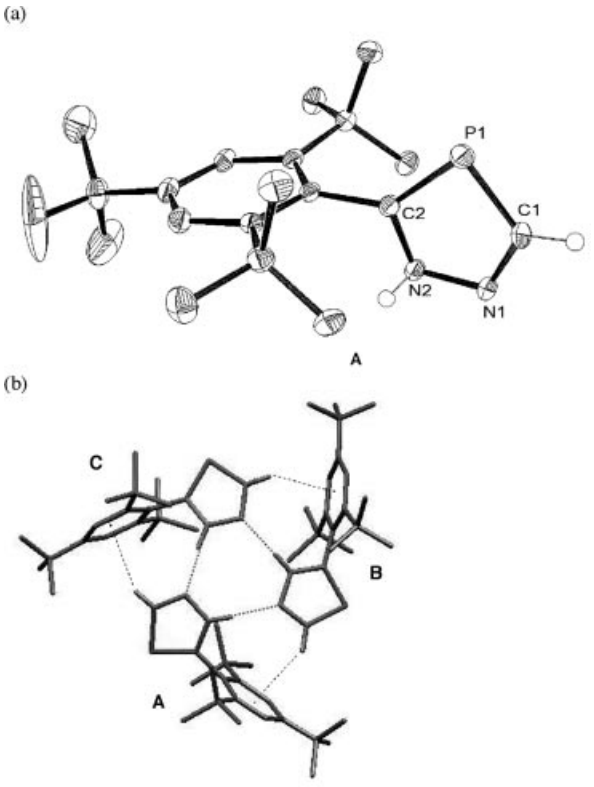


Figure 4. (a) An ORTEP drawing for **10** (50% probability ellipsoids). One of the three independent molecules (**A**) is displayed. Hydrogen atoms in the Mes* group are omitted for clarity. Atom numbering is independent of the nomenclature of 1,2,4-diazaphosphole. (b) Hydrogen-bonded trimer structure of **10** in the crystalline state. ····· NH···N interaction. - - - CH···$\pi_{Mes*}$ interaction.

Table 1. Selected bond lengths [Å] and angles [°] of **10**.

| Parameter | Molecule A | Molecule B | Molecule C |
|---|---|---|---|
| P1–C1 | 1.753(2) | 1752(2) | 1.754(2) |
| P1–C2 | 1.740(2) | 1.742(2) | 1.745(2) |
| N1–N2 | 1.350(2) | 1.344(2) | 1.349(2) |
| N1–C1 | 1.324(3) | 1.329(3) | 1.328(3) |
| N2–C2 | 1.344(2) | 1.340(2) | 1.343(3) |
| C2–$C_{Mes*}$ | 1.499(3) | 1.498(3) | 1.493(3) |
| C1–P1–C2 | 86.45(9) | 86.36(9) | 86.61(9) |
| N2–N1–C1 | 108.4(2) | 108.0(2) | 108.4(2) |
| N1–N2–C2 | 117.7(2) | 117.8(2) | 118.1(2) |
| P1–C1–N1 | 116.6(2) | 116.8(1) | 116.4(2) |
| P1–C2–N2 | 110.9(1) | 111.0(1) | 110.6(1) |
| P1–C2–$C_{Mes*}$ | 135.0(1) | 134.7(1) | 134.9(1) |
| N2–C2–$C_{Mes*}$ | 114.1(2) | 114.3(2) | 114.5(2) |

### Preparation and Structure of Bulky 3-Trimethylsilyl-1,2,4-diazaphosphole 12

The reaction of **1** with lithiated trimethylsilyldiazomethane [$Me_3Si(CN_2)Li$] (Scheme 2) gave a different result from that described above. Compound **1** was allowed to react with freshly prepared $Me_3Si(CN_2)Li$ to generate diazaphospholido anion **11**, which was observed by $^{31}P$ NMR ($\delta_P$ = 135.0 ppm), at a value close to that of a fundamental 1,2,4-diazaphospholido anion.[23,29] The anion **11** was then treated with trifluoroacetic acid to afford 3-trimethylsilyl-1,2,4-diazaphosphole **12** in a moderate yield together with a small amount of **10**. The formation of **10** would also have been possible by using nonlithiated trimethylsilyldiazomethane (Scheme 1).

The crystal structure of **12** (Figure 5) is a dimer connected by two N–H···N hydrogen bonds (H···N 2.105 Å; N···N 2.817 Å). A similar dimer structure was known for 3,5-di-*tert*-butyl-1,2,4-diazaphosphole,[23] and the silyl group appears to be effective in constructing the dimer structure of 1,2,4-diazaphosphole. The P–C1 bond is longer than the P–C2 distance, indicating the predominance of the 5-substituted 1*H*-1,2,4-diazaphosphole structure. On the other hand, almost the same bond lengths were observed for N1–C1 and N2–C2, probably because of the π-accepting effect of the silyl group to stabilize the polarized $N^-H^+$ structure.[30] In the $^{13}C$ NMR spectrum, the C($sp^2$) atoms in the five-membered ring did not give sharp signals because of signal broadening, probably indicating effects of

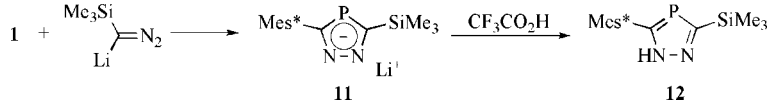


Scheme 2. Reaction of **1** with lithiated trimethylsilyldiazomethane.

 © 2007 Wiley-VCH Verlag GmbH & Co. KGaA, Weinheim 

the dimer structure of **12** in solution. The five-membered ring is planar [$\Theta$(P–C1–N1–N2) = 0.1(4)°, $\Theta$(P–C2–N1–N2) = 0.3(4)°], and the Mes* ring is perpendicular to the five-membered ring (dihedral angle: 90.0°). Compound **12** is an isomer of **9**, and the silyl- and hydrogen rearrangements of **8** can be formally controlled by the reaction conditions.[9] In contrast to the observed predominant migratory aptitude of the silyl group in the rearrangement from **8** to **9** (Scheme 1), the Si–C bond was tolerant to alcoholysis with wet thf in ethanol.

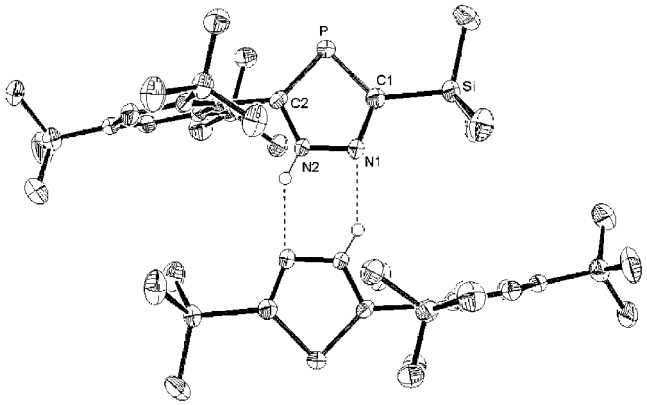


Figure 5. An ORTEP drawing for **12** with dimer structure (50% probability ellipsoids). Hydrogen atoms in the Mes* and the $SiMe_3$ groups are omitted for clarity. Atom numbering is independent from the nomenclature of 1,2,4-diazaphosphole. Typical bond lengths [Å] and angles [°]: P–C1 1.763(4), P–C2 1.744(3), Si–C1 1.886(4), N1–N2 1.349(4), N1–C1 1.340(4), N2–C2 1.337(4), C2–$C_{Mes*}$ 1.500(5), C1–P–C2 87.8(2), N2–N1–C1 109.2(3), N1–N2–C2 118.7(3), P–C1–Si 129.2(2), P–C1–N1 114.4(3), Si–C1–N1 116.4(3), P–C2–N2 109.9(3), P–C2–$C_{Mes*}$ 136.5(3), N2–C2–$C_{Mes*}$ 113.6(3).

## Conclusions

We have demonstrated ordinary [2+3] cycloadditions of phosphaalkyne **1** with diazomethane derivatives affording 1,2,4-diazaphospholes in spite of the presence of an extremely bulky Mes* group. Neutral or lithiated trimethylsilyldiazomethane operated on the structure of the [2+3] adduct to give almost selectively **10** or **12**, respectively. The crystal structure of **10** exhibits the first example of a trimer structure of 1,2,4-diazaphosphole resulting from the presence of the bulky aryl substituent, whereas **12** forms a dimer structure. Although 1,2,4-diazaphosphole is an inherently stable compound and does not require kinetic stabilization, the Mes* group might be effective in discovering novel characteristics of 1,2,4-diazaphospholes which operate molecular assemblies. Attempts to utilize **9**–**12** as unique P-heterocyclic reagents for coordination chemistry are in progress.[1,12,24,31]

## Experimental Section

**General Methods:** All manipulations were carried out under an argon atmosphere by means of standard Schlenk techniques or in a glove box. All solvents employed were dried by appropriate methods. $^1H$, $^{13}C\{^1H\}$ and $^{31}P\{^1H\}$ NMR spectra were recorded with a Bruker Avance 400 spectrometer with $Me_4Si$ ($^1H$, $^{13}C$) and $H_3PO_4$ ($^{31}P$) as internal or external standards. Mass spectra were recorded with a Bruker APEX3 spectrometer. Compound **1** was prepared by the procedures described in the literature.[8a,8b]

**Reaction of 1 with $Me_3Si(CN_2)H$:** To a solution of **1** (91.4 mg, 0.317 mmol) in thf (5 mL) was added trimethylsilyldiazomethane (0.38 mmol, 2.0 M solution in hexane,) at room temperature. After stirring for 30 min, volatiles were removed, and the residual amorphous solid **9** was characterized by NMR spectroscopy. Ethanol (2 mL) was added to **9**, and the volatiles were removed. The residual solid containing **10** was dissolved in chloroform (20 mL), and insoluble materials were filtered off. The chloroform solution was concentrated, and the residue was washed with hexane to obtain **10** as colorless crystals. Compound **10** was purified by silica-gel column chromatography (hexane/EtOAc = 1:1) (total 77.4 mg, 74%). **9**: Colorless amorphous solid: $^{31}P\{^1H\}$ NMR (162 MHz, $C_6D_6$): $\delta$ = 116.6 ppm. $^1H$ NMR (400 MHz, $C_6D_6$): $\delta$ = 0.19 (s, 9 H, $SiMe_3$), 1.25 (s, 18 H, *o*-*t*Bu), 1.32 (s, 9 H, *p*-*t*Bu), 7.65 (s, 2 H, Mes*), 8.42 (d, $^2J_{PH}$ = 39.5 Hz, 1 H, CH) ppm. $^{13}C\{^1H\}$ NMR (101 MHz, $C_6D_6$): $\delta$ = –0.63 (s, $SiMe_3$), 31.9 (s, *p*-C*Me*$_3$), 34.2 (d, $^5J_{PC}$ = 3.5 Hz, *o*-C*Me*$_3$), 35.3 (s, *p*-*C*Me$_3$), 38.3 (s, *o*-*C*Me$_3$), 122.6 (s, *m*-Mes*), 133.2 (d, $^2J_{PC}$ = 21.3 Hz, *ipso*-Mes*), 149.3 (s, *p*-Mes*), 149.6 (d, $^3J_{PC}$ = 3.0 Hz, *o*-Mes*), 162.1 (d, $^1J_{PC}$ = 53.7 Hz, *C*H), 182.0 (d, $^1J_{PC}$ = 59.7 Hz, *C*Mes*) ppm. ESI-MS: calcd. for $[M + Na]^+$ ($C_{23}H_{39}N_2PSi$ + Na) 425.2512; found 425.2511. **10**: Colorless prisms (hexane), m.p. 255–256 °C; $^{31}P\{^1H\}$ NMR (162 MHz, $CDCl_3$): $\delta$ = 106.7 ppm. $^1H$ NMR (400 MHz, $CDCl_3$): $\delta$ = 1.12 (s, 18 H, *o*-*t*Bu), 1.38 (s, 9 H, *p*-*t*Bu), 7.56 (s, 2 H, Mes*), 8.32 (d, $^2J_{PH}$ = 45.3 Hz, 1 H, CH), 12.0 (brs, 1 H, NH) ppm. $^{13}C\{^1H\}$ NMR (101 MHz, $CDCl_3$): $\delta$ = 31.8 (s, *p*-C*Me*$_3$), 33.4 (d, $^5J_{PC}$ = 3.7 Hz, *o*-C*Me*$_3$), 35.6 (s, *p*-*C*Me$_3$), 38.1 (s, *o*-*C*Me$_3$), 122.7 (s, *m*-Mes*), 127.7 (d, $^2J_{PC}$ = 16.2 Hz, *ipso*-Mes*), 150.7 (d, $^3J_{PC}$ = 3.6 Hz, *o*-Mes*), 151.0 (s, *p*-Mes*), 162.5 (d, $^1J_{PC}$ = 68.5 Hz, *C*Mes*), 174.7 (d, $^1J_{PC}$ = 49.3 Hz, *C*H) ppm. ESI-MS: calcd. for $[M + Na]^+$ ($C_{20}H_{31}N_2P$ + Na) 353.2117, found 353.2116. $C_{20}H_{31}N_2P$ (330.45): calcd. C 72.69, H 9.46, N 8.48; found C 72.52, H 9.46, N 8.50.

**Reaction of 1 with $Me_3Si(CN_2)Li$:** To a solution of trimethylsilyldiazomethane (0.10 mmol) in thf (2 mL) was added butyllithium (0.10 mmol, 1.6 M solution in hexane) at –78 °C and stirred for 5 min. To the mixture was added **1** (30 mg, 0.10 mmol) in thf (1 mL) at –78 °C and stirred for 5 min. The reaction mixture was warmed to room temperature and an aliquot was removed via syringe to observe **11** by $^{31}P$ NMR ($\delta_P$ = 135.0). The mixture was treated with trifluoroacetic acid (0.20 mmol) and volatiles were removed in vacuo. The residual materials were purified by silica-gel column chromatography (hexane/EtOAc = 1:1) to afford **12** (28 mg, 66%) and **10** (3 mg, 9%). Pure **12** was obtained by dissolving in hexane (**10** is less soluble in hexane). **12**: Colorless prisms (hexane), m.p. 251–253 °C; $^{31}P\{^1H\}$ NMR (162 MHz, $CDCl_3$): $\delta$ = 141.2 (br) ppm. $^1H$ NMR (400 MHz, $CDCl_3$): $\delta$ = 0.39 (s, 9 H, $SiMe_3$), 1.13 (s, 18 H, *o*-*t*Bu), 1.37 (s, 9 H, *p*-*t*Bu), 7.53 (s, 2 H, Mes*), 11.2 (brs, 1 H, NH) ppm. $^{13}C\{^1H\}$ NMR (101 MHz, $CDCl_3$): $\delta$ = 0.04 (s, $SiMe_3$), 31.8 (s, *p*-C*Me*$_3$), 33.8 (d, $^5J_{PC}$ = 2.9 Hz, *o*-C*Me*$_3$), 35.4 (s, *p*-*C*Me$_3$), 38.1 (s, *o*-*C*Me$_3$), 122.6 (s, *m*-Mes*), 149.7 (s, *p*-Mes*), 149.9 (s, *o*-Mes*, *ipso*-Mes*, 3- and 5-C atoms were unclear) ppm. ESI-MS: calcd. for $[M + Na]^+$ ($C_{23}H_{39}N_2PSi$ + Na) 425.2512; found 425.2513. $C_{23}H_{39}N_2PSi$ (402.63): calcd. C 68.61, H 9.76, N 6.96; found C 68.62, H 9.62, N 7.00.

**X-ray Crystallography:** A Rigaku RAXIS-IV imaging plate detector with graphite-monochromated Mo-$K_\alpha$ radiation ($\lambda$ = 0.71070 Å) was used. The structure was solved by direct methods

 © 2007 Wiley-VCH Verlag GmbH & Co. KGaA, Weinheim 

(SIR92),[32] expanded using Fourier techniques (DIRDIF94).[33] A symmetry-related absorption correction using the program ABSCOR[34] was applied for **10**. The non-hydrogen atoms were refined anisotropically. Hydrogen atoms were refined isotropically. The data were corrected for the Lorentz polarization effect. Structure solution, refinement, and graphical representation were carried out with the teXsan package.[35] The data are summarized in Table 2. CCDC-635494 (**10**) and CCDC-635495 (**12**) contain the supplementary crystallographic data for this paper. These data can be obtained free of charge from The Cambridge Crystallographic Data Centre via www.ccdc.cam.ac.uk/data request/cif.

Table 2. X-ray data for compounds **10** and **12**.

| Compound | **10** | **12** |
|---|---|---|
| Formula | $C_{20}H_{31}N_2P$ | $C_{23}H_{39}N_2PSi$ |
| Fw /g mol$^{-1}$ | 330.45 | 402.63 |
| Crystal system | triclinic | monoclinic |
| Space group | $P\bar{1}$ (no. 2) | $P2_1/c$ (no. 14) |
| $a$ /Å | 15.3082(2) | 12.583(1) |
| $b$ /Å | 17.4576(3) | 10.1014(9) |
| $c$ /Å | 15.2989(5) | 20.1680(9) |
| $\alpha$ /° | 112.328(2) | 90 |
| $\beta$ /° | 106.479(1) | 90.087(3) |
| $\gamma$ /° | 112.335(2) | 90 |
| $V$ /Å$^3$ | 3029.0(2) | 2563.4(3) |
| $Z$ | 6 | 4 |
| $T$ /K | 140 | 150 |
| $\rho_{calc}$ /g cm$^{-3}$ | 1.087 | 1.043 |
| $\mu$ /mm$^{-1}$ | 0.138 | 0.163 |
| $2\theta_{max}$ /° | 55 | 55 |
| Observed reflections | 23356 | 19885 |
| Unique reflections | 12523 | 5612 |
| $R_{int}$ | 0.031 | 0.067 |
| $R_1$ [$I > 2\sigma(I)$] | 0.052 | 0.054 |
| $R_w$ (all data) | 0.162 | 0.077 |
| Parameters | 622 | 361 |
| GOF | 1.124 | 1.020 |

**Theoretical Calculation:** A Gaussian 03 (Revision D.01) was used for DFT calculations for **8x**, **9x**, **9xx**, **9meA**, and **9meB**.[36]

**Supporting Information** (see footnote on the first page of this article): Cartesian coordinates and total energies of the calculated structures and an energy diagram of the [1,5] rearrangements.

## Acknowledgments

This work was supported in part by Grants-in-Aid for Scientific Research from the Ministry of Education, Culture, Sports, Science and Technology, Japan (No. 13303039 and 14044012). One of the authors (S. I.) acknowledges the Support for Young Researchers, Graduate School of Science, Tohoku University.

[1] a) *Multiple Bonds and Low Coordination in Phosphorus Chemistry* (Eds.: M. Regitz, O. J. Scherer), Georg Thieme Verlag, Stuttgart, **1990**; b) K. B. Dillon, F. Mathey, J. F. Nixon, *Phosphorus: The Carbon Copy*, Wiley, Chichester, **1998**; c) M. Regitz, *Chem. Rev.* **1990**, *90*, 191; d) A. Mack, M. Regitz, *Chem. Ber./Recueil* **1997**, *130*, 823; e) M. Regitz, P. Binger, *Angew. Chem. Int. Ed. Engl.* **1988**, *27*, 1484.

[2] Recent reports on P-heterocycles prepared from *t*-BuC≡P: a) F. G. N. Cloke, J. C. Green, N. Hazari, P. B. Hitchcock, P. Mountfold, J. F. Nixon, D. J. Wilson, *Organometallics* **2006**, *25*, 3688; b) C. M. Forsyth, G. B. Deacon, L. D. Field, C. Jones, P. C. Junk, D. L. Kay, A. F. Masters, A. F. Richards, *Chem. Commun.* **2006**, 1003; c) M. Scheer, S. Deng, O. J. Scherer, M. Sierka, *Angew. Chem. Int. Ed.* **2005**, *44*, 3755; d) C. Fish, M. Green, J. C. Jeffery, R. J. Kilby, J. M. Lynam, C. A. Russell, C. E. Willans, *Organometallics* **2005**, *24*, 5789.

[3] G. Märkl, H. Sejpka, *Tetrahedron Lett.* **1986**, *27*, 171.

[4] MesC≡P (Mes = 2,4,6-$Me_3C_6H_2$) is reported to react with dienes to give [2+4] adducts: A. Mack, E. Pierron, T. Allspach, U. Bergsträßer, M. Regitz, *Synthesis* **1998**, 1305.

[5] M. Yoshifuji, Y. Kawai, M. Yasunami, *Tetrahedron Lett.* **1990**, *31*, 6891.

[6] a) S. Ito, H. Sugiyama, M. Yoshifuji, *Angew. Chem. Int. Ed.* **2000**, *39*, 2781; b) S. Ito, H. Miyake, H. Sugiyama, M. Yoshifuji, *Heterocycles* **2004**, *63*, 2591.

[7] a) S. Ito, H. Sugiyama, M. Yoshifuji, *Chem. Commun.* **2002**, 1744; b) S. Ito, H. Miyake, H. Sugiyama, M. Yoshifuji, *Heteroat. Chem.* **2005**, *16*, 357.

[8] a) H. Sugiyama, S. Ito, M. Yoshifuji, *Angew. Chem. Int. Ed.* **2003**, *42*, 3802; b) H. Sugiyama, S. Ito, M. Yoshifuji, *Chem. Eur. J.* **2004**, *10*, 2700; c) M. Yoshifuji, H. Sugiyama, S. Ito, *J. Organomet. Chem.* **2005**, *690*, 2515; d) S. Ito, M. Kikuchi, H. Sugiyama, M. Yoshifuji, *J. Organomet. Chem.* **2007**, *692*, 2761; e) S. Ito, M. Kikuchi, M. Yoshifuji, A. J. Arduengo, T. A. Konovalova, L. D. Kispert, *Angew. Chem. Int. Ed.* **2006**, *45*, 4341.

[9] D. Bourissou, G. Bertrand, *Tetrahedron Lett.* **1999**, *40*, 883.

[10] L. Nyulászi, *Chem. Rev.* **2001**, *101*, 1229.

[11] L. Nyulászi, T. Veszprémi, J. Réffy, *J. Phys. Chem.* **1993**, *97*, 4011.

[12] T. A. Riley, S. B. Larson, T. L. Avery, R. A. Finch, R. K. Robins, *J. Med. Chem.* **1990**, *33*, 572.

[13] W. Rösch, U. Hees, M. Regitz, *Chem. Ber.* **1987**, *120*, 1645.

[14] a) H. Keller, M. Regitz, *Tetrahedron Lett.* **1988**, *29*, 925; b) D. Bourissou, P. Le Floch, F. Mathey, G. Bertrand, *C. R. Acad. Sci. Paris, IIC* **1999**, *2*, 351; c) W. Schnurr, M. Regitz, *Synthesis* **1989**, 511.

[15] Previous theoretical studies on diazaphospholes: L. Nyulászi, P. Várnai, W. Eisfeld, M. Regitz, *J. Comput. Chem.* **1997**, *18*, 609.

[16] Previous theoretical studies on silyl migration: T. J. Barton, J. Lin, S. Ijadi-Maghsoodi, M. D. Power, X. Zhang, Z. Ma, H. Shimizu, M. S. Gordon, *J. Am. Chem. Soc.* **1995**, *117*, 11695.

[17] The STQN process using the optimized structures of 3-silyl-3*H*-1,2,4-diazaphosphole, 1-silyl-1*H*-1,2,4-diazaphosphole, and 5-silyl-1*H*-1,2,4-diazaphosphole estimates activation energies of 7.1 and 30.9 kcal mol$^{-1}$ for the $SiH_3$- and H-migration, respectively [B3LYP/6-31+G(d) level]. The total energy of 3-silyl-1*H*-1,2,4-diazaphosphole is close to that of 5-silyl-1*H*-1,2,4-diazaphosphole. See Supporting Information.

[18] In Scheme 1, the 5-substituted isomer is shown as the structure of **9** although tautomerism might occur between the 5- and 3-substituted forms with trimethylsilyl group shift. Note, however, that 5-methyl-1-trimethylsilyl-1*H*-1,2,4-diazaphosphole (**9meA**) is less stable than the corresponding 3-methyl-1-trimethylsilyl-1*H*-1,2,4-diazaphosphole (**9meB**) by 3.9 kcal mol$^{-1}$ at the B3LYP/6-31+G(d) level of calculation because of the steric repulsion between methyl and trimethylsilyl groups.

[19] 3-Trimethylsilyl-1*H*-1,2,4-diazaphosphole, a tautomeric isomer of **9xx**, possesses lower total energy by 1.4 kcal mol$^{-1}$ at the B3LYP/6-31+G(d) level. See Supporting Information.

[20] In the previous studies on symmetrically 3,5-disubstituted 1*H*-1,2,4-diazaphospholes, the C-3 position was assigned on the basis of the slightly smaller $^1J_{PC}$ constant: R. M. Claramunt, C. López, A. Schmidpeter, A. Willhalm, J. Elguero, I. Alkorta, *Spectroscopy* **2001**, *15*, 27.

[21] L. Nyulászi, *J. Organomet. Chem.* **2005**, *690*, 2597.

[22] Compound **10** was alternatively obtained from **1** and diazomethane in 79% yield: Y. Kawai, Dissertation, Tohoku University, 1990.

 © 2007 Wiley-VCH Verlag GmbH & Co. KGaA, Weinheim 

[23] K. Polborn, A. Schmidpeter, G. Märkl, A. Willhalm, *Z. Naturforsch. Teil B* **1999**, *54*, 187. See also: R. E. Marsh, *Acta Crystallogr., Sect. B* **2002**, *58*, 893.
[24] L. Szarvas, Z. Bajko, S. Fusz, S. Burck, J. Daniels, M. Nieger, D. Gudat, *Z. Anorg. Allg. Chem.* **2002**, *628*, 2303.
[25] J. Grobe, D. Le Van, M. Hegemann, B. Krebs, M. Läge, *Chem. Ber.* **1992**, *125*, 411.
[26] In the structures of pyrazoles, molecular aggregation for the sake of hydrogen bonds and C–H···π interactions has been observed: a) A. Haghiri, H.-W. Lerner, M. Wagner, J. W. Bats, *Acta Crystallogr., Sect. E* **2002**, *58*, o1378; b) C. Foces-Foces, I. Alkorta, J. Elguero, *Acta Crystallogr., Sect. B* **2000**, *56*, 1018; c) H. V. R. Dias, X. Wang, *Polyhedron* **2004**, *23*, 2533.
[27] A helix (catemer) and a dimer structure were characterized by X-ray crystallography of nonsubstituted 1,2,4-diazaphosphole and 3,5-di-*tert*-butyl-1,2,4-diazaphosphole, respectively; see ref.[21].
[28] a) S. Ito, S. Sekiguchi, M. Yoshifuji, *Eur. J. Org. Chem.* **2003**, 4838; b) S. Ito, S. Sekiguchi, M. Yoshifuji, *J. Org. Chem.* **2004**, *69*, 4181.
[29] A. Schmidpeter, B. Wrackmeyer, *Z. Naturforsch., Teil B* **1986**, *41*, 553.
[30] Bond lengths of 1.33280 and 1.35033 Å were theoretically determined for the two C=N bonds of **9xx** at the B3LYP/6-31+G(d) level.
[31] W. Zheng, G. Zhang, K. Fan, *Organometallics* **2006**, *25*, 1548.
[32] A. Altomare, M. C. Burla, M. Camalli, M. Cascarano, C. Giacovazzo, A. Guagliardi, A. G. Polidori, *J. Appl. Crystallogr.* **1994**, *27*, 435.
[33] P. T. Beurskens, G. Admiraal, G. Beurskens, W. P. Bosman, R. de Gelder, R. Israel, J. M. M. Smits, *The DIRDIF94 Program System*, Technical Report of the Crystallography Laboratory, University of Nijmegen, The Netherlands, **1994**.
[34] T. Higashi, *Program for Absorption Correction*, Rigaku Corporation, Tokyo, **1995**.
[35] *Crystal Structure Analysis Package*, Molecular Structure Corporation, The Woodlands, TX, **1985** and **1999**.
[36] M. J. Frisch, G. W. Trucks, H. B. Schlegel, G. E. Scuseria, M. A. Robb, J. R. Cheeseman, J. A. Montgomery Jr, T. Vreven, K. N. Kudin, J. C. Burant, J. M. Millam, S. S. Iyengar, J. Tomasi, V. Barone, B. Mennucci, M. Cossi, G. Scalmani, N. Rega, G. A. Petersson, H. Nakatsuji, M. Hada, N. Ehara, K. Toyota, R. Fukuda, J. Hasegawa, M. Ishida, T. Nakajima, Y. Honda, O. Kitao, H. Nakai, M. Klene, X. Li, J. E. Knox, H. P. Hratchian, J. B. Cross, V. Bakken, C. Adamo, J. Jaramillo, R. Gomperts, R. E. Stratmann, O. Yazyev, A. J. Austin, R. Cammi, C. Pomelli, J. W. Ochterski, P. Y. Ayala, K. Morokuma, G. A. Voth, P. Salvador, J. J. Dannenberg, V. G. Zakrzewski, S. Dapprich, A. D. Daniels, M. C. Strain, O. Farkas, D. K. Malick, A. D. Rabuck, K. Raghavachari, J. B. Foresman, J. V. Ortiz, Q. Cui, A. G. Baboul, S. Clifford, J. Cioslowski, B. B. Stefanov, G. Liu, A. Liashenko, P. Piskorz, I. Komaromi, R. L. Martin, D. J. Fox, T. Keith, M. A. Al-Laham, C. Y. Peng, A. Nanayakkara, M. Challacombe, P. M. M. Gill, B. Johnson, W. Chen, M. W. Wong, C. Gonzalez, J. A. Pople, *Gaussian 03*, Revision D.01, Gaussian Inc., Wallingford CT, **2004**.

Received: February 7, 2007
Published Online: June 18, 2007

 © 2007 Wiley-VCH Verlag GmbH & Co. KGaA, Weinheim 

DOI: 10.1002/ejic.200700341

# Surface-Assisted Synthesis and Behavior of Dimetallic Mixed-Metal Complexes $[M_2Cl_2(\mu\text{-}Cl)_4(CO)_6M'(L)_2]$ (M = Ru, Os; M′ = Fe, Co; L = $CH_3CH_2OH$, $H_2O$)

**Minna Jakonen,[a] Pipsa Hirva,[a] Taina Nivajärvi,[a] Mirja Kallinen,[a] and Matti Haukka*[a]**

**Keywords:** Ruthenium / Osmium / Cobalt / Iron / Synthesis design

The reductive carbonylation of ruthenium and osmium halides in the presence of cobalt and iron surfaces was studied. In these surface-assisted reactions the metal surface plays an active role in releasing metal ions, which can be used for the in situ synthesis of mixed-metal compounds. A linear, dimetallic, chlorido-bridged, trinuclear complex $[Ru_2Cl_2(\mu\text{-}Cl)_4(CO)_6Co(CH_3CH_2OH)_2]$ was obtained by the interaction between reducing $RuCl_3$ and the cobalt surface. In the reaction the $RuCl_3$ is reduced with carbon monoxide in the presence of a solid cobalt surface in ethanol solution. During the reduction of the $RuCl_3$ the cobalt surface was simultaneously corroded, releasing cobalt cations. In addition to $[Ru_2Cl_2(\mu\text{-}Cl)_4(CO)_6Co(CH_3CH_2OH)_2]$, the reaction also produced other trinuclear complexes and mononuclear products, such as a bent and linear dimetallic, chlorido-bridged complex with the aqua ligand $[Ru_2Cl_2(\mu\text{-}Cl)_4(CO)_6Co(H_2O)_2]$ and ionic $[RuCl_3(CO)_3]_2[Co(H_2O)_6]$. The carbon monoxide reduction of $RuI_3$ produced the ionic complex $[RuI_3(CO)_3]_2[M'(H_2O)_6]$ (M′ = Fe, Co) in the presence of iron, stainless steel or cobalt. Iodido-bridged trinuclear mixed-metal complexes were not observed. The surface-assisted process proved to be useful with other metal combinations as well. When $RuCl_3$ was replaced with $OsCl_3$, a variety of trinuclear mixed-metal complexes, such as $[Os_2Cl_2(\mu\text{-}Cl)_4(CO)_6Co(CH_3CH_2OH)_2]$ and ionic $[OsCl_3(CO)_3]_2[M(H_2O)_6]$ (M = Fe, Co), were obtained, depending on the metal surface used. Due the lability of the chlorido-bridged trinuclear complexes, the possible decomposition steps of $[M_2Cl_2(\mu\text{-}Cl)_4(CO)_6M'(CH_3CH_2OH)_2]$ (M = Ru, Os; M′ = CO, Fe) were studied computationally, using DFT methods.
(© Wiley-VCH Verlag GmbH & Co. KGaA, 69451 Weinheim, Germany, 2007)

## Introduction

Sacrificial anodes, most commonly used in corrosion protection,[1] have a variety of applications in synthetic chemistry[2] and in biochemistry.[3] The sacrificial anode donates metal cations in a reaction solution when current is applied to the anode material by an external power source. These released cations can then be used to form organometallic[4] or inorganic complexes,[5] or inorganic nanomaterial.[6] Nanomaterials prepared by means of sacrificial anodes have been used, for example, in catalytic applications[6a] and as the inhibitors in biochemical applications.[6b] Sacrificial anodes are also useful in the applications of organic chemistry:[7] in the polymerisation of organic monomers,[7c] in the preparation of organic compounds and also in electrocarboxylation reactions.[7d,7e] There also exists an example of the electrosynthesis of the Grignard reagent using sacrificial magnesium.[7g] The typical sacrificial anode materials in electrosynthesis are magnesium, zinc, cadmium and aluminum, but examples involving cobalt, copper, nickel, palladium, silver, tin and iron are also available.[4–7]

Although it is known that solid metal surfaces can also participate in the formation of the products without external current, this phenomenon has not been widely used in the synthesis of organometallic compounds. In fact, carbonylmetal chemistry started to develop via the corrosion products formed under harsh conditions.[8] Mond was the first to report the formation of toxic $Ni(CO)_4$ in nickel pipes carrying carbon monoxide gas.[8] In our earlier study, we suggested that the release of the metal from a metal surface by corrosion, without the use of an externally applied current, could be used for the synthesis of other carbonyl-containing metal complexes. Such an approach was applied in the synthesis of mixed-metal trinuclear Ru-Fe-Ru complexes, which were prepared by reducing $RuCl_3$ with carbon monoxide in the presence of an iron-containing metal surface.[9] In this synthesis method, ruthenium(III) salt and the iron-containing metal surface form a metal pair suitable for redox processing, which releases the less noble metal ions from the surface. The metal cations released can then be used in the in situ synthesis of the trinuclear mixed-metal complexes $[Ru_2Cl_2(\mu\text{-}Cl)_4(CO)_6Fe(L)_2]$ (L = $H_2O$, $CH_3CH_2OH$) and a mixture of mononuclear ions $[RuCl_3(CO)_3]_2[Fe(H_2O)_6]$. The potential difference between the metal surface and the reducing metal salt determines the rate of dissolution of the metal cations from the metal surface into the reaction system.

[a] University of Joensuu, Department of Chemistry, P. O. Box 111, 80101, Joensuu, Finland
E-mail: matti.haukka@joensuu.fi
Supporting information for this article is available on the WWW under http://www.eurjic.org or from the author.

 © 2007 Wiley-VCH Verlag GmbH & Co. KGaA, Weinheim 

In the current paper we have extended the use of sacrificial metal surfaces from Ru-Fe systems into the other metal combinations. The goal of the study was to examine whether complexes such as $[Ru_2Cl_2(\mu\text{-}Cl)_4(CO)_6Fe(L)_2]$, shown in Figure 1, could be synthesized using the metal systems Ru-Co, Os-Fe and Os-Co. In addition, the influence of the halide on the reaction progress was studied using $RuCl_3$ and $RuI_3$ as the reducing components.

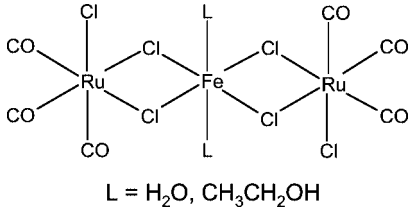


Figure 1. Schematic picture of the chlorido-bridged trinuclear ruthenium-iron complex.[6]

## Results and Discussion

The reductive carbonylation of ruthenium(III) trichloride is typically performed in alcohol solutions either under reflux or in high-pressure carbon monoxide. The reduction produces complexes with partially or fully reduced ruthenium centers.[10–15] Normally, the final reduction product is the zero-valent ruthenium cluster $Ru_3(CO)_{12}$ but several compounds containing carbonyl and halide ligands such as $[RuCl_2(CO)_3]_2$ can also be obtained.[11,14,16] Further exposure to carbon monoxide tends to reduce these species eventually to the highly stable $Ru_3(CO)_{12}$ cluster.[15,17] Like $RuCl_3$, the CO reduction of $OsCl_3$ is commonly carried out in alcohol solutions either under reflux or in a pressurized vessel under elevated CO pressure. Such reactions again produce a variety of halide-containing carbonyl products and, finally, $Os_3(CO)_{12}$.[18–20] A different type of surfaces has been used to assist the reduction process. For example, it has been found that reductive carbonylation of silica-supported $MCl_3$ (M = Ru,Os) produces several halide-containing carbonylmetal(II) compounds as well as the $M_3(CO)_{12}$ cluster.[21]

If metal surfaces are used, this opens up possibilities for synthesizing mixed-metal compounds. For example, if the reductive carbonylation of ruthenium trichloride is carried out in the presence of an iron-containing surface, it acts as a sacrificial source of iron. The active participation of the metal surface permits the formation of mixed-metal products such as trinuclear $[Ru_2Cl_2(\mu\text{-}Cl)_2(CO)_6Fe(L)_2]$ (L = $H_2O$ or $CH_3CH_2OH$) and also the ionic monomeric $[RuCl_3(CO)_3]_2[Fe(H_2O)_6]$,[6] where the cations and anions are bound together by hydrogen bonds. It is believed that during the reduction of $Ru^{3+}$, iron from the surface is simultaneously oxidized and released, which leads to the formation of labile trinuclear dimetallic chlorido-bridged compounds $[Ru_2Cl_2(\mu\text{-}Cl)_2(CO)_6Fe(L)_2]$ (L = $H_2O$ or $CH_3CH_2OH$) with $Ru^{2+}$ and $Fe^{2+}$ centres. The same approach can be applied to other metal combinations using $RuCl_3$ or $OsCl_3$ as the reducing component and iron or cobalt metal as the oxidizing component. The complexes synthesized in this work are summarized in Figure 2.

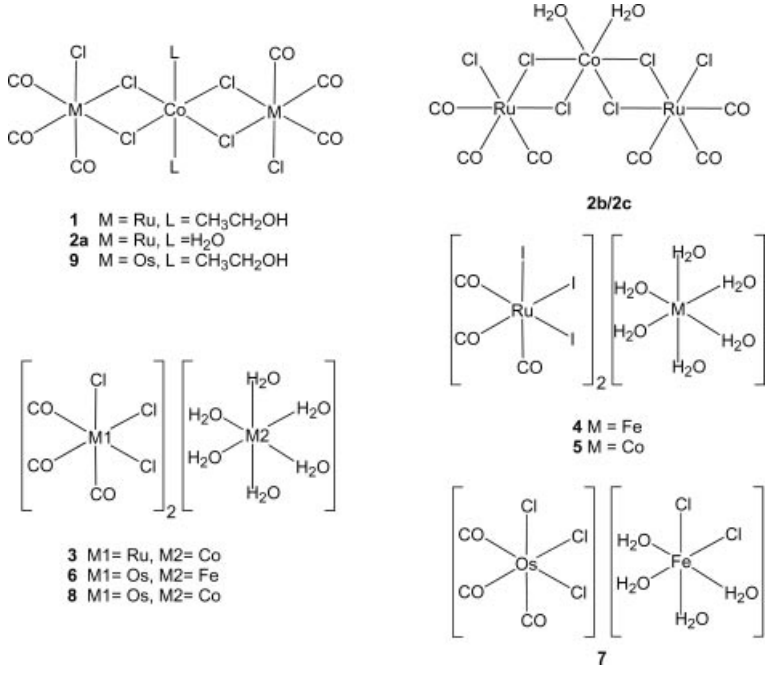


Figure 2. Schematic drawing of the main products involved in the reductive carbonylation reaction of $MX_3$ in the presence of a sacrificial metal surface.

 © 2007 Wiley-VCH Verlag GmbH & Co. KGaA, Weinheim 

Corrosion of the metal plate could be detected with all of the metals used as an oxidizing surface. Both iron and cobalt surfaces and also stainless steel do corrode. In the reactions with iron or stainless steel, the initially black reaction solution turned greenish-yellow during the carbonylative reduction of $MCl_3$. Green or a greenish color was typical for all reactions involving an iron-containing surface, indicating the release of iron ions. When stainless steel was used as the source of iron ions, the type of corrosion produced was pitting, which is typical of metals and metal alloys with a passive oxide layer on their surface.[22] Fairly uniform corrosion was observed when pure metal, iron or cobalt, was used. In a typical reaction with cobalt surface, the reductive carbonylation of $RuCl_3$ produced a blue solution. Again, the metal surface was clearly worn down. A blue coloration indicates the release of cobalt ions into the reaction solution.

### Formation of Ruthenium-Cobalt Mixed-Metal Complexes

The carbonylative reduction of $RuCl_3$ in the presence of a cobalt plate consistently produced a mixture of various mixed-metal complexes and mononuclear metal complexes with carbonyl and halide ligands. The ratio of the different products varied with each reaction. Because the yields of the individual products were rather low, single-crystal X-ray diffraction was used as the principal method of analysis. In order to crystallize the products, the reaction solutions were concentrated to dryness and the solid products were recrystallized from dichloromethane by means of slow concentration or by adding hexane to the $CH_2Cl_2$ solution. In the case of $RuCl_3$ reduction with a cobalt surface, the crystallization produced a mixture of pale pink crystals and colorless crystals. X-ray analysis of the pink crystals revealed trinuclear $[Ru_2Cl_2(\mu\text{-}Cl)_4(CO)_6Co(CH_3CH_2OH)_2]$, as shown in Figure 3.

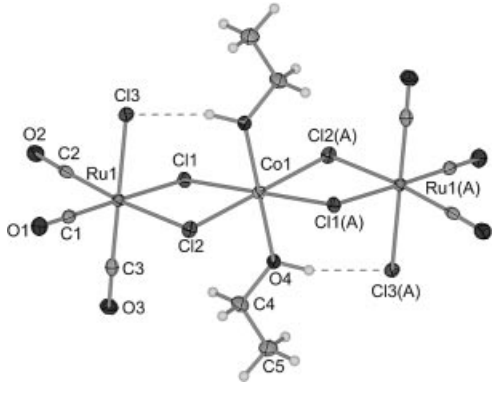


Figure 3. Thermal ellipsoid plot (50% probability level) of $[Ru_2Cl_2(\mu\text{-}Cl)_4(CO)_6Co(CH_3CH_2OH)_2]$ (**1**). Hydrogen bond [Å, °]: O4–H4O 0.95, H4O···Cl3(A) 2.15, O4···Cl3(A) 3.073(2), O4–H4O···Cl3(A) 164.6. Symmetry transformations used to generate equivalent atoms: (A) $-x + 1, -y, -z + 1$.

Structurally, $[Ru_2Cl_2(\mu\text{-}Cl)_4(CO)_6Co(CH_3CH_2OH)_2]$ closely resembles $[Ru_2Cl_2(\mu\text{-}Cl)_4(CO)_6Fe(CH_3CH_2OH)_2]$, as reported earlier.[6] The trinuclear structure is supported by hydrogen bonding between the hydroxy hydrogen atom of the ethanol ligand and the terminal chlorido ligand of the ruthenium moiety. The pink crystals of $[Ru_2Cl_2(\mu\text{-}Cl)_4(CO)_6Co(CH_3CH_2OH)_2]$ could be isolated from the solid product, which was obtained after recrystallization from dichloromethane. The yield of complex **1** was ca. 10–15%. Complex **1** could be obtained both from high-pressure reactions in an autoclave and from low-pressure reactions under reflux. A reasonable yield of the complex **1** permitted further analysis. In order to verify the results, the elemental content of the product was analyzed using both elemental analysis and EDS (Energy Dispersive Spectroscopy). The latter confirmed the presence of cobalt and ruthenium. A pale violet trinuclear complex with aqua ligand, $[Ru_2Cl_2(\mu\text{-}Cl)_4(CO)_6Co(H_2O)_2]$ (**2**), could also be isolated from the product, although the formation of complex **1** seemed to be preferred. The yield of complex **2** remained rather low at ca. 8%. Again, the structural features of $[Ru_2Cl_2(\mu\text{-}Cl)_4(CO)_6Co(H_2O)_2]$ were very similar to $[Ru_2Cl_2(\mu\text{-}Cl)_4(CO)_6Fe(H_2O)_2]$.[6] Two different structures were found: linear **2a**, presented in Figure 4, and bent **2b**, presented in Figure 5. In both structures the intramolecular hydrogen bonds between the coordinated water molecule and the terminal chlorido ligand further support the trinuclear arrangement of the metal atoms. It was found that the formation of the bent type of isomer **2b** was preferred over linear **2a** when the cobalt plate was replaced by cobalt powder. Such an observation may suggest that the morphology of the surface plays an important role in the formation of trinuclear mixed-metal products.

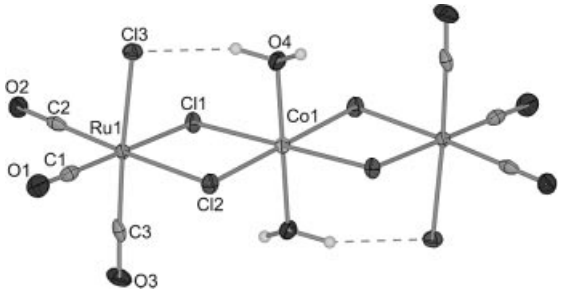


Figure 4. Thermal ellipsoid plot (50% probability level) of $OsCl_2(CO)_3(H_2O)$ (**2a**). Hydrogen bonds [Å, °]: O4–H4 0.98, H4···Cl3 2.30, O4···Cl3 3.242(3), O4–H4···Cl2(A) 161.8.

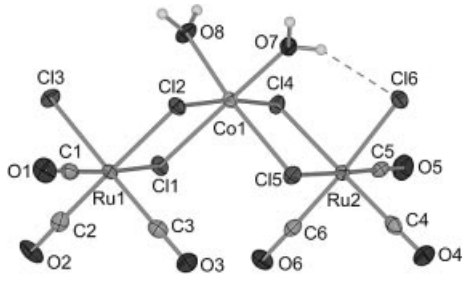


Figure 5. Thermal ellipsoid plot (50% probability level) of the bent $[Ru_2Cl_2(\mu\text{-}Cl)_4(CO)_6Co(H_2O)_2]$ (**2b**), crystallized in the triclinic space group $P\bar{1}$. Hydrogen bond [Å, °]: O7–H7A 0.79, H7A···O2 2.59, O7···O2 3.187(3), O7–H7A···O2 133.2.

 © 2007 Wiley-VCH Verlag GmbH & Co. KGaA, Weinheim 

The chlorido-bridged trinuclear mixed-metal complexes of types **1** and **2** are labile and sensitive towards moisture. Previous results suggest that the exposure of $[Ru_2Cl_2(\mu\text{-}Cl)_4(CO)_6Fe(CH_3CH_2OH)_2]$ to moisture leads first to ligand exchange on the central metal atom and then to the formation of $[Ru_2Cl_2(\mu\text{-}Cl)_4(CO)_6Fe(H_2O)_2]$. Additional exposure to moisture finally breaks down the chlorido bridges and pulls the metal atoms apart, yielding ionic $[Ru(CO)_3Cl_3]_2[Fe(H_2O)_6]$.[6] Similar behavior was also observed with complex **1**. As in the case of the $RuCl_3$/Fe reaction, the $RuCl_3$/Co reaction produced an ionic decomposition product, $[Ru(CO)_3Cl_3]_2[Co(H_2O)_6]$ (**3**), with variable ratios (Figure 6).

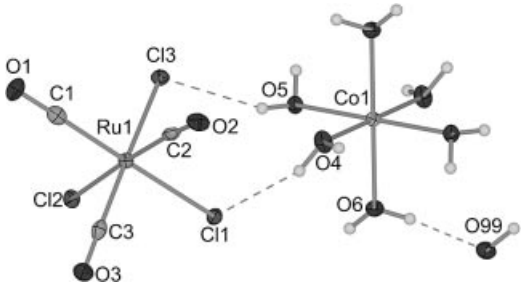


Figure 6. Thermal ellipsoid plot (50% probability level) of $[RuCl_3(CO)_3]_2[Co(H_2O)_6]\cdot 2(H_2O)$ (**3**). The symmetry-related water molecule is not shown. Hydrogen bonds [Å, °]: O4–H4A 0.85, H4A···Cl1 2.36, O4···Cl1 3.140(2), O4–H4A···Cl1 152.8, O5–H5B 0.84, H5B···Cl3 2.44, O5···Cl3 3.220(2), O5–H5B···Cl3 153.8, O6–H6B 0.84, H6B···O99 1.88, O6···O99 2.716(2), O6–H6B···O99 173.3.

Compared to $[Ru_2Cl_2(\mu\text{-}Cl)_4(CO)_6Fe(CH_3CH_2OH)_2]$ and $[Ru_2Cl_2(\mu\text{-}Cl)_4(CO)_6Fe(H_2O)_2]$, the decomposition of complexes **1** and **2** into the ionic product **3** seems to be slightly slower. For example, complex **1** can be stored in air much longer than the corresponding iron compound without severe decomposition.

In addition to complexes **1**, **2**, and **3**, crystallographic analysis of the reaction products obtained after the reduction of $RuCl_3$ in the presence of cobalt revealed other types of mononuclear products as well such as neutral $RuCl_2(H_2O)(CO)_3$ and $CoCl_2(H_2O)_4$, which could be identified by means of single-crystal X-ray diffraction. This suggests that an alternative decomposition route for trinuclear Ru-Co-Ru may also be possible. The formation of corresponding neutral mononuclear species has been observed in $RuCl_3$/Fe systems earlier, which means that a similar alternative route also exists in the case of $RuCl_3$/Co systems. However, it should be mentioned that, according to the very low yields of the neutral products, this route seems not to be very feasible. Actually, neutral products such as $RuCl_2(H_2O)(CO)_3$ were found only occasionally in some of the reaction products. Each reaction was repeated several times, and the main decomposition product was always found to be ionic $[Ru(CO)_3Cl_3]_2[Co(H_2O)_6]$.

The product distribution of the carbonylative reduction of $RuCl_3$ depends strongly on the reaction conditions. If the reaction is carried out without metal surfaces and if the CO pressure is high enough (> 20 bar) and the reaction time long enough (> 17 h), the dominating carbonylation product is zero-valent, fully carbonylated and reduced $Ru_3(CO)_{12}$. This seems to be true for both reactions, with or without the presence of the solid metal surface. The solvent also has an effect on the progression of the reaction and on the products formed during the reduction. If the alcohol solvent is replaced with water, the final carbonylation product is polymeric $[Ru(CO)_4]_n$.[23] However, the presence of the metal surface tends to favor the partially reduced and carbonylated ruthenium species. If $RuCl_3$ was simply heated under reflux in ethanol and in a CO flow in the presence of an iron or cobalt plate (17 h), $Ru_3(CO)_{12}$ was not detected at all. After 3 h of reaction with 20 bar of CO, the cluster product was still not observable. Increasing the reaction temperature from 125 °C to 150 °C led to the formation of $Ru_3(CO)_{12}$ after only 3 h of reaction with 20 bar of carbon monoxide, but under these conditions $Ru_3(CO)_{12}$ was only a minor product. At 50 bar of CO, ≥ 125 °C and ≥ 3 h reaction times with or without the presence of a metal surface, the principal product was an $Ru_3(CO)_{12}$ cluster. Cluster formation under similar conditions without metal surface is well known and reported by Bruce et al.[24] Nevertheless, it should be noted that partially carbonylated species can still be found even with elevated pressures (50 bar) and long reaction times (17–20 h), where $Ru_3(CO)_{12}$ is already the main product, including in reactions with a metal surface. It seems likely that products with partially reduced ruthenium centres $[Ru_2Cl_2(\mu\text{-}Cl)_4(CO)_6M(L)_2]$, and $[Ru(CO)_3Cl_3]_2[M(H_2O)_6]$ (M = Fe, Co and L = $H_2O$, $CH_3CH_2OH$) are stable enough to interfere with the reduction of ruthenium in the zero-valent state.

From the synthetic point of view, the formation of an unpredictable mixture of products is the main setback, which complicates the use of metal surfaces for synthetic purposes. The yields of the most interesting products, the mixed-metal trinuclear $[Ru_2Cl_2(\mu\text{-}Cl)_4(CO)_6Co(L)_2]$ complexes, consistently remained rather low at around 8–15%. This is mainly due to the lability of the trinuclear compounds in the presence of moisture. However, compared to its Ru-Fe-Ru equivalent, $[Ru_2Cl_2(\mu\text{-}Cl)_4(CO)_6Co(L)_2]$ can certainly be synthesized with better reproducibility and enhanced yields.

The reaction products **1**–**3**, which were obtained with adequate yields, were also analysed using IR spectroscopy. The common feature of all these compounds is that the arrangement of the carbonyl ligands around the ruthenium center is very similar in all of them. The facial arrangement of the CO ligands in each compound gives a ν(CO) pattern with two strong bands: a sharp band at higher wavenumbers around 2140–2145 $cm^{-1}$ and a broad- or double-headed one at lower wavenumbers at ca. 2055–2065 $cm^{-1}$. Two pairs of ν(CO) signals were found at 2143 $cm^{-1}$ and 2077 $cm^{-1}$ in the $CH_2Cl_2$ solution immediately after reaction, when ethanol is evaporated from the Ru-Co reaction solution and the solid material is dissolved in $CH_2Cl_2$. Typically, the higher band was sharp and the lower band much broader. The result closely resembles those found in reactions conducted with iron-containing surfaces, where the

 © 2007 Wiley-VCH Verlag GmbH & Co. KGaA, Weinheim 

corresponding signals have been reported to be at 2143 $cm^{-1}$ and 2078 $cm^{-1}$.[6]

ATR-IR (Attenuated Total Reflectance IR) measurements were performed for the chlorido-bridged Ru-Co-Ru complexes **1** and **2**, and for ionic **3**. In the IR measurements of the reaction solutions different complexes could not be assigned, but with the ATR technique the complexes could be identified. In the case of the ATR measurements two bands were detected again, and as with the FTIR spectra the peak at the higher wavenumber was once again strong and rather sharp. The lower peak was double-headed and actually a combination of two peaks. In the spectrum of complex **1** the highest signal is at the wavenumber 2137 $cm^{-1}$, while the lower band has two peaks, at 2075 and 2054 $cm^{-1}$. Similar patterns can be found also in the spectra of the compounds **2** and **3** with the wavenumbers 2135, 2070, and 2054 $cm^{-1}$ for **2** and 2139, 2075, and 2056 $cm^{-1}$ for **3**.

### The Effect of the Halide in the Reducing Salt

In order to study the role of the halide in the reducing salt, the $RuCl_3$ was replaced with $RuI_3$. Otherwise, the reductive carbonylation reaction with cobalt or iron surfaces was carried out under conditions similar to those used for a typical $RuCl_3$ reduction (20 bar of CO, 125 °C, 3 h). Again, the release of iron and cobalt cations was observed in the reaction. The most noticeable feature of these reactions was the absence of halide-bridged trinuclear mixed-metal products. They were detected in reduction reactions with either of the metals (Fe, Co) used. This may indicate that the trinuclear iodido-bridged products are less stable than their chlorido-bridged analogues. The reaction with $RuI_3$ produced variable amounts of $[RuI_3(CO)_3]_2[Fe(H_2O)_6]$ (**4**), $[RuI_3(CO)_3]_2[Co(H_2O)_6]$ (**5**), $[RuI_2(CO)_3]_2$ (**11**) and $Ru(CO)_4I_2$ (**12**), which were characterized by single-crystal X-ray diffraction. Structurally, compounds **4** and **5** are isostructural with the corresponding complex **3** formed in the reduction reactions of $RuCl_3$. The structures of **4**, **11** and **12** are shown in Figures 7, 8, and 9.

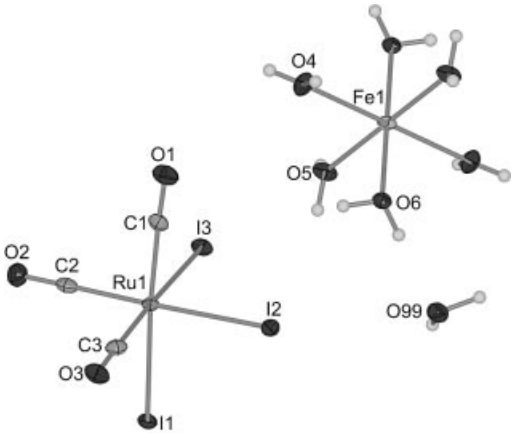


Figure 7. Thermal ellipsoid plot (50% probability level) of $[RuI_3(CO)_3]_2[Fe(H_2O)_6]\cdot 2(H_2O)$ (**4**). The symmetry-related second $[RuI_3(CO)_3]^-$ anion and the solvent water molecule are not shown. Hydrogen bonds [Å, °]: O4–H4A 0.78, H4A···O1 3.14, O4···O1 3.534(6), O4–H4A···O1 114.2, O5–H5A 0.81, H5A···I2 2.83, O5···I2 3.602(4), O5–H5A···I2 159.3, O5–H5B 0.79, H5B···I3 3.32, O5···I3 3.721(4), O5–H5B···I3 176.1, O6–H6A 0.85, H6A···O(99) 1.90, O6···O99 2.752(5), O6–H6A···O99 176.1.

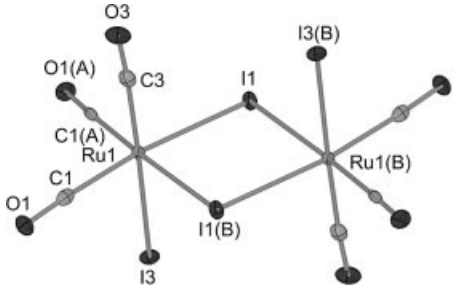


Figure 8. Thermal ellipsoid plot (50% probability level) of $[RuI_2(CO)_3]_2$ (**11**). Symmetry transformations were used to generate equivalent atoms: (A) $x, -y, z$; (B) $-x, -y, -z + 1$.

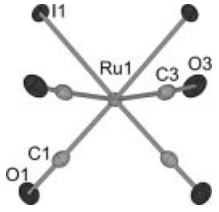


Figure 9. Thermal ellipsoid plot (50% probability level) of $RuI_2(CO)_4$ (**12**).

Another difference between the $RuI_3$ reactions and the reduction reactions of $RuCl_3$ was the strongly decreased formation of $Ru_3(CO)_{12}$. In fact, this was not observed at all even at higher pressures (50 bar) and with long reaction times (20 h). In the reactions under 50 bar pressure of carbon monoxide, the reduction reaction (125 °C, 3–20 h) produced $[RuI_2(CO)_3]_2$ (**11**), presented in Figure 8. The $RuI_2(CO)_4$ (**12**) presented in Figure 9 was found only in the reactions with iodine salt, while no equivalent chloride product was observed in the $RuCl_3$ reactions.

### The Carbon Monoxide Reduction of $OsCl_3$ in the Presence of a Sacrificial Metal Surface

The carbonylative reduction of $OsCl_3$ follows the general lines of the reduction of $RuCl_3$. The final reduction product is the zero-valent cluster $Os_3(CO)_{12}$, especially under high pressures.[18–21] In the current study, the reduction reactions were performed in an alcohol solution either under reflux with a CO stream passing through the reaction solution or in a pressurized autoclave. In both of the reaction setups a sacrificial metal plate (stainless steel, Fe or Co) was added to the system. During the reduction reaction the colour of the solution turned from black to brownish-yellow when an iron-containing plate was used, and greenish-blue when cobalt was used. In all of the osmium reactions, either under reflux or in an autoclave, a dark brown-grey metallic powder was formed. The powder was removed from the solution by filtering prior to crystallization of the carbon-

 © 2007 Wiley-VCH Verlag GmbH & Co. KGaA, Weinheim 

ylation products. The metallic powder material was characterized with the aid of EDS measurements, which confirmed that the solid material consisted mainly of metallic osmium. The filtrate was analyzed after it had been concentrated and redissolved in dichloromethane. IR analysis revealed two peaks in the ν(CO) region with both Os-Fe and Os-Co systems. In solutions containing Os-Fe, the higher band at 2135 $cm^{-1}$ was again sharp and the lower one at 2058 $cm^{-1}$ was broader. A similar pattern was also found with the Os-Co reaction solution, which produced corresponding peaks at 2135 $cm^{-1}$ and 2054 $cm^{-1}$. In comparison with the Ru-Fe/Co bands, the Os-Fe/Co bands shifted towards lower wavenumbers, but the shape and relative intensities of the bands remained the same in all cases.

The crystallization of the osmium-iron and osmium-cobalt products was much more difficult than that of the ruthenium-iron or, in particular, of the ruthenium-cobalt products. In consequence, the final yields of the separated products remained very low. This also prevented further analysis of the isolated products. Crystallization was performed according to the same procedure as for the ruthenium reactions. Only the mononuclear products could be isolated and characterized from the Os-Fe reactions. Ionic $[OsCl_3(CO)_3]_2[Fe(H_2O)_6]$ (**6**) is the structural equivalent of $[RuCl_3(CO)_3]_2[Co(H_2O)_6]$ (**3**) and another ionic product $[OsCl_3(CO)_3][FeCl_2(H_2O)_4]$ (**7**). In **7**, the osmium atom is in an oxidation state of 2+ and the iron atom is in an oxidation state of 3+. However, this minor product was obtained only from one reaction. The equivalent of complex **7** was observed neither in any of the Ru-Co or Ru-Fe reactions nor in the Os-Co reactions. Another mononuclear reduction product of $OsCl_3$ with no ruthenium counterpart was $OsCl_2(CO)_3(CH_3CH_2OH)$ (**10**). This product was also a minor product found only from one reaction. The solid-state structure of **10** consists of two osmium moieties bound together with a hydrogen bond (Figure 10).

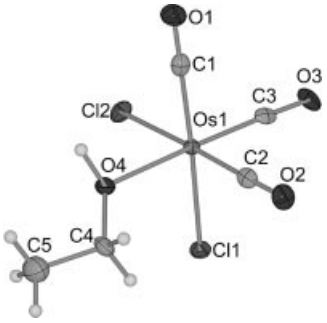


Figure 10. Thermal ellipsoid plot (50% probability level) of $OsCl_2(CO)_3(EtOH)$ (**10**).

From the osmium-cobalt reaction, $[OsCl_3(CO)_3]_2[Co(H_2O)_6]$ (**8**) could be isolated and characterized by means of the single-crystal X-ray diffraction (Figure 11). ATR measurements of the analysed complex **8a** revealed a pattern of signals that was similar to those found by means of the measurements of the Ru-Co complexes **1**, **2** and **3**. The higher band was again sharp at a wavenumber of 2126 $cm^{-1}$, and the lower peak was a combination of two peaks at wavenumbers of 2043 $cm^{-1}$ and 2024 $cm^{-1}$. Compared with the ATR-IR spectra of ruthenium analogues, the signals are shifted to a lower wavenumber, but the shape and intensity of the signals remained the same.

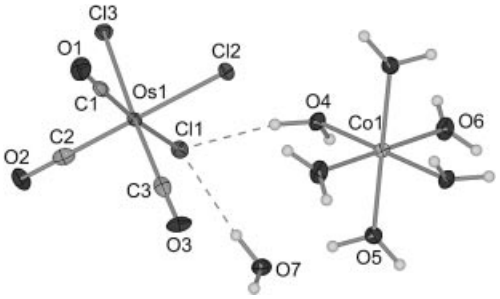


Figure 11. Thermal ellipsoid plot (50% probability level) of $[OsCl_3(CO)_3]_2[Co(H_2O)_6]\cdot 2(H_2O)$ (**8a**). The symmetry-related second $[OsCl_3(CO)_3]^-$ anion and the second water molecule are not shown. Hydrogen bonds [Å, °]: O4–H4B 0.99, H4B···Cl1 2.27, O4···Cl1 3.216(3), O4–H4B···Cl(1) 159.9, O7(A)–H7(A) 0.94, H7(A)···Cl1 2.36, O7(A)···Cl1 3.292(3), O7–H7(A)···Cl1 173.5.

An ethanol-containing trinuclear complex with chlorido bridges, $[Os_2Cl_2(\mu\text{-}Cl)_4(CO)_6Co(CH_3CH_2OH)_2]$ (**9**), could also be found in the osmium-cobalt reactions. Structurally, **9** is similar to $[Ru_2Cl_2(\mu\text{-}Cl)_4(CO)_6M(CH_3CH_2OH)_2]$ (M = Fe, Co) (Figure 12).

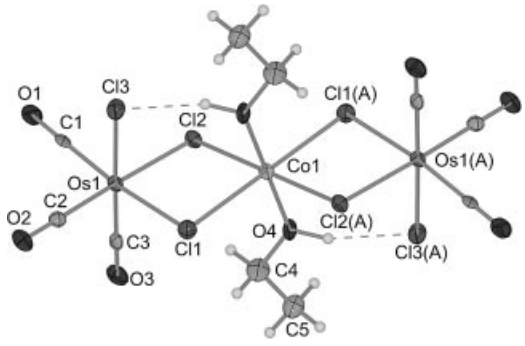


Figure 12. Thermal ellipsoid plot (50% probability level) of $[Os_2Cl_2(\mu\text{-}Cl)_4(CO)_6Co(CH_3CH_2OH)_2]$ (**9**). Hydrogen bond [Å, °]: O4–H4 0.95, H4···Cl3(A) 2.15, O4···Cl3(A) 3.072(6), O4–H4···Cl3(A) 162.4.

The formation of trinuclear halide-bridged compounds is not as favorable with Os/Fe and Os/Co metal pairs as it is with the Ru/Co pair. Complex **9** was separated in some of the reactions, but significantly more rarely than with the ruthenium analogue **1**. Although Os/Co trinuclear halide-bridged complexes were rare and Os/Fe analogues were not detected during our study, this does not necessarily mean that such a compound cannot be formed at all. Such a product may either be less stable, or the absence of these complexes may simply be due to the fact that the reaction setup as it now exists is unsuitable for osmium reactions. In addition, it can be stated that control of the products in the $OsCl_3$ reactions was undoubtedly more difficult than with $RuCl_3$.

 © 2007 Wiley-VCH Verlag GmbH & Co. KGaA, Weinheim 

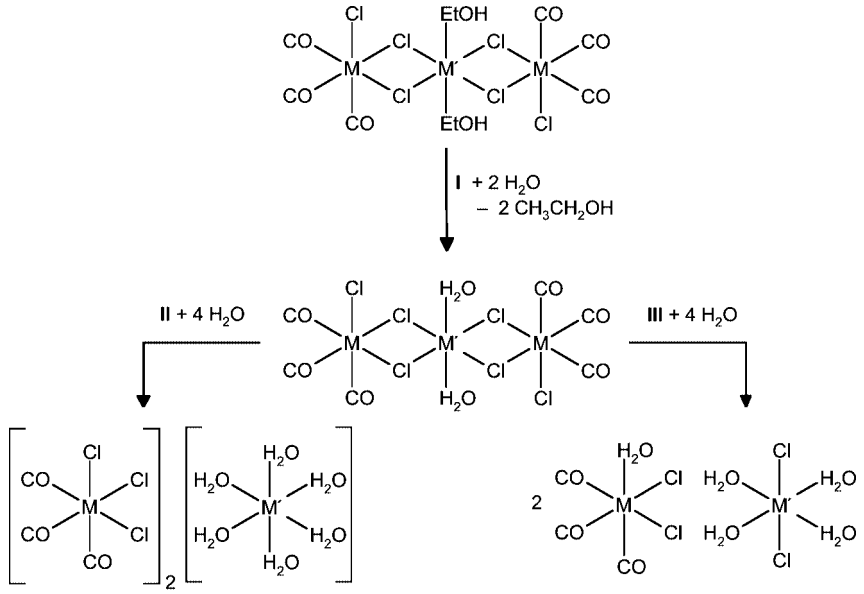


Scheme 1. Decomposition steps of μ-Cl dimetallic trinuclear complexes.

### Stability of the Trinuclear Complexes

Computational work was done to investigate the stability of the complexes by means of their relative energies. In our previous study we investigated[6] the decomposition path of $[Ru_2Cl_2(\mu\text{-}Cl)_4(CO)_6Fe(CH_3CH_2OH)_2]$. The presence of water launches the decomposition of the halide-bridged trinuclear mixed-metal complexes. The decomposition pathway proceeds by the replacement of the ethanol ligands with water and the formation of $[Ru_2Cl_2(\mu\text{-}Cl)_4(CO)_6Fe(H_2O)_2]$ and its eventual decomposition into the mononuclear products $[RuCl_3(CO)_3][Fe(H_2O)_6]$, $[RuCl_2(CO)_3(H_2O)]$ and $[FeCl_2(H_2O)_4]$. In the current study we have investigated a similar decomposition route for the Ru/Co, Os/Fe and Os/Co systems by using computational DFT methods. The decomposition steps involved are summarized in Scheme 1 and in Table 1.

Table 1. Calculated DFT energies of the decomposition routes presented in Scheme 1. Values in bold are taken from ref.[9]

| M | M′ | $E_I$ (kJ/mol) | $E_{II}$ (kJ/mol) | $E_{III}$ (kJ/mol) |
|---|---|---|---|---|
| **Ru** | **Fe** | **–34** | **–325** | **67** |
| Ru | Co | –31 | –287 | 68 |
| Os | Fe | –33 | –327 | 92 |
| Os | Co | –29 | –287 | 106 |

The first step in the decomposition of $[M_2Cl_2(\mu\text{-}Cl)_4(CO)_6M'(CH_3CH_2OH)_2]$, the replacement of $CH_3CH_2OH$ with $H_2O$ at the bridging metal atom (either Fe or Co), is favourable with all of the metal combinations. The reaction energy of the ligand exchange is around –30 kJ/mol. The two possible structural isomers of $[M_2Cl_2(\mu\text{-}Cl)_4(CO)_6M'(H_2O)_2]$, bent and linear, are energetically very similar to each other, which explains the co-existence of both structures. The relative energy between the bent and linear isomers for all the metal combinations is ca. 4 kJ/mol.

The decomposition of $[M_2Cl_2(\mu\text{-}Cl)_4(CO)_6M'(H_2O)_2]$ can follow two different main steps (steps **II** and **III** in Scheme 1). The addition of 4 equiv. of $H_2O$ breaks down the chlorido bridges and results in ionic $[MCl_3(CO)_3]_2[M'(H_2O)_6]$ or $[MCl_2(CO)_3(H_2O)]$ and $[M'Cl_2(H_2O)_4]$. According to our calculations, the relative energies of the decomposition products formed along step **II** are around 300 kJ/mol more favourable than for the trinuclear chlorido-bridged complexes. The result agrees well with the experimental results: $[MCl_3(CO)_3]_2[M'(H_2O)_6]$ is the favoured product, although $[MCl_2(CO)_3(H_2O)]$ and $[M'Cl_2(H_2O)_4]$ have been observed from reactions of the ruthenium-cobalt system. It also seems that decomposition step **III** is around 40 kJ/mol more favourable with iron than with cobalt, which is also consistent with experimental observations. According to our calculations, in $M'Cl_2(H_2O)_4$ the most favourable isomer is the *trans*(Cl) structure when the metal atom is iron and the *cis*(Cl) structure when the metal atom is cobalt, although the energy difference between the isomers is less than 5 kJ/mol for both metal chlorides. There are no notable differences in the calculation results between the Ru-Fe, Ru-Co, Os-Fe and Os-Co systems.

## Conclusions

The reductive carbonylation of $MCl_3$ (M = Ru or Os) in the presence of a metal surface (Fe or Co) produces a variety of mixed-metal products, whose components originate from the reducing $MCl_3$ and from the oxidizing surface. The metal ions released from the oxidizing surface can be used for an in situ complex formation. Although this approach produces a mixture of products, it nevertheless provides a useful method for synthesizing trinuclear mixed-metal compounds of the type $[M_2Cl_2(\mu\text{-}Cl)_4(CO)_6M'(L)_2]$

 © 2007 Wiley-VCH Verlag GmbH & Co. KGaA, Weinheim 

(M = Ru, Os; M′ = Fe, Co; L = $CH_3CH_2OH$, $H_2O$). For example, a synthesis of $[Ru_2Cl_2(\mu\text{-}Cl)_4(CO)_6Co(CH_3CH_2OH)_2]$ can be repeated with moderate yields. The main problem in the production of $[M_2Cl_2(\mu\text{-}Cl)_4(CO)_6M'(CH_3CH_2OH)_2]$ is that this can be decomposed relatively easily by moisture into mononuclear species such as $[MCl_3(CO)_3]_2[M'(H_2O)_6]$, $[MCl_2(CO)_3(H_2O)]$ and $[M'Cl_2(H_2O)_4]$.

Mechanistically, the reductive carbonylation of $MCl_3$ (M = Ru or Os) in the presence of a metal surface (Fe or Co) follows similar reaction pathways regardless of the reducing metal halide and oxidizing metal surface used. Further, the decomposition of the mixed-metal trinuclear $[M_2Cl_2(\mu\text{-}Cl)_4(CO)_6M'(L)_2]$ by moisture is similar in all studied cases. In the case of $[M_2Cl_2(\mu\text{-}Cl)_4(CO)_6M'(CH_3CH_2OH)_2]$, the first step in the decomposition is the replacement of the ethanol ligands by water at the central metal atom (Fe or Co). This is followed by cleavage of the chlorido bridges and the formation of mononuclear products. Energetically, the most favorable decomposition products are ionic compounds of the type $[MCl_3(CO)_3]_2[M'(H_2O)_6]$.

The iodide salt $RuI_3$ can be used instead of $RuCl_3$ in the preparation of ionic products, but no trinuclear compounds of the type $[M_2I_2(\mu\text{-}I)_4(CO)_6M'(L)_2]$ have been obtained so far. This is probably due to the poorer stability of $[M_2I_2(\mu\text{-}I)_4(CO)_6M'(L)_2]$ compared to its chlorido equivalents.

## Experimental Section

**Materials and Measurements:** $RuCl_3{\cdot}x(H_2O)$ (99.9%) was purchased from Alfa Aesar, $OsCl_3{\cdot}x(H_2O)$ from Sigma Aldrich and $RuI_3$ from Strem. The metal plates Co (99.9%, CO000279/3), Fe (99.5%, FE000400/11) and stainless steel were from GoodFellow. The cobalt powder (99.995%) was a product from Aldrich. MeOH (p.a.) and $CH_2Cl_2$ (p.a.) were obtained from Fluka, hexane (p.a.) from Merck, and ethanol (99.5%) from Primalco. The carbon monoxide (98%) used in reactions was purchased from Messer and AGA. The FTIR spectra were measured with a Nicolet Magna IR Spectrometer 750, and ATR-IR measurements were performed using an FTS 7000 Series DIGILAB FTIR spectrometer equipped with a UMA 600 DIGILAB microscope. CE Instruments EA 110 CHNS-O was used in the elemental analyses. Qualitative analyses of cobalt and osmium were conducted using an FE-SEM Hitachi S-4800 Scanning Electron Microscope equipped with a Norman System Six EDS.

**Syntheses**

**High-Pressure Reactions:** Metal trichloride [$RuCl_3{\cdot}x(H_2O)$, $RuI_3$ or $OsCl_3{\cdot}x(H_2O)$] reduction reactions were carried out in a Berghof autoclave equipped with a PTF liner. The solid metals (Co, Fe, stainless steel, $7 \times 7$ mm $\times$ 0.02–0.03 mm or 50 mg of cobalt powder) and 100 mg of metal trichloride reagent were placed in the liner together with 4 mL of ethanol. The autoclave was pressurized with 10, 20 or 50 bar of carbon monoxide (in a typical reaction the CO pressure was 20 bar), quickly heated to 125 °C, and maintained at that temperature for 3 h. After the reaction, the autoclave was cooled in an ice bath. The reaction solution was filtered to remove any possible solid metallic precipitations formed during the reaction. The filtrate was concentrated to dryness and the solid residue dissolved in $CH_2Cl_2$. Crystallization was performed using the $CH_2Cl_2$ solution by slow concentration or by adding hexane to the $CH_2Cl_2$ solution.

**Reactions under Reflux:** Metal trichloride [$RuCl_3{\cdot}n(H_2O)$ or $OsCl_3{\cdot}3(H_2O)$, 250 mg] was placed in a two-necked round-bottom vessel with a metal plate (Co or Fe or stainless steel, $7 \times 7$ mm). $MCl_3$ was diluted in 40 mL of ethanol and the reaction mixture was refluxed in a carbon monoxide stream for 17–20 h, until the reaction solution was yellowish with iron and blue or green with cobalt. Any solid material formed during the reduction was filtered off and the filtrate was placed in a 100 mL round-bottom vessel. The solution was concentrated to dryness and the residue dissolved in $CH_2Cl_2$. The products were crystallized as described above.

All of the reactions produced a mixture of products with variable ratios depending on the reaction time and conditions. In the cases of complexes **1**, **2**, **3**, **8** and **11**, the yields were very low and varied

Table 2. Crystallographic data for **1**–**2**.

| | **1** | **2a** | **2b** | **2c** |
|---|---|---|---|---|
| Empirical formula | $C_{10}H_{12}Cl_6CoO_8Ru_2$ | $C_6H_4Cl_6CoO_8Ru_2$ | $C_6H_4Cl_6CoO_8Ru_2$ | $C_6H_4Cl_6CoO_8Ru_2$ |
| Formula mass | 733.97 | 677.86 | 677.86 | 677.86 |
| Temperature [K] | 100(2) | 120(2) | 150(2) | 150(2) |
| $\lambda$ [Å] | 0.71073 | 0.71073 | 0.71073 | 0.71073 |
| Crystal system | monoclinic | monoclinic | triclinic | monoclinic |
| Space group | $P2_1/c$ | $P2_1/n$ | $P\bar{1}$ | $P2_1/c$ |
| $a$ [Å] | 9.1922(3) | 7.0428(15) | 6.3339(2) | 10.1061(3) |
| $b$ [Å] | 10.9226(3) | 15.489(3) | 10.4649(3) | 6.3789(2) |
| $c$ [Å] | 11.0099(4) | 8.4505(15) | 14.3176(5) | 27.6699(9) |
| $\alpha$ [°] | 90 | 90 | 87.315(2) | 90 |
| $\beta$ [°] | 96.482(2) | 96.808(15) | 81.818(2) | 95.5550(10) |
| $\gamma$ [°] | 90 | 90 | 74.300(2) | 90 |
| $V$ [Å$^3$] | 1098.36(6) | 915.3(3) | 904.28(5) | 1775.39(10) |
| $Z$ | 2 | 2 | 2 | 4 |
| $\rho_{calcd.}$ [Mg/m$^3$] | 2.219 | 2.459 | 2.490 Mg/m$^3$ | 2.536 |
| $\mu$(Mo-$K_a$) [mm$^{-1}$] | 2.866 | 3.428 | 3.470 mm$^{-1}$ | 3.535 |
| No. of reflections | 22720 | 8499 | 6593 | 8861 |
| Unique reflections | 2499 | 2090 | 4070 | 3797 |
| $R_{int}$ | 0.0580 | 0.0564 | 0.0256 | 0.0342 |
| $R_1$[a] ($I \geq 2\sigma$) | 0.0245 | 0.0309 | 0.0289 | 0.0294 |
| $wR_2$[b] ($I \geq 2\sigma$) | 0.0571 | 0.0507 | 0.0601 | 0.0511 |

[a] $R_1 = \Sigma||F_o| - |F_c||/\Sigma|F_o|$. [b] $wR_2 = \{\Sigma[w(F_o^2 - F_c^2)^2]/\Sigma[w(F_o^2)^2]\}^{1/2}$.

 © 2007 Wiley-VCH Verlag GmbH & Co. KGaA, Weinheim 

from reaction to reaction. In these cases the identification of the products was based on single-crystal X-ray analysis.

**Analysis of Separated and Purified Complexes 1–3, 8 and 11**

**$[Ru_2Cl_2(\mu\text{-}Cl)_4(CO)_6Co(CH_3CH_2OH)_2]$ (1):** $C_{10}H_{12}Cl_6CoO_8Ru_2$ (733.99): calcd. C 16.36, H 1.65; found C 16.24, H 1.69. ATR-IR $\tilde{\nu}$(CO) = 2137 (vs), 2075 (vs), 2054 $cm^{-1}$ (vs). Yield: 10–15%.

**$[Ru_2Cl_2(\mu\text{-}Cl)_4(CO)_6Co(H_2O)_2]\cdot(H_2O)$ (2):** $C_6H_6Cl_6CoO_9Ru_2$ (695.90): calcd. C 10.36, H 0.87; found C 10.11, H 0.97. ATR-IR $\tilde{\nu}$(CO) = 2135 (vs), 2070 (vs), 2054 $cm^{-1}$ (vs). Yield: 8%.

**$[RuCl_3(CO)_3]_2[Co(H_2O)_6]\cdot(H_2O)$ (3):** $C_6H_{14}Cl_6CoO_{13}Ru_2$ (767.96): calcd. C 9.38, H 1.84; found 9.34, H 2.01. ATR-IR $\tilde{\nu}$(CO) = 2139 (vs), 2075 (vs), 2056 $cm^{-1}$ (vs). Yield: 16%.

**$[OsCl_3(CO)_3]_2[Co(H_2O)_6]$ (8):** $C_6H_{12}Cl_6CoO_{12}Os_2$ (928.21): calcd. C 7.76, H 1.30; found C 7.70, H 1.31. ATR-IR $\tilde{\nu}$(CO) = 2126 (vs), 2043 (vs), 2024 $cm^{-1}$ (vs). Yield: 24%.

**$[RuI_2(CO)_3]_2$ (11):** $C_{60}I_4O_6Ru_2$ (877.82): calcd. C 8.21; found C 8.21. IR ($CH_2Cl_2$): $\tilde{\nu}$(CO) = 2118 (s) , 2055 (sh, s) $cm^{-1}$.

**X-ray Crystal Structure Determinations:** The crystals were immersed in cryo-oil, mounted in a Nylon loop and measured at a temperature of 100–150 K. The X-ray diffraction data was collected by means of a Nonius KappaCCD diffractometer using Mo-$K_\alpha$ radiation ($\lambda$ = 0.71073 Å). The Denzo-Scalepack[25] or EvalCCD[26] program packages were used for cell refinements and data reductions. The structures were solved by direct methods or by the heavy-atom method using SHELXS-97,[27] SIR-97,[28] or

Table 3. Crystallographic data for **3**–**6**.

| | **3** | **4** | **5** | **6** |
|---|---|---|---|---|
| Empirical formula | $C_6H_{16}Cl_6CoO_{14}Ru_2$ | $C_6H_{16}FeI_6O_{14}Ru_2$ | $C_6H_{16}CoI_6O_{14}Ru_2$ | $C_6H_{12}Cl_6FeO_{12}Os_2$ |
| Formula mass | 785.96 | 1331.58 | 1334.66 | 925.11 |
| Temperature [K] | 100(2) | 100(2) | 110(2) | 120(2) |
| $\lambda$ [Å] | 0.71073 | 0.71073 | 0.71073 | 0.71073 |
| Crystal system | triclinic | monoclinic | monoclinic | triclinic |
| Space group | $P\bar{1}$ | $P2_1/c$ | $P2_1/c$ | $P\bar{1}$ |
| $a$ [Å] | 6.2044(3) | 12.6166(2) | 12.6371(4) | 6.2890(14) |
| $b$ [Å] | 7.1225(2) | 9.5667(2) | 9.5821(3) | 6.3520(10) |
| $c$ [Å] | 14.7970(7) | 12.4005(2) | 12.4173(5) | 13.939(3) |
| $\alpha$ [°] | 91.603(3) | 90 | 90 | 87.901(7) |
| $\beta$ [°] | 98.438(2) | 109.3620(10) | 109.3740(10) | 77.217(5) |
| $\gamma$ [°] | 115.186(3) | 90 | 90 | 80.630(7) |
| $V$ [Å$^3$] | 582.33(5) | 1412.08(4) | 1418.47(9) | 535.8(2) |
| $Z$ | 1 | 2 | 2 | 1 |
| $\rho_{calcd.}$ [Mg/m$^3$] | 2.241 | 3.132 | 3.125 | 2.867 |
| $\mu$(Mo-$K_\alpha$) [mm$^{-1}$] | 2.729 | 8.170 | 8.207 | 13.293 |
| No. of reflections | 8390 | 9461 | 12152 | 6598 |
| Unique reflections | 2634 | 3177 | 3217 | 1840 |
| $R_{int}$ | 0.0241 | 0.0606 | 0.0408 | 0.0820 |
| $R_1$[a] ($I \geq 2\sigma$) | 0.0219 | 0.0333 | 0.0242 | 0.0523 |
| $wR_2$[b] ($I \geq 2\sigma$) | 0.0536 | 0.0791 | 0.0582 | 0.1215 |

[a] $R_1 = \Sigma||F_o| - |F_c||/\Sigma|F_o|$. [b] $wR_2 = \{\Sigma[w(F_o^2 - F_c^2)^2]/\Sigma[w(F_o^2)^2]\}^{1/2}$.

Table 4. Crystallographic data for **7**–**9**.

| | **7** | **8a** | **8b** | **9** |
|---|---|---|---|---|
| Empirical formula | $C_3H_{12}Cl_5FeO_9Os$ | $C_6H_{16}Cl_6CoO_{14}Os_2$ | $C_6H_{12}Cl_6CoO_{12}Os_2$ | $C_{10}H_{12}Cl_6CoO_8Os_2$ |
| Formula mass | 615.43 | 964.22 | 928.19 | 912.23 |
| Temperature[K] | 120(2) | 120(2) | 120(2) | 120(2) |
| $\lambda$ [Å] | 0.71073 | 0.71073 | 0.71073 | 0.71073 |
| Crystal system | monoclinic | triclinic | triclinic | monoclinic |
| Space group | $P2_1/n$ | $P\bar{1}$ | $P\bar{1}$ | $P2_1/c$ |
| $a$ [Å] | 11.7840(12) | 6.2144(2) | 6.2750(12) | 9.1912(5) |
| $b$ [Å] | 9.4780(11) | 7.1074(2) | 6.3310(13) | 10.9224(6) |
| $c$ [Å] | 15.1490(11) | 14.8771(6) | 13.877(3) | 11.0355(6) |
| $\alpha$ [°] | 90 | 91.495(2) | 87.455(11) | 90 |
| $\beta$ [°] | 108.032(6) | 98.393(2) | 77.067(11) | 96.174(3) |
| $\gamma$ [°] | 90 | 115.275(2) | 80.810(12) | 90 |
| $V$ [Å$^3$] | 1608.9(3) | 584.95(3) | 530.39(19) | 1101.43(10) |
| $Z$ | 4 | 1 | 1 | 2 |
| $\rho_{calcd.}$ [Mg/m$^3$] | 2.541 | 2.737 | 2.906 | 2.751 |
| $\mu$(Mo-$K_\alpha$) [mm$^{-1}$] | 9.650 | 12.277 | 13.527 | 13.012 |
| No. of reflections | 11930 | 10546 | 6704 | 11536 |
| Unique reflections | 3663 | 2673 | 1824 | 2164 |
| $R_{int}$ | 0.0474 | 0.0306 | 0.0788 | 0.0437 |
| $R_1$[a] ($I \geq 2\sigma$) | 0.0308 | 0.0231 | 0.0496 | 0.0319 |
| $wR_2$[b] ($I \geq 2\sigma$) | 0.0603 | 0.0517 | 0.1200 | 0.0693 |

[a] $R_1 = \Sigma||F_o| - |F_c||/\Sigma|F_o|$. [b] $wR_2 = \{\Sigma[w(F_o^2 - F_c^2)^2]/\Sigma[w(F_o^2)^2]\}^{1/2}$.

 © 2007 Wiley-VCH Verlag GmbH & Co. KGaA, Weinheim 

Table 5. Crystallographic data for **10**–**12**.

| | **10** | **11** | **12** |
|---|---|---|---|
| Empirical formula | $C_5H_6Cl_2O_4Os$ | $C_6I_4O_6Ru_2$ | $C_4I_2O_4Ru$ |
| Formula mass | 391.20 | 877.80 | 466.91 |
| Temperature [K] | 120(2) K | 100(2) | 110(2) |
| $\lambda$ [Å] | 0.71073 Å | 0.71073 | 0.71073 |
| Crystal system | Monoclinic | Monoclinic | Monoclinic |
| Space group | $P2_1/n$ | $C2/m$ | $C2/c$ |
| $a$ [Å] | 6.0129(5) | 11.0765(4) | 7.1062(3) |
| $b$ [Å] | 16.5884(8) | 7.6845(3) | 10.9172(4) |
| $c$ [Å] | 9.7260(4) | 9.6081(4) | 12.5486(3) |
| $\alpha$ [°] | 90 | 90 | 90° |
| $\beta$ [°] | 96.584(5) | 107.759(2) | 92.399(3)° |
| $\gamma$ [°] | 90 | 90 | 90 |
| $V$ [Å$^3$] | 963.72(10) | 778.85(5) | 972.66(6) |
| $Z$ | 4 | 2 | 4 |
| $\rho_{calcd.}$ [Mg/m$^3$] | 2.696 | 3.743 | 3.188 |
| $\mu$(Mo-$K_\alpha$) [mm$^{-1}$] | 13.758 | 9.877 | 7.927 |
| No. of reflections | 7892 | 4707 | 4190 |
| Unique reflections | 2197 | 832 | 952 |
| $R_{int}$ | 0.0469 | 0.0284 | 0.0228 |
| $R_1$[a] ($I \geq 2\sigma$) | 0.0274 | 0.0132 | 0.0180 |
| $wR_2$[b] ($I \geq 2\sigma$) | 0.0379 | 0.0282 | 0.0336 |

[a] $R_1 = \Sigma||F_o| - |F_c||/\Sigma|F_o|$. [b] $wR_2 = \{\Sigma[w(F_o^2 - F_c^2)^2]/\Sigma[w(F_o^2)^2]\}^{1/2}$.

Table 6. Selected bond lengths [Å] and bond angles [°] of the complexes **1**, **2a**, **2b**, **3**, **4**, presented in Figures 4, 5, 6, and 7.

| Bond length [Å] | **1** | **2a** | **2b** | **3** | **4** |
|---|---|---|---|---|---|
| C1–M1 | 1.900(3) | 1.909(4) | 1.916(3) | 1.907(2) | 1.913(6) |
| C2–M1 | 1.916(3) | 1.899(5) | 1.8994 | 1.921(2) | 1.908(6) |
| C3–M1 | 1.908(3) | 1.901(4) | 1.904(3) | 1.901(2) | 1.916(6) |
| C4–M2 | | | 1.911(4) | | |
| C5–M2 | | | 1.908(3) | | |
| C6–M2 | | | 1.911(4) | | |
| X1–M1 | 2.4208(6) | 2.4251(10) | 2.4166(7) | 2.4239(5) | 2.7441(5) |
| X2–M1 | 2.4275(6) | 2.4083(11) | 2.4221(9) | 2.4105(5) | 2.7471(5) |
| X3–M1 | 2.4186(6) | 2.4129(11) | 2.4154(8) | 2.4275(6) | 2.7357(5) |
| O4–M1 | | | | | |
| X4–M2 | | | 2.4082(8) | | |
| X5–M2 | | | 2.4284(8) | | |
| X6–M2 | | | 2.4120(9) | | |
| X1–M′1 | 2.4844(6) | | 2.4876(10) | | |
| X2–M′1 | 2.5172(6) | | 2.4646(8) | | |
| X4–M′1 | | | 2.4353(8) | | |
| X5–M′1 | | | 2.4711(9) | | |
| O4–M′1 | | 2.053(3) | | 2.0823(16) | 2.142(4) |
| O5–M′1 | | | | 2.0775(16) | 2.077(4) |
| O6–M′1 | | | | 2.0988(16) | 2.132(4) |
| O7–M′1 | | | 2.057(3) | | |
| O8–M′1 | | | 2.019(2) | | |
| **Bond angle [°]** | **1** | **2a** | **2b** | **3** | **4** |
| C1–M1–C2 | 91.45(11) | 91.4(2) | 92.07(14) | 93.40(9) | 93.4(2) |
| C1–M1–X1 | | | | | |
| C1–M1–C3 | | | | | |
| C5–M2–C6 | | | 92.32(15) | | |
| C3–M1–X3 | 179.15(8) | 176.85(12) | 178.89(11) | 174.92(7) | 177.5(2) |
| C4–M2–X4 | | | 176.44(10) | | |
| C3–M1–O4 | | | | | |
| X1–M1–X2 | 84.95(2) | 86.18(3) | 85.28(3) | 90.76(2) | |
| X4–Ru2–X5 | | | 87.15(3) | | |
| O4–M′1–X1 | 90.61(5) | | | | |
| O4–M′1–X2 | 92.02(5) | | | | |
| X1–M′1–X2 | 81.77(2) | 84.76(3) | 82.89(3) | | 92.010(16) |
| X4–M′1–X5 | | | 85.61(3) | | |
| O4–M′1–O5 | | | | 90.88(6) | 87.40(15) |
| O4–M′1–O6 | | | | 92.16(7) | 87.57(15) |
| O5–M′1–O6 | | | | 89.68(7) | 89.97(14) |
| O8–M′1–O7 | | | 87.32(10) | | |
| C1(A)–M1–C1 | | | | | |
| X1(B)–M1–X1 | | | | | |

SIR2004[29] with a WinGX[30] graphical user interface. An empirical absorption correction was applied to all of the data (XPREP in SHELXTL v.6.14–1[31] or SADABS v.2.10[32]). Structural refinements were carried out using SHELXL-97.[33] In **1**, **2a**, **2c**, **3**, **4**, **5**, **7**, **8a**, **9** and **10** the $H_2O$ and OH hydrogen atoms were located from the difference Fourier map but constrained to ride on their parent atom with $U_{iso}$ = 1.5 $U_{iso}$(parent atom). In **2b** the $H_2O$ hydrogen atoms were also located from the difference Fourier map and refined with fixed coordinates and fixed $U_{iso}$ = 0.05. In **6** and **8b** the idealized positions of the $H_2O$ hydrogen atoms were estimated using the HYDROGEN[34] program and they were constrained to ride on their parent atom by means of $U_{iso}$ = 1.5 $U_{iso}$(parent atom). Other hydrogen atoms were positioned geometrically and were also constrained to ride on their parent atoms by means of C–H 0.98–0.99 Å and $U_{iso}$ = 1.2–1.5 $U_{iso}$(parent atom). The structure of **12** is known and has been previously published in the early 1960s by Dahl and Wampler.[35] The crystallographic details are summarized in Tables 2, 3, 4 and 5. The thermal ellipsoid plots and selected bond lengths and angles for structures **1**, **2a**, **3**, **4**, **8a** and **9**–**12** are given in Figures 3, 4, 5, 6, 7, 8, 9, 10, 11, and 12 and Tables 6 and 7; for the other structures, see the Supporting Information. CCDC-630761 to -630775 (**1**–**12**, respectively) contain the supplementary

Table 7. Selected bond lengths [Å] and bond angles [°] of the complexes **8a** and **9**–**12** presented in Figures 8, 9, 10, 11, and 12.

| Bond length [Å] | **8a** | **9** | **10** | **11** | **12** |
|---|---|---|---|---|---|
| C1–M1 | 1.897(5) | 1.905(10) | 1.909(5) | 1.907(3) | 1.933(4) |
| C2–M1 | 1.902(5) | 1.896(8) | 1.892(5) | | |
| C3–M1 | 1.918(5) | 1.912(9) | 1.896(6) | 1.933(4) | 1.982(4) |
| C4–M2 | | | | | |
| C5–M2 | | | | | |
| C6–M2 | | | | | |
| X1–M1 | 2.4359(10) | 2.436(2) | 2.3908(12) | 2.7292(3) | 2.7332(4) |
| X2–M1 | 2.4329(10) | 2.429(2) | 2.4154(12) | | |
| X3–M1 | 2.4165(10) | 2.424(2) | | 2.7355(4) | |
| O4–M1 | | | 2.133(3) | | |
| X4–M2 | | | | | |
| X5–M2 | | | | | |
| X6–M2 | | | | | |
| X1–M′1 | | 2.514(2) | | | |
| X2–M′1 | | 2.486(2) | | | |
| X4–M′1 | | | | | |
| X5–M′1 | | | | | |
| O4–M′1 | 2.078(3) | 1.996(6) | | | |
| O5–M′1 | 2.107(3) | | | | |
| O6–M′1 | 2.080(3) | | | | |
| O7–M′1 | | | | | |
| O8–M′1 | | | | | |
| **Bond angle [°]** | **8a** | **9** | **10** | **11** | **12** |
| C1–M1–C2 | 92.1(2) | 91.2(4) | 92.3(2) | | |
| C1–M1–X1 | | | | | 178.68(12) |
| C1–M1–C3 | | | | | 92.90(16) |
| C5–M2–C6 | | | | | |
| C3–M1–X3 | 177.05(13) | 178.7(2) | | 178.36(11) | |
| C4–M2–X4 | | | | | |
| C3–M1–O4 | | | 173.75(15) | | |
| X1–M1–X2 | 87.53(3) | 81.22(6) | 88.13(4) | | |
| X4–Ru2–X5 | | | | | |
| O4–M′1–X1 | | | | | |
| O4–M′1–X2 | | | | | |
| X1–M′1–X2 | | | | | |
| X4–M′1–X5 | | | | | |
| O4–M′1–O5 | 90.26(12) | | | | |
| O4–M′1–O6 | 89.58(12) | | | | |
| O5–M′1–O6 | 92.11(13) | | | | |
| O8–M′1–O7 | | | | | |
| C1(A)–M1–C1 | | | | 95.46(15) | |
| X1(B)–M1–X1 | | | | 85.632(11) | |

 © 2007 Wiley-VCH Verlag GmbH & Co. KGaA, Weinheim 

crystallographic data for this paper. These data can be obtained free of charge from The Cambridge Crystallographic Data Centre via www.ccdc.cam.ac.uk/data_request/cif.

**Computational Work:** Full geometry optimization of the complexes was performed using the DFT method with a non-local hybrid functional B3PW91. The Stuttgart-Dresden ECP basis set was used for the metals (Fe, Co, Ru and Os)[36] and 6-31G* for others (C, H, O and Cl). The calculations were made with the Gaussian03 program package.[37]

**Supporting Information** (see footnote on the first page of this article): Figures S1–S5: Thermal ellipsoid plots (at 50% probability level) of **2c**, **5**, **6**, **7**, **8a** and **10**; Figures S6 and S7: ATR-IR spectra of complexes **1**, **2**, **3** and **8**.

## Acknowledgments

Financial support in the form of a grant (grant no. 210265) provided by the Academy of Finland is gratefully acknowledged. The authors would also like to thank Dr. Sari Suvanto for the EDS and ATR measurements, Ritva Romppanen for the elemental analysis measurements, and Dr. Larisa Oresmaa for her valuable comments.

[1] a) R. Brittain, A. L. Hickman, *Brit. UK Pat. Appl.* 20504727 19810107, **1981**; b) L. Bertolini, M. Gastaldi, M. P. Pedeferri, E. Redaelli, *Corros. Sci.* **2002**, *44*, 1497–1513; c) S. Paul, K. Basu, P. Mitra, *Bull. Electrochem.* **2005**, *21*, 269–273; d) G. Glass, *PCT Int. Appl.* WO 2006003473, **2006**.

[2] a) A. M. Vecchio-Sadus, *J. Appl. Electrochem.* **1993**, *23*, 401–416; b) M. T. Reetz, M. Winter, R. Breinbauer, T. Thurn-Albrecht, W. Vogel, *Chem. Eur. J.* **2001**, *7*, 1084–1094.

[3] A. Shantaram, H. Beyenal, R. R. A. Veluchamy, Z. Lewandowski, *Environ. Sci. Technol.* **2005**, *39*, 5037–5042.

[4] a) M. A. Méndez-Rojas, F. Cordova-Lozano, G. Gojon-Zorilla, E. González-Vergara, M. A. Quiroz, *Polyhedron* **1999**, *18*, 2651–2658; b) B. I. Kharisov, L. M. Blanco, A. D. Garnovskii, A. S. Burlov, L. I. Kuznetsova, L. V. Korovina, D. A. Garnovskii, T. Dieck, *Polyhedron* **1998**, *17*, 381–389; c) J. M. Paratian, E. Labbé, S. Sibile, J. Y. Nédélec, J. Périchon, *J. Organomet. Chem.* **1995**, *487*, 61–64; d) J. Sánchez-Piso, A. Carcía-Vázquez, J. Romero, M. L. Durán, A. Sousa-Pedras, E. Labisbal, O. R. Nascimento, *Inorg. Chim. Acta* **2002**, *328*, 111–122; e) H. Fillon, C. Gosmini, J.-Y. Nédélec, J. Périchon, *Tetrahedron Lett.* **2001**, *42*, 3843–3846.

[5] J. Castro, S. Cabaleiro, P. Pérez-Lourido, J. Romero, J. A. Garcia-Vásquez, A. Sousa, *Z. Anorg. Allg. Chem.* **2002**, *628*, 1210–1217.

[6] a) M. Faticanti, N. Cioffi, S. De Rossi, N. Ditaranto, P. Porta, L. Sabbatini, T. Bleve-Zacheo, *Appl. Catal., B* **2005**, *60*, 73–82; b) N. Cioffi, N. Ditaranto, L. Torsi, R. A. Picca, E. De Giglio, L. Sabbatini, L. Novello, G. Tantillo, T. Bleve-Zacheo, P. G. Zambonin, *Anal. Bioanal. Chem.* **2005**, *382*, 1912–1918.

[7] a) E. Duñach, S. Dérien, J. Périchon, *J. Organomet. Chem.* **1989**, *364*, C33–C36; b) C. Moreau, F. Serein-Spirau, M. Bordeau, C. Biran, *J. Organomet. Chem.* **1998**, *570*, 147–154; c) T.-Y. Lin, T.-C. Chou, *J. Appl. Electrochem.* **1999**, *29*, 489–496; d) C. Gosmini, J. Y. Nédélec, J. Périchon, *Tetrahedron Lett.* **2000**, *41*, 5039–5042; e) A. A. Isse, A. Gennaro, *J. Electrochem. Soc.* **2002**, *149*, D113–D117; f) A. Palma, B. A. Frontana-Uribe, J. Cárdenas, M. Saloma, *Electrochem. Commun.* **2003**, *5*, 455–459; g) H. Lund, H. Svith, S. U. Pedersen, K. Daasbjerg, *Electrochim. Acta* **2005**, *51*, 655–664; h) O. Scialdone, A. Galia, C. La Rocca, G. Filardo, *Electrochim. Acta* **2005**, *50*, 3231–3242.

[8] L. Mond, C. Langer, F. Quincke, *J. Chem. Soc. Trans.* **1890**, *57*, 749–753.

[9] M. Haukka, M. Jakonen, N. Nivajärvi, M. Kallinen, *Dalton Trans.* **2006**, 3212–3220.

[10] J. Chatt, B. L. Shaw, A. E. Field, *Chem. Ind.* **1964**, 3466–3475, and ref.[1] cited therein.

[11] M. L. Berch, A. Davison, *J. Inorg. Nucl. Chem.* **1973**, *35*, 3763–3767.

[12] C. R. Eady, P. F. Jackson, B. F. G. Johnson, J. Lewis, M. C. Malatesta, *J. Chem. Soc. Dalton Trans.* **1980**, 383–392.

[13] A. J. Deeming, M. Karim, *Polyhedron* **1991**, *10*, 837–840.

[14] H. A. Mirza, J. J. Vittal, R. J. Puddephatt, *Inorg. Chem.* **1993**, *32*, 1327–1332.

[15] E. Lucenti, E. Cariati, C. Dragonetti, D. Roberto, *J. Organomet. Chem.* **2003**, *669*, 44–47.

[16] M. Fauré, L. Maurette, B. Donnadieu, G. Lavigne, *Angew. Chem. Int. Ed.* **1999**, *38*, 518–522.

[17] M. Fauré, C. Saccavini, G. Lavigne, *Chem. Commun.* **2003**, 1578–1579.

[18] J. P. Collman, W. R. Roper, *J. Am. Chem. Soc.* **1966**, *88*, 3504–3508.

[19] M. Aracama, M. A. Esteruelas, F. J. Lahoz, J. A. Lopez, U. Meyer, L. A. Oro, H. Werner, *Inorg. Chem.* **1991**, *30*, 288–293.

[20] S. Dev, J. P. Selegue, *J. Organomet. Chem.* **1994**, *469*, 107–110.

[21] a) D. Roberto, R. Psaro, R. Ugo, *Organometallics* **1993**, *12*, 2292–2296; b) D. Roberto, R. Psaro, R. Ugo, *J. Mol. Catal.* **1994**, *86*, 109–120; c) E. Lucenti, D. Roberto, R. Ugo, *Organometallics* **2001**, *20*, 1725–1733; d) D. Roberto, E. Cariati, R. Psaro, R. Ugo, *Organometallics* **1994**, *13*, 734–737; e) D. Roberto, E. Cariati, R. Ugo, R. Psaro, *Inorg. Chem.* **1996**, *35*, 2311–2316; f) D. Roberto, E. Cariati, E. Lucenti, M. Respini, R. Ugo, *Organometallics* **1997**, *16*, 4531–4539; g) C. Roveda, E. Cariati, E. Lucenti, D. Roberto, *J. Organomet. Chem.* **1999**, *580*, 117–127.

[22] H. H. Uhlig, R. W. Revie, *Corrosion and Corrosion Control, An Introduction to Corrosion Science and Engineering*, 3rd ed., John Wiley & Sons, New York, **1985**, p. 78–87 and references cited therein.

[23] P. Hirva, M. Haukka, M. Jakonen, T. A. Pakkanen, *Inorg. Chim. Acta* **2006**, *359*, 853–862.

[24] M. I. Bruce, C. M. Jensen, N. L. Jones, *Inorg. Synth.* **1989**, *26*, 259–261.

[25] Z. Otwinowski, W. Minor, in *Methods in Enzymology*, vol. 276 ("Macromolecular Crystallography"), part A (Eds.: C. W. Carter, J. Sweet), Academic Press, New York, USA, **1997**, pp. 307–326.

[26] A. J. M. Duisenberg, L. M. J. Kroon-Batenburg, A. M. M. Schreurs, *J. Appl. Crystallogr.* **2003**, *36*, 220–229.

[27] G. M. Sheldrick, *SHELXS-97, Program for Crystal Structure Determination, University of Göttingen*, Göttingen, Germany, **1997**.

[28] A. Altomare, M. C. Burla, M. C. Camalli, C. Giacovazzo, A. Guagliardi, A. G. G. Moliterni, G. Polidori, R. Spagna, *J. Appl. Crystallogr.* **1999**, *32*, 115–119.

[29] M. C. Burla, M. Camalli, B. Carrozzini, G. L. Cascarano, C. Giacovazzo, G. Polidori, R. Spagna, *J. Appl. Crystallogr.* **2005**, *38*, 381–388.

[30] L. J. Farrugia, *J. Appl. Crystallogr.* **1999**, *32*, 837.

[31] G. M. Sheldrick, *SHELXTL*, v. 6.14-1, Bruker Analytical X-ray Systems, Bruker AXS, Inc., Madison, Wisconsin, USA, **2005**.

[32] G. M. Sheldrick, *SADABS, Bruker Nonius scaling and absorption correction*, v. 2.10, Bruker AXS, Inc., Madison, Wisconsin, USA, **2003**.

[33] G. M. Sheldrick, *SHELXL-97, Program for Crystal Structure Refinement*, University of Göttingen, Göttingen, Germany, **1997**.

[34] M. Nardelli, *J. Appl. Crystallogr.* **1999**, *32*, 563–571.

[35] L. F. Dahl, D. F. Wampler, *Acta Crystallogr.* **1962**, *15*, 946–950.

[36] The basis set was obtained from the Extensible Computational Chemistry Environment Basis Set Database, version 9/12/01,

 © 2007 Wiley-VCH Verlag GmbH & Co. KGaA, Weinheim 

as developed and distributed by the Molecular Science Computing Facility, Environmental and Molecular Sciences Laboratory, which is part of the Pacific Northwest Laboratory, P. O. Box 999, Richland, Washington 99352, USA, and funded by the U. S. Department of Energy. The Pacific Northwest Laboratory is a multi-program laboratory operated by the Battelle Memorial Institute for the U. S. Department of Energy under contract DE-AC06-76RLO 1830. Contact David Feller or Karen Schuchardt for further information.

[37] M. J. Frisch, G. W. Trucks, H. B. Schlegel, G. E. Scuseria, M. A. Robb, J. R. Cheeseman, J. A. Montgomery, Jr., T. Vreven, K. N. Kudin, J. C. Burant, J. M. Millam, S. S. Iyengar, J. Tomasi, V. Barone, B. Mennucci, M. Cossi, G. Scalmani, N. Rega, G. A. Petersson, H. Nakatsuji, M. Hada, M. Ehara, K. Toyota, R. Fukuda, J. Hasegawa, M. Ishida, T. Nakajima, Y. Honda, O. Kitao, H. Nakai, M. Klene, X. Li, J. E. Knox, H. P. Hratchian, J. B. Cross, V. Bakken, C. Adamo, J. Jaramillo, R. Gomperts, R. E. Stratmann, O. Yazyev, A. J. Austin, R. Cammi, C. Pomelli, J. W. Ochterski, P. Y. Ayala, K. Morokuma, G. A. Voth, P. Salvador, J. J. Dannenberg, V. G. Zakrzewski, S. Dapprich, A. D. Daniels, M. C. Strain, O. Farkas, D. K. Malick, A. D. Rabuck, K. Raghavachari, J. B. Foresman, J. V. Ortiz, Q. Cui, A. G. Baboul, S. Clifford, J. Cioslowski, B. B. Stefanov, G. Liu, A. Liashenko, P. Piskorz, I. Komaromi, R. L. Martin, D. J. Fox, T. Keith, M. A. Al-Laham, C. Y. Peng, A. Nanayakkara, M. Challacombe, P. M. W. Gill, B. Johnson, W. Chen, M. W. Wong, C. Gonzalez, J. A. Pople, *Gaussian 03*, revision C.02, Gaussian, Inc., Wallingford, CT, **2004**.

Received: March 27, 2007
Published Online: June 5, 2007

 © 2007 Wiley-VCH Verlag GmbH & Co. KGaA, Weinheim 

DOI: 10.1002/ejic.200700414

# Precursors for Assembly of Supramolecules Containing Quadruply Bonded $Cr_2^{4+}$ Units: Systematic Preparation of $Cr_2$(formamidinate)$_n$(acetate)$_{4-n}$ ($n$ = 2–4)

**F. Albert Cotton,[a][†] Zhong Li,[a] and Carlos A. Murillo*[a]**

**Keywords:** Metal–metal bonds / Supramolecular chemistry / Chromium / Corner piece precursors

Four quadruply bonded dichromium complexes with mixed-ligand sets, $Cr_2$(formamidinate)$_n$(acetate)$_{4-n}$ ($n$ = 2–4), were synthesized from reactions of anhydrous $Cr_2(O_2CCH_3)_4$ and formamidinate anions. The Cr–Cr bond lengths fall in the range for "supershort" Cr–Cr bonds as they vary from 1.8897(5) Å to 2.012(1) Å. The distance variation depends on the presence or absence of weak axial interactions. Because formamidinate ligands are less labile than acetate groups, these compounds may be useful building blocks for the construction of neutral supramolecules having dichromium units linked by polydentate dianions.

(© Wiley-VCH Verlag GmbH & Co. KGaA, 69451 Weinheim, Germany, 2007)

## Introduction

There is emerging interest in the use of metal atoms (or ions) as key elements in the self-assembly of metal-organic supramolecular arrays.[1] Most of these studies have focused on systems with single-metal building blocks of the type $ML_2$, where the L ligands are usually diamine, diphosphane or dicarboxylate and the metal atoms are Pt, Pd, Zn or Cd.[2] These species usually have ions with large charges. The introduction of metal–metal bonded dinuclear units into this field have enriched the diversity of the geometry and properties of the supramolecular systems and allowed the syntheses of neutral molecules.[3] Appropriate selection of the metal containing units and suitable linkers have led to the formation of a variety architectures, including dimers of dimers, loops, triangles, squares, complex polygons and extended 2D and 3D materials.[4]

One of the best strategies for construction of large molecules containing metal–metal bonds has been the use of precursors having subunits containing paddlewheel species with mixed ligands in which some of the paddles are nonlabile formamidinate groups, while the remaining coordination sites are occupied by easily displaceable ligands, such as acetonitrile molecules or carboxylate groups. The labile ligands are then replaced by polydentate linkers to assemble the target supramolecules whose structures depend on the dimensions of the linkers and shape of the corner piece precursors. On the basis of the appropriate choice of subunits and linkers, three basic assembly schemes have been generally employed: (1) Two metal–metal bonded units supported by three formamidinate groups are linked to give dimers of dimers as shown in Scheme 1. Examples are the dimers of dimolybdenum compounds that have been obtained by reactions of $Mo_2(DAniF)_3(CH_3CN_{eq})_2^+$ species (DAniF = *N*,*N*′-di-*p*-anisylformamidinate) with tetraalkylammonium salts of various dicarboxylates.[5] When $Mo_2(DAniF)_3(O_2CCH_3)$ was used as starting material, even the more basic diamidate or the all-nitrogen-donor linker fluoflavinate may be used as linkers and these ligands enable very high intramolecular electronic communication.[6] Compounds having two $Ru_2(DAniF)_3$ units linked by terephthalate anions have also been made by reaction of $(NBu_4)_2O_2CC_6H_4CO_2$ with the building block $Ru_2(DAniF)_3(O_2CCH_3)Cl$[7] and analogous $Ru_2$ compounds with diphenylformamidinate have also been made.[8] (2) Dimetal units with two *cisoid* formamidinate groups with rigid dianions allow the formation of squares, triangles (Scheme 2) and, under some circumstances, loops. Examples are the series of molecular squares assembled by reactions of [*cis*-$M_2(DAniF)_2(CH_3CN_{eq})_4]^{2+}$ (M = Mo, Rh) and dicarboxylate linkers.[9] Sometimes equilibria between triangles and the corresponding squares exist in solution because of entropy-dominated processes.[10] (3) Precursors with structures having *transoid* nonlabile formamidinate groups are expected to give one-dimensional polymers (Scheme 3). Current work in our laboratory involves the synthesis of ladder structures from *trans*-$M_2(DAniF)_2(O_2CCH_3)_2$ compounds. In addition, by utilizing the axial coordination and a combination of these linkage modes, more complex architectures can be made.[11] What is clear from this discussion is that building blocks with mixed-ligand sets of different

[a] Department of Chemistry and Laboratory for Molecular Structure and Bonding, Texas A&M University,
P. O. Box 3012, College Station, Texas 77842-3012, USA
E-mail: murillo@tamu.edu
[†] Deceased February 20, 2007.

 © 2007 Wiley-VCH Verlag GmbH & Co. KGaA, Weinheim 

labilities allow selective substitution of the more labile ligands, and preparation of such species is critical for the successful assembly of large molecules.

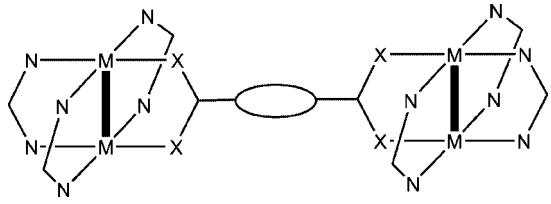

Scheme 1.

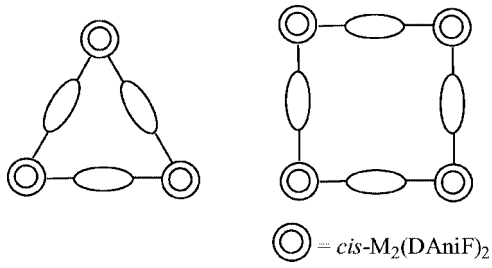


Scheme 2.

An additional advantage of using M–M bonded units in building supramolecules is that a wide selection of transition metal atoms are available and their electronic structures are generally well understood, which allow the introduction of internal spectroscopic probes. Thus far, most of the studies have been limited to dimolybdenum compounds and a handful of molecules containing $W_2$, $Ru_2$ and $Rh_2$ units. Even though the first-row transition metal, chromium, is prone to support metal–metal bonds, and hundreds of compounds with $Cr_2^{4+}$ core have been studied no efforts have been devoted to the methodical construction of appropriate corner pieces.[12] It should be noted that generally chromium compounds are useful in a variety of applications such as catalysts in organic synthetic applications[13] and are also found to be of importance in biosystems.[14] Recently an interesting compound with a Cr-to-Cr bond of order 5 has been reported, in a work that should encourage further exploration of the chemistry of this element.[15]

As a first step in the syntheses of large molecules containing $Cr_2^{4+}$ units, here we report the systematic syntheses of dichromium compounds of the type $Cr_2(formamidinate)_n(acetate)_{4-n}$ ($n$ = 2–4). The compounds are a pair of isomers, namely *cis*-$Cr_2(DPh^{Cl}F)_2(O_2CCH_3)_2$, **1**, [$DPh^{Cl}F$ = (*o*-$ClC_6H_4N)_2CH$], and *trans*-$Cr_2(DPh^{Cl}F)_2(O_2CCH_3)_2$ (**2**), as well as $Cr_2(DAniF)_3(O_2CCH_3)$ (**3**) and the parent compound $Cr_2(DAniF)_4$ (**4**). All of these compounds have been characterized structurally and by various spectroscopic techniques.

## Results and Discussion

### Syntheses

Reaction of 2 equiv. of $LiDPh^{Cl}F$ with 1 equiv. of anhydrous $Cr_2(O_2CCH_3)_4$ in THF at –70 °C affords **1** and **2** as shown by the isolation of two types of crystals when a benzene solution of the isomer mixture was layered with isomeric hexanes: red acicular crystals of *cis*-$Cr_2(DPh^{Cl}F)_2(O_2CCH_3)_2$ (**1**) and yellow-orange block crystals of *trans*-$Cr_2(DPh^{Cl}F)_2(O_2CCH_3)_2$ (**2**). Because of their distinctive shape and color, these isomers can be manually separated in a relatively easy manner and isolated in reasonable yields. It should be mentioned that the appropriate selection of the formamidinate ligands is important as earlier studies had shown that an analogous reaction of $Cr_2(O_2CCH_3)_4$ with 2 equiv. of $LiDPh^{OMe}F$ [$DPh^{OMe}F$ = (*o*-$CH_3OC_6H_4N)_2CH$] gave only the *cis* product,[16] while reaction of the heavier congener $Mo_2(O_2CCH_3)_4$ and 2 equiv. of HDAniF in the presence of $NaOCH_3$ exclusively produced the *trans* species, namely *trans*-$Mo_2(DAniF)_2(O_2CCH_3)$.[17] In the latter study, the *cis* isomer, *cis*-$Mo_2(DAniF)_2(O_2CCH_3)_2$, was obtained from a two-step reaction in which first $Mo_2(DAniF)_4$ and $(Et_3O)BF_4$ in $CH_3CN$ reacted to produce *cis*-$Mo_2(DAniF)_2(CH_3CN_{eq})_4^{2+}$. This reaction was followed by addition of acetate anions which replaced the acetonitrile molecules in the intermediate.

Once **1** and **2** are formed and isolated, these isomers are stable as the $^1H$ NMR spectra of these isomers in $CDCl_3$, which are significantly different from each other, do not change over a period of many hours. The spectra are thus consistent with retention of the geometry in solution.

An analogous reaction between $Cr_2(O_2CCH_3)_4$ but with 3 equiv. of LiDAniF gave complex **3** which has three DAniF groups and one acetate ligand. It should be noted that even when only 2 equiv. of LiDAniF were used, the isolated product was $Cr_2(DAniF)_3(O_2CCH_3)$ and under such conditions no species having the formula $Cr_2(DAniF)_2(O_2CCH_3)_2$ was observed. Furthermore, when traces of water were present in the reaction mixture or whenever an excess of LiDAniF was used, compound **4** was the only isolated species.[18] This compound can also be prepared conveniently and in better yield by reaction of LiDAniF and $CrCl_2$. Compounds **1**–**4** are soluble in common solvents such as THF, dichloromethane, toluene and benzene.

The CVs of **1**–**4** were recorded in $CH_2Cl_2$ using scan rates of 100 mV/s and 0.1 M $Bu_4NPF_6$ as electrolyte. The oxidation processes are irreversible and the potentials ranged from 0.62 V to 1.00 V. This is not unusual for $Cr_2^{4+}$ species which usually decompose upon oxidation. The only $Cr_2^{5+}$ product known so far was produced by oxidation of

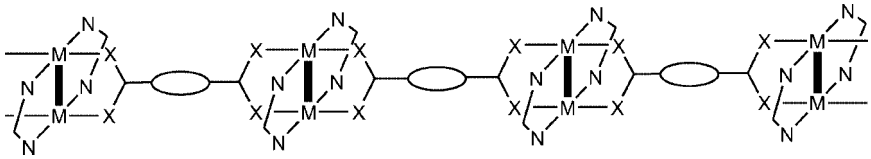

Scheme 3.

 © 2007 Wiley-VCH Verlag GmbH & Co. KGaA, Weinheim 

$Cr_2(DPPC)_4$ (DPPC is the guanidinate-type species *N*,*N*′-diphenyl-1-pyrrolidine carbodiimidate). For $Cr_2(DPPC)_4$ two quasi-reversible waves were observed in the CV having $E_{1/2}$ values of 0.02 and 1.10 V.

### Structural Results

Compounds **1**–**4** have been structurally characterized by single crystal X-ray diffraction and their structures are shown in Figure 1. Compound **1** crystallized in the space group $P2_1/n$ with the molecule residing on a general position. The Cr–Cr bond length of 2.0010(6) Å (Table 1) falls in the range of 1.83–2.60 Å found for Cr–Cr distances in paddlewheel species.[12] For such compounds, the metal–metal distances are affected not only by the identity of the supporting ligand but are very sensitive to the presence or absence of axial interactions. For example, the Cr–Cr distance for the $Cr_2(O_2CCH_3)_4$ molecule in gas phase is 1.97 Å, but this distance increases to 2.369(2) Å when two pyridine molecules coordinate to the axial sites.[19] In **1**, there is no direct axial coordination, however, there are weak axial interactions because the two *cis* formamidinate ligands provide one chlorine atom each at distances of 2.817 and 2.864 Å for Cr(1)···Cl(1) and Cr(2)···Cl(4), respectively. For comparison, in the paddlewheel compound of $Cr_2(DPh^{Cl}F)_4$, [Cr–Cr 2.208(2) Å] the distances between the chlorine and chromium atoms (2.766 Å) are shorter than those in **1**.[20] As a consequence, the Cr–Cr bond length in $Cr_2(DPh^{Cl}F)_4$ [2.208(2) Å] is considerably longer than that in **1** [2.0010(6) Å]. The effect of weak axial interactions on dichromium units has also been documented in compounds with ligands such as 2,6-bis(phenylimino)piperidine, 2,2′-dipyridylamine.[21]

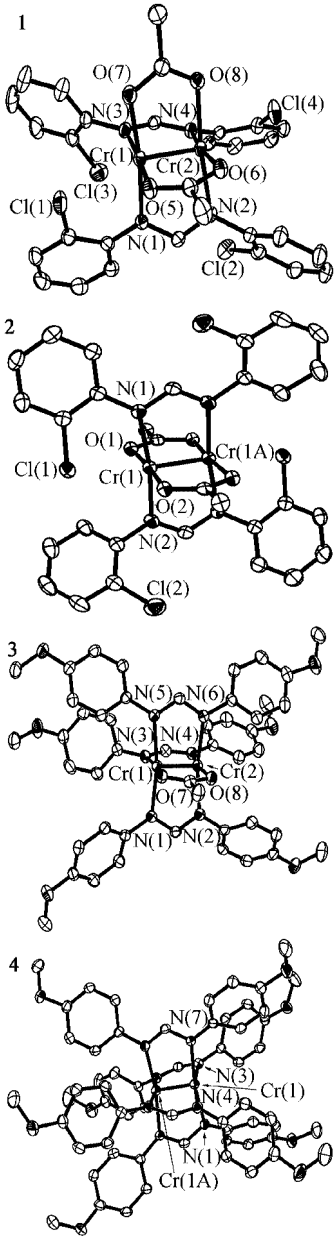


Figure 1. Structures of **1**–**4** with displacement ellipsoids drawn at the 40% probability level. Note the presence of weak Cr···Cl axial interactions in **1** and **2** and the absence of axial interactions in **3** and **4**. The Cr–Cr distances [2.0010(6) and 2.012(1) Å] for **1** and **2**, respectively, are longer than for **3** and **4** [1.8897(5) and 1.924(1) Å, respectively].

Table 1. Selected bond lengths [Å] for **1**–**4**.

| | **1** | **2**·$C_6H_6$ | **3** | **4** |
|---|---|---|---|---|
| Cr(1)–Cr(2) | 2.0010(6) | | 1.8897(5) | |
| Cr(1)–Cr(1a) | | 2.012(1) | | 1.924(1) |
| Cr(1)–N(1) | 2.051(2) | 2.068(3) | 2.049(2) | 2.067(2) |
| Cr(1)–O(1) | | 2.004(3) | | |
| Cr(1)–N(3) | 2.051(2) | | 2.019(2) | 2.049(2) |
| Cr(1)–O(3) | | | | |
| Cr(1)–N(5) | | | 2.044(2) | |
| Cr(1)–O(5) | 2.018(2) | | | |
| Cr(1)–N(7) | | | | 2.050(2) |
| Cr(1)–O(7) | 2.001(2) | | 2.027(2) | |
| Cr(2)–N(2) | 2.055(2) | 2.049(3) | 2.027(2) | |
| Cr(2)–O(2) | | 2.017(3) | | |
| Cr(2)–N(4) | 2.043(2) | | 2.048(2) | 2.054(2) |
| Cr(2)–N(6) | | | 2.033(2) | |
| Cr(2)–O(6) | 1.992(2) | | | |
| Cr(2)–O(8) | 2.015(2) | | 2.025(2) | |

Compound **2**, an isomer of **1**, crystallized in the space group $P\bar{1}$ with the molecule residing on an inversion center. The Cr–Cr bond length of 2.012(1) Å is very similar to that in **1**. Again the two *trans* formamidinate ligands provide one chlorine donor atom capable of interacting with a chromium atom at a distance of 2.793 Å.

For **3**, which crystallized in the space group $P2_1/c$ with $Z$ = 4, the Cr–Cr bond length of 1.8897(5) Å is within the range found in *super-short* quadruply bonded compounds. This is due to the lack of axial coordination by either solvent or other donor atoms in the formamidinate ligand. The bulky formamidinate groups also prevent intermolecular interactions between Cr and O atoms which tend to lengthen the Cr–Cr distances such in the structure of anhydrous $Cr_2(O_2CR)_4$, in which weak intermolecular Cr···O interactions allow the association of $Cr_2(O_2CR)_4$ molecules to form a polymer.[12]

 © 2007 Wiley-VCH Verlag GmbH & Co. KGaA, Weinheim 

In compound **4**, which crystallized in the space group *C*2/*c* with $Z = 4$, the molecule is located on a general position. The Cr–Cr bond length of 1.924(1) Å resembles that of 1.9178(11) Å in the $Cr_2(DPh^{m\text{–}OMe}F)_4$ analogue[22] and it is consistent for a species without axial interactions. It should be noted that the Cr–Cr distance in the $Cr_2(DPho^{\text{–}OMe}F)_4$ isomer, which has *o*-methoxy groups providing axial interactions, is 2.140(2) Å.[20] This distance is about 0.22 Å longer than that in **4**.

## Concluding Remarks

Systematic syntheses and characterization are reported for a series of dichromium compounds with mixed ligand sets of formamidinate and acetate groups, $Cr_2$(formamidinate)$_n$(acetate)$_{4-n}$ ($n$ = 2–4). The Cr–Cr bond lengths are strongly influenced by the presence or absence of axial interactions. These compounds are expected to serve as precursors for the preparation of supramolecules with different architectures utilizing selective ligand substitution based on the fact that acetate groups are generally more labile than formamidinate groups.

## Experimental Section

**Materials and Methods:** All reactions and manipulations were performed under nitrogen, using either a dry box or standard Schlenk line techniques. Solvents were purified under argon using a Glass Contour solvent purification system or distilled under nitrogen over appropriate drying agents. Anhydrous $Cr_2(O_2CCH_3)_4$[23] and the formamidinate precursors[24] were synthesized following reported procedures; other commercially available chemicals were used as received.

**Analytical and Physical Measurements:** Elemental analyses were performed by Robertson Microlit Laboratories, Madison, New Jersey. Electronic spectra were measured on a Shimadzu UV–2501PC spectrometer in $CH_2Cl_2$ solution. $^1$H NMR spectra were recorded on a Inova–300 NMR spectrometer with chemical shifts ($\delta$, ppm) referenced to residual $CHCl_3$ in $CDCl_3$. Cyclic voltammograms (CVs) were collected on a CH Instruments electrochemical analyzer with Pt working and auxiliary electrodes, Ag/AgCl reference electrode, scan rate of 100 mV/s, and 0.10 M $Bu_4NPF_6$ (in $CH_2Cl_2$) as electrolyte.

**Preparation of *cis*-$Cr_2(DPh^{Cl}F)_2(O_2CCH_3)_2$ (1) and *trans*-$Cr_2(DPh^{Cl}F)_2(O_2CCH_3)_2$ (2):** To a solution of $HDPh^{Cl}F$ (265 mg, 1.00 mmol) in THF (20 mL) at –70 °C, methyllithium in diethyl ether (0.32 mL, 1.6 M) was added slowly with stirring. The yellow solution was warmed to 0 °C and then transferred to a suspension of anhydrous chromium acetate (170 mg, 0.500 mmol) in THF (20 mL). The color of the brown suspension turned gradually to orange. After 4 h, the solvent was removed under reduced pressure and the solid residue was extracted with benzene (15 mL). The benzene solution was filtered through a Celite-packed frit, and the filtrate was layered with isomeric hexanes. Two types of crystals formed within 7 d: red acicular crystals of *cis*-$Cr_2(DPh^{Cl}F)_2(O_2CCH_3)_2$ (**1**) and yellow-orange block crystals of *trans*-$Cr_2(DPh^{Cl}F)_2(O_2CCH_3)_2$ (**2**). These were manually separated.

**For 1:** Yield: 138 mg (37%). $^1$H NMR ($C_6D_6$): 8.62 (s, 2 H, –NC*H*N–), 7.18 (d, 4 H, aromatic C–*H*), 6.80 (m, 8 H, aromatic C–*H*), 6.48 (t, 4 H, aromatic C–*H*), 2.33 (s, 6 H, –C$H_3$). UV-vis: $\lambda_{max}$ ($\varepsilon$, $M^{-1}mol^{-1}$) = 400 ($1.5 \times 10^3$) nm. **1**·$2H_2O$: $C_{30}H_{26}Cl_4Cr_2N_4O_5$ (786): calcd. C 45.82, H 3.58, N 7.12; found C 46.02, H 3.96, N 6.92.

**For 2:** Yield: 104 mg (28%). $^1$H NMR ($C_6D_6$): 8.67 (s, 2 H, –NC*H*N–), 7.03 (d, 4 H, aromatic C–*H*), 6.80 (m, 8 H, aromatic C–*H*), 6.55 (t, 4 H, aromatic C–*H*), 2.25 (s, 6 H, –C$H_3$). UV-vis: $\lambda_{max}$ ($\varepsilon$, $M^{-1}mol^{-1}$) = 450 ($1.1 \times 10^3$) nm. **2**·$H_2O$: $C_{30}H_{24}Cl_4Cr_2N_4O_4$ (768): calcd. C 46.89, H 3.43, N 7.26; found C 47.08, H 4.07, N 6.87.

**Preparation of $Cr_2(DAniF)_3(O_2CCH_3)$ (3):** A procedure analogous to that described above for **1** and **2** but using HDAniF (383 mg, 1.50 mmol) and $Cr_2(O_2CCH_3)_4$ (170 mg, 0.500 mmol) in THF gave an orange product. Crystals were obtained by layering a benzene solution of **3** with hexanes. Yield: 315 mg (68%). $^1$H NMR ($C_6D_6$): 8.94 (s, 2 H, –NC*H*N–), 8.76 (s, 1 H, –NC*H*N–), 6.68 (d, 16 H, aromatic C–*H*), 6.40 (d, 8 H, aromatic C–*H*), 6.24 (d, 8 H, aromatic C–*H*), 3.22 (s, 12 H, –OC$H_3$), 3.10 (s, 6 H, –C$H_3$ in DAniF). UV-vis: $\lambda_{max}$ ($\varepsilon$, $M^{-1}mol^{-1}$) = 410 ($1.3 \times 10^3$) nm. $Cr_2C_{47}H_{48}N_6O_8$ (929): calcd. C 60.77, H 4.62, N 9.05; found C 60.88, H 4.36, N 9.14.

**Preparation of $Cr_2(DAniF)_4$ (4):** To a suspension of anhydrous $CrCl_2$ (130 mg, 1.00 mmol) and HDAniF (510 mg, 2.00 mmol) in THF (30 mL) at –78 °C, a solution of methyllithium in diethyl ether

Table 2. X-ray crystallographic data for **1**–**4**.

| | **1** | **2**·$C_6H_6$ | **3** | **4**·$2C_6H_6$ |
|---|---|---|---|---|
| Empirical formula | $C_{30}H_{24}Cl_4Cr_2N_4O_4$ | $C_{36}H_{30}Cl_4Cr_2N_4O_4$ | $C_{47}H_{48}Cr_2N_6O_8$ | $C_{72}H_{72}Cr_2N_8O_8$ |
| *Fw* | 750.33 | 828.44 | 928.91 | 1281.38 |
| Space group | $P2_1/n$ | $P\bar{1}$ | $P2_1/c$ | $C2/c$ |
| *a* [Å] | 19.062(3) | 8.342(4) | 21.648(5) | 33.293(10) |
| *b* [Å] | 7.662(1) | 10.701(5) | 10.750(3) | 10.002(3) |
| *c* [Å] | 22.258(3) | 10.967(5) | 18.945(5) | 20.914(6) |
| *a* [°] | 90 | 102.929(8) | 90 | 90 |
| *β* [°] | 102.687(2) | 91.142(8) | 92.235(4) | 111.888(6) |
| *γ* [°] | 90 | 111.594(7) | 90 | 90 |
| Volume [Å$^3$] | 3171.6(7) | 881.6(7) | 4405.(4) | 6462(3) |
| *Z* | 4 | 1 | 4 | 4 |
| *T* [K] | 213 | 213 | 213 | 213 |
| *λ* [Å] | 0.71073 | 0.71073 | 0.71073 | 0.71073 |
| $d_{calcd.}$ [g/cm$^3$] | 1.571 | 1.560 | 1.401 | 1.317 |
| *μ* [mm$^{-1}$] | 1.064 | 0.966 | 0.555 | 0.399 |
| $R_1$,[a] $wR_2$[b] | 0.0392, 0.0874 | 0.0569, 0.1453 | 0.0431, 0.1045 | 0.0831, 0.1087 |

[a] $R_1 = \Sigma||F_o| - |F_c||/\Sigma|F_o|$. [b] $wR_2 = [\Sigma[w(F_o^2 - F_c^2)^2]/\Sigma[w(F_o^2)^2]]^{1/2}$.

 © 2007 Wiley-VCH Verlag GmbH & Co. KGaA, Weinheim 

(0.65 mL, 1.6 M) was added slowly with stirring. The gray suspension changed gradually to a turbid orange dispersion. After 3 h, the solvent was removed under reduced pressure and the residue washed with hexanes (3 × 15 mL). The dry solid was dissolved in benzene (15 mL) and filtered through a Celite-packed frit, and then the filtrate was layered with hexanes. Yield: 420 mg (75%). $^1$H NMR ($\delta$, ppm in $C_6D_6$): 8.69 (s, 4 H, –NC*H*N–), 6.62 (d, 16 H, aromatic C–*H*), 6.38 (d, 16 H, aromatic C–*H*), 3.19 (s, 24 H, –C$H_3$ in DAniF). UV-vis: $\lambda_{max}$ ($\varepsilon$, $M^{-1}$ $mol^{-1}$) = 502 (1.2 × $10^3$) nm. $Cr_2C_{60}H_{60}N_8O_8$ (1125.17): calcd. C 64.05, H 5.37, N 9.96; found C 63.89, H 4.86, N 9.64.

**X-ray Structural Determinations:** Single crystals suitable for X-ray analysis were mounted on the tips of cryoloops attached to a goniometer head. Data for **1**, **2**·$C_6H_6$, **3** and **4** were collected at –60 °C with a Bruker SMART 1000 CCD area detector system. Cell parameters were determined using the program SMART.[25] Data reduction and integration were performed with the software SAINT,[26] while the absorption corrections were applied by using the program SADABS.[27] The structures were solved by direct methods and refined using the SHELXS–97 program.[28] Non-hydrogen atoms, except for those of disordered solvent molecules, were refined with anisotropic displacement parameters. Hydrogen atoms were added in calculated positions. Crystallographic data are given in Table 2 and selected bond lengths in Table 1.

CCDC-641377 to -641380 (for **1**–**4**) contain the supplementary crystallographic data for this paper. These data can be obtained free of charge from The Cambridge Crystallographic Data Centre via www.ccdc.cam.ac.uk/data_request/cif.

## Acknowledgments

We thank the Robert A. Welch Foundation and Texas A&M University for financial support.

[1] See for example: a) M. Fujita, *Acc. Chem. Res.* **1999**, *32*, 53–61; b) J. A. R. Navarro, B. Lippert, *Coord. Chem. Rev.* **1999**, *185–186*, 653–667; c) J.-M. Lehn, *Supramolecular Chemistry – Concepts and Perspectives*, VCH, Weinheim, Germany, **1995**; d) G. F. Swiegers, T. J. Malefetse, *Chem. Rev.* **2000**, *100*, 3483–3538; e) B. J. Holliday, C. A. Mirkin, *Angew. Chem. Int. Ed.* **2001**, *40*, 2022–2043.

[2] a) C. A. Schalley, A. Lützen, M. Albrecht, *Chem. Eur. J.* **2004**, *10*, 1072–1080; b) S. R. Seidel, P. J. Stang, *Acc. Chem. Res.* **2002**, *35*, 972–983; c) K. K. Klausmeyer, S. R. Wilson, T. B. Rauchfuss, *J. Am. Chem. Soc.* **1999**, *121*, 2705–2711; d) O. R. Evans, W. Lin, *Acc. Chem. Res.* **2002**, *35*, 511–522; e) B. J. Holliday, C. A. Mirkin, *Angew. Chem., Int. Ed.* **2001**, *40*, 2022–2043; f) S. Leininger, B. Olenyuk, P. J. Stang, *Chem. Rev.* **2000**, *100*, 853–908; g) P. Espinet, K. Soulantica, J. P. H. Charmant, A. G. Orpen, *Chem. Commun.* **2000**, 915–916; h) J. A. R. Navarro, B. Lippert, *Coord. Chem. Rev.* **1999**, *185–186*, 653–667; i) M. Scherer, D. L. Caulder, D. W. Johnson, K. N. Raymond, *Angew. Chem. Int. Ed.* **1999**, *38*, 1587–1592; j) S.-W. Lai, M. C.-W. Chan, S.-M. Peng, C.-M. Che, *Angew. Chem. Int. Ed.* **1999**, *38*, 669–671.

[3] a) M. H. Chisholm, A. M. Macintosh, *Chem. Rev.* **2005**, *105*, 2949–2976; b) F. A. Cotton, C. Lin, C. A. Murillo, *Acc. Chem. Res.* **2001**, *34*, 759–771; c) G. L. Xu, G. Zou, Y. H. Ni, M. C. DeRosa, R. J. Crutcheley, T. Ren, *J. Am. Chem. Soc.* **2003**, *125*, 10057–10065; d) J. K. Bera, P. Angaridis, F. A. Cotton, M. A. Petrukhina, P. E. Fanwick, R. A. Walton, *J. Am. Chem. Soc.* **2001**, *123*, 1515–1516.

[4] See for example: a) R. H. Cayton, M. H. Chisholm, J. C. Huffman, E. B. Lobkovsky, *J. Am. Chem. Soc.* **1991**, *113*, 8709–8724; b) F. A. Cotton, J. P. Donahue, C. Lin, C. A. Murillo, *Inorg. Chem.* **2001**, *40*, 1234–1244; c) F. A. Cotton, C. Lin, C. A. Murillo, *Inorg. Chem.* **2001**, *40*, 472–477; d) F. A. Cotton, C. A. Murillo, S.-E. Stiriba, X. Wang, R. Yu, *Inorg. Chem.* **2005**, *44*, 8223–8233; e) F. A. Cotton, L. M. Daniels, C. Lin, C. A. Murillo, *Chem. Commun.* **1999**, 841–842; f) Y. Ke, D. J. Collins, H. C. Zhou, *Inorg. Chem.* **2005**, *44*, 4154–4156.

[5] a) F. A. Cotton, P. J. Donahue, C. A. Murillo, *J. Am. Chem. Soc.* **2003**, *125*, 5436–5450; b) F. A. Cotton, P. J. Donahue, C. A. Murillo, L. M. Pérez, *J. Am. Chem. Soc.* **2003**, *125*, 5486–5492.

[6] a) F. A. Cotton, C. Y. Liu, C. A. Murillo, D. Villagrán, X. Wang, *J. Am. Chem. Soc.* **2003**, *125*, 13564–13575; b) F. A. Cotton, C. Y. Liu, C. A. Murillo, D. Villagrán, X. Wang, *J. Am. Chem. Soc.* **2004**, *126*, 14822–14831; c) F. A. Cotton, Z. Li, C. Y. Liu, C. A. Murillo, D. Villagrán, *Inorg. Chem.* **2006**, *45*, 767–778.

[7] P. Angaridis, J. F. Berry, F. A. Cotton, P. Lei, C. Lin, C. A. Murillo, D. Villagrán, *Inorg. Chem. Commun.* **2004**, *7*, 9–13.

[8] M. C. Barral, S. Herrero, R. Jiménez-Aparicio, M. R. Torres, F. A. Urbanos, *Inorg. Chem. Commun.* **2004**, *7*, 42–46.

[9] a) F. A. Cotton, C. Lin, C. A. Murillo, *Inorg. Chem.* **2001**, *40*, 478–484; b) F. A. Cotton, C. Lin, C. A. Murillo, S. Y. Yu, *J. Chem. Soc. Dalton Trans.* **2001**, 502–504.

[10] F. A. Cotton, C. Lin, C. A. Murillo, *Inorg. Chem.* **2001**, *40*, 575–577.

[11] F. A. Cotton, C. Lin, C. A. Murillo, *Chem. Commun.* **2001**, 11–12.

[12] F. A. Cotton, in *Multiple Bonds between Metal Atoms*, 3rd ed. (Eds.: F. A. Cotton, C. A. Murillo, R. A. Walton), Springer Science and Business Media, Inc., New York, **2005**, p. 35–68.

[13] a) K. M. Smith, *Coord. Chem. Rev.* **2006**, *250*, 1023–1031; b) T. Ueno, T. Koshiyama, M. Oshashi, K. Kondo, M. Kono, A. Suzuki, T. Yamane, Y. Watanabe, *J. Am. Chem. Soc.* **2005**, *127*, 6556–6562; c) K. Srinivasan, J. K. Koshi, *Inorg. Chem.* **1985**, *24*, 4671–4679.

[14] a) J. B. Vincent, *Acc. Chem. Res.* **2000**, *33*, 503–510; b) J. B. Vincent, *Polyhedron* **2001**, *20*, 1–26.

[15] T. Nguyen, A. D. Sutton, M. Brynda, J. C. Fettinger, G. J. Long, P. P. Power, *Science* **2005**, *310*, 844–847.

[16] F. A. Cotton, L. M. Daniels, C. A. Murillo, P. Schooler, *J. Chem. Soc. Dalton Trans.* **2000**, 2001–2005.

[17] F. A. Cotton, C. Y. Liu, C. A. Murillo, *Inorg. Chem.* **2004**, *43*, 2267–2276.

[18] The byproducts were not identified.

[19] a) S. N. Ketkar, M. Fink, *J. Am. Chem. Soc.* **1985**, *107*, 338–340; b) F. A. Cotton, G. W. Rice, *Inorg. Chem.* **1978**, *17*, 2004–2009.

[20] F. A. Cotton, L. M. Daniels, C. A. Murillo, P. Schooler, *J. Chem. Soc. Dalton Trans.* **2000**, 2007–2012.

[21] F. A. Cotton, L. M. Daniels, C. A. Murillo, I. Pascual, H.-C. Zhou, *J. Am. Chem. Soc.* **1999**, *121*, 6856–6861.

[22] K. M. Carlson-Day, J. L. Eglin, C. Lin, L. T. Smith, R. J. Staples, D. O. Wipf, *Polyhedron* **1999**, *18*, 817–824.

[23] L. R. Ocone, B. P. Block, *Inorg. Synth.* **1966**, *8*, 125–132.

[24] R. Anulewicz, I. Wawer, T. M. Krygowski, F. Mannle, H. H. Limbach, *J. Am. Chem. Soc.* **1997**, *119*, 12223–12230.

[25] *SMART V 5.05 Software for the CCD Detector System*; Bruker Analytical X-ray System, Inc., Madison, WI, **1998**.

[26] *SAINT*, Data Reduction Software, version 6.36A; Bruker Advanced X-ray Solution, Inc., Madison, WI, **2001**.

[27] *SADABS*, Area Detector Absorption and other Correction Software, version 2.05; Bruker Advanced X-ray Solution, Inc., Madison, WI, **2000**.

[28] G. M. Sheldrick, *SHELXTL*, version 6.12; Advanced X-ray Solutions, Inc., Madison, WI, **2002**.

Received: April 16, 2007
Published Online: June 18, 2007

 © 2007 Wiley-VCH Verlag GmbH & Co. KGaA, Weinheim 

DOI: 10.1002/ejic.200700048

# New Open-Framework Mixed-Valence Chromium(III) Cerium(III)/(IV) Sulfate: $CrCe^{III}_7Ce^{IV}_6(HSO_4)_6(SO_4)_{21}\cdot 75H_2O$

**Barbara M. Casari*[a] and Vratislav Langer[b]**

**Keywords:** Mixed-valent compounds / Lanthanides / Cerium sulfate / X-ray diffraction

The title compound, synthesized from $Cr^{VI}$ and $Ce^{IV}$ species, crystallizes in the space group $P6_3$ with $a$ = 19.3015(2), $c$ = 25.2684(4) Å, and $Z$ = 2. The structural design of the title compound differs essentially from structures of known mixed-valence cerium compounds which all form three-dimensional networks. In the title compound the cerium atoms, interlinked by sulfate groups, extend to form layers held together by hydrogen-bonding contacts. Perpendicular to these layers there are 10 Å wide channels. One third of the channels host solvent water only, while the other two thirds of the channels also host $[Cr(H_2O)_6]^{3+}$ and $[Ce(SO_4)_3(H_2O)_6]^{3-}$ units, blocking each of these channels once per unit cell, resulting in 14 Å long voids.

(© Wiley-VCH Verlag GmbH & Co. KGaA, 69451 Weinheim, Germany, 2007)

## Introduction

Currently, there is interest in rare-earth compounds because of their important physical properties and advances achieved in the syntheses of new materials[1] with interesting applications.[2] Rare-earth materials are intriguing due to the complexity of their structural arrangements with high coordination numbers and a variety of coordination geometries. Structural investigations on hydrated rare-earth sulfates are quite numerous[3] and many of these compounds are isomorphic, with the ninefold coordinated rare-earth atoms interlinked by sulfate groups. There is structural information on anhydrous as well as hydrous ternary rare-earth sulfates with all alkaline ions for nearly all of the lanthanide series,[3] but not much work has been done combining transition metals with rare-earth metals to form double salts. Cerium compounds attract research attention owing to their applications as ion conductors, catalysts, magnetic and fluorescence materials. The existence of alterable oxidation states for the cerium ion will result in compounds with new structural frameworks and interesting properties.[4] There are six mixed-valence cerium compounds in the ICSD Database (version 2006-2):[5] $Ce_4O_4S_3$,[6] $Ce_3O_3S_2$,[7] $Ce_{10}(GeO_4)_3(Ge_2O_7)_2(Ge_3O_{10})$,[8] $(H_3O)[Ce_2(SeO_4)_4]$,[9] $KCe_2(SO_4)_4$,[10] and $Ce_{0.968}H_{10.432}O_{12.924}S_2$.[11] Here we present an open-framework structure of a new mixed-valence chromium(III) cerium(III)/(IV) sulfate.

[a] Department of Chemistry, Inorganic Chemistry, Göteborg University,
41296 Göteborg, Sweden
Fax: +46-317722853
E-mail: casari@chem.gu.se
[b] Environmental Inorganic Chemistry, Department of Chemical and Biological Engineering, Chalmers University of Technology,
41296 Göteborg, Sweden

## Results and Discussion

### Synthesis of $CrCe^{III}_7Ce^{IV}_6(HSO_4)_6(SO_4)_{21}\cdot 75H_2O$

The title compound was synthesized from $Cr^{VI}$ and $Ce^{IV}$ species in diluted sulfuric acid. Cerium(IV) in acidic aqueous solutions is metastable with respect to the oxidation of water. The attainment of equilibrium is kinetically controlled, and the reaction is observed only in the presence of a catalyst.[12] Added ions or even the glass vessel may act as the catalytic agent.[12] Thus, in acidic aqueous media cerium(III) will be formed. Cerium(III) is known to inhibit chromium(VI) oxidation of organic compounds, and this effect is attributed to the chromic acid oxidation of the cerium(III) species[13] encountered also in our previous work.[14] The chromium system is able to produce a variety of transient and intermediate species, and several competing redox reactions can take place,[13,14] but the redox equilibria involved in this case can be written as the following total reactions:

$$2\ Ce^{4+} + H_2O \rightarrow 2\ Ce^{3+} + 2\ H^+ + 1/2\ O_2$$

$$[CrO_4]^{2-} + 3\ Ce^{3+} + 8\ H^+ \rightarrow Cr^{3+} + 3\ Ce^{4+} + 4\ H_2O$$

Purbaix diagrams on cerium and chromium species have been revised recently[15] showing that the first reaction occurs in acidic solutions, while the second reaction is dominant in neutral and basic solutions. Hence, in acidic aqueous solutions mixed-valence cerium species as well as mixed-valence chromium species may form.

### Structural Description of $CrCe^{III}_7Ce^{IV}_6(HSO_4)_6(SO_4)_{21}\cdot 75H_2O$

The title compound crystallizes in the space group $P6_3$ with $a$ = 19.3015(2), $c$ = 25.2684(4) Å, and $Z$ = 2. There

 © 2007 Wiley-VCH Verlag GmbH & Co. KGaA, Weinheim 

are two atoms, $Cr^{III}$ and $Ce^{III}$, in special positions (on the threefold axis) while the remaining content of the asymmetric unit, two $Ce^{III}$ atoms, two $Ce^{IV}$ atoms, two $HSO_4^-$ groups, seven $SO_4^{2-}$ groups, and approximately 25 water molecules, are in general positions. The structure is noncentrosymmetric mainly due to $Ce1^{III}$ and $Cr^{III}$ atoms that do not respect an additional mirror plane leading to space group $P6_3/m$. The crystal was centrosymmetrically twinned with the twin volume ratio refined to 0.692(10):0.308(10).

The $Cr^{III}$ atom is sixfold coordinated to water molecules, as in known structures of chromium alums.[16] The $Ce^{III}$ atoms are in contact with nine oxygen atoms belonging to three corner-sharing sulfate groups and six water molecules. The $Ce^{III}$ coordination polyhedra are best described as tricapped trigonal prisms for the $Ce^{III}$ atom in a special position and as singly capped tetragonal antiprisms for the two $Ce^{III}$ atoms in general positions. The $Ce^{IV}$ atoms are ninefold coordinated to oxygen atoms belonging to three edge-sharing and three corner-sharing sulfate groups. The $Ce^{VI}$ coordination polyhedra are slightly distorted tricapped trigonal prisms. Coordination numbers such as nine are expected for the large $Ce^{III}$ ion but are rarely encountered for the smaller $Ce^{IV}$ ion.[17] The $Cr^{III}$–O, $Ce^{III}$–O, and $Ce^{IV}$–O distances average to 1.97(1), 2.53(4), and 2.39(9) Å, respectively (Table 1) as in known $Cr^{III}$, $Ce^{III}$, and $Ce^{IV}$ compounds.[16,17] The bond-valence sums for $Cr^{III}$, $Ce1^{III}$, $Ce2^{III}$, $Ce3^{IV}$, $Ce4^{IV}$, and $Ce5^{III}$ are 3.13, 2.85, 2.95, 4.00, 3.98, and 2.95 valence units, respectively (using parameters from Brese and O'Keefe[18] for Cr and Trzesowska et al.[19] for Ce). The S–O distances within the nine sulfate groups average to 1.48(2) Å (Table 1), and as expected, due to the restrained bite angle, the edge-sharing sulfate groups (S6, S7, S8, S12, S13, and S14) show a departure from the ideal tetrahedral symmetry, the angles ranging from 102.4(2) to 111.7(2)°. One of the sulfate groups is partly disordered (S9A, O91A, O92A and S9B, O91B, O92B) occupying 0.563(7) and 0.437(7) of two sets in a general position. All the sulfate groups link two cerium atoms, except for the S3 sulfate unit that is bridging by corner sharing from $Ce1^{III}$ to $Ce3^{IV}$ and $Ce4^{IV}$. It is difficult to distinguish by analyzing the terminal S–O bond length which two of the nine sulfate groups may be protonated to give hydrogen sulfate groups. Hence, the location of these protons may be disordered.

Table 1. Bond lengths [Å].

| | | | |
|---|---|---|---|
| Ce1–O11 | 2.511(4) | Cr–O1 | 1.975(5) |
| Ce1–O11$^{ii}$ | 2.511(4) | Cr–O1$^{iv}$ | 1.975(5) |
| Ce1–O12 | 2.492(4) | Cr–O1$^{v}$ | 1.975(5) |
| Ce1–O12$^{i}$ | 2.492(4) | Cr–O2 | 1.955(5) |
| Ce1–O12$^{ii}$ | 2.492(4) | Cr–O2$^{iv}$ | 1.955(5) |
| Ce1–O11$^{i}$ | 2.511(4) | Cr–O2$^{v}$ | 1.955(5) |
| Ce1–O101$^{i}$ | 2.636(4) | S6–O61 | 1.463(4) |
| Ce1–O101 | 2.636(4) | S6–O62 | 1.461(4) |
| Ce1–O101$^{ii}$ | 2.636(4) | S6–O63 | 1.497(4) |
| Ce2–O21 | 2.512(4) | S6–O64 | 1.502(4) |
| Ce2–O22 | 2.522(4) | S7–O71 | 1.447(4) |
| Ce2–O23 | 2.559(4) | S7–O72 | 1.476(4) |
| Ce2–O24 | 2.521(4) | S7–O73 | 1.509(4) |
| Ce2–O25 | 2.547(4) | S7–O74 | 1.496(4) |
| Ce2–O26 | 2.541(4) | S8–O81 | 1.465(4) |
| Ce2–O62 | 2.492(4) | S8–O82 | 1.457(4) |
| Ce2–O72$^{ii}$ | 2.530(4) | S8–O83 | 1.492(4) |
| Ce2–O81$^{iii}$ | 2.540(4) | S8–O84 | 1.495(4) |
| Ce3–O63 | 2.383(4) | S9A–O91A | 1.480(8) |
| Ce3–O64 | 2.519(4) | S9A–O92A | 1.449(8) |
| Ce3–O73 | 2.391(4) | S9A–O93 | 1.516(5) |
| Ce3–O74 | 2.455(4) | S9A–O94 | 1.513(5) |
| Ce3–O83 | 2.409(4) | S9B–O91B | 1.458(10) |
| Ce3–O84 | 2.478(4) | S9B–O92B | 1.453(10) |
| Ce3–O94 | 2.267(4) | S9B–O93 | 1.459(5) |
| Ce3–O111 | 2.270(4) | S9B–O94 | 1.472(5) |
| Ce3–O104 | 2.330(4) | S10–O101 | 1.456(4) |
| Ce4–O93 | 2.272(4) | S10–O102 | 1.498(4) |
| Ce4–O102 | 2.255(4) | S10–O103 | 1.469(3) |
| Ce4–O114 | 2.294(4) | S10–O104 | 1.484(4) |
| Ce4–O122 | 2.503(4) | S11–O111 | 1.490(4) |
| Ce4–O124 | 2.409(4) | S11–O112 | 1.460(3) |
| Ce4–O133 | 2.431(4) | S11–O113 | 1.462(3) |
| Ce4–O134 | 2.509(4) | S11–O114 | 1.500(4) |
| Ce4–O143 | 2.385(4) | S12–O121 | 1.460(4) |
| Ce4–O144 | 2.490(4) | S12–O122 | 1.482(4) |
| Ce5–O51 | 2.519(5) | S12–O123 | 1.475(4) |
| Ce5–O52 | 2.508(4) | S12–O124 | 1.500(4) |
| Ce5–O53 | 2.529(4) | S13–O131 | 1.460(4) |
| Ce5–O54 | 2.488(4) | S13–O132 | 1.461(4) |
| Ce5–O55 | 2.587(4) | S13–O133 | 1.505(4) |
| Ce5–O56 | 2.534(4) | S13–O134 | 1.491(4) |
| Ce5–O121$^{ii}$ | 2.528(4) | S14–O141 | 1.460(4) |
| Ce5–O132$^{iii}$ | 2.541(4) | S14–O142 | 1.463(4) |
| Ce5–O141 | 2.509(4) | S14–O143 | 1.504(4) |
| | | S14–O144 | 1.486(4) |

Symmetry transformations for equivalent atoms: (i): $-x + y + 1$, $-x + 1$, $z$; (ii): $-y + 1$, $x - y$, $z$; (iii): $x + y + 1$, $-x + 2$, $z$; (iv): $-x + y$, $-x + 1$, $z$; (v): $-y + 1$, $x - y + 1$, $z$.

The structural design of the title compound differs from structures of known mixed-valence cerium compounds, all of which form three-dimensional networks.[6–11] In the title compound the cerium atoms, interlinked by sulfate groups, extend to form layers parallel to the *ab* plane (Figure 1a). These layers (ca. 11.5 Å thick) are held together by hydrogen-bonding contacts (Figure 1b). Perpendicular to the layers, in the *c* direction, there are channels (ca. 9.7 Å in diameter), shown in Figure 1a. One of the channels, at (0,0,*z*), hosts solvent water only, while the other two channels, at (1/3,2/3,*z*) and (2/3,1/3,*z*), also host $[Cr(H_2O)_6]^{3+}$ and $[Ce(SO_4)_3(H_2O)_6]^{3-}$ units, blocking each of these channels once per unit cell. Thus, there are voids in the latter two channels, approximately 14 Å long. The $[Cr(H_2O)_6]^{3+}$ cations, located in the channels (Figure 2), are situated between the layers participating in the hydrogen-bonding network that are connecting one layer to an adjacent layer, shown in Figures 1b and 2.

There are four crystallographically different water molecules inside the voids, OW1–OW4. We believe that the OW1 water molecule acts as a hydrogen-bond donor towards O122 (S12 sulfate oxygen atom) and towards O53 (a water molecule attached to Ce5), the OW2 molecule acts as a hydrogen-bond donor towards O72 (S7 sulfate oxygen atom) and towards O11 (a water molecule attached to Ce1), the OW3 water molecule acts as a hydrogen-bond donor towards O12 and O55 (water molecules attached to Ce1 and Ce5, respectively), and that the OW4 water molecule acts

 © 2007 Wiley-VCH Verlag GmbH & Co. KGaA, Weinheim 

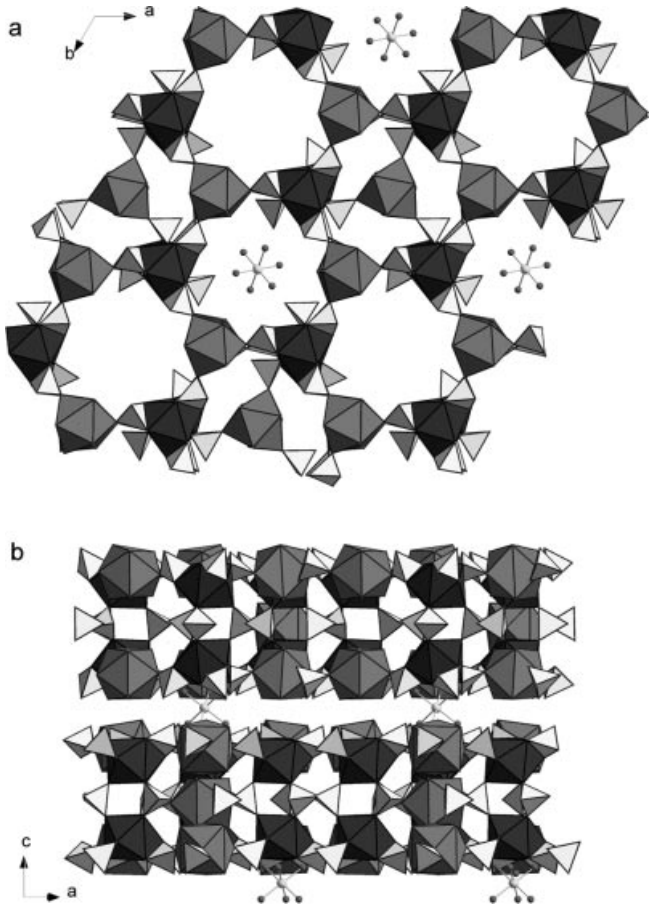


Figure 1. Packing diagrams of the title compound, the $Ce^{III}$ polyhedra are shown in light shades and the $Ce^{IV}$ polyhedra are shown in dark shades. The solvent water molecules are not shown. (a) One single layer extending through sulfate bridges forming channels. (b) There are two layers per unit cell. Adjacent layers are held together by hydrogen-bonding contacts from $[Cr(H_2O)_6]^{3+}$ and from water molecules coordinated to $Ce^{III}$ towards terminal sulfate oxygen atoms.

as a hydrogen-bond donor towards O91 and O103 (oxygen atoms belonging to the S9 and S10 sulfate groups, respectively), in addition, it acts as a hydrogen-bond acceptor from O24 and O53 (water molecules attached to Ce2 and Ce5, respectively). The water molecules coordinated to the $Cr^{III}$ and $Ce^{III}$ ions all participate in the hydrogen-bonding network connecting adjacent layers. Furthermore, there are approximately five additional water molecules that are disordered (see Experimental Section) within the open channel and the two voids, corresponding to 18 water molecules per unit cell in the channel (volume: 861 $Å^3$) plus 12 water molecules per unit cell in the two voids (volume: $2 \times 257$ $Å^3$).

According to the Robin and Day classification,[20] this compound could belong to Class II since the oxidized and reduced cerium ions occupy sites of similar geometry. The structure of the title compound can be regarded as consisting of six $[Ce^{III}(H_2O)_6(SO_4)_{3/2}]$, six $[Ce^{IV}(HSO_4)_{2/2}(SO_4)_{1/3}(SO_4)_{3/2}]^{2/3-}$, $[Ce^{III}(H_2O)_6(SO_4)_{3/3}]^{+}$, $[Cr(H_2O)_6]^{3+}$, and solvent water molecules as the main structural units.

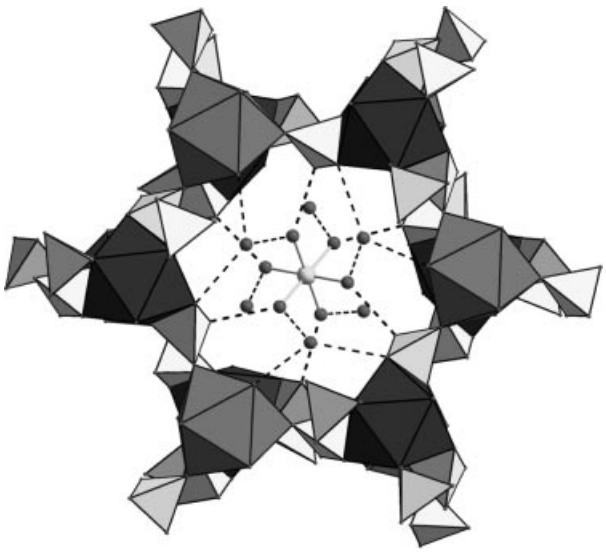

Figure 2. View through one of the channels showing one $[Cr(H_2O)_6]^{3+}$ ion, solvent water molecules, and part of the hydrogen-bonding network. The $Ce^{III}$ polyhedra are shown in light shades and the $Ce^{IV}$ polyhedra are shown in dark shades.

Hence, a possible donor–acceptor couple could be $[Ce^{III}(H_2O)_6(SO_4)_{3/2}]$ and $[Ce^{IV}(HSO_4)_{2/2}(SO_4)_{1/3}(SO_4)_{3/2}]^{2/3-}$ which are linked by one sulfate bridge, $Ce^{III}$–O–S–$O_2$–$Ce^{IV}$. The geometrical distance between the metal sites (>6.5 Å) is sufficiently large to decline direct overlap of the electronic wave functions. Prior to an electron transfer, the nuclear configurations of the reactants and the surrounding medium must adjust to an intermediate configuration with no energy change when the electron moves from the donor to the acceptor.[21] For metal complexes in a polar solvent, the nuclear configuration changes involve adjustments in the metal–ligand bond lengths and angles, and changes in the orientations of the surrounding solvent molecules.[21] Similar adjustments are also required in the stiffer inorganic solid state. Therefore, due to the difference in bond lengths at the donor and acceptor sites, a substantial energy barrier to their interconversion exists, and since electronic coupling with orbitals of appropriate symmetry in the sulfate bridge probably is negligible, this mixed-valence cerium compound presumably is a Class I compound. If there is no electronic interaction between the acceptor and donor sites then the properties of this compound are essentially those of the separate acceptor and donor sites. However, a small portion of Class II character cannot be completely dismissed since the geometry of the donor site, $[Ce^{III}(H_2O)_6(SO_4)_{3/2}]$, is quite flexible due to the coordinated water molecules and further, the oxidizing ability of the acceptor site, $[Ce^{IV}(HSO_4)_{2/2}(SO_4)_{1/3}(SO_4)_{3/2}]^{2/3-}$, may increase if it becomes protonated by the adjacent slightly acidic $[Cr(H_2O)_6]^{3+}$ species. Class II compounds generally possess new optical and electronic properties in addition to those of the separate sites and might be semiconductors or ionic conductors.

There are two structurally related compounds $H_9Nd_7Ce_6(SO_4)_{27}\cdot 72.33H_2O$[22] and $H_9Tb_7Ce_6(SO_4)_{27}\cdot$

 © 2007 Wiley-VCH Verlag GmbH & Co. KGaA, Weinheim 

$72.2H_2O$.[23] These compounds contain channels and voids of comparable dimensions but they are not mixed-valence compounds and do not contain any hydrated transition-metal ions participating in the hydrogen-bonding network. One compound containing chromium(III) combined with a rare-earth element is samarium chromium silicon oxynitride[24] (space group $P6_3$), but its crystal structure differs from the title compound as it is apatite-like and extends through silicate bridges forming a compact three-dimensional network.

## Experimental Section

**Sample Preparation:** $Ce(SO_4)_2{\cdot}4H_2O$ (0.50 g, 1.27 mmol), $CrO_3$ (0.38 g, 3.8 mmol), and water (5.0 mL) were mixed in a round-bottomed microflask connected to a reflux water condenser. The reaction mixture was refluxed for 24 h until orange crystals of $Ce(CrO_4)_2(H_2O)_2$ were formed. These crystals were dissolved in sulfuric acid (4 M). Concentration at room temperature gave light yellow crystals shaped as hexagonal needles. The title compound may also be produced from $Ce(OH)_4$ and $CrO_3$ in diluted sulfuric acid solution but the best single crystals were achieved with the former description.

**Single Crystal X-ray Analysis:** Data were collected with a Siemens SMART CCD diffractometer equipped with a Siemens LT-2A low-temperature device at –100 °C. A full sphere of the reciprocal space was scanned by 0.3° steps with a crystal-to-detector distance of 3.97 cm and an exposure time per frame of 2 s. A preliminary orientation matrix was obtained using the SMART software.[25] The collected frames were integrated with the orientation matrix which was updated every 100 frames. Final cell parameters were obtained by refinement from 8192 reflections with $I > 10\sigma(I)$ after integration of all the data using the SAINT software.[25] The data were corrected empirically for absorption and other effects using the SADABS software.[26] The structure was solved by direct methods and refined by full-matrix least squares on $F^2$ using the SHELXTL software package.[27] Disordered solvent water molecules (five water molecules in the asymmetric unit) were removed using the PLATON[28] (version 1.10) squeeze instruction. All non-hydrogen atoms were refined anisotropically. Details on data collection and refinement are given in Table 2. Further details of the crystal structures may be obtained from the Fachinformationszentrum Karlsruhe, 76344 Eggenstein-Leopoldshafen, Germany, on quoting the depository number CSD-417583. Molecular graphics were drawn with the DIAMOND software package.[29]

Table 2. Crystal data and structure refinement.

| | |
|---|---|
| Empirical formula | $H_{156}Ce_{13}CrO_{183}S_{27}$ |
| Formula mass | 5824.48 |
| Temperature | 173(2) K |
| Wavelength | 0.71073 Å |
| Crystal system | hexagonal |
| Space group | $P6_3$ |
| Unit cell dimensions | $a$ = 19.3015(2) Å, $c$ = 25.2684(4) Å |
| Volume | 8152.49(18) Å$^3$ |
| $Z$ | 2 |
| Density (calcd.) | 2.395 Mg/m$^3$ |
| Absorption coefficient | 4.106 mm$^{-1}$ |
| $F$(000) | 5720 |
| Crystal size | 0.40 × 0.10 × 0.08 mm |
| $\theta$ range for data collection | 2.11–33.02° |
| Index ranges | $-29 \le h \le 28$, $-26 \le k \le 29$, $-38 \le l \le 38$ |
| Reflections collected | 102247 |
| Independent reflections | 19680 [$R$(int) = 0.0406] |
| Completeness to $\theta$ = 31.00° | 99.9% |
| Absorption correction | Multi-scan |
| Max./min. transmission | 0.7347/0.2904 |
| Refinement method | Full-matrix least squares on $F^2$ |
| Data/restraints/parameters | 19680/1/657 |
| Goodness-of-fit on $F^2$ | 1.006 |
| Final $R$ indices [$I > 2\sigma(I)$] | $R_1$ = 0.0362, $wR_2$ = 0.0930 |
| $R$ indices (all data) | $R_1$ = 0.0460, $wR_2$ = 0.0997 |
| Twin volume ratio | 0.692(10):0.308(10) on 9462 Friedel pairs |
| Largest diff. peak/hole | 2.603/–2.104 eÅ$^{-3}$ |


[1] a) R. Yu, D. Wang, Y. Chen, X. Xing, S. Ishiwata, T. Saito, M. Takano, *Chem. Lett.* **2004**, *33*, 1186–1187; b) I. V. Ogorodnyk, I. V. Zatovsky, V. N. Baumer, N. S. Slobodyanik, O. V. Shishkin, *Acta Crystallogr., Sect. C* **2006**, *62*, i100–i102; c) I. Krügermann, M. S. Wickleder, J. Wontcheu, T. Schleid, *Anorg. Allg. Chem.* **2006**, *632*, 901–904.

[2] a) J. Perles, C. Fortes-Revilla, E. Gutiérrez-Puebla, M. Iglesias, M. Á. Monge, C. Ruiz-Valero, N. Snejko, *Chem. Mater.* **2004**, *16*, 2701–2706; b) Z. He, E.-Q. Gao, Z.-M. Wang, C.-H. Yan, M. Kurmoo, *Inorg. Chem.* **2005**, *44*, 862–874; c) F. Li, G. Yuan, *Chem. Commun.* **2005**, *17*, 2238–2240; d) M. A. Jakupec, P. Unfried, B. K. Keppler, *Rev. Physiol. Biochem. Pharmacol.* **2005**, *153*, 101–111.

[3] M. S. Wickleder, *Chem. Rev.* **2002**, *102*, 2011–2087.

[4] a) Y. K. Gun'ko, S. D. Elliott, P. B. Hitchcock, M. F. Lappert, *J. Chem. Soc. Dalton Trans.* **2002**, 1852–1856; b) L. A. J. Garvie, H. Xu, Y. Wang, R. L. Putnam, *J. Phys. Chem. Solids* **2005**, *66*, 902–905; c) S. Arai, S. Muto, T. Sasaki, K. Tatsumi, Y. Ukyo, K. Kurodad, H. Saka, *Solid State Commun.* **2005**, *135*, 664–667.

[5] Inorganic Crystal Structure Database (version 2006-2), Fachinformationszentrum Karlsruhe, Germany, **2006**.

[6] W. Wichelhaus, *Angew. Chem.* **1978**, *90*, 476–476; *Angew. Chem. Int. Ed. Engl.* **1978**, *17*, 451–452.

[7] J. Dugue, D. Carre, M. Guittard, *Acta Crystallogr., Sect. B* **1979**, *35*, 1550–1554.

[8] J. Felsche, G. Huttner, O. Scheidsteger, *Z. Naturforsch., Teil B* **1985**, *b40*, 755–761.

[9] L. D. Iskhakova, A. I. Tursina, *Kristallografiya* **1989**, *34*, 1414–1418.

[10] V. Y. Kuznetsov, L. M. Dikareva, D. L. Rogachev, M. A. Porai-Koshits, *Zh. Strukt. Khim.* **1990**, *31*, 14–18.

[11] O. S. Filipenko, G. V. Shilov, L. S. Leonova, V. I. Ponomarev, L. O. Atovmyan, *Dokl. Akad. Nauk* **2001**, *380*, 208–212.

[12] D. Grant, *J. Inorg. Nucl. Chem.* **1964**, *26*, 337–345.

[13] a) A. C. Chatterji, S. K. Mukherjee, *J. Am. Chem. Soc.* **1958**, *80*, 3600; b) A. C. Chatterji, S. K. Mukherjee, *Z. Phys. Chem.* **1959**, *210*, 255–259; c) J. F. Perez-Benito, C. Arias, *Can. J. Chem.* **1993**, *71*, 649–666; d) J. Y. Tong, E. L. King, *J. Am. Chem. Soc.* **1960**, *82*, 3805–3809; e) M. Doyle, R. J. Swedo, J. Rocek, *J. Am. Chem. Soc.* **1973**, *95*, 8352–8357.

[14] a) B. M. Casari, E. Wingstrand, V. Langer, *J. Solid State Chem.* **2006**, *179*, 296–301; b) B. M. Casari, A. K. Eriksson, V. Langer, *Z. Anorg. Allg. Chem.* **2006**, *632*, 101–106.

[15] a) B. Beverskog, I. Puigdomenech, *Corros. Sci.* **1997**, *39*, 43–57; b) S. A. Hayes, P. Yu, T. J. O'Keefe, M. J. O'Keefe, J. O. Stoffer, *J. Electrochem. Soc.* **2002**, *149*, 623–630; c) P. Yu, S. A. Hayes, T. J. O'Keefe, M. J. O'Keefe, J. O. Stoffer, *J. Electrochem. Soc.* **2006**, *153*, 74–79.

[16] N. Rempfer, H.-W. Lerner, M. Bolte, *Acta Crystallogr., Sect. E* **2004**, *60*, i80–i81.

[17] a) O. Lindgren, *Acta Chem. Scand.* **1977**, *A31*, 167–170; b) O. Lindgren, *Acta Chem. Scand.* **1977**, *A31*, 453–546; c) O.


 © 2007 Wiley-VCH Verlag GmbH & Co. KGaA, Weinheim 

Lindgren, *Acta Chem. Scand.* **1977**, *A31*, 591–594; d) U. Kolitsch, K. Schwendtner, *Acta Crystallogr., Sect. C* **2004**, *60*, i89–i90.
[18] N. E. Brese, M. O'Keefe, *Acta Crystallogr., Sect. B* **1991**, *47*, 192–197.
[19] A. Trzesowska, R. Kruszynski, T. J. Bartczak, *Acta Crystallogr., Sect. B* **2006**, *62*, 745–753.
[20] M. B. Robin, P. Day, *Adv. Inorg. Chem. Radiochem.* **1967**, *10*, 247–422.
[21] K. D. Demadis, C. M. Hartshorn, T. J. Meyer, *Chem. Rev.* **2001**, *101*, 2655–2685.
[22] J. C. Barnes, J. D. Paton, K. F. Seaward, *Acta Crystallogr., Sect. C* **1993**, *49*, 2057–2060.
[23] J. C. Barnes, *Acta Crystallogr., Sect. C* **1995**, *51*, 2466–2469.
[24] M. Maunaye, C. Hamon, P. l'Haridon, Y. Laurent, *Bull. Soc. Fr. Mineral. Cristallogr.* **1976**, *99*, 203–205.
[25] *SMART* and *SAINT*, Siemens Analytical X-ray Instruments Inc., Madison, Wisconsin, USA, **1995**.
[26] G. M. Sheldrick, *SADABS*, version 2.03, University of Göttingen, Germany, **2002**.
[27] Bruker, *SHELXTL*, version 6.10, Bruker AXS Inc., Madison, Wisconsin, USA, **2003**.
[28] A. L. Spek, *PLATON, A Multipurpose Crystallographic Tool*, Utrecht University, Utrecht, The Netherlands, **2005**.
[29] K. Brandenburg, *DIAMOND*, version 2.1c, Crystal Impact GbR, Bonn, Germany, **2000**.

Received: January 15, 2007
Published Online: June 14, 2007

 © 2007 Wiley-VCH Verlag GmbH & Co. KGaA, Weinheim 

DOI: 10.1002/ejic.200700141

# Synthesis, Characterization, and Electrochemical and Electrical Properties of Novel Pentaerythritol-Bridged Cofacial Bismetallophthalocyanines and Their Water-Soluble Derivatives

**Metin Özer,[a] Ahmet Altındal,[b] Ali Rıza Özkaya,[a] Bekir Salih,[c] Mustafa Bulut,[a] and Özer Bekaroğlu*[d]**

**Keywords:** Phthalocyanines / Cofacial configuration / Synthesis / Cyclic voltammetry / Thermopower

Novel cofacial bismetallophthalocyanines and their water-soluble derivatives were prepared. The precursor 4,4′-(2-phenyl-1,3-dioxane-5,5-diyl)bis(methylene)bis(oxy)-diphthalonitrile **3** was obtained by the reaction of [5-(hydroxymethyl)-2-phenyl-1,3-dioxan-5-yl] methanol **1** and 4-nitrophthalonitrile **2** with $K_2CO_3$ in DMF at 50 °C. Cyclotetramerization was achieved by heating the homogenized mixture of the precursor, bisphthalonitrile, and $Zn(OAc)_2{\cdot}2H_2O$ or $Co(OAc)_2{\cdot}4H_2O$ at 300 °C, which was followed by catalytic hydrogenation of the resulting product with Pd/C(10 %) in DMF. The target water-soluble phthalocyanines were acquired from boiling suspensions of the compounds bearing eight OH side groups in aqueous KOH (20 %) solution. The structure of the target compounds was confirmed by elemental analysis, FTIR, UV/Vis, $^1$H NMR, ICP-MS, and MALDI-TOF spectroscopic methods. The electrochemical and spectroelectrochemical measurements suggested the formation of various mixed-valent oxidation and reduction species, as a result of the strong intramolecular interactions between the two cofacial phthalocyanine units in the compounds. Impedance spectroscopy, dc conductivity, and thermopower measurements were performed using spin-coated films of these compounds as a function of temperature (290–440 K) and frequency (40–$10^5$ Hz). Dc conductivity showed typical Arrhenius behavior for all compounds. At low temperatures, a curved line was observed for the complex plane plots of impedance for all phthalocyanines. These curved lines transformed into a full semicircle with increasing temperature. The dependency of frequency exponent *s* on temperature suggested hopping-type conduction. A positive Seebeck coefficient was observed for all compounds, which indicates that the compounds behave as a *p*-type semiconductor.
(© Wiley-VCH Verlag GmbH & Co. KGaA, 69451 Weinheim, Germany, 2007)

## Introduction

Phthalocyanine (Pc) dimers and multimers have been the subject of great interest in areas such as electrocatalysis,[1,2] semiconductors,[3] nonlinear optics,[4] electrochromic displays,[5–7] and liquid crystals.[8,9] In this respect, various phthalocyanine,[10–12] porphyrin,[13,14] and mixed phthalocyanine-porphyrin dimers and oligomers[15] having various kinds of linkage have been reported to date. These compounds, especially those with rigid cofacial configurations,[16,17] often show spectroscopic, electrical, and electrochemical properties which differ significantly from the parent monomers. A strong interaction between the face-to-face Pc rings or two metal centers in these types of complexes was usually detected with spectroscopic and electrochemical evidence.[18]

Thin films of organic molecular crystals are promising materials for electronic and optoelectronic devices like solar cells,[19] gas sensors,[20] and light-emitting diodes[21] due to their unique electrical properties. The determination of true fundamental parameters such as the majority carrier type and electronic structure is crucial in order to optimize their potential utility for optical or electronic applications. Optical methods such as ultraviolet photoemission and inverse photoemission spectroscopy are used to determine the electronic structure of phthalocyanine thin films.[22] On the other hand, Hall effect and thermopower measurements are used for the determination of the charge carrier type. The most reliable method to investigate their conduction type is the measurement of thermoelectric power, characterized by the Seebeck coefficient *S*.

The synthesis and properties of cofacial bismetallophthalocyanines with a number of cross-links have been rarely reported in the literature.[23,24] Our interest in the design of novel macrocycles with potential applicability in various technological areas prompted us to synthesize new bridged metallated bisphthalocyanines with four linking

[a] Department of Chemistry, Marmara University, Istanbul, 34722, Turkey
[b] Department of Physics, Marmara University, Istanbul, 34722, Turkey
[c] Department of Chemistry, Hacettepe University, Ankara, 06532, Turkey
[d] Department of Chemistry, Istanbul Technical University, Maslak-Istanbul, 34469, Turkey
Fax: +90-216-3860824
E-mail: obek@itu.edu.tr
obekaroglu@gmail.com

 © 2007 Wiley-VCH Verlag GmbH & Co. KGaA, Weinheim 

arms between two Pc rings and to investigate their electrochemical and electrical properties.[18,25] Recently, we reported the synthesis, characterization, and electrical and spectroelectrochemical properties of 1,1′-methylenedinaphthalene-bridged cofacial metal-free bisphthalocyanines and bismetallophthalocyanines.[18]

In our continuing efforts, we now report the synthesis and characterization of novel pentaerythritol-bridged cofacial bismetallophthalocyanines and their water-soluble derivatives. The electrochemical and electrical properties of the compounds are also investigated.

## Results and Discussion

### Synthesis

The preparation of the pentaerythritol monoacetal **1** was accomplished by the condensation of pentaerythritol with benzaldehyde in DMF at 25–30 °C according to the given method.[26,27] The original precursor **3** for the synthesis of phthalocyanines was obtained by nitro displacement reaction of **1** and **2** using $K_2CO_3$ as catalyst in DMF with stirring at 50–60 °C. In this work, for the synthesis of the cofacial bismetallophthalocyanines, we developed a solid-phase method in the absence of catalysts. The preparation of phthalocyanine derivatives **4** and **5** was achieved by heating the homogenized mixture of **3** with $Zn(OAc)_2{\cdot}2H_2O$ or $Co(OAc)_2{\cdot}4H_2O$, respectively, in the ratio 1:1 through the cyclotetramerization reaction in a sealed tube at 300 °C for 10 min. The mixtures of Pc **4** or **5** and Pd/C(10%) in DMSO were hydrogenated at room temperature under 1 atm hydrogen pressure for 8 h according to the given procedure.[27] The catalyst was filtered off, and the mixtures were precipitated with the addition of ethanol to give Pc **6** or **7**. Water-soluble Pcs **8** and **9** were achieved by boiling suspensions of **6** or **7**, respectively, in aqueous KOH (20%) solutions (Scheme 1).

The crude Pcs **4**–**7** were dissolved in DMF and precipitated again with a mixture of $CHCl_3$ and ethanol which easily dissolved the starting material and the other impurities. After filtration, each precipitate was washed with boiling acetone and ethanol. The purification of the target Pcs **4**–**7** was achieved with a silica gel column using a THF/DMF gradient system as the eluent. On the other hand, **8**

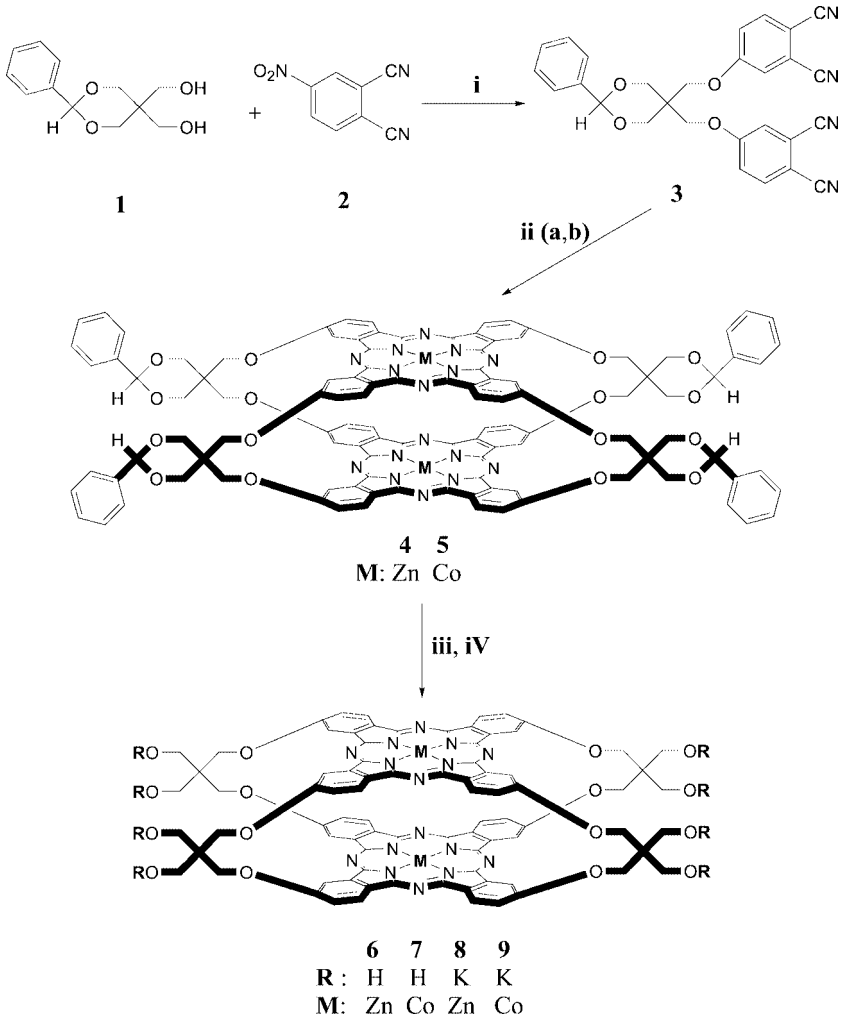


Scheme 1. (i) $K_2CO_3$, DMF; (ii) a: $Zn(CH_3COO)_2{\cdot}2H_2O$, b: $Co(CH_3COO)_2{\cdot}4H_2O$; (iii) $H_2$, Pd/C(10%); (iv) KOH (20%).

 © 2007 Wiley-VCH Verlag GmbH & Co. KGaA, Weinheim 

or **9** were dissolved in water, and they were precipitated again several times in ethanol until the solution was neutral. The precipitates were washed with ethanol and diethyl ether, and then dried in vacuo.

After purification, the compounds were characterized by elemental analysis, FTIR, $^1$H NMR, UV/Vis, MALDI-MS, and ICP-MS spectroscopy. The results of the analyses showed that the compounds were pure enough for the other measurements.

The IR spectra were derived from potassium bromide disks. The existence of C≡N groups appeared at 2231 cm$^{-1}$ as a single peak in the spectrum of **3**. Formation of dinuclear phthalocyanine complexes **4** and **5** starting from the corresponding bisphthalodinitrile derivative was verified by the disappearance of the C≡N stretching vibration band at 2231 cm$^{-1}$. After conversion of **4** and **5** into **6** and **7**, respectively, by the cleavage of the acetal groups, O–H stretching vibrations came out typically around 3402 and 3396 cm$^{-1}$ as strong absorptions.

The UV/Vis spectra of **4**–**7** in DMF display characteristic absorptions around 625 and 680 nm in the Q-band region (Figure 1). The Q-band was attributed to $\pi \rightarrow \pi^*$ transition from the highest occupied molecular orbital (HOMO) to the lowest unoccupied molecular orbital (LUMO) of the Pc ring. The other bands (B) in the UV region at 330–353 nm are observed due to the transitions from the deeper π levels to the LUMO. When aggregation occurs, a band at ca. 630 nm arises in the electronic spectrum as a result of the intramolecular interactions between the Pc units.[18,28] Thus, the band at around 625 nm can be attributed to intramolecular interactions, although the Q-band is not split. The aggregation degree of Pcs is highly affected by the surrounding conditions, one of which is the solvent media. Figures 2 and 3 show the absorption spectra of water-soluble Pcs **8** and **9**, respectively, at different concentrations [$C_8$ = $(5.28\times10^{-6})$–$(4.8\times10^{-7})$ and $C_9$ = $(7.52\times10^{-6})$–$(8.22\times10^{-7})$]. It should be noted that the absorption at around 630 nm, corresponding to aggregation, for **8** and **9** is the main band in water.[29] This observation suggests that aggregation occurs to a greater extent in water as compared with that in organic solvent.[30,31] In addition, although the concentrations of dinuclear water-soluble phthalocyanines **8** and **9** decrease, there is no significant change in the relative intensity of the aggregation band to the Q-band at ca. 685 nm. This situation is consistent with the intramolecular coupling between the rings in dinuclear phthalocyanines.

In addition to these results, the $^1$H NMR ([D$_6$]DMSO) spectra of **3**, **4**, and **6** exhibit the characteristic chemical shifts for the proposed structures as expected. The $^1$H NMR spectrum of **6**, the hydrogenolysis product of **4**, provides supporting evidence for the structure. Removal of the benzylidene acetal in **4** is confirmed by the loss of the singlet proton signal of acetal at $\delta$ = 6.14 ppm in the $^1$H NMR spectrum of **6**. A broad signal at $\delta$ = 11.35 ppm in the $^1$H NMR spectrum of **6** disappeared with $D_2O$ exchange. The $^1$H NMR spectra of **3**, **4**, and **6** exhibit the aromatic protons as multiplets at 7.73–7.21, 8.42–7.03, and 8.31–6.94 ppm, respectively. On the other hand, aliphatic proton signals appeared at 4.88–3.64 ppm for **3**, 4.81–3.57 ppm for **4**, and 4.12–3.13 ppm for **6**.

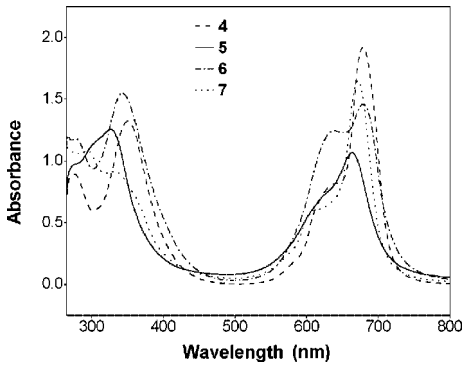


Figure 1. UV/Vis spectra of bis(metallophthalocyanine) derivatives **4**–**7** in DMF.

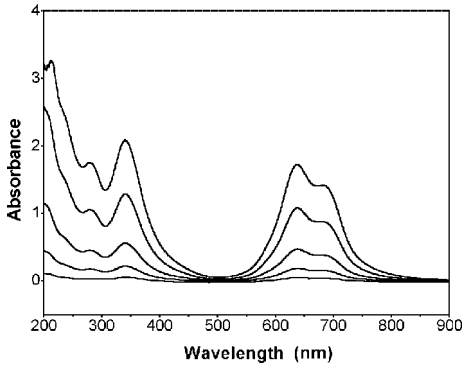


Figure 2. UV/Vis spectra of bis(metallophthalocyanine) derivative **8** in water at different concentrations.

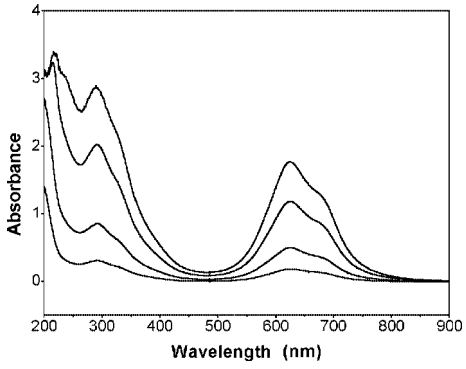


Figure 3. UV/Vis spectra of bis(metallophthalocyanine) derivative **9** in water at different concentrations.

A close investigation of the MALDI-TOF mass spectra of the Pcs confirmed the proposed structures. The protonated molecular ion peaks of **4** and **5** are observed at low intensity, but sodium adduct peaks for both **4** and **5** complexes are found to be dominant intense peaks in the linear mode MALDI-TOF mass spectra using the 3-indoleacrylic acid matrix. Sodium adduct peak stabilities of these complexes were found to be very high in the gas phase compared to the stability (following the intensity of the peaks) of the protonated molecular ion peaks, even if the sodium content in the complexes was lower than 0.1% (data not

 © 2007 Wiley-VCH Verlag GmbH & Co. KGaA, Weinheim 

shown). On the other hand, protonated molecular ion peaks of **6** and **7** complexes are observed at 1685 and 1672 Da, respectively, which exactly overlap with the mass of the protonated complexes calculated from the elemental composition of the compounds. Following the protonated molecular ion peak of **6**, a peak, 88 Da mass lower than the protonated molecular ion peak, is observed at 1596 Da. This peak resulted from the $C_4H_8O_2$ side group elimination from the protonated ion peak of the complex. Also the second $C_4H_8O_2$ side group elimination is observed at low intensity. However, no fragmentation was observed for **7** in the MALDI-TOF mass spectrum. When the MALDI-TOF mass spectra of **6** and **7** were evaluated at low-mass range between 100 and 500 Da, no meaningful intensity peak was observed representing impurities, but mainly matrix species peaks were followed. These results show that either **6** or **7** complexes were very pure. Many different MALDI matrices were tested to obtain highly resolved spectra. The best matrix for **6** and **7** was α-cyano-4-hydroxycinnamic acid for MALDI-MS analyses. Because of the short life time of the protonated complexes **6** and **7** in MALDI-MS, highly resolved spectra could not be obtained in reflectron mode. Beyond the protonated and two fragment ion peaks of **6** and the only protonated ion peak of **7**, MALDI mass spectra of the complexes showed very clear and low fragmentations in MALDI-MS (Figures 4 and 5).

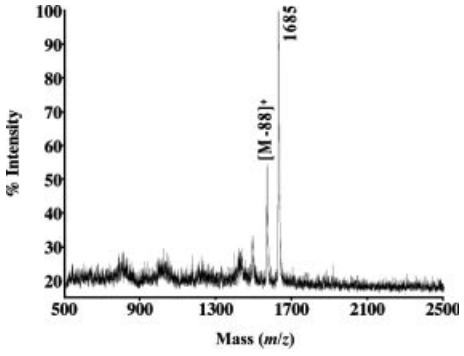


Figure 4. Positive ion mode MALDI-MS spectrum of **6** in α-cyano-4-hydroxycinnamic acid MALDI matrix using nitrogen laser accumulating 50 laser shots.

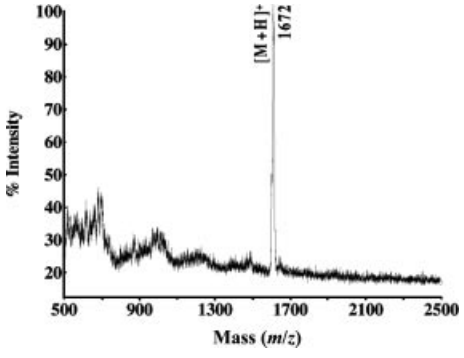


Figure 5. Positive ion mode MALDI-MS spectrum of **7** in α-cyano-4-hydroxycinnamic acid MALDI matrix using nitrogen laser accumulating 50 laser shots.

The ICP-MS measurements were obtained for the determination of the quantities of potassium, zinc, and cobalt atoms in **8** and **9** as described in the literature.[32] The results of ICP-MS analysis provide additional support for the molecular structures of **8** and **9**.

### Electrochemistry and Spectroelectrochemistry

The electrochemical properties of the complexes **4**–**7** were examined by cyclic voltammetry, controlled potential coulometry, and spectroelectrochemistry in DMSO/TBAP. Cyclic voltammetry of each complex displayed four reductions and an oxidation couple. Typical cyclic voltammograms of **4** and **5** in DMSO/TBAP (tetrabutylammonium perchlorate) are shown in Figure 6. The number of electrons transferred for each redox process is determined by the controlled potential electrolysis at the suitable potentials. Coulometric studies of broadly separated voltammetric couples showed that the number of electrons transferred for each redox process ($p$) is approximately equal to unity ($1 > p \geq 0.92$). Thus, the reactions corresponding to all waves in the voltammograms are stepwise one-electron processes of the two cofacial phthalocyanine rings and metal centers. The voltammetric data and the assignment of the redox couples for **4**–**7** are summarized in Table 1. The occurrence of stepwise one-electron processes for these complexes involving two Pc rings and two metal centers, and the comparison of their half-peak potentials with those of monophthalocyanines imply the formation of mixed-valent first- and second-reduced and first-oxidized species during the voltammetric measurements.[33,18] It can be concluded from the results of this study that the binding of two Pc rings at two sides rigidly with four linking arms leads to remarkable intramolecular cofacial coupling and thus to the splitting of the classical monophthalocyanine redox processes. For instance, for complexes **4** and **6**, the Pc(–2)/Pc(–3) redox process is split into the $[Pc(-2)]_2/[Pc(-2)\cdot Pc(-3)]$ and $[Pc(-2)\cdot Pc(-3)]/[Pc(-3)]_2$ processes, forming the mixed-valent $[Pc(-2)\cdot Pc(-3)]$ species. All the redox processes for **4** and **6** should be ligand-based since the $Zn^{II}$ ion is not redox-active in metallophthalocyanines. The difference between the first oxidation and the first reduction potentials for complexes **4** and **6** is remarkably low relative to that of monophthalocyanines (1.34 V for **4**, 1.33 V for **6**, but 1.50–1.70 V for monophthalocyanines). This is in harmony with the cofacial structures of **4** and **6**, leading to the strong electronic coupling and the splitting of molecular orbitals. Previous reports on the electrochemistry of $Co^{II}$ Pcs suggested that both the first reduction and the first oxidation processes in these complexes are metal-based in polar coordinating solvents such as DMSO and DMF.[32] Since complexes **5** and **7** involve two $Co^{II}$ centers, the oxidation and the first two reductions probably correspond to $[Co^{II}Pc(-2)\cdot Co^{III}Pc(-2)]^+/[Co^{II}Pc(-2)]_2$, $[Co^{II}Pc(-2)]_2/[Co^{II}Pc(-2)\cdot Co^{I}Pc(-2)]^-$, and $[Co^{II}Pc(-2)\cdot Co^{I}Pc(-2)]^-/[Co^{I}Pc(-2)]_2^{2-}$ redox processes, respectively. On the other hand, the third and fourth reductions should be related to the splitting of the Pc(–2)/Pc-

 © 2007 Wiley-VCH Verlag GmbH & Co. KGaA, Weinheim 

(–3) couple and thus ligand-based $[Co^{I}Pc(-2)]_2^{2-}/[Co^{I}Pc(-2)\cdot Co^{I}Pc(-3)]^{3-}$ and $[Co^{I}Pc(-2)\cdot Co^{I}Pc(-3)]^{3-}/[Co^{I}Pc(-3)]_2^{4-}$ redox processes, respectively.

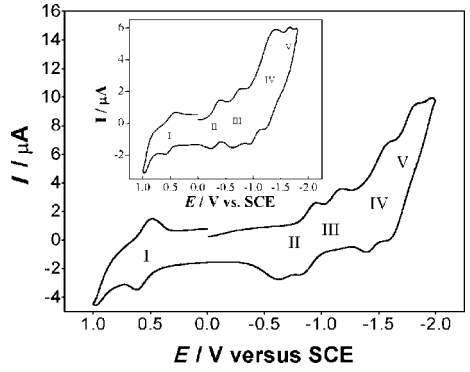


Figure 6. Cyclic voltammograms of **4** and **5** (inset) at 0.100 V/s in TBAP/DMSO.

Table 1. Electrochemical data for 4–7 in DMSO.[a]

| Pc | Redox processes | | $E_{1/2}$ [V] | $\Delta E_p$ [V] | $\Delta E$ [V] | $\Delta E_s$ [V] |
|---|---|---|---|---|---|---|
| **4** | $[Zn(II)Pc(-2)\cdot Zn(II)Pc(-1)]^{+}$ / $[Zn(II)Pc(-2)]_2$ | I | 0.55 | 0.12 | 1.34 | |
| | $[Zn(II)Pc(-2)]_2$ / $[Zn(II)Pc(-2)\cdot Zn(II)Pc(-3)]$ | II | –0.79 | 0.30 | | 0.21 |
| | $[Zn(II)Pc(-2)\cdot Zn(II)Pc(-3)]^{-}$ /$[Zn(II)Pc(-3)]_2^{2}$ | III | –1.00 | 0.32 | | |
| | $[Zn(II)Pc(-3)]_2^{2-}/[Zn(II)Pc(-3)\cdot Zn(II)Pc(-4)]^{3}$ | IV | –1.47 | 0.18 | | 0.24 |
| | $[Zn(II)Pc(-3)\cdot Zn(II)Pc(-4)]^{3-}/[Zn(II)Pc(-4)]_2^{4-}$ | V | –1.71 | 0.22 | | |
| **5** | $[Co(II)Pc(-2)\cdot Co(III)Pc(-2)]^{+}/[Co(II)Pc(-2)]_2$ | I | 0.50 | 0.18 | 0.80 | |
| | $[Co(II)Pc(-2)]_2$ / $Co(II)Pc(-2)\cdot Co(I)Pc(-2)]^{-}$ | II | –0.30 | 0.16 | | 0.43 |
| | $[Co(II)Pc(-2)\cdot Co(I)Pc(-2)]^{-}/[Co(I)Pc(-2)]_2^{2-}$ | III | –0.73 | 0.12 | | |
| | $[Co(I)Pc(-2)]_2^{2-}/[Co(I)Pc(-2)\cdot Co(I)Pc(-3)]^{3-}$ | IV | –1.17 | 0.46 | | 0.26 |
| | $[Co(I)Pc(-2)\cdot Co(I)Pc(-3)]^{3-}/[Co(I)Pc(-3)]_2^{4-}$ | V | –1.43 | 0.42 | | |
| **6** | $[Zn(II)Pc(-2)\cdot Zn(II)Pc(-1)]^{+}/[Zn(II)Pc(-2)]_2$ | I | 0.52 | 0.14 | 1.33 | |
| | $[Zn(II)Pc(-2)]_2/[Zn(II)Pc(-2)\cdot Zn(II)Pc(-3)]^{-}$ | II | –0.81 | 0.32 | | 0.24 |
| | $[Zn(II)Pc(-2)\cdot Zn(II)Pc(-3)]^{-}/[Zn(II)Pc(-3)]_2^{2-}$ | III | –1.05 | 0.42 | | |
| | $[Zn(II)Pc(-3)]_2^{2-}/[Zn(II)Pc(-3)\cdot Zn(II)Pc(-4)]^{3}$ | IV | –1.48 | 0.20 | | 0.25 |
| | $[Zn(II)Pc(-3)\cdot Zn(II)Pc(-4)]^{3-}/[Zn(II)Pc(-4)]_2^{4-}$ | V | –1.73 | 0.22 | | |
| **7** | $[Co(II)Pc(-2)\cdot Co(III)Pc(-2)]^{+}/[Co(II)Pc(-2)]_2$ | I | 0.48 | 0.16 | 0.80 | |
| | $[Co(II)Pc(-2)]_2/[Co(II)Pc(-2)\cdot Co(I)Pc(-2)]^{-}$ | II | –0.32 | 0.16 | | 0.43 |
| | $[Co(II)Pc(-2)\cdot Co(I)Pc(-2)]^{-}/[Co(I)Pc(-2)]_2^{2-}$ | III | –0.75 | 0.34 | | |
| | $[Co(I)Pc(-2)]_2^{2-}/[Co(I)Pc(-2)\cdot Co(I)Pc(-3)]^{3-}$ | IV | –1.20 | 0.10 | | 0.26 |
| | $[Co(I)Pc(-2)\cdot Co(I)Pc(-3)]^{3-}/[Co(I)Pc(-3)]^{4-}$ | V | –1.46 | 0.12 | | |

[a] Potentials are reported with respect to the SCE. Half-wave potentials in DMSO vs. $Fc/Fc^{+}$ couple correspond approximately with the given **4**–**7** data minus 0.45 V. $E_{1/2}$ values were measured by cyclic voltammetry [$E_{1/2} = (E_{pa} + E_{pc})/2$]. The peak separation values ($\Delta E_p = E_{pa} - E_{pc}$) are reported at 0.100 V/s. $\Delta E$ is the potential difference between the first oxidation and first reduction potentials. It represents the HOMO–LUMO gap for **4** and **6**, but the charge-transfer transition for **5** and **7** involving redox-active metal centers. $\Delta E_s$ indicates mixed-valent splitting energy for the relevant split redox couple.

The spectroelectrochemical measurements in solution have a vital importance in confirming the assignment of the redox processes in the Pcs, especially in metallo Pcs involving a redox-active metal center. The formation of electrochemically generated species involving a $Co^{I}$ center is confirmed by the appearance of a new intense absorption in the region of 400–500 nm. Figure 7 shows in situ UV/Vis spectral changes during the first and second reductions and the first oxidation of **5** in TBAP/DMSO. Upon the first reduction, a new intense band appears at 488 nm, confirming the formation $Co^{II}\cdot Co^{I}$ mixed-valent species.[34,35] This band can be assigned to metal-to-ligand charge transfer (MLCT) from $Co^{I}$ to the Pc ring. During the second reduction, the absorption of the newly formed MLCT peak continues to increase, forming a quite intense band with a redshift in the Q-band. It is known from the literature[36,37] that both $Co^{II}\cdot Co^{I}$ and $Co^{I}\cdot Co^{I}$ species show Q-band and MLCT absorption (near 500 nm) redshifted relative to less electronically coupled dimers or monophthalocyanines. Thus, the spectral changes observed during the second reduction process indicate the formation of $Co^{I}\cdot Co^{I}$ species. The spectrum of the mixed-valent $Co^{II}\cdot Co^{I}$ species obtained during the first reduction is different from that of the fully reduced $Co^{I}\cdot Co^{I}$ species obtained during the second reduction. The $Co^{II}\cdot Co^{I}$ mixed-valent species has a much weaker MLCT band. This implies that the added first electron may be delocalized over the extended ring system. This type of behavior was observed previously for the (–1)-bridged dinuclear $[CoTRNPc]_2$ (TRN = trineopentoxy).[12] The spectroelectrochemistry of **5** provides additional support for the fact that the reduction of **5** and **7** over the first and second reduction couples proceeds by two distinct one-electron steps, corresponding to the stepwise reduction of each of the cobalt atoms to $Co^{I}$.

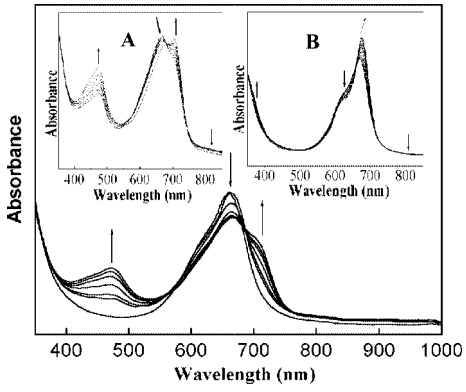


Figure 7. In situ UV/Vis spectral changes during the first reduction, the second reduction (inset A), and the first oxidation (inset B) processes of **5** in TBAP/DMSO.

## Electrical Conductivity and Thermopower Measurements

Dc conductivity of the spin-coated films was determined from the slope of the measured current–voltage (*I*–*V*) measurements by using the following relation:

$$\sigma_{dc} = \frac{I}{V}\cdot\frac{d}{(2n-1)lh}$$

where *I* is the measured current, *V* is the bias voltage, *d* is the electrode spacing, *n* is the number of electrode finger

 © 2007 Wiley-VCH Verlag GmbH & Co. KGaA, Weinheim 

pairs, $l$ is the overlap length of the electrode fingers, and $h$ is the thickness of the electrodes. Measurements of $I$–$V$ were carried out in the range of –1 to 1 V. Linear $I$–$V$ behavior was found in this voltage range, indicating no rectifying properties. The variation of the measured dc conductivity with temperature suggests the presence of only one conduction mechanism, assuming that the dominant levels are the conduction and valence bands, in the whole temperature range for the films of **4**–**9**. Arrhenius plots (logarithms of dc conductivity versus inverse temperature) indicated that the compounds are semiconducting in nature. The highest value of conduction activation energy was obtained for the film of **8** and the lowest for **5**. The difference between the electrical conductivity of the films can be attributed to the differences in the stacking arrangements and interplanar spacing.

The frequency-dependent conductivity (ac conductivity) measurements were also performed on thin films of compounds in the frequency range 40–$10^5$ Hz at temperatures between 290 and 440 K. The frequency dependence of the electrical conductivity for a large variety of materials can be expressed as $\sigma = \sigma_0 + \sigma(\omega)$, where $\sigma_0$ is the dc conductivity. The frequency-dependent part of the total conductivity, $\sigma(\omega)$, is given by the power law of the form[38] $\sigma(\omega) = A\omega^s$ where $A$ and $s$ are temperature-dependent parameters. For temperatures above 350 K, frequency-independent conductivity at low frequencies and after a certain characteristic frequency increasing with the power law, was observed. Various models such as tunelling and hopping have been proposed to explain this type of behavior. It is not easy to decide which of these mechanisms is responsible for the observed conduction mechanism. However, the behavior of the exponent $s$ with temperature can help in determining the possible conduction mechanism. The values of $s$ are calculated from the slope of the $\ln\sigma(\omega,T)$ versus $\ln\omega$ graphs and were generally found to decrease with increasing temperature. It was observed that the calculated values of the frequency exponent $s$ are in agreement with the hopping model.

The measured impedance spectra, when plotted in a complex plane plot, appeared in the form of a succession of semicircles representing the contributions to the electrical properties due to bulk material, grain boundry effect, and interfacial polarization phenomena. So, the impedance spectra technique enabled us to separate the effects due to each component. At low temperatures, the impedance spectra consist of a quasivertical line. The existence of semicircular-shaped curves in the Nyquist plot means that the impedance becomes capacitive, even at relatively high frequency. The effect of temperature on the impedance spectra of the films becomes clearly visible with a rise in temperature. On the complex plane plot at high temperatures, only a depressed semicircle with a different radius is observed (Figure 8) for the compounds **4**–**9** at higher temperatures, indicating deviation from the Debye dispersion relation. In the case of a depressed semicircle in the impedance spectra, the relaxation time is considered as a distribution of values, rather than a single relaxation time.

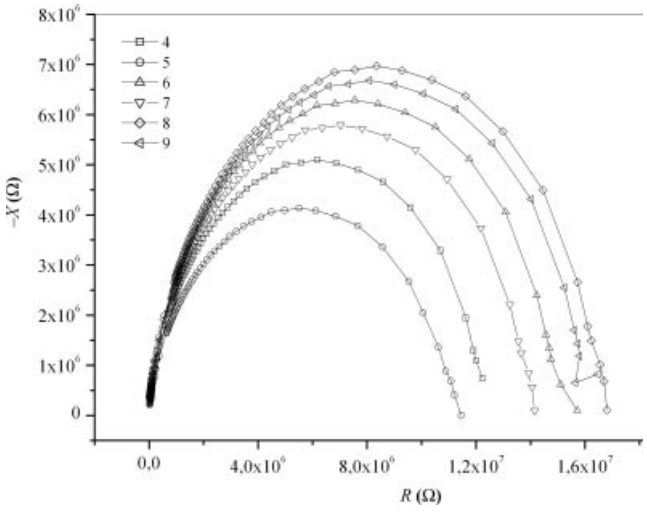


Figure 8. Nyquist plot (imaginary part vs. real part of complex impedance) of the spin-coated films of **4**–**9** at 385 K.

The Seebeck coefficient $S$ provides the transport type by its sign and provides the energetic difference between the Fermi level and transport level by its value. To determine the type of majority carrier, the temperature dependence of the thermoelectric power was also studied for thin films of **4**–**9**. The measured thermopower varied approximately exponentially with temperature for all samples investigated. Figure 9 shows the Seebeck ceefficient $S$ of the samples. Its sign is always positive. Compared to **8**, the absolute value of the thermopower for the film of **5** is larger by nearly a factor of 3. The positive sign of $S$ confirms that the thin films of the compounds behave as a $p$-type semiconductor.

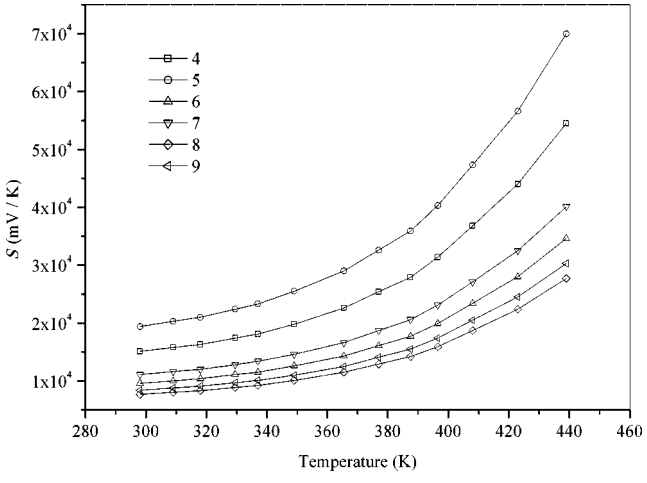


Figure 9. Seebeck coefficient vs. temperature for the films of **4**–**9**.

## Experimental Section

**General:** Compound **1** was synthesized by the methods previously described in the literature.[21,22] 4-Nitrophthalonitrile, pentaerythritol, benzaldehyde, $Zn(AcO)_2{\cdot}2H_2O$, $Co(AcO)_2{\cdot}4H_2O$, and Pd/C(10%) were obtained from commercial suppliers.

Routine IR and UV/Vis spectra were recorded with a Shimadzu FTIR-8300 spectrophotometer as KBr pellets and with a Shimadzu

 © 2007 Wiley-VCH Verlag GmbH & Co. KGaA, Weinheim 

UV-1601 UV/Vis spectrophotometer, respectively. Elemental analyses were performed with the LECO CHNS 932. $^1$H NMR spectra were obtained with a Varian Mercury-Vx 400 MHz spectrometer. Mass spectra were acquired with a Voyager-DE™ PRO MALDI-TOF mass spectrometer (Applied Biosystems, USA) equipped with a nitrogen UV-Laser operating at 337 nm. Spectra were recorded in linear mode with an average of 50 shots. 3-Indole acrylic acid (IAA) (20 mg/mL in acetonitrile) MALDI matrix for **4** and **5**, and α-cyano-4-hydroxycinnamic acid (ACCA) (15 mg/mL in 1:1 water/acetonitrile) MALDI matrix for **6** and **7** were prepared. MALDI samples were prepared by mixing the complex (2 mg/mL in dimethyl sulfoxide) with the matrix solution (1:10, v/v) in a 0.5-mL Eppendorf® microtube. Finally this mixture (1 μL) was deposited on the sample plate, dried at room temp. and then analyzed. The potassium, zinc, and cobalt contents in the digested mixtures were determined using external standards with an Agilent 7500a inductively coupled plasma mass spectrometer (ICP-MS). For the ICP-MS measurements, compounds **8** and **9** (10 mg) were digested by a mixture of acids ($HNO_3$/$HClO_4$/HF, 8:2:2, v/v) at 170 °C for 1 h.

**4,4′-(2-Phenyl-1,3-dioxane-5,5-diyl)bis(methylene)bis(oxy)diphthalonitrile (3):** A mixture of **1** (1.79 g, 8 mmol), **2** (2.77 g, 16 mmol), and $K_2CO_3$ (6.62 g, 48 mmol) in DMF (80 mL) was heated with stirring at 50 °C under argon for 30 h. The cooled reaction mixture was poured into cold water (100 mL) with stirring. The formed precipitate was filtered, washed with water, and dried in vacuo. The separation of the prepared compounds was achieved by column chromatography using silica gel with $CHCl_3$. The white powder product was obtained by evaporation of the solvent. This compound is readily soluble in $CHCl_3$, $CH_2Cl_2$, acetone, and THF. Yield 1.82 g (48%). M.p. 223 °C. $^1$H NMR ($CDCl_3$): $\delta$ = 7.73–7.21 (m, 11 H, arom. CH), 5.51 (s, 1 H, acetal CH), 4.88–3.64 (m, 8 H, aliph. $CH_2$) ppm. IR (KBr): $\tilde{\nu}$ = 3074–3038 (arom. CH), 2926–2851 (aliph. CH), 2231 (C≡N), 1595 (arom. C=C), 1483, 1390, 1309, 1246 (aliph.–O–arom.), 1165, 1093 cm$^{-1}$. $C_{28}H_{20}N_4O_4$: calcd. C 70.58, H 4.23, N 11.76; found C 70.81, H 4.29, N 11.62.

**2′,10′,16′,24′-[Tetrakis(2-phenyl-1,3-dioxan-5,5-diyl)bis(methylene)bis(oxy)]bis(phthalocyaninato)dizinc(II) (4) and 2′,10′,16′,24′-[Tetrakis(2-phenyl-1,3-dioxan-5,5-diyl)bis(methylene)bis(oxy)]bis(phthalocyaninato)dicobalt(II) (5):** Compound **3** (0.24 g, 0.5 mmol) and $Zn(OAc)_2{\cdot}2H_2O$ (0.22 g, 1 mmol) or $Co(OAc)_2{\cdot}4H_2O$ (0.13 g, 0.5 mmol) were ground in a mortar. Then the mixture was put in a glass tube, and the tube was purged with argon. After being sealed, the mixture was heated at 300 °C for 10 min. After cooling to room temp., the deep turquoise blue **4** or deep blue **5** were powdered by grinding. The crude products were dissolved in DMF (5 mL) and reprecipitated with a mixture of acetone/ethanol (1:1, v/v). After filtration, the precipitates were washed successively with hot water, ethanol, and acetone, and dried in vacuo. Compounds **4** and **5** were isolated using silica gel and a gradient of THF/DMF (10:0.1 to 10:2, v/v) as the eluent. These compounds are soluble in THF, DMSO, DMF, and DMA. Yield (**4**): 58 mg (23%). M.p. >300 °C. UV/Vis (DMF): $\lambda$ (log $\varepsilon$) = 680 (5.29), 638 (4.92), 353 (5.12) nm (Figure 1). $^1$H NMR ([D$_6$]DMSO): $\delta$ = 8.42–7.03 (m, 44 H, arom. CH), 6.14 (s, 4 H, acetal CH), 4.81–3.57 (m, 32 H, aliph. $CH_2$) ppm. IR (KBr): $\tilde{\nu}$ = 3067 (arom. CH), 2926 (aliph. CH), 1607 (arom. C=C), 1232 (aliph.–O–arom.), 1090, 1065 cm$^{-1}$. MALDI-TOF MS: $m/z$ = 2038 [M + H]$^+$, 2082 [M – H + 2Na]$^+$. $C_{112}H_{80}N_{16}O_{16}Zn_2$: calcd. C 66.05, H 3.96, N 11.00; found C 65.84, H 3.89, N 11.12. Yield (**5**): 46 mg (18%). M.p. >300 °C. UV/Vis (DMF): $\lambda$ (log $\varepsilon$) = 665 (5.03), 625 (4.88), 330 (5.10), 278 (4.99) nm (Figure 1). IR (KBr): $\tilde{\nu}$ = 3045 (arom. CH), 2941–2850 (aliph. CH), 1603 (arom. C=C), 1265, 1228 (aliph.–O–arom.), 1095, 1057 cm$^{-1}$. MALDI-TOF MS: $m/z$ = 2023 [M + H]$^+$, 2045 [M + Na]$^+$, 2091 [M + 3Na]$^+$. $C_{112}H_{80}Co_2N_{16}O_{16}$: calcd. C 66.47, H 3.98, N 11.07; found C 67.14, H 4.11, N 11.32.

**2′,10′,16′,24′-[Tetrakis(4,4′-2,2-bis(hydroxymethyl)propane-1,3-diyl)bis(oxy)]bis(phthalocyaninato)dizinc(II) (6) and 2′,10′,16′,24′-[Tetrakis(4,4′-2,2-bis(hydroxymethyl)propane-1,3-diyl)bis(oxy)]bis(phthalocyaninato)dicobalt(II) (7):** A suspension of **4** (0.11 g, 0.06 mmol) or **5** (0.12 g, 0.054 mmol) and Pd/C(10%) (30 mg) in DMSO (20 mL) was hydrogenated at room temp. under 1 atm hydrogen pressure for 8 h. The catalyst was filtered off, and the mixture was precipitated with the addition of ethanol to give **6** or **7**. Compounds **6** or **7** were dissolved in DMF (2 mL) and reprecipitated with a mixture of acetone/ethanol (1:1, v/v). After filtration, the precipitates were washed successively with hot acetic acid, water, and alcohol, and dried in vacuo. The purification of **6** and **7** was carried out using silica gel columns with a THF/DMF system changing from 10:0.1 to 10:1 (v/v). These compounds are soluble in THF, DMSO, DMF, and DMA. Yield (**6**): 69 mg (76%). M.p. >300 °C. UV/Vis (DMF): $\lambda$ (log $\varepsilon$) = 680 (5.08), 639 (5.02), 344 (5.11) nm (Figure 1). $^1$H NMR ([D$_6$]DMSO): $\delta$ = 11.35 (br s, 8 H, aliph. OH, disappeared with $D_2O$ exchange), 8.31–6.94 (m, 24 H, arom. CH), 4.12–3.13 (m, 32 H, aliph. $CH_2$) ppm. IR (KBr): $\tilde{\nu}$ = 3402 (aliph. OH), 3059 (arom. CH), 2926–2851 (aliph. CH), 1603 (arom. C=C), 1466, 1228 (aliph.–O–arom.), 1089, 1045 cm$^{-1}$. MALDI-TOF MS: $m/z$ = 1685 [M + H]$^+$, 1596 [M – 88]$^+$ (Figure 4). $C_{84}H_{64}N_{16}O_{16}Zn_2$: calcd. C 59.90, H 3.83, N 13.31; found C 60.44, H 3.79, N 13.63. Yield (**7**): 62 mg (63%). M.p. >300 °C. UV/Vis (DMF): $\lambda$ (log $\varepsilon$) = 674 (5.13), 610 (4.69), 336 (4.88) nm (Figure 1). IR (KBr): $\tilde{\nu}$ = 3396 (aliph. OH), 3053 (arom. CH), 2933–2874 (aliph. CH), 1603 (arom. C=C), 1468, 1232 (aliph.–O–arom.), 1094, 1056 cm$^{-1}$. MALDI-TOF MS: $m/z$ = 1672 [M + H]$^+$ (Figure 5). $C_{84}H_{64}Co_2N_{16}O_{16}$: calcd. C 60.36, H 3.86, N 13.41; found C 61.01, H 3.80, N 13.11.

**2′,10′,16′,24′-[{Tetrakis(4,4′-2,2-bis(oxidomethyl)propane-1,3-diyl)-bis(oxy)}]bis(phthalocyaninato)dizinc(II)] Octapotassium (8) and 2′,10′,16′,24′-[{Tetrakis(4,4′-2,2-bis(oxidomethyl)propane-1,3-diyl)-bis(oxy)}]bis(phthalocyaninato)dicobalt(II)] Octapotassium (9):** Compound **6** (0.034 g, 0.02 mmol) or **7** (0.017 g, 0.01 mmol) was suspended in aqueous KOH solution (20%, 5 mL) and boiled for 10 min. The solution of the compound **8** or **9** was cooled, and the mixture was poured into ethanol (100 mL). The formed precipitate was filtered off, dissolved in water and reprecipitated in ethanol several times until the solution was neutral. The products were then washed with ethanol and diethyl ether, and dried in vacuo. Both compounds are soluble in water at room temp. Yield (**8**): 0.031 g (77%). M.p. >300 °C. UV/Vis (water): $\lambda$ (log $\varepsilon$) = 687 (4.62), 637 (4.70), 338 (4.53) nm (Figure 2). IR (KBr): $\tilde{\nu}$ = 3061 (arom. CH), 2939–2870 (aliph. CH), 1605 (arom. C=C), 1489, 1226 (aliph.–O–arom.), 1095, 1044 cm$^{-1}$. $C_{84}H_{56}N_{16}O_{16}K_8Zn_2$: calcd. C 50.72, H 2.84, N 11.27; found C 51.08, H 2.79, N 11.31. ICP-MS (Zn, K): Anal. calcd. for $C_{84}H_{56}N_{16}O_{16}K_8Zn_2$: Zn 6.58, K 15.73; found Zn 6.47, K 15.91. Yield (**9**): 0.013 g (65%). M.p. >300 °C. UV/Vis (Water): $\lambda$ (log $\varepsilon$) = 685 (4.36), 623 (4.47), 279 (4.67) nm (Figure 3). IR (KBr): $\tilde{\nu}$ = 3067 (arom. CH), 2931–2865 (aliph. CH), 1601 (arom. C=C), 1482, 1224 (aliph.–O–arom.), 1093, 1047 cm$^{-1}$. $C_{84}H_{56}Co_2N_{16}O_{16}K_8$: calcd. C 51.06, H 2.86, N 11.34; found C 50.81, H 2.79, N 11.18. ICP-MS (Co, K): Anal. calcd. for $C_{84}H_{56}Co_2N_{16}O_{16}K_8$: Co 5.96, K 15.83; found Co 6.07, K 15.79.

**Electrochemistry and Spectroelectrochemistry:** The cyclic voltammetry (CV) and controlled potential coulometry (CPC) measurements were carried out with a Princeton Applied Research Model VersaStat II potentiostat/galvanostat, which was controlled by an external PC and utilized a three-electrode configuration at 25 °C.

 © 2007 Wiley-VCH Verlag GmbH & Co. KGaA, Weinheim 

The working electrode was a Pt plate with a surface area of 0.10 $cm^2$. The surface of the working electrode was polished with a $H_2O$ suspension of $Al_2O_3$ before each run. The last polishing was done with a particle size of 50 nm. A Pt wire served as the counter electrode. Saturated calomel electrode (SCE) was employed as the reference electrode and was separated from the bulk of the solution by a double bridge. The ferrocene/ferrocenium couple ($Fc/Fc^+$) was also used as an internal standard. Electrochemical grade tetrabutylammonium perchlorate (TBAP) in extra pure DMSO was employed as the supporting electrolyte at a concentration of 0.10 mol/$dm^3$. High purity $N_2$ was used for deoxygenating the solution at least 20 min prior to each run and for maintaining a nitrogen blanket during the measurements. For CPC studies, Pt gauze working electrode (10.5 $cm^2$ surface area), Pt-wire counter electrode separated by a glass bridge, and SCE as a reference electrode were used. The spectroelectrochemical measurements were carried out with an Agilent Model 8453 diode array spectrophotometer equipped with the potentiostat/galvanostat and utilized a three-electrode configuration of thin-layer quartz spectroelectrochemical cell at 25 °C. The working electrode was transparent Pt gauze. Pt-wire counter electrode separated by a glass bridge and a SCE reference electrode separated from the bulk of the solution by a double bridge were used.

**Conductivity and Thermopower Measurements:** The electrodes used in the conductivity and thermopower measurements consisted of an interdigital array of metal electrodes photolithographically patterned on pre-cleaned glass substrate. The films were prepared by spin-coating method. The substrate temperature was kept constant at 290 K during deposition of the materials over the electrodes. Dc conductivity and impedance spectra measurements were performed between 290 and 440 K by using a Keithley 617 electrometer. Ac conductivity and impedance measurements were carried out with a Keithley 3330 LCZ meter in the frequency range 40 to $10^5$ Hz, in the temperature range 290 to 440 K. Both dc and ac conductivity measurements were performed under $10^{-3}$ mbar in the dark. The conductivity data were recorded using an IEEE 488 data acquisition system incorporating a personal computer. The thermopower was determined independently from the electrical conductivity measurements. Thermopower measurements were carried out on the same samples, which were prepared for electrical conductivity measurements. The Seebeck coefficient $S$ was determined by measuring the voltage for a temperature gradient over the samples by using a Keithley 2000 digital multimeter. The temperature difference between the two sides of the film was measured by a Ni/CrNi thermocouple.

## Acknowledgments

This work was supported by the Research Funds of DPT (Project No: 2003K120810) and Marmara University, and partly by the Turkish Academy of Sciences (TUBA).

[1] N. Kobayashi, P. Janda, A. B. P. Lever, *Inorg. Chem.* **1992**, *31*, 5172.
[2] B. Agboola, T. Nyokong, *Electrochim. Acta*, DOI: 10.1016/j.electacta.2007.02.017.
[3] J. Simon, T. Toupance, in *Supramolecular Technology* (Ed.: D. N. Reinhoudt), Pergamon, Exeter, **1996**, vol. 10.
[4] G. de la Torre, T. Torres, F. Aqullo-Lopez, *Adv. Mater.* **1997**, *9*, 265.
[5] N. Toshima, T. Tominaga, S. Kawamura, *Bull. Chem. Soc. Jpn.* **1996**, *69*, 245.
[6] B. Lukas, J. Silver, D. Lovett, M. J. Cook, *Chem. Phys. Lett.* **1995**, *241*, 351.
[7] Ş. Abdurrahmanoğlu, A. R. Özkaya, M. Bulut, Ö. Bekaroğlu, *Dalton Trans.* **2004**, 4022.
[8] H. Eichhorn, D. Wöhrle, D. Pressner, *Liq. Cryst.* **1997**, *22*, 643.
[9] D. Lelievre, M. A. Petit, J. Simon, *Liq. Cryst.* **1989**, *4*, 707.
[10] C. C. Leznoff, A. B. P. Lever, *Phthalocyanines: Properties and Applications*, VCH, NewYork, **1996**, vols. 1–4.
[11] Ö. Bekaroğlu, *Appl. Organomet. Chem.* **1996**, *10*, 605 and references cited therein.
[12] N. Kobayashi, H. Lam, W. A. Nevin, P. Janda, C. C. Leznoff, T. Koyama, A. Monden, H. Shirai, *J. Am. Chem. Soc.* **1994**, *116*, 879.
[13] Y. Lemest, M. Lher, N. H. Hendricks, K. Kim, J. P. Collman, *Inorg. Chem.* **1992**, *31*, 835.
[14] J. P. Collman, J. E. Hutchison, M. A. Lopez, A. Tabard, R. Guilard, W. K. Seok, J. A. Ibers, M. Lher, *J. Am. Chem. Soc.* **1992**, *114*, 9869.
[15] N. Kobayashi, *Coord. Chem. Rev.* **2002**, *227*, 129.
[16] N. Kobayashi, H. Lam, W. A. Nevin, P. Janda, C. C. Leznoff, A. B. P. Lever, *Inorg. Chem.* **1990**, *29*, 3415.
[17] N. Kobayashi, Y. Yanagisawa, T. Osa, H. Lam, C. C. Leznoff, *Anal. Sci.* **1990**, *6*, 813.
[18] Z. Odabaş, A. Altındal, A. R. Özkaya, B. Salih, Ö. Bekaroğlu, *Polyhedron* **2007**, *26*, 695.
[19] D. Wöhrle, L. Kreienhoop, G. Schnurpfeil, J. Elbe, B. Tennigkeit, S. Hiller, D. Schlettwein, *J. Mater. Chem.* **1995**, *5*, 1819.
[20] A. Altındal, Z. Z. Öztürk, S. Dabak, Ö. Bekaroğlu, *Sens. Actuators B* **2001**, *77*, 389.
[21] D. Hohnholz, S. Steinbrecher, M. Hanack, *J. Mol. Struct.* **2000**, *521*, 231.
[22] R. Murdey, N. Sato, M. Bouvet, *Mol. Cryst. Liq. Cryst.* **2006**, *455*, 211.
[23] A. Y. Tolbin, A. V. Ivanov, L. G. Tomilova, N. S. Zefirov, *Mendeleev Commun.* **2002**, 96.
[24] A. Y. Tolbin, A. V. Ivanov, L. G. Tomilova, N. S. Zefirov, *J. Porphyr. Phthalocyanines* **2003**, *7*, 162.
[25] T. Ceyhan, A. Altındal, A. R. Özkaya, M. K. Erbil, B. Salih, Ö. Bekaroğlu, *Chem. Commun.* **2006**, 320.
[26] C. H. Issidorides, R. Gulen, *Org. Synth.* **1963**, *Coll. vol. IV*, 679.
[27] N. G. Lukyanenko, O. T. Melnik, T. I. Kirichenko, *Synth. Commun.* **1986**, *16*, 930.
[28] V. Manivannan, W. A. Nevin, C. C. Leznoff, A. B. P. Lever, *J. Coord. Chem.* **1988**, *19*, 139.
[29] J. R. Darwent, I. McCubbin, G. Porter, *J. Chem. Soc. Faraday Trans. 2* **1982**, *78*, 903.
[30] N. Ishikawa, O. Ohno, Y. Kaizu, H. Kobayashi, *J. Phys. Chem.* **1992**, *96*, 8832.
[31] D. Wöhrle, A. Wendt, A. Weitemeyer, J. Stark, W. Spiller, G. Schneider, S. Müller, U. Michelsen, H. Kliesch, A. Heuermann, A. Ardeschirpur, *Russ. Chem. Bull.* **1994**, *43*, 1953.
[32] M. Özer, A. Altındal, A. R. Özkaya, M. Bulut, Ö. Bekaroğlu, *Synth. Met.* **2005**, *155*, 222.
[33] A. B. P. Lever, E. R. Milaeva, G. Speier, in *Phthalocyanines: Properties and Applications* (Eds.: C. C. Leznoff, A. B. P. Lever), VCH Publishers, New York, **1993**, vol. 3.
[34] W. A. Nevin, W. Liu, S. Greenberg, M. R. Hempstead, S. M. Marcuccio, M. Melnik, C. C. Leznoff, A. B. P. Lever, *Inorg. Chem.* **1987**, *26*, 891.
[35] M. J. Stillman, A. J. Thompson, *J. Chem. Soc. Faraday Trans. 2* **1974**, *70*, 790.
[36] C. C. Leznoff, S. M. Marcuccio, S. Greenberg, A. B. P. Lever, K. B. Tomer, *Can. J. Chem.* **1985**, *63*, 623.
[37] W. A. Nevin, M. R. Hempstead, W Liu, C. C. Leznoff, A. B. P. Lever, *Inorg. Chem.* **1987**, *26*, 570.
[38] W. K. Lee, J. F. Liu, S. Walker, *Phys. Rev. Lett.* **1991**, *67*, 1559.

Received: January 31, 2007
Published Online: June 19, 2007

 © 2007 Wiley-VCH Verlag GmbH & Co. KGaA, Weinheim 

DOI: 10.1002/ejic.200700217

# Steric and Electronic Effects in the Dimerization of Wanzlick Carbenes: The Alkyl Effect[‡]

**Michael K. Denk,*[a] Azardokht Hezarkhani,[a] and Feng-Lan Zheng[a]**

**Keywords:** Carbenes / Thiourea / Thermochemistry / Dimerization / Enetetramine / Steric hindrance / DFT calculations / Steric effects / Electronic effects

The steric and electronic influence of *N*-alkyl substituents on the dimerization energies $\Delta G°$ of Wanzlick carbenes (imidazolidin-2-ylidenes) was investigated experimentally and through DFT methods for a series of non-symmetrically substituted Wanzlick carbenes. A series of 3-alkyl-1-*tert*-butylimidazolidin-2-ylidenes with decreasing steric demand of the alkyl substituent (isopropyl, ethyl and methyl) were obtained in four steps from the commercially available *N*-alkylaminoethanol compounds. The carbenes are hydrolytically sensitive, colorless oils that can be distilled without decomposition and show no sign of dimerization to the respective enetetramines, even after prolonged heating. Calculations at the B98/6-31G(d) level confirm that the dimerization of all three carbenes is thermodynamically unfavorable. To separate the steric and electronic stabilization of Wanzlick carbenes by *N*-alkyl substituents, the formation energies of $R,H_3$ mono-alkyl enetetramines were used to derive electronic increments for the *N*-alkyl substituents. The computational data show that all alkyl substituents electronically stabilize Wanzlick carbenes vs. their dimerization products with increments ranging from 2.97 kcal mol$^{-1}$ (*N*-methyl) to as high as 6.28 kcal mol$^{-1}$ (*N*-*tert*-butyl). For combinations of *N*-methyl, *N*-ethyl and *N*-isopropyl substituents, the increments are additive and the dimerization energies were found to be free of noticeably steric effects. Significant steric strain was found for all *t*Bu-substituted carbenes with strain energies of the dimerization products ranging from 6.92 kcal mol$^{-1}$ [formation of (*E*)-$Me_2tBu_2$-enetetramine] to 24.23 kcal mol$^{-1}$ (formation of $tBu_4$ enetetramine). The *tert*-butyl substituent thus assumes a unique position by strongly stabilizing the carbenes electronically as well as sterically.

(© Wiley-VCH Verlag GmbH & Co. KGaA, 69451 Weinheim, Germany, 2007)

## 1. Introduction

A limit to the steadily growing number of thermodynamically stable diamino carbenes[1] obtained since the isolation of a imidazol-2-ylidene (**A**, R = 1-adamantyl) in 1991 by Arduengo et al.[2] is their dimerization[3–5] to the respective enetetramines,[6] the very reaction preventing the isolation of 1,3-diphenylimidazolidin-2-ylidene investigated by Wanzlick's group more than 40 years ago.[3] While dimerization of the aromatically stabilized[7] carbenes of type **A** is thermodynamically unfavorable even for small substituents like R = Me, and has only been observed for the special case of the covalently tethered bis-carbene (formation of **B=B**)[8] all other diamino carbenes like **C** and **D** require sterically demanding substituents to be thermodynamically stable towards dimerization.[5–11] A notable exception may be the benzo-annellated carbene **E** that has recently been obtained by Metallinos et al.[12]

The crucial role of steric protection is particularly obvious from the behavior of Wanzlick carbenes **D** which dimerize for R = phenyl, the substituent originally chosen by Wanzlick's group, but are thermodynamically stable towards dimerization for R = *tert*-butyl[4] and mesityl.[13] For alkyl substituents, even a slight relaxation of the steric demand (R = isopropyl, ethyl, or methyl) the Wanzlick carbenes dimerize although the dimerization is slow enough to be observed by NMR methods.[4,5] The slow nature of the dimerization has since been strikingly highlighted by the successful isolation and structural characterization of a series of thermodynamically unstable amino carbenes like the tetramethyl analog of **C**,[10a] the tetraethyl analog of **C**[10b] and even the monoamino carbene **F** (Scheme 1).[10c] Irrespective of the kinetic aspect of the reaction, the presence of bulky substituents remains a prerequisite for the design of thermodynamically stable carbenes. For Wanzlick carbenes bearing identical *N*-substituents, the demarcation line separating stable from unstable carbenes is now established as $tBu_2/iPr_2$[4] and $Mes_2/Ph_2$.[13] Wanzlick carbenes bearing only *one* bulky *N*-alkyl substituent should dimerize to the (E)-enetetramines in which steric repulsion is minimized due to the large-small combination of alkyl substituents facing each other across the double bond (Scheme 2).

[‡] Presented in part (experimental part) at the OMCOS conference, July 27–31, 2005, Geneva, Switzerland.

[a] Guelph–Waterloo Centre For Graduate Research in Chemistry, Guelph Campus
50 Stone Road, Guelph, Ontario N1G 2W1, Canada
Fax: +1-519-766-1499
E-mail: mdenk@uoguelph.ca
michaeldenk@mac.com

Supporting information for this article is available on the WWW under http://www.eurjic.org or from the author.

 © 2007 Wiley-VCH Verlag GmbH & Co. KGaA, Weinheim 

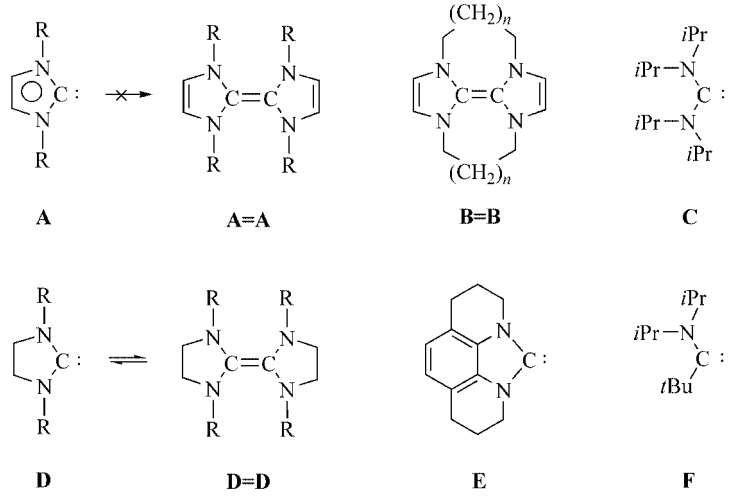


Scheme 1. Dimerization of aminocarbenes.

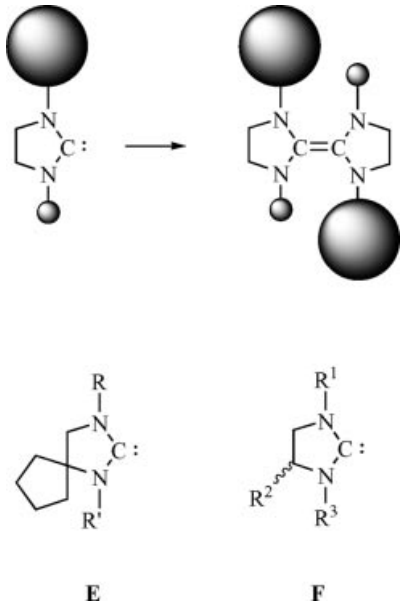


Scheme 2. Steric matching in non-symmetric Wanzlick carbenes.

To examine this prediction experimentally, we have obtained a series of 3-alkyl-1-*tert*-butylimidazolidin-2-ylidenes with alkyl substituents of decreasing size (R: *i*Pr, Et and Me). Much to our surprise, all three carbenes are perfectly stable and do not show any sign of dimerization even for the smallest substituent (Me). While surprising, the observed lack of dimerization is in good agreement with the behavior of 1,3,4-trisubstituted Wanzlick carbenes **E** and **F** (Scheme 2) which have been obtained via a new elegant synthetic protocol by Hahn's group while this work was in progress.[14]

The observed lack of dimerization is nevertheless hard to rationalize on purely steric grounds so that a more detailed computational examination of the steric and electronic influence of *N*-alkyl groups on the dimerization of Wanzlick carbenes seemed desirable.

## 2. Results and Discussion

The synthesis of Wanzlick carbenes **4** bearing dissimilar substituents R, R′ on the nitrogen atoms is of obvious interest to understand the fine interplay of steric and electronic effects in the Wanzlick equilibrium but is also desirable to broaden the repertoire of N-heterocyclic carbenes used as steering ligands in catalysis. While the symmetrically substituted ethylenediamines RNH-$CH_2CH_2$-NHR′ (R = R′) are commercially available and are also readily accessible from 1,2-dibromoethane and primary amines,[15] ethylenediamines RNH-$CH_2CH_2$-NHR′ bearing dissimilar substituents are less well explored and accessible only through multistep reactions.[16] Except for R, R′ = Me,H the diamines are not commercially available.

Among the number of possible synthetic approaches tested in our group, only the reaction of primary amines with 2-chloroethylamines[17] proved to be the most useful (Scheme 3). Apart from being adaptable to a great variety of substituents R,R′ the reactions are readily scaled up and deliver acceptable yields and purities of the diamines.

The disadvantage of using the rather toxic 2-chloroethylamines is diminished by the fact that the stable and non-volatile hydrochloride salts can be used instead of the volatile free bases.

Reaction of 2-(*tert*-butylamino)ethanol with $SOCl_2$ followed by reaction with the respective primary amine thus gave the *N*-*tert*-butyl-*N*′-(alkyl)ethylenediamines (**1**). To obtain good yields of the respective ethylenediamines, the use of an excess of the primary amine (5 equiv. or more) as well as high reaction temperatures (180 °C) were found to be crucial. Lowering the amount of primary amine lead to the predominant formation of *N*,*N*′-di-*tert*-butylpiperazine through the competing self-condensation of the 2-chloroamine, while lower reaction temperatures were found to be inadequate to achieve complete conversion (detection of the free 2-chloroamine by GC-MS). The synthesis of the respective thioureas from the ethylenediamines turned out to be an additional obstacle. As we noted previously for

 © 2007 Wiley-VCH Verlag GmbH & Co. KGaA, Weinheim 

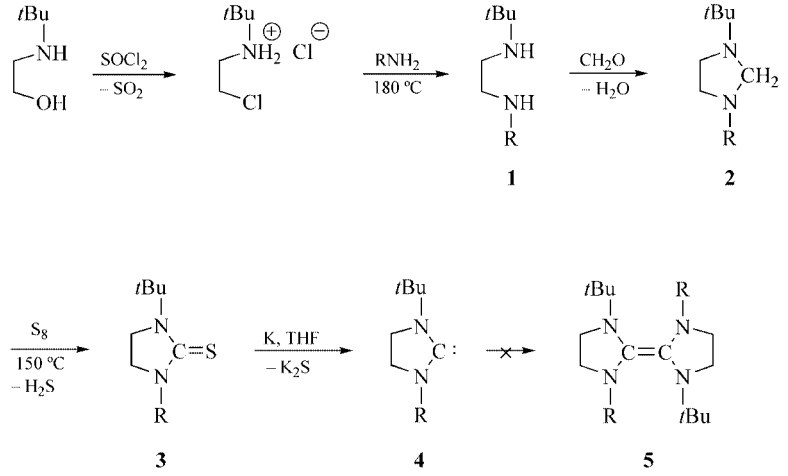

Scheme 3. Synthesis of 3-alkyl-1-*tert*-butylimidazolidin-2-ylidenes from 2-(*tert*-butylamino)ethanol.

ethylenediamines bearing *two* bulky *N*-alkyl substituents, the respective thioureas can only be obtained in poor yields via the textbook $CS_2$ route or its many variations.[18] The reaction of the ethylenediamines **1a**–**1c** with $CS_2$ gave likewise only trace amounts (GC-MS) of the thioureas **3a**–**3c**. The presence of only *one* sterically demanding substituent (*tert*-butyl) is obviously sufficient to block the $CS_2$ route.[18] To circumvent these problems, the thioureas **3a**–**3c** were obtained by oxidation of the respective formaldehyde aminals (imidazolidines) **2a**–**2c** with elemental sulfur, $S_8$, a two-step one-pot approach recently developed in our group to overcome the problems of the $CS_2$ method.[18] Reductive desulfurization of the thioureas with potassium (Kuhn method)[19] gave the respective carbenes in high yields (85–95%).

The carbenes were obtained as spectroscopically pure ($^1$H NMR, $^{13}$C NMR) oils that are readily distilled without decomposition. In line with the previously examined Wanzlick and Arduengo carbenes[20] the carbenes **4a**–**4c** were found to be unreactive towards dry oxygen but readily hydrolyze in air.[21] Most remarkably, the carbenes did not show any sign of dimerization either as such or in $C_6D_6$ at room temperature or at 100 °C even after 12 months. The dimerization of the carbenes **4a**–**4b** can in principle lead to the formation of either the respective (*E*)- or the (*Z*)-enetetramines (Scheme 4).

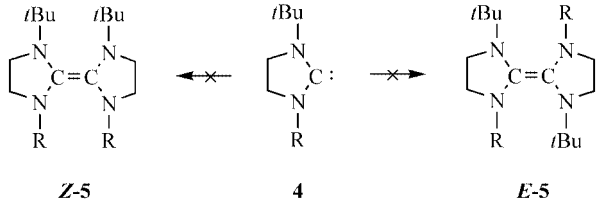

Scheme 4. Potential formation of enetetramines **5** from carbenes **4a**–**4c**.

While the (*Z*)-enetetramine is likely to suffer from significant steric front-strain due to the interaction of the *tert*-butyl groups and might be unstable for steric reasons, the argument cannot be applied to the (*E*)-isomer. The fact that neither of the two possible dimerization products could be observed is therefore hard to justify on purely steric grounds and points towards the importance of electronic effects in the stabilization of **4**. To clarify this issue, the steric and electronic influence of different *N*-alkyl substituents on the dimerization energies of Wanzlick carbenes was investigated through DFT calculations.

## Computational Studies

DFT calculations of symmetrically substituted diamino carbenes have already generated significant insight into the nature of the dimerization reaction,[5] and have recently been reviewed by Alder et al.[1a] Of particular importance is the conclusion that calculated dimerization energies $\Delta G°$ are in good qualitative agreement with the experimentally observed dimerization behavior.[1a] The precise balance of steric and electronic effects on the stability of the carbenes towards dimerization on the other hand is less clear. DFT calculations at the B98/6-31G(d) level were carried out to establish if the dimerization of the carbenes **4a**–**4c** has a thermodynamic basis and to quantify steric and electronic effects of the respective *N*-alkyl substituents. The B98 functional was selected because it offers improved thermochemical accuracy over the B3LYP method without adding computational cost.[23] To obtain a benchmark for the accuracy of the DFT calculations, the dimerization energy of the hypothetical unsubstituted carbene **4H** was calculated with the high precision CBS-Q[26] and G3[27] methods. All calculations were carried out with the Gaussian03 suite of programs.[22] Local minima were confirmed through the absence of virtual frequencies. The geometry selected for the enetetramines **5** is that found experimentally for all solid-state structures of *N*-alkyl-substituted enetetramines.[28]

The surprisingly strong effect of *N*-alkyl substituents on the dimerization of Wanzlick carbenes is readily apparent from a comparison of the dimerization energies $\Delta G°$ of *N*,*N*′-dimethylimidazolidin-2-ylidene (**4e**) with that of the unsubstituted carbene **4H** (Scheme 5). The dimerization energies reveal a net stabilizing effect caused by the presence

 © 2007 Wiley-VCH Verlag GmbH & Co. KGaA, Weinheim 

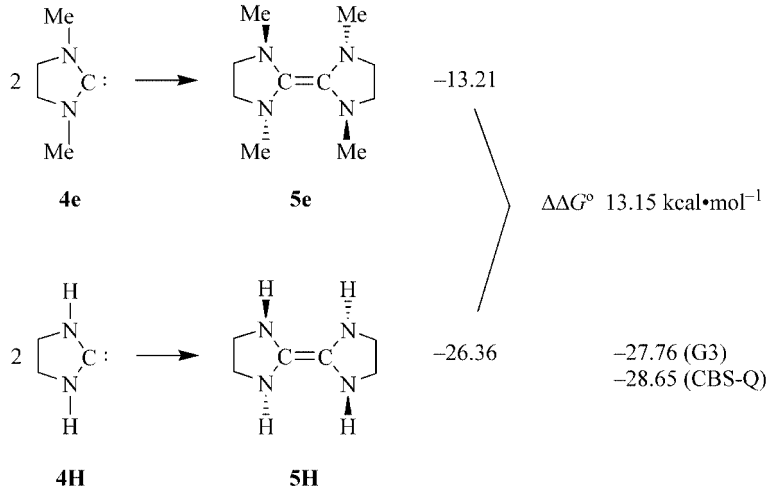


Scheme 5. Influence of *N*-methyl substitution on the dimerization energy of imidazolidin-2-ylidene. Dimerization energies $\Delta G°$ (in kcal mol$^{-1}$) at the B98/6-31G(d), CBS-Q and G3 level.

of four methyl groups ca. 13 kcal mol$^{-1}$. The high accuracy of the B98/6-31G(d) approach can be inferred by the excellent agreement of the dimerization energy of **1H** (–26.4 kcal mol$^{-1}$) with the respective G3 (–27.8 kcal mol$^{-1}$) and CBS-Q data (–28.7 kcal mol$^{-1}$).

The lack of dimerization observed for the carbenes **4a**–**4c** can in principle have thermodynamic reasons ($\Delta G° > 0$) or kinetic reasons (high $\Delta G^{‡}$). The kinetic stabilization of Wanzlick carbenes bearing only *one* sterically demanding substituent may in fact be expected from the orbital symmetry required non-least-motion pathway.[24] The calculations do however reveal that the dimerization of the carbenes **4a**–**4d** is in fact thermodynamically unfavorable: dimerization is predicted to be thermodynamically unfavorable for **4b** and **4c** and close to thermoneutral for **4a** (Scheme 6). The stable carbene **4d** which was obtained earlier in our group[4] has been included for comparison as the sterically most crowded member of the series.

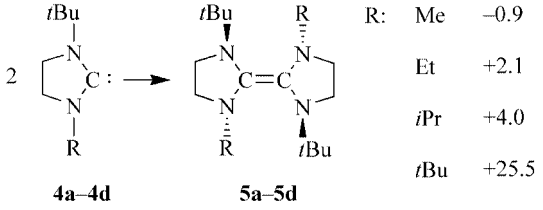


Scheme 6. Dimerization energies $\Delta G°$ (in kcal mol$^{-1}$) of imidazolidin-2-ylidenes **4a**–**4d** at the B98/6-31G(d) level of theory.

A comparison of the individual reaction energies is instructive. While the dimerization energies $\Delta G°$ show only small incremental changes from **4a**–**4c** a steep rise of ca. 20 kcal mol$^{-1}$ occurs from **4c** to **4d**. While it is tempting to assign this discontinuous change in the dimerization energy to the onset of steric crowding, a rational, quantitative separation of steric and electronic factors is desirable.

To reveal the electronic effects of *N*-alkyl substituents on the dimerization reaction, the formation of the mono-alkyl enetetramines **5h**–**5l** from the respective carbenes were examined (Scheme 7). The presence of only *one* alkyl substituent in the enetetramines **5h**–**5l** eliminates the possibility of steric effects resulting from alkyl–alkyl repulsion. The variation in the dimerization energies will thus reflect the electronic effect of the *N*-alkyl substituent.

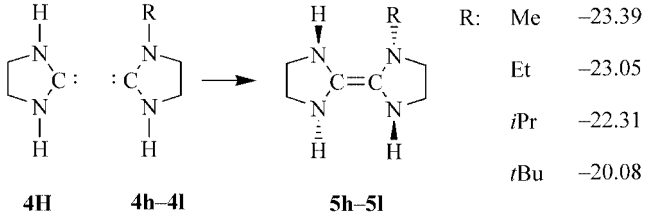


Scheme 7. Formation of mono-substituted enetetramines **5h**–**5l** from the respective carbenes **4H**, **4f**–**4i**. Energies $\Delta G°$ at the B98/6-31G(d) level.

Comparison of the dimerization energies in Scheme 7 with those obtained for the unsubstituted enetetramine **5H** (Scheme 5, $\Delta G° = –26.4$ kcal mol$^{-1}$) leads to electronic increments of the *N*-alkyl substituents as +2.97 kcal mol$^{-1}$ (Me), +3.31 kcal mol$^{-1}$ (Et), +4.04 kcal mol$^{-1}$ (*i*Pr) and +6.28 kcal mol$^{-1}$ (*t*Bu). While all four *N*-alkyl substituents electronically stabilize the carbene vs. the dimer, the effect increases along the series Me < Et < *i*Pr < *t*Bu. Although the electronic influence of the individual alkyl substituents may appear small, it must be born in mind that the overall effect is anything but negligible for the fully substituted enetetramines. The electronic effect of replacing four methyl substituents with four *tert*-butyl substituents amounts to 13 kcal mol$^{-1}$, a large caloric change considering that the dimerization reactions are close to equilibrium.

The electronic increments obtained above can now be used to separate electronic and steric effects of the *N*-alkyl substituents.

Addition of four electronic increments to the base value corresponding to the formation of unsubstituted enetetramine **5H** from the unsubstituted carbene **4H** (–26.36 kcal) will give the strain-free, electronic component $\Delta G_{el}$ of the dimer-

 © 2007 Wiley-VCH Verlag GmbH & Co. KGaA, Weinheim 

ization energies. Comparison of $\Delta G_{el}$ with the fully optimized values $\Delta G_{FC}$ leads to the quantitative estimate of strain energies $\Delta G_{st}$ according to $\Delta G_{FC} = \Delta G_{el} + \Delta G_{st}$. Scheme 8 shows the results for the symmetrically substituted carbenes.

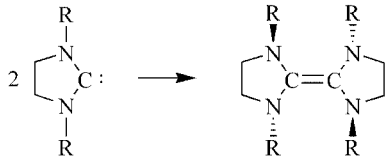

**4d–4h** **5d–5g**

| R | $\Delta G_{fc}$ | $\Delta G_{el}$ | $\Delta G_{st}$ |
|---|---|---|---|
| Me | –13.21 | –14.48 | + 1.27 |
| Et | –12.73 | –13.12 | + 0.39 |
| *i*Pr | –9.65 | –10.20 | + 0.55 |
| *t*Bu | + 25.47 | +1.24 | + 24.23 |

Scheme 8. Dimerization energies $\Delta G°$ (in kcal mol$^{-1}$) of symmetrically substituted Wanzlick carbenes at the B98/6-31G(d) level. Comparison of fully optimized energies ($\Delta G_{FC}$) with those derived from the addition of electronic alkyl increments ($\Delta G_{el}$). Steric contributions $\Delta G_{st}$ derived according to $\Delta G_{FC} = \Delta G_{el} + \Delta G_{st}$.

The dimerization energies obtained from full calculations ($\Delta G_{FC}$) and those obtained through the increment approach ($\Delta G_{el}$) are practically identical for R = Me, Et, and *i*Pr which rules out the presence of significant steric strain for these alkyl substituents. For R = *t*Bu, the pronounced difference between $\Delta G_{FC}$ (+25.47 kcal mol$^{-1}$) and $\Delta G_{el}$ (+1.24 kcal mol$^{-1}$) confirms a strong steric destabilization (+24.23 kcal mol$^{-1}$) of the enetetramine. The same approach can now be used to check if the enetetramines **5a**–**5c** are indeed free from steric strain as the large-small size match of the alkyl substituents (Scheme 2) seems to suggest.

The quantitative analysis (Scheme 9) contradicts this simplistic pictorial prediction by revealing strain energies $\Delta G_{st}$ ranging from +6.92 kcal mol$^{-1}$ (*t*Bu,Me) to +10.25 kcal mol$^{-1}$ (*t*Bu,*i*Pr). Steric strain is in fact a crucial factor for the thermodynamic stability of the carbenes **4a**–**4c** because dimerization would occur otherwise ($\Delta G_{el} < 0$).

The thermodynamic stability of Wanzlick carbenes **4** towards dimerization can in principle be ascribed to an inherent stabilization of the carbenes **4**, a destabilization of the enetetramines **5** or a combination of both. While dimerization energies, experimental or computational, cannot differentiate between these two possibilities, a comparison of other relevant data with the dimerization energies may nevertheless provide some insight. Table 1 compares the influence of the *N*-alkyl substituent on the $^{13}$C NMR shifts and dimerization energies of Wanzlick carbenes **4**, with the calculated length of the carbon–carbon double bond and the associated valence vibrations in the dimers **5** arranged in order of decreasing carbene dimerization energies $\Delta G°$.

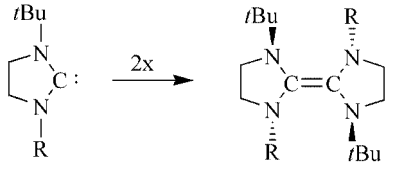

**4** **5a–5c**

| R | $\Delta G_{fc}$ | $\Delta G_{el}$ | $\Delta G_{st}$ |
|---|---|---|---|
| Me | –0.94 | –7.86 | +6.92 |
| Et | +2.13 | –7.18 | +9.31 |
| *i*Pr | +4.54 | –5.72 | +10.25 |

Scheme 9. Dimerization energies $\Delta G°$ (in kcal mol$^{-1}$) of non-symmetrically substituted Wanzlick carbenes at the B98/6-31G(d) level. Comparison of fully optimized energies ($\Delta G_{FC}$) with those derived from the addition of electronic alkyl increments. Steric contributions $\Delta G_{st}$ derived according to $\Delta G_{FC} = \Delta G_{el} + \Delta G_{st}$.

Table 1. Dimerization of Wanzlick carbenes: comparison of $^{13}$C NMR shifts and calculated dimerization energies $\Delta G°$ of carbenes **4** with calculated double bond lengths and valence vibrations of the corresponding (*E*)-enetetramines **5**.

| R | | $\delta$ $N_2C$ [ppm] | | $\nu$(C=C) [cm$^{-1}$] | *d*(C=C) [pm] | $\Delta G°$ [kcal mol$^{-1}$] |
|---|---|---|---|---|---|---|
| Me,Me | **4e** | 239.8 | **5e** | 1771 | 135.23 | –13.21 |
| Et,Et | **4f** | 237.7 | **5f** | 1765 | 135.28 | –12.73 |
| *i*Pr,*i*Pr | **4g** | 236.8 | **5g** | 1746 | 135.80 | –9.65 |
| *t*Bu,Me | **4a** | 239.7 | **5a** | 1715 | 136.45 | –0.94 |
| *t*Bu,Et | **4b** | 238.8 | **5b** | 1710 | 136.43 | +2.13 |
| *t*Bu,*i*Pr | **4c** | 237.6 | **5c** | 1704 | 136.70 | +4.54 |
| *t*Bu,*t*Bu | **4d** | 238.3 | **5d** | 1671 | 137.47 | +25.47 |

The increase in double bond lengths and decrease in the C=C stretching frequencies of the enetetramines **5** correlates well with the dimerization energies of **4**. The $^{13}$C NMR shifts ($N_2C$) of the carbenes **4** on the other hand show only a negligible variation regardless of whether the respective carbene dimerizes (**4e**, **4f**, **4g**) or not (**4a**–**4d**). It therefore seems likely, that the variation in dimerization energies is predominantly caused by a progressive destabilization of the enetetramines **5** rather than a stabilization of the carbenes **4**. The thermodynamic stability of Wanzlick carbenes **4** towards dimerization may thus reflect the stability of the dimers **5** rather than those of the carbenes **4**.[25]

A comparable analysis of how the respective activation energies of the dimerization are influenced by steric and electronic factors would be very desirable and will be the subject of future studies.

## 3. Conclusions

The stability of Wanzlick carbenes towards dimerization is the result of a complex interplay between electronic and steric effects of the nitrogen substituents. There is a smooth increase of stability along the series R = Me, Et, *i*Pr, *t*Bu,

 © 2007 Wiley-VCH Verlag GmbH & Co. KGaA, Weinheim 

the *tert*-butyl substituent occupies a special position by strongly stabilizing the carbenes electronically as well as sterically. A comparison of spectroscopic and computational data suggests that the dimerization energies of Wanzlick carbenes may in fact reflect variations in the stabilities of the enetetramines rather than that of the carbenes themselves.

## 4. Experimental Section

Melting points were recorded in sealed capillaries and are uncorrected. EI-MS spectra were obtained with a Varian CP-3800 GC/Saturn 2000 MS combination at an ionizing voltage of 70 eV and a 30 × 0.25 mm Varian CP 5860 low-bleed phenyl(dimethyl)siloxane column (5% phenyl). Temperature program: 4 min 50 °C; 10 min constant heating rate of 20 °C/min; 6 min 250 °C. NMR spectra were recorded with Bruker 400 MHz ($^1$H) and 500 MHz ($^{13}$C) NMR spectrometers at room temperature. All NMR spectra are referenced vs. tetramethylsilane (internal). 2-(*tert*-Butylamino)ethanol, isopropylamine, ethylamine, methylamine, sulfur, paraformaldehyde and potassium were obtained from Aldrich Inc., thionyl chloride from Johnson Mathey. All operations were carried out under inert gas (99.999% Argon) unless indicated otherwise. [2-(*tert*-butylamino)ethyl chloride] hydrochloride was obtained from 2-(*tert*-butylamino)ethanol and thionyl choride according to ref.[17]

**Synthesis of *N*,*N*′-Disubstituted Ethylenediamines 1a–c:** 2-(*tert*-Butylamino)ethyl chloride hydrochloride (50 g, 0.29 mol), the primary amine (1.45 mol) and water (250 mL) were sealed in a 1-L stainless-steel autoclave and heated to 180 °C for 48 h. After cooling the autoclave to room temperature, water (100 mL) and NaOH pellets (75 g) were added to the autoclave. The resulting biphasic crude solutions were extracted with $Et_2O$ (3 × 100 mL). The combined organic phases were dried by addition of NaOH pellets and decanting from the freshly forming aqueous phase until the NaOH pellets remained undissolved. After removal of the solvent in vacuo, the pure *N*,*N*′-dialkylethylenediamines were obtained by fractional distillation over a 20 cm Vigreux column under normal pressure.

**Synthesis of 3-Alkyl-1-*tert*-butylimidazolidines 2a–c:** A mixture of the respective *N*,*N*′-disubstituted ethylenediamine (**1a**, **1b** or **1c**, 30 mmol), ether (15 mL), and paraformaldehyde (1.2 g, 40 mmol) was stirred at room temperature for 24 h. The resulting turbid solutions were stirred with $MgSO_4$ (ca. 1 g, 24 h) and the imidazolidines isolated by filtration and subsequent evaporation of the solvent in vacuo. Yield quantitative.

**Synthesis of 3-Alkyl-1-*tert*-butylimidazolidine-2-thiones 3a–b:** Elemental sulfur $S_8$ (2.21 g, 8.64 mmol), the respective imidazolidine (34.5 mmol) and ether (15 mL) were sealed in a stainless steel autoclave and heated to 160 °C for 12 h. The cold reaction mixtures were extracted with methanol (3 × 10 mL), filtered, and the thioureas precipitated by dropwise addition of water (ca. 30 mL) to the methanol solution. Crystallization was typically completed after standing at room temperature for 24 h. A second crop of the thioureas could be obtained by cooling the mother liquor to –20 °C. After vacuum drying for 24 h, both fractions were adequate for the subsequent reduction to the carbenes.

**Synthesis of 3-Alkyl-1-*tert*-butylimidazolidin-2-ylidenes 4a–c:** A solution of the respective 3-alkyl-1-*tert*-butylimidazolidine-2-thione (75 mmol) in THF (200 mL) was boiled with potassium (8.80 g, 226 mmol) for 2 h. The slightly yellowish solutions were filtered through a medium-porosity glass frit and the carbenes isolated by removal of the solvent in vacuo.

***N*-*tert*-Butyl-*N*′-methyl-1,2-diaminoethane (1a):** Colorless oil, b.p. 151 °C, 12.9 g (34%). $^1$H NMR ($CDCl_3$): $\delta$ = 1.09 [s, 9 H, C(C$H_3$)$_3$], 2.43 [s, 3 H, C$H_3$], 2.68 [s, 2 H + 2 H, identical shift, NHC$H_2$] ppm. $^{13}$C NMR ($CDCl_3$): $\delta$ = 29.1 [C(*C*H$_3$)$_3$], 36.4 [N*C*H$_3$], 41.8 [*t*BuN*C*H$_2$], 50.1 [*C*(CH$_3$)$_3$], 52.6 [MeN*C*H$_2$] ppm. GC-MS: $t_r$ = 5.2 min. *m*/*z* (rel. int.%) = 131 (100), 115 (23), 100 (8), 86 (55), 72 (23), 58 (74), 44 (76).

***N*-*tert*-Butyl-*N*′-ethyl-1,2-diaminoethane (1b):** Colorless oil, b.p. 165 °C, 27 g (64%), $^1$H NMR ($CDCl_3$): $\delta$ = 1.10 [s, 9 H, C(C$H_3$)$_3$], 1.11 [t, $^3J$(H,H) = 7 Hz, 3 H, CH$_2$C$H_3$], 2.65 [q, 2 H, C$H_2$CH$_3$], 2.71 [m, 4 H, NHC$H_2$ C$H_2$] ppm. $^{13}$C NMR ($CDCl_3$): $\delta$ = 15.3 [CH$_2$**C**H$_3$], 29.0 [C(*C*H$_3$)$_3$], 42.1 [*t*BuN*C*H$_2$], 44.1 [EtN*C*H$_2$], 50.2 [*C*(CH$_3$)$_3$], 50.3 [*C*H$_2$CH$_3$] ppm. GC-MS: $t_r$ = 6.1 min, *m*/*z* (rel. int.%) = 145 (100), 129 (18), 101 (10), 86 (50), 72 (85), 58 (92).

***N*-*tert*-Butyl-*N*′-isopropyl-1,2-diaminoethane (1c):** Colorless oil, b.p. 181 °C, 32 g (70%). $^1$H NMR ($CDCl_3$): $\delta$ = 1.06 [d, $^3J$(H,H) = 6 Hz, 6 H, CH(C$H_3$)$_2$], 1.10 [s, 9 H, C(C$H_3$)$_3$], 2.68 [m, 4 H, NC$H_2$], 2.78 [sept, $^3J$(H,H) = 6, Hz, 1 H, C*H*(CH$_3$)$_2$] ppm. $^{13}$C NMR ($CDCl_3$): $\delta$ = 23.1 [CH(*C*H$_3$)$_2$], 29.2 [C(*C*H$_3$)$_3$], 42.6 [*t*BuN*C*H$_2$], 48.2 [*i*PrN*C*H$_2$], 48.8 [*C*H(CH$_3$)$_2$], 50.2 [*C*(CH$_3$)$_3$] ppm. GC-MS: $t_r$ = 7.4 min, *m*/*z* (rel. int.%) = 159 (28), 143 (5), 100 (18), 86 (75), 72 (100), 57 (32).

**1-*tert*-Butyl-3-methylimidazolidine (2a):** Colorless oil, no CAS. $^1$H NMR ($CDCl_3$): $\delta$ = 1.10 [s, 9 H, C(C$H_3$)$_3$], 2.37 [s, 3 H, NC$H_3$], 2.76 [m, 2 H, MeNC$H_2$], 2.92 [m, 2 H, *t*BuNC$H_2$], 3.50 [NC$H_2$N] ppm. $^{13}$C NMR ($CDCl_3$): $\delta$ = 26.0 [C(*C*H$_3$)$_3$], 39.9 [*t*BuN*C*H$_2$], 45.8 [MeN*C*H$_2$], 52.8 [*C*(CH$_3$)$_3$], 55.2 [*C*H$_3$], 71.6 [N*C*H$_2$N] ppm. GC-MS: $t_r$ = 6.19 min, *m*/*z* (rel. int.%) = 141 (100), 127 (48), 112 (47), 85 (73), 57 (18), 42 (37).

**1-*tert*-Butyl-3-ethylimidazolidine (2b):** Colorless oil, no CAS. $^1$H NMR ($CDCl_3$): $\delta$ = 1.09 [s, 9 H, C(C$H_3$)$_3$], 1.10 [t, $^3J$ = 7 Hz, 3 H, CH$_2$-C$H_3$], 2.52 [q, $^3J$ = 7 Hz, 2 H, C$H_2$CH$_3$], 2.76 [m, 2 H, C$H_2$CH$_3$], 2.88 [m, 2 H, C$H_2$C$H_2$], 3.50 [s, 2 H, NC$H_2$N] ppm. $^{13}$C NMR ($CDCl_3$): $\delta$ = 13.9 [CH$_2$*C*H$_3$], 26.0 [C(*C*H$_3$)$_3$], 45.0 [*t*BuN*C*H$_2$], 49.0 [EtN*C*H$_2$], 52.4 [*C*(CH$_3$)$_3$], 52.8 [*C*H$_2$-CH$_3$], 69.6 [N*C*H$_2$N] ppm. GC-MS: $t_r$ = 7.0 min, *m*/*z* (rel. int.%) = 155 (100), 141 (25), 126 (13), 100 (5), 99 (52), 84 (43), 42 (25).

**1-*tert*-Butyl-3-isopropylimidazolidine (2c):** Colorless oil, no CAS. $^1$H NMR ($CDCl_3$): $\delta$ = 1.08 [d, $^3J$(H,H) = 7.0 Hz, 6 H, CH-(C$H_3$)$_2$], 1.09 [s, 9 H, C(C$H_3$)$_3$], 2.41 [sept, $^3J$(H,H) = 7.0 Hz, 1 H, C*H*(CH$_3$)$_2$], 2.84 [m, 4 H, NC$H_2$C$H_2$], 3.54 [NC$H_2$N] ppm. $^{13}$C NMR ($CDCl_3$): $\delta$ = 21.9 [CH(*C*H$_3$)$_2$], 26.0 [C(*C*H$_3$)$_3$], 45.2 [*t*BuN*C*H$_2$], 51.1 [*i*PrN*C*H$_2$], 52.2 [*C*H(CH$_3$)$_2$], 54.1 [*C*(CH$_3$)$_3$], 68.6 [N$_2$*C*H$_2$] ppm. GC-MS: $t_r$ = 8.4 min, *m*/*z* (rel. int.%) = 169 (100), 155 (22), 140 (6), 113 (81), 98 (8), 84 (25), 71 (26), 55 (13).

**1-*tert*-Butyl-3-methylimidazolidine-2-thione (3a):** Colorless crystals, m.p. 96.5–97 °C (hexane). Yield 2.37 g, (40%). No CAS. $^1$H NMR ($CDCl_3$): $\delta$ = 1.60 [s, 9 H, C(C$H_3$)$_3$], 3.09 [s, 3 H, N*C*H$_3$], 3.43 [m, 4 H, NC$H_2$], 3.60 [m, 4 H, NC$H_2$C$H_2$] ppm. $^{13}$C NMR ($CDCl_3$): $\delta$ = 27.9 [C(*C*H$_3$)$_3$], 35.0 [N-*C*H$_3$], 44.7 [*t*BuN*C*H$_2$], 48.2 [MeN*C*H$_2$], 56.4 [*C*(CH$_3$)$_3$], 183.1 [*C*S] ppm. GC-MS: $t_r$ = 10.7 min, *m*/*z* (rel. int.%) = 172 (100), 157 (20), 116 (55), 83 (12), 44 (30).

**1-*tert*-Butyl-3-ethylimidazolidine-2-thione (3b):** Colorless crystals, m.p. 57.5–58 °C (hexane). Yield 0.96 g (15%) No CAS. $^1$H NMR ($CDCl_3$): $\delta$ = 1.15 [t, $^3J$(H,H) = 7 Hz, 3 H, CH$_2$C$H_3$], 1.61 [s, 9 H, C(C$H_3$)$_3$], 3.38–3.43 [m, 2 H, NC$H_2$], 3.43 [m, 2 H, NC$H_2$], 3.57 [m, 2 H, NC$H_2$], 3.66 [q, $^3J$(H,H) = 7 Hz, C$H_2$CH$_3$] ppm. $^{13}$C NMR ($CDCl_3$): $\delta$ = 11.8 [CH$_2$*C*H$_3$], 28.0 [C(*C*H$_3$)$_3$], 42.0 [*t*BuN*C*H$_2$], 44.8 [N*C*H$_2$], 45.0 [N*C*H$_2$], 56.4 [*C*(CH$_3$)$_3$], 182.3 [*C*S]

 © 2007 Wiley-VCH Verlag GmbH & Co. KGaA, Weinheim 

ppm. GC-MS: $t_r$ = 11.0 min, *m*/*z* (rel. int.%) = 186 (100), 171 (13), 157 (5), 129 (45), 115 (43), 56 (13), 42 (16).

**1-*tert*-Butyl-3-isopropylimidazolidine-2-thione (3c):** Colorless crystals, m.p. 102.5–103.5 °C (hexane). Yield 2.84 g (41%) No CAS. $^1$H NMR ($CDCl_3$): $\delta$ = 1.14 [d, $^3J$(H,H) = 7 Hz, 6 H, CH(C$H_3$)$_2$], 1.61 [s, 9 H, C(C$H_3$)$_3$], 3.33 [m 2 H, NC$H_2$], 3.56 [m, 2 H, NC$H_2$], 4.98 [sept, $^3J$(H,H) = 6.8 Hz, 1 H, C$H$(CH$_3$)$_2$] ppm. $^{13}$C NMR ($CDCl_3$): $\delta$ = 20.0 [CH(*C*H$_3$)$_2$], 28.1 [C(*C*H$_3$)$_3$], 40.0 [*t*BuN*C*H$_2$], 44.9 [*i*PrN*C*H$_2$], 46.3 [*C*H(CH$_3$)$_2$], 56.4 [*C*(CH$_3$)$_3$], 181.8 [*C*S] ppm. GC-MS: $t_r$ = 11.8 min, *m*/*z* (rel. int.%) = 200 (71), 185 (78), 157 (5), 143 (43), 129 (100), 111 (8), 102 (7), 84 (10), 70 (12).

**1-*tert*-Butyl-3-methylimidazolidin-2-ylidene (4a):** 8.7 g (83%). Colorless oil, b.p. 65 °C/0.1 Torr $^1$H NMR ($C_6D_6$): $\delta$ = 1.35 [s, 9 H, C(C$H_3$)$_3$], 2.80 [m, 2 H, NC$H_2$], 2.98 [m, 2 H, NC$H_2$], 3.01 [s, 3 H, C$H_3$]. $^{13}$C ($C_6D_6$): $\delta$ = 30.0, [C(*C*H$_3$)$_3$], 37.9 [N*C*H$_3$], 45.3 [*t*BuN*C*H$_2$], 50.8 [CH$_3$N*C*H$_2$], 53.7 [*C*(CH$_3$)$_3$], 239.7 [N$_2$*C*:] ppm.

**1-*tert*-Butyl-3-ethylimidazolidin-2-ylidene (4b):** 10.5 g (91%) Colorless oil, b.p. 67 °C/0.1 Torr. $^1$H NMR ($C_6D_6$): $\delta$ = 1.07 [t, $^3J$ = 7 Hz, 3 H, CH$_2$-C$H_3$], 1.35 [s, 9 H, C(C$H_3$)$_3$], 2.90 [m, 2 H, NC$H_2$], 3.03 [m, 2 H, NC$H_2$], 3.46 [q, $^3J$ = 7 Hz, 2 H, C$H_2$CH$_3$]. $^{13}$C ($C_6D_6$): $\delta$ = 14.8 [CH$_2$*C*H$_3$], 30.1 [C(*C*H$_3$)$_3$], 44.9 [*t*BuN*C*H$_2$], 45.7 [EtN*C*H$_2$], 48.1 [*C*H$_2$CH$_3$], 53.9 [*C*(CH$_3$)$_3$], 238.8 [N$_2$*C*:] ppm.

**1-*tert*-Butyl-3-isopropylimidazolidin-2-ylidene (4c):** 11.7 g (93%). Colorless oil, b.p. 70 °C/0.1 Torr. $^1$H NMR ($C_6D_6$): $\delta$ = 1.16, [d, 6.7 Hz, 6 H, CH(C$H_3$)$_2$], 1.36 [s, 9 H, C(C$H_3$)$_3$], 2.93 [m, 2 H, NC$H_2$], 2.99 [m, 2 H, NC$H_2$], 4.00 [sept, 6.7 Hz, 1 H, C$H$(CH$_3$)$_2$]. $^{13}$C ($C_6D_6$): $\delta$ = 22.1 [CH(*C*H$_3$)$_2$], 29.9 [C(*C*H$_3$)$_3$], 44.2 [*t*BuN*C*H$_2$], 44.9 [*i*PrN*C*H$_2$], 50.8 [*C*H(CH$_3$)$_2$], 53.8 [*C*(CH$_3$)$_3$], 237.6 [N$_2$*C*:] ppm.

**Supporting Information** (see also the footnote on the first page of this article): A table listing the energies, point groups and lowest frequencies of the calculated diamino carbenes **4** and enetetramines **5**.

## Acknowledgments

We thank the Natural Sciences and Engineering Research Council of Canada (NSERC) for support of this work and Professor Gord Lange for valuable comments.

[1] For reviews on stable carbenes, see: a) R. Alder, M. E. Blake, L. Chaker, J. N. Harvey, F. Paolini, J. Schutz, *Angew. Chem. Int. Ed.* **2004**, *43*, 5896–5911; b) D. Bourissou, O. Guerret, F. P. Gabbaï, G. Bertrand, *Chem. Rev.* **2000**, *100*, 39–91; c) G. Bertrand, C. Buron, H. Gornitzka, V. Romanenko, G. Bertrand, *Science* **2000**, *288*, 834–836; d) A. J. Arduengo, *Acc. Chem. Res.* **1999**, *32*, 913–921; e) A. J. Arduengo, R. Krafczyk, *Chem. Unserer Zeit* **1998**, *32*, 6–14; f) W. A. Herrmann, C. Köcher, *Angew. Chem. Int. Ed. Engl.* **1997**, *36*, 2163–2187; g) M. Regitz, *Angew. Chem. Int. Ed. Engl.* **1996**, *35*, 725–728; *Angew. Chem.* **1996**, *108*, 791–794; h) W. Sander, *Angew. Chem. Int. Ed. Engl.* **1990**, *29*, 344–354.

[2] A. J. Arduengo, R. L. Harlow, M. Kline, *J. Am. Chem. Soc.* **1991**, *113*, 361–362.

[3] a) H.-W. Wanzlick, F. Esser, H.-J. Kleiner, *Chem. Ber.* **1963**, *96*, 1208–1212; b) H.-W. Wanzlick, B. Lachmann, E. Schikora, *Chem. Ber.* **1965**, *98*, 3170–3177; c) H.-W. Wanzlick, H.-J. Kleiner, I. Lasch, H. U. Füldner, *Angew. Chem. Int. Ed. Engl.* **1966**, *5*, 126–127; *Angew. Chem.* **1966**, *78*, 115–116; H.-W. Wanzlick, E. Schikora, *Angew. Chem.* **1960**, *72*, 494; d) H.-W. Wanzlick, E. Schikora, *Chem. Ber.* **1961**, *94*, 2389–2393; e) H.-W. Wanzlick, H.-J. Kleiner, *Angew. Chem.* **1961**, *73*, 493; f) H.-W. Wanzlick, *Angew. Chem.* **1962**, *74*, 128–134; g) H.-W. Wanzlick, H.-J. Kleiner, *Angew. Chem. Int. Ed. Engl.* **1964**, *3*, 65; *Angew. Chem.* **1963**, *75*, 1204; h) H.-W. Wanzlick, B. Lachmann, *Z. Naturforsch., Teil B* **1969**, *24*, 574–576; i) B. Lachmann, H. Steinmaus, H.-W. Wanzlick, *Tetrahedron* **1971**, *27*, 4085–4090.

[4] a) M. K. Denk, A. Thadani, K. Hatano, A. J. Lough, *Angew. Chem. Int. Ed. Engl.* **1997**, *36*, 2607–2609; *Angew. Chem.* **1997**, *109*, 2719–2721; b) M. K. Denk, K. Hatano, M. J. Ma, *Tetrahedron Lett.* **1999**, *40*, 2057–2060.

[5] For computational studies of the dimerization, see: a) D. C. Graham, K. J. Cavell, B. F. Yates, *J. Phys. Org. Chem.* **2005**, *18*, 298–309; b) D. C. Graham, B. F. Yates, *Aust. J. Chem.* **2004**, *57*, 359–364; c) J. Cheng, C.-L. Lai, C.-H. Hu, *Mol. Phys.* **2004**, *102*, 2617–2621; d) R. W. Alder, M. E. Blake, J. M. Oliva, *J. Phys. Chem. A* **1999**, *103*, 11200–11211; e) R. W. Alder, M. E. Blake, L. Chaker, J. N. Harvey, F. Paolini, J. Schutz, *Angew. Chem. Int. Ed.* **2004**, *43*, 5896–5911; f) J. M. Oliva, *Chem. Phys. Lett.* **1999**, *302*, 35–42.

[6] a) D. Ülkü, M. N. Tahir, B. Çetinkaya, I. Özdemir, *Acta Crystallogr., Sect. C* **1997**, *53*, 240–241; b) A. Schönberg, E. Singer, W. Stephan, *Chem. Ber.* **1987**, *120*, 1581–1588; c) Schönberg, E. Singer, W. Stephan, *Chem. Ber.* **1987**, *120*, 1589–1591; d) Schönberg, E. Singer, W. Stephan, *Chem. Ber.* **1983**, *116*, 2068–2073; for reviews on enetetramines see: e) E. Haug, W. Kantlehner, in: *Methoden Org. Chem., Houben-Weyl*, 4th ed. **1952**, vol. E15, 2898–2904, Thieme, Stuttgart, **1993**; f) M. Regitz, *Methoden Org. Chem. (Houben-Weyl)*, 4th ed. 1952, vol. E19b, Thieme, Stuttgart, **1989**; g) M. F. Lappert, *J. Organomet. Chem.* **1988**, *358*, 185–214; h) B. Çetinkaya, E. Çetinkaya, J. A. Chamizo, P. B. Hitchcock, H. A. Jasim, H. Küçükbay, M. F. Lappert, *J. Chem. Soc. Perkin Trans. 1* **1998**, 2047–2054; i) B. Çetinkaya, E. Çetinkaya, P. B. Hitchcock, M. F. Lappert, I. Özdemir, *J. Chem. Soc. Dalton Trans.* **1997**, 1359–1362; j) E. Çetinkaya, P. B. Hitchcock, H. Küçükbay, M. F. Lappert, S. Al-Juaid, *J. Organomet. Chem.* **1994**, *481*, 89–95; k) E. Çetinkaya, P. B. Hitchcock, H. A. Jasim, M. F. Lappert, K. Spyropoulos, *J. Chem. Soc. Perkin Trans. 1* **1992**, 561–567; l) P. B. Hitchcock, M. F. Lappert, P. L. Pye, *J. Chem. Soc. Dalton Trans.* **1977**, 2160–2172; m) M. F. Lappert, P. L. Pye, *J. Chem. Soc. Dalton Trans.* **1977**, 2172–2181; n) B. Çetinkaya, P. Dixneuf, M. F. Lappert, *J. Chem. Soc. Chem. Commun.* **1973**, 1827–1833; o) J. Hocker, R. Merten, *Angew. Chem.* **1972**, *84*, 1022; *Angew. Chem. Int. Ed. Engl.* **1972**, *11*, 964–973; p) N. Wiberg, *Angew. Chem.* **1968**, *80*, 809–833; *Angew. Chem. Int. Ed. Engl.* **1968**, *7*, 766–779; q) R. W. Hoffmann, *Angew. Chem. Int. Ed. Engl.* **1967**, *7*, 754–765; *Angew. Chem.* **1968**, *80*, 823; r) H. Quast, S. Hünig, *Chem. Ber.* **1966**, *99*, 2017–2038.

[7] a) M.-D. Su, S.-Y. Chu, *Chem. Phys. Lett.* **1999**, *308*, 283–288; b) J. F. Lehmann, S. G. Urquhart, L. E. Ennis, A. P. Hitchcock, K. Hatano, S. Gupta, M. K. Denk, *Organometallics* **1999**, *18*, 1862–1872; c) S. Urquhart, A. P. Hitchcock, M. K. Denk, *Organometallics* **1998**, *17*, 2352–2360; d) C. Boehme, G. Frenking, *J. Am. Chem. Soc.* **1996**, *118*, 2039–2046; e) C. Heinemann, T. Müller, Y. Apeloig, H. Schwartz, *J. Am. Chem. Soc.* **1996**, *118*, 2023–2038; f) R. R. Sauers, *Tetrahedron Lett.* **1996**, *37*, 149–152; g) C. Heinemann, W. Thiel, *Chem. Phys. Lett.* **1994**, *217*, 11–16; h) J. Cioslowski, *Int. J. Quantum Chem.* **1993**, *27*, 309–319.

[8] a) T. A. Taton, P. Chen, *Angew. Chem.* **1996**, *108*, 1098–1100; *Angew. Chem. Int. Ed. Engl.* **1996**, *35*, 1011–1013; b) Z. Shi, V. Goulle, R. G. Thummel, *Tetrahedron Lett.* **1996**, *37*, 2357–2360; c) G. V. Tormos, M. G. Bakker, P. Wang, M. V. Lakshmikantham, M. P. Cava, R. M. Metzger, *J. Am. Chem. Soc.* **1995**, *117*, 8528–8535.

[9] a) R. W. Alder, P. R. Allen, M. Murray, A. G. Orpen, *Angew. Chem.* **1996**, *108*, 1211–1213; *Angew. Chem. Int. Ed. Engl.* **1996**, *35*, 1121–1122; b) R. W. Alder, M. E. Blake, *Chem. Commun.* **1997**, 1513–1514; c) R. W. Alder, M. E. Blake, C. Bortolotti, S.

 © 2007 Wiley-VCH Verlag GmbH & Co. KGaA, Weinheim 

Bufali, C. Butts, E. Linehan, J. M. Oliva, A. G. Orpen, M. J. Quayle, *Chem. Commun.* **1999**, 241–242; J. M. Oliva, *Chem. Phys. Lett.* **1999**, *302*, 35–42.

[10] a) M. Otto, S. Conejero, Y. Canac, V. D. Romanenko, V. Rudzevitch, G. Bertrand, *J. Am. Chem. Soc.* **2004**, *126*, 1016–1017; b) R. W. Alder, L. Chaker, F. P. V. Paolini, *Chem. Commun.* **2004**, 2172; c) V. Lavallo, J. Mafhouz, Y. Canac, B. Donnadieu, W. W. Schoeller, G. Bertrand, *J. Am. Chem. Soc.* **2004**, *126*, 8670–8671.

[11] a) F. E. Hahn, L. Wittenbecher, D. L. Van, R. Fröhlich, *Angew. Chem. Int. Ed.* **2000**, *39*, 541–544; b) F. E. Hahn, L. Wittenbecher, R. Boese, D. Bläser, *Chem. Eur. J.* **1999**, *5*, 1931–1935; c) F. E. Hahn, M. Foth, *J. Organomet. Chem.* **1999**, *585*, 241–245; d) Y. Liu, P. E. Lindner, D. M. Lemal, *J. Am. Chem. Soc.* **1999**, *121*, 10626–10627.

[12] C. Metallinos, F. B. Barrett, J. L. Chaytor, M. E. A. Heska, *Org. Lett.* **2004**, *6*, 3641–3644. DFT calculations at the B98/6-31G(d) level carried out in our group suggest that the dimerization is exothermic ($\Delta G° = -6.1$ kcal mol$^{-1}$).

[13] A. J. Arduengo, R. Goerlich, W. J. Marshall, *J. Am. Chem. Soc.* **1995**, *117*, 11027–11028.

[14] a) F. E. Hahn, D. Le Van, M. Paas, R. Fröhlich, *Dalton Trans.* **2006**, 860–864; b) F. E. Hahn, M. Paas, D. L. Van, T. Lügger, *Angew. Chem. Int. Ed.* **2003**, *42*, 5243–5246; c) F. E. Hahn, M. Paas, D. L. Van, R. Fröhlich, *Chem. Eur. J.* **2005**, *11*, 5080–5085.

[15] M. K. Denk, M. J. Krause, D. F. Niyogi, N. K. Gill, *Tetrahedron* **2003**, *59*, 7565–7570.

[16] a) Y. Hirokawa, H. Harada, T. Yoshikawa, N. Yoshida, S. Kato, *Chem. Pharm. Bull.* **2002**, *50*, 941–959; b) G. Gelbard, P. Rumpf, *Bull. Soc. Chim. Fr.* **1969**, 1161–1170.

[17] P. Foster, J. C. W. Chien, M. D. Rausch, *J. Organomet. Chem.* **1997**, *545–546*, 35–38.

[18] M. K. Denk, S. Gupta, J. Brownie, S. Tajammul, A. J. Lough, *Chem. Eur. J.* **2001**, *7*, 4477–4486.

[19] a) N. Kuhn, E. Niquet, M. Steimann, I. Walker, *Z. Naturforsch., Teil B* **1999**, *54*, 1181–1187; b) N. Kuhn, T. Kratz, *Synthesis* **1993**, 561–562.

[20] a) M. K. Denk, J. Rodezno, S. Gupta, A. J. Lough, *J. Organomet. Chem.* **2001**, *617–618*, 242–253; b) M. K. Denk, J. Rodezno, *J. Organomet. Chem.* **2001**, *617–618*, 737–740.

[21] The outcome of the hydrolysis reaction does not seem to be controlled by the *N*-alkyl substituent: examination of the hydrolysis mixtures of **4a**–**c** reveals the presence of the respective *N*-formyl and *N*′-formyl products in similar quantities ($^1$H NMR).

[22] *Gaussian 03*, Revision D.01, M. J. Frisch, G. W. Trucks, H. B. Schlegel, G. E. Scuseria, M. A. Robb, J. R. Cheeseman, J. A. Montgomery Jr, T. Vreven, K. N. Kudin, J. C. Burant, J. M. Millam, S. S. Iyengar, J. Tomasi, V. Barone, B. Mennucci, M. Cossi, G. Scalmani, N. Rega, G. A. Petersson, H. Nakatsuji, M. Hada, M. Ehara, K. Toyota, R. Fukuda, J. Hasegawa, M. Ishida, T. Nakajima, Y. Honda, O. Kitao, H. Nakai, M. Klene, X. Li, J. E. Knox, H. P. Hratchian, J. B. Cross, V. Bakken, C. Adamo, J. Jaramillo, R. Gomperts, R. E. Stratmann, O. Yazyev, A. J. Austin, R. Cammi, C. Pomelli, J. W. Ochterski, P. Y. Ayala, K. Morokuma, G. A. Voth, P. Salvador, J. J. Dannenberg, V. G. Zakrzewski, S. Dapprich, A. D. Daniels, M. C. Strain, O. Farkas, D. K. Malick, A. D. Rabuck, K. Raghavachari, J. B. Foresman, J. V. Ortiz, Q. Cui, A. G. Baboul, S. Clifford, J. Cioslowski, B. B. Stefanov, G. Liu, A. Liashenko, P. Piskorz, I. Komaromi, R. L. Martin, D. J. Fox, T. Keith, M. A. Al-Laham, C. Y. Peng, A. Nanayakkara, M. Challacombe, P. M. W. Gill, B. Johnson, W. Chen, M. W. Wong, C. Gonzalez, and J. A. Pople, Gaussian, Inc., Wallingford CT, **2004**.

[23] M. Bienati, C. Adamo, V. Barone, *Chem. Phys. Lett.* **1999**, *311*, 69–76.

[24] R. Hoffmann, R. Gleiter, F. B. Mallory, *J. Am. Chem. Soc.* **1970**, *92*, 1460–1466.

[25] Hydrogenation energies of Wanzlick carbenes (**4** + $H_2$ → **2**) at the B98/6-31G(d) level showed only a small variation (ca. 1 kcal mol$^{-1}$) with the *N*-alkyl substituent.

[26] a) M. R. Nyden, G. A. Petersson, *J. Chem. Phys.* **1981**, *75*, 1843–1862; b) G. A. Petersson, M. A. Al-Laham, *J. Chem. Phys.* **1991**, *94*, 6081–6090; c) G. A. Petersson, T. Tensfeldt, J. A. Montgomery, *J. Chem. Phys.* **1991**, *94*, 6091–6101; d) J. A. Montgomery, J. W. Ochterski, G. A. Petersson, *J. Chem. Phys.* **1994**, *101*, 5900–5909.

[27] a) L. A. Curtiss, K. Raghavachari, P. C. Redfern, V. Rassolov, J. A. Pople, *J. Chem. Phys.* **1998**, *109*, 7764–7776; b) L. A. Curtiss, P. C. Redfern, K. Raghavachari, J. A. Pople, *Chem. Phys. Lett.* **1999**, *313*, 600–607.

[28] In solution, rapid nitrogen inversion equilibrates this geometry with other isomers (singlet for the ethylene ring protons of enetetramines **5**).[4,20] For X-ray data of enetetramines **5**, see: a) P. B. Hitchcock, M. F. Lappert, P. L. Pye, *J. Chem. Soc. Dalton Trans.* **1977**, 2160; b) P. B. Hitchcock, *Acta Crystallogr., Sect. A* **1978**, *34*, S102; c) E. Çetinkaya, P. B. Hitchcock, H. A. Jasim, M. F. Lappert, K. Spyropoulos, *J. Chem. Soc. Perkin Trans. 1* **1992**, 561; d) P. B. Hitchcock, *J. Chem. Soc. Dalton Trans.* **1979**, 1314; e) E. Çetinkaya, P. B. Hitchcock, H. A. Jasim, M. F. Lappert, K. Spyropoulos, *J. Chem. Soc. Perkin Trans. 1* **1992**, 561.

Received: February 16, 2007
Published Online: June 14, 2007

 © 2007 Wiley-VCH Verlag GmbH & Co. KGaA, Weinheim 

DOI: 10.1002/ejic.200601156

# Anomeric Interactions in Pentafluoroethylimidosulfurous Dichloride, $CF_3CF_2N{=}SCl_2$: Structural, Conformational and Configurational Properties in the Gaseous and Condensed Phases

**Norma L. Robles,[a][‡] Rosa M. S. Álvarez,[a][‡‡] Edgardo H. Cutin,[a][‡‡] Carlos O. Della Védova,*[b,c][‡‡] Mauricio F. Erben,[b][‡‡] Roland Boese,[d] Helge Willner,[e] and Rüdiger Mews[f]**

**Keywords:** Imides / Conformation analysis / Structural analysis / Hyperconjugation / Sulfur

The structural, conformational, and configurational properties of pentafluoroethylimidosulfurous dichloride ($CF_3CF_2N{=}SCl_2$) have been studied by vibrational spectroscopy [IR (vapor) and Raman (liquid)] and quantum chemical calculations [HF, B3LYP and MP2 approximations using the 6-311+G(d) and 6-311+G(2df) basis sets]. $CF_3CF_2N{=}SCl_2$ exists in the liquid phase as a single (*Z*) form (C–N bond synperiplanar with respect to the Cl–S–Cl plane; $C_1$ symmetry). The structure was also determined by X-ray diffraction analysis of a single crystal grown in situ at low temperature. The crystalline solid at 159 K (monoclinic, $P2_1/c$, $a$ = 5.2466(10), $b$ = 15.376(3), $c$ = 18.730(3) Å, $\beta$ = 96.391(3)°, $Z$ = 8) consists of two crystallographically inequivalent (*Z*) forms. The results are discussed in terms of both hyperconjugative electronic effects and of natural bond orbital (NBO) calculations.

(© Wiley-VCH Verlag GmbH & Co. KGaA, 69451 Weinheim, Germany, 2007)

## Introduction

Theoretical studies performed in the last twenty years have concluded that more than one single effect should be considered in order to understand the factors stabilizing the staggered conformation of ethane. Hyperconjugation, or the anomeric effect, which is a stereoelectronic effect derived from the overlap of σ-bonding orbitals with an adjacent empty or partially filled antibonding orbital, has been proposed as the most significant factor responsible for stabilizing staggered ethane in a definite molecular conformation.[1–3] This concept has also been applied to fluoroethane species,[4] which have recently attracted much attention, and ultrafast carbon–carbon single-bond isomerization of 1-fluoro-2-isocyanatoethane in solution at room-temperature has been analyzed by two-dimensional infrared vibrational echo spectroscopy.[5]

It is well known that conjugation between lone-pair orbitals and π bonds plays an important role in structural chemistry (the resonance effect) and that the conformational preference is strongly influenced by the presence of perfluorinated groups.[6,7] For instance, conjugation in methyl vinyl ether [$CH_3OC(H){=}CH_2$][8–10] results in a sterically unfavorable synperiplanar orientation of the O–C($sp^3$) bond relative to the double bond, whereas the O–C($sp^3$) bond in $CF_3OC(F){=}CF_2$[11] is nearly perpendicular to the plane of the vinyl group [$\phi$(C=C–O–C) = 104(2)°]. An orbital interaction occurs between the oxygen lone-pair orbital and the π*(C=C) antibonding orbital [lpπ(O)→π*(C=C)] in $CH_3OC(H){=}CH_2$, whereas no conjugation is present in the perfluorinated compound.

Structural, configurational, and conformational studies in compounds such as sulfur imides ($R^1NSR^2R^3$)[12] are scarce, and little is known about the factors affecting these properties. In principle, depending on the orientation of the $R^1$–N bond with respect to the $R^2$–S–$R^3$ bisector angle, two forms [(*E*)/(*Z*)] can be expected (Scheme 1).

[a] Instituto de Química Física, Facultad de Bioquímica, Química y Farmacia, Universidad Nacional de Tucumán, San Lorenzo 456, 4000 Tucumán, Argentina
[b] CEQUINOR (CONICET-UNLP). Departamento de Química, Facultad de Ciencias Exactas, Universidad Nacional de La Plata, 47 esq. 115 (B1900AJL) C. C. 962, La Plata, Buenos Aires, Argentina
E-mail: carlosdv@quimica.unlp.edu.ar
[c] Laboratorio de Servicios a la Industria y al Sistema Científico (UNLP-CIC-CONICET), Camino Centenario, Gonnet, Buenos Aires, Argentina
[d] Institut für Anorganische Chemie, Universität Duisburg-Essen, Universitätsstrasse 5–7, 45117 Essen, Germany
[e] FB C, Anorganische Chemie, Bergische Universität Wuppertal, Gaußstrasse 20, 42119 Wuppertal, Germany
[f] Institut für Anorganische und Physikalische Chemie, Universität Bremen, 28334 Bremen, Germany
[‡] N. L. R. is a doctoral fellow of CONICET.
[‡‡]R. M. S. Á., E. H. C., M. F. E. and C. O. D. V. are members of the Carrera del Investigador of CONICET, República Argentina.

 © 2007 Wiley-VCH Verlag GmbH & Co. KGaA, Weinheim 

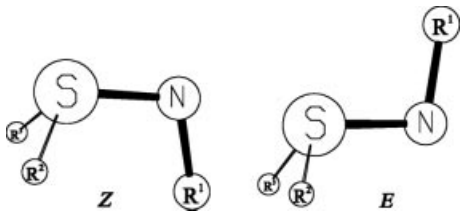


Scheme 1. Representation of the (*Z*) and (*E*) forms of $R^1NSR^2R^3$.

Vibrational spectroscopy, gas electron diffraction, X-ray crystallography, quantum chemical calculations, and other techniques have proved to be powerful tools to understand the structural properties of sulfur imide molecules containing fluorine atoms or fluorinated substituents groups. Thus, the structure and conformational and configurational properties of molecules of the type $R_FN{=}SF_2$ [$R_F$ = $CF_3$,[13–16] FC(O),[17,18] NC,[19] $CF_3C(O)$,[20] and $FSO_2$[21,22]] and $R_FN{=}SCl_2$ [$R_F$ = $CF_3$[23,24] and FC(O)[25]] have been studied, all of which show only a (*Z*) configuration around the putative N=S double bond. It is interesting to note that compounds with different substituents attached at the sulfur atom of the N=S group favor the (*E*) form. Thus, FC(O)N=S(F)$CF_3$[26] and $CF_3C(O)N{=}S(F)CF_3$[27] exist in the vapor as a mixture of (*E*) and (*Z*) forms, with the former predominating.

The question of the nature of the S–N bond in sulfur imides has not yet been resolved, and there is still some controversy as to whether the sulfur imide linkage is a double bond or a semipolar bond.[28] As noted by Protashchuk et al.[29] the relative stabilization of the (*Z*) and (*E*) forms of the simple molecule $HNSH_2$ depends mainly on the effectiveness of the following interactions: (1) the lone pair attached at the nitrogen atom with the σ* antibonding orbitals of the $SH_2$ fragment [lp(N)→σ*(S–H)], (2) the lone pair of the sulfur atom with the σ* antibonding orbital of the NH fragment [lp(S)→σ*(N–H)], and (3) the lone pairs of the nitrogen and sulfur atoms with each other. Both the stabilizing [(1) and (2)] and destabilizing [(3)] interactions are more effective in the (*Z*) than in the (*E*) form, and the destabilizing interaction energy between both lone pairs attached at the nitrogen and sulfur atoms in the (*Z*) form is lower than the stabilizing effects of the negative hyperconjugation, which results in the greater stability of the (*Z*) form for $HNSH_2$. A quantitative evaluation of these effects has been reported recently by Kumar et al.[30] for $HNSH_2$ and also for fluorinated derivatives, by using the NBO population analysis approach.

In order to gain additional experimental and theoretical information about the structural properties of sulfur imides, we report here a study of $CF_3CF_2N{=}SCl_2$ species that draws on its vibrational spectra [IR (vapor) and Raman (liquid)] and single-crystal structure. The presence of the $CF_3CF_2$ group is useful to analyze the effect of a fully fluorinated carbon chain on the molecular structure. Moreover, quantum chemical calculations have been performed in order to assist the interpretation of the experimental data, and Natural Bond Orbital (NBO) population analyses have been applied to rationalize the effect of electronic interactions on the structural, conformational, and configurational properties of $CF_3CF_2N{=}SCl_2$.

## Results and Discussion

### Quantum Chemical Calculations

According to the precedents found in the literature for *S*,*S*-dihalo-substituted sulfur imides $R_1N{=}SX_2$ (X = F, Cl; see above), the presence of the (*Z*) form might be expected for $CF_3CF_2N{=}SCl_2$. In order to gain further insight into this molecule, the potential function for internal rotation around the sulfur–imide bond was calculated by geometry optimizations at fixed torsional dihedral angles (steps of 30°) using the HF, B3LYP, and MP2 methods with the 6-311+G(d) basis sets. The derived curves obtained with the HF and MP2 approximations show two minima: a global minimum that corresponds to the (*Z*) structure and a local minimum located about 7.5 kcal mol$^{-1}$ higher in energy which corresponds to the (*E*) form of $CF_3CF_2N{=}SCl_2$ [(*Z*) and (*E*) orientation of the C–N bond with respect to the Cl–S–Cl bisector angle, respectively]. A more complicated picture of the potential energy surface for the mentioned angles was obtained by the hybrid method B3LYP, which shows the same global minimum structure as the former approximations but with a flat region near the local minimum assigned to the (*E*) form. Similar calculations performed by varying the dihedral angle around the C–N bond showed only one minimum at about –150°. Thus, both (*Z*) and (*E*) forms belong to the $C_1$ symmetry point group. Full geometry optimizations and frequency calculations for the two feasible conformers were performed with the more extended 6-311+G(2df) basis sets. The relative energies are summarized in Table 1.

Table 1. Calculated relative energies (corrected for the zero-point energy) in kcal mol$^{-1}$ for stable conformers of $CF_3CF_2N{=}SCl_2$.

| | HF/6-311+G(d) $\Delta E°$[a] | B3LYP/6-311+G(d) $\Delta E°$[a] | MP2/6-311+G(d) $\Delta E°$[a,b] |
|---|---|---|---|
| *syn* | 0.00 | 0.00 | 0.00 |
| *anti* | 5.55 | 7.34 | 7.62 |

[a] Energy differences $\Delta E° = E°_{(E)} - E°_{(Z)}$. [b] Zero-point corrections calculated at the B3LYP/6-311+G(d) level.

Since the perfluoroethyl group ($CF_3CF_2$) can adopt either a staggered or an eclipsed geometry (see Scheme 2),

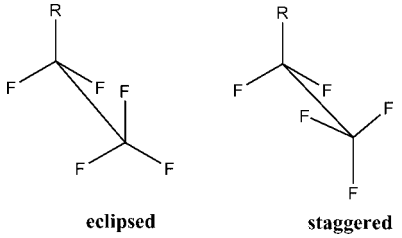


Scheme 2. Representation of the eclipsed and staggered forms in substituted perfluoroethane molecules.

 © 2007 Wiley-VCH Verlag GmbH & Co. KGaA, Weinheim 

the potential function for internal rotation around the C–C bond was calculated by full geometry optimization at fixed $\phi$(FC–CN) torsional angles. The staggered form corresponds to the preferred conformation, with $\Delta E$ ($E_{eclipsed} - E_{staggered}$) values of 5.67 and 4.10 kcal mol$^{-1}$ for the HF and B3LYP methods with the 6-311+G* basis set, respectively.

### Vibrational Spectra

Figure 1 shows the IR (vapor) and Raman (liquid) spectra of $CF_3CF_2N{=}SCl_2$. Table 2 lists the experimental frequencies together with the calculated values and a tentative assignment of the 27 expected normal modes of vibration. The vibrational spectra can be interpreted satisfactorily on the basis of the presence of only one form. Assignment of the bands related to the $N{=}SCl_2$ moiety was performed on the basis of the corresponding features for similar *S*,*S*-dichlorosulfur imide derivatives such as $CF_3N{=}SCl_2$,[23] $FC(O)N{=}SCl_2$,[25] and $ClSO_2N{=}SCl_2$.[31] The corresponding *S*,*S*-difluoro derivatives $CF_3N{=}SF_2$,[32] $FC(O)N{=}SF_2$,[23] and $ClSO_2N{=}SF_2$[22] were also taken into account to establish a correlation between the different modes. The fundamental vibrational modes related to the $CF_3CF_2$ moiety were assigned on the basis of calculated frequencies for the title molecule and taking into account the recently reported data for $CF_3CF_2COOH$.[33] All theoretical frequencies show good agreement with the experimental values, which gives confidence to the assignment of the fundamental features.

According to reported data found in the literature for sulfur imide molecules containing a $CF_3$ group as substituent, the region between 1400 and 1100 cm$^{-1}$ shows bands related to the fundamental stretching modes corresponding to both the N=S and the $CF_3$ groups.[23,32] Thus, the presence of several intense and narrow bands in that region in the gas FTIR spectra and weak and broad bands in the liquid Raman spectrum is directly related to those vibrational modes. The frequency of the N=S stretching is directly related to the electron-withdrawing properties of the substituents attached at the nitrogen and sulfur atoms. In fact, an increase in the electron-withdrawing properties of the substituents attached to any of the atoms of the N=S bond increases the bond order of this bond. Taking into account that the band centered at 1314 cm$^{-1}$ in the IR spectrum (1300 cm$^{-1}$, Raman) of $CF_3N{=}SCl_2$[23] was assigned to the N=S stretching, and postulating that the $CF_3$ group is more electronegative than $CF_3CF_2$, the band appearing at 1292 cm$^{-1}$ in the gas FTIR spectrum (1286 cm$^{-1}$ in the liquid Raman spectrum) was assigned to the N=S stretching vibration, in perfect agreement with the theoretical

Table 2. Observed and calculated vibrational data for $CF_3CF_2N{=}SCl_2$ [cm$^{-1}$].

| Mode | Approximate description[a] | Experimental[b] | | | | Calculated[c] | | | |
|---|---|---|---|---|---|---|---|---|---|
| | | IR (gas) | | Raman (liquid) | | HF/ 6-311+G(2df)[d] | | B3LYP/ 6-311+G(2df) | |
| $\nu_1$ | C–C stretch | 1380 | (20) | 1378 | (5) | 1403 | (2) | 1365 | (16) |
| $\nu_2$ | N=S stretch | 1292 | (98) | 1286 | (6) | 1292 | (100) | 1292 | (100) |
| $\nu_3$ | $CF_3$ sym stretch | 1235 | (100) | 1218 | (2) | 1262 | (31) | 1212 | (31) |
| $\nu_4$ | $CF_3$ asym stretch | | | | | 1256 | (22) | 1210 | (40) |
| $\nu_5$ | $CF_2$ asym stretch | 1158 | (65) | 1151 | (2) | 1183 | (24) | 1122 | (24) |
| $\nu_6$ | $CF_3$ sym stretch | 1133 | (76) | 1124 | (2) | 1143 | (31) | 1116 | (27) |
| $\nu_7$ | $CF_2$ sym stretch | 1029 | (78) | 1025 | (3) | 1027 | (18) | 1028 | (29) |
| $\nu_8$ | C–N stretch | 770 | (2) | 771 | (36) | 767 | (<1) | 766 | (<1) |
| $\nu_9$ | $CF_3$ sym def | 709 | (47) | 709 | (3) | 709 | (12) | 708 | (15) |
| $\nu_{10}$ | $C_2F_5$ asym def | 622 | (3) | 626 | (3) | 620 | (<1) | 613 | (<1) |
| $\nu_{11}$ | $C_2F_5$ sym def | 582 | (10) | 584 | (3) | 581 | (2) | 576 | (2) |
| $\nu_{12}$ | $C_2F_5$ asym def | 544 | (6) | 545 | (3) | 544 | (2) | 539 | (3) |
| $\nu_{13}$ | $C_2F_5$ sym def | 501 | (6) | – | – | 517 | (3) | 521 | (1) |
| $\nu_{14}$ | $SCl_2$ sym stretch | 442 | (4) | 445 | (100) | 460 | (10) | 434 | (10) |
| $\nu_{15}$ | $SCl_2$ asym stretch | 429 | (60) | 424 sh | (42) | 456 | (15) | 413 | (14) |
| $\nu_{16}$ | $C_2F_5$ sym def | | | 395 | (48) | 400 | (2) | 391 | (4) |
| $\nu_{17}$ | $C_2F_5$ sym def | | | 362 sh | (9) | 391 | (2) | 384 | (8) |
| $\nu_{18}$ | $C_2F_5$ asym def | | | – | | 357 | (<1) | 354 | (1) |
| $\nu_{19}$ | $SCl_2$ wag | | | 298 | (42) | 295 | (<1) | 291 | (2) |
| $\nu_{20}$ | $SCl_2$ twis | | | 242 sh | (24) | 247 | (<1) | 227 | (<1) |
| $\nu_{21}$ | $C_2F_5$ asym def | | | – | | 220 | (<1) | 215 | (<1) |
| $\nu_{22}$ | $SCl_2$ sym def | | | 206 | (62) | 209 | (<1) | 196 | (<1) |
| $\nu_{23}$ | C–C–N def | | | 156 | (44) | 149 | (<1) | 142 | (<1) |
| $\nu_{24}$ | C–N–S def | | | 115 | (42) | 112 | <1) | 95 | (<1) |
| $\nu_{25}$ | $SCl_2$ torsion | | | 82 | (32) | 72 | (<1) | 75 | (<1) |
| $\nu_{26}$ | $CF_3$ torsion | | | | | 55 | (<1) | 53 | (<1) |
| $\nu_{27}$ | C–N torsion | | | | | 15 | (<1) | 11 | (<1) |

[a] Stretch = stretching, def = deformation, wag = wagging, twis = twisting, sym = symmetric, asym = asymmetric, sh = shoulder; see Figure 2 for atom numbering. [b] Gas: $P$ = 15.0 mbar (glass cell, 200 mm optical path length, Si windows, 0.5 mm thick), relative absorbance at band maximum in parentheses; liquid: room temperature, relative band intensity in parentheses. [c] Relative band strength in parentheses; 100%: 968 and 703 km mol$^{-1}$ for the (*Z*) form calculated at the HF and B3LYP methods, respectively. [d] Scaled by a factor of 0.9.

 © 2007 Wiley-VCH Verlag GmbH & Co. KGaA, Weinheim 

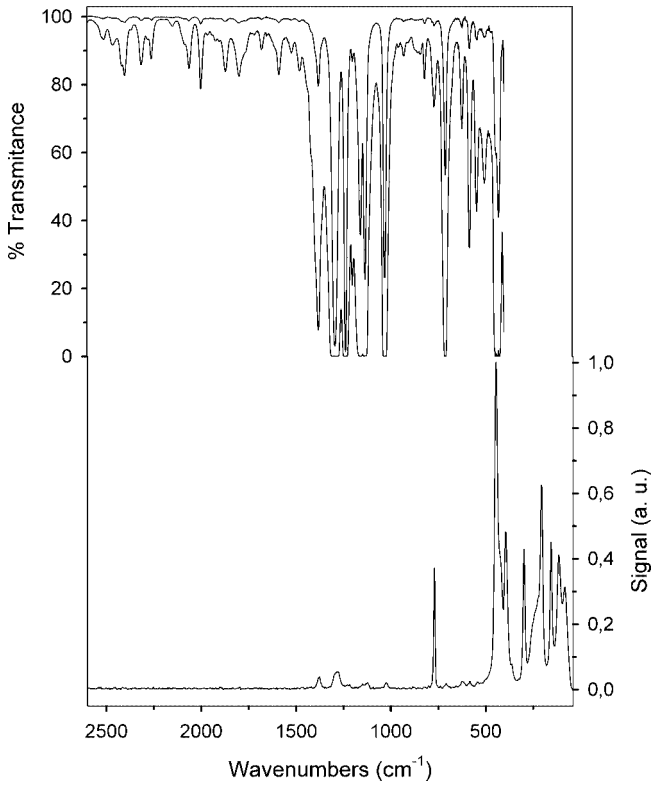


Figure 1. Gas IR (at 15.0 and 1.6 mbar; glass cell with a 200 mm optical path length and 0.5 mm thick Si windows) and liquid Raman spectra for $CF_3CF_2N{=}SCl_2$.

value. Analysis of the IR spectra obtained for seven alkyl esters of pentafluoropropionic acid [$CF_3CF_2C(O)OR$] by Crowder[34] concluded that different R groups do not affect the characteristic stretching and deformation frequency values of the $CF_3CF_2$ group. Thus, taking into account the reported data for $CF_3CF_2COOH$,[33] where the band located at 1334.7 $cm^{-1}$ in the gas FTIR spectrum has been assigned to the C–C stretching mode, the medium intensity feature centered at 1380 $cm^{-1}$ in the IR spectrum (Raman: 1378 $cm^{-1}$) of $CF_3CF_2N{=}SCl_2$ can be assigned to the ν(C–C) stretching mode.

Although theoretical calculations predict a strong coupling between the stretching modes belonging to the $CF_3CF_2$ group, their assignments were performed by considering the $CF_3$ and $CF_2$ groups individually. Only one band is found for the $CF_3$ symmetric and the antisymmetric stretching vibrational normal modes at 1235 and 1218 $cm^{-1}$ in the vapor IR and liquid Raman spectra, respectively. This coincidence in the frequencies of these two modes is also in agreement with our calculations as differences of 6 and 2 $cm^{-1}$ are calculated (HF and B3LYP methods, respectively) for the values of the two normal vibrational modes (Table 2). The second $CF_3$ symmetric stretching appears at 1133 and 1124 $cm^{-1}$ (vapor IR and liquid Raman, respectively). Similarly, the bands centered at 1158 and 1029 $cm^{-1}$ (Raman: 1151 and 1025 $cm^{-1}$) were assigned to the antisymmetric and symmetric stretching modes belonging to the $CF_2$ group, respectively. The medium-intensity bands observed in the IR spectrum at 442 and 429 $cm^{-1}$ (Raman: 445 and 424 $cm^{-1}$) were assigned to the symmetric and antisymmetric stretching modes in the $SCl_2$ group, respectively. This assignment is straightforward because the frequency values as well as the shape of the bands in the vibrational spectra of $CF_3CF_2N{=}SCl_2$ can be directly correlated with the reported features for $CF_3N{=}SCl_2$.[23] Theoretical values also confirm this proposed assignment. The medium-intensity bands found at 770 and 771 $cm^{-1}$ in the IR and Raman spectra, respectively, were assigned to the C–N stretching mode. The theoretical values calculated for this mode (HF: 767 $cm^{-1}$; B3LYP: 766 $cm^{-1}$) again support this assignment.

According to our calculated frequencies, the expected deformation modes related to the $CF_3CF_2$ group are strongly coupled. For this reason, it is not possible to assign the observed features in the vibrational spectra in a straightforward manner. However, by comparison with the assignment reported for $CF_3N{=}SCl_2$,[23] the band located at 709 $cm^{-1}$ in both the IR and Raman spectra could be assigned to the totally symmetric deformation of the $CF_3$ group.

## Crystal Structure

$CF_3CF_2N{=}SCl_2$ crystallizes in the monoclinic space group $P2_1/c$ with eight molecules per unit cell. Table 3 lists the relevant crystal data. In accordance with the theoretical calculations and the spectroscopic investigations, the most stable conformer – the (*Z*) conformer – is observed in the solid state at 159 K (Figure 2). Two nonequivalent molecules are present in the crystal (forms I and II), both of which have similar bond lengths and angles. However, some remarkable differences in the $\phi$(C–C–N=S) torsional angles between both nonequivalent forms are observed. Thus, these values are 146.5° and 160.6° for forms I and II, respectively. In order to illustrate this difference, Figure 3 shows a superimposed picture of both forms.

Table 4 lists the experimental geometrical parameters for $CF_3CF_2N{=}SCl_2$ together with the corresponding values obtained from HF and B3LYP calculations using the 6-311+G(2df) basis set, and the MP2/6-311+G(d) approximation. Contractions of polar bonds are expected on going from the gas to the solid phase. Nevertheless, taking into account the difference in the physical state of the substance, there is good agreement between the theoretical and the experimental data obtained for the (*Z*) conformer of $CF_3CF_2N{=}SCl_2$. The methods reproduce the bond lengths and angles reasonably well in general, except for some values around the sulfur atom. Thus, even with large basis sets (6-311+G(2df)), the B3LYP and MP2 methods predict the S–Cl bond to be too long by up to 0.060 and 0.074 Å, respectively. The theoretical methods used in the current work give similar values for the CN=SCl dihedral angle to those obtained from the X-ray analysis. A staggered conformation for the perfluoroethyl group is found in the crystal, which is well reproduced by the computational methods. However, some differences were observed for the CC–N=S

 © 2007 Wiley-VCH Verlag GmbH & Co. KGaA, Weinheim 

Table 3. Crystal data and structure refinement for $CF_3CF_2N{=}SCl_2$.

| | |
|---|---|
| Empirical formula | $C_2Cl_2F_5NS$ |
| Formula mass | 235.99 |
| Density (calcd.) [g cm$^{-3}$] | 2.088 |
| $F$(000) | 912 |
| Temperature [K] | 159(2) |
| Crystal size [mm] | 0.3 |
| Crystal color | colorless |
| Crystal description | cylindrical |
| Wavelength [Å] | 0.71073 |
| Crystal system | monoclinic |
| Space group | $P2_1/c$ |
| $a$ [Å] | 5.2466(10) |
| $b$ [Å] | 15.376(3) |
| $c$ [Å] | 18.730(3) |
| $\alpha$ [°] | 90 |
| $\beta$ [°] | 96.391(3) |
| $\gamma$ [°] | 90 |
| Volume [Å$^3$] | 1501.6(5) |
| $Z$ | 8 |
| Cell measurement reflections used | 3134 |
| Cell measurement $\theta_{min/max}$ [°] | 2.19–28.22 |
| Completeness to $\theta$ = 28.27° [%] | 68.5 |
| Index ranges | $-3 \le h \le 3$ |
| | $-20 \le k \le 13$ |
| | $-24 \le l \le 24$ |
| Absorption coefficient [mm$^{-1}$] | 1.166 |
| Max./min. transmission | 1.00/0.84 |
| $R$(merg) before/after correction | 0.0316/0.0195 |
| Reflections collected | 5893 |
| Independent reflections [$R_{(int)}$ = 0.0206] | 2540 |
| Data/restraints/parameters | 2150/0/199 |
| Goodness-of-fit on $F^2$ | 1.047 |
| Final $R$ indices [$I > 2\sigma(I)$] | $R_1$ = 0.0319, $wR_2$ = 0.0794[a] |
| $R$ indices (all data) | $R_1$ = 0.0393, $wR_2$ = 0.0837[a] |
| Largest diff. peak/hole [e Å$^{-3}$] | 0.703/–0.536 |

[a] $w = 1/[\sigma^2(F_o^2) + (0.0313P)^2 + 1.2107P]$, where $P = (F_o^2 + 2F_c^2)/3$.

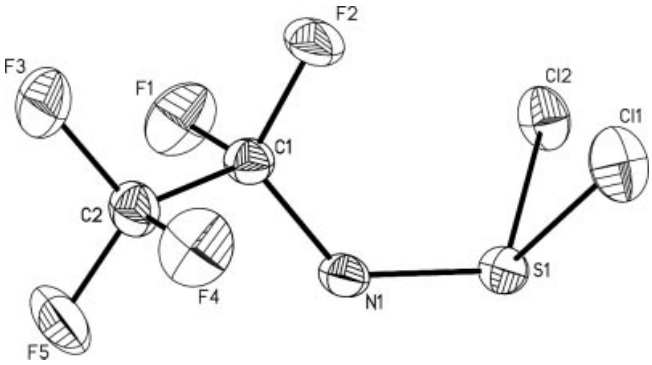


Figure 2. Molecular model, with atom numbering, showing the single-crystal structure of $CF_3CF_2N{=}SCl_2$.

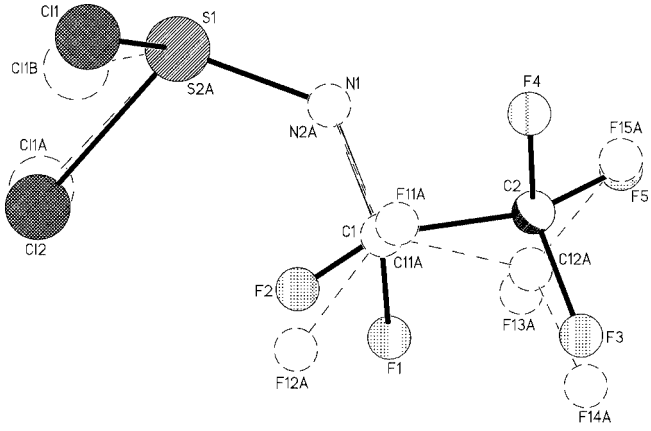


Figure 3. Molecular structures for nonequivalent forms of $CF_3CF_2N{=}SCl_2$ in the crystal.

dihedral angle: the experimental value is –147.0° whereas the computed values are –151.3°, –168.5°, and –123.7° for the HF, B3LYP, and MP2 methods, respectively.

The crystal packing along the *ac* plane is shown in Figure 4. Crystallographic studies on molecules containing halogen–halogen bonds or halogen–halogen contacts have attracted a great deal of attention because they are considered to be one of the important factors that determine the structural features in molecular crystals and may play an important role in crystal engineering as supermolecular synthons.[35–37] The term "halogen bonding" has been defined by Legon to refer to these interactions.[38] Intermolecular interactions dominated by F···F contacts are also common for fluorinated molecules where there is no other choice for stabilizing the packing. According to quantum chemical calculations, F···F contacts in aromatic systems

Table 4. Experimental and calculated geometric parameters for the $Z$ form of $CF_3CF_2N{=}SCl_2$.[a]

| Parameter | X-ray[b] | HF 6-311+G(2df) | B3LYP 6-311+G(2df) | MP2 6-311+G(d) |
|---|---|---|---|---|
| C1–F | 1.342(3) | 1.324 | 1.354 | 1.331 |
| C–C | 1.530(4) | 1.538 | 1.558 | 1.543 |
| C2–F | 1.316(4) | 1.304 | 1.333 | 1.348 |
| C–N | 1.399(4) | 1.400 | 1.410 | 1.422 |
| N=S | 1.507(2) | 1.488 | 1.510 | 1.513 |
| S–Cl | 2.072(10) | 2.054 | 2.132 | 2.146 |
| C–C–N | 110.5(2) | 110.0 | 109.6 | 109.4 |
| C–N=S | 129.13(18) | 130.7 | 132.9 | 130.1 |
| N=S–Cl | 110.98(10) | 111.0 | 111.7 | 111.4 |
| Cl–S–Cl | 95.78(4) | 96.7 | 96.5 | 96.2 |
| C–C–N=S | –147.0(3) | –151.3 | –168.5 | –123.7 |
| C–N=S–Cl1 | 56.1(5) | 60.0 | 49.7 | 53.6 |
| C–N=S–Cl2 | –49.3(5) | –46.3 | –57.1 | –52.5 |

[a] Bond lengths in Å and angles in °. See Figure 2 for atom numbering. [b] Mean values for parameters that are not unique, with σ uncertainties.

 © 2007 Wiley-VCH Verlag GmbH & Co. KGaA, Weinheim 

can contribute up to 14 kcal mol$^{-1}$ of local stabilization energy.[39] The two independent molecules in the crystal of $CF_3CF_2N{=}SCl_2$ are linked to the surrounding molecules by different intermolecular interactions. For example, $CF_3CF_2N{=}SCl_2$ forms chains with short N=S···F–CF nonbonding distances along the *a* axis. These chains formed by molecules in form I show an S1···F1′ distance of 3.168 Å, whereas their analogues in form II (S2···F12′) are slightly longer (3.222 Å). The chains form a parallel array in the *ab* plane. These planes are interconnected with each other in the *c* axis orientation through two distances, an S···N′ electrostatic interaction at 3.315 Å and a Cl···Cl′ nonbonding distance of 3.479 Å (Figure 5).

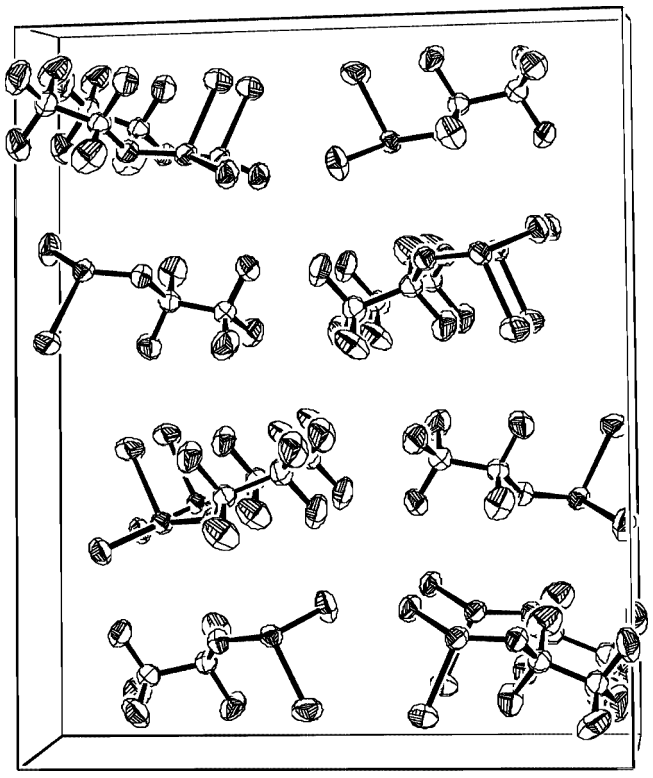

Figure 4. Stereoscopic illustration of the crystal packing of $CF_3CF_2N{=}SCl_2$ at 159 K.

**Natural Bond Orbital Analysis**

NBO analysis for the (*Z*) form of the $CF_3CF_2N{=}SCl_2$ molecule suggests that the formal N=S double bond has only σ-bond character. Indeed, this analysis clearly indicates the presence of two lone-pair orbitals at the nitrogen atom. The nature of these two orbitals is $sp^2$- [lp($Nsp^2$)] and pure p-type [lp(Np)]. Their electron occupancies are low: 1.83 and 1.67 e, respectively, thus indicating the electron-donating capacity of both orbitals, in agreement with the experimental evidence relating the sulfur imide bond order with the electron-withdrawing properties of the substituents attached at the nitrogen and sulfur atoms. Delocalizing interactions evaluated by a second-order perturbation approach reveal that the first lone-pair orbital contributes to a negative hyperconjugative interaction with the S–Cl σ-antibonding orbitals [lp($Nsp^2$)→σ*(S–Cl)], with a stabilizing energy $E^{(2)}$ of 37.71 kcal mol$^{-1}$. The second lone-pair orbital contributes to two stronger lp(Np)→σ*(S–Cl) negative hyperconjugative interactions ($E^{(2)}$ = 97.46 kcal mol$^{-1}$). This interaction corresponds to an electron donation from the formally doubly occupied HOMO to the vacant LUMO in $CF_3CF_2N{=}SCl_2$. Thus, the energy difference between lp(Np)→σ*(S–Cl) and lp($Nsp^2$)→σ*(S–Cl) interactions is mainly related to the different denominator in the expression

$$\Delta E^{(2)}_{\phi\phi^*} = -2\frac{\left\langle \phi \middle| \hat{F} \middle| \phi^* \right\rangle^2}{\varepsilon_{\phi^*} - \varepsilon_{\phi}}$$

in which $\hat{F}$ is the Fock operator, $\phi$ and $\phi^*$ the donating and acceptor orbitals, respectively, and $\varepsilon$ the NBO orbital energy.

This strong electron donation into the σ*(S–Cl) antibonding orbitals is also reflected in the high electronic occupancy of the σ*(S–Cl) orbital of about 0.23 e. The lone-pair orbital at the sulfur atom, on the other hand, donates electron density mainly into the vacant C–N antibonding orbital by a negative hyperconjugation interaction, lp(S)→σ*(C–N), with an $E^{(2)}$ value of 10.82 kcal mol$^{-1}$. All these anomeric interactions decrease on going from the (*Z*)

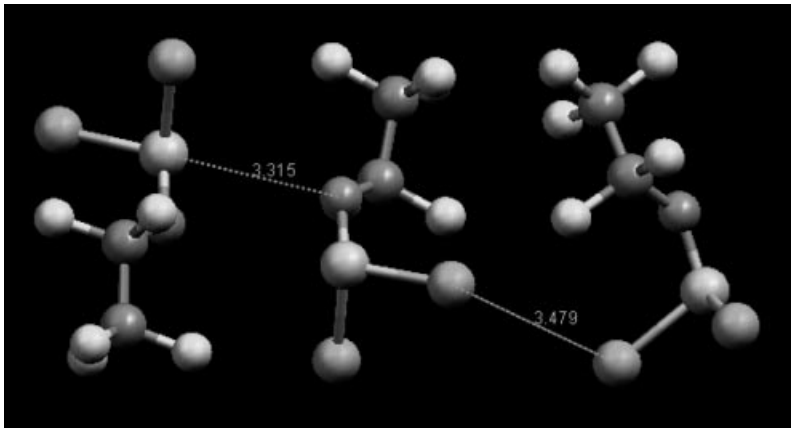


Figure 5. Short nonbonding distances in crystalline $CF_3CF_2N{=}SCl_2$ at 159 K.

 © 2007 Wiley-VCH Verlag GmbH & Co. KGaA, Weinheim 

to the (*E*) form, similar to the behavior calculated for $H_2SNH$.[30] Thus, the thermodynamic preference of the (*Z*) form for $CF_3CF_2N{=}SCl_2$ can be rationalized as originating from the dominant influence of the stabilizing anomeric interactions.

The atomic charges obtained using the Natural Population Analysis (NPA) approach for (*Z*)-$CF_3CF_2NSCl_2$ reveal that a strong positive charge (+1.25) is located at the sulfur and almost a unit negative charge (–0.99) at the nitrogen atom. These data indicate that, in addition to the negative hyperconjugation, the semipolar character of the S–N bond in sulfur imides can be attributed to this polar attraction rather than to an S–N dπ-pπ orbital interaction. It is known that the S–N rotational barrier in sulfur imide species is expected to be small in comparison with the formal double bonds depicted in their formulae because of the hypervalent nature of the sulfur atom.[40] This value has been estimated to be 8.50 kcal mol$^{-1}$ (after including thermal corrections at the G2 level) for the simple molecule $HNSH_2$.[30] This value increases for the *S*,*S*-disubstituted sulfur imides $HN{-}SX_2$ (X = F, Cl, and Me) mainly due to the fact that the S–N bond strength increases with an enhancement in the electronegativity of the substituent bonded to the sulfur atom. Following this trend, the torsional transition state calculated for $CF_3CF_2NSCl_2$ amounts to 8.45 kcal mol$^{-1}$ [B3LYP/6-311+G(d)], a value which is compatible with the rotational barrier expected for sulfur imides.[41]

## Conclusions

Only the (*Z*) conformer around the sulfur imide bond is observed in both gaseous and condensed $CF_3CF_2N{=}SCl_2$. This structural behavior seems to be a general feature in *S*,*S*-difluoro- and *S*,*S*-dichloro-substituted sulfur imides, whereas for related compounds with two different substituents attached at the sulfur atom the (*E*) conformer is favored. The conformational and configurational properties of these molecules can be rationalized on the basis of the anomeric effect, mainly by invoking electron-donating interactions between the sulfur and nitrogen lone-pair orbitals to opposite σ* orbitals. Thus, the sterically unfavorable (*Z*) orientation is stereoelectronically stabilized mainly by lp(N)→σ*(S–Cl) and, to a minor extent, by lp(S)→σ*(N–C) interactions.

The description of the central sulfur imide bond from the NBO analysis agrees with a semipolar $S^+{-}N^-$ bond with strong hyperconjugative interactions. This analysis indicates a negatively charged nitrogen atom with two lone pairs for the $CF_3CF_2NSCl_2$ molecule, in which the sulfur atom is $sp^3$-hybridized. Thus, valence expansion to more than eight electrons at the sulfur atom can be excluded to explain the bonding. An inspection of the orbital shapes involved in the sulfur imide bond is given in Figure 6, which supports a redistribution of the electronic density from the negatively charged nitrogen atom to the S–N bond. These findings are in agreement with MO calculations on second-row atoms in "hypervalent" molecules. Theoretical studies of $SO_2$, a molecule with the sulfur atom possessing the same formal oxidation state of +IV as in $CF_3CF_2N{=}SCl_2$, show that the S–O bond has a highly ionic character, the octet rule is not violated, and it is not necessary to invoke the term "hypervalency".[42]

## Experimental Section

**Synthesis:** $CF_3CF_2N{=}SCl_2$ was prepared by the reaction between $AlCl_3$ and $CF_3CF_2N{=}SF_2$ according to a literature procedure.[43] The product was purified by several trap-to-trap distillations.

**Vibrational Spectroscopy:** Gas-phase IR spectra were recorded with a resolution of 1 cm$^{-1}$ in the range 4000–400 cm$^{-1}$ with a Bruker IFS 66v FTIR instrument. FT Raman spectra of liquid $CF_3CF_2N{=}SCl_2$ were recorded with a Bruker RFS 100/S FT Raman spectrometer. The sample in a 6-mm (o.d.) glass tube was excited with 150 mW from a 1064-nm Nd:YAG laser (ADLAS, DPY 301, Lübeck, Germany).

**X-ray Diffraction at Low Temperature:** An appropriate crystal of $CF_3CF_2N{=}SCl_2$ about 0.3 mm in diameter was obtained on the diffractometer at a temperature of 159(2) K with a miniature zone-melting procedure using focused infrared laser radiation.[44] The diffraction intensities were measured at low temperature with a Nicolet R3m/V four-circle diffractometer. Intensities were collected with graphite-monochromatized Mo-$K_\alpha$ radiation using the $\omega$-scan technique. The crystallographic data, conditions, and some features of the structure are listed in Table 3. The structure was solved by Patterson syntheses, and refined by the full-matrix least-squares method on *F* with the SHELTXL-Plus program.[45] All atoms were assigned to anisotropic thermal parameters. Atomic coordinates, equivalent isotropic displacement coefficients, and anisotropic displacement parameters ($Å^2 \times 10^3$) for $CF_3CF_2N{=}SCl_2$ have been deposited; further details of the crystal structure investigation may be obtained from the Fachinformationzentrum Karlsruhe, 76344 Eggenstien-Leopoldshafen, Germany (Fax: +49-7247-808-666; E-mail: crysdata@fiz-karlsruhe.de) on quoting the depository number CSD-417110.

**Theoretical Calculations:** All the quantum chemical calculations were performed using the GAUSSIAN03 program.[46] Geometry optimizations were performed with the HF and MP2 approximations and the B3LYP methods using 6-311+G(d) and 6-311+G(2df) basis sets and standard gradient techniques with simultaneous relaxation of all the geometric parameters. Natural population analysis and second-order donor→acceptor interaction energies were estimated at the MP2/6-31+G(d) level by using the NBO analysis[47] as implemented in the GAUSSIAN03 program.

Figure 6. NBO orbitals [MP2/6-31+G(d)] for the sulfur imide bond of $CF_3CF_2N{=}SCl_2$: (a) lp(Np), MO = 57 (HOMO); (b) lp($Nsp^2$), MO = 54; (c) lp(S) MO = 39; (d) σ(N–S) MO = 34.

 © 2007 Wiley-VCH Verlag GmbH & Co. KGaA, Weinheim 

## Acknowledgments

Financial support by the Volkswagen Stiftung (I/78724) is gratefully acknowledged. The Argentinean authors acknowledge the Fundación Antorchas, the Alexander von Humboldt Stiftung, the Deutscher Akademischer Austauschdienst (DAAD), Germany, the Agencia Nacional de Promoción Científica y Técnica (ANPCYT), the Consejo Nacional de Investigaciones Científicas y Técnicas (CONICET), the Comisión de Investigaciones de la Provincia de Buenos Aires (CIC), the Facultad de Ciencias Exactas (UNLP), and the Universidad Nacional de Tucumán (UNT). C. O. D. V. specially acknowledges the DAAD, which generously sponsors the DAAD Regional Program of Chemistry of the Republic of Argentina and supports Latin-American students earning their PhDs in La Plata.

[1] F. Weinhold, *Nature* **2001**, *411*, 539–541.
[2] V. Pophristic, L. Goodman, *Nature* **2001**, *411*, 565–568.
[3] P. R. Schreiner, *Angew. Chem. Int. Ed.* **2002**, *41*, 3579–3581.
[4] L. Goodman, H. Gu, V. Pophristic, *J. Phys. Chem. A* **2005**, *109*, 1223–1229.
[5] J. Zheng, K. Kwak, J. Xie, M. D. Fayer, *Science* **2006**, *313*, 1951–1955.
[6] F. Trautner, T. Abe, H. Oberhammer, *J. Am. Chem. Soc.* **2001**, *123*, 2865–2869.
[7] A. Hermann, F. Trautner, K. Gholivand, S. von Ahsen, E. L. Varetti, C. O. Della Védova, H. Willner, H. Oberhammer, *Inorg. Chem.* **2001**, *40*, 3979–3985.
[8] N. L. Owen, H. M. Seip, *Chem. Phys. Lett.* **1970**, *5*, 162–164.
[9] S. Samdal, H. M. Seip, *J. Mol. Struct.* **1975**, *28*, 193–203.
[10] M. Fujitake, M. Hayashi, *J. Mol. Struct.* **1985**, *127*, 21–33.
[11] C. Leibold, S. Reinemann, R. Minkwitz, P. R. Resnik, H. Oberhammer, *J. Org. Chem.* **1997**, *62*, 6160–6163.
[12] International Union of Pure and Applied Chemistry, *Nomenclature of Organic Chemistry IUPAC*, Butterworths, London, **1965**, section C.
[13] J. E. Griffiths, D. F. Sturman, *Spectrochim. Acta Part A* **1969**, *25*, 1355–1363.
[14] F. Trautner, D. Christen, R. Mews, H. Oberhammer, *J. Mol. Struct.* **2000**, *525*, 135–139.
[15] N. L. Robles, E. H. Cutín, C. O. Della Védova, *J. Mol. Struct.* **2006**, *784*, 265–268.
[16] R. R. Karl, J. S. H. Bauer, *Inorg. Chem.* **1975**, *14*, 1859–1861.
[17] C. Leibold, E. Cutin, C. O. Della Védova, H.-G. Mack, R. Mews, H. Oberhammer, *J. Mol. Struct.* **1996**, *375*, 207–211.
[18] R. M. S. Álvarez, E. H. Cutin, R. M. Romano, C. O. Della Védova, *Spectrochim. Acta Part A* **1996**, *52*, 667–673.
[19] R. S. M. Alvarez, E. H. Cutin, C. O. Della Vedova, R. Mews, R. Haist, H. Oberhammer, *Inorg. Chem.* **2001**, *40*, 5188–5191.
[20] M. I. Mora Valdez, E. H. Cutin, C. O. Della Védova, R. Mews, H. Oberhammer, *J. Mol. Struct.* **2002**, *607*, 207–215.
[21] R. Haist, R. S. M. Alvaréz, E. H. Cutin, C. O. Della Védova, H. Oberhammer, *J. Mol. Struct.* **1999**, *484*, 249–257.
[22] R. M. S. Álvarez, E. H. Cutín, R. M. Romano, H.-G. Mack, C. O. Della Védova, *J. Mol. Struct.* **1998**, *443*, 155–161.
[23] R. M. S. Alvarez, E. H. Cutin, R. M. Romano, C. O. Della Védova, *Spectrochim. Acta Part A* **1999**, *55*, 2615–2622.
[24] R. Haist, E. H. Cutin, C. O. Della Védova, H. Oberhammer, *J. Mol. Struct.* **1999**, *475*, 273–277.
[25] C. Leibold, R. M. S. Álvarez, E. H. Cutin, C. O. Della Védova, H. Oberhammer, *Inorg. Chem.* **2003**, *42*, 4071–4075.
[26] F. Trautner, E. H. Cutin, C. O. Della Védova, R. Mews, H. Oberhammer, *Inorg. Chem.* **2000**, *39*, 4833–4837.
[27] A. Hermann, M. I. Mora-Valdez, E. H. Cutin, C. O. Della Védova, H. Oberhammer, *J. Phys. Chem. A* **2003**, *107*, 7874–7878.
[28] D. Leusser, J. Henn, N. Kocher, B. Engels, D. Stalke, *J. Am. Chem. Soc.* **2004**, *126*, 1781–1793.
[29] S. I. Protashchuk, N. P. Bezverkhii, A. V. Prosyanik, *J. Struct. Chem.* **1991**, *32*, 963–965.
[30] P. S. Kumar, P. Singh, P. Uppal, P. V. Bharatam, *Bull. Chem. Soc. Jpn.* **2005**, *78*, 1417–1424.
[31] R. M. S. Álvarez, E. H. Cutin, R. M. Romano, H. G. Mack, C. O. Della Védova, *J. Raman Spectrosc.* **1998**, *29*, 257–261.
[32] N. L. Robles, E. H. Cutin, C. O. Della Védova, *J. Mol. Struct.* **2006**, *784*, 265–268.
[33] N. Rontu, V. Vaida, *J. Mol. Spectrosc.* **2006**, *237*, 19–26.
[34] G. A. Crowder, *J. Fluorine Chem.* **1973**, *2*, 217–224.
[35] J. A. R. P. Sarma, G. R. Desiraju, *Acc. Chem. Res.* **1986**, *19*, 222–228.
[36] M. B. Zaman, K. A. Udachin, J. A. Ripmeester, *Cryst. Growth Des.* **2004**, *4*, 585–589.
[37] A. Matsumoto, T. Tanaka, T. Tsubouchi, K. Tashiro, S. Saragai, S. Nakamoto, *J. Am. Chem. Soc.* **2002**, *124*, 8891–8902.
[38] A. C. Legon, *Angew. Chem. Int. Ed.* **1999**, *38*, 2686–2714.
[39] C. F. Matta, N. Castillo, R. J. Boyd, *J. Phys. Chem. A* **2005**, *109*, 3669–3681.
[40] A. E. Reed, P. v. R. Schleyer, *J. Am. Chem. Soc.* **1990**, *112*, 1434–1445.
[41] T. L. Gilchrist, C. J. Moody, *Chem. Rev.* **1977**, *77*, 409–435.
[42] J. Cioslowski, S. T. Mixon, *Inorg. Chem.* **1993**, *32*, 3209–3216.
[43] M. Lustig, *Inorg. Chem.* **1966**, *5*, 1317–1319.
[44] R. Boese, M. Nussbaumer, "In situ crystallization Techniques", in *Organic Crystal Chemistry* (Ed.: D. W. Jones), Oxford University Press, Oxford, UK, **1994**, pp. 20–37.
[45] *SHELTX-Plus Version SGI IRIS Indigo, a Complex Software Package for Solving, Refining and Displaying Crystal Structures*, Siemens, Germany, **1991**.
[46] M. J. Frisch, G. W. Trucks, H. B. Schlegel, G. E. Scuseria, M. A. Robb, J. R. Cheeseman, J. A. Montgomery Jr, T. Vreven, K. N. Kudin, J. C. Burant, J. M. Millam, S. S. Iyengar, J. Tomasi, V. Barone, B. Mennucci, M. Cossi, G. Scalmani, N. Rega, G. A. Petersson, H. Nakatsuji, M. Hada, M. Ehara, K. Toyota, R. Fukuda, J. Hasegawa, M. Ishida, T. Nakajima, Y. Honda, O. Kitao, H. Nakai, M. Klene, X. Li, J. E. Knox, H. P. Hratchian, J. B. Cross, C. Adamo, J. Jaramillo, R. Gomperts, R. E. Stratmann, O. Yazyev, A. J. Austin, R. Cammi, C. Pomelli, J. W. Ochterski, P. Y. Ayala, K. Morokuma, G. A. Voth, P. Salvador, J. J. Dannenberg, V. G. Zakrzewski, S. Dapprich, A. D. Daniels, M. C. Strain, O. Farkas, D. K. Malick, A. D. Rabuck, K. Raghavachari, J. B. Foresman, J. V. Ortiz, Q. Cui, A. G. Baboul, S. Clifford, J. Cioslowski, B. B. Stefanov, G. Liu, A. Liashenko, P. Piskorz, I. Komaromi, R. L. Martin, D. J. Fox, T. Keith, M. A. Al-Laham, C. Y. Peng, A. Nanayakkara, M. Challacombe, P. M. W. Gill, B. Johnson, W. Chen, M. W. Wong, C. Gonzalez, J. A. Pople, *GAUSSIAN03*, Revision B.04 ed., Gaussian, Inc., Pittsburgh, PA, **2003**.
[47] A. E. Reed, L. A. Curtiss, F. Weinhold, *Chem. Rev.* **1988**, *88*, 899–926.

Received: December 7, 2006
Published Online: June 19, 2007

 © 2007 Wiley-VCH Verlag GmbH & Co. KGaA, Weinheim 

DOI: 10.1002/ejic.200700075

# Thiodiacetate and Oxydiacetate Cobalt Complexes: Synthesis, Structure and Stereochemical Features

**Abdessamad Grirrane,[a,b] Antonio Pastor,[a] Eleuterio Álvarez,[b] Carlo Mealli,[c] Andrea Ienco,[c] Patrick Rosa,[d,e] and Agustín Galindo*[a]**

**Keywords:** Cobalt / Thiodiacetate / Oxydiacetate / Tridentate Ligands / Coordination modes

A series of cobalt complexes containing the dianionic ligands $X(CH_2COO)_2^{2-}$ (X = S, tda; or X = O, oda) is reported. The complexes [Co(tda)(bipy)($H_2O$)]·4$H_2O$ (**2**), which was characterised by X-ray crystallography, [Co(tda)(phen)($H_2O$)] (**3**), [Co(tda){($MeO)_2$bipy}($H_2O$)]·2$H_2O$ (**4**) and [Co(tda)(dpp)($H_2O$)]·2$H_2O$ (**5**) are obtained by reaction of the precursor complex [Co(tda)($H_2O$)]$_n$ (**1a**) with the bidentate N-donor ligands 2,2′-bipyridine (bipy), *o*-phenanthroline (phen), 4,4′-dimethoxy-2,2′-bipyridine [($MeO)_2$bipy] and 2,3-bis(2-pyridyl)pyrazine (dpp), respectively. The reaction of **1a** with di(2-pyridyl) ketone unexpectedly displaces tda from the coordination sphere and leads to the $Co^{III}$ species [Co{OC(OH)(2-pyridyl)$_2$}$_2$]$^+$[Htda]$^-$·3$H_2O$ (**6**), as confirmed by an X-ray analysis. Three new oxydiacetate complexes of cobalt are also synthesised by treating the known complex [{Co(oda)($H_2O$)$_2$}·$H_2O$]$_n$ with 4,4′-di-*tert*-butyl-2,2′-bipyridine (*t*$Bu_2$bipy), 2,3-bis(2-pyridyl)pyrazine (dpp) and 4,4′-bipyridine (4,4′-bipy). The complexes [Co(oda)(*t*$Bu_2$bipy)($H_2O$)]·1.5$H_2O$ (**7**), [Co(oda)(dpp)($H_2O$)]·2$H_2O$ (**8**) and [{Co(oda)($H_2O$)$_2$}$_2$(μ-4,4′-bipy)]·2$H_2O$ (**9**) are structurally characterised (**8** as a methanol solvate). Complex **9** is binuclear, in contrast to **7** and **8** (mononuclear), and magnetic susceptibility measurements down to 2 K for this complex show high-spin noncorrelated $Co^{II}$ ions with a typical Curie–Weiss behaviour. The Co(oda) fragment in **7**–**9** adopts a planar (*mer*) rather than a folded (*fac*) conformation, the latter of which is common to all the M(tda) complexes but is only occasionally observed in the M(oda) ones. In the final section of the paper, the key geometric parameters that control the stereochemistry of the two ligands are determined from a statistical analysis based on the structurally characterised Co(oda) and Co(tda) complexes.
(© Wiley-VCH Verlag GmbH & Co. KGaA, 69451 Weinheim, Germany, 2007)

## Introduction

The thiodiacetate (tda) and oxydiacetate (oda) dianions $X(CH_2COO)_2^{2-}$ (X = S and O, respectively) are versatile ligands that have been widely explored as multidentate and chelating units for one or more metals of a different nature. They contain five atoms that are potential donors, four of which come from two carboxylate groups and one from the thioether or ether function. These ligands can bind a single metal in a tridentate manner, with the two "exo" oxygen donor atoms of the carboxylate groups being capable of additional coordination of another metal or external electrophiles. This permits the formation of homo- and heterometallic extended solids or the formation of stabilizing hydrogen bonds.

The chemistry of thiodiacetate transition metal complexes is comparatively less developed than that of the related oxydiacetate complexes. As a matter of fact, the number of X-ray characterised metal derivatives is smaller for tda than for oda derivatives (160 and 55 hits for the $O(CH_2COO)_2^{2-}$ and $S(CH_2COO)_2^{2-}$ fragments, respectively[1]). Due to our interest in this area of chemistry,[2,3] we started to explore the behaviour of thiodiacetate toward cobalt as no structure of tda-Co complexes had been reported and there were only references in the literature to the solution behaviour of tda-$Co^{II}$ species.[4] The first structural characterisation of a tda-$Co^{II}$ complex was simultaneously presented by us[5] and by Zhu and co-workers[6] (complex [Co(tda)(phen)($H_2O$)]). Some additional examples, namely [Co(tda)(N-N)($H_2O$)]·2$H_2O$ and [Co(tda)($N)_3$]·2$H_2O$, where N and N-N are nitrogen ligands, were published soon afterwards by Xu and co-workers.[7]

In this paper we present a complete report of our studies together with the synthesis and properties of new cobalt

[a] Departamento de Química Inorgánica, Universidad de Sevilla, Aptdo 1203, 41071 Sevilla, Spain
Fax: +34-95-455-7153
E-Mail: galindo@us.es
[b] Instituto de Investigaciones Químicas, CSIC-Universidad de Sevilla,
Avda. Américo Vespucio 49, 41092 Sevilla, Spain
[c] ICCOM, CNR,
Via Madonna del Piano 10, 50019 Sesto Fiorentino, Firenze, Italy
[d] LAMM, Dipartimento di Chimica, Università degli Studi di Firenze,
Via della Lastruccia 3, 50019 Sesto Fiorentino, Firenze, Italy
[e] Institut de Chimie de la Matière Condensée de Bordeaux ICMCB-CNRS, Université Bordeaux, Groupe de Sciences Moleculaires,
87 Av. Dr. A. Schweitzer, 33608 PESSAC Cedex, France
Supporting information for this article is available on the WWW under http://www.eurjic.org or from the author.

 © 2007 Wiley-VCH Verlag GmbH & Co. KGaA, Weinheim 

oxydiacetate complexes. The general coordination capabilities of both the tda and oda ligands are compared, with particular emphasis on the structural data now available for cobalt.

## Results and Discussion

### Cobalt Thiodiacetate Complexes

Treatment of aqueous solutions of cobalt dichloride with a 1:1 mixture of $Na_2CO_3$ and thiodiacetic acid, $S(CH_2COOH)_2$, affords, after the appropriate work up, dark pink block-shaped microcrystals of the complex $[Co(tda)(H_2O)]_n$ (**1a**) in good yields. Closely related thiodiacetate complexes of manganese and zinc, $[M(tda)(H_2O)]_n$, could also be synthesised by this route.[3] Complex **1a** is air-stable and soluble in water but not in solvents of low polarity. Its IR spectrum displays a very strong and broad absorption band at about 1589 $cm^{-1}$, which corresponds to the antisymmetric vibrations of the tda carboxylate groups. Another strong band at 1399 $cm^{-1}$ is assigned to the corresponding symmetric vibrations.[8] The IR spectrum is identical to that of the structurally characterised polymeric complexes $[Cd(tda)(H_2O)]_n$[9] and $[Zn(tda)(H_2O)]_n$[3c,10] and, consequently, we proposed a similar crystalline structure for **1a**. During the preparation of **1a**, some dark-pink, needle-shaped crystals were also occasionally observed. The IR spectrum of this second compound, **1b**, shows only minor differences with respect that of **1a**, mainly in the region of coordinated water (see Supporting Information). This spectrum is identical to that of the already reported[11] complex $[Ni(tda)(H_2O)_3]$, therefore taking into account the analytical data, the formula of **1b** is suggested to be $[Co(tda)(H_2O)_3]$.

Complex $[Co(tda)(H_2O)]_n$ (**1a**) exists as $[Co(tda)(H_2O)_3]$ (that is **1b**) in aqueous solution. Two coordinated water molecules can easily be displaced from this species upon reaction with several bidentate N-donor ligands (see Scheme 1). In fact, aqueous solutions of **1a** react with 2,2′-bipyridine (bipy), *o*-phenanthroline (phen), 4,4′-dimethoxy-2,2′-bipyridine [$(MeO)_2$bipy] and 2,3-bis(2-pyridyl)pyrazine (dpp) to give new complexes of general formula $[Co(tda)(N\text{-}N)(H_2O)]$ (N-N = bidentate N-donor ligand). These complexes can be isolated in good yields as crystalline solids containing a variable number of water molecules of hydration {namely, $[Co(tda)(bipy)(H_2O)]\cdot 4H_2O$ (**2**), $[Co(tda)(phen)(H_2O)]$ (**3**), $[Co(tda)\{(MeO)_2bipy\}(H_2O)]\cdot 2H_2O$ (**4**) and $[Co(tda)(dpp)(H_2O)]\cdot 2H_2O$ (**5**)}. All complexes are soluble in water (but not in low polarity solvents) and are air-stable both in solution and in the solid state. Their IR spectra are characterised, besides the absorptions due to the N-donor co-ligands, by two broad absorptions corresponding to the tda carboxylate groups (for instance at 1599 and 1400 $cm^{-1}$ for **2**). The measured effective magnetic moments (in the solid state and at room temperature) are typical of high-spin mononuclear $d^7$-cobalt complexes (4.3–4.9 $\mu_B$).[12]

The crystal structures of complexes $[Co(tda)(bipy)(H_2O)]\cdot 4H_2O$ (**2**) and $[Co(tda)(phen)(H_2O)]$ (**3**) were determined by X-ray diffraction methods. The structure of the latter was published while our work was in progress,[6] therefore some of its features are illustrated here but considered only for comparative purposes (see below). As for complex **2**, the coordination polyhedron around the cobalt atom is a distorted octahedron in which the metal atom is coordinated by the tridentate tda ligand in a typical *fac* arrangement. The coordination sphere is completed by the bidentate bipy ligand and one water molecule, which is bound *trans* to the sulfur donor atom of tda (Figure 1). Complex **2** is isomorphous with the known nickel,[11a] zinc[13] and copper analogues.[14] Selected bond lengths and angles of **2** are collected in Table 1.

Although coordinatively similar (also in terms of Co–O, Co–S and Co–N bond lengths), the pseudo-octahedral complexes **2** and **3** differ in two main aspects: the former features four hydration molecules while the latter has none, and the relative orientation of the N-donor group with respect to the tda ligand is different (Scheme 1). In spite of the similar coordination properties of the bipy and phen bidentate ligands, bipy lies coplanar with the coordinated oxygen donors of tda in **2** (the water ligand lies *trans* to the

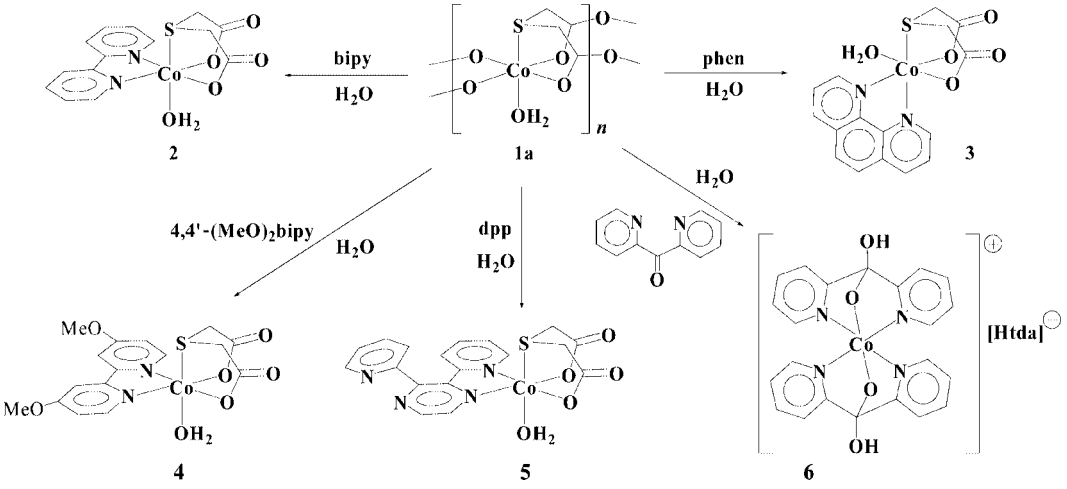


Scheme 1.

 © 2007 Wiley-VCH Verlag GmbH & Co. KGaA, Weinheim 

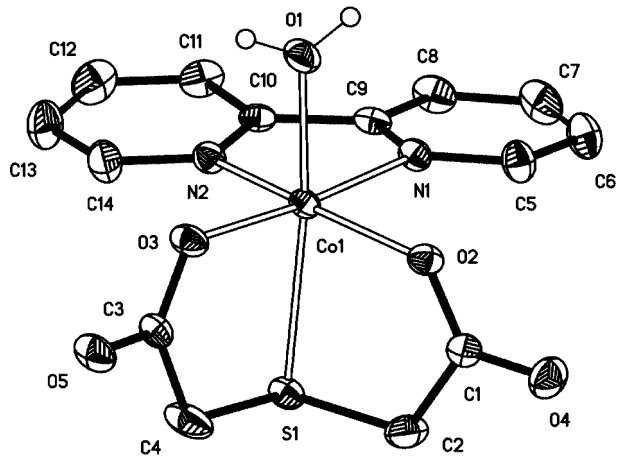


Figure 1. Molecular structure of $[Co(tda)(bipy)(H_2O)]\cdot 4H_2O$ (**2**). The hydrogen atoms, except those of the water ligand, and the crystallisation water molecules are not shown.

Table 1. Selected bond lengths [Å] and angles [°] for **2**.

| | | | |
|---|---|---|---|
| Co(1)–O(3) | 2.0289(15) | S(1)–C(4) | 1.796(3) |
| Co(1)–O(2) | 2.0456(15) | O(2)–C(1) | 1.270(3) |
| Co(1)–O(1) | 2.0911(17) | O(3)–C(3) | 1.254(3) |
| Co(1)–S(1) | 2.5077(10) | O(4)–C(1) | 1.229(3) |
| Co(1)–N(2) | 2.1100(19) | O(5)–C(3) | 1.242(3) |
| Co(1)–N(1) | 2.1549(18) | C(1)–C(2) | 1.516(3) |
| S(1)–C(2) | 1.791(3) | C(3)–C(4) | 1.518(4) |
| O(3)–Co(1)–O(2) | 96.56(7) | N(2)–Co(1)–N(1) | 76.36(7) |
| O(3)–Co(1)–O(1) | 85.78(7) | O(3)–Co(1)–S(1) | 81.83(5) |
| O(2)–Co(1)–O(1) | 95.44(7) | O(2)–Co(1)–S(1) | 82.02(5) |
| O(3)–Co(1)–N(2) | 97.83(7) | O(1)–Co(1)–S(1) | 166.96(5) |
| O(2)–Co(1)–N(2) | 163.56(7) | N(2)–Co(1)–S(1) | 92.18(6) |
| O(1)–Co(1)–N(2) | 93.51(8) | N(1)–Co(1)–S(1) | 100.33(5) |
| O(3)–Co(1)–N(1) | 173.82(7) | C(2)–S(1)–C(4) | 104.07(18) |
| O(2)–Co(1)–N(1) | 89.49(7) | C(2)–S(1)–Co(1) | 94.86(9) |
| O(1)–Co(1)–N(1) | 92.41(7) | | |

sulfur atom), although the same does not apply to phen, which adopts an upright position in **3**. In other words, it lies coplanar with the S atom while the coordinated water molecule is *trans* to one tda oxygen donor. This situation is similar to that found for the Zn-tda system, for which the bipy[13] and phen[3c] derivatives show different structures.

The crystalline solids **4** and **5** were characterised by analytical and spectroscopic methods as $[Co(tda)\{(MeO)_2\text{-}bipy\}(H_2O)]\cdot 2H_2O$ and $[Co(tda)(dpp)(H_2O)]\cdot 2H_2O$, respectively. The potentially tridentate dpp ligand coordinates in a bidentate fashion in **5**. This also occurs in the oxydiacetate derivative **8**, which has been structurally characterised (see below). The correct structure of **4** and **5** cannot be safely anticipated, however, because two isomers are also possible in this case. Their energies should be rather similar and the adoption of a specific geometry may be caused by subtle factors. For example, the presence or absence of water of crystallisation can clearly affect the final crystal structure since hydrogen bonding is a key feature in oxydiacetate and thiodiacetate metal complexes. Coordinated and solvent water molecules fix the crystal packing of most of these derivatives by interacting with the coordinated or uncoordinated oxygen atoms of tda or oda. In actual fact, complex **2** features a 3D network of hydrogen bonding between the water ligand O1, the water solvent molecules and some oxygen atoms of the carboxylate groups of tda ligand (see Figure S2 in the Supporting Information). Consequently, we propose similar structures for **4** and **5** to that observed for **2** (Scheme 1).

An attempt to obtain an additional cobalt complex with tda was made by treating **1a** with the ligand di(2-pyridyl) ketone. The deep-red crystals obtained after the appropriate work-up have properties that are different to those observed for complexes **2**–**6**. Thus, their diamagnetism suggests the presence of a $Co^{III}$ centre and their analytical data are consistent with a 1:1:2 Co:tda:di(2-pyridyl) ketone ratio. An X-ray structure determination (Figure 2) indicated that the tda ligand is protonated not coordinated, in other words it acts as a counterion. Thus, the species has the unexpected stoichiometry $[Co\{OC(OH)(2\text{-pyridyl})_2\}_2]^+[Htda]^-\cdot 3H_2O$ (**6**). Essentially, two di(2-pyridyl) ketone molecules have been hydrolysed and deprotonated in a process that has already been described (Scheme 2).[15] The latter molecules act as two staggered tridentate *fac* ligands that confer a pseudo-octahedral geometry to the oxidized $Co^{III}$ centre. Selected bond lengths and angles of **6** are collected in Table 2. The

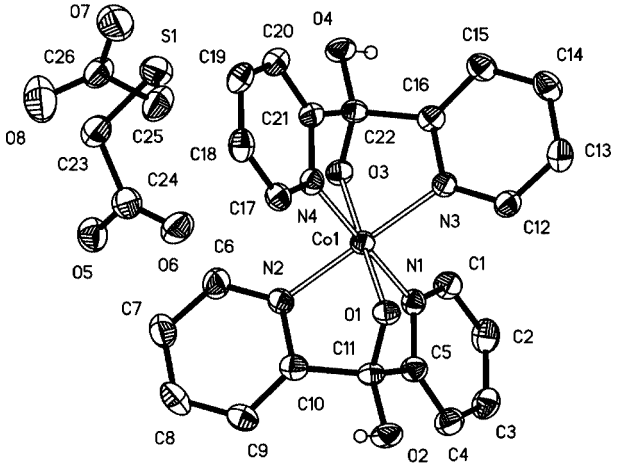


Figure 2. Crystal structure of $[Co\{OC(OH)(2\text{-pyridyl})_2\}_2]^+[Htda]^-\cdot 3H_2O$ (**6**). Solvent water molecules are not shown.

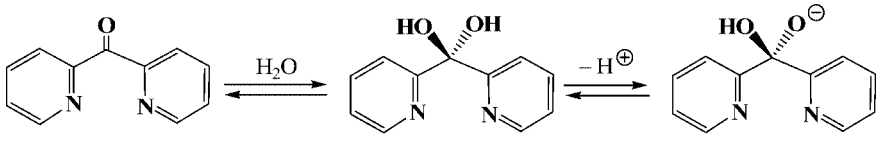


Scheme 2.

 © 2007 Wiley-VCH Verlag GmbH & Co. KGaA, Weinheim 

cationic part of **6**, $[Co\{OC(OH)(2\text{-pyridyl})_2\}_2]^+$, has been previously characterised for other cobalt complexes with different counterions.[16] There is good structural consistency among the latter, so their geometrical features do no require further comment.

Table 2. Selected bond lengths [Å] and angles [°] for **6**.

| | | | |
|---|---|---|---|
| Co(1)–O(1) | 1.886(3) | O(3)–C(22) | 1.395(7) |
| Co(1)–O(3) | 1.886(3) | O(1)–C(11) | 1.404(7) |
| Co(1)–N(1) | 1.913(4) | O(2)–C(11) | 1.382(6) |
| Co(1)–N(4) | 1.922(4) | O(4)–C(22) | 1.376(6) |
| Co(1)–N(3) | 1.926(4) | O(5)–C(24) | 1.293(8) |
| Co(1)–N(2) | 1.932(4) | O(6)–C(24) | 1.217(8) |
| S(1)–C(23) | 1.794(7) | O(7)–C(26) | 1.227(8) |
| S(1)–C(25) | 1.816(8) | O(8)–C(26) | 1.221(9) |
| O(1)–Co(1)–O(3) | 179.48(16) | N(1)–Co(1)–N(3) | 91.24(18) |
| O(1)–Co(1)–N(1) | 82.90(17) | N(4)–Co(1)–N(3) | 88.31(18) |
| O(3)–Co(1)–N(1) | 96.70(17) | O(1)–Co(1)–N(2) | 82.81(17) |
| O(1)–Co(1)–N(4) | 97.67(17) | O(3)–Co(1)–N(2) | 97.51(17) |
| O(3)–Co(1)–N(4) | 82.73(17) | N(1)–Co(1)–N(2) | 88.99(18) |
| N(1)–Co(1)–N(4) | 179.32(17) | N(4)–Co(1)–N(2) | 91.46(19) |
| O(1)–Co(1)–N(3) | 96.53(17) | N(3)–Co(1)–N(2) | 179.27(16) |
| O(3)–Co(1)–N(3) | 83.15(17) | C(23)–S(1)–C(25) | 101.8(3) |

### Cobalt Oxydiacetate Compounds

The number of structurally characterised cobalt oxydiacetate complexes has grown considerably in the last few years. Some crystallographic reports of Co-oda complexes have appeared,[17] and it is worth mentioning, in particular, that the structure of complex $[\{Co(oda)(H_2O)_2\}\cdot H_2O]_n$[18] has been re-determined twice.[19] Additionally, Jiang and Wang have pointed out a topological isomerism between this complex and $[\{Co(oda)(H_2O)\}\cdot H_2O]_n$, and discussed their interconversion.[19a] Since our original report on this chemistry,[2a] we have continued our studies of the chemical reactivity of $[\{Co(oda)(H_2O)_2\}\cdot H_2O]_n$ and we can now describe here the synthesis and structural characterisation of three new Co-oda complexes.

The reaction of aqueous solutions of the complex $[\{Co(oda)(H_2O)_2\}\cdot H_2O]_n$ with 4,4′-di-*tert*-butyl-2,2′-bipyridine ($t$Bu$_2$bipy), 2,3-bis(2-pyridyl)pyrazine (dpp) and 4,4′-bipyridine (4,4′-bipy) yields, after the appropriate work-up, crystals of $[Co(oda)(t\text{Bu}_2\text{bipy})(H_2O)]\cdot 1.5H_2O$ (**7**), $[Co(oda)(dpp)(H_2O)]\cdot 2H_2O$ (**8**) and $[\{Co(oda)(H_2O)_2\}_2(\mu\text{-}4,4'\text{-bipy})]\cdot 2H_2O$ (**9**), respectively, with good yields (see Scheme 3). These complexes are air-stable both in solution and in the solid state. They are soluble in water and complex **7** is also soluble in ethanol. The IR spectra show an intense broad absorption around 1600 cm$^{-1}$ due to the antisymmetric vibrations of the coordinated carboxylate groups of oxydiacetate. We have shown in previous work[2a,2d] that the position of the COC stretch of the oxydiacetate ligand (a characteristic sharp and strong absorption) depends on the disposition of the ligand in the coordination sphere. Thus, when the signal appears above 1100 cm$^{-1}$ the oda ligand adopts a planar conformation (*mer*), whereas in other cases the arrangement is non-planar. Bands above the latter limit for complexes **7**–**9** clearly indicate a planar coordination mode (*mer*), and this was validated by the X-ray analyses. Interestingly, while the known Co(oda) fragments can adopt either a *fac* or a *mer* arrangement, the M(tda) analogue is, to date, invariably *fac* for cobalt as well as for all known transition metal complexes (see below).

Complex **7** is monomeric (Figure 3), and selected structural data are reported in Table 3. The coordination geometry of the cobalt atom is distorted octahedral due to the low bite angle of oda [*transoid* O1–Co–O5 angle of 150.42(10)°].

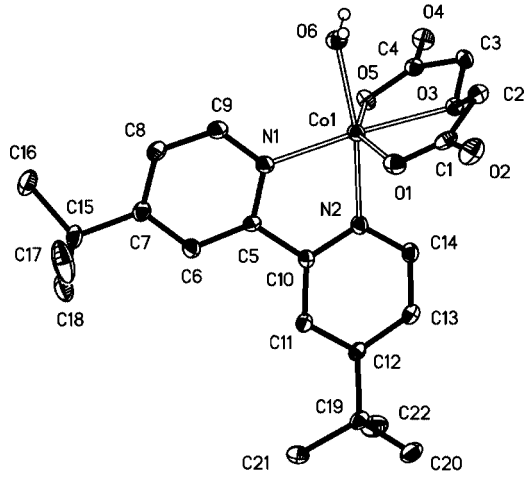


Figure 3. Drawing of one of the two independent molecules in the asymmetric unit of $[Co(oda)(t\text{Bu}_2\text{bipy})(H_2O)]\cdot 1.5H_2O$ (**7**). The hydrogen atoms, except those of the water ligand, and the crystallisation water molecules are not shown.

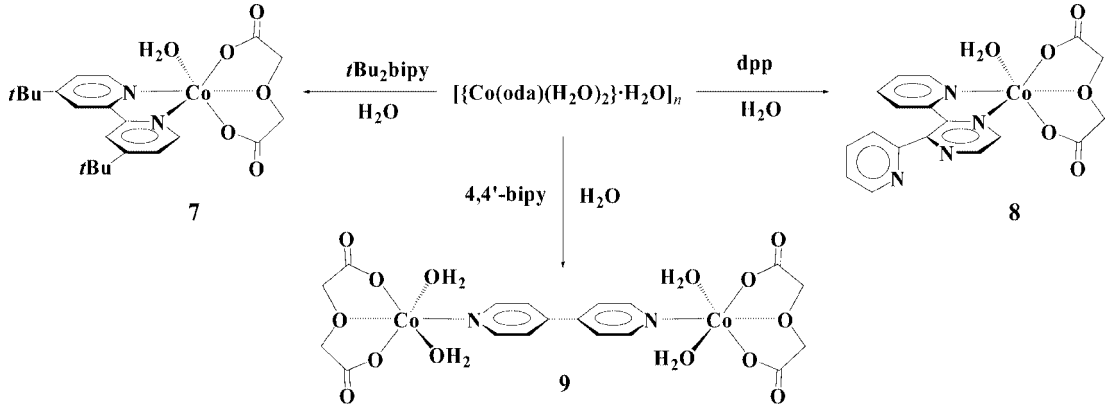


Scheme 3.

 © 2007 Wiley-VCH Verlag GmbH & Co. KGaA, Weinheim 

Although the $t$Bu$_2$bipy ligand is common in coordination chemistry (187 hits in the Cambridge Structural Database,[1a] CSD), it appears that complex **7** is the first structure of a cobalt complex with this ligand.

Table 3. Selected bond lengths [Å] and angles [°] for **7**.

| Molecule 1 | | | |
|---|---|---|---|
| Co(1)–O(5) | 2.055(2) | O(5)–Co(1)–N(2) | 87.99(10) |
| Co(1)–O(1) | 2.056(2) | O(1)–Co(1)–N(2) | 90.20(10) |
| Co(1)–N(1) | 2.080(3) | N(1)–Co(1)–N(2) | 77.04(10) |
| Co(1)–N(2) | 2.112(3) | O(5)–Co(1)–O(6) | 89.96(10) |
| Co(1)–O(6) | 2.120(2) | O(1)–Co(1)–O(6) | 96.35(10) |
| Co(1)–O(3) | 2.169(2) | N(1)–Co(1)–O(6) | 94.50(10) |
| O(1)–C(1) | 1.262(4) | N(2)–Co(1)–O(6) | 170.05(10) |
| O(2)–C(1) | 1.242(4) | O(5)–Co(1)–O(3) | 76.40(8) |
| O(3)–C(2) | 1.429(4) | O(1)–Co(1)–O(3) | 74.95(9) |
| O(3)–C(3) | 1.439(4) | N(1)–Co(1)–O(3) | 173.57(10) |
| O(4)–C(4) | 1.245(4) | N(2)–Co(1)–O(3) | 100.75(9) |
| O(5)–C(4) | 1.265(4) | O(6)–Co(1)–O(3) | 88.21(9) |
| C(1)–C(2) | 1.535(5) | C(2)–O(3)–C(3) | 116.8(2) |
| C(3)–C(4) | 1.533(4) | O(2)–C(1)–O(1) | 125.0(4) |
| O(5)–Co(1)–O(1) | 150.42(10) | O(2)–C(1)–C(2) | 118.1(3) |
| O(5)–Co(1)–N(1) | 109.39(10) | O(4)–C(4)–O(5) | 124.9(3) |
| O(1)–Co(1)–N(1) | 98.92(11) | | |
| **Molecule 2** | | | |
| Co(2)–O(11) | 2.070(2) | N(3)–Co(2)–O(12) | 94.06(10) |
| Co(2)–N(3) | 2.082(2) | O(11)–Co(2)–O(7) | 150.95(9) |
| Co(2)–O(12) | 2.090(2) | N(3)–Co(2)–O(7) | 106.58(10) |
| Co(2)–O(7) | 2.103(2) | O(12)–Co(2)–O(7) | 90.34(9) |
| Co(2)–N(4) | 2.108(3) | O(11)–Co(2)–N(4) | 94.15(10) |
| Co(2)–O(9) | 2.113(2) | N(3)–Co(2)–N(4) | 77.15(10) |
| O(7)–C(23) | 1.256(4) | O(12)–Co(2)–N(4) | 169.90(10) |
| O(8)–C(23) | 1.251(4) | O(7)–Co(2)–N(4) | 87.48(10) |
| O(9)–C(25) | 1.420(4) | O(11)–Co(2)–O(9) | 75.16(8) |
| O(9)–C(24) | 1.423(4) | N(3)–Co(2)–O(9) | 172.85(10) |
| O(10)–C(26) | 1.249(4) | O(12)–Co(2)–O(9) | 92.64(9) |
| O(11)–C(26) | 1.253(4) | O(7)–Co(2)–O(9) | 75.84(9) |
| C(23)–C(24) | 1.529(4) | N(4)–Co(2)–O(9) | 96.38(9) |
| C(25)–C(26) | 1.535(4) | C(25)–O(9)–C(24) | 117.2(2) |
| O(11)–Co(2)–N(3) | 102.03(10) | O(8)–C(23)–O(7) | 125.5(3) |
| O(11)–Co(2)–O(12) | 92.54(9) | O(10)–C(26)–O(11) | 125.7(3) |

Complex **8** was obtained in the solid state as [Co(oda)(dpp)(H$_2$O)]·2H$_2$O, although the X-ray characterisation was carried out with crystals of the methanol solvate [Co(oda)(dpp)(H$_2$O)]·H$_2$O·1/2MeOH that is formed upon recrystallisation from a MeOH/H$_2$O mixture. Complex **8** is also a monomer, with the cobalt atom octahedrally coordinated by three O atoms of the oda ligand in a quasi-planar arrangement, two N atoms of the 2,3-bis(2-pyridyl)pyrazine molecule and one water molecule (Figure 4). As seen in Table 4, the Co–O bonds range between 2.05 and 2.16 Å and the Co–N bonds are as long as 2.095(3) and 2.131(3) Å. Despite possessing three N donor atoms, the dpp ligand is bidentate in **8** since one of the two pyridyl substituents remains uncoordinated. There is one previous structurally characterised example of a Co-ddp complex[20] in which the dpp ligand bridges two cobalt atoms in a $\mu,\kappa^2,\kappa^2$ coordination mode. Interestingly, all attempts to force coordination of the N atom at the free pyridine ring failed. In fact, further reaction of complex **8** with [{Co(oda)(H$_2$O)$_2$}·H$_2$O]$_n$ or the reaction of two equivalents of the latter starting material with 2,3-bis(2-pyridyl)pyrazine did not produce the expected coordination. The geometry of **8** is related to that of **7** and other complexes of formula [Co(oda)(N-N)(H$_2$O)],[21] therefore no further comment is necessary.

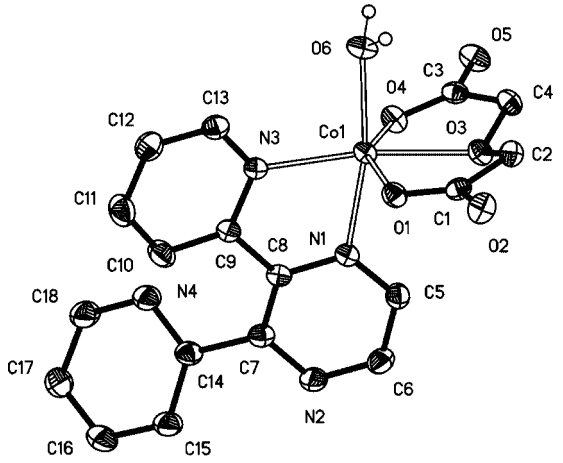


Figure 4. ORTEP drawing of **8** as the methanol solvate [Co(oda)(dpp)(H$_2$O)]·H$_2$O·1/2MeOH. The hydrogen atoms, except those of the water ligand, and the solvent molecules are not shown.

Table 4. Selected bond lengths [Å] and angles [°] for **8**.

| | | | |
|---|---|---|---|
| Co(1)–O(1) | 2.077(2) | O(1)–C(1) | 1.269(4) |
| Co(1)–O(3) | 2.159(2) | O(2)–C(1) | 1.230(4) |
| Co(1)–O(4) | 2.055(2) | O(3)–C(2) | 1.419(4) |
| Co(1)–O(6) | 2.099(2) | O(3)–C(4) | 1.432(4) |
| Co(1)–N(1) | 2.131(3) | O(4)–C(3) | 1.257(4) |
| Co(1)–N(3) | 2.095(3) | O(5)–C(3) | 1.245(4) |
| O(1)–Co(1)–O(3) | 74.76(8) | N(3)–Co(1)–O(6) | 93.65(10) |
| O(1)–Co(1)–O(6) | 93.45(9) | O(4)–Co(1)–N(1) | 87.13(10) |
| O(4)–Co(1)–O(1) | 148.98(9) | N(3)–Co(1)–N(1) | 76.51(10) |
| O(4)–Co(1)–O(3) | 74.61(8) | O(6)–Co(1)–N(1) | 168.69(10) |
| O(4)–Co(1)–O(6) | 92.08(9) | N(3)–Co(1)–O(3) | 169.13(9) |
| O(6)–Co(1)–O(3) | 91.42(9) | N(1)–Co(1)–O(3) | 99.23(10) |
| O(4)–Co(1)–N(3) | 114.75(10) | O(5)–C(3)–O(4) | 125.5(3) |
| O(1)–Co(1)–N(3) | 95.33(10) | O(2)–C(1)–O(1) | 126.1(3) |
| O(1)–Co(1)–N(1) | 93.02(10) | | |

4,4′-Bipyridine was selected as a ligand on the basis of its capacity to afford coordination polymers.[22] However, complex **9** is a binuclear species in which the 4,4′-bipy ligand bridges two cobalt centres (Figure 5). The coordination geometry of each cobalt atom is pseudo-octahedral, with the ethereal oxygen atom of the planar oda ligand O4 occupying a *trans* position with respect to the N-donor atom N1 and the two water ligands mutually *trans*. Selected structural data are collected in Table 5. Complex **9** is isostructural with the zinc analogue [{Zn(oda)(H$_2$O)$_2$}$_2$(μ-4,4′-bipy)]·2H$_2$O.[23] Other cobalt complexes containing a tridentate dianionic ligand may be related to the present species.[24]

The magnetic characterisation of complex **9** was performed with a SQUID susceptometer in the range 1.9–300 K. Magnetisations were measured up to 6 T and showed that loose powder samples have a strong tendency to align with the imposed field, therefore measurements were re-performed with a pellet. The behaviour of both the

 © 2007 Wiley-VCH Verlag GmbH & Co. KGaA, Weinheim 

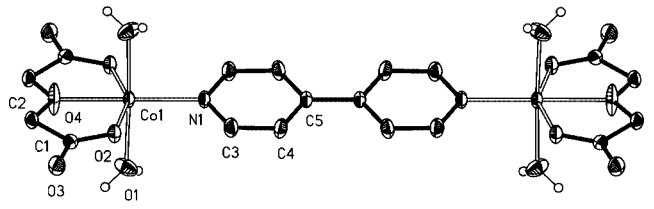


Figure 5. Molecular structure of binuclear complex $[\{Co(oda)(H_2O)_2\}_2(\mu\text{-}4,4'\text{-bipy})]\cdot 2H_2O$ (**9**). The hydrogen atoms, except those of the water ligand, and the crystallisation water molecules are not shown.

Table 5. Selected bond lengths [Å] and angles [°] for **9**.

| | | | |
|---|---|---|---|
| Co(1)–O(1) | 2.080(3) | O(4)–C(2) | 1.385(3) |
| Co(1)–O(2) | 2.063(2) | N(1)–C(3) | 1.333(3) |
| Co(1)–O(4) | 2.067(3) | C(1)–C(2) | 1.525(4) |
| Co(1)–N(1) | 2.082(3) | C(3)–C(4) | 1.371(4) |
| O(2)–C(1) | 1.262(3) | C(4)–C(5) | 1.385(4) |
| O(3)–C(1) | 1.232(3) | C(5)–C(5)[b] | 1.478(7) |
| O(1)–Co(1)–N(1) | 91.20(8) | O(2)[a]–Co(1)–O(1) | 91.11(11) |
| O(1)–Co(1)–O(2) | 88.35(11) | O(1)[a]–Co(1)–O(1) | 177.61(15) |
| O(1)–Co(1)–O(4) | 88.80(8) | O(2)–Co(1)–N(1) | 103.03(5) |
| O(2)–Co(1)–O(4) | 76.97(5) | O(4)–Co(1)–N(1) | 180.0 |
| O(2)[a]–Co(1)–O(2) | 153.94(11) | O(3)–C(1)–O(2) | 124.7(3) |
| O(4)–Co(1)–O(1)[a] | 88.80(8) | | |

[a] Symmetry transformations used to generate equivalent atoms: $-x + 2, y, -z + 1$. [b] $-x + 2, -y + 1, -z + 1$.

susceptibility $\chi_m$ and its product with temperature ($\chi_m T$) are typical of a paramagnetic system, as shown in Figure 6. The $\chi_m T$ value (5.15 emu K mol$^{-1}$ at 300 K) is consistent with two nearly uncorrelated high-spin $Co^{II}$ ions, with corresponding factors of 2.35. On lowering the temperature, $\chi_m T$ starts to decrease significantly below 60 K, while $\chi_m$ rises monotonically without reaching any maximum. A plot of the inverse susceptibility $1/\chi_m$ vs. $T$ gives a Curie–Weiss temperature $\theta$ of +4.4 K above 50 K. High-spin $Co^{II}$ has a $^4T_{1g}$ ground state and, with spin-orbit coupling leaving the orbital moment unquenched, large deviations of $g$ from the free-electron value and large zero-field splittings are expected. The latter, along with possibly some weak exchange interaction between the two cobalt atoms, accounts for the observed decrease of $\chi_m T$ at lower temperatures.

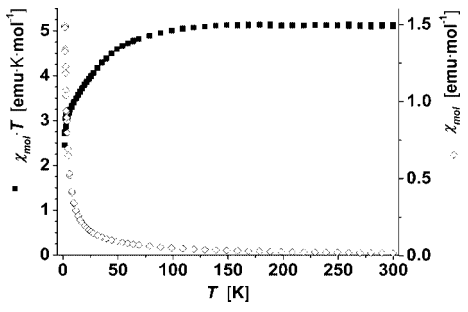


Figure 6. Molar magnetic susceptibility $\chi_m$ (✧, cgs units) and its product with temperature $\chi_m T$ (■, cgs units) of complex **9** between 1.9 and 300 K.

## Factors Governing the Stereochemical Features of the tda and oda Ligands

Although we have published several contributions concerning the coordination chemistry of tda and oda,[2,3,5] this is the first paper in which we address the behaviour of both ligands toward the same metal centre. By exploiting the small but not insignificant number of CSD structures[1a] for all the known cobalt compounds,[25] we have been able to determine the structural parameters that affect the wrapping mode of both types of ligands toward cobalt.

In spite of their similar structures, the presence of a central sulfur or oxygen atom in tda and oda, respectively, has a significant effect on the bonding modes at the metal centres. To date, it has been found that when tda acts as a tridentate ligand it is invariably folded about the M–S vector (*fac* coordination), while oda can adapt to both the folded and planar (*mer*) modes (Scheme 4). We have previously determined the energy differences between the two possible oda conformations in models such as $[Ni(oda)(H_2O)_3]$ and $[VO(oda)(H_2O)_2]$ by DFT calculations[2a,2d] and concluded that there is a small $\Delta E$ value between the two isomers (of the order of 2 kcal mol$^{-1}$ for the Ni compound). Under these circumstances, intermolecular interactions, such as the hydrogen-bond networks involving water crystallisation molecules, probably determine the specific conformation of oxydiacetate.

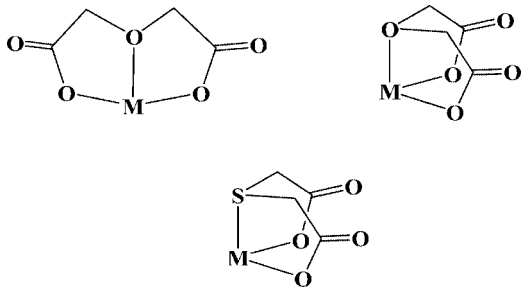


Scheme 4.

Different sets of geometric parameters are involved in the two possible coordination modes of the ligands. Among these parameters, significant variations are observed for the Co–X (X = O or S) coordination bonds, the $O_{carbox.}$–Co–$O_{carbox.}$ and Co–X–C angles at cobalt and at the heteroatom (C–X–C) and the torsion angles about the X–C and C–C bonds. Thus, it is interesting to determine which parameters exercise most control over the stereochemical features. The Co–S distances fall in the small range 2.508–2.560 Å, with a mean value of 2.52(2) Å (see Figure S3 in the Supporting Information). The corresponding Co–O distances are shorter of course, although their range is wider [2.074–2.269 Å, with a mean value of 2.13(5) Å]. In this case the data refer to both ligand conformations but, in spite of an evident overlap zone, the longer Co–O distances are associated with ligand folding. Beside the Co–X distance, the C–X–C angle is also important since its flexibility is related to the ultimate parameters of folding, in other words the $O_{carbox.}$–Co–$O_{carbox.}$ coordination angle and the

 © 2007 Wiley-VCH Verlag GmbH & Co. KGaA, Weinheim 

$O_{carbox.}$–Co–X–C torsion angle. The latter parameters should simultaneously approach the limiting values of 90° or 180° for the folded and planar conformations, respectively. Figure 7 shows a quasi-linear interdependence between M–X and C–X–C.

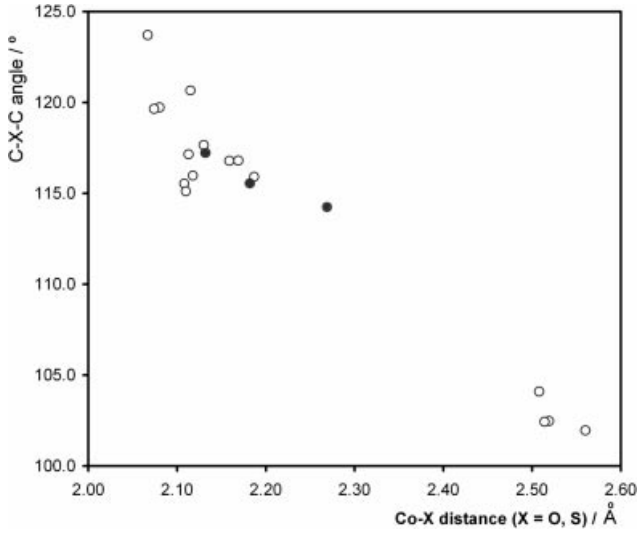


Figure 7. Plot of the Co–X distance [Å] vs. the C–X–C angle [°] showing two separate regions for oda and tda cobalt complexes (black circles are the *fac*-oda compounds).

The question remains, however, as to why the ligand tda never adopts the planar conformation. The average value for the C–O–C angle in uncoordinated ethers is higher than the corresponding C–S–C one in thioethers. Such a difference has a simple theoretical justification based on the different electronegativities of oxygen and sulfur.[26] In the cobalt complexes analysed these angles are within the range 102.0–104.1° for the tda ligand and 114.2–120.7° for the oda ligand. It is evident that ligand folding/unfolding accompanies a significant remodulation of the Co–X and C–X–C parameters, which also depend on electronic constraints (ionic radius, oxidation and spin state of the metal, electronegativity of the X atom, different hard/soft character of the X atom). According to Figure 7, a Co–S distance within the observed range or even shorter should accompany an acute C–S–C angle, which is not yet suitable for conferring the *mer* conformation to tda. This can be verified by considering the correlation diagram between the C–X–C and $O_{carbox.}$–Co–$O_{carbox.}$ angles (Figure 8), from which it becomes evident that there cannot be sufficient opening of the coordination angle at the metal centre for the C–S–C values in question. In conclusion, the planar arrangement (*mer*) is essentially unattainable for Co(tda) complexes, in fact it is impossible to build a model with tolerable distances and angles. Similar graphs to that shown in Figure 8, in which a clear separation of the three coordination modes is observed, can be obtained by plotting the Co–X–$CH_2$ angles against the $O_{carbox.}$–Co–$O_{carbox.}$ angle or against the $O_{carbox.}$–Co–X–C torsion angle (see Supporting Information).

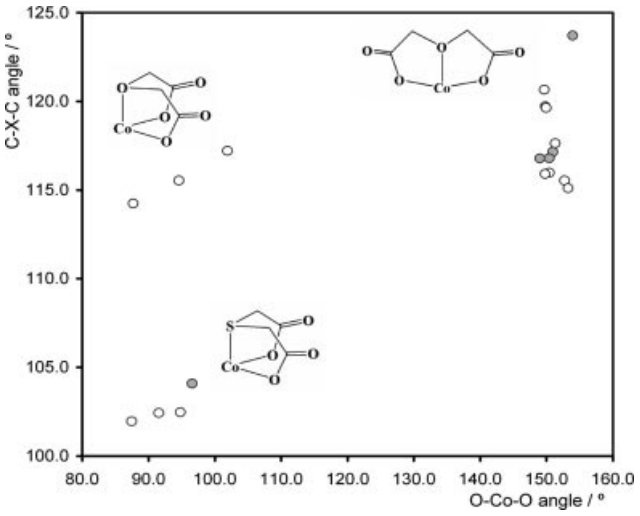


Figure 8. Plot of the C–X–C angle [°] vs. the $O_{carbox.}$–Co–$O_{carbox.}$ angle [°] (shaded circles represent the complexes reported in this paper).

## Experimental Section

**General:** All preparations and other operations were carried out under aerobic conditions. Thiodiacetic acid, oxydiacetic acid and other chemicals were obtained from commercial sources and were used without further purification. $[\{Co(oda)(H_2O)_2\}\cdot H_2O]_n$ was prepared according to the procedure previously reported by us.[2a] Microanalyses (C, H, N) were carried out by the Microanalytical Service of CITIUS. IR spectra were recorded with a Perkin–Elmer Model 883 spectrophotometer (Nujol emulsion in NaCl plates). Magnetic moments were measured in the solid state, at room temperature, with a Sherwood Scientific (Cambridge Research Laboratory) magnetic balance, and between 1.9 and 300 K with a Cryogenic S600 SQUID magnetometer. Molar susceptibilities were corrected using Pascal's constants.[27] For the pellet measurement, the measure had to be corrected for some ferromagnetic impurities. The corrected curve agreed well with a zero-field cooled measurement done on a loose powder sample prior to magnetisation measurements. No significant temperature-independent paramagnetism was found.

**$[Co(tda)(H_2O)]_n$ (1a):** $Na_2CO_3$ (0.63 g, 6 mmol) was added to a solution of $S(CH_2COOH)_2$ (0.90 g, 6 mmol) in water (20 mL). The mixture was stirred until the evolution of $CO_2$ ceased and then added to a solution of $CoCl_2\cdot 6H_2O$ (1.42 g, 6 mmol) in water (15 mL). The resulting solution was stirred for 10 min, then acetone was added and the solution was kept at room temperature overnight. The dark pink crystals of **1a** that formed were filtered off, washed with acetone and diethyl ether and air dried (1.3 g, 96% yield). IR: $\tilde{\nu}$ = 3548–3087 (br), 1637 (vs), 1589 (vs), 1459 (s), 1399 (vs), 1376 (vs), 1243 (m), 1180 (w), 917 (m), 873 (w), 806 (m), 779 (s), 698 (s) $cm^{-1}$. $C_4H_6CoO_5S$ (225.09): calcd. C 21.34, H 2.69; found C 20.86, H 3.00. Small amounts of pink needle crystals of complex $[Co(tda)(H_2O)_3]$ (**1b**) were observed and manually separated in some of the preparations of **1a**. IR: $\tilde{\nu}$ = 3548 (s), 3482–3018 (br), 1635 (vs), 1585 (vs), 1406 (s), 1376 (vs), 1254 (w), 1229 (m), 1204 (w), 1178 (w), 939 (m), 865 (m), 790 (s), 763 (s), 705 (s), 663 (m) $cm^{-1}$. $C_4H_{10}CoO_7S$ (261.12): calcd. C 18.40, H 3.86; found C 18.73, H 3.96.

**$[Co(tda)(bipy)(H_2O)]\cdot 4H_2O$ (2):** Bipy (0.156 g, 1 mmol) was added to a suspension of **1a** (0.261 g, 1 mmol) in water. This mixture,

 © 2007 Wiley-VCH Verlag GmbH & Co. KGaA, Weinheim 

which turned deep pink, was heated with stirring until all the solid had dissolved and then concentrated. Complex **2** crystallised upon evaporation of the solvent at room temperature after a few days. The pink crystals were filtered off, washed with water, acetone and diethyl ether and air dried (0.38 g, 84% yield). IR: $\tilde{\nu}$ = 3660–3036 (br), 1599 (vs), 1492 (s), 1462 (s), 1442 (vs), 1400 (s), 1375 (vs), 1338 (s), 1316 (s), 1253 (m), 1233 (m), 1196 (w), 1179 (w), 1157 (w), 1102 (w), 1061 (m), 1043 (w), 1021 (m), 1011 (w), 969 (w), 932 (s), 899 (m), 875 (w), 764 (vs), 735 (s), 698 (s), 648 (s), 626 (m) $cm^{-1}$. $\mu_{eff}$ = 4.5 $\mu_B$ at 25 °C. $C_{14}H_{22}CoN_2O_9S$ (453.33): calcd. C 37.09, H 4.89, N 6.18; found C 37.11, H 4.69, N 6.61.

**[Co(tda)(phen)(H$_2$O)] (3):** A solution of *o*-phen·$H_2O$ (0.198 g, 1 mmol) in 10 mL of methanol was added to a suspension of **1a** (0.230 g, 1 mmol) in 20 mL of water. This mixture, which turned deep pink immediately, was stirred and heated (90 °C) until all the solids had dissolved. It was then concentrated to a volume of about 15 mL. Slow evaporation of the solvent resulted in the formation of crystals of **3**, which were collected by filtration, washed with cold water, acetone and diethyl ether and dried in air (0.38 g, 90%). IR: $\tilde{\nu}$ = 3552–3088 (br), 3063 (w), 1644 (vs), 1584 (vs), 1516 (m), 1494 (w), 1426 (w), 1313 (m), 1213 (m), 1183 (w), 1136 (m), 1101 (m), 988 (w), 933 (m), 918 (m), 868 (m), 846 (s), 788 (m), 773 (m), 758 (m), 723 (s), 665 (m), 640 (m) $cm^{-1}$. $\mu_{eff}$ = 4.3 $\mu_B$ at 25.5 °C. $C_{16}H_{14}CoN_2O_5S$ (405.29): calcd. C 47.42, H 3.48, N 6.91; found C 46.97, H 3.38, N 6.76.

**[Co(tda){(MeO)$_2$bipy}(H$_2$O)]·2H$_2$O (4):** $(MeO)_2$bipy (0.108 g, 0.5 mmol) was added to a suspension of **1a** (0.120 g, 0.5 mmol) in 15 mL of water. This mixture, which turned red, was heated at 90 °C with stirring until all the solid had dissolved and was then poured into a crystallisation dish. Slow evaporation of water resulted in the formation of red crystals of **4**, which were collected by filtration, washed with acetone and diethyl ether and dried in air (0.18 g, 75% yield). IR: $\tilde{\nu}$ = 3669–3951 (br), 1602 (vs), 1496 (s), 1460 (s), 1451 (s), 1413 (s), 1402 (s), 1375 (s), 1339 (s), 1281 (s), 1245 (s), 1224 (s), 1186 (w), 1161 (w), 1130 (w), 1096 (w), 1038 (s), 1004 (m), 921 (m), 865 (m), 838 (s), 793 (m), 766 (m), 732 (m), 694 (m), 665 (m) $cm^{-1}$. $C_{26}H_{30}CoN_4O_{11}S$ (665.53): calcd. C 40.24, H 4.60, N 5.87; found C 40.24, H 4.45, N 5.95.

**[Co(tda)(dpp)(H$_2$O)]·2H$_2$O (5):** This complex was obtained as red crystals (0.11 g, 74% yield) following a similar synthetic procedure as described for **4** but with 2,3-bis(2-pyridyl)pyrazine (0.07 g, 0.3 mmol). IR: $\tilde{\nu}$ = 3601–3039 (br), 1593 (vs), 1529 (m), 1475 (s), 1452 (s), 1394 (vs), 1376 (vs),1298 (m), 1253 (m), 1238 (m), 1215 (m), 1164 (s), 1139 (m), 1121 (m), 1099 (m), 1083 (w), 1059 (w), 1038 (s), 1021 (m), 996 (m), 969 (w), 938 (s), 920 (s), 873 (m), 819 (m), 788 (vs), 761 (s), 752 (s), 705 (s), 662 (m), 647 (m), 624 (s) $cm^{-1}$. $C_{18}H_{20}CoN_4O_7S$ (495.37): calcd. C 43.60, H 4.03, N 11.30; found C 43.95, H 3.90, N 11.70.

**[Co{OC(OH)(2-pyridyl)$_2$}$_2$][Htda]·3H$_2$O (6):** Di(2-pyridyl) ketone (0.184 g, 1 mmol) was added to a suspension of **1a** (0.13 g, 0.5 mmol) in 15 mL of water. This mixture was heated at 90 °C for 0.5 h and then filtered. Slow evaporation of the filtrate resulted in the formation of red crystals of **3**, which were collected by filtration, washed with acetone and diethyl ether and dried in air (0.25 g, 75% yield). IR: $\tilde{\nu}$ = 3666–3080 (br), 1589 (vs), 1443 (vs), 1403 (s), 1376 (s), 1287 (vs), 1235 (vs), 1200 (m), 1164 (s), 1130 (w), 1085 (s), 1059 (w), 1023 (s), 933 (m), 886 (w), 868 (w), 806 (s), 768 (s), 701 (s), 667 (s) $cm^{-1}$. $C_{26}H_{29}CoN_4O_{11}S$ (664.53): calcd. C 46.95, H 4.36, N 8.43; found C 46.83, H 4.48, N 8.33.

**[Co(oda)(*t*Bu$_2$bipy)(H$_2$O)]·1.5H$_2$O (7):** A solution of 4,4′-*t*$Bu_2$bipy (0.147 g, 0.5 mmol) in 10 mL of ethanol was added to a solution of [{Co(oda)$(H_2O)_2$}·$H_2O$]$_n$ (0.122 g, 0.5 mmol) in 15 mL of water. This mixture, which turned deep pink immediately, was stirred and heated (90 °C) until all the solid had dissolved. It was then concentrated to a volume of about 15 mL. Slow evaporation of the solvent resulted in the formation of crystals of **7**, which were washed with cold water, acetone and diethyl ether and dried in air (0.20 g, 72% yield). IR: $\tilde{\nu}$ = 3496–3037 (br), 1613 (vs), 1547 (s), 1408 (vs), 1348 (m), 1305 (s), 1265 (w), 1250 (m), 1200 (m), 1131 (s), 1111 (s), 1038 (w), 1015 (s), 917 (s), 897 (m), 858 (s), 668 (w), 604 (s) $cm^{-1}$. $\mu_{eff}$ = 4.5 $\mu_B$ at 20 °C. $C_{22}H_{33}CoN_2O_{7.5}$ (504.44): calcd. C 52.37, H 6.15, N 5.55; found C 52.03, H 6.47, N 5.68.

**[Co(oda)(dpp)(H$_2$O)]·2H$_2$O (8):** 2,3-Bis(2-pyridyl)pyrazine (0.117 g, 0.5 mmol) was added to an aqueous solution of [{Co(oda)-$(H_2O)_2$}·$H_2O$]$_n$ (0.122 g, 0.5 mmol). This mixture, which turned red immediately, was stirred at 90 °C until the solid had dissolved and was then concentrated. Slow evaporation of water gave red crystals of **8**, which were collected by filtration, washed with cold water, acetone and diethyl ether and dried in air (0.15 g, 63% yield). IR: $\tilde{\nu}$ = 3636–32980 (br), 1605 (vs), 1436 (s), 1422 (s), 1398 (s), 1346 (m), 1305 (s), 1238 (m), 1169 (m), 1122 (s), 1096 (m), 1061 (m), 1038 (m), 1023 (s), 993 (m), 969 (w), 919 (m), 872 (m), 824 (w), 790 (s), 770 (m), 744 (m), 725 (m), 666 (w), 639 (m), 621 (m) $cm^{-1}$. $C_{18}H_{20}CoN_4O_8$ (479.31): calcd. C 45.07, H 4.17, N 11.68; found C 45.09, H 4.14, N 11.90. Good quality crystals of this complex were obtained by recrystallisation from a water/methanol mixture. They were obtained as the methanol solvate [Co(oda)(dpp)$(H_2O)$]·$H_2O$·1/2MeOH and analysed by X-ray crystallography.

**[{Co(oda)(H$_2$O)$_2$}$_2$(μ-4,4′-bipy)]·2H$_2$O (9):** A solution of 4,4′-bipy (0.078 g, 0.5 mmol) in 25 mL of water was added to a solution of [{Co(oda)$(H_2O)_2$}·$H_2O$]$_n$ (0.244 g, 1 mmol) in 25 mL of water. The resulting pink solution was stirred for a few minutes. Complex **9** crystallised upon slow evaporation of the solvent at room temperature. The solid was filtered off, washed with cold water, acetone and diethyl ether and dried in air (0.27 g, 84% yield). Recrystallisation of the product from water resulted in the formation of crystals suitable for an X-ray study. IR: $\tilde{\nu}$ = 3520–3034 (br), 1642 (s), 1600 (vs), 1534 (w), 1492 (m), 1442 (m), 1407 (s), 1346 (w), 1303 (m), 1226 (w), 1132 (s), 1075 (m), 1028 (m), 922 (m), 814 (m), 725 (w), 638 (m) $cm^{-1}$. $\mu_{eff}$ = 4.4 $\mu_B$ at 23 °C. $C_9H_{14}CoNO_8$ (323.14): calcd. C 33.43, H 4.33, N 4.33; found C 33.58, H 4.31, N 4.51.

**X-ray Crystallographic Studies:** A summary of the crystal data of complexes **2** and **6**–**9** is given in Table 6. The X-ray data were collected with three different equipments: an Enraf–Nonius CAD4 diffractometer equipped with a graphite monochromator and Mo-$K_\alpha$ radiation (for **2**, **8** and **9**), a Phillips PW1100 FEBO diffractometer equipped with a graphite monochromator and Cu-$K_\alpha$ radiation (for **6**) and a Bruker–Nonius X8APEX-II CCD diffractometer equipped with a graphite monochromator and Mo-$K_\alpha$ radiation (for **7**). The intensities collected for complexes **2**, **6**, **8** and **9** were corrected for Lorenz and polarisation effects. Three standard reflections were monitored every 2 h during the data collection. The atomic scattering factors are those reported by Cromer and Waber.[28] The structures were solved by direct methods using the SIR97 program.[29] The refinements were made by full-matrix least-squares on all $F^2$ data using SHELXL97.[30] Anisotropic thermal parameters were allotted to all non-hydrogen atoms. The hydrogen atoms of the water bonded to the metal as well as in the free water, when found in the Fourier maps, were refined with an isotropic structure factor, while the other hydrogen atoms were introduced in their calculated positions. The data set for complex **7** was reduced[31] and corrected for Lorentz polarisation effects and absorption by multiscan method applied by SADABS.[32] The structure was solved by direct methods (SIR-2002)[33] and refined

 © 2007 Wiley-VCH Verlag GmbH & Co. KGaA, Weinheim 

Table 6. Crystal data and structure refinement for complexes **2** and **6**–**9**.

| | **2** | **6** | **7** | **8** | **9** |
|---|---|---|---|---|---|
| Formula | $C_{14}H_{22}CoN_2O_9S$ | $C_{26}H_{29}CoN_4O_{11}S$ | $C_{44}H_{66}Co_2N_4O_{15}$ | $C_{37}H_{40}Co_2N_8O_{15}$ | $C_{18}H_{28}Co_2N_2O_{16}$ |
| $M$ | 453.33 | 664.53 | 1008.87 | 954.63 | 646.28 |
| Crystal system | triclinic | triclinic | monoclinic | monoclinic | monoclinic |
| Space group | $P\bar{1}$ | $P\bar{1}$ | $P2_1$ | $P2_1/n$ | $C2/_m$ |
| $a$ [Å] | 9.1205(14) | 8.646(5) | 13.547(2) | 7.231(3) | 10.138(3) |
| $b$ [Å] | 10.793(3) | 11.991(5) | 10.5035(17) | 10.367(2) | 20.4555(19) |
| $c$ [Å] | 11.5570(12) | 14.537(5) | 17.916(3) | 26.772(9) | 6.130(8) |
| $\alpha$ [°] | 101.777(15) | 99.960(5) | 90 | 90 | 90 |
| $\beta$ [°] | 103.166(12) | 104.174(5) | 105.889(6) | 94.28(3) | 103.829(19) |
| $\gamma$ [°] | 113.85(2) | 93.015(5) | 90 | 90 | 90 |
| $V$ [Å]$^3$ | 955.4(3) | 1432.1(11) | 2451.8(7) | 2001.3(11) | 1234.3(17) |
| $Z$ | 2 | 2 | 2 | 2 | 2 |
| $D_{calcd.}$ [Mg m$^{-3}$] | 1.576 | 1.541 | 1.367 | 1.584 | 1.739 |
| $\mu$ [mm$^{-1}$] | 1.057 | 5.972 | 0.745 | 0.911 | 1.426 |
| $T$ [K] | 293(2) | 293(2) | 173(2) | 293(2) | 293(2) |
| $F$(000) | 470 | 688 | 1064 | 984 | 664 |
| Independent reflections | 3352 | 3600 | 14711 | 3511 | 1127 |
| $R$ [$I > 2\theta(I)$] | 0.0273 | 0.0624 | 0.0452 | 0.0428 | 0.0320 |
| $wR_2$ (all data) | 0.0762 | 0.1605 | 0.1340 | 0.1296 | 0.0890 |

against all $F^2$ data by full-matrix least-squares techniques.[34] All the non-hydrogen atoms were refined with anisotropic displacement parameters. The hydrogen atoms were included from calculated positions and refined as riding on their respective carbon atoms with isotropic displacement parameters.

CCDC-263308, -263309, -629951, -629952, and -629953 (for **2** and **6**–**9**, respectively) contain the supplementary crystallographic data for this paper. These data can be obtained free of charge from The Cambridge Crystallographic Data Centre via www.ccdc.cam.ac.uk/data_request/cif.

**Supporting Information** (see also the footnote on the first page of this article): IR spectra of complexes **1a** and **1b**, hydrogen-bonding network of **2** and several plots of structural analyses for cobalt oda and tda compounds.

## Acknowledgments

Thanks are expressed to the the Ministerio de Educación y Ciencia (MEC) (BQU2001-3715 and CTQ2004-0084) and the Junta de Andalucía for financial support and to Mr. Dante Masi for X-ray technical assistance.

[1] a) *Cambridge Structural Database System*, Cambridge Crystallographic data Centre, 12 Union Road, Cambridge, CB2 1EZ, UK (updated May **2006**); b) F. H. Allen, *Acta Crystallogr., Sect. B* **2002**, *58*, 380.

[2] Oxydiacetate compounds: a) A. Grirrane, A. Pastor, A. Ienco, C. Mealli, A. Galindo, *J. Chem. Soc. Dalton Trans.* **2002**, 3771; b) A. Grirrane, A. Pastor, C. Mealli, A. Ienco, P. Rosa, R. Prado-Gotor, A. Galindo, *Inorg. Chim. Acta* **2004**, *357*, 4215; c) A. Grirrane, A. Pastor, E. Álvarez, C. Mealli, A. Ienco, P. Rosa, F. Montilla, A. Galindo, *Eur. J. Inorg. Chem.* **2004**, 707; d) D. del Río, A. Galindo, R. Vicente, C. Mealli, A. Ienco, D. Masi, *Dalton Trans.* **2003**, 1813.

[3] Thiodiacetate compounds: a) A. Grirrane, A. Pastor, A. Galindo, D. del Río, A. Orlandini, C. Mealli, A. Ienco, A. Caneschi, J. Fernández Sanz, *Angew. Chem. Int. Ed.* **2005**, *44*, 3429; b) A. Grirrane, A. Pastor, A. Galindo, A. Ienco, C. Mealli, P. Rosa, *Chem. Commun.* **2003**, 512; c) A. Grirrane, A. Pastor, E. Álvarez, C. Mealli, A. Ienco, A. Galindo, *Inorg. Chem. Commun.* **2006**, *9*, 160.

[4] a) J. Podlaha, J. Podlahova, *Inorg. Chim. Acta* **1970**, *4*, 521; b) J. Podlaha, J. Podlahova, *Inorg. Chim. Acta* **1970**, *4*, 549; c) K. Suzuki, K. Yamasaki, *J. Inorg. Nucl. Chem.* **1966**, *28*, 473.

[5] A. Grirrane, A. Pastor, E. Álvarez, C. Mealli, A. Ienco, D. Masi, A. Galindo, *Inorg. Chem. Commun.* **2005**, *8*, 463.

[6] J.-Y. Wu, L.-M. Xie, H.-Y. He, X. Zhou, L.-G. Zhu, *Acta Crystallogr., Sect. E* **2005**, *61*, m568.

[7] a) B.-X. Liu, J.-Y. Yu, D.-J. Xu, *Acta Crystallogr., Sect. E* **2005**, *61*, m1978; b) L. Cao, J.-G. Liu, D.-J. Xu, *Acta Crystallogr., Sect. E* **2006**, *62*, m579.

[8] For an analysis of the IR bands of thiodiacetate see: H. Ramsis, E. Perez-Ruiz, J. Roger, J. L. Delarbre, L. Maury, *J. Raman Spectrosc.* **1996**, *27*, 637.

[9] S. H. Whitlow, *Acta Crystallogr., Sect. B* **1975**, *31*, 2531.

[10] M.-C. Wu, C.-S. Lee, *Inorg. Chem.* **2006**, *45*, 9634.

[11] a) P. Kopel, Z. Travnicek, J. Marek, J. Mrozinski, *Polyhedron* **2004**, *23*, 1573; b) C. Alarcón-Payer, T. Pivetta, D. Choquesillo-Lazarte, J. M. González-Pérez, G. Crisponi, A. Castiñeiras, J. Niclós-Gutiérrez, *Inorg. Chem. Commun.* **2004**, *7*, 1277.

[12] See for example: L. Banci, A. Bencini, C. Benelli, D. Gatteschi, C. Zanchini, *Struct. Bonding (Berlin)* **1982**, *52*, 37.

[13] R. Baggio, M. Perec, M. T. Garland, *Acta Crystallogr., Sect. C* **1996**, *52*, 2457.

[14] R. P. Bonomo, E. Rizzarelli, N. Bresciani-Pahor, G. Nardin, *J. Chem. Soc. Dalton Trans.* **1982**, 681.

[15] See for example: G. Crundwell, B. L. Westcott, R. Coffey, M. Zeller, A. D. Hunter, *Inorg. Chim. Acta* **2003**, *355*, 432 and references cited therein.

[16] a) G. S. Papaefstathiou, A. Escuer, F. A. Mautner, C. Raptopoulou, A. Terzis, S. P. Perlepes, R. Vicente, *Eur. J. Inorg. Chem.* **2005**, 879; b) C. Hemmert, M. Renz, H. Gornitzca, S. Soulet, B. Meunier, *Chem. Eur. J.* **1999**, *5*, 1766; c) S. Sommerer, J. D. Baker, W. P. Jensen, A. Hamza, R. A. Jakobson, *Inorg. Chim. Acta* **1993**, *210*, 173; d) M. L. Tong, G. Yang, X. M. Chen, S. W. Ng, *Acta Crystallogr., Sect. C* **1998**, *54*, 217.

[17] a) B.-Y. Zhang, J.-G. Liu, D.-J. Xu, *Acta Crystallogr., Sect. E* **2005**, *61*, m1128; b) L. Cao, D.-J. Xu, *Acta Crystallogr., Sect. E* **2005**, *61*, m2127.

[18] . E. Hatfield, J. H. Helms, B. R. Rohrs, P. Singh, J. R. Wasson, R. R. Weller, *Proc. Ind. Acad. Sci., Chem. Sci.* **1987**, *98*, 23.

[19] a) C. Jiang, Z.-Y. Wang, *Polyhedron* **2003**, *22*, 2953; b) Z.-Y. Wu, D.-J. Xu, J.-Y. Wu, M. Y. Chiang, *Acta Crystallogr., Sect. E* **2002**, *58*, m634.

[20] T. Ishida, T. Kawakami, S. Mitsubori, T. Nogami, K. Yamaguchi, H. Iwamura, *J. Chem. Soc. Dalton Trans.* **2002**, 3177.

 © 2007 Wiley-VCH Verlag GmbH & Co. KGaA, Weinheim 

[21] a) Z.-Y. Wu, Y.-H. Xue, D.-J. Xu, *Acta Crystallogr., Sect. E* **2003**, *59*, m809; b) Y. Luo, D.-J. Xu, Z.-Y. Wu, J.-Y. Wu, M. Y. Chiang, *Acta Crystallogr., Sect. E* **2004**, *60*, m270; c) Y.-H. Shen, J.-G. Liu, D.-J. Xu, *Acta Crystallogr., Sect. E* **2004**, *60*, m842.
[22] See for example: K. Biradha, M. Sarkar, L. Rajput, *Chem. Commun.* **2006**, 4169.
[23] J. Tao, X. Yin, L.-S. Zheng, S. W. Ng, *Main Group Met. Chem.* **2002**, *25*, 321.
[24] a) L. G. Zhu, Y.-X. Wang, C.-Y. Duan, X.-S. Yang, X.-Z. You, J.-S. Huang, *Acta Chim. Sinica* **1992**, *50*, 583; b) X. Duanjun, C. Caorong, X. Yuanzhi, H. Shengzhi, *Chin. J. Struct. Chem.* **1989**, *8*, 81.
[25] 16 Hits, although only 15 were utilized for the statistical analysis. The refcode ETEQUP (ref.[21b]) was removed due to the observed disorder between oda and water ligands.
[26] See for example: B. M. Gimarc, *Molecular Structure and Bonding*, Academic Press, New York, **1979**.
[27] C. J. O'Connor, *Prog. Inorg. Chem.* **1982**, *29*, 20.
[28] D. T. Cromer, J. T. Waber, *Acta Crystallogr.* **1965**, *18*, 104.
[29] A. Altomare, M. C. Burla, M. Cavalli, G. L. Cascarano, C. Giavovazzo, A. Gagliardi, A. G. G. Moliterni, G. Polidori, R. Spagna, *J. Appl. Crystallogr.* **1999**, *32*, 115.
[30] G. M. Sheldrick, *SHELXL97*, *Program for Crystal Structure Refinement*, University of Göttingen, Göttingen, Germany, **1997**.
[31] *SAINT 6.02*, Bruker AXS, Inc., Madison, WI 53711–5373 USA, **1997**–**1999**.
[32] *SADABS*, G. Sheldrick, Bruker AXS, Inc., Madison, Wisconsin, USA, **1999**.
[33] M. C. Burla, M. Camalli, B. Carrozzini, G. L. Cascarano, C. Giacovazzo, G. Polidori, R. Spagna, *J. Appl. Crystallogr.* **2003**, *36*, 1103.
[34] *SHELXTL 6.14*, Bruker AXS, Inc., Madison, Wisconsin, USA, **2000**–**2003**.

Received: January 22, 2007
Published Online: June 18, 2007

 © 2007 Wiley-VCH Verlag GmbH & Co. KGaA, Weinheim 

DOI: 10.1002/ejic.200700127

# Ethynyltolan Platinum Complexes with (Arylalkynyl)phosphane Ligands

Ana García,[a] Elena Lalinde,*[a] and M. Teresa Moreno[a]

**Keywords:** Alkyne ligands / Phosphane ligands / Platinum / X-ray diffraction

The ethynyltolan mononuclear complexes *cis*-[Pt(C≡CC$_6$H$_4$C≡CPh)$_2$(PPh$_2$C≡CR)$_2$] [R = tol (**2**), C$_6$H$_4$C≡CPh (**3**)], which contain (arylalkynyl)phosphane ligands, were prepared, and the X-ray molecular structure of **2** was determined. The reaction of **2** and **3** with *cis*-[Pt(C$_6$F$_5$)$_2$(thf)$_2$] (thf = tetrahydrofuran) in the appropriate molar ratio gave the dinuclear platinum derivatives *cis*-[{Pt(PPh$_2$C≡CR)$_2$(μ-η$^1$:η$^2$-*C*$^α$,*C*$^β$-C≡CC$_6$H$_4$C≡CPh)$_2$}Pt(C$_6$F$_5$)$_2$] [R = tol (**4**), C$_6$H$_4$C≡CPh (**5**)] and the trinuclear derivatives [{Pt(μ-η$^1$:η$^2$-*C*$^α$,*C*$^β$-C≡CC$_6$H$_4$C≡CPh)$_2$(μ-1κ*P*:2η$^2$-*C*$^α$,*C*$^β$-PPh$_2$C≡CR)$_2$}{Pt(C$_6$F$_5$)$_2$}$_2$] [R = tol (**6**), C$_6$H$_4$C≡CPh (**7**)], which are stabilized by a double ethynyltolan bridging system or a mixed ethynyltolan/alkynylphosphane bridging system, respectively.

(© Wiley-VCH Verlag GmbH & Co. KGaA, 69451 Weinheim, Germany, 2007)

## Introduction

The ability of alkynylphosphanes (PPh$_2$C≡CR) to bind several metal centres through single P-complexation and/or π-coordination has been well documented.[1–16] Furthermore, these ligands have revealed an interesting reactivity in transition-metal chemistry, such as insertion into reactive M–H or M–C bonds,[17–25] intramolecular coupling reactions[10,26–29] or P–C bond cleavage to afford alkynide (C≡CR) and phosphide (PPh$_2$) fragments,[6,12,30–35] which are often involved in subsequent coupling or insertion reactions.[36–39] In addition, simple P-coordination of alkynylphosphanes polarizes the electron density of the alkyne function by concentrating it on the C$^α$ atom, which favours its interaction with electrophilic and nucleophilic substrates such as water,[40,41] ethanol,[42,43] HX,[44–46] PPh$_2$H[47] or amines.[7,48] PPh$_2$C≡C–X–C≡CR ligands are able to offer higher coordination and reactivity possibilities due to the extension of the delocalised π-system. However, they have only been used as precursors of polymetallic complexes[10,15,49–52] and in P–C bond activation or intramolecular coupling reactions[51,53–55] on a few occasions.

With the aim of exploring the η$^2$-bonding capability of two P-coordinated diphenylphosphane ligands towards a second metal centre as a way of inducing alkyne coupling, we have previously studied the reactivity of *cis*-[MX$_2$(PPh$_2$C≡CR)$_2$] (M = Pd, Pt; X = Cl,[2] C$_6$F$_5$,[4,8,11] C≡CR′;[3] R = Ph, tol, *t*Bu; R′ = Ph, *t*Bu) towards the solvate complex *cis*-[Pt(C$_6$F$_5$)$_2$(thf)$_2$] (thf = tetrahydrofuran). When X is a C$_6$F$_5$ group with a low tendency to form bridges, the η$^2$-alkyne adducts [{Pt(C$_6$F$_5$)$_2$(μ-κ*P*:η$^2$-PPh$_2$C≡CR)$_2$}{Pt(C$_6$F$_5$)$_2$}] (R = Ph, tol), which are generated at low temperature, evolve through an unexpectedly easy sequential insertion of both PPh$_2$C≡CR molecules into a Pt–C$_6$F$_5$ bond to form unusual μ-2,3-bis(diphenylphosphanyl)-1,3-butadien-1-yl dinuclear complexes.[4,8] However, when X is a group with a greater tendency to act as a bridging ligand (X = Cl, C≡CR′) these groups compete with the η$^2$-bonding capacity of the PPh$_2$C≡CR group to coordinate the "Pt(C$_6$F$_5$)$_2$" fragment and only polymetallic species with X or mixed X/PPh$_2$C≡CR bridging systems are obtained.[2,3] In particular, several homo- and heterodimetallic complexes stabilized by double alkynyl bridging systems, such as *cis*-[{Pt(PPh$_2$C≡CR)$_2$(μ-η$^1$:η$^2$-C≡CR′)$_2$}Pt(C$_6$F$_5$)$_2$], and unusual symmetrical *cis*-[{Pt(PPh$_2$C≡C*t*Bu)$_2$(μ$_3$-η$^2$-C≡CPh)$_2$}{Pt(C$_6$F$_5$)$_2$}$_2$] and *cis*-[{Pt(μ-κ*P*:η$^2$-PPh$_2$C≡CR)$_2$(μ-η$^2$-C≡C*t*Bu)$_2$}{Pt(C$_6$F$_5$)$_2$}$_2$] trimetallic species, have been isolated with the mononuclear alkynylplatinum complexes *cis*-[Pt(C≡CR′)$_2$(PPh$_2$C≡CR)$_2$] (R′, R = Ph, *t*Bu) using 1:1 or 1:2 molar ratios, respectively, thereby indicating the following order of bonding capability: C≡CR′ > P-bonded PPh$_2$C≡CR and C≡CPh > C≡C*t*Bu fragments.[3] As an extension of this work to ethynyltolan systems {when referring to ethynyltolan as ligand, its deprotonated anion [(phenylethynyl)phenyl]ethynide is meant}, we report here the preparation and characterisation of the neutral complexes *cis*-[Pt(C≡CC$_6$H$_4$C≡CPh)$_2$(PPh$_2$C≡CR)$_2$] [R = tol (**2**), C$_6$H$_4$C≡CPh (**3**)], which are stabilized by (arylalkynyl)phosphanes. Furthermore, to gain more insight into the synthetic possibilities of the ethynyltolan and (arylalkynyl)phosphane ligands, especially a comparison of the reactivity of inner and outer alkynyl functions, we have investigated the reactivity of these complexes towards *cis*-[Pt(C$_6$F$_5$)$_2$(thf)$_2$].

[a] Departamento de Química – Grupo de Síntesis Química de La Rioja, UA-CSIC Universidad de La Rioja,
26006 Logroño, Spain
Fax: +34-941-299621
E-mail: elena.lalinde@unirioja.es

 © 2007 Wiley-VCH Verlag GmbH & Co. KGaA, Weinheim 

## Results and Discussion

The precursor derivative *cis*-[Pt(C≡CC$_6$H$_4$C≡CPh)$_2$(cod)] (**1**) was obtained using a similar procedure to that used for related *cis*-[Pt(C≡CR)$_2$(cod)] (R = Ph,[56] *t*Bu[57]) derivatives. Thus, the reaction of an ethanolic suspension of [PtCl$_2$(cod)] at low temperature (–30 °C) with HC≡CC$_6$H$_4$C≡CPh (2 equiv.) in a solution of NaOEt (3.7 equiv.), prepared "in situ" from a solution of Na in absolute EtOH, yielded **1** as a white solid in low yield (32%). Treatment of **1** with 2 equiv. of the appropriate (arylalkynyl)phosphane (PPh$_2$C≡Ctol, PPh$_2$C≡CC$_6$H$_4$C≡CPh) easily led to the displacement of the cod ligand and afforded the disubstituted products *cis*-[Pt(C≡CC$_6$H$_4$C≡CPh)$_2$(PPh$_2$C≡CR)$_2$] [R = tol (**2**), C$_6$H$_4$C≡CPh (**3**); Equation (1)]. These complexes were isolated as orange-brown solids, and their spectroscopic data (see Experimental Section) unequivocally confirmed the P-coordination mode of the PPh$_2$C≡CR ligands.

*cis*-[Pt(C≡CC$_6$H$_4$C≡CPh)$_2$(cod)] (**1**)
↓ 2 PPh$_2$C≡CR
*cis*-[Pt(C≡CC$_6$H$_4$C≡CPh)$_2$(PPh$_2$C≡CR)$_2$]
R = tol (**2**), C$_6$H$_4$C≡CPh (**3**) (1)

The IR spectra of **2** and **3** show two strong ν(C≡C) bands: the high-frequency band [2171 cm$^{-1}$ (**2**, **3**)] located at slightly higher wavenumbers than that in the corresponding free (arylalkynyl)phosphane is attributed to the ν(C≡C) stretch of the phosphane ligands, whereas the low-frequency band [2121 (**2**) and 2120 cm$^{-1}$ (**3**)] is assigned to the inner C$^{\alpha}$≡C$^{\beta}$ fragment of the ethynyltolan ligand. According to this assignment, the precursor derivative *cis*-[Pt(C≡CC$_6$H$_4$C≡CPh)$_2$(cod)] (**1**) shows a medium-intensity band at 2119 cm$^{-1}$. All complexes **1**–**3** also show a very weak high-frequency band (2214 cm$^{-1}$), assigned to the outer C$^5$≡C$^6$ alkyne group of the ethynyltolan ligand [see the Experimental Section (Figure 3) for the labelling scheme]. The phosphorus resonance in complexes **2** and **3** appears as a singlet that is shifted downfield with respect to the corresponding free ligands [$\delta$ = –6.53 (**2**) and –6.27 ppm (**3**) vs. –33.42 (PPh$_2$C≡Ctol) and –33.27 ppm (PPh$_2$C≡CC$_6$H$_4$C≡CPh)], with platinum coupling constants [2350 (**2**) and 2343 Hz (**3**)] comparable to those reported for mononuclear complexes having a tertiary phosphane group *trans* to a terminal alkynide group.[3,58] The $^{13}$C{$^1$H} NMR spectra are particularly significant. The acetylenic carbon resonances for the (arylalkynyl)phosphane ligands of both complexes can clearly be seen and their assignment is mainly based on the $J_{C,P}$ coupling constants observed and also by comparison with the corresponding signals in the starting precursor **1** [$\delta$ = 96.9 (C$^{\alpha}$), 107.8 (C$^{\beta}$), 90.1, 89.4 (C$^{5,6}$) ppm; see Figure 3 for assignments]. The alkynylphosphane C$^{\alpha'}$ resonances are found as an apparent doublet at lower frequencies than those of the C$^{\beta'}$ atoms, which are found as the A part of an AXX′ system [C$^{\alpha'}$: $\delta$ = 80.1 (**2**) and 82.7 ppm (**3**); C$^{\beta'}$: $\delta$ = 108.6 (**2**) and 107.4 ppm (**3**)]. The coupling constants $|^1J_{C\alpha',P} + {}^3J_{C\alpha',P}|$ [103.4 (**2**) and 100.2 Hz (**3**)] and $|^2J_{C\beta',P} + {}^4J_{C\beta',P}|$ [15.1 (**2**) and 14.8 Hz (**3**)] could also be calculated. The C$^{\alpha}$ and C$^{\beta}$ alkynyl resonances also appear as the A part of an AXX′ system, with C$^{\alpha}$ [$\delta$ = 105.2 (**2**) and 104.5 ppm (**3**)] appearing as a doublet of doublets [$|^2J_{C\alpha,Ptrans} + {}^2J_{C\alpha,Pcis}|$ = 155.1 (**2**) and 156.2 Hz (**3**)] and C$^{\beta}$ as a three-line pattern [$\delta$ = 109.3 ($|^3J_{C\beta,Ptrans} + {}^3J_{C\beta,Pcis}|$ = 37.6 Hz; **2**) and 109.4 ($|^3J_{C\beta,Ptrans} + {}^3J_{C\beta,Pcis}|$ = 36.4 Hz; **3**) ppm]. The acetylene carbon atoms of the outer fragments [C$^5$/C$^6$ (**2**) and C$^{5,5'}$/C$^{6,6'}$ (**3**)] appear as sharp singlets [$\delta$ = 89.9, 89.4 (**2**) and 92.2, 89.8, 89.4, 88.3 ppm (**3**)] and were assigned by comparison to these signals in the precursor derivative [$\delta$ = 90.1, 89.4 ppm (**1**)]. The alkynylphosphane C$^{\alpha'}$ resonances are shifted upfield in both complexes with respect to those of free PPh$_2$C≡CR, whereas the C$^{\beta'}$ carbon resonances are very close to those of the free ligands [$\delta$(C$^{\alpha'}$/C$^{\beta'}$) = 84.6/107.9 (PPh$_2$C≡Ctol), 89.2/107.4 (PPh$_2$C≡CC$_6$H$_4$C≡CPh) ppm]. As a consequence, the resulting chemical shift difference ($\Delta$ = $\delta$C$^{\beta'}$ – $\delta$C$^{\alpha'}$), which can be related to the triple-bond polarisation,[9,13,59,60] is similar in both complexes [$\Delta$ = 28.5 (**2**) and 24.7 ppm (**3**)].

An X-ray diffraction study confirmed that **2** (Figure 1) is a slightly distorted square-planar Pt$^{II}$ complex formed by two mutually *cis*-arranged ethynyltolan (C≡CC$_6$H$_4$-C≡CPh) and (tolylethynyl)phosphane (PPh$_2$C≡Ctol) ligands. Selected bond lengths and angles are given in Table 1 and crystallographic data in the Experimental Section. Chemically equivalent Pt–C [2.017(4), 2.007(4) Å] and C≡C {1.196(6) and 1.204(6) Å [(tolylethynyl)phosphane groups]; 1.185(6), 1.198(6) and 1.194(6), 1.195(6) Å (ethynyltolan ligands)} bond lengths are identical within experimental error, while the Pt–P bond lengths differ only slightly [2.2792(11), 2.2919(11) Å]. The inner Pt–C$^{\alpha}$–C$^{\beta}$/C$^{\alpha}$–C$^{\beta}$–C(C$_6$H$_4$) [171.9(4)/176.9(5), 173.0(4)/176.5(5)°] and outer acetylenic fragments C(C$_6$H$_4$)–C$^5$–C$^6$/C$^5$–C$^6$–C(Ph) [175.5(5)/176.9(5), 178.8(6)/177.0(6)°] of the ethynyltolan ligands and the alkynyl moiety in the phosphane fragments P–C$^{\alpha'}$–C$^{\beta'}$/C$^{\alpha'}$–C$^{\beta'}$–C(C$_6$H$_4$) [171.2(4)/175.7(5), 173.6(4)/177.6(5)°] do not deviate significantly from linearity. These values are unexceptional and similar to those found in other X-ray crystallographically characterised mononuclear P-coordinated alkynylphosphane-[8,10,14,15,26,27,61,62] or σ-alkynylplatinum[63–78] complexes. The C$_6$H$_4$ group and the phenyl rings on each ethynyltolan ligand are nearly coplanar [dihedral angles: 2.89(15) and 10.81(17)°], which suggests strong π-delocalisation. However, both ethynyltolan ligands are essentially perpendicular to each other [92.18(17), 91.16(20)°]. The two PPh$_2$C≡Ctol units in this complex exhibit a *cisoidal* arrangement with a dihedral angle between the planes formed by both equivalent Pt–P–C$^{\alpha}$ atoms [Pt(1)–P(1)–C(33) and Pt(1)–P(2)–C(54)] of 51.90(15)°, which leads to a separation between both α-carbon atoms of only 3.1169(72) Å. Carty et al. have suggested a relationship between the ease of intramolecular coupling of the uncoordinated alkyne triple bonds in P-coordinated alkynylphosphane ligands and the proximity of the α-car-

 © 2007 Wiley-VCH Verlag GmbH & Co. KGaA, Weinheim 

bon atoms of the proximal alkyne units (less than 3.4 Å, twice the van der Waals radius of the carbon atom).[27] In fact, we have recently shown that compounds *cis*-[Pt($C_6F_5$)$_2$($PPh_2C{\equiv}CR$)$_2$] (R = Ph, tol) with "crossed" linear alkynyl moieties and a $C^{\alpha}$–$C^{\alpha}$ separation of 3.20(2) Å (Ph) or 3.34(2) Å (tol) evolve thermally into naphthalene-based bis(diphenylphosphane) complexes[62] *cis*-[Pt($C_6F_5$)$_2$-{$C_{10}H_5$-1-Ph-2,3-κ*PP′*($PPh_2$)$_2$}] and *cis*-[Pt($C_6F_5$)$_2$-{7-$CH_3$-$C_{10}H_4$-1-tol-2,3-κ*PP′*($PPh_2$)$_2$}] by intramolecular [2+2+2] coupling of two adjacent $PPh_2C{\equiv}CR$ ligands, in a similar manner to that previously observed by Carty et al. for related dichloridoplatinum(II) derivatives.[27] Similar naphthalene species can also be generated starting from the diynyl systems *cis*-[Pt($C_6F_5$)$_2$($PPh_2C{\equiv}CC_6H_4C{\equiv}CR$)$_2$] (R = Ph, *t*Bu), but only by photolysis. In contrast, photolysis of the monoalkynyl complexes *cis*-[Pt($C_6F_5$)$_2$($PPh_2C{\equiv}CR$)$_2$] (R = Ph, tol) proceeds with parallel formation of naphthalene species and the new chelating diphosphane complexes *cis*-[Pt($C_6F_5$)$_2${$PPh_2C(Ph){=}C(R)PPh(C{\equiv}CR)$}] (R = Ph, tol).[62] However, in contrast to this behaviour, complex **2**, which exhibits a very short separation between the alkynyl fragments, shows no evidence of coupling either under thermal (4 h at about 225 °C) or photochemical conditions (irradiation of a toluene solution for 90 min at room temperature using a 400-W Hg lamp).

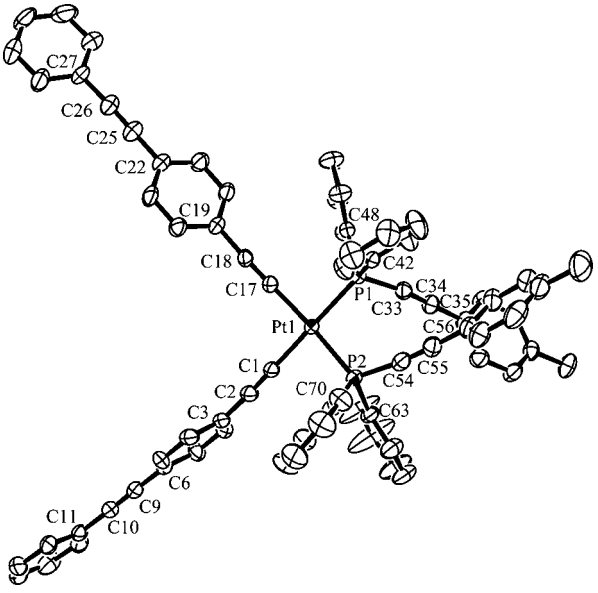


Figure 1. Molecular structure of *cis*-[Pt($C{\equiv}CC_6H_4C{\equiv}CPh$)$_2$-($PPh_2C{\equiv}Ctol$)$_2$] (**2**). Ellipsoids are drawn at the 50% probability level. Hydrogen atoms have been omitted for clarity.

To compare the coordination possibilities of the ethynyltolan ligand and the alkyne function of the P-coordinated (arylalkynyl)phosphane ligands, we studied the reactions of **2** and **3** with *cis*-[Pt($C_6F_5$)$_2$(thf)$_2$]. The results are shown in Scheme 1. Treatment of *cis*-[Pt($C{\equiv}CC_6H_4C{\equiv}CPh$)$_2$-($PPh_2C{\equiv}CR$)$_2$] [R = tol (**2**), $C_6H_4C{\equiv}CPh$ (**3**)] with 1 equiv. of *cis*-[Pt($C_6F_5$)$_2$(thf)$_2$] in $CH_2Cl_2$ at room temperature afforded the corresponding dinuclear derivatives *cis*-[{Pt($PPh_2C{\equiv}CR$)$_2$(μ-$\eta^1$:$\eta^2$-$C^{\alpha}$,$C^{\beta}$-$C{\equiv}CC_6H_4C{\equiv}CPh$)$_2$}Pt-($C_6F_5$)$_2$] [R = tol (**4**), $C_6H_4C{\equiv}CPh$ (**5**)] by $\eta^2$-complexation of the "*cis*-Pt($C_6F_5$)$_2$" fragment with both [*para*-(*para*-phenylethynyl)phenyl]alkynyl ligands. This result was not unexpected and confirms previous observations of the stronger preference of the hard $Pt^{II}$ centre towards platinaalkynyl entities rather than alkynylphosphane groups.[3,11] However, similar reactions of **2** and **3** with 2 equiv. of *cis*-[Pt($C_6F_5$)$_2$-(thf)$_2$] in $CH_2Cl_2$ yielded the trinuclear derivatives *cis*-[{Pt(μ-$\eta^1$:$\eta^2$-$C^{\alpha}$,$C^{\beta}$-$C{\equiv}CC_6H_4C{\equiv}CPh$)$_2$(μ-1κ*P*:2$\eta^2$-$C^{\alpha}$,$C^{\beta}$-$PPh_2C{\equiv}CR$)$_2$}{Pt($C_6F_5$)$_2$}$_2$] [R = tol (**6**), $C_6H_4C{\equiv}CPh$ (**7**)] in which the mononuclear precursors act as symmetrical mixed bis(*cis*-$\eta^2$:κ*P*:$\eta^2$)-chelating tetrahapto ligands of the two "*cis*-Pt($C_6F_5$)$_2$" units by binding through both an ethynyltolan group (μ-$\eta^2$-$C{\equiv}CC_6H_4C{\equiv}CPh$) and the alkyne function of the corresponding (arylethynyl)phosphane ligand (μ-κ*P*:$\eta^2$, inner for **7**).

Table 1. Selected bond lengths [Å] and angles [°] for *cis*-[Pt($C{\equiv}CC_6H_4C{\equiv}CPh$)$_2$($PPh_2C{\equiv}Ctol$)$_2$]·$C_6H_6$ (**2**·$C_6H_6$).

| | | | |
|---|---|---|---|
| Pt(1)–C(1) | 2.017(4) | C(1)–C(2) | 1.185(6) |
| Pt(1)–C(17) | 2.007(4) | C(9)–C(10) | 1.198(6) |
| Pt(1)–P(1) | 2.2792(11) | C(17)–C(18) | 1.194(6) |
| Pt(1)–P(2) | 2.2919(11) | C(25)–C(26) | 1.195(6) |
| P(1)–C(33) | 1.759(5) | C(33)–C(34) | 1.196(6) |
| P(2)–C(54) | 1.764(5) | C(54)–C(55) | 1.204(6) |
| C(1)–Pt(1)–C(17) | 89.55(17) | Pt(1)–C(17)–C(18) | 173.0(4) |
| C(1)–Pt(1)–P(2) | 88.36(12) | C(17)–C(18)–C(19) | 176.5(5) |
| C(17)–Pt(1)–P(1) | 88.34(12) | C(22)–C(25)–C(26) | 178.8(6) |
| P(1)–Pt(1)–P(2) | 95.30(4) | C(25)–C(26)–C(27) | 177.0(6) |
| Pt(1)–C(1)–C(2) | 171.9(4) | P(1)–C(33)–C(34) | 171.2(4) |
| C(1)–C(2)–C(3) | 176.9(5) | C(33)–C(34)–C(35) | 175.7(5) |
| C(6)–C(9)–C(10) | 175.5(5) | P(2)–C(54)–C(55) | 173.6(4) |
| C(9)–C(10)–C(11) | 176.9(5) | C(54)–C(55)–C(56) | 177.6(5) |

Although all attempts to obtain crystals of complexes **4**–**7** have proved fruitless so far, their spectroscopic data (see Experimental Section) are in accordance with the formulation shown in Scheme 1. Thus, complexes **4** and **5** show one strong ν(C≡C) absorption at 2173 (**4**) and 2172 $cm^{-1}$ (**5**), which confirms that the alkynyl units of the $PPh_2C{\equiv}CR$ ligands remain uncoordinated. The expected ν(C≡C) absorptions at lower frequencies, assignable to the bridging Pt(μ-$C{\equiv}CR)_2$Pt entity, are not observed, although this structural feature has been found previously in other alkynyl-bridged complexes.[57] However, both complexes show an additional very weak ν(C≡C) absorption (2216 $cm^{-1}$) that is clearly due to the outer $C^5{\equiv}C^6$ alkyne entity of these bridging alkynyl groups. The trinuclear derivatives **6** and **7** show two high-frequency bands [one sharp at 2174 (**6**) and 2173 $cm^{-1}$ (**7**) and one very weak at 2214 (**6**) and 2216 $cm^{-1}$ (**7**)] corresponding to uncoordinated alkyne units and weak bands [2019 (**6**) and 2020, 1991 $cm^{-1}$ (**7**)] assignable to the ν(C≡C) moiety of the $\eta^2$-coordinated groups.

The equivalent phosphorus atoms of the terminal alkynylphosphane ligands in the dinuclear derivatives **4** and **5** appear in the $^{31}P\{^1H\}$ NMR spectra at lower frequencies [δ = –11.20 (**4**) and –10.88 ppm (**5**)] than those in the precursors [δ = –6.53 (**2**) and –6.27 ppm (**3**)]. This high-field shift is similar to that previously observed for related dinuclear

 © 2007 Wiley-VCH Verlag GmbH & Co. KGaA, Weinheim 

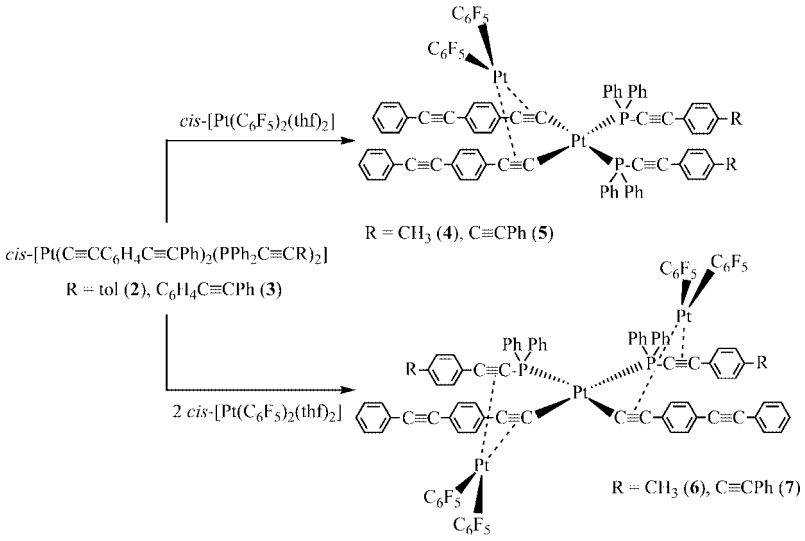


Scheme 1. Synthesis of complexes **4**–**7**.

derivatives *cis*-[{Pt(PPh$_2$C≡CR)$_2$(μ-η$^1$:η$^2$-C≡CR′)$_2$}Pt(C$_6$F$_5$)$_2$][3] and, therefore, is in keeping with the η$^2$-coordination of the "*cis*-Pt(C$_6$F$_5$)$_2$" fragment to the ethynyltolan ligands. The magnitude of $^1J_{P,Pt}$ [2682 (**4**) and 2677 Hz (**5**)] is slightly larger than that in the corresponding mononuclear derivatives with terminal ethynyltolan groups [2350 (**2**) and 2343 Hz (**3**)] due to the smaller *trans* influence of the bridging ethynyltolan ligands. In accordance with the presence of bridging four-electron (arylalkynyl)phosphane (μ-κ*P*:η$^2$) ligands in trinuclear complexes **6** and **7**, both complexes show a considerable downfield shift of the phosphorus resonance [$\delta$ = 0.19 (**6**) and 0.43 ppm (**7**)] with respect to those observed in the mononuclear precursors [$\delta$ = –6.53 (**2**) and –6.27 ppm (**3**)] and even the dinuclear derivatives, in which the PPh$_2$C≡CR molecules act only as P-donor ligands [$\delta$ = –11.20 (**4**) and –10.88 ppm (**5**)]. The platinum-phosphorus coupling constants [2514 (**6**) and 2516 Hz (**7**)] are slightly larger than those observed for the starting precursors [2350 (**2**) and 2343 Hz (**3**)] but somewhat smaller than those of the dinuclear complexes [2682 Hz (**4**) and 2677 Hz (**5**)]. It should be noted that the reaction of *cis*-[Pt(C≡CC$_6$H$_4$C≡CPh)$_2$(PPh$_2$C≡CR)$_2$] [R = tol (**2**), C$_6$H$_4$C≡CPh (**3**)] with 2 equiv. of *cis*-[Pt(C$_6$F$_5$)$_2$(thf)$_2$] could have taken place with formation of *cis*-[{Pt(PPh$_2$C≡CR)$_2$-(μ$_3$-η$^2$-*C*$^\alpha$,*C*$^\beta$-C≡CC$_6$H$_4$C≡CPh)$_2$}{Pt(C$_6$F$_5$)$_2$}$_2$], where the phosphane ligands act as terminal groups and both ethynyltolan fragments act as five-electron μ$_3$-η$^2$ bridging ligands. However, the chemical shift and coupling constant found in the related trinuclear complex *cis*-[{Pt(PPh$_2$C≡C*t*Bu)$_2$(μ$_3$-η$^2$-C≡CPh)$_2$}{Pt(C$_6$F$_5$)$_2$}$_2$] [$\delta$ = –20.55 ppm ($^1J_{P,Pt}$ = 3008 Hz)][3] are clearly different to those observed in the trinuclear derivatives **6** and **7**, with the latter being very close to those found in the symmetric isomers *cis*-[{Pt(μ-η$^1$:η$^2$-C≡C*t*Bu)$_2$(μ-1κ*P*:2η$^2$-PPh$_2$C≡CR)$_2$}{Pt(C$_6$F$_5$)$_2$}$_2$] [$\delta$ = 0.67 to –1.96 ppm ($^1J_{P,Pt}$ = 2488–2501 Hz)].[3] These results indicate that, while the phenylethynyl groups in [Pt](C≡CPh)$_2$ derivatives use both orthogonal π-acetylenic bonds in the formation of {[Pt](μ$_3$-η$^2$-C≡CPh)$_2$}{Pt(C$_6$F$_5$)$_2$}$_2$, the related ethynyltolan fragments in [Pt](C≡CC$_6$H$_4$C≡CPh)$_2$ precursors **2**, **3** only employ one in the formation of complexes **6** and **7**, thereby suggesting the lower bonding capability of these latter groups.

The variable-temperature $^{19}$F NMR spectra of dinuclear complexes **4** and **5** indicate a temperature dependence of the spectral pattern. To illustrate this, the temperature dependence of the $^{19}$F NMR spectrum of **5** in CDCl$_3$ is shown in Figure 2. As can be observed, the limiting low-temperature spectrum is compatible with a static structure. This pattern of five distinct signals (1:1:1:1:1) confirms that both C$_6$F$_5$ groups are rigid on the NMR timescale and equivalent. Upon raising the temperature, the two *o*-F doublets and the two *m*-F multiplets coalesce (above 273 K for *o*-F and 268 K for *m*-F) to only one *o*-F doublet and one *m*-F multiplet resonance. The approximate calculated activation energy is similar for the *ortho*-fluorine ($\Delta G^{\ddagger}_{273K}$ = 50.01 kJ mol$^{-1}$) and for the *meta*-fluorine atoms ($\Delta G^{\ddagger}_{268K}$ = 50.63 kJ mol$^{-1}$). The equivalence of the *o*-F atoms (and the *m*-F ones as well) at high temperature can be explained either by assuming a rapid rotation of the C$_6$F$_5$ groups around the Pt–C bonds, as previously suggested in other systems with "*cis*-Pt(C$_6$F$_5$)$_2$" fragments,[79–83] or by a fast intramolecular exchange of the "*cis*-Pt(C$_6$F$_5$)$_2$" unit below and above the platinum coordination plane. This second possibility has been suggested in related derivatives[3,57,84] stabilized by a double alkynyl bridging system and assumes the existence of a formal inversion of the PtC$_4$Pt central skeleton, which could take place via intermediate species with one or two μ-η$^1$-bonded alkynyl ligands.[85] However, we note that in these complexes (**4**, **5**) an exchange mechanism involving the inner alkynyl moieties of the (arylalkynyl)phosphane ligands cannot be discarded. The trinuclear derivatives **6** and **7** show a pattern that is consistent with two inequivalent C$_6$F$_5$ rings in which both halves are equivalent at room temperature. The two *ortho*-fluorine resonances are broad at this temperature but, unfortunately,

 © 2007 Wiley-VCH Verlag GmbH & Co. KGaA, Weinheim 

their extremely low stability in solution, even at low temperature, has prevented us from obtaining the corresponding clean variable-temperature $^{19}F$ NMR spectra.

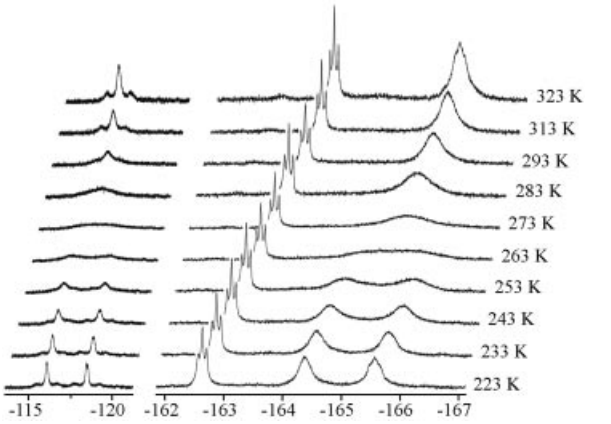


Figure 2. Variable-temperature $^{19}F$ NMR spectra (chemical shifts in ppm) of *cis*-[{Pt($PPh_2C{\equiv}CC_6H_4C{\equiv}CPh)_2$(μ-η$^1$:η$^2$-$C^{\alpha}$,$C^{\beta}$-$C{\equiv}CC_6H_4C{\equiv}CPh)_2$}Pt($C_6F_5)_2$] (**5**) in $CDCl_3$.

## Conclusion

We have reported the formation of novel (μ-$C{\equiv}CC_6H_4C{\equiv}CPh)_2$ (**4**, **5**) and mixed [μ-($C{\equiv}CC_6H_4C{\equiv}CPh$)/μ-($PPh_2C{\equiv}CR$)] (**6**, **7**) bridging di- and triplatinum complexes. In particular, the synthesis of **6** and **7**, which are stabilized by a mixed bridging system, from **2** and **3** with 2 equiv. of *cis*-[Pt($C_6F_5)_2$(thf)$_2$] instead of the isomeric *cis*-[{Pt($PPh_2C{\equiv}CR$)(μ$_3$-η$^2$-$C^{\alpha}$,$C^{\beta}$-$C{\equiv}CC_6H_4C{\equiv}CPh)_2$}{Pt($C_6F_5)_2$}$_2$] is remarkable. We have previously shown[3] that C≡CPh groups are able to act as five-electron donors (μ$_3$-η$^2$-$C^{\alpha}$,$C^{\beta}$-C≡CPh) towards "*cis*-[Pt($C_6F_5)_2$]", thus suggesting that these groups present a stronger η$^2$ capability than the more unsaturated $C{\equiv}CC_6H_4C{\equiv}CPh$ ligands.

## Experimental Section

**General Remarks:** All reactions were carried out under $N_2$ using dried solvents purified by known procedures and distilled prior to use. IR spectra were recorded with a Perkin–Elmer FT-IR 1000 spectrometer as Nujol mulls between polyethylene sheets and NMR spectra were recorded with a Bruker ARX 300 spectrometer. Chemical shifts are reported in ppm relative to external standards ($SiMe_4$, $CFCl_3$ and 85% $H_3PO_4$). Elemental analyses were carried out with a Perkin–Elmer 2400 CHNS/O microanalyzer and mass spectra were recorded with a VG Autospec spectrometer (FAB$^+$) or a Microflex MALDI-TOF Bruker spectrometer operating in the linear and reflector modes using dithranol as the matrix. $HC{\equiv}CC_6H_4C{\equiv}CPh$,[86] $PPh_2C{\equiv}Ctol$,[87] $PPh_2C{\equiv}CC_6H_4C{\equiv}CPh$[13] and *cis*-[Pt($C_6F_5)$(thf)$_2$][88] were prepared according to published procedures. Figure 3 shows the labelling scheme for the carbon atoms in the ethynyltolan ligand and in the (ethynyltolan)diphenylphosphane ligand.

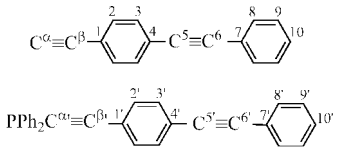


Figure 3. Labelling scheme for the carbon atoms in the ethynyltolan and (ethynyltolan)diphenylphosphane ligand.

**Synthesis of *cis*-[Pt($C{\equiv}CC_6H_4C{\equiv}CPh)_2$(cod)] (1):** A freshly prepared mixture of $HC{\equiv}CC_6H_4C{\equiv}CPh$ (432 mg, 2.138 mmol) and sodium ethoxide (prepared from 84 mg of sodium and 20 mL of ethanol) was added dropwise, with constant stirring, to a suspension of [$PtCl_2$(cod)] (400 mg, 1.069 mmol) in deoxygenated ethanol (10 mL) at –30 °C. After stirring at low temperature for 1 h, the resulting white solid was filtered and washed with successive portions of water (2 × 5 mL) and acetone (2 × 5 mL). Yield: 242 mg (32%). $C_{40}H_{30}Pt$ (705.8): calcd. C 68.07, H 4.28; found C 68.42, H 3.98. IR (Nujol): ṽ = 2214 (vw), 2119 (m) (C≡C) cm$^{-1}$. $^1H$ NMR (300.1 MHz, $CDCl_3$, 20 °C): δ = 7.50 (m), 7.38 (m), 7.32 (m) (18 H, $C_6H_4$, Ph), 5.70 (s, $J_{Pt,H}$ = 43 Hz, 4 H, =C*H*, cod), 2.58 (s, 8 H, C$H_2$, cod) ppm. $^{13}C\{^1H\}$ NMR (75.5 MHz, $CDCl_3$, 20 °C): δ = 131.5 (s), 131.2 (s), 130.8 (s), 128.0 (s, $C^{2,3,8,9}$), 127.9 (d, *J* = 16 Hz, $C^{10}$), 126.2 (s), 123.1 (s), 120.8 (s, $C^{1,4,7}$), 107.8 (s, $^2J_{C,Pt} \approx$ 370 Hz, Cβ), 104.3 (s, $J_{C,Pt}$ = 80 Hz, =*C*H, cod), 96.9 (s, Cα), 90.1 (s), 89.4 (s, $C^{5,6}$) ppm. ES (+, ionized with $Na^+$) MS: *m*/*z* (%) = 727 (38) [M$^+$ + Na – H].

**Synthesis of *cis*-[Pt($C{\equiv}CC_6H_4C{\equiv}CPh)_2$($PPh_2C{\equiv}Ctol)_2$] (2):** $PPh_2C{\equiv}Ctol$ (189 mg, 0.630 mmol) was added to a solution of *cis*-[Pt($C{\equiv}CC_6H_4C{\equiv}CPh)_2$(cod)] (**1**; 222 mg, 0.315 mmol) in $CH_2Cl_2$ (10 mL) to give an orange solution. After stirring for 1 h, the resulting solution was concentrated to a small volume, and addition of ethanol (5 mL) gave **2** as an orange-brown solid. Yield: 220 mg (58%). $C_{74}H_{52}P_2Pt$ (1198.27): calcd. C 74.18, H 4.37; found C 73.83, H 3.98. IR (Nujol): ṽ = 2214 (w), 2171 (s), 2121 (s) (C≡C) cm$^{-1}$. $^1H$ NMR (300.1 MHz, $CDCl_3$, 20 °C): δ = 7.83 (m, 8 H), 7.46 (m, 6 H), 7.28 (m) (16 H, aromatics), 7.20 (d, $J_{H,H}$ = 8.05 Hz, 4 H, $C_6H_4$), 6.97 (d, $J_{H,H}$ = 7.65 Hz, 4 H, $C_6H_4$), 6.88 (d, $J_{H,H}$ = 7.87 Hz, 4 H, $C_6H_4$), 6.84 (d, $J_{H,H}$ = 7.95 Hz, 4 H, $C_6H_4$), 2.33 (s, 6 H, C$H_3$) ppm. $^{13}C\{^1H\}$ NMR (75.5 MHz, $CDCl_3$, 20 °C): δ = 140.0 (s, $C^4$, tol), 133.3 (*A*XX′, $^{1+3}J_{C,P}$ = 12.6 Hz, *o*-C, $PPh_2$), 131.7 (s), 131.2 (s), 130.2 (s), 128.5 (s), 127.9 (s), 128.0–127.8, 127.5, 123.4 (s), 119.4 (s), 117.6 (s) (aromatics), 109.3 (*A*XX′, $^3J_{C,Ptrans} + {}^3J_{C,Pcis}$ = 37.6 Hz, Cβ, ≡*C*$^{\beta}$$C_6H_4C{\equiv}CPh$), 108.6 (*A*XX′, $^2J_{C,P} + {}^4J_{C,P}$ = 15.1 Hz, Cβ′, ≡*C*$^{\beta'}$tol), 105.2 (dd, *A*XX′, $^2J_{C,Ptrans} + {}^2J_{C,Pcis}$ = 155.1 Hz, Cα, *C*$^{\alpha}$≡), 89.9 (s), 89.4 (s, $C^{5,6}$), 80.1 (d, *A*XX′, $^1J_{C,P} + {}^3J_{C,P}$ = 103.4 Hz, Cα′, P*C*$^{\alpha'}$≡), 21.3 (s, $CH_3$) ppm. $^{31}P\{^1H\}$ NMR (121.5 MHz, $CDCl_3$, 20 °C): δ = –6.53 (s, $^1J_{P,Pt}$ = 2350 Hz) ppm. FAB(+) MS: *m*/*z* (%) = 1198 (8) [M$^+$].

**Synthesis of *cis*-[Pt($C{\equiv}CC_6H_4C{\equiv}CPh)_2$($PPh_2C{\equiv}CC_6H_4C{\equiv}CPh)_2$] (3):** Complex **3** was synthesised as an orange product according to a procedure similar to **2** but with *cis*-[Pt($C{\equiv}CC_6H_4C{\equiv}CPh)_2$(cod)] (**1**; 186 mg, 0.265 mmol) and $PPh_2C{\equiv}CC_6H_4C{\equiv}CPh$ (204 mg, 0.528 mmol). Yield: 227 mg (63%). $C_{88}H_{56}P_2Pt$ (1370.4): calcd. C 77.12, H 4.12; found C 76.92, H 3.80. IR (Nujol): ṽ = 2214 (w), 2171 (m), 2120 (s) (C≡C) cm$^{-1}$. $^1H$ NMR (300.1 MHz, $CDCl_3$, 20 °C): δ = 7.85 (m, 8 H), 7.51 (m, 12 H), 7.39–7.19 (m) (28 H, aromatics), 6.93 (d, $J_{H,H}$ = 8.05 Hz, 4 H, $C_6H_4$), 6.84 (d, $J_{H,H}$ = 8.05 Hz, 4 H, $C_6H_4$) ppm. $^{13}C\{^1H\}$ NMR (75.5 MHz, $CDCl_3$, 20 °C): δ = 133.4 (*A*XX′, $^{1+3}J_{C,P}$ = 12.4 Hz, *o*-C, $PPh_2$), 131.7 (s), 131.4 (s), 131.24 (s), 131.2 (s), 131.0 (s), 130.5 (s), 130.3 (s, *p*-C, $PPh_2$), 128.2 (s), 128.11 (d, *J* = 64 Hz, *i*-C, $PPh_2$), 128.1 (s), 128.0 (s), 127.99 (s), 124.7 (s), 123.3 (s), 122.3 (s), 119.9 (s), 119.4 (s)

 © 2007 Wiley-VCH Verlag GmbH & Co. KGaA, Weinheim 

(aromatics), 109.4 (*A*XX′, three-line pattern, $^3J_{C,Ptrans} + {}^3J_{C,Pcis}$ = 36.4 Hz, $C^{\beta}$, $\equiv C^{\beta}C_6H_4C\equiv$CPh), 107.4 (*A*XX′, $^2J_{C,P} + {}^4J_{C,P}$ = 14.8 Hz, $C^{\beta\prime}$, $\equiv C^{\beta\prime}C_6H_4C\equiv$CPh), 104.5 (dd, *A*XX′, $^2J_{C,Ptrans} + {}^2J_{C,Pcis}$ = 156.2 Hz, $C^{\alpha}$, $C^{\alpha}\equiv$), 92.2 (s), 89.8 (s), 89.4 (s), 88.3 ($C^{5,5',6,6'}$), 82.7 (d, *A*XX′, $^1J_{C,P} + {}^3J_{C,P}$ = 100.2 Hz, $C^{\alpha\prime}$, $PC^{\alpha\prime}\equiv$) ppm. $^{31}P\{^1H\}$ NMR (121.5 MHz, $CDCl_3$, 20 °C): $\delta$ = –6.27 (s, $^1J_{P,Pt}$ = 2343 Hz) ppm. MALDI-TOF(+) MS: *m*/*z* (%) = 1355 (100) [$M^+ - CH_3$], 967 (80) [$Pt(PPh_2C\equiv CC_6H_4C\equiv CPh)_2^+$].

**Synthesis of *cis*-[{Pt(PPh$_2$C≡Ctol)$_2$(μ-η$^1$:η$^2$-*C*$^α$,*C*$^β$-C≡CC$_6$H$_4$C≡CPh)$_2$}Pt(C$_6$F$_5$)$_2$] (4):** *cis*-[$Pt(C_6F_5)_2(thf)_2$] (59 mg, 0.088 mmol) was added to an orange solution of *cis*-[$Pt(C\equiv CC_6H_4C\equiv CPh)_2(PPh_2C\equiv Ctol)_2$] (**2**; 105 mg, 0.088 mmol) in $CH_2Cl_2$ (15 mL). After stirring at room temperature for 1 h, the solvent was evaporated to leave a small volume, and *n*-hexane (8 mL) was added to precipitate **4** as a brown solid. Yield: 117 mg (77%). $C_{86}H_{52}F_{10}P_2Pt_2$ (1727.5): calcd. C 59.80, H 3.03; found C 59.97, H 2.65. IR (Nujol): $\tilde{\nu}$ = 2216 (vw), 2173 (vs) (C≡C); 804 (s), 794 (s) $(C_6F_5)_{X\text{-sensitive}}$ $cm^{-1}$. $^1H$ NMR (300.1 MHz, $CDCl_3$, 20 °C): $\delta$ = 7.88 (m, 8 H, Ph), 7.50 (m, 6 H), 7.34 (m, 20 H), 7.01 (m, 8 H, $C_6H_4$), 6.84 (d, $J_{H,H}$ = 7.8 Hz, 4 H, $C_6H_4$), 2.36 (s, 6 H, $CH_3$) ppm. $^{19}F$ NMR (282.4 MHz, $CDCl_3$, 20 °C): $\delta$ = –117.2 (br. s, 4 F, *o*-F), –163.5 (t, 2 F, *p*-F), –165.6 (br. s, 4 F, *m*-F) ppm. $^{19}F$ NMR (282.4 MHz, $CDCl_3$, –30 °C): $\delta$ = –116.1 (m, $^3J_{Pt,o\text{-}F} \approx$ 340 Hz, 2 F, *o*-F), –118.4 (m, $^3J_{Pt,o\text{-}F} \approx$ 430 Hz, 2 F, *o*-F), –162.9 (t, 2 F, *p*-F), –164.6 (br. m, 2 F, *m*-F), –165.8 (br. m, 2 F, *m*-F) ppm. Signal coalescence: *o*-F (approx. 268 K), *m*-F (approx. 263 K); $\Delta G^{\ddagger} \approx$ 49.2 kJ mol$^{-1}$. $^{31}P\{^1H\}$ NMR (121.5 MHz, $CDCl_3$, 20 °C): $\delta$ = –11.20 (s, $^1J_{P,Pt}$ = 2682 Hz) ppm. FAB(+) MS: *m*/*z* (%) = 794 (55) [$Pt(PPh_2C\equiv Ctol)_2^+ - H$].

**Synthesis of *cis*-[{Pt(PPh$_2$C≡CC$_6$H$_4$C≡CPh)$_2$(μ-η$^1$:η$^2$-*C*$^α$,*C*$^β$-C≡CC$_6$H$_4$C≡CPh)$_2$}Pt(C$_6$F$_5$)$_2$] (5):** Complex **5** was prepared as a brown solid in a similar way to **4** starting from *cis*-[$Pt(C\equiv CC_6H_4C\equiv CPh)_2(PPh_2C\equiv CC_6H_4C\equiv CPh)_2$] (**3**; 112 mg, 0.082 mmol) and *cis*-[$Pt(C_6F_5)_2(thf)_2$] (55 mg, 0.082 mmol), and was recrystallised from $CH_2Cl_2$/*i*PrOH. Yield: 52 mg (43%). $C_{100}H_{56}F_{10}P_2Pt_2$ (1899.6): calcd. C 63.23, H 2.97; found C 63.12, H 2.61. IR (Nujol): $\tilde{\nu}$ = 2216 (w), 2172 (s) (C≡C); 804 (m), 794 (m) $(C_6F_5)_{X\text{-sensitive}}$ $cm^{-1}$. $^1H$ NMR (300.1 MHz, $CDCl_3$, 20 °C): $\delta$ = 7.90 (m, 8 H, Ph), 7.51–7.21 (m, 40 H, Ph), 7.00 (d, $J_{H,H}$ = 8.0 Hz, 4 H, $C_6H_4$), 6.85 (d, $J_{H,H}$ = 8 Hz, 4 H, $C_6H_4$) ppm. $^{19}F$ NMR (282.4 MHz, $CDCl_3$, 20 °C): $\delta$ = –117.1 (br. s, 4 F, *o*-F), –163.4 (t, 2 F, *p*-F), –165.6 (br. s, 4 F, *m*-F) ppm. $^{19}F$ NMR (282.4 MHz, $CDCl_3$, –50 °C): $\delta$ = –116.1 (m, $^3J_{Pt,o\text{-}F} \approx$ 340 Hz, 2 F, *o*-F), –118.5 (m, $^3J_{Pt,o\text{-}F} \approx$ 425 Hz, 2 F, *o*-F), –162.6 (t, 2 F, *p*-F), –164.4 (m, 2 F, *m*-F), –165.6 (m, 2 F, *m*-F) ppm. $^{19}F$ NMR (282.4 MHz, $CDCl_3$, +50 °C): $\delta$ = –116.9 (m, $^3J_{Pt,o\text{-}F}$ = 405 Hz, 4 F, *o*-F), –163.7 (t, 2 F, *p*-F), –165.8 (br. m, 4 F, *m*-F) ppm. Signal coalescence: *o*-F (273 K), *m*-F (approx. 268 K); $\Delta G^{\ddagger} \approx$ 50.01 (*o*-F), 50.63 kJ mol$^{-1}$ (*m*-F). $^{31}P\{^1H\}$ NMR (121.5 MHz, $CDCl_3$, 20 °C): $\delta$ = –10.88 (s, $^1J_{P,Pt}$ = 2677 Hz) ppm. MALDI-TOF(+) MS: *m*/*z* (%) = 1168 (27) [$Pt(C\equiv CC_6H_4C\equiv CPh)(PPh_2C\equiv CC_6H_4C\equiv CPh)_2^+$], 983 (50) [$Pt(C\equiv CC_6H_4C\equiv CPh)_2(PPh_2C\equiv CC_6H_4C\equiv CPh)^+$], 965 (90) [$Pt(PPh_2C\equiv CC_6H_4C\equiv CPh)_2^+ - 2H]^+$, 765 (100) [$Pt(PPh_2C\equiv CC_6H_4C\equiv CPh)(PPh_2) - H$].

**Synthesis of *cis*-[{Pt(μ-η$^1$:η$^2$-*C*$^α$,*C*$^β$-C≡CC$_6$H$_4$C≡CPh)$_2$(μ-1κ*P*:2η$^2$-*C*$^α$,*C*$^β$-PPh$_2$C≡Ctol)$_2$}{Pt(C$_6$F$_5$)$_2$}$_2$] (6):** A solution of *cis*-[$Pt(C\equiv CC_6H_4C\equiv CPh)_2(PPh_2C\equiv Ctol)_2$] (**2**; 104 mg, 0.087 mmol) in $CH_2Cl_2$ (15 mL) was treated at room temperature with *cis*-[$Pt(C_6F_5)_2(thf)_2$] (135 mg, 0.200 mmol; molar ratio 1:2.3). After stirring for 1 h, the solvent was removed in vacuo and the addition of *n*-hexane (5 mL) caused the precipitation of **6** as a brown solid. Yield: 170 mg (86%). $C_{98}H_{52}F_{20}P_2Pt_3$ (2256.7): calcd. C 52.16, H 2.32; found C 51.78, H 2.01. IR (Nujol): $\tilde{\nu}$ = 2214 (vw), 2174 (s), 2019 (w) (C≡C); 804 (m), 795 (m) $(C_6F_5)_{X\text{-sensitive}}$ $cm^{-1}$. $^1H$ NMR (300.1 MHz, $CDCl_3$, 20 °C): $\delta$ = 7.51–7.02 (m, 46 H, aromatics), 2.36 (s, 6 H, $CH_3$) ppm. $^{19}F$ NMR (282.4 MHz, $CDCl_3$, 20 °C): $\delta$ = –116.6 (br. s, 4 F, *o*-F), –117.2 (br. s, 4 F, *o*-F), –160.6 (t, 2 F, *p*-F), –161.1 (t, 2 F, *p*-F), –164.1 (br. m, 8 F, *m*-F) ppm. $^{31}P\{^1H\}$ NMR (121.5 MHz, $CDCl_3$, 20 °C): $\delta$ = 0.19 (s, $^1J_{P,Pt}$ = 2514 Hz) ppm. MALDI-TOF(+) MS: *m*/*z* (%) = 1728 (18) [$M^+$ – $Pt(C_6F_5)_2$], 1296 (50) [$Pt(C\equiv CC_6H_4C\equiv CPh)(PPh_2C\equiv Ctol)_3^+ - H$], 996 (60) [$Pt(C\equiv CC_6H_4C\equiv CPh)(PPh_2C\equiv Ctol)_2^+ - H$].

**Synthesis of *cis*-[{Pt(μ-η$^1$:η$^2$-*C*$^α$,*C*$^β$-C≡CC$_6$H$_4$C≡CPh)$_2$(μ-1κ*P*:2η$^2$-*C*$^α$,*C*$^β$-PPh$_2$C≡CC$_6$H$_4$C≡CPh)$_2$}{Pt(C$_6$F$_5$)$_2$}$_2$] (7):** Complex **7** was prepared as a brown solid according to a procedure similar to that for compound **6** starting from *cis*-[$Pt(C\equiv CC_6H_4C\equiv CPh)_2(PPh_2C\equiv CC_6H_4C\equiv CPh)_2$] (**3**; 70 mg, 0.051 mmol) and *cis*-[$Pt(C_6F_5)_2(thf)_2$] (79 mg, 0.117 mmol). Yield: 131 mg (65%). $C_{112}H_{56}F_{20}P_2Pt_3$ (2428.9): calcd. C 55.39, H 2.32; found C 55.72, H 2.61. IR (Nujol): $\tilde{\nu}$ = 2216 (w), 2173 (s), 2020 (w), 1991 (w) (C≡C); 805 (m), 796 (m) $(C_6F_5)_{X\text{-sensitive}}$ $cm^{-1}$. $^1H$ NMR (300.1 MHz, $CDCl_3$, 20 °C): $\delta$ = 7.53–7.17 (m, 56 H, aromatics) ppm. $^{19}F$ NMR (282.4 MHz, $CDCl_3$, 20 °C): $\delta$ = –116.5 (br. s, 4 F, *o*-F), –117.2 (br. s, 4 F, *o*-F), –160.2 (t, 2 F, *p*-F), –160.6 (t, 2 F, *p*-F), –163.7 (br. m, 4 F, *m*-F), –164.0 (br. m, 4 F, *m*-F) ppm. $^{31}P\{^1H\}$ NMR (121.5 MHz, $CDCl_3$, 20 °C): $\delta$ = 0.43 (s, $^1J_{P,Pt}$ = 2516 Hz) ppm. MALDI-TOF(+) MS: *m*/*z* (%) = 1899 (28) [$M^+$ – $Pt(C_6F_5)_2$], 1731 (50) [$M^+ - Pt(C_6F_5)_2 - C_6F_5 - H$], 1369 (54) [$M^+$ – 2 $Pt(C_6F_5)_2$ – H], 1151 (57) [$Pt(C_6F_5)(C\equiv CC_6H_4C\equiv CPh)_2(PPh_2C\equiv CC_6H_4C\equiv CPh^+ + H)$], 967 (64) [$Pt(PPh_2C\equiv CC_6H_4C\equiv CPh)_2^+$], 766 (25) [$Pt(PPh_2C\equiv CC_6H_4C\equiv CPh)(PPh_2)^+$].

**X-ray Crystallography:** A summary of crystal data, data collection and refinement parameters for the structural analysis is given in Table 2. Crystals of complex **2** were obtained at room temperature by slow diffusion of *n*-hexane into a solution of the compound in benzene. One molecule of benzene was found in the asymmetric

Table 2. Crystal data and structure refinement parameters for **2·C$_6$H$_6$**.

| | |
|---|---|
| Empirical formula | $C_{74}H_{52}P_2Pt\cdot C_6H_6$ |
| Formula mass | 1276.29 |
| Temperature [K] | 173(1) |
| Wavelength [Å] | 0.71073 |
| Crystal system | triclinic |
| Space group | $P\bar{1}$ |
| Crystal dimensions [mm] | 0.20 × 0.20 × 0.05 |
| *a* [Å] | 15.1950(2) |
| *b* [Å] | 15.2180(2) |
| *c* [Å] | 16.2740(2) |
| *α* [°] | 92.0880(10) |
| *β* [°] | 116.7850(10) |
| *γ* [°] | 103.1010(10) |
| *V* [Å$^3$] | 3230.12(7) |
| $D_{calcd.}$ [Mg m$^{-3}$] | 1.312 |
| *Z* | 2 |
| $\mu$(Mo-K$_\alpha$) [mm$^{-1}$] | 2.265 |
| *F*(000) | 1292 |
| $\theta$ range [°] | 1.54–27.92 |
| $T_{min/max}$ | 0.895 and 0.800 |
| No. of reflns. measd. | 52252 |
| No. of obsd. reflns. | 15294 [*R*(int) = 0.0678] |
| Goodness of fit on $F^2$[a] | 1.010 |
| Final *R* indices [$I > 2\sigma(I)$][a] | *R*1 = 0.0488, *wR*2 = 0.0976 |
| *R* indices (all data) | *R*1 = 0.0784, *wR*2 = 0.1068 |

[a] $R1 = \Sigma(|F_o| - |F_c|)/\Sigma|F_o|$; $wR2 = [\Sigma w(F_o^2 - F_c^2)^2/\Sigma wF_o^2]^{1/2}$; goodness of fit = $\{\Sigma[w(F_o^2 - F_c^2)^2]/(N_{obs} - N_{param})\}^{1/2}$; $w = [\sigma^2(F_o^2) + (g_1P)^2 + g_2P]^{-1}$, where $P = [\max(F_o^2;0) + 2F_c^2]/3$.

 © 2007 Wiley-VCH Verlag GmbH & Co. KGaA, Weinheim 

unit. This molecule of benzene was found to be disordered over two positions with two consecutive carbon atoms, C(75) and C(80), in the same position and was modelled adequately. The disordered sets of atoms were refined with a partial occupancy of 0.50 each. Data for **2**·$C_6H_6$ were collected at low temperature (173 K) with a Nonius κ-CCD area-detector diffractometer, using graphite-monochromated Mo-$K_\alpha$ radiation. Data were processed using the DENZO and SCALEPACK suite of programs.[89] The absorption correction was performed using SORTAV.[90] The structure was solved by Patterson and Fourier methods using the DIRDIF92 program,[91] and refined by full-matrix least squares on $F^2$ with SHELXL-97.[92] All non-hydrogen atoms were assigned anisotropic displacement parameters and all hydrogen atoms were constrained to idealised geometries by fixing isotropic displacement parameters at 1.2-times the $U_{iso}$ value of their attached carbon atom for the phenyl hydrogen atoms and 1.5-times for the methyl groups. There are peaks of electron density higher than 1 e Å$^{-3}$ in the final map, but they are located very close to the platinum atoms or in the vicinity of the solvent and have no chemical meaning. CCDC-634038 contains the supplementary crystallographic data for this paper. These data can be obtained free of charge from The Cambridge Crystallographic Data Centre via www.ccdc.cam.ac.uk/data_request.cif.

## Acknowledgments

This work was supported by the Ministerio de Educación y Ciencia (project CTQ2005-08606-C02-02 and a grant for A. G.).

[1] M. J. Went, *Polyhedron* **1995**, *14*, 465–481 and references cited therein.
[2] J. Forniés, E. Lalinde, A. Martín, M. T. Moreno, A. J. Welch, *J. Chem. Soc. Dalton Trans.* **1995**, 1333–1340.
[3] I. Ara, L. R. Falvello, S. Fernández, J. Forniés, E. Lalinde, A. Martín, M. T. Moreno, *Organometallics* **1997**, *16*, 5923–5937.
[4] J. P. H. Charmant, J. Forniés, J. Gómez, E. Lalinde, M. T. Moreno, A. G. Orpen, S. Solano, *Angew. Chem. Int. Ed.* **1999**, *38*, 3058–3061.
[5] E. Louattani, J. Suades, *J. Organomet. Chem.* **2000**, *604*, 234–240.
[6] J. E. Davies, M. J. Mays, P. R. Raithby, K. Sarveswaran, G. A. Solan, *J. Chem. Soc. Dalton Trans.* **2001**, 1269–1277.
[7] X. Liu, K. F. Mok, P. H. Leung, *Organometallics* **2001**, *20*, 3918–3926.
[8] I. Ara, J. Forniés, A. García, J. Gómez, E. Lalinde, M. T. Moreno, *Chem. Eur. J.* **2002**, *8*, 3698–3716.
[9] J. R. Berenguer, M. Bernechea, J. Forniés, J. Gómez, E. Lalinde, *Organometallics* **2002**, *21*, 2314–2324.
[10] T. Baumgartner, K. Huynh, S. Schleidt, A. J. Lough, I. Manners, *Chem. Eur. J.* **2002**, *8*, 4622–4632.
[11] J. Forniés, A. García, J. Gómez, E. Lalinde, M. T. Moreno, *Organometallics* **2002**, *21*, 3733–3743.
[12] M. J. Mays, K. Sarveswaran, G. A. Solan, *Inorg. Chim. Acta* **2003**, *354*, 21–28.
[13] J. R. Berenguer, M. Bernechea, J. Forniés, A. García, E. Lalinde, *Organometallics* **2004**, *23*, 4288–4300.
[14] J. R. Berenguer, M. Bernechea, J. Forniés, A. García, E. Lalinde, M. T. Moreno, *Inorg. Chem.* **2004**, *43*, 8185–8198.
[15] J. Forniés, A. García, B. Gil, E. Lalinde, M. T. Moreno, *Dalton Trans.* **2004**, 3854–3863.
[16] M. Bardají, M. T. de la Cruz, P. G. Jones, A. Laguna, J. Martínez, M. D. Villacampa, *Inorg. Chim. Acta* **2005**, *358*, 1365–1372.
[17] J. Suades, F. Dahan, R. Mathieu, *Organometallics* **1989**, *8*, 842–844.
[18] D. Montlo, J. Suades, F. Dahan, R. Mathieu, *Organometallics* **1990**, *9*, 2933–2937.
[19] L. Dupuis, N. Pirio, P. Meunier, A. Igau, D. Donnadieu, J. P. Majoral, *Angew. Chem. Int. Ed. Engl.* **1997**, *36*, 987–989.
[20] A. Mahieu, Y. Miquel, A. Igau, B. Donnadieu, J. P. Majoral, *Organometallics* **1997**, *16*, 3086–3088.
[21] P. Rosa, P. Le Floch, L. Ricard, F. Mathey, *J. Am. Chem. Soc.* **1997**, *119*, 9417–9423.
[22] Y. Miquel, A. Igau, B. Donnadieu, J. P. Mayoral, N. Pirio, P. Meunier, *J. Am. Chem. Soc.* **1998**, *120*, 3504–3505.
[23] M. A. Bennett, C. J. Cobley, A. D. Rae, E. Wenger, A. C. Willis, *Organometallics* **2000**, *19*, 1522–1533.
[24] A. J. Edwards, S. A. Macgregor, A. D. Rae, E. Wenger, A. C. Willis, *Organometallics* **2001**, *20*, 2864–2877.
[25] Y. El Harouch, V. Cadierno, A. Igau, B. Donnadieu, J. P. Majoral, *J. Organomet. Chem.* **2004**, *689*, 953–964.
[26] A. J. Carty, N. J. Taylor, D. K. Johnson, *J. Am. Chem. Soc.* **1979**, *101*, 5422–5424.
[27] D. K. Johnson, T. Rukachaisirikul, Y. Sun, N. J. Taylor, A. J. Canty, A. J. Carty, *Inorg. Chem.* **1993**, *32*, 5544–5552.
[28] M. Martin-Redondo, L. Scoles, B. T. Sterenberg, K. A. Udachin, A. J. Carty, *J. Am. Chem. Soc.* **2005**, *127*, 5038–5039.
[29] P. J. Low, T. M. Hayes, K. A. Udachin, A. E. Goeta, J. A. K. Howard, G. D. Enright, A. J. Carty, *J. Chem. Soc. Dalton Trans.* **2002**, 1455–1464.
[30] A. J. Carty, *Pure Appl. Chem.* **1982**, *54*, 113–130 and references cited therein.
[31] D. Nuccianore, S. A. MacLaughlin, N. J. Taylor, A. J. Carty, *Organometallics* **1988**, *7*, 106–117.
[32] A. A. Cherkas, L. H. Randall, S. A. MacLaughlin, G. N. Mott, N. J. Taylor, A. J. Carty, *Organometallics* **1988**, *7*, 969–977.
[33] M. H. A. Benvenutti, M. D. Vargas, D. Braga, F. Crepioni, B. E. Mann, S. Naylor, *Organometallics* **1993**, *12*, 2947–2954.
[34] G. Hogarth, S. P. Redmond, *J. Organomet. Chem.* **1997**, *534*, 221–227.
[35] A. Albinati, V. Filippi, P. Leoni, L. Marchetti, M. Pasquali, V. Passarelli, *Chem. Commun.* **2005**, 2155–2157.
[36] Y. Chi, A. J. Carty, P. Blenkiron, E. Delgado, G. D. Enright, W. Wang, S.-M. Peng, G.-H. Lee, *Organometallics* **1996**, *15*, 5269–5271.
[37] A. J. Carty, G. Hogarth, G. Enright, G. Frapper, *Chem. Commun.* **1997**, 1883–1884.
[38] J. E. Davies, M. J. Mays, P. R. Raithby, K. Sarveswaran, *Angew. Chem. Int. Ed. Engl.* **1997**, *36*, 2668–2669.
[39] E. Delgado, Y. Chi, W. Wang, G. Hogarth, P. J. Low, G. D. Enright, S.-M. Peng, G.-H. Lee, *Organometallics* **1998**, *17*, 2936–2938.
[40] S. E. Jacobson, N. J. Taylor, A. J. Carty, *J. Chem. Soc. Chem. Commun.* **1974**, 668–669.
[41] A. J. Carty, S. Jacobson, R. T. Simpson, N. J. Taylor, *J. Am. Chem. Soc.* **1975**, *97*, 7254–7262.
[42] R. J. Restivo, G. Ferguson, T. W. Ng, A. J. Carty, *Inorg. Chem.* **1977**, *16*, 172–176.
[43] M. Bardají, A. Laguna, P. G. Jones, *Organometallics* **2001**, *20*, 3906–3912.
[44] N. J. Taylor, S. Jacobson, A. J. Carty, *Inorg. Chem.* **1975**, *14*, 2648–2653.
[45] M. A. Bennett, J. Castro, A. J. Edwards, M. R. Kopp, E. Wenger, A. C. Willis, *Organometallics* **2001**, *20*, 980–989.
[46] M. A. Bennett, L. Kwan, A. D. Rae, E. Wenger, A. C. Willis, *J. Chem. Soc. Dalton Trans.* **2002**, 226–233.
[47] A. J. Carty, D. K. Johnson, S. E. Jacobson, *J. Am. Chem. Soc.* **1979**, *101*, 5612–5619.
[48] X. Liu, T. K. W. Ong, S. Selvaratnam, J. J. Vittal, A. J. P. White, D. J. Williams, P. H. Leung, *J. Organomet. Chem.* **2002**, *643*, 4–11.
[49] C. J. Adams, M. I. Bruce, E. Horn, E. R. T. Tiekink, *J. Chem. Soc. Dalton Trans.* **1992**, 1157–1164.

 © 2007 Wiley-VCH Verlag GmbH & Co. KGaA, Weinheim 

[50] C. J. Adams, M. I. Bruce, E. Horn, B. W. Skelton, E. R. T. Tiekink, A. H. White, *J. Chem. Soc. Dalton Trans.* **1993**, 3299–3312.
[51] C. J. Adams, M. I. Bruce, E. Horn, B. W. Skelton, E. R. T. Tiekink, A. H. White, *J. Chem. Soc. Dalton Trans.* **1993**, 3313–3322.
[52] D. Xu, B. Hong, *Angew. Chem. Int. Ed.* **2000**, *39*, 1826–1829.
[53] P. Blenkiron, N. J. Taylor, A. J. Carty, *J. Chem. Soc. Chem. Commun.* **1995**, 327–328.
[54] P. Blenkiron, J. F. Corrigan, D. Pilette, N. J. Taylor, A. J. Carty, *Can. J. Chem.* **1996**, *74*, 2349–2362.
[55] P. Blenkiron, G. D. Enright, P. J. Low, J. F. Corrigan, N. J. Taylor, Y. Chi, J. Y. Saillard, A. J. Carty, *Organometallics* **1998**, *17*, 2447–2458.
[56] R. J. Cross, M. F. Davidson, *J. Chem. Soc. Dalton Trans.* **1986**, 1987–1992.
[57] J. Forniés, M. A. Gómez-Saso, E. Lalinde, F. Martínez, M. T. Moreno, *Organometallics* **1992**, *11*, 2873–2883.
[58] P. S. Pregosin, R. W. Kunz, in *NMR Basic Principles and Progress* (Eds: P. Diehl, E. Fluck, R. Kosfeld), Springer-Verlay, New York, **1979**, vol. 16, pp. 43–45.
[59] E. Louattani, A. Lledós, J. Suades, A. Alvarez-Larena, J. F. Piniella, *Organometallics* **1995**, *14*, 1053–1060.
[60] E. Louattani, J. Suades, *Inorg. Chim. Acta* **1999**, *291*, 207–211.
[61] A. Díez, J. Forniés, A. García, E. Lalinde, M. T. Moreno, *Inorg. Chem.* **2005**, *44*, 2443–2453.
[62] A. García, J. Gómez, E. Lalinde, M. T. Moreno, *Organometallics* **2006**, *25*, 3926–3934.
[63] J. Manna, K. D. John, M. D. Hopkins, *Adv. Organomet. Chem.* **1995**, *38*, 79–154.
[64] R. Saha, M. D. Qaium, D. Debnath, M. Younus, N. Chawdhury, N. Sultana, G. Kociok-Köhn, L. Ooi, P. R. Raithby, M. Kijima, *Dalton Trans.* **2005**, 2760–2765.
[65] M. S. Khan, M. R. A. Al-Mandhary, M. K. Al-Suti, B. Ahrens, M. F. Mahon, L. Male, P. R. Raithby, C. E. Boothby, A. Köhler, *Dalton Trans.* **2003**, 74–84.
[66] C. J. Adams, S. L. James, X. Liu, P. R. Raithby, L. J. Yellowlees, *J. Chem. Soc. Dalton Trans.* **2000**, 63–67.
[67] S. M. Al Qaisi, K. J. Galat, M. Chai, D. G. Ray III, P. L. Rinaldi, C. A. Tessier, W. J. Youngs, *J. Am. Chem. Soc.* **1998**, *120*, 12149–12150.
[68] M. I. Bruce, K. Costuas, J. F. Halet, B. C. Hall, P. J. Low, B. K. Nicholson, B. W. Skelton, A. J. White, *J. Chem. Soc. Dalton Trans.* **2002**, 383–398.
[69] V. W. W. Yam, K. M. C. Wong, N. Zhu, *J. Am. Chem. Soc.* **2002**, *124*, 6506–6507.
[70] T. B. Peters, Q. Zheng, J. Stahl, J. C. Bohling, A. M. Arif, F. Hampel, J. A. Gladysz, *J. Organomet. Chem.* **2002**, *641*, 53–61.
[71] W. Lu, B. X. Mi, M. C. W. Chan, Z. Hui, N. Zhu, S. T. Lee, C. M. Che, *Chem. Commun.* **2002**, 206–207.
[72] W. Lu, M. C. W. Chan, N. Zhu, C. M. Che, Z. He, K. Y. Wong, *Chem. Eur. J.* **2003**, *9*, 6155–6166.
[73] M. Janka, G. K. Anderson, N. P. Rath, *Organometallics* **2004**, *23*, 4382–4390.
[74] W. Lu, B. X. Mi, M. C. W. Chan, Z. Hui, C. M. Che, N. Zhu, S. T. Lee, *J. Am. Chem. Soc.* **2004**, *126*, 4958–4971.
[75] M. I. Bruce, J. Davy, B. C. Hall, Y. J. van Galen, B. W. Skelton, A. H. White, *Appl. Organomet. Chem.* **2002**, *16*, 559–568.
[76] C. H. Tao, K. M. C. Wong, N. Zhu, V. W. W. Yam, *New J. Chem.* **2003**, *27*, 150–154.
[77] J. Vicente, M. T. Chicote, M. M. Álvarez-Falcón, P. G. Jones, *Organometallics* **2005**, *24*, 2764–2772.
[78] M. S. Khan, M. R. A. Al-Mandhary, M. K. Al-Suti, F. R. Al-Battashi, S. Al-Saadi, B. Ahrens, J. K. Bjernemose, M. F. Mahon, P. R. Raithby, M. Younus, N. Chawdhury, A. Köhler, E. A. Marseglia, E. Tedesco, N. Feeder, S. J. Teate, *Dalton Trans.* **2004**, 2377–2385.
[79] J. R. Berenguer, J. Forniés, E. Lalinde, F. Martínez, E. Urriolabeitia, A. J. Welch, *J. Chem. Soc. Dalton Trans.* **1994**, 1291–1299.
[80] I. Ara, J. R. Berenguer, J. Forniés, E. Lalinde, M. Tomás, *Organometallics* **1996**, *15*, 1014–1022.
[81] L. R. Falvello, J. Forniés, R. Navarro, A. Rueda, E. Urriolabeitia, *Organometallics* **1996**, *15*, 309–316.
[82] I. Ara, J. R. Berenguer, E. Eguizábal, J. Forniés, E. Lalinde, A. Martín, F. Martínez, *Organometallics* **1998**, *17*, 4578–4596.
[83] I. Ara, J. R. Berenguer, E. Eguizábal, J. Forniés, E. Lalinde, *Organometallics* **2001**, *20*, 2686–2696.
[84] J. R. Berenguer, E. Eguizábal, L. R. Falvello, J. Forniés, E. Lalinde, A. Martín, *Organometallics* **2000**, *19*, 490–496.
[85] J. R. Berenguer, L. R. Falvello, J. Forniés, E. Lalinde, M. Tomás, *Organometallics* **1993**, *12*, 6–7.
[86] O. Lavastre, S. Cabioch, P. H. Dixneuf, J. Vohlidal, *Tetrahedron* **1997**, *53*, 7595–7604.
[87] E. Louattani, J. Suades, R. Mathieu, *J. Organomet. Chem.* **1991**, *421*, 335–340.
[88] R. Usón, J. Forniés, M. Tomás, B. Menjón, *Organometallics* **1985**, *4*, 1912–1914.
[89] Z. Otwinowski, W. Minor, in *Methods in Enzymology* (Eds: C. V. Carter Jr, R. M. Sweet), Academic Press, New York, **1997**, vol. 276A, pp. 307.
[90] R. H. Blessing, *Acta Crystallogr., Sect. A* **1995**, *51*, 33–38.
[91] P. T. Beursken, G. Beursken, W. P. Bosman, R. de Gelder, S. García-Granda, R. O. Gould, J. M. M. Smith, C. Smykalla, *The DIRDIF92 program system*, Technical Report of the Crystallography Laboratory, University of Nijmegen, The Netherlands, **1992**.
[92] G. M. Sheldrick, *SHELX-97, Program for Crystal Structure Determination from Diffraction Data*, University of Göttingen, Germany, **1997**.

Received: January 30, 2007
Published Online: June 18, 2007

 © 2007 Wiley-VCH Verlag GmbH & Co. KGaA, Weinheim 

DOI: 10.1002/ejic.200700198

# Reactivity of InCp* Towards Transition Metal Carbonyl Clusters: Synthesis and Structural Characterization of the $Rh_6(CO)_{16-x}(InCp^*)_x$ Mixed-Metal Cluster Compounds, $x$ = 1–2

**Elena V. Grachova*[a] and Gerald Linti[b]**

**Keywords:** Rhodium / Indium / Cluster compounds

With $[Rh_6(CO)_{15}(InCp^*)]$, the first example of a transition metal carbonyl cluster with a coordinated InCp* (Cp* = $C_5Me_5$) fragment in the ligand environment is reported. This cluster with direct Rh–In bonds forms in the reaction of the hexanuclear carbonyl rhodium cluster $Rh_6(CO)_{15}(NCMe)$ with InCp* under mild conditions. This is characterized by means of IR and NMR spectroscopy and crystal structure analysis.
(© Wiley-VCH Verlag GmbH & Co. KGaA, 69451 Weinheim, Germany, 2007)

## Introduction

Creation of new materials primarily requires chemists to create new compounds with novel and unusual properties. In most cases, unusual properties are the result of the unusual composition and structure of a new compound and the combination of incompatible elements, as for example direct bonds between d- and s,p metals.

Compounds ECp* (E = group 13 metal) are used in organometallic chemistry of transition metals as "building blocks" owing to their capacity to substitute carbonyl ligands and to coordinate directly to a transition metal atom.[1,2] This enables the design of small carbonyl cluster compounds containing direct bonds between transition and non-transition metals.

Recently, we reported the synthesis and structural characterization of a series of mixed-metal rhodium and ruthenium carbonyl cluster complexes containing GaCp* fragments in the coordination environment.[3–5] Extension of these studies to InCp* complexes is directed not only to the creation of novel compounds, but to understand regular trends for the interaction of low nuclear carbonyl cluster compounds with ECp* complexes as well. This understanding is necessary to know how to create the mixed-metal carbonyl cluster compounds with a predetermined, specified relation of transition metal to group 13 metal.

[a] Department of Chemistry, St. Petersburg State University, Universitetskii pr. 26, 198504 St. Petersburg, Russia
Fax: +7-812-428-6939
E-mail: bird231102@mail.ru
[b] Anorganisch-Chemisches Institut, Ruprecht-Karls-Universität Heidelberg,
Im Neuenheimer Feld 270, 69120 Heidelberg, Germany

## Results and Discussion

Reactivity of InCp* towards transition metals has been studied and various mixed-metal complexes with InCp* as a ligand were synthesized.[6–11]

We found that the reaction of the labile $[Rh_6(CO)_{15}(NCMe)]$ cluster with a slight excess of InCp* in dry toluene results in the formation of monosubstituted $[Rh_6(\mu_3\text{-}CO)_3(\mu_3\text{-}InCp^*)(CO)_{12}]$ (**1**) and disubstituted $[Rh_6(\mu_3\text{-}CO)_2(\mu_3\text{-}InCp^*)_2(CO)_{12}]$ (**2**) cluster complexes. This is similar to the analogous reaction of the starting cluster with GaCp*.[3,4] The very curious fact is that treatment of the parent $Rh_6(CO)_{16}$ cluster with any amount of InCp* gives no substituted derivatives, which is in contrast to the behaviour of GaCp*. This fact demonstrates the lower coordination ability of $In^I$ derivatives relative to $Ga^I$ organyls.

Clusters **1** and **2** are air-sensitive and are destroyed on silica gel. Single crystals of **1** were obtained and its structure was determined by X-ray analysis. Compound **1** crystallizes

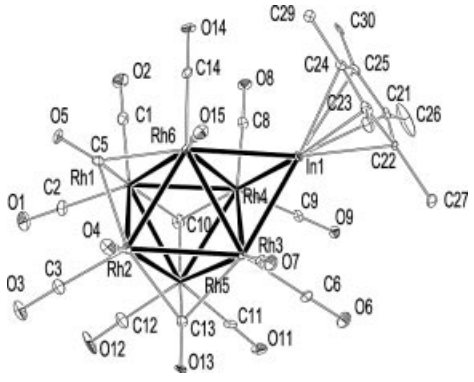


Figure 1. ORTEP view of $Rh_6(CO)_{15}(InCp^*)$ (**1**).

 © 2007 Wiley-VCH Verlag GmbH & Co. KGaA, Weinheim 

Table 1. Selected structural parameters for **1**.

| | | | | | |
|---|---|---|---|---|---|
| | | *d*(Rh–Rh), In-capped triangle [Å] | | | |
| Rh3–Rh6 | 2.8467(9) | Rh3–Rh4 | 2.8549(9) | Rh4–Rh6 | 2.8648(9) |
| | | *d*(Rh–Rh), triangles remote to In [Å] | | | |
| Rh1–Rh4 | 2.7372(10) | Rh1–Rh5 | 2.7530(9) | Rh4–Rh5 | 2.7494(9) |
| Rh1–Rh6 | 2.7464(9) | Rh1–Rh2 | 2.7532(10) | Rh2–Rh6 | 2.7373(9) |
| Rh2–Rh5 | 2.7457(9) | Rh3–Rh5 | 2.7361(9) | Rh2–Rh3 | 2.7583(10) |
| | | *d*(In–Rh) [Å] | | | |
| In1–Rh6 | 2.7072(10) | In1–Rh4 | 2.7075(9) | In1–Rh3 | 2.7196(9) |
| | | *d*(In–C) [Å] | | | |
| In1–C22 | 2.346(15) | In1–C21 | 2.442(8) | In1–C24 | 2.532(12) |
| In1–C23 | 2.461(7) | In1–C25 | 2.504(16) | | |
| | | *d*($\mu_3$-CO–Rh) [Å] | | | |
| Rh6–C5 | 2.136(8) | Rh1–C5 | 2.187(8) | Rh2–C5 | 2.217(8) |
| Rh4–C10 | 2.134(8) | Rh5–C10 | 2.178(8) | Rh1–C10 | 2.197(8) |
| Rh3–C13 | 2.146(8) | Rh2–C13 | 2.186(8) | Rh5–C13 | 2.220(7) |
| ($Cp^*_{centroid}$–In) distance [Å]: 2.153 | | (In–$Rh_{triangle}$) distance [Å]: 2.153 | | ($Cp^*_{centroid}$–In–$Rh_{triangle}$) angles [°]: 170.27 | |

together with one molecule of diethyl ether in the monoclinic crystal system and with the space group $P2_1/n$. An ORTEP view of **1** is shown in Figure 1, selected structural parameters are given in Table 1.

The cluster of **1**, provided that InCp* is a two-electron donor, has 7 skeletal electron pairs that fit the *closo* octahedral rhodium cluster skeleton that is surrounded by 16 ligands as in the parent $Rh_6(CO)_{16}$ cluster. The molecular structure of **1** demonstrates the substitution of one $\mu_3$-CO in the $Rh_6(CO)_{16}$ molecule for an InCp* fragment. As a result, the coordination environment of **1** consists of 12 terminal CO, 3 face-bridging CO and an InCp* fragment, which is coordinated to the metal core in a $\mu_3$ mode.

The InCp* ligand in **1** occupies a nearly symmetrical position over a rhodium triangle. The In–Rh distances fall in the range from 2.7072(10) to 2.7196(9) Å. This fits well with the result found in the only known cluster compound with $\mu_3$-InCp* fragments in the ligand sphere, $[Pd_3(PPh_3)_3(\mu_2\text{-InCp*})(\mu_3\text{-InCp*})_2]$.[10]

The $Cp^*_{centroid}$–In–$Rh_{triangle}$ vector in **1** deviates from linearity (170.27°). This distortion is reflected in the InCp* ligand itself, which is coordinated in a pseudo $\eta^3$ manner [In–$C_{Cp^*}$ contacts, 2.532(12), 2.346(15) Å]. Because there is some rotational disorder in the Cp* ring, which was treated as split positions of the carbon atoms in a 0.67:0.33 ratio, the results must not be overinterpreted. A similar situation was found before in the solid state for the $Rh_6(CO)_{16-x}(\mu_3\text{-GaCp*})_x$ clusters.[3,4] This outward move from the ideal symmetrical position can be formally described as a $\eta^5 \rightarrow \eta^3$ haptotropic shift in the $C_5$ rings of the ECp* fragment, but from our point of view, this phenomenon is essentially caused by steric distortions because of molecule packing in the crystal cell.

The insertion of InCp* in the coordination environment of the carbonyl cluster results in substantial distortions of the parent rhodium octahedron. These distortions are located in the vicinity of the substitution site. Thus, the mean Rh–Rh distance value in the rhodium triangle connected to In in **1** is 2.856(9) Å, whereas the mean Rh–Rh contact for the other metals in the cluster core is 2.746(8) Å (Table 1). Elongation of the Rh–Rh bonds of the indium-capped rhodium triangle looks very similar to the structural effect of weak π-acceptors, which was mentioned earlier for the terminally substituted $Rh_6(CO)_{16}$ derivatives.[12] We found the same effect for the $Rh_6(CO)_{16-x}(\mu_3\text{-GaCp*})_x$ and the $Ru_6C(CO)_{14}(GaCp^*)_3$ clusters, too. This phenomenon provides support to describe the InCp* complex as σ-donor and π-acceptor ligand toward transition metals.[13] However, InCp* is a weaker σ-donor than GaCp*, which is reflected in the lower stability of the $Rh_6(CO)_{16-x}(\mu_3\text{-InCp*})_x$ substituted cluster derivatives relative to $Rh_6(CO)_{16-x}(\mu_3\text{-GaCp*})_x$. Quantum chemical calculations on Pt–GaCp* and Pt–InCp* complexes hint to an analogous interpretation.[8]

The bonding of the face-bridging carbonyl ligands in **1** shows distortion from the highly symmetric coordination mode found in the parent $Rh_6(CO)_{16}$ cluster. This was observed earlier in $Rh_6(CO)_{15}(PR_3)$ compounds.[12] The structural effect of InCp* substitution in this case consists in a shift of all three bridging CO ligands from the idealized position over the centre of the rhodium triangles toward the Rh atoms bonded to In. Thus, one can observe a major contraction of the Rh–$\mu_3$-C bonds on the In–Rh–$\mu_3$-C line and light elongation of the Rh–$\mu_3$-C distances on the $\mu_3$-C–Rh–$\mu_3$-C line, with the average value of the six bond lengths being 2.197(17) Å. That is a little bit longer than the average of 2.186 Å in $Rh_6(CO)_{16}$ (see Table 1).

The structure of **1** as determined in the solid state is evidently maintained in solution. The $^1$H NMR spectrum of **1** displays a singlet signal at $\delta$ = 2.31 ppm, which is typical for symmetrical coordination of the Cp* moiety. This resonance is low-field shifted relative to the corresponding signals of terminally bonded InCp* fragments. This deshielding is typical for the bridging InCp* coordination.[6–11]

 © 2007 Wiley-VCH Verlag GmbH & Co. KGaA, Weinheim 

The IR spectrum (in $CH_2Cl_2$) of **1** shows peaks in the carbonyl region at 2092 (w), 2075 (sh), 2055 (s) and 2012 (sh) $cm^{-1}$, which correspond to the terminal CO groups, and the middle broad peaks at 1789 and 1778 $cm^{-1}$, which correspond to the bridging carbonyl ligands. The relative positions and intensities of the peaks in the IR spectrum of **1** agree with the spectroscopic results obtained for the $Rh_6(CO)_{15}(\mu_3$-GaCp*) cluster.[3]

We have not yet obtained crystals of **2** that are suitable for X-ray analysis, but its structure was characterized on the basis of spectroscopic data. The FD mass spectrum of **2** displays the signal of the $Rh_6(CO)_{14}(InCp^*)_2$ molecular ion. The observed isotopic distribution pattern fits completely to the calculated one.

The IR spectrum of **2** in the CO region ($CH_2Cl_2$ solution) consists of peaks at 2083 (m), 2049 (s), 2029 (m) and 2010 (w) $cm^{-1}$, which correspond to the terminal CO groups, and the middle broad peak at 1777 $cm^{-1}$, which correspond to the bridging carbonyl ligands. The relative positions and intensities of the signals in the IR spectrum of **2** agree with the spectroscopic results obtained for the $Rh_6(CO)_{14}(\mu_3$-GaCp*)$_2$ cluster, which consists of peaks at 2088 (m), 2052 (s), 2032 (m), 2008 (w) and 1774 (m br.) $cm^{-1}$ ($CHCl_3$ solution). This corroborates that these two cluster compounds comprise identical CO environments. A room temperature $^1H$ NMR spectrum of **2** shows only one signal, a singlet for the methyl groups at $\delta = 2.29$ ppm. This is 0.02 ppm shifted upfield relative to the spectrum of **1**; likewise, this was found for the pair of $Rh_6(CO)_{16-x}$-$(GaCp^*)_x$, $x$ = 1–2 clusters. These spectroscopic data clearly point to substitution of two bridging CO groups in the $Rh_6(CO)_{16}$ cluster environment. Thus, the structure of **2** can be described as a $Rh_6$ octahedron surrounded by 2 face-bridging InCp* fragments, 2 face-bridging CO ligands and 12 terminal carbonyl groups.

## Conclusions

InCp*, similar to GaCp*, is capable of occupying the $\mu_3$-bridging positions of a transition metal core in carbonyl clusters. This results in the formation of cluster compounds with direct bonds between the transition metal and the In atom. The results described above will be used to create mixed-metal cluster compounds with direct bonds between transition and group 13 metals.

## Experimental Section

**General Comments:** All operations were carried out under an atmosphere of dry argon with the use of standard Schlenk techniques. All solvents were distilled under an inert atmosphere over appropriate drying agents prior to use. The starting $Rh_6(CO)_{15}(NCMe)$[14] cluster and the InCp*[15] complex were synthesized according to literature procedures. The purity control of InCp* was carried out by $^1H$ NMR spectroscopy. Infrared spectra were recorded with a Perkin–Elmer 16PC FTIR spectrometer. $^1H$ NMR spectra were measured with a Bruker ARX200 instrument. The chemical shifts were referenced to residual solvent resonances. Microanalysis was carried out in the Microanalytical Laboratory, University of Heidelberg. FAB and FD mass spectra were obtained with a JEOL JMS-700 instrument, Institute of Organic Chemistry, University of Heidelberg.

**Synthesis of 1 and 2:** The chromatographically pure $Rh_6(CO)_{15}$-(NCMe) cluster (68 mg, 0.063 mmol) was dissolved in dry toluene (20 mL), and solid InCp* (30 mg, 0.120 mmol) was added under high stirring. The reaction mixture was kept at room temp. under an atmosphere of argon overnight, wrapped in aluminium foil for light protection. The solvent was then removed in vacuo leaving some brown material. The residue was washed with *n*-hexane (5 mL) and dried in vacuo again. The reaction mixture was extracted with $CH_2Cl_2$ (2 × 5 mL) to yield a red–brown solution with a brown oily precipitate. The solution was diluted with *n*-hexane (5 mL) and filtered through a glass filter giving a dark maroon transparent solution. The solvents were removed in vacuo leaving a dry crystalline material. It was extracted with pentane (2 × 10 mL) by using an ultrasonic bath (2 min) and then passed through a cellulose column (3 × 2 cm) to give a transparent red–brown solution. Removal of the solvent gave brown crystals of $Rh_6(CO)_{15}(InCp^*)$ (**1**); 19 mg were isolated. The residue of the pentane extraction was dissolved in $CH_2Cl_2$ (3 mL), diluted with pentane (5 mL) and passed through a cellulose column giving a transparent brown solution. Removal of the solvents gave a brown crystalline precipitate of $Rh_6(CO)_{14}(InCp^*)_2$ (**2**), 23 mg.

**1:** $^1H$ NMR (200 MHz, $CDCl_3$, ambient temperature): $\delta = 2.31$ (s, $CH_3$). IR ($CH_2Cl_2$, $\nu_{CO}$): $\tilde{\nu} = 2092$ (10), 2075 (sh), 2055 (100), 2012 (sh), 1789 (19), 1778 (21) $cm^{-1}$. IR (n-hexane, $\nu_{CO}$): $\tilde{\nu} = 2098$ (16), 2075 (33), 2064 (100), 2045 (45), 2029 (7), 2010 (6), 1820 (18), 1804 (43) $cm^{-1}$. MS (FD+): $m/z$ = 1092 $[M - 7CO]^+$ $C_{18}H_{15}InO_8Rh_6$. MS (FAB+): $m/z$ = 1148 $[M - 5CO]^+$ $C_{20}H_{15}In_1O_{10}Rh_6$, 1064 $[M - 8CO]^+$ $C_{17}H_{15}InO_7Rh_6$, 1008 $[M - 10CO]^+$ $C_{15}H_{15}InO_5Rh_6$, 952 $[M - 12CO]^+$ $C_{13}H_{15}InO_3Rh_6$, 924 $[M - 13CO]^+$ $C_{12}H_{15}InO_2Rh_6$. $C_{25}H_{15}InO_{15}Rh_6$ (1287.63): calcd. C 23.32, H 1.17; found C 23.82, H 1.88. Single crystals of **1** suitable for X-ray studies were grown from saturated pentane solution under an argon atmosphere at –25 °C.

**2:** $^1H$ NMR (200 MHz, $CDCl_3$, ambient temperature): $\delta = 2.29$ (s, $CH_3$). IR ($CH_2Cl_2$, $\nu_{CO}$): $\tilde{\nu} = 2083$ (17), 2049 (100), 2029 (22), 2010 (9), 1777 (12) $cm^{-1}$. MS (FD+): $m/z$ = 1509 $[M]^+$ $C_{34}H_{30}In_2O_{14}Rh_6$.

**X-ray Crystal Structure Determination:** Intensity data were collected at 100 K with a Bruker AXS Smart CCD diffractometer (Mo-$K_\alpha$ radiation, $\lambda = 0.71073$ Å) and corrected for absorption and other effects. The structure was solved by direct methods and refined by full-matrix least-squares based on $F^2$. All non-hydrogen atoms were given anisotropic displacement parameters. Hydrogen atoms were inserted in calculated positions. Calculations were performed by using the SHELXTL package.[16] $C_{29}H_{15}InO_{16}Rh_6$ (1361.8 $g\,mol^{-1}$), monoclinic, space group $P2_1/n$, $a$ = 12.146(2) Å, $b$ = 22.427(4) Å, $c$ = 14.402(2), $\beta$ = 100.081(3)°, $V$ = 3862(1) Å$^3$, $Z$ = 4, $\phi_{calcd.}$ = 2.342 $g\,cm^{-3}$, $\mu$ = 3.152 $mm^{-1}$, $F(000)$ = 2584, crystal dimensions 0.08 × 0.06 × 0.06 mm$^3$, $2\theta$ range for data collection 2–56°, absorption corrections: ellipsoidal, min/max transmission: 0.714/0.808, 39084 collected reflections, 9620 unique, 4940 observed [$I > 2\sigma(I)$], 508 parameters, GOOF 0.793, weighting scheme $w = 1/[\sigma^2(F_o^2) + (0.0155P)^2]$ where $P = (F_o^2 + 2F_c^2)/3$, $R_1$ = 0.044, $wR_2$ = 0.066 [$I > 2\sigma(I)$], $R_1$ = 0.114, $wR_2$ = 0.076 (all data, 0.129 for unit weights), residual electron density 1.42 e Å$^{-3}$.

CCDC-634755 contains the supplementary crystallographic data for this paper. This data can be obtained free of charge from the Cambridge Crystallographic Data Centre via www.ccdc.cam.ac.uk/data_request/cif.

 © 2007 Wiley-VCH Verlag GmbH & Co. KGaA, Weinheim 

## Acknowledgments

We are grateful to the Deutsche Forschungsgemeinschaft and to the Alexander von Humboldt Foundation (for E. V. G.) for financial support. Special thanks to Marcus Richter for the X-ray measurements.

[1] G. Linti, H. Schnöckel, *Coord. Chem. Rev.* **2000**, *206–207*, 285–319.
[2] C. Gemel, T. Steinke, M. Cokoja, A. Kempter, R. A. Fischer, *Eur. J. Inorg. Chem.* **2004**, 4161–4176.
[3] E. V. Grachova, P. Jutzi, B. Neumann, L. O. Schebaum, H.-G. Stammler, S. P. Tunik, *J. Chem. Soc. Dalton Trans.* **2002**, 302–304.
[4] E. V. Grachova, P. Jutzi, B. Neumann, H.-G. Stammler, *Dalton Trans.* **2005**, 3614–3616.
[5] E. V. Grachova, G. Linti, B. Neumann, H.-G. Stammler, S. P. Tunik, H. Wadepohl, *Eur. J. Inorg. Chem.* **2007**, 140–146.
[6] P. Jutzi, B. Neumann, G. Reumann, L. O. Schebaum, H.-G. Stammler, *Organometallics* **1999**, *18*, 2550–2552.
[7] T. Steinke, C. Gemel, M. Winter, R. A. Fischer, *Angew. Chem. Int. Ed.* **2002**, *41*, 4761–4763.
[8] D. Weiss, M. Winter, K. Merz, A. Knüfer, R. A. Fischer, N. Fröhlich, G. Frenking, *Polyhedron* **2002**, *21*, 535–542.
[9] M. Cokoja, C. Gemel, T. Steinke, F. Schröder, R. A. Fischer, *Dalton Trans.* **2005**, 44–54.
[10] T. Steinke, C. Gemel, M. Winter, R. A. Fischer, *Chem. Eur. J.* **2005**, *11*, 1636–1646.
[11] T. Steinke, C. Gemel, M. Cokoja, M. Winter, R. A. Fischer, *Dalton Trans.* **2005**, 55–62.
[12] D. H. Farrar, E. V. Grachova, A. Lough, C. Patirana, A. J. Poe, S. P. Tunik, *J. Chem. Soc. Dalton Trans.* **2001**, 2015–2019.
[13] G. Frenking, N. Fröhlich, *Chem. Rev.* **2000**, *100*, 717–774.
[14] S. P. Tunik, A. V. Vlasov, V. V. Krivykh, *Inorg. Synth.* **1997**, *31*, 239–244.
[15] O. T. Beachley Jr, R. Blom, M. R. Churchill, K. Faegri Jr, J. C. Fettinger, J. C. Pazik, L. Victoriano, *Organometallics* **1989**, *8*, 346–356.
[16] G. M. Sheldrick, *SHELXTL: Program for Crystal Structure Refinement, version 3.1*, **1997**.

Received: February 12, 2007
Published Online: June 14, 2007

 © 2007 Wiley-VCH Verlag GmbH & Co. KGaA, Weinheim 

DOI: 10.1002/ejic.200700336

# Repeated Dihydrogen Elimination from Boranes and Gallanes Stabilized by Guanidine-Type Bases: A Quantum Chemical Study Motivated by Recent Experimental Results

**Oxana Ciobanu[a] and Hans-Jörg Himmel*[a]**

**Keywords:** Hydrides / Group 13 elements / Quantum chemical calculations / Hydrogen storage

Monomeric boranes and gallanes stabilized by guanidine derivatives undergo in certain cases $H_2$ elimination reactions leading in a first step to dinuclear E(III) hydrides (E = B or Ga) and in the second step upon elimination of further $H_2$ to dinuclear compounds with the elements in the formal oxidation state +II featuring a direct E–E bond. The thermodynamics for such $H_2$ elimination reactions were calculated applying several methods and basis sets. In addition the calculations provide information about possible mechanisms. Thus the calculations suggest the first step to be an intramolecular $H_2$ elimination followed by a cycloaddition reaction. The second $H_2$ elimination, in which E–E and H–H bonds are formed at the expense of E–H bonds, is almost energy neutral, as anticipated from the small differences in electronegativity between E and H. The reaction barriers are important indicators to answer the question if $H_2$ elimination can be made reversible. Reversible $H_2$ elimination and addition would make this class of compounds in principle interesting for hydrogen storage applications, although obviously the weight percentage of stored dihydrogen is in the special systems presented herein not sufficient for mobile applications. The compounds can also be applied for dehydrocoupling and transfer hydrogenation to deliver a stoichiometric amount of $H_2$ to olefins. Finally, the possibility of elimination of a third $H_2$ leading to a dinuclear E(I) species with an E–E double bond is discussed.
(© Wiley-VCH Verlag GmbH & Co. KGaA, 69451 Weinheim, Germany, 2007)

## Introduction

Guanidine derivatives have been widely used as ligands in main group and transition metal complexes.[1] Part of the interest in these compounds stems from their potential applications in catalytic reactions. They either bind as neutral ligands, or after $H^+$ abstraction as negatively charged guanidinate ligands. Two binding modes have been observed for the guanidinate ligand. Thus it can act as a bisdentate chelating ligand to one metal atom or as a bridging ligand to two metal atoms. $Cl_2Al\{(N\mathit{i}Pr)_2CN(CH_3)_2\}$ is an example in which the chelating binding mode is realized.[2] By the use of the guanidinate hpp$^-$ (hppH = 1,3,4,6,7,8-hexahydro-2*H*-pyrimido[1,2-*a*]pyrimidine) the bridging mode can be realized, the dinuclear compound $[(CH_3)_2Al(hpp)]_2$ being one authenticated representative.[2] The hpp ligand has also been proven to be efficient in bringing two transition metals close to another in dinuclear complexes so that they engage in direct and sometimes multiple metal–metal bonding. Examples include the complexes $Nb_2(hpp)_4$ [3] and $M_2(hpp)_4Cl_2$ (e.g. M = Ru,[4] W, Os and Pt [5]).

Recently we have studied the reaction of $H_3Ga{\cdot}NMe_3$ with hppH[6] leading directly to the dinuclear hydride $[H_2Ga(hpp)]_2$ (see Scheme 1). While we were so far not able to grow crystals of $[H_2Ga(hpp)]_2$ with a quality high enough for X-ray diffraction measurements, we obtained a crystal structure for its derivative $[HClGa(hpp)]_2$. The adduct $H_3Ga{\cdot}$hppH, which is likely to be the first intermediate in this reaction, is unstable under the applied reaction conditions, readily eliminates dihydrogen and dimerises. Our experiments show that $[H_2Ga(hpp)]_2$ is also stable only below room temperature and easily loses another molecule of $H_2$ at slightly elevated temperatures to give presumably the compound $[HGa(hpp)]_2$, featuring a Ga–Ga single bond and a *cis*-bent arrangement of the H–Ga–Ga–H fragment (see Scheme 2). The two Ga atoms are thus reduced from the formal oxidation state +III to the formal oxidation state +II. Thermodynamic considerations suggest that the combined Ga–Ga and Ga–H bonds established in the product are almost similar in strength than the combined Ga–H bonds of the reactant, in line with the small difference in electronegativity between Ga and H (1.82 and 2.20 on the Allred–Rochow scale, respectively). This dihydrogen elimination and Ga–Ga bond formation has stirred our interest because we previously have studied in matrix isolation experiments the uptake of dihydrogen by the matrix isolated $Ga_2$ dimer leading to Ga–Ga bond breakage and formation of the hydride $Ga(\mu\text{-}H)_2Ga$ (see Scheme 3).[7] The barrier for this reaction, as estimated experimentally from isotopic (H/D) measurements, amounts to not more than

[a] Anorganisch-Chemisches Institut, Ruprecht-Karls-Universität Heidelberg,
Im Neuenheimer Feld 270, 69120 Heidelberg, Germany
E-mail: hans-jorg.himmel@aci.uni-heidelberg.de

 © 2007 Wiley-VCH Verlag GmbH & Co. KGaA, Weinheim 

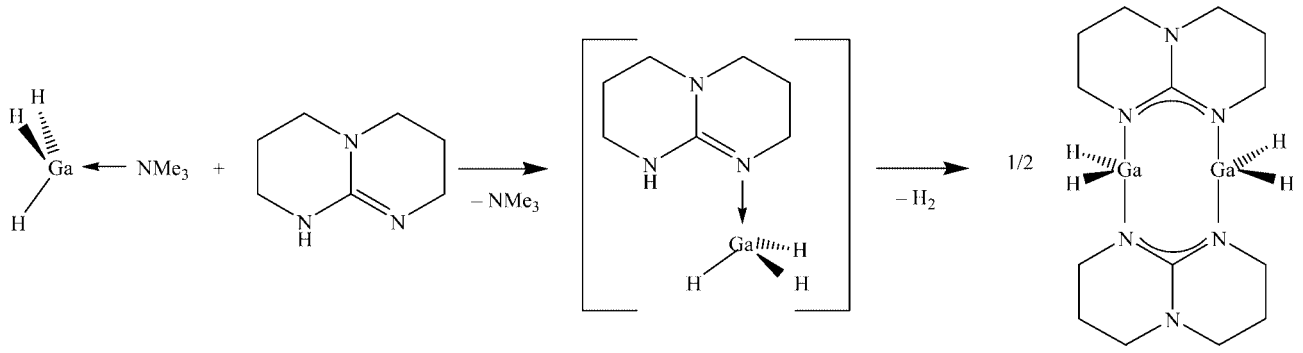

Scheme 1.

40 kJ mol$^{-1}$. The reaction of $Ga_2$ with $H_2$ to give $Ga_2H_2$ was calculated to be exothermic (–96 kJ mol$^{-1}$).[8] Thus, here again, like in the case of $[H_2Ga(hpp)]_2$, the combined Ga–Ga and H–H bonds, being now present in the reactants, are only slightly disfavoured over the two Ga–H–Ga three-center-two-electron bonds established in the product. If the barrier for $H_2$ addition in $[HGa(hpp)]_2$ is comparable with that found for the $Ga_2$ dimer, this class of dinuclear hydrides of group 13 elements is interesting for facile reversible $H_2$ activation. The compounds can certainly be applied for dehydrocoupling reactions and function as a transfer hydrogenation to deliver a stoichiometric amount of $H_2$ to olefins as was recently shown for $H_3B{\cdot}NHMe_2$.[9] Therefore it is highly desirable to get insight into the reaction mechanisms with the aid of quantum chemical calculations. In the following we report our work for B and Ga compounds.

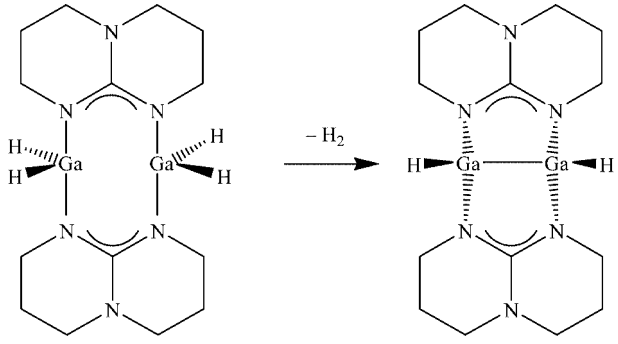

Scheme 2.

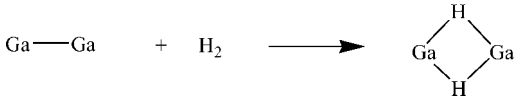

Scheme 3.

## Results and Discussion

The presentation of the results and their discussion are divided into four sections. The first is concerned with the starting reagent, the adducts of guanidine and some of its derivatives to $EH_3$ (E = B or Ga), and the thermodynamics of their formation. In the second section intramolecular $H_2$ elimination facilitated by intramolecular H···H contacts in the adducts and subsequent dimerization to give dinuclear species is analysed. We will present a detailed mechanism for this important second step on the basis of our quantum chemical calculations. The third section deals with additional $H_2$ elimination to give the dinuclear group 13 element compounds featuring four-coordinate group 13 elements in the formal oxidation state +II and a direct E–E bond. Finally, the fourth section briefly discusses the possibility of further $H_2$ eliminination leading to a compound featuring two directly connected tri-coordinated E atoms in the formal oxidation state +I. Table 1 includes the reaction energies, with and without ZPE (zero-point vibrational energy) corrections, and the changes in the standard Gibbs energy, $\Delta G^0$, for salient reactions discussed herein.

### Step 1. Formation and Structural Characterization of the Adducts of $EH_3$ to Guanidine-Type Bases

Recent experimental work by us has shown that these adducts are either the end-products or reactive intermediates formed in the course of the reaction between $H_3E{\cdot}NMe_3$ and guanidine-type bases (see Scheme 4), depending on the possibilities for intramolecular HH bonding and subsequent $H_2$ elimination.[10] The adducts could generally also be synthesized from $LiGaH_4$ and guanidine·HCl. However, herein only the base-exchange route is discussed which is more straightforward to calculate and was used in most of the experimental work carried out in our group. Table 1 compares the changes in energy and Gibbs energy accompanied by reaction between the model compounds $H_3E{\cdot}NH_3$ (E = B, Ga) and guanidine or its derivatives 1,1,3,3-tetramethylguanidine and hppH. To test the accuracy of our calculational method, we have compared the crystallographically obtained dimensions of the adduct $H_3Ga{\cdot}N(H)C(NMe_2)_2$ [10] with those calculated (see Table 2 and Figure 1). It can be seen that the general level of agreement is pleasing. According to our calculations, the B–N distances in $H_3B{\cdot}NH_3$, $H_3B{\cdot}N(H)C(NH_2)_2$, $H_3B{\cdot}N(H)$-$C(NMe_2)_2$ and $H_3B{\cdot}$hppH measure 165.4, 158.6, 159.2, and 159.0 pm. The Ga–N distances in the corresponding Ga hydrides were calculated to be 218.0, 207.8, 209.1 and 206.8 pm, respectively. The experimentally determined Ga–N bond length for $H_3Ga{\cdot}N(H)C(NH_2)_2$ measures 198.81(19) pm. For comparison, Ga–N distances of

 © 2007 Wiley-VCH Verlag GmbH & Co. KGaA, Weinheim 

206.3(4), 208.1(4), 207.9(3), and 204.24(18) pm were measured in $H_3Ga{\cdot}$quinuclidine,[11] $H_3Ga{\cdot}NMe_3$,[12] $H_3Ga{\cdot}NHMe_2$,[13] and $H_3Ga{\cdot}NH_2Me$.[14] Thus the guanidine-type bases lead to relatively short E–N bonds, in agreement to our recent experimental X-ray diffraction results for $H_3Ga{\cdot}N(H)C(NMe_2)_2$ and in line with the stronger basicity of guanidines in comparison to amines.[10] An important structural detail concerning the reactivity of adducts such as $H_3E{\cdot}N(H)C(NH_2)_2$ and $H_3E{\cdot}$hppH is the short H···H contacts established between one or two of the negatively polarised H atoms attached to E and a positively polarised H atom attached to one of the amido groups. Thus in $H_3B{\cdot}N(H)C(NH_2)_2$ and $H_3B{\cdot}$hppH, H···H separations of 175.5 and 162.5 pm are adopted. In the corresponding Ga species, the H···H separations measure 177.1 and 173.7 pm, respectively. These contacts are significantly shorter than the range of 200–240 pm normally prescribed for unconventional dihydrogen bonding of this sort.[15] For comparison, in $[H_2GaNH_2]_3$ [16] and $[H_3AlN(H)Me_2]_2$ [13] intermolecular H···H contacts of 197(2) and 192.5(1.9) pm, respectively, were measured. Particular attention was given to the intermolecular H···H contacts in crystalline $H_3B{\cdot}NH_3$, which were determined in neutron diffraction experiments to be 202 pm.[17] Work on these H···H contacts has been spurred by the search for hydrogen storage materials.[18] The contacts are the reason for the generally lower thermal stability of these compounds in the solid state in comparison to the solution. In adducts such as $H_3E{\cdot}N(H)C(NMe_2)_2$, there is no possibility for intramolecular HH bonding. The analysis of the crystal structure shows, however, that intermolecular HH contacts are established [with shortest H···H contacts of 210(5) pm].[10] Due to the absence of intramolecular H···H interactions, this experimentally verified molecule can be used as reference system to roughly estimate the strength of the H···H contacts in other adducts. As expected, formation of 1,1,3,3-tetramethylguanidine borane and gallane is slightly exothermic [energies of –19 and –18 kJ mol$^{-1}$, respectively, were calculated (see Table 1)]. Formation of $H_3E{\cdot}N(H)C(NH_2)_2$ is significantly more exothermic (reaction energies of –35 and –30 kJ mol$^{-1}$, respectively). The difference in the energy change for reactions to give the adducts of guanidine and 1,1,3,3-tetramethylguanidine should at least partially be caused by the HH bonds which can only be established in the guanidine complex. Thus, as a first estimate, the H···H contacts in $H_3B{\cdot}N(H)C(NH_2)_2$ should be ca. 12–16 kJ mol$^{-1}$ strong. For comparison, the intermolecular H···H bonds in crystalline $H_3B{\cdot}NH_3$ (with a larger bond length of 202 pm [17]) were calculated to be in average ca. 13 kJ mol$^{-1}$ strong.[19] These results demonstrate the importance of intramolecular H···H interactions in the adducts.

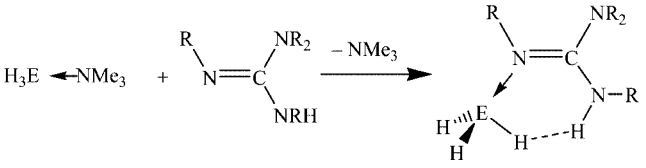


Scheme 4.

Table 1. Energy changes (in kJ mol$^{-1}$) without ($\Delta E$) and with ($\Delta E_{ZPE}$) zero-point vibrational energy corrections, and changes in the standard Gibbs energy $\Delta G^0$ (also in kJ mol$^{-1}$) as calculated for important reactions discussed in this work (fmr = four-membered ring).

| Reaction | $\Delta E$ | $\Delta E_{ZPE}$ | $\Delta G^0$ |
|---|---|---|---|
| $HNC(NH_2)_2 + H_3B{\cdot}NH_3 \rightarrow H_3B{\cdot}N(H)C(NH_2)_2 + NH_3$ | –35 | –42 | –38 |
| $HNC(NMe_2)_2 + H_3B{\cdot}NH_3 \rightarrow H_3B{\cdot}N(H)C(NMe_2)_2 + NH_3$ | –19 | –25 | –19 |
| hppH + $H_3B{\cdot}NH_3 \rightarrow H_3B{\cdot}$hppH + $NH_3$ | –48 | –55 | –47 |
| $HNC(NH_2)_2 + H_3Ga{\cdot}NH_3 \rightarrow H_3Ga{\cdot}N(H)C(NH_2)_2 + NH_3$ | –30 | –35 | –29 |
| $HNC(NMe_2)_2 + H_3Ga{\cdot}NH_3 \rightarrow H_3Ga{\cdot}N(H)C(NMe_2)_2 + NH_3$ | –18 | –21 | –14 |
| hppH + $H_3Ga{\cdot}NH_3 \rightarrow H_3Ga{\cdot}$hppH + $NH_3$ | –42 | –46 | –39 |
| $H_3B{\cdot}N(H)C(NH_2)_2 \rightarrow H_2B(\mu\text{-}NH)_2CNH_2$ (fmr) + $H_2$ | +62 | +34 | +8 |
| $H_3B{\cdot}N(H)C(NH_2)_2 \rightarrow H_2B{=}N(H)(CNH_2)NH$ (diene) + $H_2$ | +63 | +36 | +9 |
| $H_3B{\cdot}$hppH $\rightarrow H_2B$(hpp) (fmr) + $H_2$ | +70 | +46 | +14 |
| $H_3B{\cdot}$hppH $\rightarrow H_2B$(hpp) (diene) + $H_2$ | +74 | +46 | +17 |
| $H_3Ga{\cdot}N(H)C(NH_2)_2 \rightarrow H_2Ga(\mu\text{-}NH)_2CNH_2$ (fmr) + $H_2$ | +25 | +4 | –5 |
| $H_3Ga{\cdot}$hppH $\rightarrow H_2Ga$(hpp) (fmr) + $H_2$ | +22 | +1 | –25 |
| 2 $H_3BN(H)C(NH_2)_2 \rightarrow \{H_2B[HNC(NH_2)NH]\}_2$ + 2 $H_2$ | –76 | –113 | –113 |
| 2 $H_3B$(hppH) $\rightarrow [H_2B(hpp)]_2$ + 2 $H_2$ | –35 | –72 | –70 |
| 2 $H_3GaN(H)C(NH_2)_2 \rightarrow \{H_2Ga[HNC(NH_2)NH]\}_2$ + 2 $H_2$ | –74 | –110 | –109 |
| 2 $H_3Ga$(hppH) $\rightarrow [H_2Ga(hpp)]_2$ + 2 $H_2$ | –38 | –75 | –65 |
| $\{H_2B[HNC(NH_2)NH]\}_2 \rightarrow \{HB[HNC(NH_2)NH]\}_2$ (planar) + $H_2$ | +171 | +148 | +119 |
| $\{H_2B[HNC(NH_2)NH]\}_2 \rightarrow \{HB[HNC(NH_2)NH]\}_2$ + $H_2$ | +74 | +46 | +19 |
| $[H_2B(hpp)]_2 \rightarrow [HB(hpp)]_2$ + $H_2$ | +32 | +1 | –30 |
| $\{H_2Ga[HNC(NH_2)NH]\}_2 \rightarrow \{HGa[HNC(NH_2)NH]\}_2$ + $H_2$ | +7 | –7 | –33 |
| $[H_2Ga(hpp)]_2 \rightarrow [HGa(hpp)]_2$ + $H_2$ | +5 | –18 | –49 |
| $\{HB[HNC(NH_2)NH]\}_2 \rightarrow \{B[HNC(NH_2)NH]\}_2$ + $H_2$ | +254 | +231 | +202 |
| $[HB(hpp)]_2 \rightarrow [B(hpp)]_2$ + $H_2$ | +90 | +68 | +39 |

 © 2007 Wiley-VCH Verlag GmbH & Co. KGaA, Weinheim 

Table 2. Comparison between calculated and observed bond lengths (in pm) for 1,1,3,3-tetramethylguanidine-gallane (see Figure 1 for the atomic numbering).

| Bond length | Exp.[a] | BP/TZVPP | MP2/TZVPP |
|---|---|---|---|
| Ga–N1 | 198.81(19) | 209.1 | 206.1 |
| Ga–H | 161(4) | 159.4 | 157.7 |
| | 149(4) | 158.9 | 156.8 |
| | 157(4) | 159.0 | 157.0 |
| N1–C1 | 131.6(3) | 131.6 | 130.7 |
| N1–H | 78(3) | 101.9 | 101.0 |
| C1–N2,3 | 134.7(3) | 137.0 | 135.5 |
| | 136.0(3) | 138.2 | 136.7 |
| N2,3–C2,5 | 145.5(3) | 145.5 | 144.6 |
| | 145.7(3) | 146.0 | 145.0 |
| | 145.8(3) | 145.9 | 144.9 |
| | 144.8(3) | 146.0 | 145.0 |

[a] From ref.[10]

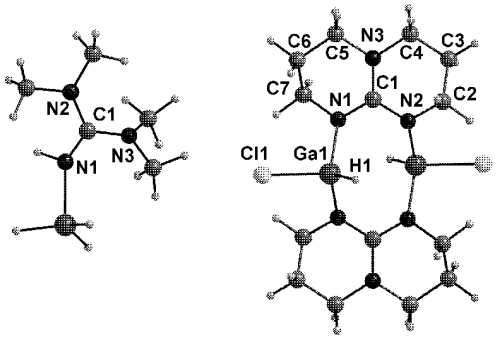


Figure 1. Molecular structures of 1,1,3,3-tetramethylguanidine gallane (left side) and $[HClGa(hpp)]_2$ (right side) as determined by X-ray diffraction.

### Step 2. Intramolecular $H_2$ Elimination Followed by Dimerization to Give Dinuclear Hydrides

The relatively strong intramolecular H···H interactions in the adducts of hppH and $HNC(NH_2)_2$ to $EH_3$ argue for facile $H_2$ elimination, in full agreement to the body of experimental results accumulated for this class of compounds in our laboratory. The final products of these first $H_2$ elimination reactions are dinuclear species featuring an eight-membered ring in which all four E–N bond lengths are almost equally long (156.9–157.2 and 199.1–199.5 pm in $\{H_2E[HNC(NH_2)NH]\}_2$, 157.8 and 200.3 pm in $[H_2E(hppH)]_2$ (E = B and Ga, respectively). They have also in common an approximately tetrahedral coordination of the group 13 element atoms. E.g. in $[H_2Ga(hpp)]_2$, the H–Ga–H, N–Ga–H and N–Ga–N angles are 123.4°, 101.4°/109.5° and 111.0°, respectively. To test the accuracy of the calculations, the calculated structure for the dimer $[HClGa(hpp)]_2$ was compared to the one determined from X-ray diffraction analysis (see Table 3). From Table 3 comparing the bond lengths it can be seen that the general level of agreement is satisfying. In agreement to our experimental findings, the overall reactions were in all cases calculated to be exothermic (see Table 1). E.g. in the case of $\{H_2B[HNC(NH_2)NH]\}_2$, a reaction energy of –76 without and –113 kJ mol$^{-1}$ with ZPE corrections was calculated. $\Delta G^0$ for this reaction amounts to –113 kJ mol$^{-1}$. The experiments indicate that the barrier for this second step is not very high. What can be said about the exact mechanism for this process?

Table 3. Comparison between calculated and observed bond lengths (in pm) for $[HClGa(hpp)]_2$ (see Figure 1 for the atomic numbering).

| Bond length | Exp.[a] | BP/TZVPP | MP2/TZVPP |
|---|---|---|---|
| Ga1–Cl1 | 220.15(15) | 225.0 | 225.2 |
| Ga1–N1 | 194.2(4) | 198.5 | 199.0 |
| Ga1–N4 | 192.8(4) | 198.4 | 198.9 |
| Ga1–H1 | 147(5) | 156.3 | 156.8 |
| N1–C1 | 135.3(6) | 135.0 | 135.4 |
| N1–C7 | 146.8(6) | 146.6 | 146.5 |
| C1–N2 | 134.7(6) | 135.0 | 135.3 |
| C1–N3 | 133.5(6) | 136.8 | 137.6 |
| N2–C2 | 147.8(7) | 146.5 | 146.5 |
| C2–C3 | 151.1(10) | 152.6 | 153.0 |
| C3–C4 | 150.7(8) | 152.4 | 152.7 |
| C4–N3 | 148.3(6) | 146.8 | 146.9 |
| N3–C5 | 147.3(6) | 146.8 | 146.9 |
| C5–C6 | 152.0(7) | 152.3 | 152.7 |
| C6–C7 | 151.2(7) | 152.6 | 153.0 |

[a] From ref.[6] Note that the molecule has a center of inversion.

At least two intermediates have to be considered (see Scheme 5).[20] The first one features a four-membered $EN_2C$ ring and can be described as a guanidinate complex to $EH_2$ in which the guanidinate unit adopts a bidentate chelating coordination mode [e.g. $H_2E(\mu\text{-}NH)_2CNH_2$ for reaction with guanidine]. These intramolecular $H_2$ eliminations represent endothermic processes (see Table 1). However, for the B compounds they are more endothermic than for the Ga homologues. Thus formation of $H_2B(\mu\text{-}NH)_2CNH_2$ is ac-

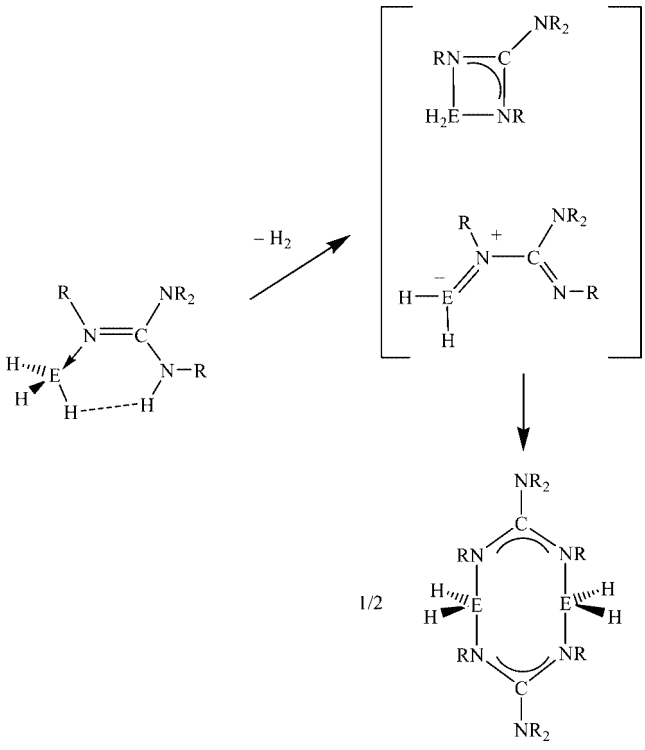


Scheme 5.

 © 2007 Wiley-VCH Verlag GmbH & Co. KGaA, Weinheim 

companied by an energy change of +62 without and +34 kJ mol$^{-1}$ with ZPE corrections. However, with +8 kJ mol$^{-1}$ the $\Delta G^0$ value is very small. In the case of formation of the four-membered ring species $H_2B$(hpp), the energies without and with ZPE are +70 and +46 kJ mol$^{-1}$, and $\Delta G^0$ amounts to not more than +14 kJ mol$^{-1}$. For Ga compounds, formation of the four-membered ring compounds is even associated with a negative $\Delta G^0$ value [–5 kJ mol$^{-1}$ for $H_2Ga(\mu\text{-}NH)_2CNH_2$ and –25 kJ mol$^{-1}$ for $H_2Ga$(hpp)].

For E = B, the four-membered ring is in equilibrium with a diene structure featuring a B=N double bond, e.g. $H_2E{=}N(H)C(NH_2){=}NH$ (E = B or Ga, see reaction Scheme 5). For E = Ga, the diene represents no minimum on the potential energy surface, in line with the lower tendency of Ga to form multiple bonds. The energy of the four-membered ring structure is by not more than 1 kJ mol$^{-1}$ favored over the diene-type intermediate in the case of $H_2B{=}N(H)C(NH_2){=}NH$, and 4 kJ mol$^{-1}$ in the case of $H_2B$(hpp). Figure 2 shows the barrier separating the model diene $H_2B{=}N(H)C(NH_2){=}NH$ from the four-membered ring $H_2B(\mu\text{-}NH)_2CNH_2$. The energy barrier amounts to +56 kJ mol$^{-1}$, and the difference in Gibbs energy between diene and transition state is +57 kJ mol$^{-1}$ under standard conditions. The diene is characterized by B–H and B–N bond lengths of 119.3/120.0 and 141.0 pm; the N–C single bond and the C–N double bond measure 141.8 and 128.0 pm, respectively. The B atom is by 295.9 pm separated from the next N atom. At the transition state, the two shortest B–N distances measure 149.4 and 222.3 pm, and the B–H and B–N bond lengths were calculated to be 119.8/120.3 and 149.4 pm, respectively. With 130.7 and 137.3 pm, the two shortest C–N distances are much closer together. Finally, in the four-membered ring, B–H, B–N, and N–C bond lengths of 121.1, 161.1, and 134.0/133.5 pm are adopted.

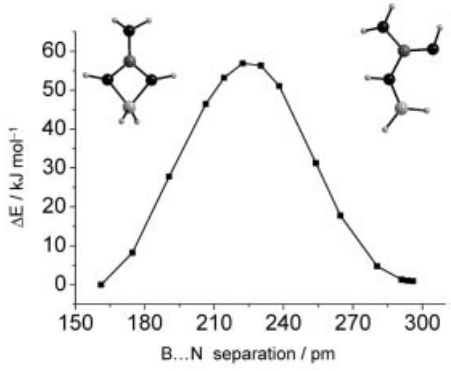


Figure 2. Energy (in kJ mol$^{-1}$) for conversion of the diene structure into the four-membered ring structure relative to that of the diene $H_2BN(H)C(NH_2)NH$ in dependence of the B···N separation.

Figure 3 illustrates the mechanism for intramolecular $H_2$ abstraction starting from the precursor $H_3B{\cdot}N(H){=}C(NH_2)_2$ and leading first to the diene structure. The transition state is reached at an H–H distance between the two eliminated H atoms of 82.0 pm. The B–N distances at this point measure 151.3 and 268.0 pm. The reaction barrier is calculated to be 97 kJ mol$^{-1}$ high. There is an abrupt change in the H–H distance after the transition state has been passed. Abrupt energy changes at the point of formation of a significant H···H interaction are typical for $H_2$ elimination reactions. We observed these abrupt changes also in the case of $H_2$ elimination from the monomeric hydrides $H_2ECl$ (E = Al, Ga or In), which can be generated in matrix isolation experiments from photolytically induced reaction between ECl and $H_2$.[21] The diene afterwards undergoes a [4+4] cycloaddition to give the dinuclear hydride.

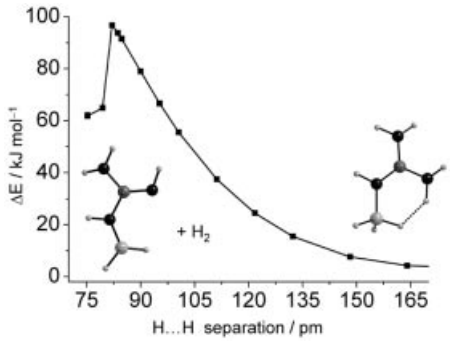


Figure 3. Relative energy (in kJ mol$^{-1}$) for intramolecular $H_2$ elimination from the adduct $H_3B{\cdot}N(H)NC(NH_2)_2$ leading to the diene structure in dependence of the H···H separation.

### Step 3. Further $H_2$ Elimination to Give Dinuclear Compounds with the Group 13 Elements in the Formal Oxidation State +II

The body of experimental results accumulated in our group shows that yet another $H_2$ molecule can be eliminated (see Scheme 6). The products of this $H_2$ elimination, $\{HE[HNC(NH_2)(NH)]\}_2$ and $[HE(hpp)]_2$, are dinuclear compounds with group 13 elements in the formal oxidation state +II and a direct E–E bond. The H–E–E–H fragment adopts a *cis*-bent arrangement. The E–E distances were calculated to be 178.1 (E = B) and 242.1 pm (E = Ga) in $HE[HNC(NH_2)NH]\}_2$. In $[HE(hpp)]_2$, E–E distances of 175.3 (E = B) and 237.6 pm (E = Ga) are adopted.

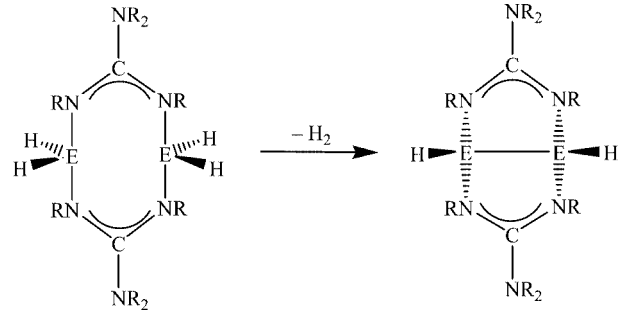


Scheme 6.

 © 2007 Wiley-VCH Verlag GmbH & Co. KGaA, Weinheim 

Thus the E–E distances lie in a region typical for E–E single bonds (e.g. 172 pm ($B_2F_4$),[22] 170.2 pm ($B_2Cl_2$),[23] 168.9 pm ($B_2Br_4$),[24] and 240.6 pm ($Ga_2Cl_4$·2 dioxane),[25] 252.5 pm $Ga_2(tmp)_4$ (tmp = 2,2,6,6-tetramethylpiperidino).[26] For the E–H distances the calculations returned 121.9 and 157.5 pm in the case of $\{HE[HNC(NH_2)NH]\}_2$, and 122.4–122.8 and 158.0 pm for $[HE(hpp)]_2$. Finally, the E–N distances are 158.0–158.2 (E = B) and 202.7 pm (E = Ga) for $\{HE[HNC(NH_2)NH]\}_2$, and 158.2–158.4 (E = B) and 203.4 pm (E = Ga) for $[HE(hpp)]_2$. Thus the E–N distances are in all cases almost identical to those established in the molecules prior to $H_2$ elimination, although there are some major structural changes.

$H_2$ elimination in all cases comes out to be endothermic, but only very weakly. The small reaction energies are in line with the small differences in electronegativity between B, Ga and H (electronegativity values of 2.01, 1.82 and 2.20, respectively, following the Allred-Rochow scale). As a consequence, $\Delta G^0$ is negative for the formation of $\{HGa[HNC(NH_2)(NH)]\}_2$ and $[HE(hpp)]_2$ (E = B or Ga). Thus for $[H_2Ga(hpp)]_2$, BP/TZVPP calculations predict $H_2$ elimination to be accompanied by an energy change of not more than +5 kJ mol$^{-1}$. With –49 kJ mol$^{-1}$, the $\Delta G^0$ value is significantly negative.

Finally, it is worth mentioning that for $\{HB[HNC(NH_2)NH]\}_2$, the calculations found another energy minimum (exhibiting $C_{2h}$ symmetry) on the potential energy surface. This minimum, with an energy exceeding that of the global minimum by almost 100 kJ mol$^{-1}$ (see Table 1), features a planar, eight-membered ring consisting of four N, two B and two C atoms (see Scheme 7). There are 10 π electrons in the ring, a situation comparable to that in the aromatic $[C_8H_8]^{2-}$ dianion. The planarity indeed argues for at least partial delocalization of the π electrons. The distances within the ring vary (from ca. 136/137 pm for the NC bonds to ca. 144 pm for the BN bonds). In ongoing work we seek to stabilize this energetically disfavoured structure by coordination to a metal fragment.

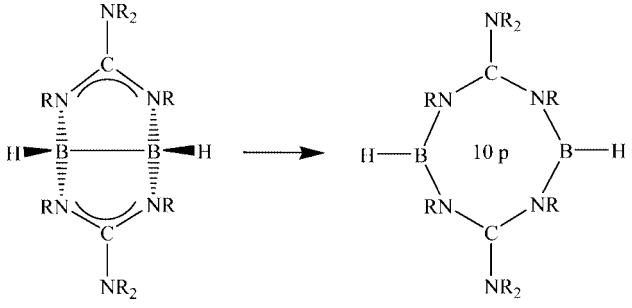


Scheme 7.

### Step 4. Final $H_2$ Elimination to Give Dinuclear E(I) Molecules

Although so far we have observed no signs of further $H_2$ elimination in our experiments, calculations were carried out for E = B to answer the question if these reactions might be possible. It has been shown previously by other groups that tetra(amino)diboranes(4) such as bis(dimethylamino)bis(pyrrolyl)diborane(4) or bis(dimethylamino)bis(indolyl)diborane(4) can be reduced with lithium powder to give the corresponding dilithium tetra(amino)diborates.[27] These diborates feature short B–B bond lengths [e.g. 158.4(4) pm for dilithium bis(dimethylamino)bis(indolyl)diborate] which can be described as double bonds.[28] The $B_2N_4$ moiety is planar, in line with the double bond description (Scheme 8). The B–B distances in $\{B[HNC(NH_2)NH]\}_2$ and $[B(hpp)]_2$ were calculated to be 159.3 and 158.7 pm, respectively and are thus also significantly shorter than those in $\{HB[HNC(NH_2)NH]\}_2$ and $[HB(hpp)]_2$ (see Figure 4). The angle sum at each of the B atoms is 343°, and the B–N distances measure 148.5 pm. With energy changes of +254 and +90 kJ mol$^{-1}$ for formation of $\{B[HNC(NH_2)NH]\}_2$ and $[B(hpp)]_2$, respectively, the reactions are endothermic, and the $\Delta G^0$ values are positive (see Table 1).

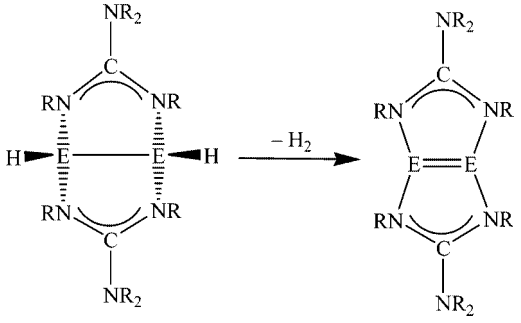


Scheme 8.

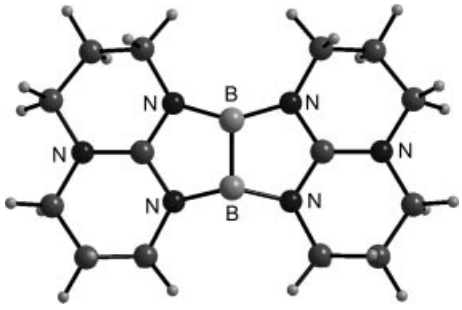


Figure 4. Molecular structure of $[B(hpp)]_2$.

## Conclusions

Quantum chemical calculations were carried out to shed light on the mechanisms of repeated $H_2$ elimination reactions of guanidine-stabilized group 13 element hydrides as recently observed in our laboratory. These repeated $H_2$ eliminations and the possibility of reversibility under mild conditions make this class of compounds attractive for applications in the fields of (i) catalysed dehydrocoupling reactions and transfer hydrogenation for olefins, and (ii) possibly also molecular hydrogen storage materials. The reactions found for this special class of compounds (hydrides

 © 2007 Wiley-VCH Verlag GmbH & Co. KGaA, Weinheim 

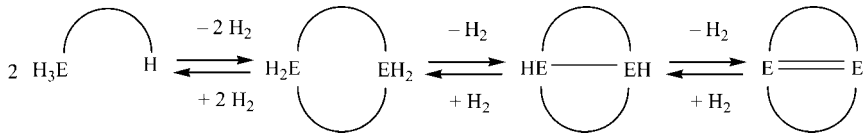


Scheme 9.

stabilized with guanidine-type bases) are examples for more general systems as illustrated in reaction Scheme 9, in the central step of which E–E and H–H bonds are formed at the expense of E–H bonds. If E has an electronegativity close to that of H, the reaction should be thermodynamically favoured. In Figure 5 the reaction sequence starting with $H_3Ga{\cdot}hppH$ is shown.[29] The standard Gibbs energy changes for almost all $H_2$ elimination steps are slightly negative. The bulk of our experimental results accumulated for this class of compounds and to some extent also the quantum chemical calculations presented herein show that the reaction barriers are relatively low ($H_2$ elimination is already observed at temperatures between 25 and 100 °C, depending on the starting adduct).

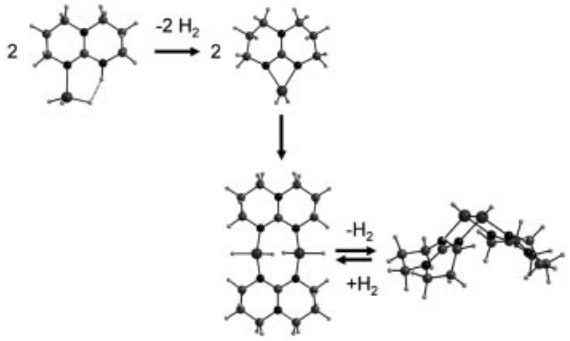


Figure 5. Repeated $H_2$ eliminations starting with the adduct $H_3Ga{\cdot}hppH$.

The calculations provide important details about each of the elimination steps. Relatively strong intramolecular H···H contacts are present in the starting compounds, adducts of the general formula $H_3E{\cdot}N(R)C(NR'R'')(NR'''H)$ (R–R''' being organic groups). These interactions facilitate elimination of a first $H_2$ molecule. Our experimental results agree with the quantum chemical calculations that the product of this $H_2$ elimination is a dinuclear hydride featuring an eight-membered ring. Two possible intermediates were discussed. In the case of boron compounds, a diene intermediate is preferred, which subsequently undergoes a [4+4] cycloaddition. The diene is in equilibrium to a second intermediate, which can be described as a $H_2E$ fragment to which a chelating guanidinate is coordinated, leading to a four-membered ENCN ring. For Ga compounds, the diene structure does not represent an energy minimum on the potential energy surface, but could nevertheless play an important role in the mechanism. The eight-membered ring compounds can eliminate another $H_2$ molecule in a redox-reaction leading to molecules with two fused five-membered rings and direct E–E bonds between E atoms in the formal oxidation state +II. This process is slightly endothermic. However, the negative sign of $\Delta G^0$ calculated for most of these reactions means that these reactions are generally spontaneous. The experimental results accumulated for this class of compounds indicate that the barrier for these $H_2$ elimination reactions is not very high so that the chances for reversibility under mild conditions are high. In a final $H_2$ elimination dinuclear B(I) species with a B–B double bond could be formed. However, $\Delta G^0$ for this process is already positive. We are currently exploring the potential applications of this class of hydrides and similar classes of compounds for dehydrocoupling reactions and hydrogen storage. They certainly can be used highly efficiently for hydrogenation of olefins in the presence of a catalyst.

## Computational Details

Quantum chemical calculations were carried out with the TURBOMOLE program package.[30] The structures and corresponding energies of all molecules were optimized using the DFT functional BP86 (BP is the short notation for Becke–Perdew and is a non-local DFT method employing the Becke exchange and Perdew correlation functionals) in combination with a TZVPP (triple-zeta valence, doubly-polarized) basis set.[31] Table 1 includes the reaction energies with and without zero point vibrational corrections (ZPE, calculated with BP86/SVP) together with the standard Gibbs energy changes, $\Delta G^0$, for all relevant reactions.

## Acknowledgments

The authors thank the Deutsche Forschungsgemeinschaft (DFG) and the Fonds der Chemischen Industrie (FCI) for their continuous support.

[1] See, for example: M. P. Coles, *Dalton Trans.* **2006**, 985–1001, and references given therein.
[2] S. L. Aeilts, M. P. Coles, D. C. Swenson, R. F. Jordan, *Organometallics* **1998**, *17*, 3265–3270.
[3] F. A. Cotton, J. H. Matonic, C. A. Murillo, *J. Am. Chem. Soc.* **1997**, *119*, 7889–7890.
[4] J. L. Bear, Y. Li, B. Han, K. M. Kadish, *Inorg. Chem.* **1996**, *35*, 1395–1398.
[5] a) R. Clérac, F. A. Cotton, L. M. Daniels, J. P. Donahue, C. A. Murillo, D. J. Timmons, *Inorg. Chem.* **2000**, *39*, 2581–2584; b) F. A. Cotton, C. A. Murillo, X. Wang, C. C. Wilkinson, *Inorg. Chim. Acta* **2003**, *351*, 191–200.
[6] G. Robinson, C. Y. Tang, R. Köppe, A. R. Cowley, H.-J. Himmel, *Chem. Eur. J.* **2007**, *13*, 2648–2654.
[7] a) H.-J. Himmel, L. Manceron, A. J. Downs, P. Pullumbi, *Angew. Chem.* **2002**, *114*, 829–832; *Angew. Chem. Int. Ed.* **2002**, *41*, 796–799; b) H.-J. Himmel, L. Manceron, A. J. Downs, P. Pullumbi, *J. Am. Chem. Soc.* **2002**, *124*, 4448–4457.
[8] A. Köhn, H.-J. Himmel, B. Gaertner, *Chem. Eur. J.* **2003**, *9*, 3909–3919.

 © 2007 Wiley-VCH Verlag GmbH & Co. KGaA, Weinheim 

[9] a) C. A. Jaska, I. Manners, *J. Am. Chem. Soc.* **2004**, *126*, 9776–9785; b) T. J. Clark, C. A. Russell, I. Manners, *J. Am. Chem. Soc.* **2006**, *128*, 9582–9583.
[10] A. R. Cowley, A. J. Downs, H.-J. Himmel, S. Marchant, S. Parsons, J. A. Yeoman, *Dalton Trans.* **2005**, 1591–1597.
[11] J. L. Atwood, S. G. Bott, F. M. Elms, C. Jones, C. L. Raston, *Inorg. Chem.* **1991**, *30*, 3792–3793.
[12] P. T. Brain, H. E. Brown, A. J. Downs, T. M. Greene, E. Johnsen, S. Parsons, D. W. H. Rankin, B. A. Smart, C. Y. Tang, *J. Chem. Soc. Dalton Trans.* **1998**, 3685–3691.
[13] C. Y. Tang, R. A. Coxall, A. J. Downs, T. M. Greene, S. Parsons, *J. Chem. Soc. Dalton Trans.* **2001**, 2141–2147.
[14] S. Marchant, C. Y. Tang, A. J. Downs, T. M. Greene, H.-J. Himmel, S. Parsons, *Dalton Trans.* **2005**, 3281–3290.
[15] a) R. H. Crabtree, P. E. M. Siegbahn, O. Eisenstein, A. L. Rheingold, T. F. Koetzle, *Acc. Chem. Res.* **1996**, *29*, 348–354; b) W. T. Klooster, T. F. Koetzle, P. E. M. Siegbahn, T. B. Richardson, R. H. Crabtree, *J. Am. Chem. Soc.* **1999**, *121*, 6337–6343.
[16] a) J.-W. Hwang, J. P. Campbell, J. Kozubowski, S. A. Hanson, J. F. Evans, W. L. Gladfelter, *Chem. Mater.* **1995**, *7*, 517–525; b) J. P. Campbell, J.-W. Hwang, V. G. Young Jr, R. B. Von Dreele, C. J. Cramer, W. L. Gladfelter, *J. Am. Chem. Soc.* **1998**, *120*, 521–531.
[17] W. T. Klooster, T. F. Koetzle, P. E. M. Siegbahn, T. B. Richardson, R. H. Crabtree, *J. Am. Chem. Soc.* **1999**, *121*, 6337–6343.
[18] See, for example: a) F. Baitalow, J. Baumann, G. Wolf, K. Jaenicke-Rossler, G. Leitner, *Thermochim. Acta* **2002**, *391*, 159–168; b) D. A. Dixon, M. Gutowski, *J. Phys. Chem. A* **2005**, *109*, 5129–5135; c) M. E. Bluhm, M. G. Bradley, R. Butterick, U. Kusari, L. G. Sneddon, *J. Am. Chem. Soc.* **2006**, *128*, 7748–7749.
[19] C. A. Morrison, M. M. Siddick, *Angew. Chem.* **2004**, *116*, 4884; *Angew. Chem. Int. Ed.* **2004**, *43*, 4780–4782.
[20] Of course, it cannot be completely excluded that an intramolecular process is the first step of the dehydrogenation reaction. However, the strong intramolecular H···H contacts favour an intramolecular process.
[21] a) H.-J. Himmel, *J. Chem. Soc. Dalton Trans.* **2002**, 2678–2682; b) H.-J. Himmel, C. Klaus, *Z. Anorg. Allg. Chem.* **2003**, *629*, 1477–1483.
[22] D. D. Danielson, J. V. Patton, K. Hedberg, *J. Am. Chem. Soc.* **1977**, *99*, 6484–6487.
[23] a) K. Hedberg, R. Ryan, *J. Chem. Phys.* **1964**, *41*, 2214–2215; b) L. H. Jones, R. R. Ryan, *J. Chem. Phys.* **1972**, *57*, 1012–1013.
[24] D. D. Danielson, K. Hedberg, *J. Am. Chem. Soc.* **1979**, *101*, 3199–3203.
[25] J. C. Beamish, R. W. H. Small, I. J. Worrall, *Inorg. Chem.* **1979**, *18*, 220–223.
[26] G. Linti, R. Freq, M. Schmidt, *Z. Naturforsch., Teil B* **1994**, *49*, 958–962.
[27] H. Nöth, J. Knizek, W. Ponikwar, *Eur. J. Inorg. Chem.* **1999**, 1931–1937.
[28] Earlier examples of molecules with B=B bonds include tris-(mesity)phenyldiborate and 1,2-bis(dimethylamino)-1,2-diphenyldiborate. See:a) A. Moezzi, M. M. Olmstead, P. P. Power, *J. Am. Chem. Soc.* **1992**, *114*, 2715–2717; b) A. Moezzi, R. A. Bartlett, P. P. Power, *Angew. Chem.* **1992**, *104*, 1075–1076; *Angew. Chem. Int. Ed.* **1992**, *31*, 1082–1083.
[29] Meanwhile we obtained crystal structures for $H_3B{\cdot}$hppH and $[HB(hpp)]_2$ (O. Ciobanu, P. Roquette, S. Leingang, H. Wadepohl, J. Mautz, H.-J. Himmel, *Eur. J. Inorg. Chem.*, in press).
[30] a) R. Ahlrichs, M. Bär, M. Häser, H. Horn, C. Kölmel, *Chem. Phys. Lett.* **1989**, *162*, 165–169; b) K. Eichkorn, O. Treutler, H. Öhm, M. Häser, R. Ahlrichs, *Chem. Phys. Lett.* **1995**, *240*, 283–289; c) K. Eichkorn, O. Treutler, H. Öhm, M. Häser, R. Ahlrichs, *Chem. Phys. Lett.* **1995**, *242*, 652–660; d) K. Eichkorn, F. Weigend, O. Treutler, R. Ahlrichs, *Theor. Chem. Acc.* **1997**, *97*, 119–124; e) F. Weigend, M. Häser, *Theor. Chem. Acc.* **1997**, *97*, 331–340; f) F. Weigend, M. Häser, H. Patzelt, R. Ahlrichs, *Chem. Phys. Lett.* **1998**, *294*, 143–152.
[31] A. Schäfer, H. Horn, R. Ahlrichs, *J. Chem. Phys.* **1992**, *97*, 2571–2577.

Received: March 26, 2007
Published Online: June 14, 2007

 © 2007 Wiley-VCH Verlag GmbH & Co. KGaA, Weinheim 

DOI: 10.1002/ejic.200700057

# Synthesis, Photophysical and Photochemical Properties of Poly(oxyethylene)-Substituted Phthalocyaninato Oxotitanium(IV) Complexes

**Devrim Atilla,[a] Mahmut Durmuş,[a,b] Özgür Yılmaz,[a] Ayşe Gül Gürek,[a] Vefa Ahsen,[a,c] and Tebello Nyokong*[b]**

**Keywords:** Phthalocyanine / Titanium / Quantum yields / Singlet oxygen / Fluorescence

The synthesis, photophysical and photochemical properties of tetra- and chlorotetrapoly(oxyethylene)-substituted oxotitanium(IV) phthalocyanines are reported for the first time. The new compounds were characterized by elemental analysis, IR, $^1$H and $^{13}$C NMR spectroscopy, electronic spectroscopy and mass spectra. These complexes showed monomeric behaviour in solution. General trends are described for photodegredation, singlet oxygen, triplet state and fluorescence quantum yields, and triplet and fluorescence lifetimes of these compounds in dimethyl sulfoxide (DMSO). Photophysical and photochemical properties of phthalocyanine complexes are very useful for PDT applications. The complexes showed high triplet quantum yields and triplet lifetimes in DMSO. The singlet oxygen quantum yields ($\Phi_\Delta$), which give an indication of the potential of the complexes as photosensitizers in applications where singlet oxygen is required (Type II mechanism), were 0.72 and 0.78 for **3a** and **5a**, respectively. Thus, these complexes show potential as Type II photosensitizers. These complexes were also quenched by benzoquinone for fluorescence quenching studies.

(© Wiley-VCH Verlag GmbH & Co. KGaA, 69451 Weinheim, Germany, 2007)

## Introduction

Recently, phthalocyanine (Pc) chemistry has undergone a renaissance because these compounds and many of their derivatives exhibit properties that are interesting for many applications in material science.[1,2] Current research on phthalocyanines (Pcs) has been rapidly expanding into several applied fields including photovoltaics, electrochromism, optical data storage, laser dyes, liquid crystals, chemical sensors and photosensitizers for photodynamic therapy.[3] Because of their properties as semiconductors as well as their large linear and nonlinear optical responses, Pcs are currently of great scientific and technological interest for designing novel electronic and photonic devices. Pcs with highly delocalized cyclic π-electron systems show intense absorptions in the red region (Q band) and these absorptions can be shifted to the near IR region by making relatively small changes in these molecules.[3,4] Fusion of additional aromatic rings (polybenzannulation) has been proposed as a practical method to enhance the conjugation of π-electrons, thus increasing the wavelength of absorbed electromagnetic radiation. However, there is a decrease in the solubility of the products obtained by increased conjugation.[5] The second way to obtain the same effect has been the addition of electron donating groups (e.g. -OR, -SR, etc.) into the periphery of Pcs.[1] The presence of substituents is an additional advantage, as they address the problem of insolubility by making the complexes soluble in most organic solvents as opposed to unsubstituted Pcs that have limited applications. Tetra-substituted Pcs are usually more soluble than the corresponding octa-substituted Pcs due to the formation of constitutional isomers and the high dipole moment that results from the unsymmetrical arrangement of the substituents at the periphery.[6–9] The other method for changing the absorption wavelength is the use of some special metals in the inner core, and $TiO^{2+}$ is one of them.[10] Unsubstituted oxotitanium phthalocyanine (OTiPc), a well-known near-IR-active photoconductive dye used as xerographic photoreceptor in copiers and laser printers,[11–13] was first synthesised by Taube.[14] Also, this material can be used in optical disc information recording. The high third order optical susceptibility values of OTiPc derivatives are well documented.[15] Specific phthalocyanines can thus be tailored such that they consist of certain properties that are required for various applications since the possibility of combining an unlimited number and type of substituents with a great number of central metals is infinite.

Thiol-derivatized metallophthalocyanine complexes show rich spectroscopic and photochemical properties. For example, they are known to absorb at longer wavelengths[16–21] than other metallo phthalocyanine complexes. To the best of our knowledge, titanium phthalocyanines

[a] Gebze Institute of Technology, Department of Chemistry, P. O. Box 141, Gebze, 41400 Kocaeli, Turkey
[b] Department of Chemistry, Rhodes University, Grahamstown 6140, South Africa
[c] TUBITAK-Marmara Research Center, Materials Institute, P. O. Box 21, Gebze, 41470 Kocaeli, Turkey

 © 2007 Wiley-VCH Verlag GmbH & Co. KGaA, Weinheim 

tetra-substituted with poly(oxyethylene) side chains containing S atoms have not been reported.

Photophysical properties of OTiPc are very useful in applications involving nonlinear optics and optical limiters as these titanyl macrocycles are known to have remarkable properties.[22–28] Herein we report the synthesis of new sterically hindered thia-bridged tetrapoly(oxyethylene)-substituted OTiPc phthalocyanine derivatives (Scheme 1). The influence of the presence of the thia bridges in the poly(oxyethylene) side chains on the photophysical (triplet quantum yields and lifetimes, fluorescence quantum yields and lifetimes) and photochemical (singlet oxygen and photodegradation quantum yields) properties were determined. The quenching of fluorescence by benzoquinone is also discussed.

## Results and Discussion

### Synthesis and Characterization

Treatment of substituted dinitriles **3** and **5** with Ti(OBu)$_4$, urea and DBU in *n*-pentanol led to the formation of corresponding metallo Pcs **3a** and **5a**, respectively (Scheme 1). This method is similar to that reported by Hanack and co-workers.[22] We expect that **3a** and **5a** were prepared as a statistical mixture of four regioisomers due to the various possible positions of the poly(oxyethylene) side chains relative to one another. The four possible isomers of molecular symmetry $D_{4h}$, $C_{4h}$, $C_{2v}$ and $C_s$ and a distribution of 1:1:2:4, respectively, can be obtained.[29] No attempt was made to separate the isomers of complexes **3a** and **5a**.

Thia-bridged tetra- and chlorotetrapoly(oxyethylene)-substituted phthalocyanines **3a** and **5a**, respectively, were purified in each case, by column chromatography (silica gel) and preparative thin-layer chromatography (silica gel) using a mixed solvent system of dichloromethane/methanol as eluent. The waxy products are very soluble in polar and apolar solvents, such as chloroform, benzene, diethyl ether, carbon tetrachloride, *N*,*N*-dimethylformamide, dimethyl sulfoxide (DMSO), ethanol and acetone. They could thus be thoroughly investigated by $^1$H and $^{13}$C NMR in solution. The mass spectra of the phthalocyanine compounds obtained by ESI (electrospray ionisation) showed relatively intense molecular ion peaks.

In the IR spectra characteristic vibrations corresponding to ether groups (C–O–C) at 1120–1100 cm$^{-1}$ and $CH_2$ stretches at ca. 2950–2850 cm$^{-1}$ are common for phthalocyanine compounds **3a** and **5a**. The disappearance of the dinitrile stretches at ca. 2230 cm$^{-1}$ and the presence of Ti=O stretches at ca. 960 cm$^{-1}$ confirmed the formation of MPc.

The $^1$H and $^{13}$C NMR spectra of phthalocyanine compounds **3a** and **5a** in $CDCl_3$ confirmed the proposed structure. The $^1$H NMR spectra of **3a** and **5a** have broad absorptions relative to those of the phthalonitrile derivative. It is likely that broadness is due to both chemical exchange caused by aggregation–disaggregation equilibria and the

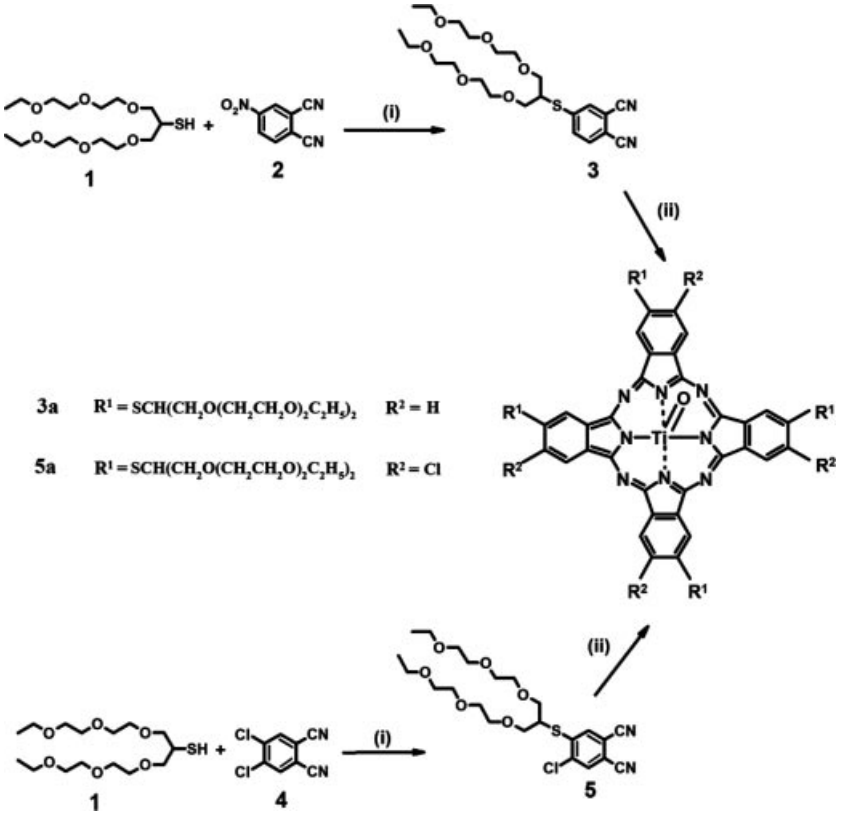


Scheme 1. Synthetic pathway for the preparation of compounds **3a** and **5a**: (i) DMSO, $K_2CO_3$, 50 °C, 48 h; (ii) 1-pentanol, urea, Ti(OBu)$_4$, DBU, reflux, 6 h.

 © 2007 Wiley-VCH Verlag GmbH & Co. KGaA, Weinheim 

fact that the product obtained in this reaction is a mixture of four positional isomers that are expected to show chemical shifts only slightly differing from each other. The poly(oxyethylene)-substituted phthalocyanines were found to be pure by $^1$H NMR spectroscopy with all the substituents and ring protons observed in their respective regions. Pc complexes **3a** and **5a** both showed the phthalocyanine ring protons as unresolved multiplets (most likely due to the presence of isomers), integrating for a total of 12 and 8 protons, respectively. The phthalocyanine ring protons were observed in the range 8.20–9.40 ppm for **3a** and 8.80–9.56 ppm for **5a**. Although the presence of isomers as well as phthalocyanine aggregation at the concentrations used for the NMR measurements may lead to broadening of the aromatic signals, the observed spectra of all the complexes were relatively well-resolved.

## Ground State Electronic Absorption and Fluorescence Spectra

The electronic spectra of phthalocyanine complexes **3a** and **5a** showed intense Q absorption bands around 715 nm (Figure 1). The spectra showed monomeric behaviour as evidenced by a single (narrow) Q band, typical of metallated phthalocyanine complexes for **3a** and **5a** in DMSO.[30] In DMSO, the Q bands were observed at 714 (**3a**) and 716 nm (**5a**), Tables 1 and 2. The B bands are broad due to the superimposition of the $B_1$ and $B_2$ bands in the 350 nm region. The shoulder between 400–500 nm (Figure 1) is tentatively assigned to charge transfer from the electron-rich ring to the electron-poor metal, but it may also be due to intraligand charge transfer between the sulfur groups and the phthalocyanine ring.

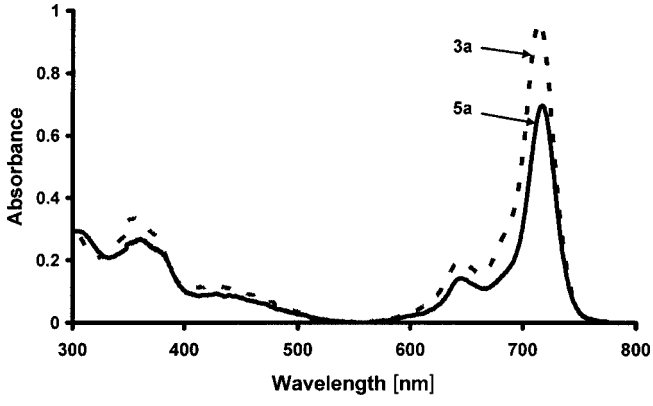


Figure 1. Absorption spectra of substituted oxotitanium phthalocyanines (OTiPc) **3a** and **5a** in DMSO. Concentration = $4\times10^{-6}$ mol dm$^{-3}$.

Aggregation is usually depicted as a coplanar association of rings progressing from monomer to dimer and higher order complexes. It is dependent on the concentration, nature of the solvent, peripheral substituents, complexed metal ions and temperature.[31,32] In the aggregated state, the electronic structure of the complexed phthalocyanine rings is perturbed resulting in alternation of the ground and excited state electronic structure.[33] In this study, the aggregation behaviour of phthalocyanine complexes **3a** and **5a** are investigated in different solvents (*n*-hexane, THF, chloroform, MeOH and DMSO), Figure 2. The complexes did not show aggregation in chloroform, THF or DMSO, whereas they showed aggregation in *n*-hexane and MeOH (Figure 2), as judged by the broadening and blueshifting of the Q band. In DMSO, the Beer–Lambert law was obeyed for all of these compounds in the concentrations ranging from $1.4\times10^{-5}$ to $4\times10^{-6}$ mol dm$^{-3}$, without any distortion of the spectra.

Table 1. UV/Vis spectroscopic data of complexes **3a** and **5a** in different solvents.

| Compound | Solvent | Q band [nm] (log $\varepsilon$) | B band [nm] | N band [nm] |
|---|---|---|---|---|
| **3a** | *n*-Hexane | 705 (4.81) | 343 | – |
| | THF | 710 (5.46) | 352 | – |
| | $CHCl_3$ | 715 (5.52) | 350 | 307 |
| | MeOH | 708 (4.96) | 344 | – |
| | DMSO | 714 (5.34) | 353 | – |
| **5a** | *n*-Hexane | 713 (4.46) | 348 | 307 |
| | THF | 716 (5.24) | 355 | 313 |
| | $CHCl_3$ | 720 (5.27) | 353 | 316 |
| | MeOH | 712 (4.70) | 349 | 314 |
| | DMSO | 716 (5.11) | 361 | 309 |

Table 2. Absorption, excitation and emission spectroscopic data for complexes **3a** and **5a** in DMSO.

| Compound | Q band $\lambda_{max}$ [nm] | log $\varepsilon$ | Excitation $\lambda_{Ex}$ [nm] | Emission $\lambda_{Em}$ [nm] | Stokes shift $\Delta_{Stokes}$ [nm] |
|---|---|---|---|---|---|
| **3a** | 714 | 5.34 | 716 | 724 | 10 |
| **5a** | 716 | 5.11 | 720 | 726 | 10 |

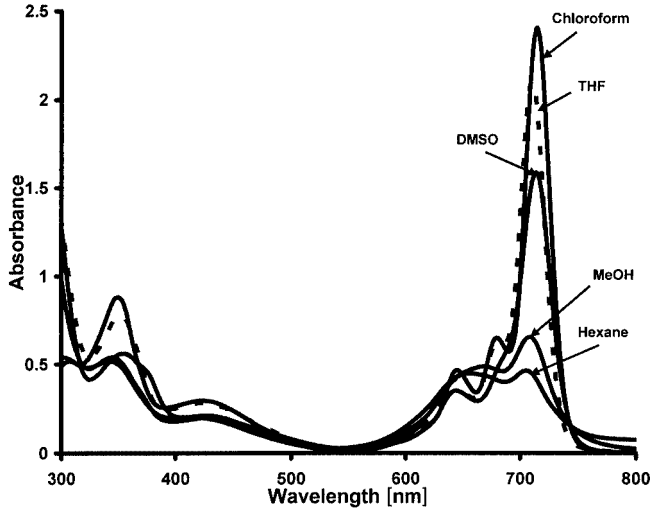


Figure 2. UV/Vis spectrum of **3a** in different solvents. Concentration = $7.20\times10^{-6}$ mol dm$^{-3}$.

Complexes **3a** and **5a** showed similar fluorescence behaviour in DMSO. Figure 3 shows the absorption, fluorescence emission and excitation spectra for complexes **3a** and **5a** in DMSO. Fluorescence emission peaks were observed at 724 nm for **3a** and 726 nm for **5a** in DMSO (Table 2). The

 © 2007 Wiley-VCH Verlag GmbH & Co. KGaA, Weinheim 

excitation spectra were similar to the absorption spectra and both were mirror images of the fluorescent spectra in DMSO (Figure 3). The proximity of the wavelength of each component of the Q band absorption to the Q band maxima of the excitation spectra for all complexes suggests that the nuclear configurations of the ground and excited states are similar and not affected by excitation in DMSO. The observed Stokes shifts (Table 2) were typical of MPc complexes in DMSO.

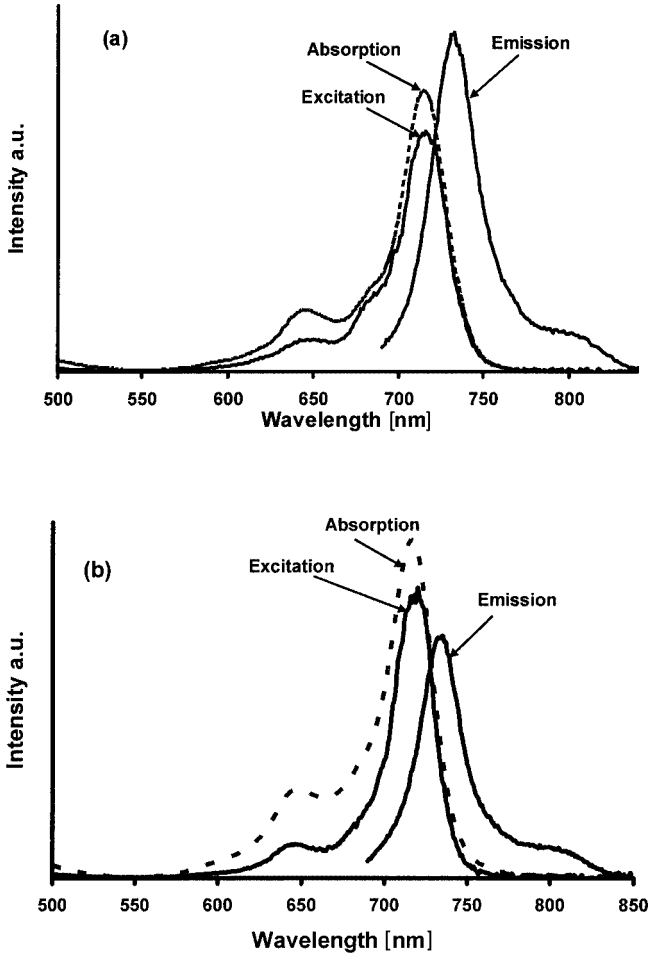


Figure 3. Absorption, excitation and emission spectra of compound **3a** (a), and **5a** (b) in DMSO. Excitation wavelength = 680 nm.

## Photophysical and Photochemical Properties

### *Fluorescence Quantum Yields and Lifetimes*

The fluorescence quantum yields ($\Phi_F$) of the complexes were similar and typical for MPc complexes, Table 3. The $\Phi_F$ value of complex **3a** was larger than that of complex **5a** in DMSO. Complex **5a** contains chlorine ligands, which would enhance intersystem crossing to the triplet state through the heavy atom effect, hence the slightly lower $\Phi_F$ value for **5a** compared to **3a**.

Table 3. Photophysical and photochemical parameters of complexes **3a** and **5a** in DMSO. Triplet absorption wavelength used = 550 nm.

| Compound | $\Phi_F$ | $\tau_T$ [μs] | $\Phi_T$ | $\Phi_{IC}$ | $\Phi_d$ [$\times 10^{-5}$] | $\Phi_\Delta$ | $S_\Delta$ |
|---|---|---|---|---|---|---|---|
| **3a** | 0.16 | 150 | 0.78 | 0.06 | 1.31 | 0.72 | 0.92 |
| **5a** | 0.10 | 220 | 0.85 | 0.05 | 3.35 | 0.78 | 0.92 |

Lifetimes of fluorescence ($\tau_F$) were calculated from the radiative lifetime using the Strickler–Berg equation and fluorescence quantum yields. Using this equation, a good correlation was[34] found for the experimentally determined fluorescence lifetimes and the theoretically determined lifetimes for the unaggregated molecules as is the case in this work. Thus we believe that the values obtained using this equation are a good measure of fluorescence lifetimes. The $\tau_F$ value for **3a** was larger than that of complex **5a** in DMSO, Table 4. The natural radiative lifetime ($\tau_0$) for **3a** was lower than that of complex **5a** in DMSO, Table 4. The rate constant value for fluorescence ($k_F$) of **3a** was larger than complex **5a** in DMSO, Table 4. The heavy atom effect due to the chlorine substituent in **5a** discussed above, will affect both the fluorescence lifetime and rate constant for this complex, hence a lower $\tau_F$ is observed for **5a** compared to **3a**. Complex **3a** showed a lower rate constant ($k_{IC}$) but showed approximately the same quantum yields for internal conversion ($\Phi_{IC}$) in DMSO when compared to complex **5a**, Tables 3 and 4. In addition, complex **3a** showed a lower rate constant for intersystem crossing ($k_{ISC}$) when compared to complex **5a** in DMSO, Table 4.

### *Triplet Lifetimes and Quantum Yields*

The transient spectrum of complex **3a** in DMSO is shown in Figure 4, and shows a maximum at 550 nm; hence the triplet lifetimes and yields were determined at this wavelength for complexes **3a** and **5a**. Figure 5 shows the triplet decay curves of the complexes (using complex **3a** in DMSO as an example). Complexes **3a** and **5a** showed typical triplet lifetimes ($\tau_T$) values for metallophthalocyanines. The triplet lifetime ($\tau_T$) value of complex **5a** was higher than complex **3a** in DMSO, Table 3. This suggests that the triplet state of complex **3a** is quenched more efficiently than that of **5a**.

Table 4. Rate constants for various excited state deactivation processes of complexes **3a** and **5a** in DMSO.

| Compound | $\tau_F$[a] [ns] | $\tau_0$[b] [ns] | $k_F$[c] [$s^{-1}$, $\times 10^8$] | $k_{ISC}$[d] [$s^{-1}$, $\times 10^8$] | $k_{IC}$[e] [$s^{-1}$, $\times 10^7$] | $k_d$[f] [$s^{-1}$, $\times 10^{-2}$] |
|---|---|---|---|---|---|---|
| **3a** | 1.39 | 8.71 | 1.15 | 5.61 | 4.31 | 8.70 |
| **5a** | 1.01 | 10.12 | 0.98 | 8.41 | 4.95 | 15.22 |

[a] Fluorescence lifetime. [b] Natural radiative lifetime. [c] Rate constant for fluorescence. Values calculated using $k_F = \Phi_F/\tau_F$. [d] Rate constant for intersystem crossing. Values calculated using $k_{ISC} = \Phi_T/\tau_F$. [e] Rate constant for internal conversion. Values calculated using $k_{IC} = \Phi_{IC}/\tau_F$. [f] Rate constant for photodegredation. Values calculated using $k_d = \Phi_d/\tau_T$.

 © 2007 Wiley-VCH Verlag GmbH & Co. KGaA, Weinheim 

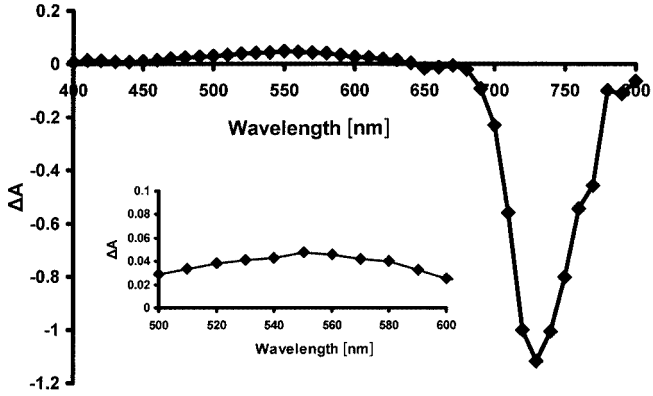


Figure 4. Transient differential spectrum of complex **3a** in DMSO. Excitation wavelength = 714 nm.

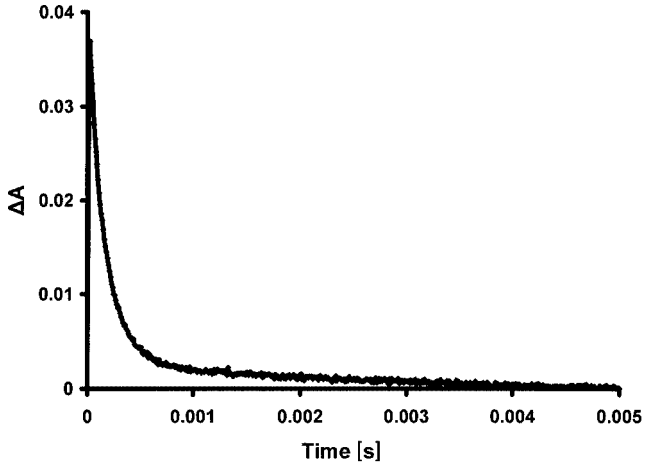


Figure 5. Triplet decay curve of **3a** in DMSO. Excitation wavelength = 714 nm.

The triplet quantum yields ($\Phi_T$) for substituted complexes **3a** and **5a** in DMSO were higher relative to typical[35] metallophthalocyanines in DMSO. For example, ZnPc standard gave $\Phi_T$ value of 0.65[36] when compared to 0.78 and 0.85 obtained in this work. Complex **5a** showed a larger $\Phi_T$ value when compared to complex **3a** in DMSO, Table 3.

### *Singlet Oxygen Quantum Yields*

Singlet oxygen quantum yields ($\Phi_\Delta$) were determined in DMSO using a chemical method [1,3-diphenylisobenzofuran (DPBF)].[37] The disappearance of DPBF was monitored using UV/Vis spectrophotometry. Many factors are responsible for the magnitude of the determined quantum yield of singlet oxygen, including triplet excited state energy, ability of substituents and solvents to quench the singlet oxygen, the triplet excited state lifetime and the efficiency of the energy transfer between the triplet excited state and the ground state of oxygen.

There was no change in the Q band intensity during the $\Phi_\Delta$ determinations, Figure 6, confirming that complexes are not degraded during singlet oxygen studies. The $\Phi_\Delta$ value of complex **3a** was lower when compared to complex **5a** in DMSO, Table 3. The magnitude of $S_\Delta$ ($= \Phi_\Delta/\Phi_T$) represents the efficiency of quenching of the triplet excited state by ground state (triplet) oxygen. Complexes **3a** and **5a** showed $S_\Delta$ of near unity (Table 3), suggesting efficient quenching of the triplet state by triplet molecular oxygen.

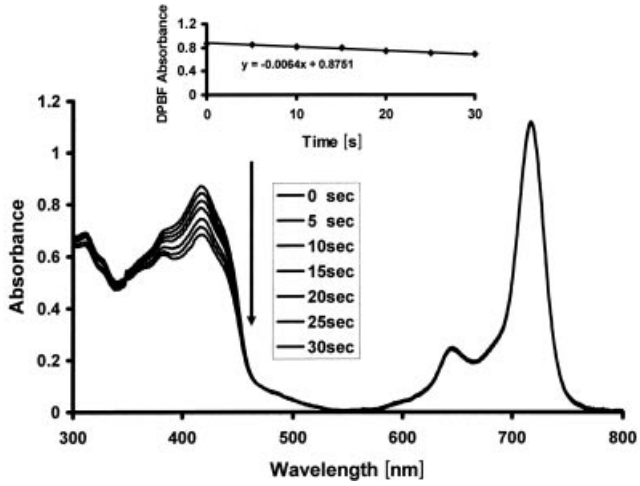


Figure 6. A typical spectrum for the determination of singlet oxygen quantum yield. This determination was for compound **5a** in DMSO at a concentration of $3 \times 10^{-5}$ mol dm$^{-3}$.

### *Photodegradation Studies*

Degradation of the molecules under irradiation can be used to study their stability and this is especially important for those molecules intended for use as photocatalysts. The collapse of the absorption spectra without any distortion of the shape confirms clean photodegradation not associated with phototransformation. The spectral changes observed for complexes **3a** and **5a** during irradiation are as shown in Figure 7 (using complex **3a** as an example in DMSO) and hence confirm that photodegradation occurred without phototransformation to new species which absorb in the Q band region. Table 3 shows that complex **3a** was more stable to degradation compared to complex **5a** in DMSO. The rate constant for photodegradation ($k_d$) of complex **3a** was also lower than that for complex **5a** in DMSO (Table 4).

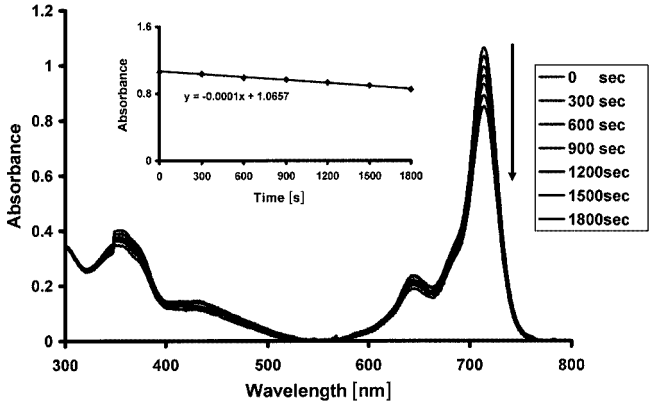


Figure 7. The photodegredation of compound **3a** in DMSO showing the disappearance of the Q band at 5 min intervals.

 © 2007 Wiley-VCH Verlag GmbH & Co. KGaA, Weinheim 

### Fluorescence Quenching Studies by Benzoquinone

In the presence of benzoquinone (BQ) quencher, a reaction takes place between the excited oxotitanium phthalocyanine complexes and the BQ molecules. The fluorescence quenching of oxotitanium phthalocyanine complexes **3a** and **5a** by BQ in DMSO was found to obey Stern–Volmer kinetics, which is consistent with diffusion-controlled bimolecular reactions. Figure 8 shows the quenching of complex **3a** and BQ in DMSO as an example. This figure shows the quenching behaviour of oxotitanium phthalocyanine complexes **3a** and **5a** typical of the nonaggregated complexes. The slope of the plots shown in Figure 9 gave $K_{SV}$ values. The $K_{SV}$ values for the BQ quenching of oxotitanium phthalocyanine complexes are listed in Table 5 in DMSO. The $K_{SV}$ value of complex **3a** was marginally lower than complex **5a** in DMSO. The bimolecular quenching constant ($k_q$) value of complex **3a** was also lower than complex **5a** in DMSO. Values of $k_q$ near $10^{10}$ M$^{-1}$s$^{-1}$ are in agreement with the theoretical Smoluchowski–Stokes-Einstein approximation at 298 K.[38]

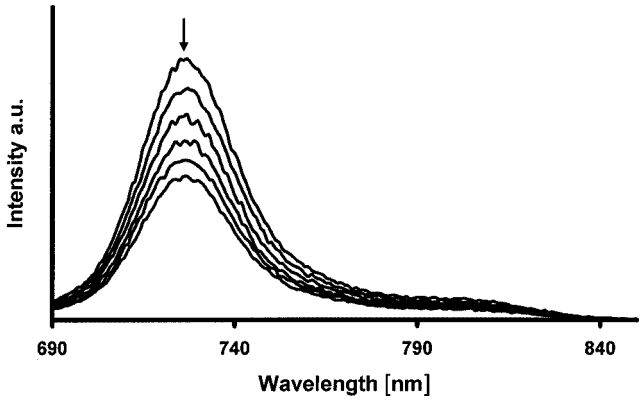


Figure 8. Fluorescence emission spectral changes of **3a** ($1.12\times10^{-5}$ mol dm$^{-3}$) on addition of different concentrations of BQ in DMSO. [BQ] = 0, 0.008, 0.016, 0.024, 0.032, 0.040 mol dm$^{-3}$. Excitation wavelength = 680 nm.

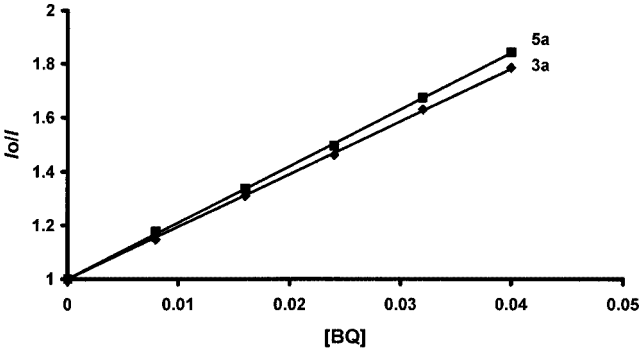


Figure 9. Stern–Volmer plots for BQ quenching of **3a** and **5a**. [MPc] ca. $1.20\times10^{-5}$ mol dm$^{-3}$ in DMSO. [BQ] = 0, 0.008, 0.016, 0.024, 0.032, 0.040 mol dm$^{-3}$. Excitation wavelength = 680 nm.

Table 5. Fluorescence quenching data for complexes **3a** and **5a** in DMSO.

| Compound | $K_{SV}$ [M$^{-1}$] | $k_q$ [dm$^3$ mol$^{-1}$ s$^{-1}$, $\times10^{10}$] |
|---|---|---|
| **3a** | 19.5 | 1.4 |
| **5a** | 21.0 | 2.0 |

## Conclusions

In the present work, the synthesis of new tetra- and chlorotetrathia(polyoxyethylene)-substituted oxotitanium phthalocyanines were described and the compounds were characterized by standard methods ($^1$H and $^{13}$C NMR spectroscopy, elemental analysis, IR and UV/Vis spectroscopy and mass spectrometry). The compounds are soluble in most solvents from *n*-hexane to methanol. In solution, the spectra showed monomeric behaviour evidenced by a single (narrow) Q band, typical of metallated phthalocyanine complexes for **3a** and **5a** in DMSO and the complexes showed charge-transfer bands around 400–500 nm as a shoulder in the UV/Vis spectra. The substituted complexes showed similar and typical fluorescence behaviour in DMSO. The complexes showed higher triplet quantum yields and triplet lifetimes in DMSO than are typical for MPc complexes. Complexes **3a** and **5a** gave high singlet oxygen quantum yields corresponding to high triplet quantum yields. The singlet oxygen quantum yields ($\Phi_\Delta$), which give an indication of the potential of the complexes as photosensitizers in applications where singlet oxygen is required (Type II mechanism), were 0.72 and 0.78 for **3a** and **5a**, respectively. Thus, these complexes show potential as Type II photosensitizers. The stability order among the substituted complexes was **3a** > **5a** in DMSO. The substituted complexes showed similar $K_{sv}$ and $k_q$ values.

## Experimental Section

**Materials:** All solvents were purified as described in Perrin and Armarego.[39] 1,3-Bis[2-(2-ethoxyethoxy)ethoxy]-2-propane-2-thiol (**1**),[40] 4-nitrophthalonitrile (**2**),[41] 4-{2-[2-(2-ethoxyethoxy)ethoxy]-1-[2-(2-ethoxyethoxy)ethoxymethyl]ethylsulfanyl phthalonitrile (**3**),[42] 1,2-dichloro-4,5-dicyanobenzene (**4**)[16] and, 4-chloro-5-{2-[2-(2-ethoxyethoxy)ethoxy]-1-[2-(2-ethoxyethoxy)ethoxymethyl]-ethylsulfanyl}phthalonitrile (**5**)[42] were prepared according to the reported procedures. Zinc phthalocyanine (ZnPc) employed as a standard was obtained from Sigma–Aldrich. All other reagents and solvents were of reagent grade quality and obtained from commercial suppliers.

**Equipment:** Elemental analyses were obtained from Carlo Erba 1106 Instrument. Infrared spectra were recorded with a Bio-Rad FTS 175C FTIR spectrophotometer. Absorption spectra in the UV/Vis region were recorded with an Shimadzu 2001 UV Pc spectrophotometer and a Varian 500 UV/Vis/NIR spectrophotometer. Fluorescence excitation and emission spectra were recorded with a Varian Eclipse spectrofluorometer using 1-cm pathlength cuvettes at room temperature. Mass spectra were recorded with a Thermo LCQ DECA XP-Max spectrometer. $^1$H and $^{13}$C NMR spectra were recorded in $CDCl_3$ solutions with a Varian 500 MHz spectrometer. Photoirradiations were performed with a General electric Quartz line lamp (300 W). A 600 nm glass cut off filter (Schott) and a water filter were used to filter off ultraviolet and infrared radia-

 © 2007 Wiley-VCH Verlag GmbH & Co. KGaA, Weinheim 

tions. An interference filter (Intor, 700 nm with a band width of 40 nm) was additionally placed in the light path before the sample. Light intensities were measured with a POWER MAX5100 (Molelectron detector incorporated) power meter. Triplet absorption and decay kinetics were recorded with a laser flash photolysis system, the excitation pulses were produced by a Quanta-Ray Nd: YAG laser providing 400 mJ, 90 ns pulses of laser light at 10 Hz, pumping a Lambda-Physik FL3002 dye (Pyridine 1 dye in methanol). Single pulse energy was 2 mJ. The analyzing beam source was from a Thermo Oriel xenon arc lamp, and a photomultiplier tube was used as a detector. Signals were recorded with a two-channel digital real-time oscilloscope (Tektronix TDS 360); the kinetic curves were averaged over 256 laser pulses. Solutions for these studies were degassed with nitrogen for at least 30 min before recording the spectra.

**Photophysical and Photochemical Parameters – Fluorescence Quantum Yields and Lifetimes:** Fluorescence quantum yields ($\Phi_F$) were determined by the comparative method outlined in Equation (1):[34,43]

$$\Phi_F = \Phi_F(\mathrm{Std}) \frac{F \cdot A_{\mathrm{Std}} \cdot \eta^2}{F_{\mathrm{Std}} A \cdot \eta^2_{\mathrm{Std}}} \quad (1)$$

where $F$ and $F_{\mathrm{Std}}$ are the areas under the fluorescence curves of samples **3a** or **5a** and the standard, respectively. $A$ and $A_{\mathrm{Std}}$ are the respective absorbances of the sample and standard at the excitation wavelengths (which was ca. 0.05), and $\eta$ and $\eta_{\mathrm{Std}}$ are the refractive indices of solvents used for the sample and standard, respectively. Unsubstituted ZnPc in DMSO ($\Phi_F = 0.18$)[44] was employed as the standard.

Natural radiative lifetimes ($\tau_0$) were determined using PhotochemCAD Program[45] which uses the Strickler–Berg equation.[46] From $\tau_0$ values, fluorescence lifetimes ($\tau_F$) were determined using Equation (2).

$$\Phi_F = \frac{\tau_F}{\tau_0} \quad (2)$$

**Triplet Quantum Yields and Lifetimes:** The deaerated solutions of the respective tetra-substituted oxotitanium phthalocyanine complexes **3a** and **5a** were introduced into a 1-cm pathlength spectrophotometric cell and irradiated at the Q band maxima with the laser system described above. Triplet quantum yields ($\Phi_T$) were determined by a comparative method using triplet decay,[47] Equation (3):

$$\Phi_T^{\mathrm{Sample}} = \Phi_T^{\mathrm{Std}} \frac{\Delta A_T^{\mathrm{Sample}} \cdot \varepsilon_T^{\mathrm{Std}}}{\Delta A_T^{\mathrm{Std}} \cdot \varepsilon_T^{\mathrm{Sample}}} \quad (3)$$

where $\Delta A_T^{\mathrm{Sample}}$ and $\Delta A_T^{\mathrm{Std}}$ are the changes in the triplet state absorbances of samples **3a** or **5a** and the standard, respectively. $\varepsilon_T^{\mathrm{Sample}}$ and $\varepsilon_T^{\mathrm{Std}}$, the triplet state extinction coefficients for samples **3a** and **5a**, and the standard, respectively. The standard employed was zinc phthalocyanine (ZnPc) in DMSO. The triplet quantum yield is $\Phi_T^{\mathrm{Std}} = 0.65$ for ZnPc[36] in DMSO.

Quantum yields of internal conversion ($\Phi_{IC}$) were obtained from Equation (4), which assumes that only three processes (fluorescence, intersystem crossing and internal conversion) jointly deactivate the excited singlet state of tetra-substituted oxotitanium phthalocyanine complexes.

$$\Phi_{IC} = 1 - (\Phi_F + \Phi_T) \quad (4)$$

Triplet lifetimes were determined by exponential fitting of the kinetic curves using OriginPro 7.5 software.

**Singlet Oxygen and Photodegradation Quantum Yields:** Singlet oxygen ($\Phi_\Delta$) and photodegradation ($\Phi_d$) quantum yield determinations were carried out using the experimental setup described above.[47–49] Typically, a 2 mL portion of the respective tetra-substituted oxotitanium phthalocyanine **3a** or **5a** solutions (absorbance ca. 1 at the irradiation wavelength) containing the singlet oxygen quencher was irradiated in the Q band region with the photoirradiation setup described in refs.[47–49] Values of $\Phi_\Delta$ were determined in air using the relative method with 1,3-diphenylisobenzofuran (DPBF) as singlet oxygen chemical quencher in DMSO [Equation (5)]:

$$\Phi_\Delta = \Phi_\Delta^{\mathrm{Std}} \frac{R \cdot I_{\mathrm{abs}}^{\mathrm{Std}}}{R^{\mathrm{Std}} \cdot I_{\mathrm{abs}}} \quad (5)$$

where $\Phi_\Delta^{\mathrm{Std}}$ is the singlet oxygen quantum yield for the standard ZnPc ($\Phi_\Delta^{\mathrm{Std}} = 0.67$ in DMSO,[50] $R$ and $R^{\mathrm{Std}}$ are the DPBF photobleaching rates in the presence of respective samples **3a** or **5a**, and the standard, respectively. $I_{\mathrm{abs}}$ and $I_{\mathrm{abs}}^{\mathrm{Std}}$ are the rates of light absorption by samples **3a** or **5a** and the standard, respectively. The concentrations of DPBF in the solutions were calculated using the determined values of log $\varepsilon = 4.36$ at 417 nm (DPBF in DMSO). The light intensity used for $\Phi_\Delta$ determinations was found to be $9.51 \times 10^{15}$ photons $s^{-1}$ $cm^{-2}$.

Photodegradation quantum yields were determined using Equation (6):

$$\Phi_d = \frac{(C_0 - C_t) \cdot V \cdot N_A}{I_{\mathrm{abs}} \cdot S \cdot t} \quad (6)$$

where $C_0$ and $C_t$ are the concentrations of samples **3a** or **5a** before and after irradiation, respectively, $V$ is the reaction volume, $N_A$ is Avogadro's constant, $S$ is the irradiated cell area and $t$ is the irradiation time. $I_{\mathrm{abs}}$ is the overlap integral of the radiation source light intensity and the absorption of samples **3a** or **5a**. A light intensity of $3.17 \times 10^{16}$ photons $s^{-1}$ $cm^{-2}$ was employed for $\Phi_d$ determinations.

**Fluorescence Quenching by BQ:** Fluorescence quenching experiments on oxotitanium phthalocyanine complexes **3a** and **5a** were carried out (in air, without degassing) by the addition of different concentrations of BQ to a fixed concentration of the complex, and the concentrations of BQ in the resulting mixtures were 0, 0.008, 0.016, 0.024, 0.032, 0.040 and 0.048 mol $dm^{-3}$. The fluorescence spectra of oxotitanium phthalocyanine complexes **3a** and **5a** at each BQ concentration were recorded, and the changes in fluorescence intensity related to BQ concentration by the Stern–Volmer (S–V) equation [Equation (7)]:[46]

 © 2007 Wiley-VCH Verlag GmbH & Co. KGaA, Weinheim 

$$\frac{I_0}{I} = 1 + K_{SV}[Q] \quad (7)$$

where $I_0$ and $I$ are the fluorescence intensities of fluorophore in the absence and presence of quencher, respectively. [$Q$] is the concentration of the quencher, and $K_{SV}$ is the Stern–Volmer constant; and is the product of the bimolecular quenching constant ($k_q$) and the fluorescence lifetime $\tau_F$ [Equation (8)].

$$K_{SV} = k_q \cdot \tau_F \quad (8)$$

The ratios $\frac{I_0}{I}$ were calculated and plotted against [BQ] according to Equation (7), and $K_{SV}$ was determined from the slope.

**Synthesis**

**Tetrakis{2-[2-(2-ethoxyethoxy)ethoxy]-1-[2-(2-ethoxyethoxy)ethoxymethyl]ethylsulfanylphthalocyaninato}titanium(IV) Oxide (3a):** Under an argon atmosphere, **3** (0.326, 0.7 mmol), urea (18 mg, 0.3 mmol) and three drops of DBU (1,8-diazabicyclo[5.4.0] undec-7-ene) were mixed in *n*-pentanol (3 mL) and heated to 120 °C. At that temperature, $Ti(OBu)_4$ (0.3 mL, 3 mmol) was added, and the reaction mixture was heated at reflux for 6 h at 155 °C. After cooling to room temperature, the mixture was poured into 100 mL hexane and precipitated. The crude product was collected by centrifugation and dried in vacuo. The obtained mixture of metallated and metal-free phthalocyanine was purified by column chromatography on silica gel. Elution with $CH_2Cl_2$/methanol (50:1) gave the metal-free Pc. The main product, oxotitanium Pc, was obtained by changing the eluent to $CH_2Cl_2$/methanol (20:1). Yield: 18 mg (11%). $^1$H NMR (500 MHz, $CDCl_3$, 25 °C): $\delta$ = 1.10 (t, $J$ = 7.1 Hz, 24 H, $CH_3$), 3.39 (m, 4 H, CH), 3.50–3.80 (m, 80 H, $CH_2$), 3.95 (m, 16 H, $CH_2$), 8.20–8.38 (br. m, 4 H, $CH_{ar}$), 8.85–9.40 (br. m, 8 H, $CH_{ar}$) ppm. $^{13}$C NMR (500 MHz, $CDCl_3$, 25 °C, decoupled): $\delta$ = 15.42 ($CH_3$), 48.75 (CH), 66.88 ($CH_2$), 70.14 ($CH_2$), 70.86–71.31 ($CH_2$), 123.27 ($CH_{ar}$), 124.32 ($CH_{ar}$), 125.28 ($CH_{ar}$), 132.94 ($C_{ar}$), 134.96 ($C_{ar}$), 137.62 ($C_{ar}$), 140.87 ($C_{ar}$), 151.43 ($C_{ar}$ *C*=N) ppm. IR (KBr pellet): $\tilde{\nu}$ = 3040, 2980–2850, 1600, 1529, 1450, 1400, 1381, 1350, 1310, 1260, 1240, 1120–1080, 959, 880 cm$^{-1}$. MS (ESI): *m/z* (%) = 1930(100) [M + 1]$^+$. $C_{92}H_{136}N_8TiO_{25}S_4$ (1929): calcd. C 57.20, H 7.10, N 5.81; found C 57.35, H 7.05, N 5.53.

**Tetrakis(2,9,16,23-{2-[2-(2-ethoxyethoxy)ethoxy]-1-[2-(2-ethoxyethoxy)ethoxymethyl]ethylsulfanyl}-3,10,17,24-chlorophthalocyaninato)titanium(IV) Oxide (5a):** Compound **5** (640 mg, 1.27 mmol), urea (36 mg, 0.6 mmol) and three drops of DBU were mixed in *n*-pentanol (5 mL) and heated at 120 °C. At that temperature, $Ti(OBu)_4$ (0.6 mL, 6 mmol) was added, and the reaction mixture was heated at reflux for 6 h at 155 °C. The *n*-pentanol was removed under reduced pressure, and the crude green product was purified by column chromatography (silica gel, $CH_2Cl_2$/methanol, 30:1) and the metallated and metal-free phthalocyanine were obtained from the crude product. Furthermore, the oxotitanium Pc was purified with preparative TLC (silica gel) using $CH_2Cl_2$/MeOH (30:1). Yield: 50 mg (9%). $^1$H NMR (500 MHz, $CDCl_3$, 25 °C): $\delta$ = 1.15 (t, $J$ = 7.2 Hz, 24 H, $CH_3$), 3.20–3.88 (m, 84 H, CH, $CH_2$), 4.12 (m, 16 H, $CH_2$), 8.80–9.56 (br. m, 8 H, $CH_{ar}$) ppm. $^{13}$C NMR (500 MHz, $CDCl_3$, 25 °C, decoupled): $\delta$ = 15.44 ($CH_3$), 49.15 (CH), 66.82 ($CH_2$), 70.08 ($CH_2$), 70.93–71.34 ($CH_2$), 123.27 ($CH_{ar}$), 125.32 ($CH_{ar}$), 126.38 ($C_{ar}$), 134.16 ($C_{ar}$), 135.86 ($C_{ar}$), 137.17 ($C_{ar}$), 141.53 ($C_{ar}$), 151.00 ($C_{ar}$ *C*=N) ppm. IR (KBr pellet): $\tilde{\nu}$ = 3040, 2980–2850, 1600, 1450, 1410, 1380, 1340, 1280, 1240, 1120–1080, 960, 880 cm$^{-1}$. MS (ESI): *m/z* (%) = 2067 (100) [M + 1]$^+$. $C_{92}Cl_4H_{132}N_8TiO_{25}S_4$ (2066): calcd. C 53.43, H 6.43, N 5.42; found C 53.80, H 6.22, N 5.60.

## Acknowledgments

This work was supported by the National Research Foundation of South Africa (NRF GUN # 2053657) as well as Rhodes University and Research Fund of Gebze Institute of Technology (2006-A-07).

[1] C. C. Leznoff, A. B. P. Lever (Eds.) *Phthalocyanines: Properties and Applications*, VCH, Weinheim, **1989**, **1993** and **1996**, vols. 1–4.
[2] M. Hanack, M. Lang, *Adv. Mater.* **1994**, *6*, 819–833.
[3] N. B. Keown, *Phthalocyanine Materials Synthesis Structure and Function*, Cambridge, **1989**.
[4] C. G. Claessens, W. J. Blau, M. J. Cook, M. Hanack, R. J. M. Nolte, T. Torres, D. Wöhrle, *Monatsh. Chem.* **2001**,*132*, 3–11.
[5] T. Sooksimuang, B. K. Mandal, *J. Org. Chem.* **2003**, *68*, 652–655.
[6] A. Beck, K. M. Mangold, M. Hanack, *Chem. Ber.* **1991**, *124*, 2315–2321.
[7] W. Eberhardt, M. Hanack, *Synthesis* **1995**, 95–100.
[8] C. C. Leznoff, S. M. Marcuccio, S. Greenberg, A. B. P. Lever, K. B. Tomer, *Can. J. Chem.* **1985**, *63*, 623–632.
[9] M. Durmuş, S. Yeşilot, V. Ahsen, *New J. Chem.* **2006**, *30*, 675–678.
[10] A. L. Thomas, F. H. Moser, *Phthalocyanine Research and Applications*, Florida, CRC Press, **1990**, pp. 15–16.
[11] W. F. Law, K. M. Lui, D. K. P. Ng, *J. Mater. Chem.* **1997**, *7*, 2063–2067.
[12] W. F. Law, R. C. W. Liu, J. Jiang, D. K. P. Ng, *Inorg. Chim. Acta* **1997**, *256*, 147–150.
[13] K.-J. Jiang, H.-Z. Chen, M. Wang, *Mater. Sci. Eng. B* **1999**, *57*, 87–91.
[14] R. Taube, *Z. Chem.* **1963**, *3*, 194–197.
[15] F. Henari, A. Davey, W. Blau, P. Haisch, M. Hanack, *J. Porphyrins Phthalocyanines* **1999**, *3*, 331–338.
[16] D. Wöhrle, M. Eskes, K. Shigehara, A. Yamada, *Synthesis* **1993**, 194–196.
[17] A. G. Gürek, Ö. Bekaroğlu, *J. Chem. Soc. Dalton Trans.* **1994**, 1419–1423.
[18] K. Ozoemena, T. Nyokong, *J. Chem. Soc. Dalton Trans.* **2002**, 1806–1811.
[19] İ. Yılmaz, A. G. Gürek, V. Ahsen, *Polyhedron* **2005**, *24*, 791–798.
[20] P. Tau, T. Nyokong, *Dalton Trans.* **2006**, 4482–4490.
[21] P. Tau, T. Nyokong, *Electrochim. Acta* **2007**, *52*, 4547–4553.
[22] M. Barthel, D. Dini, S. Vagin, M. Hanack, *Eur. J. Org. Chem.* **2002**, 3756–3762.
[23] C. G. Claessens, A. Gouloumis, M. Barthel, Y. Chen, G. Martin, F. Agulló-López, I. Ledoux-Rak, J. Zyss, M. Hanack, T. Torres, *J. Porphyrins Phthalocyanines* **2003**, *7*, 291–295.
[24] Y. Chen, M. E. El-Khouly, M. Sasaki, Y. Araki, O. Ito, *Org. Lett.* **2005**, *7*, 1613–1616.
[25] F. Fernandez-Alonso, P. Marovino, A. M. Paoletti, M. Righini, G. Rossi, *Chem. Phys. Lett.* **2002**, *356*, 607–613.
[26] B. Ballesteros, G. De la Torre, T. Torres, G. L. Hug, G. M. A. Rahman, D. M. Guldi, *Tetrahedron* **2006**, *62*, 2097–2101.
[27] M. E. El-Khouly, O. Ito, P. M. Smith, F. D'Souza, *J. Photochem. Photobiol. C* **2004**, *5*, 79–104.
[28] H. Luo, M. Fugitsuka, O. Ito, M. Kimura, *J. Photochem. Photobiol. A* **2003**, *156*, 31–38.
[29] M. Hanack, G. Schmid, M. Sommerauer, *Angew. Chem. Int. Ed. Engl.* **1993**, *32*, 1422–1424.
[30] M. J. Stillman, T. Nyokong in *Phthalocyanines: Properties and Applications* (Eds.: C. C. Leznoff, A. B. P. Lever), VCH, New York, **1989** vol. 1, ch. 3.

 © 2007 Wiley-VCH Verlag GmbH & Co. KGaA, Weinheim 

[31] J. Simon, P. Bassoul in *Phthalocyanines: Properties and Applications* (Eds.: C. C. Leznoff, A. B. P. Lever), VCH, New York, **1993**, vol.2, pp. 223–299.
[32] D. D. Dominquez, A. W. Snow, J. S. Shirk, R. G. S. Pong, *J. Porphyrins Phthalocyanines* **2001**, *5*, 582–592.
[33] H. S. Nalwa, J. S. Shirk in *Phthalocyanines: Properties and Applications* (Eds.: C. C. Leznoff, A. B. P. Lever), VCH, New York, **1996**, vol.4, pp. 79–182.
[34] D. Maree, T. Nyokong, K. Suhling, D. Phillips, *J. Porphyrins Phthalocyanines* **2002**, *6*, 6373–6376.
[35] T. Nyokong, *Coord. Chem. Rev.* **2006**, doi:10.1016/j.ccr.2006.11.011.
[36] T. H. Tran-Thi, C. Desforge, C. Thies, *J. Phys. Chem.* **1989**, *93*, 1226–1233.
[37] U. Michelsen, H. Kliesch, G. Schnurpfeil, A. K. Sobbi, D. Wöhrle, *Photochem. Photobiol.* **1996**, *64*, 694–701.
[38] S. L. Murov, I. Carmichael, G. L. Hug, *Handbook of Photochemistry*, 2nd ed., Marcel Decker, New York, **1993**, p. 207.
[39] D. D. Perrin, W. L. Armarego, *Purification of Laboratory Chemical*, 2nd ed., Pergamon Press, Oxford, **1980**.
[40] J. Vacus, J. Simon, *Adv. Mater.* **1995**, *7*, 797–800.
[41] J. G. Young, W. Onyebuagu, *J. Org. Chem.* **1990**, *55*, 2155–2159.
[42] A. G. Gürek, M. Durmuş, V. Ahsen, *New J. Chem.* **2004**, *28*, 693–699.
[43] S. Fery-Forgues, D. Lavabre, *J. Chem. Educ.* **1999**, *76*, 1260–1264.
[44] P. Jacques, A. M. Braun, *Helv. Chim. Acta* **1981**, *64*, 1800–1806.
[45] H. Du, R. A. Fuh, J. Li, A. Corkan, J. S. Lindsey, *Photochem. Photobiol.* **1998**, *68*, 141–142.
[46] S. J. Strickler, R. A. Berg, *J. Chem. Phys.* **1962**, *37*, 814–822.
[47] J. H. Brannon, D. Magde, *J. Am. Chem. Soc.* **1980**, *102*, 62–65.
[48] I. Seotsanyana-Mokhosi, N. Kuznetsova, T. Nyokong, *J. Photochem. Photobiol., A* **2001**, *140*, 215–222.
[49] A. Ogunsipe, T. Nyokong, *J. Mol. Struct.* **2004**, *689*, 89–97.
[50] N. Kuznetsova, N. Gretsova, E. Kalmkova, E. Makarova, S. Dashkevich, V. Negrimovskii, O. Kaliya, E. Luk'yanets, *Russ. J. Gen. Chem.* **2000**, *70*, 133–140.

Received: January 17, 2007
Published Online: June 14, 2007

 © 2007 Wiley-VCH Verlag GmbH & Co. KGaA, Weinheim 

DOI: 10.1002/ejic.200700083

# Localization and Delocalization of Spin Density in Mixed-Valence ($V^{IV}/V^{V}$) $[(V_2O_3)_2(PhPO_3)_4\subset F]^{-n}$ ($n$ = 1, 2): Theoretical and Experimental Studies

**Nguyen Huu Thong,[a] Jabor K. Jabor,[a] Reinhard Stößer,[a] Manfred Meisel,*[a] and Burkhard Ziemer[a]**

**Keywords:** Adsorption / DFT calculation / ESR / Hyperfine structure / Vanadium / Cage compounds

Based on XRD and optimized structures of the cage compound $[(V_2O_3)_2(PhPO_3)_4\subset F]^{-n}$ in singlet ($n$ = 1) and doublet ($n$ = 2) states DFT calculations were carried out to determine the energies and spin density distribution for the symmetries $D_{2d}$, $C_{2v}$ and $C_s$. It turned out, that the cage with $C_s$ symmetry not only represents the energetically more stable doublet system (with respect to $D_{2d}$ and $C_{2v}$-symmetries) but also corresponds to the real compound under study. The SOMO of the $S$ = 1/2 cage represents an antibonding state and the volume of the cage in this state is larger than that in the $S$ = 0 state. The calculated ESR hyperfine coupling constants are in acceptable agreement with those determined by ESR. Experimentally the localization/delocalization of spin density was determined via ESR as a function of temperature and adsorption of the cage on $Al_2O_3$, respectively. A proposal is given for the localization/delocalization of spin density based on thermally driven changes of the cage symmetry in combination with the hopping of the unpaired electron inside the cage.

(© Wiley-VCH Verlag GmbH & Co. KGaA, 69451 Weinheim, Germany, 2007)

## Introduction

Vanadium organophosphonates (VOP) represent a large group of organic-inorganic hybrid materials. They have gained increasing research interest not only due to their structural diversity and interesting redox properties but also due to potential applications in different areas, for example catalysis[1] and intercalation.[2] The anions $[(V_2O_3)_2(RPO_3)_4\subset F]^{-n}$ as mentioned in the title of the paper own cage structures and represent interesting model system for (i) spectroscopic and (ii) quantum-chemical investigations.

As a part of our research, we are interested in preparation and study of vanadium organophosphonate cages in the presence of anionic templates. In the past few years several cage structures were prepared in the presence of halide anions, e.g. $F^-$,[3–5] $Cl^-$,[6–8] and $Br^-$.[9] Up to now some questions are still not fully answered: the function of the template anion, the electronic structures including the localization/delocalization of spin density in the cages, the reversibility of the redox reactions and the potential application fields.

In principle, the one-electron reduction of the vanadium cage $[(V_2O_3)_2(RPO_3)_4\subset F]^{-1}$ (R = organic group) should result in the formation of paramagnetic species in a doublet state ($S$ = 1/2). Hardly anything is known about the extent of spin density distribution over the cage. Quantum-chemical calculation and ESR investigation at different temperature in fluid and solid matrices should provide answers to open questions. The unpaired electron in the cage structure can be localized at a single vanadium nucleus or delocalized over 2, 3 or 4 vanadium nuclei. ESR is a powerful tool to detect and monitor such kinds of paramagnetic species. A simple delocalization model will be used to elucidate the phenomena which are observed by ESR. The quantum-chemical calculations (DFT method) start with structures of forced symmetries of the cage covering $D_{2d}$, $C_{2v}$ and $C_s$ and end up with experimentally determined structures (XRD). For comparison the structurally related system $VO(acac)_2$ was investigated by both methods.

The cage compound $[(V_2O_3)_2(PhPO_3)_4\subset F]^{-n}$ in singlet and doublet states represents a suitable model not only for the study of localization/delocalization phenomena of the spin density but also for the reversibility of redox reactions.

It should be mentioned at this point, that the investigation preselected in this paper concerns chemical compounds in different states of aggregation. The quantum-chemical over the gaseous phase, the ESR over the liquid and the XRD the solid phase. But we would like to show that even in the case of the cage compounds, the cage properties will change under the influence of internal and external limiting factors. The cage itself based on its spherical structure is able to preserve most of these unique properties. Therefore, it seems to be justified to perform the investigation as outlined in this paper.

[a] Institut für Chemie, Humboldt-Universität zu Berlin, Brook-Taylor-Str. 2, 12489 Berlin, Germany
Fax: +49-30-2093-7468
E-mail: manfred.meisel@chemie.hu-berlin.de

 InterScience © 2007 Wiley-VCH Verlag GmbH & Co. KGaA, Weinheim 

## Results and Discussion

### Calculation Method

The hybrid version of the DFT method with the B3LYP-functional[10] in connection with the basis set 6-311G* of triple zeta quality for V, O and F and with the basis set 4-21G for the organic structure of the cage has been used.[11] All the calculations have been carried out with the quantum chemical code GAUSSIAN 03.[12]

Three types of structures were calculated: (i) The *simplified structures* of forced symmetry and a replacement of the organic rests by H atoms to save computer time, (ii) the *complete structures* like the simplified structures with the real organic rests and (iii) the so-called *"X-ray" structure* using structural parameters obtained from XRD measurements.

The calculations here refer to the cage anions only; the influence of the cations will not be taken into account.

### Simplified Structures with $D_{2d}$ Symmetry

The structures of both the anions $[(V_2O_3)_2(PhPO_3)_4{\subset}F]^{-n}$ in singlet ($n$ = 1) and doublet state ($n$ = 2) have been totally optimized. As displayed in parts a and b of Figure 1 the optimized geometry of the cage in the singlet state leads to an integer network with an $F^-$ anion in the centre of the cage. In contrast, for simplification the doublet structure may be thought to be composed from several fragments: two times $V_2O_3$, four times $HPO_3$ and one $F^-$.

Remarkable is the total delocalization of the additional electron in the doublet structure. Each V atom has the same spin density of 0.39 (the sum of the spin densities is greater than 1 because of the negative spin densities at some O atoms, see Table 5). The comparison between some geometry parameters of the anion cages in the singlet and the doublet state is shown in Table 1. Going from the singlet state to the doublet state both the terminal V–O and the bridging V–O bonds are almost unchanged while the V–OP and V–F distances become larger. That means, an additional electron, delocalized in the cage, causes a larger volume of the cage. This effect can be explained by the analysis of the SOMO of the doublet structure (Figure 2). All V–OP bonds in that orbital own antibonding character, and the occupation of that orbital weakens the bonds between the V atoms in $V_2O_3$ fragments and the O atoms of the $HPO_3$ fragments with the consequence of enlarging the cage. The larger V–F distance in the doublet structure is therefore caused by the enlarging of the cage based on the antibonding character of the bond between the V atoms and the O atoms of $HPO_3$ fragments and not by a weaker bond between the V and F atoms.

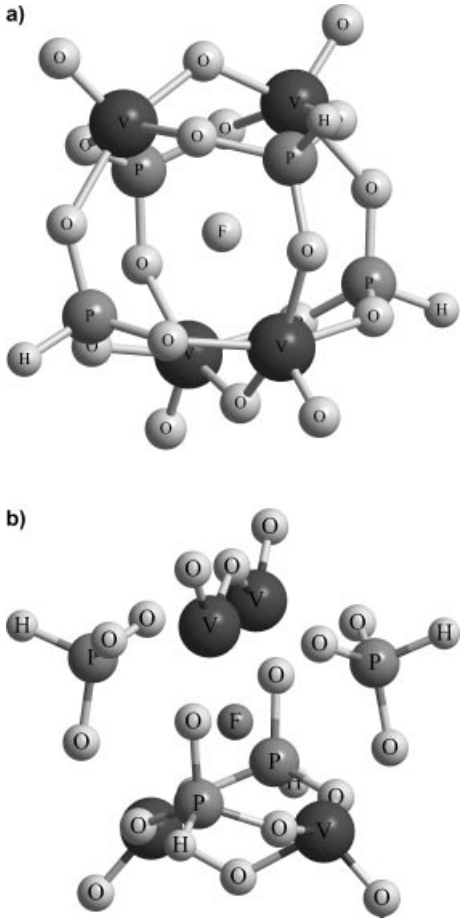


Figure 1. a) Calculated structure of the cage in the $D_{2d}$ singlet state. b) Calculated structure of the cage in the $D_{2d}$ doublet state.

Table 1. Comparison of some geometry parameters of the cage anions with $D_{2d}$ symmetry in the singlet and doublet structure.[a]

| Structural element | Distance [pm] Singlet | Doublet |
|---|---|---|
| V–O(brdg) | 179.1 | 179.0 |
| V–O(term) | 155.8 | 157.0 |
| V–O(–P on plane) | 195.1 | 197.0 |
| V–O(–P out of plane) | 194.3 | 198.0 |
| V–F | 249.0 | 250.4 |
| Energy (au) | –6599.540075 | –6599.547719 |

[a] brdg = bridging; term = terminal; on plane = the bonds on the same plane as the $V_2O_3$ fragment; out of plane = the bonds out of plane which contains the $V_2O_3$ fragment; au = atomic unit = 627.51 kcal/mol.

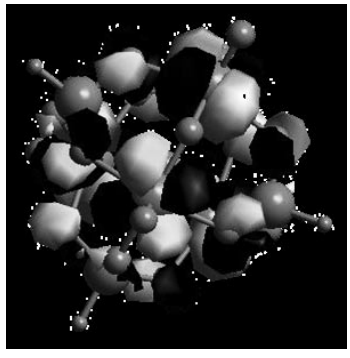

Figure 2. SOMO of the $D_{2d}$ doublet.

 © 2007 Wiley-VCH Verlag GmbH & Co. KGaA, Weinheim 

The delocalization of the unpaired electron in this model structure follows directly from the symmetry assumed. Under energetic aspects the doublet structure is a bit more stable than the singlet one (see Table 1).

### Simplified Structures with $C_{2v}$ Symmetry

The structures of both the anions $[(V_2O_3)_2(PhPO_3)_4\subset F]^{-n}$ in singlet ($n$ = 1) and doublet state ($n$ = 2) have been totally optimized. The optimized geometry of the cage in the singlet state leads to an integer network with an $F^-$ anion in the centre of the cage similar to the singlet structure in the $D_{2d}$ symmetry (Figure 1, a). While the doublet structure can be regarded as a composite of one $V_2O_3$ fragment, one $F^-$ anion in the centre of the cage and the residue of the cage (Figure 3). The unpaired electron is localized in the $V_2O_3$ fragment with equal spin densities of 0.7 for each of the two V atoms (see Table 5). Each V atom should have the oxidation number of 4.5 in this fragment. As in the case discussed above, the $V^{IV}$–OP and $V^{IV}$–$F^-$ distances are larger than the $V^V$–OP and $V^V$–F distances in the corresponding singlet structure (see Table 2). It should be noted that the $V^V$–F distances in the doublet structure are even smaller than $V^V$–F distances in the singlet structure of the same symmetry (241.0 compared with 247.0 pm). Assuming $C_{2v}$ symmetry, the doublet structure is more stable than the singlet one.

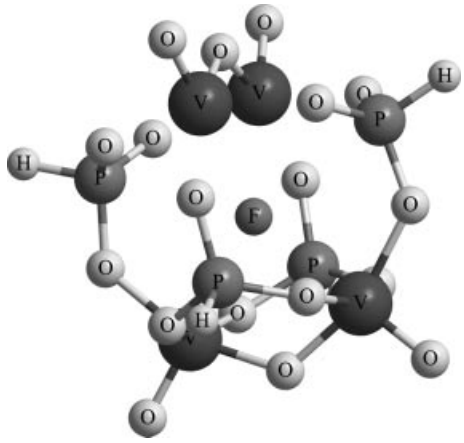

Figure 3. Calculated structure of the cage in the $C_{2v}$ doublet.

Table 2. Comparison of some geometry parameters of the cage anions with $C_{2v}$ symmetry in the singlet and doublet structure.[a]

| Structural element | Distance [pm] Singlet | Doublet |
|---|---|---|
| $V^V$–O(brdg) | 179.0 | 179.0 |
| $V^{IV}$–O(brdg) | | 178.9 |
| $V^V$–O(term) | 155.0 | 156.0 |
| $V^{IV}$–O(term) | | 157.0 |
| $V^V$–O(–P on plane) | 195.0 | 193.0 |
| $V^{IV}$–O(–P on plane) | | 202.0 |
| $V^V$–O(–P out of plane) | 194.0 | 195.0 |
| $V^{IV}$–O(–P out of plane) | | 200.0 |
| $V^V$–F | 247.0–249.0 | 241.0 |
| $V^{IV}$–F | | 260.0 |
| Energy (au) | –6599.540075 | –6599.552346 |

[a] brdg = bridging; term = terminal; on plane = the bonds on the same plane as the $V_2O_3$ fragment; out of plane = the bonds out of plane which contains the $V_2O_3$ fragment; au = atomic unit = 627.51 kcal/mol.

### Structures of $C_s$ Symmetry

#### *Simplified Structures with $C_s$ Symmetry*

The structures of both the anions $[(V_2O_3)_2(PhPO_3)_4\subset F]^{-n}$ with singlet ($n$ = 1) and doublet ($n$ = 2) states have been totally optimized. The optimized geometry of the cage in the singlet state leads to an integer network with an $F^-$ anion in the centre of the cage similar to the singlet structure in the $D_{2d}$ symmetry (Figure 1, a) while the doublet structure formal can be regarded as a composite of one $V_2O_3$ fragment, one $F^-$ anion in the centre of the cage and the residue of the cage (Figure 4). The unpaired electron appears to be localized on the $V_2O_3$ fragment which is positioned in the plane of symmetry. The consequence is, that the two V atoms are no more equivalent: two values for the spin density result: 1.07 and 0.10 (Figure 5, a). That means, the unpaired electron is more or less localized at one V atom with enlarged $V^{IV}$–F distance. The other V atom can be regarded as a "quasi $V^V$ " ion. It stands out, that the $V^{IV}$–O(brdg) and $V^{IV}$–OP distances are enlarged, but the terminal bonds $V^{IV}$–O(term) remain nearly unchanged (see Table 3). Furthermore, the distances of the $V^V$–O(brdg) in the symmetry plane is remarkable shortened (169.0 pm). The SOMO is in general of antibonding character. But there is a bonding pi-character of the bond between the $V^V$ atom and the bridging O atom in the $C_s$ plane (Figure 5, b). Under energetic aspects the doublet structure here also appears to be more stable than the singlet one.

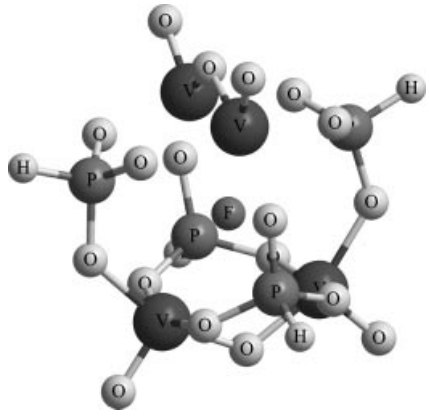

Figure 4. Calculated structure of the cage in the $C_s$ doublet state.

 © 2007 Wiley-VCH Verlag GmbH & Co. KGaA, Weinheim 

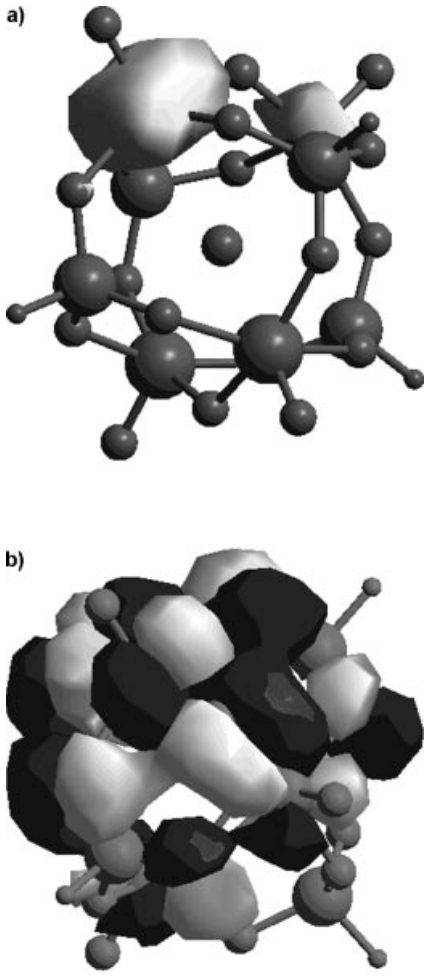


Figure 5. a) Spin density of the doublet state with $C_s$ symmetry b) SOMO of the $C_s$ doublet state.

Table 3. Comparison of some geometry parameters of the cage anions with $C_s$ symmetry in the singlet and doublet structure.

| Structural element | Distance [pm] Singlet | Doublet |
|---|---|---|
| $V^{IV}$–O(brdg)[a] | 179.0 | 193.0 |
| $V^{V}$–O(brdg)[a] | 179.0 | 169.0 |
| $V^{V}$–O(brdg)[b] | 179.0 | 179.0 |
| $V^{IV}$–O(term)[a] | 155.0 | 157.0 |
| $V^{V}$–O(term)[a] | 155.0 | 157.0 |
| $V^{V}$–O(term)[b] | 155.0 | 156.0 |
| $V^{IV}$–O(–P on plane)[a] | 195.0 | 202.0 |
| $V^{V}$–O(–P on plane)[a] | 195.0 | 203.0 |
| $V^{V}$–O(–P on plane)[b] | 195.0 | 193.0 |
| $V^{IV}$–O(–P out of plane)[a] | 194.0 | 202.0 |
| $V^{V}$–O(–P out of plane)[a] | 194.0 | 197.0 |
| $V^{V}$–O(–P out of plane)[b] | 194.0 | 194.0 |
| $V^{IV}$–F[a] | 246.0 | 260.0 |
| $V^{V}$–F[a] | 248.0 | 261.0 |
| $V^{V}$–F[b] | 250.0 | 241.0 |
| Energy (au) | –6599.540069 | –6599.556154 |

[a] On the $C_s$-plane. [b] Perpendicular to the $C_s$-plane. brdg = bridging; term = terminal; on plane = the bonds on the same plane as the $V_2O_3$ fragment; out of plane = the bonds out of plane which contains the $V_2O_3$ fragment; au = atomic unit = 627.51 kcal/mol.

### *The Complete and X-ray Doublet Structures with $C_s$ Symmetry*

The cages in the complete doublet structure with $C_s$ symmetry and the so-called X-ray doublet structure have been calculated. This has been done in order to find out what kind of influences can be expected by the organic rests of the cage. As the results of the calculation show, there is no essential influence of the phenyl substituents on the localization of the unpaired electron or on the geometry of the cage (column 2 and 3 of Table 4). The optimized parameters of the complete structure are in a good agreement with those of the XRD experiments. The calculated $C_s$ symmetry of the cage anion is compatible with that in the crystal (for related compounds see ref.[3]). But one has to note, that the spin localization at one V atom in the X-ray structure is not so strong as in the gaseous phase and that the V–F distances in the symmetry plane, determined by XRD, are remarkable shorter and more asymmetric than those in the complete structure calculated for the gaseous phase (Table 4). The most probable reason for this finding should be the packing effect in the solid state, which results in deformation of the cages and the fragments $V_2O_3$ and $HPO_3$ come closer together (see also the ESR spectra from solutions of the cage with $S = 1/2$).

Table 4. Comparison of some geometry parameters of the simplified, the complete and the X-ray doublet structures with $C_s$ symmetry.

| Structural element | Distance [pm] Simplified | Complete | X-ray |
|---|---|---|---|
| $V^{IV}$–O(brdg)[a] | 193.0 | 193.0 | 186.0 |
| $V^{V}$–O(brdg)[a] | 169.0 | 169.0 | 171.0 |
| $V^{V}$–O(brdg)[b] | 179.0 | 180.0 | 181.0 |
| $V^{IV}$–O(term)[a] | 157.0 | 158.0 | 157.0 |
| $V^{V}$–O(term)[a] | 157.0 | 158.0 | 159.0 |
| $V^{V}$–O(term)[b] | 156.0 | 157.0 | 157.0 |
| $V^{IV}$–O(–P on plane)[a] | 202.0 | 201.0 | 197.0 |
| $V^{V}$–O(–P on plane)[a] | 203.0 | 201.0 | 202.0 |
| $V^{V}$–O(–P on plane)[b] | 193.0 | 191.0 | 189.0 |
| $V^{IV}$–O(–P out of plane)[a] | 202.0 | 201.0 | 202.0 |
| $V^{V}$–O(–P out of plane)[a] | 197.0 | 197.0 | 197.0 |
| $V^{V}$–O(–P out of plane)[b] | 194.0 | 193.0 | 192.0 |
| $V^{IV}$–F[a] | 260.0 | 268.0 | 240.3 |
| $V^{V}$–F[a] | 261.0 | 267.0 | 250.4 |
| $V^{V}$–F[b] | 241.0 | 241.0 | 243.4 |

[a] On the $C_s$-plane. [b] Perpendicular to the $C_s$-plane. brdg = bridging; term = terminal; on plane = the bonds on the same plane as the $V_2O_3$ fragment; out of plane = the bonds out of plane which contains the $V_2O_3$ fragment; au = atomic unit = 627.51 kcal/mol.

### Comparison of the Simplified Doublet Structures Having Different Symmetries

Table 5 shows the energies, the spin densities and the Fermi contact coupling constants of the simplified doublet structures in regarded symmetries. A B3LYP calculation of $VO(acac)_2$ (acac = acetylacetonate) in $C_2$ symmetry has also been carried out for comparison (the last line of Table 5). First there is a tendency of delocalization of the additional electron in the higher symmetries. Second, the cage anion

 © 2007 Wiley-VCH Verlag GmbH & Co. KGaA, Weinheim 

seems energetically to prefer the less symmetric geometry $C_s$. Third, the Fermi contact coupling constants depend strongly of the forced symmetries. Fourth, both the spin densities and the Fermi contact coupling constants of the cage in $C_s$ symmetry and $VO(acac)_2$ in $C_2$ are very similar. This fact reflects the similar electronic structure of the VO groups and the similar {4+1} coordination of the V atoms in both.

Table 5. Comparison of the energies, the spin densities and the Fermi contact coupling constants between simplified doublet structures with different symmetries.

| Symmetry/ energy [au] | Spin density on the V atoms | Extent of localization | Fermi contact couplings [Gauss] |
|---|---|---|---|
| $D_{2d}$ | 0.39; 0.39 | fully | –27.54931 |
| –6599.547719 | 0.39; 0.39 | delocalized | |
| $C_{2v}$ | 0.02; 0.02 | localized on | –1.64340 |
| –6599.552346 | 0.69; 0.69 | one $V_2O_3$ fragment | –50.50854 |
| $C_s$ | 1.07; 0.10 | almost | –85.28022 |
| –6599.556154 | 0.01; 0.01 | localized on | –7.76268 |
| | | one V atom | –0.72122 |
| | | | –0.72122 |
| $C_2/VO(acac)_2$ | 1.12 on V | almost localized | –85.78522 |
| –1710.053571 | –0.13 on O | on the V atom | |

## The Experimental Findings of ESR Spectroscopy

As mentioned above, from theoretical and experimental point of view it was of interest to have a simple model system to compare the obtained results for the cage structure with those of the model. For structural reasons $VO(acac)_2$ was selected because this system has several advantages. It is well known for a long time, it bears a similar structural unit ($VO_5$), and in dilute solutions there is no doubt that only one $^{51}V$ centre is present in the molecular unit with $S = 1/2$.[13,14] The corresponding experimental and simulated ESR spectra are collected in Figure 6 and Figure 7, respectively. The spectra displayed in Figure 6 represent the resonances of $V^{IV}$ species in fluid (Figure 6, a and c) and frozen (Figure 6, b and d) solutions. The shape of the spectra in the fluid solution is characterized by an incomplete averaging out of the anisotropic hyperfine splitting by molecular motion (tumbling). It means, beside higher order hyperfine effects the typical dependence of the line width of the individual hyperfine-lines on the nuclear spin quantum number $m_I$ results.[15] The spectra could be reproduced by simulation taking into account the line width effects mentioned above together with third order effects of hyperfine splitting (Figure 7). Note that the different patterns of the spectra (Figure 6, a and c) are caused by the different viscosity and polarity of the solvents used and are manifested in the pa-

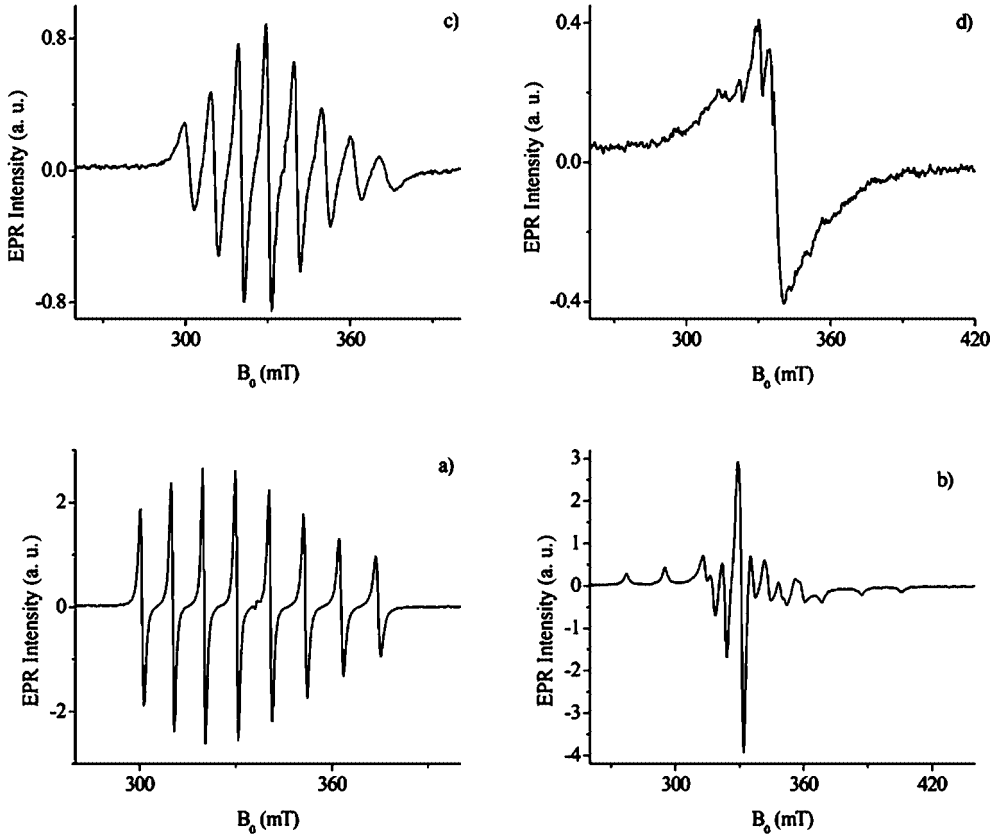


Figure 6. ESR spectra of $VO(acac)_2$, a) $CH_3CN$ solution at 293 K, b) $CH_3CN$ solution at 77 K; c) DMSO solution at 293 K; d) DMSO solution at 77 K.

 © 2007 Wiley-VCH Verlag GmbH & Co. KGaA, Weinheim 

rameters {$\alpha$, $\beta$, and $\gamma$} of the simulation[16] (see caption of Figure 7). The result of the quantum-mechanical calculations of this model system is already given in Table 5.

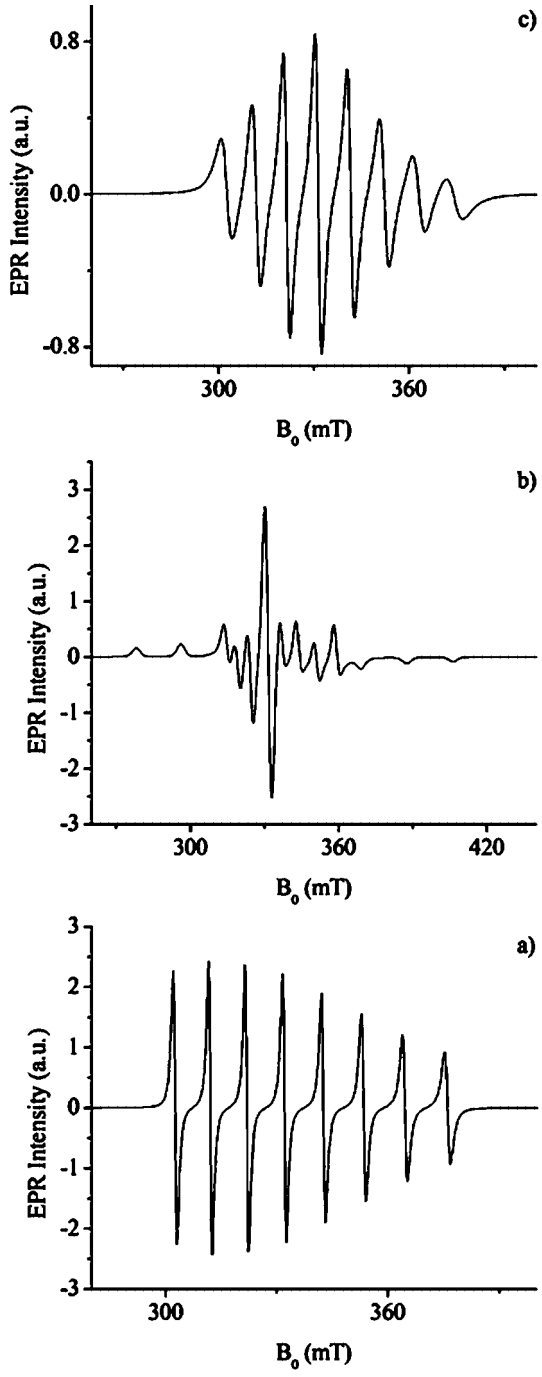


Figure 7. Simulated ESR spectra of $VO(acac)_2$, a) $CH_3CN$ solution at 293 K ($g_{iso}$ = 1.971, $A_{iso}$ = 105 G, $\alpha$ = 10.31, $\beta$ = –0.79, $\gamma$ = 0.19); b) $CH_3CN$ solution at 77 K ($g_{\|}$ = 1.956, $A_{\|}$ = 183.5 G, $g_{\perp}$ = 1.986, $A_{\perp}$ = 62.5 G); c) DMSO solution at 293 K ($g_{iso}$ = 1.969, $A_{iso}$ = 102.3 G, $\alpha$ = 21.60, $\beta$ = –2.76, $\gamma$ = 2.0).

The reduction of $[Ph_3PCH_2CH_3][(V_2O_3)_2(PhPO_3)_4 \subset F]$ with $I^-$ in $CH_3CN$ at room temperature results in the formation of paramagnetic species in a doublet state ($S$ = 1/2). The ESR spectrum of the paramagnetic species (Figure 8, a) exhibits an isotropic 29-line pattern with $g_{iso}$ = 1.964 and $A_{iso}$ = 28.6 G, due to the symmetrical interaction of the unpaired electron with 4 vanadium nuclei in the cage.[4,5,17,18] Generally, the spin density can be delocalized homogeneously, if the cage is surrounded by a symmetrical solvation shell. The consequence of that is the observation of equal values of the hyperfine coupling constant for the four vanadium nuclei ($^{51}V$, $I$ = 7/2) in the cage. A further condition for this observation is a fast reorientation of the cage ($\tau_R \approx 10$ ns) which averages out a possible residue of anisotropy of the hyperfine patterns. Under these conditions one can observe a 29 line spectrum. So, any process which will change the tumbling rate of the cage and/or make it asymmetrical should be responsible for to the change of the ESR spectra. One way to do so is to measure the ESR spectra at lower temperature. The ESR spectrum of frozen $CH_3CN$ solution (77 K) exhibits an 8 line pattern (Figure 8, b) which reflects also a large portion of anisotropic interactions. These effects are manifested in the known dependency of the intensity on the nuclear spin quantum number $m_I$.[15] It is noteworthy that the spectral change between fluid and frozen solutions is reversible.

Another way to make the cage asymmetrical is to adsorb it on the surface of e.g. alumina. The symmetry of the cage should be changed due to specific interactions between the cage and the active sites of the $Al_2O_3$ with a tendency to localize of the unpaired electron at one or two vanadium atoms assisted by the geometrical shape of the cage. The scale of these specific interactions[13,14] is of essential influence on the localization/delocalization of the spin density of the doublet state. The ESR spectrum (Figure 8, c) of $Al_2O_3$ after contact with the paramagnetic $CH_3CN$ solution shows an axial anisotropic eight-line spectrum inclusive some degree of broadening due to coupling of the unpaired electron to a single $^{51}V$ nucleus ($I$ = 7/2). The spectrum represents in its essential feature the envelope of adsorbed and aggregated cages. Broadening of the ESR signals may be attributed to the presence of a spin-spin exchange between the aggregated paramagnetic species in the solid. Lowering the temperature to 77 K yields the spectrum as displayed in Figure 8 (d).

Removing the aggregated species from the system by washing with $CH_3CN$ results in a nearly complete anisotropic 8-line spectrum (Figure 8, e) with an axial feature, $g_{\|}$ = 1.935, $A_{\|}$ = 195 G, $g_{\perp}$ = 1.986 and $A\perp$ = 72 G (compare also with the spectra displayed in Figure 6). In this case the spin density must be "fully" localized at one $^{51}V$-nucleus in the cage. Obviously, the immobilization of the cages at the surface of $Al_2O_3$ is sufficiently strong. It is evidenced by the ESR spectrum taken at 77 K (Figure 8, f) which gave no essential differences with respect to that obtained at 293 K. Furthermore these facts not only confirm the process of adsorption[13,14,19] of the cage but also the adsorption-induced localization of spin density in the cage. The solution of the cage ($S$ = 1/2) coexisting with the {adsorbence/adsorbate} yield, when separately measured at 293 K, a

 © 2007 Wiley-VCH Verlag GmbH & Co. KGaA, Weinheim 

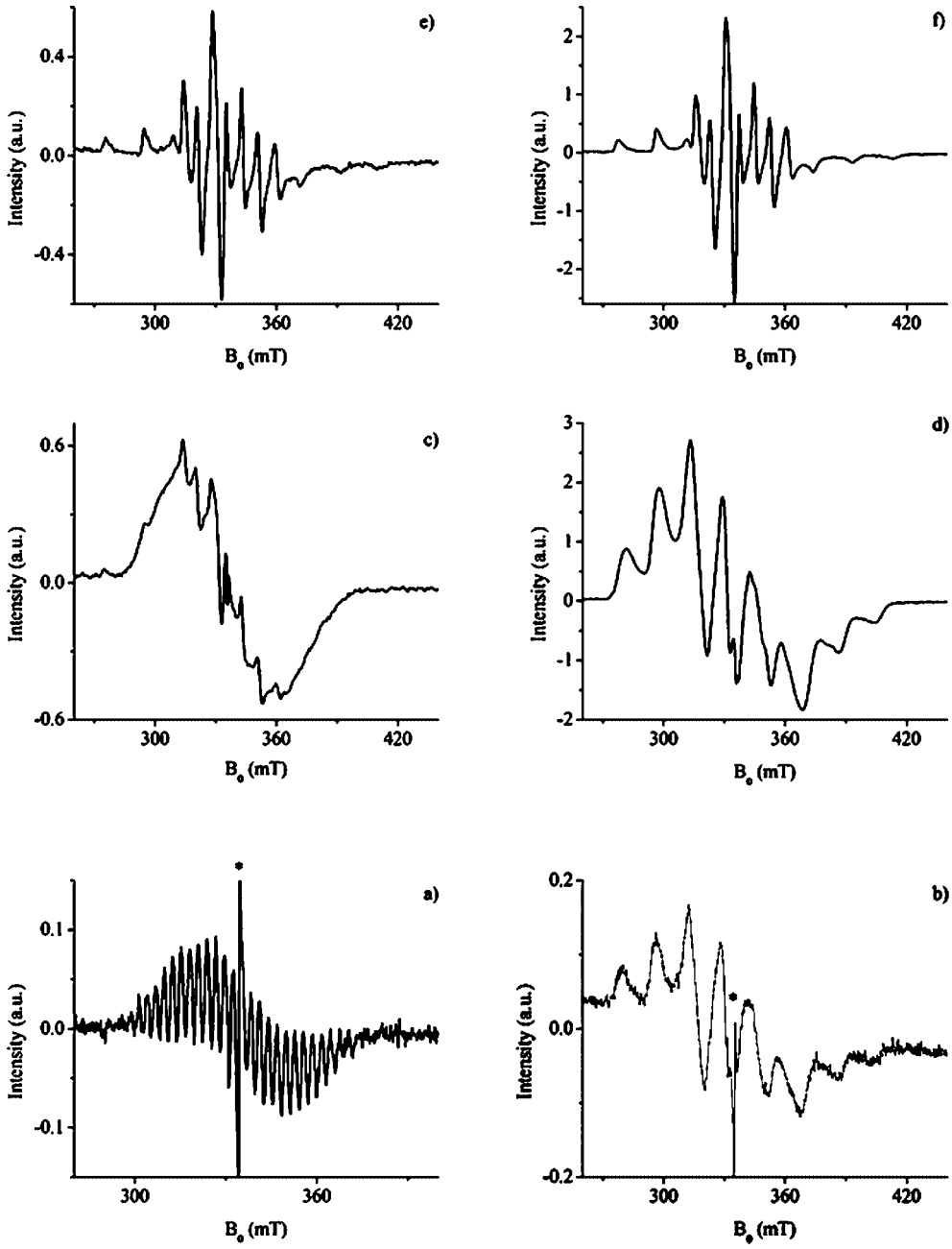


Figure 8. ESR spectra of $[(V_2O_3)_2(PhPO_3)_4 \subset F]^{2-}$ a) $CH_3CN$ solution at 293 K; b) $CH_3CN$ solution at 77 K; c) in contact with $Al_2O_3$; d) in contact with $Al_2O_3$ at 77 K; e) after washing of (c) with $CH_3CN$ at 293 K; f) after washing of (c) with $CH_3CN$ at 77 K. *: reference ($MgO:Cr^{3+}$ $g$ = 1.9796).

well-resolved hyperfine multiplet consisting of 29 lines and $A_{iso}$ = 28.6 G.

## On the Localization/Delocalization of Spin Density in the Cage with $S$ = 1/2

### *Comparison Between Experiment and Theory*

The simulation[16] of the spectra obtained for the solution of $VO(acac)_2$ in $CH_3CN$ at 293 K yields the following coupling constants: $A_0$ = 105. Because the quantum-chemical calculations refer to "free" molecules, the influence of polar or nonpolar solvents on the paramagnetic species in the experiments must be taken into account. The literature offers for $VO(acac)_2$ several values for the isotropic coupling constant in the range of 100 G.[13,14] Based on these values one can estimate a solvent-depending interval of ± 5 G for the isotropic coupling constant. Keeping in mind the general difficulties of the calculation of spin densities, there is an acceptable correspondence to the calculated value of 85 G (Table 5).

Inspecting the hyperfine coupling pattern of the solution of the cage $S$ = 1/2 in $CH_3CN$ at 293 K (Figure 8, a) the value of $A_o$ = 28.6 G reflects the delocalization of the spin

 © 2007 Wiley-VCH Verlag GmbH & Co. KGaA, Weinheim 

density in the cage because this $A$ value must be lower than ca. 100 G for a localization on one $^{51}V$ centre by factor of 1/4. But it must be taken into account that there is a negative spin density at the O atoms and small ones at the P atoms. Therefore, the experimental spectrum is governed by the splitting of the $^{51}V$. Note that a splitting by the O atom is negligible because the natural abundance of the $^{17}O$ isotope is very small.

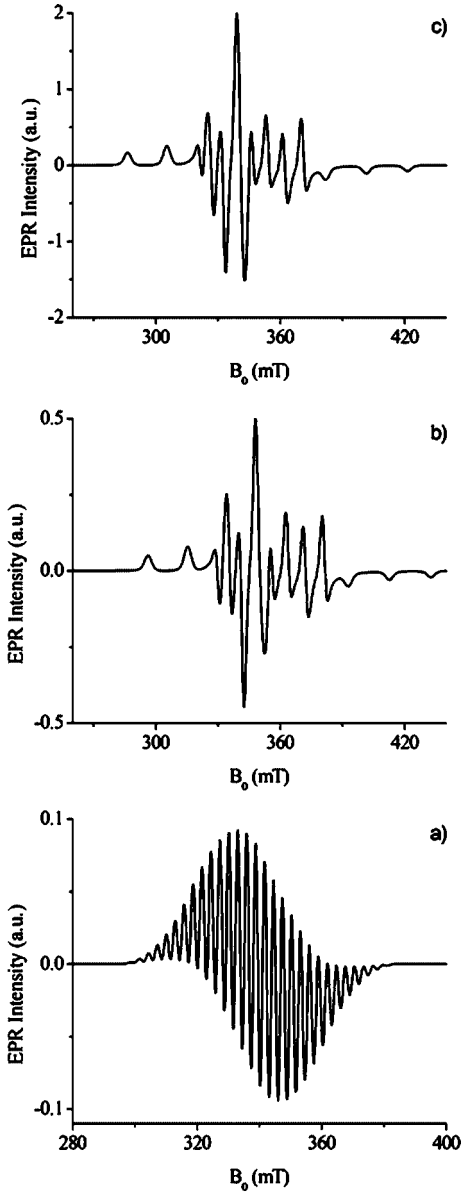


Figure 9. Simulated ESR spectra of $[(V_2O_3)_2(PhPO_3)_4\subset F]^{2-}$ a) $CH_3CN$ solution at 293 K ($g_{iso}$ = 1.964, $A_{iso}$ = 28.6 G); b) in contact with $Al_2O_3$ and washing with $CH_3CN$ at 293 K ($g_{\|}$ = 1.935, $A_{\|}$ = 195 G, $g_{\perp}$ = 1.986, $A_{\perp}$ = 72 G); c) in contact with $Al_2O_3$ and washing with $CH_3CN$ at 77 K ($g_{\|}$ = 1.934, $A_{\|}$ = 69.6 G, $g_{\perp}$ = 1.982, $A_{\perp}$ = 192.8 G).Under structural aspects ESR investigation can be performed successfully if the hyperfine structure is only less disturbed by magnetic dipole–dipole and exchange interactions. This is best realized by the use of diamagnetically diluted systems, e.g. diluted solution or diluted single complexes respectively. The latter ones bear in principle the highest content of information but there are some experimental difficulties to prepare homogeneously diluted diamagnetic solids. For the title compound it was therefore easier to make use of the advantage of the solubility of $[Ph_3PCH_2CH_3][(V_2O_3)_2(PhPO_3)_4\subset F]$ in organic solvents.

Upon cooling, the ESR spectrum became gradually broad and no coalescence temperature could be distinct even below the freezing point of $CH_3CN$ (230 K). The broad and unresolved line may due to the presence of different delocalization states i.e. 29, 21, and/or 15 lines (caused by the coupling with 4, 3 or 2 $^{51}V$ nuclei) which give the envelope of the hyperfine structure. The broad line was only found in the temperature range between the localized and fully delocalized states. However, the ESR of frozen solution (77 K) exhibits an 8 lines pattern (Figure 8, b) with a large degree of line broadening due to the anisotropy caused by the localization of the unpaired electron at one $^{51}V$ nucleus. The broad lines may indicate either that the hopping of the unpaired electron is still taking place to a small extend even at 77 K or that the electron becomes trapped on one vanadium atom with a partial spin density delocalization to other vanadium atoms in the cage (either through V–O–V and/or V–O–P–O–V). This for sure will give rise to more hyperfine lines which will contribute to the envelope. It is noteworthy that the spectral change between fluid and frozen solution is reversible which indicates that the cage compound retains its structure at these temperatures. A selection of simulated ESR spectra is given in Figure 9 together with the corresponding comments.

### *Simple Model Representation for the Delocalization of Spin Density in the Reduced Cage (S = 1/2)*

At low temperatures "packing effects" are of influence on the cage geometry and electron distribution resulting in anisotropic ESR spectra exhibiting an eight-line pattern. This implies the localization of spin density at one $^{51}V$ nucleus. The result corresponds to that of the quantum-chemical calculations forcing the cage to $C_s$ symmetry (Table 5). This configuration of the cage is represented by an energetically minimum at the potential surface which also leads to an essential localization of the spin density. The $C_s$ symmetry of the cage could be also deduced from the results of XRD. The XRD could be performed on the cage system with $S$ = 0 as well as with $S$ = 1/2. The last one bears a high concentration of unpaired electrons in the solid sample which leads to an additional effect of spin-density delocalization. The spin exchange between the cages yields a single exchange narrowed ESR line which gives no direct information about the delocalization in the individual cages of the magnetically undiluted sample.

Rising the temperature of the frozen solution of the cage in the $S$ = 1/2 state, the bond lengths and angles tend to fluctuate around temperature dependent (equilibrium) mean values. These mean values correspond to higher symmetries like $C_{2v}$ or $D_{2d}$ (see for example Table 5). In other words: driven by the thermal fluctuations these cage configurations of higher symmetry will be generated with a certain probability. The action of thermal energy induces a shift of the geometrical mean values and the bond lengths (Table 3) will be larger. It should be noted, that such states

 © 2007 Wiley-VCH Verlag GmbH & Co. KGaA, Weinheim 

of the cage must not represent minima at the potential surface. As a consequence of the admixture of such states at higher temperature (taking into account the actual solvent properties like dielectric constant, viscosity, polarity, etc.) a progressive delocalization of spin density appears in the cages. If the fluctuating $D_{2d}$ symmetry reaches a large statistical weight, the delocalization is nearly complete. This is possible, because the fluctuations of the cage geometry are followed directly by fluctuations of the spin density.

Based on a rather classical aspect the process of spin density delocalization can be regarded as a "hopping process" of the unpaired electron inside the cage with $S = 1/2$. By this hopping, transition states can be reached in the time average which are in formal correspondence to the states obtained by the quantum chemical calculations using $C_{2v}$ and $D_{2d}$ symmetries.

The patterns of the ESR spectra of the mixed-valence system $[(V_2O_3)_2(PhPO_3)_4 \subset F]^{2-}$ measured in solution at room temperature are governed at least by three processes:

i) The hopping of the unpaired electron between the $^{51}V$ atoms present in the cage.

ii) The tumbling rate of the cage: the cage possess no spherical symmetry (maximal $D_{2d}$) even at fast hopping rate[20] a tumbling rate of ca. $10^{10}$ $s^{-1}$ appears to be necessary to produce an isotropic and therefore optimal resolved ESR spectrum. This is approximately the case for the solution of the cage in the doublet state in acetonitrile ($\eta CH_3CN = 0.345$ mPas) (Figure 8, a) at 293 K.

iii) Fluctuation of the cage geometry likewise induced by thermal energy of the environment. But these fluctuations are limited by the template central $F^-$ ion which tends to preserve the cage geometry.

In solution of higher viscosity, e.g. DMSO ($\eta$ = 2.473 mPas), see also part c of Figure 6, spectral resolution of the ESR spectra will be achieved at higher temperature (e.g. 80 °C) where the tumbling of the cage is fast enough to resolve the 29-line spectrum [i.e. the coupling of the unpaired electron with 4 approximately equivalent $^{51}V$ nuclei ($I = 7/2$)].

At room temperature (Figure 8, a), the hopping is fast enough for the X-band ESR to detect the coupling with 4 equivalent $^{51}V$ nuclei. The rest anisotropy of the cage ($D_{2d}$ symmetry or lower) prevents at lower tumbling rates a high spectral resolution because the individual hyperfine lines are too broad with respect to the values of the hyperfine constant of 28.5 G.

Obviously, the hopping rate at low-temperatures is much slower (e.g. $\approx 10^8$ $s^{-1}$). Therefore the frozen solution of the cage exhibits at 77 K an eight line spectrum (Figure 8, b) with evidences the localization of the unpaired electron at one $^{51}V$ nuclei. The broad lines result from less effective hopping at 77 K, producing additional but small hyperfine splitting.

Rising the temperature (up to ≈ 150 K) the eight-line spectrum with the relatively broad lines is more or less preserved. Above ca. 150 K the hopping process will be more effective, contributing more and more to the delocalization of the unpaired electrons and the eight-line spectrum is transformed to the envelope of the 29 line spectrum. The envelope results, because at this temperature there is no real tumbling which could average out the rest of the anisotropic hyperfine coupling. Increasing the temperature even more, up to the fluid system at 293 K, the combined effect of fast hopping and fast tumbling makes the spectral resolution as displayed in Figure 8 (a) possible.

### The X-ray Structure

As shown in Figure 10 the structure of [Ag(1-methylimidazole)$_2$]$_2$[$(V_2O_3)_2(PhPO_3)_4 \subset F$] is constructed from the anionic cage fragment $[(V_2O_3)_2(PhPO_3)_4 \subset F]^{2-}$ which is already described in literature[3,4] and from two cationic [Ag(1-methylimidazole)$_2$] fragments. In each cationic frag-

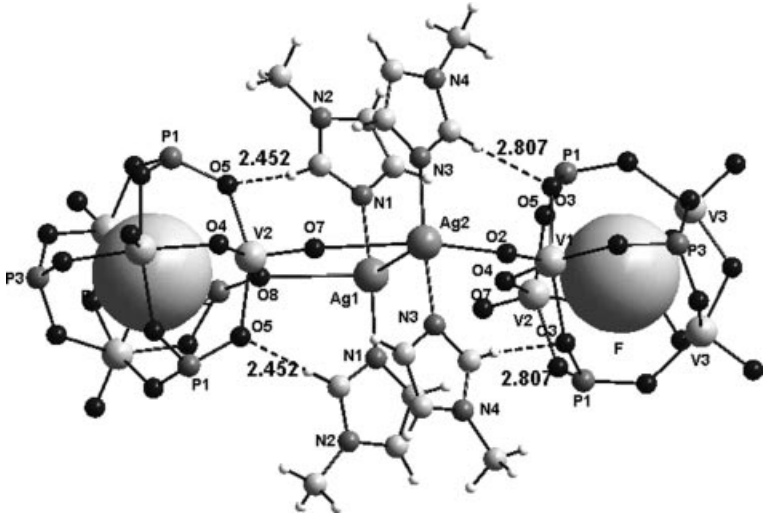


Figure 10. X-ray structure of part of 1D-chain compound [Ag(1-methylimidazole)$_2$]$_2$[$(V_2O_3)_2(PhPO_3)_4 \subset F$] showing the fluoride anion (with van der Waals radii) in the centre of the cage, hydrogen bonds between Ag(1-methylimidazole)$_2$ fragments and the O atoms of the cage and the Ag–Ag bond. Phenyl rings of the cage fragments were omitted for clarity.

 © 2007 Wiley-VCH Verlag GmbH & Co. KGaA, Weinheim 

ment, the Ag ion is coordinated by two nitrogen atoms of different 1-methylimidazole groups to make a nearly linear bond angles between N(1)–Ag(1)–N(1) (171.45°) and N(3)–Ag(2)–N(3) (173.04°). The Ag(1)–N(1) and Ag(2)–N(3) distances are 2.060 and 2.118 Å, respectively. The cationic parts are connected together through π-π stacking interactions between the methylimidazole moieties and through Ag(1)–Ag(2) bond (3.091 Å) which is shorter than the van der Waals contact distance (3.40 Å)[21] and slightly larger than Ag–Ag metallic bond (2.89 Å).[22]

The methylimidazole groups which are connected to the Ag(2) are laying in one plane while the 1-methylimidazole groups which are connected to the Ag(1) are lying in different planes (the angle between the methylimidazole planes is 24.046°). The cationic and anionic fragments are holding together through Ag–O bonds and through intermolecular hydrogen bonds to make 1D chain running along *x* axis. The Ag(2) ion is bonded to two cages through the vanadyl oxygen atoms, namely through the O(2) of one cage and through O(7) of another [Ag(2)–O(2) 2.659 Å, Ag(2)–O(7) 2.701 Å], which means that the cage acts as a ligand toward $Ag^+$ ions to create a 1D chain. Also, the cage is bonded to Ag(1) through O(8) [Ag(1)–O(8) 2.834 Å]. There are week intermolecular hydrogen bonds between the methylimidazole groups and oxygen atoms of the cage [H(19) with O(5) and H(23) with O(3)] and between hydrogen atom H(10) on the phosphonate phenyl group with Ag(2) [Ag(2)–H(10) 2.746 Å].

For Crystal data and structure refinement for [Ag(1-methylimidazole)$_2$]$_2$[$(V_2O_3)_2(PhPO_3)_4$⊂F] see Table 6. Selected bond lengths and angles are collected in Tables 7 and 8, respectively.

Table 6. Crystal data and structure refinement for [Ag(1-methylimidazole)$_2$]$_2$[$(V_2O_3)_2(PhPO_3)_4$⊂F].

| | |
|---|---|
| Empirical formula | $C_{40}H_{44}Ag_2FN_8O_{18}P_4V_4$ |
| Formula weight | 1487.21 |
| Temperature | 180(2) K |
| Wavelength | 0.71073 Å |
| Crystal system, space group | orthorhombic, *Pnma* |
| Unit cell dimensions | $a$ = 16.775(2) Å, $\alpha$ = 90° |
| | $b$ = 17.543(3) Å, $\beta$ = 90° |
| | $c$ = 18.248(3) Å, $\gamma$ = 90° |
| $V$ | 5369.9(13) Å$^3$ |
| $Z$, calculated density | 4, 1.840 Mg/m$^3$ |
| Absorption coefficient | 1.582 mm$^{-1}$ |
| $F$(000) | 2956 |
| Crystal size | 0.24 × 0.20 × 0.16 mm |
| Theta range for data collection | 2.23–25.25° |
| Limiting indices | $-20 \le h \le 20$, |
| | $-21 \le k \le 21$, |
| | $-21 \le l \le 21$ |
| Reflections collected/unique | 46121/5027 [$R$(int) = 0.0767] |
| Completeness to $\theta$ = 25.25 | 99.8% |
| Max. / min. transmission | 0.7859 / 0.7026 |
| Refinement method | full-matrix least squares on $F^2$ |
| Goodness-of-fit on $F^2$ | 1.010 |
| Final $R$ indices [$I > 2\sigma(I)$] | $R1$ = 0.0385, $wR2$ = 0.0928 |
| $R$ indices (all data) | $R1$ = 0.0610, $wR2$ = 0.1035 |
| Largest diff. peak and hole | 0.719 and –1.279 e·A$^{-3}$ |

Table 7. Selected bond lenghts.

| Atom 1 | Atom 2 | Distance [Å] |
|---|---|---|
| Ag1 | Ag2 | 3.0910(8) |
| Ag1 | N1 | 2.0600(53) |
| Ag2 | N3 | 2.1178(35) |
| V1 | O2 | 1.5869(35) |
| V1 | O4 | 1.9153(37) |
| V1 | O1 | 2.0024(38) |
| V1 | O3 | 2.0165(30) |
| V1 | O3 | 2.0165(30) |
| V1 | F | 2.4160(33) |
| V2 | O7 | 1.5972(38) |
| V2 | O4 | 1.7223(35) |
| V2 | O5 | 1.9739(33) |
| V2 | O5 | 1.9739(33) |
| V2 | O8 | 2.0285(35) |
| V2 | F | 2.5372(31) |
| V3 | O11 | 1.5807(34) |
| V3 | O10 | 1.7983(20) |
| V3 | O6 | 1.9083(32) |
| V3 | O9 | 1.9323(30) |
| V3 | O12 | 1.9367(28) |
| V3 | F | 2.4366(25) |

Table 8. Selected bond angles.

| Atom 1 | Atom 2 | Atom 3 | Angle [°] |
|---|---|---|---|
| N1 | Ag1 | N1 | 172.94(21) |
| N3 | Ag2 | N3 | 175.08(13) |
| O2 | V1 | O4 | 103.70(17) |
| O2 | V1 | O1 | 96.59(17) |
| O2 | V1 | O3 | 101.76(8) |
| O2 | V1 | O3 | 101.76(8) |
| O2 | V1 | F | 176.75(15) |
| O7 | V2 | O4 | 105.37(22) |
| O7 | V2 | O5 | 104.14(8) |
| O7 | V2 | O5 | 104.14(8) |
| O7 | V2 | O8 | 97.45(20) |
| O7 | V2 | F | 175.25(16) |
| O11 | V3 | O10 | 100.63(14) |
| O11 | V3 | O6 | 98.90(15) |
| O11 | V3 | O12 | 100.94(15) |
| O11 | V3 | O9 | 101.75(15) |

## Conclusions

For all symmetries examined in this paper it has been shown that the doublet structures are more stable than the singlet ones. The geometries of the doublet structures depend essentially on the SOMO of the additional electron. From a purely empirical point of view without referring to quantum-mechanical calculations there is no definite statement about the residence of the additional electron possible. The hybrid DFT method, at least in the B3LYP version, is able to differentiate between delocalization and localization in mixed-valence vanadium organophosphonates. It should be noted that the amount of Hartree–Fock exchange[23,24] of the DFT functional is of special influence on the values calculated for the spin density. 20% of Hartree–Fock exchange seems to be a good choice for the calculation of delocalized spin densities. Generally, it could be stated that the tendency of delocalization of spin density rises with lowering of the amount of Hartree–Fock exchange. Reduc-

 © 2007 Wiley-VCH Verlag GmbH & Co. KGaA, Weinheim 

ing the Hartree–Fock exchange to 15% the localization of the additional electron was not realized (calculated by self-defined B3LYP functional in the frame of GAUSSIAN 03).

Comparison of the experimental and calculated hyperfine coupling constants (for doublet structure with $D_{2d}$ symmetry) shows good agreement: ca. 28.6 and 27.5 G. Obviously, the stronger tendency of delocalization of spin density yields a better agreement between the results of the theoretical calculations and the experimental ones.

Lowering of the temperature down to 77 K causes localization of spin density which is announced by the eight line ESR spectrum resulting mainly from the interaction of the unpaired electron with one $^{51}$V nucleus. At least two reasons can be quoted for this behaviour: (i) states generated in freezing process deform the cage via specific interaction and can end up in $C_s$ symmetry; (ii) assuming the process of hopping for the spin-density delocalization, a lowering of the temperature diminished the rate (or the efficiency of the hopping of the unpaired electron) and the localization of spin density is favoured.

Further support for the localization results from the comparison of the spectrum with that of $VO(acac)_2$. This molecule is anisotropic (suffering from an axial perturbation) but the symmetrical cage cannot be deformed in such a way. Furthermore, one has to assume that some electron hopping occurs even at 77 K takes place in a restricted manner. This is of influence on the actual spectral pattern characterized by line widths and intensities, but they are able to change the averaged localization of spin density to a small extent.

It can be stated that the hyperfine coupling constant for the localized spin density ($A_{iso}$ = 113 G) in the cages is in acceptable corresponds to the value calculated for the cage in $C_s$ symmetry (85.3 G). No further discrete effects of the spin density localization (e.g. splitting from two or three $^{51}$V nuclei) could be observed by ESR in the temperature range between 77 and 293 K. Therefore different probabilities should result to find the unpaired electron on 4, 3, 2, or 1 $^{51}$V atom of the cage. The superposition of these probabilities yield a broad ESR line which represent the envelope of the hyperfine patterns resulting from splitting by 4, 3, 2, and 1 $^{51}$V nucleus. Lowering of the temperature starting from 293 K to the range of ca. 200 K and below more and more increases the probability to find the unpaired electron at one $^{51}$V nucleus.

## Experimental Section

The synthesis of the cage compounds was carried out by a new route of synthesis using KF as a source of the fluoride anion.[5] All chemicals were of analytical grade.

**X-ray:** Data collection was carried out on an IPDS diffractometer (Stoe & Cie) at 180 K using graphite-monochromated Mo-$K_\alpha$ radiation and a cryostream cooler (Oxford Cryosystems). The data set was collected in steps of $\Delta\phi$ = 1.1° up to 198°. The measured intensities were corrected for background, Lorentz polarization, absorption and crystal decay effects. The structure was solved[25] and refined[26] with the SHELX 97 program.

**ESR Spectroscopy:** ESR spectra (X-band) were recorded using the spectrometer ERS 300 (ZWG/Magnettech., Berlin-Adlershof, Germany). The spectra were simulated using the programs Simfonia.[16] The temperature control unit E-257/WL-257 (Varian, USA) was applied for the variation of the temperature of the samples inside the cavity. Because of the lower limit of the temperature range was of interest ($T \geq 77$ K) which bears some difficulties with respect to the stability, a simple alternative to the gas-flow apparatus E-257 was used: a Dewar flask was filled with liquid nitrogen to cool the sample down to 77 K. Afterwards the liquid nitrogen was removed and the Dewar flask was closed. The temperature was raised with a flat exponential curve caused by the transport of the heat from the environment into the sample. The temperature was monitored using a thermocouple positioned inside the sample. In the same time, the ESR spectra were measured continually in a time interval of small temperature changes.

The following experiments were performed to transform the cage into the doublet state ($S$ = 1/2) as well as to change the spatial distribution of the spin density inclusive the possible changes of the cage geometry:

i) By reaction of the cage compound $Ph_3PCH_2CH_3[(V_2O_3)_2(PhPO_3)_4F]$ with $(n\text{Bu})_4NI$ in $CH_3CN$ one electron was transferred to the cage and the system persisted in the doublet state ($S$ = 1/2). Then ESR spectra were measured at 293 and 77 K in a capillary tube (inner diameter, 1 mm).

ii) The paramagnetic solution (i) was treated with $Al_2O_3$ (Aldrich), then the solvent was removed and the ESR spectra of the solid (adsorbents/adsorbate) were measured at 293 and 77 K.

iii) The solid part of (ii) was washed with $CH_3CN$, and then the ESR spectra were measured at 293 and 77 K of both the solid and the solution.

CCDC-640689 contains the supplementary crystallographic data for this paper. These data can be obtained free of charge from The Cambridge Crystallographic Data Centre via www.ccdc.cam.ac.uk/data_request/cif.

## Acknowledgments

The Deutscher Akademischer Austausch Dienst (DAAD) is acknowledged for financial support of Jabor K. Jabor. Dr. W. Hermann and Dr. A. Zehl are kindly acknowledged for supporting parts of the experimental works. Furthermore we thank Th. Ritschel for supporting the calculations.

[1] M. Vasylyev, R. Neumann, *Chem. Mater.* **2006**, *18*, 2781–2783.
[2] W. J. Johnson, A. J. Jacobson, W. M. Butler, S. E. Rosenthal, J. F. Brody, J. T. Lewandowski, *J. Am. Chem. Soc.* **1989**, *111*, 381–383.
[3] Q. Chen, J. Zubieta, *J. Chem. Soc. Chem. Commun.* **1994**, 2663.
[4] D. Thorn, R. Harlow, N. Herron, *Inorg. Chem.* **1995**, *34*, 2629–2638.
[5] to be published.
[6] J. Salta, Q. Chen, Y.-D. Chang, J. Zubieta, *Angew. Chem. Int. Ed. Engl.* **1994**, *33*, 757.
[7] Y.-D. Chang, J. Salta, J. Zubieta, *Angew. Chem. Int. Ed. Engl.* **1994**, *33*, 325.
[8] Q. Chen, J. Zubieta, *J. Chem. Soc. Chem. Commun.* **1994**, 1635.
[9] M. Meisel, D. Wulff-Molder, in preparation.
[10] D. Becke, *J. Chem. Phys.* **1993**, *98*, 5648; C. Lee, W. Yang, R. G. Parr, *Phys. Rev. B* **1988**, *37*, 875.
[11] In general the 6-311 G* has been used with a small change of the number of polarisation functions for different atoms. For

 © 2007 Wiley-VCH Verlag GmbH & Co. KGaA, Weinheim 

the 6-311G basis set see: A. D. McLean, G. S. Chandler, *J. Chem. Phys.* **1980**, *72*, 5639.
[12] M. J. Frisch, G. W. Trucks, H. B. Schlegel, G. E. Scuseria, M. A. Robb, J. R. Cheeseman, J. A. Montgomery Jr, T. Vreven, K. N. Kudin, J. C. Burant, J. M. Millam, S. S. Iyengar, J. Tomasi, V. Barone, B. Mennucci, M. Cossi, G. Scalmani, N. Rega, G. A. Petersson, H. Nakatsuji, M. Hada, M. Ehara, K. Toyota, R. Fukuda, J. Hasegawa, M. Ishida, T. Nakajima, Y. Honda, O. Kitao, H. Nakai, M. Klene, X. Li, J. E. Knox, H. P. Hratchian, J. B. Cross, C. Adamo, J. Jaramillo, R. Gomperts, R. E. Stratmann, O. Yazyev, J. Austin, R. Cammi, C. Pomelli, J. W. Ochterski, P. Y. Ayala, K. Morokuma, G. A. Voth, P. Salvador, J. J. Dannenberg, V. G. Zakrzewski, S. Dapprich, A. D. Daniels, M. C. Strain, O. Farkas, D. K. Malick, A. D. Rabuck, K. Raghavachari, J. B. Foresman, J. V. Ortiz, Q. Cui, A. G. Baboul, S. Clifford, J. Cioslowski, B. B. Stefanov, G. Liu, A. Liashenko, P. Piskorz, Komaromi, R. L. Martin, D. J. Fox, T. Keith, M. A. Al-Laham, C. Y. Peng, A. Nanayakkara, M. Challacombe, P. M. W. Gill, B. Johnson, W. Chen, M. W. Wong, C. Gonzalez, J. A. Pople, *Gaussian 03*, Revision B.02, Gaussian, Inc., Pittsburgh PA, **2003**.
[13] C. M. Guzy, J. B. Raynor, M. C. R. Symons, *J. Chem. Soc. A* **1969**, 2791–2795.
[14] M. Baltes, P. Van Der Voort, B. M. Weckhuysen, R. Ramachandra Rao, G. Catana, R. A. Schoonheyd, E. F. Vansanta, *Phys. Chem. Chem. Phys.* **2000**, *2*, 2673–2680.
[15] D. Kivelson, *J. Chem. Phys.* **1960**, *33*, 1094–1106.
[16] *WIN-SimFonia*, Bruker.
[17] G. B. Karet, Z. Sun, D. D. Heinrich, J. K. McCusker, K. Folting, W. E. Streib, J. C. Huffman, D. N. Hendrickson, G. Christou, *Inorg. Chem.* **1996**, *35*, 6450–6460.
[18] J. Jabor, R. Stößer, Nguyen Huu Thong, B.Ziemer, M. Meisel, to be published.
[19] J. A. R. Van Veen, G. Jonkers, W. H. Hesselink, *J. Chem. Soc. Faraday Trans. 1* **1989**, *85*, 389–413.
[20] S. P. Harmalker, M. A. Leparulo, M. T. Pope, *J. Am. Chem. Soc.* **1983**, *105*, 4286–4292.
[21] A. Bondi, *J. Phys. Chem.* **1964**, *68*, 441–451.
[22] D. Venkataraman, Y. Du, S. R. Wilson, K. Hirsch, P. Zhang, J. S. Moore, *J. Chem. Educ.* **1997**, *74*, 915–918.
[23] E. Ruiz, J. Cirera, S. Alverez, *Coord. Chem. Rev.* **2005**, *249*, 2649.
[24] K. R. Asmis, G. Santambrogio, M. Brümmer, J. Sauer, *Angew. Chem.* **2005**, *117*, 3182.
[25] G. M. Sheldrick, *Acta Crystallogr., Sect. A* **1990**, *46*, 467–473, cited for SHELXS.
[26] G. M. Sheldrick, *SHELXL-97*, Program for Crystal Structure Refinement, University of Göttingen, Göttingen (Germany), **1997**.

Received: January 23, 2007
Published Online: June 18, 2007

 © 2007 Wiley-VCH Verlag GmbH & Co. KGaA, Weinheim

**The EUChemSoc Societies have taken the significant step into the future by merging their traditional journals, to form two leading chemistry journals, the *European Journal of Inorganic Chemistry* and the *European Journal of Organic Chemistry.* Three further EUChemSoc Societies (Austria, Czech Republic and Sweden) are Associates of the two journals.**

## COVER PICTURE

**The cover picture shows** the schematic structures of a 2,5-dithienylphosphole and a dithieno[3,2-*b*:2′,3′-*d*]-phosphole, as well as the fluorescence properties of materials based on the latter system. These scaffolds are two of the most promising organophosphorus-based building blocks for organic electronics to date. Extensive investigations of their structure−property relationships has laid ground for a variety of applications such as sensing or as an active component in electronic devices. Details on the syntheses, their systematic modifications, as well as the resulting (opto)-electronic properties of the materials are presented in the Microreview by M. G. Hobbs and T. Baumgartner on p. 3611ff.

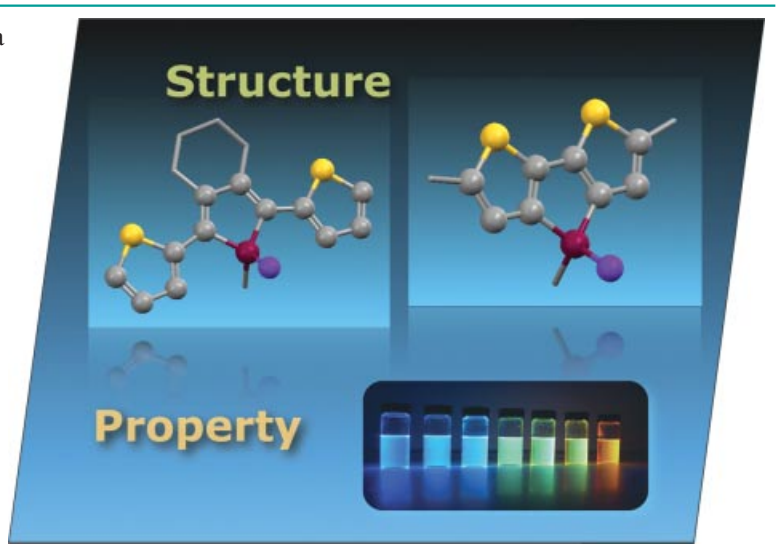


 © 2007 Wiley-VCH Verlag GmbH & Co. KGaA, Weinheim 

# CONTENTS

## MICROREVIEW


### Phosphole Materials

**M. G. Hobbs, T. Baumgartner* ..... 3611–3628**

Recent Developments in Phosphole-Containing Oligo- and Polythiophene Materials

**Keywords:** Phosphole / Thiophene / Conjugated materials / Organic electronics / Fluorescence


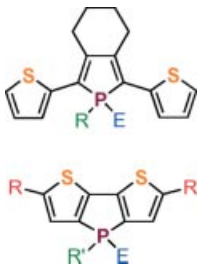


This Microreview covers the latest developments in phosphole-thiophene hybrid materials for organic electronics and describes how systematic, comprehensive investigations focusing on structure–property relationships can determine the scope and suitability of such materials for optoelectronic applications.


## SHORT COMMUNICATION


### Air-Stable Pd Catalysts

**A. L. Gottumukkala, H. Doucet* ..... 3629–3632**

Activated Aryl Chlorides: Useful Partners for the Coupling with 2-Substituted Thiazoles in the Palladium-Catalysed C-H Activation/Functionalisation Reaction

**Keywords:** Aryl chlorides / Catalysis / C-H activation / Palladium / Thiazoles


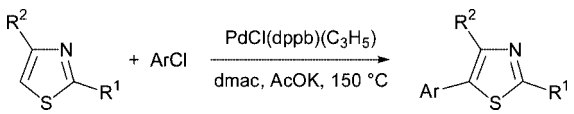



Aryl chlorides are noticeably uncommon partners in coupling reactions with heteroaromatics through C-H activation. We report herein that as little as 1 mol-% of the air-stable $PdCl(dppb)(C_3H_5)$ complex catalyses the direct coupling of electron-deficient aryl chlorides with 2-substituted thiazole derivatives.


## FULL PAPERS


### Carbohydrate Copper Complexes

**M. Gottschaldt,* R. Wegner, H. Görls, E.-G. Jäger, D. Klemm ..... 3633–3638**

Synthesis and Crystal Structure of a Heptanuclear and an Octanuclear Copper(II) Complex Derived from α-D-Glucofuranoses

**Keywords:** Carbohydrates / Copper complexes / Cluster compounds


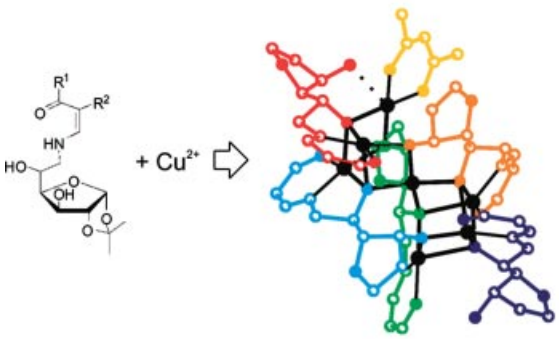



A hepta- and one octanuclear copper(II) complex could be crystallised using 6-(β-keto-enamino)-6-deoxy-1,2-*O*-isopropylidene-α-D-glucofuranoses as ligands. Due to the nature of the carbohydrate scaffold they show different and highly asymmetric structures.

## Kinetics of Complex Formation

Formation of the complexes $[Ln(DOTAM)]^{3+}$ occurs upon direct encounter between the $Ln^{3+}$ ions and the non-protonated DOTAM ligands in a second-order reaction. Contrary to the formation of $[Ln(DOTA)]^{-}$ complexes, no intermediates were detected.

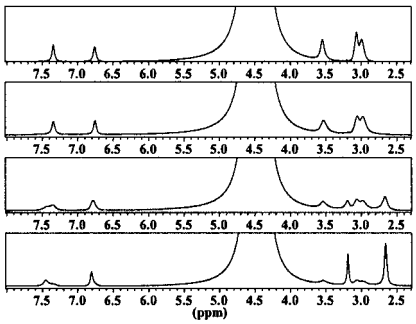


**Z. Baranyai, I. Bányai, E. Brücher,***
**R. Király, E. Terreno** ..... **3639–3645**

Kinetics of the Formation of $[Ln(DOTAM)]^{3+}$ Complexes

**Keywords:** Macrocyclic ligands / Lanthanides / Kinetics / Reaction mechanisms

## Proton Affinities

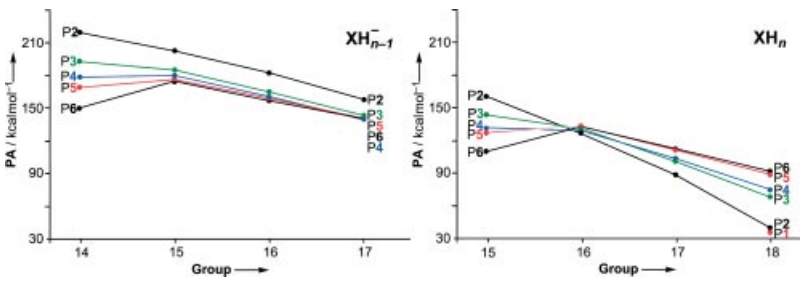


Proton affinities in water of archetypal anionic ($XH_{n-1}^-$) and neutral bases ($XH_n$) across the periodic table (groups 14–18, periods 1–6) are smaller than those in the gas phase but, importantly, they follow similar trends.

**M. Swart, E. Rösler,**
**F. M. Bickelhaupt*** ..... **3646–3654**

Proton Affinities in Water of Maingroup-Element Hydrides – Effects of Hydration and Methyl Substitution

**Keywords:** Acidity / Basicity / Density functional calculations / Periodic table / Proton affinities / Thermochemistry / Solvent effects

## Vanadium(IV/V) Complexes

The first examples of oxidotrichloridovanadium(V) thioether complexes have been prepared and fully characterised, together with vanadyl(IV) and tetrachloridovanadium(IV) analogues. The structure of a unique tetranuclear oxidovanadium(IV) thioether complex is described.

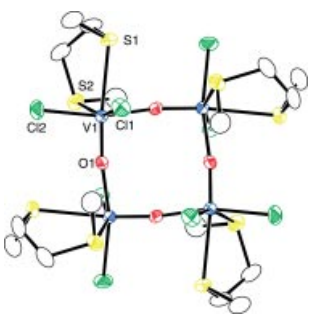


**A. L. Hector, W. Levason, A. J. Middleton,**
**G. Reid,* M. Webster** ..... **3655–3662**

Vanadium(IV) and Oxidovanadium(IV) and -(V) Complexes with Soft Thioether Coordination – Synthesis, Spectroscopic and Structural Studies

**Keywords:** Vanadium / Thioether / Structural studies

## Ferromagnetic Mn Complexes

The chlorido-bridged $[Mn(HL)(\mu\text{-}Cl)Cl]_2$ complex with intradimer ferromagnetic coupling through chlorido bridges and weak interdimer antiferromagnetic interaction through hydrogen bonding is reported. A comparison of the magnetic coupling for $[Mn(HL)(\mu\text{-}Cl)Cl]_2$ and other structurally similar compounds is discussed.

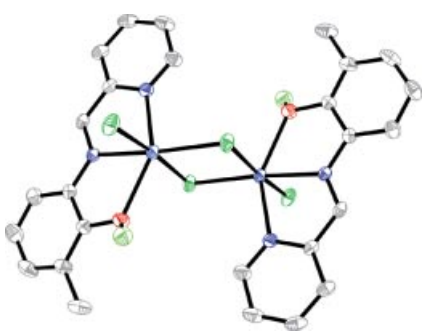

**C.-M. Qi, X.-X. Sun, S. Gao,**
**S.-L. Ma,* D.-Q. Yuan, C.-H. Fan,**
**H.-B. Huang, W.-X. Zhu** ..... **3663–3668**

Chlorido-Bridged $Mn^{II}$ Schiff-Base Complex with Ferromagnetic Exchange Interactions

**Keywords:** Manganese / Schiff bases / Magnetic properties

 © 2007 Wiley-VCH Verlag GmbH & Co. KGaA, Weinheim 

# CONTENTS


## Terdentate NSN and NNN Ligands

**L. Canovese,* F. Visentin, G. Chessa, C. Levi, A. Dolmella ..... 3669–3680**

Synthesis, Stability Constant Determination, and Structural Study of Some Complexes of a Zinc Triad Containing Pyridyl-amine-quinoline and Pyridyl-thio-quinoline

**Keywords:** Zinc / Quinoline-based ligands / Fluorescence / Formation constants

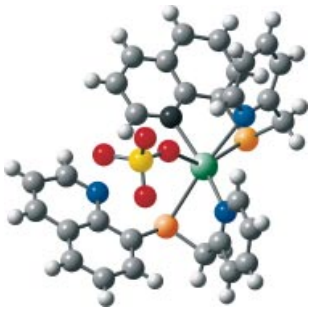

Potentially fluorescent and terdentate ligands bearing nitrogen, sulfur, and a quinoline ring were synthesized and used for the preparation of several complexes of the zinc triad. (Colour code: blue = nitrogen, orange = sulfur, green = mercury, yellow = chlorine, red = oxygen)

## Ligand Exchange Reactions

**G. Serratrice,* F. Biaso, J.-L. Pierre, S. Blanc, A.-M. Albrecht-Gary ..... 3681–3685**

Iron(III) Exchange Process between Hexadentate Tripodal Ligands: Models for the Ternary Complexes

**Keywords:** Mixed ligands / Iron / Exchange interactions / Siderophores / Tripodal ligands

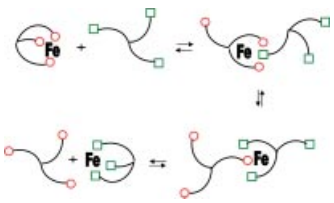


Kinetics of the iron exchange reaction between a tris(catechol) ligand (red circles) and a tris(8-hydroxyquinoline) ligand (green squares) was investigated. The mechanism shows that the reaction occurs step-by-step via ternary complexes having a mixed coordination at the iron center.

## Bioinorganic Pair Models

**S. I. Kirin, H. P. Yennawar, M. E. Williams* ..... 3686–3694**

Synthesis and Characterization of $Cu^{II}$ Complexes with Amino Acid Substituted Di(2-pyridyl)amine Ligands

**Keywords:** Bioconjugates / Bioinorganic chemistry / Copper complexes / Di(2-pyridyl)amine

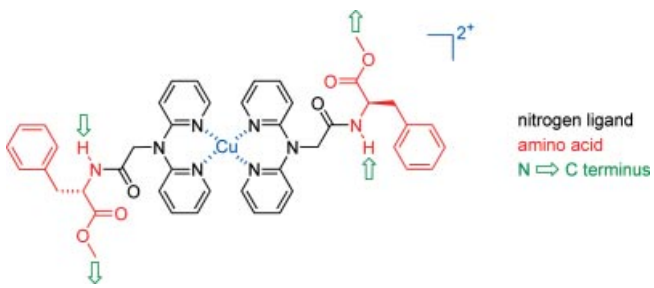


$Cu^{II}L_2$ complexes with new amino acid–nitrogen ligand derivatives are prepared as potential building blocks in the assembly of inorganic models of double-stranded nucleic acid.

## Intervalence Charge Transfer

**S. De, S. Chowdhury, J. P. Naskar, M. G. B. Drew, R. Clérac, D. Datta* ..... 3695–3700**

A Hexadecanuclear Copper(I)–Copper(II) Mixed-Valence Compound: Structure, Magnetic Properties, Intervalence Charge Transfer, EPR, and NMR

**Keywords:** Copper / High-nuclearity complexes / Aggregates / Mixed-valent compounds / Charge transfer / N,O ligands

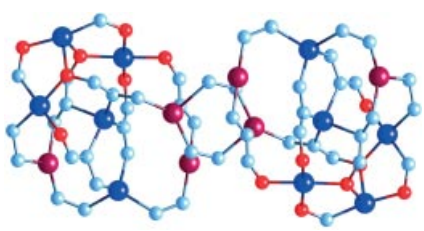

A hexadecanuclear mixed-valence copper complex containing 10 $Cu^{II}$ centers (blue) and 6 $Cu^{I}$ centers (purple), isolated with N,O donor ligands gives NMR and shows a broad intervalence charge-transfer band at 1100 nm at room temperature in methanol, and gives an EPR spectrum characteristic of mononuclear $Cu^{II}$ at 5 K.


 © 2007 Wiley-VCH Verlag GmbH & Co. KGaA, Weinheim 

## Macrocyclic Complexes

Trinuclear manganese(III) complexes of new unsymmetrical pentadentate Schiff base ligands have been prepared and characterised. The molecular structures are represented as a tripodal pyramid with a small cavity.

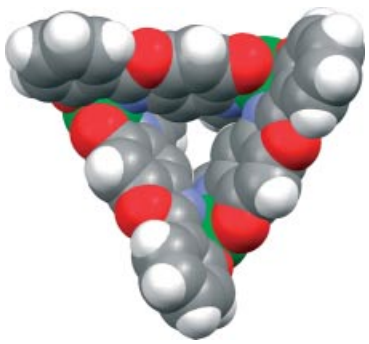

**M. Muto, N. Hatae, Y. Tamekuni, Y. Yamada, M. Koikawa,* T. Tokii* ..... 3701–3709**

Tripodal Trimanganese(III) Complexes of New Unsymmetrical Pentadentate Ligands Derived from 2-(Salicylideneamino)phenol: Syntheses, Crystal Structures and Properties

**Keywords:** Bridging ligands / Ligand design / Manganese / X-ray structures / Magnetic properties / Redox chemistry

## Magnetic Nickel Complexes

Reactions of nickel(II) salts with 4-amino-3,5-bis(pyridin-2-yl)-1,2,4-triazole (abpt) generate a tetranuclear nickel(II) rectangle box, neutral dinuclear-, and mononuclear species with two polymorphous phases. The $\mu$:$\eta^1$:$\eta^2$:$\eta^1$ coordination mode of the deprotonated $[abpt\text{-}H]^-$ ligand is observed in the rectangle box. Temperature-dependent magnetic properties of the dinuclear and tetranuclear complexes were investigated.

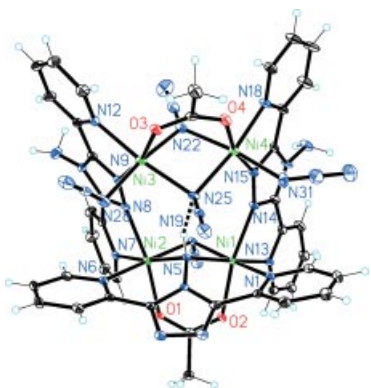


**M.-L. Tong,* C.-G. Hong, L.-L. Zheng, M.-X. Peng, A. Gaita-Ariño, J. M. Clemente Juan* ..... 3710–3717**

New Reactivity of 4-Amino-3,5-bis(pyridin-2-yl)-1,2,4-triazole: Synthesis and Structure of a Mononuclear Species, a Dinuclear Species, and a Novel Tetranuclear Nickel(II) Rectangle Box, and Magnetic Properties of the Dinuclear and Tetranuclear Complexes

**Keywords:** Nickel / Polynuclear / Azides / Magnetic properties

## Fe-Only Hydrogenase Models

The X-ray analyses show that the $PMe_2Ph$ ligand in the apical position of the starting complex rotates to the basal position of the unsymmetrically disubstituted diiron complexes when $PPh_3$ and $P(OEt)_3$ were used as incoming ligands, providing clear evidence for the conformational flexibility of the $[Fe(CO)_2L]$ subunits in the Fe-only hydrogenase model complexes in solution.

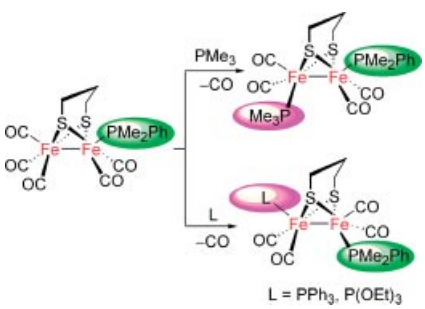


**P. Li, M. Wang,* C. He, X. Liu, K. Jin, L. Sun* ..... 3718–3727**

Phosphane and Phosphite Unsymmetrically Disubstituted Diiron Complexes Related to the Fe-Only Hydrogenase Active Site

**Keywords:** Bioinorganic chemistry / Carbonyl displacement / Diiron complexes / Fe-only hydrogenase / P ligands

## Antitumour Agents

Platinum(II) and palladium(II) complexes with 4-(2-hydroxybenzoyl)-2-(pyridin-2-yl)-1*H*-pyrazol-3-ol ($HL^1$) have been synthesised as potential anticancer compounds. Protonation constants of the ligand and solid-state structures of the complexes are reported. The cytotoxic evaluation revealed that $Pt^{II}$ and $Pd^{II}$ complexes were active in the micromolar concentration range. Color code of ORTEP drawing: blue = N; green = Cl, red = O; yellow = Pt.

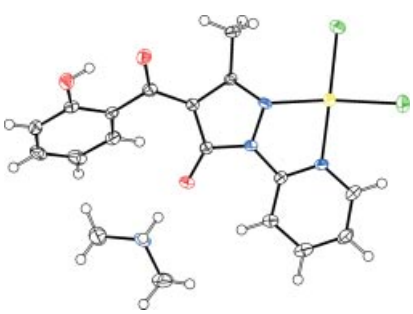

**E. Budzisz,* M. Malecka, B. K. Keppler, V. B. Arion, G. Andrijewski, U. Krajewska, M. Rozalski ..... 3728–3735**

Synthesis, Structure, Protolytic Properties, Alkylating and Cytotoxic Activity of Novel Platinum(II) and Palladium(II) Complexes with Pyrazole-Derived Ligands

**Keywords:** Metal complexes / Platinum / Palladium / Pyrazole ligands / Antitumor agents / Alkylating and cytotoxic activity

 © 2007 Wiley-VCH Verlag GmbH & Co. KGaA, Weinheim 

# CONTENTS

## C−O Activation

**G. Christian, R. Stranger,* B. F. Yates, C. C. Cummins ..... 3736−3741**

Cleavage of CO by Mo[N(R)Ar]$_3$ Complexes

**Keywords:** C−O activation / Molybdenum / Three-coordinate complexes / Density functional calculations / Bond cleavage

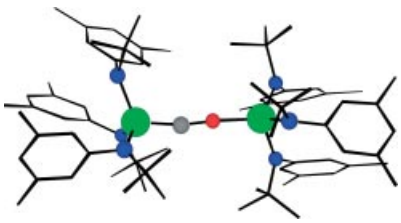

The reaction of $MoL_3$ [L = $NH_2$ and N(*t*Bu)Ar] with CO is explored using DFT in order to rationalise why C−O cleavage is not observed for this system. In contrast, the analogous $N_2$ reaction results in spontaneous cleavage of $N_2$.

## Lead Speciation

**J. S. Casas,* E. E. Castellano, J. Ellena, M. S. García-Tasende, F. Namor, A. Sánchez, J. Sordo, M. J. Vidarte ..... 3742−3750**

Methyllead(IV) Derivatives Stabilized by DAPTSC$^{2-}$: Synthesis and Structures of New Diorganolead(IV) Complexes

**Keywords:** Lead / Diorganolead (IV) complexes / Metallation

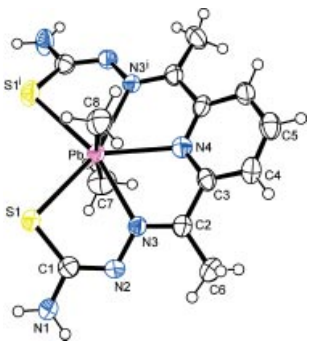


Reactions of the pentadentate ligand $H_2$DAPTSC with $PbMe_2(OAc)_2$ and $PbMePh(OAc)_2$ afforded simultaneously dimethyllead(IV) [or methylphenyllead(IV)] and lead(II) complexes. Their structures in solid state and solution were investigated.

**If not otherwise indicated in the article, papers in issue 22 were published online on July 19, 2007**

 © 2007 Wiley-VCH Verlag GmbH & Co. KGaA, Weinheim

**The EUChemSoc Societies have taken the significant step into the future by merging their traditional journals, to form two leading chemistry journals, the *European Journal of Inorganic Chemistry* and the *European Journal of Organic Chemistry.* Three further EUChemSoc Societies (Austria, Czech Republic and Sweden) are Associates of the two journals.**

## COVER PICTURE

**The cover picture shows** the schematic structures of a 2,5-dithienylphosphole and a dithieno[3,2-*b*:2′,3′-*d*]-phosphole, as well as the fluorescence properties of materials based on the latter system. These scaffolds are two of the most promising organophosphorus-based building blocks for organic electronics to date. Extensive investigations of their structure−property relationships has laid ground for a variety of applications such as sensing or as an active component in electronic devices. Details on the syntheses, their systematic modifications, as well as the resulting (opto)-electronic properties of the materials are presented in the Microreview by M. G. Hobbs and T. Baumgartner on p. 3611ff.

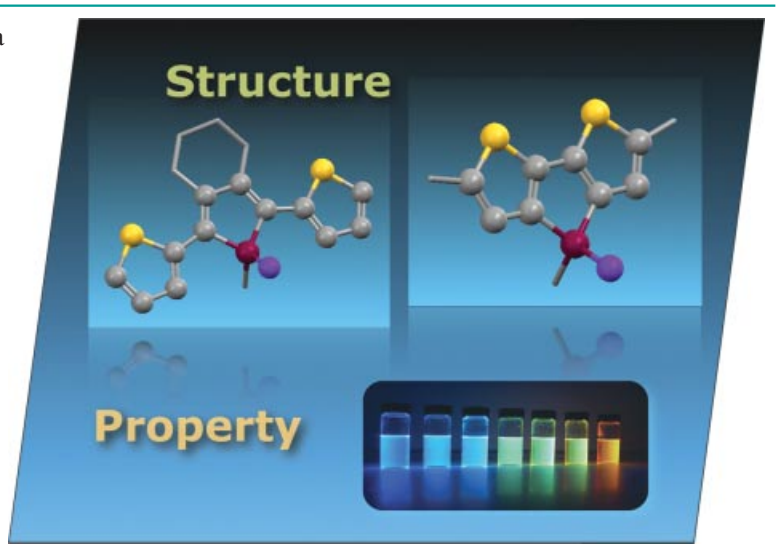


 © 2007 Wiley-VCH Verlag GmbH & Co. KGaA, Weinheim 

# SPOTLIGHTS …

## *Dialkyl Complexes*

A. S. Hock, R. R. Schrock*

**Oxidative Reactions of the $Mo^{IV}$ Dialkyl Complex $[\{(3\text{-}CF_3C_6H_4NCH_2CH_2)_2\text{-}NMe\}Mo(CH_2SiMe_3)_2]$**

*Chem. Asian J.*
DOI: **10.1002/asia.200700093**

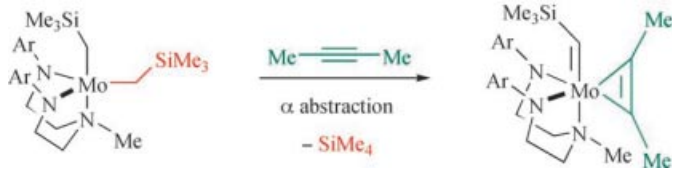


**Silicon replacement therapy**: $[(CF_3N_2NMe)Mo(CH_2SiMe_3)_2]$ ($(CF_3N_2NMe)^{2-} = [(3\text{-}CF_3C_6H_4\text{-}NCH_2CH_2)_2NMe]^{2-}$) reacts with 2-butyne, cyclohexene sulfide, and $C_2Cl_6$ to give $[(CF_3N_2NMe)Mo(CHSiMe_3)(\eta^2\text{-}MeC{\equiv}CMe)]$, $[\{(CF_3N_2NMe)MoS\}_2]$, and $[\{(CF_3N_2NMe)Mo(CSiMe_3)Cl\}_2]$, respectively. α-H abstraction of $Mo^{VI}$ to yield (initially) $Mo{=}CHSiMe_3$ and $SiMe_4$ is the proposed route for these reactions.

## *Biocatalysis*

A. Chefson, K. Auclair*

**CYP3A4 Activity in the Presence of Organic Cosolvents, Ionic Liquids, or Water-Immiscible Organic Solvents**

*ChemBioChem*
DOI: **10.1002/cbic.200700128**

**Selective hydroxylation of inactivated C–H bonds**. While tolerating only low amounts of water-miscible cosolvents or water-miscible ionic liquids, human CYP3A4 functions acceptably in organic solvents, with optimum activity in buffer/hexane biphasic solvent systems; this offers considerable potential for future applications of P450s in synthesis.

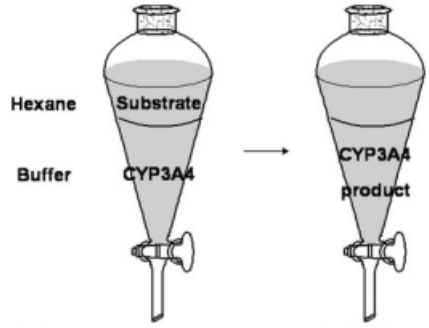


## *Computational Power*

M. Christen, C. D. Christ, W. F. van Gunsteren*

**Free Energy Calculations Using Flexible-Constrained, Hard-Constrained and Non-Constrained Molecular Dynamics Simulations**

*ChemPhysChem*
DOI: **10.1002/cphc.200700176**

**Turning the water into methanol**: One of the most important quantities that can be obtained from simulations are relative free energies. The difference in the free energy of liquid water and liquid methanol is calculated by molecular dynamics simulations using three different models for water and methanol: a flexible model, an alternative flexible model and a rigid model (see picture).

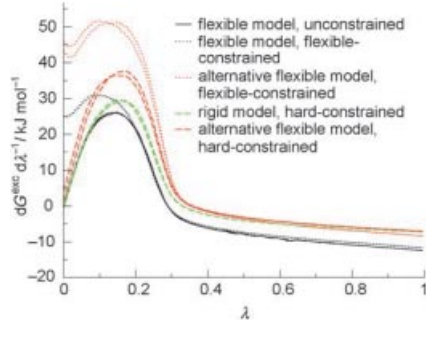


## *Compound Libraries*

A. Böcker, B. C. Sasse , M. Nietert, H. Stark, G. Schneider*

**GPCR Targeted Library Design: Novel Dopamine $D_3$ Receptor Ligands**

*ChemMedChem*
DOI: **10.1002/cmdc.200700067**

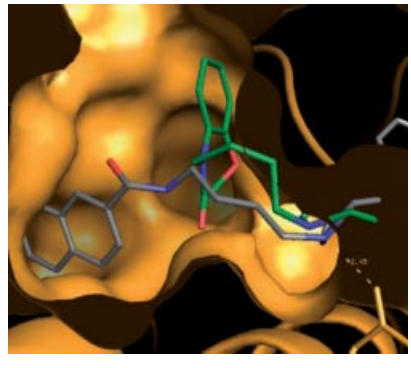

**GPCR-focused compound libraries** were designed by strategic iterative virtual screening. The most potent ligands yielded $K_i$ values of 65 nM at the dopamine $D_3$ receptor subtype. Two potential binding modes were observed for receptor antagonists in a homology-based model of the dopamine $D_3$ receptor. Results demonstrate opportunities for a combination of different virtual screening methods in early stages of GPCR drug discovery for new lead finding.

 © 2007 Wiley-VCH Verlag GmbH & Co. KGaA, Weinheim 

EurJIC European Journal of Inorganic Chemistry

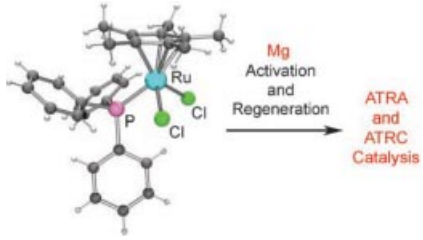


**Radical Reactions**: A combined catalyst system of the Ru complex $[RuCl_2Cp^*(PPh_3)]$ ($Cp^*$: pentamethylcyclopentadienyl) with magnesium allows atom-transfer radical addition (ATRA) and cyclization (ATRC) reactions to be performed with exceptional efficiency under mild conditions (see scheme).

***Ruthenium***

K. Thommes, B. Içli, R. Scopelliti, K. Severin*

**Atom-Transfer Radical Addition (ATRA) and Cyclization (ATRC) Reactions Catalyzed by a Mixture of $[RuCl_2Cp^*(PPh_3)]$ and Magnesium**

*Chem. Eur. J.*
DOI: **10.1002/chem.200700442**

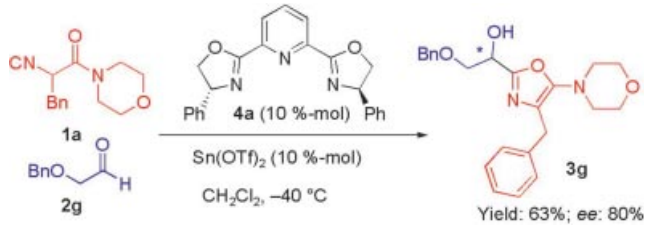


Reactions between α-isocyanoacetamides and aldehydes can be performed at low temperature in the presence of stannous chloride to furnish oxazoles in good to excellent yields. In the presence of the chiral catalyst [Sn-(*R*)-PhPyBox](OTf)$_2$, the reaction between the chelating aldehyde **2g** and **1a** afforded the corresponding 5-aminooxazole **3g** in good yield and enantioselectivity.

***Asymmetric Synthesis***

S. Wang, M.-X. Wang,* D.-X. Wang, J. Zhu*

**Asymmetric Lewis Acid Catalyzed Addition of Isocyanides to Aldehydes – Synthesis of 5-Amino-2-(1-hydroxyalkyl)oxazoles**

*Eur. J. Org. Chem.*
DOI: **10.1002/ejoc.200700340**

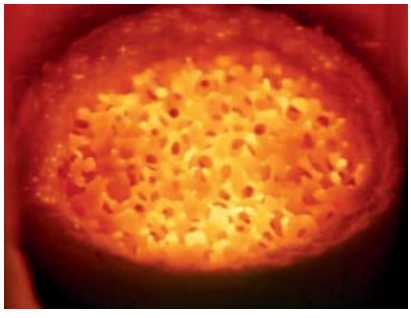

**Breaking the coke habit**: By coupling thermal decomposition with catalytic partial oxidation, an effective method has been developed to convert solid biomass such as cellulose into synthesis gas (see photo of a hot Rh catalyst surface). Not only is the process fast (<70 ms), it also avoids the formation of coke, which is known to deactivate catalyst surface sites and block surface reactions.

***Heterogeneous Catalysis***

P. J. Dauenhauer, B. J. Dreyer, N. J. Degenstein, L. D. Schmidt*

**Millisecond Reforming of Solid Biomass for Sustainable Fuels**

*Angew. Chem. Int. Ed.*
DOI: **10.1002/anie.200701238**

On these pages, we feature a selection of the excellent work that has recently been published in our sister journals. If you are reading these pages on a computer, click on any of the items to read the full article. Otherwise please see the DOIs for easy online access through Wiley InterScience.

 © 2007 Wiley-VCH Verlag GmbH & Co. KGaA, Weinheim 

DOI: 10.1002/ejic.200700236

# Recent Developments in Phosphole-Containing Oligo- and Polythiophene Materials

**Matthew G. Hobbs[a] and Thomas Baumgartner*[a]**

**Keywords:** Phosphole / Thiophene / Conjugated materials / Organic electronics / Fluorescence

The introduction of phosphorus-containing moieties into π-conjugated thiophene materials has been found to provide materials with strongly optimized and highly tunable optoelectronic features compared to their native thiophene counterparts. 2,5-Diaryl- and 2,5-bis(heteroaryl)phospholes as well as fused tricyclic dithieno[3,2-*b*:2′,3′-*d*]phospholes represent two very valuable building blocks for organic electronics as their intriguing features can be altered systematically by several, in part unique, methodologies. The potential scope of these modifications has been determined by comprehensive investigations of their structure–property relationships via suitable molecular model compounds. On several occasions, these observations could successfully be transposed to corresponding polymers that are often difficult to characterize independently. The same is true for the first organic light-emitting diodes (OLEDs) based on a phosphole scaffold, whose properties could also be predicted successfully.
(© Wiley-VCH Verlag GmbH & Co. KGaA, 69451 Weinheim, Germany, 2007)

## 1. Introduction

Organic π-conjugated polymers and oligomers have commanded a significant amount of attention as a result of the conducting (upon doping), or semiconducting properties that they exhibit.[1] Consequently, these materials have great potential for use in electronic devices such as organic or polymer-based light-emitting diodes (OLEDs/PLEDs),[2] photovoltaic cells,[3] field-effect transistors (FETs),[4] nonlinear optical (NLO) devices and polymeric sensors.[5] The development of these systems, and the optimization of their optoelectronic properties often requires the use of model systems. Well-defined model systems allow for the elucidation of important structure–property relationships through the systematic variation of the model's chemical structure, and supramolecular organization. By taking advantage of established structure–property relationships, the properties of materials may be engineered at the molecular level to suit those required by specific applications.[1]

Varying the composition of the π-conjugated backbone in such materials has proven to be a particularly "fruitful" approach to tailoring the properties of organic π-conju-

[a] Department of Chemistry, University of Calgary
2500 University Drive NW, Calgary, AB T2N 1N4, Canada
Fax: +1-403-289-9488
E-mail: thomas.baumgartner@ucalgary.ca

*Matthew G. Hobbs was born in Calgary, Alberta, Canada. He received a Bachelor of Science degree in Chemistry from the University of Calgary in 2005, where he remains as a graduate student in the group of Professor Roland Roesler. His studies involve the preparation of novel multidentate N-heterocyclic carbenes for use in catalysis and organometallic materials applications.*

*Thomas Baumgartner has joined the Department of Chemistry at the University of Calgary, Canada in July 2006 as Assistant Professor. He received his M.Sc. degree in 1996 and his Ph.D. degree in 1998 both from the University of Bonn, Germany. From 1999 to 2002 he was a postdoctoral fellow at the University of Toronto, Canada. In 2002 he was awarded a Liebig fellowship from the German chemical industry association that allowed him to start his career as independent researcher at the Johannes Gutenberg-University in Mainz (2002–2003) and at the RWTH-Aachen University (2003–2006), both Germany. His research interests are centered around organophosphorus π-conjugated materials and polymers for organic electronics as well as organometallic supramolecules and polymers.*

 © 2007 Wiley-VCH Verlag GmbH & Co. KGaA, Weinheim 

gated materials. Heterocyclopentadienes (pyrrole, furan, silole, and thiophene) have been used extensively to this end.[1] Poly- and oligothiophenes have proven to be particularly useful, and consequently form one of the most studied classes of π-conjugated polymers.[6] The ease with which thiophenes can be functionalized allows entire families of thiophene materials, displaying unique properties to be prepared. These families may be used to establish important structure-property relationships. Thiophene materials are often light emitting in the red-orange region of the visible spectrum, consistent with their ca. 2.0 eV bandgap.[6] This red emission is often difficult to obtain using other π-conjugated polymers, and implies that polythiophenes may be highly useful in LED applications. Unfortunately, the emission of polythiophenes is often quenched due to their tendency to form aggregates in the solid state, and the heavy-atom effect of sulfur. As a result, polythiophene materials display significantly lower emission efficiencies than those based on other more established π-conjugated scaffolds such as poly(fluorenes) (PFs), and poly(phenylenevinylenes) (PPVs).[6] The incorporation of other conjugated units into oligo- and polythiophenes has proven to be a reliable method to improve emission efficiency, and the performance of the light-emitting devices derived from these materials.[6]

Theoretical studies have implied that the phosphorus analog of pyrrole (phosphole) may be an excellent building block for the construction of π-conjugated materials.[7] Organophosphorus materials have received relatively little attention despite the fact that the incorporation of $\sigma^3,\lambda^3$-phosphorus centers allows for a number of facile, nearly quantitative chemical modifications to be performed. Trivalent phosphorus centers display a versatile reactivity, allowing for the preparation of entire families of materials exhibiting unique properties from a single precursor.[8] Reaction with oxidizing agents results in the formation of $\sigma^4,\lambda^5$-phosphorus centers, while the Lewis basicity of the $\sigma^3,\lambda^3$-phosphorus center allows for complexation with Lewis acids, and transition metals. The reaction of trivalent phosphorus centers with methylating agents results in the formation of a cationic $\lambda^4$-phosphorus species. Most importantly, all of these facile chemical modifications result in significant changes to the properties of the involved materials. The use of chemical modifications to tune the properties of a material is not possible in this simplicity with genuine organic systems.

The phosphole moiety **A** (Figure 1) in particular, displays a high potential for use in π-conjugated organic materials. Phosphorus centers do not readily form sp hybrids, therefore the phosphorus atom in phospholes is highly pyramidalized, and the lone pair displays a high degree of s character.[9] This prevents an efficient endocyclic interaction between the phosphorus lone pair and the phosphole's butadiene moiety. In fact, the small degree of aromaticity displayed by phospholes (an NICS value of –5.3 has been determined theoretically)[10] is actually due to a hyperconjugative overlap of the compound's butadiene system with the exocyclic P–R σ bond, and not the phosphorus lone pair.[11] This makes phosphole an ideal choice for the construction of π-conjugated materials because exocyclic delocalization along the polymer chain is favored in species exhibiting low resonance energies.[7]

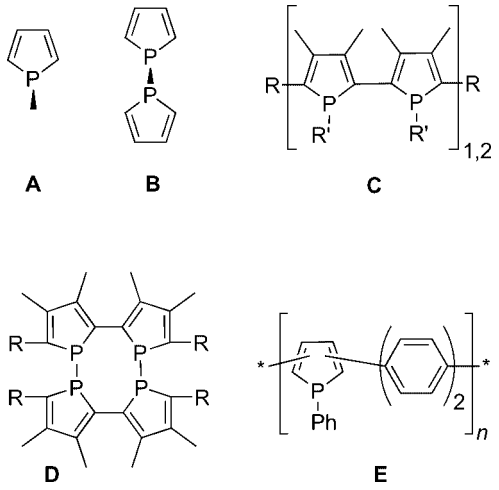


Figure 1. Phosphole-containing oligomers and polymers.

Additionally, σ–π conjugation ("through-bond" delocalization) is possible in 1,1′-biphospholes **B**, as a result of the low σ–σ* energy gap, and the high polarizability of the P–P linkage.[9] The interaction between the two phosphole π systems through the P–P σ bond in **B** may result in fascinating electronic properties that may be exploited in materials science. Although the chemistry of phospholes is well developed,[9] the incorporation of these phosphacyclopentadienes into π-conjugated materials has only been investigated quite recently. Tetrameric phosphole oligomers **C** ($n$ = 2) and **D** have been prepared from α,α′-biphospholes **C** ($n$ = 1),[12,13] however the first polymeric system to incorporate phosphole moieties **E**, was not reported until 1997 (Figure 1).[14,15] X-ray structural analyses revealed that the rings in compounds **C** were significantly twisted with respect to one another, preventing an effective overlap of the conjugated π system.[12,16]

Recently, phospholes have successfully been substituted for thiophene moieties in several well-defined oligo- and polythiophene systems. These systems display fascinating optoelectronic properties, and in some cases, unprecedented luminescence efficiencies. As a result, functional OLEDs and sensory materials have already been developed using these materials. Phosphaorganic materials have recently been comprehensively reviewed,[8] therefore the purpose of this microreview will be to provide a more detailed overview of the recent developments of the 2,5-dithienylphosphole, and the dithieno[3,2-*b*:2′,3′-*d*]phosphole systems. Related 2,5-diarylphosphole systems will also be discussed where relevant. The substitution at both the thiophene, and the phosphole moieties of these well-defined model systems may be altered, in addition to the possibility of facile chemical modifications involving the trivalent phosphorus center. Comparisons and contrasts between the properties of the obtained materials are highly dependant on the nature of the diarylphospholes or dithienophosphole based systems.

 © 2007 Wiley-VCH Verlag GmbH & Co. KGaA, Weinheim 

Consequently, structure-property relationships have been extensively investigated, and the properties of the systems have been tuned to suit potential applications.

## 2. 2,5-Diaryl- and 2,5-Bis(heteroaryl)phospholes

The incorporation of heteroaryl substituents at the α positions (2,5-positions) of a phosphole moiety provides materials displaying promising optoelectronic properties, as a result of exocyclic π conjugation present between the phosphole and the α-substituted aryl groups. Theoretical calculations have demonstrated this exocyclic π conjugation, by showing that the delocalization over the phosphole's 1,3-butadiene moiety increases [as determined using the Julg Index (JI)] upon introduction of heteroaryl substituents at the α positions of the phosphole ring.[17] This substitution was also shown to result in a concurrent reduction of the aromaticity (endocyclic π conjugation) of the phosphole ring (as measured by its calculated NICS values), demonstrating the fine balance between exocyclic and endocyclic delocalization in π-conjugated materials.[7] The 2,5-diarylphosphole system **1** developed by Réau and co-workers is a versatile model system for the development of π-conjugated materials (Figure 2).[18] It is possible to modify the chemical structure of **1** in a number of different manners, allowing for a full elucidation of the structure–property relationships displayed by the model system. Possible structural variations include the nature of the exocyclic phosphorus substituent, the size of the fused carbocycle present on the phosphole backbone, the aromatic groups present at the 2- and 5-positions of the phosphole moiety, and functionalization of the phosphorus center by facile chemical modifications (oxidation, complexation, methylation etc.). Structure–property relationships involving the 2,5-diarylphosphole system **1** have been established by examining the effects of these modifications on the system's interesting optoelectronic, and electrochemical properties. Where necessary, these effects have been rationalized theoretically.

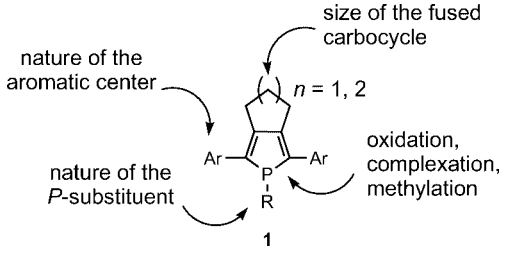


Figure 2. The π-conjugated phosphole system developed by Réau et al.

### 2.1 Modification of the π-Conjugated Framework

Compounds of type **1** are prepared using the Fagan–Nugent route,[18] a versatile method for the preparation of heteroles (Scheme 1).[19] They can be obtained by an intramolecular oxidative coupling between "zirconocene" and diynes in which the alkyne moieties are linked by a $(CH_2)_3$ or a $(CH_2)_4$ spacer. This spacer is required to promote the desired 2,5-substitution pattern.[18c] Subsequent reaction of the zirconacyclopentadienes **3** with dihalophosphanes produces the desired 2,5-diarylphospholes **1** in nearly quantitative yields. The use of different dihalophosphanes in the synthesis described above allows for the introduction of different substituents at the phosphorus center of 2,5-diarylphospholes **1**.[9] As a result of their stability in air, and their more favorable optoelectronic properties, *P*-phenyl-substituted phospholes dominate this family of 2,5-diarylphospholes, and the subsequent discussion of derivatives of **1** will focus on *P*-phenyl-substituted phospholes.

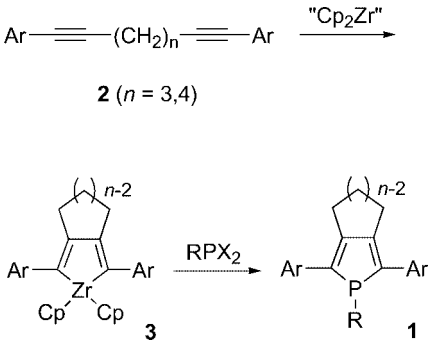


Scheme 1. Synthesis of 2,5-diaryl- and 2,5-diheteroarylphospholes.

The interaction between π chromophores in organic materials is not limited to assemblies connected by π-conjugated linkers. Indeed, the interaction of nearby π chromophores through σ linkers may occur with linkers that display high polarizabilities, and low σ–σ* gaps.[20] The electronic properties of materials displaying this form of σ–π hyperconjugation are often unique. The exocyclic P–R σ bond in phospholes is known to participate in a hyperconjugative interaction with the compound's butadiene moiety.[11] It has been suggested that P–P σ bonds display the requisite features (high polarizability and low σ-σ* gaps) to allow for an efficient interaction of the π-chromophores via a P–P σ bridge.[9] The 1,1′-biphospholes **B** (Figure 1) are a well-known family of compounds[9] that display the potential for an interaction of the phosphole π systems through the P–P σ link. The extended biphospholes **4a**,**b** were prepared according to the classical route for the preparation of 1,1′-biphospholes.[21] This route involves the reductive cleavage of the P–Ph bond in *P*-phenyl phospholes to generate intermediate phospholyl anions. Subsequent oxidation of the phospholyl anions results in the formation of the targeted 1,1′-biphospholes. The targeted biphospholes can also be prepared using an efficient "one-pot" synthesis starting from the 1,7-diyne precursors **2** (Scheme 2).[18f]

The structural parameters of **4a** suggest that the exocyclic conjugation observed between the composite heterocycles in the *P*-phenylphosphole precursor, remains in the 1,1′-biphosphole product, and the two π chromophores adopt a *gauche* conformation relative to one another (Figure 3).[18f] The absorption properties of the 1,1′-biphospholes, as determined by UV/Vis spectroscopy differ markedly from those of the corresponding phospholes. The individual 2,5-diarylphospholes display relatively simple ab-

 © 2007 Wiley-VCH Verlag GmbH & Co. KGaA, Weinheim 

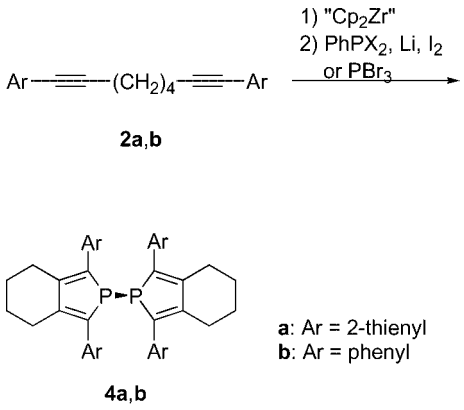


Scheme 2. Preparation of conjugated P–P biphospholes.

sorption spectra with a single band in the 400 nm range due to the π–π* transition. On the other hand, the 1,1′-biphospholes **4a**,**b** display rather complex absorption spectra, with multiple bands, including one remarkably red-shifted absorption (broad shoulder between 440–560 nm for **4a**). Quantum chemical calculations revealed that an interaction of the π chromophores through the P–P linkage results in the splitting of the HOMO and LUMO levels of the parent phospholes.[18f] The optical properties, and the presence of a P–P-mediated through-bond interaction suggest that biphosphole materials, particularly those bearing thienyl substituents, may be useful in the development of novel materials. Additionally, it was demonstrated that the optical properties of the biphospholes could still be tuned by chemical functionalization (oxidation and coordination to AuCl were investigated) of the phosphorus centers.[18f]

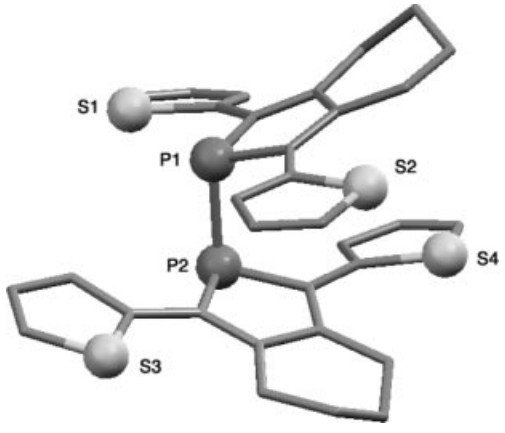


Figure 3. Molecular structure of **4a** in the solid state. Picture generated from the CSD-database file (code: BEWQAW).

Up until this point we have not been concerned with the nature of the aromatic substituents at the α positions of the phosphole moieties in Réau's 2,5-diarylphospholes **1**. In fact, a variety of aryl and heteroaryl groups have been incorporated into this system, and they display a profound influence on the optoelectronic and electrochemical properties of the system.[18] The nature of the aromatic groups can be varied by using an appropriately substituted diyne **2** in the first step of the Fagan–Nugent synthesis of the 2,5-diarylphospholes **5**–**7** (Figure 4).

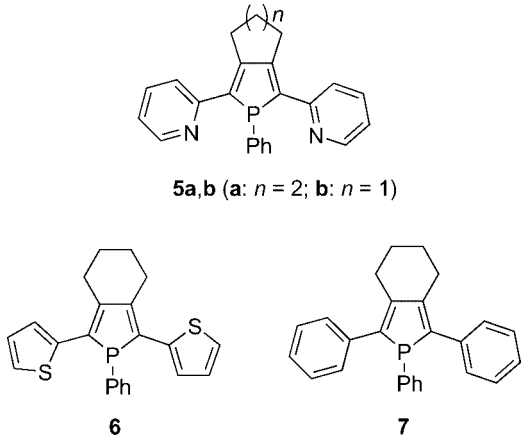


Figure 4. Variations of the aryl-/heteroaryl substituent.

2-Pyridyl groups were originally incorporated into these positions with the aim of preparing alternating electron-deficient/-rich (with the phosphole ring being considered as electron-rich heterocyclopentadiene)[22] species capable of exhibiting charge-transfer structures.[18a] It was anticipated that these charge-transfer structures would result in a more coplanar structure of the three heterocyclic rings, increasing the potential for conjugation between their π electron systems, potentially reducing the bandgaps of the corresponding materials.[23] Indeed, X-ray structural analysis of the 2,5-bis(2′-pyridyl)phosphole **5a** revealed that the twist angles between the heterocyclic rings were relatively small, and that the C–C bond lengths between the heterocyclic rings were intermediary between those expected of single and double bonds, implying an extensive π conjugation between the 2-pyridyl substituents and the central phosphole ring (Figure 5, top).[18a] Moreover, the phosphorus center in **5a** is highly pyramidalized, and the structural data indicate a rather small degree of endocyclic π conjugation, illustrating the balance between exocyclic, and endocyclic (aromatic) conjugation in these species. The oligothiophene analog **6**, in which a single thiophene ring is replaced by a phosphole ring, was prepared by Réau and co-workers shortly following their report of the preparation of **5a**.[18b] In addition to allowing for a comparison between the effects of substitution with an electron-poor heteroaromatic species (pyridine), and an electron-rich species (thiophene), the preparation of the 2,5-bis(2′-thienyl)phosphole **6** also provided an excellent model to study the effects resulting from the replacement of the central heteroatom in polythiophene with a heteroatom displaying remarkably different properties. As was observed with the 2,5-bis(2′-pyridyl)-phosphole **5a**, the structural features of **6** are consistent with an extended delocalization path incorporating the dienic moiety of the phosphole ring, and the thienyl substituents (Figure 5, bottom).[18c]

 © 2007 Wiley-VCH Verlag GmbH & Co. KGaA, Weinheim 

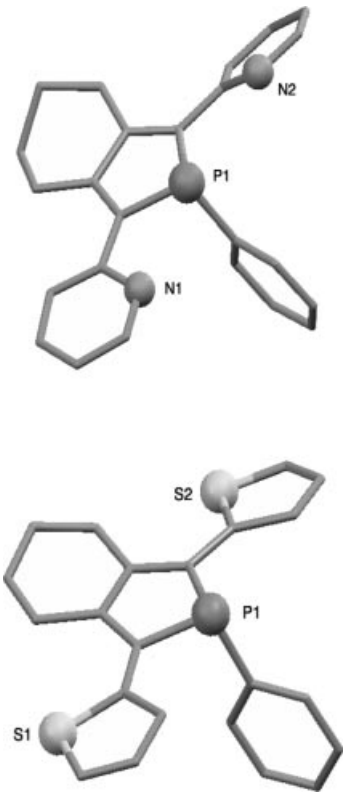


Figure 5. Molecular structures of the phospholes **5a** (top), and **6** (bottom) in the solid state. Pictures generated from the CSD-database files [codes: JOQFUQ (**5a**), MEKZEH (**6**)].

The absorbance properties of the 2,5-dithienylphosphole **6** display an even larger red shift relative to the 2,5-diphenylphosphole **7** ($\Delta\lambda_{max}$ = 58 nm, $\Delta\lambda_{onset}$ = 38 nm) than was observed with the 2,5-dipyridylphosphole **5a** ($\Delta\lambda_{max}$ = 45 nm, $\Delta\lambda_{onset}$ = 18 nm), indicating a significantly lowered HOMO–LUMO (π–π*) gap in the thienyl-substituted system. As a result, the incorporation of phosphole moieties into polythiophene materials may result in a significant optimization of the material's bandgap. Moreover, the emission of the dithienylphosphole **6** ($\lambda_{em}$ = 501 nm) is also significantly red-shifted relative to that of both the diphenyl- and the dipyridylphospholes which displayed emissions at similar wavelengths (**5a**: $\lambda_{em}$ = 463 nm; **7**: $\lambda_{em}$ = 466 nm).[18a–18c] It is important to note that the presence of terminal thiophene units in these oligomers allows for the potential preparation of dithienylphosphole polymers by electropolymerization. Importantly, the electrochemical oxidation potential of the diarylphosphole is related directly to the electron-rich or -deficient nature of the aryl substituents.[18a–18c] In summary, the optoelectronic properties of the 2,5-diarylphospholes display increasing red shifts upon substitution of pyridyl groups for phenyl substituents, and a further red shift upon introduction of thienyl substituents.

The valence π-MOs of these compounds are formed by a combination of the π-MOs of the constituent heterocycles (phosphole and either pyridine or thiophene).[17] The HOMO of 2,5-bis(2′-thienyl)phospholes arises from an antibonding combination of the thiophene, and the phosphole HOMOs, which have very nearly the same energies (the energy of the MOs differs by only 0.2 eV). In the case of the 2,5-dipyridylphospholes, however, the HOMO of the pyridine moiety is relatively high in energy. As a result, the HOMO of the phosphole moiety experiences a more efficient interaction with the HOMO-1 of the pyridine ring (the energies of these two MOs differ by 0.8 eV). Owing to the greater energy difference between the pyridine HOMO-1, and the phosphole HOMO, they experience a less-efficient interaction, and the resulting HOMO in the dipyridylphosphole is only moderately raised. The near match of the HOMO energies of thiophene and phosphole, on the other hand, result in a very efficient interaction. The resulting HOMO of the dithienylphosphole system is much more significantly raised in energy than that of the dipyridylphosphole. The same calculations predict that the LUMOs of the 2,5-bis(2′-thienyl)phosphole, and the 2,5-bis(2′-pyridyl)phosphole have very similar energies. Consequently, the observed red shift in the absorption (π–π* transition) spectrum of the dithienylphosphole relative to the dipyridylphospholes may be rationalized on the basis of its destabilized HOMO, and the resulting decreased HOMO–LUMO gap. Comparison of the experimentally obtained absorption values for the 2,5-bis(2′-thienyl)phosphole **6** ($\lambda_{max}$ = 412 nm)[18b,18c] with that the analogous oligothiophene ($\lambda_{max}$ = 353 nm)[24] reveals a significant optimization of the HOMO–LUMO gap upon substitution of the central heteroatom in the terthiophene by phosphorus.

### 2.2 Modification of the Phosphorus Center

As discussed earlier, the incorporation of phosphole moieties into materials is desirable because it may allow for the preparation of entire families of compounds from a single precursor, by taking advantage of the versatile reactivity displayed by the $\sigma^3,\lambda^3$-phosphorus center. Indeed, the phosphorus center in Réau's 2,5-dipyridylphosphole **5a**, 2,5-dithienylphosphole **6**, and 2,5-diphenylphosphole **7** has been functionalized in a number of different ways (oxidation, complexation etc.) to yield new compounds displaying significantly different optoelectronic and electrochemical properties (Scheme 3).[18,25]

The bis(heteroaryl)phosphole oxides **8** can be prepared by the quantitative reaction of the bis(heteroaryl)phosphole with trimethylsilyl peroxide. Similarly, reaction of the phosphole species with other elemental chalcogens (sulfur and selenium) results in the quantitative formation of the corresponding bis(heteroaryl)phosphole sulfides **9**, and selenides **10**.[18] This oxidative functionalization of the phosphorus center in the 2,5-bis(2-thienyl)phosphole system results in a significant red shift of both the absorption ($\Delta\lambda_{max}$ = 11–22 nm) and emission wavelengths ($\Delta\lambda_{em}$ = 46–55 nm) of these compounds.[18a–18e,18g,18h] The oxidized compounds all display a single peak in their absorption and emission spectra in both solution, and the solid state.[18g,18d] Examination of the absorption and emission data of the chalcogen series **8b**, **9b**, and **10b**, reveals that the magnitude of the

 © 2007 Wiley-VCH Verlag GmbH & Co. KGaA, Weinheim 

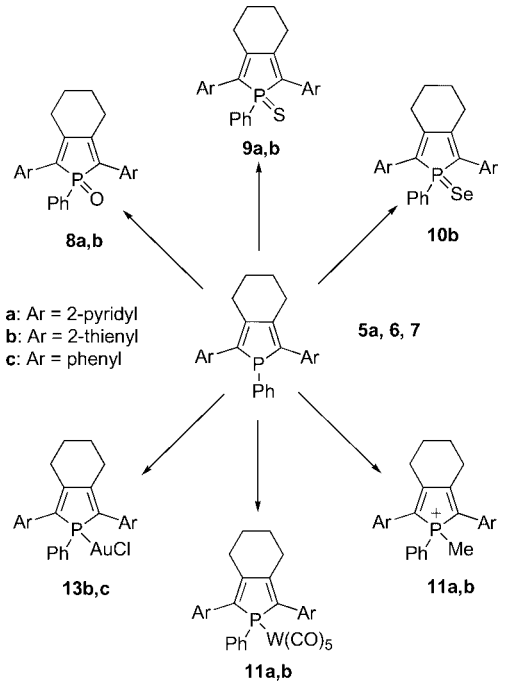


Scheme 3. Chemical modifications of the $\sigma^3,\lambda^3$-phosphorus center in 2,5-bis(heteroaryl)phospholes.

observed red shifts increases with the increasing electronegativity (O >> S > Se) of the chalcogen used.[18c] This trend has been rationalized formally on the basis of the stabilities of the ylide forms of the P=E bond ($\leftrightarrow P^+–E^–$).[26] The ylide forms, featuring a positively charged phosphorus center, are of course more stabilized for more electronegative chalcogens E. The introduction of a formal positive charge at the phosphorus center of a phosphole ring results in a shift in the aromaticity of the ring from slightly aromatic, to slightly antiaromatic. The increased antiaromatic character of the $\sigma^4$-phospholes results in a destabilization of the compound's bonding MOs, and a stabilization of the compound's antibonding MOs.[26] As a result the HOMO–LUMO gap is decreased in the less aromatic $\sigma^4$-phosphole species. DFT calculations[17] also revealed that oxidation of the phosphorus center results in a stabilization of the energy levels of both the HOMO and the LUMO of the oxidized bis(heteroaryl)phospholes, with the stabilization of the LUMO being more significant.[18b,18c] In summary, oxidation may prove to be a reliable method to reduce the bandgap of dithienylphosphole materials. It should be noted that the fluorescence efficiency, and the decomposition temperature of the 2,5-bis(2-thienyl)phosphole sulfide **9b** were reasonably high ($\phi_{PL}$ = 4.6%, $T_d$ = 254 °C),[18c] suggesting that thioxo-2,5-dithienylphospholes may be well-suited to incorporation into functional OLEDs.

Methylation of the trivalent phosphorus center in the bis(heteroaryl)phospholes to generate phospholium salts **11** proved to be another facile, and nearly quantitative means of altering the properties of the bis(heteroaryl)phosphole system (Scheme 3).[18b,18c] The functionalization resulted in relatively small red shifts in the excitation wavelengths ($\Delta\lambda_{max}$ **11a** = 4 nm; **11b** = 30 nm), and significantly larger red shifts in the emission wavelengths ($\Delta\lambda_{em}$ **11a** = 47 nm; **11b** = 92 nm) of the phospholium products. In fact, the red shifts observed upon methylation of the dithienylphosphole system are larger than those observed as a result of any other functionalization (oxidation, coordination etc.) of the phosphole's phosphorus center.[18] As discussed earlier for the dithienylphosphole chalcogenides, the presence of a positive charge at the phosphorus center in the phosphole ring reduces the aromatic stabilization of the compound, resulting in decreased HOMO–LUMO gaps.[26] The ionic nature, and the significant reduction of the HOMO–LUMO gap of the obtained phospholium products makes this modification potentially useful towards the development of functional phospholium materials.

Trivalent $\sigma^3,\lambda^3$-phosphanes are among the most versatile classes of organometallic ligands. Phospholes typically display similar coordination chemistry. Consequently, a large family of complexes can be prepared from a single phosphole precursor. The coordination chemistry of the dithienylphosphole ligand, however, has to this point been limited to its inclusion in tungsten and gold complexes **12** and **13**, respectively (Scheme 3).[18c,18d,18g] Coordination to the octahedral tungsten unit seems to have relatively little effect on the properties exhibited by the dithienylphosphole ligand.[18c] In contrast, coordination to gold produces a complex displaying dramatically different properties than those reported for the free ligand.[18d,18g] Significant red shifts in the absorption ($\Delta\lambda_{max}$ = 16 nm), and the emission wavelengths ($\Delta\lambda_{em}$ = 43 nm) are observed upon coordination to AuCl, and the fluorescence efficiency of **13b** improves to 14.0% compared to 5.0% in the free ligand. The gold complex displays a relatively high thermal decomposition temperature ($T_d$ = 218 °C), allowing thin films to be obtained upon vacuum sublimation. While the excitation properties of the complex are similar in solution and in the thin film (a small red shift of 12 nm is observed in the thin film), the emission properties of the thin film are unique,[18d,18g] displaying two broad emission bands of similar intensity. The first emission is only marginally red-shifted relative to that observed in solution ($\Delta\lambda_{em}$ = 6 nm), however the second is remarkably red-shifted ($\Delta\lambda_{em}$ = 146 nm). When the gold complexes are dispersed in a polymethacrylate matrix, the low-energy emission disappears.[18g] This observation suggests that the first emission is due to the metal-perturbed intraligand π–π* transition, while the second, remarkably red-shifted emission, is probably due to the formation of aggregates. The above observations suggest that dithienylphosphole AuCl complexes are a promising material for incorporation into OLEDs. In particular, materials displaying broad emissions may be suitable for the development of white organic light-emitting diodes (WOLEDs).[27]

### 2.3 Bis(thienyl)phosphole Oligomers and Polymers

The evolution of optoelectronic and electrochemical properties with increasing chain length is of great interest

 © 2007 Wiley-VCH Verlag GmbH & Co. KGaA, Weinheim 

in the chemistry of π-conjugated organic materials.[1] The effect of increasing chain length in the π-conjugated 2,5-dithienylphospholes has been studied through the preparation of several well-defined oligomers.[18b,18c,18e] The mixed oligomer **14** (Figure 6), containing alternating donor and acceptor units, was prepared using an appropriately substituted diyne.[18b] As with the 2,5-bis(2-pyridyl)phospholes **5b** prepared earlier, this oligomer was expected to display increased conjugation as a result of intramolecular charge transfers. Indeed, the observed wavelength of excitation ($\lambda_{max}$ = 427 nm) is red-shifted relative to either the 2,5-dipyridylphosphole **5b** or the 2,5-dithienylphosphole **6**. The emission of the mixed oligomer **15** is even more significantly red-shifted ($\Delta\lambda_{em}$ = 107 nm relative to the 2,5-dipyridylphosphole **5b**).

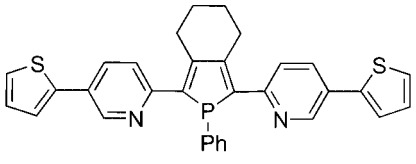


**14**

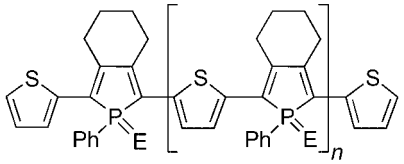


**15a** (*n* = 1), **15b** (*n* = 2)

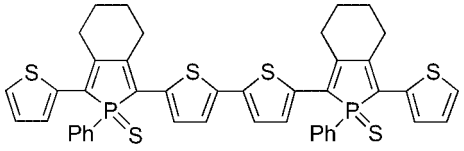


**16**

Figure 6. Well-defined 2,5-bis(heteroaryl)phosphole oligomers.

The oligo(α,α′-thiophene-phospholes) **15** (Figure 6) and their derivatives were prepared by the Fagan–Nugent route, using suitable bis- and tris(diynes).[18e] The three reported oligo(α,α′-thiophenephospholes) all display one broad band in their absorption spectra, assignable to the π–π* transitions of the thiophene-phosphole system. The excitation wavelength of the thiophene-phosphole dimer **15a** ($\lambda_{max}$ = 490 nm) is significantly red-shifted relative to that of the corresponding monomeric 2,5-dithienylphosphole **6** ($\lambda_{max}$ = 412 nm), demonstrating the successful extension of the conjugated π system in this oligomer. Sulfurization of the shorter oligomer leads to an additional red shift in the excitation wavelength. The magnitude of the red shift that occurs upon functionalization of the phosphorus centers with sulfur is similar for both the monomeric 2,5-dithienylphosphole **6**, and the bis(α,α′-thiophenephosphole) **15a** ($\Delta\lambda_{max} \approx$ 20 nm). Red shifts of similar magnitude are observed in the emission of both bis(α,α′-thiophenephospholes) **15a** and **15b**, resulting in emission in the red-orange region of the visible spectrum. Inspection of the UV/Vis spectrum of the larger tris(α,α′-thiophenephosphole) **15b** oligomer reveals an additional red shift relative to the bis-(α,α′-thiophenephosphole) **15a** ($\Delta\lambda_{max}$ = 42 nm). This red shift reveals a further extension of the conjugated π system by the coherently smaller bandgap in the longer oligomer. The bis(α,α′-thiophenephospholes) **15** were subjected to further study by CV. This study supported the extended conjugation upon chain extension, by demonstrating that oxidation and reduction potentials were decreased, and increased respectively in the longer oligomers.[18e]

Polythiophenes are often prepared by electropolymerization of thiophene monomers and oligomers.[6] The presence of terminal thiophene functionalities in the 2,5-dithienylphospholes, and their derivatives is thus interesting, because they may allow for the preparation of polymers from this well-developed family of π-conjugated oligomers. It is well known that α,α′ coupling is the major route involved in the electropolymerization of thiophenes,[6,28] therefore the "dimer" **16** (Figure 6), the product of one such coupling was prepared to examine the effects of α,α′ coupling in the 2,5-dithienylphosphole system **6**. The "dimer" was prepared using the Fagan–Nugent method with an appropriately substituted bis(diyne),[29] and was isolated as the sulfurized phosphole derivative.[18c] Absorption spectroscopy of **16** revealed significant red shifts in the excitation wavelengths relative to those displayed by the corresponding monomer **9b** ($\Delta\lambda_{max}$ = 100 nm, $\Delta\lambda_{onset}$ = 132 nm). These bathochromic shifts suggest an effective extension of the conjugated system, and imply that polymers generated electrochemically from 2,5-dithienylphosphole derivatives may display highly favorable properties, particularly with respect to bandgap.

During the electrochemical CV analyses of many of the 2,5-bis(2-thienyl)phosphole derivatives, the deposition of insoluble films was observed on the working electrode surfaces (Scheme 4).[18b,18c,18f] Repeated cycling resulted in a regular increase of the oxidation and reduction peak currents, consistent with the formation of an electroactive material on the surface of the electrode. By this method, polymeric films were obtained for the parent $\sigma^3$-dithienylphosphole **6** (E = lone pair),[18c] the $\sigma^3$-dithienyl-1,1′-biphosphole **4a**,[18f] and a large number of $\sigma^4$-dithienylphospholes,[18b,18c] including oxidized (**8**, E = O), methylated (**11**, E = $Me^+$), and transition-metal-coordinated species **13** (E = AuCl). The poor solubility of these films prevented the full characterization of most of the obtained polymers, however the optical properties of all the polymers were probed through their thin-film absorption spectra. The film obtained from the parent 2,5-bis(2-thienyl)phosphole **poly(6)** (E = lone pair) displayed two unresolved absorptions, both red-shifted relative to the corresponding monomer **6** ($\Delta\lambda_{max}$ = 51 nm, 155 nm). The absorption spectra of the functionalized dithienylphospholes all displayed red shifts relative to the appropriate monomers as well, illustrating the extension of the conjugated π system upon polymerization. The functionalized nature of the phosphorus centers in these polymers often resulted in an additional red shift in their $\lambda_{max}$ values relative to that of the parent $\sigma^3$-dithienylphos-

 © 2007 Wiley-VCH Verlag GmbH & Co. KGaA, Weinheim 

phole polymer **poly(6)**. The general trends observed for the monomers with respect to the red shift resulting from a specific functionalization of the phosphorus center were preserved in the polymers. For example, the largest red shift in both the polymer and the monomer series is observed upon methylation of the phosphorus center. Comparison between the properties displayed by the well-defined α,α′-coupled dimer **16**, and the analogous polymer suggest that the polymers obtained are in fact, longer α,α′-coupled oligomers.[18c] In summary, these results demonstrate the utility of incorporating a reactive heteroatom such as phosphorus into electroactive polythiophene materials. In addition to allowing the bandgaps of the resulting polythiophene-like materials to be tuned via facile chemical modifications of the monomeric precursors, the incorporation of the phosphorus center may result in a bandgap that is already optimized relative to that displayed by analogous, purely thiophene-containing oligomers.[17]

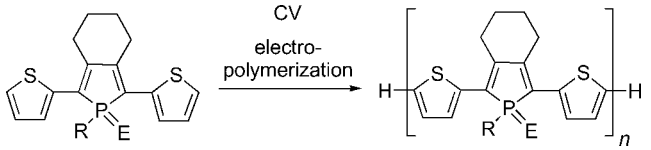


Scheme 4. Electropolymerization of 2,5-dithienylphospholes.

The presence of reactive, Lewis basic $\sigma^3,\lambda^3$-phosphorus centers in polythiophene materials such as those described above should allow for a variety of postfunctionalizations to be performed with the polymeric materials such as **poly(6)**. Functionalized dithienylphosphole polymers have been shown to display different properties than their non-functionalized analogs, therefore postfunctionalization of trivalent phosphorus-containing polythiophenes should allow them to be used as effective chemosensors.[5] In order to investigate the utility of the phosphole-modified polythiophenes as molecular sensors, the preparation of a corresponding 2,5-dithienyl-$\sigma^3,\lambda^3$-phosphole polymer film was required. This non-protonated polymer film[30] **poly(6)** was obtained using a *P*-protection/electropolymerization/deprotection sequence (Scheme 5).[18h] Protection of the phosphorus center by coordination to AuCl (**13b**), followed by electropolymerization resulted in the formation of the insoluble AuCl-coordinated dithienylphosphole polymer film **poly(13b)**. Deprotection was achieved in the presence of excess triphenylphosphane, affording [AuCl($PPh_3$)] and the deprotected polymer **poly(6)**. The $\sigma^3$-phosphole-containing polymer displayed a blue shift in its absorption band ($\Delta\lambda_{onset}$ = 41 nm), and a significant negative shift in its oxidation current offset ($\Delta E_{pa}$ = 0.26 V), consistent with the shifts observed at the molecular level for this system.[18d,18g] The polymer **poly(6)** could be treated with a AuCl solution to regenerate the protected polymer **poly(13b)**. This result effectively demonstrated that the chemistry displayed by phospholes at the molecular level could be extended to the macromolecular level, a prerequisite for the development of chemosensors from the phosphorus-modified polythiophenes. The possibility that further postfunctionalizations of the deprotected polymer might result in property shifts similar to those displayed at the molecular level, led to the investigation of the $\sigma^3$-phosphorus-containing polythiophene's reactions with chalcogens. Immersion of Pt electrode, modified with a film of the deprotected polymer **poly(6)** into a solution containing elemental sulfur resulted in the nearly quantitative sulfurization of the polymer.[18h] The polymer **poly(9b)** displayed a red shift in its absorption ($\Delta\lambda_{onset}$ = 38 nm), and an anodic shift in its oxidation current ($\Delta E_{pa}$ = 0.23 V) upon exposure to elemental sulfur. The $\sigma^3$-phosphole-modified polythiophene also displayed an anodic shift ($\Delta E_{pa}$ = 0.11 V) in the presence of elemental selenium. When the anodic shifts of the $\sigma^3$-phosphole-modified polythiophene **poly(6)** were monitored as a function of time in a sulfur-containing solution, a collective response was observed, and the degree of sulfurization could be monitored by observing the gradual shifts in the electro-

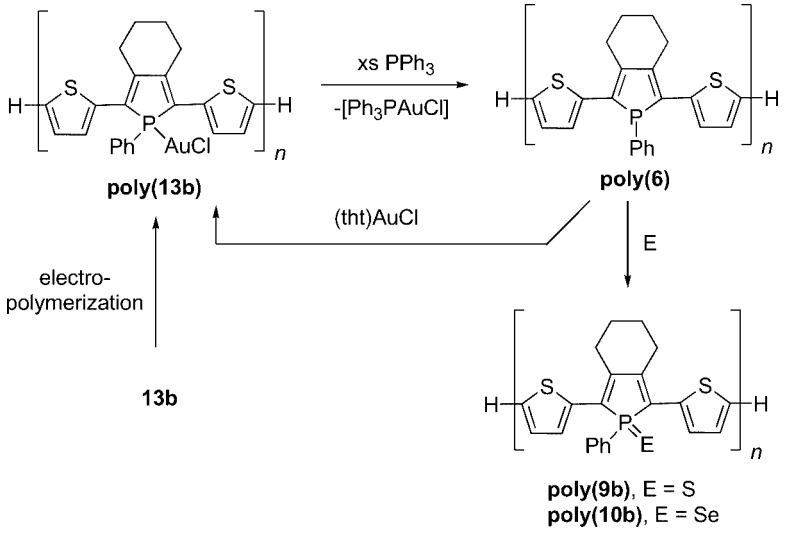


Scheme 5. Postfunctionalization of poly(2,5-thienylphospholes).

 © 2007 Wiley-VCH Verlag GmbH & Co. KGaA, Weinheim 

chemical properties of the material. This $\sigma^3,\lambda^3$-phosphorus-containing polythiophene is the first reported conjugated polymer capable of detecting chalcogens.

### 2.4 Phosphole-Based OLEDs

The development of functional OLEDs requires materials displaying several requisite features.[2] The materials must display high thermal stabilities, so that homogeneous thin films may be deposited upon vacuum sublimation. Good luminescence efficiencies are also required if a material is to be incorporated into OLEDs. Additionally, it is essential that the materials display favorable hole and electron injection, and transportation properties. It has been demonstrated that materials based on the 2,5-bis(2′-thienyl)-phosphole **6** and its derivatives display remarkable properties, with the potential for tuning by simple chemical modifications of the material's phosphorus center.[18] It is possible to tune the emission properties, the ionization potentials, and the electron affinities of these materials, allowing the color of the emission to be varied, and a good match to be obtained between the HOMO and LUMO levels of the material, and the cathode and anode (respectively) of the device. Moreover, a number of dithienylphosphole derivatives display high thermal stabilities (the thioxo- and AuCl-coordinated species **9b** and **13b** for example). These characteristics suggest that dithienylphosphole materials may be particularly well suited for incorporation into functional OLEDs. Indeed the incorporation of thioxo-dithienylphosphole, and AuCl-coordinated dithienylphosphole into functional OLEDs represented the first examples of OLEDs based on organophosphorus materials.[18d,18g] These compounds were both incorporated into single-layer OLEDs having an ITO/PEDOT:PSS/**phosphole**/Mg:Al/Ag configuration [ITO = indium-tin oxide; PEDOT = poly(3,4-ethylenedioxythiophene); PSS = polystyrene sulfonate]. The OLEDs incorporating the AuCl-functionalized phospholes displayed unique emission properties, similar to those observed for the same materials in the solid state.[18g] The long-wavelength emission of the AuCl-functionalized 2,5-diphenylphosphole **13c** was dominant, resulting in a saturated red emission from the device. This is of interest because non-doped red-emitting OLEDs are relatively rare.[31] The emission of the AuCl-coordinated dithienylphosphole **13b** on the other hand, uniformly covers a broad range ($\lambda_{EL}$ = 500–800 nm), suggesting its potential for use in WOLED applications. The performance of a number of other single-layer devices having the same configuration but incorporating other diarylphospholes were also evaluated.[18g] Importantly, the electroluminescence of these devices matched those displayed by the emissive materials in the solid state, suggesting that the luminescence mechanisms involved are similar. This result implies that the structure–property relationships established for the diarylphosphole materials, can be extended to luminescent devices, offering a predictable means of tuning the emission color of the devices. The device based on the thioxo-2,5-dithienylphosphole **9b** outshone the other devices (including those based on the AuCl-coordinated diarylphospholes **13b**) in all respects.[18g] This device displayed the lowest turn-on voltage (2.0 V), the greatest brightness (3613 cd m$^{-2}$), and the best external electroluminescence quantum efficiency (EEQE) (0.16%). Unfortunately, the EEQE values of the single-layer devices, including that based on the thioxo-dithienylphosphole **9b** were rather modest. This often occurs in single-layer devices as a result of unbalanced charge carrier injection and transport. With the aim of improving device performances, multilayer devices were prepared for all the emissive phosphole materials examined, by sandwiching the emissive layer between a hole-transporting layer (HTL), *N*,*N*′-diphenyl-*N*,*N*′-bis(1-naphthyl)-1,1′-biphenyl-4,4"-diamine (α-NPD), and an electron-transporting layer (ETL), tris(8-hydroxyquinoline)aluminum ($Alq_3$). The resulting devices displayed turn-on voltages, and emissions similar to those observed in the corresponding single-layer devices. It was therefore concluded that the diarylphospholes remained the source of emission, and not the newly introduced ETL or HTLs. The performance of the multi-layer devices were dramatically improved with respect to brightness, and EEQE, often displaying improvements of over one order of magnitude. Once again, the best performance in all aspects was obtained with the thioxo-2,5-bis(2-thienyl)phosphole **9b** based device. This device displayed a low turn-on voltage (2.2 V), and dramatically improved brightness (37830 cd m$^{-2}$), and EEQE (0.80%). As a result of the outstanding performance of the thioxo-, and the intriguing emission of the AuCl-functionalized dithienylphospholes **9b** and **13b**, these materials were evaluated as potential hosts for dopant fluorescent dyes. The problem of obtaining red emission is often solved by incorporation of a dopant such as 2-*tert*-butyl-4-(dicyanomethylene)-6-(1,1,7,7-tetramethyljulolidyl-9-enyl)-4*H*-pyran (DCJTB) into an emissive host matrix.[31] Both doped multilayer devices displayed red emission arising from the DCJTB dopant ($\lambda_{EL}$ = 617–623 nm), and not the dithienylphosphole host. Moreover, the performance of both devices was similarly exceptional. Low turn-on voltages (2.2–2.4 V), and exceptional brightness (36538 cd m$^{-2}$), and EEQEs (1.22 and 1.83%) were observed for the doped devices. These observations suggest an efficient resonant energy transfer from the dithienylphosphole emissive matrices to the DCJTB dopant. These results demonstrate that efficient luminescent devices can be prepared from phosphole-containing oligothiophenes, offering the additional ability to fine-tune the properties of the system by taking advantage of the reactive phosphorus heteroatom.

## 3. Fused Tricyclic Dithieno[3,2-*b*:2′,3′-*d*]-phospholes

Open-chain organic π-conjugated materials consisting of aromatic, or heteroaromatic rings often display a significant degree of twisting between adjacent subunits in the solid state. Because the orbital overlap of the conjugated π sys-

 © 2007 Wiley-VCH Verlag GmbH & Co. KGaA, Weinheim 

tem varies approximately with the cosine of the twist angle, this rotational disorder in open-chain systems results in a significant decrease in the degree of π conjugation displayed by oligomers and polymers of this type.[6] Annelated ring systems have the advantage of forcing the constituent rings to adopt a coplanar geometry, maximizing the overlap of the π systems of the constituent subunits. Moreover, the fused nature of the ring system in annelated materials limits the possibility of non-radiative decay processes, potentially allowing for extremely efficient emission from materials of this type. Theoretical calculations have suggested that fused polythiophene materials may display favorable bandgaps relative to their open-chain analogs.[32] Moreover, fused dithienothiophenes have recently been shown to display remarkably efficient emission.[33] Because emission is favored relative to internal conversion in the fused polythiophene system, the observed emissions of an annelated system were found to be blue-shifted relative to those of its α-coupled, open-chain polythiophene analogs. The 2,5-dithienylphospholes **1** developed by Réau et al., demonstrated that the incorporation of a phosphole moiety into the backbone of an oligothiophene results in the formation of materials displaying a number of highly favorable optoelectronic properties. Furthermore, the presence of a reactive heteroatom in these systems allows their properties to be tuned in a predictable manner following the establishment of structure–property relationships.[18,25] These results prompted Baumgartner and co-workers to develop the dithieno[3,2-*b*:2′,3′-*d*]phosphole system **17**.[34] As was seen in the 2,5-dithienylphosphole system **1**, it is possible to systematically modify the structure of **17** in a number of different ways, allowing for the establishment of structure–property relationships (Figure 7).[34] Modification of the substitution at both the phosphorus center, and the 2- and 6-positions of the dithieno unit generates a wide variety of dithienophospholes with unique properties. Moreover, the versatile reactivity of the $\sigma^3,\lambda^3$-phosphorus center allows for a number of chemically facile functionalizations (oxidation, complexation etc.) to be performed. Specific attention will be paid to the dithienophosphole's optoelectronic properties since their extraordinary nature makes this system a promising candidate for the development of materials to be used in optoelectronic applications (e.g. OLEDs, PLEDs, OFETs as well as photovoltaic cells).

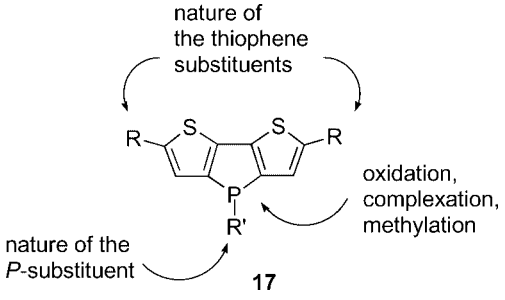


Figure 7. The dithieno[3,2-*b*:2′,3′-*d*]phosphole system developed by Baumgartner et al.

Many of the intriguing properties displayed by the dithieno[3,2-*b*:2′,3′-*d*]phosphole system can be rationalized by examining the molecule's frontier orbitals. Quantum chemical calculations revealed that both the HOMO and the LUMO of the parent dithieno[3,2-*b*:2′,3′-*d*]phosphole **17** can be easily derived from the frontier orbitals of the individual composite heterocycles, providing evidence that the π system is well-delocalized over the entire molecule (Figure 8).[34b] The HOMO of **17** is an antibonding combination of the HOMOs of the individual thiophene rings, resembling the phosphole's HOMO. The LUMO of **17** also resembles the phosphole ring's LUMO, and is comprised mainly of a bonding combination of the thiophene rings' LUMOs. It is important to note that the HOMO contains a nodal plane at the phosphorus center, while the LUMO contains a contribution from the $\sigma^*_{P-R}$ MO. As a result, chemical modifications of the phosphorus center will significantly affect the compound's LUMO. This feature will prove essential to the eventual tuning of the optoelectronic properties of dithienophosphole materials through modifications of the compound's phosphorus center.

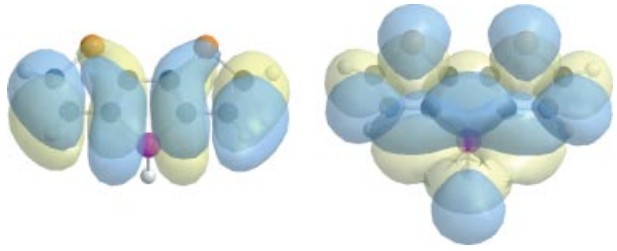

Figure 8. Frontier orbitals of the dithieno[3,2-*b*:2′,3′-*d*]phosphole (B3LYP/6-31G* level): HOMO (left), LUMO (right); P (purple), S (orange), C (black).

The dithieno[3,2-*b*:2′,3′-*d*]phospholes **17** can be accessed synthetically by lithiation of 3,3′-dibromo-2,2′-bithiophenes **18**, followed by reaction with an appropriately substituted dichlorophosphane (Scheme 6).[34] The resulting dithienophospholes display strong photoluminescence, typically in the blue region of the visible spectrum. The photoluminescence quantum yields are unprecedentedly high, ranging from 47 to 88%,[34] providing evidence that emission in these annelated systems is indeed favored relative to internal conversion.

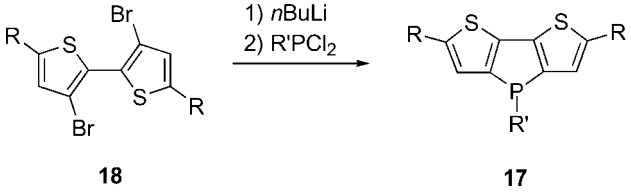


Scheme 6. Synthesis of dithieno[3,2-*b*:2′,3′-*d*]phospholes **17**.

The rigid tricyclic system of the *P*-phenyl compound **19a** is planar, and displays a high degree of π conjugation, as evidenced by the shortened C–C single bonds, and the elongated C=C double bonds present in the fused ring system (Figure 9).[34a] The observed bond shortening/elongation is significantly more pronounced in the fused tricyclic system

 © 2007 Wiley-VCH Verlag GmbH & Co. KGaA, Weinheim 

than in Réau's 2,5-dithienylphospholes. The phosphorus center is significantly pyramidalized, and the endocyclic P–C bonds are similar in length to the exocyclic P–C bond, implying a minimal involvement of the phosphorus lone pair in the molecule's delocalized π system. These observations support the reduced aromatic character of the phosphole moiety in **19a**, and the resulting increased exocyclic π conjugation within the molecule, once again illustrating the balance between endocyclic (aromaticity), and exocyclic conjugation. As a result of this feature, materials derived from the dithieno[3,2-*b*:2′,3′-*d*]phosphole scaffold display highly desirable optoelectronic properties.[34]

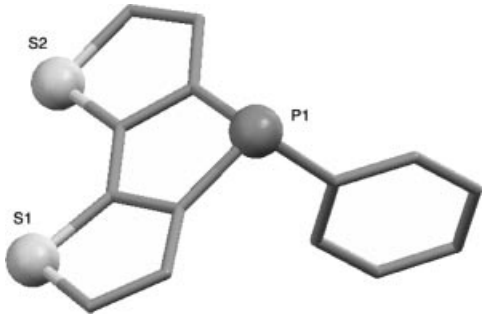


Figure 9. Molecular structure of **19a** in the solid state. Picture generated from the CSD-database file (code: FEHQAL).

### 3.1 Modification of the Phosphorus Center

The use of different dichlorophosphanes allows for the introduction of different substituents at the phosphorus center. Aromatic substituents at the phosphorus center typically result in more stable compounds than alkyl substituents due to the propensity for oxidation displayed by the latter.[9,34a] The subsequent discussion of derivatives of **17** will therefore focus on *P*-phenyl-substituted phospholes. The presence of a reactive phosphorus heteroatom in the dithieno[3,2-*b*:2′,3′-*d*]phosphole system allows the system to be tuned by taking advantage of these synthetically facile chemical modifications (Scheme 7).[34] The optoelectronic properties of the dithienophospholes **19** are particularly sensitive to such modifications as a result of the phosphorus center's contribution to the molecule's LUMO. Reaction of the Lewis basic phosphorus center in the dithieno[3,2-*b*:2′,3′-*d*]phosphole system with a Lewis acidic borane results in the formation of the phosphane–borane adducts **22** in almost quantitative yield.[34a,34b,34e]

As observed with Réau's system **1**, the phosphorus center in the dithieno[3,2-*b*:2′,3′-*d*]phosphole system may also be oxidized using a variety of oxidizing agents. The reactions are very general, and proceed in almost quantitative yields regardless of differences in the substitution at the thiophene rings. Reaction with peroxides ($H_2O_2$ or *t*BuOOH) results in the formation of $\sigma^4,\lambda^5$-dithienophosphole oxides **20**, while $\sigma^4,\lambda^5$-dithienophosphole sulfides **21** may be prepared by reaction with elemental sulfur.[34a,34b,34d,34e] Both the borane adducts, and the oxidized $\sigma^4$-dithienophospholes **22** and **20** display red-shifted excitation and emission wavelengths. The magnitude of this red shift is greater for the oxidized species than for the dithienophosphole–borane adducts ($\Delta\lambda_{max}$ = 8 nm, $\Delta\lambda_{em}$ = 9 nm). The phosphole oxides **20** and sulfides **21** display identical red shifts as a result of their similar nature, however the intensity in the observed fluorescence is significantly stronger for the dithienophosphole oxide than for the sulfide as a result of sulfur's increased quenching ability.[34b] These red shifts are larger in both the excitation ($\Delta\lambda_{max}$ = 28 nm) and emission wavelengths ($\Delta\lambda_{em}$ = 38 nm) than those observed for the corresponding borane adducts **22** as a result of the oxidized phosphorus center's increased electron-accepting ability. It should be noted that in the presence of electron-withdrawing substituents on the thiophene rings (vide infra), a cumulative effect is observed in both the excitation and emission wavelengths, resulting in larger red shifts for both the borane adducts **22**, and the oxidized $\sigma^4,\lambda^5$-dithienophospholes **20**, **21**. Quantum chemical calculations show that the oxidation of the phosphorus center in the dithieno[3,2-*b*:2′,3′-*d*]phosphole system results in a significant lowering of the LUMO energy level.[34b] Because the HOMO of the dithienophospholes **17** contains no contribution from the phosphorus center, this lowering of the LUMO's energy accounts for the observed red shifts. The experimentally observed band maxima are in good agreement with those calculated by TD-DFT means, implying that such computations may be helpful in predicting the optoelectronic properties of yet unknown dithienophospholes.[34b]

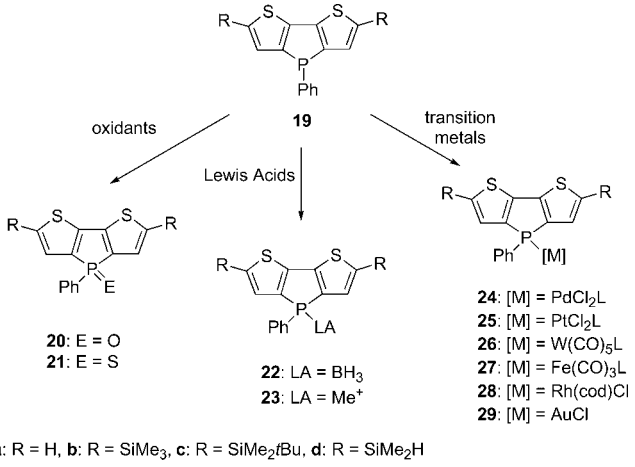


Scheme 7. Functionalization of the $\sigma^3,\lambda^3$-phosphorus center in dithienophospholes **19**.

Recently, cationic phospholium compounds **23**, based on the dithieno[3,2-*b*:2′,3′-*d*]phosphole system have been prepared by methylation of the phosphorus center (Figure 10).[34f] Treatment of the dithienophosphole with methyl triflate resulted in the formation of the cationic phospholium salt **23a** (Scheme 7). The fluorescence of the cationic dithienophosphole exhibits a pronounced red shift, emitting in the green region of the visible spectrum [$\lambda_{max}(\pi$–$\pi^*)$ = 376 nm, $\lambda_{em}$ = 467 nm].[34f] This is the largest red shift observed, due exclusively to the functionalization of the phosphorus center, and not due to a cumulative effect re-

 © 2007 Wiley-VCH Verlag GmbH & Co. KGaA, Weinheim 

sulting from functionalization of both the phosphorus and the thiophene rings in the dithieno[3,2-*b*:2′,3′-*d*]phosphole system (vide infra). The magnitude of this red shift highlights the potential utility of this simple chemical modification in terms of significantly tuning the optoelectronic properties of dithienophospholes. It should be noted in this context that the methylation of the phosphorus center provides access to species that are also water soluble.[34f]

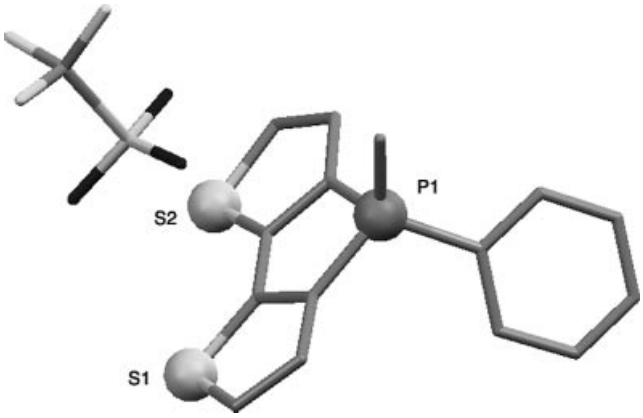


Figure 10. Molecular structure of **23a(OTf⁻)** in the solid state. Picture generated from the CIF-file.[34f]

Dibenzophospholes are known to coordinate to a variety of metal centers, behaving similarly to diphenylphosphanes.[9] The rigid tricyclic dithieno[3,2-*b*:2′,3′-*d*]phospholes **19** behave in a similar manner (Scheme 7).[34b,34c] The coordination of the dithieno-phospholes to transition metals results in an increase in the acceptor character of the dithienophosphole's phosphorus center. X-ray structure analyses of several complexes based on Pd, Pt, W, and Au revealed that the structural properties of the coordinated dithienophosphole ligands are similar to those of the free ligands. This result is in line with the poor delocalization of the phosphorus lone pair in the dithienophosphole system **17**.[9] Similarly to the free ligands, the fluorescence observed in the transition-metal complexes is due to intra-ligand π–π* transitions. As a result of the increased acceptor capacity of the phosphorus center however, red shifts in the absorption and emission wavelengths of the dithienophosphole–metal complexes relative to the free ligands are typically observed. The magnitude of these shifts is dependant on a number of factors that are not always predictable, including the nature of the metal, the substitution of the dithienophosphole ligand, and the geometry of the resulting complexes.[34c] The earlier work of Réau and co-workers had demonstrated that phosphole AuCl complexes display very promising optoelectronic properties. In fact, the complexes have been incorporated into functional OLEDs.[18d,18g] Consequently, the gold(I) complexes **29** of the dithieno[3,2-*b*:2′,3′-*d*]phosphole system were also prepared (Scheme 7). Reaction of the dithienophospholes **19** with AuCl(tht) (tht = tetrahydrothiophene) resulted in quantitative formation of the desired AuCl complexes **29**. The gold center displays a linear geometry, and shows no evidence of aurophilic interactions in the solid state (closest Au–Au distance ca. 5.639 Å) as determined by X-ray crystallography.[34c] While the optoelectronic properties of the transition metal–dithienophosphole complexes examined earlier were relatively insensitive to the nature of the metal (emission at ca. 460 nm for Pt, W, Fe, and Rh complexes **25**, **26**, **27**, and **28**), the AuCl complexes **29** display intriguing optoelectronic properties, including unique absorption and emission wavelengths.[34c] The gold complexes display two absorptions. The red-shifted absorptions have been assigned to the intraligand π–π* transition, whereas the blue-shifted absorptions observed ($\lambda_{max}$ **29b**: 375 nm; **29c**: 405 nm) are likely due to $\sigma_{AuP}$–π* transitions, although a ligand-to-metal charge transfer (LMCT) process cannot be ruled out. Typically bands in the absorption spectra of dithienophospholes are broad and poorly resolved. This is indeed the case with gold complex **29b**.[34c] The absorption spectrum of complex **29c** however, displays relatively narrow, well-resolved bands. This feature may arise as a result of poorer intermolecular interactions between the complexes in solution due to the added steric bulk of the *tert*-butyl group present in the silyl substituents on the thiophene rings of **29c**. The AuCl complex **29c** also displays a strong emission at 445 nm in the solid state, identical to that observed in solution, providing evidence that the complex does not aggregate in the solid state. The unique absorbance properties displayed by **29c** suggest that variation of the silyl functionality may allow the selective optoelectronic properties displayed by this system to be controlled. As a result, AuCl-coordinated dithienophosholes may be well-suited for the development of functional materials and devices.

### 3.2 Modification of the Dithieno-Framework

A number of different substituents may also be introduced at the 2- and 6-positions of the thiophene rings in dithieno[3,2-*b*:2′,3′-*d*]phospholes. The introduction of electron-accepting groups on the thiophene rings results in red shifts for both the excitation and emission wavelengths relative to those observed for the non-functionalized dithienophosphole **19a**.[34] This observation is in line with the further extension of the delocalized π system, and concurrent reduction in the molecule's optical HOMO–LUMO gap induced by the electron-accepting centers. This extension of the delocalized π system is further supported by spectroscopic data. Silyl groups have been used extensively to this end,[34a,34b,34c,34e] including trimethylsilyl (**19b**), *tert*-butyldimethylsilyl (**19c**), and dimethylsilyl (**19d**) groups that have been investigated systematically (Figure 11).

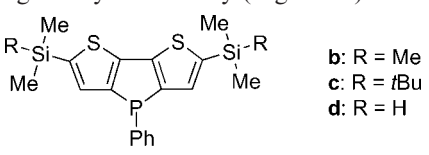


**19b,c,d**

Figure 11. Silyl-functionalized dithienophospholes.

All of these silyl-substituted dithienophospholes display similar emission wavelengths ($\lambda_{em}$ = 420–422 nm), however

 © 2007 Wiley-VCH Verlag GmbH & Co. KGaA, Weinheim 

the nature of the silyl groups has a significant effect on the excitation wavelengths.[34b,34e] The red shifts observed (R = *t*Bu: $\Delta\lambda_{max}$ = 20 nm; R = H: $\Delta\lambda_{max}$ = 22 nm) are consistent with the relative inductive effects expected for methyl, *tert*-butyl, and hydrogen (Me < *t*Bu < H) substituents at the silyl centers. The fact that the emission wavelength in these molecules is not significantly affected by the changes to the silyl centers, while the excitation wavelength is sensitive to them, allows the Stokes shifts of these dithienophospholes to be tuned in a predictable manner. Additionally, the use of the dimethylsilyl-substituted dithieno[3,2-*b*:2′,3′-*d*]phospholes **19d** allowed access to polymeric systems through hydrosilation and dehydrogenative coupling reactions (vide infra).

The introduction of bromo substituents at the 2- and 6-positions, to provide the dithienophospholium salt **23e**, can be achieved by treatment of the dithienophospholium salt **23a** with NBS in DMF (Scheme 8).[34f] As with other electron-accepting substituents, the presence of the bromo substituents results in a decrease in the compound's optical HOMO–LUMO gap. This feature becomes obvious when examining the extraordinarily red-shifted values obtained for both the absorption [$\lambda_{max}(\pi–\pi^*)$ = 411 nm] and the emission ($\lambda_{em}$ = 495 nm) wavelengths of the dibrominated dithienophosphole **23e**.

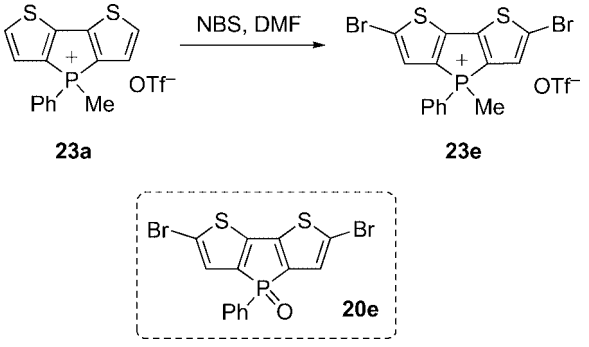


Scheme 8. Introduction of bromo functionalities to the dithienophosphole.

It should be noted that the large magnitude of the observed red shift in this compound arises as the result of the cumulative effect of the electron-accepting cationic phosphorus center, and the electron-accepting substituents on the thiophene moieties. This observation highlights the fact that considerable optimizations of the dithienophosphole system's optoelectronic properties are possible through these simple chemical modifications, or combinations of simple chemical modifications. This method has recently been extended to provide access to 2,6-dibromo-dithienophospholes oxides **20e** (Scheme 8) as well.[34g] Most importantly, in terms of the potential for the use of this system in future optoelectronic materials, is the fact that the bromo functionalities allowed for the incorporation of the dithieno-phosphole system into polymeric materials,[34f] and well-defined oligomers through palladium-catalyzed cross-coupling reactions (vide infra).[34g]

The introduction of Lewis acidic boron centers to the thiophene rings of the dithienophosphole system was possible using a different strategy. Lithiation of the 2- and 6-positions of the unsubstituted dithienophosphole **19a** with LDA, followed by addition of two equivalents of isopropoxy(pinacol)borane resulted in the formation of the boryl-functionalized dithienophosphole **19f** (Scheme 9).[34d] Similarly to other dithienophospholes, boryl-substituted compound **19f** displays blue luminescence, and the emission wavelength ($\lambda_{em}$ = 419 nm) is not significantly different from those displayed by dithienophospholes bearing electron-accepting silyl groups on the thiophene rings ($\lambda_{em}$ = 420–422 nm).[34a,34b,34e]

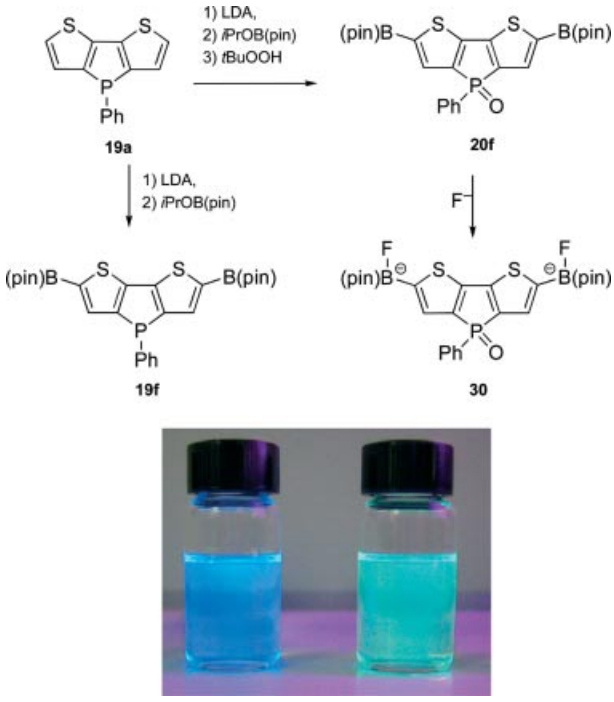


Scheme 9. Boryl-functionalized dithienophospholes – sensory materials (bottom left: **20f** - without fluoride, bottom right: **30** - with fluoride).

As a result of the high affinity of Lewis acidic boron centers for fluoride anions, the development of an effective sensory material based on the dithienophosphole system was possible.[34d] The fluorescence spectrum of the oxidized, air and moisture stable compound **20f** displays the expected red shifts in both the absorption and emission wavelengths ($\Delta\lambda_{max}$ = 22 nm, $\Delta\lambda_{em}$ = 33 nm) consistent with the increased electron-acceptor character of the phosphorus center upon oxidation. Treatment of **20f** with $Bu_4NF$ results in the formation of the ionic borate-functionalized dithienophosphole **30** (Scheme 9).[34d] The ionic borate species **30** displays significantly red-shifted absorption ($\lambda_{max}$ = 415 nm) and emission wavelengths ($\lambda_{em}$ = 485 nm) relative to its neutral borane-functionalized precursor **20f**. In fact, the emission of the compound now occurs in the blue-green region of the visible spectrum, allowing for naked-eye detection of fluoride ions under UV light. These changes in the fluorescence spectrum upon addition of fluoride can be detected at the ppm scale. Addition of $Bu_4NCl$, $Bu_4NBr$, or $Bu_4NI$ however, results in no change to the fluorescence

 © 2007 Wiley-VCH Verlag GmbH & Co. KGaA, Weinheim 

properties of the borane-functionalized dithienophosphole **20f**, consistent with the high selectivity of the boron centers for fluoride ions. As a result, the borane-functionalized dithienophospholes **19f** and **20f** function as useful, selective, and potentially quantitative sensory materials for fluoride ions.[34d]

### 3.3 Dithienophosphole Polymers

Polymeric materials based on the dithieno[3,2-*b*:2′,3′-*d*]-phosphole scaffold have been prepared with the aim of combining the favorable optoelectronic properties displayed by the monomers, with the desirable properties, such as processability (e.g. as thin films) displayed by macromolecular systems.[1] Additionally, oligomers and polymers incorporating the dithienophosphole moiety directly into the conjugated backbone may display additional delocalization between π-conjugated subunits, resulting in optimization of the material's bandgap and further tuning of the material's optoelectronic properties.

The introduction of a 4-vinylphenyl substituent at the phosphorus center of **31** allowed for the incorporation of the dithienophosphole scaffold into a polymeric system as a side-chain functionality.[34a] Radical polymerization of **31** in the presence of styrene in varying ratios provided polymers such as **32** as white amorphous solids (Scheme 10). Gel permeation chromatography (GPC) revealed a high molecular weight of $M_n$ = 147650 g mol$^{-1}$, and a polydispersity (PDI) of 2.46 for a copolymer with a 1:30 (**31**/styrene) ratio. Differential scanning calorimetry (DSC) analysis of the copolymer **32** revealed other favorable properties of the material, such as a glass transition temperature $T_g$ = 114.2 °C superior to that of polystyrene, and a high thermal decomposition temperature of $T_d$ = 428.2 °C. As expected the favorable optoelectronic properties of the dithienophosphole monomers were preserved in the copolymer **33**, which displayed absorption and emission wavelengths ($\lambda_{max}$ = 352 nm, $\lambda_{em}$ = 424 nm) nearly identical to those of the monomeric dithienophosphole **31** ($\lambda_{max}$ = 352 nm, $\lambda_{em}$ = 422 nm). Additionally, the exceptional photoluminescence efficiency of the monomers was preserved with the copolymer displaying a high photoluminescence quantum yield ($\phi_{PL}$ = 74.3%). Oxidation of the phosphorus centers is accomplished by reaction of **32** with $H_2O_2$. As was observed with the dithienophosphole monomers, oxidation of the phosphorus center results in a significant red shift in the optical spectra of the air-stable oxidized polymer **33** ($\Delta\lambda_{max}$ = 22 nm, $\Delta\lambda_{em}$ = 34 nm) relative to their $\sigma^3$-phosphole-containing analogs **32**. In order to probe the potential of the obtained copolymers as PLED materials, thin films of the copolymers were prepared. The thin film of the $\sigma^3,\lambda^3$-dithienophosphole copolymer **32** displayed red shifts in both its excitation and emission wavelengths ($\lambda_{max}$ = 374 nm, $\lambda_{em}$ = 452 nm), while surprisingly the $\sigma^4,\lambda^5$-dithienophosphole copolymer **33** displayed a slightly blue-shifted absorption ($\Delta\lambda_{max}$ = –2 nm), and a significantly blue-shifted emission ($\Delta\lambda_{max}$ = –22 nm). Both the oxidized and the non-oxidized copolymers displayed good light stability, with decreases in emission intensity of less than 5% following two hours irradiation. As a result of these favorable properties, the incorporation of the obtained copolymer into functional optoelectronic devices may be possible.

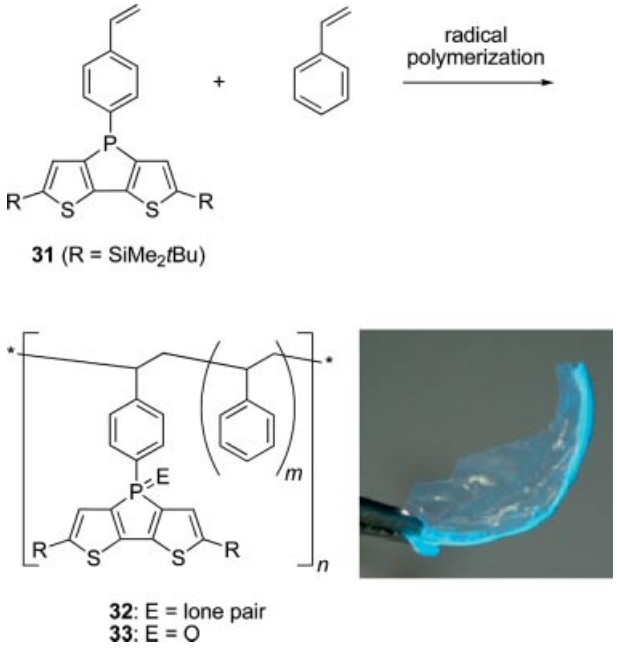


Scheme 10. Incorporation of the dithienophosphole system into polystyrene as a side-chain functionalization; right: thin film of the polymer **32**.

Recently, several copolymers containing the dithieno[3,2-*b*:2′,3′-*d*]phosphole moiety in the polymer backbone have also been prepared (Scheme 11).[34b,34e,34f] Consequently, conjugation between monomers, or comonomers may be possible, resulting in further optimization of the optoelectronic properties of the resulting dithienophosphole materials. The ability to introduce a variety of functionalities at the 2- and 6-positions of the thiophene rings of the dithienophosphole system has allowed for the preparation of a variety of copolymers using different coupling protocols. The incorporation of stannyl groups on the thiophene rings allowed for the preparation of a copolymer using Stille cross-coupling methods.[34b] Stille coupling of the oxidized stannyl-substituted dithienophosphole **20g** with 1,4-diiodo-2,5-bis(octyloxy)benzene as the aryl halide component resulted in the formation of a reddish-brown, poorly soluble material **34**. Suzuki–Miyaura coupling was used to obtain a copolymer from dithienophospholium monomers bearing bromo functionalities (**23e**) and a suitable fluorene-bis(boronic) acid.[34f] The obtained yellow copolymer was sufficiently soluble to allow for its analysis using GPC. This analysis revealed a molecular weight $M_w$ = 9800 g mol$^{-1}$, and a *PDI* of 1.70. A dibromo-functionalized dithienophosphole oxide has recently been subjected to similar reaction conditions, resulting in the formation of an insoluble dithienophosphole-fluorene copolymer.[34g] The insolubility of this material prevented a full characterization, however, the red shifts observed in its optoelectronic properties relative

 © 2007 Wiley-VCH Verlag GmbH & Co. KGaA, Weinheim 

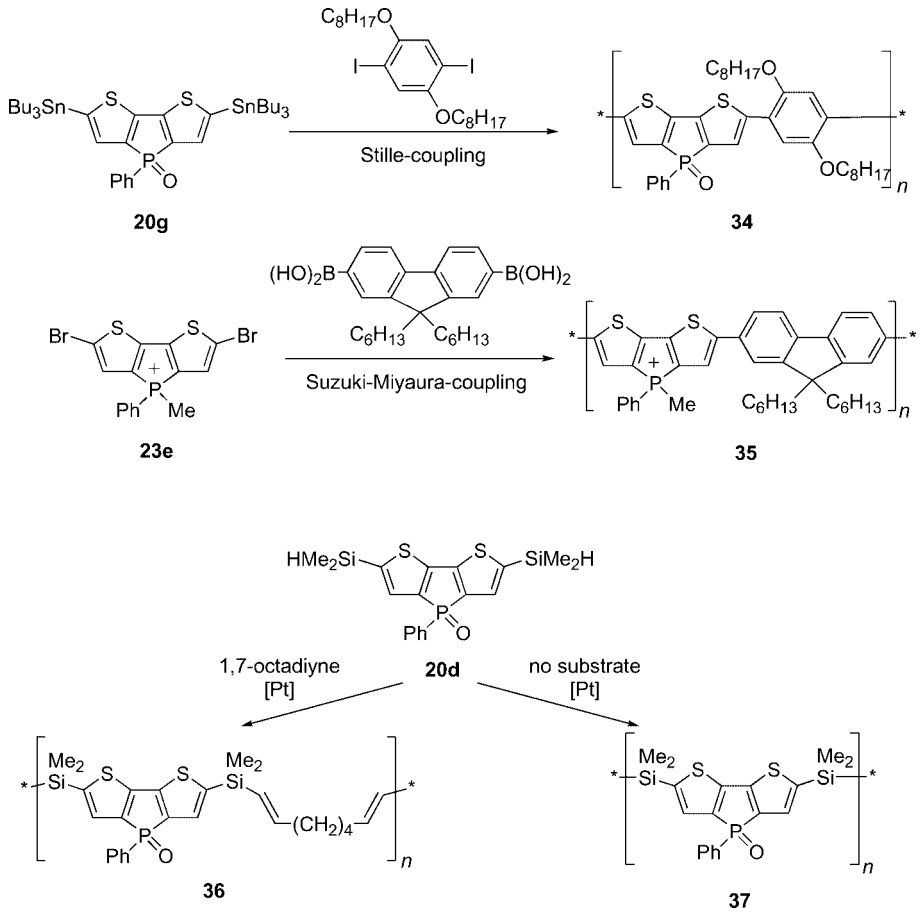


Scheme 11. Preparation of polymers containing the dithienophosphole system in the polymer backbone.

to those of the dibrominated precursor supported the successful copolymerization. The introduction of borane ester substituents in dithienophosphole **20f** should also allow for the copolymerization of this compound using Suzuki–Miyaura protocols, however to date, attempts to do so have resulted in the regeneration of the parent dithienophosphole **20a**.[34g]

Platinum-catalyzed hydrosilation has also been used to obtain copolymers from an α,ω-bis(alkyne) (1,7-octadiyne) and oxidized dimethylsilyl-substituted dithienophospholes **20d**.[34e] The use of PtDVDS ("Karstedt catalyst") resulted in conversion to the polymeric material **36**. GPC analysis of the obtained oily **36** revealed molecular weights up to $M_w$ = 8000 g mol$^{-1}$. When a similar hydrosilation reaction was attempted using an alkene (cf. alkyne) substrate with the same catalyst system, a surprising result was obtained. Instead of the expected 1,2-addition of silicon and hydrogen to the alkene, dehydrogenative homocoupling of the dimethylsilyl groups was observed, producing a polymer **37** in which the dithienophosphole moieties are linked directly by disilanylene groups.[34e] The formation of this product was also observed in the absence of alkene substrates confirming that the alkenes were not involved in its generation. The disappearance of the Si–H signal and the presence of two sets of $^{29}$Si satellites in the methyl proton signal ($^2J_{Si-H}$ = 25.4 Hz, $^3J_{Si-H}$ = 17.2 Hz) of the product's $^1$H NMR spectrum were particularly supportive of such a dehydrogenative Si–Si homocoupling. GPC analysis of the obtained polymer **37** revealed molecular weights up to $M_w$ = 10000 g mol$^{-1}$. This quantitative dehydrocoupling of a tertiary silane is unprecedented to date. The optoelectronic properties of the copolymer **36** ($\lambda_{max}$ = 378 nm, $\lambda_{em}$ = 460 nm) are not significantly different from those displayed by the corresponding monomer **20d** ($\lambda_{max}$ = 383 nm, $\lambda_{em}$ = 457 nm), indicating that the conjugated π system of the dithienophosphole is not significantly extended as a result of copolymerization. Similarly, the emission of the homopolymer **37** ($\lambda_{em}$ = 459 nm) is almost identical to that of the monomer, while the absorption experiences a slight red shift ($\Delta\lambda$ = 10 nm) relative to the dithienophosphole monomer **20d**. These observations are in line with the earlier observation that modification of the silyl substituents in dithienophospholes results in slight changes to the compound's absorption properties, but not to its emission wavelength.[34b] Both silicon-containing dithienophosphole polymers **36** and **37** display good emission intensities, and photoluminescence quantum yields of ca. 56%,[34e] in line with the preservation of the favorable optoelectronic properties of the monomers in the macromolecular systems.

In contrast to the silicon-containing dithienophosphole polymers **36** and **37**, those obtained through coupling reactions of the dithienophospholes and suitable aryl copoly-

 © 2007 Wiley-VCH Verlag GmbH & Co. KGaA, Weinheim 

mers **34** and **35** display optoelectronic properties, with emissions and absorptions that are significantly different from those of the corresponding monomers.[34b,34f] These polymers contain an exclusively π-conjugated backbone, containing the dithienophosphole moiety. As a result, narrowing of the polymer's optical HOMO–LUMO gap and a corresponding red shift in the absorption and emission wavelengths of the macromolecular systems relative to the monomeric compounds was anticipated. Indeed, the emission of the polymer **35** obtained by Suzuki–Miyaura coupling with a fluorene copolymer displays a visibly red-shifted emission, now appearing in the yellow-green region ($\lambda_{em}$ = 509 nm) of the visible spectrum (cf. the blue emission at $\lambda_{em}$ = 467 nm of the corresponding monomer **23e**).[34f] The absorption wavelength of the polymer ($\lambda_{max}$ = 485 nm) is also significantly red-shifted relative to that of the monomer ($\lambda_{max}$ = 376 nm). The photoluminescence quantum yield of polymer **35** ($\phi_{PL}$ = 47.0%) is in the same range as those reported for the dithienophosphole monomers.[34f] Although poor solubility prevented a full characterization of the copolymer **34** obtained by Stille coupling of the stannyl-functionalized dithienophosphole **20g** with an aryl halide,[34b] the obtained product displayed significantly red-shifted optoelectronic properties. The yellow emission of compound **34** at $\lambda_{em}$ = 555 nm is the most strongly red-shifted emission reported to date for polymeric materials derived from the dithieno[3,2-*b*:2,3-*d*]phosphole system. A red shift of similar magnitude is also observed in the excitation wavelength of polymer **34** ($\Delta\lambda_{max}$ = 123 nm). These results are indicative of a strongly extended π conjugation in both of the polymers discussed. As a result, dithienophosphole polymers **34** and **35**, containing exclusively π-conjugated backbones display highly intriguing optoelectronic properties, making them promising materials for future optoelectronic applications. The ionic nature of the methylated dithienophosphole fluorene copolymer **35** in particular, makes this material appealing for potential applications as a conjugated polyelectrolyte (CPE).[1]

### 3.4 Extended Dithienophosphole Molecules

To date, the emission of molecular dithieno[3,2-*b*:2′,3′-*d*]-phosphole systems has been largely limited to the blue region of the visible spectrum ($\lambda_{em}$ = 408–495 nm).[34] As was seen with Réau's system, the extension of the conjugated π system in well-defined oligomers, allows for further optimization of the bandgaps in the resulting materials. In principle, this strategy should allow access to well-defined species capable of displaying emission over a much larger range, depending on the π-conjugated system's degree of extension. Very recently, the use of 2,6-dibromodithienophosphole oxide **20e**, allowed for the incorporation of a wide variety of aryl substituents at the 2- and 6-positions of the dithienophosphole via palladium-catalyzed C–C coupling processes (Scheme 12).[34g] Stille and Suzuki–Miyaura cross-coupling protocols allowed for the preparation of a number of 2,6-diaryl-substituted dithienophospholes **38a**–**g**, displaying significantly extended π-conjugated systems (Scheme 12). Indeed the visible shift from blue-green to yellow-orange fluorescence emission could be observed in the cross-coupling reaction mixtures over the course of the reactions. The complete results of this study will be presented in a forthcoming publication.[34g] The effect of extended π conjugation on the optoelectronic properties of the resulting materials was investigated by incorporating aryl substituents displaying increasing conjugated paths. In line with the conclusion that extension of the conjugated path results in decreased HOMO–LUMO gaps, increasing red shifts in the optoelectronic properties of the products were observed with increasing conjugated path length in the aryl substituents. The effect of electron-rich, and electron-deficient aryl and heteroaryl substitution was also examined. The incorporation of thienyl groups (**38e**) was once again demonstrated to result in more favorable optoelectronic properties in the resulting materials, in line with the prediction that thienyl substituents are subject to a more favorable orbital interaction with phosphole moieties, resulting in decreased HOMO–LUMO gaps in the corresponding materials.[17]

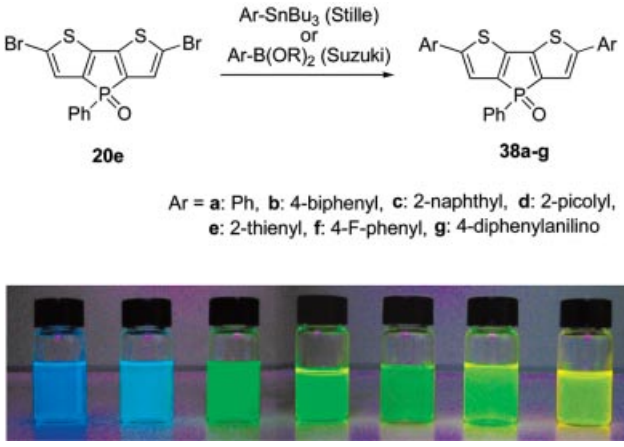


Scheme 12. Synthesis of well-defined, extended dithienophospholes with different emission colors.

The most significant red shift in the optoelectronic properties of the dithieno[3,2-*b*:2′,3′-*d*]phosphole system observed to date arises as a result of the incorporation of 4-diphenylanilino substituents at the 2- and 6-positions of the thiophene rings (**38g**). This compound displays a bright orange emission ($\lambda_{em}$ = 566 nm), and a remarkably red-shifted absorption ($\lambda_{max}$ = 527 nm). When compared with the blue emission of the parent dithienophosphole **19a** ($\lambda_{em}$ = 415 nm), this observation illustrates the versatile nature of the dithienophosphole system, and as a result the wide range of properties accessible through this system.

## 4. Conclusions

The incorporation of phosphole moieties into π-conjugated oligo- and polythiophenes has resulted in the development of new materials displaying fascinating properties. Both the 2,5-bis(2′-thienyl)phosphole, and the dithieno[3,2-

 © 2007 Wiley-VCH Verlag GmbH & Co. KGaA, Weinheim 

*b*:2′,3′-*d*]phosphole systems have proven to be versatile scaffolds as a result of the various manners in which their frameworks may be modified. Firstly, the nature of the exocyclic phosphorus substituents has profound effects on the stabilities of the obtained materials in both scaffolds. The properties of the obtained materials were also shown to be highly dependant on the nature of the 2,5-aryl substituents in Réau's diarylphosphole system, and the nature of the substituents at the 2- and 6-positions of Baumgartner's dithienophosphole system. In many respects diarylphospholes bearing thienyl substituents displayed superior properties relative to phospholes bearing alternative aryl, or heteroaryl substituents. Well-defined oligomers displaying additional π conjugation relative to the corresponding monomers have been prepared for both systems, potentially serving as useful models for larger macromolecular systems. Both families of compounds have been incorporated into such macromolecular systems, either as side-chain functionalities, or as subunits within the conjugated path. Of paramount importance in both scaffolds, the presence of a reactive trivalent phosphorus center allows for a variety of facile, quantitative chemical modifications (oxidation, complexation, methylation) to be performed. These modifications often result in significant changes to the properties of the obtained materials. As a result, large families of compounds, displaying novel properties may be prepared from single precursors. These modifications have been extended from the molecular level to the macromolecular level, allowing for a variety of postfunctionalizations of the obtained polymeric materials. Due to their intriguing properties, both phosphole-containing oligothiophene systems serve various functions in different applications: chemosensors for fluoride anions have been prepared using molecular dithienophospholes, while polymeric 2,5-dithienylphospholes were used in the development of the first polymeric chalcogen sensor. Recently, the fascinating emissive properties of the 2,5-dithienylphosphole system allowed for its incorporation in the first functional OLEDs based on organophosphorus materials. Although it is acknowledged that the study of organophosphorus π-conjugated materials such as the 2,5-diarylphosphole, and the dithieno-phosphole systems examined remains in its infancy, these promising systems represent key developments towards maturity in this field, and the development of new functional devices based on organophosphorus π-conjugated materials.


[1] a) *Handbook of Conducting Polymers 2nd Ed.* (Ed.: T. A. Skotheim, R. L. Elsenbaumer, J. R. Reynolds), Marcel Dekker, New York, **1998**; b) *Electronic Materials: The Oligomer Approach* (Ed.: K. Müllen, G. Wegner), Wiley-VCH, Weinheim, **1998**; c) P. F. H. Schwab, J. R. Smith, J. Michl, *Chem. Rev.* **2005**, *105*, 1197; d) F. J. M. Hoeben, P. Jonkheijm, A. P. H. J. Schenning, *Chem. Rev.* **2005**, *105*, 1491; e) J. Roncali, *Chem. Rev.* **1997**, *97*, 173.

[2] *Organic Light Emitting Devices* (Ed.: K. Müllen, U. Scherf), Wiley-VCH, Weinheim, **2005**.

[3] G. A. Chamberlain, *Solar Cells* **1983**, *8*, 47.

[4] H. E. Katz, Z. Bao, *J. Phys. Chem. B* **2000**, *104*, 671.

[5] D. T. McQuade, A. Pullen, T. M. Swager, *Chem. Rev.* **2000**, *100*, 2537.

[6] a) *Handbook of Oligo- and Polythiophenes* (Ed.: D. Fichou), Wiley-VCH,, Weinheim, **1998**; b) I. F. Perepichka, D. F. Perepichka, H. Meng, F. Wudl, *Adv. Mater.* **2005**, *17*, 2281.

[7] a) D. Delaere, T. N. Minh, L. G. Vanquickenborne, *Phys. Chem. Chem. Phys.* **2002**, *4*, 1522; b) J. Ma, S. Li, J. Yuansheng, *Macromolecules* **2002**, *35*, 1109; c) U. Salzner, J. B. Lagowski, P. G. Pickup, R. A. Poirier, *Synth. Met.* **1998**, *96*, 177.

[8] a) T. Baumgartner, R. Réau, *Chem. Rev.* **2006**, *106*, 4681; b) M. Hissler, P. W. Dyer, R. Réau, *Top. Curr. Chem.* **2005**, *250*, 127; c) D. P. Gates, *Top. Curr. Chem.* **2005**, *250*, 107; d) F. Mathey, *Angew. Chem. Int. Ed.* **2003**, *42*, 1578.

[9] a) L. D. Quin, G. S. Quin, *Phospholes: Recent Literature **1994**-mid 1999* in *Phosphorus-Carbon Heterocyclic Chemistry: The Rise of a New Domain* (Ed.: F. Mathey) Pergamon, New York, **2001**; b) F. Mathey, *Chem. Rev.* **1988**, *88*, 429.

[10] P. v. R. Schleyer, C. Maerker, A. Dransfeld, H. Jiao, N. J. R. V. E. Hommes, *J. Am. Chem. Soc.* **1996**, *118*, 6317.

[11] a) L. Nyulászi, *Chem. Rev.* **2001**, *101*, 1229; b) W. Schäfer, A. Schweig, F. Mathey, *J. Am. Chem. Soc.* **1976**, *98*, 407.

[12] E. Deschamps, L. Ricard, F. Mathey, *Angew. Chem. Int. Ed. Engl.* **1994**, *33*, 1158.

[13] F. Mathey, F. Mercier, F. Nief, J. Fischer, A. Mitschler, *J. Am. Chem. Soc.* **1982**, *104*, 2077.

[14] S. S. H. Mao, T. D. Tilley, *Macromolecules* **1997**, *30*, 5566.

[15] See, for the report of a more recent phosphole-containing polymer: Y. Morisaki, Y. Aiki, Y. Chujo, *Macromolecules* **2003**, *36*, 2594.

[16] O. Tissot, J. Hydrio, M. Gouygou, F. Dallemer, J.-C. Daran, G. G. A. Balavoine, *Tetrahedron* **2000**, *56*, 85.

[17] D. Delaere, M. T. Nguyen, L. G. Vanquickenborne, *J. Phys. Chem. A* **2003**, *107*, 838.

[18] a) C. Hay, D. Le Vilain, V. Deborde, L. Toupet, R. Réau, *Chem. Commun.* **1999**, 345; b) C. Hay, C. Fischmeister, M. Hissler, L. Toupet, R. Réau, *Angew. Chem. Int. Ed.* **2000**, *39*, 1812; c) C. Hay, M. Hissler, C. Fischmeister, J. Rault-Berthelot, L. Toupet, L. Nyulászi, R. Réau, *Chem. Eur. J.* **2001**, *7*, 4222; d) C. Fave, T.-Y. Cho, M. Hissler, C.-W. Chen, T.-Y. Luh, C.-C. Wu, R. Réau, *J. Am. Chem. Soc.* **2003**, *125*, 9254; e) C. Hay, C. Fave, M. Hissler, J. Rault-Berthelot, R. Réau, *Org. Lett.* **2003**, *5*, 3467; f) C. Fave, M. Hissler, T. Kárpáti, J. Rault-Berthelot, V. Deborde, L. Toupet, L. Nyulászi, R. Réau, *J. Am. Chem. Soc.* **2004**, *126*, 6058; g) H.-C. Su, O. Fadhel, C.-J. Yang, T.-Y. Cho, C. Fave, M. Hissler, C.-C. Wu, R. Réau, *J. Am. Chem. Soc.* **2006**, *128*, 983; h) M. Sebastian, M. Hissler, C. Fave, J. Rault-Berthelot, C. Odin, R. Réau, *Angew. Chem.* **2006**, *118*, 6298.

[19] P. J. Fagan, W. A. Nugent, *J. Am. Chem. Soc.* **1988**, *110*, 2310.

[20] R. Hoffman, *Acc. Chem. Res.* **1971**, *4*, 1.

[21] a) E. W. Abel, C. Towers, *J. Chem. Soc., Dalton Trans.* **1979**, 814; b) S. Holland, F. Mathey, J. Fischer, A. Mitschler, *Organometallics* **1983**, *2*, 1234.

[22] I. D. L. Albert, T. B. Marks, M. A. Ratner, *J. Am. Chem. Soc.* **1997**, *119*, 6575.

[23] E. E. Havinga, W. T. Hoeve, H. Wynberg, *Synth. Met.* **1993**, *55*, 299.

[24] S. Yamaguchi, Y. Itami, K. Tamao, *Organometallics* **1998**, *17*, 4910.

[25] a) M. Sauthier, B. Le Guennic, V. Deborde, L. Toupet, J.-F. Halet, R. Réau, *Angew. Chem. Int. Ed.* **2001**, *40*, 228; b) C. Hay, M. Sauthier, V. Deborde, M. Hissler, L. Toupet, R. Réau, *J. Organomet. Chem.* **2002**, *643–644*, 494; c) M. Sauthier, F. Leca, L. Toupet, R. Réau, *Organometallics* **2002**, *21*, 1591; d) C. Fave, M. Hissler, K. Sénéchal, I. Ledoux, J. Zyss, R. Réau, *Chem. Commun.* **2002**, 1674; e) F. Leca, M. Sauthier, V. Deborde, L. Toupet, R. Réau, *Chem. Eur. J.* **2003**, *9*, 3785; f) F. Leca, C. Lescop, L. Toupet, R. Réau, *Organometallics* **2004**, *23*, 6191; g) F. Leca, C. Lescop, E. Rodriguez-Sanz, K. Costuas, J.-F. Halet, R. Réau, *Angew. Chem. Int. Ed.* **2005**, *44*, 4362; h) F. Leca, R. Réau, *J. Catal.* **2006**, *238*, 425; i) S. Urig, K. Fritz-Wolf, R. Réau, C. Herold-Mende, K. Tóth, E. Davi-


 © 2007 Wiley-VCH Verlag GmbH & Co. KGaA, Weinheim 

oud-Charvet, K. Becker, *Angew. Chem. Int. Ed.* **2006**, *45*, 1881; j) B. Nohra, S. Graule, C. Lescop, R. Réau, *J. Am. Chem. Soc.* **2006**, *128*, 3520.
[26] L. Nyulászi, O. Hollóczki, C. Lescop, M. Hissler, R. Réau, *Org. Biomol. Chem.* **2006**, *4*, 996.
[27] B. W. D'Andrade, S. R. Forrest, *Adv. Mater.* **2004**, *16*, 1585.
[28] P. Audebert, J.-M. Catel, G. Le Coustumer, V. Duchenet, P. Hapiot, *J. Phys. Chem. B* **1998**, *102*, 8661.
[29] M. C. Suh, B. Jiang, T. D. Tilley, *Angew. Chem. Int. Ed.* **2000**, *39*, 2870.
[30] Electropolymerization of $\sigma^3,\lambda^3$-dithienylphospholes generally provides thin films with protonated phosphorus centers, see ref.[18b,18c,18f].
[31] C.-T. Chen, *Chem. Mater.* **2004**, *16*, 4389.
[32] J. M. Hong, S. Y. Hong, *J. Chem. Phys.* **1997**, *107*, 10607.
[33] a) G. Barbarella, L. Favaretto, G. Sotgiu, L. Antolini, G. Gigli, R. Cingolani, A. Bongini, *Chem. Mater.* **2001**, *13*, 4112; b) X. Zhang, A. J. Matzger, *J. Org. Chem.* **2003**, *68*, 9813.
[34] a) T. Baumgartner, T. Neumann, B. Wirges, *Angew. Chem. Int. Ed.* **2004**, *43*, 6197; b) T. Baumgartner, W. Bergmans, T. Kárpáti, T. Neumann, M. Nieger, L. Nyulászi, *Chem. Eur. J.* **2005**, *11*, 4687; c) Y. Dienes, M. Eggenstein, T. Neumann, U. Englert, T. Baumgartner, *Dalton Trans.* **2006**, 1424; d) T. Neumann, Y. Dienes, T. Baumgartner, *Org. Lett.* **2006**, *8*, 495; e) T. Baumgartner, W. Wilk, *Org. Lett.* **2006**, *8*, 503; f) S. Durben, Y. Dienes, T. Baumgartner, *Org. Lett.* **2006**, *8*, 5893; g) Y. Dienes, S. Durben, T. Kárpáti, T. Neumann, U. Englert, L. Nyulászi, T. Baumgartner, *Chem. Eur. J.*, in press.

Received: March 29, 2007
Published Online: May 10, 2007

 © 2007 Wiley-VCH Verlag GmbH & Co. KGaA, Weinheim 

DOI: 10.1002/ejic.200700420

# Activated Aryl Chlorides: Useful Partners for the Coupling with 2-Substituted Thiazoles in the Palladium-Catalysed C-H Activation/Functionalisation Reaction

**Aditya L. Gottumukkala[a] and Henri Doucet*[a]**

**Keywords:** Aryl chlorides / Catalysis / C-H activation / Palladium / Thiazoles

Aryl chlorides are noticeably uncommon partners in coupling reactions with heteroaromatics through C-H activation. We report herein that as little as 1 mol-% of the air-stable PdCl(dppb)($C_3H_5$) complex catalyses the direct coupling of electron-deficient aryl chlorides with 2-substituted thiazole derivatives. A range of functionalities on the aryl chloride such as acetyl, formyl, ester, nitro, nitrile or trifluoromethyl is tolerated.
(© Wiley-VCH Verlag GmbH & Co. KGaA, 69451 Weinheim, Germany, 2007)

## Introduction

Arylthiazole derivatives are important building blocks in organic synthesis.[1] Palladium catalysed Suzuki, Stille or Negishi cross-coupling reactions are probably the most important methods for the synthesis of such compounds.[1–4] However, these reactions require the preparation of an organometallic derivative and they provide an organometallic salt (MX) as a byproduct.

Over the last few years, very interesting results for the coupling of aryl bromides or iodides with thiazole derivatives by C-H activation have been reported and provide an economically and environmentally attractive procedure for the preparation of such compounds.[5] So far, most of the results described for this reaction were obtained with reactive, but expensive aryl bromides[6] or iodides.[7] The use of chloride substrates for cross-coupling reactions with thiazoles by C–H bond activation (Scheme 1) would be a considerable advantage for sustainable development because of their lower cost, lower mass and the wider diversity of available compounds.[8–11] However, for this coupling, aryl chlorides are noticeably uncommon partners. This is due to the fact that chlorides were generally found to be unreactive under the experimental conditions employed to activate iodide and bromide analogues. In most cases, for Suzuki, Heck or Sonogashira reactions aryl chlorides were activated using electron-rich, sterically hindered, monodentate phosphane ligands associated to palladium.[11a] Moreover, in most cases, the direct coupling of aryl chlorides with heteroaromatics such as pyridines, thiophenes or thiazoles were performed with the use of relatively large amounts of palladium or ruthenium catalysts (2.5–10 mol-%).[7–10,12] Therefore, the discovery of more effective conditions, with the use of a lower catalyst loading for the coupling of thiazoles with these challenging substrates is still subject to significant improvement.

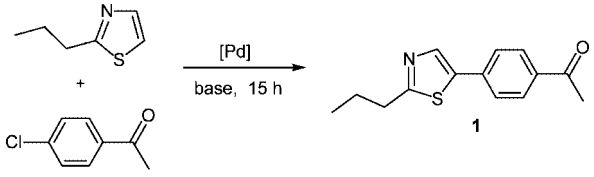


Scheme 1.

Monophosphane ligands associated to palladium were successfully used for the direct coupling of thiazoles derivatives with aryl bromides or iodides,[5] but the efficiency of bidentate phosphane ligands for such a coupling reaction has attracted less attention.[7c] In the literature, most of the couplings of heteroaryl derivatives with aryl halides were performed at elevated temperatures (140–150 °C).[5] At these temperatures, fast decomposition of the palladium complexes associated to monophosphane ligands generally occurs. In some cases, the use of polydentate ligands seems to increase the stability and longevity of the catalyst, so we could expect better conversions of aryl chlorides by using bidentate ligands.[13]

## Results and Discussion

First, we examined the efficiency of $[PdCl(C_3H_5)]_2$ associated to mono- or bidentate ligands on the yield of the direct coupling of 4-chloroacetophenone with 2-*n*-propylthiazole (Scheme 1, Table 1). $[PdCl(C_3H_5)]_2$ associated to

[a] Institut Sciences Chimiques de Rennes, UMR 6226 CNRS-Université de Rennes, "Catalyse et Organometalliques",
Campus de Beaulieu, 35042 Rennes, France
Fax: +33-2-23236939
E-mail: henri.doucet@univ-rennes1.fr
Supporting information for this article is available on the WWW under http://www.eurjic.org or from the author.

 © 2007 Wiley-VCH Verlag GmbH & Co. KGaA, Weinheim 

Table 1. Palladium-catalysed cross-coupling of 2-*n*-propylthiazole with 4-chloroacetophenone (Scheme 1). Conditions: catalyst 1 mol-%, 4-chloroacetophenone (1 equiv.), 2-*n*-propylthiazole (2 equiv.), base (4 equiv.), 15 h, GC and NMR yields.

| Entry | Catalyst | Solvent | Base | Temperature [°C] | Yield [%][a] |
|---|---|---|---|---|---|
| 1 | 0.5 $[PdCl(C_3H_5)]_2$/dppe | dmac | AcOK | 150 | 41 |
| 2 | 0.5 $[PdCl(C_3H_5)]_2$/dppf | dmac | AcOK | 150 | 10 |
| 3 | $PdCl(dppb)(C_3H_5)$ | dmac | AcONa | 150 | 72 |
| 4 | $[PdCl(C_3H_5)]_2/2PPh_3$ | dmac | AcOK | 150 | 58[b] |
| 5 | $Pd(OH)_2/C$ | dmac | AcONa | 150 | 9 |
| 6 | 10% Pd/C | dmac | AcOK | 150 | 0 |
| 7 | $Pd(OAc)_2$/dppb | dmac | AcOK | 150 | 10 |
| 8 | $Pd(OAc)_2/2PPh_3$ | dmac | AcOK | 150 | 6 |
| 9 | $PdCl(dppb)(C_3H_5)$ | dmac | AcOK | 150 | 65 (53) |
| 10 | $PdCl(dppb)(C_3H_5)$ | dmac | $Cs_2CO_3$ | 150 | 12 |
| 11 | $PdCl(dppb)(C_3H_5)$ | dmac | $K_2CO_3$ | 150 | 15 |
| 12 | $PdCl(dppb)(C_3H_5)$ | dmac | KF | 150 | 12 |
| 13 | $PdCl(dppb)(C_3H_5)$ | dmf | AcONa | 150 | 34 |
| 14 | $PdCl(dppb)(C_3H_5)$ | dmso | AcONa | 150 | 17 |
| 15 | $PdCl(dppb)(C_3H_5)$ | nmp | AcOK | 150 | 17 |
| 16 | $PdCl(dppb)(C_3H_5)$ | dioxane | AcOK | 150 | 14[c] |
| 17 | $PdCl(dppb)(C_3H_5)$ | xylene | AcOK | 150 | 5[c] |
| 18 | $PdCl(dppb)(C_3H_5)$ | dmac | AcOK | 130 | 32 |
| 19 | $PdCl(dppb)(C_3H_5)$ | dmac | AcOK | 170 | 6 |

[a] Yield in parenthesis is isolated yield. [b] The formation of side products was also observed. [c] Reaction performed in an autoclave.

the dppe or 1,1′-dppf ligands led to low conversions of 41 and 10%, respectively (Table 1, Entries 1 and 2). On the other hand, we observed that with $PdCl(C_3H_5)(dppb)$[14] as the catalyst, dmac as the solvent, AcONa as the base and heated 150 °C, 5-(4-acetylphenyl)-2-propyl-thiazole (**1**) was obtained with 72% conversion (Table 1, Entry 3). The dppb ligand is known to give sterically more hindered complexes than those of 1,1′-dppf or dppe. By using $PPh_3$ as the ligand, the formation of **1** was observed in 58% conversion together with the formation of a side product (Table 1, Entry 4). The palladium source also has a large influence on the yield. The use of $Pd(OAc)_2$ led to reactions with lower yields than those with $[PdCl(C_3H_5)]_2$ (Table 1, Entries 7 and 8). Pd/C or $Pd(OH)_2/C$ was found to be almost completely ineffective for this coupling (Table 1, Entries 5 and 6). Then, the influence of several parameters such as the base, solvent and temperature with the use of $PdCl(C_3H_5)(dppb)$ as the catalyst was examined. AcOK also led to a high yield of **1** (Table 1, Entry 9). By using carbonates or KF as bases, lower conversions were obtained (Table 1, Entries 10–12). The influence of a few other solvents such as dmf, dmso, nmp, dioxane or xylene was also examined, but in all cases, low conversions were observed (Table 1, Entries 13–17). An elevated reaction temperature (150 °C) was necessary to obtain a high yield of the product. At 130 °C, a lower conversion of 32% was obtained. On the other hand, a very high reaction temperature led to a very low conversion of 6%. This is probably due to faster decomposition of the catalyst (Table 1, Entries 18 and 19).

Then, the scope and limitations of this reaction by using $PdCl(dppb)(C_3H_5)$ in dmac with AcOK or AcONa as bases at 150 °C was investigated (Scheme 2, Table 2). The reaction

Table 2. Palladium catalysed cross-coupling with thiazole derivatives (Scheme 2). Conditions: $PdCl(dppb)(C_3H_5)$ see ref.[14], ArCl (1 equiv.), thiazole derivative (2 equiv.), AcOK or AcONa (4 equiv.), dmac, 150 °C, 15 h, GC and NMR yields.

| Entry | Thiazole | Aryl chloride | Base | Product | Yield [%][a] |
|---|---|---|---|---|---|
| 1 | 2-*n*-propylthiazole | 4-chlorobenzaldehyde | AcOK | **2** | 89 (74) |
| 2 | 2-*n*-propylthiazole | methyl 4-chlorobenzoate | AcOK | **3** | 85 (72) |
| 3 | 2-*n*-propylthiazole | 4-trifluoromethylchlorobenzene | AcOK | **4** | 63 (56)[b] |
| 4 | 2-*n*-propylthiazole | 4-chlorobenzonitrile | AcOK | **5** | 84 (75) |
| 5 | 2-*n*-propylthiazole | 4-chloronitrobenzene | AcONa | **6** | 55 |
| 6 | 2-*n*-propylthiazole | 4-chloronitrobenzene | AcOK | **6** | 100 (79) |
| 7 | 2-*n*-propylthiazole | 4-chlorofluorobenzene | AcOK | – | 0 |
| 8 | 2-*n*-propylthiazole | 3-chlorobenzonitrile | AcOK | **7** | 69 (57) |
| 9 | 2-*n*-propylthiazole | 2-chlorobenzaldehyde | AcONa | **8** | 85 (63) |
| 10 | 2-*n*-propylthiazole | 2-chlorobenzaldehyde | AcOK | **8** | 75 |
| 11 | 2-*n*-propylthiazole | 2-trifluoromethylchlorobenzene | AcOK | **9** | 13 (11) |
| 12 | 2-*n*-propylthiazole | 2-chlorobenzonitrile | AcOK | **10** | 46 (41) |
| 13 | 2-ethyl-4-methylthiazole | 4-chlorobenzonitrile | AcOK | **11** | 92 (71) |
| 14 | 2-ethyl-4-methylthiazole | 4-chloronitrobenzene | AcOK | **12** | 98 (73) |
| 15 | 2-ethyl-4-methylthiazole | 4-chlorobenzaldehyde | AcOK | **13** | 62 (52) |
| 16 | 2-ethyl-4-methylthiazole | 3-chlorobenzonitrile | AcOK | **14** | 48 (44) |
| 17 | 2-ethyl-4-methylthiazole | 2-chlorobenzaldehyde | AcOK | **15** | 82 (70) |

[a] Yields in parenthesis are isolated yields. [b] Reaction performed in an autoclave.

 © 2007 Wiley-VCH Verlag GmbH & Co. KGaA, Weinheim 

proceeds nicely with several *para*-substituted aryl chlorides. Electron-withdrawing groups in the aryl chlorides are favourable, whereas an electron-donation group is unfavourable. For example, the coupling with 4-chlorobenzaldehyde, methyl 4-chlorobenzoate, 4-chlorobenzonitrile or 4-chloronitrobenzene gave the corresponding 5-aryl-2-*n*-propylthiazoles **2**–**6** in good yields (Table 2, Entries 1–6). On the other hand, poorly activated 4-chlorofluorobenzene was recovered unreacted (Table 2, Entry 7). This result seems to indicate that with this catalyst the oxidative addition of the aryl chloride to palladium is the rate-limiting step of the catalytic cycle. As expected, quite similar reactivity was obtained by using *meta*-substituted 3-chlorobenzonitrile (Table 2, Entry 8). Sterically congested *ortho*-substituted aryl chlorides gave low-to-high yields of **8**–**10**, depending on the substituents (Table 2, Entries 9–12).

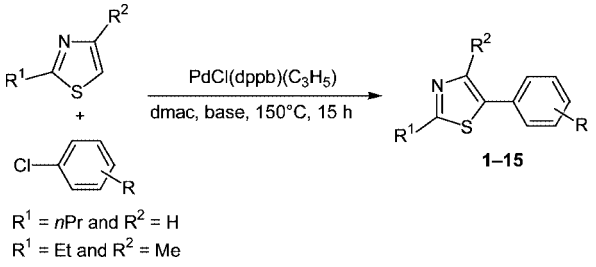


Scheme 2.

Finally, the coupling in the presence of the sterically more-hindered 2-ethyl-4-methylthiazole was studied. 2-Ethyl-5-aryl-4-methylthiazole derivatives **11**–**15** were obtained selectively in moderate-to-high yields (Table 2, Entries 13–17).

## Conclusions

In the presence 1 mol-% of the air-stable PdCl(dppb)($C_3H_5$) complex, the direct arylation of 2-substituted thiazole derivatives with the use of aryl chlorides proceeds in moderate-to-high yields. The structure of the ligand, palladium source and reaction conditions have a large influence on the yields. With this system, only electron-deficient aryl chlorides gave satisfactory results. However, it should be noted that a wide range of functionalities such as acetyl, formyl, ester, nitro, nitrile or trifluoromethyl on the aryl chloride is tolerated. This procedure is very simple, economically attractive and uses commercially available ligand and catalyst precursors. The air-stability of the catalyst and ligand make this procedure more convenient than those using bulky electron-rich phosphanes that are often employed to activate aryl chlorides in palladium-catalysed reactions.[11]

## Experimental Section

As a typical experiment, a mixture of 4-chloroacetophenone (0.154 g, 1 mmol), 2-*n*-propylthiazole (0.254 g, 2 mmol) and AcOK (0.392 g, 4 mmol) was heated at 150 °C for 15 h in dry dmac (5 mL) in the presence of PdCl(dppb)($C_3H_5$)[14] (6.1 mg, 0.01 mmol) under an atmosphere of argon. After extraction with dichloromethane, evaporation and filtration through silica gel (pentane/ether) corresponding product **1** was obtained in 53% (0.129 g) isolated yield as an oil. $^1$H NMR (200 MHz, $CDCl_3$): $\delta$ = 7.96 (d, $J$ = 8.5 Hz, 2 H), 7.92 (s, 1 H), 7.60 (d, $J$ = 8.5 Hz, 2 H), 2.99 (t, $J$ = 7.4 Hz, 2 H), 2.60 (s, 3 H), 1.85 (sext., $J$ = 7.4 Hz, 2 H), 1.03 (t, $J$ = 7.4 Hz, 3 H) ppm. $^{13}$C NMR (50 MHz, $CDCl_3$): $\delta$ = 197.1, 172.1, 138.9, 137.1, 136.2, 136.1, 129.1, 126.3, 35.6, 26.6, 23.3, 13.6 ppm. $C_{11}H_9NOS$ (203.12): C 65.00, H 4.46; found C 64.75, H 4.76.

**Supporting Information** (see footnote on the first page of this article): Experimental details for the preparation of the Pd catalyst and compounds **2**–**15**.

## Acknowledgments

A. G. is grateful to EGIDE for a grant. We thank the Centre National de la Recherche Scientifique for providing financial support.

[1] J. J. Li, G. W. Gribble, *Palladium in Heterocyclic Chemistry*, Pergamon, Amsterdam, **2000**.
[2] For selected examples of palladium cross-coupling reactions of thiazoles by Suzuki coupling, see: a) P. Vachal, L. M. Toth, *Tetrahedron Lett.* **2004**, *45*, 7157; b) K. J. Hodgetts, M. T. Kershaw, *Org. Lett.* **2002**, *4*, 1363.
[3] For selected examples of palladium cross-coupling reactions of thiazoles by Stille coupling, see: a) R. Benhida, F. Lecubin, J.-L. Fourrey, L. R. Castellanos, L. Quintero, *Tetrahedron Lett.* **1999**, *40*, 5701; b) D. Guianvarc′h, J.-L. Fourrey, R. Maurisse, J.-S. Sun, R. Benhida, *Org. Lett.* **2002**, *4*, 4209; c) P. Stanetty, M. Schnürch, M. D. Mihovilovic, *J. Org. Chem.* **2006**, *71*, 3754.
[4] For selected examples of palladium cross-coupling reactions of thiazoles by Negishi coupling, see: a) J. Jensen, N. Skjaerbaek, P. Vedsø, *Synthesis* **2001**, 128; b) O. Hara, T. Nakamura, F. Sato, K. Makino, Y. Hamada, *Heterocycles* **2006**, *68*, 1.
[5] For reviews on palladium-catalysed C-H bond activation of heteroaryls, see: a) V. Ritleng, C. Sirlin, M. Pfeffer, *Chem. Rev.* **2002**, *102*, 1731; b) D. Alberico, M. E. Scott, M. Lautens, *Chem. Rev.* **2007**, *107*, 174; c) T. Satoh, M. Miura, *Chem. Lett.* **2007**, *36*, 200.
[6] For examples of direct 5-arylation of thiazoles by using aryl bromides, see: a) A. Yokooji, T. Okazawa, T. Satoh, M. Miura, M. Nomura, *Tetrahedron* **2003**, *59*, 5685; b) A. Mori, A. Sekiguchi, K. Masui, T. Shimada, M. Horie, K. Osakada, M. Kawamoto, T. Ikeda, *J. Am. Chem. Soc.* **2003**, *125*, 1700; c) M. Parisien, D. Valette, K. Fagnou, *J. Org. Chem.* **2005**, *70*, 7578.
[7] For examples of direct 5-arylation of thiazoles by using aryl iodides, see: a) S. Pivsa-Art, T. Satoh, Y. Kawamura, M. Miura, M. Nomura, *Bull. Chem. Soc. Jpn.* **1998**, *71*, 467; b) Y. Kondo, T. Komine, T. Sakamoto, *Org. Lett.* **2000**, *2*, 3111; c) K. Masui, A. Mori, K. Okano, K. Takamura, M. Kinoshita, T. Ikeda, *Org. Lett.* **2004**, *6*, 2011; d) A. Mori, A. Sekiguchi, K. Masui, T. Shimada, K. Kobayashi, M. S. M. Ahmed, A. Mori, *Tetrahedron* **2006**, *62*, 9548.
[8] For examples of intramolecular direct arylation of heteroaromatics by using aryl chlorides, see: a) M. Smet, J. Van Dijk, W. Dehaen, *Synlett* **1999**, 495; b) T. H. M. Jonckers, B. U. W. Maes, G. L. F. Lemière, G. Rombouts, L. Pieters, A. Haemers, R. A. Dommisse, *Synlett* **2003**, *5*, 615; c) J.-P. Leclerc, M. André, K. Fagnou, *J. Org. Chem.* **2006**, *71*, 1711.
[9] For examples of bimolecular direct arylation of heteroaromatics by using aryl chlorides, see: a) K. J. Hodgetts, M. T. Kershaw, *Org. Lett.* **2003**, *5*, 2911; b) J.-P. Leclerc, K. Fagnou, *Angew. Chem. Int. Ed.* **2006**, *45*, 7781.

 © 2007 Wiley-VCH Verlag GmbH & Co. KGaA, Weinheim 

[10] Y. Aoyagi, A. Inoue, I. Koizumi, R. Hashimoto, K. Tokunaga, K. Gohma, J. Komatsu, K. Sekine, A. Miyafuji, J. Kunoh, R. Honma, Y. Akita, A. Ohta, *Heterocycles* **1992**, *33*, 257.
[11] a) A. Littke, G. Fu, *Angew. Chem. Int. Ed.* **2002**, *41*, 4176; b) H. A. Chiong, O. Daugulis, *Org. Lett.* **2007**, *9*, 1449.
[12] L. Ackermann, *Org. Lett.* **2005**, *7*, 3123.
[13] A. Battace, M. Lemhadri, T. Zair, H. Doucet, M. Santelli, *Organometallics* **2007**, *26*, 472.
[14] T. Cantat, E. Génin, C. Giroud, G. Meyer, A. Jutand, *J. Organomet. Chem.* **2003**, *687*, 365.

Received: April 18, 2007
Published Online: July 6, 2007

 © 2007 Wiley-VCH Verlag GmbH & Co. KGaA, Weinheim 

DOI: 10.1002/ejic.200600201

# Synthesis and Crystal Structure of a Heptanuclear and an Octanuclear Copper(II) Complex Derived from α-D-Glucofuranoses

**Michael Gottschaldt,*[a] Rainer Wegner,[b] Helmar Görls,[b] Ernst-G. Jäger,[a][†] and Dieter Klemm[a]**

**Keywords:** Carbohydrates / Copper complexes / Cluster compounds

$Cu^{II}$ complexes of different 6-(β-keto-enamino)-6-deoxy-1,2-*O*-isopropylidene-α-D-glucofuranoses **3a–f** have a high tendency to build up oligonuclear clusters. Two new oligonuclear copper(II) complexes could be synthesised, crystallised and their structures determined. The complex **Cu(3a)** was found to consist of a heptanuclear cluster in which two β-cubane like substructures share one copper ion. The structure is highly asymmetric and in the cluster every $Cu^{II}$ ion has a different coordination geometry. Variation of the residues of the β-ketoenaminic unit leads to the formation of the octanuclear copper(II) complex **Cu(3e)**. Similarly, this has two β-cubane subunits consisting of a heptanuclear structure with an additionally attached copper ion. In the crystal, two $Cu_8$ cluster molecules are found differing in their geometries due to intermolecular interactions responsible for the formation of a supramolecular network.
(© Wiley-VCH Verlag GmbH & Co. KGaA, 69451 Weinheim, Germany, 2007)

## Introduction

While there are a number of structurally characterised octanuclear copper clusters, examples of heptanuclear species rarely feature in the literature although recently a few compounds were synthesised and their properties determined. By complexation of 2,4,6-triallyloxy-1,3,5-triazin with CuCl or $CuCl_2$, $Cu_7$ and $Cu_8$ clusters could be isolated.[1] A dimeric tetradecanuclear copper macrocyclic complex with a heptanuclear core structure derived from 2,6-diaminomethyl-4-methylphenol and copper acetate could be synthesised and structurally characterised.[2] Heptanuclear copper subunits have been found in metal-organic frameworks comprised of 1,2,4-triazoles.[3] Addition of ethylenediamine to a D-mannopyranose containing Fehling's solution leads to a heptanuclear $Cu^{II}$ complex.[4] Further, linear "tritopic" ligands have been found to assemble copper complexes with higher orders of oligomerisation[5] such as ferromagnetic $Cu_8$ pinwheel clusters.[6] Copper(II) salts form with *N*-(2-pyridylmethyl)acetamide,[7] *N*-propyamine[8] or dipyridyl ketone and 2-hydroxypyridine[9] $Cu_8$-clusters. Octanuclear metallamacrocyclic complexes have been synthesised from the pentadentate trianionic Schiff base ligand *N*,*N*′-(2-hydroxypropane-1,3-diyl)bis(salicylaldimine)[10] or ditopic thiocarbohydrazones.[11] Efficient cleavage of supercoiled DNA in the presence of $H_2O_2$ was observed for an octanuclear copper(II) complex.[12] Derived from cytidine,[13] dithiocarbamates,[14] bis(diphenylphosphanyl)amide and

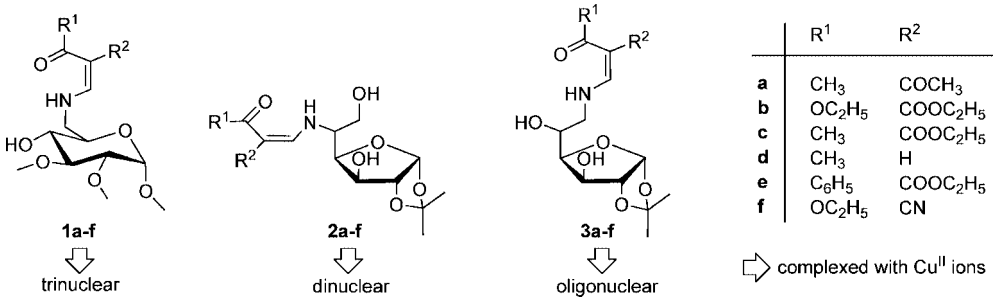


| | $R^1$ | $R^2$ |
|---|---|---|
| **a** | $CH_3$ | $COCH_3$ |
| **b** | $OC_2H_5$ | $COOC_2H_5$ |
| **c** | $CH_3$ | $COOC_2H_5$ |
| **d** | $CH_3$ | H |
| **e** | $C_6H_5$ | $COOC_2H_5$ |
| **f** | $OC_2H_5$ | CN |

Scheme 1. Influence of the sugar backbone on the oligomerisation of copper(II) complexes.

[a] Institute for Organic and Macromolecular Chemistry, Friedrich-Schiller University Jena,
Humboldtstr. 10, 07743 Jena, Germany
Fax: +49-3641-948202
E-mail: Michael.Gottschaldt@uni-jena.de
[b] Institute for Inorganic and Analytical Chemistry, Friedrich-Schiller University Jena,
Lessingstrasse 8, 07743 Jena, Germany
[†] Deceased 2006
Supporting information for this article is available on the WWW under http://www.eurjic.org or from the author.

 © 2007 Wiley-VCH Verlag GmbH & Co. KGaA, Weinheim 

$(Me_3Si)_2Se$[15] and methylsiloxane[16] different supramolecular arrangements of $Cu_8$ clusters have been be obtained. As a building block for the synthesis of heterobimetallic complexes, an octanuclear cubic copper(I) complex, exhibiting six free peripheral coordinating sites, was synthesised from 4,5-diazafluorene.[17]

Our attempts to build up oligonuclear copper complexes of β-ketoenaminic ligands based on amino carbohydrates led to very effective catalysts for the oxidation of 3,5-di-*tert*-butylcatechol.[18] Depending on the amino carbohydrate used, different types of oligomerisation could be observed. Compounds derived from 6-amino-6-deoxy-1,2,3-tri-*O*-methyl-α-D-glucopyranosides **1a**–**f** form trinuclear copper(II) complexes[19] and with 5-amino-5-deoxy-1,2-*O*-isopropylidene-α-D-glucofuranoses of type **2a**–**f** as the sugar backbone very stable dinuclear complexes could be obtained.[20] However, simply changing the position of the amino group starting from 6-amino-6-deoxy-1,2-*O*-isopropylidene-α-D-glucofuranoses **3a**–**f** lead to the formation of oligonuclear $Cu^{II}$ complexes (Scheme 1). The structures of these complexes from **3a**–**f** were very difficult to assign because of their size and their lack of suitability for NMR spectroscopy. They differ depending on the residues $R^1$ and $R^2$, the copper(II) salt used for complexation and the reaction conditions.

## Results and Discussion

By variation of the reaction conditions and after continual attempts at crystallisation, we were able to obtain crystals of the $Cu^{II}$ complexes derived from the ligands **3a** and **3e** which were suitable for single crystal X-ray structure analysis (Figure 1).

### Synthesis and Crystal Structure of Cu(3a)

Reaction of **3a** with $Cu(OAc)_2$ in a toluene/methanol mixture with an excess of triethylamine leads to the formation of **Cu(3a)**. The dark green powder obtained could be crystallised from benzene/methanol to give green crystals suitable for single-crystal X-ray structure analysis (Table 1). In the heptanuclear complex, two doubly deprotonated ligand molecules one of which acts as a tridentate ligand (D), one as a tetradentate ligand (A) and three triply deprotonated ligand molecules acting as tetradentate ligands (B, C, E) are enclosed (Figure 1, a). The Cu atom labeled Cuc is further coordinated by a 2,4-pentandionate ion which is formed from a ligand molecule during synthesis. The composition of the compound is therefore $[Cu_7(\eta^4\text{-}\mathbf{3a})_3(\eta^4\text{-}H\mathbf{3a})(\eta^3\text{-}H\mathbf{3a})(acac)]$. The elemental unit contains additional solvent molecules. The structure can be described as consisting of two β-type cubane-like cluster which share the copper atom labeled Cug. The bridging ligand atoms between the copper centres are the alkoxido oxygen atoms O2a–O2e, O6b, O6c and O6e. The triply deprotonated ligands B, C and E are coordinated to the copper atoms Cub, Cud and Cuf, while the doubly deprotonated ligands A and

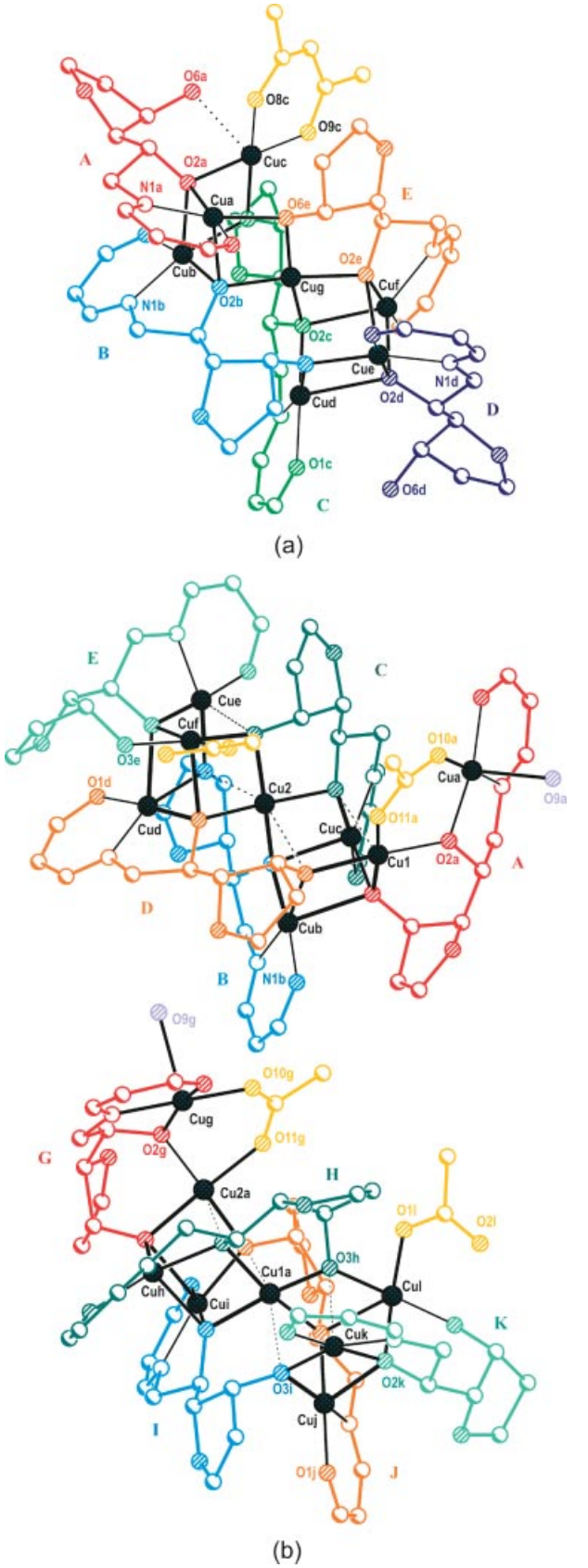


Figure 1. Representation of a) the structure of **Cu(3a)** and b) the structure of the two clusters in the crystal of **Cu(3e)**. Only the inner core, the connecting C-chain and the furanose rings are shown; for clarity all other atoms are omitted and the ligand fragments are coloured differently.

 © 2007 Wiley-VCH Verlag GmbH & Co. KGaA, Weinheim 

D are coordinated to the copper atoms Cua and Cue (Figure 2). The central copper atom Cug is surrounded by the alkoxido oxygen atoms in the 3-position of the tetradentate ligands and the corresponding alkoxido groups in the 5-position. The coordination geometry is therefore octahedral. Cuc bears the acetylacetonate ligand and is incorporated into the cubane structure by the oxygen atoms O2a (5-position of ligand A), O6c and O6e (3-position of ligands C and E). Its distorted octahedral coordination sphere is completed by the hydroxido oxygen atom O6a (3-position of ligand A). All other copper atoms are five-coordinate. Cua, Cub, Cud and Cue are surrounded by the carbonyl (O1) and 5-alkoxido oxygen (O2) atoms and the enaminic nitrogen atom of their own ligands (A, B, C and D). The fourth coordination position in the plane of the square-pyramidal geometry is occupied by one of the 3-alkoxido oxygen atoms belonging to one of the tetradentate ligands in the neighbouring cubane subunit (Cua–O6e; Cub–O6c; CuD–O6b, Cue–O6b). The 5-alkoxido oxygen atom of the neighbouring ligand in the same cubane subunit is located in the axial position. The last copper atom Cuf bears the 5-alkoxido oxygen atom O2d instead of the 3-alkoxido oxygen atom. Its coordination geometry is much more distorted than the coordination spheres of the other five-coordinate copper atoms and can be described both as distorted square-pyramidal and trigonal-bipyramidal. Preliminary studies to determine the magnetic properties of **Cu(3a)** are included in the electronic supporting information.

Table 1. Selected bond lengths [Å] and angles [°] in **Cu(3a)**.

| | | | |
|---|---|---|---|
| Cua–O1a | 1.902(11) | Cua–O2a | 2.010(10) |
| Cua–O2b | 2.394(10) | Cua–O6e | 2.000(8) |
| Cua–N1a | 1.926(13) | Cub–O1b | 1.938(9) |
| Cub–O2a | 2.369(10) | Cub–O2b | 2.037(8) |
| Cub–O6c | 1.964(10) | Cub–N1b | 1.938(11) |
| Cuc–O2a | 1.966(10) | Cuc–O6c | 1.969(10) |
| Cuc–O8c | 1.865(10) | Cuc–O9c | 1.952(11) |
| Cud–O1c | 1.964(9) | Cud–O2c | 1.980(9) |
| Cud–N1c | 1.898(12) | Cud–O6b | 1.961(9) |
| Cud–N1c | 1.898(12) | Cue–O1d | 1.929(9) |
| Cue–O2d | 1.995(9) | Cue–N1d | 1.880(11) |
| Cue–O6b | 1.939(9) | Cuf–O1e | 1.901(9) |
| Cuf–O2d | 2.099(9) | Cuf–O2e | 1.958(9) |
| Cuf–N1e | 1.924(12) | Cuf–O2 | 2.246(9) |
| Cug–O2c | 2.040(9) | Cug–O2e | 1.955(8) |
| Cug–O6e | 1.932(9) | Cug–O2b | 1.876(9) |
| O1a–Cua–O2a | 173.4(4) | O1a–Cua–O2b | 105.7(4) |
| O1a–Cua–O6e | 92.0(4) | O1a–Cua–N1a | 89.5(5) |
| O2a–Cua–O2b | 79.9(4) | O2a–Cua–O6e | 93.0(5) |
| O2a–Cua–N1a | 84.8(5) | O2b–Cua–O6e | 73.7(3) |
| O2b–Cua–N1a | 115.2(5) | O6e–Cua–N1a | 170.2(5) |
| O1b–Cub–O2a | 109.2(4) | O1b–Cub–O2b | 170.6(4) |
| O1b–Cub–O6c | 97.6(4) | O1b–Cub–N1b | 90.7(4) |
| O2a–Cub–O2b | 80.0(4) | O2a–Cub–O6c | 72.8(4) |
| O2a–Cub–N1b | 114.1(5) | O2b–Cub–O6c | 87.0(4) |
| O2b–Cub–N1b | 83.5(4) | O6c–Cub–N1b | 166.9(5) |
| O2a–Cuc–O9c | 93.0(5) | O2a–Cuc–O6c | 82.4(4) |
| O6c–Cuc–O8c | 91.4(4) | O2a–Cuc–O8c | 172.1(4) |
| O6c–Cuc–O9c | 170.6(5) | O8c–Cuc–O9c | 93.9(5) |
| O6b–Cud–N1c | 166.1(4) | O1c–Cud–O2c | 174.1(4) |
| O1c–Cud–O2d | 101.9(4) | O1c–Cud–O6b | 98.0(4) |
| O1c–Cud–N1c | 89.7(5) | O2c–Cud–O2d | 79.5(3) |
| O2c–Cud–O6b | 87.9(4) | O2c–Cud–N1c | 84.5(5) |
| O2d–Cud–O6b | 77.4(3) | O2d–Cud–N1c | 112.5(4) |
| O6b–Cue–N1d | 166.5(5) | O1d–Cue–O2d | 176.2(4) |
| O1d–Cue–O2e | 103.4(4) | O1d–Cue–O6b | 95.2(4) |
| O1d–Cue–N1d | 90.3(4) | O2d–Cue–O2e | 78.9(3) |
| O2d–Cue–O6b | 88.0(4) | O2d–Cue–N1d | 86.1(4) |
| O2e–Cue–O6b | 84.3(3) | O2e–Cue–N1d | 106.4(4) |
| O2e–Cuf–N1e | 84.3(4) | O1e–Cuf–O2c | 98.4(4) |
| O1e–Cuf–O2d | 101.8(4) | O1e–Cuf–O2e | 168.4(4) |
| O1e–Cuf–N1e | 92.2(4) | O2c–Cuf–O2d | 80.3(3) |
| O2c–Cuf–O2e | 77.9(3) | O2c–Cuf–N1e | 141.0(4) |
| O2d–Cuf–O2e | 88.5(4) | O2d–Cuf–N1e | 134.0(4) |
| O2e–Cug–O6e | 91.6(4) | O2b–Cug–O2c | 99.4(4) |
| O2b–Cug–O2e | 169.9(4) | O2c–Cug–O6e | 164.5(4) |
| O2c–Cug–O2e | 83.2(4) | O2b–Cug–O6e | 88.3(4) |

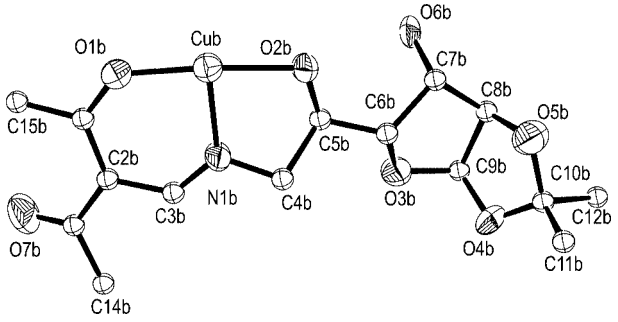


Figure 2. View of ligand B coordinated to the copper atom "Cub" in the structure of **Cu(3a)** with the crystallographic numbering and displacement ellipsoids shown at the 50% probability level; H-atoms are omitted for clarity.

### Synthesis and Crystal Structure of Cu(3e)

Heating ligand **3e** to reflux together with $Cu(OAc)_2$ and an excess of triethylamine in a mixture of toluene and hexane for several hours gives **Cu(3e)** as a dark green powder. The product was crystallised from acetone/diethyl ether to give crystals suitable for X-ray structure analysis. The compound crystallises in an orthorhombic space group and, besides several solvent molecules, the asymmetric unit of the unit cell contains two chemically identical clusters with the formula $[Cu_8(\eta^4\text{-}\mathbf{3e})_4(\eta^3\text{-H}\mathbf{3e})(OAc)(\mu\text{-}OAc)(H_2O)]$ shown in part b of Figure 1. There are only small differences in bond lengths and angles between the two cluster molecules (Table 2) so that the following copper atoms (and their ligand molecules) can be regarded as equivalent for the discussion of the structure: Cua–Cug, Cub–Cui, Cuc–Cuh, Cud–Cuj, Cue–Cuk, Cuf–Cul, Cu1–Cu2a and Cu2–Cu1a.

Seven of the eight copper atoms show similar arrangements to that of **Cu(3a)**. They form two heterocubane ($Cu_4O_4$) subunits which share one corner (Cu2). In contrast to this is the additional copper atom (Cua) which is bound to one of the cubane subunits by a bridging acetate ligand and by the second alkoxido oxygen atom (O3a) of its ligand molecule which binds to three copper atoms of the cubane subunit [O3a–Cu1 1.973(4) Å, O3a–Cub 2.399(4) Å, O3a–Cuc 2.066(4) Å]. The water oxygen atom occupies the axial position with a Cua–O9a bond length of 2.338(5) Å. Five copper atoms of the cluster carry their own ligand molecules (A–E) and the other three copper atoms (Cu1, Cu2

 © 2007 Wiley-VCH Verlag GmbH & Co. KGaA, Weinheim 

Table 2. Comparison of selected bond lengths [Å] and angles [°] of the two clusters in the crystal structure of **Cu(3e)**.

| Cluster 1 | | Cluster 2 | |
|---|---|---|---|
| Cua–N1a | 1.929(5) | Cug–N1g | 1.927(5) |
| Cua–O2a | 1.939(4) | Cug–O2g | 1.944(4) |
| Cua–O9a | 2.327(5) | Cug–O9g | 2.408(5) |
| Cua–O10a | 1.938(4) | Cug–O10g | 1.927(5) |
| Cub–O1b | 1.937(4) | Cui–O1i | 1.940(4) |
| Cub–N1b | 1.907(5) | Cui–N1i | 1.911(5) |
| Cub–O2b | 2.005(4) | Cui–O2i | 2.006(4) |
| Cub–O3a | 2.400(4) | Cui–O3g | 2.451(5) |
| Cuc–O1c | 1.909(4) | Cuh–O1h | 1.906(4) |
| Cuc–N1c | 1.927(5) | Cuh–N1h | 1.922(5) |
| Cuc–O2c | 1.958(4) | Cuh–O2h | 1.949(4) |
| Cuc–O2b | 2.285(4) | Cuh–O2i | 2.335(4) |
| Cud–O3b | 2.032(4) | Cuj–O3i | 2.018(4) |
| Cud–O2e | 2.293(5) | Cuj–O2k | 2.314(5) |
| Cue–O2e | 1.972(4) | Cuk–O2k | 1.971(4) |
| Cuf–O2e | 1.958(4) | Cul–O2k | 1.963(4) |
| Cuf–O3c | 1.982(4) | Cul–O3h | 1.975(4) |
| Cu2–O3c | 1.998(4) | Cu1a–O3h | 1.985(4) |
| Cue–O3c | 2.526(4) | Cuk–O3h | 2.537(5) |
| Cu1–O2c | 2.549(5) | Cu2a–O2h | 2.558(4) |
| Cu2–O3b | 2.446(4) | Cu1a–O3i | 2.462(5) |
| Cu2–O3d | 2.533(4) | Cu1a–O3j | 2.507(4) |
| O1a–Cua–O9a | 92.24(19) | O1g–Cug–O9g | 95.41(19) |
| O2a–Cua–O9a | 101.38(18) | O2g–Cug–O9g | 97.89(19) |
| O3a–Cub–O3d | 75.37(12) | O3g–Cui–O3j | 74.3(2) |
| O1b–Cub–N1b | 91.80(19) | O1i–Cui–N1i | 92.0(2) |
| O3a–Cuc–N1c | 144.67(15) | O3g–Cuh–N1h | 149.2(2) |
| O2b–Cuc–N1c | 132.39(16) | O2i–Cuh–N1h | 127.49(16) |
| O2e–Cud–N1d | 118.6(2) | O2k–Cuj–N1j | 114.8(2) |
| O3b–Cud–O2e | 75.31(12) | O3i–Cuj–O2k | 75.55(17) |
| O2e–Cuf–O3e | 88.32(19) | O2k–Cul–O3k | 88.31(18) |
| O3c–Cuf–O3e | 176.41(18) | O3h–Cul–O3k | 177.28(14) |
| O3d–Cu2–O2d | 168.82(16) | O3j–Cu1a–O2h | 169.16(12) |
| O2d–Cu2–O2b | 98.97(13) | O2j–Cu1a–O2i | 98.58(18) |
| O3a–Cu1–O3d | 85.18(12) | O3g–Cu2a–O3j | 85.97(13) |
| O2a–Cu1–O3d | 176.10(13) | O2g–Cu2a–O3j | 176.10(14) |
| Cu1–O3a–Cub | 91.77(15) | Cu2a–O3g–Cui | 91.2(3) |

and Cuf) are surrounded by the bridging alkoxido groups of the ligands and by an acetate oxygen atom. Except for the central copper atom (Cu2) which has a distorted octahedral environment, each copper atom has five binding partners in a more or less distorted square-planar geometry. Cub and Cuc are bound directly to each other by the alkoxido oxygen atom O2b which occupies the axial position in the environment of Cuc with a (for this position) remarkably short bond length of 2.285(4) Å. The fourth equatorial position in the ligand sphere of Cuc is occupied by one alkoxido group (O3d) of the ligand D from the other cubane subunit. The same position can be found for this atom in the ligand sphere of Cub, whereas the axial position is occupied by O3a. Cu1 is one of the atoms without its own ligand molecule. It is surrounded by the oxygen of the bridging acetate ion (O11a) and four alkoxido oxygen atoms, O3a, O3d, O2c and O2b with each pair being in the 3- and in 5-positons of their ligands. The axial ligand is the alkoxido oxygen O2c [2.549(4) Å] which makes the cubane subunit of the so-called β-type with two parallel longer Cu–O bonds perpendicular to each other. The central copper atom Cu2 is surrounded by the six alkoxido oxygen atoms of the ligands B, C and D. In the second subunit of the cluster there are two copper atoms, Cud and Cue, with their own ligands. As for Cub and Cuc, the Cu–ligand monomers are bridged by the alkoxido atom O2e which originates from the axial ligand of Cud at a relatively short distance of 2.293(5) Å. The ligand sphere of Cuc is completed by the alkoxido oxygen atoms in the 3-positions of the ligands B and C from the other subunit, with O3c in the axial position [2.526(5) Å]. O3b is the last binding partner of Cud in the fourth equatorial position. The last copper atom of the cluster Cuf is surrounded by the two alkoxido groups in the 5-positons of the neighbouring ligand molecules D and E, O3c from ligand C of the other subunit and by the oxygen atom O3e of the neighbouring ligand E. This is the only hydroxido group which is not deprotonated in the complex since it is the only one not acting as a bridging ligand and forming a hydrogen bond with the carbohydrate ring oxygen atom O4e [O···O distance 2.883(5) Å].

The copper-bound water molecule containing O9a forms a hydrogen bond with the carboxylate oxygen atom O7k of the other octanuclear cluster [O9a···O7k 2.784(5) Å; $x$, $y + 1$, $z - 1$] and the diethyl ether oxygen atom O1 [O9a···O1 2.773(6) Å; $x$, $y + 1$, $z$]. The water molecule of the other cluster (O9g) forms a corresponding hydrogen bond with the next neighbouring complex [O9g···O7e 2.827(6) Å; $x$, $y - 1$, $z$] and one ethanol oxygen atom [O9g···O4 2.827 Å; $x$, $y - 1$, $z$]. These hydrogen bonds establish chains. The next step towards a 3D network results from the water molecule containing O6 which is found at a distance of 2.896(8) Å from O9g and the next symmetry equivalent O9g at $-x - 1$, $-y - z$, $z$.

Though the bond lengths and angles in the two cluster molecules are very similar (Table 2), least-squares plane calculations on the coordinate planes show further differences – not so much in the mean deviation from planarity and in the copper distance from the plane but in the angles between them. It is striking that the highest differences between the two cluster molecules is found for the Cuc and Cuh coordinate planes [angles with Cu1 and Cu2a 33.0(2)° and 78.6(2)°, Cua/Cug 21.2(2)° and 28.2(2)°, Cud/Cuj 111.5(2)° and 80.2(2)°, Cue/Cuk 26.4(2)° and 37.2(2)° and Cuf/Cul 112.2(2)° and 98.8(2)°, respectively]. This is coincidental with the fact that the peripheral carboxylate oxygen atom of the ligand of Cuh is involved in hydrogen bonding, whereas the corresponding oxygen atom belonging to the ligand of Cuc shows no intermolecular interaction. The angles between the two cubane subunits in each cluster, at 103.8(2)° and 105.8(2)°, differ from the ideal 90(2)° but much less so than in **Cu(3a)**.

## Conclusions

In summary, the use of β-ketoenaminic ligands derived from 6-amino-6-deoxy-1,2-*O*-isopropylidene-α-D-glucofuranose provides access to polynuclear copper(II) complexes with highly asymmetric structures. Complexation of 6-[(2,2-diacetylvinyl)amino]-6-deoxy-1,2-*O*-isopropylidene-α-D-glu-

 © 2007 Wiley-VCH Verlag GmbH & Co. KGaA, Weinheim 

cofuranose (**3a**) gives a heptanuclear cluster whereas 6-[(2-ethoxycarbonyl-2-phenylcarbonylvinyl)amino]-6-deoxy-1,2-*O*-isopropylidene-α-D-glucofuranose (**3e**) leads to the formation of an octanuclear compound. The resultant structures provide insight into the coordination behaviour of this class of carbohydrate-based ligand.

## Experimental Section

**General Remarks:** All reagents and solvents were purchased from commercial sources and used as received. Electronic spectra were recorded with a Varian Cary 1 or Cary 5E spectrophotometer at room temperature. IR spectra were recorded on a Perkin–Elmer 2000 spectrometer; NMR spectra on a Bruker AC-200 instrument and mass spectra on a Finnigan MAT SSQ 710 or a Finnigan MAT 95XL TRAP machine. Elemental analyses were performed on a Leco CHNS 932.

**Heptacopper(II) Complex Cu(3a):** The ligand **3a** (0.5 mmol) and triethylamine (2 mmol) were heated to reflux together with copper(II) acetate monohydrate (0.6 mmol) in a 4:1 mixture of toluene/methanol (50 mL) for 4 h. The solution was filtered and the solvent evaporated. The residue was recrystallised from benzene/methanol to give dark green crystals suitable for X-ray structure analysis. IR (ATR): $\tilde{\nu}$ = 3372 (w), 2985 (w), 2936 (w), 2881 (w), 2845 (vw), 1645 (w), 1596 (vs), 1521 (s), 1442 (s), 1384 (vs), 1280 (s), 1214 (s), 1164 (w), 1066 (s), 1010 (s), 940 (s), 872 (s), 793 (w), 646 (s), 615 (w) cm$^{-1}$. UV/Vis (methanol): $\lambda_{max}$ = 269 (lg$\varepsilon$ = 4.8063), 304 (lg$\varepsilon$ = 4.5201), 654 nm (lg$\varepsilon$ = 2.8552). MS (ESI in methanol): *m*/*z* (%) = 2100 (3), [7 Cu] [$Cu_7L_5$ + Na]$^+$, 1648 (15), [5 Cu] [$Cu_5L_4$ + Na]$^+$, 1256 (100), [4 Cu] [$Cu_4L_3$ + Na]$^+$. $C_{80}H_{111}Cu_7N_5O_{37}$ [$Cu_7L_5$Acac] (2174.20): calcd. C 44.19, H 5.15, N 3.22; found C 44.26, H 5.54, N 3.39.

**Octacopper(II) Complex Cu(3e):** Ligand **3e** (290 mg, 0.69 mmol) together with $Cu(OAc)_2$ (125 mg, 0.69 mmol) and triethylamine (200 μL, 2.76 mmol) in 50 mL toluene/hexane, 4:1 were refluxed for 5 h. After cooling to room temperature the mixture was filtered, the solvent evaporated and the dark green powder dried. After several attempts the product could be crystallised from acetone/ether to give 105 mg (32%) of dark green crystals suitable for X-ray structure analysis. IR (ATR): $\tilde{\nu}$ = 3429 (vw), 2982 (w), 2937 (w), 1708 (vw), 1669 (s), 1620 (vs), 1568 (vs), 1554 (s), 1449 (s), 1415 (vs), 1382 (s), 1283 (s), 1262 (s), 1213 (s), 1164 (w), 1068 (s), 1010 (s), 732 (w), 699 (w), 642 (w), 617 (vw) cm$^{-1}$. UV/Vis (toluene): $\lambda_{max}$ = 299 (lg$\varepsilon$ = 4.4810), 320 (lg$\varepsilon$ = 4.4517), 615 nm (lg$\varepsilon$ = 2.6894). MS (ESI in Methanol): *m*/*z* (%) = 2618 (0.5) [8 Cu] [$Cu_8L_5$ + Na]$^+$, 2499 (1) [6 Cu] [$Cu_6L_5$ + Na]$^+$, 1994 (3) [5 Cu] [$Cu_5L_4$]$^+$, 1532 (20) [4 Cu] [$Cu_4L_3$ + Na]$^+$, 444 (100) [0 Cu] [L + Na]$^+$. $C_{109}H_{126}Cu_8N_5O_{44}$ [$Cu_8L_5(OAc)_2$] (2718.59): calcd. C 48.16, H 4.67, N 2.58; found C, 48.54; H 4.69; N, 2.64.

**X-ray Crystallographic Study:** The intensity data for the compounds were collected on a Nonius KappaCCD diffractometer using graphite-monochromated Mo-$K_\alpha$ radiation. Data were corrected for Lorentz and polarisation effects but not for absorption.[21,22] The structures were solved by direct methods (SHELXS[23]) and refined by full-matrix least-squares techniques against $F_o^2$ (SHELXL-97[24]). The hydrogen atoms of the structures were included in calculated positions with fixed thermal parameters. All non-hydrogen atoms were refined anisotropically.[16] XP (SIEMENS Analytical X-ray Instruments, Inc.) or ORTEP was used for structure representations.

CCDC-188438 (for **Cu(3a)**) and -188437 (for **Cu(3e)**) contain the supplementary crystallographic data for this paper. These data can be obtained free of charge from The Cambridge Crystallographic Data Centre via www.ccdc.cam.ac.uk/data_request/cif.

**Crystal Data for Cu(3a):** $C_{94}H_{129}Cu_7N_5O_{39}$, $M_r$ = 2397.80 g mol$^{-1}$, pink prisms, size 0.12 × 0.10 × 0.10 mm, orthorhombic, space group $P2_12_12_1$, $a$ = 19.12230(10), $b$ = 23.912(2), $c$ = 28.021(2) Å, $V$ = 12812.7(14) Å$^3$, $T$ = –90 °C, $Z$ = 4, $\rho_{calcd.}$ = 1.243 g cm$^{-3}$, $\mu$ (Mo-$K_\alpha$) = 12.11 cm$^{-1}$, $F$(000) = 4972, 20404 reflections in $h$(–17/22), $k$(–24/24), $l$(–32/31), measured in the range 1.29° ≤ $\theta$ ≤ 24.44°, completeness $\theta_{max}$ = 72.1% (due to crystal decomposition), 13374 independent reflections, $R_{int}$ = 0.0707, 8979 reflections with $F_o > 4\sigma(F_o)$, 1232 parameters, 0 restraints, $R_{1obs}$ = 0.0854, $wR_{2obs}$ = 0.2178, $R_{1all}$ = 0.1184, $wR_{2all}$ = 0.2376, GOOF = 1.010, Flack parameter 0.02(2), largest difference peak and hole: 1.051 / –0.745 e Å$^{-3}$.

**Crystal Data for Cu(3e):** $C_{114.75}H_{144.5}Cu_8N_5O_{47.5}$, $M_r$ = 2862.17 g mol$^{-1}$, blue prisms, size 0.12 × 0.10 × 0.10 mm, orthorhombic, space group $P2_12_12$, $a$ = 28.205(6), $b$ = 45.281(9), $c$ = 21.342(4) Å, $V$ = 27257(9) Å$^3$, $T$ = –90 °C, $Z$ = 8, $\rho_{calcd.}$ = 1.395 g cm$^{-3}$, $\mu$ (Mo-$K_\alpha$) = 13.06 cm$^{-1}$, $F$(000) = 11840, 70163 reflections in $h$(–36/33), $k$(–58/20), $l$(–25/24), measured in the range 1.31° ≤ $\theta$ ≤ 27.47°, completeness $\theta_{max}$ = 89.7%, 47879 independent reflections, $R_{int}$ = 0.0347, 37010 reflections with $F_o > 4\sigma(F_o)$, 3152 parameters, 0 restraints, $R_{1obs}$ = 0.0593, $wR_{2obs}$ = 0.1437, $R_{1all}$ = 0.0870, $wR_{2all}$ = 0.1610, GOOF = 1.048, Flack parameter 0.006(8), largest difference peak and hole: 1.049/–0.514 e Å$^{-3}$.

**Supporting Information** (see also the footnote on the first page of this article): Analytical data of **3a**, **3e**, selected crystal data for copper complexes, preliminary results of magnetic measurements for **Cu(3a)**.

## Acknowledgments

Financial support by the Deutsche Forschungsgemeinschaft (DFG) (Collaborative Research Center 436, Jena, Germany), the Fonds der Chemischen Industrie (Germany) and by the Thüringer Ministerium für Wissenschaft, Forschung und Kultur (Erfurt, Germany) is gratefully acknowledged.

[1] E. A. Goreshnik, L. Z. Ciunikb, Yu. K. Gorelenkoc, M. G. Mys'kivc, *Z. Anorg. Allg. Chem.* **2004**, *630*, 2743–2748.
[2] S. S. Tandon, S. D. Bunge, L. K. Thompson, *Chem. Commun.* **2007**, *8*, 798–800.
[3] S. Ferrer, E. Aznar, F. Lloret, A. Castineiras, M. Liu-Gonzalez, J. Borras, *Inorg. Chem.* **2007**, *46*, 372–374.
[4] P. Kluefers, T. Kunte, *Z. Anorg. Allg. Chem.* **2004**, *630*, 553–557.
[5] a) V. A. Milway, V. Niel, T. S. M. Abedin, Z. Xu, L. K. Thompson, H. Grove, D. O. Miller, S. R. Parsons, *Inorg. Chem.* **2004**, *42*, 1874–1884; b) S. T. Onions, S. L. Heath, D. J. Price, R. W. Harrington, W. Clegg, C. J. Matthews, *Angew. Chem. Int. Ed.* **2004**, *43*, 1814–1817.
[6] V. A. Milway, S. M. T. Abedin, L. K. Thompson, D. O. Miller, *Inorg. Chim. Acta* **2006**, *359*, 2700–2711.
[7] A. Mondal, Y. Li, M. A. Khan, J. H. Ross Jr, R. P. Houser, *Inorg. Chem.* **2004**, *43*, 7075–7082.
[8] F. Bramsen, A. D. Bond, C. J. McKenzie, R. G. Hazell, B. Moubaraki, K. S. Murray, *Chem. Eur. J.* **2005**, *11*, 825–831.
[9] M.-L. Tong, H. K. Lee, Y.-X. Tong, X.-M. Chen, Th. C. W. Mak, *Inorg. Chem.* **2000**, *39*, 4666–4669.
[10] A. Mukherjee, I. Rudra, M. Nethaji, S. Ramasesha, A. R. Chakravarty, *Inorg. Chem.* **2003**, *42*, 463–468.

 © 2007 Wiley-VCH Verlag GmbH & Co. KGaA, Weinheim 

[11] D. Dragancea, V. B. Arion, S. Shova, E. Rentschler, N. V. Gerbeleu, *Angew. Chem. Int. Ed.* **2005**, *44*, 7938–7942.
[12] K. Dhara, J. Ratha, M. Manassero, X.-Y. Wang, S. Gao, P. Banerjee, *J. Inorg. Biochem.* **2007**, *101*, 95–103.
[13] D. Armentano, T. F. Mastropietro, M. Julve, R. Rossi, P. Rossi, G. De Munno, *J. Am. Chem. Soc.* **2007**, *129*, 2740–2741.
[14] a) R. Kawajiri, T. Okubo, T. Mitani, *Polyhedron* **2006**, *25*, 2650–2654; b) D. Cardell, G. Hogarth, S. Faulkner, *Inorg. Chim. Acta* **2006**, *359*, 1321–1324.
[15] Q.-F. Zhang, Z. Yu, A. Rothenberger, D. Fenske, W.-H. Leung, *Inorg. Chim. Acta* **2007**, *360*, 1568–1574.
[16] L. Zherlitsyna, N. Auner, M. Bolte, *Acta Crystallogr., Sect. C: Cryst. Struct. Commun.* **2006**, *62*, m199–m200.
[17] S. A. Baudron, M. W. Hosseini, N. Kyritsakas, *New J. Chem.* **2006**, *30*, 1083–1086.
[18] a) R. Wegner, M. Gottschaldt, W. Poppitz, E.-G. Jäger, D. Klemm, *J. Mol. Catal. A* **2003**, *201*, 93–118; b) R. Wegner, M. Gottschaldt, H. Görls, E.-G. Jäger, D. Klemm, *Chem. Eur. J.* **2001**, *7*, 2143–2157.
[19] a) R. Wegner, M. Gottschaldt, H. Görls, E.-G. Jäger, D. Klemm, *Angew. Chem. Int. Ed.* **2000**, *39*, 595–599; b) A. Roth, J. Becher, C. Herrmann, H. Görls, G. Vaughan, M. Reiher, D. Klemm, W. Plass, *Inorg. Chem.* **2006**, *45*, 10066–10076.
[20] M. Gottschaldt, R. Wegner, H. Görls, P. Klüfers, E.-G. Jäger, D. Klemm, *Carbohydr. Res.* **2004**, *339*, 1941–1952.
[21] *COLLECT*, Data Collection Software, Nonius B. V., Netherlands, **1998**.
[22] Z. Otwinowski, W. Minor, *Processing of X-ray Diffraction Data Collected in Oscillation Mode* in: *Methods in Enzymology*, vol. 276, *Macromolecular Crystallography*, part A (Ed.: C. W. Carter, R. M. Sweet), Academic Press, San Diego, **1997**, pp. 307–326.
[23] G. M. Sheldrick, *Acta Crystallogr., Sect. A* **1990**, *46*, 467–473.
[24] G. M. Sheldrick, *SHELXL-97*, University of Göttingen, Germany, **1993**.

Received: March 6, 2006
Revised Version Received: April 24, 2007
Published Online: June 21, 2007

 © 2007 Wiley-VCH Verlag GmbH & Co. KGaA, Weinheim 

DOI: 10.1002/ejic.200700178

# Kinetics of the Formation of $[Ln(DOTAM)]^{3+}$ Complexes

**Zsolt Baranyai,[a] István Bányai,[b] Ernő Brücher,*[a] Róbert Király,[a] and Enzo Terreno[c]**

**Keywords:** Macrocyclic ligands / Lanthanides / Kinetics / Reaction mechanisms

The kinetics of the formation of lanthanide(III) complexes of the neutral ligand DOTAM differ considerably from those of DOTA and its derivatives, which contain negatively charged pendant groups. Formation of the complexes $[Ln(DOTAM)]^{3+}$ occurs upon direct encounter of the $Ln^{3+}$ ions and the fully deprotonated ligand in the pH range 4.7–5.8. The formation of a protonated intermediate, which is characteristic of the complexation of DOTA and its derivatives, was not detected. General base catalysis is not valid in the formation reactions of $[Ln(DOTAM)]^{3+}$, which also indicates the absence of protonated intermediates. The rates of the proton-exchange reactions for the ligand species $H_2DOTAM^{2+}$ and $HDOTAM^{+}$ have been studied by $^1H$ NMR spectroscopy. Proton exchange was found to be a general base-catalysed process, therefore it cannot play an important role in the formation of these complexes. The second-order rate constants, $k_L$, which characterize the formation of the complexes $[Ln(DOTAM)]^{3+}$, are lower than the analogous rate constants reported for the $Ln^{3+}$ complexes of open-chain multidentate ligands by three to four orders of magnitude. These low $k_L$ values can be interpreted by assuming an early rate-determining step (probably the second or third $Ln^{3+}$–amide bond formation) in the reaction sequence that leads to the $[Ln(DOTAM)]^{3+}$ complex.

(© Wiley-VCH Verlag GmbH & Co. KGaA, 69451 Weinheim, Germany, 2007)

## Introduction

Lanthanide(III) complexes of the different tetraamide derivatives of DOTA (Scheme 1) have attracted considerable interest in recent years because of their promising applications in different fields of biological chemistry. Positively charged complexes {e.g. $[La(DOTAM)]^{3+}$}, for example, promote or catalyse rapid RNA cleavage and hydrolysis of some biopolymers (e.g. phosphate esters),[1–3] and complexes of $Eu^{3+}$ and $Yb^{3+}$ with DOTAGly, DOTAGly-Et and other DOTA tetraamide derivatives, have been proposed as chemical exchange saturation transfer (CEST) agents in magnetic resonance imaging.[4–8] Another possible field of application for the tetraamide derivatives is the development of luminescent sensors.[9,10]

The structure of the lanthanide(III) ($Ln^{3+}$) complexes formed with the DOTA tetraamide derivatives was found to be similar to that of $[Ln(DOTA)(H_2O)]^-$,[11] with the $Ln^{3+}$ ion occupying a position in the coordination cage formed by the four ring nitrogen atoms and four amide oxygen atoms, which form a square antiprism. A water molecule is coordinated to the $Ln^{3+}$ ion in a capping position.[1,2,12–16]

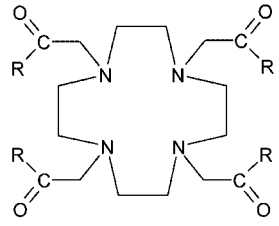


Scheme 1. Molecular structures of the ligands discussed.

The solution structure of the $Ln^{3+}$–DOTA tetraamide complexes has been studied by $^1H$, $^{13}C$ and $^{17}O$ NMR spectroscopy, and the lifetime of the inner-sphere water was found to be significantly higher than that of the complexes $[Ln(DOTA)(H_2O)]^-$.[12,16–19] The stability constants ($\log K_{ML}$) of the $Ln^{III}$ complexes formed with the DOTA tetraamide derivatives are about 10–15 orders of magnitude lower than the $\log K_{ML}$ values of the DOTA complexes.[2,15,20,21] However, the rates of the $Cu^{2+}$- and proton-assisted dissociation of the complexes $[Eu(DOTAM)]^{3+}$, $[Eu(DTMA)]^{3+}$ and $[Eu^{III}DOTTA]^{3+}$ are significantly lower than that of $[Eu(DOTA)]^-$.[1,12] The fairly large stability constants and the unusually high kinetic inertness of the complexes formed with the neutral DOTA tetraamide ligands is quite unexpected since $Ln^{3+}$ ions prefer ligands containing oxygen donor atoms with a negative charge. The moderate stability and high kinetic inertness of these complexes is probably the result of the good match between the size of the $Ln^{3+}$ ions and the preformed cavity of the neutral

[a] Department of Inorganic and Analytical Chemistry, University of Debrecen,
Egyetem tér 1, 4010 Debrecen, Hungary
Fax: +365-24-89667
E-mail: ebrucher@delfin.unideb.hu
[b] Department of Colloid and Environmental Chemistry, University of Debrecen,
4010 Debrecen, Hungary
[c] Department of Chemistry IFM & Molecular Imaging Center, University of Torino,
Via P. Giuria 7, 10125 Torino, Italy

 © 2007 Wiley-VCH Verlag GmbH & Co. KGaA, Weinheim 

ligands. The high thermodynamic and kinetic stabilities displayed by the $Ln^{3+}$ complexes of $DOTA^{4-}$ and its negatively charged derivatives can be accounted for not only in terms of the size matching between the $Ln^{3+}$ ions and the ligands but also the important role played by the electrostatic interactions. Thus, the study of the behavior of the DOTA tetraamide ligand DOTAM may give some new information about the kinetics and mechanisms of the reactions taking place between $Ln^{3+}$ ions and neutral macrocyclic ligands possessing a preformed cavity.

The formation of $Ln^{3+}$ complexes with DOTA tetraamide ligands takes place very slowly in aqueous solutions and, because of these slow reactions, the complexes in the solid state are often prepared in non-aqueous solution.[1,12–14] The kinetics of formation of the tetraamide complexes $[Ln(DOTAGly)]^-$ are very similar to those of $[Ln(DOTA)]^-$, as we have reported previously.[21] This similarity is probably due to the presence of four negatively charged functional groups in both $DOTA^{4-}$ and $DOTAGly^{4-}$, which can coordinate to $Ln^{3+}$ in the first step of the reaction and form mono- and diprotonated intermediates. The protons protonate the ring nitrogen atoms, while the $Ln^{3+}$ ion is still outside of the coordination cage. The rate-determining step of the formation of $[Ln(DOTA)]^-$ and $[Ln(DOTAGly)]^-$ is the deprotonation of the monoprotonated intermediate in a first-order reaction.[21–26] Because they isolated the diprotonated compound $[Gd(H_2DOTAM)(H_2O)_4](ClO_4)_5$ in the solid state, Parker et al. have assumed that the formation of $Gd(DOTAM)^{3+}$ occurs by a similar pathway.[27] However, as our preliminary studies have indicated, the formation of $Ln^{3+}$ complexes of the ligand DOTAM occurs by a completely different pathway as their rates of formation are directly proportional to the concentration of both $Ln^{3+}$ and DOTAM. A detailed study of the rates of the reaction shown in Equation (1) between $Ln^{3+}$ ions ($Ln^{3+}$ = $Ce^{3+}$, $Eu^{3+}$, $Gd^{3+}$, $Er^{3+}$ and $Yb^{3+}$) and DOTAM may provide new information about the role of the charged and uncharged functional groups in the reactions of a preorganized macrocyclic ligand.

$$Ln^{3+} + H_nL^{n+} \rightleftharpoons LnL^{3+} + nH^+ \ (n = 1, 2) \quad (1)$$

## Results and Discussion

### Kinetics of Complex Formation

The rates of complex formation were studied in the pH range 4.7–5.8, where the ligand species $H_2DOTAM^{2+}$ and $HDOTAM^+$ predominate [the protonation constants were found to be 6.05 and 9.07 by pH-metric titrations]. The protons presumably protonate two diagonal ring nitrogen atoms, as has been observed for $H_2DOTA^{2-}$.[28]

In the presence of an excess of $Ln^{3+}$ ions, the rate of complex formation is given by Equation (2), where $k_{obs}$ is a pseudo-first-order rate constant and $[L]_t$ and $[LnL]_t$ are the total concentrations of ligand and metal complex, respectively.

$$\frac{d[LnL]_t}{dt} = k_{obs}[L]_t \quad (2)$$

The $k_{obs}$ values obtained for the formation reactions of $Ce(DOTAM)^{3+}$ and $Eu(DOTAM)^{3+}$ are shown in Figures 1 and 2, respectively.

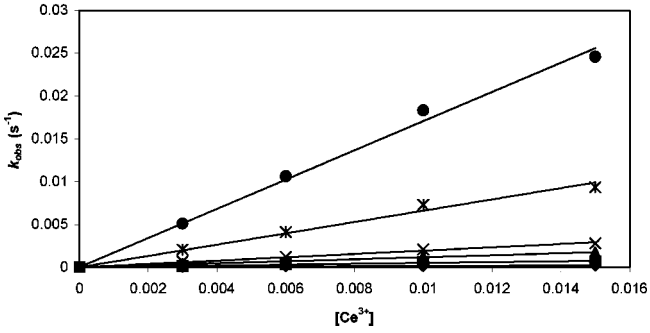


Figure 1. Rates of formation of $[Ce(DOTAM)]^{3+}$ at 25 °C in 1.0 M KCl. [DOTAM] = $3.0 \times 10^{-4}$ M, [NMP] = 0.05 M. The pH values are 4.80 (◆), 5.01 (■), 5.16 (▲), 5.30 (x), 5.53 (∗) and 5.77 (●).

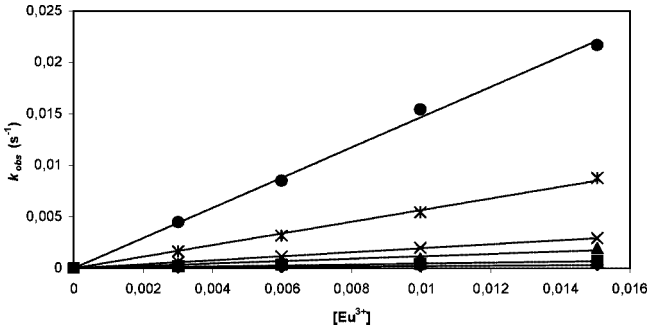


Figure 2. Rates of formation of $[Eu(DOTAM)]^{3+}$ at 25 °C in 1.0 M KCl. [DOTAM] = $3.0 \times 10^{-4}$ M, [NMP] = 0.05 M. The pH values are 4.78 (◆), 5.01 (■), 5.17 (▲), 5.30 (×), 5.56 (∗), and 5.76 (●).

As seen in Figures 1 and 2, the $k_{obs}$ values are directly proportional to the concentration of $Ce^{3+}$ and $Eu^{3+}$ over a broad concentration range. This observation differs considerably from the results obtained for the formation of DOTA and DOTA derivative complexes of $Ln^{3+}$, where similar $k_{obs}$ vs. $[Ln^{3+}]$ plots gave saturation curves, thus indicating the formation of a reaction intermediate.[21–26] The intermediates in the formation of $Ce(DOTA)^-$ and $Eu(DOTA)^-$ were detected by spectrophotometry and luminescence spectroscopy even at similar concentrations of $Ln^{3+}$ and ligand.[22,24] The absence of any intermediate in the formation of Ln(DOTAM) is particularly interesting because the diprotonated complex $[Gd(H_2DOTAM)(H_2O)_4](ClO_4)_5$, which can be regarded as an intermediate, has recently been observed in the solid state by Parker et al.[27] The X-ray crystal structure of this complex shows that the $Gd^{3+}$ion is located outside the coordination cage of the diprotonated ligand, where four amide oxygen atoms and four water molecules are coordinated to the metal ion. The authors assume that the formation of the complex [Gd-

 © 2007 Wiley-VCH Verlag GmbH & Co. KGaA, Weinheim 

(DOTAM)]$^{3+}$ could occur by deprotonation of the intermediate assisted by water as a base.[27]

The formation of an intermediate does not imply that the reaction product is formed by transformation of the intermediate. Thus, the formation of an intermediate in the complexation of DOTA with some divalent metal ions has been detected by Kasprzyk and Wilkins, although they assumed that the intermediate was not on the reaction pathway (it acted as a "dead-end" complex) and that complex formation occurred according to a simple second-order reaction.[29]

The 4f–5d UV absorption bands of $Ce^{3+}$ are suitable for detecting the formation of an intermediate in the reactions of $Ce^{3+}$ with DOTA and its derivatives.[21,23] However, the formation of an intermediate in the reaction of $Ce^{3+}$ with DOTAM could not be detected by spectrophotometry even if a 100-fold excess of $Ce^{3+}$ was used (Figure 3). The absorption of the excess $Ce^{3+}$ was compensated, but the spectrum obtained after 4 min is somewhat distorted, probably because of the imperfect compensation of one of the absorption bands of 0.05 M $Ce^{3+}$(aq), which appears at about 295 nm.

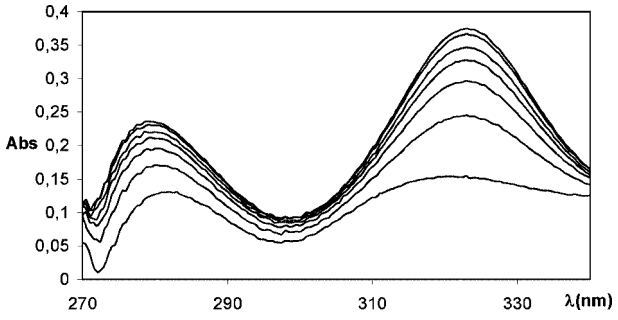


Figure 3. Absorption spectra of a $5 \times 10^{-4}$ M solution of DOTAM containing 0.05 M $Ce^{3+}$ at pH = 4.58 in the presence of 0.05 M NMP buffer 4, 8, 16, 20, 24, 28 and 32 min (in ascending order) after mixing the components (25 °C and 1.0 M KCl).

On the basis of the data presented in Figures 1 and 2, the pseudo-first-order rate constants can be expressed as $k_{obs} = k_f[Ln^{3+}]$, and the rate of formation can be given as Equation (3).

$$\frac{d[LnL]_t}{dt} = k_f[Ln^{3+}][L]_t \quad (3)$$

These findings show that the complexes Ln(DOTAM)$^{3+}$ are formed by direct encounter between the $Ln^{3+}$ ion and the ligand in a second-order reaction. In the pH range studied the ligand DOTAM is present in the form of $HL^+$ and $H_2L^{2+}$ species, and the concentration of the non-protonated species L is very low. However, it is expected that the neutral form of the ligand is the most reactive species because the $Ln^{3+}$ ion and the positive charge of the protonated species $HL^+$ and $H_2L^{2+}$ hinder the reaction.[30] However, if we assume that the reaction can take place with all ligand species, the formation rate can be expressed as Equation (4).

$$\frac{d[LnL]_t}{dt} = k_L[Ln^{3+}][L] + k_{HL}[Ln^{3+}][HL] + k_{H_2L}[Ln^{3+}][H_2L] \quad (4)$$

On the basis of Equations (3) and (4), and taking into account the protonation constants of the ligand ($K_1^H$ = [HL]/[L][H$^+$] and $K_2^H$ = [$H_2$L]/[L][H$^+$]), the second-order rate constant $k_f$ can be calculated from Equation (5), which takes into account all the possible reaction pathways, although some experimental data indicate that the reaction occurs only by encounter of the $Ln^{3+}$ ions and the neutral species L.

$$k_f = \frac{k_L + k_{HL}K_1^H[H^-] + k_{H_2L}K_1^H K_2^H[H^+]^2}{1 + K_1^H[H^-] + K_1^H K_2^H[H^+]^2} \quad (5)$$

The formation rates of the complexes [Ce(DOTAM)]$^{3+}$ and [Eu(DOTAM)]$^{3+}$ are directly proportional to the concentration of the neutral ligand L since the plots of $k_f$ vs. [L] give straight lines. In this case, according to Equation (5), $k_f = k_L/a_L$, where $a_L = 1 + K_1^H[H^+] + K_1^H K_2^H [H^+]^2$. A plot of $\log k_f$ against $\log \alpha_L$ gives a straight line with a slope of –1, which also indicates the predominance of the reaction between the neutral ligand L and the $Ln^{3+}$ ions.[22,29]

The rates of formation were also studied for the complexes of $Gd^{3+}$, $Er^{3+}$ and $Yb^{3+}$ at different pH values and at two $Ln^{3+}$concentrations. The $k_{obs}$ values obtained are presented in Table 1.

Table 1. Pseudo-first-order rate constants ($k_{obs}$, $s^{-1}$) obtained for the formation of $Gd^{3+}$, $Er^{3+}$ and $Yb^{3+}$ complexes of DOTAM ([L]$_t$ = $3 \times 10^{-4}$ M, 1.0 M KCl, 25 °C).

| | | $10^3 \times k_{obs}$ [$s^{-1}$] | |
|---|---|---|---|
| $Ln^{3+}$ | pH | $6 \times 10^{-3}$ M | $1.0 \times 10^{-2}$ M |
| $Gd^{3+}$ | 5.01 | 0.58 | 1.11 |
| | 5.35 | 1.91 | 2.81 |
| | 5.46 | 3.45 | 6.99 |
| | 5.54 | 4.78 | 10.7 |
| | 5.68 | 9.55 | 22.5 |
| $Er^{3+}$ | 5.20 | 0.13 | 0.26 |
| | 5.56 | 0.72 | 1.29 |
| | 5.71 | 1.77 | 2.63 |
| | 5.90 | 3.85 | 6.54 |
| $Yb^{3+}$ | 5.19 | 0.15 | 0.25 |
| | 5.44 | 0.49 | 0.66 |
| | 5.54 | 1.22 | 1.98 |
| | 5.66 | 2.55 | 3.69 |

The rate constants $k_L$ were calculated for the formation reactions by fitting the $k_f$ data (calculated from the $k_{obs}$ values) to the equation $k_f = k_L/a_L$. The obtained rate constants $k_L$ are presented in Table 2. The $k_f$ data were also fitted to Equation (5) when the $k_{HL}$ values obtained for the formation reaction of [Ce(DOTAM)]$^{3+}$ and [Eu(DOTAM)]$^{3+}$ were low and had a negative sign, although the $k_{H_2L}$values were also low and so the contribution of the third term of the numerator of Equation (5) to the $k_f$ values is not significant.

 © 2007 Wiley-VCH Verlag GmbH & Co. KGaA, Weinheim 

Table 2. Rate constants $k_L$ ($M^{-1}s^{-1}$) characterising the formation of $[Ln(DOTAM)]^{3+}$ complexes (25 °C, 1.0 M KCl).

| $Ln^{3+}$ | $k_L$ ($M^{-1}s^{-1}$) |
|---|---|
| $Ce^{3+}$ | $(7.7\pm0.3)\times10^3$ |
| $Eu^{3+}$ | $(2.7\pm0.1)\times10^4$ |
| $Gd^{3+}$ | $(4.0\pm0.5)\times10^4$ |
| $Er^{3+}$ | $(5.6\pm0.3)\times10^3$ |
| $Yb^{3+}$ | $(6.6\pm1.0)\times10^3$ |

The rate constants $k_L$, determined for the reactions of the $Ln^{3+}$ ions with DOTAM, are about three to four orders of magnitude lower than those reported for the complexation reactions with monodentate or open-chain multidentate ligands.[31–33] The observed reaction rates are particularly low because of the extremely low concentration (ca. $10^{-8}$ M) of the deprotonated ligand L in the pH range investigated.

To obtain further evidence that protonated intermediates do not play any role in the formation of complexes $[Ln(DOTAM)]^{3+}$, we studied the effect of changing the concentration of the buffer, *N*-methylpiperazine (NMP), on the rates of formation of $[Ce(DOTAM)]^{3+}$ and $[Eu(DOTAM)]^{3+}$. If protonated intermediates were formed and the rate-determining step of the complexation were the deprotonation of the intermediates, then an increase in the concentration of a general base like NMP ($pK_1$ = 4.83) would cause an increase in the rate of complex formation.[26,27] The rate constants $k_{obs}$ obtained for the formation of $[Ce(DOTAM)]^{3+}$ and $[Eu(DOTAM)]^{3+}$ do not show any change with an increase in the concentration of the buffer (Figure 4). These findings confirm that the formation of complexes $[Ln(DOTAM)]^{3+}$ occurs without the involvement of protonated intermediates.

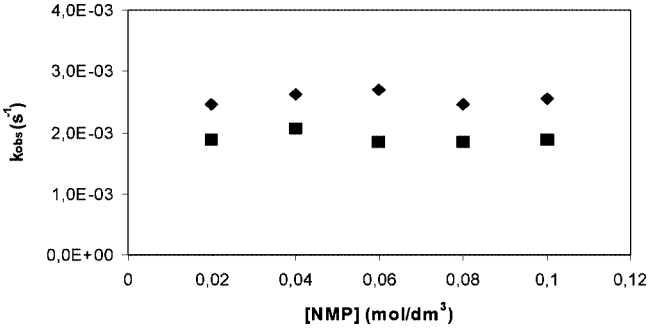


Figure 4. Rates of formation of $[Ce(DOTAM)]^{3+}$ (◆; pH = 5.32) and $[Eu(DOTAM)]^{3+}$ (■; pH = 5.2). The concentration of DOTAM and $Ln^{3+}$ ions was $3\times10^{-4}$ M and $6\times10^{-3}$ M, respectively (25 °C and 1.0 M KCl).

### Proton-Exchange Rates of the DOTAM Ligand

The $^1H$ NMR spectra of the DOTAM ligand (Figures 5 and 6) indicate that the rate of proton exchange in the species $H_2DOTAM^{2+}$ and $HDOTAM^+$ is relatively low, which could play some role in the slow formation of the $[Ln(DOTAM)]^{3+}$ complexes.

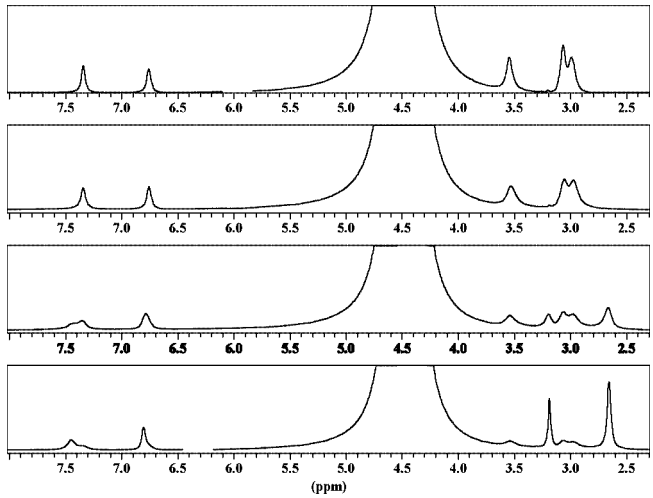


Figure 5. $^1H$ NMR spectra of the ligand DOTAM. The pH values from top to bottom are: 4.04, 5.03, 5.94 and 6.48.

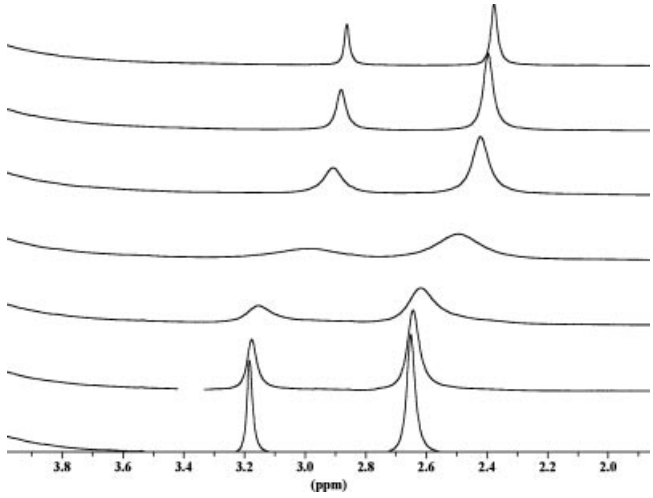


Figure 6. Variation of the $^1H$ NMR spectrum of DOTAM with pH. The pH values from top to bottom are: 7.45, 7.99, 8.53, 9.04, 9.55, 9.83 and 10.22.

At pH ≈ 4, where the species $H_2DOTAM^{2+}$ predominates, there are three broad signals in the $CH_2$ region in a 1:1:1 ratio. Two of these are assignable to the ring protons ($\delta$ = 2.98 and 3.16 ppm), while the third belongs to the amide $CH_2$ group ($\delta$ = 3.54 ppm). The signals observed between $\delta$ = 6.6 and 7.5 ppm are due to the $NH_2$ protons of the amide group. The chemical shift of the ring protons is not affected by the pH. Interestingly, the ligand $HDOTAM^+$, which predominates at pH > 7, has only two peaks in the $CH_2$ region, probably due to some fluxional motion of the molecule that averages the two signals of the ring methylene protons. Figure 6 shows that both the chemical shifts and the line widths of these signals change considerably with increasing pH. It is likely that these spectral variations are related to the proton-exchange process that occurs for the species $HDOTAM^+$ and DOTAM. Analysis

 © 2007 Wiley-VCH Verlag GmbH & Co. KGaA, Weinheim 

of the pH dependence of the proton chemical shifts allowed the determination of the $\log K_1^H$ value ($9.01 \pm 0.07$), which is in good agreement with the value obtained by pH-metry.

Exchange between the monoprotonated and nonprotonated forms of DOTAM was analysed using the simplified analytical equation reported by Piette and Anderson.[34] The exchange rate constant ($k_{ex}$) can be determined from the nonexchange linewidth and the chemical shifts of the signals in the absence of exchange. These data were obtained from the spectra, and the first-order rate constants were calculated in the pH range 8–10.[34] The proton-exchange rate is linearly proportional to the $OH^-$ concentration, as expressed by Equation (6), where the rate constant $k_0 = (1.2 \pm 0.3) \times 10^3\ s^{-1}$ refers to the rate of spontaneous deprotonation of $HDOTAM^+$, which probably takes place with the help of $H_2O$ molecules.

$$k_{ex} = k_0 + k_1[OH^-] \quad (6)$$

The rate constant $k_1 = (5.3 \pm 0.5) \times 10^8\ M^{-1}s^{-1}$ corresponds to the rate of the $OH^-$-assisted deprotonation of the species $HDOTAM^+$. The rate of proton exchange is relatively low, probably because the proton is attached to the ring nitrogen atom in the coordination cage. For the proton exchange to occur, the ligand must have a special conformation where it can donate the proton to an $H_2O$ molecule or an $OH^-$ ion. This conformation is formed by some fluxional motion of the ligand, although the experimental data are not good enough to be able to separate the contribution of fluxionality. The role of the $OH^-$-assisted deprotonation is negligible in the pH range 4.7–5.8, and the spontaneous deprotonation of $HDOTAM^+$ is much faster than complex formation, which means that this deprotonation cannot control the rate of complexation.

The $^1H$ NMR signals of the DOTAM ligand are broad because of the slow proton exchange and fluxional processes. However, the widths of the signals decrease in the presence of a general base. Thus, an increase in the concentration of sodium acetate to 0.3 M at pH = 9.0 results in a decrease of 18 and 35 Hz in the linewidths of the ring and amide methylene protons, respectively. The two ring proton signals merge into one broad signal at pH = 4.1 when the concentration of sodium formate is increased to 0.25 M. These findings indicate that the proton-exchange reactions of the species $H_2DOTAM^{2+}$ and $HDOTAM^+$ are general base catalysed processes. However, general base catalysis is not valid for the formation of $[Ln(DOTAM)]^{3+}$ (Figure 4), therefore we can conclude that the rate of proton exchange of the free ligand does not play a role in the slow complex formation.

### Mechanism of Complex Formation

The kinetic data obtained for the formation of the $[Ln(DOTAM)]^{3+}$ complexes show that the complexation occurs through a direct reaction between the $Ln^{3+}$ ions and the deprotonated ligand DOTAM that follows second-order kinetics. On this basis, since the only species formed is $[Ln(DOTAM)]^{3+}$, the rate of formation can be expressed on the basis of Equation (3) as Equation (7).

$$\frac{d[LnL]}{dt} = k_L[Ln^{3+}][L] \quad (7)$$

A low reactivity of the protonated ligands is known even for the reactions of open-chain aminocarboxylate ligands, where the ratio of the rate constants $k_L/k_{HL}$ is often as large as $10^5$–$10^6$.[30] In the case of the macrocyclic DOTA and its derivatives, the metal ion cannot enter directly into the coordination cage formed by the four ring nitrogen atoms and four oxygen donors, thus maintaining the four negatively charged pendant arms. This is due to the electrostatic repulsion caused by the presence of the protonated nitrogen atoms. Complex formation requires that this proton is shifted to another donor atom, such as the pendant carboxylate group in the case of DOTA. In the complexation of DOTAM, the proton cannot be transferred to the carboxamide moiety because it can be protonated only in very strongly acidic solutions. On this basis, the formation of complexes of DOTAM does not take place via a protonated intermediate, thus it must occur only with the participation of the fully deprotonated ligand DOTAM.

The rate constants $k_L$ reported in Table 2, are three to four orders of magnitude lower than the second-order rate constants determined for the formation of $Ln^{3+}$ complexes with murexide, oxalate or anthranilate ligands. The rate-determining step for these reactions was assumed to be the second bond formation, in other words the chelation step.[31–33]

In metal complex formation with macrocyclic ligands, formation of the first metal–ligand bond is followed by several subsequent steps in which new metal–ligand bonds are formed sequentially as the coordinated water molecules are released. Unfortunately, it is very difficult to determine which is the rate-determining step in such multi-step processes.

The very slow formation of the complexes $[Ln(DOTAM)]^{3+}$ may be tentatively interpreted in terms of the knowledge obtained for the reactions of multidentate ligands.[30] The first step of the complexation is the formation of an outer-sphere complex between the DOTAM ligand and the $[Ln(H_2O)_n]^{3+}$ ion ($n = 9$ for the ions between $La^{3+}$ and $Nd^{3+}$, $n = 8$ for the ions from $Gd^{3+}$ to $Lu^{3+}$; $n$ is between 8 and 9 for $Sm^{3+}$ and $Eu^{3+}$).[33,35] By defining the tetraamide ligand as $A_4$, this outer-sphere complex can be formulated as $Ln(H_2O)_n{\cdot}A\text{-}A_3$, which is characterized by the stability constant $K_{os}$. The subsequent steps of the formation of $[Ln(DOTAM)]^{3+}$ complexes are shown in Scheme 2, where $k_{jk}$ are first-order rate constants.

$$Ln(H_2O)_n \cdot A - A_3 \underset{k_{32}}{\overset{k_{23}}{\rightleftharpoons}} (A_3 - A)Ln(H_2O)_{n-1} \underset{k_{43}}{\overset{k_{34}}{\rightleftharpoons}} (A_2 - A_2)Ln(H_2O)_{n-2} \rightleftharpoons$$
$$\ldots \rightleftharpoons (A_4)Ln(H_2O)_{n-4} \xrightarrow{fast} Ln(H_2O)(DOTAM)$$

Scheme 2. The subsequent steps of the formation of $[Ln(DOTAM)]^{3+}$ complexes.

 © 2007 Wiley-VCH Verlag GmbH & Co. KGaA, Weinheim 

If the second bond formation were the rate-controlling step, then the expression for the second-order rate constant $k_L$ would be as shown in Equation (8).[30]

$$k_L = \frac{k_{23}k_{34}K_{os}}{k_{32} + k_{34}} \quad (8)$$

Since dissociation of the intermediate $(A_3\text{-}A)Ln(H_2O)_{n-1}$ is probably much faster than the formation of $(A_2\text{-}A_2)\text{-}Ln(H_2O)_{n-2}$, that is $k_{32} >> k_{34}$ and $k_{23} \approx k_{H_2O}$ ($k_{H_2O}$ is the water exchange rate), Equation (8) can be simplified to Equation (9).

$$k_L = k_{H_2O}K_{os}\frac{k_{34}}{k_{32}} \quad (9)$$

To obtain $k_L$ values of around $10^3$–$10^4$, the $K_{os}$ and $k_{34}/k_{32}$ values must be low, since the value of $k_{H_2O}$ is about $10^7$–$10^8$ $s^{-1}$.[31–33] The value of $K_{os}$ for an $Ln^{3+}$ ion and a neutral ligand can be estimated to be 0.3 M on the basis of the Fuoss equation.[36,37] The ratio $k_{34}/k_{32}$ must be low, and if these values were about $10^{-3}$ for the different $Ln^{3+}$ ions then the $k_L$ values would be approximately $10^3$–$10^4$, as was found experimentally. These considerations indicate that the rate-determining step for the formation of $[Ln(DOTAM)]^{3+}$ complexes must be quite early in the sequence shown in Scheme 2 (second or third bond formation) because the ratios analogous to $k_{34}/k_{32}$ are presumably lower for the later intermediates in the sequence.

The formation rate constants $k_L$ show a maximum at $Gd^{3+}$ in the series of lanthanides. Similar phenomena have often been observed for the formation of lanthanide complexes of mono- and multidentate ligands.[32,33] Since the water exchange rates of the $Ln^{3+}$(aq) ions decrease from $Gd^{3+}$ to $Yb^{3+}$, and probably also to the lighter elements, interpretation of the trend of the complexation rates is based on the assumption that the water exchange rates may influence the rates of complex formation, as expressed by Equation (9).[31–33]

## Conclusions

The complexation properties of DOTAM, which contains four uncharged acetamide functional groups, differ considerably from those of the parent ligand DOTA, which possesses four negatively charged pendant groups. The mechanisms of formation of $[Ln(DOTAM)]^{3+}$ and $[Ln(DOTA)]^-$ complexes are therefore also different. Thus, during the formation of the latter complexes, the acetate groups of the diprotonated ligand coordinate to the $Ln^{3+}$ ion to form a stable intermediate, which then undergoes transfer of the ring NH protons to the donor atoms of the pendant groups followed by entry of the metal ion into the macrocyclic cage. The complexes with DOTAM cannot be formed via protonated intermediates of this type, however, because the ring protons cannot be transferred to the amide oxygen atom. The formation of $[Ln(DOTAM)]^{3+}$ complexes therefore does not involve the formation of protonated intermediates.

The kinetic data indicate that the formation of $[Ln(DOTAM)]^{3+}$ complexes occurs in a direct reaction between the fully deprotonated DOTAM ligand and the $Ln^{3+}$ ion in a second-order reaction. Although the proton-exchange reactions of the protonated species $H_2DOTAM^{2+}$ and $HDOTAM^+$ are relatively slow on the NMR timescale, they have no effect on the rate of complex formation.

The second-order rate constants $k_L$, which characterize the formation of the $[Ln(DOTAM)]^{3+}$ complexes, are three to four orders of magnitude lower than the rate constants reported for the reactions of open-chain multidentate ligands. However, the trend of the $k_L$ values in the series of lanthanides is somewhat similar to that of the rates of complexation with some monodentate and multidentate ligands.

The formation of $[Ln(DOTAM)]^{3+}$ complexes occurs by successive replacement of the coordinated water molecules of the $Ln(H_2O)_n^{3+}$ ion. The low $k_L$ values observed can be interpreted by assuming that the rate-determining $Ln^{3+}$–amide bond formation probably occurs quite early in the reaction sequence, probably being in the second or third step of the complex formation.

The preformed coordination cage of the ligand plays an important role in determining the moderate stability constants and extremely low proton-assisted dissociation rates of the $Ln^{3+}$ complexes formed with the neutral ligand DOTAM. The neutrality of the acetamide pendant groups of the ligand has a major influence on the kinetics and mechanisms of the formation reactions; however, the rates are also influenced by the water exchange rates of the $Ln^{3+}$(aq) ions.

## Experimental Section

The chemicals used in the experiments were of the highest analytical grade. The $CeCl_3$ solution was prepared from $CeCl_3 \cdot 7H_2O$ (Aldrich, 99.9%). For the preparation of the other $LnCl_3$ solutions, $Ln_2O_3$ (Fluka, 99.9%) was dissolved in 6.0 M HCl and the excess of acid evaporated. The concentration of the $LnCl_3$ solutions was determined by complexometric titration with standardized $Na_2H_2EDTA$ and xylenol orange as indicator. The ligand DOTAM was prepared as described previously.[1] The concentration of the solution of DOTAM was determined by pH-metric titrations in the presence and absence of a large excess of $CaCl_2$. The protonation constants of DOTAM were also determined by pH-metry at 25 °C in 1.0 M KCl. The method proposed by Irving et al. was used to calculate $[H^+]$ from the measured pH values.[38] A Radiometer PHM93 pH meter, an ABU 80 autoburette and a Metrohm 6.0234.100 combined electrode were used for the pH measurements and titration. The pH-meter was calibrated with potassium hydrogen phthalate (pH = 4.005) and borax (pH = 9.180) buffers. The protonation constants were calculated with the program PSEQUAD.[39] The rates of formation of $[Ce(DOTAM)]^{3+}$ and $[Eu(DOTAM)]^{3+}$ were studied by spectrophotometry (Cary E1 spectrophotometer) at 320 and 250 nm, respectively. To study the formation of the $Gd^{3+}$, $Er^{3+}$ and $Y^{3+}$ complexes, the release of $H^+$ from the ligand was monitored by spectrophotometry at 616 nm in weakly buffered solutions with bromocresol green as indicator.[29] The decrease in pH was about 0.07–0.1 pH units in the presence of *N*-methylpiperazine (NMP) buffer. The formation of complexes was studied in the presence of a 5- to 50-fold $Ln^{3+}$ excess in order to maintain pseudo-first-order conditions. The concentration of

 © 2007 Wiley-VCH Verlag GmbH & Co. KGaA, Weinheim 

DOTAM was varied between $1 \times 10^{-4}$ and $5 \times 10^{-4}$ M. The pseudo-first-order rate constants were calculated by fitting the absorbance values to Equation (10), where $A_0$, $A_e$ and $A_t$ are the absorbance values at the start, at equilibrium and at time $t$ of the reaction.

The rates of formation [Equation (1)] were studied in the pH range 4.7–5.8 (25 °C, 1.0 M KCl). The $^1H$ NMR spectra were recorded

$$A_t = (A_0 - A_e)e^{-k_{obs}t} + A_e \quad (10)$$

with a Bruker Avance 600 spectrometer in $H_2O$ solution with a capillary containing $D_2O$ as lock and reference.

## Acknowledgments

This work was supported by the Hungarian Science Foundation (OTKA T-038364). The work was carried out in the frame of the EC COST Action D18 and the European-funded EMIL programme (LSCH-2004-503569)

[1] S. Amin, J. R. Morrow, C. H. Lake, M. R. Churchill, *Angew. Chem. Int. Ed. Engl.* **1994**, *33*, 773–775.
[2] S. Amin, D. A. Voss Jr, W. De W. Horrocks Jr, C. H. Lake, M. R. Churchill, J. R. Morrow, *Inorg. Chem.* **1995**, *34*, 3294–3300.
[3] *Metal Ions in Biological Systems* (Eds.: H. Sigel A Sigel), Marcel Dekker, New York, **2003**, vol. 40, chapters 11 and 12.
[4] S. Zhang, P. Winter, K. Wu, A. D. Sherry, *J. Am. Chem. Soc.* **2001**, *123*, 1517–1518.
[5] S. Zhang, L. Michaudet, S. Burgess, A. D. Sherry, *Angew. Chem. Int. Ed.* **2002**, *41*, 1919–1921.
[6] S. Zhang, M. Merritt, D. E. Wossner, R. E. Lenkinski, A. D. Sherry, *Acc. Chem. Res.* **2003**, *36*, 783–790.
[7] S. Aime, A. Barge, D. D. Castelli, F. Fedeli, A. Mortillaro, F. U. Nielsen, E. Terreno, *Magn. Reson. Med.* **2002**, *47*, 639–648.
[8] S. Aime, D. D. Castelli, E. Terreno, *Angew. Chem. Int. Ed.* **2002**, *41*, 4334–4336.
[9] D. Parker, P. K. Senanayake, J. A. G. Williams, *J. Chem. Soc. Perkin Trans. 2* **1998**, 2129–2140.
[10] D. Parker, R. S. Dickins, H. Puschmann, C. Crossland, J. A. Howard, *Chem. Rev.* **2002**, *102*, 1977–2010.
[11] P. Caravan, J. J. Ellison, T. J. Mc Murry, R. B. Lauffer, *Chem. Rev.* **1999**, *99*, 2293–2352.
[12] S. Aime, A. Barge, J. J. Bruce, M. Botta, J. A. K. Howard, J. M. Moloney, D. Parker, A. S. de Souza, M. Woods, *J. Am. Chem. Soc.* **1999**, *121*, 5762–5771.
[13] A. Bianchi, L. Calabi, C. Giorgi, P. Losi, P. Mariani, P. Paoli, P. Rossi, B. Vattancoli, M. Virtuani, *J. Chem. Soc. Dalton Trans.* **2000**, 697–705.
[14] S. Zhang, K. Wu, M. C. Biewer, A. D. Sherry, *Inorg. Chem.* **2001**, *40*, 4284–4290.
[15] H. Mamuela, R. D. Hancock, L. Carlton, J. H. Reibenspies, K. P. Wainwright, *J. Am. Chem. Soc.* **1995**, *117*, 6698–6707.
[16] S. Aime, A. Barge, A. S. Batsanov, M. Botta, D. D. Castelli, F. Fideli, A. Mortillaro, D. Parker, H. Puschmann, *Chem. Commun.* **2002**, 1120–1121.
[17] S. Aime, A. Barge, M. Botta, A. S. de Souza, D. Parker, *Angew. Chem. Int. Ed.* **1998**, *37*, 2673–2675.
[18] F. A. Dunand, S. Aime, A. E. Merbach, *J. Am. Chem. Soc.* **2000**, *122*, 1506–1512.
[19] S. Zhang, K. Wu, A. D. Sherry, *J. Am. Chem. Soc.* **2002**, *124*, 4226–4227.
[20] D. A. Voss Jr, E. R. Fraguhar, W. DeW. Horrocks Jr, J. R. Morrow, *Inorg. Chim. Acta* **2004**, *357*, 859–863.
[21] Z. Baranyai, E. Brücher, T. Iványi, R. Király, I. Lázár, L. Zékány, *Helv. Chim. Acta* **2005**, *88*, 604–617.
[22] X. Wang, T. Jin, V. Comblin, A. Lopez-mut, E. Merciny, J. F. Desreux, *Inorg. Chem.* **1992**, *31*, 1095–1099.
[23] É. Tóth, E. Brücher, I. Lázár, I. Tóth, *Inorg. Chem.* **1994**, *33*, 4070–4076.
[24] K. Kumar, M. F. Tweedle, *Inorg. Chem.* **1993**, *32*, 4193–4199.
[25] L. Wu, W. De W. Horrocks Jr, *Inorg. Chem.* **1995**, *34*, 3724–3732.
[26] L. Burai, I. Fábián, R. Király, E. Szilágyi, E. Brücher, *J. Chem. Soc. Dalton Trans.* **1998**, 243–248.
[27] P. A. Stenson, A. L. Thompson, D. Parker, *Dalton Trans.* **2006**, 3291–3293.
[28] J. F. Desreux, E. Merciny, M. F. Loncin, *Inorg. Chem.* **1981**, *20*, 987–991.
[29] S. P. Kasprzyk, R. G. Wilkins, *Inorg. Chem.* **1982**, *21*, 3349–3352.
[30] D. W. Margerum, G. R. Cayley, D. C. Weatherburn, G. R. Pagenkopf, *Coordination Chemistry* (Ed.: A. E. Martell), American Chemical Society, Washington, D. C., **1978**, vol. 2. p. 1–220.
[31] C. Cossy, A. E. Merbach, *Pure Appl. Chem.* **1988**, *60*, 1785–1796.
[32] S. F. Lincoln, *Advances in Inorganic and Bioinorganic Mechanisms* (Ed.: A. G. Sykes), Academic Press, London, **1986**, vol. 4. p. 217.
[33] S. F. Lincoln, A. E. Merbach, *Advances in Inorganic Chemistry* (Ed.: A. G. Sykes), Academic Press, New York, **1995**, p. 1–87.
[34] L. H. Piette, W. A. Anderson, *J. Chem. Phys.* **1959**, *30*, 899–908.
[35] D. T. Richens, *The Chemistry of Aqua Ions*, J. Wiley and Sons, Chichester, **1997**, p. 181.
[36] R. M. Fuoss, *J. Am. Chem. Soc.* **1958**, *80*, 5059–5061.
[37] I. Bányai, J. Glaser, *J. Am. Chem. Soc.* **1989**, *111*, 3186–3194.
[38] H. M. Irving, M. G. Miles, L. Pettit, *Anal. Chim. Acta* **1967**, *38*, 475–488.
[39] L. Zékány, I. Nagypál, in *Computational Methods for the Determination of Formation Constants* (Eds.: D. J. Legett), Plenum, New York, **1985**, p. 291.

Received: February 6, 2007
Published Online: June 22, 2007

 © 2007 Wiley-VCH Verlag GmbH & Co. KGaA, Weinheim 

DOI: 10.1002/ejic.200700228

# Proton Affinities in Water of Maingroup-Element Hydrides – Effects of Hydration and Methyl Substitution

Marcel Swart,[a][‡] Ernst Rösler,[a] and F. Matthias Bickelhaupt*[a]

**Keywords:** Acidity / Basicity / Density functional calculations / Periodic table / Proton affinities / Thermochemistry / Solvent effects

We have computed the proton affinities in water of archetypal anionic and neutral bases across the periodic table using the generalized gradient approximation (GGA) of density functional theory (DFT) at BP86/QZ4P//BP86/TZ2P. The main purpose of this work is to provide an intrinsically consistent set of values of the 298-K proton affinities in aqueous solution of all anionic ($XH_{n-1}^-$) and neutral bases ($XH_n$) constituted by maingroup-element hydrides of groups 14–17 and the noble gases (i.e., group 18) along the periods 1–6. Hydration has little effect on the trends in PA values, especially in the case of the neutral bases. However, in the case of the anionic bases, hydration drastically reduces the magnitude of the PA values. Finally, we have studied how proton affinities in water are affected by methyl substitution at the protophilic center.

(© Wiley-VCH Verlag GmbH & Co. KGaA, 69451 Weinheim, Germany, 2007)

## 1. Introduction

Designing new (and optimizing existing) approaches and routes in chemical synthesis requires knowledge of the thermochemistry involved in the targeted reactions. In this context, the proton affinity (PA) of a reactant or intermediate species B often plays an important role. This thermochemical quantity is defined as the enthalpy change associated with dissociation of the conjugate acid [Equation (1)].[1–8]

$$BH^+ \rightarrow B + H^+;\ \Delta H = PA \qquad (1)$$

Overall reaction enthalpies and reaction barriers (and thus reaction rates) are related to the PA, as soon as proton transfer occurs somewhere along the cascade of elementary steps of a reaction mechanism. This is often the case, as proton transfer is ubiquitous in chemical reaction mechanisms, either as simple proton transfer (PT) or as part of a more complex chemical transformation, for example, base-induced elimination reactions that may compete with nucleophilic substitution.[9–13] And, as chemical reactions are usually carried out in the condensed phase, knowledge of the *condensed-phase* PA values is vital for the understanding and prediction of (competing) reaction mechanisms.

Previously, we have studied the *gas-phase* proton affinities and trends therein of anionic and neutral maingroup-element hydrides and noble gases.[14,15] Gas-phase proton affinities are obviously directly applicable to gas-phase chemistry[3–6] but they are also relevant for chemistry occurring in the condensed phase.[1,16] On one hand, they reveal the intrinsic basicity of the protophilic species involved and, thus, they shed light on how this property is affected by the solvent. On the other hand, they can serve as a universal, solvent-independent framework of reference, from which the actual basicity of a species in solution might be obtained through correcting for the particular solvent under consideration.[17–19]

Here, we focus on the proton affinities in water and how the presence of the solvent changes the basicity of the protophilic species. The solvent environment may be taken into account using different approximations, e.g., through empirical corrections (Born, Onsager), or by including explicit solvent molecules, or through placing the solute in a dielectric continuum (COSMO[20,21]). The empirical corrections give only a rough estimate for the solvation process, while the inclusion of explicit solvent molecules necessitates sampling of the solvents' degrees of freedom in molecular simulations[22,23] (Monte Carlo, molecular dynamics). We choose the dielectric continuum (COSMO[20,21]) model as a reasonable compromise between accuracy and feasibility.

The present study has three objectives. First, we aim at setting up a complete description at BP86/QZ4P//BP86/TZ2P of the proton affinities (PA = $\Delta_{acid}H_{298}$ of reaction 1) in aqueous solution for the anionic (B = $XH_{n-1}^-$) and neutral (B = $XH_n$) maingroup-element hydrides of groups 14–17 and the noble gases, i.e. group 18, and periods 1–6.

[a] Theoretische Chemie, Scheikundig Laboratorium der Vrije Universiteit,
De Boelelaan 1083, 1081 HV Amsterdam, The Netherlands
Fax: +31-20-59-87629
E-mail: fm.bickelhaupt@few.vu.nl
[‡] Present address: ICREA (Institució Catalana de Recerca i Estudis Avançats) Researcher at Institut de Química Computacional, Universitat de Girona,
Campus Montilivi, 17071 Girona, Catalonia, Spain

Supporting information for this article is available on the WWW under http://www.eurjic.org or from the author.

 InterScience © 2007 Wiley-VCH Verlag GmbH & Co. KGaA, Weinheim 

In addition to the PA values of all bases ($\Delta_{acid}H_{298}$), we also report the corresponding 298 K reaction entropies ($\Delta_{acid}S_{298}$, provided as $-T\Delta_{acid}S_{298}$ values), and 298 K reaction free energies ($\Delta_{acid}G_{298}$). We have previously shown that this level of density functional theory (DFT)[24–32] performs well for computing gas-phase PA values.[14,15] Second, we wish to evaluate directly the effect of hydration on the PA values by comparing the condensed-phase values to the previously obtained[14,15] gas-phase values. Third, we examine the influence of stepwise methylation of the protophilic center X in species $Me_mXH_{n-m-1}^-$ and $Me_mXH_{n-m}$ (for periods 2 and 3), for example, $PH_3$, $MePH_2$, $Me_2PH$, $Me_3P$.

To the best of our knowledge, our series of in total 65 bases has never before been studied consistently with one and the same method over its full range, either experimentally or theoretically. The very consistency in the values of the present study makes our data particularly suitable for inferring accurate *trends* in condensed-phase basicity across the periodic table.

## 2. Results and Discussion

### 2.1. Effect of Hydration on Proton Affinities

The computed proton affinities in water (and the corresponding $-T\Delta_{acid}S_{298}$ and $\Delta_{acid}G_{298}$ values) of all model

Table 1. Thermodynamic acidity properties (kcal/mol) at $T$ = 298 K for anionic bases $Me_mH_{n-m}X^-$ in water.[a]

| Group 14 | | | | Group 15 | | | | Group 16 | | | | Group 17 | | | |
|---|---|---|---|---|---|---|---|---|---|---|---|---|---|---|---|
| Base | $\Delta H$ | $-T\Delta S$ | $\Delta G$ | Base | $\Delta H$ | $-T\Delta S$ | $\Delta G$ | Base | $\Delta H$ | $-T\Delta S$ | $\Delta G$ | Base | $\Delta H$ | $-T\Delta S$ | $\Delta G$ |
| **Period 2** | | | | | | | | | | | | | | | |
| $CH_3^-$ | 220.5 | –8.9 | 211.5 | $NH_2^-$ | 202.9 | –7.5 | 195.4 | $OH^-$ | 182.9 | –6.6 | 176.4 | $F^-$ | 158.1 | –5.7 | 152.4 |
| $MeCH_2^-$ | 226.6 | –8.9 | 217.7 | $MeNH^-$ | 206.6 | –7.5 | 199.1 | $MeO^-$ | 183.6 | –7.1 | 176.5 | | | | |
| $Me_2CH^-$ | 229.7 | –8.0 | 221.7 | $Me_2N^-$ | 205.1 | –7.0 | 198.1 | | | | | | | | |
| $Me_3C^-$ | 229.5 | –7.2 | 222.3 | | | | | | | | | | | | |
| **Period 3** | | | | | | | | | | | | | | | |
| $SiH_3^-$ | 193.0 | –8.2 | 184.8 | $PH_2^-$ | 185.1 | –7.5 | 177.6 | $SH^-$ | 164.9 | –6.4 | 158.5 | $Cl^-$ | 143.2 | –5.4 | 137.8 |
| $MeSiH_2^-$ | 201.6 | –7.6 | 194.0 | $MePH^-$ | 192.0 | –7.6 | 184.4 | $MeS^-$ | 171.2 | –6.3 | 164.8 | | | | |
| $Me_2SiH^-$ | 208.3 | –7.9 | 200.4 | $Me_2P^-$ | 198.2 | –7.3 | 190.9 | | | | | | | | |
| $Me_3Si^-$ | 213.4 | –7.3 | 206.0 | | | | | | | | | | | | |
| **Period 4** | | | | | | | | | | | | | | | |
| $GeH_3^-$ | 179.4 | –8.3 | 171.2 | $AsH_2^-$ | 179.8 | –7.5 | 172.3 | $SeH^-$ | 160.4 | –6.3 | 154.1 | $Br^-$ | 140.0 | –5.2 | 134.8 |
| **Period 5** | | | | | | | | | | | | | | | |
| $SnH_3^-$ | 169.7 | –8.1 | 161.6 | $SbH_2^-$ | 176.5 | –7.5 | 169.0 | $TeH^-$ | 158.7 | –6.2 | 152.5 | $I^-$ | 140.8 | –5.1 | 135.7 |
| **Period 6** | | | | | | | | | | | | | | | |
| $PbH_3^-$ | 150.4 | –7.0 | 143.3 | $BiH_2^-$ | 174.7 | –7.4 | 167.3 | $PoH^-$ | 157.3 | –6.2 | 151.1 | $At^-$ | 140.3 | –5.0 | 135.3 |

[a] Computed at BP86/QZ4P//BP86/TZ2P for the reaction $Me_mH_{n-m-1}XH \rightarrow Me_mH_{n-m-1}X^- + H^+$ with $n$ = 3, 2, 1 and 0 for groups 14, 15, 16 and 17, respectively.

Table 2. Thermodynamic acidity properties (kcal/mol) at $T$ = 298 K for neutral bases $Me_mH_{n-m}X$ in water.[a]

| Group 15 | | | | Group 16 | | | | Group 17 | | | | Group 18 | | | |
|---|---|---|---|---|---|---|---|---|---|---|---|---|---|---|---|
| Base | $\Delta H$ | $-T\Delta S$ | $\Delta G$ | Base | $\Delta H$ | $-T\Delta S$ | $\Delta G$ | Base | $\Delta H$ | $-T\Delta S$ | $\Delta G$ | Base | $\Delta H$ | $-T\Delta S$ | $\Delta G$ |
| **Period 1** | | | | | | | | | | | | | | | |
| | | | | | | | | | | | | He | 35.9 | –5.9 | 30.0 |
| **Period 2** | | | | | | | | | | | | | | | |
| $NH_3$ | 160.8 | –7.2 | 153.6 | $OH_2$ | 127.2 | –6.8 | 120.4 | FH | 88.7 | –6.6 | 82.1 | Ne | 39.9 | –5.7 | 34.3 |
| $MeNH_2$ | 164.2 | –7.6 | 156.6 | MeOH | 129.9 | –7.5 | 122.4 | MeF | 96.5 | –6.5 | 90.0 | | | | |
| $Me_2NH$ | 165.2 | –7.5 | 157.6 | $Me_2O$ | 131.2 | –7.1 | 124.2 | | | | | | | | |
| $Me_3N$ | 164.7 | –7.3 | 157.5 | | | | | | | | | | | | |
| **Period 3** | | | | | | | | | | | | | | | |
| $PH_3$ | 143.6 | –7.2 | 136.4 | $SH_2$ | 130.6 | –7.5 | 123.1 | ClH | 101.5 | –6.4 | 95.1 | Ar | 68.3 | –5.4 | 62.9 |
| $MePH_2$ | 152.7 | –7.4 | 145.4 | MeSH | 136.9 | –7.7 | 129.2 | MeCl | 108.3 | –6.3 | 102.0 | | | | |
| $Me_2PH$ | 159.3 | –7.5 | 151.8 | $Me_2S$ | 141.9 | –7.8 | 134.1 | | | | | | | | |
| $Me_3P$ | 164.2 | –7.0 | 157.2 | | | | | | | | | | | | |
| **Period 4** | | | | | | | | | | | | | | | |
| $AsH_3$ | 131.8 | –7.2 | 124.6 | $SeH_2$ | 129.6 | –7.5 | 122.1 | BrH | 103.9 | –6.3 | 97.6 | Kr | 75.4 | –5.3 | 70.1 |
| **Period 5** | | | | | | | | | | | | | | | |
| $SbH_3$ | 127.7 | –6.7 | 121.0 | $TeH_2$ | 133.6 | –6.8 | 126.7 | IH | 111.7 | –6.2 | 105.5 | Xe | 89.3 | –5.1 | 84.2 |
| **Period 6** | | | | | | | | | | | | | | | |
| $BiH_3$ | 110.4 | –6.6 | 103.8 | $PoH_2$ | 133.0 | –6.8 | 126.2 | AtH | 112.5 | –6.2 | 106.3 | Rn | 91.8 | –5.0 | 86.7 |

[a] Computed at BP86/QZ4P//BP86/TZ2P for the reaction $Me_mH_{n-m}XH^+ \rightarrow H^+ + Me_mH_{n-m}X$ with $n$ = 3, 2, 1 and 0 for groups 15, 16, 17 and 18, respectively.

 © 2007 Wiley-VCH Verlag GmbH & Co. KGaA, Weinheim 

bases are collected in Table 1 and 2 and the trends are visualized in Figure 1. The effect of solvation on the PA values is summarized in Table 3, Table 4 shows the separate contributions from solvation of the base, the proton and the conjugate acid. Before proceeding, we stress that various species for which we compute the proton affinity in water are not stable in water. For example, any anionic base with a higher PA than that of water (e.g., $NH_2^-$) will immediately abstract a proton from the latter. Access to the PA value of such in water transient species is interesting both, for the fundamental reason of having a complete trend, but also for the very practical reason to know if such a species remains intact in solution or if it directly abstracts a proton.

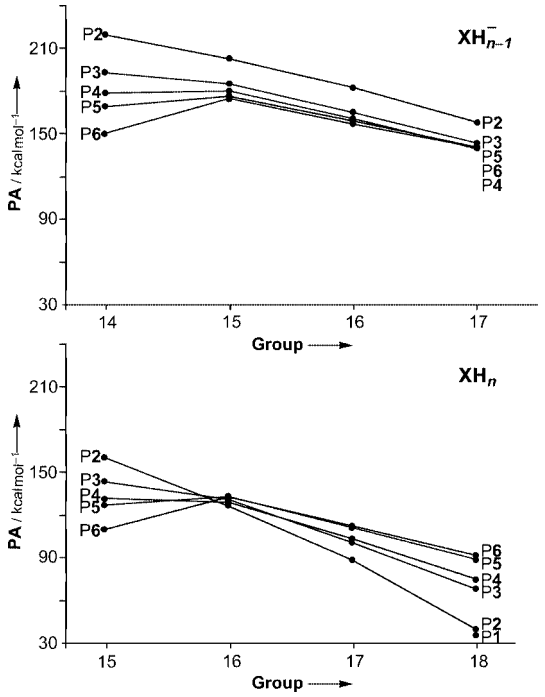


Figure 1. Proton affinities PA in water (at 298 K) of anionic bases $XH_{n-1}^-$ (upper) and neutral bases $XH_n$ (lower) constituted by the element hydrides of groups 14–18 and periods 1–6 (P1–P6), computed at BP86/QZ4P//BP86/TZ2P.

Table 4. Enthalpy of hydration (kcal/mol) for bases and their conjugate acids at $T$ = 298 K.[a]

| Base | $\Delta H_{solv}$(base) | $\Delta H_{solv}$(conj.acid) | $\Delta PA_{solv}$(base)[b] |
|---|---|---|---|
| $CH_3^-$ | –72.13 | 1.43 | –193.50 |
| $NH_2^-$ | –84.15 | –3.39 | –200.69 |
| $OH^-$ | –92.22 | –4.86 | –207.29 |
| $F^-$ | –98.12 | –3.51 | –214.54 |
| $Cl^-$ | –70.90 | –0.50 | –190.33 |
| $NH_3$ | –3.39 | –80.91 | –42.41 |
| $OH_2$ | –4.86 | –87.44 | –37.35 |
| FH | –3.51 | –94.68 | –28.76 |
| ClH | –0.50 | –85.94 | –34.49 |
| Ne | 1.45 | –105.72 | –12.76 |

[a] Computed at BP86/QZ4P//BP86/TZ2P. [b] See Equation (2). $\Delta H_{solv}(H^+)$ = –119.93 kcal/mol.

Two general observations can be made for the present PA values in aqueous solution by comparison with the corresponding PA values in the gas phase.[14,15] First, hydration reduces especially the PA values of the anionic bases and somewhat less so the PA values of the neutral bases (see Table 3). Second, the trends in PA values for either the anionic and neutral bases are only little affected by hydration, as follows from comparison of Figure 1 in the present study with that in ref.[15] (see however also the more detailed discussion in Sections 2.2 and 2.3).

The fact that the neutral bases are much less affected by hydration is easily understood if one considers that the

Table 3. Hydration effects on PA ($\Delta\Delta H$,[a] kcal/mol) for anionic bases $Me_mH_{n-m-1}X^-$ and neutral bases $Me_mH_{n-m}X$ at $T$ = 298 K.[b]

| Group 14 | | Group 15 | | Group 16 | | Group 17 | | Group 15 | | Group 16 | | Group 17 | | Group 18 | |
|---|---|---|---|---|---|---|---|---|---|---|---|---|---|---|---|
| Base | $\Delta\Delta H$ | Base | $\Delta\Delta H$ | Base | $\Delta\Delta H$ | Base | $\Delta\Delta H$ | Base | $\Delta\Delta H$ | Base | $\Delta\Delta H$ | Base | $\Delta\Delta H$ | Base | $\Delta\Delta H$ |
| **Period 1** | | | | | | | | | | | | | | | |
| | | | | | | | | | | | | | | He | –9.3 |
| **Period 2** | | | | | | | | | | | | | | | |
| $CH_3^-$ | –193.5 | $NH_2^-$ | –200.7 | $OH^-$ | –207.3 | $F^-$ | –214.6 | $NH_3$ | –42.4 | $OH_2$ | –37.3 | FH | –28.7 | Ne | –12.8 |
| $MeCH_2^-$ | –189.0 | $MeNH^-$ | –191.7 | $MeO^-$ | –193.0 | | | $MeNH_2$ | –49.8 | MeOH | –49.3 | MeF | –46.5 | | |
| $Me_2CH^-$ | –181.1 | $Me_2N^-$ | –182.0 | | | | | $Me_2NH$ | –55.3 | $Me_2O$ | –56.8 | | | | |
| $Me_3C^-$ | –174.4 | | | | | | | $Me_3N$ | –60.3 | | | | | | |
| **Period 3** | | | | | | | | | | | | | | | |
| $SiH_3^-$ | –176.1 | $PH_2^-$ | –181.1 | $SH^-$ | –186.5 | $Cl^-$ | –190.3 | $PH_3$ | –41.7 | $SH_2$ | –39.6 | ClH | –34.4 | Ar | –25.6 |
| $Me$-$SiH_2^-$ | –174.6 | $MePH^-$ | –180.9 | $MeS^-$ | –186.3 | | | $MePH_2$ | –51.1 | MeSH | –49.9 | MeCl | –48.7 | | |
| $Me_2$-$SiH^-$ | –172.9 | $Me_2P^-$ | –179.2 | | | | | $Me_2PH$ | –58.6 | $Me_2S$ | –58.5 | | | | |
| $Me_3Si^-$ | –170.3 | | | | | | | $Me_3P$ | –64.7 | | | | | | |
| **Period 4** | | | | | | | | | | | | | | | |
| $GeH_3^-$ | –176.5 | $AsH_2^-$ | –178.3 | $SeH^-$ | –181.5 | $Br^-$ | –184.3 | $AsH_3$ | –44.8 | $SeH_2$ | –42.8 | BrH | –38.0 | Kr | –30.7 |
| **Period 5** | | | | | | | | | | | | | | | |
| $SnH_3^-$ | –172.3 | $SbH_2^-$ | –172.0 | $TeH^-$ | –173.6 | $I^-$ | –175.1 | $SbH_3$ | –47.6 | $TeH_2$ | –44.7 | IH | –40.1 | Xe | –32.9 |
| **Period 6** | | | | | | | | | | | | | | | |
| $PbH_3^-$ | –174.0 | $BiH_2^-$ | –170.3 | $PoH^-$ | –171.9 | $At^-$ | –173.2 | $BiH_3$ | –51.0 | $PoH_2$ | –47.9 | AtH | –43.6 | Rn | –37.4 |

[a] $\Delta\Delta H$ is the change in PA due to solvation, i.e., $\Delta PA_{solv}$, as defined in Equation (2). [b] Computed at BP86/QZ4P//BP86/TZ2P for the reactions $Me_mH_{n-m-1}XH \rightarrow H^+ + Me_mH_{n-m-1}X^-$ with $n$ = 3, 2, 1 and 0 for groups 14, 15, 16 and 17, and $Me_mH_{n-m}XH^+ \rightarrow H^+ + Me_mH_{n-m}X$ with $n$ = 3, 2, 1 and 0 for groups 15, 16, 17 and 18, respectively.

 © 2007 Wiley-VCH Verlag GmbH & Co. KGaA, Weinheim 

main effect of solvation stems from the ionic species. The change in PA due to solvation, $\Delta PA_{solv}$, is given by Equation (2).

$$\Delta PA_{solv} = \Delta H_{solv}(base) + \Delta H_{solv}(H^+) - \Delta H_{solv}(conj.acid) \quad (2)$$

The change in enthalpy of solvation of the proton $\Delta H_{solv}(H^+)$ is large (–119.93 kcal/mol). For the neutral bases, this term is largely compensated by the strong enthalpy of solvation of their *positively charged conjugate acid*, $\Delta H_{solv}$(conj.acid). The latter ranges from –81 to –106 kcal/mol (see Table 4). Consequently, the change in proton affinity due to solvation $\Delta PA_{solv}$ is relatively small for neutral bases (see Tables 3 and 4).

The situation is different for the anionic bases. In the gas phase, they have significantly larger PA values than the neutral bases because of the charge separation, and the associated loss in Coulombic attraction, that goes with dissociating the neutral conjugate acid into the negatively charged base and the positively charge proton.[14,15] On the other hand, in solution, both the base and the proton (but not the conjugate acid) are heavily stabilized as they both carry one elementary charge. Thus, according to Equation (2), there is not a compensation but an amplification of the stabilizing effect of hydration through the terms $\Delta H_{solv}(base) + \Delta H_{solv}(H^+)$. Consequently, the reduction in proton affinity due to solvation $\Delta PA_{solv}$ is large for anionic bases (see Tables 3 and 4).

Eventually, hydration makes the PA values of the anionic bases come closer to those of the neutral bases but they remain somewhat higher than the latter (see Figure 1 and Tables 1 and 2). For instance, the difference in PA between $NH_2^-$ and $NH_3$, which is 200 kcal/mol in the gas phase, is reduced to 42 kcal/mol in water (see Tables 1 and 2). This is mainly due to the PA of the *anionic* base ($NH_2^-$) that decreases by 201 kcal/mol, while that of the *neutral* base ($NH_3$) decreases by only 42 kcal/mol (see Table 3).

### 2.2. Trends in Proton Affinities in Water

The *trends* in PA values for either the anionic and neutral bases are, as pointed out above, much less affected by hydration than the absolute values. Yet there are small but not negligible effects which are discussed in the present section. Furthermore, we note that hydration effects on trends in PA values are only small in the case of the simple element hydrides. Later on, in Section 2.3, we will see that trends can in fact be qualitatively changed by hydration in the case of the methyl-substituted bases.

First, we examine the trends in PA values in water as such before we consider the changes relative to the gas phase. For the anionic bases, we obtain the well-known trend of a decreasing basicity along the second period as the PA falls from 221 to 203 to 183 to 158 kcal/mol along $CH_3^-$, $NH_2^-$, $OH^-$ and $F^-$ (see Table 1 and Figure 1). The PA values also decrease down each group: for instance, for group 15, the PA decreases from 203 to 185 to 180 to 177 to 175 kcal/mol along $NH_2^-$, $PH_2^-$, $AsH_2^-$, $SbH_2^-$ and $BiH_2^-$. However, the changes in descending group 14 are significantly larger than those in groups 15–17. Thus, as can be seen in Figure 1, upper, the trend for monotonic decrease in PA along the second (P2) and third (P3) periods changes into a trend where the PA first increases from group 14 to group 15 and then decreases again along groups 15, 16 and 17. The corresponding reaction entropies yield a relatively small (but not entirely constant) contribution $-T\,\Delta_{acid}S_{298}$ of –5 to –9 kcal/mol for 298 K. As a consequence, the Gibbs free energies $\Delta_{acid}G_{298}$ show the same trends as the corresponding PA values (see Table 1).

For the neutral bases, we also obtain the well-known trend of decreasing basicity along the second period, just as for the anionic bases. Thus, the PA falls from 161 to 127 to 89 to 40 for $NH_3$, $OH_2$, FH, Ne. A striking change occurs from group 15 to groups 17 and 18. Descending group 15, the PA *decreases* but descending groups 17 and 18, the PA *increases* (see Table 2). Group 16 is an intermediate case with relatively constant PA values that do not show a pronounced trend. Thus, the trend of monotonic decrease of PA along the second (P2), third (P3), and fourth (P4) period changes into a trend, along the fifth (P5) and sixth (P6) period, of an initial increase of the PA from group 15 to group 16 followed by a decrease along groups 16–18 (see Figure 1, lower).

There is an interesting common feature in the trends of both anionic and neutral bases. This feature is the kink in the PA trend along a period that always occurs after the step from the tricoordinate to the dicoordinate base, that is, at group 15 for the anionic $XH_{n-1}^-$ and at group 16 for the neutral $XH_n$ (see Figure 1). The effect is most pronounced for bases with a more heavy protophilic center in which the valence *ns* AO is inactive. This suggests that the effect, that is, the sudden increase in PA from a tricoordinate to a dicoordinate base is associated with an active n*p*-type lone pair which becomes available in the latter.

The above trends of PA values in water are very similar to those in the gas phase. But, as announced above, there are differences which manifest themselves in particular in the case of the anionic bases. In the first place, the *magnitude of the hydration effect* ($\Delta PA$) on the PA values of the anionic bases $XH_{n-1}^-$ strongly *decreases down each group* (see Table 3). The largest change occurs from period 2 to period 3. This causes the PA values of $XH_{n-1}^-$ from different periods to shift closer together. The decrease in the hydration effect $\Delta PA$ on the proton affinities if one descends the periodic Table can be easily understood with the classical electrostatic Born model of a spherical ion in a dielectric continuum [Equation (3), in a.u.].[17,33]

$$\Delta E_{solv} = -\frac{q^2}{2a}\left(1-\frac{1}{\varepsilon_r}\right) \quad (3)$$

In this equation, $\varepsilon_r$ is the relative dielectric constant of the solvent (i.e. 78.4 for water). The charge $q$ is –1 for the $XH_{n-1}^-$ ion. The appearance of the effective radius $a$ of the

 © 2007 Wiley-VCH Verlag GmbH & Co. KGaA, Weinheim 

ion in the denominator leads to smaller solvation energies for larger ions. Thus, as the atomic radius of the protophilic center X (and therefore of the base $XH_{n-1}^-$) increases down a group, the stabilization due to solvation of the anionic base $\Delta\Delta H_{solv}$(base) diminishes and so does, according to Equation (2), the hydration effect ΔPA on the proton affinity.

The same simple model (i.e. Equations 2 and 3) predicts that, in the case of the neutral bases, the hydration effect increases down the periodic Table. This is indeed what happens although the effect is somewhat less pronounced than that for the anionic bases (see Table 3). Similar size effects can also be observed along a period. For example, the hydration-induced reduction of the proton affinity, ΔPA, increases from –194 to –201 to –207 to –215 kcal/mol along $CH_3^-$, $NH_2^-$, $OH^-$ and $F^-$ (see Table 3). In fact, the value of –214.6 kcal/mol for $F^-$ is the largest hydration effect on a PA value in this study. The trend in ΔPA along the second period anionic bases can again be understood in terms of the solvation stabilization becoming more effective as the anionic protophilic center becomes smaller (see equations 2 and 3).

### 2.3. Methyl Substituent Effects

Finally, we have studied the effect on the PA in water of stepwise replacing all hydrogen atoms in second- and third-period anionic bases $XH_{n-1}^-$ and neutral bases $XH_n$ by methyl substituents, for which the results are collected in Tables 1, 2 and 5 and visualized in Figures 2 and 3. Methyl substitution increases the basicity in aqueous solution as reflected by the PA in all cases, that is, for both second- and third-period anionic *and* neutral bases. For example, along $OH_2$, MeOH and $Me_2O$, the PA increases from 127 to 130 to 131 kcal/mol, and along $SH_2$, MeSH and $Me_2S$, the PA increases from 131 to 137 to 142 kcal/mol (see Table 2). In three cases the trend comes practically to a hold along the step in which the last possible methyl group is introduced, namely, from $Me_2CH^-$ to $Me_3C^-$, from $MeNH^-$ to $Me_2N^-$ and from $Me_2NH$ to $Me_3N$ (see Tables 1 and 2).

This similarity in PA trends between second- and third-period bases in water contrasts with the situation for the anionic bases in the gas phase.[14,15] In the case of the latter, methyl substitution also increases the PA of third-period bases $XH_{n-1}^-$ but it *decreases* the PA of the second-period bases $XH_{n-1}^-$. It was shown that the reduction in basicity of the second-period anionic bases is *not* the result of a stabilization of the protophilic center by methyl groups.[14] In fact, the introduction methyl groups *destabilizes in all cases* both the base and the conjugate acid. The opposite trends in the effect of methyl substitution on the gas-phase PA of second- and third-period anionic bases $XH_{n-1}^-$ originate from the fact that a *second-period base is destabilized less by introducing a methyl group* than its corresponding conjugate acid whereas a *third-period base is destabilized more* than its conjugate acid.

This difference between methyl-substituent effects on the PA of second- and third-period anionic bases obviously disappears in aqueous solution. Our analyses show that this is associated with the loss in solute–solvent interaction that goes with methyl substitution. The anionic second-period bases are particularly strongly solvated [due to the small size of their charged protophilic center, see Equation (3)], significantly more so than their neutral conjugate acid.

Table 5. Analysis of the methyl-substituent effect on PA energies $\Delta_{acid}E$ in water in terms of the partial reaction schemes in Figure 2 and Figure 3.[a]

| Base | $\Delta E_{N/C}$ | $\Delta E_{A/N'}$ | $\Delta_{acid}E$ | Base | $\Delta E_C$ | $\Delta E_{N'}$ | $\Delta_{acid}E$ |
|---|---|---|---|---|---|---|---|
| $C^{\cdots-}$ | | | 158.02 | $Si^{\cdots-}$ | | | 147.17 |
| $CH_3^-$ | –360.50 | –289.77 | 228.75 | $SiH_3^-$ | –293.12 | –241.87 | 198.42 |
| $MeCH_2^-$ | –341.36 | –264.66 | 234.72 | $MeSiH_2^-$ | –285.72 | –226.07 | 206.82 |
| $Me_2CH^-$ | –323.61 | –243.73 | 237.90 | $Me_2SiH^-$ | –277.99 | –211.76 | 213.40 |
| $Me_3C^-$ | –306.55 | –226.48 | 238.09 | $Me_3Si^-$ | –270.18 | –198.98 | 218.37 |
| $N^{\cdot\cdot-}$ | | | 201.26 | $P^{\cdot\cdot-}$ | | | 191.23 |
| $NH_2^-$ | –222.46 | –213.11 | 210.61 | $PH_2^-$ | –172.78 | –173.91 | 190.10 |
| $MeNH^-$ | –194.99 | –181.56 | 214.69 | $MePH^-$ | –158.51 | –152.70 | 197.04 |
| $Me_2N^-$ | –170.46 | –157.70 | 214.02 | $Me_2P^-$ | –145.63 | –133.69 | 203.17 |
| $O^{\cdot-}$ | | | 180.63 | $S^{\cdot-}$ | | | 168.19 |
| $OH^-$ | –129.99 | –121.34 | 189.28 | $SH^-$ | –97.85 | –96.90 | 169.14 |
| $MeO^-$ | –98.75 | –88.39 | 190.99 | $MeS^-$ | –78.50 | –71.02 | 175.67 |
| $N^{\cdots}$ | | | 61.29 | $P^{\cdots}$ | | | 84.56 |
| $NH_3$ | –425.33 | –317.38 | 169.24 | $PH_3$ | –317.23 | –252.25 | 149.54 |
| $MeNH_2$ | –401.11 | –289.91 | 172.49 | $MePH_2$ | –311.45 | –237.98 | 158.03 |
| $Me_2NH$ | –377.62 | –265.38 | 173.53 | $Me_2PH$ | –305.21 | –225.10 | 164.67 |
| $Me_3N$ | –354.46 | –242.56 | 173.19 | $Me_3P$ | –298.41 | –213.46 | 169.51 |
| $O^{\cdot\cdot}$ | | | 100.48 | $S^{\cdot\cdot}$ | | | 131.37 |
| $OH_2$ | –280.48 | –246.69 | 134.27 | $SH_2$ | –194.39 | –189.73 | 136.03 |
| MeOH | –252.05 | –215.45 | 137.08 | MeSH | –181.40 | –170.38 | 142.39 |
| $Me_2O$ | –225.94 | –187.76 | 138.66 | $Me_2S$ | –169.05 | –153.01 | 147.41 |
| $F^{\cdot}$ | | | 69.33 | $Cl^{\cdot}$ | | | 100.12 |
| FH | –174.48 | –149.90 | 93.91 | ClH | –116.06 | –110.52 | 105.66 |
| MeF | –152.63 | –119.88 | 102.08 | MeCl | –101.25 | –88.53 | 112.84 |

[a] Computed at BP86/QZ4P//BP86/TZ2P.

 © 2007 Wiley-VCH Verlag GmbH & Co. KGaA, Weinheim 

Therefore, these bases also suffer most from the shielding of the charged protophilic center from the solvent by the methyl substituents. Consequently, in water, methyl-substitution destabilizes the base more than it destabilizes the conjugate acid also in the case of the anionic second-period bases.

This leads to the well-known reversal, from gas phase to condensed phase, of the trend in basicity along a series of increasingly methyl-substituted second-period bases. For example, in the gas phase, the basicity decreases along $OH^- > MeO^-$ and along $NH_2^- > MeNH^- > Me_2N^-$. But in water, the basicity decreases in the opposite order, namely, along $MeO^- > OH^-$ and along $Me_2N^-$, $MeNH^- > NH_2^-$ (see Table 1 and ref.[14]).

Our analyses that lead to the above conclusion consist of a decomposition of the proton-affinity energies $\Delta_{acid}E$ [i.e., only the electronic-energy part, $\Delta E$, of the proton affinity, see Equation (6) in methodological section], associated with acid dissociation of the conjugate acids, into three partial reactions, as shown in the thermochemical cycles in the top panels of Figures 2 and 3. This decomposition is now explained for the anionic bases [see Equation (4)] but the situation is of course completely equivalent for the neutral bases [see Equation (5)]. The first step, which is associated with an energy change $-\Delta E_N(m)$, is dissociation of all substituents (but not the acidic proton) of the conjugate acid $Me_mH_{n-m-1}XH$ to form the radical $XH^{(n-1)\cdot}$ (see Figure 2). The energy $\Delta E_N(m)$ is the stabilization of the protophilic center X in the neutral conjugate acid $Me_mH_{n-m-1}XH$ by all substituents, i.e., the interaction with $m$ methyl groups (Me) and $n$-$m$-1 hydrogen atoms (H). Next, the unsubstituted acid $XH^{(n-1)\cdot}$ is dissociated into $X^{-(n-1)\cdot} + H^+$ (see Figure 2). The corresponding reaction energy is the proton-affinity energy $\Delta_{acid}E$ of the anionic base $X^{-(n-1)\cdot}$. The third and last step, which is associated with an energy change $\Delta E_A(m)$, is addition of all substituents to the protophilic center $X^{-(n-1)\cdot}$ to form the base $Me_mH_{n-m-1}X^-$ (see Figure 2; $m$ = number of methyl substituents). The energy $\Delta E_A(m)$ is the stabilization of the protophilic center X in the anionic base $Me_mH_{n-m-1}X^-$ by all substituents, i.e., the interaction with $m$ methyl groups (Me) and $n$-$m$-1 hydrogen atoms (H). The computed proton-affinity energies $\Delta_{acid}E$, $\Delta E_N$ and

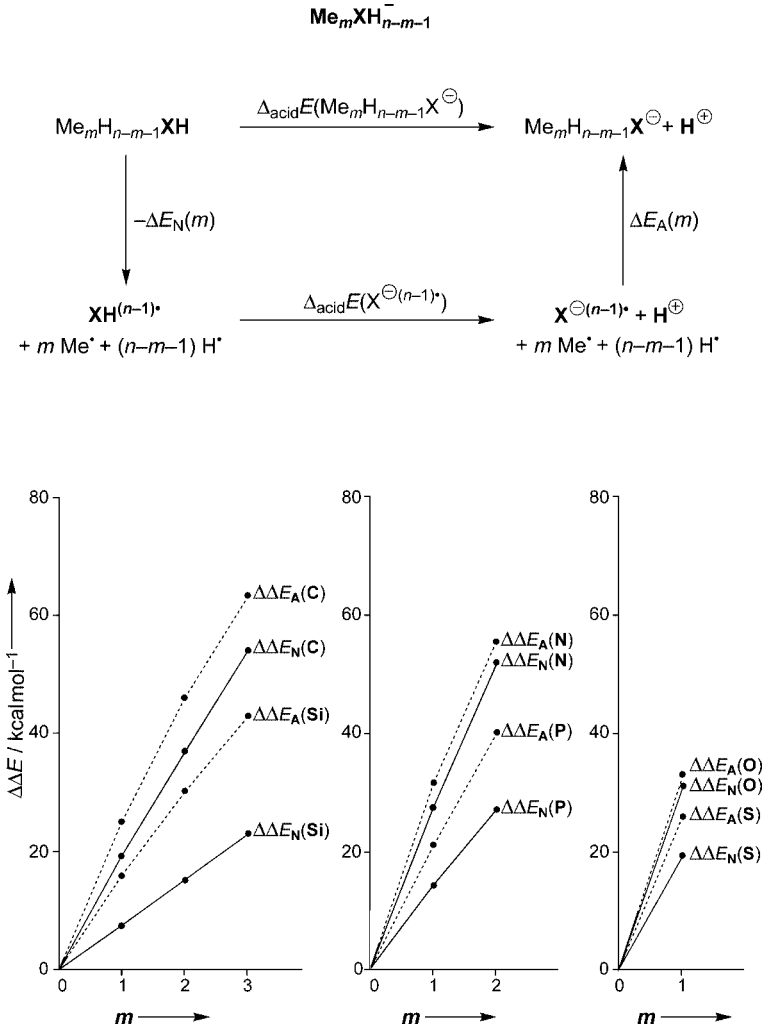


Figure 2. Effect of methyl substitution on the energies $\Delta E_N(X)$ and $\Delta E_A(X)$ of the anionic $XH_{n-1}^-$ and corresponding neutral conjugate acids $XH_n$ in water, computed at BP86/QZ4P//BP86/TZ2P [see Equation (4) and Table 5].

 © 2007 Wiley-VCH Verlag GmbH & Co. KGaA, Weinheim 

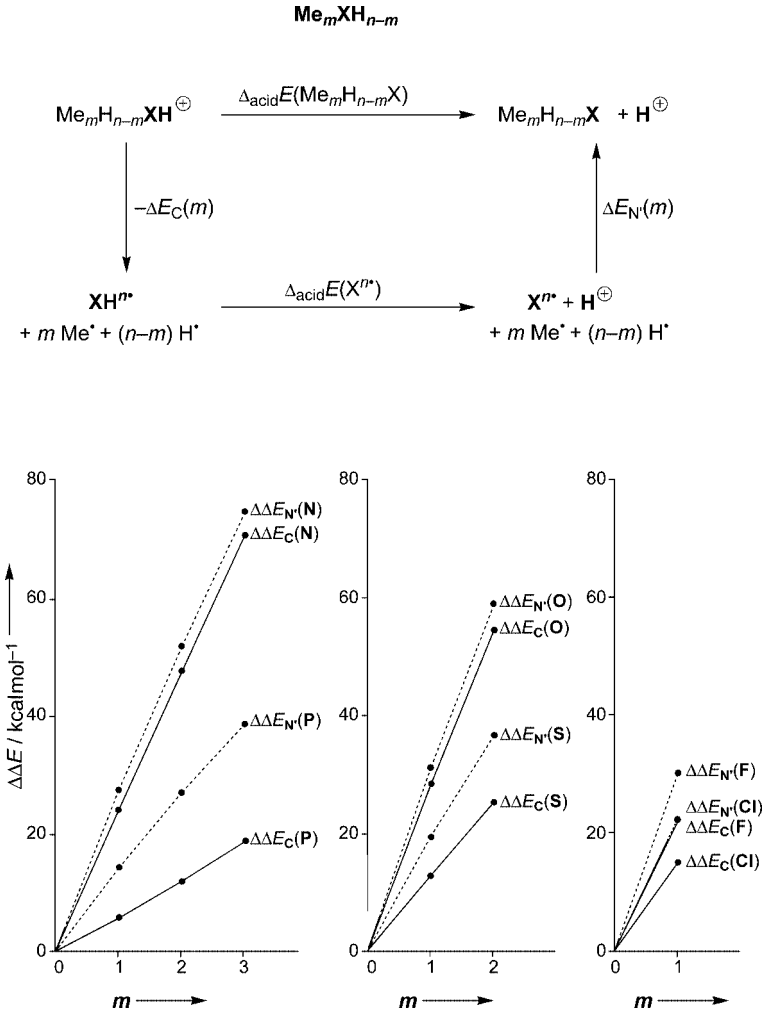


Figure 3. Effect of methyl substitution on the energies $\Delta E_C(X)$ and $\Delta E_{N'}(X)$ of the neutral $XH_n$ and corresponding cationic conjugate acids $XH_{n+1}^+$ in water, computed at BP86/QZ4P//BP86/TZ2P [see Equation (5) and Table 5].

$\Delta E_A$ of the *anionic* bases are collected in Table 5, together with corresponding energy terms $\Delta_{acid}E$, $\Delta E_C$ and $\Delta E_{N'}$ for the *neutral* bases.

The relationship between the proton-affinity energy $\Delta_{acid}E$ and the other energy terms of the thermochemical cycles shown in Figures 2 and 3 is summarized in Equations (4) and (5) ($m$ = number of methyl substituents) for the anionic ($Me_mH_{n-m-1}X^-$) and the neutral bases ($Me_mH_{n-m}X$).

$$\Delta_{acid}E(Me_mH_{n-m-1}X^-) = \Delta_{acid}E(X^{-(n-1)\bullet}) + \Delta E_A(m) - \Delta E_N(m) \quad (4)$$

$$\Delta_{acid}E(Me_mH_{n-m}X) = \Delta_{acid}E(X^{n\bullet}) + \Delta E_{N'}(m) - \Delta E_C(m) \quad (5)$$

Thus, according to Equation (4), the proton-affinity energy $\Delta_{acid}E(Me_mH_{n-m-1}X^-)$ of the base $Me_mH_{n-m-1}X^-$ is determined by the proton-affinity energy $\Delta_{acid}E(X^{-(n-1)\bullet})$ of the unsubstituted and deprotonated protophilic center $X^{-(n-1)\bullet}$ plus the *difference* in stabilization $\Delta E_A(m)$ of $X^{-(n-1)\bullet}$ in the base $Me_mH_{n-m-1}X^-$ and the stabilization $\Delta E_N(m)$ of $XH^{(n-1)\bullet}$ in $Me_mH_{n-m-1}XH$ by $m$ methyl (Me) and $n$-$m$-1 hydrogen substituents. The methyl-substituent effect on the proton-affinity energy, i.e., the change $\Delta\Delta_{acid}E(m)$ in this value if one goes from 0 to $m$ methyl substituents, therefore depends not only on the change $\Delta E_A(m) - \Delta E_A(0)$ in stabilization of the anionic base *but also on the change* $\Delta E_N(m) - \Delta E_N(0)$ *in stabilization of the neutral conjugate acid*. And, the same holds, *mutatis mutandis*, for the neutral bases, see Equation (5).

In Figure 2, lower panel, we have plotted the changes in stabilization by the substituents $\Delta\Delta E_A = \Delta E_A(m) - \Delta E_A(0)$ and $\Delta\Delta E_N = E_N(m) - \Delta E_N(0)$ for the anionic second- and third-period bases $Me_mH_{n-m-1}X^-$ and their conjugate acids $Me_mH_{n-m-1}XH$. In the lower panel of Figure 3, the corresponding plots for the neutral bases are depicted. Now it is clear that introducing a methyl substituent, i.e., replacing a hydrogen by the sterically more demanding and solvent-shielding methyl group, leads consistently in all cases to a destabilization of the system. And, contrasting the situation for the anionic bases in the gas-phase,[14] a methyl group

 © 2007 Wiley-VCH Verlag GmbH & Co. KGaA, Weinheim 

*destabilizes* the anionic base *more* than its corresponding neutral conjugate acid also for the second period and not only the third period.

## 3. Conclusions

The proton affinities (PA) in water of simple anionic bases $XH_{n-1}^-$ and neutral bases $XH_n$ (derived from or constituted by maingroup-element hydrides $XH_n$) show qualitatively similar trends along a period or down a group in the periodic table as the corresponding PA values in the gas phase, namely: a monotonic decrease along the second and third period which starting at the fourth (for $XH_{n-1}^-$) or fifth period (for $XH_n$) turns into a peak-shaped trend with an initial increase from the tri- to the dicoordinate base (e.g. from $GeH_3^-$ to $AsH_2^-$) followed again by a monotonic decrease along the rest of the period.

In the gas phase, the anionic bases $XH_{n-1}^-$ have a significantly higher PA than the neutral bases $XH_n$. Hydration however drastically reduces the PA of the anionic bases, i.e., much more so than that of the neutral bases. This causes the PA values of anionic and neutral bases to differ much less in aqueous solution than in the gas phase.

In water, methyl substitution increases practically always the PA of both the anionic bases $Me_mXH_{n-m-1}^-$ and the neutral bases $Me_mXH_{n-m}$. In the gas phase, methyl substitution has the same effect with one important exception: in the case of the anionic second-period bases $Me_mXH_{n-m-1}^-$, the gas-phase PA decreases if methyl groups are introduced. Thus, for example, $OH^-$ is more basic than $MeO^-$ in the gas phase but, in water, $MeO^-$ is more basic than $OH^-$. We have analyzed in detail why this is so.

## 4. Methods

### 4.1. Basis Sets

All calculations were performed with the Amsterdam Density Functional (ADF) program.[34,35] Molecular orbitals (MOs) were expanded using two different large, uncontracted sets of Slater-type orbitals: TZ2P and QZ4P.[36] The TZ2P basis is of triple-ζ quality, augmented by two sets of polarization functions (2*p* and 3*d* on H; *d* and *f* on heavy atoms). The QZ4P basis, which contains additional diffuse functions, is of quadruple-ζ quality, augmented by four sets of polarization functions (two 2*p* and two 3*d* sets on H; two *d* and two *f* sets on heavy atoms). Core electrons (e.g. 1*s* for 2nd period, 1*s*2*s*2*p* for 3rd period, 1*s*2*s*2*p*3*s*3*p* for 4th period, 1*s*2*s*2*p*3*s*3*p*3*d*4*s*4*p* for 5th period, 1*s*2*s*2*p*3*s*3*p*3*d*4*s*4*p*4*d* for 6th period) were treated by the frozen core (FC) approximation.[35] An auxiliary set of *s*, *p*, *d*, *f*, and *g* STOs was used to fit the molecular density and to represent the Coulomb and exchange potentials accurately in each SCF cycle. Scalar relativistic corrections were included self-consistently using the Zeroth Order Regular Approximation (ZORA).[37]

### 4.2. Density Functional

Energies and gradients were calculated using the local density approximation (LDA; Slater exchange and VWN[38] correlation) with gradient corrections[31,32] due to Becke (exchange) and Perdew (correlation) added self-consistently. This is the BP86 density functional, which is one of the three best DFT functionals for the accuracy of geometries,[39] with an estimated unsigned error of 0.009 Å in combination with the TZ2P basis set. In a previous study[14] on the proton affinity of anionic species, we compared the energies of a range of other DFT functionals, to estimate the influence of the choice of DFT functional. These functionals included the Local Density Approximation (LDA), Generalized Gradient Approximations (GGAs), *meta*-GGA and hybrid functionals. The BP86 functional emerged as one of the best functionals. The restricted and unrestricted formalisms were used for closed-shell and open-shell species, respectively. In the present study, all geometry optimizations and vibrational analyses have been done at BP86/TZ2P. Energies have been computed in a single-point fashion, on top of the BP86/TZ2P geometries, using the BP86/QZ4P level of theory. Overall, this leads to a BP86/QZ4P// BP86/TZ2P approach.

### 4.3. Solvent Effects and Thermochemistry

Solvent effects were taken into account in all calculations using the COSMO model,[20,21] used explicitly both within the solving of the SCF equations and the optimization of the geometry. The solvent radius ($R_s$) for water was taken from experimental data for the macroscopic density ($\rho$) and molecular mass ($M_m$) with the formula $R_s^3 = 2.6752 \cdot M_m/\rho$,[40] leading to a $R_s$ value of 1.9 Å for water; a value of 78.4 was used for the dielectric constant of water. Atomic radii values were taken from the MM3 van der Waals radii,[41] which are available for almost the whole periodic system, and scaled by 0.8333 (the MM3 radii are 20% larger than the normal van der Waals radii due to the specific form for the van der Waals energy within the MM3 force field). The surface charges at the GEPOL93 solvent-excluding surface[42–44] were corrected for outlying charges. This setup provides a "non-empirical" approach to including solvent effects with a dielectric continuum, and works well for solvation processes.[1] The file needed for including this setup in a COSMO computation with the ADF program (including all values of the above-mentioned atomic radii) is provided as Table S1 in the electronic supporting information.

Geometries were optimized using analytical gradient techniques until the maximum gradient component was less than $1.0 \times 10^{-4}$ atomic units (see Table S2 in the electronic supporting information). Vibrational frequencies were obtained through numerical differentiation of the analytical gradients,[35] where for most of the systems the GEPOL93 surface was recreated at each displaced geometry.

For three systems (i.e., $Me_3N$, $Me_3NH^+$ and $Me_3PH^+$), these standard settings resulted in one large imaginary frequency (in the range from –2300 to –24000 $cm^{-1}$) which, however, proved to have a positive value (of around 1200 and 2000 $cm^{-1}$) in the more accurate (automatic) PES scan afterwards. This imaginary frequency is related to the numerical differentiation in combination with the GEPOL93 surface. Thus, by creating the GEPOL93 surface in the case of the three problematic systems *only* for the initial geometry and keeping this surface (geometrically) fixed for all displaced geometries, the large imaginary frequencies do not occur. Moreover, for well-behaved systems, keeping the GEPOL93 surface fixed or recreating them at every displaced geometry has a negligible effect on the enthalpy (<0.1 kcal/mol). Thus, for the problematic cases of $Me_3N$, $Me_3NH^+$ and $Me_3PH^+$, we used the thermodynamic data from the calculations where the GEPOL93 surface was fixed.

Reaction enthalpies at 298.15 K and 1 atm ($\Delta H_{298}$) were calculated from the corresponding changes in electronic energy ($\Delta E$) according to Equation (6), assuming an ideal gas.[33]

 © 2007 Wiley-VCH Verlag GmbH & Co. KGaA, Weinheim 

$$\Delta H_{298} = \Delta E + \Delta E_{trans,298} + \Delta E_{rot,298} + \Delta E_{vib,0} + \Delta(\Delta E_{vib})_{298} + \Delta(pV) \quad (6)$$

Here, $\Delta E_{trans,298}$, $\Delta E_{rot,298}$ and $\Delta E_{vib,0}$ are the differences between products and reactants in translational, rotational and zero point vibrational energy, respectively; $\Delta(\Delta E_{vib})_{298}$ is the change in the vibrational energy difference as one goes from 0 to 298.15 K. The vibrational energy corrections are based on our frequency calculations. The molar work term for the gas-phase process, $\Delta(pV)$, is taken to be $(\Delta n)RT$; $\Delta n = +1$ for one reactant $BH^+$ dissociating into two products $B + H^+$. Thermal corrections for the electronic energy are neglected.

**Supporting Information** (see also the footnote on the first page of this article): Figures S1–S3 in color, input file (including atomic radii) for "non-empirical" COSMO solvation computations with ADF, and Cartesian coordinates of all species occurring in this study.

## Acknowledgments

We thank the Netherlands organization for Scientific Research (NWO-CW) for financial support.

[1] R. S. Bon, B. van Vliet, N. E. Sprenkels, R. F. Schmitz, F. J. J. de Kanter, C. V. Stevens, M. Swart, F. M. Bickelhaupt, M. B. Groen, R. V. A. Orru, *J. Org. Chem.* **2005**, *70*, 3542–3553.
[2] J.-F. Gal, P.-C. Maria, E. D. Raczynska, *J. Mass Spectrom.* **2001**, *36*, 699–716.
[3] E. P. L. Hunter, S. G. Lias, *J. Phys. Chem. Ref. Data* **1998**, *27*, 413–656.
[4] S. G. Lias, J. E. Bartmess, J. F. Liebman, J. L. Holmes, R. D. Levin, W. G. Mallard, *J. Phys. Chem. Ref. Data* **1988**, *17*, Suppl. No. 1.
[5] J. E. Szulejko, T. B. McMahon, *J. Am. Chem. Soc.* **1993**, *115*, 7839–7848.
[6] B. J. Smith, L. Radom, *J. Am. Chem. Soc.* **1993**, *115*, 4885–4888.
[7] K. E. Bartmess, J. A. Scott, R. T. McIver Jr, *J. Am. Chem. Soc.* **1979**, *101*, 6046–6056.
[8] S. T. Graul, R. R. Squires, *J. Am. Chem. Soc.* **1990**, *112*, 2517–2529.
[9] F. M. Bickelhaupt, *Mass Spectrom. Rev.* **2001**, *20*, 347–361.
[10] F. M. Bickelhaupt, E. J. Baerends, N. M. M. Nibbering, T. Ziegler, *J. Am. Chem. Soc.* **1993**, *115*, 9160–9173.
[11] F. M. Bickelhaupt, G. J. H. Buisman, L. J. de Koning, N. M. M. Nibbering, E. J. Baerends, *J. Am. Chem. Soc.* **1995**, *117*, 9889–9899.
[12] F. M. Bickelhaupt, G. J. H. Buisman, L. J. de Koning, N. M. M. Nibbering, E. J. Baerends, *J. Am. Chem. Soc.* **1996**, *118*, 1579–1579.
[13] F. M. Bickelhaupt, L. J. de Koning, N. M. M. Nibbering, *J. Org. Chem.* **1993**, *58*, 2436–2441.
[14] M. Swart, F. M. Bickelhaupt, *J. Chem. Theory Comput.* **2006**, *2*, 281–287.
[15] M. Swart, E. Rösler, F. M. Bickelhaupt, *J. Comput. Chem.* **2006**, *27*, 1486–1493.
[16] F. M. Bickelhaupt, E. J. Baerends, N. M. M. Nibbering, *Chem. Eur. J.* **1996**, *2*, 196–207.
[17] M. Born, *Z. Phys.* **1920**, *1*, 45–48.
[18] L. Onsager, *J. Am. Chem. Soc.* **1936**, *58*, 1486–1493.
[19] M. W. Wong, M. J. Frisch, K. B. Wiberg, *J. Am. Chem. Soc.* **1991**, *113*, 4776–4782.
[20] A. Klamt, G. Schüürmann, *J. Chem. Soc. Perkin Trans. 2* **1993**, 799–805.
[21] C. C. Pye, T. Ziegler, *Theor. Chem. Acc.* **1999**, *101*, 396–408.
[22] M. P. Allen and D. J. Tildesley, *Computer Simulation of Liquids*, Clarendon Press, Oxford, **1987**.
[23] D. Frenkel, B. Smit, *Understanding molecular simulation: from algorithms to applications*, Academic Press, **1996**.
[24] R. Dreizler, E. Gross, *Density Functional Theory*, Plenum Press, New York, **1995**.
[25] W. Koch, M. C. Holthausen, *A Chemist's Guide to Density Functional Theory*, Wiley-VCH, Weinheim, **2000**.
[26] R. G. Parr, W. Yang, *Density functional theory of atoms and molecules*, Oxford University Press, New York, **1989**.
[27] M. Ernzerhof, J. P. Perdew, K. Burke in *Density functionals: Where do they come from, why do they work?*, vol. 180 (Ed.: R. F. Nalejawski), Springer, Berlin, **1996**, pp. 1–30.
[28] S. Kurth, J. P. Perdew, P. Blaha, *Int. J. Quantum Chem.* **1999**, *75*, 889–909.
[29] J. P. Perdew, A. Ruzsinszky, J. M. Tao, V. N. Staroverov, G. E. Scuseria, G. I. Csonka, *J. Chem. Phys.* **2005**, *123*, 062201.
[30] J. P. Perdew, J. M. Tao, V. N. Staroverov, G. E. Scuseria, *J. Chem. Phys.* **2004**, *120*, 6898–6911.
[31] J. P. Perdew, *Phys. Rev. B* **1986**, *33*, 8822–8824. Erratum: *Phys. Rev. B* **1986**, *33*, 8834, 7406.
[32] A. D. Becke, *Phys. Rev. A* **1988**, *38*, 3098.
[33] P. W. Atkins, *Physical Chemistry*, Oxford University Press, Oxford, **1994**, p.
[34] E. J. Baerends, J. Autschbach, A. Bérces, C. Bo, P. L. de Boeij, P. M. Boerrigter, L. Cavallo, D. P. Chong, L. Deng, R. M. Dickson, D. E. Ellis, L. Fan, T. H. Fischer, C. Fonseca Guerra, S. J. A. van Gisbergen, J. A. Groeneveld, O. V. Gritsenko, M. Grüning, F. E. Harris, P. van den Hoek, H. Jacobsen, G. van Kessel, F. Kootstra, E. van Lenthe, D. A. McCormack, A. Michalak, V. P. Osinga, S. Patchkovskii, P. H. T. Philipsen, D. Post, C. C. Pye, W. Ravenek, P. Ros, P. R. T. Schipper, G. Schreckenbach, J. G. Snijders, M. Solà, M. Swart, D. Swerhone, G. te Velde, P. Vernooijs, L. Versluis, O. Visser, F. Wang, E. van Wezenbeek, G. Wiesenekker, S. K. Wolff, T. K. Woo, A. L. Yakovlev, T. Ziegler, *ADF 2005.01*, SCM, Amsterdam, **2005**.
[35] G. te Velde, F. M. Bickelhaupt, E. J. Baerends, C. Fonseca Guerra, S. J. A. van Gisbergen, J. G. Snijders, T. Ziegler, *J. Comput. Chem.* **2001**, *22*, 931–967.
[36] E. van Lenthe, E. J. Baerends, *J. Comput. Chem.* **2003**, *24*, 1142–1156.
[37] E. van Lenthe, E. J. Baerends, J. G. Snijders, *J. Chem. Phys.* **1993**, *99*, 4597–4610.
[38] S. H. Vosko, L. Wilk, M. Nusair, *Can. J. Phys.* **1980**, *58*, 1200–1211.
[39] M. Swart, J. G. Snijders, *Theor. Chem. Acc.* **2003**, *110*, 34–41. Erratum: *Theor. Chem. Acc.* **2003**, *110*, 111, 156.
[40] M. Swart, P. T. van Duijnen, *Mol. Simul.* **2006**, *32*, 471–484.
[41] N. L. Allinger, X. Zhou, J. Bergsma, *J. Mol. Struct. (THEOCHEM)* **1994**, *312*, 69–83.
[42] J. L. Pascual-Ahuir, E. Silla, *J. Comput. Chem.* **1990**, *11*, 1047–1060.
[43] E. Silla, I. Tunon, J. L. Pascual-Ahuir, *J. Comput. Chem.* **1991**, *12*, 1077–1088.
[44] J. L. Pascual-Ahuir, E. Silla, I. Tunon, *J. Comput. Chem.* **1994**, *15*, 1127–1138.

Received: February 21, 2007
Published Online: June 18, 2007

 © 2007 Wiley-VCH Verlag GmbH & Co. KGaA, Weinheim 

DOI: 10.1002/ejic.200700349

# Vanadium(IV) and Oxidovanadium(IV) and -(V) Complexes with Soft Thioether Coordination – Synthesis, Spectroscopic and Structural Studies

**Andrew L. Hector,[a] William Levason,[a] Annie J. Middleton,[a] Gillian Reid,*[a] and Michael Webster[a]**

**Keywords:** Vanadium / Thioether / Structural studies

$VOCl_3$ reacts with the thioethers $RS(CH_2)_2SR$ (R = Me, Et or *i*Pr) and 1,4-dithiane to form the first examples of $V^V$ thioether complexes, the highly reactive, intensely coloured $[VOCl_3(dithioether)]$ which have been characterised by $^1H$ and $^{51}V$ NMR, IR and UV/Vis spectroscopy. Combining $VOCl_3$ with $[9]aneS_3$ gives $[VOCl_3(\kappa^2\text{-}[9]aneS_3)]$ which, upon treatment with $SbCl_5$ gives $[VOCl_2(\kappa^3\text{-}[9]aneS_3)][SbCl_6]$. Vanadium *K*-edge extended X-ray absorption fine structure (EXAFS) studies on three examples provided partial structural analyses for these very unstable compounds. Reaction of $VCl_4$ with $O(SiMe_3)_2$ in $CH_2Cl_2$/MeCN followed by addition of $RS(CH_2)_2SR$ (R = Me or Et) produced $[VOCl_2\{RS(CH_2)_2SR\}]$. The crystal structure of $[\{VOCl_2(MeSCH_2CH_2SMe)\}_4]$ reveals a unique tetrameric $V_4O_4$ core with each vanadium also coordinated to a chelating dithioether and two Cl ligands to complete the distorted octahedral geometry. Under rigorously anhydrous conditions $VCl_4$ reacts with $RS(CH_2)_2SR$ (R = Me, Et, *i*Pr, Ph), 1,4-dithiane or $[9]aneS_3$ to form $[VCl_4(thioether)]$ which are assigned as six-coordinate distorted octahedral species on the basis of their spectroscopic characterisation. In some cases trace hydrolysis of these compounds provides an alternative route to the $[VOCl_2(dithioether)]$ complexes.

(© Wiley-VCH Verlag GmbH & Co. KGaA, 69451 Weinheim, Germany, 2007)

## Introduction

Vanadium has a very rich coordination chemistry owing in part to the accessibility of a range of oxidation states. However, the ease with which vanadium can undergo a redox switch between oxidation states, combined with its lability, leads to significant synthetic challenges in preparing pure materials, especially in the +4 and +5 oxidation states. These higher oxidation states of vanadium are dominated by oxido species and the majority of neutral ligand complexes known are with hard O- or N-donor ligands.[1–3] Examples of high oxidation state vanadium complexes with softer, neutral σ-donor ligands such as thio- or selenoethers are extremely rare – no $V^V$ derivatives are known and the only structurally characterised example with $V^{IV}$ is the distorted octahedral vanadyl species $[VOCl_2([9]aneS_3)]$.[4,5] The lower oxidation state $V^{III}$ and $V^{II}$ thioether complexes are well established,[5–8] but reports of $V^{IV}$ thioethers contain very limited data.[9,10] We note that much early work on phosphane complexes of $VCl_4$ is now known to be erroneous (see for example ref.[11] for a thorough discussion of the problems) due to the failure to recognise the ease of reduction to $V^{III}$ or the hydrolysis to $VOCl_2$ adducts, and the over-reliance on qualitative EPR spectra from incompletely characterised samples. In a recent paper concerned with $VOCl_3$ adducts with neutral N- or O-donor ligands,[3] we briefly noted that in dry $CH_2Cl_2$ solution $VOCl_3$ is reduced by $SR_2$ (R = Me, Et, *n*Bu or Ph), $PhSCH_2CH_2SPh$, $Me_2Se$ or $MeSeCH_2CH_2SeMe$. In an effort to investigate more fully the chemistry of $V^{IV}$ and $V^V$ precursors with soft thioether ligands and to establish whether the ligand structure is important in determining the course of the reactions, we have conducted a systematic study of $VOCl_3$, $VOCl_2$ and $VCl_4$ with the dithioethers $RSCH_2CH_2SR$ (R = Me, Et, *i*Pr), 1,4-dithiane and the macrocyclic $[9]aneS_3$ and $[18]aneS_6$. We report here the results of this investigation including the IR, UV/Vis and NMR (for $V^V$) spectroscopic characterisation of the resulting complexes, structural studies via vanadium *K*-edge EXAFS measurements, and a crystal structure of an extremely unusual metallocyclic vanadyl(IV) species, $[\{VOCl_2(MeSCH_2CH_2SMe)\}_4]\cdot CH_2Cl_2$.

## Results and Discussion

**$VOCl_3$ Complexes:** $VOCl_3$ and 2,5-dithiahexane react in anhydrous $CH_2Cl_2$ to give a dark red-brown solution from which $[VOCl_3(MeSCH_2CH_2SMe)]$ was obtained as a red-black powder by precipitation with *n*-hexane (Scheme 1). The freshly prepared complex is very soluble in chlorocarbons and extremely moisture-sensitive (turning into a blue oil in air), and decomposes even in the dark in ca. 48 h, becoming dull purple and completely insoluble in chlorocarbons. The red-black $[VOCl_3(RSCH_2CH_2SR)]$ (R = Et or

[a] School of Chemistry, University of Southampton, Southampton SO17 1BJ, UK
E-mail: wxl@soton.ac.uk
gr@soton.ac.uk

 © 2007 Wiley-VCH Verlag GmbH & Co. KGaA, Weinheim 

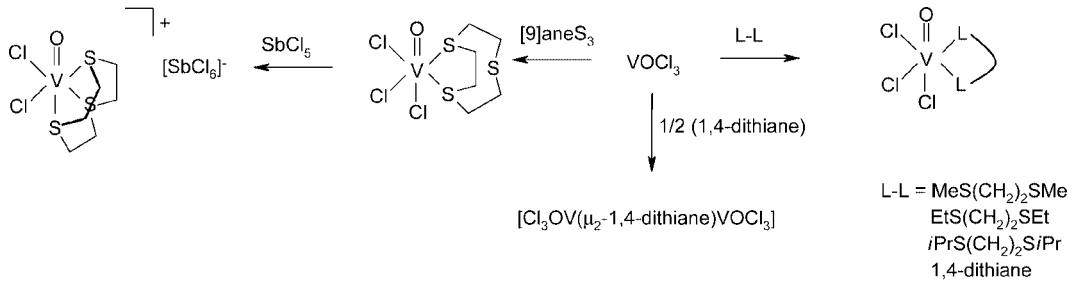


Scheme 1.

*i*Pr) are obtained similarly, although they are even less stable and decompose in a few hours, which prevented microanalytical data being obtained, but are spectroscopically very similar to the dithiahexane complex. In contrast, $VOCl_3$ in $CH_2Cl_2$ solution was immediately reduced by $PhSCH_2CH_2SPh$, *cis*-MeSCH=CHSMe or $MeS(CH_2)_3SMe$ to pinkish $V^{III}$-containing products (based upon their UV/Vis spectra). The red-black [$VOCl_3$(1,4-dithiane)] was obtained by treating a solution of 1,4-dithiane with a stoichiometric amount of $VOCl_3$ and precipitation with *n*-hexane, but using an excess of $VOCl_3$ gave the brown dinuclear [$(VOCl_3)_2$(1,4-dithiane)]. The reaction of thiacrowns with $VOCl_3$ is also very dependent on the ligand used. Both [9]aneS$_3$ and [18]aneS$_6$ react with excess $VOCl_3$ in $CH_2Cl_2$ to precipitate dark red-brown solids of composition [$VOCl_3$([9]aneS$_3$)] and [$(VOCl_3)_2$([18]aneS$_6$)] respectively, but [12]aneS$_4$ or [14]aneS$_4$ afford pale purple powders which lack any VO features in the IR spectra and their UV/Vis spectra suggest six-coordinate [$VCl_3$(thiacrown)], similar to complexes made directly from [$VCl_3(thf)_3$].[8] The [$VOCl_3$([9]aneS$_3$)] complex is stable for some weeks in the dark and the dry solid can be handled quickly in air, although it slowly turns blue in moist air (ca. 5 min) – the hydrolysis product was identified by IR and UV/Vis spectroscopy as [$VOCl_2$([9]aneS$_3$)].[4,5] Attempts to abstract chloride from [$VOCl_3$([9]aneS$_3$)] using $FeCl_3$ were unsuccessful, but when this reaction was repeated using $SbCl_5$, which is a much stronger Lewis acid, the brown-purple [$VOCl_2$([9]aneS$_3$)][$SbCl_6$] was formed in good yield. The complexes of the thiacrowns are very poorly soluble in chlorocarbons, which prevented solution spectroscopic studies.

The IR spectra of [$VOCl_3(RSCH_2CH_2SR)$] (Table 1) exhibit strong bands at ca. 970–1000 cm$^{-1}$ assigned as ν(VO), and strong features at 400–300 cm$^{-1}$ due to ν(VCl), which are similar to those observed in six-coordinate $V^V$ complexes of N- and O-donor ligands.[3] The UV/Vis spectra of the solid compounds are dominated by intense L→V charge-transfer transitions above ca. 19000 cm$^{-1}$ (usually with weak shoulders to lower energy), generally similar in band energies to those reported for N- or O-donor ligands,[3] suggesting that π(Cl)→V transitions are mainly responsible for the strong features. The insoluble materials produced by decomposition of the solids exhibited intense, poorly defined features across the visible region, presumably indicating mixed-valence materials. In anhydrous $CH_2Cl_2$ solution all three complexes exhibit single, quite sharp $^{51}$V NMR resonances with chemical shifts only slightly (5–15 ppm) to low frequency of $VOCl_3$, and the spectra are unchanged on cooling the samples to 190 K. These values compare with much more negative resonances found for complexes with N- or O-donors[3,12] and are consistent with soft V–S coordination in these complexes. Hydrolysis in solution leads to the production of $[VOCl_4]^-$ and $[VO_2Cl_2]^-$, readily identified by their $^{51}$V NMR resonances at $\delta$ +48 and –362 ppm respectively.[12] The $^1$H NMR spectrum of [$VOCl_3(MeSCH_2CH_2SMe)$] at 295 K in $CD_2Cl_2$ shows single δ(Me) and δ($CH_2$) resonances due to coordinated dithioether, to high frequency of those of the uncomplexed ligand, and the single δ(Me) and δ($CH_2$) resonances indicate a single geometric isomer with the sulfur donor atoms *trans* to Cl, giving *fac* chlorines (Scheme 1). On cooling the solution to 190 K, pyramidal inversion at the sulfur

Table 1. Selected spectroscopic data on oxidovanadium complexes.

| Complex | ν(VO) [cm$^{-1}$][a] | ν(VCl) [cm$^{-1}$][a] | δ($^{51}$V)[b] | $E_{max}$ [cm$^{-1}$][c] |
|---|---|---|---|---|
| [$VOCl_3(MeSCH_2CH_2SMe)$] | 976 | 376, 350, 327 | –14 | 14200 (sh), 18800, 21500 (sh), 27000 |
| [$VOCl_3(EtSCH_2CH_2SEt)$] | 977 | 366, 349, 323 | –7 | 15000 (sh), 20800, 27800 (sh) |
| [$VOCl_3(iPrSCH_2CH_2SiPr)$] | 998 | 370, 330, 310 | +5.5 | 15300 (sh), 20960, 28600 |
| [$VOCl_3$(1,4-dithiane)] | 988 | 374, 320 | +18 | 16100 (sh), 20000, 27400 |
| [$(VOCl_3)_2$(1,4-dithiane)] | 1012 | 402(sh), 372, 338 | +10.5 | 15530 (br), 18850, 23200, 27000 (sh) |
| [$VOCl_3$([9]aneS$_3$)] | 974 | 371, 345 | [d] | 15000 (br), 19800 (br), 29410 |
| [$VOCl_2$([9]aneS$_3$)][$SbCl_6$] | 1020 | 418 | [d] | 15600 (br), 18660, 24400 (sh) |
| [$(VOCl_3)_2$([18]aneS$_6$)] | 978 | 393, 372, 348 | [d] | 14600 (sh), 18700 (br), 30700 |
| [$VOCl_2(MeSCH_2CH_2SMe)$] | 975, 837 | 350, 319 | – | 13500 (sh), 19000, 27500 |
| [$VOCl_2(EtSCH_2CH_2SEt)$] | 985, 830 | 360, 304 | – | 13500 (sh), 18200, 27000 |

[a] Nujol mull. [b] $CH_2Cl_2$ solution relative to neat external $VOCl_3$ at 300 K. [c] Diffuse reflectance, diluted with $BaSO_4$. [d] Insufficiently soluble.

 © 2007 Wiley-VCH Verlag GmbH & Co. KGaA, Weinheim 

slows and four coordinated δ(Me) resonances and a complex pattern of overlapping δ($CH_2$) signals are present, consistent with three invertomers (*meso-1, meso-2* and *DL*) in a complex lacking axial symmetry. In the presence of added ligand, separate resonances for "free" and coordinated dithioether are seen, showing ligand exchange is slow on the NMR timescale at ambient temperatures. The $^1$H NMR spectra of the [$VOCl_3$(RS$CH_2CH_2$SR)] (R = Et or *i*Pr) exhibit generally similar behaviour, although even at the lowest temperatures studied (190 K) the $^3J_{HH}$ couplings within the Et and *i*Pr groups are not resolved, only broad singlets are observed for the different protons – this broadening may be due to the proximity to the quadrupolar $^{51}$V nucleus.

The dark red [$VOCl_3$(1,4-dithiane)] has similar physical and spectroscopic properties to the acyclic dithioether complexes, and is assigned a similar six-coordinate geometry, probably with chelating dithiane. The spectroscopic properties of the dark brown [($VOCl_3$)$_2$(1,4-dithiane)] are rather different, notably υ(VO) is at 1020 cm$^{-1}$, in the range observed for five-coordinate $VOCl_3$ adducts.[3] 1,4-Dithiane often favours a bridging coordination mode[13] and this may account for the formation of a 2:1 complex uniquely with this ligand.

The [$VOCl_3$([9]ane$S_3$)] complex is very poorly soluble in chlorocarbons, $MeNO_2$ or MeCN and decomposed by strong donor solvents such dmf, which has prevented solution spectroscopic studies. Three possible structures for this complex are the seven-coordinate [$VOCl_3$(κ$^3$-[9]ane$S_3$)], six-coordinate [$VOCl_3$(κ$^2$-[9]ane$S_3$)] or [$VOCl_2$(κ$^3$-[9]ane$S_3$)]Cl. The spectroscopic properties are similar to those of [$VOCl_3$(RS$CH_2CH_2$SR)], and the EXAFS data (below) are consistent with [$VOCl_3$(κ$^2$-[9]ane$S_3$)]. The failure of the complex to react with $FeCl_3$ (to form [$VOCl_2$(κ$^3$-[9]ane$S_3$)][$FeCl_4$]) rules out the cationic formulation, and whilst seven-coordination is known for a very small number of $V^V$ compounds, all seem to contain small bite-angle ligands such as κ$^2$-$NO_3$ or κ$^2$-$S_2CNR_2$[1] and it seems highly unlikely here. Hence the data support a [$VOCl_3$(κ$^2$-[9]ane$S_3$)] formulation. The 2:1 [18]ane$S_6$ complex probably has a similar vanadium core. The dark brown-purple [$VOCl_2$([9]ane$S_3$)][$SbCl_6$] formed by reaction of $VOCl_3$, $SbCl_5$ and [9]ane$S_3$ in anhydrous $CH_2Cl_2$ has υ(VO) at 1020 cm$^{-1}$, higher than that in the neutral [$VOCl_3$([9]ane$S_3$)] (974 cm$^{-1}$) and a very strong, broad band at 343 cm$^{-1}$ assigned as the $T_{1u}$ mode of the $[SbCl_6]^-$ ion.

The instability of the [$VOCl_3$(RS$CH_2CH_2$SR)] in solution and the insolubility of the macrocyclic complexes prevented all attempts to obtain crystals for X-ray structure determination. We therefore collected vanadium *K*-edge EXAFS data on three examples. Data were collected in transmission mode from freshly prepared (within 24 h) samples of [$VOCl_3$(MeS$CH_2CH_2$SMe)], [$VOCl_3$([9]ane$S_3$)] and [$VOCl_3$(1,4-dithiane)] diluted with BN (Experimental section). The data were all fitted to a four-shell model of 1 × O, 2 × Cl (*trans* S), 1 × Cl (*trans* O), and 2 × S, corresponding to a six-coordinate environment with the thioether sulfur atoms *trans* to Cl (see Experimental Section for details). The results are summarised in Table 2. Figure 1 shows a typical example of the background subtracted EXAFS data and the Fourier transform. The data on the three complexes are in excellent agreement. Few complexes of $VOCl_3$ have been structurally characterised but the *d*(V–O) of ca. 1.6 Å in the thioether complexes compares well with those in $[VO_2Cl_2]^-$ (1.58 (av) Å),[14] [$VOCl_2$([9]ane$S_3$)] (1.579(4) Å)[4] and [$VOCl_3${(2-nitrophenyl)pyridine-2-

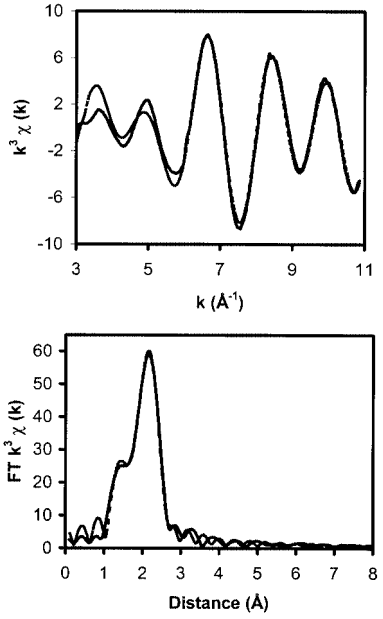


Figure 1. Vanadium *K*-edge $k^3$-weighted EXAFS (top) and Fourier-transformed EXAFS (bottom) for [$VOCl_3$(1,4-dithiane)]/boron nitride. Solid lines refer to data, dashed lines to calculated fit.

Table 2. Vanadium *K*-edge EXAFS data.[a]

| Complex | *d*(V–O) [Å] (O) | 2σ$^2$ [Å$^2$] [b] | *d*(V–Cl) [Å] (2Cl) | 2σ$^2$ [Å$^2$] [b] | *d*(V–Cl) [Å] (Cl) |
|---|---|---|---|---|---|
| [$VOCl_3$(MeS$CH_2CH_2$SMe)] | 1.583(5) | 0.002(1) | 2.249(6) | 0.009(2) | 2.385(18) |
| [$VOCl_3$(1,4-dithiane)] | 1.581(6) | 0.003(1) | 2.220(4) | 0.003(5) | 2.49(4) |
| [$VOCl_3$([9]ane$S_3$)] | 1.593(6) | 0.003(1) | 2.265(9) | 0.013(2) | 2.442(16) |
| *(continued)* | 2σ$^2$ [Å$^2$][b] | *d*(V–S) [Å] (2S) | 2σ$^2$ [Å$^2$][b] | $E_f$[c] | *R*%[d] |
| [$VOCl_3$(MeS$CH_2CH_2$SMe)] | 0.009(2) | 2.68(4) | 0.053(11) | –10.8(9) | 29.1 |
| [$VOCl_3$(1,4-dithiane)] | 0.036(12) | 2.66(5) | 0.08(3) | –12.6(9) | 20.0 |
| [$VOCl_3$([9]ane$S_3$)] | 0.013(4) | 2.69(3) | 0.052(9) | –10.5(11) | 32.0 |

[a] Standard deviations in parentheses. [b] Debye–Waller factor. [c] The difference between the calculated Fermi level energy and the theoretically known values for the element. [d] Defined as $[\int(\chi^T - \chi^E)k^3\,dk/\int \chi^E k^3\,dk] \times 100$ (where T is theoretical and E is experimental).

 © 2007 Wiley-VCH Verlag GmbH & Co. KGaA, Weinheim 

carboxamide}] (1.572(1) Å).[14] For comparison *d*(V–O) in solid molecular $VOCl_3$ (133 K) is 1.562(7) Å and *d*(V–Cl) 2.125(3) and 2.124(2) Å.[15] Two V–Cl shells were refined, the slightly shorter distances corresponding to the two chlorines *trans* to S, and the longer distance due to the one chlorine *trans* to V=O. The V–S distances at ca. 2.66–2.69 Å are significantly longer than V–$S_{trans Cl}$ in both $[\{VOCl_2(MeSCH_2CH_2SMe)\}_4]$ (2.48 Å) (Table 3) and $[VOCl_2([9]aneS_3)]$ (2.47 Å). The Ti–$S_{trans–Cl}$ distances in $[TiCl_4(dithioether)]$ are 2.60–2.65 Å.[16] The similarity of the distances within the three $V^V$ complexes and the best fit statistical data also support the six-coordinate $S_2Cl_3O$ donor sets for $[VOCl_3([9]aneS_3)]$ and $[VOCl_3(1,4\text{-dithiane})]$ proposed above based upon the spectroscopic data.

Table 3. Selected bond lengths [Å] and angles [°] for $[\{VOCl_2(MeSCH_2CH_2SMe)\}_4]\cdot CH_2Cl_2$.[a]

| | | | |
|---|---|---|---|
| V1–O1 | 1.640(3) | V1–O1c | 2.004(3) |
| V1–Cl1 | 2.288(1) | V1–Cl2 | 2.311(1) |
| V1–S1 | 2.662(1) | V1–S2 | 2.482(2) |
| S1–C1 | 1.810(6) | S1–C2 | 1.808(6) |
| S2–C3 | 1.813(5) | S2–C4 | 1.783(6) |
| O1–V1–O1c | 93.7(2) | O1–V1–Cl1 | 106.97(11) |
| O1c–V1–Cl1 | 90.89(9) | O1–V1–Cl2 | 98.29(10) |
| O1c–V1–Cl2 | 166.15(8) | Cl1–V1–Cl2 | 92.30(5) |
| O1–V1–S2 | 92.25(11) | O1c–V1–S2 | 90.50(9) |
| Cl1–V1–S2 | 160.60(5) | Cl2–V1–S2 | 82.08(5) |
| O1–V1–S1 | 168.56(11) | O1c–V1–S1 | 77.40(8) |
| Cl1–V1–S1 | 80.58(5) | Cl2–V1–S1 | 89.83(4) |
| S2–V1–S1 | 80.85(5) | V1–O1–V1b | 168.6(2) |

[a] Symmetry operations: *b* = *y*, – *x*, 2 – *z*; *c* = –*y*, *x*, 2 – *z*.

**$VOCl_2$ Complexes:** Red-brown crystals of $[\{VOCl_2(MeSCH_2CH_2SMe)\}_4]$ were initially obtained by storing a dilute $CH_2Cl_2$ solution of $VCl_4$ and $MeSCH_2CH_2SMe$ in a freezer for a few days, and were found to have the unique tetranuclear structure described below. The crystals clearly form by hydrolysis and red-brown powders of $[\{VOCl_2(RSCH_2CH_2SR)\}_4]$ (R = Me or Et) can be isolated in modest yield by storing dilute $CH_2Cl_2$ solutions of $VCl_4$ and $RSCH_2CH_2SR$ (after removal of precipitated $[VCl_4(RSCH_2CH_2SR)]$ by filtration) in a freezer for 1–2 weeks (Scheme 2). Hydrolysis does not stop at these species and after several months blue oils form. The robust (blue) $[VOCl_2([9]aneS_3)]$ can be made by hydrolytic oxidation of $[VCl_3([9]aneS_3)]$,[4] or by decomposition of $[VOCl_3([9]aneS_3)]$ (above), but these routes are not viable for the acyclic dithioethers. However, reaction of $VCl_4$ with one molequiv. of $O(SiMe_3)_2$ in anhydrous $CH_2Cl_2$ containing a small amount of MeCN, followed by addition of $RSCH_2CH_2SR$ produced the $[\{VOCl_2(RSCH_2CH_2SR)\}_4]$ in good yield. The MeCN presumably stabilises the $VOCl_2$ intermediate, since the reaction in neat $CH_2Cl_2$ does not work. Excess MeCN should be avoided since it reduces $VCl_4$ to $V^{III}$.[17] The $[\{VOCl_2(RSCH_2CH_2SR)\}_4]$ are readily hydrolysed in solution and decomposed by alcohols or acetone, but the pure, dry solids can be handled quickly in air. They are paramagnetic with $\mu_{eff}$ = 1.8 $\mu_B$ and exhibit ν(V=O) at 975, 837 (R = Me) or 985, 830 (R = Et) $cm^{-1}$ (Table 1) consistent with the V–O···V bridged structure (below).

Many vanadyl compounds are known; the majority are blue or green, discrete five-coordinate square pyramids or distorted octahedra (5 + 1 coordination), or sometimes chain polymers with *trans* O=V···O=V··· links.[1,2] A limited number of orange-brown polymers with polydentate Schiff bases are also known.[1,18] The structure of $[\{VOCl_2(MeSCH_2CH_2SMe)\}_4]$ is quite different (Table 3, Figure 2) and has a tetranuclear $V_4O_4$ core. The structure can either be described as based upon square pyramidal $VOCl_2(MeSCH_2CH_2SMe)$ units with apical chlorine, linked through asymmetric *cis* oxygen bridges into a tetramer, or as a puckered square with vanadium at the corners and asymmetric [V–O 1.640(3), 2.004(3) Å], non-linear [V–O–V 168.6(2)°] oxygen bridges along the edges. The coordination about each vanadium is completed by two terminal chlorines and a chelating dithioether [S–V–S angle 80.85(5) °]

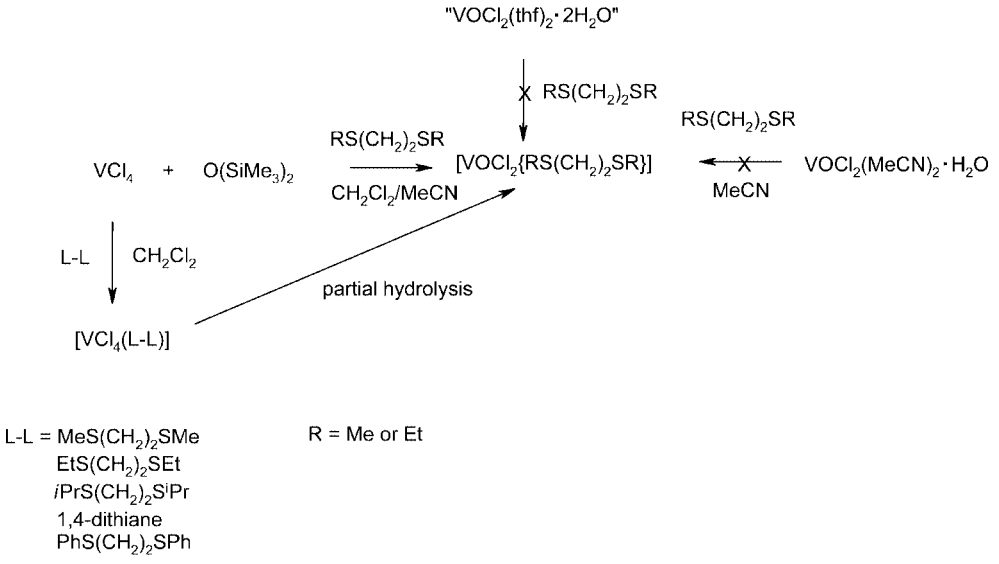


Scheme 2.

 © 2007 Wiley-VCH Verlag GmbH & Co. KGaA, Weinheim 

which has the *DL* configuration. In addition to the disparate V–O distances (the differences are 0.4 Å), the bond lengths around the vanadium centres reveal that the *trans* influence of the ligands on this hard metal is O > Cl > S. Thus V–$S_{transO}$ 2.662(1) Å, whilst V–$S_{transCl}$ 2.482(2) Å and V–$Cl_{transO}$ 2.311(1) Å, V–$Cl_{transS}$ 2.288(1) Å. For comparison, the bond lengths in the six-coordinate (5 + 1) [$VOCl_2$([9]ane$S_3$)] are V–O 1.579(4), V–Cl 2.295(5), and V–S 2.634(5), 2.470(5) Å.[4] A search of the CCDB revealed that the structure of the [{VO(SNNS)}$_4$] [SNNS = the dianion of *N*,*N*′-bis(*o*-mercaptophenyl)ethylendiamine] also contains a $V_4O_4$ core, but with a boat conformation.[19] The closest analogue to the structure of [{$VOCl_2$-($MeSCH_2CH_2SMe$)}$_4$] appears to be [{$TiOCl_2$([15]crown-5)}$_4$], a hydrolysis product of [$TiCl_4$([15]crown-5)], which contains a planar $Ti_4O_4$ ring with coordination at each Ti completed by two terminal chlorines and a $\kappa^2$-crown ether.[20]

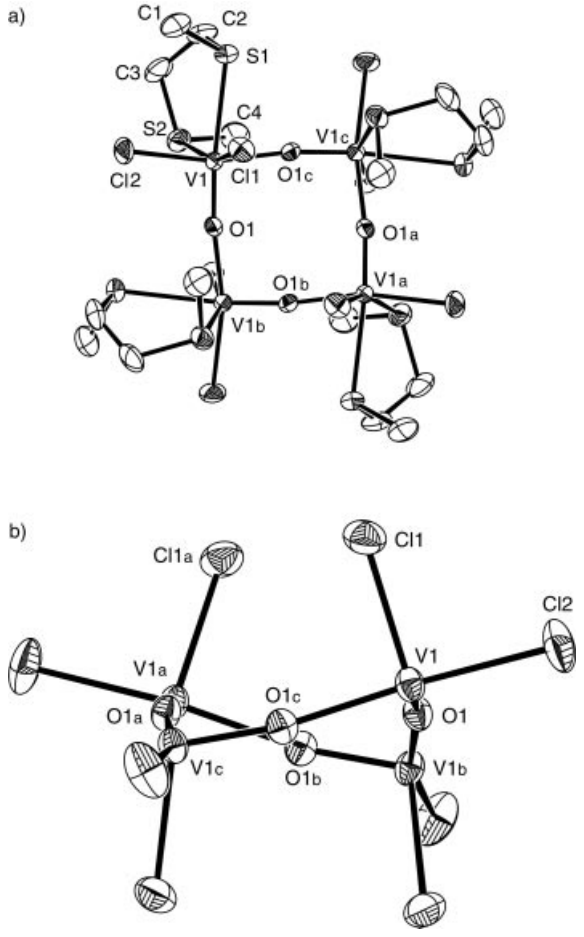


Figure 2. (a) Structure of the tetrameric molecule [{$VOCl_2$($MeSCH_2CH_2SMe$)}$_4$]·$CH_2Cl_2$. Thermal ellipsoids are drawn at the 50% probability level and H atoms are omitted for clarity. Symmetry operations: $a$ = –$x$, –$y$, $z$; $b$ = $y$, –$x$, 2 – $z$; $c$ = –$y$, $x$, 2 – $z$; (b) edge view of the $V_4O_4$ core within the tetramer.

**$VCl_4$ Complexes:** The reactions of the dithioethers $RSCH_2CH_2SR$ (R = Me, Et, *i*Pr), 1,4-dithiane and $MeS(CH_2)_3SMe$ in a 1:1 mol. ratio in rigorously anhydrous $CH_2Cl_2$ solution at or below ambient temperatures formed dark violet [$VCl_4$(dithioether)], which precipitated from the solutions. Using excess dithioether, addition of neat ligand to concentrated solutions of $VCl_4$ (which generates considerable heat) or gently heating $CH_2Cl_2$ solutions, produced lighter coloured materials, which contained substantial amounts of $V^{III}$. Gentle reflux of the $CH_2Cl_2$ preparative solutions in the presence of excess ligand produced complete reduction to pale lilac six-coordinate $V^{III}$ complexes. Using the weaker donor $PhSCH_2CH_2SPh$ produced an unstable dark purple solid [$VCl_4$($PhSCH_2CH_2SPh$)], but the related ligand $PhS(CH_2)_3SPh$ does not form a $V^{IV}$ complex; under similar reaction conditions it produced a pale lilac powder with the UV/Vis spectrum of a $V^{III}$ complex ($E_{max}$ 11970, 18500, 28570 $cm^{-1}$).[21] The reaction of $VCl_4$ with [9]ane$S_3$ in $CH_2Cl_2$ precipitates the purple solid [$VCl_4$([9]ane$S_3$)] which is insoluble in common solvents and when dry may be handled quickly in air without visible decomposition. Refluxing a mixture of $VCl_4$ with [9]ane$S_3$ in $CH_2Cl_2$ results in the known bright pink complex [$VCl_3$([9]-ane$S_3$)].[5] Repeated attempts to isolate [$VCl_4(SR_2)_2$] (R = Me, Et, *n*Bu or Ph) by reaction of $VCl_4$ with $SR_2$ in a 1:≤2 molar ratio in anhydrous $CH_2Cl_2$ solution failed. Excess thioether brings about immediate reduction to $V^{III}$, as described previously.[7,22,23]

The solid [$VCl_4$(dithioether)] are extremely moisture-sensitive, evolving yellow fumes in air and turning green-blue. However, in contrast to the $V^V$ [$VOCl_3$(dithioether)] complexes, they are stable in the dry box for several weeks. The complexes are very poorly soluble in chlorocarbons (cf. [$TiCl_4$(dithioether)])[16] and decomposed by acetone, alcohols or thf. The complexes are paramagnetic with magnetic moments $\mu_{eff}$ = 1.7–1.9 $\mu_B$, consistent with $d^1$ $V^{IV}$. The diffuse reflectance spectra show broad features at ca. 19000–20000 $cm^{-1}$ with a weaker shoulder to low energy (ca. 17000 $cm^{-1}$). The original work on these complexes assigned these features as d–d transitions and ascribed the splitting to the low symmetry ($C_{2v}$).[9] However, a d–d assignment seems at odds with the very intense colours and we propose that these bands are charge transfer π(Cl)→V (main band) and π(S)→V (shoulder), respectively. These assignments are supported by approximate calculations based upon the optical electronegativity model.[21,24,25] The spectrum of $[VCl_6]^{2-}$ contains the $^2T_{2g} \rightarrow {}^2E_g$ transition at 15500 $cm^{-1}$ and the lowest charge-transfer band, π(Cl)→V($t_{2g}$) at 20500 $cm^{-1}$.[24] The lowest energy charge-transfer band ($E_{max}$) for a $d^1$ complex in octahedral symmetry is predicted by the Equation (1):

$$E_{max}/cm^{-1} = 30000\{\chi_{opt}(L) - \chi_{opt}(M)\} - (14/3)B \quad (1)$$

Using the normal Pauling electronegativities for Cl and S, and estimating the Racah parameter ($B$) for Cl = 650 $cm^{-1}$, leads to a prediction of π(Cl)→V($t_{2g}$) ca. 20000 $cm^{-1}$ and π(S)→V($t_{2g}$) ca. 17000 $cm^{-1}$. The very significant low energy shift in the charge-transfer bands between [$TiCl_4$(dithioether)][16] and [$VCl_4$(dithioether)] is also consistent with the much greater ease of reduction of the vanadium complexes.

 © 2007 Wiley-VCH Verlag GmbH & Co. KGaA, Weinheim 

## Conclusions

The results reported here constitute the first detailed characterisation of a series of soft, neutral thioether ligand complexes of $V^{IV}$ and $V^{V}$. The architecture of the thioether ligands plays a significant role in governing the vanadium oxidation state produced and the relative stabilities of the complexes. Soft donor ligand complexes of $V^{V}$ are extremely unusual (phosphanes, arsanes, selenoethers and some thioethers bring about immediate reduction to $V^{IV}$ and/or $V^{III}$).[3,7,10] The tetrameric structure observed for $[\{VOCl_2(MeSCH_2CH_2SMe)\}_4]$ is a new structure type for vanadyl(IV), and contrasts with the discrete distorted octahedral geometry in the (coordinatively saturated) $[VOCl_2([9]aneS_3)]$. The successful isolation of these complexes indicate that under appropriate conditions and with judicious choice of ligand architecture, it may be possible to obtain limited examples of analogues with other soft donor ligands (e.g. selenoethers or arsanes).

## Experimental Section

All reactions were conducted under anhydrous conditions and under dry dinitrogen using standard vacuum line Schlenk and glovebox techniques. $VOCl_3$ and $VCl_4$ (Aldrich) were used as received. Solvents were dried by distillation from $CaH_2$ ($CH_2Cl_2$) or Na/benzophenone ketyl (hexane and diethyl ether). The thioethers $RSCH_2CH_2SR$ (R = Me, Et, *i*Pr, Ph) and $MeS(CH_2)_3SMe$ were made by literature methods[26] and dried and stored over molecular sieves. 1,4-dithiane, [9]aneS$_3$ and [18]aneS$_6$ were obtained from Aldrich and were dried by melting in vacuo immediately before use. Physical measurements were made as described previously[3] and microanalytical data were obtained from the microanalytical laboratory of Strathclyde University. All measurements were made on freshly prepared samples and the samples of the majority of the compounds were prepared several times and checked for consistency of the spectroscopic data.

**$[VOCl_3(MeSCH_2CH_2SMe)]$:** A solution of $VOCl_3$ (0.23 g, 1.3 mmol) in dry $CH_2Cl_2$ (5 mL) was added to a solution of 2,5-dithiahexane (0.16 g, 1.3 mmol) in dry $CH_2Cl_2$ (20 mL). The dark red solution was concentrated to ca. 5 mL in vacuo, dry *n*-hexane (5 mL) added and the red-black solid isolated by filtration, and dried in vacuo. Yield 0.18 g, 46%. $C_4H_{10}Cl_3OS_2V$ (295.5): calcd. C 16.3, H 3.4; found C 16.1, H 3.6. $^1$H NMR (300 MHz, $CD_2Cl_2$, 300 K): $\delta$ = 2.5 (s, 3 H, $CH_3$), 3.0 (s, 2 H, $CH_2$); (193 K): $\delta$ = 2.36, 2.39, 2.47, 2.60 (s, $CH_3$), 3.15–3.33 (br. m, $CH_2$) ppm. $^{51}$V NMR ($CH_2Cl_2$, 300 K): $\delta$ = –14 ($w_{1/2}$ = 800 Hz, sharpens on cooling but shift unchanged) ppm. UV/Vis ($CH_2Cl_2$): $E_{max}$ ($\varepsilon_{mol}$, $cm^{-1}\,dm^3\,mol^{-1}$) = 17120 (sh), 20160 (930), 21050 (1150), 25600 (1500), 31050 (sh), 33330 (2700) $cm^{-1}$.

**$[VOCl_3(EtSCH_2CH_2SEt)]$:** This compound was best made by adding excess $VOCl_3$ to the ligand in $CH_2Cl_2$ and pumping to dryness in vacuo in the dark. Yield 65%. As made it is a red-black powder, very soluble in chlorocarbons. Even in the dark in the glove box the complex decomposes in less than 24 h becoming insoluble in chlorocarbons. $^1$H NMR (300 MHz, $CD_2Cl_2$, 300 K): $\delta$ = 1.46 (br. s, 3 H, $CH_3$), 2.96 (br. s, 2 H, $CH_2$), 3.20 (br. s, 2 H, $CH_2$) ppm. $^{51}$V NMR ($CH_2Cl_2$, 300 K): $\delta$ = –7.1 ($w_{1/2}$ = 850 Hz); (223 K): $\delta$ = –7.5 ($w_{1/2}$ = 700 Hz) ppm.

**$[VOCl_3(i PrSCH_2CH_2S i Pr)]$:** This complex was made similarly to the one above, obtained as a red-black powder, yield 62%. $^1$H NMR (300 MHz, $CD_2Cl_2$, 300 K): $\delta$ = 1.2 (br., 6 H, $CH_3$), 1.40 (br., H, CH), 3.0 (br. s, 2 H, $CH_2$); (190 K): $\delta$ = 1.17, 1.18 (sh), 1.31, 1.39, 2.95, 3.08 (all broad and with no couplings resolved) ppm. $^{51}$V NMR ($CH_2Cl_2$, 300 K): $\delta$ = –5.4 ($w_{1/2}$ = 700 Hz); (213 K): $\delta$ = –6.1 ($w_{1/2}$ = 700 Hz) ppm. UV/Vis ($CH_2Cl_2$): $E_{max}$ = 15300 (sh), 20960, 28600, 30500 $cm^{-1}$.

**$[VOCl_3(1,4\text{-dithiane})]$:** A solution of $VOCl_3$ (0.23 g, 1.3 mmol) in dry $CH_2Cl_2$ (5 mL) was added to a solution of freshly sublimed 1,4-dithiane (0.16 g, 1.3 mmol) in dry $CH_2Cl_2$ (20 mL). The dark red solution was concentrated to ca. 5 mL in vacuo, dry *n*-hexane (5 mL) added and the red-black solid isolated by filtration, and dried in vacuo. Yield 0.22 g, 58%. $C_4H_8Cl_3OS_2V$ (293.5): calcd. C 16.4, H 2.8; found C 16.3, H 3.2. $^1$H NMR (300 MHz, $CD_2Cl_2$, 300 K): $\delta$ = 3.34 (br., $CH_2$); (190 K): $\delta$ = 3.63 (br., 2 H), 3.05 (br., 2 H) ppm. $^{51}$V NMR ($CH_2Cl_2$, 300 K): $\delta$ = +18 ($w_{1/2}$ = 300 Hz); (213 K): $\delta$ = +38. UV/Vis ($CH_2Cl_2$): $E_{max}$ = 16000 (sh), 18100, 21200, 26000 $cm^{-1}$.

**$[(VOCl_3)_2(1,4\text{-dithane})]$:** 1,4-Dithiane (0.12 g, 1.0 mmol) was freshly sublimed in vacuo and then dissolved in dry $CH_2Cl_2$ (15 mL) and added to a solution of $VOCl_3$ (0.36 g, 2.0 mmol) in dry $CH_2Cl_2$ (10 mL). The very dark brown solution was stirred for 1 h at room temperature and then concentrated in vacuo to ca. 5 mL. Dry *n*-hexane (5 mL) was added by cannula and the dark brown powder which separated was filtered off and dried in vacuo. Yield 0.32 g, 67%. $C_4H_8Cl_6O_2S_2V_2$ (466.8): calcd. C 10.3, H 1.7; found C 10.3, H 1.1. $^1$H NMR (300 MHz, $CD_2Cl_2$, 300 K): $\delta$ = 3.1 (s, $CH_2$) ppm. $^{51}$V NMR ($CH_2Cl_2$, 300 K): $\delta$ = +10.5 ($w_{1/2}$ = 100 Hz), little changed on cooling ppm. UV/Vis ($CH_2Cl_2$): $E_{max}$ = 18200 (sh), 21370, 27170 $cm^{-1}$.

**$[VOCl_3([9]aneS_3)]$:** [9]aneS$_3$ (0.09 g, 0.5 mmol) was dissolved in dry $CH_2Cl_2$ (15 mL) and added to a solution of $VOCl_3$ (0.09 g, 0.5 mmol) in dry $CH_2Cl_2$ (10 mL). A dark red-brown solid separated immediately. The dark suspension was concentrated to ca. 5 mL in vacuo, and the red-brown solid filtered off, rinsed with dry *n*-hexane (5 mL) and dried in vacuo. Yield 0.17 g, 94%. $C_6H_{12}Cl_3OS_3V$ (353.6): calcd. C 20.4, H 3.4; found C 20.5, H 3.7. {When the dry solid is exposed to air it turns pale green-blue in ca. 5 min and this product was identified as $[VOCl_2([9]aneS_3)]$. IR (Nujol): $\tilde{\nu}$ = 960 $cm^{-1}$ (VO), 344, 307 (sh) (VCl) $cm^{-1}$. UV/Vis (*dr* in $BaSO_4$): $E_{max}$ = 14450, 25000 sh, 30120 $cm^{-1}$.}

**$[VOCl_2([9]aneS_3)][SbCl_6]$:** $VOCl_3$ (0.09 g, 0.5 mmol) and $SbCl_5$ (0.15 g, 0.5 mmol) were dissolved in dry $CH_2Cl_2$ (15 mL), and stirred for 10 min, after which a solution of [9]aneS$_3$ (0.09 g, 0.5 mmol) in $CH_2Cl_2$ (10 mL) was added by syringe. The mixture slowly became brown and then deep purple in colour and after about 30 min contained a deep purple-brown precipitate in a pale yellow solution. The solid was filtered off, rinsed with $CH_2Cl_2$ (5 mL) and dried in vacuo. Yield 0.30 g, 91%. $C_6H_{12}Cl_8OS_3SbV$ (652.7): calcd. C 11.0, H 1.9; found C 10.7, H 2.2. IR (Nujol): $\tilde{\nu}$ = 1020 $\nu$(VO), 418 (VCl), 343 $\nu(SbCl_6)$ $cm^{-1}$.

**$[(VOCl_3)_2([18]aneS_6)]$:** Was made similarly to the [9]aneS$_3$ complex above using a 2.5:1 ratio of $VOCl_3$:[18]aneS$_6$ giving a dark red-brown powder. Yield 75%. $C_{12}H_{24}Cl_6O_2S_6V_2$ (707.3): calcd. C 20.4, H 3.4; found C 20.5, H 3.7.

**$[\{VOCl_2(MeSCH_2CH_2SMe)\}_4]$. Method 1:** $VCl_4$ (0.19 g, 1.0 mmol) was dissolved in a mixture of anhydrous $CH_2Cl_2$ (20 mL) and MeCN (0.5 mL), $Si(OMe_3)_2$ (0.18 g, 1.0 mmol) added, and the solution stirred for 15 min. $MeSCH_2CH_2SMe$ (0.12 g, 1.0 mmol) was then added, the solution stirred for 1 h and then concentrated in vacuo to ca. 5 mL. The brown solid was separated by filtration and dried in vacuo. Yield 0.15 g, 45%.

 © 2007 Wiley-VCH Verlag GmbH & Co. KGaA, Weinheim 

**Method 2:** $VCl_4$ (0.38 g, 2.0 mmol) was dissolved in anhydrous $CH_2Cl_2$ (15 mL) and $MeSCH_2CH_2SMe$ (0.24 g, 2.0 mmol) in $CH_2Cl_2$ (10 mL) added producing a very dark solution and some precipitate. The solid was filtered off and the solution stirred at room temperature under nitrogen for 24 h, and then refrigerated for 1 week. The brown solid formed was filtered off and dried in vacuo. Yields variable – typically 10–15%. $C_4H_{10}Cl_2OS_2V{\cdot}CH_2Cl_2$ (345.2): calcd. C 17.4, H 3.5; found C 17.2, H 3.7. $\mu_{eff}$ (298 K) = 1.81 $\mu_B$.

**[$VOCl_2$(EtSCH$_2$CH$_2$SEt)]:** Was made similarly by Method 1 above. Yield 55%. $C_6H_{14}Cl_2OS_2V$ (288.0): calcd. C 25.0, H 4.9; found C 24.6, H 5.3. $\mu_{eff}$ (298 K) = 1.80 $\mu_B$.

**[$VCl_4$(MeSCH$_2$CH$_2$SMe)]:** $VCl_4$ (0.38 g, 2.0 mmol) was dissolved in anhydrous $CH_2Cl_2$ (15 mL) and $MeSCH_2CH_2SMe$ (0.24 g, 2.0 mmol) in $CH_2Cl_2$ (10 mL) added producing a very dark solution and some precipitate. Concentration in vacuo to ca. 5 mL, followed by filtration produced a dark solid which became a purple-black powder on drying in vacuo. Yield 0.50 g, 80%. $C_4H_{10}Cl_4S_2V$ (315.0): calcd. C 15.2, H 3.2; found C 14.8, H 3.8. IR (Nujol): $\tilde{\nu}$ = 379 (sh), 362 (br), 316 (sh) (VCl) $cm^{-1}$. UV/Vis (*dr* in $BaSO_4$): $E_{max}$ = 17240 (sh), 19500, 29400, 38500 $cm^{-1}$. $\mu_{eff}$ (298 K) = 1.70 $\mu_B$.

**[$VCl_4$(EtSCH$_2$CH$_2$SEt)]:** Dark purple powder made similarly to the above. Yield 85%. $C_6H_{14}Cl_4S_2V$ (343.1): calcd. C 21.0, H 4.1; found C 21.4, H 4.3. IR (Nujol): $\tilde{\nu}$ = 365 (br), 346, 295 (sh) (VCl) $cm^{-1}$. UV/Vis (*dr* in $BaSO_4$): $E_{max}$ = 17000 (sh), 19650, 28400, 37750 $cm^{-1}$. $\mu_{eff}$ (298 K) = 1.68 $\mu_B$.

**[$VCl_4$(*i*PrSCH$_2$CH$_2$S*i*Pr)]:** Dark purple powder made similarly. Yield 70%. $C_8H_{18}Cl_4S_2V{\cdot}CH_2Cl_2$ (456.0): calcd. C 23.7, H 4.4; found C 22.9, H 4.0. IR (Nujol): $\tilde{\nu}$ = 389, 344 (br), 290 (VCl) $cm^{-1}$. UV/Vis (*dr* in $BaSO_4$): $E_{max}$ = 17850 (sh), 19600, 29400, 39525 $cm^{-1}$. $\mu_{eff}$ (298 K) = 1.70 $\mu_B$.

**[$VCl_4$(1,4-dithiane)]:** Dark red-black powder was made similarly. Yield 55%. $C_4H_8Cl_4S_2V$ (313.0): calcd. C 15.4, H 2.6; found C 15.3, H 2.9. IR (Nujol): $\tilde{\nu}$ = 384, 351, 312 (VCl) $cm^{-1}$. UV/Vis (*dr* in $BaSO_4$): $E_{max}$ = 17600 (sh), 20000, 28250 $cm^{-1}$. $\mu_{eff}$ (298 K) = 1.73 $\mu_B$.

**[$VCl_4${MeS(CH$_2$)$_3$SMe}]:** Dark purple powder. Yield 85%. $C_5H_{12}Cl_4S_2V$ (329.0): calcd. C 18.3, H 3.7; found C 18.3, H 3.9. IR (Nujol): $\tilde{\nu}$ = 368 (br) 330 (br) (VCl) $cm^{-1}$. UV/Vis (*dr* in $BaSO_4$): $E_{max}$ = 17000 (sh), 20100, 29100, 39600 $cm^{-1}$.

**[$VCl_4$(PhSCH$_2$CH$_2$SPh)]:** A cold solution of $VCl_4$ (0.19 g, 1.0 mmol) in $CH_2Cl_2$ (30 mL) was added slowly to a solution of $PhSCH_2CH_2SPh$ (0.25 g, 1.0 mmol) in $CH_2Cl_2$ (10 mL) with vigorous stirring. An intensely purple solution was produced, which was immediately concentrated to 10 mL in vacuo, and the dark solid which precipitated isolated by filtration, and dried in vacuo. Yield 0.28 g, 63%. If the solution is stirred for 1 h before work-up significant amounts of $V^{III}$ (UV/Vis evidence) are present. $C_{14}H_{14}Cl_4S_2V{\cdot}CH_2Cl_2$ (524.1): calcd. C 34.4, H 3.5; found C 34.5, H 3.5. IR (Nujol): $\tilde{\nu}$ = 372, 344 (br), 304 (VCl) $cm^{-1}$. UV/Vis (*dr* in $BaSO_4$): $E_{max}$ = 17250 (sh), 19200, 29400 $cm^{-1}$.

**X-ray Crystallography:** Crystals of [{$VOCl_2$(MeSCH$_2$CH$_2$SMe)}$_4$]·$CH_2Cl_2$ were obtained from a $CH_2Cl_2$ solution by cooling to about –20 °C for several days (see text). Data collection used a Nonius Kappa CCD diffractometer with confocal mirror monochromated Mo-$K_\alpha$ X-radiation ($\lambda$ = 0.71073 Å) and with the crystal held at 120 K in a cooled nitrogen gas stream. Structure solution was straightforward[27–29] with H atoms introduced into the model in calculated positions except for the dichloromethane solvate where no H atoms were included. The inclusion of the TWIN/BASF[28] commands made a small improvement to the data fit. Selected bond lengths and angles are given in Table 3 with crystallographic data in Table 4.

Table 4. Crystallographic data for [{$VOCl_2$(MeSCH$_2$CH$_2$SMe)}$_4$]·$CH_2Cl_2$.

| Formula | $C_{17}H_{42}Cl_{10}O_4S_8V_4$ |
|---|---|
| $M$ | 1125.25 |
| Crystal system | tetragonal |
| Space group (no.) | $I\bar{4}$ (82) |
| $a$ [Å] | 12.3183(17) |
| $b$ [Å] | 12.3183(17) |
| $c$ [Å] | 13.964(3) |
| $U$ [Å$^3$] | 2118.8(6) |
| $Z$ | 2 |
| $\mu$(Mo-$K_\alpha$) [$mm^{-1}$] | 1.906 |
| $F$(000) | 1132 |
| Total no. reflections | 8567 |
| Unique reflections | 2424 |
| $R_{int}$ | 0.051 |
| No. of parameters, restraints | 103, 2 |
| $R_1$[a] [$I_o > 2\sigma(I_o)$] | 0.041 |
| $R_1$ [all data] | 0.052 |
| $wR_2$[a] [$I_o > 2\sigma(I_o)$] | 0.086 |
| $wR_2$ [all data] | 0.091 |

[a] $R_1 = \Sigma\| F_o| - |F_c\|/\Sigma|F_o|$. $wR_2 = [\Sigma w(F_o^2 - F_c^2)^2/\Sigma wF_o^4]^{1/2}$.

CCDC-642012 contains the supplementary crystallographic data for this paper. These data can be obtained free of charge from The Cambridge Crystallographic Data Centre via www.ccdc.cam.ac.uk/data_request/cif

**EXAFS Data Collection and Treatment:** Vanadium *K*-edge EXAFS data were collected at ambient temperature on station 7.1 of the Daresbury SRS fitted with a silicon 110 monochromator and operating in transmission mode. Data were recorded from samples prepared <24 h previously, sealed in foil-wrapped flasks under $N_2$ and stored in the cold. Samples of the complexes were diluted ca. 1:3 with dry, powdered BN and pressed between Kapton windows in 1 mm thick cells. Two or three data sets were collected from each sample and then averaged. Background subtraction was performed with the PAXAS[30] package and the $k^3$-weighted EXAFS were fitted using Excurve.[31] The [$VOCl_3${MeS(CH$_2$)$_2$SMe}], [$VOCl_3$(1,4-dithiane)] and [$VOCl_3$($\kappa^2$-[9]ane$S_3$)] EXAFS were modelled with a cluster of $C_s$ symmetry with oxygen and one Cl on the mirror plane and an overall geometry close to octahedral. The models were tested for both five- and six-coordination, the best fit statistical data supporting six-coordination with $S_2Cl_3O$ donor sets.

## Acknowledgments

We thank the Engineering and Physical Sciences Research Council (EPSRC) for support (EP/C001176/1) and the Director of the Daresbury Laboratory for provision of facilities for EXAFS studies under award ref. 47036. We also thank Dr S. G. Fiddy for help with the EXAFS data collection and Charlotte D. Beard for some preliminary studies.

[1] F. A. Cotton, G. Wilkinson, M. Bochmann, C. A. Murillo, *Advanced Inorganic Chemistry*, 6th ed., Wiley, New York, **1998**.
[2] D. C. Crans, J. J. Smee in *Comprehensive Coordination Chemistry II* (Eds.: J. A. McCleverty, T. J. Meyer), **2004**, *4*, 175–239.
[3] C. D. Beard, R. J. Barrie, J. Evans, W. Levason, G. Reid, M. D. Spicer, *Eur. J. Inorg. Chem.* **2006**, 4391–4398 and refs. therein.

 © 2007 Wiley-VCH Verlag GmbH & Co. KGaA, Weinheim 

[4] G. R. Willey, M. T. Lakin, N. W. Alcock, *J. Chem. Soc. Chem. Commun.* **1991**, 1414–1416.
[5] S. C. Davies, M. C. Durrant, D. L. Hughes, C. Le Floc'h, S. J. A. Pope, G. Reid, R. L. Richards, J. R. Sanders, *J. Chem. Soc. Dalton Trans.* **1998**, 2191–2198.
[6] M. C. Durrant, S. C. Davies, D. L. Hughes, C. Le Floc'h, R. L. Richards, J. R. Sanders, N. R. Champness, S. J. A. Pope, G. Reid, *Inorg. Chim. Acta* **1996**, *251*, 13–14.
[7] M. W. Duckworth, G. W. A. Fowles, P. T. Greene, *J. Chem. Soc. A* **1967**, 1592–1597.
[8] C. D. Beard, L. Carr, M. F. Davis, J. Evans, W. Levason, L. D. Norman, G. Reid, M. Webster, *Eur. J. Inorg. Chem.* **2006**, 4399–4406.
[9] R. J. H. Clark, W. Errington, *Inorg. Chem.* **1966**, *5*, 650–656.
[10] K. L. Baker, D. A. Edwards, G. W. A. Fowles, R. G. Williams, *J. Inorg. Nucl. Chem.* **1967**, *29*, 1881–1885.
[11] a) F. A. Cotton, J. Lu, T. Ren, *Inorg. Chim. Acta* **1994**, *215*, 47–54; b) F. A. Cotton, J. Lu, *Inorg. Chem.* **1995**, *34*, 2639–2644.
[12] W. Priebsch, D. Rehder, *Inorg. Chem.* **1985**, *24*, 3058–3062.
[13] a) Y. Yamamoto, S. Sakamoto, Y. Ohki, A. Usuzawa, M. Fujita, T. Mochida, *Dalton Trans.* **2003**, 3534–3540; b) M. O. Santiago, J. R. Sousa, I. C. N. Diogenes, L. G. F. Lopes, E. Meyer, E. E. Castellano, J. Ellena, A. A. Batista, I. S. Moreira, *Polyhedron* **2006**, *25*, 1543–1548.
[14] a) D. Fenske, A.-F. Shihada, H. Schwab, K. Dehnicke, *Z. Anorg. Allg. Chem.* **1980**, *471*, 140–146; b) T. A. Kabanos, A. D. Keramidas, A. Papaioannou, A. Terzis, *Inorg. Chem.* **1994**, *33*, 845–846.
[15] J. Galy, R. Enjalbert, G. Jugie, J. Strähle, *J. Solid State Chem.* **1983**, *47*, 143–150.
[16] W. Levason, B. Patel, G. Reid, V.-A. Tolhurst, M. Webster, *J. Chem. Soc. Dalton Trans.* **2000**, 3001–3006.
[17] M. W. Duckworth, G. W. A. Fowles, R. A. Hoodless, *J. Chem. Soc.* **1963**, 5665–5673.
[18] M. Kojima, H. Taguchi, M. Tsuchimoto, K. Nakajima, *Coord. Chem. Rev.* **2003**, *237*, 183–196.
[19] W. Tsagkalidis, D. Rodewald, D. Rehder, *Inorg. Chem.* **1995**, *34*, 1943–1945.
[20] W. Levason, M. C. Popham, G. Reid, M. Webster, *Dalton Trans.* **2003**, 291–294.
[21] A. B. P. Lever, *Inorganic Electronic Spectroscopy*, Elsevier, Amsterdam, 2nd ed. **1984**.
[22] R. J. H. Clark, G. Natile, *Inorg. Chim. Acta* **1970**, *4*, 533–541.
[23] B. E. Bridgland, G. W. A. Fowles, R. A. Walton, *J. Inorg. Nucl. Chem.* **1965**, *27*, 383–389.
[24] R. D. Bereman, C. H. Brubaker Jr, *Inorg. Chem.* **1969**, *8*, 2480–2484.
[25] G. C. Allen, K. D. Warren, *Struct. Bonding (Berlin)* **1971**, *9*, 49–138.
[26] F. R. Hartley, S. G. Murray, W. Levason, H. E. Soutter, C. A. McAuliffe, *Inorg. Chim. Acta* **1979**, *35*, 265–277.
[27] G. M. Sheldrick, *SHELXS-97, program for crystal structure solution*, University of Göttingen, Germany, **1997**.
[28] G. M. Sheldrick, *SHELXL-97, program for crystal structure refinement*, University of Göttingen, Germany, **1997**.
[29] G. M. Sheldrick, *SADABS*, *Bruker-Nonius area detector scaling and absorption correction* (Version 2.10), Bruker AXS Inc, Madison, WI, USA, **2003**.
[30] N. Binsted, *Program for the analysis of X-ray absorption spectra, version 3.33*, University of Southampton, UK, **1998**.
[31] N. Binsted, *Excurve 9.271*, University of Southampton, UK, **2003**.

Received: March 28, 2007
Published Online: June 18, 2007

 © 2007 Wiley-VCH Verlag GmbH & Co. KGaA, Weinheim 

DOI: 10.1002/ejic.200700164

# Chlorido-Bridged $Mn^{II}$ Schiff-Base Complex with Ferromagnetic Exchange Interactions

**Chuan-Min Qi,[a] Xu-Xia Sun,[a] Song Gao,[b] Shu-Lan Ma,*[a] Da-Qiang Yuan,[c] Cui-Hong Fan,[a] Hai-Bo Huang,[a] and Wen-Xiang Zhu[a]**

**Keywords:** Manganese / Schiff bases / Magnetic properties

The preparation, crystal structure, and magnetic properties of the μ-Cl-bridged dinuclear complex $[Mn(HL)(\mu\text{-}Cl)Cl]_2$ (**1**) with the Schiff-base ligand HL, 2-methyl-6-[(pyridine-2-yl-methylene)amino]phenol, is reported. Structural studies show that **1** is binuclear with a pair of chlorine atoms bridging the manganese atoms in a central $Mn_2Cl_2$ plane, the intramolecular Mn···Mn separation being 3.694 Å. Each manganese atom in **1** is six-coordinate with two nitrogen atoms (one imine nitrogen and one pyridine nitrogen) and one phenolic oxygen from the neutral tridentate ligand, and three chlorine atoms (one terminal and two bridging) building an elongated octahedral environment. The two octahedra adopt the unique geometry sharing an equatorial-to-axial edge with parallel equatorial planes. The hydrogen bonds between the coordinated $Cl^-$ anions and hydroxy groups connect the dimeric coordinated units together forming a one-dimensional chain. Variable temperature susceptibility measurements in the temperature range of 2.0–300 K reveal a ferromagnetic coupling ($J$ = +0.94 $cm^{-1}$) in the dimer via the double chlorido bridge, and a weak antiferromagnetic coupling ($zJ'$ = –0.036 $cm^{-1}$) between the dimers through the intermolecular hydrogen bonding. A comparison of the magnetic coupling of **1** with other structurally similar $Mn(\mu\text{-}Cl)_2$-Mn compounds is discussed in detail. Complex **1** may provide useful information for the magneto-structural correlations of this kind of compounds.
(© Wiley-VCH Verlag GmbH & Co. KGaA, 69451 Weinheim, Germany, 2007)

## Introduction

The preparation and magnetic properties of discrete polynuclear molecules and coordination polymers of paramagnetic metal complexes are of considerable interest to the field of molecular magnetism.[1] In particular, the coordination chemistry of manganese has received a great deal of attention because of the variable structures of manganese complexes and the possibility of magnetic coupling interaction.[2] The magnetic behavior of $Mn^{II}$ polymers is dependent on the bridging and terminal ligands. Most magnetic studies on these $Mn^{II}$ polymers are relative to those with bridging ligands, such as azide,[3] dicyanamide,[4] and carboxylate.[5] Ferromagnetic exchange coupling among these $Mn^{II}$ compounds is rather unusual. This kind of magnetic interaction has been found in $Mn^{II}$ dinuclear complexes and polymers with end on bridging azido,[3,6] $Mn^{II}$ dinuclear complexes with diazine and some phenoxido bridging ligands.[7] Magnetically active chlorido-bridged systems are well-known in general, but relatively few investigations of the structure and magnetic properties of chlorido-bridged compounds have been carried out.[8] The angular dependence of the strength and nature of the magnetic coupling in M(μ-X)M systems was studied in detail for $Cu^{II}$ and $Cr^{III}$ systems,[1a,9] but the paucity of magneto-structural studies with dichlorido-bridged $Mn^{II}$ dimers precludes us to go further. In order to check the correlation between the angle at the bridging chlorine atom and the nature and value of magnetic coupling in $Mn^{II}$ compounds as well as to investigate the influence of additional structural factors, many more examples are needed. In this paper, we report the structural and magnetic study of the new dichlorido-bridged $Mn^{II}$ dinuclear complex $[Mn(HL)(\mu\text{-}Cl)Cl]_2$ (**1**) with the tridentate Schiff-base ligand. We will see that this six-coordinate $Mn^{II}$ dimer presents unusual ferromagnetic interactions. To establish magneto/structural correlations of $Mn^{II}$ compounds with bis(μ-chlorido) bridges, the magnetic properties of **1** were also compared to those of four structurally similar dimers, $[MnCl(\mu\text{-}Cl)(bpea)]_2$ (**2**), $[Mn(biz)_2(\mu\text{-}Cl)]_2Cl_2$ (**3**), $[Mn(mpbpa)Cl(\mu\text{-}Cl)]_2$ (**4**) and $[Mn(dpp)Cl(\mu\text{-}Cl)(H_2O)]_2$ (**5**),[8] and two one-dimensional bis(μ-chlorido) $Mn^{II}$ complexes $[Mn(\mu\text{-}Cl)_2(bpy)]_n$ (**6**) and $[Mn(\mu\text{-}Cl)_2(mppma)]_n$ (**7**).[10]

[a] College of Chemistry, Beijing Normal University, Beijing, 100875 China
Fax: +86-10-64463640
E-mail: mashulan@263.net
[b] State Key Laboratory of Rare Earth Materials Chemistry and Application, College of Chemistry and Molecular Engineering, Peking University, Beijing, 100871 China
[c] State Key Laboratory of Structural Chemistry, Fujian Institute of Research on the Structure of Matter, Chinese Academy of Sciences, Fuzhou, Fujian, 350002 China

 © 2007 Wiley-VCH Verlag GmbH & Co. KGaA, Weinheim 

## Results and Discussion

### IR and UV/Vis Spectroscopy

The IR Spectra of Schiff-base ligand HL and complex **1** provide information about the metal–ligand bonding. The strong absorption band at 1624 $cm^{-1}$ in ligand HL is assigned to the azomethine group, $\nu$(C=N).[11] The band is shifted to lower wavenumbers at 1594 $cm^{-1}$ in the complex, which can be attributed to the coordination of the C=N nitrogen atom to metal ions. In addition, the absorption band at 1582 $cm^{-1}$ assigned to the pyridine group of the ligand is shifted to 1562 $cm^{-1}$, suggesting that the coordination of the pyridine nitrogen atom group to metal ions.[12]

The UV-visible spectroscopic data for ligand HL and the complex were studied in MeOH. Schiff-base molecule HL exhibits three maxima centered at 289, 361, and 442 nm. Complex **1** exhibits three maxima centered at 240, 349, and 474 nm. The absorption bands at 200–400 nm in the complex may correspond to ligand-centered (LC) π–π* transitions, while the strong band in the range greater than 400 nm can be ascribed to the ligand-to-metal charge transfer (LMCT) transitions.[13]

### Description of the Structure

Selected bond lengths and angles of **1** are summarized in Table 1. The crystal structure of **1** consists of centrosymmetric double chlorido-bridged $[Mn(HL)(\mu\text{-}Cl)Cl]_2$ dimeric units (Figure 1). One phenolic oxygen O1, one imine nitrogen N1, one pyridine nitrogen N2 from the tridentate neutral ligand, one terminal Cl1, and two bridging $Cl^-$ anions Cl2 and Cl2A (–*x* + 1, –*y* + 1, –*z*) are coordinated to one $Mn^{II}$ ion in an elongated octahedral geometry. The best equatorial plane in the octahedron is defined by O1, N1, N2, and Cl2A set of atoms with the mean deviation of 0.0085 Å, the manganese atom being 0.1168 Å out of this mean plane. The terminal Cl1 atom occupies an axial position *trans* to the Cl2 bridge with a largest bond angle of 175.01° for Cl1–Mn1–Cl2, and a significant axial elongation (2.482 Å for Mn1–Cl1 and 2.606 Å for Mn1–Cl2) are also observed. The two small bite angles subtended at the manganese atom by the chelating ligand (69.94° for O1–Mn1–N1 and 72.92° for N1–Mn1–N2) may be considered the main reason for the distortion of the metal coordination sphere.

The Mn–$N_{imine}$, Mn–$N_{py}$ (py = pyridine), and Mn–$O_{phenol}$ distances are 2.239, 2.279, and 2.313 Å, respectively. The distance of Mn–$N_{imine}$ is close to those noted for other $Mn^{II}$ Schiff-base complexes.[14] The M–$N_{py}$ distance is longer than M–$N_{imine}$, which is comparable to other $Mn^{II}$ Schiff-base complexes.[14c,15]

The bridging $Mn_2Cl_2$ unit is constrained to be planar by the presence of the crystallographic inversion center. This $Mn_2Cl_2$ plane is practically orthogonal with the above equatorial plane O1/N1/N2/Cl2A in the octahedron, the value of the dihedral angle between both planes being 86.6°. The Mn–Cl–Mn angle of 93.80° and the different Mn–Cl distances of 2.451 and 2.606 Å show that the $Mn_2Cl_2$ core is considerably distorted from an ideal square. The two Mn–Cl bonds within the $Mn_2Cl_2$ core lie within the typical range for bridged $Mn^{II}$ chloride atoms (2.31–2.61 Å),[8c,8d,16] being longer than those terminal $Mn^{II}$–chlorido bonds (2.27–2.37 Å)[17] observed in other complexes. The two Mn–$Cl_{bridge}$ bonds in **1** are significantly different, and the terminal Mn–Cl bond (2.482 Å), essentially coplanar with the $Mn_2Cl_2$ core, is between the Mn–$Cl_{bridge}$ bonds, which is divergent from other di-μ-chlorido $Mn^{II}$ complexes containing longer Mn–$Cl_{bridge}$ bonds than Mn–$Cl_{terminal}$ bonds.[8a,18] The intramolecular Mn–Mn distance of 3.694 Å in **1** is shorter than other hexacoordinate dinuclear $Mn^{II}$ compounds with chlorido and nitrogen ligands (3.74–3.85 Å),[8a,8c,8d,18a] which points to a strong effect of the chlorido bridges in **1**. The whole Schiff-base molecule (N1/N2/O1/C1–C13) is merely an approximate plane with a deviation of 0.0695 Å. This distortion from planarity may be due to intermolecular hydrogen bonding interactions. There exist intermolecular hydrogen bonds in **1**. The hydroxy group O1–H1 of the dimer is hydrogen bonded to the Cl1B anion (–*x*, –*y* + 1, –*z*) of one adjacent dimer and forms O1–H1···Cl1B (O1···ClB 3.004 Å, H1···ClB 2.198 Å, and the O1–H1···Cl1B 157.83°), and the Cl1 anion of the

Table 1. Selected bond lengths [Å] and bond angles [°] for complex **1**.

| | | | |
|---|---|---|---|
| Mn1–O1 | 2.313(2) | Mn1–N1 | 2.239(2) |
| Mn1–N2 | 2.279(2) | Mn1–Cl1 | 2.4816(10) |
| Mn1–Cl2 | 2.6062(10) | Mn1–Cl2 #1 | 2.4511(9) |
| Mn1–Mn1 #1[a] | 3.694 | | |
| O1–Mn1–N1 | 69.94(8) | O1–Mn1–N2 | 142.70(8) |
| O1–Mn1–Cl1 | 90.55(6) | O1–Mn1–Cl2 | 84.71(6) |
| O1–Mn1–Cl2 #1 | 116.70(6) | N1–Mn1–N2 | 72.92(9) |
| N1–Mn1–Cl1 | 91.78(6) | N1–Mn1–Cl2 | 88.07(6) |
| N1–Mn1–Cl2 #1 | 170.71(7) | N2–Mn1–Cl1 | 93.93(7) |
| N2–Mn1–Cl2 | 90.80(6) | N2–Mn1–Cl2 #1 | 99.84(7) |
| Cl1–Mn1–Cl2 | 175.01(3) | Cl1–Mn1–Cl2 #1 | 94.56(3) |
| Cl2–Mn1–Cl2 #1 | 86.20(3) | Mn1–Cl2–Mn1 #1 | 93.80(3) |

[a] Symmetry transformations used to generate equivalent atoms: #1 –*x* + 1, –*y* + 1, –z.

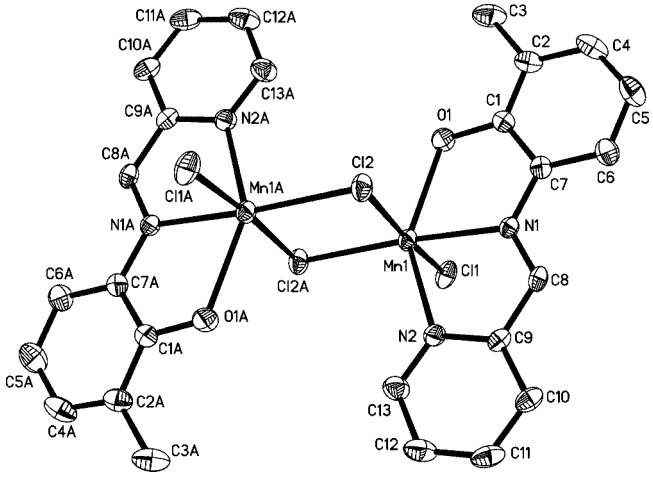


Figure 1. Molecular structure of complex **1** (thermal ellipsoids at 30% probability).

 © 2007 Wiley-VCH Verlag GmbH & Co. KGaA, Weinheim 

present dimer forms a hydrogen bond Cl1···H1B–O1B (–*x*, –*y* + 1, –z) with the hydroxy group of the adjacent unit. The hydroxy group O1A–H1A of the present dimer is again hydrogen-bonded to Cl1D (*x* + 1, *y*, *z*) of another adjacent dimer and forms O1A–H1A···Cl1D, and at the same time the Cl1A anion forms a hydrogen bond Cl1A···H1C–O1C (*x* + 1, *y*, *z*) with the hydroxy of the adjacent unit. As a result, the hydrogen bonds between coordinated $Cl^-$ anions and hydroxy groups tie the coordinated dimeric units together forming a one-dimensional zig–zag chain (Figure 2). In the chain, the shortest interdimer manganese–manganese distance is 5.523 Å for Mn1–Mn1B (–*x*, –*y* + 1, –*z*).

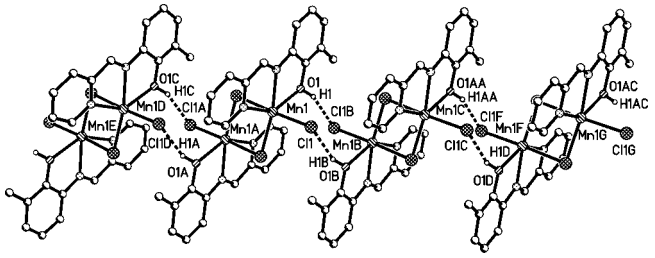


Figure 2. The one-dimensional hydrogen bond chain extending along the *a* axis of **1** (some hydrogen atoms are omitted for clarity).

## Magnetic Properties

Variable temperature magnetic susceptibility on **1** was measured in the range 2.0–300 K (Figure 3). At room temperature, the $\chi_m T$ value for the dinuclear unity is 8.73 $cm^3 mol^{-1} K$, a value which is as expected for two independent spins $S$ = 5/2 (8.75 $cm^3 mol^{-1} K$). Upon cooling from room temperature, $\chi_m T$ increases smoothly at first until around 80 K, below this temperature it increases sharply to reach a maximum of 11.24 $cm^3 mol^{-1} K$ at 6.0 K and then decreases rapidly to 9.70 $cm^3 mol^{-1} K$ at 2.0 K. The $\chi_m^{-1}$ versus $T$ plot is essentially linear, and least-squares fitting of the data to the Curie–Weiss law gave $C$ = 8.72 $cm^3 mol^{-1} K$ and $\theta$ = +1.74 K. The increase in $\chi_m T$ upon cooling and the positive Weiss constant indicates that there exists a ferromagnetic coupling between two $Mn^{II}$ centers in the dimer. The rapid decrease in $\chi_m T$ at lower temperatures is probably due to the weak antiferromagnetic interdimer interaction.[19] This latter contribution is also supported by the field dependence of the magnetization recorded at 2 K (Figure 4) with a magnetization which tends to a saturation value of 9.46 N$\beta$, slightly below the expected saturation value of 10.0 N$\beta$ for two $S$ = 5/2 spins without interactions.[20]

Keeping in mind the structure of **1**, the magnetic data were fitted through Equation (1),[8b,21] which considers both the intradimer and interdimer interactions. The additional coupling parameter, $zJ'$, was added to take into account the magnetic behavior at low temperature as a molecular field approximation.[22]

The best fitting of the data in the temperature range 2–300 K leads to the parameters $g$ = 1.98, $J$ = +0.94 $cm^{-1}$, $zJ'$ = –0.036 $cm^{-1}$. The reliability factor $R$, defined as $R(\chi_m T)$ = $\Sigma(\chi_m T_{obs} - \chi_m T_{calc})^2 / \Sigma(\chi_m T_{obs})^2$, is equal to $9.97 \times 10^{-6}$. The calculated data curve (solid line in Figure 3) matches the experimental magnetic data very well. The results indicate magnetic exchange interactions should mainly pass through the double μ-Cl bridge pathway, which exhibits a ferromagnetic coupling interaction via the double chlorido bridges. The smaller negative $zJ'$ value shows that there exists a weak antiferromagnetic interaction between the $Mn^{II}$ dimers through the intermolecular hydrogen bonding.

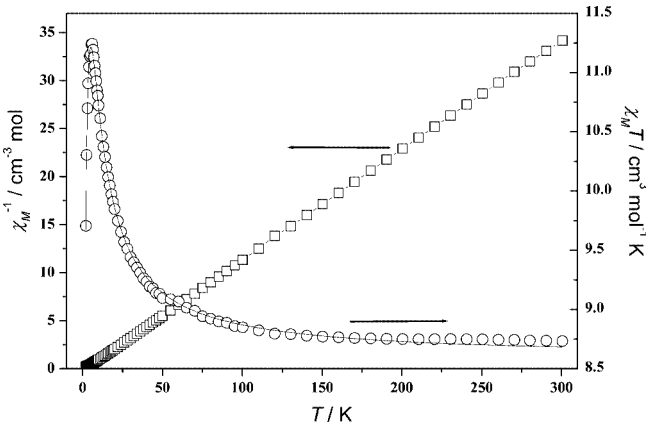


Figure 3. The plot of temperature dependence of $\chi_m^{-1}$ (□) and $\chi_m T$ (○) of **1** measured at 1000 Oe. The solid line represents the best fit of the experimental data as discussed in the text.

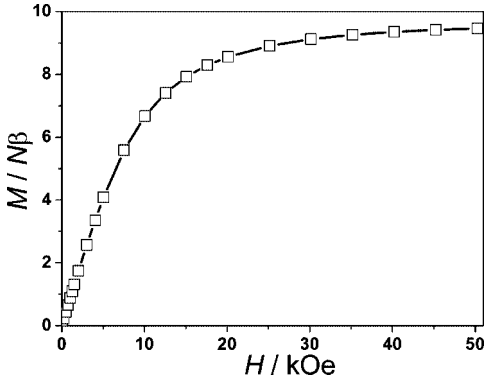


Figure 4. Magnetization vs. field up to $H$ = 50 kOe at 2.0 K. (The solid line is only a guide for the eye and does not indicate fitting).

$$\chi_M = \frac{\chi_t}{1-(2zJ'/Ng^2\beta^2)\chi_t} \quad (1)$$

*where*

$$\chi_t = \frac{2Ng^2\beta^2}{kT} \times \frac{55+30\exp(5x)+14\exp(9x)+5\exp(12x)+\exp(14x)}{11+9\exp(5x)+7\exp(9x)+5\exp(12x)+3\exp(14x)+\exp(15x)}$$

*with* $x = -J/kT$

Ferromagnetic interactions between two $S$ = 5/2 $Mn^{II}$ centers via chlorido bridges is precedented but has not been studied in detail. A spin dimer of $S$ = 5/2 $Mn^{II}$ is expected to exhibit $J$ coupling of at least 25 times less than a spin dimer of $S$ = 1/2 $Cu^{II}$,[23] and thus the values of $J$ of the dichlorido-bridged manganese(II) complexes are usually small as listed in Table 2.

 © 2007 Wiley-VCH Verlag GmbH & Co. KGaA, Weinheim 

Table 2. Structural parameters and magnetic coupling constants for $Mn^{II}$ complexes with a $[Mn_2(\mu\text{-}Cl)_2]^{2+}$ unit.

| Dinuclear complexes[a] | [b] | $a_{Mn-Cl-Mn}$ [°] | $d_{Mn-Mn}$ [Å] | $d_{Mn-Cl}$ [Å] | $J$ [$cm^{-1}$] | Geometry | $\sum\Delta_i^2$ | Ref. |
|---|---|---|---|---|---|---|---|---|
| $[Mn(HL)(\mu\text{-}Cl)Cl]_2$ (**1**) | $L_1$ = Cl | 93.8 | 3.694 | 2.61 | +0.94 | I | | this work |
| | $L_2$ = O | | | 2.45 | | | | |
| $[MnCl(\mu\text{-}Cl)(bpea)]_2$ (**2**) | $L_1$ = N | 95.7 | 3.786 | 2.57 | +0.34 | II | 0.101 | [8a] |
| | $L_2$ = Cl | | | 2.54 | | | | |
| $[Mn(biz)_2(\mu\text{-}Cl)]_2Cl_2$ (**3**) | $L_1$ = N | 93.5 | 3.740 | 2.57 | +0.33 | II | 0.181 | [8c] |
| | $L_2$ = N | | | 2.56 | | | | |
| $[Mn(mpbpa)Cl(\mu\text{-}Cl)]_2$ (**4**) | $L_1$ = N | 96.4 | 3.850 | 2.60 | +0.55 | II | 0.082 | [8d] |
| | $L_2$ = Cl | | | 2.57 | | | | |
| $[Mn(dpp)Cl(\mu\text{-}Cl)(H_2O)]_2$ (**5**) | $L_1$ = Cl | 95.6 | 3.805 | 2.61 | +0.11 | I | 0.021 | [8b] |
| | $L_2$ = O | | | 2.52 | | | | |
| One-dimensional complexes | | | | | | | | |
| $[Mn(\mu\text{-}Cl)_2(bpy)]_n$ (**6**) | $L_1$ = Cl | 96.38 | 3.835 | 2.66 | +0.19 | I | 0.021 | [10a] |
| | $L_2$ = Cl | | | 2.48 | | | | |
| $[Mn(\mu\text{-}Cl)_2(mppma)]_n$ (**7**) | $L_1$ = Cl | 95.4[c] | 3.790[c] | 2.59[c] | –0.25 | II | 0.063 | [10b] |
| | $L_2$ = Cl | | | 2.54[c] | | | | |

[a] Abbreviations: HL = 2-methyl-6-[(pyridine-2-ylmethylene)amino]phenol; bpea = *N*,*N*-[bis(2-pyridylmethyl)ethylamine]; biz = 2,2′-biimidazoline; mpbpa, *N*-(3-methoxypropyl)-*N*,*N*-bis(pyridin-2-ylmethyl)amine; dpp = 2,3-bis(2-pyridyl)pyrazine; bpy = 2,2′-bipyridine; mppma = *N*-(3-methoxypropyl)-*N*-(pyridin-2-ylmethyl)amine. [b] See Scheme 1. [c] Average values of the angles and the distances in the two nonequivalent $[Mn_2(\mu\text{-}Cl)_2]^{2+}$.

Many one-dimensional six-coordinate bis(μ-chlorido)-$Mn^{II}$ polymers are reported and most of them show antiferromagnetic coupling.[10b,24] There are few bis(μ-chlorido)-$Mn^{II}$ dinuclear complexes reported and they exhibit ferromagnetic coupling[8] or antiferromagnetic interaction.[25] Table 2 summarizes some structural parameters and magnetic coupling constants for the dinuclear and one-dimensional dichlorido-bridged complexes with similar structures of **1**. With the aim to compare the magnetic properties of these compounds, the one-dimensional systems have been considered as dinuclear complexes (Scheme 1). In all cases, a rectangular core is observed with two distinct Mn–Cl distances. In a *trans* disposition to one chlorido bridge (with the short Mn–Cl distance), there is a N-ligand, while *trans* to the other chlorido bridge (with long Mn–Cl distance) the L1 ligand could be Cl (for **1**, **5**, **6**, and **7**) or N (for **2**, **3**, and **4**) (Scheme 1). The other two positions of the octahedron are occupied by a N-ligand and by an L2 ligand. For compounds **2**, **4**, **6**, and **7** this ligand (L2) is Cl, while for **3** it is an N-ligand, and for **1** and **5** it is an O-ligand. The different kinds of ligands around the $Mn^{II}$ ions give rise to different distortions in the coordination polyhedron.

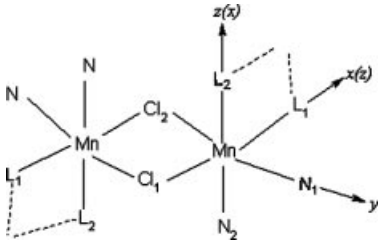


Scheme 1.

There are two types of geometries that have been characterized in the literatures: geometry I has two octahedra sharing an equatorial-to-axial edge with parallel equatorial planes, and geometry II has two octahedra sharing an equatorial edge with coplanar equatorial planes. For compounds **1**, **5**, and **6** with well-differentiated $Mn–Cl_{bridge}$ distances (Table 2), geometry I is often observed, while for compounds as **2**, **3**, **4**, and **7** containing near $Mn–Cl_{bridge}$ values, geometry II is formed. Extended Hückel calculations with the CACAO program for the six complexes (**2**–**7**) showed that for axially elongated compound **6**, the $d_{x^2-y^2}$ orbital of the manganese ions is perpendicular to the $Mn_2Cl_2$ plane and points to one chlorido bridge while the $d_{z^2}$ orbital points to the other bridge. For other compounds with smaller distortion on the octahedron the $d_{x^2-y^2}$ orbitals are in the $Mn_2Cl_2$ plane, and the magnetic interaction may be sensitive to the Mn–Cl–Mn angle.[10a] The different magnetic interaction for the two one-dimensional complexes **6** and **7** with similar structure could be attributed to the major axial elongation on the octahedron present in **6**. Important elongation of the octahedron in our complex **1** is also observed as **6**, and the two $d_{x^2-y^2}$ orbitals of the $Mn^{II}$ ions of **1** may be parallel as in **6**. The $d_{x^2-y^2} \pm d_{x^2-y^2}$ could be quite degenerated, and thus the antiferromagnetic contribution, depending on $\Delta_i$ gaps and the overlap through the bridging ligands, as being shown $J_{AF} \propto \sum\Delta_i^2$, may be smaller, which agrees with the ferromagnetic behavior observed in this case ($J$ = +0.94 $cm^{-1}$). From Table 2 we can see that for the complexes with geometry I, the values of $\sum\Delta_i^2$ are minor, and for those with geometry II, major values of $\sum\Delta_i^2$ are often shown.[10a] There should be certain correlation among the coordination geometry, the disposition of $d_{x^2-y^2}$ orbital of the metal ions, the value of $\sum\Delta_i^2$, and the magnetic interaction.

 © 2007 Wiley-VCH Verlag GmbH & Co. KGaA, Weinheim 

Another complex **5**[8b] also adopts geometry I, but no important elongation on the octahedron is observed as **6**, and the different disposition of $d_{x^2-y^2}$ orbitals may result in its small positive value of *J*.

The sign and magnitude of the coupling constant for $Cu(\mu\text{-}Cl)_2Cu$ dimers depend mainly on the Cu–Cl–Cu bridging angle, the Cu–Cl distance, the nature of the terminal ligands, and the coordination geometry.[26] An important result of the DFT study is that the presence of N-donor terminal ligands seems to favor the ferromagnetic coupling, whereas replacement by halide anions results in the antiferromagnetic behavior.[26b] These results could also explain the magnetic interaction of these chlorido-bridged $Mn^{II}$ complexes. A major value of $\sum\Delta_i^2$ was found for **3** relative to its structurally similar complexes **2** and **4**, and a minor ferromagnetic interaction should be attended. Nevertheless, the major number of N-terminal ligands and the minor Mn–Cl–Mn angle of **3** relative to other compounds may contribute its not small, positive *J* value.

Complex **1** contains quite more differentiated Mn–$Cl_{bridge}$ distances and an obvious axial elongation on the octahedron, which induce the rare octahedral geometry I with parallel equatorial planes and determine the unique disposition of $d_{x^2-y^2}$ orbital of the two $Mn^{II}$ ions. The peculiar geometry and the smallest Mn–Cl–Mn angle and shorter Mn–Mn distance of **1** compared with other compounds may induce its strongest ferromagnetic behavior.

The interesting structure and the novel ferromagnetic behavior of complex **1** might provide useful information for the magneto-structural correlations for dichlorido-bridged $Mn^{II}$ systems in the future. With continued research efforts designed to improve theoretical models and to obtain a greater number of experimental examples, the nature of the relationship between the structural properties and the exchange-coupling constant for these systems can be refined.

## Conclusions

We prepared and characterized dichlorido-bridged $Mn^{II}$ complex **1** with ferromagnetic exchange interactions. Complex **1** is binuclear with a pair of chlorine atoms bridging the manganese atoms in a central $Mn_2Cl_2$ plane, the intramolecular Mn···Mn separation being 3.694 Å. The hydrogen bonds between the coordinated $Cl^-$ anions and hydroxy groups tie the dimeric units together forming a one-dimensional chain. There are two well-differentiated Mn–$Cl_{bridge}$ bonds in the $Mn_2Cl_2$ core and obvious axial elongation on the octahedron of the metal $Mn^{II}$ ion. These structural features induce the geometry I of two octahedra sharing an equatorial-to-axial edge with parallel equatorial planes. This unique geometry may cause a parallel disposition of $d_{x^2-y^2}$ orbitals (and the $d_{z^2}$ orbitals) of the $Mn^{II}$ ions, and minor values of the antiferromagnetic contribution $\sum\Delta_i^2$ could be attended, and thus a ferromagnetic interaction is observed. The smallest Mn–Cl–Mn angle and the shorter Mn–Mn distance of **1** may also induce its maximum *J* value.

## Experimental Section

**General:** All commercially available chemicals were of analytical grade and used as received. C, H, and N analyses were determined with an Elementar vario EL elemental analyzer. UV-visible spectra were measured with a GBC Cintra 10e UV/Vis spectrophotometer in MeOH solution. The IR spectra were recorded with a Nicolet-AVATAR 360 FTIR spectrometer using KBr pellets in the 4000–400 $cm^{-1}$ regions. Variable-temperature magnetic susceptibility data for the crystalline sample of complex **1** was obtained in an external field of 1000 G with an Oxford Maglab 2000 system magnetometer in the 2–300 K temperature range. The susceptibilities were corrected for diamagnetism with Pascal's constants for all the constituent atoms.

**Ligand HL:** A mixture of pyridine-2-carbaldehyde (0.107 g, 1 mmol) and 2-amino-6-methylphenol (0.123 g, 1 mmol) was heated at reflux in anhydrous ethanol (20 mL) for 2 h. After the solvent was removed under reduced pressure, *n*-hexane (20 mL) was then added, and the mixture was heated at reflux for another 0.5 h. The reaction mixture was filtered and left to stand at room temperature and brown crystals were obtained from the filtrate after 15 min. Yield: 0.172 g, 81%. M.p. 95–96 °C. $^1H$ NMR (500 MHz, DMSO): $\delta$ = 8.76 (s, 1 H, phenol-OH), 8.74 (s, 1 H, imide-H), 8.70 (d, *J* = 4.2 Hz, 1 H, pyridine-H), 8.58 (d, *J* = 7.9 Hz, 1 H, pyridine-H), 7.96 (t, *J* = 7.6 Hz, 1 H, pyridine-H), 7.50 (t, *J* = 6.3 Hz, 1 H, pyridine-H), 7.28 (d, *J* = 7.9 Hz, 1 H, Ar-H), 7.08 (d, *J* = 7.3 Hz, 1 H, Ar-H), 6.78 (t, *J* = 7.7 Hz, 1 H, Ar-H), 2.22 (s, 3 H, -$CH_3$) ppm. IR (KBr pellet): $\tilde{\nu}$ = 3402, 3046, 2921, 1624, 1600, 1582, 1566, 1476, 1433, 1344, 1235, 1163, 1082, 1013, 991, 944, 834, 783, 742, 733, 598 $cm^{-1}$. UV/Vis (MeOH): $\lambda$ ($\varepsilon$, $10^4$ $M^{-1}cm^{-1}$) = 289(4.25), 361(4.92), 442(1.50) nm. $C_{13}H_{12}N_2O$ (212.10): calcd. C 73.56, H 5.70, N 13.20; found C 73.57, H 5.92, N 13.22.

**$[Mn(HL)(\mu\text{-}Cl)Cl]_2$ (1):** To a yellow solution of HL (0.011 g, 0.05 mmol) in $CH_2Cl_2$ (5 mL) was added a solution of $MnCl_2{\cdot}4H_2O$ (0.010 g, 0.05 mmol) in $CH_3CH_3OH$ (5 mL) dropwise with stirring for 1 h. The reaction mixture was filtered and left to stand at room temperature. On slow evaporation of the solution for several days, the deep red crystals of **1** suitable for X-ray analysis were collected. IR (KBr pellet): $\tilde{\nu}$ = 3420, 3052, 1594, 1562, 1481, 1373, 1324, 1272, 1209, 1173, 1112, 988, 894, 781, 748, 637,

Table 3. Crystal data and structure refinement details for complex **1**.

| | |
|---|---|
| Empirical formula | $C_{26}H_{24}N_4O_2Cl_4Mn_2$ |
| Formula weight | 676.17 |
| Temperature [K] | 294(2) |
| Wavelength [Å] | 0.71073 |
| Crystal system, space group | triclinic, $P\bar{1}$ |
| *a* [Å], $\alpha$ [°] | 7.6610(18), 70.347(4) |
| *b* [Å], $\beta$ [°] | 9.589(2), 70.320(4) |
| *c* [Å], $\gamma$ [°] | 11.046(3), 74.992(4) |
| Volume [$Å^3$] | 709.8(3) |
| *Z*, Calculated density [$g\,cm^{-3}$] | 1, 1.577 |
| Absorption coefficient [$mm^{-1}$] | 1.297 |
| *F*(000) | 340 |
| Crystal size [mm] | $0.20 \times 0.12 \times 0.08$ |
| $\theta$ range for data collection [°] | 2.04–25.01 |
| Limiting indices | $-8 \le h \le 9$, $-10 \le h \le 11$, $-7 \le h \le 13$ |
| Reflections collected/unique | 3598/2487 [$R_{int}$ = 0.0184] |
| Refinement method | full-matrix least squares on $F^2$ |
| Data/restraints/parameters | 2487/0/173 |
| Goodness of fit on $F^2$ | 1.053 |
| Final *R* indices [$I > 2\sigma(I)$] | $R_1$ = 0.0321, $wR_2$ = 0.0694 |
| *R* indices (all data) | $R_1$ = 0.0572, $wR_2$ = 0.0836 |

 © 2007 Wiley-VCH Verlag GmbH & Co. KGaA, Weinheim 

547 $cm^{-1}$. UV/Vis (MeOH): $\lambda$ ($\varepsilon$, $10^3$ $M^{-1}cm^{-1}$) = 240(11.75), 349(7.73), 474(3.36) nm. $C_{26}H_{24}Cl_4Mn_2N_4O_2$ (676.17): calcd. C 46.14, H 3.55, N 8.28; found C 46.28, H 3.45, N 8.20.

**X-ray Crystallographic Study:** The crystal with dimensions $0.20 \times 0.12 \times 0.08$ mm of **1** was selected for X-ray diffraction experiments. The measurements were performed with a Bruker SMART 1000 CCD diffractometer at room temperature (293 K) with graphite monochromatized *Mo-K*$_\alpha$ radiation ($\lambda$ = 0.71073 Å). Semiempirical absorption corrections were applied using the SADABS program. The structures were solved by direct methods and refined by full-matrix least-squares on $F^2$ using the SHELXS-97 and SHELXL-97 programs.[27] All non-hydrogen atoms were refined with anisotropic displacement parameters and the hydrogen atoms were generated geometrically and treated by a mixture of independent and constrained refinements. A summary of the crystallographic data and details of the structure refinements are listed in Table 3. CCDC-298016 contains the crystallographic data for this paper. These data can be obtained free of charge from The Cambridge Crystallographic Data Centre via www.ccdc.cam.ac.uk/data_request/cif.

## Acknowledgments

This work is supported by the National Natural Science Foundation of China (No. 20671014) and Key Laboratory of Radiopharmaceuticals of Beijing Normal University, Ministry of Education.

[1] a) O. Kahn, *Molecular Magnetism*, VCH, New York, **1993**; b) J. S. Miller, M. Drillon (Eds.), *Magnetism: Molecules to Materials*, Wiley-VCH, Weinheim, **2002**.

[2] a) J. D. Martin, R. F. Hess, *Chem. Commun.* **1996**, 2419–2420; b) H. Nagao, M. Nishino, Y. Shigeta, T. Soda, Y. Kitagawa, T. Onishi, Y. Yoshioka, K. Yamaguchi, *Coord. Chem. Rev.* **2000**, *198*, 265–295.

[3] a) M. A. M. Abu-Youssef, A. Escuer, D. Gatteschi, M. A. S. Goher, F. A. Mautner, R. Vicente, *Inorg. Chem.* **1999**, *38*, 5716–5723; b) E.-Q. Gao, S. Q. Bai, Y.-F. Yue, Z.-F. Wang, C.-H. Yan, *Inorg. Chem.* **2003**, *42*, 3642–3649; c) J. L. Manson, A. M. Arif, J. S. Miller, *Chem. Commun.* **1999**, 1479–1480; d) S. Han, J. L. Manson, J. Kim, J. S. Miller, *Inorg. Chem.* **2000**, *39*, 4182–4185.

[4] a) J. L. Manson, Q.-Z. Huang, J. W. Lynn, H.-J. Koo, M.-H. Whangbo, R. Bateman, T. Otsuka, N. Wada, D. N. Argyriou, J. S. Miller, *J. Am. Chem. Soc.* **2001**, *123*, 162–172; b) A. Escuer, F. A. Mautner, N. Sanz, R. Vicente, *Inorg. Chem.* **2000**, *39*, 1668–1673; c) P. M. van der Werff, S. R. Batten, P. Jensen, B. Moubaraki, K. S. Murray, *Inorg. Chem.* **2001**, *40*, 1718–1722.

[5] a) L. Yang, F. Bian, S.-P. Yan, D.-Z. Liao, P. Cheng, Z.-H. Jiang, *Inorg. Chem. Commun.* **2003**, *6*, 1188–1191; b) Y. Rodriguez-Martin, M. Hernandez-Molina, J. Sanchiz, C. Ruiz-Pérez, F. Lloret, M. Julve, *Dalton Trans.* **2003**, 2359–2365; c) P. S. Mukherjee, S. Konar, E. Zangrando, T. Mallah, J. Ribas, N. R. Chaudhuri, *Inorg. Chem.* **2003**, *42*, 2695–2703; d) S. Durot, C. Policar, G. Pelosi, F. Bisceglie, T. Mallah, J.-P. Mahy, *Inorg. Chem.* **2003**, *42*, 8072–8080.

[6] a) R. Cortes, J. L. Pizarro, L. Lezama, M. I. Arriortua, T. Rojo, *Inorg. Chem.* **1994**, *33*, 2697–2700; b) C.-M. Liu, S. Gao, D.-Q. Zhang, Z.-L. Liu, D.-B. Zhu, *Inorg. Chim. Acta* **2005**, *358*, 834–838.

[7] a) Z. Xu, L. K. Thompson, D. O. Miller, H. J. Clase, J. A. K. Howard, A. Goeta, *Inorg. Chem.* **1998**, *37*, 3620–3627; b) I. A. Koval, M. Huisman, A. F. Stassen, P. Gamez, M. Lutz, A. L. Spek, D. Pursche, B. Krebs, J. Reedijk, *Inorg. Chim. Acta* **2004**, *357*, 294–300; c) S. Koizumi, M. Nihei, H. Oshio, *Chem. Lett.* **2004**, *33*, 896–897.

[8] a) I. Romero, M.-N. Collomb, A. Deronzier, A. Llobet, E. Perret, J. Pécaut, L. Le Pape, J.-M. Latour, *Eur. J. Inorg. Chem.* **2001**, 69–72; b) D. Armentano, G. de Munno, F. Guerra, J. Faus, F. Lloret, M. Julve, *Dalton Trans.* **2003**, 4626–4634; c) G. A. Van Albada, A. Mohamadou, W. L. Driessen, R. De Gelder, S. Tanase, J. Reedijk, *Polyhedron* **2004**, *23*, 2387–2391; d) J.-Z. Wu, E. Bouwman, A. M. Mills, A. L. Spek, J. Reedijk, *Inorg. Chim. Acta* **2004**, *357*, 2694–2702.

[9] P. J. Hay, J. C. Thiebeault, R. Hoffmann, *J. Am. Chem. Soc.* **1975**, *97*, 4884–4899.

[10] a) I. Romero, M. Rodríguez, A. Llobet, M. Corbella, G. Fernández, M.-N. Collomb, *Inorg. Chim. Acta* **2005**, *358*, 4459–4465; b) J.-Z. Wu, S. Tanase, E. Bouwman, J. Reedijk, A. M. Mills, A. L. Spek, *Inorg. Chim. Acta* **2003**, *351*, 278–282.

[11] M. Vázquez, M. R. Bermejo, M. Fondo, A. M. García-Deibe, J. Sanmartín, R. Pedrido, L. Sorace, D. Gatteschi, *Eur. J. Inorg. Chem.* **2003**, 1128–1135.

[12] W. Radecka-Paryzek, V. Patroniak-Krzyminiewska, H. Litkowska, *Polyhedron* **1998**, *17*, 1477–1480.

[13] a) X. H. Bu, M. Du, L. Zhang, Z. L. Shang, R. H. Zhang, M. Shionoya, *J. Chem. Soc. Dalton Trans.* **2001**, 729–735; b) S. L. Ma, W. X. Zhu, Q. L. Guo, Y. C. Liu, M. Q. Xu, *Chin. J. Chem.* **2004**, *22*, 60–63; c) H. Asada, K. Hayashi, S. Negoro, M. Fujiwara, T. Matsushita, *Inorg. Chem. Commun.* **2003**, *6*, 193–196.

[14] a) X. M. Ouyang, B.-L. Fei, T.-A. Okamura, W. Y. Sun, W. X. Tang, N. Ueyama, *Chem. Lett.* **2002**, 362–363; b) Y. Nishida, N. Tanaka, A. Yamazaki, T. Tokii, N. Hashimoto, K. Ide, K. Iwasawa, *Inorg. Chem.* **1995**, *34*, 3616–3620; c) K. Ghosh, A. A. Eroy-Reveles, B. Avila, T. R. Holman, M. M. Olmstead, P. K. Mascharak, *Inorg. Chem.* **2004**, *43*, 2988–2997.

[15] P. S. Mukherjee, T. K. Maji, A. E. Scuer, R. Vicente, J. Ribas, G. Rosair, F. A. Mautner, N. R. Chaudhuri, *Eur. J. Inorg. Chem.* **2002**, 943–949.

[16] a) J. Chai, H. Zhu, H. W. Roesky, C. He, H.-G. Schmidt, M. Noltemeyer, *Organometallics* **2004**, *23*, 3284–3289; b) S. Bieller, M. Bolte, H.-W. Lerner, M. Wagner, *Inorg. Chem.* **2005**, *44*, 9489–9496.

[17] a) T. J. Brunker, T. Hascall, A. R. Cowley, L. H. Rees, D. O'Hare, *Inorg. Chem.* **2001**, *40*, 3170–3176; b) M. Nabika, Y. Seki, T. Miyatake, Y. Ishikawa, K. Okamoto, K. Fujisawa, *Organometallics* **2004**, *23*, 4335–4337.

[18] a) A. Garoufis, S. Kasselouri, S. Boyatzis, C. P. Raptoulou, *Polyhedron* **1999**, *18*, 1615–1620; b) J.-S. Sun, H.-H. Zhao, X. Ouyang, R. Clérac, J. A. Smith, J. M. Clemente-Juan, C. Gómez-Garcia, E. Coronado, K. R. Dunbar, *Inorg. Chem.* **1999**, *38*, 5841–5855; c) G. Pampaloni, U. Englert, *Inorg. Chim. Acta* **1995**, *231*, 167–173.

[19] S. Bhaduri, A. J. Tasiopoulos, M. A. Bolcar, K. A. Abboud, W. E. Streib, G. Christou, *Inorg. Chem.* **2003**, *42*, 1483–1492.

[20] A. Majumder, M. Westerhausen, A. N. Kneifel, J.-P. Sutter, N. Daro, S. Mitra, *Inorg. Chim. Acta* **2006**, *359*, 3841–3846.

[21] D.-G. Huang, X.-F. Zhang, C.-N. Chen, F. Chen, Q.-T. Liu, D.-Z. Liao, L.-C. Li, L.-C. Sun, *Inorg. Chim. Acta* **2003**, *353*, 284–291.

[22] C. J. O'Conner, *Prog. Inorg. Chem.* **1982**, *29*, 203–283.

[23] J. D. Martin, R. F. Hess, P. D. Boyle, *Inorg. Chem.* **2004**, *43*, 3242–3247.

[24] a) R. Caputo, R. D. Willett, B. Morosin, *J. Chem. Phys.* **1978**, *69*, 4976–4983; b) W. Zhang, J. R. Jeitler, M. M. Turnbull, C. P. Landee, M. Wie, R. D. Willett, *Inorg. Chim. Acta* **1997**, *256*, 183–198.

[25] R. D. Willett, *Acta Crystallogr., Sect. B* **1979**, *35*, 178–187.

[26] a) M. Rodríguez, A. Llobet, M. Corbella, *Polyhedron* **2000**, *19*, 2483–2491; b) A. Rodríguez-Fortea, P. Alemany, S. Alvarez, E. Ruiz, *Inorg. Chem.* **2002**, *41*, 3769–3778.

[27] G. M. Sheldrick, *SHELXS-97 and SHELXL-97*, *Program for the Solution and Refinement of Crystal Structures*, University of Göttingen, Göttingen, Germany, **1997**.

Received: February 4, 2007
Published Online: June 19, 2007

 © 2007 Wiley-VCH Verlag GmbH & Co. KGaA, Weinheim 

DOI: 10.1002/ejic.200700223

# Synthesis, Stability Constant Determination, and Structural Study of Some Complexes of a Zinc Triad Containing Pyridyl-amine-quinoline and Pyridyl-thio-quinoline

**Luciano Canovese,*[a] Fabiano Visentin,[a] Gavino Chessa,[a] Carlo Levi,[a] and Alessandro Dolmella[b]**

**Keywords:** Zinc / Quinoline-based ligands / Fluorescence / Formation constants

The potentially fluorescent and terdentate ligands containing nitrogen or sulfur as coordinating atom were synthesized and used in the formation of perchlorate or chloride complexes of the metals of the Zn triad. The reaction of the ligands with metal perchlorate salts yields the corresponding bis-chelate derivatives, whereas the same ligands react with metal chloride salts to give monochelate complexes. All of these complexes undergo NMR-scale fast fluxional rearrangement in solution. Some structural X-ray diffractometric studies were also performed and the ensuing data confirm the surmised structures and the solution rearrangement in the case of monochelate substrates and of one Hg derivative, respectively. The equilibrium constants of formation in the case of monochelate derivatives were also determined in water by means of spectrophotometric titration of the studied ligand with the metal ions. The values of the equilibrium constants were confirmed by supplementary determination taking into account the exchange between two different metals and/or dissociation equilibria. The fluorescence activity of ligands and complexes was eventually studied and notably one fluorescent silent ligand gives rise to fluorescent zinc derivatives.
(© Wiley-VCH Verlag GmbH & Co. KGaA, 69451 Weinheim, Germany, 2007)

## Introduction

The bioactivity of group-12 metal ions is well known, the toxic effects of mercury and cadmium on living organisms being widely recognized.[1] On the contrary zinc is present in traces in many enzymes and consequently it must be considered a bio-compatible metal at least when its concentration is confined within the millimolar range.[2] High concentrations of zinc could, however, entail pollution problems when industrial or human wastes in restricted areas are involved.

In this respect, the synthesis of new ligands with remarkable coordinating capabilities represents an important step for the development of chemical devices for the field monitoring of several metal ions.[3–10] For this reason, we decided to synthesize a series of new polydentate ligands and test their versatility in the identification of the group-12 metals when present in different concentrations and situations.

The synthesized ligands are reported in Scheme 1. We chose to analyze the coordinating capability of the ligands toward proton and metals in distilled water and in the presence of chloride ions since we aim at using these substrates directly in marine or lagoon waters.

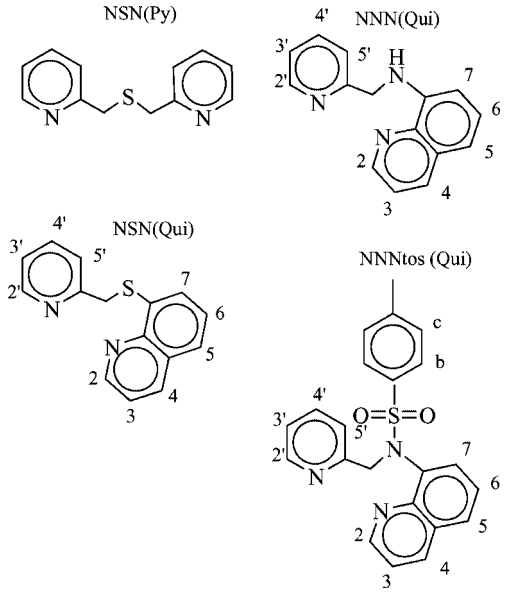


Scheme 1.

It is well known that quinoline displays remarkable properties as a photophysical fluorescent chromophore[11] and as a coordinating agent towards many transition-metal ions.

[a] Department, Dipartimento di Chimica, Università Ca' Foscari, Calle Larga S. Marta 2137, 30123 Venezia, Italy
Fax: +39-412348517
E-mail: cano@unive.it
[b] Dipartimento di Scienze Farmaceutiche, Università di Padova, Via F. Marzolo 5, 35131 Padova, Italy
Supporting information for this article is available on the WWW under http://www.eurjic.org or from the author.

 © 2007 Wiley-VCH Verlag GmbH & Co. KGaA, Weinheim 

Therefore, the synthesis of polydentate ligands bearing quinoline together with other potentially coordinating atoms could represent an important target in a strategy aiming at low cost and easy identification of several analytes.

## Results and Discussion

### General Remarks

Owing to the low solubility of the ligands and related complexes in water, all determinations of equilibrium constants were performed without ionic strength control since any addition of inert salt induces massive precipitation under our experimental conditions (i.e. the solubility of the Hg complexes in 0.01 M $NaClO_4$ dramatically drops to about $1 \times 10^{-6}$ mol dm$^{-3}$). For this reason we have determined the complex formation equilibrium constants by means of the UV/Vis technique, any potentiometric approach being inadequate. We therefore chose to privilege the use of water as solvent instead of controlling the ionic strength in mixed solvents since we expect that the ligands we synthesized should be used as metal probes in natural and waste waters.

### Synthesis of the Ligands

The ligands NSN(Py) {NSN(Py) = 2-[(2-pyridylmethyl)-thio]pyridine},[12a] NNNtos(Qui) [NNNtos(Qui) = 8-*N*-tosyl-*N*-(2-pyridylmethyl)quinoline] and NSN(Qui) [NSN-(Qui) = 8-[(2-pyridylmethyl)thio]quinoline], were synthesized according to published procedures;[12b] the ligand NNN(Qui) {NNN(Qui) = 8-[(2-pyridylmethyl) amino]-quinoline} was obtained by removing the tosyl group from the NNNtos(Qui) moiety by acid hydrolysis with concentrated $H_2SO_4$ at 110 °C.

### Synthesis of the Complexes

#### *Bis-Chelate Complexes*

Addition of the perchlorate salt $M(ClO_4)_2$ (M = Zn, Cd, Hg) to the ligand LL′L′′ [LL′L′′ = NNN(Qui), NNNtos-(Qui), NSN(Qui)] in acetonitrile or methanol yields the corresponding complex of general formula $[M(LL'L'')_2](ClO_4)_2$.

The complexes of Hg and Cd with the ligand NSN are characterized by the down-field shift of the $CH_2S$ protons and the concomitant high-field shift of the aromatic protons $H^2$ and $H^{2'}$. This phenomenon had already been observed,[13] and was traced back to the interactions occurring between the ring currents of the opposite rings of the bis coordinated ligand. A down-field shift of the aromatic protons would be otherwise observed upon ligand coordination. Moreover, in these complexes the $CH_2S$ protons resonate as a singlet and no ($^{199}Hg^1H$) and ($^{111/113}Cd^1H$) coupling even at the lowest temperature achievable (233 K) was observed. The lack of any observable coupling constants could be traced back to the small value of the constant itself or to the rapid exchange of the ligand among complexes. The authors, however, on the basis of their own experience with these kinds of ligands and according to previous observations,[14] are inclined to believe that the ligands in these cases are not firmly bound to the central metal and that a fluxional rearrangement affects these complexes in solution. As a matter of fact, the solid-state structure of the complex $[Hg(NSN)_2(OClO_3)]ClO_4$ was clearly produced by the displacement of one terminus of the potentially terdentate ligand (the quinoline nitrogen) by the oxygen of a perchlorate ion. Usually, the solid-state structure of a species cannot be considered as a warranty of its solution behavior. However, in this case the displacement of a nitrogen terminus must be definitely promoted by the rearrangement of the complex itself in solution. Furthermore, the lack of diastereotopicity of the $CH_2S$ protons indicates that the rate of sulfur absolute configuration inversion is fast with respect to the NMR time scale. The NNN(Qui) derivatives behave very similarly to those of the NSN ligand. Also in these cases no coupling between Hg, Cd, and protons is observed, the aromatic protons $H^2$ and $H^{2'}$ resonate at higher field with respect to the free ligand in both the complexes; no diastereotopicity was observed for $CH_2N$ protons which, however, resonate at field values very similar to those of the free ligand. The complexes $[Zn(LL'L)_2](ClO_4)_2$ [LL′L = NSN(Qui), NNN(Qui)] behave similarly. However, the $H^2$ and $H^{2'}$ protons of the complex $[Zn[NSN(Qui)]_2](ClO_4)_2$ resonate down field with respect to the free ligand, apparently no interference between the ring currents being operative in this case.

The most prominent features of the bis-chelate derivatives of the ligand NNNtos(Qui) are the diastereotopicity of the $CH_2N$ protons and the signals due to the $H^2$ and $H^{2'}$ protons which resonate downfield with respect to the free ligand. The tosyl group in planar tetra-coordinated complexes was shown to lie almost perpendicular to the main complex coordination plane thereby inducing an asymmetry in the $sp^3$ $CH_2N$ protons which give rise to an AB system when the rearrangement movement is slow in the NMR time scale.[12] All the $^1H$ NMR spectra of complexes $[M\{NNNtos(Qui)\}](ClO_4)_2$ (M = Hg, Cd, Zn) display for the $CH_2N$ protons an AB system indicating a slow rearrangement of the tosyl wing around the metal center. The down-field resonance of the aromatic $H^2$ and $H^{2'}$ protons is also detected in the case of Hg and Cd complexes with NNNtos(Qui) but, probably because of the compensating effect of the tosyl fragment which is orthogonal to the complex main plane, no interactions between ring currents are observable.

Moreover, in the cases of the Hg and Cd derivatives, the $^1H$ NMR low-temperature spectra display the $^{199}Hg^1H$ and $^{111/113}Cd^1H$ coupling for the signals due to the $CH_2N$ and $H^2$ and $H^{2'}$ protons.

 © 2007 Wiley-VCH Verlag GmbH & Co. KGaA, Weinheim 

### *Monochelate Dichloro Complexes*

Addition of the ligand LL′L′′ [LL′L′′ = NSN(Qui), NNN(Qui), NNNtos(Qui)] to $MCl_2$ (M = Hg, Cd, Zn) in methanol yields the corresponding monochelate dichloro complexes of general formula $[M(LL'L'')Cl_2]$. In any case a general down-field shift of the ligand signals of the $CH_2S$, $CH_2N$, and aromatic protons is observed upon coordination. The $CH_2N$ shift for both the NNN ligands is less pronounced being almost isochronous with that of the free ligand. The lack of a high-field shift of the $H^2$ and $H^{2'}$ aromatic protons induced by the currents of the opposite rings represents a useful clue to monochelation.

### X-ray Crystal Structure

The ORTEP[15] representations of the complexes $[Hg\{NSN(Qui)\}Cl_2]$ (**1**), $[Hg\{NSN(Qui)\}_2(OClO_3)](ClO_4)$ (**2**), and $[Zn\{NNN(Qui)\}Cl_2]$ (**3**) together with the employed numbering schemes are shown in Figures 1, 2, and 3, respectively. Complexes **1** and **3** are neutral and five-coordinate; complex **2** is cationic and six-coordinate.

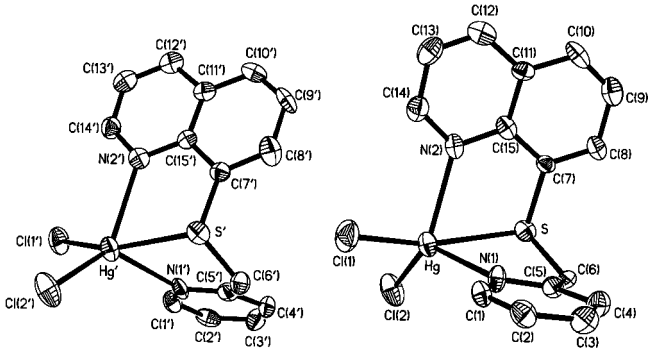


Figure 1. Anisotropic ellipsoid representation of the *TBPY*-5-12-*C* (right) and *TBPY*-5-12-*A* (left) units of complex **1**. The thermal ellipsoids are drawn at the 40% probability level. Hydrogen atoms have been omitted.

Five-coordinate complexes **1** and **3**: In complexes **1** and **3** the environment of the metal is given by a tridentate [NSN(Qui) or NNN(Qui)] ligand and by two chloride ions. Notably, in the unit cell of **1** there are two crystallographically independent complexes that are mirror images without forming, however, an enantiomeric pair (see below). The coordination geometry of both units appears intermediate between square pyramidal (*sp*) and trigonal bipyramidal (*tbp*), while it is square pyramidal in **3**. The $\tau$ angular structural index[16] (ideal values: 0 for *sp* and 1 for *tbp* geometry) was used to measure the deviation from either one of the ideal arrangements in **1** and **3**. In the two units of **1** $\tau$ = 0.59 and $\tau$ = 0.45 (average 0.52), whereas $\tau$ = 0.01 in **3**. Accordingly, we considered the two units of **1** like distorted *tbp* complexes. In this description, the apical positions around Hg are taken by the Cl(1) chloride and by the S atom of the chelate ligand, while the equatorial plane is filled by the Cl(2), N(1), and N(2) atoms. In **3**, the Cl(1) chloride takes the apical position above Zn and the basal plane is filled by the Cl(2), N(1), N(2), and N(3) atoms.

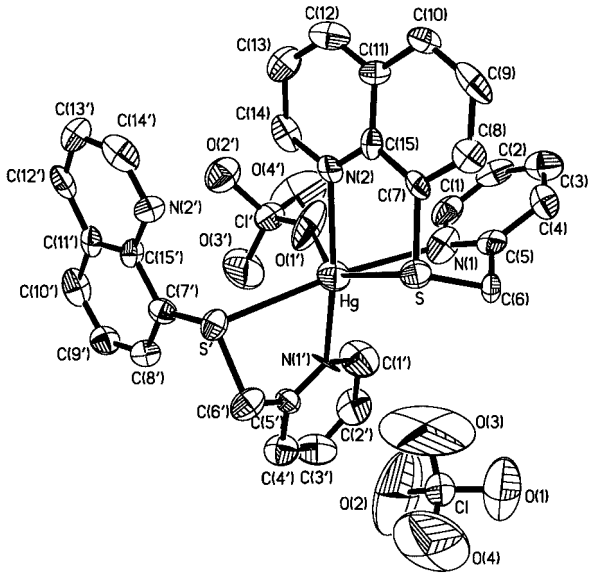


Figure 2. Anisotropic ellipsoid representation of complex **2**. The thermal ellipsoids are drawn at the 40% probability level. Hydrogen atoms have been omitted.

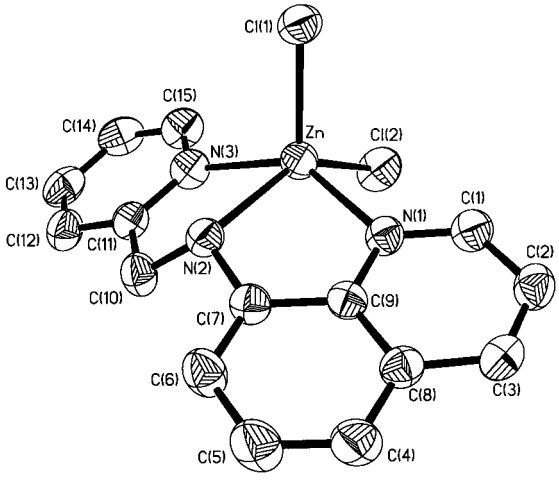


Figure 3. Anisotropic ellipsoid representation of complex **3**. The thermal ellipsoids are drawn at the 40% probability level. Hydrogen atoms have been omitted.

For the sake of clarity, in the remaining part of the discussion the two units of **1** will be named *TBPY*-5-12-*C* and *TBPY*-5-12-*A*, following the IUPAC[17] recommendations for determining the absolute configuration in inorganic compounds and the CIP (Cahn, Ingold, and Prelog) priority rules.[18] As noticed above, the two units are not alike and the difference becomes clear by comparing the angles Cl(1)–Hg–S, N(1)–Hg–N(2) (imposed by chelation), N(1)–Hg–Cl(1), N(2)–Hg–Cl(1), and S–Hg–Cl(2), whose values are 163.1(1), 95.2(3), 97.5(3), 94.6(3), and 90.8(1)° in *TBPY*-5-12-*C* and 156.5(1), 97.2(4), 93.8(3), 89.4(3), and 97.1(1)° in *TBPY*-5-12-*A*, respectively. The Hg atom also deviates from the equatorial plane by 0.42 Å in *TBPY*-5-12-*C* and 0.31 Å in *TBPY*-5-12-*A*. In **3**, the departure of the Zn atom

 © 2007 Wiley-VCH Verlag GmbH & Co. KGaA, Weinheim 

from the basal plane is even larger (0.66 Å) and such deviation implies that all the Cl(1)–Zn–equatorial donor angles are well above 90° (from 104.8 to 111.9°).

Our findings were compared with data taken from the Cambridge Crystallographic Database (CCD).[19] We searched the repository looking for (a) five-coordinate monomeric $Hg^{II}$ complexes containing a thioether ligand, (b) five-coordinate monomeric $Hg^{II}$ complexes containing at least two pyridine-like ligands, (c) five-coordinate $Zn^{II}$ complexes containing at least two pyridine-like ligands and an $N_3Cl_2$ coordination set. Search (a) returned nine entries. In these structures, the $Hg^{II}$–S(thioether) distances vary from 2.491[20] to 2.822[21] Å. The values found in *TBPY*-5-12-*C* and *TBPY*-5-12-*A* [2.759(4) and 2.748(3) Å, respectively] fit in the range and are close to those of the cations described in the literature[21,22] (2.731 and 2.727 Å, respectively).

Search (b) yielded 13 entries, in which the reported $Hg^{II}$–N(pyridyl) distances vary from 2.235[23] to 2.619[24]Å. The values found in *TBPY*-5-12-*C* and *TBPY*-5-12-*A* are 2.350(9), 2.44(1) Å and 2.38(1), 2.44(1) Å, respectively [the longer $Hg^{II}$–N bond always involving N(2)], again within the experimental range, and are similar to those found in the cation reported in ref.[25] (2.363, 2.401 Å) and in the neutral complexes reported in ref.[26] (2.373, 2.400 Å) and ref.[27] (2.372, 2.429 Å). The Hg–Cl distances are 2.455(4), 2.450(3) Å in *TBPY*-5-12-*C* and 2.494(4), 2.428(4) Å in *TBPY*-5-12-*A*. The longer Hg–Cl bond always involves the Cl(1) *trans* to S. These data agree with CCD values for 35 five-coordinate complexes (2.238–3.029 Å).

It is worth noting that complexes in which a five-coordinate $Hg^{II}$ is surrounded at the same time by pyridyl and thioether ligands are rather uncommon.[22,25] Recently, Bebout and co-workers[14] described some zinc triad complexes (with c.n. = 4, 5, or 6) of a symmetric N,S mixed ligand (L) closely related to NSN(Qui). The Hg–N, Hg–S distances found in **1** fit reasonably well with the values quoted by Bebout for six-coordinate $Hg^{II}$ complexes with pyridyl (2.352–2.557 Å) or crown-thioether ligands (2.458–2.751 Å), whereas the Hg–Cl terminal bonds are somewhat longer than those reported for either four-coordinate $Hg(L)Cl_2$ [2.4049(8), 2.4099(8) Å] or five-coordinate $Hg_2(L)Cl_4$ [2.336(2), 2.395(2) Å].[14]

Search (c) returned about 20 entries, but only 11 of these show an aliphatic amine donor atom like **3**. In the reported structures, the Zn–$N_{py}$, Zn–$N_{ali}$ ($N_{py}$ = pyridine nitrogen, $N_{ali}$ = aliphatic amine nitrogen), and Zn–Cl distances vary, respectively, in the ranges 2.039[28]–2.511,[28] 2.129[29]–2.464,[30] and 2.220[30]–2.345[29]Å. In **3**, the Zn–$N_{py}$ bonds are 2.124(3), 2.156(3) Å, Zn–$N_{ali}$ is 2.234(3) Å, and the Zn–Cl distances are 2.252(1) and 2.343(1) Å, respectively. The longer Zn–Cl bond involving the Cl(2) chloride *trans* to the aliphatic amine N(2) appears to be the second longest reported so far after 2.345 Å in ref.[29]. An overall arrangement about Zn similar to that of **3** is found in the complexes described in ref.[31,32] and to a lesser degree in those reported in refs.[29,33]

The chloride ligands of **1** and **3** are involved in a network of nonbonding interactions, which appears to be more extended in **1**. The intermolecular contacts are listed in detail in Table 2SI of the Supporting Information. The packing diagram of **1** also reveals that the quinoline rings of adjacent molecules are stacked in the solid state. The stacking occurs along the crystallographic *a* axis, in a head-to-tail arrangement. The separation between the planes is 3.47 Å as compared to 3.40 Å in graphite.

Six-coordinate complex **2**: In this cation (Figure 2) one of the two NSN(Qui) donors acts as tridentate and the other one as bidentate. The coordination position that is not occupied by the quinolyl N atom is taken by a perchlorate anion. This situation is unusual, and to the best of our knowledge, in the CCD there is no structure of general formula $[M(LL'L)_2]$ (M = six-coordinate metal, L, L′ = N, S or O, LL′L = tridentate ligand forming with the metal two adjacent five-membered rings) showing a similar arrangement. The uncommon coordinating behavior shown by one NSN donor might be due, at the first glance, to somewhat greater steric demand of the perchlorate anion, compared to the chloride one in **1**. However, we also suspect that the expected $[Hg\{NSN(Qui)\}_2](ClO_4)_2$ was represented by the colorless specimen of **2** that we could not characterize by X-ray diffraction (see Experimental Section). We will try to clarify this issue in future investigations.

The coordination environment around Hg is distorted octahedral. The dihedral angle formed by the face N(1), N(2), S with the triangle opposed to it is 30.5° (ideal value = 0°). The base plane is defined by the N(1), N(2), N(1′) and S′ atoms. The largest deviation from this plane is shown by N(1′) (–0.15 Å), while Hg itself deviates by +0.20 Å. The severe distortion of the octahedron is mainly due to the narrow S–Hg–O(1′) angle [144.1(3)°] and to the variability in Hg–N distances. In fact, in the tridentate NSN(Qui) Hg–N(1) 2.63(1) Å, Hg–N(2) 2.28(1) Å, while in the bidentate NSN(Qui) Hg–N(1′) 2.23(1) Å. Likewise, in the tridentate donor, the Hg–S–C(6) and Hg–S–C(7) angles are 97.1 and 96.1°, respectively, while the Hg–S′–C(6′) and Hg–S′–C(7′) angles in the bidentate unit are 87.7 and 113.1°, respectively.

A comparison with existing data was made searching the CCD repository for (a) six-coordinate monomeric $Hg^{II}$ complexes containing a thioether ligand, (b) six-coordinate monomeric $Hg^{II}$ complexes with the metal surrounded by at least four pyridyl ligands. Search (a) returned ten entries, in which the $Hg^{II}$–S(thioether) distance varies between 2.458[34] and 3.050[34]Å. In **2**, there is a shorter and a longer Hg–S bond [2.621(4) Å and 2.749(5) Å], a situation already found by Bebout[14] [bonds of 2.654(1) and 2.671(1) Å] and also quite similar to what was observed in the complexes described in ref.[35] (bonds of 2.654, 2.735, 2.639, 2.751 Å) and ref.[36] (distances of 2.728, 2.638, and 2.712 Å).

Search (b) returned eight entries, with $Hg^{II}$–N(pyridyl) distances ranging from 2.271[37] to 2.685[38]Å. The shorter and longer Hg–N distances found in **2** [2.23(1), 2.28(1), 2.63(1) Å] again fit into the experimental range, with the shorter bond being in fact the shortest Hg–N(pyridyl) bond so far reported, about 0.04 Å shorter than the one reported

 © 2007 Wiley-VCH Verlag GmbH & Co. KGaA, Weinheim 

in ref.[37] (2.271 Å), and the longer one being the second longest after the one found in ref.[38] (2.685 Å). A similar situation with shorter and longer Hg–N distances has been reported by Bebout[14] [2.382(4), 2.409(4) Å, 2.501(4), 2.511(4) Å] as well as in the cation described in ref.[39] (2.351, 2.418, 2.413 Å). Taken all together, these data suggest that the asymmetry of the ligand and the steric requirements of the quinolyl moiety are responsible for the NSN(Qui) donor failing to bind mercury in a bis-tridentate fashion as well as for the variation in the Hg–S, Hg–N bond lengths (Scheme 2).

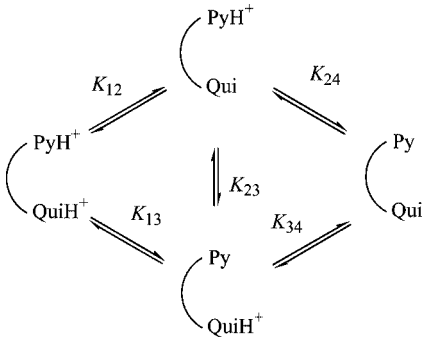


Scheme 2.

It is also worth noting that the perchlorate ligand is rather unusual in $Hg^{II}$ complexes. A search in the CCD returned only five structures, in which the Hg–O distance ranges between 2.569 and 2.932 Å. The only six-coordinate Hg complex reported[13] shows Hg–O distances of 2.569 and 2.650 Å, comparing well with our value of 2.60(1) Å. Like in **1** above, the oxygen atoms of the two perchlorate residues and the quinolyl N atom of the bidentate NSN(Qui) donor are involved in a network of nonbonding interactions. The intermolecular contacts are detailed in Table 2SI.

## Determination of the Acid Dissociation Constants

The determination of the acid dissociation constants of the ligands was performed by potentiometric titration with NaOH (0.1 M) of the conjugated acids of the ligand [NNN(Qui)·3HCl; NSN(Qui)·2HCl; NSN(Py)·2HCl] produced in situ by addition of the stoichiometric amount of HCl (0.1 M) in degassed water at controlled ionic strength (0.1 M, NaCl) under $N_2$ stream. The pH vs. titrant volume data were elaborated by means of routines appropriately written in the SCIENTIST™ environment. The macroconstant and microconstant sets are referred for each ligands to the following general schemes and are reported in Tables 1 and 2, respectively (see Supporting Information).

$LL'L''H_3^{3+} + H_2O \rightleftharpoons LL'LH_2^{2+} + H_3O^+$
$pK_{a3}$ [LL′L″ ⇌ NNN(Qui)]

$LL'L''H_2^{2+} + H_2O \rightleftharpoons LL'LH^+ + H_3O^+$
$pK_{a2}$ [LL′L″ ⇌ NNN(Qui), NSN(Qui), NSN(Py)]

$LL'L''H^+ + H_2O \rightleftharpoons LL'L + H_3O^+$
$pK_{a1}$ [LL′L″ ⇌ NNN(Qui), NSN(Qui), NSN(Py)]

Table 1. Macroconstant set determined by titration with NaOH (0.1 M) of the acid LLL·*n*HCl ($n$ = 2, 3) in degassed water ($I$ = 0.1) at 25 °C.

| LL′L″·*n*HCl | p$Ka_3$ | p$Ka_2$ | p$Ka_1$ |
|---|---|---|---|
| NSN(Py)·2HCl | / | 3.33 ± 0.04 | 5.23 ± 0.02 |
| NSN(Qui)·2HCl | / | 2.98 ± 0.14 | 4.83 ± 0.03 |
| NNN(Qui)·3HCl | <2 | 2.80 ± 0.13 | 4.84 ± 0.02 |

## Determination of the Formation Equilibrium Constants

### *Hg*

The spectrophotometric titration of the ligand NNN(Qui) with $HgCl_2$ was performed in water and resolved by means of the HYPERQUAD™ 2003 program[40] according to the model:

$$Hg^{2+} + 2Cl^- \rightleftharpoons HgCl_2 \quad (1)$$
$\log K_1 = 13.22 \pm 0.2$[41]

$$Hg^{2+} + 2Cl^- + NNN(Qui) \rightleftharpoons [Hg\{NNN(Qui)\}Cl_2] \quad (2)$$
$\log K_2 = 18.56 \pm 0.01$

$$Hg^{2+} + 2Cl^- + 2NNN(Qui) \rightleftharpoons [Hg\{NNN(Qui)\}_2Cl_2] \quad (3)$$
$\log K_3 = 23.52 \pm 0.02$

It is apparent that the formation of the species in solution is influenced by the ligand/Hg ratio and by the equilibrium constants, equilibrium (3) being the most favored at high NNN(Qui)/Hg ratios. The formulation of the complex $[Hg\{NNN(Qui)\}_2Cl_2]$ does not imply any structural preference since several attempts to produce crystals suitable for X-ray collection were unsuccessful and a mixture of uncharacterized products was always obtained. According to the structure of $[Hg\{NSN(Qui)\}_2(OClO_3)](ClO_4)$ (**2**) and to the chloride coordinating characteristics, we suggest that this species could be represented as a neutral six-coordinate octahedral complex bearing two partially coordinated NNN(Qui) fragments and two chlorides. The pH of the unbuffered solution hardly deviates from 6.5 and therefore no protonation equilibrium of the ligand occurs (see Supporting Information) and no formation of mercury hydroxide is observed. Moreover, owing to the stability of the $HgCl_2$ species the equilibrium constants are better described as shown in equations 4 and 5.

Table 2. Microconstant set determined by titration with NaOH (0.1 M) of the acid LL′L″·*n*HCl ($n$ = 2, 3).

| In degassed water ($I$ = 0.1) at 25 °C | p$K_{12}$ | p$K_{13}$ | p$K_{24}$ | p$K_{34}$ | p$K_{23}$ |
|---|---|---|---|---|---|
| NSN(Py)·2HCl | 3.63 ± 0.16 | 3.63 ± 0.16 | 4.93 ± 0.02 | 4.93 ± 0.02 | 0.00 ± 0.03 |
| NSN(Qui)·2HCl | 3.09 ± 0.02 | 3.63 ± 0.04 | 4.72 ± 0.19 | 4.18 ± 0.21 | 0.54 ± 0.06 |
| NNN(Qui)·3HCl | 2.87 ± 0.02 | 3.63 ± 0.04 | 4.77 ± 0.17 | 4.01 ± 0.19 | 0.76 ± 0.06 |

 © 2007 Wiley-VCH Verlag GmbH & Co. KGaA, Weinheim 

$HgCl_2 + NNN(Qui) \rightleftharpoons [\{HgNNN(Qui)\}Cl_2]$ (4)
$\log K_4 = 5.34 \pm 0.21$ ($\log K_4 = \log K_2 - \log K_1$)

$HgCl_2 + 2NNN(Qui) \rightleftharpoons [Hg\{NNN(Qui)\}_2Cl_2]$ (5)
$\log K_5 = 10.30 \pm 0.22$ ($\log K_5 = \log K_3 - \log K_1$)

As a matter of fact the complex $[Hg\{NNN(Qui)\}Cl_2]$ in solution dissociates according to step (4) but at variance with zinc (vide infra) the dissociation constant (ca. $6 \times 10^{-6}$) is badly determined owing to the unfavorable change of absorbance as a function of concentration.

The equilibrium constants between mercury and the NSN ligands were also determined in a similar way and a summary of the results is reported in the following Table 3.

Table 3. Log $K_2$, log $K_3$, log $K_4$, and log $K_5$ for the reaction of $HgCl_2$ with terdentate NNN or NSN ligands in $H_2O$ at 25 °C.

| Ligand | $\log K_2$ | $\log K_3$ | $\log K_4$ | $\log K_5$ |
|---|---|---|---|---|
| NNN(Qui) | $18.56 \pm 0.01$ | $23.52 \pm 0.02$ | $5.34 \pm 0.21$ | $10.30 \pm 0.22$ |
| NSN(Qui) | $18.84 \pm 0.04$ | $23.52 \pm 0.04$ | $5.62 \pm 0.24$ | $10.30 \pm 0.24$ |
| NSN(Py) | $18.60 \pm 0.07$ | $22.95 \pm 0.13$ | $5.38 \pm 0.27$ | $9.73 \pm 0.33$ |

As can be seen the equilibrium constant values are hardly influenced by the nature of the chelating ligands. However, only some complexes of the ligands NNNtos(Qui) and NNN(Qui) display fluorescence activity, the latter being the more soluble species; for this reason we decided to extend our investigation on zinc and cadmium using NNN(Qui) as the complexing agent.

### *Zn*

Analogously to the Hg case the values of the equilibrium constants were determined by direct titration of a ca. $1 \times 10^{-4}$ mol dm$^{-3}$ solution of the ligand NNN(Qui) with $ZnCl_2$. The model fitted by means of the HYPERQUAD™ 2003 program[40] was as shown in equations 1* to 3*.

$Zn^{2+} + 2Cl^- \rightleftharpoons ZnCl_2$ (1*)
$\log K_1^* = 1$[41]

$Zn^{2+} + NNN(Qui) \rightleftharpoons [Zn\{NNN(Qui)\}]^{2+}$ (2*)
$\log K_2^* = 4.58 \pm 0.02$

$Zn^{2+} + 2NNN(Qui) \rightleftharpoons [Zn\{NNN(Qui)\}_2]^{2+}$ (3*)
$\log K_3^* = 8.50 \pm 0.04$

As can be seen, chloride does not compete efficiently with oxygenated ligands ($H_2O$), thus the zinc complexes were written with vacant coordination sites which might be occupied by $H_2O$, $Cl^-$, and $OH^-$, the latter being the less probable since $pK_a\ Zn(H_2O)_x^{2+} \approx 9$.

At variance with mercury, reaction 2* can be checked by studying the dissociation of the complex $[Zn\{NNN(Qui)\}]^{2+}$ taking place upon dilution. In this case the favorable absorbance change allows the determination of $1/K_2^* = 1 \times 10^{-5}$ ($\log K_2^* = 5 \pm 0.5$) which is in substantial agreement with the value of $\log K_2^* = 4.58$ previously determined.

Moreover, it is possible to study the direct exchange between the Hg complex and $Zn(ClO_4)_2$ according to the reaction 4*.

$[Hg\{NNN(Qui)\}Cl_2] + Zn^{2+} \rightleftharpoons [Zn\{NNN(Qui)\}]^{2+} + HgCl_2$ (4*)
$\log K_4^* = -0.92 \pm 0.03$

From reactions 4 and 4* the value of $\log K_2^* = 4.42 \pm 0.24$ is obtained.

It is apparent that an internal consistency among the $K_2^*$ values is achieved. Thus, according to the previous choice the value of $\log K_2^* = 4.58 \pm 0.02$ is assumed.

### *Cd*

The direct exchange between the species $[Zn\{NNN(Qui)\}]^{2+}$ and $Cd^{2+}$ according to the model described below. Reaction 1** can be treated as a combination of 2* and 3**.

$[Zn\{NNN(Qui)\}]^{2+} + Cd^{2+} \rightleftharpoons [Cd\{NNN(Qui)\}]^{2+} + Zn^{2+}$ (1**)

$Zn^{2+} + NNN(Qui) \rightleftharpoons [Zn\{NNN(Qui)\}]^{2+}$ (2*)
$\log K_2^* = 4.58 \pm 0.02$

$Cd^{2+} + NNN(Qui) \rightleftharpoons [Cd\{NNN(Qui)\}]^{2+}$ (3**)
$\log K_3^{**} = 2.99 \pm 0.01$

In this respect from the titration of a dechlorinated solution of $[Zn\{NNN(Qui)\}]^{2+}$ (from $[Zn(NNN(Qui))Cl_2]$ treated with $AgClO_4$) with $Cd(ClO_4)_2$ it is possible to obtain the logarithm of the formation constant $K_3^{**}$ as the refined parameter, the formation constant for zinc $K_2^*$ being held constant ($4.58 \pm 0.02$) throughout the fitting process. The chloride ions were removed from the solution in order to avoid formation of cadmium complexes containing chloride bridges which might complicate the resolution of the system. Moreover, no precipitation problems arise under these conditions.

As an internal check of consistency the direct titration of $Cd^{2+}$ $\{Cd(ClO_4)_2\}$ with NNN(Qui) ligand was also performed and the value of $2.89 \pm 0.01$ for $\log K_3^{***}$ was determined by means of the customary HYPERQUAD™ 2003 program.[40] In the presence of an excess of NNN(Qui) ligand a further equilibrium takes place.

$Cd^{2+} + 2NNN(Qui) \rightleftharpoons [Cd\{NNN(Qui)\}_2]^{2+}$ (4**)
$\log K_4^{**} = 6.31 \pm 0.08$

The independently determined values for $K_3^{***}$ are in good agreement with each other, this fact confirming the model reliability and the consistency of the different approaches.

The equilibrium constants measured in the cases of $Zn^{2+}$ and $Cd^{2+}$ complexes lie among the values reported in the literature when di(2-pyridyl)amine and bis[(2-pyridyl)-methyl]amine are used as ligands.[42] The case of $Hg^{2+}$ complexes turns out to be more difficult to compare since the data in the literature are referred to complexes without chloride. The $\log K_3$ value ($23.52 \pm 0.02$), however, is in substantial agreement with that found by other authors when $Hg(NO_3)_2$ is reacting with bis[(2-pyridyl)methyl]amine.[42] In this respect it is noteworthy that the ionic strength control in the titration of the ligand with $HgCl_2$ is irrelevant since only neutral molecules are involved.

 © 2007 Wiley-VCH Verlag GmbH & Co. KGaA, Weinheim 

The titration spectra and the values of the extinction coefficients are reported in the Supporting Information (Table 3SI).

### Spectroscopic Properties of the Ligands

The spectral features of the ligands NNN(Qui) and NSN(Qui) in different solvents are summarized in Table 4.

Table 4. Absorption and emission ($\lambda_{exc}$ = 320 nm) maxima and fluorescence quantum yields of the ligands NNN(Qui) and NSN(Qui) in different solvents.

| Ligand | Solvent | $\lambda_{abs}$ [nm] | $\lambda_{em}$ [nm] | $\Phi$ |
|---|---|---|---|---|
| NNN(Qui) | *n*-hexane | 260<br>365 | 426 | <0.001 |
| | $CH_3CN$ | 258<br>360 | 489 | 0.020 ± 0.002 |
| | $H_2O$ | 252<br>337 | – | – |
| NSN(Qui) | *n*-hexane | 253<br>340 | 380 | 0.010 ± 0.001 |
| | $CH_3CN$ | 251<br>332 | 420 | 0.020 ± 0.002 |
| | $H_2O$ | 248<br>317 | 453 | 0.10 ± 0.01 |

The most prominent spectral changes observed at increasing solvent polarity for both ligands are the following: *i*) a marked blue shift of the first ππ* absorption band, *ii*) a red shift of the fluorescence emission with a concomitant increase of the Stokes shift, and *iii*) an increase of fluorescence quantum yields. These changes are consistent with a stabilization of both the ground and the first excited singlet state by polar solvents.[43] NNN(Qui) is fluorimetrically silent in $H_2O$; this could be attributed to the occurrence of a bimolecular quenching induced by the formation of an H-bond with the central amine nitrogen.

The water-insoluble NNNtos(Qui) does not show any fluorescence signal in organic solvents, probably because of an intramolecular quenching due to rotation of the tosyl moiety around the N–S bond.

### Fluorescence Properties of the Complexes

Both the complexes [Zn{NNN(Qui)}$Cl_2$] and [Zn{NNNtos(Qui)}$Cl_2$] are soluble and fluorescent in $H_2O$. Probably, metal coordination to the aliphatic nitrogen in [Zn{NNN(Qui)}$Cl_2$] prevents its interaction with the protic solvent;[44] the fluorescence quantum yield, however, is very low ($\Phi < 0.001$). On the contrary, a relatively high quantum yield $\Phi$ is observed for [Zn{NNNtos(Qui)}$Cl_2$], both in $H_2O$ [$\lambda^{max}_{em}$ (nm) = 440; $\Phi$ = 0.050 ± 0.005] and $CH_3CN$ [$\lambda^{max}_{em}$ (nm) = 375; $\Phi$ = 0.020 ± 0.002]. A plausible explanation for this behavior is that steric constraint due to metal–N chelation limits the rotational freedom of the tosyl group, thereby preventing the fluorescence quenching observed for the free ligand.

The fluorescent behavior of the ligand NNN(Qui) has also been studied with $Cd^{2+}$. A mild increase (twofold) of the fluorescent signal at $\lambda_{em}$ = 520 nm has been observed for a Cd/NNN(Qui) ratio of 2000/1. This is probably due to the high spin/orbit coupling constant of $Cd^{2+}$. For the sake of completeness a Table summarizing the photochemical properties of several complexes bearing similar ligands and the related references is reported in the Supporting Information (Table 4SI).

## Conclusions

From the present study it may be deduced that:

a) Bis-chelate complexes of the zinc triad with terdentate and potentially fluorescent ligands of the type NNN or NSN are easily obtained when perchlorate salts of the metals are used in the coordination reaction.

b) Monochelate complexes of the zinc triad with the above-mentioned ligands are easily obtained when chloride salts of the metals are used.

c) Among the X-ray determinations the structure of the complex [Hg{NSN(Qui)}$OClO_3$]$ClO_4$, which is quite unusual, bears witness to the flexibility in solution of this sort of ligand when coordinated to $d^{10}$ metals.

d) The macroscopic and microscopic set of acid dissociation constants for the terdentate NSN and NNN ligands has been determined.

e) The fluorescence of the ligands and of the corresponding metal complexes has been studied. In the case of the fluorescent silent ligands NNN(Qui) and NNNtos(Qui) the corresponding complexes with Zn were shown to be fluorescent.

## Experimental Section

**Solvents and Reagents:** $CH_3CN$, $CH_3OH$, and $H_2SO_4$ were commercial-grade chemicals and were used without further purification. HCl (0.1 M) and NaOH (0.1 M) were prepared by appropriate dilution of NORMEX solutions (Carlo Erba Reagents). $Hg(ClO_4)_2 \cdot 6H_2O$, $Cd(ClO_4)_2 \cdot 6H_2O$ (Alfa-Aesar), $Zn(ClO_4)_2 \cdot 6H_2O$, $AgNO_3$, $HgCl_2$, $CdCl_2 \cdot H_2O$, $ZnCl_2$ (Sigma–Aldrich), and $CD_3CN$ and $CD_3OD$ were commercial-grade reagents and used without further purification.

**IR, NMR, UV/Vis, and Fluorescence Measurements:** IR and $^1H$ and $^{13}C\{^1H\}$ NMR spectra were recorded with a Perkin–Elmer Spectrum One spectrophotometer and a Bruker Avance 300 spectrometer, respectively. The proton and carbon assignment was performed by $^1H$-$^{13}C$-HMQC and HMBC techniques in the case of the bis-chelate complexes $[ML_2](ClO_4)_2$ [M = Zn, Cd, Hg; L = NSN(Qui), NNN(Qui)]. The proton assignment for the chlorinated complexes $[MCl_2]$ [M = Zn, Cd, Hg; L = NSN(Qui), NNN(Qui)] and for all complexes with NNNtos(Qui) as ancillary ligand was achieved by $^1H$-$^1H$-COSY experiment because of their low solubility. UV/Vis spectra were taken with a Perkin–Elmer Lambda 40 spectrophotometer equipped with a Perkin–Elmer PTP6 (Peltier temperature programmer) apparatus. All fluorescence spectra were recorded with a Perkin–Elmer luminescence spectrometer LS 50 ($T$ = 298 K) and fluorescence quantum yields $\Phi_X$ were measured relative to quinine sulfate in $H_2SO_4$ (0.5 M) as a standard and calculated according to the following formula:

 © 2007 Wiley-VCH Verlag GmbH & Co. KGaA, Weinheim 

$$\Phi_X = \Phi_{ST} \frac{S_X}{S_{ST}} \cdot \frac{A_{ST}}{A_X} \cdot \frac{n_X^2}{n_{ST}^2}$$

where $S$ represents the area of the corrected emission fluorescence spectra ($\lambda_{exc}$ = 320 nm), $A$ is the optical density at 320 nm, and $n$ the refractive index of the solvent used.

**Synthesis of Ligands:** The synthesis of the ligands NSN(Py), NSN(Qui), and NNNtos(Qui) was carried out according to the published procedure.[12]

**8-[(Pyridylmethyl)amino]-quinoline NNN(Qui):** To concentrated $H_2SO_4$ (7.5 mL) 8-*N*-tosyl-*N*-(2-pyridylmethyl)quinoline [NNNtos-(Qui)] (2.358 g, 6.05 mmol) was added and the solution was stirred for 2 h at 110 °C. To the resulting mixture a saturated aqueous solution of NaCl (10 mL) and NaOH (6 M, 60 mL) was added. The neutral residue was extracted with $CH_2Cl_2$ and washed with a saturated aqueous solution of NaCl. The organic phase was eventually dried under vacuum. The crude product was purified by flash chromatography through a silica column with a 1:1 $CH_2Cl_2/Et_2O$ mixture as eluent. Concentration under vacuum of the eluate yields 1.088 g (4.62 mmol) of the title compound as a yellow/green oil. Yield 76%. $^1$H NMR ($CD_3CN$, $T$ = 298 K): $\delta$ = aminomethyl protons, 4.66 (d, $J_{CH2-NH}$ = 5.92 Hz, 2 H, pyr-$CH_2$N), amine protons 7.25 (br. s, 1 H, pyr-NH), pyridine and quinoline protons 6.67 (dd, 1 H, 7-$H_{qui}$), 7.11 (dd, $J$ = 7.93 Hz and $J$ = 1.15 Hz, 1 H, 5-$H_{qui}$), 7.27 (dd, $J$ = 4.83 Hz, 1 H, 3′-$H_{pyr}$), 7.36 (t, 1 H, 6-$H_{qui}$), 7.41 (d, 1 H, 5′-$H_{pyr}$), 7.48 (dd, 1 H, 3-$H_{qui}$), 7.72 (td, $J$ = 8.00 and $J$ = 1.75 Hz, 1 H, 4′-$H_{pyr}$), 8.18 (dd, $J$ = 8.33 and $J$ = 1.75 Hz, 1 H, 4-$H_{qui}$), 8.62 (d, 1 H, 2′-$H_{pyr}$), 8.79 (dd, $J$ = 4.17 Hz, 1 H, 2-$H_{qui}$) ppm. $^{13}$C NMR ($CD_3CN$, $T$ = 298 K): $\delta$ = thiomethyl carbon, 48.03 (pyr-$CH_2$N), pyridine C atoms 121.34, 121.59, 122.04 (C-5′$_{pyr}$, C-3′$_{pyr}$, C-3$_{qui}$), 136.54 (C-4′$_{pyr}$), 149.00 (C-2′$_{pyr}$), 158.50 (C-6′$_{pyr}$), quinoline C atoms 104.91 (C-5$_{qui}$), 113.90 (C-7$_{qui}$), 127.63 (C-6$_{qui}$), 128.56 (C-4a$_{qui}$), 138.05 (C-8$_{qui}$), 138.83 (C-4$_{qui}$), 144.36 (C-8a$_{qui}$), 147.14 (C-2$_{qui}$) ppm. $^1$H NMR ($CDCl_3$, $T$ = 298 K): $\delta$ = aminomethyl protons, 4.73 (d, $J$ = 5.8 Hz, 2 H, pyr-$CH_2$N), amine protons 7.03 (br. s, 1 H, pyr-NH), pyridine and quinoline protons 7.09 (dd, $J$ = 8.1 and 1.1 Hz, 1 H, 5-$H_{qui}$), 7.20 (dd, $J$ = 4.7 and = 7.6 Hz, 2 H, 3′-$H_{pyr}$), 7.34 (t, $J$ = 7.5 Hz, 1 H, 6-$H_{qui}$), 7.41 (m, 2 H, 3-$H_{qui}$, 5′-$H_{pyr}$), 7.63 (td, $J$ = 7.6 and 1.8 Hz, 1 H, 4′-$H_{pyr}$), 8.09 (dd, $J$ = 8.3 and 1.7 Hz, 1 H, 4-$H_{qui}$), 8.65 (d, 1 H, 2′-$H_{pyr}$), 8.79 (dd, $J$ = 4.2 Hz, 1 H, 2-$H_{qui}$) ppm. $^{13}$C NMR ($CDCl_3$, $T$ = 298 K): $\delta$ = thiomethyl carbon, 49.1 (pyr-$CH_2$N), pyridine C atoms 121.0, 121.4, 121.9 (C-5′$_{pyr}$, C-3′$_{pyr}$, C-3$_{qui}$), 136.6 (C-4′$_{pyr}$), 149.3 (C-2′$_{pyr}$), 158.9 (C-6′$_{pyr}$), quinoline C atoms 105.2 (C-5$_{qui}$), 114.3 (C-7$_{qui}$), 127.6 (C-6$_{qui}$), 128.6 (C-10$_{qui}$), 138.3 (C-4$_{qui}$), 144.3 (C-9$_{qui}$), 147.0 (C-2$_{qui}$) ppm.

**Synthesis of Bis-Chelate Complexes**

**[Hg[NNN(Qui)]$_2$](ClO$_4$)$_2$:** A solution of $Hg(ClO_4)_2 \cdot 6H_2O$ (0.0861 g, 0.18 mmol) in acetonitrile (4 mL) was added slowly to a stirred solution of NNN(Qui) (0.09 g, 0.38 mmol) in acetonitrile (2 mL). The resulting solution was diluted 1:1 with toluene at 0 °C. The solution was concentrated under reduced pressure and the complex precipitated. The complex was filtered off, washed with toluene, pentane, and dried under vacuum. Cream microcrystals were obtained (0.1224 g, 0.14 mmol). Yield 80%. IR (KBr): $\tilde{\nu}$ = $\nu_{N-H}$ 3289.4, $\nu_{C-H}$ 3048.0, 2920.7, $\nu_{C=N}$ 1613.4, $\nu_{C=C}$ 1512.8, 1445.8, $\nu_{ClO4^-}$ 1090.5 cm$^{-1}$. $^1$H NMR ($CD_3CN$, $T$ = 298 K): $\delta$ = aminomethyl protons, 4.69 (s, 4 H, pyr-*N*-$CH_2$), amine protons, 6.14 (br. s, 2 H, pyr-NH), pyridine and quinoline protons 7.39 (d, $J$ = 8.2 and 4.5 Hz, 2 H, 3-$H_{qui}$), 7.58 (m, 6 H, 6-$H_{qui}$, 7-$H_{qui}$, 3′-$H_{pyr}$), 7.69 (dd, $J$ = 7.35 and 2.3 Hz, 2 H, 5-$H_{qui}$), 7.75 (d, $J$ = 7.9 Hz, 2 H, 5′-$H_{pyr}$), 8.14 (td, $J$ = 7.7 and 1.7 Hz, 2 H, 4′-$H_{pyr}$), 8.25 (m, 4 H, 4-$H_{qui}$, 2-$H_{qui}$), 8.42 (d, $J$ = 4.8 Hz, 2 H, 2′-$H_{pyr}$) ppm. $^{13}$C NMR ($CD_3CN$, $T$ = 298 K): $\delta$ = aminomethyl C atoms, 51.7 (pyr-N-$CH_2$), quinoline C atoms 122.0 (C-3$_{qui}$), 125.2, 125.8 (C-5$_{qui}$, C-7$_{qui}$), 127.39 (C-6$_{qui}$), 128.2 (C-8$_{qui}$), 128.8 (C-10$_{qui}$), 138.9 (C-4$_{qui}$), 139.0 (C-9$_{qui}$), 150.3 (C-2$_{qui}$); pyridine C atoms 122.4 (C-3′$_{pyr}$), 125.8 (C-5′$_{pyr}$), 141.2 (C-4′$_{pyr}$), 149.1 (C-2′$_{pyr}$), 154.6 (C-6′$_{pyr}$) ppm. $C_{30}H_{26}Cl_2HgN_6O_8$: calcd. C 41.41, H 3.01, N 9.66; found C 41.25, H 2.97, N 9.51.

The following complexes were synthesized in an analogous way using the appropriate perchlorate salts.

**[Cd{NNN(Qui)}$_2$](ClO$_4$)$_2$:** Yield 85% (white microcrystals). IR (KBr): $\tilde{\nu}$ = $\nu_{N-H}$ 3251.4, $\nu_{C-H}$ 3078.6, 2931.4, $\nu_{C=N}$ 1613.3, $\nu_{C=C}$ 1511.0, 1440.6, $\nu_{ClO4^-}$ 1107.9 cm$^{-1}$. $^1$H NMR ($CD_3CN$, $T$ = 298 K): $\delta$ = aminomethyl protons, 4.61 (s, 4 H, pyr-N-$CH_2$), amine protons, 5.70 (br. s, 2 H, pyr-NH), pyridine and quinoline protons 7.48 (m, 4 H, 3-$H_{qui}$, 3′-$H_{pyr}$), 7.65 (d, $J$ = 7.7 Hz, 2 H, 5′-$H_{pyr}$), 7.72 (t, 2 H, 6-$H_{qui}$), 7.85 (dd, $J$ = 6.2 Hz, 2 H, 7-$H_{qui}$), 7.90 (dd, $J$ = 8.3 and 1.1 Hz, 2 H, 5-$H_{qui}$), 8.08 (td, $J$ = 7.7 Hz, 2 H, 4′-$H_{pyr}$), 8.20 (dd, $J$ = 4.6 Hz, 2 H, 4-$H_{qui}$), 8.28 (d, $J$ = 4.7 Hz, 2 H, 2′-$H_{pyr}$), 8.45 (dd, $J$ = 8.3 and 1.6 Hz, 2 H, 2-$H_{qui}$) ppm. $^{13}$C NMR ($CD_3CN$, $T$ = 298 K): $\delta$ = aminomethyl C atoms, 53.9 (pyr-N-$CH_2$), quinoline C atoms 122.6 (C-3$_{qui}$), 124.9 (C-7$_{qui}$), 126.4 (C-5$_{qui}$), 127.7 (C-6$_{qui}$), 129.2 (C-10$_{qui}$), 139.6 (C-2$_{qui}$), 139.7 (C-8$_{qui}$), 140.5 (C-9$_{qui}$), 150.3 (C-4$_{qui}$); pyridine C atoms 124.7 (C-5′$_{pyr}$), 125.0 (C-3′$_{pyr}$), 140.6 (C-4′$_{pyr}$), 148.5 (C-2′$_{pyr}$), 155.8 (C-6′$_{pyr}$). $C_{30}H_{26}CdCl_2N_6O_8$: calcd. C 46.08, H 3.35, N 10.75; found C 46.15, H 3.28, N 10.62.

**[Zn{NNN(Qui)}$_2$](ClO$_4$)$_2$:** The precipitation of the complex was induced by addition of toluene to the reaction mixture. Yield 94% (pale yellow microcrystals). IR (KBr): $\tilde{\nu}$ = $\nu_{N-H}$ 3238.6, $\nu_{C-H}$ 3085.0, 2937.8, $\nu_{C=N}$ 1619.7, $\nu_{C=C}$ 1517.4, 1440.6, $\nu_{ClO4^-}$ 1101.5 cm$^{-1}$. $^1$H NMR ($CD_3CN$, $T$ = 298 K): $\delta$ = aminomethyl protons, 4.70 (s, 4 H, pyr-N-$CH_2$), amine protons, 6.01 (br. s, 2 H, pyr-NH), pyridine and quinoline protons 7.52 (m, 6 H, 3-$H_{qui}$, 3′-$H_{pyr}$, 5′-$H_{pyr}$), 7.69 (t, 2 H, 6-$H_{qui}$), 7.81 (br. d, $J$ = 8.1 Hz, 2 H, 7-$H_{qui}$), 7.85 (br. d, $J$ = 8.4 Hz, 2 H, 5-$H_{qui}$), 8.00 (td, $J$ = 7.8 and 1.7 Hz, 2 H, 4′-$H_{pyr}$), 8.43 (d, $J$ = 8.4 Hz, 2 H, 4-$H_{qui}$), 8.49 (br. d, $J$ = 3.7 Hz, 2 H, 2′-$H_{pyr}$), 8.45 (br. d, $J$ = 5.1 Hz, 2 H, 2-$H_{qui}$) ppm. $^{13}$C NMR ($CD_3CN$, $T$ = 298 K): $\delta$ = aminomethyl C atoms, 53.9 (pyr-N-$CH_2$), quinoline C atoms 122.6 (C-3$_{qui}$), 125.9 (C-7$_{qui}$), 126.9 (C-5$_{qui}$), 128.0 (C-6$_{qui}$), 129.0 (C-10$_{qui}$), 139.6 (C-4$_{qui}$), 139.6 (C-8$_{qui}$), 140.6 (C-9$_{qui}$), 149.5 (C-2$_{qui}$); pyridine C atoms 124.9, 125.0 (C-5′$_{pyr}$, C-3′$_{pyr}$), 140.8 (C-4′$_{pyr}$), 147.7 (C-2′$_{pyr}$), 155.2 (C-6′$_{pyr}$) ppm. $C_{30}H_{26}Cl_2N_6O_8Zn$: calcd. C 49.03, H 3.57, N 11.44; found C 48.98, H 3.67, N 11.61.

**[Hg{NSN(Qui)}$_2$](ClO$_4$)$_2$:** A solution (10 mL) of $Hg(ClO_4)_2 \cdot 6H_2O$ (0.2447 g, 0.5 mmol) in methanol was added slowly to a stirred solution of NSN(Qui) (0.2650 g, 1.05 mmol) in methanol (20 mL). Acetonitrile was then added (30 mL). Volume reduction induces the precipitation of the complex which was filtered off, washed with toluene, *n*-hexane and dried under vacuum. White microcrystals were obtained (0.400 g, 0.44 mmol). Yield 88.5%. IR (KBr): $\tilde{\nu}$ = $\nu_{N-H}$ 3251.4, $\nu_{C-H}$ 3078.6, 2931.4, $\nu_{C=N}$ 1613.3, $\nu_{C=C}$ 1511.0, 1440.6, $\nu_{ClO4^-}$ 1107.9 cm$^{-1}$. $^1$H NMR ($CD_3CN$, $T$ = 298 K): $\delta$ = methylthio protons, 4.77 (s, 4 H, pyr-S-$CH_2$), pyridine and quinoline protons 7.35 (t, 2 H, 3′-$H_{pyr}$), 7.46 (d, $J$ = 7.7 Hz, 2 H, 5′-$H_{pyr}$), 7.70 (dd, $J$ = 4.40 and 7.7 Hz, 2 H, 3-$H_{qui}$), 7.86 (m, 4 H, 6-$H_{qui}$, 4′-$H_{pyr}$), 8.21 (d, $J$ = 8.1 Hz, 2 H, 5-$H_{qui}$), 8.38 (d, $J$ = 5.1 Hz, 2 H, 2′-$H_{pyr}$), 8.55 (d, $J$ = 6.6 Hz, 2 H, 7-$H_{qui}$), 8.61 (dd, $J$ = 7.7 and 1.5 Hz, 2 H, 4-$H_{qui}$), 8.79 (d, $J$ = 4.4 Hz, 2 H, 2-$H_{qui}$) ppm. $^{13}$C NMR ($CD_3CN$, $T$ = 298 K): $\delta$ = methylthio C atoms, 42.4 (pyr-S-$CH_2$), quinoline C atoms 122.9 (C-3$_{qui}$), 125.1 (C-10$_{qui}$),

 © 2007 Wiley-VCH Verlag GmbH & Co. KGaA, Weinheim 

128.1 (C-$6_{qui}$), 130.1 (C-$8_{qui}$), 132.5 (C-$5_{qui}$), 139.3 (C-$7_{qui}$), 141.1 (C-$4_{qui}$), 142.1 (C-$9_{qui}$), 152.0 (C-$2_{qui}$); pyridine C atoms 124.9 (C-$3'_{pyr}$), 126.9 (C-$5'_{pyr}$), 140.4 (C-$4'_{pyr}$), 148.9 (C-$2'_{pyr}$), 151.4 (C-$6'_{pyr}$) ppm. $C_{30}H_{24}Cl_2HgN_4O_8S_2$: calcd. C 39.85; H 2.68, N 6.20; found C 40.02, H 2.67, N 6.41.

The following complexes were synthesized in an analogous way using the appropriate ligand and perchlorate salts.

**[Cd{NSN(Qui)}$_2$](ClO$_4$)$_2$:** The complex precipitated soon after addition of $Cd(ClO_4)_2 \cdot 6H_2O$ and no reduction of the volume was necessary. Yield 97% (white microcrystals). IR (KBr): $\tilde{\nu}$ = $\nu_{C-H}$ 3073.7, 2970.8, 2919.3 $\nu_{C=N}$ 1606.6, $\nu_{C=C}$ 1497.4, 1446.0, $\nu_{ClO4^-}$ 1092.1 cm$^{-1}$. $^1$H NMR ($CD_3CN$, $T$ = 298 K): $\delta$ = methylthio protons, 4.74 (s, 4 H, pyr-S-$CH_2$), pyridine and quinoline protons 7.35 (t, 2 H, $3'$-$H_{pyr}$), 7.53 (d, $J$ = 7.7 Hz, 2 H, $5'$-$H_{pyr}$), 7.70 (dd, $J$ = 4.7 and 8.3 Hz, 2 H, 3-$H_{qui}$), 7.88 (m, 4 H, 6-$H_{qui}$, $4'$-$H_{pyr}$), 8.24 (d, $J$ = 8.4 Hz, 2 H, 5-$H_{qui}$), 8.32 (d, $J$ = 5.1 Hz, 2 H, $2'$-$H_{pyr}$), 8.55 (d, $J$ = 7.3 Hz, 2 H, 7-$H_{qui}$), 8.66 (d, $J$ = 8.4 Hz, 2 H, 4-$H_{qui}$), 8.77 (dd, $J$ = 4.7 and 1.8 Hz, 2 H, 2-$H_{qui}$) ppm. $^{13}$C NMR ($CD_3CN$, $T$ = 298 K): $\delta$ = methylthio C atoms, 42.3 (pyr-S-$CH_2$), quinoline C atoms 122.5 (C-$3_{qui}$), 125.89 (C-$10_{qui}$), 128.1 (C-$6_{qui}$), 130.0 (C-$8_{qui}$), 130.0 (C-$5_{qui}$), 139.0 (C-$7_{qui}$), 140.5 (C-$4_{qui}$), 143.5 (C-$9_{qui}$), 152.5 (C-$2_{qui}$); pyridine C atoms 124.8 (C-$3'_{pyr}$), 126.4 (C-$5'_{pyr}$), 140.5 (C-$4'_{pyr}$), 149.1 (C-$2'_{pyr}$), 153.0 (C-$6'_{pyr}$) ppm. $C_{30}H_{24}CdCl_2N_4O_8S_2$: calcd. C 44.16, H 2.96, N 6.87; found C 44.12, H 2.89, N 6.81.

**[Zn{NSN(Qui)}$_2$](ClO$_4$)$_2$:** Yield 91% (white microcrystals). IR (KBr): $\tilde{\nu}$ = $\nu_{C-H}$ 3072.0, 2993.1, 2933.8, $\nu_{C=N}$ 1604.4, $\nu_{C=C}$ 1505.7, 1485.9, 1446.4, $\nu_{ClO4^-}$ 1091.0 cm$^{-1}$. $^1$H NMR ($CD_3CN$, $T$ = 298 K): $\delta$ = methylthio protons, 4.74 (s, 4 H, pyr-S-$CH_2$), pyridine and quinoline protons 7.38 (m, 4 H, $3'$-$H_{pyr}$, $5'$-$H_{pyr}$), 7.70 (dd, $J$ = 4.8 and 8.4 Hz, 2 H, 3-$H_{qui}$), 7.81 (td, $J$ = 7.7 Hz, 2 H, $4'$-$H_{pyr}$), 7.89 (t, $J$ = 7.9 Hz, 2 H, 6-$H_{qui}$), 8.23 (d, 2 H, 5-$H_{qui}$), 8.62 (m, 6 H, $2'$-$H_{pyr}$, 4-$H_{qui}$, 7-$H_{qui}$), 8.94 (d, $J$ = 4.8 Hz, 2 H, 2-$H_{qui}$) ppm. $^{13}$C NMR ($CD_3CN$, $T$ = 298 K): $\delta$ = methylthio C atoms, 42.6 (pyr-S-$CH_2$), quinoline C atoms 123.3 (C-$3_{qui}$), 128.5 (C-$6_{qui}$), 129.7 (C-$8_{qui}$), 132.2 (C-$5_{qui}$), 139.4 (C-$7_{qui}$), 141.2 (C-$4_{qui}$), 143.3 (C-$9_{qui}$), 151.1 (C-$2_{qui}$); pyridine C atoms 125.1 (C-$3'_{pyr}$), 126.3 (C-$5'_{pyr}$), 140.4 (C-$4'_{pyr}$), 147.4 (C-$2'_{pyr}$), 152.3 (C-$6'_{pyr}$) ppm. $C_{30}H_{24}Cl_2N_4O_8S_2Zn$: calcd. C 46.86, H. 3.15, N 7.29; found C 46.72, H 3.21, N 7.31.

**[Hg{NNNtos(Qui)}$_2$](ClO$_4$)$_2$:** The precipitation of the complex was obtained by lowering the temperature (0 °C). Yield 75% (white microcrystals). IR (KBr): $\tilde{\nu}$ = $\nu_{C-H}$ 3099.3, 3061.0, 2933.2, 2862.9, $\nu_{C=N}$ 1604.2, $\nu_{C=C}$ 1508.4, 1457.3, $\nu_{ClO4^-}$ 1093.1 cm$^{-1}$. $^1$H NMR ($CD_3CN$, $T$ = 233 K): $\delta$ = methyl protons, 2.56 (s, 3 H, $CH_3$), aminomethyl protons 4.93, 5.79 (AB system, $J$ = 14.3 and 4.8 Hz, $J^3_{H-Hg}$ = 8.1 Hz, 2 H, pyr-N-$CH_2$), pyridine, quinoline, and aromatic protons 7.26 (m, $J$ = 6.7 Hz, 2 H, 5-$H_{qui}$), 7.55 (m, 7 H, $3'$-$H_{pyr}$, $5'$-$H_{pyr}$, 6-$H_{qui}$, $H_{ar}$), 8.00 (m, 2 H, $4'$-$H_{pyr}$, 3-$H_{qui}$), 8.23 (d, $J$ = 7.3 Hz, 1 H, 7-$H_{qui}$), 8.72 (d, $J$ = 4.8 Hz, 1 H, $2'$-$H_{pyr}$), 8.79 (d, $J$ = 8.4 Hz, 1 H, 4-$H_{qui}$), 8.86 (dd, $J$ = 4.0 and 1.5 Hz, $J^3_{H-Hg}$ = 9.7 Hz, 1 H, 2-$H_{qui}$) ppm. $C_{44}H_{38}Cl_2HgN_6O_{12}S_2$: calcd. C 44.85, H 3.25, N 7.13; found C 44.92, H 3.31, N 7.41.

**[Cd{NNNtos(Qui)}$_2$](ClO$_4$)$_2$:** The precipitation of the complex was obtained by lowering the temperature (0 °C). Yield 87% (white microcrystals). IR (KBr): $\tilde{\nu}$ = $\nu_{C-H}$ 3065.8, 2931.4, 2861.1, $\nu_{C=N}$ 1600.5, $\nu_{C=C}$ 1511.0, $\nu_{ClO4^-}$ 1088.7 cm$^{-1}$. $^1$H NMR ($CD_3CN$, $T$ = 233 K): $\delta$ = methyl protons, 2.56 (s, 3 H, $CH_3$), aminomethyl protons 4.93, 5.93 (AB system, $J$ = 14.1 Hz, $J^3_{H-Cd}$ = 4.3 Hz, 2 H, pyr-N-$CH_2$), pyridine, quinoline, and aromatic protons 7.30 (m, 2 H, $3'$-$H_{pyr}$, 5-$H_{qui}$), 7.57 (m, 6 H, $5'$-$H_{pyr}$, 6-$H_{qui}$, $H_{ar}$), 7.91 (td, $J$ = 7.5 and 1.3 Hz, 1 H, $4'$-$H_{pyr}$), 8.00 (dd, $J$ = 4.4 and 8.3 Hz, 1 H, 3-$H_{qui}$), 8.25 (d, $J$ = 7.9 Hz, 1 H, 7-$H_{qui}$), 8.52 (d, $J$ = 6.0, $J^3_{H-Cd}$ = 9.8 Hz, 1 H, $2'$-$H_{pyr}$), 8.84 (dd, $J$ = 8.1 and 1.1 Hz, 1 H, 4-$H_{qui}$), 8.96 (dd, $J^3_{H-Cd}$ = 6.3 Hz, 1 H, 2-$H_{qui}$) ppm. $C_{44}H_{38}CdCl_2N_6O_{12}S_2$: calcd. C 48.47, H 3.51, N 7.71; found C 48.38, H 3.60, N 7.52.

**[Zn{NNNtos(Qui)}$_2$](ClO$_4$)$_2$:** The precipitation of the complex was obtained by addition of $Et_2O$. Diethyl ether was also used to wash the precipitate. Yield 92% (white microcrystals). IR (KBr): $\tilde{\nu}$ = $\nu_{C-H}$ 3058.6, 2936.2, 2857.3, $\nu_{C=N}$ 1606.7, $\nu_{C=C}$ 1505.3, 1464.8, $\nu_{ClO4^-}$ 1091.4 cm$^{-1}$. $^1$H NMR ($CD_3CN$, $T$ = 227 K): $\delta$ = methyl protons, 2.56 (s, 3 H, $CH_3$), aminomethyl protons 5.00, 5.99 (AB system, $J$ = 14.4 Hz, 2 H, pyr-N-$CH_2$), pyridine, quinoline, and aromatic protons 7.04 (d, $J$ = 7.6 and 1.1 Hz, 2 H, 5-$H_{qui}$), 7.29 (t, 2 H, $3'$-$H_{pyr}$), 7.55 (m, 6 H, $5'$-$H_{pyr}$, 6-$H_{qui}$, $H_{ar}$), 7.94 (td, $J$ = 7.7 and 1.5 Hz, 1 H, $4'$-$H_{pyr}$), 8.10 (dd, $J$ = 5.0 and 8.3 Hz, 1 H, 3-$H_{qui}$), 8.24 (d, $J$ = 8.3 Hz, 1 H, 7-$H_{qui}$), 8.66 (d, $J$ = 5.5 Hz, 1 H, $2'$-$H_{pyr}$), 8.92 (dd, $J$ = 8.4 and 1.3 Hz, 1 H, 4-$H_{qui}$), 8.96 (dd, $J$ = 1.3 Hz, 1 H, 2-$H_{qui}$) ppm. $C_{44}H_{38}Cl_2N_6O_{12}S_2Zn$: calcd. C 50.66, H 3.67, N 8.06; found C 51.01, H 3.57, N 8.12.

### Synthesis of Monochelate Dichloro Complexes

**[Hg{NNN(Qui)}Cl$_2$]:** A solution of $HgCl_2$ (0.065 g, 0.24 mmol) in methanol (2 mL) was added slowly to a stirred solution of NNN(Qui) (0.62 g, 0.26 mmol) in methanol (2 mL). The complex, which precipitated immediately, was filtered off, washed with toluene, pentane, and dried under vacuum. Yellow microcrystals were obtained (0.086 g, 0.17 mmol). Yield 70%. IR (KBr): $\tilde{\nu}$ = $\nu_{N-H}$ 3175.4, $\nu_{C-H}$ 3081.6, 3027.9, 2914.0 $\nu_{C=N}$ 1606.7, $\nu_{C=C}$ 1506.1 cm$^{-1}$. $^1$H NMR ($CD_3OD$, $T$ = 298 K): $\delta$ = aminomethyl protons, 4.71 (s, 2 H, pyr-N-$CH_2$), amine protons, 6.59 (br. s, 1 H, pyr-NH), pyridine and quinoline protons 7.07 (d, $J$ = 7.3 Hz, 1 H, 7-$H_{qui}$), 7.44 (m, 3 H, 5-$H_{qui}$, 6-$H_{qui}$, $3'$-$H_{pyr}$), 7.55 (d, $J$ = 7.7 Hz, 1 H, $5'$-$H_{pyr}$), 7.60 (dd, $J$ = 8.3 Hz, 1 H, 3-$H_{qui}$), 7.89 (td, $J$ = 7.7 and 1.8 Hz, 1 H, $4'$-$H_{pyr}$), 8.31 (dd, $J$ = 1.7 Hz, 1 H, 4-$H_{qui}$), 8.61 (d, $J$ = 4.0 Hz, 1 H, $2'$-$H_{pyr}$), 8.86 (dd, $J$ = 4.2 Hz, 1 H, 2-$H_{qui}$) ppm. $C_{15}H_{13}Cl_2HgN_3$: calcd. C 35.55, H 2.59, N 8.29; found C 35.61, H 2.47, N 8.31.

The following complexes were synthesized in an analogous way using the appropriate ligand and chloride salts.

**[Cd{NNN(Qui)}Cl$_2$]:** Yield 82% (white microcrystals). IR (KBr): $\tilde{\nu}$ = $\nu_{N-H}$ 3144.4, $\nu_{C-H}$ 3045.7, 2927.2, $\nu_{C=N}$ 1604.4, $\nu_{C=C}$ 1505.7, 1479.3 cm$^{-1}$. $^1$H NMR ($CD_3CN$, $T$ = 333 K): $\delta$ = aminomethyl protons, 4.64 (s, 2 H, pyr-N-$CH_2$), amine protons, 5.15 (br. s, 1 H, pyr-NH), pyridine and quinoline protons 7.53 (m, 2 H, $5'$-$H_{pyr}$, $3'$-$H_{pyr}$), 7.75 (m, 2 H, 6-$H_{qui}$, 3-$H_{qui}$), 7.89 (m, 2 H, 5-$H_{qui}$, 7-$H_{qui}$), 7.98 (td, $J$ = 7.7 and 1.7 Hz, 1 H, $4'$-$H_{pyr}$), 8.55 (dd, $J$ = 8.5 and 1.5 Hz, 1 H, 4-$H_{qui}$), 8.81 (d, $J$ = 4.5 Hz, 1 H, $2'$-$H_{pyr}$), 8.86 (dd, $J$ = 4.4 Hz, 1 H, 2-$H_{qui}$) ppm. $C_{15}H_{13}CdCl_2N_3$: calcd. C 43.04, H 3.13, N 10.04; found C 43.09, H 3.20, N 10.11.

**[Zn{NNN(Qui)}Cl$_2$]:** Yield 84% (pale yellow microcrystals). IR (KBr): $\tilde{\nu}$ = $\nu_{N-H}$ 3164.2, $\nu_{C-H}$ 3078.6, 3052.3, 2920.7, 2854.8, $\nu_{C=N}$ 1611.4, $\nu_{C=C}$ 1512.2, 1453.0 cm$^{-1}$. $^1$H NMR ($CD_3CN$, $T$ = 298 K): $\delta$ = aminomethyl protons, 4.70 (br. s, 2 H, pyr-N-$CH_2$), amine protons no signal, pyridine and quinoline protons 7.59 (m, 2 H, $5'$-$H_{pyr}$, $3'$-$H_{pyr}$), 7.78 (m, 2 H, 6-$H_{qui}$, 3-$H_{qui}$), 7.95 (m, 2 H, 5-$H_{qui}$, 7-$H_{qui}$), 7.98 (br. t, $J$ = 7.4 Hz, 1 H, $4'$-$H_{pyr}$), 8.63 (br. d, $J$ = 8.3 Hz, 1 H, 4-$H_{qui}$), 8.95 (br. d, $J$ = 4.7 Hz, 1 H, $2'$-$H_{pyr}$), 9.24 (br. d, $J$ = 3.8 Hz, 1 H, 2-$H_{qui}$) ppm. $C_{15}H_{13}Cl_2N_3Zn$: calcd. C 48.49, H 3.53, N 11.31; found C 48.62, H 3.49, N 11.20.

**[Hg{NSN(Qui)}Cl$_2$]:** Yield 89% (white microcrystals). IR (KBr): $\tilde{\nu}$ = $\nu_{C-H}$ 3027.9, 2954.2, 2880.4 $\nu_{C=N}$ 1600.0, $\nu_{C=C}$ 1499.4, 1486.0, 1439.1 cm$^{-1}$. $^1$H NMR ($CD_3CN$, $T$ = 298 K): $\delta$ = methylthio protons, 4.56 (s, 2 H, pyr-S-$CH_2$), pyridine and quinoline protons 7.38

 © 2007 Wiley-VCH Verlag GmbH & Co. KGaA, Weinheim 

(dd, $J$ = 4.4 and 7.7 Hz, 1 H, 3′-$H_{pyr}$), 7.54 (d, $J$ = 7.7 Hz, 1 H, 5′-$H_{pyr}$), 7.60 (t, $J$ = 8.1 and 7.3 Hz, 1 H, 6-$H_{qui}$), 7.67 (dd, $J$ = 8.4 and 4.4 Hz, 1 H, 3-$H_{qui}$), 7.82 (td, $J$ = 7.7and 1.8 Hz, 1 H, 4′-$H_{pyr}$), 7.90 (d, 1 H, 5-$H_{qui}$), 7.98 (d, 1 H, 7-$H_{qui}$), 8.42 (dd, $J$ = 1.8 Hz, 1 H, 4-$H_{qui}$), 8.63 (d, 1 H, 2′-$H_{pyr}$), 9.06 (dd, 1 H, 2-$H_{qui}$) ppm. $C_{15}H_{12}Cl_2HgN_2S$: C 34.39, H 2.31, N 5.35; found C 34.12, H 2.27, N 5.51.

**[Cd{NSN(Qui)}Cl$_2$]:** Yield 91% (white microcrystals). IR (KBr): $\tilde{\nu}$ = $\nu_{C-H}$ 3072.0, 2966.7, 2907.5 $\nu_{C=N}$ 1597.8, $\nu_{C=C}$ 1499.1, 1485.9, 1459.6 cm$^{-1}$. $^1$H NMR ($CD_3CN$, $T$ = 333 K): $\delta$ = methylthio protons, 4.58 (s, 2 H, pyr-S-$CH_2$), pyridine and quinoline protons 7.35 (m, 2 H, 5′-$H_{pyr}$, 3′-$H_{pyr}$), 7.75 (m, 3 H, 6-$H_{qui}$, 3-$H_{qui}$, 4′-$H_{pyr}$), 8.03 (d, $J$ = 8.1 Hz, 1 H, 5-$H_{qui}$), 8.30 (d, $J$ = 6.9 Hz, 1 H, 7-$H_{qui}$), 8.42 (dd, $J$ = 8.5 and 1.8 Hz, 1 H, 4-$H_{qui}$), 8.83 (d, $J$ = 4.9 Hz, 1 H, 2′-$H_{pyr}$), 9.06 (dd, $J$ = 3.2 Hz, 1 H, 2-$H_{qui}$) ppm. $C_{15}H_{12}CdCl_2N_2S$: calcd. C 41.35, H 2.78, N 6.43; found C 41.22, H 2.87, N 6.45.

**[Zn{NSN(Qui)}Cl$_2$]:** The precipitation of the complex was achieved by volume reduction followed by toluene addition. Yield 86% (white microcrystals). IR (KBr): $\tilde{\nu}$ = $\nu_{C-H}$ 3085.2, 3052.3, 2993.1, 2914.1, 2841.7 $\nu_{C=N}$ 1611.0, $\nu_{C=C}$ 1505.7, 1485.9, 1446.4 cm$^{-1}$. $^1$H NMR ($CD_3CN$, $T$ = 298 K): $\delta$ = methylthio protons, 4.58 (s, 2 H, pyr-S-$CH_2$), pyridine and quinoline protons 7.54 (m, 2 H, 5′-$H_{pyr}$, 6-$H_{qui}$), 7.80 (dd, $J$ = 5.5 and 8.3 Hz, 1 H, 3′-$H_{pyr}$), 7.88 (dd, $J$ = 8.3 and 4.9 Hz, 1 H, 3-$H_{qui}$), 7.99 (td, $J$ = 8.3, 7.7 and 1.6 Hz, 1 H, 4′-$H_{pyr}$), 8.22 (dd, $J$ = 8.3 and 1.4 Hz, 1 H, 5-$H_{qui}$), 8.40 (dd, $J$ = 7.4 Hz, 1 H, 7-$H_{qui}$), 8.70 (dd, $J$ = 1.6 Hz, 1 H, 4-$H_{qui}$), 9.11 (d, 1 H, 2′-$H_{pyr}$), 9.75 (dd, 1 H, 2-$H_{qui}$) ppm. $C_{15}H_{12}Cl_2N_2SZn$: C 46.36, H 3.11, N 7.21; found C 46.43, H 3.07, N 7.26.

**[Hg{NNNtos(Qui)}Cl$_2$]:** Yield 64% (white microcrystals). IR (KBr): $\tilde{\nu}$ = $\nu_{C-H}$ 3068.2, 2914.0 $\nu_{C=N}$ 1606.7, $\nu_{C=C}$ 1519.1 cm$^{-1}$. $^1$H NMR ($CD_3CN$, $T$ = 233 K): $\delta$ = methyl protons, 2.44 (s, 3 H, $CH_3$), aminomethyl protons 4.71 (s, 2 H, pyr-N-$CH_2$), pyridine, quinoline, and aromatic protons 7.29 (d, $J_{b\text{-}c}$ = 8.05 Hz, 2 H, $H_{ar}$), 7.35 (t, $J$ = 5.1 Hz, 1 H, 3′-$H_{pyr}$), 7.55 (m, 4 H, 5-$H_{qui}$, 6-$H_{qui}$, $H_{ar}$), 7.62 (m, 2 H, 5′-$H_{pyr}$, 3-$H_{qui}$), 7.84 (td, $J$ = 8.0, 1.5, and 8.4 Hz, 1 H, 4′-$H_{pyr}$), 7.99 (dd, $J$ = 7.9 and 1.7 Hz, 1 H, 7-$H_{qui}$), 8.43 (dd, $J$ = 8.4 and 1.8 Hz, 1 H, 4-$H_{qui}$), 8.51 (d, 1 H, 2′-$H_{pyr}$), 8.85 (dd, $J$ = 4.4 Hz, 1 H, 2-$H_{qui}$) ppm. $C_{22}H_{19}Cl_2HgN_3O_2S$: calcd. C 39.98, H 2.90, N 6.36; found C 40.02, H 2.87, N 6.39.

**[Cd{NNNtos(Qui)}Cl$_2$]:** Yield 94% (white microcrystals). IR (KBr): $\tilde{\nu}$ = $\nu_{C-H}$ 3072.0, 2966.7, 2868.0 $\nu_{C=N}$ 1604.4, $\nu_{C=C}$ 1512.2, 1453.0 cm$^{-1}$. $^1$H NMR ($CD_3CN$, $T$ = 333 K): $\delta$ = methyl protons, 2.44 (s, 3 H, $CH_3$), aminomethyl protons 5.24 (s, 2 H, pyr-N-$CH_2$), pyridine, quinoline, and aromatic protons 7.33 (d, $J$ = 8.3 Hz, 2 H, $H_{ar}$), 7.42 (m, 4 H, 3′-$H_{pyr}$, 6-$H_{qui}$, $H_{ar}$), 7.54 (d, $J$ = 5.1 Hz, 1 H, 5-$H_{qui}$), 7.61 (d, 1 H, 5′-$H_{pyr}$), 7.72 (dd, $J$ = 4.1 and 8.3 Hz, 1 H, 3-$H_{qui}$), 7.92 (td, $J$ = 6.2 and 1.5 Hz, 1 H, 4′-$H_{pyr}$), 8.03 (dd, $J$ = 8.2 and 1.0 Hz, 1 H, 7-$H_{qui}$), 8.52 (dd, $J$ = 1.5 Hz, 1 H, 4-$H_{qui}$), 8.65 (d, $J$ = 6.2 Hz, 1 H, 2′-$H_{pyr}$), 9.04 (dd, 1 H, 2-$H_{qui}$) ppm. $C_{22}H_{19}CdCl_2N_3O_2S$: calcd. C 46.13, H 3.34, N 7.34; found C 46.21, H 3.24, N 7.42.

**[Zn{NNNtos(Qui)}Cl$_2$]:** Yield 96% (white microcrystals). IR (KBr): $\tilde{\nu}$ = $\nu_{C-H}$ 3065.4, 3032.5, 2960.1, 2927.2 $\nu_{C=N}$ 1617.6, $\nu_{C=C}$ 1512.2, 1492.5, 1439.9 cm$^{-1}$. $^1$H NMR ($CD_3OD$, $T$ = 333 K): $\delta$ = methyl protons, 2.40 (s, 3 H, $CH_3$), aminomethyl protons 5.32 (s, 2 H, pyr-N-$CH_2$), pyridine, quinoline, and aromatic protons 7.22 (d, $J$ = 7.9 Hz, 2 H, $H_{ar}$), 7.27 (td, $J$ = 7.7 and 1.1 Hz, 1 H, 3′-$H_{pyr}$), 7.48 (m, 4 H, 3-$H_{qui}$, 6-$H_{qui}$, $H_{ar}$), 7.59 (dd, $J$ = 7.4 and 1.5 Hz, 1 H, 5-$H_{qui}$), 7.71 (d, $J$ = 7.7 Hz, 1 H, 5′-$H_{pyr}$), 7.81 (td, $J$ = 1.7 Hz, 1 H, 4′-$H_{pyr}$), 7.91 (dd, $J$ = 8.2 Hz, 1 H, 7-$H_{qui}$), 8.31 (dd, $J$ = 8.4 and 1.6 Hz, 1 H, 4-$H_{qui}$), 8.43 (d, $J$ = 4.7 Hz, 1 H, 2′-$H_{pyr}$), 8.73 (dd, 1 H, 2-$H_{qui}$) ppm. $C_{22}H_{19}Cl_2N_3O_2SZn$: calcd. C 50.26, H 3.64, N 7.99; found C 50.32, H 3.73, N 8.05.

**Potentiometric Titrations and Calculations:** The potentiometric determinations were carried out by a Metrohm 654 pH-meter equipped with a Metrohm glass electrode calibrated at 25 °C by means of standard Metrohm buffer solutions (pH 4 and 7). All the measurements were carried out under $N_2$ stream in a thermostatted potentiometric cell.

The appropriate quantity of the ligands NSN(Py), NSN(Qui), and NNN(Qui) were poured into volumetric flasks (250 mL) and the appropriate volumes of HCl (0.1 M) were added to obtain NSN(Py)·2HCl, NSN(Qui)·2HCl, and NNN(Qui)·3HCl, respectively. Addition of NaCl (0.1 M) in water yielded the solutions at pre-determined concentration and ionic strength ([Ligand·$n$HCl] = $1 \times 10^{-3}$ M; $I$ = 0.1 M).

An aliquot (50 mL) of the solution under study was then titrated with NaOH (0.1 M, $I$ = 0.1 M). Evaluation of acid/base constants from the pH values vs. volume of NaOH added, was obtained by routines written using the SCIENTIST™ program. For calculation details see the Supporting Information.

**Spectrophotometric Determination of the Complex Formation Constants:** All the experiments were carried out in water (degassed under $N_2$ stream; pH ≈ 6.5) and in thermostatted (25 °C) flasks. A standard stock of solutions (50 mL; $3 \times 10^{-4}$ M) of the ligands [NNN(Qui), NSN(Qui), and NSN(Py)] was prepared by dissolving a weighted amount of the appropriate ligand in a volumetric flask and diluting to the mark with $H_2O$. The ligand solutions ($7–9 \times 10^{-5}$ M) used in the experiment were then prepared by dilution of the stock solution. The ligand solution was titrated by adding microaliquots of a standard solution of $MCl_2$ (M = Hg, Zn; [$MCl_2$] = 0.01 M) and $Cd(ClO_4)_2$ ([$Cd(ClO_4)_2$] = 0.5 M) by means of a micropipette. The ensuing absorbance values at different wavelengths were recorded at 25 °C and the evaluation of stepwise stability constants from the absorbance vs. volume of $MCl_2$ mL data was achieved by the speculative use of the program HYPERQUAD™.[40] The expected total absorbance value ($A_T$) for each solution is given as $A_T = \Sigma_i \varepsilon_i c_i$, where $\varepsilon_i$ and $c_i$ are the molar extinction coefficient and the concentration of the involved species, respectively. The iterative adjustment of calculated values of $\varepsilon_{ML}$ and $\varepsilon_{ML2}$ and subsequent refinement of the parameters was continued until the correlation matrix was minimized. The values of refined $\varepsilon_L$ are in good agreement with the values measured by the Lambert–Beer experiment. UV/Vis titration spectra are reported in the Supporting Information.

The metal exchange spectrophotometric titrations were performed by addition of a weighted amount of $Zn(ClO_4)_2 \cdot 6H_2O$ ($1 \times 10^{-4} \leq$ [$Zn(ClO_4)_2$] $\leq 1 \times 10^{-2}$ M) or of microaliquots of a standard stock solution (0.01 M) of $Cd(ClO_4)_2 \cdot 6H_2O$ to solutions of [Hg{NNN(Qui)}$Cl_2$] or [Zn{NNN(Qui)}]$^{2+}$ ($1 \times 10^{-4}$ M), respectively. The absorbance values were taken at $\lambda$ = 250 nm. The exchange constants from the absorbance vs. [$M(ClO_4)_2$] values were obtained by routines written using the SCIENTIST™ program. For calculation details see the Supporting Information.

**X-ray Structural Determination:** Well-formed crystals of the complexes [Hg{NSN(Qui)}$Cl_2$] (**1**), [Hg{NSN(Qui)}$_2${$OClO_3$}]($ClO_4$) (**2**), and [Zn{NNN(Qui)}$Cl_2$] (**3**) suitable for X-ray analysis, were mounted on the top of a glass fiber and transferred to either a STADI4 diffractometer equipped with a CCD camera (**1**, **2**) or to a Nonius DIP-1030H system (**3**). The latter was generously made available by colleagues at the Department of Chemical Sciences of the University of Trieste, Italy. During the crystallization process,

 © 2007 Wiley-VCH Verlag GmbH & Co. KGaA, Weinheim 

Table 5. Selected bond lengths [Å] and bond angles [°] for the complexes **1**–**3**.

| | **1** | | **2** | | **3** | |
|---|---|---|---|---|---|---|
| | *TBPY*-5-12-*C* | *TBPY*-5-12-*A* | | | | |
| Hg–Cl(1) | 2.455(4) | 2.494(4) | Hg–S | 2.621(4) | Zn–Cl(1) | 2.252(1) |
| Hg–Cl(2) | 2.450(4) | 2.428(4) | Hg–S′ | 2.749(5) | Zn–Cl(2) | 2.343(1) |
| Hg–S | 2.759(4) | 2.748(3) | Hg–N(1) | 2.63(1) | Zn–N(1) | 2.124(3) |
| Hg–N(1) | 2.350(9) | 2.38(1) | Hg–N(1′) | 2.23(1) | Zn–N(2) | 2.234(3) |
| Hg–N(2) | 2.44(1) | 2.44(1) | Hg–N(2) | 2.28(1) | Zn–N(3) | 2.156(3) |
| | | | Hg–O(1′) | 2.60(1) | | |
| Cl(1)–Hg–Cl(2) | 105.7(1) | 106.0(1) | S–Hg–S′ | 111.4(1) | Cl(1)–Zn–Cl(2) | 111.9(1) |
| Cl(1)–Hg–S | 163.1(1) | 156.5(1) | S–Hg–N(1) | 74.0(3) | Cl(1)–Zn–N(1) | 105.3(1) |
| Cl(1)–Hg–N(1) | 97.5(3) | 93.8(3) | S–Hg–N(1′) | 118.2(4) | Cl(1)–Zn–N(2) | 104.8(1) |
| Cl(1)–Hg–N(2) | 94.6(3) | 89.4(3) | S–Hg–N(2) | 78.0(3) | Cl(1)–Zn–N(3) | 105.9(1) |
| Cl(2)–Hg–S | 90.8(1) | 97.1(1) | S–Hg–O(1′) | 144.1(3) | Cl(2)–Zn–N(1) | 94.6(1) |
| Cl(2)–Hg–N(1) | 128.0(3) | 128.1(3) | S′–Hg–N(1) | 170.6(3) | Cl(2)–Zn–N(2) | 143.2(1) |
| Cl(2)–Hg–N(2) | 127.6(2) | 129.7(3) | S′–Hg–N(1′) | 76.3(3) | Cl(2)–Zn–N(3) | 92.6(1) |
| S–Hg–N(1) | 74.7(3) | 74.7(3) | S′–Hg–N(2) | 105.2(3) | N(1)–Zn–N(2) | 77.0(1) |
| S–Hg–N(2) | 71.6(3) | 72.2(3) | S′–Hg–O(1′) | 101.4(3) | N(1)–Zn–N(3) | 142.6(1) |
| N(1)–Hg–N(2) | 95.2(3) | 97.2(4) | N(1)–Hg–N(1′) | 94.5(4) | N(2)–Zn–N(3) | 75.3(1) |
| | | | N(1)–Hg–N(2) | 83.2(4) | | |
| | | | N(1)–Hg–O(1′) | 75.7(4) | | |
| | | | N(1′)–Hg–N(2) | 162.4(4) | | |
| | | | N(1′)–Hg–O(1′) | 82.7(4) | | |
| | | | N(2)–Hg–O(1′) | 79.9(4) | | |

complex **2** forms crystals that are either colorless or ruby-red. The data presented here refer to the ruby-red specimen, as the colorless crystals proved inadequate for the X-ray experiment.

The X-ray diffraction data were collected at room temperature using graphite-monochromatized Mo-$K_\alpha$ radiation ($\lambda$ = 0.71073 Å) and corrected for Lorentz and polarization effects (**1**–**3**) and for absorption (**1**, **2**). For **3**, a total of 36 frames were collected, each with a rotation of 6° about $\phi$, an exposure time of 20 min, and the detector position at 90 mm from the crystal, whereas data reduction and cell refinement were carried out using the programs DENZO and SCALEPACK.[45] The structures were solved by means of the heavy-atom methods (**1**, **2**) or the direct methods (**3**), using the SHELXTL-NT package,[46] and were refined by full-matrix least-squares procedure on $F^2$ with the SHELXL-97[47] program. Scattering factors incorporated in SHELXL-97 were used; no empirical extinction corrections were applied.

In the last cycles of refinement of **1** and **3**, all the non-H atoms were allowed to vibrate anisotropically. In **2** the ratio between the number of observed reflections and the number of parameters was unsatisfactory. Accordingly, the atoms belonging to the inner coordination core were refined anisotropically, while the remaining non-H atoms were refined isotropically. As for H atoms, in **1** and **2** they were placed in idealized positions and refined with the "riding model." In both structures the $U_{iso}$ values of hydrogen atoms were set at 1.2 times $U_{eq}$ of the appropriate carrier atom. In **3**, the H atoms were refined isotropically. The crystal data and refinement parameters of the three complexes are summarized in the Supporting Information (Table 1SI); none of the structures revealed any anomalous feature. Selected interatomic distances and angles are shown in Table 5.

CCDC-642237 to -642239 contain the supplementary crystallographic data for this paper. These data can be obtained free of charge from The Cambridge Crystallographic Data Centre via www.ccdc.cam.ac.uk/data_request/cif.

**Supporting Information** (see also the footnote on the first page of this article): Details on acidity macro- and micro-constant and stability constant determination, UV/Vis spectra of the spectrophotometric titrations, X-ray crystallographic data.

## Acknowledgments

The authors gratefully acknowledge the Colleagues of the Dipartimento di Scienze Chimiche of the University of Trieste (Italy), Profs. L. Randaccio, E. Zangrando, and S. Geremia, for kindly allowing access to their instrumentation for the X-ray diffraction data collection of complex **3**. We also thank Dr. F. Ricchelli of the Dipartimento di Scienze Biologiche of the University of Padova (Italy) and Dr. Peter Nikolai of the Bulgarian Academy of Sciences for the helpful discussion and suggestions about the photochemical properties of the ligands and complexes.

[1] a) M. Patra, N. Bhowmik, B. Bandopadhyay, A. Sharma, *Environ. Exp. Bot.* **2004**, *52*, 199; b) K. Vig, M. Megharaj, N. Sethunathan, R. Naidu, *Adv. Environ. Res.* **2003**, *8*, 121.
[2] D. A. Suhy, T. V. O'Halloran in *Metal-responsive Gene Regulation and the Zinc Metalloregulatory Model* (Eds: A. Sigel, H. Sigel), Marcel Dekker, Basel, **1996**, vol. 32, p. 557.
[3] E. Bakker, P. Bühlmann, E. Pretsch, *Chem. Rev.* **1997**, *97*, 3083.
[4] P. Bühlmann, E. Pretsch, E. Bakker, *Chem. Rev.* **1998**, *98*, 1593.
[5] O. S. Wolfbeis in *Biomedical Optical Instrumentation and Laser-assisted Biotechnology*, Kluwer Academic Publisher, Dordrecht, **1996**, pp. 327–337.
[6] U. E. Spichiger-Keller in *Chemical Sensors and Biosensors for Medical and Biological Application*, Wiley-VCH, Weinheim, **1997**.
[7] A. W. Czarnik (Ed.) in *Fluorescent Chemosensors for Ion and Molecule Recognition*, ACS Symposium Series 538, ACS, Washington, DC, **1992**.
[8] A. P. de Silva, H. Q. N. Gunaratne, T. Gunnlaugsson, A. J. M. Huxley, C. P. Mc Coy, C. P. J. T. Rademacher, T. E. Rice, *Chem. Rev.* **1997**, *97*, 1515.
[9] B. Valeur, I. Leray, *Coord. Chem. Rev.* **2000**, *205*, 3.
[10] a) C. Bargossi, M. C. Fiorini, M. Montalti, L. Prodi, N. Zaccheroni, *Coord. Chem. Rev.* **2000**, *208*, 17; b) L. Prodi, F. Bolletta, M. Montalti, N. Zaccheroni, *Coord. Chem. Rev.* **2000**, *205*, 59; c) M. Montalti, L. Prodi, N. Zaccheroni in *Handbook of Photochemistry and Photobiology* (Eds.: M. S. A. Abdel-Mottaleb, H. S. Nalwa), American Institute of Physics, Stevenson Ranch, **2003**, *3*, 271–371.

 © 2007 Wiley-VCH Verlag GmbH & Co. KGaA, Weinheim 

[11] a) C. J. Fahrni, T. V. O'Halloran, *J. Am. Chem. Soc.* **1999**, *121*, 11448; b) R. B. Thompson, *Curr. Opin. Chem. Biol.* **2005**, *9*, 526.
[12] a) L. Canovese, F. Visentin, G. Chessa, A. Niero, P. Uguagliati, *Inorg. Chim. Acta* **1999**, *293*, 44; b) L. Canovese, F. Visentin, G. Chessa, P. Uguagliati, C. Levi, A. Dolmella, G. Bandoli, *Organometallics* **2006**, *25*, 5355.
[13] D. C. Bebout, A. E. DeLanoy, D. E. Ehmann, M. E. Kastner, D. A. Parrish, R. J. Butcher, *Inorg. Chem.* **1998**, *37*, 2952.
[14] S. M. Berry, D. C. Bebout, R. J. Butcher, *Inorg. Chem.* **2005**, *44*, 27.
[15] C. K. Johnson, *ORTEP*, Report ORNL-5138, Oak Ridge National Laboratory, Oak Ridge, TN, **1976**.
[16] A. W. Addison, T. N. Rao, J. Reedijk, J. R. Rijn, G. C. Verschoor, *J. Chem. Soc. Dalton Trans.* **1984**, 1349.
[17] IUPAC Provisional Recommendations, Nomenclature of Inorganic Chemistry, Draft March **2004**, available at www.IUPAC.org.
[18] a) R. S. Cahn, C. Ingold, V. Prelog, *Angew. Chem. Int. Ed. Engl.* **1966**, *5*, *385*, 511; b) V. Prelog, G. Helmchen, *Angew. Chem. Int. Ed. Engl.* **1982**, *21*, 567.
[19] F. H. Allen, *Acta Crystallogr., Sect. B* **2002**, *58*, 380–388; Cambridge Structural Database (Version 5.26 of November **2004** + two updates).
[20] A. J. Blake, E. C. Pasteur, G. Reid, M. Schroder, *Polyhedron* **1991**, *10*, 1545 (refcode VUGHEK).
[21] J. Pickardt, L. von Chrzanowski, R. Steudel, M. Borowski, *Z. Naturforsch. B:. Chem. Sci.* **2004**, *59*, 1077 (refcode QAHNIX).
[22] M. E. Sobhia, K. Panneerselvam, K. K. Chacko, I. Suh, E. Weber, C. Reutel, *Inorg. Chim. Acta* **1992**, *194*, 93 (refcode KUSMAM).
[23] J. Halfpenny, *Acta Crystallogr., Sect. B* **1982**, *38*, 2049 (refcode BICMUV).
[24] E. R. T. Tiekink, *Z. Kristallogr. - New Cryst. Struct.* **2001**, *216*, 439 (refcode MIVJEG).
[25] M. Vetrichelvan, L.-H. Lai, K. F. Mok, *Eur. J. Inorg. Chem.* **2004**, 2086 (refcode AXOJAY).
[26] D. C. Craig, Y. Farhangi, D. P. Graddon, N. C. Stephenson, *Cryst. Struct. Commun.* **1974**, *3*, 155 (refcode BBPYHG).
[27] D. Matkovic-Calogovic, N. Davidovic, Z. Popovic, Z. Zugaj, *Acta Crystallogr., Sect. C* **1998**, *54*, 1766 (refcode SAVQOV).
[28] T.-F. Liu, H.-K. Lin, S.-R. Zhu, Z.-M. Wang, H.-G. Wang, H.-W. Sun, X.-B. Leng, Y.-T. Chen, *J. Mol. Struct.* **2002**, *605*, 117 (refcode UHARIE).
[29] M. Pitie, C. Boldron, H. Gornitzka, C. Hemmert, B. Donnadieu, B. Meunier, *Eur. J. Inorg. Chem.* **2003**, 528 (refcode WUTFAS).
[30] A. Angeloff, J.-C. Daran, J. Bernadou, B. Meunier, *Eur. J. Inorg. Chem.* **2000**, 1985 (refcode DUHHAP).
[31] A. Hazell, C. J. McKenzie, L. P. Nielsen, *J. Chem. Soc. Dalton Trans.* **1998**, 1751 (refcode NOZGOY).
[32] D. Schnieders, M. Merkel, S. M. Baldeau, B. Z. Krebs, *Z. Anorg. Allg. Chem.* **2004**, *630*, 1210 (refcodes OBOCIS, OBOCOY).
[33] E. Amadei, M. Carcelli, S. Ianelli, P. Cozzini, P. Pelagatti, C. Pelizzi, *J. Chem. Soc. Dalton Trans.* **1998**, 1025 (refcode PULPAN).
[34] M. Herceg, B. Matkovic, D. Sevdic, D. Matkovic-Cologovic, A. Nagl, *Croat. Chem. Acta* **1984**, *57*, 609 (refcode CUYNAL).
[35] A. J. Blake, G. Reid, M. Schroder, *Polyhedron* **1990**, *9*, 2931 (refcode VOBSEK).
[36] A. J. Blake, A. J. Holder, T. I. Hyde, G. Reid, M. Schroder, *Polyhedron* **1989**, *8*, 2041 (refcode KIFCAD).
[37] D. Matkovic-Calogovic, Z. Popovic, B. Korpar-Colig, *J. Chem. Crystallogr.* **1995**, *25*, 453 (refcode ZUWPEM).
[38] M. Saladini, L. Menabue, E. Ferrari, D. Iacopino, *J. Chem. Soc. Dalton Trans.* **2001**, 1513 (refcode QIXSUL).
[39] C. J. Baylies, L. P. Harding, J. C. Jeffery, T. Riis-Johannessen, C. R. Rice, *Angew. Chem. Int. Ed.* **2004**, *43*, 4515 (refcode IBIWAS).
[40] P. Gans, A. Sabatini, A. Vacca, *Talanta* **1996**, *43*, 1739.
[41] A. E. Martell, R. M. Smith in *Critical Stability Constants*, Plenum Press, New York, **1977**, vol. 3.
[42] a) A. E. Martell, R. M. Smith in *Critical Stability Constants*, Plenum Press, New York, **1977**, vol. 4; b) G. Anderegg, E. Hubmann, N. G. Podder, F. Wenk, *Helv. Chim. Acta* **1977**, *60*, 123.
[43] a) J. R. Lakowicz in *Principles of Fluorescence Spectroscopy*, 2nd ed., Plenum Press, New York, **1999**; b) C. A. Parker in *Photoluminescence of Solutions*, Elsevier, Amsterdam, **1968**; c) D. Sutherland, C. Compton, *J. Org. Chem.* **1952**, *17*, 1257; d) S. F. Mason, *J. Chem. Soc.* **1962**, 493; e) B. L. Van Duuren, *Chem. Rev.* **1963**, *63*, 325; f) E. A. Steck, G. W. Ewing, *J. Am. Chem. Soc.* **1948**, *70*, 3397; g) K. M. Hendrickson, T. Rodopoulos, P. A. Pittet, I. Mahadevan, S. F. Lincoln, A. D. Ward, T. Kurucsev, P. A. Duckworth, I. J. Forbes, P. Zalewski, W. H. Betts, *J. Chem. Soc. Dalton Trans.* **1997**, 3879; h) C. J. Fahrni, T. V. O'Halloran, *J. Am. Chem. Soc.* **1999**, *121*, 11448; i) S. Basu, "Theory of Solvent Effects on Molecular Electronic Spectra" in *Advances in Quantum Chemistry*, Academic Press, New York, **1964**, vol. 1.
[44] a) A. P. De Silva, H. Q. N. Gunaratne, T. Gunnlaugsson, A. J. M. Huxley, C. P. McCoy, J. T. Rademacher, T. E. Rice, *Chem. Rev.* **1997**, *97*, 1515; b) C. Bazzicalupi, A. Bencini, A. Bianchi, C. Giorgi, V. Fusi, B. Valtancoli, M. Bernardo, F. Pina, *Inorg. Chem.* **1999**, *38*, 3806; c) M. C. Aragoni, M. Arca, F. Demartin, F. A. Devillanova, F. Isaia, A. Garau, V. Lippolis, F. Jalali, U. Papke, M. Shamsipur, L. Tei, A. Yari, G. Verani, *Inorg. Chem.* **2002**, *41*, 6623; d) J. M. Castagnetto, J. W. Canary, *Chem. Commun.* **1998**, 203.
[45] Z. Otwinowski, W. Minor, "Processing of X-ray Diffraction Data Collected in Oscillation Mode" in *Methods in Enzymology*, vol. 276: *Macromolecular Crystallography* (Eds.: C. W. Carter Jr, R. M. Sweet), Academic Press, New York, **1997**, part A, pp. 307–326.
[46] G. M. Sheldrick, *SHELXTL NT*, Version 5.10, Bruker AXS Inc., Madison, WI, **1999**.
[47] G. M. Sheldrick, *SHELXL-97, Program for the Refinement of Crystal Structures*, University of Göttingen, Germany, **1997**.

Received: February 20, 2007
Published Online: June 29, 2007

*Please note that minor changes have been made to this publication in the European Journal of Inorganic Chemistry initial Early View version.*

*The Editor*

 © 2007 Wiley-VCH Verlag GmbH & Co. KGaA, Weinheim 

DOI: 10.1002/ejic.200700259

# Iron(III) Exchange Process between Hexadentate Tripodal Ligands: Models for the Ternary Complexes

Guy Serratrice,*[a] Frédéric Biaso,[a] Jean-Louis Pierre,[a] Sylvie Blanc,[b] and Anne-Marie Albrecht-Gary[c]

**Keywords:** Mixed ligands / Iron / Exchange interactions / Siderophores / Tripodal ligands

Using tripodal ligands as tools, the kinetics of iron removal from ferric complexes of the tripodal tris(hydroxyquinoline) ligands O-TRENSOX and of tris(catechol) TRENCAMS was investigated. Two hexadentate heterotripodal ligands were also examined (TRENSOX2CAMS with two hydroxyquinoline and one catechol subunits and TRENSOXCAMS2 with two catechol and one hydroxyquinoline subunits) as possible models of the ternary complexes involved in the iron exchange process. The main result of this kinetic study is the pertinence of the iron complexes of the mixed ligands as models for the transient and successive ternary complexes occurring in the iron exchange, which proceeds "arm-by-arm" between a homotopic ligand and the iron complex of another homotopic ligand.
(© Wiley-VCH Verlag GmbH & Co. KGaA, 69451 Weinheim, Germany, 2007)

## Introduction

Microbial iron bioavailability is driven by the coordination chemistry of siderophores, which are iron-chelating agents that are excreted by microorganisms to render iron soluble in the environment and favor the uptake of this metal. Iron chelation by some natural or synthetic chelators can be applied to human diseases characterized by iron overload, and water-soluble iron complexes can be used to alleviate iron deficiency in plants, preventing and even reversing iron chlorosis. The coordination chemistry of a great number of water-soluble natural or synthetic iron chelators was recently reviewed, and it is usually considered that $Fe^{III}$ removal from ferrisiderophore or from other biological complexes (transferrin carriers or storage complexes, receptor proteins, citrate, and low molecular-weight chelates) involves the formation of a ternary complex.[1] The dynamic of Fe removal from various $Fe^{III}$ complexes was studied and the formation of the ternary complex is often consistent with the kinetic data.[2–4] Nevertheless, a molecular description of the "so-called ternary" complex was never discussed to the best of our knowledge. Recently, Crumbliss et al. described the formation of a ternary complex in a redox mechanism for iron release from a siderophore.[5]

Using tripodal ligands as tools and starting from the hypothesis of a step-by-step ("arm-by-arm") exchange, we investigated the kinetics of the iron removal from the ferric complexes of the tripodal tris(hydroxyquinoline) ligands O-TRENSOX ($\mathbf{L^0}$),[6] and $\mathbf{L'^0}$,[7] where $\mathbf{L^0}$ is anchored to a tertiary amine and $\mathbf{L'^0}$ to a tertiary carbon (Figure 1), and a tris(catechol) analogue built from a tertiary amine[8] TRENCAMS ($\mathbf{L^3}$). Two hexadentate heterotripodal ligands were also examined, TRENSOX2CAMS ($\mathbf{L^1}$) with two hydroxyquinoline units and one catechol[9] unit and TRENSOXCAMS2 ($\mathbf{L^2}$) with two catechol moieties and one hydroxyquinoline[9] building block (Figure 1). Our aim was to gain insight into the step-by-step ligand exchange processes via kinetic intermediates called "ternary complexes". In addition, kinetic experiments on the iron removal from EDTA by these tripodal ligands were carried out. All the collected results allow the analysis of the influence of the structure of the ligand and of the nature of the chelating groups on the kinetic parameters.

## Results

We monitored the iron exchange reactions between two ligands using different competing ligand concentrations in pseudo first-order conditions. The global reaction of a ligand-exchange type is expressed by Equation (1) (charges omitted for clarity).

$$FeL + L' \rightarrow FeL' + L \quad (1)$$

[a] Département de Chimie Moléculaire UMR-5250, ICMG FR-2607 CNRS, Université Joseph Fourier,
B. P. 53, 38041 Grenoble Cedex 9, France
Fax: +33-4-76514836
E-mail: guy.serratrice@ujf-grenoble.fr
[b] Institut Pluridisciplinaire de Recherche sur l'Environnement et les Matériaux, UMR CNRS 5254, Université de Pau et des Pays de l'Adour,
B. P. 27540, 64075 Pau Cedex, France
[c] Laboratoire de Physico-Chimie Bioinorganique, UMR CNRS 7509, ECPM,
25, rue Becquerel, 67200 Strasbourg, France
Supporting information for this article is available on the WWW under http://www.eurjic.org or from the author.

 © 2007 Wiley-VCH Verlag GmbH & Co. KGaA, Weinheim 

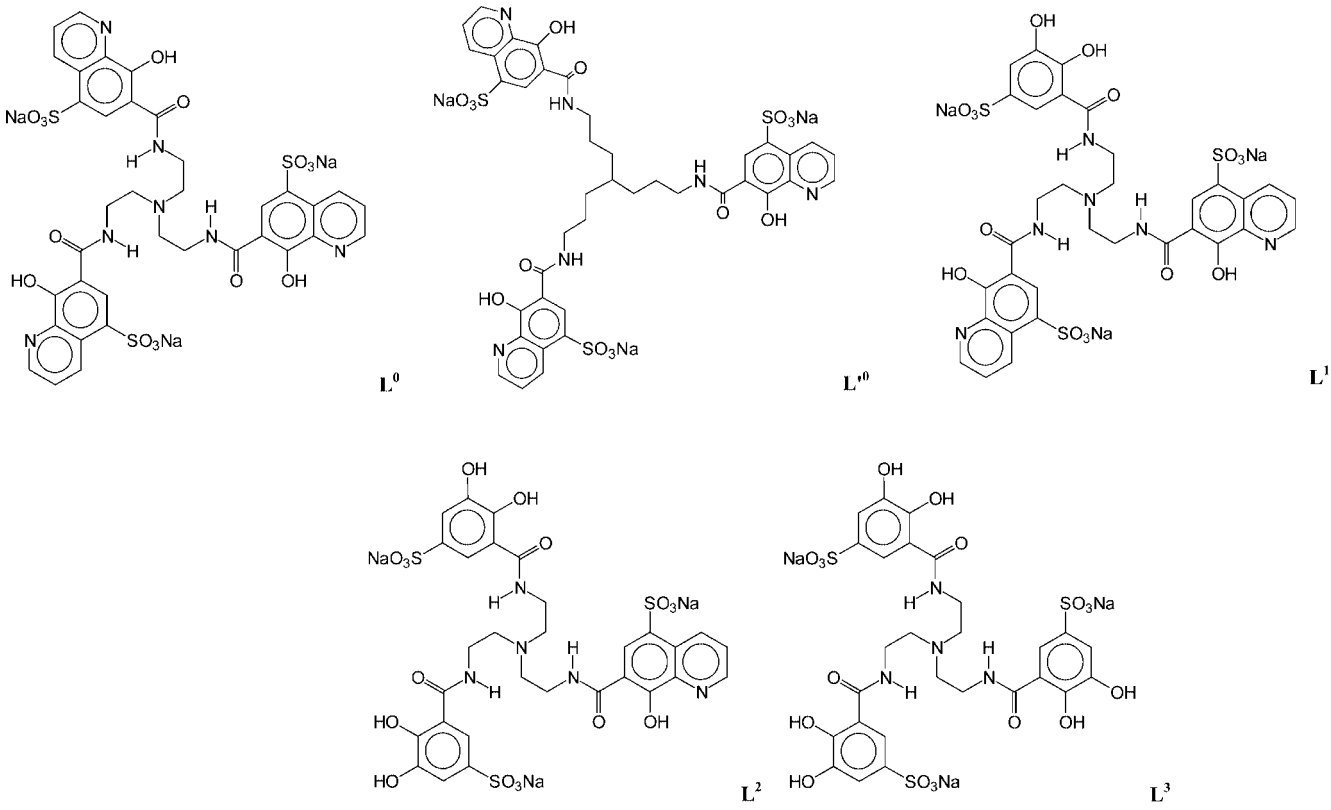


Figure 1. Chemical formulae of tripodal ligands $\mathbf{L}^n$ ($n$ refers to the number of catechol groups in the tripodal ligand).

Three FeL complexes were studied: Fe-EDTA, Fe$\mathbf{L}^0$, and Fe$\mathbf{L}^3$; L′ was $\mathbf{L}^0$, $\mathbf{L}'^0$, $\mathbf{L}^1$, $\mathbf{L}^2$, and/or $\mathbf{L}^3$. In particular, this series of exchanges allows the study of the kinetics of adding a catechol or an 8-hydroxyquinoline arm into the iron coordination sphere and the effect of the structure of the tripodal ligand (i.e. homopodal or heteropodal, anchor group). During the exchange reaction, monoexponential growth of absorbance was observed in all cases at the selected wavelength of the FeL′ complex, indicating that the reaction proceeds via a single rate-limiting step. No variation in the amplitude of the absorbance was observed during the mixing time for all the studied systems, indicating that a fast step, involving a change in the coordination sphere around $Fe^{III}$ does not occur before the first detectable step. The UV/Vis spectra were recorded as a function of the time and at the end of the kinetics. The structure of the final complex was supported by its absorption spectrum on the basis of our previous studies, particularly for the mixed coordination around $Fe^{III}$[9] related to one catechol and two 8-hydroxyquinoline groups as in Fe$\mathbf{L}^1$ or two catechol and one 8-hydroxyquinoline groups as in Fe$\mathbf{L}^2$ (see the $\lambda_{max}$ and $\varepsilon$ values in the Experimental Section).

### Iron Exchange from Fe-EDTA

The reaction was monitored with $\mathbf{L}^0$, $\mathbf{L}'^0$, $\mathbf{L}^1$, $\mathbf{L}^2$, and $\mathbf{L}^3$. The reaction was found to be complete and to occur in one distinguishable step. A linear dependence of the observed pseudo first-order rate constant $k^{obs}$ on [L′] with negligible intercept was observed [Equation (2)]. The values of $k_1$ are collected in Table 1.

$$k^{obs} = k_1 [L']_{tot} \quad (2)$$

Table 1. Kinetic data ($k_1$ values in $M^{-1}s^{-1}$) for the first step of the iron exchange reaction between FeL and L′.[a]

| Competing | Ferric complex | | |
|---|---|---|---|
| ligand | [Fe-EDTA]$^-$ | [Fe$\mathbf{L}^0$]$^{3-}$ | [Fe$\mathbf{L}^3$]$^{6-}$ |
| $\mathbf{L}^0$ | 4.0 ± 0.5 | – | 1.9 ± 0.1 |
| $\mathbf{L}^1$ | 14.2 ± 1.5 | 23 ± 1 | 5.5 ± 0.8 |
| $\mathbf{L}^2$ | 97 ± 2 | 77 ± 4 | 1.1 ± 0.15 |
| $\mathbf{L}^3$ | 145 ± 3 | 81 ± 4[b] | – |
| $\mathbf{L}'^0$ | 5.1 ± 0.4 | – | – |

[a] In aqueous 50 mM MOPS buffer, pH = 7.4, $I$ = 0.1 M ($NaClO_4$) and at temperature $T$ = 25.0 °C. [b] Intercept = $(6.6 \pm 0.6) \times 10^{-2}$ $s^{-1}$.

### Iron Exchange from Fe-O-TRENSOX

The reaction was monitored with $\mathbf{L}^1$, $\mathbf{L}^2$, and $\mathbf{L}^3$ and was found to proceed in one distinguishable step. The UV/Vis spectra recorded as the reaction proceeded exhibited isosbestic points indicating that no intermediary species were formed during the reaction. For Fe$\mathbf{L}^0$ + $\mathbf{L}^3$, the reaction was complete (see Figure S1 in the Supporting Information). For Fe$\mathbf{L}^0$/$\mathbf{L}^1$, the spectrum recorded at the equilibrium was found to be similar to that of the Fe$\mathbf{L}^1$ complex,

 © 2007 Wiley-VCH Verlag GmbH & Co. KGaA, Weinheim 

indicating the substitution of an 8-hydroxyquinoline group by a catechol group. However, the substitution by the two 8-hydroxyquinoline groups of $\mathbf{L^1}$ does not change the spectrum and cannot be detected. For Fe$\mathbf{L^0/L^2}$ the spectrum recorded at the end of the first step is similar to the spectrum of the Fe$\mathbf{L^2}$ complex, indicating the substitution of two 8-hydroxyquinoline groups by two catechol groups. Figure 2 shows the UV/Vis spectra recorded as the reaction proceeds.

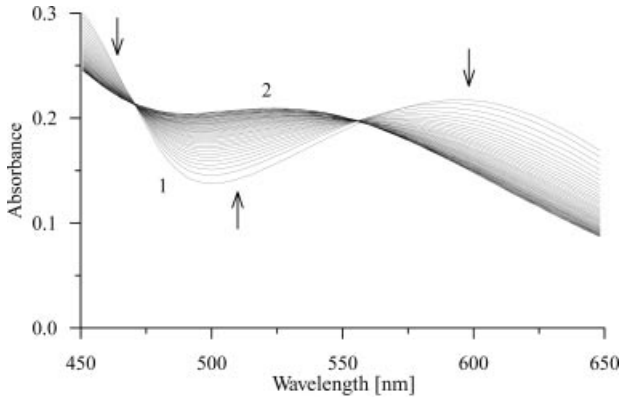


Figure 2. UV/Vis spectra recorded as a function of time for the exchange Fe$\mathbf{L^0/L^2}$; experimental conditions: [Fe$\mathbf{L^0}$] = 0.04 mM, [$\mathbf{L^2}$] = 0.4 mM, pH = 7.4 (50 mM MOPS buffer), $I$ = 0.1 M ($NaClO_4$), $T$ = 25 °C. (1) $t$ = 0 s, (2) 260 s; the arrows indicate the direction of change as the reaction proceeds.

The plots of $k^{obs}$ versus the ligand concentration show a linear dependence with a negligible intercept except for Fe$\mathbf{L^0/L^2}$. The values of $k_1$ are reported in Table 1.

### Iron Exchange from TRENCAMS

The spectrum recorded at the end of the reaction of Fe$\mathbf{L^3}$ with $\mathbf{L^1}$ or $\mathbf{L^2}$ is similar to the spectrum of the $\mathbf{FeL^2}$ complex, indicating the substitution of a catechol group by an 8-hydroxyquinoline group (see Figure S1 in the Supporting Information). The reaction was found to proceed in one detectable step. The plot of $k^{obs}$ versus the ligand concentration shows a linear dependence with negligible intercept. The values of $k_1$ are reported in Table 1.

For the reaction of Fe$\mathbf{L^3}$ with $\mathbf{L^0}$, two steps were observed as deduced from the two-exponential growth of absorbance measured at 600 nm. The spectrum recorded at the end of the first step is similar to the spectrum of the Fe$\mathbf{L^2}$ complex, indicating the substitution of a catechol group by an 8-hydroxyquinoline group (species noted $\mathbf{L^0}$Fe$\mathbf{L^3}$), and the spectrum recorded at the equilibrium after the second step is similar to the spectrum of the Fe$\mathbf{L^1}$ complex, which indicates that the substitution of a second catechol group by an 8-hydroxyquinoline group (species noted $\mathbf{L^0}$Fe$\mathbf{L^3}$*). The plot of $k_1^{obs}$ (first step) versus the ligand concentration shows a linear dependence with a nonzero intercept while $k_2^{obs}$ was found to be independent of the ligand concentration. This is consistent with the reactions according to Equations (3) and (4) and the rate law according to Equation (5) by considering the two reactions occur independently since $k_1^{obs} >> k_2^{obs}$.

$$\mathrm{Fe}\mathbf{L^3} + \mathbf{L^0} \rightleftharpoons \mathbf{L^0}\mathrm{Fe}\mathbf{L^3}\ k_1, k_{-1} \quad (3)$$

$$\mathbf{L^0}\mathrm{Fe}\mathbf{L^3} \rightarrow \mathbf{L^0}\mathrm{Fe}\mathbf{L^3}^*\ k_2 \quad (4)$$

$$k_1^{obs} = k_1[L^0] + k_{-1} \quad (5)$$

Thus, the values $k_1 = 1.9 \pm 0.1\ M^{-1}s^{-1}$, $k_{-1} = (2.1 \pm 0.2) \times 10^{-4}\ s^{-1}$, and $k_2 = (2.3 \pm 0.3) \times 10^{-5}\ s^{-1}$ were obtained.

## Discussion

The general feature resulting from the kinetic studies is that the iron exchange reactions proceed in one detectable step except for the exchange Fe$\mathbf{L^3/L^0}$ (two detectable steps). Hence, the formation of an intermediate ternary complex was only shown for this last case. In a previous investigation on the acid dissociation kinetics of the $Fe^{III}$ complexes with these tripodal ligands, we observed a very fast dissociation of one arm of the ligand which is maintained in proximity to the first coordination sphere of $Fe^{III}$.[10] This indicates that the complex has one labile arm thus favoring the formation of the precursor complex and then the substitution by one arm of the competing ligand. So, it is reasonable to propose that the kinetic rate constant $k_1$ represents the substitution rate of one arm of the initial complex by one arm of the competing ligand. In addition, this study clearly reveals the effect of the nature of the entering group, catechol or an 8-hydroxyquinoline group, on the ligand substitution rate constants.

### Iron Exchange with Homotopic Ligands $\mathbf{L^0}$, $\mathbf{L'^0}$, and $\mathbf{L^3}$

For the iron exchange from the EDTA complex, the final spectrum indicates that the reaction is complete. The same result is obtained with the heterotopic ligands. It is proposed that when the first arm of the incoming ligand is attached, EDTA dissociates rapidly and next two arms quickly coordinate to $Fe^{III}$ via catechol or the 8-hydroxyquinoline groups. The values of $k_1$ shows that the substitution rate of the catechol group ($145\ M^{-1}s^{-1}$) is about one order of magnitude faster than that of the 8-hydroxyquinoline (4.0 and $5.1\ M^{-1}s^{-1}$). Similar values for $k_1$ were obtained for the iron exchanges between Fe$\mathbf{L^0}$ and $\mathbf{L^3}$ ($81\ M^{-1}s^{-1}$) or between Fe$\mathbf{L^3}$ and $\mathbf{L^0}$ ($1.9\ M^{-1}s^{-1}$ for the first step).

### Iron Exchange with Heterotopic Ligands $\mathbf{L^1}$ and $\mathbf{L^2}$

For the exchanges Fe$\mathbf{L^0/L^1}$ and Fe$\mathbf{L^0/L^2}$, the nature of the entering group was clearly identified as a catechol group on the basis of the spectrum change. In a previous paper,[9] we determined the UV/Vis parameters for the ferric complexes with a mixed catechol/8-hydroxyquinoline coordina-

 © 2007 Wiley-VCH Verlag GmbH & Co. KGaA, Weinheim 

tion sphere. In addition, the values of $k_1$ (23 and 77 $M^{-1}s^{-1}$ for Fe**L**$^0$/**L**$^1$ and Fe**L**$^0$/**L**$^2$, respectively) are of the same order of magnitude as those for the exchanges Fe**L**$^0$/**L**$^3$ (81 $M^{-1}s^{-1}$) and Fe-EDTA/**L**$^3$ (145 $M^{-1}s^{-1}$), which correspond to the substitution by a catechol arm. For the exchanges Fe**L**$^3$/**L**$^1$ and Fe**L**$^3$/**L**$^2$, the entering group was identified as an 8-hydroxyquinoline unit according to the spectral change. The values of $k_1$ (5.5 and 1.1 $M^{-1}s^{-1}$ for Fe**L**$^3$/**L**$^1$ and Fe**L**$^3$/**L**$^2$, respectively) are of the same order of magnitude as those for the exchanges Fe**L**$^3$/**L**$^0$ (1.9 $M^{-1}s^{-1}$), Fe-EDTA/**L**$^0$ (4.0 $M^{-1}s^{-1}$), or Fe-EDTA/**L**$'^0$ (5.1 $M^{-1}s^{-1}$), which correspond to the substitution by an 8-hydroxyquinoline arm. All these results indicate that the substitution rate is mainly controlled by the nature of the entering group. Accordingly, the iron exchange rates from Fe-EDTA with **L**$^1$ and **L**$^2$, 14.2 and 97 $M^{-1}s^{-1}$, respectively, can be attributed to the substitution by the catechol arm. Table 2 summarizes the values of $k_1$ for the three series of iron exchange collected according to the nature of the chelating group that enters in the iron coordination sphere.

The fact that close $k_1$ values are obtained for one type of entering group (catechol or 8-hydroxyquinoline) in the different exchange systems suggests that the step is the substitution of one arm of the initial complex by one arm of the competing ligand, leading to the formation of an intermediate ternary complex before the substitution of the two other arms. The higher substitution rate measured for the catechol group can be attributed to its greater electron donor ability and to its lower bulkiness relative to the 8-hydroxyquinoline group. This might be also attributed to the charge of the incoming chelating group that depends on the protonation state of the ortho hydroxy groups. Indeed, a negative deprotonated hydroxy is assumed to be more reactive than the protonated one. For the catechol groups in **L**$^1$, **L**$^2$, and **L**$^3$ the lower p$K_a$ is 5.62,[9] 5.55,[9] and 5.57,[8] respectively, indicating that the hydroxy group of one arm is deprotonated at pH 7.4, whereas for the 8-hydroxyquinoline groups the lower p$K_a$ is 7.44[6] for **L**$^0$ and 6.68[7] for **L**$'^0$. For the sake of comparison, the numbers of deprotonated OH groups in the catechol and 8-hydroxyquinoline moieties are reported in Table 2. Analysis of the data shows that $k_1$ cannot be directly related to the protonation state of the OH group. It is thus suggested that the negative charge of the incoming group is not a decisive factor for the rate constant.

It should be pointed out that the substitution rate by the catechol group is decreasing as the number of 8-hydroxyquinoline groups increases (or inversely as the number of catechol groups decreases) in the competing ligand: 81, 77, or 23 $M^{-1}s^{-1}$ for Fe**L**$^0$/**L**$^3$, **L**$^2$, or **L**$^1$, respectively, and 145, 97, or 14.2 $M^{-1}s^{-1}$ for Fe-EDTA/**L**$^3$, **L**$^2$, or **L**$^1$, respectively. In contrast, the same trend is not observed for the substitution rate by the 8-hydroxyquinoline group (substitution of Fe**L**$^3$ by **L**$^0$, **L**$^1$, or **L**$^2$; 1.9, 5.5, or 1.1 $M^{-1}s^{-1}$, respectively). This indicates that steric factors rather than statistical factors occur: the 8-hydroxyquinoline group is assumed to slow down the entering of the tripodal ligand in the iron coordination sphere.

Our results suggest that iron exchange occurs step-by-step, each arm of the incoming tripodal ligand substitutes successively the leaving ligand as the coordination bonds are broken. This is clearly evidenced for the iron exchange between Fe**L**$^3$ and **L**$^0$ since the formation of an intermediate ternary complex having a mixed coordination 8-hydroxyquinolinate/catecholate could be identified from the UV/Vis spectra as previously published.[9] A probable mechanism is depicted in Figure 3. The same process is assumed to occur for the exchange between Fe**L**$^0$ and **L**$^3$, but the coordination of the second and the third catechol groups is fast relative to the first one. This can be inferred by the labilizing effect of strong electron pair donors as catechol ligands, which increases the electron density of the metal, weakening the bonds with the coordinated donor atoms. Replacement of a coordinated group by a catechol group in the first coordination shell enhances the ligand exchange of the remaining arms. In contrast, in the case of the reaction between Fe**L**$^3$ and **L**$^0$, the substitution of the second arm of the tripodal ligand is very slow ($k_2$ = 2.3 $10^{-5}$ $s^{-1}$). It is suggested that the substitution of catechol groups by poorer electron pair donors as 8-hydroxyquinoline groups diminishes the electron density at the iron center, slowing down the exchange of the remaining coordinating arms. In addition, this effect is enhanced by the steric effect of the incoming 8-hydroxyquinoline group. The sensitivity of the rate constant to the nature of the bidentate group of the incoming ligand indicates a rather associative character of the mechanism for

Table 2. Kinetic data ($k_1$ values in $M^{-1}s^{-1}$) for the first step of the iron exchange reaction between FeL and L′[a]collected according to the entering group.

| Competing ligand | Catechol as an entering group | | | 8-Hydroxyquinoline as an entering group | | |
|---|---|---|---|---|---|---|
| | [Fe**L**$^0$]$^{6-}$ | [Fe-EDTA]$^-$ | Number of OH deprotonated[b] | [Fe**L**$^3$]$^{6-}$ | [Fe-EDTA]$^-$ | Number of OH deprotonated[b] |
| **L**$^0$ | | | | 1.9 | 4.0 | 0.5 |
| **L**$^1$ | 23 | 14.2 | 1 | 5.5 | | 0 |
| **L**$^2$ | 77 | 97 | 1.5 | 1.1 | | 0 |
| **L**$^3$ | 81 | 145 | 3 | | | |
| **L**$'^0$ | | | | | 5.1 | 1.5 |

[a] In aqueous 50 mM MOPS buffer, pH = 7.4, $I$ = 0.1 M ($NaClO_4$) and at temperature $T$ = 25.0 °C. [b] at pH = 7.4; half value indicates a partially deprotonated group (pH ≈ p$K_a$).

 © 2007 Wiley-VCH Verlag GmbH & Co. KGaA, Weinheim 

these series of iron exchange. In summary, the exchange rate constants of the first step depend on the nature of the entering arm (catechol or 8-hydroxyquinoline) and on the nature of second and third arm of the incoming tripodal ligand (homotripodal or heterotripodal; Figure 3).

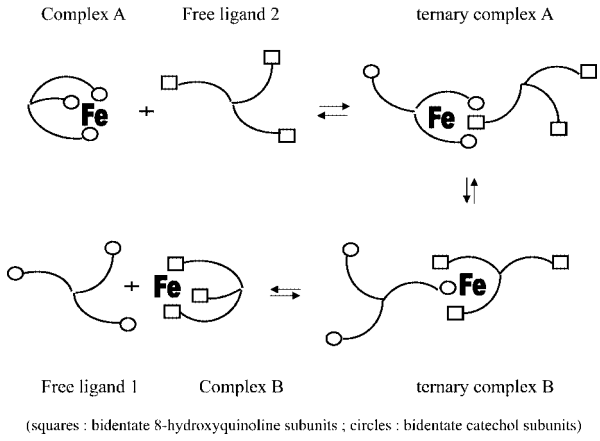


Figure 3. Successive steps for the ligand exchange at the iron center via ternary complexes.

## Conclusions

The main result of this study is the pertinence of the Fe**L**$^{1}$ and Fe**L**$^{2}$ complexes as models for the transient and successive ternary complexes occurring in the iron exchange processes between Fe**L**$^{0}$ and **L**$^{3}$ and between Fe**L**$^{3}$ and **L**$^{0}$. The results allow the first molecular description of the ternary complex formed during the iron exchange between two abiotic siderophores. Generally, ligand exchanges are slow, but they are facilitated by the formation of the so-called ternary ferric complexes with the two ligands bound to Fe$^{III}$. Our study supports this concept.

## Experimental Section

**Materials:** All commercial reagents were of the highest purity grade and used without further purification. Iron(III) stock solutions were prepared by dissolving the appropriate amount of ferric perchlorate hydrate (Aldrich) in standardized $HClO_4$ solution. The solutions were standardized for ferric ion concentration spectrophotomerically by using a molar extinction coefficient of 4160 $M^{-1}\,cm^{-1}$ at 240 nm.[11] The ligands were synthesized according to procedures previously described (**L**$^{0}$,[6] **L′**$^{0}$,[12] **L**$^{1}$,[9] **L**$^{2}$,[9] and **L**$^{3}$[8]).

**Kinetics Studies:** Iron(III) exchange kinetics between Fe**L**$^{0}$ and **L**$^{1}$, **L**$^{2}$, or **L**$^{3}$, between Fe**L**$^{3}$ and **L**$^{0}$, **L**$^{1}$, or **L**$^{2}$, and between Fe-EDTA and **L**$^{0}$, **L**$^{1}$, **L**$^{2}$, **L**$^{3}$, or **L**$^{4}$ were studied in aqueous 50 mM MOPS buffer, pH = 7.4, $I$ = 0.1 M ($NaClO_4$), and at temperature $T$ = (25.0 ± 0.2) °C. The kinetics were studied under pseudo first order conditions by using a large excess of the entering ligand over the complex. Initial concentration of the FeL complex was $2.0\times10^{-5}$ mol $L^{-1}$, initial concentration of ligand L′ was varied in a range from $2\times10^{-4}$ to $1.2\times10^{-3}$ mol $L^{-1}$. Fast kinetic measurements were performed with a KINSPEC UV (BIO-LOGIC Company, Claix, France) stopped-flow spectrophotometer equipped with a diode array detector (J & M) and connected to a microcomputer; slow kinetic measurements were performed with a Perkin–Elmer Lambda2 or Varian Cary 50 UV/Vis spectrophotometer. The kinetic data were treated on line with the commercial BIO-KINE program (BIO-LOGIC Company, Claix, France). In each run, equal volumes of solutions of the complex and of the ligand were mixed. The absorbance changes with time were recorded at the maximum of the charge-transfer band of the complex that is formed, specifically, $\lambda_{max}$ = 490, 525, and 550 nm for Fe**L**$^{3}$,[8] Fe**L**$^{2}$,[9] and Fe**L**$^{1}$,[9] respectively, and 595 nm for Fe**L**$^{0}$[6] and Fe**L′**$^{0}$.[7] Some visible spectra from 400 to 650 nm were recorded in time by using a diode array detector.

**Supporting Information** (see footnote on the first page of this article)**:** Figures S1 and S2: UV/Vis spectra recorded as a function of time for the exchanges Fe**L**$^{0}$/**L**$^{3}$ and Fe**L**$^{3}$/**L**$^{2}$. Tables S1 to S8: rate constants values for the different exchanges FeL/L′.

## Acknowledgments

The authors thank Professor P. Baret and G. Gellon for managing the syntheses of ligands **L″**.

[1] A.-M. Albrecht-Gary, A. L. Crumbliss in *Metals Ions in Biological Systems* (Eds.: A.Sigel, H. Sigel), Marcel Dekker, New-York, **1998**, vol. 35, pp. 239–327.
[2] Y. Hara, M. Akiyama, *J. Am. Chem. Soc.* **2001**, *123*, 7247–7256.
[3] A. Stinzi, C. Barnes, K. N. Raymond, *Proc. Natl. Acad. Sci. USA* **2000**, *97*, 10691–10696.
[4] B. Faller, H. Nick, *J. Am. Chem. Soc.* **1994**, *116*, 3860–3865.
[5] K. A. Mies, J. I. Wirgau, A. L. Crumbliss, *Biometals* **2006**, *19*, 115–126.
[6] G. Serratrice, H. Boukhalfa, C. Béguin, P. Baret, C. Caris, J.-L. Pierre, *Inorg. Chem.* **1997**, *36*, 3898–3910.
[7] F. Biaso, Thesis, Université Joseph Fourier Grenoble, France, **2002**.
[8] F. Thomas, C. Béguin, J. L. Pierre, G. Serratrice, *Inorg. Chim. Acta* **1999**, *291*, 148–157.
[9] A.-M. Albrecht-Gary, S. Blanc, F. Biaso, F. Thomas, P. Baret, G. Gellon, J.-L. Pierre, G. Serratrice, *Eur. J. Inorg. Chem.* **2003**, 2596–2605.
[10] G. Serratrice, F. Biaso, F. Thomas, C. Béguin, *Eur. J. Inorg. Chem.* **2004**, 1552–1565.
[11] R. Bastian, R. Weberling, F. Palilla, *Anal. Chem.* **1956**, *28*, 459–462.
[12] D. Imbert, Thesis, Université Joseph Fourier, Grenoble, France, **2000**.

Received: March 1, 2007
Published Online: June 21, 2007

 © 2007 Wiley-VCH Verlag GmbH & Co. KGaA, Weinheim 

DOI: 10.1002/ejic.200700273

# Synthesis and Characterization of $Cu^{II}$ Complexes with Amino Acid Substituted Di(2-pyridyl)amine Ligands

**Srećko I. Kirin,[a] Hemant P. Yennawar,[a] and Mary Elizabeth Williams*[a]**

**Keywords:** Bioconjugates / Bioinorganic chemistry / Copper complexes / Di(2-pyridyl)amine

The two-step syntheses of the substituted di(2-pyridyl)-amine ligands (dpa), dpa-$CH_2CO_2H$ (**1**) and dpa-$PhCO_2H$ (**2**), are described. Ligands **1** and **2** are successfully coupled to the amino acid phenylalanine, yielding the derivatives **4** and **6**, respectively. Four $Cu^{II}(dpa)_2$ complexes, [Cu(dpa-$CH_2CO_2tBu)_2(NO_3)_2$] (**$3_{Cu}$**), [Cu(dpa-$CH_2CO$-$PheOMe)_2$-$(H_2O)_2](NO_3)_2$·2MeOH (**$4_{Cu}$**), [Cu(dpa-$PhCO_2Me)_2$ $(MeOH)_2$]-$(ClO_4)_2$ (**$5_{Cu}$**) and [Cu(dpa-PhCO-$PheOMe)_2(ClO_4)_2$] (**$6_{Cu}$**) have been prepared and characterized, including their single crystal X-ray structures. Fluorescence emission at UV (for **3** and **4**) or blue (for **5** and **6**) wavelengths of the free ligands is preserved in the corresponding Cu complexes, although with lower intensity. X-band EPR spectra of **$4_{Cu}$** and **$6_{Cu}$** both revealed one axial $Cu^{II}$ signal with hyperfine and superhyperfine splittings. Complexes **$4_{Cu}$** and **$6_{Cu}$** are chiral inorganic complexes with amino acid bioconjugates that may serve as nucleoside analogs in modified peptide nucleic acids (PNA).
(© Wiley-VCH Verlag GmbH & Co. KGaA, 69451 Weinheim, Germany, 2007)

## Introduction

Inorganic nucleic acid derivatives and structural mimics have received increased attention in recent years[1] in view of their potential applications in biological and material sciences. Electrostatic attraction has been used to coat the exterior of nucleic acids with metals,[1a] and metal complexes have been inserted into double-stranded DNA (dsDNA) duplexes by intercalation and threading.[2] In contrast, metal ions have been incorporated *inside* the core of the nucleic acid duplex by replacing hydrogen bonds with metals that covalently link the nucleobases. Inclusion of metals in this manner changes the properties of the dsDNA duplex. For example, Lee et al. abstracted protons from the nucleobases of a DNA duplex at high pH, and replaced some of these H atoms with Zn cations.[3] The resulting duplex had improved electrical conductivity that was attributed to the metal-linked base pairs. Analogously, two thymine nucleobases have been shown to form a neutral complex upon complexation of a $Hg^{II}$ ion.[4] Using this coordination chemistry, dsDNA duplex formation by metal coordination of multiple $Hg^{II}$ ions along the oligonucleotide has been demonstrated. Nucleobases have also been replaced by synthetic ligands to adjust the binding affinity of metal ions. A number of common metal binding ligands and a variety of metal ions and oligomeric backbones (i.e. sugar phosphate and pseudo-peptide) have also been reported.[5–18]

Di(2-pyridyl)amine (dpa) is a well-known ligand for a range of transition metals, and structural studies on these complexes have been reported.[19] Metal dpa complexes have been used as homogeneous or heterogeneous catalysts in a number of chemical transformations including hydrolytic or oxidative DNA cleavage,[20] hydrolytic cleavage of amino acid esters,[21] oxidation of alcohols,[22] ring-opening metathesis polymerization,[23] Heck reactions,[24] and various asymmetric reactions.[25] Dpa based luminescence has been utilized for the development of new materials.[26] Given these properties of metal dpa complexes, development of methods for incorporation of the ligand into synthetically modified nucleic acids, nucleobases analogs, or bioconjugates will lead to broad applications in bioinorganic systems.

We have recently described heterocyclic ligand-containing aminoethyl glycine (aeg) oligomers,[5b,14] chains that are charge-neutral mimics of the sugar phosphate backbone of DNA. Our aeg oligomers crosslink by coordination of transition-metal ions and are synthetic inorganic structural analogs of dsDNA in which all hydrogen-bonded base pairs are replaced by metal coordination bonds. In previous studies, the aeg backbone has been successfully substituted with the acetic acid derivatives of the py,[5b,14a–5e] bpy,[14a,14c,14e] tpy,[14e] phtpy[14g] or hq[14f] ligands shown in Figure 1. Herein we extend this chemistry by introducing the fluorescent dpa ligands **1** and **2** and attach the ligands to an amino acid. Two of these ligands are crosslinked by coordination

[a] Department of Chemistry, Pennsylvania State University, 104 Chemistry Building,
University Park, PA 16802, USA
E-mail: mbw@chem.psu.edu
Supporting information for this article is available on the WWW under http://www.eurjic.org or from the author.

 © 2007 Wiley-VCH Verlag GmbH & Co. KGaA, Weinheim 

to one $Cu^{II}$ ion to form the chiral inorganic building block that could be used to replace nucleosides in modified peptide nucleic acid (PNA).[27]

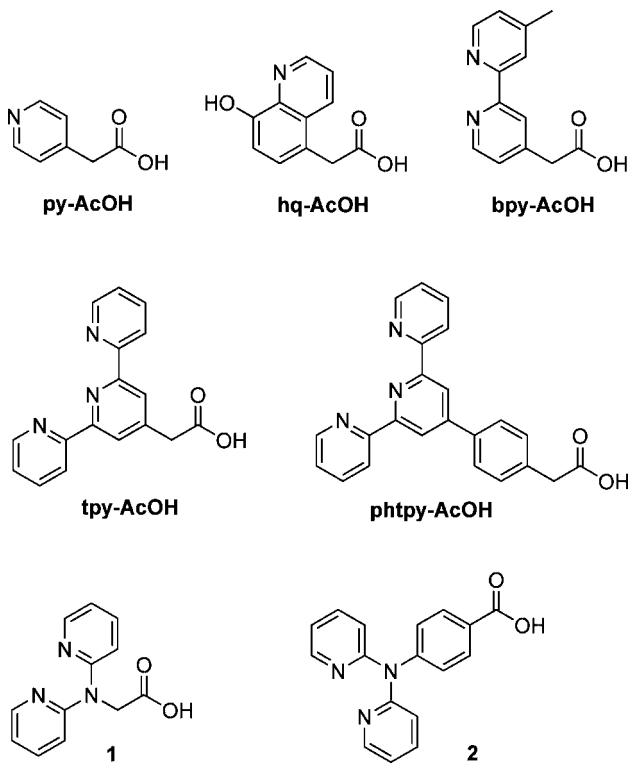


Figure 1. The heterocyclic acetic acid derivatives previously used for the synthesis of aeg-oligoligandosides[5b,14] and the dpa derivatives **1** and **2** prepared in this study.

## Results and Discussion

### Dpa Ligands and Amino Acid Conjugates

In contrast to the other ligands shown in Figure 1, dpa has not yet been used extensively in the synthesis of nucleoside analogs or bioconjugates. This is likely due to the difficult derivatization of the central amine atom. In the literature two different routes are frequently used for the synthesis of the aromatic amines like **1** and **2**: the Pd-catalyzed Buchwald–Hartwig amination[28,29] and the Ullmann condensation,[30,31] often catalyzed by $Cu^{II}$ salts. The Buchwald–Hartwig amination is strongly affected by electron-withdrawing substituents [like the *p*-methoxycarbonyl group in Scheme 2, reaction (i)],[32] while the Ullmann condensation needs aggressive conditions (high temperatures and extended reaction times), to produce only moderate yields.[30]

The Ullmann condensation was used to prepare key intermediates **3** and **5** according to Scheme 1 and Scheme 2, respectively. The ester **3** was synthesized by substitution of the commercially available dpa with *tert*-butyl bromoacetate in DMSO with KOH and catalytic KI to give the purified ester **3** in 47% yield. Deprotection of the ester proceeded smoothly to give the free acid **1** (91% yield). The synthesis of ester **5** included the construction of the dpa framework by condensation of *p*-aminobenzoic acid with two equivalents of 2-bromopyridine, $K_2CO_3$, and co-catalysts KI, $Cu(SO_4)_2$ and phenanthroline, to give the pure compound in 52% yield. Ester **5** was deprotected in standard conditions to yield the free acid **2** (89%).

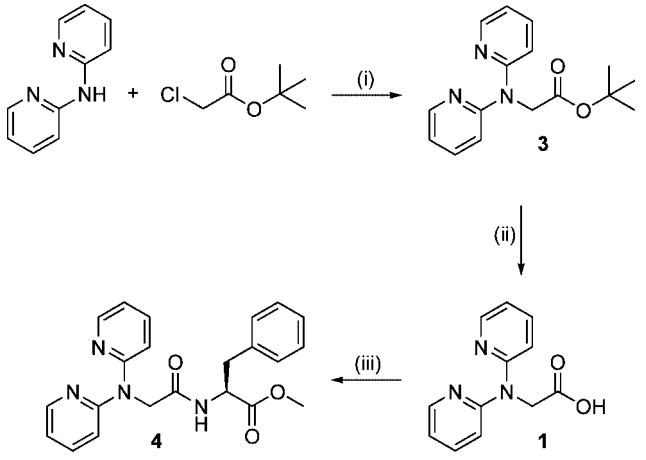


Scheme 1. Synthesis of the aliphatic side chain dpa derivatives **1**, **3** and **4**: (i) KOH, KI (cat.), DMSO/2 h, room temp. (47%); (ii) TFA, TIS, DCM/10 h, room temp. (91%); (iii) HBTU, HOBt, H-Phe-OMe·HCl, DIPEA/20 h, 0 °C→room temp. (51%).

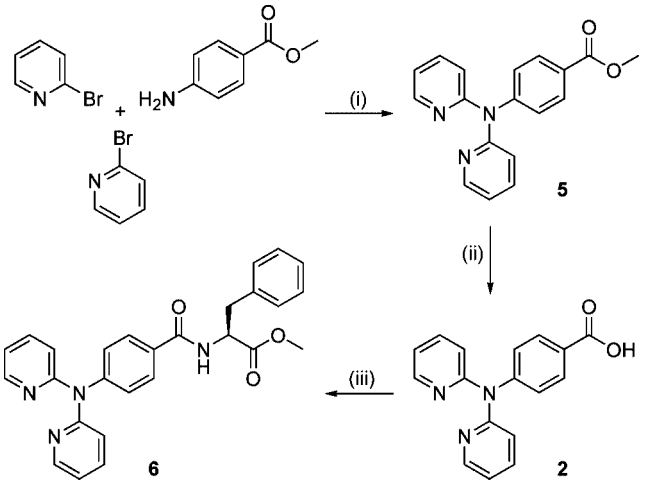


Scheme 2. Synthesis of the aromatic side chain dpa derivatives **2**, **5** and **6**: (i) $K_2CO_3$, KI (cat.), $Cu(SO_4)_2{\cdot}5H_2O$ (cat.) phen (cat.), neat/7 h, 200 °C (52%); (ii) 1 M NaOH/16 h, room temp. (89%); (iii) HBTU, HOBt, H-Phe-OMe·HCl, DIPEA/20 h, 0 °C→room temp. (56%).

The ability of the ligands **1** and **2** to react in amide condensations was tested by reaction with the primary amine group of acid-protected phenylalanine according to Scheme 1 and Scheme 2. The corresponding products **4** and **6** were obtained, strongly indicating the viability of **1** and **2**, respectively, for the construction of dpa-substituted aeg oligomers.

Interestingly, the $^1H$ NMR ($CDCl_3$) spectra of the phenylalanine conjugates **4** and **6** contain different features. The amide proton in **6** is found below 7 ppm, as expected for an amide proton not involved in H-bonding. In contrast the

 © 2007 Wiley-VCH Verlag GmbH & Co. KGaA, Weinheim 

amide proton in **4** is shifted above 7 ppm, which is indicative of H-bonding that likely is a result of the formation of the cyclic conformation of **4** in Figure 2. A hydrogen bond between the amide proton and the central dpa nitrogen atom causes the formation of a five-membered ring. This cyclic conformation is not possible for the rigid conjugate **6**.

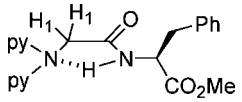


**4**

Figure 2. The cyclic conformation of dpa - amino acid conjugate **4** in $CDCl_3$ solution.

## Dpa Metal Complexes

The complexes $\mathbf{3_{Cu}}$–$\mathbf{6_{Cu}}$ have been obtained in moderate to good yields (50–75%) by mixing methanolic solutions of ligands **3** or **4** with $Cu^{II}$ nitrate and ligands **5** or **6** with $Cu^{II}$ perchlorate as shown in Scheme 3. Time of flight positive ion electrospray (TOF-ES+) mass spectra of $\mathbf{3_{Cu}}$–$\mathbf{6_{Cu}}$ contain the molecular ion peaks for the $[CuL_2]^+$ complex, where L is the corresponding ligand **3**–**6**.

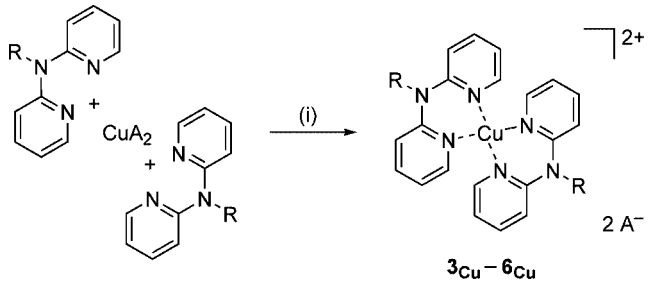


$\mathbf{3_{Cu}}$ – $\mathbf{6_{Cu}}$

$\mathbf{3_{Cu}}$, R = -$CH_2CO_2t$Bu, A = $NO_3^-$
$\mathbf{4_{Cu}}$, R = -$CH_2$CO-PheOMe, A = $NO_3^-$
$\mathbf{5_{Cu}}$, R = -*p*-$C_6H_4CO_2$Me, A = $ClO_4^-$
$\mathbf{6_{Cu}}$, R = -*p*-$C_6H_4$CO-PheOMe, A = $ClO_4^-$

Scheme 3. Synthesis of the $[Cu(dpa)_2]$ complexes $\mathbf{3_{Cu}}$–$\mathbf{6_{Cu}}$: (i) MeOH, Δ (50–75%).

Optical absorbance and emission spectroscopy were also used to characterize the Cu complexes. The UV/Vis absorbance and fluorescence spectroscopic data of complexes $\mathbf{3_{Cu}}$–$\mathbf{6_{Cu}}$ are compared to those of the free ligands **3**–**6** in Table 1. Absorption spectra of the ligands and the Cu complexes contain characteristic peaks at high energy that are due to the π–π* transition of the aryl groups ($\lambda < 320$ nm). Additional peaks in the spectra of $\mathbf{3_{Cu}}$–$\mathbf{6_{Cu}}$ are found at 375–390 nm and above 600 nm. Both the ligands and the metal complexes are emissive; the UV (for **3** and **4**) or blue (for **5** and **6**) fluorescent emission of the free ligands is attributed to π*–π relaxation in the dpa ligand.[32] The red shift of the emission bands in the aromatic side chain ligands **5** and **6** is a result of the conjugation with the adjacent phenyl ring. In contrast, the emission bands are preserved in the Cu complexes, but are weaker in intensity than in the corresponding free ligands, as has been reported for other $[Cu(dpa)_2]^{2+}$ complexes.[33]

Table 1. Compilation of spectroscopic data.

| | $\lambda_{max}$/nm[a] | | |
|---|---|---|---|
| | $\lambda_{abs}$ | $\lambda_{ex}$ | $\lambda_{em}$ |
| **3** | 228, 306 | 296 | 360 |
| **4** | 228, 303[b] | 278 | 304 |
| **5** | 223, 311 | 324 | 432 |
| **6** | 225,[b] 311 | 318 | 414 |
| $\mathbf{3_{Cu}}$ | 296, 379,[c] 621[c] | 280 | 305 |
| $\mathbf{4_{Cu}}$ | 296, 376,[c] 594[c] | 279 | 304 |
| $\mathbf{5_{Cu}}$ | 315, 390,[c,b] 679[c,d] | 324 | 434 |
| $\mathbf{6_{Cu}}$ | 309, 391,[c] 678[c,d] | 317 | 415 |

[a] The maxima ($\lambda_{max}$) of absorption ($\lambda_{abs}$), excitation ($\lambda_{ex}$) and emission ($\lambda_{em}$) were measured in methanol. [b] Shoulder. [c] These signals were measured in methanol/water = 1:1 solvent mixture due to low solubility in methanol. [d] very broad peak.

X-band EPR spectra of $\mathbf{4_{Cu}}$ and $\mathbf{6_{Cu}}$ (0.5 mM in frozen solution of a 1:1 water/methanol mixture) both show a well-resolved axial $Cu^{II}$ signal with large separation of $g_{\|}$ and $g_{\perp}$ (Figures S9 and S10 and quantitative details in the supporting information; for supporting information see also the footnote on the first page of this paper). This observation is expected for a compound containing electronically identical $Cu^{II}$ atoms separated by a distance of at least 6 Å[14a,34a] and is consistent with the geometry found by X-ray crystallography, see below. In addition, the EPR spectra show hyperfine splitting due to coupling of the unpaired electron with the copper nucleus ($I$ = 3/2 for $^{63}$Cu and $^{65}$Cu) and superhyperfine splitting due to coupling with the directly coordinated nitrogen nuclei ($I$ = 1 for $^{14}$N and $I$ = 1/2 $^{15}$N).[34b,34c]

## X-ray Crystallography

Single crystals suitable for X-ray analysis could be obtained for all four complexes in this study. Precipitation from a methanol solution was successful for $\mathbf{5_{Cu}}$, diffusion of diethyl ether in the methanol solution of the complex was used for $\mathbf{3_{Cu}}$, while slow evaporation from methanol solution was applied for $\mathbf{4_{Cu}}$ and $\mathbf{6_{Cu}}$.[35] Single crystals of the complexes were grown directly from the reaction mix-

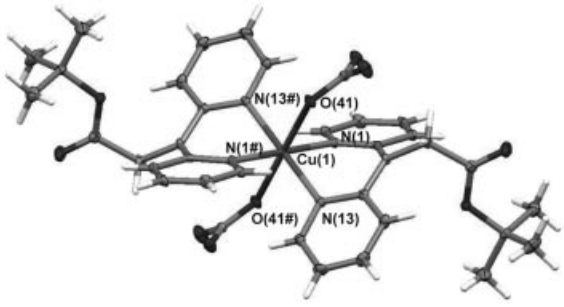


Figure 3. X-ray single crystal structure of $\mathbf{3_{Cu}}$ (thermal ellipsoids at 50% probability).

 © 2007 Wiley-VCH Verlag GmbH & Co. KGaA, Weinheim 

ture at room temperature; the solved crystal structures are shown in Figures 3, 4, 5 and 6, and the selected bond lengths and angles are collected in Table 2.

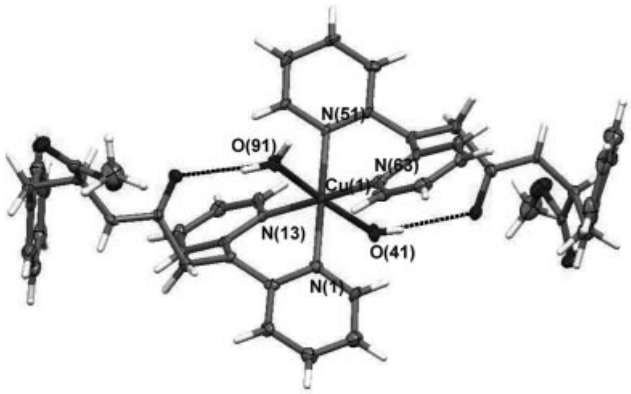


Figure 4. X-ray single crystal structure of $\mathbf{4_{Cu}}$ dication (thermal ellipsoids at 30% probability). The nitrate counterions and methanol solvent molecules are omitted for clarity.

Table 2. Selected bond lengths [Å] and angles [°] for $\mathbf{3_{Cu}}$-$\mathbf{6_{Cu}}$.

| | $\mathbf{3_{Cu}}$ | $\mathbf{4_{Cu}}$ | $\mathbf{5_{Cu}}$ | $\mathbf{6_{Cu}}$ |
|---|---|---|---|---|
| Cu(1)–N(1) | 1.994(2) | 2.011(6) | 2.007(2) | 2.006(7) |
| Cu(1)–N(51) | – | 2.029 | – | 2.008(7) |
| Cu(1)–N(13) | 2.005(2) | 2.029(6) | 1.982(2) | 2.015(7) |
| Cu(1)–N(63) | – | 1.980(6) | – | 2.007(6) |
| Cu(1)–O(41) | 2.467(2) | 2.451(5) | 2.472(2) | 2.452(7) |
| Cu(1)–O(91) | – | 2.411(6) | – | 2.477(8) |
| N(1)–Cu(1)–N(13) | 85.10(7) | 85.3(2) | 85.67(9) | 86.0(3) |
| N(51)–Cu(1)–N(63) | – | 86.4(2) | – | 84.7(3) |
| N(1)–Cu(1)–O(41) | 96.98(6) | 91.4(2) | 89.58(9) | 93.1(2) |
| N(1)–Cu(1)–O(91) | – | 84.8(3) | – | 88.5(2) |
| N(13)–Cu(1)–O(41) | 89.74(7) | 93.4(3) | 93.43(9) | 81.1(3) |
| N(13)–Cu(1)–O(91) | – | 85.5(2) | – | 87.3(3) |
| N(1)–C(6)–C(8)–C(13) | –8.8 | 3.4 | 7.2 | 5.2 |
| N(51)–C(56)–C(58)–C(63) | – | –2.8 | – | 2.1 |
| $\alpha$ [plane A/plane A′][a] | 43.6 | 53.4, 50.0 | 37.0 | 34.8, 36.9 |
| $\beta$ [plane B/plane C][a] | 38.1 | 35.6, 36.7 | 39.0 | 35.4, 41.5 |
| $\chi$ [plane D/plane Ph][a] | – | – | 73.7 | 87.4, 79.6 |

[a] See Figure 7 for explanation.

The crystal structures of $\mathbf{3_{Cu}}$–$\mathbf{6_{Cu}}$ share a number of common features that for clarity are described using $\mathbf{3_{Cu}}$ as the example (Figure 3). The structure unambiguously confirms

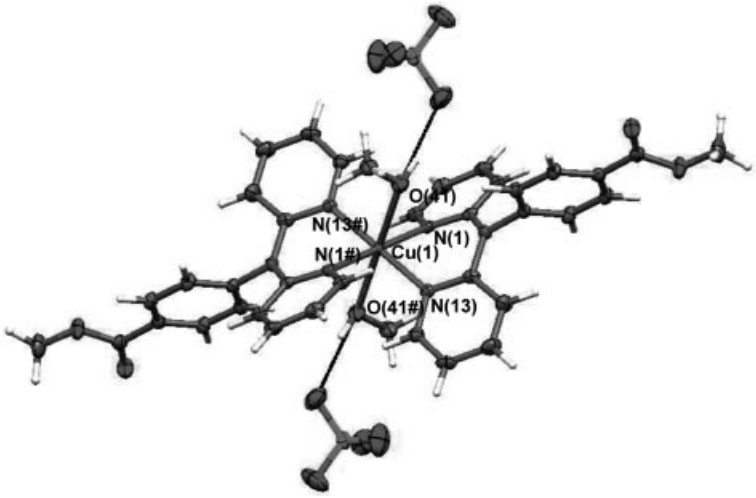


Figure 5. X-ray single crystal structure of $\mathbf{5_{Cu}}$ (thermal ellipsoids at 50% probability).

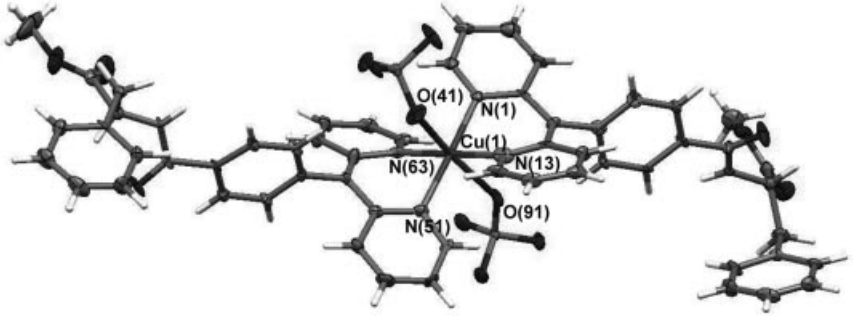


Figure 6. X-ray single crystal structure of $\mathbf{6_{Cu}}$ (thermal ellipsoids at 50% probability).

 © 2007 Wiley-VCH Verlag GmbH & Co. KGaA, Weinheim 

the [Cu(dpa)$_2$] stoichiometry as well as the bidentate nature of the dpa ligand, in which only the py nitrogen atoms coordinate to the Cu and the central dpa amine atom is not involved in metal chelation. The $N_4O_2$ coordination polyhedron is Jahn–Teller distorted square pyramidal. Four N atoms from the two dpa ligands coordinate to the Cu in the equatorial plane, *d*(Cu–N) = 1.99 and 2.01 Å, while nitrate counterions occupy the apical positions, *d*(Cu–O) = 2.47 Å. The bite angle of the dpa ligand (85.1°) indicates that there is only minimal strain in the six-membered chelate ring. Because the counterions or solvent molecules occupy apical positions, differences exist in the structures: these are nitrates in $\mathbf{3_{Cu}}$, perchlorates in $\mathbf{6_{Cu}}$, water in $\mathbf{4_{Cu}}$, and methanol in $\mathbf{5_{Cu}}$.

Selected geometrical parameters are summarized in Figure 7. The dpa moiety in $\mathbf{3_{Cu}}$ is not planar, and the angle $\alpha$ between the py rings is found to be 43.6°. In addition the central dpa chelate ring B is not coplanar with the coordination plane C and the angle between B and C is 38.1°. The conformation of the phenyl side chain with respect to the dpa moiety defined by the $\chi$ angle, specific to $\mathbf{5_{Cu}}$ and $\mathbf{6_{Cu}}$, is shown in Figure 7.[36] In both $\mathbf{5_{Cu}}$ and $\mathbf{6_{Cu}}$ $\chi$ is rather large, >70°, resulting in a "twisted" conformation in these complexes.

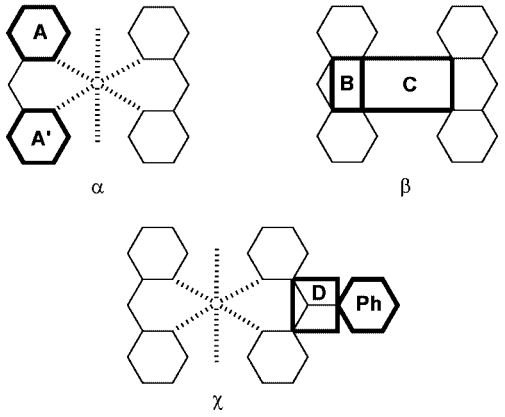


Figure 7. Selected geometrical parameters in [Cu(dpa)$_2$] complexes are defined as $\alpha$ (angle between the planes A and A′), $\beta$ (angle between B and C), and $\chi$ (angle between the planes H and Ph).

In $\mathbf{3_{Cu}}$ and $\mathbf{5_{Cu}}$ no significant intermolecular contacts are found, except the hydrogen bond between the coordinated methanol and a perchlorate counterion in $\mathbf{5_{Cu}}$. The inorganic nucleoside pair analogs $\mathbf{4_{Cu}}$ and $\mathbf{6_{Cu}}$ have more interesting intermolecular interactions. In $\mathbf{4_{Cu}}$ the amide oxygen atom of the dpa ligand coordinates to the water molecule in the apical position by hydrogen bonding. In addition, π-stacking is found between dpa ligands from neighboring molecules, which causes chains to form along the *a* crystallographic axis (Figure S11 in the electronic supporting information). Dpa π-stacking allows the Cu atoms of neighboring complexes to come as close as 8.2 Å. In $\mathbf{6_{Cu}}$, short contacts include hydrogen bonding between the coordinated perchlorate counterion of one molecule and the phenylalanine amide proton of the neighboring molecule. There is also weak π-stacking between the py substituent from one molecule with the phenyl substituent of Phe from its neighbor. These contacts cause the formation of chains along the *c* axis in the crystal of $\mathbf{6_{Cu}}$ (Figure S12 in the electronic supporting information). As a result, the Cu–Cu separation in these chains is 12.1 Å. The large separation of the copper centers in $\mathbf{4_{Cu}}$ and $\mathbf{6_{Cu}}$ is in accordance with the EPR spectra discussed above.

## Conclusions

The two new bidentate heterocyclic nitrogen ligands **3** and **5** have been prepared using the Ullmann reaction in at least 47% yield. The ester groups in **3** and **5** have been hydrolyzed in standard conditions to give the acids **1** and **2**, respectively. Ligands **1** and **2** have a carboxylic functional group that allows their use in conjugation with biological molecules. To confirm this, the bioconjugates **4** and **6** with the amino acid H-Phe-OMe have been prepared following Scheme 1 and Scheme 2.

The Cu complexes $\mathbf{3_{Cu}}$–$\mathbf{6_{Cu}}$ have been synthesized and fully characterized, including their X-ray single crystal structures. In addition to confirming the 1:2 metal to ligand stoichiometry, the X-ray structures reveal square bipyramidal geometries for all four complexes in this study. Both the free ligands and their corresponding Cu complexes are fluorescent.

Conjugates of metal complexes with amino acids or peptides have a number of biological applications,[37,38] including artificial catalysts or enzymes for biochemical reactions.[39] In this paper, we present complexes with an 1:2 metal/ligand stoichiometry that can serve as inorganic analogs of nucleic acids.[5b,14] Our current efforts are focused on the development of chiral inorganic nucleic acid models based on the aeg-oligoamide chemistry.

## Experimental Section

**General Remarks:** Chemicals were used without further purification except where indicated. UV/Vis absorption spectra were measured in 1-cm quartz cuvettes in a double-beam spectrophotometer (Varian Cary 500). Excitation and emission spectra were recorded with a Photon Technologies International fluorimeter. Positive-ion time of flight electrospray mass spectrometry (TOF ES+) was performed using a Mariner mass spectrometer (Perseptive Biosystems). For fragments containing copper only the isotopomer of the highest intensity was described. NMR spectra were collected with a 360-MHz spectrometer (Bruker AV 360). Chemical shifts, $\delta$/ppm, indicate a downfield shift from tetramethylsilane, TMS, the internal standard. Coupling constants, *J*, are given in Hz. X-band EPR spectra were obtained using a 9.5-GHz Bruker eleXsys 500 spectrometer equipped with a liquid helium cryostat. The experiments were performed in a frozen solution (0.5 mM in methanol/water = 1:1) at 20 K, with a modulation frequency of 100 kHz and a modulation amplitude of 5 G. The *g* factors were calculated as $g = 714.484\ \nu/B_0$, were $\nu$ is the microwave frequency in GHz and $B_0$ the magnetic field in gauss.

**Dpa-$CH_2CO_2t$Bu (3):** KOH (3.0 g, 53.6 mmol, 4.6 equiv.) was added to the solution of dpa (2.0 g, 11.7 mmol) in dimethyl sulfox-

 © 2007 Wiley-VCH Verlag GmbH & Co. KGaA, Weinheim 

ide (DMSO, 40 mL) and the resulting suspension was stirred overnight at room temperature. KI (200 mg, 1.2 mmol, 0.1 equiv.) and *tert*-butyl chloroacetate (4 × 0.5 mL, 14.0 mmol, 1.2 equiv.) were added. The reaction was stirred for additional 2 h and the resulting mixture was extracted with diethyl ether (3 × 50 mL). The organic extracts were dried with $Na_2SO_4$, filtered and the ether removed under reduced pressure to give a brown oil. The crude product was purified by column chromatography (silica, hexane/ethyl acetate = 8:2). Yield: 1.56 g (47%), pale yellow oil. $M_r$ (calcd. for $C_{16}H_{19}N_3O_2$) = 285.34, MS (TOF ES+): *m*/*z* = 324.5 $[M + K]^+$, 308.5 $[M + Na]^+$, 286.5 $[M + H]^+$, 230 $[M - OtBu]^+$. HR MS (TOF ES+): exp. 286.1549 and calcd. 286.1556 for $[C_{17}H_{12}N_3O_2]^+$. $^1H$ NMR ($CDCl_3$): $\delta$ = 8.32 (ddd, $^3J_{HH}$ = 1.0, 2.0 and 5.0 Hz, 2 H, $H_{py\text{-}6}$), 7.53 (ddd, $^3J_{HH}$ = 2.0, 7.2 and 8.4 Hz, 2 H, $H_{py\text{-}4}$), 7.22 (dt, $^3J_{HH}$ = 1.0 and 8.4 Hz, 2 H, $H_{py\text{-}3}$), 6.87 (ddd, $^3J_{HH}$ = 1.0, 5.0 and 7.2 Hz, 2 H, $H_{py\text{-}5}$), 4.83 (s, 2 H, $H_1$), 1.42 (s, 9 H, $H_{OtBu}$) ppm. $^{13}C$ NMR ($CDCl_3$): $\delta$ = 175.26 (C=O), 156.75 ($C_{py\text{-}2}$), 148.24 ($C_{py\text{-}6}$), 137.14 ($C_{py\text{-}4}$), 117.24 ($C_{py\text{-}5}$), 113.87 ($C_{py\text{-}3}$), 80.93 ($C_{q\text{-}tBu}$), 50.63 ($C_1$), 28.03 ($C_{Me}$) ppm.

**Dpa-$CH_2CO_2H$ (1):** Dpa-Ac-O*t*Bu (**3**, 1.5 g, 5.26 mmol) was dissolved in a mixture of dichloromethane (DCM, 12 mL), TIS (0.6 mL) and TFA (12 mL), stirred at room temperature and the reaction monitored by TLC (silica, hexane/ethyl acetate = 8:2). After the disappearance of the starting material (10 h), the DCM was evaporated under reduced pressure and cold ether (–20 °C) was added to the residue. After 1 h at –20 °C, the precipitate was collected by filtration. Yield: 1.10 g (91%) of an off-white solid. $M_r$ (calcd. for $C_{12}H_{11}N_3O_2$) = 229.23. MS (TOF ES+): *m*/*z* = 230.1 $[M + H]^+$, 252.1 $[M + Na]^+$. HR MS (TOF ES+): exp. 230.0921 and calcd. 230.0930 for $[C_{17}H_{12}N_3O_2]^+$. $^1H$ NMR ([D$_6$]DMSO): $\delta$ = 8.30 (ddd, $^3J_{HH}$ = 0.8 and 5.0 Hz, 2 H, $H_{py\text{-}6}$), 7.72 (dq, $^3J_{HH}$ = 2.0 and 8.5 Hz, 2 H, $H_{py\text{-}4}$), 7.29 (dt, $^3J_{HH}$ = 0.8 and 8.5 Hz, 2 H, $H_{py\text{-}3}$), 7.02 (dq, $^3J_{HH}$ = 0.8 and 5.0 Hz, 2 H, $H_{py\text{-}5}$), 4.82 (s, 2 H, $H_1$) ppm. $^{13}C$ NMR ([D$_6$]DMSO): $\delta$ = 170.96 (C=O), 155.22 ($C_{py\text{-}2}$), 146.83 ($C_{py\text{-}6}$), 137.99 ($C_{py\text{-}4}$), 117.33 ($C_{py\text{-}5}$), 113.70 ($C_{py\text{-}3}$), 48.91 ($C_1$) ppm.

**Dpa-$CH_2$CO-PheOMe (4):** Dpa acetic acid (**1**, 229 mg, 1 mmol), was suspended in acetonitrile (30 mL) and cooled to 0 °C with an ice bath. HBTU (379 mg, 1 mmol) and diisopropylethylamine (DIPEA, 875 μL, 5 mmol) were added. After the clear solution was stirred for 1 h at 0 °C, H-Phe-OMe·HCl (216 mg, 1 mmol) was added. The reaction mixture was allowed to reach room temperature and the stirring was continued for 20 h. After that period, the reaction mixture was concentrated under reduced pressure. The residue was dissolved in DCM (50 mL), washed with sodium hydrogen carbonate (satd. aq., 3 × 50 mL) and the organic extract was dried with sodium sulfate, filtered and evaporated under reduced pressure. The crude product was subjected to column chromatography (silica, hexane/ethyl acetate = 2:8) to yield a colorless oil (200 mg, 51%). $M_r$ (calcd. for $C_{22}H_{22}N_4O_3$) = 390.44, MS (TOF ES+): *m*/*z* = 391.2 $[M + H]^+$, 413.2 $[M + Na]^+$. HR MS (TOF ES+): exp. 391.1802 and calcd. 391.1770 for $[C_{22}H_{23}N_4O_3]^+$. $^1H$ NMR ($CDCl_3$): $\delta$ = 8.32 (ddd, $^3J_{HH}$ = 1.0, 2.0 and 5.0 Hz, 2 H, $H_{py\text{-}6}$), 7.85 (d, $^3J_{HH}$ = 8.0 Hz, 1 H, $NH_{amide}$), 7.58 (ddd, $^3J_{HH}$ = 2.0, 7.5 and 9.5 Hz, 2 H, $H_{py\text{-}4}$), 7.14–7.07 (m, 5 H, 2 $H_{Ph\text{-}m}$, 1 $H_{Ph\text{-}p}$ and 2 $H_{py\text{-}3}$), 6.96–6.91 (m, 4 H, 2 $H_{Ph\text{-}o}$ and 2 $H_{Py\text{-}5}$), 4.90 (td, $^3J_{HH}$ = 6.0 and 8.0 Hz, 1 H, $H_{Phe\text{-}a}$), 4.84 (d, $^3J_{HH}$ = 16.5 Hz, 1 H, $H_{1a}$), 4.71 (d, $^3J_{HH}$ = 16.5 Hz, 1 H, $H_{1b}$), 3.63 (s, 3 H, $H_{OMe}$), 3.11–2.99 (m, 2 H, $H_{Phe\text{-}\beta}$) ppm. $^{13}C$ NMR ($CDCl_3$): $\delta$ = 171.65 ($C_{ester}$), 170.57 ($C_{amide}$), 156.33 ($C_{py\text{-}2}$), 148.32 ($C_{py\text{-}6}$), 137.59 ($C_{ph\text{-}i}$), 135.89 ($C_{py\text{-}4}$), 129.22 ($C_{phe\text{-}m}$), 128.21 ($C_{phe\text{-}o}$), 126.78 ($C_{phe\text{-}p}$), 117.92 ($C_{py\text{-}5}$), 114.42 ($C_{py\text{-}3}$), 53.07 ($C_1$), 52.71 ($C_{OMe}$), 52.09 ($C_{Phe\text{-}\alpha}$), 37.85 ($C_{Phe\text{-}\beta}$) ppm.

**Dpa-$PhCO_2$Me (5):** Methyl *p*-aminobenzoic acid (2 g, 13.23 mmol), 2-bromopyridine (2.5 mL, 26.11 mmol), potassium carbonate (2 g), potassium iodide (200 mg), copper(II) sulfate pentahydrate (200 mg) and phenanthroline (200 mg) were mixed in a 100-mL round-bottomed flask and heated at 200 °C for 7 h. After the reaction mixture was cooled down to room temperature, it was partitioned between water (150 mL) and ethyl acetate (150 mL). The water layer was further extracted with ethyl acetate (2 × 150 mL). The combined organic extracts were dried with sodium sulfate, filtered and evaporated at reduced pressure. The crude product was subjected to column chromatography (Ø 2.5 cm, silica, 75 g), a hexane/ethyl acetate gradient (5:5 → 2:8) was used as eluent. Yield: 2.0 g (52%), pale yellow oil. $M_r$ (calcd. for $C_{18}H_{15}N_3O_2$) = 305.33. MS (TOF ES+): *m*/*z* = 306.1 $[M + H]^+$. HR MS (TOF ES+): exp. 306.1261 and calcd. 306.1243 for $[C_{18}H_{16}N_3O_2]^+$. $^1H$ NMR ($CDCl_3$): $\delta$ = 8.36 (ddd, $^3J_{HH}$ = 1.0, 2.0 and 5.0 Hz, 2 H, $H_{Py\text{-}6}$), 7.79 (d, $^3J_{HH}$ = 9.0 Hz, 2 H, $H_{Ph\text{-}3,5}$), 7.60 (ddd, $^3J_{HH}$ = 2.0, 7.5 and 8.5 Hz, 2 H, $H_{py\text{-}4}$), 7.16 (d, $^3J_{HH}$ = 9.0 Hz, 2 H, $H_{Ph\text{-}2,6}$), 6.99–7.04 (m, 4 H, $H_{py\text{-}5}$ and $H_{py\text{-}3}$), 3.89 (s, 3 H, $H_{OMe}$) ppm. $^{13}C$ NMR ($CDCl_3$): $\delta$ = 166.14 (C=O), 157.68 ($C_{py\text{-}2}$), 149.30 ($C_{Ph\text{-}1}$), 148.90 ($C_{Py\text{-}6}$), 137.86 ($C_{Py\text{-}4}$), 130.96 ($C_{Ph\text{-}3,5}$), 125.83 ($C_{Ph\text{-}2,6}$), 124.98 ($C_{Ph\text{-}4}$), 119.14 ($C_{Py\text{-}5}$), 117.88 ($C_{Py\text{-}3}$), 52.61 ($C_{OMe}$) ppm.

**Dpa-$PhCO_2$H (2):** Ligand **5** (2.0 g, 6.55 mmol) was dissolved in methanol (20 mL), 1 M NaOH (aq., 1.6 g in 20 mL) was stirred room temperature added and monitored by TLC (silica, hexane/ethyl acetate = 3:7). After the disappearance of the starting material (16 h), the reaction mixture was neutralized with HCl and the solvents evaporated to dryness. The residue was partitioned between water (150 mL) and ethyl acetate (150 mL), and the aqueous layer was further extracted with ethyl acetate (2 × 150 mL), dried with sodium sulfate, filtered and evaporated at reduced pressure. Yield: 1.63 g (89%), off white solid. The crude product was used without further purification. $M_r$ ($C_{17}H_{13}N_3O_2$) = 291.30. MS (TOF ES+): *m*/*z* = 292.1 $[M + H]^+$, 314.1 $[M + Na]^+$. HR MS (TOF ES+): exp. 292.1100 and calcd. 292.1086 for $[C_{17}H_{14}N_3O_2]^+$. $^1H$ NMR ([D$_6$]-DMSO): $\delta$ = 8.22 (m, 2 H, $H_{py\text{-}6}$), 8.85 (d, $^3J_{HH}$ = 8.5 Hz, 2 H, $H_{Ph\text{-}3,5}$), 7.66 (ddd, $^3J_{HH}$ = 2.0 Hz, 2 H, $H_{py\text{-}4}$, 7.5 and 8.5), 7.03–6.92 (m, 6 H, $H_{Ph\text{-}2,6}$, $H_{Ph\text{-}2,6}$ and $H_{py\text{-}5}$) ppm. $^{13}C$ NMR ([D$_6$]-DMSO): $\delta$ = 167.32 (C=O), 157.28 ($C_{py\text{-}2}$), 148.61 ($C_{Ph\text{-}1}$), 148.41 ($C_{Py\text{-}6}$), 138.23 ($C_{Py\text{-}4}$), 130.58 ($C_{Ph\text{-}3,5}$), 127.30 ($C_{Ph\text{-}4}$), 124.89 ($C_{Ph\text{-}2,6}$), 119.19 ($C_{Py\text{-}5}$), 117.63 ($C_{Py\text{-}3}$) ppm.

**Dpa-PhCO-Phe-OMe (6):** Dpa *p*-benzoic acid (**2**, 220 mg, 0.75 mmol), was suspended in DCM (30 mL) and cooled to 0 °C with an ice bath. HBTU (284 mg, 0.75 mmol), HOBt (125 mg, 0.75 mmol) and DIPEA (700 μL, 4 mmol) were added. After the clear solution was stirred for 1 h at 0 °C, H-Phe-OMe·HCl (165 mg, 0.75 mmol) was added. The reaction mixture was allowed to reach room temperature and the stirring was continued for 20 h. After that period, the reaction mixture was washed with sodium hydrogen carbonate (satd. aq., 3 × 50 mL) and the extracts was dried with sodium sulfate, filtered and evaporated under reduced pressure. The crude product was subjected to column chromatography (silica, hexane/ethyl acetate = 2:8) to yield an off-white solid (190 mg, 56%). $M_r$ (calcd. for $C_{27}H_{24}N_4O_3$) = 452.50. MS (TOF ES+): *m*/*z* = 453.2 $[M + H]^+$, 475.2 $[M + Na]^+$. HR MS (TOF ES+): exp. 453.1932 and calcd. 453.1940 for $[C_{27}H_{25}N_4O_3]^+$. $^1H$ NMR ($CDCl_3$): $\delta$ = 8.33 (ddd, $^3J_{HH}$ = 1.0, 2.0 and 5.0 Hz, 2 H, $H_{py\text{-}6}$), 7.68 (d, $^3J_{HH}$ = 9.0 Hz, 2 H, $H_{Ph\text{-}3,5}$), 7.58 (ddd, $^3J_{HH}$ = 2.0, 7.5 and 9.5 Hz, 2 H, $H_{py\text{-}4}$), 7.31–7.06 (m, 7 H, $H_{Ph\text{-}3,5}$, $H_{Ph\text{-}m}$, $H_{Ph\text{-}p}$ and $H_{py\text{-}3}$), 7.01–6.95 (m, 4 H, $H_{Ph\text{-}o}$ and $H_{Py\text{-}5}$), 6.49 (d, $^3J_{HH}$ = 7.5 Hz, 1 H, $NH_{amide}$), 4.90 (td, $^3J_{HH}$ = 5.5 and 7.5 Hz, 1 H, $H_{Phe\text{-}\alpha}$), 3.75 (s, 3 H, $H_{OMe}$), 3.27 (dd, $^3J_{HH}$ = 5.5 and 14.0 Hz, 1 H, $H_{Phe\text{-}\beta1}$), 3.27 (dd, $^3J_{HH}$ = 5.5 and 14.0 Hz, 1 H, $H_{Phe\text{-}\beta2}$) ppm.

 © 2007 Wiley-VCH Verlag GmbH & Co. KGaA, Weinheim 

$^{13}$C NMR ($CDCl_3$): $\delta$ = 171.95 ($C_{ester}$), 166.18 ($C_{amide}$), 157.62 ($C_{py\text{-}2}$), 148.76 ($C_{Ph\text{-}1}$), 148.23 ($C_{py\text{-}6}$), 137.80 ($C_{Ph\text{-}i}$), 135.78 ($C_{py\text{-}4}$), 129.78 ($C_{Ph\text{-}4}$), 129.25 ($C_{phe\text{-}m}$), 128.56 ($C_{Ph\text{-}3,5}$), 128.37 ($C_{phe\text{-}o}$), 127.10 ($C_{phe\text{-}p}$), 125.58 ($C_{Ph\text{-}2,6}$), 118.95 ($C_{py\text{-}5}$), 117.62 ($C_{py\text{-}3}$), 53.33 ($C_{OMe}$), 52.29 ($C_{Phe\text{-}\alpha}$), 37.73 ($C_{Phe\text{-}\beta}$) ppm.

***Caution:*** *Perchlorate salts are potentially explosive and should be handled with great care!*

**Cu Complexes, General Procedure:** Solutions containing the corresponding ligand or Cu salt were briefly heated to boiling before adding the Cu salt solution to the ligand solution reaction mixture was filtered hot and cooled to room temperature. If precipitation was observed, the vial was closed and left at room temperature for the indicated period (method 1). If no precipitation occurred, the vial was placed in a container with diethyl ether (10 mL), closed, and left at room temperature for the indicated period (method 2), or the vial was left open for slow evaporation of the solvent (method 3). In all cases the product was isolated by filtration and dried in air.

**[Cu(dpa-$CH_2CO_2t$Bu)$_2$(NO$_3$)$_2$] ($\mathbf{3_{Cu}}$):** Ligand **3** (62.7 mg, 0.22 mmol), $Cu(NO_3)_2{\cdot}2.5H_2O$ (23 mg, 0.10 mmol) and methanol (10 + 5 mL) were used, method 2. After standing for 7 d, the product was collected by filtration. Yield: 38 mg (50%) of dark brown crystals, X-ray quality. $M_r$ (calcd. for $C_{32}H_{38}N_8O_{10}Cu$) = 758.24. MS (TOF ES+): *m*/*z* = 286 [ligand **3** + H]$^+$, 317 [M – 2NO$_3$]$^{2+}$, 410 [M – NO$_3$ – ligand **3**]$^+$, 633 [M – 2NO$_3$]$^+$. HR MS (TOF ES+): *m*/*z* = exp. 633.2210 and calcd. 633.2251 for [$C_{32}H_{38}N_6O_4{}^{63}Cu$]$^+$.

**[Cu(dpa-$CH_2$CO-PheOMe)$_2$(H$_2$O)$_2$](NO$_3$)$_2{\cdot}$2MeOH ($\mathbf{4_{Cu}}$):** Ligand **4** (39 mg, 0.11 mmol), $Cu(NO_3)_2{\cdot}2.5H_2O$ (12 mg, 0.05 mmol) and methanol (10 + 5 mL) were used, method 3. After standing for 5 d, the product was collected by filtration. Yield: 40 mg (75%) of violet-blue crystals, X-ray quality. $M_r$ (calcd. for $C_{46}H_{56}N_{10}O_{16}Cu$) = 1068.54; M (TOF ES+): 391.2 [ligand **4** + H]$^+$, 413.2 [ligand **4** + Na]$^+$, 453.1 [M – 2NO$_3$ – ligand **4**]$^+$, 843.3 [M – 2NO$_3$]$^+$, 866.4 [M – 2NO$_3$ + Na]$^+$. HR MS (TOF ES+): exp. 843.2717 and calcd. 843.2680 for [$C_{44}H_{44}N_8O_6{}^{63}Cu$]$^+$; X-band EPR (9.370 GHz): $g_\parallel$ = 2.17, $A_\parallel = 189\times10^{-4}$ cm$^{-1}$, $g_\perp$ = 2.05.

**[Cu(dpa-PhCO$_2$Me)$_2$(MeOH)$_2$](ClO$_4$)$_2$ ($\mathbf{5_{Cu}}$):** Ligand **5** (33.6 mg, 0.11 mmol), $Cu(ClO_4)_2{\cdot}6H_2O$ (18.5 mg, 0.05 mmol) and methanol (5 + 5 mL) were used, method 1. After standing for 1 d, the product was collected by filtration. Yield: 35 mg (75%) of dark brown crystals, X-ray quality. $M_r$ (calcd. for $C_{36}H_{30}Cl_2N_6O_{12}Cu$) = 873.11; M (TOF ES+): 306.1 [ligand **5** + H]$^+$, 328.1 [ligand **5** + Na]$^+$, 369.2 [M – 2 ClO$_4$ – ligand **5**], 673.2 [M – 2 ClO$_4$]$^+$. HR MS (TOF ES+): exp. 673.1627 and calcd. 673.1625 for [$C_{36}H_{30}N_6O_4{}^{63}Cu$]$^+$.

**[Cu(dpa-PhCO-PheOMe)$_2$(ClO$_4$)$_2$] ($\mathbf{6_{Cu}}$):** Ligand **6** (37.3 mg, 0.0825 mmol), $Cu(ClO_4)_2{\cdot}6H_2O$ (13.9 mg, 0.0375 mmol) and methanol (10 + 5 mL) were used, method 3. After standing for 7 d, the product was collected by filtration. Yield: 27 mg (62%) of green-brown crystals, X-ray quality. $M_r$ (calcd. for $C_{54}H_{48}Cl_2N_8O_{14}Cu$) = 1167.46. MS (TOF ES+): *m*/*z* = 453.2 [ligand **6** + H]$^+$, 475.2 [ligand **6** + Na]$^+$, 967.3 [M – 2 ClO$_4$]$^+$. HR MS (TOF ES+): exp. 967.2982 and calcd. 967.2993 for [$C_{54}H_{48}N_8O_6{}^{63}Cu$]$^+$; X-band EPR (9.370 GHz): $g_\parallel$ = 2.24, $A_\parallel = 160\times10^{-4}$ cm$^{-1}$, $g_\perp$ = 2.07.

**X-ray Crystallographic Data Collection and Refinement:** A dark blue single crystal of $\mathbf{3_{Cu}}$, a blue crystal of $\mathbf{4_{Cu}}$ and dark green specimens of $\mathbf{5_{Cu}}$ and $\mathbf{6_{Cu}}$ were coated with paratone freezing oil, picked up with nylon loops and mounted in the nitrogen cold stream of the diffractometer. Intensity data were collected using a Bruker AXS APEX diffractometer equipped with a Mo-target rotating anode X-ray source and a graphite monochromator (Mo-$K_\alpha$ radiation, $\lambda$ = 0.71073 Å). Data reduction (including intensity integration, background, Lorentz and polarization corrections) was performed by use of the Bruker software package. The structure was solved by direct methods (SHELXS)[40] and refined by the full-matrix, least-squares method based on $F^2$ against all reflections (SHELXL).[41] All non-hydrogen atoms were refined anisotropically. Hydrogen atoms were placed geometrically and were refined by use of the riding model. Crystallographic data of $\mathbf{3_{Cu}}$–$\mathbf{6_{Cu}}$ are listed in Table 3.

Table 3. Crystallographic data for $\mathbf{3_{Cu}}$–$\mathbf{6_{Cu}}$.

| | $\mathbf{3_{Cu}}$ | $\mathbf{4_{Cu}}$ | $\mathbf{5_{Cu}}$ | $\mathbf{6_{Cu}}$ |
|---|---|---|---|---|
| Empirical formula | $C_{32}H_{38}CuN_8O_{10}$ | $C_{46}H_{56}CuN_{10}O_{16}$ | $C_{38}H_{38}Cl_2CuN_6O_{14}$ | $C_{54}H_{48}Cl_2CuN_8O_{14}$ |
| Formula weight | 758.25 | 1068.54 | 937.19 | 1167.46 |
| $T$ [K] | 293(2) | 133(2) | 93(2) | 105(2) K |
| $\lambda$ [Å] | 0.71073 | 0.71073 | 0.71073 | 0.71073 |
| Crystal size [mm] | 0.08 × 0.05 × 0.01 | 0.20 × 0.18 × 0.07 | 0.12 × 0.11 × 0.05 | 0.09 × 0.03 × 0.03 |
| Crystal system | monoclinic | triclinic | monoclinic | monoclinic |
| Space group | *C*2/*c* | $P\bar{1}$ | $P2_1/n$ | $P2_1$ |
| *a* [Å] | 19.953(6) | 8.2409(15) | 11.440(5) | 9.530(7) |
| *b* [Å] | 10.109(3) | 11.778(2) | 13.457(6) | 27.68(2) |
| *c* [Å] | 17.502(5) | 12.749(2) | 12.735(6) | 9.909(8) |
| $\alpha$ [°] | 90 | 82.676(3) | 90 | 90 |
| $\beta$ [°] | 102.839(5) | 84.052(3) | 99.963(10) | 103.438(16) |
| $\gamma$ [°] | 90 | 81.784(3) | 90 | 90 |
| $V$ [Å$^3$] | 3441.9(17) | 1210.2(4) | 1930.9(14) | 2542(3) |
| $Z$ | 4 | 1 | 2 | 2 |
| $\rho_{calcd.}$ [g cm$^{-3}$] | 1.463 | 1.466 | 1.612 | 1.525 |
| $\mu_{Mo\text{-}K\alpha}$ [mm$^{-1}$] | 0.704 | 0.534 | 0.784 | 0.614 |
| $\theta$ range [°] | 2.09 ≤ 28.34 | 2.51 ≤ 28.21 | 2.21 ≤ 28.45 | 2.11 ≤ 28.38 |
| Data collected | 15906 | 11582 | 15262 | 19198 |
| Independent data | 4233 [*R*(int) = 0.0503] | 9445 [*R*(int) = 0.0231] | 4804 [*R*(int) = 0.0593] | 11952 [*R*(int) = 0.0980] |
| GOF on $F^2$[a] | 1.024 | 1.019 | 1.058 | 1.093 |
| Final $R_1$ (obsd. data)[b] | 0.0455 | 0.0680 | 0.0561 | 0.1192 |
| Final $wR_2$ (all data)[c] | 0.1026 | 0.1632 | 0.1294 | 0.2702 |
| Largest diff. p/h [e Å$^{-3}$] | 0.574/–0.521 | 0.584/–0.450 | 0.452/–0.460 | 1.452/–1.837 |

[a] GOF = $[\Sigma[w(F_o^2 - F_c^2)^2]/(n-p)]^{1/2}$, where $n$ = number of reflections and $p$ = number of refined parameters. [b] $R_1 = \Sigma||F_o| - |F_c||/\Sigma|F_o|$. [c] $wR_2 = [\Sigma[w(F_o^2 - F_c^2)^2]/\Sigma[w(F_o^2)_2]]^{1/2}$, where $w = 1/\sigma^2(F_o^2) + (aP)^2 + bP$, $P = (F_o^2 + 2F_c^2)/3$.

 © 2007 Wiley-VCH Verlag GmbH & Co. KGaA, Weinheim 

CCDC-638745 to -638748 (for $\mathbf{3_{Cu}}$–$\mathbf{6_{Cu}}$) contain the supplementary crystallographic data for this paper. These data can be obtained free of charge from The Cambridge Crystallographic Data Centre via www.ccdc.cam.ac.uk/data_request/cif.

**Supporting Information** (see also the footnote on the first page of this article): ($^1$H and $^{13}$C NMR, absorption, excitation and emission spectra, EPR spectra and crystal packing views of the amino acid bioconjugates **4** and **6**, and/or their copper complexes $\mathbf{4_{Cu}}$ and $\mathbf{6_{Cu}}$).

## Acknowledgments

We are grateful to the David and Lucile Packard Foundation, the Alfred P. Sloan Foundation and the NSF Chemistry Research Instrumentation and Facilities grant CHE-0131112 for generous support of this work. We thank James R. Miller for the mass spectra and Carl P. Myers and Michael T. Green for assistance with acquisition of the EPR spectra.

[1] a) J. Richter, *Physica E* **2003**, *16*, 157–173; b) M. Shionoya, K. Tanaka, *Curr. Opin. Chem. Biol.* **2004**, *8*, 592–597; c) B. Lippert, J. Müller in *Concepts and Models in Bioinorganic Chemistry* (Eds.: H.-B. Kraatz, N. Metzler-Nolte), Wiley-VCH, Weinheim, Germany, **2006**, pp. 137–158.

[2] See for example: a) K. D. Copeland, M. P. Fitzsimons, R. P. Houser, J. K. Barton, *Biochemistry* **2002**, *41*, 343–356; b) D. R. van Staveren, N. Metzler-Nolte, *Chem. Rev.* **2004**, *104*, 5931–5985.

[3] a) P. Aich, S. L. Labiuk, L. W. Tari, L. J. T. Delbaere, W. J. Roesler, K. J. Falk, R. P. Steer, J. S. Lee, *J. Mol. Biol.* **1999**, *294*, 477–485; b) S. D. Wettig, D. O. Wood, P. Aich, J. S. Lee, *J. Inorg. Biochem.* **2005**, *99*, 2093–2101.

[4] a) A. Ono, H. Togashi, *Angew. Chem. Int. Ed.* **2004**, *43*, 4300–4302; b) A. A. Voityuk, *J. Phys. Chem. B* **2006**, *110*, 21010–21013.

[5] a) S. Atwell, E. Meggers, G. Spraggon, P. G. Schultz, *J. Am. Chem. Soc.* **2001**, *123*, 12364–12367; b) S. I. Kirin, K. Ohr, H. P. Yennawar, C. M. Morgan, L. A. Levine, M. E. Williams, *Inorg. Chem. Commun.* **2007**, *10*, 652–656.

[6] a) K. Tanaka, G. H. Clever, Y. Takezawa, Y. Yamada, C. Kaul, M. Shionoya, T. Carell, *Nat. Biotechnol.* **2006**, *1*, 190–194; b) G. H. Clever, T. Carell, *Angew. Chem. Int. Ed.* **2007**, *46*, 250–253.

[7] a) K. Tanaka, M. Shionoya, *J. Org. Chem.* **1999**, *64*, 5002–5003; b) K. Tanaka, A. Tengeiji, T. Kato, N. Toyama, M. Shionoya, *Science* **2003**, *299*, 1212–1213; c) H. Y. Zhang, A. Calzolari, R. Di Felice, *J. Phys. Chem. B* **2005**, *109*, 15345–15348.

[8] H. Weizman, Y. Tor, *Chem. Commun.* **2001**, 453–454.

[9] C. Brotschi, C. J. Leumann, *Nucleosides Nucleotides Nucleic Acids* **2003**, *22*, 1195–1997.

[10] a) D.-L. Popescu, T. J. Parolin, C. Achim, *J. Am. Chem. Soc.* **2003**, *125*, 6354–6355; b) R. M. Watson, Y. A. Skorik, G. K. Patra, C. Achim, *J. Am. Chem. Soc.* **2005**, *127*, 14628–14639; c) R. M. Franzini, R. M. Watson, G. K. Patra, R. M. Breece, D. L. Tierney, M. P. Hendrich, C. Achim, *Inorg. Chem.* **2006**, *45*, 9798–9811.

[11] a) L. Zapata, K. Bathany, J.-M. Schmitter, S. Moreau, *Eur. J. Org. Chem.* **2003**, 1022–1028; b) J. S. Choi, C. W. Kang, K. Jung, J. W. Yang, Y.-G. Kim, H. Han, *J. Am. Chem. Soc.* **2004**, *126*, 8606–8607.

[12] L. Zhang, E. Meggers, *J. Am. Chem. Soc.* **2005**, *127*, 74–75.

[13] a) C. Switzer, D. Shin, *Chem. Commun.* **2005**, 1342–1344; b) C. Switzer, S. Sinha, P. H. Kim, B. D. Heuberger, *Angew. Chem. Int. Ed.* **2005**, *44*, 1529–1532.

[14] a) B. P. Gilmartin, K. Ohr, R. L. McLaughlin, R. Koerner, M. E. Williams, *J. Am. Chem. Soc.* **2005**, *127*, 9546–9555; b) K. Ohr, B. P. Gilmartin, M. E. Williams, *Inorg. Chem.* **2005**, *44*, 7876–7885; c) B. P. Gilmartin, R. L. McLaughlin, M. E. Williams, *Chem. Mater.* **2005**, *17*, 5446–5454; d) L. A. Levine, C. M. Morgan, K. Ohr, M. E. Williams, *J. Am. Chem. Soc.* **2005**, *127*, 16764–16765; e) B. P. Gilmartin, Ph. D. Thesis, Pennsylvania State University **2006**; f) L. M. Pantzar, M. S. Thesis, Pennsylvania State University **2006**; g) K. Ohr, R. L. McLaughlin, M. E. Williams, *Inorg. Chem.* **2007**, *46*, 965–974.

[15] J. Müller, D. Böhme, P. Lax, M. Morell Cerda, M. Roitzsch, *Chem. Eur. J.* **2005**, *11*, 6246–6253.

[16] A. Küsel, J. Zhang, M. A. Gil, A. C. Stueckl, W. Meyer-Klaucke, F. Meyer, U. Diederichsen, *Eur. J. Inorg. Chem.* **2005**, 4317–4324.

[17] B. R. Babu, P. J. Hrdlicka, C. J. McKenzie, J. Wengel, *Chem. Commun.* **2005**, 1705–1707.

[18] S. J. Kim, E. T. Kool, *J. Am. Chem. Soc.* **2006**, *128*, 6164–6171.

[19] a) R. E. Shepherd, Y. Chen, R. A. Kortes, M. S. Ward, *Inorg. Chim. Acta* **2000**, *303*, 30–39; b) T. D. Coombs, B. J. Brisdon, C. P. Curtis, M. F. Mahon, S. A. Brewer, C. R. Willis, *Polyhedron* **2001**, *20*, 2935–2943; c) S. P. Foxon, O. Walter, S. Schindler, *Eur. J. Inorg. Chem.* **2002**, 111–121; d) M. J. Rauterkus, S. Fakih, C. Mock, I. Puscasu, B. Krebs, *Inorg. Chim. Acta* **2003**, *350*, 355–365; e) S. Youngme, P. Phuengphai, S. Booncoon, N. Chaichit, *Polyhedron* **2004**, *23*, 1685–1694.

[20] a) V. Uma, M. Kanthimathi, J. Subramanian, B. U. Nair, *Biochim. Biophys. Acta* **2006**, *1760*, 814–819; b) C. Tu, Y. Shao, N. Gan, Q. Xu, Z. Guo, *Inorg. Chem.* **2004**, *43*, 4761–4766.

[21] A. A. Shoukry, *Transition Met. Chem.* **2005**, *30*, 814–827.

[22] a) Y. Uozumi, R. Nakao, *Angew. Chem. Int. Ed.* **2003**, *42*, 194–197; b) B. Karimi, S. Abedi, J. H. Clark, V. Budarin, *Angew. Chem. Int. Ed.* **2006**, *45*, 4776–4779.

[23] a) F. Sinner, M. R. Buchmeiser, R. Tessadri, M. Mupa, K. Wurst, G. K. Bonn, *J. Am. Chem. Soc.* **1998**, *120*, 2790–2797; b) M. R. Buchmeiser, S. Lubbad, M. Mayr, K. Wurst, *Inorg. Chim. Acta* **2003**, *345*, 145–153.

[24] J. Silberg, T. Schareina, R. Kempe, K. Wurst, M. R. Buchmeiser, *J. Organomet. Chem.* **2001**, *622*, 6–18.

[25] C. Bolm, J.-C. Frison, J. Le Paih, C. Moessner, G. Raabe, *J. Organomet. Chem.* **2004**, *689*, 3767–3777 and references cited therein.

[26] a) W. Yang, H. Schmider, Q. Wu, Y.-s. Zhang, S. Wang, *Inorg. Chem.* **2000**, *39*, 2397–2404; b) H. Zhu, M. Ströbele, Z. Yu, Z. Wang, H.-J. Meyer, X. You, *Inorg. Chem. Commun.* **2001**, *4*, 577–581; c) N. M. Shavaleev, A. Barbieri, Z. R. Bell, M. D. Ward, F. Barigelletti, *New J. Chem.* **2004**, *28*, 398–405; d) J. Lee, Q.-D. Liu, M. Motala, J. Dane, J. Gao, Y. Kang, S. Wang, *Chem. Mater.* **2004**, *16*, 1869–1877.

[27] For the incorporation of amino acids into chiral aeg backbone see: a) M. S. Robillard, S. van Alphen, N. J. Meeuwenoord, B. A. J. Jansen, G. A. van der Marel, J. H. van Boom, J. Reedijk, *New J. Chem.* **2005**, *29*, 220–225; b) I. Dilek, M. Madrid, R. Singh, C. P. Urrea, B. A. Armitage, *J. Am. Chem. Soc.* **2005**, *127*, 3339–3345.

[28] a) F. Paul, J. Patt, J. F. Hartwig, *J. Am. Chem. Soc.* **1994**, *116*, 5969–5970; b) A. S. Guram, S. L. Buchwald, *J. Am. Chem. Soc.* **1994**, *116*, 7901–7902; c) J. Louie, J. F. Hartwig, *Tetrahedron Lett.* **1995**, *36*, 3609–3612.

[29] For examples of dpa syntheses using the Buchwald–Hartwig amination see ref.[25,26d]

[30] H. B. Goodbrand, N.-X. Hu, *J. Org. Chem.* **1999**, *64*, 670–674.

[31] For examples of dpa syntheses using the Ullmann condensation see ref.[19d,26a,26c]

[32] C. Seward, J. Pang, S. Wang, *Eur. J. Inorg. Chem.* **2002**, 1390–1399.

[33] H. C. Ahn, S. K. Yang, H. M. Kim, S. Li, S.-J. Jeon, B. R. Cho, *Chem. Phys. Lett.* **2005**, *410*, 312–315.

[34] a) E. I. Solomon, U. M. Sundaram, T. E. Machonkin, *Chem. Rev.* **1996**, *96*, 2563–2605; b) F. Neese, *J. Phys. Chem. A* **2001**, *105*, 4290–4299; c) H.-J. Scholl, J. Hüttermann, *J. Phys. Chem.* **1992**, *96*, 9684–9691.

 © 2007 Wiley-VCH Verlag GmbH & Co. KGaA, Weinheim 

[35] Only single crystals of moderate quality could be obtained for $\mathbf{6_{Cu}}$, the *R* factor is therefore relatively high. A detailed discussion of bond lenghts and angles is not possible in this case, but the data allow discussion of the coordination geometry.
[36] J.-S. Yang, Y.-D. Lin, Y.-H. Lin, F.-L. Liao, *J. Org. Chem.* **2004**, *69*, 3517–3525.
[37] a) K. Severin, R. Bergs, W. Beck, *Angew. Chem. Int. Ed.* **1998**, *37*, 1634–1654; b) R. Alberto, J. K. Pak, D. van Staveren, S. Mundwiler, P. Benny, *Biopolymers* **2004**, *76*, 324–333; c) S. I. Kirin, P. Dübon, T. Weyhermüller, E. Bill, N. Metzler-Nolte, *Inorg. Chem.* **2005**, *44*, 5405–5415; d) M. Cindrić, T. Kajfež Novak, S. Kraljević, M. Kralj, B. Kamenar, *Inorg. Chim. Acta* **2006**, *359*, 1673–1680; e) C. Schickaneder, F. W. Heinemann, R. Alsfasser, *Eur. J. Inorg. Chem.* **2006**, 2357–2363; f) M. C. Kuchta, C. Gemel, N. Metzler-Nolte, *J. Organomet. Chem.* **2007**, *692*, 1310–1314.
[38] For the interaction of metals with the peptide backbone or side chains see: a) O. Yamaguchi, A. Odani, M. Takani, *J. Chem. Soc. Dalton Trans.* **2002**, 3411–3421; b) I. Sovago, K. Osz, *Dalton Trans.* **2006**, 3841–3854.
[39] a) A. Scarso, U. Scheffer, M. Göbel, Q. B. Broxterman, B. Kaptein, F. Formaggio, C. Toniolo, P. Scrimin, *Proc. Natl. Acad. Sci. USA* **2002**, *99*, 5144–5149; b) H. Zelder, A. A. Mokhir, R. Kramer, *Inorg. Chem.* **2003**, *42*, 8618–8620; c) D. Jayasinghe, H.-B. Kraatz, *Inorg. Chim. Acta* **2006**, *359*, 3054–3065.
[40] G. M. Sheldrick, *SHELXS97*, Program for the Solution of Crystal Structures, University of Göttingen, Germany, **1997**.
[41] G. M. Sheldrick, *SHELXL97*, Program for the Refinement of Crystal Structures, University of Göttingen, Germany, **1997**.

Received: March 8, 2007
Published Online: June 22, 2007

 © 2007 Wiley-VCH Verlag GmbH & Co. KGaA, Weinheim 

DOI: 10.1002/ejic.200700369

# A Hexadecanuclear Copper(I)–Copper(II) Mixed-Valence Compound: Structure, Magnetic Properties, Intervalence Charge Transfer, EPR, and NMR

**Senjuti De,[a] Shubhamoy Chowdhury,[a] Jnan P. Naskar,[a] Michael G. B. Drew,[b] Rodolphe Clérac,[c] and Dipankar Datta*[a]**

**Keywords:** Copper / High-nuclearity complexes / Aggregates / Mixed-valent compounds / Charge transfer / N,O ligands

Hexadecanuclear copper mixed-valence complex **2** containing 10 $Cu^{II}$ centers and 6 $Cu^{I}$ centers was isolated with N,O donor ligands. From the X-ray crystal structure, **2** was found to contain a centrosymmetric dimeric cation – each monomeric unit composed of eight copper centers. It displays a very broad and weak intervalence charge-transfer band around 1100 nm at room temperature in the solid state. Variable-temperature magnetic susceptibility measurements indicate an $S = 1/2$ ground state for half of **2**, explicitly, each $Cu_8$ moiety has a $g$ value around 2.26. Complex **2** was examined by NMR spectroscopy at room temperature in solution and by EPR at low temperature; the data indicates that the valence is delocalized in **2** at room temperature but localized at low temperature.
(© Wiley-VCH Verlag GmbH & Co. KGaA, 69451 Weinheim, Germany, 2007)

## Introduction

High-nuclearity ($n > 10$) metal complexes are of much current interest as these may have applications in catalysis, bio- and nanotechnology, material science, and molecular magnetism. The most impressive example is possibly $[Mn_{84}O_{72}(CH_3COO)_{78}(CH_3O)_{24}(CH_3OH)_{12}(OH)_6(H_2O)_{42}]\cdot x H_2O\cdot y CHCl_3$, which is a single molecule magnet of nano dimension.[1] The highest nuclearity $n$ has so far been achieved in the case of Mo ($n$ = 368).[2] This $n$ may depend on the oxidation state of the metal. For example, the highest $n$ reported to date for $Cu^{I}$ is 146,[3] whereas it is 44 in the case of $Cu^{II}$.[4] Further, the situation might change in mixed-valence compounds. The highest $n$ reported so far for $Cu^{I}$–$Cu^{II}$ mixed-valence compounds is 38; this complex is made up of 36 $Cu^{II}$ centers and 2 $Cu^{I}$ centers.[5] A somewhat old review on high nuclearity $Cu^{I}$–$Cu^{II}$ mixed-valence complexes is available.[6] A general interesting feature of the mixed-valence complexes is the appearance of an intervalence charge-transfer (ICT) band in the electronic spectra.[7–9] However, such a band was not observed so far in any $Cu^{I}$–$Cu^{II}$ mixed-valence complex with $n > 3$. Herein we describe an air stable $Cu^{I}$–$Cu^{II}$ mixed-valence complex with $n$ = 16 that displays the rare ICT band.

[a] Department of Inorganic Chemistry, Indian Association for the Cultivation of Science,
Calcutta 700 032, India
Fax: +91-33-2473-2805
E-mail: icdd@mahendra.iacs.res.in
[b] School of Chemistry, University of Reading,
Whiteknights, Reading RG6 6AD, UK
[c] Université Bordeaux 1, CNRS, Centre de Recherche Paul Pascal – UPR8641,
115 avenue du Dr. A. Schweitzer, 33600 Pessac, France
Supporting information for this article is available on the WWW under http://www.eurjic.org or from the author.

Previously we reported[10] a hexanuclear $Cu^{II}$ complex of LH (H: dissociable proton; Scheme 1), the acetone condensate of L′H (3-hydrazono-butan-2-one oxime; Scheme 1), of the formulation $Cu_6L_6(O)(OH)(ClO_4)_3$ (**1**). Its X-ray crystal structure was also reported. It is a H-bonded, centrosymmetric dimer of a centrally $\mu_3$-oxido bridging $Cu_3$ complex cation $[Cu_3L_3(O)]^{2+}$ having peripheral oximato bridges. We have now found that if the crystallization of **1** is delayed in its synthesis, **1** is transformed into unique hexadecanuclear mixed-valence $Cu^{I}$–$Cu^{II}$ complex **2**. Its X-ray crystal structure, spectroscopic (electronic and magnetic resonance), and magnetic properties are described here.

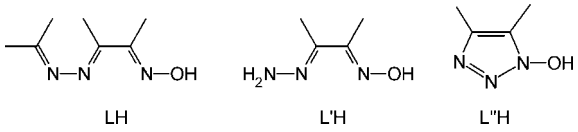


Scheme 1. Some ligands involved in the present work; H: dissociable proton.

## Results and Discussion

The unit cell of **2** contains a centrosymmetric dimer of formula $[Cu_{16}L_2L'_2L''_{16}(H_2O)_2]^{6+}$ together with 6 discrete perchlorate anions and 10 solvent water molecules. Thus, the molecular formula of **2** is $[Cu_{16}L_2L'_2L''_{16}(H_2O)_2](ClO_4)_6\cdot 10H_2O$. The cation shown in Figure 1 contains eight independent copper atoms, all with different environments; Cu1, Cu6, and Cu7 are tetrahedral, Cu2 is four-coordinate square planar, Cu3 and Cu4 are five-coordinate square pyramidal, Cu5 is two-coordinate linear, and Cu8 is three-coordinate trigonal. The numbering scheme is such that the

 © 2007 Wiley-VCH Verlag GmbH & Co. KGaA, Weinheim 

ligands are numbered 1–10 inclusive with each atom numbered by the ligand number first and then the position of the atom in the ligand; L′′ is numbered 1–8 inclusive, with L′ numbered 9 and L numbered 10. In ligand L′′, three atoms, namely N*n*1, N*n*2 and O*n*5 are found to bind to copper atoms. The acyclic ligands L and L′ both chelate to one copper atom but also bind to other copper atoms through their other available donor atoms.

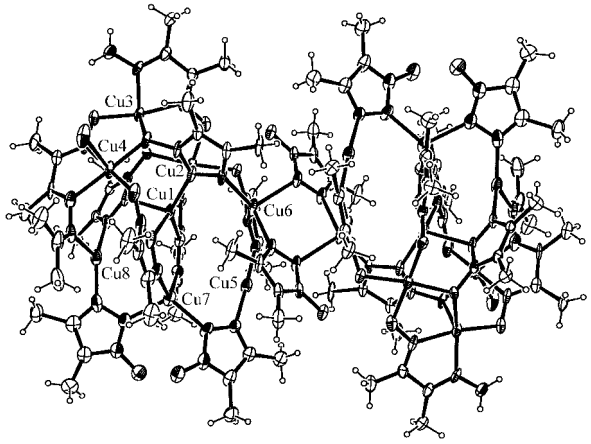


Figure 1. The structure of the centrosymmetric, dimeric cation in **2** with ellipsoids at 10% probability.

The environment of Cu1, shown in Figure 2; it is four-coordinate tetrahedral in which the metal atom is bound to four ligands through their central nitrogen atom N*n*1, where *n* is 1, 2, 7, and 8. The environment of Cu2 by contrast is four-coordinate square planar in which the metal atom is bonded to four ligands through the terminal oxygen atom O*n*5 where *n* is 5, 7, 8, and 9 (Figure 3). There is, in addition, a weak interaction with a perchlorate oxygen atom O21 at 2.53(1) Å. The environment of Cu3 is a five-coordinate square pyramid with O15 in an axial position and O105 and O85 together with the two nitrogen atoms N95 and N92 from the bidentate ligand L′ in the equatorial plane (Figure 4). Cu4 also has a five-coordinate square pyramidal geometry, but here a water molecule is in an axial position with O15 and O25 as well as two nitrogen atoms N105 and N102 from the bidentate L (Figure 5). The Cu5 atom is two-coordinate linear (Figure 6) and is bonded to N42 and N52 at 1.878(11) and 1.886(11) Å. The N42–Cu5–N52 angle is 173.4(5)°. There are no other bonding interactions for Cu5. The Cu6 atom has a tetrahedral environment but unlike Cu1 it is bonded to two N*n*1 atoms and two N*n*2 atoms. The Cu6 atom is involved in the centrosymmetric bridge as shown in Figure 7. The Cu7 atom is also tetrahedral and similar to Cu6, which is bonded to a combination of N*n*1 and N*n*2 atoms as shown in Figure 8. The Cu8 atom is three-coordinate trigonal and is bonded to N32, N82, and N101 as shown in Figure 9. Overall, the closest Cu···Cu distance in the cation $[Cu_{16}L_2L'_2L''_{16}(H_2O)_2]^{6+}$ is 3.114 Å between Cu1 and Cu2, indicating that there are no significant bonding interactions between copper atoms.

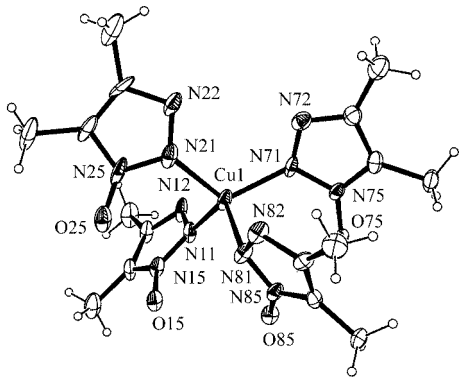


Figure 2. The environment of Cu1 with ellipsoids at 25% probability. Selected bond lengths [Å] and angles [°]: Cu1–N71 1.965(10), Cu1–N11 1.965(11), Cu1–N21 2.067(12), Cu1–N81 2.154(9), N71–Cu1–N11 135.2(4), N71–Cu1–N21 108.7(5), N11–Cu1–N21 105.9(4), N71–Cu1–N81 90.3(4), N11–Cu1–N81 112.2(4), N21–Cu1–N81 98.0(4).

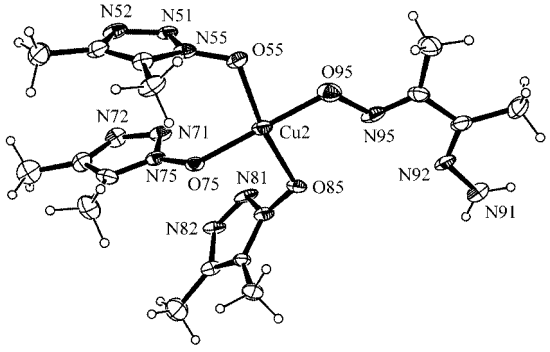


Figure 3. The environment of Cu2 with ellipsoids at 25% probability. Selected bond lengths [Å] and angles [°]: Cu2–O95 1.921(9), Cu2–O75 1.923(8), Cu2–O55 1.952(8), Cu2–O85 1.985(8), O95–Cu2–O75 170.2(4), O95–Cu2–O55 79.6(4), O75–Cu2–O55 97.0(3), O95–Cu2–O85 91.5(4), O75–Cu2–O85 92.6(3), O55–Cu2–O85 169.6(3).

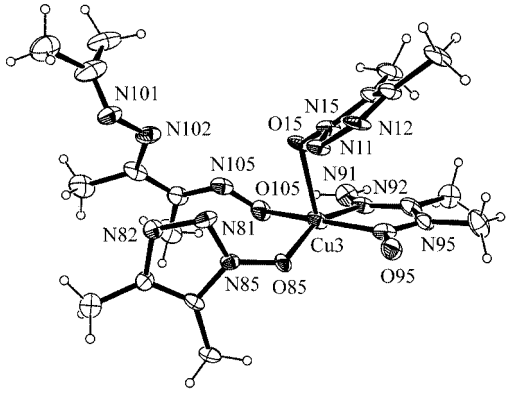


Figure 4. The environment of Cu3 with ellipsoids at 25% probability. Selected bond lengths [Å] and angles [°]: Cu3–O105 1.902(9), Cu3–N95 1.939(11), Cu3–N92 1.965(11), Cu3–O85 2.010(8), Cu3–O15 2.204(9), O105–Cu3–N95 170.4(5), O105–Cu3–N92 91.0(4), N95–Cu3–N92 79.9(5), O105–Cu3–O85 99.6(4), N95–Cu3–O85 87.9(4), N92–Cu3–O85 157.7(4), O105–Cu3–O15 88.8(4), N95–Cu3–O15 96.6(4), N92–Cu3–O15 105.2(4), O85–Cu3–O15 94.7(3).

 © 2007 Wiley-VCH Verlag GmbH & Co. KGaA, Weinheim 

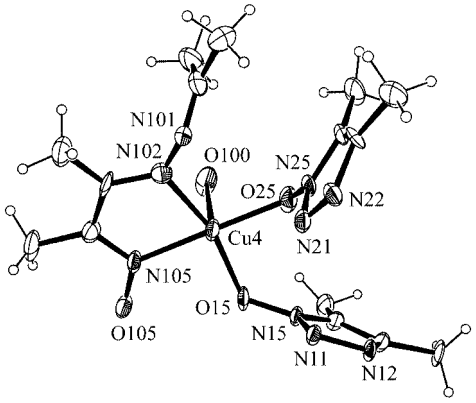


Figure 5. The environment of Cu4 with ellipsoids at 25% probability. O100 belongs to a water molecule. Selected bond lengths [Å] and angles [°]: Cu4–O25 1.914(10), Cu4–O15 1.950(10), Cu4–N105 2.007(10), Cu4–N102 2.014(13), Cu4–O100 2.313(10), O25–Cu4–O15 91.0(4), O25–Cu4–N105 179.2(5), O15–Cu4–N105 88.3(4), O25–Cu4–N102 102.5(5), O15–Cu4–N102 162.6(4), N105–Cu4–N102 78.3(5), O25–Cu4–O100 90.6(4), O15–Cu4–O100 95.8(4), N105–Cu4–O100 89.0(4), N102–Cu4–O100 94.9(4).

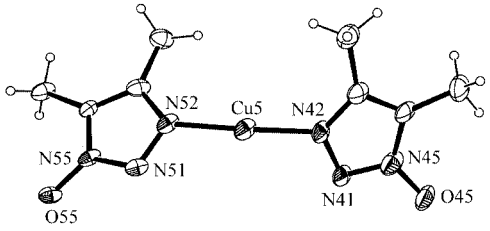


Figure 6. The environment of Cu5 with ellipsoids at 25% probability. Selected bond lengths [Å] and angles [°]: Cu5–N42 1.878(11), Cu5–N52 1.886(11), N42–Cu5–N52 173.4(5).

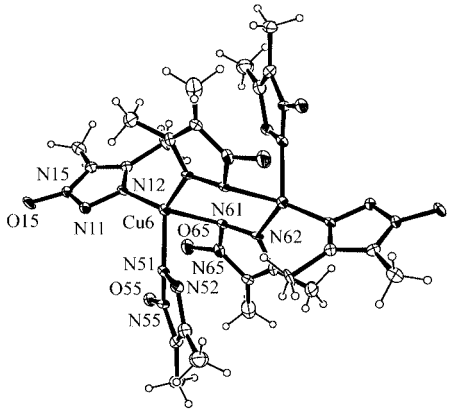


Figure 7. The environment of Cu6 with ellipsoids at 25% probability. The centrosymmetric bridge in the dimer is shown. Selected bond lengths [Å] and angles [°]: Cu6–N12 1.978(10), Cu6–N62$1 2.000(10), Cu6–N51 2.054(9), Cu6–N61 2.245(10), N12–Cu6–N62$1 125.6(4), N12–Cu6–N51 120.0(4), N62$1–Cu6–N51 105.0(4), N12–Cu6–N61 106.3(5), N62$1–Cu6–N61 102.8(4), N51–Cu6–N61 89.4(4).

We now discuss the binding nature of the three ligands occurring in **2** (Scheme 1). Of the three ligands, L and L′ are acyclic whereas L′′ is cyclic. The two acyclic ligands, L′ and L, chelate to one metal, N92 and N95 to Cu3, and

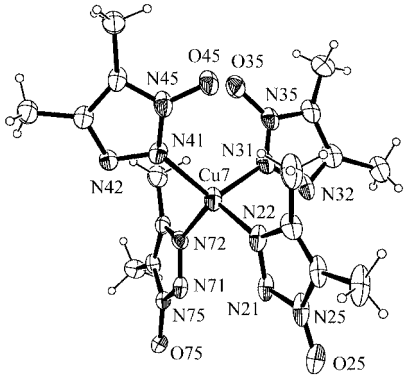


Figure 8. The environment of Cu7 with ellipsoids at 25% probability. Selected bond lengths [Å] and angles [°]: Cu7–N22 1.985(12), Cu7–N41 2.023(11), Cu7–N72 2.042(11), Cu7–N31 2.138(14), N22–Cu7–N41 122.1(5), N22–Cu7–N72 114.1(5), N41–Cu7–N72 104.1(4), N22–Cu7–N31 100.8(5), N41–Cu7–N31 113.1(5), N72–Cu7–N31 100.9(4).

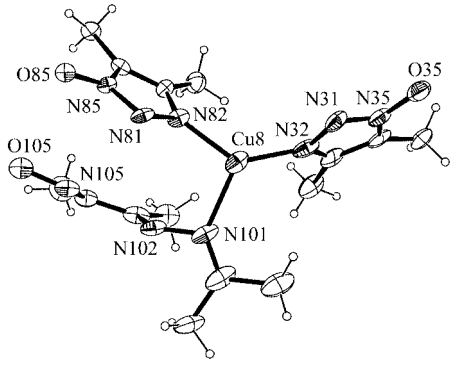


Figure 9. The environment of Cu8 with ellipsoids at 25% probability. Selected bond lengths [Å] and angles [°]: Cu8–N32 1.915(15), Cu8–N82 1.979(11), Cu8–N101 2.096(13), N32–Cu8–N82 130.3(5), N32–Cu8–N101 124.8(5), N82–Cu8–N101 102.8(5).

N102 and N105 to Cu4. In addition, O95 is bound to Cu2 within L′, N101 to Cu8, and O105 to Cu3 within L. There are eight types of L′′. Type 1 is bonded to four different metals: Cu1 through N11, Cu6 through N12, and Cu3 and Cu4 through O15. Type 2 is bonded to three copper atoms: Cu1 through N21, Cu7 through N22, and Cu4 through O25. Type 3 is bonded to two copper atoms: Cu7 through N31 and Cu8 through N32. Instead of bonding to a copper atom, O35 forms a strong hydrogen bond of 2.80 Å to solvent water O50. Type 4 is bonded to Cu7 through N41 and Cu5 through N42 but O45 remains unbonded. Type 5 is bonded to Cu6 through N51, Cu5 through N52, and Cu2 through O55. Type 6, which is adjacent to the center of symmetry, binds Cu6 through N61 and Cu61 through N62 (see Figure 7). Type 7 is bonded to Cu1 through N71, Cu7 through N72, and Cu2 through O75. Type 8 is bonded to Cu1 through N81, Cu8 through N82, and Cu2 and Cu3 through O85. Thus, for L′′, it can be concluded that its N*n*1 and N*n*2 are bound to different copper atoms, whereas its O*n*5 is bonded to two, one, or no copper atoms.

The formulation of complex **2** indicates that it consists of 10 $Cu^{II}$ and 6 $Cu^{I}$ centers. To assign the oxidations states

 © 2007 Wiley-VCH Verlag GmbH & Co. KGaA, Weinheim 

of various copper centers in **2**, we take recourse to the bond valence sum (BVS) model. BVS relates the bond lengths around a metal center to its oxidation state. In this method, originally introduced by Pauling and developed later by Brown and coworkers,[11–13] the valence $v_{ij}$ of a bond between two atoms $i$ and $j$ is given empirically by Equation (1), where $r_{ij}$ is the length (expressed in Å) and $r_0$ a parameter characteristic of the bond.

$$v_{ij} = \exp[(r_0 - r_{ij})/0.37] \quad (1)$$

The oxidation number $V_i$ of an atom $i$ is a simple algebraic sum of the $v$ values of all the bonds formed by the atom [Equation (2)]; it is also known as BVS.

$$V_i = \sum_j v_{ij} = \sum_j \exp[(r_0 - r_{ij})/0.37] \quad (2)$$

Thus, if $r_0$ is known for a particular bond type the BVS can be calculated from the crystallographically determined $r_{ij}$ values. The $r_0$ values for $Cu^{II}$–N and $Cu^{II}$–O bonds, as refined by us,[12] are 1.719 and 1.679 Å, respectively. Previously, we found[12] that with these $r_0$ values, the BVS values calculated for a number of $Cu^{II}$ complexes of N and O donor ligands are found to lie in the range of $2.00 \pm 0.35$ valence units, specifically, the oxidation number of copper in these complexes are reproduced within $\pm 0.35$ valence units. When we apply this method to **2**, we obtain the following BVS values for the eight types of copper atoms: Cu1, 1.73; Cu2, 1.95; Cu3, 2.26; Cu4, 2.10; Cu5, 1.29; Cu6, 1.61; Cu7, 1.67; and Cu8, 1.44. Thus our BVS calculations show that in the cases of Cu5, Cu6, and Cu8, the errors in the calculated oxidation states by assuming an oxidation state of II for all the copper atoms, exceed our stipulated error limit of $\pm 0.35$ valence units. Consequently, an oxidation state of I is assigned to Cu5, Cu6, and Cu8 and an oxidation state of II to other five copper centers, namely Cu1, Cu2, Cu3, Cu4, and Cu7.

In the synthesis of complex **2** from complex **1**, L is transformed to L′ and L′′. L′ is generated from L by simple hydrolysis of the acetone azine bond. Ligand L′ is then subsequently transformed into L′′. A tentative mechanism for this transformation in methanol (a protic solvent) is suggested in Scheme 2. It involves a two-electron oxidation in the last step. We believe this oxidation is brought about by two $Cu^{II}$ centers because the reaction **1**→**2** occurs under a $N_2$ atmosphere as well, and thereby some of the $Cu^{II}$ centers are reduced to $Cu^{I}$, which leads to the formation of a mixed-valence species. Interestingly, in the synthesis of [1,2,3]triazol-1-ol (the basic skeleton in L′′H) from glyoxal, proposed by Begtrup, a similar oxidation by $Cu^{2+}$ occurs in the last step.[14] X-ray crystal structures of a few of its derivatives are available. However, metal complexes of [1,2,3]triazol-1-ol are so far not known in the literature. Complex **2** illustrates the hitherto unexplored coordination behavior of [1,2,3]triazole-1-ol.

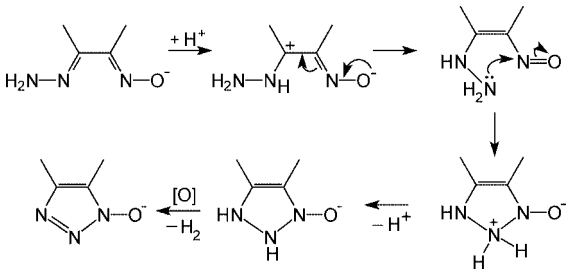


Scheme 2. A proposed mechanism for the chemical transformation of L′ into L′′ in a protic solvent.

Variable-temperature magnetic susceptibility ($\chi$) of **2** was measured and is shown in Figure 10 as a $\chi T$ versus $T$ plot. At room temperature, $\chi T$ is 0.89 $cm^3 \cdot K \cdot mol^{-1}$ and slowly decreases to 0.85 $cm^3 \cdot K \cdot mol^{-1}$ at 210 K. The value of $\chi T$ is found to be roughly constant in the temperature range 210–100 K. Then it again decreases down to an asymptotic value of 0.48 $cm^3 \cdot K \cdot mol^{-1}$ at 1.85 K. On the basis of the molecular structure of complex **2** (Figure 1), we tried to simplify the topology of the $Cu_{16}$ aggregate in order to analyze the magnetic behavior theoretically. The centrally located four diamagnetic $Cu^{I}$ centers magnetically isolate the $Cu^{II}$ ions into two distinct $Cu^{II}_5$ units (see the inset in Figure 10). In each such unit, at least four different types of magnetic interactions are present and were considered to model the magnetic property in the framework of Heisenberg's theory. However, all our attempts in this regard were unsuccessful due to the incapacity to evaluate the strong antiferromagnetic interaction between $S = 1/2$ $Cu^{II}$ metal ions present in a part of the $Cu^{II}_5$ units (likely through direct oxygen bridges). Unfortunately, the limited available temperature range between 210 and 300 K did not allow an accurate estimation of these strong interactions. The decrease in the $\chi T$ product below 100 K reveals that there are additional and weaker antiferromagnetic interactions in the $Cu^{II}_5$ units. Even if the amplitude of these interactions is not possible to determine, the asymptotic $\chi T$ value of 0.48 $cm^3 \cdot K \cdot mol^{-1}$ observed at 1.85 K suggests an $S = 1/2$ ground state for a $Cu_8$ unit with a $g$ value around 2.26.

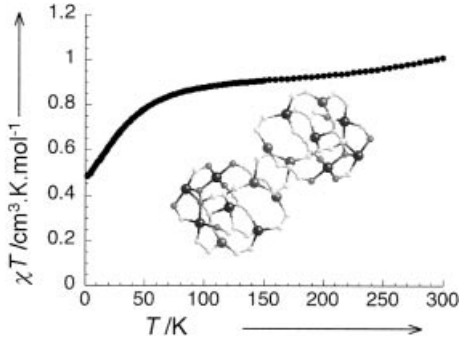


Figure 10. Temperature dependence of the $\chi T$ product at 1000 Oe (where $\chi = M/H$) for half of $[Cu_{16}L_2L'_2L''_{16}(H_2O)_2](ClO_4)_6 \cdot 10H_2O$ (**2**) shown schematically in the inset.

Complex **2** displays a very broad and weak band around 1100 nm in the solid state at room temperature (Figure 11). This band could not be observed in methanol solution at

 © 2007 Wiley-VCH Verlag GmbH & Co. KGaA, Weinheim 

room temperature. However, relative to the intensity of the 650 nm band (Figure 11), which is very well observed in methanol solution, it appears that the intensity of the 1100 nm band is much less than 2900 $M^{-1}\cdot cm^{-1}$. No copper(II) or copper(I) complex is known in the literature that displays an absorption band at such a long wavelength. We ascribe this band to an intervalence charge transfer in **2**. It is difficult to specify how many copper centers are actually involved in the intervalence charge transfer. It is possible that two-coordinate Cu5 and three-coordinate Cu8 are not involved in the intervalence charge transfer process because of geometric reasons. One of the criteria for facile intervalence charge transfer is that the coordination environments (geometries and the binding atoms) of metal centers in the two oxidation states should be close to each other.[7–9] The four-coordinate copper(I) center Cu6 is directly bridged to two four-coordinate copper(II) centers Cu1 and Cu2. Of these two, Cu1 has a distorted tetrahedral $N_4$ and Cu2 ha a square planar $O_4$ coordination sphere. Thus, geometrywise and in terms of the nature of the binding atoms, the copper(I) center Cu6 seems to be compatible only with the copper(II) center Cu1 for the involvement in the ICT process. Previously in a binuclear mixed-valence $Cu^{I}$–$Cu^{II}$ complex where both the copper centers have $N_2O_2$ coordination sphere, Long and Hendrickson[15] have observed a broad ICT band at 950 nm with an intensity of 400 $M^{-1}\cdot cm^{-1}$ in solution at room temperature.

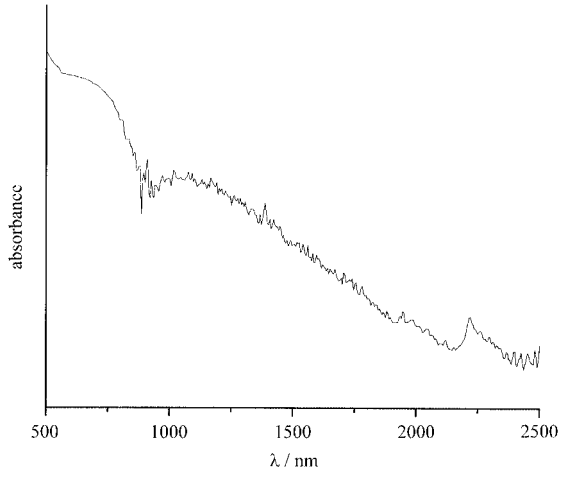


Figure 11. A portion of the absorption spectrum of **2** in nujol at room temperature.

The extensive valence delocalization in the complex of Long and Hendrickson at room temperature was established by the observation of a seven-line EPR spectrum in solution. Interestingly, their complex gives an EPR spectrum characteristic of a mononuclear copper(II) center at 100 K, to be exact, with the lowering of temperature valence gets localized.[15] In our case, valence delocalization renders the EPR signal so broad that we do not see any EPR spectrum at room temperature either in the solid state (Figure 12) or in solution. However, at low temperature (5 K) **2** displays an unsymmetrical spectrum with a *g* value of ca. 2.12. Thus in complex **2** valence is also delocalized at room temperature and localized at low temperature. The nonobservance of an EPR spectrum for **2** in methanol solution at room temperature despite being paramagnetic is supported by the observation of its $^1H$ NMR spectrum in $CD_3OD$ at room temperature (Figure 13). Resonances due to the various methyl and $NH_2$ groups and water molecules present in **2** appear within the range –5 to 15 ppm. As expected, the $^1H$ signals are somewhat broad (Figure 13).

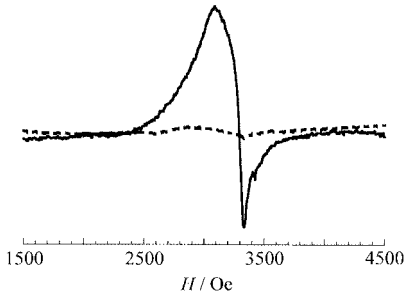


Figure 12. X-band EPR spectrum of **2** in solid state at 300 (dashed line) and 5 (full line) K.

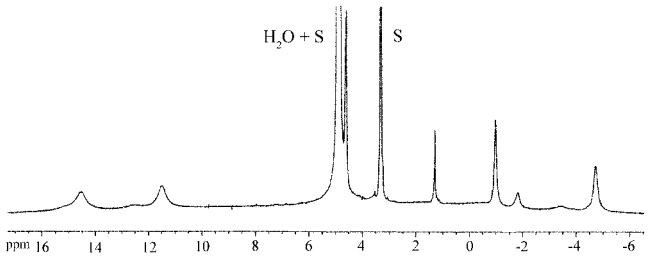


Figure 13. 300 MHz $^1H$ NMR spectrum of **2** in $CD_3OD$; peaks marked by S are due to solvent.

## Concluding Remarks

Here we have described a unique, self-assembled, paramagnetic cluster containing copper(I) and copper(II) that displays NMR in solution at room temperature and EPR at low temperature. Such magnetic resonance behavior only suggests that valence is delocalized in complex **2** at room temperature but localized at lower temperatures. This sort of valence localization–delocalization is expected intuitively. On reaching sufficiently low temperatures, a delocalized (ambient-temperature) system gets *trapped in a valence-localized state*.[16,17] Accordingly, an intervalence charge-transfer band is also observed for **2** at room temperature at a low energy (1100 nm). In Hush theory,[18,19] for a class II (valence localized) system the observed bandwidth should be close to $(2310 \times \tilde{\nu}_{max})^{1/2}$ $cm^{-1}$; when the experimental bandwidth is much lower than the calculated one, the system becomes class III (complete valence delocalization). With $\lambda_{max}$ = 1100 nm, the half-width is calculated to be 4600 $cm^{-1}$. Unfortunately, because of an intense neighboring band in the absorption spectrum of **2**, we cannot ascertain the exact half-width of the 1100 nm band experimentally, thus preventing us to categorize mixed valence complex **2** in terms of Hush theory. Self-assembly, which is

 © 2007 Wiley-VCH Verlag GmbH & Co. KGaA, Weinheim 

an important phenomenon in nature, has been a matter of extensive research in recent times.[20,21] Here it has assumed a different dimension.

## Experimental Section

**General:** Microanalyses were performed with a Perkin–Elmer 2400II elemental analyzer. FTIR spectra (KBr disc) were recorded with a Shimadzu FTIR-8400S spectrophotometer, UV/Vis/NIR spectra with a Perkin–Elmer Lambda 950 spectrophotometer, and NMR spectra with a Bruker DPX300 spectrometer. The magnetic susceptibility measurements were obtained with the use of a Quantum Design SQUID magnetometer MPMS-XL. This magnetometer works between 1.8 and 400 K for dc applied fields ranging from –7 to 7 T. Measurements were performed on finely ground crystalline samples of 31.36 mg. $M$ vs. $H$ measurements were performed at 100 K to check for the presence of ferromagnetic impurities that were found to be absent. The magnetic data were corrected for the sample holder and the diamagnetic contribution.

**Synthesis of 1:** Prepared by modifying the previously published procedure[10] in the following manner. $Cu(ClO_4)_2{\cdot}6H_2O$ (1.86 g, 5 mmol) dissolved in methanol (10 mL) was added dropwise to LH (0.77 g, 5 mmol) and anhydrous sodium acetate (0.41 g, 5 mmol), dissolved in methanol (20 mL), with stirring. A dark green compound started precipitating immediately. Stirring was continued for only 2 min. Then the compound was filtered, washed with cold methanol (5 mL) and dried in air. Yield: 0.4 g (30%).

**Synthesis of 2:** Complex **1** (0.53 g, 0.32 mmol) was dissolved in methanol (100 mL) in a conical flask to obtain a clear green solution and layered with diethyl ether (300 mL), stoppered, and left undisturbed. After three weeks, the precipitated green crystalline compound was filtered and washed with diethyl ether (single crystals suitable for X-ray crystallography were found at the upper portion). It was dried under vacuum over fused $CaCl_2$. Yield: 0.35 g (65%). $\Lambda_M$ (MeOH): 591 $\Omega^{-1}{\cdot}cm^2{\cdot}mol^{-1}$. FTIR (KBr): $\tilde{\nu}$ = 3447 (vb) $\nu$(OH), 1117 (vs), 629 (s) $\nu(ClO_4)$ $cm^{-1}$. UV/Vis/NIR (MeOH): $\lambda$ ($\varepsilon$, $M^{-1}{\cdot}cm^{-1}$) = 203 ($10.5\times10^5$), 263 ($14.3\times10^4$), 322 ($10.9\times10^4$), 642 ($2.9\times10^3$) nm. $C_{86}H_{160}Cl_6Cu_{16}N_{60}O_{56}$ (4160.01): calcd. C 24.81, H 3.88, N 20.20; found C 24.70, H 3.96, N 20.03.

***Caution!*** Though we have not met with any incident during our studies, care should be taken in handling these compounds as perchlorate salts are potentially explosive. These should not be prepared and stored in larger amounts.

**X-ray Crystallography:** Data for **2** were collected at 150 K with a Bruker SMART APEX CCD diffractometer using graphite monochromated Mo-$K_\alpha$ radiation ($\lambda$ = 0.71073 Å). Data reduction was performed with SAINT+[22] and absorption corrections applied using SADABS.[23] The structure was solved by direct methods[24] and refined[25] on $F^2$ using SHELX97. All non-hydrogen atoms were refined anisotropically and the hydrogen atoms were refined isotropically using a riding model. Of the three perchlorate anions in the asymmetric unit, two were refined with distance constraints. Five independent water molecules were located but their hydrogen atoms could not be located. Crystal Data: $C_{43}H_{80}Cl_3Cu_8N_{30}O_{28}$; $M_r$ = 2080.04; triclinic; space group $P\bar{1}$; $a$ = 13.898(4), $b$ = 16.328(5), $c$ = 18.642(6) Å; $\alpha$ = 82.144(6), $\beta$ = 72.186(5), $\gamma$ = 80.408(5)°; $V$ = 3955(2) Å$^3$; $Z$ = 2; $D_{calcd.}$ = 1.747 g·cm$^{-3}$. 18127 independent reflections were measured and were refined to $R_1$ 0.1178, $wR_2$ 0.2818 for 7300 reflections with $I>2\sigma(I)$. CCDC-600589 contains the supplementary crystallographic data for this paper. These data can be obtained free of charge from the Cambridge Crystallographic Data Center via www.ccdc.cam.ac.uk/data_request/cif.

**Supporting Information** (see footnote on the first page of this article): Figure S1 showing the 300 MHz $^1$H NMR of **2** in $CD_3OD$ after shaking with $D_2O$.


[1] A. J. Tasiopoulos, A. Vinslava, W. Wernsdorfer, K. A. Abboud, G. Christou, *Angew. Chem. Int. Ed.* **2004**, *43*, 2117–2121.
[2] A. Müller, E. Beckmann, H. Bögge, M. Schmidtmann, A. Dvess, *Angew. Chem. Int. Ed.* **2002**, *41*, 1162–1167.
[3] H. Krautscheid, D. Fenske, G. Baum, M. Semmelmann, *Angew. Chem. Int. Ed. Engl.* **1993**, *32*, 1303–1305.
[4] M. Murugesu, R. Clérac, C. E. Anson, A. K. Powell, *Inorg. Chem.* **2004**, *43*, 7269–7271.
[5] M. Murugesu, R. Clérac, C. E. Anson, A. K. Powell, *Chem. Commun.* **2004**, 1598–1599.
[6] M. Dunaj-Jurco, G. Ondrejovic, M. Melnik, J. Garaj, *Coord. Chem. Rev.* **1988**, *83*, 1–28.
[7] M. B. Robin, P. Day, *Adv. Inorg. Chem. Radiochem.* **1967**, *10*, 247–422.
[8] P. N. Schatz in *Inorganic Electronic Structure and Spectroscopy*, (Eds.: E. I. Solomon, A. B. P. Lever), Wiley, New York, **1999**, vol. 2, pp. 175–226.
[9] D. M. D'Alessandro, F. R. Keene, *Chem. Soc. Rev.* **2006**, *35*, 424–440.
[10] P. Chakrabarti, V. G. Puranik, J. P. Naskar, S. Hati, D. Datta, *Indian J. Chem. Sect. A* **2000**, *39*, 571–578.
[11] I. D. Brown, D. Altermatt, *Acta Crystallogr., Sect. B* **1985**, *41*, 244–247.
[12] S. Hati, D. Datta, *J. Chem. Soc. Dalton Trans.* **1995**, 1177–1182.
[13] S. Nag, K. Banerjee, D. Datta, *New J. Chem.* **2007**, *31*, 832–834.
[14] P. Uhlmann, J. Felding, P. Vedsø, M. Begtrup, *J. Org. Chem.* **1997**, *62*, 9177–9181.
[15] R. C. Long, D. N. Hendrickson, *J. Am. Chem. Soc.* **1983**, *105*, 1513–1521.
[16] However, at times the converse is also observed. For example, Ward and coworkers reported a mixed-valence tricopper complex where spin delocalization occurs only below 120 K with the valence-localized form becoming more prevalent at higher temperatures.[17]
[17] P. L. Jones, J. C. Jeffery, J. P. Maher, J. A. McCleverty, P. H. Rieger, M. D. Ward, *Inorg. Chem.* **1997**, *36*, 3088–3095.
[18] N. S. Hush, *Prog. Inorg. Chem.* **1967**, *8*, 391–444.
[19] C. Creutz, *Prog. Inorg. Chem.* **1983**, *30*, 1–73.
[20] V. G. Machado, P. N. W. Baxter, J. M. Lehn, *J. Braz. Chem. Soc.* **2001**, *12*, 431–462.
[21] N. Ginseppone, J. L. Schmidt, J. M. Lehn, *J. Am. Chem. Soc.* **2006**, *128*, 16748–16763.
[22] *Area Detector control and Data Integration and Reduction Software*, Bruker AXS, Madison, MI, USA, **2001**.
[23] G. M. Sheldrick, *SADABS*, University of Göttingen, Göttingen, Germany, **1997**.
[24] G. M. Sheldrick, *Acta Crystallogr., Sect. A* **1990**, *46*, 467–473.
[25] G. M. Sheldrick, *SHELX-97, Program for Crystal Structure Refinement*, University of Göttingen, **1997**.


Received: April 4, 2007
Published Online: June 21, 2007

 © 2007 Wiley-VCH Verlag GmbH & Co. KGaA, Weinheim 

DOI: 10.1002/ejic.200700061

# Tripodal Trimanganese(III) Complexes of New Unsymmetrical Pentadentate Ligands Derived from 2-(Salicylideneamino)phenol: Syntheses, Crystal Structures and Properties

**Masahiro Muto,[a] Naoya Hatae,[a] Yumi Tamekuni,[a] Yasunori Yamada,[a] Masayuki Koikawa,*[a] and Tadashi Tokii*[a]**

**Keywords:** Bridging ligands / Ligand design / Manganese / X-ray structures / Magnetic properties / Redox chemistry

Trinuclear manganese(III) complexes of new unsymmetrical pentadentate ligands, 6-hydroxy-2-(2-hydroxyphenyl)-5-(salicylideneamino)benzoxazole ($H_3L^1$) and 5-(5,6-benzosalicylideneamino)-6-hydroxy-2-(2-hydroxynaphthyl)benzoxazole ($H_3L^2$), $[Mn_3(L^1)_3(CH_3OH)_3]$ (**1**) and $[Mn_3(L^2)_3(dmf)(CH_3OH)(H_2O)]$ (**2**) (dmf = *N*,*N*-dimethylformamide), have been prepared. The structures of the ligands $H_3L^1$, $H_3L^2$ and complex **1** were determined by X-ray crystallography, which revealed that the ligands have two distant chelating sites. The molecular structure of **1** is regarded as a tripodal pyramid with a cavity of about 3 Å diameter. Each $Mn^{III}$ ion is coordinated by *ONO* atoms from a tridentate Schiff base site and *ON* atoms from a benzoxazole site of two respective $H_3L^1$ ligands. The intramolecular Mn···Mn distances for **1** are in the range 8.0683–8.1791 Å, and the nearest intermolecular Mn···Mn distance, 5.7824(15) Å, is shorter than the intramolecular values. Magnetic measurements of **1** indicate that weak antiferromagnetic interactions ($J = -0.2\ cm^{-1}$, $g = 2.0$) are dominant in the trinuclear manganese(III) core. Cyclic voltammogram of **1** in dmf showed obscure redox couples assigned to two single-electron transfer processes.

(© Wiley-VCH Verlag GmbH & Co. KGaA, 69451 Weinheim, Germany, 2007)

## Introduction

The development of nanoscale molecular architectures such as macrocyclic metal ion arrays is of considerable interest in materials science and supramolecular chemistry because these complexes often have characteristic redox, magnetic and mechanical functions and host–guest chemistry.[1–3] Moreover, the discrete macrocyclic structures can be used as secondary building units for higher-order constructions such as two- or three-dimensional network structures.[4,5] In any case, ligands that have appropriate bridging abilities and directions are used. For example, most macrocyclic metal complexes have been organised by small anions based on acetate and hydroxy anions. In this case, μ-acetato or μ-hydroxido bridges are slanted at small bending angles to the metal-to-metal direction. According to the extent of these angles, various sizes of macrocyclic metal arrangements are prepared. However, because the preparations of such complexes depend on contingency, it is rather difficult to strategically develop scientific research. Therefore, it is important that ligands that have multiple separate coordination sites, are carefully designed to obtain such nanomolecular architectures by self-assembly.

It is known that 2-(salicylideneamino)phenol ($H_2sap$)[6–11] and many other similar *ONO*-tridentate ligands form stable metal complexes.[12–20] We prepared modified ligands [$H_3L^1$: 6-hydroxy-2-(2-hydroxyphenyl)-5-(salicylideneamino)benzoxazole; $H_3L^2$: 5-(5,6-benzosalicylideneamino)-6-hydroxy-2-(2-hydroxynaphthyl)benzoxazole; $H_4L'$: 4,6-bis(salicylideneamino)benzene-1,3-diol] and introduced *ON*-bidentate or *ONO*-tridentate coordination sites into $H_2sap$ (Scheme 1). The newly designed ligands, $H_3L^1$ and $H_3L^2$, have unsymmetrical structures, and it is expected that $H_3L^n$ will lead to polynuclear complexes that have a complicated structure because the two coordination sites face different directions. These unsymmetrical multidentate ligands can generally arrange metal ions suitable for the property of each coordination site. It is possible to apply the syntheses of functional models for metalloenzymes in the field of bioinorganic chemistry.[21–23] On the other hand, the symmetrical ligand $H_4L'$, which has been known for a long time and was reported in detail in 1970,[24,25] is expected to lead to geometrically regularly structured complexes because it adapts *mer* coordination. Such symmetrical ligands are often used in studies of magnetism or electroconductivities, which require structural regularity.[25,26]

[a] Department of Chemistry and Applied Chemistry, Faculty of Science and Engineering, Saga University,
Honjo 1, Saga 840-8502, Japan
Fax: +81-952-28-8548
E-mail: koikawa@cc.saga-u.ac.jp

Supporting information for this article is available on the WWW under http://www.eurjic.org or from the author.

 © 2007 Wiley-VCH Verlag GmbH & Co. KGaA, Weinheim 

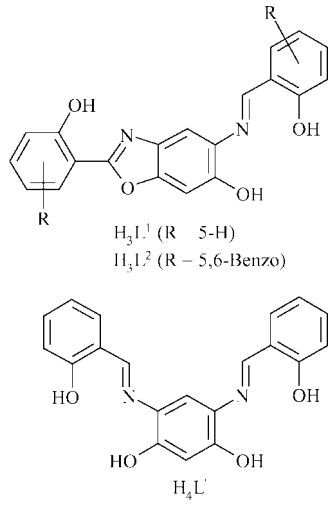


Scheme 1. Structure of the ligands.

In this study, we prepared new trinuclear manganese(III) complexes of these ligands with novel tripodal geometry. We describe here the syntheses, X-ray structural characterisation and magnetic and electrochemical properties of these newly obtained ligands and complexes.

## Results and Discussion

The ligands $H_3L^n$ and $H_4L'$ were identified by elemental analysis, FTIR, $^1$H NMR, FAB mass spectrometry and X-ray crystal structural analysis. The symmetrical ligand $H_4L'$ was temporarily obtained as the monohydrochloride, $H_4L'$·HCl, from a simple reaction of 4,6-diaminoresorcinol dihydrochloride with 2-hydroxybenzaldehyde. This ligand showed characteristic IR bands assigned to $\nu$(C=N) vibrations based on the Schiff base at 1622–1651 cm$^{-1}$ and $\nu$(OH) vibrations at 3070 and 3355 cm$^{-1}$. In the FAB mass spectrum, an intense molecular ion peak was observed at 349.1, and was assigned to the free ligand $H_4L'$. The free ligand $H_4L'$ without HCl could be isolated when two equivalents of triethylamine were used in the synthetic process. These ligands, $H_4L'$ and $H_4L'$·HCl, had similar $^1$H NMR spectra. It is considered that both ligands have a comparable structure in solution. The unsymmetrical ligand $H_3L^1$ was prepared from the filtrate obtained in the synthetic process for free $H_4L'$. On the other hand, the homologous symmetrical ligand obtained using 2-hydroxy-1-naphthaldehyde was not isolated by a similar synthetic method for $H_4L'$. The unsymmetrical ligand $H_3L^2$ was obtained as a green product under basic reaction conditions with triethylamine. The starting material, 4,6-diaminoresorcinol, can be simply oxidised to *p*-quinone imine or *p*-semiquinone imine species. In fact, the intensity of an ESR signal related to the radical in crude 4,6-diaminoresorcinol gradually increases in air. It is supposed that symmetrical Schiff base ligands, the same as $H_4L'$, are initially formed and that oxidation to a semiquinone imine form by molecular oxygen might have proceeded under such basic reaction conditions. Scheme 2 shows a reaction pathway for $H_3L^1$ formation. It is known that such radical species are stabilised by π conjugation as illustrated in Scheme 2. Consequently, the active radical species might lead to ring formation to yield benzoxazole derivatives. The free ligands $H_3L^1$ and $H_3L^2$ have characteristic IR bands assigned to $\nu$(C=N) vibrations based on Schiff base and benzoxazoline components at 1615–1634 cm$^{-1}$, and $\nu$(OH) vibrations at 3202 cm$^{-1}$ for $H_3L^1$ and at 3051 cm$^{-1}$ for $H_3L^2$. In the FAB mass spectra, intense molecular ion peaks were observed at 347.2 and 447.2.

The reaction of $H_4L'$·HCl and $H_3L^2$ with manganese(II) acetate tetrahydrate yielded trinuclear manganese(III) complexes **1** and **2**, respectively. Elemental analytical data of the complexes gave a 1:1 metal/ligand ratio. The $\nu$(C=N) vibrations observed in free ligands shifted to about 1600 cm$^{-1}$. It is suggested that both binding sites act as tridentate and bidentate chelates. At ambient conditions the manganese(III) species are produced regardless of whether manganese(II) or manganese(III) is used as the manganese source. The formation of phenoxyl radicals as shown in Scheme 2 might be accelerated by the existence of manganese(III) species. As a result, it is supposed that $H_4L'$ undergoes more facile oxidation to $H_3L1$ in these reactions. All attempts to obtain complex **1** by using $H_3L^1$ instead of

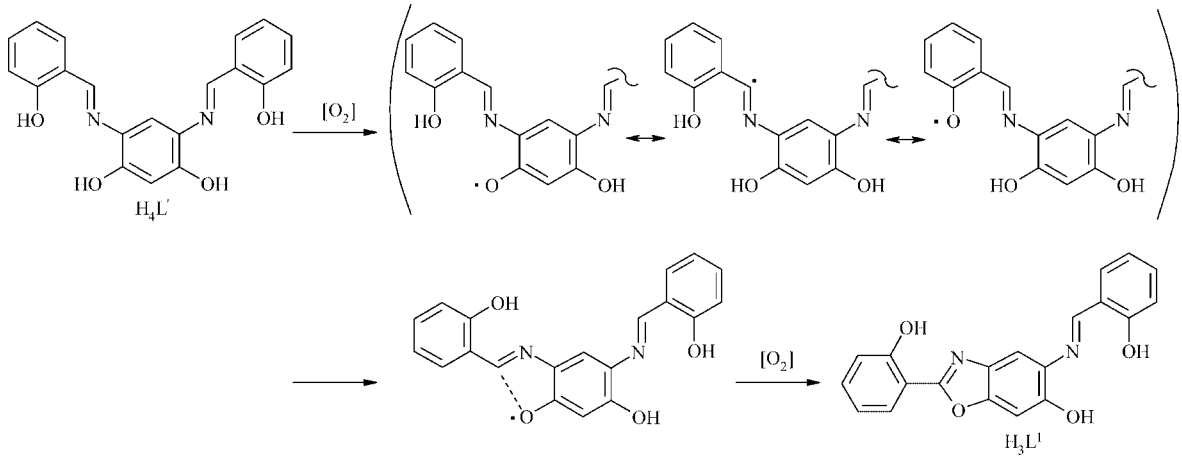


Scheme 2. Reaction pathway for the five-membered ring formation.

 © 2007 Wiley-VCH Verlag GmbH & Co. KGaA, Weinheim 

$H_4L'$ were unsuccessful. One of the reasons was considered to be the low solubility of $H_3L^1$ in organic solvents.

### X-ray Crystal Structures

Single crystals of $H_4L'$, $H_3L^1$ and $H_3L^2$, suitable for X-ray crystallography, were obtained by recrystallisation from mixed dmf solution layered with methanol or acetonitrile. All the obtained crystals were thin and fragile needles. Although the structure refinements were insufficient, the obtained results clearly revealed the ligand structures. ORTEP drawings of these are shown in Figure 1. For ligand $H_4L'$, both salicylaldehyde molecules formed Schiff base *ONO*-coordination sites such as 2-(salicylideneamino)phenol ($H_2$sap). On the other hand, $H_3L^1$ and $H_3L^2$ had *ON*-bidentate coordination sites comprising the benzoxazole substructure in addition to *ONO*-tridentate sites. The C(14)–N(2) bond length in $H_3L^1$ is 1.283(6) Å, and deviation of the five-membered ring, C(11)–C(12)–N(2)–C(14)–O(3), from planarity is very small (0.0060 Å). These data reveal the existence of a C=N double bond and the formation of a benzoxazole moiety, and prove that the ligand $H_4L'$ can undergo facile oxidation in air. The molecular structures of $H_3L^1$ and $H_3L^2$ differ in planarity from $H_2$sap frameworks. As for the dihedral angles defined by two phenyl rings binding O(1) and O(2), the angles are 10.2(2)° ($H_3L^1$) and 4.9(4)° ($H_3L^2$). It is assumed that the $H_2$sap framework in $H_3L^2$ is much more delocalised than that in $H_3L^1$. In any case, *ON*- and *ONO*-coordination sites face opposite directions. Therefore, the ligand frameworks can be regarded to have an S-shape conformation (Table 1).

Table 1. Selected bond lengths and angles of **1**.

| Bond lengths [Å] | | Angles [°] | |
|---|---|---|---|
| Mn(1)–O(1) | 1.895(5) | O(1)–Mn(1)–O(8) | 91.3(2) |
| Mn(1)–O(2) | 1.899(4) | O(1)–Mn(1)–N(1) | 90.2(2) |
| Mn(1)–O(8) | 1.901(5) | O(2)–Mn(1)–O(8) | 94.9(2) |
| Mn(1)–O(13) | 2.250(8) | O(2)–Mn(1)–N(1) | 83.6(2) |
| Mn(1)–N(1) | 1.989(6) | O(13)–Mn(1)–N(4) | 173.1(2) |
| Mn(1)–N(4) | 2.304(6) | O(5)–Mn(2)–O(12) | 95.4(2) |
| Mn(2)–O(5) | 1.916(5) | O(5)–Mn(2)–N(3) | 88.7(2) |
| Mn(2)–O(6) | 1.920(5) | O(6)–Mn(2)–O(12) | 93.5(2) |
| Mn(2)–O(12) | 1.874(5) | O(6)–Mn(2)–N(3) | 82.4(2) |
| Mn(2)–O(14) | 2.264(4) | O(14)–Mn(2)N(6) | 171.0(2) |
| Mn(2)–N(3) | 1.985(5) | O(4)–Mn(3)–O(9) | 93.2(2) |
| Mn(2)–N(6) | 2.241(6) | O(4)–Mn(3)–O(10) | 93.1(2) |
| Mn(3)–O(4) | 1.901(5) | O(9)–Mn(3)–N(5) | 90.5(2) |
| Mn(3)–O(9) | 1.895(5) | O(10)–Mn(3)–N(5) | 83.3(2) |
| Mn(3)–O(10) | 1.888(4) | O(15)–Mn(3)–N(2) | 174.5(2) |
| Mn(3)–O(15) | 2.241(8) | | |
| Mn(3)–N(2) | 2.250(6) | | |
| Mn(3)–N(5) | 2.000(5) | | |
| Mn(1)···Mn(2) | 8.1791(16) | | |
| Mn(1)···Mn(3) | 8.1081(15) | | |
| Mn(2)···Mn(3) | 8.0683(16) | | |

An ORTEP drawing of **1** is illustrated in Figure 2, and selected bond lengths and angles are listed in Table 2. The complex comprises three sets of ligands, manganese(III)

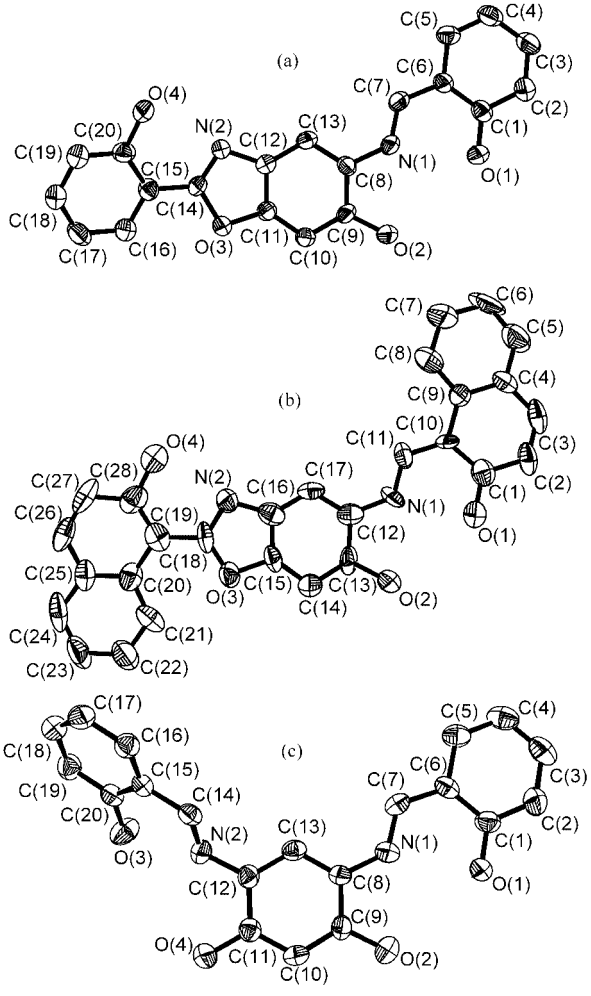


Figure 1. ORTEP drawings with the atom numbering scheme for the ligands; $H_3L^1$ (top), $H_3L^2$ (center) and $H_4L'$ (bottom).

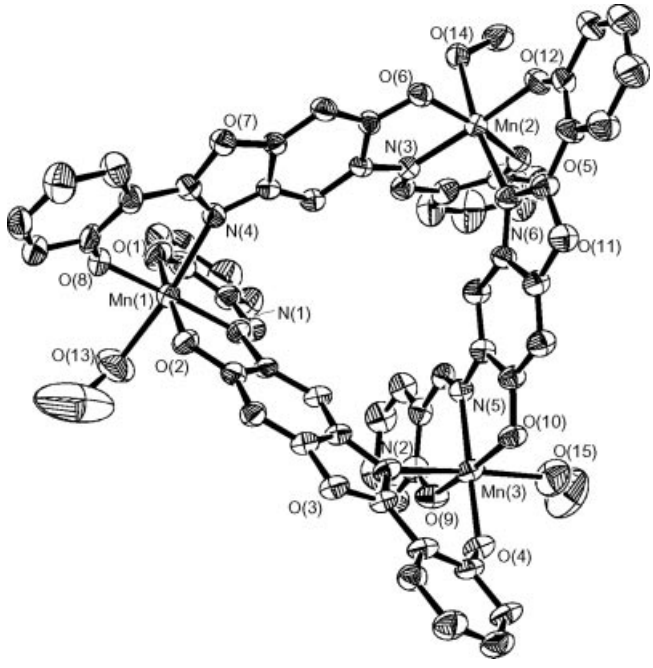


Figure 2. ORTEP view of **1** showing 30% probability.

 © 2007 Wiley-VCH Verlag GmbH & Co. KGaA, Weinheim 

Table 2. Electrochemical data of **1** and **2**.[a]

| Complex | $Mn_3$(II,III,III)/$Mn_3$(II,II,III) | | | $Mn_3$(III,III,III)/$Mn_3$(II,III,III) | | | $\Delta E$[c] |
|---|---|---|---|---|---|---|---|
| | $E_{pa}$ | $E_{pc}$ | $E_{1/2}(1)$[b] | $E_{pa}$ | $E_{pc}$ | $E_{1/2}(2)$[b] | |
| **1** | –0.68 | –0.77 | –0.73 | –0.548 | –0.64 | –0.59 | 0.14 |
| **2** | –0.70 | –0.80 | –0.75 | –0.546 | –0.71 | –0.63 | 0.12 |

[a] In V vs. $Ag/Ag^+$, scan rate 100 $mV s^{-1}$. Determined on a GC electrode in dmf. [b] $E_{1/2} = (E_{pc} + E_{pa})/2$. [c] $\Delta E = |E_{1/2}(1) - E_{1/2}(2)|$.

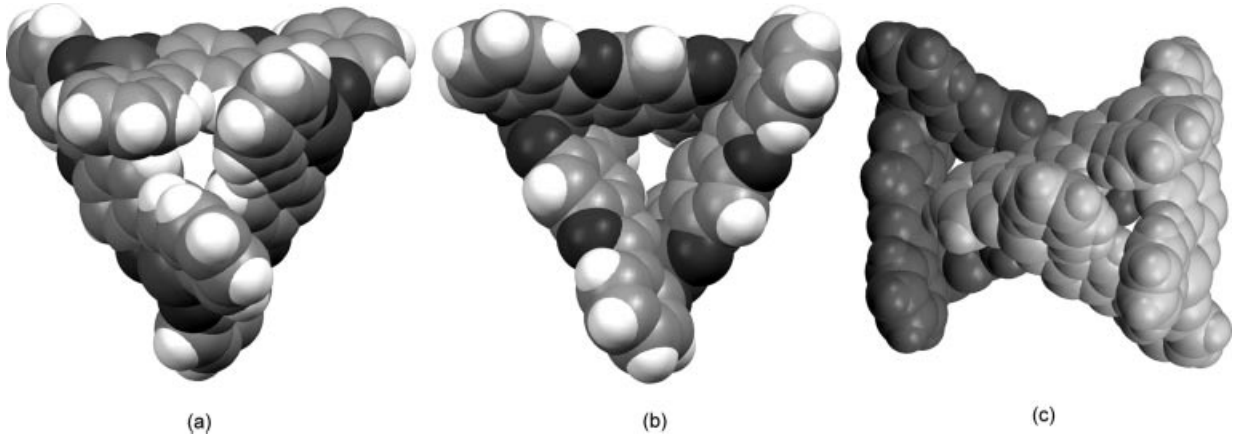


Figure 3. CPK models of **1**. Coordinating solvents are omitted for clarity; (a) view from the apex of the tripodal pyramid, (b) view from the cavity side and (c) enantiomer pairs in crystal packing; symmetry codes: ($x$, $y$, $z$) and ($1 - x$, $-y$, $1 - z$).

ions and coordinating solvents. CPK models of the $[Mn_3(L^1)_3]$ unit without the coordinating methanol molecules are shown in Figure 3. The entire molecular structure of **1** is regarded as a tripodal pyramid with a cavity. The coordination environments of the three manganese ions are very similar. Each manganese(III) ion forms a six-coordination geometry by three sets of donor components. The most effective donor set is the *ONO* one from the tridentate Schiff base binding site of $(L^1)^{3-}$. The N=C bond lengths (1.277–1.303 Å) in the Schiff base site are close to the value for standard $N(sp^2)=C(sp^2)$ double bonds. The sum of bond angles around N(1), N(3) and N(5) are 359.6, 359.3 and 359.8°, respectively. These data imply that the ligands are present in the Schiff base form, and not in the benzoxazine form. This coordination behaviour is very similar to that of 2-(salicylideneamino)phenol. The second one is the *ON* donor set from the bidentate benzoxazole site of a ligand different from the *ONO* donor. The phenolic oxygen atom coordinates to an identical plane, and the *ONO* Schiff base forms an equatorial plane. The nitrogen atom of the oxazole moiety is located in an axial position. The remaining sixth position of the manganese ion is occupied by a methanol molecule to form an $N_{oxazole}$–Mn–$O_{methanol}$ elongated axis. This axis corresponds to the Jahn–Teller axis for normal six-coordinate manganese(III) complexes. In complex **1**, the Jahn–Teller axes are defined as N(4)–Mn(1)–O(13) [Mn(1)–N(4) 2.304(6), Mn(1)–O(13) 2.250(8) Å], N(6)–Mn(2)–O(14) [Mn(2)–N(6) 2.241(6), Mn(2)–O(14) 2.264(4) Å] and N(2)–Mn(3)–O(15) [Mn(3)–N(2) 2.250(6), Mn(3)–O(15) 2.241(8) Å]. Equatorial planes comprise O(1)–N(1)–O(2)–O(8) for Mn(1) (av. 1.921 Å), O(5)–N(3)–O(6)–O(12) for Mn(2) (av. 1.924 Å) and O(9)–N(5)–O(10)–O(4) for Mn(3) (av. 1.921 Å). The bond lengths around the manganese(III) ions fall within the range observed for the manganese(III) complexes with Schiff base ligands.[16,27–31] In addition, coordination environments are very similar to that of [Mn(sap)L] [HL: 2-(2-hydroxyphenyl)benzoxazole], with a five-coordinate square-pyramidal structure, except for a coordinating methanol molecule.[17] It is well known that tridentate $H_2$sap derivatives usually form phenoxo-bridged dinuclear metal complexes.[6–9,18,20] However, when bidentate ligands such as phenanthroline are available, ternary mononuclear complexes such as [Mn(sap)L] are often reported.[11,19] In the present case, the reaction of $H_3L^1$ with manganese ions corresponds to the latter because $H_3L^1$ has both (sap) and bidentate coordination sites. As a result, $H_3L^1$ acts as an S-shaped hook to the manganese atom and locks each manganese atom to stabilise the tight triangular structure.

As for the characteristic structural properties, it is worth noting that these complexes have a cavity. The present complexes have long Mn···Mn distances arising from the unique ligand structure. The distances for **1** are 8.1791(16), 8.1081(15) and 8.0683(16) Å. Considering the van der Waals radius, a small molecule with an external diameter of about 3 Å can be held in the cavities. In fact, as shown in Figure 3, pairs of enantiomers are loosely aggregated in crystal lattices. In this pair, phenyl rings of the complexes are mutually intercalated in each cavity accompanied by π–π stacking [C(8)···$C(17)^i$ 3.411(10) Å]. It is suggested that these complexes can be expected in an application in host–guest chemistry. In the crystal packing, several intermolecular hydrogen bonds between coordinating solvents and neighbouring molecules are recognised. The distance be-

 © 2007 Wiley-VCH Verlag GmbH & Co. KGaA, Weinheim 

tween the O(14) atom of the coordinating methanol molecule and the O(8)$^{j}$ atom of $(L^1)^{3-}$ in the neighbouring molecule is 2.949(7) Å, which is regarded as a typical hydrogen bond (symmetry code j: $1 - x$, $-1/2 - y$, $1/2 - z$). As a result, the nearest intermolecular Mn···Mn distance [Mn(2)···Mn(1)$^{j}$ 5.7824(15) Å] is shorter than intramolecular Mn···Mn distances.

For complex **2**, X-ray reflection data and analytical results were insufficient for discussing structural details, because the crystals obtained were efflorescent. An identified molecular structure of **2** is very similar to that of **1** except for the coordinating solvent molecules. The estimated structure of **2** is consistent with the molecular formula suggested by the elemental analysis.

## Magnetic Properties

Powder samples of the complexes showed two ESR signals at $g \approx 9.0$ (strong) and 2.0 (weak) at room temperature. The spectra of **1** and **2** are shown in Figure 4. Generally, observation of ESR signals of mononuclear six-coordinate manganese(III) complexes are often difficult because of the fast spin relaxation and large zero-field splitting.[32] However, when the coordination geometries around the manganese(III) ion are strongly distorted, the signals can be observed as anisotropic signals. In the present complexes, the geometries of manganese(III) ions have strong axial distortion along with weakly coordinated solvent molecules. In consequence, it is assumed that these strong anisotropic signals were observed at an apparent $g$ value of about 9.0.[33] The weak signals at $g \approx 2.0$ might have arisen from manganese(II) impurities.

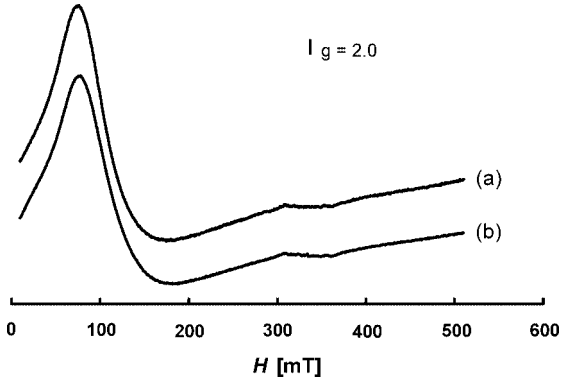


Figure 4. X-band polycrystalline ESR spectra of **1** (a) and **2** (b) at room temperature. The bar indicates the position of the weak resonance.

The magnetic moments per Mn atom of the complexes at room temperature are 4.90 (for **1**) and 4.83 (for **2**) B.M., which are close to the spin-only values (4.90) for four unpaired spins ($S = 2$). Magnetic susceptibility measurements for **1** were performed in the temperature range 2–300 K. The $\chi_A$ and $\mu_{eff}$ versus $T$ plots are shown in Figure 5. The $\mu_{eff}$ values are virtually constant from 300 K to 50 K, and then rapidly decrease with decreasing temperature and reach 3.96 B.M. at 2 K. This behaviour indicates the presence of a very weak antiferromagnetic interaction between manganese(III) ions. The magnetic property was simulated by means of the triangular spin model for $S = 2$ (Scheme 3).

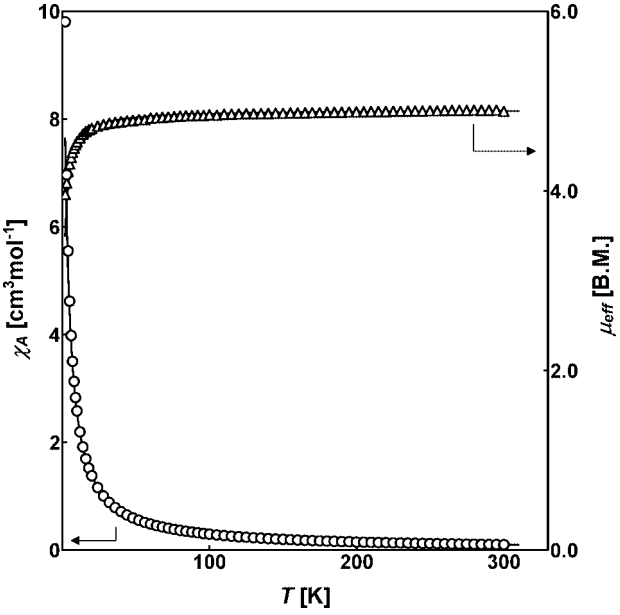


Figure 5. Temperature dependence of the magnetic susceptibilities for **1**. The solid curves were obtained as described in the text.

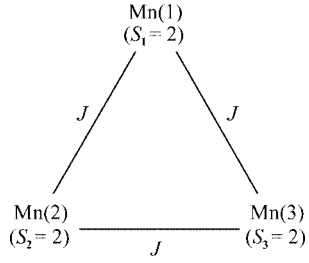


Scheme 3. Triangular spin model for **1**.

The Hamiltonian is written as in Equation (1).

$$H = -J(S_1S_2 + S_2S_3 + S_3S_1) \quad (1)$$

Magnetic susceptibilities are given by Equation (2), where $\chi_A$ is the magnetic susceptibility per manganese ion, and other symbols have their usual meanings.

$$\chi_A = \{Ng^2\beta^2/3k(T-\theta)\}\mathbf{A}/\mathbf{B} + N\alpha$$
$$\mathbf{A} = 182 + 220\exp(-12J/kT) + 180\exp(-22J/kT) + 112\exp(-30J/kT) + 50\exp(-36J/kT) + 6\exp(-40J/kT)$$
$$\mathbf{B} = 13 + 22\exp(-12J/kT) + 27\exp(-22J/kT) + 28\exp(-30J/kT) + 25\exp(-36J/kT) + 9\exp(-40J/kT) + \exp(-42J/kT) \quad (2)$$

The best fitting parameters are $J = -0.2$ cm$^{-1}$, $g = 2.00$, $N\alpha = 0$ and $\theta = -1.5$ K. For triangular complexes, spin-frustration behaviour was often observed. In the present complex **1**, the obtained $J$ value suggests that the weak antiferromagnetic interactions are dominant. However, the absolute $J$ value is too small to dispute the essence of magnetic interaction owing to the long Mn–Mn distances (av. 8.119 Å).

 © 2007 Wiley-VCH Verlag GmbH & Co. KGaA, Weinheim 

A notable result is the contribution of the $\theta$ value, which suggests that overall antiferromagnetic interactions are several times larger than the $J$ value. As shown in the crystal packing diagram, **1** has a high-order structure linked through hydrogen bonds established between the coordinated methanol and the phenolic oxygen atom of neighbouring complex molecules. Such connections are known to mediate intermolecular magnetic interactions.[34–36] In addition, because the distance between the nearest intermolecular manganese ions, 5.7824(15) Å, is shorter than the intramolecular distances (av. 8.119 Å), it is assumed that the intermolecular antiferromagnetic interaction is larger than the intramolecular interaction.

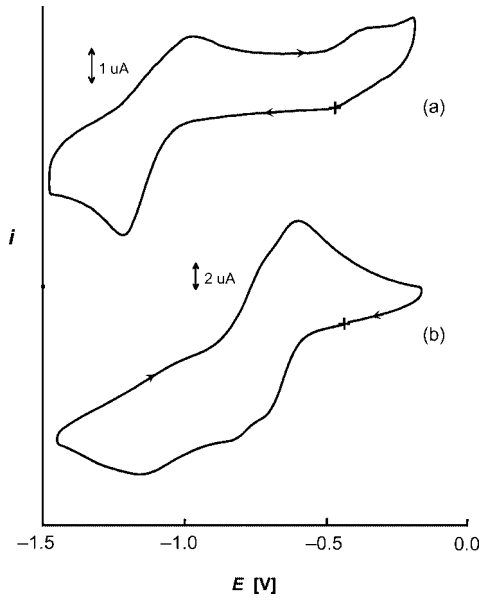


Figure 6. Cyclic voltammograms of $H_3L^1$ (a) and **1** (b); glassy-carbon electrode, scan rate 100 mV s$^{-1}$, concentration $1 \times 10^{-3}$ M, in dmf.

### Electrochemistry

Electrochemical properties of the present complexes were examined by cyclic voltammetry (CV) in dmf containing tbap (0.1 M) as the supporting electrolyte. The cyclic voltammograms of $H_3L^1$ and **1** are shown in Figure 6. When measurements were performed in the range from –0.1 to –1.4 V, three irreversible redox couples were observed at about –0.6, –0.7 and –1.0 V. The redox couples at about –1.0 V can be assigned to the reduction of the benzoxazole moiety, because the voltammogram of $H_3L^1$ also showed similar waves. In the positive range, both present complexes showed no wave except for the irreversible oxidation of phenolic oxygen atoms originating in the ligands. The electrochemical data of **1** and **2** are summarised in Table 3.

Although the first and second reduction waves are not so clear, it is assumed that they can be assigned to metal-centred one-electron transfer processes $Mn_3$(III,III,III)/$Mn_3$(II,III,III) and $Mn_3$(II,III,III)/$Mn_3$(II,II,III), respectively. The redox process of $Mn_3$(II,II,III)/$Mn_3$(II,II,II) could not be observed in the present measurements, even though we performed CV under various measurement conditions. It is considered that the effect of the ligand reduction process makes the voltammogram obscure. The potential differences ($\Delta E$) between two metal-centred redox couples are higher than 36 mV, which is expected for a purely statistical treatment in the two-electron process.[37] In multinuclear complexes, $\Delta E$ values often increase when an electronic repulsion effect exists between the redox centres. In complex **1**, the bridging ligands forming long metal-to-metal distances are expected to yield small $\Delta E$ close to the statistical case. However, the ligands have a π-conjugation system that is expected to enhance the electronic communication between manganese ions. As a result, it is assumed that the electronic repulsion effect is enhanced in **1**; large $\Delta E$ values were observed in these complexes. Such a phenomenon was also observed in other macrocyclic complexes having long metal-to-metal distances like **1**.[1,38,39]

Table 3. Crystal data and collection details for $H_3L^1$, $H_3L^2$, $H_4L'$ and complex **1**.

| Compound | $H_3L^1$ | $H_3L^2$ | $H_4L'\cdot CH_3OH$ | $\mathbf{1}\cdot 5CH_3OH\cdot 3H_2O$ |
|---|---|---|---|---|
| Empirical formula | $C_{20}H_{14}N_2O_4$ | $C_{28}H_{18}N_2O_4$ | $C_{21}H_{20}N_2O_5$ | $C_{68}H_{71}Mn_3N_6O_{23}$ |
| Formula mass | 346.34 | 446.46 | 380.40 | 1505.15 |
| Crystal size [mm] | 0.20 × 0.20 × 0.20 | 0.48 × 0.10 × 0.02 | 0.60 × 0.20 × 0.10 | 0.40 × 0.40 × 0.30 |
| Crystal system | monoclinic | monoclinic | monoclinic | monoclinic |
| Space group | $P2_1/n$ (#14) | $P2_1/n$ (#14) | $P2_1/c$ (#14) | $P2_1/c$ (#14) |
| $a$ [Å] | 11.505(7) | 17.994(9) | 13.658(5) | 12.241(6) |
| $b$ [Å] | 9.706(4) | 6.220(5) Å | 6.179(4) | 16.556(7) |
| $c$ [Å] | 14.608(4) | 20.333(14) | 22.706(5) | 36.278(8) |
| $\beta$ [°] | 103.55(4) | 111.52(3) | 103.52(2) | 93.44(4) |
| $V$ [Å$^3$] | 1585.8(13) | 2116.9(23) | 1863.1(15) | 7339.0(48) |
| $Z$ | 4 | 4 | 4 | 4 |
| $D_{calcd.}$ [g cm$^{-3}$] | 1.451 | 1.401 | 1.356 | 1.362 |
| $F$(000) | 720.00 | 928.00 | 800 | 3120.00 |
| $\mu$(Mo-$K_\alpha$) [cm$^{-1}$] | 1.028 | 0.948 | 0.977 | 5.857 |
| Number of unique reflections | 3627 ($R_{int}$ = 0.097) | 2198 ($R_{int}$ = 0.163) | 3542 ($R_{int}$ = 0.042) | 13346 ($R_{int}$ = 0.041) |
| Number of observations | 3627 | 2198 | 3542 | 13346 |
| Number of variables | 237 | 308 | 254 | 902 |
| $R$ ($I > 2\sigma$), $Rw$ (all data) | 0.0699, 0.1575 | 0.0568, 0.1450 | 0.0553, 0.1983 | 0.0685, 0.2550 |

 © 2007 Wiley-VCH Verlag GmbH & Co. KGaA, Weinheim 

## Conclusions

In the present study, it was demonstrated that the newly obtained unsymmetrical pentadentate ligands $H_3L^1$ and $H_3L^2$ support the formation of trinuclear manganese(III) complexes described as $[Mn_3(L^n)_3(solvent)_3]$. In the present complexes, the manganese atoms have six-coordinate geometries with elongated octahedral distortion. The molecular structures of the complexes are regarded as tripodal pyramids with a small cavity. The cavity is used for π–π stacking between enantiomer pairs. The magnetic interactions among trinuclear metal cores are very weak because of the long metal-to-metal distances. It is interesting that the obtained complexes are not phenoxo-bridged dinuclear complexes but trinuclear complexes. The result suggests that the present ligands can provide new applications for obtaining trinuclear macrocyclic complexes and can develop the understanding of self-assembly.

## Experimental Section

**Materials:** All ordinary reagents and solvents were purchased and used as received, unless otherwise noted. Methanol was purified by distillation from magnesium turnings.

### Preparations

**$H_4L'$·HCl:** A solution of 2-hydroxybenzaldehyde (0.976 g, 8 mmol) in dry methanol (10 mL) was added dropwise to a solution of 4,6-diaminoresorcinol dihydrochloride (0.852 g, 4 mmol) in dry methanol (40 mL) with stirring. The solution became a bright red suspension. The resulting precipitate was filtered off, washed with dry methanol and dried in vacuo. Yield of $H_4L'$·HCl·2$H_2O$: 1.36 g, 81%. $C_{20}H_{21}ClN_2O_6$ (420.85): calcd. C 57.08, H 5.03 N, 6.66; found C 56.76, H 5.04, N 6.77. IR (KBr): $\tilde{\nu}$ = 3355 and 3070 (OH), 1622–1651 (C=N), 860 and 758 (phenyl) $cm^{-1}$. $^1H$ NMR (300 MHz, dmso, tms): $\delta$ = 9.12 (s, 2 H), 7.80 (s, 1 H), 7.62 (d, 2 H), 7.45–7.39 (t, 2 H), 7.02–6.92 (m, 4 H), 6.72 (s, 1 H) ppm. FAB-MS: *m*/*z* = 349.1 [($H_4L'$)$H^+$].

**$H_4L'$:** A solution of 2-hydroxybenzaldehyde (0.976 g, 8 mmol) in dry methanol (10 mL) was added dropwise to a solution of 4,6-diaminoresorcinol dihydrochloride (0.852 g, 4 mmol) in dry methanol (40 mL) with stirring. The solution became a bright red suspension. A solution of triethylamine (0.808 g, 8 mmol) in dry methanol (5 mL) was added slowly, and the mixture was stirred at room temperature for 1 h. The resulting orange precipitate was filtered off, washed with dry methanol and dried in vacuo. Single crystals suitable for X-ray crystallography were obtained by recrystallisation from dmf solution layered with methanol. Yield of $H_4L'$·1/2MeOH·1/2$H_2O$: 1.143 g, 77%. $C_{20.5}H_{19}N_2O_5$ (373.39): calcd. C 65.94, H 5.13, N 7.50; found C 65.66, H 5.19, N 7.45. IR (KBr): $\tilde{\nu}$ = 1615–1634 (C=N), 859 and 756 (phenyl) $cm^{-1}$. $^1H$ NMR (300 MHz, dmso, tms): $\delta$ = 9.03 (s, 2 H), 7.65 (s, 1 H), 7.60 (d, 2 H), 7.35 (t, 2 H), 6.97–6.91 (m, 4 H), 6.65 (s, 1 H) ppm.

**$H_3L^1$:** The next day, ligand $H_3L^1$ precipitated from the orange solution from which the ligand $H_4L'$ had been filtered off. Single crystals suitable for X-ray crystallography were obtained by recrystallisation from dmf solution layered with acetonitrile. Yield of $H_3L^1$·4$H_2O$: 0.013 g, 0.8%. $C_{20}H_{22}N_2O_8$ (418.40): calcd. C 57.41, H 5.30, N 6.70; found C 57.27, H 5.19, N 6.78. IR (KBr): $\tilde{\nu}$ = 3202 (OH), 1615–1634 (C=N), 765 and 750 (phenyl) $cm^{-1}$. $^1H$ NMR (300 MHz, dmso, tms): $\delta$ = 9.07 (s, 1 H), 7.99 (d, 1 H), 7.91 (s, 1 H), 7.64 (d, 1 H), 7.51 (t, 1 H), 7.41 (t, 1 H), 7.34 (s, 1 H), 7.12 (d, 1 H), 7.07 (d, 1 H), 6.98 (t, 2 H) ppm. FAB-MS: *m*/*z* = 347.2 [($H_3L^1$)$H^+$].

**$H_3L^2$:** A solution of triethylamine (0.808 g, 8 mmol) in dry 1,4-dioxane (10 mL) was added dropwise to a solution of 4,6-diaminoresorcinol dihydrochloride (0.852 g, 4 mmol) and 2-hydroxy-1-naphthaldehyde (1.376 g, 8 mmol) in dry 1,4-dioxane (30 mL) with stirring. The dark green slurry was stirred at room temperature for 3 h. The resulting precipitate was filtered off and washed with dry 1,4-dioxane. Upon recrystallisation from a mixed solution of dmf/methanol, $H_3L^2$ precipitated as orange needles, was filtered off, and dried in vacuo. Single crystals suitable for X-ray crystallography were obtained by recrystallisation from dmf solution layered with methanol. Yield of $H_3L^2$·1/2$H_2O$: 0.27 g, 14.8%. $C_{28}H_{19}N_2O_{4.5}$ (455.47): calcd. C 73.84, H 4.20, N 6.15; found C 73.46, H 4.54, N 6.47. IR (KBr): $\tilde{\nu}$ = 3238 (OH), 1615–1622 (C=N), 746 (phenyl) $cm^{-1}$. $^1H$ NMR (300 MHz, dmso, tms): $\delta$ = 9.67 (s, 1 H), 8.58–8.51 (m, 3 H), 8.08 (d, 1 H), 7.96 (d, 1 H), 7.84 (d, 1 H), 7.71 (d, 1 H), 7.64 (t, 1 H), 7.54–7.44 (m, 3 H), 7.37 (d, 1 H), 7.30 (t, 1 H), 6.84 (d, 1 H) ppm. FAB-MS: *m*/*z* = 447.2 [($H_3L^2$)$H^+$].

**$[Mn_3(L^1)_3(CH_3OH)_3]$ (1):** A methanol solution (5 mL) of triethylamine (0.020 g, 0.2 mmol) was added to an orange suspension of $H_4L'$·HCl (0.077 g, 0.2 mmol) in methanol (15 mL) with stirring. A solution of manganese(II) acetate tetrahydrate (0.049 g, 0.2 mmol) in dry methanol (20 mL) was added to the resulting light brown solution, and the mixture was stirred for 10 min. The obtained dark brown solution was filtered, and the filtrate was allowed to stand at room temperature for 1 d to give dark brown crystals suitable for X-ray crystallography. Yield of **1**: 0.039 g, 45.3%. $C_{63}H_{45}Mn_3N_6O_{15}$ (1290.90): calcd. C 58.62, H 3.51, Mn 12.77, N 6.51; found C 58.47, H 3.10, Mn 13.07, N 6.74. IR (KBr): $\tilde{\nu}$ = 1606 (C=N), 1146 (C–O), 752 (phenyl) $cm^{-1}$. UV (dmf): $\lambda$ ($\varepsilon$) = 373 (37200), 503 (22900) and 800 sh (500 $dm^3 mol^{-1} cm^{-1}$) nm. $\Lambda_m$ (dmf) = 2.60 $S cm^{-2} mol^{-1}$.

**$[Mn_3(L^2)_3(dmf)(CH_3OH)(H_2O)]$ (2):** A solution of manganese(II) acetate tetrahydrate (0.025 g, 0.1 mmol) in dry methanol (10 mL) was added to an orange suspension of $H_3L^2$ (0.045 g, 0.1 mmol) in dmf (10 mL). The resulting dark brown mixture was stirred for 3 h and then filtered to remove insoluble materials. Triethylamine (0.02 g, 0.2 mmol) was added to the filtrate, and the solution was allowed to stand at room temperature for 3 d to give dark brown crystals suitable for X-ray crystallography. Yield of **2**·2dmf·$CH_3OH$: 0.029 g, 48.4%. $C_{95}H_{76}Mn_3N_9O_{18}$ (1796.51): calcd. C 63.51. H 4.26, Mn 9.17, N 7.02; found C 63.21, H 3.94, Mn 8.80, N 6.96. IR (KBr): $\tilde{\nu}$ = 1616, 1600 (C=N), 1144 (C–O), 828 and 756 (phenyl) $cm^{-1}$. UV (dmf): $\lambda$ ($\varepsilon$) = 410 sh (31600), 465 sh (20000), 526 sh (19900), 769 sh (1000) and 870 sh (500 $dm^3 mol^{-1} cm^{-1}$) nm. $\Lambda_m$ (dmf) = 1.90 $S cm^{-2} mol^{-1}$.

**Physical Measurements:** Elemental analyses for C, H and N were obtained at the Elemental Analysis Service Center, Kyushu University. Manganese was determined with a Perkin–Elmer A Analyst 100 atomic absorption spectrometer. Nuclear magnetic resonance spectra were recorded with a JNM-AL300 spectrometer in [$D_6$]-dmso using tetramethylsilane as the internal standard. FAB mass spectra for $H_3L^n$ and $H_4L'$ were recorded with a JMS-GC mate II. Infrared spectra and electronic spectra were recorded with a Perkin–Elmer Spectrum 2000 FTIR spectrometer on KBr disks and a Perkin–Elmer Lambda 19 UV/Vis/NIR spectrophotometer, respectively, at the Instrumental Analysis Center, Saga University. X-band ESR spectra were recorded with a JEOL JES-TE300 ESR spectrometer at room temperature. Magnetic susceptibilities in the temperature range 2–300 K were measured with a Quantum Design

 © 2007 Wiley-VCH Verlag GmbH & Co. KGaA, Weinheim 

MPMS XL SQUID susceptometer under an applied magnetic field of 500 G. The susceptibilities at room temperature were determined by the Gouy method with a Sherwood Scientific Magnetic Susceptibility Balance. These were corrected for the diamagnetism of the constituent atoms using Pascal's constant.[40] The effective magnetic moments were calculated from the equation $\mu_{eff} = 2.828[(\chi_A - N\alpha)T]^{1/2}$, where $\chi_\alpha$ is the atomic magnetic susceptibility and $N\alpha$ is the temperature-independent paramagnetism. Molar conductances were determined in dmf at 25 °C with a TOA EC METER CM-30G. Cyclic voltammograms (CVs) were obtained with a BAS 100B electrochemical voltammetric analyser. The CV measurements were carried out in dmf containing 0.1 M tetrabutylammonium perchlorate (tbap) as supporting electrolyte. (***Caution:*** tbap is explosive and should be handled with great care!) The three-electrode cell that was used was equipped with a glassy carbon ($\phi$ = 3 mm) working electrode, a platinum wire counter electrode, and an $Ag/Ag^+$ electrode as the reference.

**X-ray Crystal Structure Determinations:** The diffraction data were measured with a Rigaku AFC5S automated four-circle diffractometer having graphite-monochromated Mo-$K_\alpha$ ($\lambda$ = 0.71069 Å) radiation. Cell constants and an orientation matrix for data collection were obtained from a least-squares refinement using the setting angles of 25 carefully centered reflections for complexes **1**, 24 reflections for $H_3L^1$ and $H_4L'$, and 6 reflections for $H_3L^2$. The data were collected using the $\omega$-scan technique to a maximum $2\theta$ value of 55.1° for $H_3L^1$, 55.0° for $H_4L'$ and **1**, and the $\omega$-$2\theta$-scan technique to a maximum $2\theta$ value of 45.0° for $H_3L^2$. The weak reflections [$I < 10\sigma(I)$] were rescanned (maximum 5 rescans) and the counts were accumulated to assure good counting statistics. Stationary background counts were recorded on each side of the reflection. The ratio of the peak counting time was 2:1. The intensities of three representative reflections were measured after every 150 reflections. Over the course of data collections, the standards decreased by 0.7% for **1**. Polynomial correction factors were applied to the data to account for this phenomenon. Empirical absorption corrections, based on azimuthal scans of several reflections, were applied. The data were corrected for Lorentz and polarisation effects. The crystallographic data and collection details are summarised in Table 3. The structures were solved by direct methods (SIR92) and expanded using Fourier techniques.[41,42] All hydrogen atoms were located in the calculated positions and refined using the riding model. The final cycle of full-matrix least-squares refinement on $F$ using SHELXL-97 was based on observed reflections and variable parameters, and converged with unweighted and weighted agreement factors of $R$ and $R_w$.[43,44] Neutral atom scattering factors were taken from Cromer and Waber.[45] Anomalous dispersion effects were included in $F_c$;[46] the values for $\Delta f'$ and $\Delta f''$ were those of Creagh and McAuley.[47,48] All calculations were performed using the Rigaku CrystalStructure crystallographic software package, except for refinement, which was performed using SHELXL-97.[49] CCDC-625063 to -625066 contain the supplementary crystallographic data for this paper. These data can be obtained free of charge from The Cambridge Crystallographic Data Centre via www.ccdc.cam.ac.uk/data_request/cif.

**Supporting Information** (see footnote on the first page of this article): Packing diagram showing hydrogen bonding in complex **1** (Figure S1), ORTEP drawing of complex **2** (Figure S2).

## Acknowledgments

This work was supported by a Grant-in-Aid for Science Research (C) (No. 15510092) and the "Nanotechnology Support Project" of the Ministry of Education, Science, Sports and Culture of Japan.

[1] K. Severin, *Coord. Chem. Rev.* **2003**, *245*, 3–10.
[2] M. Murugesu, J. Raftery, W. Wernsdorfer, G. Christou, E. K. Brechin, *Inorg. Chem.* **2004**, *43*, 4203–4209.
[3] R. H. Fish, *Coord. Chem. Rev.* **1999**, *185–186*, 569–584.
[4] R. Wang, M. Hong, J. Luo, R. Cao, J. Weng, *Chem. Commun.* **2003**, 1018–1019.
[5] D. Moon, M. S. Lah, *Inorg. Chem.* **2005**, *44*, 1934–1940.
[6] M. Consiglo, F. Maggio, T. Pizzino, V. Romano, *Inorg. Nucl. Lett.* **1978**, *14*, 135–137.
[7] a) H. Ōkawa, M. Nakamura, S. Kida, *Bull. Chem. Soc. Jpn.* **1982**, *55*, 466–470; b) W. Kanda, M. Nakamura, H. Ōkawa, S. Kida, *Bull. Chem. Soc. Jpn.* **1983**, *56*, 744–747.
[8] H. Asada, M. Ozeki, M. Fujiwara, T. Matsushita, *Polyhedron* **2002**, *21*, 1139–1148.
[9] a) J. Qiao, L. D. Wang, L. Duan, Y. Li, D. Q. Zhang, Y. Qiu, *Inorg. Chem.* **2004**, *43*, 5096–5102; b) J. Qiao, L. D. Wang, J. F. Xie, G. T. Lei, G. S. Wu, Y. Qiu, *Chem. Commun.* **2005**, 4560–4562.
[10] S. Dutta, P. Basu, A. Chakravorty, *Inorg. Chem.* **1991**, *30*, 4031–4037.
[11] a) X. Chen, F. J. Femia, J. W. Babich, J. Zubieta, *Inorg. Chim. Acta* **2000**, *308*, 80–90; b) X. Chen, F. J. Femia, J. W. Babich, J. Zubieta, *Inorg. Chim. Acta* **2001**, *316*, 33–40.
[12] M. Mikuriya, N. Torihara, H. Ōkawa, S. Kida, *Bull. Chem. Soc. Jpn.* **1981**, *54*, 1063–1067.
[13] D. P. Kessissoglou, X. Li, W. M. Butler, V. L. Pecoraro, *Inorg. Chem.* **1987**, *26*, 2487–2492.
[14] M. Koikawa, H. Ōkawa, S. Kida, *J. Chem. Soc. Dalton Trans.* **1988**, 641–645.
[15] S. K. Chandra, P. Basu, D. Ray, S. Pal, A. Chakravorty, *Inorg. Chem.* **1990**, *29*, 2423–2428.
[16] M. Mikuriya, D. Jie, Y. Kakuta, T. Tokii, *Bull. Chem. Soc. Jpn.* **1993**, *66*, 1132–1139.
[17] H. Asada, M. Ozeki, M. Fujiwara, T. Matsushita, *Chem. Lett.* **1999**, 525–526.
[18] a) A. Elmali, I. Svoboda, *Z. Naturforsch., B: Chem. Sci.* **2001**, *56*, 897–900; b) A. Elmali, Y. Elerman, C. T. Zeyrek, I. Svoboda, *Z. Naturforsch., B: Chem. Sci.* **2003**, *58*, 433–437.
[19] P. A. N. Reddy, M. Nethaji, A. R. Chakravarty, *Eur. J. Inorg. Chem.* **2003**, 2318–2324.
[20] R. Kannappan, D. M. Tooke, A. L. Spek, J. Reedijk, *Inorg. Chim. Acta* **2006**, *359*, 334–338.
[21] E. Lambert, B. Chabut, S. Chardon-Noblat, A. Deronzier, G. Chottard, A. Bousseksou, J.-P. Tuchagues, J. Laugier, M. Bardet, J.-M. Latour, *J. Am. Chem. Soc.* **1997**, *119*, 9424–9437.
[22] D. E. Fenton, *Chem. Soc. Rev.* **1999**, *28*, 159–168.
[23] C. Belle, J.-L. Pierre, *Eur. J. Inorg. Chem.* **2003**, 4137–4146.
[24] G. Manecke, W. E. Wille, *Makromol. Chem.* **1970**, *133*, 61–82.
[25] a) Y. Kurusu, W. Storck, G. Manecke, *Makromol. Chem.* **1975**, *176*, 3185–3200; b) Y. Kurusu, *Macromol. Symp.* **1996**, *105*, 173–177.
[26] O. Waldmann, J. Massmann, P. Müller, G. S. Hanan, D. Volkmer, U. S. Schubert, J.-M. Lehn, *Phys. Rev. Lett.* **1997**, *78*, 3390–3393.
[27] L. Zhao, C. J. Matthews, L. K. Thompson, S. L. Heath, *Chem. Commun.* **2000**, 265–266.
[28] C. E. Hulme, M. Watkinson, M. Haynes, R. G. Pritchard, C. A. McAuliffe, N. Jaiboon, B. Beagley, A. Sousa, M. R. Bermejo, M. Fondo, *J. Chem. Soc. Dalton Trans.* **1997**, 1805–1814.
[29] C. Palopoli, M. González-Sierra, G. Robles, F. Dahan, J.-P. Tuchagues, S. Signorella, *J. Chem. Soc. Dalton Trans.* **2002**, 3813–3819.
[30] C. Boskovic, E. Rusanov, H. Stoeckli-Evans, H. U. Güdel, *Inorg. Chem. Commun.* **2002**, *5*, 881–886.
[31] N. Hoshino, T. Ito, M. Nihei, H. Oshio, *Inorg. Chem. Commun.* **2003**, *6*, 377–380.

 © 2007 Wiley-VCH Verlag GmbH & Co. KGaA, Weinheim 

[32] S. L. Dexheimer, J. W. Gohdes, M. K. Chan, K. S. Hagen, W. H. Armstrong, M. P. Klein, *J. Am. Chem. Soc.* **1989**, *111*, 8923–8925.
[33] K. P. Bryliakov, D. E. Babushkin, E. P. Talsi, *J. Mol. Catal. A* **2000**, *158*, 19–35.
[34] G. D. Munno, W. Ventura, G. Viau, F. Lloret, J. Faus, M. Julve, *Inorg. Chem.* **1998**, *37*, 1458–1464.
[35] C. Desplanches, E. Ruiz, A. Rodríguez-Fortea, S. Alvarez, *J. Am. Chem. Soc.* **2002**, *124*, 5197–5205.
[36] a) R. Karmakar, C. R. Choudhury, G. Bravic, J.-P. Sutter, S. Mitra, *Polyhedron* **2004**, *23*, 949–954; b) M. S. Ray, A. Ghosh, R. Bhattacharya, G. Mukhopadhyay, M. G. B. Drew, J. Ribas, *Dalton Trans.* **2004**, 252–259.
[37] G. D. Santis, L. Fabbrizzi, M. Licchelli, P. Pallavicini, *Coord. Chem. Rev.* **1992**, *120*, 237–257.
[38] N. Shan, S. J. Vickers, H. Adams, M. D. Ward, J. A. Thomas, *Angew. Chem. Int. Ed.* **2004**, *43*, 3938–3941.
[39] L. A. Berben, M. C. Faia, N. R. M. Crawford, J. R. Long, *Inorg. Chem.* **2006**, *45*, 6378–6386.
[40] Landoldt-Börnstein, Neue Serie II/11, Springer-Verlag, Berlin, **1981**.
[41] SIR92: A. Altomare, G. Cascarano, C. Giacovazzo, A. Guagliardi, M. Burla, G. Polidori, M. Camalli, *J. Appl. Crystallogr.* **1994**, *27*, 435.
[42] *DIRDIF99*: P. T. Beurskens, G. Admiraal, G. Beurskens, W. P. Bosman, R. de Gelder, R. Israel, J. M. M. Smits, *The DIRDIF-99 program system*, Technical Report of the Crystallography Laboratory, University of Nijmegen, The Netherlands, **1999**.
[43] $R = \Sigma||F_o| - |F_c||/\Sigma|F_o|$, $Rw = \{\Sigma[w(F_o^2 - F_c^2)^2]/\Sigma w(F_o^2)^2\}^{1/2}$ where $w$ = least-squares weights.
[44] G. M. Sheldrick, *SHELX97*, **1997**.
[45] D. T. Cromer, J. T. Waber (Eds.), *International Tables for X-ray Crystallography*, Kynoch Press, Birmingham, **1974**, vol. IV.
[46] J. A. Ibers, W. C. Hamilton, *Acta Crystallogr.* **1964**, *17*, 781.
[47] D. C. Creagh, W. J. McAuley in *International Tables for Crystallography* (Ed.: A. J. C. Wilson), Kluwer Academic Publishers, Boston, **1992**, vol. C, pp. 219–222.
[48] D. C. Creagh, J. H. Hubbell in *International Tables for Crystallography* (Ed.: A. J. C. Wilson), Kluwer Academic Publishers, Boston, **1992**, vol. C, pp. 200–206.
[49] *CrystalStructure 3.7.0*, Crystal Structure Analysis Package, Rigaku, Rigaku/MSC, **2000**–**2005**.

Received: January 18, 2007
Published Online: June 25, 2007

 © 2007 Wiley-VCH Verlag GmbH & Co. KGaA, Weinheim 

DOI: 10.1002/ejic.200700297

# New Reactivity of 4-Amino-3,5-bis(pyridin-2-yl)-1,2,4-triazole: Synthesis and Structure of a Mononuclear Species, a Dinuclear Species, and a Novel Tetranuclear Nickel(II) Rectangle Box, and Magnetic Properties of the Dinuclear and Tetranuclear Complexes

**Ming-Liang Tong,*[a] Chao-Gang Hong,[a] Ling-Ling Zheng,[a] Meng-Xia Peng,[a,b] A. Gaita-Ariño,[c] and Juan Modesto Clemente Juan*[c]**

**Keywords:** Nickel / Polynuclear / Azides / Magnetic properties

Reactions of $Ni(O_2CMe)_2·4H_2O$ or $NiCl_2·6H_2O$, 4-amino-3,5-bis(pyridin-2-yl)-1,2,4-triazole (abpt) and $NaN_3$ or KSCN in different molar ratios heated under reflux or hydrothermal conditions generate a mononuclear species with dimorphous phases, a dinuclear species incorporating an in situ deaminated [bpt-H]$^-$ ligand and a tetranuclear rectangle box incorporating an unprecedented $\mu:\eta^1:\eta^2:\eta^1$ coordination mode of the deprotonated [abpt-H]$^-$ ligand. Structural analysis reveals that a pair of $[Ni_2(\mu_{1,1}\text{-}N_3)(\mu\text{-}OAc)]$ motifs in $[Ni_4(abpt)_2(abpt\text{-}H)(N_3)_5(O_2CMe)_2]·5H_2O$ (**1**) are bridged by two abpt and one [abpt-H]$^-$ units into a rectangle box. $[Ni_2(bpt\text{-}H)_2(SCN)_2(H_2O)_2]·2H_2O$ (**2**) is a neutral centrosymmetric dinuclear $Ni^{II}$ complex doubly bridged by abpt ligands. The complex $[Ni(abpt)_2(N_3)_2]$ (**3**) is a neutral centrosymmetric mononuclear $Ni^{II}$ complex and crystallizes in polymorphous phases, showing an interesting example of temperature-induced polymorphism. Variable-temperature magnetic susceptibility measurements reveal that the ferromagnetic interaction via the $(\mu_{1,1}\text{-}N_3)_2(\mu\text{-}OAc)$ and $(\mu_{1,1}\text{-}N_3)(\mu_{1,1}\text{-}NH_{abpt-H})(\mu\text{-}OAc)$ bridges slightly dominates over the antiferromagnetic interaction via the abpt bridges, therefore indicative of an overall ferromagnetic coupling between $Ni^{II}$ centers in **1**, and a moderate antiferromagnetic interaction occurs in **2**.

(© Wiley-VCH Verlag GmbH & Co. KGaA, 69451 Weinheim, Germany, 2007)

## Introduction

Magnetic multimetal-centered complexes or metal clusters have attracted much attention over the past decades.[1,2] 4-Amino-3,5-bis(pyridin-2-yl)-1,2,4-triazole (abpt) is a potential multitopic ligand and its coordination chemistry has been investigating since the mid 1980s.[3] In particular, the spin-crossover system $[Fe(abpt)_2(X)_2]$ (where X = $SCN^-$, $SeCN^-$ or $N(CN)_2^-$, $TCNQ^-$) has been structurally and magnetically characterized.[4] So far, many coordination compounds of adpt have been synthesized.[5a,5b] However, most of them are mononuclear, particularly, only two examples of dinuclear nickel and copper complexes have been structurally characterized before our work,[3,5c] which indicate that the majority of these coordination compounds have relatively poor crystallization behavior in common solvents. This urged us to pursue its chemical reactivity under relatively unconventional conditions. We have recently been investigating a few in situ metal–organic reactions targeting a magnetic cluster system and furnished an interesting sandwich-type high-spin heterometallic $Ni_{12}K_4$ cluster from the reaction of di-2-pyridyl ketone with nickel acetate and azide in the presence of potassium *tert*-butoxide as a catalytic base.[6] Herein we report a tetranuclear rectangle box, a dinuclear complex and a mononuclear complex in polymorphous phases, which are synthesized by reflux and hydrothermal methods, respectively. They are $[Ni_4(abpt)_2(abpt\text{-}H)(N_3)_5(O_2CMe)_2]·5H_2O$ (**1**), $[Ni_2(bpt\text{-}H)_2(SCN)_2(H_2O)_2]·2H_2O$ (**2**) (bpt-H = 3,5-di-2-pyridyl-1,2,4-triazolate), α-$[Ni(abpt)_2(N_3)_2]$ (**3α**), and β-$[Ni(abpt)_2(N_3)_2]$ (**3β**). The [abpt-H]$^-$ in **1** resulted from the deprotonation of abpt during the reflux conditions and [bpt-H]$^-$ in **2** was formed from the deamination of abpt under solvothermal conditions.

[a] MOE Key Laboratory of Bioinorganic and Synthetic Chemistry, State Key Laboratory of Optoelectronic Materials and Technologies, School of Chemistry and Chemical Engineering, Sun Yat-Sen University,
Guangzhou, 510275 P. R. China
Fax: +86-20-8411-2245
E-mail: tongml@mail.sysu.edu.cn
[b] Department of Chemistry, Jiaying University,
514015 Meizhou, P. R. China
[c] Instituto de Ciencia Molecular, Universidad de Valencia,
C/ Dr. Moliner 50, 46100 Burjassot, Spain
E-mail: juan.m.clemente@uv.es

## Results and Discussion

### Synthesis and Characterization

In the reported metal complexes of the abpt ligand,[5a] the azide anion has not been chosen as the counterions, the azide salt is, therefore, introduced into the reaction system.

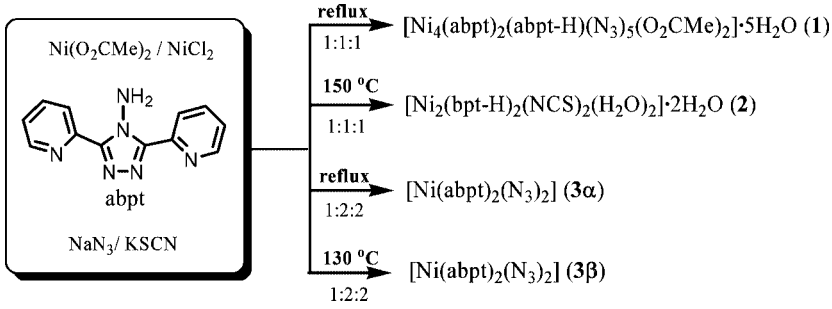


Scheme 1. Synthesis of **1**, **2**, **3α**, and **3β**.

The reaction of $Ni(O_2CMe)_2·4H_2O$, $NaN_3$ and abpt in a 1:1:1 molar ratio heated at reflux generated tetranuclear complex **1** (Scheme 1). When $NaN_3$ was replaced by KNCS, the solvothermal reaction of $NiCl_2·6H_2O$, KNCS and abpt in a 1:1:1 molar ratio led to dinuclear complex **2**. Remarkable is the deamination of abpt into bpt during the reaction probably related to the extreme conditions of the solvothermal reaction, which was also observed in the hydrothermal reaction of $[Co(abpt)_2(SCN)_2]$[3d] with $CoCl_2$. Furthermore, reactions of $NiCl_2·6H_2O$, $NaN_3$ and abpt in a 1:2:2 molar ratio heated at reflux or under solvothermal conditions led to the polymorphous mononuclear complexes of **3α** and **3β**, respectively, demonstrating that the factor of reaction temperature notably affects the final products. It should be noted that **3α** and **3β** are the first examples of ternary metal–abpt–azide complexes.

In addition to the bands of the abpt and $[abpt\text{-}H]^-$ ligands, the points of interest in the IR spectrum of the four complexes lie mainly in the bands due to the $N_3^-$ or $SCN^-$ groups. For **1**, the asymmetrical stretch $\nu_{as}(N_3)$ appears as strong bands at ca. 2070 and 2041 $cm^{-1}$, which is in good agreement with the existence of terminal and EO bridging azides in **1**; bands of weak intensity at about 1301 and 1284 $cm^{-1}$ can be ascribed to the azide symmetric stretch $\nu_s(N_3)$. Very strong bands corresponding to the characteristic $\nu_{as}$ of the azido ligands appeared at 2034 $cm^{-1}$ for **3α** and at 2053 $cm^{-1}$ for **3β**. For **2**, the stretching vibration of the $SCN^-$ group appears as a doublet at 2108 and 2058 $cm^{-1}$.

## Crystal Structure

Single-crystal X-ray structure analysis revealed that **1** is a neutral tetranuclear $Ni^{II}$ complex. A perspective view of the core part of **1** with the atom-labeling scheme is shown in Figure 1. Selected metric parameters associated with the nickel(II) center in **1** are given in Table 1. Each asymmetric unit of **1** contains four $Ni^{II}$ atoms, two abpt ligands, one anionic $[abpt\text{-}H]^-$ ligand, five $N_3^-$ ligands, two acetate ligands, and five lattice water molecules. Each $Ni^{II}$ atom is in a distorted octahedral $[NiN_5O]$ environment, of which the coordination sphere for Ni1 or Ni2 is formed by two pyridyl N atoms, one triazole N atom, one azide N atom, one amine N atom, and one acetate O atom [Ni–N = 2.001(3)–2.166(3), Ni–O = 2.050(3) and 2.052(2) Å, *cis* N–Ni–N/O = 77.53(12)–103.06(12)°, *trans* N–Ni–N/O = 166.59(12)–176.55(13)°], while the coordination sphere for Ni3 or Ni4 is formed by one pyridyl N atom, one triazole N atom, three azide N atoms, and one acetate O atom [Ni–N = 2.062(4)–2.179(3), Ni–O = 2.047(3) and 2.053(3) Å, *cis* N–Ni–N/O = 76.55(12)–105.20(12)°, *trans* N–Ni–N/O = 167.27(12)–173.10(13)°]. The Ni1 and Ni2 are triply bridged by one μ-amino [Ni–$N_{amino}$–Ni = 97.74(14)°], one $\mu_{1,1}$-azide [Ni–$N_{azide}$–Ni = 88.92(12)°], and one μ-carboxylate-O,O′ with the Ni···Ni distance of 3.0253(8) Å and the Ni3 and Ni4 are triply bridged by two $\mu_{1,1}$-azides [Ni–$N_{azide}$–Ni = 95.74(13) and 98.39(15)°] and one μ-carboxylate-O,O′ with the Ni···Ni distance of 3.138(1) Å. The Ni1 and Ni4/Ni2 and Ni3 are each singly triazole-bridged with the Ni···Ni

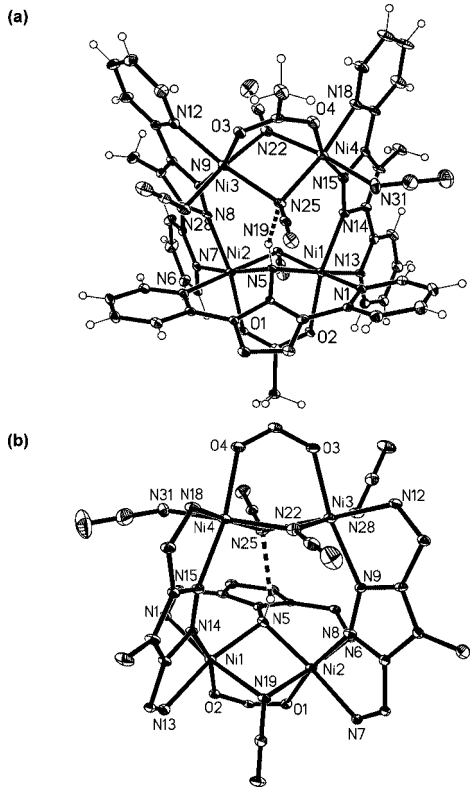


Figure 1. ORTEP plots of the molecular structure (a) and the connectivity pattern (b) in **1**. The methyl group and some of the carbon atoms of the pyridyl groups are omitted for clarity. 50% thermal ellipsoids are shown.

 © 2007 Wiley-VCH Verlag GmbH & Co. KGaA, Weinheim 

Table 1. Selected interatomic contacts [Å] and bond angles [°] for **1**.

| | | | | | | | |
|---|---|---|---|---|---|---|---|
| Ni1–N5 | 2.015(3) | Ni3–O3 | 2.053(3) | Ni2–N19 | 2.154(3) | Ni4–N15 | 2.117(3) |
| Ni1–O2 | 2.052(2) | Ni3–N12 | 2.072(3) | Ni1···Ni2 | 3.0253(8) | Ni3···Ni4 | 3.1377(8) |
| Ni1–N13 | 2.095(3) | Ni3–N22 | 2.074(3) | Ni1···Ni4 | 4.578(1) | Ni2···Ni3 | 4.6680(9) |
| Ni1–N14 | 2.116(3) | Ni3–N28 | 2.079(4) | N5···N25 | 2.871(4) | O2w···N30 | 2.919(5) |
| Ni1–N1 | 2.122(3) | Ni3–N25 | 2.123(3) | N11···N27[b] | 3.055(6) | O3w···O2w[d] | 2.889(6) |
| Ni1–N19 | 2.166(3) | Ni3–N9 | 2.179(3) | N11···O4w | 2.898(6) | O3w···N33[g] | 2.892(7) |
| Ni2–N5 | 2.001(3) | Ni4–O4 | 2.047(3) | N17···O4w[c] | 2.895(7) | O4w···O6w[a] | 2.98(1) |
| Ni2–O1 | 2.050(3) | Ni4–N31 | 2.062(4) | N17···N30[d] | 3.099(6) | O4w···O3w | 2.733(6) |
| Ni2–N7 | 2.089(3) | Ni4–N22 | 2.071(4) | O1w···N3[e] | 2.989(4) | O5w···N33 | 2.896(6) |
| Ni2–N6 | 2.092(3) | Ni4–N18 | 2.086(3) | O1w···N2 | 2.948(5) | O6w···O4w | 2.91(1) |
| Ni2–N8 | 2.100(3) | Ni4–N25 | 2.108(3) | O2w···N19[f] | 3.075(5) | | |
| | | | | | | | |
| N5–Ni1–O2 | 90.3(1) | O3–Ni3–N12 | 91.1(1) | O1–Ni2–N6 | 87.6(1) | N31–Ni4–N18 | 96.2(1) |
| N5–Ni1–N13 | 168.0(1) | O3–Ni3–N22 | 91.8(1) | N7–Ni2–N6 | 97.3(1) | N22–Ni4–N18 | 91.5(1) |
| O2–Ni1–N13 | 89.5(1) | N12–Ni3–N22 | 93.6(1) | N5–Ni2–N8 | 96.2(1) | O4–Ni4–N25 | 88.5(1) |
| N5–Ni1–N14 | 103.1(1) | O3–Ni3–N28 | 91.0(1) | O1–Ni2–N8 | 169.7(1) | N31–Ni4–N25 | 92.0(1) |
| O2–Ni1–N14 | 166.6(1) | N12–Ni3–N28 | 93.3(1) | N7–Ni2–N8 | 78.9(1) | N22–Ni4–N25 | 80.4(1) |
| N13–Ni1–N14 | 77.5(1) | N22–Ni3–N28 | 172.5(1) | N6–Ni2–N8 | 87.3(1) | N18–Ni4–N25 | 171.8(1) |
| N5–Ni1–N1 | 91.2(1) | O3–Ni3–N25 | 86.8(1) | N5–Ni2–N19 | 82.7(1) | O4–Ni4–N15 | 167.3(1) |
| O2–Ni1–N1 | 88.7(1) | N12–Ni3–N25 | 173.1(1) | O1–Ni2–N19 | 92.7(1) | N31–Ni4–N15 | 86.2(1) |
| N13–Ni1–N1 | 100.8(1) | N22–Ni3–N25 | 80.0(1) | N7–Ni2–N19 | 86.1(1) | N22–Ni4–N15 | 95.8(1) |
| N14–Ni1–N1 | 90.4(1) | N28–Ni3–N25 | 93.3(1) | N6–Ni2–N19 | 176.6(1) | N18–Ni4–N15 | 77.1(1) |
| N5–Ni1–N19 | 82.1(1) | O3–Ni3–N9 | 167.4(1) | N8–Ni2–N19 | 93.0(1) | N25–Ni4–N15 | 103.5(1) |
| O2–Ni1–N19 | 95.8(1) | N12–Ni3–N9 | 76.6(1) | N5–H5N···N25 | 148(3) | O2w–H2wb···N30 | 175(5) |
| N13–Ni1–N19 | 86.0(1) | N22–Ni3–N9 | 86.6(1) | N11–H11A···N27[b] | 154(4) | O3w–H3wa···O2w[d] | 156(6) |
| N14–Ni1–N19 | 86.8(1) | N28–Ni3–N9 | 92.2(1) | N11–H11B···O4w | 176(5) | O3w–H3wb···N33[g] | 160(5) |
| N1–Ni1–N19 | 171.9(1) | N25–Ni3–N9 | 105.2(1) | N17–H17A···O4w[c] | 164(4) | O4w–H4wa···O6w[a] | 174(5) |
| N5–Ni2–O1 | 93.1(1) | O4–Ni4–N31 | 89.2(1) | N17–H17B···N30[d] | 153(4) | O4w–H4wb···O3w | 148(5) |
| N5–Ni2–N7 | 167.5(1) | O4–Ni4–N22 | 90.4(1) | O1w–H1wa···N3[e] | 166(4) | O5w–H5w···N33 | 167(5) |
| O1–Ni2–N7 | 92.9(1) | N31–Ni4–N22 | 172.4(1) | O1w–H1wb···N2 | 164(4) | O6w–H6wa···O4w | 118(10) |
| N5–Ni2–N6 | 93.9(1) | O4–Ni4–N18 | 91.7(1) | O2w–H2wa···N19[f] | 168(4) | | |

Symmetry codes: [a] $-x + 1, y, -z + 3/2$. [b] $x, -y + 1, z + 1/2$. [c] $x, -y + 2, z - 1/2$. [d] $x, y + 1, z$. [e] $-x, y, -z + 1/2$. [f] $x, y - 1, z$. [g] $x, -y + 2, z + 1/2$.

separations of 4.578(1) and 4.6680(9) Å, respectively. A rectangle box is formed through these bridges. It is noteworthy that the dihedral angles between the coordinated pyridyl groups and the triazolato ring for the abpt and [abpt-H]$^-$ motifs are quite different. They are 24.5 and 25.2° for the anionic noncoplanar [abpt-H]$^-$ ligand, 2.3 and 22.1° for one half coplanar abpt ligand, and 6.1 and 7.0 ° for another coplanar abpt ligand, implying that there are different magnetic exchanges via the coplanar abpt, half-coplanar abpt and noncoplanar [abpt-H]$^-$ bridges. A recently reported example related to **1** was found in a tetranuclear nickel(II) rectangle box in which the long edges are spanned by the pyrazolate and each short edge is spanned by an acetate and a $\mu_{1,1}$ azide. The resulting rectangle was further capped by a $\mu_{1,1,3,3}$ bridging ligand.[7]

It is noteworthy that **1** is the first structurally characterized polynuclear cluster of the anionic [abpt-H]$^-$ ligand, in which the deprotonated 4-amino group, rather than N1 of the triazole ring, is coordinated to the Ni$^{II}$ ion, and the deprotonated amino group of the [abpt-H]$^-$ acts as a μ-bridge, and the resulting anionic [abpt-H]$^-$ ligand adopts an unprecedented $\mu:\eta^1:\eta^2:\eta^1$ coordination mode (Scheme 2d). Although the anionic [abpt-H]$^-$ form was previously found in [Rh$^I$(abpt-H)(diolefin)] (diolefin = 1,5-cyclooctadiene, 2,3-(tetrafluorobenzo)bicyclo[2.2.2]octatriene, or bicyclo-[2.2.1]heptadiene) based mainly on spectroscopic data[8a] and recently structurally characterized in [Rh(phen)$_2$(abpt-H)](PF$_6$)$_2$,[8b] it only plays a chelating role via the imine nitrogen and a pyridine nitrogen. The deprotonated amino group is also stabilized by a moderate N–H···N$_{azide}$ hydrogen bond [N···N = 2.871(4) Å, N–H···N$_{azide}$ = 148(3)°].

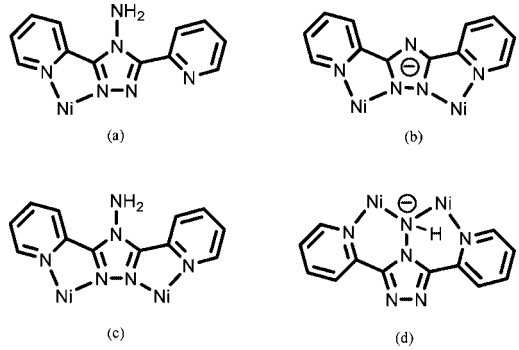


Scheme 2. Coordination modes of abpt (*a*, *c*), bpt-H (*b*), and abpt-H (*d*) in **1**, **2**, **3α**, and **3β**.

Compound **2** is a neutral centrosymmetric dinuclear Ni$^{II}$ complex (Figure 2a). Each asymmetric unit of **2** contains one Ni$^{II}$ atom, one anionic [bpt-H]$^-$ ligand, one SCN$^-$ ligand, one aqua ligand, and one lattice water molecule. The Ni$^{II}$ atom is in a distorted octahedral [NiN$_5$O] environment. The four basal nitrogen atoms coordinated to the Ni$^{II}$ atom belong to the pyridyl [N1 and N4a] and triazole [N2 and N3a] groups of two [bpt-H]$^-$ ligands. The Ni–N$_{pyridyl}$ distances are 2.220(2) and 2.193(2) Å (Table 2), respectively, which is slightly longer than those found in **1**; the

 © 2007 Wiley-VCH Verlag GmbH & Co. KGaA, Weinheim 

Ni–$N_{triazole}$ distances are 2.014(2) and 2.018(2) Å, respectively, which is shorter than those [2.110(3)–2.179(3) Å] found in **1**. The axial positions are occupied by one monodentate coordinating $SCN^-$ anion [Ni–N6 = 2.044(3) Å] and one aqua ligand (Ni–O1w = 2.062(2) Å]. The dihedral angles between the coordinated pyridyl groups and the triazolato ring are 3.0 and 4.8°, respectively. It is noteworthy to mention that recently most of the discrete and polymeric metal complexes of $[bpt\text{-}H]^-$ have been structurally characterized,[9] which probably contributes to the fact that the hydro(solvo)thermal method was widely adopted in the preparations of new metal–organic frameworks in the past decade.[10] It is also interesting that the aqua ligands and the lattice water molecules form hydrogen-bonded cyclic water tetramers [O···O = 2.729(3) and 2.755(3) Å; O–H···O = 158(4) and 169(3)°], $(H_2O)_4$ with graph set notation of $R_4^2(8)$. Theoretical studies on the basis of ab initio electronic structure calculations predicted that the cyclic $(H_2O)_4$ clusters have several configurations, $R_4^4(8)$-types of $D_{2h}$, $C_4$, or $S_4$ symmetry and $R_4^3(8)$-type of $C_s$ symmetry and most of them have widely been found in metal–organic frameworks and organic hosts.[11a,11b] The rare $R_4^2(8)$-type cyclic $(H_2O)_4$ tetramer was very recently found in an organic host.[11c] Each $(H_2O)_4$ tetramer in **2** is surrounded by four dinuclear species and each dinuclear species is surrounded accordingly by four $(H_2O)_4$ tetramers via the Ni–O coordination and O–H···N hydrogen-bonding interactions (Figure 2b).

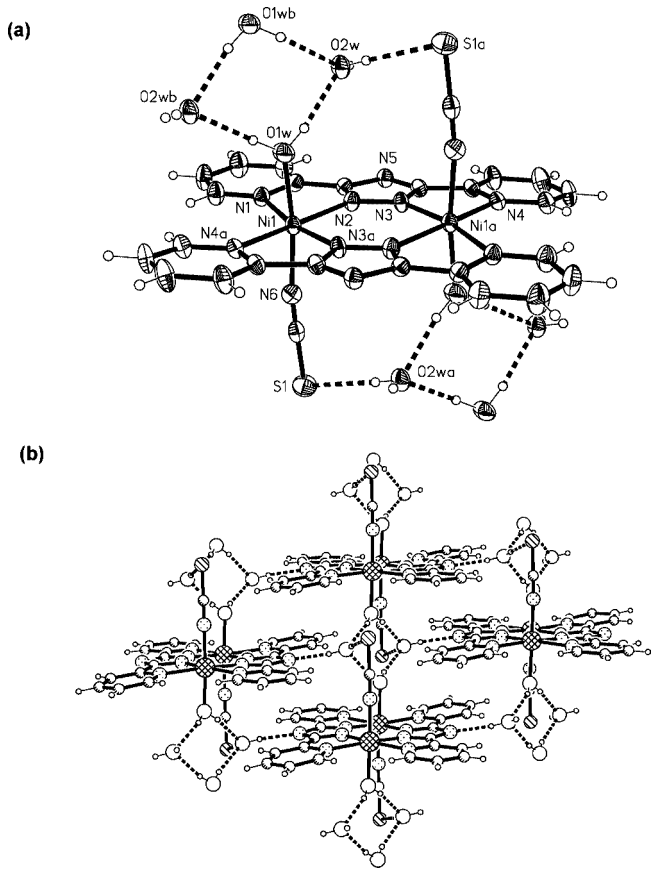


Figure 2. ORTEP plot of the molecule structure (a) and 2D hydrogen-bonded layer structure of **2**. 50% thermal ellipsoids are shown.

Table 2. Selected interatomic contacts [Å] and bond angles [°] for **2**.

| | | | |
|---|---|---|---|
| Ni1–N2 | 2.014(2) | Ni1–O1w | 2.062(2) |
| Ni1–N3[a] | 2.018(2) | Ni1–N4[a] | 2.193(2) |
| Ni1–N6 | 2.044(3) | Ni1–N1 | 2.220(2) |
| O1w···O2w[b] | 2.755(3) | O2w···N5[c] | 2.785(3) |
| O1w···O2w | 2.729(3) | O2w···S1[a] | 3.310(3) |
| | | | |
| N2–Ni1–N3[a] | 92.12(9) | N6–Ni1–N4[a] | 92.07(9) |
| N2–Ni1–N6 | 95.2(1) | O1w–Ni1–N4[a] | 83.33(9) |
| N3[a]–Ni1–N6 | 94.94(9) | N2–Ni1–N1 | 75.94(9) |
| N2–Ni1–O1w | 90.48(9) | N3[a]–Ni1–N1 | 167.99(8) |
| N3[a]–Ni1–O1w | 90.1(1) | N6–Ni1–N1 | 87.60(9) |
| N6–Ni1–O1w | 172.2(1) | O1w–Ni1–N1 | 88.7(1) |
| N2–Ni1–N4[a] | 167.00(9) | N4[a]–Ni1–N1 | 115.18(8) |
| N3[a]–Ni1–N4[a] | 76.52(8) | O2w–H2wb···N5[c] | 173(4) |
| O1w–H1wa···O2w | 158(4) | O2w–H2wa···S1[a] | 178(4) |
| O1w–H1wb···O2w | 169(3) | | |

Symmetry codes: [a] $-x, -y, -z$. [b] $-x, -y + 1, -z$. [c] $-x + 1, -y, -z$.

Both **3α** and **3β** are neutral centrosymmetric mononuclear $Ni^{II}$ complexes. Their coordination geometries are quite similar. Each asymmetric unit of **3α** and **3β** contains one-half of a $Ni^{II}$ atom, which lies on an inversion center, one abpt ligand, and one $N_3^-$ ligand. The $Ni^{II}$ atom is coordinated in a distorted octahedral $[NiN_6]$ environment. The four equatorial nitrogen atoms coordinated to the $Ni^{II}$ atom belong to the pyridyl [N1 and N1a] and triazole [N2 and N2a] groups of two abpt ligands. The Ni–$N_{pyridyl}$ distance is 2.101(2) and 2.101(3) Å for **3α** and **3β**, respectively (Tables 3 and 4), which is slightly longer than those found in **1**; the Ni–$N_{triazole}$ distances are 2.039(2) and 2.053(3) Å for **3α** and **3β**, respectively, which is shorter than those [2.110(3)–2.179(3) Å] found in **1**. The remaining two *trans*

Table 3. Selected interatomic contacts [Å] and bond angles [°] for **3α**.

| | | | |
|---|---|---|---|
| Ni1–N2 | 2.039(2) | Ni1–N7 | 2.126(2) |
| Ni1–N1 | 2.101(2) | N6···N9[b] | 2.967(2) |
| N6···N4 | 2.848(2) | | |
| | | | |
| N2–Ni1–N1[a] | 101.32(6) | N1–Ni1–N7[a] | 87.41(6) |
| N2–Ni1–N1 | 78.68(6) | N2–Ni1–N7 | 91.37(6) |
| N2–Ni1–N7[a] | 88.63(6) | N1–Ni1–N7 | 92.59(6) |
| N6–H6a···N4 | 141(2) | N6–H6b···N9[b] | 170(2) |

Symmetry codes: [a] $-x, -y, -z$. [b] $x, y - 1, z$.

Table 4. Selected interatomic contacts [Å] and bond angles [°] for **3β**.

| | | | |
|---|---|---|---|
| Ni1–N2 | 2.053(3) | Ni1–N7 | 2.126(3) |
| Ni1–N1 | 2.101(3) | N6···N9[b] | 3.095(7) |
| N6···N4 | 2.863(5) | | |
| | | | |
| N2–Ni1–N1 | 78.5(1) | N1–Ni1–N7[a] | 89.8(1) |
| N2–Ni1–N1[a] | 101.5(1) | N2–Ni1–N7 | 88.9(1) |
| N2–Ni1–N7[a] | 91.1(1) | N1–Ni1–N7 | 90.2(1) |
| N6–H6a···N4 | 122(7) | N6–H6b···N9[b] | 153(6) |

Symmetry codes: [a] $-x, -y, -z$. [b] $x, y, z - 1$.

 © 2007 Wiley-VCH Verlag GmbH & Co. KGaA, Weinheim 

positions are occupied by symmetry-related monodentate $N_3^-$ anions [Ni–N7 2.126(2) and 2.126(3) Å for **3α** and **3β**, respectively]. The dihedral angles between the coordinated pyridyl groups and the triazolato rings are 5.2(4) and 6.7(5)° for **3α** and **3β**, respectively, while those between the noncoordinating pyridyl groups and the triazolate rings are 7.1(4) and 10.2(5) ° for **3α** and **3β**, respectively. There exists intramolecular moderate N–H···N hydrogen bonding interactions between the amine groups and the noncoordinating pyridyl groups [for **3α**: N6···N4 = 2.848(2) Å; N6–H6a···N4 = 141(2)°; for **3β**: N6···N4 = 2.863(5) Å; N6–H4a···N4 = 122(7)°]. What interested us was that the orientations of the linear azide motifs in **3α** and **3β** are quite different, as shown in Figures 3a and 4a. In **3α**, the linear azide motifs run approximately parallel to the long sides of the abpt ligands, while in **3β** the linear azide motifs are approximately perpendicular to the long side of the abpt ligands. Although adjacent monoclinic $[Ni(abpt)_2(N_3)_2]$ motifs are extended via the N–H···$N_{azide}$ [N6···N9$^i$ = 2.966(3) Å, N6–H6b···N9$^i$ = 170(2)° for **3α**; N6···N9$^j$ = 3.095(7) Å, N6–H6b···N9$^j$ = 153(6)° for **3β**; symmetry codes: $i = x, y - 1, z$; $j = x, y, z - 1$] into 1D supramolecular double-stranded chains (Figures 3b and 4b), the dimensions of the cavities in 1D hydrogen-bonded chains of **3α** and **3β** are different. Particularly, the 1D chains are further extended by the nonclassical C–H···N hydrogen bonding (for **3α**: C···N = 3.442 Å and C–H···N = 150.3°; for **3β**: C···N = 3.508 Å and C–H···N = 142.5°) and offset π–π interactions (3.426–3.467 Å) into different 2D molecular layers in **3α** and **3β** (Figure 3c and 4c), and finally resulting in different 3D molecular packings in two polymorphous species. It should be noted that **3α** and **3β** represent a new interesting example showing temperature-induced polymorphism, which was observed in the case of molecular crystals of organic compounds, hydrogen bonded frameworks, and metal complexes such as L-glutamic acid, terpyridine, and $[Cu(Ph_2SNH)_4][PF_6]_2$.[12]

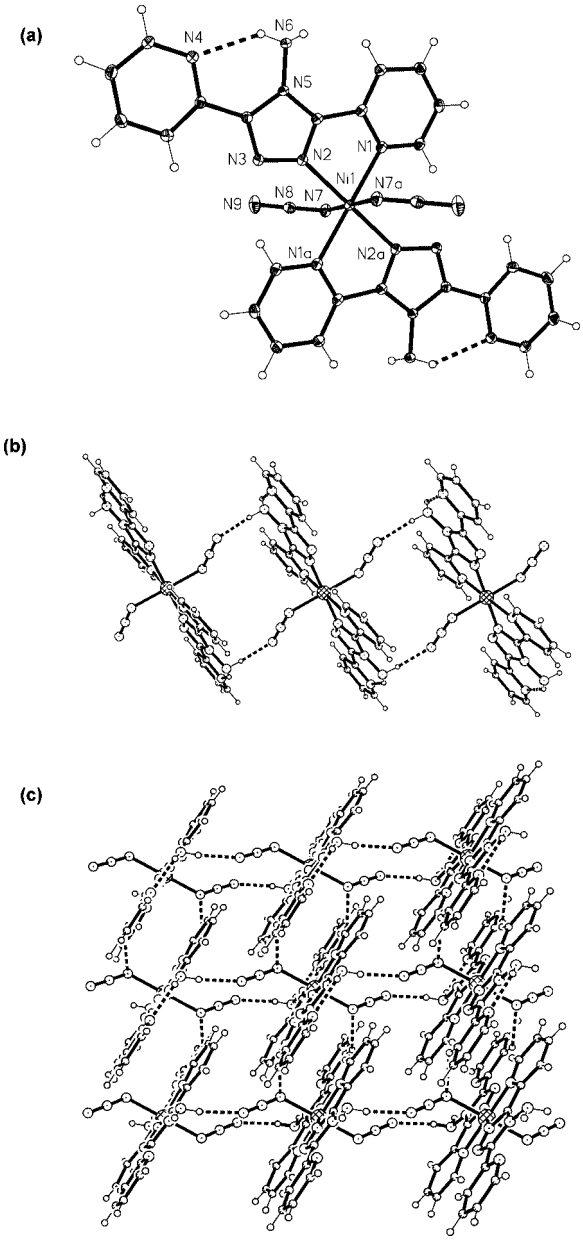


Figure 3. ORTEP plot of the coordination geometry of **3α** (a), the 1D hydrogen-bonded chain (b), and the extension of the 1D chains into 2D molecular layer by interchain π–π and C–H···N interactions in **3α**. 50% thermal ellipsoids are shown.

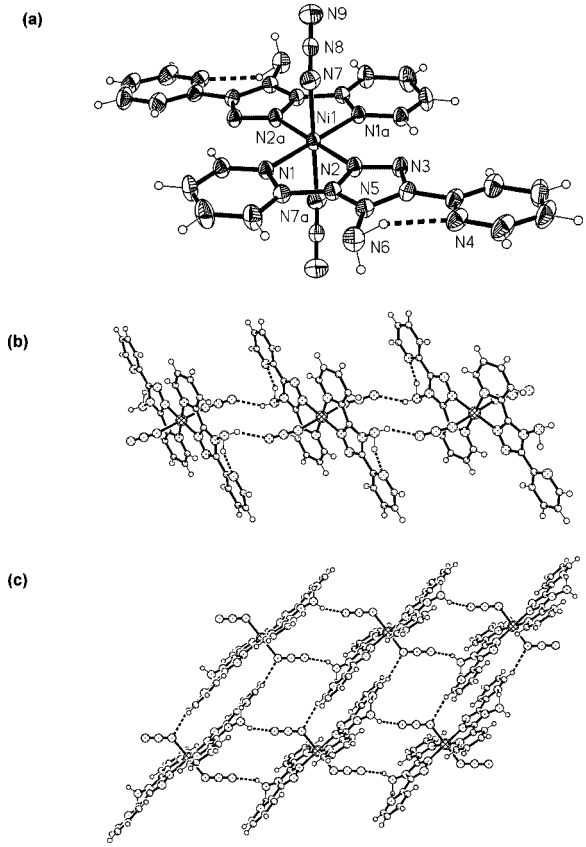


Figure 4. ORTEP plot of the coordination geometry of **3β** (a), the 1D hydrogen-bonded chain (b), and the extension of the 1D chains into 2D molecular layer by interchain π–π and C–H···N interactions in **3β**. 50% thermal ellipsoids are shown.

 © 2007 Wiley-VCH Verlag GmbH & Co. KGaA, Weinheim 

### Magnetic Properties

Magnetic susceptibility data were measured with polycrystalline samples of **1** and **2** in 1.0 KG field over the temperature range of 2–300 K.

For **1**, from room temperature down to 35 K, the $\chi_m T$ product increases continuously and reaches a maximum with 6.56 emu K mol$^{-1}$ (Figure 5). This behavior is indicative of an overall ferromagnetic coupling between the Ni$^{II}$ centers and the low temperature decrease is due to a strong zero-field splitting (ZFS) and/or the presence of a single antiferromagnetic interaction between two of the four Ni$^{II}$ centers. The magnetic data were analyzed with the spin Hamiltonian in Equation (1).

$$\hat{H} = -2J_1\hat{S}_1\hat{S}_2 - 2J_2\hat{S}_2\hat{S}_3 - 2J_3\hat{S}_3\hat{S}_4 - 2J_4\hat{S}_1\hat{S}_4 + D\left(\hat{S}_{z1}^2 + \hat{S}_{z2}^2 + \hat{S}_{z3}^2 + \hat{S}_{z4}^2\right) \quad (1)$$

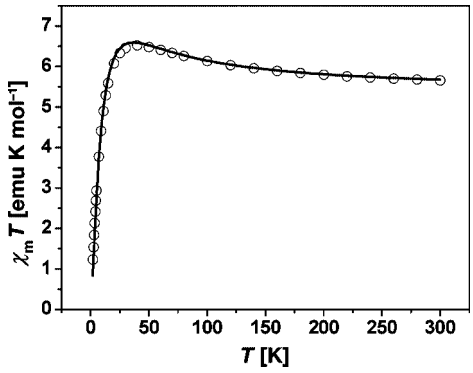


Figure 5. Plot of $\chi_M T$ vs. $T$ for **1**. Solid lines represent the best fit with the parameters given in the text.

Calculations were performed with the magnetism package MAGPACK.[13] The first best fit that was obtained from a least-squares analysis of the $\chi_m T$ implies a very big $D$ value ($D$ = 23.8 cm$^{-1}$) and unrealistic exchange parameters are $J_1$ = 2.37 cm$^{-1}$, $J_2$ = 4.84 cm$^{-1}$, $J_3$ = 15.7 cm$^{-1}$, $J_4$ = –3.95 cm$^{-1}$, and $g$ = 2.31 ($R = 7.5 \times 10^{-4}$). This solution was discarded. In order to reduce the number of parameters, we assumed that the two exchange parameters associated to the azide bridge were equal ($J_1 = J_3$) and the other two exchange parameters associated to the abpt bridge were also equal ($J_3 = J_4$). The best fit implies a zero ZFS and the parameters are $J_1 = J_3$ = 15.3 cm$^{-1}$, $J_2 = J_4$ = –2.2 cm$^{-1}$, and $g$ = 2.32. According to this calculation it is found that the ground state is $S$ = 0. Compared with those reported in our recently reported hexanuclear Ni$_6$ circle and other related species,[6] the ferromagnetic interactions ($J_1$ and $J_3$) can be assigned to the exchange pathway through the ($\mu_{1,1}$-N$_3$)$_2$(μ-OAc) and ($\mu_{1,1}$-N$_3$)($\mu_{1,1}$-N$_{abpt-H}$)(μ-OAc) bridges. The other two antiferromagnetic interactions can be assigned to the remaining exchange pathways indifferently, which is consistent with the results of X-ray structural analysis. In the future, more compounds of closely related, but significantly different, structures will be needed together with detailed magnetic studies and independent information (ab initio calculations) for a better understanding of magnetic superexchange in this type of compound.

For **2**, the magnetic data (Figure 6) were analyzed with the following spin Hamiltonian: $H = -2JS_1S_2$ ($S_1 = S_2$ = 1). From this Hamiltonian, the equation of magnetic susceptibility can be derived as $\chi = (Ng^2\beta^2/kT)[(5 + e^{4x})/(5 + 3e^{4x} + e^{6x})]$,[3a] in which $N$, β, and $k$ are fundamental constants, $g$ and $J$ are adjustable parameter, and $x = -J/kT$. The obtained parameters were fitted to be $J$ = –17.62 cm$^{-1}$ and $g$ = 2.19 ($R = 5.1 \times 10^{-4}$). The sign of $J$ in **2** is consistent with the antiferromagnetic $J_2$ and $J_4$ coupling via the abpt bridge in **1**.

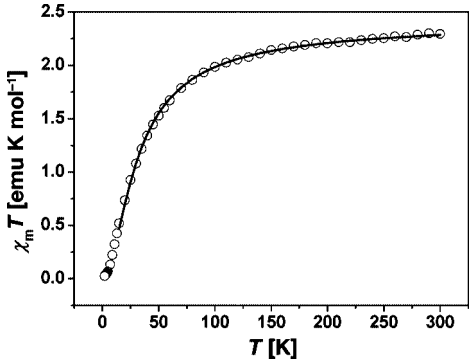


Figure 6. Plot of $\chi_M T$ vs. $T$ for **2**. Solid lines represent the best fit with the parameters given in the text.

## Conclusions

In this study, we present new reactivity of 4-amino-3,5-bis(pyridin-2-yl)-1,2,4-triazole to generate a novel tetranuclear nickel(II) rectangle box, a neutral dinuclear species, and a mononuclear species with two polymorphous phases. The μ:η$^1$:η$^2$:η$^1$ coordination mode of the deprotonated [abpt-H]$^-$ ligand in the tetranuclear nickel(II) rectangle box is for the first time observed; the anionic ligand (bpt-H) in the dinuclear nickel(II) complex was generated in situ and resulted from Ni$^{II}$-assisted deamination. The mononuclear complex represents a new interesting example showing temperature-induced polymorphism. Temperature-dependent magnetic studies revealed the presence of moderate antiferromagnetic coupling via the double μ-abpt bridges in dinuclear complex and the presence of both weak antiferromagnetic coupling via the single μ-abpt bridges and ferromagnetic coupling through the ($\mu_{1,1}$-N$_3$)$_2$(μ-OAc) and ($\mu_{1,1}$-N$_3$)($\mu_{1,1}$-N$_{abpt-H}$)(μ-OAc) bridges, all of which gives an overall ferromagnetic coupling in the tetranuclear complex.

## Experimental Section

**General Remarks:** All reagents were obtained from commercial sources and used as received, unless stated otherwise. 4-Amino-3,5-bis(pyridin-2-yl)-1,2,4-triazole (abpt) was synthesized according to the literature procedure.[14] All preparations and manipulations were performed under aerobic conditions. The C and H microanalyses were carried out with a Various EL elemental analyzer.

 © 2007 Wiley-VCH Verlag GmbH & Co. KGaA, Weinheim 

Table 5. Crystal data and structure refinement for **1**, **2**, **3α**, and **3β**.

| Compound | **1** | **2** | **3α** | **3β** |
|---|---|---|---|---|
| Formula | $C_{40}H_{45}N_{33}Ni_4O_9$ | $C_{26}H_{24}N_{12}Ni_2O_4S_2$ | $C_{24}H_{20}N_{18}Ni$ | $C_{24}H_{20}N_{18}Ni$ |
| *Fw* | 1366.93 | 750.11 | 619.29 | 619.29 |
| Temperature [K] | 123(2) | 293(2) | 123(2) | 293(2) |
| Crystal system | monoclinic | triclinic | triclinic | triclinic |
| Space group | *P*2/*c* | $P\bar{1}$ | $P\bar{1}$ | $P\bar{1}$ |
| *a* [Å] | 21.485(4) | 8.389(3) | 6.7214(8) | 8.497(2) |
| *b* [Å] | 12.072(2) | 8.905(3) | 8.321(1) | 8.610(2) |
| *c* [Å] | 21.036(4) | 11.710(4) | 11.552(1) | 10.486(2) |
| *α* [°] | 90 | 88.155(5) | 95.961(2) | 108.930(4) |
| *β* [°] | 99.399(4) | 72.679(5) | 95.340(2) | 99.064(4) |
| *γ* [°] | 90 | 66.709(4) | 98.061(2) | 104.803(4) |
| *V* [Å$^3$] | 5382.8(17) | 763.4(4) | 632.44(13) | 676.9(3) |
| Z | 4 | 1 | 1 | 2 |
| $D_{calcd.}$ [g cm$^{-3}$] | 1.687 | 1.632 | 1.626 | 1.519 |
| $\mu$(Mo-$K_\alpha$) [mm$^{-1}$] | 1.464 | 1.426 | 0.824 | 0.770 |
| *F*(000) | 2800 | 384 | 318 | 318 |
| No. unique data | 26200 | 6202 | 3439 | 5267 |
| No. data with $I > 2\sigma(I)$ | 10435 ($R_{int}$ = 0.0673) | 3276 ($R_{int}$ = 0.0260) | 2322 ($R_{int}$ = 0.0114) | 2580 ($R_{int}$ = 0.0221) |
| $R_1$, $wR_2$[a] [$I > 2\sigma(I)$] | 0.0482, 0.0913 | 0.0374, 0.0903 | 0.0303, 0.0747 | 0.0510, 0.1405 |
| $R_1$, $wR_2$[a] (all data) | 0.0788, 0.0989 | 0.0546, 0.0989 | 0.0326, 0.0762 | 0.0664, 0.1529 |

[a] $R_1 = \Sigma||F_o| - |F_c||/\Sigma|F_o|$, $wR_2 = [\Sigma w(F_o^2 - F_c^2)^2/\Sigma w(F_o^2)^2]^{1/2}$, $w = [\sigma^2(F_o)^2 + (0.1(\max(0,F_o^2) + 2F_c^2)/3)^2]^{-1}$.

The FTIR spectra were recorded from KBr pellets in the range 4000–400 cm$^{-1}$ with a Bruker-EQUINOX 55 FTIR spectrometer. Variable-temperature magnetic susceptibility data were obtained from a Quantum Design SQUID MPMS XL-7 magnetometer. The diamagnetism of the sample and sample holder were taken into account and its contributions to the susceptibility were corrected using Pascal's constants. The effective molar magnetic moments were calculated with the equation $\mu_{eff} = 2.828(\chi_M T)^{1/2}$.

**$[Ni_4(abpt)_2(abpt\text{-}H)(N_3)_5(O_2CMe)_2]\cdot 5H_2O$ (1):** To a methanolic solution (20 mL) of $Ni(O_2CMe)_2\cdot 4H_2O$ (0.120 g, 0.5 mmol) was added a solution of abpt (0.119 g, 0.5 mmol) in the same solvent (20 mL) with magnetic stirring. Once the materials were dissolved, $NaN_3$ (0.036 mg, 0.5 mmol) was slowly added. The resultant mixture was heated at reflux for 5 h and then filtered. The resulting green solution was then maintained undisturbed at ambient temperature. After 7 d, deep green crystals were collected (yield ca. 52% based on abpt). IR (KBr): $\tilde{\nu}$ = 3449 (s), (br), 3070 (m), 2070 (s), 2041 (vs), 1562 (s), 1493 (s), 1463 (s), 1430 (s), 1342 (w), 1301 (w), 1284 (w), 1258 (m), 1159 (w), 1102 (w), 1056 (w), 1015 (m), 799 (s), 751 (m), 695 (m), 641 (m), 607 (w), 467 (w) cm$^{-1}$. $C_{40}H_{45}N_{33}Ni_4O_9$ (1366.85): calcd. C 35.25, H 3.32, N 33.82; found C 35.02, H 3.25, N 33.69.

**$[Ni_2(bpt\text{-}H)_2(SCN)_2(H_2O)_2]\cdot 2H_2O$ (2):** A mixture of abpt (0.056 g, 0.25 mmol) and KNCS (0.186 g, 1.0 mmol) were added to a water/ethanol solution (1:1, 15.0 mL) of $NiCl_2\cdot 6H_2O$ (0.082 g, 0.33 mmol) and stirred. The resultant mixture was heated in a stainless steel reactor with a Teflon liner at 150 °C for 72 h. After a period of approximately 14 h cooling to room temp., green block-like crystals were obtained, isolated simultaneously by filtration, and washed with water (yield: 29%). IR (KBr): $\tilde{\nu}$ = 3745 (m), 3343 (w), 3071 (m), 2934 (m), 2358 (m), 2108 (m), 2058 (s), 1608 (s), 147 (m), 1415 (m), 1267 (m), 1152 (s), 1050 (m), 777 (s), 731 (m), 633 (s) cm$^{-1}$. $C_{26}H_{24}N_{12}Ni_2O_4S_2$: calcd. C 41.64, H 3.23, N 22.41; found C 41.25, H 3.10, N 22.32.

**α-$[Ni(abpt)_2(N_3)_2]$ (3α):** The synthetic method was similar to that of **1** by using 1:2:2 molar ratio of $Ni^{2+}$/abpt/$N_3^-$ (yield 65%). IR (KBr): $\tilde{\nu}$ = 3331 (m), 3204 (s), 3116 (m), 2034 (s), 1639 (s), 1605 (s), 1590 (s), 1569 (s), 1491 (s), 1456 (s), 1426 (s), 1302 (s), 1254 (s), 1167 (s), 1047 (m), 1015 (s), 976 (s), 785 (s), 745 (s), 697 (s) cm$^{-1}$. $C_{24}H_{20}N_{18}Ni$: calcd. C 46.55, H 3.26, N 40.71; found C 46.42, H 3.20, N 40.53.

**β-$[Ni(abpt)_2(N_3)_2]$ (3β):** A mixture of abpt (0.120 g, 0.5 mmol) and $NaN_3$ (0.036 g, 0.5 mmol) were added to an aqueous solution (15.0 mL) of $Ni(O_2CMe)_2\cdot 4H_2O$ (0.060 g, 0.25 mmol) and stirred. The resultant mixture was heated in a stainless steel reactor with a Teflon liner at 130 °C for 72 h. After a period of approximately 14 h cooling to room temp., green block-like crystals were obtained (yield: 21%). IR (KBr): $\tilde{\nu}$ = 3337 (m), 3223 (s), 3128 (m), 2053 (s), 1638 (s), 1613 (s), 1578 (s), 1557 (s), 1487 (s), 1498 (s), 1426 (s), 1302 (s), 1258 (s), 1188 (s), 1060 (m), 1025 (s), 998 (s), 774 (s), 765 (s), 666 (s), 601 (s), 426 (s) cm$^{-1}$. $C_{24}H_{20}N_{18}Ni$: calcd. C 46.55, H 3.26, N 40.71; found C 46.47, H 3.22, N 40.36.

***Safety Note:*** *Azide salts of metal complexes with organic ligands are potentially explosive. Only small amounts of material should be prepared and these should be handled with great caution.*

**X-ray Crystallographic Study:** Diffraction intensities of **1**, **2**, **3α**, and **3β** were collected with a Bruker Apex CCD area-detector diffractometer (Mo-$K_\alpha$, $\lambda$ = 0.71073 Å). For data reduction the "Bruker Saint Plus" program was used.[15] Data were corrected for Lorentz and polarization effects; empirical absorption correction was applied by using multiscan program SADABS.[16] The structures were solved with direct methods and refined with a full-matrix least-squares technique with the SHELXTL programs.[17] Non-hydrogen atoms were refined anisotropically. The positions of the hydrogen atoms for the carbon atoms were calculated assuming ideal geometries, while those for the amino, imino groups, and water molecules are located from the difference Fourier map and refined with isotropic temperature factors. A summary of the data collection and structure refinement information is provided in Table 5. Drawings were produced with SHELXTL.[18]

CCDC-285539 (for **1**), -285540 (for **2**), -294286 (for **3α**), and -294287 (for **3β**) contain the supplementary crystallographic data for this paper. These data can be obtained free of charge from The Cambridge Crystallographic Data Centre via www.ccdc.cam.ac.uk/data_request/cif.

 © 2007 Wiley-VCH Verlag GmbH & Co. KGaA, Weinheim 

## Acknowledgments

This work was supported by the NSFC (No. 20525102 and 20471069), the FANEDD of China (200122), SRFDP (20060558081), and the Scientific and Technological Project of Guangdong Province (04205405). The authors are grateful to Prof. Jin-Lin Zuo for fruitful discussions.

[1] J. S. Miller and M. Drillon (Eds.), *Magnetism: Molecules to Materials II: Molecule-Based Materials*, Wiley-VCH, Weinheim, Germany, **2001**.

[2] a) J. Ribas, A. Escuer, M. Monfort, R. Vicente, R. Cortés, L. Lezama, T. Rojo, *Coord. Chem. Rev.* **1999**, *193–195*, 1027–1068; b) A. K. Boudalis, B. Donnadieu, V. Nastopoulos, J. M. Clemente-Juan, A. Mari, Y. Sanakis, J.-P. Tuchagues, S. P. Perlepes, *Angew. Chem. Int. Ed.* **2004**, *43*, 2266–2270; c) A. Escuer, G. Aromí, *Eur. J. Inorg. Chem.* **2006**, 4721–4736.

[3] a) F. S. Keij, R. A. G. de Graaff, J. G. Haasnoot, J. Reedijk, *J. Chem. Soc. Dalton Trans.* **1984**, 2093; b) J.-C. Chen, S. Hu, A.-J. Zhou, M.-L. Tong, Y.-X. Tong, *Z. Anorg. Allg. Chem.* **2006**, *632*, 475–481; c) J.-C. Chen, A.-J. Zhou, S. Hu, M.-L. Tong, Y.-X. Tong, *J. Mol. Struct.* **2006**, *794*, 225–229; d) M.-X. Peng, C.-G. Hong, C.-K. Tan, J.-C. Chen, M.-L. Tong, *J. Chem. Crystallogr.* **2006**, *36*, 703–707.

[4] a) P. J. Kunkeler, P. J. van Koningsbruggen, J. P. Cornelissen, A. N. van der Horst, A. M. van der Kraan, A. L. Spek, J. G. Haasnoot, J. Reedijk, *J. Am. Chem. Soc.* **1996**, *118*, 2190–2197; b) N. Moliner, A. B. Gaspar, M. C. Munoz, V. Niel, J. Cano, J. A. Real, *Inorg. Chem.* **2001**, *40*, 3986–3991; c) N. Moliner, M. C. Munoz, S. Létard, J.-F. Létard, X. Solans, R. Burriel, M. Castro, O. Kahn, J. A. Real, *Inorg. Chim. Acta* **1999**, *291*, 279–288; d) A. B. Gaspar, M. C. Muñoz, N. Moliner, V. Ksenofontov, G. Levchenko, P. Gütlich, J. A. Real, *Monatsh. Chem.* **2003**, *134*, 285.

[5] a) J. G. Haasnoot, *Coord. Chem. Rev.* **2000**, *200–202*, 131–185; b) M. H. Klingele, S. Brooker, *Coord. Chem. Rev.* **2003**, *241*, 119–132; c) P. J. van Koningsbruggen, D. Gatteschi, R. A. G. de Graaff, J. G. Haasnoot, J. Reedijk, C. Zanchini, *Inorg. Chem.* **1995**, *34*, 5175–5182.

[6] M.-L. Tong, M. Monfort, J. M. Clemente Juan, X.-M. Chen, X.-H. Bu, M. Ohba, S. Kitagawa, *Chem. Commun.* **2005**, 233–235, and references cited therein.

[7] F. Meyer, P. Kircher, H. Pritzkow, *Chem. Commun.* **2003**, 774–775.

[8] a) M. P. Garcia, J. A. Manero, L. A. Oro, M. C. Apreda, F. H. Cano, C. Foces-Foces, J. G. Haasnoot, R. Prins, J. Reedijk, *Inorg. Chim. Acta* **1986**, *122*, 235–241; b) H. M. Burke, J. F. Gallagher, M. T. Indelli, J. G. Vos, *Inorg. Chim. Acta* **2004**, *357*, 2989–3000.

[9] a) J.-P. Zhang, Y.-Y. Lin, X.-C. Huang, X.-M. Chen, *J. Am. Chem. Soc.* **2005**, *127*, 5495–5506; b) J.-P. Zhang, Y.-Y. Lin, X.-C. Huang, X.-M. Chen, *Chem. Commun.* **2005**, 1258–1260.

[10] X.-M. Chen, M.-L. Tong, *Acc. Chem. Res.* **2007**, *40*, 162–170.

[11] a) S. Supriya, S. K. Das, *New J. Chem.* **2003**, *27*, 1568–1574; b) J. Tao, Z.-J. Ma, R.-B. Huang, L.-S. Zheng, *Inorg. Chem.* **2004**, *43*, 6133–6135; c) S. Pal, N. B. Sankaran, A. Samanta, *Angew. Chem. Int. Ed.* **2003**, *42*, 1741–1743.

[12] a) G. S. McGrady, M. Odlyha, P. D. Prince, J. W. Steed, *CrystEngComm* **2002**, *4*, 271–276; b) S. A. Barnett, A. J. Blake, N. R. Champness, *CrystEngComm* **2003**, *5*, 134–136; c) K. E. Holmes, P. F. Kelly, M. R. J. Elsegood, *CrystEngComm* **2004**, *6*, 56–59; d) K. E. Holmes, P. F. Kelly, S. H. Dale, M. R. J. Elsegood, *CrystEngComm* **2006**, *8*, 391–402; e) J. M. Kelleher, S. E. Lawrence, M. T. McAuliffe, H. A. Moynihan, *CrystEngComm* **2007**, *9*, 72–77.

[13] a) J. J. Borrás-Almenar, J. M. Clemente-Juan, E. Coronado, B. S. Tsukerblat, *Inorg. Chem.* **1999**, *38*, 6081–6088; b) J. J. Borrás-Almenar, J. M. Clemente-Juan, E. Coronado, B. S. Tsukerblat, *J. Comput. Chem.* **2001**, *22*, 985–989.

[14] J. F. Geldard, F. Lions, *J. Org. Chem.* **1965**, *30*, 318–321.

[15] *SMART Version 5.625 and SAINT+ Version 6.02a*, Bruker Analytical X-ray Systems, Inc., Madison, Wisconsin, US, **1998**.

[16] G. M. Sheldrick, *SADABS 2.05*, University Göttingen.

[17] *SHELXTL 6.10*, Bruker Analytical Instrumentation, Madison, Wisconsin, USA, 2000.

[18] G. M. Sheldrick, *SHELXTL Version 5*, Siemens Industrial Automation Inc., Madison, Wisconsin, US, **1995**.

Received: March 16, 2007
Published Online: June 21, 2007

 © 2007 Wiley-VCH Verlag GmbH & Co. KGaA, Weinheim 

DOI: 10.1002/ejic.200601184

# Phosphane and Phosphite Unsymmetrically Disubstituted Diiron Complexes Related to the Fe-Only Hydrogenase Active Site

**Ping Li,[a] Mei Wang,*[a] Chengjiang He,[a] Xiaoyang Liu,[a,b] Kun Jin,[a] and Licheng Sun*[a,c]**

**Keywords:** Bioinorganic chemistry / Carbonyl displacement / Diiron complexes / Fe-only hydrogenase / P ligands

A series of unsymmetrically disubstituted diiron complexes [(μ-pdt){$Fe(CO)_2L^1$}{$Fe(CO)_2L^2$}] [pdt = 1,3-propanedithiolato; $L^1 = PMe_3$, $L^2 = PMe_2Ph$, **4**; $PPh_3$, **5**; $PCy_3$, **6**; $P(OEt)_3$, **7**; $L^1 = PMe_2Ph$, $L^2 = PPh_3$, **8**; $P(OEt)_3$, **9**; $L^1 = P(OEt)_3$, $L^2 = PPh_3$, **10**; $PCy_3$, **11**] and [(μ-edt){$Fe(CO)_2PMe_3$}{$Fe(CO)_2PPh_3$}] (edt = 1,2-ethanedithiolato, **12**) were prepared by means of stepwise CO displacements of [(μ-pdt)$Fe_2(CO)_6$] and [(μ-edt)-$Fe_2(CO)_6$] by different tertiary phosphane and phosphite ligands. The interconversion of the irondithiacyclohexane ring and the rotation of the [$Fe(CO)_2PR_3$] subunit were studied using by variable-temperature $^{31}P\{^1H\}$ NMR spectroscopy of **4**, **6** and **12** in solution. The molecular structures of **4**–**6**, **8**–**10** and **12** show that complexes **4**–**6**, **8**, **9** and **12** possess an apical/basal coordination mode and complex **10** has an apical/apical conformation. The X-ray analyses indicate that the $PMe_2Ph$ ligand in the apical position of the starting complex [(μ-pdt){$Fe(CO)_3$}{$FeCO_2(PMe_2Ph)$}] rotates to the basal position on conversion to the products **8** and **9**. Cyclic voltammograms of **4**–**11** were studied both under argon and CO. The influences of the phosphane and phosphite ligands on the redox properties of the unsymmetrically disubstituted diiron complexes are discussed.
(© Wiley-VCH Verlag GmbH & Co. KGaA, 69451 Weinheim, Germany, 2007)

## Introduction

Iron-only hydrogenases with popular metals and simple diatom ligands in their active sites can catalyse the proton reduction to molecular hydrogen more efficiently than other types of hydrogenases. In recent years, synthesis of structural and functional models of the Fe-only hydrogenase active site has been a hot topic in bioinorganic and organometallic chemistry. The well-studied organometallic diiron complex [(μ-pdt)$Fe_2(CO)_6$] (pdt = 1,3-propanedithiolato) serves as a synthetic model of the Fe-only hydrogenase active site in terms of the structure revealed by X-ray crystallographic studies.[1,2] Various good donor ligands, such as $CN^-$,[3–9] $PR_3$,[8–17] CNR[18,19] and NHC (N-heterocyclic carbene)[20,21] have been successfully introduced to the model complexes by CO displacement in order to investigate the electrochemistry and protonation properties of the derivatives. Tertiary phosphane ligands, which can avoid the intricacy of the protonation process on the cyanide nitrogen atom, are widely used in many model complexes of the Fe-only hydrogenase, especially for hydridodiiron dithiolate complexes.[22–24] Although the CO displacement of [(μ-$SR)_2$-$Fe_2(CO)_6$] (R = Me, Et, Ph), [(μ-edt)$Fe_2(CO)_6$] (edt = 1,2-ethanedithiolato), [(μ-pdt)$Fe_2(CO)_6$] and [(μ-adt)$Fe_2(CO)_6$] (adt = 2-azapropane-1,3-dithiolato) by tertiary phosphanes has been extensively studied,[10–17] to the best of our knowledge the model complexes in the form of [(μ-pdt){$Fe(CO)_2$-$L^1$}{$Fe(CO)_2L^2$}] with two different π ligands have been scarcely reported.[10] To continue a systematic study of the influence of phosphane and phosphite ligands on the coordination structures, the reactivity and the redox properties of the iron centres,[15] a series of unsymmetrically disubstituted model complexes [(μ-pdt){$Fe(CO)_2L^1$}{$Fe(CO)_2L^2$}] [$L^1 = PMe_3$, $L^2 = PMe_2Ph$, **4**; $PPh_3$, **5**; $PCy_3$, **6**; $P(OEt)_3$, **7**; $L^1 = PMe_2Ph$, $L^2 = PPh_3$, **8**; $P(OEt)_3$, **9**; $L^1 = P(OEt)_3$, $L^2 = PPh_3$, **10**; $PCy_3$, **11**] and [(μ-edt){$Fe(CO)_2PMe_3$}{$Fe(CO)_2$-$PPh_3$}] (**12**) with two different tertiary phosphane and phosphite ligands were prepared and among them **4**–**6**, **8**–**10** and **12** were crystallographically characterised. Here we describe the preparation, variable-temperature $^{31}P\{^1H\}$ NMR spectra, molecular structures and cyclic voltammograms of diiron complexes unsymmetrically disubstituted by phosphane and phosphite ligands.

[a] State Key Laboratory of Fine Chemicals, DUT-KTH Joint Education and Research Centre on Molecular Devices, Dalian University of Technology (DUT),
Zhongshan Road 158-46, Dalian 116012, China
E-mail: symbueno@dlut.edu.cn
[b] State Key Laboratory of Inorganic Synthesis and Preparative Chemistry, Jilin University,
Changchun 130012, China
[c] Department of Chemistry, Royal Institute of Technology (KTH),
10044 Stockholm, Sweden
Supporting information for this article is available on the WWW under http://www.eurjic.org or from the author.

 © 2007 Wiley-VCH Verlag GmbH & Co. KGaA, Weinheim 

## Results and Discussion

### Preparation and Spectroscopic Characterisation of Complexes 4–12

The monosubstituted complexes $[(\mu\text{-pdt})Fe_2(CO)_5L^1]$ [$L^1$ = $PMe_3$, **1**; $PMe_2Ph$, **2**; $P(OEt)_3$, **3**] were prepared in moderate yields according to the previous report.[15] Treatment of **1** with $PMe_2Ph$, $PPh_3$ and $P(OEt)_3$ in toluene at reflux afforded products **4**, **5** and **7**, respectively, in good yields (Scheme 1). Complex **6** could be obtained from **1**, in a moderate yield, in the presence of 1 equiv. of $PCy_3$ using $Me_3NO$ as a CO-removing reagent. The disubstituted complexes **4**, **8** and **9** were obtained in yields of 40–70% by the replacement of CO in **2** with 1 equiv. of the corresponding tertiary phosphane or phosphite ligand in toluene at reflux (Scheme 2). Complexes **7** and **9** could also be prepared by treatment of **3** with a slight excess of $PMe_3$ and $PMe_2Ph$ under the same conditions (Scheme 3). The reaction of complex **3** with 1 equiv. or an excess of $PPh_3$ in toluene at reflux did not afford complex **10**, presumably due to the high activation energy caused by the large bulk and weak donating capability of the $PPh_3$ ligand. Consequently, $Me_3NO$ was used as CO removing reagent to prepare complex **10** (Scheme 3). Although the volume of $PCy_3$ is larger than that of $PPh_3$, complex **11** could be obtained in a good yield from a solution of **3** and 1 equiv. of $PCy_3$ in toluene at reflux. The stronger donating capability of $PCy_3$ benefits the $PCy_3$/CO displacement. Complex **12** was prepared according to a similar procedure used for **5**. The unsymmetrically disubstituted diiron dithiolate complexes **4**–**12** are relatively thermally and air-stable in the solid state.

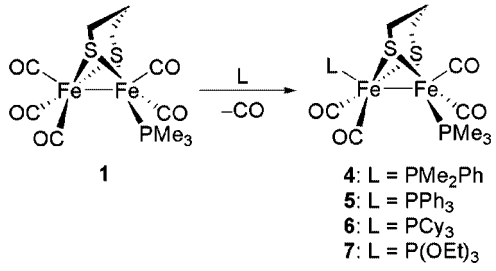


Scheme 1.

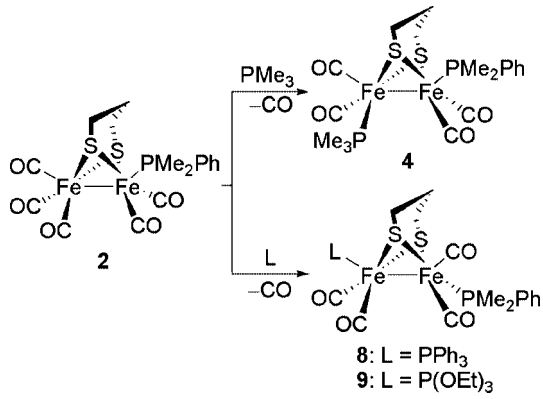


Scheme 2.

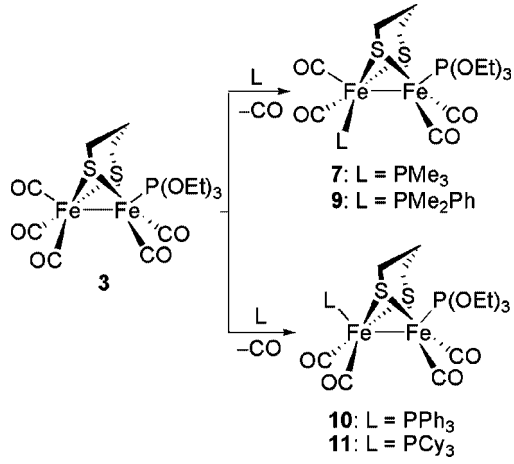


Scheme 3.

The products **4**–**12** were characterised by ESI- or APCI-MS, IR, $^1H$ and $^{31}P\{^1H\}$ NMR spectroscopy as well as elemental analysis. The results of the elemental analyses for all products are in good agreement with the proposed compositions. The $[M + H]^+$ peaks of all the diiron dithiolates were detected in the mass spectra in ESI- or APCI-positive mode. The disubstituted complexes **4**–**11** each display three $\nu$(CO) bands in the region of 1900–2000 $cm^{-1}$. The IR data of $\nu$(CO) for **4**–**11** are listed in Table 1 together with the

Table 1. A comparison of $\nu$(CO) bands of **1**–**11** and the all-CO parent complex in $CH_3CN$.

| Complex | $L^1$, $L^2$ | $\nu$(CO)/$cm^{-1}$ | $\Delta\nu(CO)_{av}$/$cm^{-1}$[a] |
|---|---|---|---|
| All-CO complex | – | 2074 (m), 2036 (s), 1995 (s) | – |
| **1** | $PMe_3$, – | 2037 (s), 1980 (s), 1919 (m) | 56 |
| **2** | $PMe_2Ph$, – | 2040 (s), 1980 (s), 1921 (m) | 55 |
| **3** | $P(OEt)_3$, – | 2046 (s), 1989 (s), 1936 (m) | 45 |
| **4** | $PMe_3$, $PMe_2Ph$ | 1981 (m), 1943 (s), 1908 (m) | 91 |
| **5** | $PMe_3$, $PPh_3$ | 1985 (s), 1946 (s), 1905 (s) | 90 |
| **6** | $PMe_3$, $PCy_3$ | 1976 (s), 1937 (s), 1901 (s) | 97 |
| **7** | $PMe_3$, $P(OEt)_3$ | 1991 (s), 1949 (s), 1907 (s) | 86 |
| **8** | $PMe_2Ph$, $PPh_3$ | 1982 (s), 1946 (s), 1913 (s) | 88 |
| **9** | $PMe_2Ph$, $P(OEt)_3$ | 1991 (s), 1952 (s), 1922 (s) | 80 |
| **10** | $P(OEt)_3$, $PPh_3$ | 1997 (s), 1955 (s), 1934 (s) | 73 |
| **11** | $P(OEt)_3$, $PCy_3$ | 1993 (s), 1943 (s), 1933 (s) | 79 |

[a] $\Delta\nu(CO)_{av} = [\Sigma\nu(CO)_{all\text{-}CO} - \Sigma\nu(CO)]/3$.

 © 2007 Wiley-VCH Verlag GmbH & Co. KGaA, Weinheim 

$\nu$(CO) data of complexes **1**–**3** and the all-CO complex.[15,25] A comparison of the $\nu$(CO) bands for the three subsets (**1** vs. **4**–**7**, **2** vs. **4**, **8** and **9**, and **3** vs. **7** and **9**–**11**) of complexes **4**–**11** shows that the introduction of the second phosphane and phosphite ligand has a considerable effect on the $\nu$(CO) bands of the diiron complexes. The variation of the $\nu$(CO) bands implies the influence of different tertiary phosphane and phosphite ligands on the electron density of the Fe centres. Compared with the all-carbonyl complex, the average values of the three strong $\nu$(CO) bands are red-shifted by 73–97 $cm^{-1}$ for **4**–**11**. The shift values [$\Delta\nu(CO)_{av}$] are consistent with the electron-donating capabilities of different phosphane and phosphite ligands.

### Variable-Temperature $^{31}P\{^1H\}$ NMR Spectra of Complexes 4, 6 and 12

The variable-temperature $^{31}P\{^1H\}$ NMR spectra of **4**, **6** and the edt-bridged analogue **12** are shown in Figures 1 and 2. Complexes **4** and **6** each display two signals at $\delta$ = 25.5 and 29.6 ppm for **4**, and $\delta$ = 23.3 and 68.1 ppm for **6**, in the $^{31}P\{^1H\}$ NMR spectra at room temperature [Figure 1(a) and (b)]. On lowering the temperature, each $^{31}P\{^1H\}$ NMR signal of complex **4** splits into two resonances ($\delta$ = 26.5, 26.8 for $PMe_3$ and $\delta$ = 32.5, 33.3 ppm for $PMe_2Ph$) at –80 °C [Figure 1(a′) and the inset]. Two resonances for the $PMe_3$ ligand and two broad signals for the $PCy_3$ ligand can be observed for complex **6** at –80 °C [Figure 1(b′)]. The broad resonance of the $PCy_3$ ligand may result from the slow rotation of the bulky $PCy_3$ ligand. The splitting of the $^{31}P\{^1H\}$ NMR signals at low temperature can be attributed to the slowing down of the interconversion of the $FeS_2C_3$ six-membered rings in complexes **4** and **6**. The resonance difference for the $PMe_3$ ligand of **6** ($\delta$ = 2.4 ppm) is apparently larger than that for the splitting of the $PMe_3$ ligand of **4** ($\delta$ = 0.3 ppm), presumably due to the large interaction between the propanedithiolato group and the bulky $PCy_3$ ligands. A similar interconversion of the irondithiacyclohexane rings in the symmetrically $PR_3$-disubstituted diiron complexes has been previously reported by Darensbourg and co-workers.[13,26]

To explore the rotation flexibility of phosphane ligands of the $[Fe(CO)_2PR_3]$ subunit and to avoid the interconversion of the S-to-S bridge, an edt-bridged analogue [(μ-edt){$Fe(CO)_2PMe_3$}{$Fe(CO)_2PPh_3$}] (**12**) was prepared for study by variable-temperature $^{31}P\{^1H\}$ NMR spectroscopy. Complex **12** displays two $^{31}P$ resonances at $\delta$ = 22.7 ppm for $PMe_3$ and $\delta$ = 60.3 ppm for $PPh_3$ at room temperature [Figure 2(top)]. When the measuring temperature was lowered to –80 °C, four $^{31}P$ signals were observed for the edt-bridged diiron complex **12** [Figure 2(bottom)], two strong signals at $\delta$ = 27.3 ppm for $PMe_3$, $\delta$ = 60.7 ppm for $PPh_3$ and two weak signals at $\delta$ = 17.0 ppm for $PMe_3$ and $\delta$ = 59.9 ppm for $PPh_3$. It is noticeable that the large resonance difference (10.3 ppm) between the two $^{31}P$ signals for the $PMe_3$ ligand of **12** can be observed, while the difference for the $PPh_3$ ligand is only 0.8 ppm. A rational explanation for the obtained variable-temperature $^{31}P\{^1H\}$ NMR spectra of **12** is that the splitting of the $^{31}P$ resonances at low temperature is caused by the slowing down of the rotation of the subunit $[Fe(CO)_2PMe_3]$,[13] and the subunit $[Fe(CO)_2PPh_3]$ does not rotate in solution within the range between –80 and 25 °C but maintains its apical position as in the crystalline state. Accordingly, the two strong signals can be attributed to the major apical ($PPh_3$)/basal ($PMe_3$) isomer of **12** and the two weak signals to the ap/ap isomer. The $^{31}P\{^1H\}$ NMR spectra of **12** suggest that the coordination

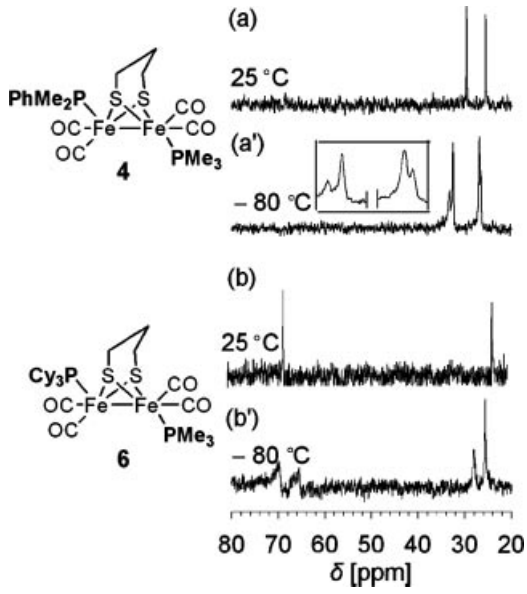


Figure 1. Variable-temperature $^{31}P\{^1H\}$ NMR spectra of **4** and **6** in $CDCl_3$.

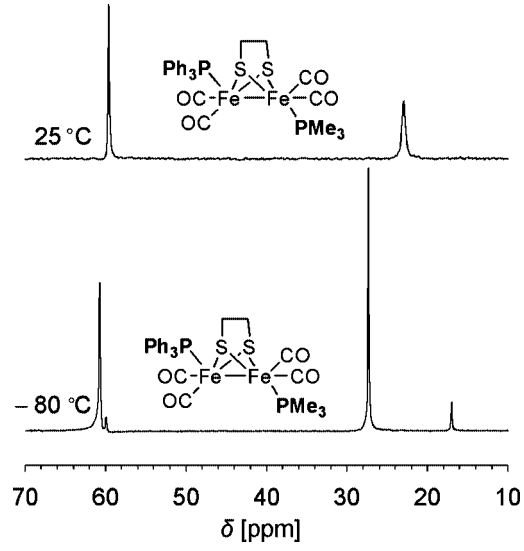


Figure 2. $^{31}P\{^1H\}$ NMR spectra of **12** at variable temperature in $CDCl_3$.

 © 2007 Wiley-VCH Verlag GmbH & Co. KGaA, Weinheim 

orientation of the $PMe_3$ ligand in the $[Fe(CO)_2PMe_3]$ subunit does not exhibit an apparent effect on the chemical shift of the $PPh_3$ ligand attached to the vicinal iron atom.

### Molecular Structures of Complexes 4–6, 8–10 and 12

Single-crystal X-ray diffraction studies were carried out on complexes **4**–**6**, **8**–**10** and **12** to determine the coordination conformations of the phosphane and phosphite ligands in the diiron complexes. The molecular structures of **4**–**6**, **8**–**10** and **12** are presented in Figure 3 and selected bond lengths and angles are listed in Table 2. The central 2Fe2S cores of complexes **4**–**6**, **8**–**10** and **12** are all in butterfly conformation as for previously reported model complexes[10–15] and each iron atom is coordinated with a distorted square-pyramidal geometry. The vertex carbon atoms of the $FeS_2C_3$ six-membered rings all orient to the phenyl-containing phosphane ligands, either in apical (**4**, **5** and **10**) or in basal (**9**) positions. In contrast, the ellipsoid of the vertex carbon atom C(14) is disordered in the crystalline state of **8** with two phenyl-containing phosphane ligands attached to two iron atoms. The distances of the Fe–Fe bonds in **4**–**6**, **8** and **9** are quite similar (2.534–2.544 Å), while the Fe–Fe bond of **10** [2.5077(5) Å] with an ap/ap conformation is apparently shorter than that of its analogous ap/ba isomers **4**–**6**, **8** and **9**. The Fe–Fe bond [2.5553(4) Å] of the edt-bridged diiron complex **12** is longer than those of the pdt-bridged complexes. The dihedral angle, defined by the S(1)Fe(1)Fe(2) and S(2)Fe(1)Fe(2) planes, increases to 73.30(2)° for **10** featuring two bulky ligands as compared to 70.89(3)° for **4** bearing two small ligands and it increases to 77.72(2)° when the pdt-bridge is replaced by the edt-bridge. The dihedral angle is affected by the steric interactions between the phosphane or phosphite ligand and the S-to-S linker.

The X-ray diffraction analyses clearly show that the conformations of the two coordinating phosphane and phosphite ligands in complexes **4**–**6**, **8**, **9** and **12** are predominantly determined by the relative sizes of the ligands. Complexes **4**–**6**, **8**, **9** and **12** feature an ap/ba conformation in the crystalline state which is a common conformation for double-CO displacement by two non-carbonyl ligands on each iron atom of $[(\mu\text{-pdt})Fe_2(CO)_6]$.[4,9,20] The size of the second phosphane or phosphite ligand determines the orientation of the $PMe_2Ph$ group in complexes **4**, **8** and **9**, which is in the apical position of **4** with $PMe_3$ as its counterpart and in the basal positions of **8** and **9** with $PPh_3$ or $P(OEt)_3$ on the other iron atom. Complex **10** containing two bulky ligands possesses an ap/ap conformation which, to the best of our knowledge, is the first structurally characterised unsymmetrically disubstituted diiron dithiolate complex of the ap/ap conformation except for the symmetrically $PMe_2Ph$-, $PPh_2(BrC_6H_4)$- and CN-*t*-Bu-disubstituted analogues.[15,19,27] Our previous crystallographic studies clarified that the ligand $PMe_2Ph$ in the starting complex **2** is in an apical orientation.[15] The basal position of the $PMe_2Ph$ ligand in **8** and **9** clearly verifies the conformational mobility of the $[Fe(CO)_2PMe_2Ph]$ subunit of the diiron dithiolate model complex in solution.

### Cyclic Voltammograms of Complexes 4–11

The cyclic voltammograms (CVs) of complexes **4**–**11** were studied to evaluate the effects of different phosphane ligands on the redox properties of the iron atoms. Except for **6** and **11**, the CV measurements were carried out in $CH_3CN$ for all complexes. The CVs of complexes **6** and **11** were recorded in toluene/$CH_3CN$ (1:3, v/v) because of the poor solubility of **6** and **11** in $CH_3CN$.

Under argon, complexes **5**, **8** and **10** containing a $PPh_3$ ligand each display two reduction peaks in the range of –1.98 to –2.26 V (vs $Ag/Ag^+$, 0.01 M $AgNO_3$) in their CVs

Table 2. Selected bond lengths [Å] and angles [°] for **4**–**6**, **8**–**10** and **12**.

| Complex | **4** | **5** | **6** | **8** | **9** | **10** | **12** |
|---|---|---|---|---|---|---|---|
| Bond lengths | | | | | | | |
| Fe–Fe | 2.5430(5) | 2.5383(6) | 2.5375(5) | 2.5437(10) | 2.5341(9) | 2.5077(5) | 2.5553(4) |
| Fe–S[a] | 2.2643(8) | 2.2636(7) | 2.2741(7) | 2.2658(11) | 2.2625(14) | 2.2745(7) | 2.2494(6) |
| $Fe–P_{ap}$ | 2.2299(7) | 2.2518(7) | 2.2822(7) | 2.2534(10) | 2.1589(13) | 2.2117(7)[b] | 2.2444(5) |
| $Fe–P_{ba}$ | 2.2335(6) | 2.2312(8) | 2.2293(8) | 2.2352(11) | 2.2278(13) | – | 2.2198(6) |
| $Fe–C_{ap}$ | 1.755(2) | 1.767(2) | 1.762(3) | 1.762(4) | 1.768(5) | – | 1.764(2) |
| $Fe–C_{ba}$[c] | 1.777(2) | 1.756(2) | 1.758(3) | 1.768(4) | 1.764(4) | 1.771(2)[d] | 1.759(2) |
| S···S | 3.053 | 3.039 | 3.039 | 3.044 | 3.039 | 3.045 | 2.877 |
| Bond angles | | | | | | | |
| S–Fe–S[e] | 84.77(2) | 84.35(2) | 83.86(3) | 84.41(4) | 84.38(5) | 84.04(2) | 79.65(2) |
| Fe–S–Fe[f] | 68.33(2) | 68.20(2) | 67.82(2) | 68.30(4) | 68.12(4) | 66.91(2) | 69.34(2) |
| Dihedral[g] | 70.89(3) | 71.65(2) | 72.75(2) | 71.47(4) | 71.68(5) | 73.30(2) | 77.72(2) |

[a] Average over four Fe–S bonds. [b] Average over two $Fe–P_{ap}$ bonds. [c] Average over three $Fe–C_{ba}$ bonds. [d] Average over four $Fe–C_{ba}$ bonds. [e] Average over two S–Fe–S angles. [f] Average over two Fe–S–Fe angles. [g] Defined by the intersection of the two $SFe_2$ planes.

 © 2007 Wiley-VCH Verlag GmbH & Co. KGaA, Weinheim 

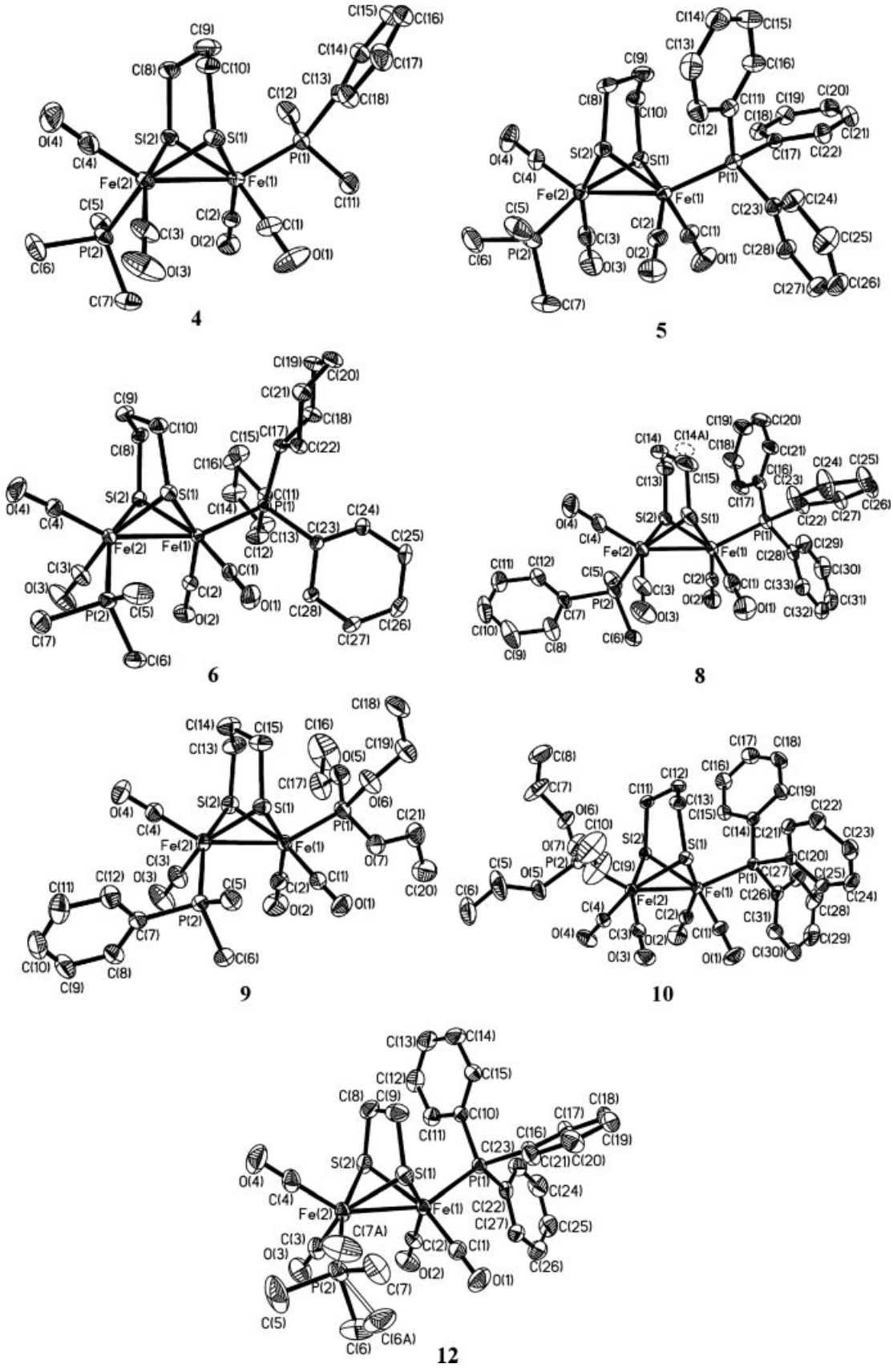


Figure 3. Molecular structures of **4**, **5**, **6**, **8**, **9**, **10** and **12** with thermal ellipsoids drawn at the 30% probability level. Hydrogen atoms have been omitted for clarity.

 © 2007 Wiley-VCH Verlag GmbH & Co. KGaA, Weinheim 

[Figure 4(a) for **5**] and the other complexes **4**, **6**, **7**, **9** and **11** without $PPh_3$ ligands each show a broad peak including two overlapping reduction events from –2.09 to –2.28 V [Figure 4(b) for **9**]. Considering the small potential differences of the two reduction peaks for each complex, the second reduction peak cannot be attributed to the further reduction process of $Fe^IFe^0$ to $Fe^0Fe^0$. In order to assign the reduction peaks, CVs of **4**–**11** were performed under CO in a CO-saturated $CH_3CN$ solution. As the two sub-groups display similar CVs under CO (complexes with a $PPh_3$ ligand and those without $PPh_3$ ligand), we chose complexes **5** and **9** as examples for comparison of the CVs recorded under argon and under CO (Figure 4). The CVs of other complexes (**4**, **6**–**8**, **10** and **11**) under argon and under CO are given in the Supporting Information.

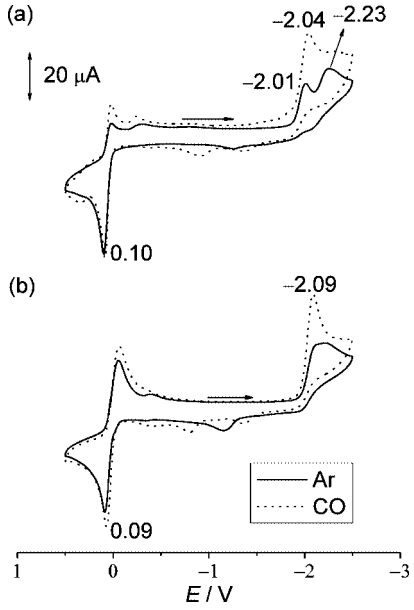


Figure 4. Cyclic voltammograms of complexes **5** (a) and **9** (b) under argon and under CO; 1.0 mM diiron complex, 0.05 M $nBu_4NPF_6$ in $CH_3CN$, scan rate 0.1 V $s^{-1}$.

The current of the first reduction peak at –2.01 V in the CV of **5**, which has been assigned to the $Fe^IFe^I/Fe^IFe^0$ process, increases under CO relative to that detected under argon. In the meantime the current height of the second reduction peak at –2.23 V apparently decreases when compared with that detected under argon. Similarly, the broad reduction peak in the range of –2.0 to –2.5 V for complex **9** under argon changes to a sharp reduction peak at –2.09 V under CO and the more cathodic overlapping peak disappears. The peak at –2.09 V can be attributed to the $Fe^IFe^I/Fe^IFe^0$ process. The different CVs recorded under argon and under CO reminded us of similar changes in the CVs reported for $PMe_2Ph$- and pta- (1,3,5-triaza-7-phosphaadamantane) -monosubstituted complexes[14,15] in which the second peaks detected under argon or $N_2$ may be attributed to a solvent-substituted species resulting from the 19-electron radical anion formed at the first reduction process. Furthermore, it was found that the current height ratio [*i*(I)/*i*(II)] of the two reduction peaks under argon varies with the scan rate. The *i*(I)/*i*(II) ratio increases when the CV is recorded at a higher scan rate. As shown in Figure 5, the values of the *i*(I)/*i*(II) ratios are ca. 1.0, 2.0 and 3.3 at scan rates of 0.1, 0.4 and 1.0 V $s^{-1}$, respectively. The CVs of multiple scans for complex **5** at a scan rate of 4.0 V $s^{-1}$ show that the current height of the second reduction peak apparently increases in the second scan cycle accompanied by a decrease in the height of the first reduction peak (see Supporting Information). After three scan cycles, the current height ratio of the two reduction peaks does not exhibit any observable change. In view of the results of the CO control experiments, the variable scan rate measurements and the CVs of multiple scans, the second reduction peak detected under argon, either as a separated peak for the complex with a $PPh_3$ ligand or as an overlapping peak for the complex without $PPh_3$, is most likely due to the reduction of a new complex, presumably generated by a quick chemical reaction following the first reduction of the diiron(I,I) complex. In comparison, the reported symmetrically disubstituted diiron analogues $[(\mu\text{-pdt})\{Fe(CO)_2L\}_2]$ [L = $PMe_3$, $PMe_2Ph$, $P(OEt)_3$, pta] each exhibit only one reduction peak in the $Fe^IFe^I/Fe^IFe^0$ region of the CVs.[14,15,27] It seems that the reductive $[Fe^IFe^0]$ intermediates formed by the unsymmetrically disubstituted diiron complexes, especially the complexes containing a $PPh_3$ ligand, are less stable than those derived from the symmetrically disubstituted diiron analogues.

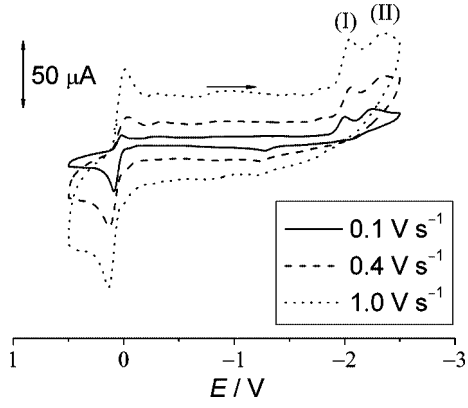


Figure 5. Cyclic voltammograms of complex **5** (1.0 mM) under argon; scan rate 0.1 [*i*(I)/*i*(II) = 1.0], 0.4 [*i*(I)/*i*(II) = 2.0] and 1.0 V $s^{-1}$ [*i*(I)/*i*(II) = 3.3].

The redox potentials under CO for complexes **4**–**11** are listed in Table 3. The anodic peaks at –0.02 to +0.21 V have been assigned to the first oxidation process of $Fe^IFe^I$ to $Fe^{II}Fe^I$ as described in the literature.[28] Complexes **6**, **7** and **9**–**11** exhibit quasi-reversible oxidation peaks, while **4**, **5** and **8** display irreversible peaks for the first oxidation process. It is interesting to notice that the $P(OEt)_3$ and $PCy_3$ ligands show a certain capability to stabilise the $Fe^{II}Fe^I$ species formed in the first oxidation process. This phenomenon was also observed in the CVs of the previously prepared

 © 2007 Wiley-VCH Verlag GmbH & Co. KGaA, Weinheim 

$P(OEt)_3$ and $PMe_2Ph$ symmetrically disubstituted complexes.[15] The $Fe^IFe^I$ to $Fe^{II}Fe^I$ oxidative peak was quasi-reversible for $[(\mu\text{-pdt})\{Fe(CO)_2P(OEt)_3\}_2]$ and totally irreversible for $[(\mu\text{-pdt})\{Fe(CO)_2PMe_2Ph\}_2]$. The redox potentials of **4**–**11** are consistent with the electron-donating capabilities of the phosphane and phosphite ligands. Complex **6** containing $PMe_3$ and $PCy_3$ displays the most negative redox potentials, –0.02 V for the oxidation process of $Fe^IFe^I$ to $Fe^{II}Fe^I$ and –2.15 V for the $Fe^IFe^I$ to $Fe^IFe^0$ process. In contrast, complex **10** featuring $P(OEt)_3$ and $PPh_3$ shows the most positive redox potentials, +0.21 V for the oxidation process of $Fe^IFe^I$ to $Fe^{II}Fe^I$ and –1.98 V for the $Fe^IFe^I$ to $Fe^IFe^0$ process. In general, the variations in the redox potentials by changing phosphane and phosphite ligands are ca. 230 mV for the first oxidation process and ca. 170 mV for the first reduction process.

Table 3. Redox potentials of complexes **4**–**11**.[a]

| Complex | $L^1$, $L^2$ | $E_{pa}$/V $Fe^IFe^I/Fe^{II}Fe^I$ | $E_{pc}$/V $Fe^IFe^I/Fe^IFe^0$ |
|---|---|---|---|
| **4** | $PMe_3$, $PMe_2Ph$ | 0.0 | –2.12 |
| **5** | $PMe_3$, $PPh_3$ | +0.10 | –2.04 |
| **6**[b] | $PMe_3$, $PCy_3$ | –0.02 | –2.15 |
| **7** | $PMe_3$, $P(OEt)_3$ | +0.11 | –2.08 |
| **8** | $PMe_2Ph$, $PPh_3$ | +0.11 | –2.01 |
| **9** | $PMe_2Ph$, $P(OEt)_3$ | +0.09 | –2.09 |
| **10** | $P(OEt)_3$, $PPh_3$ | +0.21 | –1.98 |
| **11**[b] | $P(OEt)_3$, $PCy_3$ | +0.14 | –2.14 |

[a] $nBu_4NPF_6$ (0.05 M) in a CO-saturated $CH_3CN$ solution under CO; scan rate: 0.1 $V s^{-1}$; working electrode: glassy carbon electrode of diameter 3 mm; reference electrode: non-aqueous $Ag/Ag^+$ electrode (0.01 M $AgNO_3$ in $CH_3CN$); counter electrode: platinum wire. [b] Data collected in CO-saturated toluene/$CH_3CN$ (1:3, v/v) mixture.

## Conclusions

Nine unsymmetrically disubstituted diiron dithiolate complexes **4**–**12** with various phosphane and phosphite ligands were prepared and well characterised. The rotation of the $[Fe(CO)_2PMe_3]$ subunit can be detected by the variable-temperature $^{31}P\{^1H\}$ NMR spectra of **12**, which also suggest that the $[Fe(CO)_2PPh_3]$ subunit does not rotate in solution in the range between –80 and 25 °C. In the substitution reactions of $[(\mu\text{-pdt})\{Fe(CO)_3\}\{Fe(CO)_2PMe_2Ph\}]$ (**2**) by $PPh_3$ and $P(OEt)_3$, the $PMe_2Ph$ ligand in the apical position of **2** moves to the basal position on formation of the products **8** and **9** and this provides clear evidence for the conformational flexibility of the $[Fe(CO)_2PMe_2Ph]$ subunit in solution. The CVs of complexes **4**–**11** under argon and under CO show that the reductive $[Fe^IFe^0]$ intermediates formed by the unsymmetrically disubstituted diiron complexes are not stable under argon. A considerable part of the $[Fe^IFe^0]$ intermediate is converted to a new complex by a quick chemical reaction which can be suppressed when the CV measurement is carried out under CO. The redox potentials of $PR_3$-disubstituted diiron dithiolate complexes can be adjusted in a range of ca. 200 mV.

## Experimental Section

**General Procedures:** All reactions and operations related to organometallic complexes were carried out under dry oxygen-free dinitrogen using standard Schlenk techniques. Solvents were dried and distilled prior to use according to the standard methods. Commercially available chemicals, 1,3-propanedithol, $Fe(CO)_5$ and all tertiary phosphanes and phosphite compounds were reagent grade and used as received. Compounds $[(\mu\text{-pdt})Fe_2(CO)_5L]$ [L = $PMe_3$, **1**; $PMe_2Ph$, **2** and $P(OEt)_3$, **3**] and $[(\mu\text{-edt})Fe_2(CO)_5PMe_3]$ were prepared according to previously reported procedures.[15,25] Infrared spectra were recorded in $CH_3CN$ solutions with a JASCO FT/IR 430 spectrophotometer. $^1H$ and $^{31}P\{^1H\}$ NMR spectra were recorded with a Varian INOVA 400 NMR spectrometer. Elemental analyses were performed with a Thermoquest-Flash EA 1112 elemental analyser and the mass spectra of the iron complexes were recorded with an HP1100 MSD instrument.

**Synthesis of $[(\mu\text{-pdt})\{Fe(CO)_2PMe_3\}\{Fe(CO)_2L\}]$ [L = $PMe_2Ph$ (4), $PPh_3$ (5), $P(OEt)_3$ (7)]:** Complex **1** (0.43 g, 1.0 mmol) was treated with $PMe_2Ph$ (0.14 g, 1.0 mmol) in toluene (40 mL) at reflux for 5 h. Complex **4** was obtained by column chromatography on neutral alumina with hexane and $CH_2Cl_2$ as gradient eluents. Yield: 0.11 g (40%). $C_{18}H_{26}Fe_2O_4P_2S_2$ (544.2): calcd. C 39.73, H 4.82; found C 39.77, H 4.87. $^1H$ NMR ($CDCl_3$): $\delta$ = 7.68, 7.42 (2 s, 5 H, Ph), 1.87 (s, 6 H, the $CH_3$ of $PMe_2Ph$), 1.67–1.56 (br. m, 6 H, $CH_2CH_2CH_2$), 1.45 (s, 9 H, $PMe_3$) ppm. $^{31}P\{^1H\}$ NMR ($CDCl_3$): $\delta$ = 30.99 ($PMe_2Ph$), 25.89 ($PMe_3$) ppm. IR ($CH_3CN$): $\tilde{\nu}$CO = 1981, 1943, 1907 $cm^{-1}$. APCI-MS: $m/z$ = 544.8 $[M + H]^+$. Complex **5** was prepared according to a procedure similar to that of **4**, with $PPh_3$ (0.26 g, 1.0 mmol) as the ligand. Yield: 0.40 g (60%). $C_{28}H_{30}Fe_2O_4P_2S_2$ (668.3): calcd. C 50.32, H 4.52; found C 50.24, H 4.63. $^1H$ NMR ($CDCl_3$): $\delta$ = 7.75, 7.33 (2 s, 15 H, Ph), 1.47 (d, 9 H, $PMe_3$), 1.66–1.12 (br. m, 6 H, $CH_2CH_2CH_2$) ppm. $^{31}P\{^1H\}$ NMR ($CDCl_3$): $\delta$ = 62.81 ($PPh_3$), 25.66 ($PMe_3$) ppm. IR ($CH_3CN$): $\tilde{\nu}$CO = 1985, 1946, 1905 $cm^{-1}$. APCI-MS: $m/z$ = 669.0 $[M + H]^+$. Complex **7** was prepared according to a similar procedure used for **4** but with $P(OEt)_3$ (0.17 g, 1.0 mmol) as the ligand. Yield: 0.36 g (62%). $C_{16}H_{30}Fe_2O_7P_2S_2$ (572.2): calcd. C 33.59, H 5.28; found C 33.71, H 5.18. $^1H$ NMR ($CDCl_3$): $\delta$ = 4.16 (s, 6 H, $OCH_2$), 1.46 (d, 9 H, $PMe_3$), 1.37 [s, 9 H, the $CH_3$ of $P(OEt)_3$], 1.61–1.21 (br. m, 6 H, $CH_2CH_2CH_2$) ppm. $^{31}P\{^1H\}$ NMR ($CDCl_3$): $\delta$ = 175.38 [$P(OEt)_3$], 27.10 ($PMe_3$) ppm. IR ($CH_3CN$): $\tilde{\nu}$ = CO = 1991, 1949, 1907 $cm^{-1}$. APCI-MS: $m/z$ = 572.8 $[M + H]^+$.

**Synthesis of $[(\mu\text{-pdt})\{Fe(CO)_2PMe_3\}\{Fe(CO)_2PCy_3\}]$ (6):** Complex **6** can be obtained by using $Me_3NO$ as a CO-removing reagent. A solution of complex **1** (0.43 g, 1.0 mmol) in $CH_3CN$ (10 mL) was treated with $Me_3NO{\cdot}2H_2O$ (0.11 g, 1.0 mmol) at 50 °C for 30 min and $PCy_3$ (0.28 g, 1.0 mmol) was then added to the solution. The mixture was stirred for 1 h and the resultant solution concentrated to dryness under vacuum. The crude product was purified by flash column chromatography on neutral alumina with hexane/$CH_2Cl_2$ (1:1) as eluent. Yield: 0.15 g (22%). $C_{28}H_{48}Fe_2O_4P_2S_2$ (686.42): calcd. C 48.99, H 7.05; found C 48.93, H 6.94. $^1H$ NMR ($CDCl_3$): $\delta$ = 1.47 (s, 9 H, $PMe_3$), 2.12–1.29 (br. m, 39 H, $CH_2CH_2CH_2$ and $PCy_3$) ppm. $^{31}P\{^1H\}$ NMR ($CDCl_3$): $\delta$ = 68.54 ($PCy_3$), 23.49 ($PMe_3$) ppm. IR ($CH_3CN$): $\tilde{\nu}$CO = 1976, 1937, 1901 $cm^{-1}$. ESI-MS: $m/z$ = 687.0 $[M + H]^+$.

**Synthesis of $[(\mu\text{-pdt})\{Fe(CO)_2(PMe_2Ph)\}\{Fe(CO)_2L\}]$ [L = $PPh_3$ (8), $P(OEt)_3$ (9)]:** Triphenylphosphane (0.26 g, 1.0 mmol) was added to a solution of complex $[(\mu\text{-pdt})Fe_2(CO)_5(PMe_2Ph)]$ (**2**) (0.50 g, 1.0 mmol) in toluene (40 mL). The solution was heated to reflux with stirring for 5 h, and the colour turned deep red. After the solution was concentrated by solvent evaporation under vac-

 © 2007 Wiley-VCH Verlag GmbH & Co. KGaA, Weinheim 

uum, the crude product was purified by column chromatography on neutral alumina with hexane/$CH_2Cl_2$ (2:1) as eluent. Product **8** was obtained by cooling the concentrated hexane/$CH_2Cl_2$ solution to –20 °C. Yield: 0.51 g (69%). $C_{33}H_{32}Fe_2O_4P_2S_2$ (730.4): calcd. C 54.27, H 4.42; found C 54.20, H 4.45. $^1$H NMR ($CDCl_3$): $\delta$ = 7.72, 7.39 (2 br. s, 20 H, Ph), 1.79 (d, 6 H, the $CH_3$ of $PMe_2Ph$), 1.48–1.26 (br. m, 6 H, $CH_2CH_2CH_2$) ppm. $^{31}P\{^1H\}$ NMR ($CDCl_3$): $\delta$ = 62.95 ($PPh_3$), 32.98 ($PMe_2Ph$) ppm. IR ($CH_3CN$): $\tilde{\nu}$CO = 1982, 1946, 1913 cm$^{-1}$. APCI-MS: *m*/*z* = 731.0 [M + H]$^+$. Complex **9** was prepared according to a similar procedure used for **8** or by using complex **2** as a starting compound. The reaction of **2** (0.50 g, 1.0 mmol) with $P(OEt)_3$ (0.17 g, 1.0 mmol) was carried out in toluene. Yield: 0.40 g (64%). $C_{21}H_{32}Fe_2O_7P_2S_2$ (634.2): calcd. C 39.77, H 5.09; found C 39.77, H 5.15. $^1$H NMR ($CDCl_3$): $\delta$ = 7.62, 7.38 (2 s, 5 H, Ph), 4.10 (s, 6 H, $OCH_2$), 1.77 (s, 6 H, the $CH_3$ of $PMe_2Ph$), 1.32 [s, 9 H, the $CH_3$ of $P(OEt)_3$], 1.52–1.20 (br. m, 6 H, $CH_2CH_2CH_2$) ppm. $^{31}P\{^1H\}$ NMR ($CDCl_3$): $\delta$ = 175.15 [$P(OEt)_3$], 34.38 ($PMe_2Ph$) ppm. IR ($CH_3CN$): $\tilde{\nu}$CO = 1991, 1952, 1922 cm$^{-1}$. ESI-MS: *m*/*z* = 634.8 [M + H]$^+$.

**Synthesis of [(μ-pdt){Fe(CO)$_2$P(OEt)$_3$}{Fe(CO)$_2$L}] [L = PPh$_3$ (10), PCy$_3$ (11)]:** A solution of [(μ-pdt)$Fe_2(CO)_5P(OEt)_3$] (**3**) (0.52 g, 1.0 mmol) in $CH_3CN$ (15 mL) was treated with $Me_3NO{\cdot}2H_2O$ (0.11 g, 1.0 mmol) at room temperature. The red solution was stirred for 15 min and turned dark red. Triphenylphosphane (0.26 g, 1.0 mmol) was added to the mixture in one portion with stirring. The reaction mixture was stirred for 20 min, and the resultant solution was concentrated to dryness under vacuum. The crude product was purified by flash column chromatography on neutral alumina with hexane/$CH_2Cl_2$ (1:1) as eluent. Product **10** was obtained by cooling the concentrated hexane/$CH_2Cl_2$ solution to –20 °C. Yield: 0.54 g (72%). $C_{31}H_{36}Fe_2O_7P_2S_2$ (758.4): calcd. C 49.10, H 4.78; found C 49.12, H 4.89. $^1$H NMR ($CDCl_3$): $\delta$ = 7.74, 7.41 (2 s, 15 H, Ph), 4.15 (s, 6 H, $OCH_2$), 1.55 (br. s, 6 H, $CH_2CH_2CH_2$), 1.35 [s, 9 H, $CH_3$ of $P(OEt)_3$] ppm. $^{31}P\{^1H\}$ NMR ($CDCl_3$): $\delta$ = 175.00 [$P(OEt)_3$], 64.19 ($PPh_3$) ppm. IR ($CH_3CN$): $\tilde{\nu}$CO = 1997, 1955, 1934 cm$^{-1}$. ESI-MS: *m*/*z* = 759.1 [M + H]$^+$. Complex **3** (0.52 g, 1.0 mmol) was treated with $PCy_3$ (0.14 g, 1.0 mmol) in toluene (40 mL) at reflux for 6 h. Complex **11** was obtained by column chromatography on neutral alumina with hexane and $CH_2Cl_2$ as gradient eluents. Yield: 0.51 g (65%). $C_{31}H_{54}Fe_2O_7P_2S_2$ (776.5): calcd. C 47.95, H 7.01; found C 47.68, H 6.94. $^1$H NMR ($CDCl_3$): $\delta$ = 4.18 (s, 6 H, $OCH_2$), 1.38 [s, 9 H, $CH_3$ of $P(OEt)_3$], 2.12–1.29 (br. m, 39 H, $CH_2CH_2CH_2$ and $PCy_3$) ppm. $^{31}P\{^1H\}$ NMR ($CDCl_3$): $\delta$ = 174.77 [$P(OEt)_3$], 69.97 ($PCy_3$) ppm. IR ($CH_3CN$): $\tilde{\nu}$CO = 1993, 1943, 1933 cm$^{-1}$. ESI-MS: *m*/*z* = 777.2 [M + H]$^+$.

**Synthesis of [(μ-edt){Fe(CO)$_2$PMe$_3$}{Fe(CO)$_2$PPh$_3$}] (12):** Complex [(μ-edt){$Fe(CO)_2PMe_3$}{$Fe(CO)_3$}] (0.42 g, 1.0 mmol) was treated with $PPh_3$ (0.26 g, 1.0 mmol) in toluene (40 mL) at reflux for 5 h. The workup of complex **12** was similar to that for **5**. Yield: 0.42 g (64%). $C_{27}H_{28}Fe_2O_4P_2S_2$ (654.3): calcd. C 49.56, H 4.31; found C 49.78, H 4.54. $^1$H NMR ($CD_3COCD_3$): $\delta$ = 7.65 (m, 9 H, Ph), 7.50 (s, 6 H, Ph), 1.81 (d, 2 H, $CH_2$), 1.53 (d, 9 H, $PMe_3$), 1.06 (d, 2 H, $CH_2$) ppm. $^{31}P\{^1H\}$ NMR ($CDCl_3$): $\delta$ = 60.31 ($PPh_3$), 22.68 ($PMe_3$) ppm. IR ($CH_3CN$): $\tilde{\nu}$CO = 1982, 1945, 1907 cm$^{-1}$. APCI-MS: *m*/*z* = 654.9 [M + H]$^+$.

**X-ray Structure Determination of Complexes 4–6, 8–10 and 12:** The single-crystal X-ray diffraction data were collected with an AFE5R Rigaku diffractometer for **4**, **8** and **9** and a Siemens SMART CCD diffractometer for **5**, **6**, **10** and **12**, with graphite-monochromated Mo-$K_\alpha$ radiation ($\lambda$ = 0.071073 Å) at 293 K using the $\omega$-2$\theta$ scan mode. Data processing was accomplished with the SAINT processing program.[29] Intensity data for **4**–**6** and **8**–**10** were corrected for absorption using the SADABS program.[30] All structures were solved by direct methods and refined on $F^2$ against full-matrix least-squares methods by using the SHELXTL97 program package.[31] All non-hydrogen atoms were refined anisotropically. Hydrogen atoms were located by geometrical calculation. Details of crystal data, data collections and structure refinements are summarised in Tables 4 and 5. CCDC-627499 (**4**), -627500 (**5**), -627501 (**6**), -627502 (**8**), -627503 (**9**), -627504 (**10**) and -630623 (**12**) contain the supplementary crystallographic data for this paper. These data can be obtained free of charge from The Cambridge Crystallographic Data Centre via www.ccdc.cam.ac.uk/data_request/cif.

Table 4. Crystallographic data and processing parameters for complexes **4**–**6**.

| Complex | **4** | **5** | **6** |
|---|---|---|---|
| Empirical formula | $C_{18}H_{26}Fe_2O_4P_2S_2$ | $C_{28}H_{30}Fe_2O_4P_2S_2$ | $C_{28}H_{48}Fe_2O_4P_2S_2$ |
| Formula mass | 544.15 | 668.28 | 686.42 |
| Crystal system | monoclinic | monoclinic | monoclinic |
| Space group | $P2_1/n$ | $P2_1/n$ | $P2_1/c$ |
| *a* [Å] | 14.802(3) | 8.431(2) | 11.992(1) |
| *b* [Å] | 10.337(2) | 22.350(5) | 12.077(1) |
| *c* [Å] | 16.090(3) | 16.403(4) | 22.658(3) |
| *α* [°] | 90 | 90 | 90 |
| *β* [°] | 105.53(3) | 93.598(3) | 98.146(1) |
| *γ* [°] | 90 | 90 | 90 |
| *V* [Å$^3$] | 2372.0(8) | 3085.0(12) | 3248.3(6) |
| *Z* | 4 | 4 | 4 |
| $D_{calcd.}$ [g cm$^{-3}$] | 1.524 | 1.439 | 1.404 |
| Crystal size [mm] | 0.15 × 0.28 × 0.30 | 0.08 × 0.16 × 0.22 | 0.20 × 0.26 × 0.32 |
| $\theta_{min/max}$ [°] | 3.29–27.44 | 2.21–27.00 | 1.92–27.00 |
| Reflections collected | 5395 | 6727 | 7064 |
| Unique data, $R_{int}$ | 4694, 0.0242 | 5325, 0.0262 | 5223, 0.0403 |
| Parameters | 253 | 343 | 343 |
| GOF on $F^2$ | 1.074 | 1.067 | 1.009 |
| $R_1$ [$I > 2\sigma(I)$] | 0.0278 | 0.0322 | 0.0369 |
| $wR_2$ [$I > 2\sigma(I)$] | 0.0676 | 0.0767 | 0.0793 |
| Residual electron density [e Å$^{-3}$] | 1.067,–0.501 | 0.382, –0.259 | 0.325, –0.301 |

 © 2007 Wiley-VCH Verlag GmbH & Co. KGaA, Weinheim 

Table 5. Crystallographic data and processing parameters for complexes **8**–**10** and **12**.

| Complex | **8**·0.5$C_6H_{14}$ | **9** | **10** | **12** |
|---|---|---|---|---|
| Empirical formula | $C_{33}H_{32}Fe_2O_4P_2S_2$·0.5$C_6H_{14}$ | $C_{21}H_{32}Fe_2O_7P_2S_2$ | $C_{31}H_{36}Fe_2O_7P_2S_2$ | $C_{27}H_{28}Fe_2O_4P_2S_2$ |
| Formula mass | 773.43 | 634.23 | 758.36 | 654.25 |
| Crystal system | triclinic | triclinic | orthorhombic | orthorhombic |
| Space group | $P\bar{1}$ | $P\bar{1}$ | *Pbca* | $P2_12_12_1$ |
| *a* [Å] | 10.780(5) | 8.600(2) | 20.154(3) | 12.2677(2) |
| *b* [Å] | 12.459(5) | 11.586(2) | 15.815(2) | 15.1411(3) |
| *c* [Å] | 14.972(7) | 15.036(3) | 21.852(3) | 16.1701(3) |
| *α* [°] | 79.304(14) | 96.25(3) | 90 | 90 |
| *β* [°] | 84.660(14) | 92.93(3) | 90 | 90 |
| *γ* [°] | 69.358(10) | 105.13(3) | 90 | 90 |
| *V* [Å $^3$] | 1848.2(15) | 1432.7(5) | 6965.2(18) | 3003.54(10) |
| *Z* | 2 | 2 | 8 | 4 |
| $D_{calcd.}$ [g cm$^{-3}$] | 1.390 | 1.470 | 1.446 | 1.447 |
| Crystal size [mm] | 0.12 × 0.13 × 0.25 | 0.10 × 0.24 × 0.30 | 0.12 × 0.28 × 0.30 | 0.30 × 0.40 × 0.52 |
| $\theta_{min/max}$ [°] | 2.06–28.28 | 2.99–27.45 | 1.86–26.00 | 1.84–30.00 |
| Reflections collected | 8963 | 6369 | 6852 | 8482 |
| Unique data, $R_{int}$ | 7411, 0.0174 | 4515, 0.0381 | 5741, 0.0298 | 7146, 0.0322 |
| Parameters | 425 | 307 | 398 | 353 |
| GOF on $F^2$ | 1.055 | 1.058 | 1.057 | 1.006 |
| $R_1$ [$I > 2\sigma(I)$] | 0.0464 | 0.0501 | 0.0315 | 0.0304 |
| $wR_2$ [$I > 2\sigma(I)$] | 0.1222 | 0.1378 | 0.0810 | 0.0657 |
| Residual electron density [e Å$^{-3}$] | 0.940, –0.539 | 0.857, –0.695 | 0.732, –0.551 | 0.241, –0.299 |

**Electrochemical Studies of Complexes 4–11:** Cyclic voltammograms were obtained in a three-electrode cell under argon using a BAS 100B electrochemical workstation. The working electrode was a glassy carbon disk (0.071 cm$^2$) polished with 3 and 1 μm diamond pastes and sonicated for 10 min prior to use. The reference electrode was a non-aqueous Ag/Ag$^+$ (0.01 M $AgNO_3$ in $CH_3CN$) electrode and the counter electrode was a platinum wire. A solution of 0.05 M $n$Bu$_4$NPF$_6$ (Fluka, electrochemical grade) in $CH_3CN$ was used as the supporting electrolyte for complexes **4**, **5** and **7**–**10**. A mixed solution of 0.05 M $n$Bu$_4$NPF$_6$ (Fluka, electrochemical grade) in toluene and acetonitrile (1:3, v/v) was used as supporting electrolyte for complexes **6** and **11** due to its poor solubility in pure $CH_3CN$. Acetonitrile (Aldrich, spectroscopic grade) used for electrochemical measurements was freshly distilled from $CaH_2$ under $N_2$.

**Supporting Information** (see footnote on the first page of this article): Cyclic voltammograms of complexes **4**, **6**–**8**, **10** and **11** under argon and CO, as well as the multiple scans for complex **5** at a scan rate of 4.0 V s$^{-1}$ are included.

## Acknowledgments

We are grateful to the Chinese National Natural Science Foundation (Grant nos. 20471013 and 20633020), the Swedish Energy Agency, the Swedish Research Council and the K & A Wallenberg Foundation for financial support of this work.

[1] J. W. Peters, W. N. Lanzilotta, B. J. Lemon, L. C. Seefeldt, *Science* **1998**, *282*, 1853–1858.
[2] Y. Nicolet, C. Piras, P. Legrand, C. E. Hatchikian, J. C. Fontecilla-Camps, *Structure* **1999**, *7*, 13–23.
[3] E. J. Lyon, I. P. Georgakaki, J. H. Reibenspies, M. Y. Darensbourg, *Angew. Chem. Int. Ed.* **1999**, *38*, 3178–3180.
[4] M. Schmidt, S. M. Contakes, T. B. Rauchfuss, *J. Am. Chem. Soc.* **1999**, *121*, 9736–9737.
[5] A. L. Cloirec, S. P. Best, S. Borg, S. C. Davies, D. J. Evans, D. L. Hughes, C. J. Pickett, *Chem. Commun.* **1999**, 2285–2286.
[6] E. J. Lyon, I. P. Georgakaki, J. H. Reibenspies, M. Y. Darensbourg, *J. Am. Chem. Soc.* **2001**, *123*, 3268–3278.
[7] L. Song, J. Ge, X. Zhang, Y. Liu, Q. Hu, *Eur. J. Inorg. Chem.* **2006**, 3204–3210.
[8] F. Gloaguen, J. D. Lawrence, T. B. Rauchfuss, *J. Am. Chem. Soc.* **2001**, *123*, 9476–9477.
[9] F. Gloaguen, J. D. Lawrence, M. Schmidt, S. R. Wilson, T. B. Rauchfuss, *J. Am. Chem. Soc.* **2001**, *123*, 12518–12527.
[10] F. Gloaguen, J. D. Lawrence, T. B. Rauchfuss, M. Bénard, M. Rohmer, *Inorg. Chem.* **2002**, *41*, 6573–6582.
[11] X. Zhao, I. P. Georgakaki, M. L. Miller, J. C. Yarbrough, M. Y. Darensbourg, *J. Am. Chem. Soc.* **2001**, *123*, 9710–9711.
[12] M. M. Hasan, M. B. Hursthouse, S. E. Kabir, K. M. A. Malik, *Polyhedron* **2001**, *20*, 97–101.
[13] X. Zhao, I. P. Georgakaki, M. L. Miller, R. Mejia-Rodriguez, C. Chiang, M. Y. Darensbourg, *Inorg. Chem.* **2002**, *41*, 3917–3928.
[14] R. Mejia-Rodroguez, D. Chong, J. H. Reibenspies, M. P. Soriaga, M. Y. Darensbourg, *J. Am. Chem. Soc.* **2004**, *126*, 12004–12014.
[15] P. Li, M. Wang, C. He, G. Li, X. Liu, C. Chen, B. Åkermark, L. Sun, *Eur. J. Inorg. Chem.* **2005**, 2506–2513.
[16] J. Hou, X. Peng, Z. Zhou, S. Sun, X. Zhao, S. Gao, *J. Organomet. Chem.* **2006**, *691*, 4633–4640.
[17] Y. Na, M. Wang, K. Jin, R. Zhang, L. Sun, *J. Organomet. Chem.* **2006**, *691*, 5045–5051.
[18] J. D. Lawrence, T. B. Rauchfuss, S. R. Wilson, *Inorg. Chem.* **2002**, *41*, 6193–6195.
[19] J. L. Nehring, D. M. Heinekey, *Inorg. Chem.* **2003**, *42*, 4288–4292.
[20] J. Capon, S. E. Hassnaoui, F. Gloaguen, P. Schollhammer, J. Talarmin, *Organometallics* **2005**, *24*, 2020–2022.
[21] J. W. Tye, J. Lee, H. Wang, R. Mejia-Rodriguez, J. H. Reibenspies, M. B. Hall, M. Y. Darensbourg, *Inorg. Chem.* **2005**, *44*, 5550–5552.
[22] J. I. Vlugt, T. B. Rauchfuss, C. M. Whaley, S. R. Wilson, *J. Am. Chem. Soc.* **2005**, *127*, 16012–16013.
[23] W. Dong, M. Wang, X. Liu, K. Jin, G. Li, F. Wang, L. Sun, *Chem. Commun.* **2006**, 305–307.
[24] L. Schwartz, G. Eilers, L. Eriksson, A. Gogoll, R. Lomoth, S. Ott, *Chem. Commun.* **2006**, 520–522.
[25] L. E. Bogan, D. A. Lesch, T. B. Rauchfuss, *J. Organomet. Chem.* **1983**, *250*, 429–438.
[26] M. Y. Darensbourg, E. J. Lyon, X. Zhao, I. P. Georgakaki, *Proc. Natl. Acad. Sci.* **2003**, *100*, 3683–3688.

 © 2007 Wiley-VCH Verlag GmbH & Co. KGaA, Weinheim 

[27] J. Ekström, M. Abrahamsson, C. Olson, J. Bergquist, F. B. Kaynak, L. Eriksson, L. Sun, H. Becker, B. Åkermark, L. Hammarström, S. Ott, *Dalton Trans.* **2006**, 4599–4606.
[28] D. Chong, I. P. Georgakaki, R. Mejia-Rodriguez, J. Sanabria-Chinchilla, M. P. Soriaga, M. Y. Darensbourg, *Dalton Trans.* **2003**, 4158–4163.
[29] *Software packages SMART and SAINT*, Siemens Energy & Automation Inc., Madison, Wisconsin, **1996**.
[30] G. M. Sheldrick, *SADABS, Absorption Correction Program*, University of Göttingen, Germany, **1996**.
[31] G. M. Sheldrick, *SHELXTL97, Program for the Refinement of Crystal Structure*, University of Göttingen, Germany, **1997**.
Received: December 13, 2006
Published Online: June 18, 2007

 © 2007 Wiley-VCH Verlag GmbH & Co. KGaA, Weinheim 

DOI: 10.1002/ejic.200700139

# Synthesis, Structure, Protolytic Properties, Alkylating and Cytotoxic Activity of Novel Platinum(II) and Palladium(II) Complexes with Pyrazole-Derived Ligands

**Elzbieta Budzisz,*[a] Magdalena Malecka,[b] Bernhard K. Keppler,[c] Vladimir B. Arion,[c] Grzegorz Andrijewski,[d] Urszula Krajewska,[e] and Marek Rozalski[e]**

**Keywords:** Metal complexes / Platinum / Palladium / Pyrazole ligands / Antitumor agents / Alkylating and cytotoxic activity

Novel platinum(II) and palladium(II) complexes $[PtCl_2(HL^1)]$ (**3a**), $[NH_2(CH_3)_2][PtCl_2(L^1)]$ (**3b**), $[PdCl_2(HL^1)]$ (**4a**), $[NH_2(CH_3)_2][PdCl_2(L^1)]$ (**4b**) and $[PdCl(CH_3CN)(L^1)]$ (**4c**), where $HL^1$ = 4-(2-hydroxybenzoyl)-2-(pyridin-2-yl)-1*H*-pyrazol-3-ol, have been synthesised as potential anticancer compounds. Protonation constants of the ligand were determined by pH-metric titration ($\log K_1 = 7.74 \pm 0.03$; $\log K_2 = 2.85 \pm 0.05$). The solid-state structures of complexes **3b** and **4c** have been determined by X-ray diffraction, showing square-planar coordination geometry of $Pt^{II}$ and $Pd^{II}$ ions. In addition, the compounds have been characterised by IR, $^1H$ NMR and FAB mass spectrometry. The results of preliminary studies on the cytotoxic activity in vitro against HL-60 and NALM-6 leukaemia cell lines are also reported and the $IC_{50}$ values compared with those of the metal-free ligand and cisplatin. Cytotoxic evaluation revealed that $Pt^{II}$ and $Pd^{II}$ complexes were active in the micromolar concentration range.

(© Wiley-VCH Verlag GmbH & Co. KGaA, 69451 Weinheim, Germany, 2007)

## Introduction

Cisplatin [diamminedichloroplatinum, *cis*-$PtCl_2(NH_3)_2$] is known as a DNA-modifying agent with strong anticancer potency.[1–3] Despite its wide clinical application, cisplatin causes many serious side effects, such as nephrotoxicity, ototoxicity, peripheral neuropathy and allergy.[4] In addition, the therapeutic efficacy of cisplatin is limited by inherent or treatment-induced resistance of tumour cell subpopulations.[5] Therefore, various platinum(II) and palladium(II) complexes with nitrogen-containing ligands were evaluated in the search for less toxic and more selective anticancer drugs.[6] Simple structural analogues of cisplatin were found to possess no advantages because of similar mechanism of action, structure of DNA adducts, toxicity profile, adverse effects and tumour cross-resistance.[7] Recently, attention has been focused on inert, nonleaving ligands, whose steric and electronic features may affect the mechanism of substitution at the metal centre, DNA binding and drug metabolism. It is believed that complexes containing bulky ligands are kinetically and thermodynamically more stable than simple cisplatin analogues.[8] Taking into account the structural analogy between $Pt^{II}$ and $Pd^{II}$ complexes, a variety of studies on $Pd^{II}$ complexes have been performed, including on their cytotoxicity[9] and antitumour activity.[10–12] Palladium complexes with β-carboline alkaloids,[13–15] pyrazoles[16] and DMSO[17] were tested against solid tumour cell lines, and in some cases exhibited remarkable activity. It was suggested that their biological activity depends on the nature of the ligand, the type of counterion used and the configuration of the complex.[18]

For many years the research in our laboratory has been directed towards the synthesis of chromone (benzo-γ-pyrone) and coumarin (benzo-α-pyrone) derivatives and the study of their reactivity towards nucleophilic reagents containing nitrogen, oxygen, sulfur and carbon.[19] In particular, in protolytic solvents at room temperature chromones have been converted efficiently into enamine-type compounds with a typical lemon-yellow colour.[20,21] The chromones and coumarins react with hydrazines to afford pyr-

[a] Department of Cosmetic Raw Materials Chemistry, Faculty of Pharmacy, Medical University of Lodz,
Muszynski 1, 90-151 Lodz, Poland
Fax: +48-42-678-83-98
E-mail: elora@ich.pharm.am.lodz.pl
[b] Department of Crystallography and Crystal Chemistry, University of Lodz,
Pomorska 149/153, 90-236 Lodz, Poland
E-mail: malecka@uni.lodz.pl
[c] Institute of Inorganic Chemistry, University of Vienna,
Währingerstrasse 42, 1090 Vienna, Austria
E-mail: bernhard.keppler@univie.ac.at
[d] Department of Inorganic Chemistry, University of Lodz,
Narutowicza 68, 90-136 Lodz, Poland
E-mail: grzegorz@chemul.uni.lodz.pl
[e] Department of Pharmaceutical Biochemistry, Faculty of Pharmacy, Medical University of Lodz,
Muszynski 1, 90-151 Lodz, Poland
E-mail: mrozalski@pharm.am.lodz.pl

Supporting information for this article is available on the WWW under http://www.eurjic.org or from the author.

 © 2007 Wiley-VCH Verlag GmbH & Co. KGaA, Weinheim 

azole derivatives.[22] A class of pyrazole-containing palladium(II) complexes has been reported to possess antibacterial,[23] antidepressant,[24] monoamine oxidase inhibiting[25] and antitumour activity.[26,27]

In addition, both type of compounds (chromones and coumarins) exhibit interesting biological properties,[28,29] including anticonvulsant,[30] antimicrobial,[31] spasmolytic,[32] antioxidant[33] and antitumour activities.[34] The metal complexes with coumarin as a ligand reveal anticoagulant action[35,36] and possess antiproliferative activity.[37,38] Notably, complexes with cerium(III), zirconium(IV), copper(II), zinc(II), bismuth(III) and cadmium(II) show pronounced cytotoxic activity in vitro.[39,40] The rare earth metal complexes of coumarin derivatives endowed with anticoagulant and anti-HIV activity were also documented.[41–43] Current efforts are focused on developing metal-based drugs with improved clinical effectiveness, reduced general toxicity and a broader spectrum of activity.

Herein we report the synthesis of a novel pyrazole ligand $HL^1$ by the reaction of coumarin with 2-hydrazinopyridine. Protonation constants of the ligand were determined by pH-metric titration. This ligand, as will be shown below, forms *cis* complexes with platinum(II) and palladium(II), which are often more cytotoxic than the *trans* isomers.[44] The structures of two $Pt^{II}$ and $Pd^{II}$ complexes determined by X-ray diffraction are reported. The results of preliminary studies on the alkylating and in vitro cytotoxic activity against HL-60 and NALM-6 leukaemia cell lines are also discussed.

## Results and Discussion

### Preparation of the Ligands

Pyrazole-based chelating ligands have attracted our attention, because of their ability to form *cis*-configured complexes. The anticancer activity of a metal complex depends not only on the metal itself, but also on its oxidation state, on the number and type of bound ligands, and the coordination geometry of the complex.[45]

By reaction of 3-acetyl-4-hydroxycoumarin (**2**), which was obtained from methyl ester **1**, with 2-hydrazinopyridine in a 1:1 molar ratio in refluxing methanol, we obtained 4-(2-hydroxybenzoyl)-2-(pyridin-2-yl)-1*H*-pyrazol-3-ol ($HL^1$) in 62% yield (Scheme 1).

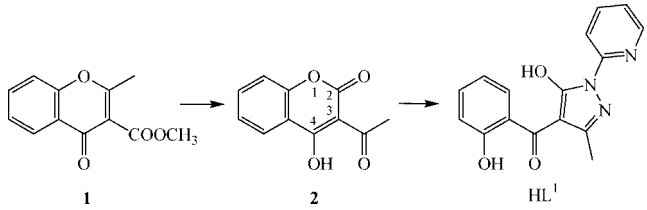


Scheme 1. Synthesis of the ligand $HL^1$.

Three different tautomeric forms (A, B and C) can be envisaged for $HL^1$ (Scheme 2). Of these, B and C are stabilised by intramolecular hydrogen bonding. The formation of $HL^1$ presumably proceeds by an attack of 2-hydrazinopyridine on the carbonyl group (C-3 position in coumarin), followed by the nucleophilic attack of the hydrazine nitrogen on the carbonyl atom at C-2 position (Scheme 3).

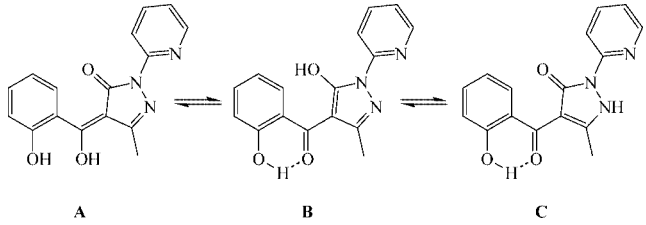


Scheme 2. Possible tautomeric forms of the ligand $HL^1$.

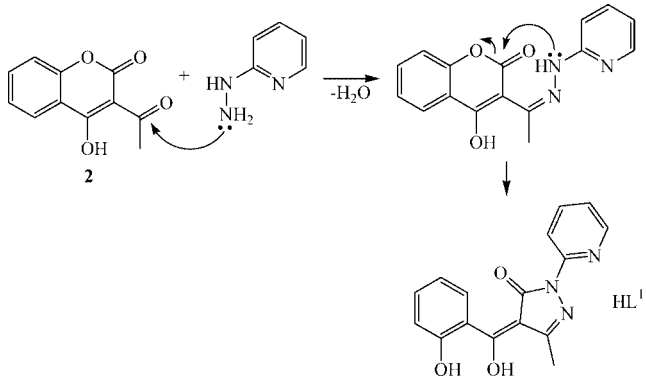


Scheme 3. Stepwise formation of $HL^1$.

The ligand has been characterised by elemental analysis, IR spectroscopy, $^1H$ and $^{13}C$ NMR spectroscopy and mass spectrometry (see Experimental Section).

### Synthesis of Complexes

The synthesised ligand $HL^1$ behaves as a strong bidentate chelating agent forming a five-membered metallocycle through coordination of the pyrazole and the pyridine nitrogen atoms to the corresponding metal ion. A review of the coordination chemistry of acylpyrazolone derivatives has been recently published.[46]

Complexes $[M^{II}Cl_2(HL^1)]$, where M = Pt (**3a**) and Pd (**4a**) (Scheme 4), were prepared at room temperature by mixing equimolar amounts of $HL^1$ and potassium tetrachloroplatinate(II) or potassium tetrachloropalladate(II), respectively, in water/methanol. Reactions of $K_2[PtCl_4]$ or $K_2[PdCl_4]$ with $HL^1$ in 1:1 molar ratio in dimethylformamide (DMF) produced (after two weeks) the complexes $[NH_2(CH_3)_2][MCl_2(L^1)]$, where M = Pt (**3b**) and Pd (**4b**). The cation $[NH_2(CH_3)_2]^+$ has been presumably formed by light-induced decomposition of DMF and protonation of the arising dimethylamine.[47] The complex $[PdCl(CH_3CN)(L^1)]$ (**4c**) resulted from the reaction of $[PdCl_2(C_6H_5CN)_2]$ with $HL^1$ in 1:1 molar ratio in chloroform/methanol (2:1), followed by recrystallisation from acetonitrile/diethyl ether.

 © 2007 Wiley-VCH Verlag GmbH & Co. KGaA, Weinheim 

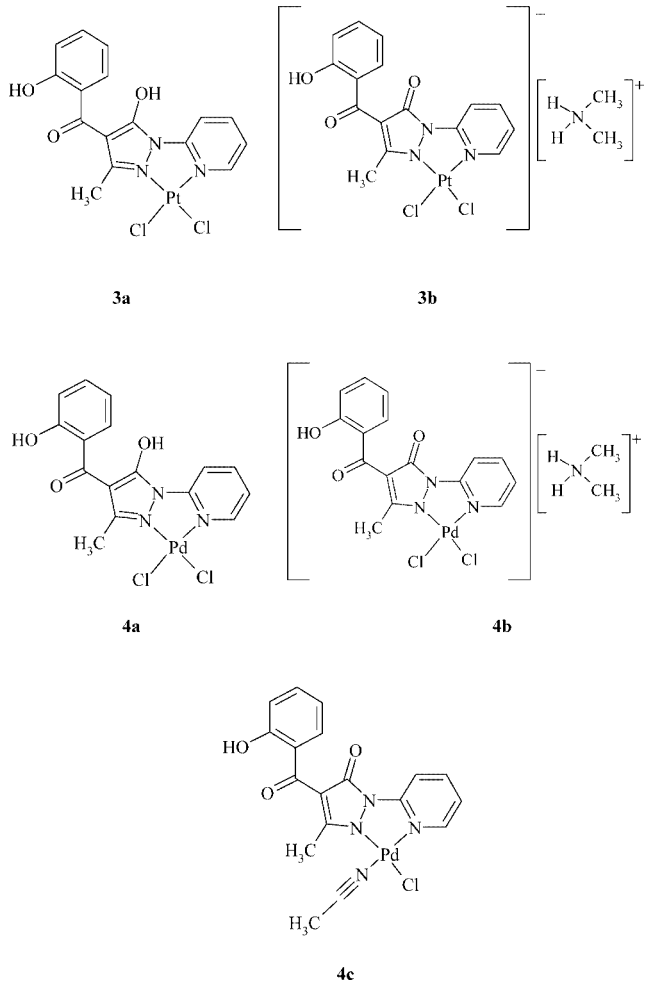


Scheme 4. The library of novel complexes prepared.

The synthesised complexes **3a** and **4a** are sparingly soluble in water, acetone and ethanol, but well soluble in DMSO and DMF.

The composition and the structure of the complexes prepared were confirmed by elemental analyses, IR spectra, $^1$H NMR spectra, mass spectrometry measurements and X-ray diffraction for compounds **3b** and **4c**. Some characteristic IR vibrations for these complexes are given in Table S1 (see Supporting Information). Significant differences in the IR spectra of complexes **3** and **4** were observed in comparison with that of ligand $HL^1$. The latter shows a strong band at 1660 cm$^{-1}$ due to $\nu$(C=O). This band is shifted by 14–32 cm$^{-1}$ to lower frequencies in the spectra of metal complexes. Moderately strong bands at 355, 334 and 328 cm$^{-1}$ can be attributed to $\nu$(M–Cl) of the complexes. Stretching vibrations of the M–N bonds were observed at 420 cm$^{-1}$. The FAB mass spectrum of **3a** recorded in positive-ion mode contains a peak at *m*/*z* 563 due to the $[M + H]^+$ ion and a strong peak at *m*/*z* 528 attributed to $[M - Cl]^+$. Analogously, the spectrum of **4a** shows two peaks at *m*/*z* 473 and 438, which were assigned to $[M + H]^+$ and $[M - Cl]^+$, correspondingly. For complex **4c** we have observed a peak at *m*/z 478 due to $[M + H]^+$. The purity of complexes **3b** and **4b** was confirmed by elemental analysis.

## The Protonation Constants of the Ligand $HL^1$

The potentiometric measurements performed within the pH range 2.5–11.0 showed that under titration with KOH, the ligand $HL^1$ acts as a weak acid with a protonation constant of about $10^8$. These acidic properties can be attributed to the hydroxy group attached to the aromatic ring. Its acidity, slightly higher than that observed for phenols, is probably enhanced by the vicinity of the carbonyl group. In the presence of a strong acid the ligand $HL^1$ acts as a weak base. However, its basicity is small and, within accessible range of concentrations, it was possible to determine potentiometrically only one additional protonation constant. Supposedly, it refers to the equilibrium of protonation of the pyridine nitrogen atom, which is expected to have a higher affinity for the proton than the pyrazole nitrogen atom.

Thus, the stepwise protonation constants of $\log K_1 = 7.74 \pm 0.03$ and $\log K_2 = 2.85 \pm 0.05$ were calculated from titration curves. This implies that, under physiological conditions, the nitrogen atoms of the ligand present in solution are unprotonated.

## X-ray Crystallography

Single crystal X-ray diffraction studies of compound **3b** were undertaken to elucidate the coordination sphere of platinum(II) and the tautomeric form of the ligand. The molecular structure of **3b** with the atom numbering scheme is shown in Figure 1. Selected bond lengths and angles are given in Table 1. The asymmetric unit consists of one $[PtCl_2(L^1)]^-$ anion and one $[NH_2(CH_3)_2]^+$ cation. The coordination environment of $Pt^{II}$ atom is planar, formed by two nitrogen atoms and two chloride ligands. The $PtN_2Cl_2$ "square" adopts a *cis* configuration. The geometry about the Pt atom deviates from the ideal square plane: the atoms N1, N3 and Cl1, Cl2 form angles smaller than 90° with the Pt atom, and consequently the N3–Pt–Cl2 and N1–Pt–Cl1 angles are larger than 90°. The distribution of electron density over the ligand backbone and the presence of a countercation indicate that $HL^1$ acts as a monodeprotonated ligand and adopts the tautomeric form C (Scheme 2).

The crystal lattice is stabilised by a net of intermolecular and intramolecular hydrogen bonds. The atom O1 participates in two O–H···O hydrogen bonds: intramolecular O1–H5···O2, which closes an extra six-membered ring, and intermolecular O5–H5···O1$^{(i)}$. In addition, N4–H16···O3 interaction is of note. The atom N4 is also involved in hydrogen bonds to the Cl atoms (see Table S2).

The packing of the molecules in the crystal lattice is stabilised by C–H···π interactions. Atom C11 is involved in a weak C–H···π intermolecular interaction with the centroid of the ring 3 (N3/C12/C13/C14/C15) [symmetry code (ii): $2 - x$, $1 - y$, $-z$] and C18 interacts with Cg4, where Cg4 is the centroid of ring C1–C6 (more details in Table S3). A number of π–π stacking interactions are observed in the crystal lattice (see Figure S2).

 © 2007 Wiley-VCH Verlag GmbH & Co. KGaA, Weinheim 

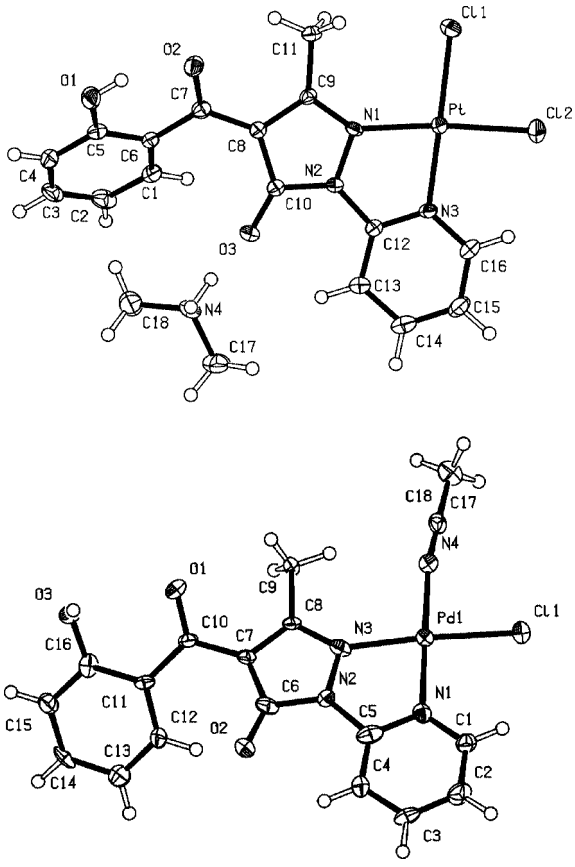


Figure 1. ORTEP drawing of **3b** (top) and of the first independent molecule of **4c** (bottom) with thermal ellipsoids depicted at 50% probability level.

Compound **4c** crystallised in the orthorhombic space group $Pca2_1$ with four crystallographically independent molecules of $[PdCl(CH_3CN)(L^1)]$ in the unit cell. In all four molecules the organic species acts as a monodeprotonated bidentate ligand coordinating to the Pd ion through two nitrogen atoms with formation of a five-membered metallocycle. The square-planar coordination geometry of each $Pd^{II}$ ion is completed by one chlorido ligand and one $CH_3CN$ molecule. The bond lengths in the coordination polyhedron of all four independent molecules are given for comparison in Table 1. The bond lengths C6–O2 of 1.243(13), C10–O1 of 1.240(12) and C16–O3 of 1.343(13) Å clearly indicate the stabilisation of tautomer C in the complex (Scheme 2). The same tendency in bond length distribution is observed in three other crystallographically independent molecules (Table 1).

## Biological Characterisation

### *Alkylating Activity*

Alkylating agents belong to the first class of cytostatics used for chemotherapy.[48] Under in vivo conditions they alkylate nucleophilic centres of nucleobases and amino acids, resulting either in cleavage or cross-linking of double-stranded DNA molecules or proteins. Such cleavage destroys DNA, while covalent cross-links prevent unwinding of nucleic acids, which is functionally important in replication and transcription processes.[49] Cisplatin and carboplatin are the nonclassical alkylating agents. These drugs interact with cellular DNA according to the same mechanism[50,51] by metallation of nucleobases of both DNA strands.

An effective drug concentration for carboplatin is 4–7-fold higher as compared to cisplatin, and the former is also less toxic.[52] The "alkylating" activities of the ligand $HL^1$ and of the complexes **3a** and **4a** were determined by the Preussmann test.[53] The level of "alkylation" of 4-(4-nitrobenzyl)pyridine (NBP) was quantified spectrophotometrically at 560 nm. The molar absorbances (A) for complexes **3a** and **4a** were 0.303 and 0.069, respectively, compared with 0.047 for $HL^1$ (Table 2). Interestingly, cisplatin in this test shows $A = 0.300$[54] and carboplatin alkylates NBP giving $A = 0.231$. According to the Preussmann scale (see footnote to Table 2), the complex **3a** and both reference compounds cisplatin and carboplatin exhibit moderate alkylating activity in this test.

Table 2. Alkylating activity of substituted pyrazoles and their $Pt^{II}$ and $Pd^{II}$ complexes.

| Compound | $\varepsilon$ [$M^{-1}cm^{-1}$] | Absorbance[a] $\lambda_{max}$ = 560 nm | Alkylation activity[b] |
|---|---|---|---|
| $HL^1$ | 47.3 | 0.0473 | – |
| **3a** | 303.4 | 0.3034 | ++ |
| **4a** | 69.0 | 0.0690 | + |
| Cisplatin[c] | 300.0 | 0.3000 | ++ |
| Carboplatin | 231.2 | 0.2312 | ++ |

[a] Means from 3 determinations. [b] According to ref.[53]: (–) $A <$ 0.05, (+) $A$ = 0.05–0.1, (++) $A$ = 0.1–0.5, (+++) $A > 0.5$. [c] According to ref.[54].

## Cytotoxicity Assay

Cytotoxicity assays for complexes **3a** and **4a** were performed on human acute leukaemia HL-60 and NALM-6 cell lines (Figure 2). Cisplatin and carboplatin were used as

Table 1. Selected bond lengths [Å] for compounds **3b** and **4c**.

| Structure **3b** | | Structure **4c** | | | | | | | |
|---|---|---|---|---|---|---|---|---|---|
| | | Molecule 1A | | Molecule 1B | | Molecule 1C | | Molecule 1D | |
| Pt–N1 | 2.019(4) | Pd1–N1 | 2.022(9) | Pd2–N5 | 2.001(10) | Pd3–N9 | 2.019(10) | Pd4–N13 | 2.003(10) |
| Pt–N3 | 2.033(3) | Pd1–N3 | 2.022(9) | Pd2–N7 | 2.007(10) | Pd3–N11 | 2.024(9) | Pd4–N15 | 2.007(10) |
| Pt–Cl2 | 2.302(2) | Pd1–N4 | 2.014(10) | Pd2–N8 | 1.989(10) | Pd3–N12 | 1.972(11) | Pd4–N16 | 1.979(10) |
| Pt–Cl1 | 2.303(2) | Pd1–Cl1 | 2.297(3) | Pd2–Cl2 | 2.286(3) | Pd3–Cl3 | 2.285(3) | Pd4–Cl4 | 2.294(3) |

 © 2007 Wiley-VCH Verlag GmbH & Co. KGaA, Weinheim 

the reference compounds. Both metal complexes exhibited relatively high cytotoxic activity with the $IC_{50}$ values in the micromolar range. Their cytotoxic effectiveness was nearly the same as that for carboplatin and only 5 (**3a**) or 10 (**4a**) times lower in comparison to cisplatin, a well-established therapeutic agent used for the treatment of leukaemia (Table 3). The most potent was the platinum(II) complex **3a**, with an $IC_{50}$ of 4.7 and 3.9 μM for HL-60 and NALM-6 cells, respectively, in line with alkylating activity towards NBP.

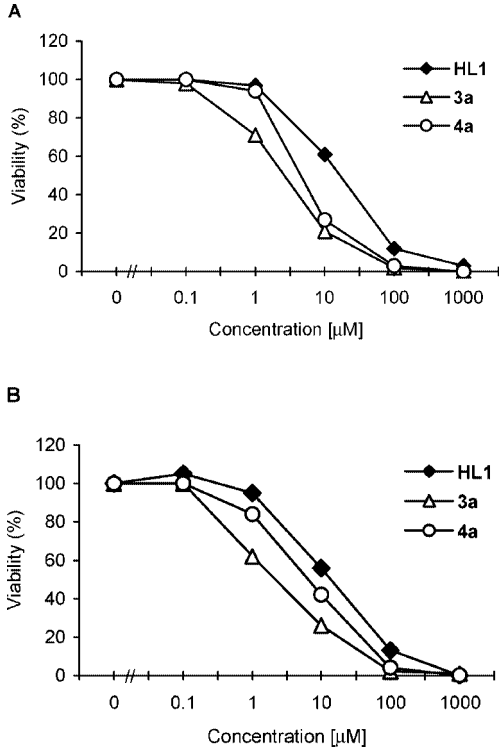


Figure 2. A: Survival curves for HL-60 and B: NALM-6 leukaemia cells exposed for 48 h to tested compounds $HL^1$, **3a** and **4a**. Each point represents the mean of four independent determinations. Standard deviations are excluded for clarity and do not exceed 20% of the mean value for each point.

Table 3. $IC_{50}$ values [μM] for $HL^1$ and complexes **3a** and **4a**.

| Compound | $IC_{50}$[a] HL-60 | NALM-6 |
|---|---|---|
| $HL^1$ | 29.9 ± 8.3 | 30.0 ± 5.3 |
| **3a** | 4.7 ± 0.6 | 3.9 ± 0.6 |
| **4a** | 7.0 ± 0.5 | 8.3 ± 0.3 |
| Cisplatin | 0.8 ± 0.1 | 0.7 ± 0.3 |
| Carboplatin | 4.3 ± 1.3 | 0.7 ± 0.2 |

[a] $IC_{50}$ – concentration of a tested compound required to reduce the fraction of surviving cells to 50% of that observed in the control, nontreated cells. Mean values of $IC_{50}$ (in μM) ± S.D. from four experiments are presented.

Comparison of the data in Table 3 clearly shows that the in vitro antiproliferative activity of complexes **3a** and **4a** exceeds that of uncomplexed ligand $HL^1$. This strongly supports the view that cytotoxicity can be quite safely ascribed to the presence of the metal centre.

## Conclusions

In this paper we have described the synthesis of a new chelating pyrazole ligand $HL^1$, which is characterised by two protonation constants determined by pH-metric titration ($\log K_1 = 7.74 \pm 0.03$; $\log K_2 = 2.85 \pm 0.05$). The ligand forms neutral complexes of the type $[MCl_2(HL^1)]$, where M = Pt (**3a**) and Pd (**4a**) in aqueous methanol. In DMF solutions the ionic species $[NH_2(CH_3)_2][PtCl_2(L^1)]$ with M = Pt (**3b**) and Pd (**4b**) have been isolated. Starting from $[PdCl_2(C_6H_5CN)_2]$ and $HL^1$, and using acetonitrile for recrystallisation, the complex $[PdCl(CH_3CN)(L^1)]$ (**4c**) has been prepared. X-ray diffraction studies of **3b** and **4c** showed that the ligand in both square-planar complexes acts as a monodeprotonated one, adopting the tautomeric form C.

Complexes **3a** and **4a** exhibit in vitro antiproliferative activity in HL-60 and NALM-6 leukaemia cells, with the cytotoxicity $IC_{50}$ values similar to those for carboplatin. The sequence in activity against HL-60 and NALM-6 leukaemia cells is as follows **3a** > **4a** > $HL^1$. The alkylating activity of the platinum compound **3a** was comparable with those of cisplatin and carboplatin.

## Experimental Section

**Materials:** All substances were used without further purification. Potassium tetrachloroplatinate(II) and potassium tetrachloropalladate(II) were purchased from Aldrich. $CDCl_3$ and $[D_6]$DMSO solvents for NMR spectroscopy were obtained from Dr. Glaser AG, Basel, Switzerland. Solvents for synthesis (toluene, methanol, dimethylformamide, acetone) were reagent-grade or better and were dried according to standard protocols.[55] The melting points were determined using an Electrothermal 1A9100 apparatus and they are uncorrected. The IR spectra were recorded with a Pye-Unicam 200G Spectrophotometer in KBr or CsI pellets. The $^1$H NMR spectra were registered at 300 MHz on a Varian Mercury spectrometer. The MS data were obtained on a LKB 2091 mass spectrometer (70 eV ionisation energy). The FAB mass spectra were recorded with a Finnigan Matt 95 mass spectrometer (NBA, $Cs^+$ gun operating at 13 keV). For the new compounds satisfactory elemental analyses (±0.3% of the calculated values) were obtained using a Perkin–Elmer PE 2400 CHNS analyser. Methyl 2-methyl-4-oxo-4*H*-chromene-3-carboxylate (**1**)[56] and 3-acetyl-4-hydroxychromen-2-one (**2**)[57,58] were prepared as described in the literature.

**4-(2-Hydroxybenzoyl)-2-pyridin-2-yl-1*H*-pyrazol-3-ol ($HL^1$):** 2-Hydrazinopyridine (0.13 g, 1.15 mmol) in methanol (5 mL) was added to a solution of **2** (0.24 g, 1.15 mmol) in methanol (15 mL) and the mixture was refluxed for 1 h. The solid crude product formed was filtered off, dried in air and recrystallised from ethanol as a white solid. Yield 0.21 g (62%); m.p. 197–198 °C, $R_f$ = 0.78 (methanol/chloroform, v/v 1:1). IR (KBr): $\tilde{\nu}$ = 3428 (OH), 1735 (C=O), 1630, 1589 (C=N), 1458 (C=C) cm$^{-1}$. $^1$H NMR (300 MHz, $CDCl_3$, 25 °C): $\delta$ = 2.47 (s, 3 H, $CH_3$), 6.88 (t, $J$ = 6.15 Hz, 1 H), 6.99 (d, $J$ = 2 Hz, 1 H), 7.22–7.26 (m, 2 H), 7.46–7.49 (m, 1 H), 7.86 (t, $J$ = 6.35 Hz, 1 H), 7.96 (d, $J$ = 3.4 Hz, 1 H), 8.26 (dt, 1 H, Ar) ppm (see Figure S1a, Supporting Information). $^{13}$C NMR (75.4 MHz, $[D_6]$DMSO, 25 °C): $\delta$ = 14.45, 103.18, 112.22, 116.25, 117.89, 119.79, 123.23, 131.33, 133.17, 141.71, 143.67 153.66, 158.77, 160.91, 190.92 ppm (Figure S1b). EI-MS: *m*/*z* (%) = 295 (51) [M$^+$],

 © 2007 Wiley-VCH Verlag GmbH & Co. KGaA, Weinheim 

175 (100%), 79 (7%). $C_{16}H_{13}N_3O_3 \cdot 1/3H_2O$ (301.29): calcd. C 63.78, H 4.57, N 13.94; found C 63.93, H 4.33, N 13.60.

**Pt Complex 3a:** A solution of $K_2PtCl_4$ (0.04 g, 0.10 mmol) in water (5 mL) was added dropwise to a solution of HL[1] (0.03 g, 0.10 mmol) in methanol (5 mL). The reaction mixture was stirred at room temperature for 48 h. The solvent was removed under reduced pressure at room temperature to half of the initial volume. After 3 h the precipitated yellow solid was filtered off, washed with methanol/water, 1:1 and dried under reduced pressure over $CaCl_2$. Yield 38.2 mg (68%); m.p. 315–317 °C. IR spectrum in CsI, selected bands: $\tilde{\nu}$ = 3428 *ν*(OH); 1631 (C=O), 1593 (C=N), 1460 (C=C), 420 (Pt–N), 384 (Pt–Cl) $cm^{-1}$. $^1H$ NMR (300 MHz, [$D_6$]-DMSO, 25 °C): $\delta$ = 2.71 (s, 3 H, $CH_3$), 6.79–6.86 (m, 2 H), 7.22 (t, 1 H), 7.34 (t, 1 H), 7.82 (d, 1 H), 8.02 (t, 1 H), 8.42 (d, 1 H), 8.78 (d, 1 H) ppm. FAB-MS: *m*/*z* (%) = 563. $C_{16}H_{13}Cl_2N_3O_3Pt$ (561.26): calcd. C 34.24, H 2.33, N 7.48; found C 34.43, H 2.16, N 7.46.

**Pt Complex 3b:** A solution of $K_2[PtCl_4]$ (0.04 g, 0.10 mmol) in DMF (10 mL) was added dropwise to a solution of HL[1] (0.03 g, 0.10 mmol) in DMF (10 mL). The mixture was stirred at room temperature for 24 h. The KCl formed was removed by filtration and the diethyl ether was allowed to diffuse into a DMF solution of the complex. After two weeks the yellow solid was filtered off, washed with diethyl ether and dried in air. The single crystals suitable for X-ray analyses were obtained directly from the synthesis. Yield 27.28 mg (45%); m.p. 251–253 °C. $C_{18}H_{20}Cl_2N_4O_3Pt$ (606.34): calcd. C 35.65, H 3.32, N 9.24; found C 35.72, H 3.41, N 9.23.

**Pd Complex 4a:** A solution of $K_2[PdCl_4]$ (0.09 g, 0.27 mmol) in water (3 mL) was added dropwise to a stirred solution of HL[1] (0.08 g, 0.27 mmol) in methanol (15 mL). A yellow solid formed immediately; the suspension was stirred for a further 30 min, then the solid was filtered off, washed with cold water, cold methanol and diethyl ether, and dried in air. Yield 93.15 mg (73%); m.p. 284–285 °C. IR spectrum in CsI, selected bands: $\tilde{\nu}$ = 3457 (OH); 1654 (C=O), 1593 (C=N), 1475(C=C), 420 (Pd–N), 338 (Pd–Cl) $cm^{-1}$. $^1H$ NMR (300 MHz, [$D_6$]DMSO, 25 °C): $\delta$ = 2.41 (s, 3 H, $CH_3$), 6.77–6.87 (m, 2 H), 7.20 (t, 1 H), 7.34 (t, 1 H), 7.81 (d, 1 H), 8.02 (t, 1 H), 8.42 (d, 1 H), 8.73 (d, 1 H) ppm (Figure S1c). FAB-MS: *m*/*z* (%) 473. $C_{16}H_{13}Cl_2N_3O_3Pd \cdot H_2O$ (490.626): calcd. C 39.16, H 3.08, N 8.56; found C 38.96, H 3.11, N 8.63.

**Pd Complex 4b:** A solution of $K_2[PdCl_4]$ (0.03 g, 0.10 mmol) in DMF (10 mL) was added dropwise to a solution of HL[1] (0.03 g, 0.10 mmol) in DMF (10 mL). The mixture was stirred at room temperature for 48 h. The KCl formed was removed by filtration and the diethyl ether was allowed to diffuse into a DMF solution of the complex. After two weeks the yellow solid was filtered off, washed with diethyl ether and dried in air. Yield 27.3 mg (45%); m.p. 253–254 °C. $C_{18}H_{20}Cl_2N_4O_3Pd$ (606.34) calcd. C 35.65, H 3.32, N 9.24; found C 35.72, H 3.41, N 9.23.

**Pd Complex 4c:** A suspension of $[Pd(C_6H_5CN)_2Cl_2]$ (0.10 g, 0.25 mmol) in chloroform (5 mL) was added to a stirred solution of HL[1] (0.074 g, 0.25 mmol) in methanol/chloroform (1:1) (5 mL). The product precipitated immediately from the reaction mixture. Stirring was continued for 30 min and the complex was filtered off, washed with cold water, cold methanol and diethyl ether, and dried in air. Recrystallisation from acetonitrile/diethyl ether (1:1) afforded a red crystalline product **4c**. Yield 53.7 mg (45%); m.p. 276.4–278.0 °C. FAB-MS: *m*/*z* (%) 478. $C_{18}H_{15}ClN_4O_3Pd$ (477.198): calcd. C 45.30, H 3.17, N 11.74; found C 45.35, H 2.98, N 11.83.

**Potentiometric Measurements:** The protonation constants of HL[1] were determined by pH-metric titrations of five identical 10-mL samples at (25.0 ± 0.1) °C. The total ligand concentration in each sample was 2.859 mmol $dm^{-3}$. The samples contained also 3 mmol $dm^{-3}$ $HClO_4$ and 0.05 mol $dm^{-3}$ $NaClO_4$. Owing to very low solubility in pure water, a mixed 70% (v/v) ethanol/water solvent was used. The titrations were carried out with carbonate-free KOH solutions of known concentration (1 mol $dm^{-3}$) using an autoburette. The drop volume during these titrations was 1 μL. The experimental value of $pK_w$ = 15.50 ± 0.03 was obtained from our acid–base calibration in the mixed solvent. The pH was measured with a combined glass electrode ESAgP-301 WM (Eurosensor) connected to computer-aided universal electrochemical meter EMU0,[59] produced by the Technical University of Wrocław, Poland. The same equipment was also used to control the autoburette, as well as for the data acquisition and their introductory treatment. The electrode was calibrated by titration of 0.01 M HCl (in 70% ethanol) with 1 M KOH at (25 ± 0.1) °C. Stepwise protonation constants were calculated with our own program based on algorithm PKAS.[60,61]

**X-ray Crystallographic Data:** X-ray diffraction data for yellow and red single crystals of **3b** and **4c**, respectively, were collected at 193 K on a STOE IPDS diffractometer and at 120 K on a Nonius Kappa CCD diffractometer. The unit cell parameters were determined from all reflection data in $\theta$ ranges 2.26–28.08° and 2.71–24.73°. 11713 and 11440 intensities were collected using graphite-monochromated Mo-$K_\alpha$ radiation. 4316 and 11440 independent reflections were measured in the ranges $-9 \le h \le 9$, $-13 \le k \le 13$, $-18 \le l \le 18$, and $-51 \le h \le 51$, $-8 \le k \le 8$, $-24 \le l \le 24$, respectively for **3b** and **4c**. In the data-reduction step, intensities were corrected for Lorentz and polarisation effect[62] for **3b** and using Denzo-SMN software[63] for **4c**. The structure was solved by direct methods using the SHELXS86[64] program and refined by full-matrix least-squares calculation on $F^2$ using SHELXL97.[65] Non-hydrogen atoms were refined with anisotropic displacement parameters. The H atoms were placed in calculated positions and allowed to ride. The molecular geometry was calculated by PLATON.[66] The drawings were made by PLATON and are presented in Figure 1. The crystal data and details of data collection for both compounds are given in Table 4.

CCDC-622068 (for **3b**) and -622067 (for **4c**) contain the supplementary crystallographic data for this paper. These data can be obtained free of charge from The Cambridge Crystallographic Data Centre via www.ccdc.cam.ac.uk/data_request/cif.

**Biological Measurements**

**Determination of Alkylating Properties:** The test compound (0.005 mmol) was dissolved in 2-methoxyethanol (1 mL) and a solution of 4-(4-nitrobenzyl)pyridine (NBP) in 2-methoxyethanol (5% solution, 1 mL) was added. The sample was heated at (100 ± 0.5) °C for 1 h and then quickly cooled to 20 °C. 2-Methoxyethanol (2.5 mL) and piperidine (0.5 mL) were added to the sample to give a total volume of 5 mL. The final concentration of the test compound was $1 \times 10^{-3}$ M. After 90 s the absorbance was measured at $\lambda_{560}$ nm in a glass cell (1 cm). 2-Methoxyethanol was used as a reference solvent.

**Cell and Cytotoxicity Assay:** The cytotoxicity was determined in the human leukaemia promyelocytic HL-60 and lymphoblastic NALM-6 cell lines. Cells were cultured in RPMI 1640 medium supplemented with 10% foetal calf serum and antibiotics (penicillin (100 U/mL) and streptomycin (100 μg/mL) in 5% $CO_2$/95% air. Exponentially growing cells were seeded at $3 \times 10^5$ per well of a 24-well plate (Nunc), and cells were then exposed to the compounds for 48 h. Stock solutions were prepared freshly in DMSO, then dilutions from $10^{-3}$ to $10^{-7}$ M in complete culture medium were

 © 2007 Wiley-VCH Verlag GmbH & Co. KGaA, Weinheim 

Table 4. Crystal data and details of data collection for **3b** and **4c**.

| | $C_{16}H_{12}Cl_2N_3O_3Pt{\cdot}C_2H_6NH_2$ (**3b**) | $C_{18}H_{15}ClN_4PdO_3$ (**4c**) |
|---|---|---|
| Formula mass | 606.37 | 477.19 |
| Space group | $P\bar{1}$ | $Pca2_1$ |
| $a$ [Å] | 7.633(2) | 44.112(9) |
| $b$ [Å] | 10.431(2) | 7.519(2) |
| $c$ [Å] | 13.763(2) | 21.226(4) |
| $\alpha$ | 105.90(2) | |
| $\beta$ | 93.17(2) | |
| $\gamma$ | 110.98(2) | |
| $V$ [Å$^3$] | 969.6(2) | 7040(3) |
| $Z$ | 2 | 16 |
| $\lambda$ [Å] | 0.71073 | 0.71073 |
| $\rho_{calcd.}$ [g cm$^{-3}$] | 2.077 | 1.801 |
| Crystal size [mm$^3$] | $0.50 \times 0.25 \times 0.06$ | $0.10 \times 0.08 \times 0.04$ |
| $\mu$ [cm$^{-1}$] | 7.539 | 12.34 |
| $R_1$[a] | 0.0391 | 0.0699 |
| $wR_2$[b] | 0.0808 | 0.1667 |
| Gof[c] | 0.981 | 1.128 |

[a] $R_1 = \Sigma||F_o| - |F_c||/\Sigma|F_o|$. [b] $wR_2 = \{\Sigma[w(F_o^2 - F_c^2)^2]/\Sigma[w(F_o^2)^2]\}^{1/2}$. [c] Gof $= \{\Sigma[w(F_o^2 - F_c^2)^2]/(n - p)\}^{1/2}$, where $n$ is the number of reflections and $p$ is the total number of parameters refined.

made. The number of viable cells was counted in a Bürker haemocytometer using trypan-blue exclusion assay.[67] The values of $IC_{50}$ (the concentration of test compounds required to reduce the cell survival fraction to 50% of the control) were calculated from concentration–response curves (as illustrated in Figure 2) and used as a measure of cellular sensitivity to a given treatment. All data were expressed as means ± SD.

**Supporting Information** (see also the footnote on the first page of this article): IR data (Table S1), $^1$H NMR, $^{13}$C NMR spectra (Figure S1, a–c), crystallographic data (Tables S2 and S3, and Figure S2).

## Acknowledgments

Financial support from the Medical University of Łódź (grant nos. 502-13-629 and 503-3066-2 to E. B. and 503-315-2 to the Department of Pharmaceutical Biochemistry) is gratefully acknowledged. The authors thank Professor Werner Massa and his group for providing the instrument for data collection at the Philipps University.

[1] J. Reedijk, *Curr. Opin. Chem. Biol.* **1999**, *3*, 236–240.
[2] M. A. Jakupec, M. Galanski, B. K. Keppler, *Rev. Physiol. Biochem. Pharmacol.* **2003**, *146*, 1–53.
[3] E. R. Jamieson, S. J. Lippard, *Chem. Rev.* **1999**, *99*, 2467–2498, and references cited therein.
[4] P. Garnuszek, J. Licinska, J. S. Skierski, M. Koronkiewicz, M. Mirowski, R. Wiercioch, A. P. Mazurek, *Nucl. Med. Biol.* **2002**, *29*, 169–175.
[5] J. Zhang, X. Zhao, *Eur. J. Med. Chem.* **2006**, *42*, 286–291.
[6] E. Wong, M. Giandomenico, *Chem. Rev.* **1999**, *99*, 2451–2466.
[7] J. Reedijk, *Proc. Natl. Acad. Sci. U. S. A.* **2003**, *100*, 3611–3616.
[8] K. M. Williams, C. Rowan, J. Mitchell, *Inorg. Chem.* **2004**, *43*, 1190–1196.
[9] M. Curic, L. J. Tusek-Bozic, D. Vikic-Topic, V. Scarcia, A. Furlani, J. Balzarini, E. De Clercq, *J. Inorg. Biochem.* **1996**, *63*, 129–142.
[10] S. Kirschner, Y. K. Wei, D. Francis, J. S. Bergman, *Med. Chem.* **1966**, *9*, 369–372.
[11] A. A. Grinberg, J. S. Warschavski, M. J. Gelfman, N. W. Kisseleva, D. B. Smolenskaya, *Zh. Neorg. Khim.* **1968**, *13*, 803–813.
[12] J. D. Higgins, L. Neely, S. Fricker, *J. Inorg. Biochem.* **1993**, *49*, 149–156.
[13] T. A. Al-Allaf, L. J. Rashan, *Boll. Chim. Farm.* **2001**, *140*, 205–210.
[14] T. A. Al-Allaf, M. T. Ayoub, L. J. Rashan, *J. Inorg. Biochem.* **1990**, *38*, 47–56.
[15] T. A. Al-Allaf, L. J. Rashan, *Eur. J. Med. Chem.* **1998**, *33*, 817–820.
[16] T. A. Al-Allaf, L. J. Rashan, R. F. Khuzaie, W. F. Halseh, *Asian J. Chem.* **1997**, *9*, 239–246.
[17] T. A. Al-Allaf, L. J. Rashan, A. S. Abu-Surrah, R. Fawzi, M. Steimann, *Transition Met. Chem.* **1998**, *23*, 403–406.
[18] E. Budzisz, M. Malecka, I.-P. Lorenz, P. Mayer, R. Kwiecień, P. Paneth, U. Krajewska, M. Rozalski, *Inorg. Chem.* **2006**, *45*, 9688–9695.
[19] M. Gabor (Ed.), *The Pharmacology of Benzopyrone Derivatives and Related Compounds*, Akademiai Kiado, Budapest, **1988**, pp. 91–126.
[20] K. Kostka, E. Zyner, *Chem. Anal. (Warsaw)* **1979**, *24*, 103–108.
[21] K. Kostka, E. Zyner, *Chem. Anal. (Warsaw)* **1980**, *25*, 61–68.
[22] E. Budzisz, U. Krajewska, M. Rozalski, A. Szulawska, M. Czyz, B. Nawrot, *Eur. J. Pharmacol.* **2004**, *502*, 59–65.
[23] B. S. Holla, P. M. Akbarali, M. K. Shivanada, *Farmaco* **2000**, *55*, 256–263.
[24] E. Plaska, M. Aytemir, T. Uzbay, D. Erol, *Eur. J. Med. Chem.* **2001**, *36*, 539–543.
[25] N. Gokham, A. Yesilada, G. Ucar, K. Erol, A. A. Bilin, *Arch. Pharm. Med. Chem.* **2003**, *336*, 362–371.
[26] K. Sakai, Y. Tomista, T. Ue, K. Goshima, M. Ohminato, T. Tsubomura, K. Matsumoto, K. Chmura, K. Kawakami, *Inorg. Chim. Acta* **2000**, *297*, 64–71.
[27] N. J. Wheate, C. Cullinane, L. K. Webster, J. G. Collins, *Anticancer Drug Des.* **2001**, *16*, 91–98.
[28] M. Gabor (Ed.), *The Pharmacology of Benzopyrone Derivatives and Related Compounds*, Akademiai Kiado, Budapest **1988**, pp. 179–223.
[29] G. Baker, G. Ellis, *J. Med. Chem.* **1973**, *6*, 87–89.
[30] A. M. El-Nagger, A. M. Abdel-El-Salam, F. S. M. Ahmed, M. S. A. Latif, *Pol. J. Chem.* **1981**, *55*, 793–798.
[31] K. A. Ohemeng, C. F. Schwender, K. P. Fu, J. F. Barrett, *Bioorg. Med. Chem. Lett.* **1993**, *3*, 225–230.
[32] G. K. Patnaik, K. K. Banaudha, K. A. Khan, A. Shoeb, B. N. Dhawan, *Planta Med.* **1987**, *53*, 517–520.
[33] X. Shao, D. H. L. Ekstrand, R. Bhikhabhai, C. F. R. Kallander, J. S. Gronowitz, *Antiviral Chem. Chemother.* **1997**, *38*, 149–159.

 © 2007 Wiley-VCH Verlag GmbH & Co. KGaA, Weinheim 

[34] E. Middleton, C. Kandaswami, "The Impact of Plant Flavonoids on Mammalian Biology: Implications for Immunity, Inflammation and Cancer", in *The Flavonoids: Advances in Research since 1986* (Ed.: J. B. Harborne), Chapman Hall, London, **1994**, pp. 619–652.
[35] D. Jiang, R. Deng, J. Wu, *Wuji Huaxue* **1989**, *5*, 21–28.
[36] R. Deng, J. Wu, L. Long, *Bull. Soc. Chim. Belg.* **1992**, *101*, 439–443.
[37] I. Kostova, I. Manolov, S. Konstantinov, M. Karaivanova, *Eur. J. Med. Chem.* **1999**, *34*, 63–68.
[38] I. Manolov, I. Kostova, T. Netzeva, S. Konstantinov, M. Karaivanova, *Arch. Pharm. Pharm. Med. Chem.* **2000**, *333*, 93–98.
[39] I. Kostova, I. Malonov, M. Karaivanova, *Arch. Pharm. Pharm. Med. Chem.* **2001**, *334*, 157–162.
[40] V. D. Karaivanova, I. Malonov, M. L. Minassyan, N. D. Danchev, S. M. Samurova, *Pharmazie* **1994**, *49*, 856–857.
[41] K. B. Gudasi, R. V. Shenoy, R. S. Vavadi, M. S. Patil, S. A. Patil, *Chem. Pharm. Bull. (Tokyo)* **2005**, *53*, 1077–1082.
[42] I. Kostova, G. Momekov, M. Zaharieva, M. Karaivanova, *Eur. J. Med. Chem.* **2005**, *40*, 542–551.
[43] I. Manolov, S. Raleva, P. Genova, A. Savov, L. Froloshka, D. Dundarova, R. Argirova, *Bioorg. Chem. Applications* **2006**, 1–7.
[44] J. Kasparkova, V. Marini, Y. Najareh, D. Gibson, V. Brabec, *Biochemistry* **2003**, *42*, 6321–6332.
[45] I. Kostova, *Anti-Cancer Agents-Med. Chem.* **2006**, *6*, 19–32.
[46] F. Marchetti, C. Pettinari, R. Pettinari, *Coord. Chem. Rev.* **2005**, *249*, 2909–2945.
[47] Y. Wan, M. Alterman, M. Larhed, A. Hallberg, *J. Org. Chem.* **2002**, *67*, 6232–6235.
[48] G. Zon, *Prog. Med. Chem.* **1982**, *19*, 205–246.
[49] H. Lindemann, E. Harbers, *Arzneim.-Forsch.* **1980**, *30*, 2075–2080.
[50] A. Lacko, P. Hudziec, G. Mazur, *Nowotwory* **2000**, *50*, 609–614.
[51] S. Rajski, R. M. Williams, *Chem. Rev.* **1998**, *98*, 2723–2795.
[52] R. J. Knox, F. Friedlos, F. D. A. Lydall, *Cancer Res.* **1986**, *46*, 1972–1979.
[53] R. Preussmann, H. Schneider, F. Epple, *Arzneim.-Forsch.* **1969**, *19*, 1059–1073.
[54] E. Zyner, J. Graczyk, J. Ochocki, *Pharmazie* **1999**, *54*, 945–946.
[55] J. T. Wrobel, *Preparatyka i elementy syntezy organicznej*, PWN, Warszawa, **1983**, pp. 9–52.
[56] G. M. Coppola, R. W. Dodsworth, *Synthesis* **1981**, *7*, 523–524.
[57] S. Klutchko, J. Shavel, M. von Strandtmann, *J. Org. Chem.* **1974**, *39*, 2436–2437.
[58] P. Babin, J. Dunogues, M. Petraud, *Tetrahedron* **1981**, *37*, 1131–1139.
[59] R. Radomski, M. Radomska, M. Dankowski, K. Szajowska, Z. Wisialski, *Comput. Chem.* **1995**, *19*, 303–323.
[60] R. J. Moteksjtis, A. E. Martell, *Can. J. Chem.* **1982**, *60*, 168–173.
[61] A. Izquierdo, J. L. Beltram, *Anal. Chim. Acta* **1986**, *181*, 87–96.
[62] Stoe, Cie, *Software for IPDS-II*, Darmstadt, Germany, **2000**.
[63] Z. Otwinowski, W. Minor, "Processing of X-ray Diffraction Data Collected in Oscillation Mode", in *Methods in Enzymology*, vol. 276: *Macromolecular Crystallography* (Eds.: C. W. Carter Jr, R. M. Sweet, Academic Press, New York, **1997**, part A, p. 307.
[64] G. M. Sheldrick, *SHELXS86 Program for Crystal Structure Solution*, University of Göttingen, Germany, **1986**.
[65] G. M. Sheldrick, *SHELX97 Programs for Crystal Structure Analysis*, University of Göttingen, Germany, **1997**.
[66] A. L. Spek, *PLATON – Molecular Geometry Program*, University of Utrecht, The Netherlands, **1998**.
[67] E. Budzisz, E. Brzezinska, U. Krajewska, M. Rozalski, *Eur. J. Med. Chem.* **2003**, *38*, 597–603.

Received: January 31, 2007
Published Online: June 21, 2007

 © 2007 Wiley-VCH Verlag GmbH & Co. KGaA, Weinheim 

DOI: 10.1002/ejic.200700304

# Cleavage of CO by Mo[N(R)Ar]$_3$ Complexes

Gemma Christian,[a] Robert Stranger,*[a] Brian F. Yates,[b] and Christopher C. Cummins[c]

**Keywords:** C–O activation / Molybdenum / Three-coordinate complexes / Density functional calculations / Bond cleavage

The reaction of $MoL_3$ [L = $NH_2$ and N(*t*Bu)Ar] with CO was explored using DFT in order to rationalize why CO cleavage is not observed experimentally for this system in contrast to the corresponding $N_2$ reaction which results in spontaneous cleavage of the N–N bond. The binding of CO to $MoL_3$ was found to be both kinetically and thermodynamically favored over the binding of $N_2$, with the formation of the encounter complex, $L_3Mo$–CO, calculated to be without barrier and exothermic. While the overall reaction to form the C–$MoL_3$ and O–$MoL_3$ products was calculated to be energetically favorable, both the encounter complex and intermediate dimer, $L_3Mo$–CO–$MoL_3$, were found to be lower in energy than the products, with the final C–O cleavage step calculated to be endothermic by 169 kJ mol$^{-1}$ and 163 kJ mol$^{-1}$ for L = $NH_2$ and N(*t*Bu)Ar, respectively. The unfavorable CO cleavage step can be attributed to the fact that Mo does not possess the optimum d-electron configuration to sufficiently stabilise the carbide and oxide products relative to the CO-bridged intermediate dimer.

(© Wiley-VCH Verlag GmbH & Co. KGaA, 69451 Weinheim, Germany, 2007)

## Introduction

One of the most significant discoveries in dinitrogen chemistry is the cleavage of $N_2$ by Mo[N(*t*Bu)Ar]$_3$ under mild conditions.[1,2] $N_2$ reacts with Mo[N(*t*Bu)Ar]$_3$ to form the intermediate dimer, [Ar(*t*Bu)N]$_3$Mo–$N_2$–Mo[N(*t*Bu)Ar]$_3$, with $N_2$ bridging the metal centers end-on, followed by N–N bond cleavage to form the nitride product N–Mo[N(*t*Bu)Ar]$_3$.[3–5] The reaction proceeds under mild conditions (1 atm of pressure and between –33 and 25 °C) compared with the extreme conditions of 200 atm and 500 °C required in the industrial Haber–Bosch process for nitrogen fixation. In addition to $N_2$ cleavage, Mo[N(*t*Bu)Ar]$_3$ is also known experimentally to cleave the stronger N–N bond in $N_2O$ to form the nitride, N–Mo[N(*t*Bu)Ar]$_3$, and nitrosyl, [Ar(*t*Bu)N]$_3$Mo–NO, products.[6,7]

Following the success of $N_2$ and $N_2O$ cleavage by Mo[N(R)Ar]$_3$ complexes under mild conditions, attention was turned to other small multiply bonded molecules such as CO and $CN^-$. Although CO and $CN^-$ are isoelectronic with $N_2$, and therefore in principle Mo[N(R)Ar]$_3$ complexes are able to provide the necessary number of electrons to reductively cleave these small molecules, to date neither C–O or C–N bond cleavage has been observed.[8–10] The carbide complex [C–Mo[N(*t*Bu)Ar]$_3$]$^-$ has been synthesized from the encounter complex, [Ar(*t*Bu)N]$_3$Mo–CO, the latter easily formed by the reaction of Mo[N(*t*Bu)Ar]$_3$ with CO.[8] However, despite the ready formation of the encounter complex, neither the intermediate dimer or C–O cleavage is observed and instead, the O atom in the [Ar(*t*Bu)N]$_3$Mo–CO complex is removed through conversion to the related methylidene complex, [HC–Mo[N(*t*Bu)Ar]$_3$], which is then deprotonated to form [C–Mo[N(*t*Bu)Ar]$_3$]$^-$.[8,9]

The resistance of CO to cleavage by Mo[N(R)Ar]$_3$ complexes may well be a consequence of the fact that the bond dissociation energy for CO is approximately 100 kJ mol$^{-1}$ greater than that for $N_2$. However, an alternative view is that the metals used to form the intermediate dimer, in this case only Mo, are not tuned to optimise the thermodynamics of the cleavage reaction. This aspect is particularly pertinent since a recent theoretical study[11] has shown that CO cleavage is predicted to be spontaneous under mild conditions when two different three-coordinate complexes Re[N(R)Ar]$_3$ and Ta[N(R)Ar]$_3$ are used. In this reaction, an intermediate dimer is formed with Re[N(R)Ar]$_3$ and Ta[N(R)Ar]$_3$ binding to the C and O atoms, respectively, and cleavage of CO proceeds without barrier.

The reaction steps of [Ar(*t*Bu)N]$_3$Mo with CO are shown in Scheme 1, assuming the cleavage of CO proceeds by a mechanism analogous to the $N_2$ cleavage reaction. The first step involves the binding of CO to form the encounter complex, [Ar(*t*Bu)N]$_3$Mo–CO, followed by binding of a second Mo[N(*t*Bu)Ar]$_3$ unit to form [Ar(*t*Bu)N]$_3$Mo–CO–Mo[N(*t*Bu)Ar]$_3$, and finally C–O bond cleavage to give the products C–Mo[N(*t*Bu)Ar]$_3$ and O–Mo[N(*t*Bu)Ar]$_3$.

[a] Department of Chemistry, Faculty of Science,
Australian National University, Canberra, ACT 0200, Australia
Fax: +61-2-6125-0760
E-mail: rob.stranger@anu.edu.au
[b] School of Chemistry, University of Tasmania,
Private Bag 75, Hobart, TAS 7001, Australia
[c] Department of Chemistry, Massachusetts Institute of Technology,
Cambridge, MA 02139, USA

Supporting information for this article is available on the WWW under http://www.eurjic.org or from the author.

 © 2007 Wiley-VCH Verlag GmbH & Co. KGaA, Weinheim 

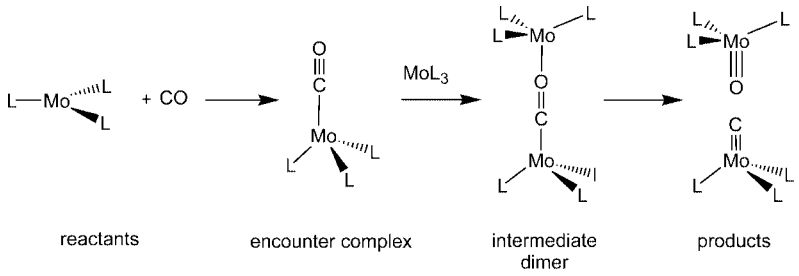


Scheme 1. The reaction of CO with $MoL_3$, L = $NH_2$ or N(*t*Bu)Ar.

In this study, the reaction mechanism shown in Scheme 1 is explored using density functional theory (DFT) for both the model, L = $NH_2$, and experimental, L = N(*t*Bu)Ar, systems in order to rationalise the experimental results. Earlier work on the analogous $N_2$ cleavage reaction by us and other groups[5,12–14] has shown that DFT methods give results in good agreement with experiment.

## Results and Discussion

### 1.1 Calculated Structures

For the model system (L = $NH_2$), calculations were carried out on the encounter complex, $[H_2N]_3Mo–CO$ and intermediate dimer, $[H_2N]_3Mo–CO–Mo[NH_2]_3$. The energies and structures of the remaining species, namely the reactant, $[H_2N]_3Mo$, and products, $[H_2N]_3Mo–C$ and $[H_2N]_3Mo–O$, have been reported in earlier studies.[13,15] In the case of the experimental system [L = N(*t*Bu)Ar], QM/MM calculations were carried out for the reactant, encounter complex, intermediate dimer and products. The optimized model and QM/MM structures are shown in Figure 1 and selected structural data from these calculations are shown in Table 1.

For the model system, the reaction of $[H_2N]_3Mo$ with CO gives rise to two possible encounter complexes, $[H_2N]_3Mo–CO$ [structure (c)] and $[H_2N]_3Mo–OC$. Both complexes have doublet ground states with approximately $C_s$ symmetry with one amide ligand rotated by 90° around the metal–ligand axis. The Mo–C–O angle of 177° indicates that the Mo–CO fragment is slightly distorted from linear geometry. Similar ligand rotation has been found for the analogous dinitrogen complex $[H_2N]_3Mo–N_2$.[13,16] The model and QM/MM structures of the CO encounter complex [structures (c) and (d)] have very similar core structures and bond lengths. Because the formation of the O-bound encounter complex was calculated to be endothermic, it is not considered further.

For the model system, the optimized $C_s$ structure of the intermediate dimer [structure (e)] has a bent Mo–C–O–Mo core with a C–O–Mo bond angle of 126° in the triplet spin state. In the QM/MM system [structure (f)], bending of the core is also observed but the larger size of the N(*t*Bu)Ar ligands restricts the C–O–Mo bond angle to 163°. Analogous to the $N_2$-bridged intermediate dimer,[13,16] ligand rotation around the metal–N(amide) axis is also observed for the CO-bridged intermediate dimer. However, while ligand rotation is observed at only one metal center for the model

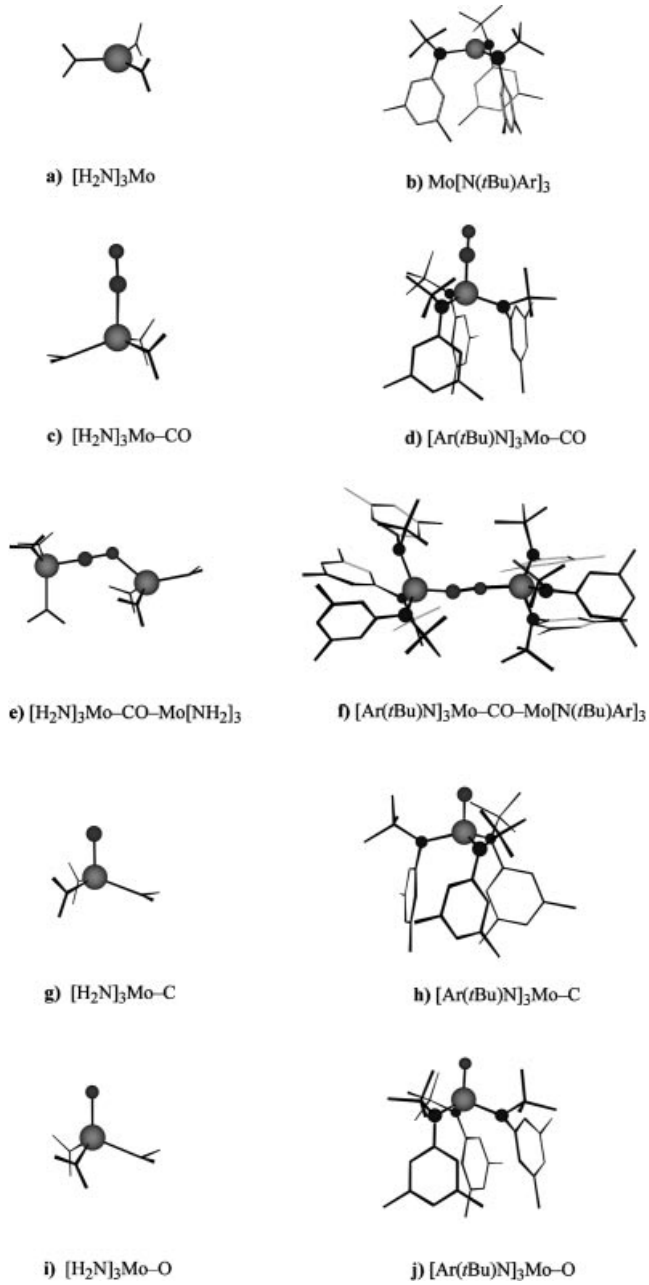


Figure 1. Optimized model and QM/MM structures.

 © 2007 Wiley-VCH Verlag GmbH & Co. KGaA, Weinheim 

Table 1. Selected geometric parameters for encounter complex, intermediate dimer and products.

| Complex | L | Spin | Bond lengths [Å] | | | Bond angles [°] | |
|---|---|---|---|---|---|---|---|
| | | | CO | Mo–C/Mo–O | Mo–$N_{amide}$ | C–Mo–N/O–Mo–N | Mo–C–O/Mo–O–C |
| $L_3Mo$ | $NH_2$ | 3/2 | | | 1.982 | | |
| | N(*t*Bu)Ar | | | | 2.004 | | |
| $L_3Mo$–CO | $NH_2$ | 1/2 | 1.184 | 1.921 | 1.969 | 103 | 177 |
| | N(*t*Bu)Ar | | 1.184 | 1.906 | 1.989 | 103 | 177 |
| $L_3Mo$–CO–$MoL_3$ | $NH_2$[a] | 0 | 1.294 | 1.774/1.960 | 1.960 | 101/115 | 178/134 |
| | N(*t*Bu)Ar | | 1.276 | 1.823/1.957 | 1.987 | 107/113 | 168/175 |
| | $NH_2$[a] | 1 | 1.278 | 1.789/2.048 | 1.974 | 100/104 | 178/126 |
| | N(*t*Bu)Ar | | 1.272 | 1.815/2.019 | 1.999 | 105/110 | 177/163 |
| $L_3Mo$–C | $NH_2$ | 1/2 | | 1.760 | 1.982 | 105 | |
| | N(*t*Bu)Ar | | | 1.737 | 1.994 | 105 | |
| $L_3Mo$–O | $NH_2$ | 1/2 | | 1.722 | 1.975 | 113 | |
| | N(*t*Bu)Ar | | | 1.717 | 1.996 | 111 | |

[a] Data has been included for the model intermediate dimer $[H_2N]_3Mo$–CO–$Mo[NH_2]_3$ even though the optimized structure is not a true minimum.

system, it occurs at both metal centers for the QM/MM system. This difference between the model and QM/MM structures is a consequence of the fact that rotation of the bulky N(tBu)Ar ligands has been shown to reduce steric crowding.[16]

The $[Ar(tBu)N]_3Mo$–C product [structure (h)] has approximately trigonal symmetry, unlike $[H_2N]_3Mo$–C, $[H_2N]_3$-Mo–O and $[Ar(tBu)N]_3Mo$–O [structures (g), (i) and (j)] which all show rotation of one or more of the amide ligands. However, the QM/MM structure for $[Ar(tBu)N]_3$-Mo–C with one ligand rotated lies only 11 kJ mol$^{-1}$ higher in energy. In general, the metal–amide distances are greater for L = N(*t*Bu)Ar than L = $NH_2$, consistent with the increased steric crowding for the former ligand. The C–O bond lengths of 1.278 and 1.276 Å in the lowest energy model and QM/MM intermediate dimer structures, respectively, indicate moderate activation compared to free CO (cf. 1.128 Å).

### 1.2 Overall Reaction Profile

The relative energies of species along the reaction pathway for the cleavage of CO by $MoL_3$ are summarized in Table 2 for both the model and QM/MM systems. The corresponding energies of species in the analogous $N_2$ cleavage reaction are also included for comparison. Overall, the CO cleavage reaction is exothermic for the model and experimental systems but the encounter complex and intermediate dimer are lower in energy than the products in both systems. Cleavage of the C–O bond to form $L_3Mo$–C and $L_3Mo$–O is highly unfavorable, and is calculated to be endothermic by 169 and 163 kJ mol$^{-1}$ for the model and experimental systems, respectively. In general, when L = N(*t*Bu)Ar, the reaction of $MoL_3$ with CO is less exothermic and the species along the reaction pathway are less stable relative to reactants than when L = $NH_2$. This is consistent with the results for the $N_2$ cleavage reaction where a similar decrease in exothermicity was found when L = N(*t*Bu)Ar due to increased steric crowding.

Table 2. Calculated energies of the encounter complex, dimer and products relative to reactants for the reaction of CO and $N_2$ with $MoL_3$ for L = $NH_2$ and N(*t*Bu)Ar.[13]

| Reaction | L | Encounter complex | Dimer | Product |
|---|---|---|---|---|
| CO | $NH_2$ | –152 | –248 | –79 |
| | N(*t*Bu)Ar | –142 | –222 | –59 |
| $N_2$ | $NH_2$ | –71 | –241 | –335 |
| | N(*t*Bu)Ar | –43 | –238 | –293 |

From the data in Table 2, the intermediate dimer is calculated to be the lowest energy species on the reaction pathway, and is 96 and 80 kJ mol$^{-1}$ lower in energy than the encounter complex for L = $NH_2$ and L = N(*t*Bu)Ar, respectively. However, under the reported experimental conditions, the intermediate dimer is not isolated, and instead the reaction is observed to cease with the formation of the encounter complex $[Ar(tBu)N]_3Mo$–CO.[8,9] Although formation of the dimer is entropically unfavorable, $\Delta S$ is calculated to be 218 J mol$^{-1}$·$T^{-1}$ which is not enough to offset $\Delta H$, even at room temperature.

### 1.3 Formation of the Encounter Complex and Intermediate Dimer

Because the calculations indicate that the intermediate dimer, $L_3Mo$–CO–$MoL_3$, should be thermodynamically stable, then it is pertinent to examine the kinetic barriers that may prevent its formation. Accordingly, the formation of both the $L_3Mo$–CO encounter complex and intermediate dimer, $L_3Mo$–CO–$MoL_3$, for L = $NH_2$ and N(*t*Bu)Ar, were investigated via linear transits, the results of which are shown in Figure 2.

The formation of the encounter complex, $L_3Mo$–CO, begins on the spin quartet surface but the spin doublet crosses below the quartet surface to become the minimum at an Mo–C distance of around 1.9 Å. There is no barrier to formation in either spin state for the model or QM/MM systems and the reaction is exothermic by 152 and 142 kJ mol$^{-1}$ for L = $NH_2$ and N(*t*Bu)Ar, respectively. To put these re-

 © 2007 Wiley-VCH Verlag GmbH & Co. KGaA, Weinheim 

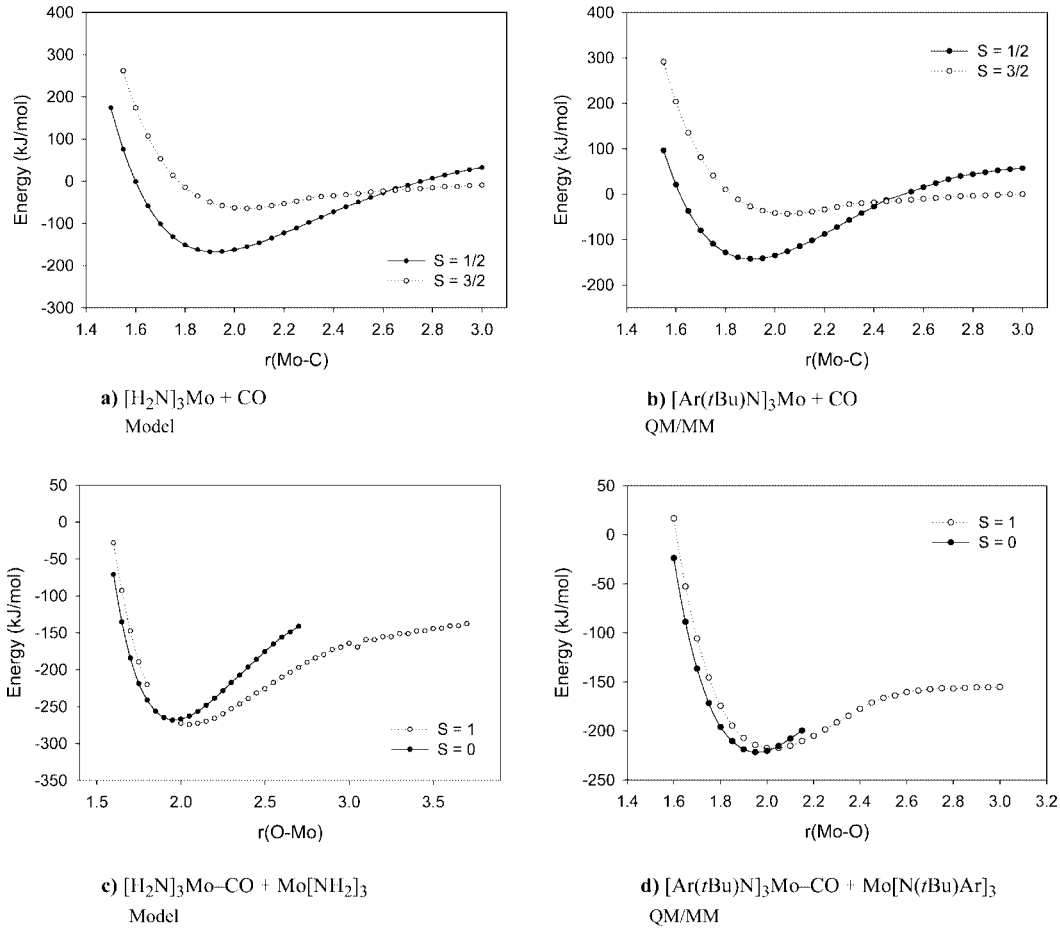


Figure 2. Linear transit results for the formation of (a) $[H_2N]_3Mo–CO$, (b) $[Ar(tBu)N]_3Mo–CO$, (c) $[H_2N]_3Mo–CO–Mo[NH_2]_3$ and (d) $[Ar(tBu)N]_3Mo–CO–Mo[N(tBu)Ar]_3$.

sults in context, the formation of the analogous $N_2$ encounter complex, $[Ar(tBu)N]_3Mo–N_2$, is exothermic by only 43 kJ mol$^{-1}$ and in addition, has a barrier of approximately 18 kJ mol$^{-1}$. The uptake of CO by $Mo[N(tBu)Ar]_3$ is therefore both kinetically and thermodynamically much more favorable than the uptake of $N_2$, consistent with experimental observations in that, while $[Ar(R)N]_3Mo–CO$ has been isolated, $[Ar(R)N]_3Mo–N_2$ has not been observed.[4,17]

Dimer formation for both $[H_2N]_3Mo–CO$ and $[Ar(tBu)N]_3Mo–CO$ through binding of a second $MoL_3$ complex end-on to O, occurs initially on the spin triplet surface. For L = N(*t*Bu)Ar, the spin singlet state crosses below the triplet when the Mo–O distance is approximately 2.0 Å with the minimum lying at approximately 1.9 Å. For the model system, the spin singlet surface also crosses the triplet around 1.9 Å, but lies higher in energy at the minimum distance of approximately 2.0 Å. As is apparent from Figure 2, there is no barrier to dimer formation for either the model or experimental system.

It is possible that the absence of dimer formation experimentally may be linked to the reaction conditions used. There are two differences in the reported reactions of $Mo[N(tBu)Ar]_3$ with $N_2$ and CO. Firstly, the solvent used in the CO reaction was tetrahydrofuran (THF) whereas non-polar solvents were used in the reaction with $N_2$. Secondly, CO, which is bound more easily than $N_2$, was in excess.

Solvent effects on the reaction energetics were investigated by performing calculations on the model system which allowed binding of THF directly to the reactant, $Mo[NH_2]_3$, encounter complex, $OC–Mo[NH_2]_3$, and the intermediate dimer, $[H_2N]_3Mo–CO–Mo[NH_2]_3$. In the case of the encounter complex, binding of THF to either the Mo or CO was explored. The results are summarized in Table 3.

Table 3. Calculated energies for the binding of THF to $Mo[NH_2]_3$, $[H_2N]_3Mo–CO$ and $[H_2N]_3Mo–CO–Mo[NH_2]_3$.

| | $\Delta E$ [kJ mol$^{-1}$] |
|---|---|
| $[H_2N]_3Mo–THF$ | –2 |
| $[H_2N]_3Mo–CO–THF$ | ca. 4 |
| THF–$[H_2N]_3Mo–CO$ (*trans*) | –37 |
| $[THF][H_2N]_3Mo–CO–Mo[NH_2]_3$ | –13 |
| $[H_2N]_3Mo–CO–Mo[NH_2]_3[THF]$ | –38 |
| $[THF][H_2N]_3Mo–CO–Mo[NH_2]_3[THF]$ | –59 |

Binding of THF to the reactant or directly to CO in the encounter complex is predicted to be weak, but binding of THF to Mo (*trans* to CO) in the encounter complex is exothermic by 37 kJ mol$^{-1}$. Binding of THF to the intermediate dimer is also favorable, particularly when THF is bound at both ends. Although binding of solvent molecules is ex-

 © 2007 Wiley-VCH Verlag GmbH & Co. KGaA, Weinheim 

pected to be weaker for the experimental system due to ligand crowding, based on these results, the intermediate dimer should be even more stable relative to reactants and encounter complex in the presence of THF. In addition to calculations involving the explicit binding of THF, the effect of the bulk properties of the solvent on the reaction pathway was also studied using the COSMO model. However, the relative energies changed by at most 10 kJ mol$^{-1}$ compared to the unsolvated calculations, and the formation of the dimer is still calculated to be exothermic.

Because the above calculations indicate that solvent effects do not favor formation of the encounter complex over the intermediate dimer, the other main difference in the reaction conditions, namely the presence of excess CO, must be significant. For the $N_2$ cleavage reaction, binding of $N_2$ to form the intermediate dimer is known to be slow experimentally,[4] and therefore there is an excess of Mo[N(*t*Bu)Ar]$_3$ available to react with the encounter complex to form the intermediate dimer. Binding of CO to form the encounter complex, [Ar(*t*Bu)N]$_3$Mo–CO, however, is fast and calculated to be more exothermic than the formation of the intermediate dimer. When CO is in excess, the rapid uptake of CO by Mo[N(*t*Bu)Ar]$_3$ will leave little remaining Mo[N(*t*Bu)Ar]$_3$ for dimer formation. However, under different reaction conditions, namely controlling the CO concentration so that it is never in excess, the formation of the [Ar(*t*Bu)N]$_3$Mo–CO–Mo[N(*t*Bu)Ar]$_3$ dimer may be possible.

## Conclusions

Calculations were carried out on the reaction of $MoL_3$ with CO for the model (L = $NH_2$) and experimental [L = N(*t*Bu)Ar] ligand systems. On the basis of these calculations, the formation of the encounter complex and intermediate dimer are predicted to be thermodynamically favorable and without barrier. Despite the overall cleavage reaction being exothermic, both the encounter complex and intermediate dimer are predicted to be more stable than the O–$MoL_3$ and C–$MoL_3$ products and therefore the final C–O cleavage step is unfavorable, being endothermic by 169 and 163 kJ mol$^{-1}$ for the model and experimental systems, respectively. The endothermic CO cleavage step can be rationalized on the basis of the electronic properties of the metal. An earlier study examining M–L bond energies in model [$NH_2$]$_3$M–L (L = N, C, O) complexes showed that the strongest M–O, M–N and M–C bonds occurred for $d^2$, $d^3$ and $d^4$ metal configurations, respectively.[15] Therefore, in the $L_3$Mo + CO system, $Mo^{III}$ does not possess the optimum d-electron configuration to sufficiently stabilise the carbide and oxide products relative to the intermediate dimer.

The intermediate dimer, $L_3$Mo–CO–$MoL_3$, is calculated to be the lowest energy species along the reaction pathway, and from both a thermodynamic and kinetic perspective, the calculations indicate that its formation is more favorable than the analogous $N_2$-bound dimer which is observed experimentally in the reaction of Mo[N(*t*Bu)Ar]$_3$ with dinitrogen. Thus, the absence of the CO-bridged intermediate dimer experimentally is attributed to the different reaction conditions employed compared to its $N_2$ counterpart, namely the use of a polar solvent and the presence of excess CO. Since calculations which investigated solvent effects were shown to favor formation of the CO-bridged intermediate dimer, it is concluded that this species is not observed experimentally due to the presence of excess CO and the ability of Mo[N(*t*Bu)Ar]$_3$ to rapidly bind CO. This conclusion is also consistent with the observation that, while [Ar(*t*Bu)]$_3$Mo–CO has been isolated, [Ar(*t*Bu)]$_3$Mo–$N_2$ has not been observed experimentally.

## Computational Section

The calculations carried out in this work were performed with the Amsterdam Density Functional (ADF)[18–20] program running on either Linux-based Pentium IV computers or the Australian National University Supercomputing Facility. All calculations used the local density approximation (LDA) to the exchange potential, the correlation potential of Vosko, Wilk and Nusair (VWN),[21] the Becke[22] and Perdew[23] corrections for non-local exchange and correlation, and the numerical integration scheme of te Velde and co-workers.[24] Geometry optimizations were performed using the gradient algorithm of Versluis and Ziegler.[25] All electron, triple-ζ Slater-type orbital basis sets (TZP) with polarization functions were used for all atoms. Relativistic effects were incorporated using the zero-order relativistic approximation (ZORA)[26–28] functionality in ADF. Frequency calculations were used to confirm that the optimized model structures of lowest energy were true minima and were computed by numerical differentiation of energy gradients in slightly displaced geometries.[29,30] Solvent-corrected calculations were carried out using the COSMO method[31] to accommodate the bulk effects of the tetrahydrofuran solvent used in the experimental work. For these calculations the solvent dielectric constant was set at 7.58 and the radius (rigid sphere) at 3.18 Å. All calculations were carried out in a spin-unrestricted manner. Optimized structures for the model system were corrected for zero-point vibrational energy. The convergence criteria for geometry optimizations were $10^{-3}$ Hartrees for energy and $10^{-2}$ Hartrees/Ångstrom for gradient. SCF convergence was set at $10^{-6}$. The integration parameter, accint, was set to 4.0 for geometry optimizations and to 6.0 for frequency calculations. For the experimental M[N(R)Ar]$_3$ system, the QM/MM[32] method implemented in ADF was used. For these calculations, the system under study was partitioned into two regions one of which was treated with DFT and the other with force field methods. The electronically important parts of the molecule were included in the QM region. Accordingly, $N_2$, CO, the N donors from the amide ligands, and Mo were treated with DFT while the *t*Bu and 3,5-$C_6H_3Me_2$ substituents were treated with molecular mechanics using the Sybyl[33] force field available in ADF. UFF van der Waals parameters[34] were used for Mo and all other parameters involving the metal atoms were set to zero. The bonds that cross the QM/MM partition, known as link bonds, were "capped" by H for the QM region. The ratio of the link bond to the length of the capping bond was kept constant throughout the calculations corresponding to the link bond parameters being fixed at values of $\alpha_{[N–C(R)]}$ = 1.489 and $\alpha_{[N–C(Ar)]}$ = 1.412. All QM/MM calculations on the experimental systems were undertaken in $C_1$ symmetry.

 © 2007 Wiley-VCH Verlag GmbH & Co. KGaA, Weinheim 

**Supporting Information** (see footnote on the first page of this article): Calculated structures and energies for $L_3Mo$, $L_3Mo$–CO, $L_3Mo$–CO–$MoL_3$, $L_3Mo$–C and $L_3Mo$–O for L = $NH_2$ and N(*t*Bu)Ar. Calculated structures and energies with THF bound to $L_3Mo$, $L_3Mo$–CO, $L_3Mo$–CO–$MoL_3$, $L_3Mo$–C and $L_3Mo$–O for L = $NH_2$ are also included.

## Acknowledgments

The authors gratefully acknowledge the Australian Research Council for financial support in the form of an Australian Postgraduate Award for G. C. and a Discovery Project Grant for R. S. and B. F. Y. The National Science Foundation of the USA is acknowledged for funding support (CHE-0316823) to C. C. C. The Australian National University is also acknowledged for access to the APAC (Australian Partnership for Advanced Computing) supercomputing facilities.

[1] C. C. Cummins, *Chem. Commun.* **1998**, 1777–1786.
[2] S. Gambarotta, J. Scott, *Angew. Chem. Int. Ed.* **2004**, *43*, 5298–5308.
[3] C. E. Laplaza, C. C. Cummins, *Science* **1995**, *268*, 861–863.
[4] C. E. Laplaza, M. J. A. Johnson, J. C. Peters, A. L. Odom, E. Kim, C. C. Cummins, G. N. George, I. J. Pickering, *J. Am. Chem. Soc.* **1996**, *118*, 8623–8638.
[5] Q. Cui, D. G. Musaev, M. Svensson, S. Sieber, K. Morokuma, *J. Am. Chem. Soc.* **1995**, *117*, 12366–12367.
[6] C. E. Laplaza, A. L. Odom, W. M. Davis, C. C. Cummins, J. D. Protasiewicz, *J. Am. Chem. Soc.* **1995**, *117*, 4999–5000.
[7] J.-P. F. Cherry, A. R. Johnson, L. M. Baraldo, Y.-C. Tsai, C. C. Cummins, S. V. Kryatov, E. V. Rybak-Akimova, K. B. Capps, C. D. Hoff, C. M. Haar, S. P. Nolan, *J. Am. Chem. Soc.* **2001**, *123*, 7271–7286.
[8] J. C. Peters, A. L. Odom, C. C. Cummins, *Chem. Commun.* **1997**, 1995–1996.
[9] J. B. Greco, J. C. Peters, T. A. Baker, W. M. Davis, C. C. Cummins, G. Wu, *J. Am. Chem. Soc.* **2001**, *123*, 5003–5013.
[10] J. C. Peters, L. M. Baraldo, T. A. Baker, A. R. Johnson, C. C. Cummins, *J. Organomet. Chem.* **1999**, *591*, 24–35.
[11] G. Christian, R. Stranger, S. Petrie, B. F. Yates, C. C. Cummins, *Chem. Eur. J.* **2007**, *13*, 4264–4272.
[12] K. M. Neyman, V. A. Nasluzov, J. Hahn, C. R. Landis, N. Rösch, *Organometallics* **1997**, *16*, 995–1000.
[13] G. Christian, J. Driver, R. Stranger, *Faraday Discuss.* **2003**, *124*, 331–341.
[14] G. Christian, R. Stranger, *Dalton Trans.* **2004**, 2492–2495.
[15] G. Christian, R. Stranger, B. F. Yates, *Inorg. Chem.* **2006**, *45*, 6851–6859.
[16] G. Christian, R. Stranger, B. F. Yates, D. C. Graham, *Dalton Trans.* **2005**, 962–968.
[17] J. C. Peters, J. P. F. Cherry, J. C. Thomas, L. Baraldo, D. J. Mindiola, W. M. Davis, C. C. Cummins, *J. Am. Chem. Soc.* **1999**, *121*, 10053–10067.
[18] G. te Velde, F. M. Bickelhaupt, E. J. Baerends, C. Fonseca Guerra, S. J. A. Van Gisbergen, J. G. Snijders, T. Ziegler, *J. Comput. Chem.* **2001**, *22*, 931–967.
[19] C. Fonseca Guerra, J. G. Snijders, G. Te Velde, E. J. Baerends, *Theor. Chem. Acc.* **1998**, *99*, 391–403.
[20] "Theoretical Chemistry" in *Amsterdam Density Functional (ADF)*, vol. SCM, **2002**.
[21] S. H. Vosko, L. Wilk, M. Nusair, *Can. J. Phys.* **1980**, *58*, 1200–1211.
[22] A. D. Becke, *Phys. Rev. A* **1988**, *38*, 3098–3100.
[23] J. P. Perdew, *Phys. Rev. B* **1986**, *33*, 8822–8824.
[24] G. T. Velde, E. J. Baerends, *J. Comput. Phys.* **1992**, *99*, 84–98.
[25] L. Versluis, T. Ziegler, *J. Chem. Phys.* **1988**, *88*, 322–328.
[26] E. van Lenthe, E. J. Baerends, J. G. Snijders, *J. Chem. Phys.* **1993**, *99*, 4597–4610.
[27] E. van Lenthe, E. J. Baerends, J. G. Snijders, *J. Chem. Phys.* **1994**, *101*, 9783–9792.
[28] E. van Lenthe, A. Ehlers, E. J. Baerends, *J. Chem. Phys.* **1999**, *110*, 8943–8953.
[29] L. Y. Fan, T. Ziegler, *J. Phys. Chem.* **1992**, *96*, 6937–6941.
[30] L. Y. Fan, T. Ziegler, *J. Chem. Phys.* **1992**, *96*, 9005–9012.
[31] C. C. Pye, T. Ziegler, *Theor. Chem. Acc.* **1999**, *101*, 396–408.
[32] T. K. Woo, L. Cavallo, T. Ziegler, *Theor. Chem. Acc.* **1998**, *100*, 307–313.
[33] M. Clark, R. D. Cramer, N. Vanopdenbosch, *J. Comput. Chem.* **1989**, *10*, 982–1012.
[34] A. K. Rappe, C. J. Casewit, K. S. Colwell, W. A. Goddard, W. M. Skiff, *J. Am. Chem. Soc.* **1992**, *114*, 10024–10035.

Received: March 20, 2007
Published Online: June 19, 2007

 © 2007 Wiley-VCH Verlag GmbH & Co. KGaA, Weinheim 

DOI: 10.1002/ejic.200700096

# Methyllead(IV) Derivatives Stabilized by $DAPTSC^{2-}$: Synthesis and Structures of New Diorganolead(IV) Complexes

**José S. Casas,*[a] Eduardo E. Castellano,[b] Javier Ellena,[b] María S. García-Tasende,[a] Facundo Namor,[a] Agustín Sánchez,[a] José Sordo,[a] and María J. Vidarte[a]**

*Dedicated to Professor Joachim Strähle on the occasion of his 70th birthday*

**Keywords:** Lead / Diorganolead(IV) complexes / Metallation

The reaction of the bis(thiosemicarbazone) of dimethyl pyridine-2,6-diyl diketone, $H_2DAPTSC$, with $PbMe_2(OAc)_2$, $PbMePh(OAc)_2$ or $PbPh_2(OAc)_2$ in MeOH afforded the complexes $[PbMe_2(DAPTSC)]$, $[PbMePh(DAPTSC)]$ or $[PbPh_2(DAPTSC)]$ (in the first two cases together with $[Pb(DAPTSC)]$). X-ray crystallography of the Pb(IV) complexes showed that the metal has a pentagonal bipyramidal coordination sphere. The $N_3,S_2$-bound $DAPTSC^{2-}$ anion occupied the equatorial plane and the organic groups were in the apical positions. These compounds retain the same coordination mode in DMSO solution. $DAPTSC^{2-}$ is also $N_3,S_2$-bound in $[Pb(DAPTSC)]$, a complex with a stereochemically active $Pb^{II}$ lone pair. The reaction of $PbPh_2Cl_2$ with $H_2DAPTSC$, also in methanol at room temperature, afforded $[PbPh_2(H_2DAPTSC)]_2[PbPh_2Cl_4]Cl_2{\cdot}6CH_3OH$. X-ray crystallography of this centrosymmetric complex showed it to consist of two $[PbPh_2(H_2DAPTSC)]^{2+}$ cations of similar structure to the neutral $[PbR_2(DAPTSC)]$ complexes, together with a *trans*-octahedral $[PbPh_2Cl_4]^{2-}$ anion and two $Cl^-$ anions. This compound decomposes in DMSO solution, probably evolving to $H_2DAPTSC$ and $PbPh_2Cl_2(DMSO)_n$. In order to evaluate the changes undergone by $H_2DAPTSC$ under metallation, the X-ray structure of the free molecule was also determined.

(© Wiley-VCH Verlag GmbH & Co. KGaA, 69451 Weinheim, Germany, 2007)

## Introduction

Structural information on methyllead(IV) coordination compounds is rather scarce. Apart from a small number of compounds with lead–metal bonds or with relatively simple anions (tetramethyllead,[1] trimethyllead chloride,[2] trimethyllead iodide,[3] trimethyllead acetate,[4] trimethyllead 2-furate,[5] trimethyllead diphenylphosphinate[6] or trimethyllead methylthiolato[7]), the only such structure in the CSD[8] is that of the complex bis(tetraphenylimidodiphosphanato)dimethyllead(IV), which was obtained in the recrystallization of the corresponding trimethyllead compound.[6] This paucity of information is probably related to the intrinsic instability of methyllead(IV) compounds, which are more unstable than the corresponding phenyl derivatives.

According to the classic papers of Huber et al.,[9] the decomposition of dimethyllead(IV) compounds occurs through redistribution of the methyl groups as shown in Equation (1).

$$2\ PbMe_2X_2 \rightarrow PbMe_3X + PbMeX_3 \quad (1)$$

This is followed by a reduction-elimination step carried out by the monomethyl derivative, see Equation (2).

$$PbMeX_3 \rightarrow MeX + PbX_2 \quad (2)$$

This evolution seems to be stimulated by the presence of Lewis bases such as DMSO, possibly because these bases stabilize the decomposition products.

As the redistribution process probably involves short distance between the lead centres,[10] we speculated that the starting organolead compound might be more stable, the bulkier the ligand X. We have investigated this idea using the potentially pentadentate bis(thiosemicarbazone) ligand ($H_2DAPTSC$, Figure 1) as $X_2$. This Schiff base coordinates well, in both neutral and deprotonated forms, to a variety of metal and organometal ions.[11] Coordination usually occurs through N(3), N(4), N(5), S(1) and S(2), and results in the occupation of a significant part of the volume around the metal centre.

Herein we describe the synthesis and structures of new complexes obtained using this strategy, including the first methylphenyllead(IV) and only the second dimethyllead(IV) coordination compounds to have been studied by X-ray diffractometry.

[a] Departamento de Química Inorgánica, Facultad de Farmacia, Universidad de Santiago de Compostela, 15782 Santiago de Compostela, Spain
E-mail: qiscasas@usc.es
[b] Instituto de Física de São Carlos, Universidade de São Paulo, CEP 13560 São Carlos, Brazil

 © 2007 Wiley-VCH Verlag GmbH & Co. KGaA, Weinheim 

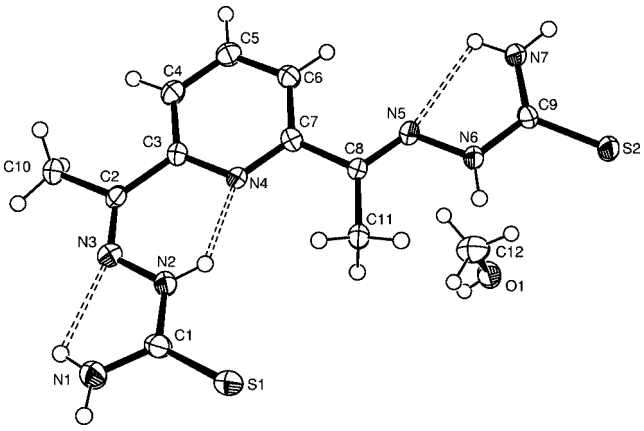


Figure 1. Molecular structure of $H_2$DAPTSC·MeOH. Ellipsoids are drawn at the 50% probability level.

## Results and Discussion

### Synthesis

$H_2$DAPTSC was combined in methanol with $PbMe_2(OAc)_2$, $PbMePh(OAc)_2$, $PbPh_2(OAc)_2$, $PbPh_3(OAc)$ and $PbPh_2Cl_2$. The reaction of the diacetates evolved as expected: the bis(thiosemicarbazone) replaced the acetate anions, the basicity of which favoured the observed deprotonation of the incoming ligand.

$$PbR_2(OAc)_2 + H_2DAPTSC \rightarrow [PbR_2(DAPTSC)] + 2\ HOAc$$

However, the additional isolation of [Pb(DAPTSC)] when the organometallic moiety had methyl groups showed that hindrance of the redistribution reaction, Equation (1), was not complete. $[PbPh_2(DAPTSC)]$ was also the product of the reaction between $H_2$DAPTSC and $PbPh_3(OAc)$, probably through a protodephenylation (acidic decomposition) reaction. Reaction of $H_2$DAPTSC with $PbPh_2Cl_2$ gave a product, the stoichiometry of which suggested that the bis(thiosemicarbazone) ligand was neutral and only replaced the chloride ligands of two-thirds of the $PbPh_2Cl_2$ molecules, the remaining third accepting half of the displaced $Cl^-$ anions, see Equation (3).

$$3\ PbPh_2Cl_2 + 2\ H_2DAPTSC \rightarrow 2\ [PbPh_2(H_2DAPTSC)]^{2+} + [PbPh_2Cl_4]^{2-} + 2\ Cl^- \quad (3)$$

This explains why unreacted $H_2$DAPTSC was recovered in spite of the reaction having being carried out in a 1:1 mol ratio. A somewhat related process has been observed[12] when $PbPh_2Cl_2$ was combined with certain monothiosemicarbazones (HTSCs), although in these cases only one chloride ligand was displaced from the coordination sphere of the metal, giving $[PbPh_2Cl(HTSC)]^+$.

### Solid-State Structures

Figure 1 shows the molecular structure of $H_2$DAPTSC·MeOH, which, unlike those of certain similar compounds (see paragraph below),[13] has not hitherto been determined by X-ray crystallography. Although the diffraction data were not of high quality, the conformations and relative orientations of the thiosemicarbazide chains are unquestionable, and this information is relevant to the analysis of the changes that occur upon deprotonation and coordination. The bond lengths and angles in these chains (Table 1) are unexceptional.[14] The chain bearing S(1) is roughly parallel to the line through C5 and N4 (named the "closed-arm" orientation in this article), and places the methyl group $C(10)H_3$ *trans* to N(4). By contrast, the chain bearing S(2) is roughly orthogonal to the line C5–N4 (the "open-arm" orientation), and places the methyl group $C(11)H_3$ *cis* to N(4). These orientations, together with the (*Z*) configuration about C(2)=N(3) in the closed arm, the (*E*) configuration about C(8)=N(5) in the open arm, and the mutually *trans* orientations of the N–N and C=S bonds in both chains, allow the stabilization of the molecule by three intramolecular hydrogen bonds (Figure 1 and Table 2). That the same structure has been observed in the dimethylthallium(III) complex $[TlMe_2(HDAPTSC)]$[15] suggests that it holds in methanol solutions of $H_2$DAPTSC as well as in the solid state.

Interestingly, the above structure differs from the structures of the three N1- or N2-substituted bis(thiosemicarbazones) derived from dimethyl pyridine-2,6-diyl diketone that were studied previously by X-ray diffractometry, namely the bis(3-hexamethyleneiminylthiosemicarbazone) ($H_2L^1$·$H_2O$),[13a] the bis(1-ethylthiosemicarbazone) ($H_2L^2$)[13b] and the bis(1-methylthiosemicarbazone) ($H_2L^3$),[13c] although these compounds differ compositionally only concerning the substituents at N(1) and N(7) ($H_2L^1$ and $H_2L^1$) or N(2) and N(5) ($H_2L^3$). Note that the lattices of $H_2L^2$ and $H_2L^3$ contain only the bis(thiosemicarbazone) molecules, whereas those of $H_2L^1$·$H_2O$ and $H_2$DAPTSC·MeOH also feature molecules of solvent. Although there is a thiosemicarbazide chain with open-arm orientation in all four molecules, the other arm is open in $H_2L^2$ and $H_2L^3$, closed in $H_2$DAPTSC·MeOH and "semi-closed" in $H_2L^1$·$H_2O$ (Scheme 1). Such variety is not unexpected given the flexibility of thiosemicarbazide chains, which readily adapt their conformations to minimize weak intra- and intermolecular forces. Together with the differences in composition and in the number and nature of intermolecular hydrogen bonds, it leads to these compounds

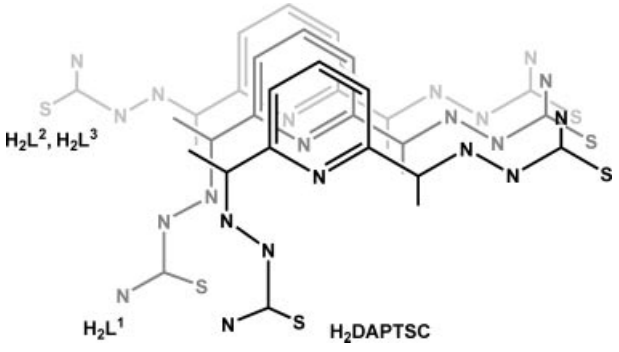


Scheme 1.

 © 2007 Wiley-VCH Verlag GmbH & Co. KGaA, Weinheim 

Table 1. Selected bond lengths [Å] and angles [°] in the ligand and complexes.

| Parameter | $H_2$DAPTSC·MeOH | [$PbMe_2$(DAPTSC)][a] | [PbPhMe(DAPTSC)]·0.45$H_2O$ |
|---|---|---|---|
| Pb–C | | 2.205(12) | 2.170(12) (Me) |
| | | 2.207(11) | 2.212(13) (Ph) |
| Pb–N(3) | | 2.533(6) | 2.540(9) |
| Pb–N(4) | | 2.509(9) | 2.473(10) |
| Pb–N(5) | | | 2.561(9) |
| Pb–S(1) | | 2.769(2) | 2.734(3) |
| Pb–S(2) | | | 2.736(3) |
| S(1)–C(1) | 1.674(4) | 1.725(7) | 1.763(13) |
| S(2)–C(9) | 1.694(4) | | 1.726(12) |
| N(1)–C(1) | 1.336(5) | 1.346(9) | 1.358(14) |
| N(2)–C(1) | 1.367(4) | 1.317(10) | 1.285(18) |
| N(3)–C(2) | 1.296(5) | 1.293(10) | 1.256(16) |
| N(3)–N(2) | 1.367(5) | 1.378(9) | 1.395(13) |
| N(4)–C(7) | 1.341(4) | | 1.351(13) |
| N(4)–C(3) | 1.353(5) | 1.351(8) | 1.367(14) |
| N(5)–C(8) | 1.288(4) | | 1.266(16) |
| N(5)–N(6) | 1.383(4) | | 1.403(13) |
| N(6)–C(9) | 1.361(4) | | 1.280(16) |
| C(2)–C(3) | 1.494(5) | 1.496(9) | 1.515(16) |
| C(7)–C(8) | 1.489(5) | | 1.378(14) |
| C–Pb–C | | 172.9(5) | 168.7(5) |
| S(1)–Pb–N(3) | | 69.58(15) | 70.0(3) |
| N(3)–Pb–N(4) | | 64.14(15) | 65.0(3) |
| N(4)–Pb–N(5) | | | 64.9(3) |
| N(5)–Pb–S(2) | | | 69.9(3) |
| S(1)–Pb–S(2) | | | 90.36(10) |
| | [$PbPh_2$(DAPTSC)]·MeOH | [$PbPh_2(H_2$DAPTSC)]$_2$[$PbPh_2Cl_4$]$Cl_2$·6$CH_3OH$[b] | [Pb(DAPTSC)][c] |
| Pb–C | 2.215(3) | 2.189(4), 2.191(4) (Pb1) | |
| | 2.218(4) | 2.201(4), 2.8023(10) (Pb2) | |
| Pb–N(3) | 2.530(3) | 2.546(3) | 2.612(18) |
| Pb–N(4) | 2.474(3) | 2.531(3) | 2.48(2) |
| Pb–N(5) | 2.543(3) | 2.580(3) | 2.67(2) |
| Pb–S(1) | 2.6598(9) | 2.7684(10) | 2.848(7) |
| Pb–S(2) | 2.6954(9) | 2.7973(11) | 2.825(8) |
| S(1)–C(1) | 1.733(4) | 1.703(4) | 1.73(4) |
| S(2)–C(9) | 1.737(4) | 1.699(4) | 1.76(3) |
| N(1)–C(1) | 1.351(4) | 1.307(6) | 1.31(3) |
| N(2)–C(1) | 1.337(5) | 1.361(5) | 1.36(5) |
| N(3)–C(2) | 1.296(4) | 1.281(5) | 1.32(4) |
| N(3)–N(2) | 1.386(4) | 1.368(5) | 1.40(3) |
| N(4)–C(7) | 1.351(4) | 1.347(5) | 1.38(3) |
| N(4)–C(3) | 1.349(4) | 1.347(5) | 1.39(3) |
| N(5)–C(8) | 1.303(5) | 1.297(6) | 1.31(3) |
| N(5)–N(6) | 1.387(4) | 1.373(5) | 1.38(3) |
| N(6)–C(9) | 1.326(5) | 1.364(6) | 1.25(4) |
| C(2)–C(3) | 1.493(5) | 1.485(6) | 1.43(3) |
| C(7)–C(8) | 1.483(5) | 1.489(6) | 1.51(4) |
| C–Pb–C | 169.57(12) | 174.67(15) | |
| S(1)–Pb–N(3) | 70.78(7) | 70.70(8) | 65.1(4) |
| N(3)–Pb–N(4) | 65.56(9) | 63.75(11) | 62.5(6) |
| N(4)–Pb–N(5) | 65.56(9) | 63.73(11) | 60.7(6) |
| N(5)–Pb–S(2) | 70.86(7) | 69.62(8) | 65.2(4) |
| S(1)–Pb–S(2) | 88.29(3) | 93.33(3) | 72.6(2) |

[a] S(1)–Pb–S(1)$^i$ 93.25(11) (i = $-x$, $y$, $z$). [b] Pb(2)–Cl(2) 2.7005(10); Pb(2)–Cl(1) 2.8023(10); C–Pb(2)–C$^i$ 180.0, Cl(1)–Pb(2)–Cl(1)$^i$ 180.0, Cl(2)–Pb(2)–Cl(2)$^i$ 180.0 (i = $-x$ + 2, $-y$, $-z$). [c] Pb–S(1)$^i$ = 3.312(8), Pb–S(2)$^i$ 3.385(8), (i = 1 + $x$, $y$, $z$).

having very different supramolecular structures: dimers in $H_2L^1$·$H_2O$ and $H_2L^3$, chains in $H_2L^2$ and two-dimensional sheets in $H_2$DAPTSC·MeOH.

The molecular structure of [$PbMe_2$(DAPTSC)] is shown, together with its numbering scheme, in Figure 2. The dideprotonated ligand coordinates to the dimethyllead(IV) unit through S1, S(1)$^i$, N(3), N(3)$^i$ and N(4) (i = $-x$, $y$, $z$). The two chains bind the lead atom symmetrically, and together with the nitrogen atom of the pyridine ring occupy the equatorial plane of a pentagonal bipyramidal coordination polyhedron in which the two methyl groups of the almost linear $PbMe_2^{2+}$ unit [C–Pb–C 172.9(5)°] are apical. The resulting [$PbC_2N_3S_2$] kernel has not hitherto been observed. The strongest Pb–N interaction is with the pyridine nitro-

 © 2007 Wiley-VCH Verlag GmbH & Co. KGaA, Weinheim 

Table 2. Intra- and intermolecular hydrogen bonds in the ligand and complexes [Å, °].

| | D–H | H···A | D···A | D–H···A |
|---|---|---|---|---|
| $H_2$DAPTSC·MeOHA[a] | | | | |
| N(1)–H(1A)···N(3) | 0.86 | 2.26 | 2.623(4) | 105.6 |
| N(1)–H(1B)···S(2)$^{i}$ | 0.86 | 2.53 | 3.385(3) | 172.8 |
| N(2)–H(2)···N(4) | 0.86 | 1.96 | 2.639(4) | 134.6 |
| N(6)–H(6A)···S(2)$^{ii}$ | 0.86 | 2.65 | 3.499(3) | 170.9 |
| N(7)–H(7A)···N(5) | 0.86 | 2.30 | 2.650(4) | 104.3 |
| N(7)–H(7A)···O(1)$^{iii}$ | 0.86 | 2.29 | 3.032(4) | 144.6 |
| N(7)–H(7B)···S(1)$^{iv}$ | 0.86 | 2.57 | 3.431(3) | 177.9 |
| O(1)–H(11)···S(1)$^{v}$ | 0.69(5) | 2.56(5) | 3.236(4) | 167(5) |
| [$PbMe_2$(DAPTSC)][b] | | | | |
| N(1)–H(1A)···S(1)$^{ii}$ | 0.8600 | 2.8374 | 3.5630(7) | 143.13 |
| N(1)–H(1B)···N(2)$^{iii}$ | 0.8600 | 2.1109 | 2.9546(9) | 166.76 |
| [PbPhMe(DAPTSC)]·0.45$H_2O$[c] | | | | |
| N(1)–H(1A)···N(6)$^{i}$ | 0.8800 | 2.1635 | 3.0368(13) | 171.63 |
| N(7)–H(7A)···N(2)$^{ii}$ | 0.8800 | 202461 | 3.1194(12) | 171.63 |
| [$PbPh_2$(DAPTSC)]·MeOH[d] | | | | |
| N(1)–H(1A)···O(1S) | 0.8800 | 2.2570 | 2.9220(4) | 132.23 |
| N(1)–H(1B)···N(6)$^{i}$ | 0.8800 | 2.2558 | 3.1229(4) | 168.46 |
| O(1S)–H(1S)···N(7) | 0.8400 | 2.3681 | 3.1760(4) | 161.51 |
| N(7)–H(7A)···O(1S)$^{ii}$ | 0.8800 | 2.1632 | 2.9283(4) | 145.06 |
| N(7)–H(7B)···N(2)$^{ii}$ | 0.8800 | 2.2244 | 3.0997(4) | 172.95 |
| [$PbPh_2$($H_2$DAPTSC)]$_2$[$PbPh_2Cl_4$]$Cl_2$·6$CH_3OH$[e] | | | | |
| N(1)–H(1A)···Cl(3)$^{ii}$ | 0.8800 | 2.4405 | 3.2540(4) | 153.92 |
| N(1)–H(1B)···O(31)$^{iii}$ | 0.8800 | 1.9695 | 2.8222(5) | 162.80 |
| N(2)–H(2)···Cl(3)$^{ii}$ | 0.8800 | 2.4104 | 3.2116(4) | 151.55 |
| N(6)–H(6)···Cl(1) | 0.8800 | 2.5243 | 3.3107(4) | 149.16 |
| N(7)–H(7A)···Cl(1) | 0.8800 | 2.4429 | 3.2686(4) | 156.45 |
| N(7)–H(7B)···Cl(3)$^{iv}$ | 0.8800 | 2.4029 | 3.2438(4) | 160.07 |
| O(31)–H(31)···Cl(3)$^{iii}$ | 0.8400 | 2.4629 | 3.2598(3) | 158.69 |
| O(41)–H(41)···O(51)$^{iii}$ | 0.8400 | 1.9029 | 2.7405(6) | 174.81 |
| O(51)–H(51)···Cl(3) | 0.8400 | 2.3474 | 3.1822(4) | 172.57 |
| [Pb(DAPTSC)][f] | | | | |
| N(1)–H(1A)···N(6)$^{ii}$ | 0.880 | 2.3178 | 3.0966(3) | 147.55 |
| N(7)–H(7A)···N(1)$^{iii}$ | 0.880 | 2.5993 | 3.1230(3) | 119.07 |
| N(7)–H(7B)···N(2)$^{iv}$ | 0.880 | 2.3379 | 3.1254(3) | 149.03 |

Symmetry operations: [a] i = $x-1$, $-y+0.5$, $z-0.5$; ii = $-x+2$, $-y+1$, $-z$; iii = $-x+2$, $-y+0.5$, $-z+0.5$; iv = $x+1$, $-y+0.5$, $z+0.5$; v = $x$, $-y+0.5$, $z+0.5$. [b] ii = $0.5-x$, $-1-y$, $-0.5+z$; iii = $0.2-x$, $-1-y$, $0.5+z$. [c] i = $x-0.5$, $-y+0.5$, $z+0.5$; ii = $x+0.5$, $-y+0.5$, $z-0.5$. [d] i = $0.5+x$, $0.5-y$, $-0.5+z$; ii = $0.5-x$, $0.5+y$, $0.5-z$. [e] ii = $0.5+x$, $0.5-y$, $-0.5+z$; iii = $0.5-x$, $0.5+y$, $0.5-z$; iv = $0.5-x$, $0.5+y$, $0.5-z$. [f] ii = $-1+x$, $y$, $-1+z$; iii = $1+x$, $y$, $1+z$; iv = $x$, $y$, $1+z$.

gen [Pb–N(4) 2.509(9)], although this bond is longer than the sum of the covalent radii, 2.35 Å.[16] The identical thiosemicarbazone chains adopt *E* conformation around C(2)–N(3) and *Z* around C(1)–N(2). The conformational changes with respect to free $H_2$DAPTSC are summarized in Scheme 2. The C–S bond is longer in the complex [1.725(7) Å] than in $H_2$DAPTSC [1.674(4) and 1.694(4) Å], showing the expected thione-to-thiol evolution upon metallation. Two hydrogen bonds involving the N(1)$H_2$ groups and the S and N(2) atoms of neighbouring molecules (see Table 2) give rise to a 2D network in the *xz* plane.

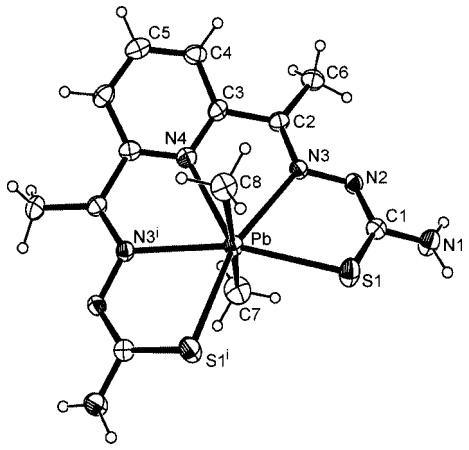


Figure 2. Molecular structure of [$PbMe_2$(DAPTSC)]. Ellipsoids are drawn at the 50% probability level.

That DAPTSC$^{2-}$, as expected, embraces the organometallic moiety, and must hamper intermolecular approach, but the observed formation of [Pb(DAPTSC)] shows that it is still possible to approach the Pb centre from above or below the equatorial coordination plane. We are currently investigating whether more enveloping ligands provide better stabilization of their methyllead(IV) complexes, so reducing the formation of lead(II) derivatives.

The structures of [PbPhMe(DAPTSC)]·0.45$H_2O$ (Figure 3) and [$PbPh_2$(DAPTSC)]·MeOH (see Figure S1 in the electronic supplementary information) are similar to that of [$PbMe_2$(DAPTSC)], showing only minor differences in certain bond lengths and angles and the expected packing differences deriving from their solvent molecules. Analysis of these small structural differences is difficult, because the esd values are not always similar and because the intermolecular forces can influence the intramolecular ones. For example, the Pb–S bonds of [$PbMe_2$(DAPTSC)] are slightly longer than those of [$PbPh_2$(DAPTSC)]·MeOH (see Table 1), but this could be due either to an intrinsically smaller acceptor capacity of the $Me_2Pb^{2+}$ moiety or to the lessening of the donor ability of the sulfur as a consequence of its intermolecular N(1)–H(1)···S bond. Also, in the diphenyllead(IV) complex the two arms of the ligand are no longer equivalent, showing small differences in the Pb–N and Pb–S bond lengths.

Figure 4 shows the molecular structure and numbering scheme of [$PbPh_2$($H_2$DAPTSC)]$_2$[$PbPh_2Cl_4$]$Cl_2$·6$CH_3OH$. This complex is centrosymmetric, consisting of two [$PbPh_2$($H_2$DAPTSC)]$^{2+}$ cations, a [$PbPh_2Cl_4$]$^{2-}$ anion and the two chloride anions. As in the [$PbR_2$(DAPTSC)] complexes (see also ref.[11c,17–20]), in the cation [$PbPh_2$($H_2$DAPTSC)]$^{2+}$ the thiosemicarbazone ligand binds to the diphenyllead(IV) fragment through its two sulfur and three nitrogen atoms. However, there are two major differences with respect to [$PbPh_2$(DAPTSC)]·MeOH: i) all the metal–ligand bonds are longer, and ii) both the C–S bond lengths suggest scant evolution of the ligand to the thiol form. Both these differences reflect weaker interaction with the organometallic cation.

 © 2007 Wiley-VCH Verlag GmbH & Co. KGaA, Weinheim 

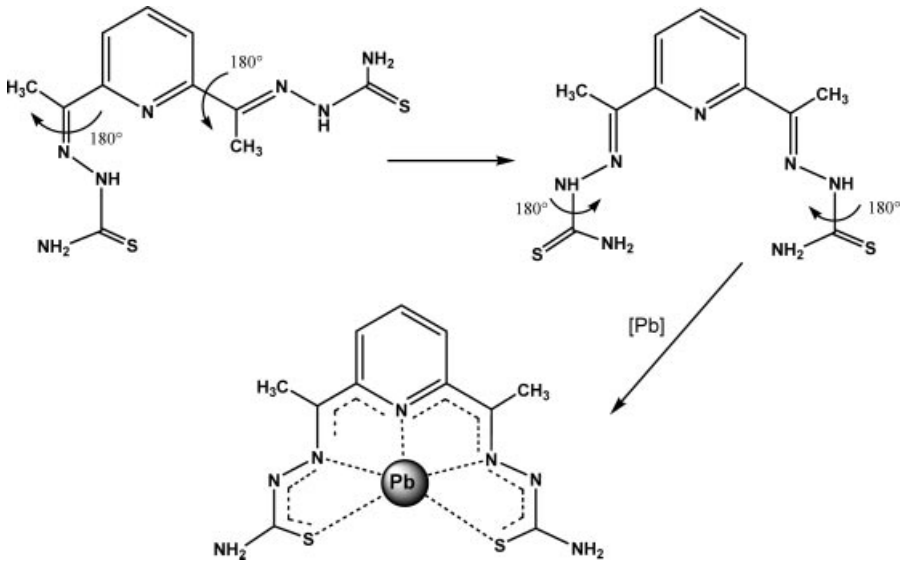


Scheme 2.

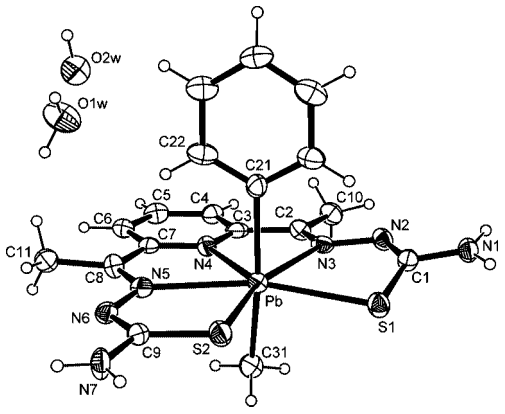


Figure 3. Molecular structure of [PbPhMe(DAPTSC)]·0.45$H_2O$. Ellipsoids are drawn at the 50% probability level.

In the anion $[PbPh_2Cl_4]^{2-}$, the Pb(2) atom is octahedrally coordinated. This fragment was previously found in $[\{PbPh_2(BPyTSC)\}_2(PbPh_2Cl_4)]$·2MeOH,[12] although in that case it interacted with the $[PbPh_2(BPyTSC)]$ moiety through chloro bridges, while in the present case it is only linked to the $[PbPh_2(H_2DAPTSC)]^{2+}$ cation by the hydrogen bonds N(6)–H(6)···Cl(1) and N(7)–H(7A)···Cl(1) (see Table 2). In keeping with this, the Pb(2)–Cl(2) bond in the present compound is shorter than any of the Pb–Cl bonds in the BPyTSC complex, in which both Cl atoms are bridges and one takes part in a hydrogen bond. By contrast, the Pb(2)–Cl(1) bond is longer than any of the Pb–Cl bonds in $[\{PbPh_2(BPyTSC)\}_2(PbPh_2Cl_4)]$·2MeOH, probably because of the two hydrogen bonds of Cl(1). These interactions, together with others involving the isolated chloride ion Cl(3) and the solvent molecules (Table 2), give rise to a complicated two-dimensional network.

Figure 5 shows the molecular structure of [Pb(DAPTSC)]. In this case, the five donor atoms of the ligand define the base of a pentagonal pyramid, and the $Pb^{II}$ cation is 1.1 Å from this plane. The location of all the metal–ligand interactions on the same side of the metal centre suggests the presence of a stereochemically active lone-

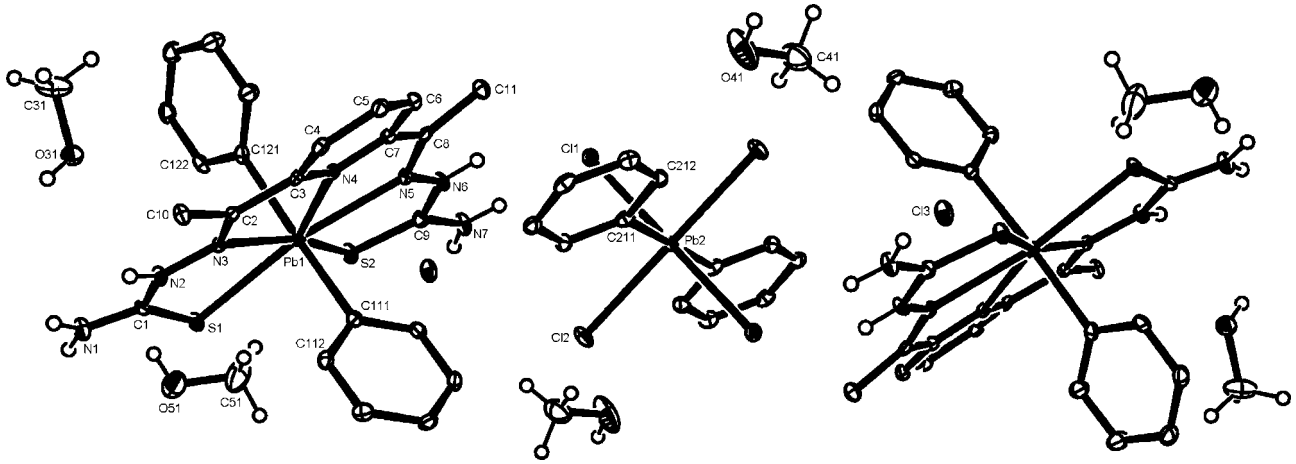


Figure 4. Crystal structure of $[PbPh_2(H_2DAPTSC)]_2[PbPh_2Cl_4]Cl_2$·6$CH_3OH$. All hydrogen atoms, except those on MeOH, and N atoms have been omitted for clarity. Ellipsoids are drawn at the 30% probability level.

 © 2007 Wiley-VCH Verlag GmbH & Co. KGaA, Weinheim 

pair on the other side. Except for minor differences in bond lengths, this is the same molecular structure as when the ligand is N(1),N(7)-dimethylated,[21] but the crystal packing is different. In the lattice of [Pb(DAPTSC)] the molecules stack along the *x* axis, each Pb centre increasing its coordination number to 7 by means of two weak Pb···S$^{i}$ interactions with the neighbouring molecule on the side opposite its own ligand (i = 1 + *x*, *y*, *z*) and giving rise to a polymeric chain (Figure 6). These polymeric chains interact by N–H···N hydrogen bonds (see Table 2) to form two-dimensional networks in the *xz* plane. In the N(1),N(7)-dimethylated complex[21] no secondary interactions are observed, and each monomer links to another two through π–π interactions between their pyridine rings and the resulting polymeric chains are linked in 2D networks by NH···S hydrogen bonds.

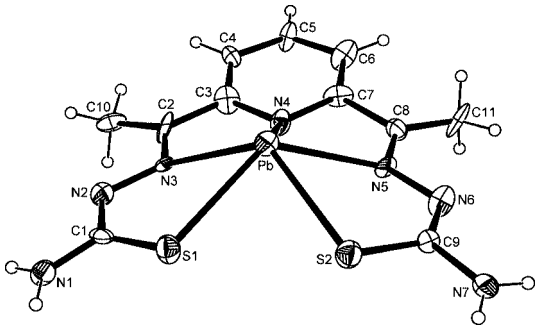


Figure 5. Molecular structure of [Pb(DAPTSC)]. Ellipsoids are drawn at the 50% probability level.

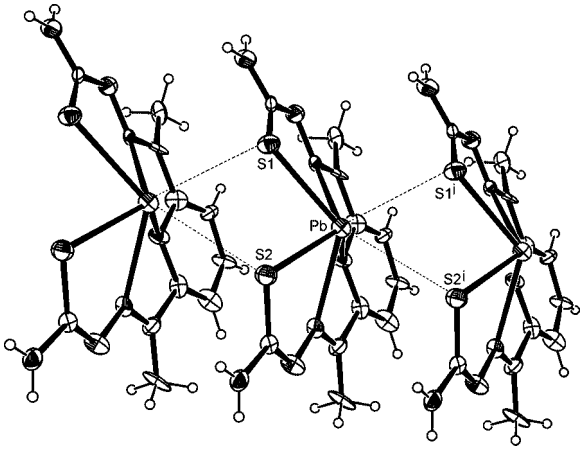


Figure 6. Intermolecular Pb···S interactions in [Pb(DAPTSC)].

## Solution Studies

The $^{1}$H, $^{13}$C and $^{207}$Pb NMR spectroscopic data for the complexes are included in the Experimental Section. Only $^{1}$H spectra could be obtained for [$PbMe_2$(DAPTSC)] (because of the small amount of solid isolated) and [Pb(DAPTSC)] (because of its poor solubility). The $^{207}$Pb NMR signal was only located for [$PbPh_2$($H_2$DAPTSC)]$_2$[$PbPh_2Cl_4$]$Cl_2$·6$CH_3OH$ and [$PbPh_2$(DAPTSC)]. $^{1}$H and $^{13}$C NMR spectra were interpreted by comparison with those of the ligand.[11a]

The $^{1}$H and $^{13}$C NMR spectra of [$PbPh_2$($H_2$DAPTSC)]$_2$[$PbPh_2Cl_4$]$Cl_2$·6$CH_3OH$ show signals in positions similar to those found in the spectra of the free ligand and $PbPh_2Cl_2$ in [$D_6$]DMSO. This suggests that Equation (3) has been shifted to the left, possibly because $PbPh_2Cl_2$ forms adducts with the solvent DMSO.[22] The $^{207}$Pb chemical shift and $^{3}J$($^{13}$C-$^{207}$Pb) coupling constant support this conclusion, their values being the same as those obtained for $PbPh_2Cl_2$ in DMSO solution.[12] The value of the molar conductivity in DMSO, 8.0 S·cm$^2$·mol$^{-1}$ ($10^{-3}$ M), rules out any ionic behaviour,[23] and is likewise in accordance with the proposed evolution.

The $^{1}$H spectra of [$PbMe_2$(DAPTSC)], [$PbPh_2$-(DAPTSC)], [PbMePh(DAPTSC)] and [Pb(DAPTSC)] are all similar. With respect to the spectrum of the free ligand, the signals corresponding to the N(2,6)H protons disappear because of the formation of DAPTSC$^{2-}$ in the complexes; the signals of the N(1,7)$H_2$ groups shift to higher fields and merge to form just one signal; the C(5)H protons become slightly deshielded and C(4,6)H is shielded. The $^{13}$C NMR spectra of [$PbPh_2$(DAPTSC)] and [PbPhMe(DAPTSC)] are also similar: in both complexes, C(1,9), C(2,8) and C(3,7) are all more shielded than in the free ligand, while C(4,6), C(5) and C(10,11) become deshielded. The shielding of C(1,9) by about 3 ppm is in accordance with evolution of the C=S group to the thiol form when S coordinates to the metal. The shielding of C(2,8) and deshielding of C(10,11) testify to the persistence of Pb–N(3) and Pb–N(5) interactions when the complexes are dissolved in DMSO, while the deshielding of the pyridine ring carbons C(4,6) and C(5) suggests that the Pb–N(4) interaction also perdures. This behaviour is similar to that of the analogous dimethyl and diphenyltin(IV) complexes, [$SnR_2$(DAPTSC)],[11a] which in the solid state show the same coordination scheme as in the lead complexes.

The above conclusions are also supported by the available NMR spectroscopic data for the diorganolead(IV) moieties. For [$PbPh_2$(DAPTSC)], a coordination of at least seven is suggested by the fact that the $^{3}J$ and $^{4}J$($^{1}$H-$^{207}$Pb) coupling constants are larger than in compounds with a coordination number of six;[24] and although the chemical shift of $^{207}$Pb for this compound, –608.9 ppm, is very close to those found in the spectra of certain diaryllead(IV) acetates, for which a coordination number of six has been postulated,[25] this chemical shift is probably not at odds with heptacoordination to C, N and S atoms, as N and S atoms exert a smaller shielding effect than O atoms.

Similarly, the $^{2}J$($^{1}$H-$^{207}$Pb) value for [$PbMe_2$(DAPTSC)], 190.0 Hz, is close to those found for other dimethyllead(IV) complexes[26] with a coordination number of seven in DMSO solution, and the $^{2}J$ value for [PbPhMe(DAPTSC)], 209.2 Hz, is even larger. To the best of our knowledge, the only previously reported $^{2}J$ value for a methylphenyllead(IV) complex is that of $PbPhMeCl_2$, 105.4 Hz, for which a coordination number of five was assumed.[27]

 © 2007 Wiley-VCH Verlag GmbH & Co. KGaA, Weinheim 

## Conclusions

The reactions of the diorganolead(IV) derivatives $PbMe_2(OAc)_2$ and $PbPhMe(OAc)_2$ with $H_2DAPTSC$ each afford two products: the corresponding dimethyllead(IV) or methylphenyllead(IV) complex, and the lead(II) compound [Pb(DAPTSC)]. Isolation of the former confirms that this bis(thiosemicarbazone) ligand can impede, albeit only partially, the decomposition of methyllead(IV) compounds to "inorganic" lead(II) derivatives. The reaction of $H_2DAPTSC$ with $PbPh_2(OAc)_2$ proceeds without any appreciable decomposition of the organometallic moiety to form $[PbPh_2(DAPTSC)]_2$, which can also be prepared by reacting $H_2DAPTSC$ with $PbPh_3(OAc)$ (probably through a protodephenylation process).

The deprotonation of the incoming ligand in the above processes is attributable to the basicity of the outgoing acetate groups. When $H_2DAPTSC$ reacts with $PbPh_2Cl_2$ it remains neutral and is only able to displace chloride from part of the substrate molecules, competing unsuccessfully with the displaced $Cl^-$ ions for the remainder. The resulting ionic compound, $[PbPh_2(H_2DAPTSC)]_2[PbPh_2Cl_4]Cl_2$, comprises $[PbPh_2(H_2DAPTSC)]^{2+}$ cations and $[PbPh_2Cl_4]^{2-}$ and $Cl^-$ anions.

The above complexes were studied by X-ray diffraction in the solid state, and by $^1H$, $^{13}C$ and $^{207}Pb$ NMR spectroscopy in DMSO solution. In the solid state, both neutral $H_2DAPTSC$ and dianionic $DAPTSC^{2-}$ behave as pentadentate ligands, although the former establishes longer, weaker bonds with the metal. The weaker donor capacity of $H_2DAPTSC$ is corroborated by its displacement by the solvent when $[PbPh_2(H_2DAPTSC)]_2[PbPh_2Cl_4]Cl_2$ is dissolved in dimethyl sulfoxide.

## Experimental Section

**Chemicals:** 2,6-Diacetylpyridine (Aldrich), thiosemicarbazide (Merck), dichlorodiphenyllead (Panreac), chlorotriphenyllead (Aldrich), lead iodide (Aldrich), methyl iodide (Aldrich) and methyllithium (Aldrich), all of reagent grade, were used without further purification.

**Physical Measurements:** Elemental analyses for C, H, N and S were performed with a Fisons 1108 microanalyzer. Melting points were determined with a Gallenkamp electrically heated apparatus. NMR spectra were recorded in DMSO using a Bruker AMX 300 spectrometer for $^1H$ spectra (at 300.14 MHz) and $^{13}C$ spectra (75.4 MHz) (these are referred to TMS through the solvent signals: $^1H$, 2.50 ppm; $^{13}C$, 39.50 ppm), and a Bruker AMX 500 at 104.58 MHz for $^{205}Pb$ spectra [using a saturated solution of $PbPh_4$ in $CDCl_3$ ($\delta$ = 178.0 ppm) ppm as external reference]. Conductance measurements ($S{\cdot}cm^2{\cdot}mol^{-1}$) were performed at room temperature using a Crison MicroMC 2202 conductivity meter and $10^{-3}$ M samples prepared in dry DMSO (Aldrich) under $N_2$ in a glovebox. Elemental analyses and spectroscopic measurements were carried out in the RIAIDT services of the University of Santiago de Compostela. X-ray data were collected at the RIAIDT services of the University of Santiago de Compostela and at the São Carlos Institute of Physics of the University of São Paulo.

**Synthesis of the Ligands and the Starting Organolead(IV) Compounds:** $H_2DAPTSC$ was prepared as described previously[28] from 2,6-diacetylpyridine and thiosemicarbazide. Crystals appropriate for X-ray study were obtained by recrystallization from MeOH. $PbMe_2Br_2$ was prepared using a published method,[29] by reaction of $PbI_2$ with IMe and LiMe in ether, and subsequent reaction of the tetramethyllead formed with $Br_2$. $C_2H_6Br_2Pb$ (397.1): calcd. C 6.05, H 1.52; found C 5.3, H 1.5. $PbPhMeCl_2$ was prepared[27] by reacting MeMgI and MeI with $PbPh_3Cl$. The $PbPh_3Me$ thus formed was dissolved in chloroform and this solution was treated with a stream of HCl(g) until a solid formed. $C_7H_8Cl_2Pb$ (370.25): calcd. C 22.71, H 2.18; found C 21.8, H 2.1. $PbR_2(OAc)_2$ (R = Me, Ph), $PbPhMe(OAc)_2$ and $PbPh_3(OAc)$ were prepared by reaction of the corresponding dihalides or monohalide with AgOAc in 1:2 or 1:1 mol ratio in methanol. The AgX formed was filtered out and the solution containing the organolead(IV) acetate was used immediately in the preparation of the complexes.

**Synthesis of the Complexes:** The complexes were prepared by reacting $H_2DAPTSC$ with $PbMe_2(OAc)_2$, $PbPhMe(OAc)_2$ $PbPh_2Cl_2$, $PbPh_2(OAc)_2$ or $PbPh_3(OAc)$ in methanol.

***Caution!*** Lead is a highly toxic cumulative poison. Lead compounds should be handled carefully.[30]

**[$PbMe_2$(DAPTSC)]:** A freshly prepared solution of $PbMe_2(OAc)_2$ (0.22 g, 0.62 mmol) in MeOH (20 mL) was slowly stirred into a yellow suspension of $H_2DAPTSC$ (0.156 g, 0.503 mmol) in the same solvent (20 mL). The orange suspension obtained was stirred for 1 h at room temperature, and the yellow-orange solid formed was filtered out. The $^1H$ NMR spectrum of this solid suggests a mixture consisting of the complex [Pb(DAPTSC)] [also formed when the ligand reacts with $PbMePh(OAc)_2$, vide infra] together with a small amount of the free ligand. A few monocrystals of [$PbMe_2$(DAPTSC)] that were suitable for X-ray study were obtained from the mother liquor after slow evaporation of the solvent. M.p. 227 °C. $^1H$ NMR ([$D_6$]DMSO): $\delta$ = 6.9 [br. s, 2 H, N(1,7)$H_2$], 7.8 [d, 2 H, C(4,6)H], 8.14 [t, 1 H, C(5)H], 2.50 [s, C(10,11)$H_3$, overlaps with solvent signal], 1.65 [s, $^2J(^1H\text{-}^{207}Pb)$ = 190.2 Hz, 6 H, $CH_3$–Pb] ppm.

**[PbPhMe(DAPTSC)]·0.45$H_2O$ and [Pb(DAPTSC)]:** A solution of freshly prepared $PbPhMe(OAc)_2$ (0.10 g, 0.24 mmol) was slowly added to a suspension of $H_2DAPTSC$ (0.07 g, 0.24 mmol) in the same solvent (10 mL). The orange suspension obtained was stirred for 12 h at room temperature. The orange solid formed was filtered out and vacuum-dried. The $^1H$ NMR spectrum of this solid indicated a mixture of [Pb(DAPTSC)] and [PbPhMe(DAPTSC)]. Evaporation of the mother liquor gave crystals of these two complexes that were suitable for X-ray diffractometry. [PbPhMe(DAPTSC)]·0.45$H_2O$. $C_{18}H_{21.9}N_7O_{0.45}PbS_2$ (614.8): calcd. C 35.13, H 3.59, N 15.95, S 10.43; found C 34.90, H 3.51, N 16.25, S 10.57. $^1H$ NMR ([$D_6$]DMSO): $\delta$ = 7.02 [br. s, 4 H, N(1,7)$H_2$], 7.78 [d, 2 H, C(4,6)*H*], 8.06 [t, 1 H, C(5)*H*], 2.50 [s, C(10,11)$H_3$, overlaps with the solvent signal], 7.51 [d, 2 H, $H_o$(Ph-Pb)], 7.20 [t, 3 H, $H_{m,p}$(Ph-Pb)], 1.79 [s, $^2J(^1H\text{-}^{207}Pb)$ = 209.2 Hz, 3 H, C$H_3$-Pb] ppm. $^{13}C$ NMR ([$D_6$]DMSO): $\delta$ = 176.8 [C(1,9)], 150.7 [C(3,7)], 146.9 [C(2,8)], 122.1 [C(4,6)], 140.3[C(5)], 14.2 [C(10,11)], 130.7 [$C_o$(Ph-Pb)], 129.1 [$C_m$(Ph-Pb)], 127.8 [$C_p$(Ph-Pb)] ppm. The signal for Me-Pb has not been located. [Pb(DAPTSC)]. M.p. 270 °C. $C_{11}H_{14}N_7PbS_2$ (515.60): calcd. C 25.62, H 2.74, N 19.02, S 12.44; found C 26.20, H 2.63, N 18.76, S 12.33. $^1H$ NMR ([$D_6$]DMSO): $\delta$ = 7.02 [br. s, 4 H, N(1,7)$H_2$], 7.83 [d, 2 H, C(4,6)*H*], 8.18 [t, 1 H, C(5)*H*], 2.50 [s, C(10,11)$H_3$, overlaps with solvent signal] ppm.

**[$PbPh_2$(DAPTSC)]:** A freshly prepared solution of $PbPh_2(OAc)_2$ (0.36 g, 0.758 mmol) in MeOH (20 mL) was slowly stirred into a suspension of $H_2DAPTSC$ (0.18 g, 0.578 mmol) in the same solvent (20 mL). The mixture was stirred for 1 h at room temperature and

 © 2007 Wiley-VCH Verlag GmbH & Co. KGaA, Weinheim 

the orange solid formed was filtered out. M.p. 230 °C. $C_{23}H_{23}N_7PbS_2$ (668.8): calcd. C 41.31, H 3.47, N 14.66, S 9.59; found C 40.48, H 3.90, N 14.02, S 9.74. $^1$H NMR ([D$_6$]DMSO): $\delta$ = 7.14 [br. s, 4 H, N(1,7)$H_2$], 7.72 [d, 2 H, C(4,6)$H$], 7.98 [t, 1 H, C(5)$H$], 2.51 [s, C(10,11)$H_3$], 7.56 [d, $^3J$($^1$H-$^{207}$Pb) = 228.2 Hz, 4 H, $H_o$(Ph-Pb)], 7.20 [t, $^4J$($^1$H-$^{207}$Pb) = 83.0 Hz, 4 H, $H_m$(Ph-Pb)], 7.13 [t, 2 H, $H_p$(Ph-Pb)] ppm. $^{13}$C NMR ([D$_6$]DMSO): $\delta$ = 176.8 [C(1,9)], 150.3 [C(3,7)], 147.2 [C(2,8)], 122.3 [C(4,6)], 40.3 [C(5)], 14.4 [C(10,11)], 173.0 [$C_{ipso}$(Ph-Pb)], 130.7 [$^2J$($^{13}$C-$^{207}$Pb) = 117.7 Hz, $C_o$(Ph-Pb)], 129.1 [$^3J$($^{13}$C-$^{207}$Pb) = 217.0 Hz, $C_m$(Ph-Pb)], 127.8 [$^4J$($^{13}$C-$^{207}$Pb) = 36.3 Hz, $C_p$(Ph-Pb)] ppm. $^{207}$Pb NMR ([D$_6$]-DMSO): $\delta$ = –608.7 ppm.

[PbPh$_2$(DAPTSC)] was also obtained by reaction of H$_2$DAPTSC with PbPh$_3$(OAc), as follows: a solution of PbPh$_3$(OAc) (0.2 g, 0.42 mmol) in MeOH (20 mL) was added to a yellow suspension of H$_2$DAPTSC (0.13 g, 0.42 mmol) in the same solvent (20 mL). The orange solution obtained was stirred overnight at room temperature and filtered to remove a small amount of H$_2$DAPTSC in suspension. Slow concentration of the filtrate afforded orange crystals of [PbPh$_2$(DAPTSC)]·MeOH that were suitable for X-ray study.

**[PbPh$_2$(H$_2$DAPTSC)]$_2$[PbPh$_2$Cl$_4$]Cl$_2$·6CH$_3$OH:** A suspension of PbPh$_2$Cl$_2$ (0.1 g, 0.23 mmol) in MeOH (10 mL) was stirred into a yellow suspension of H$_2$DAPTSC (0.071 g, 0.23 mmol) in the same solvent (10 mL). The deep yellow suspension obtained was stirred for 4 h at room temperature, after which the yellow solid in suspension was filtered out and discarded (its $^1$H NMR spectrum and elemental analysis corresponded to H$_2$DAPTSC). Slow concentration of the mother liquor afforded a yellow-green crystalline solid that was suitable for X-ray study. M.p. 197 °C. $C_{64}H_{84}Cl_6N_{14}O_6Pb_3S_4$ (2108.02): calcd. C 36.47, H 4.02, N 9.30, S 6.08; found C 35.80, H 3.90, N 10.03, S 6.94. $\Lambda_m$ (DMSO, $10^{-3}$ M) = 8.0 S·cm$^2$·mol$^{-1}$. $^1$H NMR ([D$_6$]DMSO): $\delta$ = 8.40 s, 8.13 [s, 4H N(1,7)$H_2$], 10.30 [s, 2 H, N(2,6)$H$], 8.41 [d, 2 H, C(4,6)$H$], 7.76 [t, 1 H, C(5)H], 2.43 [s, C(10,11)$H_3$], 8.12 [d, 8 H, $H_o$(Ph-Pb)], 7.60 [t, 8 H, $H_m$(Ph-Pb)], 7.43 [t, 4 H, $H_p$(Ph-Pb)] ppm. $^{13}$C NMR ([D$_6$]-DMSO): $\delta$ = 179.0 [C(1,9)], 153.4 [C(3,7)], 148.0 [C(2,8)], 120.4 [C(4,6)], 136.6 [C(5)], 12.0 [C(10,11)], 170.5 [$C_{ipso}$(Ph-Pb)], 133.5 [$C_o$(Ph-Pb)], 129.6 [$^3J$($^{13}$C-$^{207}$Pb) ≈ 200, $C_m$(Ph-Pb)], 129.5 [$C_p$(Ph-Pb)] ppm. $^{207}$Pb NMR ([D$_6$]DMSO): $\delta$ = –507.3 ppm.

**X-ray Crystallography:** Crystal data were collected at room temperature ([PbMe$_2$(DAPTSC)]) or low temperature (all others) on

Table 3. Selected crystallographic data for the ligand and complexes.

| | H$_2$DAPTSC·MeOH | [PbMe$_2$(DAPTSC)] | [PbPhMe(DAPTSC)]·0.45H$_2$O |
|---|---|---|---|
| Empirical formula | $C_{12}H_{19}N_7OS_2$ | $C_{13}H_{19}N_7PbS_2$ | $C_{18}H_{21.90}N_7O_{0.45}PbS_2$ |
| Formula mass | 341.46 | 544.66 | 614.84 |
| $T$/K | 120.00(10) | 293(2) | 120(2) |
| $\lambda$/Å | 1.54180 | 1.54184 | 0.71073 |
| Crystal system | monoclinic | orthorhombic | monoclinic |
| Space group | $P2_1/c$ | $Pmn21$ (No. 31) | $P2_1/n$ |
| $a$/Å | 10.493(5) | 15.880(2) | 10.026(2) |
| $b$/Å | 10.590(5) | 7.9249(10) | 11.996(2) |
| $c$/Å | 14.745(5) | 7.5304(8) | 17.560(3) |
| $\alpha$/° | 90.000(5) | 90 | |
| $\beta$/° | 98.420(5) | 90 | 98.924(9) |
| $\gamma$/° | 90.000(5) | 90 | |
| $V$/Å$^3$ | 1620.8(12) | 947.7(2) | 2086.4(6) |
| $Z$ | 4 | 2 | 4 |
| $\mu$/mm$^{-1}$ | 3.096 | 19.443 | 8.308 |
| Reflections collected | 10955 | 985 | 9672 |
| Independent reflections | 2734 [$R$(int) = 0.0636] | 965 [$R$(int) = 0.0208] | 3556 [$R$(int) = 0.0963] |
| Final $R_1$, $wR_2$ [$I > 2\sigma(I)$] | 0.0748, 0.1928 | 0.0241, 0.0651 | 0.0564, 0.1111 |
| Gof | 1.07 | 1.071 | 1.015 |
| | [PbPh$_2$(DAPTSC)]·MeOH | [PbPh$_2$(H$_2$DAPTSC)]$_2$[PbPh$_2$Cl$_4$]Cl$_2$·6MeOH | [Pb(DAPTSC)] |
| Empirical formula | $C_{24}H_{27}N_7OPbS_2$ | $C_{64}H_{84}Cl_6N_{14}O_6Pb_3S_4$ | $C_{11}H_{13}N_7PbS_2$ |
| Formula mass | 700.84 | 2107.96 | 514.59 |
| $T$/K | 120(2) | 110(2) | 120(2) |
| $\lambda$/Å | 0.71073 | 0.71073 | 0.71073 |
| Crystal system | monoclinic | triclinic | monoclinic |
| Space group | $P2_1/n$ | $\bar{P}$ | $P2_1$ |
| $a$/Å | 10.1550(1) | 9.4450(1) | 4.9586(7) |
| $b$/Å | 15.9560(2) | 11.1110(2) | 14.015(2) |
| $c$/Å | 15.9780(2) | 18.7520(3) | 10.5900(10) |
| $\alpha$/° | 90 | 83.462(1) | |
| $\beta$/° | 91.632(1) | 77.782(1) | 102.923(9) |
| $\gamma$/° | 90 | 77.714(1) | |
| $V$/Å$^3$ | 2587.92(5) | 1874.39(5) | 717.31(16) |
| $Z$ | 4 | 1 | 2 |
| $\mu$/mm$^{-1}$ | 6.712 | 7.104 | 12.055 |
| Reflections collected | 42027 | 52099 | 3746 |
| Independent reflections | 4559 [$R$(int) = 0.0486] | 6603 [$R$(int) = 0.1091] | 2177 [$R$(int) = 0.1079] |
| Final $R_1$, $wR_2$ [$I > 2\sigma(I)$] | 0.0259, 0.0684 | 0.0253, 0.0629 | 0.0719, 0.1495 |
| Gof | 1.092 | 1.103 | 1.052 |

 © 2007 Wiley-VCH Verlag GmbH & Co. KGaA, Weinheim 

a CCD-2000 Bruker-Nonius (RIAIDT, University of Santiago de Compostela) or on an Enraf-Nonius CAD4 or Enraf-Nonius Kappa CCD (São Carlos Institute of Physics, University of São Paulo). The data were corrected for absorption by numerical[31] [$PbMe_2$(DAPTSC)], empirical[32] ($H_2$DAPTSC) or semi-empirical[33] (all others) methods. Structures were solved by direct methods for the ligand and the Patterson method for the complexes, followed by normal difference Fourier techniques. Hydrogen atoms were included in idealized positions and refined with isotropic displacement parameters, except that the H bound to the oxygen atom in $H_2$DAPTSC·MeOH was located on the density map and refined isotropically. The program used was SHELX97.[34]

Although the data for the ligand and the $Pb^{II}$ complex were not of very good quality, successive refinements allowed the full resolution of both structures. In [PbPhMe(DAPTSC)]·0.45$H_2O$ the water molecules are disordered, their O atoms occupying two positions, O1W and O2W, with occupancy factors 3.5 and 0.1, respectively. O2W was not refined anisotropically.

Molecular graphics were obtained with ORTEP[35] and PLATON.[36] Crystal data, experimental details and refinement parameters are listed in Table 3.

CCDC-634589 (for $H_2$DAPTSC·MeOH), -634590 (for [$PbMe_2$(DAPTSC)]), -634591 (for [PbPhMe(DAPTSC)]·0.45$H_2O$), -634592 (for [$PbPh_2$(DAPTSC)]·MeOH), -634593 (for [$PbPh_2$($H_2$DAPTSC)]$_2$[$PbPh_2Cl_4$]$Cl_2$·6MeOH) and -634594 (for [Pb(DAPTSC)]) contain the supplementary crystallographic data for this paper. These data can be obtained free of charge from The Cambridge Crystallographic Data Centre via www.ccdc.cam.ac.uk/data_request/cif.

**Supporting Information** (see also the footnote on the first page of this article): Figure S1 shows the molecular structure of [$PbPh_2$(DAPTSC)]·MeOH.

## Acknowledgments

We thank the Secretariat General for Research and Development of the Xunta de Galicia (Spain), project number PGIDIT03PXIC20306PN, and the Spanish Ministerio de Ciencia y Tecnología (MCYT), project number CTQ2006-11805-BQU, for financial support.

[1] F. H. Allen, *Acta Crystallogr., Sect. B: Struct. Sci.* **2002**, *58*, 380–388.
[2] H. Fleischer, S. Parsons, C. R. Pulham, *Acta Crystallogr., Sect. E: Struct. Rep. Online* **2003**, *59*, m11–m13.
[3] D. Zhang, S. Q. Dou, A. Weiss, *Z. Naturforsch., A: Phys. Sci.* **1991**, *46*, 337–343.
[4] R. Hillwig, F. Kunkel, K. Harms, B. Neumuller, K. Dehnicke, *Z. Naturforsch., B: Chem. Sci.* **1997**, *52*, 149–152.
[5] G. M. Sheldrick, R. Taylor, *Acta Crystallogr., Sect. B: Struct. Sci.* **1975**, *31*, 2740–2741.
[6] H. Preut, P. Rohm, F. Huber, *Acta Crystallogr., Sect. C: Cryst. Struct. Commun.* **1986**, *42*, 657–658.
[7] R. A. Varga, J. E. Drake, C. Silvestru, *J. Organomet. Chem.* **2003**, *675*, 48–56.
[8] C. Pulham, I. Maley, S. Parsons, D. Messenger, private communication, CCDC-276843.
[9] a) H. J. Haupt, F. Huber, J. Gmehling, *Z. Anorg. Allg. Chem.* **1972**, *390*, 31–40; b) J. Gmehling, F. Huber, *Z. Anorg. Allg. Chem.* **1972**, *393*, 131–135.
[10] G. A. Russell, *J. Am. Chem. Soc.* **1959**, *81*, 4815–4825.
[11] a) J. S. Casas, A. Castiñeiras, A. Sánchez, J. Sordo, A. Vázquez-López, M. C. Rodríguez-Argüelles, U. Russo, *Inorg. Chim. Acta* **1994**, *221*, 61–68; b) M. C. Rodríguez-Argüelles, M. B. Ferrari, G. G. Fava, C. Pelizzi, P. Tarasconi, R. Albertini, P. P. Dall'Aglio, P. Lunghi, S. Pinelli, *J. Inorg. Biochem.* **1995**, *58*, 157–175; c) G. F. de Sousa, J. Valdés-Martínez, G. E. Pérez, R. A. Toscano, A. Abras, C. A. L. Filgueras, *J. Braz. Chem. Soc.* **2002**, *13*, 559–564; d) A. I. Matesanz, I. Cuadrado, C. Pastor, P. Souza, *Z. Anorg. Allg. Chem.* **2005**, *631*, 780–784; e) M. S. Shongwe, H. N. R. Al-Kharousi, H. Adams, M. J. Morris, E. Bill, *Inorg. Chem.* **2006**, *45*, 1103–1107 and references therein.
[12] J. S. Casas, E. E. Castellano, J. Ellena, M. S. García-Tasende, A. Sánchez, J. Sordo, M. J. Vidarte, *Inorg. Chem.* **2003**, *42*, 2584–2595.
[13] a) G. F. de Sousa, D. X. West, C. A. Brown, J. K. Swearingen, J. Valdés-Martínez, R. A. Toscano, S. Hernández-Ortega, M. Hörner, A. J. Bortoluzzi, *Polyhedron* **2000**, *19*, 841–847; b) M. Vázquez, L. Fabbrizzi, A. Taglietti, R. M. Pedrido, A. M. González-Noya, M. R. Bermejo, *Angew. Chem. Int. Ed.* **2004**, *43*, 1962–1965; c) M. A. Ali, A. H. Mirza, W. B. Ejau, P. v. Bernhardt, *Polyhedron* **2006**, *25*, 3337–3342.
[14] J. S. Casas, M. S. García-Tasende, J. Sordo, *Coord. Chem. Rev.* **2000**, *209*, 197–261.
[15] J. S. Casas, E. E. Castellano, J. Ellena, M. S. García-Tasende, A. Sánchez, J. Sordo, E. M. Vázquez-López, M. J. Vidarte, *Z. Anorg. Allg. Chem.* **2003**, *629*, 261–267.
[16] J. E. Huheey, E. A. Keiter, R. L. Keiter, *Inorganic Chemistry: Principles of Structure and Reactivity*, 4th ed., Harper Collins College Publishers, New York, **1993**.
[17] G. Dessy, V. Fares, *Cryst. Struct. Commun.* **1981**, *10*, 1025–1028.
[18] A. Bino, N. Cohen, *Inorg. Chim. Acta* **1993**, *210*, 11–16.
[19] A. H. Othman, K.-L. Lee, H.-F. Fun, B.-C. Yip, *Acta Crystallogr., Sect. C: Cryst. Struct. Commun.* **1996**, *52*, 602–605.
[20] J. S. Casas, E. E. Castellano, J. Ellena, M. S. García-Tasende, A. Sánchez, J. Sordo, M. J. Vidarte, *Inorg. Chim. Acta* **2004**, *357*, 2324–2330.
[21] R. Pedrido, M. R. Bermejo, M. J. Romero, M. Vázquez, A. M. González-Noya, M. Maneiro, M. J. Rodríguez, M. I. Fernández, *Dalton Trans.* **2005**, 572–579.
[22] A. V. Yatsenko, L. A. Aslanov, H. Schenk, *Polyhedron* **1995**, *14*, 2371–2377.
[23] W. J. Geary, *Coord. Chem. Rev.* **1971**, *7*, 81–122.
[24] S. N. Ólafsson, C. Flensbrug, P. Andersen, *J. Chem. Soc. Dalton Trans.* **2000**, 4360–4368.
[25] M. Schürmann, F. Huber, *J. Organomet. Chem.* **1997**, *530*, 121–130.
[26] T. Majima, Y. Kawasaki, *Bull. Soc. Chem. Jpn.* **1979**, *52*, 73–78.
[27] T. A. K. Al-Allaf, *J. Iraqi Chem. Soc.* **1986**, *11*, 25–40.
[28] J. S. Casas, E. E. Castellano, M. S. García-Tasende, A. Sánchez, J. Zukerman-Schpector, *Z. Anorg. Allg. Chem.* **1997**, *623*, 825–831.
[29] H. Gilman, R. Jones, *J. Am. Chem. Soc.* **1950**, *72*, 1760–1761.
[30] S. G. Schäfer, R. L. F. Davies, B. Elsenhans, W. Forth, K. Schümann in *Toxicology* (Eds.: H. Marquardt, S. G. Schäfer, R. O. McClellan, F. Welsch), Academic Press, San Diego, CA, **1999**, chapter 32.
[31] N. W. Alcock, *Cryst. Computing* **1970**, 271–278.
[32] G. M. Sheldrick, *SADABS, Program for Absorption Correction*, University of Göttingen, Germany, **1996**.
[33] R. H. Blessing, *Acta Crystallogr., Sect. A: Found. Crystallogr.* **1995**, *51*, 33–38.
[34] G. M. Sheldrick, *SHELX97*, *An Integrated System for Solving and Refining Crystal Structures from Diffraction Data*, University of Göttingen, Germany, **1997**.
[35] L. J. Farrugia, *J. Appl. Crystallogr.* **1997**, *30*, 565.
[36] A. L. Spek, *PLATON 99, A multipurpose crystallographic tool*, University of Utrecht, Utrecht, The Netherlands, **1999**.

Received: January 24, 2007
Published Online: June 18, 2007

 © 2007 Wiley-VCH Verlag GmbH & Co. KGaA, Weinheim

**The EUChemSoc Societies have taken the significant step into the future by merging their traditional journals, to form two leading chemistry journals, the *European Journal of Inorganic Chemistry* and the *European Journal of Organic Chemistry.* Three further EUChemSoc Societies (Austria, Czech Republic and Sweden) are Associates of the two journals.**

## COVER PICTURE

**The cover picture shows** an X-ray illustration of the multidentate ferrocenylpolyphosphane 1,1′,2,2′-tetrakis(diphenylphosphanyl)-4,4′-di-*tert*-butylferrocene. The cisoid conformation of the molecule, evidenced at the solid state, is conserved in solution; the phosphorus arrangement led to a rarely demonstrated multiple-coordination behaviour towards palladium, possibly useful in ultra-low catalyst loading reactions due to an improved stabilization of the metal atom. The multiple phosphane arms and their orientation resemble the elegant and intelligent creature that is the Giant Pacific Octopus (specimen from the Alaska SeaLife Centre in Seward, photo published with the kind permission of Mollie Tubbs and Jason Wettstein). The catalytic performance in palladium cross-coupling at ultra-low catalyst loading is presented in the Microreview by J.-C. Hierso et al. on p. 3767ff.

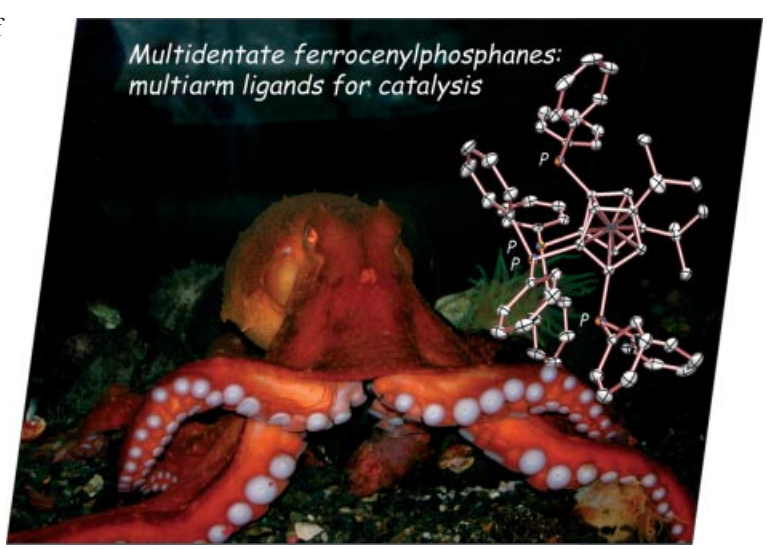


 © 2007 Wiley-VCH Verlag GmbH & Co. KGaA, Weinheim

**The EUChemSoc Societies have taken the significant step into the future by merging their traditional journals, to form two leading chemistry journals, the *European Journal of Inorganic Chemistry* and the *European Journal of Organic Chemistry.* Three further EUChemSoc Societies (Austria, Czech Republic and Sweden) are Associates of the two journals.**

## COVER PICTURE

**The cover picture shows** an X-ray illustration of the multidentate ferrocenylpolyphosphane 1,1′,2,2′-tetrakis(diphenylphosphanyl)-4,4′-di-*tert*-butylferrocene. The cisoid conformation of the molecule, evidenced at the solid state, is conserved in solution; the phosphorus arrangement led to a rarely demonstrated multiple-coordination behaviour towards palladium, possibly useful in ultra-low catalyst loading reactions due to an improved stabilization of the metal atom. The multiple phosphane arms and their orientation resemble the elegant and intelligent creature that is the Giant Pacific Octopus (specimen from the Alaska SeaLife Centre in Seward, photo published with the kind permission of Mollie Tubbs and Jason Wettstein). The catalytic performance in palladium cross-coupling at ultra-low catalyst loading is presented in the Microreview by J.-C. Hierso et al. on p. 3767ff.

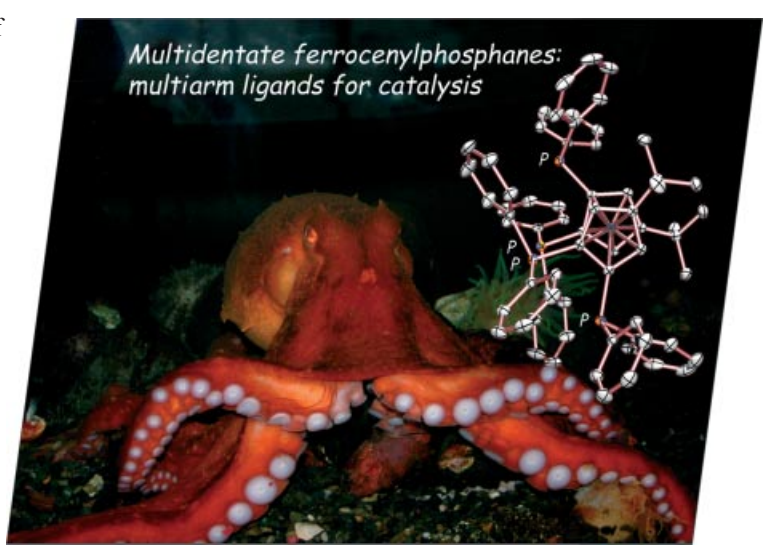


 © 2007 Wiley-VCH Verlag GmbH & Co. KGaA, Weinheim 

# CONTENTS

## MICROREVIEW


### C−C Cross-Coupling Reactions

**J.-C. Hierso,* M. Beaupérin, P. Meunier ..... 3767−3780**

Ultra-Low Catalyst Loading as a Concept in Economical and Sustainable Modern Chemistry: The Contribution of Ferrocenylpolyphosphane Ligands

**Keywords:** Sustainable chemistry / Homogeneous catalysis / P ligands / Ferrocenylphosphanes / Cross-coupling / Multidentate ligands


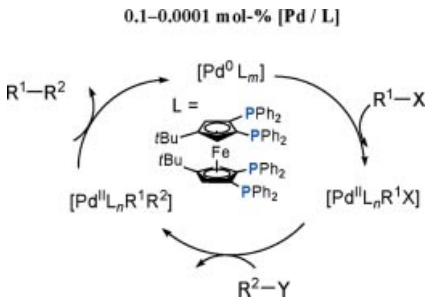



The search for catalytic longevity and ultra-low catalyst loadings on the basis of multidentarity effects and robustness of new ferrocenylphosphane ligands were focused on high-value palladium-catalyzed C−C cross-coupling reactions. Low-loading catalysis was also explored with success for C−N cross-coupling in the allylic amination of achiral substrates.


## SHORT COMMUNICATIONS


### Mo Poly(methimazolyl)borates

**A. F. Hill,* N. Tshabang, A. C. Willis ..... 3781−3785**

Poly(methimazolyl)borate Alkyne Complexes of Molybdenum and Tungsten

**Keywords:** Alkyne / Molybdenum / Tungsten / Methimazolylborates / Scorpionates

Synthetic routes are reported for the complexes [MI(alkyne)(CO){H$_n$B(mt)$_{4-n}$}] (mt = methimazolyl; $n$ = 1, 2; M = Mo, W). The reaction of [MoI(PhC≡CPh)(CO){HB(mt)$_3$}] with Na[HB(mt)$_3$] provides [Mo(PhC≡CPh)(CO){HB(mt)$_3$}$_2$] which features both κ$^3$-*S*,*S*′,*S*″ (mauve) and κ$^1$-*S* (cyan) coordination modes.



### Heteromultimetallic Complexes

**R. Packheiser, H. Lang* ..... 3786−3788**

The First Heterohexametallic Transition-Metal Complex

**Keywords:** Heteromultimetallic / Transition metal / Acetylides / Organometallic π-tweezers / Transmetallation / Mass spectrometry


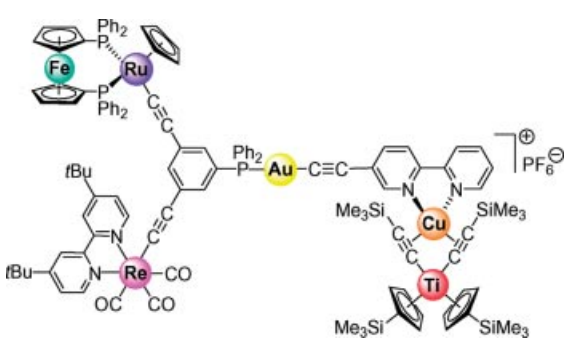



The synthesis of a heterohexanuclear Fe-Ru-Re-Au-Cu-Ti metal complex and its characterisation by $^1$H, $^{31}$P{$^1$H} NMR and IR spectroscopy, elemental analysis and ESI mass spectrometry are reported.

# FULL PAPERS

## Supramolecular Glue

Perchlorate counterions were found to act as supramolecular glue through hydrogen-bonding interactions, promoting the assembly of μ-aqua manganese−Schiff-base dimers into a 1D network of complexes.

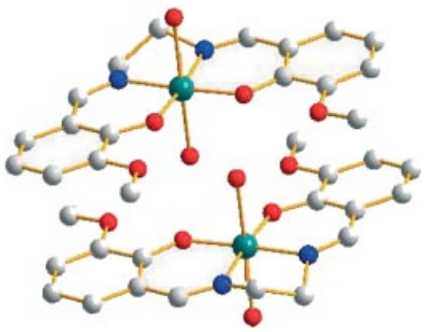

**M. R. Bermejo, M. I. Fernández,* E. Gómez-Fórneas, A. González-Noya, M. Maneiro,* R. Pedrido, M. J. Rodríguez ..... 3789−3797**

Self-Assembly of Dimeric $Mn^{III}$−Schiff-Base Complexes Tuned by Perchlorate Anions

**Keywords:** Manganese / Self-assembly / Anions / Schiff bases / Peroxidase

## Hollow Mesoporous Spheres

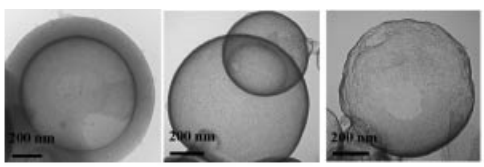


**Mesoporous Carbon Silica Metal Oxide hollow spheres**

PF−PEO polymer blend can be used as a novel organic template to synthesize mesoporous carbon or silica hollow spheres. The mesoporous carbon hollow spheres can act as a hard template for the preparation of mesoporous oxide hollow spheres.

**C.-Y. Chang-Chien, C.-H. Hsu, T.-Y. Lee, C.-W. Liu, S.-H. Wu, H.-P. Lin,* C.-Y. Tang, C.-Y. Lin ..... 3798−3804**

Synthesis of Carbon and Silica Hollow Spheres with Mesoporous Shells using Polyethylene Oxide/Phenol Formaldehyde Polymer Blend

**Keywords:** Polymer blends / Mesoporous materials / Metal oxides / Organic templates

## Amphoteric Dopants

The reaction of $Er[N(SiMe_3)_2]_3$ with a series of alcohols (HOR) in selected solvents led to the isolation of a family of $Er(OR)_3$ compounds (**1**−**19**, **11** shown). Representative members of the $Er(OR)_3$ precursors were used for the production of a PErZT precursor solution, which was subsequently used to generate thin films and nanoparticles as well as $Er_2O_3$ nanoparticles (shown).

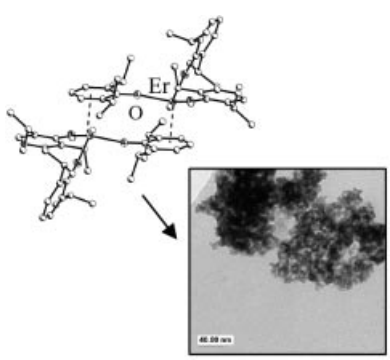


**T. J. Boyle,* L. A. M. Ottley, L. N. Brewer, J. Sigman, P. G. Clem, J. J. Richardson ..... 3805−3815**

Structurally Characterized Erbium Alkoxides for Use as an Amphoteric Dopant in PErZT Ceramic Thin Film and Nanoparticles

**Keywords:** Ceramics / Perovskites / Nanomaterials / Lanthanide alkoxides / PZT

## Ethylene Oligomerization

Nickel(II) complexes ligated by 2-(benzimidazol-2-yl)-1,10-phenanthrolines were synthesized and characterized. Upon activation with $Et_2AlCl$, these complexes exhibited excellent activities for ethylene oligomerization with high selectivities for 1-butene.

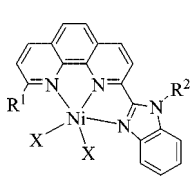


**M. Zhang, S. Zhang, P. Hao, S. Jie, W.-H. Sun,* P. Li, X. Lu ..... 3816−3826**

Nickel Complexes Bearing 2-(Benzimidazol-2-yl)-1,10-phenanthrolines: Synthesis, Characterization and Their Catalytic Behavior Toward Ethylene Oligomerization

**Keywords:** Nickel / Tridentate complexes / Phenanthrolines / Ethylene oligomerization / Oligomerization

 © 2007 Wiley-VCH Verlag GmbH & Co. KGaA, Weinheim 

# CONTENTS


## Ruthenium Complexes

**S. Y. Ng, J. Tan, W. Y. Fan, W. K. Leong, L. Y. Goh,* R. D. Webster ..... 3827–3840**

Synthetic, X-ray Diffraction, Electrochemical, and Density Functional Theoretical Studies of (Indenyl)ruthenium Complexes Containing Dithiolate Ligands

**Keywords:** Ruthenium complexes / Dithiolates / Cyclic voltammetry / Density functional calculations

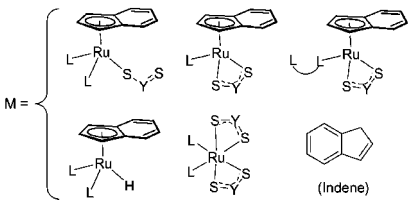


Halide substitution of the complexes [(Ind)Ru($L_2$)X] [($L_2$) = dppf, X = Cl; ($L_2$) = dppm, X = Cl; and ($L_2$) = $(CO)_2$, X = I] with the 1,1-dithiolates $^{-}S_2Y$ (Y = $CNR_2$, COR, $PR_2$) gives rise to a product mixture (M) dependent on the nature of $L_2$, $S_2Y$, and the solvent.

## Hollow Nanospheres

**M. Yang, Y. Zhang, G. Pang,* S. Feng ..... 3841–3844**

Preparation of $Cu_2O$ Hollow Nanospheres under Reflux Conditions

**Keywords:** Cuprous oxide / Nanospheres / Reflux conditions

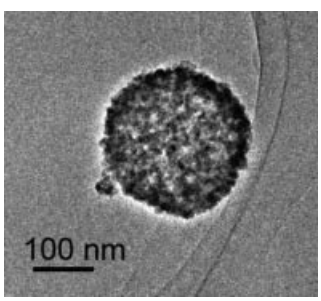


Cuprous oxide hollow nanospheres with diameters of 100–200 nm were prepared by heating a solution of copper acetate and hydrazine as a reductant in 2-propanol at reflux. The UV/Vis diffuse reflectance spectrum indicates that the optical absorption edge of the hollow $Cu_2O$ nanospheres is redshifted relative to their solid counterparts.

## $Mn^{II}$ Supramolecules

**L.-P. Sun, S.-Y. Niu,* J. Jin, L. Zhang ..... 3845–3852**

Crystal Structure and Surface Photovoltage Properties of $Mn^{II}$ Coordination Supramolecules

**Keywords:** Manganese / Hydrogen bonds / Surface photovoltage spectroscopy

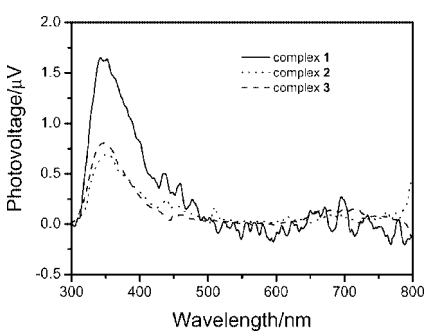


Three $Mn^{II}$ coordination supramolecules were hydrothermally synthesized and characterized by crystallography and SPS techniques. Complexes **1**–**3** exhibit positive SPV response in the range of 300–800 nm; the differences in intensities are attributable to differences in the structures of the complexes. They also possess *p*-type semiconductor characteristics.

## Ferrocenophane-Based Phosphanes

**N. Fleury-Brégeot, A. Panossian, A. Chiaroni, A. Marinetti* .... 3853–3862**

Stereospecific Synthesis, Structural Characterisation and Resolution of 2-Phospha-[3]ferrocenophane Derivatives – a New Chiral Scaffold

**Keywords:** Phosphane ligands / Ferrocenophane / Chiral resolution / Palladium

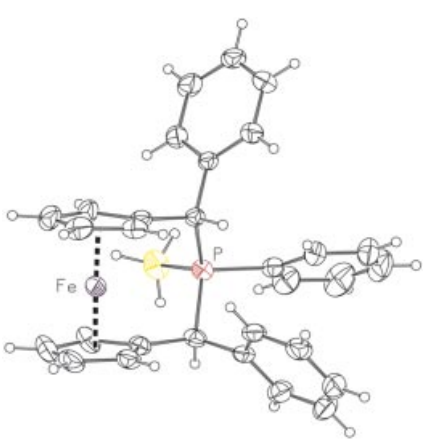


A stereospecific synthetic approach gives access to 2-phospha[3]ferrocenophane derivatives containing stereogenic carbon atoms in the three-atom bridge. The first chiral phosphane of this series has been obtained in enantiomerically pure form by resolution with a chiral cyclopalladate complex.


 © 2007 Wiley-VCH Verlag GmbH & Co. KGaA, Weinheim 

## Europium-Doped Nanodisks

Singly crystalline $LaF_3:Eu^{3+}$ nanodisks with a hexagonal structure were synthesized by a simple method. The mechanism of formation of the nanodisks was explored; furthermore, the size of the disks can be simply moderated by varying the concentration of the initial reactants.

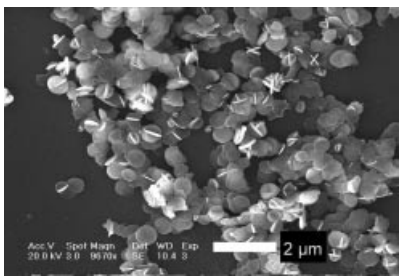


**L. Zhu, J. Meng, X. Cao* ..... 3863–3867**

Facile Synthesis and Photoluminescence of Europium Ion Doped $LaF_3$ Nanodisks

**Keywords:** Materials science / Crystal growth / Rare earths / Fluorescence

## Silver Coordination Polymers

One rigid bent bridging ligand with highly planar π-conjugated spacers, 3,6-dicyano-9-phenylcarbazole (dcphcz), was designed and synthesized. The coordination of the ligand dcphcz with a series of $Ag^I$ salts with different counterions has been investigated. Four new Ag-containing coordination polymers with different polymeric motifs, $\{[Ag(dcphcz)]BF_4\}_n$, $\{[Ag(dcphcz)]ClO_4\}_n$, $\{[Ag(dcphcz)][Ag_2(dcphcz)(H_2O)_2](SO_3CF_3)_3{\cdot}C_6H_6{\cdot}(H_2O)_2\}_n$, and $[Ag_2(dcphcz)(CF_3COO)_2]_n$, were obtained.

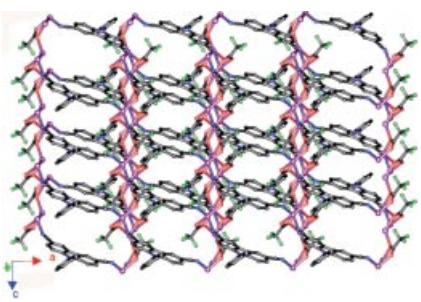

**K.-J. Wei, J. Ni, J. Gao, Y. Liu,* Q.-L. Liu* ..... 3868–3880**

Self-Assembly of Silver(I) Coordination Polymers from AgX (X = $BF_4^-$, $ClO_4^-$, $CF_3COO^-$, and $SO_3CF_3^-$) and a Rigid Bent 3,6-Dicyano-9-phenylcarbazole Ligand: The Templating Effect of Anions

**Keywords:** Silver / N ligands / Supramolecular chemistry / Luminescence / Coordination polymers / Metal-organic frameworks

## Aminophosphinic Acids

The acid–base properties of two tetraaminophosphinic acid ligands and their complexation with $Cu^{2+}$, $Ni^{2+}$, and $Zn^{2+}$ ions were studied by potentiometry. Both ligands behave similarly to linear tetraamines. The phosphinic acid moiety shows weak coordination ability. In the solid state, nitrogen atoms coordinate the metal ions mostly in a square-planar fashion.

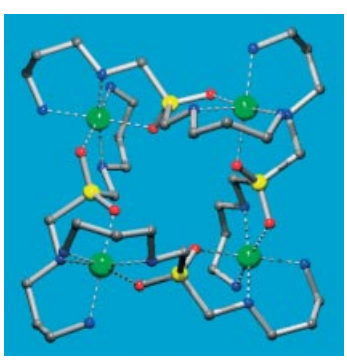

**V. Kubíček,* I. Řehoř, J. Havlíčková, J. Kotek, I. Císařová, P. Hermann, I. Lukeš ..... 3881–3891**

Synthesis and Coordination Behavior of Symmetrical Tetraamine Phosphinic Acids

**Keywords:** Aminophosphinates / Complexes / Stability constants / Potentiometry

## Hydrogen-Bonded Helices

Three metal–organic coordination polymers were synthesized under hydrothermal conditions. The bptc ligand takes part in three different coordination modes, and compound **1** exhibits a 3D network with 1D open channels that contain free solvent water molecules. Two kinds of chiral, helical, hydrogen-bonded chains exist in the neighboring holes.

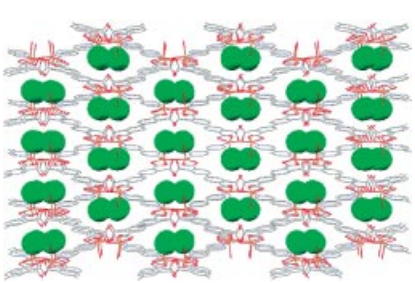

**G.-P. Yang, Y.-Y. Wang,* L.-F. Ma, J.-Q. Liu, Y.-P. Wu, W.-P. Wu, Q.-Z. Shi ..... 3892–3898**

Hydrothermal Syntheses and Characterizations of Three Coordination Polymers Based on Mixed Organic Ligands

**Keywords:** Copper / Manganese / Coordination polymers / Hydrogen bonds

 © 2007 Wiley-VCH Verlag GmbH & Co. KGaA, Weinheim 

# CONTENTS

## Mesomorphic Compounds

**J.-M. Suisse, L. Douce,***
**S. Bellemin-Laponnaz, A. Maisse-François, R. Welter, Y. Miyake, Y. Shimizu ..... 3899–3905**

Liquid Crystal Imidazolium Salts: Towards Materials for Catalysis and Molecular Electronics

**Keywords:** iquid crystals / Imidazolium ions / Pd–carbenes / Homogenous catalysis / Conducting materials

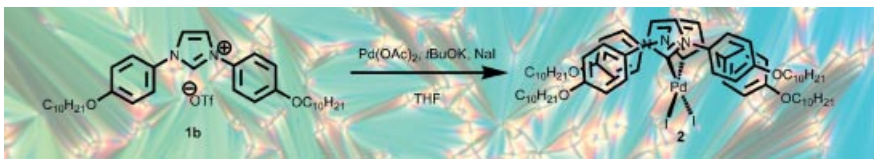


The imidazolium ion exhibits liquid crystalline behaviour over a significant temperature range and serves as a N-heterocyclic carbene ligand for Pd-catalysed cross-coupling reactions. A lamellar crystal structure of the $Pd^{II}$ *cis*-carbene with decyl tails was obtained, and the charged carrier mobilities of the $C_{10}$ salt in the smectic-A phase was measured.

## Rutile Frameworks

**F. Luo, Y.-x. Che, J.-m. Zheng* ..... 3906–3910**

Rarely Decorated Rutile Frameworks Built from Triangular Organic Spacers and Distorted Octahedral $Co_3$ Building Blocks

**Keywords:** Solvothermal syntheses / Rutile / Cobalt / Polymers

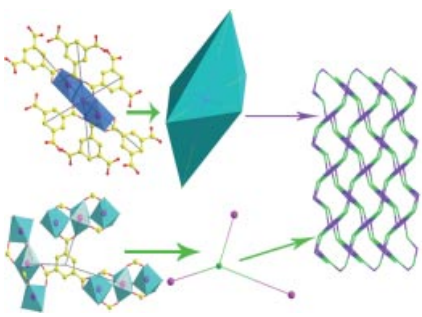

The first exploration of the synthesis of metal–organic frameworks in solutions of dmso resulted in rare noninterpenetrating decorated rutile frameworks with the $(4.6^2)_2(4^2.6^{10}.8^3)$ topology, built on three-connected organic spacers and six-connected $Co_3$ nodes.

**If not otherwise indicated in the article, papers in issue 23 were published online on July 31, 2007**

 © 2007 Wiley-VCH Verlag GmbH & Co. KGaA, Weinheim 

# SPOTLIGHTS …

## *Click Chemistry*

A. Dondoni*

**Triazole: the Keystone in Glycosylated Molecular Architectures Constructed by a Click Reaction**

*Chem. Asian J.*
DOI: **10.1002/asia.200700015**

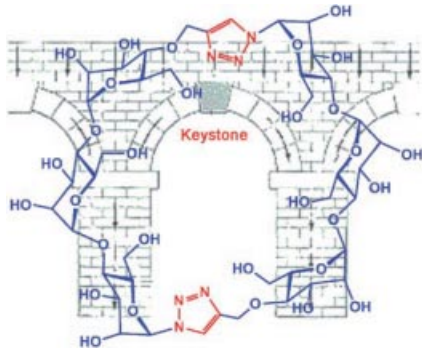


**Things don't fall apart**: Like the wedge-shaped keystone in the central part of an arch, triazole units formed by $Cu^{I}$-catalyzed azide–alkyne coupling acts as the ligation element of glycosylated molecular fragments. This structural motif is present in various complex glycoconjugates such as glycoclusters, glycodendrimers, glycopolymers, glycomacrocycles, and DNA strands.

## *Natural Products*

Y. A. Elnakady, M. Rohde, F. Sasse, C. Backes, A. Keller, H.-P. Lenhof, K. J. Weissman, R. Müller*

**Evidence for the Mode of Action of the Highly Cytotoxic *Streptomyces* Polyketide Kendomycin**

*ChemBioChem*
DOI: **10.1002/cbic.200700050**

**The first macrocyclic polyketide proteasome inhibitor**. Kendomycin is a macrocyclic polyketide recently discovered in several *Streptomyces* species. We provide evidence here that kendomycin's potent antiproliferative activity derives from inhibition of the proteasome. Kendomycin therefore represents the founding member of a new class of proteasome inhibitors with promise both in therapy and in chemical genetics.

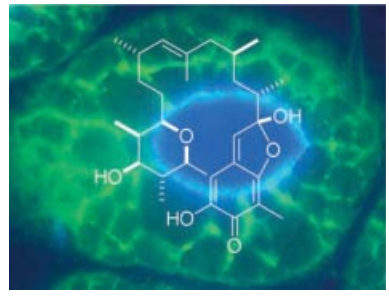

## *Single-Molecule Study*

B. I. de Bakker, F. de Lange, A. Cambi, J. P. Korterik, E. M. H. P. van Dijk, N. F. van Hulst, C. G. Figdor, M. F. Garcia-Parajo*

**Nanoscale Organization of the Pathogen Receptor DC-SIGN Mapped by Single-Molecule High-Resolution Fluorescence Microscopy**

*ChemPhysChem*
DOI: **10.1002/cphc.200700169**

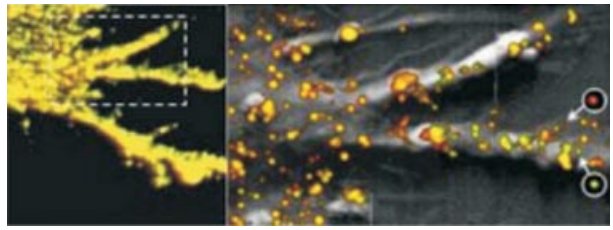

**Near-field scanning optical microscopy** (NSOM) was used to visualize the nanoscale spatial arrangement of the lectin DC-SIGN on the membrane of intact dendritic cells. Whereas the confocal image has a diffraction-limited resolution of about 350 nm (see picture, left), NSOM can visualize DC-SIGN nanodomains with a spatial resolution of less than 100 nm (right).

## *Glycomimetics*

K. Marotte, C. Sabin, C. Préville, M. Moumé-Pymbock, M. Wimmerová, E. P. Mitchell, A. Imberty,* R. Roy*

**X-ray Structures and Thermodynamics of the Interaction of PA-IIL from *Pseudomonas aeruginosa* with Disaccharide Derivatives**

*ChemMedChem*
DOI: **10.1002/cmdc.200700100**

**The disaccharide αFuc1-4GlcNAc** has been used as a scaffold toward the synthesis of a series of derivatives targeting the fucose binding lectin from *Pseudomonas aeruginosa*. High affinity has been measured by titration microcalorimetry and structural studies rationalized the difference observed for the thermodynamics of binding between the natural and the synthetic ligands.

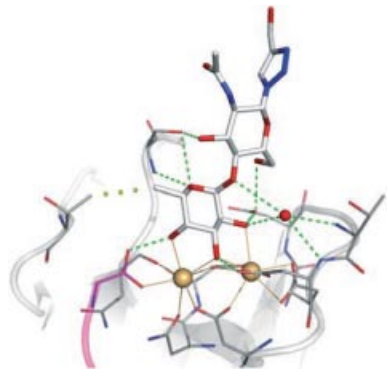

 © 2007 Wiley-VCH Verlag GmbH & Co. KGaA, Weinheim 

EurJIC European Journal of Inorganic Chemistry

**Platinum favors alpha**: Gase-phase reactions of size-selected platinum cluster cations with hydrocarbons reveal a preference for α-hydrogen atoms upon dihydrogen elimination (see scheme). These observations are in strong contrast to rhodium, which favors 1,2-elimination and explains why platinum is reactive towards methane whilst rhodium is not.

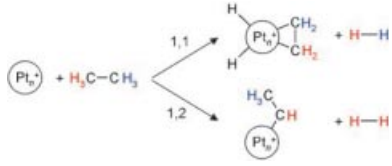


***Heterogeneous Catalysis***

C. Adlhart, E. Uggerud*

**Mechanisms for the Dehydrogenation of Alkanes on Platinum: Insights Gained from the Reactivity of Gaseous Cluster Cations, $Pt_n^+$ $n = 1–21$**

*Chem. Eur. J.*
DOI: **10.1002/chem.200700501**

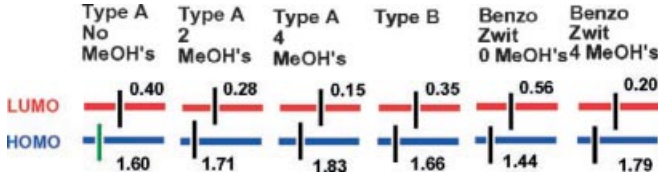


The zwitterion vs. diradical nature of the S0 intermediate in photochemical enone and dienone rearrangements has been assessed by experimental and computational means. In this study we report a number of new reactions and their mechanisms in both ground and excited states. Natural orbital analyses are used in one approach. Charge and electron density distribution are used in another. Explicit inclusion of solvent is demonstrated to be important.

***Photochemistry***

H. E. Zimmerman,* V. Suryanarayan

**Organic Photochemical Rearrangements of Triplets and Zwitterions; Mechanistic and Exploratory Organic Photochemistry**

*Eur. J. Org. Chem.*
DOI: **10.1002/ejoc.200700456**

**It's elemental**: A water-soluble polymer bearing multiple metal-chelating ligands has been used as a tag for bioassays with inductively coupled plasma mass spectrometry. The tag was covalently conjugated to antibodies, and the polymer–antibody constructs were loaded with lanthanide ions ($Ln^{3+}$) and used for the simultaneous assay of five orthogonally labeled antibodies against cell surface antigens that differ in abundance by more than two orders of magnitude.

***Bioassays***

X. Lou, G. Zhang, I. Herrera, R. Kinach, O. Ornatsky, V. Baranov,* M. Nitz,* M. A. Winnik*

**Polymer-Based Elemental Tags for Sensitive Bioassays**

*Angew. Chem. Int. Ed.*
DOI: **10.1002/anie.200700796**

On these pages, we feature a selection of the excellent work that has recently been published in our sister journals. If you are reading these pages on a computer, click on any of the items to read the full article. Otherwise please see the DOIs for easy online access through Wiley InterScience.

 © 2007 Wiley-VCH Verlag GmbH & Co. KGaA, Weinheim 

DOI: 10.1002/ejic.200700405

# Ultra-Low Catalyst Loading as a Concept in Economical and Sustainable Modern Chemistry: The Contribution of Ferrocenylpolyphosphane Ligands

**Jean-Cyrille Hierso,*[a] Matthieu Beaupérin,[a] and Philippe Meunier[a]**

**Keywords:** Sustainable chemistry / Homogeneous catalysis / P ligands / Ferrocenylphosphanes / Cross-coupling / Multidentate ligands

The challenge of sustainability in modern chemistry will be met with new technologies and processes provided significant progress is made in several key research areas, such as the expansion of chemistry from renewable feedstock, the design of environmentally benign chemicals and solvents, the minimization of depletive resources, and the development of high-performance catalysis. In this prospect, ligand chemistry is a pivotal science that links modern-organic, -inorganic, -organometallic, and -coordination chemistry through a vast number of valuable applications, precisely associated to catalysis. We review in this article our recent work on catalysis promoted by original ferrocenyl tetra-, tri-, and diphosphane ligands. New concepts, taking advantages of this family of branched multidentate ligands, have led to progress in homogeneous catalysis. The search for catalyst longevity and ultra-low catalyst loadings (high turnover numbers), on the basis of multidentarity effects and robustness of the ferrocenyl backbone were focused on high-value palladium-catalyzed C–C cross-couplings, such as Heck, Suzuki, and Sonogashira reactions. Low catalyst loading was also explored for C–N cross-coupling in the allylic amination of achiral substrates. The advantages of this newly born family of ligands in the class of multidentate compounds are discussed in light of the valuable information gathered up to now on their reactivity, structure, and mechanistic behavior.

(© Wiley-VCH Verlag GmbH & Co. KGaA, 69451 Weinheim, Germany, 2007)

## Introduction and Scope

Sustainable chemistry is expected, at the beginning of this new century, to solve many of the global environmental challenges we must face. This major societal and economic matter is now a priority of the scientific research programs in many industrialized nations,[1] and a guidance for chemists on this multiparameter question is summarized by the twelve principles of green chemistry.[2] One of these principles, which concerns explicitly catalytic chemistry, states: "Catalytic reagents (as selective as possible) are superior to stoichiometric reagents". The underlying idea of this principle is that, owing to catalysis, the minimization of the resources consumed and the economy of atoms is effective. However, a practical overview of the huge field covered by the term "catalysis" shows that the so-called "catalyst amount" ranges from substoichiometric amounts (30 mol-%) to amazingly low quantities down to $10^{-6}$ mol-%.[3,4]

Among the most fertile and innovative fields in "catalysis" for the last three decades is the formation of carbon–carbon bonds by employing active transition metals (Scheme 1). In this prospect, palladium catalysts emerged as powerful tools in reactions aimed at the coupling of organic halides with organometallic substrates that are based mainly on boron- (Suzuki–Miyaura reaction), tin- (Stille reaction), zinc- (Negishi reaction), silicon- (Hiyama reaction), or magnesium reagents (Kumada–Corriu reaction).[5]

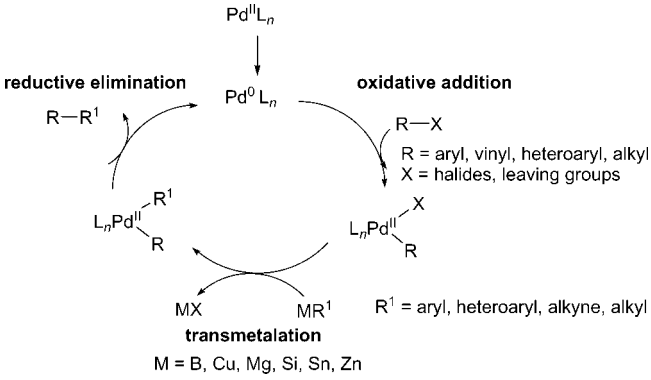


Scheme 1.

From an economic and financial point of view,[6] the catalyst turnover number (TON)[7] is a key parameter for industrial applications. Relevant recent reviews by Farina[8] and by Corbet and Mignani[5] illustrated that the efficient use of a catalytic system at less than $10^{-1}$ mol-% (TON ≥ 1000) can avoid its recovery and thus its recycling. Convergent benefits are found between industrial and sustainable development with the use of such kind of high-efficiency catalytic systems. As a consequence, in the last

[a] ICMUB (Institut de Chimie Moléculaire de l'Université de Bourgogne) – UMR CNRS 5260 – Université de Bourgogne, 9 avenue Alain Savary, 21078 Dijon, France
Fax: +33-3-80-39-36-82
E-mail: jean-cyrille.hierso@u-bourgogne.fr

 © 2007 Wiley-VCH Verlag GmbH & Co. KGaA, Weinheim 

decade the progress on ligand chemistry became a major goal in the community of the organic chemist, and creativity partnered with a better understanding of the mechanistic necessities led to the emergence of several families of useful ligands for high-turnover palladium catalytic systems. For instance, and nonexhaustively: bulky electron-rich trialkylmonophosphanes,[9] (biaryl)dialkylphosphanes,[10] di- and tridentate pincers,[11] heterostructures at the origin of various palladacycles,[12,13] carbenes,[14] or multidentate polyphosphanes (Scheme 2) were found to be very efficient catalytic auxiliaries.[15]

On this basis and ongoing since the mid 1990s we developed the design, synthesis, and characterization of original di-, tri-, and tetraphosphanes built on the ferrocenyl backbone (some representative examples of the library of ligands developed are depicted in Scheme 3). Catalytic applications of a selection of these ligands with palladium in the formation of C–C and C–N bonds are reviewed herein. The reactions explored, namely Suzuki, Heck, and Sonogashira cross-couplings, as well as the amination of allylic acetates, led either to high TONs or high turnover frequencies (TOFs) depending on the reaction and on the ligands. The general advantages of this newly born family of ligands, in the class of multidentate species, are detailed and discussed in light of the gathered structural and mechanistic information. Finally, some of the trends and properties identified could serve as a privileged starting point for the further development of the promising concepts of catalyst *longevity* and ultra-low catalyst loading.

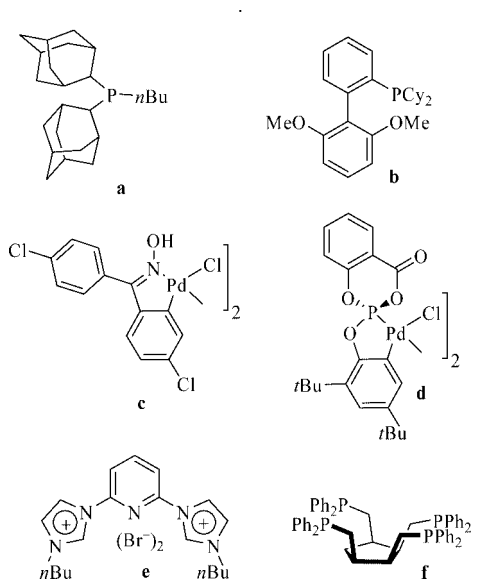


Scheme 2.

## Milestones in Ultra-Low Catalyst Loadings

In 1995 Herrmann and coworkers reported "...new, structurally defined, easy-to-handle palladium complexes, that surpass all previously known catalysts of the Heck reaction as regards stability and lifetime."[16] The authors observed from kinetic measurements that standard catalytic systems combining 1 mol-% $Pd(OAc)_2$ with 2–6 mol-% of

*Dr. Jean-Cyrille Hierso completed his Ph.D. in 1997 at the Université P. Sabatier and the National School of Engineer of Toulouse under the supervision of Prof. Ph. Kalck, after an M.S. degree with Drs. B. Chaudret and C. Amiens. He worked as a postdoctoral fellow first with Prof. M. Etienne (LCC-CNRS) then in the group of Prof. J. Reedijk (Leiden University, The Netherlands). In 2001, he was appointed Maître de Conférences at the Université de Dijon, and was awarded his Habilitation in 2006. He has coauthored about 40 papers in the fields of chemical vapor deposition, organometallic chemistry, hetero- and homogeneous catalysis, metalloligand synthesis, and coordination chemistry.*

*Matthieu Beaupérin was born in 1982 in Saint-Malo (France). In 2006, he graduated from the Graduate School of Chemistry and Chemical Engineering of Clermont-Ferrand (ENSCCF) specializing in organic chemistry. He is currently a Ph.D. student in the group of Prof. P. Meunier, where he is working under the supervision of J.-C. Hierso on the synthesis of ferrocenylphosphanes and their use in catalyzed cross-coupling reactions.*

*Prof. Philippe Meunier was born in Auxerre (France) in 1946. He obtained his Ph.D. (1979) in heterocyclic chemistry from the Université de Bourgogne after a long period of work in photoelectron spectroscopy and theoretical chemistry at the University of Pau. He then joined the group of organometallic chemistry at Dijon and began to work in group 4 organometallic chemistry. He became a full professor in 1992, and he is currently head of a research group in the Institute of Molecular Chemistry of the Université de Bourgogne (ICMUB-CNRS 5260). His research interests concern group 4 organometallic chemistry for synthesis and group 10 coordination chemistry for catalysis applications.*

 © 2007 Wiley-VCH Verlag GmbH & Co. KGaA, Weinheim 

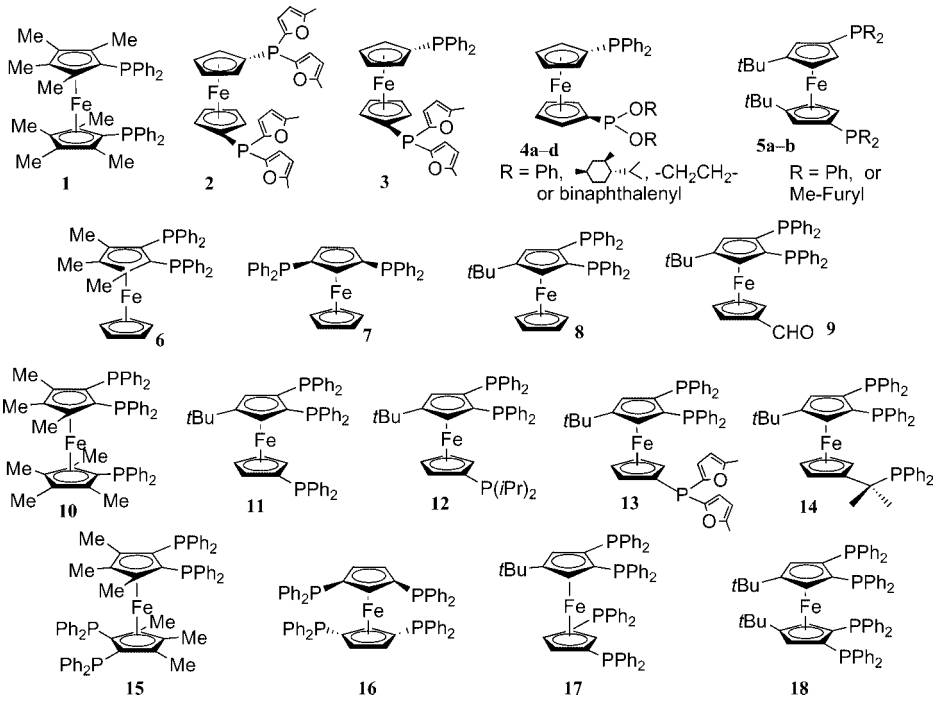


Scheme 3.

the triarylphosphane $PPh_3$ are rapidly deactivated in the Heck reaction between 4-bromoanisole and *n*-butyl acrylate above 120 °C; a temperature useful for the activation of demanding organic halides such as deactivated bromides and chlorides. The decomposition of the ligand ($P–C_{aryl}$ bond cleavage), as well as its oxidation [$P(O)Ph_3$ formation] were proposed to be responsible for the deposition of catalytically inactive palladium black. From the treatment of palladium(II) acetate with tris(*o*-tolyl)phosphane in toluene, cyclometalation afforded efficient palladacycle pre-catalyst **g** (Scheme 4).[16] In the Heck reaction of the activated 4-bromobenzaldehyde to *n*-butyl acrylate a TON of 200000 was obtained in a quantitative coupling achieved at 135 °C for 12 h ($5 \times 10^{-4}$ mol-% cat.).

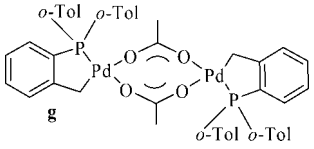


Scheme 4.

This study can be considered as a starting point in the explicit recognition of the concepts of long-term stability and increased lifetimes of the catalysts in palladium-catalyzed cross-coupling-type reactions. The mechanistic involvement of palladacycles in cross-couplings is subject of severe controversy:[8] whether palladacycles upon catalysis remain quasiunchanged and react in $Pd^{II}/Pd^{IV}$ processes, or only constitute slow-delivery reservoirs of active naked palladium, the result was a focus of the community on the ultra-low catalyst loading in C–C cross-coupling reactions.

After this work, the group of Beller[17] followed by Bedford[18] both confirmed the efficiency of palladacycles in the activation of aryl bromides for biaryl formation (in Suzuki coupling) under conditions of low catalyst loading. Palladacycle **g**, depicted in Scheme 4, allowed the coupling of phenylboronic acid to the electronically activated 4-bromoacetophenone with a TON of 74000 (yield 74%, in the presence of $10^{-3}$ mol-% cat. at 130 °C for 16 h) and to the electronically deactivated 4-bromoanisole with a TON of 7600 (yield 76%, in the presence of $10^{-2}$ mol-% cat.).[17] Orthopalladated triarylphosphite complex **h** (Scheme 5) was employed for the coupling of phenylboronic acid to 4-bromoacetophenone and 4-bromoanisole and resulted in the formation of coupling products with TONs of, respectively, 1000000 (yield 100%, in the presence of $10^{-4}$ mol-% cat. at 110 °C for 2 h) and 30000 (yield 30%, $10^{-3}$ mol-% cat. at 130 °C for 15 h).[18] The same phosphite palladacycle pre-catalyst allowed the Heck coupling of 4-bromoacetophenone to styrene, and 4-bromoanisole to *n*-butyl acrylate, with, respectively, TONs of 5700000 (yield 57%, $10^{-5}$ mol-% cat. at 180 °C for 69 h) and 9800 ($10^{-2}$ mol-% cat. at 160 °C for 65 h).[19]

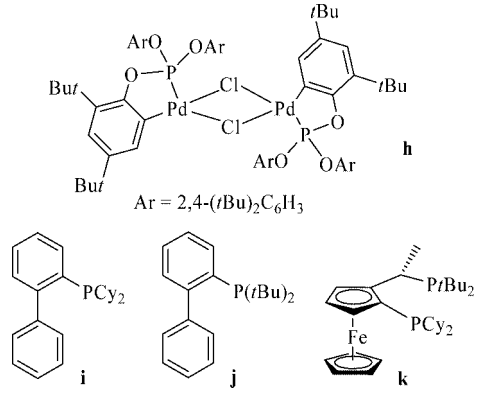


Scheme 5.

 © 2007 Wiley-VCH Verlag GmbH & Co. KGaA, Weinheim 

In 1999, Buchwald and coworkers disclosed a new family of ligands able to promote ultra-low loading catalysis with aryl bromides and chlorides.[20,21] (Biaryl)dialkylphosphanes **i** and **j** (Scheme 5) were the first of this class to be employed: the coupling of phenylboronic acid to the electronically activated 4-bromoacetophenone and the electronically deactivated 4-(*tert*-butyl)bromobenzene was effective with TONs of, respectively, 91000000 (yield 91%, $10^{-6}$ mol-% [Pd/2·**j**] at 100 °C for 24 h) and 18600 (yield 93%, $5 \times 10^{-3}$ mol-% [Pd/2·**i**] at 100 °C for 16 h). In addition, phenylboronic acid was successfully coupled to the electronically activated 4-chloroacetophenone with a TON of 4600 (yield 92%, $2 \times 10^{-2}$ mol-% [Pd/2·**j**] at 100 °C for 23 h), and to the electronically deactivated 4-chlorotoluene with a TON of 1860 (yield 93%, $5 \times 10^{-2}$ mol-% [Pd/2·**i**] at 100 °C for 25 h). These results well-illustrate the difficulties encountered when organic chlorides are preferred to bromides for cross-coupling. Interestingly, Buchwald indicated also at that time that the coupling of the electronically activated 4-bromoacetophenone was possible with $Pd(OA_C)_2$ in the absence of a ligand with a TON of 100000 (yield 100%, $10^{-3}$ mol-% Pd at 100 °C for 19 h) while "...under these conditions, Suzuki coupling reactions of other substrates give little or no products in the absence of phosphane ligands.";[21] anticipating, therefore, the future studies on ligand-free palladium low loading catalyst (see below).

After 2000, a blooming of the high-turnover palladium catalysts for the reactions of Heck, Suzuki, Stille, and Sonogashira occurred in the literature, with systems based on, for instance, ligands such as trialkylmonophosphanes,[9] modified (biaryl)dialkylphosphanes,[10] oxime palladacycles,[12] strongly π-acidic orthopalladated diarylphosphite palladacycles,[13] or carbenes[14] (respectively, **a**, **b**, **c**, **d**, and **e** in Scheme 2). The use of ferrocenyl diphosphanes, such as the electron-rich josiphos (**k**; Scheme 5) was also successful in some other low catalyst loading cross-couplings,[22] following the seminal works published by Hayashi et al. for the Kumada–Corriu reaction.[23] The high performances of the aforementioned systems were thoroughly reviewed in many recent articles,[8,24–28] and their portrayal fall out of the scope of the present review; however, two important points appeared to us as conceptual landmarks: the efficiency and scope of the multidentate diarylalkylphosphane named tedicyp (**f**; Scheme 2), and the so-called "homeopathic" ligand-free catalysis.

At the end of 2000, the first study by Doucet and Santelli appeared on the catalytic activity of the tetradentate polyphosphane ligand *cis*,*cis*,*cis*-1,2,3,4-tetrakis(diphenylphosphanylmethyl)cyclopentane (tedicyp) in C–N cross-coupling reactions.[15,29] By employing this original ligand in the palladium-catalyzed amination of allyl acetates, a TON of 680000 was obtained for the coupling of dipropylamine to allylacetate (yield 68%, $10^{-4}$mol-% cat. at 25 °C for 136 h). The authors intensively explored the catalytic performances of this multidentate ligand that is based on a cyclopentane alkyl backbone in the pallado-catalyzed reactions of allylic amination, Heck, Suzuki, and Sonogashira. This chemistry was reviewed recently,[4] nevertheless it is worthy of note that, in the reported corpus of more than 50 papers devoted to the activity of Pd/tedicyp in C–C and C–N cross-coupling, was described: (1) the coupling of phenylboronic acid to 4-bromoacetophenone and to 4-bromoanisole with TONs of, respectively, 96000000 (yield 96%, $10^{-6}$ mol-% cat. at 130 °C for 135 h) and 93000 (yield 93%, $10^{-3}$ mol-% cat. at 130 °C for 24 h);[30] (2) the Heck coupling of activated 3,5-bis(trifluoromethyl)bromobenzene to *n*-butyl acrylate with a remarkable TON of 210000000 (yield 21%, $10^{-7}$ mol-% cat. at 130 °C for 72 h) or with a TON of 78000000 and a better yield of 78% ($10^{-6}$ mol-% cat. at 130 °C for 40 h), and the coupling of deactivated 4-bromoanisole to *n*-butyl acrylate with a TON of 82000 (yield 82%, $10^{-3}$ mol-% cat. at 130 °C for 72 h);[31] (3) the Sonogashira cross-coupling of phenylacetylene to 4-bromoacetophenone and 4-bromoanisole with TONs of, respectively, 700000 (yield 70%, $10^{-4}$ mol-% cat. at 140 °C for 20 h) and 3800 (yield 38%, $10^{-2}$ mol-% cat. at 140 °C for 20 h).[32] The scope and performances of tedicyp shed light on the interest of examining the activity of multidentate phosphanes for the development of ultra-low loading catalytic processes.

The term of "homeopathic" catalyst loading has been related to the ligand-free palladium-catalyzed Heck reaction and biaryl formation.[33] Whereas this expression is objectively inappropriate for several reasons,[34] the ligand-free catalysis results that are associated with it are interesting from an economic and environmental point of view. Ligand-free $Pd(OAc)_2$ can be used as a catalyst in the Heck reaction of aryl bromides as long as the amount of catalyst is kept between $10^{-1}$ to $10^{-2}$ mol-% (TONs ranging from 1000 to 10000). For instance, in the coupling of the activated 4-bromobenzaldehyde to *n*-butyl acrylate a TON of 2000 was obtained with a quantitative coupling achieved at 135 °C in only 1 h ($5 \times 10^{-2}$ mol-% cat.). As expected, the coupling of deactivated 4-bromoanisole to *n*-butyl acrylate was more difficult, leading to a TON of 1800 in 5 h at 135 °C (yield 91%, $5 \times 10^{-2}$ mol-% cat.).[3] The authors believe that the corresponding concentration of palladium is low enough to preclude deactivation by palladium-black formation; conversely, a catalyst/substrate ratio lower than $10^{-2}$ mol-% lead to a conversion too slow to be practical. The limits of this interesting concept were found for couplings such as Negishi- (with zinc organometallics) and Kumada–Corriu reactions (with Grignard reagents), whereas the Suzuki reaction could be carried out with aryl bromides in the presence of $5 \times 10^{-1}$ to $2 \times 10^{-2}$ mol-% of $Pd(OAc)_2$: for instance, the coupling of phenylboronic acid to activated 4-bromoacetophenone was achieved with a TON of 4800 (yield 95%, $2.5 \times 10^{-2}$ mol-% cat., at 90 °C in 4 h). These results illustrate that to reach the lowest catalyst loadings (below $10^{-2}$ mol-% cat.) the stabilization and steric/electronic activation provided by the ligand chemistry remain up to now unavoidable. Table 1 summarizes the short historical perspective given above through the example of the Suzuki reactions under ultra-low catalyst loading conditions.

Finally, to develop our projects on sustainable chemistry and ultra-low catalyst loading we were inspired by a study

 © 2007 Wiley-VCH Verlag GmbH & Co. KGaA, Weinheim 

Table 1. Historical perspective of C–C coupling under ultra-low catalyst loadings in Suzuki reactions (1995–2001[a]).

| Coupling reagents | Catalyst or ligand | Class of ligand or catalyst | TON | Ref. |
|---|---|---|---|---|
| 4-Bromoacetophenone/phenylboronic acid | **g** | palladacycle | 74000 | [17] |
| 4-Bromoanisole/phenylboronic acid | **g** | | 7600 | [17] |
| 4-Bromoacetophenone/phenylboronic acid | **h** | phosphite palladacyle | 1000000 | [18] |
| 4-Bromoanisole/phenylboronic acid | **h** | | 30000 | [18] |
| 4-Bromoacetophenone/phenylboronic acid | **j** | (biaryl)dialkylphosphane | 91000000 | [20] |
| 4-*t*Bu-bromobenzene/phenylboronic acid | **j** | | 18600 | [20] |
| 4-Bromoacetophenone/phenylboronic acid | **f** | alkyl tetraphosphane | 96000000 | [28] |
| 4-Bromoanisole/phenylboronic acid | **f** | | 93000 | [28] |
| 4-Bromoacetophenone/phenylboronic acid | **18** | ferrocenyl tetraphosphane | 100000 | [b] |
| 4-Bromoanisole/phenylboronic acid | **18** | | 77000 | [b] |
| 4-Bromoacetophenone/phenylboronic acid | $Pd(OAc)_2$ | ligand-free | 4800 | [31] |
| 4-Bromoanisole/phenylboronic acid | $Pd(OAc)_2$ | ligand-free | 0 | [21] |

[a] Selected results from the first section, systematic ligand-free studies appeared after 2001. [b] Work reviewed herein.

reported in 2002 by Bedford on "...the importance of catalyst longevity".[13] The difficulties encountered in the coupling of halides other than iodides has often been ascribed to their reluctance to perform the oxidative addition to palladium. Improved catalytic activities were detected from systems that combine palladium to hindered strongly σ-electron-donating ligands (such as trialkylphosphanes); in addition, the success of bulky ligands has been suggested to be derived from the ability of these ligands to promote geometrically driven coordinative unsaturation important to the transmetalation and reductive elimination steps. The perspective of Bedford and coworkers was different when they attributed the spectacular TONs they observed (with poor σ-donor phosphonite ligand **d**; Scheme 2) not to a specific high activity of their catalyst but more to an outstanding *catalyst longevity*. This concept of catalyst longevity, and consequently the stability of the catalytic species under the reaction conditions, appeared primordial to us for sustainable chemistry and led us to employ the robust ferrocenyl backbone as a platform with a tunable flexibility to build new active ligands.

## Performances of Ferrocenylphosphanes in Heck and Suzuki Reactions

### Structural Considerations for Tetraphosphane Ferrocenic Ligands

The ferrocenyl backbone, owing to its peculiar sandwich structure, displays a number of different conformations that have to be elucidated for ferrocenyl derivatives both in the solid-state and in solution. We were specifically interested in the mutual positions adopted by the different phosphorus atoms. For instance, tetraphosphanes **15** and **18** [1,1′,2,2′-tetrakis(diphenylphosphanyl)-3,3′-4,4′,5,5′-hexamethylferrocene and 1,1′,2,2′-tetrakis(diphenylphosphanyl)-4,4′-di-*tert*-butylferrocene; Scheme 3] revealed very different geometrical features. As shown by the molecular structures in Figure 1, in the solid state the favored conformation for **15** (Figure 1, left) shows the two chelating pairs of phosphorus atoms that face opposite directions (staggered conformation).

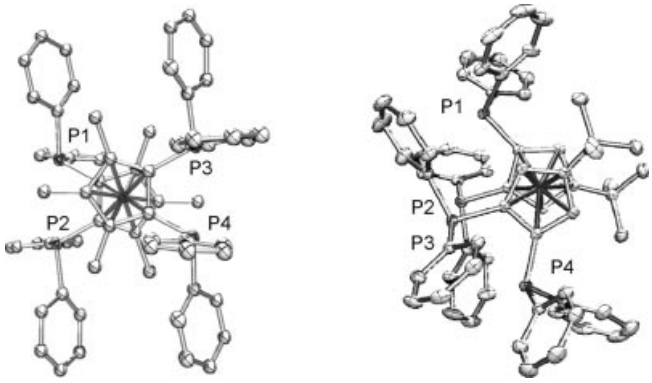


Figure 1. Molecular structures of **15** and **18** from X-ray diffraction studies (Povray illustration).

Conversely, in the favored conformation found for **18** (Figure 1, right) the four phosphorus atoms point towards the same half-space as a result of steric factors attributed to the hindering *tert*-butyl groups; the phenyl groups are also interlocked (P2 and P3 are in the eclipsed conformation).[35] In solution, NMR spectroscopic experiments indicated that the conformation of **18** is restricted, similarly to the solid state, exhibiting an AA′BB′ spin-system pattern. *The cisoid conformation for the tert-butylated tetraphosphane was conserved in solution above 90 °C, as attested by $^{31}P$ NMR spectroscopy in [$D_8$]toluene.* Therefore, in the multidentate ferrocenylphosphanes the coordination properties not only depend on the chelating possibilities of phosphorus (1,1′- or 1,2-P bonding) but also on the rotational features of the ferrocenic backbone, a rather unexploited facet prior to these studies.

### Suzuki C–C Cross-coupling and Heck Vinylation with a Ferrocenyltetraphosphane

As detailed above, in the last decade much progress in metal-catalyzed cross-coupling reactions was accomplished in the synthesis and recognition of efficient auxiliary ligands. Regarding the organic substrates now, significant advances have been reported on the activation of the relatively inert aryl bromides and chlorides relative to their iodide analogues; indeed, the relative reactivity of the aryl halides is well-established as Ar–I (65 kcal mol$^{-1}$ of bond dissoci-

 © 2007 Wiley-VCH Verlag GmbH & Co. KGaA, Weinheim 

ation energies) >> Ar–Br (81 kcal mol$^{-1}$) > Ar–Cl (96 kcal mol$^{-1}$).[36] As a consequence, we focused our efforts in the coupling of bromides and chlorides more than iodides. We verified, however, that concerning the coupling of activated or deactivated iodides all the catalytic systems described herein shows an enhancement in the activity of one or two orders of magnitude relative to bromides.

The first reaction we explored under conditions of ultra-low catalyst loading was the arylation of aryl halides with boronic acids (Scheme 6).[37] With the view to deliver more economical catalytic systems, we tested in priority nickel catalysts [$NiCl_2$, $Ni(cod)_2$, cod = 1,5-cyclooctadiene] with multidentate tetraphosphane **18** (Scheme 3), under various conditions, with unsuccessful results. Conversely, the results obtained by employing the system $[Pd(\eta^3\text{-}C_3H_5)Cl]_2$ combined with **18** were very interesting. High reaction rates were obtained with aryl bromides. TONs around 100000 were found for the coupling of phenylboronic acid to the activated 4-bromoacetophenone and 4-cyanobromobenzene (up to 150000 with 4-trifluoromethylbromobenzene) and a very good TON of 77000 was reached with deactivated 4-bromoanisole.

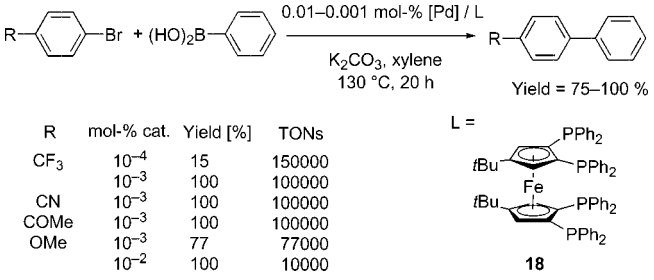


| R | mol-% cat. | Yield [%] | TONs |
|---|---|---|---|
| $CF_3$ | $10^{-4}$ | 15 | 150000 |
| | $10^{-3}$ | 100 | 100000 |
| CN | $10^{-3}$ | 100 | 100000 |
| COMe | $10^{-3}$ | 100 | 100000 |
| OMe | $10^{-3}$ | 77 | 77000 |
| | $10^{-2}$ | 100 | 10000 |

Scheme 6.

The coupling of chlorides, although successful for electronically activated substrates, did not allow reach high TONs (Scheme 7); the catalytic activity of the system, nevertheless, compared favorably to the activity of classical ligands such as $PPh_3$ or dppe [1,2-bis(diphenylphosphanyl)-ethane].[37] In the coupling of phenylboronic acid to electronically activated 4-chloroacetophenone, the systems combining [Pd/4 $PPh_3$] and [Pd/2 dppe] were found useless at low loadings of 0.1 mol-% cat. as less than 2% and only 22% yield, respectively, of the coupling products were obtained in 20 h. The catalyst [Pd/**18**] reached, under these conditions, a TON of 500 (yield 50%).

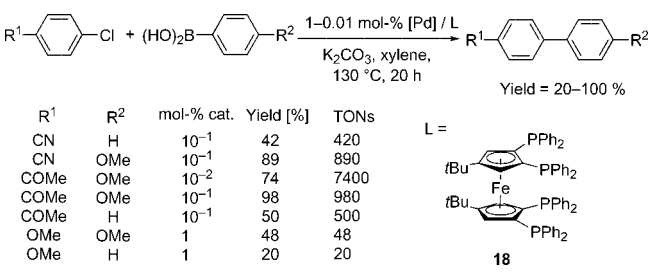


| $R^1$ | $R^2$ | mol-% cat. | Yield [%] | TONs |
|---|---|---|---|---|
| CN | H | $10^{-1}$ | 42 | 420 |
| CN | OMe | $10^{-1}$ | 89 | 890 |
| COMe | OMe | $10^{-2}$ | 74 | 7400 |
| COMe | OMe | $10^{-1}$ | 98 | 980 |
| COMe | H | $10^{-1}$ | 50 | 500 |
| OMe | OMe | 1 | 48 | 48 |
| OMe | H | 1 | 20 | 20 |

Scheme 7.

The highest TON of 7400 was obtained for the coupling of 4-methoxybenzeneboronic acid with 4-chloroacetophenone (yield 74%, $10^{-2}$ mol-%, 130 °C, 20 h). The substrate 4-cyanochlorobenzene was also efficiently coupled to 4-methoxybenzeneboronic acid with a TON of 890 (yield 89%, $10^{-1}$ mol-%). Lower TONs were obtained for the couplings with electronically deactivated 4-chloroanisole, showing the limit of the ligand, which remains nevertheless among the most active phosphanes in the class of the ligands incorporating exclusively aryl groups on the phosphorus atom (poor electron donor relative to alkyl substituents).

With the same catalytic system employed for Suzuki coupling, the Heck vinylation of aryl iodides and bromides with *n*-butyl acrylate, styrene, and *n*-butyl vinyl ether were investigated under conditions of very low catalyst loading (Scheme 8).[37] In the coupling of unactivated iodobenzene to *n*-butylacrylate, a very high TON of 1000000 was obtained (yield 100%, $10^{-4}$ mol-%, 130 °C, 48 h). With electronically deactivated 4-bromoanisole, the coupling to *n*-butyl acrylate and to styrene proceeded with high TONs of 10000 (yield 100%, $10^{-2}$ mol-%, 130 °C, 48 h) and 65000 (yield 65%, $10^{-3}$ mol-%, 130 °C, 20 h), respectively. Even the strongly deactivated electron-rich alkene *n*-butyl vinyl ether led to the corresponding adducts in the presence of 0.1 mol-% catalyst with TONs ranging from 250 to 400.

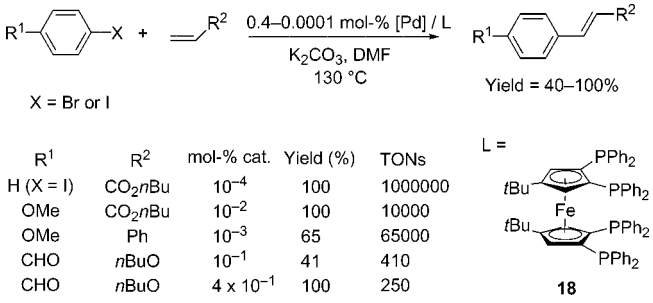


| $R^1$ | $R^2$ | mol-% cat. | Yield (%) | TONs |
|---|---|---|---|---|
| H (X = I) | $CO_2n$Bu | $10^{-4}$ | 100 | 1000000 |
| OMe | $CO_2n$Bu | $10^{-2}$ | 100 | 10000 |
| OMe | Ph | $10^{-3}$ | 65 | 65000 |
| CHO | *n*BuO | $10^{-1}$ | 41 | 410 |
| CHO | *n*BuO | $4 \times 10^{-1}$ | 100 | 250 |

Scheme 8.

The characterization of the complexes involved in the catalytic cycles is important to understand the origin of their activities under conditions of ultra-low catalyst loading. The palladium precatalyst complexes formed under the conditions employed for the Heck and Suzuki reactions in chlorinated solvents (P/Pd = 4) were identified as being ex-

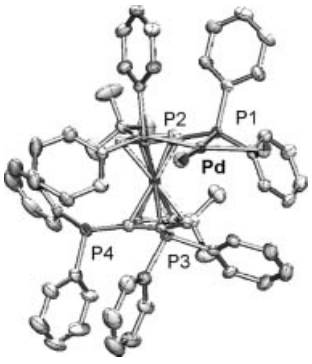


Figure 2. Molecular structure of [$PdCl_2$·**18**] from X-ray diffraction studies.

 © 2007 Wiley-VCH Verlag GmbH & Co. KGaA, Weinheim 

clusively 1,2-chelating P-bonded either mononuclear ([$PdCl_2$·**18**], see Figure 2, formed in majority above 90%) or dinuclear palladium chloride (<10%).[37]

NMR characterization in solution confirmed the solid-state X-ray analysis of the complexes, and clearly indicated that the phosphorus P3 atom is strongly oriented towards the (P1/Pd/P2) area of coordination (and especially its lone pair of electrons). The fine analysis of the unprecedented "through-space" coupling constants found between the phosphorus atoms was detailed,[38] and a theoretical model was proposed for nuclear spin transmitting.

In the course of the precatalyst characterization studies, an intriguing phenomenon was identified and investigated by variable-temperature $^{31}P$ NMR spectroscopy.[37] Under the starting conditions used for Heck and Suzuki catalysis (P/Pd = 4) was observed the occurrence of dynamic behavior at the scale rate of NMR spectroscopy. Two signals were detected between 0 and 10 ppm, an unusual range of chemical shift for the –$PPh_2$ groups (A in Figure 3).[39]

We envisioned that the four phosphorus atoms could be alternatively bonded and released from the palladium center, leading to large signals of average chemical shift. Upon cooling, the characteristic behavior of the labile compounds was confirmed with a coalescence and decoalescence (B in Figure 3) of the spin system. The dynamic phenomenon was reversible, and the labile species were stable up to 370 K. At this temperature the biligated mononuclear com-

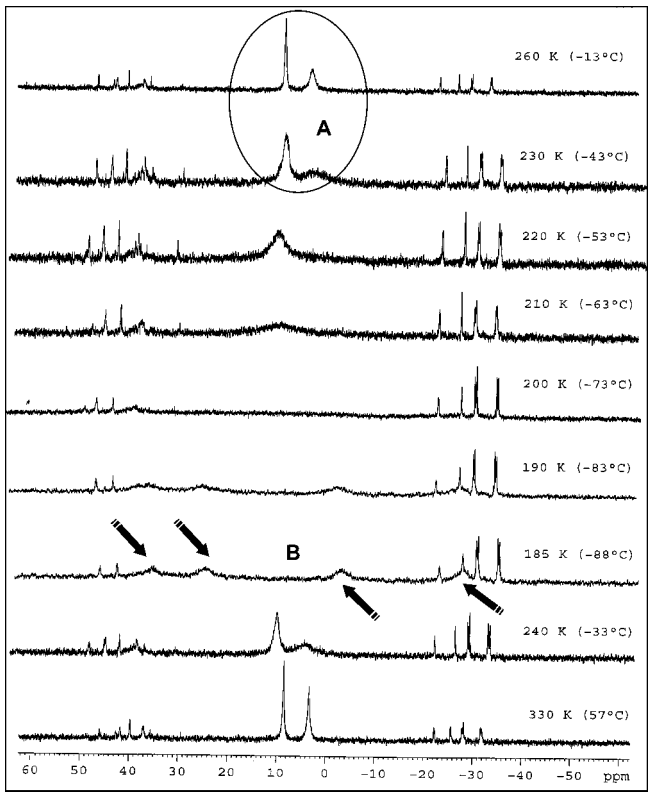


Figure 3. VT $^{31}P$ NMR spectrum of the [Pd/**18**] (1:1) catalytic system.

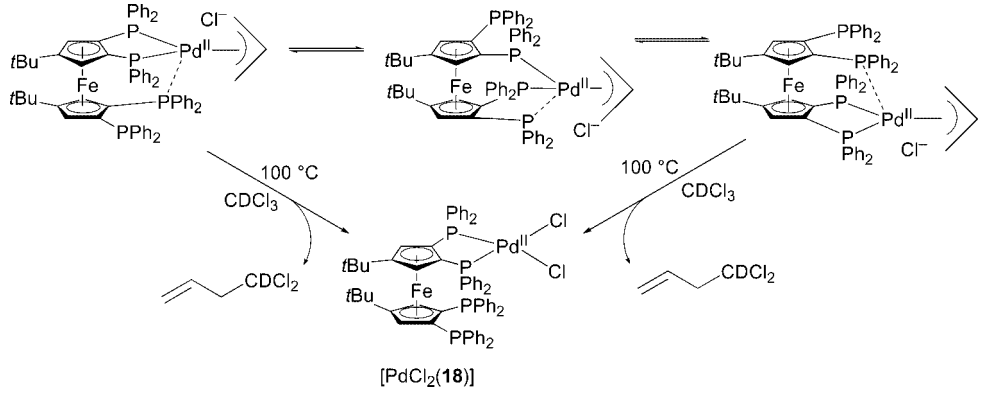


Scheme 9.

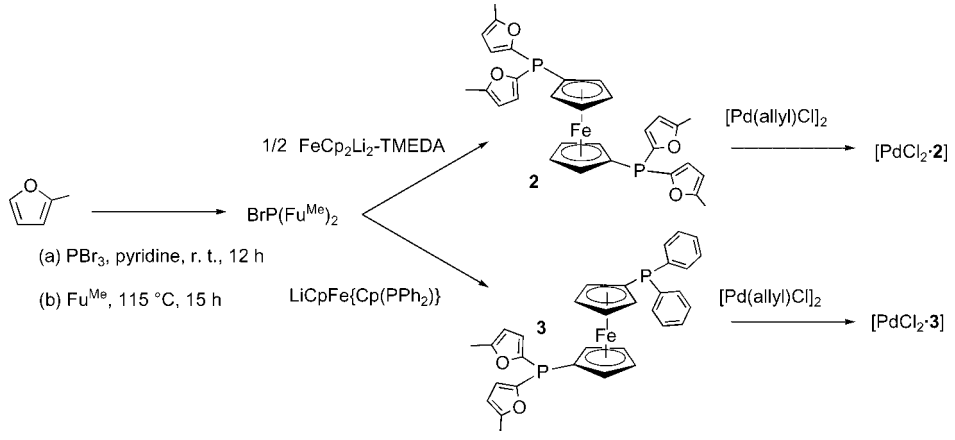


Scheme 10.

 © 2007 Wiley-VCH Verlag GmbH & Co. KGaA, Weinheim 

plex [$PdCl_2$·**18**] (Scheme 9) is quantitatively formed. Scheme 10 gives a summarized picture of the observed phenomena, which involves the chlorinated solvent.[37]

The most reasonable explanation, taking into account the ratio P/Pd, is that the palladium center "travels" between the four phosphorus donors at a high exchange rate. This constitutes a unique observation in the chemistry of multidentate compounds and the first proof of the possibility for the catalytic palladium species to be further stabilized by the close vicinity of several coordinating atoms during the successive catalytic steps. This would statistically decrease de facto the deactivation of catalysts by palladium-black formation. In addition, as postulated by Doucet and Santelli for their tetraphosphane, the "coordination pressure" around the metal center might accelerate some determining steps in cross-couplings such as the reductive elimination.[4] This "active" multidentate behavior would partly explain why, contrary to more fragile systems, polyphosphane ligands can be efficiently combined with palladium in low concentrations such as $10^{-2}$ to $10^{-4}$ mol-%.

### Performances of a Bulky π-Acidic Ferrocenyldiphosphane in Suzuki and Heck Reactions

As mentioned above, bulky phosphane ligands with high σ-donor abilities emerged as powerful ligands. Their efficiency was initially surprising since strong σ-donor ligands would not be expected to facilitate the transmetalation and reductive elimination steps. These performances revealed the importance of oxidative addition steps, particularly with substrates containing strong carbon–halide bonds. Additionally, the success of bulky phosphanes was suggested to be derived from the ability of these ligands to promote *geometrically driven* coordinative unsaturation and palladium reactivity. These geometric features appear to be important to the transmetalation and reductive elimination steps when utilizing strongly electron-donating ligands. Conversely, high activity in the cross-coupling reactions of aryl bromides and chlorides has been reported in some cases with palladium complexes incorporating various strongly electron-withdrawing phosphite ligands.[40] As a consequence of the complexity in the prediction of a rate-limiting step, it did not appear unreasonable to us to test, in more depth, a range of cross-coupling reactions using a comparatively "forgotten" π-acidic bulky ferrocenylphosphane ligand. We choose to build a weakly σ-donor phosphane on the ferrocenic backbone with phosphorus bearing heterocyclic substituents, which are notably less developed than the corresponding ferrocenyldiphosphanes bearing aryl or alkyl substituents. The new ligand 1,1′-bis[bis(5-methyl-2-furyl)phosphanyl]ferrocene (**2**; Figure 4), is obtained in 80% isolated yield from reaction of lithiated ferrocene with bis(5-methyl-2-furyl)bromophosphane (see below, amination).[41] Ligand **2** was isolated in pure form on a 10-g scale, as a crystalline orange powder, insensitive to air and moisture (Scheme 10).

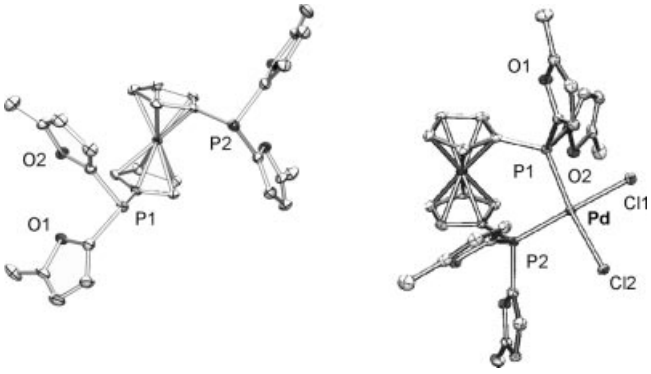


Figure 4. Molecular structures of **2** and [$PdCl_2$·**2**] from X-ray diffraction studies.

Suzuki cross-coupling with the use of activated substrate 4-bromoacetophenone with phenylboronic acid afforded the corresponding product in the presence of the in-situ-formed [$PdCl_2$·**2**] precatalyst and $K_2CO_3$ (Scheme 11).[41] Surprisingly, regarding the low basicity of phosphorus atoms, a high TON of 100000 with complete conversion was obtained in the presence of $10^{-3}$ mol-% catalyst: a result equivalent to that obtained with more electron-rich tetraphosphane **18** under identical conditions (Scheme 6). A TON of 180000 was obtained after 20 h (yield 18%, $10^{-4}$ mol-% cat. at 130 °C). Deactivated and electron-rich 4-bromoanisole gave a complete conversion with a TON of 10000 ($10^{-2}$ mol-% catalyst), but disappointingly a lower concentration did not yield any product. Under identical conditions tetraphosphane **18** facilitated a TON of 77000, in the presence of $10^{-3}$ mol-% catalyst. The preliminary experiments on the Heck reaction were conducted by using 4-bromoanisole with *n*-butyl acrylate *without* the addition of tetraalkylammonium salts, which are often used to delay palladium black formation. Here, excellent conversions were obtained in the presence of $10^{-2}$ mol-% catalyst (TON 10000), but again lowering the concentration of one order of magnitude completely inhibited the reaction.

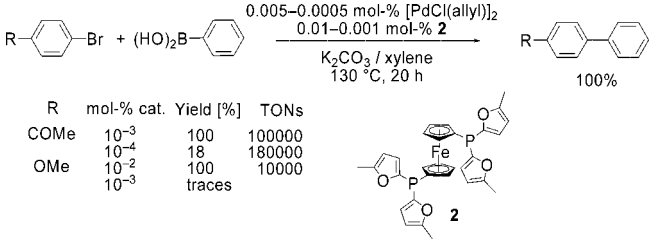


Scheme 11.

Except for the robustness of the ferrocenyl backbone, phosphane ligand **2** is very different from **18**, and obviously in this case no "multidentarity" effect was expected. To the best of our knowledge, only a few reports exist on the use of highly-efficient catalysts incorporating very poor σ-donating phosphane ligands in cross-coupling reactions.[40] One of our goals was to demonstrate the possibility of variation in the phosphorus substituents, and to explore its effects. Subtle changes in the rate-determining step *depending*

 © 2007 Wiley-VCH Verlag GmbH & Co. KGaA, Weinheim 

*on the substrate* are probably at the origin of the results obtained. For more demanding substrates, the oxidative addition is rate-determining (and disfavored by poor σ-donating ligands such **2**). In contrast, for strongly activated substrates (aryl iodides and activated bromides) where the oxidative addition is comparatively facile, the same ligands would multiply the rates of transmetalation and reductive elimination. These results led us to exploit ligand **2** in other reactions for which its π-acidic character would reveal to be more useful (see below, C–N coupling).

## Performances of Ferrocenylphosphanes in Sonogashira–Heck Alkynylations

### Structural Considerations for Triphosphane Ferrocenic Ligands

We anticipated that "geometrically simpler" ferrocenyl-*tri*phosphanes (relative to tetraphosphanes **15** or **18**) might lead, as well, to highly active systems in palladium-catalyzed C–C coupling. We developed therefore a methodology for the preparation of dissymmetric achiral trisubstituted ferrocenes (**11**–**14**; Scheme 3) from two different Cp salts: the process is efficient and complete in two simple steps.[42,43] With the view to additionally improve the performance of a ligand, we chose to electronically enrich one of the phosphorus atoms and to provide the ferrocenyl backbone with better flexibility by unblocked axial rotation. This strategy prompted us to design and synthesize ferrocenyl aryl/alkyl triphosphane **12**, 1,2-bis(diphenylphosphanyl)-1′-(diisopropylphosphanyl)-4-*tert*-butylferrocene (Scheme 12).

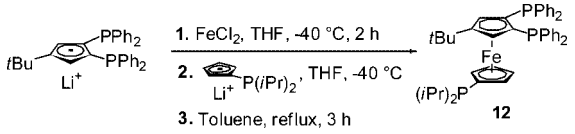


Scheme 12.

The X-ray structural characterization (Figure 5) and the solution NMR spectroscopic study revealed that,[42] as expected, the rotational flexibility of **12** was greater than that of the tetraphosphane parents; in the preferred conformation the three phosphorus atoms are not pointing in the same direction. The palladium coordination complexes were found to be preferentially 1,2-P bonded.

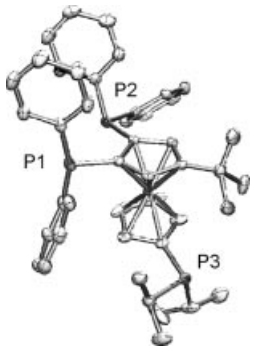


Figure 5. Molecular structure of **12** from X-ray diffraction studies.

Similar to its parent ligands, **12** is stored under air without any precaution and appeared insensitive to moisture and elevated temperatures in solution [the P(*i*Pr)$_2$ atom is not sensitive to oxidation].

### Alkynylations with a Ferrocenyltriphosphane

The examination of Suzuki cross-coupling reactions with the use of **12** was not as promising as we expected. For instance, a TON of only 10000 was obtained in the coupling of electron-poor 4-bromoacetophenone with phenylboronic acid, whereas tetraphosphane **18** gave a TON of 77000 under similar conditions (Scheme 6). We then tested the performances of the triphosphane in the more demanding reaction of aryl alkynylation in the presence of palladium and copper (Sonogashira cross-coupling).[44] The scope and

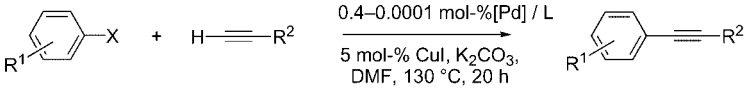


| X | $R^1$ | $R^2$ | mol-% cat. | Yield (%) | TONs |
|---|---|---|---|---|---|
| I | H | Ph | $10^{-3}$ | 95 | 95000 |
| Br | 4-COMe | Ph | $10^{-4}$ | 25 | 250000 |
| | | | $10^{-3}$ | 94 | 94000 |
| Br | 4-CN | Ph | $10^{-3}$ | 46 | 46000 |
| | | | $10^{-2}$ | 89 | 8900 |
| Br | 4-F | Ph | $10^{-3}$ | 20 | 20000 |
| | | | $10^{-2}$ | 95 | 9500 |
| Br | 2-$CF_3$ | Ph | $10^{-2}$ | 93 | 9300 |
| 9-bromoanthracene | | Ph | $10^{-1}$ | 90 | 900 |
| Br | 4-OMe | Ph | $10^{-1}$ | 52 | 520 |
| | | | 4 x $10^{-1}$ | 93 | 230 |
| Cl | 4-CN | Ph | $10^{-1}$ | 54 | 540* |
| | | | 4 x $10^{-1}$ | 86 | 215* |
| Cl | 4-COMe | Ph | 4 x $10^{-1}$ | 82 | 205* |

L =

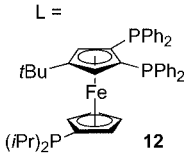


| $R^1$ | $R^2$ | mol-% cat. | Yield (%) | TON |
|---|---|---|---|---|
| COMe | $nC_8H_{17}$ | 4 x $10^{-1}$ | 62 | 620 |
| COMe | $CH_2OH$ | 4 x $10^{-1}$ | 46 | 460 |
| COMe | $CH_2OH$ | 4 x $10^{-1}$ | 92 | 230 |

(X = Br)

* Reactions performed without CuI (Heck conditions)

Scheme 13.

 © 2007 Wiley-VCH Verlag GmbH & Co. KGaA, Weinheim 

limitations of tridentate ferrocenylphosphane ligand **12** for the alkynylation of a variety of aryl bromides with alkynes is described in Scheme 13.

A very high TON of 95000 was obtained for the reaction of iodobenzene with phenylacetylene (yield 95%, $10^{-3}$ mol-% cat.).[44] In the presence of activating groups on the aryl bromide, high reaction rates were observed as well: the coupling of 4-bromoacetophenone, 4-bromobenzonitrile, and 4-fluorobromobenzene with phenylacetylene in the presence of $10^{-3}$ to $10^{-4}$ mol-% of [Pd/**12**] led to the coupling products in 94 to 20% yields (the highest TONs obtained were of 250000, 46000, and 20000, respectively). We determined the influence on the reaction of the presence of *ortho* substituents on the aryl bromide: with electronically activated 2-trifluoromethylbromobenzene: a good TON of 9300 was obtained with high conversion (yield 93%, $10^{-2}$ mol-% cat.). A lower TON of 900 was observed by using sterically congested 9-bromoanthracene (yield 90%, $10^{-1}$ mol-% cat.). The quantitative conversion of strongly deactivated 4-bromoanisole required a higher catalyst loading (0.4 mol-% cat.), consequently lower TONs of 230 to 520 were obtained. We also performed a few reactions with activated aryl chlorides such as 4-chlorobenzonitrile and 4-chloroacetophenone that were also converted in excellent yields with *less than 1 mol-%* of catalyst and in the absence of copper iodide (TONs of 540 and 205, respectively).[44] Finally, we extended the scope of the catalytic reaction to other alkynes such as dec-1-yne and but-1-yn-4-ol. With these alkynes, TONs of 620 and 460, respectively, were obtained with 4-bromoacetophenone. Consequently, this novel mixed ferrocenyl aryl/alkyl triphosphane was found thermally stable, insensitive to air and moisture, and its robustness allowed aryl alkynylation at $10^{-1}$ to $10^{-4}$ mol-% catalysts loading with iodides, bromides, and activated chlorides. Copper-free coupling with the use of phenylacetylene was also accessible in good yield. In the case of this ligand we must underline that no evidence of multidentarity (such as observed for **18**) was collected to date; nevertheless, only few multidentate ligands (tri-, tetradentate or more) have been tested for Sonogashira–Heck-type alkynylations. This is all the more surprising that, most of the time, threefold or more excess of monodentate ligands are used under the reported conditions. The emerging chemistry of multidentate ligands could be of high interest in the future development of catalyzed cross-coupling alkynylations.

### Performances of a Bulky π-Acidic Ferrocenyldiphosphane in Sonogashira Alkynylation

To our surprise, the system based on diphosphane ligand **2** also efficiently catalyzed the arylation of phenylacetylene with activated and deactivated substrates.[41] By using 4-bromoacetophenone in the presence of $10^{-4}$ mol-% catalyst a TON of 920000 *among the highest reported* with bromides was obtained. 4-Bromoanisole was quantitatively converted with a lower TON of 1000, consistently with the results observed in Suzuki/Heck reactions.[41] We found in parallel that **2** could be also a useful ligand under mild reaction conditions in allylic amination reactions (see below).

## Performances of Ferrocenylphosphanes in Allylic Amination Reactions

### Allylic Amination from Allylacetates with π-Acidic Ferrocenyldiphosphanes

Palladium-catalyzed amination of allyl acetates is recognized as being a powerful tool to form allylamine blocks. To test more efficient catalytic systems in terms of atom economy we employed the 1,1′-bis[bis(5-methyl-2-furyl)-phosphanyl]ferrocene (**2**) ligand in this reaction as well as related dissymmetric compound **3** (Scheme 10) and their coordination complexes.[45,46] Nucleophilic amination of allylic acetate was performed at r.t. with unprecedented turnover frequencies (Scheme 14, Table 2).

As seen in Table 2 (Entries 1–5): in the presence of $10^{-2}$ mol-% catalyst [Pd/**2**] the coupling of aniline to allyl acetate occurred at a high TOF of 10000 $h^{-1}$ with complete conversion and 96% selectivity in monoallylamine; under identical conditions of temperature and concentration, 60% conversion was obtained after 40 h with the more electron-rich parent ligand 1,1′-bis[diphenylphosphanyl]ferrocene (150 $h^{-1}$ TOF), the monophosphanes $PPh_3$ and $PCy_3$ were ineffective. Excellent conversions of 98 to 100% were achieved from the cyclic secondary amines pyrrolidine (TOF 4900 $h^{-1}$) and piperidine (TOF 5000 $h^{-1}$). Only a slightly decreased 85% conversion was obtained with less nucleophilic cyclic morpholine (TOF 4250 $h^{-1}$). The coupling of the primary amine benzylamine appeared more difficult and less selective (TOF 1825 $h^{-1}$ for a 75% selectivity in monoallylation product). In addition to primary amines and cyclic secondary amines, more delicate aliphatic secondary amines were efficiently coupled (Table 2, Entries 6–8). Complete conversion of the sterically demanding diisopropylamine was obtained at 80 °C in the presence of 0.1 mol-% catalyst in 2 h (TOF 480 $h^{-1}$) and of the long alkyl chain bearing dioctylamine at r.t. after 20 h (best TOF 225 $h^{-1}$). These good results prompted us to investigate the allylic amination reaction employing a much more demanding substrate, the monoterpene derivative geranyl acetate (Table 2, Entries 9–11). At r.t., 75% conversion in geranylaniline was obtained after 20 h with total selectivity. Morpholine reacted with geranyl acetate in the presence of 1 mol-% catalyst to give a 60% conversion in 1 h at r.t. and 98% after 20 h. A TOF of 333 $h^{-1}$ was obtained at 80 °C with 98% of geranylamine formed in 3 h.

This catalytic system was also found to be remarkably active and selective for the amination of substituted allylic acetates. The coupling reaction to amines of 3-phenylallyl acetate (Table 2, Entries 12–17) and (*E*)-hex-2-en-1-yl acetate (Table 2, Entries 18–22) was carried out at 0.1 and 0.01 mol-% [Pd/**2**]. 3-Phenylallyl acetate reacted with diethylamine, pyrrolidine, or morpholine to give complete con-

 © 2007 Wiley-VCH Verlag GmbH & Co. KGaA, Weinheim 

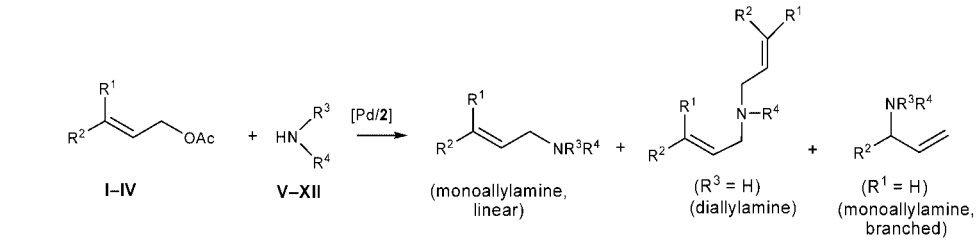


I: $R^1$, $R^2$ = H (allyl acetate)
II: $R^1$ = $CH_3$, (geranyl acetate)
$R^2$= -$CH_2$
III: $R^1$ = H, $R^2$ = Ph (cynnamyl acetate)
IV: $R^1$ = H, $R^2$= -$(CH_2)_2CH_3$ (hexenyl acetate)

V: $R^3$ = H, $R^4$ = Ph (aniline)
VI: $R^3$ = H, $R^4$ = –$CH_2$Ph (benzylamine)
VII: $R^3$-$R^4$ = –$(CH_2)_2O(CH_2)_2$– (morpholine)
VIII: $R^3$-$R^4$ = –$(CH_2)_5$– (piperidine)
IX: $R^3$-$R^4$ = –$(CH_2)_4$– (pyrrolidine)
X: $R^3$ = $R^4$ = –$CH_2CH_3$ (diethylamine)
XI: $R^3$ = $R^4$ = *n*-$(CH_2)_7CH_3$ (dioctylamine)
XII: $R^3$ = $R^4$ = *i*Pr (diisopropylamine)

Scheme 14.

Table 2. Allylic amination from acetates with [Pd/**2**].

| Entry | Acetate/Amine | mol-% of catalyst | Yield [%] | Selectivity [%][a] | TON | TOF [$h^{-1}$] |
|---|---|---|---|---|---|---|
| 1 | **I/V** | $10^{-2}$ | 100 | 96/4 (mono/di) | 10000 | 10000 |
| 2 | **I/IX** | $10^{-2}$ | 98 | 100 | 9800 | 4900 |
| 3 | **I/VIII** | $10^{-2}$ | 100 | 100 | 10000 | 5000 |
| 4 | **I/VII** | $10^{-2}$ | 85 | 100 | 8500 | 4250 |
| 5 | **I/VI** | $10^{-2}$ | 73 | 75/25 (mono/di) | 7300 | 1825 |
| 6 | **I/XII** | $10^{-1}$ | 96 | 100 | 960 | 480 |
| 7 | **I/XI** | $10^{-1}$ | 100 | 100 | 1000 | 50 |
| 8 | **I/XI** | $10^{-2}$ | 45 | 100 | 4500 | 225 |
| 9 | **II/V** | 1 | 75 | 100 | 75 | 4 |
| 10 | **II/VII** | 1 | 60 | 100 | 60 | 60 |
| 11 | **II/VII** | $10^{-1}$ | 100 | 98 | 1000 | 333 |
| 12 | **III/X** | $10^{-1}$ | 100 | 94:6 (lin/brch) | 1000 | 50 |
| 13 | **III/X** | $10^{-2}$ | 76 | 94:6 (lin/brch) | 7600 | 380 |
| 14 | **III/IX** | $10^{-1}$ | 100 | 94:6 (lin/brch) | 1000 | 50 |
| 15 | **III/IX** | $10^{-2}$ | 26 | 94:6 (lin/brch) | 2600 | 130 |
| 16 | **III/VII** | $10^{-1}$ | 100 | 93:7 (lin/brch) | 1000 | 50 |
| 17 | **III/VII** | $10^{-2}$ | 48 | 93:7 (lin/brch) | 4800 | 240 |
| 18 | **IV/X** | $4\times10^{-1}$ | 100 | 99:1 (lin/brch) | 250 | 12 |
| 19 | **IV/X** | $10^{-1}$ | 76 | 99:1 (lin/brch) | 760 | 38 |
| 20 | **IV/IX** | $10^{-1}$ | 100 | 94:6 (lin/brch) | 1000 | 50 |
| 21 | **IV/VII** | $10^{-1}$ | 98 | 94:6 (lin/brch) | 980 | 49 |
| 22 | **IV/XI** | $4\times10^{-1}$ | 59 | 100 | 245 | 12 |

[a] Total selectivity is always in linear monoallylamine (mono = linear monoallylamine, di = diallylamine, lin = linear isomer, brch = branched isomer).

version with 0.1 mol-% catalyst. Lowering the catalyst loading to 0.01 mol-% resulted in TONs of 7600, 2600, and 4800, respectively. In each case, good regioselectivity was observed for the linear product (93–94%) The selectivity was found to be higher in linear monoallylamine for the coupling of $HNEt_2$ to (*E*)-hex-2-en-1-yl acetate (99%). Coupling reactions with cyclic secondary amines proceeded in more than 90% yield by employing 0.1 mol-% catalyst (94% selectivity in linear product). Only in the course of the addition of dioctylamine were lower TONs and TOFs observed because 0.4 mol-% catalyst was required to reach 60% conversion in 20 h at 50 °C. The results obtained are certainly due to an accelerating effect on the nucleophilic substitution induced by the electron-withdrawing furyl groups on the phosphorus atoms of the ligands; we have provided a more detailed discussion on this topic.[41] The performance of the [Pd/**3**] system was found to be similar or slightly inferior to that of [Pd/**2**].[45] Finally, we have recently shown that multidentate ferrocenylphosphanes can also be useful in allylic substitution reactions.[47]

## Trends and Perspectives in Rationally Designed Ferrocenylpolyphosphane Ligands for Low Loading Catalysis

The ferrocenylphosphane species we developed present several features that are profitable to the rational design of a large number of new metalloligands. Figure 6 summarizes some of these useful points to produce adaptable systems of high-efficiency in catalytic reactions. We briefly discuss the expected effects on catalysis of the possible structural modifications (a more detailed discussion on ferrocenylpolyphosphane structural effects in catalysis was reported else-

 © 2007 Wiley-VCH Verlag GmbH & Co. KGaA, Weinheim 

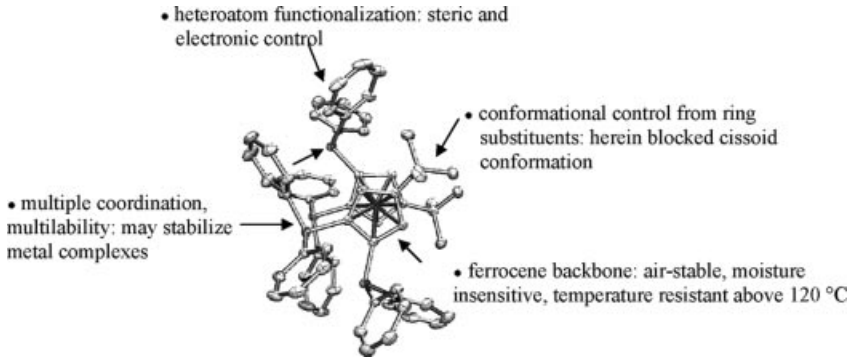


Figure 6. General features of adaptable ferrocenylphosphane ligands for high-performance catalytic reactions.

where[48]): (1) The first advantage in catalysis of these ferrocenylphosphane ligands is the robustness of the ferrocenyl backbone, which allows their handling and storage under air for years without any particular precaution. Non-glovebox conditions and temperatures above 120 °C can be used in long-term reactions without deactivation. (2) The advantage of having three or more phosphanyl groups on the ferrocene backbone is an important question. First from a practical point of view, a recent review of the use of dppf and derivatives showed that, up to now, no results matching the ultra-low loading catalysis presented herein were obtained with these diphosphanes.[48] Several reported studies from our group and others,[30–32,37,45] clearly established that classical ligands [such as $PPh_3$, dppe, dppb = 1,2-bis(diphenylphosphanyl)butane, or dppf] led to less stable catalytic systems under the conditions of low catalyst concentrations that we investigated. The ligand behavior of tetradentate phosphane **18** is expected to furnish to the $Pd^0$ species multiple coordination, as described above for $Pd^{II}$, which stabilizes the catalytic systems and therefore leads to efficient catalysis in the presence of only low loadings of the precious metal. More positions for substitution on phosphorus (or other donor atoms) are available on the ferrocenyl backbone. Therefore, polyphosphanes of higher-rank such as penta- or hexaphosphanes (or more) should be reachable. We believe that such a kind of "*enhanced multidentarity*" would permit one to pursue the effort for stabilizing catalytic systems, and promoting their longevity under ultra-low concentrations. (3) The substituents on the cyclopentadienyl rings allow the conformation of the ferrocene to be controlled, and therefore can induce a more-or-less important rigidity to the ligand as a function of their hindrance. Therefore, when a specific conformation is required, such as the orientation of several donor atoms in the same direction of space (this was shown with phosphorus atoms, but it could probably be extended to other donors, such as nitrogen atoms, etc.) very hindering substrates such as *tert*-butyl groups could be used. We envision the use of more hindered substituents (such as trityl groups, $CPh_3$) with the view to determine their influence on the conformation. Additionally, positive or negative electronic effects can be expected, as well, from the noncoordinating substituents on the Cp rings and should be worthy of further investigations. (4) We showed that the substituents on the phosphorus atoms can be modified to either more electron-donating (e.g. *i*Pr) or more electron-withdrawing groups (e.g. furyl), or to have increased bulkiness. This is a very important point as the use of modified ligands containing either electron-rich $PCy_2$ or $PtBu_2$ moieties are well-known for having induced impressive results in cross-coupling reactions (by facilitating the oxidative addition step of the catalytic cycles, see first section).

Following these trends, a number of new ligands are currently being developed in our laboratory, that incorporate other substituents on the Cp ring and on phosphorus atoms, as well as unique conformations: their features and performances are under investigation and will be reported in due time.

## Conclusions

Multidentate[49] ferrocenylphosphane ligands offer some of the highest TONs observed in Heck, Suzuki, and Sonogashira cross-coupling reactions. Demanding substrates such as aryl bromides and activated aryl chlorides were coupled with fairly good to excellent TONs from different ferrocenylpolyphosphane auxiliaries. In the achiral version of the palladium-catalyzed allylic acetate amination reaction, the modification of dppf with π-acidic furyl heterocycles provided ferrocenyldiphosphane catalysts for which high TONs were obtained together with several of the best TOFs reported to date. To obtain high TONs (>10000), relatively elevated reaction temperatures are often required for cross-coupling; under these conditions, the use of ferrocenylphosphane ligands certainly help to stabilize the catalytic species. In addition, these ligands with regard to their bulkiness would also have a positive influence as accelerators in the reductive elimination step of the cross-coupling catalytic cycle by inducing steric pressure on the active palladium center. Further mechanistic studies are absolutely necessary and in the future will certainly provide keys for the development of multidentate ligands resource-economic catalysts.

 © 2007 Wiley-VCH Verlag GmbH & Co. KGaA, Weinheim 

## Acknowledgments

Thanks are due to the Conseil regional de Bourgogne (grant to M. B.) and to the Centre National de la Recherche Scientifique (CNRS) for continuous support. We are also very thankful to R. Broussier, R. Amardeil, N. Pirio, P. H. Dixneuf, G. Erker, J. Reedijk, M. Santelli, P. Kalck, M. Urrutigoïty, and H. Doucet (at the origin of many catalysis results), as well as all our students, and particularly A. Fihri, for their interest and support in multidentate ferrocenylphosphanes chemistry. We express friendly thanks to Philippe Richard for his help since years, and its pictorial ideas.

[1] For instance, in Europe the COST program **2003**–**2006** "*Sustainable Chemical Processes: Stereoselective Transition Metal-Catalyzed Reaction"*, in the USA, the ACS-Green Chemistry Institute PRF programs, and since 2007, from the French Government, the ANR program "*Chemistry and Processes for Sustainable Development"*.

[2] P. T. Anastas, M. M. Kirchhoff, *Acc. Chem. Res.* **2002**, *35*, 686–694 and references cited therein.

[3] W. Chen, W. Du, L. Yue, R. Li, Y. Wu, L.-S. Ding, Y.-C. Chen, *Org. Biomol. Chem.* **2007**, *5*, 816–821.

[4] H. Doucet, M. Santelli, *Synlett* **2006**, *13*, 2001–2015.

[5] J.-P. Corbet, G. Mignani, *Chem. Rev.* **2006**, *106*, 2651–2710.

[6] The palladium cost was stated at 350 USD/Oz (9500 €/kg) on the New York market SE, 03/19/2007.

[7] TON defined herein as the ratio [substrate on catalyst] multiplied by the yield of conversion in the desired product (i.e. 1 for a 100% yield), that corresponds to the value (mol product per mol catalyst).

[8] V. Farina, *Adv. Synth. Catal.* **2004**, *346*, 1553–1582, this review provides an excellent overview of the challenges and advances related to the use of low loadings of catalyst.

[9] A. Zapf, A. Ehrentraut, M. Beller, *Angew. Chem. Int. Ed.* **2000**, *39*, 4153–4155.

[10] a) S. D. Walker, T. E. Barder, J. R. Martinelli, S. L. Buchwald, *Angew. Chem. Int. Ed.* **2004**, *43*, 1871–1876; b) T. E. Barder, S. D. Walker, J. R. Martinelli, S. L. Buchwald, *J. Am. Chem. Soc.* **2005**, *127*, 4685–4696.

[11] See for instance: a) C. S. Consorti, G. Ebeling, F. R. Flores, F. Rominger, J. Dupont, *Adv. Synth. Catal.* **2004**, *346*, 617–624; b) M. Ohff, A. Ohff, M. E. van der Boom, D. Milstein, *J. Am. Chem. Soc.* **1997**, *119*, 11687–11688.

[12] See, for instance: a) D. A. Alonso, C. Nájera, M.-C. Pacheco, *Org. Lett.* **2000**, *2*, 1823–1826; b) M. Ohff, A. Ohff, D. Milstein, *Chem. Commun.* **1999**, 357–358; c) H. Weissman, D. Milstein, *Chem. Commun.* **1999**, 1901–1902.

[13] R. B. Bedford, S. L. Hazelwood, M. E. Limmert, *Chem. Commun.* **2002**, 2610–2611.

[14] See, for instance: a) J. A. Loch, M. Albrecht, E. Peris, J. Mata, J. W. Faller, R. H. Crabtree, *Organometallics* **2002**, *21*, 700–706; b) D. S. McGuinness, K. J. Cavell, *Organometallics* **2000**, *19*, 741–748.

[15] D. Laurenti, M. Feuerstein, G. Pepe, H. Doucet, M. Santelli, *J. Org. Chem.* **2001**, *66*, 1633–1637.

[16] W. A. Herrmann, C. Brossmer, K. Öfele, C.-P. Reisenger, T. Priermeier, M. Beller, H. Fischer, *Angew. Chem. Int. Ed. Engl.* **1995**, *34*, 1844–1848.

[17] M. Beller, H. Fischer, W. A. Herrmann, K. Öfele, C. Brossmer, *Angew. Chem. Int. Ed. Engl.* **1995**, *34*, 1848–1849.

[18] D. A. Albisson, R. B. Bedford, S. E. Lawrence, P. Noelle Scully, *Chem. Commun.* **1998**, 2095–2096.

[19] D. A. Albisson, R. B. Bedford, P. Noelle Scully, *Tetrahedron Lett.* **1998**, *39*, 9793–9796.

[20] J. P. Wolfe, S. L. Buchwald, *Angew. Chem. Int. Ed.* **1999**, *38*, 2413–2415.

[21] J. P. Wolfe, R. A. Singer, B. H. Yang, S. L. Buchwald, *J. Am. Chem. Soc.* **1999**, *121*, 9550–9561.

[22] a) Q. Shen, S. Shekhar, J. P. Stambuli, J. F. Hartwig, *Angew. Chem. Int. Ed.* **2005**, *44*, 1371–1375; b) M. A. Fernández-Rodríguez, Q. Shen, J. F. Hartwig, *J. Am. Chem. Soc.* **2006**, *128*, 2180–2181.

[23] T. Hayashi, M. Konishi, Y. Kobori, M. Kumada, T. Higuchi, K. Hirotsu, *J. Am. Chem. Soc.* **1984**, *106*, 158–163.

[24] For general reviews on high-efficiency catalysts in C–C and C–N cross-coupling reactions, see: a) A. Zapf, M. Beller, *Chem. Commun.* **2005**, 431–440; b) R. B. Bedford, C. S. J. Cazin, D. Holder, *Coord. Chem. Rev.* **2004**, *248*, 2283–2321.

[25] U. Christmann, R. Vilar, *Angew. Chem. Int. Ed.* **2005**, *44*, 366–374 on monodentate bulky electron-rich phosphanes and carbenes for cross-coupling reactions.

[26] a) J. Dupont, C. S. Consorti, J. Spencer, *Chem. Rev.* **2005**, *105*, 2527–2571; b) I. P. Beletskaya, A. V. Cheprakov, *J. Organomet. Chem.* **2004**, *689*, 4055–4082 on palladacycle catalysis.

[27] N. T. S. Phan, M. Van der Sluys, C. W. Jones, *Adv. Synth. Catal.* **2006**, *348*, 609–679 on the nature of active species in Suzuki and Heck homogeneous catalysis.

[28] a) H. Doucet, J.-C. Hierso, *Angew. Chem. Int. Ed.* **2007**, *46*, 834–871 on palladium homogeneous and heterogeneous catalysts in Heck–Sonogashira alkynylations; b) R. Chinchilla, C. Nájera, *Chem. Rev.* **2007**, *107*, 874–922 for a review of the applications of the Sonogashira reaction.

[29] M. Feuerstein, D. Laurenti, H. Doucet, M. Santelli, *Chem. Commun.* **2001**, 43–44; on the web 15th December **2000**.

[30] a) M. Feuerstein, D. Laurenti, H. Doucet, M. Santelli, *Synthesis* **2001**, 2320–2326; b) M. Feuerstein, D. Laurenti, C. Bougeant, H. Doucet, M. Santelli, *Chem. Commun.* **2001**, 325–326.

[31] M. Feuerstein, H. Doucet, M. Santelli, *J. Org. Chem.* **2001**, *66*, 5923–5925.

[32] M. Feuerstein, F. Berthiol, H. Doucet, M. Santelli, *Org. Biomol. Chem.* **2003**, *1*, 2235–2237.

[33] a) A. H. M. de Vries, J. M. C. A. Mulders, J. H. M. Mommers, H. J. W. Henderickx, J. G. de Vries, *Org. Lett.* **2003**, *5*, 3285–3288; b) A. Alimardanov, L. Schmieder, A. H. M. de Vries, J. G. de Vries, *Adv. Synth. Catal.* **2004**, *346*, 1812–1817.

[34] First, the dilution factor 30 C (or 30 CH) commonly employed in medical homeopathy corresponds to a $10^{-60}$ volume dilution of the active substance. In addition, in the Heck reaction and C–C or C–N cross-couplings the highest catalyst dilutions reach $10^{-6}$ to $10^{-7}$ mol-% cat. and were carried out *with the assistance of phosphane ligands* (see for instance refs.[4,20] and references cited therein). Therefore, the expression "homeopathic palladium" has the advantage to strike the mind, but in our opinion should be avoided for catalyst loadings only down to $10^{-1}$ to $10^{-2}$ mol-%, *low catalyst loadings* being more acceptable; *ultra-low loading* catalysts should be reserved for loadings below $10^{-4}$ mol-% (corresponding to maximum TONs of 1000000).

[35] R. Broussier, E. Bentabet, R. Amardeil, P. Richard, P. Meunier, P. Kalck, B. Gautheron, *J. Organomet. Chem.* **2001**, *637–639*, 126–133.

[36] A. F. Littke, G. C. Fu, *Angew. Chem. Int. Ed.* **2002**, *41*, 4176–4211.

[37] J.-C. Hierso, A. Fihri, R. Amardeil, P. Meunier, H. Doucet, M. Santelli, B. Donnadieu, *Organometallics* **2003**, *22*, 4490–4499.

[38] J.-C. Hierso, A. Fihri, V. V. Ivanov, B. Hanquet, N. Pirio, B. Donnadieu, B. Rebière, R. Amardeil, P. Meunier, *J. Am. Chem. Soc.* **2004**, *126*, 11077–11087.

[39] From the stable [$PdCl_2$·**18**] and [$Pd_2Cl_4$·**18**] complexes isolated, the signals for nonbonded phosphorus atoms are found around –25 ppm, and around 40 ppm for Pd-bonded ones.

[40] See A. Zapf, M. Beller, *Chem. Eur. J.* **2000**, *6*, 1830–1833 and references cited therein.

[41] J.-C. Hierso, A. Fihri, R. Amardeil, P. Meunier, H. Doucet, M. Santelli, *Tetrahedron* **2005**, *61*, 9759–9766.

[42] J.-C. Hierso, V. V. Ivanov, R. Amardeil, P. Richard, P. Meunier, *Chem. Lett.* **2004**, *33*, 1296–1297.

 © 2007 Wiley-VCH Verlag GmbH & Co. KGaA, Weinheim 

[43] V. V. Ivanov, J.-C. Hierso, R. Amardeil, P. Meunier, *Organometallics* **2006**, *25*, 989–995.
[44] J.-C. Hierso, A. Fihri, R. Amardeil, P. Meunier, H. Doucet, M. Santelli, V. V. Ivanov, *Org. Lett.* **2004**, *6*, 3473–3476.
[45] A. Fihri, J.-C. Hierso, A. Vion, D. H. Nguyen, M. Urrutigoïty, P. Kalck, R. Amardeil, P. Meunier, *Adv. Synth. Catal.* **2005**, *347*, 1198–1202.
[46] A. Fihri, J. Boudon, J.-C. Hierso, R. Amardeil, P. Meunier, P. Richard, *Acta Crystallogr., Sect. E* **2005**, *61*, 2267–2269.
[47] D. H. Nguyen, M. Urrutigoïty, A. Fihri, J.-C. Hierso, P. Meunier, P. Kalck, *Appl. Organomet. Chem.* **2006**, *20*, 845–850.
[48] A. Fihri, P. Meunier, J.-C. Hierso, *Coord. Chem. Rev.* **2007**, doi:10.1016/j.ccr.2007.03.020.
[49] For a review of multidentate ligands, see: J.-C. Hierso, R. Amardeil, E. Bentabet, R. Broussier, B. Gautheron, P. Meunier, P. Kalck, *Coord. Chem. Rev.* **2003**, *236*, 143–206.

Received: April 12, 2007
Published Online: July 6, 2007

 © 2007 Wiley-VCH Verlag GmbH & Co. KGaA, Weinheim 

DOI: 10.1002/ejic.200700471

# Poly(methimazolyl)borate Alkyne Complexes of Molybdenum and Tungsten

**Anthony F. Hill,*[a] Never Tshabang,[a] and Anthony C. Willis[a]**

**Keywords:** Alkyne / Molybdenum / Tungsten / Methimazolylborates / Scorpionates

Synthetic routes are reported to complexes of the form [MI(alkyne)(CO){$H_nB(mt)_{4-n}$}] (mt = methimazolyl; $n$ = 1, 2; M = Mo, W) through the reactions of alkyne complexes $[WI_2(HC{\equiv}CSiMe_3)_2(CO)_2]$ or $[MI_2(RC{\equiv}CR)_2(NCMe)(CO)]$ (M = Mo, W; R = Me, Ph) with the salts $Na[H_nB(mt)_{4-n}]$. The derivative [MoI(PhC≡CPh)(CO){$HB(mt)_3$}] reacts with $Na[HB(mt)_3]$ to provide the complex [Mo(PhC≡CPh)(CO){$HB(mt)_3$}$_2$] in which the two $HB(mt)_3$ ligands adopt different non-interconverting coordination modes, $\kappa^3$-*S*,*S*′,*S*′′ and $\kappa^1$-*S*.
(© Wiley-VCH Verlag GmbH & Co. KGaA, 69451 Weinheim, Germany, 2007)

## Introduction

Alkyne complexes of divalent molybdenum or tungsten[1] in which the metal centres are either ligated by dithiocarbamato[2] or tris(pyrazolyl)borato ligands,[3] display a rich chemistry that has been extensively developed by Templeton and co-workers. Tris- and bis(methimazolyl)borate ligands, discovered respectively by Reglinski[4] and Parkin[5] (Scheme 1), might be superficially considered as hybrids of these two classes of more familiar ligand, being anionic and presenting either three or two sulfur donors. Accordingly, a similarly rich chemistry might also be anticipated for alkyne complexes of $Mo^{II}$ and $W^{II}$ bearing these ligands. In passing one might also note that alkynes are recognised substrates for the molybdenum site of nitrogenase,[6] generating interest in the nature of alkyne binding to molydbenum complexes that feature a sulfur-rich coordination sphere. It is, however, increasingly found to be the case that methimazolylborato ligands may demonstrate quite unique coordination features distinct from those offered by dithiocarbamates or poly(pyrazolyl)borates. Whilst the $HB(mt)_3$ ligand displays geometrical flexibility associated with the intrinsically chiral but readily invertible $C_3$-[3.3.3]bicyclo $HB(mt)_3M$ cage,[7] the $H_2B(mt)_2$ chelate has an emerging propensity for 3-centre, 2-electron B–H–metal interactions ($\kappa^3$-*H*,*S*,*S*′ coordination),[8–11] behaviour that has on occasion also been demonstrated by the $HB(mt)_3$ ligand.[11b,12–15] Both of these features are manifest in the chemistry to be described, which concerns the synthesis of the first alkyne complexes ligated by poly(methimazolyl)borates.

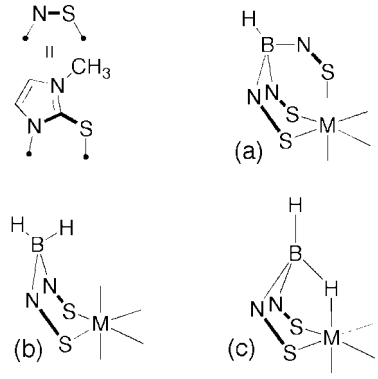


Scheme 1. Poly(methimazolyl)borato coordination. (a) $\kappa^3$-*S*,*S*′,*S*′′; (b) $\kappa^2$-*S*,*S*′; (c) $\kappa^3$-*H*,*S*′,*S*′′.

## Results and Discussion

Baker's versatile complexes $[MI_2(PhC{\equiv}CPh)_2(NCMe)(CO)_2]$ [M = Mo (**1a**), W (**1b**)] which arise from the facile reactions of tolane with $[MI_2(NCMe)_2(CO)_3]$[1b,16] appeared to be suitable substrates for the introduction of poly(methimazolyl)borate ligands (Scheme 2). However, we find that in attempting to extend this protocol to the synthesis of a tungsten complex of ethynyltrimethylsilane, nitrile substitution occurs exclusively to provide the dicarbonyl complex $[WI_2(HC{\equiv}CSiMe_3)_2(CO)_2]$ (**2**). The formulation followed from spectroscopic data and was confirmed by a crystallographic study, the results of which are summarised in Figure 1. Considering each alkyne as a single ligand, the geometry at tungsten (which lies on a crystallographic twofold axis that bisects I1–W1–I1′; symmetry generated atoms in grey), may be described as pseudo-octahedral. The geometry adopted is optimal for satisfying the π-acidic character of the carbonyl ligands and both the π-acid and π-donor functions of the alkynes. The two carbonyl ligands are bent

[a] Research School of Chemistry, Institute of Advanced Studies, Australian National University,
Canberra, Australian Capital Territory, Australia
Fax: +61-2-61253-216
E-mail: a.hill@anu.edu.au

 © 2007 Wiley-VCH Verlag GmbH & Co. KGaA, Weinheim 

away from the alkyne ligands towards the π-basic iodide ligands [C1–W1–C1′ 162.5(3)°, C1–W1–I1 82.6(2), 84.3(2) °], however, if we loosely denote this as the *z*-axis ($d^4 = d^0_{xy}d^2_{xz}d^2_{yz}$) then each of the occupied $d_{xz}$ and $d_{yz}$ orbitals are able to retrodatively interact with both carbonyls and *one* π* orbital from each alkyne. This leaves the $d_{xy}$ orbital vacant for donation from an occupied π-orbital of each alkyne.[1] Accordingly, the tungsten-alkyne bond lengths indicate a degree of W–C multiple bonding although these are significantly different (10σ), presumably due to the relative steric requirements of the silyl and hydrogen alkyne substituents.

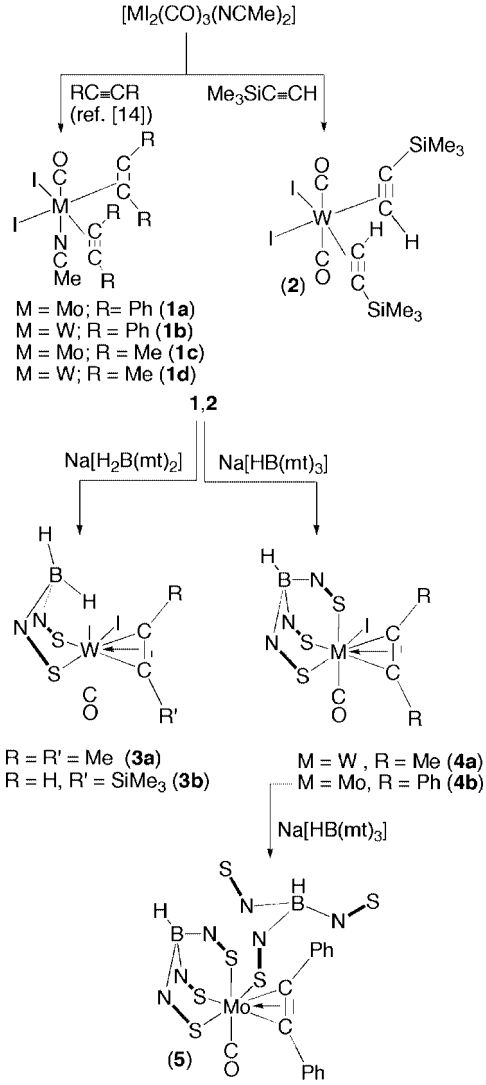


Scheme 2. Synthesis of alkyne poly(methimazolyl)borate complexes.

The complexes **1d** and **2** react with the salt Na[$H_2B$-(mt)$_2$][8a] to provide the monoalkyne complexes [WI(RC≡CR′)(CO){$H_2B$(mt)$_2$}] [R = R′ = Me (**3a**); R = H, R′ = $SiMe_3$ (**3b**)]. Simple 18-electron rule arguments require that the $H_2B$(mt)$_2$ anion (charged formalism) provide a minimum of 6 valence electrons were the alkyne to provide the maximum 4 valence electrons on offer. Thus a 3-centre 2-electron B–H–W interaction must be invoked and its occurrence is substantiated both by $^1$H NMR and IR spectroscopy: For **3b**, a high field resonance at $\delta_H$ = –5.10 ppm in the $^1$H NMR spectrum and an infrared absorption at 2261 cm$^{-1}$ ($CH_2Cl_2$) provide spectroscopic signatures for B–H–W interactions and may be compared with values of $\delta_H$ = –5.05 ppm and 2306 cm$^{-1}$ for the structurally characterised complex [Mo(η$^2$-SCNMe$_2$)(CO)$_2${κ$^3$-*H*,*S*,*S*′-$H_2B$(mt)$_2$}].[8a] The complex [W(CO){$H_2B$(mt)$_2$}$_2$] which features both bidentate (κ$^2$-*S*,*S*′) and tridentate (κ$^3$-*H*,*S*,*S*′) coordinated $H_2B$(mt)$_2$ ligands[8b] has $\delta_H$ = –3.58 ppm and $\nu_{BHW}$ = 2246 cm$^{-1}$ for the latter mode of coordination. For **3a** only one mt environment is observed on the $^1$H and $^{13}$C NMR timescales consistent with a stereochemically non-rigid molecule. For **3b**, however, whilst fluxionality is suggested by the $^1$H NMR spectrum (300 MHz), distinct "mt" environments are resolved in the $^{13}$C{$^1$H} NMR spectrum (75 MHz) at room temperature. Presumably, hemilability on the part of the B–H–W interaction allows access to a five coordinate stereochemically non-rigid intermediate.[7]

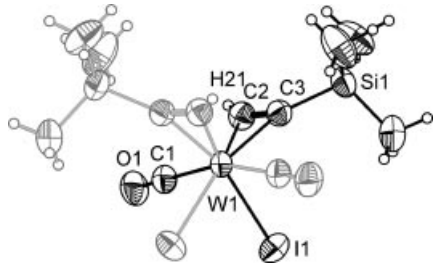


Figure 1. Geometry of **2** in a crystal of **2**·$(CH_3OH)_2$ (50% displacement ellipsoids; a rotation axis bisects I1–W–I1′; symmetry-generated atoms in grey). Selected bond lengths [Å] and angles (deg.): W1–I1 2.8547(4), W1–C1 2.081(5), W1–C2 2.099(6), W1–C3 2.148(5), Si1–C3 1.874(5), C2–C3 1.271(8), C3–W1–I1 88.43(14), C3–W1–C2 34.8(2), I1–W1–C2 89.74(15), C3–W1–C1 111.5(2), I1–W1–C1 84.33(15), C2–W1–C1 77.0(2).

In a similar manner to the syntheses of **3** a smooth reaction occurs between Na[HB(mt)$_3$] and **1d** to provide the complex [WI(CO)(MeC≡CMe){HB(mt)$_3$}] (**4a**) in moderate yields. The $^1$H NMR spectroscopic data for **4a** suggest that there is only one species present in solution and since the complex has two stereogenic components, i.e., the chiral δ/λ $C_3$-HB(mt)$_3$Mo cage and *R*/*S*-MoI(CO)(PhCCPh) pyramid, it may be assumed that a racemate of enantiomers (δ*R*/λ*S* or δ*S*/λ*R*) arises through facile inversion of the HB(mt)$_3$W cage. Similarly facile inversion has been noted for the alkylidyne complexes [W(≡CR)(CO)$_2${HB(mt)$_3$}] (R = $C_6H_4$Me-4, N*i*Pr$_2$), and purported to proceed via a dissociative (mt) mechanism.[7] The alkyne ligand in **4a** gives rise to two $^{13}$C resonances ($\delta_C$ 207.4, 206.9 ppm) (restricted rotation on the $^{13}$C NMR timescale) in the region characteristic of 4-electron (σ+π) donor alkyne coordination.[1]

Although the corresponding molybdenum tolane complex [MoI(CO)(PhC≡CPh){HB(mt)$_3$}] (**4b**) could be similarly prepared by employing a 1:1 stoichiometry of **1a** and Na[HB(mt)$_3$], invariably a small amount of poorly soluble

 © 2007 Wiley-VCH Verlag GmbH & Co. KGaA, Weinheim 

material was formed as a side product. The yield of this could be maximised by the use of two equivalents of $Na[HB(mt)_3]$ or, alternatively, the reaction of $Na[HB(mt)_3]$ with isolated **4b**. The poor solubility of the side product compromised the acquisition of spectroscopic data other than from FAB-MS and IR spectra. Mass spectrometry indicated the gross composition $[Mo(CO)(\eta\text{-}PhC{\equiv}CPh)\{HB(mt)_3\}_2]$ (**5**) but gave no indication of the connectivity of this apparently 20–22 electron complex. The geometry was eventually established by crystallographic analysis, the results of which are summarised in Figure 2. The molecular geometry of the mononuclear complex is based on a pseudo-octahedral molybdenum centre that bears one $HB(mt)_3$ ligand coordinated in a conventional tridentate manner ($\kappa^3$-*S*,*S*′,*S*′′), whilst the second binds to molybdenum through a single sulfur donor ($\kappa^3$-*S*). Monodentate $HB(mt)_3$ coordination is unprecedented in transition metal chemistry, however we have previously identifed this mode of coordination in the tin derivative $Ph_3Sn\{HB(mt)_3\}$.[17] Copious structural data exist for molybdenum alkyne complexes,[18] however consideration of the parameters of **5** with those for the exemplary complexes $[Mo(PhC{\equiv}CPh)(\eta\text{-}C_5H_5)_2]$ (a 2-electron alkyne),[19] $[Mo(MeC{\equiv}CMe)_2(S_2Cpyr)_2]$ (a homoleptic sulfur donor set)[20] and $\{Mo(PhC{\equiv}CPh)(CO)_2[HB(pz')_3]\}^{n+}$ ($n$ = 0, 1; pz′ = 3,5-dimethylpyrazol-1-yl, a redox pair),[21] reveals that the alkyne has particularly short Mo–C separations coupled with a long C–C bond. Such geometric features are typically associated with alkynes acting as "4-electron" σ+π donors to an octahedral $d^4$-metal centre. However, it is noteworthy that the $\nu_{CO}$ value for **5** (1790 $cm^{-1}$) is remarkably low and indicative of an exceptionally π-basic molybdenum centre. This contrasts dramatically with the value of 1960 $cm^{-1}$ for the alkyne complex $[W(\eta\text{-}HC{\equiv}CH)(CO)(S_2CNEt_2)_2]$.[22] In a similar manner the neutral cyclopentadienone and vinyl ketene complexes $[W(CO)(S_2CNEt_2)_2(L)]$ (L = O=C-$(C_8H_{12})_2$,[23] $H_2C{=}CHCH{=}CO$[24]) have $\nu_{CO}$ = 1921 and 1960 $cm^{-1}$, whilst even the anionic complex $[W(CO)(SPh)(\kappa^2\text{-}S_2C_2Me_2)_2]^-$ has $\nu_{CO}$ = 1933 $cm^{-1}$ although the oxidation state of the tungsten in this sulfur rich complex is open to debate.[25] Thus the very low $\nu_{CO}$ value for **5** is quite exceptional such that the geometric features of the alkyne may be as much to do with conventional retrodonation into the alkyne π* orbital as with depletion of the C≡C π-bonding orbitals.

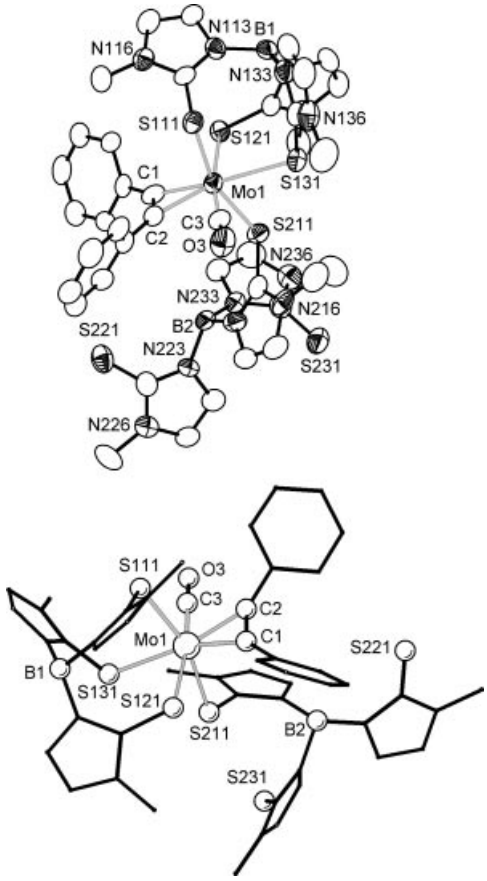


Figure 2. Top: Molecular geometry of **5**·$(CH_2Cl_2)_2$ (40% displacement ellipsoids, hydrogen atoms bound to carbon omitted). Bottom: Alternative simplified view. Selected bond lengths [Å] and angles (deg.) Mo1–S111 2.440(2), Mo1–S121 2.602(2), Mo1–S131 2.637(2), Mo1–S211 2.464(2), Mo1–C1 2.052(8), Mo1–C2 2.051(7), C1–C2 1.306(10), S111–Mo1–S121 93.74(6), S111–Mo1–S131 85.59(7), S121–Mo1–S131 85.39(6) S121–Mo1–S211 82.25(6), S131–Mo1–S211 75.97(7), C1–Mo1–C2 37.1(3), Mo1–S111–C112 107.0(2), Mo1–S121–C122 110.0(3), Mo1–S131–C132 107.7(2), Mo1–S211–C212 109.7(3), Mo1–C1–C11 148.7(6), Mo1–C2–C21 145.7(6).

## Conclusions

Synthetic routes to lead compounds for the study of alkyne derivatives of molybdenum and tungsten ligated by methimazolylborate ligands $H_nB(mt)_{4-n}$ ($n$ = 1,2) have been developed. In the case of dihydrobis(methimazolyl)borate derivatives, the propensity for 3c–2e B–H–metal interactions is manifest. In this respect, the behaviour of the $H_2B(mt)_2$ ligand is reminiscent of that first noted by Trofimenko, Kosky and Cotton[26] for the corresponding $H_2B(pzMe_2)_2$ ligand ($pzMe_2$ = 3,5-dimethylpyrazol-1-yl). However the inclusion of an extra atom in each of the arms of the $H_2B(mt)_2$ ligand (cf $pzMe_2$) results in an increased propensity for such 3c–2e B–H–metal interactions. In all cases, the alkyne coordination may be described as "4-electron," even for complex **5**, which has two alternative appended potential donors.

## Experimental Section

All manipulations of air-sensitive compounds were carried out under dry and oxygen-free nitrogen using standard Schlenk and vacuum line techniques, with dried and degassed solvents. NMR spectra were obtained at 25 °C with a Varian Gemini spectrometer 300BB ($^1H$ at 300.75 MHz, $^{13}C$ at 75.4 MHz, $^{11}B$ at 96.2 MHz). Mass Spectra were obtained with a ZAB-SEQ4F spectrometer (FAB, ACPI or ESI techniques) using matrices of either 3-nitrobenzyl alcohol (NBA) or acetonitrile and methanol (ESI). The elemental microanalysis was carried out by the microanalytical service of the Australian National University. The compounds $Na[H_2B$-

 © 2007 Wiley-VCH Verlag GmbH & Co. KGaA, Weinheim 

$(mt)_2]$,[8a] Na[HB(mt)$_3$],[27] $[MI_2(CO)_3(NCMe)_2]$[16a] and $[MoI_2(CO)(NCMe)(\eta^2\text{-PhC}{\equiv}\text{CPh})_2]$[16b] were prepared according to the indicated published procedures. Other reagents were used as received from commercial sources.

**Synthesis of $[WI_2(CO)_2(\eta^2\text{-HC}{\equiv}\text{CSiMe}_3)_2]$ (2):** Two equivalents of cold ethynyltrimethylsilane (0.70 g, 3.88 mmol) were added to a solution of $[WI_2(CO)_3(NCMe)_2]$ (1.50 g, 2.91 mmol) in $CH_2Cl_2$ (30 mL) at 0 °C in a foil-covered Schlenk tube. The reaction was warmed to room temperature, and left to stir for a further 12 h, after which time the colour had changed from brown to orange. The solvent was removed to dryness and diethyl ether (20 mL) was added and then the reaction flask was triturated for 20 min in an ultrasonic bath to provide an orange precipitate. The product was filtered and washed with diethyl ether (2 × 5 mL) and dried. The product was recrystallised from $CH_2Cl_2$ and petroleum ether (b.p. 40–60 °C). X-ray quality crystals of a methanol bis(solvate) were obtained by recrystallisation from a concentrated solution of methanol at –16 °C. Yield 1.34 g (78%). IR ($CH_2Cl_2$): $\tilde{\nu}_{CO}$ = 2089, 2070 cm$^{-1}$. (Nujol): $\tilde{\nu}_{CO}$ = 2099, 2075 cm$^{-1}$. $^1$H NMR ($CD_2Cl_2$, 25 °C): $\delta$ = 0.38 (s, 18 H, $CH_3$), 11.1 (s, 2 H, C≡CH) ppm. $^{13}$C{$^1$H}NMR ($CD_2Cl_2$, 25 °C): $\delta$ = 208.8 (CO), 195.3 (H*C*≡CSi), 173.5 (HC≡*C*Si), 0.33 ($SiCH_3$) ppm. $C_{12}H_{20}I_2O_2Si_2W$ (690.12): calcd. C 20.89, H 2.92, N 0.00; found C 21.07, H 3.05, N 0.00.

**Crystal Data:** $C_{12}H_{20}I_2O_2Si_2W{\cdot}(CH_3OH)_2$; $M_W$ = 754.20, monoclinic, *C*2/*c*, *a* = 17.1441(4), *b* = 12.1896(3), *c* = 12.8038(5) Å, $\beta$ = 97.6004(11)°, *V* = 2652.23(12) Å$^3$, *Z* = 4, $D_c$ = 1.889 Mg m$^{-3}$, $\mu$(Mo-$K_\alpha$) = 6.785 mm$^{-1}$, *T* = 200(2) K, yellow plate 0.35 × 0.28 × 0.05 mm; 3054 independent measured reflections, *F* refinement, $R_1$ = 0.027, $wR_2$ = 0.030; 2144 independent observed absorption corrected reflections [$I > 3\sigma(I)$, $2\theta \leq 55°$], 106 parameters, CCDC-284294.

**Synthesis of $[WI\{H_2B(mt)_2\}(CO)(\eta^2\text{-HC}{\equiv}\text{CSiMe}_3)]$ (3b):** A mixture of $[WI_2(CO)_2(\eta^2\text{-HC}{\equiv}\text{CSiMe}_3)_2]$ (**2**: 0.50 g, 0.72 mmol) and Na[$H_2B(mt)_2$] (0.19 g, 0.72 mmol) was stirred in $CH_2Cl_2$ (20 mL) at room temperature under nitrogen for 3 h, after which time the color of the mixture had changed from orange to green. The suspension was filtered through diatomaceous earth to remove NaI. The green filtrate was reduced to a minimum and petroleum ether (b.p. 40–60 °C) (15 mL) added resulting in the formation of a green precipitate. The product was filtered and washed with diethyl ether (2 × 5 mL) and dried. The green product was recrystallised from $CH_2Cl_2$/$Et_2O$. Yield 0.28 g (54%). IR ($CH_2Cl_2$): $\tilde{\nu}$ = 1923 ($\nu_{CO}$), 2265 ($\nu_{BHW}$), 2445 ($\nu_{BH}$) cm$^{-1}$. IR (Nujol): $\tilde{\nu}$ = 1927 ($\nu_{CO}$), 2263 ($\nu_{BHW}$), 2420 ($\nu_{BH}$) cm$^{-1}$. $^1$H NMR ($CD_2Cl_2$): $\delta$ = –0.43 (br., 1 H, BHW), 0.24 (s, 9 H, $SiCH_3$), 3.44 (s, 6 H, $NCH_3$), 6.98, 7.06 (d × 2, $^3J_{HH}$ = 1.8 Hz, 2 H, NHC=CHN), 13.1 (s, 1 H, HC≡C) ppm. $^{13}$C{$^1$H} NMR ($CD_2Cl_2$): $\delta$ = 229.5 (WCO), 203.2, 190.5 (C≡C), 161.4, (C=S), 123.6, 122.8 (NHC=CHN), 35.2 ($NCH_3$), 0.49 ($SiCH_3$) ppm. $^{11}$B{$^1$H} NMR ($CD_2Cl_2$): $\delta$ = –2.53 ppm. $C_{14}H_{22}BIN_4OS_2SiW$ (676.13): calcd. C 25.59, H 3.15, N 7.96; found C 25.56, H 3.54, N 7.99. MS (ESI): *m*/*z* (%) = 549.1 (65) [M – I]$^+$.

**Synthesis of $[MoI\{HB(mt)_3\}(CO)(\eta^2\text{-PhC}{\equiv}\text{CPh})]$ (4b):** A mixture of $[MoI_2(CO)(NCMe)(\eta^2\text{-PhC}{\equiv}\text{CPh})_2]$ (**1a**: 0.50 g, 0.65 mmol) and Na[HB(mt)$_3$] (0.24 g, 0.65 mmol) was stirred in $CH_2Cl_2$ (20 mL) at room temperature under $N_2$ for 3 h, after which time the color had changed from brown to a light green. Sodium iodide was removed by filtration through diatomaceous earth and the green filtrate was then concentrated to ca 2 mL. Dilution with petroleum spirit (b.p. 40–60 °C) (15 mL) precipitated the crude product, which was then recrystallised from $CH_2Cl_2$ and diethyl ether. Yield 0.28 g (56%). IR ($CH_2Cl_2$): $\tilde{\nu}$ = 1933 ($\nu_{CO}$), 2456 ($\nu_{BH}$) cm$^{-1}$. IR (Nujol): $\tilde{\nu}$ = 1938 ($\nu_{CO}$), 2404 ($\nu_{BH}$) cm$^{-1}$. $^1$H NMR ($CD_2Cl_2$): $\delta$ = 3.05, 3.87, 4.02 (3s, 3 × 3 H, $NCH_3$), 6.85, 6.92, 7.02 (3d, $^3J_{HH}$ = 1.8 Hz, 3 × 2 H, NHC=CHN), 7.36–7.72 (m, 10, $C_6H_5$) ppm. $^{13}$C{$^1$H} NMR ($CD_2Cl_2$): $\delta$ = 237.4 (MoCO), 207.4, 206.9 (C≡C), 162.6, 160.5, 159.8, (C=S), 126.5–129.0 ($C_6H_5$), 124.7, 123.0, 122.4, 121.2, 120.6, 120.1 (NHC=CHN), 36.4, 35.0, 34.5 ($NCH_3$) ppm. $^{11}$B{$^1$H} NMR ([$D_6$]DMSO): $\delta$ = 0.71 ppm. ESI-MS: *m*/*z* (%) = 781.9 (5) [M – $CH_3$]$^+$, 655.1 (15) [M – I]$^+$. $C_{27}H_{26}BIMoN_6OS_3$ (780.38): calcd. C 41.56, H 3.36, N 10.77; found C 41.92, H 3.66, N 10.14.

**Synthesis of $[Mo\{HB(mt)_3\}_2(CO)(\eta^2\text{-PhC}{\equiv}\text{CPh})]$ (5):** One equivalent of Na[HB(mt)$_3$] (0.25 g, 0.33 mmol) was added to a solution of $[MoI\{HB(mt)_3\}(CO)(\eta^2\text{-PhC}_2\text{Ph})]$ (**4b**: 0.12 g, 0.33 mmol) in $CH_2Cl_2$ (20 mL) and the mixture stirred at room temperature for 12 h resulting in the formation of an orange precipitate. The supernatant was then decanted and the orange product was washed with cold ethanol (20 mL) followed by cold diethyl ether (10 mL) and then dried in vacuo. N.B.: The product is poorly soluble in common organic solvents, compromising the acquisition of elemental and solution spectroscopic data. Yield 0.19 g (59%). IR (DMSO): $\tilde{\nu}$ = 1797 ($\nu_{CO}$), 2449, 2407 ($\nu_{BH}$) cm$^{-1}$. IR (Nujol): $\tilde{\nu}$ = 1790 ($\nu_{CO}$), 2433, 2406 ($\nu_{BH}$) cm$^{-1}$. APCI-MS: *m*/*z* (%) = 1029 (30) [M + Na]$^+$, 975 (25) [M – CO]$^+$. $^{11}$B{$^1$H} NMR (96.2 MHz, [$D_6$]DMSO): $\delta$ = 2.00 ppm. Storage of a dilute solution of **5** in dichloromethane at –20 °C provided crystals of a dichloromethane bis-solvate. Satisfactory elemental microanalytical data not obtained due to partial desolvation.

**Crystal Data:** $C_{39}H_{42}B_2MoN_{12}OS_6{\cdot}(CH_2Cl_2)_2$, $M_w$ = 1174.67, monoclinic, $P2_1/n$, *a* = 14.6842(3), *b* = 18.7132(6), *c* = 19.7601(6) Å, $\beta$ = 107.6683(16)°, *V* = 5173.7(3) Å$^3$, *Z* = 4, $D_c$ = 1.508 Mg m$^{-3}$, $\mu$(Mo-$K_\alpha$) = 0.749 mm$^{-1}$, *T* = 200(2) K, 9074 independent measured reflections, *F* refinement, $R_1$ = 0.064, $wR_2$ = 0.056; 4681 independent observed absorption corrected reflections [$I > 3\sigma(I)$, $2\theta \leq 50°$], 604 parameters.

CCDC-289494 and -289495 contain the supplementary crystallographic data for this paper. These data can be obtained free of charge from The Cambridge Crystallographic Data Centre via www.ccdc.cam.ac.uk/data_request/cif.

## Acknowledgments

We thank the University of Botswana for a studentship (to N. T.) and the Australian Research Council (ARC) for financial support (DP034270).

[1] a) J. L. Templeton, *Adv. Organomet. Chem.* **1989**, *29*, 1; b) P. K. Baker, *Adv. Organomet. Chem.* **1996**, *40*, 45.
[2] G. Hogarth, *Prog. Inorg. Chem.* **2005**, *53*, 71.
[3] S. Tofimenko, *Scorpionates: The Coordination Chemistry of Poly(pyrazolyl)borate Ligands*, Imperial College Press, London, **1999**.
[4] M. Garner, J. Reglinski, I. Cassidy, M. D. Spicer, A. R. Kennedy, *Chem. Commun.* **1996**, 1975.
[5] C. Kimblin, T. Hascall, G. Parkin, *Inorg. Chem.* **1997**, *36*, 5680.
[6] A. J. L. Pombiero, R. L. Richards, *Coord. Chem. Rev.* **1990**, *104*, 13.
[7] M. R. St.-J. Foreman, A. F. Hill, A. J. P. White, D. J. Williams, *Organometallics* **2003**, *22*, 3831.
[8] a) M. R. St.-J. Foreman, A. F. Hill, N. Tshabang, A. J. P. White, D. J. Williams, *Organometallics* **2003**, *22*, 5593; b) R. J. Abernethy, A. F. Hill, H. Neumann, A. C. Willis, *Inorg. Chim. Acta* **2005**, *358*, 1605; c) A. F. Hill, M. K. Smith, *Dalton Trans.* **2006**, 28; d) I. R. Crossley, A. F. Hill, A. C. Willis, *Organometallics* **2005**, *24*, 4889; e) M. R. St.-J. Foreman, A. F. Hill, M. K. Smith, N. Tshabang, *Organometallics* **2005**, *24*, 5224; f)

 © 2007 Wiley-VCH Verlag GmbH & Co. KGaA, Weinheim 

I. R. Crossley, A. F. Hill, E. R. Humphrey, M. K. Smith, *Organometallics* **2006**, *25*, 2242.
[9] a) R. Garcia, A. Domingos, A. Paulo, I. Santos, R. Alberto, *Inorg. Chem.* **2002**, *41*, 2422; b) R. Garcia, A. Paulo, A. Domingos, I. Santos, *J. Organomet. Chem.* **2001**, *632*, 41; c) R. Garcia, A. Paulo, A. Domingos, I. Santos, K. Ortner, R. Alberto, *J. Am. Chem. Soc.* **2000**, *122*, 11240.
[10] a) C. Kimblin, B. M. Bridgewater, T. Hascall, G. Parkin, *J. Chem. Soc. Dalton Trans.* **2000**, 891; b) C. Kimblin, T. Hascall, G. Parkin, *Inorg. Chem.* **1997**, *36*, 5680; c) C. Kimblin, B. M. Bridgewater, T. Hascall, G. Parkin, *J. Chem. Soc. Dalton Trans.* **2000**, 891.
[11] a) L. A. Philson, D. M. Alyounes, L. N. Zakharov, A. L. Rhenigold, D. Rabinovich, *Polyhedron* **2003**, *22*, 3461; b) H. M. Alvarez, J. M. Tanski, D. Rabinovich, *Polyhedron* **2004**, *23*, 395; c) L. A. Graham, A. R. Fout, K. R. Kuehne, J. L. White, B. Mookheri, F. M. Marks, G. P. A. Yap, L. N. Zakharov, A. L. Rheingold, D. Rabinovich, *Dalton Trans.* **2005**, 171; d) H. M. Alvarez, M. Krawiec, B. T. Donovan-Merkert, M. Fouzi, D. Rabinovich, *Inorg. Chem.* **2001**, *40*, 5736.
[12] M. R. St.-J. Foreman, A. F. Hill, G. R. Owen, A. J. P. White, D. J. Williams, *Organometallics* **2003**, *22*, 4446.
[13] C. Kimblin, D. G. Chruchill, B. M. Bridgewater, J. N. Girard, D. A. Quarless, G. Parkin, *Polyhedron* **2001**, *20*, 1891.
[14] M. Careri, L. Elviri, M. Lafranchi, M. Marchio, C. Mora, M. A. Pellinghelli, *Inorg. Chem.* **2003**, *42*, 2109.
[15] S. L. Kuan, W. K. Leong, L. Y. Goh, R. D. Webster, *Organometallics* **2005**, *24*, 4639.
[16] a) P. K. Baker, S. G. Fraser, E. M. Keyes, *J. Organomet. Chem.* **1986**, *309*, 319; b) E. M. Armstrong, P. K. Baker, M. G. B. Drew, *Organometallics* **1988**, *7*, 319.
[17] A. F. Hill, M. K. Smith, *Chem. Commun.* **2005**, 1920.
[18] Cambridge Crystallographic Data Centre, *Conquest*®, Version 1.7, November **2006** release.
[19] A. De Cian, J. Colin, M. Schappacher, L. Ricard, R. Weiss, *J. Am. Chem. Soc.* **1981**, *103*, 1850 (Mo–C: 2.142, 2.145; C–C: 1.269 Å; Mo–C–CPh: 140.5, 140.1°).
[20] R. S. Herrick, S. J. N. Burgmayer, J. L. Templeton, *Inorg. Chem.* **1983**, *22*, 3275 (Mo–C: 2.019–2.082; C–C: 1.246, 1.236 Å; Mo–C–CMe: 138.2–143.5°).
[21] I. M. Barlett, N. G. Connelly, A. G. Orpen, M. J. Quayle, J. C. Rankin, *Chem. Commun.* **1996**, 2583 ($n$ = 0: Mo–C: 2.137, 2.175; C–C: 1.282 Å; Mo–C–CPh: 144.8, 145.1°. $n$ = 1: Mo–C: 2.041, 2.070; C–C: 1.335 Å; Mo–C–CPh: 147.1, 146.5°).
[22] L. Rickard, R. Weiss, W. E. Newton, G. J.-J. Chen, J. W. McDonald, *J. Am. Chem. Soc.* **1978**, *100*, 1318.
[23] M. A. Bennett, I. A. Boyd, G. B. Robertson, W. A. Wickramasinghe, *J. Organomet. Chem.* **1985**, *290*, 181.
[24] a) R. S. Herrick, S. J. N. Burgmayer, J. L. Templeton, *Inorg. Chem.* **1983**, *22*, 3275; b) J. L. Templeton, R. S. Herrick, C. A. Rusik, C. E. McKenna, J. W. McDonald, W. E. Newton, *Inorg. Chem.* **1985**, *24*, 1383.
[25] K.-M. Sung, R. H. Holm, *Inorg. Chem.* **2000**, *39*, 1275.
[26] a) S. Trofimenko, *Inorg. Chem.* **1970**, *9*, 2493; b) S. Trofimenko, *J. Am. Chem. Soc.* **1969**, *91*, 3183; c) C. A. Kosky, P. Ganis, G. Avitabile, *Acta Crystallogr., Sect. B* **1971**, *27*, 1859; d) F. A. Cotton, M. Jeremic, A. Shaver, *Inorg. Chim. Acta* **1972**, *6*, 543.
[27] A. F. Hill, G. R. Owen, A. J. P. White, D. J. Williams, *Angew. Chem. Int. Ed.* **1999**, *38*, 2759.

Received: May 2, 2007
Published Online: July 23, 2007

 © 2007 Wiley-VCH Verlag GmbH & Co. KGaA, Weinheim 

DOI: 10.1002/ejic.200700617

# The First Heterohexametallic Transition-Metal Complex

Rico Packheiser[a] and Heinrich Lang*[a]

**Keywords:** Heteromultimetallic / Transition metal / Acetylides / Organometallic π-tweezers / Transmetallation / Mass spectrometry

The synthesis and characterisation of a first heteromultimetallic transition metal complex with six different metal atoms (Fe, Ru, Re, Au, Cu and Ti), connected through carbon-rich bridging units, are reported. Complex {1-[($\eta^2$-dppf)($\eta^5$-$C_5H_5$)RuC≡C]-3-[(bipy•)$(CO)_3$ReC≡C]-5-[$PPh_2$AuC≡C-bipy({[Ti](μ-σ,π-C≡$CSiMe_3$)$_2$}Cu)]$C_6H_3$}$PF_6$ is accessible in a consecutive reaction sequence by applying building blocks from a ligand and coordination complex library.
(© Wiley-VCH Verlag GmbH & Co. KGaA, 69451 Weinheim, Germany, 2007)

## Introduction

The linking of modular constructed transition-metal building blocks by carbon-rich bridging units to generate heteromultimetallic assemblies has increasingly gained interest during the last years.[1] A straightforward method to prepare such complexes is given by using the principle of the molecular "tinkertoy" approach.[2–4] This generally requires the prior preparation of multifunctional organic, coordination and/or organometallic molecules, which allow the stepwise synthesis of multitopic transition-metal-containing species. In particular, as different binding sites of the connecting units reactive groups, such as acetylides, phosphanes and N,N-donor systems (N,N = bi- or tridentate Lewis bases) can be used to control the synthesis of (hetero)multimetallic complexes. In context with this background, heteromultimetallic complexes with up to four different transition metals were synthesised, a hitherto scarcely explored class of compounds in transition-metal chemistry.[5] Very recently we reported the successful preparation of a heteromultimetallic species in which five different transition metals (Fe-Ru-Au-Cu-Ti) are spanned by carbon-rich organic units.[6] Extending this idea, we describe here for the first time the synthesis of an even heterohexanuclear transition-metal complex supported by applying the precoordinated multitopic organometallic building block 1-[($\eta^2$-dppf)($\eta^5$-$C_5H_5$)RuC≡C]-3-[(bipy*)$(CO)_3$ReC≡C]-5-($PPh_2$)-$C_6H_3$.

## Results and Discussion

The heterohexanuclear complex prepared was of the type {1-[($\eta^2$-dppf)($\eta^5$-$C_5H_5$)RuC≡C]-3-[(bipy*)$(CO)_3$ReC≡C]-5-[$PPh_2$AuC≡C-bipy({[Ti](μ-σ,π-C≡$CSiMe_3$)$_2$}Cu)]$C_6H_3$}-$PF_6$ (**5**) by using the versatile starting material 1-[($\eta^2$-dppf)-($\eta^5$-$C_5H_5$)RuC≡C]-3-[(bipy*)$(CO)_3$ReC≡C]-5-($PPh_2$)$C_6H_3$ (**1**) {dppf = 1,1′-bis(diphenylphosphanyl)ferrocene; bipy = 2,2′-bipyridine-5-yl; bipy* = 4,4′-di-*tert*-butyl-2,2′-bipyridine; [Ti] = ($\eta^5$-$C_5H_4SiMe_3$)$_2$Ti} and the relevant organometallic fragments. The newly synthesised transition-metal complexes and the overall synthetic methodology employed are depicted in Scheme 1.

Molecule **1** was prepared as described earlier by starting from 1,3,5-tribromobenzene.[7] Treatment of **1** with (tht)-AuC≡C-bipy (**2**), in situ generated from (tht)AuCl and 5-ethynyl-2,2′-bipyridine (tht = tetrahydrothiophene)[7] gave by replacement of the S-donor ligand tetrahydrothiophene by tertiary phosphane **1** coordination complex 1-[($\eta^2$-dppf)($\eta^5$-$C_5H_5$)RuC≡C]-3-[(bipy*)$(CO)_3$ReC≡C]-5-($PPh_2$-AuC≡C-bipy)$C_6H_3$ (**3**) (Scheme 1). After appropriate workup, compound **3** could be isolated as a yellow powder in moderate yield.

When we attempted to crystallise complex **3** by diffusion of *n*-hexane into a dichloromethane solution containing **3**, it was discovered that this complex is not stable because it decomposes to produce (bipy*)$(CO)_3$ReC≡C-bipy along with an insoluble yellow precipitate that does not dissolve in common organic solvents. This observation underlies an unexpected transmetallation reaction between the Re and Au alkynyls. The insoluble precipitate probably evinces a polymeric structure formed by the remaining phosphane gold(I) acetylide building block. Nevertheless, complex **3** with its four different transition-metal atoms is a key starting material for the synthesis of organometallic assemblies of higher nuclearity owing to the presence of a pendant 2,2′-bipyridine entity as a further N-ligating site.

{1-[($\eta^2$-dppf)($\eta^5$-$C_5H_5$)RuC≡C]-3-[(bipy*)$(CO)_3$ReC≡C]-5-[$PPh_2$AuC≡C-bipy({[Ti](μ-σ,π-C≡$CSiMe_3$)$_2$}-Cu)]$C_6H_3$}$PF_6$ (**5**) is formed in a straightforward manner when **3** is treated with the organometallic π-tweezer

[a] Technische Universität Chemnitz, Fakultät für Naturwissenschaften, Institut für Chemie, Lehrstuhl Anorganische Chemie, Straße der Nationen 62, 09111 Chemnitz, Germany
E-mail: heinrich.lang@chemie.tu-chemnitz.de
Supporting information for this article is available on the WWW under http://www.eurjic.org or from the author.

 InterScience © 2007 Wiley-VCH Verlag GmbH & Co. KGaA, Weinheim 

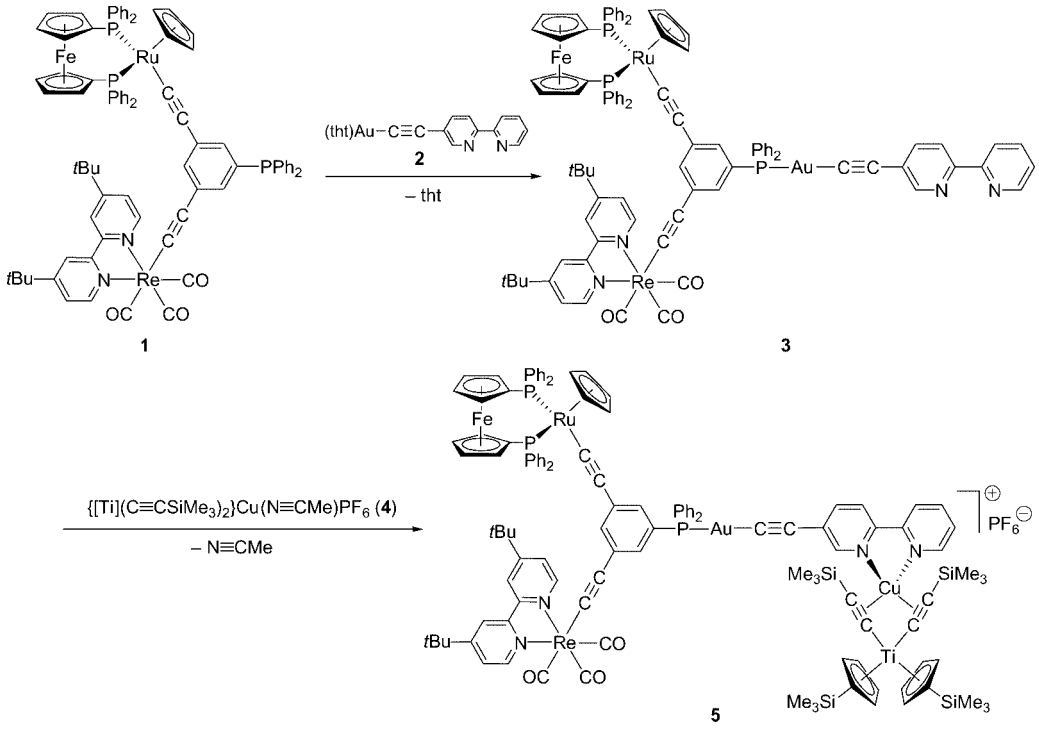


Scheme 1. Synthesis of heterotetrametallic **3** and heterohexanuclear **5** {[Ti] = ($\eta^5$-$C_5H_4SiMe_3)_2$Ti}.

[{[Ti](μ-σ,π-C≡CSiMe$_3$)$_2$}Cu(N≡CMe)]PF$_6$ (**4**), whereby the acetonitrile ligand in **4** is substituted by the bipyridine entity of **3**. Within this reaction, the coordination number at copper(I) changes from three (planar) to four (pseudo-tetrahedral).

Orange **5** is only soluble in polar solvents such as tetrahydrofuran or chloroform as a result of its ionic character. This complex is stable in the solid state, that is, no intramolecular redox processes are observed. However, it should be mentioned that all efforts to produce X-ray quality crystals of **5** failed owing to the instability of this complex in solution over prolonged periods. In **5** the appropriate transition metals Ti, Re, Fe, Ru, Cu and Au are connected by carbon-rich organic bridging units.

The synthetic protocol developed to prepare heteromutlinuclear **3** and **5** is directed to the use of modular-shaped organometallic building blocks (vide supra). In this respect, IR and NMR ($^1$H, $^{31}$P{$^1$H}) spectroscopy allow the progress of the reactions to be monitored, and thus the structure and composition of the final assemblies can be verified. In addition, ESI-TOF mass spectrometric studies were carried out with **3** and **5**.

Most characteristic in the IR spectra of **3** and **5** is the appearance of $\nu_{C\equiv C}$ and $\nu_{CO}$ vibrations typical for the individual σ alkynyl organometallic transition-metal fragments, which are diagnostic and represent a useful monitoring tool. The introduction of the gold acetylide building block at the phosphane is evidenced by the respective $\nu_{C\equiv C}$ absorption at 2117 cm$^{-1}$ (AuC≡C), which is typical for phosphane-stabilised gold(I) acetylides and also found in **5**.[8]

The $^{31}$P{$^1$H} NMR spectra of **3** and **5** show the expected resonance signals. In all complexes, a signal at $\delta \approx 54$ ppm is observed for the dppf entity. Owing to the coordination of the phosphane to gold(I), a representative shift to lower field from –5.4 (**1**) to 41.2 (**3**) ppm is observed which is, however, not influenced by further metal coordination as given in **5**.[8]

The $^1$H NMR spectroscopic properties of **3** and **5** nicely correlate with their formulations as heteromultinuclear assemblies based on the 1,3-diethynyl-5-diphenylphosphanylbenzene core, and the spectra show the respective resonance signal patterns for the organic units. Most distinctive for the formation of **5** is the chemical shift of the bipyridine protons H6/H6′ (**3**: H6′, 8.66; H6, 8.79 ppm; **5**: H6/H6′, (m) 8.49–8.58 ppm). Furthermore, as a result of the coordination of the bipyridine unit to the organometallic π-tweezer-stabilised copper(I) centre in **5**, a highfield shift of the Me$_3$SiC≡C protons is observed relative to **4**,[9] which can be explained by the ring current of the bipyridine ligand.

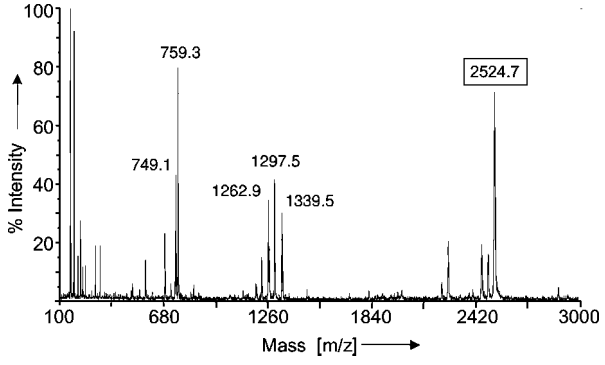


Figure 1. ESI-MS spectra of heterohexanuclear **5**.

 © 2007 Wiley-VCH Verlag GmbH & Co. KGaA, Weinheim 

The identity of heterotetranuclear **3** and heterohexametallic **5** was additionally evidenced from mass spectrometric investigations. The electrospray ionisation mass spectrum (ESI-MS) of **3** shows an ion peak at *m*/*z* = 1944.7, which corresponds to $[\mathbf{3} + H]^+$. The spectrum of **5** (Figure 1) exhibits a prominent ion peak at *m*/*z* = 2524.7, whose mass and isotope distribution pattern comply to $[\mathbf{5} - PF_6]^+$ and confirm the elemental composition and charge state.

## Conclusions

This report pertaining to the first synthesis of an organometallic complex in which a total of six different early and late transition metals, such as titanium, rhenium, iron, ruthenium, copper and gold, are connected by carbon-rich π-conjugated bridging units demonstrates that such large heteronuclear assemblies can be synthesised in a straightforward manner by combining different organic and/or organometallic building blocks of lower nuclearity from a ligand and coordination complex library that was particularly built for this purpose. This procedure allows the composition and structure of such novel molecules to be controlled, but it also should be mentioned that unexpected reactions can occur that make this field of chemistry even more challenging than initially anticipated. Similar to racing cars, from which we learn experience for everyday vehicles, the chemistry described above will surely provide the impetus for future detailed investigations in this field of chemistry, including spectroelectrochemical studies and material properties.

## Experimental Section

**Starting Materials, Reaction Conditions and Instrumentation:** All manipulations were carried out under anhydrous and anaerobic conditions by using standard Schlenk techniques. Tetrahydrofuran and *n*-hexane were purified by distillation from sodium/benzophenone. $[\{[Ti](\mu\text{-}\sigma,\pi\text{-}C{\equiv}CSiMe_3)_2\}Cu(N{\equiv}CMe)]PF_6$[9a] was prepared according to a published procedure. Infrared spectra were recorded with a Perkin–Elmer FTIR spectrometer Spectrum 1000. NMR spectra were recorded with a Bruker Avance 250 spectrometer; chemical shifts are given in $\delta$ units (parts per million) and are referenced to residual solvent resonances ($^1$H NMR: $CDCl_3$, $\delta$ = 7.26) or an external 85% $H_3PO_4$ standard ($^{31}P\{^1H\}$).

**5:** To $[\{[Ti](\mu\text{-}\sigma,\pi\text{-}C{\equiv}CSiMe_3)_2\}Cu(N{\equiv}CMe)]PF_6$ (**4**) (25 mg, 0.033 mmol) dissolved in tetrahydrofuran (25 mL) was added in a single portion 1-[($\eta^2$-dppf)($\eta^5$-$C_5H_5$)RuC≡C]-3-[(bipy*)$(CO)_3$ReC≡C]-5-($PPh_2$AuC≡C-bipy)$C_6H_3$ (**3**) (60 mg, 0.031 mmol). The resulting reaction mixture was stirred for 2 h at 25 °C, whereby the colour of the solution changed from orange to red. The solvent was reduced in volume, and the product was precipitated by the addition of *n*-hexane, washed twice with *n*-hexane and dried under vacuum to afford an orange-red solid. Yield: 70 mg (0.026 mmol, 85%). $^1$H NMR (250 MHz, $CDCl_3$, 25 °C, TMS): $\delta$ = –0.50 (s, 18 H, Si*Me*$_3$), 0.27 (br. s, 18 H, Si*Me*$_3$), 1.41 (s, 18 H, *t*Bu), 3.93 (dpt, $J_{HP}$ = 1 Hz, $J_{HH}$ = 2.4 Hz, 2 H, $C_5H_4$), 4.02 (br. s, 2 H, $C_5H_4$), 4.20 (s, 5 H, $C_5H_5$), 4.25 (br. s, 2 H, $C_5H_4$), 5.00 (br. s, 2 H, $C_5H_4$), 6.23–6.30 (m, 8 H, $C_5H_4$/$C_5H_4SiMe_3$), 6.83 (dpt, $J_{HP}$ = 12.8 Hz, $J_{HH}$ = 1.5 Hz, 1 H, $C_6H_3$), 7.00 (dpt, $J_{HP}$ = 15 Hz, $J_{HH}$ = 1.5 Hz, 1 H, $C_6H_3$), 7.06–7.53 [m, 26 H ($C_6H_5$) + 1 H ($C_6H_3$) + 2 H (*H5*/bipy*)], 7.62–7.75 [m, 4 H ($C_6H_5$) + 1 H (*H5′*/bipy)], 8.12 (dd, $^3J_{H4H3}$ = 8.4 Hz, $^4J_{H4H6}$ = 2.0 Hz, *H4*/bipy), 8.18–8.27 (m, 3 H, *H3*/bipy* + *H4′*/bipy), 8.42 (d, $^3J_{H3H4}$ = 8.4 Hz, 1 H, *H3*/bipy), 8.49–8.58 (m, 3 H, *H3′*,*H6*,*H6′*/bipy), 8.97 (d, $^3J_{H6H5}$ = 6.0 Hz, 2 H, *H6*/bipy*) ppm. $^{31}P\{^1H\}$ NMR (101.25 MHz, $CDCl_3$, 25 °C, $H_3PO_4$): $\delta$ = –145.1 (septuplet, $J_{PF}$ = 713 Hz, $PF_6$), 40.8 (Au*P*$Ph_2$), 53.7 (dppf) ppm. IR (KBr): $\tilde{\nu}$ = 1893, 1904, 2003 (s, CO), 2060 (m, *C*≡*C*Ru), 2117 (w, *C*≡*C*Au) $cm^{-1}$. MS (ESI-TOF): *m*/*z* (%) = 2524.7 (70) $[M - PF_6]^+$. $C_{120}H_{121}AuCuF_6FeN_4O_3P_4ReRuSi_4Ti$ (2669.03): calcd. C 54.00, H 4.57, N 2.10; found C 54.76, H 4.80, N 2.04.

**Supporting Information** (see footnote on the first page of this article): Synthetic details and characterisation for compounds **1** and **3**.

## Acknowledgments

We are grateful to the Deutsche Forschungsgemeinschaft and the Fonds der Chemischen Industrie for generous financial support.

[1] For example: a) V. W. W. Yam, K. K. K. Lo, K. M. C. Wong, *J. Organomet. Chem.* **1999**, *578*, 3; b) A. Ceccon, S. Santi, L. Orian, A. Bisello, *Coord. Chem. Rev.* **2004**, *248*, 683; c) P. J. Low, R. L. Roberts, R. L. Cordiner, F. Hartl, *J. Solid State Electrochem.* **2005**, *9*, 717; d) F. Paul, C. Lapinte, *Coord. Chem. Rev.* **1998**, *178–180*, 431; e) D. M. D'Alessandro, F. R. Keene, *Chem. Rev.* **2006**, *106*, 2270; f) G. Vives, A. Carella, J. P. Launay, G. Rapenne, *Chem. Commun.* **2006**, 2283; g) V. Balzani, A. Juris, M. Venturi, *Chem. Rev.* **1996**, *96*, 759; h) V. W. W. Yam, *J. Organomet. Chem.* **2004**, *689*, 1393; i) N. J. Long, A. J. Martin, A. J. P. White, D. J. Williams, M. Fontani, F. Laschi, P. Zanello, *J. Chem. Soc. Dalton Trans.* **2000**, 3387.

[2] a) J. Michl, F. Magnera, *Proc. Natl. Acad. Sci. USA* **2002**, *99*, 4788; b) M. Levin, P. Kaszynski, J. Michl, *Chem. Rev.* **2000**, *100*, 169.

[3] a) F. M. Rayoma, J. F. Stoddart, *Chem. Rev.* **1999**, *100*, 1643; b) J. F. Stoddart, *Chem. Soc. Rev.* **1992**, *21*, 215.

[4] H. Lang, R. Packheiser, B. Walfort, *Organometallics* **2006**, *25*, 1836.

[5] a) S. Back, W. Frosch, I. del Rio, G. van Koten, H. Lang, *Inorg. Chem. Commun.* **1999**, *2*, 584; b) R. Packheiser, B. Walfort, H. Lang, *Jordan J. Chem.* **2006**, *1*, 121.

[6] R. Packheiser, H. Lang, *Inorg. Chem. Commun.* **2007**, *10*, 580.

[7] R. Packheiser, Ph. D. Thesis, TU Chemnitz **2007**.

[8] a) J. Vicente, M. T. Chicote, M. M. Álvarez-Falcón, M. D. Abrisqueta, F. J. Hernandez, P. G. Jones, *Inorg. Chim. Acta* **2003**, *347*, 67; b) G. Hogarth, M. M. Álvarez-Falcón, *Inorg. Chim. Acta* **2005**, *358*, 1386; c) V. W. W. Yam, S. W. K. Choi, K. K. Cheung, *Organometallics* **1996**, *15*, 1734.

[9] a) M. D. Janssen, M. Herres, L. Zsolnai, A. L. Spek, D. M. Grove, H. Lang, G. van Koten, *Inorg. Chem.* **1996**, *35*, 2476; b) H. Lang, D. S. A. George, G. Rheinwald, *Coord. Chem. Rev.* **2000**, *206–207*, 101; c) R. Packheiser, B. Walfort, H. Lang, *Organometallics* **2006**, *25*, 4579.

Received: June 12, 2007
Published Online: July 11, 2007

 © 2007 Wiley-VCH Verlag GmbH & Co. KGaA, Weinheim 

DOI: 10.1002/ejic.200700199

# Self-Assembly of Dimeric $Mn^{III}$–Schiff-Base Complexes Tuned by Perchlorate Anions

**Manuel R. Bermejo,[a] M. Isabel Fernández,*[b] Esther Gómez-Fórneas,[b] Ana González-Noya,[b] Marcelino Maneiro,*[b] Rosa Pedrido,[a] and M. Jesús Rodríguez[b]**

**Keywords:** Manganese / Self-assembly / Anions / Schiff bases / Peroxidase

The synthesis and structural and spectroscopic characterisation of 12 manganese(III)–Schiff-base complexes of the formula $[MnL^n(H_2O/CH_3OH)_2](ClO_4)(mH_2O)$ ($m$ = 0, 1) are described. The multidentate $H_2L^n$ and $H_4L^n$ Schiff-base ligands were obtained by condensation of different diamines (1,2-diaminoethane, 1,2-diamino-2-methylethane, 1,2-diamino-2,2-dimethylethane, 1,3-diamino-2,2-dimethylpropane) and 2,3-dihydroxybenzaldehyde, 3-methoxy-2-hydroxybenzaldehyde or 3-ethoxy-2-hydroxybenzaldehyde. The crystal structures of $H_2L^3$ and $H_4L^{10}$ ligands were solved by X-ray crystallography, revealing their ability to bind metal centres. Recrystallisation of complexes **2** and **8** from methanol yielded single crystals of $[MnL^2(H_2O)_2](ClO_4)$ and $[MnL^8(H_2O)_2](ClO_4)$. Their X-ray characterisation shows a tetragonally elongated octahedral geometry for the manganese coordination sphere, formed by the chelation of the $N_2O_2$ donor set of the inner compartment of the Schiff base to the equatorial plane of the octahedron and by the binding of two water molecules in the axial positions. The octahedron entities are linked in pairs by μ-aquo bridges between neighbouring axial water molecules and also by π–π stacking interactions, establishing dimeric structures. Perchlorate anions are accommodated in the cavities of the framework and form hydrogen bonds with the aqua ligands, leading to infinite spirals of the complexes generated by a screw axis along $a$. Moreover, the peroxidase activity of the crystallographically solved complexes **2** and **8**, studied in the presence of the water-soluble trap ABTS, agrees with the predicted rate according to the activity/rhombicity correlation.

(© Wiley-VCH Verlag GmbH & Co. KGaA, 69451 Weinheim, Germany, 2007)

## Introduction

Crystal engineering of supramolecular architectures sustained by noncovalent intermolecular forces represents a rapidly expanding field that offers potential for the development of new types of functional solids.[1,2] The self-assembly of metal-organic frameworks is highly influenced by factors such as the geometric requirements of metal ions,[3,4] the ligand design,[5,6] the solvents used for crystallisation[7] or the selection of the counteranions.[8] Understanding the role of these factors may extend our knowledge of the relevant structural types and establishes proper synthetic strategies that lead to the desired species with predictable structures and properties.

In recent times one of our research goals constitutes the study of supramolecular chemistry of manganese(III).[9–11] The coordination chemistry of this species has been extensively studied[12,13] due to its rich redox behaviour, where manganese(III) complexes are the active sites of numerous enzymes,[14] but studies focusing on their multidimensional arrangements are less abundant. This paper presents new results from our intention of studying in depth the multidimensional arrangements of manganese(III) chemistry.

We have already shown how the introduction of chloride anions may induce the self-assembly of $Mn^{III}$ complexes, through a hydrogen-bonding net, to give 2D supramolecular architectures[10] when the ligand has hydroxy functional groups in adequate positions. We are now exploring the use of weakly coordinating anions such as perchlorates, nitrates, etc., to construct $Mn^{III}$ polymer networks.[15–18] The ability of these anions for establishing hydrogen bonds would allow new supramolecular architectures to be obtained and would also lead to systems of interest for the selective recognition between anions and receptors.[19,20]

Herein we report a series of $Mn^{III}$–Schiff-base complexes associated by perchlorate counteranions, using ligands with adequate OH groups. The selected Schiff-base ligands, $H_4L^n$ and $H_2L^n$ (see Scheme 1), contain six and four potential donor atoms, respectively. They have in common an inner compartment with two imine nitrogen atoms and two phenol oxygen atoms, but $H_4L^n$ ligands have an extra couple of outer phenol groups, while $H_2L^n$ ligands present two outer methoxy or ethoxy groups.

[a] Dpto. de Química Inorgánica, Facultade de Química, Universidade de Santiago de Compostela, 15782 Santiago de Compostela, Spain
[b] Dpto. de Química Inorgánica, Facultade de Ciencias, Universidade de Santiago de Compostela, 27002 Lugo, Spain

 © 2007 Wiley-VCH Verlag GmbH & Co. KGaA, Weinheim 

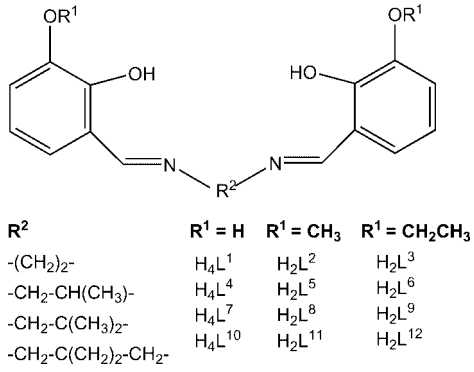


| $R^2$ | $R^1$ = H | $R^1$ = $CH_3$ | $R^1$ = $CH_2CH_3$ |
|---|---|---|---|
| -$(CH_2)_2$- | $H_4L^1$ | $H_2L^2$ | $H_2L^3$ |
| -$CH_2$-$CH(CH_3)$- | $H_4L^4$ | $H_2L^5$ | $H_2L^6$ |
| -$CH_2$-$C(CH_3)_2$- | $H_4L^7$ | $H_2L^8$ | $H_2L^9$ |
| -$CH_2$-$C(CH_2)_2$-$CH_2$- | $H_4L^{10}$ | $H_2L^{11}$ | $H_2L^{12}$ |

Scheme 1.

## Results and Discussion

### Synthesis and Spectroscopic Studies

The Schiff-base ligands were obtained in almost quantitative yield by the well-known experimental procedure, and afterwards they were characterised by elemental analysis, electrospray, IR, $^1$H- and $^{13}$C NMR spectroscopy, as well as the measurements of their melting points. Additionally, $H_2L^3$ and $H_4L^{10}$ gave crystals suitable for their characterisation by X-ray crystallography.

The manganese complexes were prepared following a variation of the Boucher method reported by us previously.[21] The manganese compounds obtained by this synthetic route, in high yield, are sparingly soluble in water and common organic solvents, but are quite soluble in MeOH, DMF and DMSO. Elemental analyses establish their general formula as $[MnL^n(H_2O/CH_3OH)_2](ClO_4)$-$(mH_2O)$ ($m$ = 0, 1).

All these complexes show similar IR spectral features (Table 1), exhibiting a strong band between 1621–1610 cm$^{-1}$ attributable to $\nu$(C=$N_{imine}$), which is shifted 7–22 cm$^{-1}$ lower than that in the free ligand. An up-frequency shift of the $\nu$($CO_{phenol}$) band to higher frequency (6–21 cm$^{-1}$) is also observed. These data suggest the coordination of the Schiff base in its dianionic form to the metal through the inner phenol oxygen and the imine nitrogen atoms.

The IR spectra also show broad unsplit bands ca. 1100 cm$^{-1}$, together with bands at 630 cm$^{-1}$, indicative of the presence of the uncoordinated perchlorate anion.

The presence of a broad band at about 3400 cm$^{-1}$ is associated with coordinated and/or solvated water/methanol molecules, but unfortunately it interferes with the observation of uncoordinated hydroxy groups.[22]

The ES mass spectra exhibit peaks relating to fragments $[MnL]^+$, which thus further corroborate coordination of the ligand to the manganese ion. The appearance of minor peaks in some complexes that could be assigned to the $[Mn_2L_2]^+$ dimeric entity (see Table 1) suggests their tendency to dimerise, although this spectroscopic technique is not sensitive enough to unambiguously detect either these dimers or the coordinated water molecules in every case.

The room temperature magnetic moments of the complexes are listed in Table 1. They exhibit values close to the spin-only value of 4.9 BM, as expected for a high-spin magnetically diluted d$^4$ manganese(III) ion, indicating little or no antiferromagnetic interaction.

The electronic spectroscopic data recorded are very similar for all compounds **1**–**12**, indicating that the $Mn^{III}$ complexes are behaving as high-spin octahedral d$^4$ systems, probably suffering a significant Jahn–Teller distortion which affects the spectra and complicates its interpretation. The characteristic UV broad band obtained at 480–490 nm ($\varepsilon$ = 2600–3300 L mol$^{-1}$ cm$^{-1}$) corresponds to the $^5E_g \leftarrow {}^5T_{2g}$ transition, and the peak appearing around 300 nm ($\varepsilon$ = 21000–23000 L mol$^{-1}$ cm$^{-1}$) can be attributed to the Schiff-base ligand → $Mn^{III}$ LMCT band.

Furthermore, the conductivity measurements in DMF give $\Lambda_M$ values of 90–60 μS cm$^{-1}$, indicating a behaviour attributable to 1:1 electrolytes.[23]

Paramagnetic $^1$H NMR spectroscopic studies of these $Mn^{III}$ complexes were undertaken using [$D_6$]dmso as the solvent. The data are presented in Table 1. The interpretation of the data was based on previous findings for manganese(III) complexes with related Schiff-base ligands.[9,24] The spectra contain proton resonances that lie outside the diamagnetic region ($\delta$ = 0–14 ppm) due to the well-known isotropically shifting of the ligand protons for high-spin $Mn^{III}$ complexes in an octahedral field. In this sense, the

Table 1. Magnetic moments, conductivity measurements, IR, $^1$H NMR and mass spectrometric data of the complexes.

| | ES [amu][a] | IR [cm$^{-1}$] | | | | $\mu$ [BM] | $\Lambda$ [μS cm$^{-1}$] | $^1$H NMR [ppm] | |
|---|---|---|---|---|---|---|---|---|---|
| | | $\nu$(O–H) | $\nu$(C=N)[b] | $N$(C–O)[b] | $\nu$(Cl–O) | | | H4 | H5 |
| $[Mn(H_2L^1)(H_2O)_2](ClO_4)(H_2O)$ (**1**) | 353 (705) | 3421 | 1621 (1633) | 1254 (1246) | 1087; 636 | 4.9 | 75 | –34.05 | –20.10 |
| $[Mn(L^2)(H_2O)_2](ClO_4)(H_2O)$ (**2**) | 382 | 3419 | 1621 (1633) | 1255 (1249) | 1087; 636 | 4.9 | 66 | –27.37 | –19.20 |
| $[Mn(L^3)(H_2O)_2](ClO_4)(H_2O)$ (**3**) | 410 (819) | 3457 | 1621 (1629) | 1258 (1250) | 1109; 623 | 5.0 | 70 | –27.72 | –19.16 |
| $[Mn(H_2L^4)(H_2O)(CH_3OH)](ClO_4)$ (**4**) | 368 | 3424 | 1619 (1626) | 1257 (1236) | 1087; 636 | 5.0 | 75 | –34.15 | –21.99 |
| $[Mn(L^5)(H_2O)_2](ClO_4)(H_2O)$ (**5**) | 396 (791) | 3417 | 1619 (1627) | 1256 (1250) | 1084; 636 | 5.0 | 60 | –27.60 | –18.93 |
| $[Mn(L^6)(H_2O)_2](ClO_4)(H_2O)$ (**6**) | 424 | 3418 | 1619 (1631) | 1259 (1249) | 1109; 624 | 5.0 | 88 | –27.64 | –18.82 |
| $[Mn(H_2L^7)(H_2O)(CH_3OH)](ClO_4)$ (**7**) | 382 | 3420 | 1610 (1624) | 1258 (1241) | 1086; 625 | 5.0 | 75 | –32.61 | –20.08 |
| $[Mn(L^8)(H_2O)_2](ClO_4)$ (**8**) | 409 (817) | 3413 | 1610 (1629) | 1255 (1249) | 1085; 625 | 5.0 | 62 | –27.80 | –18.64 |
| $[Mn(L^9)(H_2O)_2](ClO_4)$ (**9**) | 438 (875) | 3421 | 1612 (1628) | 1254 (1248) | 1120; 625 | 5.0 | 88 | –28.01 | –18.96 |
| $[Mn(H_2L^{10})(H_2O)(CH_3OH)](ClO_4)$ (**10**) | 395 | 3416 | 1620 (1639) | 1253 (1240) | 1120; 620 | 5.0 | 62 | –30.27 | –20.08 |
| $[Mn(L^{11})(H_2O)_2](ClO_4)(H_2O)$ (**11**) | 424 (846) | 3418 | 1610 (1632) | 1254 (1247) | 1108; 624 | 4.9 | 63 | –20.10 | –14.50 |
| $[Mn(L^{12})(H_2O)_2](ClO_4)$ (**12**) | 451 | 3429 | 1612 (1633) | 1256 (1250) | 1120; 625 | 4.9 | 89 | –20.72 | –16.75 |

[a] Peaks corresponding to $[MnL]^+$, and, in parentheses, to $[Mn_2L_2]^+$. [b] Bands corresponding to the free ligands in parentheses.

 © 2007 Wiley-VCH Verlag GmbH & Co. KGaA, Weinheim 

data obtained from these NMR spectroscopic studies serve to corroborate the formation of the manganese(III) complexes since two sets of upfield sharp peaks corresponding to the H4 and H5 protons of the aromatic rings (Scheme 2) are observed. Clearly the upfield signals (ranging from –20.10 to –34.15 ppm) arise from H4 protons, while the downfield resonances (–14.50 to –21.99 ppm) arise from H5 protons. Our experience shows that signals in *ortho* positions to donor atoms are not observable for these kinds of complexes by paramagnetic $^1H$ NMR spectroscopy. Since H4 signals are discernible for all complexes, including **1**, **4**, **7** and **10**, with external hydroxy groups in the aromatic rings of the Schiff bases, the NMR spectra suggest no coordination through these groups to the metal ion.

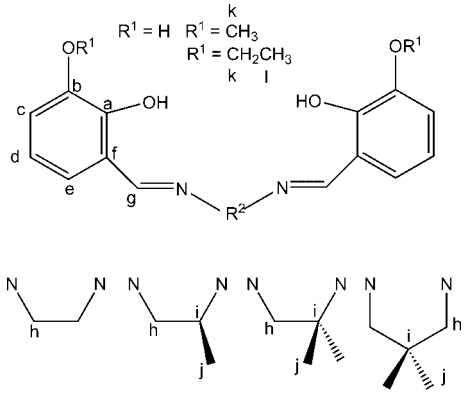


Scheme 2.

### Crystallographic Studies of Ligands $H_2L^3$ and $H_4L^{10}$

Crystals of $H_4L^{10}$ suitable for X-ray studies were obtained by slow evaporation of a methanol solution of the ligand. The crystal structure, with the numbering scheme, is shown in Figure 1. Selected bond lengths and angles are given in Table 2.

The crystal structure is made up of $H_4L^{10}$ discrete molecules. The C7–N8 and N12–C13 distances of 1.276(2) and 1.290(2) Å, respectively, are consistent with N=C double bonding. One of the four oxygen atoms, O22, lacks a hydrogen atom, appearing in the carbonyl form, which is corroborated by the C19–O22 distance of 1.2928(18) Å, in accordance with a C=O double bond. The other three oxygen

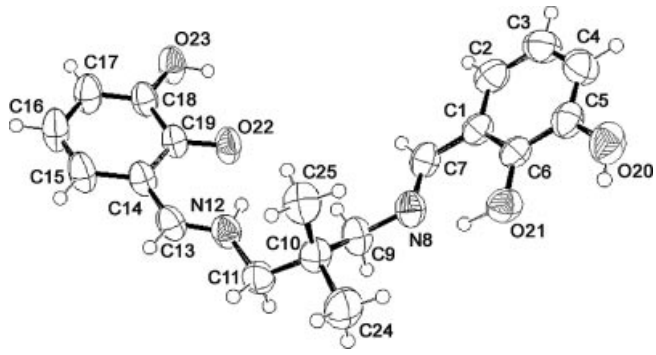


Figure 1. Molecular structure of $H_4L^{10}$ showing the atomic numbering scheme.

atoms form phenol groups, and they present longer C–O distances [C5–O20 1.365(2) Å, C6–O21 1.347(2) Å, C18–O23 1.361(2) Å], corresponding to the expected single bonds.

The study of these distances reveals the transfer of one proton from a hydroxy group of each molecule to the neighbouring nitrogen atom N12. This process is favoured by the so-called "proton-sponge" effect,[25] which consists of the increase in the basicity of the imine nitrogen atoms due to the spatial nearness of their lone pairs. The instability of a situation of proximity of these two lone pairs is then solved by the attraction of one phenol hydrogen atom by one of the nitrogen atoms. This leads to the formation of a relatively strong $[N–H\cdots O]^+$ intramolecular bond [H22···O22 1.75(2) Å, N12···O22 2.5914(19) Å and N12–H22···O22 145.2°]. Despite the symmetry of the compound, a second proton transfer to the other imine nitrogen atom does not occur since it would mean a very unfavourable situation, involving the formation of two neighbouring $[N–H]^+$ groups and preventing the $[N–H\cdots O]^+$ intramolecular hydrogen bond.

An additional intramolecular hydrogen bond exists between the N8 imine nitrogen atom and the neighbouring phenol oxygen atom [H21···N8 1.55(3) Å, O21···N8 2.5767(19) Å and O21–H21···N8 146.2°]. These intramolecular hydrogen bonds are typical of Schiff bases derived from salicylaldehydes.[26] Besides, intermolecular interactions by hydrogen bonds can also be observed between the phenol oxygen atoms of neighbouring molecules.

Table 2. Selected bond lengths [Å] and angles [°] for the ligands $H_2L^3$ and $H_4L^{10}$.

| $H_2L^3$ | | | | $H_4L^{10}$ | | | |
|---|---|---|---|---|---|---|---|
| C10–N11 | 1.272(5) | N11–C12 | 1.461(5) | C7–N8 | 1.276(2) | N8–C9 | 1.461(2) |
| C1–O13 | 1.344(4) | C6–O7 | 1.372(5) | N12–C13 | 1.290(2) | C11–N12 | 1.459(2) |
| O7–C8 | 1.417(5) | | | C5–O20 | 1.365(2) | C6–O21 | 1.347(2) |
| | | | | C18–O23 | 1.361(2) | C19–O22 | 1.2928(18) |
| N11–C10–C2 | 121.9(4) | C10–N11–C12 | 120.2(4) | N8–C7–C1 | 121.93(15) | C7–N8–C9 | 119.28(15) |
| C12B–C12–N11 | 110.5(5) | O13–C1–C2 | 121.8(4) | N8–C9–C10 | 111.63(14) | N12–C11–C10 | 112.87(14) |
| O13–C1–C6 | 118.5(4) | C5–C6–O7 | 126.6(4) | C13–N12–C11 | 124.97(15) | N12–C13–C14 | 123.76(15) |
| O7–C6–C1 | 113.9(4) | C6–O7–C8 | 117.4(4) | O20–C5–C4 | 120.35(18) | O20–C5–C6 | 119.23(17) |
| O7–C8–C9 | 106.2(4) | | | O21–C6–C5 | 118.15(15) | O21–C6–C1 | 122.08(15) |
| | | | | O22–C19–C14 | 122.78(14) | O22–C19–C18 | 120.28(14) |
| | | | | O23–C18–C17 | 119.47(16) | O23–C18–C19 | 119.44(14) |

 © 2007 Wiley-VCH Verlag GmbH & Co. KGaA, Weinheim 

According to this crystal structure study, the rather planar conformation of the set N8–N12–O21–O22 suggests that this ligand should easily act as tetradentate donor in the equatorial plane about an octahedral metal centre. However, we cannot predict the role of the outer phenol oxygen atoms of each aldehyde residue during complexation as they could coordinate, for instance, to the metal centre by an axial position, but also their role could be limited to intermolecular hydrogen-bond interactions.

Slow evaporation of a methanol solution of ligand $H_2L^3$ gives crystals, suitable for X-ray diffraction studies, of $C_{20}H_{24}N_2O_4$. The crystal structure is displayed in Figure 2 with the atom numbering scheme adopted. Selected bond lengths and angles are in Table 2.

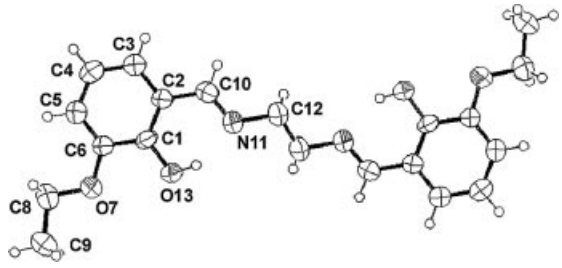


Figure 2. Molecular structure of $H_2L^3$ showing the atomic numbering scheme.

The crystal structure reveals that $H_2L^3$ exists as discrete molecules, and it is composed of two identical 3-methoxy-2-hydroxybenzylimine moieties connected by the flexible C12–C12B methylene chain (so-called spacer in supramolecular chemistry), so we will only discuss one of them. The C10–N11 distance of 1.272(5) Å is consistent with C=N double bonding. Both imine groups are fully localised in the molecule. The angle of 120.2(4)° around the N11 atom confirms its $sp^2$ character.

The disposition adopted by the free ligand in the solid state is conditioned by two strong intramolecular hydrogen-bond interactions which form two six-membered rings. These interactions arise from the contact between the hydroxy and the imine groups. In this case and contrary to the situation described for $H_4L^{10}$, both hydroxy oxygen atoms retain their hydrogen atoms. As expected, the O13–H13···N11 [H13···N11 1.59(7) Å, O13···N11 2.555(5) Å and O13–H13···N11 154(6)°] hydrogen bonding establishes an almost planar N11–C10–C2–C1–O13–H13 ring.

This kind of Schiff-base ligand, with a flexible spacer, produces this type of "open" structure as we have previously found in similar ligands.[27,28] These and other similar ligands present adequate conditions to be useful in the synthesis of octahedral complexes, occupying the equatorial positions around the metal centre.

### Crystallographic Studies of Complexes 2 and 8

Recrystallisation of $[MnL^2(H_2O)_2](ClO_4)$ (**2**) and $[MnL^8(H_2O)_2](ClO_4)$ (**8**) from methanol solutions by slow evaporation afforded brown crystals from which we determined their molecular structures. Both crystal structures show similar features; thereby, they will be discussed together. An ORTEP view of **8** with the atomic numbering scheme is shown in Figure 3. Experimental details are given in Table 5. Main bond lengths and angles are listed in Table 3.

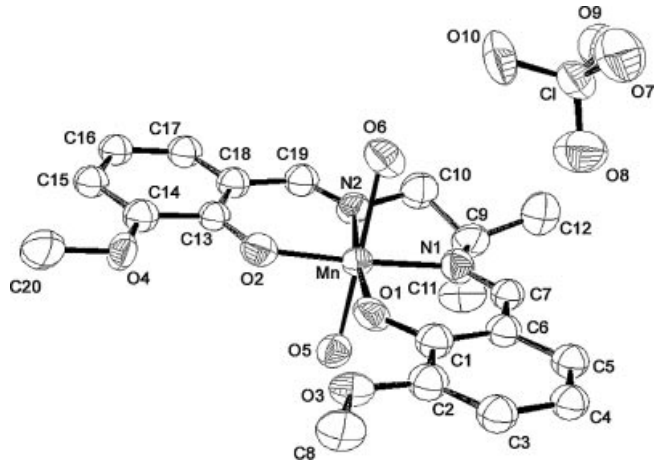


Figure 3. Molecular structure of **8** showing the atomic numbering scheme.

Table 3. Selected bond lengths [Å] and angles [°] for complexes **2** and **8**.

| | | | |
|---|---|---|---|
| Complex **2** | | | |
| Mn1–O13a | 1.864(3) | Mn1–N4 | 1.968(4) |
| Mn1–O43a | 1.866(3) | Mn1–O1W | 2.265(4) |
| Mn1–N1 | 1.961(4) | Mn1–O2W | 2.314(4) |
| Mn···Mn | 4.8886(4) | | |
| O13a–Mn1–O43a | 92.61(13) | O13a–Mn1–N1 | 92.11(15) |
| O43a–Mn1–N1 | 175.26(16) | O13a–Mn1–N4 | 174.84(15) |
| O43a–Mn1–N4 | 91.93(15) | N1–Mn1–N4 | 83.36(17) |
| O13a–Mn1–O1W | 93.84(13) | O43a–Mn1–O1W | 92.15(13) |
| N1–Mn1–O1W | 87.17(14) | N4–Mn1–O1W | 88.43(14) |
| O13a–Mn1–O2W | 88.20(15) | O43a–Mn1–O2W | 87.93(17) |
| N1–Mn1–O2W | 92.58(19) | N4–Mn1–O2W | 89.52(17) |
| O1W–Mn1–O2W | 177.95(15) | | |
| Complex **8** | | | |
| Mn–O1 | 1.8482(15) | Mn–N2 | 1.9582(18) |
| Mn–O2 | 1.8529(16) | Mn–O5 | 2.2366(17) |
| Mn–N1 | 1.9648(19) | Mn–O6 | 2.3607(19) |
| Mn···Mn | 4.8896(4) | | |
| O1–Mn–O2 | 93.21(7) | O1–Mn–N2 | 174.10(7) |
| O2–Mn–N2 | 92.07(7) | O1–Mn–N1 | 92.83(7) |
| O2–Mn–N1 | 173.80(7) | N2–Mn–N1 | 81.83(8) |
| O1–Mn–O5 | 89.04(6) | O2–Mn–O5 | 90.35(7) |
| N2–Mn–O5 | 93.55(7) | N1–Mn–O5 | 91.17(7) |
| O1–Mn–O6 | 93.81(6) | O2–Mn–O6 | 90.49(7) |
| N2–Mn–O6 | 83.51(7) | N1–Mn–O6 | 87.70(7) |
| O5–Mn–O6 | 176.97(6) | | |

The crystallographic analyses show $[MnL^n(H_2O)_2]^+$ mononuclear cationic complexes, where the geometry around each manganese(III) ion can be described as distorted octahedral. The structure of these cations comprises the planar Schiff-base ligand tightly bound to the manganese(III) ion through the inner $N_2O_2$ compartment by the $N_{imine}$ and $O_{phenol}$ atoms (Mn–$N_{imine}$ bond lengths of 1.95–1.97 Å and

 © 2007 Wiley-VCH Verlag GmbH & Co. KGaA, Weinheim 

$Mn–O_{phenol}$ of 1.84–1.87 Å are typical of such complexes and corroborate the bisdeprotonation of the ligands),[9,10,29] occupying the equatorial positions and giving rise to two six-membered chelate rings (which are nearly planar) and an additional five-membered chelate ring. The coordination sphere around each manganese centre is then completed by capping water molecules. The axial Mn–O distances (ranging from 2.23 to 2.36 Å) are considerably longer than the equatorial Mn–O bond lengths quoted earlier, indicating that the Jahn–Teller elongation expected for a high-spin $d^4$ manganese(III) ion is present among these complexes. The deviation from an ideal octahedral geometry is also revealed by the range of angles observed around the metal centre (from 81.83° to 93.84°), as well as by the interaxial angle OW–Mn–OW of 177.95° for **2** and 176.97° for **8**.

From the viewpoint of supramolecular chemistry, complexes **2** and **8** exhibit a topology constructed by hydrogen bonds, which help to stabilise the packing and induce the assembly of the mononuclear cationic complexes.

The superstructure of the complexes involves associations through a combination of π-aryl interactions and hydrogen bonds between capping water and outer phenoxy and axial water oxygen atoms of the neighbouring Schiff-base ligand. This results in Mn···Mn distances of about 4.90 Å, which are short for monomeric compounds; these types of $[MnL(H_2O)_2]_2^{2+}$ systems have been reported by us previously[30,31] as μ-aquo dimers (Figure 4). However, these Mn···Mn distances are too long to establish intermetallic interactions between neighbouring manganese ions, in accordance with the non-antiferromagnetic behaviour shown by the magnetic studies.

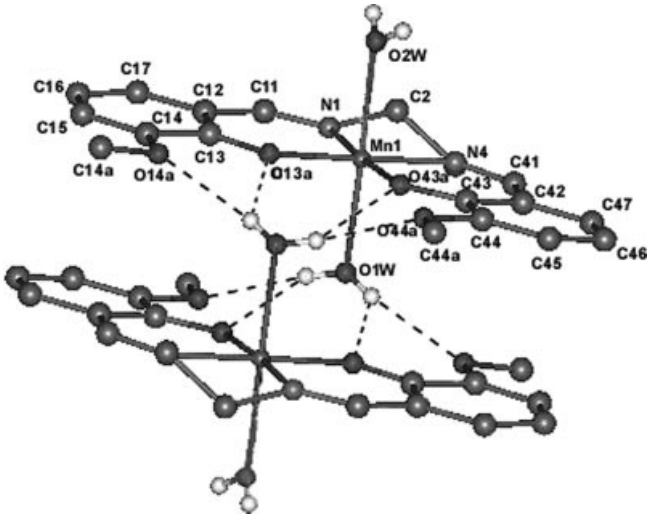


Figure 4. Ball-and-stick diagram of the μ-aqua dimer formed for **2** through hydrogen bonds.

Moreover, the μ-aquo dimers are interconnected by hydrogen bonding involving the perchlorate counterions. In this way, pairs of neighbouring μ-aquo dimers are linked by two perchlorate anions. The hydrogen-bonding interactions involving perchlorate anions with their symmetry codes for compounds **2** and **8** are given in Table 4. This hydrogen-bonding scheme arises from the interactions of two perchlorate ions which establish two pairs of hydrogen bonds to two adjacent μ-aquo dimers. Each pair is directed from the perchlorate anions to the external capping water molecule of each dimeric building unit (see Figure 5). These multiple intermolecular interactions are extended into the solid to form infinite spirals generated by a screw axis along *a*. The 1D network of manganese dimers generates a kind of tunnel along the *c* axis. Perchlorate anions are accommodated in such cavities of the framework.

Table 4. Hydrogen-bonding scheme (distances and angles) involving perchlorate counterions for complexes **2** and **8**.

| D–H···A [Å] | D–H [Å] | H···A [Å] | D···A [Å] | D–H···A [°] |
|---|---|---|---|---|
| | | Complex **2** | | |
| O2W–H12W···O2[a] | 0.80(7) | 2.47(8) | 3.10(2) | 137(7) |
| O2W–H22W···O2 | 0.74(7) | 2.01(7) | 2.71(2) | 157(7) |
| | | Complex **8** | | |
| O6–H61–O10 | 1.024(16) | 1.981(19) | 2.886(2) | 146.(2) |
| O6–H62–O9[b] | 1.074(15) | 2.178(15) | 2.998(3) | 131.3(15) |

[a] Symmetry operations: $2 - x$, $1 - y$, $1 - z$. [b] Symmetry operations: $1 - x$, $1 - y$, $1 - z$.

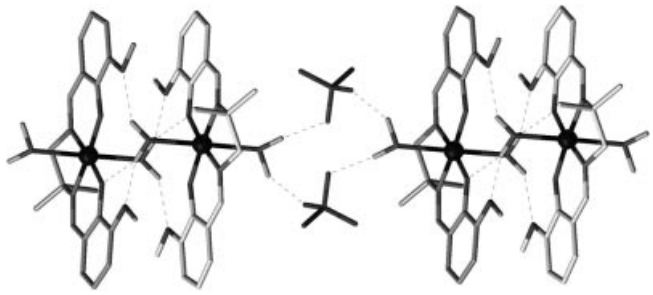

Figure 5. Stick diagram for **8** showing the hydrogen bonding between adjacent $[MnL^8(H_2O)_2]_2^{2+}$ dimeric units through perchlorate anions.

A comparison between the role of perchlorate and chloride counterions as multiple hydrogen-bond acceptors for similar manganese(III) complexes derived from $H_4L$ Schiff bases may be established. We have previously reported how each chloride ion could be involved in four O–H···Cl bonds, connecting three neighbouring cationic complexes and assembling them to constitute a 2D network.[10] In the present work, we find each perchlorate anion is only able to form two hydrogen bonds. This behaviour implies preference is given to one direction and provokes a decrease in the dimensionality of the network.

### Redox Properties and Peroxidase Essays

The electrochemical behaviour of some of the complexes (**2**, **3**, **5**, **7**, **8** and **12**) was studied by cyclic voltammetry. In all cases this technique exhibits a one-electron reduction-oxidation peak system in the 0 to –0.1 V potential range. The difference between the anodic and cathodic potentials indicates a redox reversible character. Moreover, these negative potentials belong to the range which would favour the

 © 2007 Wiley-VCH Verlag GmbH & Co. KGaA, Weinheim 

catalytic activity, as we have previously reported for other $Mn^{III}$–Schiff-base systems.[31,32]

The peroxidase-like activity of the cited complexes was followed by the oxidation of the diammonium salt of 2,2′-azinobis(3-ethylbenzothiazoline)-6-sulfonic acid (ABTS) at pH 6.8. The reaction of ABTS with $H_2O_2$ in the presence of the complexes generates $ABTS^{\cdot+}$, which can be clearly identified by its characteristic absorption bands (415, 650, 735 and 815 nm) and measured quantitatively at $\lambda$ = 650 nm since $\varepsilon$ = 12000 $M^{-1}cm^{-1}$ has been determined. The rate of formation of $ABTS^{\cdot+}$ ranges from 30–40% with respect to the initial ABTS. This shows an important capacity of hydrogen peroxide decomposition by the studied complexes. The activity is comparable to that of a previous series of Mn–Schiff-base complexes, reported by us, incorporating carboxylate ligands,[31] but is much higher than an earlier Mn–Schiff-base series with the chloride counterion.[10] Recently, we have tried to establish a correlation between peroxidase activity and the structural motifs of the complexes.[31] We have postulated what seems to be an easy approach to predict the capacity of $H_2O_2$ decomposition by these types of complexes as a finction of the tetragonal elongation of the octahedral geometry in the crystal structure. An axial water molecule in this class of distorted geometries constitutes a quite labile ligand, which would generate a vacant position in the coordination sphere to accommodate the substrate molecule.

In order to quantify the tetragonal elongation we have employed the "rhombicity" of the structure as the ratio between their manganese–axial-oxygen distances and their manganese–equatorial-oxygen distances. This correlation is also valid for the data taken for complexes **2** and **8** of this work. Their Mn–Ow/Mn–Oeq ratios of 1.24 and 1.27, respectively, are compatible with their peroxidase activity.

## Conclusions

We can conclude that these types of manganese(III) complexes, formed from Schiff bases with inner and outer O–X (X = H, $CH_3$, $CH_2CH_3$) groups, constitute suitable building units for establishing rich hydrogen-bonding networks. In the present work, the selection of the proper spacer in the Schiff-base ligand allows formation of $[MnL]_2^{2+}$ dimeric units, which can be connected through perchlorate counterions to form 1D chains. The lower dimensionality of the network with respect to the case of a chloride counterion (2D → 1D) can be interpreted in terms of the lower symmetry of the perchlorate (tetrahedral) than that of the chloride (spherical), involving a higher directionality of the network. The ability of these types of complexes to accommodate different anions in the vacancies of the framework becomes an interesting research field for selective recognition between anions and receptors, beyond their worthwhile redox behaviour.

## Experimental Section

**Physical Measurements:** Elemental analyses were performed with a Carlo Erba model 1108 CHNS-O elemental analyser. The IR spectra were recorded as KBr discs with a Bruker IFS-66V FTIR spectrophotometer and UV–Vis spectra with a Varian Cary IE. $^1$H- and $^{13}$C NMR spectra were recorded with a Bruker WH 300 MHz spectrometer using DMSO as the solvent and $SiMe_4$ as an internal reference. ES mass spectra were recorded with a Hewlett-Packard LC-MSD Series 1100a spectrometer. Conductivities of $10^{-3}$ M solutions in DMF were measured with a Crison Micro CM 2200 conductivimeter. Room-temperature magnetic susceptibilities were measured using a Faraday balance MSB-MKI by Evans; $HgCo(NCS)_4$ was employed as a susceptibility standard.

Electrochemical measurements were performed with an EG&G PAR model 273 potentiostat, controlled by EG&G PAR model 270 software. A Metrohm model 6.1204.000 graphite disc coupled to a Metrohm model 628–10 rotating electrolyte device was used as a working electrode. A saturated calomel electrode was used as a reference, and a platinum wire was used as an auxiliary electrode. All measurements were made with ca. $10^{-3}$ mol dm$^{-3}$ solutions of the complexes in dimethylformamide using 0.2 mol dm$^{-3}$ $NBu_4PF_6$ as a supporting electrode. Cyclic voltammetry measurements were performed with a static graphite electrode.

**Materials:** 2,3-Dihydroxybenzaldehyde (Sigma–Aldrich), 3-methoxy-2-hydroxybenzaldehyde (Fluka Chemika), 3-ethoxy-2-hydroxybenzaldehyde (Fluka Chemika), diamines [1,2-diaminoethane, 1,2-diamino-2-methylethane, 1,2-diamino-2,2-dimethylethane, 1,3-diamino-2,2-dimethylpropane] (Aldrich) and manganese(II) perchlorate hexahydrate (Fluka) were used as received without further purification.

**Preparation of the Ligands:** The hexadentate Schiff bases, $H_xL^n$, used in this study were prepared by condensation of the appropriate diamine with 2,3-dihydroxybenzaldehyde, 3-methoxy-2-hydroxybenzaldehyde or 3-ethoxy-2-hydroxybenzaldehyde in methanol.[33,34] They were isolated in virtually quantitative yield and satisfactorily characterised by elemental analysis, $^1$H- and $^{13}$C NMR spectroscopy, ES mass spectroscopy and IR spectroscopy. This can be typified by the following preparation of $H_4L^1$.

**$H_4L^1$:** To a methanol solution (120 mL) of 2,3-dihydroxybenzaldehyde (4.00 g, 28.96 mmol) was added 1,2-diaminoethane (0.97 mL, 14.48 mmol). This mixture was heated at reflux in a round-bottomed flask fitted with a Dean Stark trap to remove the water produced during the reaction. After heating for 3 h, the solution was concentrated to yield a yellow solid. The product was collected by filtration, washed with diethyl ether and dried in air. $C_{16}H_{16}N_2O_4$ (300.30): calcd. C 63.9, H 5.4, N 9.3; found C 63.3, H 5.6, N 9.4. $^1$H NMR (300 MHz, [D$_6$]DMSO): $\delta$ = 8.54 (s, 2 H), 6.65–6.85 (m, 6 H), 3.93 (s, 4 H) ppm. $^{13}$C NMR (75 MHz, [D$_6$]-DMSO): $\delta$ = 167.1 ($C_g$), 151.0 ($C_a$), 145.8 ($C_b$), 118.1 ($C_f$), 58.0 ($C_h$) ppm. ES-MS: *m*/*z* = 301.2. IR: $\tilde{\nu}$ = $\nu$(O–H) 3258, $\nu$(C=N) 1633, $\nu$(C–O) 1246 cm$^{-1}$. M.p. 240 °C.

**$H_2L^2$:** 3-Methoxy-2-hydroxybenzaldehyde (2.00 g, 13.15 mmol) and 1,2-diaminoethane (0.41 mL, 6.57 mmol). $C_{18}H_{20}N_2O_4$ (328.37): calcd. C 65.8, H 6.2, N 8.5; found C 65.7, H 6.2, N 8.6. $^1$H NMR (300 MHz, [D$_6$]DMSO): $\delta$ = 13.42 (br.), 8.56 (s, 2 H), 6.79–7.01 (t, d, d, 6 H), 3.92 (s, 4 H), 3.76 (s, 6 H) ppm. $^{13}$C NMR (75 MHz, [D$_6$]DMSO): $\delta$ = 167.7 ($C_g$), 152.3 ($C_a$), 148.7 ($C_b$), 59.0 ($C_h$), 56.5 ($C_k$) ppm. ES-MS: *m*/*z* = 329.3. IR: $\tilde{\nu}$ = $\nu$(O–H) 3087, $\nu$(C=N) 1633, $\nu$(C–O) 1249 cm$^{-1}$. M.p. 165 °C.

**$H_2L^3$:** 3-Ethoxy-2-hydroxybenzaldehyde (2.00 g, 12.04 mmol) and 1,2-diaminoethane (0.40 mL, 6.02 mmol). $C_{20}H_{24}N_2O_4$ (356.42): calcd. C 67.4, H 6.7, N 7.9; found C 66.9, H 6.8, N 7.1. $^1$H NMR (300 MHz, [D$_6$]DMSO): $\delta$ = 8.54 (s, 2 H), 6.72–6.99 (d, d, t, 6 H), 4.00 (q, 4 H), 3.97 (s, 4 H), 1.31 (t, 6 H) ppm. $^{13}$C NMR (75 MHz,

 © 2007 Wiley-VCH Verlag GmbH & Co. KGaA, Weinheim 

[$D_6$]DMSO): $\delta$ = 167.7 ($C_g$), 152.5 ($C_a$), 147.8 ($C_b$), 64.7 ($C_k$), 59.1 ($C_h$), 15.4 ($C_l$) ppm. ES-MS: *m/z* = 357.4. IR: $\tilde{\nu}$ = $\nu$(O–H) 3467, $\nu$(C=N) 1629, $\nu$(C–O) 1250 $cm^{-1}$. M.p. 146 °C.

**$H_4L^4$:** 2,3-Dihydroxybenzaldehyde (4.00 g, 28.96 mmol) and 1,2-diamino-2-methylethane (1.23 mL, 14.48 mmol). $C_{17}H_{18}N_2O_4$ (314.34): calcd. C 64.9, H 5.8, N 8.9; found C 64.8, H 5.8, N 8.7. $^1$H NMR (300 MHz, [$D_6$]DMSO): $\delta$ = 13.53 (br.), 9.00 (br.), 8.55 (s, 1 H), 8.52 (s, 1 H), 6.62–6.86 (m, 6 H), 3.81 (d, 2 H), 1.33 (d, 3 H), 3.75–3.89 (m, 1 H) ppm. $^{13}$C NMR (75 MHz, [$D_6$]DMSO): $\delta$ = 167.1/165.3 ($C_g$), 151.2/150.5 ($C_a$), 145.1/145.7 ($C_b$), 118.0/118.2 ($C_f$), 63.6 ($C_h$), 63.1 ($C_i$), 19.9 ($C_j$) ppm. ES-MS: *m/z* = 315. IR: $\tilde{\nu}$ = $\nu$(O–H) 3240, $\nu$(C=N) 1626, $\nu$(C–O) 1236 $cm^{-1}$. M.p. 164 °C.

**$H_2L^5$:** 3-Methoxy-2-hydroxybenzaldehyde (2.00 g, 13.15 mmol) and 1,2-diamino-2-methylethane (0.56 mL, 6.57 mmol). $C_{19}H_{22}N_2O_4$ (342.39): calcd. C 66.6, H 6.5, N 8.2; found C 66.5, H 6.8, N 8.2. $^1$H NMR (300 MHz, [$D_6$]DMSO): $\delta$ = 13.50 (br.), 8.54 (s, 1 H), 8.51 (s, 1 H), 6.73–7.01 (m, 6 H), 3.82 (m, 1 H), 3.80 (d, 2 H), 1.31 (s, 6 H) ppm. $^{13}$C NMR (75 MHz, [$D_6$]DMSO): $\delta$ = 165.8/167.7 ($C_g$), 151.3 ($C_a$), 147.5 ($C_b$), 64.8 ($C_h$), 56.4/56.5 ($C_k$), 64.0 ($C_i$), 20.5 ($C_j$) ppm. ES-MS: *m/z* = 343.1. IR: $\tilde{\nu}$ = $\nu$(O–H) 3440, $\nu$(C=N) 1627, $\nu$(C–O) 1250 $cm^{-1}$. M.p. 137 °C.

**$H_2L^6$:** 3-Ethoxy-2-hydroxybenzaldehyde (2.00 g, 12.04 mmol) and 1,2-diamino-2-methylethane (0.51 mL, 6.02 mmol). $C_{21}H_{27}N_2O_4$ (371.45): calcd. C 67.9, H 7.3, N 7.5; found C 67.3, H 7.2, N 7.5. $^1$H NMR (300 MHz, [$D_6$]DMSO): $\delta$ = 13.5 (br.), 8.53 (s, 1 H), 8.50 (s, 1 H), 6.71–6.98 (d, d, t, 6 H), 4.00 (q, 4 H), 3.96 (s, 2 H), 3.75 (m, 1 H), 1.31 (d, 3 H), 1.29 (t, 6 H) ppm. $^{13}$C NMR (75 MHz, [$D_6$]DMSO): $\delta$ = 165.8/167.8 ($C_g$), 152.4 ($C_a$), 147.7 ($C_b$), 64.9 ($C_k$), 64.0 ($C_i$), 64.1 ($C_h$), 20.6 ($C_j$), 15.4 ($C_l$) ppm. ES-MS: *m/z* = 371.4. IR: $\tilde{\nu}$ = $\nu$(O–H) 3523, $\nu$(C=N) 1631, $\nu$(C–O) 1249 $cm^{-1}$. M.p. 91 °C.

**$H_4L^7$:** 2,3-Dihydroxybenzaldehyde (4.00 g, 28.96 mmol) and 1,2-diamino-2,2-dimethylethane (1.52 mL, 14.48 mmol). $C_{18}H_{20}N_2O_4$ (328.37): calcd. C 65.8, H 6.1, N 8.5; found C 65.8, H 6.3, N 8.5. $^1$H NMR (300 MHz, [$D_6$]DMSO): $\delta$ = 13.61/14.17 (br.), 8.95 (br.), 8.56 (s, 1 H), 8.52 (s, 1 H), 6.60–6.92 (m, 6 H), 3.79 (s, 2 H), 1.38 (s, 6 H) ppm. $^{13}$C NMR (75 MHz, [$D_6$]DMSO): $\delta$ = 167.4/162.8 ($C_g$), 152.2/150.9 ($C_a$), 145.9/145.7 ($C_b$), 118.1 ($C_f$), 68.2 ($C_h$), 59.4 ($C_i$), 25.0 ($C_j$) ppm. ES-MS: *m/z* = 329. IR: $\tilde{\nu}$ = $\nu$(O–H) 3227, $\nu$(C=N) 1645–1624, $\nu$(C–O) 1241 $cm^{-1}$. M.p. 183 °C.

**$H_2L^8$:** 3-Methoxy-2-hydroxybenzaldehyde (2.00 g, 13.15 mmol) and 1,2-diamino-2,2-dimethylethane (0.69 mL, 6.57 mmol). $C_{20}H_{24}N_2O_4$ (356.42): calcd. C 67.6, H 6.9, N 7.8; found C 67.5, H 6.9, N 7.8. $^1$H NMR (300 MHz, [$D_6$]DMSO): $\delta$ = 13.57 (br.), 8.54 (s, 1 H), 8.51 (s, 1 H), 6.72–7.04 (m, 6 H), 3.77 (s, 2 H), 3.74 (s, 6 H), 1.34 (s, 6 H) ppm. $^{13}$C NMR (75 MHz, [$D_6$]DMSO): $\delta$ = 163.4/167.9 ($C_g$), 152.9 ($C_a$), 148.7 ($C_b$), 69.4 ($C_i$), 60.4 ($C_h$), 56.3/56.4 ($C_k$), 25.7 ($C_j$) ppm. ES-MS: *m/z* = 357.0. IR: $\tilde{\nu}$ = $\nu$(O–H) 3333, $\nu$(C=N) 1629, $\nu$(C–O) 1249 $cm^{-1}$. M.p. 183 °C.

**$H_2L^9$:** 3-Ethoxy-2-hydroxybenzaldehyde (2.00 g, 12.04 mmol) and 1,2-diamino-2,2-dimethylethane (0.63 mL, 6.02 mmol). $C_{22}H_{28}N_2O_4$ (384.47): calcd. C 68.7, H 7.3, N 7.3; found C 67.9, H 7.6, N 7.5. $^1$H NMR (300 MHz, [$D_6$]DMSO): $\delta$ = 8.53 (s, 1 H), 8.50 (s, 1 H), 6.69–7.00 (d, d, t, 6 H), 4.00 (q, 4 H), 3.96 (s, 2 H), 1.34 (s, 6 H), 1.30 (t, 6 H) ppm. $^{13}$C NMR (75 MHz, [$D_6$]DMSO): $\delta$ = 167.9/168.0 ($C_g$), 152.4 ($C_a$), 147.8 ($C_b$), 69.4 ($C_i$), 64.7/64.8 ($C_k$), 60.3 ($C_h$), 25.7 ($C_j$), 15.4 ($C_l$) ppm. ES-MS: *m/z* = 385.4. IR: $\tilde{\nu}$ = $\nu$(O–H) 3433, $\nu$(C=N) 1628, $\nu$(C–O) 1248 $cm^{-1}$. M.p. 88 °C.

**$H_4L^{10}$:** 2,3-Dihydroxybenzaldehyde (2.00 g, 14.48 mmol) and 1,3-diamino-2,2-dimethylpropane (0.86 mL, 7.24 mmol). $C_{19}H_{22}N_2O_4$ (342.39): calcd. C 66.7, H 6.5, N 8.2; found C 66.9, H 6.6, N 8.1. $^1$H NMR (300 MHz, [$D_6$]DMSO): $\delta$ = 13.89 (br.), 9.02 (br.), 8.52 (s, 2 H), 6.68–6.88 (t, d, d, 6 H), 3.51 (s, 4 H), 1.01 (s, 6 H) ppm. $^{13}$C NMR (75 MHz, [$D_6$]DMSO): $\delta$ = 166.0 ($C_g$), 151.3 8 ($C_a$), 145.9 ($C_b$), 118.0 ($C_f$), 65.9 ($C_k$), 35.7 ($C_i$), 23.4 ($C_j$) ppm. ES-MS: *m/z* = 343. IR: $\tilde{\nu}$ = $\nu$(O–H) 3215, $\nu$(C=N) 1639, $\nu$(C–O) 1240 $cm^{-1}$. M.p. 180 °C.

**$H_2L^{11}$:** 3-Methoxy-2-hydroxybenzaldehyde (2.00 g, 13.15 mmol) and 1,3-diamino-2,2-dimethylpropane (0.78 mL, 6.57 mmol). $C_{21}H_{26}N_2O_4$ (370.45): calcd. C 68.1, H 7.0, N 7.6; found C 67.7, H 7.2, N 7.4. $^1$H NMR (300 MHz, [$D_6$]DMSO): $\delta$ = 8.51 (s, 2 H), 6.76–7.03 (t, d, d, 6 H, ), 3.77 (s, 6 H), 3.47 (s, 4 H), 0.98 (s, 6 H) ppm. $^{13}$C NMR (75 MHz, [$D_6$]DMSO): $\delta$ = 167.3 ($C_g$), 152.6 ($C_a$), 148.8 ($C_b$), 124.0 ($C_f$), 67.4 ($C_h$), 56.6 ($C_k$), 24.3 ($C_i$, $C_j$) ppm. ES-MS: *m/z* = 371.4. IR: $\tilde{\nu}$ = $\nu$(O–H) 3439, $\nu$(C=N) 1632, $\nu$(C–O) 1247 $cm^{-1}$. M.p. 82 °C.

**$H_2L^{12}$:** 3-Ethoxy-2-hydroxybenzaldehyde (2.00 g, 12.04 mmol) and 1,3-diamino-2,2-dimethylpropane (0.72 mL, 6.02 mmol). $C_{23}H_{30}N_2O_4$ (398.50): calcd. C 69.3, H 7.5, N 7.0; found C 68.7, H 7.6, N 6.9. $^1$H NMR (300 MHz, [$D_6$]DMSO): $\delta$ = 13.85 (br.), 8.51 (s, 2 H), 6.74–7.02 (d, d, t, 6 H), 4.03 (q, 4 H), 3.48 (br.), 1.31 (t, 6 H), 0.98 (s, 6 H) ppm. $^{13}$C NMR (75 MHz, [$D_6$]DMSO): $\delta$ = 167.5 ($C_g$), 152.7 ($C_a$), 147.9 ($C_b$), 118.4 ($C_f$), 67.3 ($C_h$), 64.7 ($C_k$), 36.4 ($C_i$), 24.3 ($C_j$), 15.5 ($C_l$) ppm. ES-MS: *m/z* = 398.7. IR: $\tilde{\nu}$ = $\nu$(O–H) 3428, $\nu$(C=N) 1633, $\nu$(C–O) 1250 $cm^{-1}$. M.p. 64 °C.

**Preparation of the Complexes:** All the complexes were synthesised by air oxidation of the solution made up from $Mn(ClO_4)_2 \cdot 6H_2O$ and the Schiff base.[21] A typical preparation of these complexes is outlined.

**$[Mn(H_2L^4)(H_2O)(CH_3OH)](ClO_4)$ (4):** $H_4L^4$ (0.30 g, 0.95 mmol) was dissolved in methanol (40 mL), and then a solution of NaOH (1.90 mmol, 4 M) in methanol (0.48 mL) was added. After stirring for 10 min, a solution of $Mn(ClO_4)_2 \cdot 6H_2O$ (0.35 g, 0.95 mmol) in methanol (10 mL) was added, and the solution turned brown. (**Caution**: Although no problems were encountered in this work, perchlorates are potentially explosive and should be handled in only small quantities and with care!) The progress of the reaction was followed by TLC for 3 d, and the mixture was then filtered. The complex was obtained from the filtrate as a brown solid after crystallisation. It was isolated by filtration and washed with diethyl ether and dried in air. Yield: 0.37 g (75%). $C_{18}H_{22}ClMnN_2O_{10}$ (516.77): calcd. C 41.8, H 4.3, N 5.4; found C 42.0, H 4.1, N 5.6.

**$[Mn(H_2L^1)(H_2O)_2](ClO_4)(H_2O)$ (1):** $H_4L^1$ (0.50 g, 1.66 mmol), $Mn(ClO_4)_2 \cdot 6H_2O$ (0.60 g, 1.66 mmol) and NaOH (0.83 mL, 3.32 mmol). Yield: 0.76 g (90%). $C_{16}H_{20}ClMnN_2O_{11}$ (506.73): calcd. C 37.9, H 4.0, N 5.5; found C 38.0, H 3.9, N 5.8.

**$[Mn(L^2)(H_2O)_2](ClO_4)(H_2O)$ (2):** $H_2L^2$ (0.33 g, 1.00 mmol), $Mn(ClO_4)_2 \cdot 6H_2O$ (0.36 g, 1.00 mmol) and NaOH (0.50 mL, 2.00 mmol). Yield: 0.35 g (65%). $C_{18}H_{24}ClMnN_2O_{11}$ (534.78): calcd. C 40.4, H 4.5, N 5.2; found C 40.1, H 4.3, N 5.2. Complex **2** was recrystallised from methanol solution, affording brown crystals adequate for X-ray diffraction studies.

**$[Mn(L^3)(H_2O)_2](ClO_4)(H_2O)$ (3):** $H_2L^3$ (0.20 g, 0.56 mmol), $Mn(ClO_4)_2 \cdot 6H_2O$ (0.20 g, 0.56 mmol) and NaOH (0.28 mL, 1.12 mmol). Yield: 0.10 g (32%). $C_{20}H_{28}ClMnN_2O_{11}$ (562.84): calcd. C 42.7, H 5.0, N 5.0; found C 42.0, H 4.9, N 4.8.

**$[Mn(L^5)(H_2O)_2](ClO_4)(H_2O)$ (5):** $H_2L^5$ (0.39 g, 1.00 mmol), $Mn(ClO_4)_2 \cdot 6H_2O$ (0.36 g, 1.00 mmol) and NaOH (0.50 mL, 2.00 mmol). Yield: 0.35 g (65%). $C_{19}H_{26}ClMnN_2O_{11}$ (548.81): calcd. C 41.6, H 4.8, N 5.1; found C 41.4, H 4.6, N 5.1.

**$[Mn(L^6)(H_2O)_2](ClO_4)(H_2O)$ (6):** $H_2L^6$ (0.20 g, 0.54 mmol), $Mn(ClO_4)_2 \cdot 6H_2O$ (0.19 g, 0.54 mmol) and NaOH (0.27 mL,

 © 2007 Wiley-VCH Verlag GmbH & Co. KGaA, Weinheim 

Table 5. Crystal data and structure refinement for $H_2L^3$, $H_4L^{10}$, **2** and **8**.

| | $H_2L^3$ | $H_4L^{10}$ | **2** | **8** |
|---|---|---|---|---|
| Empirical formula | $C_{20}H_{24}N_2O_4$ | $C_{19}H_{22}N_2O_4$ | $C_{18}H_{22}ClMnN_2O_{10}$ | $C_{20}H_{26}ClMnN_2O_{10}$ |
| Formula weight | 356.41 | 342.39 | 516.77 | 544.82 |
| Temperature [K] | 293(2) | 293(2) | 293(2) | 293(2) |
| Wavelength [Å] | 1.54180 | 0.71069 | 0.71073 | 0.71073 |
| Crystal system | monoclinic | monoclinic | orthorhombic | monoclinic |
| Space group | *C*2/*c* | $P2_1/c$ | *Pbca* | $P2_1/c$ |
| *a* [Å] | 22.581(5) | 6.7030(4) | 13.990(5) | 13.4577(19) |
| *b* [Å] | 7.0115(9) | 13.8580(6) | 13.349(5) | 13.4504(17) |
| *c* [Å] | 12.4645(19) | 19.1350(10) | 22.745(5) | 14.375(2) |
| *α* [°] | 90.00 | 90.00 | 90.000(5) | 90.00 |
| *β* [°] | 108.336(15) | 91.687(4) | 90.000(5) | 116.975(19) |
| *γ* [°] | 90.00 | 90.00 | 90.000(5) | 90.00 |
| Volume [Å$^3$] | 1873.3(6) | 1776.68(16) | 4248(2) | 2319.0(6) |
| *Z* | 4 | 4 | 8 | 4 |
| $D_c$ [g cm$^{-3}$] | 1.264 | 1.280 | 1.616 | 1.560 |
| Absorption coefficient [mm$^{-1}$] | 0.721 | 0.090 | 0.807 | 0.743 |
| *F*(000) | 760 | 728 | 2128 | 1128 |
| Crystal size [mm] | 0.40 × 0.10 × 0.04 | 0.36 × 0.28 × 0.24 | 0.19 × 0.18 × 0.03 | 0.45 × 0.40 × 0.10 |
| Theta range for data collection [°] | 4.12 to 65.26 | 1.81 to 26.33 | 1.79 to 21.99 | 1.70 to 24.97 |
| Reflections collected | 1694 | 3934 | 25121 | 4235 |
| Independent reflections | 1606 [*R*(int) = 0.0922] | 3618 [*R*(int) = 0.0134] | 2602 [*R*(int) = 0.0876] | 4072 [*R*(int) = 0.0160] |
| Data/restraints/parameters | 1606/0/124 | 3618/0/253 | 2602/356/337 | 4072/0/253 |
| Goodness-of-fit on $F^2$ | 0.891 | 1.032 | 1.054 | 1.005 |
| Final *R* indices [$I > 2\sigma(I)$] | $R_1$ = 0.0599 | $R_1$ = 0.0456 | $R_1$ = 0.0444 | $R_1$ = 0.0260 |
| | $wR_2$ = 0.1353 | $wR_2$ = 0.1371 | $wR_2$ = 0.1023 | $wR_2$ = 0.0539 |
| *R* indices (all data) | $R_1$ = 0.1993 | $R_1$ = 0.0605 | $R_1$ = 0.0793 | $R_1$ = 0.0392 |
| | $wR_2$ = 0.1899 | $wR_2$ = 0.1477 | $wR_2$ = 0.1146 | $wR_2$ = 0.0642 |

1.08 mmol). Yield: 0.21 g (68%). $C_{21}H_{31}ClMnN_2O_{11}$ (577.87): calcd. C 43.7, H 5.2, N 4.9; found C 44.0, H 5.0, N 4.7.

**[Mn($H_2L^7$)($H_2O$)($CH_3OH$)]($ClO_4$) (7):** $H_4L^7$ (0.30 g, 0.91 mmol), $Mn(ClO_4)_2·6H_2O$ (0.33 g, 0.91 mmol) and NaOH (0.46 mL, 1.82 mmol). Yield: 0.29 g (60%). $C_{19}H_{24}ClMnN_2O_{10}$ (530.79): calcd. C 43.0, H 4.6, N 5.3; found C 42.7, H 4.3, N 5.3.

**[Mn($L^8$)($H_2O$)$_2$]($ClO_4$) (8):** $H_2L^8$ (0.36 g, 1.00 mmol), $Mn(ClO_4)_2·6H_2O$ (0.36 g, 1.00 mmol) and NaOH (0.50 mL, 2.00 mmol). Yield: 0.35 g (65%). $C_{20}H_{26}ClMnN_2O_{10}$ (544.82): calcd. C 44.1, H 4.8, N 5.1; found C 43.8, H 4.7, N 5.0. Single brown crystals, useful for X-ray diffraction studies, were obtained from slow evaporation of a methanol solution of complex **8**.

**[Mn($L^9$)($H_2O$)$_2$]($ClO_4$) (9):** $H_2L^9$ (0.20 g, 0.52 mmol), $Mn(ClO_4)_2·6H_2O$ (0.18 g, 0.52 mmol) and NaOH (0.26 mL, 1.04 mmol). Yield: 0.25 g (83%). $C_{22}H_{30}ClMnN_2O_{10}$ (572.87): calcd. C 46.1, H 5.2, N 4.9; found C 46.4, H 5.1, N 4.6.

**[Mn($H_2L^{10}$)($H_2O$)($CH_3OH$)]($ClO_4$) (10):** $H_4L^{10}$ (0.30 g, 0.88 mmol), $Mn(ClO_4)_2·6H_2O$ (0.32 g, 0.88 mmol) and NaOH (0.44 mL, 1.76 mmol). Yield: 0.34 g (70%). $C_{19}H_{26}ClMnN_2O_{10}$ (532.81): calcd. C 44.1, H 4.8, N 5.1; found C 44.3, H 4.6, N 5.0.

**[Mn($L^{11}$)($H_2O$)$_2$]($ClO_4$)($H_2O$) (11):** $H_2L^{11}$ (0.20 g, 0.68 mmol), $Mn(ClO_4)_2·6H_2O$ (0.20 g, 0.68 mmol) and NaOH (0.34 mL, 1.35 mmol). Yield: 0.10 g (30%). $C_{21}H_{30}ClMnN_2O_{11}$ (576.86): calcd. C 43.7, H 5.2, N 4.9; found C 43.3, H 5.0, N 4.7.

**[Mn($L^{12}$)($H_2O$)$_2$]($ClO_4$) (12):** $H_2L^{12}$ (0.20 g, 0.50 mmol), $Mn(ClO_4)_2·6H_2O$ (0.18 g, 0.50 mmol) and NaOH (0.25 mL, 1.00 mmol). Yield: 0.22 g (75%). $C_{23}H_{32}ClMnN_2O_{10}$ (586.90): calcd. C 47.1, H 5.5, N 4.8; found C 48.0, H 5.4, N 4.6.

**Peroxidase Probes:** Oxidation of 2,2′-azinobis(3-ethylbenzothiazoline-6-sulfonic acid) (ABTS) with $H_2O_2$ in the presence of the complexes was tested. An aqueous solution of ABTS (50 μL, 0.009 M, $4.5 \times 10^{-7}$ mol) and a methanol solution of the complex (10 μL, $10^{-3}$ M, $10^{-8}$ mol) were added to water (3 mL). The oxidation of ABTS started immediately after addition of an aqueous solution of $H_2O_2$ (50 μL, 10 M, $5 \times 10^{-4}$ mol).

**X-ray Crystallographic Studies:** Crystals of $H_2L^3$, $H_4L^{10}$, **2** and **8** suitable for X-ray diffraction studies were obtained by slow evaporation of methanol solutions of the cited solids. Data for $H_4L^{10}$ and **2** were collected with a Smart CCD-1000 Bruker diffractometer employing graphite-monochromated Mo-$K_\alpha$ ($\lambda$ = 0.71073 Å) radiation. Data for **8** were collected with a Nonius FR591-kappa CCD2000 diffractometer using graphite-monochromated Mo-$K_\alpha$ ($\lambda$ = 0.71073 Å) radiation. Data for $H_2L^3$ were collected with a Nonius Mach3 diffractometer employing graphite-monochromated Cu-$K_\alpha$ ($\lambda$ = 1.54180 Å) radiation. The structures were solved by direct methods[35] and finally refined by full-matrix least-squares based on $F^2$. An empirical absorption correction was applied using SADABS.[36] All non-hydrogen atoms were anisotropically refined, and all hydrogen atoms were included in the model at geometrically calculated positions. Detailed data collection and refinement of the compounds are summarised in Table 5. CCDC-636345 ($H_2L^3$), -636346 ($H_4L^{10}$), -636347 (**2**) and -636348 (**8**) contain the supplementary crystallographic data for this paper. These data can be obtained free of charge from The Cambridge Crystallographic Data Centre via www.ccdc.cam.ac.uk/data_request/cif.

## Acknowledgments

We thank Ministerio de Ciencia y Tecnología of Spain (BQU2003-00167) and Xunta de Galicia (PGIDIT06TAM26201PR) for financial support.

[1] J. M. Lehn, *Supramolecular Chemistry: Concepts and Perspectives*, Wiley-VCH, Weinheim, Germany, **1995**.
[2] S. Leininger, B. Olenyuk, P. J. Stang, *Chem. Rev.* **2000**, *100*, 853–908.

 © 2007 Wiley-VCH Verlag GmbH & Co. KGaA, Weinheim 

[3] E. C. Constable, *Chem. Commun.* **1997**, 1073–1080.
[4] G. F. Swiegers, T. J. Malafetse, *Coord. Chem. Rev.* **2002**, *225*, 91–121.
[5] D. L. Caulder, K. N. Raymond, *Acc. Chem. Res.* **1999**, *32*, 975–982.
[6] M. R. Bermejo, A. M. González-Noya, R. Pedrido, M. J. Romero, M. Vázquez, *Angew. Chem. Int. Ed.* **2005**, *44*, 4182–4187.
[7] M. R. Bermejo, M. Fondo, A. M. Gonzalez, O. L. Hoyos, A. Sousa, C. A. McAuliffe, W. Hussain, R. Pritchard, V. M. Novotorsev, *J. Chem. Soc. Dalton Trans.* **1999**, 2211–2218.
[8] L.-P. Zhang, M. Du, W.-J. Lu, T. C. W. Mak, *Inorg. Chem. Commun.* **2005**, *8*, 623–625.
[9] M. R. Bermejo, A. M. González-Noya, V. Abad, M. I. Fernández, M. Maneiro, R. Pedrido, M. Vázquez, *Eur. J. Inorg. Chem.* **2004**, 3696–3705.
[10] M. R. Bermejo, M. I. Fernández, A. M. González-Noya, M. Maneiro, R. Pedrido, M. J. Rodriguez, M. Vázquez, *Eur. J. Inorg. Chem.* **2004**, 2769–2774.
[11] J.-P. D. Costes, B. Donnadieu, M. J. Rodríguez, M. I. Fernández, A. Bousseksou, J.-P. Tuchagues, *Inorg. Chem.* **2004**, *43*, 2736–2744.
[12] V. L. Pecoraro, W.-Y. Hsieh, *Met. Ions Biol. Syst.* **2000**, *37*, 429–504.
[13] M. Maneiro, W. F. Ruettinger, E. Bourles, G. L. McLendon, G. C. Dismukes, *Proc. Natl. Acad. Sci. USA* **2003**, *100*, 3707–3712.
[14] J. D. Crowley, D. A. Traynor, D. C. Weatherburn, *Met. Ions Biol. Syst.* **2000**, *37*, 209–278.
[15] P. S. Subramanian, E. Suresh, P. Dastidar, *Polyhedron* **2004**, *23*, 2515–2522.
[16] I. Yoon, J. Seo, J.-E. Lee, M. R. Song, S. Y. Lee, K. S. Choi, O.-S. Jung, K.-M. Park, S. S. Lee, *Dalton Trans.* **2005**, 2352–2354.
[17] L. Yi, X. Yang, T. Lu, P. Cheng, *Cryst. Growth Des.* **2005**, *5*, 1215–1219.
[18] S. H. Rahaman, H. Chowdhury, D. Bose, G. Mostafa, H.-K. Fun, B. K. Ghosh, *Inorg. Chem. Commun.* **2005**, *8*, 1041–1044.
[19] P. D. Beer, *Acc. Chem. Res.* **1998**, *31*, 71–80.
[20] M. Vázquez, L. Fabbrizzi, A. Taglietti, R. M. Pedrido, A. M. González-Noya, M. R. Bermejo, *Angew. Chem. Int. Ed.* **2004**, *43*, 1962–1965.
[21] M. R. Bermejo, A. Castineiras, J. C. Garcia-Monteagudo, M. Rey, A. Sousa, M. Watkinson, C. A. McAuliffe, R. G. Pritchard, R. L. Beddoes, *J. Chem. Soc. Dalton Trans.* **1996**, 2935–2944.
[22] W. Mazurek, A. M. Bond, M. J. O'Connor, A. G. Wedd, *Inorg. Chem.* **1986**, *25*, 906–915.
[23] W. I. Geary, *Coord. Chem. Rev.* **1971**, *7*, 81–122.
[24] J. Bonadies, M. Maroney, V. L. Pecoraro, *Inorg. Chem.* **1989**, *28*, 2044–2051.
[25] A. L. Llamas-Saiz, C. Foces-Foces, J. Elguero, *J. Mol. Struct.* **1994**, *328*, 297–323.
[26] A. Filarowski, A. Koll, A. Karpfen, P. Wolschann, *Chem. Phys.* **2004**, *297*, 323–332.
[27] M. Vázquez, M. R. Bermejo, M. Fondo, A. M. González, J. Mahía, L. Sorace, D. Gatteschi, *Eur. J. Inorg. Chem.* **2001**, 1863–1868.
[28] M. Vázquez, M. R. Bermejo, M. Fondo, A. García-Deibe, A. M. González, R. Pedrido, *Eur. J. Inorg. Chem.* **2002**, 465–472.
[29] M. Watkinson, M. Fondo, M. R. Bermejo, A. Sousa, C. A. McAuliffe, R. G. Pritchard, N. Jaiboon, N. Aurangzeb, M. Naeem, *J. Chem. Soc. Dalton Trans.* **1999**, 31–41.
[30] C. A. McAuliffe, R. G. Pritchard, A. García-Deibe, A. Sousa, M. R. Bermejo, *Acta Crystallogr., Sect. C* **1992**, *48*, 364–366.
[31] M. R. Bermejo, M. I. Fernández, A. M. González-Noya, M. Maneiro, R. Pedrido, M. J. Rodríguez, J. C. García-Monteagudo, B. Donnadieu, *J. Inorg. Biochem.* **2006**, *100*, 1470–1478.
[32] M. Maneiro, M. R. Bermejo, M. I. Fernández, E. Gómez-Fórneas, A. M. González-Noya, A. M. Tyryshkin, *New J. Chem.* **2003**, *27*, 727–733.
[33] U. Casellato, P. Guerriero, S. Tamburini, P. A. Vigato, C. Benelli, *Inorg. Chim. Acta* **1993**, *207*, 39–58.
[34] J. Sanmartín, M. R. Bermejo, A. M. García-Deibe, I. M. Rivas, A. R. Fernández, *J. Chem. Soc. Dalton Trans.* **2000**, 4174–4181.
[35] G. M. Sheldrick, *SHELX-97 (SHELXS 97 and SHELXL 97), Programs for Crystal Structure Analyses*, University of Göttingen, Germany, **1998**.
[36] G. M. Sheldrick, *SADABS, Program for Scaling and Correction of Area Detector Data*, University of Göttingen, Germany, **1996**.

Received: February 12, 2007
Published Online: June 29, 2007

 © 2007 Wiley-VCH Verlag GmbH & Co. KGaA, Weinheim 

DOI: 10.1002/ejic.200700210

# Synthesis of Carbon and Silica Hollow Spheres with Mesoporous Shells using Polyethylene Oxide/Phenol Formaldehyde Polymer Blend

Chun-Yi Chang-Chien,[a] Chun-Han Hsu,[a] Tsung-Ying Lee,[a] Che-Wei Liu,[a] Sheng-Ho Wu,[a] Hong-Ping Lin,*[a,b] Chih-Yuan Tang,[c] and Chin-Yen Lin[c]

**Keywords:** Polymer blends / Mesoporous materials / Metal oxides / Organic templates

Polyethylene oxide/phenol formaldehyde silica composite hollow spheres were obtained from a fast silicification of a polymer blend, containing polyethylene oxide (PEO) as silica gelator and phenol formaldehyde (PF) polymer as carbon source, in a highly diluted silica solution at pH ≈ 5.0–6.0. The PF–PEO/silica hollow spheres can be feasibly converted to mesoporous silica hollow spheres by hydrothermal treatment and calcination, and to mesoporous carbon hollow spheres after pyrolysis under a nitrogen atmosphere and silica etching. Because the formation of the hollow spheres is kinetically controlled, the diameter of the hollow spheres is dependent on the molecular weight of the PEO polymer, pH value of the silica solution, and the PF content, and the size can be tuned within a range of a few micrometers to tens of nanometers. These mesoporous hollow spheres have high surface areas and large pore sizes and volumes. In practice, the mesoporous carbon hollow spheres with an interconnected mesostructure were used as a solid template to prepare different metal oxide hollow spheres. After impregnation of the proper metal oxide precursors and calcination, the $\gamma$-$Al_2O_3$, *anatase*-$TiO_2$, $\alpha$-$Fe_2O_3$, $ZrO_2$, MgO, and $CeO_2$ hollow spheres composed of nanoparticles were readily synthesize.

(© Wiley-VCH Verlag GmbH & Co. KGaA, 69451 Weinheim, Germany, 2007)

## Introduction

Since the discovery of mesoporous silicas by Mobil researchers and Kuroda,[1] the construction of organic templates to synthesize advanced materials has become a significant area of scientific and technological interest.[2,3] Because of potential applications in drug storage and release, confined-space catalysis, thermal and electrical insulators, separation, and biomolecule release, the fabrication of functional porous materials with hollow interiors has attracted much attention.[4–10] Typically, hollow spheres of various diameters and wall thicknesses were synthesized by using polymer or silica beads,[5,6] gold nanoparticles,[7] emulsion drops,[8–9] or multi-layers vesicles[10] as interior templates. However, a removable expensive polymer bead, silica, or a Au nanoparticle is energy-consuming and uneconomic. Moreover, fine tuning for the chemical composites and synthetic conditions (i.e. temperature, stirring rate, pH value, etc.) to prepare stable emulsions or vesicles as the morphological templates of the inorganic materials is a sophisticated approach. In addition to creating the hollow interior, introduction of porosity to the shell is also crucially important for controlling accessibility and permeability of the void interior space to the environment.[11] Up to now, the development of a convenient synthetic method and the use of cost-effective precursors to generate the materials with hollow interiors and porous shell is still of much interest.

In polymer chemistry,[12] it is well-known that thermosetting phenol formaldehyde polymers (PF) have been widely used as carbon precursors in industry and that nature-friendly polyethylene oxide (PEO) homopolymers have a high affinity to aggregate with silica species through hydrogen bonding between the ether and silanol groups. From analysis of the molecular structures of the PEO polymer and PF polymers, it can be seen that the ether groups (i.e. –O– : hydrogen-bonding acceptor) of the PEO polymers and the methylene hydroxide and phenol groups (i.e. $–CH_2OH$ and $C_6H_6–OH$: hydrogen-bonding donor) of the PF polymers have a high degree of hydrogen-bonding complementarity. Therefore, PEO and PF polymers could construct a homogeneously miscible PF–PEO polymer blend. On the basis of these concepts, in this study we used the PF–PEO polymer blend in a water/ethanol solution as the morphological and mesostructural template of the silica. When combined with a stock sodium silicate solution at pH ≈ 5.0–6.0, PF–PEO/silica hollow spheres were quickly generated. Because the synergistic PF–PEO/silica hollow spheres contain carbonizable PF polymer and silica, hollow

[a] Department of Chemistry, National Cheng Kung University, Tainan, 701, Taiwan
E-mail: hplin@mail.ncku.edu.tw
[b] Research and Education Division Center for Micro/Nanoscience and Technology, National Cheng Kung University, Tainan, 701, Taiwan
[c] Precision Instrument Center, National Taiwan University, Taipei, 106, Taiwan

Supporting information for this article is available on the WWW under http://www.eurjic.org or from the author.

 © 2007 Wiley-VCH Verlag GmbH & Co. KGaA, Weinheim 

carbon spheres with mesoporous shells were prepared after pyrolysis and silica removal. Alternatively, hollow silica spheres with porous shells were obtained from hydrothermal treatment and calcination in air.

## Results and Discussion

Figure 1 shows the representative SEM image of the as-synthesized PF–PEO6000/silica composite. It can be clearly seen that the morphology of the particle is spherical and that the diameter of the sphere ranges from 1.0 to 0.5 μm. Some broken spheres reveal that the spheres are hollow and the wall thickness is around 0.1–0.2 μm. The inner cavities of the spheres were clearly identified by TEM contrast imaging (Figure 1B). Clearly, the spheres are almost hollow (>90%). The TGA curve of the PF–PEO6000/silica composite is intermediate between the TGA curves of the PEO/silica and PF polymer (Figure 1C), which demonstrates a homogeneous blending between PEO6000 and PF polymers. This average in combustion temperature occurs commonly in homogeneous organic or polymer blends.

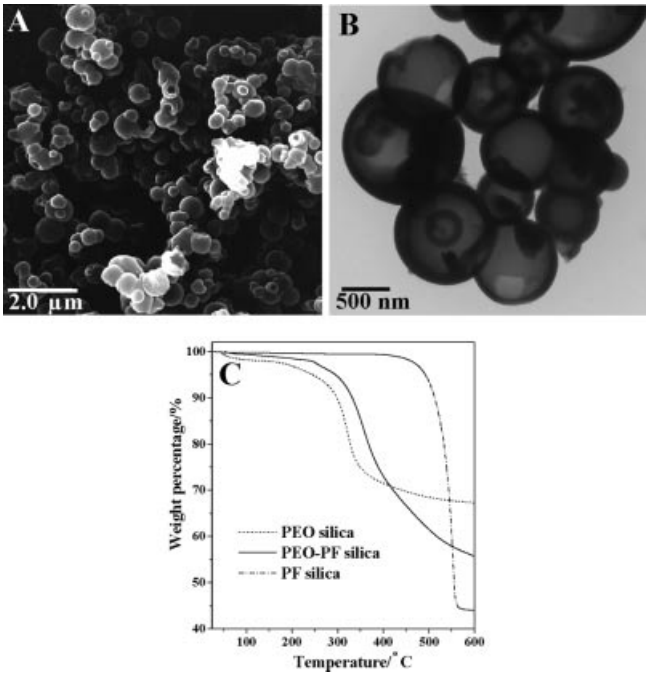


Figure 1. SEM (A) and TEM (B) images of the PF–PEO6000/silica hollow spheres prepared by using a synthetic component of PF/PEO6000/sodium silicate/$H_2O$ = 2.0: 2.0: 8.0: 315.0 g. (C). TGA curves of the PEO6000/silica, PF–PEO/silica, and PF/silica composites.

Because the PF–PEO/silica composite hollow spheres contain the carbonizable PF polymer, the mesoporous carbon hollow spheres can thus be easily obtained from high-temperature pyrolysis and silica removal by HF etching. The resulting mesoporous carbon retains the spherical morphology (Figure 2A). Some broken or folded hollow spheres reveal that the mesoporous carbon spheres are hollow.[13] The hollow interiors of the carbon spheres can be more clearly shown in a TEM image (Figure 2B). The shell thickness of the hollow mesoporous carbon spheres is around 0.1 μm. The preservation of the hollow-sphere morphology indicates that the thermosetting PF polymers disperse homogeneously within the shell, and then form a stable cross-linked framework to keep the hollow-sphere morphology. The high-magnification TEM image clearly shows that the mesostructure of the hollow sphere's shell is wormhole-like (i.e. interconnected), and the pore size is around a few nanometers (inset of Figure 2B). In parallel to the TEM observations, the hollow mesoporous carbon spheres exhibit a type IV $N_2$ adsorption–desorption isotherm with a capillary condensation occurring at $P/P_0$ = 0.3 to 0.4 (Figure 2C). By analyzing the adsorption isotherm, the mesoporous carbon hollow spheres have a high Brunauer–Emmett–Teller surface area (≈1500 $m^2 g^{-1}$), large Barrett–Joyner–Halenda pore size (≈2.6 nm), and pore volume (≈0.93 $cm^3 g^{-1}$), as do the mesoporous carbons obtained from the mesoporous silica-templating method.[4]

To obtain information about the thermal stability and carbon phase of the hollow mesoporous carbon spheres, TGA, Raman spectroscopy, and XRD investigations were performed.[14,15] The hollow mesoporous carbon spheres exhibit significant weight loss in a narrow temperature range between 600 and 650 °C (Supporting Information, Figure S1). Thus, the porous carbon of high thermal stability can be easily produced from the PF–PEO6000/silica composite. The silica residue in the porous carbon is less than 2.0 wt.-%, indicating that the silica was almost entirely removed by HF etching. The mesoporous carbon hollow spheres show two broad XRD peaks that can be indexed to (002) and (100) diffraction peaks for the amorphous carbons (Figure 2D). In addition, the Raman spectrum of the sample displays two broad vibration bands (inset of Figure 2D). One band is around 1580 $cm^{-1}$ (G-band; the interplane $sp^2$ C–C stretching) and the other band is located around 1340 $cm^{-1}$ (D-band; the defects within the carbon), which also indicate the amorphous carbon structure.[16]

In addition to producing mesoporous carbon hollow spheres, mesoporous silica hollow spheres also can be generated from the PF–PEO6000/silica composite after hydrothermal treatment at 100 °C and calcination at 560 °C in air. The microtome TEM image shows that the mesostructure of the shell of the hollow silica spheres is disordered and that the pore size is around a few nanometers (Figure 2E). Therefore, the mesoporous silica hollow sphere displays type IV $N_2$ adsorption–desorption isotherms with an apparent capillary condensation occurring at $P/P_0$ = 0.6–0.7 (Figure 2F). The mesoporous silica hollow spheres have Brunauer–Emmett–Teller surface area of 520 $m^2 g^{-1}$, a mean Barrett–Joyner–Halenda pore size of 6.2 nm, and a pore volume of 0.75 $cm^3 g^{-1}$. Consequently, the high-quality mesoporous carbon and silica hollow spheres can be conveniently obtained from the calcination and (carbonization + silica removal) of the PF–PEO/silica composite hollow spheres, respectively.

 © 2007 Wiley-VCH Verlag GmbH & Co. KGaA, Weinheim 

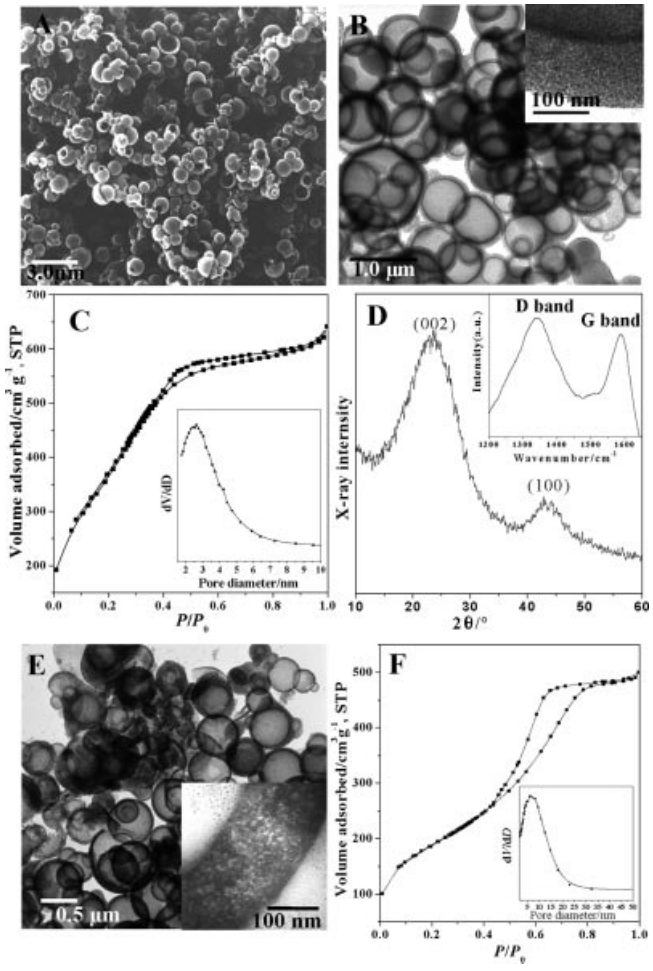


Figure 2. SEM (A) and TEM (B) micrographs of the mesoporous carbon hollow spheres. Inset is HR-TEM image of mesoporous shell of the mesoporous carbon hollow spheres. (C). $N_2$ adsorption–desorption isotherm of the mesoporous carbon hollow spheres. Inset is the BJH pore size distribution. (D) High-angle XRD pattern of the mesoporous carbon hollow spheres. Inset is the Raman spectrum. (E). TEM image of the mesoporous silica hollow spheres. Inset is the microtome TEM image. (F) $N_2$ adsorption–desorption isotherm of the mesoporous silica hollow spheres. Inset is the BJH pore-size distribution.

When using other PEO homopolymers of different molecular weights to blend with the same amount of PF polymer, the TEM images revealed that the prepared mesoporous carbon samples consisted of hollow spheres (yield > 90%) with different diameters (Figure 3). By comparing the diameters of these mesoporous carbon hollow spheres, it is clear that the average diameters and the shell thickness decrease with an increase in the PEO polymer molecular weight. According to these current results, the use of the PEO100000 or PEO300000 polymers gave hollow spheres in tens of nanometers (Figure 3B, C), and submicro- to micrometer hollow sphere were obtained with PEO10000 or PEO6000 (Figures 3A and 2B). Like the hollow mesoporous carbon spheres synthesized with PEO6000, other hollow mesoporous carbon spheres have high surface area, mesoporosity, and large pore volume (Supporting Information, Figure S2). Clearly, the mesoporous silica hollow spheres with various diameters (tens of nanometers to micrometers) were also obtained from the hydrothermal treatment and organic template removal (Supporting Information, Figure S3). To the best of our knowledge, this is the first time that the mesoporous carbon and silica hollow spheres with various diameters have been synthesize by using the commercially attractive PF–PEO polymer blend and sodium silicate.

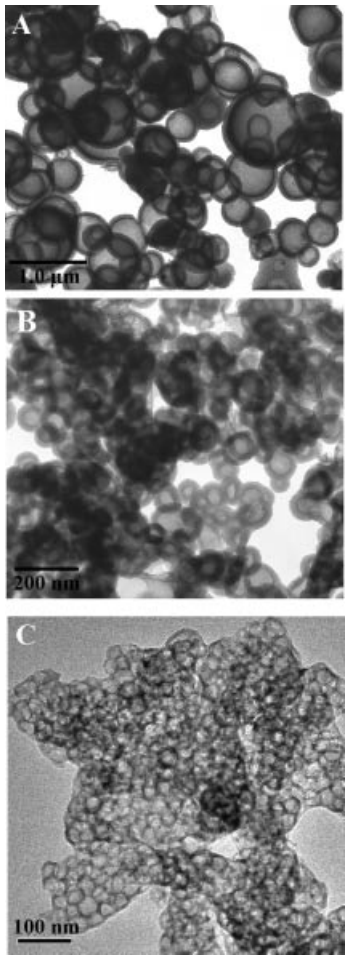


Figure 3. TEM images of the mesoporous carbon hollow spheres synthesized with PF–PEO*n* polymer blend as template. (A) $n$ = 10000; (B) $n$ = 100000; (C) $n$ = 300000. The synthetic compositions are: PF/PEO*n*/sodium silicate/$H_2O$ = 2.0: 2.0: 8.0: 315.0 g.

To understand the driving force of the formation of the hollow spheres, we poured the ethanol/water solution of the PF–PEO polymer blend into water and found that an opaque solution (i.e. PF–PEO emulsion solution) was formed at the beginning and then the hydrophobic PF polymers gradually underwent phase separation and precipitation from the aqueous phase. In contrast, when the PF–PEO polymer blend solution was added to a sodium silicate solution, a light yellow gel solution was formed in a few seconds without phase-separation and precipitation of the free PF polymers. This is because the silicate species can quickly assemble with the PEO parts in the PF–PEO polymer blend at pH around 5.0–6.0 to solidify the hydrother-

 © 2007 Wiley-VCH Verlag GmbH & Co. KGaA, Weinheim 

mally unstable PF–PEO emulsions and prohibit the self-precipitation of the hydrophobic PF polymer. Although the phase-separation approach is typically used to prepare hollow latex particles,[15] this is the first time that it was employed to synthesize porous materials.

On the basis of all the above observations, a simple plausible mechanism was proposed addressing the formation of the hollow spheres. As shown in Scheme 1, when the PF–PEO solution was added into a highly diluted sodium silicate aqueous solution, the hydrophobic PF polymers induced the formation of PF–PEO emulsions. At the same time, the silica species, which assemble with the PEO polymers, attach onto the outer surface of the PF–PEO emulsions. After fast further silica condensation, the PF–PEO emulsions were solidified prior to the PF phase-separation, and then the hollow PF–PEO/silica hollow spheres were generated. Therefore, with careful control of the condensation rate of the silica species on the PF–PEO emulsions and the coalescence rate of the PF–PEO emulsions induced by the hydrophobic PF polymer, a capsule-shaped PF–PEO/silica composite was obtained. Because the PEO homopolymer of higher molecular weight can assemble faster with the silica species than the lower molecular weight polymers, the average diameter of the trapped PF–PEO/silica hollow spheres becomes smaller (Figure 3).

According to silica chemistry, it is well-known that the silica condensation rate depends on the pH value.[17] Figure 4 exhibits the mesoporous carbon samples prepared at different pH values. It is clear that the pH value of the silicate solution must be tuned in the range of 5.0–6.0 to get the hollow spheres, where matching interaction between PEO and silica species (i.e. hydrogen bonding between $-CH_2CH_2O^{\delta-}$ of the PEO polymer and the silanol group –SiOH of the silica species) and fast silica condensation rate could prevent the self-precipitation of the PF polymers.[18] In this pH value range, the silica condensation rate increases with the pH value,[17] and thus the average diameter of the hollow spheres decreases as the pH value increases (Figures 2B, 4B, and 4D). However, outside of this pH range, the hollow spheres were no longer obtained. At pH values $<5.0$, the slow silica condensation rate led to the generation of micrometer-sized solid spheres or particles (Figure 4A). However, at pH values $>7.0$, mismatching interactions between the negatively charged silicate species and the partially negative PEO polymer resulted in the separation of the silica and the PF–PEO polymer blend, which led to the precipitation of the PF polymers.

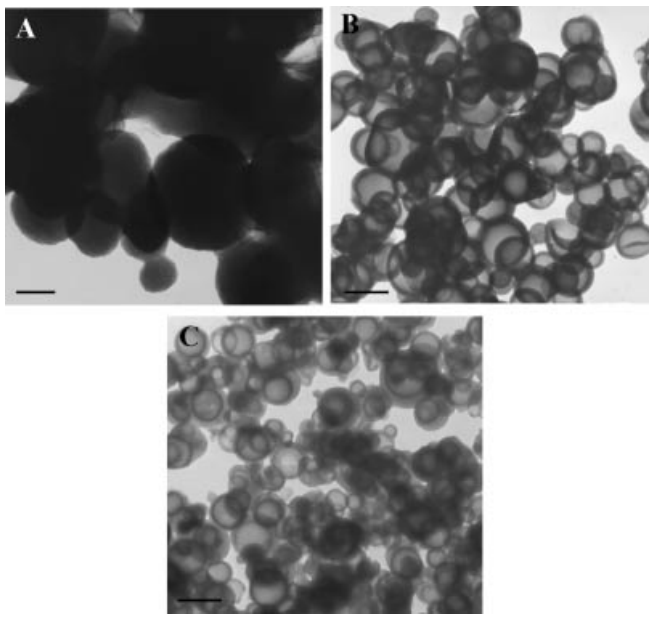


Figure 4. TEM micrographs of the mesoporous carbon hollow spheres synthesized in silica solutions at different pH value (PF/PEO6000 weight ratio = 2.0). (A) pH = 4.0; (B) pH = 5.5; (C) pH = 6.0. Scale bar = 500 nm.

In addition to studying the effect of the silica condensation rate on the diameter of the hollow spheres, we also changed the content of the PF polymer to control the coalescence rate of the PF–PEO emulsions. As expected, we found that the average diameter of the mesoporous carbon hollow spheres increased with an increase in the PF polymer content (Figure 5). When the PF/PEO6000 weight ratio is higher than 1.5, the PF polymer precipitation rate is relatively too fast to be completely trapped and some PF polymer precipitates. Moreover, it must be mentioned that the yield of the carbon is determined by the PF content. At low PF/PEO6000 weight ratios ($<0.5$), the carbon yield is very low. Consequently, the appropriate PF/PEO6000 weight ratio to obtain carbon hollow spheres in a suitable yield ranges form 0.8 to 1.5. To reduce the dispersion in the diameter of the hollow spheres, considerably kinetic and thermodynamic principles behind the formation of the hollow spheres will be further studied.

It is known that there are advantages to use mesoporous carbon as solid templates:[4,19–21] (1) The high stability of the carbon framework can stand for cruel synthetic conditions. (2) The amorphous carbon should be easily removed

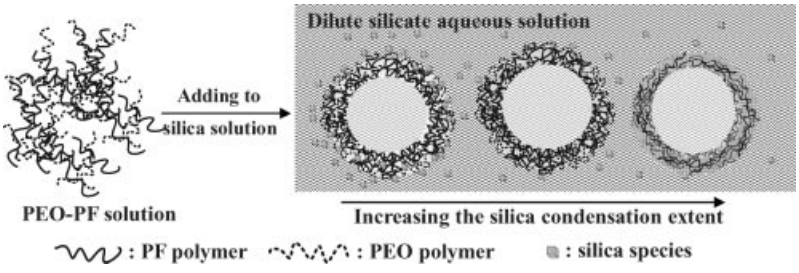


Scheme 1. Formation mechanism of the PF–PEO/silica composite hollow spheres in a highly diluted silica solution.

 © 2007 Wiley-VCH Verlag GmbH & Co. KGaA, Weinheim 

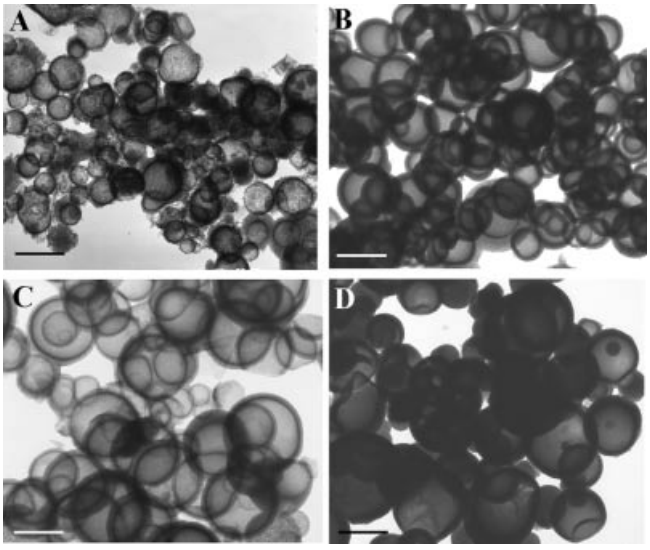


Figure 5. TEM images of the mesoporous carbon hollow spheres prepared with different PF/PEO300000 weight ratios ($r$) at pH = 5.0. (A) $r$ = 0.5; (B) $r$ = 0.8; (C) $r$ = 1.3; (D) $r$ = 1.5. Scale bar = 500 nm.

by calcination at temperatures higher than 600 °C. (3) Crystallization of the metal oxide can be readily achieved under the confinement of the mesostructure of carbon. In practice, we used the mesoporous carbon hollow spheres of interconnected mesostructure as a solid *exo* template to prepare the porous metal oxide hollow spheres.[22] Figure 6 shows the representative TEM and SEM images of the $ZrO_2$, $Al_2O_3$, $TiO_2$, and $Fe_2O_3$ hollow spheres prepared by impregnating mesoporous carbon hollow spheres with acidic ethanolic solutions of $Zr(OAc)_4$, $Al(NO_3)_3$, $Ti(OBu)_4$, and $Fe(NO_3)_3$ salts, respectively, and calcination at 600 °C in air. These images clearly demonstrate that the metal oxide hollow spheres can be easily obtained from a typical impregnation process by using mesoporous carbon hollow spheres as a solid template. In addition to preserving the hollow-sphere morphology, the HR-TEM image reveals that the shell of the metal oxide hollow spheres is composed of many nanocrystals (ca. 5–30 nm, insets of Figure 6). In combination with the high-angle XRD patterns of the metal oxide hollow spheres, all broad XRD peaks can be assigned undisputedly to the $\gamma$-$Al_2O_3$, *anatase*-$TiO_2$, $\alpha$-$Fe_2O_3$, and $ZrO_2$ nanoparticles. According to these results, we proposed a possible mechanism for the formation of the mesoporous metal oxide hollow spheres. In the first stage, the precursors of the metal oxides can be incorporated into the interconnected nanopores of the mesoporous carbon shell. Upon heat treatment, the precursors thermally decompose, and the nanoparticles derived therefrom grow larger and crystallize. In the presence of thermally stable carbon, the crystalline dimension is confined to the nanoscale. Because the nanocrystals interlink with each other and form continuous and stable frameworks, the hollow-sphere morphology is fully replicated even after the removal of the carbon template by further high temperature heat treatment. These metal oxide hollow spheres have a high surface area (100–150 $m^2 g^{-1}$), large pore size (8.0–12.0 nm), and a large volume (0.25–0.35 $cm^3 g^{-1}$; Supporting Information, Figure S4, Table S1). In addition to $ZrO_2$, $\gamma$-$Al_2O_3$, *anatase*-$TiO_2$, and $\alpha$-$Fe_2O_3$ mesoporous hollow spheres,[23–27] other metal oxide hollow spheres (e.g. MgO and $CeO_2$; Supporting Information, Figure S5) were also produced by using the mesoporous carbon hollow spheres as a solid template. Moreover, to obtain magnetic nanoparticles containing mesoporous carbon hollow spheres, the $Fe(NO_3)_3$ impregnated mesoporous carbon was heated to 900 °C under a $N_2$ atmosphere instead. Figure 6F shows that the Fe nanoparticles are embedded within the mesoporous carbon shell or in the interior of the hollow spheres. The magnetic nanoparticles containing mesoporous carbon hollow spheres demonstrate the magnetic properties (Supporting Information, Figure S6).

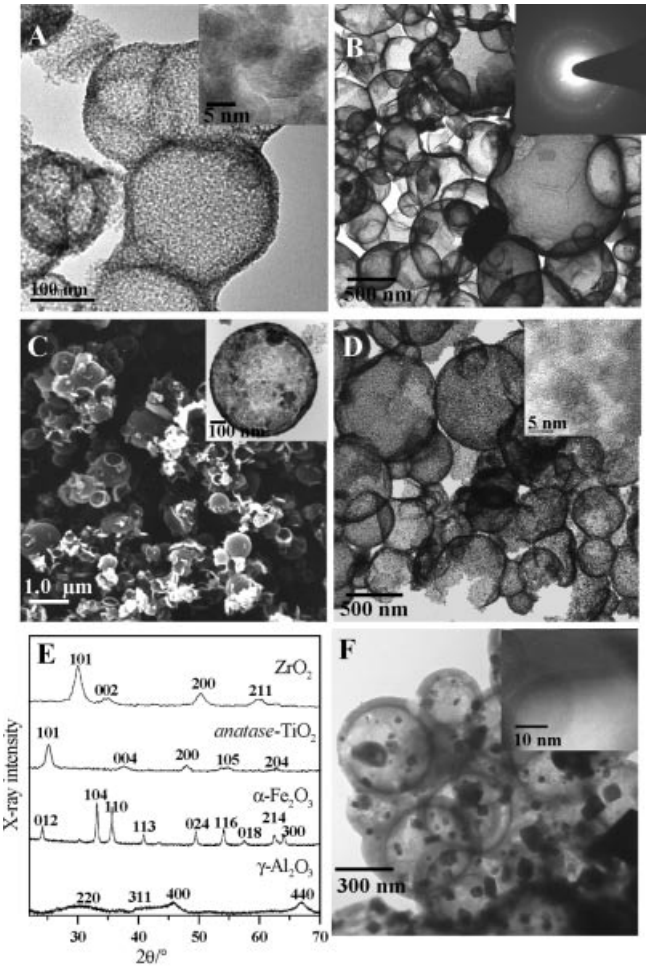


Figure 6. TEM and SEM images and XRD patterns of the mesoporous metal oxide hollow spheres prepared by using mesoporous carbon hollow spheres as hard templates. (A) $ZrO_2$; (B) $\gamma$-$Al_2O_3$; (C) $\alpha$-$Fe_2O_3$; (D) *anatase*-$TiO_2$, (E) XRD patterns; (F) The Fe nanoparticle containing mesoporous carbon hollow spheres obtained from pyrolysis of a $Fe(NO_3)_3$ impregnated mesoporous carbon hollow spheres at 700 °C under an atmosphere of $N_2$. Insets are the HR-TEM and electron-diffraction images of the metal oxides and iron nanoparticles.

 © 2007 Wiley-VCH Verlag GmbH & Co. KGaA, Weinheim 

## Conclusions

In brief, we have described a new method to conveniently synthesize PF–PEO/silica hollow spheres. The synergistic PF–PEO/silica hybrid composite can be transferred to mesoporous carbon and mesoporous silica hollow spheres as required. This synthetic method for the preparation of hollow spheres with different diameters involves the simple mixing of well-defined precursors and changing the components and pH value of the mixture; thus scale-up of the hollow spheres is readily accomplished. The phase-separation approach can be extended to different polymer blends and nonsilica metal oxides. With good control of assembling kinetics, one can judiciously select other polymer blends to manufacture hollow mesoporous spheres with high flexibility in their compositions. In addition, the use of stable mesoporous carbon hollow spheres is an alternative for the preparation of metal oxides hollow spheres of high crystallinity and magnetic mesoporous carbon hollow spheres. These hollow spheres of high composition-flexibility have potential to be applied as a catalyst, absorbent, sensor, magnetically separable carrier, microcapsule, supercapacitor, and as an aid in drug-delivery and fuel cells.

## Experimental Section

**Typical Synthesis of Mesoporous Carbon and Silica Hollow Spheres:** The PEO (Acrös) (2.0 g) and PF (0.5–3.0 g; PF2180, phenol/aldehyde, 0.8–0.9; MW ca. 96000; Chung-Chun Plastic, Taiwan) polymers were dissolved in a mixture of ethanol (20.0 g) and water (5–15 g) to form a clear solution. Then, the PF–PEO blend solution was poured quickly into an acidified sodium silicate solution aqueous solution (pH ≈ 5.0–6.0) at 40 °C, which was prepared by adjusting the pH value of a mixture of sodium silicate (27 wt.-% $SiO_2$, 8.0 g, Aldrich) and water (300.0 g) to 4.0–7.0 and aging for 3–10 min. A light-yellowed precipitate formed within a few seconds. Filtration, washing, and drying at 100 °C gave the PF–PEO/silica hollow spheres. The mesoporous carbon hollow spheres with mesoporous shells were gained after a pyrolysis at 1000 °C under a $N_2$ atmosphere for 2 h and silica removal by 6 wt.-% HF etching. Alternatively, to obtain the hollow silica spheres with a mesoporous shell, the PF–PEO/silica hollow spheres were kept static in a polypropylene bottle at 100 °C for 1 d and calcined at 580 °C for 6 h to remove the organic template.

**Synthesis of Metal Oxides Hollow Sphere:** A proper amount of metal oxide precursor (metal/carbon ≈ 1:50 in mol) was dissolved in an acidic ethanolic solution (95 wt.-% ethanol, 20.0 g, conc. $HNO_3$, 1.0 g). The $Zr(OAc)_4$, $Al(NO_3)_3$, $Ti(OBu)_4$, and $Fe(NO_3)_3$ were used as the precursors to the $ZrO_2$, $\gamma$-$Al_2O_3$, *anatase*-$TiO_2$, and $\alpha$-$Fe_2O_3$ hollow spheres, respectively. Then, the ethanolic solution was combined with the mesoporous carbon hollow sphere sample (0.4 g). After stirring for 1 d under ambient conditions and dried at 60 °C to evaporate the solvent, the dried metal oxide precursor impregnated mesoporous carbon was obtained. Calcination at 600 °C for 8 h to remove the mesoporous carbon template gave the metal oxides hollow spheres.

**Characterization:** $N_2$ adsorption–desorption isotherms were obtained at 77 K with a Micromeritics ASAP 2010 apparatus. Before analysis, the sample was degassed at 120 °C for about 6 h at $10^{-3}$ Torr. The pore size distribution was obtained from the analysis of the adsorption branch by using the BJH (Barrett–Joyner–Halenda) method. Scanning electron microscopy (SEM) and transmission electron microscopy (TEM) images were obtained with an S-800 (Hitachi) operated at an acceleration voltage of 20 keV and an H-7500 (Hitachi) operated at 100 keV, respectively. The organic content in the mesoporous silicas and the porous carbon thermostability were measured by thermogravimetric analysis (TGA). TGA tests were conducted with a TA Q-50 thermogravimetric system. In a typical experiment, ca. 10 mg of the sample was heated to 700–800 °C at 10 °C $min^{-1}$ in air. Raman spectra were obtained with a Dilor XY Raman spectrum, using an Ar laser with an excitation wavelength of 514.5 nm.

**Supporting Information** (see footnote on the first page of this article): TGA curve of the mesoporous carbon hollow spheres, $N_2$ adsorption–desorption isotherm of the PF–PEO*n* polymer blend-templated mesoporous carbon hollow spheres, SEM images of the different PF–PEO*n* polymer blend templated mesoporous silica hollow spheres, $N_2$ adsorption–desorption isotherms of the different mesoporous metal oxides hollow spheres, TEM images of mesoporous MgO and $CeO_2$ hollow spheres, photograph showing magnetic Fe@mesoporous carbon hollow sphere, and table of the precursors and properties of the metal oxides and Fe@carbon hollow spheres.

## Acknowledgments

Authors thank Pann Asia Chemical Corporation and Chung-Chun Plastic, Taiwan for providing the PEO and PF polymers. This research is financially supported by the National Science Council of Taiwan (NSC95-2113-M-006-011-MY3, NSC95-2120-M-006-009, and NSC95-2323-B-006-008).

[1] a) T. Yanagisawa, T. Shimizu, K. Kuroda, C. Kato, *Bull. Chem. Soc. Jpn.* **1990**, *63*, 988–992; b) C. T. Kresge, M. E. Leonowicz, W. J. Roth, J. C. Vartuli, J. S. Beck, *Nature* **1992**, *359*, 710–712.
[2] a) D. Zhao, J. Feng, Q. Huo, N. Melosh, G. H. Fredrickson, B. F. Chmelka, G. D. Stucky, *Science* **1998**, *279*, 548–552; b) J. Y. Ying, C. P. Mehnert, M. S. Wong, *Angew. Chem. Int. Ed.* **1999**, *38*, 56–77.
[3] a) P. T. Tanev, M. Chibwe, T. J. Pinnavaia, *Nature* **1994**, *368*, 321–323; b) P. T. Tanev, T. J. Pinnavaia, *Science* **1995**, *267*, 865–867.
[4] a) J. Lee, J. Kim, T. Hyeon, *Adv. Mater.* **2006**, *18*, 2073–2094; b) S. B. Yoon, K. Sohn, J. Y. Kim, C.-H. Shin, J.-S. Yu, T. Hyeon, *Adv. Mater.* **2002**, *14*, 19–21.
[5] a) Z. Zhong, Y. Yin, B. Gates, Y. Xia, *Adv. Mater.* **2000**, *12*, 206–209; b) S. W. Kim, M. Kim, W. Y. Lee, T. Hyeon, *J. Am. Chem. Soc.* **2002**, *124*, 7642–7643.
[6] a) F. Caruso, R. A. Caruso, H. Mohwald, *Science* **1998**, *282*, 1111–1114; b) M. Yang, J. Ma, C. Zhang, Z. Yang, Y. Lu, *Angew. Chem. Int. Ed.* **2005**, *44*, 6727–6730.
[7] a) X. Zheng, C. Liu, Y. Xie, *Eur. J. Inorg. Chem.* **2006**, 2364–2369; b) N. Singh, L. A. Lyon, *Chem. Mater.* **2007**, *19*, 719–726.
[8] a) C. I. Zoldesi, A. Imhof, *Adv. Mater.* **2005**, *17*, 924–928; b) D. Walsh, B. Lebeau, S. Mann, *Adv. Mater.* **1999**, *11*, 324–328.
[9] a) X. W. Lou, Y. Wang, C. Yuan, J. Y. Lee, L. A. Archer, *Adv. Mater.* **2006**, *18*, 2325–2329; b) R. K. Rana, V. S. Murthy, J. Yu, M. S. Wang, *Adv. Mater.* **2005**, *17*, 1145–1150.
[10] a) Y. Q. Yeh, B. C. Chen, H. P. Lin, C. Y. Tang, *Langmuir* **2006**, *22*, 6–9; b) H. P. Lin, C. Y. Mou, *Acc. Chem. Res.* **2002**, *35*, 927–935.
[11] a) H.-P. Hentze, S. R. Raghavan, C. A. McKelvey, E. W. Kaler, *Langmuir* **2003**, *19*, 1069–1074; b) D. H. Hubert, W. M. Jung, P. M. Frederik, P. H. H. Bomans, J. Meuldijk, A. L. German, *Adv. Mater.* **2000**, *12*, 1286–1290.

 © 2007 Wiley-VCH Verlag GmbH & Co. KGaA, Weinheim 

[12] M. P. Stevens, *Polymer Chemistry*, Oxford University, Oxford, New York, **1999**.
[13] P. M. Arnal, F. Schüth, F. Kleitz, *Chem. Commun.* **2006**, 1203–1205.
[14] K. Kinoshita, *Carbon: Electrochemical and Physicochemical Properties*, John Wiley & Sons, New York, **1988**.
[15] a) M. Kruk, M. Jaroniec, C. H. Ko, R. Ryoo, *Chem. Mater.* **2000**, *12*, 1961–1968; b) S. H. Joo, R. Ryoo, M. Kruk, M. Jaroniec, *J. Phys. Chem. B* **2002**, *106*, 4640–4646; c) M. Kaneda, T. Tsubakiyama, A. Carlsson, Y. Sakamoto, T. Ohsuna, O. Terasaki, *J. Phys. Chem. B* **2002**, *106*, 1256–1266.
[16] J. Roggenbuck, M. Tiemann, *J. Am. Chem. Soc.* **2005**, *127*, 1096–1097.
[17] R. K. Iler, *The Chemistry of Silica: Solubility, Polymerization, Colloid and Surface Properties and Biochemistry*, Wiley, New York, **1979**.
[18] C. J. McDonald, M. J. Devon, *Adv. Colloid Interface Sci.* **2002**, *99*, 181–213.
[19] A. Dong, N. Ren, Y. Tang, Y. Wang, Y. Zhang, W. Hua, Z. Gao, *J. Am. Chem. Soc.* **2003**, *125*, 4976–4977.
[20] Y. Xia, R. Mokaya, *J. Mater. Chem.* **2005**, *15*, 3126–3131.
[21] A.-H. Lu, W. Schmidt, N. Matoussevitch, H. Bönnemann, B. Spliethoff, B. Tesche, E. Bill, W. Kiefer, F. Schüth, *Angew. Chem. Int. Ed.* **2004**, *43*, 4303–4306.
[22] F. Schüth, *Angew. Chem. Int. Ed.* **2003**, *42*, 3604–3622.
[23] J. Lee, S. Jin, Y. Hwang, J.-G. Park, H. M. Park, T. Hyeon, *Carbon* **2005**, *43*, 2536–2543.
[24] J. Lee, D. Lee, E. Oh, J. Kim, Y.-P. Kim, S. Jin, H.-S. Kim, Y. Hwang, J. H. Kwak, J.-G. Park, C. H. Shin, J. Kim, T. Hyeon, *Angew. Chem. Int. Ed.* **2005**, *44*, 7427–7432.
[25] H. Yang, D. Zhao, *J. Mater. Chem.* **2005**, *15*, 1217–1231.
[26] S. I. Nikitenko, Y. Koltypin, O. Palchik, I. Felner, X. N. Xu, A. Gedanken, *Angew. Chem. Int. Ed.* **2001**, *40*, 4447–4449.
[27] Z. Sun, H. Yuan, Z. Liu, B. Han, X. Zhang, *Adv. Mater.* **2005**, *17*, 2993–2997.

Received: February 15, 2007
Published Online: June 29, 2007

 © 2007 Wiley-VCH Verlag GmbH & Co. KGaA, Weinheim 

DOI: 10.1002/ejic.200700314

# Structurally Characterized Erbium Alkoxides for Use as an Amphoteric Dopant in PErZT Ceramic Thin Film and Nanoparticles

**Timothy J. Boyle,*[a] Leigh Anna M. Ottley,[a] Luke N. Brewer,[b] Jennifer Sigman,[b] Paul G. Clem,[b] and Jacob J. Richardson[c]**

**Keywords:** Ceramics / Perovskites / Nanomaterials / Lanthanide alkoxides / PZT

A family of erbium alkoxides [$Er(OR)_3$] was prepared from the reaction of $Er[N(SiMe_3)_2]_3$ with a series of alcohols (HOR) in selected solvents and crystallographically characterized as: $[Er(\mu\text{-Onep})_2(Onep)]_4$, (**1**), $[Er_4(\mu_4\text{-O})(\mu_3\text{-Onep})(\mu\text{-Onep})_5(Onep)_4(py)_3]$ (**3**), $Er_3(\mu_3\text{-O}t\text{Bu})_2(\mu\text{-O}t\text{Bu})_3(O t\text{Bu})_4(HO t\text{Bu})_2$ (**4**), $Er_3(\mu_3\text{-O})(\mu\text{-O}t\text{Bu})_4(O t\text{Bu})_3(py)_3$ (**7**), $Er(dmp)_3(solv)_3$ [solv = thf (**9**), py (**10**)], $[Er(\eta\text{-dip})(dip)_2]_2$ (**11**), $Er(dip)_3(thf)_2$ (**12**), $[Er(\mu\text{-OH})(dbp)_2(thf)]_2$ (**15**), $Er(dbp)_3(py)_2$ (**16**), $[Er(\mu\text{-tps})(tps)_2]_2$ (**17**), $Er(tps)_3(solv)_3$ [solv = thf (**18**) and (py) (**19**)] where Onep = neopentoxide ($OCH_2CMe_3$), O*t*Bu = *tert*-butoxide ($OCMe_3$), dmp = 2,6-dimethylphenoxide [$OC_6H_3(Me)_2$-2,6], dip = 2,6-diisopropylphenoxide [$OC_6H_3(CHMe_2)_2$-2,6], dbp = 2,6-di-*tert*-butylphenoxide [$OC_6H_3(CMe_3)_2$-2,6], tps = triphenylsiloxide [$OSi(C_6H_5)_3$], tol = toluene, thf = tetrahydrofuran, and py = pyridine. The structures observed and data collected for the Er family of compounds are, in general, consistent with those reported previously for the Dy congeners over the range of solvated mono-, di-, tri-, and tetranuclear species. Representative members of the $Er(OR)_3$ precursors were used for the production of a PErZT precursor solution, which was subsequently used to generate thin films and nanoparticles. Further, these select Er precursors were used to generate $Er_2O_3$ nanoparticles. The full characterization of this family of compounds is reported along with the results of the materials investigations.

(© Wiley-VCH Verlag GmbH & Co. KGaA, 69451 Weinheim, Germany, 2007)

## Introduction

The perovskite phase of lead zirconium titanate (PZT) has found utility in a wide range of applications including ferroelectric nonvolatile random access memories, sports equipment, window tinting, sensors, smart cards, and numerous other electronic applications.[1–6] However, PZT ceramic materials demonstrate rapid fatigue when cycled on standard platinized silica (Pt/Si) supports. Recently, we reported on the "aliovalent cation effect" (ACE) where the PZT thin films fatigue properties were improved through selective doping with lanthanide (Ln) cations that could occupy either the A or B site.[7,8] In particular, the Dy-doped PZT films (PDyZT) were found to possess high remanent polarization ($P_r$), high dielectric constant ($\varepsilon'$), and reduced fatigue when cycled on Pt/Si wafers.[7,8] Due to the void of acceptable dysprosium alkoxide [$Dy(OR)_3$] precursors (see Table 1), it was necessary to synthesize and characterize a series of systematically varied $Dy(OR)_3$ compounds (21 new compounds) to determine the optimal Dy-dopant precursor.[8] From this novel family of compounds, the 2,6-diisopropylphenoxide (dip) derivative yielded the highest quality PDyZT films with impressive fatigue resistance. In an effort to further explore this phenomenon we were interested in determining where the edges of the ACE stopped. Fortunately, the Ln series possesses a systematic change in the +3 Ln cations, which allows for a controlled probing of the ACE phenomenon in PZT ceramic thin films. However, for the smaller lanthanides, there are surprisingly few structurally characterized alkoxides available in the literature.[9–11]

Therefore, to further develop this neglected area and identify new sol-gel precursors, we undertook the synthesis and characterization of a systematically varied family of $Er(OR)_3$ in a variety of solvents. These compounds were isolated following Equation (1), where the alcohol (H-OR) ranged from H-Onep = neopentyl alcohol ($H\text{-}OCH_2CMe_3$), H-O*t*Bu = *tert*-butyl alcohol ($H\text{-}OCMe_3$), H-dmp = 2,6-dimethylphenol [$H\text{-}OC_6H_3(Me)_2$-2,6], H-dip = 2,6-diisopropylphenol [$H\text{-}OC_6H_3(CHMe_2)_2$-2,6], H-dbp = 2,6-di-*tert*-butylphenol [$H\text{-}OC_6H_3(CMe_3)_2$-2,6], H-tps = triphenylsilanol [$H\text{-}OSi(C_6H_5)_3$] using a variety of solvents: tol = toluene, thf = tetrahydrofuran, and py = pyridine. The general matrix used in this study led to the synthesis of compounds **1**–**19** and is shown in Table 1 along with a comparison to the $Dy(OR)_3$ compounds that were previously

[a] Sandia National Laboratories, Advanced Materials Laboratory, 1001 University Boulevard SE, Albuquerque, New Mexico 87105, USA
Fax: +1-505-272-7336
E-mail: tjboyle@Sandia.gov
[b] Sandia National Laboratories, New Mexico, P. O. Box 5800, Albuquerque, NM 87185-1411, USA
[c] University of California – Santa Barbara, Materials Department, Santa Barbara, CA 93106-5050, USA

 © 2007 Wiley-VCH Verlag GmbH & Co. KGaA, Weinheim 

Table 1. List of structure types isolated for the matrix of ligands and solvents used to explore $Er(OR)_3$ and $Dy(OR)_3$ structures. The nuclearity is listed and in parentheses the type of interaction used by the ligands to form the molecule and/or the number of solvent molecules bound.

| Er | tol | thf | py | HOR |
|---|---|---|---|---|
| Onep | 1 tetra (μ, 0) | [a] | 3 tri (μ and $\mu_3$; 3) | [a] |
| O*t*Bu | [a] | [a] | 7 tri (μ and $\mu_3$; 3) | 4 tri (μ and $\mu_3$; 2) |
| dmp | [a] | 9 mono (3) | 10 mono (3) | [a] |
| dip | 11 di (π; 0) | 12 mono (2) | [a] | [a] |
| dbp | [a] | 15 di (2) | 16 mono (2) | [a] |
| tps | 17 di (μ, 0) | 18 mono (3) | 19 mono (3) | |
| **Dy** | **tol** | **thf** | **py** | **$NH_3$** |
| Onep | tetra (μ, 0) | tri (μ and $\mu_3$; 2) | tri (μ and $\mu_3$; 2) | hex |
| O*t*Bu | tri (μ and $\mu_3$) | tri (μ and $\mu_3$; 2) | tri (μ and $\mu_3$; 2) | [a] |
| dmp | di (π; 0) | mono (3) | mono (3) | linear tri (2) |
| dip | di (π; 0) | mono (2) | mono (3) | mono (2) |
| dbp | mono (0) | mono (1) | mono (2) | mono (1) |
| tps | di (μ) | mono (3) | mono (3) | [a] |

[a] No acceptable crystal solutions reported.

isolated.[8] From this matrix, the following $Er(OR)_3$ compounds were crystallographically characterized as: $[Er(\mu\text{-Onep})_2(Onep)]_4$ (**1**), $[Er_4(\mu_4\text{-O})(\mu_3\text{-Onep})(\mu\text{-Onep})_5(Onep)_4(py)_3]$ (**3**), $Er_3(\mu_3\text{-O}t\text{Bu})_2(\mu\text{-O}t\text{Bu})_3(O t\text{Bu})_4(HO t\text{Bu})_2$ (**4**), $Er_3(\mu_3\text{-O})(\mu\text{-O}t\text{Bu})_4(O t\text{Bu})_3(py)_3$ (**7**), $Er(dmp)_3(solv)_3$ [solv = thf (**9**), py (**10**)], $[Er(\eta\text{-dip})(dip)_2]_2$ (**11**), $Er(dip)_3(thf)_2$ (**12**), $[Er(\mu\text{-OH})(dbp)_2(thf)]_2$ (**15**), $Er(dbp)_3(py)_2$ (**16**), $[Er(\mu\text{-tps})(tps)_2]_2$ (**17**), $Er(tps)_3(thf)_3$ (**18**), $Er(tps)_3(py)_3$ (**19**). The synthesis and full characterization of these compounds are discussed. Suitable crystals were not isolated for compounds **2** (Onep/thf), **5** (O*t*Bu/tol), **6** (O*t*Bu/thf), **8** (dmp/tol), **13** (dip/py), **14** (dbp/tol) and additional discussion of these compounds will not be pursued since their structures were not unequivocally established.

$$Er[N(SiMe_3)_2]_3 + 3\ H\text{-}OR' \rightarrow Er(OR')_3 + 3\ H\text{-}N(SiMe_3)_2 \quad (1)$$

Representative species from this novel family of compounds were used to explore their utility for the production of ceramic materials. The ACE for PErZT thin films was probed using **11** as the dopant precursor due to the similarity with the Dy counterpart (Table 1).[7,8] Further, since new properties were expected on the nanoscale, attempts were made to generate $Er_2O_3$ and PErZT nanoceramics. With this wide variety of structurally varied species, it was possible to further explore the "precursor structure argument" (PSA)[12–16] for nanoparticle morphology predictions. A solution route to nanoparticles of $Er_2O_3$ was discovered using **1** and **11**. Full details of the synthesis, characterization, and subsequent properties of these precursors and materials are presented.

## Results and Discussion

A systematically varied series of $Er(OR)_3$ was required in order to initiate the material evaluation of Er ceramics with controlled properties. A search of the literature reveals only two $Er(OR)_3$ had been previously crystallographically characterized including $Er_5(\mu_5\text{-O})(\mu_3\text{-O}i\text{Pr})_4(\mu\text{-O}i\text{Pr})_4(O i\text{Pr})_5$[10,11] and $Er(dip)_3(thf)_2$.[9] The remainder of alkoxy-like species possess other metals,[17–21] halides,[22] or polyfunctional ligands[23] which prevents use for generation of high quality ceramic oxide materials due to the potential cross cation, anion, and/or residual ligand contamination. Due to the lack of available $Er(OR)_3$ compounds, it was necessary to synthesize a series of precursors to determine the optimal species. A study of a matrix of sterically varied precursors in different solvents was undertaken (see Table 1). For this report, only those compounds that were crystallographically characterized will be discussed.

### Synthesis

On the basis of our previous experience with the problems associated with the ammoniacal route, we elected to use the amide/alcohol metathesis route that proved beneficial for the Dy system.[8] The $Er(NR_2)_3$, where $NR_2 = N(SiMe_3)_2$, was synthesized according to established routes involving the metathesis reaction between $ErCl_3$ and 3 equiv. of $KNR_2$ in thf.[8,24–29] The resultant powder isolated from the metathesis route was sublimed and crystallized to ensure pure starting material. It is of note that purification of the $Er(NR_2)_3$ is critical to the successful isolation of crystalline material. Once isolated, this precursor was treated with a variety of alcohols as shown in Equation (1) (Table 1).

The majority of samples remained clear after stirring for 12 h; however, those that formed a precipitate, typically the more sterically demanding ligands, were warmed slightly to redissolve the powder. Crystals were either isolated by slow evaporation or rotary evaporation of the volatile portion of the reaction mixture followed by cooling the reaction mixture to –35 °C, if necessary.

FTIR data of the resultant powders revealed no amide stretches and, for the majority of samples no –OH stretches, which implies complete substitution had occurred between the amide and the alcohol. Two exceptions to this were the spectra noted for compound **4** and **15**, which showed broad IR stretches around 3000 $cm^{-1}$ associated with the bound H-O*t*Bu and the -OH, respectively. In general, elemental analyses were found to be consistent with the single-crystal X-ray structures isolated (vide infra) for these compounds. Those that were off slightly from expected values were solvated species and the high volatility of the bound solvent often causes significant problems in obtaining accurate analyses.[8,30] Due to the paramagnetic nature of the Er metal center, we were unable to get meaningful NMR spectroscopic data either in solution or solid-state. Therefore, single-crystal X-ray diffraction studies were undertaken to assist in elucidating the identity of the final products isolated.

### Crystal Structures

As mentioned only two structures of $Er(OR)_3$ have previously been reported.[9–11] Obviously, no general trends can

 © 2007 Wiley-VCH Verlag GmbH & Co. KGaA, Weinheim 

be discerned from this limited set of precursors but comparisons to literature compounds will be made when appropriate. Figures 1, 2, 3, and 4 are the structure plots of representative crystal structures for this family of compounds. The various compounds are discussed below in order of the ligand increasing steric bulk of the ligand.

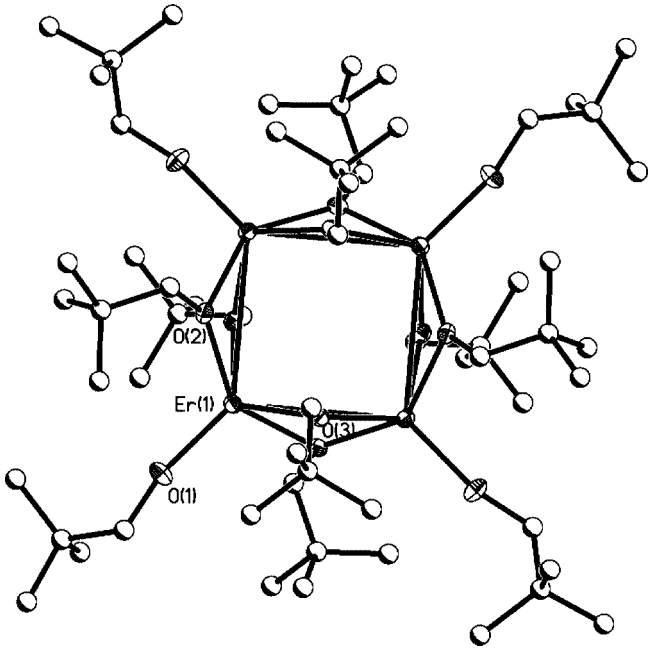


Figure 1. Structure plot of **1**. Thermal ellipsoids of heavy atoms are drawn at the 30% level and carbon atoms are shown as stick and ball for clarity. Selected bond lengths [Å]: Er(1)–O(1) 2.033(5); Er(1)–O(2) 2.241(6); Er(1)–O(3) 2.244(6). Selected bond angles [°]: O(1)–Er(1)–O(3) 122.8(3); O(1)–Er(1)–O(2) 112.9(3); O(3)–Er(1)–O(2) 72.7(2); O(1)–Er(1)–O(3) 118.3(3); O(2)–Er(1)–O(3) 89.5(3); O(1)–Er(1)–O(2) 105.8(3); O(3)–Er(1)–O(2) 86.9(2); O(3)–Er(1)–O(2) 71.7(2).

Using the more sterically demanding Onep ligand reduced the nuclearity and prevented the formation of an oxo ligand as noted for the smaller O*i*Pr derivative $Er_5(\mu_5\text{-}O)(\mu_3\text{-}OiPr)_4(\mu\text{-}OiPr)_4(OiPr)_5$.[10,11] The resultant species, identified as $[Er(\mu\text{-}Onep)_2(Onep)]_4$ (**1**), is consistent with the other Ln- and Group 3 neopentoxide species (Figure 1)[31] wherein, each of the four trigonal bipyramidal (TBP) Er metal centers possess two μ-Onep and one Onep ligand. Attempts to isolate this compound using the Lewis basic solvents thf (**2**) did not lead to X-ray quality crystals; however, from py the tetramer observed in **1** was reduced to a trinuclear species surprisingly forming an oxo species, $[Er(\mu_3\text{-}O)(\mu\text{-}Onep)_6(Onep)_4(py)_3]$ (**3**). The source of the oxo species is not known as of yet and typically not observed for the Onep derivatives, unless esterification mechanisms from side reactions with carboxylic acids occur but may be due to adventitious water in the solvent.[30–32]

Increasing the steric bulk to the O*t*Bu groups, led to crystallization of the trinuclear **4** which had additional HO*t*Bu bound to it, as shown in Figure 2. Previously, we isolated a Ce/O*t*Bu tetramer[30] that did not possess any

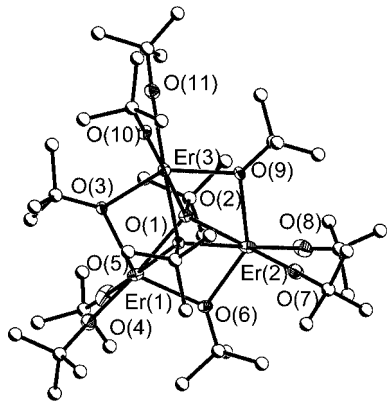


Figure 2. Structure plot of **4**. Thermal ellipsoids of heavy atoms are drawn at the 30% level and carbon atoms are shown as stick and ball for clarity. Selected bond lengths [Å]: Er(1)–O(1) 2.305(3); Er(1)–O(2) 2.371(3); Er(1)–O(3) 2.269(3); Er(1)–O(4) 2.525(4); Er(1)–O(5) 2.067(3); Er(1)–O(6) 2.250(3). Selected bond angles [°]: O(5)–Er(1)–O(6) 106.17(13); O(5)–Er(1)–O(3) 104.93(13); O(6)–Er(1)–O(3) 143.78(12); O(5)–Er(1)–O(1) 109.45(13); O(6)–Er(1)–O(1) 76.35(12); O(3)–Er(1)–O(1) 76.16(12); O(5)–Er(1)–O(2) 177.71(13); O(6)–Er(1)–O(2) 74.47(12); O(3)–Er(1)–O(2) 73.78(12); O(1)–Er(1)–O(2) 68.48(11); O(5)–Er(1)–O(4) 74.73(14); O(6)–Er(1)–O(4) 101.31(13); O(3)–Er(1)–O(4) 104.40(12); O(1)–Er(1)–O(4) 175.59(12); O(2)–Er(1)–O(4) 107.37(12).

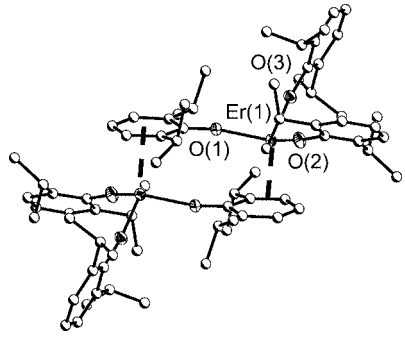


Figure 3. Structure plot of **11**. Thermal ellipsoids of heavy atoms are drawn at the 30% level and carbon atoms are shown as stick and ball for clarity. Selected bond lengths [Å]: Er(1)–O(1) 2.096(18); Er(1)–O(3) 2.069(17); Er(1)–O(2) 2.095(18); Er(1)-ring 2.81 Å. Selected bond angles [°]: O(2)–Er(1)–O(1) 109.3(7); O(2)–Er(1)–O(3) 102.5(7); O(3)–Er(1)–O(1) 106.3(7); O(1)–Er(1)–ring 108.1(9); O(2)–Er(1)–ring 83.9(9); O(3)–Er(1)–ring 140.6(8).

Lewis basic solvents (i.e., thf, py, or HO*t*Bu) however, the Er corollary could not be isolated without bound solvents as noted for the pyridine adduct, $Er_3(\mu_3\text{-}O)(\mu\text{-}OtBu)_4(OtBu)_3(py)_3$ (**7**). Again, the py adduct appears to produce the oxo which argues for water present in the py; however, numerous structures using the same solvent did not yield the oxide, so the origin of the oxo is still unproven. This complex is similar to **4** and other trinuclear species where the terminal ligands are now replaced by these stronger.

Aryl oxides are often used to control nuclearity because the steric bulk around the metal center can be easily altered.[8,12,13,30,33–36] We routinely use the most sterically demanding di-*ortho*-substituted phenoxide ligands to induce as large an effect as possible. The resulting products are again discussed in increasing steric demand (dmp, dip,

 © 2007 Wiley-VCH Verlag GmbH & Co. KGaA, Weinheim 

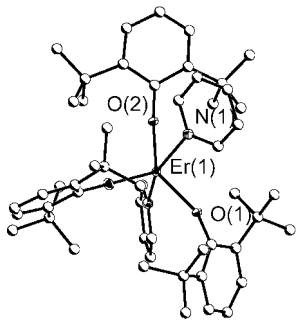


Figure 4. Structure plot of **16**. Thermal ellipsoids of heavy atoms are drawn at the 30% level and carbon atoms are shown as stick and ball for clarity. Selected bond lengths [Å]: Er(1)–O(2) 2.095(4); Er(1)–O(1) 2.161(3); Er(1)–O(1A) 2.161(3); Er(1)–N(1) 2.469(4); Er(1)–N(1A) 2.469(4). Selected bond angles [°]: O(2)–Er(1)–O(1) 112.54(8); O(2)–Er(1)–O(1A) 112.54(8); O(1)–Er(1)–O(1A) 134.92(16); O(2)–Er(1)–N(1) 101.96(9); O(1)–Er(1)–N(1) 81.96(12); O(1)–Er(1)–N(1A) 88.91(13); O(2)–Er(1)–N(1A) 101.96(9); O(1A)–Er(1)–N(1A) 88.91(13); O(1A)–Er(1)–N(1) 88.96(12); N(1)–Er(1)–N(1A) 156.08(18).

dbp). For the dmp derivative, large clear crystals were easily isolated from toluene but the diffraction was poor and an acceptable structure solution could not be garnered for **8**. Therefore, we employed the Lewis basic solvents to assist in growing acceptable crystals. For both thf and py, mononuclear species with three solvents to form an octahedral geometry were isolated as $Er(dmp)_3(solv)_3$ [solv = thf (**9**) and py (**10**)].

Increasing the steric bulk of the *ortho* substituent to isopropyl groups led to the isolation of **11** (Figure 3). The η-interaction noted for **11** is the same as previously noted for the La,[37] Nd,[9] and Dy[8] systems. Again, the η-interaction was easily disrupted using Lewis basic solvents forming the trigonal bipyramidal (TBP) monomeric species **12** for the thf adduct.

Using the most sterically demanding dbp ligand, crystals of the unsolvated species **14** could not be isolated in high quality; however, in the presence of a Lewis base, two very different species were characterized. Out of thf, a dinuclear thf adduct was isolated as **15**. Surprisingly, the dinuclear species possesses a μ-OH group which was not identified for the Dy series[8] but have been reported for other lanthanides species including, $[(\mu\text{-OH})Yb(OAr)_2(thf)]_2$ (OAr = dbp,[38] dbp-But-4,[38,39]) and $[(\mu\text{-OH})Sm(dbp\text{-Me-}4)_2(OPPh_3)]_2$.[40] Increasing the Lewis basicity of the solvent to py led to the TBP monomer **16** (Figure 4). It is most likely not due to adventitious water in the solvent or it would have been observed in the Dy system.[8]

Siloxide ligands offer the potential for the production of Si-containing materials and slightly different ligand properties both sterically and electronically. Therefore, we added the tps ligand into our structural investigation. The tps derivatives isolated for the Er system are consistent with the $Dy(tps)_3$ structure[8] wherein a dinuclear complex was isolated from tol (**17**) with μ-tps and terminal tps in standard edge-shared tetrahedral-bound metal centers. Subsequent monomers were isolated from Lewis basic solvents as **18** and **19**, for thf and py. The bulky tps ligands allow for tetrahedral (Td) arrangements for the metal centers of **17** and octahedral (Oh) geometries for **18** and **19** through the binding of three solvent molecules.

In general, the structures noted for the Er system were consistent with the $Dy(OR)_3$ precursors previously reported;[8] however, **15** does prove that unaccounted variations are possible, and probable. Surprisingly, a number of compounds could not be successfully isolated for the Er system that were easily isolated for the Dy system.[8] Subtle effects that dictate crystal growth are at play and require further investigations.

## Materials

With these compounds successfully characterized, a sufficient number and variety of species were available for systematic materials structure–property investigations. Two systems were investigated: Er-doped PZT (or PErZT) thin films for electronic properties and nanomaterials of $Er_2O_3$ and PErZT.

### *Film Characteristics*

The precursor solutions of $Pb_{0.98}(Er)_{0.04}(Zr_{0.3}Ti_{0.7})_{0.98}O_3$ [PErZT(4/30/70)] and $Pb_{0.98}(Er)_{0.04}(Zr_{0.52}Ti_{0.48})_{0.98}O_3$ [PErZT(4/52/48)] were prepared as described in the experimental section. Selection of the Er dopant on the B site of the perovskite is based on previous studies and a dopant concentration of 4% Er was selected to maximize the possible effects of the dopant without creating unwanted secondary phases. Dektak profilometer film thickness measurements were 150–180 nm after the deposition of 4 layers. X-ray diffraction patterns and hysteresis loops are shown in Figure 5, a–d. Both films were found to be polycrystalline, single-phase perovskite films (Figure 5, b and d) with an enhanced (111) orientation, attributed to the templating effects of the $Pt(111)/Ti/SiO_2/Si$ substrates. The PErZT(4/30/70) films also showed a more pronounced (100) peak than PErZT(4/52/48) films. This is consistent with the room temperature tetragonal structure of a PZT(30/70) film compared to the room temperature morphotropic structure of a PZT(52/48) film. The previously reported PZT(30/70) films isolated under identical conditions used for the PErZT films, had narrow and square loops with reasonable properties: spontaneous polarization ($P_r$) = 24 μC/cm$^2$, coercive field ($E_c$) = 93 kV/cm$^2$, a dielectric constant ($\varepsilon'$) = 396, and $\tan\delta$ = 0.007 (10 kHz, 100 mV). For the PDyZT(4/30/70) films, comparable values were obtained: $P_r$ = 26 μC/cm$^2$, $E_c$ = 126 kV/cm, $\varepsilon'$ = 343, and $\tan\delta$ = 0.009 (10 kHz, 100 mV).[8]

After top-electrodes were sputter-deposited, the ferroelectric properties were discerned for PErZT films. Hysteresis loops for the PErZT(4/30/70) and PErZT(4/52/48) films are shown in Figure 5a and Figure 5c, respectively. In agreement with the Dy-doped films, the PErZT(4/30/70) films displayed a $P_r$ = 30 μC/cm$^2$, $E_c$ = 171 kV, $\varepsilon'$ = 366 and $\tan\delta$ = 0.03. For the PErZT(4/52/48) films slightly lower ferroelectric property values were obtained, with a $P_r$ =

 © 2007 Wiley-VCH Verlag GmbH & Co. KGaA, Weinheim 

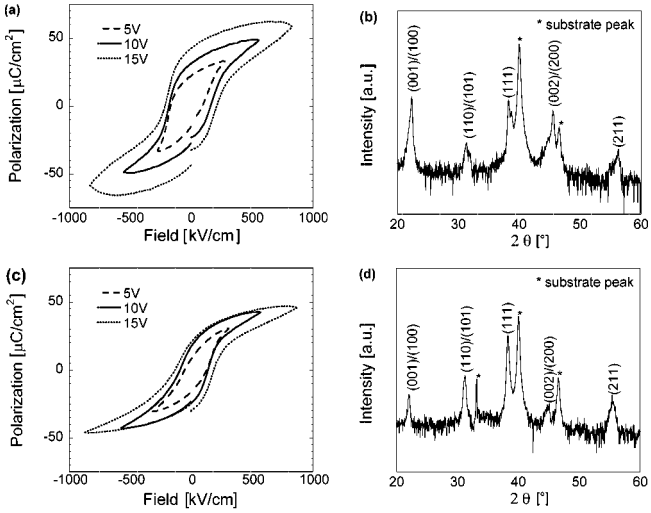


Figure 5. Characterization of PErZT(4/30/70): (a) hysteresis loop, (b) XRD; and characterization of PErZT (4/52/48): (c) hysteresis loop, (d) XRD.

20 μC/cm$^2$ and an $E_c$ = 137 kV; however, the dielectric properties improved: $\varepsilon'$ = 564 and tan $\delta$ = 0.01. The higher $P_r$ observed in the PErZT(4/30/70) is attributed to the room temperature tetragonal composition of this film while the higher $\varepsilon'$ observed in the PErZT(4/52/48) is attributed to the film's room temperature morphotropic boundary composition. Unfortunately, the fatigue testing for the Er-doped films did not show the significant improvement noted for the Dy doping.[7,8] However, this sets a lower limit for the ACE phenomenon and the slightly larger Y and Ho cations are now under investigation.

### *Nanoparticles*

With this family of well-characterized compounds in hand, it was decided to investigate their utility as precursors for nanomaterials. Nanoparticles are of interest due to the novel properties expected for materials on this size scale. In the literature, 5 to 30 nm sized erbium(III) oxide nanocrystals dispersed in titania have been previously isolated by employing $Er(NO_3)_3$ in an inverse microemulsion process followed by a heat treatment at 600 °C.[41,42] The resulting materials were identified as $Er_2O_3$ by powder XRD and photoluminescent measurements.[41,42] Recently, a solution route using decomposition of lanthanide acetylacetonate in oleic acid, oleylamine, and octadecene at 310 °C yielded $Er_2O_3$ nanoparticles.[43] We are interested in controlling the properties of nano-$Er_2O_3$ for electrooptic applications. Therefore, we undertook two different approaches to generate nanoparticles that were more amenable to large-scale syntheses: (a) solution precipitation and (b) solvothermal using our novel representative $Er(OR)_3$ precursors **1** and **11**. Both of the processing routes are greatly simplified in comparison to the microemulsion route,[41,42] are amenable to large scale synthesis, and require significantly lower processing temperatures than the Ln-acac route.[43] The results for solution precipitation of **1** and **11** are presented, followed by the results of the solvothermal routes.

### *Solution Precipitation*

The reaction pathway for both of the alkoxides appeared to follow identical pathways, wherein the pale pink solution of the precursor immediately formed a white precipitate upon injection into the refluxing solution. The subsequent isolation also proceeded in an identical manner. Therefore, all of the observed differences in the generated manner can only be attributed to the variations in pendant hydrocarbon chain of the alkoxide ligand.

For **1**, the resulting powder was found to be made of 7–8 nm highly crystalline $Er_2O_3$ (see Figure 6) particles, as found by TEM imaging, the observed SAED pattern, and only Er and O observed in the EDS spectrum (Cu is background from the grid). The PXRD spectrum was fairly broad but consistent with $Er_2O_3$ nanoparticles of 1.7 nm, based on the Scherrer equation calculations. In comparison, using **11** (Figure 7) 3–4 nm nanoparticles of $Er_2O_3$ were formed as characterized by TEM and EDS analyses with a noted decrease in crystallinity by SAED. For select grains, HRTEM images clearly show the lattice fringes of $Er_2O_3$. The PXRD was broad peaks consistent with $Er_2O_3$ wherein calculations indicated nanoparticles of 1.9 nm were formed.

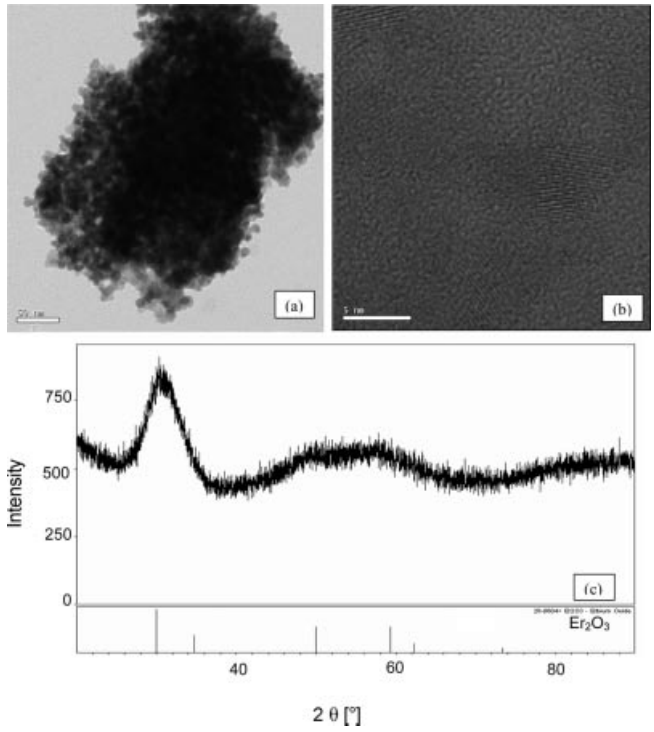


Figure 6. TEM images of $Er_2O_3$ generated from **1** using the solution precipitation route: (a) TEM image (50 nm scale bar), (b) HRTEM (5 nm scale bar), and (c) PXRD.

The difference in the observed particle sizes between the TEM and XRD measurements may be due to several factors in the X-ray diffraction measurement. Particle size affects the PXRD pattern by broadening the peak. Several

 © 2007 Wiley-VCH Verlag GmbH & Co. KGaA, Weinheim 

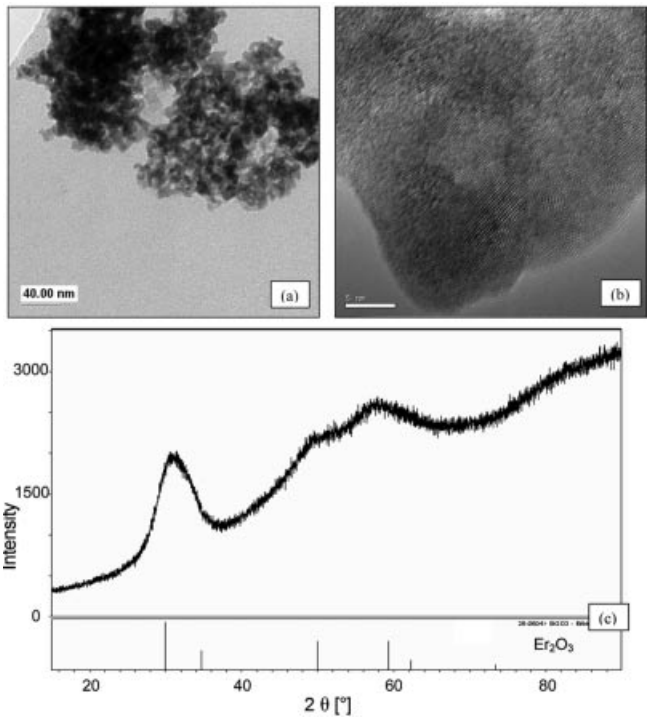


Figure 7. TEM images of $Er_2O_3$ generated from **11** using the solution precipitation route: (a) TEM image (40 nm scale bar), (b) HRTEM (5 nm scale bar), and (c) PXRD.

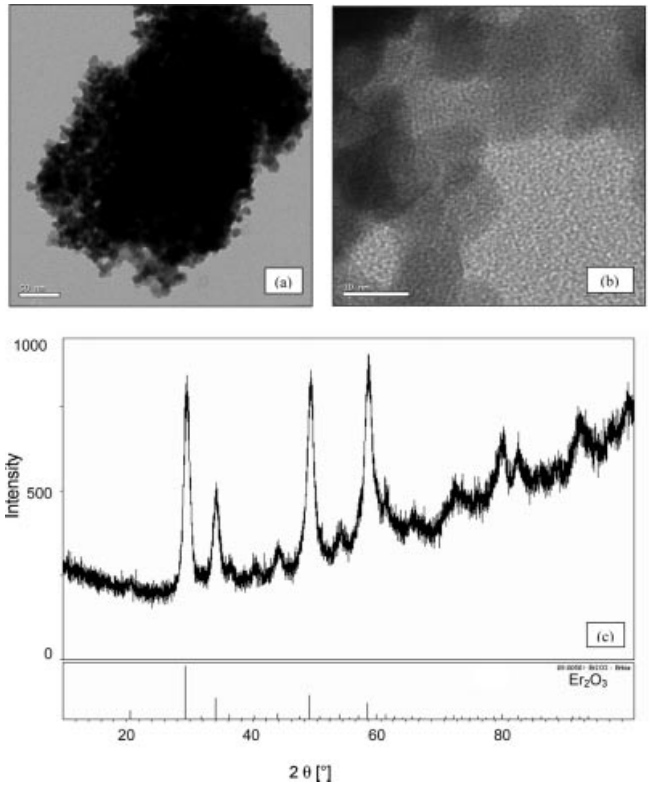


Figure 8. Nanoparticles from Parr bomb using **1**: (a) TEM image (50 nm scale bar), (b) HRTEM(10 nm scale bar), and (c) PXRD.

factors contribute to this peak broadening, including instrument line broadening, reduction in particle size, variation in particle composition, and microstrain. Of these possible effects, variation in particle composition and some instrument line broadening may account for the systematic underestimation of the particle size from the PXRD measurement. Despite this difference, the PXRD measurement of particle size is useful for efficient measurement of many samples and for particle size measurement on materials with strong agglomeration.

In general, from this study the formation of crystalline $Er_2O_3$ was more easily achieved with **1** than **11**. Upon introduction of a Lewis base, both compounds alter their original structure forming a trinuclear solvated species for **1** (as evidenced by **4**, and **7**) and a solvated monomer for **11** (**9**, **10**, **12**, **16**, **18**, and **19**). Using the PSA, the size of the resultant nanoparticles could be reasoned; however, the morphologies did not follow any trends. The faster and more uniform the nanoparticles form, the longer they will have to crystallize under the conditions we used. The particle precursor for **1** is more likely to have a larger nucleation seed in comparison to that of monomeric **11**. Thus, **1** yields higher quality nanoparticles as determined by the nature of the solvated structure.

### *Solvothermal Synthesis*

Under solvothermal conditions, a Parr digestion bomb of the same solution was investigated to determine processing variations for the same compounds. For **1**, spheroidal nanoparticles of $Er_2O_3$ were isolated ranging from 10–

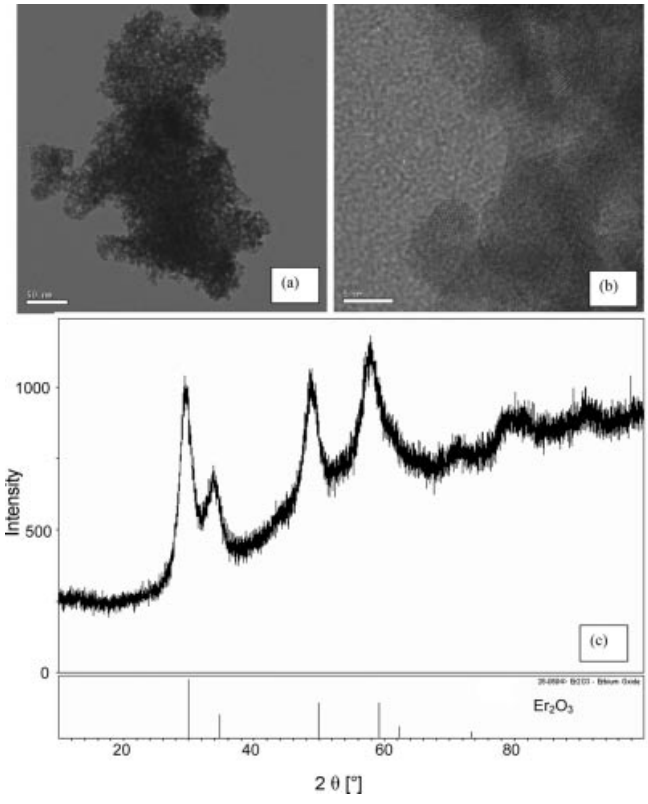


Figure 9. Nanoparticles from Parr bomb using **11**: (a) TEM image (50 nm scale bar), (b) HRTEM (5 nm scale bar), and (c) PXRD.

 © 2007 Wiley-VCH Verlag GmbH & Co. KGaA, Weinheim 

15 nm in size verified by EDS and PXRD (Figure 8). Surprisingly, the PXRD pattern was much sharper with calculated sizes of 7.0 nm. For **11**, more spherical shaped nanoparticles were isolated in the same approximate size range of 10–15 nm (Figure 9). The particles were more uniform in morphology and size in comparison to **1** but the particles appear less crystalline by PXRD pattern; however, HRTEM reveals the crystalline lattice planes. The broad peaks of PXRD pattern were calculated to generate particles of 3.7 nm. The TEM images and those calculated from the XRD pattern have a significant difference again the issues discussed previous (vide infra) may account for this variance.

In general, the structures of the precursors do not appear to play as large a role in determining the morphology of the final Ln-based nanomaterials isolated as noted for transition metals.[12–16] However, there are significant differences based on the structural considerations of **1** vs. **11**. The crystallinity of the final material appears to be higher with the bomb preparative routes vs. the solution precipitation methods.

### *PErZT Nanoparticles*

Due to the success with the simple Er system, it was of interest to determine if more complex nanoparticles could be generated from the same solution under similar conditions. Attempts to generate PErZT nanomaterials were undertaken using the same precursor thin film solution with **1** as the dopant and the process for preparing nano-$Er_2O_3$ as discussed above. The solution precipitation route yielded large nanoparticles on the order of 30 nm in size (Figure 10). EDS indicates each of the cations is present; however, the PXRD pattern shows only $ErTiO_3$ is present as a crystalline material. The absent Pb and Zr cations are probably phase separated as amorphous $PbZrO_3$, which requires significantly higher temperatures to crystallize. Alternatively, the solvothermal route led to the isolation of particles on the size of 5–10 nm (Figure 11) with each of the cations present in the EDS. Interestingly, highly crystalline particles (HRTEM with *d* spacing ca. 3.0 Å) were observed in the $PbTiO_3$ structure that is consistent with PZT (3.1 Å). Further work to improve the uniformity and consistency of the multication nanomaterial in order to explore the properties of these electroceramic materials is underway.

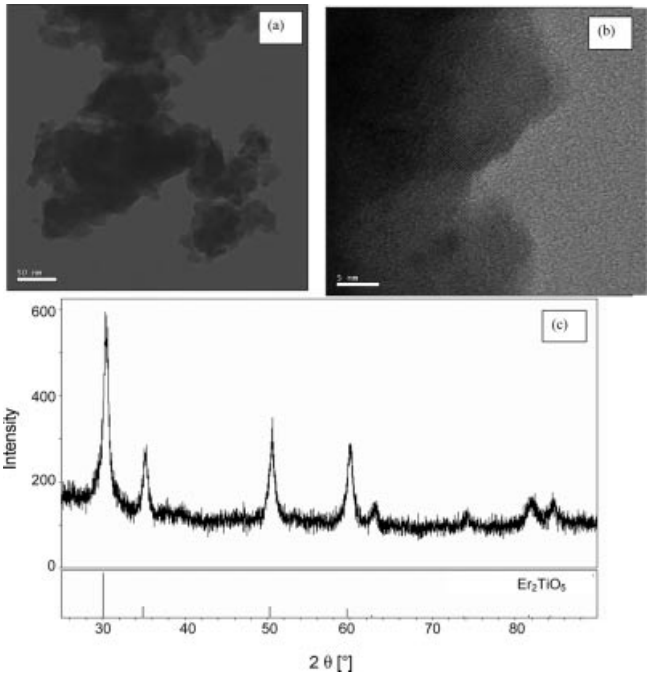


Figure 10. PErZT nanoparticles MeIM/$H_2O$ prep: calcined at 650 °C: (a) TEM image (50 nm scale bar), (b) HRTEM (5 nm scale bar), and (c) PXRD.

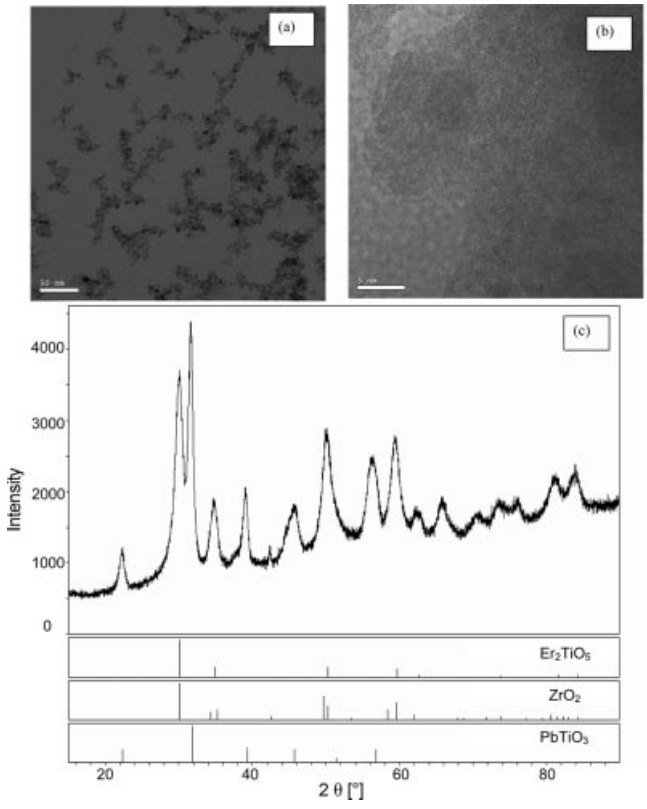


Figure 11. PErZT nanoparticles bomb prep: calcined at 650 °C: (a) TEM image (50 nm scale bar), (b) HRTEM (5 nm scale bar), and (c) PXRD.

## Conclusions

We have synthesized and fully characterized a family of $Er(OR)_3$ from the reaction of $Er[N(SiMe_3)_2]_3$ and a variety of commercially available alcohols that systematically varied in steric bulk. The isolated compounds are structurally similar to the $Dy(OR)_3$ species[8] isolated previously with nuclearity ranging from mono- (**9**, **12**, **16**, **18**, **19**), to bis- (**11**, **15**, **17**), to tri- (**6**) to tetranuclear (**1**) species. From this set of $Er(OR)_3$ compounds **11** was used to generate PErZT. The ferroelectric properties were consistent with the Dy doped PZT; however, the fatigue properties were not improved as noted for the Dy species.[7,8] Additional work to elucidate the ACE demarcation line is in progress with

 © 2007 Wiley-VCH Verlag GmbH & Co. KGaA, Weinheim 

other large Ln cations. Nanoparticles of $Er_2O_3$ were successfully synthesized and isolated; however, the more complex ternary PErZT yielded mixed size particles of various compositions.

## Experimental Section

All compounds described below were handled with rigorous exclusion of air and water using standard Schlenk line and glove box techniques. All solvents were stored under argon and used as received (Aldrich) in sure seal bottles, including hexanes (hex), tol, thf, and py. The following chemicals were used as received (Aldrich): $ErCl_3$, $KN(SiMe_3)_2$ ($KNR_2$), H-Onep, H-O*t*Bu, H-dmp, H-dip, H-dbp, H-tps, $[Zr(OiPr)_4(HOiPr)]_2$. $Ti(OiPr)_4$ was distilled immediately prior to use and stored under and inert atmosphere. $Er(NR_2)_3$ was synthesized from the reaction of $ErCl_3$ and three equivalents of $LiNR_2$ in thf and purified by sublimation and subsequent crystallization from hexanes.[8] FT-IR data were obtained on a Bruker Vector 22 Instrument using KBr pellets under an atmosphere of flowing nitrogen. Elemental analysis was performed on a Perkin–Elmer 2400 CHN-S/O Elemental Analyzer.

**General Synthesis:** The appropriate HOR was added by a pipette to a stirring mixture of $Er(NR_2)_3$ that was dissolved in desired solvent. After 12 h, if a precipitate formed, the solution was warmed until the precipitate redissolved. After cooling to room temperature, the volatile material was allowed to slowly evaporated or the volume of the reaction was drastically reduced via rotary evaporation. The reaction was then set aside or cooled to –35 °C, if necessary until crystals formed.

**$[Er(\mu\text{-Onep})_2(Onep)]_4$ (1):** See ref.[31].

**$Er(\mu\text{-O})(\mu_3\text{-Onep})(\mu\text{-Onep})_5(Onep)_4(py)_3$ (3):** Used $KNR_2$ (0.500 g, 0.771 mmol), H-Onep (0.204 g, 0.231 mmol) and ca. 10 mL of py. Yield 0.215 g (62.1%). FT-IR (KBr): $\tilde{\nu}$ = 2957 (s), 2906 (w), 2902 (m), 2809 (m), 2747 (w), 2681 (m), 2368 (m), 2348 (m), 1481 (s), 1462 (m,sh), 1394 (s), 1364 (s), 1334 (w), 1266 (m), 1216 (w), 1059 (s), 1061 (s), 1017 (s), 974 (w), 935 (m), 896 (m), 826 (m), 701 (m), 700 (m), 670 (w), 606 (s), 517 (m), 481 (s), 418 (s) $cm^{-1}$. $C_{65}H_{126}Er_4N_3O_{11}$ (1794.76): calcd. C 43.5, H 7.08, N 2.34, for $C_{75}H_{136}Er_4N_5O_{11}$ (**3** + 2py): calcd. C 46.1, H 7.02, N 3.59; found C 46.5, H 7.20, N 3.05.

**$Er_3(\mu_3\text{-O}t\text{Bu})_2(\mu\text{-O}t\text{Bu})_3(O t\text{Bu})_4(HO t\text{Bu})_2$ (4):** Used $KNR_2$ (0.500 g, 0.771 mmol), H-O*t*Bu (0.171 g, 0.231 mmol) and ca. 10 mL of tol. Yield 0.220 g (65.5%). FT-IR (KBr): $\tilde{\nu}$ = 2968 (s), 2362 (s), 2344 (s,sh), 1375 (m), 1356 (w,sh), 1203 (s), 1153 (w), 1142 (w), 1071 (w), 1039 (w,sh), 1004 (s), 938 (m), 920 (m,sh), 845 (m), 766 (w), 753 (w), 700 (m), 681 (m), 636 (w), 527 (m), 479 (m) $cm^{-1}$. $C_{44}H_{99}Er_3O_{11}$ (1306.04): calcd. C 40.47, H 7.64, for $C_{40}H_{89}Er_3O_{11}$ (**4**–1 H-O*t*Bu): calcd. C 38.49, H 7.18; found C 38.6, H 6.93.

**$Er_3(\mu_3\text{-O})(\mu\text{-O}t\text{Bu})_4(O t\text{Bu})_3(py)_3$ (7):** Used $KNR_2$ (0.500 g, 0.771 mmol), H-O*t*Bu (0.171 g, 0.231 mmol) and ca. 10 mL of py. Yield 0.25 g (76.5%). FT-IR (KBr): $\tilde{\nu}$ = 2961 (s), 2362 (s), 2344 (m), 1618 (s), 1561 (m), 1509 (m), 1378 (w), 1242 (m), 1206 (m). 1108 (s), 1061 (s), 1016 (m), 933 (w,sh), 829 (s), 748 (m), 669 (s), 594 (w), 474 (w) $cm^{-1}$. $C_{43}H_{78}Er_3N_3O_8$: cald. C 40.76, N 3.316, H 6.20. $C_{28}H_{63}Er_3O_8$ (**7**–3 py): calcd. C 32.70, H 6.17; found C 32.4, H 6.81.

**$Er(dmp)_3(thf)_3$ (9):** Used $KNR_2$ (0.500 g, 0.771 mmol), H-dmp (0.282 g, 0.231 mmol) and ca. 10 mL of thf. Yield 0.350 g (60.8%). FT-IR (KBr): $\tilde{\nu}$ = 3621 (s), 3066 (w,sh), 3039 (w,sh), 3010 (w,sh). 2957 (s), 2920 (w,sh), 2853 (w,sh), 2722 (w), 2585 (w), 2368 (w), 2345 (w), 1593 (s), 1469 (s), 1441 (s), 1428 (S). 1374 (m,sh), 1290 (s), 1269 (m,sh), 1226 (m), 1153 (m), 1092 (s), 1068 (m), 1039 (m), 1007 (m), 978 (m), 917 (m), 871 (w,sh), 849 (s), 757 (s), 748 (s), 623 (m), 569 (w), 532 (s), 489 (w), 462 (w) $cm^{-1}$. $C_{36}H_{51}ErO_6$ (747.06): calcd. C 57.9, H 6.90; found C 58.31, H 6.92.

**$Er(dmp)_3(py)_4$ (10):** Used $KNR_2$ (0.500 g, 0.771 mmol), H-dmp (0.282 g, 0.231 mmol) and ca. 10 mL of py. Yield 0.450 g (68.9%). FT-IR (KBr): $\tilde{\nu}$ = 2960 (m,sh), 2918 (s), 2850 (s), 2363 (w), 2345 (w), 1592 (m), 1466 (s), 1443 (w,sh), 1428 (w,sh), 1378 (w), 12889 (w,sh), 1264 (s), 1220 (w), 1092 (s), 1070 (w,sh), 1038 (w), 918 (w,sh), 874 (m), 847 (m), 801 (s), 756 (m), 720 (w), 704 (s), 623 (w), 534 (m) $cm^{-1}$. $C_{44}H_{47}ErN_4O_3$ (847.14): calcd. C 2.4, H 5.59, N 6.61; found C 62.1, H 5.67, N 6.68.

**$[Er(\eta\text{-dip})(dip)_2]_2$ (11):** Used $KNR_2$ (0.500 g, 0.771 mmol), H-dip (0.412 g, 0.231 mmol) and ca. 10 mL of tol. Yield 0.450 g (84.7%). 1.0618 g FT-IR (KBr): $\tilde{\nu}$ = 3063 (w,sh), 3020 (w,sh), 2961 (s), 2869 (m), 2362 (m), 2344 (w), 1601 (m,sh), 1591 (m), 1460 (w,sh), 1433 (s), 1382 (m), 1361 (m), 1333 (s), 1267 (s), 1202 (m), 1155 (w), 1069 (m), 1068 (w), 1059 (w), 1042 (m), 1007 (m), 978 (w), 924 (s), 889 (m), 864 (m,sh), 843 (*s), 797 (m), 692 (w,sh). 669 (w), 650 (w), 627 (w), 567 (m), 489 (w), 470 (w) $cm^{-1}$. $C_{71}H_{93}Er_2O_6$ (1377.03): calcd. C 61.9, H 6.82; found C 62.4, H 6.89.

**$Er(dip)_3(thf)_2$ (12):**[9] Used $KNR_2$ (0.500 g, 0.771 mmol), H-dip (0.412 g, 0.231 mmol) and ca. 10 mL of thf. Yield 0.320 g (49.2%). FT IR (KBr): $\tilde{\nu}$ = 3057 (w), 2960 (s), 2890 (w,sh), 2362 (w), 2345 (w), 1588 (s), 1450 (w,sh), 1432 (s), 1381 (m), 1357 (m,sh), 1333 (s), 1274 (s), 1210 (s), 1174 (w), 1109 (m), 1097 (m), 1042 (s), 1016 (m), 953 (w), 934 (w,sh), 888 (m,sh), 864 (s), 804 (m), 754 (s), 691 (s), 617 (w), 566 (s) $cm^{-1}$. $C_{44}H_{67}ErO_5$ (843.27): calcd. C 62.7, H 8.03; found C 61.9, H 7.98.

**$[Er(\mu\text{-OH})(dbp)_2(thf)]_2$ (15):** Used $KNR_2$ (0.500 g,0.771 mmol), H-dbp (0.477 g, 0.231 mmol) and ca. 10 mL of thf. Yield 0.380 g (73.9%). FT-IR (KBr): $\tilde{\nu}$ = 2957 (s), 2917 (w,sh), 2872 (w,sh), 2362 (s), 2344 (s), 1476 (w), 1459 (m), 1407 (s), 1385 (m,sh), 1316 (w), 1244 (s), 1200 (m), 1122 (m), 1104 (s), 1045 (w), 1007 (m), 922 (w), 865 (s), 821 (s), 796 (w), 748 (s), 708 (m), 656 (s), 527 (m), 429 (m) $cm^{-1}$. $C_{64}H_{100}Er_2O_8$ (1332.01): calcd. C 57.7, H 7.56; found C 57.1, H 7.37.

**$Er(dbp)_3(py)_2$ (16):** Used $KNR_2$ (0.500 g, 0.771 mmol), H-dbp (0.477 g, 0.231 mmol) and ca. 10 mL of py. Yield 0.390 g (53.7%). FT-IR (KBr): $\tilde{\nu}$ = 2959 (s), 2366 (w), 2345 (s), 1442 (m,sh), 1408 (s), 1384 (m,sh), 1360 (w), 1251 (s), 1219 (m,sh), 1200 (m), 1154 (w), 1104 (m), 1068 (w), 1042 (m), 866 (s), 822 (m), 749 (s), 703 (s), 655 (s), 629 (m), 545 (w), 431 (s) $cm^{-1}$. $C_{52}H_{73}ErN_2O_3$ (941.42): calcd. C 66.3, H 7.82, N 2.98; found C 66.8, H 8.10, N 2.42.

**$[Er(\mu\text{-tps})(tps)_2]_2$ (17):** Used $KNR_2$ (0.500 g, 0.771 mmol), H-tps (0.639 g, 0.231 mmol) and ca. 10 mL of tol. Yield 0.480 g (59.9%). FT-IR (KBr): $\tilde{\nu}$ = 3069 (s), 3043 (m,sh), 3021 (w), 3008 (w), 2998 (m), 2958 (s), 2366 (m), 2342 (m), 1975 (w,sh), 1958 (m), 1902 (w,sh), 1886 (m), 1818 (s), 1773 (m), 1652 (m), 1588 (s), 1560 (w), 1482 (s), 1426 (s), 1329 (w), 1301 (w,sh), 1259 (s), 1251 (w,sh), 1115 (s), 1093 (s,sh), 1027 (m,sh), 995 (w,sh), 857 (w,sh), 842 (s), 746 (s), 710 (s,sh), 698 (s), 621 (w), 571 (m), 486 (s) $cm^{-1}$. $C_{115}H_{98}Er_2O_6Si_6$ (2079.07): calcd. C 66.4, H 4.75; found C 66.6, H 5.26.

**$Er(tps)_3(thf)_3$ (18):** Used $KNR_2$ (0.500 g,0.771 mmol), H-tps (0.639 g, 0.231 mmol) and ca. 10 mL of thf. Yield 0.720 g (72.9%). FT-IR (KBr): $\tilde{\nu}$ = 3063 (m), 3045 (m), 2994 (w), 2882 (w), 1459 (m), 1450 (m), 1428 (s), 1342 (w), 1331 (w), 1296 (w), 1257 (m), 1185 (s), 1111 (s), 1068 (m), 1047 (w,sh), 1027 (s), 1000 (w,sh), 984 (s), 916 (w), 875 (s), 742 (s), 704 (s), 672 (w), 519 (s), 508 (w,sh), 452 (m), 432 (m), 413 (m) $cm^{-1}$. $C_{66}H_{69}ErO_6Si_3{\cdot}C_4H_8O$: calcd. C

 © 2007 Wiley-VCH Verlag GmbH & Co. KGaA, Weinheim 

65.6, H 6.05; for $C_{66}H_{69}ErO_6Si_3$ (**18**–1 thf): calcd. C 65.5, H 5.76; found C 65.1, H 5.96.

**$Er(tps)_3(py)_3$ (19):** Used $KNR_2$ (0.500 g, 0.771 mmol), tps(0.639 g, 0.231 mmol) and ca. 10 mL of py. Yield 0.680 g (71.7%). FT-IR (KBr): $\tilde{\nu}$ = 3063 (m), 3044 (m,sh), 3006 (w), 2363 (m), 2345 (m), 1599 (s), 1579 (w, sh), 1524 (w), 1483 (s), 1442 (s), 1427 (s), 1273 (w), 1257 (w), 1231 (w), 1217 (m), 1185 (m), 1154 (w), 1109 (s), 1067 (s), 1038 (s), 1001 (m,sh), 985 (s), 745 (s), 701 (s), 622 (s), 602 (w, sh), 520 (s), 507 (w,sh), 453 (m), 433 (m), 411 (m) $cm^{-1}$. $C_{69}H_{60}ErN_3O_3Si_3$ (1230.77): calcd. 67.3C, 4.91H, 3.42N. $C_{64}H_{55}ErN_2O_3Si_3$ (**19**–1 py): C 66.7, H 4.81, N 2.43; found C 67.0, H 4.91, N 2.80.

**General X-ray Crystal Structure Information:** [44] Crystals were mounted onto a glass fiber from a pool of Fluorolube™ and immediately placed in a cold $N_2$ vapor stream, with a Bruker AXS diffractometer equipped with a SMART 1000 CCD detector using graphite-monochromatized Mo-$K_\alpha$ radiation ($\lambda$ = 0.7107 Å). Lattice determination and data collection were carried out using SMART Version 5.054 software. Data reduction was performed using SAINTPLUS Version 6.01 software and corrected for absorption using the SADABS program within the SAINT software package.

Structures were solved by direct methods that yielded the heavy atoms, along with a number of the lighter atoms or by using the PATTERSON method, which yielded the heavy atoms. Subsequent Fourier syntheses yielded the remaining light-atom positions. The hydrogen atoms were fixed in positions of ideal geometry and refined using SHELXS software. The final refinement of each compound included anisotropic thermal parameters for all non-hydrogen atoms. It is of note that crystal structures of $M(OR)_x$ often contain disorder within the atoms of the ligand chain causing higher than normal final correlations.[24–29]

Data collection parameters for **1**–**19** are given in Table 2. Specific issues associated with individual structures are discussed below. Fully refined structures of **3** and **7** could not be obtained due to significant disorder in the Onep and O*t*Bu ligands, respectively; however, the connectivity of both compounds were unequivocally established and are in agreement with the $Dy(OR)_3$ structures reported. Structure **11** had significant disorder in the isopropoxide ligands that resulted in oblong thermal ellipsoids and a slightly higher $R_1$ value; however, the overall structure observed is in agreement with $[Dy(\eta\text{-dip})(dip)_2]_2$ in both unit cell and connectivity. For **17**, it was necessary to squeeze disorder electron density of 317.1 $A^3$ which is in agreement with ca. 1 tol molecule. Noncentrosymmetric settings were chosen for **1**, **7**, **12**, and **18** even though a mirror plane appears to exist for these molecules. By further investigation of these species, disruption in the symmetry due to nonrigid ligands, such as Onep (**1** and **7**) or disorder in coordinating solvent thf (**12** and **18**) ultimately requires refinement in noncentrosymmetric settings.

CCDC-641110 to -641120 contain the supplementary crystallographic data for this paper. These data can be obtained free of charge from The Cambridge Crystallographic Data Centre via www.ccdc.cam.ac.uk/data_request/cif.

**Film Production:** Standard spin-coat deposition routes[45] were used to generate the PErZT thin films with a brief description of the preparation and processing described below. The PZT (30/70 or 48/52) films were produced following the established "basic route to PZT" (BRP) route,[45,46] in which $Pb(OAc)_2{\cdot}(HOAc)$ (Aldrich, 95%) dissolved in pyridine (py) was added to a mixture of $Ti(O\textit{i}Pr)_4$ and $[Zr(O\textit{i}Pr)_4(HO\textit{i}Pr)]_2$ dissolved in tol to form the PZT precursor mixture. The appropriate $Er(OR)_3$ precursor was dissolved in py and then added to the PZT mixture to form the ca. 0.4 M PErZT precursor solution.

Multilayered films of the desired composition were spin-coat deposited, in air, onto Pt(1700 Å)/Ti(300 Å) coated, thermally oxidized $SiO_2$/Si substrates using a photoresist spinner (3000 rpm for 30 s). After each deposition, the films were heated on a hot plate (300 °C for ca. 5 min) and cooled to room temperature before the deposition of the next layer. After the final layer received the 300 °C treatment (for this study 2–4 layers were used), the film was crystallized in a tube furnace at 650 °C for 30 min in air. X-ray diffraction (XRD) was used to confirm the phase purity and orientation of the final films.

**Ferroelectric Testing:** To measure the electrical properties of the films, gold top electrodes (ca. 250 × 250 μm) were sputter-deposited onto the films using a shadow mask to create a parallel-plate capacitor geometry. Capacitor top electrode areas were individually measured with a calibrated optical microscope and film thicknesses were measured using a Dektak profilometer. The low-field dielectric properties were measured at 10 kHz (100 mV p–p) using an HP 4284A impedance analyzer (Palo Alto, CA). The ferroelectric properties of the PLnZT films were measured using an RT66A ferroelectric tester from Radiant Technologies (Albuquerque, NM). Accelerated ferroelectric fatigue tests were performed using a 1-MHz bipolar square wave pulse, with the applied electric field normalized to ca. 700 kV/cm.

**Nanoparticle Synthesis:** Nanoparticles of $Er_2O_3$ were formed following one of two methods using **1** or **11** which were chosen as representative members of the alkyl- and aryloxide derivatives, respectively. The BRP method was also used to generate the PErZT precursor solution for the multication nanoparticles.

Two general routes were explored to synthesize nanoparticles: (a) solution precipitation and (b) solvothermal routes. (a) *Solution Precipitation*. The first route used a mixture of 1-methyl imidazole and water (MeIm/$H_2O$) having a 14.5/0.5 mL ratio. This solution was placed in a two-neck round bottom equipped with a reflux condenser and a septum. Under flowing argon, the MeIm/$H_2O$ solution was brought to reflux conditions (ca. 200 °C) and the desired precursor dissolved in tol was injected via syringe. A white precipitate formed immediately and the mixture was stirred for 30 min at 197 °C then cooled to room temperature. The as prepared particles were collected by centrifugation and rinsed with ethanol and then calcined in a tube furnace under flowing argon at 600 °C for 1 h. (b) *Solvothermal*. The second route used was a 45 mL Parr Acid Digestion Bomb. In the glove box, the desired precursors were dissolved in ca. 15 mL of benzyl alcohol (BzOH) and the clear solutions were transferred to the Teflon™ liners and placed in the bomb. The bomb was taken out of the glove box and the reaction was heated to 200 °C for 48 h. The white precipitate was collected by centrifugation and rinsed with ethanol.

The resulting nanopowders were slurried in tol followed by placing a drop of the solution onto a holey-carbon copper grid and allowing it to air dry. Upon complete drying for the samples were then examined with a transmission electron microscope (TEM) Philips CM30 with acceleration voltage of 300 KeV to obtain images, as well as selected area electron diffraction (SAED) data when necessary. Elemental composition information was obtained with a Noran energy dispersive X-ray detector (EDX) using system 6 software. In addition, the powder was characterized using a PANalytical powder diffractometer using Cu-$K_\alpha$ radiation with step size 0.0167 degree, with 53.340 seconds dwelling time.

 © 2007 Wiley-VCH Verlag GmbH & Co. KGaA, Weinheim 

Table 2. Crystallographic data collection parameters for **1**–**19**.

| Compound | **1** | **3** | **4** | **7** | **9** |
|---|---|---|---|---|---|
| Empirical formula | $C_{15}H_{33}ErO_3$ | $C_{65}H_{126}Er_4O_{11}N_3$ | $C_{44}H_{99}Er_3O_{11}$ | $C_{43}H_{78}Er_3N_3O_8$ | $C_{36}H_{51}ErO_6$ |
| Formula weight | 428.67 | 1794.74 | 1306.01 | 1266.86 | 747.03 |
| Temp. [K] | 168(2) | 203(2) | 168(2) | 203(2) | 203(2) |
| Space group | tetragonal | monoclinic | monoclinic | hexagonal | monoclinic |
| | $P\bar{4}2_1/c$ | $P2_1/c$ | $P2_1/c$ | $P6_3/mc$ | $P2_1/n$ |
| $a$ [Å] | 20.1985(14) | 16.801(3) | 19.2913(13) | 17.239(4) | 9.8147(7) |
| $b$ [Å] | 20.1985(14) | 13.371(2) | 10.7831(8) | 17.239(4) | 27.6997(19) |
| $c$ [Å] | 12.0226(16) | 35.136(6) | 27.2513(19) | 11.269(6) | 13.1323(9) |
| $\beta$ [°] | | 90.479(3) | 99.2430(10) | | 93.4720(10) |
| $V$ [Å$^3$] | 4905.0(8) | 7893(2) | 5595.2(7) | 2900.2(17) | 3563.6(4) |
| $Z$ | 8 | 4 | 4 | 2 | 4 |
| $D_{calcd.}$ [Mg/m$^3$] | 1.161 | 4.530 | 1.550 | 1.421 | 1.392 |
| $\mu$ (Mo-$K_\alpha$) [mm$^{-1}$] | 3.424 | 4.259 | 4.506 | 4.341 | 2.395 |
| $R_1$[a] (%) (all data) | 4.10(4.77) | 12.05(12.76) | 4.41(6.33) | 7.772(9.999) | 3.03(4.34) |
| $wR_2$[b] (%) (all data) | 14.60(15.26) | 26.57(26.86) | 8.45(9.25) | 19.99(22.21) | 7.18(7.69) |

| Compound | **10** | **11** | **12** | **15** | **16** |
|---|---|---|---|---|---|
| Empirical formula | $C_{44}H_{47}ErN_4O_3$ | $C_{71}H_{93}Er_2O_6$ | $C_{44}H_{67}ErO_5$ | $C_{64}H_{100}Er_2O_8$ | $C_{52}H_{73}Er\ N_2O_3$ |
| Formula weight | 847.12 | 1376.97 | 843.24 | 1331.96 | 941.38 |
| Temp. [K] | 203(2) | 203(2) | 203(2) | 203(2) | 203(2) |
| Space group | triclinic | monoclinic | monoclinic | orthorhombic | orthorhombic |
| | $P\bar{1}$ | $P2_1/c$ | $P2_1$ | $Pbca$ | $Pbcn$ |
| $a$ [Å] | 10.8524(11) | 17.399(9) | 9.6910(6) | 19.419(4) | 20.394(3) |
| $b$ [Å] | 14.0287(15) | 21.796(12) | 19.3993(12) | 15.633(3) | 13.736(2) |
| $c$ [Å] | 27.954(3) | 9.796(5) | 12.2166(8) | 20.710(4) | 17.450(3) |
| $\alpha$ [°] | 81.924(2) | | | | |
| $\beta$ [°] | 87.581(2) | 105.827(7) | 109.6430(10) | | |
| $\gamma$ [°] | 74.401(2) | | | | |
| $V$ [Å$^3$] | 4058.4(7) | 3574(3) | 2149(3) | 6287(2) | 4888.4(14) |
| $Z$ | 4 | 2 | 2 | 4 | 4 |
| $D_{calcd.}$ [Mg/m$^3$] | 1.386 | 1.280 | 1.295 | 1.407 | 1.279 |
| $\mu$ (Mo-$K_\alpha$) [mm$^{-1}$] | 2.110 | 2.377 | 1.980 | 2.701 | 1.758 |
| $R_1$ (%) (all data) | 4.65 (7.24) | 14.33 (24.99) | 2.29 (2.34) | 2.32 (2.94) | 4.67 (9.25) |
| $wR_2$ (%) (all data) | 8.87 (9.63) | 28.59 (36.04) | 6.17 (6.20) | 5.77 (6.22) | 8.21 (9.50) |

| Compound | **17** | **18** | **19** |
|---|---|---|---|
| Empirical formula | $C_{115}H_{98}Er_2O_6Si_6$ | $C_{66}H_{69}ErO_6Si_3{\cdot}C_4H_8O$ | $C_{69}H_{60}ErN_3O_3Si_3$ |
| Form. weight | 2079.16 | 1281.85 | 1230.73 |
| Temp. [K] | 168(2) | 203(2) | 203(2) |
| Space group | triclinic | monoclinic | rhombohedral |
| | $P\bar{1}$ | $P2_1$ | $R3c$ |
| $a$ [Å] | 13.6370(15) | 14.5349(15) | 20.8803(5) |
| $b$ [Å] | 14.0918(15) | 16.4587(17) | 20.8803(5) |
| $c$ [Å] | 14.4596(15) | 14.9029(15) | 20.8803(5) |
| $\alpha$ [°] | 75.603(2) | | 66.54 |
| $\beta$ [°] | 70.595(2) | 115.687(2) | 66.54 |
| $\gamma$ [°] | 71.970(2) | | 66.54 |
| $V$ [Å$^3$] | 2459.0(5) | 3212.8(6) | 7343.8(3) |
| $Z$ | 1 | 2 | 4 |
| $D_{calcd.}$ [Mg/m$^3$] | 1.342 | 1.251 | 1.113 |
| $\mu$ (Mo-$K_\alpha$) [mm$^{-1}$] | 1.820 | 1.409 | 1.232 |
| $R_1$ (%) (all data) | 3.49 (4.11) | 6.69 (8.77) | 7.08 (9.50) |
| $wR_2$ (%) (all data) | 7.66 (7.87) | 17.15 (18.62) | 23.48 (26.26) |

[a] $R_1 = \Sigma \mid |F_o| - |F_c| \mid / \Sigma |F_o| \times 100$. [b] $wR_2 = [\Sigma\ w\ (F_o^2 - F_c^2)^2 / \Sigma\ (w\ |F_o|^2)^2]^{1/2} \times 100$.

## Acknowledgments

This work was partially funded by the Office of Basic Energy Sciences and the National Institutes of Health through the NIH Roadmap for Medical Research, Grant #1 R21 EB005365–01. Information on this RFA (Innovation in Molecular Imaging Probes) can be found at http://grants.nih.gov/grants/guide/rfa-files/RFA-RM-04–021.html. Sandia is a multiprogram laboratory operated by Sandia Corporation, a Lockheed Martin Company, for the United States Department of Energy under contract DE-AC04–94AL85000.

[1] P. Muralt, *J. Micromech. Microeng.* **2000**, *10*, 136.
[2] S. Trolier-McKinstry, P. Muralt, *J. Electroceram.* **2004**, *12*, 7.
[3] P. Muralt, *IEEE Transactions on Ultrasonics, Ferroelectrics and Frequency Control* **2000**, *47*, 903.

 © 2007 Wiley-VCH Verlag GmbH & Co. KGaA, Weinheim 

[4] T. J. Zhu, L. Lu, M. O. Lai, *Appl. Phys. A: Mater. Sci. Process.* **2005**, 701.
[5] Y. Arimoto, H. Ishiwara, *MRS Bull.* **2004**, *29*, 823.
[6] C. J. Taylor, G. N. Washington, *Smart Structures and Materials 2002*, Smart Structures and Integrated Systems, San Diego, CA, **2002**.
[7] T. J. Boyle, P. G. Clem, B. A. Tuttle, G. L. Brennecka, J. T. Dawley, M. A. Rodriguez, T. D. Dunbar, W. F. Hammetter, *J. Mater. Res.* **2002**, *17*, 871.
[8] T. J. Boyle, S. D. Bunge, P. G. Clem, J. Richardson, J. T. Dawley, L. A. M. Ottley, M. A. Rodriguez, B. A. Tuttle, G. Avilucea, R. G. Tissot, *Inorg. Chem.* **2005**, *44*, 1588.
[9] D. M. Barnhart, D. L. Clark, J. C. Gordon, J. C. Huffman, *Inorg. Chem.* **1994**, *33*, 3487.
[10] M. Kritikos, M. Moustiakimov, M. Wijk, G. Westin, *J. Chem. Soc. Dalton Trans.* **2001**, 1931.
[11] G. Westin, M. Kritikos, M. Wijk, *J. Solid State Chem.* **1998**, *141*, 168.
[12] T. J. Boyle, S. D. Bunge, T. M. Alam, G. P. Holland, T. J. Headley, G. Avilucea, *Inorg. Chem.* **2005**, *44*, 1309.
[13] T. J. Boyle, S. D. Bunge, N. L. Andrews, L. E. Matzen, K. Sieg, M. A. Rodriguez, T. J. Headley, *Chem. Mater.* **2004**, *16*, 3279.
[14] H. Gerung, T. J. Boyle, L. J. Tribby, S. D. Bunge, C. J. Brinker, S. M. Han, *J. Am. Chem. Soc.* **2006**, *128*, 5244.
[15] H. Gerung, S. D. Bunge, T. J. Boyle, C. J. Brinker, S. M. Han, *Chem. Commun.* **2005**, 1914.
[16] T. J. Boyle, B. A. Hernandez-Sanchez, C. M. Baros, L. N. Brewer, M. A. Rodriguez, *Chem. Mater.* **2007**, *1*, 2016.
[17] D. L. Clark, J. C. Gordon, J. C. Huffman, R. L. Vincent-Hollis, J. G. Watkin, B. D. Zwick, *Inorg. Chem.* **1994**, *33*, 5903.
[18] W. J. Evans, M. A. Johnston, M. A. Greci, M. A. Ansari, J. C. Brady, J. W. Ziller, *Inorg. Chem.* **2000**, *39*, 2125.
[19] M. Kritikos, M. Wijk, G. Westin, *Acta Crystallogr. Sect. C* **1998**, *54*, 576.
[20] G. Westin, R. Norrestam, M. Nygren, M. Wijk, *J. Solid State Chem.* **1998**, *135*, 149.
[21] M. Wijk, R. Norrestam, M. Nygren, G. Westin, *Inorg. Chem.* **1996**, *35*, 1077.
[22] Y.-M. Yao, Q. Shen, Y. Shang, M.-Q. Xue, *Polyhedron* **2001**, *20*, 3201.
[23] M. R. Burgstein, P. W. Roesky, *Angew. Chem. Int. Ed.* **2000**, *39*, 549.
[24] D. C. Bradley, R. C. Mehrotra, D. P. Gaur, *Metal Alkoxides*, Academic Press, New York, **1978**.
[25] D. C. Bradley, R. C. Mehrotra, I. P. Rothwell, A. Singh, *Alkoxo and Aryloxo Derivatives of Metals*, Academic Press, New York, **2001**.
[26] N. Y. Turova, E. P. Turevskaya, V. G. Kessler, M. I. Yanovskaya, *The Chemistry of Metal Alkoxide*, Kluwer Academic Publishers, Boston, **2002**.
[27] K. G. Caulton, L. G. Hubert-Pfalzgraf, *Chem. Rev.* **1990**, *90*, 969.
[28] C. D. Chandler, C. Roger, M. J. Hampden-Smith, *Chem. Rev.* **1993**, *93*, 1205.
[29] L. G. Hubert-Pfalzgraf, *New J. Chem.* **1987**, *11*, 663.
[30] T. J. Boyle, L. J. Tribby, S. D. Bunge, *Eur. J. Inorg. Chem.* **2006**, 4553.
[31] T. J. Boyle, L. A. M. Ottley, S. D. Daniel-Taylor, L. J. Tribby, S. D. Bunge, A. L. Costello, T. M. Alam, J. C. Gordon, M. McCleskey *Inorg. Chem.* **2007**, *46*, 3705.
[32] T. J. Boyle, R. P. Tyner, T. M. Alam, B. L. Scott, J. W. Ziller, B. G. Potter, *J. Am. Chem. Soc.* **1999**, *121*, 12104.
[33] T. J. Boyle, M. A. Rodriguez, D. Ingersoll, T. J. Headley, S. D. Bunge, D. M. Pedrotty, S. M. De′Angeli, S. C. Vick, H. Fan, *Chem. Mater.* **2003**, *15*, 3903.
[34] T. J. Boyle, N. L. Andrews, M. A. Rodriguez, C. Campana, T. Yiu, *Inorg. Chem.* **2003**, *42*, 5357.
[35] T. J. Boyle, D. M. Pedrotty, T. M. Alam, S. C. Vick, M. A. Rodriguez, *Inorg. Chem.* **2000**, *39*, 5133.
[36] S. D. Bunge, T. J. Boyle, H. D. Pratt, T. M. Alam, M. A. Rodriguez, *Inorg. Chem.* **2004**, *43*, 6035.
[37] R. J. Butcher, D. L. Clark, J. C. Gordon, J. G. Watkin, *J. Organomet. Chem.* **1999**, *577*, 228.
[38] G. B. Deacon, G. Meyer, D. Stellfeldt, G. Zelesny, B. W. Skelton, A. H. White, *Z. Anorg. Allg. Chem.* **2001**, *627*, 1652.
[39] G. B. Deacon, T. Feng, S. Nickel, M. I. Ogden, A. H. White, *Aust. J. Chem.* **1992**, *45*, 1992.
[40] Y.-M. Yao, K.-D. Zhang, L.-B. Yu, Q. Shen, Y.-Y. Lei, J. Sun, *Jiegou Huaxue* **2003**, *2*, 143.
[41] W. Que, Y. Zhou, Y. L. Lam, K. Ppita, Y. C. Chan, C. H. Kam, *Appl. Phys. A; Mater. Sci. Process.* **2001**, *73*, 209.
[42] W. Que, Y. Zhou, Y. L. Lam, J. Zhou, Y. C. Chan, C. H. Kam, *Appl. Phys. A; Mater. Sci. Process.* **2001**, *89*, 3058.
[43] R. Si, Y.-W. Zhang, H.-P. Zhou, L.-D. Sun, C.-H. Yan, *Chem. Mater.* **2007**, *19*, 18.
[44] The listed versions of SAINT, SMART, XSHELL, XPOW in SHELXTL, and SADABS Software from Bruker Analytical X-ray Systems Inc., 6300 Enterprise Lane, Madison, WI 53719 were used in analysis.
[45] T. J. Boyle, H. N. Al-Shareef, *J. Mater. Sci.* **1997**, *32*, 2263.
[46] Conquest Version 1.8, Cambridge Crystallographic Data Centre: support@ccdc.cam.ac.uk or www.ccdc.cam.ac.uk (**2004**, AUG **2006** update).

Received: March 21, 2007
Published Online: July 3, 2007

 © 2007 Wiley-VCH Verlag GmbH & Co. KGaA, Weinheim 

DOI: 10.1002/ejic.200700392

# Nickel Complexes Bearing 2-(Benzimidazol-2-yl)-1,10-phenanthrolines: Synthesis, Characterization and Their Catalytic Behavior Toward Ethylene Oligomerization

**Min Zhang,[a] Shu Zhang,[a] Peng Hao,[a] Suyun Jie,[a] Wen-Hua Sun,*[a] Peizhou Li,[b] and Xiaoming Lu[b]**

**Keywords:** Nickel / Tridentate complexes / Phenanthrolines / Ethylene oligomerization / Oligomerization

A series of 2-(benzimidazol-2-yl)-1,10-phenanthrolines and their nickel(II) complexes were synthesized and characterized by elemental and spectroscopic analysis along with single-crystal X-ray crystallography. X-ray diffraction analysis revealed that complexes **1a** and **6a** have a six-coordinate distorted octahedral geometry due to the coordination of solvent molecules, whereas **3a** is a centrosymmetric dimer in the solid state and **5b** displays a five-coordinate distorted trigonal-bipyramidal geometry. Upon activation with diethylaluminum chloride ($Et_2AlCl$), high catalytic activity up to $1.27 \times 10^7$ g·mol$^{-1}$(Ni)·h$^{-1}$ and high selectivity for 1-butene (90.5%) could be achieved. A higher activity up to $3.95 \times 10^7$ g·mol$^{-1}$(Ni)·h$^{-1}$ was observed in the **7a**/$Et_2AlCl$ system with addition of 20 equiv. of $PPh_3$ as an auxiliary ligand. Reaction conditions and the ligand environment significantly influenced the catalytic properties of the complexes.

(© Wiley-VCH Verlag GmbH & Co. KGaA, 69451 Weinheim, Germany, 2007)

## Introduction

Ethylene oligomerization is a major industrial process, and developing new catalysts for ethylene oligomerization is of academic and industrial interest for the synthesis of α-olefins, which are feedstocks for the preparation of detergents, plasticizers, and fine chemicals, as well as comonomers for the production of linear low-density polyethylene (LLDPE).[1] One of the major industrial processes in ethylene oligomerization, named the SHOP process, employs nickel complexes as catalysts.[2] Over the past decades, considerable research effort has been devoted to the design of new nickel complexes as catalysts for olefin reactivity.[3,4] A large number of nickel complexes have been described as active species in ethylene oligomerization. However, limited examples among them could selectively produce α-olefins, because of their fast β-hydrogen elimination and chain immigration.[5] Therefore, the current challenges of nickel complexes in ethylene oligomerization are to find suitable catalysts for better α-olefin selectivity and to improve their catalytic activities. The fundamental research in designing novel homogeneous catalysts will rely on synthesizing ligands possessing environmental coordination to metal atoms that is favorable to the formation of suitable active species. In addition to the P^O chelating nickel complexes used in the SHOP process,[2,6] there are numerous nickel catalysts being investigated with bidentate ligands, such as N^O,[7,8] P^N,[9,10] and N^N,[3,11–13] and tridentate ligands, such as N^N^O,[14] N^P^N,[15] P^N^P,[16] P^N^N,[13d,16] and N^N^N,[17,18] as well as organometallic compounds.[15a]

Considering N^N^N tridentate nickel complexes as catalysts for ethylene oligomerization, several models with high activities have been developed in our group by using 2-imino-1,10-phenanthrolines (**A**),[18b] 2-(2-benzimidazole)-6-iminopyridine (**B**) ligands,[19] and 6-imino-2-quinoxalinylpyridines.[20] Inspired by these model catalysts, our strategy for ethylene activation is to synthesize 2-(benzimidazol-2-yl)-1,10-phenanthrolines and their metal complexes (Scheme 1). A new synthetic methodology for 2-(benzimidazol-2-yl)-1,10-phenanthrolines has been developed, and a further coordination reaction with nickel halides produced their nickel complexes with dichlorides or dibromides. By

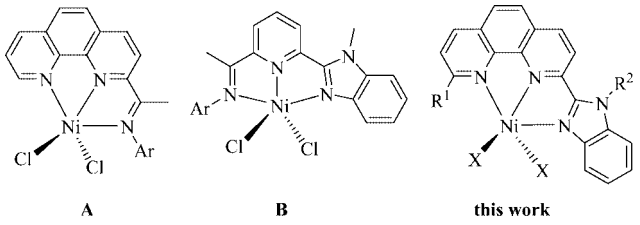


Scheme 1.

[a] Key Laboratory of Engineering Plastics and Beijing National Laboratory for Molecular Sciences, Institute of Chemistry, Chinese Academy of Sciences,
Beijing 100080, China
Fax: +86-10-62618239
E-mail: whsun@iccas.ac.cn
[b] Department of Chemistry, Capital Normal University, Beijing 100037, China


© 2007 Wiley-VCH Verlag GmbH & Co. KGaA, Weinheim

tuning the bulkiness and electronic effects of their substituents ($R^1$ and $R^2$), these nickel complexes are investigated for ethylene oligomerization, including their catalytic activities and the oligomers produced.

In the presence of $Et_2AlCl$, these nickel complexes show good catalytic activity towards ethylene oligomerization, especially with high selectivity of ethylene dimerization to 1-butene. In addition, the introduction of $PPh_3$ as an auxiliary ligand in the catalytic system greatly enhances the activity of the nickel complexes. Herein, we report the synthesis and characterization of 2-(benzimidazol-2-yl)-1,10-phenanthrolines and their nickel complexes; moreover, ethylene oligomerization of these nickel complexes is investigated in detail, along with the influence of reaction conditions and ligand environment.

## Results and Discussion

### Synthesis and Characterization of Ligands L1–L10 and Complexes 1a–10a, 1b–10b

The original organic compound 2-(1*H*-benzimidazol-2-yl)-9-methyl-1,10-phenanthroline (**L1**) is not yet reported in the literature. According to our previous work and the literature,[19,21] **L1** was synthesized by the reaction of 2,9-dimethyl-1,10-phenanthroline and *o*-phenylenediamine with sulfur as an oxidant. Another original compound, 2-(1*H*-benzimidazol-2-yl)-1,10-phenanthroline (**L6**), was synthesized by the condensation reaction of *o*-phenylenediamine with 1,10-phenanthroline-2-carboxylic acid in the presence of polyphosphoric acid (ppa) under microwave radiation.[22] The modified literature procedure was employed for the preparation of ligands **L2**–**L5** and **L7**–**L10** through the *N*-alkylation of **L1** and **L6** (Scheme 2).[19,23] All the synthesized compounds were well characterized and confirmed by elemental analysis, and $^1H$ and $^{13}C$ NMR, and IR spectroscopy. Their nickel complexes **1a**–**10a** and **1b**–**10b** were obtained in high yields by the equimolar reaction of the corresponding ligand and $NiCl_2·6H_2O$ or $(dme)NiBr_2$. These complexes were characterized by IR spectroscopy, elemental analysis, and single-crystal X-ray diffraction techniques (Figures 1–5). Some elemental data showed incorporation of solvent molecules because the samples were prepared by recrystallization. To understand their real structures, ligand **L7** and complexes **1a**, **3a**, **6a**, and **5b** were analyzed by single-crystal X-ray diffraction.

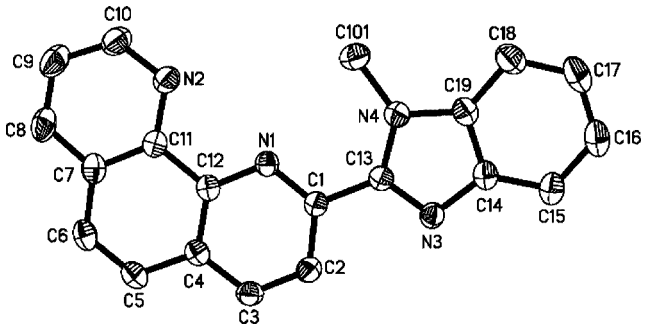


Figure 1. ORTEP drawing of ligand **L7** with thermal ellipsoids at the 30% probability level. Hydrogen atoms have been omitted for clarity. Selected bond lengths [Å] and angles [°]: N3–C13 1.3204(2), N3–C14 1.3822(2), N4–C13 1.3746(2), N4–C19 1.3863(2); N3–C13–N4 113.00(1), C13–N3–C14 105.13(1), C13–N4–C19 106.10(1).

Single crystals of ligand **L7** suitable for X-ray diffraction analysis were obtained by slow concentration of its ethyl acetate solution at room temperature. In the structure of ligand **L7** (Figure 1), the dihedral angle between the phenanthrolinyl plane and the benzimidazole plane is 7.6°, which indicates all the atoms of the ligand are almost coplanar. The N3–C13 bond [1.3204(2) Å] is longer than the typical imino C=N bond. The methyl group on the imidazole nitrogen atom stretches to the inner side of the phenanthroline ring because of the flexibility of the C1–C13 single bond.

Single crystals of complexes **1a**, **3a**, and **6a** suitable for X-ray diffraction analysis were individually grown by slow layering diffusion of diethyl ether into their methanol solutions. However, single crystals of **5b** were grown from its

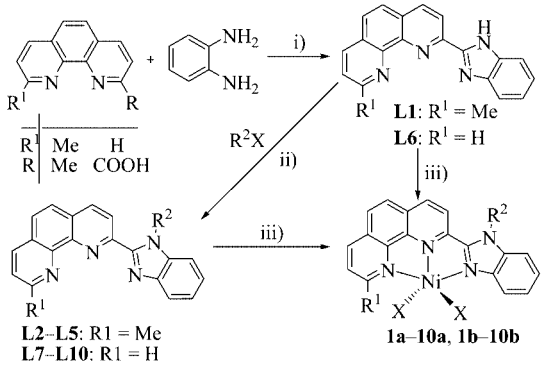


| | 1a | 2a | 3a | 4a | 5a | 6a | 7a | 8a | 9a | 10a | 1b | 2b | 3b | 4b | 5b | 6b | 7b | 8b | 9b | 10b |
|---|---|---|---|---|---|---|---|---|---|---|---|---|---|---|---|---|---|---|---|---|
| $R^1$ | Me | Me | Me | Me | Me | H | H | H | H | H | Me | Me | Me | Me | Me | H | H | H | H | H |
| $R^2$ | H | Me | Et | *i*Pr | Bn | H | Me | Et | *i*Pr | Bn | H | Me | Et | *i*Pr | Bn | H | Me | Et | *i*Pr | Bn |
| X | Cl | Cl | Cl | Cl | Cl | Cl | Cl | Cl | Cl | Cl | Br | Br | Br | Br | Br | Br | Br | Br | Br | Br |

Scheme 2. Synthesis of ligands **L1**–**L10** and nickel complexes **1a**–**10a**, **1b**–**10b**. (i) $S_8$, 170 °C for **L1**; ppa, microwave for **L6**. (ii) $K_2CO_3$, $CH_3CN$. (iii) $NiCl_2·6H_2O$, EtOH; $(dme)NiBr_2$, $CH_2Cl_2$.

 © 2007 Wiley-VCH Verlag GmbH & Co. KGaA, Weinheim 

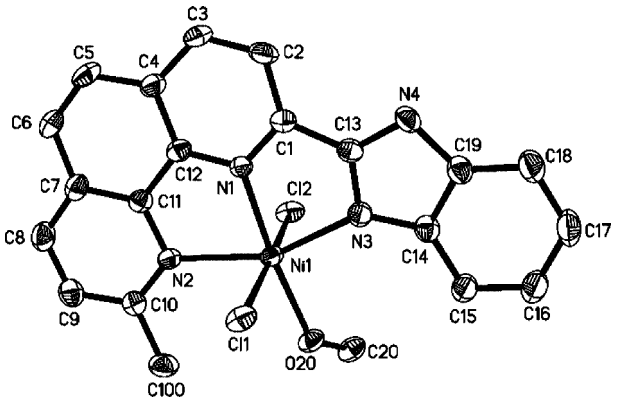


Figure 2. ORTEP drawing of complex **1a** with thermal ellipsoids at the 30% probability level. Hydrogen atoms have been omitted for clarity.

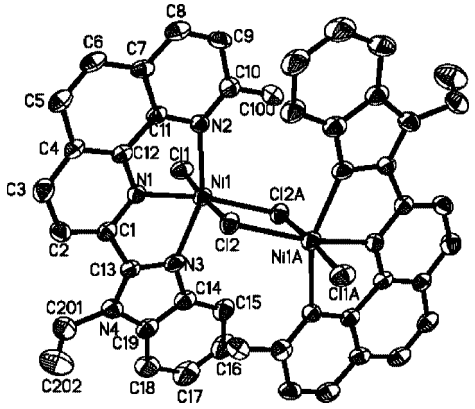


Figure 3. ORTEP drawing of complex **3a** with thermal ellipsoids at the 30% probability level. Hydrogen atoms and one molecule of $H_2O$ have been omitted for clarity.

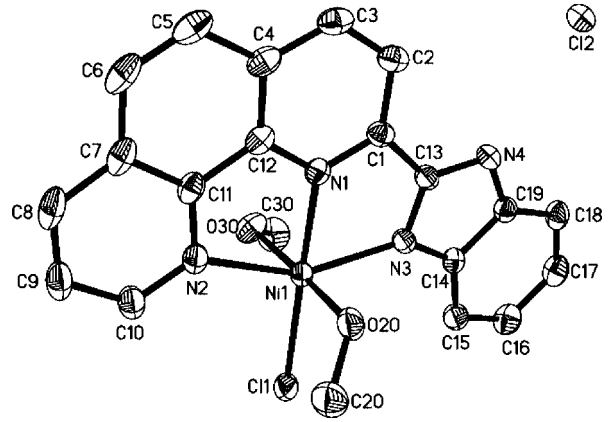


Figure 4. ORTEP drawing of complex **6a** with thermal ellipsoids at the 30% probability level. Hydrogen atoms have been omitted for clarity.

acetonitrile solution layered with diethyl ether. Their structures are depicted in Figures 2–5, and selected bond lengths and angles are collected in Table 1.

In the structure of **1a** (Figure 2), the coordination geometry around the nickel center can be described as a distorted octahedron because of the coordination of the solvent. The

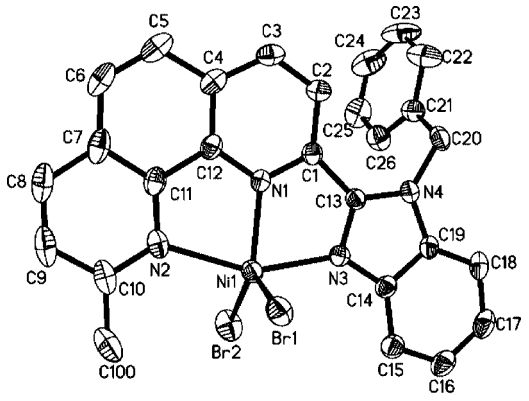


Figure 5. ORTEP drawing of complex **5b** with thermal ellipsoids at the 30% probability level. Hydrogen atoms have been omitted for clarity.

nickel center is coordinated to N1, N2 (1,10-phenanthroline), and N3 (benzimidazole), forming two fused five-membered rings with acute Ni–N angles: 77.85(1)° (N1–Ni1–N2) and 76.88(1)° (N1–Ni1–N3). The Ni1 atom deviates by 0.1149 Å from the coordinated plane. The dihedral angle between the phenanthrolinyl plane and the benzimidazole plane decreases to 5.8°, which is smaller than that of **L7** (7.6°). The bond lengths of Ni–N and Ni–Cl are significantly different: the Ni1–N1 bond [2.006(4) Å] is shorter than Ni1–N2 [2.208(4) Å] and Ni1–N3 [2.158(4) Å]; the Ni1–Cl2 bond [2.4460(2) Å] is longer than Ni1–Cl1 [2.3823(2) Å].

The structure of **3a** shows a centrosymmetric dinuclear nickel center (Figure 3) in a slightly distorted octahedral geometry. Each nickel atom is coordinated by three nitrogen atoms of the ligand, one terminal chlorine atom (Cl1), and two bridged chlorine atoms (Cl2 and Cl2A). The Ni1 atom deviates by 0.0785 Å from the plane of Cl1–N1–Cl2 and 0.0488 Å from the coordination plane (N1–N2–N3). The coordination plane incorporating N1, N2, and N3 is nearly perpendicular to the Ni1–Ni1A–Cl2–Cl2A plane, with a dihedral angle of 87.9°. The intramolecular distance of Ni···Ni is 3.658 Å, which is shorter than that in other dinuclear nickel complexes.[8c,12a] The dihedral angle between the phenanthrolinyl plane and the benzimidazole plane in **3a** ($R^2$ = Et) is 7.9°, which is wider than that in **1a** ($R^2$ = H) (5.8°). The bond lengths of Ni–N and Ni–Cl in **3a** are also different: the Ni1–N2 bond [2.202(3) Å] is longer than Ni1–N1 [2.006(3) Å] and Ni1–N3 [2.129(3) Å]; the bridged Ni1–Cl2 bond [2.5200(1) Å] is longer than Ni1–Cl1 [2.3846(1) Å].

As previously reported,[17a,18b] crystals of N^N^N tridentate nickel complexes contain not only five-coordinate species (**5b**), which are often observed in similar nickel complexes, but also six-coordinate ones, which can be realized through either the formation of dimers with bridged halogen atoms (**3a**) or the coordination of an additional solvent molecule to the metal atom (**1a**). Complex **6a** demonstrates another way of realizing the distorted octahedral coordination geometry of the Ni center (Figure 4). The six-coordinate structure of **6a** is similar to that of complexes **1a** and

 © 2007 Wiley-VCH Verlag GmbH & Co. KGaA, Weinheim 

Table 1. Selected bond lengths [Å] and angles [°] for complexes **1a**, **3a**, **6a**, and **5b**.

| | **1a** (X = Cl) | **3a** (X = Cl) | **6a** (X = Cl) | **5b** (X = Br) |
|---|---|---|---|---|
| Bond lengths [Å] | | | | |
| Ni1–N1 | 2.006(4) | 2.006(3) | 2.0328(2) | 1.994(3) |
| Ni1–N2 | 2.208(4) | 2.202(3) | 2.1722(2) | 2.181(3) |
| Ni1–N3 | 2.158(4) | 2.129(3) | 2.1338(2) | 2.094(3) |
| Ni1–X1 | 2.3823(2) | 2.3846(1) | 2.3389(6) | 2.4217(7) |
| Ni1–X2 | 2.4460(2) | 2.5200(1) | | 2.3969(8) |
| N3–C13 | 1.324(6) | 1.335(5) | 1.328(2) | 1.324(4) |
| N3–C14 | 1.383(6) | 1.396(5) | 1.381(2) | 1.384(4) |
| N4–C13 | 1.349(6) | 1.369(5) | 1.346(2) | 1.364(4) |
| N4–C19 | 1.394(6) | 1.387(5) | 1.378(3) | 1.388(4) |
| Bond angles [°] | | | | |
| N2–Ni1–N1 | 77.85(1) | 78.11(1) | 77.55(6) | 78.40(1) |
| N2–Ni1–N3 | 154.29(1) | 154.60(1) | 153.97(6) | 154.55(1) |
| N1–Ni1–N3 | 76.88(1) | 76.57(1) | 76.49(6) | 76.67(1) |
| N2–Ni1–X1 | 86.05(1) | 89.27(9) | 102.28(5) | 94.87(8) |
| N1–Ni1–X1 | 96.46(1) | 95.71(1) | 177.77(5) | 103.33(8) |
| N3–Ni1–X1 | 92.18(1) | 91.26(1) | 103.73(5) | 95.76(8) |
| N1–Ni1–X2 | 88.59(1) | 85.40(9) | | 127.54(8) |
| N2–Ni1–X2 | 88.41(1) | 87.32(9) | | 97.49(8) |
| N3–Ni1–X2 | 95.56(1) | 92.61(1) | | 93.63(8) |
| X1–Ni1–X2 | 171.55(5) | 176.12(4) | | 129.06(3) |

**3a**. However, one chlorine atom (Cl2) is replaced by one methanol molecule and acts as a counterion relatively far from the nickel atom Ni1, with an Ni1···Cl2 distance of 6.892 Å. The nickel atom and the mutually *trans*-disposed oxygen atoms are almost in the same line, with an angle of 174.85° (O20–Ni1–O30). Also, the nickel atom, N1, and Cl1 are almost in the same line, with an angle of 177.77 ° (N1–Ni1–Cl1). The Ni atom deviates slightly from the coordination plane, by 0.0459 Å. The dihedral angle between the phenanthrolinyl plane and the benzimidazole plane in **6a** is 7.5°, which is wider than that in **1a** (5.8°).

In the structure of **5b** (Figure 5), the coordination geometry of the nickel center can be best described as distorted trigonal-bipyramidal; the phenanthroline nitrogen atom (N1) and the two bromine atoms (Br1 and Br2) form the equatorial plane. The nickel atom slightly deviates from the plane, by 0.0347 Å, and equatorial angles range between 103.33(8)° and 127.54(8)°. The two axial Ni–N bonds subtend an angle of 154.55(1)°. This equatorial plane is essentially perpendicular to the phenanthrolinyl plane, with a dihedral angle of 90.1°. The sterically bulky benzyl group ($R^2$) is nearly perpendicular to the phenanthrolinyl plane, with a dihedral angle of 76.8°. It is notable that different $R^2$ substituents in the ligands have some influence on the Ni1–N3 bond length, and the Ni1–N3 bond of complex **5b** [2.094(3) Å] is shorter than those of complex **1a** [2.158(4) Å] and complex **3a** [2.129(3) Å]. The Ni1–N1 (phenanthroline) bond is shorter by about 0.1 Å than the Ni1–N3 (benzimidazole) (2.0943 Å) bond and by 0.187 Å than the Ni1–N2 (phenanthroline) (2.1813 Å) bond, which is similar to the (2-imino-1,10-phenanthrolinyl)nickel complexes.[18b] The two Ni–Br bond lengths show a slight difference between Ni1–Br2 [2.3969(8) Å] and Ni1–Br1 [2.4217(7) Å].

### Catalytic Properties of Complexes 1a–10a and 1b–10b for Ethylene Oligomerization

Ethylene oligomerization catalyzed by these nickel complexes using different cocatalysts has been systematically investigated. Treatment of complexes **6a** and **5b** with MAO, MMAO, $Et_3Al$, or $Et_2AlCl$ in toluene generates active ethylene oligomerization catalysts. The results are summarized in Table 2. In each case, the reaction produced a mixture of $C_4$ and $C_6$ components. $Et_2AlCl$ was found to be the most effective cocatalyst, which was similar to our previous N^N^N nickel system.[18b] Meanwhile, $Et_2AlCl$ generally led to slightly higher selectivities for 1-butene (Entries 4 and 8, Table 2).

In the presence of $Et_2AlCl$, complexes **6a** and **5b** were typically investigated for further optimization by varying the Al/Ni molar ratio, ethylene pressure, reaction temperature, and reaction time. The detailed results are shown in Table 3.

For the nickel chloride complex **6a**, the highest activity [$1.27 \times 10^7$ g·mol$^{-1}$(Ni)·h$^{-1}$] was observed at an Al/Ni ratio of 300 (Entry 2, Table 3), and greater loading of $Et_2AlCl$ (500–1000 equiv.) led to lower activities (Entries 3–5, Table 3). For the nickel bromide complex **5b**, the enhancement of the Al/Ni molar ratio from 200 to 800 resulted in an increase of catalytic activity (Entries 14–17, Table 3). With an Al/Ni molar ratio of 800, the catalytic activity of **5b** peaked at $4.00 \times 10^6$ g·mol$^{-1}$(Ni)·h$^{-1}$ (Entry 17, Table 3). A further increase of the Al/Ni molar ratio resulted in decreased oligomerization activity (Entry 18, Table 3). The α-$C_4$ selectivity was also affected by the Al/Ni molar ratio. When the Al/Ni molar ratio was enhanced from 200 to 1000, α-$C_4$ selectivity for both **6a** and **5b** monotonously and

 © 2007 Wiley-VCH Verlag GmbH & Co. KGaA, Weinheim 

Table 2. Ethylene oligomerization with different cocatalyst.[a]

| Entry | Complex | Cocatalyst | Activity[b] | Oligomer distribution[c] [%] | | α-$C_4$ [%] |
|---|---|---|---|---|---|---|
| | | | | $C_4/\Sigma C$ | $C_6/\Sigma C$ | |
| 1 | **6a** | $Et_3Al$ | 1.22 | 91.9 | 8.1 | 61.2 |
| 2 | **6a** | MAO | 0.92 | 93.7 | 6.3 | 54.4 |
| 3 | **6a** | MMAO | 1.13 | 93.0 | 7.0 | 59.1 |
| 4 | **6a** | $Et_2AlCl$ | 8.80 | 89.9 | 10.1 | 66.0 |
| 5 | **5b** | $Et_3Al$ | 1.01 | 91.3 | 8.7 | 68.4 |
| 6 | **5b** | MAO | 0.87 | 93.2 | 6.8 | 62.3 |
| 7 | **5b** | MMAO | 0.94 | 92.4 | 7.6 | 65.4 |
| 8 | **5b** | $Et_2AlCl$ | 3.40 | 90.2 | 9.8 | 72.5 |

[a] General conditions: 5 μmol of complex, 100 mL of toluene, $T$ = 20 °C, 30 atm of $C_2H_4$, 20 min, Al/Ni = 1000. [b] $10^6$ g·mol$^{-1}$(Ni)·h$^{-1}$. [c] Determined by GC.

Table 3. Ethylene oligomerization with **6a**/$Et_2AlCl$ and **5b**/$Et_2AlCl$ systems.[a]

| Entry | Complex | Al/Ni | $T$ [°C] | $P$ [atm] | $t$ [min] | Activity[b] | Oligomer distribution[c] [%] | | α-$C_4$ [%] |
|---|---|---|---|---|---|---|---|---|---|
| | | | | | | | $C_4/\Sigma C$ | $C_6/\Sigma C$ | |
| 1 | **6a** | 200 | 20 | 30 | 20 | 8.81 | 93.2 | 6.8 | 77.5 |
| 2 | **6a** | 300 | 20 | 30 | 20 | 12.69 | 90.1 | 9.9 | 72.6 |
| 3 | **6a** | 500 | 20 | 30 | 20 | 9.97 | 91.3 | 8.7 | 70.2 |
| 4 | **6a** | 800 | 20 | 30 | 20 | 9.73 | 89.4 | 10.6 | 68.7 |
| 5 | **6a** | 1000 | 20 | 30 | 20 | 8.80 | 89.9 | 10.1 | 66.0 |
| 6 | **6a** | 300 | 40 | 30 | 20 | 10.09 | 89.1 | 10.9 | 46.1 |
| 7 | **6a** | 300 | 60 | 30 | 20 | 1.51 | 94.0 | 6.0 | 40.8 |
| 8 | **6a** | 300 | 80 | 30 | 20 | 0.52 | 93.8 | 6.2 | 20.1 |
| 9 | **6a** | 300 | 20 | 20 | 20 | 3.55 | 90.5 | 9.5 | 61.4 |
| 10 | **6a** | 300 | 20 | 10 | 20 | 2.16 | 91.6 | 8.4 | 54.1 |
| 11 | **6a** | 300 | 20 | 30 | 30 | 9.84 | 91.0 | 9.0 | 70.5 |
| 12 | **6a** | 300 | 20 | 30 | 40 | 8.25 | 96.5 | 3.5 | 68.3 |
| 13 | **6a** | 300 | 20 | 30 | 60 | 6.17 | 90.3 | 9.7 | 64.2 |
| 14 | **5b** | 200 | 20 | 30 | 20 | 0.90 | 95.5 | 4.5 | 85.3 |
| 15 | **5b** | 300 | 20 | 30 | 20 | 1.50 | 94.0 | 6.0 | 81.1 |
| 16 | **5b** | 500 | 20 | 30 | 20 | 2.03 | 94.9 | 5.1 | 75.4 |
| 17 | **5b** | 800 | 20 | 30 | 20 | 4.00 | 91.0 | 9.0 | 74.2 |
| 18 | **5b** | 1000 | 20 | 30 | 20 | 3.40 | 90.2 | 9.8 | 72.5 |
| 19 | **5b** | 800 | 40 | 30 | 20 | 3.60 | 92.5 | 7.5 | 50.9 |
| 20 | **5b** | 800 | 60 | 30 | 20 | 0.83 | 97.1 | 2.9 | 43.8 |
| 21 | **5b** | 800 | 80 | 30 | 20 | 0.16 | 96.6 | 3.4 | 21.4 |
| 22 | **5b** | 800 | 20 | 20 | 20 | 1.03 | 96.5 | 3.5 | 70.4 |
| 23 | **5b** | 800 | 20 | 10 | 20 | 0.75 | 92.9 | 7.1 | 63.1 |
| 24 | **5b** | 800 | 20 | 30 | 30 | 2.67 | 90.3 | 9.7 | 73.1 |
| 25 | **5b** | 800 | 20 | 30 | 40 | 1.96 | 94.7 | 5.3 | 72.5 |
| 26 | **5b** | 800 | 20 | 30 | 60 | 1.28 | 92.2 | 7.8 | 72.0 |

[a] General conditions: 5 μmol of complex; 100 mL of toluene; $Et_2AlCl$ as cocatalyst. [b] $10^6$ g·mol$^{-1}$(Ni)·h$^{-1}$. [c] Determined by GC.

gradually decreased. However, the varied amounts of cocatalyst had no apparent influence on the proportion of the $C_4$ component in the oligomers produced.

As is apparent, the ethylene concentration significantly affects the catalytic behaviors of the complexes. When the ethylene pressure increased from 10 atm to 30 atm, the ethylene oligomerization activity increased sharply for both **6a** and **5b**. In addition, the α-$C_4$ selectivity also increased slightly (Entries 2, 9, 10 and Entries 17, 22, 23, Table 3). Elevating the reaction temperature of the **6a**/$Et_2AlCl$ and **5b**/$Et_2AlCl$ systems from 20 °C to 80 °C resulted in a sharp decrease of activity and α-$C_4$ selectivity, which may be attributed to the decomposition of the active catalytic sites and lower ethylene concentration at higher temperature (Entries 2, 6–8 and Entries 17, 19–21, Table 3).

The catalyst lifetime is a significant factor in industrial considerations. The oligomerization activities and selectivities for 1-butene were monitored at different time intervals in the ethylene oligomerization promoted by **6a**/$Et_2AlCl$ and **5b**/$Et_2AlCl$ systems. A slight decrease in activity was determined over a period of 20 min to 1 h for complex **6a**, indicating a rather long catalyst lifetime. Meanwhile, the α-$C_4$ selectivity decreased slightly with prolonged reaction time. This observation may be attributed to the isomerization reaction of the produced 1-butene catalyzed by the nickel complex.[9c,17b,24] However, for complex **5b**, the catalytic species showed almost no activity after 20 min.

The results of ethylene oligomerization with all the nickel complexes as precatalysts are collected in Table 4. It can be observed that the ligand environment has considerable ef-

 © 2007 Wiley-VCH Verlag GmbH & Co. KGaA, Weinheim 

fects on the catalytic behaviors, such as activity and α-$C_4$ selectivity. The introduction of a methyl group on the 9-position of the phenanthroline ring led to a dramatic decrease in oligomerization activity and a slight increase in α-$C_4$ selectivity. This could be demonstrated by comparing complexes **1a**–**5a** ($R^1$ = Me) with **6a**–**10a** ($R^1$ = H). As shown in Table 4, complexes **6a**–**10a** (Entries 6–10, Table 4) displayed higher activities and lower α-$C_4$ selectivities than their analogues **1a**–**5a** (Entries 1–5, Table 4). The same trend was also observed for the nickel dibromide complexes **1b**–**10b** (compare Entries 16–20 with Entries 11–15, Table 4).

The incorporation of an alkyl group on the nitrogen atom of the benzimidazole ligand in the complex led to a decrease in oligomerization activity and α-$C_4$ selectivity. Complexes **1a** and **1b** or **6a** and **6b** containing the N–H group showed much higher activities than their *N*-alkylated analogues (compare Entry 1 with Entries 2–5, Entry 11 with Entries 12–15, Entry 6 with Entries 7–10, and Entry 16 with Entries 17–20, Table 4). Tentatively, these results suggest that N–H functionality is essential for high activity and selectivity with this ligand system, which could be caused by their deprotonation to give anionic amide ligands when activated by $Et_2AlCl$. The anionic amide ligands could be free or form N–Al species (anion–cation pair) to increase their catalytic activity. This observation is consistent with a previous report, although the mechanism is not clear.[22a,25] Different alkyl groups such as methyl, ethyl, isopropyl, and benzyl groups had no obvious influence on α-$C_4$ selectivity. Meanwhile, the steric bulk effects of these groups on oligomerization activities are not very regular, which could be attributed to the longer distance between the alkyl group and the metal center.

The effect of the coordinated halide X (X = Cl or Br) on the ethylene reactivity seems to be rather small. With the exception of complexes **6a** and **6b**, each nickel bromide complex showed slightly higher activity than the corresponding chloride ones, which may be attributed to the better solubility in toluene for the bromide complexes.

Previous studies on nickel catalysts have demonstrated that incorporating $PPh_3$ into the catalytic system can lead to higher activity and longer lifetime. Meanwhile, the potential catalytic intermediates incorporating $PPh_3$ were observed and the relationship between the amounts of $PPh_3$ and the catalytic activity was explored.[8c,12e,18b] Complexes **2a**, **6a**, **7a**, and **1b** were selected to further study the effect of $PPh_3$ on the α-$C_4$ selectivity. The detailed results are summarized in Table 5. In the presence of 20 equiv. of $PPh_3$,

Table 4. Ethylene oligomerization with **1a**–**10a** and **1b**–**10b**/$Et_2AlCl$ systems.[a]

| Entry | Complex | Activity[b] | Oligomer distribution[c] [%] | | α-$C_4$ [%] |
|---|---|---|---|---|---|
| | | | $C_4/\Sigma C$ | $C_6/\Sigma C$ | |
| 1 | **1a** | 2.33 | 92.3 | 7.7 | 90.5 |
| 2 | **2a** | 1.06 | 93.4 | 6.6 | 85.7 |
| 3 | **3a** | 0.97 | 95.9 | 4.1 | 86.2 |
| 4 | **4a** | 0.91 | 97.1 | 2.9 | 83.6 |
| 5 | **5a** | 1.22 | 95.0 | 5.0 | 84.2 |
| 6 | **6a** | 12.69 | 90.1 | 9.9 | 72.6 |
| 7 | **7a** | 2.77 | 96.6 | 3.4 | 70.8 |
| 8 | **8a** | 4.03 | 96.2 | 3.8 | 66.4 |
| 9 | **9a** | 4.21 | 92.9 | 7.1 | 67.9 |
| 10 | **10a** | 2.00 | 95.7 | 4.3 | 70.3 |
| 11 | **1b** | 2.52 | 91.1 | 8.9 | 89.2 |
| 12 | **2b** | 1.27 | 92.5 | 7.5 | 82.8 |
| 13 | **3b** | 1.14 | 97.4 | 2.6 | 80.9 |
| 14 | **4b** | 1.02 | 94.4 | 5.6 | 86.4 |
| 15 | **5b** | 1.50 | 94.0 | 6.0 | 81.1 |
| 16 | **6b** | 10.08 | 90.4 | 9.6 | 71.3 |
| 17 | **7b** | 3.28 | 96.9 | 3.1 | 68.9 |
| 18 | **8b** | 4.24 | 94.6 | 5.4 | 67.2 |
| 19 | **9b** | 4.68 | 95.2 | 4.8 | 66.1 |
| 20 | **10b** | 2.16 | 95.6 | 4.4 | 69.0 |

[a] General conditions: 5 μmol of complex and 100 mL of toluene; $Et_2AlCl$ as cocatalyst and Al/Ni = 300. $T$ = 20 °C, 30 atm of $C_2H_4$, 20 min. [b] $10^6$ g·mol$^{-1}$(Ni)·h$^{-1}$. [c] Determined by GC.

Table 5. Ethylene oligomerization with **2a**, **6a**, **7a**, and **1b**/$Et_2AlCl$/$Ph_3P$ systems.[a]

| Entry | Complex | Activity[b] | Oligomer distribution[c] [%] | | α-$C_4$ [%] |
|---|---|---|---|---|---|
| | | | $C_4/\Sigma C$ | $C_6/\Sigma C$ | |
| 1 | **2a** | 3.78 | 92.5 | 7.5 | 19.5 |
| 2 | **6a** | 3.21 | 88.4 | 11.6 | 20.8 |
| 3 | **7a** | 3.95 | 91.8 | 8.2 | 12.1 |
| 4 | **1b** | 2.67 | 91.3 | 8.7 | 26.7 |

[a] General conditions: 5 μmol of complex; $Et_2AlCl$ as cocatalyst and Al/Ni = 300; 20 equiv. of $PPh_3$ and 100 mL of toluene; $T$ = 20 °C, 30 atm of $C_2H_4$, 20 min. [b] $10^7$ g·mol$^{-1}$(Ni)·h$^{-1}$. [c] Determined by GC.

 © 2007 Wiley-VCH Verlag GmbH & Co. KGaA, Weinheim 

the activities of all investigated complexes are much higher [up to $10^7$ g·mol$^{-1}$(Ni)·h$^{-1}$] than those of catalytic systems without $PPh_3$. For complex **7a**, a more than 10 times higher activity was achieved, reaching $3.95 \times 10^7$ g·mol$^{-1}$(Ni)·h$^{-1}$ (Entry 7 in Table 4 vs. Entry 3 in Table 5). The plausible role of $PPh_3$ is that of association and dissociation with the nickel core to activate and protect the active sites. However, it is noteworthy that analysis of the products shows that the selectivities for 1-butene are much lower (≤26.7%). Further studies to understand the effects of the auxiliary ligand on the ethylene oligomerization are in progress.

## Conclusions

A series of nickel catalysts ligated by 2-(benzimidazol-2-yl)-1,10-phenanthroline derivatives have been found to possess several characteristics that make them attractive catalysts for ethylene oligomerization. On treatment with $Et_2AlCl$, these complexes oligomerize ethylene to dimers and trimers with high activities and α-olefin selectivities. Further experimental results illustrate their sensitivity toward different ligand environments, reaction temperatures, and ethylene pressures. Complexes **1a**–**5a** and **1b**–**5b**, with a methyl group on the 9-position of the phenanthrolinyl ring ($R^1$ = Me), showed lower activities but higher selectivities for α-olefins than complexes **6a**–**10a** and **6b**–**10b** ($R^1$ = H). The incorporation of an alkyl group ($R^2$) on the nitrogen atom of the benzimidazole led to a decrease in oligomerization activity and selectivity for 1-butene (complexes **1a**, **1b**, **6a**, and **6b**). In general, higher ethylene pressure and lower temperature resulted in higher activities and α-olefin selectivities of the catalysts. Additionally, in the presence of 20 equiv. of $PPh_3$, the activities of all investigated complexes increased dramatically with lower selectivities for 1-butene.

## Experimental Section

**General Procedure:** All air- or moisture-sensitive manipulations were carried out under nitrogen using standard Schlenk techniques. Melting points were determined with a digital electrothermal apparatus without calibration. IR spectra were obtained with a Perkin–Elmer FTIR 2000 spectrophotometer by using KBr disks in the range of 4000–400 cm$^{-1}$. NMR spectra were recorded with a Bruker DMX-300 or Bruker ARX 400 spectrometer with TMS as the internal standard. Elemental analyses were performed with a Flash EA 1112 microanalyzer. GC was performed with a VARIAN CP-3800 gas chromatograph equipped with a flame ionization detector and a 30-m (0.2 mm i.d., 0.25 μm film thickness) CP-Sil 5 CB column. Toluene was refluxed in the presence of sodium/benzophenone and distilled under nitrogen prior to use. The polymerization-grade ethylene was supplied by Beijing Yansan Petrochemical Co. $Et_2AlCl$ (1.90 M) solution in toluene and triethylaluminum (diluted to 2 M in toluene for usage) were purchased from Acros Chemicals, while methylaluminoxane (MAO, 1.46 M in toluene) and modified methylaluminoxane (MMAO, 1.93 M in heptane, 3A) were purchased from Akzo Nobel Corp. All other commercial chemicals were used without further purification.

**Synthesis of Ligands:** New synthetic procedures were developed to prepare the original organic compounds, 2-(1*H*-benzimidazol-2-yl)-9-methyl-1,10-phenanthroline (**L1**) and 2-(1*H*-benzimidazol-2-yl)-1,10-phenanthroline (**L6**). The *N*-alkylation of **L1** and **L6** was subjected to different modified conditions to synthesize their derivatives, **L2**–**L5** and **L7**–**L10**, individually.

**2-(1*H*-Benzimidazol-2-yl)-9-methyl-1,10-phenanthroline (L1):** A mixture of 2,9-dimethyl-1,10-phenanthroline ($2C_{14}H_{12}N_2 \cdot H_2O$) (1.00 g, 4.80 mmol), *o*-phenylenediamine (0.58 g, 5.36 mmol), and sulfur (3.00 g, 11.70 mmol) was heated and kept at 170 °C for 8 h. After the mixture had cooled to room temperature, 200 mL of methanol was added to extract the product, and the precipitated solid was filtered off. The filtrate was concentrated and the residual brown oil was purified by column chromatography (silica gel, chloroform/ethyl acetate/methanol as elute, v/v/v = 20:20:1) to give an ivory-white powder (0.60 g) in 42% yield. M.p. 138–140 °C. IR (KBr disk): $\tilde{\nu}$ = 3419, 3051, 2950, 1620, 1590, 1466, 1435, 1337, 1189, 1065, 889, 768, 743 cm$^{-1}$. $^1$H NMR (400 MHz, $CDCl_3$): $\delta$ = 13.60 (s, 1 H, NH), 8.58 (d, $^1J$ = 8.4 Hz, 1 H, Phen), 8.18 (d, $^1J$ = 8.4 Hz, 1 H, Phen), 8.06 (d, $^1J$ = 8.4 Hz, 1 H, Phen), 7.82 (d, $^1J$ = 6.0 Hz, 1 H, Phen), 7.66 (s, 2 H, Phen), 7.49 (d, $^1J$ = 6.0 Hz, 1 H, benzimidazole), 7.36 (d, $^1J$ = 8.4 Hz, 1 H, benzimidazole), 7.24 (dd, $^1J$ = 6.0 Hz, 2 H, benzimidazole), 2.80 (s, 3 H, $CH_3$) ppm. $^{13}$C NMR (75 MHz, $CDCl_3$): $\delta$ = 157.9, 151.9, 150.6, 147.2, 143.7, 143.5, 135.8, 135.6, 127.7, 126.0, 125.5, 124.5, 123.0, 119.8, 111.9, 23.5 ppm. $C_{20}H_{14}N_4$ (310.35): calcd. C 77.06, H 4.39, N 18.55; found C 77.40, H 4.55, N 18.05.

**9-Methyl-2-(1-methyl-1*H*-benzimidazol-2-yl)-1,10-phenanthroline (L2):** $K_2CO_3$ (0.50 g, 3.62 mmol) was added to a solution of **L1** (0.25 g, 0.80 mmol) in acetonitrile (50 mL). After the mixture was refluxed for 12 h, iodomethane (0.07 mL, 1.12 mmol) was added and the mixture was stirred at room temperature for 24 h. After filtration and concentartion, an orange oil was obtained; thereafter it was dissolved in $CHCl_3$ (50 mL) and washed with water (50 mL × 3). The organic phase was separated, dried with anhydrous $MgSO_4$, and the solvents were evaporated. The residue was purified by column chromatography (silica gel, triethylamine/petroleum ether as elute, v/v = 2:1) to give a white powder (0.12 g) in 46% yield. M.p. 170–172 °C. IR (KBr disk): $\tilde{\nu}$ = 2919, 1614, 1588, 1438, 1414, 1326, 1258, 1096, 855, 728 cm$^{-1}$. $^1$H NMR (400 MHz, $CDCl_3$): $\delta$ = 8.77 (d, $^1J$ = 8.4 Hz, 1 H, Phen), 8.38 (d, $^1J$ = 8.4 Hz, 1 H, Phen), 8.17 (d, $^1J$ = 8.4 Hz, 1 H, Phen), 7.89 (d, $^1J$ = 8.0 Hz, 1 H, Phen), 7.83 (d, $^1J$ = 8.8 Hz, 1 H, Phen), 7.79 (d, $^1J$ = 8.8 Hz, 1 H, Phen), 7.55 (t, $^1J$ = 7.2 Hz, 2 H, benzimidazole), 7.40 (t, $^1J$ = 7.2 Hz, 1 H, benzimidazole), 7.35 (t, $^1J$ = 7.2 Hz, 1 H, benzimidazole), 4.78 (s, 3 H, $CH_3$), 2.94 (s, 3 H, $CH_3$) ppm. $^{13}$C NMR (75 MHz, $CDCl_3$): $\delta$ = 159.5, 150.4, 150.1, 145.7, 145.0, 142.8, 137.8, 136.7, 136.3, 127.2, 127.0, 125.3, 123.7, 123.4, 122.7, 120.2, 110.2, 33.2, 26.0 ppm. $C_{21}H_{16}N_4$ (324.38): calcd. C 77.45, H 5.23, N 17.32; found C 77.76, H 4.97, N 17.27.

**2-(1-Ethyl-1*H*-benzimidazol-2-yl)-9-methyl-1,10-phenanthroline (L3):** Ligands **L3**–**L5** and **L7**–**L10** were prepared using a similar method to that for **L2**. Iodoethane (0.09 mL, 1.12 mmol) reacted with deprotonated **L1** at 60 °C for 12 h. **L3** was obtained as a pink solid in 60% yield after purification by column chromatography (silica gel, triethylamine as elute). M.p. 128–130 °C. IR (KBr disk): $\tilde{\nu}$ = 2962, 1615, 1588, 1488, 1416, 1329, 1264, 1097, 849, 731 cm$^{-1}$. $^1$H NMR (400 MHz, $CDCl_3$): $\delta$ = 8.75 (d, $^1J$ = 8.4 Hz, 1 H, Phen), 8.37 (d, $^1J$ = 8.4 Hz, 1 H, Phen), 8.16 (d, $^1J$ = 8.4 Hz, 1 H, Phen), 7.90 (d, $^1J$ = 8.0 Hz, 1 H, Phen), 7.83 (d, $^1J$ = 8.8 Hz, 1 H, Phen), 7.79 (d, $^1J$ = 8.8 Hz, 1 H, Phen), 7.55 (t, $^1J$ = 7.2 Hz, 2 H, benzimidazole), 7.39 (t, $^1J$ = 7.2 Hz, 1 H, benzimidazole), 7.34 (t, $^1J$ = 7.2 Hz, 1 H, benzimidazole), 5.34 (q, $^1J$ = 7.2 Hz, 2 H, $CH_2CH_3$), 2.92 (s, 3 H, $CH_3$), 1.77 (t, $^1J$ = 7.2 Hz, 3 H, $CH_2CH_3$) ppm. $^{13}$C

 © 2007 Wiley-VCH Verlag GmbH & Co. KGaA, Weinheim 

NMR (75 MHz, $CDCl_3$): $\delta$ = 159.5, 150.2, 150.0, 145.9, 145.3, 143.1, 136.8, 136.6, 136.1, 128.4, 127.2, 127.0, 125.3, 123.6, 123.3, 122.6, 120.3, 110.3, 41.4, 25.8, 15.8 ppm. $C_{22}H_{18}N_4$ (338.41): calcd. C 77.81, H 5.66, N 16.53; found C 78.08, H 5.36, N 16.56.

**2-(1-Isopropyl-1*H*-benzimidazol-2-yl)-9-methyl-1,10-phenanthroline (L4):** 2-Iodopropane (0.11 mL, 1.12 mmol) reacted with deprotonated **L1** and was refluxed for 12 h. **L4** was obtained as yellow crystals in 43% yield by column chromatography (silica gel, triethylamine as elute). M.p. 130–132 °C. IR (KBr disk): $\tilde{\nu}$ = 2967, 1617, 1588, 1493, 1419, 1404, 1387, 1132, 855, 740 $cm^{-1}$. $^1H$ NMR (300 MHz, $CDCl_3$): $\delta$ = 8.63 (d, $^1J$ = 8.4 Hz, 1 H, Phen), 8.36 (d, $^1J$ = 8.4 Hz, 1 H, Phen), 8.12 (d, $^1J$ = 8.1 Hz, 1 H, Phen), 7.91 (d, $^1J$ = 8.4 Hz, 1 H, Phen), 7.78–7.75 (m, 3 H, 2 H-Phen, 1 H-benzimidazole), 7.51 (d, $^1J$ = 8.4 Hz, 1 H, benzimidazole), 7.33 (m, 2 H, benzimidazole), 6.67 (sept, $^1J$ = 6.6 Hz, 1 H, C*H*$(CH_3)_2$), 2.90 (s, 3 H, C*H*$_3$), 1.90 (d, $^1J$ = 6.6 Hz, 6 H, CH(C*H*$_3)_2$) ppm. $^{13}C$ NMR (75 MHz, $CDCl_3$): $\delta$ = 158.6, 145.0, 149.5, 144.9, 144.1, 142.8, 135.9, 135.3, 134.3, 127.4, 126.4, 126.1, 124.4, 123.2, 122.8, 122.1, 121.4, 119.8, 112.3, 48.7, 25.0, 20.9 ppm. $C_{23}H_{20}N_4$ (352.43): calcd. C 77.98, H 6.03, N 15.99; found C 78.38, H 5.72, N 15.90.

**2-(1-Benzyl-1*H*-benzimidazol-2-yl)-9-methyl-1,10-phenanthroline (L5):** Benzyl bromide (0.13 mL, 1.12 mmol) reacted with deprotonated **L1** and was refluxed for 12 h. **L5** was obtained by column chromatography (silica gel, triethylamine as elute) as an ivory-white powder in 55% yield. M.p. 122–124 °C. IR (KBr disk): $\tilde{\nu}$ = 3038, 3004, 1616, 1587, 1495, 1442, 1414, 1329, 864, 740, 720 $cm^{-1}$. $^1H$ NMR (400 MHz, $CDCl_3$): $\delta$ = 8.77 (d, $^1J$ = 8.4 Hz, 1 H, Phen), 8.36 (d, $^1J$ = 8.4 Hz, 1 H, Phen), 8.17 (d, $^1J$ = 8.0 Hz, 1 H, Phen), 7.94 (dd, $^1J$ = 6.0 Hz, 1 H, Phen), 7.80 (dd, $^1J$ = 8.4 Hz, 2 H, Phen), 7.55 (d, $^1J$ = 8.0 Hz, 2 H, benzimidazole), 7.37 (dd, $^1J$ = 6.0 Hz, 2 H, benzimidazole), 7.31 (d, $^1J$ = 6.0 Hz, 2 H, Ph), 7.13 (m, 3 H, Ph), 6.90 (s, 2 H, C*H*$_2$), 2.89 (s, 3 H, C*H*$_3$) ppm. $^{13}C$ NMR (75 MHz, $CDCl_3$): $\delta$ = 163.6, 158.5, 149.1, 145.2, 143.9, 143.6, 143.2, 142.0, 137.2, 136.4, 135.7, 135.2, 127.4, 126.2, 124.3, 122.7, 122.3, 121.9, 119.4, 110.0, 48.1, 24.8 ppm. $C_{27}H_{20}N_4$ (400.47): calcd. C 80.53, H 5.23, N 14.24; found C 80.98, H 5.03, N 13.99.

**2-(1*H*-Benzimidazol-2-yl)-1,10-phenanthroline (L6):** A mixture of 1,10-phenanthroline-2-carboxylic acid (1.12 g, 5.00 mmol), *o*-phenylenediamine (0.58 g, 5.40 mmol), and polyphosphoric acid (ppa) (7.00 g) was irradiated in a microwave oven (450 W) three times, for 2 min each time. The heated reaction mixture was poured into ice-cold water (300 mL), and the pH was adjusted to 9 by the addition of $NaHCO_3$. The precipitated solid was filtered off. After purification of the solid by column chromatography (silica gel, ethyl acetate/methanol as elute, v/v = 1:1), **L6** was obtained as white crystals (0.36 g) in 26% yield. M.p. 126–128 °C. IR (KBr disk): $\tilde{\nu}$ = 3399, 3059, 1619, 1587, 1502, 1431, 1315, 1275, 856, 740 $cm^{-1}$. $^1H$ NMR (400 MHz, $CDCl_3$): $\delta$ = 13.43 (s, 1 H, NH), 9.06 (dd, $^1J$ = 4.4 Hz, 1 H, Phen), 8.74 (d, $^1J$ = 8.4 Hz, 1 H, Phen), 8.35 (d, $^1J$ = 8.4 Hz, 1 H, Phen), 8.24 (dd, $^1J$ = 8.0 Hz, 1 H, Phen), 7.88 (t, $^1J$ = 6.4 Hz, 1 H, benzimidazole), 7.82 (dd, $^1J$ = 8.8 Hz, 2 H, Phen), 7.64 (dd, $^1J$ = 8.0 Hz, 1 H, Phen), 7.57 (m, 1 H, benzimidazole), 7.30 (m, 2 H, benzimidazole) ppm. $^{13}C$ NMR (75 MHz, $CDCl_3$): $\delta$ = 151.3, 149.0, 148.4, 145.2, 144.8, 144.2, 136.6, 136.5, 134.7, 128.8, 128.5, 126.4, 123.6, 123.0, 122.0, 120.9, 119.6, 111.6 ppm. $C_{19}H_{12}N_4$ (296.33): calcd. C 77.38, H 3.83, N 18.79; found C 77.01, H 4.08, N 18.91.

**2-(1-Methyl-1*H*-benzimidazol-2-yl)-1,10-phenanthroline (L7): L7** was obtained as a white powder in 51% yield by column chromatography (silica gel, triethylamine as elute). M.p. 186–188 °C. IR (KBr disk): $\tilde{\nu}$ = 2936, 1617, 1590, 1496, 1463, 1439, 1414, 1259, 1100, 855, 736 $cm^{-1}$. $^1H$ NMR (300 MHz, $CDCl_3$): $\delta$ = 9.23 (d, $^1J$ = 3.9 Hz, 1 H, Phen), 8.77 (d, $^1J$ = 8.4 Hz, 1 H, Phen), 8.42 (d, $^1J$ = 8.4 Hz, 1 H, Phen), 8.31 (d, $^1J$ = 8.0 Hz, 1 H, Phen), 7.92–7.88 (m, 3 H, 2 H-Phen, 1 H-benzimidazole), 7.70 (dd, $^1J$ = 7.8 Hz, 1 H, Phen), 7.55 (d, $^1J$ = 7.4 Hz, 1 H, benzimidazole), 7.41 (t, $^1J$ = 7.2 Hz, 1 H, benzimidazole), 7.36 (t, $^1J$ = 7.2 Hz, 1 H, benzimidazole), 4.72 (s, 3 H, $CH_3$) ppm. $^{13}C$ NMR (75 MHz, $CDCl_3$): $\delta$ = 149.4, 149.2, 145.1, 144.3, 144.0, 141.6, 138.0, 136.4, 135.6, 134.9, 127.9, 126.1, 125.2, 122.7, 122.4, 122.0, 121.5, 119.0, 109.0, 29.7 ppm. $C_{20}H_{14}N_4$ (310.35): calcd. C 77.18, H 4.88, N 17.94; found C 77.40, H 4.55, N 18.05.

**2-(1-Ethyl-1*H*-benzimidazol-2-yl)-1,10-phenanthroline (L8): L8** was obtained as a pale yellow powder in 62% yield by column chromatography (silica gel, triethylamine as elute). M.p. 156–158 °C. IR (KBr disk): $\tilde{\nu}$ = 3038, 2961, 1614, 1588, 1555, 1461, 1418, 1379, 1328, 1290, 1105, 845, 734 $cm^{-1}$. $^1H$ NMR (400 MHz, $CDCl_3$): $\delta$ = 9.22 (d, $^1J$ = 4.0 Hz, 1 H, Phen), 8.76 (d, $^1J$ = 8.4 Hz, 1 H, Phen), 8.42 (d, $^1J$ = 8.4 Hz, 1 H, Phen), 8.30 (d, $^1J$ = 8.0 Hz, 1 H, Phen), 7.91 (d, $^1J$ = 7.6 Hz, 1 H, benzimidazole), 7.88 (s, 2 H, Phen), 7.68 (dd, $^1J$ = 8.0 Hz, 1 H, Phen), 7.57 (d, $^1J$ = 8.0 Hz, 1 H, benzimidazole), 7.40 (t, $^1J$ = 7.2 Hz, 1 H, benzimidazole), 7.36 (t, $^1J$ = 7.2 Hz, 1 H, benzimidazole), 5.38 (q, $^1J$ = 7.2 Hz, 2 H, C*H*$_2$CH$_3$), 1.61 (t, $^1J$ = 7.2 Hz, 3 H, CH$_2$C*H*$_3$) ppm. $^{13}C$ NMR (75 MHz, $CDCl_3$): $\delta$ = 149.3, 149.1, 148.7, 145.3, 144.2, 141.8, 137.5, 135.4, 134.7, 127.8, 126.1, 125.1, 122.4, 122.3, 121.9, 121.3, 119.0, 109.0, 39.8, 14.3 ppm. $C_{21}H_{16}N_4$ (324.38): calcd. C 77.48, H 4.78, N 17.64; found C 77.76, H 4.97, N 17.27.

**2-(1-Isopropyl-1*H*-benzimidazol-2-yl)-1,10-phenanthroline (L9): L9** was obtained as a brown powder in 32% yield through column chromatography (silica gel, triethylamine as elute). M.p. 130–132 °C. IR (KBr disk): $\tilde{\nu}$ = 2973, 1617, 1586, 1495, 1457, 1422, 1336, 1282, 1254, 1136, 862, 744 $cm^{-1}$. $^1H$ NMR (300 MHz, $CDCl_3$): $\delta$ = 9.18 (d, $^1J$ = 3.3 Hz, 1 H, Phen), 8.60 (d, $^1J$ = 8.4 Hz, 1 H, Phen), 8.41 (d, $^1J$ = 8.4 Hz, 1 H, Phen), 8.27 (d, $^1J$ = 8.0 Hz, 1 H, Phen), 7.90 (d, $^1J$ = 5.4 Hz, 1 H, benzimidazole), 7.86 (s, 2 H, Phen), 7.76 (d, $^1J$ = 6.0 Hz, 1 H, benzimidazole), 7.65 (dd, $^1J$ = 7.2 Hz, 1 H, Phen), 7.32 (m, 2 H, benzimidazole), 6.45 [sept, $^1J$ = 6.9 Hz, 1 H, C*H*$(CH_3)_2$], 1.86 [d, 6 H, CH(C*H*$_3)_2$] ppm. $^{13}C$ NMR (75 MHz, $CDCl_3$): $\delta$ = 149.7, 149.5, 149.4, 145.2, 144.1, 142.5, 135.6, 134.7, 133.8, 127.8, 127.0, 126.2, 125.1, 123.2, 122.0, 121.7, 121.0, 119.5, 111.9, 48.2, 20.5 ppm. $C_{22}H_{18}N_4$ (338.41): calcd. C 78.44, H 4.93, N 16.63; found C 78.08, H 5.36, N 16.56.

**2-(1-Benzyl-1*H*-benzimidazol-2-yl)-1,10-phenanthroline (L10): L10** was obtained as a brown powder in 47% yield by column chromatography (silica gel, triethylamine as elute). M.p. 108–110 °C. IR (KBr disk): $\tilde{\nu}$ = 2928, 1605, 1588, 1496, 1434, 1351, 1259, 1163, 1078, 857, 735 $cm^{-1}$. $^1H$ NMR (300 MHz, $CDCl_3$): $\delta$ = 9.13 (d, $^1J$ = 3.2 Hz, 1 H, Phen), 8.65 (d, $^1J$ = 8.4 Hz, 1 H, Phen), 8.27 (d, $^1J$ = 8.4 Hz, 1 H, Phen), 8.18 (d, $^1J$ = 7.2 Hz, 1 H, Phen), 7.84 (t, $^1J$ = 6.0 Hz, 1 H, benzimidazole), 7.74 (s, 2 H, Phen), 7.58 (dd, $^1J$ = 8.0 Hz, 1 H, Phen), 7.47 (t, $^1J$ = 6.0 Hz, 1 H, benzimidazole), 7.28 (t, $^1J$ = 3.2 Hz, 2 H, benzimidazole), 7.22 (s, 1 H, Phen), 7.12 (d, $^1J$ = 3.2 Hz, 2 H, Ph), 6.99 (m, 3 H, Ph), 6.71 (s, 2 H, C*H*$_2$) ppm. $^{13}C$ NMR (75 MHz, $CDCl_3$): $\delta$ = 149.4, 149.2, 148.9, 145.3, 141.9, 137.0, 136.2, 135.7, 134.9, 128.0, 127.3, 126.3, 126.1, 125.2, 122.9, 122.6, 122.1, 121.8, 119.3, 109.8, 47.9 ppm. $C_{26}H_{18}N_4$ (386.45): calcd. C 81.13, H 4.82, N 14.05; found C 80.81, H 4.69, N 14.50.

**Syntheses of Nickel Complexes 1a–10a and 1b–10b:** Complexes **1a**–**10a** were prepared according to the following procedure. The corresponding ligand and 1 equiv. of $NiCl_2 \cdot 6H_2O$ were individually dissolved in ethanol and mixed together. The reaction mixture was stirred at room temperature for 8 h. The resulting precipitate was

 © 2007 Wiley-VCH Verlag GmbH & Co. KGaA, Weinheim 

filtered, washed with diethyl ether, and dried in a vacuum. Instead of $NiCl_2·6H_2O$ in the same synthetic procedure, a stoichiometric amount of (dme)$NiBr_2$ and the corresponding ligand in $CH_2Cl_2$ were stirred under nitrogen to form the nickel bromide complexes **1b**–**10b**.

**Characterization Data of Nickel Dichloride Complexes 1a–10a. 1a**: Green powder in 87% yield. IR (KBr disk): $\tilde{\nu}$ = 3254, 1624, 1588, 1504, 1429, 1321, 863, 747 $cm^{-1}$. $C_{20}H_{14}Cl_2N_4Ni·H_2O$ (457.97): calcd. C 52.19, H 3.17, N 12.66; found C 52.45, H 3.52, N 12.23. **2a**: Green powder in 82% yield. IR (KBr disk): $\tilde{\nu}$ = 1622, 1589, 1504, 1486, 1464, 862, 745 $cm^{-1}$. $C_{21}H_{16}Cl_2N_4Ni$ (453.98): calcd. C 55.14, H 3.07, N 12.55; found C 55.56, H 3.55, N 12.34. **3a**: Green powder in 86% yield. IR (KBr disk): $\tilde{\nu}$ = 3333, 1621, 1585, 1491, 1441, 1334, 862, 746 $cm^{-1}$. $C_{22}H_{18}Cl_2N_4Ni$ (468.00): calcd. C 56.14, H 3.47, N 11.65; found C 56.46, H 3.88, N 11.97. **4a**: Green powder in 91% yield. IR (KBr disk): $\tilde{\nu}$ = 3371, 2973, 1622, 1586, 1517, 1446, 1334, 1161, 865, 747 $cm^{-1}$. $C_{23}H_{20}Cl_2N_4Ni$ (482.03): calcd. C 57.62, H 4.46, N 11.33; found C 57.31, H 4.18, N 11.62. **5a**: Green powder in 90% yield. IR (KBr disk): $\tilde{\nu}$ = 3056, 1619, 1586, 1522, 1481, 1447, 1426, 1334, 857, 746 $cm^{-1}$. $C_{27}H_{20}N_4NiCl_2$ (530.07): calcd. C 61.04, H 3.57, N 10.65; found C 61.18, H 3.80, N 10.57. **6a**: Green powder in 84% yield. IR (KBr disk): $\tilde{\nu}$ = 3273, 3046, 1614, 1581, 1512, 1446, 1321, 859, 742, 706 $cm^{-1}$. $C_{19}H_{12}Cl_2N_4Ni$ (425.92): calcd. C 53.13, H 2.51, N 13.50; found C 53.58, H 2.84, N 13.15. **7a**: Green powder in 88% yield. IR (KBr disk): $\tilde{\nu}$ = 3273, 1621, 1577, 1530, 1510, 1460, 1418, 1335, 854, 743, 706 $cm^{-1}$. $C_{20}H_{14}Cl_2N_4Ni$ (439.95): calcd. C 54.11, H 3.59, N 12.47; found C 54.60, H 3.21, N 12.73. **8a**: Green powder in 85% yield. IR (KBr disk): $\tilde{\nu}$ = 3340, 1621, 1607, 1579, 1526, 1482, 1442, 1334, 853, 745 $cm^{-1}$. $C_{21}H_{16}Cl_2N_4Ni$ (453.98): calcd. C 55.17, H 3.88, N 12.11; found C 55.56, H 3.55, N 12.34. **9a**: Green powder in 89% yield. IR (KBr disk): $\tilde{\nu}$ = 2976, 1620, 1577, 1522, 1440, 1334, 857, 746 $cm^{-1}$. $C_{22}H_{18}Cl_2N_4Ni$ (468.00): calcd. C 56.09, H 3.51, N 12.32; found C 56.46, H 3.88, N 11.97. **10a**: Green powder in 90% yield. IR (KBr disk): $\tilde{\nu}$ = 3055, 1621, 1605, 1577, 1523, 1467, 1436, 1333, 857, 739 $cm^{-1}$. $C_{26}H_{18}Cl_2N_4Ni$ (516.05): calcd. C 60.14, H 3.13, N 10.59; found C 60.51, H 3.52, N 10.86.

**Characterization Data of Nickel Dibromide Complexes 1b–10b: 1b**: Green powder in 79% yield. IR (KBr disk): $\tilde{\nu}$ = 3373, 1624, 1588, 1504, 1446, 1321, 1147, 864, 745 $cm^{-1}$. $C_{20}H_{14}Br_2N_4Ni$ (528.85): calcd. C 45.66, H 2.74, N 10.35; found C 45.42, H 2.67, N 10.59. **2b**: Green powder in 77% yield. IR (KBr disk): $\tilde{\nu}$ = 2963, 1622, 1587, 1486, 1461, 1261, 1097, 1024, 861, 801, 741 $cm^{-1}$. $C_{21}H_{16}Br_2N_4Ni$ (542.88): calcd. C 46.24, H 2.65, N 10.77; found C 46.46, H 2.97, N 10.32. **3b**: Green powder in 80% yield. IR (KBr disk): $\tilde{\nu}$ = 3333, 1622, 1586, 1486, 1446, 1335, 1200, 1155, 860, 744 $cm^{-1}$. $C_{22}H_{18}Br_2N_4Ni·0.5H_2O$ (565.91): calcd. C 47.06, H 3.68, N 10.33; found C 46.69, H 3.38, N 9.90. **4b**: Green powder in 82% yield. IR (KBr disk): $\tilde{\nu}$ = 2971, 1622, 1587, 1516, 1457, 1334, 1160, 861, 752 $cm^{-1}$. $C_{23}H_{20}Br_2N_4Ni$ (570.93): calcd. C 48.67, H 3.98, N 9.41; found C 48.39, H 3.53, N 9.81. **5b**: Green powder in 73% yield. IR (KBr disk): $\tilde{\nu}$ = 3044, 1624, 1589, 1482, 1448, 1333, 1151, 859, 731 $cm^{-1}$. $C_{27}H_{20}Br_2N_4Ni$ (618.98): calcd. C 52.78, H 3.64, N 9.50; found C 52.39, H 3.26, N 9.05. **6b**: Green powder in 70% yield. IR (KBr disk): $\tilde{\nu}$ = 3363, 1623, 1580, 1514, 1446, 1320, 1144, 980, 858, 743 $cm^{-1}$. $C_{19}H_{12}Br_2N_4Ni$ (514.83): calcd. C 44.02, H

Table 6. Crystallographic data and refinement for **L7**, **1a**, **3a**, **6a**, and **5b**.

| | **L7** | **1a**·$CH_3OH$ | **3a** | **6a**·$2CH_3OH$ | **5b** |
|---|---|---|---|---|---|
| Empirical formula | $C_{20}H_{14}N_4$ | $C_{21}H_{17}Cl_2N_4NiO$ | $C_{44}H_{36}Cl_4N_8Ni_2O_2$ | $C_{21}H_{20}Cl_2N_4NiO_2$ | $C_{27}H_{20}Br_2N_4Ni$ |
| Formula mass | 310.35 | 471.00 | 967.99 | 490.02 | 619.00 |
| Temperature [K] | 293(2) | 296(2) | 293(2) | 293(2) | 293(2) |
| Wavelength [Å] | 0.71073 | 0.71073 | 0.71073 | 0.71073 | 0.71073 |
| Crystal system | orthorhombic | monoclinic | triclinic | monoclinic | monoclinic |
| Space group | *P*2(1)2(1)2(1) | $P2_1/n$ | $P\bar{1}$ | $P2_1/n$ | $P2_1/c$ |
| *a* [Å] | 6.0912(7) | 9.6962(2) | 9.7622(1) | 10.8359(4) | 12.814(3) |
| *b* [Å] | 12.4134(2) | 21.060(4) | 10.3016(2) | 20.3821(9) | 13.114(3) |
| *c* [Å] | 20.360(2) | 10.437(2) | 11.6713(2) | 10.8855(4) | 15.384(3) |
| *α* [°] | 90 | 90 | 72.086(8) | 90 | 90 |
| *β* [°] | 90 | 113.46(3) | 84.125(9) | 118.3960(1) | 107.29(3) |
| *γ* [°] | 90 | 90 | 70.165(9) | 90 | 90 |
| Volume [Å$^3$] | 1539.4(3) | 1955.2(7) | 1050.6(3) | 2114.89(1) | 2468.3(9) |
| *Z* | 4 | 4 | 1 | 4 | 4 |
| $D_{calcd.}$ [g m$^{-3}$] | 1.339 | 1.600 | 1.530 | 1.539 | 1.666 |
| $\mu$ [mm$^{-1}$] | 0.082 | 1.287 | 1.200 | 1.196 | 4.047 |
| *F*(000) | 648 | 964 | 496 | 1008 | 1232 |
| Crystal size [mm] | 0.30 × 0.10 × 0.07 | 0.13 × 0.11 × 0.10 | 0.27 × 0.19 × 0.10 | 0.45 × 0.25 × 0.20 | 0.32 × 0.16 × 0.10 |
| $\theta$ range [°] | 1.92–28.28 | 2.34–27.48 | 1.83–28.38 | 2.00–28.38 | 2.08–28.36 |
| Limiting indices | $-6 \le h \le 8$ | $-12 \le h \le 12$ | $-13 \le h \le 7$ | $-14 \le h \le 12$ | $-16 \le h \le 16$ |
| | $-16 \le k \le 13$ | $-26 \le k \le 27$ | $-13 \le k \le 10$ | $-26 \le k \le 27$ | $-17 \le k \le 17$ |
| | $-27 \le l \le 26$ | $-13 \le l \le 13$ | $-15 \le l \le 14$ | $-6 \le l \le 14$ | $-20 \le l \le 17$ |
| No. of reflections collected | 9186 | 8598 | 12212 | 19029 | 26399 |
| No. of unique reflections | 3749 | 4484 | 5144 | 5210 | 6147 |
| $R_{int}$ | 0.0175 | 0.0593 | 0.0464 | 0.0293 | 0.0569 |
| Completeness to $\theta$ (%) | 98.6 ($\theta$ = 28.28 °) | 100.0 ($\theta$ = 27.48 °) | 97.6 ($\theta$ = 28.38 °) | 98.2 ($\theta$ = 28.38 °) | 99.4 ($\theta$ = 28.36 °) |
| Absorption correction | empirical | empirical | empirical | empirical | empirical |
| No. of parameters | 217 | 268 | 271 | 279 | 307 |
| Goodness-of-fit on $F^2$ | 1.068 | 1.074 | 0.881 | 1.040 | 1.003 |
| Final *R* indices [$I > 2\sigma(I)$] | $R_1$ = 0.0361 | $R_1$ = 0.0672 | $R_1$ = 0.0522 | $R_1$ = 0.0324 | $R_1$ = 0.0429 |
| | $wR_2$ = 0.0953 | $wR_2$ = 0.1425 | $wR_2$ = 0.1151 | $wR_2$ = 0.0798 | $wR_2$ = 0.0981 |
| *R* indices (all data) | $R_1$ = 0.0480 | $R_1$ = 0.1164 | $R_1$ = 0.1754 | $R_1$ = 0.0490 | $R_1$ = 0.0968 |
| | $wR_2$ = 0.1008 | $wR_2$ = 0.1595 | $wR_2$ = 0.1457 | $wR_2$ = 0.0858 | $wR_2$ = 0.1164 |
| Largest diff. peak, hole [e Å$^{-3}$] | 0.133, –0.146 | 0.462, –0.485 | 0.355, –0.451 | 0.369, –0.356 | 0.470, –0.590 |

 © 2007 Wiley-VCH Verlag GmbH & Co. KGaA, Weinheim 

2.59, N 10.51; found C 44.33, H 2.35, N 10.88. **7b**: Green powder in 73% yield. IR (KBr disk): $\tilde{\nu}$ = 3310, 1621, 1576, 1531, 1511, 1480, 1460, 1418, 1335, 1132, 1043, 854, 742, 706 $cm^{-1}$. $C_{20}H_{14}Br_2N_4Ni$ (528.85): calcd. C 44.97, H 2.28, N 10.11; found C 45.42, H 2.67, N 10.59. **8b**: Green powder in 71% yield. IR (KBr disk): $\tilde{\nu}$ = 3369, 1620, 1607, 1577, 1525, 1481, 1441, 1334, 858, 743 $cm^{-1}$. Anal. $C_{21}H_{16}Br_2N_4Ni$ (542.88): calcd. C 46.95, H 2.52, N 10.78; found C 46.46, H 2.97, N 10.32. **9b**: Green powder in 81% yield. IR (KBr disk): $\tilde{\nu}$ = 3351, 1622, 1580, 1521, 1441, 1335, 857, 746 $cm^{-1}$. $C_{22}H_{18}Br_2N_4Ni$ (556.91): calcd. C 46.99, H 3.57, N 10.48; found C 47.45, H 3.26, N 10.06. **10b**: Green powder in 77% yield. IR (KBr disk): $\tilde{\nu}$ = 3374, 1621, 1606, 1576, 1524, 1438, 1334, 854, 737, 697 $cm^{-1}$. $C_{26}H_{18}Br_2N_4Ni$ (604.95): calcd. C 51.27, H 3.34, N 9.58; found C 51.62, H 3.00, N 9.26.

**X-ray Crystallography:** Single-crystal X-ray diffraction studies for complex **1a** were carried out on a Rigaku RAXIS Rapid IP diffractometer with graphite-monochromated Mo-$K_\alpha$ radiation ($\lambda$ = 0.71073 Å). Intensity data for crystals of ligand **L7** and complexes **3a**, **6a**, and **5b** were collected with a Bruker SMART 1000 CCD diffractometer with graphite-monochromated Mo-$K_\alpha$ radiation ($\lambda$ = 0.71073 Å). Cell parameters were obtained by global refinement of the positions of all collected reflections. Intensities were corrected for Lorentz and polarization effects and empirical absorption. The structures were solved by direct methods and refined by full-matrix least squares of $F^2$. All non-hydrogen atoms were refined anisotropically. Structure solution and refinement were performed using the SHELXL-97 package.[26] Crystal data and processing parameters are summarized in Table 6. CCDC-643354 (for **L7**), -643355 (for **1a**), -643356 (for **3a**), -643357 (for **6a**), and -643358 (for **5b**) contain the supplementary crystallographic data for this paper. These data can be obtained free of charge from the Cambridge Crystallographic Data Centre via www.ccdc.cam.ac.uk/data_request/cif.

**General Procedure for Ethylene Oligomerization:** A 250-mL stainless steel autoclave equipped with a mechanical stirrer and a temperature controller was heated in vacuo at 80 °C for 2 h. It was cooled to the required reaction temperature under ethylene, and charged with toluene, the desired amount of cocatalyst, and toluene solution of catalytic precursor; the total volume was 100 mL. The reactor was sealed and pressurized to the desired ethylene pressure, and the ethylene pressure was maintained with feeding of ethylene. After the reaction was carried out for the required period, the pressure was released. A small amount of the reaction solution was collected, the reaction in this small sample was terminated by the addition of 5% aqueous hydrogen chloride, and the organic layer was analyzed by gas chromatography (GC) for determining the composition and mass distribution of oligomers obtained.

## Acknowledgments

This work was supported by the National Natural Science Foundation of China (grant no. 20473099) and the Ministry of Science and Technology (grant no. 2006AA03Z553).

[1] a) D. Vogt in *Applied Homogeneous Catalysis with Organometallic Compounds* (Eds.: B. Cornils, W. A. Herrmann), VCH, Weinheim, Germany, **2002**, vol. 1, pp. 240–253; b) G. W. Parshall, S. D. Ittel in *Homogeneous Catalysis: The Applications and Chemistry of Catalysis by Soluble Transition Metal Complexes*, Wiley, New York, **1992**, pp. 68–72; c) J. Skupinska, *Chem. Rev.* **1991**, *91*, 613–648.

[2] a) W. Keim, F. H. Kowaldt, R. Goddard, C. Krüger, *Angew. Chem. Int. Ed. Engl.* **1978**, *17*, 466–467; b) W. Keim, A. Behr, B. Limbäcker, C. Krüger, *Angew. Chem. Int. Ed. Engl.* **1983**, *22*, 503; c) P. Braunstein, Y. Chauvin, S. Mercier, L. Saussine, A. D. Cian, J. Fisher, *J. Chem. Soc. Chem. Commun.* **1994**, 2203–2204; d) P. Braunstein, Y. Chauvin, S. Mercier, L. Saussine, *C. R. Chim.* **2005**, *8*, 31–38.

[3] a) L. K. Johnson, C. M. Killian, M. Brookhart, *J. Am. Chem. Soc.* **1995**, *117*, 6414–6415; b) L. K. Johnson, S. Mecking, M. Brookhart, *J. Am. Chem. Soc.* **1996**, *118*, 267–268; c) C. M. Killian, D. J. Tempel, L. K. Johnson, M. Brookhart, *J. Am. Chem. Soc.* **1996**, *118*, 11664–11665.

[4] a) S. D. Ittel, L. K. Johnson, M. Brookhart, *Chem. Rev.* **2000**, *100*, 1169–1204; b) S. Mecking, *Angew. Chem. Int. Ed.* **2001**, *40*, 534–540; c) V. C. Gibson, S. K. Spitzmesser, *Chem. Rev.* **2003**, *103*, 283–315; d) F. Speiser, P. Braunstein, L. Saussine, *Acc. Chem. Res.* **2005**, *38*, 784–793; e) W. Zhang, W.-H. Sun, *Prog. Chem.* **2005**, *17*, 310–319; f) S. Jie, S. Zhang, W.-H. Sun, *Petrochem. Technol. (Shiyou Huagong)* **2006**, *35*, 295–300; g) W.-H. Sun, D. Zhang, S. Zhang, S. Jie, J. Hou, *Kinet. Catal.* **2006**, *47*, 278–283; h) D. H. Camacho, E. V. Salo, J. W. Ziller, Z. Guan, *Angew. Chem. Int. Ed.* **2004**, *43*, 1821–1825.

[5] P. W. Jolly in *Comprehensive Organometallic Chemistry* (Eds.: G. Wilkinson, F. G. A. Stone, E. W. Abel), Pergamon Press, Oxford, U. K., **1982**, vol. 8, p. 384.

[6] a) W. Keim, *Angew. Chem. Int. Ed. Engl.* **1990**, *29*, 235–244; b) J. Heinicke, M. He, A. Dal, H.-F. Klein, O. Hetche, W. Keim, U. Flörke, H.-J. Haupt, *Eur. J. Inorg. Chem.* **2000**, 431–440.

[7] a) C. Wang, S. Friedrich, T. R. Younkin, R. T. Li, R. H. Grubbs, D. A. Bansleben, M. W. Day, *Organometallics* **1998**, *17*, 3149–3151; b) T. R. Younkin, E. F. Connor, J. I. Henderson, S. K. Friedrich, R. H. Grubbs, D. A. Bansleben, *Science* **2000**, *287*, 460–462; c) C. Carlini, M. Isola, V. Liuzzo, A. M. R. Galletti, G. Sbrana, *Appl. Catal., A* **2002**, *231*, 307–320; d) L. Wang, W.-H. Sun, L. Han, Z. Li, Y. Hu, C. He, C. Yan, *J. Organomet. Chem.* **2002**, *650*, 59–64.

[8] a) S. Wu, S. Lu, *Appl. Catal., A* **2003**, *246*, 295–301; b) D. Zhang, S. Jie, T. Zhang, J. Hou, W. Li, D. Zhao, W.-H. Sun, *Acta Polym. Sin.* **2004**, *5*, 758–762; c) W.-H. Sun, W. Zhang, T. Gao, X. Tang, L. Chen, Y. Li, X. Jin, *J. Organomet. Chem.* **2004**, *689*, 917–929; d) T. Hu, L.-M. Tang, X.-F. Li, Y.-S. Li, N.-H. Hu, *Organometallics* **2005**, *24*, 2628–2632.

[9] a) W. Keim, S. Killat, C. F. Nobile, G. P. Suranna, U. Englert, R. Wang, S. Mecking, D. L. Schröder, *J. Organomet. Chem.* **2002**, *662*, 150–171; b) W.-H. Sun, Z. Li, H. Hu, B. Wu, H. Yang, N. Zhu, X. Leng, H. Wang, *New J. Chem.* **2002**, *26*, 1474–1478; c) F. Speiser, P. Braunstein, L. Saussine, R. Welter, *Organometallics* **2004**, *23*, 2613–2624; d) F. Speiser, P. Braunstein, L. Saussine, *Organometallics* **2004**, *23*, 2625–2632.

[10] a) F. Speiser, P. Braunstein, L. Saussine, *Organometallics* **2004**, *23*, 2633–2640; b) F. Speiser, P. Braunstein, L. Saussine, R. Welter, *Inorg. Chem.* **2004**, *43*, 1649–1658; c) Z. Weng, S. Teo, T. S. A. Hor, *Organometallics* **2006**, *25*, 4878–4882.

[11] a) C. M. Killian, L. K. Johnson, M. Brookhart, *Organometallics* **1997**, *16*, 2005–2007; b) S. A. Svejda, M. Brookhart, *Organometallics* **1999**, *18*, 65–74; c) S. P. Meneghetti, P. J. Lutz, J. Kress, *Organometallics* **1999**, *18*, 2734–2737; d) T. V. Laine, K. Lappalainen, J. Liimatta, E. Aitola, B. Löfgren, M. Leskelä, *Macromol. Rapid Commun.* **1999**, *20*, 487–491.

[12] a) T. V. Laine, U. Piironen, K. Lappalainen, M. Klinga, E. Aitola, M. Leskelä, *J. Organomet. Chem.* **2000**, *606*, 112–124; b) Z. Li, W.-H. Sun, Z. Ma, Y. Hu, C. Shao, *Chin. Chem. Lett.* **2001**, *12*, 691–692; c) B. Y. Lee, X. Bu, G. C. Bazan, *Organometallics* **2001**, *20*, 5425–5431; d) C. Shao, W.-H. Sun, Z. Li, Y. Hu, L. Han, *Catal. Commun.* **2002**, *3*, 405–410; e) X. Tang, W.-H. Sun, T. Gao, J. Hou, J. Chen, W. Chen, *J. Organomet. Chem.* **2005**, *690*, 1570–1580; f) S. Jie, D. Zhang, T. Zhang, W.-H. Sun, J. Chen, Q. Ren, D. Liu, G. Zheng, W. Chen, *J. Organomet. Chem.* **2005**, *690*, 1739–1749.

[13] a) E. Nelkenbaum, M. Kapon, M. S. Eisen, *J. Organomet. Chem.* **2005**, *690*, 2297–2305; b) J. M. Benito, E. de Jesús, F. J. de la Mata, J. C. Flores, R. Gómez, P. Gómez-Sal, *Organome-*

 © 2007 Wiley-VCH Verlag GmbH & Co. KGaA, Weinheim 

*tallics* **2006**, *25*, 3876–3887; c) C.-L. Song, L.-M. Tang, Y.-G. Li, X.-F. Li, J. Chen, Y.-S. Li, *J. Polym. Sci., Part A: Polym. Chem.* **2006**, *44*, 1964–1974; d) C. Zhang, W.-H. Sun, Z.-X. Wang, *Eur. J. Inorg. Chem.* **2006**, *23*, 4895–4902.

[14] Q.-Z. Yang, A. Kermagoret, M. Agostinho, O. Siri, P. Braunstein, *Organometallics* **2006**, *25*, 5518–5527.

[15] a) S. Al-Benna, M. J. Sarsfield, M. Thornton-Pett, D. L. Ormsby, P. J. Maddox, P. Brès, M. Bochmann, *J. Chem. Soc. Dalton Trans.* **2000**, 4247–4257; b) F. Speiser, P. Braunstein, L. Saussine, *Dalton Trans.* **2004**, 1539–1545.

[16] J. Hou, W.-H. Sun, S. Zhang, H. Ma, Y. Deng, X. Lu, *Organometallics* **2006**, *25*, 236–244.

[17] a) L. Wang, W.-H. Sun, L. Han, H. Yang, Y. Hu, X. Jin, *J. Organomet. Chem.* **2002**, *658*, 62–70; b) F. A. Kunrath, R. F. de Souza, O. L. Casagrande Jr, N. R. Brooks, V. G. Young Jr, *Organometallics* **2003**, *22*, 4739–4743; c) N. Ajellal, M. C. A. Kuhn, A. D. G. Boff, M. Hörner, C. M. Thomas, J.-F. Carpentier, O. L. Casagrande Jr, *Organometallics* **2006**, *25*, 1213–1216.

[18] a) W.-H. Sun, S. Jie, S. Zhang, W. Zhang, Y. Song, H. Ma, *Organometallics* **2006**, *25*, 666–677; b) W.-H. Sun, S. Zhang, S. Jie, W. Zhang, Y. Li, H. Ma, J. Chen, K. Wedeking, R. Fröhlich, *J. Organomet. Chem.* **2006**, *691*, 4196–4203; c) J. D. A. Pelletier, Y. D. M. Champouret, J. Cadarso, L. Clowes, M. Gañete, K. Singh, V. Thanarajasingham, G. A. Solan, *J. Organomet. Chem.* **2006**, *691*, 4114–4123; d) S. Jie, S. Zhang, K. Wedeking, W. Zhang, H. Ma, X. Lu, Y. Deng, W.-H. Sun, *C. R. Chim.* **2006**, *9*, 1500–1509; e) S. Jie, S. Zhang, W.-H. Sun, X. Kuang, T. Liu, J. Guo, *J. Mol. Catal. A: Chem.* **2007**, *269*, 85–96.

[19] a) P. Hao, S. Zhang, W.-H. Sun, Q. Shi, S. Adewuyi, X. Lu, P. Li, *Organometallics* **2007**, *26*, 2439–2446; b) W.-H. Sun, P. Hao, S. Zhang, Q. Shi, W. Zuo, X. Tang, *Organometallics* **2007**, *26*, 2720–2734.

[20] a) S. Adewuyi, G. Li, S. Zhang, W. Wang, P. Hao, W.-H. Sun, N. Tang, J. Yi, *J. Organomet. Chem.* **2007**, *692*, 3532–3541; b) W.-H. Sun, P. Hao, G. Li, S. Zhang, W. Wang,J. Yi, M. Asma, N. Tang, *J. Organomet. Chem.*; DOI: 10.1016/j.jorganchem.2007.04.027.

[21] a) H. Saikachi, T. Hisano, *Chem. Pharm. Bull.* **1959**, *7*, 347–350; b) G. Tsukamoto, K. Yoshino, T. Kohno, H. Ohtaka, H. Kagaya, K. Ito, *J. Med. Chem.* **1980**, *23*, 734–738.

[22] a) W. Zhang, W.-H. Sun, S. Zhang, J. Hou, K. Wedeking, S. Schultz, R. Fröhlich, H. Song, *Organometallics* **2006**, *25*, 1961–1969; b) A. W. Addison, P. J. Burke, *J. Heterocycl. Chem.* **1981**, *18*, 803–805.

[23] Y. Kikugawa, *Synthesis* **1981**, 124–125.

[24] H.-P. Chen, Y.-H. Liu, S.-M. Peng, S.-T. Liu, *Organometallics* **2003**, *22*, 4893–4899.

[25] D. S. McGuinness, P. Wasserscheid, D. H. Morgan, J. T. Dixon, *Organometallics* **2005**, *24*, 552–556.

[26] G. M. Sheldrick, *SHELXTL-97, Program for the Refinement of Crystal Structures*, University of Göttingen, Germany, **1997**.

Received: April 10, 2007
Published Online: June 29, 2007

 © 2007 Wiley-VCH Verlag GmbH & Co. KGaA, Weinheim 

DOI: 10.1002/ejic.200700070

# Synthetic, X-ray Diffraction, Electrochemical, and Density Functional Theoretical Studies of (Indenyl)ruthenium Complexes Containing Dithiolate Ligands

**Sin Yee Ng,[a] Jialin Tan,[a] Wai Yip Fan,[a] Weng Kee Leong,[a] Lai Yoong Goh,*[a] and Richard D. Webster[b]**

**Keywords:** Ruthenium complexes / Dithiolates / Cyclic voltammetry / Density functional calculations

Halide substitution of the complexes [(Ind)Ru($L_2$)X] {Ind = $\eta^5$-$C_9H_7$. **1**: ($L_2$) = dppf [1,1′-bis(diphenylphosphanyl)ferrocene], X = Cl; **2**: ($L_2$) = dppm [1,1′-bis(diphenylphosphanyl)methane], X = Cl; and **18**: ($L_2$) = $(CO)_2$, X = I} with the 1,1-dithiolates $^-S_2CNR_2$ (dialkyl dithiocarbamates for R = Me, Et, and $C_5H_{10}$), $^-S_2COR$ (alkyl xanthates for R = Et and *i*Pr), and $^-S_2PR_2$ (dithiophosphinates for R = Et and Ph) showed that the lability of the indenyl ligand is influenced by the nature of both the coligand and the incoming dithiolate, as well as the solvent. In addition to dithiolate derivatives, the reactions also produced the hydride species [(Ind)Ru(diphos)H] in solvent- and stoichiometry-dependent yields. The observed dependence of lability of Ind on ($L_2$) follows the order, dppf < dppm ≈ $(CO)_2$, in agreement with the electron-donor capability of $L_2$, as well as the estimation of lowest activation energy for the $\eta^5 \rightarrow \eta^3$ ring slippage process in the series of complexes [(Ind)Ru$(L)_2(S_2COMe)$] (L = $PMeH_2$, $PH_3$, CO) for L = CO. The computational study also indicated an indenyl lability order for dithiolate substitution (dithiocarbamate > xanthate), in agreement with experimental findings. The dissociation of the indenyl ligand in chloro substitution of **1** by $^-S_2CNEt_2$ was found to be exhaustive in a polar solvent like MeOH, but only partial in $CH_2Cl_2$. Cyclic voltammetry experiments indicated that [(Ind)Ru(dppf)($\eta^1$-$S_2COiPr$)] (**10**) and [(Ind)Ru(dppf)($\eta^1$-$S_2PPh_2$)] (**13**) can be oxidized in one-electron chemical irreversible or chemical reversible processes, respectively (at a scan rate of 100 mV/s), at about 0 V versus $Fc/Fc^+$. Complex **13** underwent additional one-electron oxidation processes at +0.5 and +0.8 V versus $Fc/Fc^+$. The new complexes have all been characterized spectroscopically, and some (four containing the indenyl ligand and three of the non-indenyl type) by X-ray diffraction as well.
(© Wiley-VCH Verlag GmbH & Co. KGaA, 69451 Weinheim, Germany, 2007)

## Introduction

1,1-Dithiolate compounds represent a class of versatile ligands, owing to the occurrence of resonance phenomena, which result in electron delocalization, as depicted in Scheme 1. Their coordination chemistry with the transition metals commands much interest, on account of the rich diversity of the complexes and their numerous and potential applications in industry and agriculture.[1]

Our work on some of these ligands was directed at their reactivity in the coordination environment of $CpCr(CO)_n$ ($n$ = 2 or 3),[2] (HMB)Ru(dppf), and CpRu(dppf) (Cp = $\eta^5$-$C_5H_5$ and HMB = $\eta^6$-$C_6Me_6$).[3] A logical and interesting follow-up of these studies on Ru would be a corresponding reactivity study of the indenyl (Ind) analogue, as Ind can potentially assume bonding modes involving $\eta^5$-Cp or by

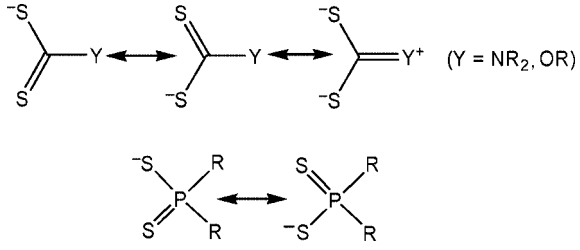


Scheme 1.

ring slippage to $\eta^3$ or $\eta^6$-$C_9H_7$.[4] Such an investigation is also timely, as there is intense interest in reactivity aspects of (Ind)Ru complexes, especially from catalytic perspectives;[5] and the bulk of the literature on (Ind)Ru complexes deals with examples containing phosphanes as coligands, with only two such complexes carrying S-donor ligands, viz. SEt and SEtMe.[6] Moreover, the outcome of the study will provide a useful comparison to our completed study of (Ind)Ru(dppf)Cl (**1**) with simple alkyl/aryl monothiolates, $SR^-$ (R = Me, Et, and Ph).[7] This paper will describe the results of reactions of **1**, its dppm analogue **2**, and (Ind)-$Ru(CO)_2I$ **18** with dialkyl dithiocarbamate, alkyl xanthate, and bis(alkyl/aryl)dithiophosphinate, together with X-ray

[a] Department of Chemistry, National University of Singapore, Kent Ridge, Singapore 117543, Singapore
Fax: +65-6779-1691
E-mail: chmgohly@nus.edu.sg
[b] Division of Chemistry and Biological Chemistry, Nanyang Technological University, Singapore 637616, Singapore
Supporting information for this article is available on the WWW under http://www.eurjic.org or from the author.

 © 2007 Wiley-VCH Verlag GmbH & Co. KGaA, Weinheim 

structural and electrochemical data of some of the new complexes, and a computational estimation of the energies involved in $\eta^5 \rightarrow \eta^3$ ring slippage of the indenyl ligand in selected molecules.

## Results and Discussion

### Reactions of [(Ind)Ru($L_2$)Cl] ($L_2$ = dppf, dppm)

#### *Reaction with Dialkyl Dithiocarbamates*

Complex [(Ind)Ru(dppf)Cl] (**1**) and its dppm analogue [(Ind)Ru(dppm)Cl] (**2**) were reacted with $NaS_2CNR_2$. The product mixture from the reaction of **1** in MeOH is both stoichiometry- and time-dependent. Thus the addition of 1 mol-equiv. of $^-S_2CNR_2$ to **1** gives complexes [Ru($\eta^2$-dppf)($\eta^2$-$S_2CNR_2$)$_2$] [R = Me (**3**), Et (**4**), $C_5H_{10}$ (**5**)], together with the hydride, [(Ind)Ru(dppf)H] **6**, which was not observed with the use of excess $^-S_2CNR_2$ (Scheme 2). The release of indene in all cases is consistent with the formation of the non-indenyl complexes **3**–**5**. In the reaction of **1** with 1 mol-equiv. of $^-S_2CNEt_2$, $^{31}$P NMR spectroscopy showed that the reaction mixture contained species **1** ($\delta$ = 51.7 ppm), **6** ($\delta$ = 62.8 ppm), **4** ($\delta$ = 47.1 ppm), and [(Ind)-Ru($\eta^1$-dppf)($\eta^2$-$S_2CNEt_2$)] **4a** ($\delta$ = –17.7 and 57.3), in an approximate 2:3:7:1 molar proportion after 4 h at room temperature, but finally only complexes **4** and **6** in 3:2 molar ratio after 16 h. A repeat of the reaction in $CH_2Cl_2$ using **1** and $NaS_2CNEt_2$ in 1:4 molar proportion yielded a final 1:1 molar mixture of **4** and **4a**, which was isolated in 35% yield. It was further demonstrated that the reaction of **4a** with $NaS_2CNEt_2$ in MeOH yielded **4** (Scheme 3).

The structure of **4a** was determined by X-ray diffraction analysis. This is consistent with its NMR spectroscopic data, which indicated the presence of $\eta^5$-Ind and $\eta^2$-$S_2CNEt_2$ ligands in the proton spectrum, and $\eta^1$-dppf in the $^{31}$P spectrum ($\delta$ = –17.7 and 57.3, with the upfield signal associated with the uncoordinated phosphorus atom).

The progression of **1** to **4** via **4a** indicates the weaker thermodynamic stability of bidentate dppf versus $^-S_2CNEt_2$, which in excess will also displace the indenyl ligand, accompanied by rechelation of the monodentate dppf ligand in **4a** to achieve the favored hexacoordination at

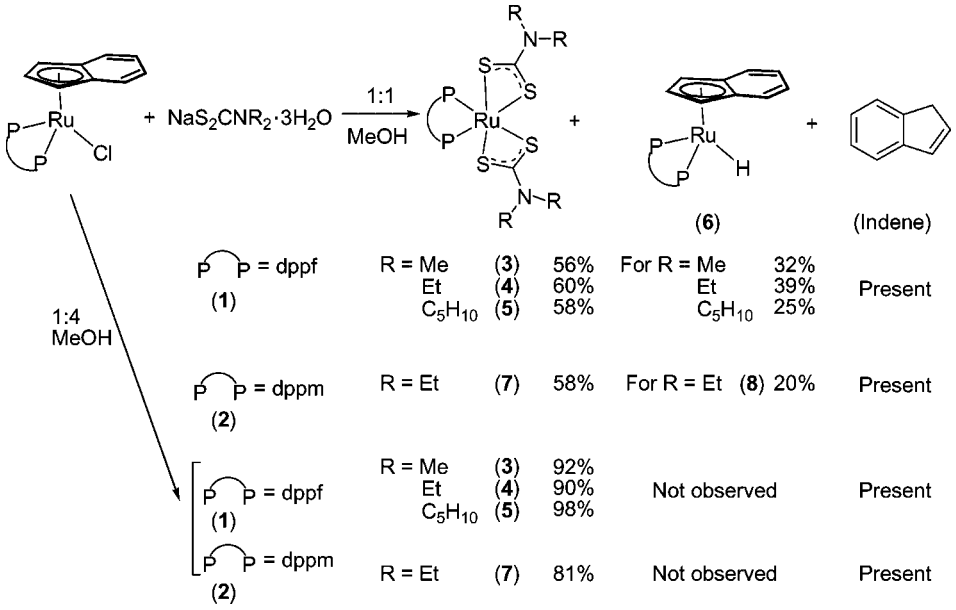


Scheme 2.

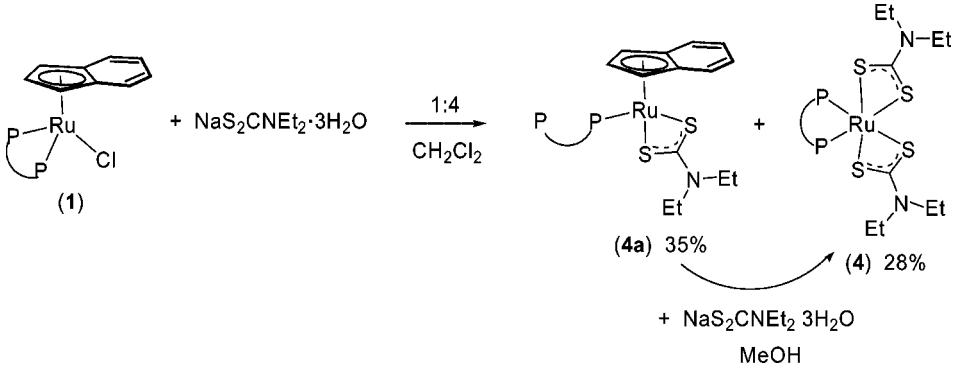


Scheme 3.

 © 2007 Wiley-VCH Verlag GmbH & Co. KGaA, Weinheim 

$Ru^{II}$. We had previously isolated complex **4** in 80% yield by displacement of triphenylphosphane in $Ru(\eta^2\text{-}S_2CNEt_2)_2(PPh_3)_2$ with dppf and have observed mono- and bidentate exchange behavior of the dithiocarbamate ligand in solution.[8]

The formation of **6** points to the role of methoxide arising from an equilibrium, as discussed before for $SR^-$ (R = Me, Et):[7]

$$^-S_2CNR_2 + MeOH \overset{K}{\rightleftharpoons} {}^-OMe + HS_2CNR_2$$

It is significant that **6** was not detected when excess $^-S_2CNR_2$ was used. Although it is probable that it was formed but underwent a facile $H^-$ and $^-S_2CNEt_2$ exchange, as found in the reactions of $CpRu(PPh_3)_2H$ with the halide and SCN anions,[9] this probability was ruled out experimentally in this case, as **6** did not react at all with excess $NaS_2CNR_2$, indicating that **6** was not the intermediate leading to **4**. As the formation of **4** requires 2 mole equiv. of $^-S_2CNEt_2$ to **1**, such a stoichiometric reaction was carried out in MeOH, in an attempt to further investigate the reaction pathways. A yellow precipitate, identified as **4**, was obtained, while the reaction of the filtrate with a new batch of **1** for 18 h at room temp. generated **6**, indicative of the presence of $^-OMe$ in the filtrate. This indirectly demonstrated that MeOH was the proton source for the conversion of the indenyl moiety to indene.

A comparative study was carried out on the reactivity of [(Ind)Ru(dppm)Cl] (**2**), the dppm analogue of **1**, towards the nucleophile $^-S_2CNR_2$. As shown in Scheme 2, similar observations were found in MeOH solvent, giving **7** (a compound similar to **4**) and **8** (a hydride similar to **6**);[10] the latter was not formed when the nucleophile was used in excess. However, the dppm equivalent of **4a**, that is, [(Ind)-$Ru(\eta^1\text{-dppm})(\eta^2\text{-}S_2CNEt_2)$], was not observed, probably because of thermodynamic instability, though complexes with monodentate dppm are known.[11]

Our previous studies showed that the outcome of the reactions of LRu(dppf)Cl [L = Cp (**A**), HMB (**B**)] with $^-S_2CNEt_2$ were very different. For L = Cp, a dinuclear complex $[CpRu(S_2CNEt_2)_2]_2(\mu\text{-dppf})$ (**C**) was formed, and for L = arene, $^-S_2CNEt_2$ displaced the arene ligand, as it displaced the indenyl ligand in complex **1**, as discussed above (see Scheme 4, a,b[3a]). In comparison, the analogous reaction of [CpRu(dppe)Cl] (**D**) was reported to give the mononuclear complex $[CpRu(dppe)(\eta^1\text{-}S_2CNEt_2)]$ (**E**) (Scheme 4, c).[12]

### *Reaction with Alkyl Xanthates*

The reaction of **1** with $KS_2COR$ (R = Et, *i*Pr) in MeOH at room temp. or in refluxing $CH_2Cl_2$ yielded $[(Ind)Ru(\eta^2\text{-dppf})(\eta^1\text{-}S_2COR)]$ in high yield [R = Et (**9**), 78% yield; R = *i*Pr (**10**), 83% yield]. On the other hand, the reaction of **2** with $KS_2CO$*i*Pr in MeOH gave only a non-indenyl complex $[Ru(\eta^2\text{-dppm})(\eta^2\text{-}S_2CO$*i*$Pr)_2]$ (**11**) (Scheme 5). There was no sign of the formation of any (Ind)Ru complex, neither $[(Ind)Ru(\eta^2\text{-dppm})(\eta^1\text{-}S_2COR)]$ nor $[(Ind)Ru(\eta^1\text{-dppm})(\eta^2\text{-}S_2COR)]$, indicative of thermodynamic instability of such indenyl compounds in MeOH. A change of solvent to $CH_2Cl_2$ was attempted; however, unlike in the case with $^-S_2CNR_2$, there was no reaction at all, even after prolonged heating.

The $^1H$ NMR spectra of **9** and **10** showed the presence of $\eta^5$-Ind [$\delta(H^2)$ 5.16–5.17, $\delta(H^{1,3})$ 5.43–5.51]. Bidentate coordination of dppf is evident from its single $^{31}P$ resonance in both **9** ($\delta$ = 54.9 ppm) and **10** ($\delta$ = 54.8 ppm). Monodentate coordination of the xanthate ligand was supported by X-ray diffraction analysis.

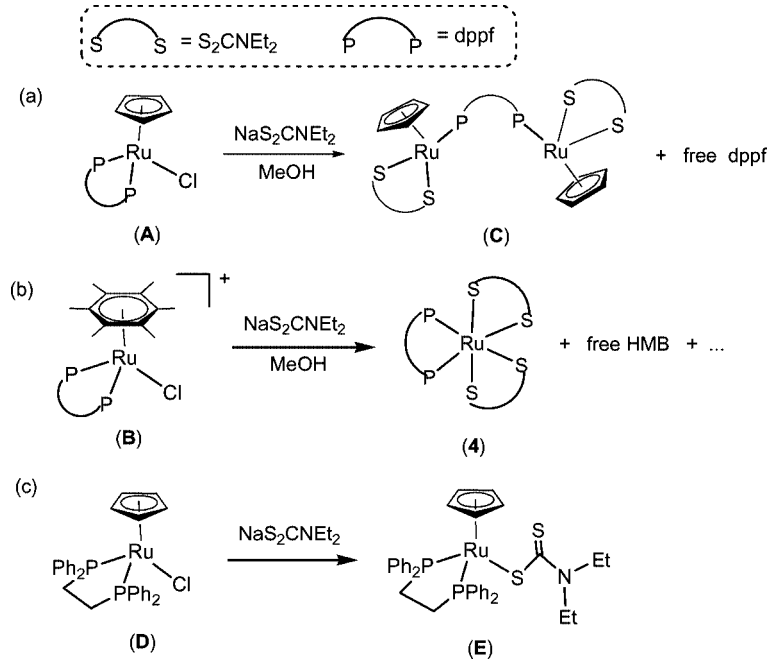


Scheme 4.[3a]

 © 2007 Wiley-VCH Verlag GmbH & Co. KGaA, Weinheim 

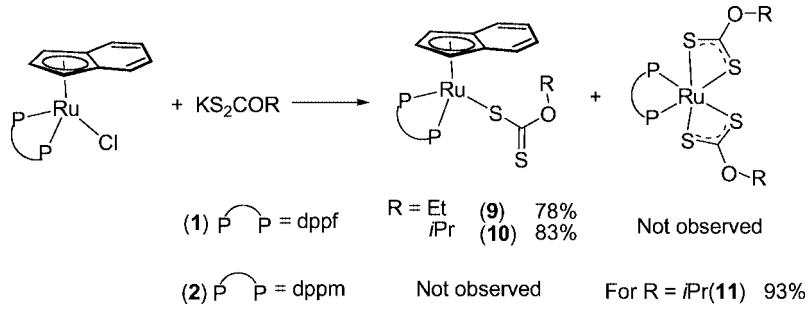


Scheme 5.

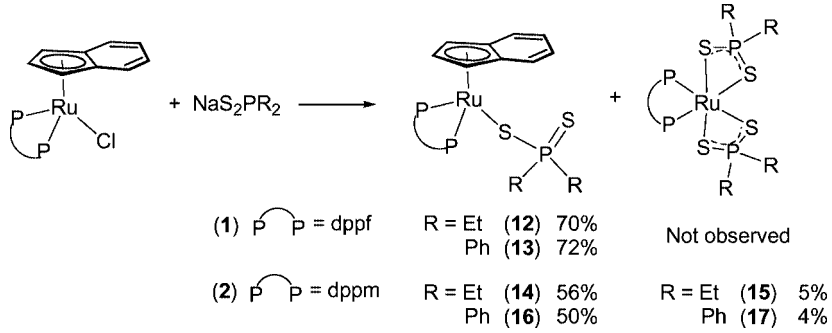


Scheme 6.

Complex **11** was formulated, based on its spectroscopic data. Its $^1$H NMR spectrum showed the absence of a $\eta^5$-Ind ligand and its $^{31}$P NMR spectrum showed a singlet at $\delta = 4.1$, assignable to chelating dppm. The FAB$^+$-mass spectrum showed the molecular ion peak at *m*/*z* 756, consistent with the presence of the non-indenyl six-coordinate complex.

### *Reaction with Dialkyl/Aryl Dithiophosphinates*

The reactions of **1** with $NaS_2PR_2$ gave high yields of [(Ind)Ru(dppf)($\eta^1$-$S_2PR_2$)] [R = Et (**12**), R = Ph (**13**)] (Scheme 6). The similar reaction of the dppm complex **2** gave the dppm analogues of **12** and **13**, viz. [(Ind)Ru(dppm)($\eta^1$-$S_2PR_2$)] [R = Et (**14**), 56%; and R = Ph (**16**), 50%], the lower yields probably arising from degradation to the non-indenyl compounds, [Ru(dppm)($\eta^2$-$S_2PR_2$)$_2$] [R = Et (**15**) and R = Ph (**17**)], which were isolated in 4–5% yields.

The $^1$H NMR spectra of **12**–**14** and **16** showed $\eta^5$-Ind bonding to the Ru center, $\delta$(H$^2$) 4.84–5.15 and $\delta$(H$^{1,3}$) 5.34–6.12. In their $^{31}$P NMR spectra, the chelating diphosphanes are seen as doublets (in the range $\delta = 53.1$–$54.8$ for $\eta^2$-dppf in **12** and **13**, and at $\delta = 12.5$–$12.6$ for $\eta^2$-dppm in **14** and **16**), while the monodentate dithiophosphinate ligand is seen as a triplet in the range $\delta = 84.9$–$87.9$ for $S_2PEt_2$ and $\delta = 70.9$–$71.1$ for $S_2PPh_2$.

The multiplet nature of these resonances is indicative of coupling between the two ligands in each of these complexes. However, for some unclear reason, such coupling is not evident in the $^{31}$P NMR spectra of the non-indenyl complexes **15** and **17**, both of which show a singlet for the dithiophosphinate ligand at $\delta = 88.0$–$105.6$, as well as for dppm at $\delta = 4.0$–$5.1$.

### Reactions of [(Ind)Ru(CO)$_2$I] (18) with $NaS_2CNEt_2$ and $KS_2CO$*i*Pr with or without Mediation by Trimethylamine *N*-Oxide

The reaction of **18** with $^-S_2CO$*i*Pr in MeOH gave, within 30 min, free indene and the six-coordinate Ru complex, [Ru($\eta^2$-$S_2CO$*i*Pr)$_2$(CO)$_2$] (**19**) (Scheme 7). It is apparent that the strong propensity of $^-S_2CO$*i*Pr towards chelation facilitated the dissociation of the weaker indenyl ligand rather than the CO ligands. Liberation of free indene was likewise observed in the reactions of **18** with thiolates, for example, $^-$SMe or $^-S_2CNC_6H_4$.[13]

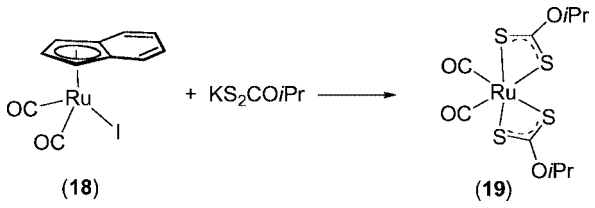


Scheme 7.

An attempt was made to hamper the dissociation of the indenyl ligand by generating a vacant site for coordination of the incoming bidentate thiolate. This was done by prior removal of CO ligands in **18** with trimethylamine *N*-oxide dihydrate, TMNO·2H$_2$O. It was found that decarbonylation of **18** resulted in a dark brown solution, from which a red

 © 2007 Wiley-VCH Verlag GmbH & Co. KGaA, Weinheim 

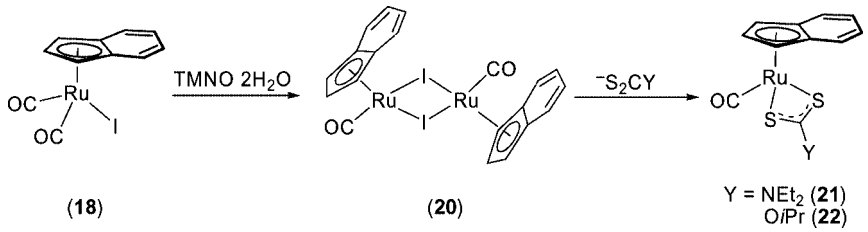


Scheme 8.

solid of $[(Ind)Ru(CO)(\mu\text{-}I)]_2$ (**20**) (70%) was obtained, undoubtedly from facile dimerization of the coordinatively unsaturated [(Ind)Ru(CO)I] species.

Complex **20** was characterized, based on its $^1H$ NMR spectrum, which showed $\eta^5$-Ind resonances at $\delta$ = 4.26 ($H^{1,3}$), 4.37 ($H^2$), and 6.54–7.59 ($H^{5-8}$), its $ESI^+$-mass spectrum, which gave the molecular ion peak at *m*/*z* 742.5 and an isotopic fragmentation pattern indicative of a $Ru_2$ moiety, and its IR spectrum, which showed a terminal CO stretch at 1925 $cm^{-1}$, in addition to an X-ray diffraction analysis.

The dark brown solution of **20** in $CH_3CN$ reacted slowly with $^-S_2CNEt_2$ or $^-S_2CO$*i*Pr giving dirty green and dirty yellow solutions, respectively, from which (Ind)Ru(CO){$\eta^2$-(S–S)} [S–S = $S_2CNEt_2$ (**21**, 55%), $S_2CO$*i*Pr (**22**, 81%)] was isolated (Scheme 8).

The infrared spectra of **21** and **22** in THF showed a new CO stretching frequency at 2031 and 2041 $cm^{-1}$, respectively. The presence of the $\eta^5$-Ind ligand was again indicated by the $^1H$ NMR signals at $\delta$ = 4.77–4.85 ($H^2$), 5.07–5.16 ($H^{1,3}$), and 6.83–7.16 ($H^{5-8}$). The molecular ions were observed at *m*/*z* 393 and 380, respectively. The structure of **21** has been determined by single-crystal X-ray diffraction analysis.

## Crystallographic Studies

The molecular structure of **4a** is illustrated in the ORTEP diagram (Figure 1, with selected bond parameters), which shows Ru coordinated to $\eta^5$-Ind, $\eta^2$-$S_2CNEt_2$, and $\eta^1$-dppf ligands. The Cp rings of dppf are almost eclipsed (anticlinal) to each other, with a torsional angle ($\tau$) of 136.58°. The slip-fold parameters of the indenyl ligand (see Table 1) suggest undistorted $\eta^5$-coordination,[14] with the benzenoid ring "flipped" towards the Ru center, probably a consequence of the relief in steric congestion around the metal center, which undoubtedly is the underlying cause for the dppf ligand to adopt a rare $\eta^1$-coordination mode, the first such case (as far as we are aware) in a structurally characterized mononuclear complex. Likewise steric demands have caused the pendant $PPh_2$ group to point away from the [(Ind)Ru($S_2CNEt_2$)] fragment. The extensive electron delocalization in the $S_2CNEt_2$ ligand can be observed in the bond lengths of S1–C10, S2–C10, and C10–N1, the values of which lie between those of a single and a double bond (C–S 1.81 Å; C=S 1.61 Å; C–N 1.47 Å; C=N 1.27 Å).[15]

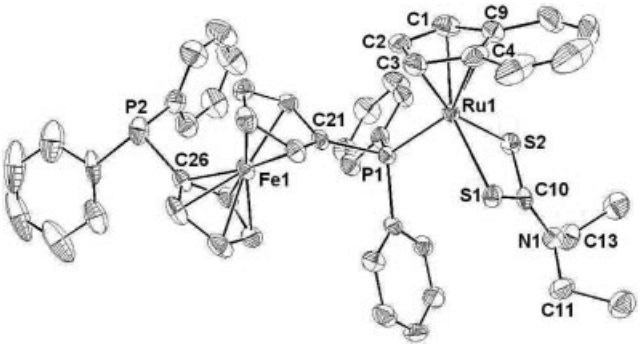


Figure 1. ORTEP diagram of **4a**. Thermal ellipsoids are drawn to 50% probability level. Hydrogen atoms are omitted for clarity. Selected bond lengths [Å] and angles [°]: Ru1–C* 1.873, Ru1–C1 2.180(5), Ru1–C2 2.159(5), Ru1–C3 2.185(5), Ru1–C4 2.309(5), Ru1–C9 2.302(5), Ru1–P1 2.2392(13), Ru1–S1 2.4068(13), Ru1–S2 2.3826(14), S1–C10 1.699(5), S2–C10 1.718(5), C10–N1 1.337(6), P1–C21 1.825(5), P2–C26 1.810(6), S1–Ru1–S2 71.85(4), S1–Ru1–P1 93.73(5), S2–Ru1–P1 88.04(5), S1–C10–S2 110.7(3), S1–C10–N1 126.3(4), S2–C10–N1 122.9(4), C10–N1–C11 121.1(4), C10–N1–C13 119.7(4), Ru1–P1–C21 111.90(16).

Table 1. Comparison of slip-fold parameters[a] of the ($\eta^5$-Ind)Ru complexes.

| Complex | Δ [Å] | HA [°] | FA [°] |
|---|---|---|---|
| [(Ind)Ru($DTC_{Et}$)($\eta^1$-dppf)] **4a** | 0.123 | 4.68 | 3.53 |
| [(Ind)Ru(dppf)($\eta^1$-$S_2COEt$)] **9** | 0.152 | 6.23 | 9.21 |
| [(Ind)Ru(dppf)($\eta^1$-$S_2PEt_2$)] **12** | 0.203 | 7.52 | 12.91 |
| [(Ind)Ru(dppm)($\eta^1$-$S_2PPh_2$)] **16** | 0.128 | 6.38 | 4.96 |
| $[(Ind)Ru(CO)I]_2$ **20** | 0.162, 0.185 | 6.32, 5.87 | 3.96, 4.18 |
| [(Ind)Ru(CO)($DTC_{Et}$)] **21** | 0.165 | 6.81 | 4.83 |
| [(Ind)Ru(CO)I{$P(CH_2Ph)_3$}] **F**[17] | 0.10 | 3.32 | 5.59 |
| $[(Ind)RuH(PPh_3)_2]$ **G**[5a] | 0.154 | 5.1 | 8.4 |

[a] Δ is the difference in the average bond lengths of the metal to the ring junction carbons, i.e., C4, C9, and of the metal to adjacent carbon atoms of the five-membered ring, i.e., C1, C3. HA is the angle between the planes defined by [C1,C2,C3] and [C1,C3,C4,C9]. FA is the angle between the planes defined by [C1,C2,C3] and [C4,C5,C6,C7,C8,C9][14] (see Figure 9 for atom numbering).

The asymmetric unit of complex **9** contains one ruthenium complex and two dichloromethane solvent molecules. The Ru center is coordinated to $\eta^5$-Ind, $\eta^2$-dppf, and a monodentate xanthate ligand. The Ru centers in **12** and **16** are similarly coordinated with a monodentate dithiophosphinate ligand. The ORTEP diagrams of complexes **9**, **12**, and **16** are shown in Figures 2, 3, and 4.

 © 2007 Wiley-VCH Verlag GmbH & Co. KGaA, Weinheim 

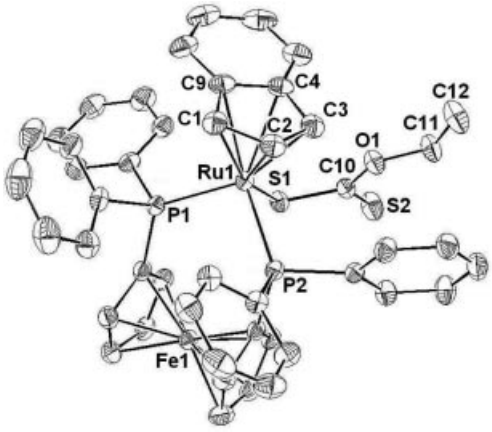


Figure 2. ORTEP diagram of **9**. Thermal ellipsoids are drawn to 50% probability level. Hydrogen atoms are omitted for clarity. Selected bond lengths [Å] and angles [°]: Ru1–C* 1.918, Ru1–C1 2.220(3), Ru1–C2 2.186(3), Ru1–C3 2.212(3), Ru1–C4 2.361(3), Ru1–C9 2.374(3), Ru1–P1 2.3110(7), Ru1–P2 2.2618(7), Ru1–S1 2.3964(7), S1–C10 1.712(3), S2–C10 1.674(3), C10–O1 1.331(4), P1–Ru1–P2 97.43(3), S1–Ru1–P1 89.31(3), S2–Ru1–P2 86.53(3), Ru1–S1–C10 116.03(10), S1–C10–S2 120.60(17), S1–C10–O1 116.4(2), S2–C10–O1 123.0(2), C10–O1–C11 118.5(2).

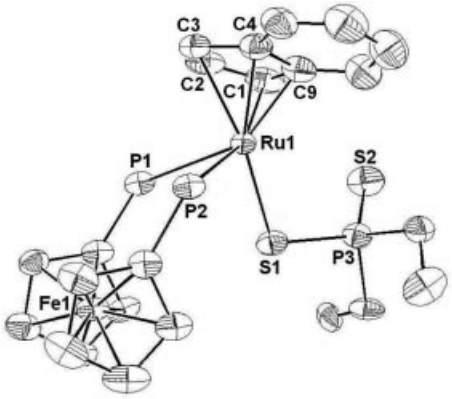


Figure 3. ORTEP diagram of **12**. Thermal ellipsoids are drawn to 50% probability level. Hydrogen atoms and phenyl groups are omitted for clarity. Selected bond lengths [Å] and angles [°]: Ru1–C* 1.941, Ru1–C1 2.244(8), Ru1–C2 2.168(7), Ru1–C3 2.182(7), Ru1–C4 2.408(7), Ru1–C9 2.424(8), Ru1–P1 2.2516(19), Ru1–P2 2.3181(18), Ru1–S1 2.4647(18), P1–Ru1–P2 98.98(7), S1–Ru1–P1 89.27(7), S1–Ru1–P2 86.07(6).

The $\eta^5$-indenyl ligands in **9** and **16** do not show noticeable distortion, while that of **12** is slightly distorted[14] (see Table 1). The fold angle of complex **16** indicates that the benzenoid ring of the indenyl ligand bends towards the ruthenium center rather than away as observed in **9** and **12**. This presumably is due to the coordination of a less sterically demanding dppm compared to dppf. Another interesting feature in the structures of complexes **9**, **12**, and **16** is the orientation of the monodentate dithiolate ligand. The noncoordinating S atom of the xanthate ligand in **9** is oriented away from the indenyl ligand, whereas those of the dithiophosphinate ligands in **12** and **16** are pointing towards the indenyl ligands, as shown in their stereo views. This probably arises from steric repulsion between the two

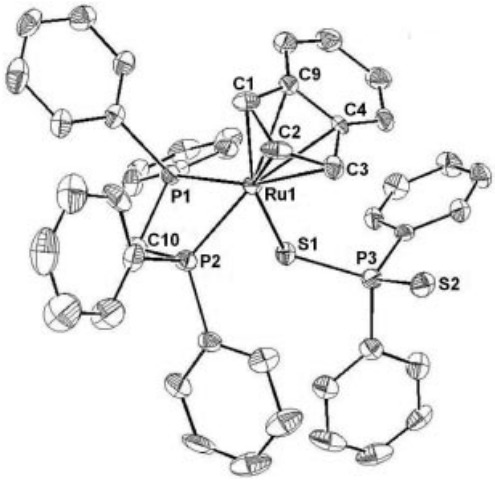


Figure 4. ORTEP diagram of **16**. Thermal ellipsoids are drawn to 50% probability level. Hydrogen atoms are omitted for clarity. Selected bond lengths [Å] and angles [°]: Ru1–C* 1.884, Ru1–C1 2.161(7), Ru1–C2 2.183(7), Ru1–C3 2.223(7), Ru1–C4 2.318(7), Ru1–C9 2.321(7), Ru1–P1 2.2695(19), Ru1–P2 2.242(2), Ru1–S1 2.439(2), S1–P3 2.044(3), S2–P3 1.965(3), C10–P1 1.848(7), C10–P2 1.848(8), P1–Ru1–P2 72.20(7), S1–Ru1–P1 84.98(7), S2–Ru1–P2 84.76(7), Ru1–S1–P3 117.45(10), S1–P3–S2 121.02(14), P1–C10–P2 92.0(3).

R groups in dithiophosphinate ligands and the indenyl ligands.

The six-coordinate complexes **7**, **11**, and **17** have also been characterized by X-ray diffraction analysis. Their molecular structures were found to be similar to those of known analogues, such as $[Ru(dppf)(S_2CNEt_2)_2]$[8] and $[Ru(L)(L')(S_2Z)_2]$ (L = CO, L = $PEt_3$, Z = $CNMe_2$, COEt, L = L′ = $PMe_2Ph$, Z = $PEt_2$)[16] (see electronic supporting information).

The molecular structure of the di-iodo-bridged complex **20** is shown in the ORTEP diagram (Figure 5). The structure exhibits crystallographic mirror symmetry, with the

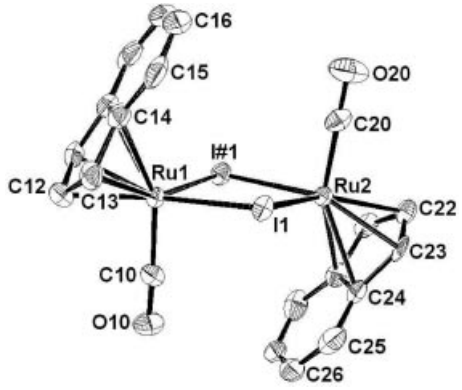


Figure 5. ORTEP drawing of $[(Ind)Ru(CO)I]_2$ **20** with 50% probability thermal ellipsoids. H atoms are omitted for clarity. Selected bond lengths [Å] and angles [°]: Ru1–C* 1.874, Ru1–C12 2.142(16), Ru1–C13 2.172(10), Ru1–C14 2.334(10), Ru2–C* 1.885, Ru2–C22 2.141(15), Ru2–C23 2.171(10), Ru2–C24 2.356(10), Ru1···Ru2 4.014, Ru1–I1 2.716(10), Ru2–I1 2.717(10), Ru1–C10 1.820(15), Ru2–C20 1.812(16), I1–Ru1–I#1 84.37(4), I1–Ru2–I#1 84.35(4), C10–Ru1–I1 93.1(4), C20–Ru2–I1 92.5(4), Ru1–I1–Ru2 95.26(3).

 © 2007 Wiley-VCH Verlag GmbH & Co. KGaA, Weinheim 

mirror plane passing through the two Ru centers, the two CO ligands and the center of the two $\eta^5$-Ind ligands through C12 and C22. As in $[(Ind)Ru(CO)_2]_2$, the structure possesses two *trans* CO ligands and two *trans* [(Ind)-Ru(CO)] fragments, but unlike it, there is no interaction between Ru1 and Ru2 (4.014 Å).

The ORTEP diagram for the molecular structure of **21** is depicted in Figure 6, together with selected bond parameters. The structure shows a three-legged piano-stool configuration at $Ru^{II}$, being coordinated to $\eta^5$-Ind, $\eta^2$-$S_2CNEt_2$, and one CO ligand. The slip-fold parameters for **21** are in agreement with $\eta^5$-coordination of Ind.[14] As in the structure of **4a**, the metric data show that there is extensive electron delocalization in the $S_2CNEt_2$ ligand.

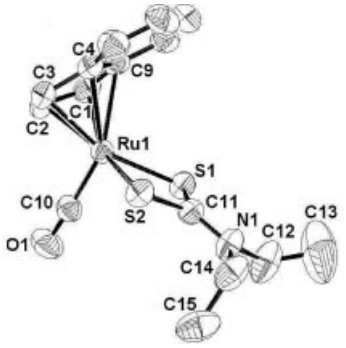


Figure 6. ORTEP drawing of $(Ind)Ru(CO)(S_2CNEt_2)$ **21** with 50% probability thermal ellipsoids. H atoms are omitted for clarity. Selected bond lengths [Å] and angles [°]: Ru1–C* 1.910, Ru1–C1 2.210(4), Ru1–C2 2.174(4), Ru1–C3 2.191(4), Ru1–C4 2.358(4), Ru1–C9 2.372(4), Ru1–S1 2.4035(10), Ru1–S2 2.3930(10), S1–C11 1.712(4), S2–C11 1.724(4), C11–N1 1.320(5), Ru1–C10 1.807(4), S1–Ru1–S2 72.22(3), S1–C11–S2 110.7(2).

An examination of slip-fold parameters of the indenyl complexes in this study and two other reported examples (Table 1) shows that complexes **4a**, **16**, **20**, and **21** possess FA values smaller than their HA values. This observation is unusual for $\eta^5$-indenyl complexes. The probable cause is the lack of a bulky ligand directly below the benzenoid ring of the Ind ligand in these complexes, unlike the structural feature found in **9**, **12**, **F**, and **G**. In these four latter phosphane complexes, the steric repulsion between the indenyl and bulky phosphane ligands forces the benzenoid ring to "flip" away from the Ru center, hence resulting in greater FA values.

### Lability of the Indenyl Ligand

The foregoing results indicate that the lability of the indenyl ligand is influenced by the incoming 1,1-dithiolate and the coligands, according to the following trends: (i) dithiolates: $^-S_2CNR_2 > {}^-S_2COR > {}^-S_2PR_2$, (ii) coligands: CO ≈ dppm > dppf. Trend (i) can be readily rationalized, based on e-density considerations of the S donor atoms. The observation of monodenticity of the $S_2PR_2$ moiety in the high-yield indenyl complexes, **12**–**14** and **16**, is significant. In this dithiolate series, the S atoms in $^-S_2PR_2$ possess the most *localized* and hence highest electron density, whereas those in $^-S_2CNR_2$ possess the *lowest* electron density because of extensive electron delocalization. Hence the increased tendency of the latter towards chelation. In the absence of a vacant site or an easily displaceable ligand, chelation of a ligand will inevitably enforce dissociation of the indenyl ligand. For rationalizing trend (ii), we note that the benzenoid ring of the indenyl ligand can be considered as an electron-withdrawing group,[18] hence an electron-rich Ru center is required for strong interaction with $\eta^5$-Ind through its fused $C_5H_3$ ring, a situation provided by strong donor coligands like dppf, while labilization of the indenyl ligand will be assisted by the presence of a strong π-acceptor coligand, like CO.

The application of density functional theory has provided an understanding of the effect of different ligands on the energetics of $\eta^5 \rightarrow \eta^3$ ring slippage of the indenyl ligand and hence on its dissociation tendency. In a recent study, Veiros et al. demonstrated that the effect of the nature of the coligands on the strength of the indenyl–metal bond plays an important role in the energetics of $\eta^5$ versus $\eta^3$ indenyl–molybdenum complexes.[19] Because of the constraints on computational time, we have selected the complexes $[(Ind)Ru(L)_2(S_2COMe)]$ (**H1**: L = $PMeH_2$, **H2**: L = $PH_3$, **H3**: L = CO), containing small phosphane ligands such as $PH_3$ and $PH_2Me$, rather than the larger diphos ligands (dppm or dppf), as the model compounds for study. In this series, complex **H1** contains the strongest σ-donor ligand, followed by **H2**, with **H3** possessing the strongest π-acceptor ligand. The dissociation of the indenyl ligand by $\eta^5 \rightarrow \eta^3 \rightarrow \eta^1$ has been considered and the results are presented in Figure 7.

It was found that $\eta^5 \rightarrow \eta^3$ indenyl ring slippage in complexes **H1** and **H2** possesses comparable activation energy (67 and 70 kJ/mol, respectively), with the process in **H1** being slightly more endothermic (7.4 kJ/mol). However, a remarkable difference was observed in the case of the strong π-acceptor CO in complex **H3**. Not only is the activation energy of the slippage almost half that for both **H1** and **H2** (33 kJ/mol), but the $\eta^3$-Ind coordination mode is more favorable, with the $\eta^5 \rightarrow \eta^3$ ring slippage process being exothermic (–13 kJ/mol). This is consistent with the expectation that stronger σ-donor ligands enhance the interaction between electron-rich Ru and the $\eta^5$-Ind ligand and vice versa. Therefore, as the dithiolate ligand tends to chelate to the electron-deficient Ru, the weak interaction of the $\eta^5$-Ind ligand and the Ru center would have facilitated the ease of $\eta^5 \rightarrow \eta^3$ slippage, and the combined effect would be the dissociation of the indenyl ligand.

A comparison between the effect of xanthate and dithiocarbamate ligands on indenyl ring slippage has also been made using the $PH_3$-containing complex **H4** as the model compound. As shown in Figure 1, the formation of the $\eta^3$-Ind isomer of the dithiocarbamate complex **H4** is a much more exothermic process. Unfortunately the transition state for this process could not be located, though it is not uncommon for activation energies of highly exothermic processes to be much lower or even close to zero, thus causing the transition state to assume a structure similar to that of

 © 2007 Wiley-VCH Verlag GmbH & Co. KGaA, Weinheim 

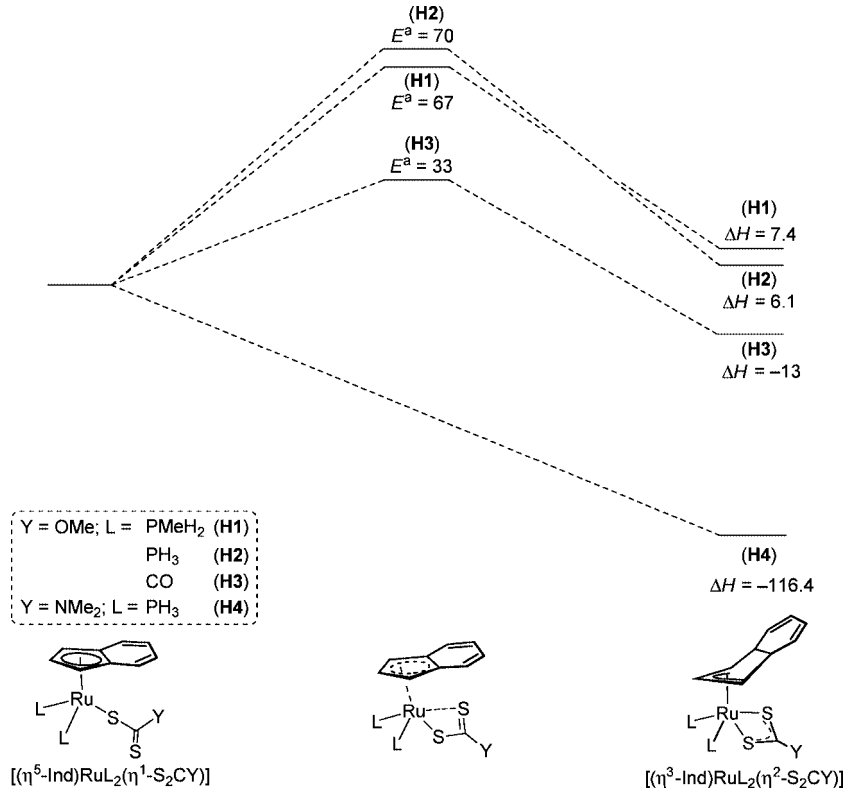


Figure 7. Energy diagram of ring slippage from $\eta^5 \rightarrow \eta^3$ ($E^a$ is activation energy in kJ/mol).

the reactant. This may have caused difficulty in optimizing the transition-state structure using computational methods. Nevertheless the calculations indicated that $^-S_2CNR_2$ exerts a stronger effect than xanthate in causing indenyl ring slippage, in good agreement with the trend observed in the experimental data.

## Electrochemical Studies

Cyclic voltammograms performed at a GC electrode in 0.5 mM solutions of **10** and **13** in $CH_2Cl_2$ at 233 K are shown in Figure 8. Complex **10** displayed one chemically irreversible oxidation process at about 0 V versus $Fc/Fc^+$. The expression "chemical reversibility" when used in connection with cyclic voltammetry experiments relates to the ratio of the oxidative ($i_p^{ox}$) to reductive peak currents ($i_p^{red}$). The $i_p^{ox}/i_p^{red}$ ratio approaches unity for a fully chemically reversible process. Complex **13** showed three oxidation processes, although the two most positive processes displayed small reverse peaks when the scan direction was reversed, suggesting instability of the highly oxidized states. Increasing the scan rate up to 5 V/s did not improve the chemical reversibility of the processes shown in Figure 8. Table 2 lists the reversible oxidation potentials ($E^r_{1/2}$) that were calculated from CV data under conditions where the $i_p^{ox}/i_p^{red}$ ratio was equal to unity and using the relationship [Equation (1)]

$$E^r_{1/2} = (E_p^{ox} + E_p^{red})/2 \quad (1)$$

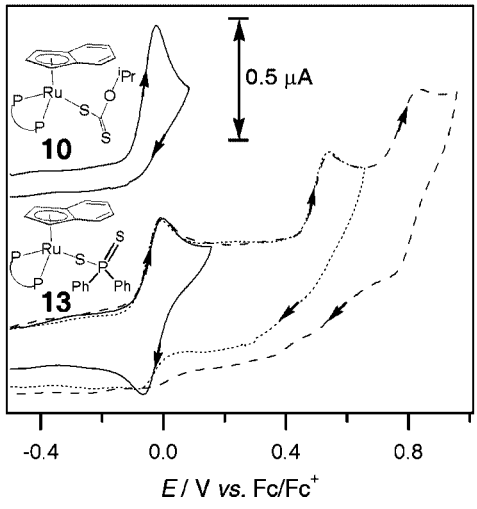


Figure 8. Cyclic voltammograms performed at a 1-mm diameter planar GC electrode in $CH_2Cl_2$ (0.25 M $Bu_4NPF_6$) at 233 K at a scan rate of 100 mV/s for 0.5 mM **10** and **13**.

where $E_p^{ox}$ and $E_p^{red}$ are the anodic and cathodic peak potentials respectively. In situations where small reverse peaks were observed, only the forward (oxidative) peak potentials are given.

The peak current intensities were similar to those obtained under identical conditions for the one-electron oxidation of **1**, [(Ind)Ru(dppf)(SMe)], [(Ind)Ru(dppf)(SPh)],[7]

 © 2007 Wiley-VCH Verlag GmbH & Co. KGaA, Weinheim 

Table 2. Cyclic voltammetric data obtained at a scan rate of 100 mV/s at a 1-mm diameter glassy carbon electrode at 233 K in $CH_2Cl_2$ with 0.25 M $Bu_4NPF_6$ as the supporting electrolyte.

| Compound | Oxidation process[a] | | | |
|---|---|---|---|---|
| | $E_p^{ox}$ [V][b] | $E_p^{red}$ [V][c] | $E^r_{1/2}$ [V][d] | $\Delta E$ [mV][e] |
| **10** | –0.023 | | | |
| **13** | –0.004 | –0.068 | –0.04 | 64 |
| | +0.540 | | | |
| | +0.830 | | | |

[a] All potentials in Table 2 are relative to the ferrocene/ferrocenium redox couple. [b] $E_p^{ox}$ is the oxidative peak potential. [c] $E_p^{red}$ is the reductive peak potential. [d] $E^r_{1/2} = (E_p^{red} + E_p^{ox})/2$. [e] $\Delta E = |E_p^{ox} - E_p^{red}|$.

**I**, and [Cp*Ru(dppf)Cl] (**VI**), indicating that **10** and **13** were also oxidized by one electron. However, **1**, [(Ind)Ru(dppf)(SMe)], [(Ind)Ru(dppf)(SPh)], **I**, and **VI** showed two or three one-electron chemically reversible oxidation processes, whilst cyclic voltammograms performed on solutions of **10** and **13** indicated that their oxidized states were relatively unstable even at low temperatures (Figure 8).[7]

Based on previous studies, it is thought that the initial oxidation process in Figure 8 for **10** and **13** is associated with $Ru^{II}$ being oxidized to $Ru^{III}$ (rather than oxidation in the region of dppf), as this process is very sensitive to the substituent (S or Ind) coordinated to the Ru. It is thought that the second process in the CV of **13** is associated with oxidation in the region of dppf, as the potential is close to that observed in other dppf-containing complexes,[7] while the third oxidation process is associated with further oxidation of the Ru ion. This would explain why the third oxidation process shows more chemical reversibility than the second process, if the individual regions (Ru and Fe) are not electronically communicating, then it is possible that the individual oxidation processes are semi-independent of one another (i.e., the first and third are associated with oxidation of the Ru ion, whilst the second process involves oxidation in the vicinity of dppf).

Both compounds displayed one chemically irreversible reduction process at very negative potentials (about –2.5 V vs. $Fc/Fc^+$), with a similar current magnitude to the first oxidation process (indicating that the same number of electrons were transferred). It is not possible to conclude whether the chemical instability of the reduced compounds is because of increased chemical reactivity due to the very high reduction potentials, or due to an $\eta^5 \rightarrow \eta^3$ ring slippage mechanism following reduction.

## Conclusions

The lability of the Ind ligand in halide substitution of [(Ind)Ru($L_2$)Cl] [$L_2$ = dppf, dppm or $(CO)_2$] with 1,1′-dithiolates is dependent on several variables: (i) the nature of the coligand $L_2$, which follows a lability order: dppf < dppm ≈ CO, in agreement with the electron donor capability of $L_2$ and calculated energetics for $\eta^5 \rightarrow \eta^3$ ring slippage in related (Ind)Ru complexes, (ii) the incoming dithiolates, which results in ease of indenyl ligand dissociation at (Ind)Ru(dppf) as follows: dithiocarbamates > xanthates > dithiophosphinates, in agreement with DFT calculations, and (iii) the solvent medium, as illustrated in complete dissociation of Ind from (Ind)Ru(dppf) in dithiocarbamate substitution in the highly polar solvent MeOH relative to partial dissociation in $CH_2Cl_2$. In the case of the (Ind)-$Ru(CO)_2$ substrate, dissociation of Ind could be averted by chemically assisted decarbonylation of the complex before reaction with 1,1-dithiolate ligands. The hydride species [(Ind)Ru(diphos)H], formed in solvent- and stoichiometry-dependent yields in the (diphos) systems, presumably arose from the presence of $OMe^-$ in MeOH, as previously observed.[7] Cyclic voltammetry experiments indicate that the (Ind)Ru(dppf) derivatives containing $\eta^1$-$S_2CO$*i*Pr and $\eta^1$-$S_2PPh_2$ can be oxidized in one-electron chemical irreversible and reversible processes, respectively, at a scan rate of 100 mV/s at about 0 V versus $Fc/Fc^+$.

## Experimental Section

**General:** All reactions were carried out using conventional Schlenk techniques under inert nitrogen or under argon in an M. Braun Labmaster 130 Inert Gas System. NMR spectra were measured on a Bruker 300 FT NMR spectrometer, $^1H$ chemical shifts were referenced to residual solvent in the deuterio-solvents, $C_6D_6$ or $CD_3CN$, and $^{31}P$ chemical shifts were referenced to external $H_3PO_4$. IR spectra in KBr pellets were measured in the range 4000–400 $cm^{-1}$ by means of a BioRad FTS-165 FTIR instrument. Mass spectra were run on a Finnigan Mat 95XL-T (FAB) or a Finnigan-MAT LCQ (ESI) spectrometer. Voltammetric experiments were conducted with a computer-controlled Eco Chemie μAutolab III potentiostat. The electrochemical cell was jacketed in a glass sleeve and cooled to 233 K using a Lauda RL6 variable-temperature methanol-circulating bath. Elemental analyses were performed by the microanalytical laboratory in-house. [(Ind)Ru(dppf)Cl] (**1**),[20] [(Ind)Ru(dppm)Cl] (**2**),[21] and [(Ind)Ru$(CO)_2$I] (**18**)[22] were prepared by published methods. All other chemicals were obtained commercially and used without any further purification. All solvents were dried with sodium/benzophenone and distilled before use. Celite (Fluka AG) and silica gel (Merck Kieselgel 60, 230–400 Mesh) were dried at 140 °C overnight before chromatographic use.

Conventional numbering of indenyl protons shown in Figure 9 is followed in the assignment of NMR signals.

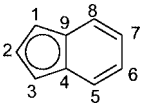


Figure 9. Atom labeling of the indenyl ligand.

### (I) Reactions of (Ind)Ru(diphosphane) Complexes

### (a) Reactions with Dialkyl Dithiocarbamates

(i) Reactions of [(Ind)Ru(dppf)Cl] (**1**) with $NaS_2CNR_2$ were carried out at stoichiometries of 1:1 and 1:4. A typical reaction for each stoichiometry is described for R = Et, as follows:

**1:$S_2CNR_2$ (1:1):** $NaS_2CNEt_2 \cdot 3H_2O$ (10 mg, 0.04 mmol) was added to a suspension of **1** (35 mg, 0.04 mmol) in MeOH (5 mL) and the mixture was stirred at room temp. for 18 h. The color of the suspen-

 © 2007 Wiley-VCH Verlag GmbH & Co. KGaA, Weinheim 

sion slowly changed from red to yellow. The suspension was filtered and the residue was extracted using toluene (2 × 5 mL). The filtrate was examined by GC/MS, which showed indene. The extract was concentrated to about 2 mL and loaded onto a silica gel column (2 × 5 cm) prepared in n-hexane. Elution gave two fractions: (i) a yellow eluate in toluene (8 mL), which yielded [(Ind)Ru(dppf)H] (**6**) (13 mg, 39% yield) (for the reaction in which R = Me, 11 mg, 32% yield, R = $C_5H_{10}$, 8 mg, 25% yield), (ii) a yellow eluate in toluene/THF (1:1, 10 mL), which yielded [Ru($\eta^2$-dppf)($\eta^2$-$S_2CNEt_2$)$_2$] **4** (25 mg, 60% yield). Similar reactions gave **3** (R = Me), 22 mg, 56% yield, and **5** (R = $C_5H_{10}$), 25 mg, 58% yield. Analytical pure samples of complexes **3**–**5** were obtained by recrystallization from THF/hexane (1:5).

**1:$S_2CNR_2$ (1:4). Reaction in MeOH:** $NaS_2CNEt_2 \cdot 3H_2O$ (40 mg, 0.16 mmol) was added to a suspension of **1** (35 mg, 0.04 mmol) in MeOH (5 mL) and the mixture was stirred at room temp. for 18 h. The color of the suspension slowly changed from red to yellow. The solvent was removed in vacuo and the residue was extracted with toluene (2 × 5 mL). The extract was concentrated to about 2 mL, addition of hexane (2 mL) at –30 °C for 1 d gave yellow crystals of **4** (37 mg, 90% yield). Similar reactions gave **3** (R = Me), 36 mg, 92% yield, and **5** (R = $C_5H_{10}$), 41 mg, 98% yield.

**Reaction in $CH_2Cl_2$:** $NaS_2CNEt_2 \cdot 3H_2O$ (60 mg, 0.24 mmol) was added to a solution of **1** (50 mg, 0.06 mmol) in $CH_2Cl_2$ (10 mL) and the mixture was refluxed for 4 h. The solution was evacuated to dryness and the residue extracted with diethyl ether (2 × 3 mL). The extract was concentrated to about 3 mL and kept at –30 °C, after 2 d, yellow microcrystals of **4** (16 mg, 28% yield) were collected. Addition of hexane (about 0.5 mL) to the mother liquor led to the isolation of red microcrystals of [(Ind)Ru($\eta^1$-dppf)($\eta^2$-$S_2CNEt_2$)] (**4a**) (20 mg, 36% yield) after two more days at –30 °C.

A small-scale reaction was carried out at stoichiometry 1:2, using **1** (5 mg, 6.2 μmol) and $NaS_2CNEt_2 \cdot 3H_2O$ (3 mg, 12 μmol) in MeOH (2 mL) and the red suspension was stirred at room temp. for 18 h. The resultant yellow suspension was filtered to give yellow solids, **4** (5 mg, 85% yield), and pale yellow filtrate. The $^1$H and $^{31}$P NMR spectra of the yellow solids (in $C_6D_6$) showed **4** as the sole product. A new batch of **1** (5 mg, 6.2 μmol) was added to the filtrate and the red suspension was stirred for another 18 h. The resultant yellow suspension was filtered and the yellow solids, **6** (4 mg, 84% yield) were obtained. The $^1$H and $^{31}$P NMR spectra of the yellow solids in $C_6D_6$ indicate the sole presence of **6**.

**Data for 3:** $^1$H NMR ($C_6D_6$): $\delta$ = 2.41 and 2.43 [each s, 3 H, $S_2CN(CH_3)_2$], 3.94, 4.04, 4.62 and 4.69 (each s, 2 H, $C_5H_4$), 7.03–7.11, 7.21–7.25, 7.95 and 8.20–8.25 (m, 20 H, Ph) ppm. $^{31}$P{$^1$H} NMR ($C_6D_6$): $\delta$ = 47.9 (s, dppf) ppm. IR (KBr): $\tilde{\nu}$ = 3053 (w), 2922 (w), 2855 (w), 1509 [m, SC(S)], 1432 [m, SC(S)], 1386 [s, SC(S)], 1262 [m, SC(S)], 1146 (m), 1086 (m), 1028 (m), 811 (w), 746 (w), 697 (m), 548 (w), 521 (w) cm$^{-1}$. FAB$^+$-MS: *m*/*z* (%) = 896 [M]$^+$, 776 [M – $S_2CNMe_2$]$^+$. $C_{40}H_{40}FeN_2P_2RuS_4 \cdot 1/4C_6H_{12}$ (917.39): calcd. C 54.3, H 4.7, N 3.1, S 14.0, found C 54.1, H 5.1, N 3.2, S 13.5.

**Data for 4a:** $^1$H NMR ($C_6D_6$): $\delta$ = 0.61 [t, $^3J_{HH}$ = 7.4 Hz, 6 H, $S_2CN(CH_2CH_3)_2$], 2.81 and 3.04 [each m, $^3J_{HH}$ = 7.4 Hz, 2 H, $S_2CN(CH_2CH_3)_2$], 4.11 and 4.33 (each s, 2 H, $C_5H_4$), 4.19 (s, 4 H, $C_5H_4$), 4.56 (t, $^3J_{HH}$ = 2.5 Hz, 1 H, H$^2$), 4.89 (d, $^3J_{HH}$ = 2.5 Hz, 2 H, H$^{1,3}$), 7.04–7.16, 7.37–7.40, 7.42–7.48 and 7.75–7.81 (each m, total 24 H, H$^{5-8}$ and Ph) ppm. $^{31}$P{$^1$H} NMR ($C_6D_6$): $\delta$ = 57.3 and –17.7 (each s, dppf) ppm. IR (KBr): $\tilde{\nu}$ = 3050 (w), 2972 (w), 2929 (w), 1484 [s, SC(S)], 1431 [vs, SC(S)], 1380 (w), 1324 (w), 1270 [m, SC(S)], 1215 (w), 1159 (m), 1092 (m), 1030 (m), 830 (w), 743 (m), 696 (vs), 543 (m), 517 (m) cm$^{-1}$. FAB$^+$-MS: *m*/*z* (%) = 804 [M – Ind]$^+$. $C_{48}H_{45}FeNP_2RuS_2$ (918.87): calcd. C 62.7, H 4.9, N 1.5, S 7.0, found C 62.6, H 5.2, N 1.3, S 6.9.

**Data for 5:** $^1$H NMR ($C_6D_6$): $\delta$ = 0.95 (br. s, 12 H, $S_2CNC_5H_{10}$), 3.02, 3.63 (each br. s, 4 H, $S_2CNC_5H_{10}$), 3.95, 4.05, 4.62 and 4.71 (each s, 2 H, $C_5H_4$), 7.00–7.23, 7.69–7.72, 8.03–8.05 and 8.19–8.24 (each m, total 20 H, Ph) ppm. $^{31}$P{$^1$H} NMR ($C_6D_6$): $\delta$ = 47.6 (s, dppf) ppm. IR (KBr): $\tilde{\nu}$ = 3048 (w), 2931 (m), 2853 (m), 1479 [s, SC(S)], 1433 [s, SC(S)], 1233 [s, SC(S)], 1129 (m), 1086 (m), 995 (m), 885 (w), 850 (w), 811 (w), 743 (m), 695 (s), 546 (m), 518 (m) cm$^{-1}$. FAB$^+$-MS: *m*/*z* (%) = 976 [M]$^+$, 816 [M – $S_2CNC_5H_{10}$]$^+$. $C_{46}H_{48}FeN_2P_2RuS_4$ (976.01): calcd. C 56.6, H 5.0, N 2.9, S 13.1, found C 56.5, H 5.0, N 2.7, S 12.9.

(ii) Reactions of [(Ind)Ru(dppm)Cl] **2** with $NaS_2CNEt_2$ were carried out at stoichiometries of 1:1 and 1:4.

**2:$S_2CNR_2$ (1:1):** $NaS_2CNEt_2 \cdot 3H_2O$ (10 mg, 0.04 mmol) was treated with **2** (20 mg, 0.04 mmol) in MeOH (5 mL). A similar workup as described above for the dppf analogue yielded [Ru(dppm)($\eta^2$-$S_2CNEt_2$)$_2$] (**7**) (18 mg, 58% yield) and [(Ind)Ru(dppm)H] (**8**) (5 mg, 20% yield), identified by its published proton NMR spectroscopic data, notably $\delta$(H) –14.21 (s) in $C_6D_6$ versus the lit. value of –14.12 (s) in $CD_2Cl_2$.[10]

**Using 2:$S_2CNR_2$ (1:4):** A similar reaction as described above for **1** was carried out, using $NaS_2CNEt_2 \cdot 3H_2O$ (20 mg, 0.08 mmol) and [(Ind)Ru(dppm)Cl] (**2**) (10 mg, 0.02 mmol) in MeOH (5 mL) and the mixture was stirred for 4 h. Similar workup procedures gave yellow crystals of [Ru(dppm)($\eta^2$-$S_2CNEt_2$)$_2$] (**7**) (10 mg, 81% yield).

**Data for 7:** $^1$H NMR ($C_6D_6$): $\delta$ = 0.63–0.68 and 0.86–0.91 (each t-like m, 6 H, $CH_3$), 2.85–3.02 (m, 2 H, $CH_2CH_3$), 3.15–3.28 (m, 2 H, $CH_2CH_3$), 3.43–3.62 (m, 4 H, $CH_2CH_3$), 4.73 (t, $^2J_{HP}$ = 9.9 Hz, 2 H, $CH_2$ of d), 6.98–7.16 (m, 14 H, Ph), 7.54–7.58 (m, 3 H, Ph), 7.93–7.95 (m, 3 H, Ph) ppm. $^{31}$P{$^1$H} NMR ($C_6D_6$): $\delta$ = 3.7 (s, dppm) ppm. IR (KBr): $\tilde{\nu}$ = 3050 (w), 2974 (w), 2929 (w), 2871 (w), 1483 [s, SC(S)], 1426 [s, SC(S)], 1303 (w), 1268 [s, SC(S)], 1214 (m), 1142 (m), 1091 (m), 997 (w), 911 (w), 848 (w), 698 (s), 535 (m) cm$^{-1}$. FAB$^+$-MS: *m*/*z* (%) 782 [M]$^+$, 634 [M – $S_2CNEt_2$]$^+$. $C_{35}H_{42}N_2P_2RuS_4$ (782.00): calcd. C 53.8, H 5.4, N 3.6, S 16.4, found C 53.8, H 5.5, N 3.7, S 16.2.

**(b) Reactions with Alkyl Xanthates**

(i) $KS_2COR$ (0.07 mmol, R = Et, 11 mg, R = *i*Pr, 12 mg) was added into a solution of **1** (15 mg, 0.02 mmol) in $CH_2Cl_2$ (10 mL) and the mixture was refluxed. The reaction was not accompanied by any color change, hence it was monitored by $^1$H and $^{31}$P NMR spectroscopy. After the reaction was complete (about 4 h), the solution was evacuated to dryness. The solid residue was extracted with toluene (2 × 2 mL) and the concentrated extract recrystallized from 1:2 THF/hexane at –30 °C. Red microcrystals of [(Ind)Ru(dppf)($\eta^1$-$S_2COR$)] [R = Et (**9**), 13 mg, 78% yield, R = *i*Pr (**10**), 14 mg, 83% yield] were obtained after one day.

**Data for 9:** $^1$H NMR ($C_6D_6$): $\delta$ = 1.06 (t, $^3J_{HH}$ = 7.4 Hz, 3 H, $S_2COCH_2CH_3$), 3.55, 3.81, 3.98 and 4.34 (each s, 2 H, $C_5H_4$), 4.41 (q, $^3J_{HH}$ = 7.4 Hz, 2 H, $S_2COCH_2CH_3$), 5.16 (s, 1 H, H$^2$), 5.43 (s, 2 H, H$^{1,3}$), 6.98–7.14, 7.26–7.30 and 7.43–7.48 (each m, total 24 H, H$^{5-8}$ and Ph) ppm. $^{31}$P{$^1$H} NMR ($C_6D_6$): $\delta$ = 54.9 (s, dppf) ppm. IR (KBr): $\tilde{\nu}$ = 3050 (w), 2978 (w), 1478 (w), 1432 (w), 1382 (w), 1165 [s, (CO)], 1105 [s, (CS)], 1030 [vs, (CS)], 858 w, 819 w, 792 w, 744 m, 697 s, 631 w, 513 m. FAB$^+$-MS: *m*/*z* (%) = 892 [M]$^+$, 777 [M – Ind]$^+$, 655 [M – Ind – $S_2COEt$]$^+$. $C_{46}H_{40}FeOP_2RuS_2$ (891.80): calcd. C 62.0, H 4.5, S 7.2, found C 61.6, H 4.8, S 7.5.

**Data for 10:** $^1$H NMR ($C_6D_6$): $\delta$ = 1.25 [d, $^3J_{HH}$ = 5.76 Hz, 6 H, $S_2COCH(CH_3)_2$], 3.55, 3.84, 3.98 and 4.46 (each s, 2 H, $C_5H_4$),

 © 2007 Wiley-VCH Verlag GmbH & Co. KGaA, Weinheim 

5.17 (s, 1 H, $H^2$), 5.51 (s, 2 H, $H^{1,3}$), 5.67 [sept, $J$ = 6.6 Hz, 1 H, $S_2COCH(CH_3)_2$] 7.00–7.47 (m, 24 H, $H^{5-8}$ and Ph) ppm. $^{31}P\{^1H\}$ NMR ($C_6D_6$): $\delta$ = 54.8 (s, dppf) ppm. IR (KBr): $\tilde{\nu}$ = 3047 (w), 2963 (w), 2923 (w), 1940 (w), 1478 (w), 1433 (w), 1382 (w), 1261 [m, (CO)], 1187 (w), 1089 [s, SC(S)], 1015 [s, SC(S)], 803 (s), 743 (m), 695 (s), 631 (w), 507 (m) $cm^{-1}$. $FAB^+$-MS: $m/z$ (%) = 906 $[M]^+$, 791 $[M - Ind]^+$, 771 $[M - S_2CO{i}Pr]^+$, 655 $[M - Ind - S_2CO{i}Pr]^+$. $C_{47}H_{42}FeOP_2RuS_2$ (905.83): calcd. C 62.3, H 4.7, S 7.0, found C 61.9, H 4.8, S 6.6.

(ii) $KS_2CO{i}Pr$ (23 mg, 0.13 mmol) was added to a solution of **2** (20 mg, 0.03 mmol) in MeOH (5 mL) and the solution was stirred at room temp. for 18 h. The color of the solution changed slowly from red to yellow in the course of reaction. The yellow product solution was evacuated to dryness and the residue extracted with toluene (2 × 2 mL). Addition of hexane (about 4 mL) into the concentrated extract (about 2 mL) at –30 °C for 1 d gave [Ru(dppm)($\eta^2$-$S_2CO{i}Pr$)$_2$] (**11**) (27 mg, 93% yield) as yellow microcrystals.

**Data for 11:** $^1H$ NMR ($C_6D_6$): $\delta$ = 0.87–0.89 and 0.95–0.97 (each d-like m, 6 H, $CH_3$), 4.67 (t, $^2J_{HP}$ = 9.9 Hz, 2 H, $CH_2$ of d), 5.34 [sept, $^3J_{HH}$ = 6.6 Hz, 2 H, $CH(CH_3)_2$], 6.95–7.02 (m, 7 H, Ph), 7.08–7.16 (m, 5 H, Ph), 7.38–7.45 (m, 4 H, Ph), 7.81–7.89 (m, 4 H, Ph) ppm. $^{31}P\{^1H\}$ NMR ($C_6D_6$): $\delta$ = 4.1 (s, dppm) ppm. IR (KBr): $\tilde{\nu}$ = 3049 (w), 2976 (w), 2930 (w), 1481 (w), 1432 (m), 1371 (w), 1231 [vs, (CO)], 1093 [vs, SC(S)], 1033 [s, SC(S)], 905 m, 723 s, 696 s, 538 m, 509 s. $FAB^+$-MS: $m/z$ (%) = 756 $[M]^+$. $C_{33}H_{36}O_2P_2RuS_4$ (755.92): calcd. C 52.4, H 4.8, S 17.0, found C 52.4, H 4.8, S 17.0.

**(c) Reactions with Dithiophosphinates**

(i) $NaS_2PR_2$ (0.04 mmol, R = Et, 7 mg, R = Ph, 11 mg) was added to a suspension of **1** (10 mg, 0.01 mmol) in MeOH and the mixture was stirred at room temp. for 18 h. The resultant red solution was evacuated to dryness and the residue extracted with toluene (2 × 3 mL). The extract was concentrated to about 2 mL and loaded on a silica gel column (1.5 × 2.0 cm). Elution with 2:1 hexane/diethyl ether (3–5 mL) and subsequent workup gave red crystals of [(Ind)Ru(dppf)($\eta^1$-$S_2PR_2$)] (R = Et (**12**), 8 mg, 70% yield, R = Ph (**13**), 9 mg, 72% yield).

**Data for 12:** $^1H$ NMR ($C_6D_6$): $\delta$ = 1.18–1.30 [m, 6 H, $S_2P(CH_2CH_3)_2$], 1.90–2.12 [m, 4 H, $S_2P(CH_2CH_3)_2$], 3.70, 3.81, 4.20 and 5.15 (each s, 2 H, $C_5H_4$), 4.84 (s, 1 H, $H^2$), 5.70 (s, 2 H, $H^{1,3}$), 6.90–6.93 and 7.58–7.61 (each 4-line m, $^3J_{HH}$ = 3.3 Hz, 2 H, $H^{5-8}$), 7.11–7.68 (m, 20 H, Ph) ppm. $^{31}P\{^1H\}$ NMR ($C_6D_6$): $\delta$ = 54.8 (d, $^3J_{PP}$ = 16 Hz, dppf), 87.5 (t, $^3J_{PP}$ = 16 Hz, $S_2PEt_2$) ppm. IR (KBr): $\tilde{\nu}$ = 3054 (w), 2966 (w), 2924 (w), 2868 (w), 1479 (w), 1433 (m), 1325 (w), 1157 (w), 1090 (m), 1030 (m), 821 (m), 746 [s, (PS)], 695 (PS), 594 [w, (PS)], 632 (m), 511 (s) $cm^{-1}$. $FAB^+$-MS: $m/z$ (%) = 924 $[M]^+$, 809 $[M - Ind]^+$, 771 $[M - S_2PEt_2]^+$, 655 $[M - Ind - S_2PEt_2]^+$. $C_{47}H_{45}FeP_3RuS_2$ (923.833): calcd. C 61.1, H 4.9, found C 61.4, H 4.7.

**Data for 13:** $^1H$ NMR ($C_6D_6$): $\delta$ = 3.60, 3.79, 4.05 and 5.20 (each s, 2 H, $C_5H_4$), 5.10 (s, 1 H, $H^2$), 5.34 (s, 2 H, $H^{1,3}$), 6.61–6.64 and 7.35–7.39 (each 4-line m, 2 H, $H^{5-8}$), 7.05–7.19, 7.26–7.33 and 7.45–7.51 (each m, total 26 H, Ph), 8.43–8.50 (4-line m, 4 H, Ph) ppm. $^{31}P\{^1H\}$ NMR ($C_6D_6$): $\delta$ = 53.1 (d, $^3J_{PP}$ = 15 Hz, dppf), 71.1 (t, $^3J_{PP}$ = 15 Hz, $S_2PPh_2$) ppm. IR (KBr): $\tilde{\nu}$ = 3052 (w), 2922 (w), 2854 (w), 1650 (w), 1477 (w), 1433 (m), 1158 (w), 1089 (m), 1033 (w), 821 (w), 745 [m, (PS)], 698 [s, (PS)], 649 [m, (PS)], 512 (m) $cm^{-1}$. $FAB^+$-MS: $m/z$ (%) = 1020 $[M]^+$, 905 $[M - Ind]^+$, 771 $[M - S_2PPh_2]^+$, 655 $[M - Ind - S_2PPh_2]^+$. $C_{55}H_{45}FeP_3RuS_2$ (1019.91): calcd. C 64.8, H 4.5, S 6.3, found C 64.8, H 4.4, S 5.8.

(ii) $NaS_2PR_2$ (0.31 mmol, R = Et, 55 mg, R = Ph, 85 mg) was added to a suspension of **2** (50 mg, 0.08 mmol) in MeOH and the red mixture was stirred at room temp. for 18 h. The red product solution was evacuated to dryness and the residue extracted with toluene (2 × 3 mL). The extract was concentrated to about 2 mL and loaded on a silica gel column (1.5 × 2.0 cm). Elution gave three fractions: (i) a yellow eluate in ether/hexane (1:2, about 4 mL), which yielded [Ru(dppm)($\eta^1$-$S_2PR_2$)$_2$] (R = Et (**15**), 3 mg, 5% yield, R = Ph (**17**), 3 mg, 4% yield), (ii) a red eluate in ether:hexane (2:1, 4–8 mL), which yielded [(Ind)Ru(dppm)($\eta^1$-$S_2PR_2$)] (R = Et (**14**), 16 mg, 56% yield, R = Ph (**16**), 33 mg, 50% yield), (iii) an orange-yellow eluate in THF (3 mL), which gave **2** in trace amounts.

**Data for 14:** $^1H$ NMR ($C_6D_6$): $\delta$ = 1.07 and 1.11 [each t, $^3J_{HH}$ = 7.4 Hz, 3 H, $S_2P(CH_2CH_3)_2$], 1.46–1.57 [m, 4 H, $S_2P(CH_2CH_3)_2$], 4.04–4.16 and 4.43–4.54 [each m, 1 H, $CH_2(PPh_2)_2$], 5.15 (t, $^3J_{HH}$ = 2.5 Hz, 1 H, $H^2$), 6.12 (d, $^3J_{HH}$ = 2.5 Hz, 2 H, $H^{1,3}$), 6.89–7.12, 7.23–7.29, 7.37–7.43 and 7.78–7.81 (each m, total 24 H, $H^{5-8}$ and Ph) ppm. $^{31}P\{^1H\}$ NMR ($C_6D_6$): $\delta$ = 12.5 (d, $^3J_{PP}$ = 19 Hz, d), 84.9 (t, $^3J_{PP}$ = 19 Hz, $S_2PEt_2$) ppm. IR (KBr): $\tilde{\nu}$ = 3052 (w), 2967 (w), 2927 (w), 1433 (m), 1324 (w), 1093 (m), 1027 (w), 730 [s, (PS)], 697 [vs, (PS)], 596 (m, (PS)], 534 m, 510 m. $FAB^+$-MS: $m/z$ (%) = 791 $[M - Ind + S_2PEt_2]^+$, 639 $[M - Ind]^+$, 601 $[M - S_2PEt_2]^+$. $C_{38}H_{39}P_3RuS_2$ (753.84): calcd. C 60.5, H 5.2, S 8.5, found C 60.6, H 5.3, S 8.3.

**Data for 15:** $^1H$ NMR ($C_6D_6$): $\delta$ = 0.45–0.57 [m, 6 H, $S_2P(CH_2CH_3)_2$], 0.87–1.02 [m, 4 H, $S_2P(CH_2CH_3)_2$], 1.14–1.25 [m, 6 H, $S_2P(CH_2CH_3)_2$], 2.18–2.45 [m, 4 H, $S_2P(CH_2CH_3)_2$], 4.78–4.85 [m, 2 H, $CH_2(PPh_2)_2$], 6.91–7.34 and 8.10–8.16 (each m, total 20 H, Ph) ppm. $^{31}P\{^1H\}$ NMR ($C_6D_6$): $\delta$ = 5.1 (s, d), 105.6 (s, $S_2PEt_2$) ppm. IR (KBr): $\tilde{\nu}$ = 3049 (w), 2967 (w), 2929 (w), 2874 (w), 1433 (m), 1096 (m), 1036 (w), 723 [s, (PS)], 699 [vs, (PS)], 674, 603 [w, (PS)], 541 (m), 510 (m) $cm^{-1}$. $FAB^+$-MS: $m/z$ (%) = 791 $[M]^+$, 639 $[M - S_2PEt_2]^+$. $C_{33}H_{42}P_4RuS_4$ (791.92): calcd. C 50.0, H 5.4, S 16.2, found C 50.2, H 5.4, S 15.7.

**Data for 16:** $^1H$ NMR ($C_6D_6$): $\delta$ = 3.94–4.06 and 4.42–4.54 [each m, 1 H, $CH_2(PPh_2)_2$], 5.15 (t, $^3J_{HH}$ = 2.5 Hz, 1 H, $H^2$), 5.82 (d, $^3J_{HH}$ = 2.5 Hz, 2 H, $H^{1,3}$), 6.66–6.69 (4-line m, 2 H, $H^{4-7}$), 6.90–7.11, 7.26–7.32, 7.47–7.53 and 8.13–8.20 [each m, total 32 H, $S_2PPh_2$, $CH_2(PPh_2)_2$, 2H of $H^{5-8}$] ppm. $^{31}P\{^1H\}$ NMR ($C_6D_6$): $\delta$ = 12.6 (d, $^3J_{PP}$ = 15 Hz, d), 70.9 (t, $^3J_{PP}$ = 19 Hz, $S_2PPh_2$) ppm. IR (KBr): $\tilde{\nu}$ = 3050 (w), 1481 (w), 1434 (s), 1306 (w), 1098 (s), 726 [m, (PS)], 703 [vs, (PS)], 568 [s, (PS)], 539 (m), 509 (m) $cm^{-1}$. $FAB^+$-MS: $m/z$ (%) 850 $[M]^+$, 735 $[M - Ind]^+$, 601 $[M - S_2PPh_2]^+$. $C_{46}H_{39}P_3RuS_2$ (849.93): calcd. C 65.0, H 4.6, S 7.6, found C 65.2, H 5.0, S 7.7.

**Data for 17:** $^1H$ NMR ($C_6D_6$): $\delta$ = 4.76–4.82 [m, 2 H, $CH_2(PPh_2)_2$], 6.91–7.34, 8.08–8.26 (each m, total 40 H, Ph) ppm. $^{31}P\{^1H\}$ NMR ($C_6D_6$): $\delta$ = 4.0 (s, d), 88.0 (s, $S_2PPh_2$) ppm. IR (KBr): $\tilde{\nu}$ = 3049 (w), 2923 (w), 2854 (w), 1480 (w), 1433 (m), 1305 (w), 1097 (s), 1025 (w), 997 (w), 845 (w), 725 [s, (PS)], 703 [vs, (PS)], 631 (w), 608 (w), 567 [s, (PS)], 538 (m), 508 (m) $cm^{-1}$. $FAB^+$-MS: $m/z$ (%) 984 $[M]^+$, 735 $[M - S_2PPh_2]^+$. $C_{49}H_{42}P_4RuS_4$ (984.09): calcd. C 59.8, H 4.3, S 13.0, found C 60.1, H 4.6, S 12.6.

**(II) Reactions of (Ind)Ru(carbonyl) Complexes**

**(a) Reaction with Isopropyl Xanthate:** A solution of [(Ind)Ru(CO)$_2$I] (**18**) (50 mg, 0.13 mmol) and $KS_2CO{i}Pr$ (45 mg, 0.26 mmol) in $CH_3OH$ (15 mL) was stirred for 30 min at ambient temperature. The red solution slowly turned orange-yellow. Solvent was removed under vacuo and extracted with toluene (about 20 mL) to afford orange-red solids of [Ru(CO)$_2$($\eta^2$-$S_2CO{i}Pr$)$_2$] (**19**) (24 mg, 50% yield).

**Data for 19:** $^1H$ NMR ($C_6D_6$): $\delta$ = 0.85 (m, 6 H, $CH_3$), 5.15 (sept, $^3J_{HH}$ = 6.1 Hz, 1 H, $CH$) ppm. $^{13}C$ NMR ($C_6D_6$): $\delta$ = 21.8 ($CH_3$),

 © 2007 Wiley-VCH Verlag GmbH & Co. KGaA, Weinheim 

78.0 (O-*C*H), 195.3 (S*C*O), 230.0 (*C*O) ppm. IR (THF): $\tilde{\nu}_{CO}$ = 2047 s, 1986 (s) $cm^{-1}$ (literature[23] values 2052 s, 1990 s in $C_6H_{12}$). $FAB^+$-MS: 429.3 $[M + H]^+$.

**(b) Reaction with Trimethylamine *N*-Oxide (TMNO):** A solution of **18** (20.0 mg, 0.05 mmol) and TMNO·$2H_2O$ (12.0 mg, 0.11 mmol) in $CH_3CN$ (10 mL) was stirred for 1 h at ambient temperature. The resulting dark brown solution was adsorbed onto Celite (150 mg). Solvent was removed under vacuo and the Celite mixture was loaded onto a silica gel column (5 × cm) prepared in *n*-hexane. Elution with toluene gave an orange-red solution (about 40 mL), which, upon removal of solvent to dryness, afforded a red solid of $[(Ind)Ru(CO)I]_2$ (**20**) (13 mg, 70% yield).

In a repeated reaction of the same scale, the resulting brown solution was evacuated to dryness. The residue was dissolved in $C_6D_6$ and filtered. The reddish brown filtrate was allowed to evaporate at room temperature. Analytical pure red microcrystals of **20** were obtained after 2 d (10 mg, 54% yield).

**Data for 20:** $^1H$ NMR ($C_6D_6$): $\delta$ = 4.26 (d, $^3J_{HH}$ = 2.5 Hz, 4 H, $H^{1,3}$), 4.37 (t, $^3J_{HH}$ = 2.5 Hz, 2 H, $H^2$), 6.54 (d, $^3J_{HH}$ = 8.2 Hz, 2 H, $H^{5-8}$), 6.77 (t, $^3J_{HH}$ = 8.1 Hz, 2 H, $H^{5-8}$), 6.90 (t, $^3J_{HH}$ = 7.9 Hz, 2 H, $H^{5-8}$), 7.59 (d, $^3J_{HH}$ = 8.2 Hz, 2 H, $H^{5-8}$) ppm. IR (KBr): $\tilde{\nu}_{CO}$ = 1925 (s) $cm^{-1}$. $ESI^+$-MS: 742.5 $[M]^+$. $C_{20}H_{14}I_2O_2Ru_2 \cdot 0.35C_6D_6$ (771.67): calcd. C 34.4, H 1.8, found C 34.8, H 2.3.

**(c) Reaction with Diethyl Dithiocarbamate in the Presence of TMNO:** A solution of **18** (30.0 mg, 0.08 mmol) and TMNO·$2H_2O$ (17.0 mg, 0.15 mmol) in $CH_3CN$ (15 mL) was stirred for 30 min at ambient temperature. The resulting dark brown solution was transferred via a cannula into a flask containing $NaS_2CNEt_2 \cdot 3H_2O$ (17.0 mg, 0.80 mmol) and the mixture was stirred for 1 h, giving a dirty green solution. This was concentrated to about 10 mL and adsorbed onto Celite (200 mg). Solvent was removed under vacuo and the Celite mixture was loaded onto a silica gel column (5 × 2 cm) prepared in *n*-hexane. Elution gave a yellow eluate in toluene (about 25 mL), which, upon removal of solvent, afforded a yellow solid of $(Ind)Ru(CO)(\eta^2\text{-}S_2CNEt_2)$ (**21**) (16 mg, 55% yield).

**Data for 21:** $^1H$ NMR ($C_6D_6$): $\delta$ = 0.61 (t, $^3J_{HH}$ = 7.1 Hz, 6 H, N-$CH_2CH_3$), 2.94 (q, $^3J_{HH}$ = 7.1 Hz, 4 H, N-$CH_2$), 4.85 (t, $^3J_{HH}$ = 2.6 Hz, 1 H, $H^2$), 5.16 (d, $^3J_{HH}$ = 2.6 Hz, 2 H, $H^{1,3}$), 6.91–6.96 (4-line m, 2 H, $H^{5-8}$), 7.12–7.16 (m, 2 H, $H^{5-8}$) ppm. $^{13}C$ NMR ($C_6D_6$): $\delta$ = 11.7 ($CH_3$), 43.1 (N–$CH_2$), 64.6 ($C^{1,3}$), 85.8 ($C^2$), 113.1 ($C^{4,9}$), 124.4, 126.3 ($C^{5,8}$ and $C^{6,7}$), 201.5 (S*C*N), 215.3 (*C*O) ppm. IR (THF): $\tilde{\nu}_{CO}$ = 1931 (s) $cm^{-1}$. $FAB^+$-MS: 393.0 $[M]^+$, 364.9 [M – CO]$^+$. $C_{15}H_{17}NORuS_2$ (392.5): calcd. C 45.9, H 4.4, N 3.6, S 16.3, found C 45.8, H 4.2, N 3.2, S 16.0.

**(d) Reaction with Isopropyl Xanthate in the Presence of TMNO:** A similar reaction using $KS_2CO$*i*Pr (14.0 mg, 0.08 mmol) to replace $NaS_2CNEt_2 \cdot 3H_2O$ resulted in a brownish yellow solution. A similar chromatographic workup gave a yellow solution in toluene (about 25 mL), which, upon removal of solvent, afforded an orange oil. Recrystallization of the orange oil in hexane gave yellow crystals of $(Ind)Ru(CO)(\eta^2\text{-}S_2CO$*i*$Pr)$ (**22**) (23.0 mg, 81% yield).

**Data of 22:** $^1H$ NMR ($C_6D_6$): $\delta$ = 0.80 (d, $^3J_{HH}$ = 6.2 Hz, 6 H,$CH_3$), 4.77 (t, $^3J_{HH}$ = 2.6 Hz, 1 H, $H^2$), 5.00 (sept, $^3J_{HH}$ = 6.2 Hz, 1 H, O-C*H*), 5.07 (d, $^3J_{HH}$ = 2.6 Hz, 2 H, $H^{1,3}$), 6.83–6.87 (4-line m, 2 H, $H^{5-8}$), 6.95–6.98 (4-line m, 2 H, $H^{5-8}$) ppm. $^{13}C$ NMR ($CD_2Cl_2$): $\delta$ = 21.4 ($CH_3$), 65.1 ($C^{1,3}$), 76.8 (O-*C*H), 85.8 ($C^2$), 111.6 ($C^{4,9}$), 124.8, 127.4 ($C^{5,8}$ and $C^{6,7}$), 199.4 (S*C*O), 231.9 (*C*O) ppm. IR (THF): $\tilde{\nu}_{CO}$ = 2041 (s) $cm^{-1}$. EI-MS: 380.1 $[M]^+$, 352.0 [M – CO]$^+$, 217.0 [M – CO–$S_2COC_3H_7$]$^+$. HR-$FAB^+$-MS for $C_{14}H_{14}O_2RuS_2$ $[M]^+$: *m*/*z* (%) = 379.9563 (found), 379.9473 (calcd.), for $C_{13}H_{14}ORuS_2$ [M – CO]$^+$: *m*/*z* (%) = 351.9599 (found), 351.9524 (calcd.). $C_{14}H_{14}O_2RuS_2$ (379.46): calcd. C 44.3, H 3.7, S 16.9, found C 44.7, H 3.7, S 16.8.

**Crystal Structure Determinations:** X-ray diffraction-quality crystals were obtained at –30 °C from solvent mixtures as follows: **7**, **9**, **11**, **16**, and **17** from $CH_2Cl_2$/hexane, **4a** from $CH_2Cl_2$/ether and **12** from THF/hexane, while those of **20** and **21** were obtained at room temperature from $C_6D_6$ and $CH_3CN/C_6D_6$, respectively. Crystals were mounted on quartz fibers. X-ray data were collected on a Bruker AXS APEX system, using Mo-$K_\alpha$ radiation, with the SMART suite of programs.[24] Data were processed and corrected for Lorentz and polarization effects with SAINT,[25] and for absorption effects with SADABS.[26] Structural solution and refinement were carried out with the SHELXTL suite of programs.[27] Crystal and structure refinement data are summarized in Table 3. The structures were solved by direct methods or Patterson maps to locate the heavy atoms, followed by difference maps for the light, non-hydrogen atoms. All non-hydrogen atoms were generally given anisotropic displacement parameters in the final model.

The crystal of **4a** contains one and a half $Et_2O$ solvent molecules. The half solvent molecule was disordered over two sites related by an inversion center, appropriate restraints on the molecular geometry were applied.

The crystal of **11** contained two half $CH_2Cl_2$ solvent molecules, both at special position and both disordered, while the crystal of **17** contained three $CH_2Cl_2$ solvent molecules. Two $CH_2Cl_2$ solvent molecules were also found and refined for **7** and **9**. The latter also contained a half molecule of hexane, which was modeled as disordered over two sites of equal occupancies, a common thermal parameter each for the $CH_2$ and $CH_3$ carbon atoms were assigned, with appropriate restraints on the bond lengths. The molecule of **7** exhibited disorder of the $NEt_2$ fragment over two alternative sites, the occupancies were allowed to refine and summed to unity, giving an approximate 65:35 ratio. The thermal parameters for the corresponding atoms were restrained to be the same, as were the bond lengths.

For complex **12**, two half molecules of THF were found. These were modeled with a common thermal parameter each for the O and C atoms, and with appropriate restraints on the bond lengths. The molecule of **12** exhibited disorder, which was modeled with two alternative sites for the Ru atom and the $PEt_2$ fragment. The occupancies were initially refined in an all-isotropic model and then fixed at 0.9 and 0.1 for the two sites, respectively, in the final model. Appropriate restraints similar to those described for the solvent molecule above were also applied. The molecular structure of **20** exhibits crystallographic mirror symmetry, with the mirror plane passing through the two Ru atoms and bisecting the $Ru_2S_2$ plane.

CCDC-626123 to -626131 contain the supplementary crystallographic data for this paper. These data can be obtained free of charge from The Cambridge Crystallographic Data Centre via www.ccdc.cam.ac.uk/data_request/cif.

**Computation:** The initial geometries of the ruthenium complexes used for the calculations were based on some of the X-ray crystal structures obtained. The structures of the reactants, products, and transition state were fully optimized at the B3LYP density functional theory together with LANL2DZ basis sets. Harmonic frequencies were calculated at the optimized geometries to characterize stationary points as equilibrium structures, with all real frequencies, or transition states with one imaginary frequency, and to evaluate zero-point energy (ZPE) corrections. For all cases in which transition states have been found, these states were verified by following the path traced by the reaction coordinate, which was the

 © 2007 Wiley-VCH Verlag GmbH & Co. KGaA, Weinheim 

Table 3. Crystal and structure refinement data.

| Compound | **4a**·1.5($Et_2O$) | **9**·2($CH_2Cl_2$)·0.5($C_6H_{14}$) | **12**·($C_4H_8O$) |
|---|---|---|---|
| Formula | $C_{54}H_{60}FeNO_{1.50}P_2RuS_2$ | $C_{51}H_{51}Cl_4FeOP_2RuS_2$ | $C_{51}H_{53}FeOP_3RuS_2$ |
| Formula mass | 1030.01 | 1104.70 | 995.88 |
| Space group (crystal system) | $P\bar{1}$ | $P\bar{1}$ | $P\bar{1}$ |
| Crystal system | triclinic | triclinic | triclinic |
| Unit cell dimensions | | | |
| $a$ [Å] | 13.7226(9) | 11.6305(7) | 11.3272(14) |
| $b$ [Å] | 13.7314(9) | 14.5322(8) | 13.4646(17) |
| $c$ [Å] | 14.4562(9) | 15.8226(9) | 16.962(2) |
| $\alpha$ [°] | 75.104(2) | 104.580(1) | 105.351(3) |
| $\beta$ [°] | 69.530(2) | 109.823(1) | 94.667(3) |
| $\gamma$ [°] | 84.632(2) | 95.273(1) | 99.352(3) |
| Cell volume [Å$^3$] | 2466.2(3) | 2388.2(2) | 2440.4(5) |
| $Z$ | 2 | 2 | 2 |
| $D_{calcd}$ (g/cm$^3$) | 1.387 | 1.536 | 1.355 |
| Absorption coefficient [mm$^{-1}$] | 0.790 | 1.036 | 0.826 |
| $F$(000) electrons | 1070 | 1130 | 1028 |
| Crystal size [mm$^3$] | 0.29 × 0.10 × 0.04 | 0.32 × 0.24 × 0.11 | 0.28 × 0.20 × 0.12 |
| $\theta$ range for data collection [°] | 2.11–26.37 | 2.17–29.69 | 2.09–26.37 |
| Index ranges | $-16 \le h \le 17$ | $-16 \le h \le 14$ | $-14 \le h \le 14$ |
| | $-16 \le k \le 17$ | $-20 \le k \le 18$ | $-16 \le k \le 16$ |
| | $0 \le l \le 18$ | $0 \le l \le 21$ | $0 \le l \le 21$ |
| Reflections collected | 33018 | 33852 | 31598 |
| Independent reflections | 10064 | 12251 | 9971 |
| Max. and min. transmission | 0.9691–0.8033 | 0.8945–0.7327 | 0.9074–0.8017 |
| Data/restraints/parameters | 10064/15/577 | 12251/4/555 | 9971/26/571 |
| Gof | 1.167 | 1.099 | 1.173 |
| Final $R$ indices [$I > 2\sigma(I)$] | $R_1$ = 0.0728 | $R_1$ = 0.0484 | $R_1$ = 0.0861 |
| | $wR_2$ = 0.1325 | $wR_2$ = 0.1162 | $wR_2$ = 0.2272 |
| $R$ indices (all data) | $R_1$ = 0.1051 | $R_1$ = 0.0540 | $R_1$ = 0.1024 |
| | $wR_2$ = 0.1434 | $wR_2$ = 0.1203 | $wR_2$ = 0.2371 |
| Largest diff. peak and hole [e/Å$^3$] | 1.058 and –0.591 | 1.462 and –0.893 | 1.512 and –1.322 |

| Compound | **16** | **20** | **21** |
|---|---|---|---|
| Formula | $C_{47}H_{41}Cl_2P_3RuS_2$ | $C_{10}H_7IORu$ | $C_{15}H_{17}NORuS_2$ |
| Formula mass | 934.80 | 371.13 | 392.49 |
| Space group (crystal system) | $P2_1/C$ | $Pnma$ | $P2_1/c$ |
| Crystal system | monoclinic | orthorhombic | monoclinic |
| Unit cell dimensions | | | |
| $a$ [Å] | 11.4645(6) | 19.462(2) | 11.6373(9) |
| $b$ [Å] | 44.244(2) | 9.5125(12) | 7.1854(5) |
| $c$ [Å] | 8.3165(5) | 19.7207(15) | 19.7207(15) |
| $\alpha$ [°] | 90 | 90 | 90 |
| $\beta$ [°] | 90.321(2) | 90 | 103.900(2) |
| $\gamma$ [°] | 90 | 90 | 90 |
| Cell volume [Å$^3$] | 4218.3(4) | 1999.2(4) | 1600.7(2) |
| $Z$ | 4 | 8 | 4 |
| $D_{calcd}$ (g/cm$^3$) | 1.472 | 2.466 | 1.629 |
| Absorption coefficient [mm$^{-1}$] | 0.745 | 4.611 | 1.234 |
| $F$(000) electrons | 1912 | 1376 | 792 |
| Crystal size [mm$^3$] | 0.20 × 0.16 × 0.10 | 0.18 × 0.11 × 0.05 | 0.34 × 0.20 × 0.14 |
| $\theta$ range for data collection [°] | 0.92–25.00 | 2.09 to 26.37 | 1.80 to 27.49 |
| Index ranges | $-11 \le h \le 13$ | $0 \le h \le 24$ | $-11 \le h \le 15$ |
| | $-52 \le k \le 52$ | $0 \le k \le 11$ | $-9 \le k \le 9$ |
| | $-9 \le l \le 9$ | $0 \le l \le 13$ | $-21 \le l \le 25$ |
| Reflections collected | 24515 | 12455 | 10941 |
| Independent reflections | 7415 | 2162 | 3648 |
| Max. and min. transmission | 0.9292–0.8653 | 0.8022–0.4908 | 0.8462–0.6790 |
| Data/restraints/parameters | 7415/0/496 | 2162/0/130 | 3648/0/183 |
| Gof | 1.310 | 1.335 | 1.172 |
| Final $R$ indices [$I > 2\sigma(I)$] | $R_1$ = 0.0916 | $R_1$ = 0.0580, | $R_1$ = 0.0414 |
| | $wR_2$ = 0.1609 | $wR_2$ = 0.1698 | $wR_2$ = 0.0985 |
| $R$ indices (all data) | $R_1$ = 0.1113 | $R_1$ = 0.0580, | $R_1$ = 0.0460 |
| | $wR_2$ = 0.1674 | $wR_2$ = 0.1698 | $wR_2$ = 0.1011 |
| Largest diff. peak and hole [e/Å$^3$] | 1.108 and –1.358 | 3.170 and –1.211 | 0.585 and –0.351 |

mode with the imaginary frequency. These displacements were indeed along the reaction pathways leading to the products (the $\eta^3$ complex) or back to the reactants (the $\eta^5$ complex). All calculations were performed using the Gaussian 03 suite of programs.[28]

 © 2007 Wiley-VCH Verlag GmbH & Co. KGaA, Weinheim 

**Supporting Information** (see also the footnote on the first page of this article): Table S1. Energies of selected molecules and transition states involved in the indenyl $\eta^5 \rightarrow \eta^3$ ring slippage process computed at B3LYP/LANL2DZ level of theory. Bond parameters of selected molecules and transition states involved in the indenyl $\eta^5 \rightarrow \eta^3$ ring slippage process computed at B3LYP/LANL2DZ level of theory. Table S2. Crystal and structure refinement data of complexes **7**, **11**, and **17**. Table S3. Selected bond lengths [Å] and angles [°] for complexes **7**, **11**, and **17**. ORTEP diagrams of **7**, **11**, and **17** with selected bond parameters.

## Acknowledgments

The authors acknowledge with thanks support from the Academic Research Fund (grant no. 143-000-209-112 to L. Y. G, the Institute of Chemical and Engineering Sciences for a research scholarship to S. Y. N, and technical assistance from Dr. L. L. Koh and Ms G. K. Tan for X-ray structure determinations of **11**, **16**, **17**, and **21**.

[1] See for instance the following and references cited therein: a) G. Hogarth, *Prog. Inorg. Chem.* **2005**, *53*, 71, b) E. R. T. Tiekink, G. Winter, *Rev. Inorg. Chem.* **1992**, *12*, 185, c) G. Winter, *Rev. Inorg. Chem.* **1980**, *2*, 254, d) D. Coucouvanis, *Prog. Inorg. Chem.* **1979**, *26*, 302, e) R. Eisenberg, *Prog. Inorg. Chem.* **1970**, *12*, 295, f) D. Coucouvanis, *Prog. Inorg. Chem.* **1970**, *11*, 234, g) I. Haiduc, L. Y. Goh, *Coord. Chem. Rev.* **2002**, *1–2*, 151.

[2] Z. Weng, L. Y. Goh, *Acc. Chem. Res.* **2004**, *37*, 187, and references therein.

[3] a) X. L. Lu, J. J. Vittal, E. R. T. Tiekink, G. K. Tan, S. L. Kuan, L. Y. Goh, T. S. A. Hor, *J. Organomet. Chem.* **2004**, *689*, 1978, b) X. L. Lu, J. J. Vittal, E. R. T. Tiekink, L. Y. Goh, T. S. A. Hor, *J. Organomet. Chem.* **2004**, *689*, 1444.

[4] a) V. Cadierno, J. Díez, M. P. Gamasa, J. Gimeno, E. Latra, *Coord. Chem. Rev.* **1999**, *193–195*, 147, b) M. J. Calhorda, L. F. Veiros, *Coord. Chem. Rev.* **1999**, *185–186*, 37, c) J. M. O'Connor, C. P. Casey, *Chem. Rev.* **1987**, *87*, 307, d) R. T. Baker, T. H. Tulip, *Organometallics* **1986**, *5*, 839, e) J. W. Faller, R. H. Crabtree, A. Habib, *Organometallics* **1985**, *4*, 929, f) M. E. Rerek, L. N. Ji, F. Basolo, *J. Chem. Soc. Chem. Commun.* **1983**, 1208.

[5] See for instance the following: a) W. K. Fung, X. Huang, M. L. Man, S. M. Ng, M. Y. Hung, Z. Lin, C. P. Lau, *J. Am. Chem. Soc.* **2003**, *125*, 11539, b) M. K. Y. Watanabe, T. Ando, M. Sawamoto, *J. Am. Chem. Soc.* **2002**, *124*, 9994, c) T. Ando, M. Kamigito, M. Sawamoto, *Macromolecules* **2000**, *33*, 5825, d) E. P. Kündig, C. M. Saudan, V. Alezra, F. Viton, G. Bernardinelli, *Angew. Chem. Int. Ed.* **2001**, *40*, 4481, e) H. Takahashi, T. Ando, M. Kamigito, M. Sawamoto, *Macromolecules* **1999**, *32*, 3820, f) B. M. Trost, R. C. Livingston, *J. Am. Chem. Soc.* **1995**, *117*, 9586, g) B. M. Trost, R. J. Kulawiec, *J. Am. Chem. Soc.* **1993**, *115*, 2027.

[6] T. Sato, M. Nishio, Y. Ishii, H. Yamazaki, M. Hidai, *J. Organomet. Chem.* **1998**, *569*, 98.

[7] S. Y. Ng, W. K. Leong, L. Y. Goh, R. D. Webster, *Eur. J. Inorg. Chem.* **2007**, 463 and references cited therein.

[8] X. L. Lu, S. Y. Ng, J. J. Vittal, G. K. Tan, L. Y. Goh, T. S. A. Hor, *J. Organomet. Chem.* **2003**, *688*, 100.

[9] a) M. I. Bruce, M. G. Humphrey, A. G. Swincer, R. C. Wallis, *Aust. J. Chem.* **1984**, *37*, 1747, b) T. Wilczewski, M. Bocheńska, J. F. Biernat, *J. Organomet. Chem.* **1981**, *215*, 87.

[10] M. P. Gamasa, J. Gimeno, C. González-Bernardo, B. M. Martín-Vaca, J. Borge, S. García-Granda, *Inorg. Chim. Acta* **2003**, *347*, 181.

[11] a) S. D. Orth, N. R. Terry, K. A. Abboud, B. Dodson, L. McElwee-White, *Inorg. Chem.* **1996**, *35*, 916, b) B. Chaudret, G. Commernges, R. Poilblanc, *J. Chem. Soc. Dalton Trans.* **1984**, 1635.

[12] A. Shaver, P.-Y. Plouffe, P. Bird, E. Livingstone, *Inorg. Chem.* **1990**, *29*, 1826.

[13] S. L. Kuan, J. Tan, W. K. Leong, L. Y. Goh, Unpublished results.

[14] A. K. Kakkar, N. J. Taylor, T. B. Marder, J. K. Shen, N. Hallinan, F. Basolo, *Inorg. Chim. Acta* **1992**, *198–200*, 219, reported for true $\eta^5$-coordination: $\Delta$ = 0.03 Å, HA = 2.5°, FA = 4.4°, for distorted $\eta^5$: $\Delta$ = 0.11–0.42 Å, HA = 7–14°, FA = 6–13°, and for true $\eta^3$-coordination: $\Delta$ = 0.8 Å, FA = 28°. In general, for indenyl complexes considered $\eta^5$: $\Delta < 0.25$ Å, HA < 10°, and for those considered $\eta^3$: $\Delta$ = 0.69–0.80 Å, HA ≈ 20–30°, and for those with slight distortion towards $\eta^3$: $\Delta$ = 0–0.22 Å, HA < 13° (see for instance, refs.[4a,4b] and M. E. Stoll, P. Belanzoni, M. J. Calhorda, M. G. B. Drew, V. Félix, W. E. Geiger, C. A. Gamelas, I. S. Goncalves, C. C. Romão, L. F. Veiros, *J. Am. Chem. Soc.* **2001**, *123*, 10595).

[15] L. Pauling, *The Nature of the Chemical Bond*, Cornell University Press, Ithaca, NY, **1960**, chapter 8.

[16] a) A. J. Deeming, C. Forth, G. Hogarth, *J. Organomet. Chem.* **2006**, *691*, 79, b) J. D. Owen, D. J. Cole-Hamilton, *J. Chem. Soc. Dalton Trans.* **1974**, 1867.

[17] M. S. Loonat, L. Carlton, J. C. A. Boeyens, M. J. Covelle, *J. Chem. Soc. Dalton Trans.* **1989**, 2407.

[18] H. W. Vos, C. MacLean, N. H. Velthorst, *J. Chem. Soc. Faraday Trans.* **1976**, *72*, 63.

[19] M. J. Calhorda, C. C. Romão, L. F. Veiros, *Chem. Eur. J.* **2002**, *8*, 868.

[20] S. Y. Ng, G. Fang, W. K. Leong, L. Y. Goh, M. Garland, *Eur. J. Inorg. Chem.* **2007**, 452.

[21] M. P. Gamasa, J. Gimeno, C. Gonzalez-Bernardo, B. M. Martin-Vaca, D. Monti, M. Bassetti, *Organometallics* **1996**, *15*, 302.

[22] P. McArdle, A. R. Manning, *J. Chem. Soc. A* **1970**, 2128.

[23] A. J. Deeming, C. Forth, G. Hogarth, *Transition Met. Chem.* **2006**, *31*, 42.

[24] *SMART* version 5.628, Bruker AXS Inc., Madison, WI, USA, **2001**.

[25] *SAINT+* version 6.22a, Bruker AXS Inc., Madison, WI, USA, **2001**.

[26] G. M. Sheldrick, *SADABS*, **1996**.

[27] *SHELXTL* version 5.1, Bruker AXS Inc., Madison, WI, USA, **1997**.

[28] M. J. Frisch, G. W. Trucks, H. B. Schlegel, G. E. Scuseria, M. A. Robb, J. R. Cheeseman, J. A. Montgomery, Jr., T. Vreven, K. N. Kudin, J. C. Burant, J. M. Millam, S. S. Iyengar, J. Tomasi, V. Barone, B. Mennucci, M. Cossi, G. Scalmani, N. Rega, G. A. Petersson, H. Nakatsuji, M. Hada, M. Ehara, K. Toyota, R. Fukuda, J. Hasegawa, M. Ishida, T. Nakajima, Y. Honda, O. Kitao, H. Nakai, M. Klene, X. Li, J. E. Knox, H. P. Hratchian, J. B. Cross, C. Adamo, J. Jaramillo, R. Gomperts, R. E. Stratmann, O. Yazyev, A. J. Austin, R. Cammi, C. Pomelli, J. W. Ochterski, P. Y. Ayala, K. Morokuma, G. A. Voth, P. Salvador, J. J. Dannenberg, V. G. Zakrzewski, S. Dapprich, A. D. Daniels, M. C. Strain, O. Farkas, D. K. Malick, A. D. Rabuck, K. Raghavachari, J. B. Foresman, J. V. Ortiz, Q. Cui, A. G. Baboul, S. Clifford, J. Cioslowski, B. B. Stefanov, G. Liu, A. Liashenko, P. Piskorz, I. Komaromi, R. L. Martin, D. J. Fox, T. Keith, M. A. Al-Laham, C. Y. Peng, A. Nanayakkara, M. Challacombe, P. M. W. Gill, B. Johnson, W. Chen, M. W. Wong, C. Gonzalez, J. A. Pople, *Gaussian 03*, Gaussian Inc., Wallingford CT, **2004**..

Received: January 20, 2007
Published Online: June 29, 2007

 © 2007 Wiley-VCH Verlag GmbH & Co. KGaA, Weinheim 

DOI: 10.1002/ejic.200700155

# Preparation of $Cu_2O$ Hollow Nanospheres under Reflux Conditions

**Muquan Yang,[a] Yingwei Zhang,[a] Guangsheng Pang,*[a] and Shouhua Feng[a]**

**Keywords:** Cuprous oxide / Nanospheres / Reflux conditions

Cuprous oxide hollow nanospheres were prepared by heating a solution of copper acetate and hydrazine as a reductant in 2-propanol at reflux. The size distribution of the nanospheres is mainly in the range 100–200 nm. The products were characterized by X-ray diffraction, UV/Vis diffuse reflectance spectroscopy, SEM, and TEM. The results indicated that the $Cu_2O$ hollow nanospheres aggregated from small nanoparticles with an average size of ca. 6.6 nm. The UV/Vis diffuse reflectance spectrum indicated that the optical absorption edge of the hollow $Cu_2O$ nanospheres is redshifted relative to their solid counterparts. The influence of the reaction conditions, such as reaction temperature, reaction time, and the amount of water, on the formation of the nanospheres as well as their morphology were studied.
(© Wiley-VCH Verlag GmbH & Co. KGaA, 69451 Weinheim, Germany, 2007)

## Introduction

In recent years, controlled architectures and the fabrication of hollow inorganic micro- and nanostructures have attracted extensive research interests owing to their unique thermal, electrical, optical, and surface properties.[1–8] Materials with hollow interiors have potential applications in many fields, such as catalyst, adsorbent, drug delivery, photonic crystals, optical imaging, low dielectric constant materials, and acoustic insulation etc. Cuprous oxide is an important *p*-type semiconductor with a direct bandgap of 2.17 eV. Owing to its unique optical property, $Cu_2O$ has potential applications in the catalytic oxidation of CO to $CO_2$,[9] photocatalytic degradation of organic pollutants, and decomposition of water into $H_2$ and $O_2$ under visible light.[10]

Various methods have been reported for the preparation of $Cu_2O$ with various morphologies and hollow structures, such as nanowire,[11] octahedral nanocages,[12] hollow cubes, and spheres.[13–16] There have been two main preparative routes for the synthesis of the hollow structure. In the template method, raw materials or target precursors are adsorbed onto the template surface and subsequently the template is removed by calcination or dissolution with solvent.[1] Another preparative strategy concerns physical phenomena such as "Ostwald ripening"[13,14,17] and the "Kirkendall effect".[2] Cetyltrimethylammonium (CTAB)[15] and gelatin[16] are used to prepare $Cu_2O$ hollow nanospheres by the template-assisted method. Here, we describe a facile template-free and surfactant-free route for the formation of hollow $Cu_2O$ nanospheres by heating a solution of copper acetate and hydrazine as the reductant in 2-propanol at reflux.

## Results and Discussion

Figure 1(a) shows the SEM image of the $Cu_2O$ nanospheres prepared by heating a solution of copper acetate and hydrazine in 2-propanol at reflux. The hollow feature of the nanospheres can be confirmed from TEM by observing that the light interior in contrast to the dark periphery as shown in the inset of Figure 1(a). The TEM image shows that the nanospheres are aggregated by small nanoparticles,

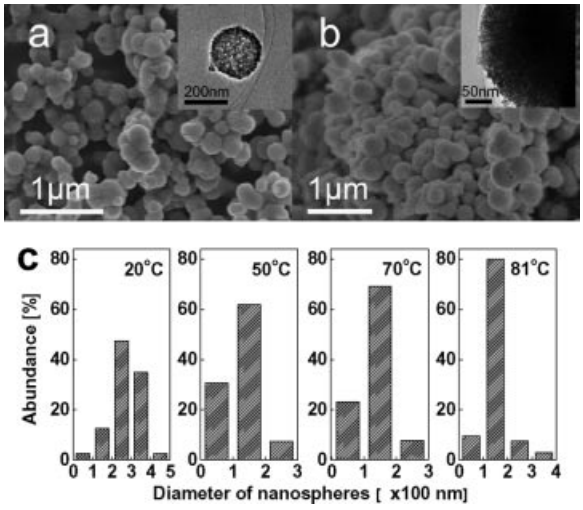


Figure 1. SEM images of $Cu_2O$ nanospheres prepared at (a) the boiling point of 2-propanol (81 °C) and (b) at room temperature (20 °C). The insets of (a) and (b) show the TEM images of $Cu_2O$ nanospheres. (c) The size distributions of $Cu_2O$ nanospheres prepared at 81, 70, 50, and 20 °C.

[a] College of Chemistry, State Key Laboratory of Inorganic Synthesis and Preparative Chemistry, Jilin University, Changchun, Jilin 130012, P. R. China
Fax: +86-0431-85168624
E-mail: panggs@jlu.edu.cn

 © 2007 Wiley-VCH Verlag GmbH & Co. KGaA, Weinheim 

and the thickness of the hollow sphere shell is estimated to be ca. 20 nm for the nanosphere with a diameter of 210 nm as shown in the inset of Figure 1(a). The size distribution of the $Cu_2O$ nanospheres is mainly in the scale of 100–200 nm as shown in Figure 1(c).

Temperature is a crucial factor in the formation of the hollow structure. The boiling point of 2-propanol is 81.5 °C, and $Cu_2O$ nanospheres can also be prepared at lower temperature. Although spherical morphology was observed in the products prepared at 20 °C, as shown in Figure 1(b), a longer reaction time of 90 min was necessary and only solid nanospheres were observed by TEM from the inset of Figure 1(b). The diameter of these solid nanospheres varies from 100 to 500 nm, and is mainly concentrated in the region 200–400 nm as shown in Figure 1(c). As the temperature was increased to 50 °C, the size distribution of the spheres narrowed, but still only solid nanospheres were observed. As the temperature was increased to 70 °C, hollow nanospheres were observed to coexist with the solid nanospheres. Figure 2 shows that all of the nanospheres prepared at 81 °C were hollow.

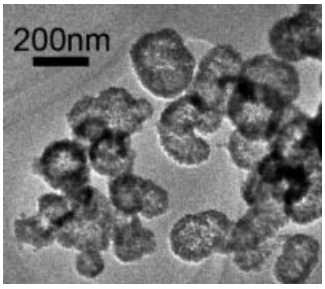


Figure 2. TEM image of $Cu_2O$ hollow nanospheres prepared at 81 °C.

Figure 3 shows the XRD patterns of the samples prepared at 20, 50, 70, and 81 °C. All the diffraction peaks can be indexed to cubic $Cu_2O$ (JCPDS card No. 05–0667). The average particle size of the primary particles that agglomerated into nanospheres was estimated from the line broadening of the XRD peak (111) by using the Scherrer equation ($D_{hkl} = k\lambda/\beta_{hkl}\cos\theta$). The results indicate that the average size of the primary particles decreased slightly from 9.6 to 7.9 nm, and then to 6.6 nm within the same reaction time of 10 min when the preparation temperature was increased from 50 to 70 °C, and then 81 °C.

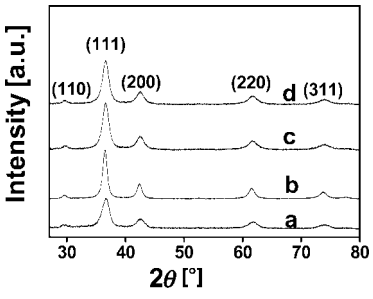


Figure 3. XRD patterns of the cubic $Cu_2O$ samples prepared at different temperatures: (a) 20 °C, (b) 50 °C, (c) 70 °C, and (d) 81 °C.

Reaction time had an influence on the morphology of the nanospheres as well as the average size of the primary particles. Figure 4 show the SEM images of the $Cu_2O$ hollow spheres prepared by heating for 20, 30, and 120 min at 81 °C in 2-propanol. In Figure 4(a), the $Cu_2O$ hollow spheres that were prepared in 20 min have smooth surfaces that are similar to the products prepared after 10 min. The spherical diameter distribution is concentrated in the range 100–300 nm as shown in Figure 4(d). When the reaction time was increased to 30 min, the surfaces of the products were relatively rough as shown in Figure 4(b), and the spherical diameter distribution was then concentrated in the region from 200 to 400 nm as shown in Figure 4(d). When the reaction time was increased to 120 min, irregular spheres with large sizes and rough surfaces were observed in Figure 4(c), and many broken particles were spread around. There was no change in the size of the primary particles when the reaction time was less than 20 min. The average size of the primary particles increased from 6.6 to 9.3 nm when the reaction time was increased from 20 to 30 min, according to the XRD line broadening.

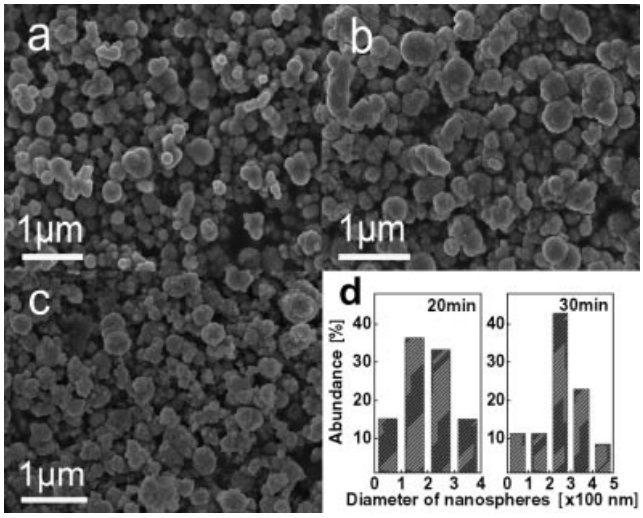


Figure 4. SEM images of hollow $Cu_2O$ nanospheres prepared at 81 °C after (a) 20 min, (b) 30 min, and (c) 2 h. (d) The size distribution of the $Cu_2O$ nanospheres.

There is a small amount of water that exists in the reaction system owing to the hydrazine aqueous solution. Although the products maintain their spherical morphology when additional water is introduced, the size of the nanospheres as well as the primary particles changed significantly. Figure 5(a) and (b) show the products prepared by adding 10 mL and 20 mL of water, respectively. The majority of the products are still hollow spheres as shown in the inset of Figure 5(a), but they have relatively small hollow interiors relative to the nanospheres that were prepared without additional water. As shown in Figure 5(c), the size distribution of the nanospheres prepared with an additional 10 mL of water is in the range 100–700 nm and is mainly concentrated around 300–400 nm. When 20 mL of water were added, we found that the size distribution of the

 © 2007 Wiley-VCH Verlag GmbH & Co. KGaA, Weinheim 

nanospheres changed to 200–800 nm and was basically concentrated around 600–700 nm. This change indicates that the size of the spheres increases by adding more water. According to the XRD line broadening, the average size of the primary particles increased to ca. 15.4 nm and ca. 14.7 nm for the samples with the additional 10 mL and 20 mL of water.

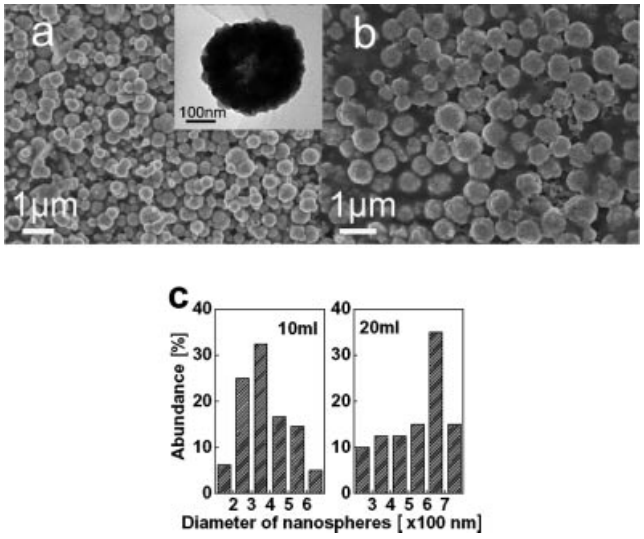


Figure 5. SEM images of hollow $Cu_2O$ nanospheres prepared with (a) 10 mL and (b) 20 mL of additional water. The inset of (a) shows a TEM image of a hollow sphere. (c) The size distribution of $Cu_2O$ nanospheres prepared with 10 mL and 20 mL of additional water.

Figure 6 shows the UV/Vis diffuse reflectance spectrum of $Cu_2O$ nanospheres that were prepared at 20, 50, 70, and 81 °C. The bandgaps of $Cu_2O$ were estimated according to the absorption edge position as shown in Figure 6 by intercepting the two linearly extrapolated lines. It is observed that the optical absorption edge of the $Cu_2O$ hollow nanospheres prepared at 81 °C occurs at about 616 nm, corresponding to a bandgap energy of 2.01 eV. The optical absorption edge of the $Cu_2O$ solid nanospheres prepared at 20 °C is at about 600 nm, corresponding to a bandgap energy of 2.07 eV. It is worth noting that the hollow nanospheres exhibit similar features in the DRS spectra (Figure 6a and b) whereas there are significant differences with that of solid nanospheres (Figure 6c and d). Relative to the solid nanospheres, the optical absorption edge of hollow the $Cu_2O$ nanospheres is redshifted. It is well known that the optical absorption would be altered considerably by the morphology and crystallinity of the nanospheres. The average particle size of the primary particles that were agglomerated into hollow and solid nanospheres is in the range of 6–10 nm, according to the XRD line broadening. The size distributions of hollow and solid nanospheres are all basically in the region of 100 to 400 nm. Hence, we speculate that the enhanced optical absorption of the nanospheres results from their hollow structure. The surface structure and adsorbed species on the surface have an influence on the optical absorption. The inner and outer surfaces of the hollow nanospheres may be different, which will result in a redshift.

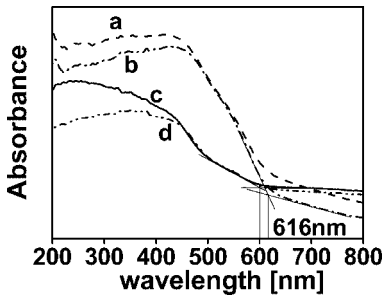


Figure 6. UV/Vis diffuse reflectance spectra of $Cu_2O$ nanospheres prepared at different reaction temperatures: (a) 81 °C, (b) 70 °C, (c) 50 °C, and (d) 20 °C.

## Conclusions

A facile template-free and surfactant-free route was developed for the preparation of hollow $Cu_2O$ nanospheres. Cuprous oxide hollow nanospheres with diameters of ca. 100–200 nm were successfully prepared by heating a solution of $Cu(OAc)_2 \cdot H_2O$ and hydrazine as a reductant in 2-propanol at reflux. The nanospheres were aggregated from small primary particles with an average size of 6–10 nm. Temperature is a critical factor in the formation of the hollow nanospheres, and hollow spheres come into being only when the temperature is close to the boiling point of the solvent. Both the reaction time and the amount of water have an influence on the formation of the $Cu_2O$ hollow structures as well as the morphology and the size of the primary particles. The UV/Vis diffuse reflectance spectrum indicated that the hollow structure enhanced the absorption of visible light relative to their solid counterpart.

## Experimental Section

All reagents (A.R) were from the Beijing Chemical Reagent Corporation and used without further purification. In a typical synthesis procedure, $Cu(OAc)_2 \cdot H_2O$ (2.0 g) was added to 2-propanol (100 mL) in a three-necked flask whilst stirring. The solution was heated at reflux (81 °C) for 20 min. and then a hydrazine (2.5 mL, 1 mol $L^{-1}$) solution was added dropwise. The resulting deep green mixture was stirred for another 10 min, and a reddish brown suspension came into being. The solid product was separated from the solution by centrifugation, washed with absolute ethanol, and dried in air.

The X-ray powder diffraction (XRD) patterns of the products were collected with a Rigaku D/MAX 2500/PC X-ray diffractometer with graphite-filtered Cu-$K_\alpha$ radiation at 40 kV and 200 mA with a scan rate of 1° $min^{-1}$. The morphologies were observed by SEM with a JSM-6700F electron microscope and TEM with a JSM-3010 electron microscope. UV/Vis diffuse reflectance spectra of the products were measured with a UV/Vis spectrometer Lambda 20.

## Acknowledgments

This research was supported by National Natural Science Foundation of China (No. 20671039 and 20121103) and the National High Technology Research and Development program of China (863 program).

 © 2007 Wiley-VCH Verlag GmbH & Co. KGaA, Weinheim 

[1] F. Caruso, R. A. Caruso, H. Möhwald, *Science* **1998**, *282*, 1111–1114.
[2] Y. Yin, R. M. Rioux, C. K. Erdonmez, S. Hughes, G. A. Somorjai, A. P. Alivisatos, *Science* **2004**, *304*, 711–714.
[3] A. P. Li, F. Müller, A. Birner, K. Nielsch, U. Gösele, *Adv. Mater.* **1999**, *11*, 483–487.
[4] Y. Sun, Y. Xia, *Science* **2002**, *298*, 2176–2179.
[5] A. D. Dinsmore, M. F. Hsu, M. G. Nikolaides, M. Marquez, A. R. Bausch, D. A. Weitz, *Science* **2002**, *298*, 1006–1009.
[6] J. Chen, F. Saeki, B. J. Wiley, H. Cang, M. J. Cobb, Z. Y. Li, L. Au, H. Zhang, M. B. Kimmey, X. D. Li, Y. Xia, *Nano Lett.* **2005**, *5*, 473–477.
[7] S. W. Kim, M. Kim, W. Y. Lee, T. Hyeon, *J. Am. Chem. Soc.* **2002**, *124*, 7642–7643.
[8] H. P. Liang, H. M. Zhang, J. S. Hu, Y. G. Guo, L. J. Wan, C. L. Bai, *Angew. Chem. Int. Ed.* **2004**, *43*, 1540–1543.
[9] B. White, M. Yin, A. Hall, D. Le, S. Stolbov, T. Rahman, N. Turro, S. O'Brien, *Nano Lett.* **2006**, *6*, 2095–2098.
[10] P. E. de Jongh, D. Vanmaekelbergh, J. J. Kelly, *Chem. Commun.* **1999**, 1069–1070.
[11] W. Z. Wang, G. H. Wang, X. S. Wang, Y. J. Zhan, Y. K. Liu, C. L. Zheng, *Adv. Mater.* **2002**, *14*, 67–69.
[12] C. H. Lu, L. M. Qi, J. H. Yang, X. Y. Wang, D. Y. Zhang, J. L. Xie, J. M. Ma, *Adv. Mater.* **2005**, *17*, 2562–2567.
[13] Y. Chang, J. J. Teo, H. C. Zeng, *Langmuir* **2005**, *21*, 1074–1079.
[14] J. J. Teo, Y. Chang, H. C. Zeng, *Langmuir* **2006**, *22*, 7369–7377.
[15] H. R. Zhang, C. M. Shen, S. T. Chen, Z. C. Xu, F. S. Liu, J. Q. Li, H. J. Gao, *Nanotechnology* **2005**, *16*, 267–272.
[16] L. S. Xu, X. H. Chen, Y. R. Wu, C. S. Chen, W. H. Li, W. Y. Pan, Y. G. Wang, *Nanotechnology* **2006**, *17*, 1501–1505.
[17] H. G. Yang, H. C. Zeng, *J. Phys. Chem. B* **2004**, *108*, 3492–3495.

Received: February 2, 2007
Published Online: June 29, 2007

 © 2007 Wiley-VCH Verlag GmbH & Co. KGaA, Weinheim 

DOI: 10.1002/ejic.200700202

# Crystal Structure and Surface Photovoltage Properties of $Mn^{II}$ Coordination Supramolecules

Li-Ping Sun,[a] Shu-Yun Niu,*[a] Jing Jin,[a] and Li Zhang[a]

**Keywords:** Manganese / Hydrogen bonds / Surface photovoltage spectroscopy

Three $Mn^{II}$ coordination supramolecular complexes $[Mn(pdc)(H_2O)]_n$ **1**, $\{[Mn(pdc)(phen)(H_2O)]\cdot 3H_2O\}_n$ **2**, and $\{[Mn(cyan)_2(H_2O)_4]\cdot 2HCl\cdot 2(Hcyan)\}$ **3** ($H_2pdc$ = pyridine-2,3-dicarboxylic acid, Hcyan = cyanuric acid, phen = 1,10-phenanthroline) were hydrothermally synthesized and their structures determined by single-crystal X-ray diffraction. The pdc group in complex **1** bridges the $Mn^{II}$ ions to form an infinite 3D structure. In complex **2**, the $Mn^{II}$ ion is bridged to a 1D infinite chain by pdc groups and the chain is further connected to a 2D structure by hydrogen bonds. The 3D structure of complex **3** is formed by hydrogen bonds and O···Cl weak interactions. Surface photovoltage spectroscopy (SPS) of complexes **1**–**3** indicate that they all possess positive SPV response in the range of 300–800 nm and show *p*-type semiconductor characteristic. The intensities of the SPV responses are obviously different, and this can mainly be attributed to the differences in their structures. Field-induced surface photovoltage spectroscopy (FISPS) of complexes **1**–**3** confirms their *p*-type semiconductor characteristic.

(© Wiley-VCH Verlag GmbH & Co. KGaA, 69451 Weinheim, Germany, 2007)

## Introduction

In recent years, the most attractive areas of research in the fields of crystal engineering and supramolecular chemistry have been aimed at creating a wide range of purpose materials with specific structures and useful properties, such as electronic, magnetic, optical, and catalytic properties.[1,2] In inorganic coordination polymers, the choice of metal–ligand combination is the main factor controlling both the supramolecular topology and dimensionality, but other factors such as hydrogen-bonding, $\pi\rightarrow\pi^*$ interactions, and metal–metal interactions can also greatly influence the crystal structure and its dimensionality.[3,4] Owing to the particularity and variety of electronic configurations possible for manganese ions, manganese coordination complexes have attracted great attention in the domain of coordination chemistry all along, though the research of $Mn^{n+}$ coordination complexes have gone across hundreds of years. Manganese complexes play an important role in some biological redox systems owing to the various oxidation states of the manganese ion;[5,6] the water oxidizing complex of photosystem II [PS (II)] involves manganese ions in various combinations of oxidation states, including $Mn^{II}$, $Mn^{III}$, and $Mn^{IV}$.[7,8] It is well-known that the electronic arrangement of the six-coordinate $Mn^{II}$ ($d^5$) ion can take the high-spin (HS) and low-spin (LS) states depending on the different ligand field. The spin conversion between HS and LS probably accompanies magnetic behaviors. When $Mn^{II}$ ion takes HS, there are more unpaired electrons, which easily leads to the behavior of paramagnetism, antiferromagnetism, and ferromagnetism.[9,10] When the $Mn^{II}$ ion takes LS, various transitions will occur, which makes the corresponding complexes appear to have photoelectric and optical properties. In addition, $Mn^{II}$ complexes coordinated by a carboxylic group have some potential application in human pharmaceuticals.[11] At present, research on the properties of $Mn^{II}$ coordination complexes is mainly focused on magnetism.[12–14] Research into photoelectric properties is mainly involved in the coordination complexes which depend on phthalocyanine and porphyrin as ligands. There are few reports on the photoelectric properties of coordination polymers.[15–17] Surface photovoltage spectroscopy (SPS) is an effective technique that can be used to investigate the photophysics of the excited states and the surface charge behavior of the sample. This technique provides information about the properties of the sample surface layer (several atomic layers), and it has a very high sensitivity. The sensitivity of this method is about $10^8$ $q\,cm^{-2}$, or about one elementary charge per $10^7$ surface atoms, which exceeds that of conventional spectroscopy such as XPS and Auger spectroscopy by many orders of magnitude. Moreover, the SPV method is a contactless and nondestructive technique. This technique has been used to investigate the photoelectric processes such as charge transfer and photocatalysis.[18,19] On the basis of the principle of SPS, Wang and coworkers developed a field-induced surface photovoltage spectroscopy (FISPS) technique,[20,21] which can demon-

[a] School of Chemistry and Chemical Engineering, Liaoning Normal University
Dalian 116029, P. R. China
E-mail: syniu@sohu.com

Supporting information for this article is available on the WWW under http://www.eurjic.org or from the author.

 © 2007 Wiley-VCH Verlag GmbH & Co. KGaA, Weinheim 

strate the photoelectric properties of semiconductors under the effect of an external electric field. In this paper we report the synthesis, structure, and properties of three $Mn^{II}$ coordination supramolecules. Meanwhile we discuss the influence of the different structures on the photoelectric properties.

## Results and Discussion

### $[Mn(pdc)(H_2O)]_n$ (1)

Single-crystal X-ray diffraction analysis reveals that complex **1** possesses a 3D infinite structure and its building unit is [Mn(pdc)($H_2O$)] (Figure 1a). The $Mn^{II}$ ion is six-coordinate with an $NO_5$ donor set in the distorted octahedron environment. One O atom and one N atom are from the same pdc group, the other four O atoms are from three different pdc ligands and one coordinated water molecule (Figure 1b). The equatorial plane is defined by the O1, O2, O3, and O5 atoms with the O4 and N1 atoms occupying the apical positions. The bond lengths of Mn–O range from 2.1464(16) to 2.2436(18) Å and the bond length of Mn–N is 2.287(2) Å. In the crystal, the pdc group plays a bridging role. The two β-carboxylic O atoms (O2, O3) bridge equivalent $Mn^{II}$ ions and the $Mn^{II}$ ion is connected to a 1D infinite chain along the *a* axis. Along the *c* axis, the two α-carboxylic O atoms (O1, O5) separately coordinate to two equivalent $Mn^{II}$ ions. The $Mn^{II}$ ions are also connected to a 1D infinite structure. Then, complex **1** is connected to a regular 2D structure in the *ac* plane (Figure 2). Moreover, along the *b* axis, the α-carboxylic O atom (O1) together with the pyridine N atom chelate to one $Mn^{II}$ ion, the β-carboxylic O atom (O2) coordinates to the other equivalent $Mn^{II}$ ion, then the $Mn^{II}$ ions are also linked to a 1D infinite chain. It can be seen that the *ab* plane is also a regular 2D web structure (Figure 3). Complex **1** is therefore webbed to a 3D infinite structure (Figure 4).

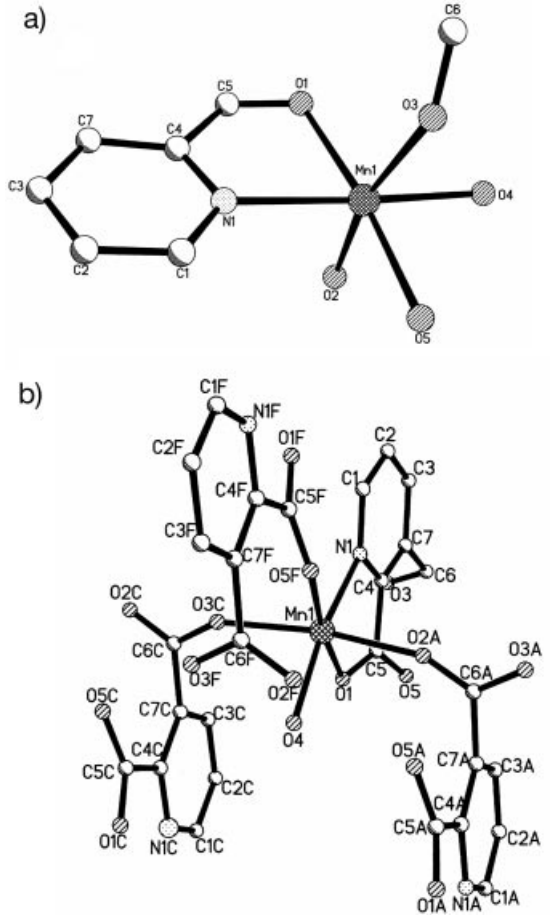


Figure 1. a) The asymmetry unit of complex **1**. b) The coordination environment of the $Mn^{II}$ ion in complex **1**.

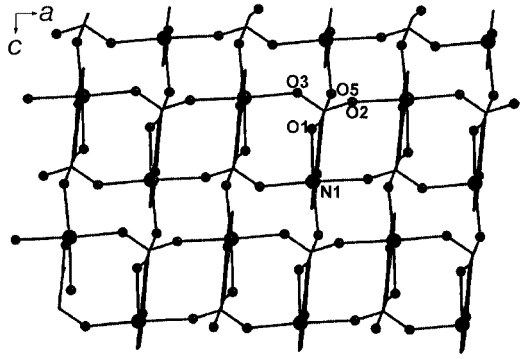


Figure 2. The 2D structure of the *ac* plane in complex **1**.

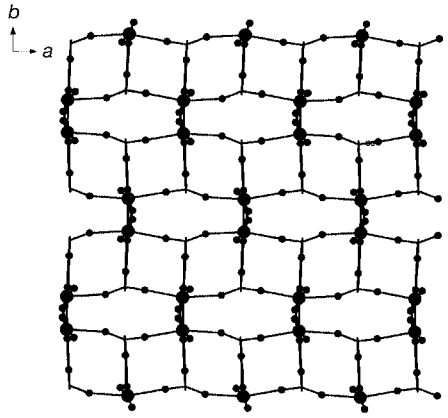


Figure 3. The 2D structure of the *ab* plane in complex **1**.

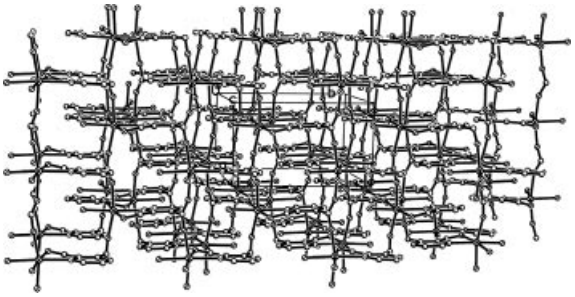

Figure 4. The 3D structure of complex **1**.

 © 2007 Wiley-VCH Verlag GmbH & Co. KGaA, Weinheim 

### {[Mn(pdc) (phen)($H_2O$)]·3$H_2O$}$_n$ (2)

Single-crystal X-ray diffraction analysis reveals that complex **2** possesses a 2D infinite structure and its building unit is {[Mn(pdc)(phen)($H_2O$)]·3$H_2O$}. The $Mn^{II}$ ion is six-coordinate by the $N_3O_3$ donor (N1, N2, N3, O1, O3, and O4) set in a distorted octahedron. The equatorial plane is defined by the N1 and N2 atoms from one phen molecule and the O3 and O4 atoms from two different pdc groups. The O1 and N3 atoms are separated from the coordinated water molecules and the pdc group occupies the apical position. The bond lengths of Mn–N range from 2.2718(16) to 2.3149(15) Å and the bond lengths of Mn–O are from 2.0963(13) to 2.1710(3) Å. The pdc group plays a bridging role: its two carboxylic groups adopt a monodentate coordination mode, one together with the pyridine N atom coordinates to one $Mn^{II}$ ion, the other coordinates to a second equivalent $Mn^{II}$ ion. Then, the $Mn^{II}$ ions are linked to a 1D infinite chain along the *b* axis (Figure 5). Two 1D infinite chains are connected to a 1D double chain through the hydrogen bond [O1–H···O2, 2.835(2) Å], which from the coordinated water molecule and uncoordinated carboxylic O atom (Figure 6). Between the different 1D double chains, there are two styles of O–H···O hydrogen bonds. They are the interactions between the lattice water molecules and the uncoordinated carboxylic O atoms [O6–H···O5, 2.854(3) Å, O7–H···O5, 2.833(3) Å] as well as lattice water molecules [O6–H···O8, 2.758(3) Å, O8–H···O7, 2.794(3) Å]. These hydrogen bonds link the multi 1D double chains to form an infinite structure along the *a* axis. Therefore, complex **2** is linked to a 2D irregular structure by hydrogen bonds (Figure 7).

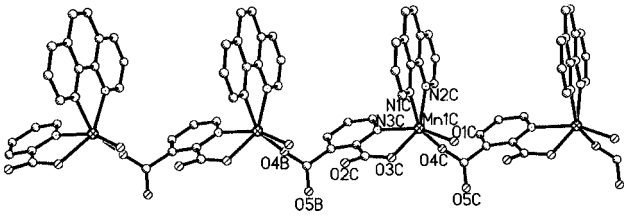


Figure 5. The 1D chain structure of complex **2**.

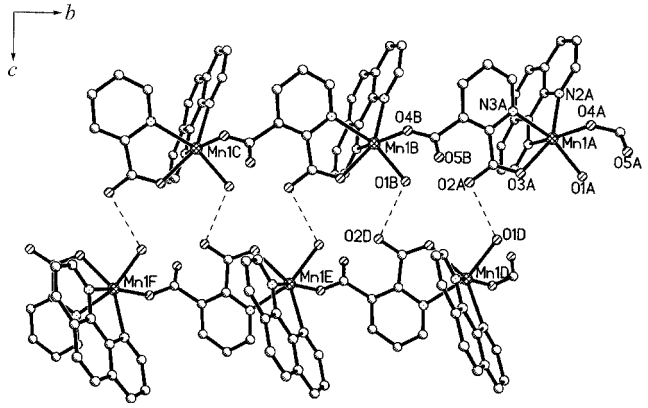


Figure 6. The 1D double chain structure of complex **2**. Dotted lines are hydrogen bonds.

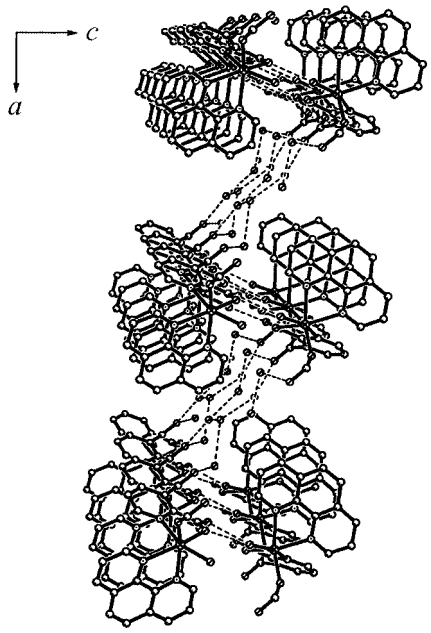


Figure 7. The 2D structure of complex **2**. Dotted lines are hydrogen bonds.

### {[Mn(cyan)$_2$($H_2O$)$_4$]·2HCl·2(Hcyan)} (3)

Complex **3** is a mononuclear coordination complex. The $Mn^{II}$ ion is six-coordinate with an $N_2O_4$ donor set in the better octahedron environment (Figure 8). Four O atoms (O6, O6A, O3, and O3A) are from four different coordinated water molecules and they comprise the equatorial plane. The bond lengths of Mn1–O3 and Mn1–O6 are 2.228(4) and 2.238(3) Å, respectively. The O6–Mn1–O6A and O3–Mn1–O3A bond angles are all 180°. The O3–Mn1–O6 and O3A–Mn1–O6 bond angles are 95.32(14)° and 84.68(14)°, respectively. The two N atoms (N1, N1A) are from two different cyan groups and they occupy the apical positions of the octahedron. The Mn1–N bond length of 2.261(4) Å and N1–Mn1–N1A bond angles of 180° means that the coordination environment of $Mn^{II}$ ion is a better octahedron. The free chloride ion is from the $MnCl_2$ reagent. The hydrogen ion comes from the coordinated Hcyan group. The N atom of the Hcyan group coordinates to the $Mn^{II}$ ion, simultaneously, the N–H bond breaks, the corresponding hydrogen ion dissociates itself from the N–H

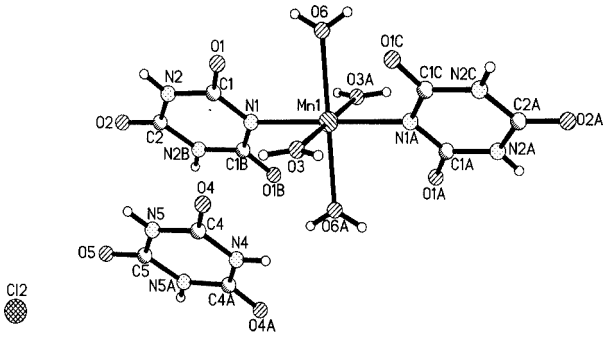


Figure 8. The molecule structure of complex **3**.

 © 2007 Wiley-VCH Verlag GmbH & Co. KGaA, Weinheim 

bond to the solution and they exactly take on the action of balancing the charge. In the crystal, there are two styles of O–H···O and O–H···N hydrogen bonds. The former is from one coordinated water molecule and a carbonyl O atom of the free Hcyan, [O3–H···O4, 2.771(3) Å], the latter is from the other coordinated water molecule and the N atom of the free Hcyan group [O6–H···N4, 2.920(4) Å]. The two styles of intermolecular hydrogen bonds link the molecule to form an infinite 1D structure along the *c* axis. In addition, there are two kinds of O···Cl weak interactions between the chlorine ion and the carbonyl O atom of the coordinated cyan group (O2···Cl, 2.867 Å) as well as the carbonyl O atom of the free Hcyan group (O5···Cl, 2.893 Å). The O···Cl weak interactions also link the molecule to form a 1D infinite structure along the *b* axis. So complex **3** is linked to a 2D regular structure at the *bc* plane (Figure 9). Moreover, the weak interactions between the free chlorine ions and the coordinated water molecules (O6···Cl, 2.949 Å; O3···Cl, 2.819 Å) as well as the carbonyl O atom of the coordinated cyan group (O1···Cl, 2.906 Å) link complex **3** to form a 1D infinite structure along the *a* axis. When projecting along the *c* axis, the *ab* plane is also a regular 2D layer (Figure 10). So complex **3** is connected to a 3D structure by hydrogen bonds and a O···Cl weak interaction (Figure 11).

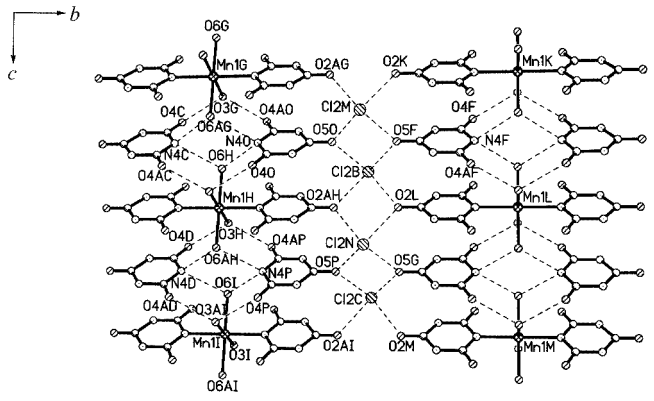


Figure 9. The 2D hydrogen-bonding structure of the *bc* plane in complex **3**. Dotted lines are hydrogen bonds.

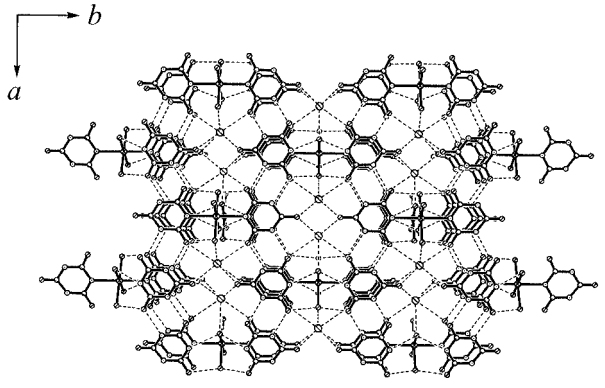


Figure 10. The 2D hydrogen-bonding structure of the *ab* plane in complex **3**. Dotted lines are hydrogen bonds.

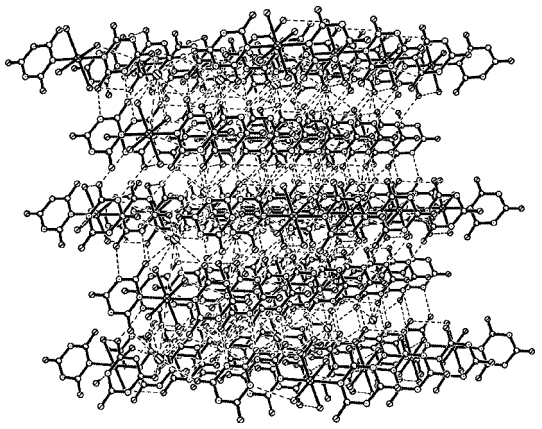

Figure 11. The 3D hydrogen-bonding structure of complex **3**. Dotted lines are hydrogen bonds.

### SPS of Complexes 1–3

The emergence of the surface photovoltage (SPV) response band indicate that when the surface of the solid sample is illuminated, the electron-hole pairs separate under a built-in field, resulting in a change in the surface potential barrier, which produces the photoelectric behavior. The detected signal by SPS is equivalent to the change in the surface potential barrier on illumination ($\delta V_s$), which is given by the equation: $\delta V_s = V_s' - V_s^o$, where $V_s'$ and $V_s^o$ are the surface potential barriers before and after illumination, respectively. As far as band-to-band transitions are concerned, a positive response in SPV ($\delta V_s > 0$) means that the sample is characterized as a *p*-type semiconductor, whereas a negative response means that the sample is an *n*-type semiconductor. The magnitude of the surface potential barrier depends on the numbers of surface net charge. Figures 12, 13, and 14 show the SPS spectra of complexes **1**–**3**, respectively. They all appear as positive SPV response bands between 300 and 800 nm. Thereinto, the signal detected by SPS at 300–500 nm is a wide peak. The signal is actually the result of overlap of several SPV response bands. To make the assignment of each SPV response band clear, we separated them by the Origin 7.0 program. Then, complexes **1** and **3** present two positive SPV responses and complex **2** appears as three positive SPV responses in the range 300–800 nm, which indicates that they all possess *p*-type semiconductor characteristics. In complex **1**, the response at $\lambda_{max}$ = 349 nm is attributed to the $\pi \rightarrow \pi^*$ transition of the ligands and the response at $\lambda_{max}$ = 403 nm is assigned to the LMCT (from ligand-to-metal charge transfer) transition. At 600–800 nm, some very weak and splitting peaks appear, this phenomenon is associated with the weak crystal-field coordination environment of the $Mn^{II}$ ion. In the six-coordinate atoms of the $Mn^{II}$ ion, there are one N atom and five O atoms. The four O atoms are from four carboxylic groups and one O atom is from one coordination water molecule. According to the spectra chemical series (–COO $<$ $H_2O$ $<$ N complexes), the $Mn^{II}$ ion ($d^5$) in complex **1** can be regarded as lying among the weak crystal field. So the $d \rightarrow d^*$ transition is forbidden. However, the microenvi-

 © 2007 Wiley-VCH Verlag GmbH & Co. KGaA, Weinheim 

ronment of the $Mn^{II}$ ion is not a strict octahedron, and there still appears to be weak splitting SPV response bands at 600–800 nm.

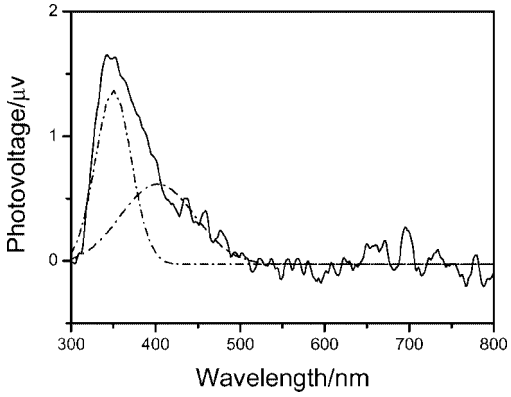


Figure 12. The SPS of complex **1**. Dotted lines are treated peak.

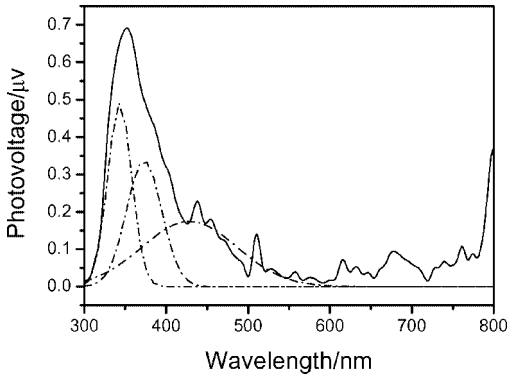


Figure 13. The SPS of complex **2**. Dotted lines are treated peak.

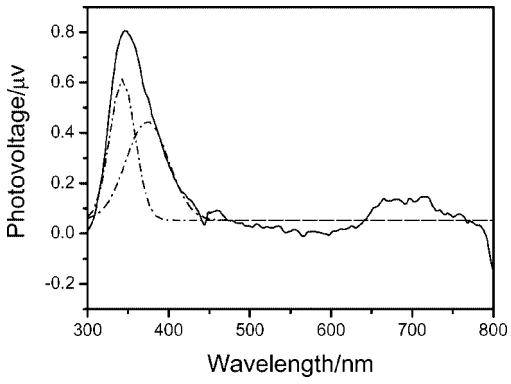


Figure 14. The SPS of complex **3**. Dotted lines are treated peak.

In complex **2**, there are three SPV responses in the range 300–800 nm. The SPV response at $\lambda_{max}$ = 349 nm is assigned to the π→π* transition of the ligand and the response at $\lambda_{max}$ = 370 nm is attributed to the LMCT transition. The response at $\lambda_{max}$ = 429 nm can be assigned to the d→d* transition ($^2T_2 \rightarrow {}^2A_2,{}^2T_2$) of the $Mn^{II}$ ion. In contrast with complex **1**, complex **2** has another SPV response band ($\lambda_{max}$ = 429 nm) that is caused by a d→d* transition, and the energy of this SPV band is very high. This can be attributed to the crystal field of the $Mn^{II}$ ion in complex **2**, which is different than that in complex **1**. The coordination atoms for the $Mn^{II}$ ion in complex **2** are three N atoms and three O atoms. So it can be regarded that the crystal field of the $Mn^{II}$ ion in complex **2** is stronger than that of in complex **1**; the d→d* transition $^2T_2 \rightarrow {}^2A_2,{}^2T_2$ can take place. The $^2T_2 \rightarrow {}^4T_1$ transition is forbidden. So only one SPV response band ($\lambda_{max}$ = 429 nm) is caused by a d→d* ($^2T_2 \rightarrow {}^2A_2,{}^2T_2$) transition. The weak and splitting SPV response band at 600–800 nm is attributed to the forbidden d→d* transition ($^2T_2 \rightarrow {}^4T_1$), owing to the microenvironment of the $Mn^{II}$ ion not being a strict octahedron.

In complex **3**, there are two positive SPV responses at 300–800 nm. The response at $\lambda_{max}$ = 340 nm is attributed to the π→π* transition of the ligand, and the response at $\lambda_{max}$ = 376 nm is assigned to the LMCT transition. Analogous with complex **1**, in the coordinated atoms with the $Mn^{II}$ ion, there are two N atoms from two cyan groups and four O atoms from four coordinated water molecules. The $Mn^{II}$ ion can be regarded as lying among a weak crystal field. The d→d* transition is forbidden. The microenvironment of the $Mn^{II}$ ion is not a strict octahedron and a weak SPV response band at 600–800 nm appears.

Comparing the SPV responses of complexes **1**–**3** at 300–500 nm (Figure 15), it can be seen that the SPV intensity of complex **1** is larger than that of complexes **2** and **3**. The differences in their intensities are maybe mainly due to the differences in their structures. Complex **1** is a 3D infinite coordination polymer. In the crystal, the 3D structure is completely formed by the coordination bonds and it can supply more transmission passages for the electrons and holes. That means that more electrons diffuse to the surface, which leads to an increase in the SPV intensity. Moreover, the 2D plane made from the *ab* and *bc* planes in complex **1** is a regular structure, and it is very favorable for the transmission of electrons and holes. Although complex **2** possesses a 2D infinite structure, the 2D structure is an irregular space structure. The irregular space structure in transferring electrons and holes is smaller than the regular structure. So the SPV intensity of complex **2** is lower than that of complex **1**. Complex **3** is a mononuclear complex and the molecule is further connected to a 3D structure by hydrogen bonds and weak interactions. Hydrogen bonds belong to the class of weak bonds and they are not as capable

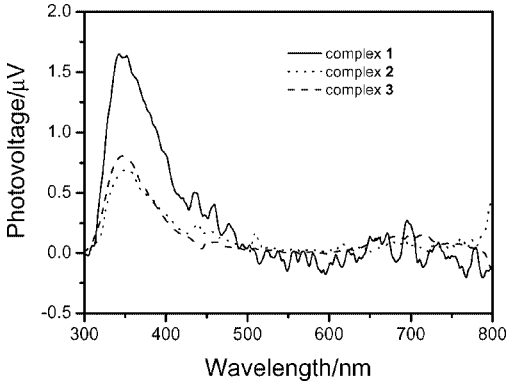


Figure 15. The contrastive SPS diagram of complexes **1**–**3**.

 © 2007 Wiley-VCH Verlag GmbH & Co. KGaA, Weinheim 

in transferring electrons and holes as coordination bonds. So the SPV intensity of complex **3** is lower than that in complex **1**. Meanwhile, the 2D structure of the *ab* and *bc* planes in complex **3** are all regular structures, which benefits to the transmission of electrons and holes. Thereby, the SPV intensity of complex **3** and complex **2** is nearly the same.

### FISPS of Complexes 1–3

FISPS can determine the direction of the built-in field and the mobile direction of photogeneration carriers. If we apply a positive electric field (the illuminated surface is positive) vertically to the *p*-type semiconductor surface, whose direction is the same as the direction of the built-in field, the separation efficiency of the photogeneration carriers are increased and the intensity of the SPV response increases in the original direction. If a negative electric field, whose direction is opposite to that of the built-in field, is applied, the separation efficiency of the photogenerated carriers reduces and the intensity of the SPV response is weakened, even in the reverse direction. In contrast to *p*-type semiconductors, the SPV response intensity of the *n*-type semiconductors increase as a negative field is applied and reduces as a positive electric field is applied. The FISPSs of complexes **1**–**3** are given in Figures 16, 17, and 18. The SPV responses in the range 300–800 nm in all three complexes increase linearly with a positive electric field, which shows that the direction of the positive electric field is consistent with the built-in field. This enhances the separation efficiency of the photoexcited electron-hole pairs and results in an increase in the surface potential; thus, the fact that complexes **1**–**3** have *p*-type semiconductor characteristics is confirmed. Otherwise, in complexes **1** and **2**, when adding a DC +2 V, some new SPV responses are produced: $\lambda_{max}$ = 442, 490 nm for complex **1** and $\lambda_{max}$ = 388, 454 nm and $\lambda_{max}$ = 700 nm for complex **2**. These new SPV response bands may be attributed to the forbidden spectroscopic term transition because the external positive electric field provides more impetus for electronic transitions, which makes the forbidden transitions take place.

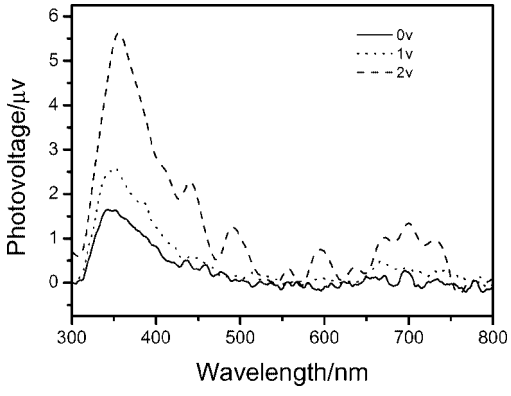


Figure 16. The FISPS of complex **1**. The intensities of the SPV response increase linearly with the external positive electric field.

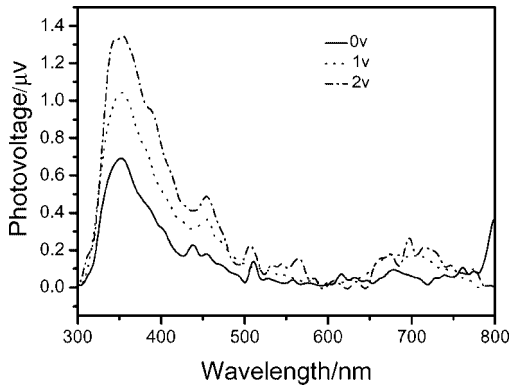


Figure 17. The FISPS of complex **2**. The intensities of the SPV response increase linearly with the external positive electric field.

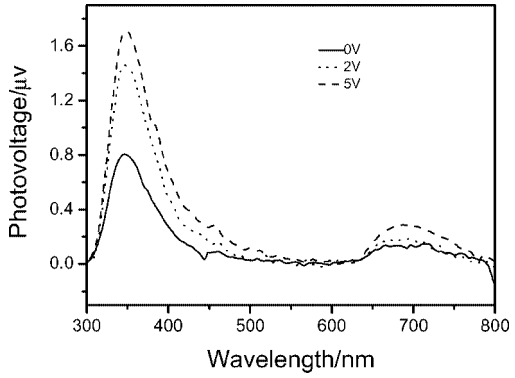


Figure 18. The FISPS of complex **3**. The intensities of the SPV response increase linearly with the external positive electric field.

## Conclusion

In this paper, three $Mn^{II}$ coordination supramolecules were synthesized by a hydrothermal method. Complex **1** possesses a 3D infinite structure. Complex **2** contains a 1D coordination chain, and the chains are further connected to a 2D infinite structure by hydrogen bonds. The 3D structure of complex **3** is completely formed by hydrogen bonds and weak interactions. The SPS of complexes **1**–**3** indicate that they all show positive SPV responses in the range 300–800 nm and all show *p*-type semiconductor characteristics. The intensities of the SPV response band at 300–500 nm in complex **1** is obviously stronger than that in complexes **2** and **3**. The differences in the intensities are attributed to the differences in their structures. The 3D structure of complex **1** is connected completely by coordination bonds and the *ab* and *bc* planes are all of regular structure. This structure style is very beneficial to the transferring of electrons and holes. Meanwhile, the microenvironment (crystal field) of the $Mn^{II}$ ion in the complexes has a certain effect on the SPV responses, especially the d→d* transition response. Due to the crystal field, complex **2** shows a stronger response than complexes **1** and **3**, and the SPV response from the d→d* transitions are obviously different. Moreover, the FISPS confirm the *p*-type semiconductor characteristic of complexes **1**–**3**.

 © 2007 Wiley-VCH Verlag GmbH & Co. KGaA, Weinheim 

## Experimental Section

**Materials and Methods:** All the reagents are A.R grade. IR spectra were recorded in the range 220–4000 $cm^{-1}$ with a JASCO FT/IR 480 spectrophotometer using KBr pellets. The elemental compositions of the complexes were determined with a PE-240C Analyzer and a PLASAM-SPEC-II instrument. The SPS and FISPS instrument was made by ourselves. Monochromatic light was obtained by passing light from a 500W xenon lamp through a double-prism monochromator. The slit width of the entrance and exit was 3 mm. A lock-in amplifier, synchronized with a light chopper, was employed to amplify the photovoltage signal. The range of modulating frequency is from 20 to 70 Hz. The spectral resolution is 1 nm. The samples were rubbed to power and were pressed between two slices of ITO glass during the SPS and FISPS measurements. The construction of the photovoltaic cell is an ITO/sample/ITO sandwich structure.[22] It was ensured that the light penetrating depth was much less than the powder layer thickness. All the measurements were performed under atmospheric pressure and at ambient temperature.

**$[Mn(pdc)(H_2O)]_n$ (1):** A solution of $MnCl_2{\cdot}4H_2O$ (0.10 g, 0.5 mmol) in water (10 mL) was added to the solution of $H_2pdc$(0.08 g,0.5 mmol) and NaOH (0.04 g,1 mmol) in water (10 mL); the solution was colorless. Then, this solution was transferred into a Teflon-lined stainless steel vessel, and the vessel was sealed and heated to 150 °C for 5 d. The mixture was cooled to room temp., and pink crystals of complex **1** were collected. $C_7H_5MnNO_5$ (238.06): calcd. C 35.31, H 2.12, N 5.89, Mn 23.08; found C 35.55, H 2.34, N 5.97, Mn 22.93. IR(KBr): $\tilde{\nu}$ = 3440, 3354

Table 1. Crystallographic data and structural refinement details for complexes **1**–**3**.

| Complex | **1** | **2** | **3** |
|---|---|---|---|
| Empirical formula | $C_7H_5MnNO_5$ | $C_{19}H_{19}MnN_3O_8$ | $C_{12}H_{20}Cl_2MnN_{12}O_{16}$ |
| $M$ | 238.06 | 472.31 | 714.24 |
| $T$ / K | 293(2) | 293(2) | 293(2) |
| $\lambda$ / Å | 0.71073 | 0.71073 | 0.71073 |
| Crystal system | monoclinic | monoclinic | monoclinic |
| Space group | $P2_1/c$ | $P2_1/n$ | $C2/m$ |
| $a$ / Å | 6.412(3) | 13.302(3) | 11.786(4) |
| $b$ / Å | 10.785(5) | 7.6274(19) | 16.064(5) |
| $c$ / Å | 11.122(5) | 19.510(5) | 7.027(2) |
| $\beta$ / ° | 94.760(5) | 91.166(3) | 116.932(4) |
| $V$ / Å$^3$ | 766.5(6) | 1979.2(8) | 1186.1(7) |
| $Z$ | 4 | 4 | 2 |
| $D_{calcd.}$ / g cm$^{-3}$ | 2.063 | 1.585 | 1.994 |
| $F$ (000) | 476 | 972 | 722 |
| Goodness-of-fit on $F^2$ | 1.066 | 1.008 | 1.060 |
| Final $R$ indices [$I > 2\sigma(I)$] | $R_1$ = 0.0275, $wR_2$ = 0.0754 | $R_1$ = 0.0351, $wR_2$ = 0.0854 | $R_1$ = 0.0629, $wR_2$ = 0.1687 |
| $R$ indices (all data) | $R_1$ = 0.0300, $wR_2$ = 0.0772 | $R_1$ = 0.0529, $wR_2$ = 0.0932 | $R_1$ = 0.0802, $wR_2$ = 0.1821 |
| Data/restraints/parameters | 1886/0/139 | 4858/8/356 | 1502/0/107 |

Table 2. Selected bond lengths [Å] and angles [°] for **1**–**3**.

| | | | | | |
|---|---|---|---|---|---|
| **1** | | | | | |
| Mn1–O3 | 2.1464(16) | Mn1–O5 | 2.1621(16) | Mn1–O4 | 2.2436(18) |
| Mn1–O2 | 2.1599(17) | Mn1–O1 | 2.1669(17) | Mn1–N1 | 2.287(2) |
| O3–Mn1–O2 | 166.25(6) | O5–Mn1–O1 | 173.06(5) | O3–Mn1–N1 | 101.13(6) |
| O3–Mn1–O5 | 88.35(6) | O3–Mn1–O4 | 84.52(6) | O2–Mn1–N1 | 92.38(5) |
| O2–Mn1–O5 | 86.44(6) | O2–Mn1–O4 | 82.40(5) | O5–Mn1–N1 | 101.40(5) |
| O3–Mn1–O1 | 96.79(6) | O5–Mn1–O4 | 85.54(6) | O1–Mn1–N1 | 73.10(5) |
| O2–Mn1–O1 | 89.54(6) | O1–Mn1–O4 | 99.54(6) | O4–Mn1–N1 | 171.09(5) |
| **2** | | | | | |
| Mn1–O4 | 2.0963(13) | Mn1–O3 | 2.1710(13) | Mn1–N2 | 2.2852(15) |
| Mn1–O1 | 2.1586(15) | Mn1–N1 | 2.2718(16) | Mn1–N3 | 2.3149(15) |
| O4–Mn1–O1 | 85.37(6) | O3–Mn1–N1 | 90.65(6) | O4–Mn1–N3 | 95.75(5) |
| O4–Mn1–O3 | 111.77(6) | O4–Mn1–N2 | 90.21(6) | O1–Mn1–N3 | 158.72(6) |
| O1–Mn1–O3 | 87.94(6) | O1–Mn1–N2 | 115.34(6) | O3–Mn1–N3 | 71.87(5) |
| O4–Mn1–N1 | 155.94(6) | O3–Mn1–N2 | 149.74(5) | N1–Mn1–N3 | 99.64(5) |
| O1–Mn1–N1 | 86.90(6) | N1–Mn1–N2 | 72.67(6) | N2–Mn1–N3 | 85.92(5) |
| **3** | | | | | |
| Mn1–O3 | 2.228(4) | Mn1–O6[a] | 2.238(3) | Mn1–N1 | 2.261(4) |
| Mn1–O3[a] | 2.228(4) | Mn1–O6 | 2.238(3) | Mn1–N1[a] | 2.261(4) |
| O3–Mn1–O3[a] | 180.0 | O6[a]–Mn1–O6 | 180.0 | O3–Mn1–N1[a] | 90.0 |
| O3–Mn1–O6[a] | 84.68(14) | O3–Mn1–N1 | 90.0 | O3[a]–Mn1–N1[a] | 90.0 |
| O3[a]–Mn1–O6[a] | 95.32(14) | O3[a]–Mn1–N1 | 90.0 | O6[a]–Mn1–N1[a] | 90.0 |
| O3–Mn1–O6 | 95.32(14) | O6[a]–Mn1–N1 | 90.0 | O6–Mn1–N1[a] | 90.0 |
| O3[a]–Mn1–O6 | 84.68(14) | O6–Mn1–N1 | 90.0 | N1–Mn1–N1[a] | 180.0 |

[a] Symmetry transformations used to generate equivalent atoms: –x, y, –z.

 © 2007 Wiley-VCH Verlag GmbH & Co. KGaA, Weinheim 

$\upsilon$(OH), 3077 $\upsilon$(ArC-H), 1614 $\upsilon$(asCOO), 1393 $\upsilon$(sCOO), 1574, 1456 $\upsilon$(ArC···C), 1241 $\upsilon$(C-N), 1153, 1104 $\upsilon$(C-C,C-O), 877, 844, 832, 784, 709, 659 $\delta$(ArC-H), 455 $\upsilon$(Mn-N), 429, 370 $\upsilon$(Mn-O) $cm^{-1}$.

**{[Mn(pdc) (phen)($H_2O$)]·3$H_2O$}$_n$ (2):** A solution of $MnCl_2·4H_2O$ (0.10 g, 0.5 mmol) in water (10 mL) was added to a solution of $H_2$pdc(0.08 g,0.5 mmol) and NaOH (0.04 g,1 mmol) in water (10 mL). An ethanol (5 mL) solution of phen (0.04 g) was then added to the above solution. The solution was yellow and clear. Then the solution was transferred into a Teflon-lined stainless steel vessel, and the vessel was sealed and heated to 170 °C for 6 d. The mixture was cooled to room temp., and pink crystals of complex **2** were collected. $C_{19}H_{19}MnN_3O_8$ (472.31): calcd. C 48.31, H 4.05, N 8.90, Mn 11.63; found C 48.52, H 4.21, N 9.12, Mn 11.49. IR (KBr): $\tilde{\nu}$ = 3395 $\upsilon$(OH), 3060 $\upsilon$(ArC-H), 1657 $\upsilon$(asCOO), 1372 $\upsilon$(sCOO), 1595, 1572, 1517, $\upsilon$(ArC···C), 1233 $\upsilon$(C-N), 1146, 1102 $\upsilon$(C-C,C-O), 844, 726 $\delta$(ArC-H), 444 $\upsilon$(Mn-N), 420 $\upsilon$(Mn-O) $cm^{-1}$.

**{[Mn(cyan)$_2$($H_2O$)$_4$]·2HCl·2(Hcyan)} (3):** A solution of $MnCl_2·4H_2O$ (0.20 g, 1 mmol) in water (10 mL) was added to a solution of Hcyan (0.13 g,1 mmol) and NaOH (0.04 g,1 mmol) in water (20 mL), and the DMF (5 mL) was added into the above solution. The solution was white and muddy. The solution was then transferred into a Teflon-lined stainless steel vessel, and the vessel was sealed and heated to 100 °C for 5 d. The mixture was cooled to room temp., and colorless crystals of complex **3** were collected. $C_{12}H_{20}Cl_2MnN_{12}O_{16}$ (714.24): calcd. C 20.18, H 2.82, N 23.54, Mn 7.69; found C 20.31, H 2.85, N 23.72, Mn 7.57. IR (KBr): $\tilde{\nu}$ = 3177, 3091 $\upsilon$(NH), 2992, 2852, $\upsilon$(OH), 1737, 1625 $\upsilon$(C=O), 1476 $\delta$(NH), 1399 $\delta$(OH), 1238, 1081, 993 $\upsilon$(C-N, C-O), 777 $\upsilon$(Cl-H), 556 $\upsilon$(Mn-N), 428 $\upsilon$(Mn-O) $cm^{-1}$.

**X-ray Crystallographic Data:** Crystallographic data for complexes **1**–**3** were collected with a Smart 1000 APEX II CCD diffractometer using graphite monochromated Mo-$K_\alpha$ radiation. ($\lambda$ = 0.71073 Å) at 293 K. All data were corrected for L-P factor and empirical absorption. The structures were solved by direct methods and refined by full-matrix least-squares calculations on $F^2$ using the SHELXTL 97 program. All non-hydrogen atoms were refined anisotropically. Hydrogen atoms were found by mixed methods. The crystal data and structure refinement of complexes **1**–**3** are summarized in Table 1. Selected bond lengths and bond angles of complexes **1**–**3** are listed in Table 2.

CCDC-634132 (for **1**), -634133 (for **2**), and -634134 (for **3**) contain the supplementary crystallographic data for this paper. These data can be obtained free of charge from The Cambridge Crystallographic Data Centre via www.ccdc.cam.ac.uk/data_request/cif.

**Supporting Information** (see footnote on the first page of this article): Two correlated structure figures of complexes **1** and **2**, IR spectra of complexes **1**–**3**, principle of the SPS, analysis of the transition assignment, and equipment of the SPV technique.

## Acknowledgments

This work was supported by the National Natural Science Foundation of China (Nos.20571037 and 90201018).

[1] J. Fan, L. Gan, H. Kawaguchi, W. Y. Sun, K. B. Yu, W. X. Tang, *Chem. Eur. J.* **2003**, *9*, 3965–3973.
[2] M. L. Tong, J. Wang, S. Hu, *J. Solid State Chem.* **2005**, *178*, 1518–1525.
[3] W. Dong, Q. L. Wang, S. F. Si, D. Z. Liao, Z. H. Jiang, S. P. Yan, P. Cheng, *Inorg. Chem. Commun.* **2003**, *6*, 873–876.
[4] C. Genre, G. S. Matouzenko, E. Jeanneau, D. Lunean, *New J. Chem.* **2006**, *30*, 1669–1674.
[5] X. H. Bu, M. L. Tong, Y. B. Xie, J. R. Li, H. C. Chang, S. Kitagawa, J. Ribas, *Inorg. Chem.* **2005**, *44*, 9837–9846.
[6] M. F. Anderlund, J. Högblom, W. Shi, P. Huang, L. Eriksson, H. Weihe, S. Styring, B. Åkermark, R. Lomoth, A. Magnuson, *Eur. J. Inorg. Chem.* **2006**, *24*, 5033–5047.
[7] V. L. Pecoraro (Ed.), *Manganese Redox Enzymes*, VCH, New York, **1992**.
[8] M. Fujiware, T. Matsushita, S. Ikeda, *J. Electron. Spectrosc. Relat. Phenom.* **1995**, *74*, 201–206.
[9] S. Ohkoshi, H. Tokoro, M. Utsunomiya, M. Mizuno, M. Abe, K. Hashimoto, *J. Phys. Chem. B* **2002**, *106*, 2423–2425.
[10] D. Dobraynska, L. B. Jeraykiewicz, J. Jezierska, M. Duczmal, *Cryst. Growth Des.* **2005**, *5*, 1945–1951.
[11] A. Murphy, G. Dubois, T. D. P. Stack, *J. Am. Chem. Soc.* **2003**, *125*, 5250–5251.
[12] X. H. Liu, M. Krott, P. Műller, C. H. Hu, H. Lueken, R. Dronskowski, *Inorg. Chem.* **2005**, *44*, 3001–3003.
[13] D. Ghoshal, A. K. Ghosh, J. Ribas, E. Zangrando, G. Mostafa, T. K. Maji, N. R. Chaudhuri, *Cryst. Growth Des.* **2005**, *5*, 941–947.
[14] J. F. Chai, H. P. Zhu, A. C. Stűckl, H. W. Roesky, J. Magull, A. Bencini, A. Caneschi, D. Gratteschi, *J. Am. Chem. Soc.* **2005**, *127*, 9201–9206.
[15] D. J. Wang, J. Zhang, T. S. Shi, B. H. Wang, X. Z. Cao, T. J. Li, *J. Photochem. Photobiol. A* **1996**, *93*, 21–25.
[16] Q. L. Zhang, D. J. Wang, J. J. Xu, J. Cao, J. Z. Sun, M. Wang, *Mater. Chem. Phys.* **2003**, *82*, 525–528.
[17] L. P. Sun, S. Y. Niu, J. Jin, G. D. Yang, L. Ye, *Eur. J. Inorg. Chem.* **2006**, 5130–5137.
[18] T. F. Xie, D. J. Wang, L. J. Zhu, C. Wang, T. J. Li, *J. Phys. Chem. B* **2000**, *104*, 8177–8181.
[19] A. Kokler, J. Gruner, R. H. Friend, K. Mullen, V. Scherf, *Chem. Phys. Lett.* **1995**, *243*, 456–461.
[20] J. Zhang, D. J. Wang, T. S. Shi, B. H. Wang, J. Z. Sun, T. J. Li, *Thin Solid Films* **1996**, *284/285*, 596–599.
[21] H. F. Mao, H. J. Tian, Q. F. Hou, H. J. Xu, *Thin Solid Films* **1997**, *300*, 208–212.
[22] K. Y. Li, D. J. Wang, F. Q. Wu, T. F. Xie, T. J. Li, *Mater. Chem. Phys.* **1999**, *60*, 226–230.

Received: February 13, 2007
Published Online: June 29, 2007

 © 2007 Wiley-VCH Verlag GmbH & Co. KGaA, Weinheim 

DOI: 10.1002/ejic.200700282

# Stereospecific Synthesis, Structural Characterisation and Resolution of 2-Phospha[3]ferrocenophane Derivatives – a New Chiral Scaffold

**Nicolas Fleury-Brégeot,[a] Armen Panossian,[a] Angèle Chiaroni,[a] and Angela Marinetti*[a]**

**Keywords:** Phosphane ligands / Ferrocenophane / Chiral resolution / Palladium

The first 2-phospha[3]ferrocenophanes containing stereogenic carbon atoms in the three-atom bridge have been synthesised from phenylphosphane by stereospecific ring-closing phosphanation reactions. Either α-substituted 1,1′-bis-(hydroxymethyl)ferrocenes or the corresponding 2-oxa-[3]ferrocenophanes have been used as diastereomerically pure starting materials. The resolution of 1,2,3-triphenyl-[2]phosphaferrocenophane has been achieved by chromatographic separation of the diastereomeric adducts of a chiral cyclopalladate complex. The X-ray crystal structures of two 2-phospha[3]ferrocenophane-borane complexes are also reported.
(© Wiley-VCH Verlag GmbH & Co. KGaA, 69451 Weinheim, Germany, 2007)

The emergence of monodentate, bulky, electron-rich phosphanes is a recent, noteworthy issue in the field of organometallic catalysis. Tris(*tert*-butyl)phosphane, biphenyl-(di-*tert*-butyl)- and dicyclohexylphosphane are prototypical compounds of this class. By showing their great potential in palladium-promoted coupling reactions,[1] the pioneering work of Nishiyama, Fu and Buchwald stimulated the active search for new catalytic applications[2] as well as for new ligand structures. Among others, the synthesis and use of ferrocenyl-based phosphanes have been considered, which combine the steric bulk of the organometallic moiety with the electron-donating properties of alkyl and/or ferrocenyl phosphorus substituents.[3] Representative examples are given in Figure 1.

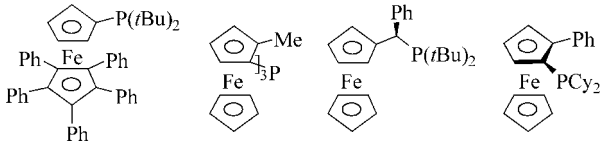


Figure 1. Ferrocenylphosphanes.

An especially attractive and favourable feature of ferrocenylphosphanes for routine bench use is their higher resistance to air oxidation with respect to other ligands with similar bulk and electron-donating ability. This is the basis of, for instance, the impressive development of ferrocenyl-based phosphanes in enantioselective catalysis,[4] and it motivates new studies in these series.

In this context, our purpose is to expand the field of monodentate, electron-rich ferrocenylphosphanes, and especially that of chiral species, to include unprecedented or neglected scaffolds. In most known ferrocenyl phosphanes, a phosphorus function and the cyclopentadienyl ring are either directly bonded or separated by a one-carbon spacer (representative examples of monodentate derivatives are shown in Figure 1). In only a few cases have two[3d,5,6] or three[3c] ferrocene moieties been connected to the same phosphorus atom, and ferrocenophane frameworks bearing phosphorus functions in a carbon-tethering chain are especially uncommon. Thus, ferrocenophane moieties of this series have been selected in this work as target compounds.

It may be interesting to recall here that, among phosphorus-containing ferrocenophanes, 1-phospha[1]ferrocenophanes are moderately stable compounds that have been extensively studied mainly as precursors for high-molecular-weight poly(ferrocenes) by thermal or photochemical ring-opening polymerisation.[7] Similarly, incorporation of phosphorus in the two-atom chain of [2]ferrocenophanes has been used to generate strained starting materials for the synthesis of polymeric materials.[8] On the other hand, three- to five-atom tethers are known to afford stable phosphorus derivatives. Thus, for instance, the synthesis and coordinating properties of a 3-phospha[5]ferrocenophane have been reported.[9] Concerning phosphorus-containing [3]ferrocenophanes, most known compounds have three heteroatom bridges. These include 1,3-distanna-,[10] 1,3-dithia-[11] and 1,3-diaza-2-phospha[3]ferrocenophanes.[12] The first [3]ferrocenophanes where phosphorus is included in a

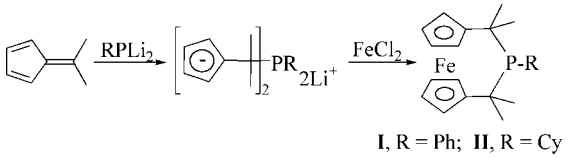


**I**, R = Ph; **II**, R = Cy

Scheme 1.

[a] Institut de Chimie des Substances Naturelles, CNRS UPR 2301,
1, av. de la Terrasse, 91198 Gif-sur-Yvette Cedex, France
E-mail: angela.marinetti@icsn.cnrs-gif.fr

 © 2007 Wiley-VCH Verlag GmbH & Co. KGaA, Weinheim 

carbon tether have only recently been isolated from the reaction of 6,6′-dimethylfulvene with, successively, the dilithiated phosphanes $PhPLi_2$ or $CyPLi_2$, and $FeCl_2$ (Scheme 1).[13]

## Results and Discussion

### Synthesis and Characterisation of 2-Phospha[3]ferrocenophanes

As far as we know, no chiral, enantiomerically pure phosphaferrocenophanes where either phosphorus or phosphorus-containing chains link the two cyclopentadienyl rings are known to date.[14] Thus, in this work, 2-phospha-[3]ferrocenophane derivatives of the general formula **1** (Figure 2), including optically pure compounds, have been targeted as new bulky, rigid and electron-rich phosphanes for use in organometallic catalysis.

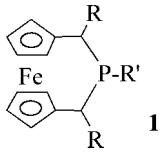


**1**

Figure 2. 2-Phospha[3]ferrocenophane derivatives **1**.

A key prerequisite for the synthesis of chiral derivatives is establishing reliable, stereospecific synthetic approaches to the [3]ferrocenophane scaffold; then convenient resolution procedures must be defined. The synthetic approach to 2-phospha[3]ferrocenophane shown in Scheme 1 is unlikely to be applied to the stereoselective synthesis of the targeted phospha[3]ferrocenophanes **1**, given that mixtures of all possible stereoisomers of **1** are expected to form as a result of such a procedure. Thus, alternative approaches that start from preformed, suitably substituted ferrocenes have been considered in this work. Known methods for the formation of P–C bonds from ferrocenylmethyl derivatives have been tested and adapted to the synthesis of the ferrocenophane derivatives **1**.

Since the pioneering work of Kumada and Hayashi, ferrocenylmethyl acetates or the corresponding ammonium salts have been routinely used for the synthesis of (ferrocenylmethyl)phosphanes through reactions with secondary phosphanes.[15] Starting from α-substituted derivatives, these highly stereospecific reactions take place with retention of the carbon configuration, because of the high configurational stability of the intermediate carbocation.

Although the use of primary phosphanes in such reactions has scarcely been reported,[6,16] the method might provide stereospecific access to 2-phospha[3]ferrocenophanes starting from 1,1′-bis(α-acetoxymethyl)ferrocenes. In preliminary experiments, however, the reaction of 1,1′-bis(α-acetoxybenzyl)ferrocene with phenylphosphane in usual experimental conditions (room temp. in acetic acid) afforded only trace amounts of the expected compounds, together with supposedly polymeric, insoluble material. We thus turned our attention to alternative starting materials and found that suitable reactants and conditions for the stereospecific synthesis of **1** must be selected for each of the targeted phosphanes. Especially, the availability of diastereomerically pure starting materials is a key prerequisite for these reactions.

For R = Ph, high-yield, stereospecific synthesis of **1a** and **1a′** has been performed from the *meso* and *dl* diols **2a′** and **2a** respectively, by their reactions with $PhPH_2$ in acetic acid (Scheme 2).

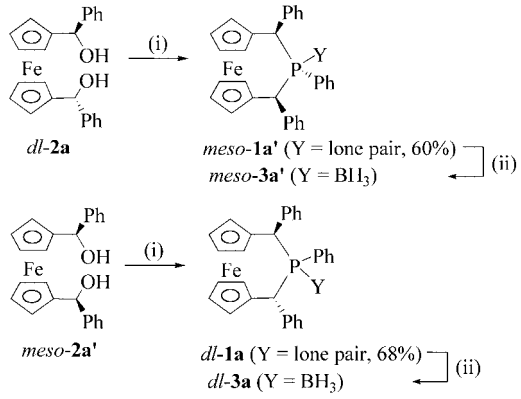


Reagents and conditions: (i) $PhPH_2$, 1 equiv., AcOH, 0°C to r.t. (ii) excess $BH_3$·THF

Scheme 2.

Diol **2a** can be obtained easily, albeit in an expensive and redundant way, by CBS reduction[17] of the corresponding diketone, 1,1′-dibenzoylferrocene. Alternatively,[18–20] diol **2a** can be obtained from the 1:1 mixture of the *meso* and *dl* diols produced by $NaBH_4$ reduction of 1,1′-dibenzoylferrocene, by repeated crystallisations from ethyl acetate/hexane. The *meso* diol **2a′** was obtained by fractional crystallisation of the *meso*/*dl* (2:1) diastereomeric mixture, which is produced when the same diketone is reduced with $LiAlH_4$ in ether.

The stereochemical course of the reactions of diols **2** with phenylphosphane (Scheme 2) follows the expected pattern: retention of the carbon configuration takes place in the first, intermolecular nucleophilic substitution step, while the intramolecular ring-closing reaction necessarily induces inversion of the carbon configuration. In both steps an iron-stabilised carbocation is formed after departure of the leaving group;[21] however, the entering nucleophiles approach the carbocation once from the face opposite the iron atom and once from the "iron face". Consequently, the *dl* diol **2a** affords the *meso* derivative, *anti*,*anti*-1,3-diphenyl-2-phospha[3]ferrocenophane **1a′**, while the *meso* diol **2a′** selectively affords the *dl* isomer **1a**.

The cyclisation reaction is best performed by adding phenylphosphane to an ice-cooled suspension of diols **2** in acetic acid and then warming the mixture to room temperature. Prolonged stirring of the diol in acetic acid should be avoided, in order to prevent epimerisation.

The [3]ferrocenophanes **1** are air-stable in the solid state and oxidise slowly in solution. These compounds, as well as the corresponding borane complexes **3**, have been fully

 © 2007 Wiley-VCH Verlag GmbH & Co. KGaA, Weinheim 

characterised. The crystal structure of the *dl* isomer **3a** has been determined by X-ray diffraction studies (see below). Phosphane **1a**′ and corresponding borane **3a**′ have been assigned as the *anti*,*anti* isomers, based on the small $^2J_{H-P}$ coupling (6.0 Hz) observed for the *CH*Ph protons in the $^1$H NMR spectrum of **1a**′.[22] This isomer is expected to be the thermodynamically favoured one.

The use of ferrocenylmethyl alcohols as precursors for phosphanes has been rather infrequently reported,[3d,16,23] the alcohols usually being converted into acetates before their reaction with phosphorus nucleophiles. Thus, having ascertained the high stereoselectivity of the reaction between diols **2a** and phenylphosphane in acetic acid, we wondered if the method could also be applied to the stereoselective synthesis of simpler phosphanes, directly from enantiomerically enriched alcohols. As a representative example, the commercially available diisobutylphosphane has been reacted with (*S*)-α-ferrocenylpentan-1-ol **4a**[24] and (*S*)-α-(ferrocenyl)benzyl alcohol **4b**.[25] In both cases the targeted phosphane could be obtained stereoselectively when suitable experimental conditions were applied.

The (α-ferrocenyl-1-pentyl)diisobutylphosphane **5a** is formed with total retention of the carbon configuration when diisobutylphosphane is added to a solution of (*S*)-**4a** in acetic acid at room temperature. However, in the same conditions, the substitution reaction on the α-(ferrocenyl)-benzyl alcohol (*S*)-**4b** induces partial racemisation of the carbon centre. Racemisation can be avoided by immediately adding the phosphane to an ice-cooled suspension of the chiral alcohol **4b** in acetic acid. This procedure avoids prolonged contact of alcohol **4b** with the acidic medium and thus allows a stereospecific substitution reaction to take place with the phosphane.

These results corroborate previous data showing lack of stereochemical control in the substitution reaction between **4b** and imidazoles in acidic medium and almost total retention of the carbon configuration in the analogous substitution on α-ferrocenylethanol at room temperature.[26] On the other hand, however, a stereospecific reaction has been reported by Hu to take place between **4b** and phenylphosphane in acetic acid at room temperature.[3d]

Taken together, the results shown in Scheme 3 and literature data afford additional evidence that the stereochemical course of the substitution reactions on the α-substituted(ferrocenyl) alcohols **4** and most particularly on α-aryl-

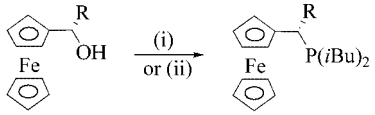


(*S*)-**4a** R = Bu (*ee* = 98%)
(*S*)-**4b** R = Ph (*ee* = 94%)
(*S*)-**4b** R = Ph (*ee* = 96%)

**5a** R = Bu, 90% yield, *ee* = 98%[(i)]
**5b** R = Ph, 65% yield, *ee* = 49%[(i)]
**5b** R = Ph, 86% yield, *ee* = 96%[(ii)]

Reagents and conditions: (i) slow addition of $i$Bu$_2$PH (1 equiv.) to a solution of **4** in AcOH, at r.t. (ii) rapid addition of $i$Bu$_2$PH (1 equiv.) to an ice-cooled suspension of **4** in AcOH.

Scheme 3.

substituted species depends on the nature of the entering nucleophile and/or on the precise experimental procedure, racemisation of the starting alcohol possibly being a competitive side reaction. Experimental conditions can be found where the substitution reaction overcomes the racemisation process induced by the acidic medium and the chiral alcohols **4** can be conveniently converted into the corresponding phosphanes by using nucleophilic phosphorus reagents.

Returning to our main aim, that is, the stereospecific synthesis of 2-phospha[3]ferrocenophanes, we next considered synthetic approaches to phosphanes **1b** (R = Me). In this case, the question arises of the availability of suitable, diastereomerically pure starting materials.[27] It is well known that the diastereomeric mixture of the 1,1′-bis(α-hydroxyethyl)ferrocenes **2b/2b**′ obtained by reduction of 1,1′-diacetylferrocene cannot be separated either by chromatography or by crystallisation. On the other hand, according to Yamakawa and Hisatome,[18] the corresponding diastereomeric 2-oxa[3]ferrocenophanes **6b/6b**′ are easily separable by column chromatography. The cyclic ethers **6**[28] have thus been selected as starting materials for the synthesis of phosphanes **1b**, which have been isolated as their borane complexes **3b**, according to the method shown in Scheme 4.

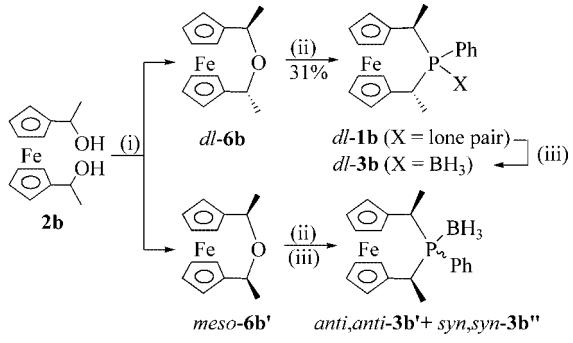


Reagents and conditions: (i) $HCl_{aq}$, column chromatography on silica gel. (ii) $PhPH_2$, $BF_3{\cdot}Et_2O$, $CH_2Cl_2$. (iii) $BH_3{\cdot}THF$

Scheme 4.

Treatment of diol **2b** (1:1 isomeric mixture) with aqueous HCl induces the ring-closure reaction and quantitatively affords the diastereomeric ethers **6**, which are easily separated by column chromatography on silica gel with hexane/ethyl acetate (9:1) as the eluent. The *meso*-**6b**′ isomer was eluted first ($R_f$ = 0.47), followed by the *dl* isomer **6b** ($R_f$ = 0.35).[29]

For the direct conversion of the cyclic ethers **6** into phosphanes, we envisioned a reaction with phenylphosphane in the presence of acid catalysts. Addition of the acid catalyst to the bridging oxygen atom is expected to generate a ferrocene-stabilised carbocation,[30] which should then react with the nucleophilic phosphane to afford a phosphonium salt intermediate. A second, intramolecular, acid-catalysed, nucleophilic substitution between the corresponding phosphane and the residual hydroxy function should then lead to the expected phospha[3]ferrocenophane **1b**. The use of both Brønsted and Lewis acid catalysts ($HBF_4$, $CF_3CO_2H$,

 © 2007 Wiley-VCH Verlag GmbH & Co. KGaA, Weinheim 

$BF_3{\cdot}Et_2O$, $SnCl_4$) has been considered. Boron trifluoride proved to be the best catalyst, affording the desired 2-phospha[3]ferrocenophanes **1b** in about 30% yield. The final phosphane–borane complexes are easily purified by column chromatography, given that the only side-products formed in the reaction are insoluble and probably polymeric.

The substitution reaction takes place with total stereoselectivity with respect to the carbon configuration, through a conceivably double inversion process. A single diastereoisomer is obtained from the *dl* ether **6b**, while a mixture of the *anti*,*anti* and *syn*,*syn* isomers **3b′** and **3b′′** respectively are formed from *meso*-**6b′**.

### X-ray Crystal Structures of the Borane Complexes of 2-Phospha[3]ferrocenophane

As compounds **1** and **3** are the first known, stereochemically defined, phosphorus-bridged ferrocenophanes, the molecular structure of one of them, the *dl*-triphenyl-substituted derivative **3a**, has been investigated by X-ray diffraction studies. Suitable single crystals of **3a** were obtained by slow crystallisation from ethyl acetate/hexane. The ORTEP drawing is presented in Figure 3.

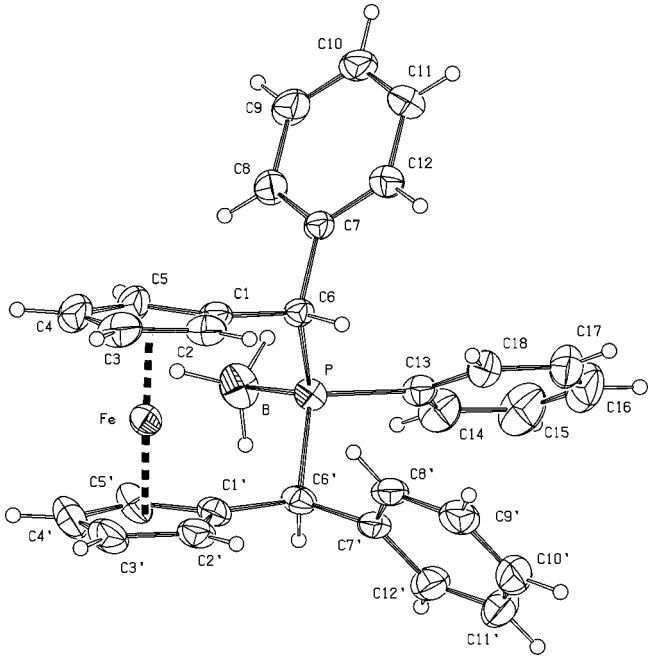


Figure 3. ORTEP drawing of *dl*-**3a**. Displacement ellipsoids are shown at the 30% probability level.

For comparison purposes, the carbon-unsubstituted *P*-phenylferrocenophane **3c** has been prepared from the corresponding oxa[3]ferrocenophane[31] and phenylphosphane (see Experimental Section) and structurally characterised (Figure 4). Comparative bond lengths and angles for compounds **3a** and **3c** are given in Table 1, together with relevant values for compound **I** from ref.[13]

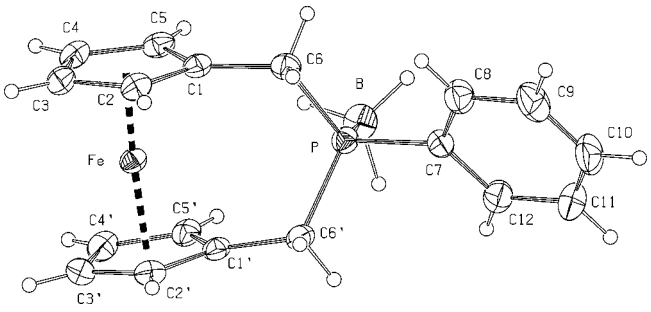


Figure 4. ORTEP view of the 2-phenyl-2-phospha[3]ferrocenophane borane complex **3c**. Displacement ellipsoids are shown at the 30% probability level.

Table 1. Selected bond lengths [Å] and angles [°] for **3a**, **3c** and **I** (see Scheme 1).

| | *dl*-**3a** | **3c** | **I**[13] |
|---|---|---|---|
| P–C6 | 1.855(2) | 1.826(3) | 1.899(2) |
| P–C6′ | 1.878(2) | 1.826(3) | 1.900(2) |
| P–C13 or P–C7 | 1.813(3) | 1.813(3) | 1.844(2) |
| P–B | 1.910(3) | 1.929(4) | |
| C1–C6 | 1.510(3) | 1.512(3) | 1.516(3) |
| C1′–C6′ | 1.515(3) | 1.508(3) | 1.516(3) |
| Fe–C1 | 2.025(2) | 2.024(3) | 2.034(2) |
| Fe–C1′ | 2.016(2) | 2.023(2) | 2.045(2) |
| C6–P–C6′ | 108.28(9) | 105.28(13) | 109.16(9) |
| B–P–C13 or C7 | 110.20(14) | 110.57(16) | |
| C7–C6–P | 110.72(14) | | 118.5(2) |
| C7′–C6′–P | 113.37(14) | | 104.8(2) |

The crystal structures of **3a** and **3c** display roughly the same preferred arrangement and geometrical features as other 2-phospha[3]ferrocenophane derivatives.[13,32]

The Cp rings of **3** and, consequently, the C1–C6 and C1′–C6′ bonds are almost perfectly eclipsed in a synperiplanar conformation. The ferrocenophane scaffold therefore shows a symmetry plane including the iron and phosphorus atoms. This symmetry plane will be lost in **3a** because of the presence of the stereogenic α-carbon atoms. The mean values for the Fe–C distances are identical in the two complexes at 2.035 Å.

In **3a**, the plane of the phenyl ring bonded to C6 forms a dihedral angle of 74.8° with the Cp ring (pseudoaxial position), while the phenyl bonded to C6′ has a dihedral angle of 40.6° with the Cp plane (pseudoequatorial position). The phenyl substituent on phosphorus occupies an *anti* position with respect to the ferrocenyl moiety, which should minimise steric repulsions.

In both phosphane–borane complexes **3**, the cyclopentadienyl rings are slightly tilted toward each other, with dihedral angles of 4.8° and 5.6° for **3a** and **3c** respectively. Moreover, the angles around the phosphorus atom are very close to the expected tetrahedral value (109.5°). This suggests a very low degree of ring strain induced by the three-atom tether.

### Resolution of *dl*-1,2,3-Triphenyl-2-phospha[3]ferrocenophane

The final aim of our work is to set up the 2-phospha[3]ferrocenophane unit as a new structural motif for the de-

 © 2007 Wiley-VCH Verlag GmbH & Co. KGaA, Weinheim 

sign of chiral ligands. Thus, within these first and preliminary studies, the last step has been the search for a suitable resolution procedure for the representative phosphane **1a**. For this resolution process we envisioned the use of *ortho*-palladate derivatives of optically active amines whose versatility as resolving agents for Lewis bases has been largely demonstrated.[33] The choice of the chiral amine auxiliary proved crucial. Attempts to separate diastereomeric palladium complexes derived from either α-methylbenzylamine, *N*,*N*-dimethyl-α-methylbenzylamine or 1-(α-naphthyl)ethylamine were unsuccessful, however better results were obtained with the (*R*)-configured cyclopalladate complex **7**.[34]

The (*R*)-configured cyclopalladate complex **7** was treated with the racemic 1,2,3-triphenyl-2-phospha[3]ferrocenophane *dl*-**1a** to afford a 1:1 mixture of the mononuclear diastereomeric complexes **8a** and **8b** by displacement of the chloride bridge (Scheme 5). Separation of the mixture proved to be straightforward: column chromatography on silica gel with a heptane/ethyl acetate (8:2) mixture as the eluent afforded **8a** and **8b** separately ($R_f$ = 0.5 and 0.3 respectively in heptane/ethyl acetate, 6:4). An X-ray crystal structure of **8a** allowed assignment of the relative configuration of the phospha[3]ferrocene ligand with respect to the known (*R*) configuration of the amine fragment. In complex **8a** the 1,2,3-triphenyl-2-phospha[3]ferrocenophane has an (*S*,*S*) configuration (Figure 5).

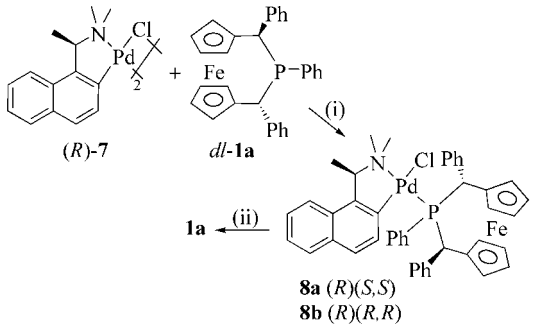


Reagents and conditions: (i) acetone, r.t., 2h, chromatographic separation of the diastereomeric complexes **8**; (ii) dppe, $CH_2Cl_2$, r.t., 3h

Scheme 5.

Compared to the X-ray structures of compounds **3a** and **3c**, the special feature of the ferrocenophane moiety in **8a** is the synclinal staggered conformation of the cyclopentadienyl rings. The dihedral angle between the Cp rings is 11.7°, that is, slightly larger than in the corresponding borane complex **3c**. This distorted conformation may result from steric constraints in the hindered palladium complex.

Decomplexation of phosphane **1a** from **8** was performed according to the standard method, by reaction with the chelating diphosphane dppe, in dichloromethane, followed by separation on a short silica column. The optically active (*S*,*S*)-1,2,3-triphenyl-2-phospha[3]ferrocenophane **1a** obtained from **8a** gave $[a]_D$ = +392 (*c* = 0.2, $CHCl_3$).

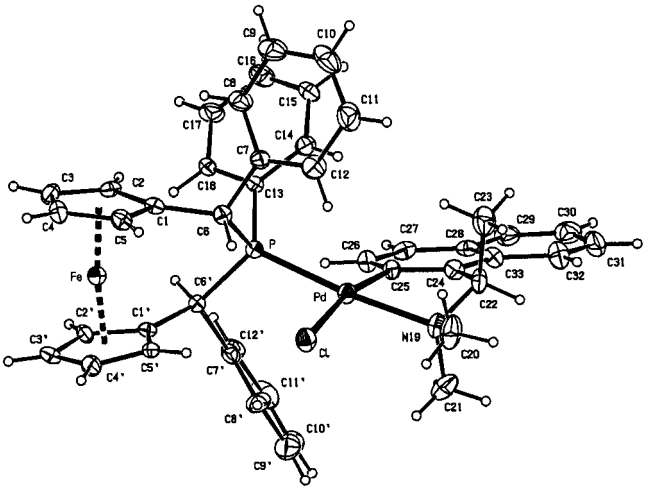

Figure 5. ORTEP view of the cyclopalladate complex **8a**. Displacement ellipsoids are shown at the 30% probability level.

## Conclusions

This work demonstrates an unprecedented synthetic approach to the 2-phospha[3]ferrocenophane scaffold, which allows the stereospecific synthesis of α,α′-disubstituted derivatives. Moreover, optical resolution of the 2-phospha[3]-ferrocenophane **1a**, which contains stereogenic carbon atoms in the three-atom bridge, has been performed. These preliminary studies open the way to the development of a new family of phosphorus ligands based on the 2-phospha[3]ferrocenophane unit as a new chiral cyclic scaffold.

## Experimental Section

NMR spectra were recorded with Bruker Avance 300 or Avance 500 spectrometers in $CDCl_3$ solutions. Chemical shifts are reported in ppm with reference to the residual solvent peak ($CHCl_3$) for $^1H$ and $^{13}C$. Mass spectra were run on LCT Waters-Micromass (Electrospray) or on a MALDI-TOF Perseptive Biosystem Voyager DE-STR (HRMS). $[a]_D$ values were recorded with a Jasco P-1010 polarimeter at 20 °C. All reactions were carried out under argon.

**General Procedure for the Synthesis of the 1,2,3-Triphenyl-2-phospha[3]ferrocenophanes 1a,1a′ and Their Borane Complexes 3a,3a′:** The known 1,1′-bis(hydroxybenzyl)ferrocenes **2a** and **2a′** were obtained according to literature methods.[18,19] NMR spectra are in good agreement with those reported previously.[17c,19] $^1H$ NMR ($CDCl_3$), *dl*-**2a**: δ = 4.17 (s, 2 H), 4.23 (s, 2 H), 4.28 (s, 2 H), 4.29 (2 H, OH), 4.46 (s, 2 H), 5.55 (s, 2 H, CHPh), 7.2–7.3 (10 H, Ph); *meso* **2a′**: δ = 4.12 (s, 2 H), 4.21 (s, 2 H), 4.25 (s, 2 H), 4.29 (2 H, OH), 4.33 (s, 2 H), 5.54 (s, 2 H, CHPh), 7.2–7.4 (10 H, Ph) ppm.

A Schlenk tube was charged with acetic acid (6 mL) and ice-cooled under argon for about 10 min. The 1,1′-bis(hydroxybenzyl)ferrocene **2** (0.2 g, 0.5 mmol) was added at once, followed by addition of phenylphosphane (60 μL, 0.6 mmol). The mixture was warmed slowly to room temperature while stirring for about 1 h. The solvent was removed under vacuum. In order to remove the residual solvents, degassed $CH_2Cl_2$ was added and removed again under vacuum to afford an orange solid. Starting from the *meso* isomer **2a′**, $^1H$ NMR of the crude mixture shows formation of *dl*-**1a** as the single diastereomer of the final product. Starting from *dl*-**2a**,

 © 2007 Wiley-VCH Verlag GmbH & Co. KGaA, Weinheim 

the thermodynamically favoured *anti*,*anti* isomer **1a′** has been obtained as the major product. Phosphanes **1a** and **1a′** have been purified by column chromatography under argon.

To obtain the borane complexes **3a** or **3a′**, the crude product isolated from the reaction above after removal of acetic acid was dissolved in THF. An excess of $BH_3$·THF adduct (1.6 mL, 1 M solution in THF) was added at room temperature. After evaporation of the solvent, the final product was purified by column chromatography.

***anti*,*syn*-1,2,3-Triphenyl-2-phospha[3]ferrocenophane (1a):** Complex **1a** was purified by column chromatography on silica gel with hexane/ethyl acetate (90:10) as the eluent ($R_f$ = 0.5). It was obtained as an orange solid in 68% yield (160 mg). $^1$H NMR ($CDCl_3$): $\delta$ = 4.00 (d, $J_{H,P}$ = 12.5 Hz, 1 H, CHPh), 4.09 (d, $J_{H,P}$ = 5.0 Hz, 1 H, CHPh), 4.13 (m, 1 H, Cp), 4.14 (m, 1 H, Cp), 4.15 (m, 1 H, Cp), 4.18 (m, 1 H, Cp), 4.22 (m, 1 H, Cp), 4.29 (m, 1 H, Cp), 4.34 (m, 1 H, Cp), 4.41 (m, 1 H, Cp), 6.80 (t, 2 H), 6.95 (4 H), 7.06 (4 H), 7.21 (3 H), 7.39 (d, $J$ = 7.5 Hz, 2 H) ppm. $^{13}$C NMR ($CDCl_3$): $\delta$ = 35.9 (d, $^1J_{P,C}$ = 18.6 Hz, PCH), 44.8 (d, $^1J_{P,C}$ = 24.0 Hz, PCH), 68.1 ($CH_{Cp}$), 68.3 ($CH_{Cp}$), 68.5 (d, $J_{P,C}$ = 6.3 Hz, $CH_{Cp}$), 68.8 ($CH_{Cp}$), 69.1 ($CH_{Cp}$), 69.5 (d, $J_{P,C}$ = 9.2 Hz, $CH_{Cp}$), 69.7 ($CH_{Cp}$), 70.4 (d, $J_{P,C}$ = 4.2 Hz, $CH_{Cp}$), 85.5 (d, $^1J_{P,C}$ = 7.4 Hz, $C_{Cp}$), 87.3 (d, $^1J_{P,C}$ = 15.5 Hz, $C_{Cp}$), 126.0, 126.1, 127.2, 127.3, 127.6, 128.3, 128.6, 128.7, 128.8, 133.2, 133.3, 134.5 (d, $^1J_{P,C}$ = 20.5 Hz, $C_{Ph}$), 137.5 (d, $^2J_{P,C}$ = 6.6 Hz, $C_{Ph}$), 141.4 (d, $^2J_{P,C}$ = 14.4 Hz, $C_{Ph}$) ppm. $^{31}$P NMR ($CDCl_3$): $\delta$ = 26 ppm. MS (MALDI): *m*/*z* (%) = 472.1 (100) [M]. HRMS: calcd. for $C_{30}H_{26}FeP$ [M + H] 473.1099; found 473.1122.

**Borane Complex of *anti*,*syn*-1,2,3-Triphenyl-2-phospha[3]ferrocenophane (3a):** Column chromatography was performed with hexane/ethyl acetate, 80:20 ($R_f$ = 0.4) to afford **3a** as a yellow-orange solid. $^1$H NMR ($CDCl_3$): $\delta$ = 4.19 (m, 1 H, Cp), 4.21 (d, $J_{H,P}$ = 4.7 Hz, 1 H, CHPh), 4.24 (m, 1 H, Cp), 4.28 (m, 1 H, Cp), 4.34 (m, 1 H, Cp), 4.37 (m, 2 H, Cp), 4.46 (d, $J_{H,P}$ = 18.3 Hz, 1 H, CHPh), 5.19 (m, 2 H, Cp), 6.9–7.2 (13 H, Ph), 7.50 (2 H, Ph) ppm. $^{13}$C NMR ($CDCl_3$): $\delta$ = 34.0 (d, $^1J_{P,C}$ = 27.3 Hz, PCH), 46.7 (d, $^1J_{P,C}$ = 26.3 Hz, PCH), 68.3 ($CH_{Cp}$), 68.4 ($CH_{Cp}$), 70.4 ($CH_{Cp}$), 70.5 ($CH_{Cp}$), 70.7 ($CH_{Cp}$), 71.0 ($CH_{Cp}$), 71.1 ($CH_{Cp}$), 81.7 ($C_{Cp}$), 83.8 ($C_{Cp}$), 127.1, 127.4, 127.5, 128.1, 129.6, 130.0, 130.1, 130.4, 132.3, 132.4 ($CH_{Ph}$), 136.6 ($C_{Ph}$) ppm. $^{31}$P NMR ($CDCl_3$): $\delta$ = 55 ppm. HRMS (MALDI): calcd. for $C_{30}H_{25}FeP$ [M – $BH_3$] 472.1043; found 472.1031.

***anti*,*anti*-1,2,3-Triphenyl-2-phospha[3]ferrocenophane (1a′):** Complex **1a** was purified by column chromatography on silica gel with hexane/ethyl acetate (90:10) as the eluent ($R_f$ = 0.5). It was obtained in 60% yield (70 mg, starting from 0.25 mmol of **2a**) as an orange solid. $^1$H NMR ($CDCl_3$): $\delta$ = 4.05 (d, $J_{H,P}$ = 6.0 Hz, 2 H, CHPh), 4.08 (m, 2 H, Cp), 4.26 (m, 2 H, Cp), 4.33 (m, 2 H, Cp), 4.88 (m, 2 H, Cp), 6.9 (t, 2 H), 7.0–7.1 (6 H), 7.2 (4 H), 7.2–7.3 (4 H) ppm. $^{13}$C NMR ($CDCl_3$): $\delta$ = 48.7 (d, $^1J_{P,C}$ = 15.8 Hz, PCH), 67.8, 68.7 (d, $J_{P,C}$ = 7.2 Hz, Cp), 69.8, 70.2 (d, $J_{P,C}$ = 3.9 Hz, Cp), 86.8 (d, $^1J_{P,C}$ = 12.8 Hz, $C_{Cp}$), 125.9, 127.6, 127.7, 128.1, 128.2, 129.0, 133.0, 133.3 ($CH_{Ph}$), 135.9 (d, $^1J_{C,P}$ = 16.0 Hz, $PC_{Ph}$), 141.5 (d, $^2J_{C,P}$ = 11.4 Hz, $C_{Ph}$) ppm. $^{31}$P NMR ($CDCl_3$): $\delta$ = 21 ppm.

**Borane Complex of *anti*,*anti*-1,2,3-Triphenyl-2-phospha[3]ferrocenophane (3a′):** Column chromatography was performed with hexane/ethyl acetate (80:20) ($R_f$ = 0.4) to afford 150 mg of **3a′** (63% yield) as a yellow-orange solid. $^1$H NMR ($CDCl_3$): $\delta$ = 4.08 (m, 2 H, Cp), 4.19 (d, $J_{H,P}$ = 17.7 Hz, 2 H, CHPh), 4.20 (m, 2 H, Cp), 4.29 (m, 2 H, Cp), 5.17 (m, 2 H, Cp), 6.9–7.0 (6 H, Ph), 7.1 (4 H, Ph), 7.1–7.33 (3 H, Ph), 7.55 (t, 2 H, Ph) ppm. $^{13}$C NMR (selected data, $CDCl_3$): $\delta$ = 45.8 (d, $^1J_{P,C}$ = 29.1 Hz, PCH), 68.6 ($CH_{Cp}$), 70.9 ($CH_{Cp}$), 71.1 ($CH_{Cp}$), 71.2 ($CH_{Cp}$), 83.1 ($C_{Cp}$), 126.8, 126.9, 127.6, 128.1, 128.2, 129.7, 129.8, 131.1, 132.4, 132.5 ($CH_{Ph}$), 136.5 ($C_{Ph}$) ppm. $^{31}$P NMR ($CDCl_3$): $\delta$ = 51 ppm. MS (MALDI): *m*/*z* (%) = 472.1 (100) [M – $BH_3$].

**(*S*)-1-Ferrocenylpentan-1-ol (4a):**[24] A solution of borane–dimethyl sulfide complex (1.0 mL, 10 mmol) in anhydrous THF (about 10 mL) was prepared under argon. A fifth of this solution (2.2 mL) was added to a solution of (*R*)-2-methyl-CBS-oxazaborolidine in toluene (1 M, 3.0 mL, 3.0 mmol) under argon. The remaining $BH_3$–$Me_2S$ solution and a solution of pentanoylferrocene (2.70 g, 10.0 mmol) in THF (10 mL) under argon were added simultaneously to this mixture at 0 °C. The addition was carried out over about 60 min. The mixture was stirred for another 60 min at 0 °C, then quenched by dropwise addition of methanol (2 mL) and satd. aqueous $NH_4Cl$ (8 mL). The aqueous layer was extracted with diethyl ether. The organic phases were combined, washed with water and brine, and dried with magnesium sulfate. Purification by column chromatography (eluent: heptane/ethyl acetate, 5:1) gave (*S*)-1-ferrocenylpentan-1-ol as an amber-orange oil. Yield: 2.51 g (92%). $^1$H NMR ($CDCl_3$): $\delta$ = 0.92 (t, $J_{H,H}$ = 7.0 Hz, 3 H, Me), 1.3–1.5 (m, 4 H, $CH_2$), 1.6–1.7 (m, 2 H, $CH_2$), 1.94 (d, $^3J_{H,H}$ = 3.5 Hz, 1 H, OH), 4.2 (m, 3 H, $CH_{Cp}$), 4.23 (s, 5 H, Cp), 4.27 (1 H, $CH_{Cp}$), 4.33 (m, 1 H, CHOH) ppm. HPLC [Chiralpak AD; *n*-hexane/isopropyl alcohol, 98:2, 1 mL/min; $t_R$/min = 17.2 (*R*), 23.7 (*S*)]: *ee* = 98%. $[\alpha]_D$ = +45 ($c$ = 1, $CHCl_3$).

**(*S*)-(α-Ferrocenylpentyl)diisobutylphosphane (5a):** Diisobutylphosphane (4 mL) in hexane (10 wt.-% solution, about 1.8 mmol) was added to a degassed solution of (*S*)-1-ferrocenylpentan-1-ol (275 mg, 1.0 mmol) in degassed acetic acid (10 mL) under argon. The mixture was stirred overnight under argon at room temperature. The solvent and the remaining diisobutylphosphane were evaporated under vacuum. The residue was purified by chromatography on a short silica gel column, under argon. Elution with heptane/ethyl acetate (5:1) gave (*S*)-(1-ferrocenylpentyl)diisobutylphosphane as an amber-coloured oil. Yield: 360 mg (90%). $^{31}$P NMR ($CDCl_3$): $\delta$ = –28 ppm. HRMS: calcd. for $C_{23}H_{38}FeP$ [M + H] 401.2041; found 401.2061. $[\alpha]_D$ = –39 ($c$ = 0.1, $CHCl_3$); *ee* = 98%. NMR characterisation has been performed on the corresponding borane complex, **5a**·$BH_3$: $^1$H NMR ($CDCl_3$): $\delta$ = 0.92 (d, $^3J$ = 6.6 Hz, 3 H, Me), 0.95 (d, $^3J$ = 6.6 Hz, 3 H, Me), 1.03 (t, 3 H, Me), 1.04 (d, $^3J$ = 6.9 Hz, 6 H, Me), 1.2–1.7 (7 H, $CH_2$, CH), 1.8–2.1 (5 H, $CH_2$, CH), 2.50 (ddd, $J$ = 8.1, $J$ = 6.6, $J$ = 4.5 Hz, 1 H, CHP), 3.97 (1 H, $CH_{Cp}$), 4.08 (1 H, $CH_{Cp}$), 4.19 (s, 5 H, Cp), 4.2 (2 H, $CH_{Cp}$) ppm. $^{13}$C NMR ($CDCl_3$): $\delta$ = 14.0 (Me), 23.0 ($CH_2$), 24.0, 24.3, 24.6 (d, $J_{P,C}$ = 2.0 Hz), 24.7 (d, $J_{P,C}$ = 1.0 Hz), 25.1 (d, $J_{P,C}$ = 7.5 Hz), 25.3 (d, $J_{P,C}$ = 7.8 Hz), 31.1 (d, $^1J_{P,C}$ = 30.1 Hz, $PCH_2$), 31.4 (d, $J_{P,C}$ = 3.5 Hz, $CH_2$), 32.7 (d, $^1J_{P,C}$ = 30.3 Hz, $PCH_2$), 33.1 (d, $J_{P,C}$ = 3.5 Hz, $CH_2$), 36.0 (d, $^1J_{P,C}$ = 26.9 Hz, PCH), 66.9 ($CH_{Cp}$), 67.2 ($CH_{Cp}$), 67.9 ($CH_{Cp}$), 68.7 ($CH_{Cp}$), 69.0 (Cp), 88.7 (d, $J_{P,C}$ = 4.1 Hz, $C_{Cp}$) ppm. $^{31}$P NMR ($CDCl_3$): $\delta$ = 23 ppm. $[\alpha]_D$ = –35 ($c$ = 0.1, $CHCl_3$). The enantiomeric excess of **5a** was determined by HPLC analysis of the corresponding oxide, which was prepared as follows: (*S*)-(1-ferrocenylpentyl)diisobutylphosphane (100 mg, 0.25 mmol) was dissolved in acetone (about 2 mL), and hydrogen peroxide (35 wt.-% solution in water) was added. The mixture was stirred overnight at room temp. After addition of water, the aqueous phase was extracted with dichloromethane. The organic layer was washed with brine, dried with magnesium sulfate and concentrated to give (*S*)-(1-ferrocenylpentyl)diisobutylphosphane oxide as a red-brown oil. $^1$H NMR ($CDCl_3$): $\delta$ = 0.98–1.07 (15 H, Me), 1.3–2.1 (12 H, $CH_2$, CH), 2.71 (ddd, $J$ = 16.2, $J$ = 6.6, $J$ = 4.5 Hz, 1 H, CHP), 4.01 (1 H, $CH_{Cp}$), 4.16 (2 H, $CH_{Cp}$), 4.17 (s, 5 H, Cp), 4.22 (1 H, $CH_{Cp}$) ppm. $^{13}$C NMR ($CDCl_3$): $\delta$ = 14.0

 © 2007 Wiley-VCH Verlag GmbH & Co. KGaA, Weinheim 

(Me), 23.3 ($CH_2$), 23.5 (d, $J_{P,C}$ = 3.5 Hz), 23.6 (d, $J_{P,C}$ = 3.6 Hz), 24.5–25.0 (5 C), 30.1 ($CH_2$), 32.7 (d, $J$ = 3.2 Hz, $CH_2$), 34.5 (d, $J$ = 61.7 Hz, $PCH_2$), 36.1 (d, $J$ = 61.8 Hz, $PCH_2$), 40.4 (d, $J$ = 58.1 Hz, PCH), 66.9 ($CH_{Cp}$), 67.3 ($CH_{Cp}$), 67.7 ($CH_{Cp}$), 68.2 ($CH_{Cp}$), 68.8 (Cp), 88.3 ($C_{Cp}$) ppm. $^{31}$P NMR ($CDCl_3$): $\delta$ = 49 ppm. HPLC (Chiralcel OD; *n*-hexane/2-propanol, 98:2, 1 mL/min) $t_R$/min = 10.0 (*R*), 11.3 (*S*).

**(*S*)-(α-Ferrocenylbenzyl)diisobutylphosphane (5b):** (a) Phosphane **5b** was first prepared by following the same procedure used for the synthesis of **5a**. Starting from (*S*)-ferrocenylbenzyl alcohol **4b**[17a,30] (290 mg, 1.0 mmol, 94% *ee*), phosphane **5b** was obtained as a pale orange solid after chromatography (silica gel, heptane/ethyl acetate, 9:1). Yield 270 mg (65%); *ee* = 49%. (b) The same phosphane **5b** was then prepared as follows: (*S*)-ferrocenylbenzyl alcohol **4b** (1 mmol, 96% *ee*) was added to ice-cooled acetic acid (10 mL) under argon, and diisobutylphosphane was added immediately to the yellow suspension without waiting for the alcohol to be dissolved. The mixture was warmed slowly to room temperature. After overnight stirring, workup was performed as described above for **5a**. Phosphane **5b** was obtained in 86% yield (360 mg); *ee* = 96%. $^1$H NMR ($CDCl_3$): $\delta$ = 0.77 (d, $^3J$ = 6.5 Hz, 3 H, Me), 0.83 (d, $^3J$ = 6.5 Hz, 3 H, Me), 0.85 (d, $^3J$ = 6.5 Hz, 3 H, Me), 0.92 (d, $^3J$ = 6.5 Hz, 3 H, Me), 1.1 (m, 3 H), 1.3 (m, 2 H), 1.38 (m, $J$ = 6.5 Hz, 1 H, CHMe), 3.39 (d, $^1J_{H-P}$ = 5.0 Hz, CHP), 3.78 (s, 5 H, Cp), 4.08 (1 H, $CH_{Cp}$), 4.12 (1 H, $CH_{Cp}$), 4.14 (1 H, $CH_{Cp}$), 4.18 (1 H, $CH_{Cp}$), 7.2–7.4 (5 H, Ph) ppm. $^{13}$C NMR ($CDCl_3$): $\delta$ = 23.8 (d, $^3J_{P,C}$ = 9.0 Hz, Me), 24.0 (d, $^3J_{P,C}$ = 9.2 Hz, Me), 24.2 (Me), 24.3 (Me), 26.18, 26.28, 26.38, 26.48 (*CH*Me), 38.7 (d, $^1J_{P,C}$ = 17.5 Hz, $PCH_2$), 38.8 (d, $^1J_{P,C}$ = 17.5 Hz, $PCH_2$), 48.3 (d, $^1J_{P,C}$ = 15.6 Hz, PCH), 66.2 ($CH_{Cp}$), 67.3 (d, $J_{C,P}$ = 5.2 Hz, $CH_{Cp}$), 68.1 ($CH_{Cp}$), 68.4 (Cp), 69.4 ($CH_{Cp}$), 91.2 (d, $^2J_{C,P}$ = 14.9 Hz, $C_{Cp}$), 126.1, 127.9, 129.0, 129.1 ($CH_{Ph}$) ppm. $^{31}$P NMR ($CDCl_3$): $\delta$ = –14 ppm. HRMS: calcd. for $C_{25}H_{34}FeP$ [M + H] 421.1748; found 421.1738. The enantiomeric excess of the phosphane was determined by HPLC analysis of the corresponding oxide, which was prepared as described above. $^1$H NMR ($CDCl_3$): $\delta$ = 0.88 (d, $^3J$ = 6.5 Hz, 3 H, Me), 0.90 (d, $^3J$ = 7.0 Hz, 3 H, Me), 0.93 (d, $^3J$ = 6.5 Hz, 3 H, Me), 0.99 (d, $^3J$ = 6.5 Hz, 3 H, Me), 1.3–1.5 (4 H), 1.8–1.9 (2 H, *CH*Me$_2$), 3.75 (d, $^1J_{H-P}$ = 12.5 Hz, CHP), 3.79 (s, 5 H, Cp), 4.15 (1 H, $CH_{Cp}$), 4.18 (1 H, $CH_{Cp}$), 4.31 (1 H, $CH_{Cp}$), 4.35 (1 H, $CH_{Cp}$), 7.34 (1 H, Ph), 7.43 (2 H, Ph), 7.54 (2 H, Ph) ppm. $^{13}$C NMR ($CDCl_3$): $\delta$ = 23.7 (dd, 2 × *CH*Me), 24.4 (Me), 24.5 (Me), 24.9 (dd, 2 × Me), 36.5 (d, $^1J_{P,C}$ = 62.0 Hz, $PCH_2$), 36.6 (d, $^1J_{P,C}$ = 61.2 Hz, $PCH_2$), 49.9 (d, $^1J_{P,C}$ = 56.1 Hz, PCH), 66.9 ($CH_{Cp}$), 68.3 (d, $J_{C,P}$ = 2.2 Hz, $CH_{Cp}$), 68.5 (Cp), 68.6 ($CH_{Cp}$), 70.0 (d, $J_{C,P}$ = 2.1 Hz, $CH_{Cp}$), 85.6 ($C_{Cp}$), 127.2 (d, $J_{C,P}$ = 1.6 Hz, $CH_{Ph}$), 128.3, 128.4, 129.7, 129.8 ($CH_{Ph}$), 138.5 (d, $J_{C,P}$ = 3.3 Hz, $C_{Ph}$) ppm. $^{31}$P NMR ($CDCl_3$): $\delta$ = 45 ppm. HPLC (Chiralpak AD column, *n*-hexane/2-propanol, 93:7, 1 mL/min) $t_R$/min = 8.3 (*S*), 13.9 (*R*).

### Syntheses of the Borane Complexes of 1,3-Dimethyl-2-phenyl-2-phospha[3]ferrocenophane (6b, 6b′ and 3b)

**(a) 1,3-Dimethyl-2-oxa[3]ferrocenophanes, 6b,b′:**[28] 1,1′-Bis(acetyl)ferrocene (3.0 g, 11 mmol) was reduced with $NaBH_4$ in methanol. After hydrolysis and extraction in ether, the ether solution of crude 1,1′-bis(α-hydroxyethyl)ferrocene was acidified with aqueous HCl (1 N). After 1 h of stirring at room temperature, the organic layer was separated, dried with $MgSO_4$ and the final product was submitted to column chromatography. Elution with hexane/ethyl acetate (9:1) afforded 1.2 g (41% yield) of *meso*-**6b′** ($R_f$ = 0.47), followed by 1.1 g (38% yield) of *dl*-**6b** ($R_f$ = 0.35). *meso*-**6b′**: $^1$H NMR ($CDCl_3$): $\delta$ = 1.54 (d, $^3J_{H,H}$ = 6.5 Hz, 6 H, Me), 3.84 (q, $^3J_{H,H}$ = 6.5 Hz, 2 H, C*H*Me), 4.05 (m, 2 H), 4.17 (m, 2 H), 4.27 (m, 4 H) ppm. HRMS: calcd. for $C_{14}H_{16}FeO$ 256.0551; found 256.0531. *dl*-**6b**: $^1$H NMR ($CDCl_3$): $\delta$ = 1.48 (d, $^3J_{H,H}$ = 7.0 Hz, 6 H, Me), 4.12 (m, 4 H), 4.22 (m, 2 H), 4.24 (m, 2 H), 4.34 (q, $^3J_{H,H}$ = 7.0 Hz, 2 H, C*H*Me) ppm. HRMS: calcd. for $C_{14}H_{16}FeO$ 256.0551; found 256.0523.

**(b) 3b:** A solution of $BF_3$·$Et_2O$ (0.28 mL, 2 mmol) in $CH_2Cl_2$ (5 mL) was added to a solution containing 1,3-dimethyl-2-oxa[3]-ferrocenophane (250 mg, 0.98 mmol) and phenylphosphane (0.12 mL, 1.1 mmol) in dichloromethane (20 mL) at room temperature. After two hours of stirring, an excess of $BH_3$·THF was added (2 mL, 1 M solution). The mixture was hydrolysed with water. The organic layer was dried with $MgSO_4$. After evaporation of the solvents, the crude product was purified by chromatography on silica gel with hexane/ethyl acetate (8:2) as the eluent. The borane complex **3b** was purified by column chromatography.

**Borane Complex of *anti*,*syn*-1,3-Dimethyl-2-phenyl-2-phospha[3]ferrocenophane (3b):** Complex **3b** was obtained in 31% yield (105 mg) as a yellow solid after column chromatography with hexane/ethyl acetate (9:1) as the eluent ($R_f$ = 0.5). $^1$H NMR ($CDCl_3$): $\delta$ = 1.15 (dd, $^3J$ = 12.5, $^3J$ = 7.5 Hz, 3 H, Me), 1.45 (dd, $^3J$ = 15.5, $^3J$ = 7.0 Hz, 3 H, Me), 2.83 (qd, $^3J$ = 7.5, $^2J_{H-P}$ = 3.0 Hz, 1 H, C*H*Me), 3.16 (dq, $^2J_{H-P}$ = 16.5, $^3J$ = 7.0 Hz, 1 H, C*H*Me), 4.04 (m, 1 H, $CH_{Cp}$), 4.11 (m, 1 H, $CH_{Cp}$), 4.14 (m, 1 H, $CH_{Cp}$), 4.16 (m, 1 H, $CH_{Cp}$), 4.23 (m, 1 H, $CH_{Cp}$), 4.25 (m, 1 H, $CH_{Cp}$), 4.72 (m, 1 H, $CH_{Cp}$), 4.87 (m, 1 H, $CH_{Cp}$), 7.54 (3 H, Ph), 7.87 (2 H, Ph) ppm. $^{13}$C NMR ($CDCl_3$): $\delta$ = 14.1 (d, $^2J_{P,C}$ = 6.9 Hz, Me), 16.8 (d, $^2J_{P,C}$ = 7.0 Hz, Me), 19.2 (d, $^1J_{P,C}$ = 32.4 Hz, *CH*Me), 29.4 (d, $^1J_{P,C}$ = 32.0 Hz, *CH*Me), 67.2 ($CH_{Cp}$), 67.6 ($CH_{Cp}$), 67.8 (d, $J_{P,C}$ = 4.1 Hz, $CH_{Cp}$), 69.8 (d, $J_{P,C}$ = 6.1 Hz, $CH_{Cp}$), 70.1 ($CH_{Cp}$), 70.2 ($CH_{Cp}$), 70.5 ($CH_{Cp}$), 71.6 ($CH_{Cp}$), 84.1 ($C_{Cp}$), 84.4 ($C_{Cp}$), 128.6, 127.8 ($CH_{Ph}$), 129.6 (d, $^1J_{C,P}$ = 43.3 Hz, $C_{Ph}$), 130.9 (d, $J_{C,P}$ = 2.2 Hz, $CH_{Ph}$), 132.1 ($CH_{Ph}$), 132.2 ($CH_{Ph}$) ppm. $^{31}$P NMR ($CDCl_3$): $\delta$ = 57 ppm. HRMS: calcd. for $C_{20}H_{21}FeP$ [M – $BH_3$] 348.0730; found 348.0741.

**Borane Complexes of *syn*,*syn*- and *anti*,*anti*-1,3-Dimethyl-2-phenyl-2-phospha[3]ferrocenophane (3b′ and 3b′′):** The diastereomeric mixture of *anti*,*anti* and *syn*,*syn* isomers of the 1,3-dimethyl-2-phenyl-2-phospha[3]ferrocenophane borane complexes **3b′** and **3b′′** was characterised by mass spectrometry and $^1$H NMR spectroscopy. ESI-MS: *m*/*z* (%) = 348 (100) [M]. A sample of pure *syn*,*syn*-**3b′′** was obtained by chromatography. *syn*,*syn*-**3b′′**: $^1$H NMR ($CDCl_3$): $\delta$ = 1.37 (dd, $^3J$ = 15.9, $^3J$ = 7.5 Hz, 6 H, Me), 2.92 (dq, $^2J_{H-P} \approx {}^3J_{H,H}$ = 7.5 Hz, 2 H, C*H*Me), 4.12 (m, 2 H, $CH_{Cp}$), 4.17 (m, 4 H, $CH_{Cp}$), 4.23 (m, 2 H, $CH_{Cp}$), 7.5 (3 H, Ph), 8.2 (2 H, Ph) ppm. $^{13}$C NMR ($CDCl_3$): $\delta$ = 17.7 (Me), 30.0 (d, $^1J_{P,C}$ = 32.9 Hz, *CH*Me), 67.6 ($CH_{Cp}$), 68.5 ($CH_{Cp}$), 69.9 ($CH_{Cp}$), 71.5 (d, $J$ = 5.2 Hz, $CH_{Cp}$), 88.7 ($C_{Cp}$), 128.5, 131.4, 134.7 ($CH_{Ph}$) ppm. *anti*,*anti*-**3b′** was characterised from the mixture of isomers: $^1$H NMR ($CDCl_3$): $\delta$ = 1.19 (dd, $^3J_{H-P}$ = 15.5, $^3J$ = 7.0 Hz, 6 H, Me), 2.85 (dq, $^2J_{H-P}$ = 16.5, $^3J_{H,H}$ = 7.0 Hz, 2 H, C*H*Me), 4.07 (m, 2 H, $CH_{Cp}$), 4.12 (m, 2 H, $CH_{Cp}$), 4.21 (m, 2 H, $CH_{Cp}$), 4.72 (m, 2 H, $CH_{Cp}$), 7.5 (3 H, Ph), 7.9 (2 H, Ph) ppm.

**Synthesis of the Borane Complex of 2-Phenyl-2-phospha[3]ferrocenophane (3c):** (a) 2-Oxa[3]ferrocenophane.[35] A solution of 1,1′-bis-(hydroxymethyl)ferrocene (107 mg, 0.43 mmol) in HCl (1 M)/ether (1:1, 12 mL) was stirred vigorously for 6 h. The layers were separated and the organic layer dried with $MgSO_4$, filtered and concentrated in vacuo. The crude product was purified by flash chromatography (hexane/ethyl acetate, 8:2) to yield 81 mg (82%) of the desired compound as an orange solid. $^1$H NMR ($CDCl_3$): $\delta$ = 3.92 (s, 4 H, $CH_2$), 4.17–4.19 ($CH_{Cp}$, 8 H, $A_2B_2$) ppm. $^{13}$C NMR

 © 2007 Wiley-VCH Verlag GmbH & Co. KGaA, Weinheim 

($CDCl_3$): $\delta$ = 64.6 ($OCH_2$), 69.9 ($CH_{Cp}$), 70.1 ($CH_{Cp}$), 83.2 ($C_{Cp}$) ppm.

(b) The same experimental procedure as for the synthesis of **3b** was applied, starting from 2-oxa[3]ferrocenophane. Compound **3c** was obtained in 17% yield as a yellow-orange solid. $^1H$ NMR ($CDCl_3$): $\delta$ = 2.55 (t, $J_{H,P} = J_{H,H}$ = 15.0 Hz, 2 H, $CH_2$), 2.65 (d, $J_{H,H}$ = 14.0 Hz, 2 H, $CH_2$), 4.02 (s, 2 H, $CH_{Cp}$), 4.11 (s, 2 H, $CH_{Cp}$), 4.22 (s, 2 H, $CH_{Cp}$), 4.61 (s, 2 H, $CH_{Cp}$), 7.56 (3 H, Ph), 7.91 (2 H, Ph) ppm. $^{13}C$ NMR ($CDCl_3$): $\delta$ = 22.5 (d, $^1J_{P,C}$ = 34.6 Hz, $PCH_2$), 68.0 ($CH_{Cp}$), 69.8 ($CH_{Cp}$), 70.8 (d, $J_{P,C}$ = 5.1 Hz, $CH_{Cp}$), 71.6 ($CH_{Cp}$), 78.5 (d, $^2J_{P,C}$ = 4.6 Hz, $C_{Cp}$), 128.9, 129.0 ($CH_{Ph}$), 130.3 (d, $^1J_{C,P}$ = 48.8 Hz, CPh), 131.3, 131.4 ($CH_{Ph}$) ppm. $^{31}P$ NMR ($CDCl_3$): $\delta$ = 46 ppm. HRMS (MALDI): calcd. for $C_{18}H_{17}PFe$ [M – $BH_3$] 320.0417; found 320.0412.

**Resolution of *dl*-1,2,3-Triphenyl-2-phospha[3]ferrocenophane (1a):** Complex **7** was obtained from the corresponding amine[36] and palladium(II) chloride, as described in the literature.[37] *anti*,*syn*-1,2,3-Triphenyl-2-phospha[3]ferrocenophane **1a** (100 mg, 0.21 mmol) and complex **7** (72 mg, 0.11 mmol) were dissolved in acetone (10 mL) under argon and the mixture was stirred at room temperature for 2 h. After evaporation of the solvent, the crude product was obtained as a diastereomeric mixture, which was separated by column chromatography on silica gel with a heptane/ethyl acetate (8:2) mixture as the eluent.

Complex **8a** was eluted first ($R_f$ = 0.5 in heptane/ethyl acetate, 6:4, 35 mg, 40% yield): $^1H$ NMR ($CDCl_3$): $\delta$ = 1.96 (d, $^3J_{H,H}$ = 6.5 Hz, 3 H, CH*Me*), 2.44 (s, 3 H, NMe), 3.08 (d, $J$ = 3.5 Hz, 3 H, NMe), 4.1–4.2 (4 H, Cp, N*CH*Me), 4.35 (1 H, Cp), 4.44 (2 H, Cp), 4.48 (1 H, Cp), 5.42 (d, $^1J_{H\text{-}P}$ = 15.0 Hz, 1 H, CHPh), 5.62 (dd, 1 H, Naph), 5.92 (1 H, Cp), 6.48 (d, $^3J$ = 7.0 Hz, 1 H, Naph), 6.91 (t, $J$ = 8.5 Hz, 1 H), 7.0–7.5 (Ar), 7.54 (d, $J$ = 8.5 Hz, 1 H), 8.16 (d, $J$ = 7.0 Hz, 2 H) ppm. $^{13}C$ NMR (selected data, $CDCl_3$): $\delta$ = 21.8 (CH*Me*), 43.4 (d, $^1J_{P,C}$ = 10.9 Hz, PCH), 46.2 (d, $^1J_{P,C}$ = 12.1 Hz, PCH), 48.0 (NMe), 50.3 (NMe), 67.3, 68.1, 68.3, 69.5, 70.5, 70.6, 70.7, 71.8, 72.1 (Cp, N*CH*Me), 84.0 (d, $^1J_{P,C}$ = 9.2 Hz, $C_{Cp}$), 86.2 ($C_{Cp}$), 121–129 (Ar), 137.4 [C-3′ (Naph)], 141.2, 145.9, 150.0 (C) ppm. $^{31}P$ NMR ($CDCl_3$): $\delta$ = 80.4 ppm. MS (MALDI): *m*/*z* (%) = 776 (100) [M – Cl]. HRMS (MALDI): calcd. for $C_{44}H_{41}FeNPPd$ 776.1361; found 776.1359. $[a]_D$ = +281 ($c$ = 0.2, $CHCl_3$).

Complex **8b** was then eluted with $R_f$ = 0.3 in heptane/ethyl acetate (6:4). $^1H$ NMR ($CDCl_3$): $\delta$ = 2.19 (d, $^3J_{H,H}$ = 6.5 Hz, 3 H, CH*Me*), 2.73 (s, 3 H, NMe), 3.13 (d, $J$ = 3.5 Hz, 3 H, NMe), 4.18, 4.21, 4.23, 4.28, (Cp), 4.31 (m, N*CH*Me), 4.35, 4.39 (Cp), 4.77 (d, $^1J_{H-P}$ = 17.0 Hz, 1 H, CHPh), 5.47 (1 H, Cp), 5.65 (dd, $^3J_{H,H}$ = 8.5 Hz, $^4J_{H,P}$ = 5.0 Hz, 1 H, Naph), 6.02 (1 H, Cp), 6.12 (d, $^3J$ = 8.5 Hz, 1 H, Naph), 6.33 (d, $^1J_{H-P}$ = 6.5 Hz, 1 H, CHPh), 6.65 (2H), 6.88 (t, $J$ = 7.5 Hz, 1 H), 7.0–7.5 (Ar), 7.67 (d, $J$ = 8.5 Hz, 1 H), 7.84 (2H). $^{13}C$ NMR (selected data, $CDCl_3$): $\delta$ = 22.4 (CH*Me*), 37.7 (d, $^1J_{P,C}$ = 15.1 Hz, PCH), 46.6 (d, $^1J_{P,C}$ = 17.3 Hz, PCH), 48.7 (NMe), 50.9 (NMe), 69.0, 69.2, 69.3, 69.6, 70.1, 70.3, 70.7, 71.5, 73.5 (Cp, N*CH*Me), 82.1 ($C_{Cp}$), 83.9 ($C_{Cp}$), 123–131 (Ar), 136.2 (CH), 136.3 (CH), 137.2, 138.1, 147.0, 148.0 (C) ppm. $^{31}P$ NMR ($CDCl_3$): $\delta$ = 75.8 ppm. $[a]_D$ = –160 ($c$ = 0.2, $CHCl_3$).

Complex **8a** (32 mg, 0.04 mmol) was treated with 1,2-bis(diphenylphosphanyl)ethane (15 mg) in $CH_2Cl_2$ (2 mL) at room temperature for 3 h. After evaporation, phosphane **1a** was isolated by filtration through a short silica gel column with heptane/ethyl acetate (8:2) as the eluent ($R_f$ = 0.6). $[a]_D$ = +392 ($c$ = 0.2, $CHCl_3$).

**X-ray Crystal Structure Analyses:** For the three structures, intensity data were measured with a Nonius Kappa-CCD area detector diffractometer using graphite-monochromated Mo-$K_\alpha$ radiation, in $\phi$- and $\omega$-scans, up to $\theta$ = 27.5° for compounds **3a** and **3c**, and only to 22° for **8c**. The structures were solved by direct methods with the program SHELXS86[38] and refined by full-matrix least-squares, on the basis of unique $F^2$, with the program SHELXL97.[39] The hydrogen atoms were located on difference Fourier maps and fitted at theoretical positions [$d$(C–H) = 0.93 or 0.98 Å], except those fixed to the B atom, which were refined. They were assigned an isotropic displacement parameter equivalent to 1.12 times that of the bonded atom.

**Crystallographic Data for Compound 3a:** A small brown-yellow prismatic crystal of 0.55 × 0.45 × 0.45 mm, cut from a larger one, was used. Empirical formula $C_{30}H_{28}BFeP$, $M$ = 486.15, $T$ = 293 K. Monoclinic system, centrosymmetric space group $P2_1/n$. The unit cell of parameters $a$ = 7.401(4), $b$ = 29.868(15), $c$ = 11.186(6) Å, $\beta$ = 93.75(2)°, $V$ = 2467 Å$^3$ contains four molecules ($Z$ = 4); $d_{calcd}$ = 1.309 g cm$^{-3}$, $F$(000) = 1016, $\mu$ = 0.692 mm$^{-1}$, $\lambda$(Mo-$K_\alpha$) = 0.71073 Å. A total of 9485 data were collected, giving 6901 monoclinic reflections, of which 4806 were unique.[40] Refinement of 307 parameters on $F^2$ led to $R_1(F)$ = 0.0382 calculated with the 3942 observed reflections having $I \geq 2\sigma(I)$ and to $wR_2(F^2)$ = 0.0946 considering all 4806 unique reflections. Goodness of fit = 1.050. The residual density was found to be between –0.36 and 0.29 e Å$^{-3}$.

**Crystallographic Data for Compound 3c:** A yellow prismatic crystal of 0.25 × 0.10 × 0.10 mm was used. Empirical formula $C_{18}H_{20}BFeP$, $M$ = 333.97, $T$ = 293 K. Monoclinic system, centrosymmetric space group $P2_1/a$. The unit cell of parameters $a$ = 10.891(4), $b$ = 7.472(4), $c$ = 19.160(6) Å, $\beta$ = 94.47(2)°, $V$ = 1554 Å$^3$ contains four molecules ($Z$ = 4); $d_{calcd}$ = 1.427 g cm$^{-3}$, $F$(000) = 696, $\mu$ = 1.062 mm$^{-1}$, $\lambda$(Mo-$K_\alpha$) = 0.71073 Å. A total of 14535 data were collected, giving 6478 monoclinic reflections, of which 3530 were unique. Refinement of 199 parameters on $F^2$ led to $R_1(F)$ = 0.0401 calculated with the 2292 observed reflections having $I \geq 2\sigma(I)$ and to $wR_2(F^2)$ = 0.0956 considering all 3530 unique reflections. Goodness of fit = 1.044. The residual density was found to be between –0.47 and 0.42 e Å$^{-3}$.

**Crystallographic Data for Compound 8a:** From very small crystals, a small orange needle of 0.20 × 0.05 × 0.012 mm was chosen. Empirical formula $C_{44}H_{41}ClFeNPPd{\cdot}C_7H_8$, $M$ = 904.58, $T$ = 293 K. Tetragonal system, chiral space group $I4_1$. The unit cell of parameters $a$ = $b$ = 27.112(7), $c$ = 11.592(5) Å, $V$ = 8521 Å$^3$ contains eight molecules ($Z$ = 8); $d_{calcd}$ = 1.410 g cm$^{-3}$, $F$(000) = 3891, $\mu$ = 0.90 mm$^{-1}$, $\lambda$(Mo-$K_\alpha$) = 0.71073 Å. A total of 26093 reflections were collected, giving 5070 unique tetragonal reflections. In addition, a toluene molecule of crystallisation solvent was found per molecule. The absolute configuration was calculated from the anomalous dispersion effects in diffraction measurements. Refinement of 510 parameters on $F^2$ led to $R_1(F)$ = 0.0440 calculated with the 3891 observed reflections having $I \geq 2\sigma(I)$ and to $wR_2(F^2)$ = 0.0768 considering all 5070 unique reflections. Goodness of fit = 1.032. The residual density was found to be between –0.28 and 0.25 e Å$^{-3}$.

CCDC-636890 (for **3a**), -636891 (for **3c**) and -636892 (for **8a**) contain the supplementary crystallographic data for this paper. These data can be obtained free of charge from The Cambridge Crystallographic Data Centre via www.cccd.cam.ac.uk/data_request/cif.

[1] Amination of aryl halides: M. Nishiyama, T. Yamamoto, Y. Koie, *Tetrahedron Lett.* **1998**, *39*, 617–620. Amination and Suzuki coupling of aryl chlorides: J. P. Wolfe, S. L. Buchwald, *Angew. Chem. Int. Ed.* **1999**, *38*, 2413–2416. Stille cross-coupling: A. F. Littke, G. C. Fu, *Angew. Chem. Int. Ed.* **1999**, *38*, 2411–2412. Aromatic C–O bond formation: A. Aranyos, D. W. Old,

 © 2007 Wiley-VCH Verlag GmbH & Co. KGaA, Weinheim 

A. Kiyomori, J. P. Wolfe, J. P. Sadighi, S. L. Buchwald, *J. Am. Chem. Soc.* **1999**, *121*, 4369–4378.

[2] Representative examples. α-Arylation of ketones: J. M. Fox, X. Huang, A. Chieffi, S. L. Buchwald, *J. Am. Chem. Soc.* **2000**, *122*, 1360–1370. Rhodium promotes addition of boronic acids to aldehydes: M. Ueda, N. Miyaura, *J. Org. Chem.* **2000**, *65*, 4450–4452. Alkyl Suzuki cross-couplings: M. R. Netherton, C. Dai, K. Neuschütz, G. C. Fu, *J. Am. Chem. Soc.* **2001**, *123*, 10099–10100. Heck reactions: A. F. Littke, G. C. Fu, *J. Am. Chem. Soc.* **2001**, *123*, 6989–7000. The use of electron-rich ferrocenylphosphanes has been extended also, albeit far less extensively to date, to organocatalytic transformations: S. I. Pereira, J. Adrio, A. M. S. Silva, J. C. Carretero, *J. Org. Chem.* **2005**, *70*, 10175–10177.

[3] a) Q. Shelby, N. Kataoka, G. Mann, J. Hartwig, *J. Am. Chem. Soc.* **2000**, *122*, 10718–10719; b) T. E. Pickett, C. J. Richards, *Tetrahedron Lett.* **2001**, *42*, 3767–3769; c) T. E. Pickett, F. X. Roca, C. J. Richards, *J. Org. Chem.* **2003**, *68*, 2592–2599; d) Z.-Y. Tang, Y. Lu, Q.-S. Hu, *Org. Lett.* **2003**, *5*, 297–300; e) J. F. Jensen, M. Johannsen, *Org. Lett.* **2003**, *5*, 3025–3028; f) C. Baillie, L. Zhang, J. Xiao, *J. Org. Chem.* **2004**, *69*, 7779–7782.

[4] For recent reviews see: a) C. J. Richards, A. J. Locke, *Tetrahedron: Asymmetry* **1998**, *9*, 2377–2407; b) T. J. Colacot, *Chem. Rev.* **2003**, *103*, 3101 and references cited therein; c) R. G. Arrayás, J. Adrio, J. C. Carretero, *Angew. Chem. Int. Ed.* **2006**, *45*, 7674–7715.

[5] J. W. Han, N. Tokunaga, T. Hayashi, *J. Am. Chem. Soc.* **2001**, *123*, 12915–12916.

[6] P. Barbaro, A. Togni, *Organometallics* **1995**, *14*, 3570–3573.

[7] Selected references: a) D. Seyferth, H. P. Withers Jr, *J. Organomet. Chem.* **1980**, *185*, C1–C5; b) A. G. Osborne, R. H. Whiteley, R. E. Meads, *J. Organomet. Chem.* **1980**, *193*, 345–357; c) C. H. Honeyman, D. A. Foucher, F. Y. Dahmen, R. Rulkens, A. J. Lough, I. Manners, *Organometallics* **1995**, *14*, 5503; d) H. Brunner, J. Klankermayer, M. Zabel, *J. Organomet. Chem.* **2000**, *601*, 211–219; e) T. Mizuta, M. Onishi, K. Miyoshi, *Organometallics* **2000**, *19*, 5005–5009.

[8] R. Resendes, J. M. Nelson, A. Fischer, F. Jäkle, A. Bartole, A. J. Lough, I. Manners, *J. Am. Chem. Soc.* **2001**, *123*, 2116–2126.

[9] a) O. J. Curnow, G. Huttner, S. J. Smail, M. M. Turnbull, *J. Organomet. Chem.* **1996**, *524*, 267–270; b) J. J. Adams, O. J. Curnow, G. Huttner, S. J. Smail, M. M. Turnbull, *J. Organomet. Chem.* **1999**, *577*, 44–57.

[10] M. Herberhold, U. Steffl, B. Wrackmeyer, *Z. Naturforsch., B: Chem. Sci.* **1999**, *54*, 57–62.

[11] A. Osborne, R. F. Bryan, S. Lockhart, *J. Organomet. Chem.* **1985**, *288*, 207–217.

[12] B. Wrackmeyer, E. V. Klimkina, W. Milius, *Inorg. Chem. Commun.* **2004**, *7*, 884–888.

[13] T. Höcher, A. Cinquantini, P. Zanello, E. Hey-Hawkins, *Polyhedron* **2005**, *24*, 1340–1346.

[14] However, chiral phosphanes based on ferrocenophane moieties have been reported where all-carbon tethers link the cyclopentadienyl rings. For representative examples see: a) T. Sturm, W. Weissensteiner, F. Spindler, K. Mereiter, A. M. López-Agenjo, B. R. Manzano, F. A. Jalón, *Organometallics* **2002**, *21*, 1766–1774; b) P. Liptau, T. Seki, G. Kehr, A. Abele, R. Fröhlich, G. Erker, S. Grimme, *Organometallics* **2003**, *22*, 2226–2232; c) P. Liptau, L. Tebben, G. Kehr, R. Fröhlich, G. Erker, F. Hollmann, B. Rieger, *Eur. J. Org. Chem.* **2005**, 1909–1918; d) R. Šebesta, A. Almassy, I. Císarova, Š. Toma, *Tetrahedron: Asymmetry* **2006**, *17*, 2531–2537.

[15] T. Hayashi, T. Mise, M. Fukushima, M. Kagotani, N. Nagashima, Y. Hamada, A. Matsumoto, S. Kawakami, M. Konishi, K. Yamamoto, M. Kumada, *Bull. Chem. Soc. Jpn.* **1980**, *53*, 1138–1151.

[16] G. Marr, T. M. White, *J. Chem. Soc. Perkin Trans. 1* **1973**, 1955–1958.

[17] a) J. Wright, L. Frambes, P. Reeves, *J. Organomet. Chem.* **1994**, *476*, 215–217; b) L. Schwink, P. Knochel, *Tetrahedron Lett.* **1996**, *37*, 25–28; c) L. Schwink, P. Knochel, *Chem. Eur. J.* **1998**, *4*, 950–968.

[18] K. Yamakawa, M. Hisatome, *J. Organomet. Chem.* **1973**, *52*, 407–424.

[19] M. N. Nefedova, I. A. Mamedyarova, P. P. Petrovski, V. I. Sokolov, *J. Organomet. Chem.* **1992**, *425*, 125–130.

[20] a) A. J. Locke, N. Gouti, C. J. Richards, D. E. Hibbs, M. B. Hursthouse, *Tetrahedron* **1996**, *52*, 1461–1472; b) A. J. Locke, C. Jones, C. J. Richards, *J. Organomet. Chem.* **2001**, *637–639*, 669–676.

[21] For detailed discussions on the stereochemistry of substitution reactions on ferrocenylmethyl cations, see: G. Wagner, R. Herrmann in *Ferrocenes* (Eds.: A. Togni, T. Hayashi), VCH, Weinheim, **1995**, Part 2, pp. 173–218.

[22] In trivalent phosphorus compounds, small $^2J_{H-P}$ coupling constants are expected for large dihedral angles between the P–C–H and P–C–lone-pair planes: J. P. Albrand, D. Gagnaire, J. B. Robert, *J. Chem. Soc. Chem. Commun.* **1968**, 1469–1470.

[23] a) J. Cabou, J. Brocard, L. Pélinski, *Tetrahedron Lett.* **2005**, *46*, 1185–1188; b) M. Lamač, I. Císařová, P. Štěpnička, *J. Organomet. Chem.* **2005**, *690*, 4285–4301; c) J. R. Garabatos Perera, R. Wartchow, H. Butenschön, *J. Organomet. Chem.* **2004**, *689*, 3541–3549.

[24] A. Ohno, M. Yamane, T. Hayashi, N. Oguni, M. Hayashi, *Tetrahedron: Asymmetry* **1995**, *6*, 2495.

[25] (*S*)-(α-Hydroxy)phenylmethylferrocene has been obtained according to ref.[17a].

[26] H. Seo, B. Y. Kim, J. H. Lee, H. J. Park, S. U. Son, Y. K. Chung, *Organometallics* **2003**, *22*, 4783–4791.

[27] The *anti*-diol **2b** could be easily obtained by enantioselective, CBS-promoted reduction of 1,1′-diacetylferrocene (see ref.[17c]). However, for our purposes, this is not an economically convenient method, as a *meso* product would result from the subsequent cyclisation reaction with the primary phosphane.

[28] T. A. Mashburn, C. R. Hauser, *J. Org. Chem.* **1961**, *26*, 1671–1672.

[29] The initial assignment of *meso* and *dl* isomers for ferrocene-based diols and oxa-ferrocenophanes (ref.[18]) was later reversed (ref.[19,20a]).

[30] The generation of transient carbocations from (ferrocenylmethyl) methyl ethers was previously performed by using either $BF_3{\cdot}OEt_2$ (see ref.[20a]) or acetic acid as the catalyst. Only the second procedure has been applied to the stereospecific synthesis of chiral phosphanes: R. J. Kloetzing, M. Lotz, P. Knochel, *Tetrahedron: Asymmetry* **2003**, *14*, 255–264.

[31] M. Hillmann, J. D. Austin, *Organometallics* **1987**, *6*, 1737–1743.

[32] Analogous structural features have been observed also in 2-phospha[3]ferrocenophanes with nitrogen atoms in the bridging chain: B. Wrackmeyer, E. V. Klimkina, W. Milius, *Inorg. Chem. Commun.* **2004**, *7*, 884–888.

[33] a) S. Otsuka, A. Nakamura, T. Tano, K. Tani, *J. Am. Chem. Soc.* **1971**, *54*, 4301; b) K. Tani, L. D. Brown, J. Ahmed, J. A. Ibers, M. Yokota, A. Nakamura, S. Otsuka, *J. Am. Chem. Soc.* **1977**, *99*, 7876. Reviews: c) S. B. Wild, *Coord. Chem. Rev.* **1997**, *166*, 291–311; d) J. Albert, J. Granell, G. J. Muller, *Organomet. Chem.* **2006**, *691*, 2101–2106.

[34] For previous uses of **7** as a resolving agent, see, for instance: a) J. M. Valk, T. D. W. Claridge, J. M. Brown, D. Hibbs, M. B. Hursthouse, *Tetrahedron: Asymmetry* **1995**, *6*, 2597–2610; b) J. Albert, R. Bosque, J. M. Cadena, S. Delgado, J. Granell, G. Muller, J. I. Ordinas, M. F. Bardia, X. Solans, *Chem. Eur. J.* **2002**, *8*, 2279–2287 and references cited therein.

[35] M. Hillman, J. D. Austin, *Organometallics* **1987**, *6*, 1737–1743.

[36] G. J. Meuzelaar, A. S. E. Karlström, M. van Klaveren, E. S. M. Persson, A. del Villar, G. van Koten, J.-E. Bäckvall, *Tetrahedron* **2000**, *56*, 2895–2903.

 © 2007 Wiley-VCH Verlag GmbH & Co. KGaA, Weinheim 

[37] D. J. Connolly, P. M. Lacey, M. McCarthy, C. P. Saunders, A.-M. Carroll, R. Goddard, P. J. Guiry, *J. Org. Chem.* **2004**, *69*, 6572–6589.
[38] G. M. Sheldrick, *Acta Crystallogr., Sect. A: Found. Crystallogr.* **1990**, *46*, 467–473.
[39] G. M. Sheldrick, *SHELXL-97*. Program for the Refinement of Crystal Structures. University of Göttingen, Germany, **1997**.
[40] *Collect*, Nonius BV, **1997–2000**; Z. Otinowski, W. Minor, *HKL Denzo and Scalepack*, **1997**.

Received: March 12, 2007
Published Online: June 29, 2007

 © 2007 Wiley-VCH Verlag GmbH & Co. KGaA, Weinheim 

DOI: 10.1002/ejic.200700390

# Facile Synthesis and Photoluminescence of Europium Ion Doped $LaF_3$ Nanodisks

**Ling Zhu,[a,b] Jian Meng,[a] and Xueqiang Cao*[a]**

**Keywords:** Materials science / Crystal growth / Rare earths / Fluorescence

$LaF_3$:$Eu^{3+}$ (5.0 mol-% $Eu^{3+}$) nanodisks with perfect crystallinity were successfully synthesized by a simple method. The synthesis was carried out in an aqueous solution at room temperature without the use of templates or organic additives. The mechanism of formation of the nanodisks was explored, and the fluoride source ($KBF_4$) is believed to play a key role in controlling the morphology of the final product. Furthermore, the size of the disk can be simply moderated by varying the concentration of the initial reactants. The room-temperature photoluminescence of $LaF_3$:$Eu^{3+}$ with different morphologies and sizes were also investigated, and the results indicate that the emission intensity of the product is strongly affected by their size, shape, and other factors.

(© Wiley-VCH Verlag GmbH & Co. KGaA, 69451 Weinheim, Germany, 2007)

## Introduction

Inorganic materials with controllable morphologies and sizes have attracted increasing attention because of their unique morphology- and size-dependent chemical and physical properties.[1–5] To date, a number of synthetic approaches including laser ablation, templating direction, electrochemical deposition, thermolysis of complex precursors in solution phase, and solvothermal/hydrothermal treatments have been developed to control the morphologies of materials.[6–11] However, the reported conventional methods suffer from the requirement of a template, high temperatures, special conditions, or tedious procedures, and therefore, facile and template-free methods are highly desired. Because of the significant advantages, such as the ease of control, low temperature, low cost, and easy scale-up, the stirring method is a powerful and practical route to prepare a great deal of inorganic materials with uniform and unique morphologies. Recently, great progress was made in the synthesis of nanodisks. Wu et al. reported the preparation of monodispersive silver nanodisks by thermolysis of the layered silver thiolate precursor.[12] Zhang et al. successfully synthesized ultrathin $WO_3$ nanodisks by using a wet chemical route with polyethylene glycol (PEG) as the surface modulator.[13] Korgel et al. developed the solvent-free thermolysis of a copper alkylthiolate molecular precursor to prepare $Cu_2S$ nanodisks.[14] Iron oxide nanodisks can also be obtained through the nonhydrolytic, surfactant-mediated thermal reaction of iron pentacarbonyl and an oxidizer.[15] The growth of $Cd(OH)_2$ nanodisks by a hydrothermal route was reported by Zhang et al.[16]

The study of rare-earth fluorides is currently an active research field in modern materials chemistry as these compounds have potential applications in optics, optoelectronics, biological labeling, catalysis fields, etc.[17–21] Rare-earth fluoride crystals with various morphologies have been prepared by different synthetic techniques, for example, fullerene-like $LnF_3$ (Ln = La, Pr, Nd, Sm, and Y),[22,23] bundle-like, rod-like, hexagonal and triangular $YF_3$ nanocrystals,[24–26] monodisperse $LaF_3$ triangular nanoplates,[27] and $EuF_3$ nanocrystals with different crystalline phases and morphologies.[28,29] Wang et al. reported a hydrothermal method for the growth of $LaF_3$ nanodisks using $KF{\cdot}2H_2O$ as the fluoride source, and then the self-assembly of these nanodisks into the plate-built cylinders through oriented aggregation.[30] However, it is still a challenge to develop a more simple method to prepare $LaF_3$:$Eu^{3+}$ with the controlled morphology under mild reaction conditions. Herein, we report a facile and fast solution-based method for the synthesis of singly crystalline $LaF_3$:$Eu^{3+}$ nanodisks without the use of templates or organic additives, and further investigate their microstructure and luminescence properties.

## Results and Discussion

### Structure and Morphology of the Product

The crystal structure of the $LaF_3$:$Eu^{3+}$ sample was characterized by XRD. As shown in Figure 1, all the peaks can be readily indexed to a hexagonal structure of $LaF_3$ [space

[a] Key Laboratory of Rare Earth Chemistry & Physics, Changchun Institute of Applied Chemistry, Chinese Academy of Sciences
Changchun, 130022 Jilin, China
Fax: +86-431-85262285
E-mail: xcao@ciac.jl.cn,
[b] Graduate School of the Chinese Academy of Sciences
Beijing 100049, China

 © 2007 Wiley-VCH Verlag GmbH & Co. KGaA, Weinheim 

group $P\bar{3}c1$ (No. 165)] with lattice constants of $a$ = 7.187 Å and $c$ = 7.350 Å (JCPDS No. 32–0483). No impurities were observed in the XRD pattern. The strong and sharp diffraction peaks indicate that the product crystallizes well.

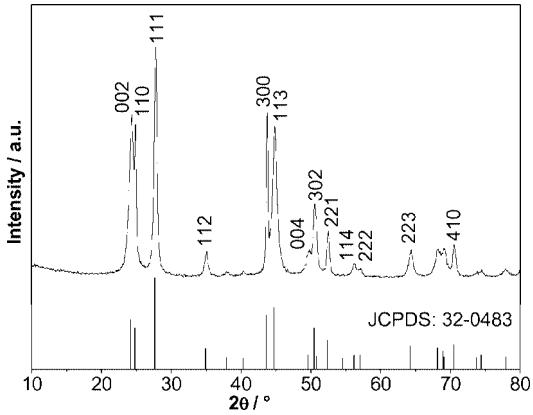


Figure 1. XRD pattern of the $LaF_3$:$Eu^{3+}$ nanodisks.

The morphology and microstructure detail of the as-synthesized sample was investigated by SEM, TEM, HRTEM, and SAED observation. The SEM image with a low magnification (Figure 2a) reveals that the $LaF_3$:$Eu^{3+}$ product is entirely comprised of disks with a uniform size and round shape. The average diameter of the disks is about 500 nm, as can be seen from the SEM with a high magnification (Figure 2b), and this is confirmed by the TEM images (Figure 2c). The thickness of the disk is about 20 nm, as observed from those disks that are perpendicular to the silicon substrate in the SEM image (Figure 2b). Furthermore, Figure 2b shows that the surfaces of the $LaF_3$:$Eu^{3+}$ nanodisks are extremely smooth. The clear lattice fringes in the HRTEM image (Figure 2d) confirm the high crystallinity of the $LaF_3$:$Eu^{3+}$ nanocrystals. The SAED image (Figure 2e) of a disk shows the regular diffraction spots and confirms that the $LaF_3$:$Eu^{3+}$ nanodisks are singly crystalline. Furthermore, the diffraction observation indicates that <1120> is the growth direction for developing the hexagonal crystals, and the $LaF_3$:$Eu^{3+}$ nanodisks are dominated by {0001} facets. These results indicate that $LaF_3$:$Eu^{3+}$ nanodisks with uniform morphology and size can be obtained by this simple and mild method, and the productivity of the product is as high as 81%.

It is well-known that lanthanum fluoride has a small solubility product constant ($K_{sp}$ = $2.0 \times 10^{-19}$ at 25 °C),[31] implying that upon direct mixing, $La^{3+}$ and $F^-$ would immediately react to form the precipitate of lanthanum fluoride. For this rapid reaction it is thus difficult to control the morphology and size of the product. Figure 3 show the TEM images of the $LaF_3$:$Eu^{3+}$ samples that were synthesized by using either NaF or $NH_4F$ as the fluoride source, and the other preparation conditions are identical to those of the disk-like product. It can be seen that the $LaF_3$:$Eu^{3+}$ samples are composed of irregular nanoparticles with serious agglomeration (Figure 3). Moreover, the SAED images of these two samples reveal that the $LaF_3$:$Eu^{3+}$ nanoparticles are polycrystalline in nature (insets of Figure 3). In the case

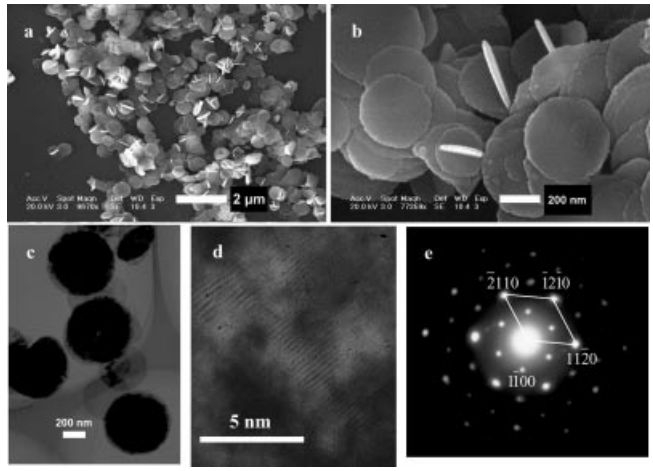


Figure 2. SEM images of the $LaF_3$:$Eu^{3+}$ nanodisks with different magnification (a, b), TEM (c), HRTEM (d), and SAED (e) images of the $LaF_3$:$Eu^{3+}$ nanodisks.

of NaF and $NH_4F$, a white precipitate appeared immediately after the lanthanum nitrate solution was mixed with sodium or ammonium fluoride, which indicated that the nucleation had taken place rapidly. These results indicate that in the current case, the rapid reaction process is not suitable to prepare $LaF_3$:$Eu^{3+}$ with controlled morphology and size. Therefore, to solve these problems, a slow reaction process was adopted. It is interesting to observe that the experimental phenomena and the morphology of the final product are different when $KBF_4$ is used as the fluoride source. When $KBF_4$ was used, the reaction solution became turbid after 40 min, and the uniform nanodisks were formed. In an aqueous solution, $KBF_4$ was slowly hydrolyzed to produce $F^-$ anions; these $F^-$ anions reacted with $Ln^{3+}$ cations (Ln = La, Eu) to form the lanthanum fluoride as described by Equations (1) and (2).

$$BF_4^- + 3H_2O \leftrightarrow H_3BO_3 + 3HF + F^- \quad (1)$$

$$Ln^{3+} + 3F^- \rightarrow LnF_3\downarrow \quad (2)$$

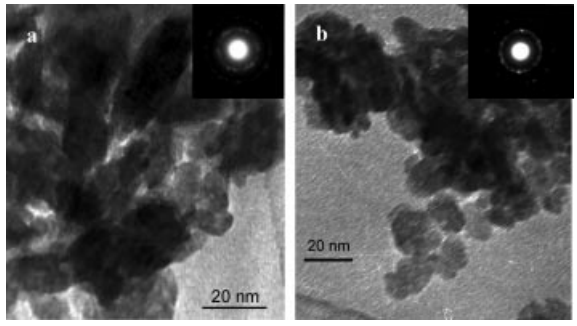


Figure 3. TEM (a) and SAED (inset a) images of the $LaF_3$:$Eu^{3+}$ nanocrystal from NaF and the TEM (b) and SAED (inset b) images of the $LaF_3$:$Eu^{3+}$ nanocrystal from $NH_4F$.

The equilibrium constant of the hydrolysis reaction [Equation (1)] is very small ($K^0$ = $6.41 \times 10^{-12}$ at 25 °C)[32], which is helpful to keep the concentration of $F^-$ ions in the reaction solution at a low level, and consequently, this leads

 © 2007 Wiley-VCH Verlag GmbH & Co. KGaA, Weinheim 

to slow crystallization of the product. The slow crystallization process can be further confirmed by the experimental observation that the reaction solution became turbid after stirring for 40 min, and the pH value of the aqueous solution gradually increased from approximately 5.0 at the beginning of the reaction to 1.5 when the reaction was complete. From the above observation, it is believed that the slow reaction process is a key factor for the synthesis of the singly crystalline $LaF_3:Eu^{3+}$ nanodisks with uniform morphology and size. Mann et al. reported the synthesis of Prussian blue nanoparticles and nanocrystal superlattices by the slow photoreduction of $[Fe(C_2O_4)_3]^{3-}$ to $Fe^{2+}$ in the presence of $[Fe(CN)_6]^{3-}$ in reverse microemulsion.[33] Hu et al. synthesized perfect α-$Fe_2O_3$ fractal dendrites by the slow decomposition and hydrolysis of $K_3Fe(CN)_6$ under hydrothermal conditions.[34] Therefore, it can be reasonably inferred that a slow reaction process is very useful to control the morphology and size of the materials, especially for those with small $K_{sp}$ values.

A crystal growth process consists of the nucleation and the growth, which are affected by the intrinsic crystal structure and the external conditions such as the kinetic energy barrier, temperature, time, and capping molecules, etc. Generally speaking, for materials with a hexagonal structure, the anisotropic growth along the *c* axis is available to form the 1D nanostructures, as the {001} planes (which are perpendicular to the *c* axis) exhibit significantly different surface energies relative to the {100} and {110} crystal planes. However, in the current case, only nanoparticles were obtained when NaF or $NH_4F$ was used as the fluoride source and 2D nanodisks were obtained if $KBF_4$ was used as the fluoride source, indicating that $KBF_4$ plays a critical role in the formation of 2D nanodisks of the $LaF_3:Eu^{3+}$ crystals. $BO_3^{3-}$ ions are produced during the hydrolysis of $KBF_4$ in aqueous solution as shown in Equation (1), and their appearance has been proven by other groups.[35] It is quite possible that these anions, such as $BF_4^-$, $NO_3^-$, and $BO_3^{3-}$, are adsorbed on the (0001) plane of the crystal seed, which slow down the crystal growth along the <0001> orientation. Accordingly, the intrinsically anisotropic growth of $LaF_3$ along the <0001> direction is substantially suppressed, and the 2D disk-like $LaF_3$ is formed. It is well-documented that adsorbed ions can change the growth kinetics and the surface energies of different crystal faces, which can ultimately lead to anisotropic growth of low-symmetry nanostructures, such as the nanodisk, the nanoplate, the nanorod, and the nanowire.[36–39] For example, Liu et al. used a seed growth procedure to obtain a complex hexagonal ZnO nanostructure with capping of the citric acid, which adsorbs preferably on the (001) surface of ZnO and slows down the crystal growth along the *c* axis.[40] Xia et al. observed that the polyvinylpyrrolidone capping agent interacted more strongly with the silver atoms on the {100} facets than those on the {111} facets, and the growth of silver could be directed into a highly anisotropic mode to form uniform nanowires.[41] Accordingly, in this work, $KBF_4$ is believed to play a key role in the formation of $LaF_3:Eu^{3+}$ nanodisks in the adopted reaction system. Therefore, through the above analysis, it is proposed that there are two key factors that allow $LaF_3:Eu^{3+}$ nanocrystals with the 2D disk-like morphology to be obtained. One is the slow reaction process, and the other is the selective absorption of anions ($BF_4^-$, $NO_3^-$, $BO_3^{3-}$) specifically on the crystal faces of the crystal seed. However, the mechanism of formation of the $LaF_3:Eu^{3+}$ nanodisks is not fully understood. Further theoretical and experimental work is required to understand the exact nature of the mechanism of growth.

Further experiments indicated that the size of the synthesized $LaF_3:Eu^{3+}$ disk depends strongly on the concentration of the initial reagents. At the fixed molar ratio of 3:1 for $KBF_4$:La(Eu)$(NO_3)_3$, the size of the product decreased from 500 to 100 nm with an increase in the initial concentration of the reactant. Figure 4a shows a typical SEM image of a $LaF_3:Eu^{3+}$ sample that was prepared from an aqueous solution in which the concentrations of La(Eu)$(NO_3)_3$ and $KBF_4$ were 0.04 and 0.12 M, respectively. The average size of the disk is 300 nm. A further increase in the concentration of La(Eu)$(NO_3)_3$ to 0.08 M and that of $KBF_4$ to 0.24 M caused the average size of the disk to be reduced to 100 nm, as illustrated in Figure 4b. Moreover, it is obvious that the surface of the nanodisk becomes coarse with an increase in the concentration of the initial reagents. The above experiments indicate that the size of the $LaF_3:Eu^{3+}$ disks could be tuned by simply changing the concentrations of the precursors.

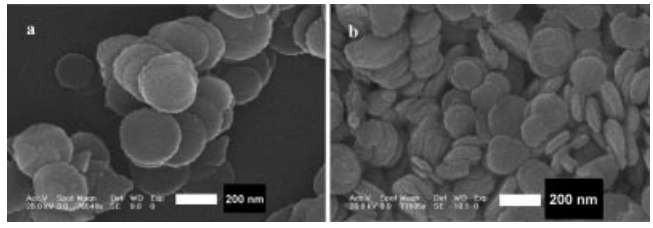


Figure 4. SEM image (a) of the $LaF_3:Eu^{3+}$ nanocrystal with La(Eu)$(NO_3)_3$ and $KBF_4$ concentrations of 0.04 and 0.12 M, respectively, and the SEM image (b) of the $LaF_3:Eu^{3+}$ nanocrystal with La(Eu)$(NO_3)_3$ and $KBF_4$ concentrations of 0.08 and 0.24 M, respectively.

### Photoluminescent (PL) Properties

Figure 5 shows the room-temperature emission spectra of $LaF_3:Eu^{3+}$ nanodisks and nanoparticles that were prepared from different fluoride sources. Both samples were measured under identical conditions with an excitation wavelength of $\lambda_{ex}$ = 399 nm. In the emission spectra, the characteristic emission peaks of $Eu^{3+}$ in the wavelength range from 520 to 720 nm were observed, corresponding to the transitions from the excited $^5D_1$ and $^5D_0$ levels to $^7F_J$ ($J$ = 0–4) levels, with the magnetic dipole $^5D_0 \rightarrow {}^7F_1$ allowed transition (589 nm) being the most prominent emission line.[42] The relative intensities of the emission peaks were similar to those reported earlier,[19] indicating that the $Eu^{3+}$ ion is located in the $La^{3+}$ crystal site with $C_2$ symmetry,

 © 2007 Wiley-VCH Verlag GmbH & Co. KGaA, Weinheim 

which is the same as that of the bulk $LaF_3$ crystals.[43] For the C2 site, the electric and magnetic dipole transitions are allowed. Therefore, both the $^5D_0 \rightarrow {}^7F_1$ and the $^5D_0 \rightarrow {}^7F_2$ transitions of $Eu^{3+}$ can be observed in the $LaF_3$:$Eu^{3+}$ nanocrystals. Although the emission positions of the major peaks of these two samples are identical, the emission intensity of the disk-like $LaF_3$:$Eu^{3+}$ product is significantly higher than that of the particle-like product. It is well-documented that the grain size, morphology, crystal structure, dimension, and surface modification of the luminescent material all influence its photoluminescent properties.[44–46] Owing to a large surface area to volume ratio, an important source of luminescence quenching in small particles is the surface where the coordination of the atom differs from that in the bulk and the site where different chemical species can be adsorbed. Because the samples were prepared in aqueous solution, the surface of the nanocrystals can be covered with hydroxy species such as lanthanum or europium hydroxides, fluorine ions, or adsorbed water molecules. Different sizes and shapes result in different combinations between the surface and the adsorbed species so as to produce different quenching abilities of the emissions of the $Eu^{3+}$ ions; therefore, the differences in the PL intensities of the samples may be attributed to the different abilities of the adsorbed species on the surface to quench the emissions from the $Eu^{3+}$ ions. The luminescence intensity of the disk-like nanocrystals is obviously stronger than that of the particle-like nanocrystals, which may be due to the factor that the nanostructure can prevent the adsorbed species on the surface from quenching the emission from the $Eu^{3+}$ ions. We also assume that the particle-like crystals would possess more defects due to the fast growth of the crystal. Some of these defects may act as the nonradiative recombination centers, and they may be responsible for the decrease in the luminescence intensity as observed in the particle-like product.

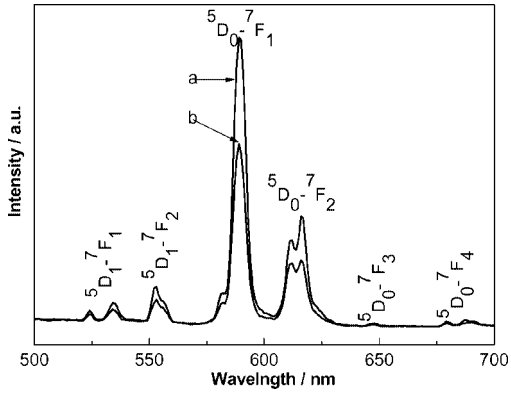


Figure 5. Emission spectra of the nanodisks (a) and nanoparticles (b) of $LaF_3$:$Eu^{3+}$ nanocrystals.

The emission spectra of $LaF_3$:$Eu^{3+}$ disks with different sizes under excitation at 399 nm were also investigated. From Figure 6 it can be seen that the emission intensity of the $LaF_3$:$Eu^{3+}$ phosphors basically increase with an increase in the size of the disks. It is well-known that a large particle size is helpful for improving the PL intensity of phosphors.[47,48] A more extensive investigation of the differences in the luminescent properties of the products with different morphologies, crystal structures, sizes, and dimensions will be further investigated in our future work.

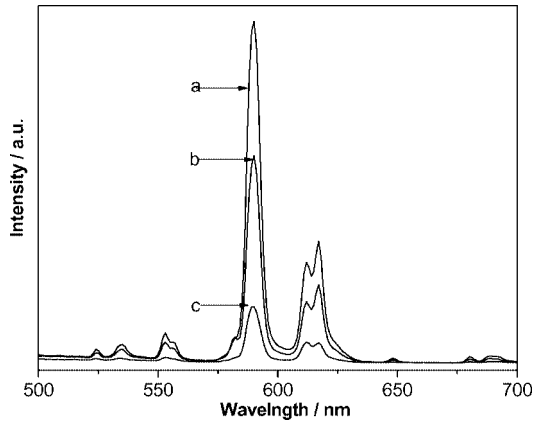


Figure 6. Emission spectra of the $LaF_3$:$Eu^{3+}$ disks with different size: 500 nm (a), 300 nm (b), and 100 nm (c).

## Conclusions

We utilized a mild and facile synthetic route to prepare $LaF_3$:$Eu^{3+}$ nanodisks from an aqueous solution of $(La,Eu)(NO_3)_3$ and $KBF_4$ without the use of templates or organic additives. The size of the $LaF_3$:$Eu^{3+}$ nanodisks can be tuned by simply controlling the concentration of the precursors. The mechanism of formation of the disk-like structures was investigated, and the fluoride source ($KBF_4$) clearly contributes to the creation of such a structure. Room-temperature photoluminescence of the $LaF_3$:$Eu^{3+}$ samples with different morphologies and sizes were also investigated, and the results reveal that all of these samples showed similar features but different luminescence intensities.

## Experimental Section

**General:** All the reagents used were of analytical grade, including $La_2O_3$ and $Eu_2O_3$ (Shanghai Chemical Reagent), $KBF_4$, NaF, and $NH_4F$ (Beijin Chemical Reagent), and used as received without further purification.

**Typical Synthesis:** Appropriate amounts of $La_2O_3$ and $Eu_2O_3$ (La:Eu = 95:5, in molar ratio) were first dissolved in nitric acid (10%) and then mixed with a $KBF_4$ solution in a 150-mL plastic flask to give a final concentration of 20 mM of $La(Eu)(NO_3)_3$ and 60 mM of $KBF_4$. The total volume of the solution was 100 mL. The resulted solution was stirred at ambient temperature for 3 h. A white precipitate was centrifuged and then washed with distilled water and absolute ethanol in sequence. The final product was dried under vacuum at 60 °C for 12 h.

**Crystal Structure Determination:** X-ray powder diffraction (XRD) was performed with a Rigaku D/MAX-2500 diffractometer with Cu-$K_\alpha$ radiation ($\lambda$ = 0.15406 nm) and a scanning rate of 5 °$min^{-1}$.

 © 2007 Wiley-VCH Verlag GmbH & Co. KGaA, Weinheim 

Scanning electron micrographs (SEM) were taken with a XL30 field-emission scanning electron microscope. Transmission electron micrographs (TEM), high-resolution transmission electron micrographs (HRTEM), and the selected area electron diffraction (SAED) were taken with a JEOL-JEM-2010, operating at 200 kV (JEOL, Japan). Samples for TEM were prepared by dropping a diluted suspension of the sample powders onto a standard carbon-coated (20–30 nm) Formvar film on a copper grid (230 mesh). Photoluminescence (PL) spectra were recorded with a Hitachi F-4500 spectrophotometer equipped with a 150 W xenon lamp as the excitation source. All the measurements were performed at room temperature.

## Acknowledgments

This work was financially supported by the National Nature Science Foundation of China (No. 20331030).

[1] M. Pal, J. G. Serrano, P. Santiago, U. Pal, *J. Phys. Chem. C* **2007**, *111*, 96–102.
[2] Y. F. Hao, G. W. Meng, C. H. Ye, L. D. Zhang, *Cryst. Growth Des.* **2005**, *5*, 1617–1621.
[3] J. Geng, Y. N. Lv, D. J. Lu, J. J. Zhu, *Nanotechnology* **2006**, *17*, 2614–2620.
[4] T. Xia, Q. Li, X. D. Liu, J. Meng, X. Q. Cao, *J. Phys. Chem. B* **2006**, *110*, 2006–2012.
[5] A. Miyazaki, I. Balint, Y. Nakano, *J. Nanopart. Res.* **2003**, *5*, 69–80.
[6] J. Q. Hu, Q. Li, X. M. Meng, C. S. Lee, S. T. Lee, *J. Phys. Chem. B* **2002**, *106*, 9536–9539.
[7] Z. F. Pu, M. H. Cao, J. Yang, K. L. Huang, C. W. Hu, *Nanotechnology* **2006**, *17*, 799–804.
[8] B. Q. Cao, Y. Li, G. T. Duan, W. P. Cai, *Cryst. Growth Des.* **2006**, *6*, 1091–1095.
[9] P. Gao, Y. Xie, L. N. Ye, Y. Chen, Q. X. Guo, *Cryst. Growth Des.* **2006**, *6*, 583–587.
[10] Z. A. Peng, X. G. Peng, *J. Am. Chem. Soc.* **2001**, *123*, 1389–1395.
[11] H. S. Qian, S. H. Yu, J. Y. Gong, L. B. Luo, L. L. Wen, *Cryst. Growth Des.* **2005**, *5*, 935–939.
[12] Y. B. Chen, L. Chen, L. M. Wu, *Inorg. Chem.* **2005**, *44*, 9817–9822.
[13] A. Wolcott, T. R. Kuykendall, W. Chen, S. W. Chen, J. Z. Zhang, *J. Phys. Chem. B* **2006**, *110*, 25288–25296.
[14] M. B. Sigman, J. A. Ghezelbash, T. Hanrath, A. E. Saunders, F. Lee, B. A. Korgel, *J. Am. Chem. Soc.* **2003**, *125*, 16050–16057.
[15] M. F. Casula, Y. W. Jun, D. J. Zaziski, E. M. Chan, A. Corrias, A. P. Alivisatos, *J. Am. Chem. Soc.* **2006**, *128*, 1675–1682.
[16] W. D. Shi, C. Wang, H. S. Wang, H. J. Zhang, *Cryst. Growth Des.* **2006**, *6*, 915–918.
[17] J. W. Stouwdam, C. J. M. van Veggel Frank, *Langmuir* **2004**, *20*, 11763–11771.
[18] L. Y. Wang, Y. D. Li, *Nano Lett.* **2006**, *6*, 1645–1649.
[19] J. W. Stouwdam, C. J. M. van Veggel Frank, *Nano Lett.* **2002**, *2*, 733–737.
[20] S. Sivakumar, P. R. Diamente, C. J. M. van Veggel Frank, *Chem. Eur. J.* **2006**, *12*, 5878–5884.
[21] J. Z. Luo, H. L. Wan, *Appl. Catal. A* **1997**, *158*, 137–144.
[22] X. Wang, Y. D. Li, *Angew. Chem. Int. Ed.* **2003**, *42*, 3497–3500.
[23] X. Wang, Y. D. Li, *Chem. Eur. J.* **2003**, *9*, 5627–5635.
[24] R. X. Yan, Y. D. Li, *Adv. Funct. Mater.* **2005**, *15*, 763–770.
[25] X. Wang, J. Zhuang, Q. Peng, Y. D. Li, *Inorg. Chem.* **2006**, *45*, 6661–6665.
[26] J. L. Lemyre, A. M. Ritcey, *Chem. Mater.* **2005**, *17*, 3040–3043.
[27] Y. W. Zhang, X. Sun, R. Si, L. P. You, C. H. Yan, *J. Am. Chem. Soc.* **2005**, *127*, 3260–3261.
[28] M. Wang, Q. L. Huang, J. M. Hong, X. T. Chen, Z. L. Xue, *Cryst. Growth Des.* **2006**, *6*, 1972–1974.
[29] M. Wang, Q. L. Huang, J. M. Hong, X. T. Chen, Z. L. Xue, *Cryst. Growth Des.* **2006**, *6*, 2169–2173.
[30] Y. Cheng, Y. S. Wang, Y. H. Zheng, Y. Qin, *J. Phys. Chem. B* **2005**, *109*, 11548–11551.
[31] T. L. Brown, H. E. LeMay Jr, B. E. Bursten, *Chemistry – The Central Science*, 8th ed., Prentice-Hall International, INC, **2000**, p. 1023.
[32] W. J. Crooks III, W. D. Rhodes, *Use of Modeling for the Prevention of Solids Formation during Canyon Processing of Legacy Nuclear Materials*, Westinghouse Savannah River Company Aiken, SC 29808,WSRC-TR-2002–00462, **2003**, p. 7.
[33] S. Vaucher, M. Li, S. Mann, *Angew. Chem. Int. Ed.* **2000**, *39*, 1793–1796.
[34] M. H. Cao, T. F. Liu, S. Gao, G. B. Sun, X. L. Wu, C. W. Hu, Z. L. Wang, *Angew. Chem. Int. Ed.* **2005**, *44*, 4197–4201.
[35] Z. J. Miao, Z. M. Liu, K. L. Ding, B. X. Han, S. D. Miao, G. M. An, *Nanotechnology* **2007**, *18*, 125605.
[36] A. Filankembo, S. Giorgio, I. Lisiecki, M. P. Pileni, *J. Phys. Chem. B* **2003**, *107*, 7492–7500.
[37] S. H. Im, Y. T. Lee, B. Wiley, Y. N. Xia, *Angew. Chem. Int. Ed.* **2005**, *44*, 2154–2157.
[38] B. Wiley, Y. G. Sun, B. Mayers, Y. N. Xia, *Chem. Eur. J.* **2005**, *11*, 454–463.
[39] K. K. Caswell, C. M. Bender, C. J. Murphy, *Nano Lett.* **2003**, *3*, 667–669.
[40] Z. R. Tian, J. A. Voigt, J. Liu, B. Mckenzie, M. J. Mcdermott, *J. Am. Chem. Soc.* **2002**, *124*, 12954–12955.
[41] Y. G. Sun, Y. D. Yin, B. T. Mayers, T. Herricks, Y. N. Xia, *Chem. Mater.* **2002**, *14*, 4736–4745.
[42] F. Wang, Y. Zhang, X. P. Fan, M. Q. Wang, *J. Mater. Chem.* **2006**, *16*, 1031–1034.
[43] W. T. Carnall, G. L. Goodman, K. Rajnak, R. S. Rana, *J. Chem. Phys.* **1989**, *90*, 3443–3457.
[44] C. Burda, X. B. Chen, R. Narayanan, M. A. El-Sayed, *Chem. Rev.* **2005**, *105*, 1025–1102.
[45] L. M. Chen, Y. N. Liu, K. L. Huang, *Mater. Res. Bull.* **2006**, *41*, 158–166.
[46] G. S. Yi, H. C. Lu, S. Y. Zhao, Y. Ge, W. J. Yang, D. P. Chen, L. H. Guo, *Nano Lett.* **2004**, *4*, 2191–2196.
[47] M. Yu, H. Wang, C. K. Lin, G. Z. Li, J. Lin, *Nanotechnology* **2006**, *17*, 3245–3252.
[48] X. Jing, T. G. Ireland, C. Gibbons, D. J. Barber, J. Silver, A. Vecht, G. Fern, P. Trogwa, D. Morton, *J. Electrochem. Soc.* **1999**, *146*, 4654–4658.

Received: April 8, 2007
Published Online: June 29, 2007

 © 2007 Wiley-VCH Verlag GmbH & Co. KGaA, Weinheim 

DOI: 10.1002/ejic.200601259

# Self-Assembly of Silver(I) Coordination Polymers from AgX (X = $BF_4^-$, $ClO_4^-$, $CF_3COO^-$, and $SO_3CF_3^-$) and a Rigid Bent 3,6-Dicyano-9-phenylcarbazole Ligand: The Templating Effect of Anions

**Kai-Ju Wei,[a] Jia Ni,[b] Jian Gao,[a] Yangzhong Liu,*[a] and Qing-Liang Liu*[a]**

**Keywords:** Silver / N ligands / Supramolecular chemistry / Luminescence / Coordination polymers / Metal-organic frameworks

One rigid bent bridging ligand with highly planar π-conjugated spacers, 3,6-dicyano-9-phenylcarbazole (dcphcz), was designed and synthesized. The coordination reactions of dcphcz with a series of $Ag^I$ salts with different counterions has been investigated. Four coordination polymers were obtained by solution reactions and characterized by IR, elemental analysis, and single-crystal X-ray diffraction. The solid-state structures of $\{[Ag(dcphcz)]BF_4\}_n$ (**1**) and $\{[Ag(dcphcz)]ClO_4\}_n$ (**2**), exhibit similar 1D "zigzag" patterns. The complex $\{[Ag(dcphcz)][Ag_2(dcphcz)(H_2O)_2](SO_3CF_3)_3 \cdot C_6H_6 \cdot (H_2O)_2\}_n$ (**3**) includes two different one-dimensional (1D) chain units: one forms double-layer two-dimensional (2D) metal–organic frameworks (MOFs) through intermolecular Ag–O–Ag bridging interactions, the other features double-layer 2D supramolecular networks through C–H···O hydrogen-bonding interactions. The complex $[Ag_2(dcphcz)(CF_3COO)_2]_n$ (**4**) features a bundle of novel nanotubular structures, which contain silver chains formed by carboxylate spacers. Furthermore, all these complexes are connected by face-to-face π···π stacking interactions between carbazolyl planes, affording a series of three-dimensional (3D) architectures with different structural geometries. The structural diversities of these complexes demonstrated that counteranions and bridging ligands play essential roles in the construction of supramolecular frameworks. In addition, the luminescence properties of the free ligand dcphcz and complexes **1**–**4** were investigated.

(© Wiley-VCH Verlag GmbH & Co. KGaA, 69451 Weinheim, Germany, 2007)

## Introduction

The design and synthesis of metal–organic coordination polymers have attracted intensive attention not only because of their novel topologies and intriguing structural diversity,[1] such as nanotubes[2] and various metal–organic frameworks (MOFs),[3] but also because of their unique chemical and physical properties and their potential applications as optoelectronic, magnetic, and porous materials.[4] In fact, the ultimate aim of supramolecular and coordination chemistry is to control the structure of the target products and investigate the relationship between the structures and physicochemical properties. Generally, the topology of a coordination polymer generated from the self-assembly of metals and ligands can be controlled by ingenious design of the organic ligand,[5] selection of proper metal ions and counterion,[6] solvent system,[7] pH value of solution,[8] and the molar ratio of the reagents.[9] On top of these factors, a bridging ligand as a "*building block*" is a pivotal point in manipulating the network structures. Because of configuration, coordination activity, and relative orientation of the donor groups, the organic spacers take important roles in determining the structure and geometry of the polymers. Rigid linear ligands have already been extensively studied[3n,10] for designing polymers; however, bent ligands still remain a challenge in self-assembly due to their unpredictable coordination geometry.

It is well recognized that the carbazole moiety not only possesses highly planar π-conjugated systems, but also can be easily functionalized at its 3-, 6-, or 9-positions and covalently linked to other functional moieties.[11] Furthermore, the thermal stability of organic compounds can be greatly improved upon incorporation of a carbazole moiety in the core structure.[12] Therefore, thermally stable molecules possessing dual functions, light-emitting and hole-transporting, should be achieved by using carbazole as the central core. Currently, compounds with highly π-conjugated systems are of great interest due to their various applications in chemical sensors, molecular optical and electronic devices.[13]

Herein, we report the design and synthesis of a new organic molecule with large angular and highly planar π-con-

[a] Department of Chemistry, University of Science & Technology of China,
Hefei, Anhui 230026, P. R. China
Fax: +86-551-3603388
E-mail: liuyz@ustc.edu.cn
qliu@ustc.edu.cn
[b] Center Lab, Shantou University,
Shantou, Guangdong 515063, P. R. China

Supporting information for this article is available on the WWW under http://www.eurjic.org or from the author.

 © 2007 Wiley-VCH Verlag GmbH & Co. KGaA, Weinheim 

jugated spacers based on carbazole, 3,6-dicyano-9-phenylcarbazole (dcphcz). In most cases, the conformation of coordination polymers from bent bidentate ligands are hardly predictable because of the variation of coordination geometry, such as *cis*, *trans*, or intermediary.[7,14] On the other hand, these variations also provide more chances for designing novel polymeric patterns. The ligand dcphcz does not have a conformational diversity owing to the particular structure of carbazole as the central core, neglecting the rotationality of the terminal phenyl ring of dcphcz. The coordination reactions of dcphcz and the $Ag^I$ ion with different counterions were investigated aiming at expanding dcphcz units through the "soft" $Ag^I$ metal ion and exploring the templating effects of counterions in the self-assembly process. It has been reported[6b,6c,10c,15] that the –CN functional group on the aromatic ring serves as a good candidate for coordination bonding in the self-assembly of Ag-supramolecular architectures. With a $d^{10}$ electronic configuration, the $Ag^I$ ion often has irregular coordination geometries and shows a strong tendency to display versatile coordinations. Thus, the $Ag^I$ ion is much more accommodating towards ligands and is expected to form polymer structures more readily than other $d^{10}$ metal ions. At the same time, the ancillary ligation by different counterions, such as $NO_3^-$, $BF_4^-$, $ClO_4^-$, $SO_3CF_3^-$, $CF_3COO^-$, $PF_6^-$, and $SbF_6^-$, may cause a significant structural change of the polymer.[6,10c,14,15] With different polymeric motifs, four new Ag-containing coordination polymers, $\{[Ag(dcphcz)]BF_4\}_n$ (**1**), $\{[Ag(dcphcz)]ClO_4\}_n$ (**2**), $\{[Ag(dcphcz)][Ag_2(dcphcz)(H_2O)_2](SO_3CF_3)_3{\cdot}C_6H_6{\cdot}(H_2O)_2\}_n$ (**3**), and $[Ag_2(dcphcz)(CF_3COO)_2]_n$ (**4**), were synthesized based on ligand 3,6-dicyano-9-phenylcarbazole and their luminescence properties were characterized in this work.

## Results and Discussion

### Synthesis and Characterization

3,6-Dicyano-9-phenylcarbazole (dcphcz) was synthesized in high yield by using the modified Ullmann condensation procedure depicted in Scheme 1, where 3,6-diiodo-9-phenylcarbazole reacts with CuCN in the presence of an HMPA catalyst. The dcphcz is very soluble in common organic solvents, such as $CH_2Cl_2$, $CHCl_3$, THF, benzene, toluene, and $CH_3CN$. The slow diffusion of a $CH_2Cl_2$ solution of dcphcz into a benzene solution of AgX (X = $BF_4^-$, $ClO_4^-$, $SO_3CF_3^-$, and $CF_3COO^-$) afforded a 3:2 ratio of $Ag^I$ salt/dcphcz ligand adduct for $SO_3CF_3^-$ and 1:1 adducts for $BF_4^-$, $ClO_4^-$, and $CF_3COO^-$, which may result from the subtle templating effects of the counterions. It was observed that the products do not depend on the ligand/metal ratio; however, increasing the metal/ligand ratio resulted in somewhat higher yields and better crystal qualities. Complexes **1**–**4** are stable in air at room temperature only for a short time. All these complexes are insoluble in $CH_2Cl_2$, $CHCl_3$, THF, benzene, and $CH_3CN$, but moderately soluble in MeOH, and soluble in DMF.

The structures of the ligand dcphcz and complexes **1**–**4** were determined by IR and elemental analysis. The IR spectrum of ligand dcphcz and complexes **1**–**4** show a –CN absorption band at 2219, 2251, 2251, 2220, and 2219 $cm^{-1}$, respectively. The rigid bidentate or tridentate ligands containing benzonitrile groups, such as 4,4′-dicyanobiphenyl,[15n] 2,5-bis{3-[(4-cyanophenyl)ethynyl]phenyl}-1,3,4-oxadiazole,[7] 1,3,5-tris[(4-cyanophenyl)ethynyl]benzene,[15n] and 1,3,5-tris{4-[(4-cyanophenyl)ethynyl]phenyl}benzene,[15k] have shown excellent bridging action to construct porous frameworks and supramolecular polymers. However, to the best of our knowledge, no supramolecular architectures based on carbazole-containing nitrile groups have been reported.

### Crystal Structures

#### *Structural Analysis of Ligand dcphcz*

The structure of dcphcz was further confirmed by single-crystal X-ray diffraction, as shown in Figure 1. The central carbazolyl group is nearly planar (with a dihedral angle of 2.9° between the two benzonitrile groups). The terminal (–CN) N···N separation is 9.631 Å, which is close to that of 1,2-bis(4-pyridyl)ethyne (9.685 Å).[16] The terminal phenyl ring is not coplanar with the carbazolyl group, as indicated by the dihedral angle of 59.5° between the terminal phenyl

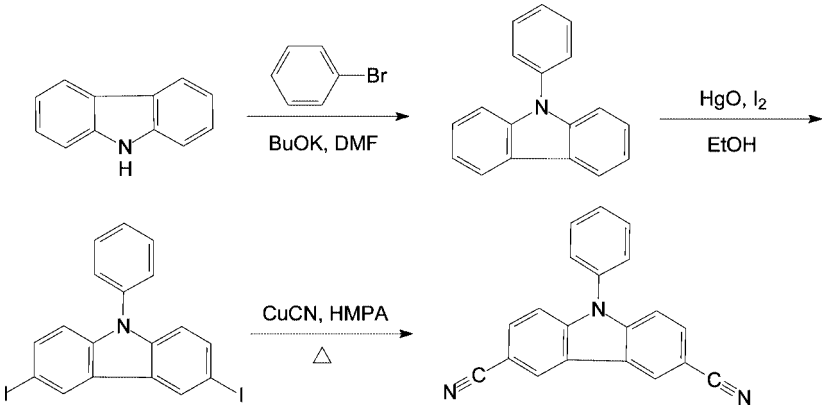


Scheme 1. Preparation of the ligand dcphcz.

 © 2007 Wiley-VCH Verlag GmbH & Co. KGaA, Weinheim 

plane and the five-membered ring of the carbazolyl group. Evidently, the nonplanarity of the ligand is caused by the steric hindrance between C–H groups in two phenyl rings.

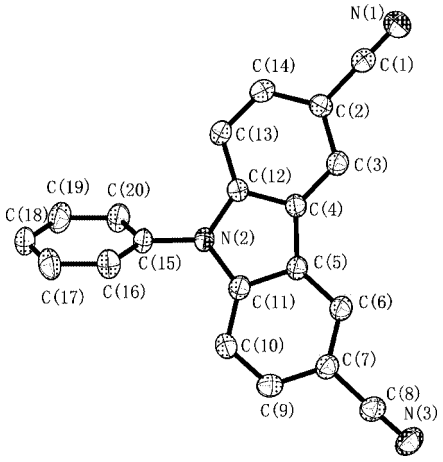


Figure 1. ORTEP diagram showing the structure of dcphcz with 30% thermal ellipsoid probability and the atom-labeling scheme. Hydrogen atoms have been omitted for clarity in this and the following figures.

Figure 2 shows several intermolecular noncovalent interactions in the dcphcz crystal that extends the packing in the solid-state structure. There are two kinds of C–H···N hydrogen-bond interactions between the –CN groups and carbazolyl groups on adjacent molecules of dcphcz, which results in the formation of 1D double chains. The distances of N(1)···H(9) and N(3)···H(3) (2.620 and 2.75 Å, respectively) are significantly shorter than the sum of the van der Waals radii for nitrogen and hydrogen (ca. 1.2 Å for H, and 1.70 Å for N).[17] The other intermolecular interaction, face-to-face π···π stacking between terminal phenyl rings, constructs 2D networks from the 1D chain (Figure 2). At the same time, the C(3)-containing phenyl ring is involved in a moderately strong[18] face-to-face π-stacking interaction with its symmetry-related equivalent, with an interplane distance of 3.47 Å. Thus, the dual interactions of π-stacking and H-bonding extend the 2D networks into 3D architectures.

### *Structural Analysis of {[Ag(dcphcz)]$BF_4$}$_n$ (1) and {[Ag(dcphcz)]$ClO_4$}$_n$ (2)*

Crystallization of dcphcz with $AgBF_4$ in a dichloromethane/benzene mixed solvent afforded **1** as an infinite 1D chain structure. As shown in Figure 3a, single-crystal analysis reveals, that there is only one $Ag^I$ center in complex **1**. Each $Ag^I$ ion is coordinated by two nitrogen atoms from two different dcphcz ligands and two fluorine atoms from the $BF_4^-$ anion. The bond lengths of Ag(1)–N(1) and Ag(1)–N(3) are 2.116 and 2.119 Å, respectively. The Ag(1)–F(1) and Ag(1)–F(2) bonds (2.654 and 2.910 Å) are significantly shorter than the sum of the van der Waals radii for Ag and F (3.19 Å),[17] which indicates the coordination between $Ag^I$ and anion $BF_4^-$.

As shown in Figure 4a, the intrapolymer chain Ag···Ag distance is 13.378 Å. Furthermore, the 1D polymeric chain of **1** is linked into a 2D double-layer network through interpolymer C–H···F hydrogen-bonding interactions (Figure 5). The hydrogen-bonding system involves F(3) of the coordinated $BF_4^-$ counterion and H(7) and H(13) on the dcphcz ligand of the neighboring chain. The F(1)···H(7) and F(1)···H(13) contacts are 2.398 and 2.563 Å, respectively. The corresponding C(7)–H(7)···F(1) and C(13)–H(13)···F(1) angles are 158.36° and 155.18°, respectively.

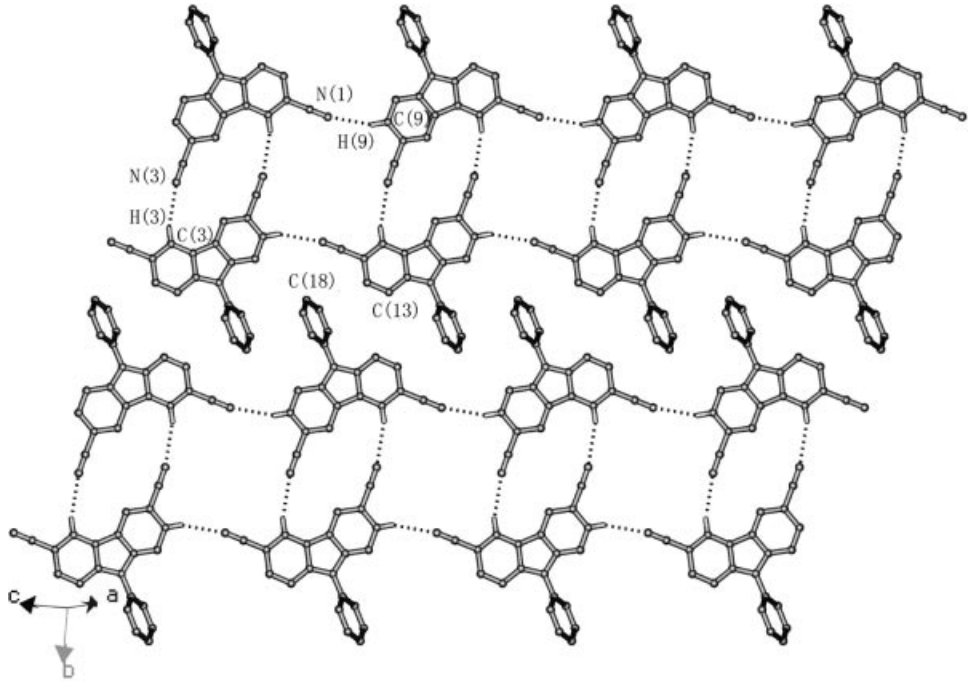


Figure 2. 2D network of dcphcz, showing the π-stacking interactions between the phenyl rings and weak C–H···N hydrogen-bond interactions.

 © 2007 Wiley-VCH Verlag GmbH & Co. KGaA, Weinheim 

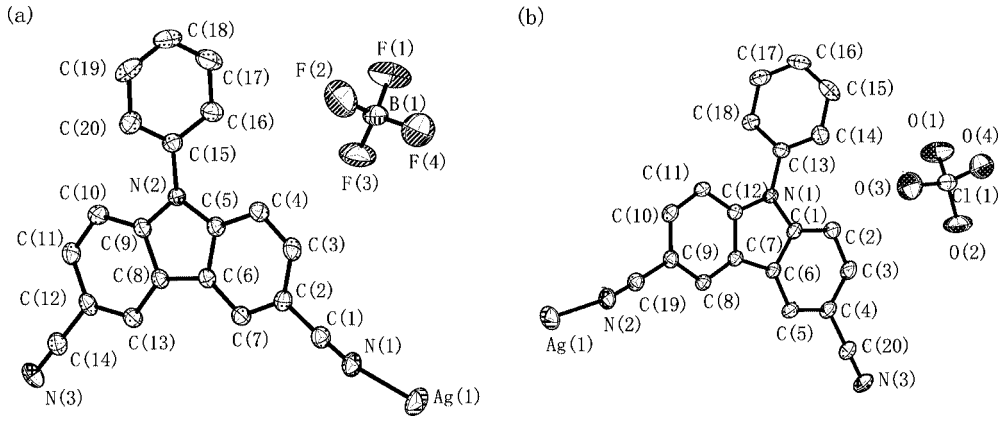


Figure 3. ORTEP diagram showing the structures of **1** (a) and **2** (b), respectively, with 30% thermal ellipsoid probability and the atom-labeling scheme.

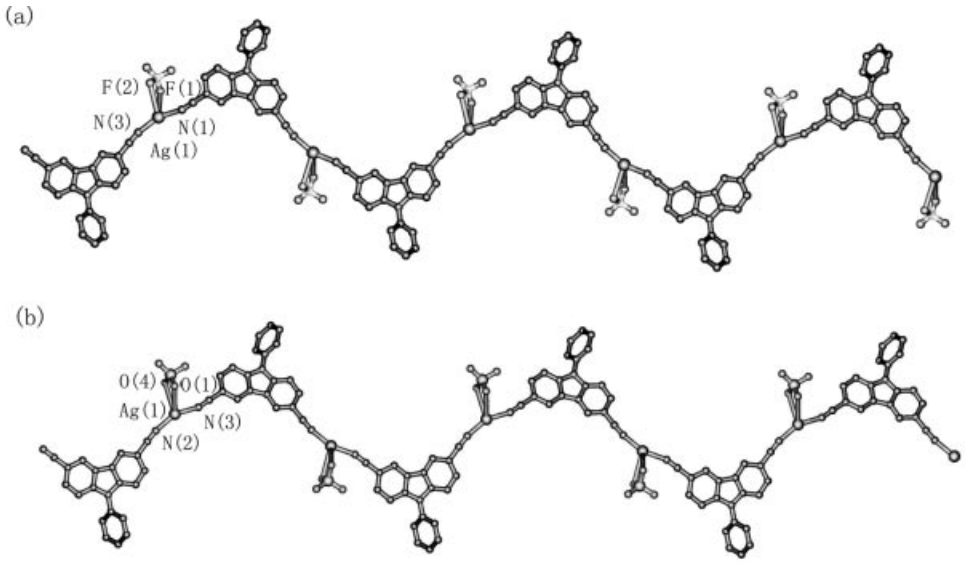


Figure 4. View of one-dimensional "zigzag" chain of **1** (a) and **2** (b).

The existence of weak C–H···X (X = F, Cl, Br, I, O, S, and N) hydrogen-bonding interactions are observed in many compounds and the structural importance is well established.[11b,11c,15d–15j,19] These weak hydrogen bonds often contribute significantly to the alignment of the supramolecular structures in the crystalline state. In complex **1**, the $BF_4^-$ anion contributes to the packing of the complex by coordinating the $Ag^I$ center in one chain and hydrogen-bonding to the F atoms in the neighboring chain. These 2D double-layer networks stack in the *ac* plane through π···π interactions between the lateral carbazolyl planes with an interplane distance of 3.391 Å. Of course, there is also a face-to-face π···π stacking in 2D double-layer networks with an interplane distance of 3.357 Å. Undoubtedly, these π-stacking interactions serve as important driving forces to cross-link the 2D double-layer networks into a 3D architecture. Some examples have shown that the organic ligands involved in the nucleation process use both coordination and π···π interactions to construct the framework.[6b,20]

The other 1D zigzag chain **2** was obtained in a similar way to **1** by using $AgClO_4$ in place of $AgBF_4$. The two complexes have very similar coordination features with two dcphcz chelating ligands (Figure 3b and Figure 4b), while the $ClO_4^-$ anion takes the place of $BF_4^-$ with two coordinating O atoms. The Ag–N bond lengths are close to those in complex **1**, whereas the two Ag–O bonds are somewhat longer (2.636 and 2.847 Å) than Ag–F and within the typical Ag–O bond lengths as reported previously.[11c] The N(1)–Ag(1)–N(3) bond angle (154.02°) and the intrapolymer Ag···Ag distance (13.257 Å) are similar to those in complex **1**. Obviously, the structural similarity of **1** and **2** is generated by the similar nature of the anions ($BF_4^-$ and $ClO_4^-$).

Recently, Ag-supramolecular complexes have been reported[6,10c,14,15,21] based on bent organic ligands with pyridyl, cyano, aminophenyl, and acetylenylphenyl groups as the terminal coordination sites. However, these bent organic ligands exhibit potentially diverse conformations on coordi-

 © 2007 Wiley-VCH Verlag GmbH & Co. KGaA, Weinheim 

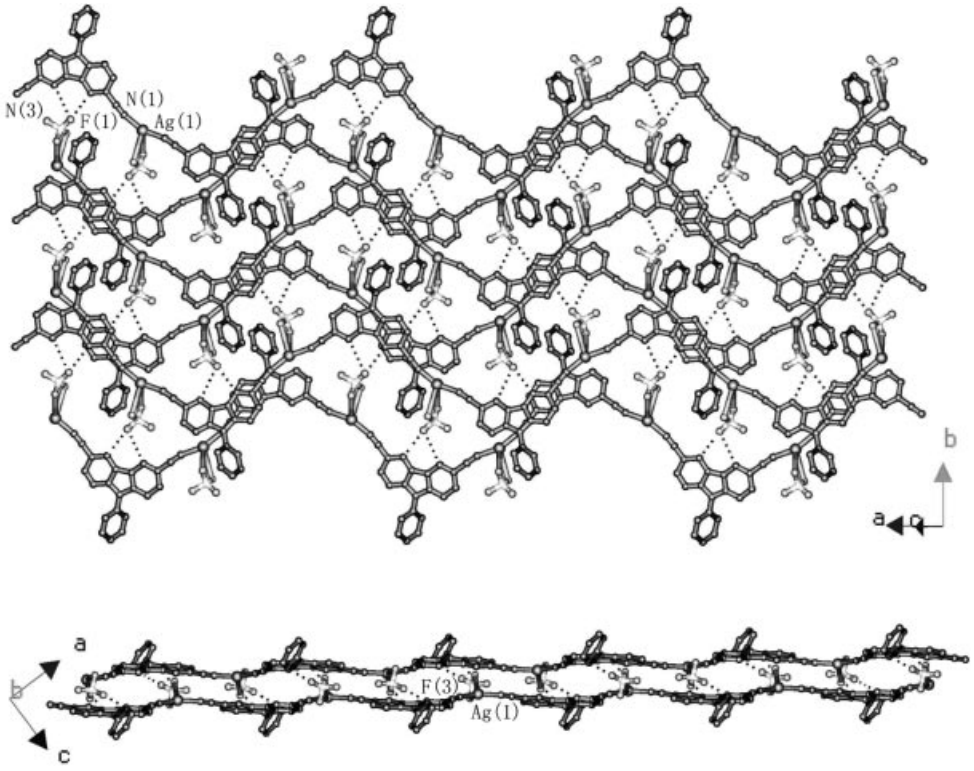


Figure 5. Top (top) and side (bottom) views of two-dimensional double-layer supramolecular networks of **1** stacked together through multiple C–H···F hydrogen-bonding interactions and face-to-face π···π stacking interactions ($d_{\pi-\pi}$ = 3.357 Å).

nation; while dcphcz has a conformation suitable for coordinating to metal centers retaining the bending geometry, making it easy to control and predict the structure and geometry of the resulting polymers.

Similar to complex **1**, a double-layer architecture is formed through multiple C–H···O hydrogen bonding [O(2)···H(5) 2.594 Å, C(5)–H(5)···O(2) 155.75°; O(2)···H(8) 2.395 Å, C(8)–H(8)···O(2) 159.68°]. The parallel carbazole rings from adjacent chains are paired to furnish face-to-face π···π stacking with an interplane distance of 3.349 Å, which extends the 2D network into 3D supramolecular architectures along the *ac* plane.

### *Structural Analysis of {[Ag(dcphcz)][$Ag_2$(dcphcz)-($H_2O$)$_2$]($SO_3CF_3$)$_3$·$C_6H_6$·($H_2O$)$_2$}$_n$ (3)*

Bright yellow single crystals of **3** were obtained by slow diffusion of a benzene solution of $AgSO_3CF_3$ into a $CH_2Cl_2$ solution of dcphcz. Single-crystal analysis reveals that there are three independent $Ag^I$ centers in **3**. The ligand dcphcz has a similar coordination mode in this complex relative to **1** and **2**, however, the different property of the anion alters the molecular architectures in **3**. Atoms Ag(1) and Ag(2) expand the dcphcz units into two independent zigzag chains a and b, respectively, whereas atom Ag(3) is locked in the chain b through a peculiar Ag–C interaction to the phenyl ring (Figure 6). The Ag–N bond lengths in the two chains are all within the range typical for Ag–N bond lengths,[15] though it is slightly longer in chain a [Ag(1)–N(3) 2.134 Å; Ag(1)–N(4) 2.148 Å] than in chain b [Ag(2)–N(1) 2.098 Å; Ag(2)–N(2) 2.119 Å]. The Ag(1) center in chain a also weakly coordinates to an anionic oxygen atom [Ag(1)–O(2) 2.803 Å], and a water oxygen atom [Ag(1)–O(11) 2.738 Å], showing tetrahedral coordination geometry with an N(3)–Ag(1)–N(4) bond angle of 174.4°. While Ag(2) in the chain b center only weakly coordinates to an anionic oxygen atom [Ag(2)–O(9) 2.660 Å], showing T-shaped coordination geometry with an N(1)–Ag(2)–N(2) bond angle of 166.3°. Although these Ag–O distances are relatively long, they are all significantly shorter than the sum of the van der Waals radii for silver and oxygen (3.24 Å).[17] The intrapolymer Ag···Ag distances are 12.559 and 12.308 Å for chains a and b, respectively, which are shorter than those of complexes **1** and **2**. Interestingly, a solvent benzene molecule is located in chain b through weak Ag···C interactions with the nearest Ag···C distance of 2.959 Å.

Sitting on the flank of chain a, Ag(3) has a coordination environment different to those of atoms Ag(1) and Ag(2). In addition to the coordination of two water molecules, Ag(3) has a strong interaction with a terminal phenyl ring from chain a. The Ag(3) atom sits above the phenyl rings and slightly off the center, resulting in a shortest Ag–$C_{benzene}$ distance of Ag(3)–C(17) (2.523 Å) which is still within the normal range for Ag–C bond lengths (2.47–2.76 Å), while the remaining Ag–C distances [Ag(3)···C(16) 2.852 Å; Ag(3)···C(18) 2.889 Å] are beyond the limits commonly observed in $Ag^I$-aromatic complexes.[14,15f–15j,22] Thus, it is concluded that the benzene ring coordinates to the Ag(3) ion with an $\eta^1$-bonding mode. The $\eta^1$-type interaction between the $Ag^I$ ion with a phenyl ring has already been observed in many complexes,[14,15j] although it is less

 © 2007 Wiley-VCH Verlag GmbH & Co. KGaA, Weinheim 

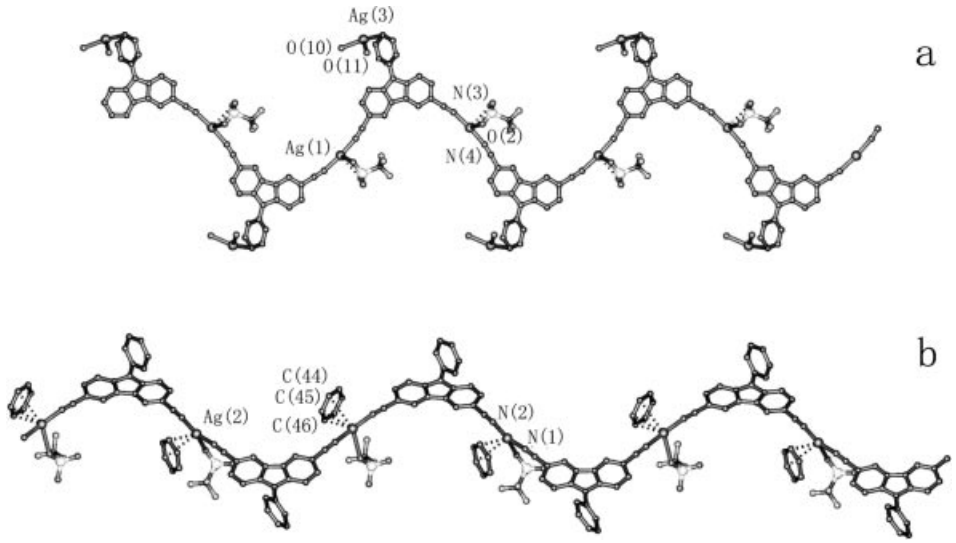


Figure 6. Views of the "zigzag" chains a (top) and b (bottom) in complex **3**.

common than the $\eta^2$-type interaction in which the metal ion interacts with one edge of the phenyl ring.

As shown in Figure 7, the packing style of **3** from chains a and b is different from **1** and **2**. Chains a extend along the crystallographic *b* axis and generate a 2D double-layer metal–organic framework containing irregular channels through Ag–(μ-$O_{water}$)–Ag and Ag–(μ-$SO_3CF_3$)–Ag bridging and face-to-face π···π stacking with an interplane distance of 3.552 Å. Chains b link together into a 2D double-layer supramolecular network through interpolymer C–H···O interactions [O(7)···H(30) 2.436 Å, C(30)–H(30)–O(7) 138.23°; O(9)···H(34) 2.656 Å, C(34)–H(34)–O(9) 125.35°] and face-to-face π···π stacking between adjacent b chains with an interplane distance of 3.485 Å (Figure 8). Consequently, chains a and b stack in an ...*ABC*... sequence along the *a* axis in complex **3**. The parallel carbazole rings from adjacent chains a and b are also paired to furnish π···π stacking with a centroid–centroid distance of 3.879 Å and a dihedral angle of 8.4°, which extend two 2D networks into a 3D architecture along the *ac* plane (Figure 9). In ad-

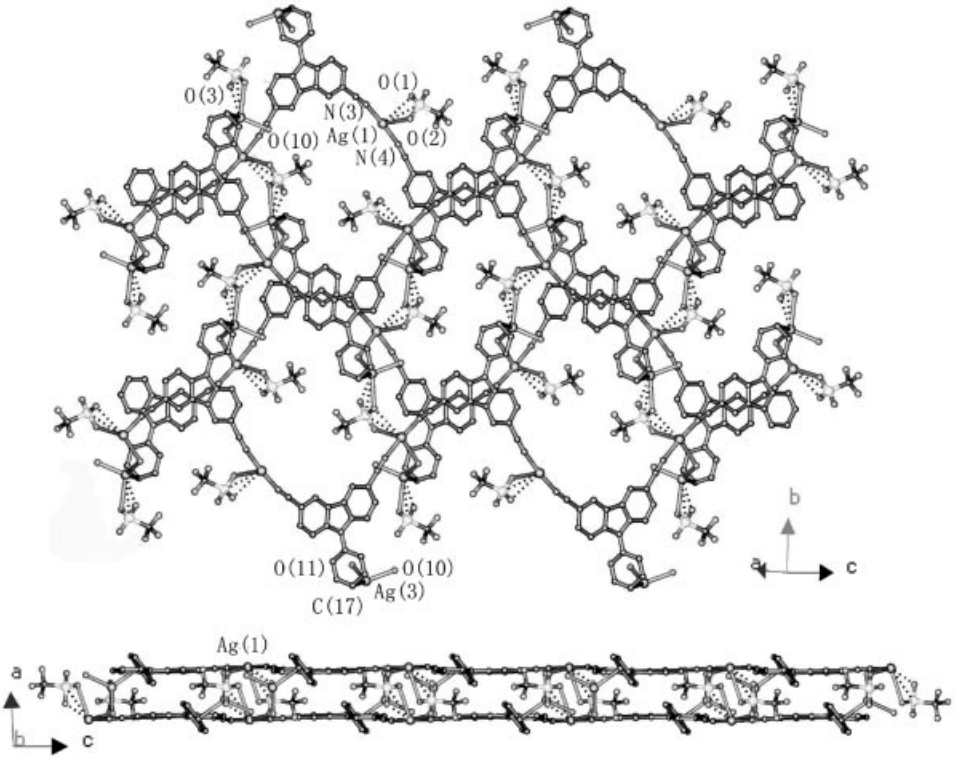


Figure 7. Top (top) and side (bottom) views of 2D double-layer metal–organic frameworks (MOFs) of chain a stacked together through μ-O and μ-$SO_3CF_3$ bridging and face-to-face π···π stacking interactions ($d_{\pi-\pi}$ = 3.552 Å).

 © 2007 Wiley-VCH Verlag GmbH & Co. KGaA, Weinheim 

dition, the chains a and b are also linked through interpolymer O···H hydrogen-bonding interactions. The O(8)···H(10A) distance of 1.945 Å and the O(8)···H(10A)–O(10) angle of 162.67° indicate a very strong hydrogen-bonding interaction. To the best of our knowledge, it is the first example that independent 2D + 1D polymers coexist in one crystal without mutual interpenetration. The shortest interchain Ag(1)···Ag(2) separation is 3.593 Å between chains a and b, which is slightly longer than the sum of the van der Waals radii of two silver atoms, 3.44 Å. It can be concluded from the architecture of the three complexes that the counterions (polar $SO_3CF_3^-$ vs. nonpolar $ClO_4^-$ and $BF_4^-$) play a key role in determining the polymeric structures of complex **3**.

### *Structural Analysis of [Ag$_2$(dcphcz)(CF$_3$COO)$_2$]$_n$ (4)*

In order to further investigate the effect of the counterion on the long-range order of the $Ag^I$-dcphcz coordination polymer, the more strongly coordinating $CF_3CO_2^-$ anion was used instead of the weakly coordinating $BF_4^-$, $ClO_4^-$, and $SO_3CF_3^-$ anions. Yellowish crystals of **4** were obtained.

Single-crystal X-ray analysis of **4** reveals a novel two-dimensional nanotube from two different crystallographic silver(I) centers. As shown in Figure 10, each Ag(1) center is coordinated by two nitrogen atoms of –CN groups and two oxygen atoms from two different $CO_2CF_3^-$ anions, resulting in a severely distorted tetrahedral environment, with the angles around the Ag(1) center ranging from 98.1 to 150.05°. The Ag(1)–N(1) and Ag(1)–O(1) bond lengths are 2.371 and 2.263 Å, respectively, while the coordination sphere around each Ag(2) center is composed of four oxygen atoms from four $CO_2CF_3^-$ anions with two different Ag–O distances (2.235 and 2.570 Å). Thus, the final coordination geometry around the Ag(2) center is irregular with bond angles ranging from 75.30 to 163.84°. The Ag(1) and

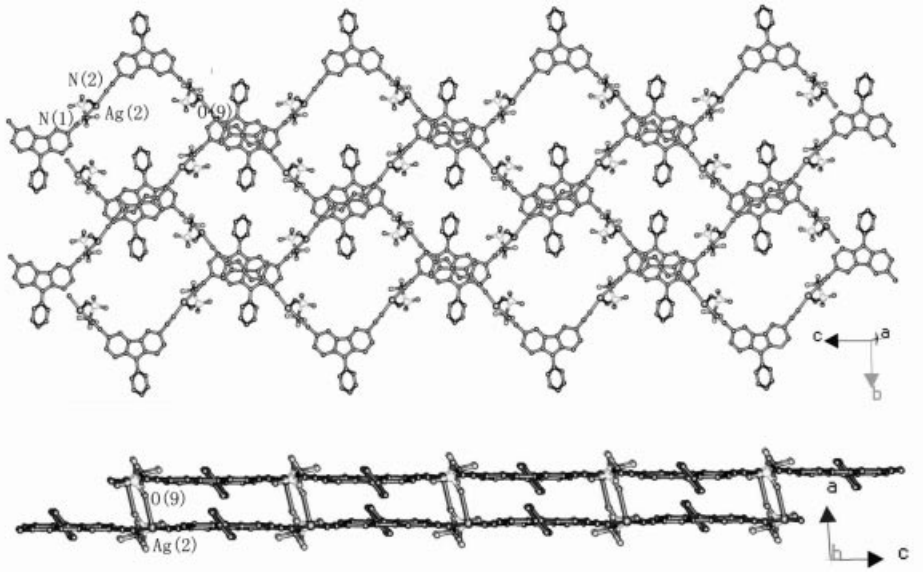


Figure 8. Top (top) and side (bottom) views of two-dimensional double-layer supramolecular networks of chain b stacked together through multiple C–H···O hydrogen-bonding interactions and face-to-face π···π stacking interactions ($d_{\pi-\pi}$ = 3.485 Å).

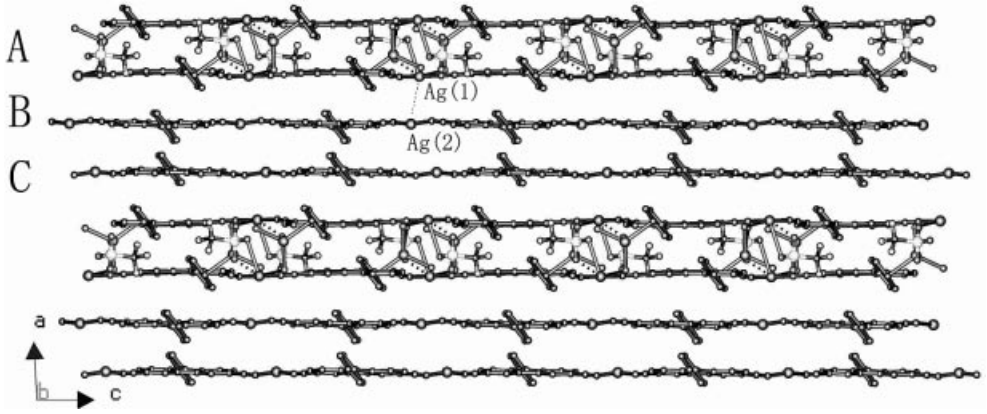


Figure 9. View of the packed structure (parallel to *ac* plane) in complex **3**, showing *...ABC...* packing sequence of chains a and b in the crystal lattice. Some of the $SO_3CF_3^-$ anions, water, and benzene molecules have been omitted for clarity in this figure.

 © 2007 Wiley-VCH Verlag GmbH & Co. KGaA, Weinheim 

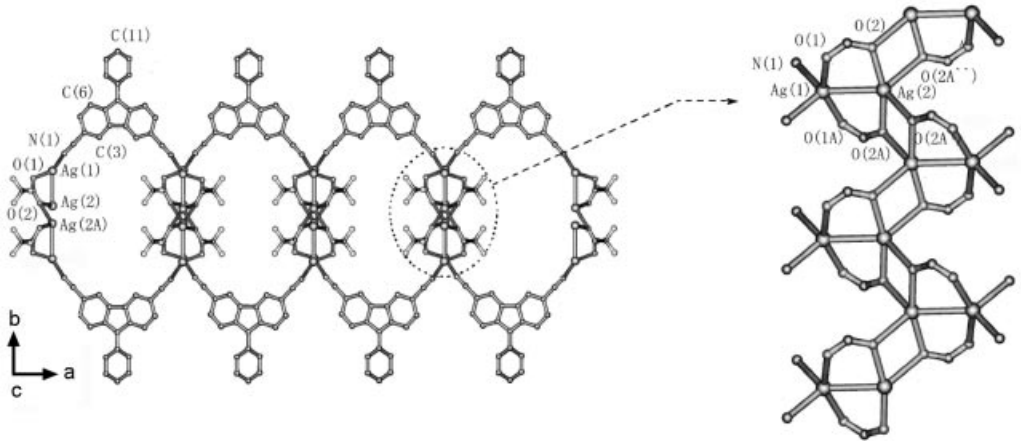


Figure 10. Perspective view of **4**, showing a one-dimensional macrocycle-containing chain.

Ag(2) atoms are bridged by two carboxyl groups with an Ag–Ag distance of 2.992 Å, which is slightly longer than for metallic silver (ranging from 2.803 to 2.987 Å) and shorter than for other reported ligand-unsupported Ag–Ag distances (ranging from 3.011 to 3.655 Å).[14,23] To form the nanotube, each carboxyl group of $CF_3CO_2^-$ connects to three Ag atoms through its two oxygen atoms: one oxygen atom bridges two Ag atoms, while another oxygen atom attaches to the third Ag atom. Therefore, $CF_3CO_2^-$ acts as a $\mu_2$-bridge and links two Ag(2) units, resulting in linear distorted ladder-like Ag chains. The ligand dcphcz is therefore bridged by Ag(1) atoms, producing a condensed nanotubular structure with dimensions of about $12 \times 13$ Å. The adjacent nanotubes are in line through multiple Ag–$O_{carbonyl}$ bonding (Figure 11). Of course, the whole structure can also be regarded as parallel Ag chains linked by dcphcz spacers.

Analogously, adjacent 2D architectures containing 1D open channels along the *c* axis direction stack in the *ab* plane through noncovalent face-to-face π···π interactions between the carbazolyl planes of dcphcz ligands with an interplane distance of 3.355 Å for **4**. However, the open channels are fully filled with the terminal phenyl group of dcphcz from adjacent 2D units. These noncovalent interactions serve again as important driving forces for cross-linking the 2D structure into a 3D architecture.

The different polymeric motifs from the four complexes indicate that the counteranions and bridging ligands are two crucial factors in designing the structure and geometry of the self-assemblies. The properties of the bridging ligands, such as π-conjugated spacers and relative orientation of the donor groups, take important roles in controlling the structural topologies of their metal–organic supramolecular architectures. In this system, the coordination conformation of dcphcz is special because of the conformational irrotationality around the central five-membered ring of the carbazolyl group. Thus, the architecture of the complexes depends greatly on the counterions. Furthermore, π···π stacking between carbazole rings is the basis of the 3D architectures in the complexes **1**–**4**.

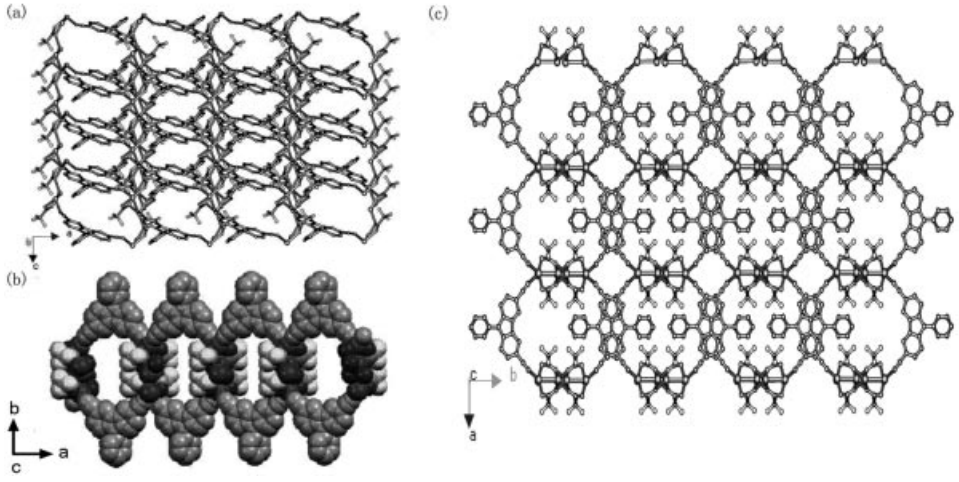


Figure 11. (a) View of two-dimensional nanotubal structure in **4** along the *ac* plane. (b) Space-filling representation of the 2D nanotubal polymer along the *c* axis. (c) View of supramolecular networks of **4** stacked together through face-to-face π···π stacking interactions ($d_{\pi-\pi}$ = 3.355 Å).

 © 2007 Wiley-VCH Verlag GmbH & Co. KGaA, Weinheim 

### Thermogravimetric Analysis

Thermogravimetric analysis of compound **3** was performed by heating the complex from 20 to 600 °C under $N_2$. The TGA curve for complex **3** showed that the first major weight loss of the lattice benzene occurred between 40 and 100 °C by 5.10% weight (calcd. 7.38%), which indicates that benzene molecules could easily escape from the crystal lattice of **3**. As shown in Figure S14, further thermogravimetric data shows the second major weight loss of the four water molecules between 110 and 145 °C by 4.11% weight (calcd. 4.78%).

### Luminescent Properties

For potential applications as luminescent materials,[24] fluorescence properties have been investigated in metal–organic coordination polymers. Because of their ability to affect the emission wavelength of organic materials, syntheses of inorganic–organic coordination polymers have employed the ingenious design of conjugated organic ligands and judicious choice of proper metal centers in order to obtain new types of luminescent materials,[25] especially for $d^{10}$ metal systems[13c,13d,26] and highly conjugated ligand-containing complexes.[11,13c,27] We have explored the luminescent properties of 3,6-bis(2,2′-dipyridylamino)-9-phenylcarbazole and its $Ag^I$ coordination polymer.[11c] The results indicated that the emission color of organic spacers ddpapcz was remarkably affected by Ag coordination compounds. Herein, the luminescent properties of 3,6-dicyano-9-phenylcarbazole and its metal complexes **1**–**4** were investigated.

The UV/Vis spectra of ligand dcphcz and complexes **1**–**4** display two intense absorption bands from π→π* electronic transitions (from 230 to 290 nm), which originate from the carbazolyl groups (Figure S15). No difference in emission colors has been observed between free ligand and complexes in methanol, which has a broad fluorescent emission band (from 340 to 420 m), with $\lambda_{max}$ = 367 nm (Figure S16). This probably implies that the polymeric complexes disaggregate in methanol solution. The dissociation of Ag-supramolecules in solvent has been reported in many other samples.[11c,14]

Despite the similarity of emission bands in solution, the emission bands of five compounds in the solid state are significantly different (Figure S17). A very strong emission of the free ligand dcphcz with a wavelength from 375 to 575 nm ($\lambda_{max}$ = 404 nm) upon excitation at 330 nm is observed, which has a redshift relative to the solution state. This can be explained by the extensive π···π stacking in the solid state, which is between the carbazolyl planes of one dcphcz and the neighboring molecules with an interplane distance of 3.47 Å. This π···π stacking lowers the excited energy of dcphcz in the solid state and causes the redshift of emission energy relative to the solution, in which the carbazolyl stacking could not exist.

Blue/green luminescence is observed with the coordination to the silver center. In the solid state, complexes **1**–**3** show broad emission bands at 499 (**1**), 515 (**2**), and 492 nm (**3**), respectively, upon 330 nm excitation, whereas **4** has also a very broad emission band (bandwidth at half-height = 110 nm) with $\lambda_{max}$ = 425 nm, which is in the blue region and yields visible blue luminescence. Thus, complex **4** may have potential applications as a luminescent material in organic light-emitting devices. Generally, the intraligand fluorescence emission wavelength is determined by the energy gap between π and π* molecular orbitals of the free ligand, which is related to the extent of π conjugation in the system.[28] Since the emission peak positions of complex **4** almost corresponded to that of the ligand dcphcz, they should be due to neither ligand-to-metal nor metal-to-ligand charge transfer and can be ascribed to the intraligand π-π* charge transfer of dcphcz. All these complexes exhibited relatively weak emissions, which may be a result of the heavy-atom effect of silver.[29]

It is clear that significantly different emission in **1**–**4** is due to the variation of anions and coordination environments, because photoluminescence behaviors closely associate with the local environments around metal ions.[20a,30] In **1** and **2**, the anions $BF_4^-$ and $ClO_4^-$ are similar in nature and also display similar weak coordination to $Ag^I$. Complex **3** has two 1D chain units, which are similar to those in **1** and **2**, and the anion $CF_3SO_3^-$ also weakly coordinates to $Ag^I$ although it has properties different from those of $BF_4^-$ and $ClO_4^-$. In contrast, each $Ag^I$ ion in complex **4** is strongly coordinated by O atoms of $CF_3CO_2^-$ and provides a coordination geometry different from those of **1**–**3**.

## Conclusions

Four $Ag^I$-dcphcz coordination polymers with one-, two-, and three-dimensional supramolecular structures have been successfully prepared by the reaction of dcphcz and $Ag^I$ salts with different counterions in solution. The roles of the counteranions in determining the molecular structures of the coordination polymers have been exhibited. The nature of the anions is the underlying reason behind the differences in the structures of this series of $Ag^I$ complexes. In complexes **1** and **2**, the weakly coordinated $BF_4^-$ and $ClO_4^-$ anions not only act as the counteranions to balance the charge but have a spatial templating effect in building up the coordination frameworks. For **3** and **4**, the bulkier $CF_3SO_3^-$ and $CF_3CO_2^-$ anions possess stronger coordination ability than $BF_4^-$ and $ClO_4^-$ and serve as linkages to bridge the 1D chains to 2D MOFs with Ag–O contacts. Moreover, the coordinated $CF_3SO_3^-$ and $CF_3CO_2^-$ ions also possess weak interactions with ligand units, probably act as templates for the formation of the network, and consequently maintain the structural stability. In addition, for the $Ag^I$-dcphcz system in this work, the conformation of dcphcz does not depend on the counterion and solvent system used in the formation of the complexes.

The self-assembly of the bent organic ligands with highly planar π-conjugated spacers provides a new approach for building metal–organic frameworks consisting of a 1D open

 © 2007 Wiley-VCH Verlag GmbH & Co. KGaA, Weinheim 

channel. We are also intrigued by the question whether the variation of the terminal group of dicyanocarbazole will lead to MOF assemblies with open channels by introducing small groups to the 9-position of the carbazole on coordination. Further work is currently ongoing in this laboratory.

## Experimental Section

**Materials and Methods:** All starting chemicals were of reagent-grade quality, obtained from commercial sources and used without further purification. Bromobenzene was freshly distilled. Benzene was freshly distilled from sodium/benzophenone; dichloromethane was dried and distilled from $P_2O_5$ under nitrogen; dmf was dried and distilled from $MgSO_4$. $^1H$ NMR spectra were recorded with a Bruker 300 Ultrashield spectrometer operating at 300 MHz. The FT-IR spectra were recorded in the region 400–4000 $cm^{-1}$ with a Bruker EQUINOX 55 VECTOR22 spectrophotometer and the samples were prepared using KBr pellets. Elemental analyses were carried out with an Elmentar Vario EL-III analyzer. Fluorescence measurements were carried out with a JOBIN YVON Analytical Instrument FLUOROLOG-3-TAU at room temperature. Thermogravimetric analyses (TGA) were performed with a TGA-50H thermoanalyzer under $N_2$ (in the temperature range 20–600 °C) at a heating rate of 10 °C/min. 9-Phenylcarbazole and 3,6-diiodo-9-phenylcarbazole were synthesized according to procedures reported earlier.[11c,31]

***Caution!*** One of the crystallization procedures involves $AgClO_4$, which is a strong oxidizer.

**Synthesis of 3,6-Dicyano-9-phenylcarbazole (dcphcz):** A mixture of 3,6-diiodo-9-phenylcarbazole (0.99 g, 0.002 mol) and CuCN powder (0.448 g, 0.005 mol) in HMPA (10 mL) was stirred under the protection of dry nitrogen at 160 °C for 6 h. The reaction mixture was cooled to ambient temperature, poured into aqueous $NaHCO_3$ (10%) and extracted with dichloromethane. The aqueous phase was discarded, the organic layer was washed with distilled water to neutral pH, dried with $MgSO_4$ and concentrated in vacuo. The residue was filtered to give the desired compound as a primrose solid. Yield: 0.55 g, 93%. IR (KBr): $\tilde{\nu}$ = 2219 (vs), 1631 (m), 1595 (s), 1502 (s), 1480 (s), 1455 (m) 1369 (m), 1292 (s), 1243 (s), 1185 (m) $cm^{-1}$. $^1H$ NMR (300 MHz, $CDCl_3$): $\delta$ = 8.48 (d, 2 H), 7.75–7.71 (d, 4 H), 7.68–7.60 (d, 1 H), 7.49–7.52 (d, 2 H), 7.42–7.44 (d, 2 H) ppm.

**Synthesis of $\{[Ag(dcphcz)]BF_4\}_n$ (1):** Upon a solution of dcphcz (0.0586 g, 0.2 mmol) in 5 mL of dichloromethane was successively layered a solution of $AgBF_4$ (0.0390 g, 0.2 mmol) in benzene (4 mL). The vial was covered with aluminum foil and the solvents were allowed to diffuse slowly. Bright yellow crystals suitable for X-ray structure analysis were obtained several days later. Yield: 0.0517 g, 53%. IR (KBr): $\tilde{\nu}$ = 2251 (vs), 1631 (m), 1591 (s), 1492 (s), 1362 (m), 1294 (s), 1244 (s), 1187 (m), 1063 (vs), 821 (m) $cm^{-1}$. $C_{20}H_{11}AgBN_3F_4$ (488.00): calcd. C 49.23, H 2.273, N 8.611; found C 49.31, H 2.274, N 8.620.

**Synthesis of $\{[Ag(dcphcz)]ClO_4\}_n$ (2):** Upon a solution of dcphcz (0.0586 g, 0.2 mmol) in 5 mL of dichloromethane was successively layered a solution of $AgClO_4$ (0.0414 g, 0.2 mmol) in benzene (5 mL). The vial was covered with aluminum foil and the solvents were allowed to diffuse slowly. Bright yellow crystals suitable for X-ray structure analysis were obtained several days later. Yield: 0.0651 g, 65%. IR (KBr): $\tilde{\nu}$ = 2251 (vs), 1628 (m), 1592 (s), 1501 (s), 1479 (s), 1367 (m), 1295 (s), 1245 (vs), 1188 (m), 1092 (vs) $cm^{-1}$. $C_{20}H_{11}AgClN_3O_4$ (500.6): calcd. C 47.98, H 2.215, N 8.393; found C 48.09, H 2.209, N 8.401.

**Synthesis of $\{[Ag(dcphcz)][Ag_2(dcphcz)(H_2O)_2](SO_3CF_3)_3 \cdot C_6H_6 \cdot (H_2O)_2\}_n$ (3):** Upon a solution of dcphcz (0.0586 g, 0.2 mmol) in 5 mL of dichloromethane was successively layered a solution of $AgSO_3CF_3$ (0.0514 g, 0.2 mmol) in benzene (5 mL). The vial was covered with aluminum foil and the solvents were allowed to diffuse slowly. Bright yellow single crystals suitable for X-ray structure analysis were obtained several days later. Yield: 0.0573 g, 57%. IR (KBr): $\tilde{\nu}$ = 2220 (vs), 1632 (m), 1596 (s), 1503 (s), 1481 (s), 1456 (m) 1369 (m), 1245 (vs), 1176 (vs), 1034 (vs) $cm^{-1}$. $C_{49}H_{36}Ag_3F_9N_6O_{13}S_3$ (1507.6): calcd. C 39.04, H 2.407, N 5.574; found C 39.01, H 2.402, N 5.583.

**Synthesis of $[Ag_2(dcphcz)(CF_3COO)_2]_n$ (4):** Upon a solution of dcphcz (0.0586 g, 0.2 mmol) in 4 mL of dichloromethane was successively layered a solution of $CF_3COOAg$ (0.0442 g, 0.2 mmol) in benzene (5 mL). The vial was covered with aluminum foil and the solvents were allowed to diffuse slowly. Bright yellow single crystals suitable for X-ray structure analysis were obtained several days later. Yield: 0.0471 g, 64%. IR (KBr): $\tilde{\nu}$ = 2219 (vs), 1682 (vs), 1595 (m), 1501 (m), 1480 (m), 1292 (m), 1209 (vs), 1132 (vs) $cm^{-1}$.

Table 1. Selected interatomic distances [Å] and angles [°] for complexes **1**–**4**.

| | | | |
|---|---|---|---|
| Complex **1** | | | |
| Ag(1)–N(1) | 2.116(3) | Ag(1)–N(3) | 2.119(3) |
| Ag(1)–F(1) | 2.654 | N(3)–Ag(1)–F(1) | 82.77 |
| N(1)–Ag(1)–N(3) | 156.89(15) | F(1)–Ag(1)–N(1) | 119.75 |
| Complex **2** | | | |
| Ag(1)–N(2) | 2.112(3) | Ag(1)–N(3) | 2.122(3) |
| Ag(1)–O(1) | 2.636 | Ag(1)–O(4) | 2.847 |
| N(2)–Ag(1)–N(3) | 154.02(11) | O(1)–Ag(1)–N(3) | 84.46 |
| N(3)–Ag(1)–O(4) | 86.06 | O(1)–Ag(1)–O(4) | 49.10 |
| N(2)–Ag(1)–O(4) | 115.07 | N(2)–Ag(1)–O(1) | 120.51 |
| Complex **3** | | | |
| Ag(1)–N(3) | 2.134(5) | Ag(1)–N(4) | 2.148(5) |
| Ag(2)–N(1) | 2.098(5) | Ag(2)–N(2) | 2.119(5) |
| Ag(3)–O(11) | 2.327(6) | Ag(3)–O(10) | 2.344(6) |
| Ag(3)–C(17) | 2.523(7) | Ag(1)–O(2) | 2.803 |
| Ag(1)–O(1) | 3.031 | Ag(1)–O(11) | 2.738 |
| Ag(3)–O(1) | 2.704 | Ag(2)–O(9) | 2.660 |
| N(3)–Ag(1)–N(4) | 174.4(2) | N(1)–Ag(2)–N(2) | 166.3(2) |
| O(11)–Ag(3)–C(17) | 123.5(2) | O(11)–Ag(3)–O(10) | 100.56(19) |
| O(10)–Ag(3)–C(17) | 119.9(2) | O(9)–Ag(2)–N(2) | 87.04 |
| O(9)–Ag(2)–N(1) | 98.67 | O(2)–Ag(1)–N(4) | 86.86 |
| O(11)–Ag(1)–O(2) | 100.47 | O(2)–Ag(1)–N(3) | 94.99 |
| O(11)–Ag(1)–N(4) | 84.00 | O(11)–Ag(1)–N(3) | 90.51 |
| Ag(1)–O(11)–Ag(3) | 118.66 | O(10)–Ag(3)–C(17) | 119.91 |
| O(1)–Ag(3)–C(17) | 80.44 | O(11)–Ag(3)–O(1) | 125.53 |
| O(10)–Ag(3)–O(1) | 106.88 | | |
| Complex **4** | | | |
| Ag(1)–O(1) | 2.263(3) | Ag(1)–N(1) | 2.371(4) |
| Ag(1)–Ag(2) | 2.9924(7) | Ag(2)–O(2) | 2.235(3) |
| Ag(2A)–O(2) | 2.570(3) | | |
| O(1)–Ag(1)–O(1A) | 150.05(16) | O(1A)–Ag(1)–N(1A) | 94.84(15) |
| O(1)–Ag(1)–N(1) | 104.74(13) | N(1)–Ag(1)–N(1A) | 98.1(2) |
| O(1)–Ag(1)–Ag(2) | 75.02(8) | N(1)–Ag(1)–Ag(2) | 130.97(11) |
| O(2)–Ag(2)–O(2A) | 163.84(17) | O(2)–Ag(2)–O(2A′) | 115.94(15) |
| O(2A)–Ag(2)–O(2A′) | 75.30(12) | O(2A′)–Ag(2)–Ag(1) | 130.76(8) |
| O(2A′)–Ag(2)–O(2A′′) | 98.48(17) | O(2)–Ag(2)–Ag(1) | 81.92(9) |
| Ag(2)–O(2A)–Ag(2A) | 104.70 | | |

 © 2007 Wiley-VCH Verlag GmbH & Co. KGaA, Weinheim 

Table 2. Crystallographic data and structure refinement summary for the ligand dcphcz and complexes **1**–**4**.

| | dcphcz | **1** | **2** | **3** | **4** |
|---|---|---|---|---|---|
| CCDC | 286976 | 608217 | 286975 | 286973 | 286974 |
| Empirical formula | $C_{20}H_{11}N_3$ | $C_{20}H_{11}AgBF_4N_3$ | $C_{20}H_{11}AgClN_3O_4$ | $C_{49}H_{36}Ag_3F_9N_6O_{13}S_3$ | $C_{24}H_{11}Ag_2F_6N_3O_4$ |
| Formula mass | 293.32 | 488.00 | 500.64 | 1507.63 | 735.1 |
| Crystal system | triclinic | monoclinic | monoclinic | monoclinic | monoclinic |
| Crystal size [mm] | $0.35\times0.33\times0.30$ | $0.41\times0.30\times0.28$ | $0.27\times0.08\times0.07$ | $0.28\times0.20\times0.15$ | $0.32\times0.30\times0.15$ |
| Space group | $P\bar{1}$ | $P2_1/c$ | $P2_1/c$ | $P2_1/c$ | $P2/c$ |
| $A$ [Å] | 8.802(5) | 10.6840(11) | 10.600(17) | 14.343(7) | 11.2145(8) |
| $b$ [Å] | 9.011(5) | 11.0728(12) | 11.076(18) | 15.873(7) | 15.2776(11) |
| $c$ [Å] | 10.104(6) | 15.3809(18) | 15.23(2) | 24.558(11) | 7.1139(5) |
| $\alpha$ [°] | 74.672(11) | 90.00 | 90.00 | 90.00 | 90.00 |
| $\beta$ [°] | 81.129(13) | 90.134(3) | 90.26(3) | 93.095(8) | 94.5540(10) |
| $\gamma$ [°] | 74.356(11) | 90.00 | 90.00 | 90.00 | 90.00 |
| $V$ [Å$^3$] | 741.2(8) | 1819.6(3) | 1788(5) | 5583(4) | 1214.98(15) |
| $D_{calcd.}$ [Mg m$^{-3}$] | 1.314 | 1.781 | 1.860 | 1.794 | 2.009 |
| $Z$ | 2 | 4 | 4 | 4 | 4 |
| $F$(000) | 304 | 960 | 992 | 2984 | 712 |
| $\mu$ [mm$^{-1}$] | 0.080 | 1.158 | 1.312 | 1.251 | 1.696 |
| Reflections collected | 3714 | 13720 | 18998 | 26453 | 7439 |
| Reflections unique | 2535 | 3209 | 4071 | 9825 | 2776 |
| $R$(int) | 0.0297 | 0.0295 | 0.0329 | 0.0402 | 0.0197 |
| Data/restraints/parameters | 2535/0/208 | 3209/0/262 | 4071/0/262 | 9825/0/748 | 2776/0/179 |
| Final $R$ indices [$I>2\sigma(I)$] | $R_1$ = 0.0620 | $R_1$ = 0.0472 | $R_1$ = 0.0457 | $R_1$ = 0.0633 | $R_1$ = 0.0390, |
| | $wR_2$ = 0.1106 | $wR_2$ = 0.1169 | $wR_2$ = 0.1213 | $wR_1$ = 0.1492 | $wR_1$ = 0.1067 |
| $R$ indices (all data) | $R_1$ = 0.1057 | $R_1$ = 0.0578 | $R_1$ = 0.0560 | $R_1$ = 0.0958 | $R_1$ = 0.0467 |
| | $wR_2$ = 0.1251 | $wR_2$ = 0.1233 | $wR_2$ = 0.1283 | $wR_1$ = 0.1710 | $wR_1$ = 0.1219 |
| GOF on $F^2$ | 1.005 | 1.050 | 1.035 | 1.035 | 1.021 |

$C_{24}H_{11}Ag_2F_6N_3O_4$ (735.1): calcd. C 39.21, H 1.509, N 5.716; found C 39.22, H 1.509, N 5.721.

**X-ray Crystallography:** X-ray diffraction data were collected with a Bruker-AXS SMART CCD area detector diffractometer at 293 K using ω-rotation scans with a scan width of 0.3° and Mo-$K_\alpha$ radiation ($\lambda$ = 0.71073 Å). The structures were solved by direct methods and refined with the full-matrix least-squares technique using SHELXTL.[32] Anisotropic thermal parameters were applied to all non-hydrogen atoms. All of the hydrogen atoms in these structures are located from the differential electron density map and constrained to the ideal positions in the refinement procedure. The crystallographic calculations were conducted using the SHELXL-97 program. Crystal data and experimental details for the crystals of the ligand dcphcz and complexes **1**–**4** are summarized in Tables 1 and 2. CCDC-286976, -608217, -286975, -286973, and -286974 contain the supplementary crystallographic data for this paper. These data can be obtained free of charge from The Cambridge Crystallographic Data Centre via www.ccdc.cam.ac.uk/data_request/cif.

**Supporting Information** (see also the footnote on the first page of this article): TGA, UV/Vis absorption spectra, emission spectra in MeOH solution and solid state.

## Acknowledgments

This work was support by the National Natural Science Foundation of China and the China Postdoctoral Science Foundation.

[1] a) B. Moulton, M. J. Zaworotko, *Chem. Rev.* **2001**, *101*, 1629–1658; b) Q. Ye, X.-S. Wang, H. Zhao, R.-G. Xiong, *Chem. Soc. Rev.* **2005**, *34*, 208–225.

[2] a) A. L. Pickering, G. Seeber, D.-L. Long, L. Cronin, *Chem. Commun.* **2004**, 136–137; b) F. Chang, Z.-M. Wang, H.-L. Sun, S. Gao, G.-H. Wen, X.-X. Zhang, *Dalton Trans.* **2005**, 2976–2978; c) Z. Fei, D. Zhao, T. J. Geldbach, R. Scopelliti, P. J. Dyson, S. Antonijevic, G. Bodenhausen, *Angew. Chem. Int. Ed.* **2005**, *44*, 5720–5725; d) S. U. Son, K. H. Park, B. Y. Kim, Y. K. Chung, *Cryst. Growth Des.* **2003**, *3*, 507–512.

[3] a) N. L. Rosi, J. Kim, M. Eddaoudi, B. Chen, M. O'Keeffe, O. M. Yaghi, *J. Am. Chem. Soc.* **2005**, *127*, 1504–1518; b) B. Chen, N. W. Ockwig, F. R. Fronczek, D. S. Contreras, O. M. Yaghi, *Inorg. Chem.* **2005**, *44*, 181–183; c) B.-H. Ye, M. L. Tong, X.-M. Chen, *Coord. Chem. Rev.* **2005**, *249*, 545–565; d) Q.-R. Fang, G.-S. Zhu, M. Xue, Q.-L. Zhang, J.-Y. Sun, X.-D. Guo, S.-L. Qiu, S.-T. Xu, P. Wang, D.-J. Wang, Y. Wei, *Chem. Eur. J.* **2006**, *12*, 3754–3758; e) D. Sun, D. J. Collins, Y. Ke, J.-L. Zuo, H.-C. Zhou, *Chem. Eur. J.* **2006**, *12*, 3768–3776; f) D. M. Shin, I. S. Lee, Y. K. Chung, *Cryst. Growth Des.* **2006**, *6*, 1059–1061; g) A. Erxleben, *Coord. Chem. Rev.* **2003**, *246*, 203–228; h) N. W. Ockwig, O. Delgado-Friderichs, M. O'Keeffe, O. M. Yaghi, *Acc. Chem. Res.* **2005**, *38*, 176–182; i) X.-L. Wang, C. Qin, E.-B. Wang, Y.-G. Li, Z.-M. Su, L. Xu, L. Carlucci, *Angew. Chem. Int. Ed.* **2005**, *44*, 5824–5827; j) T.-T. Luo, H.-L. Tsai, S.-L. Yang, Y.-H. Liu, R.-D. Yadav, C.-C. Su, C.-H. Ueng, L.-G. Lin, K.-L. Lu, *Angew. Chem. Int. Ed.* **2005**, *44*, 6063–6067; k) A. C. Sudik, A. P. Côté, A. G. Wong-Foy, M. O'Keeffe, O. M. Yaghi, *Angew. Chem. Int. Ed.* **2006**, *45*, 2528–2533; l) A. L. Grzesiak, F. J. Uribe, N. W. Ockwig, O. M. Yaghi, A. J. Matzger, *Angew. Chem. Int. Ed.* **2006**, *45*, 2553–2556; m) G. S. Papaefstathiou, L. R. MacGillivray, *Coord. Chem. Rev.* **2003**, *246*, 169–184; n) S. Shimomura, R. Matsuda, T. Tsujino, T. Kawamura, S. Kitagawa, *J. Am. Chem. Soc.* **2006**, *128*, 16416–16417; o) T. Uemura, R. Kitaura, Y. Ohta, M. Nagaoka, S. Kitagawa, *Angew. Chem. Int. Ed.* **2006**, *45*, 4112–4116; p) R.-G. Xiong, X. Xue, H. Zhao, X.-Z. You, B. F. Abrahams, Z. Xue, *Angew. Chem. Int. Ed.* **2002**, *41*, 3800–3803.

[4] a) M. Eddaoudi, D. B. Moler, H. Li, B. Chen, T. M. Reineke, M. O'Keeffe, O. M. Yaghi, *Acc. Chem. Res.* **2001**, *34*, 319–330; b) W. Lin, Z. Wang, L. Ma, *J. Am. Chem. Soc.* **1999**, *121*, 11249–11250; c) O. Kahn, *Acc. Chem. Res.* **2000**, *33*, 647–657; d) Y.-H. Kiang, G. B. Gardner, S. Lee, Z. Xu, E. B. Lobkovsky, *J. Am. Chem. Soc.* **1999**, *121*, 8204–8205; e) D. Venkataraman, G. B. Gardner, S. Lee, J. S. Moore, *J. Am. Chem. Soc.* **1995**, *117*, 11600–11601; f) D. Venkataraman, S. Lee, J. S. Moore, P.

 © 2007 Wiley-VCH Verlag GmbH & Co. KGaA, Weinheim 

Zhang, K. A. Hirsch, G. B. Gardner, A. C. Covey, C. L. Prentice, *Chem. Mater.* **1996**, *8*, 2030–2040; g) A. C. Sudik, A. R. Millward, N. W. Ockwig, A. P. Côté, J. Kim, O. M. Yaghi, *J. Am. Chem. Soc.* **2005**, *127*, 7110–7118; h) J. L. C. Rowsell, O. M. Yaghi, *Microporous Mesoporous Mater.* **2004**, *73*, 3–14; i) Q. Ye, Y.-M. Song, G.-X. Wang, K. Chen, D.-W. Fu, P. W. H. Chan, J.-S. Zhu, S. D. Huang, R.-G. Xiong, *J. Am. Chem. Soc.* **2006**, *128*, 6554–6555; j) B. I. I. Park, I. S. Chun, Y.-A. Lee, K.-M. Park, O.-S. Jung, *Inorg. Chem.* **2006**, *45*, 4310–4312; k) Y.-Q. Sun, J. Zhang, Y.-M. Chen, G.-Y. Yang, *Angew. Chem. Int. Ed.* **2005**, *44*, 5814–5817; l) T. K. Maji, K. Uemura, H.-C. Chang, R. Matsuda, S. Kitagawa, *Angew. Chem. Int. Ed.* **2004**, *43*, 3269–3272; m) C.-D. Wu, A. Hu, L. Zhang, W. Lin, *J. Am. Chem. Soc.* **2005**, *127*, 8940–8941; n) T. K. Maji, W. Kaneko, M. Ohba, S. Kitagawa, *Chem. Commun.* **2005**, 4613–4615; o) B. Zhao, X.-Y. Chen, P. Cheng, D.-Z. Liao, S.-P. Yan, Z.-H. Jiang, *J. Am. Chem. Soc.* **2004**, *126*, 15394–15395; p) D. N. Dybtsev, H. Chun, S. H. Yoon, D. Kim, K. Kim, *J. Am. Chem. Soc.* **2004**, *126*, 32–33; q) L. Pan, M. B. Sander, X. Huang, J. Li, M. Smith, E. Bittner, B. Bockrath, J. K. Johnson, *J. Am. Chem. Soc.* **2004**, *126*, 1308–1309; r) J. L. Rowsell, O. M. Yaghi, *Angew. Chem. Int. Ed.* **2005**, *44*, 4670–4679.

[5] a) X.-C. Huang, Y.-Y. Lin, J.-P. Zhang, X.-M. Chen, *Angew. Chem.* **2006**, *118*, 1587–1589; b) X.-C. Huang, J.-P. Zhang, Y.-Y. Lin, X.-M. Chen, *Chem. Commun.* **2005**, 2232–2234; c) X.-C. Huang, J.-P. Zhang, X.-M. Chen, *J. Am. Chem. Soc.* **2004**, *126*, 13218–13219.

[6] a) Z. Huang, M. Du, H.-B. Song, X.-H. Bu, *Cryst. Growth Des.* **2004**, *4*, 71–78; b) Y.-B. Dong, J.-P. Ma, R.-Q. Huang, M. D. Smith, H.-C. zur Loye, *Inorg. Chem.* **2003**, *42*, 294–300; c) Y.-B. Dong, J.-Y. Cheng, R.-Q. Huang, M. D. Smith, H.-C. zur Loye, *Inorg. Chem.* **2003**, *42*, 5699–5706.

[7] a) Y.-B. Dong, H.-X. Xu, J.-P. Ma, R.-Q. Huang, *Inorg. Chem.* **2006**, *45*, 3325–3343; b) K.-J. Wei, J. Ni, Y.-S. Xie, Q.-L. Liu, *Inorg. Chem. Commun.* **2007**, *10*, 279–283.

[8] a) M.-L. Tong, S.-L. Zheng, X.-M. Chen, *Chem. Eur. J.* **2000**, *6*, 3729–3738; b) G. A. Bowmarker, J. V. Hanna, C. E. F. Richand, A. S. Lipton, *J. Chem. Soc. Dalton Trans.* **2001**, 20–28.

[9] K.-X. Wang, J.-H. Yu, J.-J. Li, R.-R. Xu, *Inorg. Chem.* **2003**, *42*, 4597–4602.

[10] a) R. J. Hill, D.-L. Long, N. R. Champness, P. Hubberstey, M. Schröder, *Acc. Chem. Res.* **2005**, *38*, 335–348; b) A. J. Blake, N. R. Champness, P. Hubberstey, W. S. Li, M. A. Withersby, M. Schröder, *Coord. Chem. Rev.* **1999**, *183*, 117–138; c) A. N. Khlobystov, A. J. Blake, N. R. Champness, D. A. Lemenovskii, A. G. Majouga, N. V. Zyk, M. Schröder, *Coord. Chem. Rev.* **2001**, *222*, 155–192.

[11] a) H.-P. Zhou, Y.-P. Tian, J.-Y. Wu, J.-Z. Zhang, D. M. Li, Y.-M. Zhu, Z.-J. Hu, X.-T. Tao, M.-H. Jiang, Y. Xie, *Eur. J. Inorg. Chem.* **2005**, 4976–4984; b) H.-P. Zhou, Y.-M. Zhu, J.-J. Chen, Z.-J. Hu, J.-Y. Wu, Y. Xie, M.-H. Jiang, X.-T. Tao, Y.-P. Tian, *Inorg. Chem. Commun.* **2006**, *9*, 90–92; c) K.-J. Wei, Y.-S. Xie, J. Ni, M. Zhang, Q.-L. Liu, *Inorg. Chem. Commun.* **2006**, *9*, 926–930; d) H.-P. Zhou, Y.-M. Zhu, C.-M. Cui, P. Wang, H.-W. Li, J.-Y. Wu, Y. Xie, M.-H. Jiang, X.-T. Tao, Y.-P. Tian, *Inorg. Chem. Commun.* **2006**, *9*, 351–353.

[12] a) Y. Kuwabara, H. Ogawa, H. Inada, N. Noma, Y. Shirota, *Adv. Mater.* **1994**, *6*, 677–679; b) B. E. Koene, D. E. Loy, M. E. Thompson, *Chem. Mater.* **1998**, *10*, 2235–2250; c) D. F. O'Brien, P. E. Burrows, S. R. Forrest, B. E. Koene, D. E. Loy, M. E. Thompson, *Adv. Mater.* **1998**, *10*, 1108–1112.

[13] a) A. Kraft, A. C. Grimsdale, A. B. Holmes, *Angew. Chem. Int. Ed.* **1998**, *37*, 402–428; b) A. P. de Silva, H. Q. N. Gunaratne, T. Gunnlaugsson, A. J. M. Huxley, C. P. McCoy, J. T. Rademacher, T. E. Rice, *Chem. Rev.* **1997**, *97*, 1515–1566; c) C. Seward, W. L. Jia, R. Y. Wang, G. D. Enright, S.-N. Wang, *Angew. Chem. Int. Ed.* **2004**, *43*, 2933–2936; d) J. Pang, E. J. P. Marcotte, C. Seward, R. S. Brown, S. N. Wang, *Angew. Chem. Int. Ed.* **2001**, *40*, 4042–4045.

[14] Y.-B. Dong, Q. Zhang, L. Wang, J.-P. Ma, R.-Q. Huang, D.-Z. Shen, D.-Z. Chen, *Inorg. Chem.* **2005**, *44*, 6591–6593.

[15] a) F. C. Pigge, M. D. Burgard, N. P. Rath, *Cryst. Growth Des.* **2003**, *3*, 507–512; b) W. Choe, Y.-H. Kiang, Z. Xu, S. Lee, *Chem. Mater.* **1999**, *11*, 1776–1783; c) K. A. Hirsch, S. R. Wilson, J. S. Moore, *Chem. Commun.* **1998**, 13–14; d) Y.-B. Dong, G.-X. Jin, X. Zhao, B. Tang, R.-Q. Huang, *Organometallics* **2004**, *23*, 1604–1609; e) Y.-B. Dong, G.-X. Jin, M. D. Smith, R.-Q. Huang, B. Tang, H.-C. zur Loye, *Inorg. Chem.* **2002**, *41*, 4909–4914; f) Y.-B. Dong, Y. Geng, J.-P. Ma, R.-Q. Huang, *Inorg. Chem.* **2005**, *44*, 1693–1703; g) Y.-B. Dong, P. Wang, R.-Q. Huang, M. D. Smith, *Inorg. Chem.* **2004**, *43*, 4727–4739; h) Y.-B. Dong, Y. Geng, J.-P. Ma, R.-Q. Huang, *Organometallics* **2006**, *25*, 447–462; i) P. Wang, Y.-B. Dong, J.-P. Ma, R.-Q. Huang, M. D. Smith, *Cryst. Growth Des.* **2005**, *5*, 701–706; j) Y.-B. Dong, G.-X. Jin, X. Zhao, B. Tang, R.-Q. Huang, M. D. Smith, K. E. Stitzer, H.-C. zur Loye, *Organometallics* **2004**, *23*, 1604–1609; k) Y.-H. Kiang, G. B. Gardner, S. Lee, Z. Xu, E. B. Lobkovsky, *J. Am. Chem. Soc.* **1999**, *121*, 8204–8215; l) D. Venkataraman, G. B. Gardner, S. Lee, J. S. Moore, *J. Am. Chem. Soc.* **1995**, *117*, 11600–11601; m) K. A. Hirsch, S. R. Wilson, J. S. Moore, *J. Am. Chem. Soc.* **1997**, *119*, 10401–10412; n) D. Venkataraman, S. Lee, J. S. Moore, P. Zhang, K. A. Hirsch, G. B. Gardner, A. C. Covey, C. L. Prentice, *Chem. Mater.* **1996**, *8*, 2030–2040.

[16] Y.-B. Dong, R. C. Layland, N. G. Pschirer, M. D. Smith, U. H. F. Bunz, H.-C. zur Loye, *Chem. Mater.* **1999**, *11*, 1413–1415.

[17] A. Bondi, *J. Phys. Chem.* **1964**, *68*, 441–451.

[18] a) S. Tsuzuki, K. Honda, T. Uchimaru, M. Mikami, K. Tanabe, *J. Am. Chem. Soc.* **2002**, *124*, 104–112; b) M. Kamishima, M. Kojima, Y. Yoshikawa, *J. Comput. Chem.* **2001**, *22*, 835; c) C. Janiak, *J. Chem. Soc. Dalton Trans.* **2000**, 3885–3891.

[19] a) G. R. Desiraju, *Acc. Chem. Res.* **1996**, *29*, 441–449; b) G. R. Desiraju, *Nature* **2001**, *412*, 397–400; c) G. R. Desiraju, *Angew. Chem. Int. Ed. Engl.* **1995**, *34*, 2311–2327.

[20] a) K.-J. Wei, Y.-S. Xie, J. Ni, M. Zhang, Q.-L. Liu, *Cryst. Growth Des.* **2006**, *6*, 1341–1350; b) O. M. Yaghi, H. Li, T. L. Groy, *Inorg. Chem.* **1997**, *36*, 4292–4293; c) A. J. Blake, N. R. Champness, A. N. Khlobystov, D. A. Lemenovski, W.-S. Li, M. Schröder, *Chem. Commun.* **1997**, 1339–1340.

[21] Y.-B. Dong, H.-Y. Wang, J.-P. Ma, R.-Q. Huang, M. D. Smith, *Cryst. Growth Des.* **2005**, *5*, 789–800.

[22] a) M. Munakata, L. P. Wu, G. L. Ning, *Coord. Chem. Rev.* **2000**, *198*, 171–203; b) G. L. Ning, L. P. Wu, K. Sugimoto, M. Munakata, T. Kuroda-Sowa, M. Mackawa, *J. Chem. Soc. Dalton Trans.* **1999**, 2529–2536; c) S.-L. Zheng, M.-L. Tong, S.-D. Tan, Y. Wang, J.-X. Shi, Y.-X. Tong, H. K. Lee, X.-M. Chen, *Organometallics* **2001**, *20*, 5319–5325.

[23] a) S.-L. Zheng, M.-L. Tong, H.-L. Zhu, Y. Fang, X.-M. Chen, *J. Chem. Soc. Dalton Trans.* **2001**, 2049–2053; b) A. D. Burrows, M. F. Mahon, M. T. Palmer, *J. Chem. Soc. Dalton Trans.* **1998**, 1941–1942; c) M. Maekawa, H. Konaka, Y. Suenaga, T. Kuroda-Sowa, M. Munakata, *J. Chem. Soc. Dalton Trans.* **2000**, 4160–4166; d) Z. Liu, P. Liu, Y. Chen, J. Wang, M. Huang, *New J. Chem.* **2005**, *29*, 474–478; e) D. Sun, R. Cao, J. Weng, M. Hong, Y. Liang, *J. Chem. Soc. Dalton Trans.* **2002**, 291–292; f) O. Kristiansson, *Inorg. Chem.* **2001**, *40*, 5058–5059; g) M. L. Tong, X.-M. Chen, B.-H. Ye, S. W. Ng, *Inorg. Chem.* **1998**, *37*, 5278–5281; h) K. Singh, J. R. Long, P. Stavropoulos, *J. Am. Chem. Soc.* **1997**, *119*, 1942–1946; i) M.-L. Tong, X.-M. Chen, B.-H. Ye, L. N. Ji, *Angew. Chem. Int. Ed.* **1999**, *38*, 2237–2240; j) X.-M. Chen, T. C. W. Mak, *J. Chem. Soc. Dalton Trans.* **1991**, 3253–3257; k) B. L. Fei, W. Y. Sun, T. Okamura, W. X. Tang, N. Ueyama, *New J. Chem.* **2001**, *25*, 210–212; l) B. R. Bhogala, P. K. Thallapally, A. Nangia, *Cryst. Growth Des.* **2004**, *4*, 215–218; m) X. Zhang, G.-C. Guo, F.-K. Zheng, G.-W. Zhou, J.-G. Mao, Z.-C. Dong, J.-S. Huang, T. C. W. Mak, *J. Chem. Soc. Dalton Trans.* **2002**, 1344–1349.

[24] U. H. F. Bunz, *Chem. Rev.* **2000**, *100*, 1605–1644.

 © 2007 Wiley-VCH Verlag GmbH & Co. KGaA, Weinheim 

[25] a) D. M. Ciurtin, N. G. Pschirer, M. D. Smith, U. H. F. Bunz, H.-C. zur Loye, *Chem. Mater.* **2001**, *13*, 2743–2745; b) A. Burini, R. J. P. F. Bravi Jr, R. Galassi, T. A. Grant, M. A. Omary, B. R. Pietroni, R. J. Staples, *Inorg. Chem.* **2000**, *39*, 3158–3165; c) C. Seward, W.-L. Jia, H.-Y. Wang, G. D. Enright, S. Wang, *Angew. Chem. Int. Ed.* **2004**, *43*, 2933–2936; d) C.-D. Wu, H. L. Ngo, W. Lin, *Chem. Commun.* **2004**, 1588–1589; e) J. Wang, R. Wang, J. Yang, Z. Zheng, M. D. Carducci, T. Cayou, N. Peyghgambarian, G. E. Jabbour, *J. Am. Chem. Soc.* **2001**, *123*, 6179–6180.
[26] a) M.-L. Tong, X.-M. Chen, B.-H. Ye, L.-N. Ji, *Angew. Chem. Int. Ed.* **1999**, *38*, 2237–2240; b) V. W.-W. Yam, K. K.-W. Lo, *Chem. Soc. Rev.* **1999**, *28*, 323.
[27] a) N.-X. Hu, M. Esteghamatian, S. Xie, Z. Popovic, A.-M. Hor, B. Ong, S.-N. Wang, *Adv. Mater.* **1999**, *11*, 1460–1463; b) J. Wang, R. Wang, J. Yang, Z. Zheng, M. D. Carducci, T. Cayou, N. Peyghambarian, G. E. Jabbour, *J. Am. Chem. Soc.* **2001**, *123*, 6179–6180.
[28] M. W. Perkovic, *Inorg. Chem.* **2000**, *39*, 4962–4968.
[29] C. Seward, J. Chan, D. Song, S. Wang, *Inorg. Chem.* **2003**, *42*, 1112–1120.
[30] a) Z. Y. Fu, X. T. Wu, J. C. Dai, S. M. Hu, W. X. Du, H. H. Zhang, R. Q. Sun, *Eur. J. Inorg. Chem.* **2002**, 2730–2735; b) L.-L. Wen, D.-B. Dang, C.-Y. Duan, Y.-Z. Li, Z.-F. Tian, Q.-J. Meng, *Inorg. Chem.* **2005**, *44*, 7161–7170; c) R.-Q. Fan, D.-S. Zhu, Y. Mu, G.-H. Li, Y.-L. Yang, Q. Su, S.-H. Feng, *Eur. J. Inorg. Chem.* **2004**, 4891–4897.
[31] J.-Z. Zhang, C.-M. Cui, H.-P. Zhou, J.-X. Yang, J.-Y. Wu, Y.-P. Tian, X.-T. Tao, M.-H. Jiang, *Fun. Mater.* **2005**, *36*, 1624.
[32] G. M. Sheldrick, *SHELXTL*, version 6.10, Bruker Analytical X-ray Systems, Madison, WI, **2001**.

Received: December 31, 2006
Published Online: July 11, 2007

 © 2007 Wiley-VCH Verlag GmbH & Co. KGaA, Weinheim 

DOI: 10.1002/ejic.200700010

# Synthesis and Coordination Behavior of Symmetrical Tetraamine Phosphinic Acids

**Vojtěch Kubíček,*[a] Ivan Řehoř,[a] Jana Havlíčková,[a] Jan Kotek,[a] Ivana Císařová,[a] Petr Hermann,[a] and Ivan Lukeš[a]**

**Keywords:** Aminophosphinates / Complexes / Stability constants / Potentiometry

Two new tetraamine ligands, bis[*N*-(2-aminoethyl)aminomethyl]phosphinic acid ($Hen_2p$) and bis[*N*-(3-aminopropyl)-aminomethyl]phosphinic acid ($Hpn_2p$), were synthesized from the corresponding diaminoalkanes and bis(chloromethyl)phosphinic acid. Their acid–base properties and complexation with $Cu^{2+}$, $Ni^{2+}$, and $Zn^{2+}$ ions were studied by potentiometric titrations. Different chain lengths of the ligands result in significantly different coordination abilities. The five-membered chelate ring of $Hen_2p$ leads to a higher stability of its complexes. In comparison with tetraamines having the same number of the bridging atoms separating the amino groups, the presence of the phosphinic acid moiety decreases the basicity of the amine groups, and consequently, the stability of their complexes. Several solid-state structures were determined by X-ray diffraction analysis. Four nitrogen atoms coordinate the $Cu^{2+}$ or $Zn^{2+}$ ion in a square-planar fashion, whereas the phosphinic acid group is not coordinated or acts as a bridging unit between neighboring metal ions. The unexpectedly high stability of the $Ni^{2+}/Hpn_2p$ complex can be explained by the possible presence of a tetramer in solution as was found in the solid state.

(© Wiley-VCH Verlag GmbH & Co. KGaA, 69451 Weinheim, Germany, 2007)

## Introduction

The phosphinic acid group is derived from phosphoric acid by replacement of two –OH groups with hydrogen, alkyl, or aryl groups (Figure 1). In comparison with phosphonates (where only one –OH group is replaced), phosphinic acid derivatives are less studied because their synthesis is more complicated. Derivatives of phosphonic and phosphinic acids substituted in the α-position with an amino group have been intensively studied over the last 25 years as inhibitors of various enzymes.[1] Tetrahedral phosphinic (or phosphonic) acid groups mimic a transition state that is present during the hydrolysis of peptides and block efficiently the active sites of hydrolytic enzymes. Hydrolytic enzymes such as, for example, peptidases often contain a metal ion in the active site, and the inhibiting aminophosphinic acid binds the metal ion. Therefore, complexation properties of the phosphorous acid analogs have been studied in solution as well in the solid state.[2,3] Some of these compounds are produced commercially in a large scale as herbicides (Glyphosate, Bialaphos, etc.).[4]

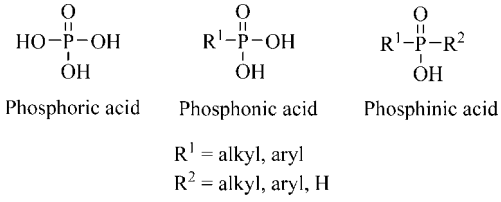


Figure 1. Phosphoric acid and its organophosphorus analogues.

Usually, an introduction of acidic fragments into a chelating molecule results in a higher stability of the complexes and decreases the overall charge of the complex formed in comparison with those of the corresponding amine. Phosphonic or phosphinic acid groups represent an alternative for the generally used carboxyl group. Relative to the carboxylate function, the presence of the phosphinic acid group decreases the basicity of the nearest amino group as well as the stability of the complexes as a result of the electron-withdrawing effect of the phosphorus atom. In the case of phosphonic acid derivatives, the doubly negative charge of the phosphonate overcompensates this disadvantage, leading to higher dissociation and, consequently, stability constants. Dissociation constants of the nitrogen atoms and stabilities of the complexes of these related ligands then follow the order: aminophosphinates < aminocarboxylates < aminophosphonates.[2,3] On the other hand, the higher acidity of the phosphonic and phosphinic acid groups causes the complexation to start at a lower pH. The lower stability

[a] Department of Inorganic Chemistry, Faculty of Science, Charles University in Prague,
Hlavova 8, 128 40 Prague 2, The Czech Republic
E-mail: vvvojta@volny.cz

Supporting information for this article is available on the WWW under http://www.eurjic.org or from the author.

 © 2007 Wiley-VCH Verlag GmbH & Co. KGaA, Weinheim 

of the phosphinate complexes can by compensated by their structural flexibility. Whereas the carboxylic and phosphonic acid groups are the terminal ones, the phosphinic acid group allows the attachment of another molecule fragment and the formation of more complicated structures and bifunctional ligands. Studies of phosphinic acid analogs of common amino acids in solution are not very frequent and confirm the above general considerations.[5–9] In addition, the solution properties depend on the kind of substituent bound to the phosphorus atom for simple aminophosphinic acids[8] as well as for their dipeptides.[10] In the complexes in the solid state, the amino group can be protonated and the metal ion is bound only by the phosphinate oxygen atom(s)[9,11–15] or the phosphinic amino acids can behave as chelating ligands bound through amino and phosphinate groups.[8,9,16,17] In addition, the phosphinate moiety serves as a bridge between two metal ions, often forming characteristic eight-membered M–(O–P–O)$_2$–M metallacycles.[8,11,13–15]

During the last decades, aminoalkylphosphinic acid groups have been used as building blocks in the design of polydentate ligands.[2,18] These compounds, usually based on acyclic[19–22] or macrocyclic[23–29] polyamine skeletons, have been studied as ligands for binding of "hard" metal ions, e.g. lanthanide(III) ions. The introduction of the methylphosphinic acid group(s) into DTPA or DOTA skeletons has led to an interesting alteration of properties of complexes of such ligands which are studied as possible contrast agents in magnetic resonance imaging,[30–37] for utilization in nuclear medicine,[38] or for luminescence imaging.[39]

Surprisingly, complexation abilities of compounds bearing two aminoalkyl substituents on one phosphorus atom have been only sparingly investigated. There are only several studies dealing with the solution[9,40–42] or solid-state[9,41,42] studies of this class of ligands. To obtain more information about the ligands, we decided to synthesize and investigate two new symmetrical polyaminophosphinic acid ligands, bis[*N*-(2-aminoethyl)aminomethyl]phosphinic acid (Hen$_2$p) and bis[*N*-(3-aminopropyl)aminomethyl]phosphinic acid (Hpn$_2$p) (Figure 2). Their acid–base and complexation properties were studied by using potentiometric titrations and UV/Vis spectroscopy. The solid-state structures of several complexes were determined by X-ray diffraction. As ligands containing the phosphinic acid group inside a macrocyclic skeleton have been previously prepared,[43] these open-chain ligands can serve for comparison of the properties of the corresponding cyclic and acyclic ligands.

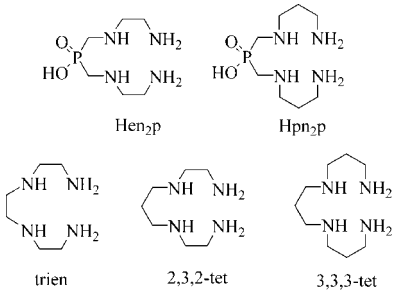


Figure 2. Ligands discussed.

## Results and Discussion

### Synthesis

The ligands Hen$_2$p and Hpn$_2$p were prepared by reaction of bis(chloromethyl)phosphinic acid (**1**) with 1,2-diaminoethane or 1,3-diaminopropane. Nucleophilic substitution of the chlorine atoms proceeds in almost quantitative yield. The formation of polymers was reduced by using a 100-fold excess of the diaminoalkane. After purification on ion-exchange resins, both ligands were isolated as their trihydrobromides; they slowly lost hydrobromic acid on storage or heating.

Neither the two ligands nor their salts are soluble in common organic solvents. For future synthetic purposes, solubility in organic solvents would be useful. Therefore, we tried to prepare an esterified form **3** by the reaction of isopropyl bis(chloromethyl)phosphinate (**2**) with the diaminoalkanes (Scheme 1). All these attempts failed, as the deesterification (by alkylation of the diaminoalkane with the isopropyl group) proceeded much faster than the substitution of chlorine atoms, and, at reflux temperature, both ligands were formed in the nonesterified form. When the reaction mixture was stirred at ambient temperature, the only product formed was bis(chloromethyl)phosphinic acid (**1**) as a result of the deesterification.

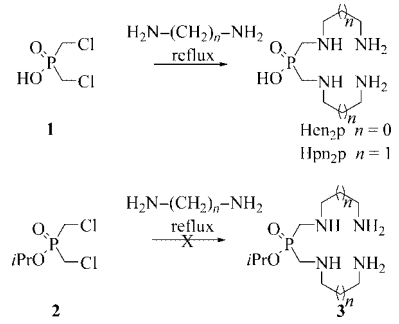


Scheme 1. Synthesis of the ligands.

### Acid–Base Properties

Both ligands, Hen$_2$p and Hpn$_2$p, contain five groups that can be protonated. The last two dissociations occur in strongly alkaline solution. The protonation constants, corresponding to proton loss from the terminal (primary) amino groups, are similar to those found in the corresponding tetraazaalkanes (Table 1). Whereas these two deprotonations are almost independent, the other two dissociations are strongly affected by the number of atoms separating the secondary amino groups from already protonated primary amino groups. The presence of propylene bridges results in a higher basicity of the secondary amino groups. In the case

 © 2007 Wiley-VCH Verlag GmbH & Co. KGaA, Weinheim 

Table 1. Dissociation constants of the ligands $Hen_2p$, $Hpn_2p$, and linear tetraamines.[44]

| | $Hen_2p$ | $Hpn_2p$ | | trien[a] | $Hen_2p$ | 2,3,2-tet[b] | $Hpn_2p$ | 3,3,3-tet[c] |
|---|---|---|---|---|---|---|---|---|
| $\log\beta_1$ | 10.10(2) | 10.60(1) | $pK_A(HL)$ | 9.95 | 10.10 | 10.25 | 10.60 | 10.46 |
| $\log\beta_2$ | 19.36(2) | 20.48(1) | $pK_A(H_2L)$ | 9.31 | 9.26 | 9.5 | 9.88 | 9.82 |
| $\log\beta_3$ | 25.06(2) | 27.89(2) | $pK_A(H_3L)$ | 6.86 | 5.70 | 7.28 | 7.41 | 8.54 |
| $\log\beta_4$ | 29.25(3) | 33.78(2) | $pK_A(H_4L)$ | 3.66 | 4.19 | 6.02 | 5.89 | 7.22 |
| $\log\beta_5$ | – | – | $pK_A(H_5L)$ | – | <1 | – | <1 | – |

[a] trien = triethylenetetraamine (1,4,7,10-tetraazadecane). [b] 2,3,2-tet = 1,4,8,11-tetraazaundecane. [c] 3,3,3-tet = 1,5,9,13-tetraazatridecane).

of ligands $Hen_2p$ and $Hpn_2p$, these two dissociation constants were found to be 1–2 orders of magnitude lower than those found for 2,3,2-tet and 3,3,3-tet. This decrease in basicity is typical for amino groups in the α-position to the phosphinate moiety.[2,3,9] Protonation of the phosphinate group occurs at very low pH (<1). The values of the dissociation constants of the fully protonated species are below the limit of the potentiometric method, and it was therefore not possible to calculate these constants.

## Complexation Properties

To simplify the following text we use a three-digit code for describing the complexes. The first digit represents the number (stoichiometric coefficient) of protons, the second one is the number of ligand molecules, and the third one is the number of metal ions. The negative value of the first digit represents a hydroxido complex. In general, complex $[H_hL_lM_m]$ is represented by [hlm], and its overall stability constant is $\beta_{hlm}$. Charges of the complexes are omitted.

Complexation properties of the ligands $Hen_2p$ and $Hpn_2p$ towards $Cu^{2+}$, $Ni^{2+}$, and $Zn^{2+}$ ions were studied by potentiometric titrations. The results are listed in Table 2. Some of the constants were not calculated. This is probably due to a simultaneous protonation of two sites and/or a very low abundance of the corresponding species (<10%).

Table 2. Overall stability constants ($\log\beta_{hml}$) of the complexes.

| Coefficient | | | $Cu^{2+}$ | | $Ni^{2+}$ | | $Zn^{2+}$ | |
|---|---|---|---|---|---|---|---|---|
| *h* | *l* | *m* | $Hen_2p$ | $Hpn_2p$ | $Hen_2p$ | $Hpn_2p$ | $Hen_2p$ | $Hpn_2p$ |
| 3 | 1 | 1 | – | 31.50(6) | – | 30.04(9) | – | – |
| 2 | 1 | 1 | – | 27.83(1) | – | 24.05(3) | – | 23.17(4) |
| 1 | 1 | 1 | 24.17(2) | 22.00(3) | 19.60(2) | 17.88(4) | – | – |
| 0 | 1 | 1 | 21.63(2) | 15.94(1) | 15.68(1) | 11.34(1) | 12.04(1) | 8.22(5) |
| – 1 | 1 | 1 | – | – | – | – | 1.36(3) | –1.99(3) |
| 3 | 2 | 1 | – | – | – | 41.73(6) | – | 40.01(2) |
| 2 | 2 | 1 | 47.76(5) | – | 38.67(8) | – | 34.29(5) | 32.51(4) |
| 1 | 2 | 1 | – | 30.50(9) | 29.56(5) | – | – | – |
| 0 | 2 | 1 | 26.45(9) | 19.94(7) | – | 13.91(7) | 15.84(7) | 11.92(6) |
| 0 | 1 | 2 | – | 20.76(2) | – | 13.61(5) | 14.09(4) | – |
| – 1 | 1 | 2 | – | 13.16(4) | – | – | – | 4.27(1) |
| – 2 | 1 | 2 | – | 5.79(2) | – | – | – | – |

### *Ligand $Hen_2p$*

In equimolar solutions, complexation of the $Cu^{2+}$ and $Ni^{2+}$ ions starts with formation of the monoprotonated

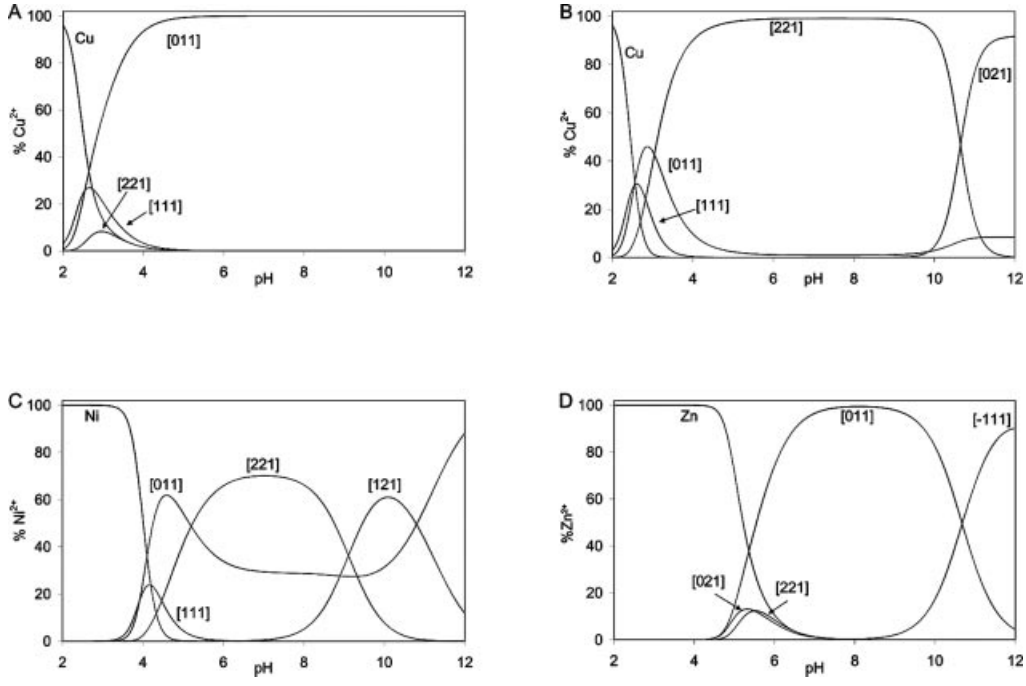


Figure 3. Distribution diagrams. (A) $Cu^{2+}/Hen_2p$ 1:1; (B) $Cu^{2+}/Hen_2p$ 1:2; (C) $Ni^{2+}/Hen_2p$ 1:2; (D) $Zn^{2+}/Hen_2p$ 1:1.

 © 2007 Wiley-VCH Verlag GmbH & Co. KGaA, Weinheim 

[111] complex at pH ≈ 2 for $Cu^{2+}$ (Figure 3A) and pH ≈ 3 for $Ni^{2+}$. The protonated complex does not exhibit a high abundance (<30%), and its deprotonation to the [011] species occurs with low p$K_A$ (p$K_{Cu}$ = 2.5, p$K_{Ni}$ = 3.9). The nonprotonated complex [011] is the only species present in the neutral and alkaline regions. Complexation of the $Zn^{2+}$ ion proceeds differently. The protonated complex [111] was not observed. Complexation starts at pH ≈ 4.5 with the formation of the [011] complex. At pH > 8, the hydroxido [–111] complexes are formed and become the main species present in the solution under the strongly alkaline conditions (Figure 3D).

In the presence of excess ligand (1:2 $M^{2+}$/L ratio), [221] complexes were formed in the neutral region (abundance >90% for $Cu^{2+}$, ca. 70% for $Ni^{2+}$, ca. 40% for $Zn^{2+}$; Figure 3B, C). Deprotonation results in the formation of [021] complexes ($Cu^{2+}$, $Zn^{2+}$) at pH ≈ 10–11 or a [121] complex ($Ni^{2+}$) at pH ≈ 9. In the presence of excess metal (2:1 $M^{2+}$/L ratio), the $M^{2+}$ hydroxides precipitated in all systems. Distributions in all systems are given in the Supporting Information (Figure S1).

### *Ligand $Hpn_2p$*

A successful fitting of titrations of all three studied systems containing the ligand $Hpn_2p$ required inclusion of the complexes with M/L ratios 1:1, 1:2, and 2:1 in various degrees of protonation (Figure 4). The complexation process starts at slightly higher pH (about 0.5 units) than that for $Hen_2p$. Complexation of $Cu^{2+}$ and $Ni^{2+}$ ions exhibits a preference for formation of the [011] complex, which is the main species present in equimolar solution (Figure 4A, B). In the presence of excess ligand, the complexes with 1:2 $M^{2+}$/L stoichiometry are formed only in the case of $Cu^{2+}$ ion in alkaline solutions (pH > 9). In the case of $Ni^{2+}$, complex [011] remains the major species in the whole alkaline region (Figure 4C). In the presence of excess $Cu^{2+}$ ions, the dinuclear [012] complex becomes dominant with an abundance of ca. 90% (at pH ≈ 6). For $Ni^{2+}$, the abundance of the [012] complex does not reach more than 30%. The $Zn^{2+}$/$Hpn_2p$ system involves a mixture of several complexes with comparable abundances in equimolar solution and with ligand in excess. In the presence of excess $Zn^{2+}$ ions, the dinuclear [–112] hydroxido complex becomes a major species. The unusually high abundance of this complex in equimolar solution (ca. 50% at pH ≈ 8) indicates a strong preference for this species (Figure 4D), where $OH^-$ probably forms a bridge between two metal ions. A similar motif of two hydroxide-bridged zinc(II) ions was observed in several types of metalloenzymes[45] and artificial catalytic centers[46] playing a role in hydrolytic processes. Distributions in all systems are given in the Supporting Information (Figure S2).

Results of the potentiometric study show that both studied ligands exhibit similar trends of coordination behavior to that of related linear tetraamines (Table 3). Stability constants of complexes of the tetraamine ligands with divalent metals increase in the order 3,3,3-tet < trien < 2,3,2-tet as a result of steric properties of the ligand. The least stable complexes are formed by 3,3,3-tet as all chelate rings in the complexes are six-membered, which is in general less convenient relative to trien and 2,3,2-tet, which form five-membered chelate rings.[47] The flexibility of the propylene bridge in 2,3,2-tet allows the formation of complexes having ideal square geometry, whereas the shorter ethylene bridge of trien is not ideal for this equatorial coordination. The lower basicity of $Hen_2p$ and $Hpn_2p$ in comparison with those of 2,3,2-tet and 3,3,3-tet (ligands having the same

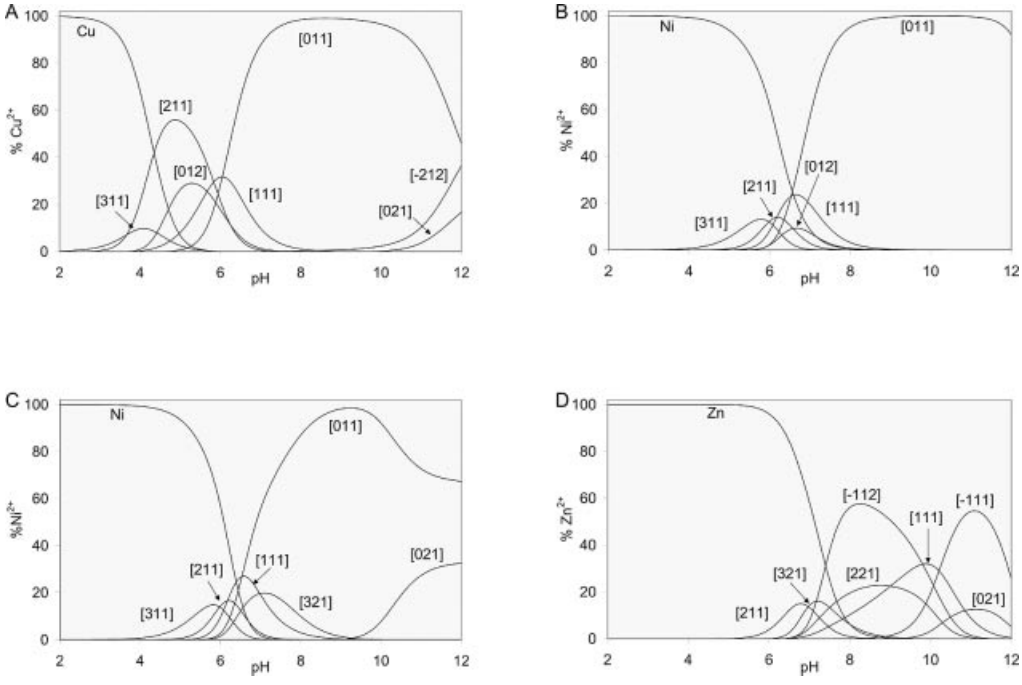


Figure 4. Distribution diagrams. (A) $Cu^{2+}$/$Hpn_2p$ 1:1; (B) $Ni^{2+}$/$Hpn_2p$ 1:1; (C) $Ni^{2+}$/$Hpn_2p$ 1:2; (D) $Zn^{2+}$/$Hpn_2p$ 1:1.

 © 2007 Wiley-VCH Verlag GmbH & Co. KGaA, Weinheim 

number of bridging atoms between amino groups) results in the decrease of the stability constants of the [011] complexes, which are 1–3 units lower than those reported for the corresponding tetraamines. The only exception is the $Ni^{2+}$/$Hpn_2p$ system, whose [011] complex exhibits a slightly higher stability than that of 3,3,3-tet. This can be explained by a possible formation of the cyclic tetrameric complex [044], which was identified in the solid state (see further). As this complex shows very similar potentiometric behavior to the [011] complex, the presence of the [044] complex cannot be confirmed by potentiometry, mainly because of the rather complex chemical model of the system. The possible presence of the tetramer in the solution is supported by the similarity of the UV/Vis spectra in the solution ($Ni^{2+}$/$Hpn_2p$ 1:1, pH = 10, 100% abundance of [011] species according to the distribution diagram, see Figure 4B) and in the solid state (complex [044], see crystallographic part). The UV/Vis spectra are shown in Figure 5 (maxima in the solution at 364, 581, and 947 nm; maxima in the solid state at 366, 587, and 970 nm).

Table 3. Comparison of stability constants $\log\beta_{011}$ of complexes found for $Hen_2p$ and $Hpn_2p$ with those reported for linear tetraamines.[44]

| Ion | $Hen_2p$ | $Hpn_2p$ | trien[a] | 2,3,2-tet[b] | 3,3,3-tet[c] |
|---|---|---|---|---|---|
| $Cu^{2+}$ | 21.63 | 15.94 | 20.2 | 23.9 | 17.3 |
| $Ni^{2+}$ | 15.68 | 11.34 | 14.4 | 16.4 | 10.65 |
| $Zn^{2+}$ | 12.04 | 8.22 | 12.1 | 12.8 | 9.41 |

[a] trien = triethylenetetraamine (1,4,7,10-tetraazadecane). [b] 2,3,2-tet = 1,4,8,11-tetraazaundecane. [c] 3,3,3-tet = 1,5,9,13-tetraazatridecane.

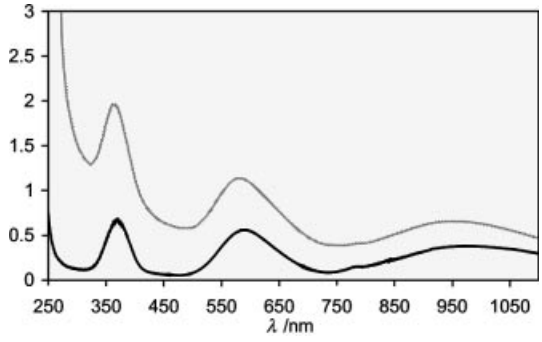


Figure 5. Comparison of the UV/Vis spectra of the $[Ni_4(pn_2p)_4]^{4+}$ complex in solution (dashed line) and in the solid state (solid line). The *y* axis shows absorbance units for solution and Kubelka–Munk units for the solid state.

Comparison of the $Hen_2p$ and $Hpn_2p$ systems can nicely document the different selectivity of these ligands. The higher stability of $Hen_2p$ complexes and the simpler models for the $M^{2+}$/$Hen_2p$ systems (4–5 species, strong preference for [011] complexes) indicate that the stereochemical properties of this ligand are much more suitable for the complexation of the studied divalent metal ions than those of the ligand $Hpn_2p$ (7–9 species in each system).

## Crystallography

The crystal structures of three salts of the $H_4en_2p$ cation, two $Hen_2p$ and two $Hpn_2p$ complexes were determined by X-ray diffraction. In contrast to the simplest bis(aminomethyl)phosphinic acid,[9] the phosphinic acid groups of the studied ligands are not coordinated in acid solution, and the ligand behaves only as an organic base. In the presence of a bulky anion, e.g. tetrachlorocuprate(II), the simple salts crystallize. In neutral and alkaline solutions, both ligands behave in a similar manner as the corresponding tetraamines; four nitrogen atoms of one ligand molecule are coordinated in equatorial positions around the transition-metal ion. In the solid state, the phosphinic acid group is mostly coordinated to another metal center and plays the role of the bridging unit. In simple systems [ligand, metal(II) chloride, hydrochloric acid, sodium hydroxide], crystallization experiments were not successful – oily and glassy products were formed. Single crystals were obtained after bulky anions (perchlorate, hexafluorophosphate) and ammonium cations (forming a hydrogen-bond network) were added and the pH was adjusted to the value of the maximum abundance of the species in solution (according to the distribution diagrams). In addition, in most cases, only several single crystals, which decomposed on standing in air, were obtained. Therefore, microanalytical data are not provided (the rest of the solution formed only oils).

### *Ligand Salt Structures (4, 5, 6)*

In all three structures, all four amino groups are protonated, and the phosphinic acid group is deprotonated. The distances between the phosphorus atom and the two oxygen atoms in the structure of $(H_4en_2p)Cl_3$ (**4**) are the same (1.49 Å), which indicates full delocalization of the phosphinate negative charge. The two side arms of the ligand are almost planar. Both compounds $(H_4en_2p)[CuCl_4]Cl$ (**5**) and $(H_4en_2p)[ZnCl_4]Cl$ (**6**) are almost isostructural. All amino groups are protonated, whereas the phosphinic acid group is deprotonated. In contrast to the structure of **4**, the ligand side-arms are not arranged in one plane. Torsion angles around the phosphorus atom (C–P–C–N) are 73–75° (for **4**), 155–158° (for **5**), and 160° (for **6**). The torsion angles about the P–C–N–C bonds are antiperiplanar (170–180°). Other bonds in the chain are in the synclinal conformation (torsion angles of 61–82°) probably because of the presence of the hydrogen-bond network between the protonated amino groups and the anions. The coordination sphere of both tetrachloroanions is a distorted tetrahedron. The structure of the $(H_4en_2p)^{3+}$ cation in $(H_4en_2p)Cl_3$ (Figure S3), the independent unit found in the crystal structure of $(H_4en_2p)[CuCl_4]Cl$ (Figure S4), and selected geometric parameters (Table S1) are given in the Supporting Information.

### *$Na_2(NH_4)_4[Cu(en_2p)]_4Br_4(PF_6)_6\cdot H_2O$ (7)*

The structural unit has a plane of symmetry. The structurally independent part consists of four halves of the complex molecules. Their central atoms ($Cu^{1a}$, $Cu^{1b}$, $Cu^{1c}$, and

 © 2007 Wiley-VCH Verlag GmbH & Co. KGaA, Weinheim 

$Cu^{1d}$) are situated in a plane. Three complex units (with central ions $Cu^{1a}$, $Cu^{1b}$, and $Cu^{1c}$) are coordinated to one $Na^+$ cation ($Na^1$) through phosphinate oxygen atoms. The fourth complex forms a coordination bridge between $Cu^{1b}$ and $Cu^{1c\#}$ (of the neighboring crystal unit) through the two bromide anions $Br^2$ and $Br^3$. In all complexes, amino groups occupy equatorial positions, and the $N_4Cu$ plains are perpendicular to the crystallographic plane of symmetry. The $Cu^{2+}$ ions $Cu^{1a}$ and $Cu^{1b}$ have an octahedral coordination sphere with one bromide anion ($Br^1$ or $Br^2$) and one phosphinate oxygen atom ($O^{61b}$ or $O^{61c}$ coming from ligand molecules coordinated to the neighboring $Cu^{2+}$ ions) in axial positions. The coordination sphere of $Cu^{1c}$ is square-pyramidal with bromide anion $Br^{3\#}$ in the axial position. $Cu^{1d}$ has an octahedral coordination sphere with two bromide anions ($Br^2$ and $Br^3$) in the axial position. Part of the crystal structure of complex **7** is shown in Figure 6. Cocrystallized water molecules as well as ammonia cations fill the empty cavities of the structure, forming a system of hydrogen bonds. The remaining spaces in the coordination sphere of the $Na^+$ ion are occupied by fluorine atoms of the hexafluorophosphate anion, phosphinate oxygen atoms $O^{61a}$, $O^{61d}$, $O^{62d}$, and the bromide ion $Br^4$. Selected geometric parameters are given in the Supporting Information (Table S2).

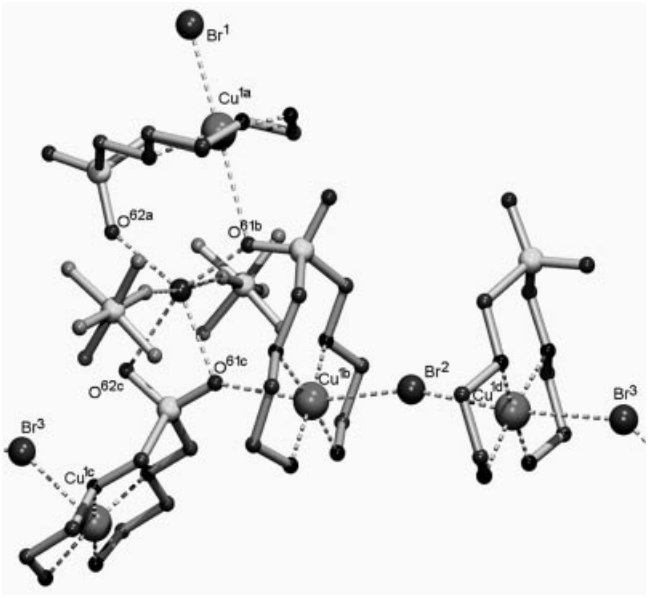


Figure 6. Complex framework found in the crystal structure of $Na_2(NH_4)_4[Cu(en_2p)]_4Br_4(PF_6)_6{\cdot}H_2O$ (**7**).

### *$Na_{3/2}(NH_4)_2[Zn(en_2p)]_3Br_{5/2}(PF_6)_4{\cdot}3H_2O$ (8)*

The structural unit has a plane of symmetry. Three halves of complex molecules form an independent part. Three central atoms ($Zn^{1a}$, $Zn^{1b}$, and $Zn^{1c}$) form three vertexes of the virtual square at the center of which is the $Na^+$ ion $Na^1$. The $N_4Zn$ planes in all complexes are perpendicular to the plane of symmetry. The first complex ($Zn^{1a}$) shows tetragonal pyramidal geometry. The axial position is occupied by the bromide anion $Br^{1a}$. The distance to another bromide anion $Br^1$ is too long (3.22 Å) to expect there to be a direct coordination bond in the remaining axial position. $Zn^{1b}$ has octahedral geometry. The axial positions are occupied by the phosphinate oxygen atom $O^{61a}$ and bromide anion $Br^2$. The bromide anion $Br^2$ plays the role of bridging ligand and it is coordinated to the atom $Zn^{1b\#}$ from the neighboring trimeric unit. The third complex molecule whose central atom is $Zn^{1c}$ has tetragonal pyramidal geometry with the phosphinate oxygen atom $O^{61b}$ in the axial position. Similarly to the first complex molecule, there

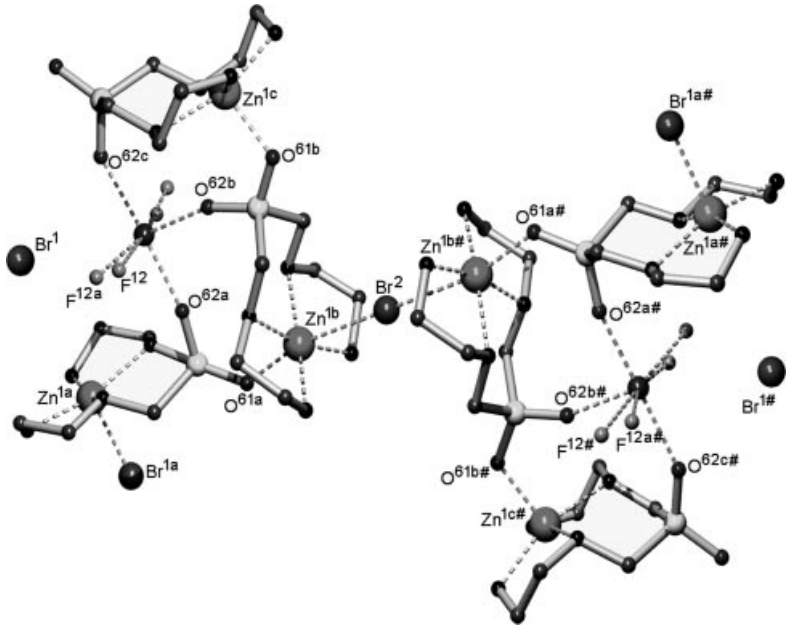


Figure 7. Complex framework found in the crystal structure of $Na_{3/2}(NH_4)_2[Zn(en_2p)]_3Br_{5/2}(PF_6)_4{\cdot}3H_2O$ (**8**). Two structural units are displayed. Fluorine atoms coordinated to the $Na^+$ ion belong to the hexafluorophosphate anions.

 © 2007 Wiley-VCH Verlag GmbH & Co. KGaA, Weinheim 

is a bromide anion ($Br^{1\#}$) in the direction of the second axial position, but too far from the metal center to be assigned as directly coordinated (3.23 Å). The square-pyramidal coordination sphere of the $Na^+$ ion $Na^1$ is occupied by three phosphinate oxygen atoms ($O^{62a}$, $O^{62b}$, and $O^{62c}$) and two fluorine atoms coming from hexafluorophosphate anions. Other $PF_6^-$, $NH_4^+$, and $Br^-$ ions are bound into the structure by a framework of hydrogen bonds. The framework of the complex molecules found in the crystal structure of **8** is shown in Figure 7. Selected geometric parameters are given in the Supporting Information (Table S3).

### *$Na_2[Cu(pn_2p)]_4Br_2(ClO_4)_4\cdot 3H_2O$ (9)*

The structural unit has again a plane of symmetry. Four halves of the complexes (with central atoms $Cu^{1a}$, $Cu^{1b}$, $Cu^{1c}$, and $Cu^{1d}$) form an independent unit. The copper atoms are located in the corners of the virtual square at whose center is the $Na^1$ atom. The motif of four nitrogen atoms in the equatorial plane of the complexes is similar with that found in the previous structures; ligand equatorial planes are perpendicular to the crystallographic plane of symmetry. The coordination spheres of $Cu^{1a}$ and $Cu^{1b}$ have tetragonal pyramidal geometry, where the axial position is occupied by a phosphinate oxygen atom ($O^{71b}$ and $O^{71c}$, respectively) coming from the neighboring complex. The octahedral coordination sphere of the $Cu^{1c}$ atom is completed in the axial positions with the bromide anion $Br^{1c}$ and the disordered phosphinate oxygen atom $O^{71d}$ coming again from the neighboring complex unit. The trimethylene bridge of the ligand exhibits disorder into two positions. The last complex unit $Cu^{1d}$ has square-pyramidal geometry whose axial position is occupied by the oxygen atom of a water molecule, $O^{1d}$. The octahedral coordination sphere of the $Na^1$ consists of four oxygen atoms from four phosphinate groups in the equatorial plane ($O^{72a}$, $O^{72b}$, $O^{72c}$, and $O^{72d}$). Oxygen atoms coming from perchlorate anions occupy the axial positions. Cocrystallized water molecules and bromide anions are fixed in the structure by the hydrogen-bond network. The complex framework found in the crystal structure of $Na_2[Cu(pn_2p)]_4Br_2(ClO_4)_4\cdot 3H_2O$ (**9**) is shown in Figure 8. Selected geometric parameters are given in the Supporting Information (Table S4).

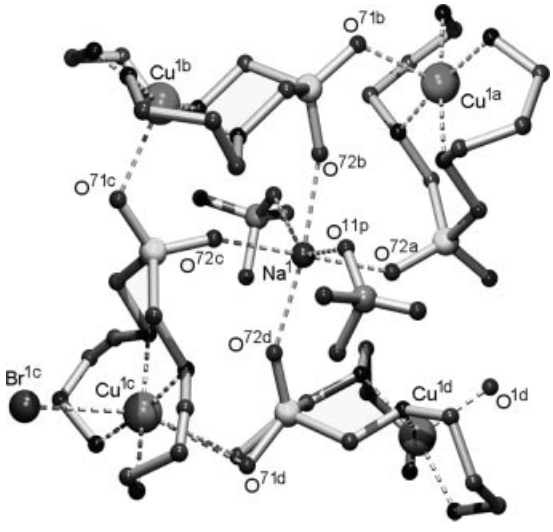


Figure 8. Complex framework found in the crystal structure of $Na_2[Cu(pn_2p)]_4Br_2(ClO_4)_4\cdot 3H_2O$ (**9**).

### *$[Ni_4(pn_2p)_4](ClO_4)_4\cdot 7H_2O$ (10)*

In comparison with the previous complexes, the structure of this coplex is exceptional, as a structural unit is formed by an isolated $[Ni_4L_4]$ tetramer. The $Ni^{2+}$ ions are connected by four ligand molecules to a supramolecular crown. Two nitrogen atoms of a propylenediamine fragment and one oxygen atom of a deprotonated phosphinate are coordinated to the metal ion in the meridional configuration. The second propylenediamine fragment and the second phosphinate oxygen atom are coordinated in the same way to the neighboring metal ion. The planes of those two groups of donor atoms are almost perpendicular. The remaining three positions around the metal ion are occupied by another ligand molecule. The $Ni^{2+}$ ions can be viewed as the vertexes of an intermediate shape between a square and a tetrahedron, as their mutual position shows almost perfect $D_{2v}$ symmetry with dihedral angles just between an ideal square and an ideal tetrahedron (Table 4; dihedral angles in the ideal tetrahedron are 70.5°, in square-planar geometry, the four angles are equal to 0°, and the remaining two are 180°). The positive charge is compensated for by four per-

Table 4. Dihedral angles [°] of the flattened tetrahedron formed by $Ni^{2+}$ ions found in the structure of the $[Ni_4(pn_2p)_4]^{4+}$ cation.

| Edge of the polyhedron | Angle /° | Square /° | Tetrahedron /° |
|---|---|---|---|
| Ni1···Ni2 | 51.9 | 0 | 70.5 |
| Ni1···Ni3 | 103.4 | 180 | 70.5 |
| Ni1···Ni4 | 52.0 | 0 | 70.5 |
| Ni2···Ni3 | 52.3 | 0 | 70.5 |
| Ni2···Ni4 | 103.4 | 180 | 70.5 |
| Ni3···Ni4 | 51.7 | 0 | 70.5 |

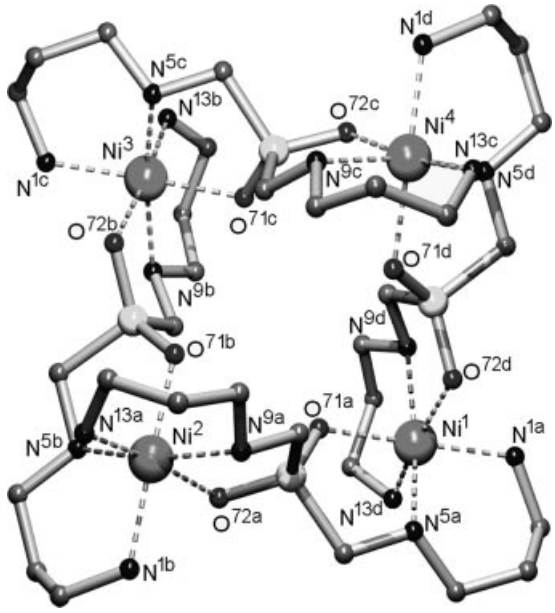


Figure 9. Structure of the $[Ni_4(pn_2p)_4]^{4+}$ complex cation.

 © 2007 Wiley-VCH Verlag GmbH & Co. KGaA, Weinheim 

chlorate anions, which are connected to water molecules by hydrogen bonds and ligand amino groups. The structure of the $[Ni_4(pn_2p)_4]^{4+}$ complex cation is presented in Figure 9, and selected geometric parameters are given in the Supporting Information (Table S5).

## Conclusions

Two new symmetrical tetraazaphosphinic acids, bis[*N*-(2-aminoethyl)aminomethyl]phosphinic acid ($Hen_2p$) and bis[*N*-(3-aminopropyl)aminomethyl]phosphinic acid ($Hpn_2p$), were prepared by reaction of bis(chloromethyl)phosphinic acid with excess 1,2-diaminoethane or 1,3-diaminopropane. Their protonation constants and the stability constants of their complexes with $Cu^{2+}$, $Ni^{2+}$, and $Zn^{2+}$ ions were determined by potentiometry. The presence of the electron-withdrawing phosphinic acid group decreases the basicity of the amino groups in the α-position in comparison with the linear tetraamines. The lower basicity results in the lower stability of the complexes with the divalent metal ions studied relative to that of the linear tetraamines containing the same number of bridging atoms between the amine groups. Chemical models for $M^{2+}/Hen_2p$ systems are simpler than those of systems containing $Hpn_2p$, with a high preference for complexes with a M/L ratio of 1:1 as a result of the better stereochemical properties and the higher selectivity of $Hen_2p$. In single crystals of the complexes obtained from neutral and alkaline solutions, all nitrogen atoms show equatorial coordination, whereas the phosphinic acid group is coordinated to the neighboring metal center. A different motif was found in the structure of the $[Ni_4(pn_2p)_4](ClO_4)_4{\cdot}7H_2O$, where four $Ni^{2+}$ ions and four ligand molecules form a cyclic supramolecular crown.

## Experimental Section

**Materials:** Commercially available chemicals had synthetic purity and were used as received. Bis(chloromethyl)phosphinic acid (**1**) and isopropyl bis(chloromethyl)phosphinate (**2**) were prepared according to the reported procedures.[48,49] Elemental analyses were performed in the Institute of Macromolecular Chemistry (Academy of Sciences of the Czech Republic, Prague).

**NMR Spectroscopy:** $^1H$ (400.0 MHz), $^{13}C$ (100.6 MHz) and $^{31}P$ (161.9 MHz) NMR spectra were recorded with a Varian $^{UNITY}$PLUS-400 spectrometer in 5 mm sample tubes. NMR experiments were performed at 298 K. For the measurements in $D_2O$, *tert*-butyl alcohol was used as an internal standard, the methyl signal being referenced to 1.2 ppm ($^1H$) and 31.2 ppm ($^{13}C$). For the measurements in $CDCl_3$, tetramethylsilane was used as an internal standard; the methyl signal was referenced to 0.0 ppm ($^1H$). The $^{31}P$ chemical shifts were measured with respect to 1% $H_3PO_4$ in $D_2O$ as an external standard (substitution method).

**Mass Spectrometry:** Mass spectra were recorded by using a Bruker Esquire 3000 spectrometer equipped with an electrospray ion source and an ion trap. All measurements were carried out in the positive-ion mode.

**General Procedure for Ligands $Hen_2p$ and $Hpn_2p$:** Bis(chloromethyl)phosphinic acid (**1**) (5.0 g, 30 mmol) was dissolved in diaminoalkane (3.0 mol). The solution was refluxed for 24 h. After removal of excess diaminoalkane in a rotary evaporator, the resulting oil was purified on a strong anion exchange resin (Dowex 1×8, 100–200 mesh, $OH^-$-form, elution with $H_2O$ followed with 20% aq. HCl) and a strong cation exchange resin (Dowex 50×4, 100–200 mesh, $H^+$-form, elution with $H_2O$ followed with 5% aq. $NH_3$). After evaporation of the volatiles, the resulting oily products were dissolved in 30% HBr (20 mL) and treated with charcoal. After filtration, the volatiles were removed in a rotary evaporator, the residue was dissolved in water (5 mL), and the resulting solution was slowly dropped into anhydrous EtOH (800 mL) with vigorous stirring. After 3 h, the precipitate was filtered, washed with EtOH, and dried with $P_2O_5$ under reduced pressure.

**Bis[*N*-(2-aminoethyl)aminomethyl]phosphinic Acid Trihydrobromide, $(H_4en_2p)Br_3$:** Yield 9.8 g (72%). $C_6H_{22}Br_3N_4O_2P$ (452.95): calcd. C 15.91, H 4.90, Br 52.92, N 12.37; found C 16.02, H 4.86, Br 48.55, N 11.47. $^1H$ NMR ($D_2O$): $\delta$ = 3.34 (m, 8 H, $NH_2$–C$H_2$–C$H_2$–NH), 3.44 (m, 4 H, C$H_2$–P) ppm. $^{31}P$ NMR ($D_2O$): $\delta$ = 19.0 (p, $^2J_{PH}$ = 9.7 Hz) ppm. $^{13}C\{^1H\}$ NMR ($D_2O$): $\delta$ = 37.9 (s, $NH_2$–C$H_2$), 48.5 (d, $^3J_{CP}$ = 21.8 Hz, NH–C$H_2$–$CH_2$), 49.2 (d, $^1J_{CP}$ = 103.2 Hz, C$H_2$–P) ppm. MS: calculated for [M + $Na^+$] 233.2; found 233.6.

**Bis[*N*-(3-aminopropyl)aminomethyl]phosphinic Acid Trihydrobromide, $(H_4pn_2p)Br_3$:** Yield 10.0 g (69%). $C_8H_{26}Br_3N_4O_2P$ (481.00): calcd. C 19.98, H 5.45, N 11.65, Br 49.84; found C 20.35, H 5.44, N 11.11, Br 47.76. $^1H$ NMR ($D_2O$): $\delta$ = 2.03 (m, 4 H, $CH_2$–C$H_2$–$CH_2$), 3.02 (t, $^3J_{HH}$ = 8.0 Hz, 4 H, $NH_2$–C$H_2$–$CH_2$), 3.17 (t, $^3J_{HH}$ = 8.0 Hz, 4 H, NH–C$H_2$–$CH_2$), 3.26 (d, $^2J_{PH}$ = 10.0 Hz, 4 H, NH–C$H_2$–P) ppm. $^{31}P$ NMR ($D_2O$): $\delta$ = 19.7 (p, $^2J_{PH}$ = 9.9 Hz) ppm. $^{13}C\{^1H\}$ NMR ($D_2O$): $\delta$ = 25.2 (s, $CH_2$–C$H_2$–$CH_2$), 38.1 (s, $NH_2$–C$H_2$), 47.7 (d, $^1J_{CP}$ = 101.9 Hz, C$H_2$–P), 48.1 (s, NH–C$H_2$–$CH_2$) ppm. MS: calculated for [M + $Na^+$] 261.3; found 261.5.

**Preparation of Single Crystals for X-ray Analysis**

**$(H_4en_2p)Cl_3$ (4):** $(H_4en_2p)Br_3$ (0.10 g, 0.31 mmol) was evaporated with HCl (10 mL, 6 M). The resulting oil was dissolved in HCl (2 mL, 6 M). Colorless single crystals were prepared by slow vapor diffusion of EtOH into the solution.

**$(H_4en_2p)[CuCl_4]Cl$ (5):** $(H_4en_2p)Br_3$ (0.1 g, 0.31 mmol) and $CuCl_2{\cdot}2H_2O$ (0.053 g, 0.31 mmol) were dissolved in HCl (2 mL, 12 M). Volatiles were removed in a rotary evaporator, and the resulting oil was dissolved in $H_2O$ (5 mL). Yellow single crystals of the product were obtained in 1 h.

**$(H_4en_2p)[ZnCl_4]Cl$ (6):** $(H_4en_2p)Br_3$ (0.10 g, 0.31 mmol) and $ZnCl_2$ (0.043 g, 0.31 mmol) were dissolved in HCl (2 mL, 12 M). Volatiles were removed in a rotary evaporator, and the resulting oil was dissolved in $H_2O$ (5 mL). Colorless single crystals were obtained by slow evaporation over a week.

**$Na_2(NH_4)_4[Cu(en_2p)]_4Br_4(PF_6)_6{\cdot}H_2O$ (7):** $(H_4en_2p)Br_3$ (0.048 g, 0.11 mmol) and $CuCl_2{\cdot}2H_2O$ (0.018 g, 0.11 mmol) were dissolved in water (0.75 mL). The pH of the solution was increased to 8.5 by using NaOH (5% aq.), and a concentrated solution of $NH_4PF_6$ in EtOH (0.5 mL) was added. Blue single crystals were obtained by slow evaporation over two weeks.

**$Na_{3/2}(NH_4)_2[Zn(en_2p)]_3Br_{5/2}(PF_6)_4{\cdot}3H_2O$ (8):** $(H_4en_2p)Br_3$ (0.048 g, 0.11 mmol) and $ZnCl_2$ (0.015 g, 0.11 mmol) were dissolved in water (0.75 mL). The pH of the solution was increased to 8.0 by using NaOH (5% aq.), and a concentrated solution of $NH_4PF_6$ in EtOH (0.5 mL) was added. Colorless single crystals were obtained by slow evaporation over a week.

**$Na_2[Cu(pn_2p)]_4Br_2(ClO_4)_4{\cdot}3H_2O$ (9):** $(H_4pn_2p)Br_3$ (0.055 g, 0.11 mmol) and $CuCl_2{\cdot}2H_2O$ (0.019 g, 0.11 mmol) were dissolved

 © 2007 Wiley-VCH Verlag GmbH & Co. KGaA, Weinheim 

in water (0.75 mL). The pH of the solution was increased to 8.5 by using NaOH (5% aq.), and a concentrated solution of $NaClO_4$ in EtOH (0.5 mL) was added. Blue single crystals were obtained by slow evaporation over a week.

**$[Ni_4(pn_2p)_4](ClO_4)_4·7H_2O$ (10):** $(H_4pn_2p)Br_3$ (0.055 g, 0.11 mmol) and $NiCl_2·6H_2O$ (0.026 g, 0.11 mmol) were dissolved in water (0.75 mL). The pH of the solution was increased to 9.0 by using NaOH (5% aq.), and a concentrated solution of $NaClO_4$ in EtOH (0.5 mL) was added. Light blue single crystals were obtained from the mixture that was kept in a closed vial for a week.

**Crystal Structure Determination:** The selected crystals were mounted on glass fibers in random orientation by using silicone grease. Diffraction data were collected by using graphite-monochromated Mo-$K_\alpha$ radiation with an Enraf–Nonius KappaCCD diffractometer at 150(1) K [Cryostream Cooler (Oxford Cryosystems)] and analyzed with the HKL DENZO program package (ref.[50]). Cell parameters were determined from all data with the same program package.[50] The structure was solved by direct methods and refined by full-matrix least-squares techniques (SIR92,[51] SHELXL97[52]). The scattering factors used for neutral atoms were included in the SHELXL97 program. In the structures of $(H_4en_2p)Cl_3$ (**4**), $(H_4en_2p)[CuCl_4]Cl$ (**5**), and $(H_4en_2p)[ZnCl_4]Cl$ (**6**), all non-hydrogen atoms were refined anisotropically. The hydrogen atoms were localized in the difference map of electronic density and refined isotropically. In the structure of $Na_2(NH_4)_4[Cu(en_2p)]_4Br_4(PF_6)_6·H_2O$ (**7**), all non-hydrogen atoms of the complex units were refined anisotropically. The hydrogen atoms were placed in theoretical (C–H, N–H of amino groups) or original (O–H, N–H of ammonia cations) positions and treated by using a riding model with thermal parameters $U_{eq}(H) = 1.2U_{eq}(X)$. All copper(II) ions, phosphinate phosphorus and oxygen atoms, and bromide and sodium ions occupy the special positions (lying in the plane of symmetry). Two of the hexafluorophosphate anions were disordered. One was treated in two staggered positions (having axial fluorine atoms nondisordered, and equatorial ones with ca. 80:20 occupancies). All fluorine atoms of the second disordered hexafluorophosphate were refined in two positions in ca. 80:20 occupancies. More occupied fluorine atoms were refined anisotropically, less occupied atoms were refined isotropically. In the structure of $Na_{3/2}(NH_4)_2[Zn(en_2p)]_3Br_{5/2}(PF_6)_4·3H_2O$ (**8**), all non-hydrogen atoms were refined anisotropically. The hydrogen atoms were placed in theoretical (C–H, N–H of amino groups) or original (O–H, N–H of ammonia cations) positions and treated by using a riding model with thermal parameters $U_{eq}(H) = 1.2U_{eq}(X)$. All zinc(II) ions, phosphinate phosphorus and oxygen atoms, and bromide and sodium ions occupy special positions (lying in the plane of symmetry). Both hexafluorophosphate anions were disordered, and all their fluorine atoms were refined in two positions with occupancies of ca. 60:40 and ca. 50:50, respectively. To obtain reliable thermal parameters, one bromide and one sodium(I) ion were treated as half-occupied. In the structure of $Na_2[Cu(pn_2p)]_4Br_2(ClO_4)_4·3H_2O$ (**9**), all non-hydrogen atoms were refined anisotropically. The hydrogen atoms were placed in theoretical positions and treated by using a riding model with thermal parameters $U_{eq}(H) = 1.2U_{eq}(X)$. All copper(II) ions, phosphinate phosphorus and oxygen atoms, and bromide and sodium ions occupy special positions (lying in the plane of symmetry). Perchlorate oxygen atoms were disordered; the anion was found to be staggered in two positions with occupancies of ca. 70:30 (one oxygen atom was not disordered, the remaining three were disordered). The propylene backbone of one ligand molecule was refined in two positions with ca. 50:50 occupancies. Water oxygen atoms were treated as half-occupied to obtain reasonable thermal factors. In the structure of $[Ni_4(pn_2p)_4](ClO_4)_4·7H_2O$ (**10**), all non-hydrogen atoms were refined anisotropically. The hydrogen atoms belonging to the ligand molecules were localized in the difference map of electronic density and refined isotropically. Three perchlorate anions were disordered, and their oxygen atoms were refined with ca. 70:40–60:40 occupancies. Some water oxygen atoms were treated as half-occupied to obtain reliable thermal factors; hydrogen atoms belonging to cocrystallized water molecules were not found. Relatively high electronic maxima peaks

Table 5. Experimental data for the reported crystal structures (**4**, **5**, **6**, and **7**).

| Parameter | **4** | **5** | **6** | **7** |
|---|---|---|---|---|
| Formula | $C_6H_{24}Cl_3N_4O_3P$ | $C_6H_{22}Cl_5CuN_4O_2P$ | $C_6H_{22}Cl_5N_4O_2PZn$ | $C_{24}H_{90}Br_4Cu_4F_{36}N_{20}Na_2O_9P_{10}$ |
| $M$ | 337.61 | 454.04 | 455.87 | 2416.64 |
| Crystal system | monoclinic | monoclinic | monoclinic | monoclinic |
| Space group | $Cc$ (No. 9) | $Cc$ (No. 9) | $Cc$ (No. 9) | $P2_1/m$ (No. 11) |
| $a$ /Å | 15.407(1) | 8.3447(2) | 8.1077(2) | 12.9522(4) |
| $b$ /Å | 10.791(1) | 19.7531(6) | 19.6706(4) | 17.6610(5) |
| $c$ /Å | 10.148(1) | 10.4301(3) | 10.6603(2) | 16.9828(3) |
| $\beta$ /° | 116.151(4) | 94.089(1) | 94.2672(8) | 91.5128(16) |
| $V$ /Å$^3$ | 1514.48(16) | 1714.86(8) | 1695.43(6) | 3883.44(18) |
| $Z$ | 4 | 4 | 4 | 2 |
| $D_c$ /g cm$^{-3}$ | 1.481 | 1.759 | 1.786 | 2.067 |
| $\mu$ /mm$^{-1}$ | 0.714 | 2.147 | 2.332 | 3.498 |
| $F(000)$ | 712 | 924 | 928 | 2396 |
| $\theta$ range /° | 2.80–27.48 | 3.40–27.50 | 2.82–27.51 | 1.20–27.49 |
| Index ranges | $-19 < h < 19$; $-13 < k < 11$; $-13 < l < 13$ | $-10 < h < 10$; $-21 < k < 25$; $-13 < l < 13$ | $-10 < h < 10$; $-25 < k < 25$; $-13 < l < 13$ | $-16 < h < 16$; $-22 < k < 22$; $-21 < l < 21$ |
| Reflections total | 2210 | 3321 | 3783 | 9041 |
| Reflections observed [$I > 2\sigma(I)$] | 2134 | 2975 | 3685 | 6268 |
| Data; restraints; parameters | 2210; 0; 249 | 3321; 2; 224 | 3783; 2; 225 | 9041; 0; 586 |
| GOF | 1.086 | 1.072 | 1.057 | 1.024 |
| $R_1$, $R_2$ [$I \geq 2\sigma(I)$] | 0.0258, 0.0238 | 0.0384, 0.0312 | 0.0346, 0.0336 | 0.0917, 0.0552 |
| w$R_1$, $wR_2$ [$I \geq 2\sigma(I)$] | 0.0612, 0.0593 | 0.0714, 0.0677 | 0.0857, 0.0846 | 0.1573, 0.1367 |
| Max shift /e.s.d. | 0.000 | 0.001 | 0.000 | 0.001 |
| Highest diff. peaks/holes /e A$^{-3}$ | 0.198, –0.252 | 0.307, –0.441 | 2.418, –0.593 | 0.918, –2.217 |

 © 2007 Wiley-VCH Verlag GmbH & Co. KGaA, Weinheim 

Table 6. Experimental data of reported crystal structures (**8**, **9**, and **10**).

| Parameter | **8** | **9** | **10** |
|---|---|---|---|
| Formula | $C_{18}H_{69}Br_{2.5}F_{24}N_{14}Na_{1.5}O_{9.5}P_7Zn_3$ | $C_{16}H_{48}BrCl_2Cu_2N_8NaO_{14}P_2$ | $C_{32}H_{102}Cl_4N_{16}Ni_4O_{31}P_4$ |
| $M$ | 1737.07 | 939.44 | 1707.82 |
| Crystal system | monoclinic | monoclinic | monoclinic |
| Space group | $C2/m$ (No. 12) | $P2_1/m$ (No. 11) | $P2_1/c$ (No. 14) |
| $a$ /Å | 24.3305(4) | 13.2960(3) | 19.7233(2) |
| $b$ /Å | 18.6827(2) | 18.0898(5) | 13.6071(2) |
| $c$ /Å | 14.0651(2) | 15.3909(4) | 25.5459(3) |
| $\beta$ /° | 110.9460(10) | 110.4499(14) | 92.1856(8) |
| $V$ /Å$^3$ | 5970.93(14) | 3468.55(15) | 6850.94(15) |
| $Z$ | 4 | 4 | 4 |
| $D_c$ /g cm$^{-3}$ | 1.932 | 1.799 | 1.656 |
| $\mu$ /mm$^{-1}$ | 3.195 | 2.708 | 1.424 |
| $F$(000) | 3463 | 1920 | 3576 |
| $\theta$-range /° | 1.84–27.47 | 1.81–25.03 | 1.60–27.09 |
| Index ranges | $-31 < h < 31$;<br>$-24 < k < 24$;<br>$-18 < l < 18$ | $-15 < h < 15$;<br>$-21 < k < 21$;<br>$-18 < l < 18$ | $-25 < h < 25$;<br>$-17 < k < 17$;<br>$-32 < l < 32$ |
| Reflections total | 7045 | 6334 | 15092 |
| Reflections observed [$I > 2\sigma(I)$] | 6142 | 4446 | 11683 |
| Data; restraints; parameters | 7045; 0; 474 | 6334; 0; 469 | 11683; 0; 1301 |
| GOF | 1.065 | 1.040 | 1.039 |
| $R_1$, $R_2$ [$I \geq 2\sigma(I)$] | 0.0848, 0.0771 | 0.1165, 0.0830 | 0.0655, 0.0455 |
| w$R_1$, $wR_2$ [$I \geq 2\sigma(I)$] | 0.2443, 0.2364 | 0.2529, 0.2288 | 0.1304, 0.1169 |
| Max shift/e.s.d. | 0.009 | 0.016 | 0.001 |
| Highest diff. peaks/holes /e A$^{-3}$ | 1.859, –5.444 | 1.759, –2.462 | 1.251, –1.112 |

and holes in the structures of the compounds (**4**)–(**10**) are associated mainly with disordered hexafluorophosphate (or perchlorate) anions, as they are located in close proximity to phosphorus (or chlorine) atoms, respectively. Table 5 and Table 6 give the pertinent crystallographic data.

CCDC-627266 (**4**), -627267 (**5**), -627268 (**6**), -627269 (**7**), -627270 (**8**), -627271 (**9**), and -627272 (**10**) contain the supplementary crystallographic data for this paper. These data can be obtained free of charge from The Cambridge Crystallographic Data Centre via www.ccdc.cam.ac.uk/data_request/cif.

**Potentiometric Titrations:** The methodology of the potentiometric titrations and processing of the experimental data were similar to those previously reported.[9] Titrations were carried out in a vessel thermostatted at 25 ± 0.1 °C, at ionic strength $I$ ($KNO_3$) = 0.1 mol dm$^{-3}$. Ligand-to-metal ratios were 1:1, 1:2, and 2:1. Titrations were carried out at least four times, each titration yielding about 40 data points. The water ion product, p$K_w$ = 13.78, and stability constants of $M^{2+}$/$OH^-$ systems were taken from ref.[53] The protonation constants $\beta_n$ calculated are concentration constants and are defined by $\beta_n = [H_nL]/([H]^n \times [L])$ (p$K_1$ = log$\beta_1$; p$K_n$ = log$\beta_n$ – log$\beta_{n-1}$); the stability constant are defined by $\beta_{pqr} = [M_pH_qL_r]/[M]^p \times [H]^q \times [L]^r$. The constants (with standard deviations) were calculated with the program OPIUM.[54] Throughout the paper, pH means –log[$H^+$]. As hydrobromides of the ligands slowly lose HBr upon standing, the stock solutions for potentiometry were prepared from freshly isolated materials. The ligand and the proton concentrations in the stock solution determined together with the calculation of the protonation constants, is in perfect agreement with a 1:3 ligand/HBr stoichiometry. In all systems, equilibrium was established quickly (< 20 s) at all data points.

**UV/Vis Spectroscopy:** Solution spectra were recorded with a Cary 1E (Varian) spectrometer in the 200–1100-nm range at room temperature. $NiCl_2 \cdot 6H_2O$ and ligand $(H_4pn_2p)Br_3$ (one equivalent) were dissolved in water, and the pH of the sample was adjusted with dilute KOH solution to a value of ca. 10, where the maximum abundance of the $[ML]^+$ species occurs according to the distribution diagram. Reflection spectra of the microcrystalline sample diluted with $BaSO_4$ were recorded with a Lambda 19 (Perkin–Elmer) spectrometer by using an integration sphere in the 200–1100-nm range at room temperature.

**Supporting Information** (see footnote on the first page of this article): Distribution diagrams of all studied systems are shown in Figures S1 and S2. Geometric parameters of coordination polyhedrons in the crystal structures are listed in Tables S1–S5. Colored structures and ORTEP representations of compounds **4**–**10** are shown in Figures S3 to S8.

## Acknowledgments

Support from the Grant Agency of the Czech Republic (203/06/0467) and the Grant Agency of the Academy of Science of the Czech Republic (KAN201110651) is acknowledged. The work was carried out in the frame of COST D38 and the "Network of Excelence" projects EMIL (No. LSHC-2004–503569) and DiMI (No. LSHB-2005–512146).

[1] V. P. Kukhar, H. R. Hudson(Eds.), *Aminophosphonic and Aminophosphinic Acids. Chemistry and Biological Activity*, John Wiley and Sons, New York, **2000**.
[2] I. Lukeš, J. Kotek, P. Vojtíšek, P. Hermann, *Coord. Chem. Rev.* **2001**, *216–217*, 287–312.
[3] T. Kiss, I. Lázár. in *Aminophosphonic and Aminophosphinic Acids. Chemistry and Biological Activity* (Eds.: V. P. Kukhar, H. R. Hudson), John Wiley and Sons, New York, **2000**, ch. IX, pp. 285–326.
[4] J. E. Franz, M. K. Mao, J. A. Sikorski, *Glyphosate. A Unique Global Herbicide*, Oxford University Press, Oxford, **1997**.
[5] T. Kiss, E. Farkas, M. Jezowska-Bojczuk, H. Kozlowski, E. Kowalik, *J. Chem. Soc. Dalton Trans.* **1990**, 377–379.
[6] K. B. Yatsimirskii, L. B. Tsimbal, E. I. Sinyavskaya, *Zh. Neorg. Khim.* **1990**, *35*, 117–123.

 © 2007 Wiley-VCH Verlag GmbH & Co. KGaA, Weinheim 

[7] T. Kiss, M. Jezowska-Bojczuk, H. Kozlowski, P. Kafarski, K. Antczak, *J. Chem. Soc. Dalton Trans.* **1991**, 2275–2279.
[8] J. Rohovec, I. Lukeš, P. Vojtíšek, I. Císařová, P. Hermann, *J. Chem. Soc. Dalton Trans.* **1996**, 2685–2691.
[9] V. Kubíček, P. Vojtíšek, J. Rudovský, P. Hermann, I. Lukeš, *Dalton Trans.* **2003**, 3927–3938.
[10] M. Lukáš, M. Kývala, P. Hermann, I. Lukeš, D. Sanna, G. Micera, *J. Chem. Soc. Dalton Trans.* **2001**, 2850–2857.
[11] T. Glowiak, W. Sawka-Dobrowolska, *Acta Crystallogr., Sect. B* **1977**, *33*, 2648–2650.
[12] T. Glowiak, W. Sawka-Dobrowolska, *Acta Crystallogr., Sect. B* **1977**, *33*, 2763–2766.
[13] Z. Žák, J. Kožíšek, T. Z. Glowiak, *Z. Anorg. Allg. Chem.* **1981**, *477*, 221–224.
[14] W. Sawka-Dobrowolska, T. Glowiak, *Acta Crystallogr., Sect. C* **1983**, *39*, 345–347.
[15] T. Glowiak, *Acta Crystallogr., Sect. C* **1986**, *42*, 62–64.
[16] I. Lukeš, I. Císařová, P. Vojtíšek, K. Bazakas, *Polyhedron* **1995**, *14*, 3163–3166.
[17] J. F. Britten, C. J. L. Lock, Z. Y. Wang, *Acta Crystallogr., Sect. C* **1993**, *49*, 881–884.
[18] D. Parker, J. A. G. Williams, *J. Chem. Soc. Dalton Trans.* **1996**, 3613–3628.
[19] M. P. Lowe, S. J. Rettig, C. Orvig, *J. Am. Chem. Soc.* **1996**, *118*, 10446–10456.
[20] M. P. Lowe, P. Caravan, S. J. Rettig, C. Orvig, *Inorg. Chem.* **1998**, *37*, 1637–1647.
[21] M. S. Kovacs, V. Monga, B. O. Patrick, C. Orvig, *Dalton Trans.* **2006**, 31–38.
[22] J. Kotek, F. K. Kálmán, P. Hermann, E. Brücher, K. Binnemans, I. Lukeš, *Eur. J. Inorg. Chem.* **2006**, 1976–1986.
[23] K. Bazakas, I. Lukeš, *J. Chem. Soc. Dalton Trans.* **1995**, 1133–1137.
[24] J. Rohovec, M. Kývala, P. Vojtíšek, P. Hermann, I. Lukeš, *Eur. J. Inorg. Chem.* **2000**, 195–203.
[25] I. Lázár, A. D. Sherry, R. Ramasamy, E. Brücher, R. Király, *Inorg. Chem.* **1991**, *30*, 5016–5019.
[26] J. Huskens, A. D. Sherry, *Inorg. Chem.* **1996**, *35*, 5137–5143.
[27] J. Huskens, A. D. Sherry, *J. Am. Chem. Soc.* **1996**, *118*, 4396–4404.
[28] J. Huskens, A. D. Sherry, *J. Chem. Soc. Dalton Trans.* **1998**, 177–184.
[29] J. Huskens, D. A. Torres, Z. Kovacs, J. P. André, C. F. G. C. Geraldes, A. D. Sherry, *Inorg. Chem.* **1997**, *36*, 1495–1503.
[30] J. Kotek, P. Lebdušková, P. Hermann, L. Vander Elst, R. N. Muller, C. F. G. C. Geraldes, T. Maschmeyer, I. Lukeš, J. A. Peters, *Chem. Eur. J.* **2003**, *9*, 5899–5915.
[31] P. Lebdušková, J. Kotek, P. Hermann, L. Vander Elst, R. N. Muller, I. Lukeš, J. A. Peters, *Bioconjugate Chem.* **2004**, *15*, 881–889.
[32] J. Rudovský, J. Kotek, P. Hermann, I. Lukeš, V. Mainero, S. Aime, *Org. Biomol. Chem.* **2005**, *3*, 112–117.
[33] J. Rudovský, P. Hermann, M. Botta, S. Aime, I. Lukeš, *Chem. Commun.* **2005**, 2390–2392.
[34] J. Rudovský, M. Botta, P. Hermann, A. Koridze, S. Aime, *Dalton Trans.* **2006**, 2323–2333.
[35] J. Rudovský, M. Botta, P. Hermann, K. I. Hardcastle, I. Lukeš, S. Aime, *Bioconjugate Chem.* **2006**, *17*, 975–987.
[36] P. Lebdušková, A. Sour, L. Helm, E. Tóth, J. Kotek, I. Lukeš, A. E. Merbach, *Dalton Trans.* **2006**, 3399–3406.
[37] M. Försterová, I. Svobodová, P. Lubal, P. Táborský, J. Kotek, P. Hermann, I. Lukeš, *Dalton Trans.* **2007**, 535–549.
[38] K. P. Pullukkody, T. M. Norman, D. Parker, L. Royle, C. J. Broan, *J. Chem. Soc. Perkin Trans. 2* **1993**, 605–620.
[39] D. Parker, *Coord. Chem. Rev.* **2000**, *205*, 109–130.
[40] N. V. Nagy, T. Szabó-Plánka, G. Tircsó, R. Király, Z. Arkosi, A. Rockenbauer, E. Brücher, *J. Inorg. Biochem.* **2004**, *98*, 1655–1666.
[41] L. Xu, S. J. Rettig, C. Orvig, *Inorg. Chem.* **2001**, *40*, 3734–3738.
[42] G. Tircso, A. Benyei, R. Kiraly, I. Lazar, R. Pal, E. Brucher, *Eur. J. Inorg. Chem.* **2007**, 701–713.
[43] B. Song, T. Storr, S. Liu, C. Orvig, *Inorg. Chem.* **2002**, *41*, 685–692.
[44] A. E. Martell, R. M. Smith, *Critical Stability Constants*, Plenum Press, New York, **1974–1989**, vols. 1–6; NIST Standard Reference Database 46 (*Critically Selected Stability Constants of Metal Complexes*), Version 7.0, **2003**.
[45] W. N. Lipscomb, N. Sträter, *Chem. Rev.* **1996**, *96*, 2375–2433.
[46] N. V. Kaminskaia, Ch. He, S. J. Lippard, *Inorg. Chem.* **2000**, *39*, 3365–3373.
[47] R. D. Hanckock, *Acc. Chem. Res.* **1990**, *23*, 253–257.
[48] L. Maier, *Helv. Chim. Acta* **1969**, *52*, 827–845.
[49] L. Maier, *J. Organomet. Chem.* **1979**, *178*, 157–169.
[50] Z. Otwinowski, W. Minor, *HKL Denzo and Scalepack Program Package*, Nonius BV, Delft, **1997**. For a reference see: Z. Otwinowski, W. Minor, *Methods Enzymol.* **1997**, *276*, 307–326.
[51] A. Altomare, G. Cascarano, C. Giacovazzo, A. Guagliardi, M. C. Burla, G. Polidori, M. Camalli, *J. Appl. Crystallogr.* **1994**, *27*, 435.
[52] G. M. Sheldrick, *SHELXL97. Program for Crystal Structure Refinement from Diffraction Data*, University of Göttingen, Göttingen, **1997**.
[53] C. F. Baes Jr, R. E. Mesmer, *The Hydrolysis of Cations*, Wiley, New York, **1976**.
[54] M. Kývala, I. Lukeš, *International Conference, Chemometrics '95*, p. 63. Pardubice, Czech Republic, **1995**; the full version of *"OPIUM"* is available (free of charge) on http://www.natur.cuni.cz/~kyvala/opium.html.

Received: January 4, 2007
Published Online: June 27, 2007

 © 2007 Wiley-VCH Verlag GmbH & Co. KGaA, Weinheim 

DOI: 10.1002/ejic.200700156

# Hydrothermal Syntheses and Characterizations of Three Coordination Polymers Based on Mixed Organic Ligands

Guo-Ping Yang,[a] Yao-Yu Wang,*[a] Lu-Fang Ma,[a,b] Jian-Qiang Liu,[a] Ya-Pan Wu,[a] Wei-Ping Wu,[a] and Qi-Zhen Shi[a]

**Keywords:** Copper / Manganese / Coordination polymers / Hydrogen bonds

Three new coordination polymers, namely $\{[Cu_2(bptc)(4,4'\text{-bpy})(H_2O)_2]\cdot 2H_2O\}_n$ (**1**), $\{Cu_2(bptc)(bpe)(H_2O)_6\}_n$ (**2**), and $\{[Mn(H_2bptc)(H_2O)_4]\cdot 2bpe\}_n$ (**3**) [$H_4$bptc = 3,3′,4,4′-biphenyltetracarboxylic acid, 4,4′-bpy = 4,4′-bipyridine, bpe = *trans*-1,2-bis(4-pyridyl)ethene], were rationally designed and hydrothermally synthesized at different pH values. Their structures were determined by X-ray diffraction on single crystals. Compound **1** exhibits a 3D network with 1D open channels that contain free solvent water molecules, and two kinds of chiral, helical, hydrogen-bonded chains exist in the neighboring holes. Both compounds **2** and **3** show a 3D supramolecular network that is connected through hydrogen bonds. Compound **2** also shows weak Cu···O semicoordinated interactions that are based on 1D chains. Importantly, bptc reveals three different coordination modes in these compounds: the four carboxylic groups combine with metal ions by bis(monodentate) and bis(chelate) fashions in **1**, whereas only two carboxylic groups are bis(monodentate) in **2** and **3**, respectively, and the 4,4′-carboxylic groups are protonated in **3**. The elemental analysis, IR spectra, UV/Vis spectra, and TG analysis for compounds **1**, **2**, and **3** are discussed. Additionally, the XRPD is also studied for compound **1**.
(© Wiley-VCH Verlag GmbH & Co. KGaA, 69451 Weinheim, Germany, 2007)

## Introduction

The design and construction of metal–organic coordination polymers is of current interest in the fields of supramolecular chemistry and crystal engineering.[1] Major reasons for this interest stem from their intriguing variety of topologies and structural diversity,[2] such as helixes[3]and diamondoid nets[4] and because of their potential applications as functional materials,[5] such as heterogeneous catalysis,[6] molecular recognition,[7] magnetism,[8] gas storage,[9] ion exchange,[10] nonlinear optics,[11] and electrical conductivity.[12] In order to build these molecular architectures, polycarboxylates are often employed as bridging ligands to construct coordination polymers owing to their versatile coordination modes and high structural stability.[13] These polymeric solids can be essentially regarded as a class of metal polycarboxylate salts. Hence, the structures of the resulting compounds are influenced by the degree of deprotonation, the coordination modes and capabilities, the size and shape of the polycarboxylic acids, as well as by the coordination spheres of the metal centers. Thus, it is possible to synthesize polymeric frameworks with interesting topologies through the appropriate choice of ligand, tailoring, and manipulation of the reaction conditions, including pH, temperature, stoichiometry, and the addition of templates or structure-directing agents. For resolving the poor solubility of reactants and products, the hydrothermal reaction technique offers a powerful synthetic route to prepare polymeric solids with better crystallinity[14] than traditional solution techniques such as evaporation, diffusion, and cooling etc. In most cases, water is not only a solvent but also acts as a competing ligand in these hydrothermal reactions. This phenomenon is observed in many coordination polymers that are constructed from polycarboxylate ligands where the water molecules usually act as terminal or bridging ligands in the coordination sphere of the metal; thus, the variety of the assembled structural topologies of the polymers increases.

According to the above strategy, 3,3′,4,4′-biphenyltetracarboxylic acid ($H_4$bptc, Scheme S1, Supporting Information), which has eight potential donor oxygen atoms, is undoubtedly a better choice as the ligand for the construction of novel metal–organic coordination polymers owing to its quadruple carboxylic dentate arms. However, to the best of our knowledge, polymers containing bptc have been scarcely studied so far.[15] With the aim to understand the coordination chemistry of bptc and to prepare new materials with interesting structures and excellent physical properties, we recently started to research this kind of coordination polymer. We also notice that the introduction of N-containing auxiliary ligands, such as 4,4′-bipyridine (4,4′-

[a] Department of Chemistry, Shaanxi Key Laboratory of Physico-Inorganic Chemistry, Northwest University, Xi'an 710069, P. R. China
Fax: +86-29-88303798
E-mail: wyaoyu@nwu.edu.cn
[b] Department of Chemistry, Luoyang Normal University, Luoyang 471022, P. R. China
Supporting information for this article is available on the WWW under http://www.eurjic.org or from the author.

 © 2007 Wiley-VCH Verlag GmbH & Co. KGaA, Weinheim 

bpy) and *trans*-1,2-bis(4-pyridyl)ethene (bpe), into the {M-bptc}(M = transition metal) system may lead to the structural evolution of these metal–organic compounds and their structural motifs may ultimately be fine-tuned. Herein, we report three interesting coordination polymers with mixed organic ligands, $\{[Cu_2(bptc)(4,4'\text{-bpy})(H_2O)_2]\cdot 2H_2O\}_n$ (**1**), $\{Cu_2(bptc)(bpe)(H_2O)_6\}_n$ (**2**), and $\{[Mn(H_2bptc)(H_2O)_4]\cdot 2bpe\}_n$ (**3**). Our results demonstrate that bptc adopts various coordination modes in the three compounds (Scheme S2, Supporting Information). Interestingly, two kinds of hydrogen-bonded-directed chiral helices exist in 1D open channels of compound **1**.

## Results and Discussion

### General Synthesis

Because the mixing of metal salts and carboxylate solutions usually resulted in precipitation in traditional aqueous reactions, which makes the growth of crystals difficult, the hydrothermal method was adopted in these reactions. The use of hydrothermal conditions causes a reaction to shift from the kinetic to the thermodynamic domain. By performing parallel experiments, it was found that the pH values of the reaction solutions play an important role in the isolation of the three compounds, as is the case for some other metal polycarboxylate coordination polymers reported.[15b,16] The three compounds were prepared at different pH values: compound **1** at pH 6, compound **2** at pH 7, and compound **3** at pH 4. If the pH values of the reactions were lower or higher than those listed in the Experimental Section, no products could be obtained. Besides the pH, a suitable steric geometry of the reactants is also very important for the fabrication of the resulting coordination architectures. As described in the Experimental Section, although the synthetic conditions are very similar, only a small difference in the steric demands of the reactants, for example between 4,4′-bpy and bpe, results in the different coordination architectures of compounds **1** and **2**. However, we found that the above reactions were not sensitive to the reaction temperature. If the reaction temperature was set 10 °C above or below 145 °C, the intended crystals still formed.

### Description of the Structures

#### *$\{[Cu_2(bptc)(4,4'\text{-bpy})(H_2O)_2]\cdot 2H_2O\}_n$ (1)*

Single-crystal X-ray structural analysis showed that compound **1** crystallizes in the monoclinic space group $P2_1/c$, with two copper(II) atoms, one hexadentate bptc ligand, one 4,4′-bpy ligand, two coordinated waters, and two lattice water molecules in each crystallographic unit (Figure 1). Each copper atom has a distorted square-pyramidal environment (tetragonality parameter $\tau = 0.55$)[17] and binds equatorially to three oxygen atoms (O1, O3A and O4A) of two different bptc ligands and one nitrogen atom (N1) of 4,4′-bpy; a water molecule ($O_w5$) coordinates in the apical position. The equatorial plane of the copper atom is tetrahedrally distorted (maximum atomic deviation 0.046 Å), with the metal atom displaced by 0.207 Å from the best mean plane toward the apical ligand.

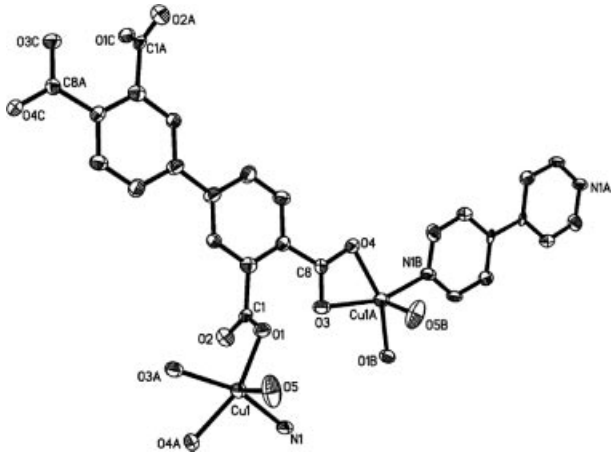


Figure 1. ORTEP representation (30% thermal probability ellipsoids) of the crystal structure of compound **1**. Hydrogen atoms and the lattice waters are omitted for clarity.

Compound **1** exhibits an extended 3D framework involving 1D open channels when viewed along the crystallographic *c* axis (Figure 2). The approximate dimensions of these channels are $15.55 \times 8.81$ Å (calculated from the distance of the neighboring $Cu^{II}$ atoms),[18] which are large enough to encapsulate guest solvent water molecules. When viewed along the crystallographic *b* axis, the bptc and 4,4′-bpy ligands alternate one by one in each layer to form huge "infinite sandwiches"[19] (Figure S1, Supporting Information). The planes of the pyridyl rings and phenyl rings are offset between the adjacent layers with a face-to-face separation with a center-to-center distance of 3.844 Å and a dihedral angle of 8.43°. To the best of our knowledge, compound **1** represents the first example of a perfect molecular network building upon ligands bptc and 4,4′-bpy with copper in which the four carboxylate groups of bptc take part in coordination: the two carboxylate groups (3,3′-$COO^-$) adopt bis(monodentate) coordination with two different copper ions, the other carboxylate groups (4,4′-$COO^-$) are bis(chelated) with two dissimilar copper cations, and the 4,4′-bpy ligands are coordinatively bridged with them.

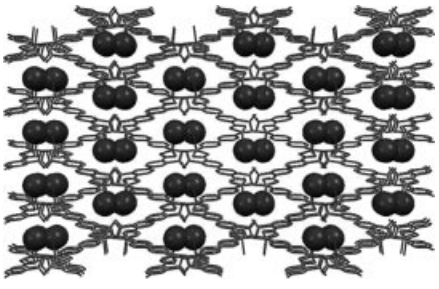

Figure 2. A perspective view of the 3D network of compound **1** containing 1D open channels encapsulating water molecules.

 © 2007 Wiley-VCH Verlag GmbH & Co. KGaA, Weinheim 

Multiple hydrogen bonds are known to cooperatively exert a dramatic influence on the control of molecular self-assembly in chemical and biological systems,[13b,20] and some examples of hydrogen-bonded helices have been reported.[21] The most fascinating structural feature of compound **1** is that chiral, helical, hydrogen-bonded (lengths and angles are listed in Table S1, Supporting Information) chains also exist in 1D open channels. Interestingly, when viewed along the crystallographic *a* axis, we found that the hydrogen-bonded chains, which are composed of coordinated water molecules (O5), carboxylate oxygen atoms (O2), and lattice water molecules (O6), show two different kinds of chiral helices (one is left-handed and the other is right-handed) in the neighboring holes (Figure 3) and that the winding axes are parallel to the *c* axis. The two parallel helices exist concurrently, and they are enchased in 1D channels by hydrogen bonds. So far, the examples that have two kinds of helices are still few.[3e,21c,22] Obviously, these strong hydrogen bonds undoubtedly steer the rotational direction of the helix.[23] It is worth noting that the use of hydrogen bonds as a steering force is becoming a very important strategy in crystal engineering.[24] To date, studies on this aspect are unprecedented with respect to the bptc ligand. Additionally, the O6 atom donates a hydrogen bond towards carboxyl oxygen atom O1 [$O_w6\cdots O_{COO}1$ = 2.903(2) Å] that is situated on the bptc ligand of the host framework. This additional interaction has an important effect on the stability of the 1D chiral, helical, hydrogen-bonded chains.

Figure 3. The right-handed (a) and left-handed (b) chiral helical hydrogen-bonded chains in the neighboring holes of compound **1** containing free solvent water molecules (light gray balls, O6), coordinated waters (dark gray balls, O5), and uncoordinated oxygen atoms (black balls,O2).

### *{Cu$_2$(bptc)(bpe)(H$_2$O)$_6$}$_n$ (2)*

The crystal structure of compound **2** consists of a neutral 1D zigzag chain based on alternating bptc and bpe ligands and crystallizes in the $P\bar{1}$ space group. As shown in Figure 4, in each asymmetry unit, compound **2** is composed of two copper(II) atoms, one bis(monodentate) bptc ligand, one bpe ligand, and six coordinated water molecules. The coordinated sphere of each copper atom is a distorted trigonal bipyramid with three water molecules in the equatorial plane, and a carboxylate oxygen atom (4,4′-COO$^-$) of bptc and a nitrogen atom of bpe occupy the apical positions.

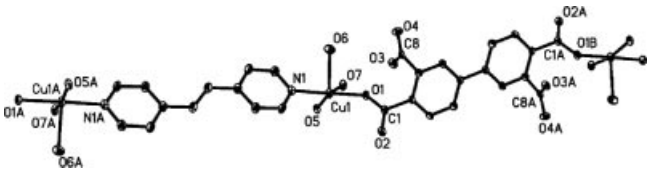


Figure 4. View of the 1D zigzag coordination polymer with alternating bptc and bpe ligands in compound **2** (30% thermal probability ellipsoids).

However, the copper atoms have a weak equatorial connection to semicoordinated centrosymmetrically related water molecules [Cu1···O5 = 2.896(4) Å, symmetry code: $1 - x,1 - y,1 - z$], resulting in a 5 + 1 coordination sphere for the copper atom (Figure 5). The equatorial plane of the copper atom has a moderate tetrahedral distortion (maximum atomic deviation 0.074 Å), the copper atom is displaced by only 0.073 Å from this plane towards the nitrogen atom. The dihedral angles between the equatorial plane and the planes of bptc and bpe are 87.62 and 73.18°, respectively. Furthermore, two pyridyl rings of bpe are parallel with each other at the distance of 0.528 Å.

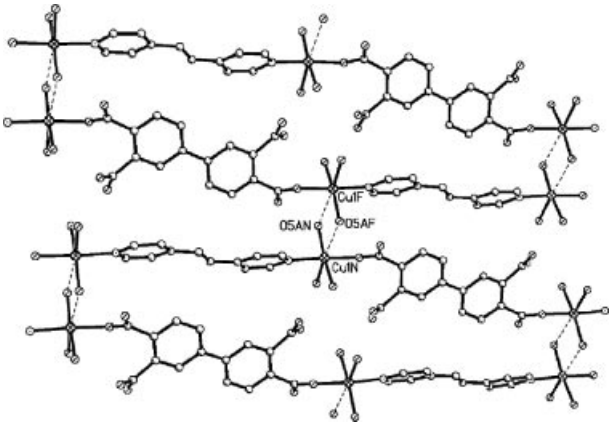


Figure 5. The 2D layer of compound **2** by Cu···O$_w$ semicoordination and hydrogen bonds. Hydrogen bonds are deleted for clarity.

The shortest intermolecular metal···metal distance is Cu1F···Cu1N and measures 3.862 Å. It occurs between the pairs of 1D staggered chains (···ABAB··· fashion) that are connected through the semicoordination mentioned above and simultaneously the chains form a 2D network that including interlocking of hydrogen bonds. In other reported papers,[25] we found that only the lower dimensional architectures (1D chains or dimers) existed by weak Cu···O interactions. Because compound **2** possesses multiuncoordinated carboxylate oxygen atoms and coordinated water molecules, hydrogen bonds connect the 2D layers into a 3D supramolecular framework.

 © 2007 Wiley-VCH Verlag GmbH & Co. KGaA, Weinheim 

### *{[Mn(H$_2$bptc)(H$_2$O)$_4$]·2bpe}$_n$ (3)*

Compounds **3** and **2** have the same space group, $P\bar{1}$. The crystal structure of compound **3** also contains a neutral 1D chain, but here the chain is only based on bptc and the bpe ligands just exist as free solvent molecules in it. At the same time, different from **2**, two pyridyl rings of the bpe ligand are not parallel and have a dihedral angle of 2.72°. The manganese atoms are 4 + 2 six-coordinate in a slightly distorted octahedral coordination environment with four water molecules located in the equatorial plane and the two oxygen atoms (3,3′-COO) from the bptc ligand occupy the apical positions, as depicted in Figure 6. The best equatorial plane is defined by the O1, O2, O1A, and O2A atoms, which are perfectly planar (no deviation in the four atoms) and the manganese atom lies in this plane.

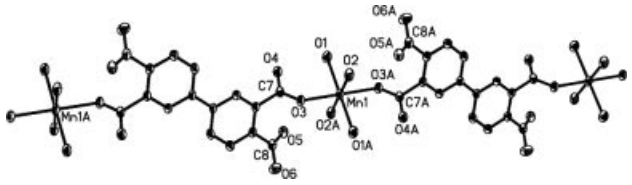


Figure 6. View of the coordination environment of $Mn^{II}$ in compound **3**. Hydrogen atoms and free bpe ligands are deleted for clarity.

According to the results of X-ray diffraction, there are two uncoordinated carboxylate groups of the bptc ligand that are protonated in compound **3**. This is dissimilar from compound **2** where two carboxylate groups do not take part in coordination even though they are deprotonated. The neighboring 1D chains are connected through hydrogen bonds between the coordinated water molecules and the oxygen atoms of the carboxylate groups [$O_w1\cdots O_{COO}6$ = 2.751(5) Å] (Figure S2, Supporting Information). The resulting wavelike 2D network contains almost rhombic holes in which the Mn···Mn distance through the bptc is 14.584 Å, whereas the distance through the water oxygen atoms of the bptc bridge is 7.970 Å, and there are no solvent molecules in the rhombic holes. The bpe ligands act as pillars, as in the case of the 4,4′-bpy ligand,[26] and link the 2D layers together to form a 3D network by using hydrogen-bonding recognition [$O_w2\cdots N1$ = 2.809(5) Å and $O_{COO}6\cdots N2$ = 2.560(4) Å] (Figure 7) as in compound **2**.

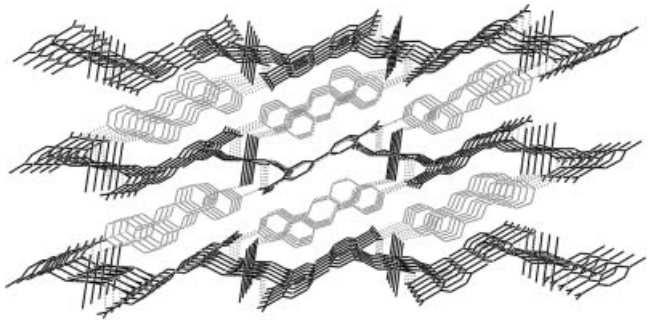

Figure 7. The 3D network of compound **3** constructed from 2D layers with bpe ligands as the pillars. The bpe ligands are represented in grey.

### Spectroscopic Characterization, Thermal Gravimetric Analysis, and XRPD Measurement

The IR spectra of the three compounds were performed as KBr pellets in the range 4000–400 cm$^{-1}$.These compounds show the characteristic bands of the carboxylate groups in the usual region[27] at 1630–1550 cm$^{-1}$ for the asymmetric vibration and at 1410–1360 cm$^{-1}$ for the symmetric, and the value $\Delta[\nu_{as}(COO^-) - \nu_s(COO^-)] > 200$ cm$^{-1}$ for the three compounds reveals that the carboxylate group is coordinated in a monodentate fashion,[28] which is consistent with the results of the X-ray analysis. Also observed were the bands for the 4,4′-bpy ligand at 1593, 1571, and 1494 cm$^{-1}$ for **1**, the bands of the bpe ligand at 1551 cm$^{-1}$ for **2** and 1574 cm$^{-1}$, 1506 cm$^{-1}$ for **3**. The splitting of $\nu_{as}(COO^-)$ in **1** confirms that the carboxylate groups have a variety of coordination fashions. These proposals are in accordance with the crystal structures. The UV/Vis spectra of the three compounds were recorded in *N*,*N*-dimethylformamide at room temperature and are characterized by several spectral regions (Figures S3, S4, and S5, Supporting Information). The maximum absorption band at 276 nm for the bptc ligand is ligand-centered (LC) due to π–π* transitions. The peaks at 286, 289, and 288 nm for compounds **1**, **2**, and **3**, respectively, are due to d–d transitions and the low-energy bands at 283, 299, and 298 nm, respectively, are assigned to metal-to-ligand charge-transfer transitions (MLCT).[29] This slight shift in absorption bands of the compounds relative to that of the bptc ligand is caused by the effect of metal-to-ligand charge-transfer transitions.

To examine the thermal stability of the three compounds, thermal gravimetric analyses (TGA) were carried out between 50–800 °C. As shown in Figure 8, for **1** a total weight loss of 11.58% occurred over the temperature range 67–158 °C, corresponding to the loss of four water molecules (calcd. 10.57%). When the temperature was increased to ca. 268 °C, the product began to lose the bptc and 4,4′-bpy ligands. Finally, the remaining weight of 19.10% corresponds to the percentage (calcd. 20.99%) of Cu and O components, indicating that the final product is $Cu_2O$. The TGA traces of **2** and **3** are much like that observed for **1**: compound **2** loses six water molecules between 74 and 171 °C (observed 15.61%, calcd. 14.54%), and compound

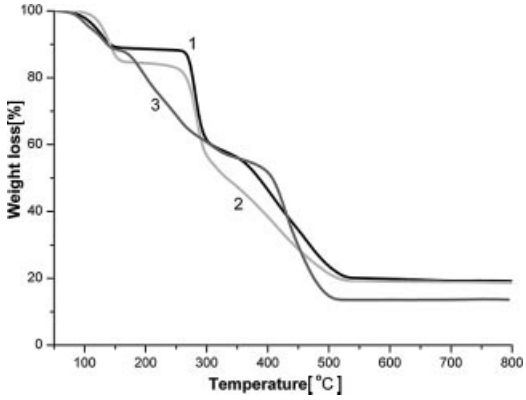


Figure 8. The TG curves of compounds **1**, **2**, and **3**.

 © 2007 Wiley-VCH Verlag GmbH & Co. KGaA, Weinheim 

**3** loses two bpe ligands and four water molecules between 79 and 384 °C (observed 46.27%, calcd. 46.90%), respectively. The remaining weight of 18.71% (calcd. 19.24%) for **2** (observed 13.33%, calcd. 12.55% for **3**) indicates that the final product is $Cu_2O$ ($MnO_3$). Additionally, to confirm the phase-pure and the stable framework of compound **1**, the original sample and dehydrated sample were characterized by X-ray powder diffraction (XRPD) at room temperature. The pattern that was simulated from the single-crystal X-ray data of compound **1** was in good agreement with those that were observed, thus compound **1** was obtained as a single phase. For compound **1**, after heating at 85 °C for 3 h, the guest water molecules were removed (the evacuated frameworks are defined as **1′**). The XRPD pattern of **1′** is similar to compound **1**, although minor differences can be seen in the positions, intensities, and widths of some peaks (Figure S6, Supporting Information), which indicates that the framework of compound **1** is retained after the removal of the guest molecules.

## Conclusions

As described above, we successfully designed and synthesized three coordination polymers constructed from bptc and N-containing auxiliary ligands (4,4′-bpy, bpe) at different pH values. Comparing the structure of compounds **1**, **2**, and **3**, it was found that the different coordination modes of the bptc ligand may have a significant effect on the formation and dimension of the resulting structures. The successful preparation of three compounds provides a valuable approach for the construction of many other coordination polymers with different dimensional structures by the introduction of another kind of organic ligand. More significantly, compound **1** contains 1D open channels that contain free water molecules and chiral hydrogen bonded helices exist.

## Experimental Section

**Materials:** All chemicals purchased were of reagent grade and used without further purification. The bptc ligand was obtained by hydrolyzing 4,4′-biphthalic anhydride that is bought from Alfa Aesar. All syntheses were carried out in 25-mL Teflon-lined autoclaves under autogenous pressure. The reaction vessels were filled to approximately 60% volume capacity. Distilled water was used in all reactions.

**$\{[Cu_2(bptc)(4,4'\text{-bpy})(H_2O)_2]\cdot 2H_2O\}_n$ (1):** A mixture of $Cu(NO_3)_2\cdot 8H_2O$ (332 mg, 1.0 mmol), $H_4$bptc (165 mg, 0.5 mmol), 4,4′-bpy (78 mg, 0.5 mmol), and water (15 mL) was adjusted to pH 6 with a 1 M NaOH solution and then heated at 145 °C for 4 d. Well-shaped blue block crystals were obtained when the mixture was cooled to room temp. at 10 °C h$^{-1}$. Yield: 61.3%. IR (KBr): $\tilde{\nu}$ = 3472 (s), 3215 (m), 1613 (s), 1593 (s), 1571 (m), 1494 (m), 1423 (s), 1384 (s), 1221 (m), 1166 (w), 1096 (w), 1071 (m), 873 (s), 846 (s), 822 (s), 649 (m), 568 (m), 552 (w), 460 (w) cm$^{-1}$.$C_{26}H_{22}Cu_2N_2O_{12}$ (681.55): calcd. C 45.82, H 3.25, N 4.11; found C 45.69, H 3.22, N 4.20.

**$\{Cu_2(bptc)(bpe)(H_2O)_6\}_n$ (2):** A mixture of $Cu(OAc)_2\cdot H_2O$ (200 mg, 1.0 mmol), $H_4$bptc (165 mg, 0.5 mmol), bpe (91 mg, 0.5 mmol), and water (15 mL) was adjusted to pH 7 with a 1 M NaOH solution and then heated at 145 °C for 4 d. Blue-green crystals were obtained when the mixture was cooled to room temp. at 10 °C h$^{-1}$. Yield: 65.8%. IR (KBr): $\tilde{\nu}$ = 3397 (s), 3155 (m), 2921 (m), 1608 (s), 1551 (s), 1483 (m), 1370 (s), 1294 (m), 1159 (w), 1097 (w), 978 (m), 891 (w), 838 (m), 790 (m), 697 (w), 662 (m), 552 (m), 470 (m) cm$^{-1}$. $C_{28}H_{28}Cu_2N_2O_{14}$ (743.60): calcd. C 45.22, H 3.80, N 3.77; found C 45.35, H 3.62, N 3.64.

**$\{[Mn(H_2bptc)(H_2O)_4]\cdot 2bpe\}_n$ (3):** A mixture of $Mn(OAc)_2\cdot 4H_2O$ (123 mg, 0.5 mmol), $H_4$bptc (165 mg, 0.5 mmol), bpe (182 mg, 1.0 mmol), and water (15 mL) was adjusted to pH 4 with a 1 M NaOH solution and then heated at 145 °C for 4 d. Pale yellow crystals were obtained when the mixture was cooled to room temp. at 10 °C h$^{-1}$. Yield: 53.1%. IR (KBr): $\tilde{\nu}$ = 3333 (s), 3085 (m), 2225 (w), 1940 (w), 1626 (m), 1574 (s), 1506 (m), 1480 (m), 1403 (s), 1360 (m), 1250 (w), 1184 (w), 1094 (m), 944 (m), 899 (m), 868 (w), 793 (s), 694 (m), 636 (m), 544 (w), 450 (w) cm$^{-1}$. $C_{40}H_{36}MnN_4O_{12}$ (819.67): calcd. C 62.82, H 4.74, N 7.33; found C 62.73, H 4.89, N 7.21.

**Physical Measurements:** Elemental analyses (C, H, and N) were determined with a PE 2400 Elemental analyzer. Infrared spectra of KBr pellets were recorded with a BRUKER EQUINOX-55 spectrometer in the range of 4000–400 cm$^{-1}$. Thermal analyses were performed with a NETZSCH STA 449C microanalyzer with a heating rate of 10 °C min$^{-1}$ under a nitrogen atmosphere. Electronic spectra were recorded with a Cary 300 Bio UV/Vis spectrophotometer in the range 270–450 nm at ambient temperature. The XRPD pattern was recorded with a Pigaku D/Max 3III diffractometer.

**Crystal Data Collection and Refinement:** Diffraction experiments for **1**, **2**, and **3** were carried out with Mo-$K_\alpha$ radiation by using a BRUKER SMART APEX-CCD diffractometer at 291(2) (for **1**, **2**) and 296(2) (for **3**) K. A summary of the crystallographic data and structure refinement details are given in Table 1, and selected bond

Table 1. Crystallographic data and structure refinement details for compounds **1**, **2**, and **3**.

| Compound | **1** | **2** | **3** |
|---|---|---|---|
| Empirical formula | $C_{26}H_{22}Cu_2N_2O_{12}$ | $C_{28}H_{28}Cu_2N_2O_{14}$ | $C_{40}H_{36}MnN_4O_{12}$ |
| Formula weight | 681.55 | 743.60 | 819.67 |
| Crystal system | monoclinic | triclinic | triclinic |
| Space group | $P2_1/c$ | $P\bar{1}$ | $P\bar{1}$ |
| Crystal size [mm] | 0.14×0.08×0.05 | 0.13×0.10×0.05 | 0.31×0.19×0.08 |
| $a$ [Å] | 6.696(7) | 7.541(2) | 7.9703(2) |
| $b$ [Å] | 17.504(1) | 8.345(2) | 9.6846(2) |
| $c$ [Å] | 11.322(2) | 11.793(3) | 12.6091(1) |
| $\alpha$ [°] | 90.00(1) | 106.204(4) | 87.237(2) |
| $\beta$ [°] | 95.445(1) | 90.862(4) | 87.197(2) |
| $\gamma$ [°] | 90.00(2) | 97.673(4) | 74.492(2) |
| $V$ [Å$^3$] | 1321(2) | 705.2(3) | 936.1(2) |
| $Z$ | 2 | 1 | 1 |
| $T$ [K] | 291(2) | 291(2) | 296(2) |
| $D_{calcd.}$ [g cm$^{-3}$] | 1.713 | 1.751 | 1.454 |
| $\mu$ [mm$^{-1}$] | 1.681 | 1.587 | 0.424 |
| $F$(000) | 692 | 380 | 425 |
| Limiting indices | $-7\le h\le 7$ | $-9\le h\le 9$ | $-9\le h\le 8$ |
| | $-20\le k\le 20$ | $-10\le k\le 10$ | $-11\le k\le 5$ |
| | $-13\le l\le 13$ | $-14\le l\le 14$ | $-15\le l\le 15$ |
| $\lambda$ [Å] | 0.71073 | 0.71073 | 0.71073 |
| $\theta$ Range [°] | 2.95–25.10 | 2.57–25.50 | 1.62–25.10 |
| Reflections collected | 9257 | 5099 | 4804 |
| Goodness-of-fit on $F^2$ | 0.942 | 1.041 | 1.097 |
| $R_1$[a], $wR_2$[b] [$I>2\sigma(I)$] | 0.0737, 0.1413 | 0.0492, 0.0984 | 0.0584, 0.1292 |
| $R_1$[a], $wR_2$[b] [all data] | 0.1686, 0.1832 | 0.0793, 0.1128 | 0.1050, 0.1604 |

[a] $R_1 = \Sigma||F_o| - |F_c||/\Sigma|F_o|$. [b] $wR_2 = [\Sigma w(F_o^2 - F_c^2)^2/\Sigma w(F_o^2)^2]^{1/2}$.

 © 2007 Wiley-VCH Verlag GmbH & Co. KGaA, Weinheim 

Table 2. Selected bond lengths [Å] and angles [°] of compounds **1**, **2**, and **3**.

| **1** | | **2** | | **3** | |
|---|---|---|---|---|---|
| Cu1–O1 | 1.948(6) | Cu1–O7 | 1.956(3) | Mn1–O1 | 2.176(3) |
| Cu1–N1 | 1.973(7) | Cu1–O5 | 1.962(3) | Mn1–O2 | 2.216(3) |
| Cu1–O4[a] | 1.990(6) | Cu1–O1 | 1.971(3) | Mn1–O3 | 2.150(2) |
| Cu1–O3[a] | 2.050(6) | Cu1–N1 | 2.019(4) | Mn1–O1[b] | 2.176(3) |
| Cu1–O5 | 2.216(7) | Cu1–O6 | 2.324(4) | Mn1–O2[b] | 2.216(3) |
| | | | | Mn1–O3[b] | 2.150(2) |
| O1–Cu1–N1 | 98.1(3) | O7–Cu1–O5 | 167.72(1) | O1–Mn1–O2 | 87.12(1) |
| O1–Cu1–O4[a] | 158.3(3) | O7–Cu1–O1 | 88.11(1) | O1–Mn1–O3 | 86.89(2) |
| N1–Cu1–O4[a] | 96.7(3) | O5–Cu1–O1 | 91.46(2) | O1–Mn1–O2[b] | 92.89(2) |
| O1–Cu1–O3[a] | 98.0(2) | O7–Cu1–N1 | 88.18(2) | O1–Mn1–O3[b] | 93.12(1) |
| N1–Cu1–O3[a] | 160.1(3) | O5–Cu1–N1 | 92.26(1) | O2–Mn1–O3 | 89.72(2) |
| O4[a]–Cu1–O3[a] | 64.8(2) | O1–Cu1–N1 | 176.26(2) | O2–Mn1–O1[b] | 92.89(2) |
| O1–Cu1–O5 | 94.9(3) | O7–Cu1–O6 | 92.94(2) | O2–Mn1–O3[b] | 90.28(2) |
| N1–Cu1–O5 | 97.6(3) | O5–Cu1–O6 | 99.32(1) | O3–Mn1–O1[b] | 93.12(1) |
| O4[a]–Cu1–O5 | 98.8(3) | O1–Cu1–O6 | 87.43(1) | O3–Mn1–O2[b] | 90.28(2) |
| O3[a]–Cu1–O5 | 92.7(3) | N1–Cu1–O6 | 92.46(2) | O1[b]–Mn1–O2[b] | 87.12(1) |

[a] Symmetry codes: $x$, $-y + 3/2$, $z + 1/2$. [b] Symmetry codes: $-x$, $1 - y$, $2 - z$.

lengths and angles are listed in Table 2. Both structures were solved by direct methods and refined with the full-matrix least-squares technique on $F^2$ by using SHELXS-97[30] and SHELXL-97.[31] All non-hydrogen atoms were refined anisotropically. The water H atoms were located in a different Fourier map and refined with restrained O–H bond lengths [0.82(2) Å] in **1**. CCDC-634976 (for **1**), -634977 (for **2**), and -634978 (for **3**) contain the supplementary crystallographic data for this paper. These data can be obtained free of charge from The Cambridge Crystallographic Data Centre via www.ccdc.cam.ac.uk/data_request/cif.

**Supporting Information** (see footnote on the first page of this article): Coordination modes of the bptc ligand, table of hydrogen bond lengths and angles, UV/Vis spectra for the three compounds, XRPD pattern for compound **1**, and additional plots of the structures.

## Acknowledgments

This work was supported by the National Natural Science Foundation of China (No. 20471048) and TRAPOYT, and Specialized Research Fund for the Doctoral Program of Higher Education (No. 20050697005).

[1] a) G. F. Swiegers, T. Malefetse, *J. Chem. Rev.* **2000**, *100*, 3483–3538; b) M. Albrecht, *Chem. Rev.* **2001**, *101*, 3457–3498; c) J. P. Zhang, X. M. Chen, *Chem. Commun.* **2006**, 1689–1699; d) A. Y. Robin, K. M. Fromm, *Coord. Chem. Rev.* **2006**, *250*, 2127–2157; e) J. Mrozinski, *Coord. Chem. Rev.* **2005**, *249*, 2534–2548; f) M. J. Rosseinsky, *Microporous Mesoporous Mater.* **2004**, *73*, 15–30; g) J. L. Serrano, T. Sierra, *Coord. Chem. Rev.* **2003**, *242*, 73–85.

[2] B. Moulton, M. J. Zaworotko, *Chem. Rev.* **2001**, *101*, 1629–1658.

[3] a) O. Mamula, A. von Zelewsky, T. Bark, G. Bernardinelli, *Angew. Chem. Int. Ed.* **1999**, *38*, 2945–2948; b) X. M. Chen, G. F. Liu, *Chem. Eur. J.* **2002**, *8*, 4811–4817; c) P. Grosshans, A. Jouaiti, V. Bulach, J. M. Planeix, M. W. Hosseini, J. F. Nicoud, *Chem. Commun.* **2003**, 1336–1337; d) X. J. Luan, Y. Y. Wang, D. S. Li, P. Liu, H. M. Hu, Q. Z. Shi, S. M. Peng, *Angew. Chem. Int. Ed.* **2005**, *44*, 3864–3867; e) D. R. Xiao, E. B. Wang, H. Y. An, Y. G. Li, Zh. M. Su, Ch. Y. Sun, *Chem. Eur. J.* **2006**, *12*, 6528–6541.

[4] a) L. R. MacGillivray, S. Subramanion, M. J. Zaworotko, *J. Chem. Soc. Chem. Commun.* **1994**, 1325–1326; b) O. M. Yaghi, H. Li, *J. Am. Chem. Soc.* **1995**, *117*, 10401–10402; c) O. R. Evans, R. G. Xiong, Z. Y. Wang, G. K. Wong, W. B. Lin, *Angew. Chem.* **1999**, *111*, 557–559; *Angew. Chem. Int. Ed.* **1999**, *38*, 536–538.

[5] C. Janiak, *Dalton Trans.* **2003**, 2781–2804.

[6] a) J. S. Seo, D. Whang, H. Lee, S. I. Jun, J. Oh, Y. J. Jeon, K. Kim, *Nature* **2000**, *404*, 982–986; b) B. Gomez-Lor, E. Gutiérrez-Puebla, M. Iglesias, M. A. Monge, C. Ruiz-Valero, N. Snejko, *Inorg. Chem.* **2002**, *41*, 2429–2432; c) D. Fiedler, D. H. Leung, R. G. Bergman, K. N. Raymond, *Acc. Chem. Res.* **2005**, *38*, 351–360; d) W. Tsai, Y. H. Liu, S. M. Peng, S. T. Liu, *J. Organomet. Chem.* **2005**, *690*, 415–421.

[7] a) S. S. Y. Chui, S. M. F. Lo, J. P. H. Charmant, A. G. Orpen, I. D. Williams, *Science* **1999**, *283*, 1148–1150; b) C. D. Wu, W. Lin, *Angew. Chem. Int. Ed.* **2005**, *44*, 284–287.

[8] a) Q. Ye, Y. M. Song, G. X. Wang, K. Chen, D. W. Fu, P. W. H. Chan, J. S. Zhu, S. D. Huang, R. G. Xiong, *J. Am. Chem. Soc.* **2006**, *128*, 6554–6555; b) C. Beghidja, G. Rogez, J. Kortus, M. Wesolek, R. Welter, *J. Am. Chem. Soc.* **2006**, *128*, 3140–3141.

[9] a) O. M. Yaghi, M. O'Keeffe, N. W. Ockwig, H. K. Chae, M. Eddaoudi, J. Kim, *Nature* **2003**, *423*, 705–714; b) B. Kesanli, W. Lin, *Coord. Chem. Rev.* **2003**, *246*, 305–326; c) S. Kitagawa, R. Kitaura, S. I. Noro, *Angew. Chem. Int. Ed.* **2004**, *43*, 2334–2375; d) L. Pan, B. Parker, X. Huang, D. H. Olson, J. Lee, J. Li, *J. Am. Chem. Soc.* **2006**, *128*, 4180–4181; e) J. L. C. Rowsell, O. M. Yaghi, *J. Am. Chem. Soc.* **2006**, *128*, 1304–1315.

[10] a) D. N. Dybtsev, H. Chun, S. H. Yoon, D. Kim, K. Kim, *J. Am. Chem. Soc.* **2004**, *126*, 32–33; b) L. Pan, M. B. Sander, X. Huang, J. Li, M. Smith, E. Bittner, B. Bockrath, J. K. Johnson, *J. Am. Chem. Soc.* **2004**, *126*, 1308–1309; c) M. Oh, C. A. Mirkin, *Angew. Chem. Int. Ed.* **2006**, *45*, 5492–5494.

[11] a) H. Hou, Y. Wei, Y. Song, L. Mi, M. Tang, L. Li, Y. Fan, *Angew. Chem. Int. Ed.* **2005**, *44*, 6067–6074; b) X. P. Yang, R. A. Jones, W. K. Wong, V. Lynch, M. M. Oyec, A. L. Holmes, *Chem. Commun.* **2006**, 1836–1838; c) J. P. Zhang, Y. Y. Lin, X. C. Huang, X. M. Chen, *J. Am. Chem. Soc.* **2005**, *127*, 5495–5506.

[12] a) S. L. Zheng, J. H. Yang, X. L. Yu, X. M. Chen, W. T. Wong, *Inorg. Chem.* **2004**, *43*, 830–838; b) X. Wang, C. Qin, E. Wang, Y. Li, N. Hao, C. Hu, L. Xu, *Inorg. Chem.* **2004**, *43*, 1850–1856; c) Y. Z. Tang, X. F. Huang, Y. M. Song, P. W. H. Chan, R. G. Xiong, *Inorg. Chem.* **2006**, *45*, 4868–4870.

[13] a) M. Eddaoudi, D. B. Moler, H. Li, B. Chen, T. M. Reineke, M. O'Keeffe, O. M. Yaghi, *Acc. Chem. Res.* **2001**, *34*, 319–330; b) D. Sh. Li, Y. Y. Wang, X. J. Luan, P. Liu, C. H. Zhou, M. R. Ma, Q. Z. Shi, *Eur. J. Inorg. Chem.* **2005**, 2678–2684; c) X. J. Luan, X. H. Cai, Y. Y. Wang, D. S. Li, C. J. Wang, P. Liu, H. M. Hu, Q. Z. Shi, S. M. Peng, *Chem. Eur. J.* **2006**, *12*, 6281–

 © 2007 Wiley-VCH Verlag GmbH & Co. KGaA, Weinheim 

6289; d) Sh, Q. Zang, Y. Su, Ch. Y. Duan, Y. Zh. Li, H. Zh. Zhu, Q. J. Meng, *Chem. Commun.* **2006**, 4997–4999.
[14] a) O. M. Yaghi, H. L. Li, C. Davis, D. Richardson, T. L. Groy, *Acc. Chem. Res.* **1998**, *31*, 474–484; b) S. Feng, R. Xu, *Acc. Chem. Res.* **2001**, *34*, 239–247.
[15] a) X. L. Wang, Ch. Qin, E. B. Wang, L. Xu, *Eur. J. Inorg. Chem.* **2005**, 3418–3421; b) X. L. Wang, Ch. Qin, E. B. Wang, *Cryst. Growth Des.* **2006**, *6*, 439–443; c) J. J. Wang, M. L. Yang, H. M. Hu, G. L. Xue, D. Sh. L, Q. Z. Sh, *Z. Anorg. Allg. Chem.* **2007**, *633*, 341–345.
[16] a) J. C. Dai, X. T. Wu, Z. Y. Fu, C. P. Cui, S. M. Hu, W. X. Du, L. M. Wu, H. H. Zhang, R. Q. Sun, *Inorg. Chem.* **2002**, *41*, 1391–1396; b) J. C. Dai, X. T. Wu, S. M. Hu, Z. Y. Fu, J. J. Zhang, W. X. Du, H. H. Zhang, R. Q. Sun, *Eur. J. Inorg. Chem.* **2004**, 2096–2106.
[17] A. W. Addison, T. N. Rao, J. Reedijk, J. Vin Rijin, G. C. Verschoor, *J. Chem. Soc. Dalton Trans.* **1984**, 1439–1456.
[18] a) R. Vaidhyanathan, S. Natarajan, C. N. Rao, *Dalton Trans.* **2003**, 1459–1464; b) L. Han, X. H. Bu, Q. C. Zhang, P. Y. Feng, *Inorg. Chem.* **2006**, *45*, 5736–5738; c) Q. Fang, G. S. Zhu, J. Y. Sun, F. X. Sun, S. L. Qiu, *Inorg. Chem.* **2006**, *45*, 3582–3587.
[19] A. K. Ghosh, D. Ghoshal, G. Mostafa, T. H. Lu, N. Ray Chaudhuri, *Cryst. Growth Des.* **2004**, *4*, 851–857.
[20] a) J. R. Fredericks, A. D. Hamilton, "Hydrogen Bonding Control of Molecular Self-Assembly: Recent Advances in Design, Synthesis and Analysis" in *Comprehensive Supramolecular Chemistry* (Eds.: J. P. Sauvage, M. W. Hosseini), Pergamon, Oxford, **1996**, vol. 9, ch. 16; b) J. M. Lehn, *Science* **2002**, *295*, 2400–2403; c) J. Zhang, Z. J. Li, Y. Kang, J. K. Cheng, Y. G. Yao, *Inorg. Chem.* **2004**, *43*, 8085–8091; d) S. K. Ghosh, P. K. Bharadwaj, *Eur. J. Inorg. Chem.* **2005**, 4886–4889; e) L. J. Zhou, Y. Y. Wang, C. H. Zhou, C. J. Wang, Q. Z. Shi, X. M. Peng, *Cryst. Growth Des.* **2007**, *7*, 300–306.
[21] a) Y. Song, J. H. Yu, Y. Li, G. H. Li, R. R. Xu, *Angew. Chem. Int. Ed.* **2004**, *43*, 2399–2402; b) Y. Wang, J. H. Yu, Y. Li, S. Zhan, R. R. Xu, *Chem. Eur. J.* **2003**, *9*, 5045–5055; c) D. R. Xiao, E. B. Wang, H. Y. An, Y. G. Li, L. Xu, *Cryst. Growth Des.* **2007**, *7*, 506–512.
[22] a) L. Han, M. C. Hong, R. H. Wang, J. H. Luo, Z. Z. Lin, D. Q. Yuan, *Chem. Commun.* **2003**, 2580–2581; b) S. Zang, Y. Su, Y. Li, Z. Ni, H. Zhu, Q. Meng, *Inorg. Chem.* **2006**, *45*, 3855–3857; c) Y. Q. Sun, J. Zhang, Y. M. Chen, G. Y. Yang, *Angew. Chem. Int. Ed.* **2005**, *44*, 5814–5817.
[23] a) I. Boldog, E. B. Rusanov, A. N. Chernega, J. Sieler, K. V. Domasevitch, *Angew. Chem. Int. Ed.* **2001**, *40*, 3435–3438; b) K. V. Domasevitch, I. Boldog, E. B. Rusanov, J. Hunger, S. Blaurock, M. Schröder, J. Sieler, *Z. Anorg. Allg. Chem.* **2005**, *631*, 1095–1100.
[24] a) J. W. Steed, J. L. Atwood, *Supramolecular Chemistry*, Wiley, Chichester, **2000**; b) J. L. Atwood, J. W. Steed, *Encyclopedia of Supramolecular Chemistry*, Marcel Dekker, New York, **2004**; c) K. Adachi, Y. Sugiyama, K. Yoneda, K. Yamada, K. Nozaki, A. Fuyuhiro, S. Kawata, *Chem. Eur. J.* **2005**, *11*, 6616–6628.
[25] a) J. Carranza, H. Grove, J. Sletten, F. Lloret, M. Julve, P. E. Kruger, C. Eller, D. P. Rillema, *Eur. J. Inorg. Chem.* **2004**, 4836–4848; b) H. Grove, N. Å. Frystein, L. J. Sthre, J. Sletten, *J. Mol. Struct.* **2006**, *800*, 1–17.
[26] a) M. Kondo, T. Okubo, A. Asami, S. I. Noro, T. Yoshitomi, S. Kitagawa, T. Ishii, H. Matsuzaka, K. Seki, *Angew. Chem. Int. Ed.* **1999**, *38*, 140–141; b) Zh. Shi, L. R. Zhang, Sh. Gao, G. Y. Yang, J. Hua, L. Gao, Sh. H. Feng, *Inorg. Chem.* **2000**, *39*, 1990–1993; c) Y. Q. Zheng, J. L. Lin, Z. P. Kong, *Inorg. Chem.* **2004**, *43*, 2590–2596; d) C. J. Li, Sh. Hu, W. Li, Ch. K. Lam, Y. Zh. Zh, M. L. Tong, *Eur. J. Inorg. Chem.* **2006**, 1931–1935.
[27] L. J. Bellamy, *The Infrared Spectra of Complex Molecules*: John Wiley & Sons, New York, **1958**.
[28] V. Zeleňák, I. Císařová, P. Llewellyn, *Inorg. Chem. Commun.* **2007**, *10*, 27–32.
[29] A. Volger, H. Kunkely, *Coord. Chem. Rev.* **1998**, *177*, 81–96.
[30] G. M. Sheldrick, *SHELXS*, University of Göttingen, Germany, **1997**.
[31] G. M. Sheldrick, *SHELXL, Program for the Refinement of Crystal Structures*, University of Göttingen, Germany, **1997**.

Received: February 2, 2007
Published Online: June 28, 2007

 © 2007 Wiley-VCH Verlag GmbH & Co. KGaA, Weinheim 

DOI: 10.1002/ejic.200700251

# Liquid Crystal Imidazolium Salts: Towards Materials for Catalysis and Molecular Electronics

Jean-Moïse Suisse,[a] Laurent Douce,*[a] Stéphane Bellemin-Laponnaz,[b] Aline Maisse-François,[b] Richard Welter,[b] Yasuo Miyake,[c,d] and Yo Shimizu[c]

**Keywords:** Liquid crystals / Imidazolium ions / Pd–carbenes / Homogenous catalysis / Conducting materials

1,3-Bis(4-alkyloxyphenyl)-3*H*-imidazol-1-ium trifluoromethanesulfonates, alkyl = $CH_3(CH_2)_{n-1}$, $n$ = 8, 10, 12, 14 and 16, can be derived from the analogous 4-alkyloxyphenylamines. These imidazolium salts exhibit a lamellar liquid-crystal mesophase between 99 °C and 191 °C. The smectic-A phase was fully characterised by polarising optical microscopy, differential scanning calorimetry and X-ray diffraction. We report also the synthesis, lamellar crystal structure and catalytic activity of the $Pd^{II}$ complex of the (deprotonated) carbene form of one of these salts. In addition, we measured the charged carrier mobilities in the mesophase.

(© Wiley-VCH Verlag GmbH & Co. KGaA, 69451 Weinheim, Germany, 2007)

## Introduction

Extensive studies of ionic liquids have revealed their many useful properties such as their extremely low volatility, high thermal stability, nonflammability, high chemical stability, high ionic conductivity and wide electrochemical window.[1] Such salts are extremely versatile in that changes in both the cation and its counteranion can be used to tune their properties, which for imidazolium salts in particular includes their mesomorphism.[2] The merging of imidazolium ionic liquids and liquid-crystal chemistry has indeed begun to lead to a new range of materials[1d,3] with applications in, for example, dye-sensitised solar cells,[4] electron transport systems[3b] and nanoparticle electrosynthesis.[5] Variation of the imidazolium N-substituents is a facile means of creating this range. Of additional interest is the fact that the salts can be readily deprotonated to give, formally, N-heterocyclic carbenes that are excellent ligands for transition-metal-based catalysts.[6]

Herein, we wish to report the synthesis of imidazolium liquid crystals as well as the synthesis and catalytic activity of a $Pd^{II}$ carbene complex derived from a mesomorphic imidazolium species.

## Results and Discussion

### Synthesis

Compounds **1a**–**e** were obtained − as described previously for **1c**[7] − in a two-step procedure from aniline derivatives (Scheme 1). Condensation of the aniline derivatives with glyoxal followed by treatment with chloromethyl pivalate in the presence of 1 equiv. of silver triflate gave corresponding imidazolium salts **1a**–**e** in good yields, all of which were unequivocally characterised by $^1H$ and $^{13}C\{^1H\}$ NMR, UV and FTIR spectroscopy, as well as elemental analysis.

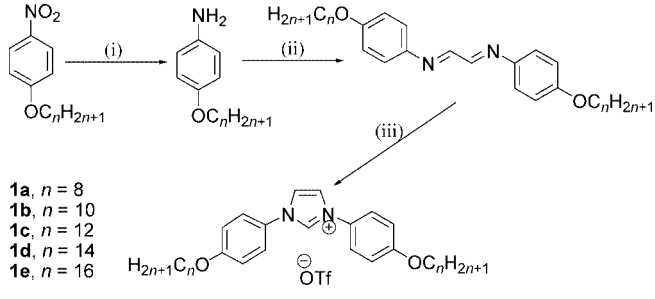


Scheme 1. Reagents and conditions: (i) hydrazine/C; (ii) glyoxal, ethanol, reflux; (iii) AgOTf, chloromethyl pivalate, $CH_2Cl_2$, 48 h reflux under inert atmosphere.

[a] Institut de Physique et Chimie des Matériaux de Strasbourg, Groupe des Matériaux Organiques, UMR 7504, CNRS-Université Louis Pasteur,
B. P. 43, 23 rue du Loess, 67034 Strasbourg Cedex 2, France
Fax: +33-388-107-246
E-mail: laurent.douce@ipcms.u-strasbg.fr
[b] Institut de Chimie, Université Louis Pasteur, UMR CNRS 7177-LC003, Laboratoire DECOMET,
4 rue Blaise Pascal, 67000 Strasbourg, France
[c] Synthetic Nano-Function Materials Group, Nanotechnology Research Institute, National Institute of Advanced Industrial Science and Technology (AIST), Kansai centre,
Midorigaoka 1-8-31, Ikeda, Osaka, 563-8577 Japan
[d] Graduate School of Engineering, Osaka Electro-Communication University,
Hatscho, Neyagawa, Osaka, 572-8530 Japan

 © 2007 Wiley-VCH Verlag GmbH & Co. KGaA, Weinheim 

### Mesomorphic Properties

The mesomorphic behaviour and phase-transition temperatures were characterised by polarising optical microscopy (POM), differential scanning calorimetry (DSC) and X-ray diffractometry (XRD). The phase-transition temperatures and their corresponding enthalpy changes for compounds **1a**–**e** are compiled in Table 1, whereas typical results are displayed in Figure 1.

Table 1. Phase-transition temperatures (°C) and corresponding enthalpies $\Delta H$ (J/mmol) were determined from the first heating; abbreviations: Cr = crystalline phase, LC = smectic-A phase, I = isotropic phase.

| Compound | $T$ [°C] Cr → LC | $T$ [°C] LC → I |
|---|---|---|
| **1a** | 120.0 (48.51) | 126.0 (3.09) |
| **1b** | 116.0 (57.55) | 158.0 (3.78) |
| **1c** | 117.0 (80.03) | 175.7 (4.60) |
| **1d** | 118.3 (71.91) | 183.9 (3.87) |
| **1e** | 113.4 (108.44) | 191.1 (3.46) |

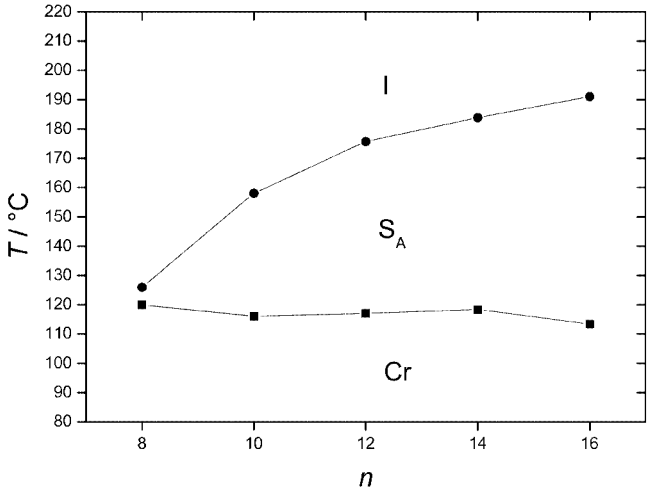


Figure 1. Phase diagram of compounds **1a**–**e** (I: isotropic liquid; $S_A$: smectic-A phase; Cr: crystalline phase).

The high stability of the compounds was demonstrated by the absence of significant perturbation of the DSC patterns following several heating–cooling cycles. The peak occurring at the lowest temperature (see Table 1 and Figure 1) corresponds to the melting of the crystal into a smectic-A phase. Determined by random motions of the paraffinic moiety, this peak involves an important enthalpy change that increases linearly with the number of carbon atoms of the tails (see Figure 2, ■).

The corresponding slope (7.2 ± 0.9) KJ/mol gives a value of the melting enthalpy of the methylene groups of (258 ± 32) J/g, comparable to that found for the complete melting of linear paraffins (289 J/g)[8] or for the transition of crystalline mesogens into a smectic phase (272[9a] and 238[9b] J/g).

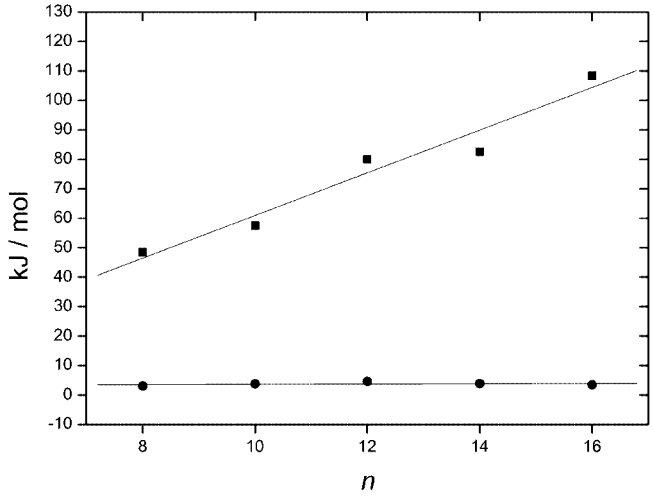


Figure 2. Phase transition enthalpies as a function of the number of carbon atoms in the alkyl chains; ■, Cr–$S_A$; ●, $S_A$–I.

The peak corresponding to the transition from the smectic-A phase to the isotropic liquid, related to the disordering of the aromatic cores of the molecules, involves an enthalpy that is independent of the length of the molecules, as expected and observed (see Figure 2, ●).

The liquid-crystalline phase was also confirmed by optical microscopy. The optical textures observed during slow cooling from isotropic melt showed the emergence of a smectic-A phase (see Figure 3a–b, initial appearance of rods turning into wide, fan-like, focal-conic textures).

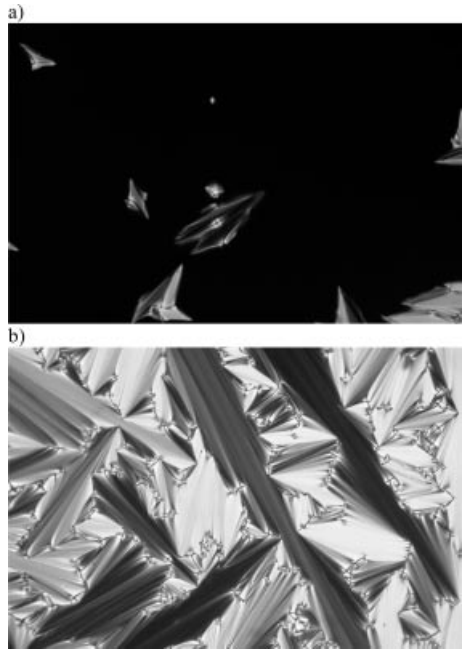


Figure 3. a) Polarising optical microscope image observed upon slow cooling of the isotropic melt clearly show the emergence of Batônnets with positive units. b) Typical smectic-A phase obtained from **1c** between 117 and 175 °C.

 © 2007 Wiley-VCH Verlag GmbH & Co. KGaA, Weinheim 

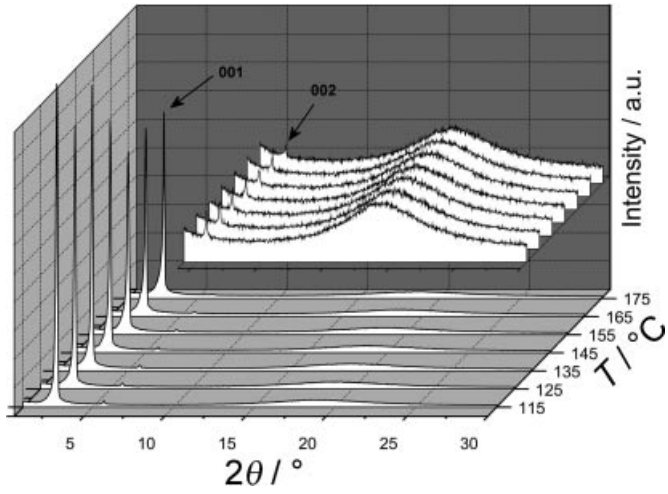


Figure 4. X-ray diffraction pattern of the smectic-A phase of **1c** at different temperatures. For clarity the intensities of the peak 002 and the broad band at Bragg angles $2\theta \geq 5°$ have been magnified.

The smectic-A arrangement is definitively established by the presence of two sharp, equidistant reflections (ratio 1:2) in the small angle region, related to smectic layering, and a broad band in the wide angle region, related both to the disordered conformation of the alkyl chains and the liquid-like lateral correlations of the aromatic core within the layers (Figure 4).

This mesophase was also evident in the XRD patterns, allowing determination of the *d*-spacing values for the smectic-A phase as shown in Figure 5. It is important to note that the smectic period increases in a linear manner with the molecular size.

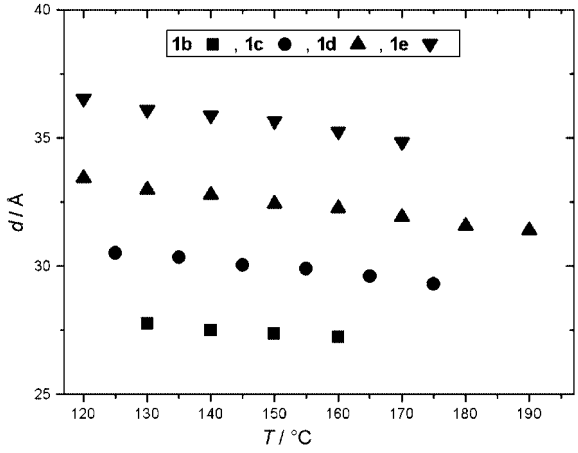


Figure 5. Variation of the smectic period of **1a**–**e** in the smectic-A state as a function of the number of carbon atoms in the alkyl chains and at different temperatures.

## Palladium(II) Carbene Complex

Transformation of imidazolium salts **1a**–**e** into N-heterocyclic carbene complexes was of interest in regard to possible applications in catalysis. Thus, palladium(II) complex **2** was obtain by deprotonation of imidazolium **1b** in the presence of the palladium salt precursor $Pd(OAc)_2$, KO*t*Bu (1 equiv.) and NaI (4 equiv.) (Scheme 2).[10] The formulation of complex **2** was confirmed by elemental analysis. The presence of a carbene centre was established by the observation of a signal at $\delta$ = 167.0 ppm in the $^{13}C$ NMR spectra, which was assigned to the 2C-imidazol-2-ylidene carbon nucleus, and by the absence of the resonance for the 2H-imidazolium proton in the $^{1}H$ NMR spectra. The details of the molecular structure of palladium carbene complex **2** in the solid state were established by a single-crystal X-ray diffraction study. The molecular unit present in the crystal is shown in Figure 6.

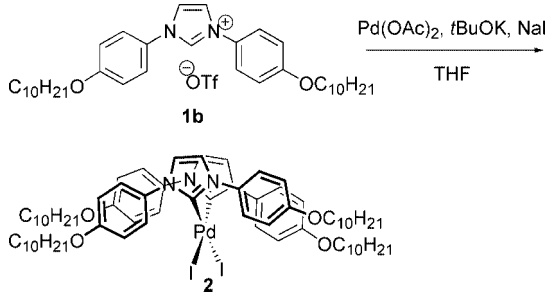


Scheme 2. Conditions: 12 h at room temp.

As shown in Figure 6, the $Pd^{II}$ centre is bound to two carbene ligands with a *cis* coordination geometry. The metal has a square-planar coordination sphere [C1–Pd–C36, 89.8(1)°; I–Pd–I, 92.42(4)°], with the heterocyclic rings near-perpendicular to the coordination plane and to one another.

The Pd–I [2.6788(3) and 2.6620(8) Å] and Pd–C bond lengths [2.009(3) and 2.000(4) Å] are similar to those in related complexes.[11] The *cis* geometry is probably favoured by a combination of steric and electronic factors involving the Pd centre as well as π–π interactions between the phenyl groups of the two heterocyclic ligands[12] [centroid distances of 3.54(2) and 3.66(2) Å for C20–C25/C55–C60 and C4–C9/C39–C44, respectively, labelled *x* in Figure 7). This in-

 © 2007 Wiley-VCH Verlag GmbH & Co. KGaA, Weinheim 

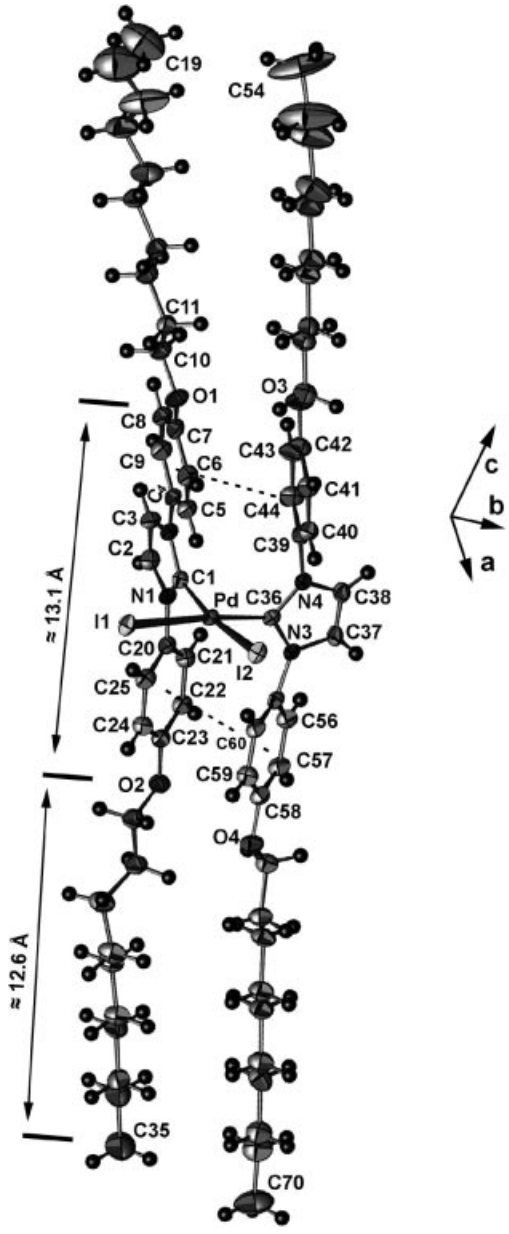


Figure 6. ORTEP view of the crystal structure asymmetric unit of complex **2** with partial labelling scheme. Thermal ellipsoids enclose 50% of the electronic density. Dashed lines indicate the intramolecular phenyl–phenyl π–π interactions.

teraction may also account for the orientation of the phenyl rings towards the heterocyclic carbene. The length of the rigid part of the molecule is around 13.1 Å, whereas the length of the alkoxy chain is around 12.6 Å (see Figure 6).

No classical hydrogen bonds were detected in this crystal structure. Nevertheless, careful analysis of the intermolecular approaches provided evidence for three nonclassical hydrogen bonds involving the iodine and carbon atoms of both the phenyl and heterocyclic rings.

These presumably weak hydrogen contacts[13] are listed in Table 2. The crystal packing can be interpreted in terms of a combination of CH–π and π–π interactions.[13] The intermolecular π–π interactions (labelled *y* in Figure 7) occurring between the heterocycles force them to be strictly parallel. Another π–π weak interaction is detected between both C36–N3–C37–C38–N4 rings of two adjacent molecules along the *b* axis [with a centroid distance of 3.90(2) Å].

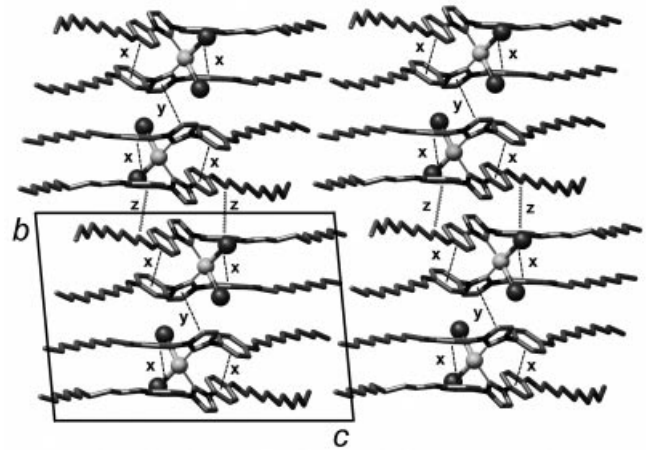


Figure 7. Solid-state packing diagram of complex **2** in projection on the (*b*,*c*) plane. The π–π and CH–π interactions are labelled with *x* (intramolecular π–π), *y* (intermolecular π–π) and *z* (intermolecular CH–π).

Table 2. Weak hydrogen interactions with iodine atoms.

| C–H···I | $d_{C–H}$ [Å] | $d_{H–I}$ [Å] | $d_{C–I}$ [Å] | C–H–I angle [°] |
|---|---|---|---|---|
| C25–H25···I1 | 0.95 | 2.99 | 3.8954 | 159 |
| C37–H37···I2 | 0.95 | 3.02 | 3.8384 | 146 |
| C60–H60···I2 | 0.95 | 2.93 | 3.8223 | 156 |

Finally, the CH–π interactions (C10–H10B···phenyl group and C11–H11A···phenyl group; labelled *z* in Figure 7) probably explain the form of the array along the crystallographic *b* axis.

## Catalysis Behaviour

Cross-coupling reactions represent an extremely versatile tool in organic synthesis. In order to explore the potential of our imidazolium salts as a source of N-heterocyclic carbene ligands for palladium-catalysed cross-coupling reactions, we decided to investigate the Suzuki–Miyaura reaction with imidazolium **1b** (Scheme 3).[14] Optimised conditions were used for the Suzuki–Miyaura cross-coupling: $Pd(OAc)_2$/imidazolium salt (2 equiv.), $Cs_2CO_3$ as base and dioxane as solvent (80 °C).[15]

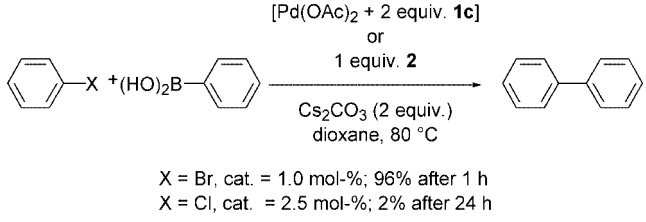


Scheme 3. Suzuki–Miyaura reaction.

 © 2007 Wiley-VCH Verlag GmbH & Co. KGaA, Weinheim 

The coupling of bromobenzene and phenylboronic acid proceeds quite rapidly in high yields with a catalyst loading of 1.0 mol-% (96% GC yield after 1 h). However, we were not able to observe catalysis for the coupling of chlorobenzene and phenylboronic acid even with a higher catalyst loading (2.5 mol-%). Similar results were obtained by using palladium complex **2**. It is known that steric factors dictate the catalytic activity since bulky N-substituents in the imidazolium salt are required to get good catalytic activity. The presence of the alkoxy chain in the *para* position of the *N*-aryl imidazolylidene does not change the efficiency of the ligand in the cross-coupling. Therefore, imidazolium **1b** with two $C_{10}H_{21}$ alkyl tails acts as a ligand with the same reactivity as 1,3-bis(4-methylphenyl)imidazolylidene.[15]

### Mobility of Charged Carriers in the Mesophase

The carrier mobility measurements were carried out for the smectic-A phase of **1b** by using the time-of-flight (TOF) technique (Figure 8). As preliminary data, the mobility for the positive electrode illumination was estimated to be in the order of $10^{-4}$ $cm^2/Vs$, which is comparable to those of nematic liquid crystals ($10^{-4}$–$10^{-6}$ $cm^2/Vs$)[16] and the lower ordered smectic liquid crystals.[17–19]

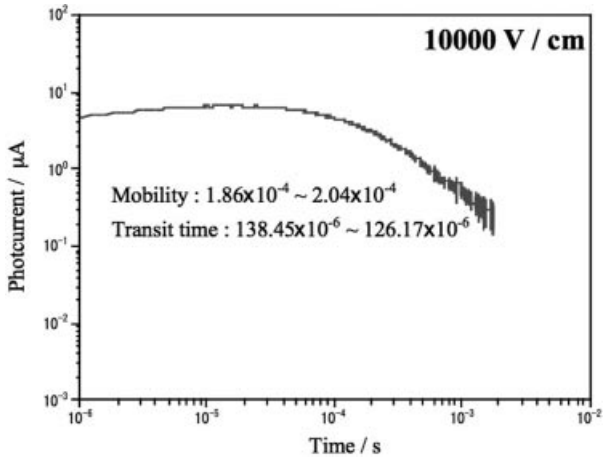


Figure 8. Typical decay curve of the transient photocurrent observed in the TOF measurements (bias: 10000 V/cm). The mesophase is smectic-A phase (131 °C) and the compound was not uniformly aligned in the cell gap (2.56 μm-thick).

This mobility is in a region where both electronic and ionic transports of charged carriers should be considered. It might indicate that both ionic transport and electronic hopping could be realised in the liquid-crystalline phase of this compound, though the reality of carriers is unknown for this mobility.

## Conclusions

We report the full characterisation of new mesomorphic compounds based on an imidazolium unit with different alkyls tails. We investigated the ability of the conjugate base of the cation to form carbene complexes with palladium(II). Preliminary measurements of the charged carrier mobility in the mesophase suggest electronic as well as ionic transports. To evaluate the influence of the supramolecular architecture on catalysis or palladium-catalysed reactions, we are now investigating the ability of this palladium(II) carbene complex to be dissolved in an ionic liquid crystal.

## Experimental Section

**Synthesis:** All commercially available chemicals were used without further purification. Dichloromethane (DCM) was carefully dried and distilled prior to use. Full details of the salt and $Pd^{II}$ complex syntheses will be given elsewhere, though all bisimines were obtained as indicated in Figure 1.[7] The new compounds were characterised by NMR spectroscopy and elemental analyses. With appropriate variations of the alkoxyphenyl diimine starting material (Figure 1), all imidazolium triflates were prepared by the method described below for octyloxy species **1a**.

**1,3-Bis(4-octyloxyphenyl)-3*H*-imidazol-1-ium Trifluoromethanesulfonate (1a):** To a mixture of the octyloxy bisimine (0.521 g, 1.12 mmol) and AgOTf (0.317 g, 1.23 mmol) was added dry $CH_2Cl_2$ (25 mL) and then chloromethyl pivalate (305 μL, 2.103 mmol). The mixture was stirred in the dark at 50 °C, under an argon atmosphere, for 20 h. The solution was cooled to room temp., the mixture was filtered through Celite, the solvent was evaporated and the crude product was purified by silica gel column chromatography ($CH_2Cl_2$ then $CH_2Cl_2$/MeOH, 95:5). The compound was subsequently crystallised from dichloromethane by the addition of hexane. The imidazolium triflate deposited as colourless crystals. (0.413 g, 59%). $^1$H NMR (300 MHz, $CDCl_3$, 20 °C): $\delta$ = 9.64 (t, $^4J$ = 1.23 Hz, N–CH–N imidazolium), 7.67 (d, $^4J$ = 1.60 Hz, 2 H, N–CH–CH–N imidazolium), 7.65 (m, $^3J$ = 9.0 Hz, 2 H, aromatic, AA′ system), 7.04 (m, $^3J$ = 9.0 Hz, 2 H, aromatic, BB′ system), 3.90 (t, $^3J$ = 6.60 Hz, 2 H, $CH_2$–O), 1.80 (m, 2 H, $CH_2$–$CH_2$–O), 1.44 (m, 2 H, $CH_2$–$CH_2$–$CH_2$–O), 1.32 (br. s, 16 H, aliphatic), 0.90 (t, $^3J$ = 7.0 Hz, 3 H, $CH_3$) ppm. $^{13}$C NMR (75 MHz, $CDCl_3$, 20 °C): $\delta$ = 14.04 (–$CH_3$), 22.61, 25.91, 29.03 29.17, 29.29, 31.76, 68.59 (O–$CH_2$), 115.90, 120.63 (q, $J$ = 320 Hz, $CF_3$) 121.98, 123.39, 124.82, 126.88, 132.35, 160.58 ppm. IR (KBr pellet): $\tilde{\nu}$ = 3141 and 3102 (C–H aromatic), 2918 and 2852 (C–H aliphatic), 1555 and 1513 (C=N imidazolium), 1266 ($OTf^-$) $cm^{-1}$. $\lambda$ ($\varepsilon$) = 277 (16375) nm. $C_{32}H_{45}F_3N_2O_5S$ (626.77): calcd. C 61.32, H 7.24, N 4.47; found C 61.36, H 7.25, N 4.44.

**1,3-Bis(4-decyloxyphenyl)-3*H*-imidazol-1-ium Trifluoromethanesulfonate (1b):** Yield crystalline solid (4.39 g; 82%) $^1$H NMR (300 MHz, $CDCl_3$, 20 °C): $\delta$ = 9.64 (t, $^4J$ = 1.56 Hz, N–CH–N imidazolium), 7.66 (d, $^4J$ = 1.74 Hz, 2 H, N–CH–CH–N imidazolium), 7.65 (m, $^3J$ = 6.78 Hz, 2 H, aromatic, AA′ system), 7.03 (m, $^3J$ = 6.78 Hz, 2 H, aromatic, BB′ system), 3.97 (t, $^3J$ = 6.36 Hz, 2 H, $CH_2$–O), 1.80 (m, 2 H, $CH_2$–$CH_2$–O), 1.43 (m, 2 H, $CH_2$–$CH_2$–$CH_2$–O), 1.29 (br. s, 24 H, aliphatic), 0.89 (t, $^3J$ = 6.97 Hz, 3 H, $CH_3$) ppm. $^{13}$C NMR (75 MHz, $CDCl_3$, 20 °C): $\delta$ = 14.05 (–$CH_3$), 22.62, 22.85, 25.90, 26.11, 29.04, 29.27, 29.35, 29.52, 31.84, 68.55 (O–$CH_2$), 115.84, 120.65 (q, $J$ = 320 Hz, $CF_3$), 122.09, 123.30, 126.87, 132.02, 160.49 ppm. IR (KBr pellet): $\tilde{\nu}$ = 3143 and 3102 (C–H aromatic), 2917 and 2851 (C–H aliphatic), 1555 and 1513 (C=N imidazolium), 1265 ($OTf^-$) $cm^{-1}$. $\lambda$ ($\varepsilon$) = 277 (21977) nm. $C_{36}H_{53}F_3N_2O_5S$ (682.88): calcd. C 63.32, H 7.82, N 4.10, S 4.70; found C 63.10, H 7.97, N 3.89, S 4.75.

**1,3-Bis(4-dodecyloxyphenyl)-3*H*-imidazol-1-ium Trifluoromethanesulfonate (1c):** Yield crystalline solid (0.600 g, 61%). $^1$H NMR

 © 2007 Wiley-VCH Verlag GmbH & Co. KGaA, Weinheim 

(300 MHz, $CDCl_3$, 20 °C): $\delta$ = 9.59 (t, $^4J$ = 1.65 Hz, N–CH–N imidazolium), 7.67 (d, $^4J$ = 1.60 Hz, 2 H, N–CH–CH–N imidazolium), 7.64 (m, $^3J$ = 9.0 Hz, 2 H, aromatic, AA′ system), 7.01 (m, $^3J$ = 9.0 Hz, 2 H, aromatic, BB′ system), 3.95 (t, $^3J$ = 6.6 Hz, 2 H, $CH_2$–O), 1.79 (m, 2 H, $CH_2$–$CH_2$–O), 1.43 (m, 2 H, $CH_2$–$CH_2$–$CH_2$–O), 1.28 (br. s, 32 H, aliphatic), 0.89 (t, $^3J$ = 7.0 Hz, 3 H, $CH_3$) ppm. $^{13}$C NMR (75 MHz, $CDCl_3$, 20 °C): $\delta$ = 14.10 (–$CH_3$), 22.69, 25.97, 29.10, 29.36, 29.41, 29.60, 29.63, 29.65, 29.68, 31.92, 68.65 (O–$CH_2$), 120.68 (q, $J$ = 320 Hz, $CF_3$), 122.02, 123.44, 126.86, 132.40, 160.64 ppm. IR (KBr pellet): $\tilde{\nu}$ = 3141 and 3102 (C–H aromatic), 2917 and 2852 (C–H aliphatic), 1555 and 1513 (C=N imidazolium), 1266 ($OTf^-$) $cm^{-1}$. $\lambda$ ($\varepsilon$) = 276 (18400) nm. $C_{40}H_{61}F_3N_2O_5S$ (738.98): calcd. C 65.01, H 8.32, N 3.79, S 4.34; found C 64.78, H 8.58, N 4.25, S 3.56.

**1,3-Bis(4-tetradecyloxyphenyl)-3*H*-imidazol-1-ium Trifluoromethanesulfonate (1d):** Yield crystalline solid (0.479 g; 58%). $^1$H NMR (300 MHz, $CDCl_3$, 20 °C): $\delta$ = 9.64 (t, $^4J$ = 1.74 Hz, N–CH–N imidazolium), 7.66 (d, $^4J$ = 1.70 Hz, 2 H, N–CH–CH–N imidazolium), 7.64 (m, $^3J$ = 7.02 Hz, 2 H, aromatic, AA′ system), 7.03 (m, $^3J$ = 6.99 Hz, 2 H, aromatic, BB′ system), 3.97 (t, $^3J$ = 6.57 Hz, 2 H, $CH_2$–O), 1.80 (m, 2 H, $CH_2$–$CH_2$–O), 1.43 (m, 2 H, $CH_2$–$CH_2$–$CH_2$–O), 1.27 (br. s, 40 H, aliphatic), 0.88 (t, $^3J$ = 7.02 Hz, 3 H, $CH_3$) ppm. IR (KBr pellet): $\tilde{\nu}$ = 3143 and 3101 (C–H aromatic), 2917 and 2850 (C–H aliphatic), 1555 and 1513 (C=N imidazolium), 1265 ($OTf^-$) $cm^{-1}$. $\lambda$ ($\varepsilon$) = 277 (27047) nm. $C_{44}H_{69}F_3N_2O_5S$ (795.09): calcd. C 66.47, H 8.75, N 3.52, S 4.03; found C 66.35, H 8.77, N 3.48, S 4.17.

**1,3-Bis(4-hexadecyloxyphenyl)-3*H*-imidazol-1-ium Trifluoromethanesulfonate (1e):** Yield crystalline solid (0.376 g; 34%). $^1$H NMR (300 MHz, $CDCl_3$, 20 °C): $\delta$ = 9.72 (t, $^4J$ = 1.53 Hz, N–CH–N imidazolium), 7.65 (d, $^4J$ = 1.53 Hz, 2 H, N–CH–CH–N imidazolium), 7.67 (m, $^3J$ = 7.03 Hz, 2 H, aromatic, AA′ system), 7.03 (m, $^3J$ = 7.0 Hz, 2 H, aromatic, BB′ system), 3.99 (t, $^3J$ = 6.57 Hz, 2 H, $CH_2$–O), 1.81 (m, 2 H, $CH_2$–$CH_2$–O), 1.41 (m, 2 H, $CH_2$–$CH_2$–$CH_2$–O), 1.27 (br. s, 40 H, aliphatic), 0.89 (t, $^3J$ = 7.0 Hz, 3 H, $CH_3$) ppm. $^{13}$C NMR (75 MHz, $CDCl_3$, 20 °C): $\delta$ = 14.06 (–$CH_3$), 22.64, 25.91, 29.02, 29.31 29.53, 29.60, 29.57, 29.66, 31.87, 68.65 (O–$CH_2$), 116.05, 121.82, 123, 126.78, 132.26, 160.80 ppm. IR (KBr pellet): $\tilde{\nu}$ = 3141 and 3102 (C–H aromatic), 2918 and 2852 (C–H aliphatic), 1555 and 1513 (C=N imidazolium), 1266 ($OTf^-$) $cm^{-1}$. $\lambda$ ($\varepsilon$) = 277 (18438) nm. $C_{48}H_{77}F_3N_2O_5S$ (851.20): calcd. C 67.73, H 9.12, N 3.29; found: C 67.75, H 8.98, N 3.39.

**Palladium–Carbene Complex 2:** Compound **1b** (250.0 mg, 0.367 mmol), $Pd(OAc)_2$ (41.2 mg, 0.183 mmol) and NaI (55.0 mg, 0.367 mmol) were suspended in THF (15 mL). *t*BuOK (41.1 mg, 0.367 mmol) was added to the suspension under an atmosphere of nitrogen. The resulting solution was stirred for 1.5 d at 40 °C. After evaporation of the solvent, the residue was extracted with dichloromethane/water. After drying the DCM layer over $Na_2SO_4$ and evaporating it to dryness, the orange solid was purified by flash column chromatography ($SiO_2$, $CH_2Cl_2$/pentane). Yield: 116 mg, 44%. $^1$H NMR (300 MHz, $CDCl_3$): $\delta$ = 7.51 (d, $J$ = 8.9 Hz, 4 H), 6.96 (s, 2 H), 6.75 (d, $J$ = 8.9 Hz, 4 H), 4.05 (t, $J$ = 6.6 Hz, 4 H), 1.86 (m, 4 H), 1.53–1.26 (m, 28 H), 0.89 (t, $J$ = 6.7 Hz, 6 H) ppm. $^{13}$C NMR (75 MHz, $CDCl_3$): $\delta$ = 167.0 ($C_{carbene}$), 158.5 ($C_q$), 133.0 ($C_q$), 127.8 (CH), 123.8 (CH), 114.5 (CH), 68.2, 31.9, 29.7, 29.6, 29.5, 29.4, 29.3, 26.2, 22.7, 14.1 ($CH_3$) ppm. $C_{71}H_{105}I_2N_3O_4Pd$ (1424.84): calcd. C 59.0, H 7.3, N 3.9; found C 58.95, H 7.45, N 3.80.

**General Procedure for the Suzuki-Type Coupling Reactions:** Palladium acetate (1–2.5 mol-%), imidazolium salt (2–5 mol-%), $Cs_2CO_3$ (652 mg, 2 mmol) and phenylboronic acid (183 mg, 1.5 mmol) were added to a small Schlenk tube under an atmosphere of nitrogen. Dioxane (3 mL) and the aryl halide (1 mmol) were then added, and the mixture was heated in an oil bath at 80 °C. At the conclusion of the reaction, the reaction mixture was cooled and analysed by GC–MS.

**Carrier Mobility Measurements:** The charge carrier mobility in the mesophase was measured by TOF (time-of-flight) measurement apparatus equipped with a polarising microscope and a hot stage. The light source was a pulsed nitrogen gas laser (Nippon Laser, $\lambda$ = 337 nm, 0.8 ns). The cells consisting of ITO- and $TiO_2$-coated glasses for an asymmetric structure of sandwich-type cells were mounted on the hot stage and electric bias was applied by a stabilised DC power supply. The resulting photocurrent was detected with a digital oscilloscope with a homemade preamplifier.

**X-ray Crystallography:** The selected crystal was mounted on a Nonius Kappa-CCD area detector diffractometer (Mo-$K_\alpha$, $\lambda$ = 0.71073 Å). The complete conditions of data collection (Denzo software) and structure refinements are given below. The cell parameters were determined from reflections taken from one set of ten frames (1.0° steps in phi angle), each at 20 s exposure. The structures were solved by direct methods (SHELXS97) and refined against $F^2$ using the SHELXL97 software. All non-hydrogen atoms were refined anisotropically. Hydrogen atoms were generated according to stereochemistry and refined by using a riding model in SHELXL97.[20] CCDC-628899 contains the supplementary crystallographic data for this paper. These data can be obtained free of charge from The Cambridge Crystallographic Data Centre via www.ccdc.cam.ac.uk/data_request/cif. Colourless single crystal; crystal dimension: $0.10 \times 0.08 \times 0.05$ mm$^3$. $C_{70}H_{104}I_2N_4O_4Pd$, $M$ = 1425.77 g/mol; Triclinic; space group $P\bar{1}$; $a$ = 10.7060(1) Å; $b$ = 15.8080(2) Å; $c$ = 21.6950(3) Å; $Z$ = 2; $D_{calcd.}$ = 1.354 g/cm; $\mu$ (Mo-$K_\alpha$) = 1.195 mm$^{-1}$; a total of 20389 reflections; $1.34° < \theta < 30.06°$, 1842 independent reflections with 12376 having $I > 2\sigma(I)$; 730 parameters; Final results: $R_1$ = 0.0460; $wR_2$ = 0.1287, *Goof* = 0.996, maximum residual electronic density = 1.887 e/Å$^3$.

## Acknowledgments

We are especially grateful to D. Guillon and J. Harrowfield for the critical evaluation of this manuscript, we also thank A. De Cian for the X-ray diffraction studies. This work was supported by the Institut for Physics and Chemistry of Materials Strasbourg (I. P. C. M. S), the Institut of Chemistry and Louis Pasteur University.

[1] a) P. Wasserscheid, T. Welton in *Ionic Liquids in Synthesis*, Wiley-VCH, Weinheim, **2003**; b) J. Dupont, R. F. de Souza, P. A. Suarez, *Z. Chem. Rev.* **2002**, *102*, 3667–3692; c) C. E. Song, *Chem. Commun.* **2004**, 1033–1043; d) H. Ohno, *Electrochemical Aspects of Ionic Liquids*, Wiley-Interscience, **2005**; e) J. M. Crosthwaite, S. N. V. K. Aki, E. J. Maginn, J. F. Brennecke, *J. Phys. Chem. B* **2004**, *108*, 5113–5119; f) M. Yoshizawa, W. Xu, C. A. Angell, *J. Am. Chem. Soc.* **2003**, *125*, 15411–15419; g) A. J. Fry, *J. Electroanal. Chem.* **2003**, *546*, 35–39.

[2] a) R. B. Rogers, K. R. Seddon (Eds.), *ACS Symposium Series No. 901: Ionic Liquids IIIA: Fundamental, Progress, Challenges and Opportunities*, American Chemical Society, Washington DC, **2005**; b) R. B. Rogers, K. R. Seddon (Eds.), *ACS Symposium Series No. 902:Ionic Liquids IIIB: Fundamental, Progress, Challenges and Opportunities*, American Chemical Society, Washington DC, **2005**.

[3] a) K. Binnemans, *Chem. Rev.* **2005**, *105*, 4148–4204; b) M. Yoshio, T. Mukai, H. Ohno, T. Kato, *J. Am. Chem. Soc.* **2004**, *126*, 994–995; c) C. J. Bowlas, D. W. Bruce, K. R. Seddon,

 © 2007 Wiley-VCH Verlag GmbH & Co. KGaA, Weinheim 

*Chem. Commun.* **1996**, 1625–1626; d) C. M. Gordon, J. D. Holbrey, A. R. Kennedy, K. R. Seddon, *J. Mater. Chem.* **1998**, *8*, 2627–2636; e) A. E. Bradley, C. Hardacre, J. D. Holbrey, S. Johnston, S. E. J. McMath, M. Nieuwenhuyzen, *Chem. Mater.* **2002**, *14*, 629–635; f) J. De Roche, C. M. Gordon, C. T. Imrie, M. D. Ingram, A. R. Ingram, A. R. Kennedy, F. LoCelso, A. Triolo, *Chem. Mater.* **2003**, *15*, 2003; g) K.-M. Lee, Y.-T. Lee, J. B. Lin, *J. Mater. Chem.* **2003**, *13*, 1079–1084; h) J. Y. Z. Chiou, J. N. Chen, J. S. Lei, I. J. B. Lin, *J. Mater. Chem.* **2006**, *16*, 2972–2977; i) W. Dobbs, L. Douce, L. Allouche, A. Louati, F. Malbocs, R. Welter, *New J. Chem.* **2006**, *30*, 528–532.

[4] a) J. Motoyanagi, T. Fukushima, T. Aida, *Chem. Commun.* **2005**, 101–103; b) S. Kumar, S. Kumar Pal, *Tetrahedron Lett.* **2005**, *46*, 2607–2610.

[5] a) A. Taubert, P. Steiner, A. Mantion, *J. Phys. Chem. B* **2005**, *109*, 15542–15547; b) A. Taubert, *Acta Chim. Slov.* **2005**, *52*, 183–186; c) A. Taubert, *Angew. Chem. Int. Ed.* **2004**, *43*, 5380–5382; d) W. Dobbs, J.-M. Suisse, L. Douce, R. Welter, *Angew. Chem. Int. Ed.* **2006**, *45*, 4179–4182.

[6] a) W. A. Herrmann, *Angew. Chem. Int. Ed.* **2002, 41**, *8*, 1290–1309; b) D. Bourissou, O. Guerret, F. Gabbaï, G. Bertrand, *Chem. Rev.* **2000**, *100*, 39–92; c) W. A. Herrmann, C. Köcher, *Angew. Chem. Int. Ed. Engl.* **1997**, *36*, 2162–2187; d) V. César, S. Bellemin-Laponnaz, L. H. Gade, *Chem. Soc. Rev.* **2004**, 619–636.

[7] J.-M. Suisse, S. Bellemin-Laponnaz, L. Douce, A. Maisse-François, R. Welter, *Tetrahedron Lett.* **2005**, *46*, 4303–4305.

[8] R. C. Weast, *Handbook of Chemistry and Physics*, 64th ed., CRC Press, Cleveland, **1983**.

[9] a) P. Seurin, D. Guillon, A. Skoulios, *Mol. Cryst. Liq. Cryst.* **1981**, *71*, 51; b) L. Douce, R. Ziessel, R. Seghrouchni, A. Skoulios, E. Campillo, R. Deschenaux, *Liq. Cryst.* **1996**, *20*, 235–242.

[10] F. Glorius, G. Altenhoff, R. Goddard, C. Lehmann, *Chem. Commun.* **2002**, 2704–2705.

[11] M. Poyatos, A. Maisse-François, S. Bellemin-Laponnaz, L. H. Gade, *Organometallics* **2006**, *25*, 2634–2641.

[12] PLATON, A Multipurpose Crystallographic Tool, A. L. Spek, *J. Appl. Crystallogr.* **2003**, *36*, 7–13.

[13] R. G. Pearson, *Inorg. Chem.* **1973**, *12*, 712–713.

[14] For a review of metal-catalyzed cross-coupling reactions, see: F. Diederich, P. J. Stang (Eds.), *Metal-Catalyzed Cross-Coupling Reactions*, Wiley-VCH, New York, **1998**; J. Dupont, R. F. de Souza, P. A. Z. Suarez, *Chem. Rev.* **2002**, *102*, 3667–3692; J.-C. Xiao, B. Twamley, J. M. Shreeve, *Org. Lett.* **2004**, *6*, 3845–3847.

[15] G. A. Grasa, M. S. Viciu, J. Huang, C. Zhang, M. L. Trudell, S. P. Nolan, *Organometallics* **2002**, *21*, 2866–2873.

[16] K. Okamoto, S. Nakajima, A. Itaya, S. Kusabayashi, *Bull. Chem. Soc. Jpn.* **1983**, *56*, 3830–3832.

[17] H. Tokuhisa, M. Era, T. Tsutsui, *Adv. Mater.* **1998**, *10*, 404–406.

[18] M. Funahashi, J. Hanna, *Appl. Phys. Lett.* **1997**, *71*, 602–604.

[19] M. Funahashi, J. Hanna, *Phys. Rev. Lett.* **1997**, *78*, 2184–2187.

[20] G. M. Sheldrick, *SHELXL97*, University of Göttingen, Germany, **1997**.

Received: February 27, 2007
Published Online: June 28, 2007

 © 2007 Wiley-VCH Verlag GmbH & Co. KGaA, Weinheim 

DOI: 10.1002/ejic.200700285

# Rarely Decorated Rutile Frameworks Built from Triangular Organic Spacers and Distorted Octahedral $Co_3$ Building Blocks

Feng Luo,[a] Yun-xia Che,[a] and Ji-min Zheng*[a]

**Keywords:** Solvothermal syntheses / Rutile / Cobalt / Polymers

Under mild temperatures, the self-assembly of $CoCl_2$ and $H_3BTC$ in a solution of dmso generates a guest-free metal–organic polymer, namely $Co_3(BTC)_2(\mu_1\text{-dmso})_2(\mu_2\text{-dmso})_2$(**1**: dmso = dimethylsulfoxide, $H_3BTC$ = 1,3,5-benzenetricarboxylic acid). In **1**, the $Co^{II}$ ions show the six-coordinate octahedral geometry completed by the $BTC^{3-}$ ions and the dmso oxygen atoms; remarkably, the coordinated dmso ligands not only act as terminal ligands to complete the octahedral geometry of the $Co^{II}$ ions, but also play an important role in bridging $Co^{II}$ ions together to give the $Co_3$ secondary building units (SBUs). From a topological viewpoint, this novel polymer is classified to be the decorated (3,6)-connected rutile net with the $(4.6^2)_2(4^2.6^{10}.8^3)$ topology, where $BTC^{3-}$ ligands and $Co_3$ SBUs are viewed to be the 3- and 6-connected nodes, respectively. In addition, the magnetic properties of **1** are explored by using a linear trinuclear cobalt mode, thus leading to $g = 2.41$, $J = -34.92$ cm$^{-1}$, TIP = $340 \times 10^{-6}$ cm$^3$ mol$^{-1}$, $\theta = -6$ K (a $\theta$ parameter was included to take into account intertrinuclear interactions).

(© Wiley-VCH Verlag GmbH & Co. KGaA, 69451 Weinheim, Germany, 2007)

## Introduction

The design and synthesis of metal-organic frameworks (MOFs) is now of great interest owing to the potential applications and unusual topologies of these new materials.[1] Although this relatively new field of chemistry is aimed at the discovery and synthesis of new materials for practical applications with an emphasis on their functional aspects, it would be difficult to achieve true advancements without an understanding of the structural aspects of these materials at the molecular or atomic levels; however, recent remarkable research results and reviews on framework topologies and other geometrical characteristics of network solids reflect this importance.[2] It seems that for the majority of 3D metal–organic framework topologies, we can find the well-known prototypes in metallic or binary inorganic solids. For example, diamond or diamond-related nets that are composed of tetrahedral nodes are the most common, and they allow the highest interpenetration. A primitive cubic (**pcu**) net/or α-Po net, based on octahedral nodes is also frequently observed and shows the relatively lower two- or threefold interpenetration.[2a,3] Other 3D structures have recently been reported to have the following topologies: boracite, $CdSO_4$, $CaB_6$, feldspar, NbO, perovskite, $Pt_3O_4$, PtS, pyrite, quartz, rutile (**rtl**), sodalite, $SrSi_2$, and tungsten bronze.[4] Among the most important and frequently encountered mixed connectivity types, the rutile form of $TiO_2$ is an important (3,6)-connected net structure. To construct such a net, it appears that assembling triangular building blocks with octahedral building blocks will realize it. In this regard, several compounds with expanded (increased spacing between vertices in a network) **rtl** nets were constructed, most of which are interpenetrating structures constructed with cyano ligands.[5] By contrast, the decorated (replacement of a vertex in a net by a group of vertices) **rtl** nets are less developed. To the best of our knowledge, there are only four interpenetrating decorated and one noninterpenetrating such species.[3b,6] Hence, further investigation into the self-assembly of MOFs characterized by the noninterpenetrating decorated **rtl** nets is needed.

Very recently, most of the significant MOFs were prepared by solvothermal syntheses in $CH_3OH$, $C_2H_5OH$, and $CH_3CN$ solutions, but especially in DMF solution.[7] However, the solvothermal synthesis of MOFs in dmso solution is unexplored. Herein, we report such a reaction, and the resulting elegant MOF presents as the second noninterpenetrating decorated **rtl** net.

## Results and Discussion

The as-synthesized samples are air-stable and insoluble in water and common organic solvents, such as $CH_3OH$, $C_2H_5OH$, $CH_3CN$, and DMF. Incidentally, dmso decomposes at high temperature and emits a terrible odor; hence, we must be careful to obtain crystal samples from the reaction vessel.

### Crystal Structure and Network Topology

Single-crystal X-ray structural analysis revealed that **1** crystallizes in the monoclinic system, space group $P2(1)/c$.

[a] Department of Chemistry, Nankai University, Tianjin, 300071 China
E-mail: jmzheng@nankai.edu.cn

 © 2007 Wiley-VCH Verlag GmbH & Co. KGaA, Weinheim 

There are two crystallographically independent cobalt ions in this structure. The local coordination geometry for the six-coordinate Co1 center is close to an octahedron coordinated by four $BTC^{3-}$ oxygen atoms and two dmso oxygen atoms. Co2 located at an inverse center is also surrounded by four $BTC^{3-}$ oxygen atoms and two dmso oxygen atoms to give the $CoO_6$ octahedral geometry. The $Co–O_{dmso}$ bond lengths vary from 2.097 to 2.243 Å, which are comparable to the $Co–O_{carboxylate}$ bond lengths in the range of 2.034–2.228 Å, and both of them are comparable with those observed in other Co–BTC compounds;[13] thus, the distortion parameter of the $CoO_6$ octahedra is $8.8 \times 10^{-4}$ for Co1 and $2.2 \times 10^{-3}$ for Co2.[8] As for each $BTC^{3-}$ ligand, it shows a pentadentate-coordinated mode with one carboxyl group chelated to the Co1 ion and two carboxyl groups bridging Co1 with Co2.

The Co1, Co2, and symmetry-related Co1′ ions are combined together by the *syn-syn* carboxyl groups of the $BTC^{3-}$ ligands and $\mu_2$-dmso bridges thus leading to the linear $Co_3$ SBU of corner-sharing octahedra (Figure 1). The intratrinuclear Co1–Co2 distance is 3.562 Å, and the $Co1–O_{dmso}–Co2$ angle is 109.04°. Furthermore, each SBU connects six $BTC^{3-}$ ligands in six directions (Figure 2), whereas each $BTC^{3-}$ ligand ligates three SBUs (Figure 3); consequentially, such a connectivity pattern is repeated infinitely to construct the infinite (3, 6)-connected net (Figure 4). For perspicuous representation, the $Co_3$ SBUs are represented by distorted octahedral nodes, as each carboxyl group is more-or-less offset from the phenyl plane and not all the vertices of each octahedral $Co_3$ SBU are symmetrically equivalent, whereas the $BTC^{3-}$ ligands are described as triangular units.

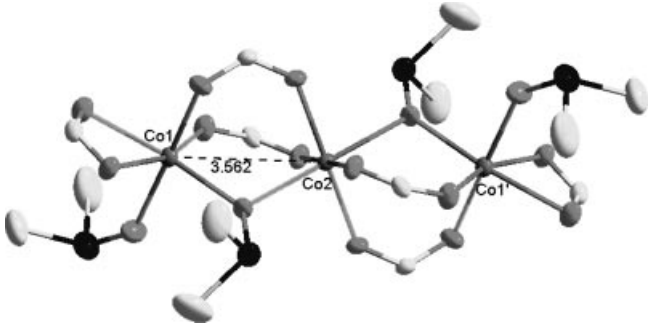


Figure 1. Schematic description of the $Co_3$ SBU and its coordinated environment: C is light grey, S is black, and O is dark grey. The atoms are drawn at the 50% probability level.

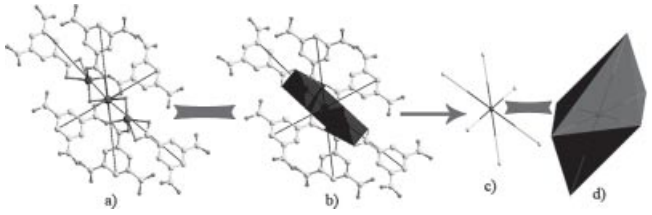


Figure 2. a) Ball-and-stick mode of the six-connected $Co_3$ SBU; b) polyhedral illustration of the $Co_3$ core; c) the simplified node-to-node fashion of the six-connected SBU; d) polyhedral illustration of the distorted octahedral SBU.

Hence, the framework should be viewed as a noninterpenetrating decorated **rtl** net with the $(4.6^2)_2(4^2.6^{10}.8^3)$ topology, where six-connected $Co_3$ SBUs and three-connected $BTC^{3-}$ units correspond to the Ti atoms and the O atoms in the **rtl** net structure, respectively.

Figure 3. a) Ball-and-stick mode of the three-connected $BTC^{3-}$ unit; b) polyhedral illustration of the $Co_3$ core; c) the simplified node-to-node fashion of the triangle $BTC^{3-}$ node.

Figure 4. View of the noninterpenetrating decorated rutile net with the $(4.6^2)_2(4^2.6^{10}.8^3)$ topology and constructed from distorted octahedral $Co_3$ SBUs and triangle $BTC^{3-}$ units.

Carefully checking the reported decorated **rtl** nets, we find that most of them are built from octahedral $M_2$ (M = metal ion) SBUs and triangular organic units. Obviously, the present one contains the biggest octahedral SBUs ($Co_3$).

## Magnetic Properties

The $\chi_M T$ product of crystal samples of **1** was measured in the temperature range 2–300 K with applied magnetic fields of 500 Oe (Figure 5). At room temp., the $\chi_M T$ value of 6.37 $cm^3 K mol^{-1}$ is slightly higher than that of three high-spin $Co^{II}$ ion (5.63 $cm^3 mol^{-1} K$, $S = 3/2$, $g = 2.0$) as a magnetically noninteracting center owing to orbital contribution from the octahedral high-spin $Co^{II}$ ions. Upon cooling from room temp., the $\chi_M T$ product linearly decreases to 2.30 $cm^3 K mol^{-1}$ at 10 K, which is due to the spin-orbit coupling effects of the high-spin octahedral $Co^{II}$ ions with an orbital degenerate $^4T_1$ ground term and the antiferromagnetic exchange coupling between $Co^{II}$ ions. The $\chi_M T$ values then sharply decrease to 1.19 $cm^3 K mol^{-1}$ at 2 K as a result of the ZFS (zero field splitting) and/or other fac-

 © 2007 Wiley-VCH Verlag GmbH & Co. KGaA, Weinheim 

tors, such as intertrinuclear interactions. In the $1/\chi_M$ versus $T$ plot, above 75 K, the plot is exactly a straight line well-fitted by the Curie–Weiss law [$\chi_M = C/(T - \theta)$], with $C$ = 8.3 $cm^3 mol^{-1} K$ and $\theta$ = –83.0 K. This is consistent with three $S$ = 3/2 $Co^{II}$ ions with moderate antiferromagnetic coupling to yield an average $g$ value of 2.4. This large Weiss constant indicates a dominated antiferromagnetic coupling between the $Co^{II}$ ions.

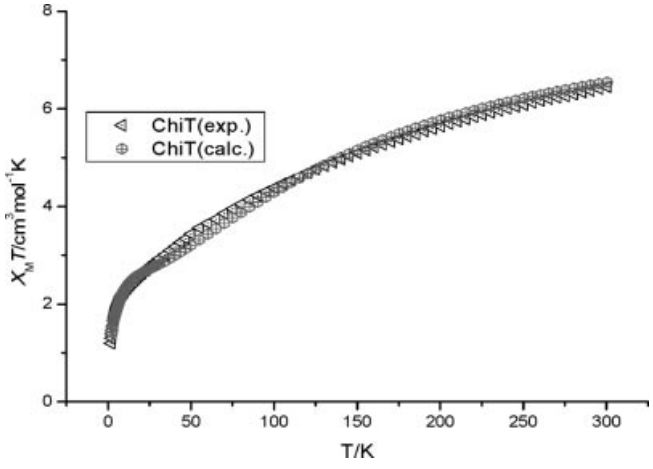


Figure 5. The plot of $\chi_M T$ vs. $T$: open triangle is the experimental curve and the crossed circle is the simulated curve.

As mentioned above, in this linear $Co_3$ unit, Co1 and Co1′ are symmetrical, and the closest distance of Co1–Co1′ is 7.124 Å; hence, we chose a "one $J$" mode to analyze the experimental magnetic data.[9] A least-squares fit to the data leads to $g$ = 2.41, $J$ = –34.92 $cm^{-1}$, TIP = $340 \times 10^{-6}$ $cm^3 mol^{-1}$, $\rho$ = 0.09 $cm^3 mol^{-1} K$, and $\theta$ = –6 K: $J$ is the magnetic coupling parameter between Co1–Co2 and Co1′–Co2, $g$ is the Zeeman factor, TIP is the temperature-independent paramagnetism, $\rho$ is the paramagnetic impurity, and $\theta$ is the intertrinuclear interactions. It is not surprising to find important TIP contributions and such a strong Zeeman factor. Indeed, the combined influences of the local distortion of the coordination sphere around the $Co^{II}$ ion and the spin-orbit coupling are known to produce this set of local parameters.[10]

Relative to the pyridazine-bridging Co3 compounds,[11] the preset compound bridged by $\mu_2$-O atoms displays the obviously bigger antiferromagnetic interactions, but comparable with the cobalt(II)–hydroxy compounds.[12]

### TGA Research of 1

The TG research (30–800 °C) of **1** shows that at 30–300 °C, there is no weight loss, which is consist with the structure of **1**, and polymer **1** then starts to perform the process of chemical decomposition (Figure 6). The remains may be $Co_2O_3$ (calcd. 28%; found 30%).

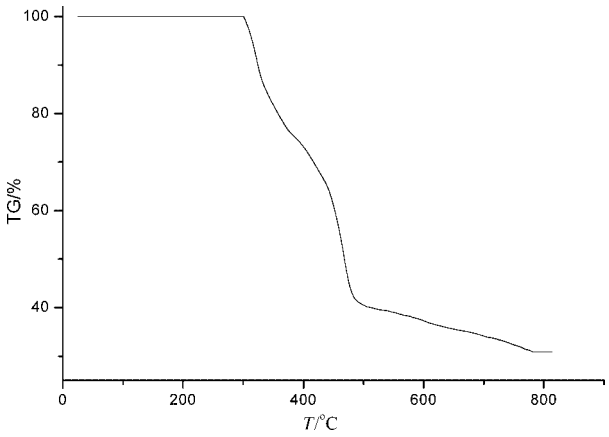


Figure 6. The TG plot of **1** (to our surprise, we found that the TG plot is straight until 300 °C; maybe, the former treatment such as heating to avoid the absorbed water molecules and $N_2$ protection are the main reason.

## Conclusions

Through this original research, we initiated the solvothermal synthesis of MOFs in dmso solution. The resulting MOF, defined as a noninterpenetrating decorated rutile net with the $(4.6^2)_2(4^2.6^{10}.8^3)$ topology, is built from distorted octahedral $Co_3$ SBUs and triangular $BTC^{3-}$ units. To the best of knowledge, this distorted octahedral $Co_3$ SBU is the biggest relative to those ($M_2$ SBU) observed in other similar instances. In addition, it should be highlighted that the dmso molecules in polymer **1** display two different ligand coordination modes: terminal and $\mu_2$-bridging; however, this phenomenon has never been observed in the literature. Thus, this study will largely enrich the field of MOFs and further understand the coordinated behavior of $H_3BTC$ ligands, especially the dmso molecules.

## Experimental Section

**Materials and Instrumentation:** All reagents were bought from commercial sources and used without further purification. Elemental analysis was carried out with an Elementar Vario ELIII microanalyzer. Magnetic measurements were carried out with a Quantum

Table 1. Crystal and structure refinement data for **1**.

| Complex | **1** |
|---|---|
| Formula | $C_{26}H_{30}Co_3O_{16}S_4$ |
| *Fw* | 903.53 |
| Crystal system | monoclinic |
| Space group | $P2_1/c$ |
| *a* / Å | 10.107(2) |
| *b* / Å | 10.258(2) |
| *c* / Å | 16.276(3) |
| $\beta$ / ° | 95.38(3) |
| *V* / $Å^3$ | 1680.0(6) |
| *Z* | 2 |
| $D_{calcd.}$ / $g cm^{-3}$ | 1.786 |
| *S* | 1.032 |
| $R_1$[a] | 0.0625 |
| $\omega R_2$[b] | 0.1406 |

[a] $R_1 = \Sigma|F_o - F_c|/\Sigma|F_o|$. [b] $\omega R_2 = \Sigma[\omega(F_o^2 - F_c^2)^2]/\Sigma[\omega(F_o^2)^2]^{1/2}$.

 © 2007 Wiley-VCH Verlag GmbH & Co. KGaA, Weinheim 

Table 2. Selected bond lengths [Å] and angles [°] for **1**.[a]

| | | | |
|---|---|---|---|
| Co1–O1 | 2.034(4) | O4#2-Co1–O6#3 | 86.34(16) |
| Co1–O4#2 | 2.054(4) | O7–Co1–O6#3 | 90.48(17) |
| Co1–O7 | 2.096(4) | O1–Co1–O8#4 | 97.16(15) |
| Co1–O6#3 | 2.113(4) | O4#2-Co1–O8#4 | 90.22(16) |
| Co1–O8#4 | 2.131(4) | O7–Co1–O8#4 | 89.97(15) |
| Co1–O5#3 | 2.228(4) | O6#3-Co1–O8#4 | 102.19(15) |
| Co2–O3#5 | 2.042(3) | O1–Co1–O5#3 | 99.97(15) |
| Co2–O3#2 | 2.042(3) | O4#2-Co1–O5#3 | 86.38(16) |
| Co2–O8#4 | 2.243(4) | O7–Co1–O5#3 | 92.49(16) |
| Co2–O8 | 2.243(4) | O6#3-Co1–O5#3 | 60.64(14) |
| O3–Co2#6 | 2.042(3) | O8#4-Co1–O5#3 | 162.66(14) |
| O4–Co1#6 | 2.054(4) | O2#4-Co2–O2 | 180.0(3) |
| O5–Co1#1 | 2.228(4) | O2#4-Co2–O3#5 | 89.76(16) |
| O1–Co1–O(4)#2 | 92.37(16) | O2–Co2–O3#5 | 90.24(16) |
| O1–Co1–O7 | 90.79(18) | O2#4-Co2–O8#4 | 88.48(15) |
| O4#2-Co1–O7 | 176.78(18) | O2–Co2–O8#4 | 91.52(15) |
| O1–Co1–O6#3 | 160.61(15) | O3#5-Co2–O8#4 | 84.18(14) |
| | | O3#2-Co2–O8#4 | 95.82(14) |

[a] Symmetry transformations used to generate equivalent atoms: #1: $x - 1$, $y$, $z$; #2: $-x + 2$, $y - 1/2$, $-z + 1/2$; #3: $x + 1$, $y$, $z$; #4: $-x + 2$, $-y$, $-z$; #5: $x$, $-y + 1/2$, $z - 1/2$; #6: $-x + 2$, $y + 1/2$, $-z + 1/2$.

Design (SQUID) magnetometer MPMS-XL-5. Thermal gravimetric analysis was completed with a NETZSCH TG 209 instrument.

**Preparation of 1:** A mixture of $CoCl_2 \cdot 6H_2O/H_3BTC$ (1:0.8) in a solution of dmso (10 mL) was placed in a Teflon reactor (23 mL) and heated at 160 °C for 3 d. The mixture was then cooled to room temp. at 5 °C $h^{-1}$. Purple crystals were obtained in 75% yield based on Co. $C_{26}H_{30}Co_3O_{16}S_4$ (903.53): calcd. C 34.56, H 3.35; found C 34.52, H 3.26.

**X-ray Crystallographic Studies:** Intensity data were collected with a rigaku r-axis rapid IP area detector with Mo-$K_\alpha$ monochromated radiation ($\lambda$ = 0.71073 Å) at room temp. Empirical absorption correction was applied. The structures of these polymers were solved by direct method and refined by full-matrix least-squares on $F^2$ by using the SHELXL-97 software. All of the non-hydrogen atoms were refined anisotropically. The organic hydrogen atoms were generated geometrically and refined with isotropic temperature factors. Crystal data and structure refinement for these polymers are summarized in Table 1. Selected bond lengths and angels are listed in Table 2. CCDC-638904 contains the supplementary crystallographic data for this paper. These data can be obtained free of charge from The Cambridge Crystallographic Data Centre via www.ccdc.cam.ac.uk/data_request/cif.

## Acknowledgments

This work was supported by the National Natural Science Foundation of China under Project 50572040.

[1] a) P. J. Hagrman, D. Hagrman, J. Zubieta, *Angew. Chem. Int. Ed.* **1999**, *38*, 2638; b) A. J. Blake, N. R. Champness, P. Hubberstey, W. S. Li, M. A. Withersby, M. Schröder, *Coord. Chem. Rev.* **1999**, *183*, 117; c) B. Moulton, M. J. Zaworotko, *Chem. Rev.* **2001**, *101*, 1629; d) O. R. Evans, W. Lin, *Acc. Chem. Res.* **2002**, *35*, 511; e) O. M. Yaghi, M. O'Keeffe, N. W. Ockwig, H. K. Chae, M. Eddaoudi, J. Kim, *Nature* **2003**, *423*, 705; f) C. N. R. Rao, S. Natarajan, R. Vaidhyanathan, *Angew. Chem. Int. Ed.* **2004**, *43*, 1466; g) S. Kitagawa, R. Kitaura, S. I. Noro, *Angew. Chem. Int. Ed.* **2004**, *43*, 2334.

[2] a) S. R. Batten, R. Robson, *Angew. Chem. Int. Ed.* **1998**, *37*, 1460; b) M. O'Keeffe, M. Eddaoudi, H. Li, T. Reineke, O. M. Yaghi, *J. Solid State Chem.* **2000**, *152*, 3; c) R. Robson, *J. Chem. Soc. Dalton Trans.* **2000**, 3735; d) M. Eddaoudi, D. B. Moler, H. Li, B. Chen, T. M. Reineke, M. O'Keeffe, O. M. Yaghi, *Acc. Chem. Res.* **2001**, *34*, 319; e) B. Moulton, M. Zaworotko, *Chem. Rev.* **2001**, *101*, 1629; f) O. R. Evans, W. Lin, *Acc. Chem. Res.* **2002**, *35*, 511; g) O. M. Yaghi, M. O'Keeffe, N. W. Ockwig, H. K. Chae, M. Eddaoudi, J. Kim, *Nature* **2003**, *423*, 705; h) S. L. James, *Chem. Soc. Rev.* **2003**, *32*, 276.

[3] a) D. S. Reddy, T. Dewa, K. Endo, Y. Aoyama, *Angew. Chem. Int. Ed.* **2000**, *39*, 4266; b) V. A. Blatov, L. Carlucci, G. Cianib, D. M. Proserpio, *CrystEngComm* **2004**, *6*, 377; c) F. Luo, S. R. Batten, Y. X. Che, J. M. Zheng, *Chem. Eur. J.* **2007**, *13*, 4948; d) F. Luo, Y. X. Che, J. M. Zheng, *Cryst. Growth Des.* **2006**, *6*, 2432.

[4] a) M. Eddaoudi, J. Kim, D. Vodak, A. Sudik, J. Wachter, M. O'Keeffe, O. M. Yaghi, *Proc. Natl. Acad. Sci. USA* **2002**, *99*, 4900; b) J. Kim, B. Chen, T. M. Reineke, H. Li, M. Eddaoudi, D. B. Moler, M. O'Keeffe, O. M. Yaghi, *J. Am. Chem. Soc.* **2001**, *123*, 8239; c) M. Eddaoudi, J. Kim, M. O'Keeffe, O. M. Yaghi, *J. Am. Chem. Soc.* **2002**, *124*, 376; d) B. Chen, M. Eddaoudi, S. T. Hyde, M. O'Keeffe, O. M. Yaghi, *Science* **2001**, *291*, 1021; e) B. Chen, M. Eddaoudi, T. M. Reineke, J. W. Kampf, M. O'Keeffe, O. M. Yaghi, *J. Am. Chem. Soc.* **2000**, *122*, 11559.

[5] a) S. R. Batten, B. F. Hoskins, R. Robson, *J. Chem. Soc. Chem. Commun.* **1991**, 445; b) S. R. Batten, B. F. Hoskins, B. Moubaraki, K. S. Murray, R. Robson, *J. Chem. Soc. Dalton Trans.* **1999**, 2977; c) P. Jensen, D. J. Price, S. R. Bateen, B. Moubaraki, K. S. Murray, *Chem. Eur. J.* **2000**, *6*, 3186; d) L. Carlucci, G. Ciani, F. Porta, D. M. Proserpio, L. Santagostini, *Angew. Chem. Int. Ed.* **2002**, *41*, 1907; e) F. C. Liu, Y. F. Zeng, J. Jiao, X. H. Bu, J. Ribas, S. R. Batten, *Inorg. Chem.* **2006**, *45*, 2776; f) D. B. Cordes, L. R. Hanton, *Inorg. Chem.* **2007**, *46*, 1634; g) S. Hu, A. J. Zhou, Y. H. Zhang, S. Ding, M. L. Tong, *Cryst. Growth Des.* **2006**, *6*, 2543; h) J. Luo, X. G. Zhou, X. F. Hou, H. X. Wu, L. H. Weng, Y. R. Li, *Chin. J. Chem.* **2005**, *23*, 310; i) C. Qin, X. L. Wang, E. B. Wang, Z. M. Su, *Inorg. Chem.* **2005**, *44*, 7122; j) J. A. Schlueter, J. L. Manson, U. Geiser, *Inorg. Chem.* **2005**, *44*, 3194.

[6] a) I. Ino, P. L. Wu, M. Munakata, Y. Maekawa, Y. Suenaga, I. Kuroda-Sowa, Y. Kitamori, *Inorg. Chem.* **2000**, *39*, 2146; b) M. Schwarten, J. Chomic, J. Cernak, D. Babel, *Z. Anorg. Allg. Chem.* **1996**, *622*, 1478; c) L. H. Xie, S. X. Liu, B. Gao, C. D. Zhang, C. Y. Sun, D. H. Li, Z. M. Su, *Chem. Commun.* **2005**, 2402; d) C. Qin, X. L. Wang, L. Carlucci, M. L. Tong, E. B. Wang, C. W. Hu, L. Xu, *Chem. Commun.* **2004**, 1876.

[7] a) H. Chun, D. Kim, D. N. Dybtsev, K. Kim, *Angew. Chem. Int. Ed.* **2004**, *43*, 971; b) X. S. Wang, S. Ma, D. Sun, S. Parkin,

 © 2007 Wiley-VCH Verlag GmbH & Co. KGaA, Weinheim 

H. C. Zhou, *J. Am. Chem. Soc.* **2006**, *128*, 16474; c) B. Chen, S. Ma, F. Zapata, E. B. Lobkovsky, J. Yang, *Inorg. Chem.* **2006**, *45*, 5718.
[8] N. E. Khayati1, R. C. El Moursli, J. RodrÍguez-Carvajal, G. André, N. Blanchard, F. Bourée, G. Collin, T. Roisnel, *Eur. Phys. J. B* **2001**, *22*, 429.
[9] MAGMUN was developed by Dr. Zhiqiang Xu and OW01.exe by Dr. O. Waldmann.
[10] a) O. Kahn, *Molecular Magnetism*, VCH, New York, **1993**; b) N. Benbellat, K. S. Gavrilenko, Y. Le Gal, O. Cador, S. Golhen, A. Gouasmia, J. M. Fabre, L. Ouahab, *Inorg. Chem.* **2006**, *45*, 10440; c) A. Rodriguez-Dieguez, R. Kivekas, R. Sillanpaa, J. Cano, F. Lloret, V. McKee, H. Stoeckli-Evans, E. Colacio, *Inorg. Chem.* **2006**, *45*, 10537.
[11] a) S. Brooker, D. J. de Geest, R. J. Kelly, P. G. Plieger, B. Moubaraki, K. S. Murray, G. B. Jameson, *J. Chem. Soc. Dalton Trans.* **2002**, 2080; b) U. Beckmann, S. Brooker, *Coord. Chem. Rev.* **2003**, *245*, 17.
[12] Y. Z. Zheng, M. L. Tong, W. X. Zhang, X. M. Chen, *Chem. Commun.* **2006**, 165.
[13] Y. Y. Liu, J. F. Ma, J. Yang, Z. M. Su, *Inorg. Chem.* **2007**, *46*, 3027.

Received: March 13, 2007
Published Online: June 29, 2007

 © 2007 Wiley-VCH Verlag GmbH & Co. KGaA, Weinheim

**The EUChemSoc Societies have taken the significant step into the future by merging their traditional journals, to form two leading chemistry journals, the *European Journal of Inorganic Chemistry* and the *European Journal of Organic Chemistry.* Three further EUChemSoc Societies (Austria, Czech Republic and Sweden) are Associates of the two journals.**

## COVER PICTURE

**The cover picture shows** a novel method for producing mesoporous zeolite single crystals by using cheap and easily prepared porous carbon as the mesopore template. The porous carbon template was obtained by carbonization in Ar of a hydrothermally treated sucrose/ammonia mixture, and it was successfully applied as an inert carbon matrix during zeolite crystallization. After hydrothermal crystallization, combustion of the carbon embedded in the zeolite crystals yielded mesoporous zeolite single crystals. Details are discussed in the article by C. H. Christensen et al. on p. 3955ff.

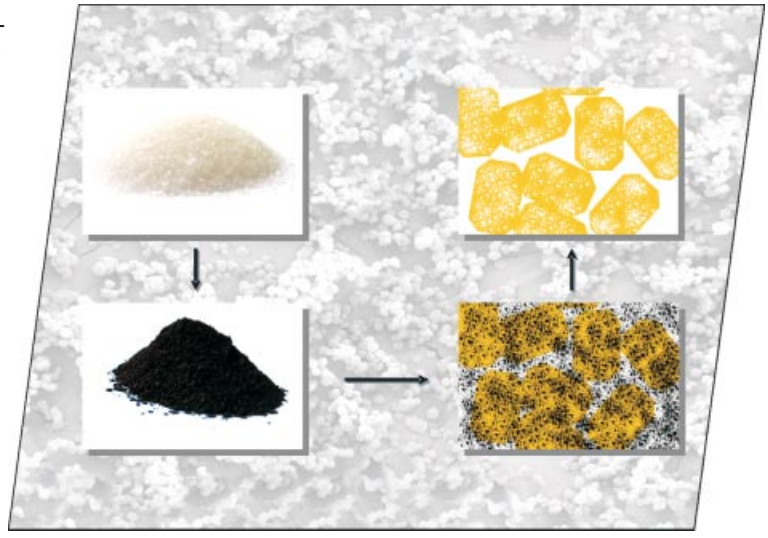

 © 2007 Wiley-VCH Verlag GmbH & Co. KGaA, Weinheim

**The EUChemSoc Societies have taken the significant step into the future by merging their traditional journals, to form two leading chemistry journals, the *European Journal of Inorganic Chemistry* and the *European Journal of Organic Chemistry.* Three further EUChemSoc Societies (Austria, Czech Republic and Sweden) are Associates of the two journals.**

## COVER PICTURE

**The cover picture shows** a novel method for producing mesoporous zeolite single crystals by using cheap and easily prepared porous carbon as the mesopore template. The porous carbon template was obtained by carbonization in Ar of a hydrothermally treated sucrose/ammonia mixture, and it was successfully applied as an inert carbon matrix during zeolite crystallization. After hydrothermal crystallization, combustion of the carbon embedded in the zeolite crystals yielded mesoporous zeolite single crystals. Details are discussed in the article by C. H. Christensen et al. on p. 3955ff.

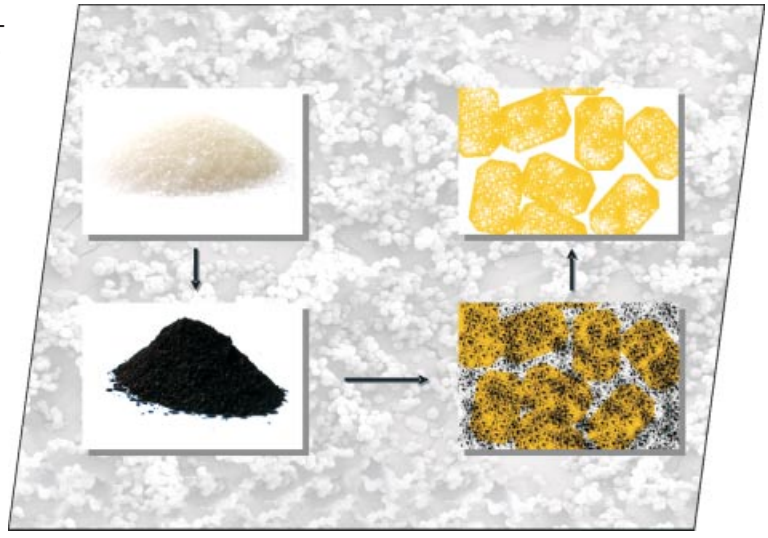

 © 2007 Wiley-VCH Verlag GmbH & Co. KGaA, Weinheim 

# CONTENTS

## MICROREVIEW


### $CO_2$ Conversion

**Y. Himeda* ..... 3927–3941**

Conversion of $CO_2$ into Formate by Homogeneously Catalyzed Hydrogenation in Water: Tuning Catalytic Activity and Water Solubility through the Acid–Base Equilibrium of the Ligand

**Keywords:** Carbon dioxide fixation / Catalyst tuning / Ligand design / Substituent effects / Catalyst recycling

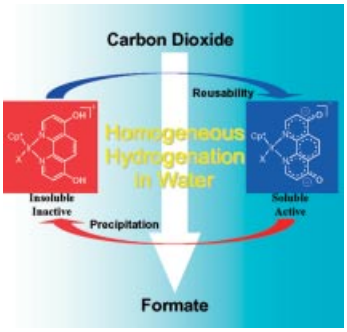


Highly efficient, waste-free, and catalyst-recyclable conversion of $CO_2$ into formate in water was achieved by tuning the catalytic activity and water solubility of the catalyst ligands 4,4′-dihydroxy-2,2′-bipyridine (dhbp) and 4,7-dihydroxy-1,10-phenanthroline (dhpt) by monitoring their acid–base equilibrium.


## SHORT COMMUNICATIONS


### C–C Bond Activation

**M. J. Shaw,* S. W. Bryant, N. Rath ..... 3943–3946**

$\eta^1$-Vinylidene Formation from Internal Alkynones by C–C Bond Migration

**Keywords:** Ruthenium / Alkynes / Isomerization / Vinylidene bond activation / Unsaturated complexes

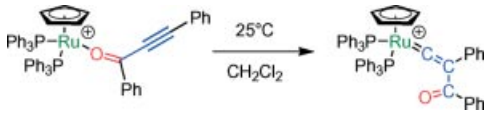


The formal 16-electron $[CpRu(PPh_3)_2]^+$ fragment was shown to react with three nonterminal acetylenic ketones to form $\eta^1$-vinylidene complexes. These reactions involve C–C bond activation and apparently proceed through $\eta^1$-ketone intermediates.

### Chain-Like CoNi Alloys

**L.-P. Zhu, H.-M. Xiao, S.-Y. Fu* ..... 3947–3951**

Surfactant-Assisted Synthesis and Characterization of Novel Chain-Like CoNi Alloy Assemblies

**Keywords:** Alloy / Assemblies / Hydrothermal method / Ferromagnetism / Coercivity

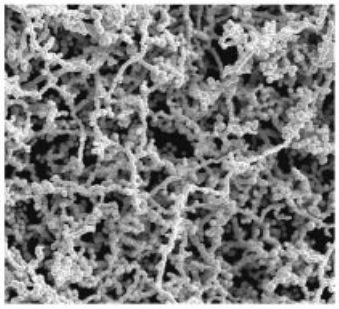

Novel chain-like CoNi alloy assemblies with a length of up to 6–7 μm were successfully prepared by a surfactant-assisted hydrothermal synthetic route. The results show that chain-like CoNi alloy assemblies composed of well-aligned CoNi alloy submicrospheres have a diameter of about 400–500 nm. Magnetic hysteresis measurements revealed that the chain-like CoNi alloy assemblies display ferromagnetic behavior.

### Hexamolybdates

**M. R. Pedrosa,* R. Aguado, V. Díez, J. Escribano, R. Sanz, F. J. Arnáiz* ..... 3952–3954**

Unprecedented Rearrangement of Molybdenum(VI) Oxide to ($\mu_2$-Oxido)bis[dioxidomolybdenum(VI)] Hexamolybdate

**Keywords:** Molybdenum / Hexamolybdates / O ligands / Polyoxometalates

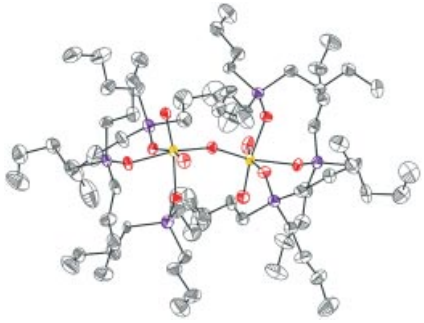

$MoO_2(acac)_2$ reacts in methanol under mild conditions to afford a new family of molybdates of composition $[Mo_2O_5L_6]$-$[Mo_6O_{19}]$ (L = $H_2O$, amides, sulfoxides, and phosphane oxides); the $OPBu_3$ derivative is the first hexamolybdate in a noncentrosymmetric polar crystal class.


 © 2007 Wiley-VCH Verlag GmbH & Co. KGaA, Weinheim 

# FULL PAPERS

## Hierarchical Zeolites

A mesoporous carbon prepared from sucrose was successfully employed as a hard template to produce hierarchical silicalite-1, thus providing a very simple and inexpensive route to desirable zeolite catalysts.

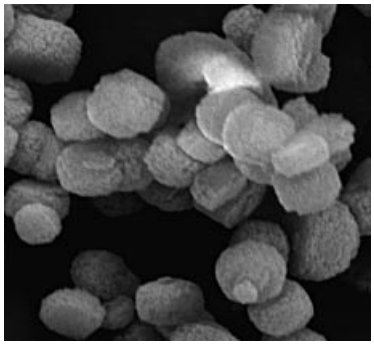

**K. Zhu, K. Egeblad, C. H. Christensen* ..... 3955–3960**

Mesoporous Carbon Prepared from Carbohydrate as Hard Template for Hierarchical Zeolites

**Keywords:** Zeolite / Templating / Hierarchical materials / Sucrose / Porosity

## (Arene)ruthenium(II) Complexes

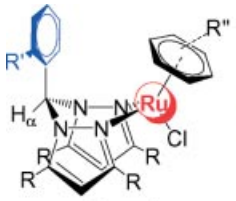

Isomer A

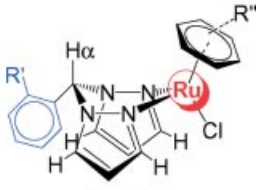

Isomer B

A new and safer method for the synthesis of differently substituted bis(pyrazolyl)-methane ligands has been developed. Arene–Ru derivatives containing these ligands were obtained. The relative stability of isomers A and B has been analysed. The activity in transfer hydrogenation of benzophenone has been studied. Better results are obtained with ligands that contain methylated pyrazoles.

**M. C. Carrión, F. A. Jalón, B. R. Manzano,* A. M. Rodríguez, F. Sepúlveda, M. Maestro ..... 3961–3973**

(Arene)ruthenium(II) Complexes Containing Substituted Bis(pyrazolyl)methane Ligands – Catalytic Behaviour in Transfer Hydrogenation of Ketones

**Keywords:** Ruthenium / Arene ligands / Homogeneous catalysis / Bis(pyrazolyl)-methane / Transfer hydrogenation / X-ray structure determination

## $Zn^{II}$-cyclen-pyridine Complexes

Binary and ternary systems containing $Zn^{2+}$, cyclen and/or pyridine derivatives (picolinic, nicotinic and dipicolinic acids and nicotinamide) were investigated in solution and in the solid state, and the stability of the ternary complexes was determined.

**Z. Vargová,* J. Kotek, J. Rudovský, J. Plutnar, R. Gyepes, P. Hermann, K. Györyová, I. Lukeš* ..... 3974–3987**

Ternary Complexes of Zinc(II), Cyclen and Pyridinecarboxylic Acids

**Keywords:** Cyclen complexes / N ligands / Stability constants / Zinc

## Metathesis Polymerization

Several $Ru^{II}$–N-heterocyclic carbene complexes were investigated for their use as pre-catalysts for the ring-opening metathesis polymerization of enantiomerically pure *exo* and *endo* norbornene derivatives. Differences in reactivity between the *exo* and *endo* derivatives were elucidated by quantum chemical calculations. These revealed different potential reaction pathways.

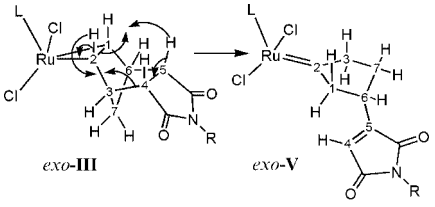

*exo*-**III** *exo*-**V**

**M. R. Buchmeiser,* D. Wang, Y. Zhang, S. Naumov, K. Wurst ..... 3988–4000**

Novel Ruthenium(II) N-Heterocyclic Carbene Complexes as Catalyst Precursors for the Ring-Opening Metathesis Polymerization (ROMP) of Enantiomerically Pure Monomers: X-ray Structures, Reactivity, and Quantum Chemical Considerations

**Keywords:** Carbene ligands / Ruthenium / ROMP / Quantum chemistry

 © 2007 Wiley-VCH Verlag GmbH & Co. KGaA, Weinheim 

# CONTENTS


## Tetranuclear Gold(I) Complexes

**E. J. Fernández,* A. Laguna,* J. M. López-de-Luzuriaga, M. Monge, M. Montiel, M. E. Olmos, R. C. Puelles, E. Sánchez-Forcada ..... 4001–4005**

Tetranuclear (Phosphane)(thiolato)gold(I) Complexes: Synthesis, Characterization and Photoluminescent Properties

**Keywords:** Phosphanes / Thiolates / Gold / Luminescence / Aurophilicity

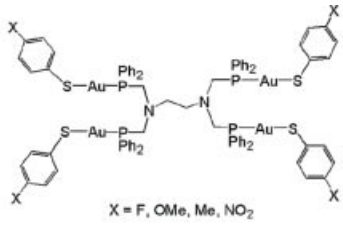


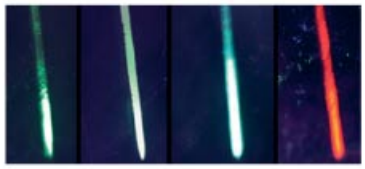

Tetranuclear (benzenethiolato)(phosphane)-gold(I) complexes were prepared from tetradentate P donor ligands with an ethylenediamine core, and aurophilic Au···Au interactions were found for $[Au_4(SC_6H_4OMe)_4\{(Ph_2PCH_2)_2NCH_2CH_2N(CH_2PPh_2)_2\}]$. The luminescent properties of these complexes display bright emissions at 77 K in the solid state.

## Silicon Carbide Nanowires

**B. J.-J. Niu,* J.-N. Wang ..... 4006–4010**

An Approach to the Synthesis of Silicon Carbide Nanowires by Simple Thermal Evaporation of Ferrocene onto Silicon Wafers

**Keywords:** Silicon / Carbides / Thermal evaporation / Ferrocene / Nanowires

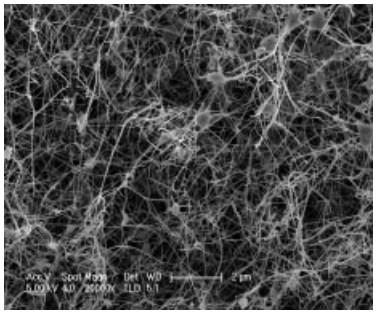

Scales of silicon carbide nanowires (SiC-NWs) were synthesized by thermal evaporation of ferrocene onto silicon wafers at high temperature. The SiC-NWs have diameters of ≈ 20 nm and lengths of several μms. A tentative growth model on the basis of a vapor–liquid–solid (VLS) mechanism was proposed.

## Metallophosphaalkene Chelates

**L. Weber,* G. Noveski, S. Uthmann, H.-G. Stammler, B. Neumann ... 4011–4016**

Phosphaalkenes $R^1C(O)-P=C(NMe_2)_2$ ($R^1$=Ph, 4-$EtC_6H_4$): Versatile Reagents for 1,3-Dipolar Cycloadditions to Phosphenium Complexes $[Cp(CO)_2M = PPh_2]$ (M = Mo, W)

**Keywords:** Phosphaalkenes / Phosphenium Complexes / Molybdenum / Tungsten

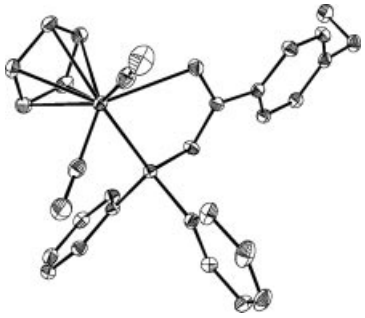

The synthesis of the metallophosphaalkenes $[Cp(CO)_2M^a-P=C(aryl)-O-P^bPh_2-(M^a-P^b)]$ [M = Mo, W; aryl = Ph (**4a**,**b**); M = Mo, W; aryl = 4-$EtC_6H_4$ (**6a**,**b**)] was effected by treating phosphenium complexes $[Cp(CO)_2M = PPh_2]$ (M = Mo, W) with an excess of the phosphaalkenes aryl-$C(O)-P=C(NMe_2)_2$.

## Uranyl Activation

**J.-C. Berthet,* G. Siffredi, P. Thuéry, M. Ephritikhine* ..... 4017–4020**

Controlled Chemical Reduction of Uranyl Salts into $UX_4(MeCN)_4$ (X = Cl, Br, I) with $Me_3SiX$ Reagents

**Keywords:** Uranyl salts / Reduction / Silanes / Uranium

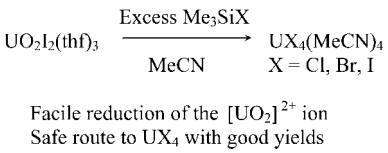


Facile deoxygenation and reduction of the robust $[UO_2]^{2+}$ entity is carried out by treating $UO_2I_2(thf)_2$ or $UO_2(OTf)_2$ with $Me_3SiX$ (X = Cl, Br, I) in acetonitrile. The tetravalent $UX_4(MeCN)_4$ products, obtained in good yields, are useful precursors in uranium chemistry.


 © 2007 Wiley-VCH Verlag GmbH & Co. KGaA, Weinheim 

## Mixed-Valent Ru Complexes

The kinetics of axial ligand substitution of $[Ru_2(\mu\text{-}O_2CCH_3)_4(MeCN)_2]^+$ by two phosphane ligands were measured for the first time as well as the variable-temperature magnetic susceptibility of the corresponding phosphane diadducts, which shows a Boltzmann distribution of states in both cases that is supported by low-temperature X-ray diffraction data.

**T. J. Burchell, T. S. Cameron, D. H. Macartney, L. K. Thompson, M. A. S. Aquino* ..... 4021–4027**

Kinetics and Magnetism of Phosphane Diadducts of Diruthenium(II,III) Tetraacetate

**Keywords:** Carboxylate ligands / P ligands / Ruthenium / Kinetics / Magnetic properties

## Self-Assembled Monolayers

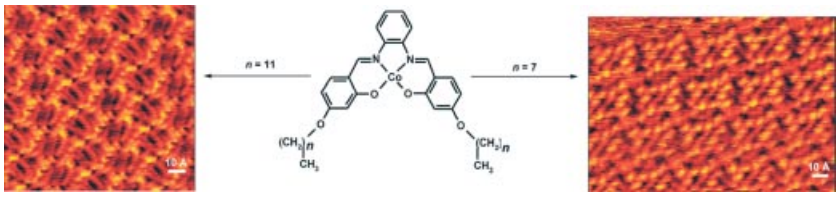


As demonstrated here for a series of $Co^{II}$, $Cu^{II}$ and $Ni^{II}$ salophen complexes, alkyl chain length defines the favoured 2D structure for each metal complex on a liquid–graphite interface.

**M. T. Räisänen, F. Mögele, S. Feodorow, B. Rieger, U. Ziener, M. Leskelä, T. Repo* ..... 4028–4034**

Alkyl Chain Length Defines 2D Architecture of Salophen Complexes on Liquid–Graphite Interface

**Keywords:** Metal-containing monolayers / Nanopatterning / Scanning tunnelling microscopy (STM) / Self-assembly

## Efficient Molecular Wires

A particularly short and efficient preparation of conjugated oligo(phenyleneethylene) thiols bearing redox-active ferrocene moieties is described. For the bis(ferrocenyl) derivatives, the nature of the substituents may lead to an inverted series of electrode potentials, causing a single two-electron wave to occur. The ultrafast cyclic voltammetry of the adsorbed species onto gold electrodes confirms that these compounds are indeed very efficient molecular wires.

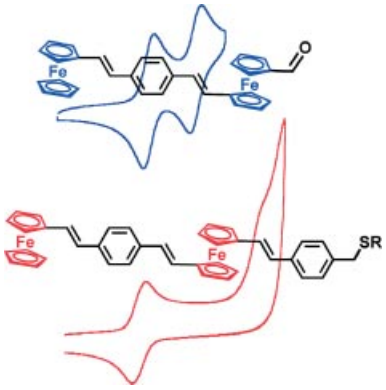


**C. Amatore,* S. Gazard, E. Maisonhaute, C. Pebay, B. Schöllhorn,* J.-L. Syssa-Magalé, J. Wadhawan ..... 4035–4042**

Ferrocenyl Oligo(phenylene-vinylene) Thiols for the Construction of Self-Assembled Monolayers

**Keywords:** Molecular wires / SAMs / Ferrocenes / Thiols / Redox chemistry / Self-assembly

## Fluorogallophosphates

A 2D fluorogallophosphate, named Mu-35, was synthesized hydrothermally by in situ generation of the ethylamine structure-directing agent from ethylformamide. Protonated ethylamine molecules are located inside pseudo 12 MR, in opposition to those observed inside pseudo 8 MR.

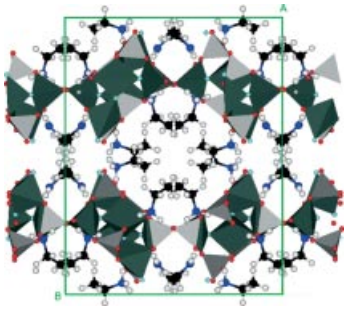


**L. Lakiss, A. Simon-Masseron,* F. Porcher, S. Rigolet, J. Patarin ..... 4043–4049**

Mu-35: A Fluorogallophosphate Obtained by In Situ Generation of the Template

**Keywords:** Fluorine / Gallophosphate / Structure elucidation / Hydrothermal synthesis

 © 2007 Wiley-VCH Verlag GmbH & Co. KGaA, Weinheim 

# CONTENTS


## Intelligent Materials

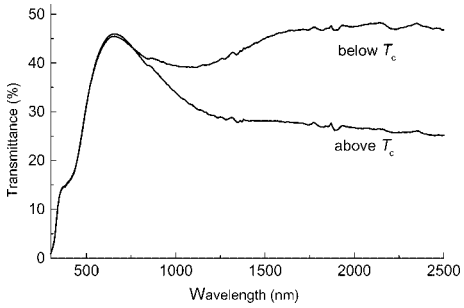


**C. Piccirillo, R. Binions, I. P. Parkin* ..... 4050–4055**

Nb-Doped $VO_2$ Thin Films Prepared by Aerosol-Assisted Chemical Vapour Deposition

**Keywords:** Intelligent materials / Vanadium dioxide (M) / Transition temperature / Niobium doping

Niobium-doped vanadium dioxide ($V_xNb_{1-x}O_2$, $x = 0-0.037$) thin films were prepared by aerosol-assisted chemical vapour deposition (AACVD) of vanadyl-(IV) acetonate and niobium(V) ethoxide in ethanol. The thin films showed thermochromic behaviour, with a marked change in optical properties above and below the switching.

## Luminescent Ru Complexes

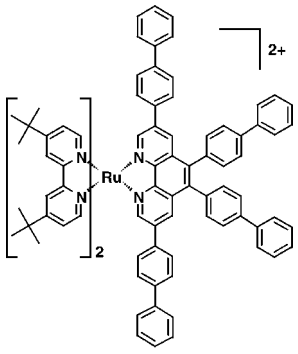


**B. Schäfer, H. Görls, S. Meyer, W. Henry, J. G. Vos, S. Rau* ..... 4056–4063**

Synthesis and Properties of Tetrasubstituted 1,10-Phenanthrolines and Their Ruthenium Complexes

**Keywords:** Ruthenium / Phenanthroline / Luminescence / Photochemistry

Novel phenanthroline-type ligands with extended aromatic substitutions and the corresponding ruthenium complexes were characterised. The luminescence properties indicate potential applications as luminescent oxygen sensors.

## Metal–Carbonyl Clusters

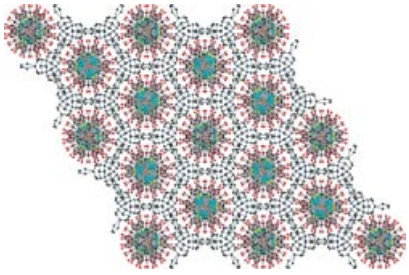

**C. Femoni, M. C. Iapalucci, G. Longoni, F. Ranuzzi, S. Zacchini,* S. Fedi, P. Zanello ..... 4064–4070**

Condensation of Nickel–Carbonyl Clusters with Soft Lewis Acids: Synthesis and Characterisation of the $\{Cd_2Cl_3[Ni_6(CO)_{12}]_2\}^{3-}$ Dimer

**Keywords:** Cluster compounds / Carbonyl ligands / Structure elucidation / Lewis acids / Cyclic voltammetry

Reaction of $[Ni_6(CO)_{12}]^{2-}$ with $CdCl_2 \cdot 2.5H_2O$ gives the $\{Cd_2Cl_3[Ni_6(CO)_{12}]_2\}^{3-}$ dimer, confirming that the basic character of the $M_3(CO)_6$ triangular faces can be exploited to obtain oligomers or polymers based on metal–carbonyl clusters. These dimers are pillared along the crystallographic *c* axis, forming infinite columns of alternating cluster anions and thf molecules.

## Silicon Pnictogen Cages

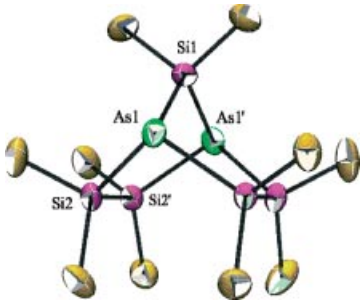


**G. Tekautz, J. Baumgartner, A. Dransfeld, K. Hassler* ..... 4071–4077**

Silicon–Phosphorus and Silicon–Arsenic Cage Compounds with Bicyclo[2.2.1]-heptane, Bicyclo[3.2.1]octane and Tricyclo-[3.3.3.1.$0^{3,7}$]nonane Backbones

**Keywords:** Cage compounds / Crystal structures / Ab initio calculations / Silicon

In the reaction of chlorooligosilanes $MeSi(SiMe_2Cl)_3$ or $[MeSi(SiMe_2Cl)_2]_2$ with $Na_xP/K_xP$ and $Na_xAs/K_xAs$, bi- and tricyclic cage compounds are formed alongside polymeric materials. To explain the observed product distributions, the Gimarc concept of thermodynamic preference of topomers was positively verified with the help of quantum chemical calculations.


**If not otherwise indicated in the article, papers in issue 24 were published online on August 8, 2007**

 © 2007 Wiley-VCH Verlag GmbH & Co. KGaA, Weinheim 

# SPOTLIGHTS …

## *Fullerene Complexes*

Y. Matsuo, T. Fujita, E. Nakamura*

**Hoop-Shaped Condensed Aromatic Systems: Synthesis and Structure of Iron– and Ruthenium–;Hepta-(organo)[60]fullerene Complexes**

*Chem. Asian J.*
DOI: **10.1002/asia.200700124**

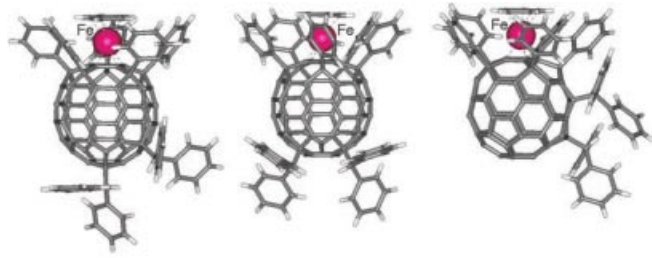


**We don't just do balls**: Hoop- and bowl-shaped aromatic systems can be synthesized by reductive alkylation of buckyferrocene and ruthenocene with metallic potassium. Physical methods such as X-ray crystallography reveal the structures of these iron– and ruthenium–hepta(organo)[60]fullerenes.

## *Cyclotide Biosynthesis*

J. A. Camarero,* R. H. Kimura, Y.-H. Woo, A. Shekhtman, J. Cantor

**Biosynthesis of a Fully Functional Cyclotide inside Living Bacterial Cells**

*ChemBioChem*
DOI: **10.1002/cbic.200700183**

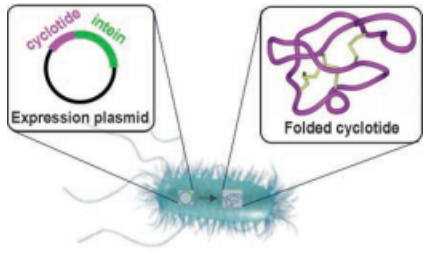


**Perfect circle**. We report the biosynthesis of a natively folded cyclotide, MCoTI-II, in *E. coli* by intracellular backbone cyclization of a linear cyclotide–intein fusion precursor. The cyclized peptide then spontaneously folds into its native conformation. Biosynthetic access to correctly folded cyclotides allows the possibility of generating cell-based combinatorial libraries that can be screened, inside living cells, for their ability to modulate or inhibit cellular processes.

## *Ultrafast Spectroscopy*

E. van Veldhoven, C. Khurmi, X. Zhang, M. A. Berg*

**Time-Resolved Optical Spectroscopy with Multiple Population Dimensions: A General Method for Resolving Dynamic Heterogeneity**

*ChemPhysChem*
DOI: **10.1002/cphc.200700088**

**Dynamic heterogeneity:** A new type of multidimensional experiment is demonstrated that distinguishes between heterogeneous and homogeneous causes of nonexponential relaxation. By varying the duration of an initial time period $\tau_1$, fast-relaxing molecules are removed from the decay during a second period $\tau_2$ (see figure).

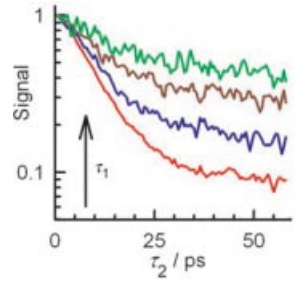


## *SAR of SERMs*

M. Touaibia, A. Wellens, T. C. Shiao, Q. Wang, S. Sirois, J. Bouckaert,* R. Roy*

**Mannosylated G(0) Dendrimers with Nanomolar Affinities to *Escherichia coli* FimH**

*ChemMedChem*
DOI: **10.1002/cmdc.200700063**

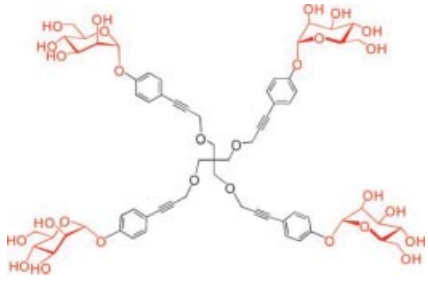

**Mannosylated dendrimers:** Pentaerythritol and bis-pentaerythritol scaffolds were used for the preparation of first generation glycodendrimers bearing aryl α-D-mannopyranoside residues assembled using Sonogashira and click chemistry. Surface Plasmon Resonance measurements showed these two mannosylated clusters as the best ligands known towards FimH from *Escherichia coli* at subnanomolar concentrations.


© 2007 Wiley-VCH Verlag GmbH & Co. KGaA, Weinheim

EurJIC European Journal of Inorganic Chemistry

## *Asymmetric Catalysis*

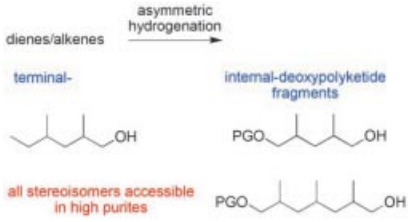


**Interplay** of catalyst and substrate vectors allow application of asymmetric hydrogenations to facilitate formation of terminal- and internal-deoxypolyketide chirons (see scheme). Two of the tools used to achieve this were: DFT calculations to understand the abnormal mechanism for hydrogenation of α,β-unsaturated esters and double asymmetric syntheses (Horeau's principle) in reduction of dienes.

J. Zhou, J. W. Ogle, Y. Fan, V. Banphavichit(Bee), Y. Zhu, K. Burgess*

**Asymmetric Hydrogenation Routes to Deoxypolyketide Chirons**

*Chem. Eur. J.*
DOI: **10.1002/chem.200700390**

## *Organoiron Intermediates*

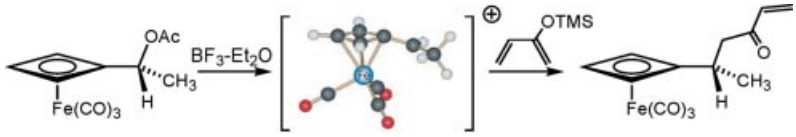


The configurational stability of reactive intermediates derived from ethylcyclobutadiene–$Fe(CO)_3$ by the formal abstraction of a hydride ion, a hydrogen atom or a proton from the pseudobenzylic position was investigated theoretically (DFT, Becke3LYP), and rotational barriers for rotation around the exocyclic C–C bond were probed experimentally.

A. Pfletschinger, U. Schneider, J. Lex, H.-G. Schmalz*

**Stereospecific Side Chain Activation in Cyclobutadiene–$Fe(CO)_3$ Chemistry: A Theoretical and Experimental Study on the Structure and Configurational Stability of Cationic, Radical and Anionic Intermediates**

*Eur. J. Org. Chem.*
DOI: **10.1002/ejoc.200700342**

## *Nanostructure Growth*

**Length made to order**: Controlled reduction of $[Pt(acac)_2]$ and decomposition of $[Fe(CO)_5]$ in a mixture of oleylamine and octadecene leads to the facile synthesis of FePt nanowires and nanorods with diameters of 2–3 nm (see TEM image). The length of the nanowires/nanorods is tunable from greater than 200 nm down to 20 nm by simply controlling the volume ratio of oleylamine and octadecene.

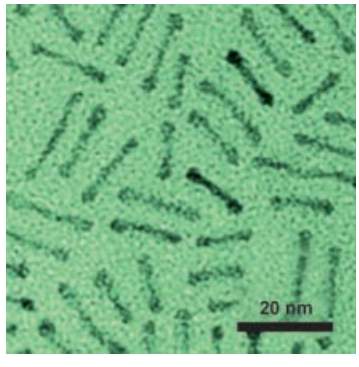


C. Wang, Y. Hou,* J. Kim, S. Sun*

**A General Strategy for Synthesizing FePt Nanowires and Nanorods**

*Angew. Chem. Int. Ed.*
DOI: **10.1002/anie.200702001**

On these pages, we feature a selection of the excellent work that has recently been published in our sister journals. If you are reading these pages on a computer, click on any of the items to read the full article. Otherwise please see the DOIs for easy online access through Wiley InterScience.

 © 2007 Wiley-VCH Verlag GmbH & Co. KGaA, Weinheim 

DOI: 10.1002/ejic.200700494

# Conversion of $CO_2$ into Formate by Homogeneously Catalyzed Hydrogenation in Water: Tuning Catalytic Activity and Water Solubility through the Acid–Base Equilibrium of the Ligand

**Yuichiro Himeda*[a]**

**Keywords:** Carbon dioxide fixation / Catalyst tuning / Ligand design / Substituent effects / Catalyst recycling

This Microreview focuses on the recently developed hydrogenation of $CO_2$ and hydrogen carbonate catalyzed by half-sandwich complexes with 4,4′-dihydroxy-2,2′-bipyridine (dhbp) and 4,7-dihydroxy-1,10-phenanthroline (dhpt). An unprecedented high catalytic activity and reusability of the catalyst without waste generation were achieved by automatic tuning of the catalytic activity and water solubility of the catalyst through the acid–base equilibrium of the catalyst ligand. The oxyanion generated from the phenol hydroxy group played significant roles in the electronic effect and polarity. The catalyst design concept and the excellent properties of the ligands are expected to have significantly broader implications for the design of new homogeneous catalysts.

(© Wiley-VCH Verlag GmbH & Co. KGaA, 69451 Weinheim, Germany, 2007)

## Introduction

The conversion of $CO_2$ into useful organic products still remains an intriguing and challenging subject.[1–6] In nature, an enormous amount of $CO_2$ is transformed into carbohydrate in metal centers of enzymatic systems in an aqueous environment. However, the industrial application of $CO_2$ as a source of $C_1$ instead of carbon monoxide and phosgene is limited: a recent topic of interest is polycarbonate production by using $CO_2$ as a starting material.[7] From an academic viewpoint, the activation of inert $CO_2$ has attracted considerable interest. Many attempts to convert $CO_2$ by using transition-metal catalysts have focused on the photochemical[8–13] and electrochemical[14–16] reduction of $CO_2$. In addition, there have been significant advances in the homogeneously catalyzed hydrogenation of $CO_2$ in the last decade, although the primary products are limited, in general, to formic acid and its derivatives (Table 1).

The homogeneous hydrogenation of $CO_2$ to formic acid was first reported by Inoue et al. in 1976.[17] They used phosphane complexes of group 8, 9, and 10 metals, including Wilkinson's catalyst, in benzene in the presence of water and base. Recently, Ezhova and co-workers studied the hydrogenation by Wilkinson's catalyst in detail.[18] They reported that the rhodium catalysts required phosphane ligands for the hydrogenation of $CO_2$, whereas the complex with bipyridine as a ligand was inactive.

In 1994, Noyori and co-workers reported that the use of supercritical carbon dioxide ($scCO_2$) greatly improved the catalytic efficiency of $Ru^{II}$–phosphane complexes in the presence of amine.[19,20] They obtained TOFs (Please see the list of abbreviations at the end.) up to 95000 $h^{-1}$ at 19 MPa by the use of pentafluorophenol as the additive.[21] The good results are explained by the characteristic properties of $scCO_2$, such as its extremely high miscibility with $H_2$ and its good mass-transfer capability. However, a $scCO_2$-soluble catalyst and a relatively high pressure are required.

[a] National Institute of Advanced Industrial Science and Technology,
Tsukuba Central 5–2, 1–1-1 Higashi, Tsukuba, Ibaraki 305–8565, Japan
Fax: +81-29-861-4687
E-mail: himeda.y@aist.go.jp

*Yuichiro Himeda was born in 1966 in Ehime, Japan. He studied organic chemistry at the School of Science, Osaka University (1984–1991). Then, he moved to the present National Institute of Advanced Industrial Science and Technology. He received his Ph. D. degree from Osaka University under the supervision of Prof. Ikuo Ueda in 1994. After a postdoctoral stay with Prof. Andrew D. Hamilton at the University of Pittsburgh (1995–1996), he worked on the development of homogeneous catalysis for $CO_2$ conversion. His research is focused on the development of new and potentially useful catalytic reactions.*

 © 2007 Wiley-VCH Verlag GmbH & Co. KGaA, Weinheim 

Table 1. Homogeneous catalyst precursors for the hydrogenation of $CO_2$ to formic acid.

| Catalyst precursor | Solvent | Additives | $P(H_2/CO_2)$/MPa | $T$/°C | $t$/h | TON | TOF/$h^{-1}$ | Ref. |
|---|---|---|---|---|---|---|---|---|
| $RuH_2(PPh_3)_4$ | $C_6H_6$ | $NEt_3$, $H_2O$ | 2.5/2.5 | r.t. | 20 | 87 | 4 | [17] |
| $RuH_2(PMe_3)_4$ | $scCO_2$ | $NEt_3$, $H_2O$ | 8.5/12 | 50 | 1 | 1400 | 1400 | [19] |
| $RuCl(OAc)(PMe_3)_4$ | $scCO_2$ | $NEt_3/C_6F_5OH$ | 7/12 | 50 | 0.3 | 31700 | 95000 | [21] |
| K[RuCl(edta-H)] | $H_2O$ | – | 0.3/1.7 | 40 | 0.5 | | 250 | [24] |
| $RhCl(tppts)_3$ | $H_2O$ | $NHMe_2$ | 2/2 | 81 | 0.5 | | 7260 | [22] |
| | | | 2/2 | r.t. | 12 | 3439 | | [23] |
| $[RuCl_2(tppms)_2]_2$ | $H_2O$ | $NaHCO_3$ | 6/3.5 | 80 | 0.03 | 320 | 9600 | [29] |
| | | | 0.2/0.8 | 50 | 1 | | 50 | [29] |
| $RuCl_2(pta)$ | $H_2O$ | $NaHCO_3$ | 6/– | 80 | | | 807[a] | [31] |

[a] The initial TOF was calculated by nonlinear least-squares fitting of the experimental data obtained from the initial part of the reaction.

Leitner and co-workers reported that the water-soluble analogue of Wilkinson's catalyst, $[RhCl(tppts)_3]$ (Ligand abbreviations are in lowercase letters according to IUPAC recommendations; they may be in capital letters in some of the articles cited in this review.), serves as an effective catalyst in water.[22,23] In aqueous systems, an amine additive is required, and the final concentration of formic acid never exceeds that of the added amine. Moreover, the problem of separating the base from the reaction medium still exists. Khan and co-workers reported that $[RuCl(edta-H)]^+$ catalyzed the hydrogenation of $CO_2$ in pure water.[24] Although the initial rate of the reaction was relatively high (TOF of 250 $h^{-1}$), the decomposition of formic acid and formaldehyde as a reverse reaction occurred readily. Joo and Katho performed extensive studies on the hydrogenation of $CO_2$ and hydrogen carbonate in amine-free aqueous solutions. The use of rhodium and ruthenium complexes with widely used water-soluble phosphane ligands (i.e., tppms, tppts, and pta) were investigated in detail.[25–32] The rate of hydrogenation strongly depends on the central metal, the phosphane ligand, and the pH of the reaction solution. A high TOF of 9600 $h^{-1}$ was obtained by using $[RuCl_2(tppms)_2]_2$ at 9.5 MPa and 80 °C. More interestingly, in the hydrogenation of $CaCO_3$, the final formate concentration reached 143% (the calculation is based on the amount of added base). It was revealed that the hydrogenation proceeds in the absence of base. Their detailed kinetic, mechanistic, and theoretical investigations[25] provided useful information on the hydrogenation of $CO_2$ and hydrogen carbonate in water.

According to excellent reviews encompassing the literature until 2003,[5,33–35] almost all the active catalysts for the hydrogenation of $CO_2$ to formic acid are rhodium- and ruthenium-based complexes with phosphane ligands. On the other hand, there are a few, less active examples of other metals (e.g., Ir,[17] Pd,[36] and Ni[37]) and ligands (e.g., edta-H,[24] 6,6′-dichloro-2,2′-bipyridine[38]). Although an aqueous-phase catalyst might not be expected to be active on the basis of mass-transfer rates, a number of active catalysts were found from aqueous systems. On the other hand, an active catalyst promotes the decomposition of formic acid as a reverse process.[27,39] Therefore, the yield of formate is strongly dependent on the equilibrium between formic acid and $CO_2$. Furthermore, recovery and reusability of catalyst are serious concerns from the viewpoint of process cost, because highly active catalysts are restricted to the complexes of precious metals.[37] Several attempts have been made by Baiker and Ikariya to achieve reusability by immobilizing the catalyst for dmf synthesis under $scCO_2$.[40–44]

This Microreview focuses on aqueous catalysts containing rhodium, ruthenium, and, in particular, iridium with 4,4′-dihydroxy-2,2′-bipyridine (dhbp) and 4,7-dihydroxy-1,10-phenanthroline (dhpt) as ligands. In addition, catalyst recycling as well as improvement in catalytic efficiency is considered. For a more sophisticated process, the catalytic activity and water solubility of the metal complexes are controlled through the acid–base equilibrium of the catalyst ligand.

## The Use of Water as a Solvent

Water is innocuous, abundant, and cheap. Furthermore, in the hydrogenation of $CO_2$ and hydrogen carbonate into formic acid and formate, water serves not only as a bulk solvent but also as a participant. The solvation effect of water can significantly influence the thermodynamics of the reaction. Although the hydrogenation of $CO_2$ into formic acid [Equation (1)] in the gas phase is endergonic ($\Delta G°_{298}$ = +33 kJ mol$^{-1}$), the reaction in the aqueous phase is exergonic ($\Delta G°_{298}$ = –4 kJ mol$^{-1}$).[22] Similarly, on the basis of theoretical calculation, the hydrogenation of a hydrogen carbonate into formate in water [Equation (2)] is exergonic.[25] Thus, water is believed to be an ideal reaction medium for the hydrogenation of $CO_2$ and hydrogen carbonate.

$$CO_2 + H_2 \rightleftharpoons HCO_2H \quad (1)$$

$$HCO_3^- + H_2 \rightleftharpoons HCO_2^- + H_2O \quad (2)$$

The equilibriums of both $CO_2$ and formic acid in water must be considered [Equations (3) and (4)].

 © 2007 Wiley-VCH Verlag GmbH & Co. KGaA, Weinheim 

$$CO_2 + H_2O \rightleftharpoons H_2CO_3 \overset{pK_1 = 6.35}{\rightleftharpoons} HCO_3^- + H^+ \overset{pK_2 = 10.33}{\rightleftharpoons} CO_3^{2-} + 2H^+ \quad (3)$$

$$HCO_2H \overset{pK_a = 3.6}{\rightleftharpoons} HCO_2^- + H^+ \quad (4)$$

$CO_2$ reaches an equilibrium with hydrogen carbonate and carbonate, and this is strongly dependent on pH, temperature, and $CO_2$ pressure.[45,46] It is believed that, in acidic conditions, hydrogenation converts $CO_2$ into formic acid [Equation (1)], whereas in alkaline conditions, it converts hydrogen carbonate into formate [Equation (2)]. The presence of the base makes the hydrogenation of $CO_2$ more favorable.[33,39] Thus, the hydrogenation usually fails or provides only a small yield in the absence of a base, because the decomposition of formic acid as a reverse reaction might occur easily under acidic conditions. Joo reported an interesting result: the generation of formate exceeds the amount of added base, in other words, the product mixture contains formic acid, and the reaction solution changes from a basic solution into an acidic one.[27]

On the other hand, the catalysis in water requires the development of water-soluble ligands. Thus far, imparting water solubility to complexes for aqueous catalysis can be achieved by the introduction of charged or polar substituents such as acidic (-$SO_3H$, -$CO_2H$) and basic (-$NR_2$) functionalities into the ligands.[47,48] Although various phosphane ligands (e.g., tppms, tppts, and pta) have been the subject of considerable research in the area of aqueous catalysts, other types of water-soluble ligands have hardly been investigated.

## Background

Numerous studies have investigated half-sandwich bipyridine complexes $[(C_nR_n)M(ppy)X]^{k+}$ [ppy = 2,2′-bipyridine or 1,10-phenanthroline; R = H, Me, and alkyl; X = halogen, $H_2O$; M = Rh, Ir ($n$ = 5); M = Ru ($n$ = 6)], which are isoelectronic complexes of each other, because of their interesting properties.[49–55] In particular, the transfer hydrogenation of NAD catalyzed by rhodium complexes in water by using a formate as the hydrogen donor was extensively investigated by Steckhan et al.[56–60] The reaction of rhodium complexes with a formate provides the corresponding hydrido complex $[Cp^*RhH(bpy)]^+$ through a β-elimination reaction to produce $CO_2$. Direct hydride transfer from the hydrido complex to a ketone results in low yields under neutral conditions.[60] However, we found that transfer hydrogenation is strongly dependent on the pH value, and the yields were significantly improved under acidic formate conditions.[61,62] In addition, the decomposition of formic acid to $CO_2$ and $H_2$ (i.e., the reverse reaction of the hydrogenation of $CO_2$) catalyzed by $[Cp^*Rh(bpy)Cl]Cl$ proceeded smoothly with a TOF of 238 $h^{-1}$ at 40 °C.[63]

Caix and co-workers reported that rhodium and iridium complexes $[Cp^*MCl(bpy)]^+$ (M = Rh, Ir) serve as electrocatalysts for the reduction of $CO_2$ to formate in an aqueous organic medium.[16,64] It has been observed that the electrochemical reduction involves the formation of hydrido complexes $[Cp^*MH(bpy)]^+$, followed by the insertion of $CO_2$ into the metal–hydrogen bond.

Previous studies by us and others prompted us to investigate the hydrogenation of $CO_2$ or hydrogen carbonate by using the half-sandwich bipyridine complexes in water. Table 2 shows the results of the hydrogenation of $CO_2$ or hydrogen carbonate; the reaction proceeded in aqueous solution without the use of amine additives.[65] Interestingly, the hydrogenation proceeded under neutral and acidic conditions (entries 2 and 3), although these conditions are less suitable for activity than basic conditions. However, the decomposition of the formate as a reverse reaction occurred easily after pressure release, particularly in acidic solutions. It is noteworthy that the iridium complexes showed a catalytic activity similar to those of the rhodium and ruthenium complexes (entry 4). However, the catalytic activities of the half-sandwich bipyridine complexes were far from satisfactory.

Table 2. Hydrogenation catalyzed by half-sandwich bipyridine complexes in aqueous solution.[a]

| Entry | Complex | Solution | TON |
|---|---|---|---|
| 1 | $[Cp^*Rh(bpy)Cl]Cl$ | 1 M KOH aq. | 216 |
| 2 | $[Cp^*Rh(bpy)Cl]Cl$ | 1 M $NaH_2PO_4$ aq. | 76 |
| 3 | $[Cp^*Rh(bpy)Cl]Cl$ | $H_2O$ | 31 |
| 4 | $[Cp^*Ir(bpy)Cl]Cl$ | 1 M KOH aq. | 105 |
| 5 | $[(C_6Me_6)Ru(bpy)Cl]Cl$ | 1 M KOH aq. | 68[b] |

[a] The reaction was carried out by using a catalyst (0.1 mM) at 4 MPa ($CO_2/H_2$ = 1:1) and 80 °C for 20 h. [b] The catalyst concentration was 0.2 mM.

Sakaki's theoretical studies[66] and Jessop's experimental results[67] had the important implication that electron-donating ligands would improve the catalytic efficiency. The electronic substituent effect in a bipyridine ligand, in which the coordinated nitrogen atoms are incorporated in the aromatic ring, may have a stronger influence on the central metal atom than that in a triphenylphosphane ligand. In order to improve the catalytic activity and recover the catalyst, we designed a novel catalyst based on bipyridine complexes.

## Catalyst Design

Recently, extensive efforts have been undertaken to optimize an entire chemical process consisting of reaction and separation steps in order to minimize economical and environmental costs.[68–70] Control or switching of catalyst properties (e.g., reactivity and solubility) is one of the strategies employed for this purpose.[71] The pioneering reports of Wrighton demonstrated that catalytic activity can be electrochemically controlled by changing the oxidation state of the redox-active ligand by addition of stoichiometric amounts of simple redox reagents (Scheme 1a).[72,73] In the

 © 2007 Wiley-VCH Verlag GmbH & Co. KGaA, Weinheim 

hydrogenation of cyclohexene, the reduced form of the diphosphanylcobaltocene-stabilized rhodium complex is approximately 16 times faster than its oxidized form. On the other hand, there are many reports of the use of an amphiphilic ligand for controlling the solubility of the complexes by varying the pH of the system.[74] For example, catalyst recycling was achieved by addition of acid or base to the solution after the reaction, followed by extraction or filtration.[75,76] Recently, the interesting work of Sussner demonstrated the recycling of the Grubbs–Hoveyda catalyst with two ferrocene moieties by using the redox-switching concept (Scheme 1b).[77] However, the simultaneous and effective control of two or more functions of a catalyst has never been demonstrated.

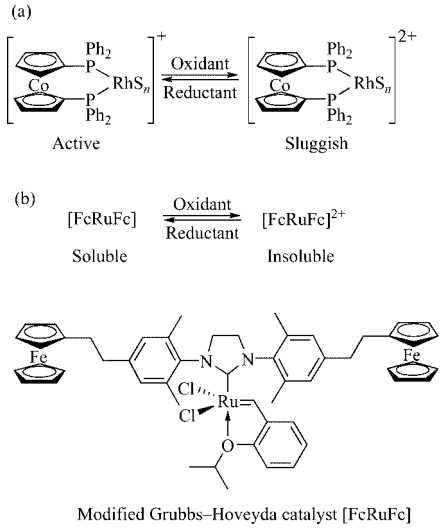


Scheme 1. Control of catalytic properties by switching of the redox-active ligand: (a) Electrochemical control of catalytic activity.[72] (b) Control of solubility for recyclability of catalyst.[77]

We focused our attention on catalyst tuning through the acid–base equilibrium between pyridinol and pyridinolate (Scheme 2). The interconversion leads to simultaneous changes in both electronic and polar properties, which are attributed to the difference between the hydroxy group in pyridinol and the oxyanion in pyridinolate (Scheme 2a). In comparison with the acid–base equilibrium of carboxylic acid and sulfonic acid, the interconversion of the phenol hydroxy group causes a drastic change in the electronic status on the benzene ring through the resonance structure. From the Hammett constant,[78] a substantial difference in the electronic effects of the oxyanion ($\sigma_p^+ = -2.30$) and the hydroxy group ($\sigma_p^+ = -0.91$) can be observed. Thus, the control of the electronic effect through the acid–base equilibrium of catalyst ligands provides a desirable reactivity of the catalyst, i.e., activation in the reaction step and deactivation in the separation step in order to prevent the reverse reaction. In addition, it should be noted that the $\sigma_p^+$ value of the oxyanion is much lower than those of the amine and alkoxy groups, which are widely used electron-donating substituents. On the other hand, it is known that the dipole moment of pyridone is much greater than that of pyridinol.[79,80] Accordingly, when pyridinol is used as a part of a complex ligand, the interconversion will provide an excellent opportunity for controlling the electronic effect and polarity of a catalyst by varying only the pH (Scheme 2b).

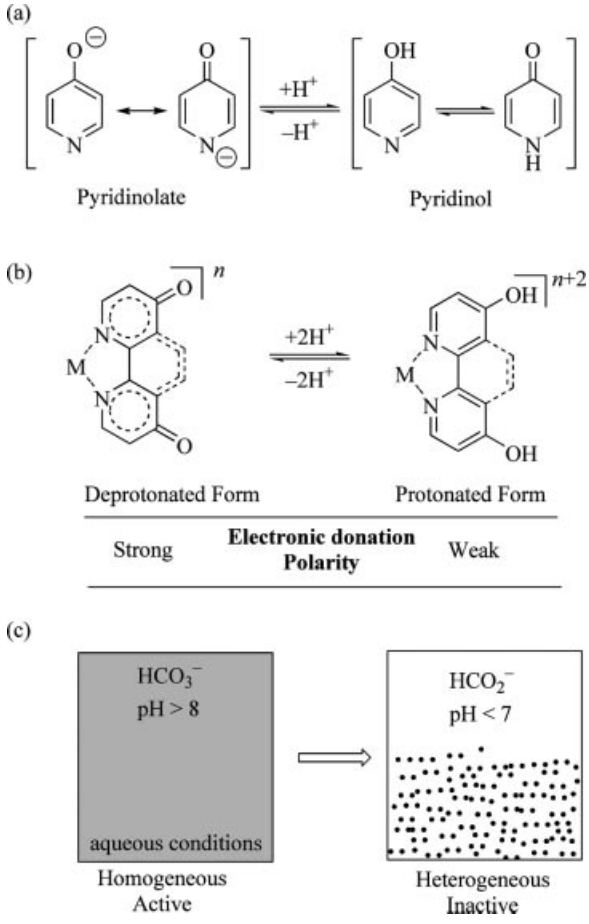


Scheme 2. Catalyst design for catalyst tuning: (a) Acid–base equilibrium between pyridinol and pyridinolate. (b) Interconversion between the deprotonated and protonated forms. (c) Catalyst state at the beginning and at the end of the hydrogenation of hydrogen carbonate in water.

It is noteworthy that our catalyst design based on the acid–base equilibrium of catalyst ligands is closely correlated with the change in the pH of the reaction solution during the hydrogenation of hydrogen carbonate. In other words, as the reaction proceeds, the reaction solution changes from basic to acidic. Therefore, it is expected that the catalyst may spontaneously transform from the homogeneous and active deprotonated form at the beginning of the reaction into the heterogeneous and inactive protonated form at the end (Scheme 2c). Our system has the advantages of heterogeneous catalysis (i.e., the simplicity of catalyst separation) and biocatalysis (i.e., aqueous reaction and pH dependence) as well as those of homogeneous catalysis (i.e., high catalytic performance).

This paper reviews catalysis with complexes of the 4,4′-dihydroxy-2,2′-bipyridine (dhbp: $H_2L^1$) and 4,7-dihydroxy-1,10-phenanthroline (dhpt: $H_2L^2$) ligands that succeeded in the activation and reusability of the catalyst for the hydro-

 © 2007 Wiley-VCH Verlag GmbH & Co. KGaA, Weinheim 

genation of $CO_2$ and hydrogen carbonate in water. In addition, our studies on catalyst tuning through the acid–base equilibrium of the catalyst ligand can be expected to provide valuable insights into the development of homogeneous catalysts.

## Properties of dhbp and dhpt Complexes

The most significant feature of dhbp and dhpt is that they have two acidic phenol hydroxy groups. While both ligands are soluble in an alkaline aqueous solution, dhpt is insoluble in water and common organic solvents except dmf and dmso. Hence, half-sandwich dhbp complexes $[(C_nMe_n)M(H_2L^1)Cl]Cl$ **1**–**3** [M = Rh, Ir ($n$ = 5), M = Ru ($n$ = 6)] were prepared from $[(C_nMe_n)MCl_2]_2$ in water or alcohol, but dhpt complexes $[(C_nMe_n)M(H_2L^2)Cl]Cl$ **4**–**6** were prepared in dmf.

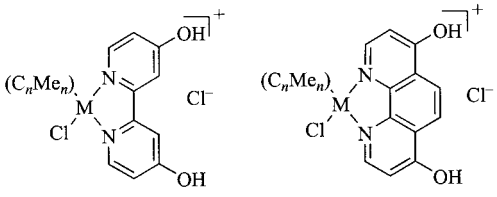

**1:** M = Rh ($n$ = 5)
**2:** M = Ir ($n$ = 5)
**3:** M = Ru ($n$ = 6)

**4:** M = Rh ($n$ = 5)
**5:** M = Ir ($n$ = 5)
**6:** M = Ru ($n$ = 6)

The $^1H$ and $^{13}C$ NMR spectra of aqua complex $[Cp^*Ir(H_2O)(H_2L^1)]^{2+}$ (**7**) were strongly dependent on the pH of the environment (Table 3).[81] The substantial shifts are attributed not only to the transformation from the aqua ligand to the hydroxido ligand,[82] but also to the deprotonation of the hydroxy groups (Scheme 3).[83] The downfield shift in the $^{13}C$ NMR signal for the carbon atoms attached to oxygen strongly suggests the generation of the oxyanion. On the other hand, the complex with 3,3′-dihydroxy-2,2′-bipyridine (**8**) allows the formation of an intramolecular O–H–O hydrogen bond.[84]

Table 3. $^1H$ and $^{13}C$ NMR spectroscopic data for iridium complexes in $D_2O$ (chemical shifts in ppm).

| Signal | In acidic solution | In basic solution |
|---|---|---|
| *C*-4,4′ in **7** | 170.37 | 178.59 |
| 3,3′-*H* in **7** | 7.24 | 6.63 |
| 5,5′-*H* in **7** | 7.77 | 7.13 |
| 6,6′-*H* in **7** | 8.77 | 8.25 |
| 6,6′-*H* in $[Cp^*Ir(H_2O)bpy]^{2+}$ [a] | 9.14 | 9.00 |
| 6,6′-*H* in $[Cp^*Ir(H_2O)(Me_2L^1)]^{2+}$ [a] | 8.88 | 8.76 |

[a] Ref.[82]

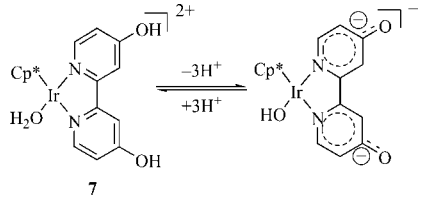

**7**

Scheme 3. Acid–base equilibrium of **7**.

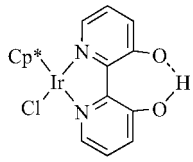

**8**

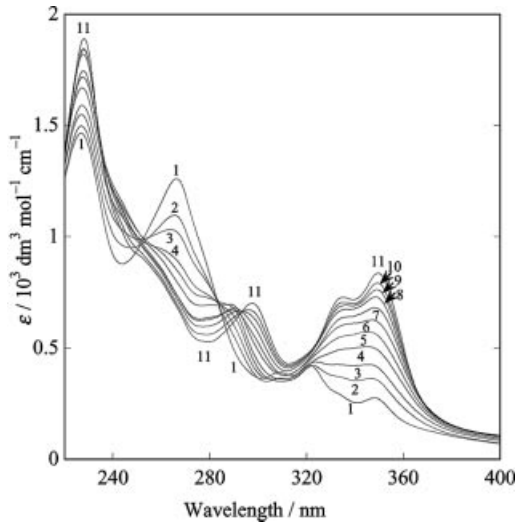


Figure 1. Absorption spectra of rhodium complex **4** (50 μM) in an aqueous solution containing 2.5% methanol at pH values of 1.9–2.3 (1), 3.3 (2), 3.6 (3), 4.0 (4), 4.2 (5), 4.5 (6), 4.8 (7), 4.9 (8), 5.2 (9), 5.5 (10), and 5.6–9.0 (11).

The electronic spectra of ruthenium dhpt complexes $[Ru(dhpt)(ppy)_2]^{2+}$ were studied in detail.[83,85,86] As a result of an acid–base equilibrium of the phenol hydroxy group in dhpt, the absorption spectra of the complexes are dependent on the pH of the environment. Similarly, in half-sandwich complexes **1**–**6**, spectral changes were observed with variations in the pH. Representative absorption spectra of rhodium dhpt complex **4** as a function of pH are shown in Figure 1. Plots of percent change in optical density against pH for iridium and ruthenium complexes are shown in Figure 2. Although the complexes have two acidic protons, only one inflection point is observed in the plots. The values of the overall dissociation constant $pK_a$ estimated from the pH at the inflection point are given in Table 4.[83] The result indicates that the dhpt complexes were obviously more acidic than the dhbp complexes, and the iridium complexes were slightly acidic relative to other complexes.

The structural features of ruthenium complex **3** obtained by single-crystal X-ray crystallographic analysis are similar to those of its 4,4′-dimethoxy-2,2′-bipyridine and bipyridine analogs (Figure 3).[87,88]

The water solubilities of chlorido complexes **1**–**6** are pH dependent: chlorido complexes are highly soluble in basic solution but poorly soluble under acidic and neutral conditions (Scheme 4). When an alkaline solution of deprotonated complexes **1**–**6** was acidified, it precipitated as the protonated complexes. However, the complexes remained par-

 © 2007 Wiley-VCH Verlag GmbH & Co. KGaA, Weinheim 

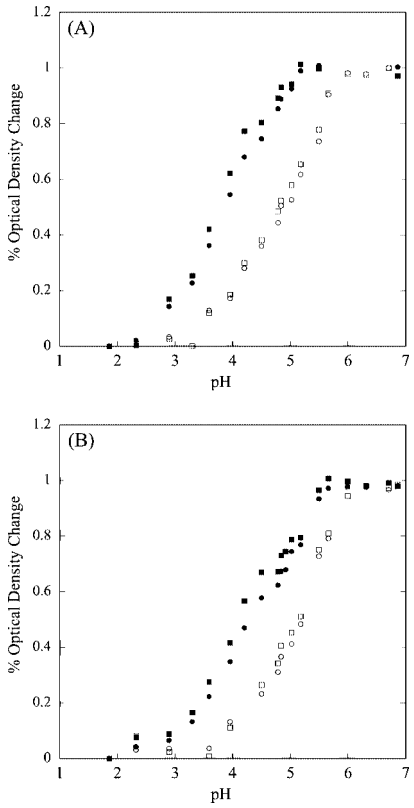


Figure 2. Absorbance change as a function of pH for: (A) iridium complexes **2** at 328 (empty circle) and 258 nm (empty square) and **5** at 353 (filled circle) and 340 nm (filled square); (B) ruthenium complexes **3** at 318 (empty circle) and 247 nm (empty square) and **6** at 358 (filled circle) and 345 nm (filled square).

Table 4. p$K_a$ for complexes with dhbp or dhpt.

| Complex | p$K_a$[a] |
|---|---|
| **2** | 9.6 |
| **3** | 10.2 |
| **4** | 8.4 |
| **5** | 7.7 |
| **6** | 8.4 |

[a] Observed p$K_a$ is twice the pH at the inflection point in the curve.

tially in the mother liquor as a result of the generation of aqua complexes by the aquation of the chlorido complexes. It is highly probable that the dhpt complexes could be recovered more efficiently than the dhbp complexes. On the other hand, aqua complex **7** is water soluble. However, when HCl was added to a solution of **7**, chlorido complex **2** precipitated as a result of the anation of the aqua complex. This result shows that anation is preferable to aquation in half-sandwich bipyridine complexes.[53,89]

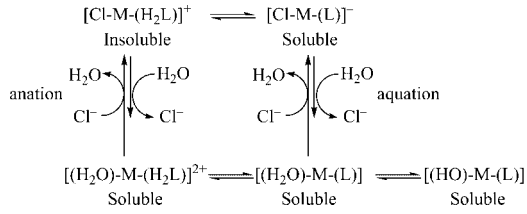


Scheme 4. Behavior of the dhbp and dhpt complexes in aqueous solution. [M = Cp*Rh, Cp*Ir, or ($C_6Me_6$)Ru; L = $L^1$ or $L^2$].

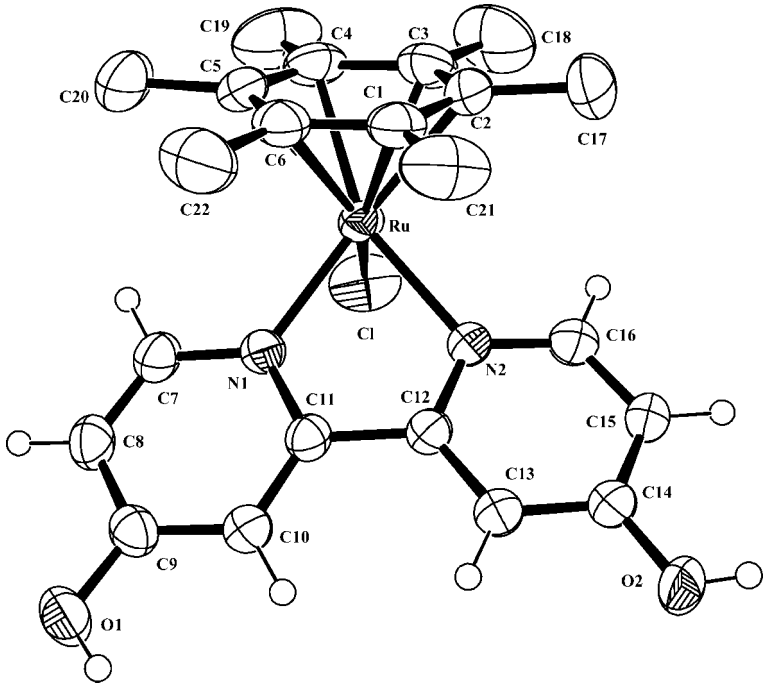


Figure 3. ORTEP view of **3**. The counteranion ($Cl^-$), methanol, and hydrogen atoms of $\eta_6$-$C_6Me_6$ are omitted for clarity.

 © 2007 Wiley-VCH Verlag GmbH & Co. KGaA, Weinheim 

The pH-dependent solubility of the complexes in formate solutions was investigated.[90] An alkaline solution of the complex was added to the formate solution at various pH values. After the resulting solution was allowed to stand overnight, the metal concentrations of the filtrates were measured by ICP-MAS. Figure 4 shows the iridium concentrations of **2** and **5** at various pH values. In both of the complexes, the solubility decreased sharply below pH 8. In particular, the concentration of dhpt complex **5** was as low as 0.12 ppm in the pH range 4.5 to 5.5, which is almost one seventh that of the dhbp complex **2** (0.80 ppm at pH 7.4). Since it is known that half-sandwich bipyridine complexes form hydrido complexes under certain conditions in a formate solution,[61] the recovered solids may be mixtures of hydrido complexes, which consist of monoprotonated and fully protonated complexes. On the other hand, at pH 3.5 and below, the solubility of both the complexes increased; this was probably due to the generation of aqua complexes.[91,92] In the rhodium and ruthenium complexes, precipitation was not observed under these conditions, probably because of the instability of the hydrido complexes.

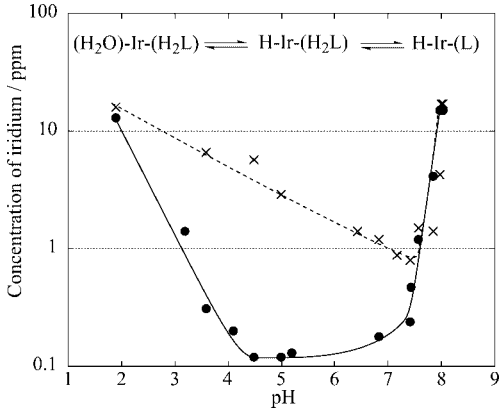


Figure 4. Iridium concentration in an aqueous formate solution (1 M) of **2** (crosses/dotted line) and **5** (filled circles/solid line). Ir = Cp*Ir, $H_2L$ = dhbp($H_2L^1$), dhpt($H_2L^2$).

## Electronic Effect on Catalytic Activity

Numerous studies have established a dependence of both stoichiometric and catalytic activity on electronic substituent effects in the range from the electron-withdrawing nitro group to the electron-donating amine groups.[93–95] The substituent effects on the electrochemical properties of the half-sandwich bipyridine rhodium and iridium complexes have been investigated.[59,96] Sakaki[66] and Jessop[67] suggested that electron-donating ligands would improve the catalytic efficiency for the hydrogenation of $CO_2$. On the other hand, a high catalytic activity might promote the reverse reaction after the release of pressure.[27,39] Such a conflicting requirement can be satisfied by controlling the electronic properties of the catalyst ligand (i.e., the catalytic activity) through the acid–base equilibrium of pyridinol.

The electronic substituent effect on the hydrogenation of hydrogen carbonate was investigated by using a series of iridium complexes [Cp*Ir(4,4′-$X_2$-2,2′-bpy)Cl]Cl [X = H, $CO_2H$, Me, OMe, OH(**2**)].[90,97,98] The time courses of formate generation are shown in Figure 5. The catalytic activities of the iridium complexes are strongly dependent on the substituent on the bipyridine ligand. The correlation between the substituent and the initial TOF can be explained on the basis of Hammett's rule. Note that the deprotonation of the phenol hydroxy group and the carboxyl group occurs under basic reaction conditions. Thus, the $\sigma_p^+$ value for the hydroxy complex is –2.30 and that for the carboxylic acid complex is –0.02, and they correspond to the oxyanion (-$O^-$) and carboxylato (-$CO_2^-$) values, respectively.[78] The Hammett plots of the initial TOF vs. the $\sigma_p^+$ value of X in [Cp*Ir(4,4′-$X_2$-2,2′-bpy)Cl]Cl at 4 MPa and 1 MPa and 80 °C are shown in Figure 6. Both plots have high correlation coefficients, and the reaction constants ($\rho$) are very similar. The electronic trend is in agreement with Sakaki's theoretical prediction[66] and Jessop's experimental results[67] for the catalytic hydrogenation of $CO_2$. The large $\sigma_p^+$ value of –2.30 and the $\rho$ value of –1.3 resulted in a remarkably high initial TOF for **2**, which was ca. 100 times greater than that of a methoxy complex (X = OMe) and over 1000 times greater than that of an unsubstituted complex (X = H). Similarly, a similar reactivity trend (H < OMe < OH) was observed for the series of disubstituted phenanthroline complexes.[63] This was the first example of a strong electronic oxyanion effect on catalytic activity in the field of complex catalysts.

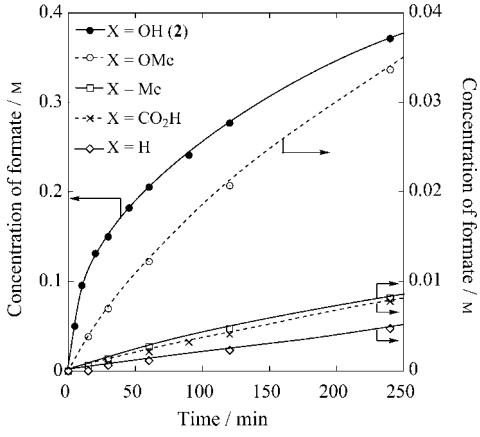


Figure 5. Time course of formate concentration during the hydrogenation of hydrogen carbonate catalyzed by [Cp*Ir(4,4′-$X_2$-2,2′-bpy)Cl]Cl (0.2 mM) at 4 MPa ($H_2$:$CO_2$ = 1:1) and 80 °C in an aqueous KOH solution (1 M).

Surprisingly, no significant activation was observed in *meta*-substituted analogue **8**, although one negative charge existed on the ligand.[63] One possible explanation is that the resonance structures of 3-hydroxypyridine cannot increase the π-electron density on the nitrogen atoms. This hypothesis is consistent with the data reported for the nucleophilicity of the nitrogen atom in the 3- and 4-hydroxypyridine anions.[99]

 © 2007 Wiley-VCH Verlag GmbH & Co. KGaA, Weinheim 

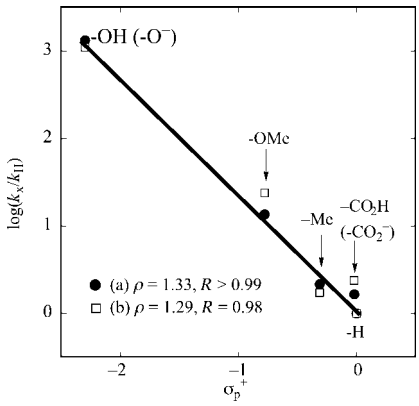


Figure 6. Hammett plot of initial TOF (= $k$) vs. the $\sigma_p^+$ value of substituent (X) in [Cp*Ir(4,4′-$X_2$-2,2′-bpy)Cl]Cl. The reaction was carried out with the catalyst (0.02–0.2 mM) at 80 °C in an aqueous KOH solution (1 M) at (a) 4 MPa and (b) 1 MPa.

Table 5 summarizes the results for the iridium complexes with dhbp, **2**, and dhpt, **5**, under various conditions. The catalysts were relatively stable at a high temperature. Unprecedented high activities [TOF = 42000 $h^{-1}$ (entry 3) and TON = 222000 (entry 11)] were obtained at 6 MPa and 120 °C in a highly diluted solution of the catalyst (<2 μM). As compared with $[RuCl_2(tppms)_2]_2$ under the same conditions (TOF = 30–50 $h^{-1}$ at 1 MPa and 50 °C),[29] **2** showed a far superior catalytic activity [TON = 740 after 1 h (entry 5)].[81] Furthermore, the hydrogenation of hydrogen carbonate proceeded at ambient pressure and 60 °C (entries 6 and 9) and even at 30 °C (entry 10). The results show that the corresponding hydrido complexes can be easily generated at ambient pressure, because the color of the solution changed immediately from pale yellow into deep yellow when $H_2$ was admitted. To the best of our knowledge, there is only one other report on homogeneously catalyzed hydrogenation of $CO_2$ that occurs at ambient pressure at room temperature (TON = 3 per day).[22]

Activation by the introduction of the hydroxy group into the bipyridine ligand as a catalyst ligand were also observed in ruthenium and rhodium complexes (Table 6).[63] In the (arene)ruthenium complexes $[(C_6Me_6)Ru(L)Cl]Cl$, the TONs for complexes with dhbp, **3**, and dhpt, **6**, were ca. 60 times greater than those of the unsubstituted ones. The detailed results under various conditions are summarized in Table 7. The ruthenium complexes yielded higher concentrations of formate relative to the iridium complexes, although their TOF and TON values were moderate (entries 2–5). The formate concentrations increased steadily with increasing pressure from 1.08 M at 2 MPa to 1.54 M at 6 MPa (entries 3–5). The TOFs increased with an increase in the

Table 6. Substituent effect on TON for the hydrogenation of hydrogen carbonate.[a]

| Cat.[b] L = | TON bpy | dhbp | phen | TON dhpt |
|---|---|---|---|---|
| Ru | 68 | 4400 | 78[c] | 5100 |
| Rh | 216[c] | 1800 | 220 | 2300 |

[a] The reactions were carried out at 4 MPa ($CO_2/H_2$ = 1:1) and 80 °C for 20 h in an aqueous KOH solution (1 M) containing the complex (0.1 mM). [b] Catalyst: Rh = [Cp*Rh(L)Cl]Cl, Ru = $[(C_6Me_6)Ru(L)Cl]Cl$. [c] The catalyst concentration was 0.2 mM.

Table 7. Hydrogenation of hydrogen carbonate using the rhodium and ruthenium complexes with the dhbp or dhpt ligand.[a]

| Entry | Catalyst | $T$ /°C | $P$ /MPa | $t$ /h | Initial TOF[b] /$h^{-1}$ | TON | Final conc. of formate /M |
|---|---|---|---|---|---|---|---|
| 1 | **3** | 80 | 4 | 20 | 720 | 4400 | 0.44 |
| 2 | **3**[c] | 120 | 6 | 8 | 4400 | 13620 | 1.36 |
| 3 | **6**[c] | 80 | 4 | 165 | 370 | 12500 | 1.25 |
| 4 | **6**[c] | 120 | 6 | 24 | 3600 | 15400 | 1.54 |
| 5 | **6**[c] | 100 | 2 | 92 | 600 | 10800 | 1.08 |
| 6 | **1** | 80 | 4 | 12 | 790 | 1800 | 0.18 |
| 7 | **1** | 80 | 1 | 24 | 170 | 1200 | 0.12 |
| 8 | **1** | 50 | 1 | 30 | 24 | 500 | 0.05 |
| 9 | **4** | 80 | 4 | 32 | 270 | 2400 | 0.24 |

[a] The reaction was carried out by using the catalyst (0.1 mM) in an aqueous KOH solution (1 M) at the desired $CO_2/H_2$ (1:1) pressure. [b] The initial TOFs were calculated by nonlinear least-squares fits of the experimental data from the initial part of the reaction.[36] [c] The reaction was carried out in an aqueous KOH solution (2 M).

Table 5. Hydrogenation of hydrogen carbonate with iridium complexes **2** and **5**.[a]

| Entry | Catalyst (Conc./μM) | $T$/°C | $P$/MPa | $t$/h | Initial TOF[b]/$h^{-1}$ | TON | Final conc. of formate/M |
|---|---|---|---|---|---|---|---|
| 1 | **2** (100) | 80 | 4 | 140 | 4000 | 8000 | 0.80 |
| 2 | **2** (20) | 120 | 6 | 32 | 41000 | 33500 | 0.67 |
| 3 | **2** (0.5) | 120 | 6 | 57 | 42000 | 190000 | 0.095 |
| 4 | **2** (20) | 120 | 1 | 30 | 14200 | 13500 | 0.27 |
| 5 | **2** (20) | 50 | 1 | 30 | 820 | 9500 | 0.19 |
| 6 | **2** (200)[c] | 60 | 0.1 | 50 | 33 | 376 | 0.075 |
| 7 | **5** (100) | 80 | 4 | 116 | 3000 | 7300 | 0.73 |
| 8 | **5** (20) | 120 | 6 | 32 | 35000 | 26000 | 0.52 |
| 9 | **5** (200)[c] | 60 | 0.1 | 50 | 32 | 444 | 0.089 |
| 10 | **5** (200)[c] | 30 | 0.1 | 30 | 3.5 | 81 | 0.016 |
| 11 | **5** (2) | 120 | 6 | 48 | 33000 | 222000 | 0.44 |

[a] The reaction was carried out in an aqueous KOH solution (1 M) at the desired $CO_2/H_2$ (1:1) pressure. [b] The initial TOFs were calculated by nonlinear least-squares fits of the experimental data from the initial part of the reaction.[36] [c] The reaction was carried out in an aqueous $K_2CO_3$ solution (0.1 M).

 © 2007 Wiley-VCH Verlag GmbH & Co. KGaA, Weinheim 

reaction temperature from 60 to 120 °C without a decrease in the product yield (Figure 7). However, at ambient pressure, only a small amount of formate was generated (TOF = 1.8 at 60 °C).

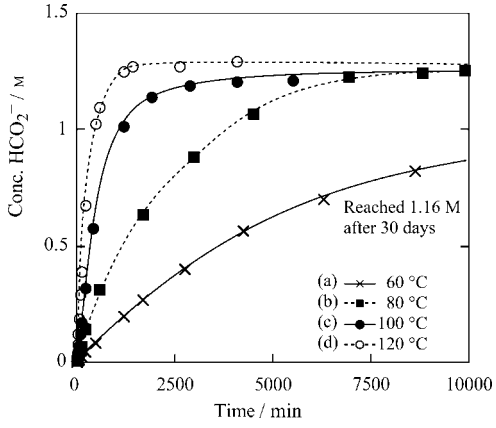


Figure 7. Time course of formate concentration during the hydrogenation of hydrogen carbonate catalyzed by ruthenium complex **6** (0.1 mM) at 4 MPa ($H_2/CO_2$ = 1:1) and (a) 60 °C, (b) 80 °C, (c) 100 °C, and (d) 120 °C in aqueous KOH solution (2 M).

Among rhodium complexes [Cp*Rh(L)Cl]Cl, the TOFs of the unsubstituted ones were the highest among those of all unsubstituted complexes. However, the TOFs for rhodium complexes **1** and **4** were ordinary, and the rates of increase against the unsubstituted complexes were moderate (8–10 times). In addition, the final concentrations of the formate were lower than those of the other metal complexes, probably because of the instability of the catalyst.[61]

The catalytic efficiencies (i.e., TOF, TON, and the concentration of formate) were strongly affected by the central metals. The effects of the metal in complexes with phosphane ligands were also reported.[17,31,32] Interestingly, in the series of the catalysts, the iridium complexes were superior to the rhodium and ruthenium complexes, which have so far dominated in the hydrogenation of $CO_2$. On the other hand, the difference between the effects of the dhbp and dhpt ligands on the catalytic efficiency is relatively small.

Interestingly, no significant decomposition of formate, which is sometimes a problem in the hydrogenation of $CO_2$ and hydrogen carbonate after pressure release, was observed.[39] This suggests that the catalyst activity decreases considerably at the end of the reaction, since it is highly probably that by the acidification of the reaction solution, the catalyst changes from the active deprotonated form into the sluggish protonated form, in which its activity might be lower relative to that of the methoxy analogue.

In this manner, the results demonstrated the usefulness of the concept of catalyst tuning through the acid–base equilibrium of dhbp and dhpt as a catalyst ligand for the hydrogenation of hydrogen carbonate. In other words, the catalyst in the deprotonated form showed an enormously high activity that can be attributed to the strong electron-donating ability of the oxyanion group. On the other hand, the decrease in the activity by the transformation from the deprotonated form into the protonated form restrained the reverse reaction at end of the reaction.

## Catalyst Recycling

Homogeneous catalysis generally has many advantages with respect to the reaction step; however, there are considerable difficulties involved in the separation of a catalyst from the product and/or solvent as compared with heterogeneous catalysis. There have been numerous attempts to recycle catalysts by using multiphase[100–105] and immobilized[106–111] catalysts; however, these often reduce the mixing efficiency between catalyst and substrate. Recently, in order to keep homogeneity in a reaction step, significant attention has been given to stimuli-responsive catalysts such as redox-switchable,[77] magnetic-,[112] temperature-,[113] and pH-responsive,[75] and self-assembly-supported[114] catalysts.[115] However, many concerns (e.g., reduced activity and selectivity, catalyst leaching, waste generation, and use of environmentally suspected solvents) still remain. In particular, a sophisticated design generally results in increasingly expensive complexes.

Reusability of the catalyst was achieved by tuning its water solubility through the acid–base equilibrium of the ligand.[116] In the hydrogenation of hydrogen carbonate in water, it is noteworthy that the reaction solution changes from basic to acidic during the course of the reaction, because the hydrogenation of a basic hydrogen carbonate yields a formate and then formic acid after the consumption of the added base.[27] Thus, it is expected that the catalyst may spontaneously transform from the water-soluble deprotonated form at the beginning of the reaction into the poorly water-soluble protonated form at the end. In particular, iridium–dhpt complex **5** will become favorable for catalyst recycling because of its water insolubility between pH 4 and 7 (Figure 4).

The hydrogenation of hydrogen carbonate catalyzed by **5** was strongly affected by the concentration of KOH, i.e., the pH of the solution. Figure 8 shows the time course of the

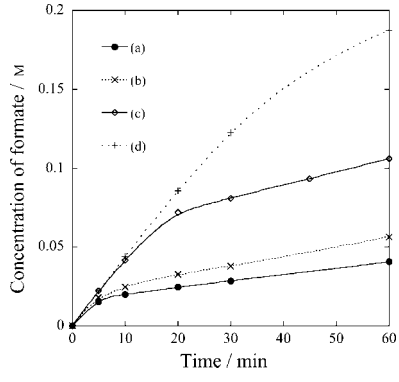


Figure 8. Time course of formate concentration during the hydrogenation of hydrogen carbonate with **5** (0.05 mM) at 6 MPa ($CO_2$/$H_2$ = 1:1) and 60 °C in (a) 0.1-M, (b) 0.2-M, (c) 0.5-M, and (d) 1.0-M aqueous KOH solution.

 © 2007 Wiley-VCH Verlag GmbH & Co. KGaA, Weinheim 

Table 8. Hydrogenation of hydrogen carbonate catalyzed by **5** in various KOH concentrations.[a]

| KOH/M | *t*/h | Leaching [Ir][b]/ppm | Final conc. of formate/M | pH of the final solution |
|---|---|---|---|---|
| 0.5 | 72 | 0.61 | 0.476 | 7.5 |
| 0.2 | 48 | 0.19 | 0.201 | 6.8 |
| 0.1 | 20 | 0.11 | 0.105 | 5.5 |

[a] The reaction was carried out by using **5** (0.05 mM) at 6 MPa ($CO_2/H_2$ = 1:1) and 60 °C. [b] The iridium concentration was measured by ICP-MS analysis.

formate concentration in a KOH solution (0.1–1.0 M). At the beginning of the reaction, the maximum TOFs (ca. 5000 $h^{-1}$) were observed in all the reactions. However, in 0.1- and 0.2-M KOH solutions, the reaction rates decreased drastically after 5 min. In a 1.0-M KOH solution, the rate was steady till 30 min, and it then decreased gradually. The results reveal that **5** exhibited high activity at the beginning of the reaction (i.e., basic conditions), in which **5** might exist in a homogeneous and activated deprotonated form.

On the other hand, prolongation of the reaction time to 72 h in 0.5-M KOH solution did not lead to complete consumption of the added base (Table 8). In other words, the reaction medium was not neutralized (pH = 7.5). Although most of the catalyst precursor was precipitated spontaneously and recovered by filtration of the obtained suspension, 0.61 ppm iridium remained in the filtrate. By using 0.2-M solutions, the added base was consumed completely, and the solution was neutralized. Hence, the remaining iridium decreased to 0.19 ppm. In particular, in 0.1-M KOH solutions, the concentration of the generated formate (0.105 M) exceeded that of the added base to give a weakly acidic suspension (pH = 5.5). The catalyst precursor was separated by filtration. As expected, the colorless filtrate was found to contain only 0.11 ppm iridium, which was 1.2% of the loaded catalyst. The value for iridium leaching was consistent with its solubility in the formate solution, as shown in Figure 4. Furthermore, the concentration of the filtrate and drying under vacuum at 100 °C resulted in pure potassium formate (>98% pure). These results imply the possibility of catalyst recycling in the conversion of $CO_2$ into formate without waste generation.

Subsequently, **5** was recycled in a batchwise cycle (Table 9). The above-mentioned recovered catalyst precursor was dissolved in a 0.1 M degassed aqueous KOH solution, from which 93% iridium was recovered [the loss of iridium was due to the sampling for assay (2%) and handling losses]. While all the four cycles could be performed without a significant loss of the catalytic activity, leaching increased and recovery decreased with an increase in the recycling of the catalyst. However, thermal degradation was observed. It appears that thermal stress and exposure to air lead to an increase in catalyst leaching.

The solubility behavior of **5** during the course of the reaction was visually observed by using a glass reactor. Complex **5** (0.05 mM) was completely soluble in the KOH solution with pressurized $CO_2$. When the reactor was recharged with 3 MPa of $H_2/CO_2$ (1:1) at 60 °C, the pale yellow solution immediately turned to orange, which might indicate the formation of a hydrido complex.[117] After 30 min, a yellow

Table 9. Batchwise recycling of **5** for the conversion of $CO_2$.[a]

| Cycle | Loaded [Ir] /ppm | Recovery efficiency/% | Leaching [Ir][b] /ppm | Final conc. of formate/M |
|---|---|---|---|---|
| 1 | 9.0 | – | 0.11 | 0.105 |
| 2 | 8.4 | 93 | 0.22 | 0.104 |
| 3 | 7.7 | 92 | 0.42 | 0.103 |
| 4 | 7.0 | 91 | 0.61 | 0.103 |

[a] The reaction was carried out at 6 MPa ($CO_2/H_2$ = 1:1) and 60 °C in aqueous KOH solution (0.1 M). No hydrogen carbonate was detected in all the four cycles. [b] The iridium concentration was measures by ICP-MS analysis.

precipitate was formed. After a further 2.5 h, the resulting suspension was filtered to give a clear pale yellow filtrate and yellow precipitate. The filtrate (pH = 7.9) was found to contain 0.05 M of the formate (50% conversion) and 1.0 ppm iridium (ca. 10% of the loaded iridium). The precipitate was readily converted to a deprotonated form by the addition of an aqueous base. Figure 9 shows the photographs of the reaction solution, in which ten times catalyst concentration (0.5 mM) was used for clarity. The pale yellow solution (Figure 9a) at the beginning of the reaction turned into a yellow suspension (Figure 9b) at the end of the reaction. By filtration of the suspension, a colorless solution (Figure 9c) was obtained.

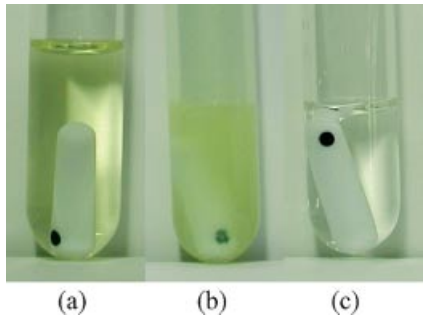


Figure 9. Photographs of the reaction solution (a) before reaction, (b) after reaction, and (c) after filtration. The reaction was carried out with **5** (0.5 mM) in an aqueous KOH solution (0.1 M) at 6 MPa ($CO_2/H_2$ = 1:1) and 60 °C for 15 h.

In this manner, the reusability of **5** was achieved by self-precipitation without a significant loss of catalytic activity. It is interesting to note that the three components (i.e., catalyst, product, and solvent) can be easily separated by using conventional filtration and evaporation without waste generation (Scheme 5). This catalytic system is characterized by interconversion between an active and homogeneous deprotonated form at the beginning of the reaction and an inac-

 © 2007 Wiley-VCH Verlag GmbH & Co. KGaA, Weinheim 

tive and heterogeneous protonated form at the end of the reaction, which is achieved through the acid–base equilibrium of the ligand; the catalyst is easily recovered, and the reverse reaction is suppressed in this system.

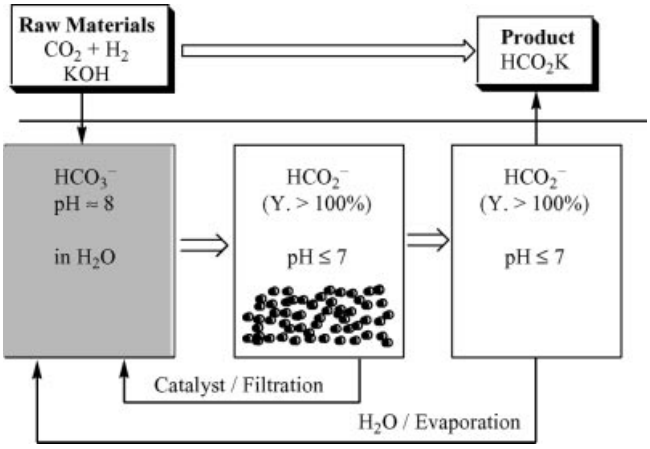


Scheme 5. Recycling system for the conversion of $CO_2/H_2$ and KOH into $HCO_2K$ with **5** in water.

## Mechanistic and Kinetic Studies

The mechanisms of the hydrogenation of hydrogen carbonate catalyzed by ruthenium and rhodium complexes with water-soluble phosphane ligands have been studied extensively by Joo and Katho.[26–32] Recently, a theoretical investigation with the density functional theory was reported.[25] Although these studies increased their mechanistic understanding, the pH-dependent catalysts with dhbp and dhpt ligands in our system are distinct from water-soluble phosphane complexes.

Deprotonated dhpt complexes [Cp*Ir($L^2$)Cl]K (**9**) and [($C_6Me_6$)Ru($L^2$)Cl]K (**10**) were isolated from an alkaline ethanol solution by the addition of ethyl ether (Scheme 6). Similar to the dhbp complex **7**, significant shifts of the deprotonated forms **9** and **10** were observed in the $^1H$ and $^{13}C$ NMR spectra in [$D_6$]dmso relative to those of the protonated forms **5** and **6**, respectively.[63] The $^1H$ NMR spectrum of **9** in $D_2O$ was nearly identical to that of **5** in KOD/$D_2O$ (i.e., the deprotonated form of **5**).

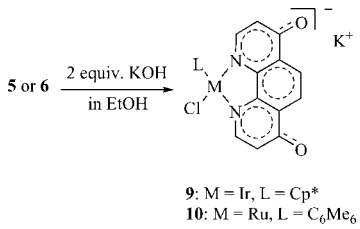


Scheme 6. Preparation of deprotonated complexes **9** and **10**.

The properties of the hydrido complexes [($C_nR_n$)-MH(ppy)]$^+$ [M = Rh, Ir ($n$ = 5), M = Ru ($n$ = 6)] are dependent on the central metal (M). Hydrido(iridium) complexes with bipyridine and phenanthroline were prepared by a reaction with $NaBH_3CN$ or a formate and were isolated.[92,118,119] The hydrido(iridium) complexes appear to be relatively stable.[55,117] Hydrido complexes [Cp*IrH-($L^1$)]$^-$ (**11**) and [Cp*IrH($L^2$)]$^-$ (**12**) were quantitatively generated under $H_2$ pressure. In comparison with the hydrido complexes with unsubstituted and methoxy-substituted bipyridine, significant upfield shifts of the aromatic protons in **11** and **12** were observed due to the oxyanion (Table 10). Hydrido(ruthenium) complex [($C_6Me_6$)RuH(bpy)]$^+$ was isolated by Ogo.[91] Under $H_2$ pressure, hydrido complexes [($C_6Me_6$)RuH($L^1$)]$^-$ (**13**) and [($C_6Me_6$)RuH($L^2$)]$^-$ (**14**) were generated as a mixture of the corresponding deprotonated forms, whose ratios depended on the $H_2$ pressure. However, the hydrido(rhodium) complex has never been isolated. Indeed, the corresponding hydrido complexes from **1** and **4** were not detected spectroscopically.

The reaction of the hydrido(iridium) complexes with $KHCO_3$ in aqueous solution led to the production of formate in an atmosphere of $H_2$. However, no formate was generated in the reaction with $K_2CO_3$. In the hydrogenation catalyzed by **2**, there was no induction period in the solution saturated by $CO_2$ prior to the reaction (Figure 10).[81] Conversely, an induction period was observed in the solution saturated by $H_2$ prior to the reaction. This indicates that the overall rate of the generation of hydrido complexes from **2** and the subsequent reaction with hydrogen carbonate was extremely rapid, when compared with the rate of hydration of $CO_2$ in aqueous KOH solution.

Scheme 7 shows the proposed pathway for the generation of hydrido complexes, which is marked by the acid–base equilibrium of dhbp and dhpt. The protonated form (**PX**: X = Cl) as the catalyst precursor was transformed into the deprotonated form (**DX**) in an alkaline solution. The reaction of **DX** with $H_2$ yielded the deprotonated hydrido complex (**DH**), which probably is the actual catalyst. The strong electron-donating ability of oxyanion on **DH** will play a significant role in the activation of the hydrido complexes. The generation of **DH** is strongly dependent on the central metal (M): under $H_2$ pressure, the iridium hydrido complexes are formed quantitatively, but the ruthenium complexes attain equilibrium between **DH** and **DX**. It is likely that the hydride-formation step is one of the factors that affect the catalyst activity of the hydrogenation of hydrogen carbonate. This hypothesis is consistent with the mechanistic investigation of Ogo: the rate-determining step for the hydrogenation of $CO_2$ in an acidic solution by using the methoxy ruthenium analog [($C_6Me_6$)Ru($Me_2L^1$)($H_2O$)]$^{2+}$ is the formation of a hydrido complex, whereas it is the reaction of the hydrido complex with $CO_2$ in the methoxy iridium analog [Cp*Ir($Me_2L^1$)($H_2O$)]$^{2+}$.[82]

The actual substrate could be established as hydrogen carbonate under basic conditions and as $CO_2$ under acidic conditions (Scheme 8).[33] It is known that $CO_2$ readily gets inserted into the metal–hydrogen bond to give a formato complex in nonaqueous media.[66,120–123] Similarly, the formato complex is believed to be generated by the insertion of $CO_2$ into the metal–hydrogen bond in an acidic aqueous solution and a water/amine mixture.[22,82] Indeed, the for-

 © 2007 Wiley-VCH Verlag GmbH & Co. KGaA, Weinheim 

Table 10. $^1$H NMR spectroscopic data for hydrido complexes.

| Complex | Solvent | M–*H* | Cp*/$C_6Me_6$ | $\delta$/ppm [bpy(3,3′;4,4′;5,5′;6,6′)/ phen(2,9;3,8;4,7;5,6)] | Ref. |
|---|---|---|---|---|---|
| $[Cp^*IrH(bpy)]^+$ | $[D_6]$acetone | –11.45 | 1.93 | 8.55; 8.16; 7.72; 9.11 | [118] |
| $[Cp^*IrH(phen)]^+$ | $[D_6]$acetone | –11.35 | 2.00 | 9.48; 8.10; 8.80; 8.28 | [118] |
| $[Cp^*IrH(bpy)]^+$ | $D_2O$ | –11.80 | 1.78 | 8.29; 8.11; 7.62; 8.90 | [92] |
| $[Cp^*IrH(Me_2L^1)]^+$ | dmso | –11.25 | 1.79 | 8.33; –; 7.33; 8.65 | [82] |
| $[Cp^*IrH(L^1)]^-$ (**11**) | KOD/$D_2O$ | –11.09 | 1.75 | 7.15; –; 6.58; 8.15 | [90] |
| $[Cp^*IrH(L^2)]^-$ (**12**) | KOD/$D_2O$ | –11.10 | 1.69 | 8.40; 6.75; –; 7.92 | [90] |
| $[(C_6Me_6)RuH(bpy)]^+$ | $D_2O$ | –7.45 | 2.14 | 8.19; 7.93; 7.48; 8.57 | [91] |
| $[(C_6Me_6)RuH(L^1)]^-$ (**13**) | KOD/$D_2O$ | –7.46 | 2.03 | 7.03; –; 6.49; 7.83 | [90] |
| $[(C_6Me_6)RuH(L^2)]^-$ (**14**) | KOD/$D_2O$ | –7.58 | 2.02 | 8.12; 6.66; –; 7.83 | [90] |

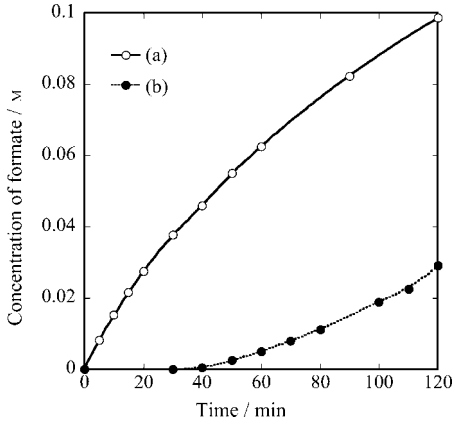


Figure 10. Time course of formate concentration during the hydrogenation of hydrogen carbonate catalyzed by **2** (20 μM) at 1 MPa ($CO_2/H_2$ = 1:1) and 80 °C after the reaction solution was saturated by (a) $CO_2$ and (b) $H_2$.[81]

mato(ruthenium) complex was isolated in aqueous formate solution.[87] In contrast, the key intermediate has not been observed experimentally in the basic aqueous solution. However, it is assumed that the hydrogen carbonate is inserted into the metal–hydrogen bond, after which a formato intermediate is generated with the accompanying release of a hydroxide ion.[29,31]

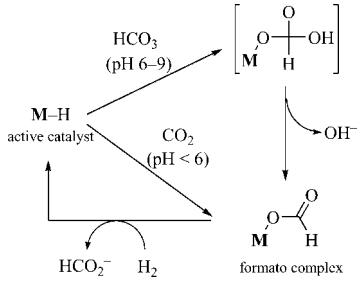


Scheme 8. Suggested pathway for the hydrogenation steps of $HCO_3^-/CO_2$ in water.

During the course of the reaction, the acidification due to formate generation might cause the deprotonated form (**D**) to transform into the monoprotonated (**N**) or fully protonated form (**P**). Hence, this results in less catalytic activity and prevention of the decomposition of the formate as a reverse reaction. In particular, iridium–dhpt complexes,

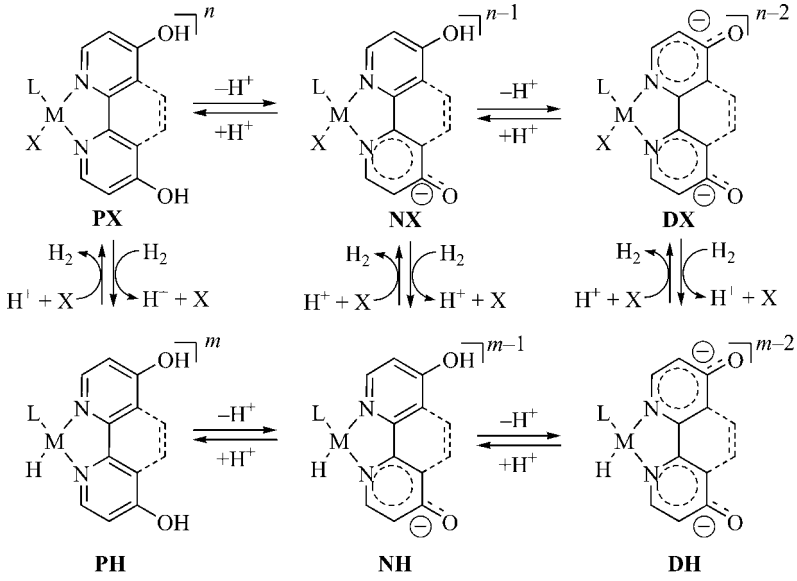


Scheme 7. Proposed pathway for the generation of hydrido complexes in the hydrogenation of $HCO_3^-/CO_2$ in water.

 © 2007 Wiley-VCH Verlag GmbH & Co. KGaA, Weinheim 

whose solubility is negligible under weak acidic formate conditions, can be recovered almost quantitatively at the end of the reaction. Further studies are required to clarify the interesting catalytic system for the conversion of $CO_2$ in detail.

## Summary and Outlook

The $CO_2$ conversion system that uses the half-sandwich complexes with dhbp and dhpt has significant features (high efficiency, catalyst recycling by self-precipitation, easy isolation of product, waste-free process, aqueous reaction, and prevention of reverse reaction); further, the system overcomes almost all of the problems occurring in the homogeneously catalyzed hydrogenation of $CO_2$ into formate. It should be noted that over a 1000-fold increase in catalytic activity was achieved as a result of the strong electron-donating ability of the oxyanion on the catalyst ligand. In addition, the three components (i.e., catalyst, product, and solvent) could be easily separated by conventional filtration and evaporation without waste generation. Our next goal will be the conversion of $CO_2$ into products other than formate (e.g., methanol or oxalic acid) by the homogeneously catalyzed hydrogenation of $CO_2$.

More importantly, the tuning of the catalyst through the acid–base equilibrium of dhbp or dhpt as a catalyst ligand offers a novel tool for the simultaneous control of the activity and water solubility of complex catalysts. It was shown that the properties of iridium complexes were strongly dependent on the pH of the aqueous solution. These significant features are attributed to the electronic effect and polarity of the oxyanion generated from the phenol hydroxy group. Consequently, the system combines the advantages of homogeneous catalysis (i.e., high catalytic performance) with those of heterogeneous catalysis (i.e., simplicity of catalyst separation) and biocatalysis (aqueous reaction and pH dependence). The control of catalyst properties through the acid–base equilibrium between pyridinol and pyridinolato as a ligand has not been explored previously in catalyst systems. For these features to appear, only the introduction of a hydroxy group into the pyridine and subsequent pH control are required. This catalyst design concept is expected to have significantly broader implications for the design of new homogeneous catalysts (e.g., strong electronic effect and water-soluble ligand). The idea of catalyst tuning will become increasingly important and will be an extremely challenging field of study.

**Abbreviations**: dhbp, 4,4′-dihydroxy-2,2′-bipyridine; dhpt, 4,7-dihydroxy-1,10-phenanthroline; edta-H, protonated ethylenediaminetetraacetic acid; pta, 1,3,5-triaza-7-phosphaadamantane; TON, turnover number (mole product per mol catalyst); TOF, turnover frequency (TON per hour); tppms, sodium 3-(diphenylphosphanyl)benzenesulfonate; tppts, triphenylphosphane-3,3′,3′′-trisulfonic acid trisodium salt.

## Acknowledgments

The author thanks Dr Nobuko Onozawa–Komatsuzaki, Dr Hideki Sugihara, and Dr Kazuyuki Kasuga at AIST for their many helpful suggestions and discussions related to this work.

[1] H. Arakawa, M. Aresta, J. N. Armor, M. A. Barteau, E. J. Beckman, A. T. Bell, J. E. Bercaw, C. Creutz, E. Dinjus, D. A. Dixon, K. Domen, D. L. DuBois, J. Eckert, E. Fujita, D. H. Gibson, W. A. Goddard, D. W. Goodman, J. Keller, G. J. Kubas, H. H. Kung, J. E. Lyons, L. E. Manzer, T. J. Marks, K. Morokuma, K. M. Nicholas, R. Periana, L. Que, J. Rostrup-Nielson, W. M. H. Sachtler, L. D. Schmidt, A. Sen, G. A. Somorjai, P. C. Stair, B. R. Stults, W. Tumas, *Chem. Rev.* **2001**, *101*, 953–996.
[2] E. Dinjus, R. Fornika, S. Pitter, T. Zevaco in *Applied Homogeneous Catalysis with Organometallic Compounds: A Comprehensive Handbook, Vol. 3* (Eds.: B. Cornils, W. A. Herrmann), Wiley-VCH, Weinheim, **2002**, pp. 1189–1213.
[3] I. Omae, *Catal. Today* **2006**, *115*, 33–52.
[4] M. Aresta in *Activation of Small Molecules: Organometallic and Bioinorganic Perspectives* (Ed.: W. B. Tolman), Wiley-VCH, Weinheim, **2006**, pp. 1–41.
[5] P. G. Jessop in *Handbook of Homogeneous Hydrogenation, Vol. 1* (Eds.: J. G. De Vries, C. J. Elsevier), Wiley-VCH, Weinheim, **2007**, pp. 489–511.
[6] S. K. Ritter, *Chem. Eng. News* **2007**, *85*, 11–17.
[7] S. Fukuoka, M. Kawamura, K. Komiya, M. Tojo, H. Hachiya, K. Hasegawa, M. Aminaka, H. Okamoto, I. Fukawa, S. Konno, *Green Chem.* **2003**, *5*, 497–507.
[8] R. Ziessel, J. Hawecker, J. M. Lehn, *Helv. Chim. Acta* **1986**, *69*, 1065–1084.
[9] T. Ogata, S. Yanagida, B. S. Brunschwig, E. Fujita, *J. Am. Chem. Soc.* **1995**, *117*, 6708–6716.
[10] E. Fujita, *Coord. Chem. Rev.* **1999**, *186*, 373–384.
[11] B. Gholamkhass, H. Mametsuka, K. Koike, T. Tanabe, M. Furue, O. Ishitani, *Inorg. Chem.* **2005**, *44*, 2326–2336.
[12] T. Hirose, Y. Maeno, Y. Himeda, *J. Mol. Catal. A* **2003**, *193*, 27–32.
[13] N. Komatsuzaki, Y. Himeda, T. Hirose, H. Sugihara, K. Kasuga, *Bull. Chem. Soc. Jpn.* **1999**, *72*, 725–731.
[14] J. P. Collin, J. P. Sauvage, *Coord. Chem. Rev.* **1989**, *93*, 245–268.
[15] K. Tanaka, D. Ooyama, *Coord. Chem. Rev.* **2002**, *226*, 211–218.
[16] C. Caix, S. ChardonNoblat, A. Deronzier, *J. Electroanal. Chem.* **1997**, *434*, 163–170.
[17] Y. Inoue, H. Izumida, Y. Sasaki, H. Hashimoto, *Chem. Lett.* **1976**, 863–864.
[18] N. N. Ezhova, N. V. Kolesnichenko, A. V. Bulygin, E. V. Slivinskii, S. Han, *Russ. Chem. Bull.* **2002**, *51*, 2165–2169.
[19] P. G. Jessop, T. Ikariya, R. Noyori, *Nature* **1994**, *368*, 231–233.
[20] P. G. Jessop, Y. Hsiao, T. Ikariya, R. Noyori, *J. Am. Chem. Soc.* **1996**, *118*, 344–355.
[21] P. Munshi, A. D. Main, J. C. Linehan, C. C. Tai, P. G. Jessop, *J. Am. Chem. Soc.* **2002**, *124*, 7963–7971.
[22] W. Leiner, E. Dinjus, F. Gassner in *Aqueous-Phase Organometallic Catalysis, Concepts and Applications* (Eds.: B. Cornils, W. A. Herrmann), Wiley-VCH, Weinheim, **1998**, pp. 486–498.
[23] F. Gassner, W. Leitner, *J. Chem. Soc. Chem. Commun.* **1993**, 1465–1466.
[24] M. M. T. Khan, S. B. Halligudi, S. Shukla, *J. Mol. Catal.* **1989**, *57*, 47–60.
[25] G. Kovacs, G. Schubert, F. Joo, I. Papai, *Catal. Today* **2006**, *115*, 53–60.
[26] H. Horvath, G. Laurenczy, A. Katho, *J. Organomet. Chem.* **2004**, *689*, 1036–1045.
[27] I. Joszai, F. Joo, *J. Mol. Catal. A* **2004**, *224*, 87–91.
[28] A. Katho, Z. Opre, G. Laurenczy, F. Joo, *J. Mol. Catal. A* **2003**, *204*, 143–148.

 © 2007 Wiley-VCH Verlag GmbH & Co. KGaA, Weinheim 

[29] J. Elek, L. Nadasdi, G. Papp, G. Laurenczy, F. Joo, *Appl. Catal., A* **2003**, *255*, 59–67.
[30] F. Joo, G. Laurenczy, P. Karady, J. Elek, L. Nadasdi, R. Roulet, *Appl. Organomet. Chem.* **2000**, *14*, 857–859.
[31] G. Laurenczy, F. Joo, L. Nadasdi, *Inorg. Chem.* **2000**, *39*, 5083–5088.
[32] F. Joo, G. Laurenczy, L. Nadasdi, J. Elek, *Chem. Commun.* **1999**, 971–972.
[33] P. G. Jessop, F. Joo, C. C. Tai, *Coord. Chem. Rev.* **2004**, *248*, 2425–2442.
[34] W. Leitner, *Angew. Chem. Int. Ed. Engl.* **1995**, *34*, 2207–2221.
[35] P. G. Jessop, T. Ikariya, R. Noyori, *Chem. Rev.* **1995**, *95*, 259–272.
[36] K. Kudo, N. Sugita, Y. Takezaki, *Nippon Kagaku Kaishi* **1977**, 302–309.
[37] C. C. Tai, T. Chang, B. Roller, P. G. Jessop, *Inorg. Chem.* **2003**, *42*, 7340–7341.
[38] C. P. Lau, Y. Z. Chen, *J. Mol. Catal. A* **1995**, *101*, 33–36.
[39] W. Leitner, E. Dinjus, F. Gassner, *J. Organomet. Chem.* **1994**, *475*, 257–266.
[40] O. Krocher, R. A. Koppel, A. Baiker, *Chem. Commun.* **1997**, 453–454.
[41] O. Krocher, R. A. Koppel, A. Baiker, *Chem. Commun.* **1996**, 1497–1498.
[42] L. Schmid, M. Rohr, A. Baiker, *Chem. Commun.* **1999**, 2303–2304.
[43] O. Krocher, R. A. Koppel, M. Froba, A. Baiker, *J. Catal.* **1998**, *178*, 284–298.
[44] Y. Kayaki, Y. Shimokawatoko, T. Ikariya, *Adv. Synth. Catal.* **2003**, *345*, 175–179.
[45] R. J. Bonilla, B. R. James, P. G. Jessop, *Chem. Commun.* **2000**, 941–942.
[46] K. P. Zeller, P. Schuler, P. Haiss, *Eur. J. Inorg. Chem.* **2005**, 168–172.
[47] N. Pinault, D. W. Bruce, *Coord. Chem. Rev.* **2003**, *241*, 1–25.
[48] T. Dwars, G. Oehme, *Adv. Synth. Catal.* **2002**, *344*, 239–260.
[49] F. Hollmann, P. C. Lin, B. Witholt, A. Schmid, *J. Am. Chem. Soc.* **2003**, *125*, 8209–8217.
[50] P. A. Gosling, J. H. Vanesch, M. A. M. Hoffmann, R. J. M. Nolte, *J. Chem. Soc. Chem. Commun.* **1993**, 472–473.
[51] U. Kolle, B. S. Kang, P. Infelta, P. Comte, M. Grätzel, *Chem. Ber.* **1989**, *122*, 1869–1880.
[52] W. Kaim, R. Reinhardt, M. Sieger, *Inorg. Chem.* **1994**, *33*, 4453–4459.
[53] L. Dadci, H. Elias, U. Frey, A. Hornig, U. Koelle, A. E. Merbach, H. Paulus, J. S. Schneider, *Inorg. Chem.* **1995**, *34*, 306–315.
[54] R. Ziessel, *J. Am. Chem. Soc.* **1993**, *115*, 118–127.
[55] A. Gabrielsson, P. van Leeuwen, W. Kaim, *Chem. Commun.* **2006**, 4926–4927.
[56] R. Ruppert, S. Herrmann, E. Steckhan, *Tetrahedron Lett.* **1987**, *28*, 6583–6586.
[57] R. Ruppert, S. Herrmann, E. Steckhan, *J. Chem. Soc. Chem. Commun.* **1988**, 1150–1151.
[58] E. Steckhan, S. Herrmann, R. Ruppert, J. Thommes, C. Wandrey, *Angew. Chem. Int. Ed. Engl.* **1990**, *29*, 388–390.
[59] E. Steckhan, S. Herrmann, R. Ruppert, E. Dietz, M. Frede, E. Spika, *Organometallics* **1991**, *10*, 1568–1577.
[60] D. Westerhausen, S. Herrmann, W. Hummel, E. Steckhan, *Angew. Chem. Int. Ed. Engl.* **1992**, *31*, 1529–1531.
[61] Y. Himeda, N. Onozawa-Komatsuzaki, H. Sugihara, H. Arakawa, K. Kasuga, *J. Mol. Catal. A* **2003**, *195*, 95–100.
[62] Y. Himeda, N. Onozawa-Komatsuzaki, H. Sugihara, H. Arakawa, K. Kasuga in *The 50th Symposium on Coordination Chemistry of Japan*, Japan Society of Coordination Chemistry, Kusatsu, **2000**.
[63] Y. Himeda, N. Onozawa-Komatsuzaki, H. Sugihara, H. Arakawa, K. Kasuga, *Organometallics* **2004**, *23*, 1480–1483.
[64] C. M. Bolinger, B. P. Sullivan, D. Conrad, J. A. Gilbert, N. Story, T. J. Meyer, *J. Chem. Soc. Chem. Commun.* **1985**, 796–797.
[65] Y. Himeda, N. Onozawa-Komatsuzaki, H. Sugihara, H. Arakawa, K. Kasuga, Japan Patent 3968431, **2007**.
[66] Y. Y. Ohnishi, T. Matsunaga, Y. Nakao, H. Sato, S. Sakaki, *J. Am. Chem. Soc.* **2005**, *127*, 4021–4032.
[67] C. C. Tai, J. Pitts, J. C. Linehan, A. D. Main, P. Munshi, P. G. Jessop, *Inorg. Chem.* **2002**, *41*, 1606–1614.
[68] M. Poliakoff, J. M. Fitzpatrick, T. R. Farren, P. T. Anastas, *Science* **2002**, *297*, 807–810.
[69] D. J. Cole-Hamilton, *Science* **2003**, *299*, 1702–1706.
[70] C. C. Tzschucke, C. Markert, W. Bannwarth, S. Roller, A. Hebel, R. Haag, *Angew. Chem. Int. Ed.* **2002**, *41*, 3964–4000.
[71] A. M. Allgeier, C. A. Mirkin, *Angew. Chem. Int. Ed.* **1998**, *37*, 894–908.
[72] I. M. Lorkovic, R. R. Duff, M. S. Wrighton, *J. Am. Chem. Soc.* **1995**, *117*, 3617–3618.
[73] C. K. A. Gregson, V. C. Gibson, N. J. Long, E. L. Marshall, P. J. Oxford, A. J. P. White, *J. Am. Chem. Soc.* **2006**, *128*, 7410–7411.
[74] P. C. J. Kamer, J. N. H. Reek, P. W. N. M. van Leeuwen in *Aqueous-Phase Organometallic Catalysis, Concepts and Applications*, 2nd ed. (Eds.: B. Cornils, W. A. Herrmann), Wiley-VCH, Weinheim, **2004**, pp. 686–698.
[75] J. C. Bayon, J. Real, C. Claver, A. Polo, A. Ruiz, *J. Chem. Soc. Chem. Commun.* **1989**, 1056–1057.
[76] M. Karlsson, M. Johansson, C. Andersson, *J. Chem. Soc. Dalton Trans.* **1999**, 4187–4192.
[77] M. Sussner, H. Plenio, *Angew. Chem. Int. Ed.* **2005**, *44*, 6885–6888.
[78] C. Hansch, A. Leo, R. W. Taft, *Chem. Rev.* **1991**, *91*, 165–195.
[79] J. Gao, L. Shao, *J. Phys. Chem.* **1994**, *98*, 13772–13779.
[80] J. Wang, R. J. Boyd, *J. Phys. Chem.* **1996**, *100*, 16141–16146.
[81] Y. Himeda, S. Miyazawa, T. Hirose, T. Gunji, Y. Abe, N. Onozawa-Komatsuzaki, H. Sugihara, K. Kasuga, unpublished result.
[82] S. Ogo, R. Kabe, H. Hayashi, R. Harada, S. Fukuzumi, *Dalton Trans.* **2006**, 4657–4663.
[83] P. J. Giordano, C. R. Bock, M. S. Wrighton, *J. Am. Chem. Soc.* **1978**, *100*, 6960–6965.
[84] A. Thompson, J. C. Jeffery, D. J. Liard, M. D. Ward, *J. Chem. Soc. Dalton Trans.* **1996**, 879–884.
[85] C. M. Chan, C. S. Fung, K. Y. Wong, W. H. Lo, *Analyst* **1998**, *123*, 1843–1847.
[86] J. M. Price, W. Y. Xu, J. N. Demas, B. A. DeGraff, *Anal. Chem.* **1998**, *70*, 265–270.
[87] S. Ogo, T. Abura, Y. Watanabe, *Organometallics* **2002**, *21*, 2964–2969.
[88] H. Hayashi, S. Ogo, S. Fukuzumi, *Chem. Commun.* **2004**, 2714–2715.
[89] T. Poth, H. Paulus, H. Elias, C. Ducker-Benfer, R. van Eldik, *Eur. J. Inorg. Chem.* **2001**, 1361–1369.
[90] Y. Himeda, N. Onozawa-Komatsuzaki, H. Sugihara, K. Kasuga, *Organometallics* **2007**, *26*, 702–712.
[91] S. Ogo, K. Uehara, T. Abura, Y. Watanabe, S. Fukuzumi, *Organometallics* **2004**, *23*, 3047–3052.
[92] T. Abura, S. Ogo, Y. Watanabe, S. Fukuzumi, *J. Am. Chem. Soc.* **2003**, *125*, 4149–4154.
[93] P. E. A. Ribeiro, C. L. Donnici, E. N. dos Santos, *J. Organomet. Chem.* **2006**, *691*, 2037–2043.
[94] B. P. Sullivan, T. J. Meyer, *Organometallics* **1986**, *5*, 1500–1502.
[95] G. J. ten Brink, I. Arends, M. Hoogenraad, G. Verspui, R. A. Sheldon, *Adv. Synth. Catal.* **2003**, *345*, 497–505.
[96] C. Caix, S. ChardonNoblat, A. Deronzier, R. Ziessel, *J. Electroanal. Chem.* **1996**, *403*, 189–202.
[97] Y. Himeda, N. Onozawa-Komatsuzaki, H. Sugihara, K. Kasuga, *J. Photochem. Photobiol., A* **2006**, *182*, 306–309.
[98] Y. Himeda, N. Onozawa-Komatsuzaki, H. Sugihara, H. Arakawa, K. Kasuga, *Stud. Surf. Sci. Catal.* **2004**, *153*, 263–266.

 © 2007 Wiley-VCH Verlag GmbH & Co. KGaA, Weinheim 

[99] L. W. Deady, W. L. Finlayson, C. H. Potts, *Aust. J. Chem.* **1977**, *30*, 1349–1352.
[100] B. Cornils, W. A. Herrmann, *Aqueous-Phase Organometallic Catalysis, Concepts and Applications*, 2nd ed., Wiley-VCH, Weinheim, **2004**.
[101] P. B. Webb, M. F. Sellin, T. E. Kunene, S. Williamson, A. M. Z. Slawin, D. J. Cole-Hamilton, *J. Am. Chem. Soc.* **2003**, *125*, 15577–15588.
[102] M. Solinas, A. Pfaltz, P. G. Cozzi, W. Leitner, *J. Am. Chem. Soc.* **2004**, *126*, 16142–16147.
[103] I. T. Horvath, *Acc. Chem. Res.* **1998**, *31*, 641–650.
[104] P. G. Jessop, D. J. Heldebrant, X. W. Li, C. A. Eckert, C. L. Liotta, *Nature* **2005**, *436*, 1102–1102.
[105] D. J. Heldebrant, P. G. Jessop, *J. Am. Chem. Soc.* **2003**, *125*, 5600–5601.
[106] J. Yoshida, K. Itami, *Chem. Rev.* **2002**, *102*, 3693–3716.
[107] H. P. Dijkstra, G. P. M. Van Klink, G. Van Koten, *Acc. Chem. Res.* **2002**, *35*, 798–810.
[108] G. J. Deng, Q. H. Fan, X. M. Chen, D. S. Liu, A. S. C. Chan, *Chem. Commun.* **2002**, 1570–1571.
[109] D. E. Bergbreiter, *Chem. Rev.* **2002**, *102*, 3345–3383.
[110] Y. Liang, Q. Jing, X. Li, L. Shi, K. L. Ding, *J. Am. Chem. Soc.* **2005**, *127*, 7694–7695.
[111] A. Hu, H. L. Ngo, W. B. Lin, *J. Am. Chem. Soc.* **2003**, *125*, 11490–11491.
[112] A. G. Hu, G. T. Yee, W. B. Lin, *J. Am. Chem. Soc.* **2005**, *127*, 12486–12487.
[113] M. Wende, J. A. Gladysz, *J. Am. Chem. Soc.* **2003**, *125*, 5861–5872.
[114] J. H. Yoon, Y. J. Park, J. H. Lee, J. Yoo, C. H. Jun, *Org. Lett.* **2005**, *7*, 2889–2892.
[115] V. K. Dioumaev, R. M. Bullock, *Nature* **2003**, *424*, 530–532.
[116] Y. Himeda, N. Onozawa-Komatsuzaki, H. Sugihara, K. Kasuga, *J. Am. Chem. Soc.* **2005**, *127*, 13118–13119.
[117] D. Sandrini, M. Maestri, R. Ziessel, *Inorg. Chim. Acta* **1989**, *163*, 177–180.
[118] M. T. Youinou, R. Ziessel, *J. Organomet. Chem.* **1989**, *363*, 197–208.
[119] S. Ogo, N. Makihara, Y. Kaneko, Y. Watanabe, *Organometallics* **2001**, *20*, 4903–4910.
[120] J. C. Tsai, K. M. Nicholas, *J. Am. Chem. Soc.* **1992**, *114*, 5117–5124.
[121] T. Matsubara, *Organometallics* **2001**, *20*, 19–24.
[122] K. W. Huang, J. H. Han, C. B. Musgrave, E. Fujita, *Organometallics* **2007**, *26*, 508–513.
[123] Y. Y. Ohnishi, Y. Nakao, H. Sato, S. Sakaki, *Organometallics* **2006**, *25*, 3352–3363.

Received: May 8, 2007

 © 2007 Wiley-VCH Verlag GmbH & Co. KGaA, Weinheim 

DOI: 10.1002/ejic.200700588

# $\eta^1$-Vinylidene Formation from Internal Alkynones by C–C Bond Migration

Michael J. Shaw,*[a] Steven W. Bryant,[a] and Nigam Rath[b]

**Keywords:** Ruthenium / Alkynes / Isomerization / Vinylidene bond activation / Unsaturated complexes

The $[\mu^2\text{-}N_2\{CpRu(PPh_3)_2\}_2]^{2+}$ ($\mathbf{1}^{2+}$) dication is a source of the formal 16-electron $[CpRu(PPh_3)_2]^+$ fragment, and it reacts with internal alkynes such as 1,3-diphenylpropynone, 4-phenyl-3-butyn-2-one, and 3-cyclopropyl-1-phenylpropynone to yield $\eta^1$-vinylidene complexes $\mathbf{2a}^+$–$\mathbf{2c}^+$ by C–C bond activation. In the case of 1,3-diphenylpropynone, the $\eta^1$-ketone complex $[CpRu(PPh_3)_2\{PhC(\eta^1\text{-}O)C{\equiv}CPh\}]^+$ ($\mathbf{3a}^+$) was isolated as its $PF_6^-$ salt, and it is apparently an intermediate in the formation of the vinylidene complex. Complexes $\mathbf{2a}^+$–$\mathbf{2c}^+$ were characterized as their $BAr^F{}_4^-$ [ArF = 3,5-bis(trifluoromethyl)phenyl] salts by NMR and IR spectroscopic methods, ESI-MS, and EA. The single crystal X-ray diffraction structure of $\mathbf{2a}BAr^F{}_4$ is presented. These reactions represent the first examples where an internal alkyne undergoes C–C bond migration to form an $\eta^1$-vinylidene complex.
(© Wiley-VCH Verlag GmbH & Co. KGaA, 69451 Weinheim, Germany, 2007)

## Introduction

Terminal vinylidene complexes have an established role in the catalytic and stoichiometric transformation of alkynes into elaborated structures.[1] The isomerization of alkyne ligands to vinylidenes has been examined in detail by experimental[2] and theoretical techniques[3] and this reaction continues to generate interest.[4] A net 1,2-H atom shift is common,[5] but the migration of other functional groups is limited to $-SiMe_3$, –SR, and –I,[1,6] which means that further reactions are necessary to produce disubstituted vinylidenes. In only one case has C–C bond activation been observed in an alkyne-to-vinylidene conversion,[7] although C–C bond migration in vinylidene-to-alkyne isomerization has been reported.[8] This communication details the formation of terminal vinylidene complexes through C–C bond activation of acetylenic ketones by electrophilic cations derived from $[CpRu(PPh_3)_2Cl]$, a well-known starting material for the formation of vinylidene ligands from terminal alkynes.[9]

## Results and Discussion

Halide abstraction of $Cl^-$ by silver salts from $[CpRu(L)_2Cl]$ (L = phosphane) results in the formation of unsaturated cationic complexes that absorb $N_2$ even from high-purity argon.[10a] Thus, a solution that behaves as "$[CpRu(PPh_3)_2]PF_6$" can be prepared in situ from $[CpRu(PPh_3)_2Cl]$ and $AgPF_6$ in $CH_2Cl_2$, but the actual metal species has proved difficult to isolate and characterize, a circumstance previously described for several related unsaturated metal complexes.[10] A tractable material that serves as a synthon for the "$[CpRu(PPh_3)_2]^+$" unit is $[\mu^2\text{-}N_2\{CpRu(PPh_3)_2\}_2](BAr^F{}_4)_2$ [$\mathbf{1}(BAr^F{}_4)_2$, $Ar^F$ = 3,5-bis(trifluoromethyl)phenyl]. The addition of 1,3-diphenylpropynone, 4-phenyl-3-butyn-2-one, or 3-cyclopropyl-1-phenylpropynone to $CH_2Cl_2$ or $CDCl_3$ solutions of $\mathbf{1}(BAr^F{}_4)_2$ immediately and cleanly yield the $\eta^1$-vinylidene complexes $\mathbf{2a}BAr^F{}_4$–$\mathbf{2c}BAr^F{}_4$, respectively (Scheme 1).

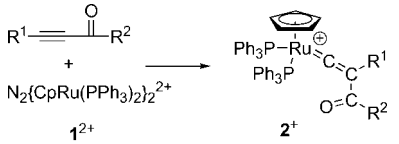


**2a**$^+$: $R^1$ = Ph; $R^2$ = Ph
**2b**$^+$: $R^1$ = Ph; $R^2$ = Me
**2c**$^+$: $R^1$ = cyclopropyl; $R^2$ = Ph

Scheme 1. Formation of vinylidene complexes from acetylenic ketones.

The single-crystal X-ray diffraction study (Figure 1)[11] of $\mathbf{2a}BAr^F{}_4$ reveals the vinylidene cation $\mathbf{2a}^+$ and clearly shows that an unexpected C–C bond migration has taken place. This rearrangement represents an unprecedented rearrangement for an internal alkyne in a monometallic compound.

The structure of $\mathbf{2a}^+$ is comparable to similar structures of $[CpRu(L)_2(vinylidene)]^+$ cations (L = phosphane) with a Ru=C bond length of 1.818(4) Å, a C=C bond length of 1.335(5) Å, and P–Ru–C bond angles of 94.65(11)° and 98.30(3)°.[12] This structure clearly establishes that C–C bond migration occurs, which transforms 1,3-diphenylpro-

[a] Department of Chemistry, Box 1652, Southern Illinois University Edwardsville,
Edwardsville, IL 62025-1652, USA
Fax: +1-618-650-3556
E-mail: michsha@siue.edu
[b] Department of Chemistry and Biochemistry,
315 Benton Hall, One University Blvd., St. Louis, MO 63121, USA
Supporting information for this article is available on the WWW under http://www.eurjic.org/ or from the author.

 © 2007 Wiley-VCH Verlag GmbH & Co. KGaA, Weinheim 

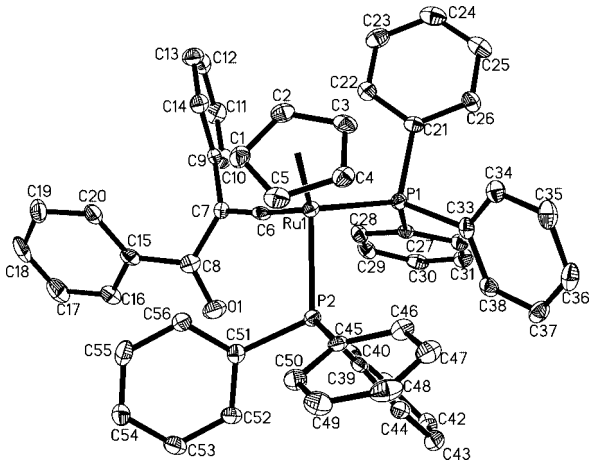


Figure 1. Projection view of complex $\mathbf{2a}^+$ with 50% thermal ellipsoids. The counterion and H atoms are omitted for clarity.

pynone into the 2-phenyl-2-benzoylvinylidene ligand. Cation $\mathbf{2a}^+$ is close in size to the $BAr^F{}_4^-$ anion (Supporting Information, Figure S1), a factor that often aids in the crystallization process. The solubility of the $BAr^F{}_4^-$ salts in $CDCl_3$ and $Et_2O$ is higher than the corresponding $PF_6^-$ salts, which tend to form oily masses rather than X-ray quality crystals.

Complexes $\mathbf{2a}^+$–$\mathbf{2c}^+$ were spectroscopically characterized by $^1H$, $^{13}C$, $^{31}P$, and $^{19}F$ NMR spectroscopy, IR spectroscopy, and ESI-MS as their $BAr^F{}_4^-$ salts. For example, the NMR spectra of $\mathbf{2a}BAr^F{}_4$ show the expected features such as a single resonance due to the $C_5H_5$ group in the $^1H$ and $^{13}C$ NMR spectra, and a single resonance due to the two equivalent phosphane ligands and the $BAr^F{}_4^-$ anion, respectively, in the $^{31}P$ and $^{19}F$ NMR spectra. Of note is the resonance at $\delta$ = 349.53 ppm in the $^{13}C$ NMR spectrum, which is due to the vinylidene carbon atom attached directly to the Ru atom.[13] Similarly, terminal vinylidenes $\mathbf{2b}BAr^F{}_4$ and $\mathbf{2c}BAr^F{}_4$ show diagnostic peaks in the $^{13}C$ NMR spectra at 351.91 and 353.29 ppm, respectively (see Supporting Information). For $\mathbf{2a}BAr^F{}_4$, a feature in the IR spectrum at 1658 $cm^{-1}$ is attributed to the vinylidene stretching vibration,[12b] but this vibration also appears to couple with the ketone stretching frequency that should occur in a similar position. The ESI-MS spectrum of $\mathbf{2a}BAr^F{}_4$ reveals the $P^+$ peak at 897 *m*/*z* with the expected pattern of Ru-isotope peaks.

The nature of the "$[CpRu(PPh_3)_2]^+$" cation in these reactions is an important factor. Solid samples of $\mathbf{1}(BAr^F{}_4)_2$ can be prepared by treating $[CpRu(PPh_3)_2Cl]$ with $NaBAr^F{}_4$ in $CH_2Cl_2$ under an argon atmosphere, followed by filtration of the mixture to remove NaCl and recrystallization (see Supporting Information). The Raman spectra of solid samples of $\mathbf{1}(BAr^F{}_4)_2$ show a peak at 2062 $cm^{-1}$, which is due to the bridging $N_2$ ligand.[10a,14] Exposure of this material in solution to nitrogen gas results in a band at 2192 $cm^{-1}$ in the KBr-pellet IR spectrum of the resulting solid as a result of the formation of a terminal $N_2$ ligand.[10a,14] However, exposure to excess $N_2$ appears to have no effect on the reactions of isolated $\mathbf{1}(BAr^F{}_4)_2$ with alkynones. Additionally, a $CH_2Cl_2$ signal ($\delta$ =5.32 ppm) is observed in the $^1H$ NMR spectrum of samples of $\mathbf{1}(BAr^F{}_4)_2$, so this solid is formulated as $\mathbf{1}(BAr^F{}_4)_2{\cdot}CH_2Cl_2$, which is consistent with the microanalytical data. As yet, X-ray quality crystals of this material are not available.

In $CDCl_3$ solution, $\mathbf{1}(BAr^F{}_4)_2$ appears to change into two species. As expected, there is no evidence of interaction between the noncoordinating $BAr^F{}_4^-$ anion and cation $\mathbf{1}^{2+}$ in the $^{19}F$ NMR spectrum. The $^1H$ NMR spectra of $\mathbf{1}(BAr^F{}_4)_2$ in $CDCl_3$ reveal two broad resonances at 4.53 and 5.16 ppm attributable to $C_5H_5$ protons, which indicates that the bulk of the ruthenium complex exists in two forms. There are also broad $^1H$ NMR signals at 7.01 and 10.11 ppm assigned to the *ortho* hydrogen atoms of the $PPh_3$ ligands. The $^1H$ NMR signal at 10.11 ppm disappears upon addition of alkynone with a corresponding increase in the usual Ph region of the spectrum. We suggest that the 10.11 ppm signal indicates that some of the ruthenium complex converts to a monometallic species agostically stabilized in solution by *ortho* C–H interactions as depicted in Scheme 2. Crystallographically characterized examples of related complexes with and without agostic interactions are known.[15] It is unlikely that this second cation exists as a true 16-electron species, as such compounds are known to have intense blue color.[14]

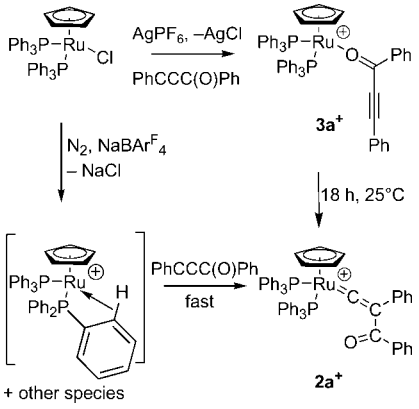


Scheme 2. The reaction of 1,3-diphenylpropynone with $\mathbf{1}BAr^F{}_4$ and in-situ-generated $\mathbf{1}PF_6$.

The reaction conditions play a considerable role in this alkyne-to-vinylidene conversion. Solutions of $\mathbf{1}(BAr^F{}_4)_2$ under an atmosphere of argon react immediately with 1,3-diphenylpropynone to form $\mathbf{2a}BAr^F{}_4$. Solutions of "$CpRu(PPh_3)_2PF_6$" generated in situ under an atmosphere of $N_2$ react over several hours to yield a mixture of products, in which $\mathbf{2a}PF_6$ can be observed spectroscopically by IR and $^1H$ NMR spectroscopy. Under these conditions an additional isomer of $\mathbf{2a}PF_6$ can be isolated (Scheme 2). The $\eta^1$-ketone complex $\mathbf{3a}PF_6$ can be isolated as a red-brown powder by fractional crystallization at –30 °C. Compound $\mathbf{3a}PF_6$ was characterized by NMR and IR spectroscopic methods and ESI-MS. These data establish that cation $\mathbf{3a}^+$ is an isomer of $\mathbf{2a}^+$. The definitive evidence for the $\eta^1$-ketone structure of $\mathbf{3a}PF_6$ comes from its IR spectrum

 © 2007 Wiley-VCH Verlag GmbH & Co. KGaA, Weinheim 

where an alkyne band at 2202 $cm^{-1}$ is almost unchanged from that of 1,3-diphenylpropynone (2207 $cm^{-1}$), whereas the ketone band moves to 1524 $cm^{-1}$, a shift of 116 $cm^{-1}$ lower than that of the free ligand.[16] The $^{13}C$ NMR spectra support this assignment with alkyne C atoms observable in their usual range, and the carbonyl C atom resonates at almost the same chemical shift as in the free ligand.[16]

It thus appears that the presence of ligands that coordinate more strongly than $BAr^F_4^-$ (such as $PF_6^-$) is a factor that can slow the formation of the vinylidene cation. $CH_2Cl_2$ solutions of "$[CpRu(PPh_3)_2]PF_6$" generated in situ by halide abstraction and then exposed to $N_2$ slowly develop IR bands at 2181 $cm^{-1}$, which are due to terminal $N_2$ ligands, as previously observed for similar Ru species.[14] The addition of 1,3-diphenylpropynone to such solutions (Scheme 2) immediately induces a change in the burgundy of **3a**$PF_6$. Over a period of hours, the color reverts to orange-brown. Progress monitored by FTIR spectroscopy indicates the immediate conversion of some "$[CpRu(PPh_3)_2]PF_6$" into **3a**$PF_6$, as evidenced by the appearance of a strong IR band at 1532 $cm^{-1}$. However, the alkyne band and the bound ketone band are very slowly consumed, whereas features due to vinylidene complex **2a**$PF_6$ increase in intensity (see Supporting Information). No features due to an η²-alkyne complex are observed in the region 1800–2000 $cm^{-1}$. From these results is it clear that the ketone complex **3a**$PF_6$ slowly isomerizes in $CH_2Cl_2$ to form the vinylidene complex **2a**$PF_6$.

An η²-alkyne intermediate cannot be ruled out at present. The conversion of η¹-ketone to η²-alkyne complexes was previously observed and is facile.[17] Calculations on $[Cp(PMe_3)_2(\eta^2\text{-}HC{\equiv}CR)]^+$ (R = H, $CH_3$) complexes show that initial slippage of the Ru atom from the alkyne triple bond to the terminal C–H bond is a necessary step in the isomerization process.[4d] It is likely that activation of the C(O)R group occurs in these reactions by a similar interaction of the Ru atom with the C–C bond that links the alkyne to the C=O unit. Ph group migration is unlikely because the addition of diphenylacetylene to **1**$BAr^F_4$ yields no vinylidene (monitored by NMR spectroscopy) and at least one related η²-PhC≡CPh complex was crystallographically characterized.[18] In the formation of the cyclopropyl complex **2c**$BAr^F_4$, no sign of ring-opening occurs during isomerization. If the cyclopropyl ring migrates, then migration must occur without a significant amount of positive charge or unpaired electron density build up on the migrating group, as these factors would encourage ring opening. Detailed calculations on this reaction pathway are currently underway.

## Conclusions

This report describes the reaction of an internal alkyne with a commonly encountered $d^6$-Ru complex cation that results in C–C bond migration to form a vinylidene complex. This migration represents a new path to disubstituted terminal vinylidene complexes, which are currently of intense theoretical and applied interest, and it may represent a general method for the activation of internal alkynes found in acetylenic ketones. Further theoretical and experimental studies are underway to establish a pathway for the activation of the acetylenic ketone ligand.

## Experimental Section

All manipulations were carried out under an atmosphere of prepurified nitrogen or argon. All solvents were distilled from appropriate drying agents (e.g. $CaH_2$ or K) and freeze–pump–thaw degassed before use.

**Preparation of 2a$BAr^F_4$:** Under an atmosphere of dry argon, $[CpRu(PPh_3)_2Cl]$ (1.40 g, 1.93 mmol) was mixed with $AgPF_6$ (0.487 g, 1.78 mmol) in $CH_2Cl_2$ (50 mL). The solution was stirred for 30 min and then 1,3-diphenylpropynone (0.45 g, 2.18 mmol) was added. The mixture was stirred in the dark for 5 d whereupon it was filtered, concentrated, and cooled to –30 °C. After 2 d, white crystals of AgCl had formed, and the solution was transferred to another vessel, further concentrated, and cooled again to –30 °C. This procedure was repeated until no more white precipitate formed, and then a crude solid (1.30 g) was precipitated from the solution by the addition of $Et_2O$ (50 mL). Half of the crude solid (0.62 g) was dissolved in $CH_2Cl_2$ (2.0 mL) to which $NaBAr^F_4$ (0.61 g, 0.69 mmol) was added. The solution was stirred for 30 min, filtered, and $Et_2O$ (10 mL) was added. The solution was concentrated under reduced pressure and cooled to –30 °C overnight whereupon **2a**$BAr^F_4$ precipitated from the solution as bright-orange crystals that were suitable for x-ray diffraction studies. Further concentration of the mother liquor resulted in four more crops of **2a**$BAr^F_4$ {0.521 g total, estimate 15% yield based on original $[CpRu(PPh_3)_2Cl]$}. $^1H$ NMR (300 MHz, $CDCl_3$, 25 °C): $\delta$ = 5.12 (s, $C_5H_5$), 6.80–7.78 (m, aromatic) ppm. $^{13}C$ NMR (75 MHz, $CDCl_3$, 25 °C): $\delta$ = 349.53 (s, Ru=*C*=C), 188.57 (s, *C*=O), 95.29 (s, $C_5H_5$), 82.00 (s, Ru=C=*C*) ppm. $^{31}P$ NMR (121.46 MHz, $CDCl_3$, 25 °C): $\delta$ = 40.48 (s) ppm. IR (KBr): $\tilde{\nu}$ = 1657, 1557, 1439, 1360, 1281, 1128 $cm^{-1}$. ESI-MS: *m*/*z* = 987 $[P - BAr^F_4^-]^+$. $[C_{88}H_{57}BF_{24}OP_2Ru]$ (1760.21): calcd. C 60.05, H 3.26; found C 60.07, H 3.28.

**Preparation of 3a$PF_6$:** $[CpRuCl(PPh_3)_2]$ (0.38 g, 0.50 mmol), $CH_2Cl_2$ (20 mL), and $AgPF_6$ (0.13 g, 0.50 mmol) were placed in a 100-mL Schlenk tube. The mixture was stirred under inert conditions, and a voluminous white precipitate formed. The mixture was stirred for 30 min and 1,3-diphenylpropynone (0.11 g, 0.50 mmol) was then added. The mixture was stirred overnight in the dark and then filtered through a 1-cm layer of Celite supported on a medium porous glass frit. Toluene (2 mL) was then added to induce crystallization, and the mixture was concentrated under reduced pressure. The solution was cooled overnight to –30 °C, and a small amount of solid was isolated. Three small crops of solid were obtained first, all between ca. 2 and 5 mg, which corresponded to impure AgCl and **1**$PF_6$. After these crops were obtained, the solution began to form a separate layer of oil. The oil was concentrated under reduced pressure and $Et_2O$ was added (10 mL), and the solution was stirred overnight. The resulting powder of **3**$PF_6$ (0.22 g, 42%) was isolated by filtration, rinsed with $Et_2O$, and dried under vacuum. $^1H$ NMR (300 MHz, $CDCl_3$): $\delta$ = 6.9–7.6 (40 H, Ph), 5.22 (5 H, $C_5H_5$) ppm. $^{13}C$ NMR (75 MHz, $CDCl_3$): $\delta$ = 189.0 (*C*=O), 98 ($C_5H_5$) ppm. IR ($CH_2Cl_2$): $\tilde{\nu}$ = 2207 [ν(C≡C)], 1524 [ν(C=O)] $cm^{-1}$. FAB-MS: *m*/*z* = 897.1 $[P]^+$, 690.9 $[P - dpp]^+$, 634.8 $[P - PPh_3]^+$. $C_{56}H_{45}OF_6P_3Ru$ (1041.95): C 64.55, H 4.35; found C 64.44, H 4.27.

 © 2007 Wiley-VCH Verlag GmbH & Co. KGaA, Weinheim 

**IR Spectroscopic Monitoring of the Reaction of $[CpRu(PPh_3)_2]PF_6$ with 1,3-Diphenylpropynone:** Under an atmosphere of dry argon, $[CpRu(PPh_3)_2Cl]$ (0.40 g, 0.96 mmol) was mixed with $AgPF_6$ (0.24 g, 0.96 mmol) in $CH_2Cl_2$ (50 mL). The solution was stirred for 30 min, and a portion (7.0 mL) of the mixture was then transferred by syringe into a cell equipped with a fiber optic FTIR probe. Two spectra were recorded that showed a flat baseline and a peak at 2181 $cm^{-1}$ [ν(N≡N)] and then 1,3-diphenylpropynone (0.14 g, 0.67 mmol) was added. Thirty spectra were recorded over 20 min: the spectra contained peaks at 2197 and 1532 $cm^{-1}$ that decreased in intensity and at 1658, 1596, 1580, and 1558 $cm^{-1}$ that increased in intensity; a strong peak at 1641 $cm^{-1}$ decreased slightly in intensity; and an isosbestic point at 1528 $cm^{-1}$. These spectra are plotted in Figure S2 (Supporting Information). A KBr-pellet IR spectrum of **2**$BAr^F{}_4$ is plotted in Figure S3.

**Supporting Information** (see footnote on the first page of this article): Experimental procedures and characterization data for the three vinylidene cations **2**$BAr^F{}_4$, crystal structure of **2**$BAr^F{}_4$, and IR spectra.

## Acknowledgments

This work was supported by an award to M. J. S. from the United States National Science Foundation (CHE-0514745) and by the Southern Illinois University Edwardsville (SIUE) Graduate School. The X-ray diffractometer was purchased with a grant from NSF (CHE0420497). We are grateful for the assistance of the Richter-Addo group at the University of Oklahoma for assistance in obtaining ESI-MS.

[1] C. Bruneau, P. H. Dixneuf, *Acc. Chem. Res.* **1999**, *32*, 311–323.
[2] a) J. Ipaktschi, J. Hohsseni-Ala, S. Uhlig, *Eur. J. Inorg. Chem.* **2003**, 4313–4320 and references cited therein; b) D. B. Grotjahn, X. Zeng, A. L. Cookst, *J. Am. Chem. Soc.* **2006**, *128*, 2798–2799; c) H. Katayama, K. Onitsuka, F. Ozawa, *Organometallics* **1996**, *15*, 4642–4645.
[3] a) C. H. Suresh, N. Koga, *J. Theor. Comput. Chem.* **2005**, *4*, 59–73 and references cited therein; b) V. Cadierno, M. P. Gamasa, J. Gimeno, C. Gonzalez-Bernardo, E. Perez-Carreno, S. Garcia-Granda, *Organometallics* **2001**, *20*, 5177–5188; c) F. De Angelis, A. Sgamellotti, N. Re, *Organometallics* **2002**, *21*, 5944–5950; d) F. De Angelis, A. Sgamellotti, N. Re, *Organometallics* **2002**, *21*, 2715–2723; e) R. Stegmann, G. Frenking, *Organometallics* **1998**, *17*, 2089–2095.
[4] a) Y.-S. Yen, Y.-C. Lin, S.-L. Huang, Y.-H. Liu, H.-L. Sung, Y. Wang, *J. Am. Chem. Soc.* **2005**, *127*, 18037; b) H. Kim, C. Lee, *J. Am. Chem. Soc.* **2005**, *127*, 10180–10181; c) J. A. Varela, C. Gonzalez-Rodriguez, S. G. Rubin, L. Castedo, C. Saa, *J. Am. Chem. Soc.* **2006**, *128*, 9576–9577; d) E. Bustelo, M. Jimenez-Tenorio, M. C. Puerta, P. Valerga, *Organometallics* **2006**, *25*, 4019–4025.
[5] M. C. Puerta, P. Valerga, *Coord. Chem. Rev.* **1999**, *99*, 193–195; M. C. Puerta, P. Valerga, *Coord. Chem. Rev.* **1999**, *99*, 977–1025 and references cited therein.
[6] N. G. Connelly, W. E. Geiger, C. Lagunas, B. Metz, A. L. Rieger, P. H. Rieger, M. J. Shaw, *J. Am. Chem. Soc.* **1995**, *117*, 12202–12208.
[7] P. J. King, S. A. R. Knox, M. S. Legge, A. G. Orpen, J. N. Wilkinson, E. A. Hill, *J. Chem. Soc. Dalton Trans.* **2000**, 1547–1548.
[8] a) R. S. Bly, Z. Zhong, C. Kane, R. K. Bly, *Organometallics* **1994**, *13*, 899–905; b) A. Ebrahimi, F. Deyhimi, H. Roohi, *J. Mol. Struct., Theochem* **2001**, *546*, 207–215.
[9] M. I. Bruce, C. Hameister, A. G. Swincer, R. C. Wallis, S. D. Ittel, *Inorg. Synth.* **1990**, *28*, 270–272.
[10] For examples, see: a) H. Aneetha, M. Jimenez-Tenorio, M. C. Puerta, P. Valerga, K. Mereiter, *Organometallics* **2002**, *21*, 628–635; b) P. Legzdins, W. S. McNeil, E. G. Vessey, R. J. Batchelor, F. W. B. Einstein, *Organometallics* **1992**, *11*, 2718–2723; c) R. P. Stewart, G. T. Moore, *Inorg. Chem.* **1975**, *14*, 2699–2703; d) M. Rosenbloom, D. Scheck, *Organometallics* **1982**, *1*, 397–399; e) M. J. Shaw, J. Mertz, *Organometallics* **2002**, *21*, 3434–3442.
[11] Single crystals were grown by cooling a saturated $Et_2O$ solution to –30 °C. Data for **2a**$BAr^F{}_4$ at 100 K: $C_{88}H_{57}BF_{24}OP_2Ru$ 1760.16 g $mol^{-1}$, triclinic, space group $P\bar{1}$, $a$ = 12.3691(8) Å, $b$ = 17.6970(10) Å, $c$ = 18.1997(11) Å, $\alpha$ = 104.163(3)°, $\beta$ = 92.766(4)°, $\gamma$ = 99.179(3)°, $V$ = 3797.4(4) $Å^3$, $Z$ = 2, $D_{calcd.}$ = 1.539 Mg $m^{-3}$, $R_1$ = 0.0656 for 12197 reflections with $I > 2\sigma(I)$, $wR_2$ = 0.1199 for 17959 reflections ($R_{int}$ = 0.074, with a measured total number of 64083 reflections), GOF on $F^2$ = 1.024, largest diff. peak (hole) = 1.046 (–0.830) e $Å^{-3}$. CCDC-647871 contains the supplementary crystallographic data for this paper. These data can be obtained free of charge from The Cambridge Crystallographic Data Centre via www.ccdc.cam.ac.uk/data_request/cif.
[12] a) E. Bustelo, J. J. Carbó, A. Lledó, K. Mereiter, M. C. Puerta, P. Valerga, *J. Am. Chem. Soc.* **2003**, *125*, 3311; b) J. R. Lomprey, J. P. Selegue, *J. Am. Chem. Soc.* **1992**, *114*, 5518; c) P. Haquette, N. Pirio, D. Touchard, L. Loïc-Toupet, P. H. Dixneuf, *J. Chem. Soc. Chem. Commun.* **1993**, 163; d) S. G. Davies, A. J. Smallridge, *J. Organomet. Chem.* **1990**, *395*, C39.
[13] N. J. Beach, H. A. Jenkins, G. J. Spivak, *Organometallics* **2003**, *22*, 5179.
[14] M. Jiménez-Tenorio, K. Mereiter, M. C. Puerta, P. Valerga, *J. Am. Chem. Soc.* **2000**, *122*, 11230–11231.
[15] K. Urtel, A. Frick, G. Huttner, L. Zsolnai, P. Kircher, P. Rutsch, E. Kaifer, A. Jacobi, *Eur. J. Inorg. Chem.* **2000**, 33–50.
[16] J. A. Gladysz, Y. H. Huang, *J. Chem. Ed.* **1988**, *65*, 298–303.
[17] H. Aneetha, M. Jiménez-Tenorio, M. C. Puerta, P. Valerga, K. Mereiter, *Organometallics* **2003**, *22*, 1779–1782.
[18] Y. Wang, F. Agbossou, D. M. Dalton, Y. Liu, A. M. Arif, J. A. Gladysz, *Organometallics* **1993**, *12*, 2699–2713.

Received: June 6, 2007
Published Online: July 27, 2007

 © 2007 Wiley-VCH Verlag GmbH & Co. KGaA, Weinheim 

DOI: 10.1002/ejic.200700558

# Surfactant-Assisted Synthesis and Characterization of Novel Chain-Like CoNi Alloy Assemblies

**Lu-Ping Zhu,[a,b] Hong-Mei Xiao,[a,b] and Shao-Yun Fu*[a]**

**Keywords:** Alloy / Assemblies / Hydrothermal method / Ferromagnetism / Coercivity

Novel chain-like CoNi alloy assemblies with a length of up to 6–7 μm were successfully prepared by a surfactant-assisted hydrothermal synthetic route at 100 °C for 2 h. The individual submicrospheres built from smaller CoNi nanoparticles had a diameter of about 400–500 nm. These microspheres were then integrated to form the novel chain-like CoNi alloy assemblies. The effects of synthetic parameters such as surfactant and solvent on the formation and morphology of CoNi samples were investigated. The experimental results showed that $N_2H_4{\cdot}H_2O$ and $CTA^+$ play important roles in the formation of the novel chain-like CoNi alloy assemblies. Based on the structural information provided by X-ray powder diffraction, scanning electron microscopy, transmission electron microscopy, selected-area electron diffraction and energy-dispersive X-ray analysis, a growth mechanism was tentatively proposed for the formation of chain-like CoNi alloy assemblies. Magnetic hysteresis measurement revealed that the chain-like CoNi alloy assemblies display ferromagnetic behavior with a saturation magnetization of 96.15 emu/g and a coercivity of 144.75 Oe at room temperature.
(© Wiley-VCH Verlag GmbH & Co. KGaA, 69451 Weinheim, Germany, 2007)

## Introduction

Transition metal nanoparticles, especially those of Fe, Co and Ni, are considered to be very important for technological applications, such as electronic, optical and mechanic devices, magnetism, catalysis, superconductors and ferrofluids etc.[1–5] It is claimed by Ung et al.[6] that, as far as magnetic storage is concerned, very high storage density requires high magnetic anisotropy to overcome thermal effects and to prevent superparamagnetic behavior. Several kinds of magnetic anisotropy can be considered to meet this requirement, including (a) shape anisotropy of elongated magnetic particles, such as rods and wires;[7] (b) magnetocrystalline anisotropy (for example: CoPt, FePt, CuNi, $FeNi_3$, etc.);[8–12] and (c) exchange anisotropy of ferromagnetic/antiferromagnetic core-shell particles.[13]

As important transition metal alloys, CoNi alloys have been widely used for decoration, corrosion resistance and magnetic recording devices, etc.[14–17] Therefore, much effort has been made in preparation of CoNi alloys. Micro- and nanosized CoNi alloy particles were prepared by electrochemical reduction,[18–20] thermal decomposition of organometallic precursors,[21] sol-gel routes,[22] polyols of metal salts[23] and leaching technology.[24] Nanosized amorphous CoNi alloy powders were also obtained by sonochemical decomposition methods.[25] Using the cationic water-in-oil (W/O) microemulsion of water/butanol/cetyltrimethyl bromide (CTAB)/*n*-octane, Zheng and co-workers synthesized CoNi needle-like alloys of different compositions with aspect ratios of 10–20.[26] Zhang and co-workers fabricated CoNi nanowires within nanochannel alumina (NCA) templates.[27] The magnetic behavior of the nanowires showed strong temperature dependence. Furthermore, Ung et al. synthesized CoNi nanowires by heterogeneous nucleation in liquid polyol.[6] In our previous work, we reported the synthesis of submicro-sized spherical ferromagnetic CoNi alloy particles by a polyol process assisted by solvothermal treatment.[28] However, chain-like CoNi alloy assemblies have received much less attention, although they are (i) members of the family of one-dimensional structural materials, which are likely to play a critical role in the improvement of the efficiencies of various devices based on single particles or their composites and (ii) are of considerable interest in fundamental research since they provide a direct bridge between nanometer-scale objects and the macroscale world.[29]

Herein, we report the preparation of high-density chain-like CoNi assemblies by a surfactant-assisted hydrothermal method and characterize the size, structure and composition of the resultant particles by transmission electron microscopy, selected-area electron diffraction, scanning electron microscopy, energy-dispersive X-ray analysis and X-ray powder diffraction.

[a] Technical Institute of Physics and Chemistry, Chinese Academy of Sciences,
Beijing 100080, China
Fax: +86-10-82543752
E-mail: syfu@mail.ipc.ac.cn
syfu@cl.cryo.ac.cn
[b] Graduate School of Chinese Academy of Sciences,
Beijing 100039, China

 © 2007 Wiley-VCH Verlag GmbH & Co. KGaA, Weinheim 

## Results and Discussion

The phase and purity of the as-prepared product formed at 100 °C for 2 h was determined by X-ray diffraction (XRD), as shown in Figure 1 for $2\theta$ angle values of 20–80°. The feature peaks of the as-prepared arise at $2\theta$ = 44.44, 51.72 and 76.32°, which match the (111), (200) and (220) characteristics of a face-centered cubic (fcc) structure, respectively. No characteristic peaks due to the impurities of $NiCl_2$, $CoCl_2$ or NaCl were detected, indicating that the as-obtained product was pure. In addition, there were no observable peaks in the XRD spectra corresponding to those of pure cobalt and nickel. If the homogeneous solid solution of CoNi were not formed, XRD peaks of pure Co or Ni should be observed simultaneously in the spectrum. These facts confirm that Co and Ni formed an alloy, rather than separate grains.

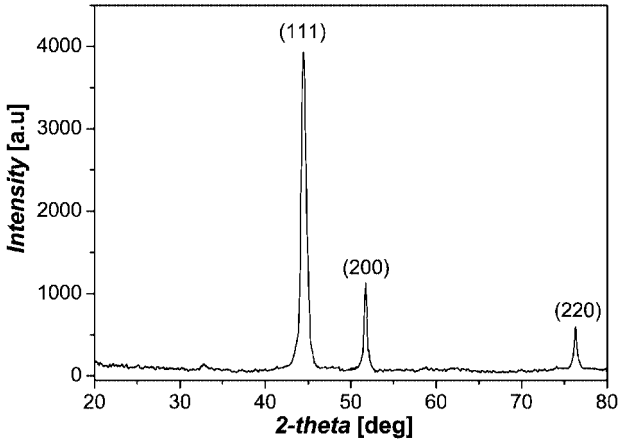


Figure 1. XRD pattern of the as-prepared sample obtained at 100 °C for 2 h.

Figure 2(a)–(c) shows SEM images of the as-synthesized product formed at 100 °C for 2 h. Figure 2(a) is the overall morphology of the sample, which indicates that the obtained product consists of large-scale chain-like assemblies. The magnified SEM image as shown in Figure 2(b) clearly displays that all of the CoNi chains are in the size range of 400–500 nm and in close contact with each other, forming branched, necklace-like chains with lengths of 6–7 μm. A close observation, as shown in Figure 2(c), reveals that the surface of the individual CoNi alloy submicroparticle is quite rough, and it presents a fine hierarchical nanostructure. On the basis of the above results, we conclude that the rough surfaces of these submicrospheres in the chain-like CoNi alloy assemblies are formed by attachment of nanoparticles, which may be related to the natural property and the presence of a surfactant. The morphology of the as-synthesized product was further determined by TEM as shown in Figure 2(d), which is consistent with that observed by SEM. The corresponding electron-diffraction pattern, displaying considerably sharp ring-like features of the selected area of the sample [Figure 2(e)], indicates that the as-obtained product is polycrystalline. The as-prepared alloy compositions were determined by EDX analysis under $N_2$. Figure 2(f) shows EDX spectra taken from the as-prepared products. The only detectable elements by EDX are cobalt and nickel, and the corresponding elemental analysis reveals that the atomic ratio of Co/Ni in the alloys is up to 1.0 which is very close to the designed composition, and hence the reduction reaction should be rather complete.

To investigate the influence of the surfactant on the formation feature of chain-like CoNi alloy assemblies, a synthetic experiment without CTAB was carried out. No chain-like materials that appeared in the experiment with the surfactant were observed [Figure 3(a)]. In addition, in the presence of CTAC, a similar result [Figure 3(b)] was obtained as in the presence of CTAB. These suggested that $CTA^+$ is a prerequisite to form the chain-like CoNi alloy assemblies. Other synthetic parameters were also examined. It was found that by introducing glycol into the present

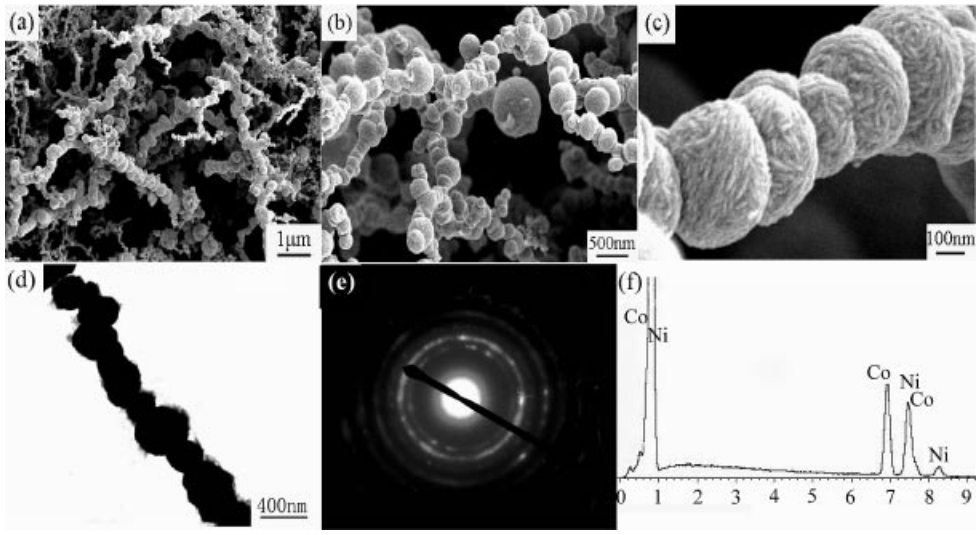


Figure 2. (a), (b), (c) SEM images at different magnifications of the as-prepared product. (d) TEM image, (e) the corresponding SAED pattern, (f) EDX spectrum of the as-prepared sample.

 © 2007 Wiley-VCH Verlag GmbH & Co. KGaA, Weinheim 

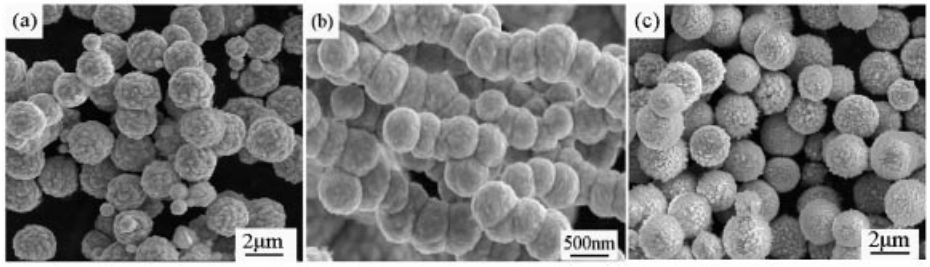


Figure 3. SEM images of the as-prepared product. (a) CoNi microspheres in the absence of surfactant. (b) CoNi submicrospheres in the presence of CTAC. (c) CoNi microspheres in the present system, with a water/polyol ratio of 1:2 (v/v).

system with a water/polyol ratio of 1:2 (v/v), CoNi microspheres rather than chain-like assemblies were obtained [Figure 3(c)]. Furthermore, the temperature rise did not show any additional effect on the morphology of the final products.

Regarding the mechanism for the growth of highly branched CoNi chain-like assemblies, we believe that both $N_2H_4{\cdot}H_2O$ and $CTA^+$ play important roles. In the experiment, hydrazine hydrate and sodium hydroxide were chosen as the reductant and buffer agent, respectively. The cobalt and nickel salts were reduced by hydrazine hydrate in concentrated basic media. The solution was blue before being reduced and afterwards became colorless. The reactions can be expressed as Equations (1) and (2).

$$2\ Ni^{2+} + N_2H_4 + 4\ OH^- \rightarrow 2\ Ni + N_2\uparrow + 4\ H_2O \quad (1)$$

$$2\ Co^{2+} + N_2H_4 + 4\ OH^- \rightarrow 2\ Co + N_2\uparrow + 4\ H_2O \quad (2)$$

Metallic cobalt and nickel give an intermetallic phase Equation (3).

$$Ni + Co \rightarrow CoNi \quad (3)$$

During the course of the reaction, the reduction of cobalt and nickel ions is effectively achieved by $N_2H_4$, which is a potent reducing agent in alkali solution.[12] A possible formation mechanism of chain-like CoNi alloy assemblies is proposed, as shown in Figure 4. Initially, cobalt(II) and nickel(II) ions react with hydroxy ions in the solution to form an intermediate phase consisting of cobalt and nickel hydroxide. Then, the redissolution of the intermediate solid phase takes place and the reduction of $Co^{II}$ and $Ni^{II}$ occurs according to Equations (1) and (2) and primary nuclei [Figure 4(a)] are formed in the presence of CTAB [see Equation (3)]. With the increase of the reaction time, presumably, the small CoNi primary nuclei diffuse and aggregate to form larger CoNi submicrospheres with a hierarchical nanostructure [Figure 4(b)] due to the magnetic dipole–dipole interaction[30] and effects of the $CTA^+$ templates. The larger CoNi submicrospheres are then assembled into chain-like assembles with multiple branches [Figure 4(e)] because of the stronger anisotropic magnetic forces.[31] This process is possible only when the magnetization of the particle does not fluctuate during the time of magnetic interaction in the suspension.[30] On the basis of the proposed mechanism for the growth of 1D nanostructure under the confinement of a capping reagent,[32,33] the surfactants CTAB or CTAC were necessary in the present procedure for the synthesis of chain-like CoNi alloy assemblies. It is assumed that the surfactants CTAB or CTAC play roles in at least two aspects. CTAB or CTAC are cationic surfactants, which can form $CTA^+$ in the solution. On the one hand, the surfactant could act as a template, which forms a $CH_3–CH_2–CH_2–N$ chain-like structure;[34,35] on the other hand, it could form a shell surrounding the particles to prevent them from aggregating to larger particles during the reduction process of the intermediate solid phase. Though

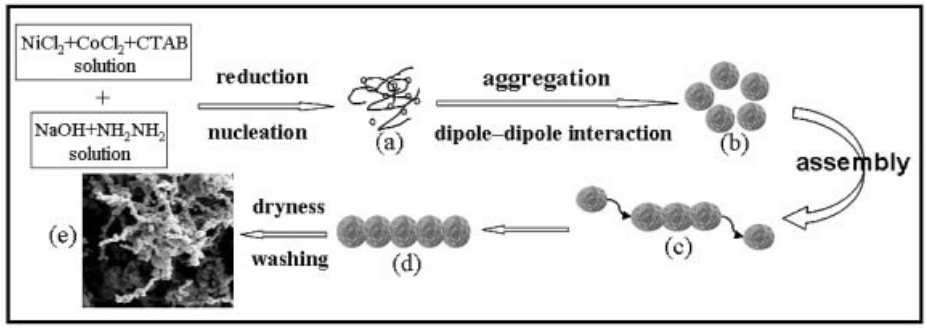


Figure 4. Schematic illustration of the formation and shape evolution of the CoNi alloy chain in the whole synthetic process: (a) Dissociative $CTA^+$ and CoNi primary nuclei, (b) CoNi submicrospheres with hierarchical nanostructure, (c) assembly of $CTA^+$ and CoNi alloy into a chain-like structure, (d) part of $CTA^+$ and CoNi alloy chain-like assemblies. (e) Removal of surfactant molecules to form chain-like CoNi alloy assemblies.

 © 2007 Wiley-VCH Verlag GmbH & Co. KGaA, Weinheim 

cobalt and nickel are easily oxidized, some possible oxides such as CoO, $Co_2O_3$ or NiO were not observed from the phase analysis by XRD. This might be due to the fact that the reaction was carried out at appropriate pH, temperature and hydrazine concentration and created under inert $N_2$ which does not favor cobalt and nickel oxidation.

The magnetic hysteresis measurement of the CoNi alloy was carried out at room temperature in an applied magnetic field sweeping from –10 to 10 kOe. Figure 5 shows magnetic hysteresis curves of the as-synthesized samples carried out at room temperature. The hysteresis loop of CoNi alloy samples reveals a ferromagnetic behaviour with a saturation magnetization ($M_s$) of 96.15 emu/g and a coercivity ($H_c$) of 144.75 Oe. Compared with the spherical CoNi alloy powders with a similar size of 200–500 nm in diameter in our previous work,[28] the coercivity increased from 108.23 to 144.75 Oe; on the other hand, the saturation magnetization decreased from 123.21 to 96.15 emu/g. It is well known that the size, structure and shapes of magnetic particles have effects on the magnetic properties of the products. The shape of the $M/H$ curve, or the shape of the hysteresis loop, may be strongly affected not only by the specific particle surface area but also by the magnetic anisotropy.[36] The magnetic anisotropy includes magnetocrystalline anisotropy, shape anisotropy, stress anisotropy, induced anisotropy and exchange anisotropy.[36] Cullity has given an expression for the magnetostatic energy $E_{ms}$ of the magnetic materials in the shape of a prolate spheroid with semimajor axis $c$ and semiminor axes of equal length a as in Equation (4),[36] where $M$ is the level of magnetization of an applied field, $\theta$ is the angle of the applied field to $c$, $N_a$ and $N_c$ are demagnetizing coefficients along $a$ and $c$, respectively.

$$E_{ms} = 1/2M^2N_c + 1/2(N_a - N_c)M^2\sin^2\theta \quad (4)$$

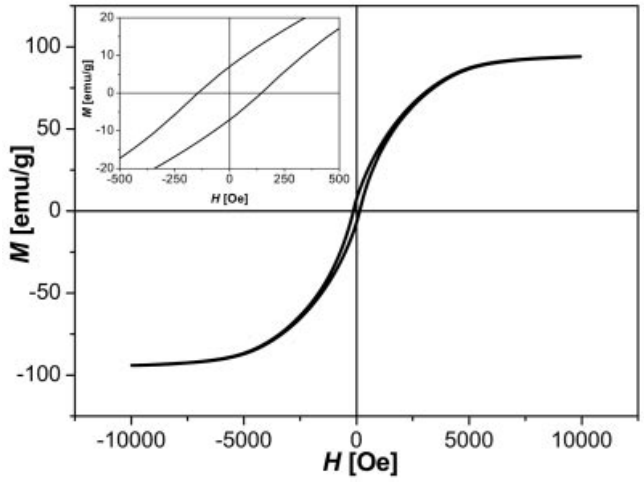


Figure 5. Hysteresis loop for the sample at room temperature.

The shape-anisotropy constant $K_s$ is given by Equation (5).

$$K_s = 1/2(N_a - N_c)M^2 \quad (5)$$

As Equation (5) shows, the strength of the shape anisotropy depends on the axial ratio $c/a$ of the specimen. Symmetrically shaped nanoparticles, such as spheres, do not have any net shape anisotropy. However, the synthesized representative chain-like CoNi alloy assemblies with an aspect ratio of about 15 on average would have shape anisotropy, which should increase the coercivity. So, the different coercivity may be attributed to the shape anisotropy of chain-like CoNi alloy assemblies, which prevent them from magnetizing in directions other than along their easy magnetic axes,[37] hence leading to the different saturation magnetization and coercivity.

## Conclusions

Novel chain-like CoNi alloy assemblies have been successfully prepared by the surfactant-assisted hydrothermal method. XRD, SEM, EDX, TEM, SAED, and VSM analyses have been employed for the characterization of the as-synthesized chain-like CoNi alloy assemblies. The results showed that $CTA^+$ plays an important role in the formation of chain-like CoNi alloy assemblies. The hysteresis loop of CoNi alloy samples revealed ferromagnetic behaviors with a saturation magnetization of 96.15 emu/g and a coercivity of 144.75 Oe at room temperature. A possible formation mechanism of the as-synthesized chain-like assemblies was proposed.

## Experimental Section

All reagents were of analytical grade from Beijing Chemical Reagent Ltd. and used without further purification. In a typical experiment, 0.50 g of $CoCl_2{\cdot}6H_2O$, 0.50 g of $NiCl_2{\cdot}6H_2O$, and 1 g of cetyltrimethylamonium bromide (CTAB) were dissolved in 30 mL of deionized water, and the mixture was strongly stirred for 5 min; then ultrasound sonication was applied for 30 min to ensure that all the reagents were dispersed homogeneously in the solution. Afterwards, a certain amount of a hydrazine hydrate ($N_2H_4{\cdot}H_2O$) solution in sodium hydroxide (NaOH) was added dropwise to the mixture whilst stirring. The obtained blue latex was then transferred into a 50 mL Teflon-lined stainless steel autoclave, sealed and maintained at 100 °C for 2 h after strongly stirring for 10 min. After being cooled to room temperature, the precipitates were collected and washed with deionized water and ethanol for several times. Finally, the precipitates were dried in vacuo at 40 °C for 12 h. The phase purity of the products was examined by X-ray powder diffraction (XRD) using a Rigaku D/max 2500 diffractometer at a voltage of 40 kV and a current of 200 mA with Cu-$K_\alpha$ radiation ($\lambda$ = 1.5406 Å), employing a scanning rate of 0.02°/s in the $2\theta$ range from 10 to 80°. Scanning electron microscopy (SEM) images and energy-dispersive X-ray (EDX) analysis were obtained using a HITACHI S-4300 microscope. Transmission electron microscopy (TEM) images and the corresponding selected-area electron-diffraction (SAED) pattern were taken with a HITACHI-600 transmission electron microscope at an accelerating voltage of 200 kV. Magnetic measurements for the samples were carried out at room temperature using a vibrating sample magnetometer (VSM, Lakeshore 7307, USA) with a maximum magnetic field of 10 kOe.

 © 2007 Wiley-VCH Verlag GmbH & Co. KGaA, Weinheim 

## Acknowledgments

We appreciate the financial support of the Overseas Outstanding Scholar Foundation of Chinese Academy of Sciences (Grant Nos. 2005-1-3 and 2005-2-1) and National Natural Science Foundation of China (Grant No. 50573090).

[1] T. Kato, *Ind. Mater.* **1983**, *31*, 18–21.
[2] M. Ozaki, *Mater. Res. Soc. Bull.* **1989**, *14*, 35–41.
[3] M. L. Wagner, L. D. Schmidt, *J. Phys. Chem.* **1995**, *99*, 805–815.
[4] G. Schmid, L. F. Chi, *Adv. Mater.* **1998**, *10*, 515–526.
[5] M. Giersig, M. Hilgendorff, *Eur. J. Inorg. Chem.* **2005**, 3571–3583.
[6] D. Ung, G. Viau, C. Ricolleau, *Adv. Mater.* **2005**, *17*, 338–344.
[7] A. Fert, L. Piraux, *J. Magn. Magn. Mater.* **1999**, *200*, 338–358.
[8] M. Yu, Y. Liu, D. J. Sellmyer, *J. Appl. Phys.* **2000**, *87*, 6959–6961.
[9] J. A. Christodoulides, Y. Huang, Y. Zhang, G. C. Hadjipanayis, I. Panagiotopoulos, D. Niarchos, *J. Appl. Phys.* **2000**, *87*, 6938–6940.
[10] S. H. Sun, C. B. Murray, D. Weller, L. Folks, A. Moser, *Science* **2000**, *287*, 1989–1992.
[11] J. Feng, C.-P. Zhang, *J. Colloid Interface Sci.* **2006**, *293*, 414–420.
[12] Q. Liao, R. Tannenbaum, Z. L. Wang, *J. Phys. Chem. B* **2006**, *110*, 14262–14265.
[13] V. Skumryev, S. Stoyanov, Y. Zhang, G. Hadjipanayis, D. Givord, J. Nogues, *Nature* **2003**, *423*, 850–853.
[14] Z. Tang, B. Ozturk, Y. Wang, N. A. Kovtov, *J. Phys. Chem. B* **2004**, *108*, 6927–6931.
[15] R. L. Penn, *J. Phys. Chem. B* **2004**, *108*, 12707–12712.
[16] M. Giersig, I. Pastoriza-Santos, L. M. Liz-Marzan, *J. Mater. Chem.* **2004**, *14*, 607–610.
[17] J. Polleux, N. Pinna, M. Antonietti, M. Niederberger, *Adv. Mater.* **2004**, *16*, 436–439.
[18] D. Golodnitsky, Y. Rosenberg, A. Ulus, *Electrochim. Acta* **2002**, *47*, 2707–2714.
[19] S. Armyanov, *Electrochim. Acta* **2000**, *45*, 3323–3335.
[20] G. Qiao, T. Jing, N. Wang, Y. Gao, X. Zhao, J. Zhou, W. Wang, *Electrochim. Acta* **2005**, *51*, 85–92.
[21] Syukri, T. Ban, Y. Ohya, Y. Takahashi, *Mater. Chem. Phys.* **2003**, *78*, 645–649.
[22] C. Sangregorio, C. de Julián Fernández, G. Battaglin, G. De, D. Gatteschi, G. Mattei, P. Mazzoldi, *J. Magn. Magn. Mater.* **2004**, *272–276*, e1251–e1252.
[23] P. Elumalai, H. N. Vasan, M. Verelst, P. Lecante, V. Carles, P. Taihades, *Mater. Res. Bull.* **2002**, *37*, 353–363.
[24] M. Uzawa, A. Inoue, T. Masumoto, *Mater. Sci. Eng., A* **1994**, *181–182*, 1176–1183.
[25] K. V. P. M. Shafi, A. Gedanken, R. Prozorov, *J. Mater. Chem.* **1998**, *8*, 769–773.
[26] D. E. Zhang, X. M. Ni, X. J. Zhang, H. G. Zheng, *J. Magn. Magn. Mater.* **2006**, *302*, 290–293.
[27] X. Y. Zhang, L. H. Xu, J. Y. Dai, H. L. W. Chan, *Phys. B* **2004**, *353*, 187–191.
[28] X. M. Liu, S. Y. Fu, C. J. Huang, *Mater. Lett.* **2005**, *59*, 3791–3794.
[29] Z. Y. Tang, N. A. Kotov, *Adv. Mater.* **2005**, *17*, 951–962.
[30] V. Salgueirino-Maceira, M. A. Correa-Duarte, A. Hucht, M. Farle, *J. Magn. Magn. Mater.* **2006**, *303*, 163–166.
[31] C.-M. Liu, L. Guo, R.-M. Wang, Y. Deng, H.-B. Xua, S. Yang, *Chem. Commun.* **2004**, 2726–2727.
[32] Y. Xia, P. Yang, Y. Sun, Y. Wu, B. Mayers, B. Gates, Y. Yin, F. Kim, H. Yan, *Adv. Mater.* **2003**, *15*, 353–389.
[33] Z. Liu, S. Li, Y. Yang, S. Peng, Z. Hu, Y. Qian, *Adv. Mater.* **2003**, *15*, 1946–1948.
[34] Z. J. Jia, L. P. Zhu, G. H. Liao, Y. Yu, Y. W. Tang, *Solid State Commun.* **2004**, *132*, 78–82.
[35] R. Zielinski, S. Ikeda, H. Nomura, S. Kato, *J. Colloid Interface Sci.* **1988**, *125*, 497–507.
[36] B. D. Cullity (Ed.), *Introduction to Magnetic Materials*, Addison-Wesley, London, UK, **1972**, pp. 240–243, 386–389.
[37] J. Wang, Q. W. Chen, C. Zeng, B. Y. Hou, *Adv. Mater.* **2004**, *16*, 137–140.

Received: May 28, 2007
Published Online: July 24, 2007

 © 2007 Wiley-VCH Verlag GmbH & Co. KGaA, Weinheim 

DOI: 10.1002/ejic.200700653

# Unprecedented Rearrangement of Molybdenum(VI) Oxide to ($\mu_2$-Oxido)-bis[dioxidomolybdenum(VI)] Hexamolybdate

**María R. Pedrosa,*[a] Rafael Aguado,[a] Virginia Díez,[a] Jaime Escribano,[a] Roberto Sanz,[a] and Francisco J. Arnáiz*[a]**

**Keywords:** Molybdenum / Hexamolybdates / O ligands / Polyoxometalates

$MoO_2(acac)_2$ reacts with water, amides, sulfoxides, and phosphane oxides in aqueous methanol, under mild conditions, to afford a new family of molybdates of composition $[Mo_2O_5L_6][Mo_6O_{19}]$ (L = $H_2O$, dimethylformamide, dimethylacetamide, dimethyl sulfoxide, dibutyl sulfoxide, tributylphosphane oxide, triphenylphosphane oxide, hexamethylphosphoramide). The crystal and molecular structures of the two first structurally characterized ($\mu_2$-oxido)bis[dioxidomolybdenum(VI)] hexamolybdates were established by X-ray diffraction analysis.
(© Wiley-VCH Verlag GmbH & Co. KGaA, 69451 Weinheim, Germany, 2007)

Polymolybdates have played a significant role in molybdenum chemistry for more than a century. The contemporary interest in these compounds arises from their compositional range and structural versatility, as well as important optical, magnetic, catalytic, and medicinal properties.[1] The formation of a particular polymolybdate depends on the nature of the cation and the reaction conditions.[2] Hexamolybdates, despite their low relevance in aqueous media, are an important class of polyoxometalates because of the high symmetry of the anion and their concomitant capability to form interesting derivatives.[3]

Here we report the easy formation of several ($\mu_2$-oxido)-bis[dioxidomolybdenum(VI)] hexamolybdates of composition $[Mo_2O_5L_6][Mo_6O_{19}]$ [L = $H_2O$ (**1**), dimethylformamide (dmf) (**2**), dimethylacetamide (dma) (**3**), dimethyl sulfoxide (dmso) (**4**), dibutyl sulfoxide (dbso) (**5**), tributylphosphane oxide ($OPBu_3$) (**6**), triphenylphosphane oxide ($OPPh_3$) (**7**), hexamethylphosphoramide (hmpa) (**8**)], as well as the crystal and molecular structure of the dmso and $OPBu_3$ derivatives, **4** and **6**, respectively. To the best of our knowledge, these compounds are the first hexamolybdates with dioxidomolybdenum(VI) cations reported to date, and **6** is the first to crystallize in a noncentrosymmetric polar crystal class. These compounds are of high potential interest since: (1) the possibility of functionalization of both anion[4] and cation through substitution of the terminal oxido groups opens up the way to new materials with unexplored properties, (2) the expected different capability of anion and cation to work as oxido transfer catalysts may enable selective transformations, and (3) the ionic nature of the compounds and the tuning of the cation by coordinated ligands expand the options to work in a wide range of conditions.

As part of an ongoing study on the reactivity of $MoO_2(acac)_2$ (acac = acetylacetonate), it was soon evident that the diketonate hydrolyzes rapid and completely in aqueous methanol to yield a white solid for which molybdenum analysis and weight difference after heating were consistent with a composition very close to $MoO_3 \cdot 0.75H_2O$. We propose the formulation **1** for this compound because the IR spectrum showed the characteristic pattern of dioxidomolybdenum compounds, along with bands that strongly support the presence of the hexamolybdate anion,[5] and the $^1H$ NMR spectrum in [$D_4$]methanol only showed the presence of water.

To further elucidate the nature of this product we performed several reactions of $MoO_2(acac)_2$ in methanol in the presence of various O-donor ligands that are either able to stabilize oxidomolybdenum(VI) hydrates as previously reported[6] or to replace water from the coordination sphere of molybdenum.[7] In this manner we were able to isolate in high yield compounds **2**–**8**.

We also studied the reactivity of a suspension of freshly precipitated $MoO_3 \cdot nH_2O$ in methanol with the same ligands. In all cases partial formation of the corresponding $[Mo_2O_5L_6][Mo_6O_{19}]$ compounds was observed; the best result was obtained with the most basic ligand, hmpa.

According to these observations, the hydrolysis of $MoO_2(acac)_2$ in aqueous methanol leads to a hydrated molybdenum(VI) oxide that rearranges to the metastable $[Mo_2O_5(H_2O)_6][Mo_6O_{19}]$, which in turn reacts with strong O-donor ligands, such as amides, sulfoxides, and phosphane oxides, through replacement of coordinated water while respecting the preformed $[Mo_2O_5]$ and $[Mo_6O_{19}]$ cores.

[a] Departamento de Química, Universidad de Burgos,
Pz. Misael Bañuelos s/n, 09001 Burgos, Spain
Fax: +34-947-25-88-31
E-mail: mpedrosa@ubu.es
farnaiz@ubu.es

Supporting information for this article is available on the WWW under http://www.eurjic.org or from the author.

 © 2007 Wiley-VCH Verlag GmbH & Co. KGaA, Weinheim 

This process can be rationalized by assuming that the mentioned hydrolysis proceeds through a sequence of reactions as shown in Scheme 1, in which the formation of dinuclear species must play a relevant role, as evidenced by the easy formation of $Mo_2O_5(H_2O)_2(acac)_2$, which was recently characterized,[8] and the persistence of $[Mo_2O_5L_6]^{2+}$ cations in all compounds isolated.

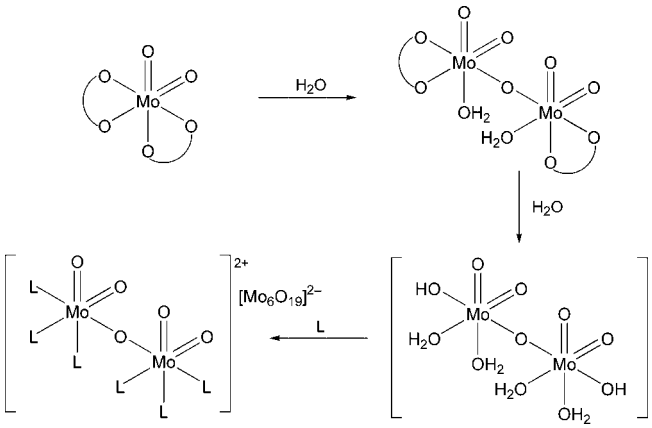


Scheme 1. Suggested stepwise formation of $[Mo_2O_5L_6][Mo_6O_{19}]$.

Condensation and deprotonation of the dinuclear species $Mo_2O_5(H_2O)_4(OH)_2$ may lead to the formation of the $[Mo_6O_{19}]^{2-}$ anion, which could coexist for a while with the hydrated dinuclear cation $[Mo_2O_5(H_2O)_6]^{2+}$, which in turn is formed by protonation. According to this, when water is replaced by strong coordinating ligands $[Mo_2O_5L_6][Mo_6O_{19}]$ (**2**–**8**) were formed.

Compounds **1**–**8** were fully characterized by elemental analysis, and IR and $^1H$ NMR spectroscopy. The molecular structures of **4** and **6** were also confirmed by single-crystal X-ray diffraction,[9] and their dinuclear cations are shown in Figures 1 and 2, respectively.

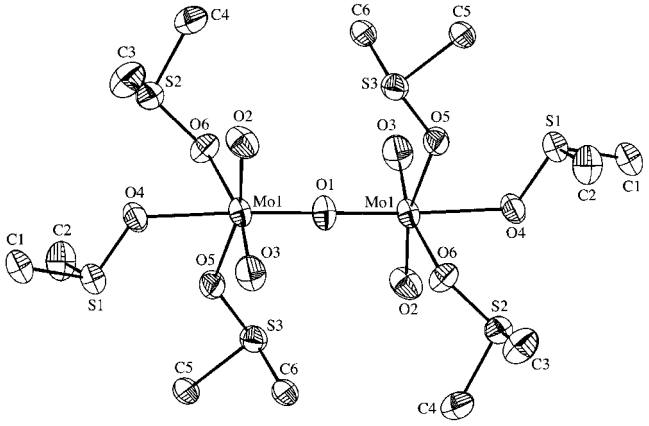


Figure 1. Crystal structure and atom-labeling scheme for $[Mo_2O_5(dmso)_6]^{2+}$ with thermal ellipsoids at the 50% probability level. The minor disorder component and hydrogen atoms are omitted for clarity.

Well-characterized compounds with the dication $[Mo_2O_5]^{2+}$ are rare, and to the best of our knowledge they are limited to $[Mo_2O_5L_2]^{2+}$ (L = *N*,*N*′,*N*′′-trimethyl-1,4,7-triazacyclononane, *N*,*N*′,*N*′′-tri-*tert*-butyl-1,4,7-triazacyclononane)[10–12] and $[Mo_2O_5L_6]^{2+}$ (L = $OPPh_3$).[13] For the cations from **4** and **6**, the Mo–O(t) and Mo–O($\mu_2$) bond lengths are similar to those reported for related cat-

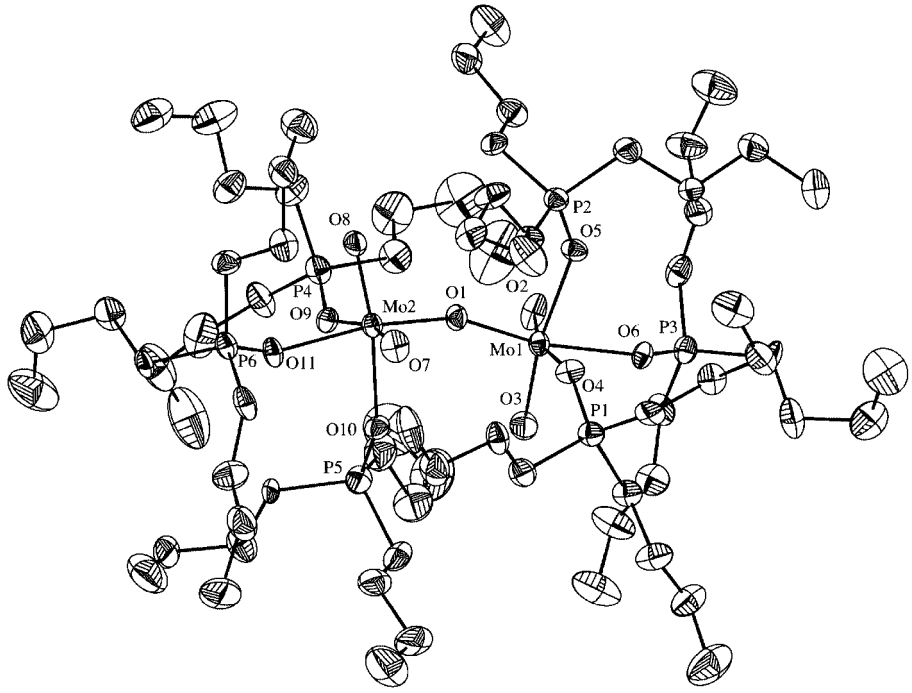


Figure 2. Crystal structure and atom-labeling scheme for $[Mo_2O_5(OPBu_3)_6]^{2+}$ with thermal ellipsoids at the 50% probability level. The minor disorder component and hydrogen atoms are omitted for clarity.

 © 2007 Wiley-VCH Verlag GmbH & Co. KGaA, Weinheim 

ions.[10–13] The cation from **4** has an inversion center at the oxygen bridge, which is analogous to cations reported in the literature; however, the angle Mo–O–Mo for the cation from **6** is 158.8(3)°, and this species is the first example of this type of cation that does not possess an inversion center.

The polyoxidoanion $[Mo_6O_{19}]^{2-}$ in **4** and **6** displays the well-known Lindqvist structure. The anion from **4** is highly symmetric, whereas that from **6** can be described as a distorted octahedron.

Whereas **4** crystallizes in the space group $P2_1/c$, quite common among the hexamolybdates previously reported, **6** crystallizes in the more interesting space group $P2(1)$. To the best of our knowledge, this is the first hexamolybdate in an acentric space group that falls in a noncentrosymmetric polar crystal class.[14] This kind of material possesses all four of the noncentrosymmetric symmetry-dependent properties,[15] specifically enantiomorphism, optical activity, pyroelectricity, and piezoelectricity.

The catalytic activity of compounds **1**–**8** for oxido transfer processes from several oxygen sources to $PPh_3$ was been measured and compared with that of the prototypical $[Bu_4N]_2[Mo_6O_{19}]$. It is noteworthy that full oxidation of $PPh_3$ to $OPPh_3$ could be achieved under mild conditions with these compounds when oxygen was used as the oxidant, whereas $[Bu_4N]_2[Mo_6O_{19}]$ proved to be inactive in the same conditions.

In summary, we have developed a simple reaction route to prepare ($\mu_2$-oxido)bis[dioxidomolybdenum(VI)] hexamolybdates from $MoO_2(acac)_2$. This easy procedure allows the reactions to be carried out in high yields under mild conditions. We have structurally characterized the two first members of this new family of hexamolybdates; one of them is the first hexamolybdate in a noncentrosymmetric polar crystal class. All these compounds show catalytic activity in oxidation processes with molecular oxygen as the oxidant. Further studies are currently being carried out in our laboratory.

**Supporting Information** (see footnote on the first page of this article): Full experimental details, structure refinement data and tables of bond lengths and bond angles for **4** and **6**.

## Acknowledgments

The authors thank Prof. H. D. Flack and Dr. G. Bernardinelli for assistance during the refinement of the crystal structures. This research was funded by Junta de Castilla y León (BU033A06 and BU012A06). J. E. thanks Junta de Castilla y León for a fellowship.

[1] a) M. T. Pope, A. Müller, *Angew. Chem.* **1991**, *103*, 56–70; *Angew. Chem. Int. Ed. Engl.* **1991**, *30*, 34–48; b) D.-L. Long, E. Burkholder, L. Cronin, *Chem. Soc. Rev.* **2007**, *36*, 105–121.
[2] M. T. Pope in *Comprehensive Coordination Chemistry II* (Eds: J. A. McCleverty, T. H. Meyer, A. G. Wedd), Elsevier Pergamon, Amsterdam, **2004**, vol. 4, pp. 635–678.
[3] a) J. B. Strong, B. S. Haggerty, A. L. Rheingold, E. A. Maatta, *Chem. Commun.* **1997**, 1137–1138; b) Y. Wei, B. Xu, C. L. Barnes, Z. Peng, *J. Am. Chem. Soc.* **2001**, *123*, 4083–4084.
[4] a) P. Wu, Q. Li, N. Ge, Y. Wey, Y. Wang, P. Wang, H. Guo, *Eur. J. Inorg. Chem.* **2004**, 2819–2822; b) Y. Xia, Y. Wey, Y. Wang, H. Guo, *Inorg. Chem.* **2005**, *44*, 9823–9828; c) K. Pavani, S. E. Lofland, K. V. Ramanujachary, A. Ramanan, *Eur. J. Inorg. Chem.* **2007**, 568–578.
[5] R. I. Buckley, R. J. H. Clark, *Coord. Chem. Rev.* **1985**, *65*, 167–218.
[6] a) F. J. Arnáiz, R. Aguado, J. Sanz-Aparicio, M. Martínez-Ripoll, *Polyhedron* **1994**, *13*, 2745–2749; b) F. J. Arnáiz, R. Aguado, M. R. Pedrosa, J. Mahía, M. A. Maestro, *Polyhedron* **2001**, *20*, 2781–2785; c) F. J. Arnáiz, M. R. Pedrosa, R. Aguado in *Inorganic Synthesis* (Ed.: J. R. Shapley), Wiley-Interscience, New Jersey, **2004**, vol. 34, pp. 49–53.
[7] a) F. J. Arnáiz, R. Aguado, M. R. Pedrosa, J. Mahía, M. A. Maestro, *Polyhedron* **2002**, *21*, 1635–1642; b) F. J. Arnáiz, R. Aguado, M. R. Pedrosa, A. De Cian, *Inorg. Chim. Acta* **2003**, *347*, 33–40.
[8] M. R. Pedrosa, J. Escribano, R. Aguado, V. Díez, R. Sanz, F. J. Arnáiz, *Polyhedron*, **2007**, DOI 10.1016/j.poly.2007.03.062.
[9] CCDC-639298 (for **4**) and -639299 (for **6**) contain the supplementary crystallographic data for this paper. These data can be obtained free of charge from The Cambridge Crystallographic Data Centre via www.ccdc.cam.ac.uk/data_request/cif.
[10] K. Wieghardt, G. Backes-Dahmann, W. Herrmann, J. Weiss, *Angew. Chem.* **1984**, *96*, 890–891; *Angew. Chem. Int. Ed. Engl.* **1984**, *23*, 899–900.
[11] K. S. Bürger, G. Haselhorst, S. Stotzel, T. Weyhermuller, K. Wieghardt, B. Nuber, *J. Chem. Soc. Dalton Trans.* **1993**, 1987–1997.
[12] D. V. Partyka, R. J. Staples, R. H. Holm, *Inorg. Chem.* **2003**, *42*, 7877–7886.
[13] G. Wang, G. Chen, R. L. Luck, Z. Wang, Z. Mu, D. G. Evans, X. Duan, *Inorg. Chim. Acta* **2004**, *357*, 3223–3229.
[14] a) A. M. Glazer, K. Steadnicka, *Acta Crystallogr., Sect. A* **1989**, *45*, 234–238; b) H. D. Flack, G. Bernardinelli, D. A. Clemente, A. Linden, A. L. Spek, *Acta Crystallogr., Sect. B* **2006**, *62*, 695–701; c) H. D. Flack, G. Bernardinelli, *Inorg. Chim. Acta* **2006**, *359*, 383–387.
[15] P. S. Halasyamani, K. R. Poeppelmeier, *Chem. Mater.* **1998**, *10*, 2753–2769.

Received: May 23, 2007
Published Online: July 27, 2007

 © 2007 Wiley-VCH Verlag GmbH & Co. KGaA, Weinheim 

DOI: 10.1002/ejic.200700218

# Mesoporous Carbon Prepared from Carbohydrate as Hard Template for Hierarchical Zeolites

**Kake Zhu,[a] Kresten Egeblad,[a] and Claus Hviid Christensen*[a]**

**Keywords:** Zeolite / Templating / Hierarchical materials / Sucrose / Porosity

A mesoporous carbon prepared from sucrose was successfully employed as a hard template to produce hierarchical silicalite-1, thus providing a very simple and inexpensive route to desirable zeolite catalysts from widely available raw materials. The porous carbon was prepared by hydrothermal treatment of a mixture of sucrose and ammonia followed by carbonization of the mixture in $N_2$ at high temperatures. The porous carbon produced by this method was subsequently applied as a hard template in the synthesis of mesoporous silicalite-1 and removed by combustion after synthesis. X-ray diffraction (XRD), scanning electron microscopy (SEM), transmission electron microscopy (TEM), selected-area electron diffraction (SAD), thermal gravimetry (TG), differential scanning calorimetry (DSC), $N_2$ physisorption measurements, Hg porosimetry and CHN elemental analysis techniques were applied to investigate the porous carbon template as well as the mesoporous zeolite single-crystal material.
(© Wiley-VCH Verlag GmbH & Co. KGaA, 69451 Weinheim, Germany, 2007)

## Introduction

Zeolites constitute an important class of crystalline microporous solids due to their widespread application in adsorption, separation and catalysis. Their importance stems from their unique pore structures, which make them highly selective to adsorbed molecules for separation purposes, or towards product molecules in catalysis. Moreover, they exhibit good thermal and hydrothermal stabilities during heterogeneous catalytic reactions.[1,2] However, the pore sizes of zeolites or zeolite-type materials, which are smaller than 1.5 nm, often restrict their applications due to diffusion limitations.[3]

Many strategies have been developed to overcome this problem, e.g. synthesizing larger-pore zeolite structures[4] and mesoporous molecular sieves,[5] reducing the size of the individual zeolite crystals,[6] subjecting the prepared zeolite to post-treatments like dealumination[7] and desilication,[8] as well as various hard template routes, where the template is removed after synthesis.[9] Naturally, pores created by post synthesis chemical treatments are highly dependant on the composition and structure of the original material, and a zeolite material consisting of nanosized crystals causes problems with handling during its applications. On the other hand, hard-template methods produce mesoporous zeolites with controlled porosity independent of their composition and structure, and have thus provided a general approach to solve this problem. So far, carbon blacks,[10] multiwalled carbon nanotubes,[11] carbon nanofibers,[12] carbon mesoporous molecular sieves,[13] carbon aerogels,[14–15] polymer aerogels,[16] and very recently mesoscale cationic polymers[17] have been utilized to fabricate zeolite materials which have a hierarchical pore system of intracrystalline mesopores interconnected with the conventional micropores.

Recently, mesoporous carbons have found application as hard templates for the production of very porous metal oxides such as $Al_2O_3$[18] and MgO.[19] Furthermore, also binary metal oxides like $MgAl_2O_4$ have been successfully prepared by this strategy.[20] More importantly, mesoporous carbons can also be employed to cast hierarchical-porous zeolites with tailored mesoporosities.[14–16] Mesoporous carbons are conventionally prepared by carbonization of a carbon precursor on a mesoporous silica template such as MCM-48,[21] SBA-15,[22] or amorphous silica,[23,24] which is subsequently removed by dissolving it in either HF or NaOH. Another category of mesoporous carbons are the carbon aerogels, which are prepared by pyrolysis of resorcinol/formaldehyde aerogels in an inert gas at high temperatures.[25–27] These methods are very costly and/or tedious. Preparation of an aerogel, for instance, entails supercritical fluid treatments making it both expensive and complex in preparation. In this paper, we report a simple and convenient way to prepare a mesoporous carbon template and its application in the synthesis of mesoporous silicalite-1. Contrary to the previously reported methods that typically rely on the availability of special and often expensive mesoporous carbons obtained from only a few suppliers, the present method only involves chemicals that are widely

[a] Center for Sustainable and Green Chemistry, Department of Chemistry, Technical University of Denmark, Building 206, 2800 Lyngby, Denmark
E-mail: chc@kemi.dtu.dk

 © 2007 Wiley-VCH Verlag GmbH & Co. KGaA, Weinheim 

available. The starting materials used here, sucrose and ammonia, are very inexpensive in comparison with aerogel precursors, and no sacrificial silica is needed. As carbon blacks are normally 100 times more expensive than sucrose, the outstanding features of the reported method are its simplicity, convenience and inexpensiveness.

## Results and Discussion

### Mesoporous Carbon Template

After hydrothermal treatment of a mixture of sucrose and ammonia for 2 d, a brown solid was obtained. $N_2$ physisorption measurements of this brown solid showed that it has a surface area of 34 $m^2/g$. In Figure 1 is shown a photographic image of the brown solid. It can be seen, that the brown solid retains the shape of the Teflon beaker in which it was produced and this allows for formation of larger zeolite objects though controlled templating.

Figure 1. Photographic image of the brown solid obtained after hydrothermal treatment of a mixture of sucrose and ammonia in a Teflon beaker. The porous carbon maintains the shape of the beaker.

From the TG and DSC measurements of the brown solid, shown in Figure 2, it can be seen that a major weight loss occurs between 400 and 500 °C. This is due to dehydration of the sucrose during decomposition. Above 500 °C, several endothermic peaks appear in the DSC profile. These are due to carbonization of the decomposed sucrose, since carbonization is an endothermic process. Hydrothermal treatment of the sucrose and ammonia mixture is necessary to obtain a porous carbon, because heating of sucrose directly causes melting and more complex decomposition, which results in non-porous carbon after thermal decomposition.

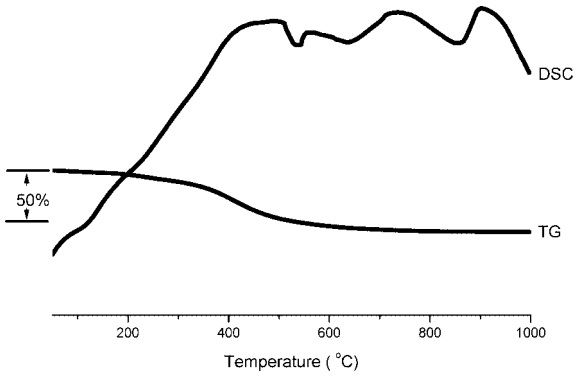


Figure 2. TG and DSC profiles of the solid obtained after hydrothermal treatment of a mixture of sucrose and ammonia.

Thermal decomposition of the brown solid at 850 °C in $N_2$ resulted in a porous black solid. This solid contained (by weight) 86.5% C, 1.17% N and 1.25% H, as examined by CHN elemental analysis. Thus, even after carbonization, minor amounts of nitrogen and hydrogen are present in the carbonaceous material. The remaining mass of the sample is most likely oxygen, which is not detected by this technique. Oxygen could easily be present in the carbonaceous material in the form of hydroxy groups.

$N_2$ adsorption and desorption isotherms of the porous black solid are shown in Figure 3. It can be seen that the isotherm contains a hysteresis loop which starts at a relative pressure of 0.8 and then rises dramatically with increasing pressure. According to the IUPAC classification of physisorption isotherms, isotherms featuring this type of hysteresis loops are classified as type IV isotherms, and are characteristic of mesoporous materials. From Figure 3 it is also evident, that the pore size distribution of the porous carbon is quite broad beginning at 10 nm and ending at more than 100 nm. Since the BET surface area of the carbon material presented here is only 416 $m^2/g$ (further results from the physisorption analyses are listed in Table 1), the material is not superior to the known carbon aerogels, which possess surface areas above 1000 $m^2/g$ and narrow pore size distributions.[27]

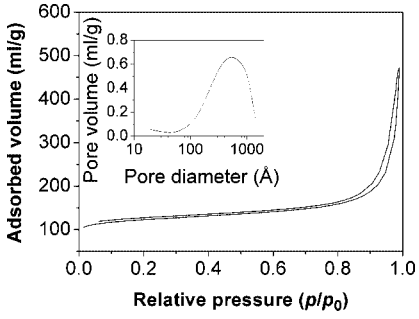


Figure 3. Nitrogen adsorption/desorption isotherms of the porous carbon obtained by carbonizing sucrose. The inset shows the pore size distribution obtained from the desorption branch of the isotherm using the BJH method.

 © 2007 Wiley-VCH Verlag GmbH & Co. KGaA, Weinheim 

Table 1. Surface area and porosity analyses of the mesoporous carbon template and the mesoporous silicalite-1 material obtained from it.[a]

| | $S_{BET}$ [$m^2$/g] | Micropore vol. [$cm^3$/g] | Meso- + macropore vol. [$cm^3$/g] | Mesopore size [nm] |
|---|---|---|---|---|
| Carbon | 416 | 0.13 | 0.60 | ca. 53 |
| Meso silicalite-1 | 403 | 0.09 | 0.37 | ca. 31 |

[a] The micropore volume is estimated from a *t* plot (DeBoer) and total pore volumes were calculated based on volume adsorbed at a relative pressure of $p/p_o = 0.99$, volumes of mesoporosity and macroporosity are calculated accordingly.[15]

However, given that the mesoporous carbon prepared in this way works well as a template in the synthesis of hierarchical zeolites, as will be shown later, the specific porosity properties of the material are not important.

### Mesoporous Silicalite-1

After crystallization of a zeolite gel mixture adsorbed on the porous carbon and subsequent calcination of the crude product in air, a white powder was obtained. The XRD pattern obtained for this powder is shown in Figure 4: the material contains exclusively highly crystalline MFI-structured material, since no peaks from other crystalline materials are observed in the pattern and there is no amorphous background. Thus, the prepared sample is a phase-pure silicalite-1 material. The peaks in the XRD diagram shown in Figure 4 are broader than the peaks observed in XRD patterns of conventional microporous ZSM-5 samples (also of MFI framework structure). This appears to be a general phenomenon in all XRD patterns of mesoporous zeolites produced by carbon templating. Even though the overall crystal sizes are similar in conventional and mesoporous samples, the XRD line width of the mesoporous samples always shows significant broadening. Thus, it is not possible to differentiate between nanosized and mesoporous zeolite samples from XRD analyses alone. However, the line broadening is still indicative of the porous carbon functioning as a chemically inert hard template during the crystallization of the zeolite.

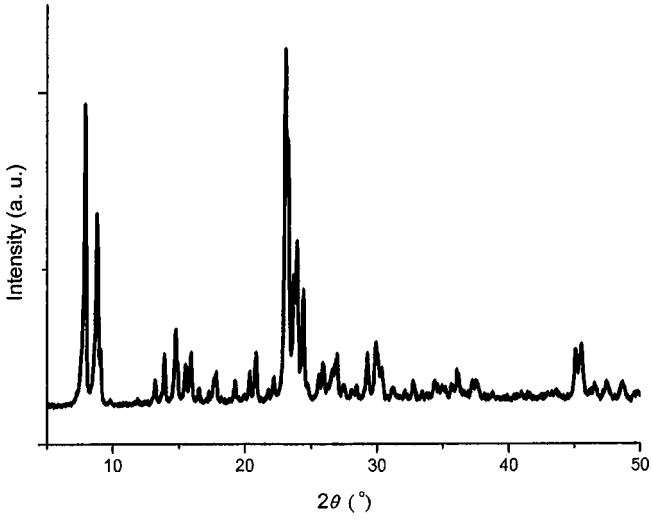


Figure 4. XRD pattern of the prepared silicalite-1 material.

In Figure 5 is shown the nitrogen physisorption isotherms of the mesoporous silicalite-1 material. It can be seen, that the isotherms contain two hysteresis loops, one at relative pressure below 0.4 and one starting at relative pressure 0.9. The hysteresis loop at a low relative pressure is commonly observed for microporous silicalite-1 and results from a phase transformation of dinitrogen inside the micropores of the pure silica MFI structure.[9] The hysteresis loop starting at a relative pressure of 0.9 is a type IV isotherm, which indicates that the material contains mesoporosity. Besides a micropore volume of 0.09 mL/g, the material contains an additional pore volume of 0.37 mL/g, attributable to mesopores and macropores. This is calculated from the total volume of $N_2$ adsorbed by the material at a relative pressure of $P/P_o = 0.99$. The pore size distribution of the mesoporous silicalite-1 is relatively narrow and centered at 31 nm, which is comparable to mesoporous zeolites prepared from other carbon templates.[10,14–16] The findings from nitrogen physisorption are completely verified by Hg intrusion data, which also reveal that some larger macropores, which cannot be seen efficiently by physisorption, are present. They are attributed to intercrystal voids in the material. The similarity of the physisorption data and the Hg porosimetry data confirms what has been found before: the pore system of the zeolite consists of an interconnected and homogeneously distributed system of intracrystalline mesopores that completely penetrate the crystals. Thus, since the newly developed procedure presented here clearly produces a hierarchical microporous/mesoporous material, which exhibits porosity similar to that of mesoporous silicalite-1 materials prepared using carbon blacks[10] and carbon aerogels as templates,[14–16] it is preferable when considering the complex nature of the carbon aerogel preparation and its high cost.

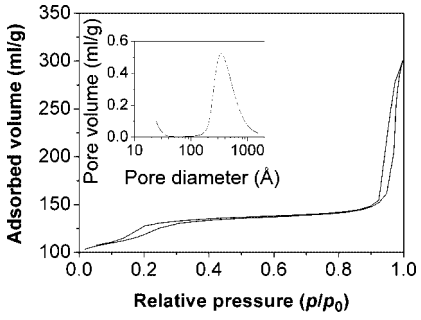


Figure 5. Nitrogen adsorption/desorption isotherms of the mesoporous zeolite silicalite-1 material after combustion of the carbon and organic templates. The inset shows the pore-size distribution obtained from the desorption branch of the isotherm using the BJH method.

 © 2007 Wiley-VCH Verlag GmbH & Co. KGaA, Weinheim 

A comparison of the pore-size distributions of the porous carbon and the silicalite-1 material (Figures 3 and 5) clearly points out that a mesoporous zeolite with a relatively narrow pore size distribution can be produced from a porous carbon having a much more broad pore size distribution. This suggests that the mesoporous silicalite-1 crystals start to grow inside the pores of the carbon matrix and during crystallization gradually encapsulate the carbon. Thus, since the porosity of the zeolite is a negative replica of the carbon template, the specific pore size distribution of this template is less important. This tendency has also been observed for mesoporous zeolites templated from different carbon blacks, since not all carbon blacks are able to efficiently produce mesoporous zeolites.[12] In this light, the route to mesoporous zeolites presented here is superior to carbon-black-based methods because, using the method reported here, it is not possible to alter the porosity of the carbon matrix by pushing aside the carbon particles during zeolite growth.

Figure 6 shows the results of SEM analyses of the prepared mesoporous silicalite-1 after combustion of the carbon and organic templates. Figure 6a shows a low-magnification SEM image of the prepared material: the sample contains only impressively homogeneously sized single crystals, which can be seen all over the sample. From the higher resolution images, shown in Figure 6b–d, it can easily be seen that the single crystals are all sponge-like in appearance, which is a characteristic feature of mesoporous zeolites. Moreover, the coffin-like morphology exhibited by the mesoporous single crystals is typical of MFI-structured crystals. Furthermore, this mesoporous silicalite-1 material is quite similar to the one reported by Jacobsen using commercially available carbon black as hard template,[10] and it is different from carbon-aerogel-templated mesoporous silicalite-1 which contains a mixture of nanosized crystals and larger mesoporous monocrystals.[14] However, in the carbon-aerogel-templated systems the zeolite properties can be influenced by the crystallizations conditions.[14–16] This can probably be ascribed to different crystallization kinetics in the various carbon matrix materials. Thus, zeolite crystallization in the confined space of the carbons leads to nanosized crystals instead of the mesoporous crystals obtained when the zeolite encapsulates the carbon particles. From the SEM analyses of the prepared zeolite material it is concluded that the present sample contains exclusively mesoporous silicalite-1 single crystals. Here, we only show the use of a specific carbon produced by carbohydrate decomposition. However, it can be envisaged that a wide range of different carbons can be produced with this approach, and that could lead to possibilities for tuning the zeolite mesopore size just as it is possible with different carbon black materials.

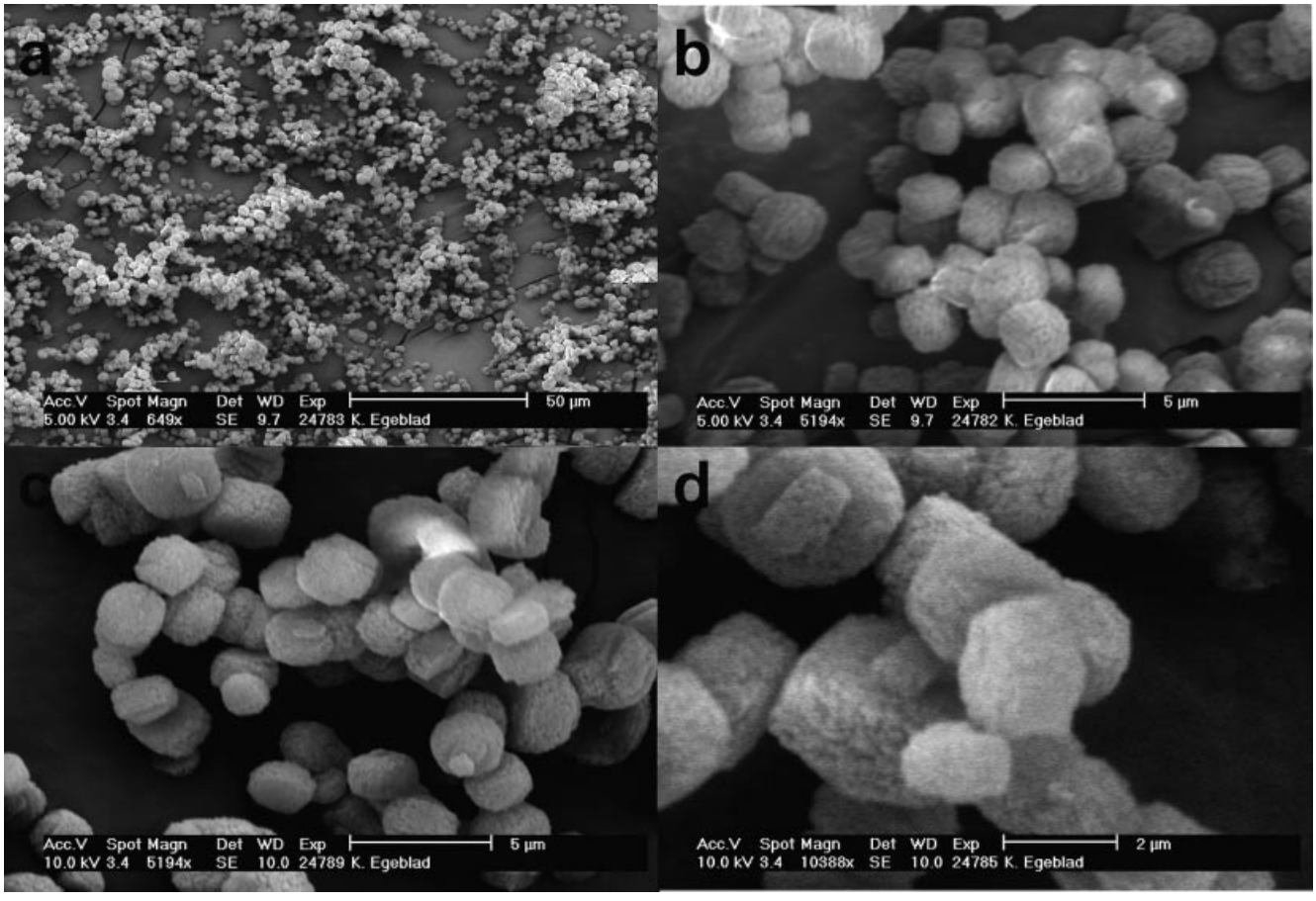


Figure 6. SEM images of the mesoporous silicalite-1 single crystals at different magnifications.

 © 2007 Wiley-VCH Verlag GmbH & Co. KGaA, Weinheim 

From the TEM images of the prepared mesoporous silicalite-1 material shown in Figure 7 it is evident, that the material does indeed consist of mesoporous single crystals as the sponge-like coffin shape is readily identifiable in these images. The close-up TEM image shown in Figure 7b along with the SAD pattern shown in its inset unambiguously confirms the single-crystalline nature of the materials.

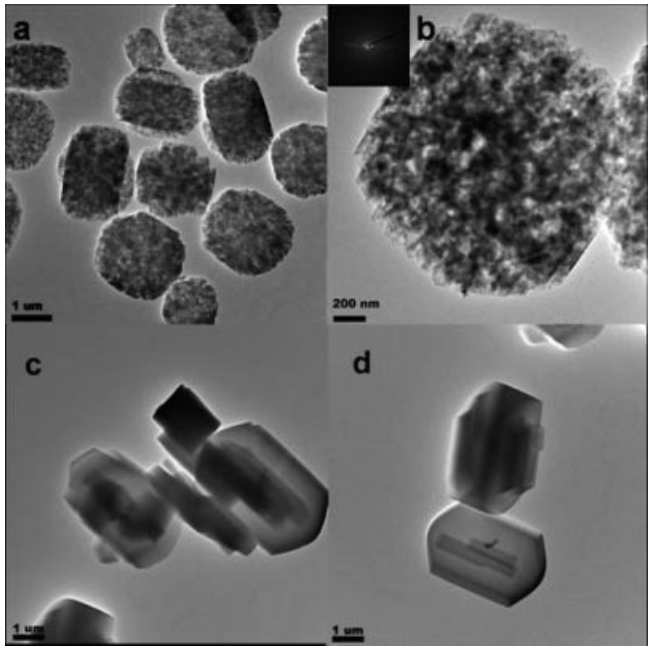


Figure 7. TEM images of the mesoporous silicalite-1 single crystals. The inset in (b) shows the SAD pattern of the area marked by a circle in the image, c) and d) show images of analogously prepared zeolite without the carbon template.

## Conclusions

Mesoporous zeolite single crystals of MFI structure were synthesized from cheap and readily available starting materials using a newly developed and very simple procedure in which an in-situ prepared mesoporous carbon is used as a mesopore template during synthesis and subsequently removed by combustion. XRD, SEM, TEM, SAD and $N_2$ physisorption measurements of the prepared zeolite material showed that the material contained exclusively mesoporous silicalite-1 single crystals, which are very similar to those obtained using much more expensive carbon black as the mesopore template. $N_2$ physisorption measurements of the carbon template showed that this material was in fact mesoporous, although not as porous as carbon aerogels. However, since the carbon template can obviously be used for the synthesis of mesoporous zeolite single crystals, the specific porosity of the carbon template is perhaps not so important. Nevertheless, understanding the mechanisms leading to the mesoporous carbon as well as its specific role in templating mesoporous zeolites might lead to mesoporous zeolites with even better properties. In all, the simple procedure presented here, combined with the comparatively cheap carbon matrix, make this method attractive for the synthesis of other zeolite or zeolite-type structures or perhaps even other oxide materials.

## Experimental Section

Hierarchical microporous/mesoporous silicalite-1 single crystals were obtained after combustion of a zeolite/carbon composite material, prepared by first producing a mesoporous carbon template material onto which the necessary zeolite gel components were impregnated and subjected to hydrothermal conditions.

The porous carbon template was prepared by dissolving 13.1 g of sucrose (98%, Aldrich) in a mixture of 9.6 mL of EtOH (absolute), 7.5 mL of $H_2O$ (deionized) and 1.0 mL of ammonia (25 wt.-%, Fluka) whilst stirring at 50 °C for 1.5 h. The material was transferred to a Teflon beaker and hydrothermally treated at 180 °C for 2 d, producing a brown solid which retained the shape of the beaker. The brown solid was crushed in a mortar and transferred to a horizontal tube furnace and heated to 850 °C in a flow of $N_2$ for 5 h to afford a porous black carbonaceous solid.

Mesoporous silicalite-1 single crystals were prepared by sequentially impregnating the necessary zeolite gel components onto the porous black carbonaceous solid. First, a mixture of 3.4 g of TPAOH (tetrapropylammonium hydroxide, 40 wt.-%, Aldrich) and 2.0 mL of EtOH was impregnated onto 2.5 g of porous black solid and the mixture was dried in air under ambient conditions overnight. Then, the material was impregnated with 3.0 mL of TEOS (tetraethyl orthosilicate, 98%, Aldrich) which was allowed to hydrolyze in air for 1 d. After aging, the material was transferred to a Teflon beaker which was placed inside a Teflon-lined autoclave with 10.0 mL of $H_2O$ added outside the beaker. The autoclave was hydrothermally treated at 180 °C for 3 d before the carbon and organic templates were removed by combustion at 550 °C for 24 h.

XRD was performed with a Philips PW 3710 X-ray diffractometer using Cu-$K_\alpha$ radiation ($\lambda$ = 0.154 nm) in the $2\theta$ range between 5 and 50° at a scanning speed of 0.6°/min.

Nitrogen adsorption/desorption isotherms were collected at liquid-nitrogen temperature (–196 °C) with a Micromeritics ASAP 2020. All samples were outgassed under vacuum at 200 °C overnight prior to measurement. The total surface area was calculated according to the BET method. Mesopore volumes were determined by the BJH method from the desorption branch of the isotherms, while micropore volumes and external surface areas were determined by using a *t*-plot analysis.

Hg porosimetry was measured by intrusion using a Quantachrome equipment.

SEM was performed with a Philips XL20 FEG. The calcined zeolite samples were placed on a carbon film and Pt was evaporated onto the sample for approximately 20 min to achieve sufficient conductivity.

TEM was performed with a JEM 2000FX using an accelerating voltage of 300 kV. SAD was used to obtain electron diffraction patterns from individual grains of powder. A few mg of the powdered samples were suspended in 2 mL of ethanol, and the suspension was sonicated for 1 h. Then, the suspension was allowed to settle for 15 min, before a drop was taken and dispersed on a 300 mesh copper grid coated with holey carbon film.

TG and DSC were conducted with NETZSCH STA 409 PC/PG equipment with a ramp of 20 °C/min under a nitrogen flow of 20 mL/min.

 © 2007 Wiley-VCH Verlag GmbH & Co. KGaA, Weinheim 

CHN elemental analysis was performed with a CE Instruments FLASH 1112 Series EA.

## Acknowledgments

The Center for Sustainable and Green Chemistry is sponsored by the Danish National Research Foundation.

[1] D. W. Breck, *Zeolite Molecular Sieves*, Wiley, New York, **1974**.
[2] A. Corma, *Chem. Rev.* **1997**, *97*, 2373–2420.
[3] J. Kaerger, D. M. Ruthven, *Diffusion in Zeolites and Other Microporous Materials*, Wiley, New York, **1992**.
[4] A. G. Dong, Y. J. Wang, Y. Tang, Y. H. Zhang, N. Ren, Z. Gao, *Adv. Mater.* **2002**, *14*, 1506–1510.
[5] C. T. Kresge, M. E. Leonowicz, W. J. Roth, J. C. Vartuli, J. S. Beck, *Nature* **1992**, *359*, 710–712; D. Y. Zhao, J. L. Feng, Q. S. Huo, N. Melosh, G. H. Fredrickson, B. F. Chmelka, G. D. Stucky, *Science* **1998**, *279*, 548–552.
[6] L. Tosheva, V. P. Valtchev, *Chem. Mater.* **2005**, *17*, 2494–2513.
[7] M. Boveri, C. Marquez-Alvarez, M. A. Laborde, E. Sastre, *Catal. Today* **2006**, *114*, 217–225.
[8] J. C. Groen, J. A. Moulijn, J. Perez-Ramirez, *J. Mater. Chem.* **2006**, *16*, 2121–2131.
[9] Y. S. Tao, H. Kanoh, L. Abrams, K. Kaneko, *Chem. Rev.* **2006**, *106*, 896–910.
[10] C. J. H. Jacobsen, C. Madsen, J. Houzvicka, I. Schmidt, A. Carlsson, *J. Am. Chem. Soc.* **2000**, *122*, 7116–7117.
[11] I. Schmidt, A. Boisen, E. Gustavsson, K. Stahl, S. Pehrson, S. Dahl, A. Carlsson, C. J. H. Jacobsen, *Chem. Mater.* **2001**, *13*, 4416–4418.
[12] A. H. Janssen, I. Schmidt, C. J. H. Jacobsen, A. J. Koster, K. P. de Jong, *Microporous Mesoporous Mater.* **2003**, *65*, 59–75.
[13] Z. Yang, Y. Xia, R. Mokaya, *Adv. Mater.* **2004**, *16*, 727–732.
[14] Y. Tao, H. Kanoh, K. Kaneko, *J. Am. Chem. Soc.* **2003**, *125*, 6044–6045.
[15] W. C. Li, A. H. Lu, R. Palkovtis, W. Schmidt, B. Spliethoff, F. Schuth, *J. Am. Chem. Soc.* **2005**, *127*, 12595–12600.
[16] Y. Tao, H. Kanoh, K. Kaneko, *Langmuir* **2005**, *21*, 504–507.
[17] F. S. Xiao, L. F. Wang, C. Y. Yin, K. F. Lin, Y. Di, J. X. Li, R. R. Xu, D. S. Su, R. Schlogl, T. Yokoi, T. Tatsumi, *Angew. Chem. Int. Ed.* **2006**, *45*, 3090–3093.
[18] W. C. Li, A. H. Lu, W. Schmidt, F. Schuth, *Chem. Eur. J.* **2005**, *11*, 1658–1664.
[19] J. Roggenbuck, M. Tiemann, *J. Am. Chem. Soc.* **2005**, *127*, 1096–1097.
[20] W. C. Li, M. Comotti, A. H. Lu, F. Schuth, *Chem. Commun.* **2006**, 1772–1774.
[21] M. Kruk, M. Jaroniec, R. Ryoo, S. H. Joo, *J. Phys. Chem. B* **2000**, *104*, 7960–7968.
[22] H. J. Shin, R. Ryoo, M. Kruk, M. Jaroniec, *Chem. Commun.* **2001**, 349–350.
[23] S. J. Han, M. Kim, T. Hyeon, *Carbon* **2003**, *41*, 1525–1532.
[24] K. Bohme, W. D. Einicke, O. Klepel, *Carbon* **2005**, *43*, 1918–1925.
[25] V. Bock, A. Emmerling, R. Saliger, J. Fricke, *J. Porous Mater.* **1997**, *4*, 284–297.
[26] R. W. Pekala, C. T. Alviso, F. M. Kong, S. S. Hulsey, *J. Non-Cryst. Solids* **1992**, *145*, 90–98.
[27] Y. Tao, H. Tanaka, T. Ohkubo, H. Kanoh, K. Kaneko, *Adsorpt. Sci. Technol.* **2003**, *21*, 199–203.

Received: February 17, 2007
Published Online: May 29, 2007

 © 2007 Wiley-VCH Verlag GmbH & Co. KGaA, Weinheim 

DOI: 10.1002/ejic.200700267

# (Arene)ruthenium(II) Complexes Containing Substituted Bis(pyrazolyl)methane Ligands – Catalytic Behaviour in Transfer Hydrogenation of Ketones

**M. Carmen Carrión,[a] Félix A. Jalón,[a] Blanca R. Manzano,*[a] Ana M. Rodríguez,[b] Francisco Sepúlveda,[a] and Miguel Maestro[c]**

*Dedicated to the memory of Prof. S. Trofimenko*

**Keywords:** Ruthenium / Arene ligands / Homogeneous catalysis / Bis(pyrazolyl)methane / Transfer hydrogenation / X-ray structure determination

A new and safer methodology has been developed for the synthesis of bis(pyrazol-1-yl)methane ligands (NN). Several ligands containing different phenyl groups on the central carbon atom have been obtained. Ruthenium derivatives of the type [Ru(arene)Cl(NN)]$BPh_4$ (arene = benzene, *p*-cymene) have been synthesised using these ligands. One or two isomers that differ regarding the axial or equatorial disposition of the phenyl group on the metallacycle have been obtained. Their formation is rationalised by considering steric effects. The structures of five derivatives were determined by X-ray diffraction. In four complexes the phenyl substituent is in the axial disposition of the metallacycle and in one case in the equatorial orientation. The dihedral angle formed by the planes of the two pyrazole rings is always bigger for the complexes containing unsubstituted pyrazolyl heterocycles. The behaviour of the new derivatives in the transfer hydrogenation of benzophenone in the presence of KOH was studied. The benzene derivatives showed higher activity than the *p*-cymene complexes. A marked and positive effect of the methyl groups on the pyrazolyl rings was observed. The effect of the substituents on the benzyl carbon atom was also important. It has been observed that the benzophenone hydrogenation was possible without the addition of complexes. The effect of the KOH concentration was evaluated and a concentration that leads to negligible conversion in a base-only process was chosen.
(© Wiley-VCH Verlag GmbH & Co. KGaA, 69451 Weinheim, Germany, 2007)

## Introduction

(Arene)ruthenium(II) complexes constitute an important group of derivatives that have applications in numerous catalytic processes. Although some ruthenium derivatives containing poly(pyrazolyl)borate[1] or poly(pyrazolyl)methane[2] ligands have been reported, arene complexes with these groups[3] are extremely scarce. One of the catalytic applications of arene–ruthenium derivatives is in the transfer hydrogenation of ketones. This process gives high yields and enantiomeric excesses with some ketones and has the advantage over the traditional use of $H_2$ pressure of greater operational simplicity.[4] Different Ru–arene systems have been described for this process including PP, NN, NO and NPN ligands.[5] In this context, one of the most important breakthroughs was discovered by Noyori and involves the use of "$Ru^{II}$(arene)" precursors with chiral amino alcohols or diamines[6] in processes that lead to excellent activities and enantioselectivities. Because of the participation of the ligand in the catalytic reaction, Noyori has proposed the term bifunctional metal-ligand catalysis for this kind of process. He performed theoretical calculations concerning the mechanism and the origin of enantioselectivity.[7] Other groups have also developed systems based on Ru–arene fragments with amino alcohols,[8] amino amide[9] or amino carboxylate[10] ligands. Interesting papers concerning mechanisms have also appeared.[11] Besides the metal ligand bifunctional mechanism, other mechanisms involving monohydride or dihydride species have been proposed. Although not involving arene derivatives, it is worth noting that recently Baratta et al.[12] designed a new type of $Ru^{II}$ catalyst, containing the ligand 2-(aminomethyl)pyridine or its derivatives, that was active in the transfer hydrogenation of acetophenone, using NaOH as cocatalyst with TOF up to $4.0 \times 10^5$ $h^{-1}$.

[a] Departamento de Química Inorgánica, Orgánica y Bioquímica, Universidad de Castilla-La Mancha, Facultad de Químicas, Avda. C.J. Cela 10, 13071 Ciudad Real, Spain
[b] Departamento de Química Inorgánica, Orgánica y Bioquímica, Universidad de Castilla-La Mancha, Escuela Técnica Superior de Ingenieros Industriales, Avda. C.J. Cela 3, 13071 Ciudad Real, Spain
[c] Departamento de Química Fundamental, Universidade da Coruña, 15071 A Coruña, Spain
Supporting information for this article is available on the WWW under http://www.eurjic.org or from the author.

 © 2007 Wiley-VCH Verlag GmbH & Co. KGaA, Weinheim 

In recent years we have worked with a series of bis(pyrazolyl)methane derivatives.[2a,13] These compounds offer the possibility of modulating the steric and electronic properties by introducing substituents in the pyrazole rings and at the central carbon atom. We used ligands that contained differently substituted phenyl rings and pyrazole (pz) or 3,5-dimethylpyrazole (pz*) heterocycles attached to the central carbon atom. We have also explored the coordination chemistry of these ligands, mainly with palladium fragments.[13] An endobidentate coordination with the formation of metallacycles with a boat conformation has always been found. Interestingly, in all cases the phenyl substituent occupies the axial position in this metallacycle (see Scheme 1a). This is probably due to the steric hindrance that these groups would cause if they were in an equatorial position with respect to the pyrazole rings (Scheme 1b) and also the absence of other interactions in the axial position because of the square-planar environment of the metal centre. We found that with substituted pyrazolyl rings, the bite angle and the dihedral angle formed by the planes NPdN/$N_4$ were smaller and this influenced the dynamic behaviour of some derivatives.[13c] These data were rationalised by means of theoretical calculations.[14] Bis(pyrazolyl)methane complexes in which the substituent (pyrazole or thienyl) on the central CH group is situated in an equatorial position correspond to octahedral derivatives of ruthenium(II)[15] or platinum(IV).[16] In both cases, the pyrazolyl rings were unsubstituted.

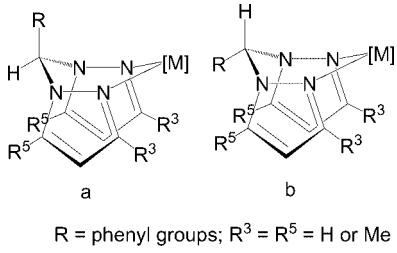


Scheme 1.

In the work described here we decided to synthesise a series of bis(pyrazolyl)methane ligands in which the central carbon atom bears phenyl rings that have different functional substituents such as $OCH_3$, $NO_2$ or $NH_2$. One objective was to find a method of synthesis that avoided the use of toxic phosgene. The purpose was also the synthesis of new arene (benzene, *p*-cymene) ruthenium derivatives that contain these ligands. Ultimately, we were interested in evaluating the stereochemistry of these complexes and, in particular, the preference for an equatorial or axial disposition of the phenyl ring and the relationship of this fact with the substitution on the pyrazolyl groups and the steric requirements of the arene. An open question concerned whether the change in the type of pyrazole present would also force the same type of distortions found in the related palladium chemistry.

Taking into account that Ru–arene complexes with poly(pyrazolyl)methane ligands have never been studied in hydrogenation transfer of ketones, another goal was the use of the new complexes as precatalysts in these processes using 2-propanol as the solvent and reducing agent. Preliminary tests will be presented. The NN ligands are clearly different to those used by Noyori because of the absence of NH groups as donor centres. In any case, it was of interest to evaluate the effect of the functional groups on the benzyl carbon atom outside the coordination centre including the $NH_2$ fragment.

## Results and Discussion

### Synthesis of the Ligands and Complexes

The ligands used in this work and their abbreviations are summarised in Scheme 2.

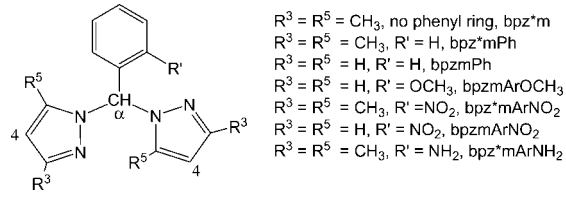


Scheme 2.

The ligands bpz*mPh,[17] bpzmPhOCH$_3$[13c] and bpz*m[18] have been described previously. The ligands bpz*mArNO$_2$, bpzmArNO$_2$ and bpz*mArNH$_2$ are described in this work for the first time. Until now, the intermediate bis(pyrazol-1-yl)ketone that is necessary for the preparation of these types of ligand, was synthesised by the reaction of pyrazole (substituted or not) and phosgene. In this work we tried to develop a greener method that could avoid the use of this highly toxic gas. The alternative that we have found is the use of the solid triphosgene. Thus, the synthesis of the ligands bpzmPh, bpz*mArNO$_2$ and bpzmArNO$_2$ was carried out in the following way. Firstly, the bis(pyrazol-1-yl)ketone species were obtained through the reaction of the corresponding pyrazole with triphosgene in the presence of triethylamine (Scheme 3).

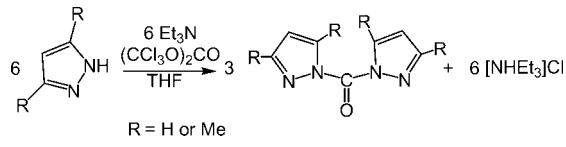


Scheme 3.

The resulting ketone subsequently reacted with the corresponding aldehyde in toluene under reflux for 24 h (Scheme 4).

 © 2007 Wiley-VCH Verlag GmbH & Co. KGaA, Weinheim 

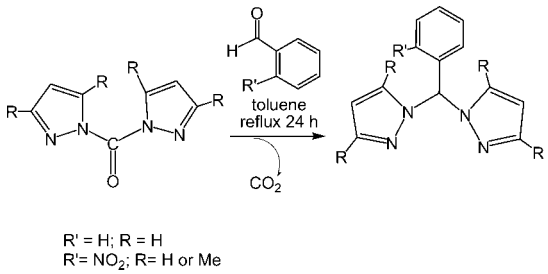


Scheme 4.

The ligand bpz*mArNH$_2$ was obtained by hydrogenation of bpz*mArNO$_2$ using a Pd/C catalyst.

The Ru$^{II}$–arene (arene = benzene, *p*-cymene) complexes used in this work were obtained by treating the corresponding Ru$^{II}$ starting material, the nature of which depends on the arene, with the desired ligand in MeOH with the addition of Na[BPh$_4$] at the end of the reaction [see Equations (1) and (2)].

$$[RuCl_2(benzene)(CH_3CN)] + NN \xrightarrow{NaBPh_4} [RuCl(benzene)(NN)]BPh_4 + NaCl + CH_3CN \quad (1)$$

NN = bpz*m, **1**; bpz*mPh, **3**; bpzmPh, **5**; bpzmArOCH$_3$, **7**; bpz*mArNO$_2$, **9**; bpzmArNO$_2$, **11**; bpz*mArNH$_2$, **13**.

$$1/2\ [RuCl_2(p\text{-cymene})]_2 + NN \xrightarrow{NaBPh_4} [RuCl(p\text{-cymene})(NN)]BPh_4 + NaCl \quad (2)$$

NN = bpz*m, **2**; bpz*mPh, **4**; bpzmPh, **6**; bpzmArOCH$_3$, **8**; bpz*mArNO$_2$, **10**; bpzmArNO$_2$, **12**; bpz*mArNH$_2$, **14**.

In cases where the nitrogenated ligands contained methylated pyrazolyl groups, only one isomer was obtained for the corresponding ruthenium complexes. A different situation was found when the ligand contained unsubstituted pyrazoles. Apart from the complexes containing bpzmPh, where only one isomer was found, the other derivatives exist as a mixture of two isomers (A and B). The relative ratios of these isomers, determined by NMR before recrystallisation, are shown, where applicable, in the Experimental Section.

The new complexes were characterised by elemental analysis as well as IR, $^1$H and $^{13}$C NMR spectroscopy and, in some cases, by X-ray diffraction. The bands corresponding to the stretching vibrations of the NO$_2$ and NH$_2$ groups were observed in the IR spectra (see Exp. Sect.).

## NMR Study

A careful NMR analysis of the new ligands and complexes was carried out. The assignment of the resonances was possible with the help of $^1$H,$^1$H-COSY, NOESY and *g*-HMQC spectra (in some cases also with *g*-HMBC) and by considering the values of coupling constants. The $^1$H NMR spectroscopic data are gathered in Table S1 of the Supporting Information. Coordination of the nitrogenated ligand to the [RuCl(arene)]$^+$ fragment results in shifts that, in some cases, were greater than 1 ppm towards higher frequencies for the pyrazolyl ring proton resonances. The same trend was observed for the $^{13}$C NMR resonances in cases where the appropriate data for direct comparison are available. This effect was attributed in general to the electron donation of the ligand to the metal cation (the effect of other groups in the molecule on specific protons will be detailed below). The increased electron deficiency of the heterocyclic rings also leads to an increase in the $^1$H,$^1$H coupling constants.[19] The assignment of structures to the complexes was done mainly by means of the NOESY spectra. The two possible structures are shown in Scheme 5. These compounds differ in the axial or equatorial orientation of the phenyl ring in the metallacycle. The arrows represent the most important NOEs observed. The disposition of the arene ring bonded to Ru and the chloride proposed in the scheme is thought to be the only possible situation for steric reasons. In the complexes obtained with methylated ligands and the isomers labelled A for the nonmethylated ones, an NOE is always observed between H$_\alpha$ and H$^5$ (or Me$^5$) of the pyrazolyl groups. In some cases, an NOE is also observed between resonances of the arene groups and the H atom of the phenyl group *ortho* to the benzyl carbon atom. These data indicate that in these complexes the phenyl ring is situated in an axial position. The structures in which the phenyl ring is in an equatorial disposition are assigned to isomers B. In fact, in complex **12B** an NOE was observed between H$_\alpha$ and the proton H$^3$ of the *p*-cymene ring. Although it does not provide structural information, a noticeable NOE is frequently observed in both types of isomer between the H$^3$ or Me$^3$ pyrazole resonances and signals from the arenes. This must be a consequence of the large dihedral angle NRuN/N$_4$ in the metallacycle having the boat conformation (see X-ray structures described below).

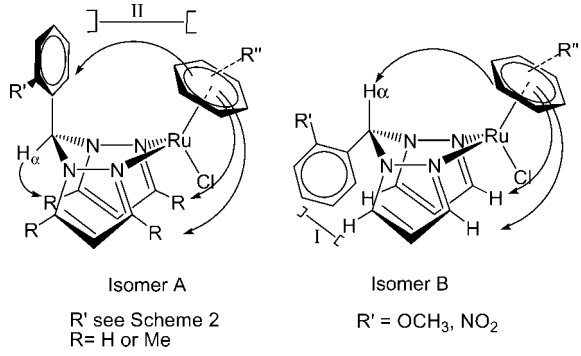


Scheme 5. Isomers A and B for the arene–Ru$^{II}$ derivatives. The most important NOEs are indicated with arrows. The steric interactions used to rationalise the isomer ratio are indicated by the roman numerals I and II. R′′ means that the arene ring is benzene or *p*-cymene.

Concerning the $^1$H NMR chemical shifts of the resonances of the two isomers, it is expected that the resonances of the H$^5$ pyrazole protons or even those of the arene rings would be affected by the position of the phenyl groups. In

 © 2007 Wiley-VCH Verlag GmbH & Co. KGaA, Weinheim 

fact, the $H^5$ (pz) protons for isomers A appear in the range 8.23–8.50 ppm and those of isomers B in the range 7.69–7.80 ppm. When the phenyl groups are in an equatorial position, it is clear that these $H^5$ protons are more shielded. This must be due to the effect of the current anisotropy of the aromatic rings. A similar effect is observed for the aromatic resonances of the arenes. For example, the benzene signals of isomers A are in the region 4.90–5.75 ppm whereas isomers B give rise to signals in the range 6.24–6.27 ppm. This observation implies that, although the phenyl rings will rotate around the C(*ipso*)–$C_\alpha$ bond, the preferred orientation for the A isomers is that in which the ring forms an angle of approximately 90° with the $H_\alpha$–$C_\alpha$–C(*ipso*) plane. This orientation also leads to an upfield shift of the phenyl resonances of the protons situated *ortho* to $C_\alpha$, a situation due to the anisotropy effect of the pyrazole rings. These resonances could serve as a way of identifying the structure of a specific isomer. In the case of the $^{13}C\{^1H\}$ NMR resonances, a clear difference is also observed in the $C^5$ pyrazole signals, similar to that observed in the $^1H$ NMR spectra. For example, a higher chemical shift (difference of about 3–4 ppm) is observed for isomer A than isomer B.

The formation of a single isomer or a mixture of isomers, and even the ratio of isomers, can be rationalised on the basis of steric effects alone. Steric hindrance between the arene rings and the pyrazolyl groups exists in both isomers and probably will not influence their ratio (see Scheme 5). Steric hindrance I will be important in isomers B while steric hindrance II will be operating in isomers A. When the pyrazolyl groups are methylated, interaction I must predominate to induce the unique formation of complexes of type A. For the case of nonmethylated pyrazolyl groups, interaction I will be less important and both interactions may be competitive. In fact, both isomers are formed (see isomer ratio of complexes **7**, **8**, **11** and **12**; complexes **5** and **6** with bpzmPh constitute an exception, see Exp. Sect.), albeit in a ratio that depends on the nature of the arene. For the benzene complexes, isomers of type A are dominant, while for the bulkier *p*-cymene the ratio is nearly 1. In conclusion, in benzene derivatives interaction I is dominant while for the *p*-cymene complexes both interactions must be comparable. In the case of complexes with the ligand bpzmPh where the phenyl group does not have a functional group, it seems that interaction of type II is not very significant and only isomers of type A are formed.

It is interesting to compare these data with those found in square-planar palladium complexes,[13] in which the phenyl ring is always situated in an axial position, even for methylallyl derivatives.[13a,13b] The reason must be that in these types of derivatives the geometry of the metal centre means that interactions of type II do not exist or are not important.

In the case of complex **8** we obtained a crystallised sample that was enriched in isomer B and we monitored the evolution of this sample at 50 °C in a $[D_6]$acetone solution. Figure 1 reflects the changes that were observed with time. The initial ratio **8B/8A** of 77:23 changed to 55:45 after 90 min, which constitutes a clear indication that interconversion between isomers is possible. There is no signal coalescence or broadening of the resonances. Consequently, the energy of the process is high enough not to be observable by coalescence methods. This process cannot take place through a boat-to-boat interconversion of the metallacycle, because, although the axial or equatorial position of the phenyl rings will change with this process, it would not lead to the other isomer but to a species that we consider unstable for steric reasons (see Scheme 6). A possible way of isomer interconversion is through a partial decoordination of the nitrogenated ligand.

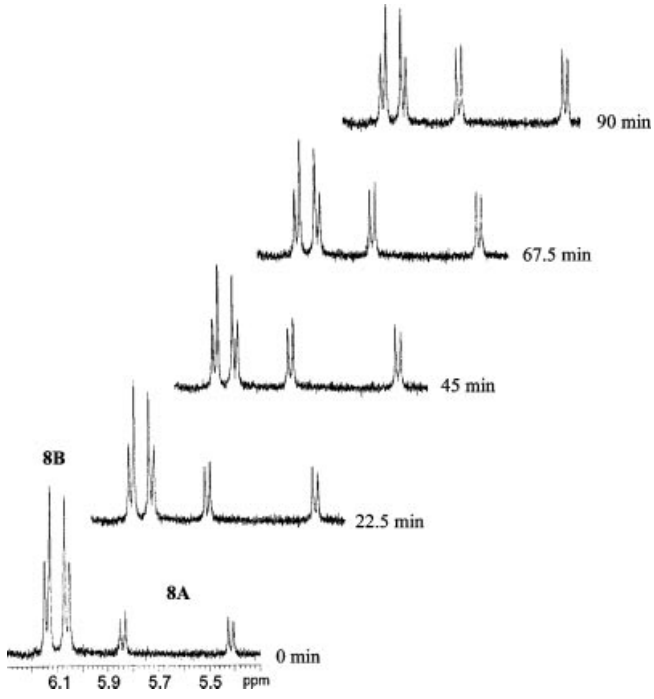


Figure 1. $^1H$ NMR monitoring of the evolution of a **8A/8B** mixture with time.

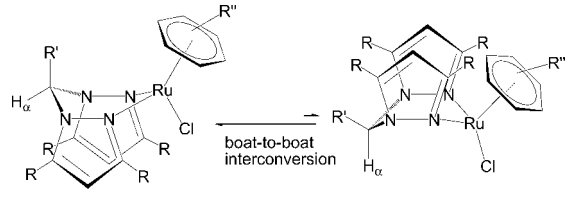


Scheme 6.

## X-ray Structure Determinations

The molecular structures of complexes **7A**·$0.5C_2H_4Cl_2$, **8B**, **9**, **10**·$0.5C_2H_4Cl_2$ and **12A** were determined by X-ray diffraction analysis. The crystallographic data are gathered in Table 1 and the most important bond lengths and angles, including some dihedral angles, are given in Table 2. The corresponding ORTEP drawings are shown in Figures 2, 3, 4, 5 and 6. In the case of **10**, two independent molecules exist in the asymmetric unit. The data for both are very

 © 2007 Wiley-VCH Verlag GmbH & Co. KGaA, Weinheim 

similar and only those of one molecule are given, in Table 2. All complexes have a half-sandwich structure consisting of the coordinated arene, a chloride and the bidentate nitrogenated ligand. In complexes **7**, **9**, **10** and **12** the phenyl group has an axial disposition on the metallacycle having the boat conformation. However, in the case of **8** we were fortunate to crystallise isomer B, in which this group is in an equatorial disposition. The distances between the Ru centre and the coordinated atoms are in the expected range. The average Ru–C distances are slightly longer for the *p*-cymene derivatives than for those containing benzene. The Ru–N distances are shorter for the nonmethylated pyrazolyl rings. The bite angle is in the range 83.4–85.5°. The values of the dihedral angles $NRuN/N_4$, which are listed in Table 2, are in the range 151–169°. In contrast to the palladium derivatives, there is no relationship in these ruthenium complexes between the bite angle or the stated dihedral angle and the nature of the substituent on the pyrazolyl rings. However, it is clear that the dihedral angle formed by the planes of the two pyrazole rings is always bigger for the complexes containing unsubstituted pyrazolyl heterocycles. We propose that this effect is due to steric hindrance be-

Table 1. Crystallographic data for complexes **7A**·0.5$C_2H_4Cl_2$, **8B**, **9**, **10**·0.5$C_2H_4Cl_2$ and **12A**.

| | **7A**·0.5$C_2H_4Cl_2$ | **8B** | **9** | **10**·0.5$C_2H_4Cl_2$ | **12A** |
|---|---|---|---|---|---|
| Empirical formula | $C_{45}H_{42}BCl_2N_4ORu$ | $C_{48}H_{48}BClN_4ORu$ | $C_{47}H_{45}BClN_5O_2Ru$ | $C_{52}H_{55}BCl_2N_5O_2Ru$ | $C_{47}H_{45}BClN_5O_2Ru$ |
| Formula mass | 837.61 | 844.23 | 859.21 | 964.79 | 859.21 |
| Temperature [K] | 130(2) | 130(2) K | 298(2) | 293(2) | 298(2) |
| Wavelength [Å] | 0.71073 | 0.71073 | 0.71073 | 0.71073 | 0.71073 |
| Crystal system | monoclinic | monoclinic | monoclinic | triclinic | monoclinic |
| Space group | $P2_1/n$ | $P2_1/n$ | $P2_1/c$ | $P\bar{1}$ | $P2_1/c$ |
| $a$ [Å] | 9.8348(2) | 9.5852(4) | 16.6942(6) | 10.0732(5) | 18.022(1) |
| $b$ [Å] | 35.361(1) | 34.987(2) | 12.3963(5) | 15.1007(8) | 9.6950(8) |
| $c$ [Å] | 11.8454(3) | 12.3711(6) | 20.9589(8) | 32.086(2) | 23.868(2) |
| $\alpha$ [°] | | | | 79.224(1) | 90 |
| $\beta$ [°] | 106.500(1) | 95.854(4) | 107.375(1) | 82.557(1) | 99.785(2) |
| $\gamma$ [°] | | | | 82.630(1) | 90 |
| $V$ [Å$^3$] | 3949.8(2) | 4127.1(3) | 4139.5(3) | 4727.1(4) | 4109.8(6) |
| $Z$ | 4 | 4 | 4 | 4 | 4 |
| $D_{calcd}$ [Mg·m$^{-3}$] | 1.409 | 1.359 | 1.379 | 1.356 | 1.389 |
| $F(000)$ | 1724 | 1752 | 1776 | 2004 | 1776 |
| Crystal size [mm] | 0.26 × 0.22 × 0.18 | 0.57 × 0.20 × 0.13 | 0.50 × 0.21 × 0.16 | 0.18 × 0.17 × 0.12 | 0.32 × 0.24 × 0.13 |
| Limiting indices | $-9 \le h \le 12$ | $-13 \le h \le 13$ | $-20 \le h \le 16$ | $-13 \le h \le 13$ | $-19 \le h \le 24$ |
| | $-44 \le k \le 44$ | $-49 \le k \le 49$ | $-13 \le k \le 15$ | $-18 \le k \le 20$ | $-12 \le k \le 11$ |
| | $-14 \le l \le 14$ | $-17 \le l \le 14$ | $-25 \le l \le 26$ | $-25 \le l \le 42$ | $-31 \le l \le 30$ |
| Data/restraints/parameters | 8053/0/488 | 12548/0/509 | 8458/0/514 | 21595/0/1115 | 9754/0/514 |
| $\theta$ range for data collection (°) | 2.13–26.39 | 2.83–30.53 | 1.93–26.37 | 1.30–28.31 | 1.73–28.35 |
| Goodness-of-fit on $F^2$ | 1.058 | 1.043 | 1.014 | 0.997 | 1.014 |
| Final $R$ indices [$I > 2\sigma(I)$] | $R_1$ = 0.0444 | $R_1$ = 0.0465 | $R_1$ = 0.0345 | $R_1$ = 0.0750 | $R_1$ = 0.0461 |
| | $wR_2$ = 0.0971 | $wR_2$ = 0.1019 | $wR_2$ = 0.0789 | $wR_2$ = 0.1577 | $wR_2$ = 0.0920 |
| Largest diff. peak/hole [e·Å$^{-3}$] | 1.064, –0.622 | 1.494, –0.909 | 0.363, –0.403 | 1.439, –1.255 | 0.665, –0.636 |

Table 2. Selected bond lengths [Å], bond angles [°] and dihedral angles [°] for complexes **7A**·0.5$C_2H_4Cl_2$, **8B**, **9**, **10**·0.5$C_2H_4Cl_2$ and **12A**.

| **7A**·0.5$C_2H_4Cl_2$ | | **8B** | | **9** | | **10**·0.5$C_2H_4Cl_2$ | | **12A** | |
|---|---|---|---|---|---|---|---|---|---|
| Ru1–N3 | 2.090(3) | Ru1–N1 | 2.089(2) | Ru1–N1 | 2.116(2) | Ru1–N1 | 2.140(5) | Ru1–N3 | 2.101(3) |
| Ru1–N2 | 2.101(3) | Ru1–N3 | 2.069(2) | Ru1–N3 | 2.128(2) | Ru1–N3 | 2.141(5) | Ru1–N1 | 2.105(3) |
| Ru1–Cl2 | 2.3940(8) | Ru1–Cl2 | 2.4019(6) | Ru1–Cl1 | 2.3896(8) | Ru1–Cl1 | 2.381(2) | Ru1–Cl1 | 2.4134(9) |
| Ru1–$C_{average}$ | 2.183 | Ru1–$C_{average}$ | 2.197 | Ru1–$C_{average}$ | 2.185 | Ru1–$C_{average}$ | 2.211 | Ru1–$C_{average}$ | 2.198 |
| N3–Ru1–N2 | 85.54(10) | N3–Ru1–N1 | 83.41(8) | N1–Ru1–N3 | 85.40(8) | N1–Ru1–N3 | 83.6(2) | N3–Ru1–N1 | 83.8(1) |
| | | | | | | | 84.66 | | |
| N3–Ru1–Cl2 | 82.67(7) | N3–Ru1–Cl2 | 84.78(6) | N1–Ru1–Cl1 | 84.49(6) | N1–Ru1–Cl1 | 84.7(1) | N1–Ru1–Cl1 | 84.05(7) |
| N2–Ru1–Cl2 | 84.90(7) | N1–Ru1–Cl2 | 84.49(6) | N3–Ru1–Cl1 | 85.23(6) | N3–Ru1–Cl1 | 84.6(1) | N3–Ru1–Cl1 | 85.56(7) |
| $\varepsilon$[a] | 143.9 | $\varepsilon$[a] | 131.7 | $\varepsilon$[a] | 119.4 | $\varepsilon$[a] | 110.9 | $\varepsilon$[a] | 126.4 |
| | | | | | | | 117.5 | | |
| $NRuN/N_4$[b] | 168.8 | $NRuN/N_4$[b] | 151.2 | $NRuN/N_4$[b] | 160.3 | $NRuN/N_4$[b] | 152.0 | $NRuN/N_4$[b] | 161.8 |
| $NCN/N_4$[c] | 133.5 | $NCN/N_4$[c] | 131.7 | $NCN/N_4$[c] | 129.1 | $NCN/N_4$[c] | 134.0 | $NCN/N_4$[c] | 133.1 |
| $\zeta$[d] | 56.1 | $\zeta$[d] | 10.8 | $\zeta$[d] | 85.9 | $\zeta$[d] | 87.6 | $\zeta$[d] | 78.3 |
| | | | | $\eta$[e] | 65.9 | $\eta$[e] | 68.8 | $\eta$[e] | 54.4 |

[a] Dihedral angle between both pyrazole rings. [b] Dihedral angle between the plane formed by the four nitrogen atoms and the angle formed by Ru and the two coordinated nitrogen atoms. [c] Dihedral angle between the plane formed by the four nitrogen atoms and the angle formed by the benzyl carbon atom and the two noncoordinated nitrogen atoms. [d] Dihedral angle formed by the plane of the phenyl ring and the plane formed by the atoms H–C–C(*ipso*) (phenyl ring). [e] Dihedral angle formed by the phenyl ring and the plane of the $NO_2$ group.

 © 2007 Wiley-VCH Verlag GmbH & Co. KGaA, Weinheim 

tween the methyl groups of the pyrazoles and the arene groups. When the angle between the pyrazoles decreases, this interaction may be reduced. This is clearly reflected in the structure drawing and the space-filling representations in Figure 7.

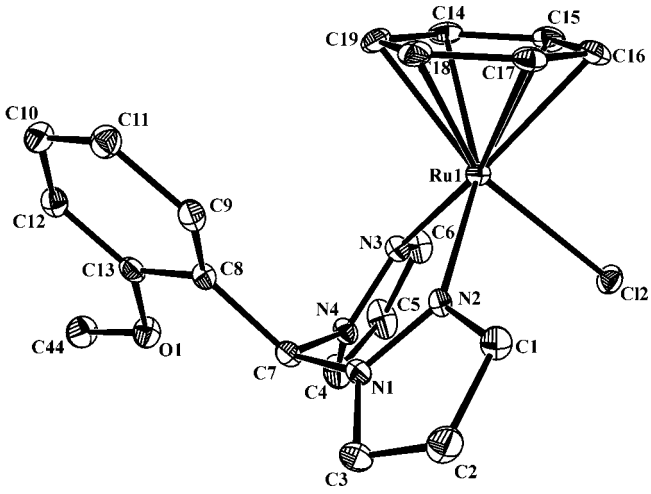


Figure 2. ORTEP view of the cation of complex **7A**·0.5$C_2H_4Cl_2$. Displacement ellipsoids are drawn at the 30% probability level. Hydrogen atoms have been omitted for clarity.

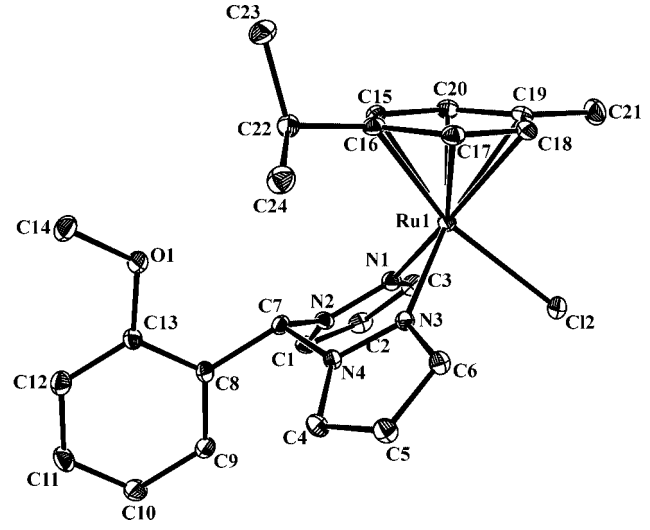


Figure 3. ORTEP view of the cation of complex **8B**. Displacement ellipsoids are drawn at the 30% probability level. Hydrogen atoms have been omitted for clarity.

The orientation of the phenyl ring with respect to the plane formed by the atoms $H_\alpha$–$C_\alpha$–C(*ipso*) is mainly dependent on the axial or equatorial disposition of this ring. When it is axial, the dihedral angle is very close to 90° (in the case of **7A** it is smaller: 56.12°), while for **8B** (where the group is equatorial) the value is only 10.79°.

The methoxy group is approximately in the plane of the phenyl ring. However, it is worth noting the orientation of the $NO_2$ plane with respect to the corresponding phenyl ring. Unexpectedly, these planes are not parallel, and the values for the dihedral angle are in the range 65–68° for the methylated complexes and 54.4° for the nonmethylated

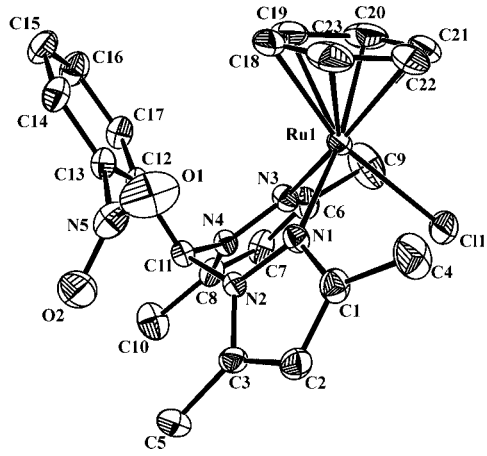


Figure 4. ORTEP view of the cation of complex **9**. Displacement ellipsoids are drawn at the 30% probability level. Hydrogen atoms have been omitted for clarity.

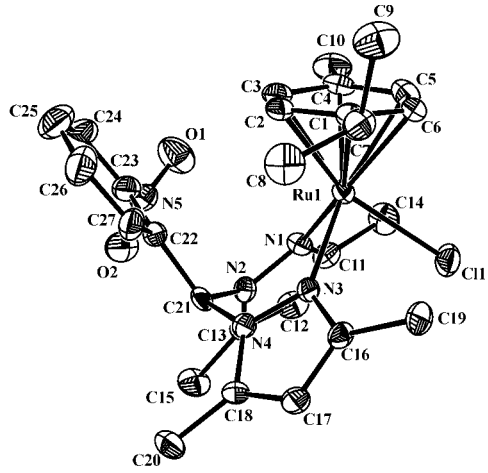


Figure 5. ORTEP view of the cation of complex **10**·0.5$C_2H_4Cl_2$. Displacement ellipsoids are drawn at the 30% probability level. Hydrogen atoms have been omitted for clarity.

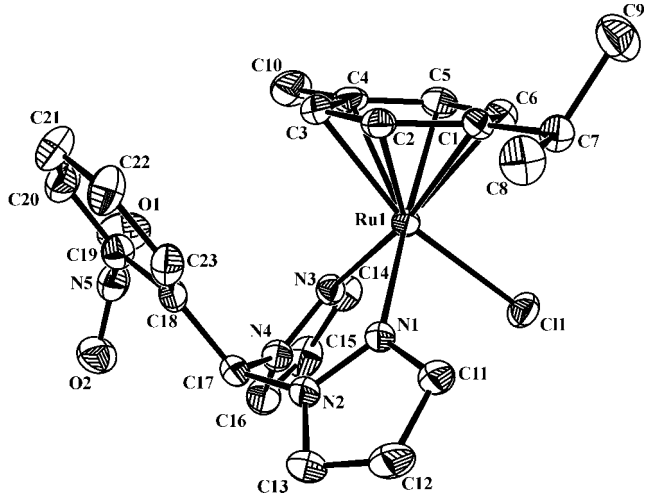


Figure 6. ORTEP view of the cation of complex **12A**. Displacement ellipsoids are drawn at the 30% probability level. Hydrogen atoms have been omitted for clarity.

 © 2007 Wiley-VCH Verlag GmbH & Co. KGaA, Weinheim 

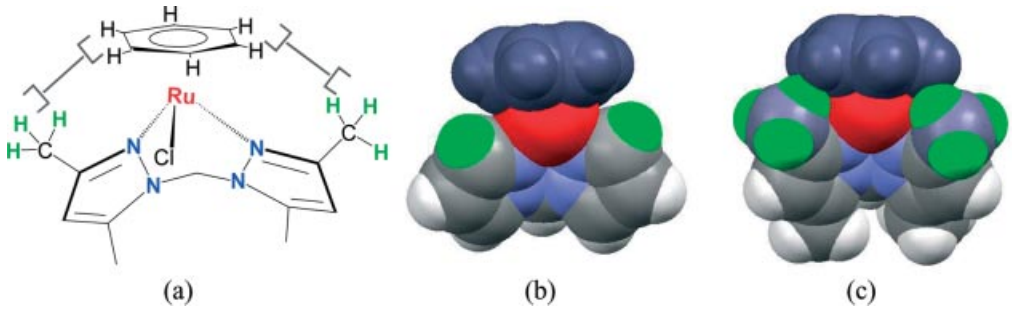


Figure 7. (a) Drawing scheme showing the steric interaction between the pyrazole $Me^3$ groups and the CH bonds of the coordinated benzene that influences the pz–pz interplanar angle (the same is applicable to the *p*-cymene derivatives). (b and c) Comparison of such interactions in a space-fill drawing of the X-ray structures of complexes **7** and **9** respectively (Cl ligands and benzyl groups on the $C_\alpha$ atom have been omitted for clarity).

system. A closer inspection of the structure provides a plausible explanation for this observation. If the $NO_2$ plane was parallel to the phenyl ring, one of the oxygen atoms (with a negative charge density) would be situated very close to the π electron density of one pyrazole ring, and the aim of the torsion is probably to prevent this repulsive interaction. On the other hand, another orientation of the phenyl ring to minimise this problem would involve greater steric hindrance, because the phenyl ring would be too close to the arene that is bonded to the ruthenium centre (see Scheme 7).

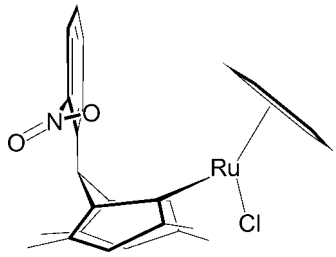


Scheme 7.

As far as the orientation of the *p*-cymene ring in complexes **8B**, **10** and **12A** is concerned, there are two situations that are clearly different. In the case of complexes **10** and **12A**, where the phenyl ring has an axial orientation, the disposition of the *p*-cymene is such that the steric hindrance with this ring is reduced. The orientation in the case of **8B**, where the anisole ring is in an equatorial position, is clearly different and the isopropyl group is oriented towards the methoxy group. Closer inspection of the structure of **8B** reveals the existence of a hydrogen bond between the C–H fragment of the isopropyl group and the oxygen atom of the methoxy group. The C···O distance is 3.427 Å and the angle C–H–O is 142°. These data allow us to conclude that this hydrogen bond is weak.[20]

## Hydrogen Transfer Catalytic Tests

Preliminary tests were done concerning the behaviour of some of the new derivatives in catalytic transfer hydrogenation reactions of benzophenone using 2-propanol as the reducing agent and solvent in the presence of KOH as the base [Equation (3)]:

$$PhCOPh + iPrOH \rightarrow PhCHOHPh + Me_2CO \quad (3)$$

Conversion was not observed at room temperature. For example, on using complex **7** there was no conversion after 36 h (see Exp. Sect. for conditions). Consequently, the boiling point of the solvent (85 °C) was used as the temperature in all the experiments. Initially we performed catalytic tests with complexes **1** and **3** with a substrate/KOH/complex ratio of 1000:100:1. Only moderate yields of the alcohol were obtained after 24 h of reaction (28% for **1** and 15% for **3**). We decided to evaluate the influence of the base concentration and we increased the number of equivalents of KOH without changing other factors. We performed tests with 250, 500 and 1000 of KOH per mole of complex and a steady increase in the TOF number and yield was observed. At this point it is necessary to consider the possibility of a high effect of the base that could obscure the catalytic effect of the complex. Processes of hydrogenation have been described with molecular hydrogen of benzophenone with a base (mainly *tert*-butoxide) in the absence of a catalyst, but using very drastic conditions (about 200 °C, >100 bar $H_2$).[21] Regarding transfer hydrogenation, a conversion of 60% of acetophenone to the corresponding alcohol in boiling 2-propanol with NaOH 0.5 M[22] in 4 h and very low activity in 0.02 M KOH solutions has been reported.[23] Our highest concentration was 0.2 M. In any case, we decided to perform an analysis of the base-only reaction at different KOH concentrations. We found that KOH is able to catalyse the benzophenone hydrogenation with 2-propanol at 85 °C. When the alcohol yield is represented against different KOH concentrations, a straight line with positive slope (% yield = 0.91894 + 306.60015[KOH]; $R$ = 0.99421) is obtained. The results are reflected in Table 3. In Figure 8 a representation of conversion against time is reflected for two experiments without a catalyst (KOH 0.008 M and 0.2 M) and another two experiments with KOH 0.2 M in the presence of complexes **3** or **13** (substrate/KOH/complex ratio of 1000:1000:1). It is clear that when working with KOH concentrations of 0.2 M the effect of our complexes is very

 © 2007 Wiley-VCH Verlag GmbH & Co. KGaA, Weinheim 

small and other conditions must be chosen. We think that these studies must be taken into account before performing reactions of transfer hydrogenation in the presence of KOH.

Table 3. Transfer hydrogenation of benzophenone with KOH without Ru complexes.[a]

| [KOH] [mol·L$^{-1}$] | Mol KOH [500 mol substrate] | Yield [b] [%] |
|---|---|---|
| 0.004 | 10 | 0 |
| 0.006 | 15 | 2 |
| 0.008 | 20 | 3 |
| 0.016 | 40 | 7 |
| 0.04 | 100 | 10 |
| 0.1 | 250 | 36 |
| 0.2 | 500 | 68 |
| 0.3 | 750 | 88 |

[a] Conditions: 2 mmol of benzophenone, 10 mL of *i*PrOH, reflux (82 °C). [b] Yield of diphenylmethanol after 13 h.

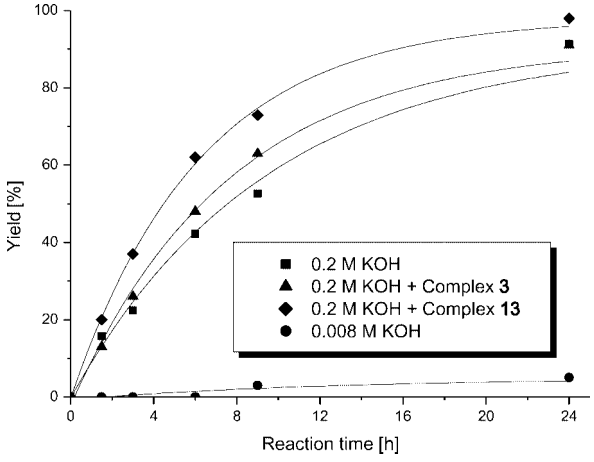


Figure 8. Yield of diphenylmethanol against time for the hydrogenation of benzophenone. Conditions: 2 mmol of benzophenone, 10 mL of *i*-PrOH, reflux (82 °C), 0.004 mmol precatalyst (when applicable).

Considering these results we decided to study the behaviour of our different derivatives with a base concentration of 0.008 M and a substrate/KOH/complex ratio of 500:20:1. The yields and the turnover frequencies evaluated at 20% conversion ($TOF_{20}$) are reflected in Table 4. The conversion for the TOF number was chosen in order to minimise the influence on the rate of decreases in substrate concentration and increases in product concentration. Several clear conclusions can be drawn from the analysis of the results. (i) Better behaviour of the benzene derivatives (those with an odd number) against *p*-cymene complexes (even number) is observed (in some cases the differences are not large). (ii) The introduction of methyl substituents on the pyrazole rings has a dramatic and positive effect (compare runs 4/6, 5/7, 11/13 and 12/14). For example, in the case of complexes **4** and **6**, the improvement is from 10 to 82% in the product yield (see Figure 9 to observe both effects). (iii) The introduction of a phenyl group at the benzyl carbon atom (compare runs 2/4 and 3/5) also increases the activity of the system. (iv) When the existence of functional groups on this ring is considered, a negative effect of the $NH_2$ (runs 4/15 and 5/16) or $NO_2$ groups (runs 4/11 and 5/12 for methylated pyrazoles and runs 6/13 and 7/14 for nonmethylated pyrazoles) is observed. However, a large increase in the activity is observed when the $OCH_3$ group is introduced on the phenyl ring (runs 6/8 and 7/10). In all the experiments samples were taken at 1.5, 3, 6, 9 and 24 h (see Supporting Information for the corresponding data).

Table 4. Transfer hydrogenation of benzophenone with Ru precatalysts.[a]

| Run | Complex | NN ligand | $TOF_{20}$[b] [h$^{-1}$] | Yield[c] [%] |
|---|---|---|---|---|
| 1[d] | – | – | – | 5 |
| 2 | **1** | bpz*m | 35 | 62 |
| 3 | **2** | bpz*m | 25 | 61 |
| 4 | **3** | bpz*mPh | 62 | 97 |
| 5 | **4** | bpz*mPh | 31 | 82 |
| 6 | **5** | bpzmPh | 8 | 37 |
| 7 | **6** | bpzmPh | – | 10 |
| 8 | **7** | bpzmAr$OCH_3$ | 125 | 90 |
| 9[e] | **7** | bpzmAr$OCH_3$ | 125 | 82 |
| 10 | **8** | bpzmAr$OCH_3$ | 50 | 90 |
| 11 | **9** | bpz*mAr$NO_2$ | 18 | 60 |
| 12 | **10** | bpz*mAr$NO_2$ | 15 | 60 |
| 13 | **11** | bpzmAr$NO_2$ | – | 18 |
| 14 | **12** | bpzmAr$NO_2$ | – | 8 |
| 15 | **13** | bpz*mAr$NH_2$ | 45 | 74 |
| 16 | **14** | bpz*mAr$NH_2$ | 29 | 66 |

[a] Conditions: 2 mmol of benzophenone, 0.004 mmol precatalyst, 10 mL of *i*PrOH, reflux (82 °C), 0.008 M in KOH, substrate/KOH/complex ratio of 500:20:1. [b] Catalyst turnover frequency at 20% conversion. [c] Yield of diphenylmethanol at 24 h of reaction. [d] No precatalyst was added. [e] 300 equiv. of Hg was added.

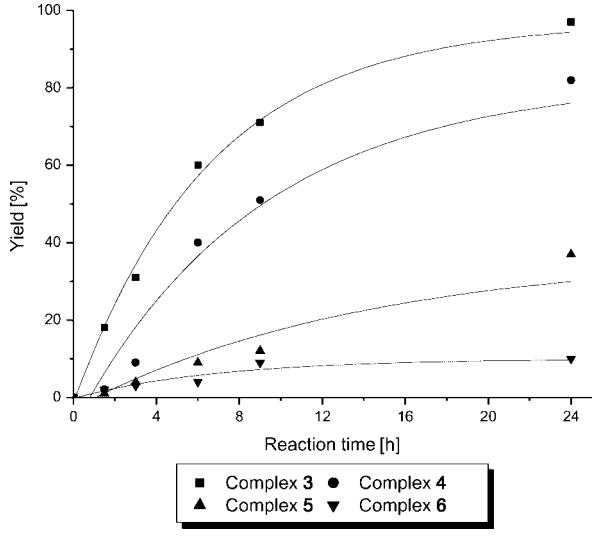


Figure 9. Yield of diphenylmethanol against time for the hydrogenation of benzophenone. Conditions: 2 mmol of benzophenone, 0.004 mmol precatalyst, 10 mL of *i*PrOH, reflux (82 °C), 0.008 M in KOH, substrate/KOH/complex ratio of 500:20:1.

We subjected complex **7** to the mercury drop test during the hydrogenation of benzophenone. Several authors[24] found that the addition of excess metallic mercury (with respect to the metal complex) to the reaction mixture led to the amalgamation of the surface of a heterogeneous metal particle, thus poisoning it, but did not affect a homogeneous catalyst. When we added 300 equiv. of Hg(0) to the

 © 2007 Wiley-VCH Verlag GmbH & Co. KGaA, Weinheim 

reaction mixture at $t = 0$ min, the catalytic system only suffered a slight decrease in activity (compare runs 8/9), indicating the existence of a homogeneous system.

We also carried out a catalytic test with complex **7** (0.004 mmol), analysing samples at short times of 5, 10, 15, 30, 45 and 60 min. No induction period was observed. We also subjected complex **7** to a pretreatment of one hour, during which the precatalyst was heated at reflux in the presence of the base (base:**7** = 20:1) prior to the addition of the substrate (2 mmol), and the outcome of the reaction was the same as that without this treatment.

The precatalysts are not active in the hydrogenation of styrene. Thus, they exhibit selectivity towards the ketone unsaturation.

According to previous mechanistic proposals,[11a–11e] and considering the formulae and type of ligand present in our derivatives, the most plausible mechanism is that involving a monohydride intermediate generated after β elimination from an isopropoxide complex. In principle, the vacant coordination site necessary for the ketone coordination could be generated by partial decoordination of the nitrogenated ligand or by slippage of the arene moiety. Our study of the isomer interconversion and the fact that the methylated ligands that exhibit longer Ru–N distances have much higher activity point to the former possibility. Transfer of the hydride and reaction with 2-propanol will yield the dibenzyl alcohol.

More studies concerning the catalytic behaviour of these complexes are in progress. We will study complexes with the bpz*PhOCH$_3$ ligand that predictably will give better results than those reported in Table 4 and we will also consider the possibility of obtaining ligands that have pyrazoles containing more bulky substituents. Other parameters such as the introduction of other functional groups on the phenyl ring and the use of asymmetric ligands will also be analysed.

## Conclusions

New bis(pyrazol-1-yl)methane ligands containing different substituents on the central carbon atom have been synthesised using a new and safer methodology. Ru derivatives of the type [Ru(arene)Cl(NN)]BPh$_4$ (arene = benzene, *p*-cymene) have been synthesised from these ligands. The formation of two isomers is possible depending on the axial or equatorial disposition of the substituent on this carbon. The formation of only one isomer (axial) or a mixture of two (including their ratio) can be rationalised in terms of steric repulsions (effect of the methyl groups on the pyrazolyl rings or of the arene). A full NMR analysis was performed and a clear effect of the type of isomer on the chemical shifts of certain resonances was found. The structures of five derivatives were determined by X-ray diffraction. In four complexes the benzyl substituent is in the axial disposition and in one case in the equatorial disposition. A relationship between the dihedral angle formed by the planes of the two pyrazole rings and the substituent on these rings was found. The behaviour of the new derivatives in the transfer hydrogenation of benzophenone in the presence of KOH was studied. The influence of the arene, the functional group on the phenyl ring and the substitution on the pyrazole ring has been evaluated. A marked positive effect of the methyl groups on the pyrazole rings and of the methoxy group on the phenyl ring has been found. The hydrogenation of benzophenone without the addition of a complex in the presence of KOH is possible and the effect of the base concentration has been analysed.

## Experimental Section

**General:** All manipulations were carried out under dry oxygen-free nitrogen using standard Schlenk techniques. Solvents were distilled from the appropriate drying agents and degassed before use. Elemental analyses were performed with a Thermo Quest FlashEA 1112 microanalyser. IR spectra were recorded as KBr pellets or Nujol solutions with a Perkin–Elmer PE 883 IR spectrometer and on a Shimadzu IRPrestige-21 IR spectrometer equipped with a Pike Technologies ATR. $^1$H and $^{13}$C{$^1$H} NMR spectra were recorded with a Varian Unity 500 spectrometer. Chemical shifts (ppm) are relative to TMS ($^1$H, $^{13}$C NMR). $^1$H-$^1$H COSY spectra: standard pulse sequence with an acquisition time of 0.214 s, pulse width 10 ms, relaxation delay 1 s, number of scans 16, number of increments 512. For $^1$H-$^{13}$C *g*-HMBC and *g*-HMQC spectra the standard VARIAN pulse sequences were used (VNMR 6.1 C software). The spectra were acquired using 7996-Hz ($^1$H) and 25133.5-Hz ($^{13}$C) widths; 16 transients of 2048 data points were collected for each of the 256 increments. NOESY spectra were acquired using 8000-Hz width; 16 transients of 2048 data points were collected for each of the 256 increments; pulse time of 1 s and mixing time of 1 s. *o*-, *m*- and *p*- stand for *ortho*, *meta* and *para*. s, d, t and p stand for singlet, doublet, triplet and apparent for the NMR resonances. Unless otherwise stated, the $^{13}$C{$^1$H} NMR signals are singlets. The ligands bpz*m[18] and bpzmArOCH$_3$[13c] were prepared according to the methods described in the literature. For the preparation of the ligands bpzmPh and bpz*mPh[17] the ketone bpz*CO was synthesised as described below.

**bpz*CO:** 3,5-Dimethylpyrazole (1.5 g, 15.6 mmol) was dissolved in thf (20 mL) and NEt$_3$ (2.13 mL) was added afterwards. Triphosgene, Cl$_3$COCOOCCl$_3$ (772 mg, 2.60 mmol), was dissolved in thf (20 mL) and the resulting solution was added as quickly as possible to the initial one. After 16 h of stirring at room temperature, the white solid formed was filtered off and washed twice with thf. The thf fractions were combined and the solvent evaporated. The yellowish oil obtained was washed with pentane and a white solid was formed. The solid was recrystallised from toluene/hexane obtaining white crystals. Yield 1.4 g (80%).

**bpzCO:** The method was similar to that used for bpz*CO. Amounts were as follows: pyrazole (1 g, 15.6 mmol), NEt$_3$ (2.13 mL) and triphosgene (772 mg, 2.60 mmol). bpzCO was obtained as a white solid. Yield 948.6 mg (75%).

**bpz*mArNO$_2$:** bpz*CO (500 mg, 2.29 mmol) and 2-nitrobenzaldehyde (346 mg, 2.29 mmol) were mixed in toluene (25 mL). After refluxing for 24 h, the yellowish solution was evaporated and the residue was washed with pentane (3 × 10 mL), obtaining a white solid of bpz*mArNO$_2$. Yield 506.7 mg (68%). $^1$H NMR (500 MHz, CDCl$_3$, 298 K): $\delta$ = 2.08 (s, 6 H, Me$^5$-Pz), 2.15 (s, 6 H, Me$^3$-Pz), 5.89 (s, 2 H, H$^4$-Pz), 6.60 (d, $J$ = 7.7 Hz, 1 H, H$^3$-ArNO$_2$), 7.53 (td, $J$ = 7.7, 1.5 Hz, 1 H, H$^5$-ArNO$_2$), 7.57 (td, $J$ = 7.7, 1.5 Hz, 1 H, H$^4$-ArNO$_2$), 8.04 (dd, $J$ = 7.7, 1.5 Hz, 1 H, H$^6$-ArNO$_2$), 8.22

 © 2007 Wiley-VCH Verlag GmbH & Co. KGaA, Weinheim 

(s, 1 H, $H_\alpha$) ppm. $^{13}C\{^1H\}$ NMR (125 MHz, $CDCl_3$, 298 K): $\delta$ = 11.16 (2 C, $Me^5$-Pz), 13.97 (2 C, $Me^3$-Pz), 71.57 (1 C, $C_\alpha$), 107.22 (2 C, $C^4$-Pz), 122.25 (1 C, $C^6$-$ArNO_2$), 128.80 (1 C, $C^3$-$ArNO_2$), 129.78 (1 C, $C^5$-$ArNO_2$), 131.90 (1 C, $C^2$-$ArNO_2$), 133.86 (1 C, $C^4$-$ArNO_2$), 141.17 (2 C, $C^5$-Pz), 148.27 (1 C, $C^1$-$ArNO_2$), 148.76 (2 C, $C^3$-Pz) ppm. IR (KBr): $\tilde{\nu}$ = 1563 (CN); 1528, 1360, 1317 (NO) $cm^{-1}$.

**bpzmArNO$_2$:** The method was similar to that used for bpz*mArNO$_2$. Amounts were as follows: bpzCO (300 mg, 1.85 mmol) and 2-nitrobenzaldehyde (280 mg, 1.85 mmol). Yield 382.3 mg (62%). $^1H$ NMR (500 MHz, $CDCl_3$, 298 K): $\delta$ = 6.38 (pt, $J$ = 2.1 Hz, 2 H, $H^4$-Pz), 6.71 (dd, $J$ = 7.3, 1.7 Hz, 1 H, $H^3$-$ArNO_2$), 7.52 (d, $J$ = 2.2 Hz, 2 H, $H^5$-Pz), 7.57 (td, $J$ = 7.6, 1.7 Hz, 1 H, $H^5$-$ArNO_2$), 7.62 (td, $J$ = 7.6, 1.7 Hz, 1 H, $H^4$-$ArNO_2$), 7.63 (d, $J$ = 1.7 Hz, 2 H, $H^3$-Pz), 8.11 (dd, $J$ = 7.6, 1.9 Hz, 1 H, $H^6$-Ar $NO_2$), 8.52 (s, 1 H, $H_\alpha$) ppm. $^{13}C\{^1H\}$ NMR (125 MHz, $CDCl_3$, 298 K): $\delta$ = 74.42 (1 C, $C_\alpha$), 107.42 (2 C, $C^4$-Pz), 125.64 (1 C, $C^6$-$ArNO_2$), 129.40 (1 C, $C^3$-$ArNO_2$), 130.58 (1 C, $C^5$-$ArNO_2$), 130.92 (2 C, $C^5$-Pz), 131.79 (1 C, $C_2$-$ArNO_2$), 134.10 (1 C, $C^4$-$ArNO_2$), 141.44 (2 C, $C^3$-Pz), 147.52 (1 C, $C^1$-$ArNO_2$) ppm. IR (KBr): $\tilde{\nu}$ = 1580 (CN); 1526, 1350, 1312 (NO) $cm^{-1}$.

**bpz*mArNH$_2$:** bpz*mArNO$_2$ (745.1 mg, 2.29 mmol) was solved in toluene (30 mL) in a Fischer-Porter tube. A suspension of Pd/C (10%) catalyst (200 mg) in toluene (10 mL) was added to the initial solution. When the system was under dry oxygen-free nitrogen, hydrogen was introduced under pressure (about 3 kg·$cm^{-2}$). After 5.5 h of reaction at room temperature, the suspension was filtered off in a column filled with Kieselguhr. The solution was evaporated, obtaining a bright yellow oil, which was left under vacuum overnight, and a pale yellow solid was obtained. After recrystallisation in toluene/pentane, colourless crystals were obtained. Yield: 491.8 mg (90%). $^1H$ NMR (500 MHz, $CDCl_3$, 298 K): $\delta$ = 2.14 (s, 6 H, $Me^5$-Pz), 2.22 (s, 6 H, $Me^3$-Pz), 3.51 (br. s, 2 H, $NH_2$), 5.87 (s, 2 H, $H^4$-Pz), 6.42 (d, $J$ = 7.8 Hz, 1 H, $H^3$-$ArNH_2$), 6.65 (d, $J$ = 7.3 Hz, 1 H, $H^6$-$ArNH_2$), 6.68 (t, $J$ = 7.6 Hz, 1 H, $H^4$-$ArNH_2$), 7.13 (t, $J$ = 7.1 Hz, 1 H, $H^5$-$ArNH_2$), 7.40 (s, 1 H, $H_\alpha$) ppm. $^{13}C\{^1H\}$ NMR (125 MHz, $CDCl_3$, 298 K): $\delta$ = 11.93 (2 C, $Me^5$-Pz), 14.08 (2 C, $Me^3$-Pz), 72.58 (1 C, $C_\alpha$), 107.19 (2 C, $C^4$-Pz), 116.48 (1 C, $C^6$-$ArNH_2$), 118.63 (1 C, $C^4$-$ArNH_2$), 121.53 (1 C, $C^2$-$ArNH_2$), 127.64 (1 C, $C^3$-$ArNH_2$), 129.88 (1 C, $C^5$-$ArNH_2$), 141.43 (2 C, $C^5$-Pz), 144.49 (1 C, $C^1$-$ArNH_2$), 148.96 (2 C, $C^3$-Pz) ppm. IR (KBr): $\tilde{\nu}$ = 3395, 3312 ($NH_2$); 1554 (CN) $cm^{-1}$.

**[RuCl(benzene)(bpz*m)][BPh$_4$] (1):** [$RuCl_2(C_6H_6)(CH_3CN)$] (93 mg, 0.32 mmol) and bpz*m (65.4 mg, 0.32 mmol) were mixed in MeOH (10 mL). After stirring for 12 h, a solution of $NaBPh_4$ (200 mg, 0.6 mmol) in MeOH (10 mL) was added to the initial orange solution, changing the colour to yellow. After 30 min, the solution was partially evaporated up to 5 mL and the solid obtained was filtered off. The light yellow solid was washed once with MeOH. The product was recrystallised from 1,2-dichloroethane/hexane. Yield 210.2 mg (89%). $C_{41}H_{42}BClN_4Ru{\cdot}C_2H_4Cl_2$ (837.11): calcd. C 61.70, H 5.54, N 6.69; found C 61.41, H 5.41, N 6.94. $^{13}C\{^1H\}$ NMR (125 MHz, $CDCl_3$, 298 K): $\delta$ = 11.38 (2 C, $Me^5$-Pz), 15.76 (2 C, $Me^3$-Pz), 55.67 (1 C, $C_\alpha$), 85.46 (6 C, *C*-benzene), 109.35 (2 C, $C^4$-Pz), 122.11 [4 C, $C_p$-Ph($BPh_4$)], 125.81 [8 C, $C_m$-Ph($BPh_4$)], 136.19 [8 C, $C_o$-Ph($BPh_4$)], 142.99 (2 C, $C^5$-Pz), 156.28 (2 C, $C^3$-Pz), 164.31 [q, $J_{C-^{11}B}$ = 49.4 Hz, 4 C, $C_{ipso}$-Ph($BPh_4$)] ppm. IR: $\tilde{\nu}$ = 1558 (CN) $cm^{-1}$.

**[RuCl(*p*-cymene)(bpz*m)][BPh$_4$] (2):** [$RuCl_2$(*p*-cymene)]$_2$ (128 mg, 0.21 mmol) and bpz*m (85.8 mg, 0.42 mmol) were stirred in MeOH (10 mL) for 12 h. Afterwards, a solution of MeOH (10 mL) with $NaBPh_4$ (200 mg, 0.6 mmol) was added to the initial reddish solution, obtaining a yellow suspension. The solution was partially evaporated up to 5 mL and the solid obtained was filtered off. The yellow solid was washed once with MeOH. The product was recrystallised from 1,2-dichloroethane/hexane. Yield 293.5 mg (88%). $C_{45}H_{50}BClN_4Ru{\cdot}C_2H_4Cl_2$ (893.22): calcd. C 63.20, H 6.09, N 6.27; found C 63.51, H 6.06, N 6.37. $^{13}C\{^1H\}$ NMR (125 MHz, $CDCl_3$, 298 K): $\delta$ = 11.64 (2 C, $Me^3$-Pz), 16.02 (2 C, $Me^5$-Pz), 18.72 (1 C, Me-Tol), 22.77 (2 C, Me-*i*Pr), 31.87 (1 C, *C*H-*i*Pr), 56.01 (1 C, $C_\alpha$), 81.71 (2 C, $CH^{2/2'}$-*p*-cym), 84.86 (2 C, $CH^{3/3'}$-*p*-cym), 99.74 (1 C, $C^4$-*p*-cym), 107.38 (1 C, $C^1$-*p*-cym), 109.75 (2 C, $C^4$-Pz), 122.29 [4 C, $C_p$-Ph($BPh_4$)], 125.96 [8 C, $C_m$-Ph($BPh_4$)], 136.52 [8 C, $C_o$-Ph($BPh_4$)], 143.32 (2 C, $C^5$-Pz), 156.86 (2 C, $C^3$-Pz), 164.32 [q, $J_{C-^{11}B}$ = 49.4 Hz, 4 C, $C_{ipso}$-Ph($BPh_4$)] ppm. IR: $\tilde{\nu}$ = 1560 (CN) $cm^{-1}$.

**[RuCl(benzene)(bpz*mPh)][BPh$_4$] (3):** The method was similar to that used for complex **1**. Amounts were as follows: [$RuCl_2(C_6H_6)(CH_3CN)$] (93 mg, 0.32 mmol) and bpz*m (89.7 mg, 0.32 mmol). Complex **3** was obtained as a yellowish solid. The product was recrystallised from 1,2-dichloroethane/hexane. Yield 221.5 mg (85%). $C_{47}H_{46}BClN_4ORu{\cdot}0.5C_2H_4Cl_2$ (863.73): calcd. C 66.75, H 5.60, N 6.49; found C 66.45, H 5.66, N 7.20. $^{13}C\{^1H\}$ NMR (125 MHz, $CD_3COCD_3$, 298 K): $\delta$ = 10.98 (2 C, $Me^5$-Pz), 16.10 (2 C, $Me^3$-Pz), 68.78 (1 C, $C_\alpha$), 86.31 (6 C, *C*-benzene), 109.61 (2 C, $C^4$-Pz), 121.63 [4 C, $C_p$-Ph($BPh_4$)], 125.41 [8 C, $C_m$-Ph($BPh_4$)], 125.56 (2 C, $C_o$-Ph), 130.25 (1 C, $C_p$-Ph), 130.282 (2 C, $C_m$-Ph), 136.38 [8 C, $C_o$-Ph($BPh_4$)], 136.757 (1 C, $C^1$-Ph), 146.48 (2 C, $C^5$-Pz), 157.86 (2 C, $C^3$-Pz), 164.31 [q, $J_{C-^{11}B}$ = 49.4 Hz, 4 C, $C_{ipso}$-Ph($BPh_4$)] ppm. IR: $\tilde{\nu}$ = 1558 (CN) $cm^{-1}$.

**[RuCl(*p*-cymene)(bpz*mPh)][BPh$_4$] (4):** The method was similar to that used for complex **2**. Amounts were as follows: [$RuCl_2$(*p*-cymene)]$_2$ (128 mg, 0.21 mmol) and bpz*mPh (117.8 mg, 0.42 mmol). Complex **4** was obtained as an orange solid, which was washed once with MeOH. Yield 325.3 mg (89%). $C_{51}H_{54}BClN_4Ru{\cdot}CH_3OH$ (902.40): C 69.21, H 6.48, N 6.21; found C 69.13, H 6.45, N 6.23. $^{13}C\{^1H\}$ NMR (125 MHz, $CD_3COCD_3$, 298 K): $\delta$ = 11.23 (2 C, $Me^5$-Pz), 16.44 (2 C, $Me^3$-Pz), 17.63 (1 C, Me-Tol), 21.76 (1 C, *C*H-*i*Pr), 22.38 (2 C, Me-*i*Pr), 66.62 (1 C, $C_\alpha$), 82.20 (2 C, $CH^{2/2'}$-*p*-cym), 84.42 (2 C, $CH^{3/3'}$-*p*-cym), 101.97 (1 C, $C^4$-*p*-cym), 107.23 (1 C, $C^1$-*p*-cym), 109.93 (2 C, $C^4$-Pz), 121.58 [4 C, $C_p$-Ph($BPh_4$)], 125.34 [8 C, $C_m$-Ph($BPh_4$)], 126.23 (2 C, $C_o$-Ph), 130.13 (2 C, $C_m$-Ph), 130.35 (1 C, $C_p$-Ph), 135.99 (1 C, $C^1$-Ph), 136.41 [8 C, $C_o$-Ph($BPh_4$)], 146.55 (2 C, $C^5$-Pz), 157.87 (2 C, $C^3$-Pz), 164.32 [q, $J_{C-^{11}B}$ = 49.4 Hz, 4 C, $C_{ipso}$-Ph($BPh_4$)] ppm. IR: $\tilde{\nu}$ = 1566 (CN) $cm^{-1}$.

**[RuCl(benzene)(bpzmPh)][BPh$_4$] (5):** The method was similar to that used for complex **2**. Amounts were as follows: [$RuCl_2(C_6H_6)(CH_3CN)$] (37.8 mg, 0.13 mmol) and bpzmPh (29.1 mg, 0.25 mmol). The yellow solid obtained was washed once with MeOH. The product was recrystallised from 1,2-dichloroethane/hexane. Yield: 161.1 mg (85%). $C_{43}H_{38}BClN_4Ru{\cdot}0.5C_2H_4Cl_2$ (807.62): calcd. C 65.44, H 4.99, N 6.94; found C 65.88, H 4.88, N 7.08. $^{13}C\{^1H\}$ NMR (125 MHz, $CD_3COCD_3$, 298 K): $\delta$ = 75.26 (1 C, $C_\alpha$), 86.48 (6 C, *C*-benzene), 108.80 (2 C, $C^4$-Pz), 121.62 [4 C, $C_p$-Ph($BPh_4$)], 125.36 (2 C, $C_o$-Ph), 125.42 [8 C, $C_m$-Ph($BPh_4$)], 129.97 (2 C, $C_m$-Ph), 130.38 (1 C, $C_p$-Ph), 136.39 [8 C, $C_o$-Ph($BPh_4$)], 130.67 (2 C, $C^5$-Pz), 150.98 (2 C, $C^3$-Pz), 164.29 [q, $J_{C-^{11}B}$ = 49.4 Hz, 4C, $C_{ipso}$-Ph($BPh_4$)] ppm. IR: $\tilde{\nu}$ = 1577 (CN) $cm^{-1}$.

**[RuCl(*p*-cymene)(bpzmPh)][BPh$_4$] (6):** The method was similar to that used for complex **2**. Amounts were as follows: [$RuCl_2$(*p*-cymene)]$_2$ (36.7 mg, 0.06 mmol) and bpzmPh (29.1 mg, 0.13 mmol) in MeOH (5 mL). Complex **6** was obtained as a light yellow solid,

 © 2007 Wiley-VCH Verlag GmbH & Co. KGaA, Weinheim 

which was washed once with MeOH. Yield: 95.3 mg (90%). $C_{47}H_{46}BClN_4Ru$ (814.25): calcd. C 69.33, H 5.69, N 6.88; found C 69.42, H 5.61, N 6.92. $^{13}C\{^1H\}$ NMR (125 MHz, $CD_3COCD_3$, 298 K): $\delta$ = 17.80 (1 C, Me-Tol), 21.79 (1 C, *C*H-*i*Pr), 22.07 (2 C, Me-*i*Pr), 75.29 (1 C, $C_\alpha$), 80.77 (2 C, *C*H$^{3/3'}$-*p*-cym), 88.75 (2 C, *C*H$^{2/2'}$-*p*-cym), 101.92 (1 C, *C*$^4$-*p*-cym), 104.32 (1 C, *C*$^1$-*p*-cym), 108.99 (2 C, *C*$^4$-Pz), 121.58 [4 C, $C_p$-Ph(BPH$_4$)], 125.34 [8 C, $C_m$-Ph(BPh$_4$)], 125.70 (2 C, $C_o$-Ph), 130.05 (2 C, $C_m$-Ph), 130.49 (1 C, $C_p$-Ph), 136.41 [8 C, $C_o$-Ph(BPh$_4$)], 137.65 (2 C, *C*$^5$-Pz), 149.96 (2 C, *C*$^3$-Pz), 164.32 [q, $J_{C-^{11}B}$ = 49.4 Hz, 4 C, $C_{ipso}$-Ph(BPh$_4$)] ppm. IR: $\tilde{\nu}$ = 1577 (CN) cm$^{-1}$.

**[RuCl(benzene)(bpzmArOCH$_3$)][BPh$_4$] (7):** The method was similar to that used for complex **1**. Amounts were as follows: [RuCl$_2$(C$_6$H$_6$)(CH$_3$CN)] (37.8 mg, 0.13 mmol) and bpzmArOCH$_3$ (33.1 mg, 0.13 mmol) in MeOH (5 mL). Complex **7** was obtained as a yellow solid. Yield: 86.6 mg (83%). Ratio of isomers A/B = 4.8:1. $C_{44}H_{40}BClN_4ORu{\cdot}0.5C_2H_4Cl_2$ (837.65): calcd. C 64.53, H 5.05, N 6.69; found C 64.58, H 5.09, N 6.58. Crystals for the X-ray structure determination were obtained from 1,2-dichloroethane/hexane. ***Isomer A*:** $^{13}C\{^1H\}$ NMR ($CD_3COCD_3$, 125 MHz, 298 K): $\delta$ = 55.51 (1 C, Me-ArOCH$_3$), 73.30 (1 C, $C_\alpha$), 86.61 (6 C, *C*-benzene), 108.12 (2 C, *C*$^4$-Pz); 121.60 (4 C, $C_p$-Ph(BPh$_4$)), 125.36 [8 C, $C_m$-Ph(BPh$_4$)], 127.96 (1 C, *C*$^3$-ArOCH$_3$), 136.39 [8 C, $C_o$-Ph(BPh$_4$)], 137.89 (2 C, *C*$^5$-Pz), 150.53 (2 C, *C*$^3$-Pz), 164.29 [q, $J_{C-^{11}B}$ = 49.4 Hz, 4 C, $C_{ipso}$-Ph(BPh$_4$)] ppm. ***Isomer B*:** $^{13}C\{^1H\}$ NMR ($CD_3COCD_3$, 125 MHz, 298 K): $\delta$ = 87.04 (6 C, *C*-benzene), 121.60 [4 C, $C_p$-Ph(BPh$_4$)], 125.36 [8 C, $C_m$-Ph(BPh$_4$)], 136.39 [8 C, $C_o$-Ph(BPh$_4$)], 164.29 [q, $J_{C-^{11}B}$ = 49.4 Hz, 4 C, $C_{ipso}$-Ph(BPh$_4$)] ppm. IR: $\tilde{\nu}$ = 1580 (CN) cm$^{-1}$.

**[RuCl(*p*-cymene)(bpzmArOCH$_3$)][BPh$_4$] (8):** The method was similar to that used for complex **2**. Amounts were as follows: [RuCl$_2$(*p*-cymene)]$_2$ (36.7 mg, 0.06 mmol) and bpzmArOCH$_3$ (33.1 mg, 0.13 mmol) in MeOH (5 mL). Complex **8** was obtained as a yellow solid. Yield: 56.1 mg (78%). Ratio of isomers A/B = 1.1:1. $C_{48}H_{48}BClN_4ORu$ (844.28): calcd. C 68.29, H 5.73, N 6.64; found C 68.25, H 5.77, N 6.68. Crystals for the X-ray structure determination were obtained from 1,2-dichloroethane/pentane. ***Isomer A*:** $^{13}C\{^1H\}$ NMR (125 MHz, $CD_3COCD_3$, 298 K): $\delta$ = 17.73 (1 C, Me-Tol), 22.25 (2 C, Me-*i*Pr), 31.14 (1 C, *C*H-*i*Pr), 55.75 (1 C, Me-ArOCH$_3$), 73.73 (1 C, $C_\alpha$), 84.77 (2 C, *C*H$^{2/2'}$-*p*-cym), 85.94 (2 C, *C*H$^{3/3'}$-*p*-cym), 105.64 (1 C, *C*$^1$-*p*-cym), 108.65 (2 C, *C*$^4$-Pz), 112.77 (1 C, *C*$^6$-ArOCH$_3$), 121.43 (1 C, *C*$^4$-ArOCH$_3$), 122.02 [4 C, $C_p$-Ph(BPh$_4$)], 125.75 [8 C, $C_m$-Ph(BPh$_4$)], 128.61 (1 C, *C*$^3$-ArOCH$_3$), 133.05 (1 C, *C*$^5$-ArOCH$_3$), 136.84 [8 C, $C_o$-Ph(BPh$_4$)], 138.39 (2 C, *C*$^5$-Pz), 150.34 (2 C, *C*$^3$-Pz), 158.23 (1 C, *C*$^1$-ArOCH$_3$), 164.29 [q, $J_{C-^{11}B}$ = 49.4 Hz, 4 C, $C_{ipso}$-Ph(BPh$_4$)] ppm. ***Isomer B*:** $^{13}C\{^1H\}$ NMR (125 MHz, $CD_3COCD_3$, 298 K): $\delta$ = 18.37 (1 C, Me-Tol), 22.21 (2 C, Me-*i*Pr), 31.72 (1 C, *C*H-*i*Pr), 85.46 (br. s, 4 C, *C*H$^{2/2'}$, *C*H$^{3/3'}$-*p*-cym), 108.69 (2 C, *C*$^4$-Pz), 122.02 [4 C, $C_p$-Ph(BPh$_4$)], 125.75 [8 C, $C_m$-Ph(BPh$_4$)], 135.48 (br. s, 3 C, *C*$^5$-ArOCH$_3$, *C*$^5$-Pz), 136.84 [9 C, $C_o$-Ph(BPh$_4$), *C*$^6$-ArOCH$_3$], 164.29 [q, $J_{C-^{11}B}$ = 49.4 Hz, 4 C, $C_{ipso}$-Ph(BPh$_4$)] ppm. IR: $\tilde{\nu}$ = 1580 (CN) cm$^{-1}$.

**[RuCl(benzene)(bpz*mArNO$_2$)][BPh$_4$] (9):** The method was similar to that used for complex **1**. Amounts were as follows: [RuCl$_2$(C$_6$H$_6$)(CH$_3$CN)] (72.8 mg, 0.25 mmol) and bpz*mArNO$_2$ (81.3 mg, 0.25 mmol) in MeOH (10 mL). Complex **9** was obtained as a bright yellow solid. The product was recrystallised from 1,2-dichloroethane/hexane (X-ray crystals). Yield: 159.0 mg (74%). $C_{47}H_{45}BClN_5O_2Ru$ (859.25): calcd. C 65.70, H 5.28, N 8.15; found C 65.79, H 5.22, N 8.18. $^{13}C\{^1H\}$ NMR (125 MHz, $CDCl_3$, 298 K): $\delta$ = 11.17 (2 C, Me$^3$-Pz), 16.32 (2 C, Me$^5$-Pz), 66.35 (1 C, $C_\alpha$), 86.01 (6 C, *C*-benzene), 110.14 (2 C, *C*$^4$-Pz), 121.60 [4 C, $C_p$-Ph(BPh$_4$)], 125.22 (1 C, *C*$^6$-ArNO$_2$), 125.35 [8 C, $C_m$-Ph(BPh$_4$)], 128.86 (1 C, *C*$^2$-ArNO$_2$), 129.55 (1 C, *C*$^3$-ArNO$_2$), 132.36 (1 C, *C*$^4$-ArNO$_2$), 133.07 (1 C, *C*$^5$-ArNO$_2$), 136.39 [8 C, $C_o$-Ph(BPh$_4$)], 149.29 (1 C, *C*$^1$-ArNO$_2$), 164.29 [q, $J_{C-^{11}B}$ = 49.4 Hz, 4 C, $C_{ipso}$-Ph(BPh$_4$)] ppm. IR (Nujol): $\tilde{\nu}$ = 1563 (CN); 1542 (NO) cm$^{-1}$.

**[RuCl(*p*-cymene)(bpz*mArNO$_2$)][BPh$_4$] (10):** The method was similar to that used for complex **2**. Amounts were as follows: [RuCl$_2$(*p*-cymene)]$_2$ (76.5 mg, 0.125 mmol) and bpz*mArNO$_2$ (81.3 mg, 0.25 mmol) in MeOH (10 mL). Complex **10** was obtained as a cream-coloured solid. The product was recrystallised from 1,2-dichloroethane/hexane (X-ray crystals). Yield: 178.5 mg (78%). $C_{51}H_{53}BClN_5O_2Ru{\cdot}0.5C_2H_4Cl_2$ (964.84): calcd. C 64.73, H 5.75, N 7.26; found C 64.76, H 5.83, N 7.21. $^{13}C\{^1H\}$ NMR ($CDCl_3$, 125 MHz, 298 K): $\delta$ = 12.00 (2 C, Me$^5$-Pz), 17.35 (2 C, Me$^3$-Pz), 18.51 (1 C, Me-Tol), 23.06 (2 C, Me-*i*Pr), 31.11 (1 C, *C*H-*i*Pr), 65.22 (1 C, $C_\alpha$), 81.91 (2 C, *C*H$^{2/2'}$-*p*-cym), 83.35 (2 C, *C*H$^{3/3'}$-*p*-cym), 103.08 (1 C, *C*$^4$-*p*-cym), 106.49 (1 C, *C*$^1$-*p*-cym), 110.69 (2 C, *C*$^4$-Pz), 121.67 [4 C, $C_p$-Ph(BPh$_4$)], 124.81 (1 C, *C*$^6$-ArNO$_2$), 125.47 [8 C, $C_m$-Ph(BPh$_4$)], 126.61 (1 C, *C*$^2$-ArNO$_2$), 129.16 (1 C, *C*$^3$-ArNO$_2$), 132.62 (1 C, *C*$^4$-ArNO$_2$), 133.54 (1 C, *C*$^5$-ArNO$_2$), 136.11 [8 C, $C_o$-Ph(BPh$_4$)], 146.34 (2 C, *C*$^5$-Pz), 148.35 (1 C, *C*$^1$-ArNO$_2$), 159.21 (1 C, *C*$^3$-Pz), 163.89 [q, $J_{C-^{11}B}$ = 49.4 Hz, 4 C, $C_{ipso}$-Ph(BPh$_4$)] ppm. IR (Nujol): $\tilde{\nu}$ = 1562 (CN); 1531 (NO) cm$^{-1}$.

**[RuCl(benzene)(bpzmArNO$_2$)][BPh$_4$] (11):** The method was similar to that used for complex **1**. Amounts were as follows: [RuCl$_2$(C$_6$H$_6$)(CH$_3$CN)] (72.8 mg, 0.25 mmol) and bpzmArNO$_2$ (67.3 mg, 0.25 mmol) in MeOH (10 mL). Complex **11** was obtained as a pale yellow solid. Ratio of isomers A/B = 4.2:1. The product was recrystallised from 1,2-dichloroethane/hexane. Yield: 162.6 mg (81%). $C_{43}H_{37}BClN_5O_2Ru{\cdot}0.5C_2H_4Cl_2$ (852.62): calcd. C 61.98, H 4.61, N 8.21; found C 62.32, H 4.34, N 8.18. ***Isomer A*:** $^{13}C\{^1H\}$ NMR (125 MHz, $CD_3COCD_3$, 298 K): $\delta$ = 72.41 (1 C, $C_\alpha$), 86.41 (6 C, *C*-benzene), 108.98 (2 C, *C*$^4$-Pz), 121.61 [4 C, $C_p$-Ph(BPh$_4$)], 125.36 [8 C, $C_m$-Ph(BPh$_4$)], 125.49 (1 C, *C*$^6$-ArNO$_2$), 128.61 (1 C, *C*$^2$-ArNO$_2$), 129.60 (1 C, *C*$^3$-ArNO$_2$), 132.60 (1 C, *C*$^4$-ArNO$_2$), 133.19 (1 C, *C*$^5$-ArNO$_2$), 136.39 [8 C, $C_o$-Ph(BPh$_4$)], 139.07 (2 C, *C*$^5$-Pz), 148.85 (1 C, *C*$^1$-ArNO$_2$), 151.99 (2 C, *C*$^3$-Pz), 164.56 [q, $J_{C-^{11}B}$ = 49.4 Hz, 4 C, $C_{ipso}$-Ph(BPh$_4$)] ppm. ***Isomer B*:** $^{13}C\{^1H\}$ NMR (125 MHz, $CD_3COCD_3$, 298 K): $\delta$ = 72.00 (1 C, $C_\alpha$), 87.08 (6 C, *C*-benzene), 108.47 (2 C, *C*$^4$-Pz), 121.61 [4 C, $C_p$-Ph(BPh$_4$)], 125.36 [8 C, $C_m$-Ph(BPh$_4$)], 126.96 (1 C, *C*$^6$-ArNO$_2$), 133.64 (1 C, *C*$^3$-ArNO$_2$), 134.15 (1 C, *C*$^5$-ArNO$_2$), 135.23 (1 C, *C*$^4$-ArNO$_2$), 135.50 (2 C, *C*$^5$-Pz), 136.39 [8 C, $C_o$-Ph(BPh$_4$)], 149.54 (2 C, *C*$^3$-Pz), 164.56 [q, $J_{C-^{11}B}$ = 49.4 Hz, 4 C, $C_{ipso}$-Ph(BPh$_4$)] ppm. IR (Nujol): $\tilde{\nu}$ = 1579 (CN); 1530 (NO) cm$^{-1}$.

**[RuCl(*p*-cymene)(bpzmArNO$_2$)][BPh$_4$] (12):** The method was similar to that used for complex **2**. Amounts were as follows: [RuCl$_2$(*p*-cymene)]$_2$ (76.5 mg, 0.125 mmol) and bpzmArNO$_2$ (67.3 mg, 0.25 mmol) in MeOH (10 mL). Complex **12** was obtained as a yellowish orange solid, as a mixture of the isomers. Yield: 139.6 mg (65%). Ratio of isomers A/B = 1.2:1. The product was recrystallised from 1,2-dichloroethane/hexane (X-ray crystals). $C_{47}H_{45}BClN_5O_2Ru$ (859.25): calcd. C 65.70, H 5.28, N 8.15; found C 65.62, H 5.19, N 8.21. ***Isomer A*:** $^{13}C\{^1H\}$ NMR (125 MHz, $CD_3COCD_3$, 298 K): $\delta$ = 17.70 (1 C, Me-Tol), 21.97 (2 C, Me-*i*Pr), 30.51 (1 C, *C*H-*i*Pr), 72.25 (1 C, $C_\alpha$), 81.26 (2 C, *C*H$^{2/2'}$-*p*-cym), 88.13 (2 C, *C*H$^{3/3'}$-*p*-cym), 102.52 (1 C, *C*$^4$-*p*-cym), 103.69 (1 C, *C*$^1$-*p*-cym), 109.16 (2 C, *C*$^4$-Pz), 121.61 [4 C, $C_p$-Ph(BPh$_4$)], 125.47 [8 C, $C_m$-Ph(BPh$_4$)], 125.52 (1 C, *C*$^6$-ArNO$_2$), 128.52 (1 C, *C*$^2$-ArNO$_2$), 129.80 (1 C, *C*$^3$-ArNO$_2$), 132.79 (1 C, *C*$^4$-ArNO$_2$), 133.48 (1 C, *C*$^5$-ArNO$_2$), 136.38 [8 C, $C_o$-Ph(BPh$_4$)], 139.04 (2 C, *C*$^5$-Pz), 151.04 (2 C, *C*$^3$-Pz), 149.05 (1 C, *C*$^1$-ArNO$_2$), 164.29 [q, $J_{C-^{11}B}$ =

 © 2007 Wiley-VCH Verlag GmbH & Co. KGaA, Weinheim 

49.4 Hz, 4 C, $C_{ipso}$-Ph($BPh_4$)] ppm. ***Isomer B*:** $^{13}C\{^1H\}$ NMR (125 MHz, $CD_3COCD_3$, 298 K): $\delta$ = 17.93 (1 C, Me-Tol), 21.97 (2 C, Me-*i*Pr), 30.97 (1 C, *C*H-*i*Pr), 71.93 (1 C, $C_\alpha$), 83.39 (2 C, *C*H$^{2/2'}$-*p*-cym), 87.03 (2 C, *C*H$^{3/3'}$-*p*-cym), 102.58 (1 C, *C*$^4$-*p*-cym), 105.32 (1 C, *C*$^1$-*p*-cym), 108.64 (2 C, *C*$^4$-Pz), 121.61 [4 C, $C_p$-Ph($BPh_4$)], 121.79 (1 C, *C*$^2$-Ar$NO_2$), 125.47 [8 C, $C_m$-Ph($BPh_4$)], 126.88 (1 C, *C*$^6$-Ar$NO_2$), 133.86 (1 C, *C*$^3$-Ar$NO_2$), 134.23 (1 C, *C*$^4$-Ar$NO_2$), 135.16 (1 C, *C*$^5$-Ar$NO_2$), 135.77 (2 C, *C*$^5$-Pz), 136.38 [8 C, $C_o$-Ph($BPh_4$)], 148.88 (2 C, *C*$^3$-Pz), 150.76 (1 C, *C*$^1$-Ar$NO_2$), 164.29 [q, $J_{C-^{11}B}$ = 49.4 Hz, 4 C, $C_{ipso}$-Ph($BPh_4$)] ppm. IR: $\tilde{\nu}$ = 1580 (CN), 1533 (NO) $cm^{-1}$.

**[RuCl(benzene)(bpz*mArNH$_2$)][BPh$_4$] (13):** The method was similar to that used for complex **1**. Amounts were as follows: [$RuCl_2(C_6H_6)(CH_3CN)$] (72.8 mg, 0.25 mmol) and bpz*mArNH$_2$ (73.8 mg, 0.25 mmol) in MeOH (10 mL). Complex **13** was obtained as a yellow solid. The product was recrystallised from 1,2-dichloroethane/hexane. Yield: 165.8 mg (80%). $C_{47}H_{47}BClN_5Ru\cdot 0.5C_2H_4Cl_2$ (878.75): calcd. C 65.61, H 5.62, N 7.97; found C 65.88, H 5.34, N 8.04. $^{13}C\{^1H\}$ NMR (125 MHz, $CDCl_3$, 298 K): $\delta$ = 11.48 (2 C, Me$^3$-Pz), 16.29 (2 C, Me$^5$-Pz), 67.97 (1 C, $C_\alpha$), 86.28 (6 C, *C*-benzene), 109.87 (2 C, *C*$^4$-Pz), 119.08 (1 C, *C*$^4$-Ar$NH_2$), 119.35 (1 C, *C*$^6$-Ar$NH_2$), 121.45 [4 C, $C_p$-Ph($BPh_4$)], 125.21 [8 C, $C_m$-Ph($BPh_4$)], 127.64 (1 C, *C*$^3$-Ar$NH_2$), 130.98 (1 C, *C*$^5$-Ar$NH_2$), 136.24 [8 C, $C_o$-Ph($BPh_4$)], 145.65 (1 C, *C*$^1$-Ar$NH_2$), 145.88 (2 C, *C*$^5$-Pz), 157.97 (2 C, *C*$^3$-Pz), 164.07 [q, $J_{C-^{11}B}$ = 49.4 Hz, 4 C, $C_{ipso}$-Ph($BPh_4$)] ppm. IR: $\tilde{\nu}$ = 1562 (CN), 3464 ($NH_2$) $cm^{-1}$.

**[RuCl(*p*-cymene)(bpz*mArNH$_2$)][BPh$_4$] (14):** The method was similar to that used for complex **2**. Amounts were as follows: [$RuCl_2$(*p*-cymene)]$_2$ (76.5 mg, 0.125 mmol) and bpz*mArNH$_2$ (73.8 mg, 0.25 mmol) in MeOH (10 mL). Complex **14** was obtained as a reddish orange solid. Yield: 157.16 mg (71%). $C_{51}H_{55}BClN_5Ru\cdot 1.5CH_3OH$ (933.44): calcd. C 67.56, H 6.59, N 7.50; found C 67.55, H 6.40, N 7.14. $^{13}C\{^1H\}$ NMR (125 MHz, $CDCl_3$, 298 K): $\delta$ = 12.42 (2 C, Me$^5$-Pz), 17.27 (2 C, Me$^3$-Pz), 18.43 (1 C, Me-Tol), 23.22 (2 C, Me-*i*Pr), 30.79 (1 C, *C*H-*i*Pr), 67.28 (1 C, $C_\alpha$), 83.01 (2 C, *C*H$^{2/2'}$-*p*-cym), 83.81 (2 C, *C*H$^{3/3'}$-*p*-cym), 102.14 (1 C, *C*$^4$-*p*-cym), 107.56 (1 C, *C*$^1$-*p*-cym), 110.76 (2 C, *C*$^4$-Pz), 118.26 (1 C, *C*$^2$-Ar$NH_2$), 119.78 (1 C, *C*$^4$-Ar$NH_2$), 120.27 (1 C, *C*$^6$-Ar$NH_2$), 122.09 [4 C, $C_p$-Ph($BPh_4$)], 125.86 [8 C, $C_m$-Ph($BPh_4$)], 127.56 (1 C, *C*$^3$-Ar$NH_2$), 132.16 (1 C, *C*$^5$-Ar$NH_2$), 136.54 [8 C, $C_o$-Ph($BPh_4$)], 145.30 (1 C, *C*$^1$-Ar$NH_2$), 145.06 (2 C, *C*$^5$-Pz), 158.00 (2 C, *C*$^3$-Pz), 164.37 [q, $J_{C-^{11}B}$ = 49.4 Hz, 4 C, $C_{ipso}$-Ph($BPh_4$)] ppm. IR (Nujol): $\tilde{\nu}$ = 1562 (CN), 3467 ($NH_2$) $cm^{-1}$.

**Hydrogen-Transfer Catalysis:** A typical procedure for the catalytic hydrogen-transfer reaction is as follows. A mixture of benzophenone (368.1 mg, 2 mmol), KOH (10 mL, 0.008 M in *i*PrOH) and the catalyst (0.004 mmol) was heated to reflux under nitrogen. At the desired reaction times, aliquots were extracted from the reaction vessel, obtaining the yields by $^1H$ NMR spectroscopy.

**X-ray Crystallography:** A summary of crystal data collection and refinement parameters for all compounds is given in Table 1. The single crystals for **7A**·$0.5C_2H_4Cl_2$ and **8B** were mounted on a glass fibre and transferred to a Bruker X8 APPEX II CCD-based diffractometer equipped with a graphite-monochromated Mo-$K_\alpha$ radiation source ($\lambda$ = 0.71073 Å). Data were integrated using the SAINT[25] program and an absorption correction was performed with the program SADABS.[26] The software package SHELXTL version 6.12[27] was used for space group determination, structure solution and refinement by full-matrix least-squares methods based on $F^2$. All non-hydrogen atoms were refined with anisotropic thermal parameters. Hydrogen atoms were placed using a "riding model" and included in the refinement at calculated positions.

Prismatic crystals of complexes **9**, **10**·$0.5C_2H_4Cl_2$ and **12A** were selected and mounted on a Bruker SMART-CCD area diffractometer. Intensities were collected with graphite-monochromated Mo-$K_\alpha$ radiation ($\lambda$ = 0.71073 Å). Lorentz polarisation and absorption corrections were made.[26] The structures were solved by direct methods, using the SHELXS computer program[28] and refined by full-matrix least-squares method with the SHELX97 computer program.[28] All hydrogen atoms were computed and refined using a riding model.

CCDC-631606 to -631610 contain the supplementary crystallographic data for complexes **7A**·$0.5C_2H_4Cl_2$, **8B**, **9**, **10**·$0.5C_2H_4Cl_2$ and **12A**. These data can be obtained free of charge from The Cambridge Crystallographic Data Centre via www.ccdc.cam.ac.uk/data_request/cif.

**Supporting Information** (see footnote on the first page of this article): Tables S1 and S2 contain the $^1H$ NMR spectroscopic data and the results of the catalytic tests at different times, respectively.

## Acknowledgments

Financial support from the Junta de Castilla-La Mancha-FEDER Funds (PBI-05-003) and the Spanish DGES/MCyT (CTQ2005-01430/BQU) is acknowledged.

[1] S. Trofimenko, *Scorpionates, The Coordination Chemistry of Polypyrazolylborate Ligands*, Imperial College Press, London, **1999**.

[2] a) A. Caballero, M. C. Carrión, G. Espino, F. A. Jalón, B. R. Manzano, *Polyhedron* **2004**, *23*, 361–371; b) D. C. Wilson, J. H. Nelson, *J. Organomet. Chem.* **2003**, *682*, 272–289; c) B. A. Messerle, V. Tolhurst, P. Turner, *Eur. J. Inorg. Chem.* **2003**, *2*, 293–300; d) C. Zuccaccia, G. Bellachioma, G. Cardaci, A. Macchioni, *J. Am. Chem. Soc.* **2001**, *123*, 11020–11028; e) M. H. Huynh, J. M. Lasker, M. Wetzler, B. Mort, L. Szczepura, L. M. Witham, J. M. Cintron, A. C. Marschilok, L. J. Ackerman, R. K. Castellano, D. L. Jameson, M. R. Churchill, A. J. Jircitano, K. J. Takeuchi, *J. Am. Chem. Soc.* **2001**, *123*, 8780–8784; f) L. D. Field, B. A. Messerle, L. Soler, I. E. Buys, T. W. Hambley, *J. Chem. Soc. Dalton Trans.* **2001**, *13*, 1959–1965; g) M. Yamaguchi, T. Iida, T. Yamagishi, *Inorg. Chem. Commun.* **1998**, *1*, 299–301; h) A. Macchioni, G. Bellachioma, G. Cardaci, V. Gramlich, H. Rueegger, S. Terenzi, L. M. Venanzi, *Organometallics* **1997**, *16*, 2139–2145; i) F. A. Jalón, A. Otero, A. Rodríguez, M. Pérez-Manrique, *J. Organomet. Chem.* **1996**, *508*, 69–74; j) M. Fajardo, A. de la Hoz, E. Diez-Barra, F. A. Jalón, A. Otero, A. Rodríguez, J. Tejeda, D. Belletti, M. Lanfranchi, M. A. Pellinghelli, *J. Chem. Soc. Dalton Trans.* **1993**, *13*, 1935–1939.

[3] a) S. Bhambri, D. A. Tocher, *Polyhedron* **1996**, 2763–2770; S. Bhambri, D. A. Tocher, *J. Chem. Soc. Dalton Trans.* **1997**, 3367–3372; b) S. Bhambri, A. Bishop, N. Kaltsoyannis, D. A. Tocher, *J. Chem. Soc. Dalton Trans.* **1998**, 3379–3390.

[4] a) V. Rautenstrauch, X. Hoang-Cong, R. Churlaud, K. Abdur-Rashid, R. H. Morris, *Chem. Eur. J.* **2003**, *9*, 4954–4967; b) R. Noyori, T. Ohkuma, *Angew. Chem. Int. Ed.* **2001**, *40*, 40–73; c) H.-U. Blaser, C. Malan, B. Pugin, F. Spindler, H. Steiner, M. Studer, *Adv. Synth. Catal.* **2003**, *345*, 103–151.

[5] a) K. Y. Ghebreyessus, J. H. Nelson, *J. Organomet. Chem.* **2003**, *669*, 48–56; b) R. K. Rath, M. Nethaji, A. R. Chakravarty, *Polyhedron* **2001**, *20*, 2735–2739; c) P. Braunstein, M. D. Fryzuk, F. Naud, S. J. Rettig, *J. Chem. Soc. Dalton Trans.* **1999**, 589–594; d) P. Braunstein, F. Naud, S. J. Rettig, *New J. Chem.* **2001**, *25*, 32–39; e) S. Ogo, T. Abura, Y. Watanabe, *Organometallics* **2002**, *21*, 2964–2969; f) M. T. Reetz, X. Li, *J. Am. Chem. Soc.* **2006**, *128*, 1044–1045.

 © 2007 Wiley-VCH Verlag GmbH & Co. KGaA, Weinheim 

[6] a) T. Ohkuma, H. Ooka, S. Hashiguchi, T. Ikariya, R. Noyori, *J. Am. Chem. Soc.* **1995**, *117*, 7562–7563; b) A. Fujii, S. Hashiguchi, N. Uematsu, T. Ikariya, R. Noyori, *J. Am. Chem. Soc.* **1996**, *118*, 2521–2522; c) R. Noyori, S. Hashiguchi, *Acc. Chem. Res.* **1997**, *30*, 97–102; d) K.-J. Haack, S. Hashiguchi, A. Fujii, T. Ikariya, R. Noyori, *Angew. Chem. Int. Ed. Engl.* **1997**, *36*, 285–288; e) T. Ohkuma, N. Utsumi, K. Tsutsumi, K. Murata, C. Sandoval, R. Noyori, *J. Am. Chem. Soc.* **2006**, *128*, 8724–8725.

[7] a) M. Yamakawa, H. Ito, R. Noyori, *J. Am. Chem. Soc.* **2000**, *122*, 1466–1478; b) M. Yamakawa, I. Yamada, R. Noyori, *Angew. Chem. Int. Ed.* **2001**, *113*, 2900–2903; c) R. Noyori, M. Yamakawa, S. Hashiguchi, *J. Org. Chem.* **2001**, *66*, 7931–7944.

[8] a) S. J. M. Nordin, P. Roth, T. Tarnai, D. A. Alonso, P. Brandt, P. G. Andersson, *Chem. Eur. J.* **2001**, *7*, 1431–1436; b) J. W. Faller, A. R. Lavoie, *Organometallics* **2002**, *21*, 3493–3495; c) M. Pastó, A. Riera, M. A. Pericàs, *Eur. J. Org. Chem.* **2002**, 2337–2341; d) K. Everaere, A. Mortreux, J. F. Carpentier, *Adv. Synth. Catal.* **2003**, *345*, 67–77; e) D. G. I. Petra, P. C. J. Kamer, P. W. N. M. Van Leeuwen, K. Goubitz, A. M. Van Loon, J. G. De Vries, H. E. Schoemaker, *Eur. J. Inorg. Chem.* **1999**, 2335–2341.

[9] P. Pelagatti, M. Carcelli, F. Calbiani, C. Cassi, L. Elviri, C. Pelizzi, U. Rizzotti, D. Rogolino, *Organometallics* **2005**, *24*, 5836–5844.

[10] a) D. Carmona, M. P. Lamata, L. A. Oro, *Eur. J. Inorg. Chem.* **2002**, 2239–2251; b) D. Carmona, M. P. Lamata, F. Viguri, I. Dobrinovich, F. J. Lahoz, L. A. Oro, *Adv. Synth. Catal.* **2002**, *344*, 499–502.

[11] a) J. S. M. Samec, J.-E. Bäckvall, P. G. Anderson, P. Brandt, *Chem. Soc. Rev.* **2006**, *35*, 237–248; b) S. E. Clapham, A. Hadzovic, R. H. Morris, *Coord. Chem. Rev.* **2004**, *248*, 2201–2237; c) O. Pàmies, J.-E. Bäckvall, *Chem. Eur. J.* **2001**, *7*, 5052–5058; d) Y. R. S. Laxmi, J.-E. Bäckvall, *Chem. Commun.* **2000**, 611–612; e) J.-E. Bäckvall, *J. Organomet. Chem.* **2002**, *652*, 105–111; f) D. G. I. Petra, J. N. H. Reek, J.-W. Handgraaf, E. J. Meijer, P. Dierkes, P. C. J. Kamer, J. Brussee, H. E. Schoemaker, P. W. N. M. Van Leeuwen, *Chem. Eur. J.* **2000**, *6*, 2818–2829.

[12] a) W. Baratta, J. Schütz, E. Herdtweck, W. A. Herrmann, P. Rigo, *J. Organomet. Chem.* **2005**, *690*, 5570–5575; b) W. Baratta, E. Herdtweck, K. Siega, M. Toniutti, P. Rigo, *Organometallics* **2005**, *24*, 1660; c) W. Baratta, G. Chelucci, S. Gladiali, K. Siega, M. Toniutti, M. Zanette, E. Zangrando, P. Rigo, *Angew. Chem. Int. Ed.* **2005**, *44*, 6214–6219.

[13] a) N. Arroyo, F. Gómez-de la Torre, F. A. Jalón, B. R. Manzano, B. Moreno-Lara, A. M. Rodríguez, *J. Organomet. Chem.* **2000**, *603*, 174–184; b) M. C. Carrión, A. Díaz, A. Guerrero, F. A. Jalón, B. R. Manzano, A. Rodríguez, L. P. Rowena, J. C. Jeffery, *J. Organomet. Chem.* **2002**, *650*, 210–222; c) M. C. Carrión, A. Díaz, A. Guerrero, F. A. Jalón, B. R. Manzano, A. Rodríguez, *New J. Chem.* **2002**, *26*, 305–312.

[14] M. C. Carrión, F. A. Jalón, I. López-Solera, B. R. Manzano, F. Sepúlveda, L. Santos, A. Rodríguez, M. Moreno, M. Martínez-Ripoll, *Can. J. Chem.* **2005**, *83*, 2106–2119.

[15] E. Iengo, E. Zangrando, E. Baiutti, E. Alessio, *Eur. J. Inorg. Chem.* **2005**, 1019–1031.

[16] A. J. Canty, R. T. Honeyman, B. W. Skelton, A. H. White, *J. Organomet. Chem.* **1990**, *396*, 105–113.

[17] a) K. I. The, L. K. Peterson, *Can. J. Chem.* **1973**, *51*, 422–426; b) K. I. The, L. K. Peterson, E. Kiehlmann, *Can. J. Chem.* **1973**, *51*, 2448–2451; c) L. K. Peterson, E. Kiehlmann, A. R. Sanger, K. I. The, *Can. J. Chem.* **1974**, *52*, 2367–2374.

[18] J. Sebastian, P. Sala, J. Del Mazo, M. Sancho, C. Ochoa, J. Elguero, T. A. Fayet, M. C. Vertut, *J. Heterocycl. Chem.* **1982**, *19*, 1141–1145.

[19] H. Günter, *NMR Spectroscopy: Basic Principles, Concepts and Applications in Chemistry*, 2nd ed., John Wiley and Sons, New York, **1995**.

[20] G. A. Jeffrey, *An Introduction to Hydrogen Bonding*, Oxford University Press, Oxford, **1997**.

[21] a) C. Waalling, L. Bollyky, *J. Am. Chem. Soc.* **1964**, *86*, 3750–3752; b) A. Berkessel, T. J. S. Schubert, T. N. Müller, *J. Am. Chem. Soc.* **2002**, *124*, 8693–8698.

[22] M. D. Le Page, B. R. James, *Chem. Commun.* **2000**, 1647–1648.

[23] D. Amoroso, A. Jabri, G. P. A. Yap, D. G. Gusev, E. N. dos Santos, D. E. Fogg, *Organometallics* **2004**, *23*, 4047–4054.

[24] a) D. R. Anton, R. H. Crabtree, *Organometallics* **1983**, *2*, 855–859; b) P. Foley, R. DiCosimo, G. M. Whitesides, *J. Am. Chem. Soc.* **1980**, *102*, 6713–6725; c) M. R. Eberhard, *Org. Lett.* **2004**, *6*, 2125–2128.

[25] *SAINT+ v7.12a. Area-Detector Integration Program*, Bruker-Nonius AXS, Madison, WI, USA, **2004**.

[26] G. M. Sheldrick, *SADABS version 2004/1. A Program for Empirical Absorption Correction*, University of Göttingen, Göttingen, Germany, **2004**.

[27] *SHELXTL-NT version 6.12. Structure Determination Package*, Bruker-Nonius AXS, Madison, WI, USA, **2001**.

[28] G. M. Sheldrick, *SHELXS-97, A Program for Solving Crystal Structures and Crystal Structure Refinement*, University of Göttingen, Germany, **1997**.

Received: March 7, 2007
Published Online: July 6, 2007

 © 2007 Wiley-VCH Verlag GmbH & Co. KGaA, Weinheim 

DOI: 10.1002/ejic.200700183

# Ternary Complexes of Zinc(II), Cyclen and Pyridinecarboxylic Acids

**Zuzana Vargová,*[a] Jan Kotek,[b] Jakub Rudovský,[b] Jan Plutnar,[b] Robert Gyepes,[b] Petr Hermann,[b] Katarina Györyová,[a] and Ivan Lukeš*[b]**

**Keywords:** Cyclen complexes / N ligands / Stability constants / Zinc

Binary and ternary systems containing $Zn^{2+}$, cyclen and/or pyridinecarboxylic acids and amides [picolinic ($HL^1$), nicotinic ($HL^2$) and dipicolinic ($H_2L^3$) acids and nicotinamide ($L^4$)] have been investigated in solution and in the solid state. Dissociation and stability constants for the ligands and binary systems, respectively, are in accordance with literature results. Both picolinic and dipicolinic acids form stable ternary complexes with the $[Zn(cyclen)]^{2+}$ species; a weak interaction is observed for nicotinic acid and nicotinamide. The formation of ternary complexes stabilizes the products of protonation at the cyclen nitrogen atom, and these protonated complexes are found even up to pH = 7. The structures of the complexes in solution correlate well with those found in the solid state and by molecular modelling calculations. The solid-state structures of several complexes are determined. The zinc atom in the $[Zn(cyclen)(NO_3)]^+$ complex is bound in an $N_4O$ tetragonal-pyramidal environment. The nicotinic acid anion forms a bridge in the $[\{Zn(cyclen)\}_2(\mu\text{-}L^2\text{-}N,O)]^{3+}$ cation, and both $[Zn(cyclen)]^{2+}$ units exhibit tetragonal-pyramidal arrangements. An unusual coordination mode is found in the $[\{Zn(cyclen)\}_2(\mu\text{-}L^1\text{-}O{:}N,O')]^{3+}$ cation, where the picolinic acid anion also bridges two $[Zn(cyclen)]^{2+}$ units but is coordinated monodentately through one oxygen atom to one unit ($N_4O$ tetragonal pyramid) and chelates through the other pyridine nitrogen and carboxylate oxygen atoms. Nicotinamide in the $[Zn(cyclen)(L^4\text{-}N)]^{2+}$ cation is bound to the $[Zn(cyclen)]^{2+}$ unit through the pyridine nitrogen atom in the axial position of the tetragonal pyramid. This is the first fully quantitative assessment of $Zn^{2+}$-cyclen-ligand ternary systems, and the results, namely the presence of protonated cyclen in the ternary species even at high pH, are relevant for evaluation of the $[Zn(cyclen)]^{2+}$ unit as a model complex for zinc-containing enzymes.

(© Wiley-VCH Verlag GmbH & Co. KGaA, 69451 Weinheim, Germany, 2007)

## Introduction

Zinc is an essential element for all forms of life and plays a critical role in various functions, both structural and catalytic, in proteins and enzymes.[1] Typically, the metal ion is coordinatively saturated by four donor atoms from amino acid side-chains of the protein when playing a structural role. On the other hand, if the functional catalytic role is examined, the ion in the active site is mostly three- or four-coordinate or, less commonly, the coordination number can also reach four, five and rarely even six, although this is always accompanied by coordination of labile ligands.[2] There are two basic mechanisms by which zinc(II) exerts its catalytic function. The first is exemplified by carbonic anhydrase (CA) and involves delivery of a metal-bound hydroxido nucleophile, which can exist at pH values where the concentration of free hydroxide ion is extremely low. The second takes advantage of the strong Lewis acid character of zinc(II) to polarize a susceptible bond for substitution,[3] and thus zinc(II) appears to be the most abundant metal centre present in phosphatases and nucleases.[4] In addition, the zinc enzymes remain a central issue in the area of molecular recognition.[5] For example, CA recognizes not only its normal substrates ($CO_2$ and $HCO_3^-$) but also substrates such as phosphoric esters, carboxylic esters, aldehydes and binds halide anions, $SCN^-$, acetate, sulfonamides, carboxamides, phenol, imidazole and alcohols as inhibitors. Up-to-date information regarding zinc(II) functions in biological systems has been collated recently.[6]

An important contribution to the detailed understanding of the catalytic activity and molecular recognition of the enzyme has been made by experimental investigations with suitable model systems. Several ligands, usually with three or four nitrogen donor atoms, have been used to mimic the rigid and stable coordination centre of the active zinc(II) part of an enzyme. Various azacycles, especially 1,4,7,10-tetraazacyclododecane (cyclen) and its derivatives, have been used to model the protein environment of carbonic anhydrase,[7,8] phosphatases,[9–11] β-lactamase,[12] flavoenzymes[13] or NADH models.[14] A flavin-$[Zn(cyclen)]^{2+}$ complex has also been used as a catalyst for the photooxidation

[a] Department of Inorganic Chemistry, P. J. Šafárik University, Moyzesova 11, 04154 Košice 1, Slovak Republic
Fax: +421-556-222-124
E-mail: vargovaz@upjs.sk
[b] Department of Inorganic Chemistry, Charles University (Universita Karlova), Hlavova 2030, 12840 Prague 2, Czech Republic
Fax: +420-221-951-253
E-mail: lukes@natur.cuni.cz

Supporting information for this article is available on the WWW under http://www.eurjic.org or from the author.

 © 2007 Wiley-VCH Verlag GmbH & Co. KGaA, Weinheim 

of methoxybenzyl alcohol.[15] Cyclen ligands modified with other functionalities in the pendant arms, such as sulfonamides, carboxamides, phenols, alcohols or phosphoric esters, are also commonly used in these studies.[5]

There are only a few examples in the literature in which interactions or reactions of an unmodified $[Zn(cyclen)]^{2+}$ complex with another molecule have been studied. In addition to the examples of carbonic anhydrase mentioned above,[7,8] this complex has also been used to investigate the interaction and hydrolysis behaviour of phosphate esters[9,16] and has been found to catalyze the hydrolysis of *N*-benzylpenicillin.[17]

Most of the papers dealing with models based on $[Zn(cyclen)]^{2+}$ complexes are oriented towards the molecular recognition of nucleobases. These biomimetic studies, which have been summarised recently,[18,19] show that the $[Zn(cyclen)]^{2+}$ complex can be used as a novel receptor for imide-containing nucleobases such as thymine (T) and uracil (U) in aqueous solution and at physiological pH. Coordination of a nucleobase through a $Zn^{2+}$–N ("imide") bond is enforced by interaction of the "urea" carbonyl groups with the hydrogen atoms of the ring NH groups in the complementary positions. The dissociation constants, $K_d$, determined for ternary complexes of zinc(II), substituted cyclen and T or U are of the order of 10 μM, and for analogous systems containing bis($[Zn(cyclen)]^{2+}$) or tris($[Zn(cyclen)]^{2+}$) complexes (mononuclear complex units linked covalently through *p*-xylene or mesitylene spacers) with corresponding di- and trinucleotides (TpTp or TpTpTp) are even in a nanomolar range. In addition, bis- or tris($[Zn(cyclen)]^{2+}$) complexes connected through an imidazole group[20] and the formation of assembled three-dimensional supramolecules have also been studied.[21–25] Recently, a polymer containing $[Zn(cyclen)]^{2+}$ units was synthesised and investigated as a creatine receptor.[26]

As mentioned above, in contrast to the large number of papers dealing with modified cyclen complexes, only a few works have focused on the complexation and formation of ternary cyclen complexes,[7,8] which would be crucial for modelling the complexation at the active centre of the enzymes. Thus, in this paper we report a detailed investigation of the formation of ternary complexes of $[Zn(cyclen)]^{2+}$ and picolinic ($HL^1$), nicotinic ($HL^2$), and dipicolinic ($H_2L^3$) acids or nicotinamide ($L^4$) as the approaching ligands. This series helps to explain the complexing properties of the $[Zn(cyclen)]^{2+}$ species towards aromatic heterocycles and/or carboxylate coordination, their preference, and possible interactions of non-coordinated groups with the cyclen skeleton.

## Results and Discussion

### Preparation of the Complexes $[Zn(cyclen)(NO_3)]ClO_4$, $[\{Zn(cyclen)\}_2(\mu\text{-}L^2\text{-}N,O)](ClO_4)_3$, $[\{Zn(cyclen)\}_2(\mu\text{-}L^1\text{-}O:N,O')](ClO_4)_3\cdot H_2O$, $[Zn(cyclen)(L^4\text{-}N)](ClO_4)_2$ and Their X-ray Crystal Structures

To assess the coordination modes in the ternary complexes formed with $Zn^{2+}$, cyclen and pyridinecarboxylic acids or nicotinamide in solution we tried to prepare single crystals suitable for X-ray analysis by slow evaporation of the solvent from mixed solutions of $Zn^{2+}$, cyclen and the corresponding pyridine-based ligand in an equimolar ratio at a concentration of about 0.1–0.2 M at various pH values. We succeeded in several cases, and the crystal structures of four crystalline materials were determined. The bond lengths found in the coordination spheres of the zinc(II) complexes and the deviations from planarity observed for the cyclen nitrogen atoms are given in Table 1. Further bond lengths and angles are listed in Table S1 (see Supporting Information).

Table 1. Selected bond lengths [Å] found in the crystal structures.

| $[Zn(cyclen)(NO_3)]ClO_4$ | | | | $[Zn(cyclen)(L^4\text{-}N)](ClO_4)_2$ | | | |
|---|---|---|---|---|---|---|---|
| Coordination sphere | | Distance from $N_4$ plane | | Coordination sphere | | Distance from $N_4$ plane | |
| Zn–O1 | 1.998(3) | N11, N17 | –0.037(2) | Zn–N1 | 2.029(3) | N11, N17 | –0.005(2) |
| Zn–N11 | 2.097(4) | N14, N110 | 0.037(2) | Zn–N11 | 2.112(3) | N14, N110 | 0.005(2) |
| Zn–N14 | 2.148(5) | Zn | 0.786(2) | Zn–N14 | 2.139(4) | Zn | 0.786(2) |
| Zn–N17 | 2.124(4) | | | Zn–N17 | 2.136(3) | | |
| Zn–N110 | 2.124(5) | | | Zn–N110 | 2.164(3) | | |
| $[\{Zn(cyclen)\}_2(\mu\text{-}L^2\text{-}N,O)](ClO_4)_3$ | | | | $[\{Zn(cyclen)\}_2(\mu\text{-}L^1\text{-}O:N,O')](ClO_4)_3\cdot H_2O$ | | | |
| Coordination sphere | | Distance from $N_4$ plane | | Coordination sphere | | Distance from $N_4$ plane | |
| Zn1–N1 | 2.026(2) | N11, N17 | –0.0075(13) | Zn2–O2 | 1.945(8) | N21, N27 | –0.006(9) |
| Zn1–N11 | 2.123(2) | N14, N110 | 0.0075(13) | Zn2–N21 | 2.079(16) | N24, N210 | 0.006(9) |
| Zn1–N14 | 2.129(3) | Zn1 | 0.7849(13) | Zn2–N24 | 2.157(18) | Zn2 | 0.805(9) |
| Zn1–N17 | 2.146(2) | N21 | –0.0069(14) | Zn2–N27 | 2.110(15) | Distance from O1,N11,N17,N1,Zn1 plane | |
| Zn1–N110 | 2.139(2) | N24 | 0.0068(14) | Zn2–N210 | 2.127(17) | O1 | –0.084(6) |
| Zn2–O1 | 1.924(2) | N27 | –0.0068(13) | Zn1–N1 | 2.154(9) | N1 | 0.059(6) |
| Zn2–N21 | 2.137(2) | N210 | 0.0069(14) | Zn1–O1 | 2.232(8) | N11 | 0.051(5) |
| Zn2–N24 | 2.133(3) | Zn2 | 0.7880(14) | Zn1–N11 | 2.128(10) | N17 | –0.064(5) |
| Zn2–N27 | 2.168(3) | | | Zn1–N14 | 2.143(12) | Zn1 | 0.038(5) |
| Zn2–N210 | 2.111(2) | | | Zn1–N17 | 2.201(11) | N14 | 2.091(14) |
| | | | | Zn1–N110 | 2.142(11) | N110 | –2.055(13) |

 © 2007 Wiley-VCH Verlag GmbH & Co. KGaA, Weinheim 

First, we obtained a single crystal of the parent $Zn^{2+}$-cyclen complex. $[Zn(cyclen)(NO_3)]ClO_4$ contains a five-coordinate $Zn^{2+}$ ion (Figure 1) with four nitrogen atoms of the macrocycle and one oxygen atom of nitrate ion coordinated to the metal centre to form a slightly distorted tetragonal pyramid ($\tau$ = 0.097; this parameter should be 1.000 for an ideal trigonal bipyramid and 0.000 for an ideal tetragonal pyramid[27]). The zinc atom is placed above the plane containing the four nitrogen atoms of cyclen (0.750 Å). All four five-membered chelate rings of cyclen have the same conformation (δδδδ in the independent unit), as is usual in similar complexes. The bond lengths and angles around the $Zn^{2+}$ ion (Tables 1 and S1) are as expected.

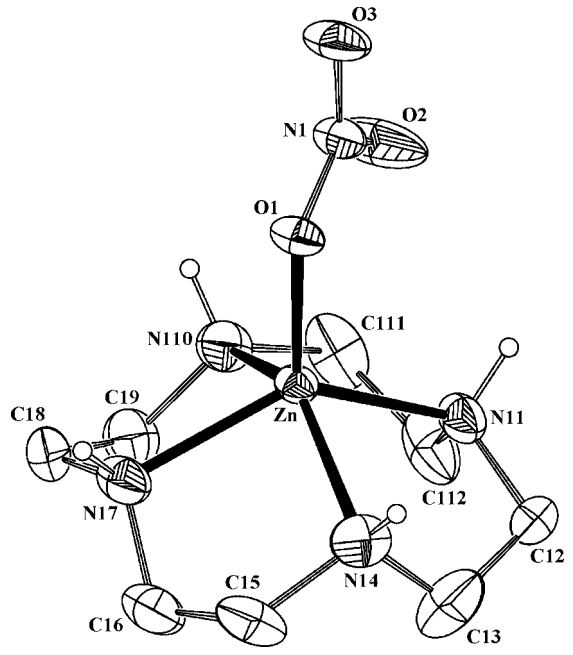


Figure 1. ORTEP drawing of the $[Zn(cyclen)(NO_3)]^+$ cation found in the structure of $[Zn(cyclen)(NO_3)](ClO_4)$. Hydrogen atoms bound to carbon atoms have been omitted for clarity.

$[\{Zn(cyclen)\}_2(\mu\text{-}L^2\text{-}N,O)](ClO_4)_3$ contains two $[Zn(cyclen)]^{2+}$ complex subunits bridged by nicotinate (Figure 2). All five-membered chelate rings of both cyclen ligands show the same conformation (λλλλ for both subunits in the independent unit). The fifth coordination sites are occupied by a pyridine nitrogen atom (N1–Zn1) and a carboxylate oxygen atom (O1–Zn2) to form slightly distorted tetragonal pyramids [the $\tau$ values for the coordination polyhedrons $Zn1(N_5)$ and $Zn2(N_4O)$ are 0.015 and 0.002, respectively]. The planar pyridine ring of the nicotinate anion is perpendicular to the cyclen plane formed by N11, N14, N17 and N110. The distances of Zn1 and Zn2 from the tetragonal basal planes formed by the nitrogen atoms of cyclen are 0.793 and 0.781 Å, respectively; these values are slightly longer than that observed in $[Zn(cyclen)(NO_3)]ClO_4$. The apical Zn1–N1 and Zn2–O1 bond lengths (2.026 and 1.924 Å, respectively) are shorter than the average Zn–N length (2.135 Å) in the basal plane of the cyclen units. Nevertheless, the bond lengths fall into the expected range for such complexes (Tables 1 and S1).[28]

$[\{Zn(cyclen)\}_2(\mu\text{-}L^1\text{-}O{:}N,O')](ClO_4)_3{\cdot}H_2O$ also contains two independent zinc atoms with two different coordination geometries, namely a distorted tetragonal bipyramid $[Zn1(N_5O)$ coordination sphere] and a slightly distorted tetragonal pyramid [$Zn2(N_4O)$ coordination sphere with a $\tau$ value of 0.002; Figure 3]. The distance of Zn2 from the tetragonal basal plane formed by the nitrogen atoms of the cyclen ring (0.790 Å) is very close to that found in the previous structure; the picolinate oxygen atom O2 is coordinated in the apical position. The central Zn1 atom is surrounded by four nitrogen atoms of cyclen, and the coordination sphere is completed by *cis* coordination of the picolinate nitrogen atom N1 and oxygen atom O1. The atoms form an axially elongated tetragonal bipyramid, with the

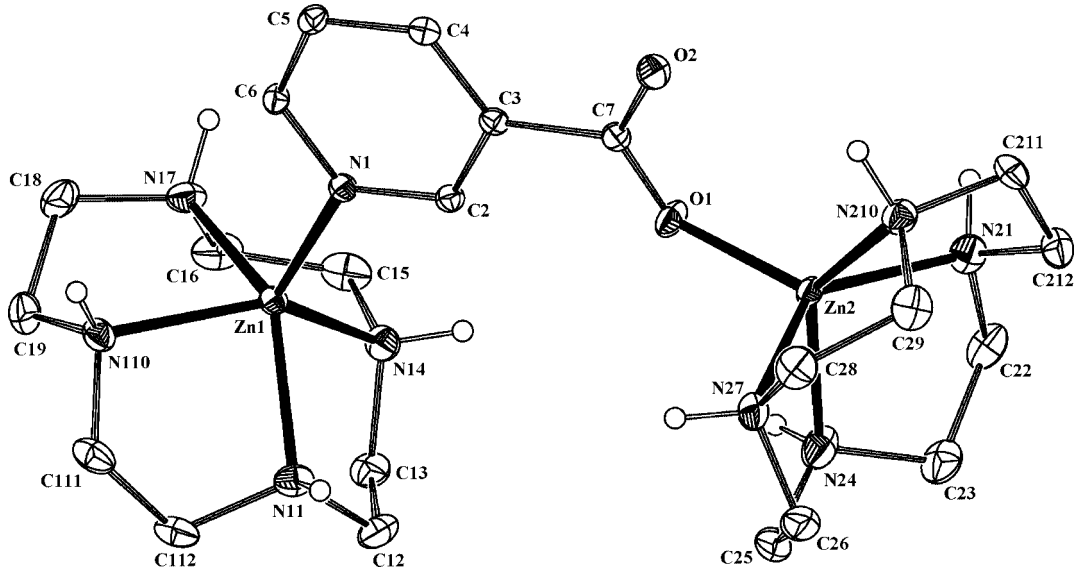


Figure 2. ORTEP drawing of the $[\{Zn(cyclen)\}_2(\mu\text{-}L^2\text{-}N,O)]^{3+}$ cation found in the structure of $[\{Zn(cyclen)\}_2(\mu\text{-}L^2\text{-}N,O)](ClO_4)_3$. Hydrogen atoms bound to carbon atoms have been omitted for clarity.

 © 2007 Wiley-VCH Verlag GmbH & Co. KGaA, Weinheim 

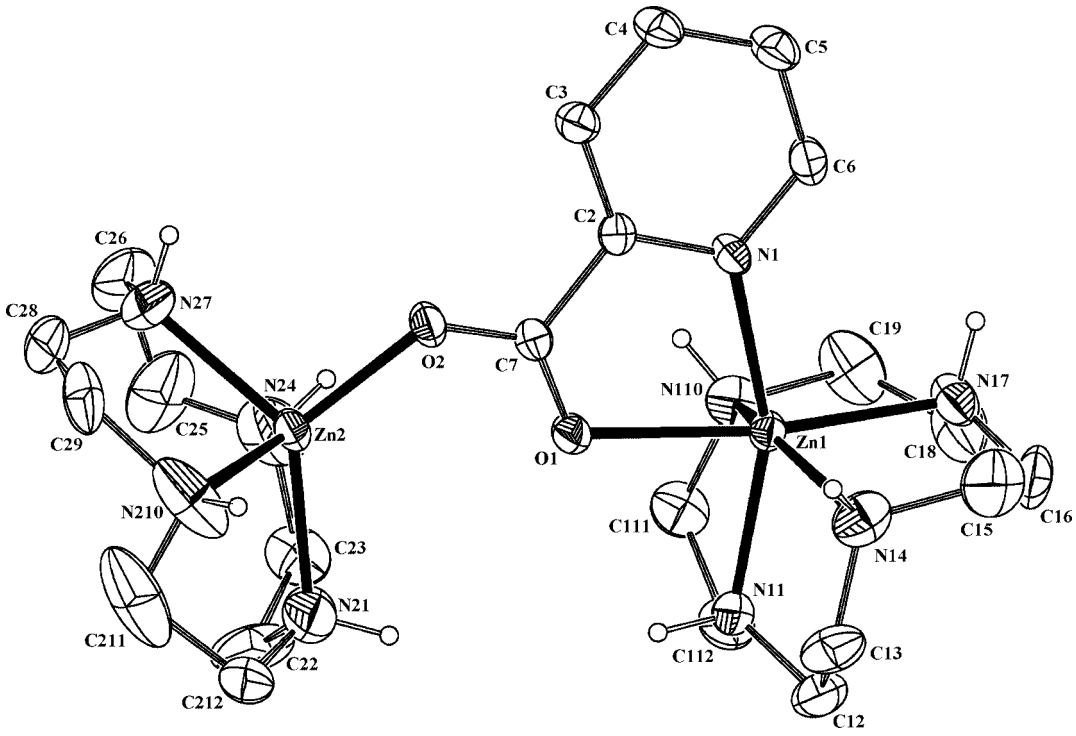


Figure 3. ORTEP drawing of the $[\{Zn(cyclen)\}_2(\mu\text{-}L^1\text{-}O{:}N,O')]^{3+}$ cation found in the structure of $[\{Zn(cyclen)\}_2(\mu\text{-}L^1\text{-}O{:}N,O')](ClO_4)_3\cdot H_2O$. Hydrogen atoms bound to carbon atoms have been omitted for clarity.

equatorial plane formed by three cyclen nitrogen atoms N11, N17 and N110 together with O1 from picolinate. However, the bond angles show large deviations from the corresponding ideal values. The coordination spheres of the Zn1 and Zn2 atoms contain different conformations of the cyclen. In the Zn2 sphere a λ conformation is observed for all four five-membered chelate rings formed due to coordination of the nitrogen atoms, whereas the nitrogen atoms of cyclen coordinated to Zn1 do not form a plane as in the other structures and the chelate rings adopt δλδλ conformations (see Figure S2 in the Supporting Information). Selected geometric parameters for this complex are listed in Table 1.

$[Zn(cyclen)(L^4\text{-}N)](ClO_4)_2$ contains monomeric units with a five-coordinate zinc atom (Figure 4). Four nitrogen atoms of the macrocycle and the nitrogen atom of nicotinamide are coordinated to the zinc atom in an approximately tetragonal-pyramidal sphere ($\tau = 0.017$). All four five-membered chelate rings of cyclen have the same conformation (λλλλ in the independent unit). Four cyclen nitrogen atoms N11, N14, N17 and N110 form a plane with a similar distance to the zinc atom as found in the previous structures (0.794 Å). The pyridine ring of nicotinamide is perpendicular to this plane. Selected geometric parameters are listed in Tables 1 and S1.

Two structural motifs are observed in the compounds studied. Thus, if the approaching ligand is monodentately coordinated to the $[Zn(cyclen)]^{2+}$ unit, the central $Zn^{2+}$ ion is placed above the plane formed by the four nitrogen atoms of cyclen and the conformation of all four five-membered chelate rings is the same, either all-δ or all-λ. The distance

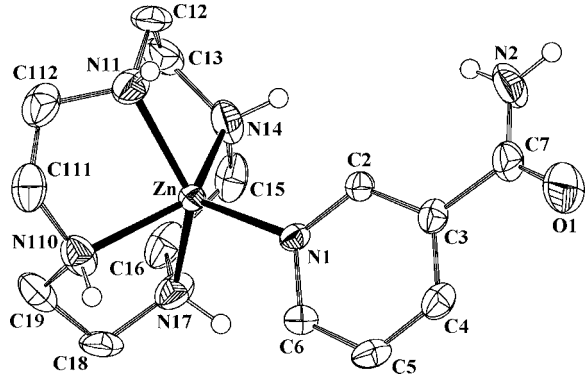


Figure 4. ORTEP drawing of the $[Zn(cyclen)(L^4\text{-}N)]^{2+}$ cation found in the structure of $[Zn(cyclen)(L^4\text{-}N)](ClO_4)_2$. Hydrogen atoms bound to carbon atoms have been omitted for clarity.

from the $N_4$ plane is 0.75 Å for $[Zn(cyclen)(NO_3)]ClO_4$ and about 0.79 Å for the ternary complexes, which means that it falls into the range 0.75–0.80 Å found in the CCDC[28,29] for $Zn^{2+}$ complexes of cyclen derivatives with no coordinated pendant. If the pendant group of cyclen is coordinated, however, the $N_4$–Zn distance is usually longer. Formation of an $N_4$ plane containing the cyclen nitrogen atoms has also been observed in structures with higher coordination numbers, such as in the $Zn^{2+}$ complexes with *N*,*N*′,*N*′′,*N*′′′-tetrakis(carbamoylmethyl)cyclen (dotam),[30] which has a coordination number of six, or with *N*,*N*′,*N*′′-tris(pyrazol-1-ylmethyl)cyclen,[31] which has a coordination number of seven. When the approaching ligand is bidentately coordinated to form a chelate, as found in

 © 2007 Wiley-VCH Verlag GmbH & Co. KGaA, Weinheim 

$[\{Zn(cyclen)\}_2(\mu\text{-}L^1\text{-}O{:}N,O')](ClO_4)_3\cdot H_2O$ (the coordination number of $Zn^{2+}$ is six), this results in a different δλδλ conformation of cyclen. This conformation is relatively rare among $Zn^{2+}$-cyclen complexes and is found, for example, in $[Zn(H_2dota)]$ ($H_4dota$ = 1,4,7,10-tetraazacyclododecane-1,4,7,10-tetraacetic acid)[32] and $[Zn(cyclen\text{-}R\text{-}O)(H_2O)]^{2+}$ (R = $CH_2COC_6H_4Br$-4).[33]

Pyridinecarboxylic acids also show a tendency to bridge the $[Zn(cyclen)]^{2+}$ units in dinuclear complexes. A similar bridging motif through another ligand has also been found for carbonate,[34] phosphate[35] and imidazole.[20] Crystallisation of the bridged dinuclear complexes from equimolar solutions is surprising but is probably due to their lower solubility due to the relatively hydrophobic surrounding sphere formed by the cyclen ligands.

## Potentiometric Study

To prevent misunderstandings and to clarify the following text, both the protonation and stability constants are concentration constants and are defined by the general term:

$$\beta_{pqrs} = [H_p(cyclen)_q(L^n)_rZn_s]/[H]^p \times [cyclen]^q \times [L^n]^r \times [Zn]^s$$

This definition will be used for proton-ligand speciation and for all binary systems ($Zn^{2+}$-cyclen and $Zn^{2+}$-$H_xL^n$) as well as for the ternary systems. The relevant stoichiometric coefficient for the missing component is taken to be zero. In this formalism, each species can be represented by the four-digit code *pqrs*; for example, the $[Zn(cyclen)]^{2+}$ complex can be viewed as 0101, and $[Zn(Hcyclen)(HL^1)]^{2+}$ as 2111. The charges are omitted from the general formulae for the sake of clarity.

### *Protonation Constants of $HL^1$, $HL^2$, $H_2L^3$ and $L^4$ and Their Stability Constants with $Zn^{2+}$ Ions*

Although the protonation constants of pyridinecarboxylic acids and nicotinamide have already been reported and summarised,[36] we determined them under our experimental conditions (25 °C and $I$ = 0.1 M $KNO_3$) by potentiometric titration. All values are listed in Table 2 together with the literature data for comparison. The $\log\beta_{1010}$ values correspond to the protonation of nitrogen atoms of the pyridine ring and the difference $\log\beta_{2010} - \log\beta_{1010}$ to the dissociation ($\log K_A$) of a proton from the carboxylic group.[36] In addition to the published protonation/dissociation constants, we were able to determine the $\log\beta_{3010}$ value for dipicolinic acid associated with protonation of the second carboxylate group.

The pyridine derivatives form complexes with a $Zn^{2+}$/$H_xL^n$ molar ratio of 1:1 and 1:2 in the presence of $Zn^{2+}$; $HL^1$ also forms a complex with a 1:3 ratio. The species determined for each system together with their stability constants and literature values are listed in Table 2; representative distribution diagrams are shown in Figure S3 (see the Supporting Information). It is clear that there are no significant differences between our data and the literature data for the systems with picolinic and dipicolinic acids.[36] The slight differences found for the 1:2 and 1:3 ratios are probably caused by variants in ionic strength and electrolyte. In addition, these values are a little higher than those expected for these ratios from the values determined for the 1:1 (or 1:2) species, although they still lie in the expected range of 3σ variance. The formation of a zinc(II) hydroxide precipitate was observed at pH > 8.0 in both systems. Both picolinic and dipicolinic acids form chelates through the nitrogen atom and the carboxylate group (see below) in the pH range 2–7, which means that these complexes are more stable than those found for nicotinic acid and nicotinamide. Nicotinic acid forms very weak complexes with a low abundance in aqueous solution, and in acid solution the main species seems to be $[Zn(HL^2)]^{2+}$, probably with a protonated pyridine nitrogen atom and coordinated through the carboxylate group and, in the neutral region, $[Zn(L^2)]^+$ species with a coordinated nitrogen atom. The abundance of these species is only about 20% (Figure S3). The uppermost estimate of $\log\beta_{0011}$ for the $[Zn(L^4)]^{2+}$ complex is one, which corresponds to the value found in the literature.[36]

### *Protonation Constants of Cyclen and Stability Constants of Its $Zn^{2+}$ Complexes*

The protonation constants of cyclen are given in Table 3. From the best fits of our experimental data, it appears that

Table 3. Protonation constants of cyclen and stability constants of $Zn^{2+}$-cyclen complexes (25 °C, $I$ = 0.1 M $KNO_3$).[a]

| $\log\beta_{1100}$ | $\log\beta_{2100}$ | $\log\beta_{3100}$ | $\log\beta_{4100}$ | $\log\beta_{0101}$ | $\log\beta_{1101}$ |
|---|---|---|---|---|---|
| 10.67(1) | 20.25(2) | – | 22.59(6) | 14.77(2) | 7.36(5) |
| *10.65* | *20.29* | *21.69* | *22.39* | *16.2* | *7.75* |

[a] Values in italics are taken from ref.[36]

Table 2. Protonation constants of pyridinecarboxylic acids and nicotinamide and the stability constants of their $Zn^{2+}$ complexes (25 °C, $I$ = 0.1 M $KNO_3$).[a]

| Ligand | $\log\beta_{1010}$ | $\log\beta_{2010}$ | $\log\beta_{3010}$ | $\log\beta_{1011}$ | $\log\beta_{0011}$ | $\log\beta_{1011}$ | $\log\beta_{2011}$ | $\log\beta_{1021}$ | $\log\beta_{0021}$ | $\log\beta_{0031}$ |
|---|---|---|---|---|---|---|---|---|---|---|
| $HL^1$ | 5.22(1) | 6.39(1) | – | – | 5.33(2) | –2.56(2) | –12.37(3) | – | 9.60(7) | 14.06(7) |
| | *5.21* | *6.16* | | | *5.23* | | | | *9.56* | *12.9* |
| $HL^2$ | 4.66(1) | 6.77(1) | – | 6.18(3) | 1.72(4) | – | – | – | – | – |
| | *4.69* | *6.77* | | | | | | | | |
| $H_2L^3$ | 4.70(2) | 6.72(3) | 8.08(4) | – | 6.50(8) | – | – | 14.98(10) | 13.18(6) | – |
| | *4.66* | *6.73* | | | *6.35* | | | | *11.88* | |
| $L^4$ | 3.26(2) | – | – | – | <1 | – | – | – | – | – |
| | *3.31* | | | | *0.78* | | | | *1.15* | |

[a] Values in italics are taken from ref.[36]

 © 2007 Wiley-VCH Verlag GmbH & Co. KGaA, Weinheim 

Table 4. Stability constants of ternary $Zn^{2+}$-cyclen-$H_xLn$ complexes (25 °C, $I$ = 0.1 M $KNO_3$).

| Ternary system | $\log\beta_{0111}$ | $\log\beta_{1111}$ | $\log\beta_{2111}$ | $pK_A(1111)$ | $pK_A(2111)$ | $\log\beta_{0111} - \log\beta_{0101}$[a] |
|---|---|---|---|---|---|---|
| Zn-cyclen-$HL^1$ | 18.68(6) | 24.09(7) | 27.63(12) | 6.22 | 3.53 | 3.91 |
| Zn-cyclen-$HL^2$ | 16.72(18) | 21.95(7) | 25.62(17) | 5.22 | 3.68 | 1.95 |
| Zn-cyclen-$H_2L^3$ | 19.20(11) | 26.09(11) | 29.62(13) | 6.89 | 3.53 | 4.43 |
| Zn-cyclen-$L^4$ | 15.5(6) | 20.3(2) | – | 4.8 | – | 0.7 |

[a] Equilibrium constant for the reaction: $[Zn(cyclen)]^{2+} + (L^n)^{x-} \rightleftharpoons [Zn(cyclen)(L^n)]^{(2-x)+}$.

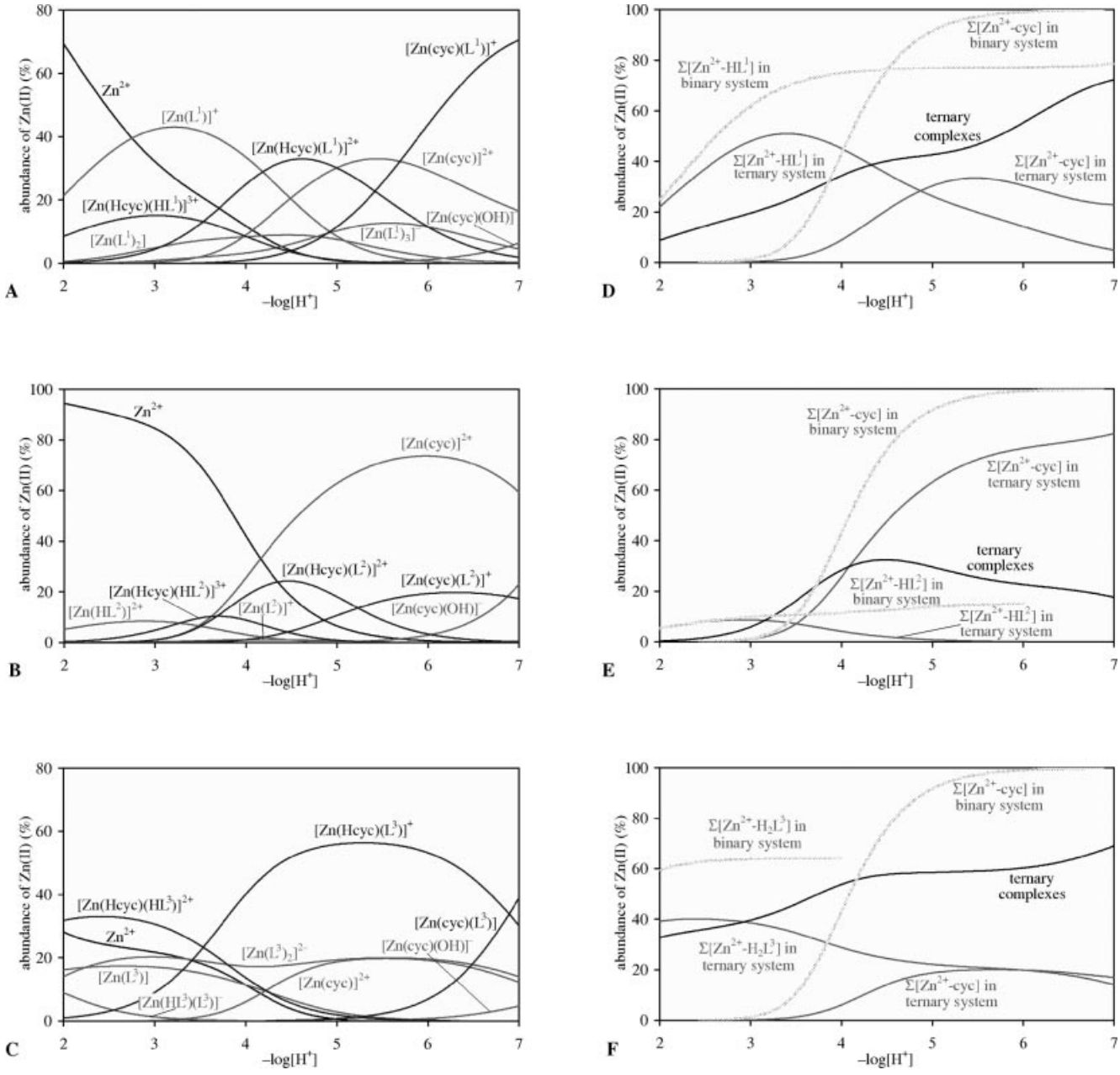


Figure 5. Calculated distribution of $Zn^{2+}$ in the ternary $Zn^{2+}$-cyclen-$H_xL^n$ systems as a function of –log[$H^+$] for a $Zn^{2+}$/cyclen/$H_xL^n$ molar ratio of 1:1:1: (A) $HL^1$, (B) $HL^2$, (C) $H_2L^3$ [binary $Zn^{2+}$-cyclen species and binary $Zn^{2+}$-$H_xL^n$ species (light grey) and ternary $Zn^{2+}$-cyclen-$H_xL^n$ species (dark grey)]. A comparison of the total abundance of all binary $Zn^{2+}$-cyclen species and all binary $Zn^{2+}$-$H_xL^n$ species in the ternary 1:1:1 mixtures (grey) and all ternary complexes (black) with total abundance of $Zn^{2+}$-cyclen and $Zn^{2+}$-$H_xL^n$ (dotted) complexes found in the binary mixtures for $Zn^{2+}$/cyclen = 1:1 and $Zn^{2+}$/$H_xL^n$ = 1:1: (D) $HL^1$, (E) $HL^2$, (F) $H_2L^3$. cyc = cyclen; $c(Zn^{2+})$ = 0.004 M in all cases.

 © 2007 Wiley-VCH Verlag GmbH & Co. KGaA, Weinheim 

binding of the third and fourth protons to the cyclen molecule occurs simultaneously. However, the value of $\log\beta_{4100} - \log\beta_{2100}$ (2.34) corresponds well with the sum of the $pK_A$ values (1.4 + 0.7 = 2.1) reported in the literature.[36] The out-of-cell method had to be used for potentiometric titrations of the $Zn^{2+}$-cyclen system due to the slow rate of the complex formation. The dominant species is $[Zn(cyclen)(H_2O)]^{2+}$, whose deprotonation starts at pH > 6.0, and the hydroxido complex $[Zn(cyclen)(OH)]^{+}$ is the main species in solution at pH = 8. The determined stability constants together with the literature values are also listed in Table 3 and the distribution diagram is shown in Figure S4 (see the Supporting Information).

### *Stability Constants in Ternary Systems*

The potentiometric titrations were performed by the out-of-cell method, as described in the Experimental Section. The determined stability constants are listed in Table 4 and the calculated distribution diagrams are shown in Figure 5A–C (except for the nicotinamide system, where the very low complex stabilities result in a very low abundance of the complex species). The distribution diagrams indicate the presence of binary $[Zn(L^n)]$ and $[Zn(cyclen)]^{2+}$ species. The abundance of the binary $[Zn(L^n)]$ species corresponds to their stability constant values, which are higher for the chelating ligands (picolinic and dipicolinic acids) than for nicotinic acid. The distribution of $Zn^{2+}$ between the binary and ternary species is evident from Figure 5D–F. The total abundance of ternary $[H_{0-2}(cyclen)(L^n)Zn]$ complexes in the systems with picolinic and dipicolinic acids increases with pH up to 70% in the neutral region as the abundance of the binary species decreases. The total abundance of $[H_{0-2}(cyclen)(L^2)Zn]$ in the nicotinic acid system is only 30%. The distributions in the binary systems are also included in Figure 5D–F for comparison. The nicotinamide system is different, and only the values of stability constants for the monoprotonated and non-protonated complexes were estimated here. Its value is close to the lower limit of the used method, so the interaction between $[Zn(cyclen)(H_2O)]^{2+}$ and nicotinamide is very weak, if any.

Formation of the 2111, 1111 and 0111 ternary complexes was observed in the systems with picolinic, dipicolinic and nicotinic acids. The acidic and basic groups of both ligands offer several possible protonation schemes and their corresponding dissociation constants. Comparison of the $pK_A$ values determined for the ternary systems with those found for the acids indicates the following scheme: formation of the diprotonated 2111 species starts at pH ≈ 2. These species deprotonate to the 1111 species with a $pK_A(2111)$ of about 3.5. These values are higher than the $pK_A$ values of carboxylic acid groups but lower than those corresponding to the pyridine nitrogen atoms. The proton is released from the pyridine nitrogen atom of the diprotonated 2111 species, and the dissociation constants decrease (compared with the free ligands), probably due to simultaneous coordination to $Zn^{2+}$. However, $pK_A(1111)$ is even higher than $pK_A$ of the protonated nitrogen atom of the pyridine ligands themselves (5–7), and thus this proton should be released from the cyclen amino group. The monoprotonated species can therefore be viewed as $[Zn(Hcyclen)(L^n)]$ and the diprotonated species as $[Zn(Hcyclen)(HL^n)]$; other microspecies with protonated carboxylic and pyridine functions could also be present.

The stability constants of the $[Zn(Hcyclen)(HL^n)]$, $[Zn(Hcyclen)(L^n)]$ and $[Zn(cyclen)(L^n)]$ species decrease in the order dipicolinic > picolinic > nicotinic acids (Table 4), in agreement with the stability constants of the binary systems (Table 2). The contribution of the acids to the stability of the ternary complexes {expressed as the equilibrium constant for the reaction $[Zn(cyclen)]^{2+} + (L^n)^{x-} \rightleftharpoons [Zn(cyclen)(L^n)]^{(2-x)+}$; $\log\beta_{0111} - \log\beta_{0101}$} is obviously lower than that of the $[Zn(L^n)]$ species for picolinic and dipicolinic acids. As these constants have a similar value to that corresponding to the formation of the $[Zn(cyclen)(imidazole)]^{2+}$ species ($\log K$ = 3.0),[37] which contains the more basic imidazole as a co-ligand, an extra stabilisation due to formation of the chelate ring should be assumed. These values are low (at the limit of potentiometry) in the case of nicotinic acid and nicotinamide and are therefore roughly comparable (see Table 4).

A structural motif in which the pyridinecarboxylic acid bridges two $[Zn(cyclen)]^{2+}$ subunits is observed in the complexes isolated in the solid state. All attempts to include a species of the $[\{Zn(cyclen)\}_2L^n]$ type into the chemical model to fit the potentiometric data failed. Thus, the presence of these species in solution is expected to be negligible; they crystallise in preference because of their low solubility.

### $^1$H NMR Study

To confirm the complexation behaviour suggested in the potentiometric section above, we monitored the changes in the $^1$H NMR spectra of a cyclen solution and its mixtures with $Zn^{2+}$. In the NMR spectra of cyclen itself, one peak of the $CH_2$ groups changes its position from $\delta$ = 3.03 ppm at pH = 1.9 to $\delta$ = 2.98 (pH = 9.0) and 2.66 ppm (pH = 12.2). The observed changes with pH correspond to the determined protonation constants.

A peak with a chemical shift close to that of free cyclen is observed for the system with $Zn^{2+}$ at pH ≈ 2, therefore no complexation is expected (Figure 6A). At pH > 2.55, a set of peaks attributable to the $[Zn(cyclen)(H_2O)]^{2+}$ species, namely two multiplets at $\delta$ = 2.65–2.87 ppm ($CH_2$ groups) and a broad singlet at $\delta$ = 3.67 ppm (NH groups), appear in addition to the signal for free cyclen. One can therefore conclude that the complex formed is rigid and that free and complexed ligand do not mutually exchange on the NMR timescale. The signal attributed to free cyclen disappears at pH > 5.0, which corresponds to full complexation of $Zn^{2+}$. The NMR spectra also indicate deprotonation of the coordinated water. The formation of the $[Zn(cyclen)(OH)]^{+}$ hydroxido complex does not influence the multiplets of the $CH_2$ groups, although the position of the signal corresponding to the NH proton is shifted from $\delta \approx 3.6$ ppm at pH = 6.99 to $\delta \approx 3.3$ ppm at pH = 8.97. The changes ob-

 © 2007 Wiley-VCH Verlag GmbH & Co. KGaA, Weinheim 

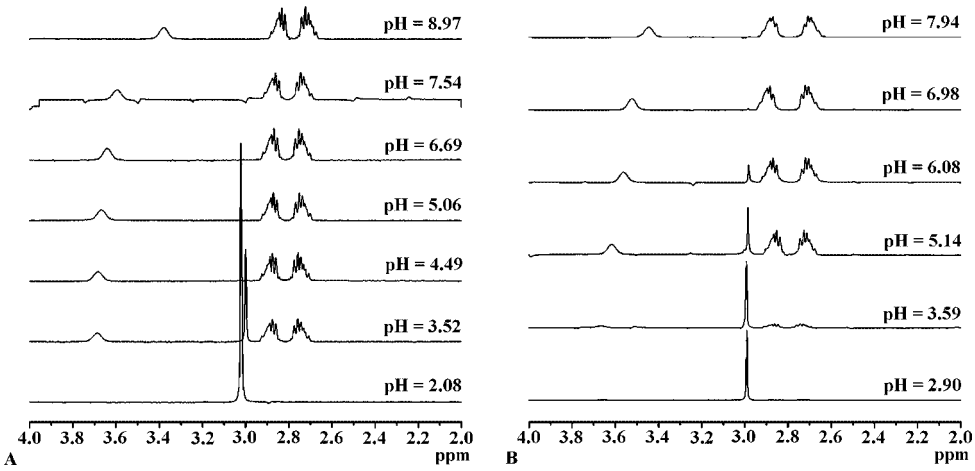


Figure 6. Examples of the $^1$H NMR spectra of the studied systems at different pH values: (A) $Zn^{2+}$-cyclen (1:1 mixture); (B) $Zn^{2+}$-cyclen-$HL^1$ (1:1:1 mixture).

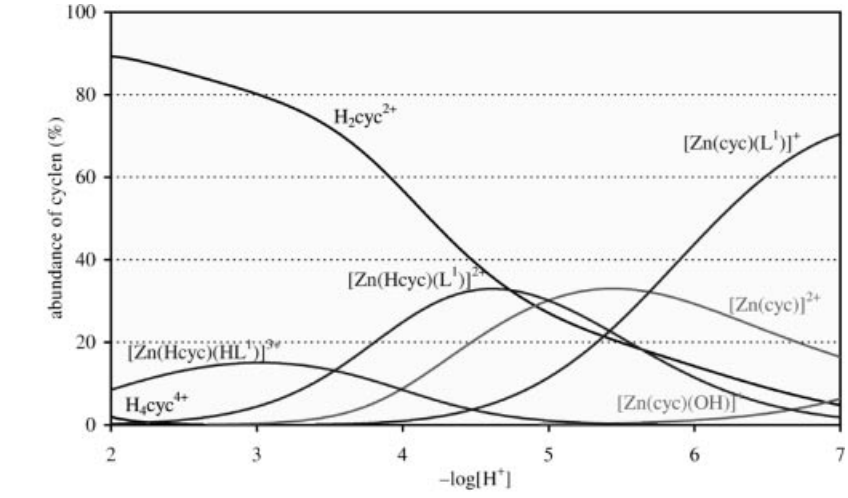


A

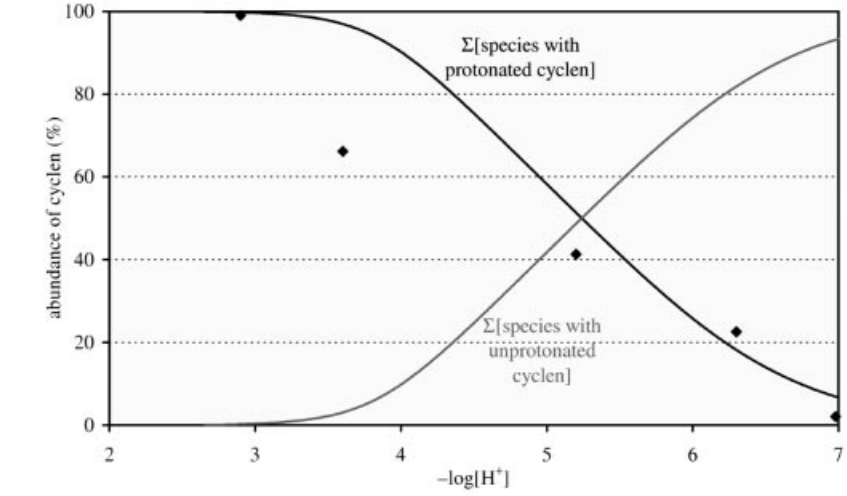


B

Figure 7. (A) Abundance of cyclen-containing species in the $Zn^{2+}$/cyclen/$HL^1$ (1:1:1) system; $c(Zn^{2+})$ = 0.004 M (ternary species: dark grey; binary species: light grey). (B) Comparison of the sum of the $^1$H NMR signal integrals of protonated cyclen species (diamonds) and the total abundance of protonated cyclam species (black line) and the deprotonated $[Zn(cyclen)]^{2+}$ complex (grey line), as calculated by potentiometry.

 © 2007 Wiley-VCH Verlag GmbH & Co. KGaA, Weinheim 

served in the NMR spectra correspond well to the speciation determined by potentiometry.

The changes in the cyclen region of the $^1$H NMR spectra of the ternary complexes as the pH is varied are also shown in Figure 6B for the system with picolinic acid. The trends in the spectra of the other ternary systems are similar. As is the case with the binary $[Zn(cyclen)]^{2+}$ species, the multiplets found close to $\delta$ = 2.8 ppm for all ternary systems can be assigned to deprotonated species of the type [Zn(cyclen)($L^n$)]. On the other hand, a singlet close to $\delta$ = 3 ppm is found in the ternary systems and is present even up to pH ≈ 6 for picolinic acid and 7 for dipicolinic acid; its position is slightly shifted at pH ≈ 5 from $\delta$ = 3.02 (free cyclen) to 2.95 ppm. Distribution diagrams B and E in Figure 6 show that about 80% of cyclen should be taken up in the complexes and that the protonated species [Zn(Hcyclen)($HL^n$)] and [Zn(Hcyclen)($L^n$)] should also be present at this pH along with the [Zn(cyclen)($L^n$)] species mentioned above. In contrast to [Zn(cyclen)($L^n$)], however, these protonated species are not likely to be rigid. Thus, the signal

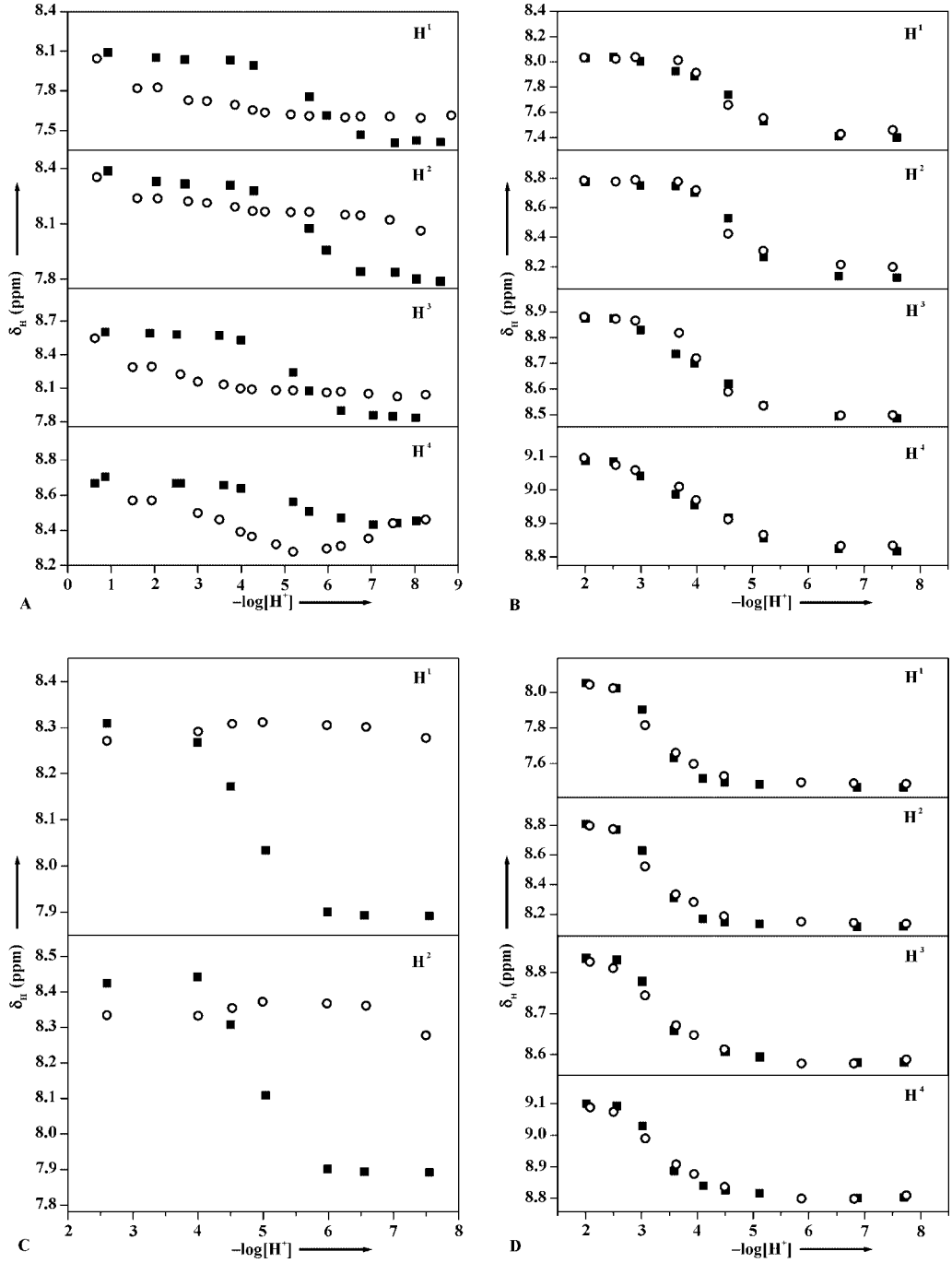


Figure 8. Comparison of $^1$H NMR chemical shifts of $HL^1$ (A), $HL^2$ (B), $H_2L^3$ (C) and $L^4$ (D) as a function of –log[$H^+$] for the free ligands (filled squares) and for the ligands in the ternary mixtures with $[Zn(cyclen)]^{2+}$ (open circles; see Figure 9 for assignment).

 © 2007 Wiley-VCH Verlag GmbH & Co. KGaA, Weinheim 

at $\delta$ = 2.95 ppm can be attributed to free cyclen and the protonated ternary [Zn(Hcyclen)(HL$^n$)] and [Zn(Hcyclen)(L$^n$)] complexes in fast chemical exchange. This assignment corresponds with the integration of the $^1$H NMR signals, as the relative intensities of the singlet at $\delta \approx$ 2.95 ppm {suggested for species protonated at the cyclen amino groups, such as free cyclen and [Zn(Hcyclen)(HL$^n$)] and [Zn(Hcyclen)(L$^n$)] complexes} and the signals of the deprotonated ternary complex {[Zn(cyclen)(L$^n$)], multiplets at $\delta \approx$ 2.8 ppm} nicely correlate with the speciation suggested by potentiometry (Figure 7). The signal at $\delta$ = 2.95 ppm also appears in the spectrum after addition of picolinic acid to a solution of [Zn(cyclen)]$^{2+}$ at pH ≈ 6.

The formation of ternary complexes with pyridine ligands bound in the axial position is also evident from a small but distinct change of the position of the amine proton signal at $\delta \approx$ 3.5 ppm. Unlike to the binary Zn$^{2+}$-cyclen system, where $\delta_H$(NH) starts to change with the formation of the hydroxido complex (at pH > 7), in the ternary systems the amine proton signal (Figure 6) moves from pH ≈ 4 due to formation of the deprotonated ternary species (Figure 7). The chemical shift of the amine protons seems to be sensitive to the replacement of the water molecule in the axial position with a hydroxide anion and/or a pyridine ligand.

The changes in the aromatic region of the $^1$H NMR spectra of both Zn$^{2+}$-cyclen-H$_x$L$^n$ systems and free ligands H$_x$L$^n$ as the pH changes are plotted in Figure 8. Assignment of the protons is shown in Figure 9. It is clear from the plots of the free acids that distinct breaks of the chemical shifts correspond to deprotonation of the pyridine nitrogen atom. The estimated p$K_A$ values for this reaction correspond to those determined from potentiometry (see Table 2). Deprotonation of the carboxylic groups causes only small changes of the spectra.

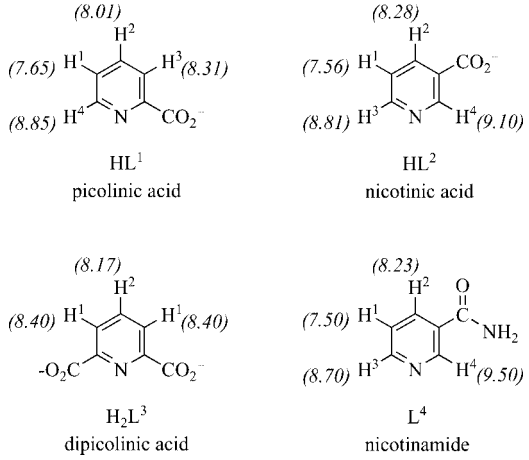


Figure 9. Assignment of the aromatic hydrogen atoms of HL$^1$, HL$^2$, H$_2$L$^3$ and L$^4$; $^1$H NMR chemical shifts for the protons (in ppm) in the free ligands are given in parentheses.

The plots of signals of the free ligands and the ligands in the ternary systems with nicotinic acid and nicotinamide are quite similar. This similarity indicates that deprotonation of the nitrogen atom is not significantly influenced by complexation and therefore that the interactions of both the ligands with [Zn(cyclen)]$^{2+}$ and in the acid region with free Zn$^{2+}$ are weak.

A different situation results from an analogous comparison of the systems with picolinic or dipicolinic acids. The chemical-shift changes of of free picolinic acid and its ternary system point to two deprotonation steps and simultaneous coordination: one in the pH range 1–2 and the other at pH = 3–5. The observed shapes of the $\delta_H$ vs. pH plots indicate that picolinic acid coordinates in the acid region through the carboxylic group whereas in the pH region 3–5 it forms a chelate through the carboxylate group and the nitrogen atom. This is especially evident from the signal of the H$^4$ proton, which is strongly influenced by the deprotonation of the pyridine nitrogen atom. In this case, the change in the signal position of the free acid and the ligand in the ternary system in the acid region is significant. For dipicolinic acid, the $\delta_H$ vs. pH plot indicates a similarity in the region of pH = 2–4 and, as above, the shape also points to the formation of a chelate. Thus, in both systems Zn$^{2+}$ is hexacoordinate in the [Zn(cyclen)(L$^n$)] species due to the bidentate coordination of the pyridinecarboxylic acids and tetradentate coordination of cyclen.

## Molecular Modelling

The minimal total energies, $E_{min}$, of both protonated and non-protonated [Zn(Hcyclen)(L$^n$)] and [Zn(cyclen)(L$^n$)] species were calculated to estimate an alternative Zn$^{2+}$ coordination by nitrogen or oxygen atoms and also to compare the energies of the protonated and non-protonated ternary complexes (see Table 5). As we concluded from the NMR results, monodentate coordination is found for nicotinic acid and nicotinamide and chelate formation for picolinic and dipicolinic acids. These coordination modes were therefore considered. The coordination sphere was completed with a molecule of water to give a coordination number of five where necessary.

Table 5. Minimised energies calculated for the ternary complexes.

| Species | $E_{min}$ [kJ mol$^{-1}$] Coordination of (L$^n$)$^{x-}$ through | | |
|---|---|---|---|
| | pyridine | oxygen | chelate |
| [Zn(cyclen)(L$^4$)]$^{2+}$ | 30.8 | 31.0 | |
| [Zn(Hcyclen)(H$_2$O)(L$^4$)]$^{3+}$ | 43.9 | 40.2 | |
| [Zn(cyclen)(L$^2$)]$^{+}$ | 29.1 | 28.8 | |
| [Zn(Hcyclen)(H$_2$O)(L$^2$)]$^{2+}$ | 43.5 | 39.2 | |
| [Zn(cyclen)(L$^1$)]$^{+}$ | | | 46.0 |
| [Zn(Hcyclen)(L$^1$)]$^{2+}$ | | | 43.9 |
| [Zn(cyclen)(L$^3$)] | | | 58.0 |
| [Zn(Hcyclen)(L$^3$)]$^{+}$ | | | 53.8 |

The $E_{min}$ values found for [Zn(Hcyclen)(H$_2$O)(L$^2$)]$^{2+}$ and [Zn(Hcyclen)(H$_2$O)(L$^4$)]$^{3+}$ are higher than those of [Zn(cyclen)(L$^2$)]$^{+}$ and [Zn(cyclen)(L$^4$)]$^{2+}$. As expected, species with fully coordinated cyclen are more stable than those in which one nitrogen atom is protonated (and non-coordi-

 © 2007 Wiley-VCH Verlag GmbH & Co. KGaA, Weinheim 

nated). Both protonated species prefer to coordinate through the carbonyl oxygen atom rather than through the pyridine nitrogen atom. On the other hand, the $E_{min}$ values of the $[Zn(cyclen)(L^2)]^+$ and $[Zn(cyclen)(L^4)]^{2+}$ are virtually the same for both coordination modes, therefore an equilibrium between interactions through nitrogen and oxygen atoms is assumed in these species. The species $[Zn(Hcyclen)(H_2O)(L^2)]^{2+}$ and $[Zn(Hcyclen)(H_2O)(L^4)]^{3+}$ are present in acid solution (pH ≈ 3–4). There are no significant differences in the chemical shifts of the aromatic proton signals between the free ligands and the ligands in the ternary mixtures in this region, which indicates only a weak interaction between $[Zn(cyclen)]^{2+}$ and $HL^2$ or $L^4$.

As mentioned above, the formation of chelates for both $(L^1)^-$ and $(L^3)^{2-}$ is assumed in both protonated ($[Zn(Hcyclen)(L^1)]^{2+}$ and $[Zn(Hcyclen)(L^3)]^+$) and deprotonated ($[Zn(cyclen)(L^1)]^+$ and $[Zn(cyclen)(L^3)]$) species, and these types were included in our treatment. In contrast to the systems with nicotinic acid and nicotinamide, the values of $E_{min}$ in systems containing picolinic and dipicolinic acids are lower for the protonated complexes than for the deprotonated species. This corresponds to NMR titrations in which the presence of the protonated species was confirmed even at pH ≈ 7.

These results support the potentiometric conclusions, which suggest that the formation of an additional chelate in the $[Zn(cyclen)]^{2+}$ moiety destabilizes the tetradentate coordination of cyclen. Thus, the $Zn^{2+}$ complexes with coordination number six seem to be less stable than those with coordination number five.

In addition, we searched for intramolecular hydrogen bonds between the cyclen amino group and the carboxylate groups of the coordinated acids similar to those found in the $Zn^{2+}$-cyclen-thymine system.[38] The only interaction found was in the $[Zn(cyclen)(L^3)]$ species, with an estimated $H_{amine}\cdots O_{carboxylate}$ distance of around 2.16 Å (which corresponds to a weak hydrogen bond).

## Conclusions

The central $Zn^{2+}$ ion in the $[Zn(cyclen)(L^n)]$ complexes of nicotinic acid or nicotinamide is pentacoordinate in the solid state. This corresponds to the known structural motif of analogous complexes containing the $[Zn(cyclen)]^{2+}$ fragment. Picolinic acid forms a $[\{Zn(cyclen)\}_2(\mu\text{-}L^1\text{-}O{:}N,O')]^{3+}$ cation in the solid state, where one zinc atom is pentacoordinate and the other hexacoordinate. A hexacoordinate motif has not yet been observed for the $[Zn(cyclen)]^{2+}$ fragment and is present in only a few complexes with *N*-substituted cyclen derivatives.

The NMR results in solution indicate that $Zn^{2+}$ is also hexacoordinate in the $[Zn(cyclen)(L^n)]$ species with picolinic and dipicolinic acids, and protonated $[Zn(Hcyclen)(HL^n)]$ and $[Zn(Hcyclen)(L^n)]$ species have also been identified. The cyclen ligand in these species should be protonated and only tridentate coordination is assumed from a comparison of $pK_A$ values; the coordination number of the central ion should therefore be five. Unfortunately, all attempts to prepare crystals of the protonated species to confirm this hypothesis failed.

The difference between the stability constants of $[Zn(cyclen)]^{2+}$ and $[Zn(L^{1,3})]$ is 9–10 orders of magnitude and between $[Zn(cyclen)]^{2+}$ and $[Zn(L^2)]^+$ 13 orders of magnitude (Tables 2 and 3). When comparing the stability constants of the binary systems, it is surprising that coordination of $H_xL^n$ to $[Zn(cyclen)]^{2+}$ causes the protonation of cyclen in the $[Zn(Hcyclen)(HL^n)]$ and $[Zn(Hcyclen)(L^n)]$ species even though the $[Zn(Hcyclen)]^+$ ion has not been identified in the binary system. This comparison suggests the preference for a coordination number of five in $Zn^{2+}$ complexes. This corresponds to Hancock's conclusion based on a comparison of the binding properties of $[Zn(cyclen)]^{2+}$ and [Zn(1,5,9-triazacyclododecane)]$^{2+}$ complexes.[39] The structures of the known zinc enzymes[6] also indicate the preference of $Zn^{2+}$ to form only three coordination bonds when anchored in the catalytic site of proteins. From this point of view, the [Zn(1,5,9-triazacyclododecane)]$^{2+}$ complex would be more convenient for modelling the zinc enzymes. On the other hand, the observed protonation of the $[Zn(cyclen)]^{2+}$ fragment could be utilized to model hydrolases in which one basic site is required. In addition, the affinity of $[Zn(cyclen)]^{2+}$ for picolinic and dipicolinic acids indicates potential inhibition properties of their derivatives for zinc enzymes. Generally, the possibility of protonating cyclen in its $Zn^{2+}$ complexes should be taken into account when considering the $[Zn(cyclen)]^{2+}$ fragment as a model for the above enzymes.

## Experimental Section

**General:** The pyridine derivatives were purchased from Fluka and recrystallised from water before use. Cyclen was obtained from Strem and purified by vacuum sublimation for potentiometric measurements. Elemental analyses were performed at the Department of Organic Chemistry, P. J. Šafárik University, Košice. The zinc content was determined by complexometric titration with $Na_2H_2$edta after sample mineralisation. The water used in physicochemical measurements was purified using the Milli-Q System (Millipore). $Zn(ClO_4)_2\cdot 6H_2O$ and $Zn(NO_3)_2\cdot 6H_2O$ (Lachema) were recrystallised from slightly acidified water. The other chemicals were of analytical purity.

### Preparation of the Zinc(II) Complexes

**$[Zn(cyclen)(NO_3)]ClO_4$:** A solution of cyclen (345 mg, 2.00 mmol) in water (20 mL) was acidified with dilute $HNO_3$ [378 mg of concentrated acid (6.00 mmol) in 20 mL of water]. An aqueous solution (20 mL) of zinc perchlorate hexahydrate (745 mg, 2.00 mmol) was then added, and the pH was adjusted with 1 M NaOH to 5.9. The mixture was allowed to stand for 24 h and then an equal volume of ethanol was added. Colourless crystals were obtained after a few days. Yield: 0.55 g (69%). $C_8H_{20}ClN_5O_7Zn$ (399.11): calcd. C 24.07, H 5.05, N 17.55, Zn 16.38; found C 20.38, H 4.42, N 13.52, Zn 17.85.

**$[\{Zn(cyclen)\}_2(\mu\text{-}L^1\text{-}N{:}O,O')](ClO_4)_3\cdot H_2O$:** Zinc perchlorate hexahydrate (172 mg, 0.462 mmol) in water (5 mL) was slowly added to an aqueous solution (5 mL) of cyclen (80 mg, 0.462 mmol). After standing for 24 h, an equimolar amount of picolinic acid (58 mg,

 © 2007 Wiley-VCH Verlag GmbH & Co. KGaA, Weinheim 

0.462 mmol) in water (5 mL) was added, and, after a further 2 h, the pH was adjusted with 1 M NaOH to 5.6. The solution was left to stand in air for 24 h, then acetone (10 mL) was added, and colourless crystals were obtained after a few days. Yield: 0.14 g (66%). $C_{22}H_{46}Cl_3N_9O_{15}Zn_2$ (913.78): calcd. C 29.50, H 4.95, N 14.07, Zn 14.60; found C 29.14, H 4.78, N 12.95, Zn 13.75.

**[{Zn(cyclen)}$_2$(μ-L$^2$-*N*,*O*)](ClO$_4$)$_3$:** Zinc perchlorate hexahydrate (86 mg, 0.232 mmol) in water (3 mL) was slowly added to an aqueous solution (7 mL) of cyclen (40 mg, 0.232 mmol). After standing for 24 h, an equimolar amount of nicotinic acid (29 mg, 0.232 mmol) in water (10 mL) was added, and the solution was left to stand at room temperature (pH = 4.3). Colourless and transparent crystals were obtained after several days. Yield: 0.065 g (63%). $C_{22}H_{44}Cl_3N_9O_{14}Zn_2$ (895.76): calcd. C 29.50, H 4.95, N 14.07, Zn 14.60; found C 29.49, H 4.51, N 12.99, Zn 15.75.

**[Zn(cyclen)(L$^4$-*O*)](ClO$_4$)$_2$:** Zinc perchlorate hexahydrate (172 mg, 0.462 mmol) in water (5 mL) was slowly added to an aqueous solution (5 mL) of cyclen (80 mg, 0.462 mmol). After standing for 24 h, an equimolar amount of nicotinamide (56 mg, 0.462 mmol) in water (5 mL) was added. After another 2 h, once the pH of the solution had stabilized at 5.9, acetone (10 mL) was added. The colourless product crystallised over several days. Yield: 0.19 g (74%). $C_{14}H_{26}Cl_2N_6O_9Zn$ (558.68): calcd. C 30.10, H 4.69, N 15.04 Zn 11.70; found C 29.90, H 4.39, N 14.33, Zn 10.93.

**X-ray Crystallography:** Colourless prismatic crystals of the complexes selected from the bulk before filtration were used for data collection. Unit cell determination and data collection were carried out with a Nonius KappaCCD diffractometer using graphite-monochromated Mo-$K_\alpha$ radiation ($\lambda$ = 0.71070 Å). The phase problem was solved with SIR-97[40] and structure refinement was carried out by the full-matrix least-squares method on $F^2$ using the SHELXL-97[41] program. All non-hydrogen atoms were refined anisotropically. Experimental crystallographic parameters of all complexes are listed in Table 6. CCDC-633924 for [Zn(cyclen)(NO$_3$)]ClO$_4$, -633926 for [{Zn(cyclen)}$_2$(μ-L$^1$-*O:N,O′*)](ClO$_4$)$_3$·H$_2$O, -634730 for [{Zn(cyclen)}$_2$(μ-L$^2$-*N*,*O*)](ClO$_4$)$_3$ and -633925 for [Zn(cyclen)(L$^4$-*O*)](ClO$_4$)$_2$ contain the supplementary crystallographic data for this paper. These data can be obtained free of charge from The Cambridge Crystallographic Data Centre via www.ccdc.cam.ac.uk/data_request/cif.

**$^1$H NMR Titrations:** $^1$H NMR spectra were recorded with a Varian–Unity Inova 400 spectrometer. Samples were prepared in $H_2O$ and the spectra recorded relative to a $D_2O$ insert containing 0.5% *t*BuOH ($\delta$ = 1.25 ppm) as reference and lock. Four FIDs were accumulated for each spectrum using a standard-transmitter water-presaturated pulse sequence. The initial volume of solutions for each titration point was 0.7 mL. In the titration experiments, solutions contained aliquots of Zn(NO$_3$)$_2$·6H$_2$O, cyclen and an appropriate ligand. The initial concentration of individual species was 0.1 M for the ternary Zn$^{2+}$-cyclen-HL$^{1,2}$ and Zn$^{2+}$-cyclen-HL$^4$ mixtures and 0.05 M for the Zn$^{2+}$-cyclen-H$_2$L$^3$ system. The required pH values of the solutions were attained by adding aqueous 0.1 M NaOH or 0.1 M HNO$_3$ solutions.

**Potentiometric Titrations:** Stock solutions of pyridine derivatives were prepared by dissolving solid samples in deionised water. Their concentrations were calculated from the weight of samples and agreed well with those found in calculations of protonation constants of the ligands. The cyclen stock solution (approx. 0.02 M) was prepared by dissolving the solid in deionised water followed by addition of a standardised HNO$_3$ solution (final concentration of acid in the stock solution of cyclen was 0.06 M); the exact concentration of cyclen was calculated together with the determination of protonation constants. The preparation of standard solutions, titrations and calculation were performed as published previously.[42] Potentiometric measurements were carried out with a PHM 84 pH-meter, ABU 80 autoburette and a GK 2401 B combination electrode (Radiometer) in a glass vessel (10 mL) thermostatted at 25.0 ± 0.1 °C at an ionic strength $I$(KNO$_3$) of 0.1 M. An inert atmosphere was ensured by a constant flow of argon saturated with the solvent vapour. For determination of the protonation constants, the concentration of ligands was 0.004 M and the initial volume was 5 mL. In the case of Zn$^{2+}$ complexes with HL$^1$, HL$^2$, H$_2$L$^3$ and L$^4$, the volume of the initial solution was also 5 mL and the ligand concentration ranged from 0.002 to 0.004 M. The Zn$^{2+}$/ligand ratio was 2:1, 1:1, 1:2 and 1:4, with [Zn$^{2+}$] = 0.001–0.004 M. At least three parallel titrations were carried out for each ratio; each titration consisted of 40–50 points. The total dataset consisted of approximately 500 data points per given Zn-H$_x$L$^n$ system. Equilibration was slow for the Zn$^{2+}$-cyclen and ternary mixtures; therefore the out-of-cell method was used. Around 4 h was required to attain equilibrium in the binary Zn$^{2+}$-cyclen system. For the ter-

Table 6. Crystallographic parameters of the studied complexes.

| | [Zn(cyclen)(NO$_3$)]ClO$_4$ | [{Zn(cyclen)}$_2$(μ-L$^1$-*O:N,O′*)](ClO$_4$)$_3$·H$_2$O | [{Zn(cyclen)}$_2$(μ-L$^2$-*N*,*O*)](ClO$_4$)$_3$ | [Zn(cyclen)(L$^4$-*N*)](ClO$_4$)$_2$ |
|---|---|---|---|---|
| Empirical formula | $C_8H_{20}ClN_5O_7Zn$ | $C_{22}H_{48}Cl_3N_9O_{15}Zn_2$ | $C_{22}H_{44}Cl_3N_9O_{14}Zn_2$ | $C_{14}H_{26}Cl_2N_6O_9Zn$ |
| $M_r$ | 399.11 | 913.78 | 895.75 | 558.68 |
| Crystal colour | colourless | colourless | colourless | colourless |
| Crystal dimensions [mm] | unknown | 0.13 × 0.15 × 0.23 | 0.3 × 0.25 × 0.25 | 0.15 × 0.25 × 0.55 |
| Crystal system | monoclinic | monoclinic | monoclinic | monoclinic |
| Space group | $P2_1/n$ | $P2_1/c$ | $P2_1/c$ | $P2_1/n$ |
| Lattice parameters | $a$ = 8.8470(3) Å | $a$ = 8.6920(4) Å | $a$ = 15.5830(2) Å | $a$ = 8.8030(2) Å |
| | $b$ = 14.9780(9) Å | $b$ = 22.9190(8) Å | $b$ = 17.1720(2) Å | $b$ = 18.7180(5) Å |
| | $c$ = 12.0220(6) Å | $c$ = 18.9450(8) Å | $c$ = 14.4250(2) Å | $c$ = 13.3320(4) Å |
| | $\beta$ = 93.512(3)° | $\beta$ = 90.747(3)° | $\beta$ = 114.4890(9)° | $\beta$ = 96.0560(15)° |
| $V$ [Å]$^3$ | 1590.05(14) | 3773.75(3) | 3512.76(8) | 2184.51(10) |
| $Z$ | 4 | 4 | 4 | 4 |
| $D_{calcd.}$ [g cm$^{-3}$] | 1.667 | 1.612 | 1.694 | 1.699 |
| $\mu$ [mm$^{-1}$] | 1.753 | 1.558 | 1.670 | 1.43 |
| $2\theta_{max}$ [°] | 50.01 | 50.05 | 55.00 | 55.03 |
| Measured reflections | 11268 | 17483 | 57756 | 28957 |
| Independent reflections [$I > 2\sigma(I)$] | 2814 | 6565 | 8048 | 4157 |
| $R_1$ | 0.0471 | 0.1211 | 0.039 | 0.0542 |
| $wR_2$ | 0.1213 | 0.3286 | 0.1021 | 0.1417 |

 © 2007 Wiley-VCH Verlag GmbH & Co. KGaA, Weinheim 

nary systems, the $Zn^{2+}$-cyclen complex was formed first (overnight equilibration), then a solution of the second ligand was added along with an appropriate amount of hydroxide solution. The final reaction mixture was left to stand for at least 15 h for equilibration. The molar ratios used were 1:1 for $Zn^{2+}$-cyclen and 1:1:1 for the ternary systems, with concentrations of the components in the range 0.003–0.004 M. The initial volume of the solution (before addition of the hydroxide solution) for each titration point was 1 mL. The titrations were performed at least in duplicate with 25 points per titration. A typical dataset consisted of around 70 data points for each system. Precise calibration of the electrode was carried out by titration of 0.03 M $HNO_3$ with 0.2 M KOH in the range $-\log[H^+] = 1.8–12.0$, with the pH-meter yielding $E$ values. The relation between $E$ and $-\log[H^+]$ is expressed by Equation (1) where the term $E_0$ contains the standard potentials of the electrodes used and the contribution of inert ions to the liquid-junction potential. $S$ corresponds to the Nernstian slope, the value of which should be close to the theoretical value, and $j_1 \times [H^+]$ and $j_2 \times [OH^-] = j_2 \times K_w/[H^+]$ are contributions of the $H^+$ and $OH^-$ ions, respectively, to the liquid-junction potential. The $pK_w$ value was 13.78 [Equation (1)].

$$E = E_0 - S \times (-\log[H^+]) + j_1 \times [H^+] + j_2 \times K_w/[H^+] \quad (1)$$

It is clear that $j_1$ and $j_2$ cause deviation from a linear dependence between $E$ and $-\log[H^+]$ only in strongly acid and strongly alkaline solutions. The protonation and stability constants were calculated with the OPIUM software package.[43]

**Molecular Modelling Calculations:** The calculations were carried out with a Pentium® IV 2.0 GHz PC using Hyperchem Pro™ version 7.04.[44] The Conformational Search module was used to find the lowest energy conformation of the coordinated cyclen, analyzing the systems in 1000 cycles. The energy of the systems in vacuo was minimised using molecular mechanics employing the MM+ force field and the Polak–Ribiere (conjugate gradient) algorithm, ending at an energy gradient of 0.01 kJ mol$^{-1}$. The geometry was optimised without any constraints by allowing all atoms, bonds and dihedral angles to change simultaneously.

**Supporting Information** (see footnote on the first page of this article): Colour versions of Figures 5 and 7; selected geometric parameters found in the studied crystal structures; arrangement of the chelate rings in the $[\{Zn(cyclen)\}_2(\mu\text{-}L^1\text{-}O{:}N,O')]^{3+}$ cation; distribution of the complex species formed in the $Zn^{2+}$-$H_xL^n$ systems as a function of $-\log[H^+]$; distribution of the complex species formed in the $Zn^{2+}$-cyclen system as a function of $-\log[H^+]$.

## Acknowledgments

Financial support from the Ministry of the Education of the Slovak Republic (VEGA 1/2474/05 and MVTS 9), a bilateral contract between the Czech Republic and the Slovak Republic (SK-77/CZ-81) and the long-term research plan of the Ministry of Education, Youth and Sports of the Czech Republic (MSM0021620857) is acknowledged.

[1] a) W. N. Lipscomb, N. Straeter, *Chem. Rev.* **1996**, *96*, 2375–2434; b) A. Neuberger, K. Brocklehurst, *Hydrolytic Enzymes*, Elsevier, Amsterdam, **1987**; c) T. G. Spiro, *Zinc Enzymes*, Wiley, New York, **1983**.
[2] B. L. Vallee, D. S. Auld, *Biochemistry* **1990**, *29*, 5647–5659.
[3] D. W. Christianson, W. N. Lipscomb, *Acc. Chem. Res.* **1989**, *22*, 62–69.
[4] B. L. Vallee, D. S. Auld, *Acc. Chem. Res.* **1993**, *26*, 543–551.
[5] E. Kimura, *Acc. Chem. Res.* **2001**, *34*, 171–179.
[6] S. Aoki, E. Kimura in *Comprehensive Coordination Chemistry* (Eds.: J. A. McCleverty, T. J. Meyer), Elsevier, Amsterdam, **2004**, vol. 8, pp. 601–640.
[7] X. Zhang, R. van Eldik, *Inorg. Chem.* **1995**, *34*, 5606–5614.
[8] M. Brauer, J. L. Perez-Lustres, J. Weston, E. Anders, *Inorg. Chem.* **2002**, *41*, 1454–1463.
[9] T. Koike, E. Kimura, *J. Am. Chem. Soc.* **1991**, *113*, 8935–8941.
[10] M. Kalesse, A. Loos, *Liebigs Ann.* **1996**, 935–939.
[11] E. Kimura, Y. Kodama, T. Koike, M. Shire, *J. Am. Chem. Soc.* **1995**, *117*, 8304–8311.
[12] T. Koike, M. Takamura, E. Kimura, *J. Am. Chem. Soc.* **1994**, *116*, 8443–8449.
[13] B. König, M. Pelka, R. Reichenbach-Klinke, J. Schelter, J. Daub, *Eur. J. Org. Chem.* **2001**, 2297–2303.
[14] R. Reichenbach-Klinke, M. Kruppa, B. König, *J. Am. Chem. Soc.* **2002**, *124*, 12999–13007.
[15] a) R. Cibulka, R. Vasold, B. König, *Chem. Eur. J.* **2004**, *10*, 6223–6231; b) S. C. Ritter, M. Eiblmaier, V. Michlová, B. König, *Tetrahedron* **2005**, *61*, 5241–5251.
[16] T. Walenzyk, B. König, *Inorg. Chim. Acta* **2005**, *358*, 2269–2274.
[17] T. Koike, S. Kajitani, I. Nakamura, E. Kimura, M. Shiro, *J. Am. Chem. Soc.* **1995**, *117*, 1210–1219.
[18] S. Aoki, E. Kimura, *Chem. Rev.* **2004**, *104*, 769–787.
[19] S. Aoki, E. Kimura, *Rev. Mol. Biotechnol.* **2002**, *90*, 129–155.
[20] C. Pariya, T.-Y. Chi, T. K. Mishra, C.-S. Chung, *Inorg. Chem. Commun.* **2002**, *5*, 119–123.
[21] S. Aoki, M. Shiro, T. Koike, E. Kimura, *J. Am. Chem. Soc.* **2000**, *122*, 576–584.
[22] S. Aoki, M. Shiro, E. Kimura, *Chem. Eur. J.* **2002**, *8*, 929–939.
[23] S. Aoki, E. Kimura, *J. Am. Chem. Soc.* **2000**, *122*, 4542–4548.
[24] D. S. Turygin, M. Subat, O. A. Raitman, V. V. Arslanov, B. König, M. A. Kalinina, *Angew. Chem. Int. Ed.* **2006**, *45*, 5340–5344.
[25] Y. Yamada, S. Aoki, *J. Inorg. Biol. Chem.* **2006**, *11*, 1007–7023.
[26] M. Subat, A. S. Borovik, B. König, *J. Am. Chem. Soc.* **2004**, *126*, 3185–3190.
[27] A. W. Addison, T. N. Rao, J. Reedijk, J. van Rijn, G. C. Verschoor, *J. Chem. Soc. Dalton Trans.* **1984**, 1349–1356.
[28] F. H. Allen, *Acta Crystallogr., Sect. B* **2002**, *58*, 380–388.
[29] I. J. Bruno, J. C. Cole, P. R. Edgington, M. Kessler, C. F. Macrae, P. McCabe, J. Pearson, R. Taylor, *Acta Crystallogr., Sect. B* **2002**, *58*, 389–397.
[30] H. Maumela, R. D. Hancock, L. Carlton, J. H. Reibenspies, K. P. Wainwright, *J. Am. Chem. Soc.* **1995**, *117*, 6698–6707.
[31] G. M. Norante, M. Di Vaira, F. Mani, S. Mazzi, P. Stoppioni, *Inorg. Chem.* **1990**, *29*, 2822–2829.
[32] A. Riesen, M. Zehnder, T. A. Kaden, *Acta Crystallogr., Sect. C* **1991**, *47*, 531–532.
[33] E. Kimura, T. Gotoh, T. Koike, M. Shiro, *J. Am. Chem. Soc.* **1999**, *121*, 1267–1274.
[34] A. Schrodt, A. Neubrand, R. van Eldik, *Inorg. Chem.* **1997**, *36*, 4579–4584.
[35] E. Kimura, S. Aoki, T. Koike, M. Shiro, *J. Am. Chem. Soc.* **1997**, *119*, 3068–3076.
[36] A. E. Martell, R. M. Smith, R. J. Motekaitis, *NIST Standard Reference Database 46 (Critically Selected Stability Constants of Metal Complexes)*, Version 7.0, NIST Standard Reference Data, Gaithersburg, MD 20899, U. S. A., **2003**.
[37] M. Kruppa, D. Frank, H. Leffler-Schuster, B. König, *Inorg. Chim. Acta* **2006**, *359*, 1159–1168.
[38] E. Kimura, N. Katsube, T. Koike, M. Shiro, S. Aoki, *Supramol. Chem.* **2002**, *14*, 95–102.
[39] M. H. Salter Jr, J. H. Reibenspies, S. B. Jones, R. D. Hancock, *Inorg. Chem.* **2005**, *44*, 2791–2797.

 © 2007 Wiley-VCH Verlag GmbH & Co. KGaA, Weinheim 

[40] A. Altomare, M. C. Burla, M. Camalli, G. Cascarano, C. Giacovazzo, A. Guagliardi, G. Polidori, *J. Appl. Crystallogr.* **1994**, *27*, 435–435.
[41] G. M. Sheldrick, *SHELXL-97, Program for the Refinement of Crystal Structures*, University of Göttingen, Germany, **1997**.
[42] P. Táborský, P. Lubal, J. Havel, J. Kotek, P. Hermann, I. Lukeš, *Collect. Czech. Chem. Commun.* **2005**, *70*, 1909–1942.
[43] M. Kývala, I. Lukeš, *Proceedings of the International Conference on Chemometrics 95*, Pardubice, Czech Republic, p. 63, University of Pardubice, Pardubice **1995**; the full version of "OPIUM" is available free of charge from http://www.natur.cuni.cz./~kyvala/opium.htm.
[44] *Hyperchem Pro*™, release 7.04 for Windows, Molecular Modelling System, Hypercube, Inc., Gainesville, Florida, USA, **2002**.
Received: February 8, 2007
Published Online: July 6, 2007

 © 2007 Wiley-VCH Verlag GmbH & Co. KGaA, Weinheim 

DOI: 10.1002/ejic.200700041

# Novel Ruthenium(II) N-Heterocyclic Carbene Complexes as Catalyst Precursors for the Ring-Opening Metathesis Polymerization (ROMP) of Enantiomerically Pure Monomers: X-ray Structures, Reactivity, and Quantum Chemical Considerations

**Michael R. Buchmeiser,*[a,b] Dongren Wang,[a] Yan Zhang,[a] Sergej Naumov,[a] and Klaus Wurst[c]**

**Keywords:** Carbene ligands / Ruthenium / ROMP / Quantum chemistry

Four chiral, enantiomerically pure monomers, *exo*,*exo*-*N*,*N*-(norborn-5-ene-2,3-dicarbimido)-L-valine ethyl ester (*exo*-**1**), *endo*,*endo*-*N*,*N*-(norborn-5-ene-2,3-dicarbimido)-L-valine ethyl ester (*endo*-**1**), *exo*,*exo*-*N*,*N*-(norborn-5-ene-2,3-dicarbimido)-L-valine-*tert*-butylamide (*exo*-**2**), and *endo*,*endo*-*N*,*N*-(norborn-5-ene-2,3-dicarbimido)-L-valine-*tert*-butylamide (*endo*-**2**), were subjected to ring-opening metathesis polymerization (ROMP) with $Ru(CF_3CO_2)_2(IMesH_2)$(*p*-cymene) (**3**), $Ru(CF_3CO_2)_2$(IMes)(*p*-cymene) (**4**), $RuCl_2$(IMes)(*p*-cymene) (**5**), $Ru(PCy_3)(CF_3CO_2)_2$(*p*-cymene) (**6**), $Ru(CF_3CO_2)_2$(*p*-cymene)·$CF_3COOAgPCy_3$(**6a**),$Ru(CF_3CO_2)_2(PPh_3)$(*p*-cymene) (**7**), $Ru(CF_3CO_2)_2$(IMes)$(PhNC)_3$ (**8**), and $Ru(CF_3CO_2)_2(IMesH_2)(PhNC)_3$ (**9**) (IMes = 1,3-dimesitylimidazol-2-ylidene, $IMesH_2$ = 1,4-dimesityl-4,5-diyhdroimidazolin-2-ylidene, $PCy_3$ = tricyclohexylphosphane). X-ray structures of precatalysts **3** and **6**–**9** are presented. Compounds **3** and **4** displayed significant ROMP activity, allowing for the controlled, yet nonliving synthesis of the corresponding polymers with polydispersity indices (PDIs) in the range of 1.17–2.14. In all cases the *exo* isomers of compounds **1** and **2** were polymerized by preference. While poly(*endo*-**1**) was formed in an all-*trans* form, poly(*exo*-**1**) and poly(*exo*-**2**) were produced in their *cis*/*trans* forms with a *cis* content of around 40%. Calculations carried out at the B3LYP/LACVP* level suggest two possible mechanisms for the increased reactivity of the 2,3-$R_2$-*exo*,*exo* isomers of norborn-5-ene-2,3-dicarbimido derivatives resulting in the formation of the ROMP-active $Ru^{IV}$ alkylidene.
(© Wiley-VCH Verlag GmbH & Co. KGaA, 69451 Weinheim, Germany, 2007)

## Introduction

The first reports on the activity of ruthenium(II) complexes in ring-opening metathesis polymerization (ROMP) were published some 15 years ago[1] and may certainly be regarded as the basis for the development of well-defined ruthenium(IV)–alkylidene complexes.[1,2] In 1997, Hafner et al. reported on the photo- and thermal activation of $Ru^{II}$ and $Os^{II}$ arene complexes of the general formula $MCl_2(PR_3)$(*p*-cymene) (M = Ru, Os) in the polymerization of norborn-2-ene.[3] Thermal initiation of the ROMP of norborn-2-ene was also observed by Lindner et al. for Ru(arene)H[P–O] complexes.[4] Noels et al. showed that complexes of the general formula $RuCl_2(PCy_3)$(arene) can be activated by treatment with diazo compounds to form ROMP-active Grubbs-type catalysts.[5] $RuCl_2$(IMes)(*p*-cymene) (**5**) (IMes = 1,3-dimesitylimidazol-2-ylidene) was first reported by Nolan et al., who showed that this complex was capable of performing ring-closing metathesis (RCM) reactions.[6] Later, Dixneuf et al. reported on the in situ formation of **5** and $RuCl_2(IMesH_2)$(*p*-cymene) ($IMesH_2$ = 1,4-dimesityl-4,5-diyhdroimidazolin-2-ylidene) and their use in RCM, enyne metathesis reactions,[7–10] and later in ROMP.[11] Noels et al. suggested the use of **5**, $RuCl_2(IMesH_2)$(*p*-cymene), and derivatives thereof as photoinitiators that can be activated by visible light.[12,13] However, in view of their inherent activity even *in the absence of light*,[14] they appear less suitable for these applications. As a matter of fact, calculations at the B3LYP/LACVP* level indicate a dissociation energy $E_{diss}$ of only 8.7 kcal/mol for the dissociation of the *p*-cymene ligand in $RuCl_2(IMesH_2)$(*p*-cymene).

In an ongoing project we are interested in the synthesis of novel latent metathesis catalysts[15,16] that may be converted into the active species in the presence of a monomer either thermally or by the action of (UV) light.[14] Key properties of such compounds are high thermal stability of

[a] Leibniz-Institut für Oberflächenmodifizierung e.V. (IOM), Permoserstr. 15, 04318 Leipzig, Germany
Fax: +49-341-235-2584
E-mail: michael.buchmeiser@iom-leipzig.de
dongren.wang@iom-leipzig.de
chem_yzhang@yahoo.com
sergej.naumov@iom-leipzig.de
[b] Institut für Technische Chemie, Universität Leipzig, Linnéstr. 3, 04103 Leipzig, Germany
[c] Institut für Allgemeine, Anorganische und Theoretische Chemie, Leopold-Franzens-Universität Innsbruck, Innrain 52 a, 6020 Innsbruck, Austria
E-mail: klaus.wurst@uibk.ac.at
Supporting information for this article is available on the WWW under http://www.eurjic.org or from the author.

 © 2007 Wiley-VCH Verlag GmbH & Co. KGaA, Weinheim 

the precatalyst at least up to 45 °C and prolonged storability of ready-to-use monomer–precatalyst mixtures up to this temperature. Vice versa, either by the action of UV light or by thermal treatment, the precatalyst should, together with the monomer, form the active species to initiate ROMP. Despite selected reports on such systems,[3,17–20] these suffer from drawbacks such as thermal or visible light activation and significant metathesis activity *at room temperature and below*. In view of the pronounced changes in reactivity observed for bis(trifluoroacetate)-derived Grubbs and Grubbs–Hoveyda systems,[21–27] we were interested to what extent the replacement of the chlorine groups by trifluoroacetate groups would have influence on the ROMP activity of the resulting precatalysts. Instead of using norborn-2-ene, which is polymerized to some extent by virtually any metathesis catalyst, we focused on more complex molecules. On the basis of previous reports on the superiority of *exo* isomers in ROMP,[1] we prepared enantiomerically pure *exo* and *endo* isomers of two monomers, *exo*,*exo*-*N*,*N*-(norborn-5-ene-2,3-dicarbimido)-L-valine ethyl ester (*exo*-**1**), *endo*,*endo*-*N*,*N*-(norborn-5-ene-2,3-dicarbimido)-L-valine ethyl ester (*endo*-**1**), *exo*,*exo*-*N*,*N*-(norborn-5-ene-2,3-dicarbimido)-L-valine-*tert*-butylamide (*exo*-**2**), *endo*,*endo*-*N*,*N*-(norborn-5-ene-2,3-dicarbimido)-L-valine-*tert*-butylamide (*endo*-**2**) and investigated their polymerization using $Ru(CF_3CO_2)_2(IMesH_2)$(*p*-cymene) (**3**), $Ru(CF_3CO_2)_2$(IMes)(*p*-cymene) (**4**), $RuCl_2$(IMes)(*p*-cymene) (**5**), $Ru(PCy_3)(CF_3CO_2)_2$(*p*-cymene) (**6**), $Ru(CF_3CO_2)_2$(*p*-cymene)·$CF_3COOAgPCy_3$ (**6a**), $Ru(CF_3CO_2)_2(PPh_3)$(*p*-cymene) (**7**), $Ru(CF_3CO_2)_2$(IMes)$(PhNC)_3$ (**8**), and $Ru(CF_3CO_2)_2(IMesH_2)(PhNC)_3$ (**9**) (IMes = 1,3-dimesitylimidazol-2-ylidene, $IMesH_2$ = 1,3-dimesityl-4,5-diyhdroimidazolin-2-ylidene, $PCy_3$ = tricyclohexylphosphane). In addition, the structure of the final polymers was investigated. Finally, we performed theoretical calculations at the B3LYP/LACVP* level and propose a model that explains the superior reactivity of *exo* isomers compared to their *endo* analogues in ROMP.

## Results and Discussion

### Synthesis of Monomers and Catalyst Precursors

The synthesis of the *endo* monomers *endo*-**1** and *endo*-**2**,[28] the $CF_3COO$-derived precatalysts **3**, **4**, **8**, and **9**,[14] as well as of precatalyst **5**,[6] is described elsewhere. Monomer *exo*-**1** was prepared by esterification of *exo*,*exo*-(norborn-5-ene-2,3-dicarbimido)-L-valine with ethanol. Monomer *exo*-**2** was synthesized by reaction of L-valine-*exo*,*exo*-*N*,*N*-(norborn-2-ene-5,6-dicarbimide) with dicyclohexyldicarbodiimide (DCC) followed by the reaction of *tert*-butylamine. All structures are shown in Figure 1. In addition to the data already reported, the X-ray structures of compounds **3**, **6a**, **7**, **8**, and **9** are presented here. Thus, compound **3** crystallizes in the triclinic space group $P\bar{1}$ with $a$ = 11.3770(4) Å, $b$ = 12.1632(5) Å, $c$ = 14.5978(6) Å, $\alpha$ = 104.636(2)°, $\beta$ = 96.217(2)°, $\gamma$ = 113.276(2)°, $Z$ = 2. The distance Ru(1)–C(11) is 2.109(2) Å; the complex exists in a distorted octahedral form (Figure 2).

Precatalyst **6** was prepared from $[RuCl_2(p\text{-cymene})]_2$ by reaction with 2 equiv. of $PCy_3$ followed by reaction with 2 equiv. of $CF_3COOAg$. The compound crystallizes as the $CF_3COOAg{\cdot}PCy_3$ adduct **6a** in the triclinic space group $P\bar{1}$ with $a$ = 10.2007(4) Å, $b$ = 13.8886(4) Å, $c$ = 14.9130(6) Å, $\alpha$ = 107.497(2)°, $\beta$ = 94.569(2)°, $\gamma$ = 95.552(2)°, $Z$ = 2. The complex again exists with a distorted octahedral coordination for the Ru and a distorted tetrahedral coordination for the Ag center (Figure 3).

In a similar manner, precatalyst **7** was prepared from $[RuCl_2(p\text{-cymene})]_2$ by reaction with 2 equiv. of $PPh_3$ fol-

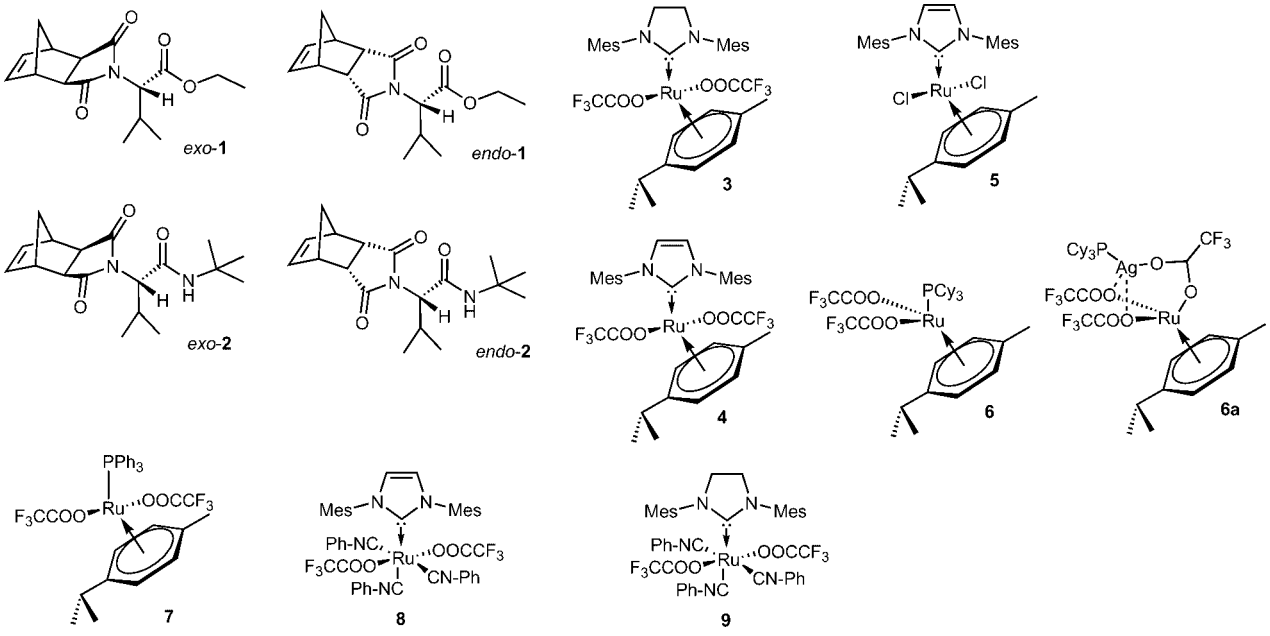


Figure 1. Monomers *exo*-**1**, *endo*-**1**, *exo*-**2**, *endo*-**2**, and precatalysts **3**–**10** used.

 © 2007 Wiley-VCH Verlag GmbH & Co. KGaA, Weinheim 

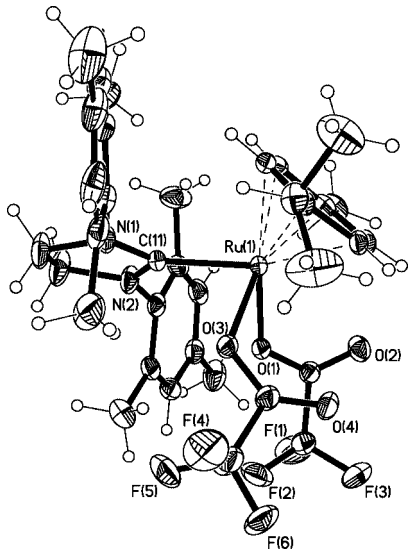


Figure 2. X-ray structure of **3**. Selected bond lengths [Å] and angles [°]: Ru(1)–C(11) 2.109(2), Ru(1)–O(1) 2.113(2), Ru(1)–O(3) 2.113(2), Ru(1)–C(5) 2.174(3), Ru(1)–C(6) 2.175(3), Ru(1)–C(4) 2.208(3), Ru(1)–C(1) 2.216(3), Ru(1)–C(2) 2.262(3), Ru(1)–C(3) 2.266(2); C(11)–Ru(1)–O(1) 87.37(9), C(11)–Ru(1)–O(3) 82.52(9), O(1)–Ru(1)–O(3) 76.20(8).

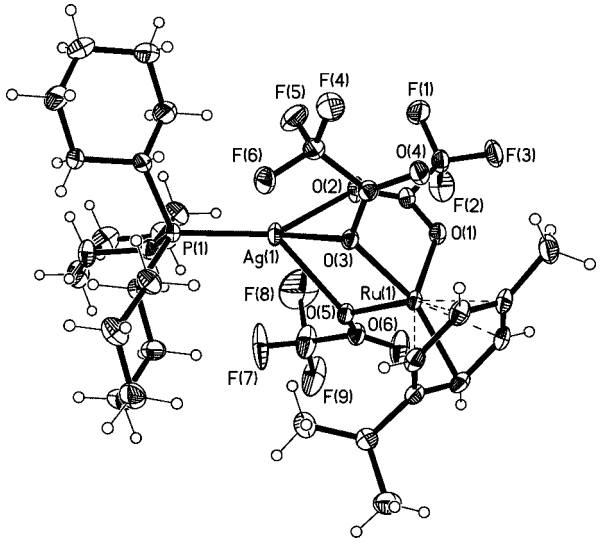


Figure 3. X-ray structure of **6a**. Selected bond lengths [Å] and angles [°]: Ru(1)–O(1) 2.1082(18), Ru(1)–O(3) 2.121(2), Ru(1)–O(5) 2.131(2), Ru(1)–C(3) 2.155(3), Ru(1)–C(2) 2.156(3), Ru(1)–C(5) 2.166(2), Ru(1)–C(1) 2.168(3), Ru(1)–C(6) 2.169(2), Ru(1)–C(4) 2.185(2), Ag(1)–O(2) 2.348(2), Ag(1)–P(1) 2.362(1), Ag(1)–O(3) 2.478(2), Ag(1)–O(5) 2.507(2); O(1)–Ru(1)–O(3) 86.44(7), O(1)–Ru(1)–O(5) 84.57(7), O(3)–Ru(1)–O(5) 80.29(6), O(2)–Ag(1)–P(1) 143.72(5), O(2)–Ag(1)–O(3) 74.93(6), P(1)–Ag(1)–O(3) 132.63(4), O(2)–Ag(1)–O(5) 75.94(6), P(1)–Ag(1)–O(5) 132.12(4), O(3)–Ag(1)–O(5) 66.70(5).

lowed by reaction with 2 equiv. of $CF_3COOAg$. Compound **7** crystallized in the monoclinic space group $C2/c$ with $a$ = 27.0985(3) Å, $b$ = 14.4321(4) Å, $c$ = 20.3053.(5) Å, $\alpha = \gamma$ = 90°, $\beta$ = 109.654(2)°, $Z$ = 8 (Figure 4).

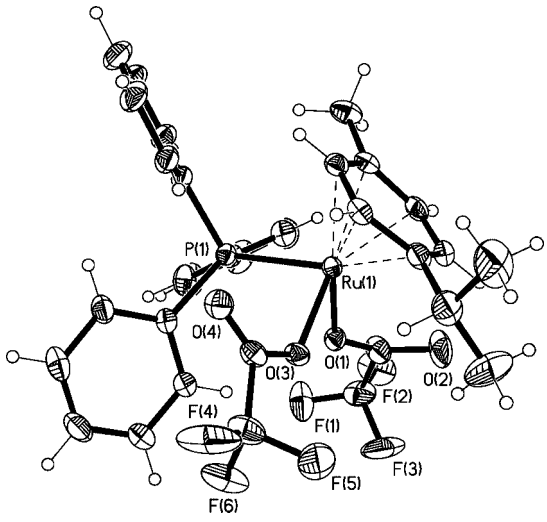


Figure 4. X-ray structure of **7**. Selected bond lengths [Å] and angles [°]: Ru(1)–O(3) 2.093(2), Ru(1)–O(1) 2.107(2), Ru(1)–C(6) 2.169(2), Ru(1)–C(5) 2.179(2), Ru(1)–C(3) 2.189(2), Ru(1)–C(2) 2.230(3), Ru(1)–C(4) 2.240(2), Ru(1)–C(1) 2.265(3), Ru(1)–P(1) 2.3654(7); O(3)–Ru(1)–O(1) 78.89(7), O(3)–Ru(1)–P(1) 89.59(5), O(1)–Ru(1)–P(1) 79.71(5).

Again, the complex exists with a distorted octahedral coordination of the Ru core. Compound **8** was prepared by reaction of **4** with excess phenylisonitrile.[14] It crystallizes in the orthorhombic space group $P2_12_12_1$ with $a$ = 10.8932(2) Å, $b$ = 16.4398(4) Å, $c$ = 26.9136(7) Å, $\alpha = \beta = \gamma$ = 90°, $Z$ = 4 (Figure 5). The Ru center again shows a slightly distorted octahedral coordination sphere with all angles close to 90 and 180°, respectively. One of the three phenylisonitrile ligands is arranged in a position *trans* to

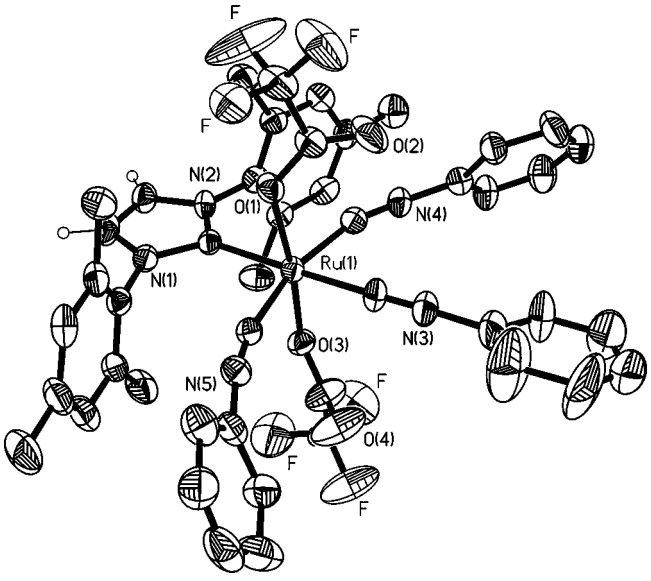


Figure 5. X-ray structure of **8**. Selected bond lengths [Å] and angles [°]: Ru(1)–C(27) 1.968(6), Ru(1)–C(20) 1.980(7), Ru(1)–C(34) 1.986(7), Ru(1)–O(3) 2.091(4), Ru(1)–O(1) 2.096(4), Ru(1)–C(1) 2.112(5); C(20)–Ru(1)–C(34) 164.9(2), O(3)–Ru(1)–O(1) 172.1(2), C(27)–Ru(1)–C(1) 178.5(2), Ru(1)–C(20)–N(3) 166.1(5), Ru(1)–C(27)–N(4) 177.2(6), Ru(1)–C(34)–N(5) 162.3(5).

 © 2007 Wiley-VCH Verlag GmbH & Co. KGaA, Weinheim 

the N-heterocyclic carbene ligand. The two trifluoroacetate ligands are *trans* to each other.

Because of its structural similarity to **8**, compound **9** again crystallizes in the orthorhombic space group $P2_12_12_1$ with $a$ = 10.8403(2) Å, $b$ = 16.5038(3) Å, $c$ = 27.1075(4) Å, $\alpha = \beta = \gamma = 90°$, $Z$ = 4 (Figure 6). The arrangement of the two phenylisonitrile and trifluoroacetate ligands is identical to that in **8**.

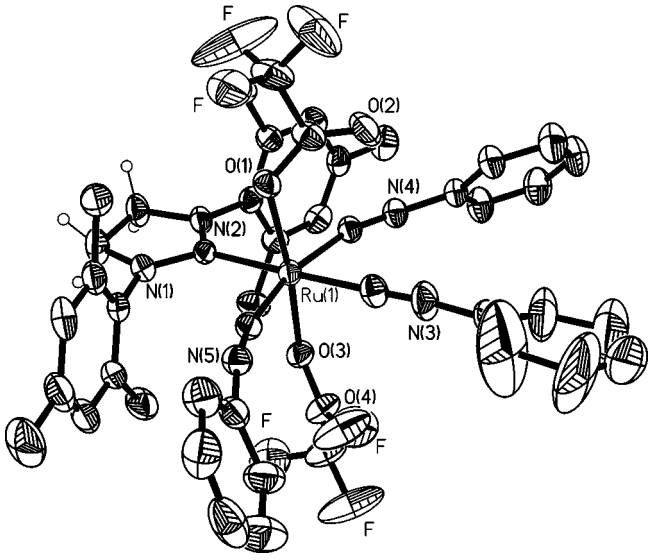


Figure 6. X-ray structure of **9**. Selected bond lengths [Å] and angles [°]: Ru(1)–C(27) 1.967(5), Ru(1)–C(20) 1.986(5), Ru(1)–C(34) 1.986(5), Ru(1)–O(3) 2.096(3), Ru(1)–O(1) 2.102(3), Ru(1)–C(1) 2.123(4), C(20)–Ru(1)–C(34) 164.4(2); O(3)–Ru(1)–O(1) 172.6(1), C(27)–Ru(1)–C(1) 178.5(2), Ru(1)–C(20)–N(3) 166.1(4), Ru(1)–C(27)–N(4) 178.4(5), Ru(1)–C(34)–N(5) 161.8(4).

## Reactivity in ROMP

All precatalysts, **3**–**9**, were investigated for their activity in ROMP using the monomers *exo*-**1**, *endo*-**1**, *exo*-**2**, and *endo*-**2**. In all cases, only precatalysts **3** and **4** were found to possess significant polymerization activity. Poly(*endo*-**1**) was prepared by the action of both precatalysts **3** and **4** (Table 1, entries 1–13) in the molecular weight range of 25000–160000 g/mol and polydispersity indices (PDIs) in the range of 1.17–1.54. A graph of the number of equivalents of the monomer with respect to the precatalyst ($N$) versus $M_n$ illustrates these results (Figure 7).

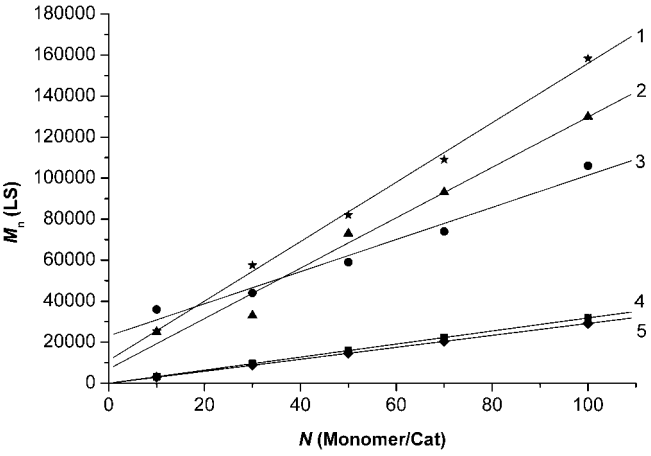


Figure 7. Plot of $M_n$ vs. number of monomer equivalents ($N$). 1: precatalyst **3** with *endo*-**1**; 2: precatalyst **4** with *exo*-**2**; 3: precatalyst **3** with *exo*-**2**; 4: calculated values for monomer **2**; 5: calculated values for monomer **1**.

As can be deduced therefrom, polymerization proceeds in a *controlled* manner, that is, the values of $M_n$ increase linearly with increasing $N$. The stepwise synthesis of poly-(*endo*-**1**)$_{100}$ (Table 1, entry 13) yields a polymer similar to the one prepared in a one-step procedure (Table 1, entry 9), however with higher PDI. This suggests that the polymerization does not proceed in a truly living[29] manner. The fact that the values for $M_n$ as determined by light scattering

Table 1. Polymerization results for *endo*-**1** and *exo*-**1** catalyzed by the action of precatalysts **3** and **4**. Solvent: $ClCH_2CH_2Cl$, 70 °C, 8 h.

| Entry | Monomer | Catalyst | $N$ | $M_n$ (theor.)[a] | $M_n$ (LS) | PDI | Yield [%] |
|---|---|---|---|---|---|---|---|
| 1 | *endo*-**1** | **4** | 10 | 2913 | – | – | oligomer |
| 2 | *endo*-**1** | **4** | 30 | 8740 | – | – | oligomer |
| 3 | *endo*-**1** | **4** | 50 | 14567 | 40000 | 1.37 | 10 |
| 4 | *endo*-**1** | **4** | 70 | 20393 | 85000 | 1.25 | 23 |
| 5 | *endo*-**1** | **4** | 100 | 29134 | 91000 | 1.38 | 43 |
| 6 | *endo*-**1** | **3** | 10 | 2913 | 25300 | 1.17 | 52 |
| 7 | *endo*-**1** | **3** | 30 | 8740 | 57500 | 1.24 | 72 |
| 8 | *endo*-**1** | **3** | 50 | 14567 | 82000 | 1.34 | 80 |
| 9 | *endo*-**1** | **3** | 70 | 20393 | 109000 | 1.35 | 80 |
| 10 | *endo*-**1** | **3** | 100 | 29134 | 158300 | 1.38 | 85 |
| 11 | *endo*-**1** | **3** | 50[b] | 14567 | 50800 | 1.40 | 48 |
| 12 | *endo*-**1** | **3** | 50 | 14567 | 88000 | 1.39 | [c] |
| 13 | *endo*-**1** | **3** | 50–100 | 29134 | 166000 | 1.54 | 80 |
| 14 | *exo*-**1** | **4** | 10 | 2913 | – | – | oligomer |
| 15 | *exo*-**1** | **4** | 30 | 8740 | – | – | oligomer |
| 16 | *exo*-**1** | **4** | 50 | 14567 | 64500 | 2.00 | 42 |
| 17 | *exo*-**1** | **4** | 70 | 20393 | 55700 | 1.94 | 60 |
| 18 | *exo*-**1** | **4** | 100 | 29134 | 152000 | 1.71 | 78 |
| 19 | *exo*-**1** | **3** | 50 | 14567 | 58600 | 2.09 | 100 |
| 20 | *exo*-**1** | **3** | 100 | 29134 | 116000 | 2.14 | 100 |

[a] Without end groups. [b] 1 equiv. of pyridine. [c] Taken from experiment entry 13 prior to addition of second 50 equiv. of monomer.

 © 2007 Wiley-VCH Verlag GmbH & Co. KGaA, Weinheim 

are much higher than the calculated ones also suggests a nonquantitative initiation of the precatalysts. Not unexpectedly, addition of pyridine (Table 1, entry 11) reduces the molecular weight of the polymer.

It is worth noting that **3** is far more reactive than **4**, as illustrated by the comparably low yields (≤43%) obtained with the latter. The lower activity of **4** in comparison to **3** may be rationalized by the fact that precatalyst **3** is believed

Table 2. Polymerization results for *endo*-**2** and *exo*-**2** catalyzed by the action of precatalysts **3** and **4**. Solvent: $ClCH_2CH_2Cl$, 70 °C, 8 h.

| Entry | Monomer | Catalyst | *N* | $M_n$ (theor.)[a] | $M_n$ (LS) | PDI | Yield [%] |
|---|---|---|---|---|---|---|---|
| 1 | *endo*-**2** | **4** | 10 | 3182 | insoluble | – | 8 |
| 2 | *endo*-**2** | **4** | 30 | 9546 | insoluble | – | 10 |
| 3 | *endo*-**2** | **4** | 50 | 15910 | insoluble | – | 10 |
| 4 | *endo*-**2** | **4** | 70 | 22274 | insoluble | – | 15 |
| 5 | *endo*-**2** | **4** | 100 | 31820 | insoluble | – | 18 |
| 6 | *endo*-**2** | **3** | 50 | 15910 | – | – | oligomer |
| 7 | *endo*-**2** | **3** | 100 | 31820 | – | – | oligomer |
| 8 | *exo*-**2** | **4** | 10 | 3182 | 25000 | 1.83 | 52 |
| 9 | *exo*-**2** | **4** | 30 | 9546 | 33000 | 2.05 | 53 |
| 10 | *exo*-**2** | **4** | 50 | 15910 | 73000 | 1.91 | 61 |
| 11 | *exo*-**2** | **4** | 70 | 22274 | 93200 | 1.88 | 75 |
| 12 | *exo*-**2** | **4** | 100 | 31820 | 130000 | 1.68 | 77 |
| 13 | *exo*-**2** | **3** | 10 | 3182 | 36000 | 1.25 | 35 |
| 14 | *exo*-**2** | **3** | 30 | 9546 | 44000 | 1.50 | 68 |
| 15 | *exo*-**2** | **3** | 50 | 15910 | 59000 | 1.56 | 61 |
| 16 | *exo*-**2** | **3** | 70 | 22274 | 74000 | 1.55 | 74 |
| 17 | *exo*-**2** | **3** | 100 | 31820 | 106000 | 1.49 | 73 |

[a] Without end groups.

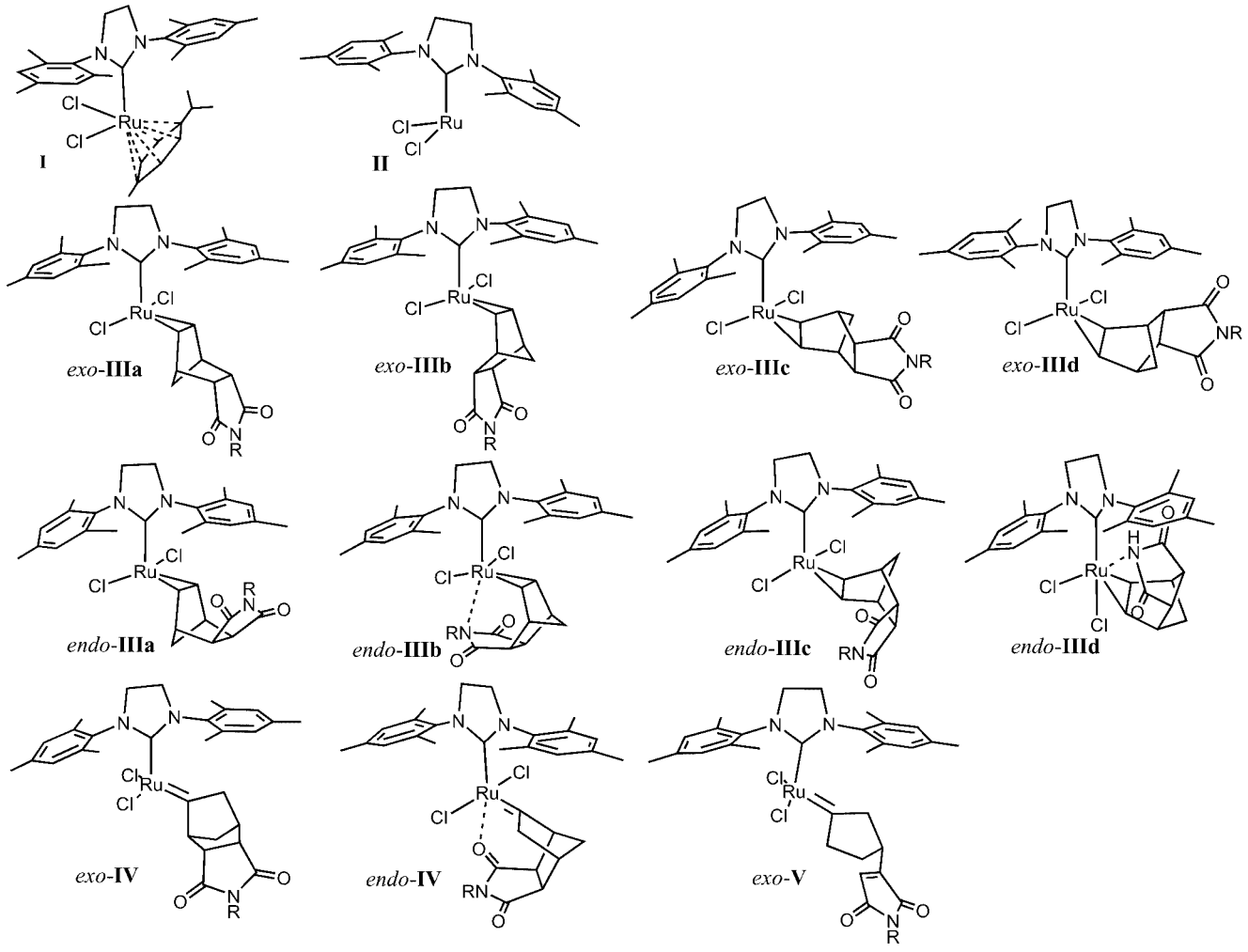


Figure 8. Structures of the studied complexes for the reaction of the *exo* and *endo* isomers with $RuCl_2(IMesH_2)$(*p*-cymene).

 © 2007 Wiley-VCH Verlag GmbH & Co. KGaA, Weinheim 

to form a 1,3-dimesityl-3,4-dihydroimidazolin-2-ylidene-based propagating species. These types of initiators have been reported to be far more active than the corresponding 1,3-dimesitylimidazol-2-ylidene-derived ones.[30] An important finding is the fact that the parent complex **5** is virtually inactive in the ROMP of *exo*-**1**, *endo*-**1**, *exo*-**2**, and *endo*-**2**. Thus, the exchange of both chlorine ligands by trifluoroacetates appears to be a necessary prerequisite for the formation of an active precatalyst. Similar behavior has been observed in the Ru–alkylidene-initiated cyclopolymerization of 1,6-heptadiynes, where substitution of both chlorines of the Grubbs-[24] and Grubbs–Hoveyda-type initiators[21–23,31] by trifluoroacetate groups was necessary to generate polymerization-active systems. Precatalysts **6** and **6a**, as well as **7**, apparently decompose upon heating the polymerization mixture prior to any initiation. Finally, both precatalysts **8** and **9** are composed upon heating in the presence of any monomer. We tentatively assign this finding to an imine-type metathesis-type reaction[32,33] of dissociated phenylisonitrile with any in situ formed Ru–alkylidene complex resulting in cleavage of the Ru moiety from the polymer chain.

Polymerization results similar to those obtained for *endo*-**1** were observed for *exo*-**1**. Again, precatalyst **3** turned out to be more reactive than **4**. The values for $M_n$ of poly(*exo*-**1**) as determined by LS (Table 1, entries 19 and 20) were significantly lower than those for poly(*endo*-**1**) (Table 1, entries 8 and 10), indicative of a higher initiation efficiency of the precatalyst for the *exo* monomer. Such higher reactivity of *exo* isomers versus Grubbs-type initiators was also reported by other groups.[34] In contrast to *endo*-**1**, polymerization of *endo*-**2** with either **3** or **4** resulted only in oligomeric or insoluble products that were isolated in low yields, typically <20% (Table 2, entries 1–7).

However, *exo*-**2** may be polymerized by both precatalysts **3** and **4** in a controlled way (Table 2, entries 8–17). PDIs were in the range of 1.69–2.05 for precatalyst **4** and 1.25–1.56 for precatalyst **3**. An illustration is given in Figure 8.

## Polymer Structure

The structure of poly(*endo*-**1**) prepared by the action of either **3** or **4** was identical to the one published previously.[35] An atactic, all-*trans* structure was assigned to this polymer. In contrast to poly(*endo*-**1**), poly(*exo*-**1**) and poly(*exo*-**2**), whether prepared by the action of **3** or **4**, showed a *cis* content of roughly 40%, as evidenced by signals in the $^1$H NMR at $\delta$ = 5.44 ppm and in the $^{13}$C NMR spectrum around $\delta$ = 132 ppm and 52 ppm, respectively. For NMR assignment of signals, see refs.[36–38]

## Theoretical Considerations

Quantum chemical calculations were carried out to shed some light on the possible mechanism of the formation of ROMP-active Ru–alkylidene complexes and to provide an explanation for the different reactivity of the *exo* and *endo* forms of *N*,*N*-(norborn-5-ene-2,3-dicarbimide)-L-valine ethyl ester (NB-R1) and *N*,*N*-(norborn-5-ene-2,3-dicarbimide)-L-valine-*tert*-butylamide (NB-R2). For these calculations, the catalyst $RuCl_2(IMesH_2)$(*p*-cymene) was chosen as a model compound. Calculations revealed that the *exo* forms of both monomers studied are only insignificantly more stable (<2 kcal/mol) than the corresponding *endo* forms. Additionally, there is no essential effect of the substituent R {H, $CH_3$, 2-propyl, $CH[CH(CH_3)_2]COOEt$, $CH[CH(CH_3)_2]CONH$-*t*Bu} and conformation (*exo* vs. *endo*) on the Mulliken atomic charges and electron density at the C=C double bond of monomers. Thus, the calculated Mulliken atomic charges at the C atoms forming the double bond are –0.106/–0.104 and –0.119/–0.118 for the *exo* and *endo* forms, respectively (R = $CH_3$/R = H). Additionally, the calculated relative energies of the different Ru–alkylidene complexes for NB-R1 {R = $CH[CH(CH_3)_2]COOEt$} differ only slightly (<1 kcal/mol) from those calculated for R = H and $CH_3$. Therefore, a simplified form of the monomers with R = H, which is not too time-consuming in frequency analysis, was used for further calculations.

After dissociation of the *p*-cymene ligand ($\Delta U_{tot}$ = 6.2 kcal/mol), the formation of the corresponding Ru–alkylidene complexes was calculated. In the case of the *exo*-form, four possible stable structures for the catalyst–monomer complexes (*exo*-**IIIa**, *exo*-**IIIb**, *exo*-**IIIc**, and *exo*-**IIId**) (Figure 8) were optimized, with *exo*-**IIIa** with C7 in proximity to the Ru center being the most stable one.

Complexes *exo*-**IIIa** and *exo*-**IIIb** are characterized by monomer C=C double bonds orthogonal to the Ru–NHC bond. In contrast, the C=C double bond in *exo*-**IIIc** and *exo*-**IIId** (Figure 8) is almost parallel to the Ru–NHC bond. The calculated relative stabilities of different structures are given in Table 3.

All four *exo*-monomer–Ru complexes are stable ($\Delta U_{tot}$ is negative) and their possible transformations were further analyzed (Scheme 1).

Similar to the *exo* form, two stable catalyst–*endo*-monomer complexes with the C=C double bond of the monomer orthogonal to the Ru–NHC bond (*endo*-**IIIa** and *endo*-**IIIb**, Figure 8) were identified, *endo*-**IIIa** with C7 in proximity to the Ru center being the most stable one (Scheme 2). In addition, two structures, that is, *endo*-**IIIc** and *endo*-**IIId** with the C=C double bond of the monomer almost parallel to the Ru–NHC bond, are stable. Because of a strong steric interaction with the norborn-2-ene moiety, the Cl atom is *trans* to the N-heterocyclic carbene in *endo*-**IIId**. The calculated relative stabilities of the Ru–*endo*-monomer complexes (Table 3) indicate that formation of the structures *endo*-**IIIa**, *endo*-**IIIb**, *endo*-**IIIc**, and *endo*-**IIId** is exothermic ($\Delta U_{tot}$ is negative) and their possible transformations were therefore further analyzed (Scheme 2). In addition, it could be argued that the existence of an additional interaction between Ru and the N atom of the monomer in the case of the *endo* form (structure *endo*-**IIIb**, Figure 8, Ru–N = 0.2407 nm) may prevent further transformation. Here the question arose whether an additional interaction between the Ru and the N atoms of the monomer calculated for the cut-down

 © 2007 Wiley-VCH Verlag GmbH & Co. KGaA, Weinheim 

Table 3. Relative energies [kcal/mol] of the different Ru complexes and activation energies $U_{act}(E_0 + E_{ZP})$ [kcal/mol] for intramolecular C1–C2 H-shift. $U_{act}$ was estimated for a simplified structure of the NHC (Supporting Information).

| | Structure *exo* | Relative energy | Structure *endo* | Relative energy |
|---|---|---|---|---|
| $\Delta E_0$ | **I** | –8.73 | **I** | –8.73 |
| $\Delta U_{tot}$ ($E_0 + E_{ZP}$) | | –6.24 | | –6.24 |
| $\Delta G_{tot}$ ($U_{tot} - TS$) | | 9.71 | | 9.71 |
| $\Delta E_0$ | **II** | 0 | **II** | 0 |
| $\Delta U_{tot}$ ($E_0 + E_{ZP}$) | | 0 | | 0 |
| $\Delta G_{tot}$ ($U_{tot} - TS$) | | 0 | | 0 |
| $\Delta E_0$ | *exo*-**IIIa** | –28.4 | *endo*-**IIIa** | –28.44 |
| $\Delta U_{tot}$ ($E_0 + E_{ZP}$) | | –26.00 | | –26.05 |
| $\Delta G_{tot}$ ($U_{tot} - TS$) | | –11.85 | | –11.31 |
| $\Delta E_0$ | *exo*-**IIIb** | –20.05 | *endo*-**IIIb** | –13.82 |
| $\Delta U_{tot}$ ($E_0 + E_{ZP}$) | | –18.24 | | –11.53 |
| $\Delta G_{tot}$ ($U_{tot} - TS$) | | –3.55 | | +5.19 |
| $\Delta E_0$ | *exo*-**IIIc** | –15.64 | *endo*-**IIIc** | –13.76 |
| $\Delta U_{tot}$ ($E_0 + E_{ZP}$) | | –13.11 | | –11.46 |
| $\Delta G_{tot}$ ($U_{tot} - TS$) | | +2.42 | | +3.40 |
| $\Delta E_0$ | *exo*-**IIId** | –5.45 | *endo*-**IIId** | –9.1 |
| $\Delta U_{tot}$ ($E_0 + E_{ZP}$ | | –3.27 | | –7.0 |
| $\Delta G_{tot}$ ($U_{tot} - TS$) | | +12.02 | | +11.2 |
| $\Delta E_0$ | *exo*-**IV** | –28.38 | *endo*-**IV** | –27.25 |
| $\Delta U_{tot}$ ($E_0 + E_{ZP}$) | | –26.40 | | –25.33 |
| $\Delta G_{tot}$ ($U_{tot} - TS$) | | –12.78 | | –9.02 |
| $\Delta E_0$ | *exo*-**V** | –17.96 | | |
| $\Delta U_{tot}$ ($E_0 + E_{ZP}$) | | –17.36 | | |
| $\Delta G_{tot}$ ($U_{tot} - TS$) | | –4.33 | | |
| $U_{act}$ ($E_0 + E_{ZP}$) | TS(I) *exo*-**3a** → **4** | 73 | TS(I) *endo*-**3a** → **4** | 74 |
| $U_{act}$ ($E_0 + E_{ZP}$) | TS(II) *exo*-**3a** → **4** | 41 | TS(II) *endo*-**3a** → **4** | 46 |
| $U_{act}$ ($E_0 + E_{ZP}$) | TS(I) *exo*-**3b** → **4** | 67 | TS(I) *endo*-**3b** → **4** | – |
| $U_{act}$ ($E_0 + E_{ZP}$) | TS(II) *exo*-**3b** → **4** | 33 | TS(II) *endo*-**3b** → **4** | 38 |
| $U_{act}$ ($E_0 + E_{ZP}$) | TS(II) *exo*-**3c** → **4** | 28 | TS(II) *endo*-**3c** → **4** | 34 |
| $U_{act}$ ($E_0 + E_{ZP}$) | TS(II) *exo*-**3d** → **4** | 18 | TS(II) *endo*-**3d** → **4** | 36 |

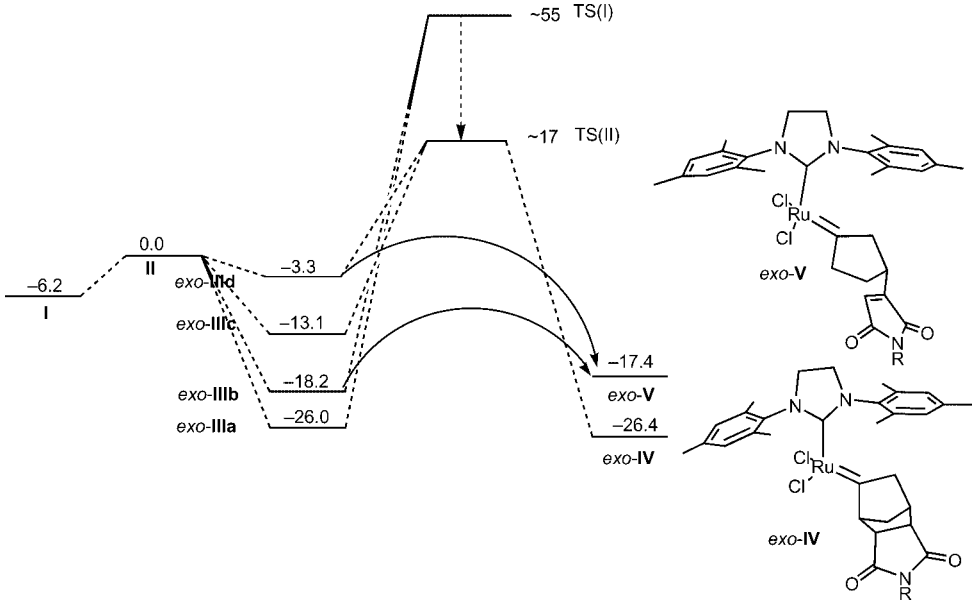


Scheme 1. Energy diagram and two possible reaction pathways calculated at the B3LYP/LACVP* level for the reaction of an *exo* isomer with $RuCl_2(IMesH_2)$(*p*-cymene). Transition-state energies TS(I) and TS(II) are estimated for a simplified structure of the NHC (Supporting Information).

 © 2007 Wiley-VCH Verlag GmbH & Co. KGaA, Weinheim 

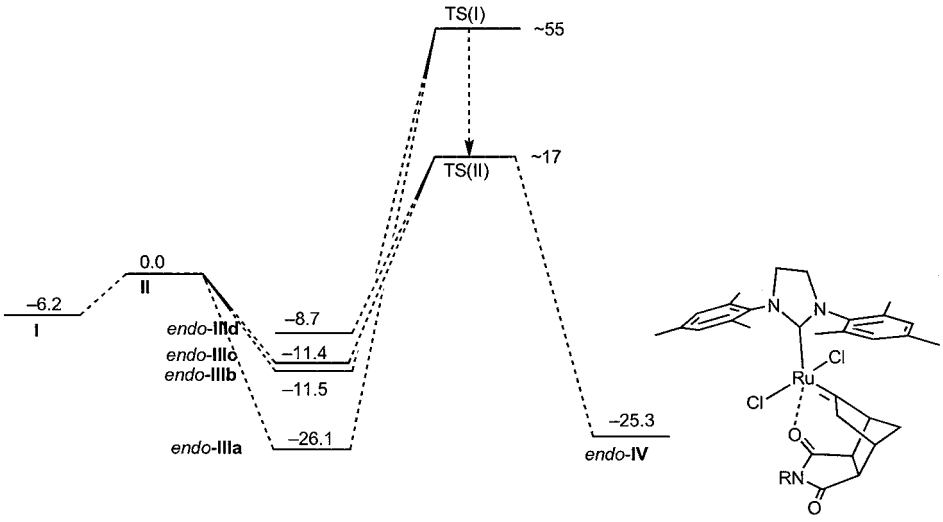


Scheme 2. Energy diagram and possible reaction pathways calculated at the B3LYP/LACVP* level for the reaction of an *endo* isomer with $RuCl_2(IMesH_2)$(*p*-cymene). Transition-state energies TS(I) and TS(II) are estimated for a simplified structure of the NHC (Supporting Information).

model *N*-R-norborn-5-ene-2,3-dicarboximide (R = H, $CH_3$) existed also for the actual monomers {R = $CH[CH(CH_3)_2]$-COOEt, $CH[CH(CH_3)_2]$CONH-*t*Bu} or whether other steric effects would dominate. To shed light on this point, calculations were carried out on the unrestricted monomers NB-R1 and NB-R2. As a matter of fact, these not only confirmed that this extra interaction exists, but revealed that the oxygen atom from the 2,3-dicarbimide group interacts very strongly with the Ru atom, thus forming an additional O–Ru bond. In due consequence, these two additional N–Ru and O–Ru interactions should aggravate any further transformation of *endo*-**IIIb** and thus further explain the reduced reactivity of the *endo*-monomer. The calculated *endo*-**IIIb** structures for NB-R1 and NB-R2 are given in Figure S2 in the Supporting Information.

To form the ROMP-active Ru–alkylidene complexes, the following mechanism may be proposed: one H atom from the C1=C2 double bond shifts from C1 to C2 followed by formation of the Ru–alkylidene complex, leading to structures *exo*-**IV** or *endo*-**IV** (Schemes 2 and 3).

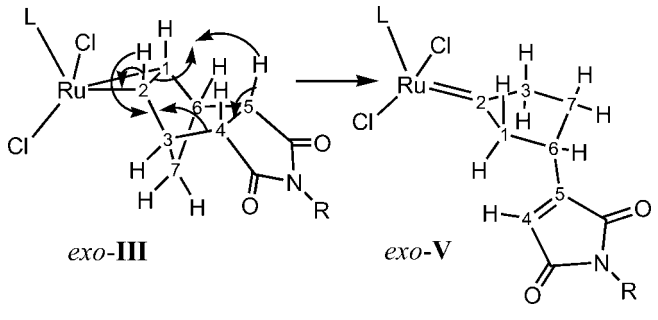


Scheme 3. Proposed reaction cascade for the formation of a ROMP-active $Ru^{IV}$ alkylidene (structure *exo*-**5**).

Though structures *exo*-**IV** and *endo*-**IV** are energetically possible, the intramolecular C1 → C2 H-shift proceeds with a high activation barrier and should therefore be analyzed. However, in contrast to stable structures, the optimization of transition states for such large molecules is comparably complicated. So, we were forced to use simplified molecular structures for the estimation of the barrier for possible models of intramolecular H-shifts. Thus, in the search of the transition state for the H-shift from C1 to C2 of the double bond we started from the corresponding *exo* and *endo* monomers (i.e., *exo*- and *endo*-*N*-R-norborn-5-ene-2,3-dicarboximide, respectively; R = H, $CH_3$) *not* bonded to the Ru moiety. We found no effect of the substituents R on the nitrogen of the monomer on the structure and activation energy for the H-shift from C1 to C2. The calculated activation energy was very high (73 kcal/mol, 70 kcal/mol with Zero Point Energy correction). Transition structures of the monomer obtained that way were used as initial transition structures for the modeling of the different Ru–monomer complexes. A simplified catalyst structure with N–H instead of *N*-mesityl substituents was used.

Starting from the stable structures *exo*-**3a** and *exo*-**3b** (Scheme S1, Supporting Information), the transition structures [TS(I)] for the H-shift from C1 to C2 could be localized. The activation energy (given in Table 3) was again, as in the case of the nonbonded monomer, comparably high (up to 73 kcal/mol). However, when the H-shift from C1 to C2 was in conjunction with a concomitant formation of a Ru–alkylidene complex [TS(II)], the activation energy was essentially reduced, to 41 kcal/mol and 33 kcal/mol for *exo*-**3a** and *exo*-**3b**, respectively. Starting from the stable structures *exo*-**3c** and *exo*-**3d** (Scheme S1, Supporting Information), the transition structures [TS(I)] could not be localized and transformed directly into the corresponding sec-

 © 2007 Wiley-VCH Verlag GmbH & Co. KGaA, Weinheim 

ond transition structures [TS(II)]. This is a consequence of the geometries of TS(II), which have the alkylidene parallel to the Ru–NHC bond and do not need any additional rotation of the ruthenacyclopropane ring as is the case in *exo*-**3a** and *exo*-**3b**. Vice versa, the ruthenacyclopropane rings in *exo*-**3c** and *exo*-**3d** also already occupy a parallel orientation with respect to the Ru–NHC bond. The analysis of the TS(II) structures showed that in the case of the *exo* form only two structures of the TS(II) with very small differences in energy (<1 kcal/mol) exist. Here, the *exo*-**3a** structure is identical to *exo*-**3c** and *exo*-**3b** is identical to *exo*-**3d** (Supporting Information).

Starting from the stable structure *endo*-**3a** (Scheme S2, Supporting Information), the transition structure [TS(I)] for the H-shift from C1 to C2 could be localized with a very high activation energy (74 kcal/mol). In case the H-shift occurs concomitantly to a rotation of the ruthenacyclobutane, formation of a Ru–alkylidene complex occurs, and the activation energy is again essentially reduced to 46 kcal/mol [TS(II)] (Scheme S2, Supporting Information). TS(I) could not be localized for *endo*-**3b**, *endo*-**3c**, and *endo*-**3d** and transformed directly into the second transition structure [TS(II)]. Again, the TS(II) of *endo*-**3a** is identical to that of *endo*-**3c**. Formation of the TS(II) of *endo*-**3b**, being identical to that of *endo*-**3d**, was calculated to be slightly more favorable (about 2 kcal/mol) than the TS(II) of *endo*-**3a** and *endo*-**3c**.

Activation energies for the intramolecular C1 → C2 H-shift were calculated for the simplified structure of the NHC ligand with N–H instead of *N*-mesityl groups. These were further used for the analysis of the possible transformations of the Ru–alkylidene complexes (Table 3). However, it should be noted that the calculated activation energies for the 1,2-H-shift for the simplified form of the monomer (R = H) should be used on a qualitative rather than on a quantitative base. From the analysis of the data summarized in Table 3 it can be seen that the formation of TS(II) is particularly favorable (18 kcal/mol) in case the reaction proceeds via the *exo*-**IIId** structure.

From the analysis of the formation of the ROMP-active structures *exo*-**IV** and *endo*-**IV** through $C_1 \rightarrow C_2$ H-shift (Schemes 1 and 2) follows: (i) the ROMP-active structure *exo*-**IV** can be built starting from all four stable structures *exo*-**IIIa**, *exo*-**IIIb**, *exo*-**IIIc**, and *exo*-**IIId**; its formation is energetically favorable ($\Delta U_{tot}$ = –26.0 kcal/mol, –18.2 kcal/mol, –13.1 kcal/mol, and –3.3 kcal/mol, respectively); (ii) the transformation starting from the less stable complex *exo*-**IIId** occurs with lower activation energy (only 18 kcal/mol) than from the most stable structure *exo*-**IIIa**, indicating a low-energy pathway; (iii) the formation of *endo*-**IV** by the low-energy pathway starting from the less stable structure *endo*-**IIIc** occurs with activation energy 31 kcal/mol, which is 13 kcal/mol higher than that for the pathway starting from *exo*-**IIId**. Moreover, the structure *endo*-**IIIb** seems to be inactive because of additional Ru–N bonding. Finally, the structure *endo*-**IV** must be further expected to be virtually ROMP-inactive because of the formation of an additional Ru–O bond (Scheme 2, bond length = 0.240 nm). All these findings may be indicative of a lower activity of the *endo* forms of the monomers investigated in comparison to the corresponding *exo* forms.

An additional, alternative *activation mechanism* for the formation of Ru–alkylidene complexes necessary for ROMP may explain the different reactivity of the *exo* and *endo* forms of **1** and **2**. While there is no essential difference between the *exo* and *endo* forms of monomers in the electronic parameters, such as charge and electron density at the double bond, there is a deciding contrast in geometry. As can be seen in Figure 9, there is a significant difference in the distances between the C1 atom of the double bond and the H5 atom at the *exo* or *endo* position (0.269 nm and 0.367 nm, for *exo* or *endo* respectively).

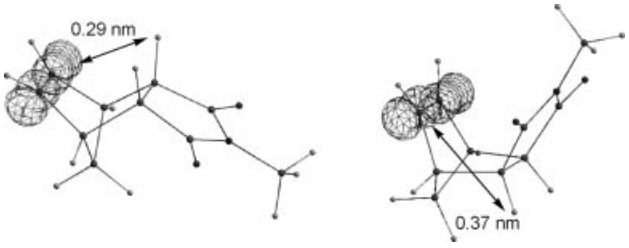


Figure 9. Distances between C1/C2 atoms of the double bond (the $p_z$ orbitals) and the H atoms at C4/C5 in the *exo* and *endo* forms.

Consequently, the positively charged H atom in the *exo* position interacts strongly with the $p_z$ orbital on the negatively polarized C1, thus facilitating the intramolecular C5 → C1 (or C4 → C2) H-shift to the double bond. As geometry optimization reveals, the weakening of the C3–C4 bond could be followed by ring opening, concomitant intramolecular H-shift from C2 to C1, and formation of a Ru=C double bond. All these intramolecular transformations can apparently occur concomitantly (Scheme 3) with low activation energies leading to the structure *exo*-**V**. However, such transformation is impossible in the case of the *endo* form. For this reaction pathway, the starting complexes *exo*-**IIIb** and especially *exo*-**IIId** appear to be more favorable than complexes *exo*-**IIIa** and *exo*-**IIIc** for two reasons. First, as a consequence of the interaction between the double bond and the Ru center, the geometry on C1 and C2 is no longer planar (there is some admixture of $sp^3$ hybridization), thus leading to the deformation of $p_z$ electron density from the C atoms in the direction of the H atom at C4 and C5, respectively. This facilitates the interaction with the H atom and consequently the H-shift. This also explains the stability of the monomer in the absence of any catalyst. Second, as revealed by calculations, complexes *exo*-**IIIb** and *exo*-**IIId** are also energetically favorable for transformation into the activated catalyst *exo*-**V** ($\Delta G_{tot}$ = –0.8 kcal/mol and $\Delta G_{tot}$ = –16.35 kcal/mol respectively).

It should be emphasized that so far the discussed mechanism through the possible H-shift from C4 to C2 is only *qualitative* because of computational restrictions in the search for transition structures that operate through a concerted transformation (H-shifts and ring opening). However, such transformations are expected to occur easily be-

 © 2007 Wiley-VCH Verlag GmbH & Co. KGaA, Weinheim 

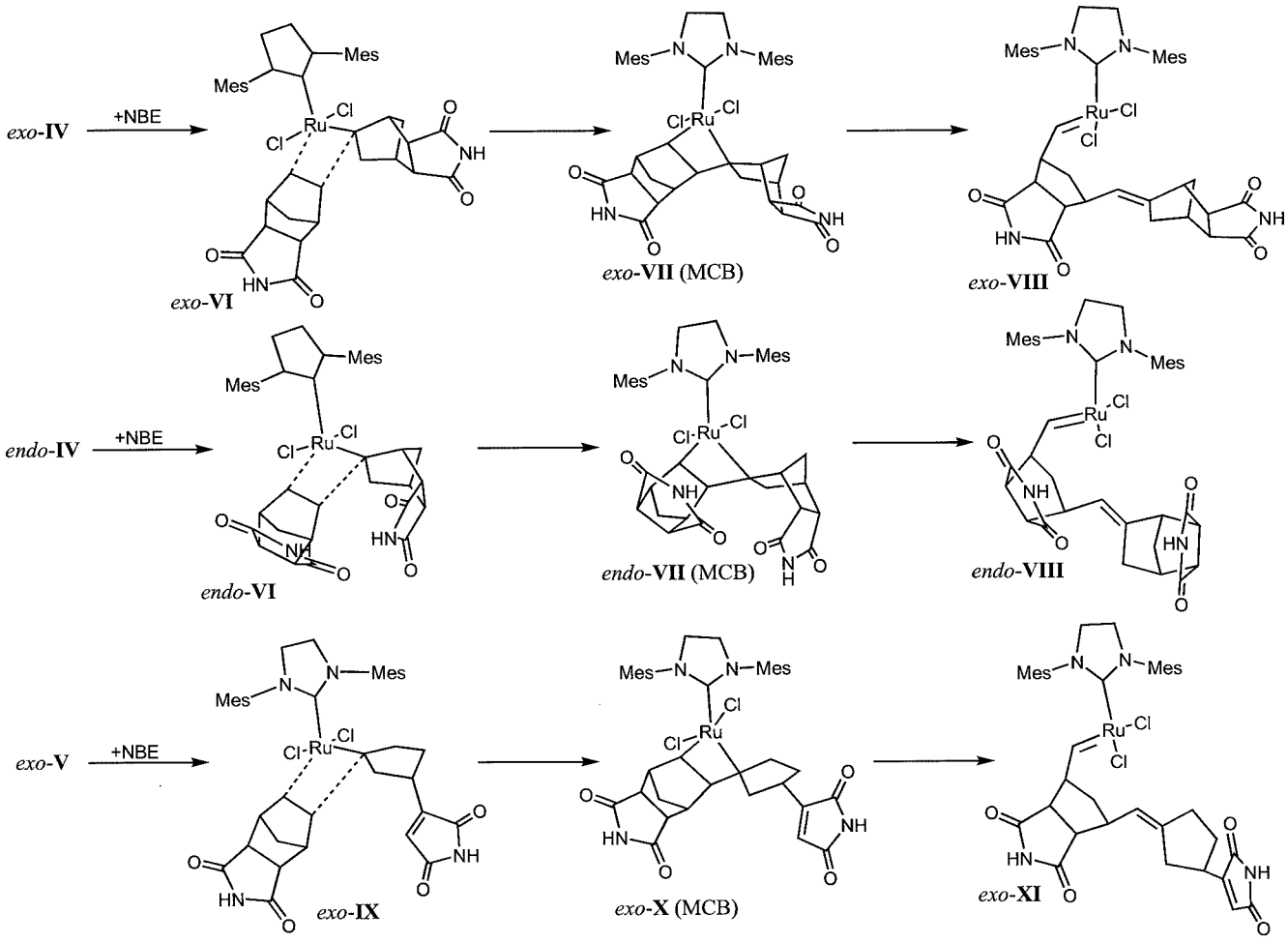


Scheme 4. Most stable structures of Ru–alkylidene complexes (B3LYP/LACVP*).

cause of a favorable geometry for the H-shift in the *exo*-**IIIb** and *exo*-**IIId** complexes and the better interaction of the proton with the $p_z$ electrons of the double bond.

The mechanism discussed so far for the formation of Ru–alkylidene complexes (structures *exo*-**IV**, *exo*-**V**, and *endo*-**IV**) necessary for ROMP clearly shows the difference between the *exo* and *endo* forms. However, it might be of interest to identify the rate-determining step of the overall polymerization reaction. To understand differences in reactivities of the *exo* and *endo* forms, further insertion reactions of a second norborn-2-ene monomer into *exo*-**IV**, *exo*-**V**, and *endo*-**IV** were calculated. The calculated structures are shown in Scheme 4.

It was found that both active complexes *exo*-**IV** and *endo*-**IV** form stable π complexes (structures *exo*-**VI** and *endo*-**VI**) with stabilization energies of 2.6 kcal/mol and 0.6 kcal/mol respectively. The active complex *exo*-**V** can form a stable π complex (*exo*-**IX**) with norborn-2-ene (stabilization energy 3.1 kcal/mol) too. However, the next steps, that is, the conversion of the π complex into the corresponding metallacyclobutane (MCB) structures *exo*-**VII** (MCB), *exo*-**X** (MCB), and *endo*-**VII** (MCB) (Scheme 4) followed by ring opening (structures *exo*-**VIII**, *exo*-**XI**, and *endo*-**VIII**), proceed energetically differently for the *exo* and *endo* forms. Thus, though the ring-opening reaction is energetically favorable in all three cases, the formation of the MCB structure is very different for *exo* and *endo* forms. In the cases of *exo*-**IV** and *exo*-**V**, stable structures of the MCB were calculated with reaction enthalpies around –1.0 kcal/mol and –2.5 kcal/mol for *exo*-**VII** (MCB) and *exo*-**X** (MCB) respectively. On the contrary, *endo*-**VII** (MCB) is only a transition structure requiring an activation energy for MCB formation of about 17 kcal/mol. Such different behavior of the *endo* form is apparently caused by a strong steric interaction of the Cl ligand with the substituents at the *N*-imido group. In due consequence, the large activation energy for the MCB formation in the case of the *endo* form may be the rate-determining step of the overall polymerization reaction. A comprehensive study on the different reactivity of various *exo*- and *endo*-norborn-5-ene-2,3-dicarbimides is now in progress.

## Conclusions

A series of novel $Ru^{II}$-derived precatalysts have been investigated for their polymerization behavior in the ROMP of *exo*- and *endo*-norborn-5-ene-2,3-dicarbimides. Our in-

 © 2007 Wiley-VCH Verlag GmbH & Co. KGaA, Weinheim 

vestigations revealed that precatalysts containing an N-heterocyclic carbene ligand, two trifluoroacetate groups, and one labile ligand are best suited for the thermal initiation of ROMP. The *exo* isomer was preferentially polymerized in both cases. Quantum chemical calculations propose possible mechanisms for the formation of ROMP-active structures, which could also explain the experimental findings of the better reactivity of the *exo* form. Additionally, the different activation energies for MCB formation of the *exo* and *endo* forms may be the rate-determining step of the overall polymerization reaction. Further work will focus on the construction of suitable labile ligands that allow for a *quantitative initiation* of the precatalysts.

## Experimental Section

All manipulations were performed under nitrogen in a glovebox (MBraun LabMaster 130) or by standard Schlenk techniques. Purchased starting materials were used without any further purification. Dichloroethane was distilled from calcium hydride under nitrogen. Tetrahydrofuran (THF), pentane, diethyl ether, toluene, and dichloromethane were dried by an MBraun solvent purification system (SPS). NMR spectroscopic data were obtained at 250.13 MHz for proton and 62.90 MHz for carbon in the indicated solvent at 25 °C on a Bruker Spectrospin 250 and are listed in parts per million downfield from tetramethylsilane for proton and carbon. IR spectra were recorded with a Bruker Vector 22 using ATR technology. Molecular weights and polydispersity indices (PDIs) of the polymers were determined by GPC at 30 °C on Polymer laboratories columns (PLgel 10 μm MIXED-B, 7.5 × 300 mm) in THF at 25 °C using a Waters Autosampler, a Waters 484 UV spectrometer detector (254 nm), an Optilab Rex refractive index detector (Wyatt), and a MiniDawn light-scattering detector (Wyatt). Synthesis and structural data of compounds *endo*-**1** and *endo*-**2**,[28] **3**, **4**, **9**, **10**,[14] and **5**[6] have been reported elsewhere. Values for *dn*/*dc* for *endo*-**1**, *exo*-**1**, and *exo*-**2** were 0.119, 0.126, and 0.116, respectively.

***exo*,*exo*-*N*,*N*-(Norborn-5-ene-2,3-dicarbimido)-L-valine Ethyl Ester (*exo*-1):** *exo*,*exo*-*N*,*N*-(Norborn-5-ene-2,3-dicarbimido)-L-valine (575 mg, 2.18 mmol) and *p*-toluenesulfonic acid (17 mg, 0.08 mmol) were dissolved in dry ethanol and refluxed for 8 h. The ethanol was evaporated and the residue was dissolved in diethyl ether. The ether solution was subject to flash chromatography over silica gel 60 (diethyl ether/pentane, 5:1). Recrystallization gave *exo*-**1** as white needles in 35% yield (220 mg). IR (ATR): $\tilde{\nu}$ = 2975 (w), 1739 (m), 1693 (s), 1526 (m), 1380 (s), 1352 (m), 1281 (w), 1186 (s), 1097 (m), 1050 (m), 1018 (m), 969 (m), 892 (m), 825 (m), 771 (m), 724 (w), 673 (m) cm$^{-1}$. $^1$H NMR ($CDCl_3$): $\delta$ = 6.30 (s, 2 H), 4.34 (d, $^1J$ = 8.1 Hz, 1 H), 4.25–4.08 (m, 2 H), 3.31 (br. s, 2 H), 2.78–2.57 (m, 3 H), 1.53 (m, 2 H), 1.20 (t, $^2J$ = 7.17 Hz, 3 H, $CH_3$), 1.10 (d, $^2J$ = 6.67 Hz, 3 H, $CH_3$), 0.84 (d, $^2J$ = 6.84 Hz, 3 H, $CH_3$) ppm. $^{13}$C NMR ($CDCl_3$): $\delta$ = 177.4, 177.26, 168.3, 137.9, 61.37, 57.7, 47.8, 47.3, 45.6, 45.37, 42.8, 27.9, 22.3, 21.03, 19.34, 14.01 ppm. MS: calcd. for $C_{16}H_{21}NO_4$ $[M^{\cdot}]^+$ 291.15; found 291.

***exo*,*exo*-*N*,*N*-(Norborn-5-ene-2,3-dicarbimido)-L-valine-*tert*-butylamide (*exo*-2):** Dicyclohexyldicarbodiimide (DCC, 1.96 g, 0.95 mmol) was added to L-valine-*exo*,*exo*-*N*,*N*-(norborn-2-ene-5,6-dicarbimide) (5.0 g, 1.9 mmol) dissolved in acetonitrile. Soon after addition of DCC, dicyclohexylurea (DCU) precipitated, and the reaction mixture was stirred for a further 6 h. DCU was filtered off, *tert*-butylamine (2.0 mL, 1.9 mmol) was added to the filtrate, and the reaction mixture was stirred for 12 h. Finally, the ammonium salt was filtered off. Acetonitrile was evaporated under reduced pressure until an oily residue remained, which was dissolved in diethyl ether. The ether solution was subsequently washed with 0.1 M hydrochloric acid and saturated aqueous sodium hydrogen carbonate and finally dried with sodium sulfate. The solution was concentrated, and about the same amount of pentane was added. Crystallization was performed at –18 °C. Yield: 2.6 g (43%). IR (ATR-mode): $\tilde{\nu}$ = 3353 (m), 2965 (w), 2929 (m), 2864 (m), 1690 (s), 1523 (m), 1454 (m), 1376 (s), 1352 (s), 1212 (w), 1182 (s), 1044 (m), 927 (m), 891 (m), 858 (m), 823 (m), 777 (m), 720 (w) cm$^{-1}$. $^1$H NMR ($CDCl_3$): $\delta$ = 6.63 (br. s, 1 H, NH), 6.11 (m, 2 H), 3.94 (d, $^2J$ = 11.54 Hz, 1 H, CH), 3.42 (br., 2 H), 3.29 (m, 2 H), 2.60 (m, 1 H), 1.74 (d, $^1J$ = 8.8 Hz, 1 H), 1.54 (d, $^1J$ = 8.9 Hz, 1 H), 1.30 (s, 9 H, *t*Bu), 0.98 (d, $^2J$ = 6.67 Hz, 3 H, $CH_3$), 0.75 (d, $^2J$ = 6.52 Hz, 3 H, $CH_3$) ppm. $^{13}$C NMR ($CDCl_3$): $\delta$ = 178.31, 177.83, 167.50, 134.89, 134.6, 65.03, 52.35, 51.03, 45.58, 45.41, 45.12, 28.53, 26.50, 19.54 ppm. MS: calcd. for $C_{18}H_{26}N_2O_3$ $[M^{\cdot}]^+$ 318.19; found 276 $[M^{\cdot} - H_3C{-}CH{=}CH_2]^+$.

**[Ru(CF$_3$CO$_2$)($p$-cymene)PCy$_3$] (6):** $[RuCl_2(p\text{-cymene})]_2$[39] was treated with 2 equiv. of $PCy_3$ and $[RuCl_2(p\text{-cymene})PCy_3]$ was obtained in 90% yield according to ref.[5]. $^1$H NMR ($CDCl_3$): $\delta$ = 5.58 (br. s, 4 H, ArH), 2.83 [pent, $^2J$ = 6.9 Hz, 1 H, $CH(CH_3)_2$], 2.42 (q, $J$ = 22.3, 11.4 Hz, 3 H, cyclohexyl), 2.14 (s, 3 H, $CH_3$), 2.09 (br., 6 H, cyclohexyl), 1.88–1.66 (m, 9 H, cyclohexyl), 1.30 [d, $^2J$ = 7.0 Hz, 6 H, $CH(CH_3)_2$], 1.56–1.10 (m, 15 H, cyclohexyl) ppm. $^{13}$C NMR ($CDCl_3$): $\delta$ = 106.7, 94.2, 88.2 ($J_{^{31}P-^{13}C}$ = 3.8 Hz), 83.7 ($J_{^{31}P-^{13}C}$ = 4.9 Hz), 35.7 ($J_{^{31}P-^{13}C}$ = 17.9 Hz, cyclohexyl), 30.4 (s, cyclohexyl), 29.5 ($J_{^{31}P-^{13}C}$ = 2.1 Hz, cyclohexyl), 27.4 ($J_{^{31}P-^{13}C}$ = 9.8 Hz, cyclohexyl), 26.3 $[CH(CH_3)_2]$, 22.3 $[CH(CH_3)_2]$, 17.7 ($CH_3$) ppm.

$[RuCl_2(p\text{-cymene})PCy_3]$ (114 mg, 0.20 mmol) was dissolved in THF and added to a solution of silver trifluoroacetate (97.2 mg, 0.44 mmol) in THF, both cooled to –36 °C. After mixing, the solution was stirred for another 4 h, allowing it to reach room temperature. During that time a white precipitate of AgCl formed. The mixture was filtered through celite and the THF was removed in vacuo. Methylene chloride was added to dissolve the residue and the solution was again concentrated in vacuo. Diethyl ether and *n*-pentane were successfully layered over the red, saturated solution. Yield: 82%. FTIR (ATR mode): $\tilde{\nu}$ = 2934, 2853, 2052, 1701, 1448, 1396, 1187, 1126, 1006, 837, 784, 725, 672 cm$^{-1}$. $^1$H NMR ($CDCl_3$): $\delta$ = 6.14 (d, $^2J$ = 5.9 Hz, 2 H, ArH), 6.14 (d, $^2J$ = 6.1 Hz, 2 H, ArH), 2.60 [pent, $^2J$ = 6.9 Hz, 1 H, $CH(CH_3)_2$], 2.25 (q, $J$ = 11.9 Hz, 3 H, cyclohexyl), 2.07 (s, 3 H, $CH_3$), 1.98–1.69 (m, 15 H, cyclohexyl), 1.56–1.22 (m, 15 H, cyclohexyl), 1.18 [d, $^2J$ = 6.9 Hz, 6 H, $CH(CH_3)_2$] ppm. $^{13}$C NMR ($CDCl_3$): $\delta$ = 163.0 [dq, $^2J_{^{19}F-^{13}C}$ = 36.3, 2.5 Hz, CO], 114.6 (q, $^1J_{^{19}F-^{13}C}$ = 291.1 Hz, $CF_3$), 107.2, 94.8, 84.2 ($J_{^{31}P-^{13}C}$ = 3.0 Hz), 81.8 ($J_{^{31}P-^{13}C}$ = 3.9 Hz), 35.6 ($J_{^{31}P-^{13}C}$ = 17.0 Hz, cyclohexyl), 31.5 (cyclohexyl), 29.3 ($J_{^{31}P-^{13}C}$ = 2.2 Hz, cyclohexyl), 27.7 ($J_{^{31}P-^{13}C}$ = 9.9 Hz, cyclohexyl), 26.4 $[CH(CH_3)_2]$, 22.5 $[CH(CH_3)_2]$, 18.8 ($CH_3$) ppm. $C_{32}H_{47}F_6O_4PRu$ (742.22): calcd. C 51.82, H 6.39; found C 51.87, H 6.50. Crystals of compound **6** were obtained in the form of its $CF_3COOAg$ adduct (**6a**).

**[Ru(CF$_3$CO$_2$)$_2$($p$-cymene)PPh$_3$] (7):** $[RuCl_2(p\text{-cymene})]_2$ was treated with $PPh_3$ (2 equiv.) according to the literature to give $[RuCl_2(p\text{-cymene})PPh_3]$ in 98% yield.[33] $^1$H NMR ($CDCl_3$): $\delta$ = 7.87–7.79 (m, 6 H, Ph), 7.40–7.32 (m, 9 H, Ph), 5.24 (d, $^2J$ = 6.2 Hz, 2 H, ArH), 4.98 (dd, $^2J$ = 6.2, 1.2 Hz, 2 H, ArH), 2.85 [pent, $^2J$ = 6.2 Hz, 1 H, $CH(CH_3)_2$], 1.86 (s, 3 H, $CH_3$), 1.09 [d, $^2J$ = 6.2 Hz, 6 H, $CH(CH_3)_2$] ppm. $^{13}$C NMR ($CDCl_3$): $\delta$ = 134.3 ($^2J_{^{31}P-^{13}C}$ = 9.4 Hz, Ph), 133.7 ($^1J_{^{31}P-^{13}C}$ = 45.7 Hz, Ph), 130.2 ($^4J_{^{31}P-^{13}C}$ = 2.2 Hz, Ph),

 © 2007 Wiley-VCH Verlag GmbH & Co. KGaA, Weinheim 

127.9 ($^3J_{^{31}P-^{13}C}$ = 9.9 Hz, Ph), 111.2 ($^2J_{^{31}P-^{13}C}$ = 3.3 Hz, *p*-Cym), 95.9 (*p*-Cym), 89.0 ($^2J_{^{31}P-^{13}C}$ = 3.3 Hz, *p*-Cym), 87.1 ($^2J_{^{31}P-^{13}C}$ = 3.3 Hz, *p*-Cym), 30.2, 21.8, 17.7 (mesityl) ppm.

[$RuCl_2$(*p*-cymene)$PPh_3$] (56.8 mg, 0.10 mmol) was dissolved in THF and added to a solution of silver trifluoroacetate (44.2 mg, 0.20 mmol) in THF, both cooled to –36 °C. After mixing, the solution was stirred for another 4 h, allowing it to reach room temperature. During that time a white precipitate of AgCl formed. The mixture was filtered through celite and the THF was removed in vacuo. Methylene chloride was added to dissolve the residue and the solution was again concentrated in vacuo. Diethyl ether and *n*-pentane were successfully layered over the red, saturated solution. Red crystals formed at –36 °C. Yield: 62.2 mg, 86%. FTIR: $\tilde{\nu}$ = 3057, 1679, 1436, 1405, 1183, 1139, 1095, 845, 788, 750, 694, 620 $cm^{-1}$. $^1H$ NMR ($CDCl_3$): $\delta$ = 7.51–7.43 (m, 9 H, Ph), 7.40–7.34 (m, 6 H, Ph), 6.26 (d, $^2J$ = 5.1 Hz, 2 H, ArH), 4.98 (d, $^2J$ = 5.1 Hz, 2 H, ArH), 2.58 [pent, $^2J$ = 6.9 Hz, 1 H, $CH(CH_3)_2$], 1.68 (s, 3 H, $CH_3$), 1.26 (d, $^2J$ = 6.9 Hz, 6 H, $CH_3$) ppm. $^{13}C$ NMR ($CDCl_3$): $\delta$ = 163.6 (dq, $^2J_{^{19}F-^{13}C}$ = 36.6, 1.8 Hz, CO), 134.4 ($^2J_{^{31}P-^{13}C}$ = 10.4 Hz, Ph), 130.9 ($^4J_{^{31}P-^{13}C}$ = 2.3 Hz, Ph), 129.5 ($^1J_{^{31}P-^{13}C}$ = 47.2 Hz, Ph), 128.4 ($^3J_{^{31}P-^{13}C}$ = 10.4 Hz, Ph), 114.8 (q, $^1J_{^{19}F-^{13}C}$ = 291.1 Hz, $CF_3$), 115.2 ($^2J_{^{31}P-^{13}C}$ = 8.4 Hz, *p*-Cym), 95.7 (*p*-Cym), 86.6, 86.5 ($^2J_{^{31}P-^{13}C}$ = 3.4 Hz, *p*-Cym), 82.8 (*p*-Cym), 31.4 [$CH(CH_3)_2$], 21.8, 18.1 ($CH_3$) ppm.

**Typical Procedure for ROMP:** Polymerizations were performed under argon. A solution of the corresponding initiator (5 mg) in $ClCH_2CH_2Cl$ (1 mL) was added to a solution of the monomer in $ClCH_2CH_2Cl$ (3 mL). The mixture was stirred at 70 °C for 8 h, then concentrated to about 1 mL, then the polymer was precipitated by dropwise addition of the solution to 30 mL of acidic methanol. The product was then filtered and dried in vacuo to give an off-white to light yellow powder.

**Poly(*exo*-1) Prepared by the Action of 3:** $M_n$ = 88000 g/mol; $M_w$ = 209000 g/mol; PDI = 2.36. IR (ATR): $\tilde{\nu}$ = 2964, 1740, 1702, 1456, 1375, 1269, 1182, 1129, 1025, 968, 812, 650 $cm^{-1}$. $^1H$ NMR ($CDCl_3$): $\delta$ = 5.76 (br. s), 5.44 (br. s), 4.28–4.16 (m, 3 H), 3.04 (m, 3 H), 2.62 (m, 2 H), 2.15 (m, 1 H), 1.62 (m, 1 H), 1.23 (t, $^2J$ = 7.1 Hz, 3 H), 1.10 (d, $^2J$ = 6.5 Hz, 3 H), 0.83 (d, $^2J$ = 6.7 Hz, 3 H) ppm. $^{13}C$ NMR ($CDCl_3$): $\delta$ = 177.6, 168.3, 132 (unresolved m), 131.6, 61.3, 57.5, 52.0 (unresolved), 50.6, 45.9, 41.8, 27.7, 21.2, 19.3, 14.1 ppm. NMR spectra of poly(*exo*-**1**) prepared by the action of **4** ($M_n$ = 130200 g/mol; $M_w$ = 225800 g/mol; PDI = 1.73) were identical.

**Poly(*endo*-1) Prepared by the Action of 3:** $M_n$ = 158300 g/mol; $M_w$ = 218900 g/mol; PDI = 1.38. IR (ATR): $\tilde{\nu}$ = 2967, 1739, 1700 (s), 1461, 1380, 1274, 1188, 1133, 1028, 969, 922, 821, 715, 661 $cm^{-1}$. $^1H$ NMR ($CDCl_3$): $\delta$ = 5.65 (br. m, 2 H), 4.33 (m, 1 H), 4.14 (m, 2 H), 3.24 (br. s, 3 H), 2.93 (br. s, 1 H), 2.58 (br. s, 1 H), 1.86 (br. s, 1 H), 1.35–1.22 (m, 4 H), 1.08 (br. s, 3 H), 0.79 (br. s, 3 H) ppm. $^{13}C$ NMR ($CDCl_3$): $\delta$ = 176.1, 175.3, 168.3, 129.3, 61.4, 57.7, 48.4, 45.5, 40.3, 37.3 (br), 27.5, 21.2, 19.4, 14.1 ppm. NMR spectra of poly(*endo*-**1**) prepared by the action of **4** ($M_n$ = 90900 g/mol; $M_w$ = 125600 g/mol; PDI = 1.39) were identical.

**Poly(*exo*-2) Prepared by the Action of 3:** $M_n$ = 106000 g/mol; $M_w$ = 158000 g/mol; PDI = 1.49. IR (ATR): $\tilde{\nu}$ = 2963, 1772, 1697, 1536, 1455, 1360, 1183, 1131, 967, 650 $cm^{-1}$. $^1H$ NMR ($CDCl_3$): $\delta$ = 6.75 (br. s), 5.75–5.48 (m), 4.05 (m, 1 H), 3.02 (br. s, 3 H), 2.68 (br. s, 2 H), 2.15 (br. s, 1 H), 1.62 (m, 1 H), 1.31 (s, 9 H), 1.03 (d, $^2J$ = 6.24 Hz, 3 H), 0.79 (d, $^2J$ = 6.18 Hz, 3 H) ppm. $^{13}C$ NMR ($CDCl_3$): $\delta$ = 178.4, 167.4, 132 (unresolved m), 131.6, 64.8, 51.2 (unresolved), 50.4, 46.2, 41.8, 28.5, 26.7, 19.6, 19.3 ppm. NMR spectra of poly(*exo*-**2**) prepared by the action of **4** ($M_n$ = 130000 g/mol; $M_w$ = 218500 g/mol; PDI = 1.68) were identical.

**Computational Methods:** Density Functional Theory (DFT) calculations were carried out using Becke's three-parameter functional (B3)[40,41] in combination with the Lee, Yang, and Parr (LYP) correlation functional[42] with the LACVP* basis set (Jaguar, version 6.5 program[43]). The LACVP* basis set uses the standard 6-31G* basis set for light elements and the LAC pseudopotential[44] for the Ru atom. The molecular geometries and energies of all calculated structures were obtained at the same B3LYP/LACVP* level of theory. The B3LYP/LACVP* method has already been successfully used in many studies.[45–48] To prove the ability of this method, the calculated molecular structure of precatalyst **3** was compared with its X-ray structure.

The calculated parameters of structure **3** were in good agreement with those of the X-ray structure (given in Supporting Information Figure S1 and Table S1). Frequency analysis was used throughout for identification of the stationary points, which is especially important for the search of the transition states, and to obtain thermochemistry parameters such as zero point energy ($E_{ZP}$), entropy ($S$), total internal energy ($U_{tot}$), total enthalpy ($H_{tot}$), and total Gibbs free energy ($G_{tot}$) at 298 K. The relative stability of the different structures was calculated as a balance of both $U_{tot}$ and $G_{tot}$ relative to those of the intermediary $RuCl_2$(IMes$H_2$) complex (structure II in Scheme 1).

**X-ray Measurement and Structure Determination of 3, 6a, and 7–9:** Data collection was performed with a Nonius Kappa CCD equipped with graphite-monochromated Mo-$K_\alpha$ radiation ($\lambda$ = 0.71073 Å) and a nominal crystal-to-area detector distance of 36 mm. Intensities were integrated using DENZO and scaled with SCALEPACK.[49] Several scans in $\phi$ and $\omega$ directions were made to increase the number of redundant reflections, which were averaged in the refinement cycles. This procedure replaces in a good approximation an empirical absorption correction. The structures were solved with direct methods SHELXS86 and refined against $F^2$ SHELXL97.[50] The function minimized was $\Sigma[w(F_o^2 - F_c^2)^2]$ with the weight defined as $w^{-1} = [\sigma^2(F_o^2) + (xP)^2 + yP]$ and $P = (F_o^2 + 2F_c^2)/3$. All non-hydrogen atoms were refined with anisotropic displacement parameters. Positions of hydrogen atoms were calculated using a riding model. Compound **3**: Triclinic space group $P\bar{1}$ (no. 2), $a$ = 11.3770(4) Å, $b$ = 12.1632(5) Å, $c$ = 14.5978(6) Å, $\alpha$ = 104.636(2)°, $\beta$ = 96.217(2)°, $\gamma$ = 113.276(2)°, $V$ = 1745.50(12) Å$^3$, $Z$ = 2, $\rho_{calcd}$ = 1.461 g/cm$^3$, $T$ = 233 K, $\mu$ = 0.521 mm$^{-1}$, orange prism, 6121 reflections > 2$\sigma(I)$, $R_1$ = 0.0350, and $\omega R_2$ = 0.0804. Compound **6a**: Triclinic space group $P\bar{1}$, $a$ = 10.2007(4) Å, $b$ = 13.8886(4) Å, $c$ = 14.9130(6) Å, $\alpha$ = 107.497(2)° $\beta$ = 94.569(2)° $\gamma$ = 95.552(2)°, $V$ = 1992.37(13) Å$^3$, $Z$ = 2, $\rho_{calcd}$ = 1.605 g/cm$^3$, $T$ = 233 K, $\mu$ = 0.993 mm$^{-1}$, orange prism, 6844 reflections > 2$\sigma(I)$, $R_1$ = 0.0282, and $\omega R^2$ = 0.0648. Compound **7**: Monoclinic space group $C2/c$ (no. 15), $a$ = 27.0985(3) Å, $b$ = 14.4321(4) Å, $c$ = 20.3053(5) Å, $\beta$ = 109.654(2)°, $V$ = 7478.5(3) Å$^3$, $Z$ = 8, $\rho_{calcd}$ = 1.413 g/cm$^3$, $T$ = 233 K, $\mu$ = 0.528 mm$^{-1}$, orange prism, 5820 reflections > 2$\sigma(I)$, $R_1$ = 0.0348, and $\omega R^2$ = 0.0784. Compound **8**: Orthorhombic space group $P2_12_12_1$ (no. 19), $a$ = 10.8932(2) Å, $b$ = 16.4398(4) Å, $c$ = 26.9136(7) Å, $\alpha = \beta = \gamma$ = 90°, $V$ = 4819.74(19) Å$^3$, $Z$ = 4, $\rho_{calcd}$ = 1.414 g/cm$^3$, $T$ = 233 K, $\mu$ = 0.506 mm$^{-1}$, colorless prism, 6183 reflections > 2$\sigma(I)$, $R_1$ = 0.0548, and $\omega R_2$ = 0.1203. Compound **9**: Orthorhombic space group $P2_12_12_1$, $a$ = 10.8403(2) Å, $b$ = 16.5038(3) Å, $c$ = 27.1075(4) Å, $\alpha = \beta = \gamma$ = 90°, $V$ = 4849.70(14) Å$^3$, $Z$ = 4, $\rho_{calcd}$ = 1.408 g/cm$^3$, $T$ = 233 K, $\mu$ = 0.503 mm$^{-1}$, colorless prism, 7510 reflections > 2$\sigma(I)$, $R_1$ = 0.0461, and $\omega R_2$ = 0.1181.

 © 2007 Wiley-VCH Verlag GmbH & Co. KGaA, Weinheim 

**Supporting Information** (see footnote on the first page of this article): Comparison of the calculated most stable structure of **3** with its X-ray structure; the most stable structure of *endo*-**IIIb**-type Ru–alkylidene complexes; energy diagram and structures of the transition states for the H-shift from C1 to C2 for both *exo*-**3a** and *endo*-**3a**.

CCDC-631369 to -631371, -631373, and -631374 (for compounds **3**, **6a** and **7**–**9**) contain the supplementary crystallographic data for this paper. These data can be obtained free of charge from The Cambridge Crystallographic Data Centre via www.ccdc.cam.ac.uk/data_request/cif.

## Acknowledgments

Our work was supported by grants from the Deutsche Forschungsgemeinschaft (DFG, BU2174/2-1) and the Freistaat Sachsen.

[1] R. H. Grubbs, *Handbook of Metathesis*, 1st ed., Wiley-VCH, Weinheim, **2003**, vols. 1–3.
[2] T. M. Trnka, R. H. Grubbs, *Acc. Chem. Res.* **2001**, *34*, 18–29.
[3] A. Hafner, A. Mühlebach, P. A. van der Schaaf, *Angew. Chem.* **1997**, *109*, 2213–2216; *Angew. Chem. Int. Ed. Engl.* **1997**, *36*, 2121–2123.
[4] E. Lindner, S. Pautz, R. Fawzi, M. Steimann, *Organometallics* **1998**, *17*, 3006–3014.
[5] A. Demonceau, A. W. Stumpf, E. Saive, A. F. Noels, *Macromolecules* **1997**, *30*, 3127–3136.
[6] L. Jafarpour, J. Huang, E. D. Stevens, S. P. Nolan, *Organometallics* **1999**, *18*, 3760–3763.
[7] L. Ackermann, C. Bruneau, P. H. Dixneuf, *Synlett* **2001**, *3*, 397–399.
[8] D. Sémeril, C. Bruneau, P. H. Dixneuf, *Helv. Chim. Acta* **2001**, *84*, 3335–3341.
[9] D. Sémeril, M. Cléran, C. Bruneau, P. H. Dixneuf, *Adv. Synth. Catal.* **2001**, *343*, 184–187.
[10] D. Sémeril, C. Bruneau, P. H. Dixneuf, *Adv. Synth. Catal.* **2002**, *344*, 585–595.
[11] R. Castarlenas, I. Alaoui-Abdallaoui, D. Sémeril, B. Mernari, S. Guesmi, P. H. Dixneuf, *New J. Chem.* **2003**, *27*, 6–8.
[12] L. Delaude, A. Demonceau, A. F. Noels, *Chem. Commun.* **2001**, 986–987.
[13] L. Delaude, M. Szypa, A. Demonceau, A. F. Noels, *Adv. Synth. Catal.* **2002**, *344*, 749–756.
[14] Y. Zhang, D. Wang, P. Lönnecke, T. Scherzer, M. R. Buchmeiser, *Macromol. Symp.* **2006**, *236*, 30–37.
[15] T. Ung, A. Hejl, R. H. Grubbs, Y. Schrodi, *Organometallics* **2004**, *23*, 5399–5401.
[16] A. Hejl, M. W. Day, R. H. Grubbs, *Organometallics* **2006**, *25*, 6149–6154.
[17] P. A. van der Schaaf, R. Kolly, H. J. Kirner, F. Rime, A. Mühlebach, A. Hafner, *J. Organomet. Chem.* **2000**, *606*, 65–74.
[18] A. Hafner, P. van der Schaaf, A. Mühlebach, P. Bernhard, U. Schaedeli, T. Karlen, A. Ludi, *Prog. Org. Coat.* **1997**, *32*, 89–96.
[19] G. Bhukta, R. Manivannan, G. Sundarajan, *J. Organomet. Chem.* **2000**, *601*, 16–21.
[20] B. Gita, G. Sundararajan, *J. Mol. Catal. A* **1997**, *115*, 79–84.
[21] J. O. Krause, M. T. Zarka, U. Anders, R. Weberskirch, O. Nuyken, M. R. Buchmeiser, *Angew. Chem.* **2003**, *115*, 6147–6151; *Angew. Chem. Int. Ed.* **2003**, *42*, 5965–5969.
[22] J. O. Krause, O. Nuyken, M. R. Buchmeiser, *Chem. Eur. J.* **2004**, *10*, 2029–2035.
[23] J. O. Krause, D. Wang, U. Anders, R. Weberskirch, M. T. Zarka, O. Nuyken, C. Jäger, D. Haarer, M. R. Buchmeiser, *Macromol. Symp.* **2004**, *217*, 179–190.
[24] T. S. Halbach, S. Mix, D. Fischer, S. Maechling, J. O. Krause, C. Sievers, S. Blechert, O. Nuyken, M. R. Buchmeiser, *J. Org. Chem.* **2005**, *70*, 4687–4694.
[25] T. S. Halbach, J. O. Krause, O. Nuyken, M. R. Buchmeiser, *Macromol. Rapid Commun.* **2005**, *26*, 784–790.
[26] T. S. Halbach, J. O. Krause, O. Nuyken, M. R. Buchmeiser, *Polym. Prepr. (Am. Chem. Soc., Div. Polym. Chem.)* **2005**, *46*, 615–616.
[27] L. Yang, M. Mayr, K. Wurst, M. R. Buchmeiser, *Chem. Eur. J.* **2004**, *10*, 5761–5770.
[28] M. R. Buchmeiser, F. Sinner, M. Mupa, K. Wurst, *Macromolecules* **2000**, *33*, 32–39.
[29] K. Matyjaszewski, *Macromolecules* **1993**, *26*, 1787–1788.
[30] C. W. Bielawski, R. H. Grubbs, *Angew. Chem.* **2000**, *112*, 3025–3028; *Angew. Chem. Int. Ed.* **2000**, *39*, 2903–2906.
[31] J. O. Krause, K. Wurst, O. Nuyken, M. R. Buchmeiser, *Chem. Eur. J.* **2004**, *10*, 777–784.
[32] G. K. Cantrell, S. J. Geib, T. Y. Meyer, *Organometallics* **2000**, *19*, 3562–3568.
[33] J. Zhang, T. B. Gunnoe, *Organometallics* **2003**, *22*, 2291–2297.
[34] J. D. Rule, J. S. Moore, *Macromolecules* **2002**, *35*, 7878–7882.
[35] D. Wang, L. Yang, U. Decker, M. Findeisen, M. R. Buchmeiser, *Macromol. Rapid Commun.* **2005**, *26*, 1757–1762.
[36] K. J. Ivin, J. Kress, J. A. Osborn, *J. Mol. Catal.* **1988**, *46*, 351–358.
[37] E. Khosravi, A. A. Al-Hajaji, *Polymer* **1998**, *39*, 5619–5625.
[38] E. Khosravi, A. A. Al-Hajaji, *Eur. Polym. J.* **1998**, *34*, 153–157.
[39] R. A. Zelonka, M. C. Baird, *Can. J. Chem.* **1972**, *50*, 3063–3072.
[40] A. D. Becke, *J. Chem. Phys.* **1993**, *98*, 5648–5652.
[41] A. D. Becke, *J. Chem. Phys.* **1996**, *104*, 1040–1046.
[42] C. T. Lee, W. T. Yang, R. G. Parr, *Phys. Rev. B: Condens. Matter* **1988**, *37*, 785–789.
[43] *Jaguar*, Schrodinger LLC, New York, **2005**.
[44] W. R. Wadt, P. J. Hay, *J. Chem. Phys.* **1985**, *82*, 284–298.
[45] S. Fomine, S. M. Vargas, M. A. Tlenkopatchev, *Organometallics* **2003**, *22*, 93–99.
[46] S. Fomine, J. V. Ortega, M. A. Tlenkopatchev, *J. Mol. Catal. A* **2005**, *236*, 156–161.
[47] S. Fomine, J. V. Ortega, M. A. Tlenkopatchev, *Organometallics* **2005**, *24*, 5696–5701.
[48] B. F. Straub, *Angew. Chem.* **2005**, *117*, 6129–6132; *Angew. Chem. Int. Ed.* **2005**, *44*, 5974–5978.
[49] Z. Otwinowski, W. Minor, *Methods in Enzymology*, Academic Press, New York, **1997**, vol. 276.
[50] G. M. Sheldrick, *Program package SHELXTL V.5.1*, Bruker Analytical X-ray Instruments Inc, Madison, USA, **1997**.

Received: January 12, 2007
Published Online: July 6, 2007

 © 2007 Wiley-VCH Verlag GmbH & Co. KGaA, Weinheim 

DOI: 10.1002/ejic.200700529

# Tetranuclear (Phosphane)(thiolato)gold(I) Complexes: Synthesis, Characterization and Photoluminescent Properties

**Eduardo J. Fernández,*[a] Antonio Laguna,*[b] José M. López-de-Luzuriaga,[a] Miguel Monge,[a] Manuel Montiel,[a] M. Elena Olmos,[a] Raquel C. Puelles,[a] and Eva Sánchez-Forcada[a]**

*Dedicated to Professor Vicente Gotor on the occasion of his 60th birthday*

**Keywords:** Phosphanes / Thiolates / Gold / Luminescence / Aurophilicity

The reactions of the tetraphosphane donor ligand $(Ph_2PCH_2)_2NCH_2CH_2N(CH_2PPh_2)_2$ with the gold precursors [AuCl(tht)] or [Au($C_6F_5$)(tht)] (tht = tetrahydrothiophene) leads to complexes $[Au_4R_4\{(Ph_2PCH_2)_2NCH_2CH_2N(CH_2PPh_2)_2\}]$ [R = Cl (**1**) or $C_6F_5$ (**2**)]. Further substitution of the chlorine atoms in **1** by the corresponding 4-substituted benzenethiolates gives rise to the tetranuclear (phosphane)(thiolato)gold(I) complexes $[Au_4(S\text{-}C_6H_4\text{-}X)_4\{(Ph_2PCH_2)_2NCH_2CH_2N(CH_2PPh_2)_2\}]$ [X = F (**3**), MeO (**4**), Me (**5**) and $NO_2$ (**6**)]. Complexes **2** and **4** were characterized by X-ray diffraction studies showing Au···Au interactions in the case of complex **4**. Complexes **3**–**6** display intense emissions in the solid state at 77 K with lifetimes in the microsecond range. The observed phosphorescent emissions are attributed to metal-to-ligand charge-transfer transitions. Nevertheless, the influence in the emission energies of gold–gold interactions or the contribution of the substituent in the 4-position of the benzenethiolate ring to the excited state cannot be neglected.
(© Wiley-VCH Verlag GmbH & Co. KGaA, 69451 Weinheim, Germany, 2007)

## Introduction

Polynuclear gold(I) complexes have attracted much interest in the last years mainly due to their intriguing structural dispositions, their rich photoluminescent properties[1] or even their potential applications in different fields as pharmaceutics, optical sensors, chemosensing, etc. In this sense, much of the interest has been generated by the clinical use of the mononuclear (phosphane)(thiolato)gold complex Auranofin,[2] employed in the treatment of reumathoid arthritis. Also, these types of complexes can be used as optical sensors for volatile organic compounds (VOCs) as shown by Eisenberg and coworkers[3] or as specific sensors for several cations as reported by Yam et al.[4]

(Thiolato)gold(I) complexes containing multidentate phosphane ligands can be considered an important class of polynuclear compounds, as the presence of several P–Au–S structural units in their structures permits the formation of aurophilic interactions. These interactions, which are comparable in strength with hydrogen bonding, are recognized as a structural motif that governs the amazing molecular and supramolecular arrangements found in the solid state for many types of gold(I) compounds.[5] Moreover, several (phosphane)(thiolato)gold(I) compounds also display very interesting photoluminescent properties over a wide range of the visible spectrum (400–700 nm), and the observed emissions are usually attributed to ligand-to-metal charge-transfer (LMCT) excited states that can be perturbed by the presence of the above-mentioned $Au^I\cdots Au^I$ interactions.[6]

In spite of several literature reports[7] on the synthesis of (phosphane)(thiolato)gold(I) complexes, the quest for high nuclearity compounds is often pursued through the use of

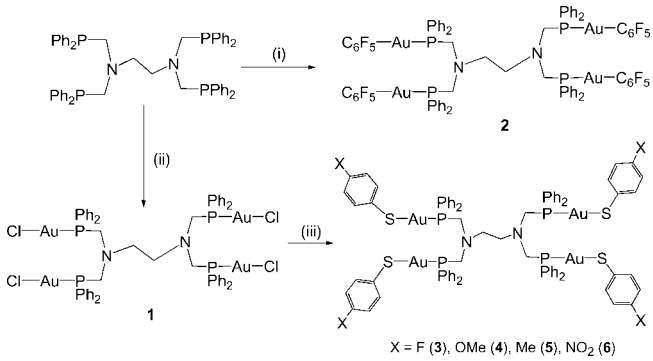


Scheme 1. Synthesis of complexes **1**–**6**. (i) [Au($C_6F_5$)(tht)]; (ii) [AuCl(tht)]; (iii) NaOMe, SH–$C_6H_4$–X (X = F, OMe, Me or $NO_2$).

[a] Departamento de Química, Universidad de La Rioja, Grupo de Síntesis Química de La Rioja, UA-CSIC – Complejo Científico-Tecnológico,
26004 Logroño, Spain
Fax: +34-941-299-621
E-mail: eduardo.fernandez@unirioja.es
[b] Departamento de Química Inorgánica, Instituto de Ciencia de Materiales de Aragón, Universidad de Zaragoza – CSIC,
50009 Zaragoza, Spain
Fax: +34-976-761-187
E-mail: alaguna@unizar.es

 © 2007 Wiley-VCH Verlag GmbH & Co. KGaA, Weinheim 

bi- or tridentate phosphorus donor ligands. We focused a part of our outgoing research on the synthesis of high nuclearity gold(I) complexes through the reaction of the appropriate gold(I) precursors with the tetradentate P donor ligand $(Ph_2PCH_2)_2NCH_2CH_2N(CH_2PPh_2)_2$[8] that permits the synthesis of tetranuclear (phosphane)(thiolato)gold(I) compounds (Scheme 1).

In this paper we report the synthesis of tetranuclear (phosphane)(thiolato)gold(I) compounds that are brightly luminescent in the solid state at 77 K. We analyzed the mechanism responsible for the luminescence in this type of complex by taking into account the presence of intramolecular aurophilic interactions or the electronic influence of the substituent in the 4-position of the benzenethiolato ligands bonded to gold.

## Results and Discussion

### Synthesis and Characterization

The tetranuclear gold(I) compounds $[Au_4R_4\{(Ph_2PCH_2)_2NCH_2CH_2N(CH_2PPh_2)_2\}]$ [R = Cl (**1**) or $C_6F_5$ (**2**)] were prepared by the reaction of 4 equiv. of the corresponding [AuCl(tht)] or $[Au(C_6F_5)(tht)]$ (tht = tetrahydrothiophene) precursors and 1 equiv. of the tetradentate phosphane ligand $(Ph_2PCH_2)_2NCH_2CH_2N(CH_2PPh_2)_2$ (Scheme 1) in quantitative yields by displacement of the labile tht ligand as crystalline white solids. All analytical and spectroscopic data are in agreement with the proposed stoichiometries. Their $^{31}P\{^1H\}$ NMR spectra display a singlet at 17.7 (**1**) or 24.7 ppm (**2**), which shows a large shift downfield upon coordination of the four Cl–Au or $C_6F_5$–Au units to the tetraphosphane ligand (–28.5 ppm). The $^{19}F$ NMR spectrum of complex **2** shows the expected pattern of the $C_6F_5$ groups bonded to $Au^I$ with three signals at –115.4, –157.7 and –161.8 ppm, which correspond to the fluorine atoms in the *ortho*, *para* and *meta* positions, respectively. Both complexes show the corresponding signals of the different methylene groups that are present in the phosphane ligand in their $^1H$ NMR spectra, and they are also shifted downfield relative to those of the free ligand. Their IR spectra show absorptions arising from the Au–Cl or Au–$C_6F_5$ groups that appear at 326 or at 1504, 954 and 792 $cm^{-1}$.

The reaction of complex **1** with different 4-substituted benzenethiols affords the corresponding compounds $[Au_4(S–C_6H_4\text{-}X)_4\{(Ph_2PCH_2)_2NCH_2CH_2N(CH_2PPh_2)_2\}]$ [X = F (**3**), MeO (**4**), Me (**5**) and $NO_2$ (**6**)] as stable crystalline solids. The thiolato ligands are prepared in situ by the reaction of the benzenethiols with an excess amount of sodium methoxide. The analytical and spectroscopic properties are in accordance with the proposed formulations. Their $^{31}P\{^1H\}$ NMR spectra show very similar shifts for the corresponding singlets as a result of the similar chemical and magnetic environments around the P atoms at 23.5, 23.4, 23.5 and 23.5 ppm for complexes **3**–**6**, respectively. In all cases, their IR spectra display the characteristic absorptions due to $\nu$(C–S) at 1103, 857 (for **3**), 1101, 867 (for **4**), 1101, 867 (for **5**) and 1103, 857 $cm^{-1}$(for **6**).

### X-ray Structural Determination of Derivatives 2 and 4

Single crystals suitable for X-ray diffraction studies were obtained by layering diethyl ether or hexane into a solution of the complex in dichloromethane (for **2**) or toluene (for **4**). Both **2** and **4** crystallize in the $P\bar{1}$ space group of the triclinic system with one molecule of the complex and one half of a molecule of diethyl ether (for **2**) or one molecule of toluene (for **4**) in the unit cell. Both structures consists of tetranuclear molecules in which each phosphorus atom of the tetradentate phosphane binds a (pentafluorophenyl)-gold(I) unit or a (thiolato)gold(I) unit for **2** and **4**, respectively (Figures 1 and 2), with Au–P distances of 2.2725(14) and 2.2799(14) Å for **2** and 2.260(2) and 2.267(2) Å for **4**, which compare well to those found in other related (pentafluorophenyl)-[9] or (benzenethiolato)(phosphane)-gold(I)[6a,10,12] complexes. The gold(I) centres complete their usual lineal environment with the coordination of a carbon atom of the anionic ligand $C_6F_5$ or a sulfur atom of S–$C_6H_4$–OMe for **2** or **4**, respectively. The Au–C bonds

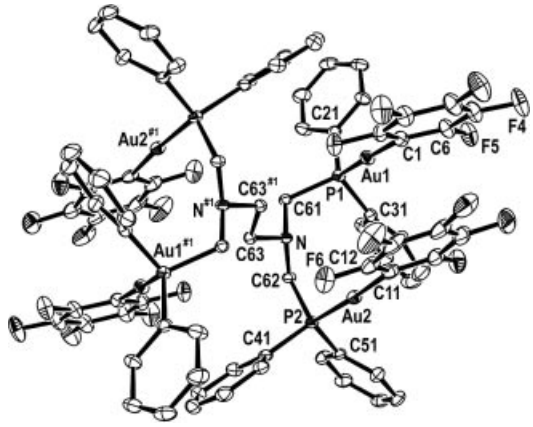


Figure 1. Molecular structure of complex **2**. Selected bond lengths [Å] and angles [°]: Au1–C1 2.049(6), Au2–C11 2.051(6), Au1–P1 2.2725(14), Au2–P2 2.2799(14), C1–Au1–P1 174.74(15), C11–Au2–P2 175.81(16).

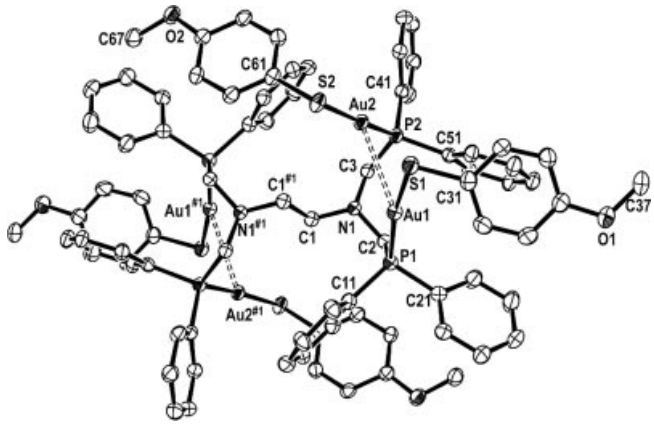


Figure 2. Molecular structure of complex **4**. Selected bond lengths [Å] and angles [°]: Au1–S1 2.318(2), Au2–S2 2.313(2), Au1–P1 2.260(2), Au2–P2 2.267(2), Au1–Au2 3.1485(4), S1–Au1–P1 169.13(8), S2–Au2–P2 173.13(7).

 © 2007 Wiley-VCH Verlag GmbH & Co. KGaA, Weinheim 

in **2**, of 2.049(6) and 2.051(6) Å, show typical values for pentafluorophenylphosphane gold(I) complexes,[9] whereas the Au–S bond lengths in **4** [2.318(2) and 2.313(2) Å] are slightly longer than the values found in a great number of (benzenethiolato)(phosphane)gold(I) complexes, but they are nearly identical to those observed in some derivatives containing the fragment Ph–S–Au–P.[6a,10a,10b,11] The main difference between these two structures is that whereas in **4** the metals associate into pairs through weak intramolecular Au···Au interactions of 3.1485(4) Å, the same disposition is not found in the case of complex **2**, in which the shortest Au–Au distance is 4.264 Å. The Au–Au distance in **4** is shorter than that in the related (diphosphane)(thiolato)-gold(I) complexes $[Au_2(S–B15C5)_2(dcmp)]$ [dcmp = bis(dicyclohexylphosphanyl)methane, S–B15C5 = 4′-mercaptobenzo-15-crown-5] [3.2556(8) Å] or $[Au_2(dcmp)(S–B18C6)_2]$ (S–B18C6 = 4′-mercaptobenzo-18-crown-6) [3.284(1) Å],[12] but it is longer than that in $[Au_2(m\text{-tc})_2\{Ph_2P(o\text{-}C_6H_4)O(o\text{-}C_6H_4)\ PPh_2\}]$ (tc = thiocresol) [3.0065(15) Å],[13] $[Au_2(S–C_6H_4NH_2\text{-}2)_2(dppm)]$ [3.1346(4) Å][6b] or $[Au_2(S–C_6H_4\text{-}CONH_2\text{-}2)_2(dppp)]$ [dppp = bis(diphenylphosphanyl)propane] [2.9997(7) Å].[10a]

### Photophysical Studies

The four phosphane–sulfide complexes display luminescence under UV light at 77 K, but they are not luminescent at room temperature or in solution. Thus, by excitation at 375 nm (complexes **3**–**5**) or 475 nm (complex **6**), emissions at 497, 508, 510 or 625 nm, respectively, are observed. The large Stokes shifts observed (>6500 for **3**, 6900 for **4**, 7000 for **5** and 5000 for **6**) implies that there is a large distortion in the excited state relative to the ground state, which is consistent with a charge transfer transition. In fact, in luminescent complexes containing S(thiolato)–Au–P(phosphane) units, the emissions are assigned to metal-to-ligand charge transfer (MLCT) transitions and, therefore, we propose a similar origin.[6] Nevertheless, the presence of phenyl groups in the ligands raises an alternative assignment, because emission bands near 500 nm in phenylphosphane metal complexes have previously been reported. These have their origin in π–π* transitions,[14] although this possibility appears remote as the chloro- and pentafluorophenylgold(I) derivatives **1** and **2**, which contain the same diphenylphosphane ligand, do not show luminescence neither in the solid state at different temperatures nor in solution.

The four complexes have long lifetimes in the microsecond range with values of 28.7 and 107.5 ($R^2$ = 0.997) for **3**, 32.4 ($R^2$ = 0.991) for **4**, 30.1 ($R^2$ = 0.991) for **5** and 399.7 μs ($R^2$ = 0.994) for **6**, suggesting that the excited states are of triplet parentage and, therefore, consistent with phosphorescent emissions (Figure 3).

As regards the position of the emission bands, previous studies in thiolate–phosphane–gold complexes carried out originally by Bruce et al.[15] and Fackler et al.[6a] point out two main factors that are responsible for the luminescent behaviour: electron-withdrawing groups on the thiolato ligands and the presence or absence of gold–gold interactions in the complexes. Electron-withdrawing groups on the thiolato ligand stabilize the sulfur orbital, which makes the ligand more difficult to oxidize and shifts the emissions to higher energies. By contrast, from these studies it was also concluded that the "gold–gold interaction is not a necessary condition for luminescence",[15] but "in some circumstances shift the emission maxima to lower energies".[6a] In our case, only the methoxy derivative was structurally characterized, and the metal–metal distance is 3.15 Å. As the emission band of the methyl derivative appears at similar energy and the electron withdrawing capability is similar for both groups, it is likely that this complex will display a similar gold–gold interaction. Nevertheless, when a fluorine atom is the substituent on the thiolato ligand its much higher electron-withdrawing ability only slightly shifts the emission band to higher energy; this can be attributed to a decreased effectiveness of this ability in the *para* position. Finally, the nitro derivative displays the longest wavelength emission in spite of its large electron-withdrawing ability. By taking into account that it is also placed in the *para* position where this effect is diminished, it is likely that the nitro group importantly contributes to the excited state or that this derivative presents a very short gold–gold interaction in the solid state.

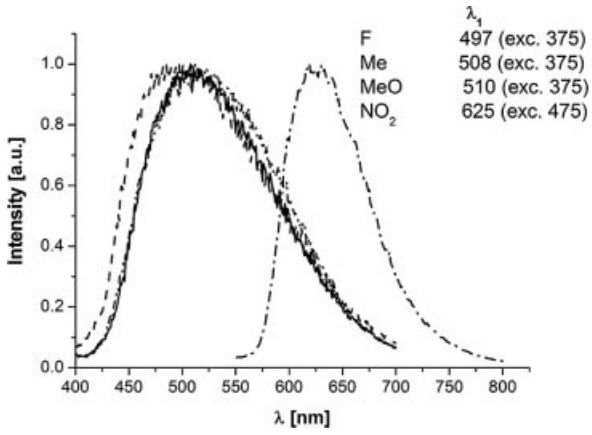


Figure 3. Emission spectra of complexes **3**–**6**.

## Conclusions

We report here the synthesis and characterization of new tetranuclear (phosphane)(thiolato)gold(I), in which a tetradentate phosphane with an ethylenediamine core and 4-substituted benzenethiols are employed as ligands. The X-ray structure of the precursor gold(I) complex with pentafluorophenyl groups bonded to gold does not show aurophilic interactions; meanwhile the corresponding (benzenethiolato)(phosphane)gold(I) complex **4** displays two $Au^I\cdots Au^I$ interactions leading to two pairs of P–Au–S units.

From the photophysical measurements it was shown that these (benzenethiolato)(phosphane)gold(I) tetranuclear derivatives display intense luminescence in the solid state at 77 K with lifetimes in the microsecond range. Both the pres-

 © 2007 Wiley-VCH Verlag GmbH & Co. KGaA, Weinheim 

ence of aurophilic interactions as well as the electron-withdrawing ability of the substituents in the 4-position of the benzenethiolato ligands were studied. It seems plausible that the electron-withdrawing abilities of the substituents in 4-position of the benzenethiolato ligand do not play a key role as it is not possible to correlate it with the emission energies. The results obtained could be more likely related to the presence of aurophilic interactions in the complexes, although the possibility of a contribution of the substituents to the excited state cannot be neglected.

## Experimental Section

**General:** The compounds [AuCl(tht)],[16] [Au($C_6F_5$)(tht)][17] and $(Ph_2PCH_2)_2NCH_2CH_2N(CH_2PPh_2)_2$[8] were synthesized by standard literature procedures. The starting materials $Ph_2PH$, *p*-formaldehyde and $NH_2CH_2CH_2NH_2$ were purchased from Sigma–Aldrich and used as received without further purification.

**Instrumentation:** Infrared spectra were recorded in the 4000–200 $cm^{-1}$ range with a Perkin–Elmer FTIR Spectrum 1000 spectrophotometer by using Nujol mulls between polyethylene sheets. C, H and N analyses were carried out with a C.E. Instrument EA-1110 CHNS-O microanalyzer. Mass spectra were recorded with a MICROFLEX MALDI-TOF spectrometer by using dithranol (DIT) as matrix. $^1H$, $^{19}F$ and $^{31}P\{^1H\}$ NMR spectra were recorded with a Bruker ARX 300 in $CDCl_3$. Chemical shifts are quoted relative to $SiMe_4$ ($^1H$ external), $CFCl_3$ ($^{19}F$ external) and $H_3PO_4$ (85%) ($^{31}P$ external), respectively. Excitation and emission spectra as well as lifetime measurements were recorded with a Jobin–Yvon Horiba Fluorolog 3–22 Tau-3 spectrofluorimeter.

**$[Au_4Cl_4\{(Ph_2PCH_2)_2NCH_2CH_2N(CH_2PPh_2)_2\}]$ (1):** To a dichloromethane solution (20 mL) of [AuCl(tht)] (0.20 g, 0.624 mmol) in dichloromethane (20 mL) was added $(Ph_2PCH_2)_2NCH_2CH_2N(CH_2PPh_2)_2$ (0.13 g, 0.145 mmol). After 30 min of stirring at room temp., the solvent was evaporated to ca. 5 mL. The addition of *n*-hexane (20 mL) led to the precipitation of compound **1** as a white solid. Yield: 83%. $^1H$ NMR (300 MHz, $CDCl_3$): $\delta$ = 7.80–7.20 (m, 40 H, aromatic protons), 3.87 (s, 8 H, P-$CH_2$-N), 2.60 (s, 4 H, N-$CH_2CH_2$-N) ppm. $^{31}P\{^1H\}$ NMR (121 MHz, $CDCl_3$): $\delta$ = 17.7 (s, $PPh_2$) ppm. IR: $\tilde{\nu}$ = 1573 $\nu$(C–N), 327 $\nu$(Au–Cl) $cm^{-1}$. MS (MALDI+): *m/z* (%) = 1747.1 (100) $[M - Cl]^+$. $C_{54}H_{52}Au_4Cl_4N_2P_4$ (1782.57): calcd. C 36.38, H 2.94, N 1.57; found C 36.52, H 2.97, N 1.59.

**$[Au_4(C_6F_5)_4\{(Ph_2PCH_2)_2NCH_2CH_2N(CH_2PPh_2)_2\}]$ (2):** To a dichloromethane solution (20 mL) of [Au$C_6F_5$(tht)] (0.15 g, 0.332 mmol) in dichloromethane (20 mL) was added $(Ph_2PCH_2)_2NCH_2CH_2N(CH_2PPh_2)_2$ (0.071 g, 0.083 mmol). After 30 min of stirring at room temp., the solvent was evaporated to ca. 5 mL. The addition of *n*-hexane (20 mL) led to the precipitation of compound **2** as a white solid. Yield: 75%. $^1H$ NMR (300 MHz, $CDCl_3$): $\delta$ = 7.70–7.20 [m, 40 H, aromatic protons], 3.70 (s, 8 H, P-$CH_2$-N), 3.02 (s, 4 H, N-$CH_2CH_2$-N) ppm. $^{31}P\{^1H\}$ NMR (121 MHz, $CDCl_3$): $\delta$ = 24.7 (s, $PPh_2$) ppm. $^{19}F$ NMR (283 MHz, $CDCl_3$): $\delta$ = –115.36 (m, 8 F, $F_{ortho}$), –157.71 (t, $^3J_{Fp\text{-}Fm}$ = 19 Hz, 4 F, $F_{para}$), –161.82 (m, 8 F, $F_{meta}$) ppm. IR: $\tilde{\nu}$ = 1586 $\nu$(C–N), 1504, 954, 792 $\nu$(Au–$C_6F_5$) $cm^{-1}$. MS (MALDI+): *m/z* (%) = 1777.9 (100) $[M - Au(C_6F_5)_2]^+$. $C_{78}H_{52}Au_4F_{20}N_2P_4$ (2308.99): calcd. C 40.57, H 2.27, N 1.21; found C 40.96, H 2.38, N 1.25.

**General Procedure for the Preparation of $[Au_4(S\text{-}C_6H_4\text{-}X)_4\{(Ph_2PCH_2)_2NCH_2CH_2N(CH_2PPh_2)_2\}]$ [X = F (3), MeO (4), Me (5) and $NO_2$ (6)]:** To a dichloromethane solution (20 mL) of the benzenethiol (0.337 mmol) was added an excess amount of NaOMe (0.073 g, 1.34 mmol). After 15 min of stirring, complex $[Au_4Cl_4\{(Ph_2PCH_2)_2NCH_2CH_2N(CH_2PPh_2)_2\}]$ **1** was added (0.15 g, 0.084 mmol). The reaction mixture was stirred for 2 h, generating a white solid (NaCl) that was separated by filtration. The filtrate was evaporated to ca. 5 mL, and the addition of diethyl ether (20 mL) led to the precipitation of the compounds.

**3:** From 4-fluorobenzenethiol (0.043 g). Yield: 45%, white solid. $^1H$ NMR (300 MHz, $CDCl_3$): $\delta$ = 7.70–7.20 (m, 40 H, Ph rings), 6.77 (m, 8 H, 3-H and 5-H in S-$C_6H_4$-F), 3.83 (s, 8 H, $PCH_2N$), 2.61 (s, 4 H, $NCH_2CH_2N$) ppm.$^{31}P\{^1H\}$ NMR (121 MHz, $CDCl_3$): $\delta$ = 23.5 (s) ppm. $^{19}F$ NMR (283 MHz, $CDCl_3$): $\delta$ = –120.70 (s, 4 F) ppm. IR: $\tilde{\nu}$ = 1584 $\nu$(C–N), 1103, 857 $\nu$(C–S) $cm^{-1}$. MS (MALDI+): *m/z* (%) = 2022 (1.5) $[M - (S\text{-}C_6F_4\text{-}F)]^+$, 1698 (17) $[M - Au(S\text{-}C_6H_4\text{-}F)_2]^+$. $C_{78}H_{68}Au_4F_4N_2P_4S_4$ (2149.41): calcd. C 43.58, H 3.19, N 1.30, S 5.97; found C 43.33, H 3.16, N 1.35, S 5.90.

**4:** From 4-methoxybenzenethiol (0.047 g). Yield: 63%, yellow solid. $^1H$ NMR (300 MHz, $CDCl_3$): $\delta$ = 7.70–7.20 (m,40 H, Ph rings), 7.41 (m, 8 H, 2-H and 6-H in S-$C_6H_4$-$OCH_3$), 6.64 (m, 8 H, 3-H and 5-H in S-$C_6H_4$-$OCH_3$), 3.83 (s, 8 H, $PCH_2N$), 3.69 (s, 12 H, MeO), 2.57 (s, 4 H, $NCH_2CH_2N$) ppm. $^{31}P\{^1H\}$ NMR (121 MHz, $CDCl_3$): $\delta$ = 23.4 (s) ppm. IR: $\tilde{\nu}$ = 1589 $\nu$(C–N), 1101, 867 $\nu$(C–S) $cm^{-1}$. MS (MALDI+): *m/z* (%) = 2058 (4) $[M - (S\text{-}C_6H_4\text{-}OCH_3)]^+$, 1722 (28) $[M - Au(S\text{-}C_6H_4\text{-}OCH_3)_2]^+$. $C_{82}H_{80}Au_4N_2O_4P_4S_4$ (2197.55): calcd. C 44.82, H 3.67, N 1.27, S 5.84; found C 44.58, H 3.45, N 1.26, S 5.54.

**5:** From 4-methylbenzenethiol (0.042 g). Yield: 51%, yellow solid. $^1H$ NMR (300 MHz, $CDCl_3$): $\delta$ = 7.70–7.20 (m,40 H, Ph rings), 7.42 (m, 8 H, 2-H and 6-H in S-$C_6H_4$-$CH_3$), 6.87 (m, 8 H, 3-H and 5-H in S-$C_6H_4$-$CH_3$), 3.82 (s, 8 H, $PCH_2N$), 2.59 (s, 4 H, $NCH_2CH_2N$), 2.21 (s, 12 H, Me) ppm. $^{31}P\{^1H\}$ NMR (121 MHz, $CDCl_3$): $\delta$ = 23.5 (s) ppm. IR: $\tilde{\nu}$ = 1587 $\nu$(C–N), 1101, 867 $\nu$(C–S) $cm^{-1}$. MS (MALDI+): *m/z* (%) = 2010 (1) $[M - (S\text{-}C_6H_4\text{-}CH_3)]^+$, 1690 (2) $[M - Au(S\text{-}C_6H_4\text{-}CH_3)_2]^+$. $C_{82}H_{80}Au_4N_2P_4S_4$ (2133.55): calcd. C 46.16, H 3.78, N 1.31, S 6.01; found C 46.12, H 3.62, N 1.36, S 5.98.

**6:** From 4-nitrobenzenethiol (0.052 g). Yield: 80%, orange solid. $^1H$ NMR (300 MHz, $CDCl_3$): $\delta$ = 7.60–7.40 (m,40 H, Ph rings), 7.82 (m, 8 H, 3-H and 5-H in S-$C_6H_4$-$NO_2$), 7.37 (m, 8 H, 2-H and 6-H in S-$C_6H_4$-$NO_2$), 3.81 (s, 8 H, $PCH_2N$), 2.89 (s, 4 H, $NCH_2CH_2N$) ppm. $^{31}P\{^1H\}$ NMR (121 MHz, $CDCl_3$): $\delta$ = 23.5 (s) ppm. IR: $\tilde{\nu}$ = 1569 $\nu$(C–N), 1499, 1328 $\nu$(C–$NO_2$), 1103, 857 $\nu$(C–S) $cm^{-1}$. MS (MALDI+): *m/z* (%) = 2103 (1) $[M - (S\text{-}C_6H_4\text{-}NO_2)]^+$, 1752 (11) $[M - Au(S\text{-}C_6H_4\text{-}NO_2)_2]^+$. $C_{78}H_{68}Au_4N_6O_8P_4S_4$ (2257.43): calcd. C 41.49, H 3.03, N 3.72, S 5.68; found C 41.46, H 2.93, N 3.91, S 5.89.

**Crystallography:** The crystals were mounted in inert oil on glass fibres and transferred to the cold gas stream of a Nonius Kappa CCD diffractometer equipped with an Oxford Instruments low-temperature attachment. Data were collected by monochromated Mo-$K_\alpha$ radiation ($\lambda$ = 0.71073 Å). Scan type $\omega$ and $\phi$. Absorption corrections: numerical (based on multiple scans). The structures were solved by direct methods and refined on $F^2$ by using the program SHELXL-97.[18] All non-hydrogen atoms were anisotropically refined with the exception of the solvent (diethyl ether) molecule in **2**. Hydrogen atoms were included using a mixed model. CCDC-647628 to -647629 contain the supplementary crystallographic data for this paper. These data can be obtained free of charge from The Cambridge Crystallographic Data Centre via www.ccdc.cam.ac.uk/data_request/cif.

 © 2007 Wiley-VCH Verlag GmbH & Co. KGaA, Weinheim 

**Crystal Data for 2:** $C_{78}H_{52}Au_4F_{20}N_2P_4{\cdot}0.5Et_2O$, $Mr$ = 2346.02, triclinic, $P\bar{1}$, $a$ = 12.183(2) Å, $b$ = 14.667(2) Å, $c$ = 14.991(2) Å, $\alpha$ = 116.97(10)°, $\beta$ = 110.67(10)°, $\gamma$ = 92.13(10)°, $V$ = 2170.4(5) Å$^3$, $Z$ = 1, $\rho_{calcd.}$ = 1.795 g cm$^{-3}$, $\mu$(Mo-$K_\alpha$) = 6.897 mm$^{-1}$, $R_1$ = 0.0388, $wR_2$ = 0.1144 for 10286 observed reflections [$I > 2\sigma(I)$].

**Crystal Data for 4:** $C_{82}H_{80}Au_4N_2O_4P_4S_4{\cdot}C_7H_8$, $Mr$ = 2289.60, triclinic, $P\bar{1}$, $a$ = 9.173(2) Å, $b$ = 13.844(3) Å, $c$ = 18.582(5) Å, $\alpha$ = 105.40(1)°, $\beta$ = 89.69(1)°, $\gamma$ = 95.99(1)°, $V$ = 2261.89(9) Å$^3$, $Z$ = 1, $\rho_{calcd.}$ = 1.681 g cm$^{-3}$, $\mu$(Mo-$K_\alpha$) = 6.677 mm$^{-1}$, $R_1$ = 0.0510, $wR_2$ = 0.1400 for 9289 observed reflections [$I > 2\sigma(I)$].

## Acknowledgments

The Dirección General de Investigación MEC/FEDER (CTQ2004-05495) and European Commission, Interreg III A (NANORET, I3A-7-341-O) are thanked for financial support. M. Monge thanks the Ministerio de Educación y Ciencia-Universidad de La Rioja for his research contract "Ramón y Cajal". M. Montiel and R. C. Puelles thank the Comunidad Autónoma de La Rioja and the Ministerio de Educación y Ciencia for a grant, respectively.

[1] J. M. Forward, J. P. Fackler Jr, Z. Assefa in *Optoelectronic Properties of Inorganic Compounds* (Eds.: D. M. Roundhill, J. P. Fackler Jr), Plenum, **1999**, New York, pp. 195–226.
[2] C. F. Shaw III in *Gold: Progress in Chemistry, Biochemistry and Technology* (Ed.: H. Schmidbaur), John Wiley & Sons, **1999**, Chichester, pp. 259.
[3] M. A. Mansour, W. B. Connick, R. J. Lachicotte, H. J. Gysling, R. Eisenberg, *J. Am. Chem. Soc.* **1998**, *120*, 1329.
[4] a) V. W. W. Yam, C. L. Chan, C. K. Li, K. M. C. Wong, *Coord. Chem. Rev.* **2001**, *216–217*, 173; b) V. W. W. Yam, C. K. Li, C. L. Chan, *Angew. Chem. Int. Ed.* **1998**, *37*, 2857.
[5] a) H. Schmidbaur, *Nature* **2001**, *413*, 31; b) P. Pyykkö, *Chem. Rev.* **1997**, *97*, 597; c) R. J. Puddephatt, *Coord. Chem. Rev.* **2001**, *216–217*, 313.
[6] a) J. M. Forward, D. Bohmann, J. P. Fackler Jr, R. J. Staples, *Inorg. Chem.* **1995**, *34*, 6330; b) M. Bardají, M. J. Calhorda, P. J. Costa, P. G. Jones, A. Laguna, M. R. Pérez, M. D. Villacampa, *Inorg. Chem.* **2006**, *45*, 1059; c) S. Y. Ho, E. C. C. Cheng, E. R. T. Tiekink, V. W. W. Yam, *Inorg. Chem.* **2006**, *45*, 8165; d) A. Pintado-Alba, H. de la Riva, M. Niewenhuyzen, D. Bautista, P. R. Raithby, H. A. Sparkes, S. J. Teat, J. M. López-de-Luzuriaga, M. C. Lagunas, *Dalton Trans.* **2004**, 3459; e) V. W. W. Yam, E. C. C. Cheng, Z. Y. Zhou, *Angew. Chem. Int. Ed.* **2000**, *39*, 1683; f) Y. Lee, R. Eisenberg, *J. Am. Chem. Soc.* **2003**, *125*, 7778; g) V. W. W. Yam, K. K.-W. Lo, *Chem. Soc. Rev.* **1999**, *28*, 323.
[7] M. C. Gimeno, A. Laguna in *Comprehensive Coordination Chemistry II* (Eds.: J. A. MacCleverty, T. J. Meyer), Elsevier Pergamon, **2003**, New York, pp. 911–1145 and references cited therein.
[8] S. O. Grim, L. J. Matienzo, *Tetrahedron Lett.* **1973**, *14*, 2951.
[9] For example, see: a) J. E. Aguado, S. Canales, M. C. Gimeno, P. G. Jones, A. Laguna, M. D. Villacampa, *Dalton Trans.* **2005**, 3005; b) E. J. Fernández, M. C. Gimeno, P. G. Jones, A. Laguna, M. Laguna, M. E. Olmos, *J. Chem. Soc. Dalton Trans.* **1994**, 2891; c) M. Bardají, P. G. Jones, A. Laguna, M. D. Villacampa, N. Villaverde, *Dalton Trans.* **2003**, 4529; d) M. A. Bennett, D. C. R. Hockless, A. D. Rae, L. L. Welling, A. C. Willis, *Organometallics* **2001**, *20*, 79; e) O. Crespo, E. J. Fernández, P. G. Jones, A. Laguna, J. M. López-de-Luzuriaga, M. Monge, M. E. Olmos, J. Pérez, *Dalton Trans.* **2003**, 1076.
[10] For example, see: a) D. R. Smyth, E. R. T. Tiekink, *Z. Kristallogr., New Cryst. Struct.* **2002**, *217*, 363; b) J. D. E. T. Wilton-Ely, A. Schier, N. W. Mitzel, H. Schmidbaur, *J. Chem. Soc. Dalton Trans.* **2001**, 1058; c) T. Yoshida, S. Onaka, M. Shiotsuka, *Inorg. Chim. Acta* **2003**, *342*, 319; d) W. J. Hunks, M. C. Jennings, R. J. Puddephatt, *Inorg. Chim. Acta* **2006**, *359*, 3605; e) B.-C. Tzeng, J. Zank, A. Schier, H. Schmidbaur, *Z. Naturforsch., Teil B* **1999**, *54*, 825.
[11] a) K. Nunokawa, K. Okazaki, S. Onaka, M. Ito, T. Sunahara, T. Ozeki, H. Imai, K. Inoue, *J. Organomet. Chem.* **2005**, *690*, 1332; b) R. Narayanaswamy, M. A. Young, E. Parkhurst, M. Ouellette, M. E. Kerr, D. M. Ho, R. C. Elder, A. E. Bruce, M. R. M. Bruce, *Inorg. Chem.* **1993**, *32*, 2506.
[12] C. K. Li, X. X. Lu, K. M. C. Wong, C. L. Chan, N. Zhu, V. W. W. Yam, *Inorg. Chem.* **2004**, *43*, 7421.
[13] H. de la Riva, A. Pintado-Alba, M. Niewenhuyzen, C. Hardacre, M. C. Lagunas, *Chem. Commun.* **2005**, 4970.
[14] J. F. Fife, K. W. Morse, W. M. Moore, *J. Photochem.* **1984**, *24*, 249.
[15] W. B. Jones, B. J. Yuan, R. Narayanaswamy, M. A. Young, R. C. Elder, A. E. Bruce, M. R. M. Bruce, *Inorg. Chem.* **1995**, *34*, 1996.
[16] E. A. Allen, W. Wilkinson, *Spectrochim. Acta* **1972**, *28A*, 2257.
[17] R. Usón, A. Laguna, J. Vicente, *J. Chem. Soc. Chem. Commun.* **1976**, 353.
[18] G. M. Sheldrick, *SHELXL-97: Program for Crystal Structure Refinement*, University of Göttingen, Germany, **1997**.

Received: May 21, 2007
Published Online: July 12, 2007

 © 2007 Wiley-VCH Verlag GmbH & Co. KGaA, Weinheim 

DOI: 10.1002/ejic.200700454

# An Approach to the Synthesis of Silicon Carbide Nanowires by Simple Thermal Evaporation of Ferrocene onto Silicon Wafers

**Jun-Jie Niu*[a] and Jian-Nong Wang[a]**

**Keywords:** Silicon / Carbides / Thermal evaporation / Ferrocene / Nanowires

Scales of silicon carbide nanowires (SiC-NWs) with high quality were synthesized by direct thermal evaporation of ferrocene onto silicon wafers at high temperature. Ferrocene decomposed into iron and carbon, which was subsequently treated with silicon to form SiC-NWs at high temperature. The SiC-NWs possess small diameters of ≈ 20 nm and lengths of several μms. Furthermore, the samples show a uniform morphology, crystalline structure, and a very thin oxide layer. The main crystal direction of [111] was confirmed by high-resolution field-emission-transmission electron microscopy (HR-FETEM). The Raman scattering spectra showed two peaks at ≈ 796 (TO) and ≈ 980 $cm^{-1}$ (LO) with varying intensity ratios at different positions. The band line fluctuation was contributed to the Raman selection rules. With reference to the experimental results, we suggested a tentative growth model according to the vapor–liquid–solid (VLS) mechanism. (© Wiley-VCH Verlag GmbH & Co. KGaA, 69451 Weinheim, Germany, 2007)

## Introduction

Silicon carbide presents wide applications in many harsh conditions such as high temperature and high frequency due to the high mechanical strength, high chemical stability, low induced activity, and so forth.[1] Many high-performance silicon carbide based devices are now commercially available, including metal semiconductor field-effect transistors and Schottky rectifiers. One-dimensional nanomaterials deserve special attention, as they are expected to play a crucial role as building blocks of future molecular electronic applications.[2–4] Silicon carbide nanowires (SiC-NWs), possessing a special geometrical and wide band-gap semiconductor structure, show the considerable advantage of a high electrical conductance and excellent mechanical stability, which makes them extremely interesting in many electrical and mechanical fields. Much effort has been focused in the miniaturization of electronic devices by using SiC-NWs in the last decade.[5–7] It was demonstrated that the SiC-NWs displayed excellent field emission and optical properties due to their remarkable structural and chemical stabilities.[6,8–10] Furthermore, SiC-NWs also exhibit good mechanical features in reinforcing the strength of ceramic–matrix composite.[11–12]

A number of existing techniques can be used for the synthesis of SiC-NWs, including carbon nanotube confined reactions,[5,13–16] carbothermal reduction,[17–21] metal-assisted vapor–liquid–solid (VLS) growth,[8,22–25] etc. Among them, a process based upon the carbon nanotube (CNTs) solid–vapor reaction with volatile oxides and/or halide species, was reported.[5] By using the floating catalyst ferrocene with the $SiCl_4$–$C_6H_6$–$H_2$–Ar system, SiC nanorods with sizes of ≈ 100 nm were obtained.[23] If the ferrocene on the silicon wafer was reacted at 600 °C with an ultrahigh vacuum (UHV) system, SiC nanodots will be formed.[24] Lee and coworkers have synthesized crystalline β-SiC-NWs with diameters of 10–30 nm by hot filament chemical vapor deposition (HFCVD), and these nanowires possessed good field-emitting properties.[22,26] Yang et al. proposed the synthesis of SiC-NWs by the thermal decomposition of a polymeric precursor with a thickness ranging from 80 to 200 nm.[27] Needle SiC-NWs were successfully prepared by thermal evaporation of SiC powder and iron powder at a high temperature of 1700 °C.[28] Moreover, Deng et al. found that single crystalline SiC-NWs could be grown directly on the surface of bulk SiC ceramic substrates in a catalyst-assisted thermal heating process.[29] However, most of the synthetic methods involved complex processes and manipulations. Furthermore, the as-produced SiC-NWs were usually over 30 nm in size and a contained a thick oxide layer. It is desirable to fabricate crystalline SiC-NWs with small diameters that are free of oxide layers by a simple process. Furthermore, the Raman scattering spectra of SiC-NWs are seldom studied and need to be further investigated.

Herein we report an alternative approach in which scales of high-quality SiC-NWs were synthesized by the simple thermal evaporation of ferrocene onto silicon wafers. Iron as a catalyst and carbon pyrrolyzed by ferrocene at high temperatures deposited on the surface of silicon wafers and reacted with silicon to generate SiC-NWs. The as-formed

[a] School of Materials Science and Engineering, Shanghai Jiao Tong University
Shanghai 200030, P. R. China
Tel.: +86-21-62932050
E-mail: jjniu@sjtu.edu.cn

 © 2007 Wiley-VCH Verlag GmbH & Co. KGaA, Weinheim 

SiC-NWs with small diameters of ≈ 20 nm and lengths of several μms show a well-crystalline structure, uniform size distribution, and thin oxide layer. Furthermore, the crystal direction of [111] is clearly observed. Two peaks at ≈ 796 (TO) and ≈ 980 $cm^{-1}$ (LO) in the Raman scattering spectra show varying intensity ratios at different positions. The intensity fluctuation is attributed to the Raman selection rules. Finally, we suggest a possible growth model that is related to the vapor–liquid–solid (VLS) mechanism.

## Results and Discussion

Figure 1 displays the FESEM image of scales of SiC-NWs with diameters of ≈ 20 nm and lengths of several μms. Relatively straight SiC-NWs with uniform size distributions and smooth surfaces can be clearly observed from the enlarged image in Figure 1b. It also can be seen that the surface of the SiC-NWs is clean and free of impurities. Shown in Figure 1c is an interesting FESEM image of as-grown SiC-NWs sticking to the silicon wafer. As can be seen from the figure, the homogeneous SiC-NWs closely contact to the surface of the silicon wafer, indicating a different growth procedure relative to Figure 1a and b. The possible chemical composition of the sample was analyzed through the EDS data recorded from several pure nanowires (Figure 1d). The presence of peaks demonstrates that the nanowires are composed of silicon, carbon, and small amount of oxygen. The quantitative element analysis shows a Si/C ratio of 1:1, which corresponds well to the standard SiC (1:1) and thus confirms the composition of the SiC nanowires. The small quantity of oxygen may come from the resident oxide layer or the adsorbed oxygen in the air. The Fe peak was not detected because of the weak concentration. Shown in Figure 2 are the TEM images of several SiC-NWs with mean diameters of ≈ 20 nm and lengths of 2–3 μms. It is clear that the SiC-NWs are structurally uniform and dislocation free. We estimated the diameter distribution of the SiC-NWs by calculating hundreds of nanowires from the TEM images. As can be seen from Figure 4b, the majority of SiC-NWs show a concentrated diameter arrangement of ≈ 20 nm. Some of the SiC-NWs have sizes that are less than 10 nm and very few are over 25 nm. The high-magnification TEM image in Figure 2b more clearly shows a smooth morphology and homogeneous size distribution of the SiC-NWs. Moreover, the SiC-NWs are of high quality with free of defects such as stacking faults. The selected area electric diffraction (SAED) pattern corresponding to the SiC-NWs indicates a crystalline structure (Figure 2a inset). The (111) face that is confirmed in the figure suggests a main growth direction of [111] because of the lowest energy theory. Otherwise, the fluctuant brightness of black and white in the TEM image synchronously indicates a crystalline nature. The lattice structure of the SiC-NWs can be viewed in the HR-FETEM image (Figure 3). As can be seen from Figure 3, the regular interplanar spacing of 0.25 nm shows good agreement with SiC growth along the [111] direction, indicating a single-crystalline structure. Otherwise, it is observed that the lattice fringes are parallel to the nanowire axes, which indicates a [220] growth direction. It can also be observed that the surfaces

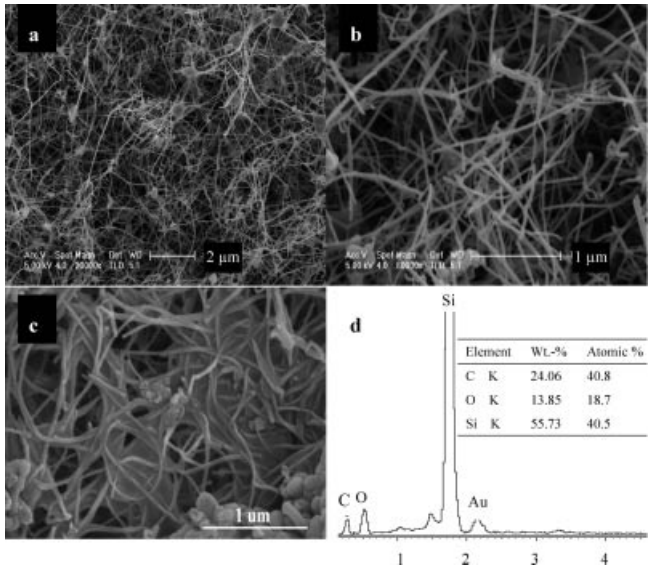


Figure 1. (a) The low-magnification, (b) high-magnification, and (c) special-structure FESEM images of the SiC-NWs with mean diameters of ≈ 20 nm and lengths of several μms. (d) The EDS spectrum and quantitative elemental analysis recorded from the pure SiC-NWs. The weak Au and unmarked peaks come from sample preparation during the FESEM measurements.

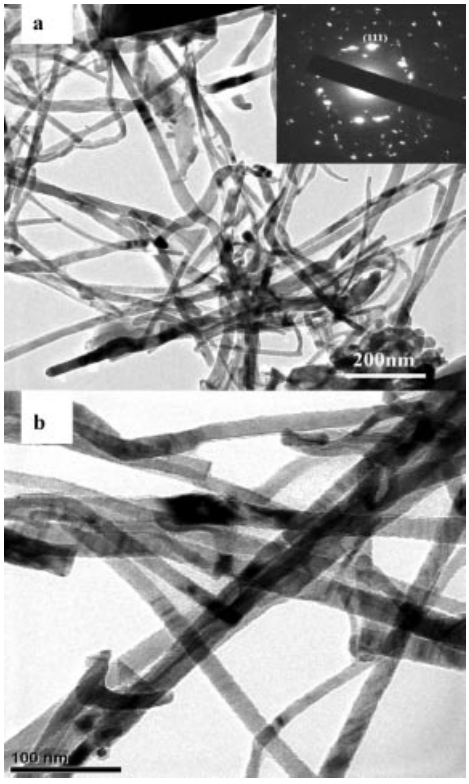


Figure 2. (a) The low-magnification and (b) high-magnification TEM images of the SiC-NWs. The inset in (a) is the corresponding SAED pattern.

 © 2007 Wiley-VCH Verlag GmbH & Co. KGaA, Weinheim 

of the SiC-NWs are smooth and clean and possess only a very thin oxide layer of less than 1 nm. As a result, the SiC-NWs are structurally uniform, singly crystalline, and have only a thin oxide layer.

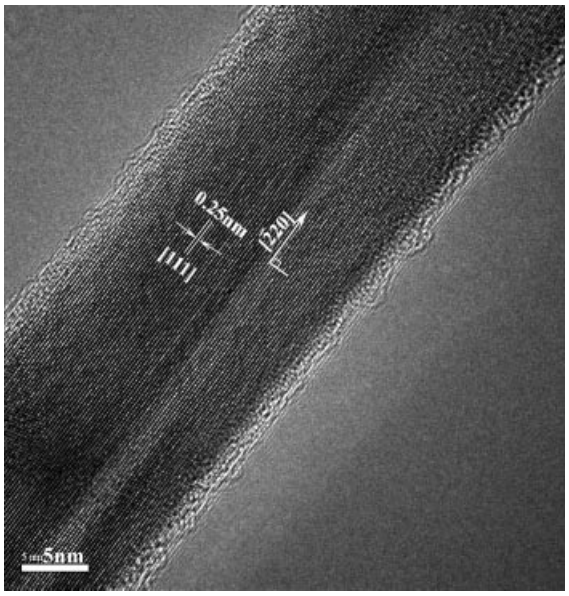


Figure 3. HR-FETEM image of a SiC-NW with the lattice orientation of [111].

Shown in Figure 4a is the XRD data of the sample, which is used for analyzing the crystalline structure. As can be seen from the pattern, the peaks of (111), (200), (220), (311), and (222) are completely consistent to the standard face-centered cubic (fcc) cell of SiC with the lattice constant of $a$ = 0.4349 nm (JCPDS card No. 73–1665). The strong intensity and narrow width of the lines also indicate an excellent crystal structure, which is also shown in the HR-FETEM image. Except for the peaks of SiC, several peaks of $Si_2N_2O$ with a low intensity are synchronously observed. These reflection lines are believed to be derived from weak nitrification and oxidation during the procedure.

Figure 5A displays the Raman scattering spectrum of a typical SiC-NW sample at room temperature. There is a prominent band line at ≈ 796 $cm^{-1}$ and a low intensity line at ≈ 980 $cm^{-1}$; these two lines correspond well to the band lines of a zincblende structure of bulk SiC. Furthermore, these bands normally result from the first-order phonon frequencies of the transverse optical (TO) and longitudinal optical (LO) modes, respectively.[30] Between these two lines, the lines at 729 and 887 $cm^{-1}$ can also be distinguished. These two peaks may be attributable to special SiC-NWs Raman-active modes or to impurities. As can be seen from the figure, the symmetry and narrow width of the lines indicate a crystalline nature of the high-quality SiC-NWs. The lines in this Raman spectrum are consistent with those reported for SiC nanorods or nanowires,[25,31] but they are different to those of bulk materials or films of SiC.[32–33]

It is known that the LO band line is usually higher than the TO band line near the zone center in bulk SiC.[34] However, in this Raman scattering spectrum, the TO band

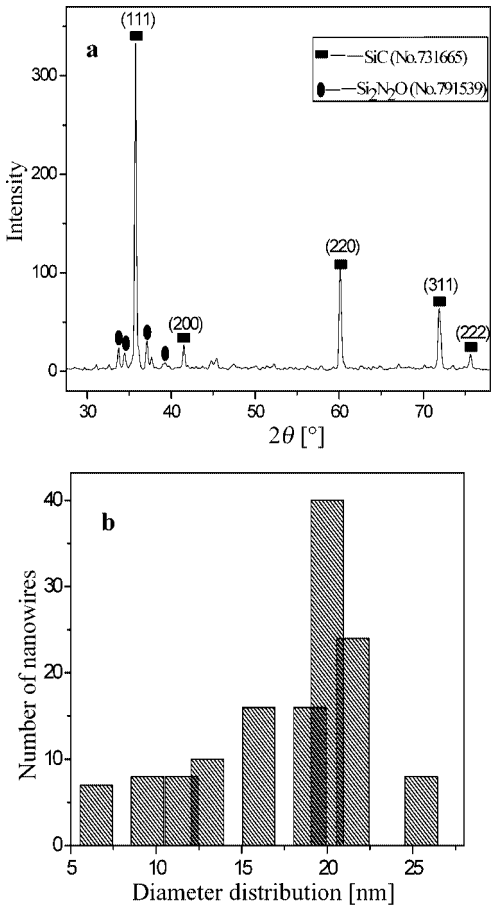


Figure 4. (a) XRD pattern of the SiC-NW sample. (b) Diameter distribution of the SiC-NWs.

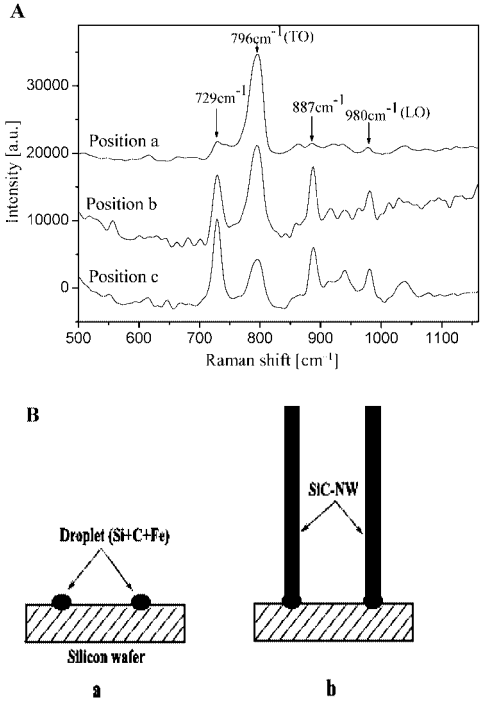


Figure 5. (A) Raman scattering spectra of the SiC-NWs with different positions. (B) Schematic illustration of the SiC-NWs growth model.

 © 2007 Wiley-VCH Verlag GmbH & Co. KGaA, Weinheim 

shows a stronger intensity than the LO band (Figure 5A). As depicted in the figure, the SiC-NWs sample exhibits a fluxional intensity ratio of the various band lines when it was irradiated at different positions. The intensity of the TO band at ≈ 796 $cm^{-1}$ continually decreases whereas the LO band at ≈ 980 $cm^{-1}$ increases when the radiation is moved from position a to c. These phenomena may be explained by the Raman selection rules. During the Raman measurements, the radiated SiC-NWs were randomly arranged and had no unique predominant crystalline direction, although the [111] will be the major orientation of growth. Therefore, the polarization of the incident and scattered wave vectors such as the (011) face, which is perpendicular to the quasi-backscattering geometry face (100), was not strictly obeyed.[21,31] Consequently, the TO and LO band lines in the Raman spectrum of our sample were not completely forbidden or allowed but showed a varying intensity ratio with different positions.

The growth of SiC-NWs with a metal catalyst normally results from the VLS mechanism. In the current process, ferrocene was used to serve as the iron catalyst and a source of carbon whereas the silicon wafer was used as a silicon source and the substrate. Here we propose a possible growth model corresponding to the VLS mechanism. During the process, ferrocene [$(C_5H_5)_2Fe$] will favorably be pyrolyzed into iron and carbon at high temperature. The decomposed Fe and C atoms will then be deposited onto the surface of the silicon wafer to form an alloy droplet with Si atoms along the VLS mechanism (Figure 5B, a). Once the Si and C atoms reach supersaturation, the excess atoms will precipitate out from the nuclear (alloy droplet) and grow up to a SiC-NW (Figure 5B, b). In theory, it is also possible for the catalyst to serve as an anchor on the tip of the nanowire. During this step, the one-dimensional SiC-NW structure usually grows along the direction of [111] because of the lowest-energy principle. Here one case should be mentioned; a small quantity of silicon may be oxidized to $SiO_2$ or SiO. The produced silicon oxide will simultaneously react with the deposited carbon and form the structure of SiC-NW. Furthermore, some silicon or generated silicon oxide will possibly be nitrified by nitrogen gas at high temperature (as shown in Figure 4a). It is noted that the as-formed SiC-NWs are not easy to be nitrified because of their high stability in the present experiments. It is believed that if another inert gas, such as argon, was used, the nitrification will not happen. During the current process, the C, Si, and catalytic Fe sources are supplied simultaneously by ferrocene and the silicon substrate, which obviously simplifies the synthesis process. Thus, a useful technique for synthesizing scales of crystalline SiC-NWs is suggested.

## Conclusions

Scales of high-quality crystalline silicon carbide nanowires with small diameters of ≈ 20 nm and lengths of several μms were synthesized by direct thermal evaporation of ferrocene onto a silicon wafer at high temperature. The samples possessed a uniform size, crystalline structure, and a thin oxide layer. The HR-FETEM image showed a main single-crystal direction of [111]. The Raman scattering spectra of the sample showed varying intensity ratios at different positions, which is attributed to the Raman selection rules. Finally, a tentative growth model according to the vapor–liquid–solid (VLS) mechanism was suggested. The simple synthetic process presented here suggests a useful route for the fabrication of crystalline SiC-NWs with high quantity.

## Experimental Section

**General Procedure:** A ceramic boat containing pieces of silicon wafers (n-type Si (100) with a resistivity of about 4.1 Ωcm) and an amount of ferrocene powder was placed on a silicon surface and put in the center of a high-temperature chemical-vapor-deposition furnace. The furnace was heated to 1550 °C at a rate of 10 °C/min. A nitrogen gas flow was initiated at a rate of 70 mL/min at the beginning. After heating for ca. 2 h, the samples were taken out for the next measurements. The morphology and lattice structure of the samples were checked by field emission scanning electric microscopy (FESEM, FEI Sirion) and high-resolution field emission transmission electron microscopy (HR-FETEM, JEM 2010F). The possible chemical composition was investigated by using energy-dispersive X-ray spectroscopy (EDS) attached to the FESEM. The crystalline structure was measured by X-ray diffraction using Cu-$K_\alpha$ radiation (XRD, D8 DISCOVER, Bruker). Raman scattering spectra were measured with a Raman microscope (Renishaw inVia plus) with a 514.5 nm laser as the excitation source at room temperature.

## Acknowledgments

This work was supported by the Shanghai-Applied Materials Research and Development Fund (No. 06SA06) and Youth Teacher Fund of Shanghai Jiao Tong University (A2306B). We would like to thank the Instrumental Analysis Center of Shanghai Jiao Tong University for their great help in obtaining the measurements.

[1] J. B. Casady, R. W. Johnson, *Solid-State Electron.* **1996**, *39*, 1409.
[2] Y. Cui, C. M. Lieber, *Science* **2001**, *291*, 851.
[3] C. M. Lieber, *Nano Lett.* **2002**, *2*, 81.
[4] R. Rurali, *Phys. Rev. B* **2005**, *71*, 205405.
[5] H. J. Dai, E. W. Wong, Y. Z. Lu, S. S. Fan, C. M. Lieber, *Nature* **1995**, *375*, 769.
[6] Z. Pan, H. L. Lai, F. C. K. Au, Z. Duan, W. Zhou, W. Shi, N. Wang, C. S. Lee, N. B. Wong, S. T. Lee, S. Xie, *Adv. Mater.* **2000**, *12*, 1186.
[7] Z. J. Li, H. J. Li, X. L. Chen, A. L. Meng, K. Z. Li, Y. P. Xu, L. Dai, *Appl. Phys. A: Mater. Sci. Process* **2003**, *76*, 637.
[8] C. H. Liang, G. W. Meng, L. D. Zhang, Y. C. Wu, Z. Cui, *Chem. Phys. Lett.* **2000**, *329*, 323.
[9] H. K. Seong, H. J. Choi, S. K. Lee, J. I. Lee, D. J. Choi, *Appl. Phys. Lett.* **2004**, *85*, 1256.
[10] B. Yan, G. Zhou, W. Duan, J. Wu, B. Gu, *Appl. Phys. Lett.* **2006**, *89*, 023104.
[11] E. W. Wong, P. E. Sheehan, C. M. Lieber, *Science* **1997**, *277*, 1971.
[12] W. Yang, H. Araki, C. Tang, S. Thaveethavorn, A. Kohyama, H. Suzuki, T. Noda, *Adv. Mater.* **2005**, *17*, 1519.

 © 2007 Wiley-VCH Verlag GmbH & Co. KGaA, Weinheim 

[13] W. Q. Han, S. S. Fan, Q. Q. Li, W. J. Liang, B. L. Gu, D. P. Yu, *Chem. Phys. Lett.* **1997**, *265*, 374.
[14] A. I. Kharlamov, S. V. Loichenko, N. V. Kirillova, V. V. Fomenko, M. E. Bondarenko, Z. A. Zaitseva, *Inorg. Mater.* **2003**, *39*, 260.
[15] Y. Xia, P. Yang, Y. Sun, Y. Wu, B. Mayers, B. Gates, Y. Yin, F. Kim, H. Han, *Adv. Mater.* **2003**, *15*, 353.
[16] C. C. Tang, S. S. Fan, H. Y. Dang, J. H. Zhao, Z. Zhang, P. Li, Q. Gu, *J. Cryst. Growth* **2000**, *210*, 595.
[17] G. W. Meng, L. D. Zhang, C. M. Mo, S. Y. Zhang, Y. Qin, S. P. Feng, H. J. Li, *J. Mater. Res.* **1998**, *13*, 2533.
[18] Z. X. Yang, Y. D. Xia, R. Mokaya, *Chem. Mater.* **2004**, *16*, 3877.
[19] H. Ye, N. Titchenal, Y. Gogotsi, F. Ko, *Adv. Mater.* **2005**, *17*, 1531.
[20] J. We, K. Z. Li, H. J. Li, Q. G. Fu, L. Zhang, *Mater. Chem. Phys.* **2006**, *95*, 140.
[21] G. Gundiah, G. V. Madhav, A. Govindaraj, M. M. Seikh, C. N. R. Rao, *J. Mater. Chem.* **2002**, *12*, 1606.
[22] X. T. Zhou, N. Wang, H. L. Lai, H. Y. Peng, I. Bello, N. Wong, C. S. Lee, S. T. Lee, *Appl. Phys. Lett.* **1999**, *74*, 3942.
[23] Y. Zhang, N. Wang, R. He, X. Chen, J. Zhu, *Solid State Commun.* **2001**, *118*, 595.
[24] K. Kametani, K. Sudoh, H. Iwasaki, *Thin Solid Films* **2004**, *467*, 50.
[25] H. Y. Kim, J. Park, H. Yang, *Chem. Commun.* **2003**, 256.
[26] K. W. Wong, X. T. Zhou, F. C. K. Au, H. L. Lai, C. S. Lee, S. T. Lee, *Appl. Phys. Lett.* **1999**, *75*, 2918.
[27] W. Yang, H. Miao, Z. Xie, L. Zhang, L. An, *Chem. Phys. Lett.* **2004**, *383*, 441.
[28] Z. S. Wu, S. Z. Deng, N. S. Xu, J. Chen, J. Zhou, J. Chen, *Appl. Phys. Lett.* **2002**, *80*, 3829.
[29] S. Z. Deng, Z. B. Li, W. L. Wang, N. S. Xu, J. Zhou, X. G. Zheng, H. T. Xu, J. Chen, J. C. Lee, *Appl. Phys. Lett.* **2006**, *89*, 023118-1.
[30] H. Okumura, E. Sakuma, J. H. Lee, H. Mukaida, S. Misawa, K. Endo, S. Yoshida, *J. Appl. Phys.* **1987**, *61*, 1134.
[31] S. Zhang, B. Zhu, F. Huang, Y. Yan, E. Shang, S. Fan, W. Han, *Solid State Commun.* **1999**, *111*, 647.
[32] W. Feldman, J. H. Parker Jr, W. J. Choyke, L. Patrick, *Phys. Rev.* **1968**, *173*, 790.
[33] Z. C. Feng, C. C. Tin, R. Hu, J. Willianms, *Thin Solid Films* **1995**, *266*, 1.
[34] D. Olego, M. Cardona, *Phys. Rev. B* **1982**, *25*, 3889.
Received: April 26, 2007
Published Online: July 12, 2007

 © 2007 Wiley-VCH Verlag GmbH & Co. KGaA, Weinheim 

DOI: 10.1002/ejic.200700440

# Phosphaalkenes $R^1C(O)–P=C(NMe_2)_2$ ($R^1$=Ph, 4-Et$C_6H_4$): Versatile Reagents for 1,3-Dipolar Cycloadditions to Phosphenium Complexes $[Cp(CO)_2M = PPh_2]$ (M = Mo, W)

**Lothar Weber,*[a] Gabriel Noveski,[a] Stefan Uthmann,[a] Hans-Georg Stammler,[a] and Beate Neumann[a]**

**Keywords:** Phosphaalkenes / Phosphenium Complexes / Molybdenum / Tungsten

Reaction of $[Cp(CO)_2M = PPh_2]$ [where M = Mo (**2a**), W (**2b**)] with an excess of the phosphaalkenes arylC(O)P=C$(NMe_2)_2$ [where aryl = Ph (**3**), 4-Et$C_6H_4$ (**5**)] afforded the metallophosphaalkenes $[Cp(CO)_2M^a–P=C(aryl)–O–P^bPh_2(M^a–P^b)]$ [where M = Mo, aryl = Ph (**4a**); M = W, aryl = Ph (**4b**); M = Mo, aryl = 4-Et$C_6H_4$ (**6a**); M = W, aryl = 4-Et$C_6H_4$ (**6b**)] as orange crystals. Compounds **4a**,**b** and **6a**,**b** were characterized by means of spectroscopy (IR, $^1$H, $^{13}$C and $^{31}$P NMR spectroscopy and MS). Moreover, the molecular structures of **3**, **4a**, and **6b** were determined by X-ray diffraction analysis.
(© Wiley-VCH Verlag GmbH & Co. KGaA, 69451 Weinheim, Germany, 2007)

## Introduction

During the course of our studies on phosphaalkenes R–P=C$(NMe_2)_2$ (R = *t*Bu, Cy, Ph), we observed a facile metal-assisted cleavage of the PC multiple bond and the formal transfer of phosphanediyls (RP) on suitable complexes with electrophilic ligands.[1] Thus, reaction with selected Fischer carbene complexes gave rise to the formation of coordination compounds **I** with novel $\eta^1$-phosphaalkene ligands,[2] whereas treatment with vinylidene complexes resulted in the formation of $\eta^2$(P,C)-phosphaallene complexes **II**.[3] $\eta^3$-1,2-Diphosphaallyl complexes **III** were obtained from the combination of phosphaalkenes and phosphavinylidene complexes.[4] Only recently we disclosed the generation of $\eta^2$-diphosphanyl complexes **IV** by reacting phosphaalkenes and phosphenium complexes[5] (Scheme 1).

## Results and Discussion

The purpose of this work was to study the reactivity of the *P*-benzoylphosphaalkenes PhC(O)P=C$(NMe_2)_2$ (**3**)[6] and 4-Et$C_6H_4$C(O)P=C$(NMe_2)_2$ (**5**) with the phosphenium complexes $[Cp(CO)_2M = PPh_2]$ (**2a**: M = Mo; **2b**: W). The latter were generated in situ by the dehydrochlorination of the functionalized phosphane complexes $[Cp(CO)_2ClMP(H)Ph_2]$[7] (**1a**: M = Mo; **1b**: W) with diazabicycloundecene (DBU). Phosphaalkene **5** was synthesized as a yellow powder in 81% yield from 4-ethylbenzoylchloride and $Me_3SiP=C(NMe_2)_2$[8] (Scheme 2).

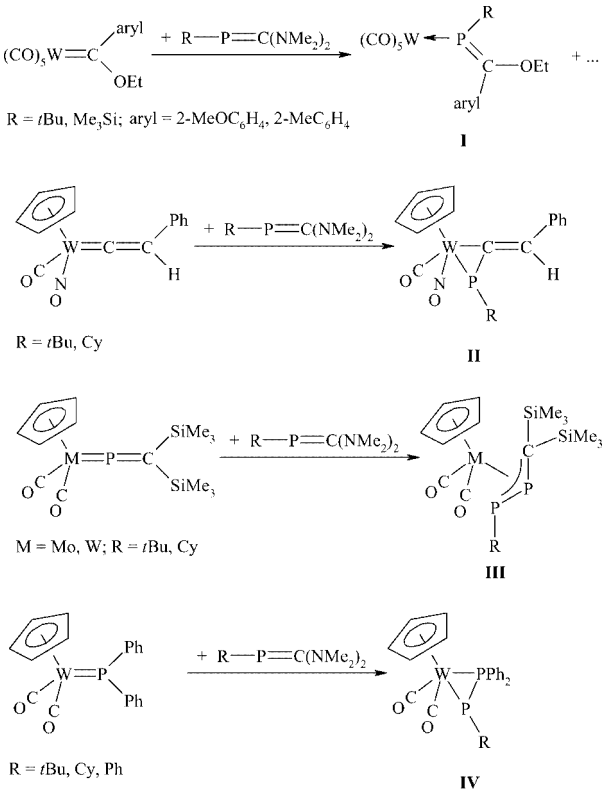


Scheme 1. Phosphanediyl-transfer from phosphaalkenes onto selected organometallic electrophiles.

Treatment of freshly prepared complexes **2a**,**b** with an excess of the phosphaalkenes in toluene solution over a temperature range of –30 to 20 °C afforded orange crystalline metallophosphaalkenes **4a**,**b** and **6a**,**b** in modest yields (Scheme 3).

[a] Fakultät für Chemie der Universität Bielefeld
Universitätsstrasse 25, 33615 Bielefeld, Germany
Fax: +49-521-106-6146
E-Mail: lothar.weber@uni-bielefeld.de

 © 2007 Wiley-VCH Verlag GmbH & Co. KGaA, Weinheim 

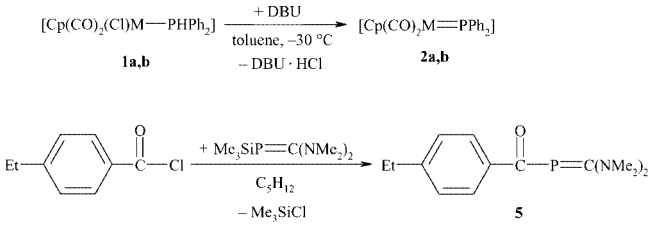


Scheme 2. Preparation of **2a**,**b** and **5**.

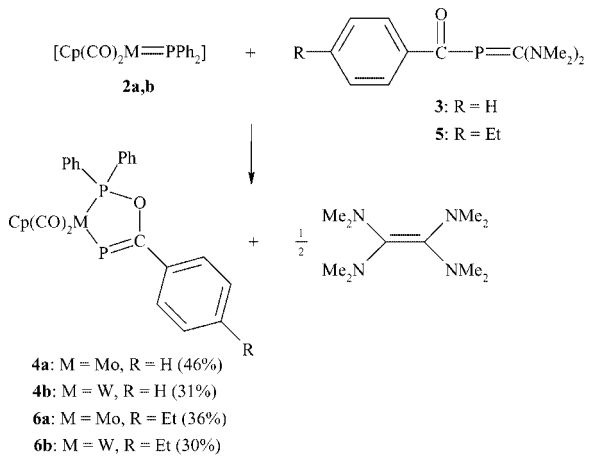


Scheme 3. Synthesis of metallophosphaalkenes **4a**,**b** and **6a**,**b**.

Isolation of the products was effected by column chromatography on Florisil with mixtures of pentane/diethylether as the eluents. Subsequent crystallization furnished analytically pure compounds.

The $^{31}P\{^1H\}$ NMR spectra of **4a** and **6a** show two doublets. The tetracoordinate P atoms give rise to signals at $\delta$ = 199.9 and 198.7 ppm, whereas the dicoordinate P atoms are observed at markedly lower field [**4a**: 235.5 (d); **6a**: 225.9 (d)] with PP coupling constants of 21.8 and 20.7 Hz, respectively. As expected, the corresponding doublets in tungsten complex **4b** and **6b** are more shielded and appear at $\delta$ = 170.7 (d, $PPh_2$) and 170.1 (d, $PPh_2$) ppm and $\delta$ = 209.4 (d, P=C) and 199.9 (d, P=C) with PP coupling constants of 21.8 and 22.5 Hz. Only tetracoordinate P atoms of **4b** and **6b** exhibit $^{183}W$ satellites with $^1J_{WP}$ = 329.3 and 330.4 Hz.

In the $^{13}C\{^1H\}$ NMR spectra of the products, the carbon atoms of the P=C bonds give rise to doublets of doublets in the typical low field region [**4a**: $\delta$ = 193.6 ppm ($^1J_{PC}$ = 85.6 Hz, $^2J_{PC}$ = 17.8 Hz); **4b**: $\delta$ = 192.9 ppm ($^1J_{PC}$ = 82.9 Hz, $^2J_{PC}$ = 18.2 Hz); **6a**: $\delta$ = 194.1 ppm ($^1J_{PC}$ = 86.2 Hz, $^2J_{PC}$ = 17.5 Hz); **6b**: $\delta$ = 193.4 ppm ($^1J_{PC}$ = 82.8 Hz, $^2J_{PC}$ = 18.4 Hz)]. The $^{13}C\{^1H\}$ NMR spectra of **4a**,**b** and **6a**,**b** show in the region of the carbonyl carbon atoms two markedly separated resonances at $\delta$ = 223.9 (s; **4b**, **6b**) and $\delta$ = 231.5 (d, $^2J_{PC}$ = 17.5 Hz; **4b**), 231.8 (d, $^2J_{PC}$ = 18.4 Hz; **6b**) and in the molybdenum compounds at $\delta$ = 234.3 (d, $^2J_{PC}$ = 12.7 Hz), 241.3 (d, $^2J_{PC}$ = 26.4 Hz) and at 234.3 (d, $^2J_{PC}$ = 12.1 Hz), 241.5 (d, $^2J_{PC}$ = 25.6 Hz) for **4a** and **6a**, respectively. We assign the resonances at higher field to the carbonyl group in the *trans* disposition of the $PPh_2$ unit. In keeping with the increased donor capability of the phosphaalkenyl group, the resonance of the carbonyl ligand in its *trans* disposition is attributed to the more deshielded signal. The $[M(CO)_2]$ group gives rise to two intense bands in the IR spectra at $\tilde{\nu}$ = 1935–1943 and 1864–1881 $cm^{-1}$, which are due to the symmetric and asymmetric CO stretching vibrations. Interestingly, the novel bidentate chelating ligand exhibits a decreased donor capacity relative to the $\eta^2$-diphosphanido ligand in complexes of the type $[Cp(CO)_2MPR^1–PR^2R^3]$, **IV** ($\tilde{\nu}$ = 1918–1933; 1837–1849 $cm^{-1}$).[5] The carbonyl vibration of the aryl group in precursor **4** was observed at $\tilde{\nu}$ = 1535 $cm^{-1}$, and does not show up in the products any longer, which means that it was involved in a cycloaddition process.

## X-ray Structural Investigations

Single crystals of phosphaalkene **2** suitable for X-ray diffraction studies were grown from *n*-pentane at –30 °C. The analysis (Figure 1, Table 1) shows a benzoyl-stabilized carbenium phosphanide, in which the planar carbenium center C(8) (sum of angles is 359.6°) displays multiple bonding to planarly configured nitrogen atoms [N(1)–C(8) = 1.344(2) Å, N(2)–C(8) = 1.356(2) Å].

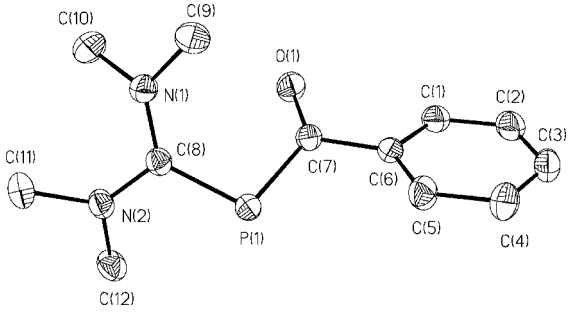


Figure 1. Molecular crystal structure of **2**. Selected bond lengths [Å] and angles [°]: P(1)–C(8) 1.800(1), P(1)–C(7) 1.806(1), O(1)–C(7) 1.240(2), N(1)–C(8) 1.344(2), N(1)–C(9) 1.462(2), N(1)–C(10) 1.468(2), N(2)–C(8) 1.356(2), N(2)–C(11) 1.461(2), N(2)–C(12) 1.457(2), C(6)–C(7) 1.511(2). C(8)–P(1)–C(7) 101.34(6), C(8)–N(1)–C(9) 123.0(1), C(8)–N(1)–C(10) 122.5(1), C(9)–N(1)–C(10) 113.4(1), C(8)–N(2)–C(11) 122.9(1), C(8)–N(2)–C(12) 123.3(1), C(11)–N(2)–C(12) 113.8(1), N(1)–C(8)–N(2) 116.8(1), N(1)–C(8)–P(1) 124.6(1), N(2)–C(8)–P(1) 118.2(1), P(1)–C(7)–O(1) 127.0(1), O(1)–C(7)–C(6) 118.0(1), C(6)–C(7)–P(1) 115.0(1).

The former P=C bond of the precursor [cf. $HP=C(NMe_2)_2$; *d*(P=C) = 1.740(1) Å] is markedly lengthened to 1.800(1) Å. A bond length of 1.806(1) Å is found between the phosphorus atom and the carbon atom of the carbonyl group in **2**, which compares well with the other PC bond of the molecule. Both bonds are best regarded as single bonds. The bonds between the phosphorus atom and the carbon atoms of both carbonyl groups in bis(pivaloyl)-phenylphosphane $[tBuC(O)]_2PPh$, however, are much longer [1.893(4) and 1.922(5) Å].[9] The CO double bond in **2** [1.240(1) Å] is slightly elongated relative to the CO bonds in $[tBuC(O)]_2PPh$ [1.201(6) and 1.217(6) Å]. The backbone of the compound defined by the atoms N(2), C(8), P(1), C(7), and C(6) deviates severely from a plane, as indicated

 © 2007 Wiley-VCH Verlag GmbH & Co. KGaA, Weinheim 

Table 1. Crystal data and data collection parameters.

| Compound | **3** | **4a** | **6b** |
|---|---|---|---|
| Empirical formula | $C_{12}H_{17}N_2OP$ | $C_{26}H_{20}MoO_3P_2$ | $C_{28}H_{24}O_3P_2W$ |
| $M_r$ [g mol$^{-1}$] | 236.25 | 538.30 | 654.26 |
| Crystal dimensions [mm] | $1.1 \times 1.0 \times 0.6$ | $0.27 \times 0.16 \times 0.07$ | $0.30 \times 0.30 \times 0.24$ |
| Crystal system | monoclinic | monoclinic | triclinic |
| Space group | *C*2/*c* | $P2_1/n$ | $P\bar{1}$ |
| *a* [Å] | 18.295(7) | 9.2032(7) | 8.6693(10) |
| *b* [Å] | 7.867(2) | 16.8512(9) | 11.5833(14) |
| *c* [Å] | 17.562(5) | 14.8462(9) | 13.0253(3) |
| $\alpha$ [°] | 90 | 90 | 90.573(6) |
| $\beta$ [°] | 96.62(3) | 95.457(5) | 103.736(5) |
| $\gamma$ [°] | 90 | 90 | 101.577(16) |
| *V* [Å$^3$] | 2510.8(14) | 2292.0(3)) | 1242.4(2) |
| *Z* | 8 | 4 | 2 |
| $\rho_{calcd.}$ [g cm$^{-3}$] | 1.250 | 1.560 | 1.749 |
| $\mu$ [mm$^{-1}$] | 0.201 | 0.738 | 4.806 |
| *F*(000) | 1008 | 1088 | 640 |
| $\theta$ [°] | 2.24–30.00 | 3.01–27.50 | 3.23–30.00 |
| refl. collected | 3720 | 37211 | 45461 |
| refl. unique | 3619 | 5237 | 7238 |
| *R* (int) | 0.0262 | 0.0294 | 0.0553 |
| Refined parameters | 213 | 289 | 309 |
| GOF | 1.067 | 1.079 | 1.091 |
| $R_F$ [$I > 2\sigma(I)$] | 0.0404 | 0.0215 | 0.0155 |
| $wR_{F2}$ [all Data] | 0.1073 | 0.0489 | 0.0388 |
| $\Delta\rho$ max/min [e Å$^{-3}$] | 0.521/–0.350 | 0.406/–0.496 | 0.686/–0.771 |

by the torsion angles O(1)–C(7)–P(1)–C(8) (–16.2°) and C(6)–C(7)–P(1)–C(8) (167.3°) and an interplanar angle of 40.5° between the plane defined by the atoms N(1),N(2), C(8) and P(1), C(7), C(8). From the X-ray structural data it can be concluded that compound **2** is best described by the zwitterionic limiting formula **A** and not by **B** or **C** (Scheme 4).

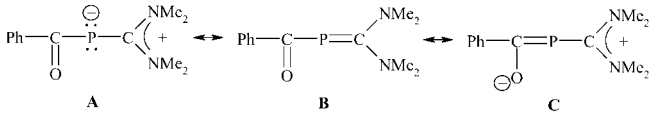


Scheme 4. Canonical formulae for phosphaalkene **3**.

Single crystals of **4a** suitable for X-ray diffraction analysis were grown from *n*-pentane at +4 °C. The analysis (Figure 2, Table 1) displays a molecule with a distorted four-legged piano-stool geometry [C(6)–Mo(1)–C(7) 78.79(7)°, C(6)–Mo(1)–P(2) 72.86(5)°, C(7)–Mo(1)–P(1) 80.57(5)°, P(1)–Mo(1)–P(2) 70.86(1)°] with two nearly linear carbonyl ligands [Mo(1)–C(6)–O(1) 177.9(2), Mo(1)–C(7)–O(2) 177.8(2)°]. The remaining two legs are represented by a 1,4,2-diphosphaoxabuten-3-yl ligand, which is chelating the metal atom through bonds Mo(1)–P(1) [2.3754(4) Å] and Mo(1)–P(2) [2.5602(5) Å]. The latter bond length compares well to the Mo–P distance in the metallophosphaalkene [$Cp(CO)_3Mo$–P=$C(SiMe_3)_2$] [2.568(1) Å].[10] The bond length between the metal atom and the tetracoordinated phosphorus atom of 2.3754(4) Å is slightly longer than the Mo–P contact in [$Cp(CO)_2Mo^a$–$PMe_2$–$C^b(SiMe_3)_2$(*Mo*$^a$–*C*$^b$)] [2.348(2) Å].[11]

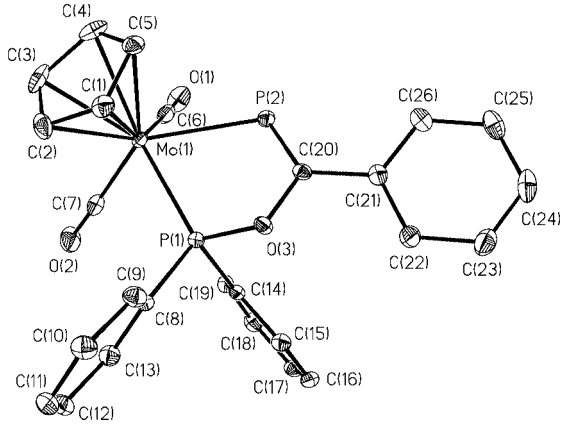


Figure 2. Molecular crystal structure of **4a**. Selected bond lengths [Å] and angles [°]: Mo(1)–C(6) 1.974(2), Mo(1)–C(7) 1.971(2), Mo(1)–P(1) 2.3754(4), Mo(1)–P(2) 2.5602(5), P(2)–C(20) 1.707(2), C(20)–O(3) 1.402(2), C(20)–C(21) 1.472(2), P(1)–O(3) 1.666(1), P(1)–C(8) 1.819(2), P(1)–C(14) 1.830(2); C(6)–Mo(1)–C(7) 78.8(1), C(6)–Mo(1)–P(2) 72.9(1), C(7)–Mo(1)–P(1) 80.6(1), P(1)–Mo(1)–P(2) 70.86(1), Mo(1)–P(1)–O(3) 112.51(4), P(1)–O(3)–C(20) 107.5(1), O(3)–C(20)–P(2) 121.7(1), Mo(1)–P(2)–C(20) 105.3(1), O(3)–C(20)–C(21) 112.7(1), P(2)–C(20)–C(21) 125.3(1), Mo(1)–C(6)–O(1) 177.9(2), Mo(1)–C(7)–O(2) 177.8(2)°.

Repulsion between the lone pair of electrons at P(2) and the electron-rich Mo atom may be responsible for the increased bond length relative to the Mo(1)–P(1) distance. This novel chelating ligand features the double bond P(2)–C(20) [1.707(2) Å], which compares well to the PC separation in the ferriophosphaalkene [$Cp(CO)_2Fe$–P=C-($OSiMe_3$)*t*Bu] [1.701(4) Å],[12] but it is markedly longer than that in the molybdophosphaalkene [$Cp(CO)_3Mo$–

 © 2007 Wiley-VCH Verlag GmbH & Co. KGaA, Weinheim 

P=C(SiMe$_3$)$_2$] [1.665(3) Å]. The contact P(1)–O(3) [1.666(1) Å] is shorter than the sum of the covalent radii (1.76 Å) but still reflects a bond order of unity.[13] Bond C(20)–O(3), which in precursor **2** exists as a carbonyl group with a bond length of 1.240(2) Å, is lengthened to a single bond of length 1.402(2) Å. The metalloheterocycle is slightly puckered (sum of endocyclic angles 517.9°).

Single crystals of **6b** were grown from *n*-pentane/diethyl ether at + 4 °C (Figure 3). Like **3a**, this complex has the geometry of a four-legged piano stool [C(6)–W(1)–C(7) 79.1(1), C(6)–W(1)–P(2) 72.9(1), C(7)–W(1)–C(7) 79.9(1), P(1)–W(1)–P(2) 72.77(2)°]. A 1,4,2-diphosphaoxabuten-3-yl ligand chelates the tungsten atom through bonds W(1)–P(1) [2.3632(5) Å] and W(1)–P(2) [2.5556(5) Å]. The former bond length is slightly shorter than the coordinative W–P bond in **7** [2.432(2) Å][7] or **8** [2.434(2) Å].[14]

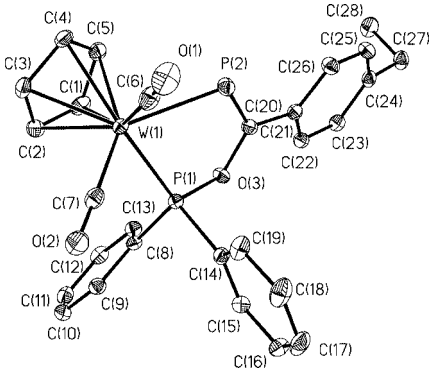


Figure 3. Molecular crystal structure of **6b**. Selected bond lengths [Å] and angles [°]: W(1)–C(6) 1.980(2), W(1)–C(7) 1.966(2), W(1)–P(1) 2.3632(5), W(1)–P(2) 2.5556(5), P(2)–C(20) 1.700(2), C(20)–O(3) 1.402(2), C(20)–C(21) 1.468(2), P(1)–C(8) 1.824(2), P(1)–C(14) 1.827(2); C(6)–W(1)–C(7) 79.1(1), C(6)–W(1)–P(2) 74.0(1), C(6)–W(1)–P(1) 116.2(1), C(7)–W(1)–P(1) 79.9(1), C(7)–W(1)–P(2) 127.1(1), P(1)–W(1)–P(2) 72.77(2), W(1)–P(1)–O(3) 113.64(4), P(1)–O(3)–C(20) 111.2(1), O(3)–C(20)–P(2) 121.7(1), W(1)–P(2)–C(20) 105.3(1), O(3)–C(20)–C(21) 112.0(1), P(2)–C(20)–C(21) 126.1(1), W(1)–C(6)–O(1) 177.4(2), W(1)–C(7)–O(2) 178.8(2).

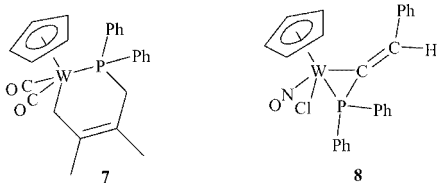


Bonding parameters within the chelating ligand of **6b** are close to those in **4a** and merit no particular discussion at this point. The five-membered metalloheterocycle of **6b** is more flattened (sum of endocyclic angles 529.6°) relative to that of **4a** (517.9°).

### Mechanisms

It is conceivable that the path towards the formation of complexes **4a**, **4b**, **6a**, and **6b** begins with nucleophilic attack of phosphaalkenes **2**,**3** by its electron-abundant phosphorus atom at the phosphenium center of **1a**,**b**, which affords zwitterion **A**. Release of a carbene unit and metal–phosphorus bond formation then affords intermediate **B**. Finally, ring enlargement leads to the final products; however, intermediates **A** and **B** were not detected by $^{31}$P NMR spectroscopic monitoring of the reaction (Scheme 5).

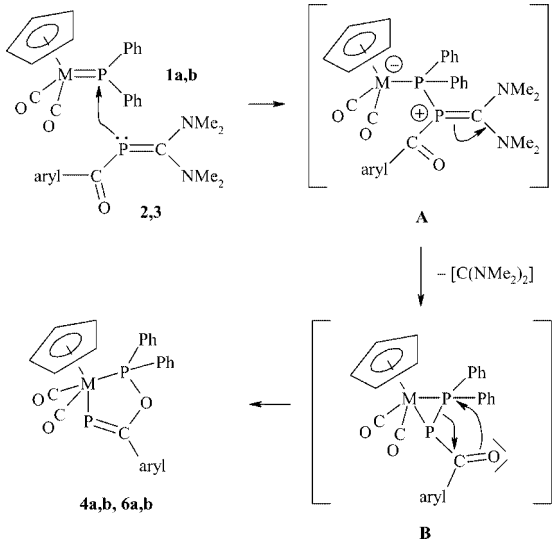


Scheme 5. Proposed mechanism for the synthesis of **4a**,**b** and **6a**,**b**.

## Conclusions

Transition-metal-induced cleavage of inversely polarized phosphaalkenes with concomitant transfer of the phosphanediyl unit on carbene- or phosphenium ligands to give $\eta^1$-phosphaalkene[2] and $\eta^2$-diphosphanido complexes[5] have previously been described. Here the smooth generation of complexes **4a**,**b** and **6a** featuring the chelating 1,4,2-diphosphaoxabutene-3-yl ligand underlines the ability of phosphaalkenes to act as convenient sources for phosphanediyl units under mild conditions.

## Experimental Section

**General:** All experiments were performed under a dry, oxygen-free nitrogen atmosphere by using standard Schlenk techniques. Solvents were carefully dried with an appropriate drying agent and freshly distilled under an atmosphere of $N_2$ before use. The following compounds were prepared according to literature procedures: [Cp(CO)$_2$ClMo–PHPh$_2$] (**1a**),[7] [Cp(CO)$_2$ClW–PHPh$_2$] (**1b**),[7] PhC(O)P=C(NMe$_2$)$_2$ (**3**),[6] and Me$_3$SiP=C(NMe$_2$)$_2$.[8] Diazabicycloundecene (DBU), 4-Et$C_6H_4$C(O)Cl, and Florisil (0.150–0.250 mm) were purchased commercially. IR spectra were recorded with a Bruker FTIR VECTOR 22 spectrometer. $^1$H-, $^{13}$C-, and $^{31}$P NMR spectra were recorded at room temp. with a Bruker AM Avance DRX 500 instrument. References: SiMe$_4$ ($^1$H, $^{13}$C) and 85% $H_3PO_4$ ($^{31}$P). MS was conducted with a Bruker Esquire Ion trap mass spectrometer autospec, sector field.

**4-Et$C_6H_4$C(O)P=C(NMe$_2$)$_2$ (5):** A solution of Me$_3$SiP=C(SiMe$_3$)$_2$ (0.25 g, 1.20 mmol) in *n*-pentane (20 mL) was added dropwise at –30 °C to the solution of 4-Et$C_6H_4$C(O)Cl (0.20 g, 1.20 mmol) in *n*-pentane(20 mL), whereby a yellow precipitate formed. Stirring was continued at –30 °C for 1 h. The cold slurry was filtered, and

 © 2007 Wiley-VCH Verlag GmbH & Co. KGaA, Weinheim 

the filtercake was washed with cold *n*-pentane (3 × 20 mL, –30 °C). The filtercake was dried at $10^{-3}$ bar to afford **5** as a bright yellow powder (yield: 0.26 g, 81%). $^1$H NMR (500.13 MHz, $C_6D_6$): $\delta$ = 0.99 (t, $^3J_{HH}$ = 7.5 Hz, 3 H, $CH_2CH_3$), 2.36 (q, $^3J_{HH}$ = 7.5 Hz, 2 H, $CH_2CH_3$), 2.59 (s, 12 H, $NCH_3$), 7.05 (m, 2 H, *m*-H-Ph), 8.54 (m, 2 H, *o*-H-Ph) ppm. $^{13}$C{$^1$H} NMR (125.75 MHz, $C_6D_6$): $\delta$ = 15.7 (s, $CH_2CH_3$), 29.0 (s, $CH_2CH_3$), 42.8 (d, $^3J_{PC}$ = 4.6 Hz, $NCH_3$), 126.9 (s, Ph), 127.0 (s, Ph), 142.9 (d, $^2J_{PC}$ = 48.3 Hz, *i*-C-Ph), 147.1 (s, *p*-C-Ph), 200.2 (d, $^1J_{PC}$ = 78.2 Hz, P=*C*), 215.4 (d, $^1J_{PC}$ = 78.2 Hz, PC=O) ppm. $^{31}$P{$^1$H} NMR (202.46 MHz, $C_6D_6$): $\delta$ = 30.8 (s) ppm. IR (KBr): $\tilde{\nu}$ = 1535 [s (CO)] cm$^{-1}$. MS (EI): *m*/*z* = 264 [M]$^+$, 133 [4 – $EtC_6H_4CO$]$^+$, 131 [P=C$(NMe_2)_2$]$^+$, 105 [4 – $EtC_6H_4$]$^+$. $C_{14}H_{21}N_2OP$ (264.30): calcd. C 63.62, H 8.01, N 10.60; found C 63.13, H 8.15, N 10.60.

**[Cp(CO)$_2$Mo$^a$–P=C(Ph)O–P$^b$Ph$_2$(*Mo$^a$–P$^b$*)] (4a):** A solution of [Cp(CO)$_2$ClMoPHPh$_2$] (**1a**; 0.80 g, 1.82 mmol) in toluene (40 mL) was added dropwise to a chilled solution (–30 °C) of PhC(O)-P=C$(NMe_2)_2$ (**3**; 1.29 g, 5.46 mmol) and DBU (0.42 g, 2.76 mmol) in toluene (30 mL). After 2 h, the addition was complete, and stirring at –30 °C was continued for 1 h. The mixture was then warmed to room temp. and stirred overnight. Solvent and volatile components were removed in vacuo. To the residue was added Florisil (3 g) and toluene (15 mL), and the slurry was evaporated to dryness. The remaining powder was brought on a column filled with Florisil and pentane (*l* = 5 cm, *d* = 2 cm). First the column was developed with pentane/diethyl ether (30:1) to separate a yellow zone. This zone was eluted with pentane/diethyl ether (30:5, ca. 250 mL). Concentration of the elute to ca. 120 mL and storage for 12 h at –30 °C furnished product **4a** as orange crystals (yield: 0.45 g, 46%). $^1$H NMR (500.13 MHz, $C_6D_6$): $\delta$ = 4.56 (s, 5 H, Cp), 6.80–7.08 (m, 9 H, Ph), 7.64 (m, 2 H, Ph), 7.81 (m, 2 H, Ph), 8.23 (m, 2 H, Ph) ppm. $^{13}$C{$^1$H} NMR (125.75 MHz, $C_6D_6$): $\delta$ = 93.0 (s, $C_5H_5$), 125.4, 125.5, 127.9, 128.1, 128.3, 128.4, 128.5, 128.6, 128.7, 129.8, 129.9, 130.3, 131.7, 132.4, 132.5, 137.9 (s, Ph), 138.2 (m, Ph), 141.7, 142.1 (s, Ph), 193.6 (dd, $^1J_{PC}$ = 85.6 Hz, $^2J_{PC}$ = 17.8 Hz, P=C), 234.3 (d, $^2J_{PC}$ = 12.7 Hz, CO), 241.3 (d, $^2J_{PC}$ = 26.4 Hz, CO) ppm. $^{31}$P{$^1$H} NMR (202.46 MHz, $C_6D_6$): $\delta$ = 199.3 (d, $^2J_{PP}$ = 21.8 Hz, $PPh_2$), 235.5 (d, $^2J_{PP}$ = 21.8 Hz, P=C) ppm. IR (KBr): $\tilde{\nu}$ = 1943 [s (CO)], 1874 [s (CO)] cm$^{-1}$. MS (EI): *m*/*z* = 540 [M]$^+$, 484 [M – 2 CO]$^+$. $C_{26}H_{20}MoO_3P_2$ (538.32): calcd. C 58.01, H 3.74; found C 57.20, H 3.42.

**[Cp(CO)$_2$W$^a$–P=C(Ph)O–P$^b$Ph$_2$(*W$^a$–P$^b$*)] (4b):** A solution of [Cp-(CO)$_2$ClWPHPh$_2$] (**1b**; 0.86 g, 1.63 mmol) in toluene (40 mL) was added dropwise (2 h) to a cold solution (–10 °C) of PhC(O)-P=C$(NMe_2)_2$ (**3**; 0.39 g, 1.63 mmol) and DBU (0.42 g, 2.76 mmol) in toluene (20 mL). The mixture was warmed to ambient temperature and stirred for 12 h. Volatile components were removed in vacuo, and the oily residue was combined with Florisil (2 g) and toluene and then chromatographed on Florisil as described above. A yellow zone was eluted with pentane/diethyl ether (3:2, ca. 300 mL). The elute was concentrated, and the residue was crystallized from toluene/pentane (1:1, 20 mL) at –30 °C over 24 h. The product separated as orange crystals (yield: 0.31 g, 31%). $^1$H NMR (500.13 MHz, $C_6D_6$): $\delta$ = 4.55 (s, 5 H, Cp), 6.82 (m, 1 H, Ph), 6.89 (m, 2 H, Ph), 6.99–7.11 (m, 6 H, Ph), 7.64 (m, 2 H, Ph), 7.81 (m, 2, Ph), 8.24 (m, 2 H, Ph) ppm. $^{13}$C{$^1$H} NMR (125.75 MHz, $C_6D_6$): $\delta$ = 91.6 (s, $C_5H_5$), 125.6, 125.8, 130.0, 130.1, 130.4, 131.8, 132.9, 133.0 (s, Ph), 192.9 (dd, $^1J_{PC}$ = 82.9 Hz, $^2J_{PC}$ = 18.2 Hz, P=C), 223.9 (s, CO), 231.5 (d, $^2J_{PC}$ = 17.5 Hz, CO) ppm. $^{31}$P{$^1$H} NMR (202.46 MHz, $C_6D_6$): $\delta$ = 170.7 (d, $J_{PP}$ = 21.8 Hz, $^1J_{WP}$ = 329.3 Hz, $PPh_2$), 209.4 (d, $^2J_{PP}$ = 21.8 Hz, P=C) ppm. IR (KBr): $\tilde{\nu}$ = 1935 [s (CO)], 1864 [s (CO)] cm$^{-1}$. MS (EI): *m*/*z* = 626 [M]$^+$, 570 [M – CO]$^+$. $C_{26}H_{20}O_3P_2W$ (626.22): calcd. C 49.87, H 3.22; found C 48.97, H 3.10.

**[Cp(CO)$_2$Mo$^a$–P=C(4-Et-C$_6$H$_4$)O–P$^b$Ph$_2$(*Mo$^a$–P$^b$*)] (6a):** As described above, solutions of [Cp(CO)$_2$ClMoPHPh$_2$] (**1a**; 0.68 g, 1.55 mmol) in toluene (30 mL), 4-$EtC_6H_4C$(O)P=C$(NMe_2)_2$ (**5**; 0.41 g, 1.55 mmol), and DBU (0.36 g, 2.33 mmol) in toluene (20 mL) were combined at –30 °C. Stirring was continued for 1 h at –30 °C and 12 h at 20 °C. The solvent and the volatile components were removed in vacuo, and the residue was chromatographed on Florisil. A yellow zone was eluted with a pentane/diethyl ether (10:3, ca. 350 mL). The elute was concentrated to ca. 50 mL and stored at –30 °C for 12 h. Product **6a** separated as orange crystals (yield: 0.32 g, 36%). $^1$H NMR (500.13 MHz, $C_6D_6$): $\delta$ = 0.98 (t, $^3J_{HH}$ = 7.5 Hz, 3 H, $CH_2CH_3$), 2.31 (q, $^3J_{HH}$ = 7.5 Hz, 2 H, $CH_2CH_3$), 4.59 (s, 5 H, Cp), 6.84 (m, 1 H, Ph), 6.89–6.91 (m, 4 H, Ph), 7.05–7.11 (m, 4 H, Ph), 7.66 (m, 2 H, Ph), 7.84 (m, 2 H, Ph), 8.19 (m, 2 H, Ph) ppm. $^{13}$C{$^1$H} NMR (125.75 MHz, $C_6D_6$): $\delta$ = 15.6 (s, $CH_2CH_3$), 28.9 (s, $CH_2CH_3$), 93.0 (s, $C_5H_5$), 125.6, 125.8, 128.3, 128.4, 128.7, 128.8, 129.9, 130.1, 131.7, 132.5, 132.6 (s, Ph), 194.1 (dd, $^1J_{PC}$ = 86.2 Hz, $^2J_{PC}$ = 17.5 Hz, P=C), 234.3 (d, $^2J_{PC}$ = 12.1 Hz, CO), 241.5 (d, $^2J_{PC}$ = 25.6 Hz, CO) ppm. $^{31}$P{$^1$H} NMR (202.46 MHz, $C_6D_6$): $\delta$ = 198.7 (d, $^2J_{PP}$ = 20.7 Hz, $PPh_2$), 225.9 (d, $^2J_{PP}$ = 20.7 Hz, P=C) ppm. IR (KBr): $\tilde{\nu}$ = 1942 [s (CO)], 1881 [s (CO)] cm$^{-1}$. MS (EI): *m*/*z* = 568 [M]$^+$, 540 [M – CO]$^+$, 512 [M – 2 CO]$^+$. $C_{28}H_{24}MoO_3P_2$ (566.38): calcd. C 59.38, H 4.27; found C 59.50, H 4.24.

**[Cp(CO)$_2$W$^a$–P=C(4-Et-C$_6$H$_4$)O–P$^b$Ph$_2$(*W$^a$–P$^b$*)] (6b):** As described above, a solution of [Cp(CO)$_2$ClWPHPh$_2$] (**1b**; 0.91 g, 1.73 mmol) in toluene (40 mL) was combined with a mixture of 4-$EtC_6H_4C$-(O)P=C$(NMe_2)_2$ (**5**; 0.47 g, 1.78 mmol) and DBU (0.36 g, 2.33 mmol) in chilled toluene (20 mL, –10 °C). After stirring at room temp. for 14 h, the mixture was evaporated to dryness, and the residue was chromatographed on Florisil. A yellow zone was eluted with pentane/diethyl ether (10:3, 250 mL; then 2:1, 200 mL). The elute was concentrated to ca. 120 mL and stored at –30 °C for 24 h, whereby product **6b** separated as yellow crystals (yield: 0.34 g, 30%). $^1$H NMR (500.13 MHz, $C_6D_6$): $\delta$ = 0.98 (t, $^3J_{HH}$ = 7.5 Hz, 3 H, $CH_2CH_3$), 2.31 (q, $^3J_{HH}$ = 7.5 Hz, 2 H, $CH_2CH_3$), 4.58 (s, 5 H, Cp), 6.83 (m, 1 H, Ph), 6.91 (m, 4 H, Ph), 7.03–7.11 (m, 3 H, Ph), 7.68 (m, 2 H, Ph), 7.84 (m, 2 H, Ph), 8.23 (m, 2 H, Ph) ppm. $^{13}$C{$^1$H} NMR (125.75 MHz, $C_6D_6$): $\delta$ = 15.6 (s, $CH_2CH_3$), 28.9 (s, $CH_2CH_3$), 91.6 (s, $C_5H_5$), 125.8, 125.9, 127.9, 128.3, 128.4, 128.6, 128.7, 130.1, 130.2, 130.4, 131.7, 132.9, 133.1, 135.7, 135.9, 136.0, 137.6, 138.0, 141.4, 141.8, 144.9, 145.0 (s, Ph), 193.4 (dd, $^1J_{PC}$ = 82.8 Hz, $^2J_{PC}$ = 18.4 Hz, P=C), 223.9 (br., CO), 231.8 (d, $^2J_{PC}$ = 18.4 Hz, CO) ppm. $^{31}$P{$^1$H} NMR (202.46 MHz, $C_6D_6$): $\delta$ = 170.1 (d, $J_{PP}$ = 22.5 Hz, $J_{PW}$ = 330.4 Hz, $PPh_2$), 199.9 (d, $J_{PP}$ = 22.5 Hz, P=C) ppm. IR (KBr): $\tilde{\nu}$ = 1935 [s (CO)], 1870 [s (CO)] cm$^{-1}$. MS (EI): *m*/*z* = 654 [M]$^+$, 626 [M – CO]$^+$, 598 [M – 2 CO]$^+$. $C_{28}H_{24}O_3P_2W$ (654.28): calcd. C 51.40, H 3.69; found C 51.47, H 3.51.

**X-ray Crystallography**: Crystallographic data for **3** was collected with a Siemens P3 diffractometer with Mo-$K_\alpha$ at 173 K, data for **4a** and **6b** were collected with a Nonius Kappa CCD diffractometer with Mo-$K_\alpha$ (graphite monochromator, $\lambda$ = 0.71073 Å) at 100 K. Crystallographic programs used for the structure solution and refinement were from SHELX-97.[15] The structures were solved by direct methods and refined by using full-matrix least-squares on $F^2$ of all unique reflections with anisotropic thermal parameters for all non-hydrogen atoms. Hydrogen atoms for **3** were refined isotropically, for **4a** and **6b** they were included at calculated positions with $U$(H) = 1.2 $U_{eq}$ for $CH_2$ groups, $U$(H) = 1.5 $U_{eq}$ for $CH_3$ groups. Crystal data of the compounds are listed in Table 1.[16]

 © 2007 Wiley-VCH Verlag GmbH & Co. KGaA, Weinheim 

[1] Review: L. Weber, *Eur. J. Inorg. Chem.* **2000**, 2425–2441.
[2] a) L. Weber, M. Meyer, H.-G. Stammler, B. Neumann, *Chem. Eur. J.* **2001**, *7*, 5401–5408; b) L. Weber, M. Meyer, H.-G. Stammler, B. Neumann, *Organometallics* **2003**, *22*, 5063–5068.
[3] L. Weber, G. Noveski, U. Lassahn, H.-G. Stammler, B. Neumann, *Eur. J. Inorg. Chem.* **2005**, 1940–1946.
[4] L. Weber, G. Noveski, T. Braun, H.-G. Stammler, B. Neumann, *Eur. J. Inorg. Chem.* **2007**, 562–567.
[5] L. Weber, G. Noveski, H.-G. Stammler, B. Neumann, *Z. Anorg. Allg. Chem.* **2007**, *633*, 994–999.
[6] L. Weber, S. Uthmann, H. Bögge, A. Müller, H.-G. Stammler, B. Neumann, *Organometallics* **1998**, *17*, 3593–3598.
[7] W. Malisch, K. Grün, A. Fried, W. Reich, M. Schmeußer, U. Weis, C. Abd. El Baky, C. Krüger, *Z. Naturforsch., Teil B* **1998**, *53*, 1506–1510.
[8] L. Weber, O. Kaminski, *Synthesis* **1995**, 158.
[9] G. Becker, B. Becker, M. Birkhahn, O. Mundt, R. E. Schmidt, *Z. Anorg. Allg. Chem.* **1985**, *529*, 97–110.
[10] D. Gudat, E. Niecke, W. Malisch, U. Hofmockel, S. Quashie, A. H. Cowley, A. M. Arif, B. Krebs, M. Dartmann, *J. Chem. Soc. Chem. Commun.* **1985**, 1687–1688.
[11] C. J. Carrano, A. H. Cowley, C. M. Nunn, M. Pakulski, S. Quashie, *J. Chem. Soc. Chem. Commun.* **1988**, 170–171.
[12] L. Weber, K. Reizig, M. Frebel, R. Boese, M. Polk, *J. Organomet. Chem.* **1986**, *306*, 105–114.
[13] A. Holleman, E. Wiberg, *Lehrbuch der Anorganischen Chemie*, 91st to 100th ed., Berlin, **1985**, p. 133.
[14] J. Ipaktschi, T. Klotzbach, A. Dülmer, *Organometallics* **2000**, *19*, 5281–5286.
[15] G. M. Sheldrick, *SHELX-97: Programs for Solution and Refinement of Crystal Structures*, University of Göttingen, Germany, **1997**.
[16] CCDC-141724, -644445, and -644446 contain the supplementary crystallographic data for this paper. These data can be obtained free of charge from The Cambridge Crystallographic Data Centre via www.ccdc.cam.ac.uk/data_request/cif.

Received: April 23, 2007
Published Online: July 4, 2007

 © 2007 Wiley-VCH Verlag GmbH & Co. KGaA, Weinheim 

DOI: 10.1002/ejic.200700272

# Controlled Chemical Reduction of Uranyl Salts into $UX_4(MeCN)_4$ (X = Cl, Br, I) with $Me_3SiX$ Reagents

**Jean-Claude Berthet,*[a] Gérald Siffredi,[a] Pierre Thuéry,[a] and Michel Ephritikhine*[a]**

**Keywords:** Uranyl salts / Reduction / Silanes / Uranium

$UO_2I_2(thf)_3$ or $UO_2(OTf)_2$ are easily reduced by $Me_3SiX$ (X = Cl, Br, I) in acetonitrile into the tetravalent $UX_4(MeCN)_4$ complexes, which are useful precursors in uranium chemistry.

(© Wiley-VCH Verlag GmbH & Co. KGaA, 69451 Weinheim, Germany, 2007)

## Introduction

A variety of methods have been designed for the preparation of the uranium tetrahalides $UX_4$ (X = Cl, Br, I) and their Lewis base adducts, which are ordinary and convenient precursors for the synthesis of a large range of uranium derivatives.[1] Most of the usual procedures are based on the treatment of solid $UO_2$ or $UO_3$ with gaseous $X_2$ or HX at high temperature, or with halogenated liquid reagents under reflux conditions, which releases very toxic side-on gases.[1] In an attempt to avoid the thermal decomposition of $UI_4$, the synthesis of $UI_4(PhCN)_4$ was performed by the oxidation of uranium turnings with iodine in benzonitrile,[2] but a similar reaction in acetonitrile failed to produce pure $UI_4(MeCN)_4$,[2,3] which was conveniently obtained by metathesis of $UCl_4$ in acetonitrile by using excess $Me_3SiI$.[4] The $Me_3SiX$ molecules are versatile reagents that have found numerous applications in organic and inorganic syntheses.[5] In addition to being very efficient in metathesis reactions of d- and f-transition-metal halides,[4–6] they are also capable of inducing redox transformations.[5] Thus, $UF_6$ was reduced into $UF_5$ or $UF_4$ with $Me_3SiCl$;[7] $RuCl_3$ reacted with $Me_3SiI$ to give the $Ru^{II}$ compound $[Ru(MeCN)_6][I_4]$,[5] and $CrCl_2$ was oxidized with $Me_3SiI$ into the $Cr^{III}$ iodide $[CrI_2(MeCN)_4][CrI_4(MeCN)_2]$.[5] However, it seems surprising, in view of the strength of the Si–O bond, that the $Me_3SiX$ reagents have seldom been considered for the deoxygenation of metal oxides and their conversion into the corresponding halides.[8]

Activation of the reputedly inert U=O bond of the uranyl ion $[UO_2]^{2+}$ and the controlled reduction of this species represent a particularly active field of research that attracts much attention for both its fundamental aspects and applications.[9] Although the photosensitivity of the $[UO_2]^{2+}$ ion to UV light is a well-documented feature, leading generally to insoluble $UO_2$ or rare $U^{IV}$ coordination complexes,[10] chemical reduction of uranyl salts into interesting derivatives remains a challenging goal. Such transformations have mostly been observed serendipitously,[11,12] and it is only recently that some smooth and controlled reactions of the $[UO_2]^{2+}$ ion proved successful, revealing new aspects of uranyl chemistry.[13] These advances were made possible by the use of strictly anhydrous experimental conditions. Here we report the reduction of $UO_2I_2(thf)_3$[14] or $UO_2(OTf)_2$[15] with $Me_3SiX$ (X = Cl, Br, I) in acetonitrile, which provides a novel and convenient synthetic route to tetrahalides $UX_4(MeCN)_4$. These reactions, which involve deoxygenation, halide exchange and reduction processes, are much influenced by the nature of the solvent, the $Me_3SiX$ reagent and the uranyl salt.

## Results and Discussion

We previously reported that treatment of $UO_2(OTf)_2$ with pure $Me_3SiI$ led to the formation of $UO_2I_2$ in almost quantitative yield.[14] This compound, which likely has a polymeric structure, is quite insoluble and stable in $Me_3SiI$. However, after dissolution of $UO_2I_2$ in coordinating solvents, the molecular Lewis base adducts $UO_2I_2L_n$ (L = thf, py, MeCN) were found to react with the iodosilane. Reactions of $UO_2I_2(thf)_3$ with a large excess of $Me_3SiX$ (X = Cl, Br, I) were first examined in thf at 25° or 100 °C. Metathetical exchange with $Me_3SiCl$ afforded the uranyl chloride, which was inert in the presence of the chlorosilane, as previously observed in the dehydration of $UO_2Cl_2(H_2O)_n$.[16] However, $UO_2I_2(thf)_3$ was found to react with $Me_3SiBr$, as shown by the colour change of the solution, from red to green, characteristic of uranium(IV) compounds. Similar treatment of $UO_2I_2(thf)_3$ with $Me_3SiI$ gave a mixture of

[a] Service de Chimie Moléculaire, DSM, DRECAM, CNRS URA 331, Laboratoire Claude Fréjacques, CEA Saclay, Gif-sur-Yvette, 91191, France
Fax: +33-169-08-66-40
E-mail: jean-claude.berthet@cea.fr
michel.ephritikhine@cea.fr

 © 2007 Wiley-VCH Verlag GmbH & Co. KGaA, Weinheim 

complexes among which red crystals of $[U(O\{CH_2\}_4I)_2(thf)_5][I_3]_2[I_2]$ were characterized by X-ray diffraction analysis;[17] this alkoxide derivative obviously resulted from thf ring-opening reaction, which is currently initiated by $Me_3SiI$ and iodo uranium complexes.[18,19] The uranyl iodide $UO_2I_2(thf)_3$ was more reactive towards $Me_3SiX$ in pyridine, but the reduction led to a mixture of the two uranium(IV) complexes $UX_4(py)_4$ and $[UX_6]^{2-}$ (X = Cl, Br).[17]

Eventually, the uranium(IV) tetrahalides $UX_4(MeCN)_4$ [X = Cl (**1**), Br (**2**), I (**3**)] were simply obtained by the addition of an excess of $Me_3SiX$ to a solution of $UO_2I_2$ or $UO_2I_2(thf)_3$ in acetonitrile at room temperature [Equation (1)]; **1** and **2** were deposited as light green crystals and **3** as an orange powder in good yields (68– 93%).

$$UO_2I_2(thf)_3 \xrightarrow[MeCN]{\text{Excess } Me_3SiX} UX_4(MeCN)_4 \quad \begin{matrix}\mathbf{1}\text{: X = Cl}\\ \mathbf{2}\text{: X = Br}\\ \mathbf{3}\text{: X = I}\end{matrix} \qquad (1)$$

The rate of the reaction was found to depend markedly on X and followed the unusual order Br >> I > Cl. Thus, $UO_2I_2(thf)_3$ was immediately transformed into **2**, whereas its complete conversion into **1** and **3** required 24 h at 25 °C. The reasons for this trend, which could be related to opposite electronic and steric effects,[20] are not obvious.

While $MoO_2X'_2$ or $CrO_3$ reacted with $Me_3SiX$ to give the partially deoxygenated derivatives $MoOX_2X'_2$ or $CrO_2Cl_2$, respectively,[8a,8c] complete deoxygenation of the uranyl ion was achieved, as shown by the absence in the IR spectra of the reaction products of any band that could be assigned to the $\nu_{asym}(UO)$ frequency.

Compounds **1**–**3** were characterized by their elemental analyses (C, H, N) and their IR spectra. These spectra, which are identical to those of $UX_4(MeCN)_4$ that was prepared from the uranium tetrahalides, show two bands in the CN region; the strong stretching frequencies (2275–2277 $cm^{-1}$) correspond to those previously reported for $UX_4(MeCN)_4$ (X = Cl, Br, I),[3,21] and they show a ca. 25 $cm^{-1}$ increase in the coordinated nitrile CN stretching frequency relative to $\nu$(CN) = 2249 $cm^{-1}$ for free acetonitrile.[21]

Crystals of **2** were characterized by X-ray diffraction analysis; a view of the complex is shown in Figure 1 together with selected bond lengths. The structure is identical to that of $UCl_4(MeCN)_4$,[22] and the uranium atom is in a dodecahedral configuration defined by the two orthogonal trapezia Br1–N1–N1′–Br1′ and Br2–N2–N2′–Br2′, with the nitrogen atoms in the A sites.[23] The average U–N and U–Br distances of 2.56(3) and 2.80(2) Å, respectively, are comparable to those measured in $UCl_4(MeCN)_4$ [2.531(17) Å][22] and $UBr_4(OPPh_3)_2$ [2.771(2) Å].[24]

$UO_2(OTf)_2$ is a more accessible precursor than the iodide counterpart and access to the $UX_4(MeCN)_4$ compounds directly from $UO_2(OTf)_2$ would be a much more convenient route.[14] In agreement with previous observations on the distinct reactivities of analogous halide and triflate metal

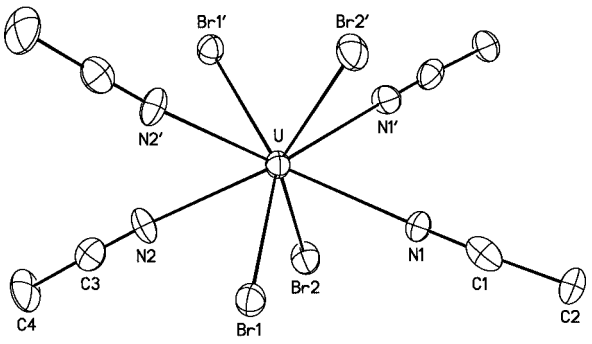


Figure 1. View of $UBr_4(MeCN)_4$ (**2**). Displacement ellipsoids are drawn at the 50% probability level. Symmetry code: ′ = *y*, *x*, 2 – *z*. Selected bond lengths [Å]: U–Br1 2.7751(6), U–Br2 2.8157(5), U–N1 2.527(4), U–N2 2.583(4), N1–C1 1.150(7), N2–C3 1.143(6).

compounds,[14–16,18,19] reactions of $UO_2(OTf)_2$ with $Me_3SiX$ in acetonitrile at 20 °C were slower than those of $UO_2I_2$ and required heating to go to completion. Whereas $UO_2(OTf)_2$ was inert towards an excess of $Me_3SiCl$ in acetonitrile at 100 °C, its treatment under the same conditions with $Me_3SiX$ led to the formation of $UX_4(MeCN)_4$ (X = Br, I) and the successful preparation of tetrabromide **2**, which was isolated in 72% yield. These results demonstrate that the nature of the uranyl precursor has a major influence on the course of its reactions with the halogenosilanes. The lower reactivity of $UO_2(OTf)_2$ likely reflects the weaker lability of $OTf^-$ versus $I^-$; however, the facile access to **2** constitutes the most convenient synthesis of this $U^{IV}$ compound.

## Conclusions

Reactions of $UO_2I_2(thf)_3$ or $UO_2(OTf)_2$ with $Me_3SiX$ provide rare examples of the controlled activation and reduction of the $[UO_2]^{2+}$ ion and new convenient and safe routes to the tetrahalides $UX_4(MeCN)_4$. In particular, the facile synthesis of **2** is attractive for extending the poorly developed chemistry of uranium bromides, which are susceptible to display solubility, structural and reactivity patterns different from those of the other halides and triflate species.[4,14,25]

## Experimental Section

**General:** All experiments were carried out under an atmosphere of argon (<5 ppm oxygen or water) by using standard Schlenk-vessel and vacuum-line techniques or in a glove box. Solvents were dried by standard methods and distilled immediately before use. IR samples were prepared as Nujol mulls between KBr round cell windows, and the spectra were recorded with a Perkin-Elmer FTIR 1725X spectrometer. Elemental analyses were performed by Analytische Laboratorien at Lindlar (Germany). The $Me_3SiX$ reagents (Aldrich) were distilled and stored over 4-Å molecular sieves; $UO_2I_2(thf)_3$[13] and $UO_2(OTf)_2$[14] were prepared by published methods.

**$UCl_4(MeCN)_4$ (1):** A flask was charged with $UO_2I_2(thf)_3$ (200 mg, 0.27 mmol), MeCN (6 mL) and $Me_3SiCl$ (6 mL, 49 mmol). After 24 h at 25 °C, light green crystals of **1** were deposited from the dark brown solution. After filtration, the crystals were washed with

 © 2007 Wiley-VCH Verlag GmbH & Co. KGaA, Weinheim 

MeCN/$Et_2O$ (1:4, 25 mL) and dried under vacuum (99 mg, 68%). IR: $\tilde{\nu}$ = 2277 (s) (NC), 2307(m) (NC) $cm^{-1}$. $C_8H_{12}Cl_4N_4U$ (544.05): calcd. C 17.66, H 2.22, N 10.29; found C 17.41, H 2.22, N 10.12.

**Synthesis of $UBr_4(MeCN)_4$ (2)**

**(a) From $UO_2I_2(thf)_3$:** A flask was charged with $UO_2I_2(thf)_3$ (200 mg, 0.27 mmol) and MeCN (6 mL). The dark red solution immediately turned colourless upon the addition of $Me_3SiBr$ (6 mL, 46 mmol) at 25 °C, and light green crystals of **2** were deposited. The crystals were filtered off, washed with pentane and dried under vacuum (181 mg, 93%). IR: $\tilde{\nu}$ = 2275 (s) (NC), 2307(m) (NC) $cm^{-1}$. $C_8H_{12}Br_4N_4U$ (721.85): calcd. C 13.31, H 1.67, N 7.76; found C 13.41, H 1.87, N 7.90.

**(b) From $UO_2(OTf)_2$:** A flask was charged with $UO_2(OTf)_2$ (40 mg, 0.07 mmol) and MeCN (0.4 mL). The initially yellow solution immediately turned orange upon the addition of $Me_3SiBr$ (0.4 mL, 3 mmol) at 25 °C, and an orange powder was deposited. After 24 h at 100 °C, light green crystals of **2** were deposited from the dark brown solution, and another crop of crystals was collected after the addition of $Et_2O$ (1.5 mL) onto the concentrated MeCN solution (0.2 mL). The crystals were washed with MeCN/$Et_2O$ (1:4, 5 mL) and dried under vacuum (36.7 mg, 72%). IR: $\tilde{\nu}$ = 2275(s) (NC), 2307(m) (NC) $cm^{-1}$. $C_8H_{12}Br_4N_4U$ (721.85): calcd. C 13.31, H 1.67, N 7.76; found C 13.46, H 1.75, N 7.82.

**Synthesis of $UI_4(MeCN)_4$ (3)**

**(a) From $UO_2I_2(thf)_3$:** A flask was charged with $UO_2I_2(thf)_3$ (200 mg, 0.27 mmol) and MeCN (6 mL). The addition of $Me_3SiI$ (6 mL, 42 mmol) to the dark red solution immediately led to an orange precipitate. After 24 h at 25 °C, $Et_2O$ (30 mL) was condensed in, which induced increased precipitation of **3**. Product **3** (212 mg, 87%) was recovered as an orange powder after filtration, washing with pentane and drying under vacuum. IR: $\tilde{\nu}$ = 2275(s) (NC), 2301(m) (NC) $cm^{-1}$. $C_8H_{12}I_4N_4U$ (909.85): calcd C 10.56, H 1.33, N 6.15; found C 10.35, H 1.54, N 5.99.

**(b) From $UO_2(OTf)_2$:** An NMR tube was charged with $UO_2(OTf)_2$ (10 mg, 0.018 mmol) and acetonitrile (0.2 mL). The addition of $Me_3SiI$ (0.2 mL, 1.4 mmol) at 25 °C to the yellow solution gave immediately a dark red solution from which red-brown crystals of **3** were deposited in a few minutes. Further precipitation was induced by heating the mixture at 100 °C for 24 h.

**X-ray Crystallography:** The data were collected at 110(2) K with a Nonius Kappa-CCD area-detector diffractometer with Mo-$K_\alpha$ radiation and processed with HKL2000.[26] The structure was solved by direct methods and refined by full-matrix least-squares on $F^2$ with SHELXTL.[27] Absorption effects were corrected with SCALEPACK.[26] All non-hydrogen atoms were refined with anisotropic displacement parameters. Crystal data for **2**: $C_8H_{12}Br_4N_4U$, $M$ = 721.89, trigonal, space group $P3_221$, $a = b$ = 8.7269(3) Å, $c$ = 20.6198(10) Å, $V$ = 1359.99(9) $Å^3$, $Z$ = 3, $D_{calcd.}$ = 2.644 $g\,cm^{-3}$, $\mu$ = 17.753 $mm^{-1}$, $F(000)$ = 960, 31861 measured reflections, 1732 independent ($R_{int}$ = 0.085), 1703 with $I > 2\sigma(I)$, 81 parameters, $R_1$ = 0.025, $wR_2$ = 0.049, S = 1.054, $\Delta\rho_{min}$ = –1.47, $\Delta\rho_{max}$ = 1.18 $e\,Å^{-3}$.

CCDC-637174 contains the supplementary crystallographic data for this paper. These data can be obtained free of charge from the Cambridge Crystallographic Data Centre via www.ccdc.cam.ac.uk/data_request/cif.

## Acknowledgments

We thank the Direction de l'Energie Nucléaire of the Commissariat à l'Energie Atomique (DSOE) for its financial support.

[1] I. Grenthe, J. Drozdzynski, T. Fujino, E. C. Buck, T. E. Albrecht-Schmitt, S. F. Wolf in *The Chemistry of the Actinide and the Transactinide Elements*, 3rd ed., (Eds: L. R. Morss, N. M. Edelstein, J. Fuger), Springer, Dordrecht, The Netherlands, **2006**, vol. 1, ch. 5, pp. 420–499.
[2] A. E. Enriquez, B. L. Scott, M. P. Neu, *Inorg. Chem.* **2005**, *44*, 7403–7413.
[3] J. G. H. Du Preez, B. Zeelie, *Inorg. Chim. Acta* **1986**, *118*, L25–L26.
[4] J. C. Berthet, P. Thuéry, M. Ephritikhine, *Inorg. Chem.* **2005**, *44*, 1142–1146.
[5] G. J. Leigh, J. R. Sanders, P. B. Hitchcock, J. S. Fernandes, M. Togrou, *Inorg. Chim. Acta* **2002**, *330*, 197–212.
[6] a) G. R. Giesbrecht, J. C. Gordon, D. L. Clark, B. L. Scott, *Inorg. Chem.* **2004**, *43*, 1065–1071; b) W. W. Lukens, S. M. Beshouri, L. L. Blosch, A. L. Stuart, R. A. Andersen, *Organometallics* **1999**, *18*, 1235–1246.
[7] a) D. Brown, J. A. Berry, J. H. Holloway, R. F. Holland, G. M. Staunton, *J. Less-Common Met.* **1983**, *92*, 149–153; b) F. A. Cotton, G. Wilkinson, C. A. Murillo, M. Bochmann, *Advanced Inorganic Chemistry*, 6th ed., John Wiley and Sons, Chichester, **1999**, ch. 20, p. 1147.
[8] a) H. Teruel, Y. Y. Moret, B. Perillot, *Polyhedron* **1999**, *18*, 419–422; b) H. Arzoumanian, H. Krentzien, C. Corao, R. Lopez, G. Agrifoglio, *Polyhedron* **1995**, *14*, 2887–2891; c) P. Stavropoulos, N. Bryson, M.-T. Youinou, J. A. Osborn, *Inorg. Chem.* **1990**, *29*, 1807–1811; d) D. L. Hughes, U. Kleinkes, G. J. Leigh, M. Maiwald, J. R. Sanders, C. Sudbrake, J. Weisner, *J. Chem. Soc. Dalton Trans.* **1993**, 3093–3096; e) G. Parkin, J. E. Bercaw, *J. Am. Chem. Soc.* **1989**, *111*, 391–393; f) R. H. Holm, *Chem. Rev.* **1987**, *87*, 1401–1449.
[9] a) T. Toraishi, T. Kimura, M. Arisaka, *Chem. Commun.* **2007**, 240–2041; b) J. C. Renshaw, L. J. C. Butchins, F. R. Livens, I. May, J. M. Charnock, J. R. Lloyd, *Environ. Sci. Technol.* **2005**, *39*, 5657–5660; c) L. V. Moskaleva, S. Kruger, A. Spörl, N. Rösch, *Inorg. Chem.* **2004**, *43*, 4080–4090.
[10] a) Chagnon, J. Huré in *Nouveau Traité de Chimie Minérale* (Ed.: P. Pascal), Masson, Paris, **1960**, vol. XV, ch. 9, pp. 596–600; b) G. H. John, I. May, C. A. Sharrad, A. D. Sutton, D. Collison, M. Helliwell, M. J. Sarsfield, *Inorg. Chem.* **2005**, *44*, 7606–7615 and references cited therein.
[11] V. A. Golovnya, G. T. Bolotova, *Russ. J. Inorg. Chem.* **1966**, *11*, 1419–1424.
[12] a) L. Natrajan, F. Burdet, J. Pécaut, M. Mazzanti, *J. Am. Chem. Soc.* **2006**, *128*, 7152–7153; b) L. M. Mokry, N. S. Dean, C. J. Carrano, *Angew. Chem. Int. Ed. Engl.* **1996**, *35*, 1497–1498; c) H. Greiwing, B. Krebs, A. A. Pinkerton, *Inorg. Chim. Acta* **1995**, *234*, 127–130.
[13] a) J. C. Berthet, G. Siffredi, P. Thuéry, M. Ephritikhine, *Chem. Commun.* **2006**, 3184–3186; b) J. C. Berthet, P. Thuéry, M. Ephritikhine, *Chem. Commun.* **2005**, 3415–3417; c) S. Kannan, A. E. Vaughn, E. M. Weiss, C. L. Barnes, P. B. Duval, *J. Am. Chem. Soc.* **2006**, *128*, 14024–14025; d) P. B. Duval, C. J. Burns, W. E. Buschmann, D. C. Clark, D. E. Morris, B. L. Scott, *Inorg. Chem.* **2001**, *40*, 5491–5496.
[14] J. C. Berthet, P. Thuéry, M. Ephritikhine, *Chem. Commun.* **2004**, 870–871.
[15] J. C. Berthet, M. Lance, M. Nierlich, M. Ephritikhine, *Eur. J. Inorg. Chem.* **2000**, 1969–1973.
[16] M. P. Wilkerson, C. J. Burns, R. T. Paine, B. L. Scott, *Inorg. Chem.* **1999**, *38*, 4156–4158.
[17] The X-ray crystal structures of these compounds will be reported separately.
[18] H. Van der Heijden, C. J. Schaverien, A. G. Orpen, *Organometallics* **1989**, *8*, 255–258.
[19] a) L. R. Avens, D. M. Barnhart, C. J. Burns, S. D. McKee, *Inorg. Chem.* **1996**, *35*, 537–539; b) J. Collin, A. Pires de Matos, I. Santos, *J. Organomet. Chem.* **1993**, *463*, 103–107.
[20] K. I. Kanno, M. Kira, *Chem. Lett.* **1999**, *16*, 1127–1128.

 © 2007 Wiley-VCH Verlag GmbH & Co. KGaA, Weinheim 

[21] a) K. W. Bagnall, D. Brown, P. J. Jones, *J. Chem. Soc. A* **1966**, 1763–1766; b) P. Gans, J. Marriage, *J. Chem. Soc. Dalton Trans.* **1972**, 46–48.
[22] G. Van den Bossche, J. Rebizant, M. R. Spirlet, J. Goffart, *Acta Crystallogr., Sect. C* **1986**, *42*, 1478–1480.
[23] D. L. Keppert in *Inorganic Stereochemistry*, *Inorganic Chemistry Concepts*, Springer, Heidelberg, **1982**, vol. 6.
[24] G. Bombieri, F. Benetollo, K. W. Bagnall, M. J. Plews, D. Brown, *J. Chem. Soc. Dalton Trans.* **1983**, 343–348.
[25] a) J. Maynadié, J. C. Berthet, P. Thuéry, M. Ephritikhine, *J. Am. Chem. Soc.* **2006**, *128*, 1082–1083; b) C. D. Sofield, R. A. Andersen, *J. Organomet. Chem.* **1995**, *501*, 271–276; c) G. A. Lawrance, *Chem. Rev.* **1986**, *86*, 17–33.
[26] Z. Otwinowski, W. Minor, *Methods Enzymol.* **1997**, *276*, 307–326.
[27] G. M. Sheldrick, *SHELXTL*, version 5.1, Bruker AXS Inc., Madison, WI, USA, **1999**.

Received: March 8, 2007
Published Online: July 6, 2007

 © 2007 Wiley-VCH Verlag GmbH & Co. KGaA, Weinheim 

DOI: 10.1002/ejic.200700400

# Kinetics and Magnetism of Phosphane Diadducts of Diruthenium(II,III) Tetraacetate

**Tara J. Burchell,[a] T. Stanley Cameron,[b] Donal H. Macartney,[c] Laurence K. Thompson,[d] and Manuel A. S. Aquino*[a]**

**Keywords:** Carboxylate ligands / P ligands / Ruthenium / Kinetics / Magnetic properties

The kinetic parameters for the axial-ligand-substitution reactions of $[Ru_2(\mu\text{-}O_2CCH_3)_4(MeCN)_2]^+$ in acetonitrile (MeCN) with $PCy_3$ and $PCy_2Ph$ (Cy = cyclohexyl and Ph = phenyl) were investigated under pseudo first-order conditions of excess phosphane. The rate-determining formation of $[Ru_2(\mu\text{-}O_2CCH_3)_4(MeCN)(PCy_2R]^+$ appears independent of the nature of the incoming phosphane with an average $k_1$ (25.0 °C) = $(1.25 \pm 0.06) \times 10^3$ $M^{-1} s^{-1}$. A dissociatively activated mechanism is proposed for substitution of the axially coordinated acetonitrile, and the rate parameters are compared to earlier measurements carried out on $[Rh_2(\mu\text{-}O_2CCH_3)_4(MeCN)_2]$. Variable-temperature magnetic susceptibility measurements were carried out on the two phosphane diadducts, $[Ru_2(\mu\text{-}O_2CCH_3)_4(PCy_3)_2]PF_6$, (**1**) and $[Ru_2(\mu\text{-}O_2CCH_3)_4(PCy_2Ph)_2]PF_6$ (**2**), and showed behaviour unique to a Boltzmann distribution of states over the temperature range 2–300 K. To support the magnetic measurements, the single-crystal X-ray structure of **1** was redetermined at various temperatures down to –150 °C and showed a distinct decrease in the Ru–Ru bond length with decreasing temperature, consistent with a $\sigma^2\pi^4\delta^2\pi^{*3}$ configuration at low temperature (ground state) and a $\sigma^2\pi^4\delta^2\pi^{*2}\delta^{*1}$ configuration at room temp. In addition, the structure redeterminations of **1** were better resolved than the earlier reported structure and also corrected a minor error in that the molecule of solvation was found to be 1,2-dichloroethane instead of dichloromethane.
(© Wiley-VCH Verlag GmbH & Co. KGaA, 69451 Weinheim, Germany, 2007)

## Introduction

Diruthenium tetracarboxylates, both in their homovalent $Ru_2(II,II)$ and valent-averaged $Ru_2(II,III)$ forms, have received considerable attention in the past 20 years owing primarily to their interesting electronic and magnetic properties.[1–4] The basic diruthenium tetracarboxylate "building block", $[Ru_2(\mu\text{-}O_2CR)_4]^{+/0}$, has been modified in a wide variety of ways leading to compounds with mesomorphic, catalytic and cytotoxic properties. Numerous extended polymeric and network structures based on these building blocks have also been assembled and display properties ranging from gas-occlusion[5–7] to ferrimagnetic ordering[8,9] and significant electronic delocalization.[10]

We recently reported the structure and electrochemistry of the first axial phosphane diadduct of diruthenium(II,III) tetraacetate.[11] We were able to isolate and crystallographically characterize what, in essence, was a kinetic product, $[Ru_2(\mu\text{-}O_2CCH_3)_4(PCy_3)_2]PF_6$ (**1**), by using the bulky phosphane, $PCy_3$ (Cy = cyclohexyl), which has a Tolman cone angle of 170°.[12] The bulkiness of the phosphane slowed down its thermodynamically favoured migration to the equatorial positions and subsequent displacement of the carboxylate groups. This process eventually leads to Ru–Ru bond cleavage and a total disassembly of the dimer into mononuclear fragments.[13] The structure revealed the longest Ru–Ru bond length in a diruthenium tetracarboxylate to date at 2.427(1) Å. In addition, we were able to generate, by cyclic voltammetry, the one-electron oxidation product, $[Ru_2(\mu\text{-}O_2CCH_3)_4(PCy_3)_2]^{2+}$, in which we have a $Ru_2(III,III)$ core. This is unprecedented for any diruthenium *tetracarboxylate*. Unfortunately we have, to date, not been able to isolate X-ray quality crystals of this oxidized species.

The extraordinarily long Ru–Ru bond length, as well as a small but significant redshift in the $\pi^*(Ru_2)\leftarrow\pi(RuO,Ru_2)$ visible transition when the phosphane diadduct is formed, motivated us to study both the variable-temperature magnetic susceptibility behaviour and the ligand substitution kinetics of complex **1** as well as those of the related complex, $[Ru_2(\mu\text{-}O_2CCH_3)_4(PPhCy_2)_2]PF_6$ (**2**). In addition, we have redetermined the structure of **1** at various temperatures in order to be able to correlate the Ru–Ru bond length/temperature dependence with the magnetic behaviour. The re-

[a] Department of Chemistry, St. Francis Xavier University, P. O. Box 5000, Antigonish, Nova Scotia B2G 2W5, Canada
Fax: +1-902-867-2414
E-mail: maquino@stfx.ca
[b] Department of Chemistry, Dalhousie University, Halifax, Nova Scotia B3H 4J3, Canada
[c] Department of Chemistry, Queen's University, Kingston, Ontario K7L 3N6, Canada
[d] Department of Chemistry, Memorial University of Newfoundland, St. John's, Newfoundland A1B 3X7, Canada
Supporting information for this article is available on the WWW under http://www.eurjic.org or from the author.

 © 2007 Wiley-VCH Verlag GmbH & Co. KGaA, Weinheim 

determination also corrects a minor mistake in the earlier structural formulation, replacing the original dichloromethane (DCM) of solvation with 1,2-dichloroethane (DCE). We report here as well the fully corrected structure, determined at –150 °C.

## Results and Discussion

### Synthesis

We found that the reaction of $[Ru_2(\mu\text{-}O_2CCH_3)_4(H_2O)_2]^+$, in which we exchanged the axial waters with modest and strong π-acid ligands, must be carried out stoichiometrically and reasonably fast. This is due to the fact that any excess of ligand or reaction times greater than 10 min will result in decomposition (disassembly) of the diruthenium core, which would lead to mononuclear ruthenium(II) complexes or a disproportionation reaction leading to a μ-oxido $Ru_2$(III,III) dimer and mononuclear $Ru^{II}$ complex. These reactions have been seen, and exploited, by our group and others.[13,14] In a previous paper we synthesized a series of diadducts with modest π-acid N-heterocycles, $[Ru_2(\mu\text{-}O_2CCH_3)_4(\text{N-heterocycle})_2]^+$, by a rapid reaction of the diaqua adduct and 2 equiv. of the appropriate N-heterocycle in 2-propanol.[15] This reaction gave rapid precipitation of the desired product, which we were able to isolate, usually within 10 min.

We applied a similar strategy in trying to isolate adducts with the stronger π-acid phosphane ligands. It appears that for the reactions with phosphanes, $PPh_3$ in particular, a relatively rapid disproportionation occurs even when a relatively small excess of phosphane is employed.[14] The phosphane initially binds at the axial site and then performs an intramolecular migration to the equatorial positions leading to carboxylate displacement and Ru–Ru bond rupture. In our preliminary paper[11] we were able to somewhat slow down this migration process by using a significantly bulkier phosphane, $PCy_3$ (Cy = cyclohexyl), and hence we were able to isolate, purify and structurally characterize this diadduct. The electrochemistry was also reported. The detailed synthesis of this complex is given here. The bulkiness of the phosphane evidently slowed the axial–equatorial migration enough to allow us to isolate the diadduct. We can gauge the bulkiness of the phosphanes by looking at their Tolman cone angles.[12] For $PPh_3$, the angle is 145°, whereas for $PCy_3$, it is 170°. We also attempted to synthesize the $PPh_3$ diadduct along with diadducts involving phosphanes of intermediate cone angle, namely $PPh_2Cy$ (cone angle = 153°) and $PPhCy_2$ (cone angle = 162°). In all three cases we were able to obtain some solid products; however, the $PPh_3$ and $PPh_2Cy$ "products" gave very inconsistent elemental analyses, IR spectra and electrochemistry and could not be purified further, either by column chromatography or recrystallization, without appreciable decomposition. The $PPhCy_2$ reaction product **2** was more promising, and we were able to get reproducible analyses and spectra; however, X-ray quality crystals are still elusive.

The elemental analyses for adducts **1** and **2** are consistent with the formulations given. The IR spectra showed characteristic C–H stretching modes (primarily from the phenyl and cyclohexyl rings) in the range 2850–3070 $cm^{-1}$, asymmetric O–C–O stretching at 1440 $cm^{-1}$, symmetric O–C–O stretching at ≈ 1350 $cm^{-1}$, P–F stretching (from the $PF_6^-$ counterion) at ≈ 840 $cm^{-1}$ and the C–$CH_3$ bending mode at 692 $cm^{-1}$. The UV/Vis spectra were similar to the diaqua adduct except for a small bathochromic shift in the $\pi^*(Ru_2)\leftarrow\pi(RuO,Ru_2)$ band, a shift from 430 nm (in the diaqua complex) to 473 nm in **1** and 478 nm in **2** (Supporting Information, Figure S1).

### Ligand Substitution Kinetics

The redshifting of the $\pi^*(Ru_2)\leftarrow\pi(RuO,Ru_2)$ band in **1** and **2** allowed us to monitor the ligand substitution process using stopped-flow techniques at 475 nm in dry acetonitrile (0.100 M $TBAPF_6$). Owing to our inability to differentiate exactly the $\lambda_{max}$ value of the mono- from the diphosphane adduct (and hence determine accurately the absorptivity coefficients, $\varepsilon$) and the inherent instability of the diphosphane adduct once it is formed (particularly at high phosphane concentrations), we were not able to calculate successive equilibrium constants with sufficient accuracy to report here. Despite this fact, we assumed, as was the case with phosphane substitution reactions on the dirhodium(II,II) core in $Rh_2(\mu\text{-}O_2CCH_3)_4L_2$ complexes,[16] that the process should be dissociative with the substitution of the first axial ligand being rate determining, the second phosphane substituting rapidly owing to the *trans* effect (i.e. $k_2 >> k_1$). The steps required for substitution by $PCy_3$ are outlined in Equations (1) and (2).

$$[Ru_2(O_2CCH_3)_4(MeCN)_2] + PCy_3 \underset{k_{-1}}{\overset{k_1}{\rightleftharpoons}} [Ru_2(O_2CCH_3)_4(MeCN)(PCy_3)] + MeCN \quad (1)$$

$$[Ru_2(O_2CCH_3)_4(MeCN)(PCy_3)] + PCy_3 \underset{k_{-2}}{\overset{k_2}{\rightleftharpoons}} [Ru_2(O_2CCH_3)_4(PCy_3)_2] + MeCN \quad (2)$$

The formation of $[Ru_2(\mu\text{-}O_2CCH_3)_4(PCy_3)_2]^+$ was therefore monitored and, under pseudo first-order reaction conditions of excess phosphane concentrations {concentration of $[Ru_2(O_2CCH_3)_4(MeCN)_2]^+$ is $5.08\times10^{-4}$ M} the rate expression can be given as that shown in Equation (3).

$$d[Ru_2(O_2CCH_3)_4(PCy_3)_2]^+ / dt = k_{obs}[Ru_2(O_2CCH_3)_4(MeCN)_2]^+ \quad (3)$$

and $k_{obs} = k_1[PCy_3]$. It should be noted at this point that as soon as the diadduct is formed it begins to disassemble/disproportionate with the rate of disassembly increasing as the concentration of the phosphane increases. In fact, at high phosphane concentrations (>35 mM) this subsequent decay can be seen at the end of the stopped-flow trace. However, at none of the concentrations used here does this

 © 2007 Wiley-VCH Verlag GmbH & Co. KGaA, Weinheim 

slower decay interfere with the initial rapid pseudo first-order formation (phosphane binding axially). Plots of $k_{obs}$ against phosphane concentration are linear for the reactions with each of the two phosphanes. The plot for $PCy_3$ is shown in Figure 1a and, from the slope of the line, a value of $k_1(25\,°C) = 1.29(3) \times 10^3\ M^{-1}s^{-1}$ ($R^2 = 0.9981$) is obtained. Measurements of $k_{obs}$ at various temperatures at a constant concentration of $PCy_3$ yielded a reasonably linear ($R^2 = 0.9843$) Eyring plot (Figure 1b) from which the activation parameters $\Delta H^{\neq}$ and $\Delta S^{\neq}$ could be determined. Identical treatment was used for the substitution with $PPhCy_2$. The basic rate data are reported in Table 1 with the second-order rate constants and activation parameters summarized in Table 2.

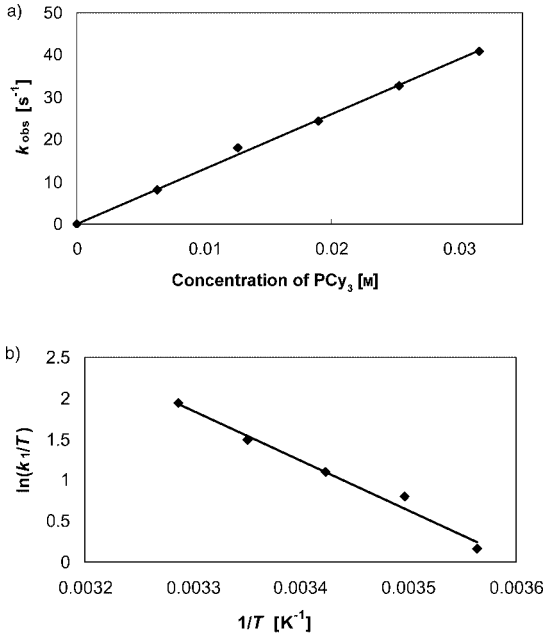


Figure 1. a) Plot of $k_{obs}$ vs. [$PCy_3$] for the reaction of $[Ru_2(O_2CCH_3)_4(MeCN)_2]^+$ with $PCy_3$ in acetonitrile. b) Eyring plot for the reaction in a) with [$PCy_3$] = 0.0210 mM.

Table 1. Kinetic data for the reaction of $[Ru_2(\mu\text{-}O_2CCH_3)_4(MeCN)_2]^+$ with $PCy_3$ and $PPhCy_2$. Lig = $PCy_3$ or $PPhCy_2$.

| T [°C] | [Lig] × $10^2$ [M] | $k_{obs}$ for $PCy_3$ [$s^{-1}$] | $k_{obs}$ for $PPhCy_2$ [$s^{-1}$] | $k_1 \times 10^{-3}$ for $PCy_3$ [$M^{-1}s^{-1}$] | $k_1 \times 10^{-3}$ for $PPhCy_2$ [$M^{-1}s^{-1}$] |
|---|---|---|---|---|---|
| 7.4 | 2.10 | 6.94 | 6.81 | 0.330(3) | 0.325(2) |
| 12.8 | 2.10 | 13.30 | 9.70 | 0.633(2) | 0.462(3) |
| 19.0 | 2.10 | 18.36 | 16.46 | 0.874(3) | 0.784(3) |
| 25.0 | 0.632 | 8.00 | 7.71 | 1.26(3) | 1.22(4) |
| 25.0 | 1.28 | 16.90 | 16.01 | 1.31(4) | 1.25(2) |
| 25.0 | 1.90 | 24.47 | 22.61 | 1.29(3) | 1.19(4) |
| 25.0 | 2.53 | 32.64 | 30.11 | 1.29(2) | 1.19(3) |
| 25.0 | 3.16 | 40.83 | 39.18 | 1.29(3) | 1.24(3) |
| 25.3 | 2.10 | 28.04 | 26.54 | 1.34(3) | 1.26(4) |
| 31.1 | 2.10 | 44.62 | 47.49 | 2.12(5) | 2.26(6) |

The rate law in Equation (3) implies that the formation of the monoadduct is the rate-determining step and that the redshifting of the $\pi^*(Ru_2) \leftarrow \pi(RuO,Ru_2)$ band is primarily due to the formation of $[Ru_2(\mu\text{-}O_2CCH_3)_4(PCy_3)(MeCN)]^+$, and the subsequent rapid formation of $[Ru_2(\mu\text{-}O_2CCH_3)_4(PCy_3)_2]^+$ causes little further change in the electronic spectrum. Because phosphanes lie higher than nitriles in the *trans* effect (and *trans* influence) series, a rapid second step would appear most likely. The Ru–P bond length in $[Ru_2(\mu\text{-}O_2CCH_3)_4(PCy_3)_2]^+$ is the longest of any Ru–L bond in complexes of this type, consistent with its *trans* influence. Unfortunately, attempts to measure the substitution of $[Ru_2(\mu\text{-}O_2CCH_3)_4(PCy_3)_2]^+$ with $PPhCy_2$ did not meet with any success as there was no noticeable change in the electronic spectrum.

Table 2. Rate and activation parameters for the substitution reactions of diruthenium(II,III) tetraacetate with $PCy_3$ and $PPhCy_2$ in acetonitrile and their comparison to similar reactions involving dirhodium(II,II) tetraacetate.

| Ligand | $k_1$ [$M^{-1}s^{-1}$][a] | $\Delta H^{\neq}$ [kcal $mol^{-1}$] | $\Delta S^{\neq}$ [cal $K^{-1}mol^{-1}$] | Ref. |
|---|---|---|---|---|
| | | $Ru_2$(II,III) | | |
| $PCy_3$ | $1.29(3) \times 10^3$ | 12.1(9) | –3.6(3.0) | [b] |
| $PPhCy_2$ | $1.22(3) \times 10^3$ | 13.3(6) | 0.3(2.3) | [b] |
| | | $Rh_2$(II,II) | | |
| $PPh_3$ | $1.07(2) \times 10^5$ | 11.6(1) | 3.4(4) | [16] |
| $P(OPh)_3$ | $1.05(3) \times 10^5$ | 10.5(9) | –0.5(2.7) | [16] |

[a] Measured at 25 °C. [b] This work.

Except for the *actual* value of the second-order rate constant, the substitution behaviour of the mixed-valent $[Ru_2(\mu\text{-}O_2CCH_3)_4(MeCN)_2]^+$ complex is remarkably similar to that of $[Rh_2(\mu\text{-}O_2CCH_3)_4(MeCN)_2]$.[16] The lack of dependence of $k_1$ on the nature of the phosphane would seem to imply a dissociatively activated formation of the monophosphane adduct. In addition, the highest occupied molecular orbitals (HOMO) of $[Ru_2(\mu\text{-}O_2CCH_3)_4(MeCN)_2]^+$ are the partially filled, near-degenerate, Ru–Ru-based $\pi^{*2}\delta^{*1}$. The electron density in these orbitals, which would be situated somewhere between the Ru–O(acetate) and Ru–L(axial ligand) bond axes, as well as the inherent steric bulk of the phosphanes, should prevent any significant associative attack by an incoming ligand. The activation parameters for the two complexes tell us little about the mechanism, the error in $\Delta S^{\neq}$ being too large to tell whether it is significantly positive (dissociative) or negative (associative).

The rate of axial ligand substitution (acetonitrile for phosphane) is two orders of magnitude slower in the present diruthenium system than in the aforementioned dirhodium complex. This can, presumably, be attributed to the higher charge on the metal centres (+2.5 in diruthenium vs. +2 in dirhodium) and the decreased number of antibonding electrons in the metal-centred HOMO (3 vs. 6).

Only one previous study dealt with ligand substitution in $[Ru_2(\mu\text{-}O_2CCH_3)_4L_2]^+$-type complexes. Dema and Bose[17] reported the anation reaction in acidic aqueous solution (pH = 1) of $[Ru_2(\mu\text{-}O_2CCH_3)_4(H_2O)_2]^+$ with $Cl^-$. They were able to determine successive equilibrium constants ($K_1$ = 15 $M^{-1}$, $K_2$ = 3.7 $M^{-1}$) because of the stability of the $[Ru_2(\mu\text{-}O_2CCH_3)_4Cl_2]^-$ diadduct and their ability to go to very high

 © 2007 Wiley-VCH Verlag GmbH & Co. KGaA, Weinheim 

concentrations of $Cl^-$, up to 2.0 M. Unfortunately, they were unable to measure the rates of anation, as more than 95% of the reaction was over in the time of mixing (4 ms) of their stopped-flow apparatus, which led them to estimate a lower limit for $k_1$ of $10^4\ M^{-1}s^{-1}$. This is not surprising (assuming a dissociative mechanism) as $H_2O$ is a more labile leaving group than MeCN. Substitution rate constants of $Rh_2(\mu\text{-}O_2CCH_3)_4(H_2O)_2$ versus $Rh_2(\mu\text{-}O_2CCH_3)_4(MeCN)_2$ in most cases tend to be one or two orders of magnitude higher.[16,18]

### Variable-Temperature Magnetic Susceptibility

Variable-temperature magnetic susceptibility measurements (2–300 K) were performed on complexes **1** and **2** as well as $[Ru_2(\mu\text{-}O_2CCH_3)_4(H_2O)_2]PF_6$. Figure 2 shows the plot of $\mu_{eff}$ vs. $T$ for all three complexes. The plot for $[Ru_2(\mu\text{-}O_2CCH_3)_4(H_2O)_2]PF_6$ shows a decrease in $\mu_{eff}$ at low temperature owing to a large zero-field splitting parameter typical of many diruthenium complexes of this form.[4] We have fit the data to a model previously developed by Drago[19] and adapted by Maldivi and co-workers[20] to fit the magnetic data for $[Ru_2(\mu\text{-}O_2CCH_3)_4(H_2O)_2]BF_4$ (see ref[20] for details) and determined the $g$ factor ($g$), zero-field splitting parameter ($D$) and temperature independent paramagnetism (TIP). The parameters obtained for our $PF_6^-$ salt were $g = 2.186$, $D = 70.4\ cm^{-1}$ and TIP $< 10^{-6}\ cm^3\,mol^{-1}$ compared with $g = 2.190$, $D = 71.8\ cm^{-1}$ and TIP $< 10^{-6}\ cm^3\,mol^{-1}$ for the $BF_4^-$ salt. This data is consistent with a ground-state configuration of $\sigma^2\pi^4\delta^2\pi^{*2}\delta^{*1}$, which displays significant zero-field splitting as the temperature is lowered, and the π* and δ* orbitals are essentially degenerate and often written as $(\pi^*\delta^*)^3$.

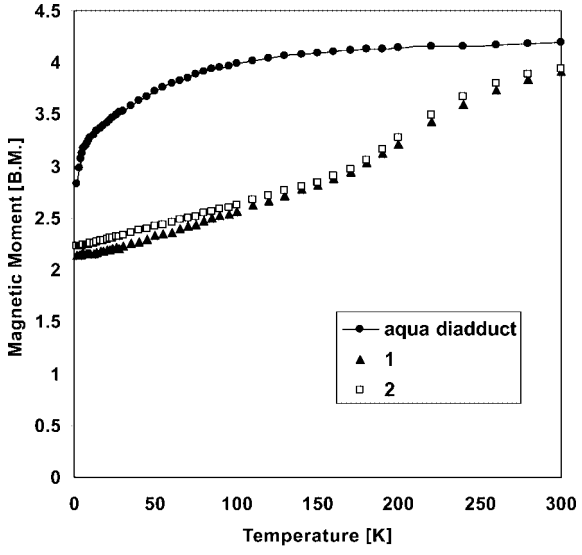


Figure 2. Plot of magnetic moment (B.M.) vs. temperature [K] for complexes **1**, **2** and $[Ru_2(\mu\text{-}O_2CCH_3)_4(H_2O)_2]PF_6$ (aqua diadduct).

The plots for **1** and **2** are quite similar to each other but distinctly different from the diaqua complex. In both cases the curves assume a sigmoidal shape with a long tail at low temperatures. The $\mu_{eff}$ value for **1** is 3.92 B.M. at 300 K (consistent with three unpaired electrons) and drops to 2.14 B.M. at 2 K (consistent with one unpaired electron), and similarly for **2**, the $\mu_{eff}$ is 3.94 B.M. at 300 K and 2.23 B.M. at 2 K. The shallow break in both curves occurs in the range 180–220 K. The values of $\mu_{eff}$ at 200 K are 3.22 B.M. for **1** and 3.27 B.M. for **2**, consistent with two unpaired electrons and a spin-crossover from an $S = 3/2$ to $S = 1/2$ state.

A wide variety of variable temperature magnetic behaviour has been ascribed to various diruthenium(II,III) complexes over the years: (1) high-spin (three unpaired electrons)[1–4] with ZFS (similar to the diaqua complex above), (2) low-spin (one unpaired electron),[21] (3) quantum mechanical spin admixed,[22] (4) Boltzmann distribution between $\pi^{*3}$ and $\pi^{*2}\delta^*$ homoelectronic configurations[23] and (5) physical spin mixture.[24] From the temperature dependence and overall shape of our plots for complexes **1** and **2**, a Boltzmann distribution of configurations similar to what Cotton and co-workers[23] saw for the *para* isomer of the *N*,*N*′-diarylformamidinate derivative, $Ru_2(DArF)_4Cl$ with Ar = *p*-$C_6H_4OMe$, would seem reasonable. In this case, the π* orbital is somewhat more stable than the δ*, and one sees a Boltzmann distribution between the less stable $\pi^{*2}\delta^{*1}$ configuration (seen at room temp.) and the more stable $\pi^{*3}$ configuration. Unfortunately, similar behaviour can also be ascribed to the situation where the δ* orbital is somewhat more stable than the π* orbital, and a Boltzmann distribution between the more stable $\delta^{*2}\pi^{*1}$ and less stable $\delta^{*1}\pi^{*2}$ occurs. To resolve the issue, Cotton looked at the structural changes that would need to take place for the two different Boltzmann distributions to be possible. When the π* orbital is more stable than the δ* orbital, a δ* electron is lost and a π* electron is gained as the temperature is lowered. Because a π* electron has a greater effect on the Ru–Ru bond than a δ* electron, the bond length will increase by 0.02–0.05 Å (on going from room temp. to 3 K). When the δ* orbital is more stable than the π* orbital, a δ* electron is gained at the expense of a π* electron, and the Ru–Ru bond length should decrease by 0.02–0.03 Å over the same temperature range.

In order to resolve this problem in our case we have redetermined the X-ray structure of **1** at various temperatures.

### Redetermination of the X-ray Structure of Complex 1

The structure of **1** was redetermined at –150, –75, –60, –40, –25, –10, +20 and +50 °C. The redeterminations, performed on the same crystal we used in our earlier study,[11] were all better resolved than the original, and they also corrected an error in the nature of the molecule of solvation, with 1,2-dichloroethane replacing the dichloromethane (1,2-dichloroethane is often an impurity in dichloromethane). The new formulation is therefore $[Ru_2(\mu\text{-}O_2CCH_3)_4(PCy_3)_2]PF_6{\cdot}1,2\text{-}C_2H_4Cl_2$. Figure S2 (Supporting Information) shows the molecular structure, Table 3 gives the

 © 2007 Wiley-VCH Verlag GmbH & Co. KGaA, Weinheim 

crystal parameters and Table 4 includes selected bond lengths and angles for the structure redetermination of **1** at –150 °C.

Table 3. Crystal parameters for **1**·DCE at –150 °C.

| Parameter | **1**·DCE |
|---|---|
| Empirical formula | $C_{46}H_{82}F_6O_8P_3Ru_2Cl_2$ |
| Formula weight | 1243.11 |
| Crystal system | triclinic |
| Space group | $P\bar{1}$ |
| $T$ [K] | 123.1(5) |
| $a$ [Å] | 10.5082(10) |
| $b$ [Å] | 11.4258(9) |
| $c$ [Å] | 12.6953(5) |
| $\alpha$ [°] | 77.06(2) |
| $\beta$ [°] | 68.40(2) |
| $\gamma$ [°] | 71.33(2) |
| Volume [Å$^3$] | 1332.8(2) |
| $Z$ | 1 |
| $D_{calcd.}$ [g cm$^{-1}$] | 1.549 |
| $\mu$ [cm$^{-1}$] | 8.26 |
| $F$(000) | 643 |
| Crystal size [mm] | 0.03 × 0.15 × 0.20 |
| $\theta$ range [°] | 3.2 to 72.4 |
| Index ranges | $-26 \le h \le 20$<br>$-29 \le k \le 29$<br>$-26 \le l \le 31$ |
| Collected reflections | 63056 |
| Independent reflections | 39488 ($R_{int}$ = 0.026) |
| Refinement method | full-matrix least squares on $F^2$ |
| Data / restraints / parameters | 7724 / 0 / 495 |
| Goodness-of-fit on $F^2$ | 1.157 |
| Final $R$ values [$I > 2\sigma(I)$] | $R1$ = 0.026, $wR2$ = 0.070 |
| $R$ values (all data) | $R1$ = 0.027, $wR2$ = 0.070 |
| Largest diff. peak/hole [e Å$^{-3}$] | 0.49 / –0.71 |

Table 4. Selected bond lengths [Å] and angles [°] for **1**·DCE at –150 °C.

| | | | |
|---|---|---|---|
| Ru(1)–Ru(1) | 2.44222(15) | Ru(1)–P(1) | 2.3445(5) |
| Ru(1)–O(1) | 2.0320(12) | Ru(1)–O(2) | 2.0128(7) |
| Ru(1)–O(3) | 2.0645(12) | Ru(1)–O(4) | 2.0930(8) |
| O(1)–C(19) | 1.2693(18) | O(2)–C(21) | 1.2735(15) |
| O(3)–C(19) | 1.2721(14) | O(4)–C(21) | 1.2668(15) |
| P(1)–C(1) | 1.8515(16) | P(1)–C(7) | 1.8433(10) |
| P(1)–C(13) | 1.8627(12) | O(1)–C(19) | 1.2693(18) |
| O(4)–C(21) | 1.2668(15) | C(19)–C(20) | 1.500(2) |
| C(21)–C(22) | 1.4942(19) | C(1)–C(2) | 1.5396(16) |
| | | | |
| Ru(1)–Ru(1)–P(1) | 160.265(8) | Ru(1)–Ru(1)–O(1) | 89.34(2) |
| Ru(1)–Ru(1)–O(2) | 94.99(2) | Ru(1)–Ru(1)–O(3) | 85.40(2) |
| Ru(1)–Ru(1)–O(4) | 79.88(2) | P(1)–Ru(1)–O(1) | 96.14(2) |
| P(1)–Ru(1)–O(2) | 104.05(2) | P(1)–Ru(1)–O(3) | 89.75(2) |
| P(1)–Ru(1)–O(4) | 81.11(2) | O(1)–Ru(1)–O(2) | 88.74(4) |
| O(1)–Ru(1)–O(3) | 174.04(3) | O(1)–Ru(1)–O(4) | 90.70(4) |
| O(2)–Ru(1)–O(3) | 88.91(4) | O(2)–Ru(1)–O(4) | 174.84(3) |
| O(3)–Ru(1)–O(4) | 91.14(4) | Ru(1)–P(1)–C(1) | 111.32(3) |
| Ru(1)–P(1)–C(7) | 108.11(3) | Ru(1)–P(1)–C(13) | 117.74(4) |
| C(1)–P(1)–C(7) | 105.28(6) | C(1)–P(1)–C(13) | 106.88(5) |
| C(7)–P(1)–C(13) | 106.75(5) | Ru(1)–O(1)–C(19) | 118.57(8) |
| Ru(1)–O(2)–C(21) | 113.99(7) | Ru(1)–O(3)–C(19) | 121.25(10) |
| Ru(1)–O(4)–C(21) | 126.44(7) | O(1)–C(19)–O(3) | 125.14(15) |

All of the bond length and angle values for the redetermination at 20 °C are very similar to those of the earlier room temp. structure. For example, the redetermined bond length value for Ru–Ru is 2.42825(16) Å, for Ru–P it is 2.3717(4) Å and the Ru–Ru–P bond angle is 160.331(13)°. The values for the previous determination are 2.427(1) and 2.369(2) Å and 160.40(5)°, respectively.

Only two parameters, the Ru–Ru and Ru–P bond lengths, change significantly over the temperature range studied (50 to –150 °C) and this is shown in Figure 3. The Ru–Ru bond *increases* from 2.42373(15) Å at 50 °C to 2.44222(15) Å at –150 °C, a difference of +0.0185 Å. Despite the fact that we could not make measurements below –150 °C (123 K), this bond length *increase* is clearly significant and consistent with a $\pi^{*3}$ configuration at low temperature and a $\pi^{*2}\delta^{*1}$ configuration at room temp., as concluded by Cotton. In addition, the Ru–P bond length *decreases* from 2.3735(4) Å at 50 °C to 2.3445(3) Å at –150 °C, a difference of –0.029 Å, indicative of increased back-donation from the now more populated Ru–Ru-based π* orbital to the phosphane.

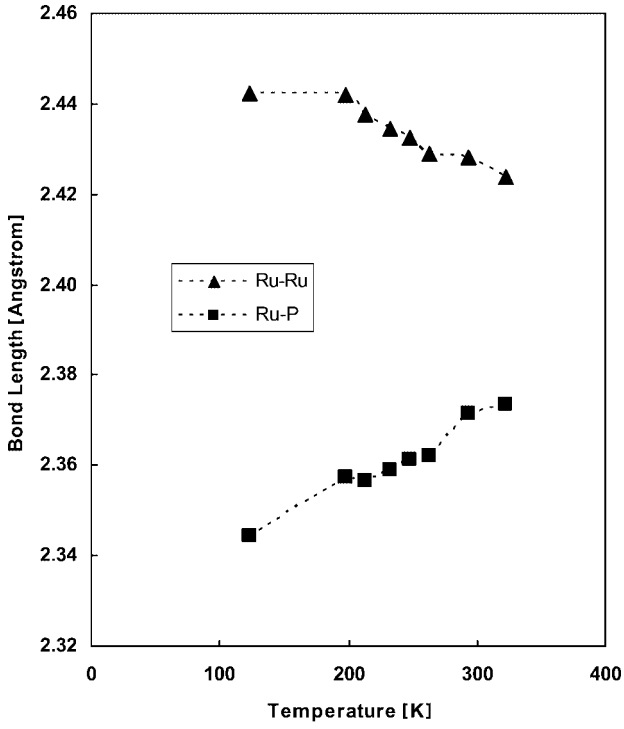


Figure 3. Plots of bond length vs. temperature for the Ru–Ru and Ru–P bonds in **1**.

It should be noted that no other major structural changes occur as the temperature is lowered. The space group is $P\bar{1}$ at all temperatures measured, and the unit cell volume contracts by about 3.7% over the range 50 °C to –150 °C, which is consistent with normal unit cell contraction as the temperature is lowered.

## Conclusions

In this paper we reported the rate constants and activation parameters for the axial-ligand-substitution reactions of $[Ru_2(\mu\text{-}O_2CCH_3)_4(MeCN)_2]^+$ with the phosphanes $PCy_3$ and $PCy_2Ph$. This is the first time rate constants were

 © 2007 Wiley-VCH Verlag GmbH & Co. KGaA, Weinheim 

measured for any substitution reaction on the $[Ru_2(\mu\text{-}O_2CR)_4L_2]^+$ core. The rate constants are found to be about two orders of magnitude less than similar axial-ligand substitutions on the $[Rh_2(\mu\text{-}O_2CR)_4L_2]$ core. The two phosphane diadducts thus formed, $[Ru_2(\mu\text{-}O_2CCH_3)_4(PCy_3)_2]PF_6$ (**1**) and $[Ru_2(\mu\text{-}O_2CCH_3)_4(PCy_2Ph)_2]PF_6$ (**2**) were further investigated for their variable-temperature magnetic susceptibility properties and both displayed behaviour consistent with a Boltzmann distribution between a low temperature $\sigma^2\pi^4\delta^2\pi^{*3}$ doublet (ground-state) and a high temperature $\sigma^2\pi^4\delta^2\pi^{*2}\delta^{*1}$ quartet state. This conclusion is supported by the variable-temperature X-ray diffraction data of complex **1**, which shows an increase in the Ru–Ru bond length upon decreasing temperature, which is consistent with a metal–metal centred π* orbital being populated at the expense of a δ* orbital. Whereas Jiménez-Aparicio and co-workers[22] showed that the variation of the axial ligand in $[Ru_2(\mu\text{-}O_2CCH_3)(\mu\text{-}DPhF)_3X](BF_4)_n$-type systems ($DPhF^-$ = *N*,*N*′-diphenylformamidinate) can lead to high-spin (X = $Cl^-$, *n* = 0), low-spin (X = $SCN^-$, *n* = 0) or spin-admixed (X = $H_2O$, *n* = 1) complexes, Cotton and co-workers[23] showed that the variation of the equatorial ligand in $Ru_2(\mu\text{-}DArF)_4Cl$ systems ($DArF^-$ = *N*,*N*′-diarylformamidinate) can lead to a high-spin (Ar = *m*-$C_6H_4OMe$) complex or one showing a Boltzmann distribution of states (Ar = *p*-$C_6H_4OMe$); ours is the first example of a Boltzmann distribution being induced in a diruthenium(II,III) paddle-wheel-style complex by the variation of the *axial* ligand.

## Experimental Section

**General Remarks:** Unless otherwise indicated all reactions were carried out under an inert (Ar) atmosphere. Tricyclohexylphosphane, $PCy_3$, and dicyclohexylphenylphosphane, $PPhCy_2$, were obtained from Aldrich and used as received. $[Ru_2(\mu\text{-}O_2CCH_3)_4(H_2O)_2]PF_6$ was prepared by a literature procedure.[25] IR spectra were recorded as KBr discs with a Bio-Rad FTS-175 spectrophotometer. UV/Vis spectra were recorded in 1-cm Hellma quartz cells with a Varian 100 spectrometer. C, H and P elemental analyses were performed by Canadian Microanalytical Service Ltd., Delta, BC, Canada. The variable temperature magnetic susceptibility data were recorded with a Quantum Design MPMS5S2 Superconducting Quantum Interference Device (SQUID) susceptometer at Memorial University over a temperature range of 2 to 300 K. Corrections for the diamagnetic contribution to the susceptibility of the samples and sample holder were performed on the raw data. The molar diamagnetic corrections for the complexes were calculated on the basis of Pascal's constants. The kinetics measurements were performed in acetonitrile with 0.100 M tetrabutylammonium hexafluorophosphate ($TBAPF_6$) with a SX-17MV stopped-flow spectrophotometer (Applied Photophysics), and the kinetic traces were fit to first-order reactions (4–6 replicate runs) by using the Applied Photophysics software on an Acorn A5000 workstation. The temperature was maintained at ±0.1 °C over the temperature range of 7–32 °C by using an external circulating water bath (VWR Scientific Model 1166).

**$[Ru_2(\mu\text{-}O_2CCH_3)_4(PCy_3)_2]PF_6$ (1):** A brief outline of this synthesis was reported earlier.[11] $[Ru_2(\mu\text{-}O_2CCH_3)_4(H_2O)_2]PF_6$ (0.100 g, 0.16 mmol) was dissolved in 2-propanol (7 mL). A solution of tricyclohexylphosphane (0.090 g, 0.32 mmol) in 2-propanol (3 mL) was added, with stirring, at room temp. and allowed to react for no more than 5 min. The dark brown precipitate that formed was immediately filtered off in vacuo and washed with 2-propanol (30 mL) after which it was dried in vacuo. Crystals could be grown under an atmosphere of argon by rapid evaporation from DCM. Yield: 0.15 g (80%). IR (KBr): $\tilde{\nu}$ = 2931 (s), 2854 (s), 1440 (s), 1345 (s), 1271 (m), 1113 (m), 1005 (m), 843 (s), 731 (m), 692 (s), 558 (m), 510 (m) $cm^{-1}$. UV/Vis (1,2-dichloroethane): $\lambda$ ($\varepsilon$, $L\,mol^{-1}\,cm^{-1}$) = 473 (≈ 900) nm. $C_{44}H_{78}F_6O_8P_3Ru_2$ (1144.58): calcd. C 46.17, H 6.87, P 8.12; found C 45.84, H 6.55, P 8.08.

**$[Ru_2(\mu\text{-}O_2CCH_3)_4(PPhCy_2)_2]PF_6$ (2):** This diadduct was prepared in a similar fashion to **1** except that dicyclohexylphenylphosphane (0.088 g, 0.32 mmol) was used. Yield: 0.15 g (81%). IR (KBr): $\tilde{\nu}$ = 3064 (w), 2931 (s), 2852 (s), 1440 (s), 1355 (s), 1274 (m), 1189 (m), 1112 (m), 1003 (m), 843 (s), 692 (s), 558 (m) $cm^{-1}$. UV/Vis (1,2-dichloroethane): $\lambda$ ($\varepsilon$, $L\,mol^{-1}\,cm^{-1}$) = 479 (≈ 900) nm. $C_{44}H_{66}F_6O_8P_3Ru_2$ (1132.05): calcd. C 46.68, H 5.88, P 8.21; found C 46.84, H 6.13, P 8.01.

**X-ray Crystallographic Study:** All measurements were made with a Rigaku RAXIS RAPID imaging plate area detector with graphite monochromated Mo-$K_\alpha$ radiation. Indexing was performed from 4 oscillations that were exposed for 600 seconds. The data were collected at temperatures of (–150, –75, –60, –40, –25, –10, +20 and +50) ± 0.5 °C to a maximum $2\theta$ value of 145.2 °. The crystal-to-detector distance was 127.40 mm. Readout was performed in the 0.100 mm pixel mode. The data were corrected for Lorentz and polarization effects. A correction for secondary extinction was applied.[26] The structures were solved by direct methods[27] and expanded by using Fourier techniques.[28] The non-hydrogen atoms were refined anisotropically. Some hydrogen atoms were refined isotropically and the rest were refined by using the riding model. The final cycle of full-matrix least-squares refinement was on $F^2$.

Neutral atom scattering factors were taken from Cromer and Waber.[29] Anomalous dispersion effects were included in $F_{calcd.}$;[30] the values for $\Delta f'$ and $\Delta f''$ were those of Creagh and McAuley.[31] The values for the mass attenuation coefficients are those of Creagh and Hubbell.[32] All calculations were performed by using the CrystalStructure[33–34] crystallographic software package except for the refinement, which was performed with SHELXL-97.[35] CCDC-640710 to -640717 (for **1** at the various temperatures) contain the supplementary crystallographic data for this paper. These data can be obtained free of charge from The Cambridge Crystallographic Data Centre via www.ccdc.cam.ac.uk/data_request/cif.

**Supporting Information** (see footnote on the first page of this article): Electronic spectra of **1** and its precursor and the ORTEP diagram of $\mathbf{1}^+$.

## Acknowledgments

M. A. S. A. acknowledges the Natural Sciences and Engineering Research Council (Canada) for financial support.

[1] M. A. S. Aquino, *Coord. Chem. Rev.* **1998**, *170*, 141–202.
[2] M. A. S. Aquino, *Coord. Chem. Rev.* **2004**, *248*, 1025–1045.
[3] F. A. Cotton, C. A. Murillo, R. A. Walton, *Multiple Bonds Between Metal Atoms*, 3rd ed., Springer Science and Business Media, New York, **2005**.
[4] M. Mikuriya, D. Yoshioka, M. Handa, *Coord. Chem. Rev.* **2006**, *250*, 2194–2211.

 © 2007 Wiley-VCH Verlag GmbH & Co. KGaA, Weinheim 

[5] S. Takamizawa, K. Yamaguchi, W. Mori, *Inorg. Chem. Commun.* **1998**, *1*, 177–178.
[6] S. Takamizawa, T. Ohmura, Y. Yamaguchi, W. Mori, *Mol. Cryst. Liq. Cryst.* **2000**, *342*, 199–204.
[7] T. Ohmura, W. Mori, H. Hiraga, M. Ono, Y. Nishimoto, *Chem. Lett.* **2003**, *32*, 468–469.
[8] Y. Liao, W. W. Shum, J. S. Miller, *J. Am. Chem. Soc.* **2002**, *124*, 9336–9337.
[9] D. Yoshioka, M. Mikuriya, M. Handa, *Chem. Lett.* **2002**, 1044–1045.
[10] H. Miyasaka, C. S. Campos-Fernández, R. Clérac, K. R. Dunbar, *Angew. Chem. Int. Ed.* **2000**, *39*, 3831–3835.
[11] G. G. Briand, M. W. Cooke, T. S. Cameron, H. M. Farrell, T. J. Burchell, M. A. S. Aquino, *Inorg. Chem.* **2001**, *40*, 3267–3268.
[12] C. A. Tolman, *Chem. Rev.* **1977**, *77*, 313–348.
[13] I. W. Wyman, T. J. Burchell, K. N. Robertson, T. S. Cameron, M. A. S. Aquino, *Organometallics* **2004**, *23*, 5353–5364.
[14] M. C. Barral, R. Jiménez-Aparicio, E. C. Royer, F. A. Urbanos, A. Monge, C. Ruiz-Valero, *Polyhedron* **1991**, *10*, 113–120.
[15] G. Vamvounis, J. F. Caplan, T. S. Cameron, K. N. Robertson, M. A. S. Aquino, *Inorg. Chim. Acta* **2000**, *304*, 87–98.
[16] M. A. S. Aquino, D. H. Macartney, *Inorg. Chem.* **1987**, *26*, 2696–2699.
[17] A. C. Dema, R. N. Bose, *Inorg. Chem.* **1989**, *28*, 2711–2713.
[18] K. Das, E. L. Simmons, J. L. Bear, *Inorg. Chem.* **1977**, *16*, 1268–1271.
[19] J. Telser, R. S. Drago, *Inorg. Chem.* **1984**, *23*, 3114–3120.
[20] F. D. Cukiernik, A.-M. Giroud-Godquin, P. Maldivi, J.-C. Marchon, *Inorg. Chim. Acta* **1994**, *215*, 203–207.
[21] M. C. Barral, R. González-Prieto, S. Herrero, R. Jiménez-Aparicio, J. L. Priego, E. C. Royer, M. R. Torres, F. A. Urbanos, *Polyhedron* **2004**, *23*, 2637–2644.
[22] M. C. Barral, S. Herrero, R. Jiménez-Aparicio, M. R. Torres, F. A. Urbanos, *Angew. Chem. Int. Ed.* **2005**, *44*, 305–307.
[23] P. Angaridis, F. A. Cotton, C. A. Murillo, D. Villagrán, X. Wang, *J. Am. Chem. Soc.* **2005**, *127*, 5008–5009.
[24] M. C. Barral, T. Gallo, S. Herrero, R. Jiménez-Aparicio, M. R. Torres, F. A. Urbanos, *Inorg. Chem.* **2006**, *45*, 3639–3647.
[25] K. D. Drysdale, E. J. Beck, T. S. Cameron, K. N. Robertson, M. A. S. Aquino, *Inorg. Chim. Acta* **1997**, *256*, 243–252.
[26] A. C. Larson in *Crystallographic Computing* (Ed.: F. R. Ahmed), Munksgaard, Copenhagen, **1970**, pp. 291–294.
[27] *SIR92*: A. Altomare, G. Cascarano, C. Giacovazzo, A. Guagliardi, M. Burla, G. Polidori, M. Camalli, *J. Appl. Cryst.* **1994**, *27*, 435.
[28] *DIRDIF99*: P. T. Beurskens, G. Admiraal, G. Beurskens, W. P. Bosman, R. de Gelder, R. Israel, J. M. M. Smits, *The DIRDIF-99 Program System*, Technical Report of the Crystallography Laboratory, University of Nijmegen, The Netherlands, **1999**.
[29] D. T. Cromer, J. T. Waber, *International Tables for X-ray Crystallography*, The Kynoch Press, Birmingham, England, **1974**, vol. IV, Table 2.2A.
[30] J. A. Ibers, W. C. Hamilton, *Acta Crystallogr.* **1964**, *17*, 781–782.
[31] D. C. Creagh, W.J McAuley, *International Tables for Crystallography* (Ed.: A. J. C. Wilson), Kluwer Academic Publishers, Boston, **1992**, vol. C, Table 4.2.6.8, pp. 219–222.
[32] D. C. Creagh, J. H. Hubbell, *International Tables for Crystallography* (Ed.: A. J. C. Wilson), Kluwer Academic Publishers, Boston, **1992**, vol. C, Table 4.2.4.3, pp. 200–206.
[33] *CrystalStructure 3.6.0*: *Crystal Structure Analysis Package*, Rigaku and Rigaku/MSC, 9009 New Trails Dr., The Woodlands, TX, 77381 USA, **2000**–**2004**.
[34] *CRYSTALS Issue 10*: D. J. Watkin, C. K. Prout, J. R. Carruthers, P. W. Betteridge, Chemical Crystallography Laboratory, Oxford, UK, **1996**.
[35] G. M. Sheldrick, *SHELXL97*, University of Göttingen, **1997**.

Received: April 11, 2007
Published Online: July 6, 2007

 © 2007 Wiley-VCH Verlag GmbH & Co. KGaA, Weinheim 

DOI: 10.1002/ejic.200700154

# Alkyl Chain Length Defines 2D Architecture of Salophen Complexes on Liquid–Graphite Interface

**Minna T. Räisänen,[a] Florian Mögele,[b] Santeri Feodorow,[a] Bernhard Rieger,[b] Ulrich Ziener,[c] Markku Leskelä,[a] and Timo Repo*[a]**

**Keywords:** Metal-containing monolayers / Nanopatterning / Scanning tunnelling microscopy (STM) / Self-assembly

A series of $Cu^{II}$, $Ni^{II}$ and $Co^{II}$ salophen [salophen = *N*,*N*′-(*o*-phenylene)bis(salicylideneimine)] complexes were prepared, and their two-dimensional (2D) assemblies on a liquid–graphite interface were studied by scanning tunnelling microscopy (STM). Depending on their varying alkyl chain lengths ($C_8$, $C_{10}$ or $C_{12}$), two different new adlayers, parallelogram and honeycomb, were recorded. According to STM data, the driving force for these assemblies is a subtle interplay between a maximum amount of attractive van der Waals interaction of the alkyl chains and weak hydrogen bonding of the phenoxy moieties. Thus, the alkyl chain length defines the favoured 2D structure for each metal complex. As shown here, the self-assembled monolayers of the salophen complexes studied provide an attractive approach to varying the surface architecture.

(© Wiley-VCH Verlag GmbH & Co. KGaA, 69451 Weinheim, Germany, 2007)

## Introduction

The formation of self-assembled monolayers (SAMs) is a useful methodology for the preparation of surfaces with well-defined composition, structure and thickness.[1] SAMs have found use in chemical sensors,[2] electrochemistry,[3] catalysis,[4] corrosion protection,[5] lubrication,[6] adhesion[7] and wetting.[7,8] Lately, SAMs of metal complexes on highly oriented pyrolytic graphite (HOPG) have captured significant interest,[9] as they provide a platform for the highly ordered metal-decorated surfaces required in such uses as functional nano devices and data storage.[10] For example, the controlled 2D or 3D assembly of [2 × 2] $M^{II}$ grid-type complexes of Co[11] and Fe[12] is important, as these complexes have many technologically interesting properties.[13] Furthermore, redox-active $Ru^{II}$ and $Pt^{II}$ Fréchet dendrons have been assembled on HOPG.[14] In addition to assemblies on HOPG, several metal–organic coordination networks have been studied on single crystalline Cu, Au and Ag surfaces for the preparation of functional nanomaterials.[15]

For application purposes, the highly oriented SAMs must be kinetically and thermodynamically stable in the long run in order to maintain their desired function. Intermolecular van der Waals interactions – especially those of long alkyl chains – as well as hydrogen bonding and adsorbate–substrate interactions within the 2D arrays provide strong driving forces for the formation of highly ordered surface structures. Long alkyl chains play a considerable role in the mutual recognition and stabilisation of the patterns formed and act as easily variable spacers.[9d,9f] In this context, we report herein a study of 2D assemblies for a series of $Co^{II}$, $Cu^{II}$ and $Ni^{II}$ salophen complexes (**1**–**9**) on a liquid–graphite interface (Figure 1). Depending on their varying alkyl chain lengths ($C_8$, $C_{10}$ or $C_{12}$), the salophen complexes formed two different new adlayers on HOPG.

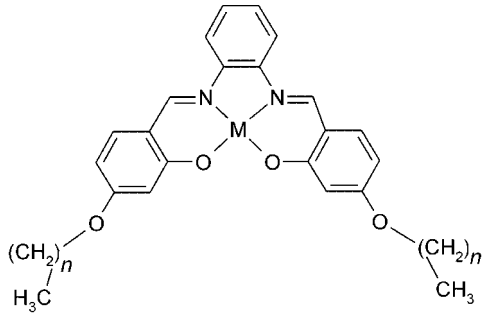


**1**: M = $Cu^{2+}$, *n* = 11; **2**: M = $Cu^{2+}$, *n* = 9; **3**: M = $Cu^{2+}$, *n* = 7;
**4**: M = $Ni^{2+}$, *n* = 11; **5**: M = $Ni^{2+}$, *n* = 9; **6**: M = $Ni^{2+}$, *n* = 7;
**7**: 1: M = $Co^{2+}$, *n* = 11; **8**: 1: M = $Co^{2+}$, *n* = 9; **9**: M = $Co^{2+}$, *n* = 7.

Figure 1. Schematic structures of salophen complexes **1**–**9**.

[a] Laboratory of Inorganic Chemistry, Department of Chemistry, University of Helsinki
P.O. Box 55, 00014 University of Helsinki, Finland
Fax: +358-9-191-50198
E-Mail: timo.repo@helsinki.fi
[b] Department of Materials and Catalysis, University of Ulm
Albert-Einstein-Allee 11, 89081 Ulm, Germany
[c] Department of Organic Chemistry III, Macromolecular Chemistry, University of Ulm
Albert-Einstein-Allee 11, 89081 Ulm, Germany

Supporting information for this article is available on the WWW under http://www.eurjic.org or from the author.

 © 2007 Wiley-VCH Verlag GmbH & Co. KGaA, Weinheim 

## Results and Discussion

Salophen ligand precursors with varying alkyl chain lengths and their $Co^{II}$, $Cu^{II}$ and $Ni^{II}$ complexes (**1**–**9**) were prepared by standard synthetic procedures (see Exp. Sect.). The self-assembled monolayers of **1**–**9** were measured at room temperature in saturated 1,2,4-trichlorobenzene (TCB) solutions by STM at the liquid–solid interface on HOPG.[16] The images were measured in a constant-current mode, and the aromatic parts of the molecules appear brighter than the alkyl chains because of their higher electron density. In addition to the SAMs of the metal complexes, those of the uncomplexed salophen ligand **E** with $C_{12}$ alkyl chains were imaged. The surface structure formed was of lamellar type with interdigitating alkyl chains (Figure 2) and clearly distinct from those of the complexes deposited on HOPG from the same solvent (TCB). In the case of ligands with shorter alkyl chains ($C_{10}$ and $C_8$), no images were obtained under the same conditions as those used for the metal complexes.[16]

So far the most common 2D structure reported for metal complexes on HOPG is a highly ordered lamellar structure similar to that measured here for the uncomplexed salophen ligand.[9a,9b,9e–9g] Therefore, it was quite unexpected that all salophen complexes bearing short ($C_{10}$ or $C_8$) alkyl chains would assemble on the HOPG surface by forming an array of almost distinct parallelograms rather than striped lamellar structures (Figure 3). The attribution of the bright features to the aromatic parts of the molecule leads to a proposed model where each parallelogram consists of four salophen complexes. Detailed analysis of the 2D structure revealed its novelty.

The interatomic distances between neighbouring molecules in the structure can be estimated from the model coinciding with the high-resolution STM pattern. As shown

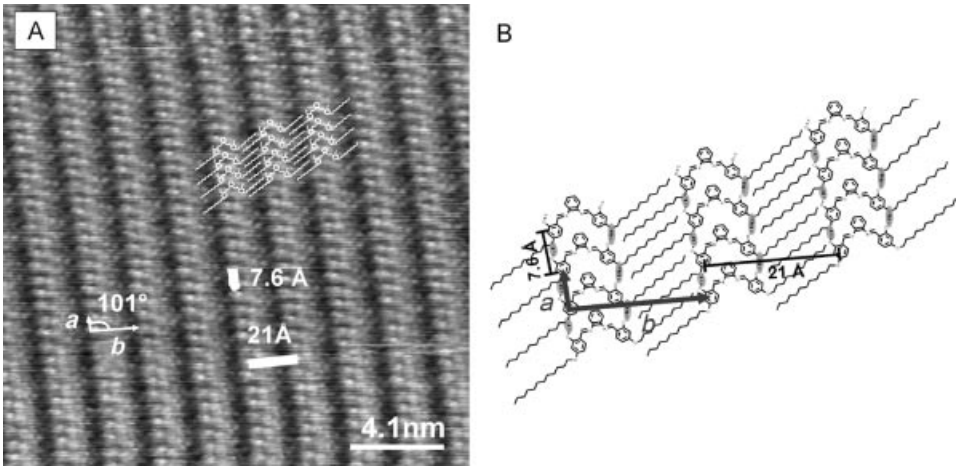


Figure 2. The STM image (A) and the proposed molecular model (B) for *N*,*N*′-(*o*-phenylene)bis(4-decyloxysalicylideneimine) (**E**) on HOPG. The image was obtained from saturated 1,2,4-trichlorobenzene solution. Image area: 203 Å × 203 Å; $U_{set}$ = –259 mV; $I_{set}$ = 18.2 pA. Unit cell dimensions: $a = 7.6 \pm 0.2$ Å; $b = 21.0 \pm 0.2$ Å; angle $101 \pm 2$ °. The hydrogen bonding of molecules is shown by the dotted lines and the grey overlay.

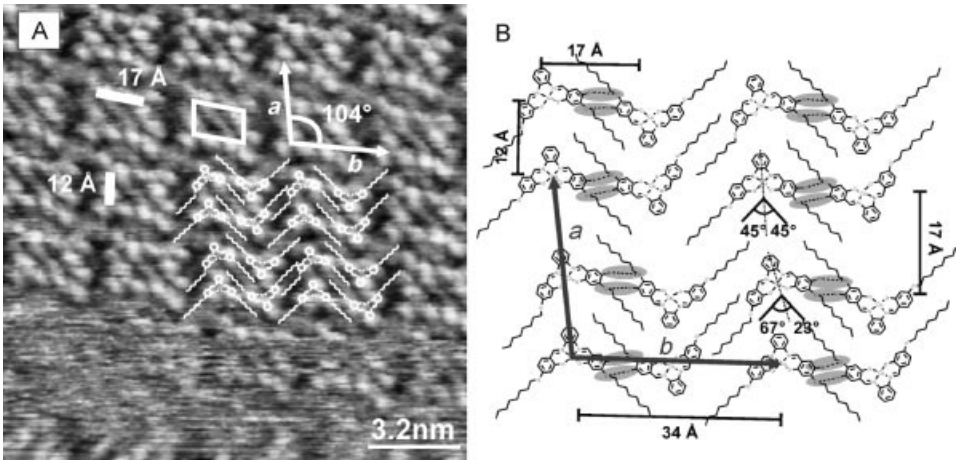


Figure 3. The high-resolution STM image (A) and the proposed molecular model (B) for complex **3** at the liquid–HOPG interface. Image area: 161 Å × 161 Å; $U_{set}$ = –630 mV; $I_{set}$ = 29.3 pA. Unit cell dimensions: $a = 28.5 \pm 0.2$ Å; $b = 34.0 \pm 0.2$ Å; angle $104 \pm 2$ . The hydrogen bonding in a parallelogram is shown by the dotted lines and the grey overlay.

 © 2007 Wiley-VCH Verlag GmbH & Co. KGaA, Weinheim 

here for **3**, intermolecular metal–metal distances within a parallelogram alternate between $12.0 \pm 0.2$ Å (*a* axis) and $17.0 \pm 0.2$ Å (*b* axis), while the shortest metal–metal distances between the parallelograms, regardless of the axis, are constant at a value of $17.0 \pm 0.2$ Å (Figure 3). The metal–metal distances along the *b* axis can be considered as the distances between the lamellae. This structure consists of two different, alternating lamellae that differ from each other by the relative orientation of the salophen complexes. In the proposed structural model, every second complex within a lamella is also twisted by 18° with respect to the preceding molecule, which further distorts the classical lamellar structure. If a parallelogram is considered to be a unit, it can be seen that the periodicity of this structure is 34 Å along the *b* axis and 29 Å along the *a* axis. Specifically, the differing orientation of the molecules and the resulting loss of symmetry within a lamella distinguish this parallelogram-like structure from the traditional lamellar structure. A parallelogram-like structure similar to that of **3** was also obtained for Ni and Co complexes **5**, **6**, **8** and **9** bearing $C_{10}$ and $C_8$ alkyl chains (see Supporting Information). As illustrated in Table 1, the variation of the alkyl chain length and central metal ion has an observable influence on the geometry of the 2D structure obtained. For example, the Co complexes **8** ($C_{10}$) and **9** ($C_8$) have a rather constant *b* axis, whereas the change in the alkyl chain length has a substantial influence on the *a* axis. Similarly, the difference in the *b* axis is only ca. 1 Å in Ni complexes **5** ($C_{10}$) and **6** ($C_8$), whereas the *a* axis is longer by ca. 3 Å in the complex with the longer alkyl chain. Although the image resolutions of **5**, **6**, **8** and **9** do not facilitate the interpretation of the 2D fine structures, it is clear that the length of the alkyl chain and the nature of the metal ion play an interactive role in the formation of these structures.

Table 1. Unit cell dimensions of salophen complexes **3**, **5**, **6**, **8** and **9** with parallelogram-like 2D structures.

| Complex | Unit cell dimensions | | |
|---|---|---|---|
| | *a* [Å] | *b* [Å] | Angle [°] |
| $CuC_8$ (**3**) | $28.5 \pm 0.2$ | $34.0 \pm 0.2$ | $104 \pm 2$ |
| $NiC_{10}$ (**5**) | $28.0 \pm 0.2$ | $28.0 \pm 0.2$ | $90 \pm 2$ |
| $NiC_8$ (**6**) | $25.0 \pm 0.2$ | $27.0 \pm 0.2$ | $95 \pm 2$ |
| $CoC_{10}$ (**8**) | $28.0 \pm 0.2$ | $33.5 \pm 0.2$ | $92 \pm 2$ |
| $CoC_8$ (**9**) | $22.0 \pm 0.2$ | $34.0 \pm 0.2$ | $100 \pm 2$ |

The measured lamellar periodicities suggest that the alkyl chains of neighbouring lamellae interdigitate. The darker regions in Figure 3A exhibit a striped pattern that approximates the distance between the alkyl chains, which averages $5.0 \pm 0.2$ Å. This is a rather typical value for close-packed alkyl chains in van der Waals contact.[17] The alkyl chains need to adjust themselves to the adjacent molecule; this results in different angles (23°, 45° or 67°) between the alkyl chains and the bisectors of the molecules. As a result of the distorted lamellar structure, the interdigitation of the alkyl chains also varies in the assembly. In a parallelogram, one alkyl chain of a complex in the upper left-hand corner and one of a complex in the lower right-hand corner fully interdigitate with alkyl chains of complexes in two neighbouring parallelograms, and this particular interaction actually joins the individual parallelograms together to form a continuous pattern. Further on, the remaining alkyl chains of these complexes fully interdigitate with each other. Interdigitation of the alkyl chains of complexes in the lower left-hand and upper right-hand corners, even to a relatively low degree, with the molecules of neighbouring parallelograms provides additional stabilisation for the assembly.

In addition to the above-described van der Waals interactions, the parallelogram-like structure appears to be further stabilised by intermolecular $C_{Ar}H\cdots O_{alkoxy}$ hydrogen bonding. Inside a given parallelogram are two pairs of hydrogen-bond-coupled salophen complexes (Figure 3). The observed hydrogen bond lengths of ca. $2.7 \pm 0.2$ Å fall within the range of weak hydrogen bonds.[18] According to the molecular symmetry, these hydrogen-bonded couples inside each parallelogram are identical. In this respect, the 2D assembly can also be seen as an arrangement of those hydrogen-bonded couples rather than that of individual salophen complexes. It is noteworthy that there is no interparallelogram hydrogen bonding. We assume that the hydrogen bonding is essential in stabilising the 2D structure, which represents the global energetic minimum gained by a compromise between the hydrogen bonding and the maximum amount of van der Waals contacts. Both of these intermolecular interactions are known to be important structural parameters in 2D assemblies,[9a,19,20] and the influence of alkyl chain length on the 2D structure was described previously for the co-adsorption of trimesic acid with even- and odd-numbered alcohols on HOPG.[20]

In this series of salophen complexes, an increase in the alkyl chain length from $C_{10}$ to $C_{12}$ leads exclusively to a new, honeycomb-type network pattern consisting of hexagons with six molecules.[21] A structural model in which each molecule has its three nearest neighbours within a range of $12.0 \pm 0.2$ Å to $15.0 \pm 0.2$ Å is proposed (Figure 4). In this assembly, the alkyl chains of each molecule are parallel to the bisector of the salophen complex and interdigitate perfectly with those of the opposite molecule within each hexagon. Thus, in the honeycomb assembly, the alkyl chains only form van der Waals contacts inside the hexagons, whereas in the classical lamellar assembly as well as in the parallelogram-like one described above, they form a continuous network throughout the 2D structures. Instead, here the hydrogen-bonding network continues throughout the structure, and every complex has two intermolecular $C_{Ar}H\cdots O_{alkoxy}$ hydrogen bonds at an approximate distance of $2.6 \pm 0.2$ Å. This distance was estimated by applying typical geometric parameters to the structural model in Figure 4B. Apparently, both van der Waals contacts and hydrogen bonding are needed to stabilise this assembly.

The substantial differences in the 2D packings of the salophen-$C_{12}$ ligand **E** and its $Co^{II}$ complex **7** can be explained by the effect of the $Co^{II}$ ion on the ligand geometry upon complex formation. When the salophen ligand coordinates to the $Co^{II}$ ion, both hydroxy groups are forced towards the metal ion, and the complex acquires an overall $C_2$ symmetry. On the contrary, in the free ligand **E**, the OH groups

 © 2007 Wiley-VCH Verlag GmbH & Co. KGaA, Weinheim 

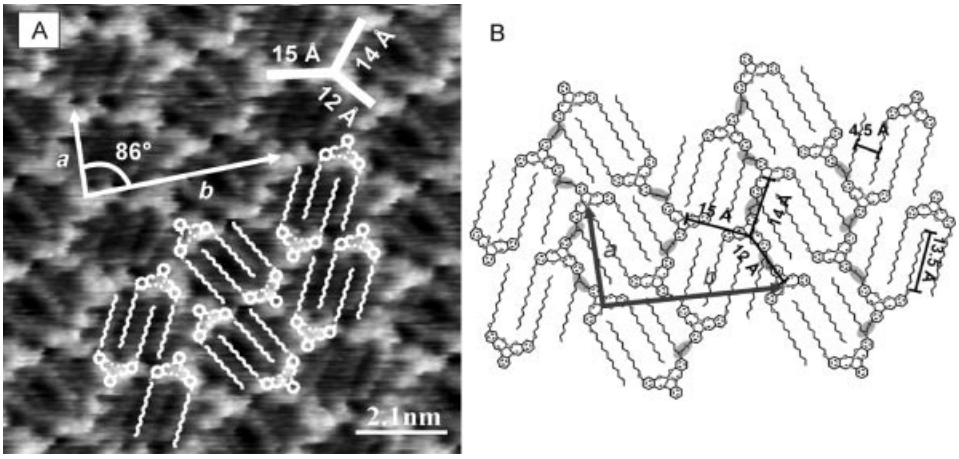


Figure 4. The high-resolution STM image (A) and the proposed molecular model (B) for complex **7**. Image area: 104 Å × 104 Å; $U_{set}$ = –180 mV; $I_{set}$ = 12.8 pA. Unit cell dimensions: $a = 19.5 \pm 0.2$ Å; $b = 46.0 \pm 0.2$ Å; angle = 86 ± 2 °. The hydrogen bonding in a honeycomb is shown by the dotted lines and the grey overlay.

can be located independently either inside or outside the ligand cavity as a result of rotation. In the 2D structure of **E** (Figure 2), both hydroxy groups point outwards, forming hydrogen bonds with the adjacent molecule.

Clear differences can be noted in the stabilisation of the 2D parallelogram-like and honeycomb structures. In the parallelogram-like structure the van der Waals forces are reduced as a result of the twisted orientation of every second complex in a lamella, but this reduced stability is compensated for by hydrogen bonds inside the parallelogram. The van der Waals interactions network the structure. In the honeycomb assembly, alkyl chains of an individual complex fully interdigitate with alkyl chains of another complex, but further networking is prohibited by the surrounding ligand frameworks. Hydrogen bonds form the required network and are essential in stabilising the honeycomb structure. Apparently, by tuning the alkyl chain length in salophen complexes, the balance between van der Waals and hydrogen bonding interactions can be controlled. As a consequence, the 2D assembly of the complexes changes. These findings are summarised in Table 2 to illustrate the interactive effects of van der Waals interactions, i.e. the alkyl chain length, and hydrogen bonding on the 2D morphology of the SAMs. Furthermore, metal ions have clear effects on the 2D assemblies, as shown by the formation of a lamellar structure by the uncomplexed $C_{12}$ ligand (Figure 2).

Table 2. The van der Waals interactions and number of hydrogen bonds in parallelogram-like and honeycomb structures.

| 2D structure | van der Waals interactions | H bonds per molecule | Networking by |
|---|---|---|---|
| Parallelogram-like: $CoC_8$, $CuC_8$, $NiC_8$, $CoC_{10}$, $NiC_{10}$ | Alkyl chains of every second molecule are fully interdigitating. | 2 | van der Waals interactions |
| Honeycomb: $CoC_{12}$, $NiC_{12}$ | Alkyl chains of each molecule are fully interdigitating. | 2 | Hydrogen bonds |

Regardless of the surface architecture and hence different metal ion patterning on the surface, both structures exhibit rather similar metal ion densities. The parallelogram-like assembly has a packing where the average metal ion coverage is ca. 0.52/nm$^2$, whereas in the honeycomb structure the value is ca. 0.48/nm$^2$ (values are estimated from a 5 nm × 5 nm area).

## Conclusions

STM studies of salophen complexes on liquid–graphite interfaces revealed new parallelogram-like and honeycomb structures. As demonstrated here, the alkyl chain length can have a significant influence in determining the assembly of the salophen complexes. Complexes bearing $C_8$ or $C_{10}$ alkyl chains assemble in the parallelogram-like 2D structure, while those with $C_{12}$ alkyl chains form the honeycomb assembly. The driving force for these new assemblies is a subtle interplay between a maximum amount of attractive van der Waals interactions of the alkyl chains and weak hydrogen bonding. Because of the ease of the methodology of SAM formation and the straightforward synthesis of salophen complexes, the SAMs of these compounds provide an attractive approach for the fine tuning of the surface architecture.

## Experimental Section

**General Methods and Materials:** $^1$H NMR spectra were recorded with a Varian Gemini 200 apparatus, and IR spectra were taken with a PerkinElmer Spectrum One. EI$^+$ and HRMS (ESI$^+$ TOF) mass spectra were recorded with a JEOL JMS-SX 102 (ionising voltage 70 eV) and with a Bruker micrOTOF mass spectrometer, respectively. Elemental analyses were performed with an EA 1110 CHNS-O CE instrument. For STM measurements, a low-current RHK scanning tunnelling microscope was used, which was operated in a constant-current mode under ambient conditions. STM tips were mechanically sharpened from Pt/Ir (80:20) wire, and HOPG was used as a substrate for the adlayers. The compounds

 © 2007 Wiley-VCH Verlag GmbH & Co. KGaA, Weinheim 

were dissolved in 1,2,4-trichlorobenzene, and a droplet of the saturated solution was placed on freshly cleaved HOPG. All chemicals required for complex synthesis were purchased from Aldrich and used as received. STM images were processed with WSxM©.

**Ligands:** 4-dodecyloxy-2-hydroxybenzaldehyde (**A**), 4-decyloxy-2-hydroxybenzaldehyde (**B**) and 4-octyloxy-2-hydroxybenzaldehyde (**C**) were prepared with moderate yields according to a procedure by Binnemans et al.[22]

***N,N′*-(*o*-Phenylene)bis(4-dodecyloxysalicylideneimine) (D):** (*o*-Phenylene)diamine (1.412 g, 13 mmol) in MeOH (20 mL) was added to compound **A** (8.005 g, 26 mmol) dissolved in *n*-hexane (20 mL). A yellow colour immediately appeared, and the solution was stirred at room temperature for 18 h. The viscous product obtained was stirred in MeOH for 2 h, and the yellow powder that was formed was filtered, washed with MeOH and finally dried in vacuo (isolated yield 7.156 g, 40%). Analytical data for $C_{44}H_{64}N_2O_4$: $^1$H NMR (200 MHz, $CDCl_3$, 25 °C, TMS): $\delta$ = 0.94 (t, $^3J_{H,H}$ = 7.0 Hz, 6 H, $CH_3$), 1.32 (s, 36 H, $CH_2$), 1.76–1.90 (m, 4 H, $CH_2$), 4.03 (t, $^3J_{H,H}$ = 6.7 Hz, 4 H, $OCH_2$), 6.51 (dd, $J_{H,H}$ = 2.4 Hz, $^3J_{H,H}$ = 8.5 Hz, 2 H, Ar-H), 6.58 (d, $^3J_{H,H}$ = 2.2 Hz, 2 H, Ar-H), 7.23–7.36 (m, 6 H, Ar-H), 8.58 (s, 2 H, HC=N) ppm. IR: $\tilde{\nu}$ = 1609 (C=N), 1583 (C=C), 1246 (C–O) cm$^{-1}$. HRMS (ESI-TOF): calcd. for $[M + H]^+$ 685.4939; found 685.4938; error 0.08 ppm.

Salophen ligands **E** and **F** were synthesised in the same manner as ligand **D**.

***N,N′*-(*o*-Phenylene)bis(4-decyloxysalicylideneimine) (E):** Yellow powder (isolated yield 31%). Analytical data for $C_{40}H_{56}N_2O_4$: $^1$H NMR (200 MHz, $CDCl_3$, 25 °C, TMS): $\delta$ = 0.89 (t, $^3J_{H,H}$ = 6.9 Hz, 6 H, $CH_3$), 1.28 (s, 28 H, $CH_2$), 1.71–1.85 (m, 4 H, $CH_2$), 3.98 (t, $^3J_{H,H}$ = 6.7 Hz, 4 H, $OCH_2$), 6.38 (dd, $J_{H,H}$ = 2.4 Hz, $^3J_{H,H}$ = 8.9 Hz, 2 H, Ar-H), 6.45 (d, $^3J_{H,H}$ = 2.3 Hz, 2 H, Ar-H), 7.18–7.31 (m, 6 H, Ar-H), 8.53 (s, 2 H, HC=N) ppm. IR: $\tilde{\nu}$ = 1608 (C=N), 1582 (C=C), 1240 (C–O) cm$^{-1}$. HRMS (ESI-TOF): calcd. for $[M + H]^+$ 629.4313; found 629.4330; error –2.66 ppm.

***N,N′*-(*o*-Phenylene)bis(4-octyloxysalicylideneimine) (F):** Yellow powder (isolated yield 56%). Analytical data for $C_{36}H_{48}N_2O_4$: $^1$H NMR (200 MHz, $CDCl_3$, 25 °C, TMS): $\delta$ = 0.89 (t, $^3J_{H,H}$ = 6.9 Hz, 6 H, $CH_3$), 1.30 (s, 20 H, $CH_2$), 1.72–1.85 (m, 4 H, $CH_2$), 3.98 (t, $^3J_{H,H}$ = 6.5 Hz, 4 H, $OCH_2$), 6.46 (dd, $J_{H,H}$ = 2.4 Hz, $^3J_{H,H}$ = 8.4 Hz, 2 H, Ar-H), 6.53 (d, $^3J_{H,H}$ = 2.0 Hz, 2 H, Ar-H), 7.18–7.31 (m, 6 H, Ar-H), 8.53 (s, 2 H, CH=N) ppm. IR: $\tilde{\nu}$ = 1608 (C=N), 1582 (C=C), 1240 (C–O) cm$^{-1}$. HRMS (ESI-TOF): calcd. for $[M + H]^+$ 573.3687; found 573.3701; error –2.44 ppm.

**Complexes:** Cobalt complexes were prepared under an Ar atmosphere by using standard Schlenk techniques. Copper and nickel complexes were synthesised under ambient conditions. Dry solvents were used in the preparation of cobalt complexes. Crude products of nickel and copper complexes were washed with MeOH and *n*-hexane, and they were finally recrystallised from $CHCl_3$ or $CH_2Cl_2$. Crude products of the cobalt complexes were washed with MeOH.

***N,N′*-(*o*-Phenylene)bis(4-dodecyloxysalicylideneiminato)copper(II) (1):** A warmed solution of $Cu(OOCCH_3)_2$ (0.133 g, 0.73 mmol) in MeOH (40 mL) was added to a solution of **D** (0.500 g, 0.74 mmol) in $CH_2Cl_2$ (10 mL). A brown suspension immediately formed and was stirred at room temperature for 20 h. A green precipitate was filtered and washed with MeOH and *n*-hexane. Finally the crude product was recrystallised from $CH_2Cl_2$, and the precipitate that formed was dried in vacuo. Complex **1** was obtained as a green powder (isolated yield 68%). $C_{44}H_{62}CuN_2O_4{\cdot}H_2O$ (746.5·$H_2O$): calcd. C 69.12, H 8.44, N 3.66; found C 69.41, H 8.57, N 3.72. IR: $\tilde{\nu}$ = 1610 (C=N), 1577 (C=C), 1244 (C–O) cm$^{-1}$. HRMS (ESI-TOF): calcd. for $[M + H]^+$ 746.4078; found 746.4070; error 1.18 ppm.

Complexes **2**–**6** were prepared similarly to **1**.

***N,N′*-(*o*-Phenylene)bis(4-decyloxysalicylideneiminato)copper(II) (2):** Green powder (isolated yield 57%). $C_{40}H_{54}CuN_2O_4{\cdot}2H_2O$ (690.4·2$H_2O$): calcd. C 66.13, H 8.05, N 3.86; found C 65.87, H 8.07, N 3.51. IR: $\tilde{\nu}$ = 1606 (C=N), 1578 (C=C), 1244 (C–O) cm$^{-1}$. HRMS (ESI-TOF): calcd. for $[M + H]^+$ 690.3452; found 690.3462; error –1.45 ppm.

***N,N′*-(*o*-Phenylene)bis(4-octyloxysalicylideneiminato)copper(II) (3):** Green powder (isolated yield 73%). $C_{36}H_{46}CuN_2O_4{\cdot}2H_2O$ (634.3·2$H_2O$): calcd. C 64.50, H 7.52, N 4.18; found C 65.06, H 7.61, N 3.66. IR: $\tilde{\nu}$ = 1604 (C=N), 1578 (C=C), 1239 (C–O) cm$^{-1}$. HRMS (ESI-TOF): calcd. for $[M + H]^+$ 634.2826; found 634.2821; error 0.81 ppm.

***N,N′*-(*o*-Phenylene)bis(4-dodecyloxysalicylideneiminato)nickel(II) (4):** Orange powder (isolated yield 57%). Analytical data for $C_{44}H_{62}N_2NiO_4$: $^1$H NMR (200 MHz, $CDCl_3$, 25 °C, TMS): $\delta$ = 0.88 (t, $^3J_{H,H}$ = 6.6 Hz, 6 H, $CH_3$), 1.27 (s, 36 H, $CH_2$), 1.70–1.85 (m, 4 H, $CH_2$), 3.95 (t, $^3J_{H,H}$ = 6.5 Hz, 4 H, $OCH_2$), 6.31 (dd, $J_{H,H}$ = 2.4 Hz, $^3J_{H,H}$ = 8.8 Hz, 2 H, Ar-H), 6.61 (d, $^3J_{H,H}$ = 2.0 Hz, 2 H, Ar-H), 7.13–7.21 (m, 4 H, Ar-H), 7.59–7.66 (m, 2 H, Ar-H), 8.06 (s, 2 H, HC=N) ppm. $C_{44}H_{62}N_2NiO_4{\cdot}H_2O$ (741.7·$H_2O$): calcd. C 69.56, H 8.49, N 3.69; found C 69.76, H 8.65, N 3.47. IR: $\tilde{\nu}$ = 1604 (C=N), 1575 (C=C), 1252 (C–O) cm$^{-1}$. HRMS (ESI-TOF): calcd. for $[M + H]^+$ 741.4136; found 741.4147; error –1.56 ppm.

***N,N′*-(*o*-Phenylene)bis(4-decyloxysalicylideneiminato)nickel(II) (5):** Reddish-orange powder (isolated yield 48%). Analytical data for $C_{40}H_{54}N_2NiO_4$: $^1$H NMR (200 MHz, $CDCl_3$, 25 °C, TMS): $\delta$ = 0.89 (t, $^3J_{H,H}$ = 6.9 Hz, 6 H, $CH_3$), 1.28 (s, 32 H, $CH_2$), 1.71–1.85 (m, 4 H, $CH_2$), 3.95 (t, $^3J_{H,H}$ = 6.6 Hz, 4 H, $OCH_2$), 6.30 (dd, $J_{H,H}$ = 2.3 Hz, $^3J_{H,H}$ = 8.8 Hz, 2 H, Ar-H), 6.60 (d, $^3J_{H,H}$ = 2.0 Hz, 2 H, Ar-H), 7.13–7.19 (m, 4 H, Ar-H), 7.58–7.67 (m, 2 H, Ar-H), 8.04 (s, 2 H, HC=N) ppm. $C_{40}H_{54}N_2NiO_4{\cdot}H_2O$ (685.6·$H_2O$): calcd. C 68.28, H 8.02, N 3.98; found C 68.65, H 7.95, N 3.71. IR: $\tilde{\nu}$ = 1603 (C=N), 1575 (C=C), 1250 (C–O) cm$^{-1}$. HRMS (ESI-TOF): calcd. for $[M + H]^+$ 685.3510; found 685.3518; error –1.18 ppm.

***N,N′*-(*o*-Phenylene)bis(4-octyloxysalicylideneiminato)nickel(II) (6):** Orange powder (isolated yield 37%). Analytical data for $C_{36}H_{46}N_2NiO_4$: $^1$H NMR (200 MHz, $CDCl_3$, 25 °C, TMS): $\delta$ = 0.90 (t, $^3J_{H,H}$ = 6.4 Hz, 6 H, $CH_3$), 1.30 (s, 20 H, $CH_2$), 1.71–1.85 (m, 4 H, $CH_2$), 3.95 (t, $^3J_{H,H}$ = 6.5 Hz, 4 H, $OCH_2$), 6.28 (d, $^3J_{H,H}$ = 8.6 Hz, 2 H, Ar-H), 6.59 (s, 2 H, Ar-H), 7.11–7.16 (m, 4 H, Ar-H), 7.59–7.64 (m, 2 H, Ar-H), 8.00 (s, 2 H, HC=N) ppm. $C_{36}H_{46}N_2NiO_4{\cdot}H_2O$ (629.5·$H_2O$): calcd. C 66.78, H 7.47, N 4.33; found: C 66.33, H 7.10, N 4.05. IR: $\tilde{\nu}$ = 1602 (C=N), 1574 (C=C), 1249 (C–O) cm$^{-1}$. HRMS (ESI-TOF): calcd. for $[M + H]^+$ 629.2884; found 629.2876; error 1.30 ppm.

In a typical procedure for $Co^{II}$ salophen complex synthesis, a solution of **D** (1.000 g, 1.46 mmol) in $CH_2Cl_2$ (5 mL) was added to a warm solution of $Co(OOCCH_3)_2{\cdot}4H_2O$ (0.482 g, 1.94 mmol) in MeOH (10 mL). A brown suspension immediately formed and was stirred for 4 h. The suspension was filtered, and the powder obtained was washed with MeOH. After drying in vacuo, the product was obtained as a dark brown powder.

***N,N′*-(*o*-Phenylene)bis(4-dodecyloxysalicylideneiminato)cobalt(II) (7):** Isolated yield 51%. $C_{44}H_{62}CoN_2O_4{\cdot}H_2O$ (741.9·$H_2O$): calcd. C 69.54, H 8.49, N 3.69; found C 69.58, H 8.79, N 3.39. IR: $\tilde{\nu}$ = 1606 (C=N), 1578 (C=C), 1240 (C–O) cm$^{-1}$. HRMS (ESI-TOF): calcd. for $[M]^+$ 741.4036; found 741.4037; error –0.10 ppm.

 © 2007 Wiley-VCH Verlag GmbH & Co. KGaA, Weinheim 

***N*,*N*′-(*o*-Phenylene)bis(4-decyloxysalicylideneiminato)cobalt(II) (8):** Isolated yield 68%. $C_{40}H_{54}CoN_2O_4 \cdot 2H_2O$ (685.8·$2H_2O$): calcd. C 66.56, H 8.10, N 3.88; found C 66.43, H 8.10, N 3.72. IR: $\tilde{\nu}$ = 1604 (C=N), 1577 (C=C), 1241 (C–O) $cm^{-1}$. HRMS (ESI-TOF): calcd. for $[M]^+$ 685.3410; found 685.3400; error 1.41 ppm.

***N*,*N*′-(*o*-Phenylene)bis(4-octyloxysalicylideneiminato)cobalt(II) (9):** Isolated yield 41%. $C_{36}H_{46}CoN_2O_4 \cdot H_2O$ (629.7·$H_2O$): C 66.76, H 7.47, N 4.32; found C 66.98, H 7.53, N 3.90. IR: $\tilde{\nu}$ = 1603 (C=N), 1579 (C=C), 1239 (C–O) $cm^{-1}$. HRMS (ESI-TOF): calcd. for $[M]^+$ 629.2790; found 629.2775; error 2.32 ppm.

**Supporting Information** (see footnote on the first page of this article): STM images of complexes **5**, **6**, **8** and **9**.

## Acknowledgments

We gratefully acknowledge the financial support of the Magnus Ehrnrooth Foundation, TEKES and Academy of Finland as well as the "Sonderforschungsbereich" SFB 569 ("Hierarchic structure formation and function of organic-inorganic nano systems") of the German Science Foundation DFG.

[1] a) A. Ulman, S. D. Evans, Y. Shnidman, R. Sharma, J. E. Eilers, J. C. Chang, *J. Am. Chem. Soc.* **1991**, *113*, 1499–1506; b) A. Ulman, J. F. Kang, Y. Shnidman, S. Liao, R. Jordan, G.-Y. Choi, J. Zaccaro, A. S. Myerson, M. Rafailovich, J. Sokolov, C. Fleischer, *Rev. Mol. Biotechnol.* **2000**, *74*, 175–188; c) G. C. Herdt, D. R. Jung, A. W. Czanderna, *Prog. Surf. Sci.* **1995**, *50*, 103–129.

[2] a) R. Izumi, K. Hayama, K. Hayashi, K. Toko, *Chem. Sens.* **2004**, *20*, 50–51; b) J. Ladd, C. Boozer, Q. Yu, S. Chen, J. Homola, S. Jiang, *Langmuir* **2004**, *20*, 8090–8095; c) S. Huan, G. Shen, R. Yu, *Electroanalysis* **2004**, *16*, 1019–1023; d) F. Maya, A. K. Flatt, M. P. Stewart, D. E. Shen, J. M. Tour, *Chem. Mater.* **2004**, *16*, 2987–2997.

[3] S. Flink, B. A. Boukamp, A. van den Berg, F. C. J. M. van Veggel, D. N. Reinhoudt, *J. Am. Chem. Soc.* **1998**, *120*, 4652–4657.

[4] G. A. Somorjai, *Chemistry in Two Dimensions: Surfaces*, Cornell University Press, Ithaca NY, **1981**.

[5] a) C. M. Whelan, M. Kinsella, H. M. Ho, K. Maex, *J. Electrochem. Soc.* **2004**, *151*, B33–B38; b) Z. Quan, S. Chen, X. Cui, Y. Li, *Corrosion (Houston, TX, U. S.)* **2002**, *58*, 248–256; c) S. Ramachandran, B.-L. Tsai, M. Blanco, H. Chen, Y. Tang, W. A. Goddard III, *Langmuir* **1996**, *12*, 6419–6428.

[6] Q. Zhang, L. A. Archer, *J. Phys. Chem. B* **2003**, *107*, 13123–13132.

[7] a) M. K. Chaudhury, G. M. Whitesides, *Science* **1992**, *255*, 1230–1232; b) R. K. Smith, P. A. Lewis, P. S. Weiss, *Prog. Surf. Sci.* **2004**, *75*, 1–68.

[8] a) C. D. Bain, G. M. Whitesides, *Angew. Chem. Int. Ed. Engl.* **1989**, *28*, 506–512; b) G. M. Whitesides, P. E. Laibinis, *Langmuir* **1990**, *6*, 87–96; c) P. E. Laibinis, R. G. Nuzzo, G. M. Whitesides, *J. Phys. Chem.* **1992**, *96*, 5097–5105.

[9] a) T. Ikeda, M. Asakawa, M. Goto, K. Miyake, T. Ishada, T. Shimizu, *Langmuir* **2004**, *20*, 5454–5459; b) P. Qian, H. Nanjo, N. Sanada, T. Yokoyama, T. M. Suzuki, *Chem. Lett.* **2000**, 1118–1119; c) I. Sakata, K. Miyamura, *Chem. Commun.* **2003**, 156–157; d) X. Qiu, C. Wang, Q. Zeng, B. Xu, S. Yin, H. Wang, S. Xu, C. Bai, *J. Am. Chem. Soc.* **2000**, *122*, 5550–5556; e) T. Ohshiro, T. Ito, P. Bühlmann, Y. Umezawa, *Anal. Chem.* **2001**, *73*, 878–883; f) P. Zell, F. Mögele, U. Ziener, B. Rieger, *Chem. Eur. J.* **2006**, *12*, 3847–3857; g) S. De Feyter, M. M. S. Abdel-Mottaleb, N. Schuurmans, B. J. V. Verkuijl, J. H. van Esch, B. L. Feringa, F. C. De Schryver, *Chem. Eur. J.* **2004**, *10*, 1124–1132.

[10] D. Yin, S. Horiuchi, M. Morita, A. Takahara, *Langmuir* **2005**, *21*, 9352–9358.

[11] a) M. S. Alam, S. Strömsdörfer, V. Dremov, P. Müller, J. Kortus, M. Ruben, J.-M. Lehn, *Angew. Chem. Int. Ed.* **2005**, *44*, 7896–7900; b) A. Semenov, J. P. Spatz, M. Möller, J.-M. Lehn, B. Sell, D. Schubert, C. H. Weidl, U. S. Schubert, *Angew. Chem. Int. Ed.* **1999**, *38*, 2547–2550; c) N. Lin, S. Stepanow, F. Vidal, K. Kern, M. S. Alam, S. Strömsdörfer, V. Dremov, P. Müller, A. Landa, M. Ruben, *Dalton Trans.* **2006**, 2794–2800; d) U. Ziener, J.-M. Lehn, A. Mourran, M. Möller, *Chem. Eur. J.* **2002**, *8*, 951–957.

[12] A. Mourran, U. Ziener, M. Möller, E. Breuning, M. Ohkita, J.-M. Lehn, *Eur. J. Inorg. Chem.* **2005**, 2641–2647.

[13] a) G. S. Hanan, D. Volkmer, U. S. Schubert, J.-M. Lehn, G. Baum, D. Fenske, *Angew. Chem. Int. Ed. Engl.* **1997**, *36*, 1842–1844; b) M. Ruben, E. Breuning, J.-P. Gisselbrecht, J.-M. Lehn, *Angew. Chem. Int. Ed.* **2000**, *39*, 4139–4142; c) E. Breuning, M. Ruben, J.-M. Lehn, F. Renz, Y. Garcia, V. Ksenofontov, P. Gütlich, E. Wegelius, K. Rissanen, *Angew. Chem. Int. Ed.* **2000**, *39*, 2504–2507; d) O. Waldmann, J. Hassmann, P. Müller, G. S. Hanan, D. Volkmer, U. S. Schubert, J.-M. Lehn, *Phys. Rev. Lett.* **1997**, *78*, 3390–3393; e) M. Ruben, J.-M. Lehn, G. Vaughan, *Chem. Commun.* **2003**, 1338–1339; f) M. Ruben, E. Breuning, J.-M. Lehn, V. Ksenofontov, F. Renz, P. Gütlich, G. B. M. Vaughan, *Chem. Eur. J.* **2003**, *9*, 4422–4429; g) M. Ruben, U. Ziener, J.-M. Lehn, V. Ksenofontov, P. Gütlich, G. B. M. Vaughan, *Chem. Eur. J.* **2005**, *11*, 94–100.

[14] B. A. Hermann, L. J. Scherer, C. E. Housecroft, E. C. Constable, *Adv. Funct. Mater.* **2006**, *16*, 221–235.

[15] a) M. Surin, P. Samorì, A. Jouaiti, N. Kyritsakan, M. W. Hosseini, *Angew. Chem. Int. Ed.* **2007**, *46*, 245–249; b) L. Pirondini, A. G. Stendardo, S. Geremia, M. Campagnolo, P. Samorì, J. P. Rabe, R. Fokkens, E. Dalcanale, *Angew. Chem. Int. Ed.* **2003**, *42*, 1384–1387; c) A. P. Seitsonen, M. Lingenfelder, H. Spillmann, A. Dmitriev, S. Stepanow, N. Lin, K. Kern, J. V. Barth, *J. Am. Chem. Soc.* **2006**, *128*, 5634–5635; d) S. Clair, S. Pons, S. Fabris, S. Baroni, H. Brune, K. Kern, J. V. Barth, *J. Phys. Chem. B* **2006**, *110*, 5627–5632; e) T. Classen, G. Fratesi, G. Costantini, S. Fabris, F. L. Stadler, C. Kim, S. de Gironcoli, S. Baroni, K. Kern, *Angew. Chem. Int. Ed.* **2005**, *44*, 6142–6145; f) S. Clair, S. Pons, H. Brune, K. Kern, J. V. Barth, *Angew. Chem. Int. Ed.* **2005**, *44*, 7294–7297; g) S. Stepanow, N. Lin, J. V. Barth, K. Kern, *J. Phys. Chem. B* **2006**, *110*, 23472–23477; h) A. Dmitriev, H. Spillmann, N. Lin, J. V. Barth, K. Kern, *Angew. Chem. Int. Ed.* **2003**, *42*, 2670–2673; i) H. Spillmann, A. Dmitriev, N. Lin, P. Messina, J. V. Barth, K. Kern, *J. Am. Chem. Soc.* **2003**, *125*, 10725–10725; j) S. Stepanow, N. Lin, J. V. Barth, K. Kern, *Chem. Commun.* **2006**, 2153–2155.

[16] Though solvent molecules can be coordinated to the axial positions of the metal centres in the 2D assemblies of the studied complexes, this is believed to have only a minor influence on the surface patterns created. Also, attempts at imaging the corresponding salen complexes and the salophen complexes with hexyloxy side chains were not successful. We therefore propose that in particular, salen complexes with $C_6$–$C_{12}$ chains, salophen complexes with $C_6$ chains and salophen ligands with alkyl chains shorter than 12 carbons are too mobile on HOPG for successful STM imaging. It has been previously reported that even if the molecules are easily adsorbed on the surface, high-resolution images may be difficult to obtain because of the mobility of the molecules within the basal plane. Also, the scanning tip may introduce a perturbation which would interfere with the imaging. [see ref.[9a,9c,9d]] and D. M. Cyr, B. Venkataraman, G. W. Flynn, *Chem. Mater.* **1996**, *8*, 1600–1615].

[17] C. L. Claypool, F. Faglioni, W. A. Goddard III, H. B. Gray, N. S. Lewis, R. A. Marcus, *J. Phys. Chem. B* **1997**, *101*, 5978–5995.

[18] a) G. R. Desiraju, *Chem. Commun.* **2005**, 2995–3001; b) C. Meier, U. Ziener, K. Landfester, P. Weihrich, *J. Phys. Chem. B* **2005**, *109*, 21015–21027.

[19] a) J. H. Chou, M. E. Kosal, H. S. Nalwa, N. A. Rakow, K. S. Suslick, *The Porphyrin Handbook*, Academic Press: New York,

 © 2007 Wiley-VCH Verlag GmbH & Co. KGaA, Weinheim 

**2000**, *6*, 43–131; b) A. Zlatkin, S. Yudin, J. Simon, M. Hanack, H. Lehmann, *Adv. Mater. Opt. Electron.* **1995**, *5*, 259–263; c) L. Scudiero, D. E. Barlow, K. W. Hipps, *J. Phys. Chem. B* **2002**, *106*, 996–1003.

[20] K. G. Nath, O. Ivasenko, J. A. Miwa, H. Dang, J. D. Wuest, A. Nanci, D. F. Perepichka, F. Rosei, *J. Am. Chem. Soc.* **2006**, *128*, 4212–4213.

[21] Cu complexes with $C_{10}$ and $C_{12}$ alkyl chains formed another new 2D pattern on the liquid–graphite interface. The only difference in these patterns is the periodicity in one of the directions which varies predictably with the alkyl chain length. Even though a high-resolution STM image was obtained for complex **2**, the resolution was still not high enough to allow us to propose a proper structural model.

[22] K. Binnemans, Y. G. Galyametdinov, R. Van Deun, D. W. Bruce, S. R. Collinson, A. P. Polishchuk, I. Bikchantaev, W. Haase, A. V. Prosvirin, L. Tinchurina, I. Litvinov, A. Gubajdullin, A. Rakhmatullin, K. Uytterhoeven, L. van Meervelt, *J. Am. Chem. Soc.* **2000**, *122*, 4335–4344.

Received: February 2, 2007
Published Online: July 6, 2007

 © 2007 Wiley-VCH Verlag GmbH & Co. KGaA, Weinheim 

DOI: 10.1002/ejic.200700266

# Ferrocenyl Oligo(phenylene-vinylene) Thiols for the Construction of Self-Assembled Monolayers

**Christian Amatore,*[a] Stephen Gazard,[a] Emmanuel Maisonhaute,[a] Cécile Pebay,[a] Bernd Schöllhorn,*[a] Jean-Laurent Syssa-Magalé,[a] and Jay Wadhawan[a]**

**Keywords:** Molecular wires / SAMs / Ferrocenes / Thiols / Redox chemistry / Self-assembly

A short and efficient preparation of conjugated oligo(phenylene-ethylene) thiols bearing redox-active ferrocene moieties is described. While minimising the number of synthetic steps, the proposed strategy permits the development of sets of oligomers with varying chain length. The redox properties of the compounds in solution are determined. Preliminary studies of self-assembled monolayers (SAMs) on gold electrodes are discussed, and indicate that electron transfer through the SAMs is indeed rapid.

(© Wiley-VCH Verlag GmbH & Co. KGaA, 69451 Weinheim, Germany, 2007)

## Introduction

There is growing interest in nanotechnologies for attaching and wiring conductive molecules onto surfaces for a wide series of applications. Electrochemical systems may be promising for developing, for example, molecular electronic devices,[1] efficient artificial photosynthetic systems,[2] organic liquid crystal light-emitting diodes[3] or biosensors. The use of self-assembly allows easy formation of monolayers of a redox-active species over an electrode by soaking an appropriate electrode surface in a nonaqueous solution of the suitably derivatised redox-active compound to enable it to tether to the surface. Typically, an electroactive moiety is located at one end of the molecule, whilst the grafting end is terminated by a Lewis base.[4] When using gold electrodes, such compounds often terminate with thiol moieties, owing to the exquisite affinity of sulfur groups for gold. This methodology is also highly attractive for electroanalytical sensors, as this method requires little preparative work, and furnishes a reagent-immobilised electrode relatively inexpensively. The attached compounds are able to carry electrons back and forth from the electrode to redox enzymes.

In this context, the investigation of electron transfer through molecular bridges has revealed that the rates usually decrease exponentially as the distance to the electrode decreases. The attenuation factor is typically 10 $nm^{-1}$ (i.e., 1 $Å^{-1}$) for alkyl bridges, a value that may be too high for fast signal processing over long distances. Recent contributions by the groups of Chidsey,[5] Creager[6] and Finklea[7] illustrate the tendency to use conjugated bridges because π-delocalisation increases the coupling between the redox probe and the electrode. For this reason conjugated π-systems are potentially the most adapted and most promising molecular wires, assuring fast electron transfer kinetics over distances up to 20 Å and longer. Hitherto, oligo(*p*-phenylene-*trans*-vinylene) chains have exhibited the fastest electron transfer rates of all investigated systems.[5] Ferrocene has been used in various studies as a convenient electroactive centre showing fast and reversible one-electron oxidation. Furthermore, ferrocenes may act as a local molecular switch as their Cp/Cp conduction (Cp = cyclopentadienyl ligand) is poor in the reduced state and effective in the ferricinium cations. It is thus important to develop rapid and efficient access for sets of ferrocenyl oligo(phenylene-ethylene) thiols with varying chain length. Our synthetic strategy described herein also permits the insertion of additional ferrocenyl groups into the bridge itself and thus the building of more complex structures leading eventually to more sophisticated signal processing functions such as field-effect transistors. We wish to report here the rapid access to a set of three ferrocenyl oligo(*p*-phenylene-*trans*-vinylene) derivatives, **1**, **2** and **3**, bearing a mercaptomethyl group on the terminating phenyl ring. The peculiar electrochemical properties of **3** will also be described.

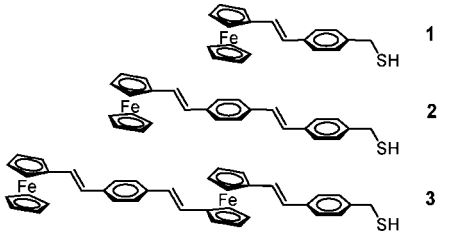


[a] Ecole Normale Supérieure, Département de Chimie, UMR CNRS 8640 "PASTEUR", Université Pierre et Marie Curie-Paris 6,
24 rue Lhomond, 75231 Paris cedex 05, France
Fax: +33-144-32-38-63
E-mail: christian.amatore@ens.fr

 © 2007 Wiley-VCH Verlag GmbH & Co. KGaA, Weinheim 

## Results and Discussion

Two main approaches are commonly used in the synthesis of free thiol derivatives: either the use of a protective group or the late introduction of the thiol group as a final step so as to avoid interferences during the earlier synthetic steps. In the case of benzyl derivatives, a possible approach involves masking a hydroxy group by an aldehyde, which, after reduction to the corresponding primary alcohol, can be converted in several steps to the desired thiol. Compounds **1** and **2** have been prepared in this way.[8] As an alternative, we opted for the late introduction of a thioester group. We chose the *S*-protected 4-iodobenzylthiol **4**, as this useful building block significantly reduces the number of synthetic steps. In a more convergent approach, **4a** can be easily obtained by treatment of 4-iodobenzyl bromide with sodium thioacetate.[9] As an alternative route, we tried to exploit the 4-iodobenzyl alcohol as a starting material, thus favouring the direct conversion of the generally more stable and readily available alcohol into the corresponding thioester without any preceding halogenation. The Mitsunobu reaction of 4-iodobenzyl alcohol with thioacetic acid affords **4a** in only low yield (30%) (Scheme 1). Hughes and Reamer[10] showed evidence for improved yields in the Mitsunobu esterification of alcohols in the presence of acids stronger than acetic acid. Accordingly, we employed thiobenzoic acid instead of thioacetic acid so that, under the same conditions, the thiobenzoic acid ester **4b** is obtained in high yield (95%).

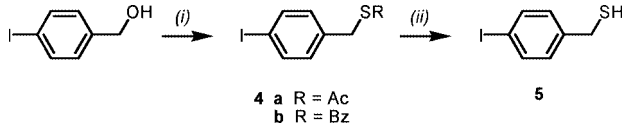


Scheme 1. Synthesis of the precursors **4a** and **4b**: (i) AcSH (for **4a**), BzSH (for **4b**), $PPh_3$, DEAD, THF, 0 °C; (ii) $LiAlH_4$, THF, 0 °C.

The thiobenzoates **6b** and **7b** are also formed in satisfactory yields (84 and 63%) from the respective hydroxymethyl derivatives **6a** and **7a**. The reaction of alcohol **8a** to the thioacetate **8b**[8] shows a low yield (20%) compared to the thiobenzoate **8c** (75%), confirming the observed tendency. All of the thiobenzoic acid esters discussed above were successfully converted into the respective free thiols **5**, **6c**, **7c** and **1** through reduction with sodium borohydride (Scheme 1). Both of the building blocks **4a** and **4b** were employed in the following syntheses leading to the target compounds **1**, **2** and **3**.

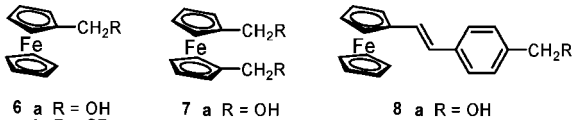


The preparation of the short ferrocenyl-vinylene-phenylene thiol **1** was achieved in only two steps. The Heck coupling of **4b** with vinylferrocene afforded thiobenzoate **8c** directly (Scheme 2). The subsequent reduction of the latter compound with sodium borohydride in a mixture of methanol and tetrahydrofuran afforded the desired free thiol (88%). The use of lithium aluminium hydride (LAH) as a reducing agent gave thiol **1** in only a 46% yield. Even with an excess of LAH, the aldehyde **9** was isolated as an unexpected sideproduct. Whilst the analytical characterisation data of **9** are consistent with previously published data for this compound,[11] it is important to note that in contrast to the earlier work, we also prepared compound **9** by Heck reaction of vinylferrocene with 4-iodobenzaldehyde, thus unambiguously identifying the structure of **9**.

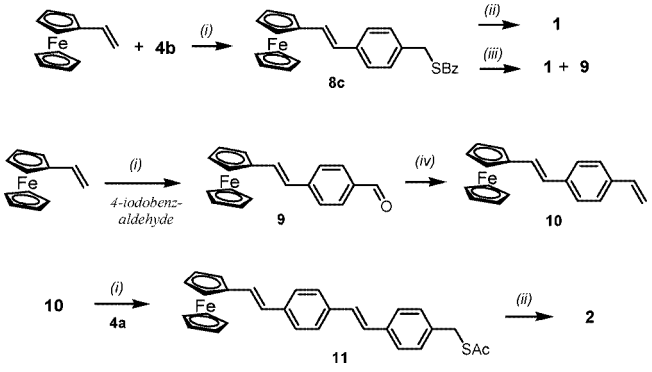


Scheme 2. Synthesis of compounds **1** and **2**: (i) $Pd(OAc)_2$, $P(Tol)_3$, tributylamine, dimethylacetamide; (ii) $NaBH_4$, THF, MeOH, 0 °C; (iii) $LiAlH_4$, THF, 0 °C.

Access to the ferrocene thiol **2** is achieved in only 3 steps starting from aldehyde **9** (Scheme 2). The Heck coupling of the olefin **10** and **4a** leads directly to the thioacetate **11**, which was subsequently converted into the free thiol **2** through reduction with lithium aluminium hydride.

Taking into account our previous results, we performed the synthesis of the bis(ferrocenyl) thiol **3** in only 6 steps involving Heck coupling, standard methyl Wittig conversion and a final reduction (Scheme 3). Our synthetic strategy is based on the monofunctionalisation of 1,1′-ferrocenedicarbaldehyde leading, in two steps, to the key intermediate **13**. The methyl Wittig conversion of ferrocenedicarbaldehyde in dioxane allows for its selective monoolefination. Upon using the less polar tetrahydrofuran as a solvent, the reaction is faster (TLC analysis) but less selective, indicative of a strong kinetic control depending on the solvent polarity. In the following Heck reaction of **12** with a twofold excess of 1,4-diiodobenzene, the monoiodo derivative **13** was obtained as the major product. Only small amounts of the symmetric bis(ferrocenyl) derivative **17** (2%) are isolated. Inversion of the molar ratio of the starting compounds should afford this potential precursor of a tris(ferrocenyl) derivative in reasonable yields. An alternative, but longer and less efficient, synthesis of **13** involving a protective group is described in the literature.[12,13] A second Heck reaction of compound **13** with vinylferrocene affords the dissymmetric bis(ferrocenyl) monocarbaldehyde **14**. The

 © 2007 Wiley-VCH Verlag GmbH & Co. KGaA, Weinheim 

$R_f$ values of starting material **13** and product **14** are very similar, and it is difficult to monitor the reaction by TLC. In order to obtain a complete conversion, a higher temperature has to be maintained during the reaction. The relatively low yield (53%) is probably due to a competitive degradation of either starting material or product under these conditions. A methyl Wittig conversion of **14** leads to the corresponding vinyl derivative **15**. This highly conjugated and relatively apolar compound displays low solubility in solvents such as diethyl ether or chloroform. The use of dichloromethane is necessary for the purification steps in the workup following the reaction. Unreacted starting compound **14** was recovered and the reaction repeated in order to improve the total yield to 60%. The thiobenzoate **16** was obtained by a third Heck reaction of **15** with **4b**. In the final step, **16** is reduced with sodium borohydride to the target compound **3**. The use of LAH as a reducing agent considerably lowers the yield and affords the aldehyde **18** as a side product, like in the reduction of **8c**.

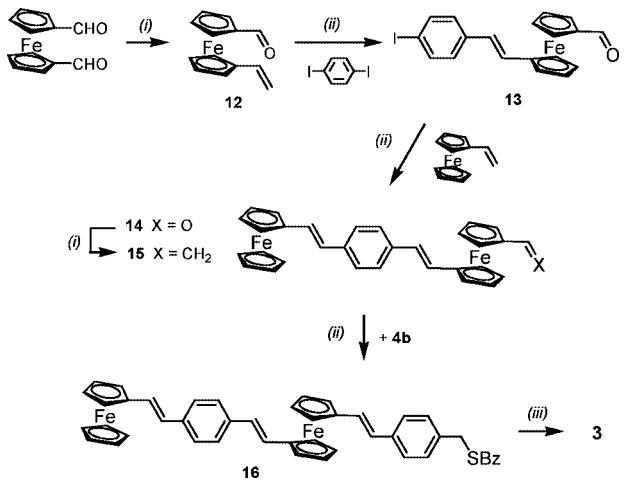


Scheme 3. Synthesis of compound **3**: (i) methyltriphenylphosphonium bromide, *tert*-butoxide, dioxane/water; (ii) $Pd(OAc)_2$, $P(Tol)_3$, tributylamine, dimethylacetamide; (iii) $NaBH_4$, THF, MeOH, 0 °C.

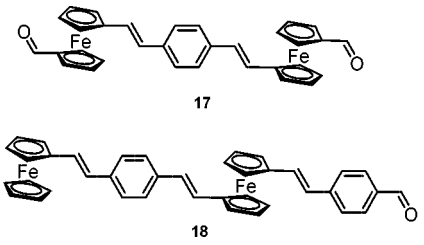


## Exploring the Electron Transfer Properties of the Ferrocene-Based Compounds in Homogeneous Solution

We resorted to cyclic voltammetry to explore the electrochemical properties of **1**, **2**, **3**, **14**, **16** and **17**. Owing to the low solubility of some of the compounds in conventional electrochemical solvents, investigations were undertaken in dichloromethane with tetrabutylammonium tetrafluoroborate ($TBABF_4$) at 0.1 M concentration as the supporting electrolyte. In a preliminary study, we checked that **1** and **2**, bearing a single redox centre, behave similarly to ferrocene. Each gave a monoelectronic reversible wave whose current intensity was proportional to $v^{1/2}$, where $v$ is the scan rate. This is typical of a diffusive behaviour. The average of the forward and backward peak currents allows evaluation of a standard potential of $(0.55 \pm 0.01)$ V versus SCE for **1** and $(0.54 \pm 0.01)$ V versus SCE for **2**. Figure 1a depicts a cyclic voltammogram at a scan rate of 200 $mV\,s^{-1}$ of a 0.38 mM solution of **14** at a glassy carbon electrode. This bis(ferrocenyl) monocarbonyl species gives rise to two apparently reversible waves centred at $E°_1 = (0.54 \pm 0.01)$ V versus SCE and $(0.81 \pm 0.01)$ V versus SCE, both waves being of the same height. Given that the first wave occurs at the same potential as that of the nonderivatised ferrocene, we infer that this wave represents the one-electron oxidation of the ferrocene moiety within the conjugated chain to yield the corresponding ferricinium cation. The second wave is related to oxidation of the terminal ferrocenyl group bearing an electron-withdrawing substituent.

Conversely, the voltammetry of the thiobenzoate **16** (cf. Figure 1b) reveals a single oxidation wave, despite the presence of two redox centres. Complex **16** is a larger molecule

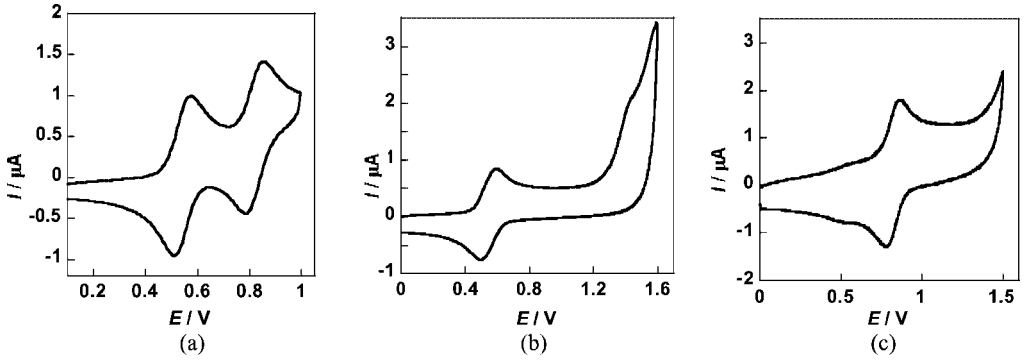


Figure 1. Cyclic voltammogram of (a) **14** ($3.8 \times 10^{-4}$ M), (b) **16** ($2.5 \times 10^{-4}$ M), (c) **17** ($2.7 \times 10^{-4}$ M) in dichloromethane containing 0.1 M $TBABF_4$ at a scan rate of 0.2 $V\,s^{-1}$.

 © 2007 Wiley-VCH Verlag GmbH & Co. KGaA, Weinheim 

than **14**, so that its diffusion coefficient is necessarily smaller. Hence, we infer from the peak current intensities that two electrons are involved in the oxidation. Unfortunately, free thiol **3** adsorbs slightly even onto a carbon electrode, which prevents its full characterisation in solution. However, a single wave was also observed. This unusual behaviour may seem counterintuitive as the electrostatic repulsion should destabilise the dication and thus raise the potential of the second oxidation. In fact, such behaviour has already been observed by Launay et al. for polyvinylferrocenes,[14] and by Saveant et al. for carotenoids.[15] These authors proposed a rationalisation of this effect. As the monocationic species are in a mixed-valence state, the charge is delocalised inside the large volume defined between both redox centres, so that the solvation is necessarily weak. Conversely, in the dication, because of coulombic repulsion, the charges are localised onto the two redox centres, thus minimising the electrostatic repulsion and also allowing a much stronger stabilisation by the solvent. In some cases, this effect may balance the electrostatic repulsion and may result in a potential inversion. A single two-electron process then occurs, being thermodynamically and kinetically controlled by the first electron transfer. This effect corresponds with previous observations by Amatore and Kochi, revealing that for common aromatic compounds, there is a linear correlation between the standard potential $E°_1$ and the ionisation potential IP [Equation (1)],[16] where $0 < \mu < 1$ and $C^{te}$ is a constant depending on the reference electrode:

$$E° \approx \mu IP + C^{te} \quad (1)$$

Here, $\mu$ reflects how the variations in IP are transmitted to $E°$; $\mu = 1$ would mean that any variation in IP is fully reflected in the condensed phase. In this study, the electroactive moieties were normally solvated and $\mu = 0.71$ was obtained; $(1 - \mu)$ reflects the effects of solvation. For the monocation, the charge is only poorly solvated, so that $\mu$ should be close to 1 so that [Equation (2)]:

$$E°_1 \approx IP + C^{te} \quad (2)$$

Conversely, in the dication, the charges are normally solvated, so that in a very approximate model [Equation (3)], where $\Delta E_{coul}$ is the electrostatic contribution, we can evaluate that:

$$E°_2 - E°_1 \approx -2(1 - \mu)IP + \Delta E_{coul} \quad (3)$$

This formulation leads to [Equation (4)]:

$$E°_2 \approx (2\mu - 1)IP + \Delta E_{coul} + C^{te} \quad (4)$$

We can then predict that there is a potential inversion when [Equation (5)]:

$$IP > \Delta E_{coul}/(2 - 2\mu) \quad (5)$$

If the compound is dissymmetrical (for example **14**), another term, $\Delta E_{chim}$, should be added to Equation (2), taking into account the different chemical nature of both electroactive moieties. Agreeing with this analysis, the voltammetry of **17**, which is totally symmetrical, also reveals a single peak (cf. Figure 1c). The weak signal around 0.55 V may be attributed to an impurity in the crude product **17**.

In Figure 1b a second wave is observed as a shoulder on the medium discharge, reflecting an oxidative degradation of compound **16**, probably due to the irreversible thiobenzoate oxidation.

The electrochemical behaviour of **3** while attached to a gold electrode will be described elsewhere.[17] As a preliminary result, Figure 2 illustrates typical cyclic voltammograms for **3**, coadsorbed with diphenyl disulfide or pentanethiol diluents. A single two-electron wave is still observed as anticipated. Although the scan rate is high (cf. Figure 2b), the relatively low peak-to-peak potential difference confirms that electron transfer inside this molecule is indeed very fast.

## Conclusions

A particularly short and efficient preparation of conjugated oligo(phenylene-ethylene) thiols bearing redox-active ferrocene moieties is described. The proposed strategy to introduce the sulfur group by Heck reaction of a vinyl group with the key synthone **4** readily yields a set of oligomers with varying chain length in only 2 (compound **1**) or 4

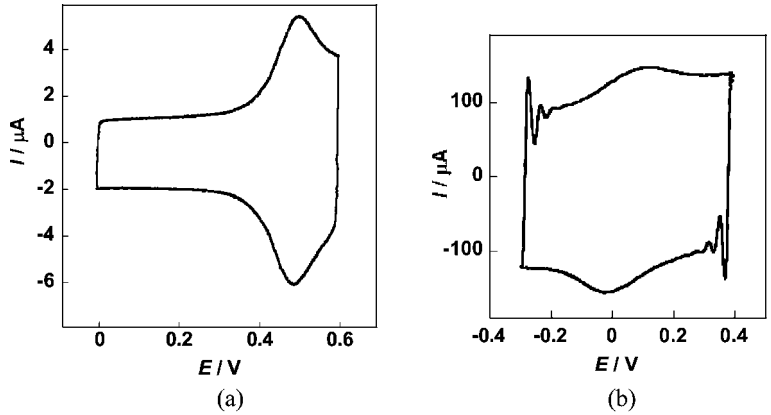


Figure 2. Cyclic voltammogram in 1 M perchloric acid of **3** coadsorbed (a) with pentanethiol onto a 111 gold single-crystal electrode, scan rate: 12 $V s^{-1}$; (b) with diphenyl disulfide onto a gold ball ultramicroelectrode, scan rate: 220000 $V s^{-1}$.

 © 2007 Wiley-VCH Verlag GmbH & Co. KGaA, Weinheim 

synthetic steps (compound **2**). The preparation of the thioesters by Mitsunobu reaction of benzyl alcohol was improved by replacing thioacedic acid with thiobenzoic acid. The additional insertion of ferrocenyl units into the conjugated bridge can be easily achieved by the use of 1′-vinylferrocene-1-carbaldehyde (**12**), a key intermediate in the synthesis of the bis(ferrocenyl) derivative **3**. For the bis(ferrocenyl) derivatives, the nature of the second side chain attached to the second ferrocene species may have a significant effect on the redox thermodynamics, leading to an inverted series of electrode potentials, causing a single two-electron wave to occur. The ultrafast cyclic voltammetry of **1**, **2** and **3** when they are adsorbed onto gold electrodes confirms that these compounds are indeed very efficient molecular wires. A full kinetic analysis of electrochemical results for monolayers of these compounds will be published elsewhere.[17]

## Experimental Section

**General:** All reactions were performed with previously dried solvents under argon, if not stated otherwise. The compounds ferrocene, ferrocenemonocarbaldehyde, ferrocenylmethanol (**6a**) and ferrocene-1,1′-diyldimethanol (**7a**) were bought from Sigma/Aldrich (France). The commercially available vinylferrocene was obtained in larger quantities from ferrocenemonocarbaldehyde in a Wittig reaction with methyltriphenylphosphonium bromide. Ferrocene-1,1′-dicarbaldehyde was prepared from freshly sublimed ferrocene.[18] Thin layer chromatography (TLC) was performed on aluminium sheets precoated with 60 $F_{254}$ silica gel. Preparative flash column chromatography was performed on silica gel 60 (0.040–0.063 mm, Merck). $^1H$ and $^{13}C$ NMR spectra were recorded with a Bruker AC 250 or a Bruker DRX 400 spectrometer. Chemical shifts are reported using the deuterated ($^{13}C$ NMR) or the residual monoprotonated ($^1H$ NMR) solvent signals as reference, based on the values published by Gottlieb and Nudelman.[19] Mass spectra were recorded with a Jeol JMS-700 spectrometer and UV/Vis spectra with a Beckman DU 7400 spectrophotometer. Elemental analyses were conducted at the University of Pierre and Marie Curie (Paris, Jussieu, France) or the Centre Nationale de Recherche Scientifique (Gif-sur-Yvette, France).

**Electrochemistry:** The electrochemical experiments in dichloromethane were conducted in an air-tight, three-electrode glass cell, controlled by a commercially available computer-controlled potentiostat (AUTOLAB PGSTAT 30, Eco Chemie, the Netherlands). A platinum wire and an aqueous saturated calomel electrode (SCE) were used as a counter and a reference electrode, respectively. The reference electrode was kept in a side arm separated from the electrochemical cell by a porous frit. The side arm was filled with the solvent/supporting electrolyte solution. A glassy carbon disk electrode, having a disk radius of 0.5 mm, was used as the working electrode. The working electrode was polished prior to each experiment on successively finer grades of carborundum paper (P1200 down to P4000), and then using a 0.3 μM aqueous alumina slurry on a wetted, napped polishing cloth. The supporting electrolyte employed was a 0.1 M solution of tetrabutylammonium tetrafluoroborate ($TBAF_4$) in dichloromethane (distilled from barium oxide). $TBABF_4$ had been recrystallised and dried at 70 °C for at least 24 h before use. Prior to experimentation, argon gas was bubbled into the electrolyte solution to remove oxygen, and was flushed over the cell solution during the electrochemical measurements. Cyclic voltammograms (CV) were recorded at room temperature [(22 ± 1) °C] and at a potential sweep rate of 0.2 $V s^{-1}$. To form self-assembled monolayers, we left gold electrodes to bathe for one night in a mixture of **1** and pentanethiol or **1** and diphenyl disulfide in chloroform. Either a 111 Au single crystal or a gold ball ultramicroelectrode (made by melting a 10 μm diameter wire in a blue flame)[17] were used. Cyclic voltammograms were then recorded in $H_2O$ + 1 M $HClO_4$. For Figure 2b, a home-built potentiostat allowing scan rates up to 2.5 $MV s^{-1}$ was used.[20,21] A full analysis of the electrochemical behaviour of self-assembled monolayers will be described elsewhere.

**Synthesis**

**4-[(*E*)-2-Ferrocenylvinyl]benzylthiol (1). (a)** A solution of **8b** (45 mg, 0.12 mmol) in tetrahydrofuran (THF) (2 mL) was chilled with a water/ice bath. A 1 M solution of lithium aluminium hydride (LAH) in diethyl ether (0.24 mL, 0.24 mmol) was added slowly. The reaction mixture was stirred at room temperature for 30–60 min, and the reaction progress was monitored by thin layer chromatography (TLC). The mixture was neutralised with 1 M hydrochloric acid, and extracted with dichloromethane. The organic phase was washed with water, brine and then dried with magnesium sulfate. Purification by chromatography (silica gel, dichloromethane/petroleum ether using a solvent gradient of 20:80 to 50:50) yielded **1** as a red solid (39 mg, 97%). **(b) 8c** (45 mg, 0.10 mmol) was dissolved in a mixture of methanol (2 mL) and tetrahydrofuran (1 mL). Sodium borohydride (8 mg, 0.21 mmol) was added. The reaction mixture was stirred at room temperature for 12 h, and the reaction progress was monitored by TLC. The mixture was neutralised with 1 M hydrochloric acid, and extracted with dichloromethane. The organic phase was washed with water, brine and then dried with magnesium sulfate. Purification by chromatography (silica gel, dichloromethane/petroleum ether using a solvent gradient of 20:80 to 50:50) yielded **1** as a red solid (32 mg, 93%). **(c)** Compound **1** (10 mg, yield 47%) was prepared from **8c** (28 mg, 0.064 mmol) and lithium aluminium hydride as described. Compound **9** was found to be a sideproduct (7.4 mg, yield 36%).

**Compound 1:** $^1H$ NMR ($CDCl_3$, 250 MHz): $\delta$ = 7.39 (d, $J$ = 8.2 Hz, 2 H, aromatic), 7.28 (d, $J$ = 8.2 Hz, 2 H, aromatic), 6.86 (d, $J$ = 16 Hz, 1 H, vinyl), 6.67 (d, $J$ = 16 Hz, 1 H, vinyl), 4.46 (t, $J$ = 1.7 Hz, 2 H, Cp), 4.28 (t, $J$ = 1.7 Hz, 2 H, Cp), 4.13 (s, 5 H, unsubstituted Cp), 3.74 (d, $J$ = 7.4 Hz, 2 H, $CH_2$), 1.76 (t, $J$ = 7.4 Hz, 1 H, SH) ppm. $^{13}C$ NMR ($CDCl_3$, 400 MHz): $\delta$ = 139.6, 136.8, 128.3, 127.0, 126.0, 125.5, 69.2, 69.1, 66.8, 28.8 ppm. MS ($CI^+$, $NH_3$): $m/z$ (%) = 335 (95) [M + 1], 303 (100). HRMS ($CI^+$, $CH_4$): calcd. for $[C_{19}H_{19}FeS]^+$ 335.0551; found 335.0546. UV ($CH_3Cl$): $\lambda$ ($\varepsilon$) = 456 (908) nm (br.).

**4-[(*E*)-2-{4-[(*E*)-2-Ferrocenylvinyl]phenyl}vinyl]benzylthiol (2):** Compound **2** (74 mg, yield 71%) was prepared from **11** (114 mg, 0.24 mmol) and lithium aluminium hydride as described for the preparation of **1** (procedure a). $^1H$ NMR ($CDCl_3$, 250 MHz): $\delta$ = 7.45–7.19 (m, 10 H, aromatic, vinyl), 6.83 (d, $J$ = 16 Hz, 1 H, vinyl), 6.62 (d, $J$ = 16 Hz, 1 H, vinyl), 4.42 (d, $J$ = 2.7 Hz, 2 H, Cp), 4.23 (d, $J$ = 2.7 Hz, 2 H, Cp), 4.08 (s, 5 H, unsubstituted Cp), 3.68 (d, $J$ = 7.5 Hz, 2 H, $CH_2$), 1.60 (t, $J$ = 7.5 Hz, 1 H, SH) ppm. MS ($CI^+$, $CH_4$): $m/z$ (%) = 437 (50) [M + 1], 405 (100). HRMS ($CI^+$, $CH_4$): calcd. for $[C_{27}H_{25}FeS]^+$ 437.1021; found 437.1024.

**4-[(*E*)-2-{1′-[(*E*)-2-{4-[(*E*)-2-Ferrocenylvinyl]phenyl}vinyl]ferrocen-1-yl}vinyl]benzylthiol (3). (a)** Compound **3** (14 mg, yield 81%) was prepared from **16** (20 mg, 0.026 mmol) and sodium borohydride as described for the preparation of **1** (procedure b). Compound **16** is soluble in dichloromethane, whereas its solubility is very low in diethyl ether. Chromatography (silica gel; dichloromethane/petro-

 © 2007 Wiley-VCH Verlag GmbH & Co. KGaA, Weinheim 

leum ether gradient of 20:80 to 40:60) to yield pure compound **3**. **(b)** Compound **3** (7 mg, yield 46%) was prepared from **16** (18 mg, 0.023 mmol) and lithium aluminium hydride as described for the preparation of **1** (procedure a). Aldehyde **18** was isolated as a side-product {MS (CI; $NH_3$): *m*/*z* (%) = 648 (37) [M + 1], 631 (33), 613 (100)}.

**Compound 3:** $^1$H NMR ($CD_2Cl_2$, 400 MHz): $\delta$ = 7.25 (m, 6 H, aromatic), 7.14 (m, 2 H, aromatic), 6.88 (d, *J* = 16Hz, 1 H, vinyl), 6.76 (d, *J* = 16 Hz, 1 H, vinyl), 6.73 (d, *J* = 16 Hz, 1 H, vinyl), 6.68 (d, *J* = 16 Hz, 1 H, vinyl), 6.61 (d, *J* = 16 Hz, 1 H, vinyl), 6.59 (d, *J* = 16 Hz, 1 H, vinyl), 4.48 (t, *J* = 1.8 Hz, 2 H, Cp), 4.42 (m, 4 H, Cp), 4.28 (t, *J* = 1.8 Hz, 2 H, Cp), 4.25 (m, 4 H, Cp), 4.13 (s, 5 H, unsubst. Cp), 3.68 (m, 2 H, $CH_2$), 0.88 (t, *J* = 7.6 Hz, 1 H, SH) ppm. MS ($CI^+$, $NH_3$): *m*/*z* (%) = 647 (100) [M + 1], 615 (65). HRMS ($FAB^+$, $NH_3$): calcd. for $[C_{39}H_{35}FeS]^+$ 647.1153; found 647.1157. UV ($CH_3Cl$): $\lambda$ ($\varepsilon$) = 463 (4311) nm (br.).

***S*-(4-Iodobenzyl) Thioacetate (4a):** A solution of 4-iodobenzyl alcohol (200 mg, 0.85 mmol), triphenylphosphane (448 mg, 1.71 mmol) and thioacetic acid (122 μL, 1.71 mmol) in tetrahydrofuran (3.5 mL) was cooled to 0 °C, and diethyl diazodicarboxylate (298 mg, 1.71 mmol, 40% mixture in toluene) was added dropwise. The reaction mixture was stirred for 12 h. Diethyl ether was added and the organic phase was washed with aqueous sodium hydrogen carbonate solution, water and brine and then dried with magnesium sulfate. After evaporation of the solvent, the residue was purified by column chromatography (silica gel; 40% dichloromethane in petroleum ether) to yield **4a** as a colourless oil (72 mg, 29%). $^1$H NMR ($CDCl_3$, 250 MHz): $\delta$ = 7.62 (d, *J* = 8.3 Hz, 2 H, aromatic) 7.03 (d, *J* = 8.3 Hz, 2 H, aromatic), 4.04 (s, 2 H, $CH_2$), 2.35 (s, 3 H, $CH_3$) ppm.

***S*-(4-Iodobenzyl) Thiobenzoate (4b):** A solution of 4-iodobenzyl alcohol (200 mg, 0.85 mmol), triphenylphosphane (448 mg, 1.71 mmol) and thiobenzoic acid (222 μL) in tetrahydrofuran (3.5 mL) was cooled to 0 °C, and diethyl diazodicarboxylate (298 mg, 1.71 mmol, 40% mixture in toluene) was added dropwise. The reaction mixture was stirred for 4–12 h (TLC control). Diethyl ether was added and the organic phase was washed with aqueous sodium hydrogen carbonate solution, water and brine and then dried with magnesium sulfate. After evaporation of the solvent, the residue was purified by column chromatography (silica gel; 40% dichloromethane in petroleum ether) to yield **4b** as a colourless oil (287 mg, 95%). $^1$H NMR ($CDCl_3$, 250 MHz): $\delta$ = 7.95 (d, 2 H, *J* = 7.4 Hz, aromatic), 7.63 (d, 2 H, *J* = 8.2 Hz, aromatic), 7.58 (t, 1 H, *J* = 7.4 Hz, aromatic), 7.44 (t, 2 H, *J* = 7.4 Hz, aromatic), 7.12 (d, 2 H, *J* = 8.2 Hz, aromatic), 4.24 (s, 2 H, $CH_2$) ppm. $^{13}$C NMR ($CDCl_3$, 250 MHz): $\delta$ = 191.0, 137.7, 137.4, 136.7, 133.6, 130.9, 128.7, 127.3, 32.8 ppm. MS ($CI^+$, $NH_3$): *m*/*z* (%) = 372 (100) [M + $NH_4$], 355 (8) [M + 1], 246 (33) [M – I + $NH_4$]. $C_{14}H_{11}IOS$ (354.21): calcd. C 47.47, H 3.13; found C 47.40, H 3.13.

**(4-Iodophenyl)methanethiol (5):** Compound **5** (32 mg, yield 91%) was prepared from **4b** (50 mg, 0.14 mmol) and sodium borohydride as described for the preparation of **1** (procedure b). $^1$H NMR ($CDCl_3$, 250 MHz): $\delta$ = 7.64 (d, *J* = 8.2 Hz, 2 H, aromatic), 6.96 (d, *J* = 8.2 Hz, 2 H), 3.54 (s, 2 H, $CH_2$), 1.85 (s, 1 H, SH) ppm.

***S*-(Ferrocenylmethyl) Thiobenzoate (6b):** Compound **6b** (208 mg, yield 84%) was prepared from ferrocenylmethanol **6a** (159 mg, 0.74 mmol) and thiobenzoic acid as described for the preparation of **4b**. $^1$H NMR ($CDCl_3$, 250 MHz): $\delta$ = 7.93 (d, *J* = 7.4 Hz, 2 H, aromatic), 7.54 (t, *J* = 7.4 Hz, 1 H, aromatic), 7.41 (t, *J* = 7.4 Hz, 2 H, aromatic), 4.33 (m, 2 H, Cp), 4.26 (m, 2 H, Cp), 4.22 (s, 5 H, Cp), 4.13 (s, 2 H, $CH_2$) ppm.

**Compound 7b:** Compound **7b** (194 mg, yield 63%) was prepared from **7a** (156 mg, 0.63 mmol) and thiobenzoic acid as described for the preparation of **4b**. $^1$H NMR ($CDCl_3$, 250 MHz): $\delta$ = 7.96 (d, *J* = 7.4 Hz, 4 H, aromatic), 7.56 (m, 2 H, aromatic), 7.44 (m, 4 H, aromatic), 4.27 (s, 4 H, Cp), 4.18 (s, 4 H, Cp), 4.15 (s, 4 H, $CH_2$) ppm. MS ($CI^+$, $NH_3$): *m*/*z* (%) = 504 (62) [M + $NH_4$], 349 (96), 213 (100).

**{4-[(*E*)-2-Ferrocenevinyl]phenyl}methanol (8a):** Compound **8a** (436 mg, yield 85%) was prepared from **9** (510 mg, 1.61 mmol) and sodium borohydride as described for the preparation of **1** (procedure b). Chromatography (silica gel; dichloromethane) yielded a red-orange solid. $^1$H NMR ($CDCl_3$, 250 MHz): $\delta$ = 7.44 (d, *J* = 8.1 Hz, 2 H, aromatic), 7.33 (d, *J* = 8.1 Hz, 2 H, aromatic), 6.89 (d, *J* = 16.1 Hz, 1 H, vinyl), 6.69 (d, *J* = 16.1 Hz, 1 H, vinyl), 4.68 (d, *J* = 5 Hz, 2 H, $CH_2$), 4.47 (s, 2 H, Cp), 4.29 (s, 2 H, Cp), 4.14 (s, 5 H, unsubstituted Cp), 1.61 (t, *J* = 5 Hz, 1 H, OH) ppm.

**S-{4-[(*E*)-2-Ferrocenylvinyl]benzyl} Thioacetate (8b):** Compound **8b** (78 mg, yield 22%), a red solid, was prepared from **8a** (300 mg, 0.94 mmol) and thioacetic acid as described for the preparation of **4a**. Chromatography: silica gel; dichloromethane/petroleum ether, 40:60 v/v. $^1$H NMR ($CDCl_3$, 250 MHz): $\delta$ = 7.36 (d, *J* = 8.2 Hz, 2 H, aromatic), 7.24 (d, *J* = 8.2 Hz, 2 H, aromatic), 6.85 (d, *J* = 16.1 Hz, 1 H, vinyl), 6.66 (d, *J* = 16.1 Hz, 1 H, vinyl), 4.45 (t, *J* = 1.6 Hz, 2 H, Cp), 4.29 (t, *J* = 1.6 Hz, 2 H, Cp), 4.13 (s, 5 H, unsubstituted Cp), 4.11 (s, 2 H, $CH_2$), 2.35 (s, 3 H, $CH_3$) ppm. The $^1$H NMR data described in the literature[8] confirms the above data.

***S*-{4-[(*E*)-2-Ferrocenylvinyl]benzyl} Thiobenzoate (8c):** A solution of vinylferrocene (106 mg, 0.50 mmol), **4b** (176 mg, 0.50 mmol), palladium acetate (11 mg, 0.014 mmol) and tributylamine (180 μL, 0.75 mmol) in *N*,*N*-dimethylacetamide (10 mL) was stirred at room temperature for 1 h. Tri(*ortho*-tolyl)phosphane (3 mg, 0.01 mmol) was added. After 3 h of stirring at room temperature, the reaction mixture was heated at 100 °C for 12 h. After extraction with diethyl ether, the organic phase was washed with 1 M hydrochloric acid, water, brine and then dried with magnesium sulfate. After evaporation of the solvent, the residue was purified by column chromatography (silica gel; 50% dichloromethane in petroleum ether) to yield **8c** (138 mg, 63%). $^1$H NMR ($CDCl_3$, 250 MHz): $\delta$ = 7.97 (d, *J* = 7.2 Hz, 2 H, aromatic), 7.31–7.57 (m, 7 H, aromatic), 6.85 (d, *J* = 16 Hz, 1 H, vinyl), 6.66 (d, *J* = 16 Hz, 1 H, vinyl), 4.46 (m, 2 H, Cp), 4.31 (s, 2 H, $CH_2$), 4.28 (m, 2 H, Cp), 4.12 (s, 5 H, unsubstituted Cp) ppm. $^{13}$C NMR ($CDCl_3$, 250 MHz): $\delta$ = 185.0, 133.4, 129.3, 128.6, 127.3, 127.1, 126.0, 125.5, 69.2, 69.1, 66.9, 33.3 ppm. MS ($CI^+$, $NH_3$): *m*/*z* (%) = 456 (12) [M + $NH_4$], 439 [17] [M + 1], 303 (100).

**{4-[(*E*)-2-Ferrocenevinyl]phenyl}carbaldehyde (9):** Compound **9** (406 mg, yield 56%) was prepared from vinylferrocene (486 mg, 2.30 mmol) and 4-iodobenzaldehyde (532 mg, 2.29 mmol) as described for the preparation of **8c**. $^1$H NMR ($CDCl_3$, 250 MHz): $\delta$ = 9.98 (s, 1 H, CHO), 7.84 (d, *J* = 8.2 Hz, 2 H, aromatic), 7.56 (d, *J* = 8.2 Hz, 2 H, aromatic), 7.08 (d, *J* = 16.1 Hz, 1 H, vinyl), 6.72 (d, *J* = 16.1 Hz, 1 H, vinyl), 4.52 (s, 2 H, Cp), 4.36 (s, 2 H, Cp), 4.16 (s, 5 H, unsubstituted Cp) ppm. $^{13}$C NMR ($CDCl_3$, 250 MHz): $\delta$ = 191.6, 131.5, 130.3, 126.0, 124.6, 69.8, 69.5, 69.4, 67.4 ppm. MS ($CI^+$, $NH_3$): *m*/*z* (%) = 317 (100) [M + 1].

**4-[(*E*)-2-Ferrocenylvinyl]styrene (10):** Compound **10** (301 mg, yield 86%) was prepared from aldehyde **9** (352 mg, 1.11 mmol) as described for the preparation of **12**. $^1$H NMR ($CDCl_3$, 250 MHz): $\delta$ = 7.40 (s, 4 H, aromatic), 6.88 (d, *J* = 16.2 Hz, 1 H, vinyl), 6.70 (dd, *J* = 16.2, 10.7 Hz, 1 H, vinyl), 6.67 (d, *J* = 16.2 Hz, 1 H, vinyl), 5.75 (d, *J* = 17.5 Hz, 1 H, vinyl), 5.22 (d, *J* = 10.7 Hz, 1 H, vinyl),

 © 2007 Wiley-VCH Verlag GmbH & Co. KGaA, Weinheim 

4.46 (t, *J* = 1.6 Hz, 2 H, Cp), 4.3 (m, 2 H, Cp), 4.15 (s, 5 H, Cp) ppm.

***S*-{4-[(*E*)-2-{1′-[(*E*)-2-{4-[(*E*)-2-Ferrocenylvinyl]phenyl}vinyl]-ferrocen-1-yl}vinyl]benzyl} Thioacetate (11):** Compound **11** (152 mg, yield 83%) was prepared from **10** (120 mg, 0.38 mmol) and **4a** (233 mg, 0.80 mmol) as described for the preparation of **8c**. $^1$H NMR ($CDCl_3$, 250 MHz): $\delta$ = 7.45 (m, 8 H, aromatic), 7.20 (2d, *J* = 17 Hz, 2 H, vinyl), 6.85 (2d, *J* = 16.1 Hz, 2 H, vinyl), 4.65 (s, 2 H, $CH_2$) 4.45 (d, *J* = 2.67 Hz, 2 H, Cp), 4.30 (d, *J* = 1.6 Hz, 2 H, Cp), 4.15 (s, 5 H, unsubstituted Cp), 3.95 (s, 3 H, $CH_3$) ppm. The $^1$H NMR data described in the literature[8] confirms the above data. MS ($CI^+$, $NH_3$): *m*/*z* (%) = 479 (20) [M + 1], 295 (100). MS ($FAB^+$): *m*/*z* (%) = 478 (10) [M], 295 (100).

**1′-Vinylferrocene-1-carbaldehyde (12):** A solution of ferrocene-1,1′-dicarbaldehyde (0.849 g, 3.51 mmol) and methyltriphenylphosphonium bromide (1.25 g, 3.51 mmol) in dioxane (20 mL) was treated with potassium *tert*-butoxide (0.39 g, 3.5 mmol) and water (100 μL). After stirring at room temperature for 3 h, the reaction mixture was extracted with diethyl ether. The organic phase was washed with water and dried with magnesium sulfate. Purification by chromatography (silica gel; dichloromethane) yielded **12** as a brown oil (0.37 g, 44%). $^1$H NMR ($CDCl_3$, 250 MHz): $\delta$ = 9.88 (s, 1 H, CHO), 6.37 (dd, *J* = 17.5, 10.7 Hz, 1 H, vinyl), 5.40 (d, *J* = 17.5 Hz, 1 H, vinyl), 5.14 (d, *J* = 10.7 Hz, 1 H), 4.72 (s, 2 H, Cp), 4.54 (s, 2 H, Cp), 4.51 (s, 2 H, Cp), 4.31 (s, 2 H, Cp) ppm. MS ($CI^+$, $NH_3$): *m*/*z* (%) = 241 (100) [M + 1], 215 (12), 124 (7).

**1′-[(*E*)-2-(4-Iodophenyl)vinyl]ferrocene-1-carbaldehyde (13):** Compound **13** (276 mg, 57%) was prepared from **12** (271 mg, 1.1 mmol) and 1,4-diiodobenzene (0.74 g, 2.3 mmol), as described for the preparation of **8c**. However, the reaction mixture was not heated but stirred at room temperature for 3 d (chromatography: silica gel; dichloromethane). $^1$H NMR ($CDCl_3$, 400 MHz): $\delta$ = 9.90 (s, 1 H, CHO), 7.65 (d, *J* = 8.4 Hz, 2 H, aromatic), 7.17 (d, *J* = 8.4 Hz, 2 H, aromatic), 6.76 (d, *J* = 16.2 Hz, 1 H, vinyl), 6.63 (d, *J* = 16.2 Hz, 1 H, vinyl), 4.76 (t, *J* = 1.9 Hz, 2 H, Cp), 4.55 (multiplet, *J* = 1.9 Hz, 4 H, Cp), 4.38 (t, *J* = 1.9 Hz, 2 H, Cp) ppm. MS ($CI^+$, $NH_3$): *m*/*z* (%) = 443 (100) [M + 1], 317 (33). Only a small amount of the symmetrical bis(ferrocene) dicarbaldehyde **17** was isolated (12 mg, 2%). $^1$H NMR ($CDCl_3$, 250 MHz): $\delta$ = 9.90 (s, 2 H, CHO), 7.42 (s, 4 H, aromatic), 6.67 (s, 2 H, vinyl), 6.66 (s, 2 H, vinyl), 4.77 (t, *J* = 1.8 Hz, 4 H, Cp), 4.57 (m, 8 H, Cp), 4.39 (t, *J* = 1.8 Hz, 4 H, Cp) ppm. $^{13}$C NMR ($CDCl_3$, 250 MHz): $\delta$ = 193.8, 136.4, 127.8, 126.4, 124.8, 85.5, 79.9, 74.4, 70.7, 70.5, 68.2 ppm. MS ($CI^+$, $CH_4$): *m*/*z* (%) = 455 (15) [M + 1], 241 (100).

**1′-[(*E*)-2-{4-[(*E*)-2-Ferrocenylvinyl]phenyl}vinyl]ferrocene-1-carbaldehyde (14):** Compound **14** (180 mg, 55%) was prepared from **13** (276 mg, 0.63 mmol) and vinylferrocene (265 mg, 1.25 mmol) as described for the preparation of **8c** (chromatography: silica gel; dichloromethane/petroleum ether, 40:60 v/v). $^1$H NMR ($CDCl_3$, 250 MHz): $\delta$ = 9.91 (s, 1 H, CHO), 7.40 (s, 4 H, aromatic), 6.90 (d, *J* = 16 Hz, 1 H, vinyl), 6.72 (s, 2 H, vinyl), 6.66 (d, *J* = 16 Hz, 1 H, vinyl), 4.76 (t, *J* = 1.8 Hz, 2 H, Cp), 4.57 (t, *J* = 1.6 Hz, 4 H, Cp), 4.47 (t, *J* = 1.5 Hz, 2 H, Cp), 4.38 (t, *J* = 1.7 Hz, 2 H, Cp), 4.29 (t, *J* = 1.5 Hz, 2 H, Cp), 4.14 (s, 5 H, unsubstituted Cp) ppm. MS ($CI^+$, $CH_4$): *m*/*z* (%) = 527 (100) [M + 1], 391 (12), 345 (12), 317 (30), 279 (27). $C_{31}H_{26}Fe_2O$ (526.32): calcd. C 70.75, H 4.98; found C 69.78, H 4.87.

**1′-[(*E*)-2-{4-[(*E*)-2-Ferrocenylvinyl]phenyl}vinyl]-1-vinylferrocene (15):** A solution of **14** (127 mg, 0.20 mmol) and methyltriphenylphosphonium bromide (90 mg, 0.25 mmol) in dioxane (3 mL) was treated with potassium *tert*-butoxide (28 mg, 0.25 mmol) and the mixture stirred at room temperature for 12 h (TLC control). The reaction mixture was extracted with dichloromethane. The organic phase was washed with water and dried with magnesium sulfate. After evaporation of the solvent, the brown solid residue was purified by column chromatography (silica gel; dichloromethane/petroleum ether, 35:65 v/v) to yield **15** (56 mg, 44%). Repetition of the experiment with the recovered starting material afforded another 37 mg of **15**, increasing the total yield to 64%. $^1$H NMR ($CDCl_3$, 250 MHz): $\delta$ = 7.4 (s, 4 H, aromatic), 6.9 (d, *J* = 16 Hz, 1 H, vinyl), 6.81 (d, *J* = 16 Hz, 1 H, vinyl), 6.68 (d, *J* = 16 Hz, 1 H, vinyl), 6.64 (d, *J* = 16 Hz, 1 H, vinyl), 6.38 (dd, *J* = 17.5, 10.7 Hz, 1 H, C*H*=$CH_2$), 5.24 (d, *J* = 17.5 Hz, 1 H, CH=C$H_2$), 5.0 (d, *J* = 10.7 Hz, 1 H, CH=C$H_2$), 4.47 (t, *J* = 1.3 Hz, 2 H, Cp), 4.39 (t, *J* = 1.6 Hz, 2 H, Cp), 4.30 (t, *J* = 2.3 Hz, 4 H, Cp), 4.23 (t, *J* = 1.7 Hz, 2 H, Cp), 4.19 (t, *J* = 1.6 Hz, 2 H, Cp), 4.14 (s, 5 H, Cp) ppm. MS ($CI^+$, $NH_3$): *m*/*z* (%) = 525 (100) [M + 1], 391 (5), 315 (7).

***S*-{4-[(*E*)-2-{1′-[(*E*)-2-{4-[(*E*)-2-Ferrocenylvinyl]phenyl}vinyl]-ferrocen-1-yl}vinyl]benzyl} Thiobenzoate (16):** Compound **16** (24 mg, 91%) was prepared from **15** (22 mg, 0.035 mmol) and **4b** (30 mg, 0.084 mmol) as described for the preparation of **8c** (chromatography: silica gel; 50% dichloromethane in petroleum ether). $^1$H NMR ($CD_2Cl_2$, 400 MHz): $\delta$ = 7.99 (dd, *J* = 7.1, 1.4 Hz, 2 H, aromatic), 7.58 (tt, *J* = 7.4, 1.4 Hz, 1 H, aromatic), 7.45 (m, 2 H, aromatic), 7.29 (aromatic, *J* = 8.3 Hz, 2 H, d), 7.23 (s, 4 H, aromatic), 7.21 (aromatic, *J* = 8.3 Hz, 2 H, d), 6.9 (d, *J* = 16 Hz, 1 H, vinyl), 6.75 (d, *J* = 16 Hz, 2 H, vinyl), 6.68 (d, *J* = 16 Hz, 1 H, vinyl), 6.60 (d, *J* = 16 Hz, 2 H, vinyl), 4.47 (t, *J* = 1.8 Hz, 2 H, Cp), 4.41 (t, *J* = 1.8 Hz, 4 H Cp), 4.29 (s, 2 H, $CH_2$), 4.27 (t, *J* = 1.8 Hz, 2 H, Cp), 4.25 (t, *J* = 1.8 Hz, 4 H, Cp), 4.12 (s, 5 H, Cp) ppm. MS (CI+, $CH_4$): *m*/*z* (%) = 751 (62) [M + 1], 242 (100), 186 (40). HRMS ($CI^+$, $NH_3$): calcd. for $[C_{46}H_{39}Fe_2OS]^+$ 751.1415; found 751.1412.

## Acknowledgments

This work was supported by the CNRS, the Ecole Normale Supérieure, the Universite Pierre et Marie Curie and the French Ministry of Research (ACI Nanosciences-Nanotechnologies). J. W. gratefully thanks The Leverhulme Trust, London, UK for financial support through a postdoctoral studentship (GR/N SAS/30105). We gratefully thank Prof. Juan Feliu and Dr. Victor Climent (University of Alicante) for providing a 111 Au single crystal.

[1] a) J. Chen, M. A. Reed, A. M. Rawlett, J. Tow, *Science* **1999**, *286*, 1550; b) L. A. Bumm, J. J. Arnold, M. T. Cygan, T. D. Dunbar, T. P. Burgin, L. Jones, D. L. Allara, J. M. Tow, P. S. Weiss, *Science* **1996**, *271*, 1705; c) R. J. Forster, T. E. Keyes, J. G. Vos, *Interfacial Supramolecular Assemblies*, Wiley-VCH, Weinheim, **2003**.

[2] a) M. R. Wasielewski, *Chem. Rev.* **1992**, *92*, 435; b) A. F. Collings, C. Critchley, *Artificial Photosynthesis*, Wiley-VCH, Weinheim, **2005**.

[3] a) J. H. Burroughs, D. D. C. Bradley, A. R. Brown, R. N. Marks, K. Mackay, R. H. Friend, P. L. Burns, A. B. Holmes, *Nature* **1990**, *347*, 539; b) M. O'Neill, S. M. Kelly, *Adv. Mater.* **2003**, *15*, 1135.

[4] H. O. Finklea in *Electroanalytical Chemistry* (Eds.: A. J. Bard, I. Rubenstein), Marcel Dekker, New York, **1996**, vol. 19, pp. 109–335.

[5] H. D. Sikes, J. F. Smalley, S. P. Dudek, A. R. Cook, M. D. Newton, C. E. D. Chidsey, S. W. Feldberg, *Science* **2001**, *291*, 1519; D. B. Robinson, C. E. D. Chidsey, *J. Phys. Chem. B* **2002**, *106*, 10706.

 © 2007 Wiley-VCH Verlag GmbH & Co. KGaA, Weinheim 

[6] S. Creager, C. J. Yu, C. Bamdad, S. O'Conner, T. MacLean, E. Lam, Y. Chong, G. T. Olsen, J. Y. Luo, M. Gozin, J. F. Kayyem, *J. Am. Chem. Soc.* **1999**, *121*, 1059.
[7] a) H. O. Finklea, M. S. Ravenscroft, D. A. Snider, *Langmuir* **1993**, *9*, 223; b) H. O. Finklea, M. S. Ravenscroft, *J. Phys. Chem.* **1994**, *98*, 3843; c) H. O. Finklea, L. Liu, M. S. Ravenscroft, S. Punturi, *J. Phys. Chem.* **1996**, *100*, 18852; d) D. A. Brevnov, H. O. Finklea, H. van Ryswyk, *J. Electroanal. Chem.* **2001**, *500*, 100; e) M. D. Newton, *Chem. Rev.* **1991**, *91*, 767.
[8] S. P. Dudek, H. D. Sikes, C. E. D. Chidsey, *J. Am. Chem. Soc.* **2001**, *123*, 8033–8038.
[9] D. T. Gryko, C. Clausen, K. M. Roth, N. Dontha, D. F. Bocian, W. G. Kuhr, J. S. Lindsey, *J. Org. Chem.* **2000**, *65*, 7345–7355.
[10] D. L. Hughes, R. A. Reamer, *J. Org. Chem.* **1996**, *61*, 2967–2971; see refs therein.
[11] A. J. Moore, A. Chesney, M. R. Bryce, A. S. Batsanov, J. F. Kelly, J. A. K. Howard, I. F. Perepichka, D. F. Perepichka, G. Meshulam, G. Berkovic, Z. Kotler, R. Mazor, V. Khodorkovsky, *Eur. J. Org. Chem.* **2001**, 2671–2687.
[12] J.-G. Rodriguez, S. Pleite, *J. Organomet. Chem.* **2001**, *637–639*, 230–239.
[13] G. Iftime, C. Moreau-Bossuet, E. Manoury, G. G. A. Balavoine, *Chem. Commun.* **1996**, 527–528.
[14] A. Hradsky, B. Bildstein, N. Schuler, H. Schottenberger, J. Jaitner, K. H. Ongania, K. Wurst, J. P. Launay, *Organometallics* **1997**, *16*, 392.
[15] P. Hapiot, L. D. Kispert, V. V. Konovalov, J. M. Saveant, *J. Am. Chem. Soc.* **2001**, *123*, 6669.
[16] J. O. Howell, J. M. Goncalves, C. Amatore, L. Klasinc, R. M. Wightman, J. K. Kochi, *J. Am. Chem. Soc.* **1984**, *106*, 3968–3976.
[17] C. Amatore, E. Maisonhaute, B. Schöllhorn, J. Wadhawan, *ChemPhysChem* **2007**, *8*, 1321–1329.
[18] G. G. A. Balavoine, G. Doisneau, T. Fillebeen-Khan, *J. Organomet. Chem.* **1991**, *412*, 381–382; U. T. Mueller-Westerhoff, Z. Yang, G. Ingram, *J. Organomet. Chem.* **1993**, *463*, 163–167.
[19] H. E. Gottlieb, V. Kotlyar, A. Nudelman, *J. Org. Chem.* **1997**, *62*, 7512–7515.
[20] C. Amatore, E. Maisonhaute, G. Simonneau, *J. Electroanal. Chem.* **2000**, *486*, 141–155.
[21] C. Amatore, E. Maisonhaute, G. Simonneau, *Electrochem. Commun.* **2000**, *2*, 81–84.

Received: March 7, 2007
Published Online: July 11, 2007

 © 2007 Wiley-VCH Verlag GmbH & Co. KGaA, Weinheim 

DOI: 10.1002/ejic.200700262

# Mu-35: A Fluorogallophosphate Obtained by In Situ Generation of the Template

**Louwanda Lakiss,[a] Angélique Simon-Masseron,*[a] Florence Porcher,[b] Séverinne Rigolet,[a] and Joël Patarin[a]**

**Keywords:** Fluorine / Gallophosphate / Structure elucidation / Hydrothermal synthesis

A two-dimensional microporous fluorogallophosphate, named Mu-35, closely related to ULM-8, was hydrothermally synthesized by in situ generation of the structure-directing agent. The precursor of the structure-directing agent is ethylformamide, which is generated in situ by decomposition, and goes on to form ethylamine molecules that act as templates in the medium used for the synthesis. The fluorogallophosphate Mu-35 (Mu is Mulhouse), $Ga_3(PO_4)_2(HPO_4)F_3(C_2H_8N)_2$-$(C_2H_7N)_{0.5}$ ($Z$ = 8), crystallizes in the orthorhombic space group *Pbcn* with the following unit cell parameters: $a$ = 22.117(1), $b$ = 17.3740(8), $c$ = 10.1550(4) Å. The structure of fluorogallophosphate Mu-35 was determined from single-crystal XRD data. It exhibits anionic layers composed of an unusual arrangement of three-, five-, and eight-membered rings (MR) [$Ga_2PO_2F$, $Ga_3P_2O_4F$, and $Ga_3P_3O_8$, respectively], and intercalated by protonated and nonprotonated ethylamine molecules. Mu-35 was also characterized by powder XRD, SEM, elemental and thermal analyses, and solid-state NMR spectroscopy ($^1$H, $^{13}$C, $^{19}$F, and $^{31}$P MAS and $^1$H-$^{31}$P HETCOR experiments).
(© Wiley-VCH Verlag GmbH & Co. KGaA, 69451 Weinheim, Germany, 2007)

## Introduction

In the last years, the search for new microporous materials has attracted special interest due to their potential uses as molecular sieves, heterogeneous catalysts, or ion exchangers.[1] After the discovery of the aluminophosphates by Wilson et al.,[2] research in the field of microporous phosphates was extended to different metals. The substitution of aluminium by other metals (Zn, Ga, etc.) has been reported. Among these materials, gallophosphates have attracted special attention; they allow a wide variety of structures to be formed owing to the gallium atoms, which can adopt four-, five-, and six-coordinations. Moreover the use of fluorine in the starting mixture enabled us to investigate new systems.[3] By introducing fluorine in the medium used for the synthesis, numerous fluorogallophosphates were obtained[4–5] such as cloverite, which is molecular sieves that contain a large 3D pore channel system.[6] In most cases, $F^-$ was found to be present in the inorganic framework as terminal Ga–F groups, bridging gallium atoms, or trapped into small building units such as the so-called double four rings (D4R units). In this case, it seems that fluorine, besides its mineralizing role, plays a templating role and stabilizes these units.[5–8] A large number of metallophosphates with 0D, 1D, 2D, or 3D frameworks have been reported.[3–15] One way to obtain new materials is to exploit the in situ generation of the structure-directing agent. By this synthetic route, solvent or precursors of the templates are introduced into the starting mixtures, and during the synthesis, they partly decompose into molecules that act as templates. Few applications of such a synthetic technique have been reported; for instance, the in situ generation of structure-directing agents from 1,5-diaminopentane,[16] guanidinium cations,[17–19] piperazine,[20] dichloride of benzylviologen,[21] or urea derivatives.[22,23] In 1998, a new type of template precursor (i.e. alkylformamide molecules) was tested in the laboratory. Thus, it was possible to produce the two-layered aluminophosphates Mu-4[9] and Mu-7[10] and, more recently, the gallophosphates MIL30,[11] Mu-30,[12] Ea-TREN-GaPO,[13] Mu-33,[14] and Mu-34.[15]

In this paper, we report the synthesis, the structure determination, and the characterization of a new porous 2D fluorogallophosphate named Mu-35 that was obtained by using ethylformamide (EFD) as a precursor of ethylamine, which acts as the structure-directing agent (SDA).

## Results and Discussion

### Synthesis and Crystal Morphology

The results concerning the synthesis of fluorogallophosphate Mu-35 are summarized in Table 1. The fluoro-

[a] Laboratoire de Matériaux à Porosité Contrôlée, UMR CNRS 7016, Université de Haute Alsace, ENSCMu,
3 rue Alfred Werner, 68093 Mulhouse Cedex, France
Fax: +33-3-89336885
E-mail: Angelique.Simon-Masseron@uha.fr
[b] Laboratoire de Cristallographie et Modélisation des Matériaux Minéraux et Biologiques UMR CNRS 7036, Faculté des Sciences, Université Henri Poincaré Nancy 1,
B. P. 239, 54506 Vandoeuvre-lès-Nancy Cedex, France
Supporting information for this article is available on the WWW under http://www.eurjic.org or from the author.

 © 2007 Wiley-VCH Verlag GmbH & Co. KGaA, Weinheim 

Table 1. Syntheses performed in the system $GaOOH/H_3PO_4/HF/ethylformamide$ (EFD)/tripropylamine (TPA)/$H_2O$.

| Sample (Heating time, d) | Molar composition of the starting mixture | | | | | | | XRD results |
|---|---|---|---|---|---|---|---|---|
| | GaOOH | $H_3PO_4$ | HF | EFD | $H_2O$ | TPA | $T$ [°C] | |
| **A** (7) | 1 | 2 | 2 | 6 | 5.8[a] | – | 170 | Mu-35 |
| **B** (7) | 1 | 2 | – | 6 | 5.8[a] | – | 170 | $GaPO_4$-$C_4$ |
| **C** (7) | 1 | 2 | 2 | 6 | 5.8[a] | – | 200 | Phase A + impurity[b] |
| **D** (4) | 1 | 2 | 2 | 6 | 5.8[a] | – | 130 | Phase B[c] |
| **E** (4) | 2 | 2 | 2 | 2 | 80 | – | 170 | Quartz |
| **F** (4) | 2 | 2 | 2 | 2 | 16.3 | 1 | 170 | Mu-35[d] |

[a] $H_2O$ arising from orthophosphoric (85% $H_3PO_4$) and hydrofluoric acid (40% HF). [b] Unknown phase. [c] Structure in progress. [d] Impurity eliminated by ultrasound.

gallophosphate Mu-35 was first prepared as white powder in a fluorine quasinonaqueous medium with a Ga/P molar ratio equal to 0.5 (sample A). The presence of fluorine is crucial as the $GaPO_4$-$C_4$[24] crystallizes when fluorine is not present in the mixture (sample B). A change in the heating temperature (samples A, C, and D) influences the nature of the crystallized phase. For a similar starting molar composition, but with a higher heating temperature (200 °C, sample C), a nonidentified phase (phase A) with traces of an impurity crystallizes. Moreover, for a lower heating temperature (130 °C, sample D), another phase, namely phase B, was obtained. Experiments were also performed in aqueous medium. In a diluted medium (sample E, 80 $H_2O$) a quartz-type gallophosphate was obtained, whereas in a more concentrated medium (sample F, 16.3 $H_2O$) large crystals of Mu-35 suitable for single crystal XRD determination were formed.

As shown in Figure 1, the crystals of the fluorogallophosphate Mu-35-sample A and Mu-35-sample F display rectangular shapes, with average sizes of $150 \times 20$ and $150 \times 30$ μm$^2$, respectively.

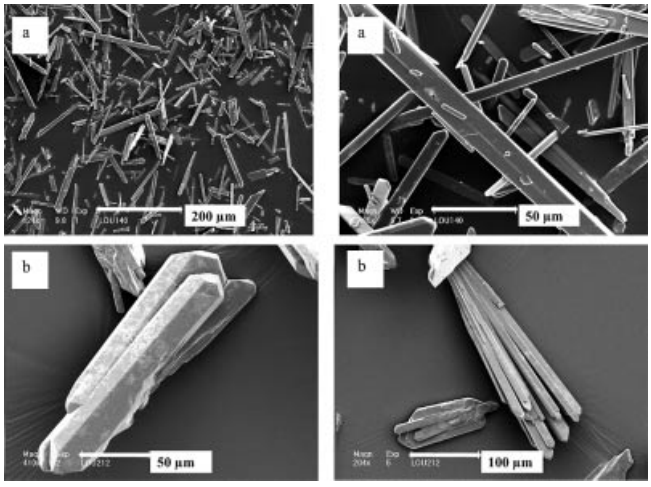


Figure 1. Scanning electron micrographs of (a) the fluorogallophosphate Mu-35-sample A, (b) the fluorogallophosphate Mu-35-sample F.

## XRD Analysis

The experimental powder diffraction pattern of the fluorogallophosphate Mu-35 is reported in Figure 2a. It was indexed in orthorhombic symmetry with the following unit cell parameters: $a$ = 22.410(3), $b$ = 17.478(3), $c$ = 10.2060(18) Å. For comparison, the simulated XRD pattern of Mu-35 is reported in Figure 2b.

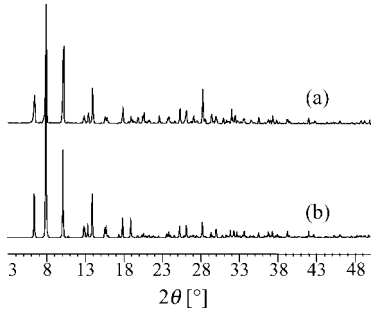


Figure 2. XRD patterns of the fluorogallophosphate Mu-35: (a) experimental pattern, (b) simulated pattern (radiation Cu-$K_{\alpha 1}$).

## Chemical and Thermal Analyses

According to elemental analyses, the as-synthesized Mu-35 sample has the following composition: Ga 30, P 15, F 8, N 5, C 9 wt.-%. Such results are in agreement with the composition obtained from the structure determined: Ga 31, P 14, F 8, N 5, C 9 wt.-%. The experimental C/N molar ratio equal to 2 is different from the value expected for ethylformamide (3C:1N), which proves that the solvent partly decomposes into ethylamine (EA) (3C:1N) during the synthesis. This was later confirmed by $^{13}C$ NMR spectroscopy (see below). As previously shown for other phosphate-based materials synthesized in the presence of alkylformamide,[9–15] the in situ release of the corresponding protonated amine during the synthesis appears to be a key step in the crystallization of this lamellar fluorogallophosphate. Indeed, experiments using ethylamine directly introduced in the starting mixture led to the crystallization of a quartz-type gallophosphate.

The thermal behavior of the fluorogallophosphate Mu-35 was investigated by TG/DTA thermal analyses. The TG and DTA curves of the as-synthesized material are reported in Figure 3. The total weight loss occurs mainly in two steps. A small weight loss close to 3 wt.-% appears before 250 °C. It might correspond to the removal of water molecules physisorbed and arise from the dehydroxylation reaction. The main weight loss (18.3 wt.-%) occurs between 250

 © 2007 Wiley-VCH Verlag GmbH & Co. KGaA, Weinheim 

and 500 °C. It is associated with endothermic components on the DTA curve, and can be attributed to desorption and decomposition of the ethylamine molecules and to the removal of the fluorine atoms (probably under the form of HF). After heating at 800 °C, the XRD analysis of the residue shows that the starting material was transformed by an amorphization–recrystallization process into a cristobalite-type gallophosphate.

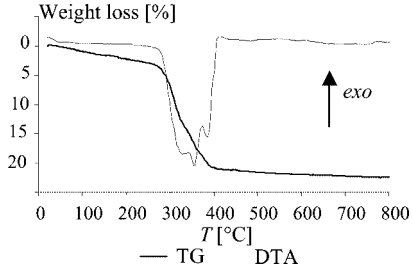


Figure 3. Thermal analyses (TG and DTA) under air of the fluorogallophosphate Mu-35.

## Structure Description

The structure of the fluorogallophosphate Mu-35 displays macroanionic layers composed of an arrangement of 3, 5, and 8 MR [$Ga_2PO_2F$, $Ga_3P_2O_4F$, and $Ga_4P_4O_8$, respectively]. These layers can be observed as the results of the condensation of fluorogallophosphate zig–zag chains (AAA) connected together along the *b* axis by the O5 oxygen atom (Figure 4). These zig–zag chains are built up from $GaO_4F$, $GaO_3F_2$, and $GaO_4F_2$ polyhedra linked by $PO_4$ tetrahedra. The asymmetric unit, reported in Figure 5, contains three crystallographically distinct Ga sites, two in fivefold coordination (Ga2 and Ga3) and one in sixfold coordination (Ga1). The structure also contains three crystallographically distinct P sites: the P1 and P2 sites share all their oxygen atoms with gallium neighbors, whereas P3 displays a hydroxy group O12, which points towards the layers. It should be noted that this oxygen atom, in addition to others (O1, O2, and O8), interact strongly with ethylamine molecules that are located between the layers through hydrogen bonds (‹N1–H1b···O1› = 1.92, N2–H2b···O2 = 2.02, ‹N2–H2c···O8› = 1.91, ‹N1–H1c···O12› = 1.85 Å). The structure could also be described as an arrangement of hexameric units ($Ga_3P_3$). These hexameric units are common in fluorinated gallium phosphates, as it has been observed in many 2D and 3D structures (ULM-8,[25] MIL-30,[11] MIL-50[26]). These units are joined together by two opposite orientations, which then generates the pseudo-membered rings described below. It is noteworthy that the structure of the Mu-35 is closely related to that of the fluorogallophosphate ULM-8.[25] Indeed, in comparison to the ULM-8 compound, the hexameric unit here possesses three fluorine ions instead of the usual two, and one hydroxy group P–OH. Furthermore, in our compound the sheets are shifted by a factor of *b*/2. Such a displacement could be a key factor for the transformation of the 2D Mu-35 compound into the 3D TREN-GaPO phase. To confirm this hypothesis, experimental study of the 2D Mu-35/3-D TREN-GaPO transformation, by hydrothermal treatment, is in progress.

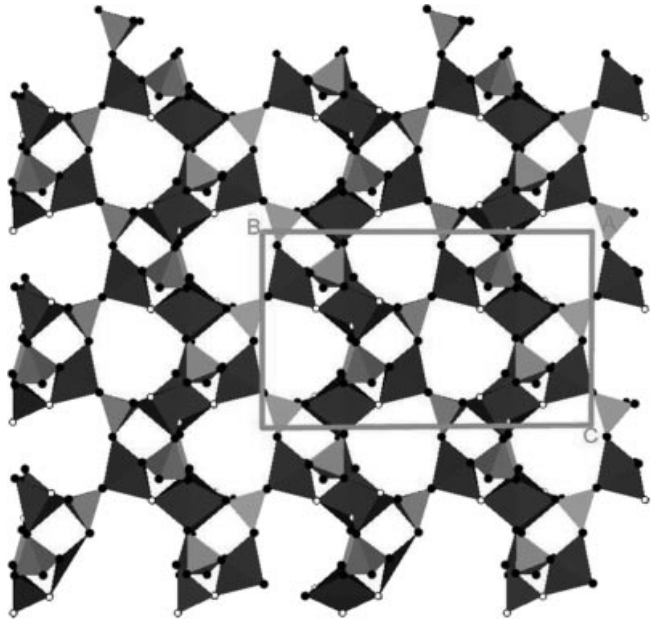


Figure 4. Projection of the structure of the fluorogallophosphate Mu-35 along the *a* axis, which shows the inorganic chains connected by O5 with 8-MR openings. Black spheres: O, open circles: F, dark grey polyhedra: Ga, light grey polyhedra: P.

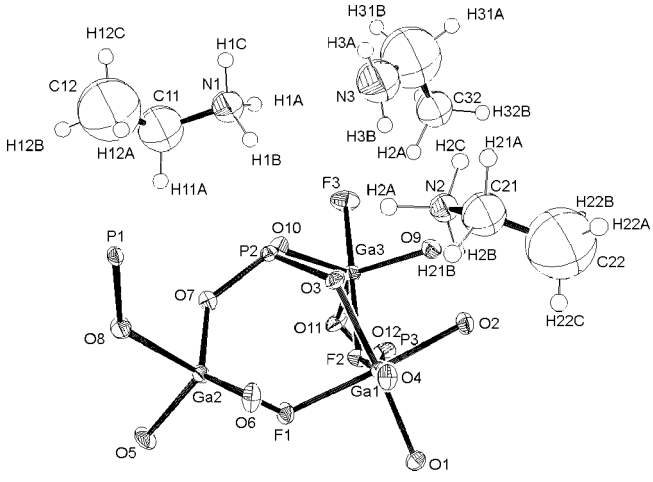


Figure 5. The asymmetric building unit of the fluorogallophosphate Mu-35.

The fluorine atoms are located on three nonequivalent crystallographic sites: two correspond to bridging species F1 and F2, which interact with the ethylamine molecules through hydrogen bonds [‹N2–H2a···F2› = 2.06(4), ‹N2–H2a···F1› = 2.22(4) Å; Table 2]. The third one (F3), which is connected to Ga3, is observed in the terminal position. The average ‹Ga–F› bond length is in good agreement with those reported for fluorogallophosphates.[15]

 © 2007 Wiley-VCH Verlag GmbH & Co. KGaA, Weinheim 

Table 2. Ethylamine-framework contacts with $d$(D···A) < 3.40 Å, $d$(H···A) < 2.33 Å, D–H···A > 100.0°. H···A distances and D–H···A angles are indicative only (H atoms fixed at their standard positions).

| Donor | H | Acceptor | D–H | H···A | D···A | D–H···A |
|---|---|---|---|---|---|---|
| N1 | H1A | F3 | 1.03(4) | 1.80(4) | 2.729(8) | 149(4) |
| N1 | H1B | O1 | 1.03(4) | 1.92(4) | 2.839(8) | 147(4) |
| N1 | H1B | O10 | 1.03(4) | 2.30(4) | 3.1071(8) | 134(4) |
| N1 | H1C | O12 | 1.03(3) | 1.85(4) | 2.861(8) | 168(4) |
| N2 | H2A | F1 | 1.02(3) | 2.22(4) | 2.835(7) | 117(2) |
| N2 | H2A | F2 | 1.02(3) | 2.06(4) | 3.049(7) | 160(2) |
| N2 | H2B | O2 | 1.02(2) | 2.02(3) | 3.029(7) | 168(2) |
| N2 | H2C | O8 | 1.03(3) | 1.91(3) | 2.887(7) | 158(3) |
| C32 | H32A | F3 | 1.04(8) | 1.85(9) | 2.74(2) | 142(1) |
| C32 | H32B | O6 | 1.02(9) | 2.26(9) | 3.10(2) | 138(5) |

To compensate for the negative charges of the framework, two of the three ethylamine molecules that are intercalated between the layers (N1 and N2, 8 × 2 molecules), are protonated. These molecules, which occupy a general position, are located inside the pseudo 12-membered ring (Figure 6). The remaining ethylamine molecule, which occupies the special N3 position, has an occupancy factor of 0.5, and it is nonprotonated and localized in the pseudo 8 MR.

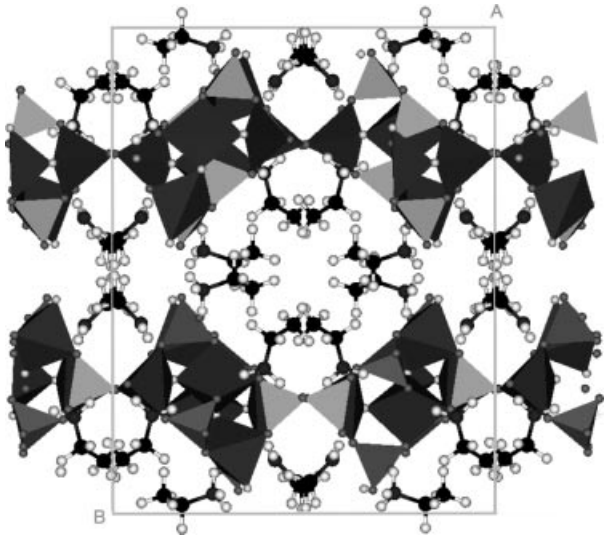


Figure 6. Projection of the structure of the fluorogallophosphate Mu-35 along the *c* axis, which shows the localization of the amine (black spheres). For a colored version of this figure see the Supporting Information.

### $^{13}$C CP MAS NMR Spectroscopy

Figure 7 shows the proton decoupled $^{13}$C MAS NMR spectrum of the fluorogallophosphate Mu-35. It displays two main signals located at ca. 13.1 and 35.2 ppm, which can be assigned to the $CH_3$ and $CH_2$ groups of the ethylamine molecules, respectively.[27] No carbonyl group is observed in this spectrum (resonance expected at about 160 ppm), which means that EFD is partly decomposed into ethylamine (EA) under our experimental conditions. The signal at $\delta$ = 13.1 ppm, which has a shoulder at $\delta$ = 14.1 ppm, can be attributed to the methyl groups of the ethylamine molecules. According to the $^{13}$C isotropic chemical shifts ($\delta$) known from liquid-state $^{13}$C NMR [$\delta(CH_3)$ protonated molecules: 12.5 ppm and $\delta(CH_3)$ nonprotonated molecules: 19 ppm], these two signals could be assigned to the $CH_3$ groups of protonated and nonprotonated EA, respectively. Such a result confirms with agreement with the structure determination: the hypothesis of amine protonation. Indeed the relative areas of the two signals are close to 4 ($\delta$ = 13.1 ppm):1 ($\delta$ = 14.1 ppm).

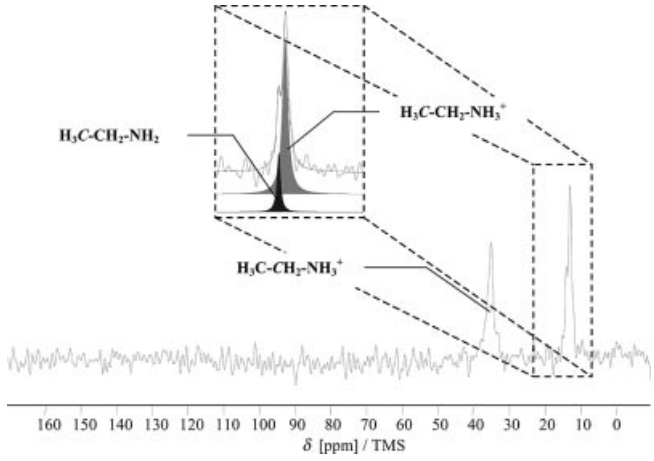


Figure 7. $^{1}$H decoupled $^{13}$C MAS spectrum of the fluorogallophosphate Mu-35 and its decomposition.

### $^{19}$F MAS NMR Spectroscopy

As shown in the Figure 8, the $^{19}$F MAS NMR spectrum of the as-synthesized product exhibits two signals located at –106.2 and –140.2 ppm. After decomposition, the relative areas are close to 2:1, respectively, indicating, in agreement with the structure determination, the existence of three crystallographically distinct fluorine sites. As observed for other fluorogallophosphates,[28–30] these signals could be assigned to the bridging fluorine species F1 and F2 and to the terminal fluorine species F3, respectively.

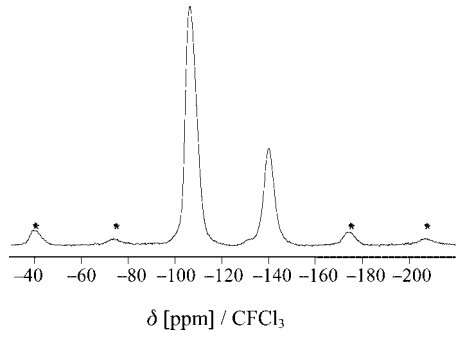


Figure 8. $^{19}$F MAS NMR spectrum of the fluorogallophosphate Mu-35. * Spinning side bands.

 © 2007 Wiley-VCH Verlag GmbH & Co. KGaA, Weinheim 

### $^{1}H$, $^{31}P$ and $^{1}H$-$^{31}P$ HETCOR NMR Spectroscopy

The $^{31}P$ MAS NMR spectrum of the fluorogallophosphate Mu-35, reported in Figure 9, displays three main signals at –3.4, –7, and –13.8 ppm. The relative areas are close to 1:1:1, which confirms, in agreement with the structure determination, the existence of three distinct crystallographic phosphorus sites. The decomposition shows that the signal at –7 ppm could be decomposed into two components (–6.2 and –7.2 ppm). It was noted that the intensity areas ratio between these two components varies with the amount of physisorbed water. This means that at the local order, the symmetry is probably lower, and the P3 phosphorus site splits into two different crystallographic sites.

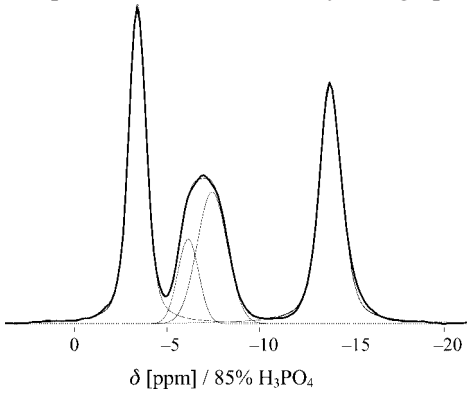


Figure 9. $^{31}P$ MAS NMR spectrum of the fluorogallophosphate Mu-35 and its decomposition.

The $^{1}H$ MAS NMR spectrum reported in Figure 10, displays at least four resonances at ca. 1.4, 3.4, 7.4, and 15.1 ppm. The resonances at $\delta$ = 1.4 and 3.4 ppm could be attributed to the $CH_3$ and $CH_2$ groups of the ethylamine molecules. According to the $^{1}H$ liquid-state NMR spectroscopic data, the signal located at 7.4 ppm could be assigned to the $NH_3^+$ and $NH_2$ groups. It is noteworthy that protons of $NH_2$ groups might be shielded because of the existence of hydrogen bonds with the oxygen atoms of physisorbed water molecules, which is expected to be observed at 4.7 ppm. The remaining signal at ca. 15.1 ppm could be assigned to the proton of the hydroxy group bound to the phosphorus atom (P–OH) that is in strong interaction with a water molecule through a hydrogen bond.

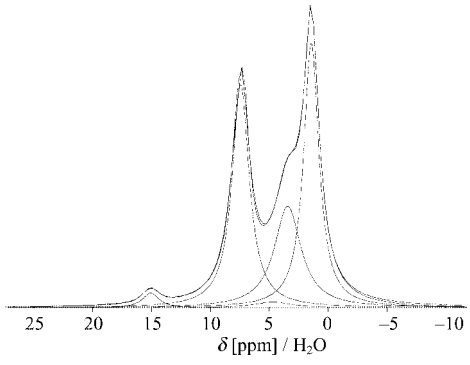


Figure 10. $^{1}H$ MAS NMR spectrum of the fluorogallophosphate Mu-35 and its decomposition.

A $^{1}H$-$^{31}P$ CP MAS NMR experiment was performed (spectrum not reported) to reveal the presence of the hydroxy group. For a contact time of 0.1 ms, an increase in the signal located at –7.0 ppm (Figure 9) was observed between the MAS and CP MAS spectra, which means, in agreement with the structure determination, that the corresponding phosphorus site is close to the proton and could be considered as a P–OH group. In Mu-35, this site could be assigned to P3.

To assign the different phosphorus signals, a 2D $^{1}H$-$^{31}P$ HETCOR experiment was performed. The 2D spectrum, shown in Figure 11, displays three signals for the P atoms located at –3.4, –7.0, and –13.8 ppm, which are characteristic of P*i*-H*j* interaction. It should be noted that only the phosphorus site associated to $\delta$ = –7.0 ppm has a strong interaction with the proton signal at ca. 15.1 ppm. Such a result confirms the assignment of the signal at –7.0 ppm to the phosphorus crystallographic P3 site. Unfortunately, it was not possible to clearly discriminate between P2 and P1.

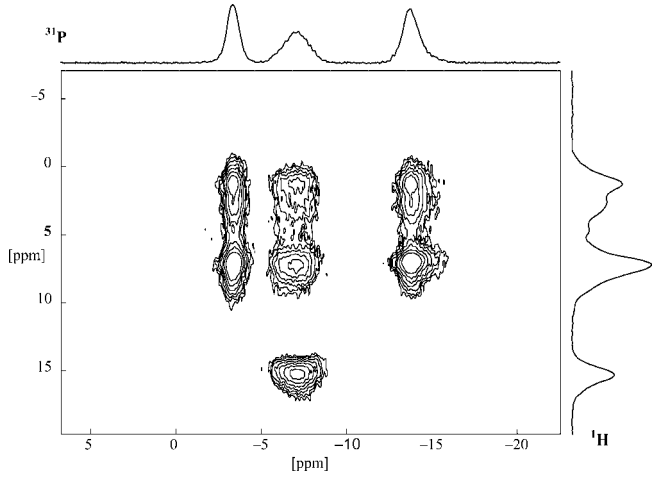


Figure 11. $^{1}H$-$^{31}P$ 2D HETCOR spectrum of the fluorogallophosphate Mu-35.

## Conclusion

In this paper the synthesis and the characterization of a fluorogallophosphate Mu-35, with a rather unusual structure, was reported. It was prepared in an aqueous medium by using ethylformamide as the precursor of the structure-directing agent. As in several similar syntheses, ethylformamide decomposes during the synthesis, and the corresponding amine is found occluded in the final structure. The in situ release of the amine during the synthesis appears to be a key step in the crystallization of this lamellar fluorogallophosphate. Indeed, experiments using ethylamine directly in the starting mixture did not lead to the crystallization of this material.

The fluorogallophosphate Mu-35 displays anionic layers closely related to ULM-8, built from three-, five- and eight-membered rings. To compensate for the negative charges of the anionic layers, the ethylamine molecules that are located inside the pseudo 12 MR are protonated, which is in contrast to the ones observed inside the pseudo 8 MR.

 © 2007 Wiley-VCH Verlag GmbH & Co. KGaA, Weinheim 

## Experimental Section

**General:** The fluorogallophosphate Mu-35 was prepared in an aqueous fluoride medium at 170 °C from a mixture containing ethylformamide as a precursor of the SDA (ethylamine). The molar composition of the starting mixture was 2 GaOOH/2 $H_3PO_4$/2 HF/2 ethylformamide (EFD)/16 $H_2O$. The water amount arises from the phosphorus and the fluoride sources. The pH value of the reaction mixture was adjusted to 2.5 with tripropylamine (TPA, Fluka 98 wt.-%), the latter presenting no structure-directing effect in the fluorine-containing gallophosphate system.[31] The amorphous gallium oxyhydroxide GaOOH was prepared by heating a gallium nitrate aqueous solution at 250 °C for 24 h. The other reactants were orthophosphoric acid (Labosi 85 wt.-%), hydrofluoric acid (Prolabo 40 wt.-%), and ethylformamide (EFD, Fluka 99 wt.-%).

**Synthesis:** The starting mixture was prepared by adding the amorphous gallium source (0.45 g) to water (0.36 g) under magnetic stirring. Then, ethylformamide (0.29 g), orthophosphoric acid (0.46 g), and hydrofluoric acid (0.2 g) were introduced. To increase the pH value of the solution to 2.5, tripropylamine (0.29 g) was added, and the mixture was stirred until homogeneous. Then, it was transferred to a 20-mL PTFE-lined stainless-steel autoclave and heated at 170 °C for 4 d. The product was filtered, washed with distilled water, and dried at 60 °C overnight.

**Characterization:** The as-synthesized product was characterized by powder X-ray diffraction (XRD) with a STOE STADI-P diffractometer equipped with a curved germanium (111) primary monochromator and a linear position-sensitive detector using Cu-$K_\alpha 1$ radiation ($\lambda$ = 1.5406 Å). The morphology and average size of the crystals were determined by scanning electron microscopy (SEM) with a Philips XL30 microscope. Elemental analyses were performed with an induced coupled plasma technique by using atomic energy spectroscopy (ICP AES) for Ga and P, and by coulometric and catharometric methods for C and N quantifications, respectively. Thermogravimetric (TGA) and differential thermal (DTA) analyses were performed under air with a Setaram Labsys thermoanalyser with a heating rate of 5 °C min$^{-1}$ up to 1000 °C. Solid-state NMR experiments were performed at r.t. with a Bruker DSX 400 spectrometer operating at $B_0$ = 9.4 T and a Bruker double channel high-speed 2.5 mm probe. The recording conditions are reported in Table 3. As the typical $T_1$ values measured for our sample by using inversion recovery was slightly less than 0.6 and 2.8 s for the $^1$H and $^{19}$F, respectively, the corresponding recycle delays were fixed to 3 and 15 s, respectively. Furthermore the $^{31}$P spin lattice relaxation times ($T_1$) was measured with the saturation-recovery pulse sequence and it was found to be less than 68 s. Decompositions of the spectra were performed with WINFIT programs.[32]

Table 3. Recording conditions of the NMR spectra.

| | $^1$H MAS | $^1$H decoupled $^{13}$C MAS | $^{31}$P MAS | $^1$H-$^{31}$P CP MAS | $^1$H-$^{31}$P HETCOR | $^{19}$F MAS |
|---|---|---|---|---|---|---|
| Chemical shift reference | TMS | TMS | 85% $H_3PO_4$ | 85% $H_3PO_4$ | 85% $H_3PO_4$ | $CFCl_3$ |
| Frequency [MHz] | 400.2 | 100.6 | 161.98 | 161.98 | 161.98 | 376.5 |
| Pulse width [μs] | 5.5 | 2.5 | 3.5 | 4.5 | 4 | 4 |
| Flip angle | π/2 | π/4 | π/2 | π/2 | π/2 | π/2 |
| Contact time [ms] | – | – | – | 0.05–0.1 | 0.05 | – |
| Recycle time [s] | 3 | 60 | 30 | 10 | 3 | 20 |
| Spinning rate [Hz] | 25000 | 5000 | 25000 | 25000 | 25000 | 25000 |
| Number of scans | 8 | 832 | 64 | 64 | 200 | 32 |

Table 4. Experimental single-crystal XRD data and structure analysis of the fluorogallophosphate Mu-35.

| | |
|---|---|
| Compound name | Mu-35 |
| Chemical formula (asymmetric unit) | $[Ga_3(HPO_4)\ (PO_4)_2F_3(C_2H_8N)_{2.0}(C_2H_7N)_{0.5}]$ |
| Cell parameters | $a$ = 22.1170(11), $b$ = 17.3740(8), $c$ = 10.1550(4) Å<br>$\alpha$ = 90°, $\beta$ = 90°, $\gamma$ = 90° |
| $V$ [Å$^3$] | 3902.2(3) |
| Space group, $Z$ | *Pbcn*, 8 |
| Density (calculated) | 2.336(5) |
| Crystal size [μm] | 170 × 90 × 50 |
| Diffractometer | Oxford diffraction Xcalibur 2 + Sapphire CCD |
| Radiation source, Wavelength | Mo($K\alpha$) $\lambda$ = 0.71073 Å |
| Absorption coefficient [mm$^{-1}$] | 4.45 |
| Transmission $T_{min}/T_{max}$ | 0.53/0.85 |
| Temperature [K] | 293 |
| Reflections measured, independent | 58820, 10701 |
| Unique reflections Observed [$I > 3\sigma(I)$] | 4642 |
| Overall completeness ($sin\theta/\lambda_{max}$ = 0.88 Å$^{-1}$) | 90% |
| Internal agreement $R_{int}$[a] | 0.078 |
| Agreement factors after structural refinement [$I > 3\sigma(I)$] | $R$ = 0.054, $Rw$ = 0.058, goof = 2.53 |

[a]

$$R = \left( \sum_H \left\| F_{obs.} \right| - \left| kF_{calc.} \right\| \right) \Big/ \left( \sum_H \left| F_{obs.} \right| \right), \quad Rw = \left\{ \left( \sum_H w\left( \left| F_{obs.} \right| - \left| kF_{calc.} \right| \right)^2 \right) \Big/ \left( \sum_H w \left| F_{obs.} \right|^2 \right) \right\}^{1/2}$$

$$Goof = \left\{ \left( \sum_H w\left( \left| F_{obs.} \right| - \left| kF_{calc.} \right| \right)^2 \right) \Big/ (m-n) \right\}^{1/2}, \quad w = 1 \Big/ \sigma^2 \left( F_{obs.} \right),$$ $m$ is the number of reflections used, $n$ the number of parameters.

 © 2007 Wiley-VCH Verlag GmbH & Co. KGaA, Weinheim 

**Crystal Structure Determination:** A crystal plate was cut out of a larger aggregate and selected after optical examination under crossed polars. The single-crystal X-ray diffraction experiment was performed at r.t. with an Oxford diffraction Xcalibur diffractometer equipped with a CCD detector. A full redundant Ewald sphere was collected with Mo($K_\alpha$) radiation up to a maximum resolution $sin\theta/\lambda max = 0.88$ Å$^{-1}$. Bragg intensities were integrated with Crysalis software,[33] and averaged in Laue point group mmm with SORTAV program[34] after an absorption correction ($\mu = 4.45$ mm$^{-1}$) based on the crystal shape. Data collection details are summarized in Table 4. The crystal structure was solved by direct methods using SHELXS[35] and refined with JANA2000.[36] The positions of all non-hydrogen atoms were found straightforwardly on successive Fourier maps. Hydrogen atoms were introduced in the structural model by assuming ideal conformations for all ethylamine molecules. Atomic displacement parameters of H atoms were restrained to 1.5 times the value of that of the heavy atom they were attached to. All bond lengths and bond angles of ethylamine molecules were also restrained to the expected values observed in $CH_3$ (methyl), $CH_2$ (methylene), and $NH_3$ (amine) groups.[37] The refinement converged to $R = 0.054$ and $R_W = 0.058$ for the 4642 observed reflections [$I > 3\sigma(I)$]. Selected bond lengths are given in Table 5. CCDC-645100 contains the supplementary crystallographic data for this paper. These data can be obtained free of charge from The Cambridge Crystallographic Data Centre via www.ccdc.cam.ac.uk/data_request/cif.

Table 5. Selected bond lengths [Å] in the fluorogallophosphate Mu-35.

| Bond | Length [Å] | Bond | Length [Å] | Bond | Length [Å] |
|---|---|---|---|---|---|
| Ga1–O1 | 1.911(4) | Ga2–O5 | 1.826(4) | Ga3–O9 | 1.837(4) |
| Ga1–O3 | 1.924(4) | Ga2–O7 | 1.846(4) | Ga3–O10 | 1.860(4) |
| Ga1–O2 | 1.929(4) | Ga2–O6 | 1.849(4) | Ga3–O11 | 1.866(4) |
| Ga1–O4 | 1.933(4) | Ga2–O8 | 1.943(4) | | |
| Ga1–F1 | 1.977(3) | Ga2–F1 | 2.025(3) | Ga3–F2 | 2.009(3) |
| Ga1–F2 | 1.981(3) | | | | |
| | | | apical F | Ga3–F3 | 1.864(4) |
| P1–O5 | 1.524(4) | P2–O3 | 1.521(4) | P3–O4 | 1.517(4) |
| P1–O2 | 1.532(4) | P2–O1 | 1.526(4) | P3–O11 | 1.537(4) |
| P1–O8 | 1.534(4) | P2–O7 | 1.530(4) | P3–O6 | 1.540(4) |
| P1–O9 | 1.538(4) | P2–O10 | 1.544(4) | | |
| | | | apical O | P3–O12 | 1.533(4) |

**Supporting Information** (see footnote on the first page of this article): Atomic coordinates and displacement parameters at the end of structural refinement as well as selected angles. Projection of the structure of the fluorogallophosphate Mu-35 along the *c* axis in color.


[1] M. E. Davis, *Nature* **2002**, *417*, 813.
[2] S. T. Wilson, B. M. Lok, C. A. Messina, T. R. Cannan, E. M. Flanigen, *J. Am. Chem. Soc.* **1982**, *104*, 1146.
[3] H. Kessler, J. Patarin, C. Schott-Darie, "Advanced Zeolite Science and Applications" in *Studies in Surface Science and Catalysis* (Eds.: J. C. Jansen, M. Stöcker, H. G. Karge, J. Weitkamp), Elsevier, Amsterdam, **1994**, vol. 85, p. 75.
[4] G. Férey, *J. Fluorine Chem.* **1995**, *72*, 187.
[5] J. Patarin, J. L. Paillaud, H. Kessler in *Synthesis of AlPO4s and Other Crystalline Materials, Handbook of Porous Solids* (Eds.: F. Schüth, K. S. Sing, J. Weitkamp), Wiley-VCH, Germany, **2002**, vol. 2, ch. 4.2.3, p. 815.
[6] M. Estermann, L. B. McCusker, Ch. Baerlocher, A. Merrouche, H. Kessler, *Nature* **1991**, *352*, 320.
[7] A. Matijasic, P. Reinert, L. Josien, A. Simon, J. Patarin, "Zeolites and Mesoporous Materials at the Dawn of the 21st Century" in *Studies in Surface Science and Catalysis* (Eds.: A. Galarneau, F. Direnzo, F. Fajula, J. Vedrine), Elsevier, Amsterdam, vol. 135, **2001**, p. 142.
[8] P. Caullet, J. L. Paillaud, A. Simon-Masseron, M. Soulard, J. Patarin, *C. R. Chimie* **2005**, *8*, 245.
[9] L. Vidal, V. Gramlich, J. Patarin, Z. Gabelica, *Eur. J. Solid State Inorg. Chem.* **1998**, *35*, 545.
[10] L. Vidal, V. Gramlich, J. Patarin, Z. Gabelica, *Chem. Lett.* **1999**, 201.
[11] C. Paulet, T. Loiseau, G. Férey, *J. Mater. Chem.* **2000**, *10*, 1225.
[12] L. Lakiss, A. Simon-Masseron, V. Gramlich, J. Patarin, *J. Solid State Sci.* **2005**, *7*, 141.
[13] L. Lakiss, A. Simon-Masseron, J. Patarin, *Microporous Mesoporous Mater.* **2005**, *84*, 50.
[14] C. Marichal, J. M. Chézeau, M. Roux, J. Patarin, J. Luis Jorda, L. B. McCusker, C. Baerlocher, P. Pattison, *Microporous Mesoporous Mater.* **2006**, *90*, 5.
[15] L. Lakiss, A. Simon-Masseron, F. Porcher, J. Patarin, *Eur. J. Inorg. Chem.* **2006**, 237.
[16] A. M. Chippindale, S. Natarajan, J. M. Thomas, R. H. Jones, *J. Solid State Chem.* **1994**, *111*, 18.
[17] T. Loiseau, G. Férey, *Eur. J. Solid State Inorg. Chem.* **1994**, *31*, 575.
[18] T. Loiseau, C. Paulet, N. Simon, V. Munch, F. Taulelle, G. Férey, *Chem. Mater.* **2000**, *12*, 1393.
[19] R. N. Devi, K. Vidyasagar, *J. Chem. Soc. Dalton Trans.* **2000**, *10*, 1605.
[20] J. N. Behera, C. N. R. Rao, *J. Am. Chem. Soc.* **2006**, *128*, 9334.
[21] S. J. Weigel, R. E. Morris, G. D. Stucky, A. K. Cheetham, *J. Mater. Chem.* **1998**, *8*, 1607.
[22] E. R. Cooper, C. D. Andrews, P. S. Wheatley, P. B. Webb, P. Wormald, R. E. Morris, *Nature* **2004**, *430*, 1012.
[23] E. R. Parnham, E. A. Drylie, P. S. Wheatley, A. M. Z. Slawin, R. E. Morris, *Angew. Chem.* **2006**, *118*, 5084.
[24] S. Feng, R. Xu, *Chem. J. Chinese Univ.* **1988**, *4*, 1.
[25] F. Serpaggi, T. Loiseau, D. Riou, G. Férey, M. W. Hosseini, *Eur. J. Solid State Inorg. Chem.* **1994**, *31*, 595.
[26] L. Beitone, J. Marrot, T. Loiseau, G. Férey, M. Henry, C. Huguenard, A. Gansmuller, F. Taulelle, *J. Am. Chem. Soc.* **2003**, *125*, 1912.
[27] H. O. Kalinowski, S. Berger, S. Braun, *$^{13}$C NMR Spektroskopie*, Georg Thieme, Stuttgart, New York, **1984**, p. 189.
[28] A. Matijasic, V. Gramlich, J. Patarin, *J. Solid State Sci.* **2001**, *3*, 155.
[29] A. Matijasic, V. Gramlich, J. Patarin, *J. Mater. Chem.* **2001**, *11*, 2553.
[30] L. Josien, A. Simon-Masseron, V. Gramlich, J. Patarin, *Chem. Eur. J.* **2002**, *8*, 1614.
[31] C. Schott-Darie, PhD Thesis, University of Haute Alsace, Mulhouse, **1994**.
[32] http://crmht-europe.cnrs-orleans.fr/dmfit/, D. Massiot, F. Fayon, M. Capron, I. King, S. Le Calvé, B. Alonso, J. O. Durand, B. Bujoli, Z. Gan, G. Hoatson, *Magn. Reson. Chem.* **2002**, *40*, 70.
[33] *Crysalis Software system*, Version 1.170, Oxford Diffraction Ltd, **2003**.
[34] R. H. Blessing, *J. Appl. Crystallogr.* **1997**, *30*, 421.
[35] G. M. Sheldrick, *SHELXS86: Program for the Solution of Crystal Structures*, Institut für Anorganische Chemie der Universität, Göttingen, Germany, **1986**.
[36] V. Petříček, M. Dušek, *The Crystallographic Computing System JANA2000*, Institute of Physics, Praha, Czech Republic, **2000**.
[37] *International Tables for X-ray Crystallography – Vol. C*. Kluwer Academic Publishers, Dordrecht.


Received: March 5, 2007
Published Online: July 11, 2007

 © 2007 Wiley-VCH Verlag GmbH & Co. KGaA, Weinheim 

DOI: 10.1002/ejic.200700284

# Nb-Doped $VO_2$ Thin Films Prepared by Aerosol-Assisted Chemical Vapour Deposition

Clara Piccirillo,[a] Russell Binions,[a] and Ivan P. Parkin*[a]

**Keywords:** Intelligent materials / Vanadium dioxide (M) / Transition temperature / Niobium doping

Niobium-doped vanadium dioxide ($V_xNb_{1-x}O_2$, $x$ = 0–0.037) thin films were prepared by aerosol-assisted chemical vapour deposition (AACVD) of vanadyl(IV) acetonate and niobium(V) ethoxide in ethanol. Samples were analysed by EDX, XRD, Raman, XPS and SEM. The analyses confirmed the deposition of niobium, even if no separated phase was formed; the morphological structure of the films was affected by the dopant presence. The thin films showed thermochromic behaviour, with a marked change in optical properties above and below the switching temperature.
(© Wiley-VCH Verlag GmbH & Co. KGaA, 69451 Weinheim, Germany, 2007)

## Introduction

Vanadium(IV) oxide ($VO_2$) is a material with many interesting characteristics, including a thermochromic phase transition. At room temperature, the most stable phase is the monoclinic $VO_2$ (M); at higher temperature the rutile phase $VO_2$ (R) is stabilised. Above a certain temperature, there is a spontaneous transition from the monoclinic to the rutile form, a metal-to-semiconductor transition (MST), that is completely reversible and takes place at 68 °C.[1] A remarkable change in the physical properties is detected on passing through the MST transition; $VO_2$ (M) behaves as a semiconductor and does not reflect much solar energy, whereas $VO_2$ (R) is a semimetal and shows markedly higher electrical conductivity and a much higher reflectance, particularly in the infrared range.[2]

Vanadium dioxide represents an ideal material for use as an intelligent window coating, that is a coating that modifies its behaviour in response to an external stimulus, i.e. heat. The low reflectance of the monoclinic phase assures that a coated window allows maximum solar gain on cooler days ($T$ below $T_c$). The transition to the rutile phase, on the other hand, can help to reduce the heat gain in hot days. The effect would be to have a comfortable environment with reduced air-conditioning costs, which has economical and environmental benefits.[2]

For practical application an intelligent window coating should have its phase-transition temperature closer to a comfortable room temperature value. It has been reported previously that a change in the transition temperature can be obtained by doping metal ions into the $VO_2$ lattice; doping with titanium, for instance, raises the value of $T_c$[3] while tungsten, molybdenum and niobium lower it.[4,5]

Up to now, the best reduction in the transition temperature has been obtained by the use of tungsten; in fact W-doped $VO_2$ thin films have been prepared with different methodologies such as sputtering,[6,7] sol-gel,[8] atmospheric-pressure and aerosol-assisted chemical vapour deposition (APCVD and AACVD).[2,9] These films show a decrease in the transition temperature that is proportional to the amount of tungsten incorporated; samples containing about 1% tungsten, show a decrease of 20–25 °C.[2,6,7] Considering in particular the AACVD methodology, films with values of $T_c$ close to room temperature were deposited.[9]

Niobium-doped $VO_2$ thin films have been prepared by sol-gel[10] and APCVD methodologies.[5] The results seemed particularly encouraging for APCVD samples; in fact, above the transition temperature, they showed a remarkable decrease in the transmittance in the infrared region, fulfilling the requirement for intelligent window coatings. The problem, however, was the difficulty to incorporate large enough amounts of niobium into the $VO_2$ films, in fact the highest niobium concentration achieved was 0.4%, corresponding to a $T_c$ value of 55 °C.[11]

In this paper we report the first synthesis of Nb-doped $VO_2$ thin films with AACVD. With this methodology the precursor is dissolved in a solvent and an aerosol generated ultrasonically. An inert carrier gas transports the precursor (within the aerosol droplets) to the deposition reactor where the reaction takes place. The main advantage of AACVD deposition is that, unlike for APCVD, the precursor does not need to be volatile but just soluble in a solvent appropriate for the aerosol formation.[12] In this way it is possible to use different precursors, not normally used in APCVD.[13,14] Previous work indicates a strong correlation between metal ratios in the precursor solution and those found in the resultant film.[9] AACVD provides an easy method to prepare multi-component and/or doped films.

[a] University College London, Chemistry Department, Christopher Ingold Laboratories,
20 Gordon Street, London, WC1H 0AJ, UK
E-mail: i.p.parkin@ucl.ac.uk

 InterScience © 2007 Wiley-VCH Verlag GmbH & Co. KGaA, Weinheim 

Previous experiments were carried out by our group to deposit $VO_2$ (M) using AACVD methodology (Figure 1). The effect of different experimental parameters such as solvent, deposition temperature and gas-flow rate was studied and the deposition conditions were optimised to deposit $VO_2$(M) as the only phase and with no contamination.[15] The same experimental conditions were used to deposit Nb-doped $VO_2$, with $[Nb(OC_2H_5)_5]$ added as a niobium precursor. Depositions with different Nb/V ratios were performed; the deposited films were analysed to determine their composition, their structure and their behaviour as an intelligent window material.

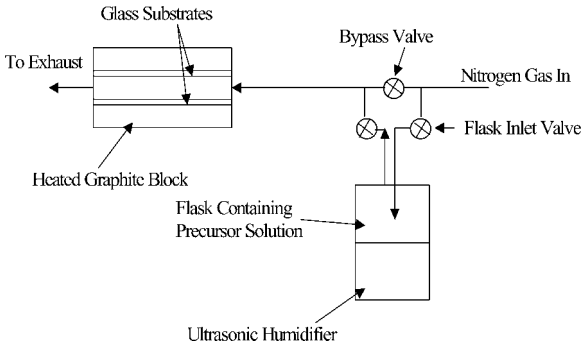


Figure 1. Schematic representation of AACVD experimental apparatus.

## Results and Discussion

### Film Deposition and Characterisation (Deposited Phases and Morphology)

Vanadium dioxide thin films with different amounts of niobium were deposited, by AACVD of a solution containing $[VO(acac)_2]$ and $[Nb(OEt)_5]$. Table 1 reports the Nb/V precursors ratio employed for the depositions. All deposited films were yellow in colour with some trace of brown, identical to undoped $VO_2$ films.[15] They all showed good adherence; they passed the Scotch tape test, but they could be scratched by a scalpel and were stable in air.

Table 1. Niobium/vanadium molar ratio for the initial solution and the deposited samples.

| Sample | Nb/V solution molar ratio (%) | Nb/V film molar ratio (%) | $T_c \pm$ hysteresis width (°C) |
|---|---|---|---|
| **1** | 1.3 | 0 | 58 ± 3 |
| **2** | 5.2 | 0 | 58 ± 3 |
| **3** | 7.5 | 2.6 | 42 ± 3.5 |
| **4** | 10.3 | 2.4 | 44 ± 3 |
| **5** | 12.4 | 2.2 | 35 ± 3 |
| **6** | 13.8 | 3.7 | 37 ± 3 |
| **7** | 14 | 3.0 | 35 ± 4 |
| **8** | 17 | 2.7 | 37 ± 3.5 |
| **9** | 18.9 | 2.8 | 41 ± 3 |

To determine the films' composition, i.e. the amount of niobium deposited in each film, EDX analyses were taken. The results are listed in Table 1. It can be seen that for precursor ratios in solution up to 5.2%, there is no niobium detected in the films. The reason for this behaviour is not clear, it is likely that the niobium precursor has to reach a critical concentration before it interacts with the vanadium; this would explain the sudden increase in the Nb/V film ratio from 0 to 2.6%.

For higher concentrations in solution, there is an increase of the niobium concentration in the deposits; however, the value reaches a plateau and it remains stable (within experimental error), despite the increase in concentration of niobium in solution. An explanation for these results can be that the value of the solubility limit on niobium in vanadium is reached; however, no data are available in literature to confirm this.

From this data it can be seen that niobium behaves very differently from tungsten in $VO_2$ films deposited by AACVD; in fact a linear correlation was observed for tungsten between the amounts of precursor in solution and the metal in the film.[9] Furthermore, a much greater proportion of the tungsten precursor was included in the $VO_2$ film as metal dopant (e.g. a W/V atom ratio of about 6% in solution corresponded to about 2% in the film).

The different behaviour of niobium confirms the difficulties previously reported with this metal already observed in APCVD.[11] In comparison a much greater amount of metal was deposited in the AACVD samples; this indicates the suitability of the technique for the deposition of multicomponent/doped films.

The XRD patterns of all samples were recorded to determine the nature of the phases present; Figure 2 shows the XRD spectrum of sample **5**. It can be seen, despite the glass background signal, that the deposited film is unambiguously $VO_2$(M).[2] Similarly to undoped $VO_2$ and W-doped $VO_2$ deposited by AACVD, no preferential orientation is observed.[9] No other phase was detected, neither for niobium nor for other vanadium oxides. Other areas of the same film showed the same pattern, indicating good homogeneity of the film. All the thin films investigated, with different niobium concentration, had the same characteristics; this indicates that the amount of dopant does not affect the nature of the phase deposited and that, under these conditions, it does not favour the formation of mixed phases.

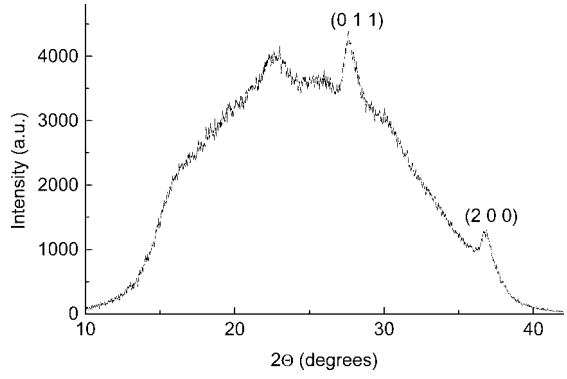


Figure 2. XRD spectrum of sample **5**.

 © 2007 Wiley-VCH Verlag GmbH & Co. KGaA, Weinheim 

The Raman spectrum of sample **5** is shown in Figure 3. It can be seen that it shows the characteristics $VO_2$ pattern. In fact all the detected signals can be assigned to $VO_2$ (M); furthermore, there is no signal corresponding to graphitic carbon (i.e. at 1355 $cm^{-1}$), indicating no carbon contamination of the film.

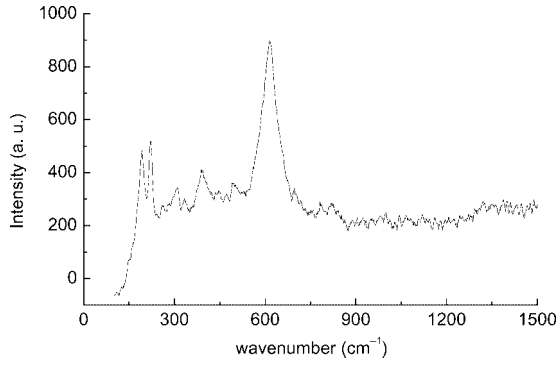


Figure 3. Raman spectrum for sample **5**.

XPS spectra of Nb-doped $VO_2$ samples were acquired to detect the possible other elements deposited in the film as impurities and to determine the oxidation states of the main film components. From the analysis of the survey spectrum (registered on the surface of the film), it was seen that the only additional element detected in the film is carbon. However, the intensity of the carbon signals decreased remarkably moving from the surface into the bulk of the film; this indicates the carbon is present only on the surface as contaminant from the external environment, but it is not present in the bulk of the film. This is in agreement with what was observed by Raman spectroscopy; in fact the signals in the Raman spectra are related to the bulk of a material and not just to its surface.

Figure 4(a) and (b) show the sections of the spectrum corresponding to the niobium and vanadium, respectively, for sample **5**; as mentioned above, the spectrum was registered on the surface of the film. The niobium peaks were detected for $Nb3d_{5/2}$ and $Nb3d_{3/2}$ at the binding energies of 207.0 and 209.2 eV. These values correspond to the binding energies of $Nb_2O_5$, therefore it follows that the niobium oxidation state is +5.[16] This is in agreement with previously published data,[11] hence it confirms that niobium does not change its oxidation state during the deposition. Spectra acquired in the bulk of the film show that niobium has the same oxidation state throughout the film.

The analysis of the part of the spectrum corresponding to vanadium shows that the main signal consists of two overlapping peaks at 516.2 and 517.4 eV (the deconvolution is shown in Figure 4). These two binding energies correspond to $V2p_{3/2}$ (+4) and $V2p_{3/2}$ (+5).[16] This indicates that, on the surface of the film, $VO_2$ is partly oxidised to $V_2O_5$.

Moving to the bulk of the film, however, only the peak corresponding to $V^{IV}$ is detected (spectrum is not shown). These results are in agreement with the XRD and Raman results; in fact no $V_2O_5$ signal was observed by either technique (see Figures 2 and 3), because they analyse the bulk of the film and not just the surface.

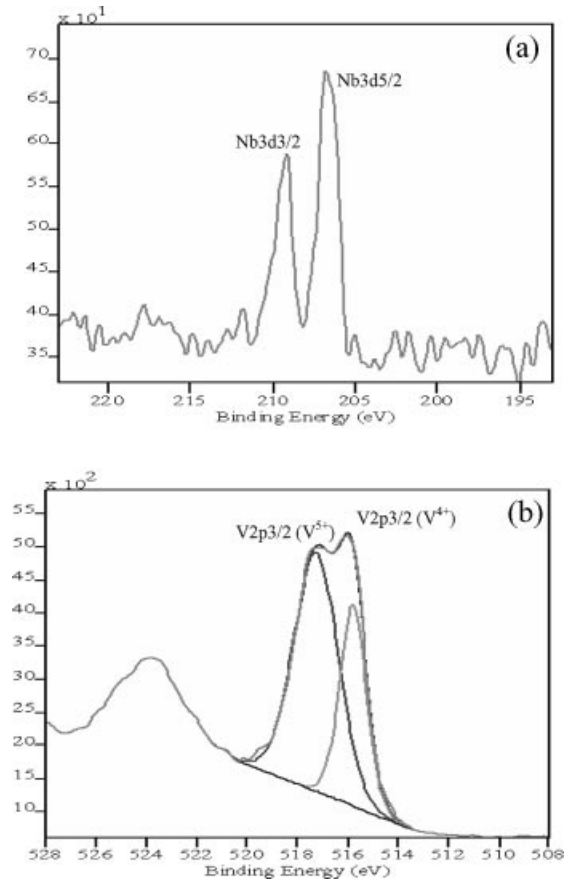


Figure 4. XPS spectrum for sample **5**: (a) niobium section; (b) vanadium section.

The morphology of the Nb-doped $VO_2$ thin films was studied by scanning electron microscopy (SEM). Figure 5 compares the surface structure of undoped $VO_2$ [Figure 5(a)] with the one of Nb-doped $VO_2$ [sample **7**, Fig-

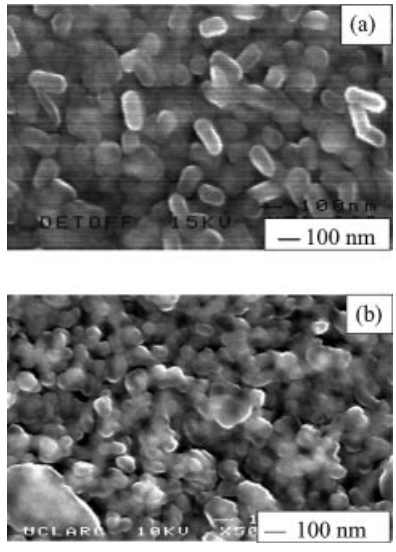


Figure 5. SEM images for (a) undoped $VO_2$; (b) sample **7**.

 © 2007 Wiley-VCH Verlag GmbH & Co. KGaA, Weinheim 

ure 5(b)], both deposited using AACVD. It can be observed that they look quite different, indicating the effect of niobium on the film structure. Other films with different niobium concentrations have a similar morphology, indicating that the amount of niobium does not have any influence on the morphology.

### Film Characterisation: Functional Properties

The optical properties of the samples were investigated and their thermochromic change through the monoclinic-rutile phase transition studied. The change in transmittance and reflectance above and below the transition temperature was measured to assess the efficiency and the suitability of this material as an intelligent window coating.

Figure 6 shows the transmittance and reflectance spectra above and below the transition temperature for sample **9**. Considering the transmittance [Figure 6(a)], there is a significant decrease above the transition temperature (up to 30%) in the infrared range. The spectra of all the other samples showed the same features, with some changes in the extent of the decrease in the transmittance, which was dependant on the thickness of the films. This behaviour is analogous to the one shown by both undoped and W-doped $VO_2$.[9,15]

The change in the reflectance, however, has different characteristics depending on the niobium content of the film; Figure 6(b) and (c) show the reflectance spectra of samples **5** and **9**, respectively. For sample **5**, an increase above $T_c$ can be observed for the full infrared range; for sample **9**, on the contrary, such increase can be seen only for wavelengths larger than 1650 nm. At about 1650 nm the two lines cross over, therefore the curve corresponding to the reflectance above $T_c$ is slightly less intense than the one representing the reflectance below $T_c$. Similar to the Raman spectra, this different behaviour was observed for samples **6**, **7**, **8** and **9**, when the niobium concentration in the films is about 3%; the two curves cross over in a range of energy between 1550 and 1650 nm. The comparison of these results suggests that probably the presence of another phase affects the change in the reflectance, limiting it to a smaller energy range.

The value of the transition temperature was also determined for each sample. This was done by measuring the transmittance at 4000 $cm^{-1}$ as a function of the temperature. Figure 7 shows as an example the measurements for samples **4** and **7** (Nb/V = 2.4 and 3.0%, respectively). As shown in Figure 7, the transition temperature was determined considering the average value of the transmittance; the midpoint of the hysteresis loop for this value of transmittance is the transition temperature. It can be seen that the larger the Nb/V ratio, the lower is the value of the temperature. This shows the effectiveness of niobium to decrease $T_c$. Table 1 reports the value of $T_c$ for every sample ± the width of the hysteresis loop. Similarly to what is observed for W-doped $VO_2$ deposited with AACVD, the width of the hysteresis loop does not change with the decrease of the transition temperature which is constant between 3 and 4 °C.

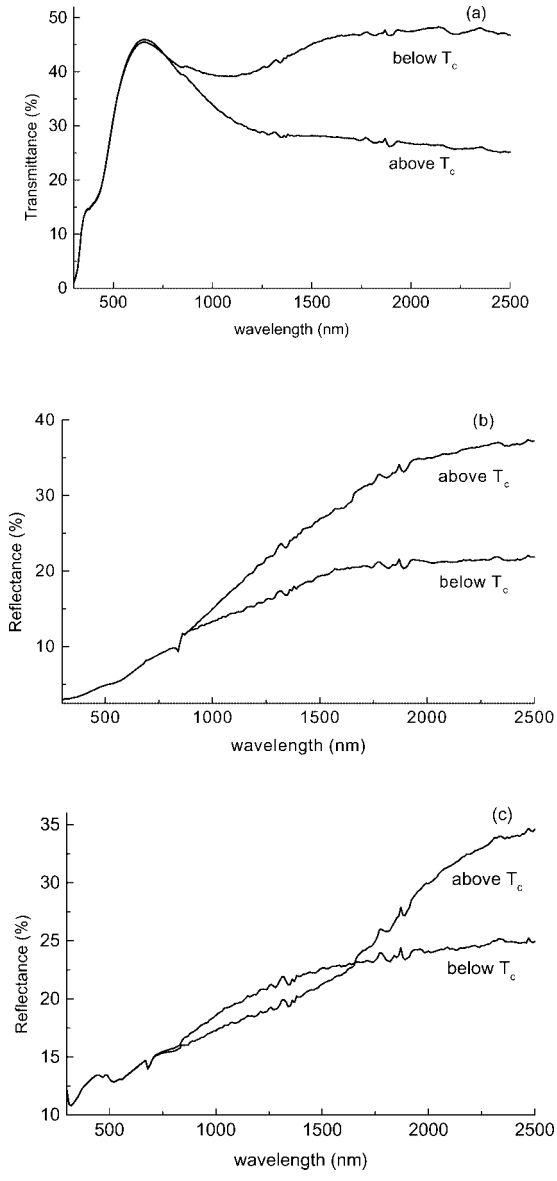


Figure 6. Optical properties above and below $T_c$. (a) Transmittance for sample **9**; (b) reflectance for sample **5**; (c) reflectance for sample **9**.

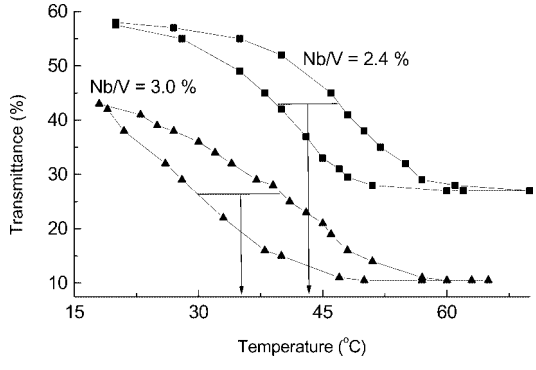


Figure 7. Transmittance at 4000 $cm^{-1}$ as a function of the temperature for samples **4** and **7** (Nb/V atom ratio 2.4 and 3%, respectively).

 © 2007 Wiley-VCH Verlag GmbH & Co. KGaA, Weinheim 

Figure 8 shows the value of $T_c$ as a function of the niobium content in the film and that a good linear correlation is established. From this data it can be seen that an amount of niobium in the film of 2% lowers the transition temperature by 15 °C. It follows that niobium is less effective than tungsten to decrease the value of $T_c$ (for tungsten, 1% of dopant decreases $T_c$ by about 22 °C);[9] it is, however, still possible to achieve values of transition temperatures close to room temperature.

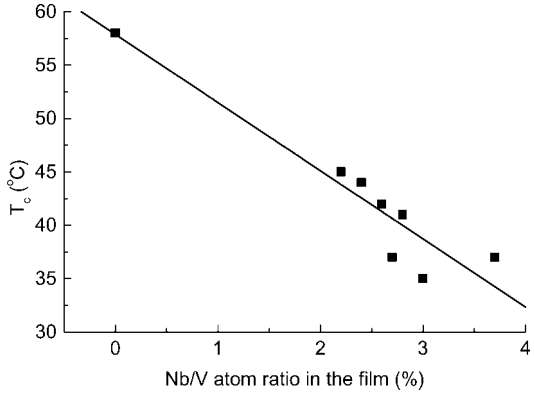


Figure 8. Transition temperature vs. the Nb/V atom ratio in the films.

## Conclusions

Nb-doped $VO_2$ thin films were successfully deposited by *A*erosol-*A*ssisted *C*hemical *V*apour *D*eposition (AACVD). EDX analysis showed that an increase in the niobium concentration in solution correlates to an increase in niobium in the film as well, until a plateau is reached. Samples with a niobium content up to 3.7% (atom ratio) were prepared, $VO_2$ films with such high niobium concentrations were never deposited before. This indicates the suitability of the AACVD methodology to deposit doped thin films.

Films were characterised by several analytical techniques (XRD, Raman, SEM, XPS) to determine the nature of the deposited phase and to detect possible impurities. The functional properties of the films (reflectance/transmittance, transition temperature) were studied as well, to test their application as an intelligent material for window coating. Significant changes in the transmittance and reflectance properties were observed on passing the transition temperature; furthermore, a decrease in the transition temperature was observed, with a linear correlation, between the films' niobium content and the value of the temperature. These features indicate Nb-doped $VO_2$ as a suitable material for application in smart windows.

## Experimental Section

**Film Deposition:** Vanadyl(IV) acetylacetonate $[VO(C_5H_8O_2)_2]$ = $[VO(acac)_2]$ and $Nb^V$ ethoxide $[Nb(OC_2H_5)_5]$ were purchased from Aldrich Chemical Co and used as supplied. The aerosol solution was prepared by dissolving both precursors in ethanol. For $[VO(acac)_2]$, a constant concentration of 0.05 mol dm$^{-3}$ was used. Different molar amounts of $[Nb(OC_2H_5)_5]$ were used, in order to have a varying Nb/V molar ratio (5.2–17 mol-%). An aerosol was generated from 50 mL of precursor solution using a Mountain Breeze humidifier; a nitrogen flow of 1.5 L min$^{-1}$ (BOC, 99.9%) was passed through the aerosol mist, directing the aerosol to a horizontal bed cold wall CVD reactor. Sheets of float glass ($150 \times 45 \times 4$, Pilkington Glass Plc.) were used as deposition substrates; an $SiO_2$ layer, about 50 nm thick, was used to suppress the diffusion of ions from the bulk glass. Prior to the deposition, the substrates were cleaned using water, acetone and 2-propanol and then dried in air. A Tempatron TC4800 thermostat was used to heat the substrates, with the temperature monitored by a Pt-Rh thermocouple. The substrates were heated to a temperature of 500 °C. The aerosol passed between the heated substrate and a glass top plate, placed 8 mm above the substrate and parallel to it. The exhaust was vented into a fume cupboard. The gas flow was continued until all the precursor solution had passed through the reactor; it normally took between 40 and 50 min. At the end of the deposition, the nitrogen flow through the aerosol was diverted and only nitrogen passed over the substrate. A schematic representation of the AACVD deposition apparatus is shown in Figure 1.

**Film Characterisation:** X-ray powder diffraction patterns were measured with a Bruker D8 diffractometer using filtered (Cu-$K_{\alpha 1+\alpha 2}$) radiation in the reflection mode using glancing angle incidence (1.5°). SEM was carried out with a Hitachi filament scanning microscop. EDAX was determined with a Philips XL30 ESEM instrument, data was quantified using Oxford Inca Software. Raman measurements were carried out with a Renishaw system 1000 Raman spectrometer, with an Ar laser excitation source (514 nm). The Raman system was calibrated against the emission lines of argon. X-ray photoelectron spectroscopy (XPS) measurements were carried out with a VG ESCALAB 220i XL instrument using monochromatic Al-$K_\alpha$ radiation. Binding energies were referenced to surface elemental carbon at 284.6 eV. Depth profiling was carried out using a 3-kV argon ion gun operating at 0.5 μA to sputter the surface of the film. Reflectance and transmission spectra were recorded between 300 and 2500 nm with a Perkin–Elmer Lambda 950 UV/Vis spectrometer. Measurements were standardised relative to a Spectralon® standard (reflectance) and air (transmission). For measurements at different temperatures, an aluminium temperature cell, controlled by RS resistive heaters, Eurotherm temperature controllers and k-type thermocouples were used to manipulate the sample temperature. The sample temperature was measured using a k-type thermocouple taped directly onto the film surface.

## Acknowledgments

This research was financially supported by the EU project Termoglaze COOP-CT-2005-017761. The authors would like to thank Pilkington Glass for providing the deposition substrates, Mr. Kevin Reeves for the help with scanning electron microscopy, Dr. Steve Firth for the help with Raman spectroscopy. I. P. P. thanks the Royal Society/Wolfson Trust for a merit award.

[1] F. J. Morin, *Phys. Rev. Lett.* **1959**, *3*, 34–36.
[2] T. D. Manning, I. P. Parkin, R. J. H. Clark, D. Sheel, M. E. Pemble, D. Vernadou, *J. Mater. Chem.* **2002**, *12*, 2936–2939.
[3] F. Beteille, R. Morineau, J. Livage, M. Nagano, *Mater. Res. Bull.* **1997**, *32*, 1109–1117.
[4] T. D. Manning, I. P. Parkin, M. E. Pemble, D. Sheel, D. Vernardou, *Chem. Mater.* **2004**, *16*, 744–749.

 © 2007 Wiley-VCH Verlag GmbH & Co. KGaA, Weinheim 

[5] T. D. Manning, I. P. Parkin, C. Blackman, U. Qureshi, *J. Mater. Chem.* **2005**, *15*, 4560–4566.
[6] W. Burkhardt, T. Christmann, B. K. Meyer, W. Niessner, D. Schalch, A. Scharmann, *Thin Solid Films* **1999**, *345*, 229–235.
[7] P. Jin, S. Nakao, S. Tanemura, *Thin Solid Films* **1998**, *324*, 151–158.
[8] I. Takahashi, M. Hibino, T. Kudo, *Jpn. J. Appl. Phys.* **2001**, *40*, 1391–1395.
[9] C. Piccirillo, R. Binions, I. P. Parkin, *Thin Sol. Films*, submitted for publication.
[10] C. B. Greenberg, *Thin Solid Films* **1983**, *110*, 73–82.
[11] T. D. Manning, Ph. D. Thesis, London, **2004**.
[12] K. L. Choy, *Prog. Mater. Sci.* **2003**, *48*, 57–170.
[13] W. B. Cross, I. P. Parkin, *Chem. Commun.* **2003**, *14*, 1696–1697.
[14] R. Binions, C. J. Carmalt, I. P. Parkin, *Thin Solid Films* **2004**, *469–470*, 416–419.
[15] C. Piccirillo, I. P. Parkin, R. Binions, *Chem. Vap. Depos.*, in press.
[16] C. D. Wagner, A. V. Naumkin, A. Kraut-Vass, J. W. Allison, C. J. Powell, J. R. Rumble, *NIST X-ray Photoelectron Spectroscopy Database*, version 3.4 (web version), NIST, **2003**, http://srdata.nist.gov/xps/.

Received: March 12, 2007
Published Online: July 11, 2007

 © 2007 Wiley-VCH Verlag GmbH & Co. KGaA, Weinheim 

DOI: 10.1002/ejic.200600933

# Synthesis and Properties of Tetrasubstituted 1,10-Phenanthrolines and Their Ruthenium Complexes

**Bernhard Schäfer,[a] Helmar Görls,[a] Susann Meyer,[b] William Henry,[c] Johannes G. Vos,[c] and Sven Rau*[a]**

**Keywords:** Ruthenium / Phenanthroline / Luminescence / Photochemistry

The synthesis and the photophysical properties of a series of tetrasubstituted phenanthroline (phen) ruthenium complexes of the type $[Ru(tbbpy)_2(phen\text{-}R_4)]^{2+}$ (tbbpy = 4,4′-di-*tert*-butyl-2,2′-bipyridine; phen = 1,10-phenanthroline; R represents the substitution at 3-, 5-, 6- and 8-positions with phenyl, 4-*tert*-butylphenyl and *para*-biphenyl) and of a homoleptic $[Ru(phen\text{-}R'_4)_3]^{2+}$ (R′ = 4-*tert*-butylphenyl) are described. The phen-$R_4$ ligands were obtained in high yields using Suzuki-type coupling reactions. The solid-state structure of 3,5,6,8-tetraphenylphenanthroline is reported. The investigation of the photophysical properties of the free ligands reveals a pronounced effect of the aryl substitution on absorption and emission properties. These properties are mirrored in the corresponding complexes, which possess room-temperature emission lifetimes of up to 2833 ns.

(© Wiley-VCH Verlag GmbH & Co. KGaA, 69451 Weinheim, Germany, 2007)

## Introduction

Luminescent polypyridyl–metal complexes, especially of ruthenium and osmium, have received considerable attention due to their favourable combination of interesting photophysical properties such as long-lived excited triplet states ($^3$MLCT) and high chemical stability.[1] This has also allowed them to play an important role in artificial photosynthesis,[2] dye sensitised solar cells[3] or luminescent sensors, for instance, for oxygen.[4] The photophysical properties of the ruthenium and osmium complexes can be easily tuned by variation of the ligand $\pi$-system.[5] Modification of the topology of the ligand structure allows the construction of elaborate supramolecular architectures containing multiple metal centres.[6] Within this context it is essential to be able to introduce substituents at a potential ligand at a predefined position and in variable numbers. Beside bipydines and terpyridines, derivatives of 1,10-phenanthroline (Figure 1) have received increasing attention since they can be easily transformed into various bridging ligands such as tetrapyridophenazins[7] or ligands which form the basis for luminescent DNA sensors.[8]

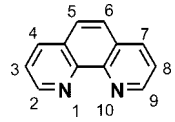


Figure 1. 1,10-Phenanthroline and the numbering scheme employed.

Strong effects on the electronic transitions of the 1,10-phenanthroline ligand and its $Ru^{II}$ complexes have been observed, which depend on the nature and position of the substituents of the phenanthroline scaffold.[9–11] In general, 1,10-phenanthroline ligands substituted at the 2,9- and the 4,7-positions are accessible using various synthetic pathways.[12–15]

However, access to phenanthrolines substituted in the 3- and 3,8-positions is rather limited and often requires tedious work up.[16–19] Tor and co-workers have shown that a multitude of different phenanthrolines can be synthesised by organometallic reactions starting from 3-bromo- and 3,8-dibromo-1,10-phenanthrolines.[20] Using this methodology, Br-phen ligands and the corresponding complexes have been employed in the construction of luminescent sensors for metal ions,[10] multinuclear metal complexes possessing interesting photophysical properties[10,11,16–22] and nucleotide labelled luminescent complexes.[23–25]

Substitutions at the 5,6-positions of the phenanthroline are very rarely reported.[26] 5,6-Bis-thiophenyl-1,10-phenanthrolines, which were obtained by a Suzuki coupling, were employed for the construction of light-driven switches.[27]

[a] Institut für Anorganische und Analytische Chemie, Friedrich Schiller Universität,
Lessingstr. 8, 07743 Jena, Germany
Fax: +49-3641-948102
E-mail: sven.rau@uni-jena.de
[b] Institut für Technische und Umweltchemie, Friedrich Schiller Universität,
Lessingstr. 12, 07743 Jena, Germany
[c] National Centre for Sensor Research, School of Chemical Sciences, Dublin City University,
Dublin 9, Ireland

 © 2007 Wiley-VCH Verlag GmbH & Co. KGaA, Weinheim 

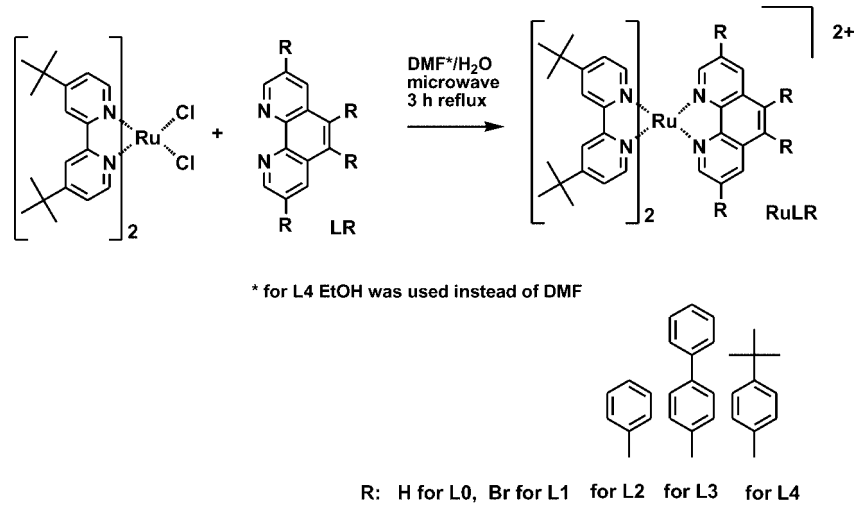


Figure 2. Naming of ruthenium complexes and corresponding ligands.

Recently we reported a bromination reaction of 1,10-phenanthroline which allowed the selective formation of 3,5,6,8-tetrabromophenanthroline (phen-$Br_4$) in an one-step multigram reaction.[28] There we showed that the regioselective nucleophilic substitution of phen-$Br_4$ in the $[Ru(tbbpy)_2(phen\text{-}Br_4)]^{2+}$ complex in the 3,8-position was possible under mild conditions and at room temperature. Furthermore, the synthesis of tetraalkynyl-substituted phenanthrolines based on phen-$Br_4$ was observed using Negishi-type conditions. Preliminary investigations showed that the tetraalkynyl-substituted phenanthrolines may serve as ligands for ruthenium(II) centres.[29]

It is noteworthy that the introduction of alkynyl functional groups in bipyridine or phenanthroline frames leads to the expansion of the conjugated π-system which will have a dramatic impact on the metal-to-ligand charge-transfer excited state of ruthenium complexes. The introduction of aryl substituents, however, does not necessarily lead to the expansion of the conjugated π-system since the torsion angle of these substituents relative to the phenanthroline main frame can be substantial, thus limiting delocalisation.[30] The extremely long lifetimes of the tris-(4,7-diphenylphenanthroline)ruthenium(II) complex of up to 9640 ns which is extensively used in oxygen sensing is, however, worth noting.[31]

In this contribution we present a series of tetraaryl-substituted 1,10-phenanthroline ligands, which were prepared by Suzuki reactions, and their corresponding ruthenium–polypyridyl complexes (see Figure 2).

To avoid solubility problems we utilised the bis(4,4′-di-*tert*-butyl-2,2′-bipyridine)$Ru^{II}$ core, $(tbbpy)_2Ru^{2+}$, since this ensures high solubility in organic solvents.[32] The novel ligands L**2** to L**4** were prepared to illustrate the potential of the building-block approach utilising organometallic C–C coupling reactions. We will focus this investigation on the synthetic accessibility of differently substituted ruthenium complexes with tetrasubstituted phenanthrolines and the preliminary characterisations of their photophysical properties.

## Results and Discussion

### Synthesis

All prepared complexes contain 4,4′-di-*tert*-butyl-2,2′-bipyridine (tbbpy) to increase the solubility of the ruthenium complexes in less polar organic solvents. The new ligands L**2** to L**4** rely on the accessibility of 3,5,6,8-tetrabromophenanthroline (L**1**, phen-$Br_4$) which was conveniently prepared using literature methods.[28] All four bromine functionalities in L**1** were easily substituted by aromatics using conventional Suzuki reactions utilising $Pd(PPh_3)_4$ as catalyst, yielding L**2**–L**4** in good yields (see Figure 3).

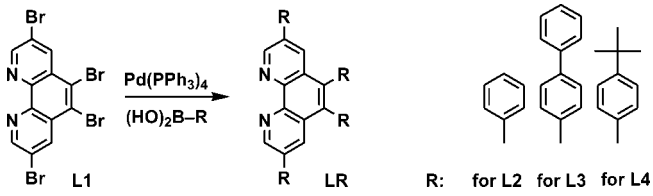


Figure 3. Synthetic route to tetraaryl-substituted phen ligands.

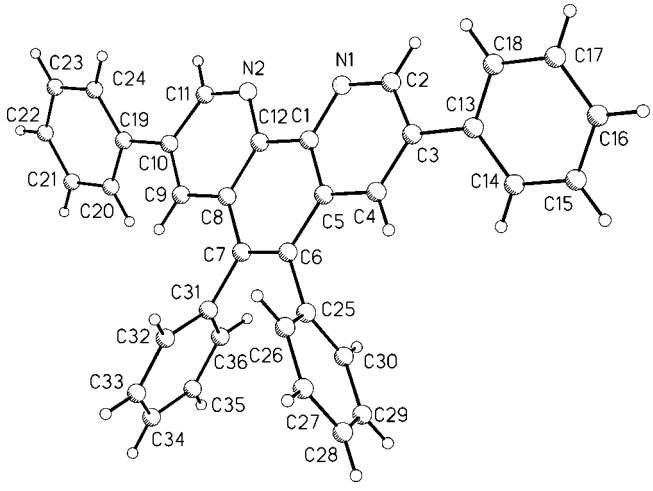


Figure 4. Solid-state structure of L**2**.

 © 2007 Wiley-VCH Verlag GmbH & Co. KGaA, Weinheim 

The nature of the products was unambiguously identified using multidimensional NMR spectroscopic methods, MS and UV-Vis/emission spectroscopy. The nature of the reaction products and the interaction between the hydrogen substituents of the phenanthroline frame and the aryl substituents was confirmed by the solid-state structure obtained for **L2** shown in Figure 4.

The phenanthroline frame is nearly ideally planar (deviation from planarity is 0.015 Å), whereas the two phenyl substituents in the 3,8-positions of the phenanthroline are twisted out of the plane by 29° (C4, C3, C13, C14) and 33° (C9, C10, C19, C20). The two other phenyl substituents in the 5- and 6-positions of the phenanthroline are twisted even more relative to the plane by 82° (C5, C6, C25, C26) and 71° (C7, C8, C31, C32). The strong twisting of the 5,6-substituents is a consequence of the repulsion imposed by the two neighbouring phenyl rings on each other. The smaller steric pressure for the phenyl substituents in the 3,8-positions is a consequence of the interaction of the hydrogen atoms of the phenanthroline pyridine ring with the

Table 1. Photophysical properties of **L2**–**L4**, $[Ru(tbbpy)_2(LR)]^{2+}$ (R = 0, 1, 2, 3, 4) and $[Ru(\mathbf{L4})_3]^{2+}$.

| Compound | Solvent | Absorption | Emission | $\tau$ [ns] | $\tau$ [ns] |
|---|---|---|---|---|---|
| | | $\lambda_{max}$ [nm] ($\varepsilon$ [1000 L mol$^{-1}$ cm$^{-1}$]) | $\lambda_{max}$ [nm] | aerated | deaerated |
| **L0**[a] | DCM | sh[b] 280 (14), 265 (30), 233 (40) | 359 | – | – |
| **L2** | DCM | sh 330 (27), 290 (53), sh 271 (43) | 400 | – | – |
| **L3** | DCM | sh 340 (48), 308 (62), 279 (60) | 406 | – | – |
| **L4** | DCM | sh 335 (29), 300 (47), 265 (37) | 408 | – | – |
| Ru**L0** | ACN | 454 (16), sh 431 (15), 287 (63), 265 (53), 214 (60) | 610 | 211 | 1423 |
| Ru**L1** | ACN | sh 486 (12), 441 (15), 340 (9), 288 (101), 250 (48), 210 (84), 193 (74) | 672 | 100 | 1336 |
| Ru**L2** | ACN | 442 (13), sh 347 (22), 288 (80), 248 (46) | 633 | 189 | 2833 |
| | DCM | 445 (14), 347 (28), 289 (74), 259 (41), 252 (41) | 618 | 529 | 1448 |
| Ru**L3** | ACN | 444 (18), 355 (53), sh 316 (62), 286 (117), 258 (105) | 640 | 201 | 1477 |
| | DCM | 448 (18), 362 (53), sh 318 (54), 286 (113), 261 (100) | 625 | 550 | 1308 |
| Ru**L4** | ACN | 444 (15), 351 (36), sh 313 (46), 288 (80), 243 (53) | 628 | 153 | 1551 |
| | DCM | 462 (15), sh 428 (13), 352 (34), sh 310 (38), 289 (74), 251 (44) | 613 | 468 | 823 |
| $Ru(\mathbf{L4})_3$ | ACN | 465 (19), sh 435 (16), sh 348 (83), 315 (111), 268 (93), 242 (126) | 604 | 151 | 1017 |
| | DCM | 462 (19), 430 (17), 329 (92), 274 (82), 246 (110) | 594 | 198 | 283 |
| $Ru(\mathbf{L0})_3$ | ACN | 445 (16), sh 417 (15), 313 (5), sh 291 (22), 263 (105), 223 (81) | 593 | 460[a] | – |
| | DCM | 448 (17), 422 (15), 314 (5), sh 290 (21), 264 (100) | 578 | 150[a] | – |

[a] The data for **L0** and $Ru(\mathbf{L0})_3$ is given for comparison, see ref.[34] [b] Shoulder = sh.

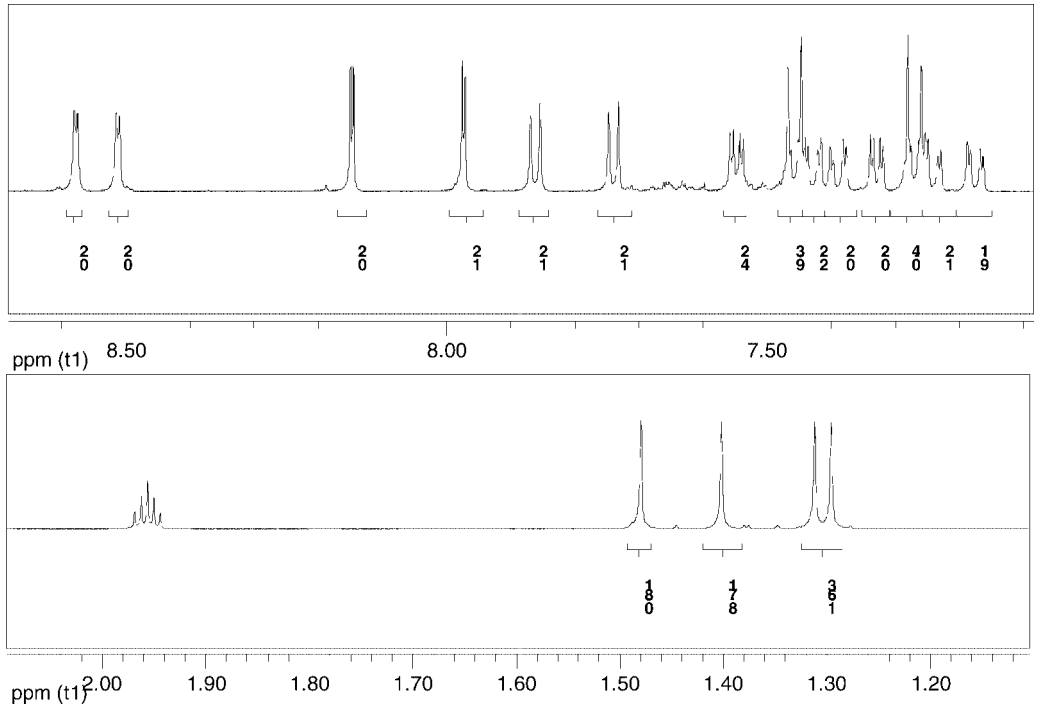


Figure 5. $^1$H NMR spectrum of Ru**L4**.

 © 2007 Wiley-VCH Verlag GmbH & Co. KGaA, Weinheim 

neighbouring phenyl ring which results in significantly smaller torsion angles.

Complexation of **L0**–**L4** to $(tbbpy)_2Ru^{2+}$ fragments [Ru] was achieved using microwave irradiation.[33] Because of the poor solubility of **L2** and **L3**, DMF had to be used. The short reaction times made possible by the use of the microwave ensured that no significant formation of ruthenium–carbonyl complexes from the decomposition of the DMF occurred. The full characterisation of all complexes by multidimensional NMR spectroscopic methods, MS and UV-Vis/emission spectroscopy is outlined in the Experimental Section and in Table 1. The $^1H$ NMR spectrum of the heteroleptic complex Ru**L4** is depicted in Figure 5, and it shows four *tert*-butyl signals between 1.2 and 1.6 ppm. Two *tert*-butyl signals are tbbpy-based, with the third and the fourth stem from the *tert*-butyl groups of the substituents in the 3,8- and 5,6-positions, respectively. The signals in the aromatic region could be assigned to the two *tert*-butyl bipyridine ligands and to the phenanthroline ligand **L4** by H,H COSY NMR spectroscopy.

The compositions of the complexes Ru**L0**–Ru**L4** were additionally confirmed by ESI mass spectroscopy. The spectra always contained the $[M - PF_6]^+$ and $[M - 2PF_6]^{2+}$ peaks. These peaks were assigned to the corresponding molecular ion with the aid of a matching isotopic pattern as depicted for $[RuL4 - PF_6]^+$ in Figure 6.

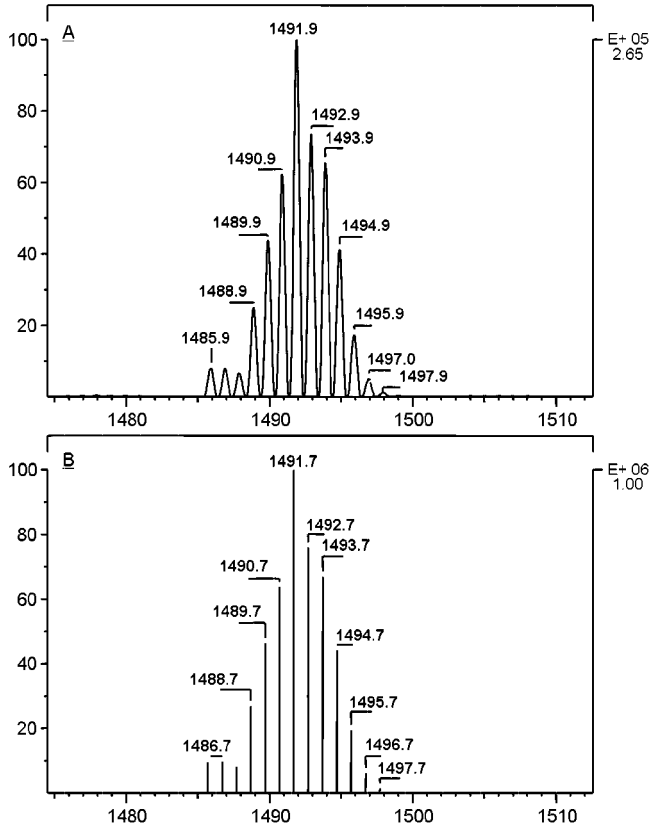


Figure 6. $[RuL4 - PF_6]^+$ peak of the ESI-MS of Ru**L4** in MeOH (A) and the corresponding isotopic pattern (B) of $C_{88}H_{104}N_6RuPF_6$.

We obtained the homoleptic complex $Ru(L4)_3$ using standard microwave-assisted reaction conditions. Attempts to synthesise $Ru(L1)_3$ did not yield any product that could be characterised but rather a mixture of different decomposition products.

## Electronic Spectra

All three new ligands **L2**–**L4** display redshifted absorption maxima relative to that of 1,10-phenanthroline, **L0**, at around 300 nm and a shoulder at around 340 nm and for **L3** up to 370 nm. A clear influence of the peripheral substitution pattern on the shape of the long wavelength maxima is observed (Figure 7). The absorption spectrum of **L0** features two distinct maxima at 265 and 233 nm.[34] All three aromatically substituted ligands (**L2** to **L4**) show relatively strong emission between 400 nm (**L2**) and 408 nm (**L4**) in dichloromethane (DCM). The influence of the aromatic substitution on the emission is obvious by a pronounced redshift of about 40 nm between **L0** and **L2** to **L4**.

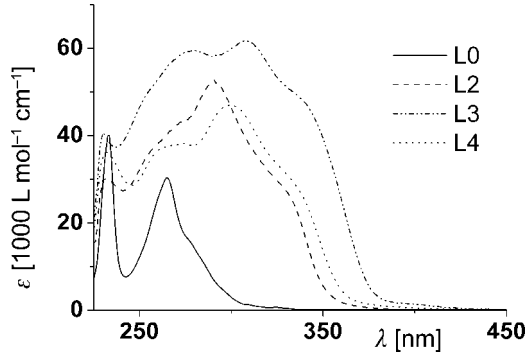


Figure 7. Absorption spectra of LR (R = 0, 2, 3, 4) in $CH_2Cl_2$ (DCM).

The absorption and emission data of **L2** to **L4** indicate that the substitution of the phenanthroline frame with aromatic moieties results in significant changes in the electronic properties of the ligands. A similar observation was previously made for substituted dipyrido[3,2-*a*:2′,3′-*c*]phenazine ligands.[35]

All four complexes Ru**L1** to Ru**L4** show absorption properties which are common for this class of ruthenium–polypyridyl compounds. The absorption spectra in acetonitrile (ACN) of the new complex Ru**L3** and Ru**L0** (for comparison) are depicted in Figure 8. The shape of the long wavelength maxima of the new complexes show an influence of the peripheral substitution pattern since shoulders of these MLCT bands appear slightly redshifted with regard to that of the related compound $[Ru(tbbpy)_2(phen)]^{2+}$ (Ru**L0**). The intensity of the phenanthroline-based transitions at ca. 286 nm increases from Ru**L0** ($63 \times 10^3$ M$^{-1}$ cm$^{-1}$) to Ru**L3** ($117 \times 10^3$ M$^{-1}$ cm$^{-1}$). The introduction of more extensive aromatic substituents leads to a new π–π* transition around 350 nm which decreases in energy and increases in intensity from Ru**L2** (347 nm, $22 \times 10^3$ M$^{-1}$ cm$^{-1}$) to Ru**L4** (351 nm, $36 \times 10^3$ M$^{-1}$ cm$^{-1}$) to Ru**L3** (355 nm, $53 \times 10^3$ M$^{-1}$ cm$^{-1}$).

 © 2007 Wiley-VCH Verlag GmbH & Co. KGaA, Weinheim 

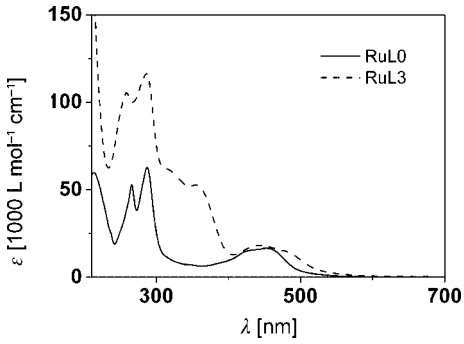


Figure 8. Absorption spectra of Ru**L0** and Ru**L3** in $CH_3CN$.

The homoleptic complex Ru(**L4**)$_3$ has a bathochromically shifted absorption maximum of 465 nm. The next highest energy transition is observed at 348 nm, similar to that of Ru**L4**, but with a higher extinction coefficient as expected. This allows the assignment of this band to a π–π* transition in the tetra(*tert*-butylphenyl)-substituted phenanthroline ligand **L4**. The absorption intensity of the band at 243 nm of the bisheteroleptic Ru**L4** is almost half of the homoleptic Ru(**L4**)$_3$ complexes which can also be considered as a **L4**-based transition. The investigation in dichloromethane shows that no significant changes in the absorption characteristics are observed except for Ru**L4** which displays a redshift of the long wavelength absorption maximum of 18 nm.

The luminescence data for all four complexes were obtained in acetonitrile and dichloromethane. The influence of the solvent on emission wavelength is evident by the ca. 15 nm redshift of the emission maxima upon going from dichloromethane to acetonitrile, which correlates to the increased polarity of the solvent and the nature of the MLCT transition. Similar effects of solvent polarity on the emission wavelength in substituted phenanthroline–ruthenium complexes have been observed.[36] The impact of the substitution at the phen core is observed for the phosphorescence maxima in $CH_3CN$ that shifts from 610 nm for Ru**L0** to 640 nm for Ru**L3** (see Table 1). The emission of the homoleptic Ru(**L4**)$_3$ slightly redshifts to 604 nm relative to the emission of Ru(**L0**)$_3$ (Table 1). Currently it is not possible to give a conclusive explanation for the observed effects of solvent polarity and substitution at the phenanthroline ligand; more detailed investigations using spectroscopic techniques such as resonance Raman and time-resolved spectroscopy in combination with theoretical methods might aid in the interpretation and characterisation of the nature of the emitting state. The information obtained so far indicates that the expansion of the 1,10-phenanthroline frame by aryl substituents does lead to a moderate change in the energies of the excited states which might be caused by limited delocalisation of the resulting aromatic frame due to the twisting of the aryl substituents caused by steric hindrance by neighbouring hydrogen atoms. A higher degree of delocalisation could be obtained by introduction of alkyne substituents like tri(isopropyl)silylacetylene.[29] In this case, the MLCT absorption of $[Ru(tbbpy)_2(L^*)]^{2+}$ {L* = 3,5,6,8-tetrakis[tri(isopropylsilyl)acetylene]phenanthroline} has a maximum at 439 nm with a shoulder at 505 nm and an emission maximum at 692 nm in acetonitrile.

The lifetimes of the excited states of all complexes in aerated solution lie in the expected range. Generally, longer lifetimes are identified in aerated dichloromethane solutions if compared with those in aerated acetonitrile solutions. Deaeration leads in both solvents to increasing lifetimes of the excited triplet MLCT as expected. However, this effect is more pronounced for acetonitrile solutions. In acetonitrile solution a nearly 15-fold increase from 189 to 2833 ns is detected for Ru**L2** upon removal of oxygen. This significant increase in lifetime renders the tetraaryl-substituted phenanthroline complexes potential candidates for applications as oxygen sensors.[4] In contrast to the data obtained for the heteroleptic complexes, the homoleptic complex Ru(**L4**)$_3$ shows relatively short lifetimes of 150 ns, especially if compared with the parent phenanthroline complex Ru(**L0**)$_3$ with 460 ns.

Photometric investigation of a solution of Ru**L2** which had been irradiated in acetonitrile for 72 hours with visible light $\lambda > 450$ nm showed that no significant photobleaching was detected.

## Electrochemistry

The electrochemical behaviour of the complexes was studied in acetonitrile and in DMF (Table 2). The reductions of complexes Ru**L3** and Ru(**L4**)$_3$ are not well-behaved in acetonitrile solution, probably due to the adsorption of the reduced species onto the surface of the electrode, and show abrupt and sharp adsorption and desorption spikes. In DMF this phenomenon disappears in the case of Ru**L3**. The behaviour of Ru(**L4**)$_3$ will be the subject of further investigations. A representative cyclic voltammogram for Ru**L2** is depicted in Figure 9.

Table 2. Electrochemical data for the complexes $[Ru(LR)]^{2+}$ (R = 0, 2, 3, 4).

| Complex | *Solvent* | $E_{1/2}$ox [V]; ($Ru^{II}/Ru^{III}$ vs. $Fc/Fc^+$) | $E_{1/2}$red [V] vs. $Fc/Fc^+$ | | | |
|---|---|---|---|---|---|---|
| Ru**L0** | ACN | 0.74 | –1.77 | –1.98 | –2.25 | – |
| Ru**L1** | ACN | 0.92[a] | – | – | – | – |
| Ru**L2** | ACN | 0.82 | –1.63 | –1.96 | –2.18 | –2.47 |
| Ru**L3** | ACN | 0.82 | – | – | – | – |
| Ru**L4** | ACN | 0.80 | –1.65 | –1.96 | –2.19 | –2.56 |
| Ru**L0** | DMF | 0.76 | –1.78 | –1.99 | –2.24 | – |
| Ru**L2** | DMF | 0.77 | –1.60 | –1.94 | –2.18 | – |
| Ru**L3** | DMF | 0.78 | –1.58 | –1.95 | –2.18 | –2.43 |
| Ru**L4** | DMF | 0.76 | –1.62 | –1.95 | –2.19 | –2.57 |

[a] Data taken from ref.[28]

The oxidation potentials of the ruthenium complexes Ru**L2**–Ru**L4** are only slightly affected by the peripheral substitution at the phen ligand (Table 2). This can be observed by the increase in the oxidation potential of Ru**L0** (0.74 V) over Ru**L4** (0.80 V) followed by Ru**L2** (0.82 V) and Ru**L3** (0.82 V) vs. $Fc/Fc^+$. The presence of four bromo sub-

 © 2007 Wiley-VCH Verlag GmbH & Co. KGaA, Weinheim 

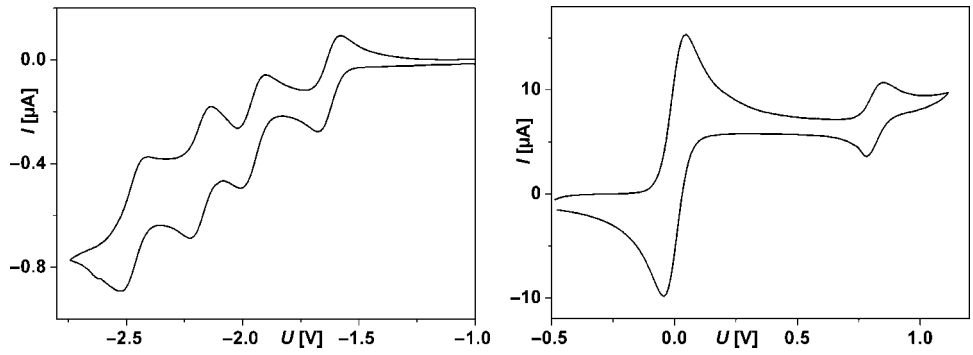


Figure 9. Cyclic voltammograms of RuL**2** (1 mM) in $CH_3CN$ containing $Bu_4NBF_4$ (0.1 M) vs. $Fc/Fc^+$ at 0.0 V (scan rate 0.05 $Vs^{-1}$, step potential 0.01 V).

stituents in RuL**1** shifts the oxidation potential of the ruthenium centre by 0.18 to 0.92 V. This suggests that the introduction of the aryl substituents has a relatively small influence on the metal-based ground state. The value observed for the first reduction potential suggests that L**2**–L**4** are easier to reduce than L**0**.

The reduction events of the complexes RuL**2**–RuL**4** in DMF show only small differences in their potentials of maximal 40 mV for the first reduction and ca. 10 mV for the second and third reduction processes. In contrast to this, the potentials of the ligand reduction of the unsubstituted RuL**0** show a cathodic shift with regard to the potentials of RuL**2**–RuL**4**. The differences of these shifts are 180 mV for the first, 40 mV for the second and 60 mV for the third reduction process.

## Conclusions

In conclusion we have shown that it is possible to introduce four substituents into a phenanthroline frame using Suzuki coupling reactions starting from the free ligand phen-$Br_4$, L**1**. The absorption spectra of the free ligands are highly dependent on the substitution pattern. Importantly, with increasing aryl character the ligand-centred π–π* transition of the LR ligand moves to lower energy. The substituted ligands form heteroleptic complexes in high yields. It is also possible to form a homoleptic complex with a *tert*-butyl-substituted 3,5,6,8-tetraphenylphenanthroline, Ru(L**4**)$_3$. The UV/Vis spectra of the complexes RuL**2**–RuL**4** show a redshift of the MLCT bands and the appearance of intensive π–π* transitions between 300 and 400 nm. The excited-state lifetimes of tetrasubstituted Ru–phenanthroline complexes are very sensitive to oxygen; the lifetime is almost 3 µs for RuL**2**. If compared with that of the unsubstituted phenanthroline complex RuL**0**, this represents an increase of 100% in the lifetime of the excited state. The synthetic accessibility of various tetrasubstituted phenanthrolines makes them ideal targets for further developments as building blocks for the construction of tuneable luminescent sensors or oligonuclear complexes.

## Experimental Section

Unless otherwise noted, all Pd-catalysed cross-coupling reactions were conducted under dry, deoxygenated argon using standard Schlenk techniques. Ru(tbbpy)$_2Cl_2$[33] and 3,5,6,8-tetrabromo-1,10-phenanthroline[28] were prepared using literature methods. Toluene was distilled from sodium benzophenone ketyl under argon prior to use. All other solvents were used as received. Boronic acids were purchased from Fluka, Aldrich and Lancaster.

$^1$H NMR spectra were recorded with a Bruker 400 MHz/200 MHz spectrophotometer. The mass spectra were obtained using a SSQ 170, Finnigan MAT at the Friedrich Schiller University, Jena. Electrospray mass spectra were recorded with a Finnigan MAT, MAT 95 XL. The positive ES mass spectra were obtained with voltages of 3–4 kV applied to the electrospray needle. The microwave-assisted reactions were carried out using the Microwave Laboratory Systems MLS EM-2 microwave system.

**Typical Procedure for Preparation of LR (R = 2, 3, 4) from phen-$Br_4$ (L1):** A Schlenk vessel was charged with phen-$Br_4$ (0.3 g, 0.61 mmol) and the corresponding boronic acid (2.54 mmol), $Pd(PPh_3)_4$ [0.044 g, $n = 3.81 \times 10^{-5}$ mol (1.5 mol-%)] in dry toluene (60 mL) and oxygen-free solution of 2 M aqueous $Na_2CO_3$ (20 mL). The suspension was refluxed under argon for 3 d. After cooling to room temp., the reaction mixture was taken up in water (100 mL) followed by extraction with chloroform. The solvent of the combined organic layers was removed, and the crude product was dried under vacuum. Column chromatography was performed using silica and a gradient eluent system starting with $CHCl_3$ and changing to $CHCl_3$/MeOH (99:1 and later to 9:1). The main fluorescent band was collected and yielded the pure ligand.

**3,5,6,8-Tetraphenylphenanthroline (L2):** Yield: 71%. $^1$H NMR ($CD_2Cl_2$): $\delta$ = 7.24–7.65 (m, 20 H, phenyl), 8.07 [s, long-range coupling (lc), $^4J$ = 2 Hz, 2 H, H4,H7-phen], 9.41 [s(lc), $^4J$ = 2 Hz, 2 H, H2,H9-phen] ppm. MS (DEI, EI+Q1MS): *m*/*z* (%) = 484 (100) [$M^+$]. $C_{36}H_{24}N_2 \cdot 1CH_3OH$ (516.61): calcd. C 86.02, H 5.46, N 5.42; found C 85.93, H 5.25, N 5.14.

**3,5,6,8-Tetra(*para*-biphenyl)phenanthroline (L3):** Yield: 82%. $^1$H NMR ($CDCl_3$): $\delta$ = 7.30–7.75 (m, 36 H, phenyl), 8.36 (s, 2 H, H4,H7-phen), 9.68 [s(lc), 2 H, H2,H9-phen] ppm. MS (DEI, EI+Q1MS): *m*/*z* (%) = 788 (28) [$M^+$]. Recrystallisation from $CH_2Cl_2$. $C_{60}H_{40}N_2 \cdot 0.5CH_2Cl_2$ (831.43): calcd. C 87.4, H 4.97, N 3.37; found C 87.8, H 5.32, N 2.99.

**3,5,6,8-Tetra(4-*tert*-butylphenyl)phenanthroline (L4):** Yield: 76%. $^1$H NMR ($CDCl_3$): $\delta$ = 1.28 (s, 18 H, $CH_3$ *tert*-butyl), 1.35 (s, 18

 © 2007 Wiley-VCH Verlag GmbH & Co. KGaA, Weinheim 

H, $CH_3$ *tert*-butyl), 7.05 (d, $^3J$ = 8 Hz, 4 H, phenylA), 7.25 (d, $^3J$ = 8 Hz, 4 H, phenylA), 7.51 (d, $^3J$ = 8.4 Hz, 4 H, phenylB), 7.57 (d, $^3J$ = 8.4 Hz, 4 H, phenylB), 8.34 (s, 2 H, H4,H7-phen), 9.57 (s, 2 H, H2,H9-phen) ppm. MS (DEI, EI+Q1MS): *m*/*z* (%) = 709 (4) [$M^+$]. $C_{52}H_{56}N_2{\cdot}1CH_3OH$ (741.05): calcd. C 85.9, H 8.16, N 3.78; found C 85.81, H 7.72, N 3.33.

**Preparation of RuL2 and RuL3:** $Ru(tbbpy)_2Cl_2$ (0.1 g, 0.14 mmol) and the corresponding ligand (0.14 mmol) were suspended in DMF/$H_2O$ (80 mL/10 mL) and heated at reflux for 3 h using microwave irradiation (150 W). Afterwards the reaction mixture was filtered, and the solvent was removed under reduced pressure. The complexes were recrystallised from a mixture of ethanol and aqueous $NH_4PF_6$, and further purified by column chromatography using a stationary silica phase and a gradient changing from EtOH to EtOH/$H_2O$/$KNO_3$. The novel ruthenium complexes based on the aryl-substituted phenanthroline ligands did not yield satisfactory elemental analysis results, which might be due to the presence of multiple flexible substituents retaining varying amounts of solvents.

**$[Ru(tbbpy)_2(L2)](PF_6)_2$ (RuL2):** Yield 84%. $^1$H NMR ($CD_3CN$, 400 MHz): $\delta$ = 1.38 (s, 18 H, $CH_3$ *tert*-butyl), 1.45 (s, 18 H, $CH_3$ *tert*-butyl), 7.25–7.45 (m, 22 H, phenyl, H5-bpy), 7.52 (d, $^3J$ = 6 Hz, $^4J$ = 2 Hz, 2 H, H5′-bpy), 7.73 (d, $^3J$ = 6 Hz, 2 H, H6-bpy), 7.83 (d, $^3J$ = 6 Hz, 2 H, H6′-bpy), 8.00 (s, $^4J$ = 1.6 Hz, 2 H, phen), 8.11 (s, $^4J$ = 2 Hz, 2 H, phen), 8.49 (s, $^4J$ = 2 Hz, 2 H, H3-bpy), 8.56 (s, $^4J$ = 1.6 Hz, 2 H, H3′-bpy) ppm. MS (ESI, MeOH): *m*/*z* = 1267.5 ($[M - PF_6]^+$, 100% with matching isotopic pattern).

**$[Ru(tbbpy)_2(L3)](PF_6)_2$ (RuL3):** Yield: 70%. $^1$H NMR ($CD_3CN$, 400 MHz): $\delta$ = 1.39 (s, 18 H, $CH_3$ *tert*-butyl), 1.47 (s, 18 H, $CH_3$ *tert*-butyl), 7.3–7.5 (m, 18 H, phenyl, H5-bpy), 7.55 [d(lc), $^3J$ = 5.8, $^4J$ = 1.8 Hz, 2 H, H5′-bpy], 7.58–7.70 (m, 20 H, phenyl), 7.77 (d, $^3J$ = 6 Hz, 2 H, H6-bpy), 7.86 (d, $^3J$ = 5.6 Hz, 2 H, H6′-bpy), 8.09 [s(lc), $^4J$ = 2 Hz, 2 H, phen], 8.26 [s(lc), $^4J$ = 2 Hz, 2 H, phen], 8.517 [s(lc), $^4J$ = 2 Hz, 2 H, H3-bpy], 8.58 [s(lc), $^4J$ = 2 Hz, 2 H, H3′-bpy] ppm. MS (ESI, MeOH): *m*/*z* = 1571.5 ($[M - PF_6]^+$, 74%), 713.3 ($[M - 2PF_6]^{2+}$, 100% with matching isotopic pattern).

**Preparation of $[Ru(tbbpy)_2(L4)](PF_6)_2$ (RuL4):** $Ru(tbbpy)_2Cl_2$ (0.2 g, 0.282 mmol) and the corresponding ligand (0.282 mmol) were suspended in EtOH/$H_2O$ (60 mL/20 mL) and heated at reflux for 1 h using microwave irradiation (150 W). Afterwards the reaction mixture was filtered. The work-up procedure used was the same as that for Ru**L2** and Ru**L3**. Yield: 89%. Silica and chloroform were used for column chromatography. $^1$H NMR ($CD_3CN$, 400 MHz): $\delta$ = 1.27 (s, 18 H, $CH_3$ *tert*-butyl), 1.28 (s, 18 H, $CH_3$ *tert*-butyl), 1.38 (s, 18 H, $CH_3$ *tert*-butyl), 1.46 (s, 18 H, $CH_3$ *tert*-butyl), 7.15 (d, $^3J$ = 8 Hz, $^4J$ = 1.8 Hz, 2 H, phenylA), 7.22 (d, $^3J$ = 8 Hz, $^4J$ = 1.6 Hz, 2 H, phenylA), 7.25 (d, $^3J$ = 8.4 Hz, 4 H, phenylB), 7.31 (d, $^3J$ = 6.4 Hz, $^4J$ = 2 Hz, 2 H, H5-bpy), 7.36 (d, $^3J$ = 8.4 Hz, $^4J$ = 1.8 Hz, 2 H, phenylA), 7.40 (d, $^3J$ = 8 Hz, $^4J$ = 2.2 Hz, 2 H, phenylA), 7.44 (d, $^3J$ = 8.8 Hz, 4 H, phenylB), 7.53 (d, $^3J$ = 6, $^4J$ = 2 Hz, 2 H, H5′-bpy), 7.72 (d, $^3J$ = 6 Hz, 2 H, H6-bpy), 7.84 (d, $^3J$ = 6 Hz, 2 H, H6′-bpy), 7.95 (s, $^4J$ = 2 Hz, 2 H, H4,H7-phen), 8.12 (s, $^4J$ = 1.6 Hz, 2 H, H2,H9-phen), 8.49 (s, $^4J$ = 1.6 Hz, 2 H, H3-bpy), 8.55 (s, $^4J$ = 1.6 Hz, 2 H, H3′-bpy) ppm. MS (ESI, MeOH): *m*/*z* = 1491.5 ($[M - PF_6]^+$, 100% with matching isotopic pattern), 673.3 ($[M - 2PF_6]^{2+}$, 55% with matching isotopic pattern).

**Synthesis of the Homoleptic Complex of L4, $[Ru(L4)_3](PF_6)_2$ $[Ru(L4)_3]$:** A mixture of $RuCl_3{\cdot}3H_2O$ (0.012 g, 45.9 μmol) and L**4** (0.101 g, 0.143 mmol) was suspended in ethanol (30 mL), methanol (20 mL), DMF (15 mL) and water (15 mL). The reaction mixture was refluxed in a microwave oven for 3 h at 200 W and cooled down. Afterwards the solution was filtered, and the solvent was removed by rotary evaporation. The crude product was purified using column chromatography [silica, $CHCl_3$/heptane (v/v = 2)]. While the amount of heptane in the gradient was decreased, a violet band and a red main band were gathered from the column. Switching the eluent to $CHCl_3$/MeOH led to the collection of a brown band. The red band was recrystallised from acetone and aqueous $NH_4PF_6$ solution. Yield: 46%. $^1$H NMR ($CD_3CN$, 400 MHz): $\delta$ = 1.24 (s, 54 H, $CH_3$ *tert*-butyl), 1.29 (s, 54 H, $CH_3$ *tert*-butyl), 7.23 (d, $^3J$ = 8.4 Hz, 12 H, phenyl), 7.39 (d, $^3J$ = 8.4 Hz, 12 H, phenyl), 8.20 [s(lc), $^4J$ = 2 Hz, 6 H, phen], 8.47 [s(lc), $^4J$ = 2 Hz, 6 H, phen] ppm. MS (ESI, MeOH): *m*/*z* = 2372 ($[M - PF_6]^+$, 26% with matching isotopic pattern), 1114.4 ($[M - 2PF_6]^{2+}$, 100% with matching isotopic pattern).

**Crystal Structure Determination:** The intensity data for the compound were collected with a Nonius KappaCCD diffractometer using graphite-monochromated Mo-$K_\alpha$ radiation. Data were corrected for Lorentz and polarisation effects but not for absorption.[37,38] The structures were solved by direct methods (SHELRS[39]) and refined by full-matrix least-squares techniques against $F_o^2$ (SHELRL-97[40]). The hydrogen atoms of the structures were included at calculated positions with fixed thermal parameters. All non-hydrogen atoms were refined anisotropically.[40] XP (SIEMENS Analytical X-ray Instruments, Inc.) was used for structure representations. CCDC-617531 (L**2**) contains the supplementary crystallographic data for this paper. These data can be obtained free of charge from The Cambridge Crystallographic Data Centre via www.ccdc.cam.ac.uk/data_request/cif.

**Crystal Data for L2:** $C_{36}H_{24}N_2{\cdot}2CHCl_3$, $M_r$ = 723.31 g mol$^{-1}$, colourless prism, size 0.05 × 0.05 × 0.04 mm$^3$, triclinic, space group $P\bar{1}$, *a* = 12.8649(8), *b* = 12.9330(6), *c* = 12.9950(7) Å, *α* = 64.525(3), *β* = 64.591(3), *γ* = 68.457(3)°, *V* = 1718.31(16) Å$^3$, *T* = –90 °C, *Z* = 2, $\rho_{calcd.}$ = 1.398 g cm$^{-3}$, $\mu$(Mo-$K_\alpha$) = 5.31 cm$^{-1}$, *F*(000) = 740, 12260 reflections in *h*(–16/16), *k*(–15/16), *l*(–14/16), measured in the range 2.02° ≤ *Θ* ≤ 27.46°, completeness $\Theta_{max}$ = 98.7%, 7758 independent reflections, $R_{int}$ = 0.0281, 5185 reflections with $F_o > 4\sigma(F_o)$, 415 parameters, 0 restraints, $R_1$(obs) = 0.0527, $wR_2$(obs) = 0.1134, $R_1$(all) = 0.0933, $wR_2$(all) = 0.1338, GOOF = 1.003, largest difference peak and hole = 0.462/–0.492 e Å$^{-3}$.

**Electronic Spectroscopy:** UV/Vis absorption spectra (accuracy ±2 nm) were recorded with an Analytikjena Specord S 600 spectrometer with standard software-based tools. Emission spectra (accuracy ±5 nm) were recorded at 298 K using a Perkin–Elmer LS50B luminescence spectrophotometer, which was equipped with a red-sensitive Hamamatsu R298 PMT detector and interfaced with an Elonex PC466 employing Perkin–Elmer FlWinLab custom-built software. Emission spectra are uncorrected for photomultiplier response. 10-mm path length quartz cells were used for recording spectra.

**Emission Lifetime Measurements:** Luminescence lifetime measurements were obtained using an Edinburgh Analytical Instruments (EAI) time-correlated single photon counting apparatus (TCSPC) comprised of two model J-yA monochromators (emission and excitation), a single photon photomultiplier detection system model 5300 and a F900 nanosecond flashlamp (nitrogen filled at 1.1 atm pressure, 40 kHz or 0.3 atm pressure, 20 kHz) interfaced with a personal computer by a NorlandMCA card. A 410 nm cut-off filter was used in emission to attenuate scatter of the excitation light (337 nm); luminescence was monitored at the $k_{max}$ of the emission. Data correlation and manipulation was carried out using EAI F900 software version 6.24. Samples were de-aerated using argon for 30 min prior to measurements, followed by repeated purging to en-

 © 2007 Wiley-VCH Verlag GmbH & Co. KGaA, Weinheim 

sure complete oxygen exclusion. Emission lifetimes were calculated using a single-exponential fitting function, Levenberg–Marquardt algorithm with iterative deconvolution (Edinburgh instruments F900 software). The reduced $v2$ and residual plots were used to judge the quality of the fits. Lifetimes are ±5%.

**Electrochemistry:** The electrochemical measurements were executed with a PGSTAT booth (manufacturer: Autolab) with the aid of the appropriate GPES software. The experiments were carried out by means of a three-electrode technique in degassed acetonitrile with tetrabutylammoniumtetrafluoroborate (0.1 mol $L^{-1}$) as the conducting salt. A Hg-dropping electrode or a rotating-disc platinum electrode was used as the working electrode. The reference electrode was a Ag/AgCl electrode. The electrode's calibration took place according to the ferrocene standard potential in acetonitrile for which a value of +0.827 V was assumed. The concentration of the complexes measured was 1 mmol $L^{-1}$.

## Acknowledgments

Financial support by the DFG (SFB 436) is gratefully acknowledged. S. R. acknowledges financial support by the DFG (RA 1017/1-1 and 1-2). W. H. would like to thank Enterprise Ireland (Grant Number SC/2003/74) for financial support. We would like to thank Professor D. Walther for helpful discussions and encouragement.

[1] V. Balzani, A. Credi, M. Venturi, *Molecular Devices and Machines*, Wiley-VCH, Weinheim, **2003**.
[2] J. Hawecker, J.-M. Lehn, R. Ziessel, *J. Chem. Soc. Chem. Commun.* **1983**, 536; J.-M. Lehn, J.-P. Sauvage, *Nouv. J. Chim.* **1977**, *1*, 449.
[3] B. Oregan, M. Gratzel, *Nature* **1991**, *353*, 737.
[4] B. D. Macraith, C. McDonagh, G. O'Keeffe, T. E. Keyes, J. G. Vos, B. O'Kelly, J. F. McGilp, *Analyst* **1993**, *118*, 385.
[5] J. H. Alstrum-Acevedo, M. K. Brennaman, T. J. Meyer, *Inorg. Chem.* **2005**, *44*, 6802 and references cited therein.
[6] J.-M. Lehn, *Supramolecular Chemistry: Concepts and Perspectives*, VCH, Weinheim, **1995**.
[7] S. Rau, B. Schäfer, D. Gleich, E. Anders, M. Rudolph, M. Friedrich, H. Görls, W. Henry, J. G. Vos, *Angew. Chem. Int. Ed.* **2006**, *45*, 6215.
[8] A. E. Friedman, J. C. Chambron, J.-P. Sauvage, N. J. Turro, J. K. Barton, *J. Am. Chem. Soc.* **1990**, *112*, 4960.
[9] C.-T. Lin, W. Böttcher, M. Chou, C. Creutz, N. Sutin, *J. Am. Chem. Soc.* **1976**, *98*, 6536.
[10] H. S. Joshi, R. Jamshidi, Y. Tor, *Angew. Chem. Int. Ed.* **1999**, *38*, 2721.
[11] H. Suzuki, T. Kanbara, T. Yamamoto, *Inorg. Chim. Acta* **2004**, *357*, 4335.
[12] C. O. Dietrich-Buchecker, J. Guilhem, A.-K. Khemiss, J.-P. Kintzinger, C. Pascard, J. P. Sauvage, *Angew. Chem. Int. Ed. Engl.* **1987**, *26*, 661.
[13] N. Armaroli, L. De Cola, V. Balzani, J. P. Sauvage, C. O. Dietrich-Buchecker, J.-M. Kern, *J. Chem. Soc. Faraday Trans.* **1992**, *88*, 553.
[14] F. Vögtle, I. Lüer, V. Balzani, N. Armaroli, *Angew. Chem. Int. Ed. Engl.* **1991**, *30*, 1333; J. Suffert, R. Ziessel, *Tetrahedron Lett.* **1991**, *32*, 757.
[15] M. Sjörgren, S. Hansson, P.-O. Norrby, B. Akermank, M. Cucciolito, A. Vitagliano, *Organometallics* **1992**, *11*, 3954.
[16] D. Tzalis, Y. Tor, *Tetrahedron Lett.* **1995**, *36*, 6017.
[17] D. Tzalis, Y. Tor, *J. Am. Chem. Soc.* **1997**, *119*, 852.
[18] D. Tzalis, Y. Tor, *Angew. Chem. Int. Ed. Engl.* **1997**, *36*, 2666.
[19] D. J. Hurley, J. R. Roppe, Y. Tor, *Chem. Commun.* **1999**, 993.
[20] Y. Tor, *Synlett* **2002**, *7*, 1043.
[21] P. J. Connors Jr, D. Tzalis, A. L. Dunnick, Y. Tor, *Inorg. Chem.* **1998**, *37*, 1121.
[22] R. Ziessel, C. Stroh, *Tetrahedron Lett.* **2004**, *45*, 4051.
[23] E. C. Glazer, D. Magde, Y. Tor, *J. Am. Chem. Soc.* **2005**, *127*, 4190.
[24] D. J. Hurley, Y. Tor, *J. Am. Chem. Soc.* **1998**, *120*, 2194.
[25] D. J. Hurley, Y. Tor, *J. Am. Chem. Soc.* **2002**, *124*, 3749.
[26] V. W.-W. Yam, C.-C. Ko, L. X. Wu, K. M. C. Wong, K. K. Cheng, *Organometallics* **2000**, *19*, 1820.
[27] V. W.-W. Yam, C.-C. Ko, N. Zhu, *J. Am. Chem. Soc.* **2004**, *126*, 12734.
[28] S. Rau, R. Fischer, M. Jäger, B. Schäfer, S. Meyer, G. Kreisel, H. Görls, M. Rudolph, W. Henry, J. G. Vos, *Eur. J. Inorg. Chem.* **2004**, 2001.
[29] S. Rau, K. Lamm, H. Görls, J. Schöffel, D. Walther, *J. Organomet. Chem.* **2004**, *689*, 3582.
[30] R. Passalacqua, F. Loiseau, S. Campagna, Y.-Q. Fang, G. S. Hanan, *Angew. Chem. Int. Ed.* **2003**, *42*, 1608.
[31] K. F. Mongey, J. G. Vos, B. D. MacCraith, C. M. McDonagh, C. Coates, J. J. McGarvey, *J. Mater. Chem.* **1997**, *7*, 1473.
[32] S. Rau, M. Ruben, T. Büttner, C. Temme, S. Dautz, H. Görls, M. Rudolph, D. Walther, A. Brodkorb, M. Duati, C. O'Connor, J. G. Vos, *J. Chem. Soc. Dalton Trans.* **2000**, 3649.
[33] S. Rau, B. Schäfer, A. Grüßing, S. Schebesta, K. Lamm, J. Vieth, H. Görls, D. Walther, M. Rudolph, U. W. Grummt, E. Birkner, *Inorg. Chim. Acta* **2004**, *357*, 4496.
[34] A. Juris, V. Balzani, F. Barigelletti, S. Campagna, P. Belser, A. von Zelewsky, *Coord. Chem. Rev.* **1988**, *84*, 85.
[35] B. Schäfer, H. Görls, M. Presselt, M. Schmitt, J. Popp, W. Henry, J. G. Vos, S. Rau, *Dalton Trans.* **2006**, *18*, 2225.
[36] B. Higgins, B. A. DeGraff, J. N. Demas, *Inorg. Chem.* **2005**, *44*, 6662.
[37] *COLLECT, Data Collection Software*, Nonius B. V., Netherlands, **1998**.
[38] Z. Otwinowski, W. Minor, "Processing of X-ray Diffraction Data Collected in Oscillation Mode" in *Methods in Enzymology Vol. 276 (Macromolecular Crystallography Part A)* (Eds.: C. W. Carter, R. M. Sweet), Academic Press, San Diego, **1997**.
[39] G. M. Sheldrick, *Acta Crystallogr., Sect. A* **1990**, *46*, 467.
[40] G. M. Sheldrick, *SHELXL-97 (Release 97–2)*, University of Göttingen, Germany, **1997**.

Received: October 3, 2006
Published Online: July 12, 2007

 © 2007 Wiley-VCH Verlag GmbH & Co. KGaA, Weinheim 

DOI: 10.1002/ejic.200700159

# Condensation of Nickel–Carbonyl Clusters with Soft Lewis Acids: Synthesis and Characterisation of the $\{Cd_2Cl_3[Ni_6(CO)_{12}]_2\}^{3-}$ Dimer

**Cristina Femoni,[a] Maria Carmela Iapalucci,[a] Giuliano Longoni,[a] Fabrizio Ranuzzi,[a] Stefano Zacchini,*[a] Serena Fedi,[b] and Piero Zanello[b]**

**Keywords:** Cluster compounds / Carbonyl ligands / Structure elucidation / Lewis acids / Cyclic voltammetry

Reaction of $[Ni_6(CO)_{12}]^{2-}$ in thf with 2 equiv. of the soft Lewis acid $CdCl_2{\cdot}2.5H_2O$ gives the new dimeric species $\{Cd_2Cl_3[Ni_6(CO)_{12}]_2\}^{3-}$. The formation of the latter is not the result of direct addition of $CdCl_2$ to $[Ni_6(CO)_{12}]^{2-}$, but it involves some intermediate species, i.e. $[Ni_9(CO)_{18}]^{2-}$ and $[Ni_9(CO)_{18}Cd_2Cl_4]^{2-}$. The crystal structure of $[NBu_4]_3\{Cd_2Cl_3[Ni_6(CO)_{12}]_2\}{\cdot}$thf was ascertained by X-ray crystallography. In the solid state, the $\{Cd_2Cl_3[Ni_6(CO)_{12}]_2\}^{3-}$ cluster anions are pillared along the crystallographic *c* axis, forming infinite columns of perfectly alternating cluster anions and thf molecules. The chemical and electrochemical behaviours of $\{Cd_2Cl_3[Ni_6(CO)_{12}]_2\}^{3-}$ are also reported and compared to those of the parent $[Ni_6(CO)_{12}]^{2-}$ dianion.

(© Wiley-VCH Verlag GmbH & Co. KGaA, 69451 Weinheim, Germany, 2007)

## 1. Introduction

Several low-valent metal clusters, stabilised mainly or uniquely by carbonyl ligands, apart from being molecules or molecular ions perfectly defined in composition and all structural details, trespass by size in the field of nanomaterials (1–1000 nm) from the lowest limit.[1] Pseudo 1D molecular carbonyl clusters (MCC) possessing nanometric size have been known for a long time. For instance, the $[Pt_{15}(CO)_{30}]^{2-}$[2] dianion has a metal frame length of ca. 1.5 nm. More-or-less spherical or ellipsoidal clusters, such as $[Ni_{32}Pt_{24}(CO)_{56}]^{6-}$,[3] $[Ni_{26}Pd_{20}(CO)_{54}]^{6-}$,[4] $Pd_{59}(CO)_{32}(PMe_3)_{21}$,[5] $Pd_{69}(CO)_{36}(PEt_3)_{18}$[6] and the giant three-shell $Pd_{145}(CO)_x(PEt_3)_{30}$ ($x \approx 30$),[7] display metallic core diameters in the 1–2-nm range. Moreover, several MCC aggregates close to or trespassing in the nanofield can be prepared, for instance by the fusion of two or more anionic clusters with a central core constituted by a single cation, for example $\{Hg[Os_{10}C(CO)_{24}]_2\}^{2-}$,[8] or cationic moieties, such as $[H_2Ru_{12}Cu_6Cl_2(CO)_{34}]^{2-}$,[9] $[H_4Ru_{20}Cu_6Cl_2(CO)_{48}]^{4-}$[10] and $[Ag_3Ru_{10}C_2(CO)_{28}Cl]^{2-}$.[11] The existence in solution of several fused MCC moieties such as $\{Ag[Rh_6C(CO)_{15}]_2\}^{3-}$ and higher $\{Ag_{n-1}[Rh_6C(CO)_{15}]_n\}^{n-}$ oligomers was demonstrated several years ago by multinuclear NMR spectroscopy,[12] and envisions the possibility to isolate MCC aggregates well beyond 2 nm. For instance, an infinite $\{[AgRu_6C(CO)_{16}]^-\}_\infty$ superwire was quantitatively assembled by the reaction of $[Ru_6C(CO)_{16}]^{2-}$ with $Ag^+$ ions.[13] Miscellaneous 1D and 2D arrays assembled through $\eta^2$-carbonyl groups of the previously unknown $[Co_4(CO)_{11}]^{2-}$ dianion with $Yb^{II}$ or $Eu^{II}$ cations were obtained by the reaction of $Hg[Co(CO)_4]_2$ with Yb or Eu metals.[14]

Recently, we reported two different strategies for the polymerisation of MCC. First, the controlled oxidation of $[Pt_6(CO)_{12}]^{2-}$ affords the $[Pt_{18}(CO)_{36}]^{2-}$ and $[Pt_{24}(CO)_{48}]^{2-}$ dianions that self-assemble by formation of homometallic Pt–Pt bonds into 1D $\{[Pt_{18}(CO)_{36}]^{2-}\}_\infty$ and $\{[Pt_{24}(CO)_{48}]^{2-}\}_\infty$ infinite wires upon crystallisation.[15] Secondly, the reaction of $[NBu_4]_2[Pt_9(CO)_{18}]$ with the soft Lewis acid $CdCl_2$ gives the $[Pt_9(CO)_{18}(\mu_3\text{-}CdCl_2)_2]^{2-}$ adduct, which self-assembles upon crystallisation into a 1D $\{[Pt_9(CO)_{18}(\mu_3\text{-}CdCl_2)_2]^{2-}\}_\infty$ polymer through the formation of chloride bridges.[16]

Nickel is known to have a more limited chemistry than platinum for what concerns homometallic carbonyl clusters. For instance, nickel displays only the first two species in the series $[Ni_{3n}(CO)_{6n}]^{2-}$ ($n$ = 2, 3),[17,18] whereas several compounds were prepared and characterised in the $[Pt_{3n}(CO)_{6n}]^{2-}$ ($n$ = 2–10) series.[2] Therefore, self-assembly of $[Ni_{3n}(CO)_{6n}]^{2-}$ ($n$ = 2, 3) units into 1D infinite wires seems unlikely owing to excessive electrostatic repulsion between anions, even if $[Ni_6(CO)_{12}]^{2-}$ in its $[NMe_4]^+$ salt gives rise to columnar stacks.[19] For this reason, we focused our attention on the possibility of building-up oligomeric species based on nickel MCC following the second route described above, i.e. the assembly of nickel clusters with Lewis acids. We report here our results on the oligomerisation of $[Ni_6(CO)_{12}]^{2-}$ with the soft Lewis acid $CdCl_2$.

[a] Dipartimento di Chimica Fisica ed Inorganica, Università di Bologna,
Viale Risorgimento 4, 40136 Bologna, Italy
Fax: +39-0512093690
E-mail: zac@ms.fci.unibo.it
[b] Dipartimento di Chimica dell'Università di Siena
Via Aldo Moro, 53100 Siena, Italy

 InterScience © 2007 Wiley-VCH Verlag GmbH & Co. KGaA, Weinheim 

## 2. Results and Discussion

### 2.1 Synthesis of $\{Cd_2Cl_3[Ni_6(CO)_{12}]_2\}^{3-}$

The reaction of $[Ni_6(CO)_{12}]^{2-}$ in thf with 2 equiv. of $CdCl_2{\cdot}2.5H_2O$ directly affords the $\{Cd_2Cl_3[Ni_6(CO)_{12}]_2\}^{3-}$ oligomer in good yields (ca. 60% based on Ni). The IR spectrum shows $\nu$(CO) at higher frequencies [2025(vs), 1844(m) and 1819(m) $cm^{-1}$, in thf] relative to the parent $[Ni_6(CO)_{12}]^{2-}$ [1980(s), 1810(m) and 1790(m) $cm^{-1}$, in thf], in agreement with the lower negative charge per $[Ni_6(CO)_{12}]$ unit. Despite the fact that the formation of $\{Cd_2Cl_3[Ni_6(CO)_{12}]_2\}^{3-}$ could appear to be the result of the addition of $CdCl_2$ to one triangular face of $[Ni_6(CO)_{12}]^{2-}$ followed by condensation of two of these units and loss of one $Cl^-$ ligand, according to Equation (1), this does not seem to be the case.

$$2\ [Ni_6(CO)_{12}]^{2-} + 2\ CdCl_2 \rightarrow \{Cd_2Cl_3[Ni_6(CO)_{12}]_2\}^{3-} + Cl^- \quad (1)$$

In fact, careful study of the course of the reaction after the addition of $CdCl_2{\cdot}2.5H_2O$ in small portions to a solution of $[Ni_6(CO)_{12}]^{2-}$ indicates a more complex pathway. The first product formed is, in fact, the previously reported $[Ni_9(CO)_{18}]^{2-}$ anion,[17,18] which is the main species present in solution after the addition of ca. 0.5–1 equiv. of $CdCl_2{\cdot}2.5H_2O$. The formation of $[Ni_9(CO)_{18}]^{2-}$ can in principle arise by either the oxidation due to the $Cd^{2+}/Cd$ or the $H^+/H_2$ redox couple consequent to the Bronsted acidity of the water molecules that are coordinated to $Cd^{II}$. As detailed below in Section 2.4, the first oxidation of $[Ni_6(CO)_{12}]^{2-}$ irreversibly occurs at –0.22 V, and the oxidation potential is only slightly affected by the solvent and the nature of the electrode. By taking this potential and the standard redox potential in water of the $Cd^{2+}/Cd$ couple (–0.40 V) as very rough references, it may be suggested that reduction of $Cd^{II}$ to $Cd^0$ by $[Ni_6(CO)_{12}]^{2-}$ is not thermodynamically favoured. Therefore, the oxidation of $[Ni_6(CO)_{12}]^{2-}$ to $[Ni_9(CO)_{18}]^{2-}$ can probably be ascribed to the $H^+/1/2H_2$ redox couple brought about by the acidity of the coordinated water of the $CdCl_2{\cdot}2.5H_2O$ salt. Indeed, though the p$K_a$ of the hydrated $Cd^{II}$ ion is relatively high (10.1), it is known that $[Ni_6(CO)_{12}]^{2-}$ is converted into $[Ni_9(CO)_{18}]^{2-}$ and $[H_{4-n}Ni_{12}(CO)_{21}]^{n-}$ by weak protonic acids and even upon hydrolysis in neutral water.[20] Considering Equation (2), this process would require 0.67 mol of $CdCl_2{\cdot}2.5H_2O$ per mole of $[Ni_6(CO)_{12}]^{2-}$, in fair agreement with our experimental findings.

$$3\ [Ni_6(CO)_{12}]^{2-} + 2\ CdCl_2 + 2\ H_2O \rightarrow 2\ [Ni_9(CO)_{18}]^{2-} + H_2 + 2\ Cd(OH)Cl + 2\ Cl^- \quad (2)$$

Further addition of $CdCl_2{\cdot}2.5H_2O$ to the solution results in the formation of a new species that displays $\nu$(CO) in thf at 2036(vs) and 1824(ms) $cm^{-1}$. This species could not bet isolated and identified, as it was always obtained as a mixture with either $[Ni_9(CO)_{18}]^{2-}$ or $\{Cd_2Cl_3[Ni_6(CO)_{12}]_2\}^{3-}$. Nonetheless, considering the fact that this species displays $\nu$(CO) at higher frequencies relative to both $[Ni_9(CO)_{18}]^{2-}$ and $\{Cd_2Cl_3[Ni_6(CO)_{12}]_2\}^{3-}$, we speculatively assume that it could consist of an adduct between $[Ni_9(CO)_{18}]^{2-}$ and $CdCl_2$, probably featuring a $[Ni_9(CO)_{18}Cd_2Cl_4]^{2-}$ formula. Indeed, the species displays an IR spectrum almost coincident with that of the related $[Pt_9(CO)_{18}Cd_2Cl_4]^{2-}$ species, which was fully characterised.[16] Further addition of $CdCl_2{\cdot}2.5H_2O$, reaching the overall $Cd/Ni_6$ ratio of ca. 2 results in the complete conversion of this adduct into the final $\{Cd_2Cl_3[Ni_6(CO)_{12}]_2\}^{3-}$. The suggestion that $[Ni_9(CO)_{18}]^{2-}$ is an intermediate during the formation of $\{Cd_2Cl_3[Ni_6(CO)_{12}]_2\}^{3-}$ was examined by the reaction of $CdCl_2{\cdot}2.5H_2O$ with a preformed sample of $[Ni_9(CO)_{18}]^{2-}$ prepared by literature methods.[17,20] As shown by IR spectroscopic monitoring, this latter reaction occurs with elimination of $Ni_3(CO)_6$ moieties as $[Ni_3(CO)_6Cl]^-$, according to Equation (3). The $[Ni_3(CO)_6Cl]^-$ byproduct is very unstable and readily decomposes to Ni, chloride ions and $Ni(CO)_4$, which is indeed observed as the only carbonyl final byproduct:

$$2\ [Ni_9(CO)_{18}]^{2-} + 3\ CdCl_2 \rightarrow \{Cd_2Cl_3[Ni_6(CO)_{12}]_2\}^{3-} + 2\ [Ni_3(CO)_6Cl]^- + CdCl^+ \quad (3)$$

The sum of Equations (2) and (3) suggests that the most plausible formal stoichiometry for the formation of $\{Cd_2Cl_3[Ni_6(CO)_{12}]_2\}^{3-}$ requires 1.67 mol of $CdCl_2{\cdot}2.5H_2O$ per mole of $[Ni_6(CO)_{12}]^{2-}$, in fair agreement with the experimentally required ratio between the starting materials [Equation (4].

$$3\ [Ni_6(CO)_{12}]^{2-} + 5\ CdCl_2 + 2\ H_2O \rightarrow \{Cd_2Cl_3[Ni_6(CO)_{12}]_2\}^{3-} + 2\ [Ni_3(CO)_6Cl]^- + CdCl_3^- + H_2 + 2\ Cd(OH)Cl \quad (4)$$

The fact that Ni carbonyl moieties are partially lost during this process explains why the yields based on Ni are not very high (ca. 60%). By considering the overall Equation (4), in fact, it is possible to conclude that the yield in $\{Cd_2Cl_3[Ni_6(CO)_{12}]_2\}^{3-}$ based on Ni cannot exceed 67%.

### 2.2 Crystal Structure of $[NBu_4]_3\{Cd_2Cl_3[Ni_6(CO)_{12}]_2\}{\cdot}thf$

The crystal structure of $[NBu_4]_3\{Cd_2Cl_3[Ni_6(CO)_{12}]_2\}{\cdot}$thf was ascertained by X-ray crystallography. The unit cell contains 6 cluster anions, 18 $[NBu_4]^+$ cations and 6 thf molecules. Some short contacts (below the sum of the van der Waals radii) exist between the carbonyl ligands of the cluster anions and the C–H groups of the $[NBu_4]^+$ cations and the thf molecules. Owing to the high symmetry of the $R\bar{3}c$ space group, only one sixth of one $\{Cd_2Cl_3[Ni_6(CO)_{12}]_2\}^{3-}$ anion, one half of $[NBu_4]^+$ and one thf molecule are independent. Moreover, both $\{Cd_2Cl_3[Ni_6(CO)_{12}]_2\}^{3-}$ and thf lay along the $\bar{3}$ axis, and they display some disorder. In particular, the thf molecule is disordered over six positions, the $[Ni_3(CO)_6]$ triangle bonded to Cd is disordered over three positions and the bridging Cl ligand is statistically disordered over six positions. All above positions are related by $\bar{3}$ symmetry and give an overall count of three chloride ligands and one thf molecule per cluster anion. As shown in Figure 1, the $\{Cd_2Cl_3[Ni_6(CO)_{12}]_2\}^{3-}$ cluster can be described as being

 © 2007 Wiley-VCH Verlag GmbH & Co. KGaA, Weinheim 

composed of two $[Ni_6(CO)_{12}]^{2-}$ units joined by a $Cd_2Cl_3^+$ bridge. Therefore, $\{Cd_2Cl_3[Ni_6(CO)_{12}]_2\}^{3-}$ can be regarded as a Lewis acid–base adduct between the soft acid $Cd_2Cl_3^+$ and the soft basic sites of two $[Ni_6(CO)_{12}]^{2-}$ units, represented by the $Ni_3$ faces. Regarding the $[Ni_6(CO)_{12}]^{2-}$ units, these surprisingly display a distorted trigonal prismatic geometry, rather than the usual antiprismatic configuration found in the crystal structure of $[Ni_6(CO)_{12}]^{2-}$,[17] and for this it rather resembles the analogous platinum compound $[Pt_6(CO)_{12}]^{2-}$.[2,19] As shown in Table 1, which collects the most significant molecular parameters, the intratriangular Ni–Ni distances fall in the narrow range 2.349(6)–2.381(6) Å [average 2.366(10) Å], as previously found in $[Ni_6(CO)_{12}]^{2-}$ and $[Ni_9(CO)_{18}]^{2-}$.[17,18] Conversely, the intertriangular Ni–Ni distances span quite a wide range [2.416(4)–2.712(4) Å], showing also an unusually short contact; by comparison the average intertriangular distances is 2.77 Å in the antiprismatic cluster $[Ni_6(CO)_{12}]^{2-}$ and 2.766 Å and 2.719 Å for the antiprismatic and prismatic moieties of $[Ni_9(CO)_{18}]^{2-}$,[17,18] respectively. The unusually short Ni–Ni intertriangular distances displayed by $\{Cd_2Cl_3[Ni_6(CO)_{12}]_2\}^{3-}$ are due to its distorted trigonal prismatic structure. In particular, the distortion involves the inner triangle, which is slightly shifted and tilted with respect to the outer one, and this explains the very short Ni(1)–Ni(2) distance [2.416(4) Å]. As a consequence of this short bond, the diagonal contact of the corresponding distorted square face of the prism is quite shortened [Ni(2)–Ni(1)#1 2.982(5) Å] relative to the other diagonals [3.171(5)–3.854(4) Å]. Because the centre of the inner $Ni_3(CO)_6$ triangle is shifted with respect to the symmetry axis in which the Cd atom lies, three different Ni–Cd distances are present in the range 2.656(3)–2.802(4) Å. As far as we are aware, the only example of a structurally characterised molecule containing a Ni–Cd interaction is $Cp_2Ni_2Cd_3(GePh_3)_4$,[21] for which the bond lengths are 2.459 and 2.476 Å. The fact that the Ni–Cd bonds in $\{Cd_2Cl_3[Ni_6(CO)_{12}]_2\}^{3-}$ are considerably longer can be explained on the basis of the fact that in the latter the Cd atom is coordinated to a $Ni_3$ triangle probably by a 4c–2e bond, whereas it is connected to single Ni atoms in $Cp_2Ni_2Cd_3(GePh_3)_4$.

The $Cd_2Cl_3$ bridge shows a relatively short Cd–Cd distance [3.236(1) Å]. This contact is shorter than the Cd–Cd distances displayed by other compounds containing the $Cd_2(\mu\text{-}Cl)_3$ group [3.283–3.647 Å],[22] and even the loosest Cd–Cd contacts in metallic cadmium [3.286 Å]. Direct Cd–Cd bonds in molecular compounds, with distances below the sum of Pauling's single-bond metallic radii for cadmium [2.82 Å], are very rare and, as far as we are aware, the only two species structurally characterised so far are the $Cd^I$ derivatives of formula Ar′CdCdAr′ [Ar′ = $C_6H_3$-2,6-($C_6H_3$-2,6-*i*$Pr_3$)$_2$; Cd–Cd 2.6257(5) Å][23a] and $[Cd_2][AlCl_4]_2$ [Cd–Cd 2.576(1) Å].[23b] Therefore, even though the Cd–Cd contact in the $\{Cd_2Cl_3[Ni_6(CO)_{12}]_2\}^{3-}$ anion is shorter than that in other $Cd_2(\mu\text{-}Cl)_3$ moieties, its length seems to argue against the presence of a significant direct bonding interaction. It may be speculated that electron donation from the $[Ni_6(CO)_{12}]^{2-}$ units would increase electron density onto the $Cd^{II}$ ions and may shorten the Cd–Cd distance, formally owing to their partial reduction. It is well-known that reduction of $Hg^{II}$ to $Hg^I$ results in the formation of a Hg–Hg bond.

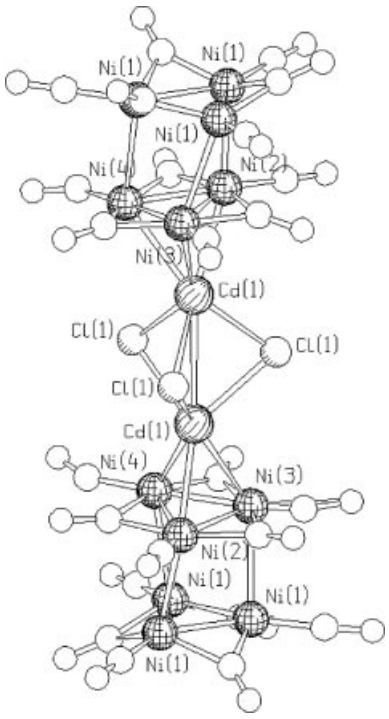


Figure 1. Molecular structure of $\{Cd_2Cl_3[Ni_6(CO)_{12}]_2\}^{3-}$.

Table 1. Bond lengths [Å] in the $\{Cd_2Cl_3[Ni_6(CO)_{12}]_2\}^{3-}$ cluster anion.

| | | | |
|---|---|---|---|
| Ni(1)–Ni(1)[a]1 | 2.365(2) | Ni(2)–C(8) | 1.873(10) |
| Ni(1)–Ni(2) | 2.416(4) | Ni(2)–C(6) | 1.874(9) |
| Ni(1)–Ni(3)[a]2 | 2.680(5) | Ni(3)–C(4) | 1.756(10) |
| Ni(1)–Ni(4)[a]1 | 2.712(4) | Ni(3)–C(7) | 1.862(10) |
| Ni(2)–Ni(3) | 2.349(6) | Ni(3)–C(6) | 1.867(10) |
| Ni(2)–Ni(4) | 2.381(6) | Ni(4)–C(5) | 1.758(10) |
| Ni(3)–Ni(4) | 2.374(4) | Ni(2)–C(3) | 1.767(10) |
| Ni(2)–Cd(1) | 2.656(3) | Ni(4)–C(7) | 1.858(10) |
| Ni(3)–Cd(1) | 2.802(4) | Ni(4)–C(8) | 1.860(10) |
| Ni(4)–Cd(1) | 2.749(4) | C(1)–O(1) | 1.145(8) |
| Ni(1)–Ni(2)[a]2 | 2.982(5) | C(2)–O(2) | 1.163(8) |
| Cd(1)–Cl(1) | 2.590(15) | C(3)–O(3) | 1.161(10) |
| Cd(1)–Cl(1)[a]3 | 2.597(15) | C(4)–O(4) | 1.142(10) |
| Cd(1)–Cd(1)[a]3 | 3.236(1) | C(5)–O(5) | 1.140(10) |
| Ni(1)–C(1) | 1.753(11) | C(6)–O(6) | 1.166(10) |
| Ni(1)–C(2) | 1.826(11) | C(7)–O(7) | 1.145(10) |
| Ni(1)–C(2)[a]1 | 1.931(10) | C(8)–O(8) | 1.165(10) |

[a] Symmetry transformations used to generate equivalent atoms: #1: $-y + 1, x - y, z$; #2: $-x + y + 1, -x + 1, z$; #3: $y + 1/3, x - 1/3, -z + 13/6$.

The $\{Cd_2Cl_3[Ni_6(CO)_{12}]_2\}^{3-}$ cluster anions are pillared along the crystallographic *c* axis, forming infinite columns of perfectly alternating cluster anions and thf molecules (Figure 2). Viewing the packing of $[NBu_4]_3\{Cd_2Cl_3[Ni_6(CO)_{12}]_2\}$·thf along the crystallographic *c* axis (Figure 3) shows a perfect 2D hexagonal arrangements of these infinite columns, which are separated by the $[NBu_4]^+$ cat-

 © 2007 Wiley-VCH Verlag GmbH & Co. KGaA, Weinheim 

ions. Moreover, all the consecutive $\{Cd_2Cl_3[Ni_6(CO)_{12}]_2\}\cdot$thf columns in this 2D arrangement are shifted along the *c* axis to optimise the crystal packing. The distance between the centroids of the outer $Ni_3(CO)_6$ triangles of two consecutive $\{Cd_2Cl_3[Ni_6(CO)_{12}]_2\}^{3-}$ cluster anions is 8.338 Å, whereas the analogous separation of the two inner triangles of the same anion is 7.893 Å, suggesting that replacement of the thf molecule with a second $Cd_2Cl_3^+$ bridge could result in the formation of a perfectly alternated copolymer.

Figure 2. View along the *b* axis of the crystal packing of $[NBu_4]_3\{Cd_2Cl_3[Ni_6(CO)_{12}]_2\}\cdot$thf.

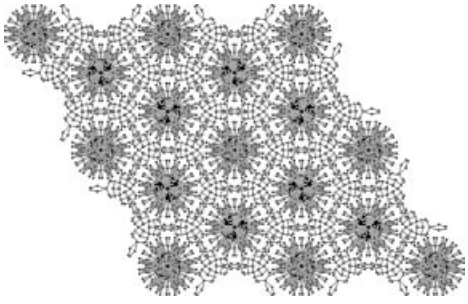

Figure 3. View along the *c* axis of the crystal packing of $[NBu_4]_3\{Cd_2Cl_3[Ni_6(CO)_{12}]_2\}\cdot$thf.

### 2.3. Reactivity of $\{Cd_2Cl_3[Ni_6(CO)_{12}]_2\}^{3-}$

With the aim to prepare the above-suggested alternating copolymer, the $\{Cd_2Cl_3[Ni_6(CO)_{12}]_2\}^{3-}$ cluster was treated in thf with excess $CdCl_2$, but without any major success, apart from the formation of a small amount of an amorphous precipitate that was partially soluble only in dmf. IR spectra of the latter solution indicate the presence of uncoordinated $[Ni_6(CO)_{12}]^{2-}$. Because most of its salts are also well-soluble in less polar solvents, such as thf and acetone, the scarce solubility of the above material could be an indication of the formation of some Cd-rich copolymer containing intact $[Ni_6(CO)_{12}]^{2-}$ units, which is dismantled by dmf. ESI-MS spectra of dmf suspensions of this compound show the presence of $\{CdCl[Ni_6(CO)_{12}]\}^-$ (*m*/*z* = 836) and $[CdCl_3]^-$ (*m*/*z* = 219) ions, which could result from the fragmentation of a $\{Cd_2Cl_3[Ni_6(CO)_{12}]^-\}_\infty$ copolymer. The conclusion drawn from electrochemical studies of $\{Cd_2Cl_3[Ni_6(CO)_{12}]_2\}^{3-}$ (see next section) did not encourage further attempts to prepare $\{Cd_2X_3[Ni_6(CO)_{12}]^-\}_\infty$ copolymers, as evidently the presence of Ni–Ni, Ni–Cd and chloride bridges (and perhaps, incipient Cd–Cd bonds) is not sufficient to guarantee electron communication between the $Ni_6(CO)_{12}$ moieties and, therefore, should not enable relevant electron conduction along the intertriangular axis.

The reaction of $\{Cd_2Cl_3[Ni_6(CO)_{12}]_2\}^{3-}$ with [TBA]Cl results in the formation of $[Ni_6(CO)_{12}]^{2-}$ as outlined in Equation (5).

$$\{Cd_2Cl_3[Ni_6(CO)_{12}]_2\}^{3-} + 5\ Cl^- \rightarrow 2\ [Ni_6(CO)_{12}]^{2-} + 2\ CdCl_4^{2-} \quad (5)$$

This is a further indication of the acid–base interaction existing in $\{Cd_2Cl_3[Ni_6(CO)_{12}]_2\}^{3-}$, which is broken because of the attack of the Lewis base $Cl^-$ at $Cd^{II}$.

Finally, $\{Cd_2Cl_3[Ni_6(CO)_{12}]_2\}^{3-}$ is nearly completely decomposed by a CO atmosphere into $Ni(CO)_4$ and $Cd^{II}$ salts. By carrying out the CO-induced decomposition of $\{Cd_2Cl_3[Ni_6(CO)_{12}]_2\}^{3-}$ in thf, the formation of very small amounts of a brown precipitate was noticed. This is soluble in acetonitrile and displays *ν*(CO) at 1983(s) and 1798(m) $cm^{-1}$, fairly similar to those of the $[Ni_6(CO)_{10}(In_2Br_5)_2]^{4-}$ species [*ν*(CO) 1976(s) and 1784(m) $cm^{-1}$], which was previously obtained from the reaction of $[Ni_6(CO)_{12}]^{2-}$ with $InBr_3$.[24] Its very meagre yields hampered further characterisation.

Aiming to extend the chemistry of bimetallic Ni–Cd carbonyl clusters, the reactions of $[Ni_6(CO)_{12}]^{2-}$ with other $Cd^{II}$ salts, such as $CdF_2$, $CdI_2$ and $[Cd(H_2O)_6][BF_4]_2$, were investigated. No reaction at all was observed with $CdF_2$, whereas the other two reactions on the basis of IR monitoring completely parallel those with $CdCl_2$. Thus, the final products can be formulated as $\{Cd_2I_3[Ni_6(CO)_{12}]_2\}^{3-}$ [*ν*(CO) in thf at 2021(s), 1846(m) and 1822(m) $cm^{-1}$] and $\{Cd_2(OH)_3[Ni_6(CO)_{12}]_2\}^{3-}$ [*ν*(CO) in thf at 2030(s), 1841(m) and 1819(m) $cm^{-1}$].

### 2.4. Electrochemical Studies

Figure 4 shows the redox activity of the trianion $[Cd_2Cl_3\{Ni_6(CO)_{12}\}_2]^{3-}$ in thf solution.

 © 2007 Wiley-VCH Verlag GmbH & Co. KGaA, Weinheim 

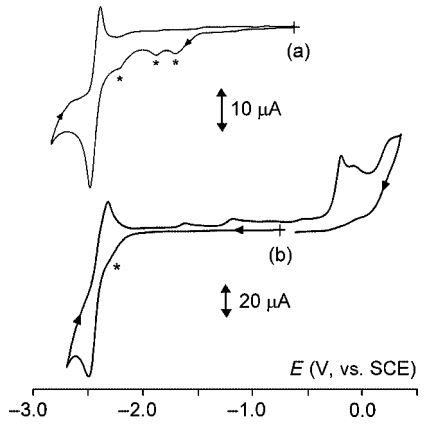


Figure 4. Cyclic voltammograms recorded at a gold electrode in thf solution of: (a) $[NBu_4]_3[Cd_2Cl_3\{Ni_6(CO)_{12}\}_2]$ ($1.7 \times 10^{-3}$ mol dm$^{-3}$); (b) $[NBu_4]_2[Ni_6(CO)_{12}]$ ($2.8 \times 10^{-3}$ mol dm$^{-3}$). $[NBu_4][PF_6]$ (0.2 mol dm$^{-3}$) supporting electrolyte. Scan rate 0.2 V s$^{-1}$.

Apart from a few unidentified processes (asterisked peaks) probably due to minor traces of impurities, the cyclic voltammogram exhibits one reduction, which displays features of partial chemical reversibility in the cyclic voltammetric timescale. In fact, analysis of the cyclic voltammetric responses with scan rates varying from 0.02 to 1.00 V s$^{-1}$ showed that the current ratio $i_{pa}/i_{pc}$ is about 0.7 at the lowest scan rate and progressively increases up to about 0.9 at the highest scan rate. Concomitantly, the peak-to-peak separation tends to increase progressively from 64 to 180 mV, and the current function $i_{pc}v^{-1/2}$ decreases by about 10% for a 10-fold increase in the scan rate. Such parameters are diagnostic for a (substantially) electrochemically reversible electron transfer coupled to slow chemical complications.[25] Unfortunately, the very negative potential value of such a cathodic process ($E°'$ = –2.43 V, vs. SCE) prevented any reliable coulometric determination of the number of electrons involved.

To better define the nature of such a process, it seemed useful to look at the redox properties of the precursor dianion $[Ni_6(CO)_{12}]^{2-}$. As illustrated in Figure 4b, the voltammogram exhibits two main irreversible oxidations ($E_{pa}$ = –0.22 and +0.25 V, respectively), and one reduction displaying features of chemical reversibility in the cyclic voltammetric timescale ($E°'$ = –2.41 V, vs. SCE), which is quite reminiscent of the cathodic process exhibited by $[Cd_2Cl_3\{Ni_6(CO)_{12}\}_2]^{3-}$.

Cyclic voltammetric tests recorded in correspondence of the first anodic step at scan rates varying from 0.02 to 2.00 V s$^{-1}$ showed that the process is rather complex, in that at high scan rates it splits into two separate processes, whereas the close-spaced minor peak ($E_{pa}$ = –0.08 V) tends to disappear. In addition, no directly associated response was detected in the backscan even at the highest scan rate.

Controlled potential coulometry ($E_w$ = 0.0 V) afforded a sudden decline in the electrolysis current after the consumption of about 0.6–0.7 electrons per molecule. Therefore, even if the process seems affected by electrode poisoning effects probably caused by electrogenerated byproducts, it does not seem too ventured to assign it as a one-electron step. Interestingly, a cyclic voltammogram recorded on the solution resulting from the incomplete exhaustive oxidation showed a quite untouched cathodic pattern, thus indirectly supporting that, as reported above, the dimeric trianion $[Cd_2Cl_3\{Ni_6(CO)_{12}\}_2]^{3-}$ arises from chemical oxidation of $[Ni_6(CO)_{12}]^{2-}$.

Also in this case, analysis of the cathodic cyclic voltammetric responses with scan rates varying from 0.02 to 1.00 V s$^{-1}$ showed that: (1) the current ratio $i_{pa}/i_{pc}$ is about 0.7 at the lowest scan rate and progressively increases up to about 0.9 at the highest scan rate, (2) the peak-to-peak separation tends to increase progressively from 75 to 165 mV and (3) the current function $i_{pc}v^{-1/2}$ decreases by about 10% for a 10-fold increase in the scan rate. In both cases, Osteryoung square-wave voltammetry did not appreciably improve the resolution of the voltammetric profiles.

On the basis of the above-mentioned coulometric measurements on the oxidation process of the monomeric dianion (which in cyclic voltammetry exhibits a peak-height substantially similar to that of the cathodic step), on the widths of the square wave peaks at half height (at 25°, $\Delta E_{p/2} = 126/n$ (mV),[25] which are 129 mV for $[Ni_6(CO)_{12}]^{2-}$ and 91 mV for $[Cd_2Cl_3\{Ni_6(CO)_{12}\}_2]^{3-}$, and upon the fact that, under the same concentrations, the peak height of the dimer is about two times that of the monomer, we assign the reduction processes as a one-electron step in the case of the monomeric dianion and as a two-electron step in the case of the dimeric trianion. On this basis, it seems plausible to deduce that the two $[Ni_6(CO)_{12}]$ subunits in $[Cd_2Cl_3\{Ni_6(CO)_{12}\}_2]^{3-}$ are electronically noninteracting.

## 3. Conclusions

The work reported in this paper confirms the Lewis base donor ability of the triangular faces of the clusters $[M_{3n}(CO)_{6n}]^{2-}$ (M = Ni, Pt) and the possibility of exploiting it to obtain oligomers and polymers based on MCC.[16] The use of soft Lewis acids is of paramount importance to address the reaction directly on the metal core of the MCC, rather than on the harder basic sites represented by the CO ligands. These reactions result in new direct heteronuclear M–M′ bonds that, together with ancillary bridging halides ligands M′–$X_n$–M′, cooperate at the formation of oligomers or polymers held together by M–M′–$X_n$–M′–M bridges.

The formation of the $\{Cd_2Cl_3[Ni_6(CO)_{12}]_2\}^{3-}$ dimer indicates some important differences between the reactions of $[Ni_6(CO)_{12}]^{2-}$ and $[Pt_6(CO)_{12}]^{2-}$ with $CdCl_2$. In both cases, the reactions first proceeds by oxidation of $[M_6(CO)_{12}]^{2-}$ (M = Ni, Pt) to give $[M_9(CO)_{12}]^{2-}$ followed by addition of the Lewis acid to the metal frame of the cluster and resulting in the formation of the adducts $[M_9(CO)_{18}Cd_2Cl_4]^{2-}$. Nonetheless, when M = Pt, this adduct is stable and it self-assembles upon crystallisation into a 1D $\{[Pt_9(CO)_{18}(\mu_3\text{-}CdCl_2)_2]^{2-}\}_\infty$ polymer by the formation of chloride brid-

 © 2007 Wiley-VCH Verlag GmbH & Co. KGaA, Weinheim 

ges.[16] Conversely, the nickel analogue loses very easily a $[Ni_3(CO)_6Cl]^-$ unit and is transformed into the $\{Cd_2Cl_3[Ni_6(CO)_{12}]_2\}^{3-}$ dimer. Intrinsically weaker Ni–Ni bonds relative to the Pt–Pt bonds and increasing intraunit steric repulsion between the carbonyl groups upon dimerisation may account for the observed difference.

The different products isolated in the case of Ni and Pt, i.e. $\{Cd_2Cl_3[Ni_6(CO)_{12}]_2\}^{3-}$ and $\{[Pt_9(CO)_{18}(\mu_3\text{-}CdCl_2)_2]^{2-}\}_\infty$, display two alternative bridging modes of the $Cd^{II}$ chloride derivatives, i.e. $[Cd(\mu\text{-}Cl)_3Cd]^+$ and $Cd(Cl)(\mu\text{-}Cl)_2Cd(Cl)$, and suggest that $CdCl_2$ can be a versatile reagent used to assemble MCC.

The redox condensation of $[Ni_6(CO)_{12}]^{2-}$ with halides $MX_n$ of transition metals (e.g. Fe, Co, Rh, Pd, Pt, Cu, Ag, Au) and main group elements (e.g. C, Ge, Sn, Sb, Bi) has been widely exploited to obtain bi- and heterometallic MCC.[1,26] The formation of acid–base adducts, i.e. $[Ni_6(CO)_6(\mu_3\text{-}CO)_5(\mu_3\text{-}InBr_3)(\eta^2\text{-}\mu_6\text{–}In_2Br_5)]^{3-}$, $[Ni_{12}(CO)_{12}(\mu\text{-}CO)_{10}(\mu_6\text{-}In)(\eta^2\text{-}\mu_6\text{–}In_2Br_4OH)]^{4-}$ and $[Ni_6(CO)_{11}(In_2Br_5)_2]^{4-}$,[24] was previously observed only in the case of $InX_3$. This can be explained by the fact that both $Cd^{II}$ and $In^{III}$ are electropositive elements quite difficult to reduce, which form very weak homometallic bonds and with a high affinity for halides

Electrochemistry suggests that the two $[Ni_6(CO)_{12}]$ subunits present in the dimer are electronically independent. Attempts will be made in the future to replace the bridging $Cd_2Cl_3$ fragment with proper units that might favour the electronic interactions between the two peripheral clusters.

## Experimental Section

**General:** All reactions and sample manipulations were carried out by using standard Schlenk techniques under an atmosphere of nitrogen and in dried solvents. The $[Ni_6(CO_{12}]^{2-}$ and $[Ni_9(CO)_{18}]^{2-}$[17,18] salts were prepared according to the literature. Analysis of Ni and Cd were performed by atomic absorption with a Pye-Unicam instrument. Analyses of C, H and N were obtained with a ThermoQuest FlashEA 1112NC instrument. IR spectra were recorded with a Perkin–Elmer SpectrumOne interferometer in $CaF_2$ cells. ESI mass spectra were recorded with a Waters Micromass ZQ4000 instrument. Cyclic voltammetry was performed in a three-electrode cell containing a platinum working electrode surrounded by a platinum-spiral counter electrode, and an aqueous saturated calomel reference electrode (SCE) mounted with a Luggin capillary. A BAS 100W electrochemical analyser was used as the polarising unit. All the potential values are referred to the saturated calomel electrode (SCE). Under the present experimental conditions, the one-electron oxidation of ferrocene occurs at $E°' = +0.59$ V in thf solution. Controlled potential coulometry was performed in an H-shaped cell with anodic and cathodic compartments separated by a sintered-glass disk. The working macroelectrode was a platinum gauze; a mercury pool was used as the counter electrode. Structure drawings were performed with SCHAKAL99.[27]

**$[NBu_4]_3\{Cd_2Cl_3[Ni_6(CO)_{12}]_2\}$:** $CdCl_2·2.5H_2O$ (0.82 g, 3.59 mmol) was added in portions to a solution of $[NBu_4]_2[Ni_6(CO)_{12}]$ (2.01 g, 1.71 mmol) in thf (40 mL) with stirring. The mixture was left to react for 2 h, and the resulting dark red solution was evaporated to dryness. The residue was washed with water (40 mL) and extracted into thf (30 mL). Precipitation by slow diffusion of *n*-hexane (50 mL) gave a red crystalline precipitate composed of crystals of $[NBu_4]_3\{Cd_2Cl_3[Ni_6(CO)_{12}]_2\}$·thf (yield 1.32 g, 61.5% based on Ni). The salt is soluble in thf, acetone, acetonitrile, dmf and dmso, sparingly soluble in alcohols and insoluble in nonpolar solvents. IR (thf, 293 K): $\tilde{\nu}$ = 2025 (vs), 1844 (m), 1819(m) $cm^{-1}$. $C_{76}H_{116}Cd_2Cl_3N_3Ni_{12}O_{25}$ (2507.39): calcd. C 36.41, H 4.66, N 1.68, Ni 28.09, Cd 8.97; found C 36.28, H 4.82, N 1.56, Ni 27.95, Cd 9.02.

**X-ray Crystallographic Study:** Crystal data and collection details for $[NBu_4]_3\{Cd_2Cl_3[Ni_6(CO)_{12}]_2\}$·thf are reported in Table 2. The diffraction experiments were carried out with a Bruker APEX II diffractometer equipped with a CCD detector using Mo-$K_\alpha$ radiation. Data were corrected for Lorentz polarisation and absorption effects (empirical absorption correction SADABS).[28] Structures were solved by direct methods and refined by full-matrix least-squares based on all data using $F^2$.[29] Hydrogen atoms were fixed at calculated positions and refined by a riding model. All non-hydrogen atoms were refined with anisotropic displacement parameters, unless otherwise stated. The $[Ni_3(CO)_6]$ unit bonded to Cd is disordered over three equally populated positions related by symmetry; similarly, the bridging chloride atom is disordered over two symmetry-related positions. Finally, the thf molecule appears disordered around the $\bar{3}$ axis over six symmetry-related positions. Only the independent part of the disordered groups were refined by using the following occupancy factors: 0.33333 for $[Ni_3(CO)_6]$, 0.5 for Cl(1) and 0.16667 for thf. The overall occupancy for each group is one, after applying the related symmetry operations. All the disordered atoms were refined isotropically, except the three Ni and the Cl atoms which were refined anisotropically. Restraints were applied to the C–O distances of the anion, the C–N and C–C dis-

Table 2. Crystal data and experimental details for $[NBu_4]_3\{Cd_2Cl_3[Ni_6(CO)_{12}]_2\}$·thf.

| | |
|---|---|
| Formula | $C_{76}H_{116}Cd_2Cl_3N_3Ni_{12}O_{25}$ |
| *Fw* | 2507.39 |
| *T* [K] | 193(2) |
| $\lambda$ [Å] | 0.71073 |
| Crystal system | rhombohedral |
| Space group | $R\bar{3}c$ |
| *a* [Å] | 20.3179(8) |
| *b* [Å] | 20.3179(8) |
| *c* [Å] | 42.532(3) |
| $\alpha$ [°] | 90 |
| $\beta$ [°] | 90 |
| $\gamma$ [°] | 120 |
| Cell volume [Å$^3$] | 15205.5(15) |
| *Z* | 6 |
| $D_{calcd.}$ [g cm$^{-3}$] | 1.643 |
| $\mu$ [mm$^{-1}$] | 2.725 |
| *F*(000) | 7656 |
| Crystal size [mm] | 0.22 × 0.16 × 0.13 |
| $\theta$ limits [°] | 1.50–25.03 |
| Index ranges | $-24 \le h \le 24$ |
| | $-24 \le k \le 24$ |
| | $-50 \le l \le 50$ |
| Reflections collected | 46319 |
| Independent reflections | 2994 [$R_{int}$ = 0.0340] |
| Completeness to $\theta$ = 25.03° | 100% |
| Data/restraints/parameters | 2994/79/–230 |
| Goodness on fit on $F^2$ | 1.026 |
| $R_1$ [$I > 2\sigma(I)$] | 0.0551 |
| $wR_2$ (all data) | 0.1765 |
| Largest diff. peak and hole [e Å$^{-3}$] | 0.669/–0.786 |

 © 2007 Wiley-VCH Verlag GmbH & Co. KGaA, Weinheim 

tances of the $NBu_4^+$ cation and to the C–O and C–C distances of the thf molecule to obtain a satisfactory model.

CCDC-633786 contains the supplementary crystallographic data for this paper. These data can be obtained free of charge from The Cambridge Crystallographic Data Centre via www.ccdc.cam.ac.uk/data_request/cif.

## Acknowledgments

This work was supported by the EU Integrated Project NAIMO (No NMP4-CT-2004-500355) and PRIN2006.

[1] C. Femoni, M. C. Iapalucci, F. Kaswalder, G. Longoni, S. Zacchini, *Coord. Chem. Rev.* **2006**, *250*, 1580–1604.
[2] J. C. Calabrese, L. F. Dahl, P. Chini, G. Longoni, S. Martinengo, *J. Am. Chem. Soc.* **1974**, *96*, 2614–2616; G. Longoni, P. Chini, *J. Am. Chem. Soc.* **1976**, *98*, 7225–7231.
[3] C. Femoni, M. C. Iapalucci, G. Longoni, P. H. Svensson, *Chem. Commun.* **2004**, 2274–2275.
[4] C. Femoni, M. C. Iapalucci, G. Longoni, P. Svensson, J. Wolowska, *Angew. Chem. Int. Ed.* **2000**, *39*, 1635–1637.
[5] N. T. Tran, M. Kawano, D. R. Powell, L. F. Dahl, *J. Am. Chem. Soc.* **1998**, *120*, 10986–10987.
[6] N. T. Tran, L. F. Dahl, *Angew. Chem. Int. Ed.* **2003**, *42*, 3533–3537.
[7] N. T. Tran, D. R. Powell, L. F. Dahl, *Angew. Chem. Int. Ed.* **2000**, *39*, 4121–4125.
[8] L. H. Gade, B. F. G. Johnson, J. Lewis, M. McPartlin, H. R. Powell, *J. Chem. Soc. Chem. Commun.* **1990**, 110–111.
[9] M. A. Beswick, J. Lewis, P. R. Raithby, M. C. Ramirez de Arellano, *Angew. Chem. Int. Ed. Engl.* **1997**, *36*, 291–293.
[10] M. A. Beswick, J. Lewis, P. R. Raithby, M. C. Ramirez de Arellano, *Angew. Chem. Int. Ed. Engl.* **1997**, *36*, 2227–2228.
[11] D. S. Shephard, T. Maschmeyer, B. F. G. Johnson, J. M. Thomas, G. Sankar, D. Ozkaya, W. Zhou, R. D. Oldroyd, R. G. Bell, *Angew. Chem. Int. Ed. Engl.* **1997**, *36*, 2242–2245.
[12] B. T. Heaton, L. Strona, S. Martinengo, D. Strumolo, V. G. Albano, D. Braga, *J. Chem. Soc. Dalton Trans.* **1983**, 2175–2182.
[13] T. Nakajima, A. Ishiguro, Y. Wakatsuki, *Angew. Chem. Int. Ed.* **2001**, *40*, 1066–1068.
[14] C. E. Plechnik, S. Liu, X. Chen, E. A. Meyers, S. G. Shore, *J. Am. Chem. Soc.* **2004**, *126*, 204–213.
[15] a) C. Femoni, F. Kaswalder, M. C. Iapalucci, G. Longoni, M. Mehlstäubl, S. Zacchini, A. Ceriotti, *Angew. Chem. Int. Ed.* **2006**, *45*, 2060–2062; b) C. Femoni, F. Kaswalder, M. C. Iapalucci, G. Longoni, S. Zacchini, *Eur. J. Inorg. Chem.* **2007**, 1483–1486.
[16] C. Femoni, F. Kaswalder, M. C. Iapalucci, G. Longoni, S. Zacchini, *Chem. Commun.* **2006**, 2135–2137.
[17] a) J. C. Calabrese, L. F. Dahl, A. Cavalieri, P. Chini, G. Longoni, S. Martinengo, *J. Am. Chem. Soc.* **1974**, *96*, 2616–2618; b) G. Longoni, P. Chini, A. Cavalieri, *Inorg. Chem.* **1976**, *15*, 3025–3027.
[18] a) G. Longoni, P. Chini, L. D. Lower, L. F. Dahl, *J. Am. Chem. Soc.* **1975**, *97*, 5034–5036; b) G. Longoni, P. Chini, *Inorg. Chem.* **1976**, *15*, 3029–3031.
[19] D. Braga, F. Grepioni, P. Milne, E. Parisini, *J. Am. Chem. Soc.* **1993**, *115*, 5115–5122.
[20] A. Ceriotti, P. Chini, R. Della Pergola, G. Longoni, *Inorg. Chem.* **1983**, *22*, 1595–1598.
[21] S. N. Titova, V. T. Bychkov, G. A. Domrechev, G. A. Razuvaev, M. T. Strachkov, L. N. Zacharov, *J. Organomet. Chem.* **1980**, *187*, 167–174.
[22] a) A. Washowska, T. Lis, U. Krewska, Z. Czapla, *Acta Crystallogr., Sect. C* **1990**, *46*, 1768–1770; b) U. Walther, D. Brinkmann, G. Chapuis, H. Arend, *Solid State Commun.* **1978**, *27*, 901–905; c) S. Kashida, S. Sato, *J. Phys. Soc. Jpn.* **1985**, *54*, 2934–2939; d) A. B. Corradi, M. R. Cramarossa, M. Saladini, *Inorg. Chim. Acta* **1997**, *257*, 19–26; e) A. B. Corradi, M. R. Cramarossa, M. Saladini, L. B. Battaglia, J. Giusti, *Inorg. Chim. Acta* **1995**, *230*, 59–65; f) S. Kashhida, Y. Ito, S. Sato, *J. Solid State Chem.* **1987**, *69*, 258–266.
[23] a) Z. Zhu, R. C. Fischer, J. C. Fettinger, E. Rivard, M. Brynda, P. P. Power, *J. Am. Chem. Soc.* **2006**, *128*, 15068–15069; b) R. Faggiani, R. J. Gillespie, J. E. Vekris, *J. Chem. Soc. Chem. Commun.* **1986**, 517–518.
[24] F. Demartin, M. C. Iapalucci, G. Longoni, *Inorg. Chem.* **1993**, *32*, 5536–5543.
[25] P. Zanello in *Inorganic Electrochemistry: Theory, Practice and Application*, RSC, Cambridge, UK, **2003**.
[26] P. D. Mlynek, M. Kawano, M. A. Kozee, L. F. Dahl, *J. Cluster Sci.* **2001**, *12*, 313–338.
[27] E. Keller, *SCHAKAL99*, University of Freiburg, Germany, **1999**.
[28] G. M. Sheldrick, *SADABS: Program for Empirical Absorption Correction*, University of Göttingen, Germany, **1996**.
[29] G. M. Sheldrick, *SHELX97: Program for Crystal Structure Determination*, University of Göttingen, Germany, **1997**.

Received: February 2, 2007
Published Online: July 11, 2007

 © 2007 Wiley-VCH Verlag GmbH & Co. KGaA, Weinheim 

DOI: 10.1002/ejic.200700416

# Silicon–Phosphorus and Silicon–Arsenic Cage Compounds with Bicyclo[2.2.1]heptane, Bicyclo[3.2.1]octane and Tricyclo[3.3.3.1.0$^{3,7}$]nonane Backbones

**Günter Tekautz,[a] Judith Baumgartner,[a] Alk Dransfeld,[a] and Karl Hassler*[a]**

**Keywords:** Cage compounds / Crystal structures / Ab initio calculations / Silicon

The reaction of tris(chlorodimethylsilyl)methylsilane (**1**) and 1,1,2,2-tetrakis(chlorodimethylsilyl)-1,2-dimethyldisilane (**2**) with sodium/potassium arsenide $Na_3As/K_3As$ afforded decamethyl-2,3,5,6,7-pentasila-1,4-diarsabicyclo[2.2.1]heptane (**3**) and dodecamethyl-2,3,4,6,7,8,9-heptasila-1,5-diarsatricyclo-[3.3.1.0$^{3,7}$]nonane (**4**). Compounds **3** and **4** were isolated from the reaction mixture by fractional crystallization and structurally characterized by single-crystal X-ray crystallography. The reaction of **1** with an excess amount of sodium/potassium phosphide ($Na_3P/K_3P$) afforded the cage-shaped anion sodium hexamethyl-2,4,6,7-tetrasila-1-phosphanido-3,5-diphosphabicyclo[3.2.1]octane (**5**), which reacts with chlorotrimethylsilane to form trimethylsilyl-substituted derivative **6**. The molecular structures of **5** and **6** were established by X-ray crystallography. Cages **3**–**6** were also characterized by $^{29}$Si- and $^{31}$P NMR spectroscopy. Owing to indirect spin–spin coupling between the $^{29}$Si and $^{31}$P nuclei, the resonances of the $^{29}$Si nuclei in the spectra of **5** and **6** are only of first order approximately. To account for the observed preferences of the cage structures in these reactions, extensive B3LYP/6-31G* quantum chemical calculations of relative energies of bicyclo[2.2.2] and bicyclo[3.2.1] isomers of $Si_8H_{14}$, $PSi_7H_{13}$, $P_2Si_6H_{12}$ and $P_3Si_5H_{11}$ were conducted. On the basis of the computed charge distributions, the concept of topological charge stabilization was used to predict the relative stabilities.

(© Wiley-VCH Verlag GmbH & Co. KGaA, 69451 Weinheim, Germany, 2007)

## Introduction

The exceptional tendency of the elements silicon (group 14) and phosphorus (group 15) to form rings and cages is well-known and has been reviewed extensively in the past.[1] Much less experimental and theoretical material is available for the heavier elements of these two groups, which are Ge, Sn and Pb and As, Sb and Bi, respectively. As the metallic character of the elements increases with increasing atomic number, the thermal stability of $E_nR_m$ (where R is an organic substituent, for example) decreases considerably. They easily decompose into the metal, thereby forming R–R bonds, as shown in Equation (1). Flasks with metallic-black coatings are a common sight with this type of chemistry.

$$E_nR_m \rightarrow E_{metal} + m/2\ (R_2) \quad (1)$$

It is clear that rings and cages composed of elements of both group 14 and 15 (for instance Si and P, As, Sb or Bi) will behave similarly in this respect. An important difference, however, is in the polar bonds that are present in these cage compounds as a result of the electronegativity difference between the two elements. Not only does this lead to increased chemical reactivity, but also to interesting electronic effects. For instance, in small ring systems such as 1,3-disiladiphosphabicyclobutanes, the ring-strain energy is considerably increased by the electropositive Si atoms, which is reflected in a unusually large P–P distance of 238 pm.[2] Moreover, cage compounds that are composed of elements from group 15 and silicon that also possess Si–Si bonds show unusual electronic interactions between the lone pairs of electrons of the group 15 element and the Si–Si σ electrons. A n→σ* interaction was shown by NBO ab initio calculations and photoelectron spectra of dodecamethyl-2,3,5,6,7,8-hexasila-1,4-diphosphabicyclo[2.2.2]-octane to be responsible for these interactions. X-ray analysis of the molecular structure confirmed the increased Si–Si bond length in the cage, which is reported as 235.9 and 236.3 pm.[3,4] Normal Si–Si bond lengths are 232–234 pm.

Previously, we have reported on the synthesis and molecular structure of decamethyl-2,3,5,6,7-pentasila-1,4-dibismuthabicyclo[2.2.1]heptane from $Na_3Bi/K_3Bi$ and dichlorodimethylsilane,[5] which decomposes quickly at room temperature forming metallic bismuth. We also reported the synthesis and structure of decamethyl-2,3,5,6,7-pentasila-1,4-diphosphabicyclo[2.2.1]heptane from $Na_3P/K_3P$ and 1,2-dichlorotetramethyldisilane.[4] These syntheses show that in the reactions between sodium/potassium pnictides and halogenated mono- and oligosilanes, Si–Si bonds are not only cleaved, but new bonds are formed depending on

[a] Institute of Inorganic Chemistry, University of Technology, Stremayrgasse 16, 8010 Graz, Austria
E-mail: günter.tekautz@tugraz.at
baumgartner@tugraz.at
alk.dransfeld@tugraz.at
karl.hassler@tugraz.at

 © 2007 Wiley-VCH Verlag GmbH & Co. KGaA, Weinheim 

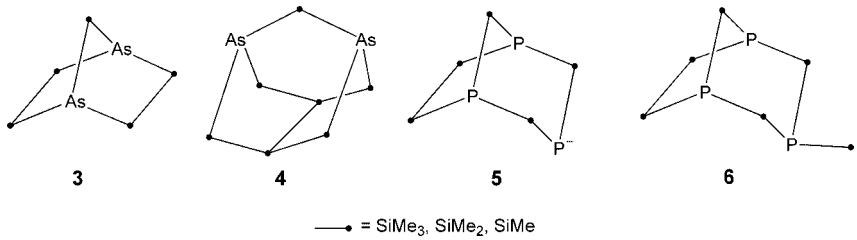


Figure 1. Cage compounds prepared in this work.

the reaction conditions. This was also reported for the reaction of $t$BuSi($SiMe_2Cl$)$_3$ with $LiPH_2$, which resulted in the formation of a hexasila-1,5-diphosphabicyclo[3.2.1]octane.[6]

These findings prompted us to not only use halogenated isotetrasilanes but larger oligosilanes as well to form novel cage compounds. Moreover, by varying the stoichiometric ratio between the halosilane and the sodium/potassium pnictide, we expected the formation of novel anionic species with cage-like structures. We were pleased to learn that this is indeed possible. Herein we report the synthesis of hitherto unknown silicon–arsenic cages **3** and **4** as well as anionic silicon–phosphorus cage **5** and its trimethylsilyl derivative **6** as shown in Figure 1 starting from the oligosilanes MeSi($SiMe_2Cl$)$_3$ (**1**) and ($SiMe_2Cl$)$_2$MeSiSiMe($SiMe_2Cl$)$_2$ (**2**) and $Na_xP/K_xP$ or $Na_xAs/K_xAs$.

## Results and Discussion

### Synthesis

As mentioned in the introduction, the products formed in the reactions between sodium/potassium pnictides and multiply halogenated oligosilanes depend strongly on the reaction conditions, and the largest influence comes from the solvent that is used. In polar solvents such as dimethoxyethane (dme), Si–Si bonds of the oligosilane are broken and reformed to a certain extent to give -E$SiMe_2$E- and even -E$Me_2$Si$SiMe_2$E atom arrangements when MeSi($SiMe_2Cl$)$_3$ is used. Even traces of ($SiMe_2$)$_6$ can be detected in the reaction mixtures with $^{29}$Si NMR spectroscopy. Of course, considerable quantities of polymers are also formed in these reactions. Whereas insoluble polymers are removed in the workup process, the soluble fraction may severely hamper successful crystallization of the cage compounds. We also found that the quantities of polymers that are formed are much larger for arsenic compounds than for phosphorus compounds, which we attribute to the much greater reducing power of sodium/potassium arsenide. So far, no systematic experimental studies on the influence of the solvent and the pnictogen/alkali metal ratio on the product distribution of these reactions have been described.

The mechanisms of these reactions are not known. The formation of silylenoide species $Me_2SiNaCl$ or dimethylsilylene, $SiMe_2$, as intermediates through Si–Si bond cleavage seems plausible. For instance, the formation of such species is thought to play a major role during the reduction of dichlorodimethylsilane with alkali metals.[7]

The silylenes can then insert into Si–Si, Si–P, Si–As or Si–Cl bonds to give a plethora of compounds. When $Na_3As/K_3As$ reacts with **1** at r.t., cage **3** can be isolated in about 5% yield. We did not attempt to optimize the reaction conditions. Cage **3** is not the only cage that forms under these conditions, because in the $^{29}$Si NMR spectrum of the reaction mixture we observed, besides the signal of hexasila-1,4-diarsabicyclo[2.2.2]octane, three resonances at –70.0, –17.1 and 5.0 ppm, which we attribute to an adamantane-like structure, as shown in Figure 2. So far, we were unable to purify this compound by crystallization. In this molecule, the $Si_4$ atom arrangement of **1** is still present.

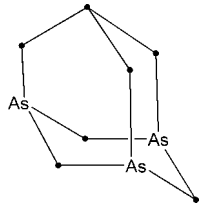


Figure 2. Proposed structure for adamantane $As_3Si_7Me_{13}$.

When $Na_3As/K_3As$ reacts with **2**, tricyclononane **4** forms in about 5% yield and can be separated by crystallization. Here again we performed no optimization of the reaction conditions. From the $^{29}$Si NMR spectra it can be concluded that there are other cage compounds present in the reaction mixture, such as bicycloheptane **3**, which can be identified unambiguously. So far, all attempts to isolate other cage compounds by fractional crystallization have failed.

Noteworthy is that the tricyclononane structure established for **5** by X-ray diffraction can also be found as $P_9$ groups (alternating with $P_8$ groups) in Hittorf's violet monoclinic phosphorus allotrope, as shown in Figure 3.[8] Recently, the crystal structure of a fibrous variation of violet phosphorus, which also contains the $P_8$ and $P_9$ units, was reported.[9] For us, the $P_2Si_7$ cage (analogous to **4**) and the

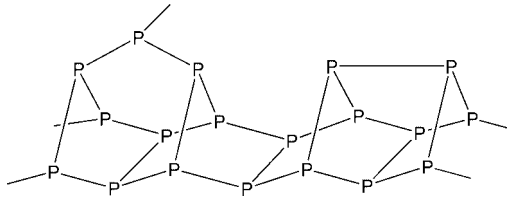

Figure 3. $P_9$ and $P_8$ substructures in violet phosphorus and in its fibrous variation.

 © 2007 Wiley-VCH Verlag GmbH & Co. KGaA, Weinheim 

tricyclooctanes $E_2Si_6$ (E = As, P) analogous to $P_8$ are tempting synthetic targets that we are currently pursuing by reaction of **2** with $Na_3E/K_3E$ under various conditions.

When a suspension of an excess amount of $Na_3P/K_3P$ in dme is added to a solution of **1** in dme heated at reflux, anionic cage **5** can be separated by crystallization from pentane/dme. As a byproduct, decamethyl-2,3,5,6,7-pentasila-1,4-diphosphabicyclo[2.2.1]heptane is formed in considerable quantities.

## X-ray Crystallography

Crystals of cages **3**, **4**, **5** and **6** in a quality suitable for X-ray experiments could be obtained as described in the Experimental Section. Figure 4 presents the molecular structures of these compounds, and Table 1 summarizes selected bond lengths and bond angles by employing the numbering scheme of Figure 4. The molecular symmetry of all four molecules is $C_s$, characterized by a mirror plane bisecting the cages.

The Si–As and Si–P bond lengths are all within the expected range found in acyclic silylphosphanes and their arsenic analogues. Si–Si distances are longer than the normal 232–234 pm by about 30 pm for P cages **5** and **6**, and by about 10 pm for arsenic cage **3**, which reflects the decreasing n→σ* interaction of arsenic relative to phosphorus. The Si(2)–Si(3) bond length in **4** is in the normal range because just one As atom is available for this interaction. The central Si–Si bond in **4** is somewhat longer (235.2 pm), which certainly is due to steric reasons.

Table 1. Selected bond lengths [pm] and bond angles [°] for **3**, **4**, **5** and **6**.

| | **3** | **4** | **5** | **6** |
|---|---|---|---|---|
| Si(1)–E(1) | 236.73(9) | 237.19(16) | 224.83(30) | 226.25(11) |
| Si(2)–E(1) | 236.46(9) | 236.24(18) | 225.00(30) | 227.09(11) |
| Si(3)–P(1) | | | 228.45(30) | 226.03(13) |
| Si(3)–P(2) | | | 218.70(20) | 226.05(13) |
| Si(4)–P(2) | | | | 226.57(13) |
| Si(2)–Si(2′) | 235.53(10) | | 236.35(20) | 237.50(11) |
| Si(2)–Si(3) | | 233.80(20) | | |
| Si(3)–Si(3′) | | 235.20(20) | | |
| E(1)–Si(1)–E(1′) | 111.07(3) | 126.74(7) | 114.59(10) | 114.11(4) |
| E(1)–Si(2)–Si(2′) | 109.10(3) | | 108.39(9) | 108.24(4) |
| As(1)–Si(2)–Si(3) | | 105.38(7) | | |
| Si(2)–Si(3)–Si(3′) | | 103.80(8) | | |
| Si(1)–E(1)–Si(2) | 92.12(3) | 102.33(6) | 93.93(9) | 95.17(4) |
| Si(1)–P(1)–Si(3) | | | 103.39(9) | 104.13(4) |
| Si(2)–As(1)–Si(2′′) | 101.38(3) | 94.46(6) | | |
| Si(2)–P(1)–Si(3) | | | 103.16(9) | 103.40(4) |
| Si(4)–P(2)–Si(3) | | | | 106.35(4) |
| Si(3)–P(2)–Si(3′) | | | | 105.78(4) |
| C–Si(1)–C | 106.86(14) | 106.40(30) | 104.42(4) | 105.81(13) |

## NMR Spectra

Because of the quadrupole moment of the $^{75}As$ nucleus, the $^{29}Si$ NMR spectra of **3** and **4** are simple and consist of

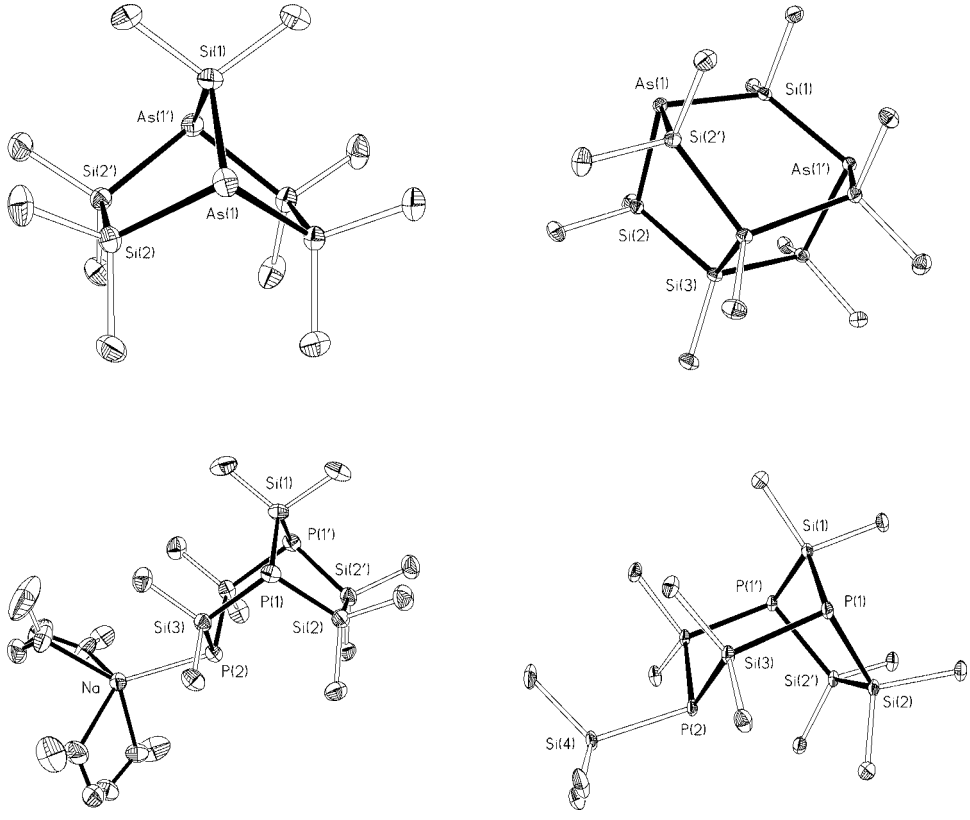


Figure 4. ORTEP plots (30% probabilities) of the molecular structures for **3** (top, left), **4** (top, right), **5** (bottom, left) and **6** (bottom, right).

 © 2007 Wiley-VCH Verlag GmbH & Co. KGaA, Weinheim 

Table 2. Chemical shifts [ppm, $\delta(^{29}Si)$ against TMS, $\delta(^{31}P)$ against 85% $H_3PO_4$] and coupling constants [Hz] for cages **3**, **4**, **5** and **6**.

| | **3** | **4** | **5** | | | | **6** | | | |
|---|---|---|---|---|---|---|---|---|---|---|
| | $\delta$ | $\delta$ | $\delta$ | $J$ | | | $\delta$ | $J$ | | |
| | | | | P1 | P1′ | P2 | | P1 | P1′ | P2 |
| Si(1) | 26.6 | –1.7 | 17.1 | 50.9 | 50.9 | 0 | 13.9 | 47.9 | 47.9 | 0 |
| Si(2) | 1.2 | –3.2 | –4.2 | 39.5 | 6.2 | 0 | –4.7 | 40.5 | 4.8 | 3.0 |
| Si(3) | | –73.8 | 4.9 | 39.7 | 0 | 81.4 | 1.3 | 46.4 | 0 | 49.5 |
| Si(4) | | | | | | | 2.4 | 0 | 0 | 39.8 |
| P(1) | | | –247.1 | | | 2.1 | –238.9 | | | 8.3 |
| P(2) | | | –261.9 | | | | –231.0 | | | |

just two signals for **3** and three signals for **4**. Table 2 summarizes the $\delta(^{29}Si)$ values with reference to the atom numbers that are used in Figure 4.

The spectra of phosphorus cages **5** and **6** are different, as not all signals are necessarily of first order as a result of indirect spin–spin coupling between the $^{29}Si$ and $^{31}P$ nuclei. For instance, Si(2) is part of an ABX system with $\delta(A) \approx \delta(B)$ because the shift differences between P(1) and P(1′) is due to isotopic effects only. The ABX system itself is weakly coupled to phosphorus atom P(2). From spectra simulations with various fixed values for $^2J_{P1,P1'}$ it is quickly deduced that this coupling constant must be quite small (<2–4 Hz), and that the spectra can be evaluated by using first-order rules to a very good accuracy. The g NMR software package was used for this purpose.

Figure 5 presents the measured $^{29}Si$ NMR spectra of **5** (top left) and **6** (top right), as well as the simulated spectra. The spectrum of **5** consists of a triplet of doublets for Si(1) at +17ppm, a doublet of doublets for Si(3) at +5 ppm and doublet of doublets of doublets for Si(3) at –4 ppm. The spectrum for **6** is very similar except that the resonance for Si(4) (the $SiMe_3$ group) overlaps the multiplet of Si(3). A view of the expanded spectrum for **6** is given at the bottom of Figure 5 and illustrates the effects of two- or three-bond couplings. All chemical shifts and coupling constants, treating all spectra as first order, are presented in Table 2.

The Si,P coupling constants of **5** and **6** are very similar, except between Si(3) and P(2). In anionic cage **5**, a $J$ value of 81.4 Hz was measured, but this value was only 49.5 Hz in cage **6** where the negative charge is replaced by the trimethylsilyl group. Bond lengths P(2)–Si(3), which are 218.7 and 226.1 pm, respectively (Table 1), are also quite different. A shortening of the Si–P bonds by 6–10 pm upon substitution of a $SiMe_3$ group with a negative charge is also observed for $P(SiMe_3)_3$ and the phosphanides $MP(SiMe_3)_2$, M = K, Rb and Cs.[10,11]

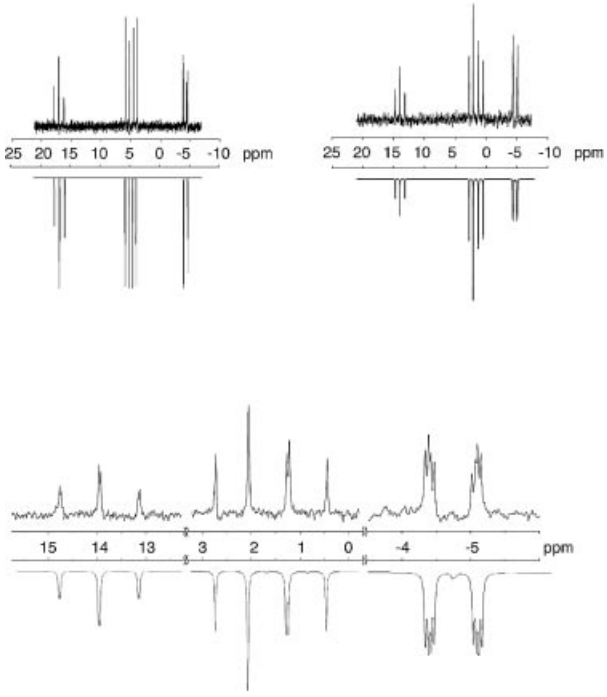


Figure 5. Proton decoupled $^{29}Si$ NMR spectra of **5** (top left) and **6** (top right), including simulated spectra shown with negative intensities. An expanded spectrum of **6** is presented at the bottom and illustrates the splitting due to two- and three-bond $^{29}Si,^{31}P$ couplings.

## Ab Initio Calculations

The number of different anionic species that are present in the "Zintl phases" prepared from the elements P or As and sodium/potassium alloy in a solvent such as dme is unknown. Most certainly, not all P–P or As–As bonds are broken in this reaction, and an equilibrium between the various anions is established depending on the stoichiometric ratio of phosphorus/alkaline metals used. For instance, $(Me_3Si)_2PP(SiMe_3)_2$ and $P_7(SiMe_3)_3$ are just two minor by-products in the synthesis of $P(SiMe_3)_3$ from "$Na_3P/K_3P$" and $Me_3SiCl$. An even larger variety of $Si_mP_n$ frameworks can be formed when Si–Si bonds in reagents **1** and **2** are broken under the attack by "$Na_3P/K_3P$". Because only a few of the potential species are observed, the question arises whether the obtained product distribution can be deduced from simple considerations. Cages such as diphosphabicyclo[2.2.1]heptanes and diphosphabicyclo[2.2.2]octanes are prevalent in the reaction mixtures, whereas triphosphabicyclo[2.2.2]octanes A or B shown in Scheme 1 do not form at all in the reaction with $Me_2SiClSiClMe_2$ or $Me_2SiCl_2$.

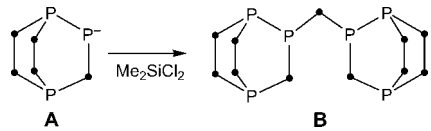


Scheme 1. Cages that are not formed.

 © 2007 Wiley-VCH Verlag GmbH & Co. KGaA, Weinheim 

Because the major products obtained experimentally comprise eight second-row atoms, the computational study focuses on bicyclic $Si_8$, $PSi_7$, $P_2Si_6$ and $P_3Si_5$ structures. Our approach to rationalize the observations is the concept of topological charge stabilization advocated by Gimarc 20 years ago.[12] It predicts that by replacing a silicon atom in one of the $Si_nP_m$ cages by an atom of higher electronegativity, P, at the site with the highest electron density leads to the most stable isomer.

We first calculated minimum structures, energies and Mulliken charges for the isomeric $Si_8H_{14}$ structures. The five lowest-energy isomers are shown in Figure 6 together with the Mulliken charge of the Si atom possessing the highest electron density. Replacing it by P should result in the best $PSi_7H_{13}$ structure. Only the two best homonuclear frameworks, the bicyclo[2.2.2] and bicyclo[3.2.1] cages that differ by just 0.9 kJ mol$^{-1}$, are considered in the further replacement study.[13] With a value of about 40 kJ mol$^{-1}$, the relative energies of the bicyclo[4.2.0] and bicyclo[4.1.1] structures are large. The bicyclo[5.1.0] cage has an even higher energy of 117 kJ mol$^{-1}$. These large values can be used to rationalize why we never observed their formation.

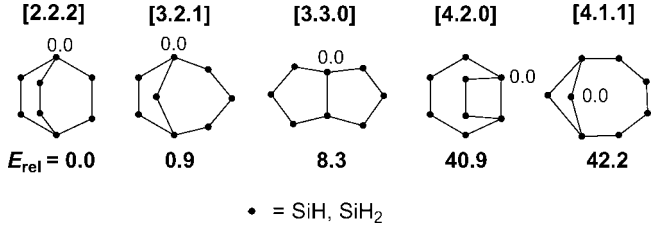


Figure 6. Relative energies [kJ mol$^{-1}$] of bicyclic $Si_8H_{14}$ isomers and the position of the Si atom possessing the smallest Mulliken charge. Relative energies are given for the most favourable stereoisomer or conformer. A dot represents a $SiH_2$ or SiH group.

As shown in Figure 7 (1st row), the relative energies of the two bicyclo[2.2.2] and the three bicyclo[3.2.1] topomers of $PSi_5H_{13}$ demonstrate the validity of the Gimarc rule. The Mulliken charges (the position with the smallest value is indicated in Figure 7) predict that the diphospha[2.2.2] and diphospha[3.2.1] cages with P atoms in 1,4- and 1,5-positions will be preferred, which is just what we observed in numerous experiments. In the second row of Figure 7, the relative energies of the two sets of $P_2Si_6H_{12}$ topomers are presented, again confirming the predictions of the Gimarc rules.

Although the bicyclo[2.2.2] structure is higher in energy than bicyclo[3.2.1] by 6.7 kJ mol$^{-1}$, both are considered in the final replacement for obtaining the energies of the triphospha cages. The results are summarized in the third row of Figure 7. The charge distribution in bicyclo[2.2.2] $P_2Si_6H_{12}$ clearly suggests that the 1,2,4-triphospha isomer will be preferred. Consequently, its energy relative to the 1,2,3- and 1,2,6-triphospha isomer is predicted to be lower by more than 45 kJ mol$^{-1}$. The situation is less clear for the bicyclo[3.2.1] framework, because in the lowest energy isomer the two smallest atomic charges differ by merely 0.01 units. According to Gimarc's rule, the 1,3,5- and the 1,5,8-

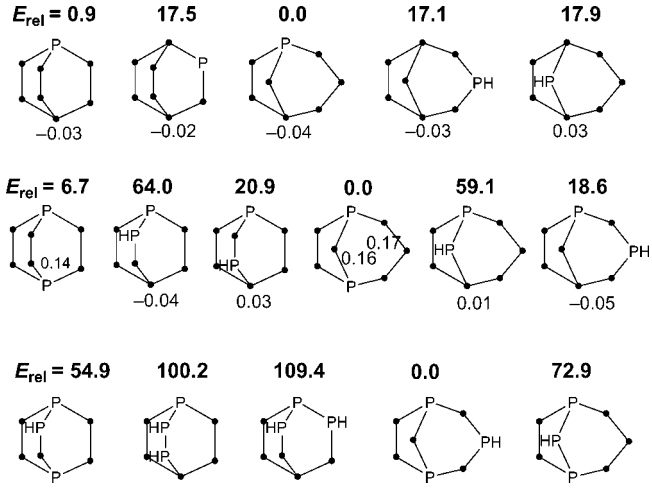


Figure 7. Relative energies [kJ mol$^{-1}$] of the bicyclic $PSi_7H_{13}$, $P_2Si_6H_{12}$ and $P_3Si_5H_{11}$ isomers, and the position of the Si atom possessing the smallest Mulliken charge. Relative energies are given for the most favourable stereoisomer or conformer.

isomer are predicted to possess very similar energies, and both should be present in the reaction mixture. Nevertheless, the charges in the second best structure indicate that the 1,3,5-$P_3Si_5$ backbone is preferred. The calculated relative energy of 72.9 kJ mol$^{-1}$ for the 1,5,8-structure provides clear preference for 1,3,5-isomer, which is what we found in the experiment.

Our ab initio calculations indicate that isomers with P–P bonds generally have higher energies. This agrees with the lack of observation of these isomers in the synthesis. Owing to $^{31}P,^{31}P$ one bond coupling, their presence would have been detected very easily by using NMR spectroscopy.

The general conclusion that the polar Si–P bond is favoured over the nonpolar Si–Si as well as the P–P bond was quantified by the comparative calculation of two saturated $P_2Si_2H_8$ isomers. $H_3Si–SiH_2–PH–PH_2$ has a relative energy of 32.8 kJ mol$^{-1}$ with respect to $H_3Si–PH–SiH_2–PH_2$, which both have the same number of Si–H and P–H bonds. In conclusion, the Si–P bond is favoured by about 16 kJ mol$^{-1}$ over a Si–Si or a P–P bond in phosphasilanes. Analysis of all investigated cage isomers deposited at nmr-sharc.tugraz.at shows that the relative energies are positively related to the $(n_{SiSi} + n_{PP})/n_{SiP}$ ratio, where $n_{SiSi}$, $n_{PP}$ and $n_{SiP}$ are the number of Si–Si, P–P and Si–P bonds, respectively. Therefore, it can be generalized that cage isomers with a maximum number of Si–P bonds will be energetically preferred.

## Conclusions

In the present publication we showed that by reaction of sodium/potassium phosphide and arsenide with chlorooligosilanes containing $SiMe_2Cl$ end groups, anionic and neutral cage compounds containing E–$SiMe_2$–E and E–$SiMe_2$–$SiMe_2$–E atom arrangements can be obtained. A plausible reaction mechanism explaining Si–Si bond cleavage involves dimethylsilylene as a reaction intermediate. In that case, a donor interaction with a P atom on the surface of the solid

 © 2007 Wiley-VCH Verlag GmbH & Co. KGaA, Weinheim 

must be assumed. Noteworthy, chlorodisilanes disproportionate by such a donor mechanism in the presence of amines, even in heterogeneous phase.[14]

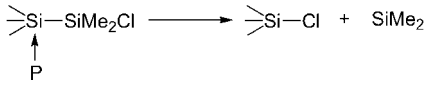


The preferred formation of 1,4-diphosphahexasilabicyclo[2.2.2]octanes and 1,3,5-triphosphapentasilabicyclo-[3.2.1]octanes over other topological isomers could be rationalized by using the concept of topological charge stabilization.

## Experimental Section

**General:** All experiments were performed under anaerobic conditions by using standard Schlenk techniques. Solvents were dried with sodium or potassium and distilled under an atmosphere of $N_2$ prior to use. Starting materials **1** and **2** were prepared as described in the literature. $^{31}P$ and $^{29}Si$ NMR spectra were recorded with a BRUKER MSL 300 spectrometer (59.627 MHz for $^{29}Si$, 121.451 MHz for $^{31}P$). Chemical shifts are given in ppm relative to 85% aq. $H_3PO_4$ for $^{31}P$ and $SiMe_4$ for $^{29}Si$ (external). Elemental analyses were performed with a HERAEUS VARIO EL. As compounds **3**–**5** are extremely sensitive towards traces of oxygen and moisture, the quality of the elemental analyses is not as good as usually achieved.

**Decamethyl-2,3,5,6,7-pentasila-1,4-diarsabicyclo[2.2.1]heptane (3):** To a suspension of "$Na_xAs/K_xAs$" [prepared from Na (1.10 g, 48.22 mmol), K (1.50 g, 38.58 mmol) and As (5.0 g, 74.92 mmol) by a modified procedure described by Becker[15]] in dme (300 mL) was added dropwise a solution of **1** (9.37 g, 28.9 mmol) in dme (70 mL) over a period of 60 min. During the reaction, which is exothermic, the black colour of the suspension changed to yellow-green. The reaction mixture was then heated at reflux for 8 h, and the precipitated salts were separated by filtration. The solvent was then removed by evaporation in vacuo and replaced by heptane. Subsequently, the solution was decanted from the remaining salts, and **3** (1.7 g, 5%) was obtained by fractional crystallization at –30 °C. $C_{10}H_{30}As_2Si_5$ (440.62): calcd. C 27.26, H 6.86; found C 28.57, H 7.28.

**Dodecamethyl-2,3,4,6,7,8,9-heptasila-1,5-diarsatricyclo[3.3.1.0$^{3,7}$]-nonane (4):** To a suspension of "$Na_xAs/K_xAs$" [prepared from Na (1.71 g, 74.4 mmol), K (2.18 g, 55.8 mmol) and As (9.76 g, 130.25 mmol)] in dme (500 mL) was added a solution of **2** (15.0 g, 32.56 mmol) in dme (70 mL) over a period of 1 h. The reaction mixture was then submitted to the same procedure as described above. Crystallization from heptane at –30 °C gave **4** (1.7 g, 5%) as colourless crystals. $C_{12}H_{36}As_2Si_7$ (526.88): calcd. C 27.36, H 6.89; found C 28.05, H 7.08.

**Sodium Hexamethyl-2,4,6,7-tetrasila-1-phosphanido-3,5-diphosphabicyclo[3.2.1]octane (5):** To a solution of **1** (12.69 g, 39.2 mmol) in dme (150 mL) was added dropwise a suspension of "$Na_xP/K_xP$" [prepared from Na (1.53 g, 66.73 mmol), K (3.48 g, 88.97 mmol) and white phosphorus $P_4$ (3.30 g, 106.5 mmol] in dme (300 mL)

Table 3. Crystal data and structure refinement for compounds **3**, **4**, **5** and **6**.

| | **3** | **4** | **5** | **6** |
|---|---|---|---|---|
| Formula | $C_{10}H_{30}As_2Si_5$ | $C_{12}H_{36}As_2Si_7$ | $C_{18}H_{50}NaO_4P_3Si_5$ | $C_{13}H_{39}P_3Si_6$ |
| Formula weight | 440.62 | 526.88 | 586.93 | 456.89 |
| T [K] | 293(2) | 98(2) | 223(2) | 100(2) |
| Wavelength [Å] | 0.71073 | 0.71073 | 0.71073 | 0.71073 |
| Crystal system | monoclinic | tetragonal | orthorhombic | monoclinic |
| Space group | $P2_1/n$ | I4(1)/a | Pca2(1) | $P2_1/c$ |
| $a$ [Å] | 12.906(3) | 33.100(6) | 21.554(4) | 9.6779(19) |
| $b$ [Å] | 22.413(5) | 33.100(6) | 10.747(2) | 26.177(5) |
| $c$ [Å] | 14.551(3) | 9.379(2) | 30.410(6) | 11.028(2) |
| $\alpha$ [°] | 90 | 90 | 90 | 90 |
| $\beta$ [°] | 96.39(3) | 90 | 90 | 108.02(3) |
| $\gamma$ [°] | 90 | 90 | 90 | 90 |
| V [Å$^3$] | 4183.0(15) | 10276(3) | 7044(2) | 2656.9(9) |
| Z | 4 | 16 | 4 | 4 |
| $\rho_{calcd.}$ [g cm$^{-3}$] | 1.399 | 1.362 | 1.106 | 1.142 |
| Absorption coefficient [mm$^{-1}$] | 3.466 | 2.923 | 0.371 | 0.491 |
| $F(000)$ | 1808 | 4352 | 2524 | 984 |
| $\theta$ range [°] | $1.68 < \theta < 26.30$ | $2.57 < \theta < 25.00$ | $1.89 < \theta < 24.71$ | $2.09 < \theta < 26.34$ |
| $h$, $k$, $l$ indices range | $-16 < h < 16$ | $0 < h < 39$ | $-25 < h < 15$ | $-12 < h < 12$ |
| | $-27 < k < 27$ | $-2 < k < 39$ | $-12 < k < 12$ | $32 < k < 32$ |
| | $-17 < l < 18$ | $-2 < l < 11$ | $-35 < l < 33$ | $-13 < l < 13$ |
| Reflections collected/unique | 32221/8449 | 6461/4525 | 33203/11690 | 20473/5392 |
| Completeness to $\theta$ = 28.35° [%] | 99.7 | 99.9 | 99.9 | 99.7 |
| Absorption correction | SADABS | None | SADABS | SADABS |
| Refinement method | Full-matrix least-squares on $F^2$ | Full-matrix least-squares on $F^2$ | Full-matrix least-squares on $F^2$ | Full-matrix least-squares on $F^2$ |
| Data/restraints/parameters | 8449/0/327 | 4525/0/202 | 11690/1/587 | 5392/0/212 |
| Goodness-of-fit on $F^2$ | 1.052 | 1.020 | 0.968 | 1.138 |
| Final $R$ indices | $R_1$ = 0.0295 | $R_1$ = 0.0524 | $R_1$ = 0.0584 | $R_1$ = 0.0550 |
| $[I > 2\sigma(I)]$ | $wR_2$ = 0.0702 | $wR_2$ = 0.1170 | $wR_2$ = 0.1045 | $wR_2$ = 0.1360 |
| $R$ indices (all data) | $R_1$ = 0.0372 | $R_1$ = 0.0746 | $R_1$ = 0.1091 | $R_1$ = 0.0644 |
| | $wR_2$ = 0.0730 | $wR_2$ = 0.1285 | $wR_2$ = 0.1218 | $wR_2$ = 0.1416 |
| Largest diff. peak/hole [e Å$^{-3}$] | 0.956/–0.313 | 0.928/–0.493 | 0.289/–0.176 | 0.809/–0.536 |

 © 2007 Wiley-VCH Verlag GmbH & Co. KGaA, Weinheim 

heated at reflux. After heating for 24 h, a considerable quantity of unreacted **1** was detected by $^{29}Si$ NMR spectroscopy, even after treatment in an ultrasonic bath. Therefore, the suspension of "$Na_xP/K_xP$" and the salts were removed by decantation, and a suspension of freshly prepared "$Na_xP/K_xP$" (from 3.3 g of white phosphorus) was added dropwise to the solution heated at reflux. The reaction mixture was heated at reflux for another 40 h and separated from the salts by filtration. The solvent was removed by evaporation in vacuo and replaced by pentane. The insoluble residue was dissolved in hexane/dme (1:1). At –30 °C, **5** (4.9 g, 23%) was obtained as colourless crystals. $C_{18}H_{50}NaO_4P_3Si_5$ (586.93): calcd. C 36.83, H 8.59; found C 35.74, H 7.92.

**Decamethyl-3-trimethylsilyl-1,3,5-triphospha-2,4,6,7-tetrasilabicyclo[3.2.1]octane (6):** To a solution of **5** (2.70 g, 4.6 mmol) in pentane/dme (1:1) at –80 °C was added dropwise chlorotrimethylsilane (0.5 g, 4.6 mmol). The reaction mixture was allowed to reach r.t., and the solvents are removed completely by evaporation in vacuo. *n*-Pentane was added, and the solid precipitates were separated by decantation. At –30 °C, **6** (1.2 g, 57%) was obtained as colourless crystals. $C_{13}H_{39}P_3Si_6$ (456.89): calcd. C 34.17, H 8.60; found C 33.52, H 8.41.

**X-Ray Crystal Structure Analysis:** Crystals were mounted onto the tip of a glass fibre, and the data collection was performed with a BRUKER-AXS SMART APEX CCD diffractometer for compounds **3**, **5** and **6**, and a STOE four-circle diffractometer for **4**. Graphite-monochromated Mo-$K_\alpha$ radiation (71.073 pm) was used for the measurements. Crystal data and details of the structure refinement are summarized in Table 3. The data were reduced to $F^2_o$ and corrected for absorption effects with SAINT[16] and SADABS.[17] The structures were solved by direct methods and refined by full-matrix least-squares method (SHELXL97).[18] All non-hydrogen atoms were refined with anisotropic displacement parameters. All hydrogen atoms were located in calculated positions to correspond to standard bond lengths and angles.

CCDC-637289 (for **3**), -637287 (for **4**), -637288 (for **5**) and -637290 (for **6**) contain the supplementary crystallographic data for this paper. These data can be obtained free of charge from The Cambridge Crystallographic Data Centre via www.ccdc.cam.ac.uk/data_request/cif.

**Quantum Chemical Calculations:** All considered geometries were optimized at the B3LYP/6-31G* level by using the Gaussian 03 software package.[19] The conformers with the lowest energy were considered in the discussion with their atomic charges as defined by Mullican.[20]

## Acknowledgments

The authors thank the Fond zur Förderung der wissenschaftlichen Forschung, FWF, for financial support (project P 15366-NO3).

[1] For a review on polycyclic phosphanes, see for instance: M. Baudler, K. Glinka, *Chem. Rev.* **1993**, *93*, 1623; for polycyclic silanes, see: E. Hengge, R. Janoschek, *Chem. Rev.* **1995**, *95*, 1495; A. Sekiguchi, H. Sakurai, *Adv. Organomet. Chem.* **1995**, *37*, 1.
[2] See, for instance: M. Driess, A. D. Fanta, D. Powell, R. West, *Angew. Chem.* **1989**, *101*, 1087; *Angew. Chem. Int. Ed. Engl.* **1989**, *28*, 1038.
[3] U. Winkler, M. Schieck, H. Pritzkow, M. Driess, I. Hyla-Kryspin, H. Lange, R. Gleiter, *Chem. Eur. J.* **1997**, *3*, 874.
[4] G. M. Kollegger, U. Katzenbeisser, K. Hassler, C. Krüger, D. Brauer, R. Gielen, *J. Organomet. Chem.* **1997**, *543*, 103.
[5] G. M. Kollegger, H. Siegl, K. Hassler, K. Gruber, *Organometallics* **1996**, *15*, 4337.
[6] M. Driess, M. Reisgys, H. Pritzkow, *Z. Anorg. Allg. Chem.* **1998**, *624*, 1886.
[7] See, for instance: K. Tamao, A. Kawachi, *Angew. Chem. Int. Ed. Engl.* **1995**, *34*, 818; A. Kawachi, K. Tamao, *Bull. Chem. Soc. Jpn.* **1997**, *70*, 945.
[8] N. N. Greenwood, A. Earnshaw, *Chemistry of the Elements*, Pergamon Press, Oxford, **1985**.
[9] M. Ruck, D. Hoppe, B. Wahl, P. Simon, Y. Wang, G. Seifert, *Angew. Chem.* **2005**, *117*, 7788.
[10] J. Bruckmann, C. Krüger, *Acta Crystallogr., Sect. C* **1995**, *51*, 1152.
[11] U. Englich, K. Hassler, K. Ruhland-Senge, F. Uhlig, *Inorg. Chem.* **1998**, *37*, 3532.
[12] B. M. Gimarc, J. J. Ott, *J. Am. Chem. Soc.* **1983**, *105*, 1979.
[13] The relative energy of the [3.2.1] isomer with a $Si_6$ boat conformation is 7.6 kJ mol$^{-1}$.
[14] See, for instance: N. Schulze, G. Roewer in *Organosilicon Chemistry IV – From Molecules to Materials* (Eds.: N. Auner, J. Weis), Wiley-VCH, Weinheim, **2000**.
[15] G. Becker, G. Gutekunst, H. J. Wessely, *Z. Anorg. Allg. Chem.* **1980**, *462*, 113.
[16] *SAINTPLUS: Software Reference Manual*, Version 6.45, Bruker-AXS, Madison, WOI, **1997**–**2003**.
[17] R. H. Blessing, *Acta Crystallogr., Sect. A* **1995**, *51*, 33; *SADABS*, Version 2.1, Bruker-AXS, **1998**.
[18] G. M. Sheldrick, *SHELXL97: Programs for Crystal Structure Analysis (Release 97–2)*, University of Göttingen, Göttingen, Germany **1998**.
[19] M. J. Frisch, G. W. Trucks, H. B. Schlegel, G. E. Scuseria, M. A. Robb, J. R. Cheeseman, J. A. Montgomery Jr, T. Vreven, K. N. Kudin, J. C. Burant, J. M. Millam, S. S. Iyengar, J. Tomasi, V. Barone, B. Mennucci, M. Cossi, G. Scalmani, N. Rega, G. A. Petersson, H. Nakatsuji, M. Hada, M. Ehara, K. Toyota, R. Fukuda, J. Hasegawa, M. Ishida, T. Nakajima, Y. Honda, O. Kitao, H. Nakai, M. Klene, X. Li, J. E. Knox, H. P. Hratchian, J. B. Cross, C. Adamo, J. Jaramillo, R. Gomperts, R. E. Stratmann, O. Yazyev, A. J. Austin, R. Cammi, C. Pomelli, J. W. Ochterski, P. Y. Ayala, K. Morokuma, G. A. Voth, P. Salvador, J. J. Dannenberg, V. G. Zakrzewski, S. Dapprich, A. D. Daniels, M. C. Strain, O. Farkas, D. K. Malick, A. D. Rabuck, K. Raghavachari, J. B. Foresman, J. V. Ortiz, Q. Cui, A. G. Baboul, S. Clifford, J. Cioslowski, B. B. Stefanov, G. Liu, A. Liashenko, P. Piskorz, I. Komaromi, R. L. Martin, D. J. Fox, T. Keith, M. A. Al-Laham, C. Y. Peng, A. Nanayakkara, M. Challacombe, P. M. W. Gill, B. Johnson, W. Chen, M. W. Wong, C. Gonzalez, J. A. Pople, *Gaussian 03*, Revision B.03, Gaussian, Inc., Pittsburgh, PA, **2003**.
[20] R. S. Mulliken, *J. Chem. Phys.* **1962**, *36*, 3428.

Received: April 17, 2007
Published Online: July 6, 2007

 © 2007 Wiley-VCH Verlag GmbH & Co. KGaA, Weinheim

**The EUChemSoc Societies have taken the significant step into the future by merging their traditional journals, to form two leading chemistry journals, the *European Journal of Inorganic Chemistry* and the *European Journal of Organic Chemistry.* Three further EUChemSoc Societies (Austria, Czech Republic and Sweden) are Associates of the two journals.**

## COVER PICTURE

**The cover picture shows** the reaction between the phosphavinylidene complexes $[(\eta^5\text{-}C_5H_5)(CO)_2M{=}P{=}C(SiMe_3)_2]$ and the inversely polarized phosphaalkene $t$BuP=C(NMe$_2$)$_2$, which affords $\eta^3$-1,2-diphosphaallyl complexes by smooth transfer of the phosphinidene unit onto the electrophilic ligand of the precursors. The molecular structure underlines the unsymmetrical $\eta^3$-ligation of the heteroallyl ligand to the metal with the *tert*-butyl substituent *syn* to the central phosphorus atom. Treatment of the phosphavinylidene complexes with *P*-aroylphosphaalkenes leads to decomposition. In contrast, phosphavinylidene complexes and *As*-aroylarsaalkenes yield complexes featuring cyclic phosphenium ligands with an As=C bond. It is believed that the first step of this process is a formal [2+1] cycloaddition between the P=C bond and the aroylarsinidine to give a three-membered ring, which subsequently incorporates the CO unit to afford the final product. In all cases, tetrakis(dimethylamino)ethene is formed as a byproduct. Details are presented in the Microreview by L. Weber on p. 4095 ff.

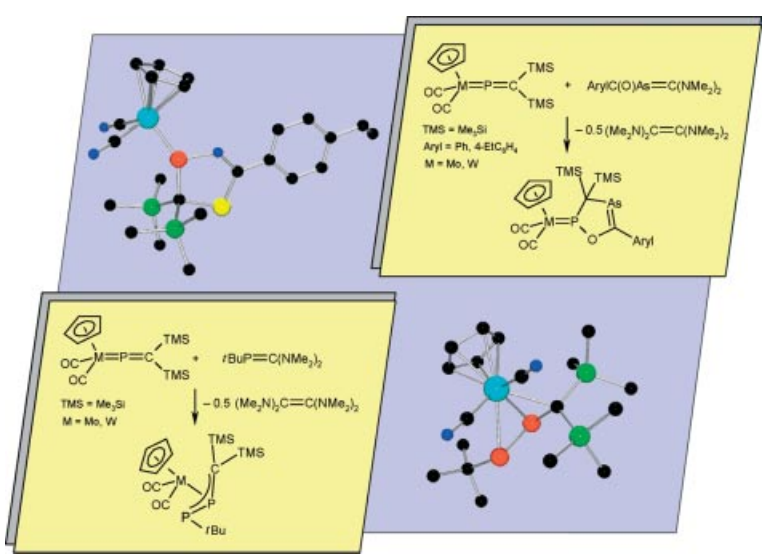

 © 2007 Wiley-VCH Verlag GmbH & Co. KGaA, Weinheim 

# CONTENTS

## MICROREVIEW


### Inversely Polarized Phosphaalkenes

**L. Weber* ..... 4095–4117**

Phospha- and Arsaalkenes $RE{=}C(NMe_2)_2$ (E = P, As) as Novel Phosphinidene- and Arsinidene-Transfer Reagents

**Keywords:** Phosphaalkenes / Arsaalkenes / Phosphinidene / Arsinidene


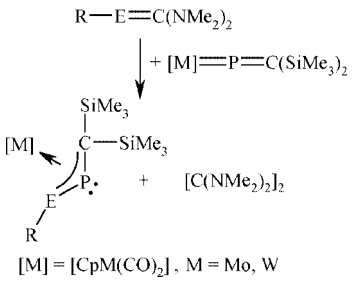


Inversely polarized phosphaalkenes $RP{=}C(NMe_2)_2$ serve as convenient sources of the phosphinidene unit PR, which can be transferred onto a broad variety of electrophilic ligands in transition-metal complexes such as complexes with carbene, vinylidene, phosphenium, and phosphavinylidene ligands. Similarly, inversely polarized arsaalkenes behave as arsinidene transfer reagents under mild conditions.

## SHORT COMMUNICATIONS


### Click Assemblies

**J. Tang, J. S. Costa, G. Aromí, I. Mutikainen, U. Turpeinen, P. Gamez, J. Reedijk* ..... 4119–4122**

Supramolecular Click Assembly of a Fused Double-Stranded $[Mn^{II}_3]$ Dihelicate

**Keywords:** Self-assembly / Helicates / Click chemistry / Manganese / Ferromagnetic interactions


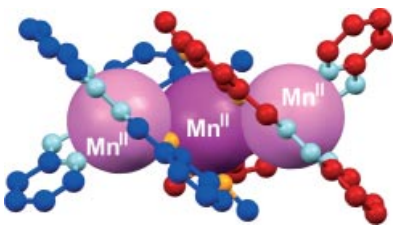


The self-assembly between 2-methoxy-6-(pyridine-2-ylhydrazonomethyl)phenol and $Mn^{II}$ ions leads to a remarkable supramolecular arrangement, where two helicates are "clicked" together to produce a bent linear metal array with ferromagnetic interactions.


### Carbonate Apatites

**L.-F. Olsson, K. Sandin, R. Odselius, L. Kloo* ..... 4123–4127**

In Vitro Formation of Nanocrystalline Carbonate Apatite – A Structural and Morphological Analogue of Atherosclerotic Plaques

**Keywords:** Carbonate apatite / Crystallization / Calcification / Nanocrystalline / Calcium


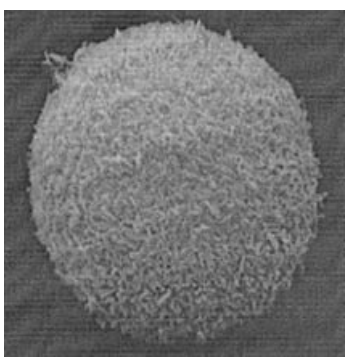

Carbonate apatites, analogous to the so-called bioapatites presumed only to precipitate in vivo, were also shown to form spontaneously in vitro in solutions mimicking the ion concentrations in human blood serum. The formed precipitates display a hierarchical morphology made from nanocrystalline building blocks into a spherical precipitate.

 © 2007 Wiley-VCH Verlag GmbH & Co. KGaA, Weinheim 

### A Redox Switch

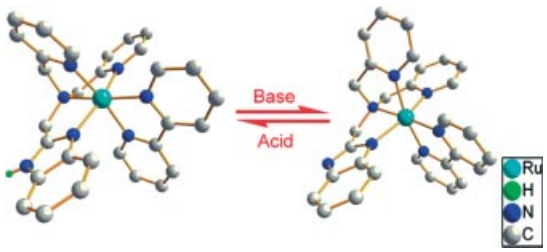


A monoruthenium(II) complex of the benzimidazolyl ligand and its deprotonated counterpart were prepared and structurally characterized. The reversible protonation/deprotonation process of the ancillary ligand switches the redox potential of the ruthenium(II) core from 0.69 to 0.26 V vs. $Ag/AgNO_3$.

**H. Sun, M. Wang,* K. Jin, C. Ma, R. Zhang, L. Sun* ..... 4128–4131**

Effect of Deprotonation of a Benzimidazolyl Ligand on the Redox Potential and the Structures of Mononuclear Ruthenium(II) Complexes

**Keywords:** Benzimidazolyl ligand / Redox switch / Reversible protonation and deprotonation / $Ru^{II}$ complex


## FULL PAPERS


### Al-Bridged [3,3,3]Cyclophanes

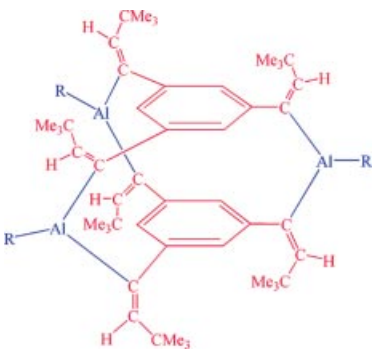

The addition of Al–H bonds of dialkylaluminum hydrides to the C≡C bonds of 1,3,5-tris(*tert*-butylethynyl)benzene (hydroalumination) did not result in the formation of the expected simple addition products, but yielded cyclophane-type molecules by condensation and release of the corresponding trialkylaluminum compounds.

**W. Uhl,* A. Hepp, M. Matar, A. Vinogradov ..... 4133–4137**

Facile Synthesis of Aluminum-Bridged [3,3,3]Cyclophanes by Hydroalumination

**Keywords:** Aluminum / Hydroalumination / Cage compounds / Cyclophanes

### Iron(III) Porphyrins

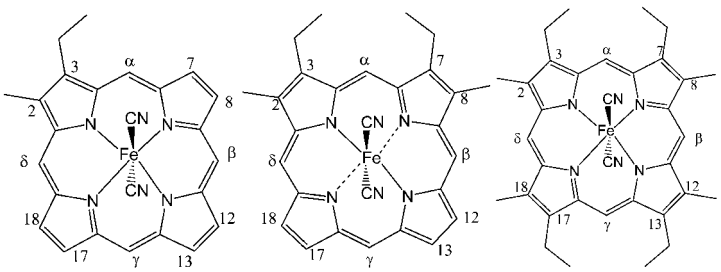

Paramagnetic $^1H$ and $^{13}C$ NMR spectroscopy were used to characterize the influence of small alkyl groups on the spin density of a series of high-spin and low-spin iron(III) porphyrins. Analysis of the chemical shifts of the pyrrole proton and *meso*-carbon of porphyrins reveals that all complexes show a low-spin $(d_{xy})^2(d_{xz},d_{yz})^3$ electronic ground state.

**S. Juillard, A. Bondon, G. Simonneaux* ..... 4138–4144**

Proton NMR Study of Low-Spin *meso*-Unsubstituted β-Substituted Alkyl Iron Porphyrins: Remarkable Influence of Peripheral Substitution on Spin Density

**Keywords:** NMR spectroscopy / Porphyrinoids / Iron / HMBC / Saturation transfer

### Single-Molecule Magnets

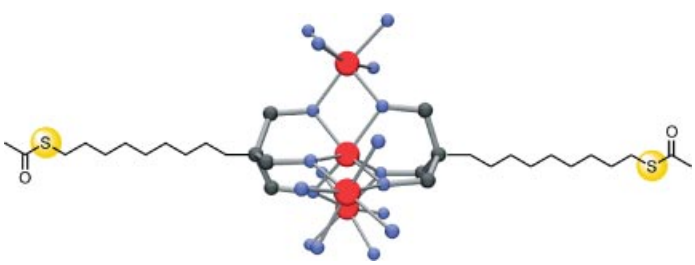

Single-molecule magnets of the $Fe_4$ family have been functionalized with terminal "alligator clips" by exploiting the site-specific coordinating ability of 2-(hydroxymethyl)propane-1,3-diol derivatives. The complexes have an $S = 5$ ground state and energy barriers exceeding 15 K.

**A.-L. Barra, F. Bianchi, A. Caneschi, A. Cornia,* D. Gatteschi, L. Gorini, L. Gregoli, M. Maffini, F. Parenti, R. Sessoli,* L. Sorace, A. M. Talarico ..... 4145–4152**

New Single-Molecule Magnets by Site-Specific Substitution: Incorporation of "Alligator Clips" into $Fe_4$ Complexes

**Keywords:** Iron / Ligand design / Magnetic properties / EPR spectroscopy / Single molecule magnets


 © 2007 Wiley-VCH Verlag GmbH & Co. KGaA, Weinheim 

# CONTENTS


## Asymmetric Catalysis

**L. Eberhardt, D. Armspach,* D. Matt,* L. Toupet, B. Oswald ..... 4153–4161**

Synthesis of Chiral, Monodentate Aminophosphane and Phosphoramidite Ligands Derived from Amino Acid Esters: Application in Rh-Catalysed Asymmetric Olefin Hydrogenation Reactions

**Keywords:** Phosphoramidites / Binol / Asymmetric catalysis / Rhodium / Olefin hydrogenation / Amino acid esters

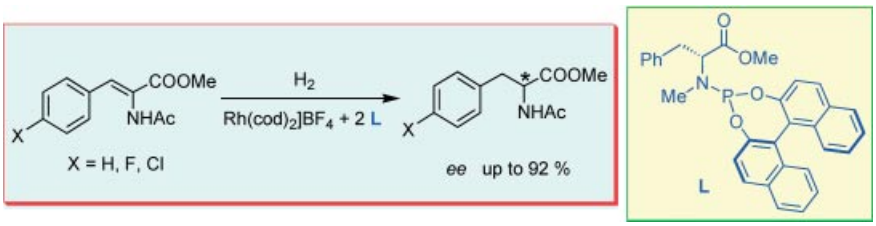


A series of chiral monodentate ligands combining a 3,5-dioxa-4-phosphacycloheptadinaphthyl unit either with a phenylalanine- or with an alanine-derived fragment were synthesised and tested in the hydrogenation of 2-(acetylamino)-3-(aryl)propenoic methyl esters.

## Understanding Clathrate-I Structures

**A. Kaltzoglou, S. D. Hoffmann, T. F. Fässler* ..... 4162–4167**

Order-Disorder Phase Transition in Type-I Clathrate $Cs_8Sn_{44}\square_2$

**Keywords:** Clathrates / Order-disorder transitions / Single-crystal structure analysis / Thermoelectricity / Tin

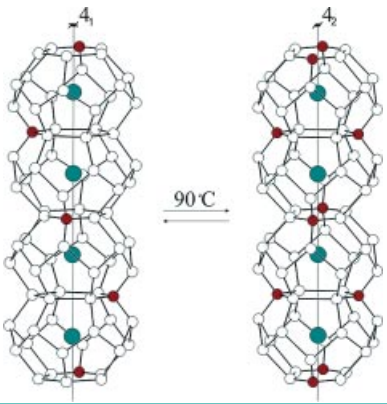


$Cs_8Sn_{44}\square_2$ adopts a $2 \times 2 \times 2$ superstructure of the type-I clathrate ($Ia\bar{3}d$) at room temperature and exhibits a high ordering of the vacancies (□) in the Sn framework (left). Its single crystals transform at 90 °C to a high-temperature modification ($Pm\bar{3}n$) with a lower ordering of the defects (right). DTA corroborates the totally reversible character of the phase transition.

## Zinc(II) Complexes

**Q. Su, W. Gao, Q.-L. Wu, L. Ye, G.-H. Li, Y. Mu* ..... 4168–4175**

Syntheses, Characterization, and Luminescent Properties of Monoethylzinc Complexes with Anilido–Imine Ligands

**Keywords:** Luminescence / N ligands / Quinoline / Zinc

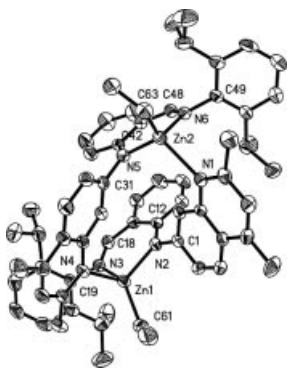


Dinuclear four-coordinate zinc complexes were synthesized from the alkane elimination reaction of $ZnEt_2$ with the corresponding anilido–imine ligands. The molecular structures of **3b** and **3c** were characterized by spectroscopy and X-ray crystallography. Luminescent properties of four zinc complexes in both solution and the solid state were explored.

## Ligand Properties

**C. Makedonas, C. A. Mitsopoulou* ..... 4176–4189**

Introduction of Modified Electronic Parameters – Searching for a Unified Ligand Properties Scale through the Electrophilicity Index Concept

**Keywords:** Modified electronic parameters / Electrophilicity index / Diimine complexes / Reduction potential / Charge-transfer bands

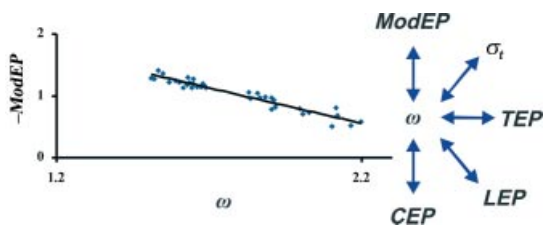


The contribution of the diimine ligands to the electronic properties of the corresponding metal complexes is quantified by two novel indices, namely Modified Electronic Parameters, *ModEP*, and the electrophilicity, $\omega$. The latter correlates well with all known electronic parameters, such as *CEP*, *LEP*, *TEP*, *ModEP* and the Hammett constant. The method in which it is calculated avoids any experimental limitation; thus, it can be employed even for ligands that have not yet been synthesized, and its correlation with the known scales could provide the properties of the corresponding complexes.


 © 2007 Wiley-VCH Verlag GmbH & Co. KGaA, Weinheim 

## Ferraphosphacarboranes

Room-temperature reactions of the phosphadicarbollide anion $[7,8,9\text{-}PC_2B_8H_{10}]^-$ with $[(C_5R_5)Fe]^+$ cations afford the expected 12-vertex ferraphosphadicarbollides $[1\text{-}C_5R_5\text{-}1,2,3,4\text{-}FePC_2B_8H_{10}]$, which undergo polyhedral rearrangement at 150 °C. The calculated value of the root-mean-square-amplitude-of-vibration of the iron atom, based on the Mössbauer effect data, is in good agreement with crystallographic data.

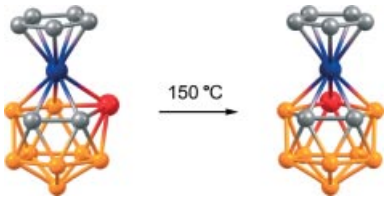


**A. R. Kudinov,* R. H. Herber,* P. Zanello,* D. S. Perekalin, I. V. Glukhov, I. Nowik, M. Corsini, S. Fedi, F. Laschi ..... 4190–4196**

Synthesis, Structure, Electrochemistry, and Mössbauer Effect Studies of the Ferraphosphadicarbollides $[(C_5R_5)Fe(PC_2B_8H_{10})]$ (R = H, Me)

**Keywords:** Iron / Carboranes / Electrochemistry / X-ray diffraction / Mössbauer spectroscopy

## Copper Complexes for Catalysis

Pyrazole-pyridine and pyrazole-naphthol ligands have been used in the [copper/TEMPO]-catalysed oxidation of benzyl alcohol to benzaldehyde. The results so far obtained suggest that the combination of pyrazole/pyridine coordinating groups is crucial to generate active copper catalysts.

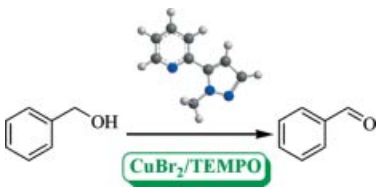


**J. Salinas Uber, Y. Vogels, D. van den Helder, I. Mutikainen, U. Turpeinen, W. T. Fu, O. Roubeau, P. Gamez, J. Reedijk* ..... 4197–4206**

Pyrazole-Based Ligands for the [Copper–TEMPO]-Mediated Oxidation of Benzyl Alcohol to Benzaldehyde and Structures of the Cu Coordination Compounds

**Keywords:** Copper(I) and copper(II) complexes / Catalysis / Oxidation / Luminescence / Bioinorganic chemistry

## Iridium Complexes

The synthesis, structures, thermal stabilities and photophysical properties of a series of heteroleptic iridium(III) complexes of the type bis[$\kappa^2(C^2,N)$-2-phenylpyridine]-[$\kappa^2(N,O)$-8-quinolinolato]iridium(III) are discussed. Substitution of the quinolinolato ligand with electron-withdrawing functional groups results in absorption features in the visible and quinolinolato-governed emission of the complexes.

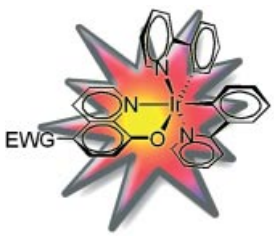


**S. Kappaun, S. Eder, S. Sax, K. Mereiter, E. J. W. List, C. Slugovc* ..... 4207–4215**

Organoiridium Quinolinolate Complexes: Synthesis, Structures, Thermal Stabilities and Photophysical Properties

**Keywords:** Iridium / N,O ligands / Luminescence / Nitrogen heterocycles

## Coordination Oligomers

Tetra- and pentanuclear lanthanide clusters $HNEt_3^+[Ln_5(\mu_3\text{-}OH)_4(\mu_4\text{-}OH)(Ph_2acac)_7(o\text{-}O_2NC_6H_4O)_3Cl]^-$ (Ln = Er, Tm) and $[Ln_4(\mu_3\text{-}OH)_2(Ph_2acac)_8(o\text{-}O_2NC_6H_4O)_2]$ (Ln = Yb, Lu) having dibenzoylmethanido and *o*-nitrophenolato as ligands in the coordination sphere were prepared.

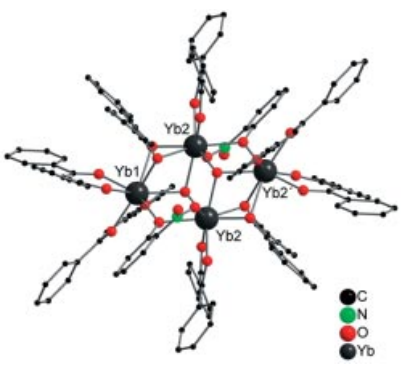


**S. Datta, V. Baskar, H. Li, P. W. Roesky* ..... 4216–4220**

Synthesis and Structural Characterization of Tetra- and Pentanuclear Lanthanide Hydroxido Clusters

**Keywords:** Cage compounds / Cluster compounds / Coordination modes / Bridging ligands / Lanthanides

 © 2007 Wiley-VCH Verlag GmbH & Co. KGaA, Weinheim 

# CONTENTS


## Selective Ethylene Dimerization

**T. Irrgang, S. Keller, H. Maisel, W. Kretschmer, R. Kempe* .... 4221–4228**

Sterically Demanding Iminopyridine Ligands

**Keywords:** Ethylene polymerization / N ligands / Cobalt / Iron / Nickel / Palladium

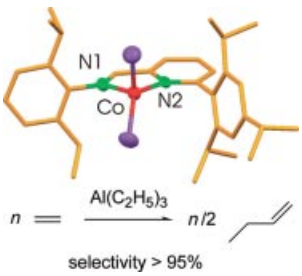


Sterically demanding iminopyridine ligands were prepared by Kumada-type coupling. Ethylene polymerization/oligomerization behavior of the dichlorido complexes (Co, Fe, Ni, and Pd) after activation with methylaluminoxane or triethylaluminum revealed ethylene dimerization selectivity greater than 95% for Co.

## Multifunctional Rotaxanes

**M. Narita, I. Yoon, M. Aoyagi, M. Goto, T. Shimizu, M. Asakawa* ..... 4229–4237**

Transition Metal(II)–Salen and –Salophen Macrocyclic Complexes for Rotaxane Formation: Syntheses and Crystal Structures

**Keywords:** Rotaxanes / Ring opening / Ring closing / Transition metals / Porphyrinoids

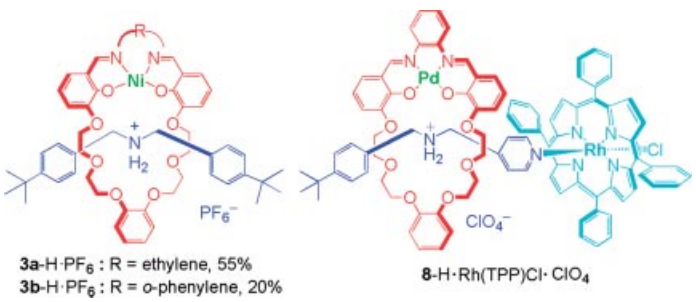


A "threading-followed-by-shrinking" approach afforded [2]rotaxanes **3a/b**-H·$PF_6$ possessing nickel(II)–salen and –salophen moieties; the salen-containing rotaxane was prepared in remarkably high yields. [2]Rotaxane **8**-H·Rh(TPP)Cl·$ClO_4$ has potential as a next-generation molecular machine exhibiting catalytic function.

## Photoluminescent Lanthanides

**P. I. Girginova, F. A. Almeida Paz, P. C. R. Soares-Santos, R. A. Sá Ferreira, L. D. Carlos, V. S. Amaral, J. Klinowski, H. I. S. Nogueira, T. Trindade* ..... 4238–4246**

Synthesis, Characterisation and Luminescent Properties of Lanthanide-Organic Polymers with Picolinic and Glutaric Acids

**Keywords:** Lanthanide complexes / Picolinic acid / Glutaric acid / Luminescence

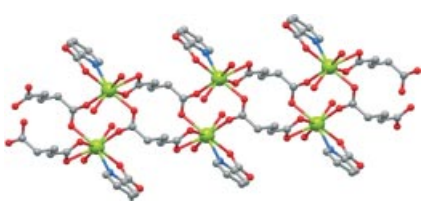

Lanthanide ($Sm^{3+}$, $Eu^{3+}$, $Tb^{3+}$) coordination polymers containing a flexible bridging ligand and a chelating aromatic ligand have been synthesised and characterised. In these compounds the aromatic ligand acts as an antenna, efficiently transferring energy to the Ln emitting centre and the dicarboxylato ligand controls, to some extent, the dimensionality of the final product.


# CORRECTION


**E. Pacholska-Dudziak, L. Latos-Grażyński* ..... 4247**

NMR Studies of Paramagnetic Metallocarbaporphyrinoids

**Keywords:** Carbaporphyrinoids / Porphyrinoids / NMR spectroscopy / Organometallic chemistry



**If not otherwise indicated in the article, papers in issue 25 were published online on August 21, 2007**

**The EUChemSoc Societies have taken the significant step into the future by merging their traditional journals, to form two leading chemistry journals, the *European Journal of Inorganic Chemistry* and the *European Journal of Organic Chemistry.* Three further EUChemSoc Societies (Austria, Czech Republic and Sweden) are Associates of the two journals.**

## COVER PICTURE

**The cover picture shows** the reaction between the phosphavinylidene complexes $[(\eta^5\text{-}C_5H_5)(CO)_2M{=}P{=}C(SiMe_3)_2]$ and the inversely polarized phosphaalkene $t$BuP=C(NMe$_2$)$_2$, which affords $\eta^3$-1,2-diphosphaallyl complexes by smooth transfer of the phosphinidene unit onto the electrophilic ligand of the precursors. The molecular structure underlines the unsymmetrical $\eta^3$-ligation of the heteroallyl ligand to the metal with the *tert*-butyl substituent *syn* to the central phosphorus atom. Treatment of the phosphavinylidene complexes with *P*-aroylphosphaalkenes leads to decomposition. In contrast, phosphavinylidene complexes and *As*-aroylarsaalkenes yield complexes featuring cyclic phosphenium ligands with an As=C bond. It is believed that the first step of this process is a formal [2+1] cycloaddition between the P=C bond and the aroylarsinidine to give a three-membered ring, which subsequently incorporates the CO unit to afford the final product. In all cases, tetrakis(dimethylamino)ethene is formed as a byproduct. Details are presented in the Microreview by L. Weber on p. 4095 ff.

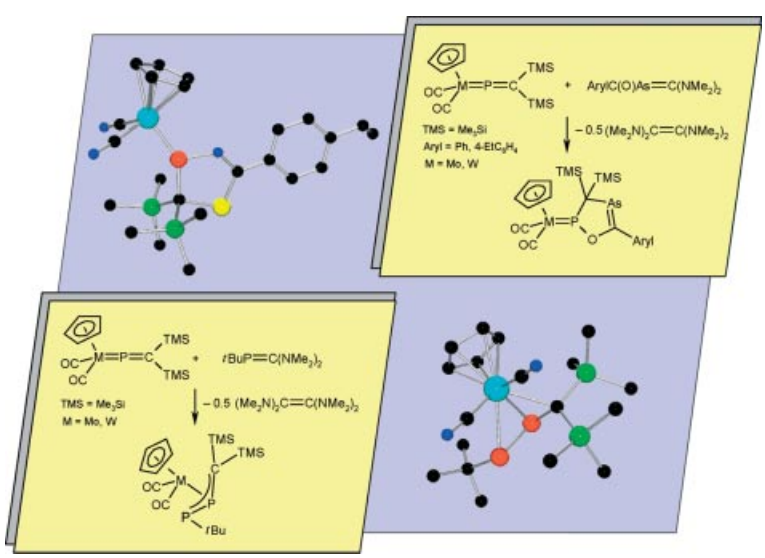

 © 2007 Wiley-VCH Verlag GmbH & Co. KGaA, Weinheim 

# SPOTLIGHTS …

## *Organocatalysis*

T. Kano, Y. Tanaka, K. Maruoka*

**_exo_-Selective Asymmetric Diels–Alder Reaction Catalyzed by Diamine Salts as Organocatalysts**

*Chem. Asian J.*
DOI: **10.1002/asia.200700122**

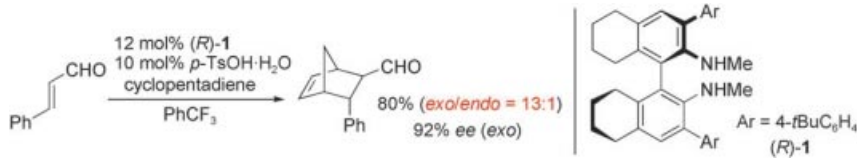


**It's cool to be different**: The axially chiral diamine (*R*)-**1** was designed and used successfully with *p*-TsOH·$H_2O$ as an organocatalyst in the Diels–Alder reaction of cyclopentadiene with α,β-unsaturated aldehydes. Although the Diels–Alder reaction of such compounds is inherently *endo* selective, (*R*)-**1** exhibits unprecedented levels of *exo* selectivity. Ts = toluenesulfonyl.

## *Library Screening*

Y.-W. Kim, H.-M. Chen, J. H. Kim, J. Müllegger, D. Mahuran, S. G. Withers*

**Thioglycoligase-Based Assembly of Thiodisaccharides: Screening as β-Galactosidase Inhibitors**

*ChemBioChem*
DOI: **10.1002/cbic.200700263**

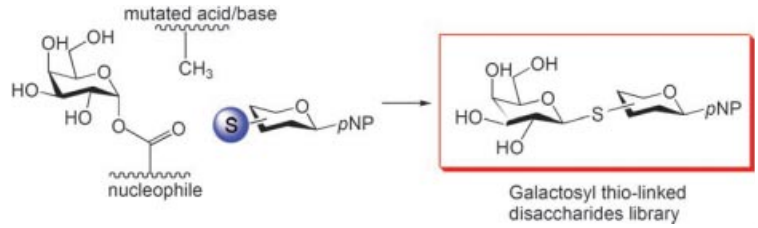


**New way of doing things**. An efficient inhibitor of a human lysosomal acid β-galactosidase was identified through screening of a small collection of thioglycosides created by using a thioglycoligase derived from a bacterial β-galactosidase (see scheme). The results described here open the interesting possibility of finding novel and unpredicted inhibitors of enzymes of interest through the relatively simple strategy of library generation by using thioglycoligases.

## *Primary Photoreaction*

C. Schumann, R. Groß, N. Michael, T. Lamparter, R. Diller*

**Sub-Picosecond Mid-Infrared Spectroscopy of Phytochrome Agp1 from *Agrobacterium tumefaciens***

*ChemPhysChem*
DOI: **10.1002/cphc.200700210**

**Isomerization**: Light sensing by phytochrome photoreceptors is initiated via *Z–E* isomerization of the chromophore, an open chain tetrapyrrole molecule (see picture). The vibrational dynamics of this primary photoreaction in the bacterial phytochrome Agp1 from *Agrobacterium tumefacines* are followed by means of ultrafast infrared spectroscopy.

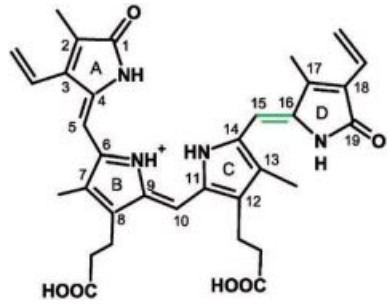


## *Inhibitor Screening*

J. Trapp, R. Meier, D. Hongwiset, M. U. Kassack, W. Sippl, M. Jung*

**Structure–Activity Studies on Suramin Analogues as Inhibitors of NAD$^+$-Dependent Histone Deacetylases (Sirtuins)**

*ChemMedChem*
DOI: **10.1002/cmdc.200700003**

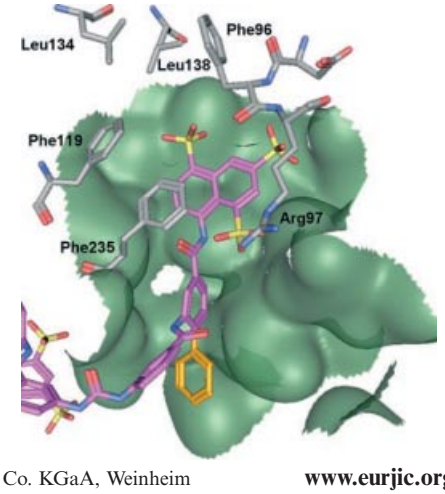


**New inhibitors for sirtuins**: Suramin emerged as an inhibitor of the NAD$^+$-dependent histone deacetylase SIRT1. We found suramin-related compounds to be much more potent than the parent molecule and established structure–activity relationships for a large set of suramin derivatives. Molecular modeling accompanied the screening process and gives new insight into suramin binding on sirtuins.


© 2007 Wiley-VCH Verlag GmbH & Co. KGaA, Weinheim

# … ON OUR SISTER JOURNALS

EurJIC European Journal of Inorganic Chemistry

## Macrocycles

**A new bis-macrocycle** has been prepared via two different routes and used for the synthesis of an intricate topology. The spectroscopic and electrochemical properties of this bis-copper(I) catenane have been explored.

J. Frey, T. Kraus, V. Heitz,* J.-P. Sauvage*

**Synthesis of a Bis-macrocycle Containing Two Back-to-Back Rigidly Connected 1,10-Phenanthroline Units as a Central Core and its Incorporation in a Handcuff-Like Catenane**

*Chem. Eur. J.*
DOI: **10.1002/chem.200700671**

## Carbaporphyrinoid Chemistry

Tetraarylazuliporphyrins with $2^3$-*tert*-butyl- or $2^3$-phenyl substituents were found to undergo oxidative rearrangements with *t*BuOOH and KOH to give substituted benzocarbaporphyrins. The data indicate that these reactions are triggered by nucleophilic attack at the positions adjacent to the azulene substituents.

J. A. El-Beck, T. D. Lash*

**Synthesis and Reactivity of $2^3$-*tert*-Butyl- and $2^3$-Phenyltetraarylazuliporphyrins: an Analysis of the Effect of Bulky Substituents on Oxidative Ring Contractions to Benzocarbaporphyrins**

*Eur. J. Org. Chem.*
DOI: **10.1002/ejoc.200700526**

## Coordination Polymers

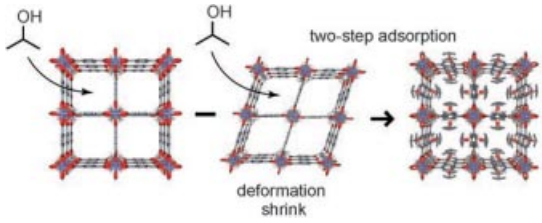


**Flexible frameworks:** Unique two-step isotherms were observed for the adsorption/desorption of propan-2-ol on [{$Zn_2$(1,4-benzenedicarboxylate)$_2$(1,4-diazabicyclo[2.2.2]octane)}$_n$] with hydrophobic open spaces. The isotherms were characterized by means of thermal analysis and single-crystal X-ray diffraction (see picture).

K. Uemura,* Y. Yamasaki, Y. Komagawa, K. Tanaka, H. Kita

**Two-Step Adsorption/Desorption on a Jungle-Gym-Type Porous Coordination Polymer**

*Angew. Chem. Int. Ed.*
DOI: **10.1002/anie.200702390**

On these pages, we feature a selection of the excellent work that has recently been published in our sister journals. If you are reading these pages on a computer, click on any of the items to read the full article. Otherwise please see the DOIs for easy online access through Wiley InterScience.

 © 2007 Wiley-VCH Verlag GmbH & Co. KGaA, Weinheim 

DOI: 10.1002/ejic.200700483

# Phospha- and Arsaalkenes RE=C(NMe$_2$)$_2$ (E = P, As) as Novel Phosphinidene- and Arsinidene-Transfer Reagents

**Lothar Weber*[a]**

**Keywords:** Phosphaalkenes / Arsaalkenes / Phosphinidene / Arsinidene

Phosphinidenes (phosphanylidenes) (RP) are electronically and coordinatively unsaturated phosphorus compounds, which, as six-electron species, are formally analogous to the more familiar carbenes and nitrenes. In contrast to carbenes ($CR_2$), the extremely reactive phosphinidenes cannot be isolated without decomposition. Thus, our knowledge on phosphinidenes is mainly limited to trapping reactions and quantum-chemical calculations. There are a number of synthetic methods for phosphinidenes available, for example photolysis or thermolysis of cyclic phosphanes and oligophosphanes, dehalogenation of organodihalophosphanes, liberation of dinitrogen from organodiazidophosphanes, or decomposition of phosphoranylidene-$\sigma^4$-phosphoranes (arylP=PMe$_3$). A plethora of information is available on the generation of highly reactive terminal phosphinidene complexes [RPW(CO)$_5$] and their chemistry. Many of these methods suffer from comparatively harsh conditions (strong base, heat, etc.) which limit their preparative use.
(© Wiley-VCH Verlag GmbH & Co. KGaA, 69451 Weinheim, Germany, 2007)

## 1. Introduction

Phosphinidenes R–P (phosphanylidenes) are elusive six-electron species, which can only be evidenced by interception reactions or by their oligomerization to oligocyclophosphanes.[1]

The chemistry of unsupported phosphinidenes is only poorly developed in comparison to the rich chemistry displayed by free carbenes. One reason might be sought in the limited number of suitable precursors for these electron-deficient molecules. Moreover, general difficulties in the unambiguous identification of phosphinidenes as key compounds in reactions have to be noted at this point. Often it has not been sufficient to draw a conclusion about their identity solely from an observed product pattern.

Phosphinidenes occur as singlet and triplet species, whereby, like in the case of methylene, the parent compound [PH] has a triplet ground state with an experimentally determined triplet–singlet separation of 22 kcal mol$^{-1}$. Quantum chemical calculations have evidenced that, with π-donor substituents at the phosphorus atom, the energy of the open-shell particles approach the singlet state.

[a] Fakultät für Chemie der Universität Bielefeld,
Universitätsstrasse 25, 33615 Bielefeld, Germany
Fax: +49-521-106-6146
E-mail: lothar.weber@uni-bielefeld.de

## 2. Synthesis and Trapping Reactions of Phosphinidenes

Convincing arguments for the intermediacy of phosphinidenes where obtained from their photochemical generation. Photolysis of Mes*P(N$_3$)$_2$ (**1**) (Mes* = 2,4,6-*t*Bu$_3$C$_6$H$_2$) with UV light (254 nm) afforded phosphaindane **3**, the formation of which was rationalized by the insertion of the P atom into a C–H bond of one *tert*-butyl group in the *ortho* position of the arene ring (Scheme 1).[2]

When the photolysis of **1** was conducted in deuterated solvents, *no* deuterium incorporation into product **3** was observed. Obviously, the intramolecular rearrangement of transient **2** into **3** occurred very rapidly. Photolyses of Mes*P=C=O and Mes*P=PMes* also gave compound **3** as the final product in high yields.[2]

*Lothar Weber was born in 1944 in Langenöls in Schlesien. He studied at the University of Marburg and received his doctorate there under the direction of Professor Günter Schmid in 1973. Afterwards, he carried out postdoctoral studies with Professor Barry M. Trost at the University of Wisconsin in Madison, USA. On his return to Marburg, he began the experimental work leading to his Habilitation, which was completed in 1982 at the University of Essen. His work focused on the coordination chemistry of sulfur ylides. In 1985, he became a C2 Professor and then joined the Fakultät für Chemie der Universität Bielefeld. His research interests include the chemistry of compounds with low-coordinate elements of the fifth main group, the synthesis of homo- and heterocycles with heavy elements, as well as new aspects in boron chemistry.*

 © 2007 Wiley-VCH Verlag GmbH & Co. KGaA, Weinheim 

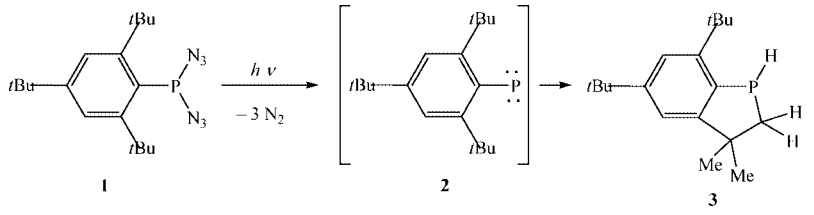

Scheme 1. Generation of phosphaindane **3** by photolysis of **1**.

The "retro-addition strategy" seemed to be particularly useful for the synthesis of phosphinidenes. Thus, photolysis of 3-methyl-1-phenyl-3-phospholene (**4**) in the presence of 2,3-dimethylbutadiene furnished phospholene **5** in addition to a *cis*/*trans* mixture of 4,5-dimethyl-1,2-diphenyl-1,2-diphosphacyclohexenes **6** (Scheme 2).

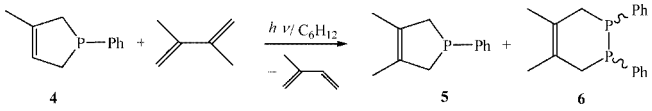

Scheme 2. Photolysis of **4** in the presence of 2,3-dimethylbutadiene.

These observations were explained by invoking the photochemical extrusion of phenylphosphinidene from **4** and its subsequent cheletropic [1+4] cycloaddition to the diene. In a competing process, the phosphinidene dimerized to a diphosphene which underwent a Diels–Alder reaction to give isomers **6**.[3]

Irradiation of 3,4-dimethyl-1-supermesityl-3-phospholene (**7**) afforded phosphinidene **2**, which isomerized to **3**. Compound **3** was obtained in 68% yield upon photolysis of **8** even in the presence of potential trapping reagents such as alkenes, dienes, or alkynes. Only traces of diphosphene Mes*P=PMes* were observed (Scheme 3).

Photolysis of mesitylphosphirane **9** furnished a mixture of cyclophosphanes **10** (40%) and **11** (11%) in addition to mesitylvinylphosphane **12** (8%) and mesitylphosphane **13** (1%) (Scheme 3). In the presence of alkenes, dienes or alkynes, the yield of the oligocyclophosphanes decreased in favor of the formation of three-membered rings.

Frozen solutions of phosphirane **15** in methylcyclohexane at 77 K turned yellow upon irradiation with UV light ($\lambda$ = 254 nm). Thawing the glass in the absence of trapping reagents gave cyclotriphosphane **10** in 30% yield. In the presence of 3-hexyne, phosphirene **14** was formed in yields up to 88%, which was rationalized by the initial liberation of mesitylphosphinidene. In an ESR experiment at 4 K, the yellow glass displayed a strong signal at 11492 Gauss, which was assigned to the free [Mes–P] in the triplet ground state.[4a] A recent careful theoretical analysis of the fragmentation reaction demonstrated that free [Mes–P] was probably not generated in the presence of alkenes.[4b]

Phosphanylphosphinidene [$t$Bu$_2$P–P] has been known for some time.[5a] Its chemistry as well as theoretical calculations[5b] on it agree with a singlet ground state of the molecule.

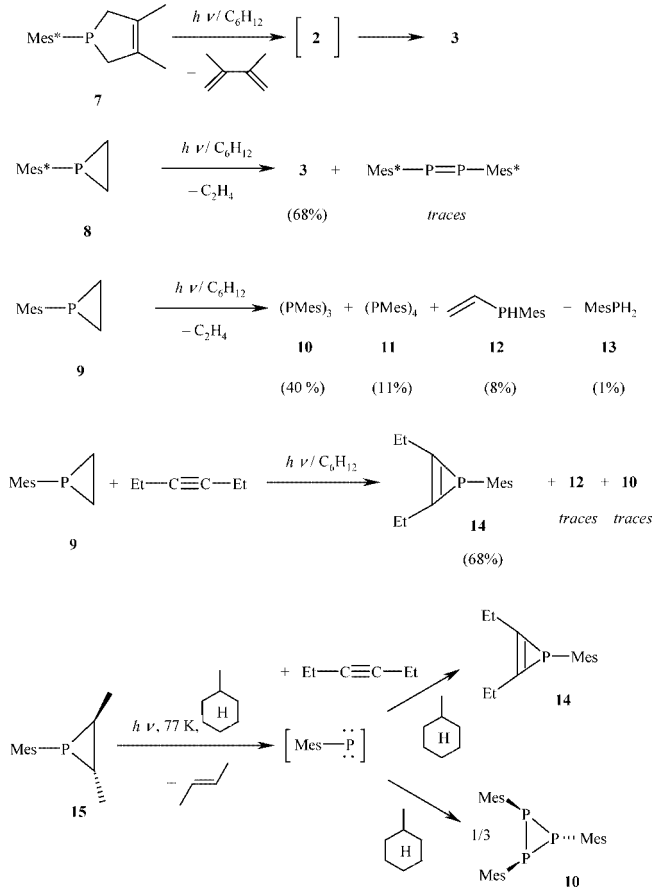

Scheme 3. Photolysis of phospholene **7** and phosphiranes **8**, **9**, and **15**.

Stimulated by the work of Burg and Mahler, who studied the decomposition of $CF_3P{=}PMe_3$,[6] Protasiewicz et al. photolyzed the phosphinidenephosphoranes **16**–**18** (Scheme 4).[7] Release of $PMe_3$ from derivative **16** gave phosphinidene **2**, which rearranged immediately to **3**.

In contrast, irradiation of **17** afforded diphosphene **20** in 90–95% yield, which was explained by an attack of phosphinidene **19** at the precursor. The photochemical treatment of phosphinidenephosphorane **18** led to phosphafluorene **22** as the product of the insertion of the P atom of transient **21** into the carbon–carbon bond of an *ortho*-isopropyl group. Interestingly, compound **22** was also formed in 68% yield during the magnesium reduction of 2,6-trip$_2$C$_6$H$_3$PCl$_2$.[7b,8] The reductive dechlorination of aryl-PCl$_2$, however, does not necessarily proceed via free phos-

 © 2007 Wiley-VCH Verlag GmbH & Co. KGaA, Weinheim 

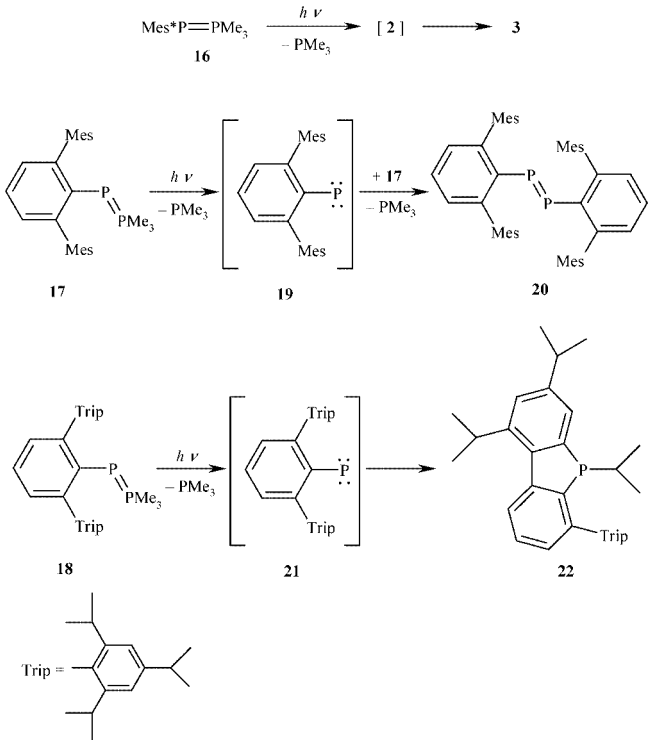


Scheme 4. Photolysis of phosphinidenephosphoranes **16**–**18**.

phinidenes as intermediates. It is equally conceivable that this process may involve radicals or species of the type arylP(Cl)MgCl.

## 3. Phosphinidene Complexes as Phosphinidene Transfer Reagents

A rich area of transition-metal complexes featuring terminal phosphinidene ligands contrasts with the scarcely developed chemistry of free phosphinidenes.[9] There was a considerable effort to develop a phosphinidene chemistry analogous to the well familiar carbene complex chemistry.[10] Here, however, it proved troublesome to employ synthetic methods that proved fruitful in carbene chemistry. In contrast, one had to face the task of individually modifying the reaction conditions according to the demands of the substituents at the P atoms. A useful approach was the stabilization and fixation of singlet phosphinidene in the coordination sphere of d-block metals. At this point, two different types of terminal phosphinidene complexes may be discriminated: coordination compounds with phosphinidenes as two electron donors with a nonlinear M–P–R arrangement (e.g. **23**)[11] or those with phosphinidenes that serve as four electron donors with a linear M–P–R skeleton (e.g. **24**).[12] It is obvious that complexes with $sp^2$-hybridized phosphorus atoms show $^{31}P$ NMR resonances at very low field, which is in sharp contrast to those with sp-hybridized phosphorus.

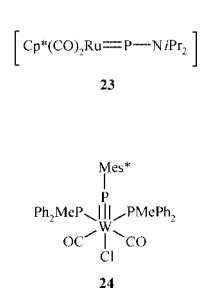


| | |
|---|---|
| $d$(Ru=P) | 2.2654(5) Å |
| ∢ Ru–P–N | 119.6° |
| $\delta(^{31}P)$ | + 932 ppm |
| $d$(W≡P) | 2.169(1) Å |
| ∢ W–P–C | 168.2° |
| $\delta(^{31}P)$ | + 193.0 ppm |

### 3.1 Nucleophilic Phosphinidene Complexes

The discrimination between nucleophilic and electrophilic phosphinidene complexes is mainly justified by their reactivity. Early transition metals with an electron-abundant coordination sphere favor a polarity $P^{\delta-}$–$M^{\delta+}$ of the metal–phosphorus bond. Thereby the gradual variation of the ancillary ligands to some extent allows tuning of the mode of reactivity of the PR ligand from nucleophilic to electrophilic. This aspect was analyzed in a theoretical study.[13]

The first stable transition-metal complexes having nucleophilic phosphinidene ligands [$Cp_2M$=PMes*] (**26a**,**b**) (M = Mo, W) were synthesized as red solids by the reaction of Mes*$PCl_2$ with the hydridolithium species **25a**,**b** (Scheme 5).

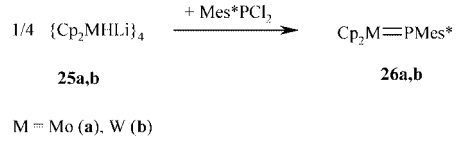


Scheme 5. Synthesis of **26a**,**b**.

According to an X-ray structural analysis of the molybdenum complex **26a** the M–P–R skeleton is bent [115.8(2)°] with a MoP double bond of 2.370(2) Å.[14]

A bent terminal phosphinidene derivative, [$Cp_2$Zr(=PMes*)($PMe_3$)] (**27**), was isolated from the reaction of [$Cp_2ZrCl_2$] with LiPHMes* in the presence of $PMe_3$ (Scheme 6).

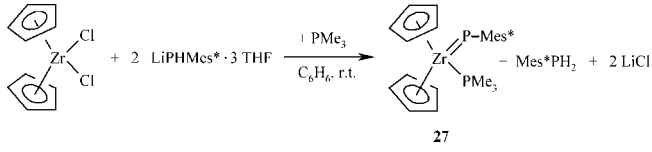


Scheme 6. Synthesis of **27**.

The outcome of such a protocol is crucially dependent on the steric requirements of the ligands at the metal and the phosphorus atom.[15] According to a comparable protocol, the synthesis of the first terminally bonded phosphanylphosphinidene complex [$Cp_2$Zr{=P–P($t$Bu)$_2$}($PPhMe_2$)] (**28**) was achieved. The ZrP contact to the phosphinidene ligand was considerably shorter [2.488(3) Å] than that to the phosphane ligand [2.734(3) Å] (Scheme 7).[16]

 © 2007 Wiley-VCH Verlag GmbH & Co. KGaA, Weinheim 

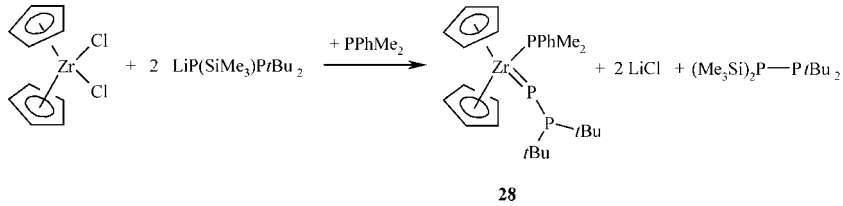


Scheme 7. Synthesis of **28**.

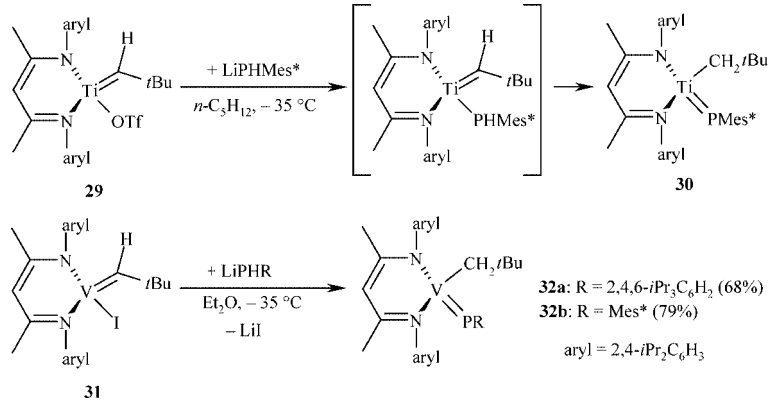


Scheme 8. Titanium and vanadium complexes with nucleophilic terminal phosphinidene ligands.

Until 2004, $\eta^2$-coordination was found to be essential to stabilize the $t$Bu$_2$PP ligand, whose source is phosphanylphosphinidine-$\sigma^4$-phosphoranes.[5a,17]

A strategy for preparing a terminal titanium phosphinidene complex, **30**, involved treatment of the nucleophilic and four-coordinate titanium alkylidene complex [(Nacnac)-Ti=CH$t$Bu(OTf)] (**29**) [Nacnac = 2,6-$i$Pr$_2$C$_6$H$_3$NC(Me)-CHC(Me)N-C$_6$H$_3$-$i$Pr$_2$-2,6] with LiPHMes* in pentane at –35 °C (Scheme 8). The structure of the molecule in the crystal displays a four-coordinate titanium–phosphinidene complex with an exceptionally short Ti=P bond [2.183(4) Å] and a nearly linear Ti=P–C$_{ipso}$ angle [164.44(5) Å].[18a]

Dark blocks of crystalline **32a** and **32b** were obtained in good yield from the layering of a cold ethereal solution (–35 °C) of the lithium phosphide onto a similarly cold ether solution of vanadium(IV) complex **31** (Scheme 8).[18b]

In contrast to a series of phosphinidene complexes, which owe their stability to very bulky substituents, Schrock developed a synthetic procedure for stable tantalum phosphinidenes **33**, which tolerate Ph, Cy, and $t$Bu groups as substituents. This is due to the bulky tetradentate amido ligand $\{N(CH_2CH_2NSiMe_3)_3\}^{3-}$ (Scheme 9).

The X-ray diffraction study of **33c** displays a nearly linear Ta–P–C unit with a short Ta–P bond of 2.145(7) Å. The $^{31}$P NMR resonances of the complexes range from 175.1 to 227.3 ppm.[19] Tantalum phosphinidene complex **35** ($\delta^{31}$P = 334.6 ppm) resulted from a 1,2-H$_2$-elimination of phosphanido complex ($t$Bu$_3$SiO)$_3$(H)Ta–P(H)Ph (**34**), (Scheme 10).[20] The angle Ta–P–C in **35** is 110.2(4)°, and the Ta=P bond length is 2.317(4) Å.

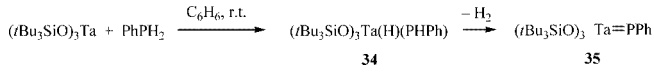


Scheme 10. Synthesis of **35**.

Terminal nucleophilic complexes of group 8 (**36**) and group 9 (**37**) transition metals were synthesized by Lammertsma et al. by the base-induced dehydrohalogenation of appropriate precursor complexes in the presence of stabilizing ligands. $^{31}$P NMR resonances of the Ru complexes were observed between 801 and 846 ppm, and in the Os compounds they range from 668 to 744 ppm. The $p$-cymene(PPh$_3$)Os complex displays a bent Os–P–C backbone [106.56(9)°] with an Os–P bond of 2.2195(7) Å (Scheme 11).[21]

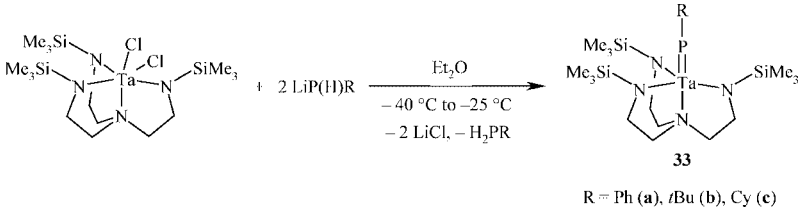


Scheme 9. Synthesis of **33a**–**c**.

 © 2007 Wiley-VCH Verlag GmbH & Co. KGaA, Weinheim 

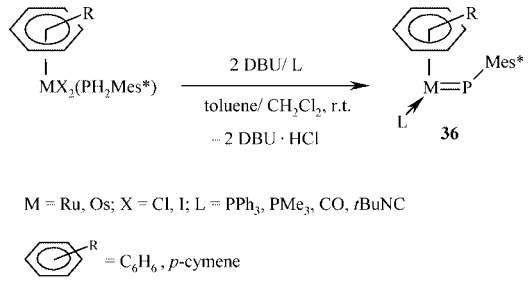


**36**

Scheme 11. Synthesis of phosphinidene complexes of Ru and Os.

Similarly, iridium complexes [Cp*(L)Ir=Paryl] (aryl = Mes, Is, Mes*), L = $PR_3$, $P(OR)_3$, $AsR_3$, dppe, RNC, and CO,[22] and the corresponding cobalt and rhodium complexes [Cp*($R_3P$)Rh=Paryl] (**37**) [aryl = Mes*, Is (Is = 2,4,6-$iPr_3C_6H_2$); R = Me, Ph], and [Cp*Co($PPh_3$)=PMes*][23] were synthesized (Scheme 12).

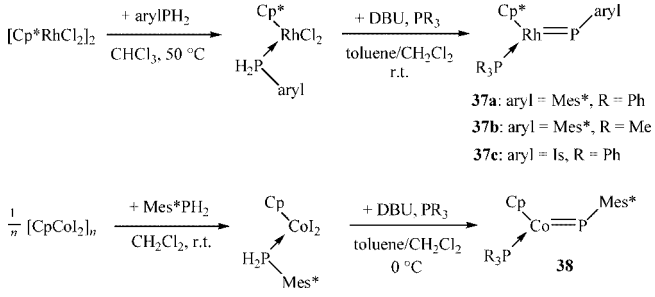


Scheme 12. Synthesis of phosphinidene complexes of Rh and Co.

Ether solutions of lithium-2,6-dimesitylphenylphosphanide [LiP(H)dmpp] reacted cleanly with **39** to give the paramagnetic primary phosphanido complex **40**, which, after oxidation to **41** by tropylium hexafluorophosphate and deprotonation, afforded the nickel–phosphinidene complex **42** as bright green crystals in 86% yield (Scheme 13).[24]

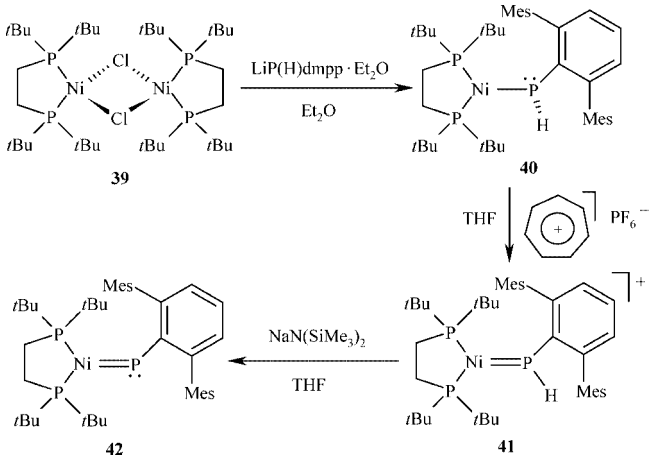


**39** **40** **41** **42**

Scheme 13. Synthesis of Ni–phosphinidene complex **42**.

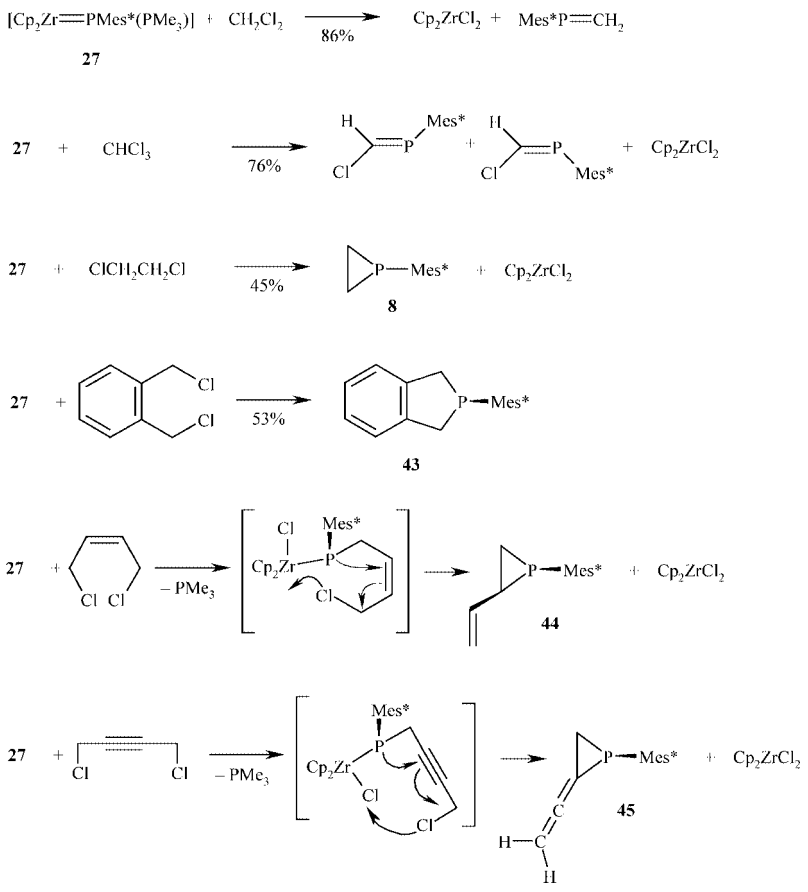


Scheme 14. Reactions of **27** with organic dichlorides.

 © 2007 Wiley-VCH Verlag GmbH & Co. KGaA, Weinheim 

The terminal phosphinidene complex [$Cp_2Zr$=PMes*-($PMe_3$)] (**27**) proved useful in delivering the phosphinidene [PMes*] to suitable acceptors. The high oxo- and chlorophilicity of the zirconium center in **27** allows exchange of its phosphinidene unit for two chlorine atoms or an oxygen atom of a substrate to form either [$Cp_2ZrCl_2$] or [$Cp_2ZrO$]$_n$, respectively. For example, reactions of **27** with dichloromethane or chloroform readily afforded the phosphaalkenes Mes*P=$CH_2$ and (*E*/*Z*)-Mes*P=CHCl[25] (Scheme 14).

With 1,2-dichloroethane phosphirane **8** was formed in addition to [$Cp_2ZrCl_2$]. The use of *o*-dichloroxylene produced the new phospholane **43** in 53% yield. In contrast to these results, the reaction of **27** with 1,4-dichloro-2-butene did not produce the anticipated five-membered ring, but rather the *cis*-isomer of vinyl-substituted phosphirane **44** in 38% yield. Likewise, the reaction of **27** with 1,4-dichloro-2-butyne produced the vinylidenephosphirane **45** (53% yield). The reactions with alkyl halides were thought to involve phosphanide–halide intermediates of the form [$Cp_2Zr$(PMes*R)Cl].

In a Wittig-type process, compound **27** reacted with benzaldehyde to give an insoluble colorless precipitate {presumably [($Cp_2ZrO$)$_n$]}, free $PMe_3$ and (*E*)-Mes*P=CHPh. An analogous synthetic procedure using benzophenone provided an 82% yield of Mes*P=$CPh_2$, and in the same manner the use of 2 equiv. of **27** and isophthalaldehyde furnished exclusively the *E*,*E* isomer of the bis(phosphaalkene) **46** in 86% yield. The related transformation of **27** with phenylisothiocyanate gave the heteroallene *trans*-PhN=C=P–Mes* **47** (81% yield) along with the crystalline blue byproduct [$Cp_2ZrS$]$_2$[25] (Scheme 15).

The reaction of **27** with benzonitrile afforded the red compounds **48** as a 55:45 isomeric mixture. The addition of **27** with dicyclohexyl carbodiimide (DCC) led to the phosphoguanidino complex **49**[23] (Scheme 16).

Phosphiranes **50a** and **50b** were derived from reactions of **27** with *trans*-stilbene oxide and styrene oxide, respectively. In the related reaction with propylene oxide, complex **51**, with a secondary phosphanido and a propenolato ligand, was obtained. This process probably involves precoordination of the epoxide to the zirconium center followed by abstraction of the enolizable proton and ring opening[25] (Scheme 17).

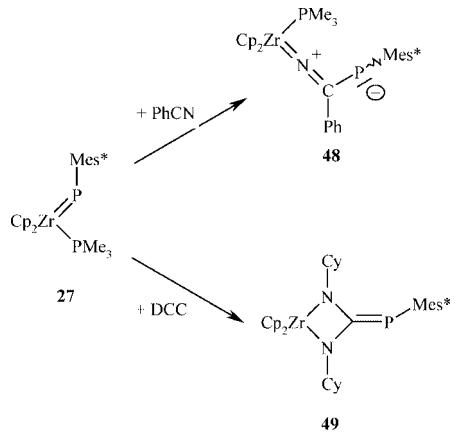


Scheme 16. Reaction of **27** with PhCN and DCC.

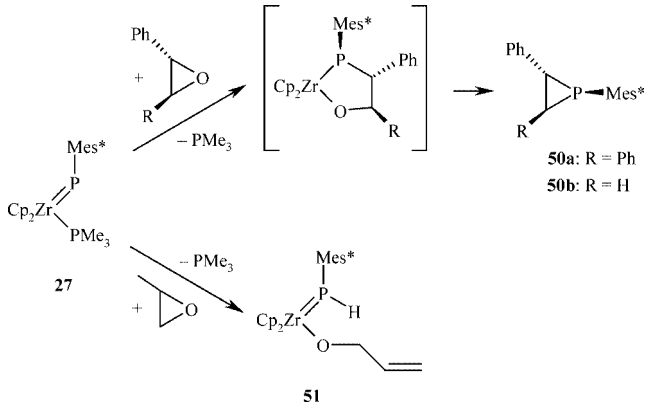


Scheme 17. Reaction of [$Cp_2Zr$=PMes*($PMe_3$)] (**27**) with epoxides.

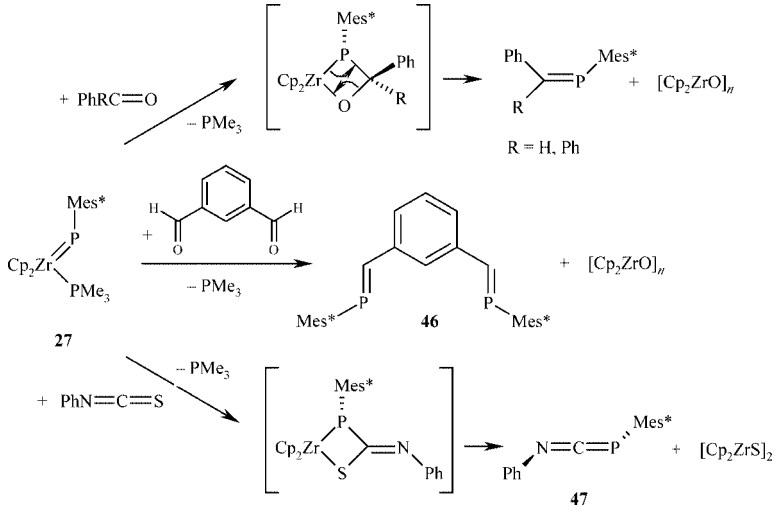


Scheme 15. Reaction of **27** with carbonyl compounds and isothiocyanate.

 © 2007 Wiley-VCH Verlag GmbH & Co. KGaA, Weinheim 

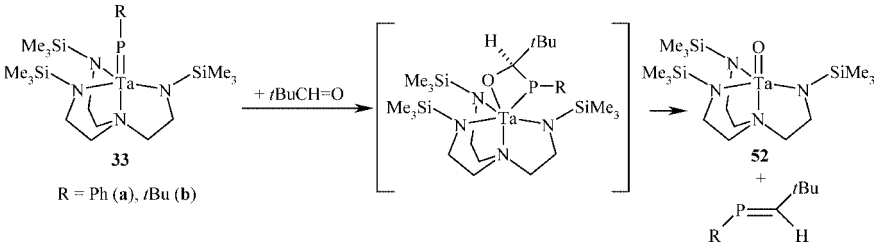


Scheme 18. Synthesis of phosphaalkenes from complex **33** and aldehydes.

Aldehydes react cleanly with tantalum–phosphinidene complexes **33**, providing the stable oxotantalum complex **52** in addition to the corresponding phosphaalkenes. The reaction of **33b** with pivaldehyde took 7 h at 95 °C to reach completion and furnished (*E*)-*t*BuP=CH*t*Bu. Phosphaalkene (*E*)-PhP=CH*t*Bu resulted as an oil in 83% yield from the treatment of **33a** with pivaldehyde[19a] (Scheme 18).

### 3.2 Electrophilic Phosphinidene Complexes

The synthetically most valuable phosphinidene complexes are unstable species exhibiting the [M(CO)$_5$] (M = Cr, Mo, W) fragment. In two recent reviews, is has been reported that these complexes almost always mirror the chemistry of singlet carbenes in Fischer-type complexes.[9,10] Thus, only a brief survey of this area with selected aspects is presented at this point. The most prominent access to these reagents involved the pyrolysis of [W(CO)$_5$] adducts of 7-phosphanorbornadienes **53** (Scheme 19).[9]

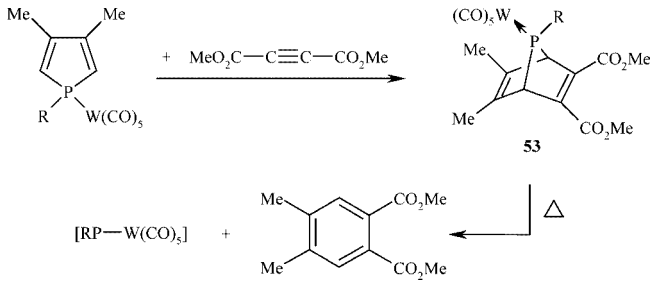


Scheme 19. Generation of [RP–W(CO)$_5$].

The concomitant interception of [RP–W(CO)$_5$] with alkenes proceeded with retention of stereochemistry (Scheme 20).[26] Reaction with alkynes preferentially afforded phosphirene complexes.[27] With 1,3-butadiene, vinyl phosphirane and 2,2′-bisphosphiranyl complexes were obtained.[26,28]

Recently, Lammertsma et al. used the thermolysis of benzophosphepine complexes **54** for the generation and trapping of [PhP–W(CO)$_5$] at 75–80 °C (Scheme 21). Apart from considerably milder reaction conditions, better yields were achieved than with other precursors.[29]

A striking difference between carbenes and electrophilic phosphinidene complexes became evident in their reactivity towards aromatic compounds. In contrast to the reaction of methylene [:CH$_2$] with benzene to afford mainly norcaradiene, which rearranges to cycloheptatriene and toluene, phosphinidene complexes are inert and may be generated in arenes such as toluene. Nevertheless, [RP–W(CO)$_5$] reacted with several selected aromatic compounds. The nucleophilic cyclopentadienyl ligand of ferrocene is an attractive target for the electrophilic phosphinidene, and the reaction results in C–H insertion.[30] Another rare example is the unique [1+4] cycloaddition to ansa compound **55** (Scheme 22) to afford **56**, because it describes the reverse of the cheletropic elimination of [RP–W(CO)$_5$].

The reaction of [PhP–W(CO)$_5$] generated from **53** in the presence of CuCl at 60 °C leads to C–H-insertion product **57a** (55%) and the formal 1,4 adducts **58a** and **58b** (45%) (Scheme 23). The analogous transformation with guaiazulene favors the formation of the 1,4 adducts **58c** and **58d** (77%) (Scheme 23).[31a]

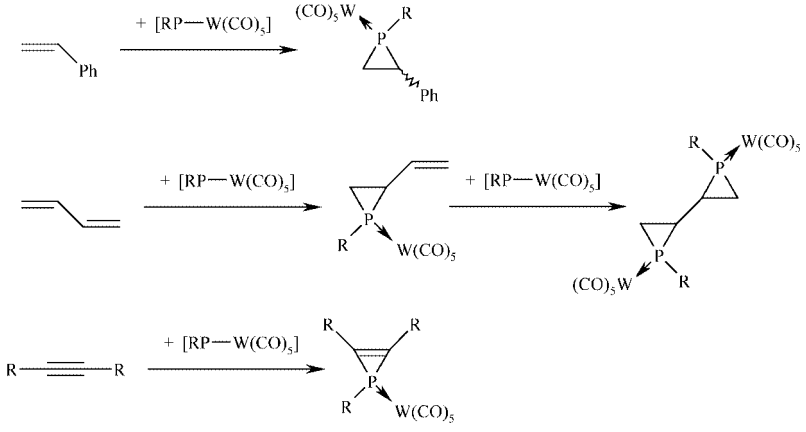


Scheme 20. Addition reactions of [RP–W(CO)$_5$].

 © 2007 Wiley-VCH Verlag GmbH & Co. KGaA, Weinheim 

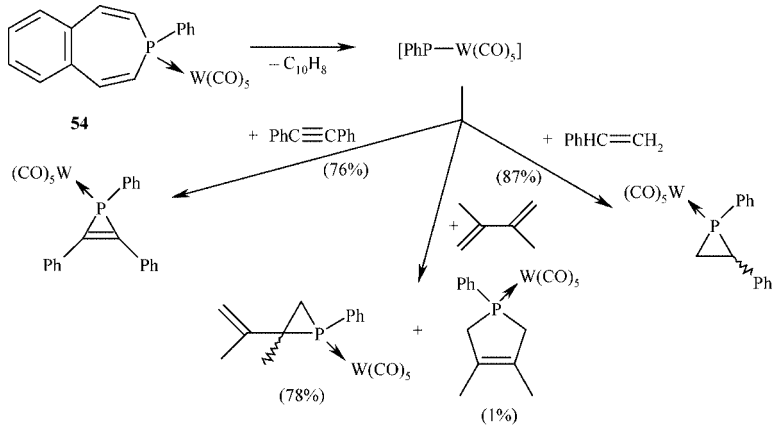

Scheme 21. Thermolysis of **54** and selected trapping reactions of [PhP–W(CO)$_5$].

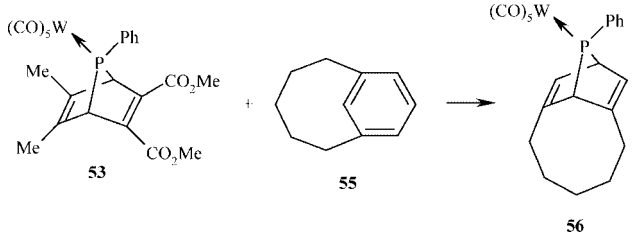

Scheme 22. Synthesis of **56**.

The reaction of electrophilic phosphinidene complex [MeP–W(CO)$_5$] with 1,6-methano[10]annulene (**59**) resulted in the exclusive formation of the isomeric C–C-insertion products **60a** (main) and **60b** (minor)[31b] (Scheme 24).

Treatment of [(CO)$_5$W–PPh] with 2,4,6-tri-*tert*-butyl-1,3,5-triphosphinine **61** in toluene at 110 °C unexpectedly afforded products **62** and **63a** in 25% and 39% isolated yields (Scheme 25).[32]

The reaction of [MeP–W(CO)$_5$] with **61**, however, resulted in a mixture of tetraphosphanorbornadiene **64**, a formal 1,4 adduct, and its corresponding quadricyclane **63b** as a 1:8 mixture.[32]

Interception of complexed phosphinidenes generated from **65** with 1-ethoxy-2-(triorganostannyl)acetylene afforded phosphaallene **66** in addition to the expected cycloadduct **67**, which was rationalized by the intermediacy of a zwitterion[33] (Scheme 26).

The reaction of tungsten–phosphinidene complexes with ketones and nitriles furnished zwitterionic 1,3-dipolar adducts whose structure depended on the substitution pattern at the P atom[34–36] (Scheme 27).

Functionalized phosphinidene complexes are frequently involved in interesting intramolecular rearrangement processes, which impressively underline the great versatility of the P-substituents[30,37–39] (Scheme 28).

Another type of intramolecular addition of a coordinated phosphinidene was realized by heating complex **68a** in tolu-

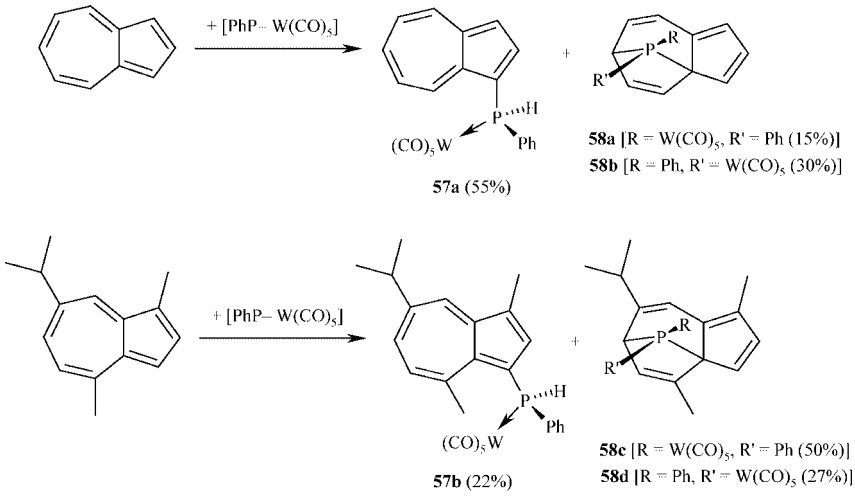

Scheme 23. Reaction of [RP–W(CO)$_5$] with azulenes.

 © 2007 Wiley-VCH Verlag GmbH & Co. KGaA, Weinheim 

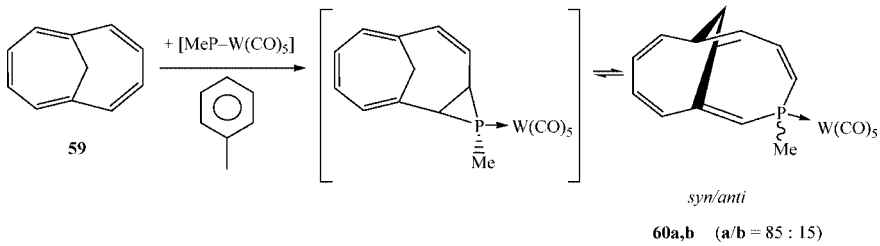


Scheme 24. Phosphinidene addition to **59**.

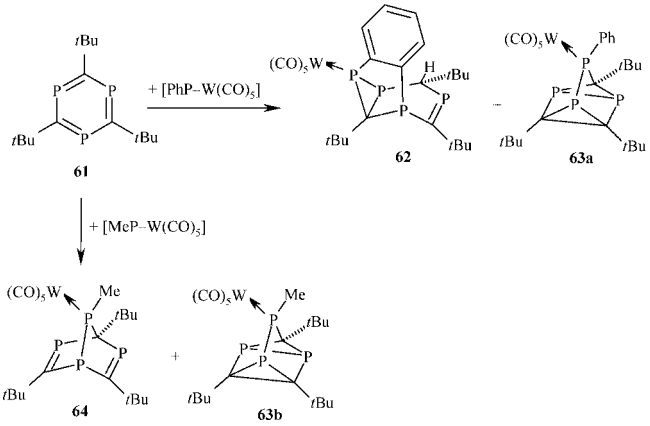


Scheme 25. Reaction of triphosphinine **61** with phosphinidene complexes.

ene at 80 °C to give the diphosphane basket **69a** as the sole isolable product in 66% yield. Similarly, the diphosphane baskets **69b**,**c** were obtained (Scheme 29).[40]

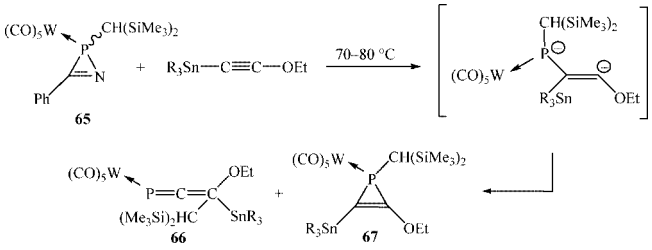


Scheme 26. Synthesis of **66** and **67**.

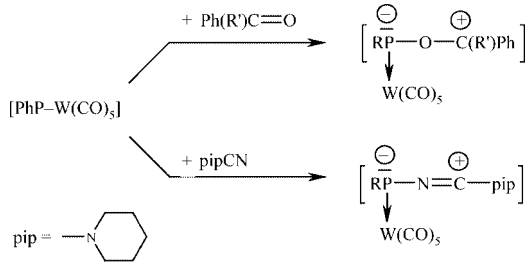


Scheme 27. Zwitterions from phosphinidene addition to ketones and nitriles.

A different route to electrophilic "Fischer Type" phosphinidene complexes of molybdenum, tungsten, ruthenium and cobalt was devised by Carty et al.[11,41,42] Their approach was based on the chloride abstraction from preformed chloro(diisopropylamino)phosphanido complexes **70a**,**b**, **72**, and **74** by using the Lewis acid aluminum chloride (Scheme 30).

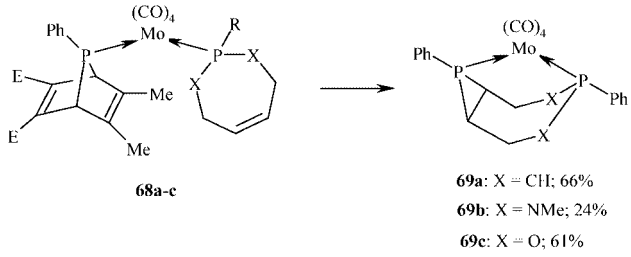


Scheme 29. Formation of **69a**–**c**.

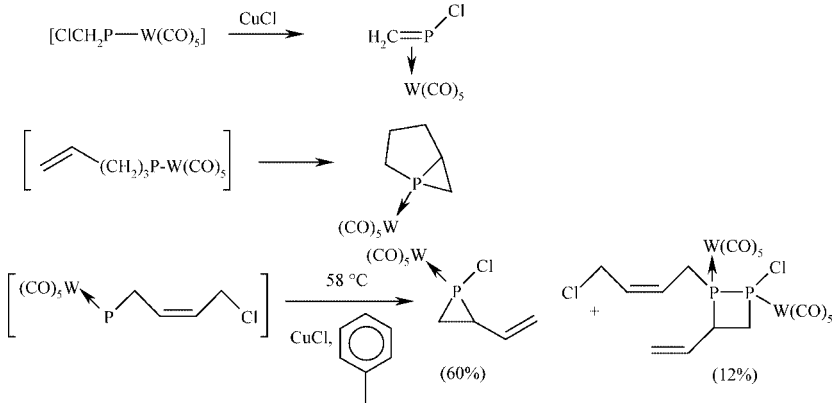


Scheme 28. Rearrangement reactions of functionalized phosphinidene complexes.

 © 2007 Wiley-VCH Verlag GmbH & Co. KGaA, Weinheim 

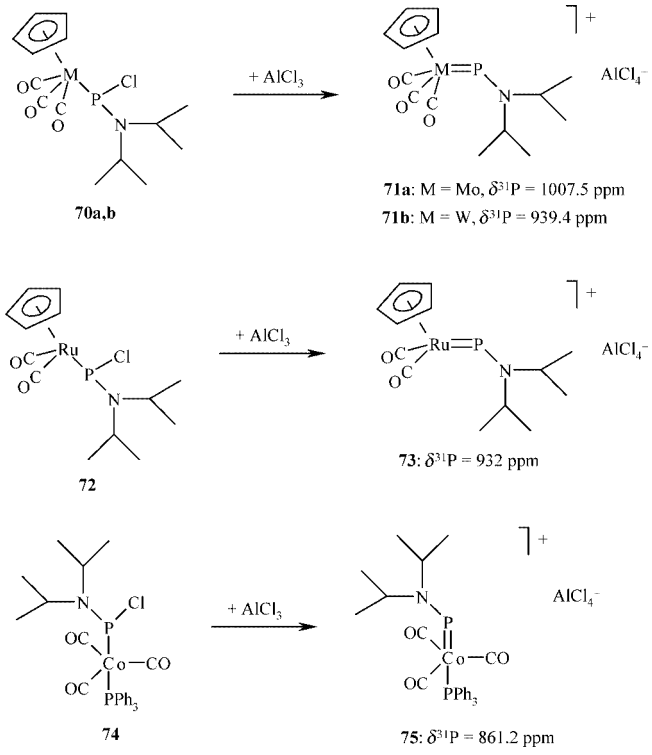


Scheme 30. Formation of cationic phosphinidene complexes.

So far, the reactivity studies of these cations are limited to alkyne additions.

## 4. Phosphinidene Transfer from Phospha-Wittig Reagents

The Wittig reaction between phosphorus ylides $Ph_3P{=}CHR^1$ – these reagents may also be considered as carbanions with an α-phosphonium center – and aldehydes and ketones furnished alkenes. Particularly in the light of the diagonal relationship C/P in the periodic table, the quest for an analogous phospha-Wittig reaction was obvious. The required reagents $R^1{}_3P{=}PR^2$ are formed by a formal phosphinidene addition to a Lewis basic tertiary phosphane, and they are easily accessible by the reaction of dichlorophosphanes, trialkylphosphanes, and zinc metal. With aldehydes they form phosphaalkenes.[43–45]

This approach was extended to the preparation of fluorescent (*E*)-poly-*p*-phenylenephosphaalkenes **76**[46] (Scheme 31).

A serious limitation of this protocol is the need of bulky substituents to provide the phospha-Wittig reagents with sufficient stability. This hurdle was circumvented by the coordination of the phosphinidene group to a transition-metal-complex fragment, preferentially to pentacarbonyltungsten, which stabilizes the organophosphorus precursor as well as the resulting phosphaalkene[47,48] (Scheme 32).

This type of reaction can only be performed with aldehydes and usually failed with ketones. This limitation can be overcome by the employment of anionic phosphorylphosphane complexes in a process analogous to the Horner–Wittig reaction[49,50] (Scheme 33).

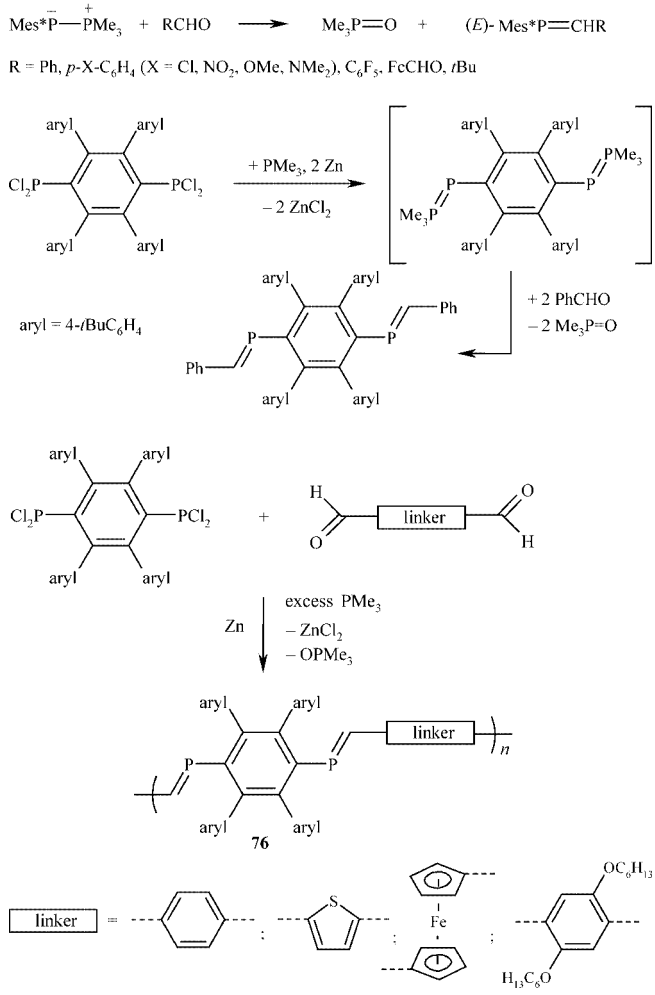


Scheme 31. Phospha-Wittig reactions.

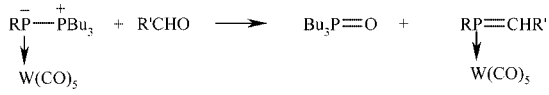


Scheme 32. Phospha-Wittig reactions with $[W(CO)_5]$-supported phosphinidenephosphoranes.

A different type of reaction was observed when phosphinidene-$\sigma^4$-phosphoranes arylP=$PMe_3$ (aryl = 2,6-$Mes_2C_6H_3$ or 2,4,6-$tBu_3C_6H_2$) were combined with selected *o*-quinones. The formation of 1,3,2-dioxophospholanes **79** and **80** was observed[51] (Scheme 34).

## 5. Phosphinidene Transfer from Inversely Polarized Phosphaalkenes

### 5.1 To Diphenylketene

The phosphorus atom of inversely polarized phosphaalkenes such as R–P=$C(NR'_2)_2$ (R = H, alkyl, aryl, $SiMe_3$; R′

 © 2007 Wiley-VCH Verlag GmbH & Co. KGaA, Weinheim 

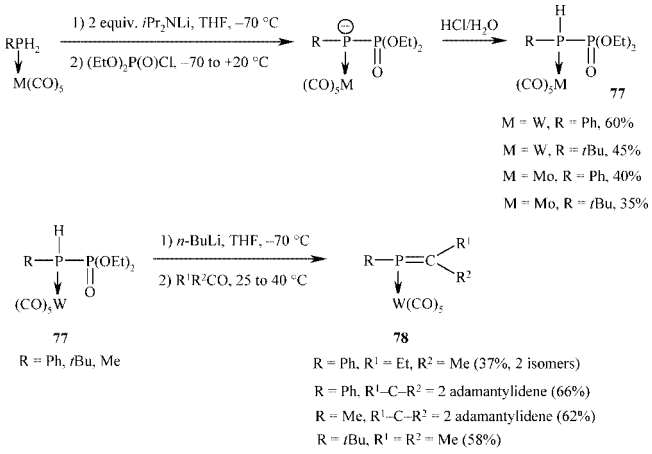


Scheme 33. Selected Phospha-Horner–Wittig reactions.

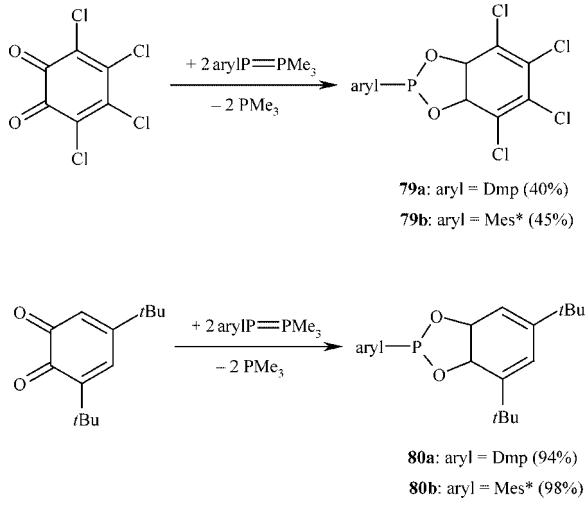


Scheme 34. Reaction of phosphinidenephosphorane with *o*-quinones.

= Me, Et) is highly nucleophilic, which is rationalized by an effective π-electron delocalization of the lone pair of electrons at the trigonal-planar amino substituents into the P–C multiple bond[52] (Scheme 35).

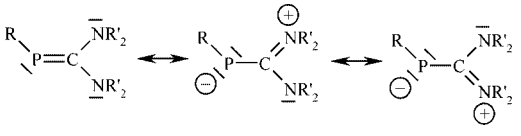

Scheme 35. Limiting formulae of amino-substituted phosphaalkenes.

Quantum chemical calculations were performed on the parent methylenephosphane and its amino-substituted derivatives $(H_2N)(H)C{=}PH$ and $(H_2N)_2C{=}PH$ at the B3LYP/6-31g* level. The parent compound has a σ + π NBO charge of +0.387 *e* at the phosphorus atom and –0.810 *e* at the carbon atom, whereas its P–C π-bond is essentially nonpolar (+0.030 *e* at P; –0.039 *e* at C). The calculations on the C-amino-substituted phosphaalkenes predict a strong polarization of the π-bond. One, and to a greater extent, two amino groups at the carbon atom induce an inverse electron density distribution at the π-bond [for example, in $(H_2N)(H)C{=}PH$ a π NBO charge of –0.285 *e* at phosphorus and +0.013 *e* at carbon; in $(H_2N)_2C{=}PH$ values of –0.504 *e* at phosphorus and +0.059 *e* at carbon were determined].[52] This effect is mirrored in the P=C-double bond lengths, which in nonconjugated phosphaalkenes range from 1.65–1.67 Å, whereas in C-amino-functionalized phosphaalkenes P–C distances of 1.72–1.76 Å are frequently measured. $^{31}$P NMR shifts in normally polarized phosphaalkenes $R^1P^{\delta+}{=}C^{\delta-}R^2R^3$ are mainly governed by a paramagnetic contribution, which is influenced by the HOMO–LUMO gaps in such molecules. Small HOMO–LUMO gaps are responsible for low field shifts in the range between $\delta$ = 740 ppm in $[Cp^*(PEt_3)Ni{-}P{=}C(SiMe_3)_2]$ and $\delta$ = 233 ppm in $MesP{=}CPh_2$. In inversely polarized phosphaalkenes, where π-conjugation of the nitrogen lone pair with the P=C-double bond operates, the P atom in β-position to the N atoms experiences additional negative charge, which causes a pronounced high-field shift [e.g. $\delta$ = –62.6 ppm in $HP{=}C(NMe_2)_2$].[52]

Protonation,[53] alkylation,[53,54] silylation,[54] and coordination to metal centers occur at the P atom with increase of the coordination number.[53,55,56] With regard to the diagonal relationship in the periodic table between the elements carbon and phosphorus, these electron-abundant C-amino phosphaalkenes are formally analogous to the tetraamino-substituted alkenes of the Wanzlick-type.[57] Accordingly, the homolytic cleavage of phosphaalkene should furnish a relatively stable bis(amino)carbene[58] and a highly reactive phosphinidene. Thus, the quest for Wanzlick-type reactions of the electron-rich bis(amino)phosphaalkenes was obvious. Thereby the reaction of 1,1′,3,3′-tetraphenyl-2,2′-bis(imidazolidinylidene) with diphenyl ketene to afford adduct **81**, performed previously by Regitz et al., served as a model reaction[59] (Scheme 36).

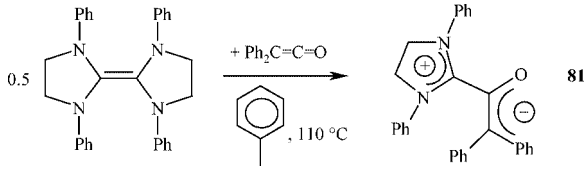


Scheme 36. Formation of a carbene/ketene adduct **81**.

Combination of the phosphaalkenes $R{-}P{=}C(NMe_2)_2$ (**82**) [R = *t*Bu (**a**), Cy (**b**), 1-Ad (**c**), Ph (**d**), Mes (**e**)] with an excess of diphenyl ketene in *n*-pentane led to the precipitation of the light yellow zwitterionic compound **83** in about 85% yield. After removal of **83** and destruction of $Ph_2C{=}C{=}O$ with powdered NaOH, 3,5-dibenzhydrylidene-1,4,2-dioxophospholanes **84a**–**e** were isolated as colorless waxes in 45–53% yield[60] (Scheme 37).

 © 2007 Wiley-VCH Verlag GmbH & Co. KGaA, Weinheim 

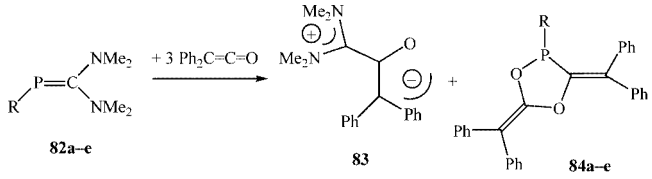


Scheme 37. Formation of compounds **83** and **84a**–**e**.

When the reaction of a concentrated solution **82a** was performed with neat $Ph_2C=C=O$, a dark-violet emulsion was formed, from which product **83** was obtained as previously from the pentane solution. Moreover, a few crystals of 5-benzhydrylidene-2-*tert*-butyl-4,4-diphenyl-1,2-oxaphospholan-3-one (**85a**) were isolated as a byproduct.

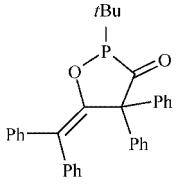

**85a**

According to a series of exchange experiments, transient, free electron-sextet species have to be excluded as intermediates. The following mechanism, invoking 1,3-dipolar species **86**, was proposed to explain the formation of **84a**–**c** and **85a** (Scheme 38).

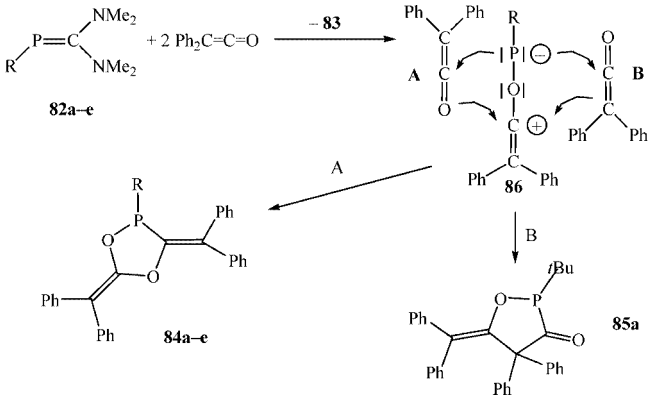


Scheme 38. Proposed mechanism for the formation of compounds **84a**–**e** and **85a**.

It is conceivable that zwitterion **86** and **83** were first formed from **82a**–**e** and two equiv. of ketene. Intermediate **86** then underwent a 1,3-dipolar addition to the C=O bond of another ketene molecule to yield major product **84** (path A). Alternatively, the 1,3-cycloaddition to the C=C double bond of the ketenes afforded **85a** (path B).[52] Reaction of inversely polarized phosphaalkenes with aldehydes did not succeed as yet.

### 5.2 To Coinage Metal Complexes

In a recent study, the coordination behavior of inversely polarized phosphaalkenes towards copper and gold compounds were investigated. The reaction of equimolar amounts of $tBuP=C(NMe_2)_2$ (**82a**) and copper(I) chloride afforded the complex $[Cu_3Cl_3\{\mu_3\text{-}P(tBu)C(NMe_2)_2\}_3]$ (**87**) as the formal result of the cyclotrimerization of a 1:1 adduct (76% yield).[61] Analogously, complex **88** was synthesized in 66% yield from phosphaalkene $PhP=C(NMe_2)_2$ (**82d**) and $[Cu\{P(OMe)_3\}_3Cl]$ [38] (Scheme 39). Similarly, the analogous complexes $[Cu_3X_3\{\mu\text{-}P(tBu)C(NMe_2)_2\}_3]$ (X = Br, I) were generated.[62]

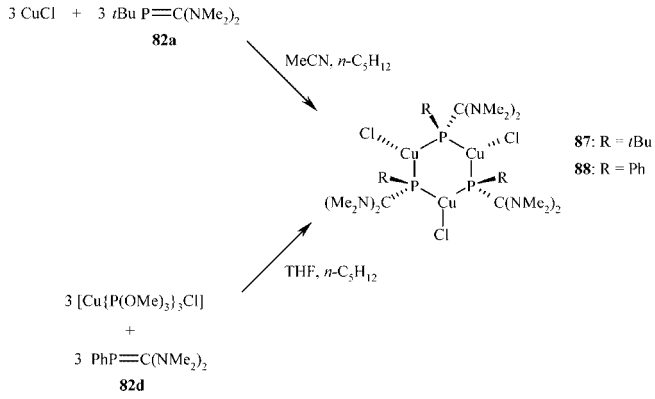


Scheme 39. Synthesis of complexes **87** and **88**.

Treatment of **82a** with [Cu(L)Cl] (L = P*i*Pr$_3$; Sb*i*Pr$_3$) led to the formation of compounds $[CuCl(L)\{P(tBu)C(NMe_2)_2\}]$ **89a** (L = P*i*Pr$_3$) and **90** (L = Sb*i*Pr$_3$)[62] (Scheme 40). The reaction of $[(MeCN)_4Cu]BF_4$ with 2 equiv. of $PhP=C(NMe_2)_2$ (**82d**) yields compound $[Cu\{P(Ph)C(NMe_2)_2\}_2]BF_4$ (**91d**). Similarly, complexes $[Cu\{P(aryl)C(NMe_2)_2\}_2]BF_4$ (**91e**: aryl = Mes; **91f**: aryl = Mes*) are obtained from $arylP=C(NMe_2)_2$ [aryl = Mes (**82e**) and Mes* (**82f**)].

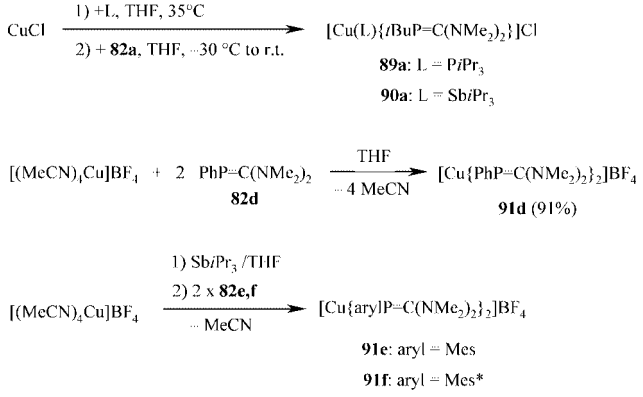


Scheme 40. Formation of the copper complexes **89a**, **90a**, and **91d**–**f**.

A different situation was observed with gold complexes. Combination of the gold complexes [Au(Cl)L] [**a**: L = $PPh_3$; **b**: L = tetrahydrothiophene(THF); **c**: L = CO] with two molar equivalents of phosphaalkene $HP=C(NMe_2)_2$ (**82g**) in THF at 20 °C led to the yellow mononuclear complex **92**[63] (Scheme 41).

 © 2007 Wiley-VCH Verlag GmbH & Co. KGaA, Weinheim 

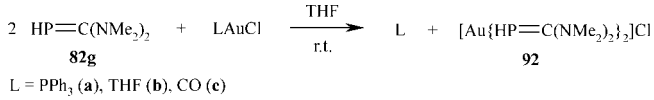


Scheme 41. Reaction of $HP=C(NMe_2)_2$ with [LAuCl].

The reaction of complexes [LAuCl] with the more bulky and more basic phosphaalkene $t$BuP=C(NMe$_2$)$_2$ (**82a**) under analogous conditions produced a mixture of cationic complexes **93** and **94** as an amorphous green-yellow precipitate (Scheme 42).

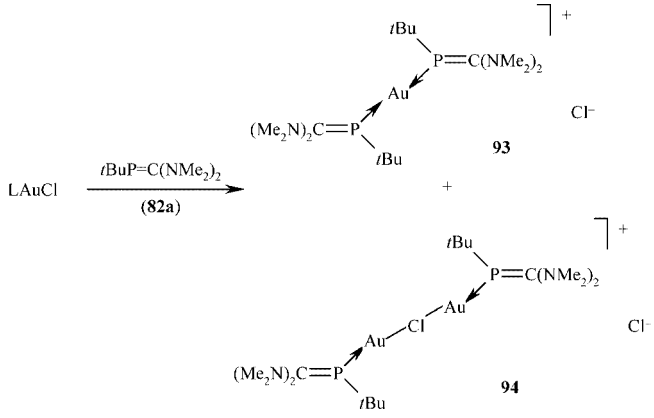


Scheme 42. Reaction of $t$BuP=C(NMe$_2$)$_2$ with [LAuCl].

Attempts to separate the compounds by crystallization from dichloromethane or acetonitrile led to the complete transformation of **93** and **94** into the yellow salt **95** with a decanuclear cluster cation (Scheme 43).

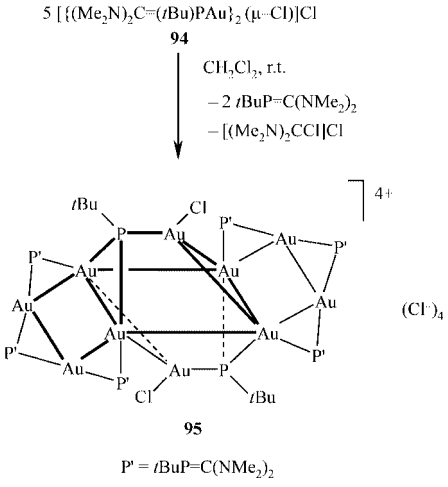


Scheme 43. Formation of **95** from **94** (idealized).

The cation $[(Me_2N)_2CCl]^+$ was formed from an unprecedented nucleophilic cleavage of a P=C double bond by a chloride. According to an X-ray structure analysis, eight gold atoms form a puckered ladder made up of three quadrangles. The central quadrangle is capped on both faces by a [$t$BuPAuCl] entity. Three edges of each peripheral rectangle are bridged by phosphaalkene ligands.

### 5.3 To Fischer Carbene Complexes

Fischer carbene complexes are organometallic electrophiles with a carbene ligand highly susceptible to nucleophilic attack, which renders them extremely useful as reagents and catalysts in modern preparative chemistry. Thus, the question of the reactivity of inversely polarized phosphaalkenes towards these compounds became relevant.

Ferriophosphaalkene **96** was allowed to react with two molar equivalents of carbene complexes **97a** and **97b** in diethyl ether, forming the novel ferriophosphaalkene complexes **98a**,**b** and β-aminoalkenyl(ethoxy)carbene complexes **99a**,**b** (Scheme 44).

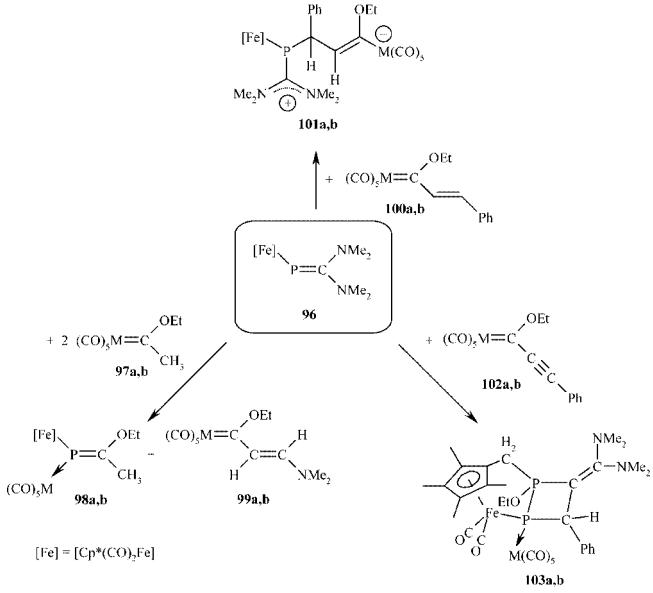


Scheme 44. Reaction of **96** with several Fischer carbene complexes.

Combination of **96** and the alkenyl carbene complexes **100a**,**b** in a mixture of $n$-pentane and diethyl ether at –30 °C led to the precipitation of orange zwitterionic Michael-type adducts **101a**,**b** (Scheme 44).

In sharp contrast to the synthesis of **98a**,**b** and **101a**,**b**, treatment of **96** with an equimolar amount of ethynyl(phenyl) carbene complexes **102a**,**b** in $n$-pentane at –60 °C afforded the yellow pentacarbonylmetal adducts **103a**,**b** of a 1-ferriophosphetane as the only tractable phosphorus-containing products (ca. 20% yield)[64] (Scheme 44).

When the ethoxy($o$-tolyl)carbene complex **104** was subjected to reaction with $Me_3SiP=C(NMe_2)_2$ (**82h**) in $n$-pentane at –40 °C, the yellow complex **105** (38%) was obtained in addition to the novel orange crystalline $\eta^1$-phosphaalkene complex **106** and alkene **107** (Scheme 45). No reaction oc-

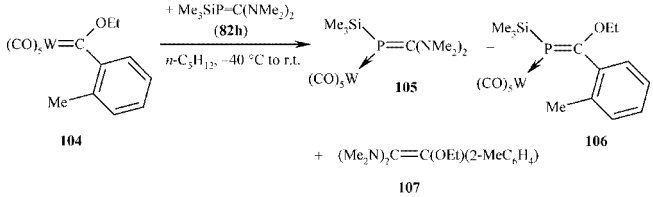


Scheme 45. Reaction of **104** with phosphaalkene $Me_3SiP=C(NMe_2)_2$.

 © 2007 Wiley-VCH Verlag GmbH & Co. KGaA, Weinheim 

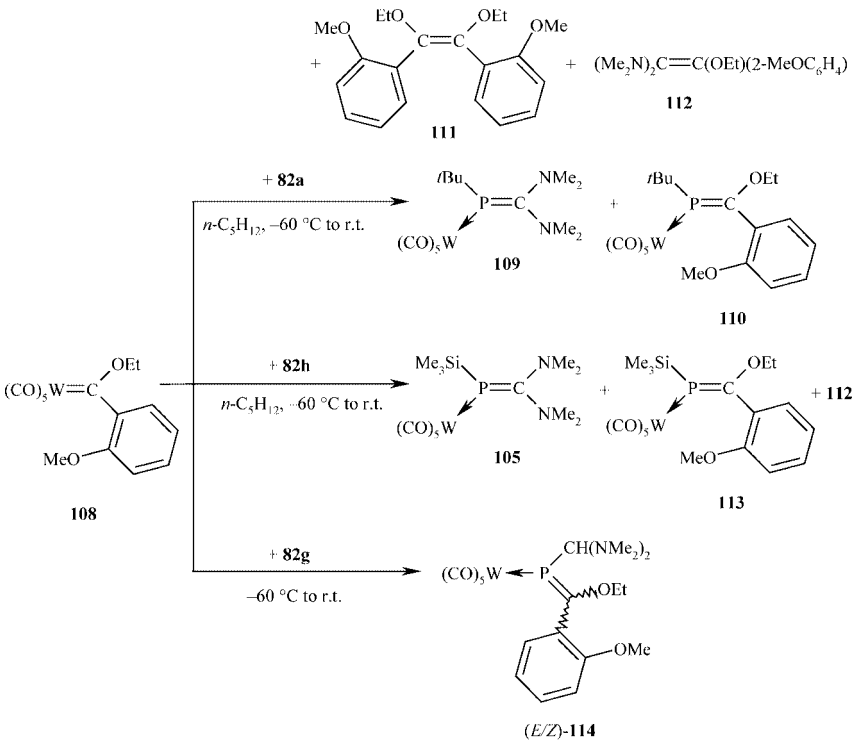


Scheme 46. Reaction of **108** with the phosphaalkenes $RP{=}C(NMe_2)_2$ (**82a**: R = *t*Bu; **82h**: R = $Me_3Si$; **82g**: R = H).

curred between **104** and *t*BuP=C(NMe$_2$)$_2$ (**82a**). Precursor **104** was decomposed by exposure to HP=C(NMe$_2$)$_2$ (**82g**).[65]

The reaction of *o*-methoxyphenyl carbene complex **108** with *t*BuP=C(NMe$_2$)$_2$ (**82a**) under comparable conditions yielded the yellow $\eta^1$-phosphaalkene complex **109** (29%) and the orange $\eta^1$-phosphaalkene complex **110** (39%), after fractioning crystallization from pentane. Small amounts of an oily 1:1 mixture of alkenes [(*E*/*Z*)-2-MeOC$_6$H$_4$(EtO)C]$_2$ (**111**) and (Me$_2$N)$_2$C=C(OEt)(2-MeOC$_6$H$_4$) (**112**) were identified as byproducts[65] (Scheme 46).

Similarly, combination of **108** with $Me_3SiP{=}C(NMe_2)_2$ (**82h**) gave rise to the formation of **105** (51%) and the metathesis product [{$Me_3SiP{=}C(OEt)(2\text{-}MeOC_6H_4)$}W(CO)$_5$] (**113**), which was isolated as an orange solid in 21% yield. Alkene **112** was also identified in the reaction residue (Scheme 46). The course of the reaction of carbene complex **108** with HP=C(NMe$_2$)$_2$ (**82g**) was completely different. Here [(CO)$_5$W] complexes of the two geometric isomers of the phosphaalkene (Me$_2$N)$_2$CH–P=C(OEt)(2-MeOC$_6$H$_4$) (*E*/*Z*)-**114** were obtained as orange crystals in 80% yield. The *E*/*Z* ratio was 1:2[65] (Scheme 46).

As pointed out, the course of the reaction and the product pattern of the processes under discussion are sensitively governed by the nature of substituents at the carbene ligand as well as at the P atom of the organophosphorus reagent. In keeping with this, yet different, results were obtained in the reaction of inversely polarized phosphaalkenes **82** with Fischer carbene complexes having secondary alkyl or cycloalkyl substituents at the carbene carbon atom, which are less electron-withdrawing than aryl groups, but cannot be involved in condensations as primary alkyl substituents at the carbene center. When cyclopropyl carbene complex **115a** was treated with an equimolar amount of phosphaalkene HP=C(NMe$_2$)$_2$ (**82g**) in *n*-pentane in the range –40 °C to room temperature, phosphaalkene complex **116** separated from the filtered reaction mixture at –16 °C as orange crystals in 47% yield, and dimethylamine was identified as a byproduct. The fate of the cyclopropyl moiety remained unclear (Scheme 47).

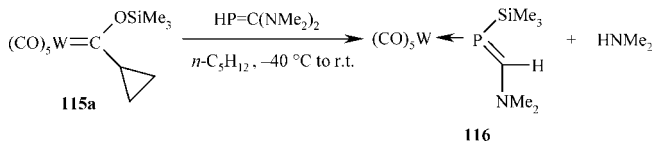


Scheme 47.

In contrast to this, cyclopropyl(methoxy)- and cyclopropyl(ethoxy)carbene complexes **115b** and **115c** were converted by HP=C(NMe$_2$)$_2$ (**82g**) into the 1,3-bis(pentacarbonyltungsten)-1,3-diphosphetane complexes **117b** and **117c**, which separated from pentane solutions at –16 °C as yellow-to-orange crystals in 60% and 72% yields, respectively.[66] In many cases 1,3-diphosphetanes result from a [2+2] head-to-tail dimerization of relatively unhindered phosphaalkenes. Accordingly, it is most likely that phosphaalkene complexes analogous to **116** were initially generated and subsequently suffered from self-dimerization[66] (Scheme 48).

 © 2007 Wiley-VCH Verlag GmbH & Co. KGaA, Weinheim 

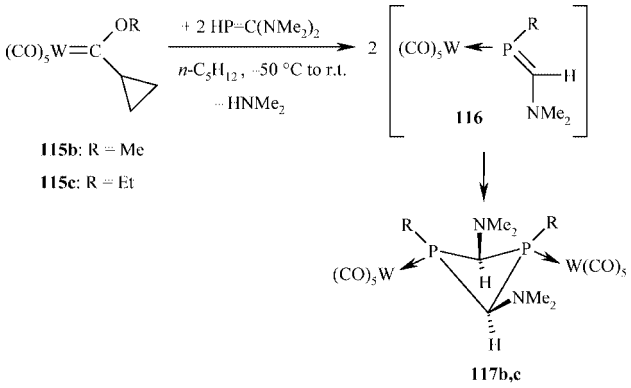


Scheme 48. Preparation of **117b,c**.

Cyclopentyl(ethoxy)carbene complex **115d** and $XP=C(NMe_2)_2$ (X = H, D) did not react to afford the expected 1,3-diphosphetane **117c**. Instead, the PH-functionalized 1,3-diphosphetane complex **118** was isolated from *n*-pentane at –16 °C as colorless crystals (42%) (Scheme 49). With $DP=C(NMe_2)_2$ product **[D$_2$]118** resulted, where the ring carbon atoms are deuterated. Thus the phosphaalkene cannot be the source of the hydrogen atom at phosphorus in the 1,3-diphosphetane.

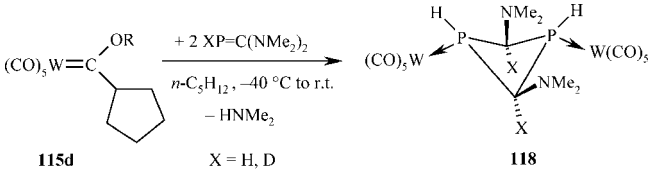


Scheme 49. Synthesis of **118**.

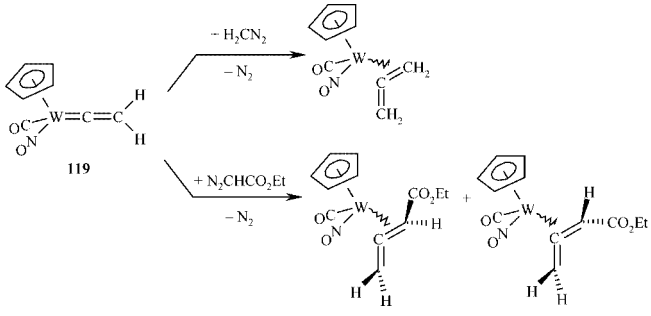


Scheme 50.

## 5.4 To Vinylidene Complexes

The obvious next step was to study the nucleophilic transfer of phosphinidenes from inversely polarized phosphaalkenes to the electrophilic ligand of vinylidene complexes, which are closely related to transition-metal carbenes. A motivation for this came from a recent paper of Ipaktschi et al. who succeeded in the transformation of vinylidene complex **119** into $\eta^2$-allene complexes by exposing it to diazomethane and ethyl diazoacetate[67] (Scheme 50).

Treatment of [Cp(CO)(NO)W=C=C(H)Ph] (**120**) with half a molar equivalent of phosphaalkenes $RP=C(NMe_2)_2$ **82** (**a**: R = *t*Bu; **b**: *c*-$C_6H_{11}$) in ethereal solvents at 0 °C to 20 °C afforded the crystalline $\eta^2$-1-phosphaallene complexes **121** (20% yield) and **122** (19%) after chromatography[68] (Scheme 51). Red crystalline carbene complex **123** was formed as a byproduct in these reactions.

Similarly, yellow crystalline **124** (R = *t*Bu) resulted from the reaction of **82a** and vinylidene complex **119** in THF at 20 °C (30% yield). The synthesis of **125** (R = $C_6H_{11}$) from **119** and **82b** was accomplished in diethyl ether at –30 °C (12% yield) (Scheme 52).

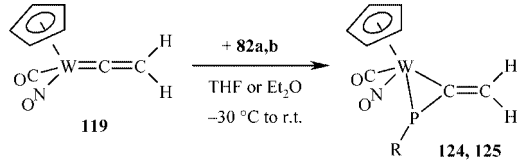


Scheme 52. Preparation of the 1-phosphaallene complexes **124** and **125**.

## 5.5 To Phosphenium Complexes

From a formal point of view, carbene $CR_2$- and phosphenium ligands [$PR_2^+$] are isolobal, both exhibiting pronounced electrophilic character. Thus it was obvious to also include transition-metal–phosphenium complexes in the investigations on the nucleophilicity and on the phosphinidene-transfer tendency of inversely polarized phosphaalkenes. Phosphenium complexes [$Cp(CO)_2W=PPh_2$] (**126**), [$Cp(CO)_2W=P(H)tBu$] (**127**), and [$Cp(CO)_2MoP(H)tBu$] (**128**) were freshly prepared by the dehydrochlorination of the chlorophosphane complexes [$Cp(CO)_2(Cl)W–P(H)Ph_2$], [$Cp(CO)_2(Cl)W–P(H)_2tBu$], and [$Cp(CO)_2(Cl)Mo–P(H)_2tBu$] with

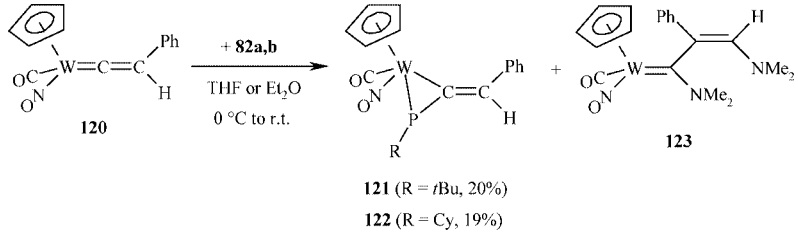


Scheme 51. Preparation of $\eta^2$-1-phosphaallene complexes **121** and **122**.

 © 2007 Wiley-VCH Verlag GmbH & Co. KGaA, Weinheim 

DBU or triethylamine at –78 °C and subsequently combined with phosphaalkenes $RP{=}C(NMe_2)_2$ **82** (**a**: R = *t*Bu; **b**: R = Cy; **d**: R = Ph; **g**: R = H). Alternatively, the isolated compound $[Cp(CO)_2W{=}P(Ph)N(SiMe_3)_2]$ (**132**) was directly subjected to reaction with $HP{=}C(NMe_2)_2$. Thereby $\eta^2$-diphosphanyl complexes **129a**,**b**,**d**, **130**, **131**, and **133** were generated and isolated as crystalline compounds after column chromatography in 24–30% yield[69] (Scheme 53).

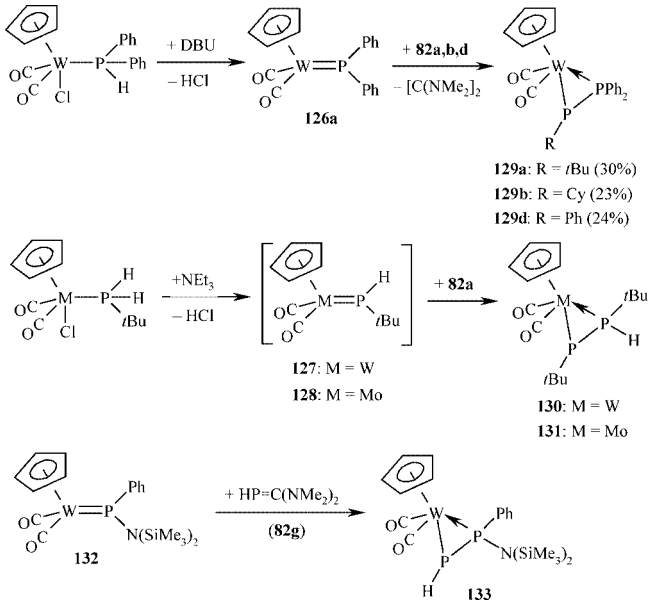


Scheme 53. Preparation of the $\eta^2$-diphosphanyl complexes **129a,b,d**, **130**, **131**, and **133**.

The reaction of **126a**,**b** was also conducted with an excess of carbonyl-stabilized phosphaalkenes $arylC(O)P{=}C(NMe_2)_2$ (**134**: aryl = Ph; **135**: aryl = 4-Et$C_6H_4$) in toluene in the range –30 °C to room temperature to afford metallophosphaalkenes **136a**,**b** and **137a**,**b** in modest yields (30–46%)[70] (Scheme 54).

As a mechanism for the formation of the chelates, an initial attack of the phosphaalkene onto the phosphenium center with formation of transient **A** was postulated. Extrusion of carbene $[C(NMe_2)_2]$ was accompanied by ring closure to give diphosphanyl complex **B**. Insertion of the C=O moiety of **B** into the P–P bond furnished the final products.

### 5.6 To Phosphavinylidene Complexes

Phosphavinylidene complexes $[Cp(CO)_2M{=}P{=}C(SiMe_3)_2]$ (**138**: M = Mo; **139**: M =W) are organometallic electrophiles closely related to vinylidene as well as to phosphenium complexes. The reaction of phosphavinylidene complex **138** with an equimolar amount of phosphaalkene $tBuP{=}C(NMe_2)_2$ (**82a**) in toluene afforded the yellow $\eta^3$-1,2-diphosphaallyl complex **140a** by a phosphinidene transfer process from the phosphaalkene onto the ligand (31% yield). Similarly, **138** was converted into orange product **140b** when allowed to react with $CyP{=}C(NMe_2)_2$ (**82b**) (49% yield). The reaction of **139** with **82a** under comparable conditions led to the formation of complex **141** (Scheme 55).

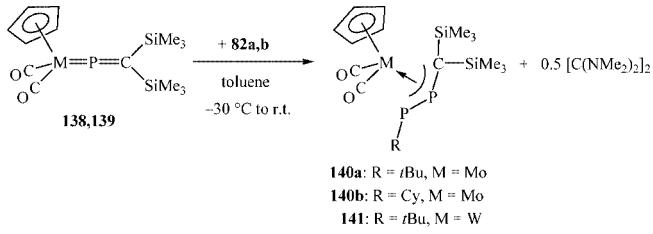


Scheme 55. Synthesis of 1,2-diphosphaallyl complexes.

The reaction of **138** and **139** with an equivalent amount of phosphaalkene $HP{=}C(NMe_2)_2$ (**82g**) in diethyl ether in the range –30 °C to room temperature took another course. Here, a proton transfer from the phosphorus atom on to the disilylmethylene unit of the precursor complex led to the formation of the unsymmetrical diphosphene complexes **142** and **143** as yellow-to-orange crystals[71] (Scheme 56).

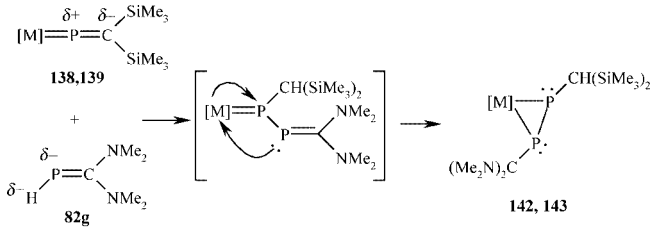


Scheme 56. Formation of complexes **142** and **143**.

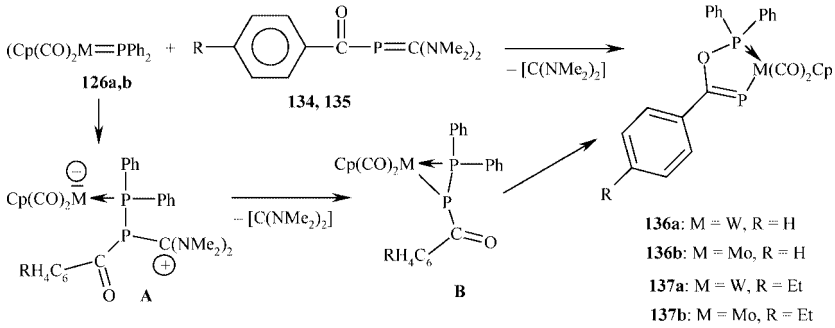


Scheme 54. Formation of **136a**,**b** and **137a**,**b**.

 © 2007 Wiley-VCH Verlag GmbH & Co. KGaA, Weinheim 

## 6. Arsinidenes

In comparison to the well-developed chemistry of phosphinidenes, little attention has been addressed to the homologous arsinidenes. A few adducts of arsinidenes to carbenes and trimethylphosphane have been prepared recently. Carbene **144** was treated with hexaphenylcyclohexaarsane to form the adduct **145** as a yellow crystalline solid melting at 148–152 °C with decomposition[72] (Scheme 57).

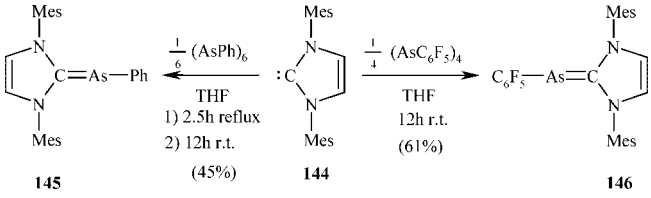


Scheme 57. Preparation of **145** and **146**.

Compound **146** was prepared similarly from **144** and tetrakis(pentafluorophenyl)cyclotetraarsane as a yellow solid in 61% yield.[72]

An arsa-Wittig reagent (arsanylidene-$\sigma^4$-phosphorane) was synthesized by the zinc reduction of 2,6-Trip$_2$C$_6$H$_3$AsCl$_2$ (Trip = 2,4,6-*i*Pr$_3$C$_6$H$_2$) in the presence of excess of PMe$_3$. The labile product decomposed upon attempted purification to the diarsene 2,6-Trip$_2$C$_6$H$_3$As=AsC$_6$H$_3$Trip$_2$-2,6. Thus, when heated in THF for a few minutes, the arsa-Wittig reagent was quantitatively converted into the diarsene. Attempts to synthesize the arsa-Wittig reagent 2,6-Mes$_2$C$_6$H$_3$-As=PMe$_3$ by reduction of 2,6-Mes$_2$C$_6$H$_3$AsCl$_2$ with zinc and PMe$_3$ gave only the corresponding diarsene in quantitative yield[73] (Scheme 58).

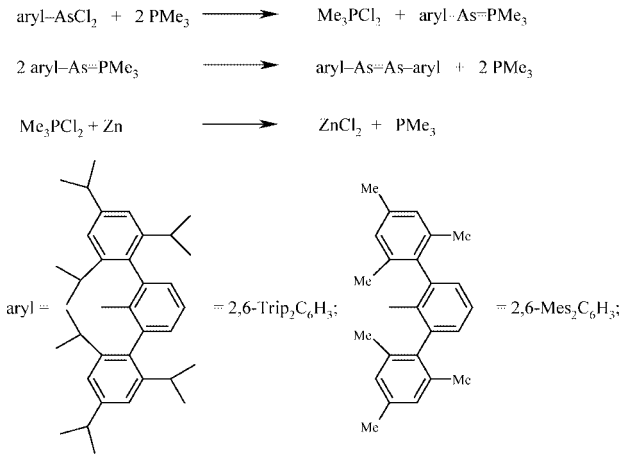


Scheme 58. Synthesis of diarsenes by using arsa-Wittig reagents.

Huttner et al.,[74] conducted pioneering studies of $\mu_2$-arsinidene complexes L$_n$M=As(R)=ML$_n$; however, only little information on complexes with terminal arsinidene ligands is available to date.

The need to employ bulky groups for the kinetic stabilization of the reactive metal–arsenic multiple bond was also fulfilled by the employment of sterically encumbering ancillary ligands at the metal. Thus, Wolczanski et al. have used the (*t*Bu$_3$SiO)$_3$Ta fragment to support the terminal AsPh group. This first terminal arsinidene complex **148** was prepared by a two-step process, the first of which was an oxidative addition reaction of (*t*Bu$_3$SiO)$_3$Ta with phenylarsane to afford the arsenido complex **147**[20] (Scheme 59).

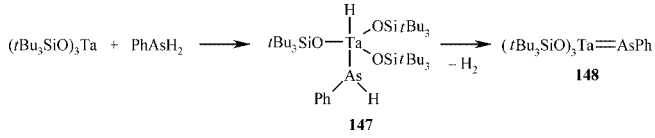


Scheme 59. Synthesis of **148**.

In benzene solution, the arsenido tantalum hydride **147** underwent loss of dihydrogen to yield the terminal arsinidene complex **148**.

The reaction between [N$_3$N]MoCl complex **149** and 2 equiv. of LiAsPhH in the absence of light afforded orange diamagnetic [N$_3$N]Mo≡As complex **150** in ca. 30% yield in addition to an equal amount of [N$_3$N]Mo–Ph, whereby no intermediates could be detected[75] (Scheme 60).

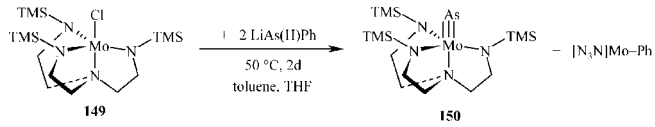


Scheme 60. Preparation of arsenido complex **150**.

The tungsten analogue **152** could not be prepared by a protocol analogous to Scheme 60. Instead, the treatment of phenyl tungsten complex **151** with phenylarsine led to the desired tungsten–arsenido complex[75] (Scheme 61).

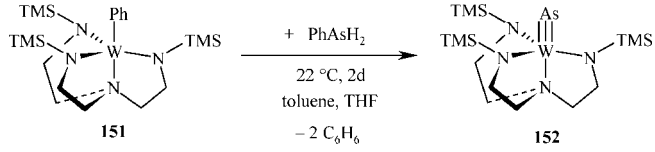


Scheme 61. Synthesis of arsenido complex **152**.

This tungsten arsenido complex reacted readily with methyl triflate in toluene to give the cationic arsinidene complex **153**[75] (Scheme 62).

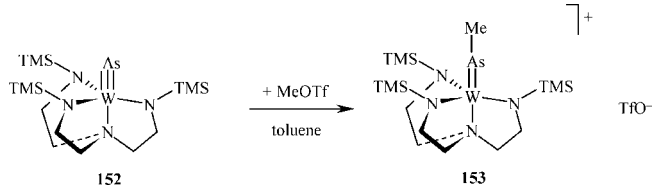


Scheme 62. Methylation of **152** to yield arsinidene complex **153**.

The most interesting features in the molecular structure of **153** are the essentially linear arsinidene ligand [W–As–C = 173.3(6)°] and a W=As bond length of 2.2494(14) Å, which is virtually the same as the Mo≡As bond length in [N$_3$N]Mo≡As. The linearity of the arsinidene ligand in **153** contrasts strongly with the dramatically bent phenylarsinidene li-

 © 2007 Wiley-VCH Verlag GmbH & Co. KGaA, Weinheim 

gand [107(4)°] and longer Ta=As bond length [2.428(2) Å] in $[(t\mathrm{Bu_3SiO})_3\mathrm{Ta{=}AsPh}]$.[20]

## 7. Arsinidene Transfer from Inversely Polarized Arsaalkenes

### 7.1 With the Formation of $(RAs)_n$ ($n$ = 2, 3)

A first evidence for the facile cleavage of the As=C bond of arsaalkenes was observed in the reaction of $[Cp^*(CO)_2Fe{-}As{=}C(NMe_2)_2]$ (**154**) with $CpRh(CO)_2$ to afford an $\eta^2$-diarsene rhodium complex **155** as dark-red crystals in 63% yield[76] (Scheme 63).

This is in sharp contrast to the behavior of the analogous ferriophosphaalkene **96**, which, upon reaction with the rhodium complex, furnished compound **156** as the result of a condensation process of one methyl group of the Cp* ligand and the tricoordinate C atom of the P=C double bond[76] (Scheme 63).

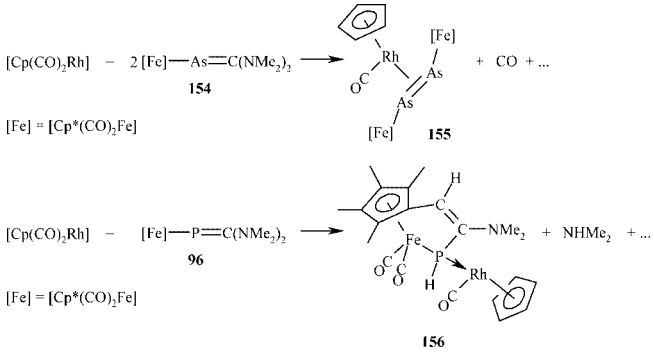


Scheme 63. Formation of **155** and **156**.

During the studies on $[HB(3,5\text{-}Me_2HC_3N_2)_3(CO)_2M{\equiv}C{-}As{=}C(NMe_2)_2]$ (**157a**: M = Mo; **157b**: M = W) a facile metal-assisted cleavage of the As=C multiple bond was observed in the reaction of the arsaalkene was allowed to react with [(CO)AuCl]. Cyclotriarsanes **158a**,**b** resulted from the formal trimerization of the respective arsinidenes $[HB(3,5\text{-}Me_2HC_3N_2)_3(CO)_2M{\equiv}C{-}As]$. Thereby the carbene fragment $[C(NMe_2)_2]$ was intercepted as the known carbene complex $[(Me_2N)_2C{\rightarrow}AuCl]$[77] (Scheme 64).

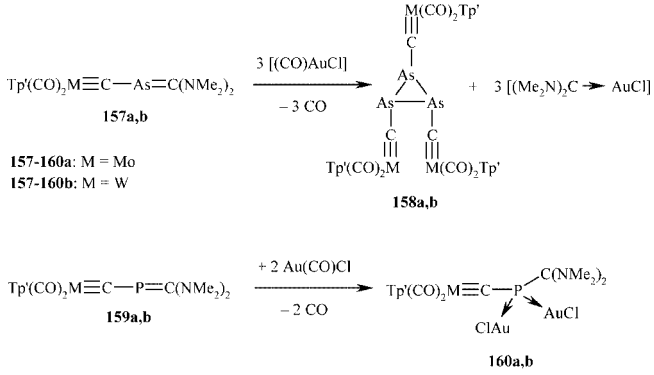


Scheme 64. Preparation of **158a**,**b** and **160a**,**b**.

Again, a completely different behavior was encountered in the reaction of phosphaalkenes **159a**,**b** with the gold compound, where simply a twofold addition of AuCl to the phosphorus atom occurred[77] (Scheme 64).

### 7.2 With Vinylidene Complexes

In order to explore the scope and limitations of inversely polarized arsaalkenes to formally act as a source for arsinidene species, the investigations were extended to vinylidene complexes. Treatment of complex [Cp(CO)(NO)W=C=C(H)($t$Bu)] (**161**) with an equimolar amount of arsaalkenes $R{-}As{=}C(NMe_2)_2$ {**162**: R = $t$BuC(O); **154**: R = $Cp^*(CO)_2Fe$} in diethyl ether solution in the range –30 °C to room temperature afforded the crystalline $\eta^1$-1-arsaallene complexes **163** (50% yield) and **164** (73% yield), respectively after chromatography. Compound **164** was obtained as a mixture of two isomers[78] (Scheme 65).

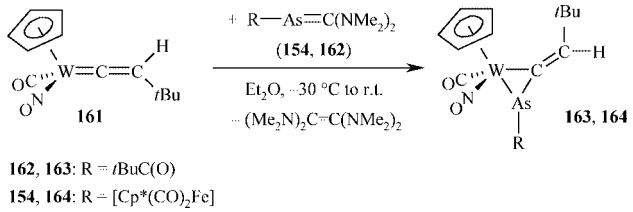


Scheme 65. Formation of the 1-arsaallene complexes **163** and **164**.

An analogous treatment of vinylidene complex **120** with the pivaloylarsaalkene **162** afforded the thermolabile complex **165** as orange crystals in 29% yield (Scheme 66).

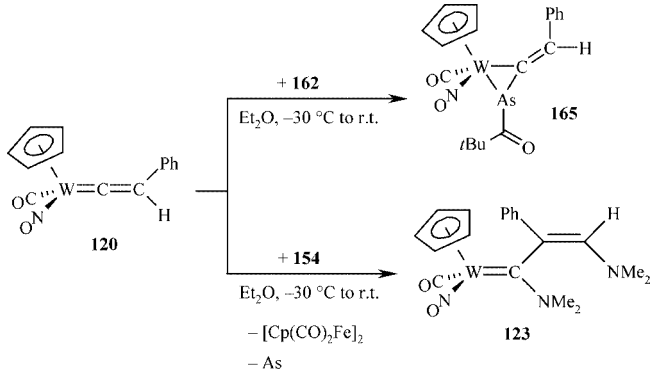


Scheme 66. Reaction of **120** with arsaalkenes **154** and **162**.

In sharp contrast to this, reaction of **120** with ferrioarsaalkene **154** did not lead to the anticipated arsaallene system. Instead, red crystalline carbene complex **123** was isolated in 69% yield. Elemental arsenic and complex $[Cp^*Fe(CO)_2]_2$ were also obtained (82% yield).[78] The generation of carbene complex **123** was previously observed in the reaction of **120** with phosphaalkenes $RP{=}C(NMe_2)_2$ **82** (**a**: R = $t$Bu; **b**: Cy).[68]

### 7.3 With Phosphavinylidene Complexes

Combination of complexes $[Cp(CO)_2M{=}P{=}C(SiMe_3)_2]$ (**138**: M = Mo; **139**: M = W) with an equimolar amount of

 © 2007 Wiley-VCH Verlag GmbH & Co. KGaA, Weinheim 

ferrioarsaalkene [Cp*(CO)$_2$Fe–As=C(NMe$_2$)$_2$] (**154**) in toluene afforded the deep red crystalline η$^3$-2-phosphaarsaallyl complexes **166** and **167**. Analogously, reaction of compound **162** with an equimolar amount of **139** gave rise to the formation of heteroallyl complex **168** as an orange solid (63% yield). Tetrakis(dimethylamino)ethane was formed as a by-product[79] (Scheme 67).

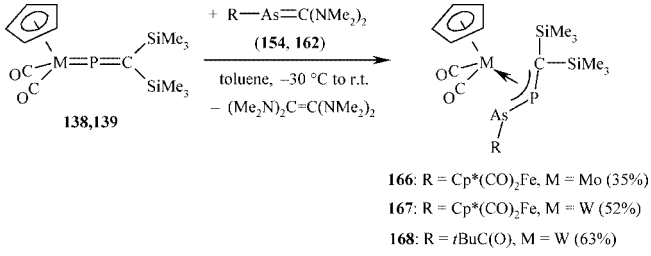


Scheme 67. Formation of the 2-phospha-1-arsaallyl complexes **166**–**168**.

The outcome of the reaction between precursors **138**, **139** and *t*BuC(O)As=C(NMe$_2$)$_2$ proved to be crucially dependent on the respective stoichiometry employed.[80] Thus, when the reaction of [Cp(CO)$_2$W=P=C(SiMe$_3$)$_2$] (**139**) was conducted with twice the molar equivalent of arsaalkene under otherwise comparable conditions, complex **168** was isolated in only 22% yield from the first orange-red zone of the column. From the second deep-red zone, dark-red crystals were obtained, which, according to an X-ray analysis, were disclosed as an inseparable 81:19 mixture of the η$^3$-2-phospha-1,3-diarsaallyl complex **169a** and the η$^3$-1,2,3-triarsaallyl complex **170a**. The employment of a 10-fold amount of arsaalkene in this process afforded a 35:65 mixture of **169a** and **170a**[80] (Scheme 68).

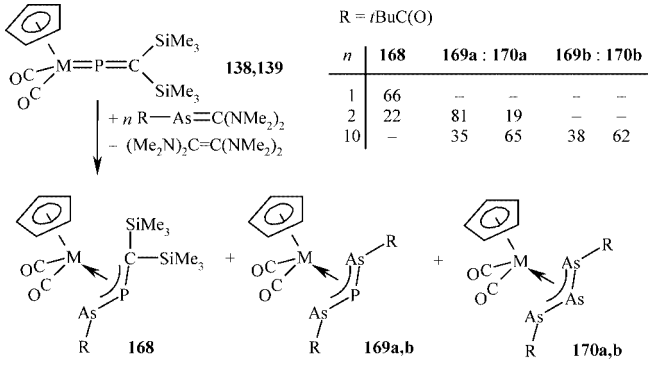


Scheme 68. Reactions of **138** and **139** with *t*BuC(O)As=C(NMe$_2$)$_2$.

Analogously, the reaction of **138** (M = Mo) with a 10-fold excess of arsaalkene gave a 38:62 mixture of [Cp(CO)$_2$-Mo{η$^3$-*t*BuC(O)AsPAsC(O)*t*Bu}] (**169b**) and [Cp(CO)$_2$-Mo{η$^3$-*t*BuC(O)AsAsAsC(O)*t*Bu}] (**170b**). A proposal for the mechanism of the formation of **169a**,**b** involves the initial formation of adduct **A**, which extrudes the putative alkene (Me$_2$N)$_2$C=C(SiMe$_3$)$_2$ with the formation of [Cp(CO)$_2$-M=P=As–C(O)(*t*Bu)] (**B**). The latter arsaphosphene adds a second equivalent of arsaalkene to give intermediate **C**. Liberation of [C(NMe$_2$)$_2$] to form **D** and rearrangement furnish the final products **169a**,**b**. The mechanism of the formation of **170** remained unclear[80] (Scheme 69).

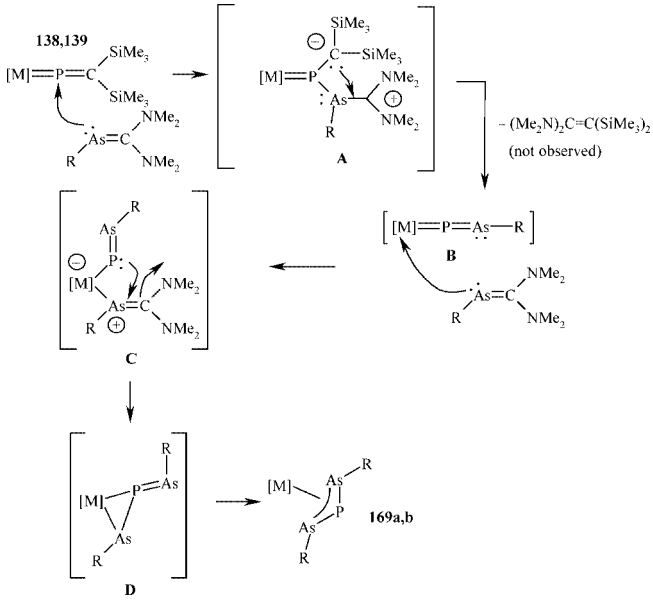


Scheme 69. Proposed mechanism for the formation of compounds **169a**,**b**.

In contrast to this, the more reactive arsaalkene 4-EtC$_6$H$_4$C(O)As=C(NMe$_2$)$_2$ and the tungsten complex **139** underwent reaction to afford the cyclic phosphenium complex **171** as red crystals in 41% yield[79b] (Scheme 70).

The reaction of complex **171** with a second equivalent of 4-EtC$_6$H$_4$C(O)As=C(NMe$_2$)$_2$ or, alternatively, treatment with **139** with two molar equivalents of arsaalkene led to the formation of the bicyclic metalloarsaalkene **172** as yellow crystals in 71% yield (Scheme 71).

Similarly, treatment of complexes **138**, **139** with 2 equiv. of freshly prepared arsaalkene PhC(O)As=C(NMe$_2$)$_2$ in diethyl ether solution afforded the yellow microcrystalline metalloarsaalkenes **173** (80%) and **174** (75%). In the case of the reaction of the molybdenum complex **138** with PhC(O)-As=C(NMe$_2$)$_2$, a few crystals of a second product, **175**, were isolated from the mother liquor after chromatography and

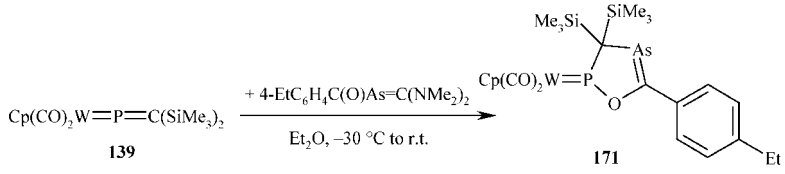


Scheme 70. Formation of phosphenium complex **171**.

 © 2007 Wiley-VCH Verlag GmbH & Co. KGaA, Weinheim 

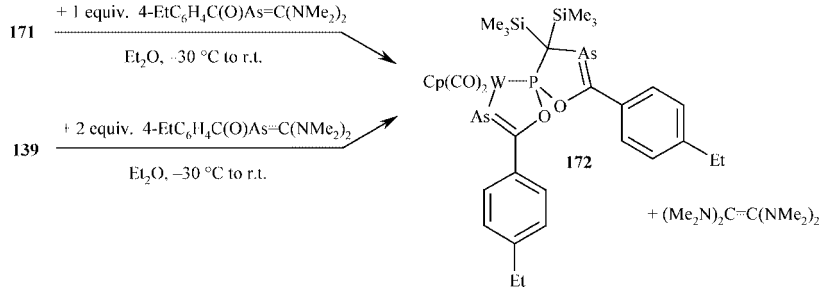


Scheme 71. Formation of spiro compound **172**.

separation of **173**. According to an X-ray structural analysis, compound **175** has to be regarded as the yet unknown {Cp(CO)$_2$Mo}$\eta^3$(1–3):$\eta^3$(3–6)-2,5-diphospha-3,4-diarsadiallyl system[80] (Scheme 72).

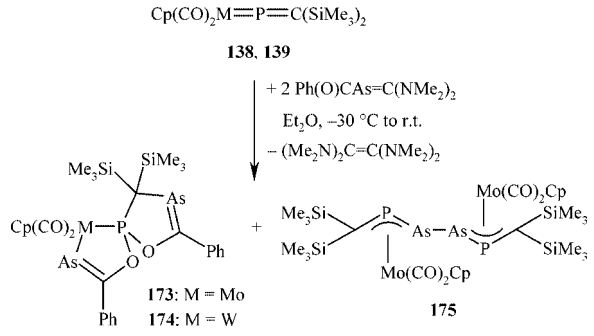


Scheme 72. Formation of **173**–**175**.

For a mechanism, it was suggested that adduct **A** is formed from the precursors, which lose [C(NMe$_2$)$_2$] with formation of intermediate **E**. Insertion of the carbonyl unit into the P–As bond of the three membered ring in **E** afforded the phosphenium complex **171**. Attack of the arsaalkene at the metal center of **171** would lead to intermediate **F**, which extrudes [C(NMe$_2$)$_2$] to give transient **G**.

The attack of the carbonyl oxygen atom at the P atom is responsible for the ring enlargement to give final products **172**–**174**[79,80] (Scheme 73).

The increase of the steric demand of the substituent on going from the benzoyl and 4-ethylbenzoyl derivatives to MesC(O)As=C(NMe$_2$)$_2$ provided a situation where hetero-

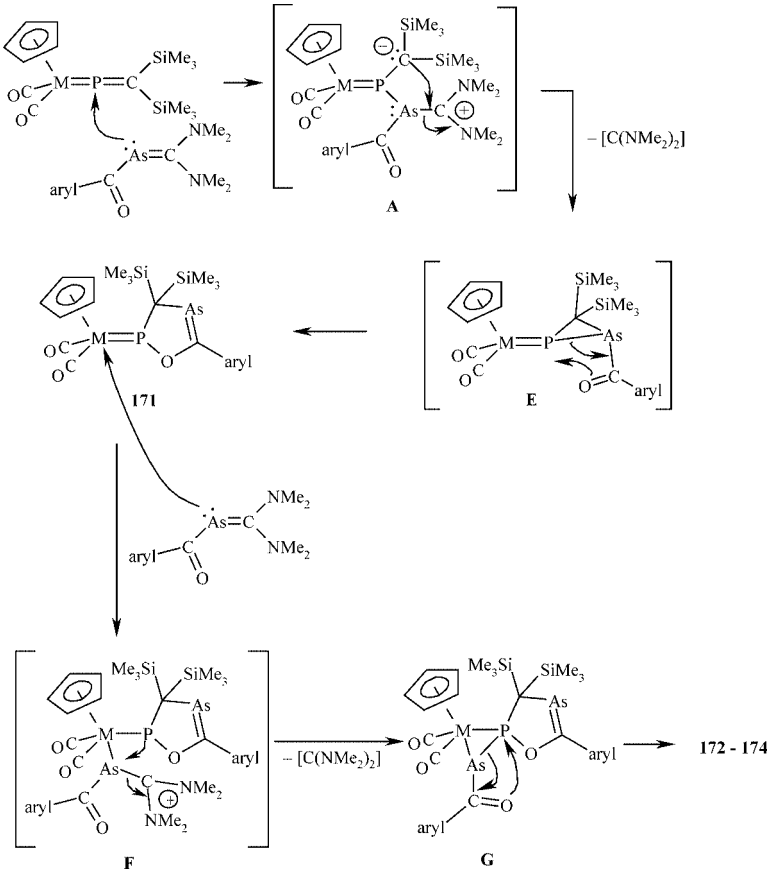


Scheme 73. Proposed mechanism for the formation of **172**–**174**.

 © 2007 Wiley-VCH Verlag GmbH & Co. KGaA, Weinheim 

cyclic ligands (e.g. in **178**) are no longer formed by CO incorporation. Instead, treatment of **139** with 1 equiv. of this arsaalkene generated the labile phosphenium complex **176**, which rearranged in solution within a few hours to the orange crystalline 2-phospha-1-arsaallyl complex **177** in 54% yield[80] (Scheme 74).

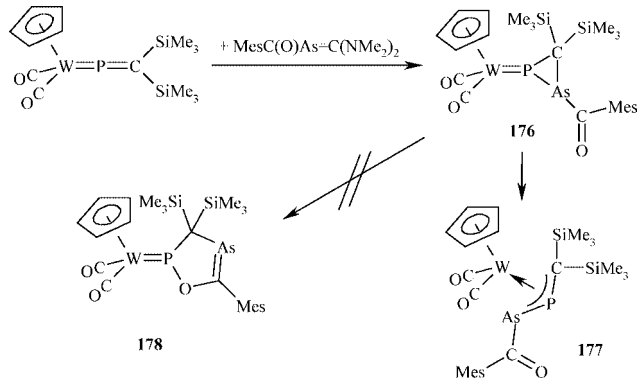


Scheme 74. Formation of 2-phospha-1-arsaallyl complex **177**.

The reaction of arsaalkene $Me_3SiAs=C(NMe_2)_2$ with molybdenum complex **138** proceeded with yet a different result. Combination of the reactants in a 2:1 molar ratio in diethyl ether at –100 to 20 °C afforded the As-free complex **179** as dark-red crystals after chromatographic work-up (yield 64%) [80] (Scheme 75).

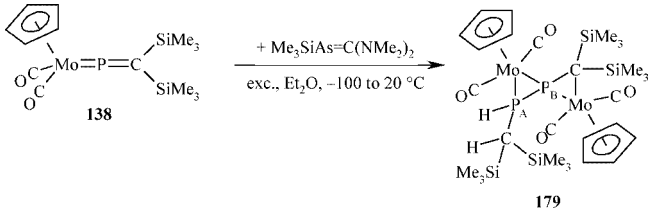


Scheme 75. Formation of **179** from **138** and $Me_3SiAs=C(NMe_2)_2$.

## 8. Conclusions and Perspectives

Inversely polarized phosphaalkenes $RP=C(NMe_2)_2$ serve as convenient sources of the phosphinidene unit PR, which can be transferred onto a broad variety of electrophilic ligands in transition-metal complexes. Their combination with Fischer carbene complexes affords $\eta^1$-phosphaalkene complexes. This synthetic principle was extended to vinylidene complexes [$L_nM=CR'H$] and phosphenium complexes [$L_nM=PRR'$], which are cleanly converted into $\eta^1$-phosphaallene and diphosphanido complexes, respectively. Phosphaalkenes, in which the phosphorus atom carries benzoyl-type substituents, reacted with phosphenium complexes with the incorporation of the CO group into five-membered metalloheterocycles. Phosphavinylidene complexes [$L_nM=P=C(SiMe_3)_2$] are transformed into coordination compounds featuring the novel $\eta^3$-1,2-diphosphaallylic ligand. Inversely polarized arsaalkenes $RAs=C(NMe_2)_2$ also display a rich chemistry when allowed to react with organometallic electrophiles such as vinylidene and phosphavinylidene complexes. Here, the synthesis of phosphaallene, phosphaarsaallyl, diarsaphosphaallyl, and triarsaallyl complexes was achieved. Carbonyl-functionalized arsaalkenes led to phosphenium and spiro complexes featuring five-membered heterocycles.

Thus phospha- and arsaalkenes are valuable and versatile reagents in the arsenal of elementorganic and coordination chemists.


[1] a) F. Mathey in *Multiple Bonds and Low Coordination in Phosphorus Chemistry* (Eds.: M. Regitz, O. J. Scherer), Thieme, Stuttgart **1990**, pp. 33–47; b) F. Mathey, *Angew. Chem.* **2003**, *115*, 1616–1643; *Angew. Chem. Int. Ed.* **2003**, *42*, 1578–1604; c) F. Mathey, *Dalton Trans.* **2007**, 1861–1868; d) R. Streubel, *Coord. Chem. Rev.* **2002**, *227*, 175–192; e) K. Lammertsma, *Top. Curr. Chem.* **2003**, *229*, 95–119.

[2] A. H. Cowley, F. Gabbai, R. Schluter, D. Atwood, *J. Am. Chem. Soc.* **1992**, *114*, 3142–3144.

[3] X. Li, D. Lei, M. Y. Chiang, P. P. Gaspar, *J. Am. Chem. Soc.* **1992**, *114*, 8526–8531.

[4] a) X. Li, S. I. Weisman, T.-S. Liu, P. P. Gaspar, A. H. Cowley, A. I. Smirnow, *J. Am. Chem. Soc.* **1994**, *116*, 7899–7900; b) W. H. Lam, P. P. Gaspar, D. A. Hrovat, D. A. Trieber II, E. R. Davidson, W. T. Borden, *J. Am. Chem. Soc.* **2005**, *127*, 9886–9894.

[5] a) Review: J. Olkowska-Oetzel, J. Pikies, *Appl. Organomet. Chem.* **2003**, *17*, 28–35; b) M. T. Nguyen, A. Vankeer, L. G. Nanquickenborne, *J. Org. Chem.* **1996**, *61*, 7077–7084.

[6] A. B. Burg, W. Mahler, *J. Am. Chem. Soc.* **1961**, *83*, 2388–2389.

[7] a) S. Shah, M. C. Simpson, R. C. Smith, J. D. Protasiewicz, *J. Am. Chem. Soc.* **2001**, *123*, 6925–6926; b) R. C. Smith, S. Shah, J. D. Protasiewicz, *J. Organomet. Chem.* **2002**, *646*, 255–256.

[8] B. Twamley, C. D. Sofield, M. M. Olmstead, P. P. Power, *J. Am. Chem. Soc.* **1999**, *121*, 3357–3367.

[9] A. H. Cowley, *Acc. Chem. Res.* **1997**, *30*, 445–451.

[10] Reviews: a) F. Mathey, N. H. T. Huy, A. Marinetti, *Helv. Chim. Acta* **2001**, *84*, 2938–2957; b) K. Lammertsma, M. J. M. Vlaar, *Eur. J. Org. Chem.* **2002**, 1127–1138.

[11] B. T. Sterenberg, K. A. Udachin, A. J. Carty, *Organometallics* **2001**, *20*, 2657–2659.

[12] A. H. Cowley, B. Pellerin, J. L. Atwood, S. G. Bott, *J. Am. Chem. Soc.* **1990**, *112*, 6734–6735.

[13] A. W. Ehlers, E. J. Baerends, K. Lammertsma, *J. Am. Chem. Soc.* **2002**, *124*, 2831–2838.

[14] P. B. Hitchcock, M. F. Lappert, W.-P. Leung, *J. Chem. Soc. Chem. Commun.* **1987**, 1282–1283.

[15] a) Z. Hou, T. L. Breen, D. W. Stephan, *Organometallics* **1993**, *12*, 3158–3167; b) J. Ho, R. Rousseau, D. W. Stephan, *Organometallics* **1994**, *13*, 1918–1926.

[16] J. Pikies, E. Baum, E. Matern, J. Chojuacki, R. Grubba, A. Robaszkiewicz, *Chem. Commun.* **2004**, 2478–2479.

[17] G. Fritz, P. Scheer, *Chem. Rev.* **2000**, *100*, 3341–3402.

[18] a) F. Basuli, J. Tomaszewski, J. C. Huffman, D. J. Mindiola, *J. Am. Chem. Soc.* **2003**, *125*, 10170–10171; b) F. Basuli, B. C. Bailey, J. C. Huffman, M. H. Baik, D. J. Mindiola, *J. Am. Chem. Soc.* **2004**, *126*, 1924–1925.

[19] a) C. C. Cummins, R. R. Schrock, W. M. Davies, *Angew. Chem.* **1993**, *105*, 758–761; *Angew. Chem. Int. Ed. Engl.* **1993**, *32*, 756–759; b) P. P. Power, *Angew. Chem.* **1993**, *105*, 893–894; *Angew. Chem. Int. Ed. Engl.* **1993**, *32*, 850–851.

[20] J. B. Bonanno, P. T. Wolczanski, E. B. Lobkovsky, *J. Am. Chem. Soc.* **1994**, *116*, 11159–11160.

[21] A. T. Termaten, T. Nijbacker, M. Schakel, M. Lutz, A. L. Spek, K. Lammertsma, *Chem. Eur. J.* **2003**, *9*, 2200–2208.


 © 2007 Wiley-VCH Verlag GmbH & Co. KGaA, Weinheim 

[22] A. T. Termaten, T. Nijbacker, M. Schakel, M. Lutz, A. L. Spek, K. Lammertsma, *Organometallics* **2002**, *21*, 3196.–3202.
[23] A. T. Termaten, H. Aktas, M. Schakel, A. W. Ehlers, M. Lutz, A. L. Spek, K. Lammertsma, *Organometallics* **2003**, *22*, 1827–1834.
[24] a) R. Melenkivitz, D. J. Mindiola, G. L. Hillhouse, *J. Am. Chem. Soc.* **2002**, *124*, 3846–3847; b) R. Waterman, G. L. Hillhouse, *J. Am. Chem. Soc.* **2003**, *125*, 13350–13351; c) R. Waterman, G. L. Hillhouse, *Organometallics* **2003**, *22*, 5182–5184.
[25] T. L. Breen, D. W. Stephan, *J. Am. Chem. Soc.* **1995**, *117*, 11914–11921.
[26] A. Marinetti, F. Mathey, *Organometallics* **1984**, *3*, 456–461.
[27] A. Marinetti, F. Mathey, J. Fischer, A. Mitschler, *J. Am. Chem. Soc.* **1982**, *104*, 4484–4485.
[28] A. Marinetti, F. Mathey, J. Fischer, A. Mitschler, *J. Chem. Soc. Chem. Commun.* **1982**, 667–668.
[29] M. L. Borst, R. H. Bulo, C. W. Winkel, D. J. Gibney, A. W. Ehlers, M. Schakel, M. Lutz, A. L. Spek, K. Lammertsma, *J. Am. Chem. Soc.* **2005**, *127*, 5800–5801.
[30] J. Svara, A. Marinetti, F. Mathey, *Organometallics* **1986**, *5*, 1159–1161.
[31] a) R. E. Bulo, A. W. Ehlers, F. J. J. de Kanter, M. Schakel, M. Lutz, A. L. Spek, K. Lammertsma, B. Wang, *Chem. Eur. J.* **2004**, *10*, 2732–2738; b) R. E. Bulo, L. Trion, A. W. Ehlers, F. J. J. de Kanter, M. Schakel, M. Lutz, A. L. Spek, K. Lammertsma, *Chem. Eur. J.* **2004**, *10*, 5332–5337.
[32] a) M. J. M. Vlaar, A. W. Ehlers, M. Schakel, S. B. Clendenning, J. F. Nixon, M. Lutz, A. L. Spek, K. Lammertsma, *Angew. Chem.* **2001**, *113*, 4524–4527; *Angew. Chem. Int. Ed.* **2001**, *40*, 4412–4415; b) M. J. M. Vlaar, A. W. Ehlers, M. Schakel, S. B. Clendenning, J. F. Nixon, M. Lutz, A. L. Spek, K. Lammertsma, *Chem. Eur. J.* **2001**, *7*, 3545–3550.
[33] R. Streubel, H. Wilkens, P. G. Jones, *Chem. Commun.* **1998**, 1761–1762.
[34] Y. Inubuchi, N. H. Tran Huy, L. Ricard, F. Mathey, *J. Organomet. Chem.* **1997**, *533*, 83–86.
[35] R. Streubel, A. Ostrowski, H. Wilkens, F. Ruthe, J. Jeske, P. G. Jones, *Angew. Chem.* **1997**, *109*, 409–413; *Angew. Chem. Int. Ed. Engl.* **1997**, *36*, 378–381.
[36] R. Streubel, U. Schiemann, P. G. Jones, N. H. Tran Huy, F. Mathey, *Angew. Chem.* **2000**, *112*, 3845–3847; *Angew. Chem. Int. Ed.* **2000**, *39*, 3686–3688.
[37] N. H. Tran Huy, T. V. Gryaznova, L. Ricard, F. Mathey, *Organometallics* **2005**, *24*, 2930–2934.
[38] B. Deschamps, F. Mathey, *J. Chem. Soc. Chem. Commun.* **1985**, 1010–1012.
[39] B. Deschamps, F. Mathey, *J. Organomet. Chem.* **1988**, *354*, 83–90.
[40] S. G. A. van Assema, A. W. Ehlers, F. J. J. de Kanter, M. Schakel, A. L. Spek, M. Lutz, K. Lammertsma, *Chem. Eur. J.* **2006**, *12*, 4333–4340.
[41] B. T. Sterenberg, A. J. Carty, *J. Organomet. Chem.* **2001**, *617/618*, 696–701.
[42] J. Sanchez-Nieves, B. T. Sterenberg, K. Udachin, A. J. Carty, *J. Am. Chem. Soc.* **2003**, *125*, 2404–2405.
[43] S. Shah, J. D. Protasiewicz, *Coord. Chem. Rev.* **2000**, *210*, 181–201.
[44] S. Shah, J. D. Protasiewicz, *Chem. Commun.* **1998**, 1585–1586.
[45] S. Shah, T. Concolino, A. L. Rheingold, J. D. Protasiewicz, *Inorg. Chem.* **2000**, *39*, 3860–3867.
[46] R. C. Smith, X. Chen, J. Protasiewicz, *Inorg. Chem.* **2003**, *42*, 5468–5470.
[47] P. Le Floch, A. Marinetti, L. Ricard, F. Mathey, *J. Am. Chem. Soc.* **1990**, *112*, 2407–2410.
[48] P. Le Floch, F. Mathey, *Synlett* **1990**, 171–172.
[49] A. Marinetti, F. Mathey, *Angew. Chem.* **1988**, *100*, 1435–1437; *Angew. Chem. Int. Ed. Engl.* **1988**, *27*, 1382–1384.
[50] A. Marinetti, S. Bauer, L. Ricard, F. Mathey, *Organometallics* **1990**, *9*, 793–798.
[51] X. Chen, R. C. Smith, J. D. Protasiewicz, *Chem. Commun.* **2004**, 146–147.
[52] Review: L. Weber, *Eur. J. Inorg. Chem.* **2000**, 2425–2441.
[53] L. Weber, S. Uthmann, H.-G. Stammler, B. Neumann, W. W. Schoeller, R. Boese, D. Bläser, *Eur. J. Inorg. Chem.* **1999**, 2369–2381.
[54] L. Weber, M. H. Scheffer, H.-G. Stammler, B. Neumann, W. W. Schoeller, A. Sundermann, K. K. Laali, *Organometallics* **1999**, *18*, 4216–4221.
[55] L. Weber, O. Kaminski, B. Quasdorff, H.-G. Stammler, B. Neumann, *J. Organomet. Chem.* **1997**, *529*, 329–341.
[56] L. Weber, M.-H. Scheffer, H.-G. Stammler, A. Stammler, *Eur. J. Inorg. Chem.* **1999**, 1607–1611.
[57] a) H. W. Wanzlick, E. Schikora, *Angew. Chem.* **1960**, *72*, 494; b) H. W. Wanzlick, E. Schikora, *Chem. Ber.* **1961**, *94*, 2389–2393; c) H. W. Wanzlick, *Angew. Chem.* **1962**, *74*, 129–134; *Angew. Chem. Int. Ed. Engl.* **1962**, *1*, 75–80.
[58] R. W. Alder, L. Chaker, F. P. V. Paolini, *Chem. Commun.* **2004**, 2172–2173.
[59] M. Regitz, J. Hocker, B. Weber, *Angew. Chem.* **1970**, *82*, 394–395; *Angew. Chem. Int. Ed. Engl.* **1970**, *9*, 375–376.
[60] L. Weber, U. Lassahn, H.-G. Stammler, B. Neumann, *Eur. J. Inorg. Chem.* **2005**, 4590–4597.
[61] L. Weber, J. Krümberg, H.-G. Stammler, B. Neumann, *Z. Anorg. Allg. Chem.* **2004**, *630*, 2478–2482.
[62] L. Weber, J. Krümberg, H.-G. Stammler, B. Neumann, *Z. Anorg. Allg. Chem.* **2006**, *632*, 879–884.
[63] L. Weber, U. Lassahn, H.-G. Stammler, B. Neumann, K. Karaghiosoff, *Eur. J. Inorg. Chem.* **2002**, 3272–3277.
[64] L. Weber, B. Quasdorff, H.-G. Stammler, B. Neumann, *Chem. Eur. J.* **1998**, *4*, 469–475.
[65] L. Weber, M. Meyer, H.-G. Stammler, B. Neumann, *Chem. Eur. J.* **2001**, *7*, 5401–5408.
[66] L. Weber, M. Meyer, H.-G. Stammler, B. Neumann, *Organometallics* **2003**, *22*, 5063–5068.
[67] J. Ipaktschi, P. Rooshenas, A. Dülmer, *Eur. J. Inorg. Chem.* **2006**, 1456–1459.
[68] L. Weber, G. Noveski, T. Braun, H.-G. Stammler, B. Neumann, *Eur. J. Inorg. Chem.* **2007**, 562–567.
[69] L. Weber, G. Noveski, H.-G. Stammler, B. Neumann, *Z. Anorg. Allg. Chem.* **2007**, *633*, 994–999.
[70] L. Weber, G. Noveski, H.-G. Stammler, B. Neumann, *Eur. J. Inorg. Chem.* **2007**, 4011–4016.
[71] L. Weber, G. Noveski, U. Lassahn, H.-G. Stammler, B. Neumann, *Eur. J. Inorg. Chem.* **2005**, 1940–1946.
[72] A. J. Arduengo III, J. C. Calabrese, A. H. Cowley, H. V. Rasika Dias, J. R. Goerlich, W. J. Marshall, B. Riegel, *Inorg. Chem.* **1997**, *36*, 2151–2158.
[73] R. C. Smith, P. Gantzel, A. L. Rheingold, J. D. Protasiewicz, *Organometallics* **2004**, *23*, 5124–5126.
[74] a) G. Huttner, H. G. Schmid, *Angew. Chem.* **1975**, *87*, 454–455; *Angew. Chem. Int. Ed. Engl.* **1975**, *14*, 433; b) J. von Seyerl, U. Moering, A. Wagner, A. Frank, G. Huttner, *Angew. Chem.* **1978**, *90*, 912; *Angew. Chem. Int. Ed. Engl.* **1978**, *17*, 844; c) B. Sigwarth, C. Zsolnai, U. Scheidsteger, G. Huttner, *J. Organomet. Chem.* **1982**, *235*, 43–58; d) K. Plöße, G. Huttner, L. Zsolnai, *Angew. Chem.* **1989**, *101*, 482–483; *Angew. Chem. Int. Ed. Engl.* **1989**, *28*, 446; e) A. Strube, G. Huttner, L. Zsolnai, *Z. Anorg. Allg. Chem.* **1989**, *577*, 263–269; f) A. Strube, G. Huttner, L. Zsolnai, W. Imhof, *J. Organomet. Chem.* **1990**, *399*, 281–290; g) Ch. Emmerich, G. Huttner, *J. Organomet. Chem.* **1993**, *448*, 81–83; h) Ch. Emmerich, G. Huttner, *J. Organomet. Chem.* **1993**, *447*, 81–83; i) Ch. Emmerich, G. Huttner, A. Asam, *J. Organomet. Chem.* **1993**, *447*, 71–79.
[75] N. C. Mösch-Zanetti, R. R. Schrock, W. M. Davis, K. Wanninger, S. W. Seidel, M. B. O'Donoghue, *J. Am. Chem. Soc.* **1997**, *119*, 11037–11048.
[76] L. Weber, M. H. Scheffer, H.-G. Stammler, B. Neumann, *Inorg. Chim. Acta* **1999**, *291*, 311–316.

 © 2007 Wiley-VCH Verlag GmbH & Co. KGaA, Weinheim 

[77] L. Weber, G. Dembeck, P. Lönnecke, H.-G. Stammler, B. Neumann, *Organometallics* **2001**, *20*, 2288–2293.
[78] L. Weber, P. Bayer, G. Noveski, H.-G. Stammler, B. Neumann, *Eur. J. Inorg. Chem.* **2006**, 2299–2305.
[79] a) L. Weber, P. Bayer, H. G. Stammler, B. Neumann, *Chem. Commun.* **2005**, 1595–1597; b) L. Weber, P. Bayer, S. Uthmann, T. Braun, H.-G. Stammler, B. Neumann, *Eur. J. Inorg. Chem.* **2006**, 137–143.
[80] L. Weber, P. Bayer, T. Braun, H.-G. Stammler, B. Neumann, *Organometallics* **2006**, *25*, 1786–1794.

Received: May 4, 2007
Published Online: August 23, 2007

 © 2007 Wiley-VCH Verlag GmbH & Co. KGaA, Weinheim 

DOI: 10.1002/ejic.200700697

# Supramolecular Click Assembly of a Fused Double-Stranded [$Mn^{II}_3$] Dihelicate

**Jinkui Tang,[a] José Sánchez Costa,[a] Guillem Aromí,[b] Ilpo Mutikainen,[c] Urho Turpeinen,[c] Patrick Gamez,[a] and Jan Reedijk*[a]**

**Keywords:** Self-assembly / Helicates / Click chemistry / Manganese / Ferromagnetic interactions

A trinuclear $Mn^{II}$ complex was obtained by reaction of manganese(II) perchlorate with the ligand 2-methoxy-6-(pyridine-2-ylhydrazonomethyl)phenol in methanol. The X-ray crystal structure of $[Mn_3L_4](ClO_4)_2(H_2O)_2$ (**1**) reveals that the "bent" chain of the $Mn^{II}$ ions is assembled by a unique click-assembly of two double-stranded helicates. Magnetic susceptibility measurements show weak ferromagnetic interactions between the metal ions.
(© Wiley-VCH Verlag GmbH & Co. KGaA, 69451 Weinheim, Germany, 2007)

## Introduction

The self-assembly between metal centres and selected ligands into predetermined molecular architectures is now ubiquitous in chemistry.[1] This is especially relevant in the field of magnetic materials,[2–4] as remarkable metal–metal interactions may be achieved through the formation of such supramolecular architectures.[5] In this context, helicates are amazing metallosupramolecular assemblies that have been comprehensively investigated during the past two decades, both for their aesthetic nature and for their potential physical properties.[6–9] Most multistranded helicates reported feature two metal centres.[10] Examples containing a trinuclear (or higher) array of metal ions are less common, but they are increasingly described.[11]

In the course of our investigations on the design and preparation of polynuclear metal complexes with attractive magnetic properties, the potentially tetradentate, rigid N,O-ligand 2-methoxy-6-(pyridine-2-ylhydrazonomethyl)phenol[12] (HL) was used to generate metal clusters. We report here a new structural type in metallosupramolecular chemistry, namely, a double-stranded trinuclear dihelicate.

## Results and Discussion

The reaction of two equivalents of hydrated manganese(II) perchlorate with one equivalent of HL in methanol

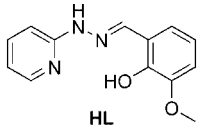


produces orange block-shaped crystals of $[Mn_3L_4](ClO_4)_2(H_2O)_2$ (**1**), whose X-ray structure is depicted in Figures 1 and S1. The structure of **1** shows a dicationic trinuclear "bent" chain of $Mn^{II}$ ions [angle Mn1–Mn2–Mn3 147.6(1)°] assembled by four deprotonated $L^-$ ligands. Each $L^-$ ligand acts as a tetradentate and tris-chelating donor, and the pyridyl and imine N atoms and both the methoxy and phenoxide O atoms are used for coordination.

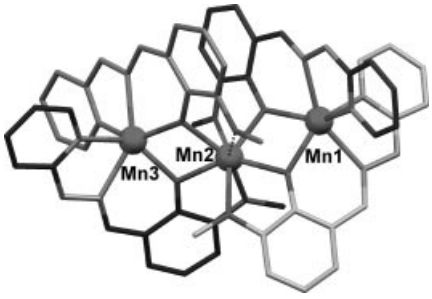


Figure 1. Representation of the trinuclear complex cation of **1**, which shows the three manganese(II) ions coordinated by four different deprotonated **L** ligands.

The bending of the metal array is most likely due to steric constraints around the central Mn2 ion. The charge of the complex is compensated by two $ClO_4^-$ anions. The oxidation state of +2 for the three manganese ions is corroborated by valence bond sum analysis[13] and the magnetic behaviour of the compound (see below). The external six-coordinate metal centres, Mn1 and Mn3, exhibit rare distorted trigonal-prismatic geometries with $N_4O_2$ donor sets.[14,15] This unusual coordination geometry is most likely

[a] Leiden Institute of Chemistry, Gorlaeus Laboratories, Leiden University,
P.O. Box 9502, 2300 RA Leiden, The Netherlands
Fax: +31715274671
E-mail: reedijk@chem.leidenuniv.nl
[b] Departament de Química Inorgànica, Grup d'interaccions Magnètiques, Universitat de Barcelona,
Diagonal 647, 08028 Barcelona, Spain
[c] Department of Chemistry, Laboratory of Inorganic Chemistry, University of Helsinki,
P.O. Box 55 (A.I. Virtasenaukio 1), 00014 Helsinki, Finland
Supporting information for this article is available on the WWW under http://www.eurjic.org/ or from the author.

 © 2007 Wiley-VCH Verlag GmbH & Co. KGaA, Weinheim 

due to: (1) the small NN bite angles of the ligands [the N–Mn–N angles range from 70.8(2) to 71.6(2)°], (2) the rigidity of the dinucleating ligand HL and (3) steric constraints resulting from the coordination of four ligands to the central Mn2 ion (for instance, two ligands coordinated to Mn2 are stacked; Figures 1 and 2). The Mn–N and Mn–O bond lengths (Table S1) are within the usual ranges found for this type of coordination environment.[16] The coordination angles (Table S1) reflect the distortion of the trigonal prisms. Thus, the trigonal twist angles[17] (Figure S2) vary from 4.65 to 23.60° for Mn1 and from 4.07 to 26.47° for Mn3. These values suggest that the distortion of the trigonal prismatic geometry is more pronounced in Mn3. The central Mn2 ion is in fact heptacoordinated (Figure S3), and it has one additional Mn–O contact at a rather long distance of 2.616(5) Å [see bond lengths in Table S1; a longer bond at 3.022(7) Å neither is nor considered as coordination]. The unusual geometry around the Mn2 ion is best described as highly distorted capped trigonal-prismatic; the capping atom is O27 (Figure S4). The trigonal twist angles vary from 5.10 to 32.70°. The Mn–O bond lengths are comparable to those of seven-coordinate $Mn^{II}$ centres reported earlier.[18,19]

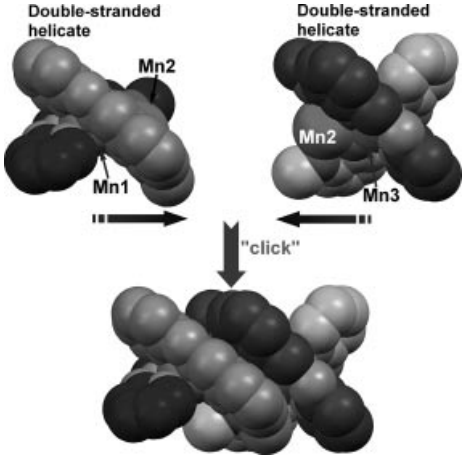


Figure 2. Fused double-stranded trinuclear dihelicate generated by supramolecular click self-assembly.

This compound exhibits fascinating features from a supramolecular point of view. It results from the fusion of two double-stranded helicates to form a unique trinuclear double-stranded dihelicate (Figure 2). Actually, the manganese(II) ions Mn1 and Mn2 are bridged by two $L^-$ ligands (Figure 2, top left), which constitutes a double-stranded bimetallic helicate with a Δ configuration[20] (Figure 3). Similarly, Mn2 and Mn3 can be regarded as a Δ-configured helicate together with two other $L^-$ ligands (Figure 2, top right). Because Mn2 belongs to both double-stranded helicates, it acts as a link between them, and it is thus coordinated by four different $L^-$ ligands (Figure 2 bottom and Figure 3). This "click self-assembly" leads to an unprecedented trinuclear helical structure (Figures 2 and 3). Indeed, to the best of our knowledge, all linear trimetallic helicates so far described in the literature exhibit metal arrays whose formation is achieved by trinucleating ligands.[8] In the present example, the trimetallic chain is assembled with only dinucleating ligands.

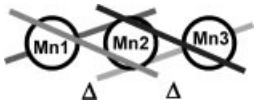


Figure 3. Schematic representation of the double-stranded dihelicate, which shows the stereochemistry of each helical subunit.

The X-band EPR spectrum of compound **1** (Figure S5), recorded at 77 K on a powdered sample, shows an intense and broad signal centred at $g = 2.14$ ($\Delta H_{pp} = 990$ G). A weaker line is also detected at 95 mT (Figure S5), which suggests that there are weak interactions between the Mn centres within complex **1**. Variable-temperature magnetic susceptibility measurements were performed on powdered **1** in the 3–300 K range under a constant magnetic field of 0.5 T. The results are shown in Figure 4 in form of a $\chi_M T$ vs. $T$ curve ($\chi_M$ is the molar paramagnetic susceptibility). The $\chi_M T$ value increases from 16.15 $cm^3 K mol^{-1}$ at 300 K (the expected value for three uncoupled $Mn^{II}$ ions with $S = 5/2$ and $g = 2.2$) and reaches a maximum value of 16.6 $cm^3 K mol^{-1}$ at 10 K, followed by a sudden drop at lower temperatures down to 13.95 $cm^3 K mol^{-1}$ at 3 K. To interpret this behaviour, the experimental data were simulated through a least-squares fitting procedure by using the isotropic Heisenberg Hamiltonian in Equation (1).

$$H = -2J_1(S_1S_2 + S_2S_3) - 2J_2(S_1S_3) \quad (1)$$

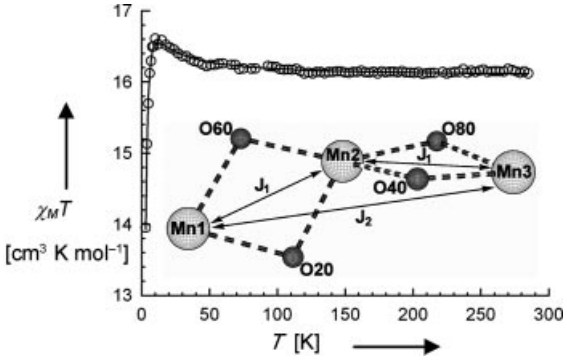


Figure 4. Plot of $\chi_M T$ vs. $T$ per mol of complex **1**. The solid line is a fit to the experimental data. The inset shows the core of the complex, together with the spin coupling scheme.

In this Hamiltonian (see inset of Figure 4 for coupling scheme), $S_1 = S_3 = S_2 = 5/2$, whereas the respective interactions within the Mn1–Mn2 and Mn2–Mn3 pairs were considered to be equal. This model does not include any effect arising from zero-field splitting. This approximation is reasonable here, as the $Mn^{II}$ ion ($d^5$) is quite isotropic, and thus, it does not usually conduce to any significant magnetoanisotropy. The solutions of the above Hamiltonian can be found analytically, and correspond to 27 $|S_A,S_T\rangle$ states ($S_A = S_1 + S_3$, $S_T$ = total spin) with a total degeneracy of 216. With these eigenvalues and their corresponding energies, a $\chi_M = f(T)$ expression can then be constructed by

 © 2007 Wiley-VCH Verlag GmbH & Co. KGaA, Weinheim 

using the van Vleck equation.[21] Initially, a term considering the effect of intermolecular magnetic interactions, $-2zJ'$, was added to the Hamiltonian and treated according to the molecular-field approximation approach.[22] The fit resulting from this model (Figure 4) produced the following parameters: $J_1 = +0.23\ cm^{-1}$, $J_2 = -0.03\ cm^{-1}$, $-zJ' = -0.07\ cm^{-1}$ and $g = 2.2$, which leads to a spin ground state of $S_T = 15/2$. These results reveal that all magnetic exchange interactions in this system are very weak (involving energies of less than $1\ cm^{-1}$) and also suggest that the coupling between Mn1 and Mn3 is negligible. A less satisfactory fit is obtained by fixing $zJ'$ to zero, which led to $J_1 = +0.31\ cm^{-1}$, $J_2 = -0.44\ cm^{-1}$ and $g = 2.2$, which conduces to a ground state $S_T = 7/2$. This solution was considered unlikely, because it attributes more weight to the interaction between the external Mn ions than to the coupling of adjacent metals, and therefore, the first solution was preferred. In both cases, the value of $g$ is slightly higher than normal. The $g$ values as obtained from bulk magnetization studies are affected by small experimental errors associated with the sample weight and the molecular mass. In this sense, the value obtained from EPR is more reliable. The above results add to a small collection of data relative to the nature and magnitude of the magnetic exchange between $Mn^{II}$ ions bridged only by two phenolate moieties. In all reported cases the coupling revealed itself to be very weak and examples have been found of both types of interactions, ferro-[23–27] and antiferromagnetic.[28–32]

This investigation is currently being extended to other metals to ascertain whether the concept of interconnected double-stranded trinuclear dihelicates can be generalized.

## Experimental Section

**Compound 1:** Prepared from $Mn(ClO_4)_2 \cdot 6H_2O$ (0.50 mmol) and HL (0.25 mmol) in methanol (10 mL). The resulting yellow solution was left unperturbed to allow slow evaporation of the solvent. Orange crystals, suitable for X-ray diffraction analysis, were formed after 1 d. Yield: 35 mg, 41% (based on the ligand HL). IR (neat): $\tilde{\nu}$ = 3266 (w), 1616 (vs), 1538 (s), 1485 (s), 1464 (s), 1456 (s), 1427 (vs), 1375 (w), 1346 (s), 1286 (s), 1220 (vs), 1074 (vs), 1004 (w), 980 (s), 850 (w), 772 (s), 732 (vs), 622 (vs), 499 (w), 448 (vs), 410 (s) $cm^{-1}$. $C_{52}H_{52}Cl_2Mn_3N_{12}O_{18}$ (1368.77): calcd. C 45.63, H 3.83, N 12.28; found C 45.60, H 3.49, N 12.11.

**X-ray Crystallographic Analysis:** Intensity data were recorded with a Nonius Kappa CCD diffractometer with Mo-$K_\alpha$ radiation ($\lambda$ = 0.71073 Å) at 173(2) K and were corrected for Lorentz and polarization effects and for absorption. The programs COLLECT,[33] SHELXS-97[34] and SHELXL-97[35] were used for data reduction, structure solution and structure refinement, respectively. All non-hydrogen atoms were refined anisotropically. The H atoms were introduced in calculated positions and refined with fixed geometry with respect to their carrier atoms. The H atoms were not located for the disordered water molecules. Crystal data for **1**: Monoclinic, $C2/c$; $a$ = 37.332(5) Å, $b$ = 15.075(3) Å, $c$ = 24.610(5) Å, $V$ = 12721(4) $Å^3$, $Z = 8$, $\rho_{calcd.} = 1.439\ g\,cm^{-3}$, $\mu = 0.747\ mm^{-1}$, final $R_1 = 0.0775$ for $I \geq 2\sigma(I)$, $wR_2 = 0.1806$ for all data. CCDC-648621 contains the supplementary crystallographic data for this paper. These data can be obtained free of charge from the Cambridge Crystallographic Data Centre via www.ccdc.cam.ac.uk/data_request/cif.

X-band EPR studies were carried out with a JEOL electron spin resonance spectrometer equipped with an Esprit 330 data system, with dpph as an internal reference ($g$ = 2.0036).

Magnetic susceptibility measurements on **1** were performed with a Quantum Design MPMS-5 5T SQUID magnetometer at 5000 Oe in the temperature range 3–300 K. Data were corrected for the diamagnetic contributions estimated from Pascal's Tables.[22]

**Supporting Information** (see footnote on the first page of this article): Schematic representations of the coordination environments of the three $Mn^{II}$ centres of **1**. Selected bond lengths and angles for **1**, as well as X-ray data. Solid-state EPR spectrum of complex **1**.

## Acknowledgments

The work described here was supported by the Leiden University Study Group Werkgroep Fundamenteel Materialen-Onderzoek (WFMO). The European Cooperation in the Field of Science and Technology (COST) Action D35/0011 and coordination by the FP6 Network of Excellence "Magmanet" (contract number 515767) are also kindly acknowledged.

[1] G. M. Whitesides, M. Boncheva, *Proc. Natl. Acad. Sci. USA* **2002**, *99*, 4769–4774.
[2] L. N. Dawe, T. S. M. Abedin, T. L. Kelly, L. K. Thompson, D. O. Miller, L. Zhao, C. Wilson, M. A. Leech, J. A. K. Howard, *J. Mater. Chem.* **2006**, *16*, 2645–2659.
[3] J. R. Long, "Molecular Cluster Magnets" in *Chemistry of Nanostructured Materials* (Ed.: P. Yang), World Scientific, Hong Kong, **2003**.
[4] G. Aromí, E. K. Brechin, *Struct. Bond.* **2006**, *122*, 1–67.
[5] C. J. Milios, A. Vinslava, W. Wernsdorfer, S. Moggach, S. Parsons, S. P. Perlepes, G. Christou, E. K. Brechin, *J. Am. Chem. Soc.* **2007**, *129*, 2754–2755.
[6] B. Champin, P. Mobian, J. P. Sauvage, *Chem. Soc. Rev.* **2007**, *36*, 358–366.
[7] J. R. Nitschke, *Acc. Chem. Res.* **2007**, *40*, 103–112.
[8] M. Albrecht in *Topics in Current Chemistry Vol. 248: Templates in Chemistry I* (Eds.: C. A. Schalley, F. Vögtle, K. H. Dötz), Springer, Berlin, **2004**, pp. 105–139.
[9] C. Piguet, M. Borkovec, J. Hamacek, K. Zeckert, *Coord. Chem. Rev.* **2005**, *249*, 705–726.
[10] K. Zeckert, J. Hamacek, J. M. Senegas, N. Dalla-Favera, S. Floquet, G. Bernardinelli, C. Piguet, *Angew. Chem. Int. Ed.* **2005**, *44*, 7954–7958.
[11] M. Albrecht, *Chem. Rev.* **2001**, *101*, 3457–3497.
[12] M. Mohan, N. S. Gupta, L. Chandra, N. K. Jha, R. S. Prasad, *Inorg. Chim. Acta* **1988**, *141*, 185–192.
[13] W. T. Liu, H. H. Thorp, *Inorg. Chem.* **1993**, *32*, 4102–4105.
[14] C. Desroches, G. Pilet, S. A. Borshch, S. Parola, D. Luneau, *Inorg. Chem.* **2005**, *44*, 9112–9120.
[15] R. van Gorkum, F. Buda, H. Kooijman, A. L. Spek, E. Bouwman, J. Reedijk, *Eur. J. Inorg. Chem.* **2005**, 2255–2261.
[16] D. F. Xiang, C. Y. Duan, X. S. Tan, Y. J. Liu, W. X. Tang, *Polyhedron* **1998**, *17*, 2647–2653.
[17] E. L. Muetterties, L. J. Guggenberger, *J. Am. Chem. Soc.* **1974**, *96*, 1748–1756.
[18] E. Coronado, J. R. Galán-Mascarós, C. Martí-Gastaldo, A. M. Martínez, *Dalton Trans.* **2006**, 3294–3299.
[19] Z. A. D. Lethbridge, A. F. Congreve, E. Esslemont, A. M. Z. Slawin, P. Lightfoot, *J. Solid State Chem.* **2003**, *172*, 212–218.
[20] C. Piguet, G. Bernardinelli, G. Hopfgartner, *Chem. Rev.* **1997**, *97*, 2005–2062.

 © 2007 Wiley-VCH Verlag GmbH & Co. KGaA, Weinheim 

[21] S. Menage, S. E. Vitols, P. Bergerat, E. Codjovi, O. Kahn, J. J. Girerd, M. Guillot, X. Solans, T. Calvet, *Inorg. Chem.* **1991**, *30*, 2666–2671.
[22] O. Kahn, *Molecular Magnetism*, VCH, New York, **1993**.
[23] J. C. Jeffery, P. Thornton, M. D. Ward, *Inorg. Chem.* **1994**, *33*, 3612–3615.
[24] E. O. Gao, S. Q. Bai, Z. He, C. H. Yan, *Inorg. Chem.* **2005**, *44*, 677–682.
[25] M. Mikuriya, K. Nakadera, T. Tokii, *Inorg. Chim. Acta* **1992**, *194*, 129–131.
[26] H. R. Chang, S. K. Larsen, P. D. W. Boyd, C. G. Pierpont, D. N. Hendrickson, *J. Am. Chem. Soc.* **1988**, *110*, 4565–4576.
[27] D. Luneau, J. M. Savariault, P. Cassoux, J. P. Tuchagues, *J. Chem. Soc. Dalton Trans.* **1988**, 1225–1235.
[28] T. C. Higgs, K. Spartalian, C. J. O'Connor, B. F. Matzanke, C. J. Carrano, *Inorg. Chem.* **1998**, *37*, 2263–2272.
[29] C. Hureau, E. Anxolabehere-Mallart, M. Nierlich, F. Gonnet, E. Riviere, G. Blondin, *Eur. J. Inorg. Chem.* **2002**, 2710–2719.
[30] I. A. Koval, M. Huisman, A. F. Stassen, P. Gamez, M. Lutz, A. L. Spek, D. Pursche, B. Krebs, J. Reedijk, *Inorg. Chim. Acta* **2004**, *357*, 294–300.
[31] M. Qian, S. H. Gou, S. Chantrapromma, S. S. S. Raj, H. K. Fun, Q. D. Zeng, Z. Yu, X. Z. You, *Inorg. Chim. Acta* **2000**, *305*, 83–90.
[32] G. Aromí, G. Gamez, C. Boldron, H. Kooijman, A. L. Spek, J. Reedijk, *Eur. J. Inorg. Chem.* **2006**, 1940–1944.
[33] Nonius, *COLLECT*, Nonius BV, Delft, The Netherlands, **2002**.
[34] G. M. Sheldrick, *SHELXS-97 Program for Crystal Structure Determination*, University of Göttingen, Germany, **1997**.
[35] G. M. Sheldrick, *SHELXL-97-2 Program for Crystal Structure Refinement*, University of Göttingen, Germany, **1997**.

Received: July 4, 2007
Published Online: August 8, 2007

 © 2007 Wiley-VCH Verlag GmbH & Co. KGaA, Weinheim 

DOI: 10.1002/ejic.200700654

# In Vitro Formation of Nanocrystalline Carbonate Apatite – A Structural and Morphological Analogue of Atherosclerotic Plaques

**Lars-Fride Olsson,[a] Karin Sandin,[a] Rolf Odselius,[b] and Lars Kloo*[c]**

**Keywords:** Carbonate apatite / Crystallization / Calcification / Nanocrystalline / Calcium

The in vitro formation of carbonate apatite in solutions with ion concentrations comparable to those in human serum was studied. The composition and morphology of the resulting apatite precipitate displayed a hierarchical assembly of elongated plate-shaped nanocrystals of carbonate apatite analogous to previously characterized bioapatites formed in vivo. The main conclusion is that so-called bioapatites may form in vitro and that precipitation inhibitors most likely are essential for the prevention of spontaneous calcification at normal human serum ion concentrations.
(© Wiley-VCH Verlag GmbH & Co. KGaA, 69451 Weinheim, Germany, 2007)

## Introduction

Biological mineralization of solid calcium phosphates occurs in humans both under normal conditions, such as in bone and teeth formation, and under pathological conditions, such as vascular calcification related to advanced atherosclerosis,[1] diabetes[2] and chronic renal failure,[3] where the latter also includes end-stage renal disease pertinent to patients on hemodialysis.[4] Giachelli[5] recently published a comprehensive review on possible mechanisms behind vascular calcification, in which several mechanisms were discussed.

From a purely solution chemistry point of view, vascular calcification is expected: normal human serum calcium and inorganic phosphate concentrations are such that supersaturation exists with respect to hydroxyapatite, $Ca_5(PO_4)_3OH$, (OHAp),[6] octacalcium phosphate (OCP), and carbonate apatite (dahllite);[7] the latter is often denoted bioapatite, a name suggesting that it can be formed only in vivo. Investigations of atherosclerotic plaques show that bioapatite is an apatite with a significant amount of carbonate included[7,8] (cf. Table 2). Also, comparisons between synthetically made and biological apatites showed that phosphate, to a varying degree, was exchanged for carbonate in the latter type.[9]

Biomineralization of apatites has been host to renewed interest. The main reason is the hierarchical crystallization and observation of nano- and mesocrystalline features, especially in combination with composite formation. Spherical precipitates were identified and shown to consist of bundles of small crystallites.[11–13]

Despite supersaturation, spontaneous calcification under normal human serum conditions does not occur. This indicates that inhibitors must be present to maintain metastability. With regard to pathological vascular calcification, a pathway involving a lack of inhibition seems to be the most important of the mechanisms listed by Giachelli.[5] Both in vitro and mice in vivo experiments support this mechanism.[14] In vivo mice experiments with a reduced concentration of calcification inhibitors in the serum were shown to give calcification;[15,16] the "knock-out mice" that lacked inhibitors were severely calcified despite having normal mice serum ionized calcium and inorganic phosphate concentrations. However, applied to human vascular calcification, the mice results are inconclusive. The reason is that even though mice serum contains the same total calcium concentration as human serum, the inorganic phosphate concentrations are two to three times higher.[16,17] From a solution chemistry point of view, this mice and human serum phosphate concentration difference is essential, as it is related to the details of calcium phosphate precipitation; more precisely, this value is related to supersaturation with respect to brushite, $CaHPO_4{\cdot}2H_2O$. A number of in vitro studies have shown that once this species is formed,[18] it is transformed to the less-soluble OCP and in turn transformed into OHAp at physiological pH. Even formation of bioapatite as the end product is possible; according to LeGeros, OCP is transformed into carbonated apatite in the presence of hydrogen carbonate.[19] However, in normal human serum the calcium ion and inorganic phosphate concentrations are so low that the saturation limit for brushite is never exceeded. This was verified experimentally by Eidelman et al.,[20] who showed that brushite dissolves in ultrafiltered human serum, and by model equilibrium calculations.[21]

[a] Gambro Corporate Research
Lund, Sweden
[b] Electron Microscopy Unit, Lund Univ. Hospital,
Lund, Sweden
[c] Division of Inorganic Chemistry, Royal Institute of Technology,
10044 Stockholm, Sweden
Fax: +46-879-09-349
E-mail: Larsa@kth.se
Supporting information for this article is available on the WWW under http://www.eurjic.org or from the author.

 © 2007 Wiley-VCH Verlag GmbH & Co. KGaA, Weinheim 

Table 1. Composition of solutions, concentrations in mmol/L; calcium–phosphate product, $Ca \times P_i$; calcium–phosphate molar ratio in precipitate (Ca/P, ppt), number of vessels and vessel material [glass (G) or polypropylene (PPye)].[a]

| | 2 × 44, G (low hydrogen carbonate) | | 4 × 25 PPye, 4 × 5 G | | | | 25 PPye | Normal human serum[27] |
|---|---|---|---|---|---|---|---|---|
| $P_i$ | 1.30 | 1.84 | 0.99 | 1.29 | 1.59 | 1.90 | 1.90 | 0.84–1.45 |
| Ca, total | 1.30 | 1.30 | 1.56 | 1.56 | 1.56 | 1.56 | 1.64 | 2.1–2.6 |
| $(Ca \times P_i) \times 10^6$ [mol/L]$^2$ | 1.7 | 2.4 | 1.5 | 2.0 | 2.5 | 3.0 | 3.1 | (1.8–3.8) |
| $NaHCO_3$ | 0.18 | 0.11 | 24.7 | 24.7 | 24.9 | 24.6 | 24.9 | 22–26 |
| $Na^+$, total | 145 | 146 | 146 | 148 | 148 | 146 | 146 | 135–145 |
| $K^+$ | | | | | | | | 3.5–5.0 |
| $Mg^{2+}$ | | | | | | | | 0.7–1.0 |
| $Cl^-$ | 145 | 145 | 124 | 125 | 125 | 123 | 122 | 100–108 |
| iCa = $[Ca^{2+}]$, calcd. | 1.2 | 1.2 | 1.2 | 1.2 | 1.2 | 1.2 | 1.2 | 1.14–1.30 |
| $CaHPO_4$(aq.), calcd. | 0.1 | 0.1 | 0.1 | 0.1 | 0.1 | 0.1 | 0.1 | – |
| $CaHCO_3^+$, calcd. | – | – | 0.3 | 0.3 | 0.3 | 0.3 | 0.3 | – |
| pH, at preparation | 7.67 | 7.41 | 7.38 | 7.36 | 7.16 | 7.21 | 7.43 | 7.35–7.45 |
| Sign of 1:st ppt (weeks) | no precipitate | | 6 | 3 | 3 | 3 | 1–2 | – |
| pH, after ppt | | | 7.43 | 7.43 | 7.43 | 7.42 | 7.37 | |
| Ca/P, ppt | – | – | 1.85 | 1.79 | 1.76 | 1.73 | 1.73 | – |

[a] For calculated values, see Supporting Information.

To test the mechanism based on the lack of inhibition in the case of human serum, we here report a study of salt solutions supersaturated with respect to OHAp, OCP, and carbonate apatite (cf. bioapatite), but not brushite, and with temperature, buffer (sodium hydrogen carbonate), and thus pH, ionic medium, and strength as close as possible to human serum conditions (cf. Table 1). These conditions ensure that the chemical potentials of all individual ionic species involved in the hypothetical precipitation process are close to those in human serum.

Our study is an extension of an earlier investigation, in which we characterized a carbonated apatite formed in solution with inorganic phosphate corresponding to hyperphosphatemic concentrations and determined the stoichiometry to be $Ca_5(PO_4)_3HCO_3 \cdot 4H_2O$.[22]

In the experiments reported here, phosphate was varied from human normal to hyperphosphatemic concentrations. To the best of our knowledge there is no experimental study published about in vitro formation of carbonate apatite (analogous to bioapatite) in solutions with calcium, phosphate, and hydrogen carbonate concentrations comparable to those in human serum. Even though the solutions in the experiments reported by Boskey et al. contained equally low concentrations of calcium and phosphate, hydrogen carbonate was not present thus excluding carbonate apatite as a potential mineral deposit.[23]

For the sake of completeness we have included experiments in a physiological sodium chloride medium containing very low hydrogen carbonate concentrations aimed at giving precipitation of a carbonate-free apatite, i.e. OHAp.

## Results

The time from preparation of the solution until a precipitate was visually observed in the polypropylene tubes amounted to 2–3 weeks for all phosphate concentrations, except $P_i$ = 0.99 mmol/L, for which the delay time was 5–6 weeks. After seven weeks all tubes contained precipitate. The precipitate observed in the glass flasks occur as relatively large half-spheres, few in number, and with a diameter of about 1 mm, similar to those found in glass flasks with an initial phosphate concentration of 1.8 mmol/L reported earlier and displayed in Figure 1.[21] Those in the polypropylene tubes occur as considerably smaller and more numerous half-spheres (Figure 2). However, for $P_i$ = 0.99 mmol/L, in a few polypropylene tubes we observed precipitates consisting solely of a few half-spheres with a diameter of about 0.3 mm.

In an earlier publication we showed that the precipitates formed in glass flasks with an initial phosphate concentration of 1.8 mmol/L consist of a hydrated carbonate apatite. A plausible formula was suggested, $Ca_5(PO_4)_3(HCO_3) \cdot 4H_2O$.[22] Our results reported here (cf. Figures 1, 2, and 3), show that the precipitates in the polypropylene tube are also calcium phosphates that contain carbon.

The EDS spectrum of a half-sphere removed from a glass flask with an initial phosphate concentration of 1.8 mmol/L is displayed in Figure 1. A comparison between that and the EDS spectra in Figures 2 and 3 shows that the atomic composition of the precipitates in the polypropylene tubes is approximately the same as that in the glass flask with an initial phosphate concentration of 1.8 mmol/L. Signals from calcium, phosphorus, oxygen carbon, and sodium are present, but those of chlorine are not. The IR spectrum in Figure 4 was not assigned in detail but only compared to the published and assigned IR spectra of OCP by Fowler et al.,[24] and to those of OHAp and high-temperature carbonate apatite by Nelson et al.;[25] our IR spectrum was also compared to that of calcified vascular deposits by Tomazic.[7] The spectrum by Nelson et al. with 6.7 wt.-% carbonate and that by Tomazic compare favorably with regard to both the positions and shapes of the bands and to the relative magnitude of the strong carbonate and phosphate bands. It should be noted that the strong band observed in the OHAp spectrum at 631 $cm^{-1}$ and assigned to hydroxy

 © 2007 Wiley-VCH Verlag GmbH & Co. KGaA, Weinheim 

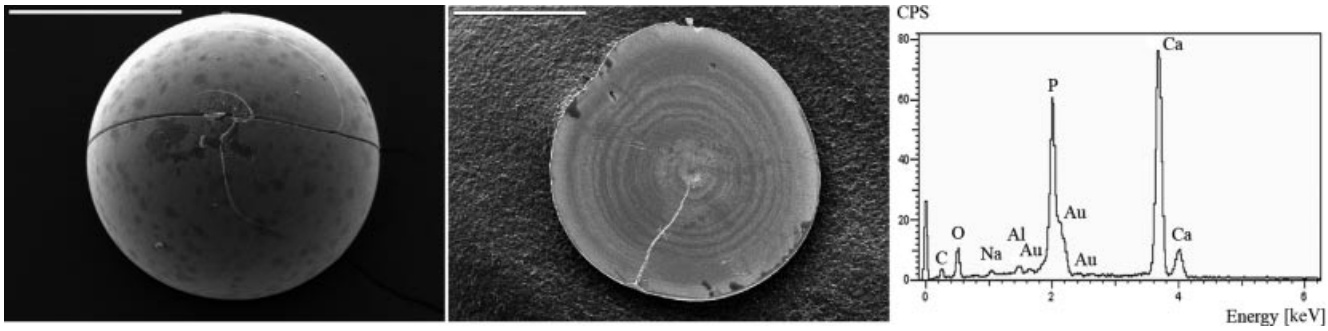


Figure 1. Scanning electron micrographs of two gold-coated samples grown in a glass bottle. The diameter is approximately 1 mm. The scale bar corresponds to 500 μm. The EDS spectrum is from the central to the right part of the flat surface of the sample. Original solution phosphate concentration: 1.8 mmol/L.

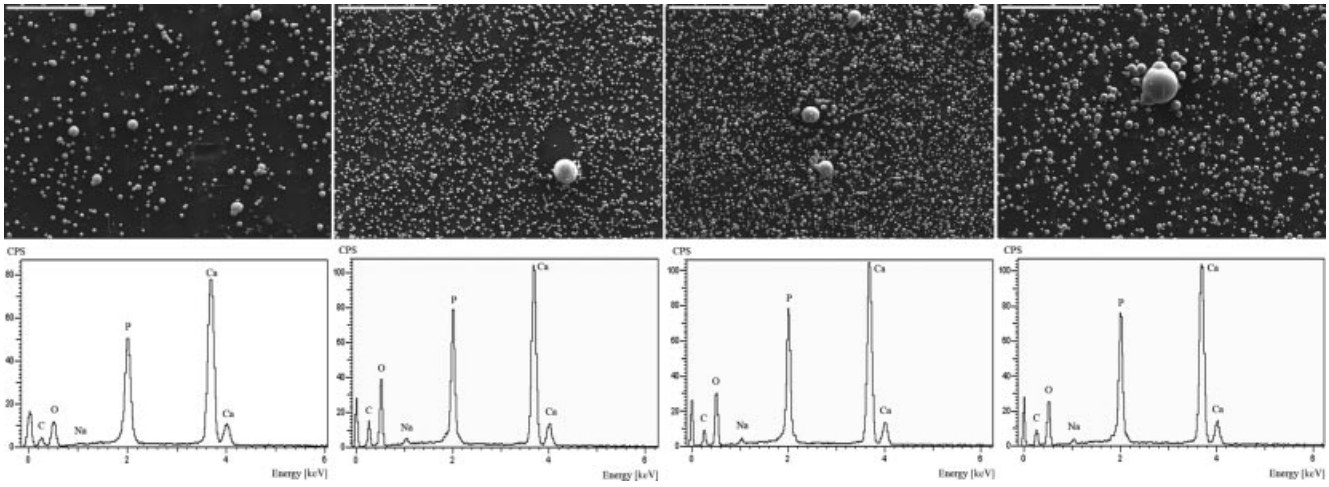

Figure 2. Scanning electron micrographs (top) and accompanying EDS spectra (bottom) of carbonated apatite samples grown in polypropylene tubes. The scale bars correspond to 500 μm. The EDS spectra are from the central to the right part of the flat surface of the samples. Original solution phosphate concentrations from left to right: 0.99, 1.29, 1.59, and 1.90 mmol/L.

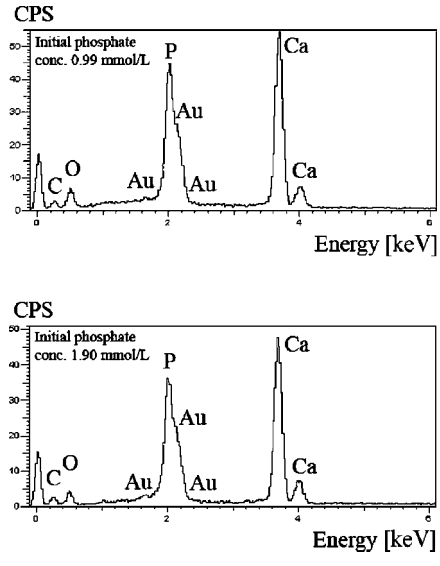


Figure 3. EDS spectra from gold-coated samples grown in polypropylene tubes. Original solution phosphate concentrations: 0.99 (top) and 1.90 (bottom) mmol/L. Note the presence of the carbon peak.

(OH) liberation is hardly discernible in our spectrum,[25] which indicates a low amount of OH. Tomazic made a similar observation concerning his reported IR spectrum of cardiovascular deposits.[7] We can safely conclude that the precipitate formed in vitro and reported here has approxi-

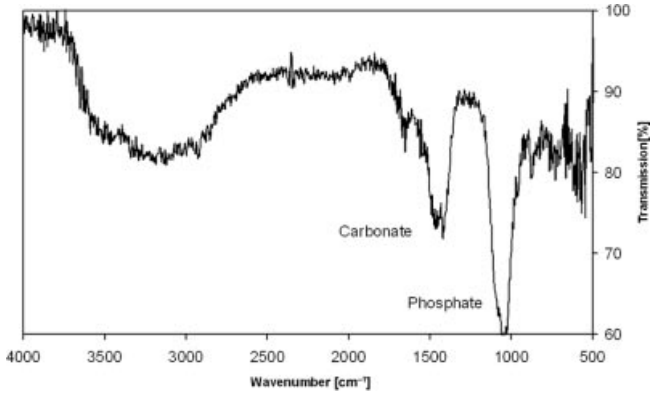


Figure 4. FTIR spectrum of precipitate grown in a polypropylene tube. Original solution phosphate concentration: 1.90 mmol/L.

 © 2007 Wiley-VCH Verlag GmbH & Co. KGaA, Weinheim 

Table 2. Composition (wt.-%) and Ca/P molar ratio of apatites and human vascular calcium phosphate deposits.

| Calcium phosphate stoichiometry | Ref. | Ca | $PO_4$ | $CO_3$ | Ca/P |
|---|---|---|---|---|---|
| OHAp, $Ca_5(PO_4)_3OH$ | | 39.9 | 56.7 | – | 1.67 |
| In vitro precipitated carbonate apatite, $Ca_5(PO_4)_3HCO_3{\cdot}4H_2O$ | [22] | 32.4 | 46.0 | 9.7 | 1.67 |
| Human atherosclerotic thoracic and abdominal aortas 4 samples. Recalculated assuming 15% protein. | [8] | 33.5–36.6 | 47.3–50.5 | 7.2–14.2 | 1.61–1.77 |
| Human atherosclerotic cardiovascular deposits (average) $Ca_{8.66}Mg_{0.22}Na_{0.32}H_{0.14}(PO_4)_5(CO_3)_{1.22}(OH,F,Cl)_{0.80}$ | [7] | 37.4 | 51.2 | 7.9 | 1.73 |

mately the same relative amounts of carbonate and phosphate as the cardiovascular deposits investigated by Tomazic.

The Ca/P molar ratios based on chemical analysis of the precipitates in the polypropylene tubes are consistently higher than those of OHAp and $Ca_5(PO_4)_3(HCO_3){\cdot}4H_2O$ (Ca/P = 1.67; cf. Table 1). The Ca/P molar ratio varies with the initial phosphate concentrations in the solution: the lower the phosphate concentration, the higher the ratio. This indicates that the composition of the precipitates to some extent varies as far as the relative amount of calcium and phosphate is concerned. Thus, from the electroneutrality requirement we can conclude that even the carbonate content may vary. An upper limit for the carbonate content can be calculated. For example, if Ca/P = 1.75 = 7/4, the electroneutrality condition requires one carbonate, stoichiometry $Ca_7(PO_4)_4CO_3$ (Ca/C = 7) or two hydrogen carbonates $Ca_7(PO_4)_4(HCO_3)_2$ (Ca/C = 3.5), and with Ca/P = 1.80 = 9/5, either two carbonates, $Ca_9(PO_4)_5(CO_3)(HCO_3)$ (Ca/C = 4.5) or, if also hydroxide is included, one carbonate $Ca_9(PO_4)_5(CO_3)OH$ (Ca/C = 9). The wt.-% calcium, phosphate, and carbonate of the in vivo calcified vascular deposits from atherosclerotic plaque $Ca_5(PO_4)_3(HCO_3){\cdot}4H_2O$ and OHAp are summarized in Table 2.

With respect to OHAp, which is assumed to form in the solutions with a very low amount of hydrogen carbonate, it does not show any tendency to precipitate in vitro after more than 16 months, neither under the prevailing conditions occurring in a so-called physiological salt solution (150 mmol/L sodium chloride and pH 7.4), nor in the presence of physiological amounts of hydrogen carbonate, where solely a carbonate apatite is formed. This is consistent with the finding that the composition of mineral deposits reported by Tomazic[7] and Schmid et al.[8] cannot be represented by the OHAp stoichiometry.

## Discussion

In a water solution with inorganic phosphate concentrations corresponding to normal human serum values, spontaneous precipitation of calcium phosphate occurs. Higher phosphate concentrations, corresponding to human hyperphosphatemic conditions, are not necessary to induce precipitation, even though they may accelerate it. The composition of the in vitro formed carbonate apatite precipitate agrees strikingly well with the findings of Tomazic[7] and Schmid et al.[8] with regard to calcified atherosclerotic plaque in a number of human blood vessels (cf. Table 2). The morphological characteristics of the precipitated carbonate apatite in vitro and in vivo are also comparable: small – a few μm – spherically shaped deposits depicted in Figures 2 and 5 are very similar to those found in human vascular deposits, see Schmid et al.,[8] Tomazic,[7] and Mohr.[26] The spherical shape thus exists both in calcification in vivo and in vitro. From the high magnification image displayed in Figure 5 it can be concluded that the spherical particles are built from units consisting of elongated plate-shaped "crystals", with a size of about a few hundred nm. Figure 5 gives the impression that there is successive assemblage of these small units first into rather irregular shaped aggregates and then, with an increasing number of units, a spherical shape. These results are in good agreement with old electron microscopy investigations and those observed for fluorapatites grown in gelatin media.[10–12]

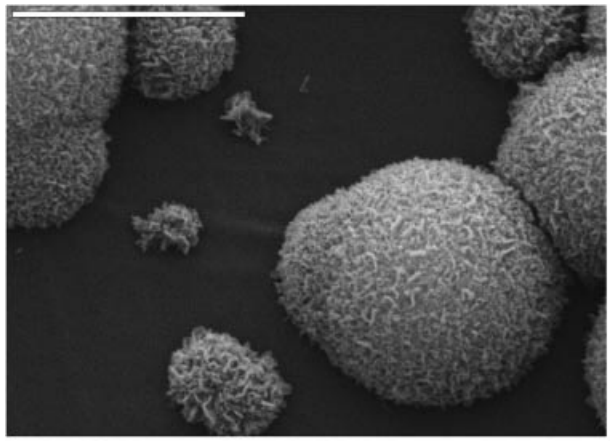

Figure 5. Assemblage of spherically shaped particles from small plate-shaped particles. The scale bar corresponds to 5 μm. Sample grown in a polypropylene tube. Original solution phosphate concentration: 1.90 mmol/L.

Our study shows that from a thermodynamic point of view we can assume that the in vitro and in vivo conditions required to induce precipitation are similar: the chemical potentials of the relevant individual ionic species are highly related and the precipitate formed in vitro is strikingly similar to that formed in vivo vascular deposits. We cannot, however, say anything about the details of the chemical reactions leading to in vitro precipitation, although we can exclude an "inorganic" mechanism assuming brushite as precursor. We can also exclude biological mechanisms that actively promote calcification, even though we obviously cannot exclude such mechanisms in vivo. From our study,

 © 2007 Wiley-VCH Verlag GmbH & Co. KGaA, Weinheim 

we can also conclude that the absence of calcification in human serum with normal clinical levels of calcium and phosphate ions unconditionally requires at least one species that prevents the precipitation process to take place. From our work and the above-mentioned in vitro[14] and mice in vivo[14,15] experiments it follows that calcification is solely due to the presence of calcium, phosphate, and hydrogen carbonate ions and decreased levels of those specific proteins that act as calcification inhibitors. Other serum components may influence the rate of the precipitation process, but not the final outcome.

Our study shows that spontaneous calcification occurs at normal human serum ion concentrations of calcium, inorganic phosphate, and hydrogen carbonate and a lack of calcification inhibitors is the simplest explanation to pathological calcification. Biological processes regulating the serum concentration of these inhibitors are of vital importance for the prevention of vascular calcification.

## Experimental Section

All concentrations were chosen to give pH and ionic medium and strength similar to those in human serum, cf. Table 1. The expected solid deposit components, calcium, phosphate, and carbonate (from the buffer) were included, and carbon dioxide was present in the atmosphere surrounding the solutions with a partial pressure either corresponding to serum conditions or equal to that of air. Two hydrogen carbonate concentrations, one high physiological and one low were used, cf. Table 1.

False indications of precipitation due to bacterial growth were suppressed and bacterial growth was never observed. Solution preparation was designed to prevent precipitation of calcium phosphate or calcium carbonate at the time of mixing. The tubes and flasks were either stored in a climate chamber at $37.0 \pm 0.2$ °C, 5% $CO_2$(g), and 99% relative humidity (high hydrogen carbonate concentration) or in a heat chamber at $37 \pm 1$ °C with 65% relative humidity (low hydrogen carbonate concentration). The calcium and phosphate ion concentrations were determined by reflectance spectrophotometry with a KODAK Ektachem DTII (Eastman Kodak Company, Rochester, New York, US) instrument.

All tubes were periodically visually checked for precipitation and a few removed for pH, calcium, and phosphate ion analysis. Precipitates were dissolved and the calcium content was determined by atomic absorption spectrometry with a Varian SpectrAA 220FS with a hollow cathode lamp at 422.7 nm, and phosphate spectrophotometrically in the form of its molybdenum complex at 882 nm with a Perkin–Elmer Lambda 20 spectrophotometer. Precipitates were also characterized by energy-dispersive spectrometry (EDS) in a scanning electron microscope (SEM) and with Fourier transformation infrared (FTIR) spectroscopy. A Philips SEM 515, operated at 20 kV was used for imaging, and calcium, phosphorus, oxygen, and carbon contents were detected with a Link ISIS EDS. An IR transmission spectrum for the qualitative determination of carbonate and phosphate was recorded with a Perkin–Elmer Spectrum BX FTIR instrument with a spectral range from 450 to 4400 $cm^{-1}$.

**Supporting Information** (see footnote on the first page of this article): Full description of the experimental procedures.

## Acknowledgments

This work was supported by the Swedish Research Council.

[1] H. C. Stary, *Virchows Arch.* **1992**, *421*, 277.
[2] N. X. Chen, S. M. Moe, *Curr. Diabetes Rep.* **2003**, *3*, 28.
[3] D. Russo, G. Palmiero, A. P. De Blasio, M. M. Balletta, V. E. Andreucci, *Am. J. Kidney Dis.* **2004**, *44*, 1024.
[4] G. A. Block, F. K. Port, *Am. J. Kidney Dis.* **2000**, *35*, 1226.
[5] C. M. Giachelli, *J. Am. Soc. Nephrol.* **2004**, *15*, 2959.
[6] M. Epple, P. Lanzer, *Z. Kardiol.* **2001**, *90*, III/2.
[7] B. B. Tomazic, *Z. Kardiol.* **2001**, *90*, III/68.
[8] K. Schmid, W. O. McSharry, C. H. Pameijer, J. P. Binette, *Atherosclerosis* **1980**, *37*, 199.
[9] S. Chakraborty, S. Bag, S. Pal, A. K. Mukherjee, *Appl. Crystallogr.* **2006**, *39*, 385.
[10] R. A. Robinson, *J. Bone Joint Surgery* **1952**, *34A*, 389.
[11] S. Busch, H. Dolhaine, A. DuChesne, S. Heinz, O. Hochrein, F. Laeri, O. Podebrad, U. Vietze, T. Weiland, R. Kniep, *Eur. J. Inorg. Chem.* **1999**, 1643.
[12] H. Tlatlik, P. Simon, A. Kawska, D. Zahn, R. Kniep, *Angew. Chem. Int. Ed.* **2006**, *45*, 1905.
[13] H. Cölfen, M. Antonietti, *Angew. Chem. Int. Ed.* **2005**, *44*, 5576.
[14] M. Ketteler, P. Bongartz, R. Westenfeld, J. E. Wildberger, A. H. Mahnken, R. Böhm, T. Metzger, W. Wanner, W. Jahnen-Dechent, *Lancet* **2003**, *361*, 827.
[15] G. Luo, P. Ducy, M. D. McKee, G. J. Pinero, E. Loyer, R. R. Behringer, G. Karsenty, *Nature* **1997**, *386*, 78.
[16] C. Schäfer, A. Heiss, A. Schwarz, R. Westenfeld, M. Ketteler, J. Floege, W. Muller, W. Esterl, T. Schinke, J. Jahnen-Dechent, *J. Clin. Invest.* **2003**, *112*, 357.
[17] R. Varghese, A. D. Gagliardi, P. E. Bialek, S. Yee, G. F. Wagner, G. E. Dimattia, *Endocrinology* **2002**, *143*, 868.
[18] S. Mann in *Biomineralization: Principles and Concepts in Bioinorganic Materials Chemistry*, Oxford University Press, Oxford, **2001**, p. 62.
[19] R. Z. LeGeros, *Z. Kardiol.* **2003**, *90*, III/116.
[20] N. Eidelman, L. C. Chow, W. E. Brown, *Calcif. Tissue Int.* **1987**, *41*, 18.
[21] K. Sandin, J. Hegbrant, L. Kloo, L.-F. Olsson, *J. Appl. Biomater. Biomech.* **2006**, *4*, 80.
[22] K. Sandin, L. Kloo, R. Odselius, L.-F. Olsson, Manuscript to be submitted for publication, **2007**.
[23] A. Boskey, A. S. Posner, *J. Phys. Chem.* **1976**, *80*, 40.
[24] B. O. Fowler, M. Markovic, W. E. Brown, *Chem. Mater.* **1993**, *5*, 1417.
[25] D. G. A. Nelson, B. E. Williamson, *Aust. J. Chem.* **1982**, *35*, 715.
[26] W. Mohr, E. Götz, *Z. Kardiol.* **2003**, *92*, 60.
[27] A. Kratz, K. B. Lewandrowski, *N. Engl. J. Med.* **1998**, *339*, 1063.

Received: June 25, 2007
Published Online: August 3, 2007

 © 2007 Wiley-VCH Verlag GmbH & Co. KGaA, Weinheim 

DOI: 10.1002/ejic.200700549

# Effect of Deprotonation of a Benzimidazolyl Ligand on the Redox Potential and the Structures of Mononuclear Ruthenium(II) Complexes

**Hongfei Sun,[a] Mei Wang,*[a] Kun Jin,[a] Chengbing Ma,[b] Rong Zhang,[a] and Licheng Sun*[a,c]**

**Keywords:** Benzimidazolyl ligand / Redox switch / Reversible protonation and deprotonation / $Ru^{II}$ complex

A monoruthenium(II) complex of the benzimidazolyl ligand and its deprotonated counterpart were prepared and structurally characterized. The reversible protonation/deprotonation process of the ancillary ligand switches the redox potential of the ruthenium(II) core from 0.69 to 0.26 V vs. Ag/$AgNO_3$.
(© Wiley-VCH Verlag GmbH & Co. KGaA, 69451 Weinheim, Germany, 2007)

## Introduction

Reversible protonation/deprotonation of an ancillary ligand at a site remote from the metal–ligand bond is a simple reaction but a crucial step in some complicated biological processes. Many metal-containing proteins and enzymes, such as photosystem II,[1,2] cytochrome *c* oxidase[3,4] and non-heme iron enzymes,[5] play their function involving proton-coupled electron transfer (PCET) reactions. To understand the relationship between electron transfer and proton motion, the PCET reactions and the modulation of the redox potential of biomimetic model complexes by deprotonation of the ligand have been intensively studied.[6–9] In most cases, imidazole, benzimidazole and biimidazoline ligands were used as proton carriers because the metal centres of many metalloenzymes are coordinated by imidazole units from histidine residues.[10–12] The effect of the distal deprotonation of the ligands bearing imidazole and benzimidazole units on the physical and chemical properties of mono- and dinuclear ruthenium and osmium complexes has been reported.[13–19] In addition to the imidazole-containing ligands, mono- and dinuclear ruthenium complexes with ligands bearing triazole and pyrazole units were also extensively studied for their interesting electrochemical and photophysical properties.[20–24] In this communication, we describe the preparation of the mononuclear ruthenium(II) complex $[Ru(bbpaH)(bpy)](PF_6)_2$ [bbpaH = (2-benzimidazolylmethyl)bis(2-pyridylmethyl)amine, bpy = bipyridine], the influence of reversible protonation/deprotonation of the coordinated benzimidazolyl ligand on the redox potential of the ruthenium(II) complex, and the molecular structures of $[Ru(bbpaH)(bpy)](PF_6)_2$ (**1**) and its deprotonated species $[Ru(bbpa)(bpy)](PF_6)$ (**2**). This proton-coupled redox process might be relevant to some metalloenzymes active sites, such as the oxygen evolving complex (OEC) in photosystem II.

## Results and Discussion

The starting complex $[Ru(bbpaH)(dmso)Cl](PF_6)_2$ was prepared by the reaction of $Ru(dmso)_4Cl_2$[25] and the bbpaH ligand[26] according to the literature procedure for the preparation of the analogous complex $[Ru(tpa)(dmso)Cl](PF_6)$ [tpa = tris(2-pyridylmethyl)amine].[27] The subsequent reaction of $[Ru(bbpaH)(dmso)Cl](PF_6)$ with bipyridyl as ligand at room temperature afforded the target complex $[Ru(bbpaH)(bpy)](PF_6)_2$ in moderate yield. The deprotonated species $[Ru(bbpa)(bpy)](PF_6)$ was readily obtained by dissolving $[Ru(bbpaH)(bpy)](PF_6)_2$ in an acetone/water (1:1, v/v) mixture with pH = 11. Both complexes are stable in polar aprotic solvent such as acetone and acetonitrile.

The molecular structures of $[Ru(bbpaH)(bpy)]^{2+}$ and its deprotonated species $[Ru(bbpa)(bpy)]^{+}$ were determined at –80 °C by X-ray diffraction analyses. To the best of our knowledge, these are the first crystallographically characterized protonation/deprotonation pair of ruthenium complexes containing an imidazolyl ligand. The overall structures of both complexes are very similar (Figure 1), with distorted octahedral coordination geometry around their ruthenium centres. In both complexes, two $N_{py}$ atoms, one from the bbpaH or bbpa ligand and another from the bpy

[a] State Key Laboratory of Fine Chemicals, DUT-KTH Joint Education and Research Centre on Molecular Devices, Dalian University of Technology,
Zhongshan Road 158-46, Dalian 116012, P. R. China
Fax: +86-411-83702185
E-Mail: symbueno@dlut.edu.cn
[b] State Key Laboratory of Structural Chemistry, Fujian Institute of Research on the Structure of Matter,
Fuzhou 350002, P. R. China
[c] Organic Chemistry, Royal KTH Chemical Science and Engineering,
10044, Stockholm, Sweden
Supporting information for this article is available on the WWW under http://www.eurjic.org or from the author.

 © 2007 Wiley-VCH Verlag GmbH & Co. KGaA, Weinheim 

ligand, an $N_{benz}$ and an $N_{amine}$ atom are located in a tetragonal plane. The remaining two $N_{py}$ atoms occupy the vertexes of the octahedron. The ruthenium atom in each complex lies slightly out of the tetragonal plane towards the pyridyl group of the bpy ligand, 0.0351 Å for $[Ru(bbpaH)(bpy)]^{2+}$ and 0.0314 Å for $[Ru(bbpa)(bpy)]^{+}$. The Ru(1)–N(1) bond length increases significantly in the deprotonated species, 2.058(6) Å for $[Ru(bbpaH)(bpy)]^{2+}$ and 2.100(3) Å for $[Ru(bbpa)(bpy)]^{+}$. In parallel, the Ru(1)–N(5) bond [2.064(3) Å] of $[Ru(bbpa)(bpy)]^{+}$, *trans* to the Ru(1)–N(1) bond, considerably shortens as compared to that [2.088(6) Å] of $[Ru(bbpaH)(bpy)]^{2+}$. The bond angles increase by ca. 18° for N(1)–Ru(1)–N(4) and 5° for N(1)–Ru(1)–N(6), while the N(1)–Ru(1)–N(7), N(1)–Ru(1)–N(3) and N(1)–Ru(1)–N(5) angles decrease by ca. 8, 4 and 1°, respectively, in the deprotonated complex. The other corresponding Ru–N bond lengths and N–Ru–N angles in the coordination sphere of two ruthenium complexes are quite similar. To the best of our knowledge there are only two examples of crystallographically characterized iron and cobalt complexes containing deprotonated imidazolylate and benzimidazolylate ligands.[8,9] The deprotonation of 2,6-bis(2-imidazolyl)pyridine as ligand in the iron complex leads to the oxidation of the iron(II) centre from $Fe^{II}$ to $Fe^{III}$,[9] while the formal oxidation state of the cobalt(II) centre in the cobalt complex of the tris(2-benzimidazolylmethyl)amine ligand does not change before and after deprotonation. During deprotonation, the ruthenium complex $[Ru(bbpaH)(bpy)]^{2+}$ behaves like the cobalt complex. Compared with the molecular structures of the reported cobalt complexes, there are two noteworthy points in the molecular structure of the deprotonated ruthenium complex. First, the lengthening of 0.042 Å for the $Ru–N_{benzimidazolylate}$ bond is contrary to the shortening of 0.026 Å for the $Co–N_{benzimidazolylate}$ bond.[8] Second, the length of the $Ru–N_{py}$ bond *trans* to the $Ru–N_{benzimidazolylate}$ bond decreases by 0.024 Å in the deprotonated ruthenium complex, while one of the $Co–N_{benz}$ bonds neighbouring the $Co–N_{benzimidazolylate}$ bond increases by 0.053 Å. These apparent contrasts in the changes of the M–N bond lengths after deprotonation of the prepared ruthenium complex and the reported cobalt complex are assumed to result from the strong coordination ability of the pyridyl group and from different coordination geometries of the ruthenium and cobalt complexes. In spite of the differences in the aforementioned two aspects, the lengthening (0.005 Å) of the average distance of the Ru–N bonds in the tetragonal plane of $[Ru(bbpa)(bpy)]^{+}$, as compared to that of the parent ruthenium complex, is consistent with the 0.009 Å increase in that of the Co–N bonds in the trigonal plane for the deprotonated cobalt complex.

The reversible protonation/deprotonation process was monitored by ESI mass spectrometry and $^1H$ NMR spectroscopy. The ESI mass spectra of $[Ru(bbpaH)(bpy)]^{2+}$ and the deprotonated complex $[Ru(bbpa)(bpy)]^{+}$ show signature peaks at $m/z$ = 293.6 and 586.1, respectively. Figure 2 shows the curves of relative intensities of the peaks for $[Ru(bbpaH)(bpy)]^{2+}$ and $[Ru(bbpa)(bpy)]^{+}$ vs. the equiv. of $NEt_3$ in the acetone solution of complex **1**. As shown in Figure 2, the peak at $m/z$ = 586.1 for $[Ru(bbpa)(bpy)]^{+}$ is enhanced gradually with the addition of $NEt_3$, and the peak at $m/z$ = 293.6 for $[Ru(bbpaH)(bpy)]^{2+}$ eventually disappears in the presence of 2 equiv. of $NEt_3$. No peak for dinuclear or larger cluster is found in mass spectra in the presence of $NEt_3$.

The $^1H$ NMR spectra of a selected region for $[Ru(bbpaH)(bpy)](PF_6)_2$ and the deprotonated complex $[Ru(bbpa)(bpy)](PF_6)$ in $[D_6]$acetone are shown in Figure 3. The six methylene protons are all inequivalent with respect to their chemical environment, and each $CH_2$ group displays an AB quartet (Figure 3a). Compared with the $^1H$ NMR spectra of the reported complex coordinated by the ligands bearing 2-pyridylmethyl moieties,[28] the quartet centered at $\delta$ = 5.08 is attributed to the $CH_2$ group attached to the benzimidazolyl unit, and the other two quartets to the $CH_2$ groups of the pyridylmethyl units. Upon addition

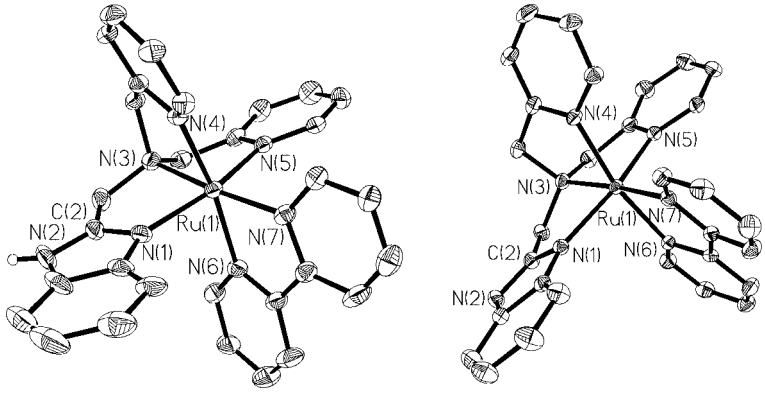


Figure 1. Thermal ellipsoid diagram of $[Ru(bpbaH)(bpy)]^{2+}$ (left) and $[Ru(bpba)(bpy)]^{+}$ (right). The ellipsoids are drawn at the 30% probability level, and only the benzimidazolyl hydrogen atom is shown. Selected bond lengths [Å] and angles [°] for $[Ru(bpbaH)(bpy)]^{2+}$ and $[Ru(bpba)(bpy)]^{+}$ [in brackets]: Ru(1)–N(1), 2.058(6) [2.100(3)]; Ru(1)–N(3), 2.119(6) [2.113(3)]; Ru(1)–N(4), 2.088(6) [2.100(3)]; Ru(1)–N(5), 2.088(6) [2.064(3)]; Ru(1)–N(6), 2.090(6) [2.090(3)]; Ru(1)–N(7), 2.072(6) [2.076(3)]; C(2)–N(1), 1.343(9) [1.366(4)]; C(2)–N(2), 1.354(10) [1.334(5)]; N(1)–Ru(1)–N(3), 82.2(2) [78.69(11)]; N(1)–Ru(1)–N(4), 82.3(2) [100.53(11)]; N(1)–Ru(1)–N(5), 161.4(2) [160.55(11)]; N(1)–Ru(1)–N(6), 86.6(2) [91.50(10)]; N(1)–Ru(1)–N(7), 103.1(2) [95.39(10)].

 © 2007 Wiley-VCH Verlag GmbH & Co. KGaA, Weinheim 

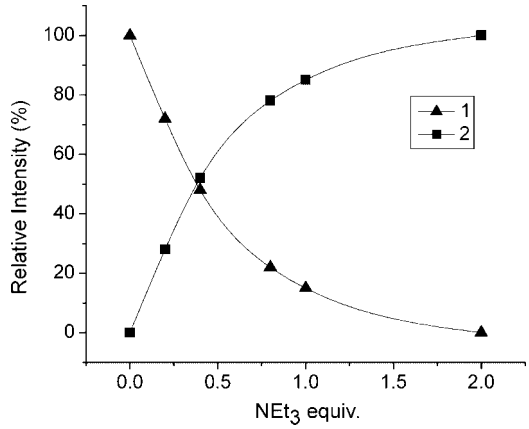


Figure 2. Plot of relative intensities of the peaks for $[Ru(bbpaH)(bpy)]^{2+}$ (trigonal) and $[Ru(bbpa)(bpy)]^{+}$ (square) vs. the equiv. of $NEt_3$ (0, 0.2, 0.4, 0.6, 1.0, 2.0 equiv.) in an acetone solution of complex **1** ($5 \times 10^{-4}$ M) monitored by ESI-MS.

of 2 equiv. of $NEt_3$, the signals for $[Ru(bbpaH)(bpy)](PF_6)_2$ completely disappear, and only the signals for $[Ru(bbpa)(bpy)](PF_6)$ are detected (Figure 3b), which suggests that no other reaction or decomposition occurs during the deprotonation process. Significant upfield shifts are observed in Figure 3b for the corresponding signals of three $CH_2$ groups of the deprotonated complex, which are expected for the monoanionic $bbpa^-$ ligand. The quartet at $\delta$ = 5.08 in the $^1H$ NMR spectrum of $[Ru(bbpaH)(bpy)](PF_6)_2$ changes to a singlet at $\delta$ = 4.78 upon deprotonation, indicating that the two protons on the $CH_2$ group of the benzimidazolylmethyl arm gain better symmetry in the deprotonated complex. The signals for the benzene ring of the deprotonated benzimidazolylmethyl ligand also apparently shift upfield. Sequential addition of 1 equiv. of $HClO_4$ recovers the original $^1H$ NMR spectrum of $[Ru(bbpaH)(bpy)](PF_6)_2$ as depicted in Figure 3a. This clearly indicates the complete reversibility of deprotonation and protonation.

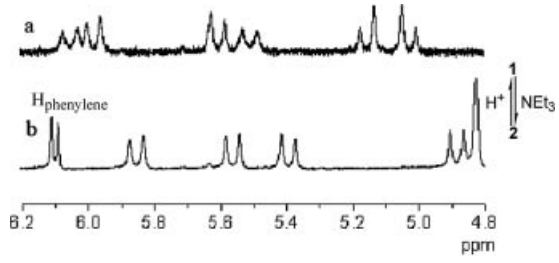


Figure 3. $^1H$ NMR spectra of a selected region: (a) $[Ru(bbpaH)(bpy)](PF_6)_2$ (**1**) and (b) $[Ru(bbpa)(bpy)](PF_6)$ (**2**) in $[D_6]$acetone.

The influence of deprotonation of the coordinated bbpaH ligand on the redox potential of the ruthenium centre was explored by cyclic voltammograms. The reversible $Ru^{II}/Ru^{III}$ oxidation wave of $[Ru(bbpaH)(bpy)](PF_6)_2$ appears at 0.69 V ($E_{1/2}$) vs. $Ag/AgNO_3$ in $CH_3CN$ and the deprotonated ruthenium complex $[Ru(bbpa)(bpy)](PF_6)$ displays the reversible oxidation wave at 0.26 V (Figures S1 and S2, see Supporting Information). It shows that the deprotonation of the coordinated bbpaH ligand can shift the redox potential of the ruthenium centre by 430 mV, which is larger than the shift (ca. 300–350 mV per proton) of the redox potentials reported for ruthenium, osmium and iron complexes with the ligands bearing multi-imidazolyl and -benzimidazolyl units,[9,14–16] but similar to the shift (350–420 mV) of the $Ru^{II}/Ru^{III}$ oxidation potentials reported for monoruthenium complexes with two bpy ligands and one triazole- or pyrazole-containing ligand.[21,23,29,30]

## Conclusions

We have prepared a pair of novel monoruthenium(II) complexes (**1** and **2**) with bpbaH or bpba and bipyridine as ligands. The structures of (benzimidazole)ruthenium complexes **1** and **2** were crystallographically characterized. The NH group of the bpbaH ligand readily undergoes a reversible protonation/deprotonation process, which is proven by spectroscopic and electrochemical evidence. The reversible protonation/deprotonation regulates the oxidation potential of the $Ru^{II}/Ru^{III}$ redox couple around 430 mV without changing the framework of the ruthenium complex.

## Experimental Section

**General Procedures:** All reactions and operations related to organometallic complexes were carried out under dry, oxygen-free dinitrogen with standard Schlenk techniques. Solvents were distilled prior to use with routine drying agents. Tetra-*n*-butylammonium hexafluorophosphate (TBAH) and bipyridine were used as received. Ligand (2-benzimidazolylmethyl)bis(2-pyridylmethyl)amine (bbpaH) and $[Ru(bbpa)(dmso)Cl](PF_6)$ were synthesized according to literature procedures for preparation of similar compounds.[25–27] $^1H$ NMR spectra were collected with a Varian INOVA 400 NMR spectrometer. Elemental analyses were performed with a Thermoquest-Flash EA 1112 elemental analyzer. Mass spectra were recorded with an HP 1100 MSD instrument.

**Complex $[Ru(bbpaH)(bpy)](PF_6)_2$ (1):** Complex **1** was synthesized according to a literature procedure for the preparation of the analogous complex $[Ru(TPA)(bpy)](PF_6)_2$.[27] The subsequent recrystallization of the crude product from acetone/diethyl ether afforded red crystals. Yield: 94 mg (37%). $^1H$ NMR ($CDCl_3$, 400 MHz): $\delta$ = 10.21 (d, 1 H, *J* = 5.6 Hz, Py of bbpaH), 9.47 (d, *J* = 6.0 Hz, 1 H, Py of bpy), 9.44 (d, *J* = 6.0 Hz, 1 H, Py of bpy), 8.80 (d, *J* = 8.2 Hz, 1 H, Py of bbpaH), 8.59 (d, *J* = 8.0 Hz, 1 H, Py of bbpaH), 8.42 (t, *J* = 8.2, 7.4 Hz, 1 H, Py of bbpaH), 8.21 (t, *J* = 5.6, 7.4 Hz, 1 H, Py of bbpaH), 7.96 (t, *J* = 8.0, 6.4 Hz, 1 H, Py of bbpaH), 7.94 (t, *J* = 5.8, 7.2 Hz, 1 H, Py of bpy), 7.78 (d, *J* = 7.8 Hz, 1 H, Py of bbpaH),7.77 (d, *J* = 5.8 Hz, 1 H, Py of bpy), 7.73 (t, *J* = 6.4, 6.4 Hz, 1 H, Py of bpy), 7.59 (d, *J* = 6.4 Hz, 1 H, Py of bpy), 7.53 (t, *J* = 7.8, 6.4 Hz, 1 H, Py of bbpaH), 7.53 (d, *J* = 6 Hz, 1 H, Py of bpy), 7.43 (d, *J* = 8.4 Hz, 1 H, Ph of bbpaH), 7.33 (t, *J* = 6.0, 6.4 Hz, 1 H, Py of bpy), 7.15 (t, *J* = 8.4, 7.2 Hz, 1 H, Ph of bbpaH), 7.00 (t, *J* = 7.2, 8.0 Hz, 1 H, Ph of bbpaH), 6.50 (d, *J* = 8.0 Hz, 1 H, Ph of bbpaH), 6.02 (d, *J* = 18.4 Hz, 1 H, CH of bbpaH), 5.96 (d, *J* = 18.4 Hz, 1 H, CH of bbpaH), 5.58 (d, *J* = 16.8 Hz, 1 H, CH of bbpaH), 5.48 (d, *J* = 17.6 Hz, 1 H, CH of bbpaH), 5.13 (d, *J* = 16.8 Hz, 1 H, CH of bbpaH), 5.01 (d, *J* = 17.6 Hz, 1 H, CH of bbpaH) ppm. ESI-MS: *m*/*z* = 293.5 $[Ru(bbpaH)(bpy)]^{2+}$.

 © 2007 Wiley-VCH Verlag GmbH & Co. KGaA, Weinheim 

$C_{31.5}H_{30}F_{12}N_7O_{0.5}P_2Ru$ (905.62): calcd. C 41.72, H 2.82, N 10.83; found C 41.75, H 2.73, N 10.83.

**Complex [Ru(bbpa)(bpy)](PF$_6$) (2):** Complex **1** (50 mg, 0.057 mmol) was dissolved in an NaOH-containing acetone/water (1:1, v/v) mixture with pH = 11. A majority of the acetone was removed in a rotary evaporator and the product precipitated as the fully deprotonated species [Ru(bbpa)(bpy)](PF$_6$). The solid was dissolved in hot $CHCl_3$. After cooling, dark-red crystals were obtained. Yield: 13 mg (31%). $^1$H NMR ($CDCl_3$, 400 MHz): $\delta$ = 10.15 (d, 1 H, $J$ = 6.0 Hz, Py of bbpa), 9.37 (d, $J$ = 5.6 Hz, 1 H, Py of bbpa), 9.32 (d, $J$ = 6.0 Hz, 1 H, Py of bpy), 8.71 (d, $J$ = 8.0 Hz, 1 H, Py of bbpa), 8.49 (d, $J$ = 8.0 Hz, 1 H, Py of bbpa), 8.30 (t, $J$ = 6.8, 8.0 Hz, 1 H, Py of bbpa), 8.07 (t, $J$ = 6.0, 6.8 Hz, 1 H, Py of bbpa), 7.98 (d, $J$ = 5.6 Hz, 1 H, Py of bpy), 7.81 (t, $J$ = 7.2, 8.0 Hz, 1 H, Py of bbpa), 7.68 (t, $J$ = 7.2, 7.6 Hz, 1 H, Py of bpy), 7.58 (t, $J$ = 7.6, 6.8 Hz, 1 H, Py of bpy), 7.57 (d, $J$ = 7.6 Hz, 1 H, Py of bpy), 7.39 (t, $J$ = 5.6, 7.2 Hz, 1 H, Py of bbpa), 7.38 (d, $J$ = 6.8 Hz, 1 H, Py of bpy), 7.20 (d, $J$ = 8.4 Hz, 1 H, Ph of bbpa), 7.17 (t, $J$ = 6.0, 7.2 Hz, 1 H, Py of bpy), 7.14 (t, $J$ = 5.6, 7.6 Hz, 1 H, Py of bpy), 6.64 (t, $J$ = 8.4, 7.6 Hz, 1 H, Ph of bbpa), 6.51 (t, $J$ = 7.6, 7.6 Hz, 1 H, Ph of bbpa), 6.10 (d, $J$ = 7.6 Hz, 1 H, Ph of bbpa), 5.85 (d, $J$ = 16.8 Hz, 1 H, CH of bbpa), 5.56 (d, $J$ = 16.4 Hz, 1 H, CH of bbpa), 5.39 (d, $J$ = 16.8 Hz, 1 H, CH of bbpa), 4.89 (d, $J$ = 16.4 Hz, 1 H, CH of bbpa), 4.83 (s, 2 H, $CH_2$ of bbpa) ppm. ESI-MS: $m/z$ = 586.1 [Ru(bbpa)(bpy)]$^+$. $C_{31}H_{27}Cl_3F_6N_7PRu$ (849.99): calcd. C 43.80, H 3.20, N 11.54; found C 44.79, H 3.27, N 11.68.

**X-ray Structure Determination:** The single-crystal X-ray diffraction data were collected with a Siemens SMART CCD diffractomer, with graphite-monochromated Mo-$K_\alpha$ radiation ($\lambda$ = 0.071073 Å) at 153 K using the $\omega$-2$\theta$ scan mode. Data processing was accomplished with the SAINT processing program.[31] Intensity data were corrected for absorption by the SADABS program.[32] All structures were solved by direct methods and refined on $F^2$ by full-matrix least-squares methods using the SHELXTL 97 program package.[33] All non-hydrogen atoms were refined anisotropically. Hydrogen atoms were located by geometrical calculation. Crystal data for [Ru(bbpaH)(bpy)](PF$_6$)$_2$ (**1**): $C_{30.50}H_{29}F_{12}N_7O_{0.50}P_2Ru$, $M$ = 892.62, monoclinic, space group $P2(1)/n$, $a$ = 12.4535(14), $b$ = 19.742(2), $c$ = 13.6163(15) Å, $\beta$ = 91.270°, $V$ = 3346.8(6) Å$^3$, $Z$ = 4, $\rho_{calcd.}$ = 1.772 g cm$^{-3}$, $\mu$ = 0.67 mm$^{-1}$, $T$ = 153(2) K, 6565 reflections measured, 4243 unique, $R_{int}$ = 0.0650, $R_1$ = 0.0787 and $wR_2$ = 0.1138 (all data), GOF = 1.017. CCDC-641251. Crystal data for [Ru(bbpa)(bpy)](PF$_6$) (**2**): $C_{32}H_{29}Cl_5F_6N_7PRu$, $M$ = 934.91, triclinic, space group $P1$, $a$ = 10.6539(7), $b$ = 13.1807(9), $c$ = 13.9109(9) Å, $\alpha$ = 75.291, $\beta$ = 75.424, $\gamma$ = 84.229°, $V$ = 1827.2(2) Å$^3$, $Z$ = 2, $\rho_{calcd.}$ = 1.699 g cm$^{-3}$, $\mu$ = 0.91 mm$^{-1}$, $T$ = 153(2) K, 7046 reflections measured, 5985 unique, $R_{int}$ = 0.0192, $R_1$ = 0.0531, $wR_2$ = 0.1123 (all data), GOF = 1.028. CCDC-641252. These data can be obtained free of charge from The Cambridge Crystallographic Data Centre via www.ccdc.cam.ac.uk/data_request/cif.

**Supporting Information** (see footnote on the first page of this article): Figures S1 and S2 give cyclic voltammograms of [Ru(bbpaH)(bpy)](PF$_6$)$_2$ (**1**) and [Ru(bbpa)(bpy)](PF$_6$) (**2**).

## Acknowledgments

We are grateful to the Chinese National Natural Science Foundation (Grant nos. 20471013 and 20633020), the Swedish Energy Agency, the Swedish Research Council and K & A Wallenberg Foundation for financial support of this work.

[1] M. Y. Okamura, G. Feher, *Annu. Rev. Biochem.* **1992**, *61*, 861–896.
[2] G. T. Babcock, B. A. Barry, R. J. Debus, C. W. Hoganson, M. Atamian, L. McIntosh, I. Sithole, C. F. Yocum, *Biochemistry* **1989**, *28*, 9557–9565.
[3] B. Maison-Peteri, B. G. Malmstrom, *Biochemistry* **1989**, *28*, 3156–3160.
[4] J. E. Morgan, M. Wikstrom, *Biochemistry* **1991**, *30*, 948–958.
[5] A. L. Feig, S. J. Lippard, *Chem. Rev.* **1994**, *94*, 759–805.
[6] T. Claudia, C. K. Chang, G. E. Leroi, R. I. Cukier, D. G. Nocera, *J. Am. Chem. Soc.* **1992**, *114*, 4013–4015.
[7] J. P. Kirby, J. A. Roberts, D. G. Nocera, *J. Am. Chem. Soc.* **1997**, *119*, 9230–9236.
[8] B. S. Hammes, M. T. Kieber-Emmons, R. Sommer, A. L. Rheingold, *Inorg. Chem.* **2002**, *41*, 1351–1353.
[9] R. F. Carina, L. Verzegnassi, A. F. Williams, *Chem. Commun.* **1998**, 2681–2682.
[10] S. Han, L. D. Eltis, K. N. Timmis, S. W. Muchmore, J. T. Bolin, *Science* **1995**, *270*, 976–980.
[11] J. C. Boyington, B. J. Gaffney, M. Arnzel, *Science* **1993**, *260*, 1482–1486.
[12] P. L. Roach, I. J. Clifton, V. Fülöp, K. Harlos, G. J. Barton, J. Hajdu, I. Andersson, C. J. Schofield, J. E. Baldwin, *Nature* **1995**, *375*, 700–704.
[13] A. M. Bond, M. Haga, *Inorg. Chem.* **1986**, *25*, 4507–4514.
[14] M. Haga, T. Ano, K. Kano, S. Yamabe, *Inorg. Chem.* **1991**, *30*, 3843–3849.
[15] M. Haga, T. Ano, K. Kano, K. Nozaki, T. Ohno, *J. Chem. Soc. Dalton Trans.* **1994**, 263–272.
[16] M. Haga, M. M. Ali, A. S. Koseki, K. Fujimoto, A. Yoshimura, K. Nozaki, T. Ohno, K. Nakajima, D. J. Stufkens, *Inorg. Chem.* **1996**, *35*, 3335–3347.
[17] S. Baitalik, U. Flörke, K. Nag, *Inorg. Chem.* **1999**, *38*, 3296–3308.
[18] S. Baitalik, P. Bag, K. Nag, *Polyhedron* **2002**, *21*, 2481–2488.
[19] S. Baitalik, B. Dutta, K. Nag, *Polyhedron* **2004**, *23*, 913–919.
[20] R. Hage, J. G. Haasnoot, J. Reedijk, R. Wang, J. G. Vos, *Inorg. Chem.* **1991**, *30*, 3263–3269.
[21] H. E. B. Lempers, J. G. Haasnoot, J. Reedijk, R. Hage, F. M. Weldon, J. G. Vos, *Inorg. Chim. Acta* **1994**, *225*, 67–74.
[22] C. D. Pietro, S. Serroni, S. Campagna, M. T. Gandolfi, R. Ballardini, S. Fanni, W. R. Browne, J. G. Vos, *Inorg. Chem.* **2002**, *41*, 2871–2878.
[23] C. Sens, M. Rodríguez, I. Romero, A. Llobet, *Inorg. Chem.* **2003**, *42*, 2040–2048.
[24] C. Sens, M. Rodríguez, I. Romero, A. Llobet, *Inorg. Chem.* **2003**, *42*, 8385–8394.
[25] I. P. Evans, A. Spencer, G. Wilkinson, *J. Chem. Soc. Dalton Trans.* **1973**, 204–209.
[26] M. Psacaly, M. Duda, F. Schweppe, K. Zurlinden, F. K. Müller, B. Krebs, *J. Chem. Soc. Dalton Trans.* **2001**, 828–837.
[27] J. Bjernemose, A. Hazell, C. J. McKenzie, M. F. Mahon, L. P. Nielsen, P. R. Raitby, O. Simonsen, H. Toftlund, J. A. Wolny, *Polyhedron* **2003**, *22*, 875–885.
[28] T. Kojima, T. Sakamoto, Y. Matsuda, *Inorg. Chem.* **2004**, *43*, 2243–2245.
[29] B. D. J. R. Fennema, R. Hage, J. G. Haasnoot, J. Reedijk, *Inorg. Chim. Acta* **1990**, *171*, 223–228.
[30] H. A. Nieuwenhuis, J. G. Hassnoot, R. Hage, J. Reedijk, T. L. Snoeck, D. J. Stufkens, J. G. Vos, *Inorg. Chem.* **1991**, *30*, 48–54.
[31] Software packages *SMART* and *SAINT*, Siemens Energy & Automation Inc., Madison, Wisconsin, **1996**.
[32] G. M. Sheldrick, *SADABS, Absorption Correction Program*, University of Göttingen, Germany, **1996**.
[33] G. M. Sheldrick, *SHELXTL 97, Program for the Refinement of Crystal Structure*, University of Göttingen, Germany, **1997**.

Received: May 25, 2007
Published Online: August 7, 2007

 © 2007 Wiley-VCH Verlag GmbH & Co. KGaA, Weinheim 

DOI: 10.1002/ejic.200700481

# Facile Synthesis of Aluminum-Bridged [3,3,3]Cyclophanes by Hydroalumination

**Werner Uhl,*[a] Alexander Hepp,[a] Madhat Matar,[a] and Andrej Vinogradov[a]**

**Keywords:** Aluminum / Hydroalumination / Cage compounds / Cyclophanes

The reaction of 1,3,5-tris(3,3-dimethyl-1-butinyl)benzene $C_6H_3(C{\equiv}C{-}CMe_3)_3$ with the dialkylaluminum hydrides $HAl(CMe_3)_2$ and $HAl(CH_2CMe_3)_2$ gave the addition of one Al–H bond to each C–C triple bond (hydroalumination). Spontaneous condensation by the release of the corresponding trialkylaluminum derivatives afforded [3,3,3]cyclophane derivatives **6** and **7** in which three tricoordinate Al atoms are in the bridging positions between two functionalized benzene rings. The aluminum atoms behave as Lewis acids, and treatment with thf yielded adduct **6**·3thf.
(© Wiley-VCH Verlag GmbH & Co. KGaA, 69451 Weinheim, Germany, 2007)

## Introduction

The addition of Al–H bonds to unsaturated compounds containing C=C and C≡C bonds (hydroalumination) is a powerful method for the reduction of organic compounds and the generation of new hydrocarbons.[1,2] In most cases, the organoaluminum intermediates were not isolated, but the organic components were released by hydrolysis. Other derivatives are accessible by particular oxidative workup such as halogenation.[3] Thus, suggestions concerning the structure of the organoaluminum intermediates are rather speculative in most cases. A preferred *cis* addition was postulated owing to the constitutions of the finally isolated hydrocarbons.[1] As was shown by our group only recently,[4,5] silyl-substituted alkynes gave the predicted products of hydroalumination with a dialkylaluminum group attached to that carbon atom that also bears the trimethylsilyl group (**1** and **2** in Scheme 1). This particular constitution may be favored by two reasons. Owing to the electronegativity difference between both elements, the carbon atom attached to silicon bears a negative partial charge and, hence, may be attacked preferentially by the positively charged alumi-

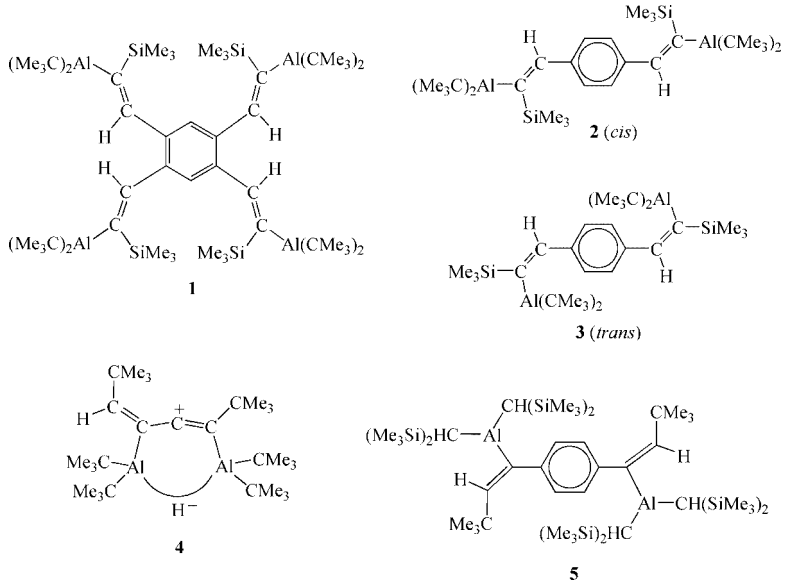


Scheme 1.

num ions. Furthermore, the enhanced negative charge at this position in the product, which is introduced by the polarity of the freshly formed Al–C bond, can be stabilized by

[a] Institut für Anorganische und Analytische Chemie der Universität Münster
Corrensstraße 30, 48149 Münster, Germany
Fax: +49-251-8336660

 © 2007 Wiley-VCH Verlag GmbH & Co. KGaA, Weinheim 

hyperconjugation with the Si–C bonds. In all cases the *cis* addition products are formed with the hydrogen and aluminum atoms on the same side of the C=C bonds. A *cis*/*trans* rearrangement was observed only for **3** (Scheme 1) upon elongated heating of solutions in benzene.[4] In contrast, spontaneous rearrangement occurred upon the similar addition of Ga–H bonds to silylalkynes (hydrogallation).[6] Exceptions were observed only for the reactions of the sterically shielded di(*tert*-butyl)gallium hydride. The products of these reactions contain up to three coordinatively unsaturated, tricoordinate aluminum or gallium atoms; however, only the *trans* isomers are able to act as powerful chelating Lewis acids. Secondary reactions with the release of trialkylaluminum derivatives occurred upon treatment of dialkylaluminum alkynides with dialkylaluminum hydrides. Clusters similar to carbaboranes were formed that contained aluminum and carbon atoms and had a delocalized bonding situation.[7] Analogous reactions of gallium compounds afforded heteroadamantane-type molecules possessing localized Ga–C bonds.[8] An unexpected and unprecedented product was formed upon treatment of di(*tert*-butyl)butadiyne with di(*tert*-butyl)aluminum hydride. C–H bond activation by hyperconjugation with Al–C bonds and the chelating coordination of the resulting hydride anion by two aluminum atoms afforded **4** as a singular, persistent butadienyl cation (Scheme 1), which was zwitterionic and did not require the application of a strictly noncoordinating counterion for its stabilization.[9] In contrast, benzene centered *tert*-butylethynes showed a more complicated reaction behavior. Secondary reactions occurred that could be clarified completely for the more selective hydrogallation reactions only.[10] Bulky substituents attached to the aluminum atoms as in $R_2Al–H$ [R = $CH(SiMe_3)_2$] prevented these secondary processes.[11] The persistent simple addition products, **5** (Scheme 1), had the aluminum atoms attached to the carbon atoms in the α position to the aromatic ring. This particular constitution may allow optimum mesomeric stabilization of the negative charge, which is localized at these atoms and resulted from the polarity of the Al–C bonds. We report here the first successful reactions of that type conducted with sterically less-shielded dialkylaluminum hydrides.

## Results and Discussion

Complete consumption of the starting compounds was observed when mixtures of 1,3,5-tris(*tert*-butylethynyl)benzene and the corresponding dialkylaluminum hydrides in *n*-pentane or *n*-hexane were stirred at r.t. for about 20 h [Equation (1)]. Thus, the hydroalumination reactions are much faster than hydrogallation reactions, which do not start at ambient temperature at all and require boiling *n*-hexane over a period of about 16 h for completion.[6,10] The difference in the reaction behaviors of the hydrides may depend on the lower polarity of the Ga–H bond relative to the Al–H bonds. Two aluminum hydrides $R_2Al–H$ (R = $CMe_3$, $CH_2CMe_3$) were employed. The $^1H$ NMR spectroscopic analysis of the reaction courses verified the release of the corresponding trialkylaluminum derivatives, tri(*tert*-butyl)- and trineopentylaluminum, respectively, in both cases. The reaction of di(*tert*-butyl)aluminum hydride proved to be complicated. Unknown byproducts were formed, and the yield of compound **6** varied between 10 and 80%. Despite intensive efforts with dozens of experiments, we did not succeed in finding suitable conditions for a more reproducible reaction course. A second problem arose from the poor crystallization behavior, which made the purification by recrystallization from different solvents rather difficult. Sometimes solutions of **6** must be stored at –45 °C for several weeks to isolate colorless crystals of the product. In contrast, the reaction of dineopentylaluminum hydride with the trialkyne was rather unproblematic. Colorless product **7** precipitated directly from the reaction mixture after concentration and cooling to –30 °C. The pure compound was isolated in 63% yield. Smaller substituents attached to aluminum such as methyl or ethyl groups or the application of the dialkyne 1,4-bis(*tert*-butylethynyl)benzene resulted in the formation of insoluble products or complicated reaction mixtures. Thus far, we were not able to isolate any product in a pure form or to unambiguously identify one component of the reaction mixtures.

Schematic drawings of the molecular structures are given in Equation (1). The integration ratio of the $^1H$ NMR spectra clearly confirms the condensation reaction and the formation of cyclophane-type molecules. The resonances of the vinylic hydrogen atoms and the protons attached to the aromatic ring are close together and resonate at $\delta$ = 6.00 and 6.32 ppm for **6** and at $\delta$ = 6.24 and 6.22 ppm for **7**. The

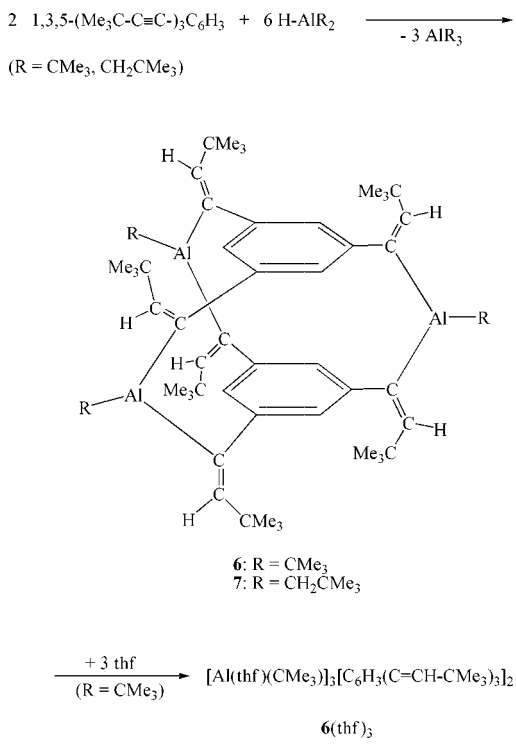


(1)

 © 2007 Wiley-VCH Verlag GmbH & Co. KGaA, Weinheim 

carbon atoms of the C=C bonds show chemical shifts of $\delta$ = 152 and 156 ppm on average; the resonances at higher field belong to the carbon atoms attached to the phenyl rings and to the aluminum atoms. This situation is in complete accordance with data obtained for the corresponding gallium compounds.[10]

Crystal-structure determinations verified the condensation reactions by the release of the corresponding trialkylaluminum derivatives and the formation of cyclophane-type molecules. All C≡C bonds of the starting trialkyne were reduced by the addition of Al–H bonds to yield alkenyl groups containing C=C bonds. The aluminum atoms attacked exclusively those carbon atoms of the triple bonds that are in the α position to the aromatic ring. Aluminum and hydrogen adopt a *cis* configuration across the double bonds, which is the expected arrangement under kinetically controlled conditions. Spontaneous *cis*/*trans* rearrangement with the formation of the *trans* products occurred only with the addition of Ga–H bonds to trimethylsilyl-substituted alkynes.[6] Condensation and release of trialkylaluminum species from the hypothetical intermediates containing dialkylaluminum groups attached to the C=C bonds gave three C–Al–C bridges between two aromatic rings with coordinatively unsaturated three-coordinate aluminum atoms. Thus, these compounds may be described as [3,3,3]cyclophanes. The molecular structures are depicted in Figures 1, 2, and 3. Considerable problems occurred with respect to the generation of single crystals and the determination of the molecular structure of compound **6** (see Experimental Section). Severe disorder was observed for two of the three independent molecules, which prevents a concise discussion of all the structural parameters. However, the result can be taken as clear structural evidence for the suggested constitution. Further evidence was achieved by the generation and structural characterization of the thf adduct, **6**·3thf, in which the cyclophane-type structure is retained and one thf molecule is bonded to each of its aluminum atoms. This compound is not only valuable for the structural characterization of **6**. It impressively shows that this particular type of compound is suitable to act as multipodal Lewis acids. Relevant bond lengths and angles of the adduct are quite similar to those of the ether-free products. The phenyl rings are almost ideally coplanar with angles between the normals of both rings smaller than 1°. They are not in an ideal

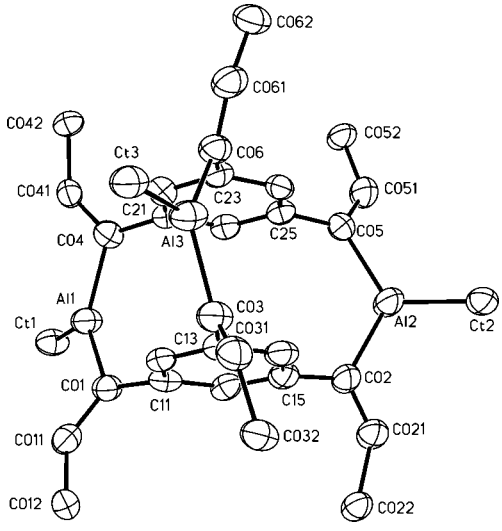


Figure 1. Molecular structure and numbering scheme of compound **6**. The thermal ellipsoids are drawn at the 40% probability level. Methyl groups and hydrogen atoms are omitted for clarity. The molecule located on a general position (see Experimental Section) is considered only. Selected bond lengths [pm] and angles [°]: Al*x*–C0*y* (*x* = 1 to 3; *y* = 1 to 6) 195.7 (av.), Al*x*–Ct*x* 198.4 (av.), C0*y*=C0*y*1 134.6 (av.), C0*y*–Al*x*–C0*y* 120.6 (av.), Al*x*–C0*y*–C0*y*1 115.9 (av.), C0*y*–C0*y*1–C0*y*2 133.0 (av.).

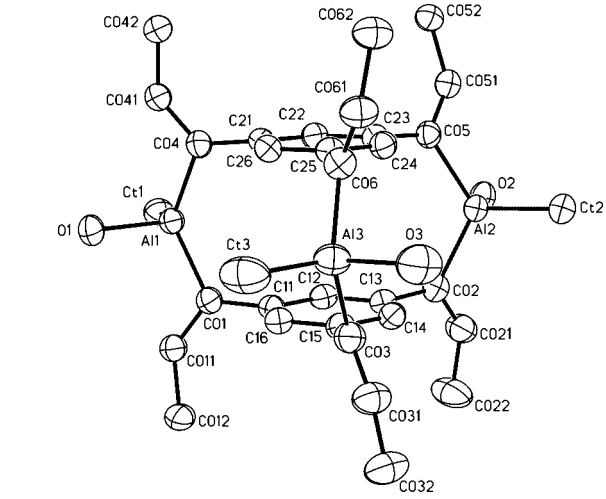


Figure 2. Molecular structure and numbering scheme of compound **6**·3thf. The thermal ellipsoids are drawn at the 40% probability level. Methyl groups and hydrogen atoms are omitted for clarity. Only the oxygen atoms of the thf molecules are considered. Selected bond lengths [pm] and angles [°]: Al*x*–C0*y* (*x* = 1 to 3, *y* = 1 to 6) 198.8 (av.), Al*x*–Ct*x* 201.2(av.), Al*x*–O*x* 193.0 (av.), C0*y*=C0*y*1 134.6 (av.), C0*y*–Al*x*–C0*y* 119.8 (av.), Al*x*–C0*y*–C0*y*1 115.3 (av.), C0*y*–C0*y*1–C0*y*2 133.9 (av.).

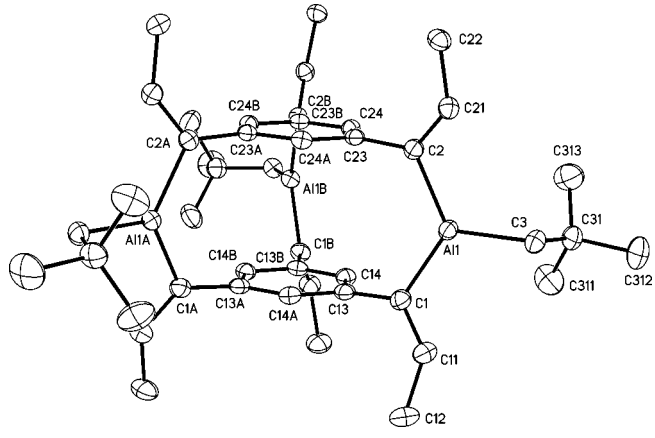


Figure 3. Molecular structure and numbering scheme of compound **7**. The thermal ellipsoids are drawn at the 40% probability level. Methyl groups and hydrogen atoms are omitted for clarity. Selected bond lengths [pm] and angles [°]: Al1–C1 195.6(2), Al1–C2 196.2(1), Al1–C3 196.9(2), C1–C11 134.6(2), C2–C21 134.6(2), C1–Al1–C2 122.40(6), Al1–C1–C11 114.7(1), Al1–C2–C21 112.9(1), C1–C11–C12 132.6(2), C2–C21–C22 132.6(1).

 © 2007 Wiley-VCH Verlag GmbH & Co. KGaA, Weinheim 

eclipsed arrangement. This may also be deduced from the fact that the normals of the planes of the benzene rings and the C–Al–C groups deviate considerably from the ideal value of 90° (75 to 87°). The distance between the benzene rings of one molecule is close to 360 pm on average, which is in the characteristic range of van der Waals interactions.[12] Thus, the cavity seems to be suitable for the coordination of transition-metal atoms, and it may be an interesting task for future work to generate those products containing an encapsulated metal atom. The C=C bond lengths (135 pm on average) correspond to standard values.[13] The inner cage Al–C distances are quite similar to those including the terminal alkyl groups. Thus, there is no hint of steric stress in the cages. The angles at the aluminum atoms are close to 120°. Expectedly, only in the thf adduct did we observe an approach of the angles to the ideal tetrahedral angle with the exception of the inner cage angle, which remained unchanged relative to the ether-free compounds (about 120° on average).

## Experimental Section

**General:** All procedures were carried out under an atmosphere of purified argon. Cyclopentane, *n*-pentane, and *n*-hexane were dried with $LiAlH_4$; thf with Na/benzophenone. Di(*tert*-butyl)aluminum hydride,[14] dineopentylaluminum hydride[15] and 1,3,5-tris(*tert*-butylethynyl)benzene[10] were obtained according to literature procedures. The assignments of the signals in the NMR spectra were made on the basis of HMBC, HSQC, ROESY, and DEPT135 data.

**6:** A solution of 1,3,5-tris(*tert*-butylethynyl)benzene (0.227 g, 0.714 mmol) in *n*-hexane (20 mL) was added dropwise to a cooled (–10 °C) solution of di(*tert*-butyl)aluminum hydride (0.304 g, 2.14 mmol) in *n*-hexane (20 mL). The mixture was stirred at r.t. for 24 h. The solvent was distilled off in vacuo, and the residue was thoroughly evacuated ($10^{-3}$ Torr) to partially remove the tri(*tert*-butyl)aluminum byproduct. The oily product was dissolved in cyclopentane and stored at –45 °C for several weeks to afford **6** as a colorless solid. Yield: 0.080 g (25%). M.p. (argon, sealed capillary): 185 °C. $^1$H NMR (400 MHz, $C_6D_6$): $\delta$ = 1.11 (s, 54 H, $CMe_3$ of alkenyl group), 1.37 (s, 27 H, Al-$CMe_3$), 6.00 (s, 6 H, vinylic H), 6.32 (s, 6 H, benzene H) ppm. $^{13}$C NMR (100 MHz, $C_6D_6$): $\delta$ = 19.6 (Al-*C*Me$_3$), 30.9 (Al-C*Me*$_3$), 32.0 (*C*Me$_3$ of the alkenyl group), 37.4 (C*Me*$_3$ of the alkenyl group), 122.0 (CH of the aromatic rings), 145.9 (*ipso*-C), 150.1 (Al-*C*=C), 154.8 (Al-C=*C*) ppm. IR (CsBr plates, paraffin): $\tilde{\nu}$ = 1580 (vs, *v*C=C), phenyl, 1460 (vs, paraffin), 1404 (m, $\delta CH_3$), 1381 (s, paraffin), 1359 (vs, $\delta CH_3$), 1223 (s), 1200 (vs), 1135 (w), 1034 (m), 991 (s), 934 (m), 912 (s), 882 (s), 808 (s), 734 (s), 710 (s, *v*CC, $\delta$CH), 624 (vs), 573 (m), 538 (vw), 487 (s), 439 (w), 386 (m), 361 (s, *v*AlC, phenyl, $\delta$CC) cm$^{-1}$. $C_{60}H_{93}Al_3$ (895.3): C 80.5, H 10.5; found C 79.8, H 10.3.

**6·3thf:** An oily residue out of the synthesis of compound **6** was dissolved in thf. Slow concentration of the solution at r.t. over several days afforded crystals of the thf adduct of compound **6**. M.p. (argon, sealed capillary): **6**·3thf did not melt below 230 °C. $^1$H NMR (400 MHz, [D$_8$]thf): $\delta$ = 0.89 (s, 54 H, $CMe_3$ of alkenyl group), 1.08 (s, 27 H, Al-$CMe_3$), 1.77 (m, 12 H, thf), 3.62 (m, 12 H, thf), 5.54 (s, 6 H, vinylic H), 5.92 (s, 6 H, benzene H) ppm. $^{13}$C NMR (100 MHz, [D$_8$]thf): $\delta$ = 15.5 (Al-*C*Me$_3$), 26.3 (thf), 31.8 (Al-C*Me*$_3$), 32.7 (*C*Me$_3$ of the alkenyl group), 37.0 (C*Me*$_3$ of the alkenyl group), 68.2 (thf), 119.9 (CH of the aromatic rings), 147.1 (*ipso*-C), 147.8 (Al-*C*=C), 155.9 (Al-C=*C*) ppm. IR (CsBr plates, paraffin): $\tilde{\nu}$ = 1578 (vs), 1556 (vs, *v*C=C), phenyl, 1465 (vs, paraffin), 1403 (m, $\delta CH_3$), 1380 (vs, paraffin), 1355 (vs), 1318 (w), 1299 (w), 1281 (w), 1248 (m, $\delta CH_3$), 1224 (vs), 1200 (vs), 1181 (s), 1133 (m), 1071 (m), 1037 (vs), 1003 (vs), 970 (vs), 959 (m), 934 (s), 911 (vs), 893 (vs), 854 (vs), 795 (s), 733 (s), 707 (s, *v*CC, *v*CO, $\delta$CH), 688 (m), 651 (m), 616 (vs), 571 (s), 549 (s), 484 (vs), 442 (s), 394 (vs), 359 (vs), 336 (s, *v*AlC, *v*AlO, phenyl, $\delta$CC) cm$^{-1}$.

**7:** A solution of 1,3,5-tris(*tert*-butylethynyl)benzene (0.244 g, 0.767 mmol) in *n*-pentane (10 mL) was treated with a solution of dineopentylaluminum hydride (0.392 g, 2.30 mmol) in *n*-pentane (20 mL) at r.t. The mixture was stirred under these conditions for 20 h. After concentration and cooling of the solution to –30 °C, product **7** precipitated as a colorless amorphous powder. Yield: 0.227 g (63%). M.p. (argon, sealed capillary): 140 °C (dec.). $^1$H NMR (400 MHz, $C_6D_6$): $\delta$ = 0.76 (s, 6 H, Al-$CH_2$), 1.13 (s, 54 H, $CMe_3$ of alkenyl group), 1.31 (s, 27 H, $CMe_3$ of neopentyl), 6.22 (s, 6 H, benzene H), 6.24 (s, 6 H, vinylic H) ppm. $^{13}$C NMR (100 MHz, $C_6D_6$): $\delta$ = 25.2 (Al-$CH_2$), 31.9 (*C*Me$_3$ of neopentyl and C*Me*$_3$ of the alkenyl groups), 35.8 (C*Me*$_3$ of neopentyl), 37.4 (*C*Me$_3$ of the alkenyl group), 121.1 (CH of the aromatic rings), 145.3 (*ipso*-C), 153.3 (Al-*C*=C), 157.7 (Al-C=*C*) ppm. IR (CsBr plates, paraffin): $\tilde{\nu}$ = 1574 (s, br. *v*C=C, phenyl), 1454 (vs, paraffin), 1410 (w, $\delta CH_3$), 1373 (s, paraffin), 1293 (w), 1254 (w, $\delta CH_3$), 1225 (s), 1202 (s), 1136 (m), 1115 (s), 1094 (m), 1028 (vs), 910 (s), 895 (s), 880 (s), 824 (m), 802 (m), 739 (s), 710 (s, *v*CC, $\delta$CH), 682 (s), 646 (s), 620 (w), 600 (m), 590 (s), 570 (m), 527 (m), 517 (m), 467 (s), 430 (s, *v*AlC, phenyl, $\delta$CC) cm$^{-1}$. MS (EI, 20 eV): *m*/*z* = 937 (100), 938 (72) $[M + H]^+$, 866 (28), 867 (17) $[M - CH_2CMe_3]^+$. $C_{63}H_{99}Al_3$ (937.4): calcd. C 80.7, H 10.6, Al 8.6; found C 80.2, H 11.3, Al 8.2.

**Crystal Structure Determinations of 6, 6·3thf, and 7:** Single crystals of solvent-free **6** could only be obtained with enormous difficulties by recrystallization from *n*-pentane (20/–15 °C). It crystallized in the hexagonal space group $P6_3/m$ with 20 molecules in the unit cell. Twelve symmetry related molecules are in general positions. The molecular structure of that species could be refined to reasonable final structural parameters. Six molecules are localized on crystallographic mirror planes. They are severely disordered in particular with respect to the bridging C–Al–C groups. The refinement was done by severe restrictions and gave an insufficient result only, but verified clearly the occurrence of a structure identical to that of the molecule on a general position. Two further molecules are localized on $\bar{6}$ axes. They show a similar disorder of the C–Al–C bridges, but the refinement gave a more consistent result. Overall, the value of that structure determination should be seen in structural evidence only; it clearly does not meet the standard requirement of a sufficiently high quality. Crystals of **6**·3thf were generated by slow concentration of a thf solution at r.t. over several days. The crystals enclosed a thf molecule per formula unit of the adduct, which was refined with atomic occupation factors of 0.5. Recrystallization of the amorphous solid product from *n*-pentane afforded single crystals of **7**, which enclose strongly disordered solvent molecules. The cyclophane molecules of **7** reside on crystallographic threefold rotation axes. Crystal data, data collection parameters, and structure refinement details are given in Table 1. The crystallographic data of **6** and **6**·3thf were collected with a STOE image plate diffractometer, those of **7** were determined with a BRUKER apex diffractometer. The structures were solved by direct methods and refined with the program SHELXL-97[18] by a full-matrix least-squares method based on $F^2$.

 © 2007 Wiley-VCH Verlag GmbH & Co. KGaA, Weinheim 

Table 1. Crystal data and structure refinement for compounds **6**, **6**·3thf, and **7**.[a]

| | **6** | **6**·3thf | **7** |
|---|---|---|---|
| Formula | $C_{60}H_{93}Al_3$ | $C_{74}H_{121}Al_3O_{3.5}$ | $C_{64.67}H_{99}Al_3$ |
| Crystal system | hexagonal | monoclinic | rhombohedral |
| Space group[16] | $P6_3/m$ (no. 176) | $P2_1/c$ (no. 14) | $R\bar{3}$ (no. 148) |
| $Z$ | 20 | 4 | 6 |
| $T$ [K] | 193(2) | 193(2) | 153(2) |
| $d_{calcd.}$ [g cm$^{-3}$] | 0.984 | 0.980 | 0.978 |
| $a$ [pm] | 2803.53(9) | 2327.5(2) | 1647.47(6) |
| $b$ [pm] | 2803.53(9) | 2320.7(1) | 1647.47(6) |
| $c$ [pm] | 4438.7(2) | 1444.4(1) | 4150.3(2) |
| $\alpha$ [°] | 90 | 90 | 90 |
| $\beta$ [°] | 90 | 94.084(7) | 90 |
| $\gamma$ [°] | 120 | 90 | 120 |
| $V$ [$10^{-30}$ m$^3$] | 30213(2) | 7782.0(9) | 9755.4(7) |
| $\mu$ [mm$^{-1}$] | 0.095 | 0.089 | 0.092 |
| Crystal size [mm] | $0.24 \times 0.16 \times 0.10$ | $0.26 \times 0.14 \times 0.09$ | $0.37 \times 0.33 \times 0.26$ |
| Radiation | Mo-$K_\alpha$; graphite monochromator | Mo-$K_\alpha$; graphite monochromator | Mo-$K_\alpha$; graphite monochromator |
| $\theta$ range [°] | $1.24 \le \theta \le 24.01$ | $1.24 \le \theta \le 26.31$ | $1.73 \le \theta \le 31.26$ |
| Index ranges | $-32 \le h \le 32$ | $-28 \le h \le 28$ | $-23 \le h \le 23$ |
| | $-32 \le k \le 31$ | $-28 \le k \le 28$ | $-23 \le k \le 23$ |
| | $-50 \le l \le 50$ | $-18 \le l \le 17$ | $-60 \le l \le 59$ |
| Independent reflections | 16024 [$R_{int}$ = 0.2221] | 15640 [$R_{int}$ = 0.1161] | 6632 [$R_{int}$ = 0.0418] |
| Reflections $I > 2\sigma(I)$ | 5435 | 6413 | 4908 |
| Parameters | 1107 | 776 | 255 |
| $R = \Sigma\|\|F_o\| - \|F_c\|\|/\Sigma\|F_o\|$ [$I > 2\sigma(I)$] | 0.1005 | 0.0608 | 0.0635 |
| $wR_2 = \{\Sigma w(\|F_o\|^2 - \|F_c\|^2)^2/\Sigma\|F_o\|^2\}^{1/2}$ (all data) | 0.2740 | 0.1735 | 0.1875 |
| Max./min. residual [$10^{30}$ e m$^{-3}$] | 0.908/–0.373 | 0.728/–0.273 | 0.472/–0.260 |

[a] Program SHELXL-97;[17] solutions by direct methods, full-matrix refinement with all independent structure factors.

## Acknowledgments

We are grateful to the Deutsche Forschungsgemeinschaft and the Fonds der Chemischen Industrie for generous financial support.

[1] a) E. Winterfeldt, *Synthesis* **1975**, *10*, 617–630; b) J. Marek, J.-F. Normant, *Chem. Rev.* **1996**, *96*, 3341–3367; c) J. J. Eisch in *Comprehensive Organic Chemistry* (Eds.: B. Frost, J. Flemming), Pergamon, Oxford **1991**, vol. 8, p. 773.

[2] a) G. Wilke, H. Müller, *Chem. Ber.* **1956**, *89*, 444–447; G. Wilke, H. Müller, *Justus Liebigs Ann. Chem.* **1960**, *629*, 222–240; b) J. J. Eisch, M. W. Foxton, *J. Org. Chem.* **1971**, *36*, 3520–3526; c) J. J. Eisch, W. C. Kaska, *J. Am. Chem. Soc.* **1966**, *88*, 2213–2220; d) J. J. Eisch, W. C. Kaska, *J. Am. Chem. Soc.* **1963**, *85*, 2165–2166. Some recent publications on general aspects of hydroalumination: e) U. Dümichen, T. Gelbrich, J. Sieler, *Z. Anorg. Allg. Chem.* **2001**, *627*, 1915–1920; f) J. A. Francis, S. G. Bott, A. R. Barron, *Main Group Chem.* **1999**, *3*, 53–57; g) M. G. Gardiner, S. M. Lawrence, C. L. Raston, *Inorg. Chem.* **1999**, *38*, 4467–4472; h) M. Hoshi, K. Shirakawa, *Chem. Commun.* **2002**, 2146–2147; i) W. Uhl, M. Matar, *Z. Naturforsch.* **2004**, *59b*, 1214–1222; j) W. Uhl, J. Molter, B. Neumüller, *J. Organomet. Chem.* **2001**, *634*, 193–197; k) V. V. Burlakov, P. Arndt, W. Baumann, A. Spannenberg, U. Rosenthal, *Organometallics* **2004**, *23*, 4160–4165.

[3] L. Aufauvre, P. Knochel, J. Marek, *Chem. Commun.* **1999**, 2207–2208.

[4] W. Uhl, F. Breher, *J. Organomet. Chem.* **2000**, *608*, 54–59.

[5] W. Uhl, M. Matar, *J. Organomet. Chem.* **2002**, *664*, 110–115.

[6] W. Uhl, H. R. Bock, F. Breher, M. Claesener, S. Haddadpour, B. Jasper, A. Hepp, *Organometallics* **2007**, *26*, 2363–2369.

[7] a) W. Uhl, F. Breher, *Angew. Chem.* **1999**, *111*, 1578–1580; *Angew. Chem. Int. Ed.* **1999**, *38*, 1477–1479; b) W. Uhl, F. Breher, A. Lützen, W. Saak, *Angew. Chem.* **2000**, *112*, 414–416; *Angew. Chem. Int. Ed.* **2000**, *39*, 406–409; c) W. Uhl, F. Breher, J. Grunenberg, A. Lützen, W. Saak, *Organometallics* **2000**, *19*, 4536–4543; d) W. Uhl, F. Breher, A. Mbonimana, J. Gauss, D. Haase, A. Lützen, W. Saak, *Eur. J. Inorg. Chem.* **2001**, 3059–3066.

[8] W. Uhl, L. Cuypers, B. Neumüller, F. Weller, *Organometallics* **2002**, *21*, 2365–2368.

[9] W. Uhl, J. Grunenberg, A. Hepp, M. Matar, A. Vinogradov, *Angew. Chem.* **2006**, *118*, 4465–4467; *Angew. Chem. Int. Ed.* **2006**, *45*, 4358–4361.

[10] a) W. Uhl, F. Breher, S. Haddadpour, *Organometallics* **2005**, *24*, 2210–2213; b) W. Uhl, S. Haddadpour, M. Matar, *Organometallics* **2006**, *25*, 159–163.

[11] W. Uhl, M. Matar, *Z. Anorg. Allg. Chem.* **2005**, *631*, 1177–1180.

[12] a) G. D. Smith, R. L. Jaffke, *J. Phys. Chem.* **1996**, *100*, 9624–9630; b) W. Uhl, F. Hannemann, R. Wartchow, *Organometallics* **1998**, *17*, 3822–3825.

[13] J. March, *Advanced Organic Chemistry*, 3rd ed., Wiley, New York, **1985**, p. 19.

[14] W. Uhl, L. Cuypers, R. Graupner, J. Molter, A. Vester, B. Neumüller, *Z. Anorg. Allg. Chem.* **2001**, *627*, 607–614.

[15] O. T. Beachley Jr, L. Victoriano, *Organometallics* **1988**, *7*, 63–67.

[16] T. Hahn (Ed.), *International Tables for Crystallography, Space-Group Symmetry*, Kluwer Academic, Dordrecht-Boston-London, **1989**, vol. A.

[17] CCDC-645566 (for **6**), -645565 (for **6**·3thf), and -645564 (for **7**) contain the supplementary crystallographic data for this paper. These data can be obtained free of charge from The Cambridge Crystallographic Data Centre via www.ccdc.cam.ac.uk/data_request/cif.

[18] *SHELXTL-Plus*, REL. 4.1, Siemens Analytical X-RAY Instruments Inc., Madison, WI, **1990**; G. M. Sheldrick, *SHELXL-97: Program for the Refinement of Structures*, University of Göttingen, **1997**.

Received: May 3, 2007
Published Online: July 12, 2007

 © 2007 Wiley-VCH Verlag GmbH & Co. KGaA, Weinheim 

DOI: 10.1002/ejic.200700503

# Proton NMR Study of Low-Spin *meso*-Unsubstituted β-Substituted Alkyl Iron Porphyrins: Remarkable Influence of Peripheral Substitution on Spin Density

**Sandrine Juillard,[a] Arnaud Bondon,[b] and Gérard Simonneaux*[a]**

**Keywords:** NMR spectroscopy / Porphyrinoids / Iron / HMBC / Saturation transfer

Paramagnetic NMR spectroscopy was used to characterize the influence of small alkyl groups on the spin density of a series of high-spin and low-spin iron(III) porphyrins. Assignment of the resonances was obtained by using a variety of NMR techniques including heteronuclear multiple bond correlation and saturation transfer experiments.
(© Wiley-VCH Verlag GmbH & Co. KGaA, 69451 Weinheim, Germany, 2007)

## Introduction

Heme is one of the most versatile prosthetic groups in metalloproteins, and different types of heme have been found in proteins.[1] The reconstitution of heme proteins with modified heme is a useful method for understanding the physiological function and creating a new function in heme proteins.[2] Many heme modifications with different substituents have been designed to optimize heme/apoprotein interaction and even an iron porphine complex has been employed as the smallest prosthetic group of heme protein to modify intensively the heme–globin interactions.[3] Recently, we prepared myoglobin (rMb) reconstituted with the iron complex of 3,7-diethyl-2,8-dimethylporphyrin[4] in which two ethyl groups were found to be large enough to avoid the free rotation movement of the heme.[5] However, to discuss the contribution of individual pyrroles in myoglobin, it is quite interesting to design smaller porphyrins such as 3-ethyl-2-methylporphyrin. In this study, we used paramagnetic NMR spectroscopy to characterize the influence of small alkyl groups on the spin density of a series of high-spin and low-spin iron(III) porphyrins, including low-spin bis(cyanido)-3-ethyl-2-methylporphyriniron(III).

## Results and Discussion

The synthesis of β-pyrrole-substituted porphyrins has been reported elsewhere,[4] and iron was inserted to produce $Fe^{III}Cl$ porphyrins as outlined in the Experimental Section. The UV/Vis spectra of these complexes are compatible with high-spin, five coordinate structures. The structures of the compounds are summarized in Figures 1 and 2.

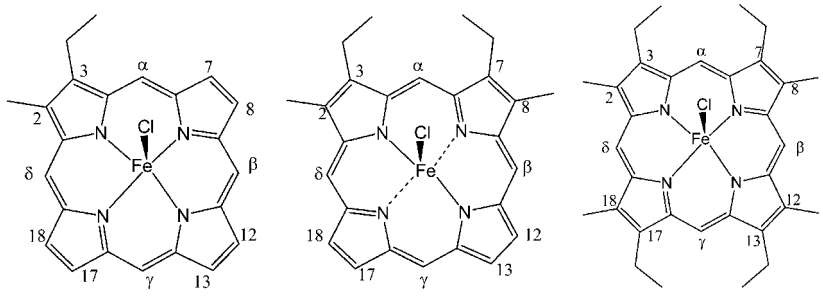


**1**·$Fe^{III}Cl$ **2**·$Fe^{III}Cl$ **3**·$Fe^{III}Cl$

Figure 1. The structures of β-pyrrole-substituted FeCl porphyrin complexes.

[a] Laboratoire de Chimie Organométallique et Biologique, UMR CNRS 6226 Campus de Beaulieu,Université de Rennes 1, 35042 Rennes, France
[b] RMN-ILP, UMR CNRS 6026, IFR 140 PRISM, Campus de Villejean, Université de Rennes 1, 35043 Rennes, France

### High-Spin Complexes

The $^1H$ NMR spectrum of **1**·FeCl in [$D_1$]chloroform at 298 K is shown in Figure 3a. The relative intensities of the peaks and their comparison with $^1H$ NMR spectroscopic

 © 2007 Wiley-VCH Verlag GmbH & Co. KGaA, Weinheim 

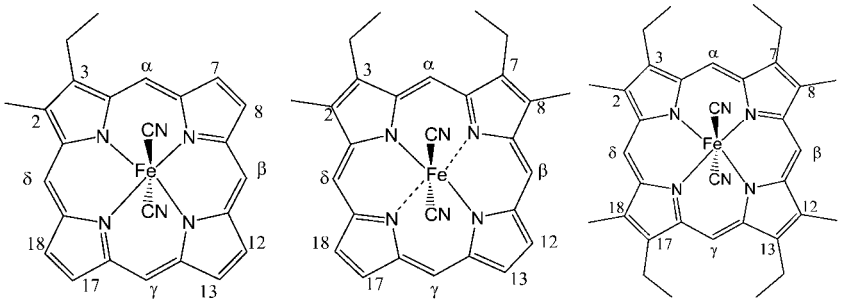


Figure 2. The structures of β-pyrrole-substituted $Fe(CN)_2$ porphyrin cmplexes.

results previously reported for octaethylporphyriniron chloride[6–8] determined their assignment. Two resonances for the *meso* protons are observed in the highfield region at $\delta$ = –63.3 and –58.3 ppm. In the downfield part of the spectrum, three resonances are found at $\delta \approx 78$ ppm for the β-pyrrole protons as a result of accidental overlap, as the absence of symmetry dictates that there should be six β-pyrrole resonances. Also in the downfield part of the spectrum, one resonance at $\delta$ = 51.3 ppm for 2-$CH_3$ and two resonances at $\delta$ = 39.9 and 43.7 ppm for the ethyl group of 3-$CH_2CH_3$ appear owing to diastereoisomerism. The $CH_3$ resonance of the ethyl group is not assigned because of its presence under the diamagnetic area. The $^1$H NMR spectra of the other complexes of this type **2**·FeCl and **3**·FeCl have related features, although the presence of idealized $C_s$ symmetry greatly simplifies the spectrum. Thus, **2**·FeCl has three *meso* protons with a 1:2:1 intensity ratio in the upfield region, two resonances at $\delta$ = 76.8 and 79.1 ppm for the β-pyrrole protons as a result of accidental overlap, two resonances at $\delta$ = 40.4 and 43.3 ppm for the 3,7-$CH_2CH_3$ group owing to diastereoisomerism, and a resonance at $\delta$ = 54 ppm for the 2,8-$CH_3$ group. As expected for **3**·FeCl, only two broad resonances are observed at $\delta$ = –54.9 and –56.6 ppm for the *meso* protons. The chemical shifts for the three complexes are summarized in Table 1 (298 K), and all of them are compatible with a high-spin state, $S$ = 5/2.[9]

Table 1. $^1$H NMR chemical shifts [ppm] of high-spin iron porphyrin chloride in $CDCl_3$ (298 K).

| Complex | *meso*-H | $CH_2CH_3$ | $CH_2CH_3$ | β-pyrrole-H |
|---|---|---|---|---|
| **1**·$Fe^{III}Cl$ | –58.3 | 39.9 | 51.3 | 76.8 |
| | –63.3 | 43.7 | | 77.7 |
| | | | | 78.6 |
| **2**·$Fe^{III}Cl$ | –53.8 | 40.4 | 54.0 | 76.8 |
| | –59.3 | 43.3 | | 79.1 |
| | –63.3 | | | |
| **3**·$Fe^{III}Cl$ | –54.9 | 40.5 | 52.5 | – |
| | –56.6 | 43.9 | | |
| $TPPFe^{III}Cl$[a] | – | – | – | –72.4 |
| $OEPFe^{III}Cl$[b] | –55.5 | 41.6 | – | – |
| | | 43.7 | | |

[a] At 293 K, TPP: tetraphenylporphyrin.[33] [b] At 298 K, OEP: octaethylporphyrin.[8]

The typical spin delocalization pathways for high-spin iron(III) porphyrins produce resonances for the β-pyrrole and α-$CH_2$ protons that are strongly shifted downfield.[10] Accordingly, all the iron(III) chloride complexes **1**·FeCl, **2**·FeCl, and **3**·FeCl showed this behavior. This downfield shift is mainly a result of the σ-contact contribution that results from delocalization through the σ-framework by way of σ-donation to the half-occupied $d_{x^2-y^2}$ iron(III) orbital. Comparison of the $^1$H NMR spectroscopic data of the high-spin, five coordinate iron(III) complexes shown in Table 1 also shows that substitution produces a small effect on the chemical shift of the *meso* resonances with electron-donating groups (alkyl groups), shifting these resonances in a downfield fashion. The β-pyrrole protons are found to resonate in a narrow window from $\delta$ = 76 to 79 ppm.

## Low-Spin Complexes

The addition of an excess amount of potassium cyanide to the iron chloride complexes in the NMR tube gave the low-spin bis(cyanido)iron complexes (see Experimental Section). Thus the $^1$H NMR spectrum of K[**1**·$Fe(CN)_2$] in methanol/chloroform at 308 K (Figure 3b) shows six resonances for the β-pyrrole protons in the high-field region, as expected from the absence of symmetry in the structure. Because HMBC spectra were not informative in this particular case, assignments of these protons were obtained by means of 1D NOE difference spectroscopy as well as 2D COSY spectroscopy. For example, all required cross peaks were identified in the COSY spectrum (Figure 4), allowing notably the identification of each pair of the β-pyrrole protons. The NOE difference spectrum, recorded at 308 K (Figure 5a), outlines the increase in intensity for the *meso* proton α-H at $\delta$ = 2.93 ppm and the β-pyrrole proton 7-H at $\delta$ = –11.75 ppm when the ethyl group at $\delta$ = 8.51 ppm was irradiated. Following the COSY spectrum, this situation identifies the proton 8-H at $\delta$ = –14.75 ppm. To complete the assignment, the NOE difference spectrum showed an increase in the intensity for the *meso* proton δ-H at $\delta$ = 2.56 ppm and the β-pyrrole proton 18-H at $\delta$ = –11.89 ppm when the methyl group (2-$CH_3$) at $\delta$ = 18.46 ppm was irradiated (Figure 5b). The signal at $\delta$ = –14.37 ppm was as-

 © 2007 Wiley-VCH Verlag GmbH & Co. KGaA, Weinheim 

signed to 17-H, whereas the last two *meso* protons at $\delta$ = 0.32 and 0.38 ppm were assigned to β-H and γ-H without a respective assignment. The last two β-pyrrole protons at $\delta$ = –12.96 and –13.05 ppm were assigned to 12-H and 13-H without a respective assignment. The chemical shift values obtained at 298 and 308 K for K[**1**·Fe(CN)$_2$] are summarized in Table 2. They are all compatible with a low-spin state, $S$ = 1/2.

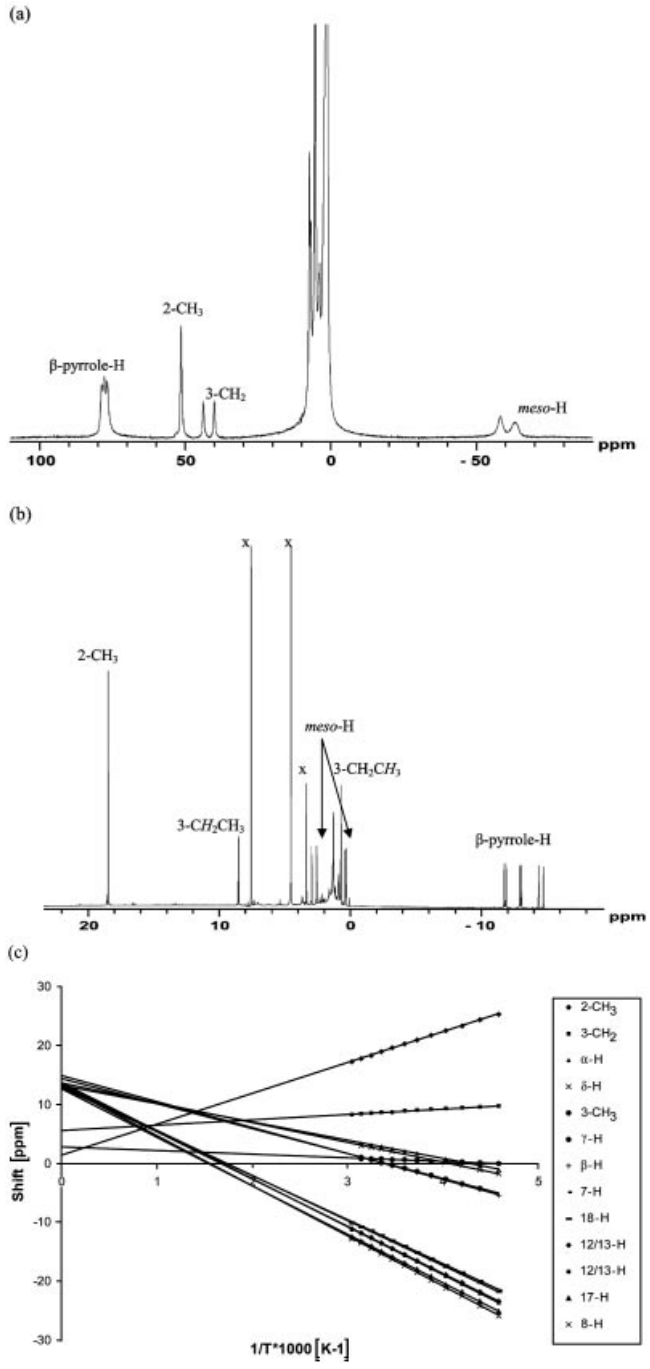


Figure 3. $^1$H NMR spectrum for (a) **1**·Fe$^{III}$Cl in $CDCl_3$ at 298 K, (b) K[**1**·Fe(CN)$_2$] in $CDCl_3$/MeOD (60:40) at 308 K, x: solvent peaks, and (c) Curie plots for K[**1**·Fe(CN)$_2$].

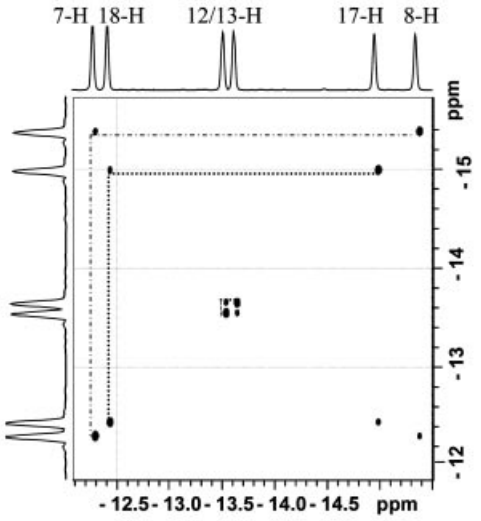


Figure 4. Part of the COSY spectrum showing β-pyrrole protons for K[**1**·Fe(CN)$_2$] (298 K).

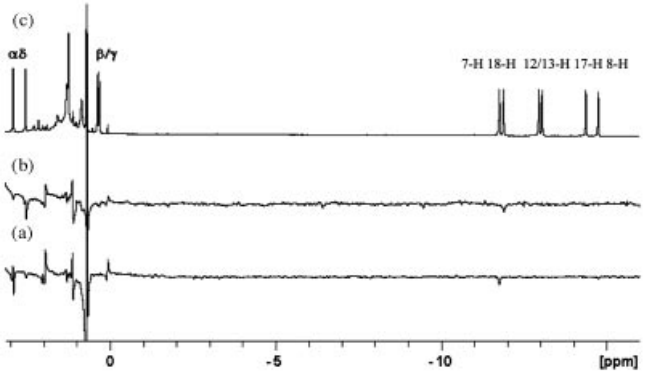


Figure 5. 1D NOE difference spectra for K[**1**·Fe(CN)$_2$] at 308 K: (a) irradiation of the $CH_2$ group at $\delta$ = 8.51 ppm, (b) irradiation of the $CH_3$ group at $\delta$ = 18.46 ppm, (c) high-field part of the spectrum.

The $^1$H NMR spectrum of K[**2**·Fe(CN)$_2$] in methanol/chloroform at 298 K (Figure 6a) shows two resonances for the β-pyrrole protons in the highfield region, as expected from the symmetry of the structure. A complete assignment of all the protons was obtained by means of heteronuclear correlation spectroscopy (HMQC and HMBC) as well as 2D COSY spectroscopy. The relative intensities of the resonances and the COSY spectrum allowed the assignment of all the protons except for the two *meso* protons, α and γ, and the β-pyrrole protons. It was previously reported that HMQC spectroscopy of paramagnetic iron porphyrins provides the scalar heterocorrelation under natural abundance conditions of $^{13}$C.[11] In the present study, this correlation technique offers a route to identify the β-pyrrole resonances by taking advantage of the fact that the full assignment of the proton signals of the β-$^{13}$C-$^1$H pairs has been established. Thus, the signal assignment of the carbons with directly bonded protons such as β-pyrrole protons and *meso* protons ($^{13}$C-$^1$H) was done on the basis of HMQC experiments. The assignment was then completed with the

 © 2007 Wiley-VCH Verlag GmbH & Co. KGaA, Weinheim 

Table 2. $^1$H chemical shifts [ppm] of low-spin bis(cyanido)iron porphyrins in $CDCl_3/CD_3OD$ (60:40) (298 K).

| Complex | β-pyrrole-H | *meso*-H | $CH_3$ | $CH_2CH_3$ | $CH_2CH_3$ |
|---|---|---|---|---|---|
| K[**1**·Fe(CN)$_2$] | –15.32 (–14.75)[d] | 0.07 (0.32) | 18.89 | 8.62 | 0.68 |
| | –14.93 (–14.37) | 0.12 (0.38) | (18.46) | (8.51) | (0.71) |
| | –13.59 (–13.05) | 2.38 (2.56) | | | |
| | –13.49 (–12.96) | 2.77 (2.93) | | | |
| | –12.38 (–11.89) | | | | |
| | –12.25 (–11.75) | | | | |
| K[**2**·Fe(CN)$_2$] | –14.49 | –0.66 | 18.87 | 7.02 | 0.50 |
| | –11.73 | 1.29 | | | |
| | | 3.72 | | | |
| K[**3**·Fe(CN)$_2$] | – | 1.43 | 16.71 | 7.30 | 0.44 |
| | | 2.18 | | | |
| K[Fe(OEP)CN$_2$][a] | – | 3.32 | – | 7.35 | |
| K[Fe(TPP)CN$_2$][b] | –11.68 | | | | |
| K[Fe(Porphine)CN$_2$][c] | –13.8 | 1.8 | | | |

[a] OEP: octaethylporphyrin in $CD_3OD$.[8] [b] TPP: tetraphenylporphyrin in $CD_2Cl_2/CD_3OD$ at 202 K.[21] [c] At 298 K.[23] [d] At 308 K.

HMBC spectrum (Figure 7). For example, the $^{13}$C signal at $\delta$ = 76.18 ppm (a β-pyrrole carbon) that showed correlation peaks with the proton signal at +1.29 ppm (*meso* β,δ-H) was assigned to C-12 and C-18. Consequently, the proton resonance at $\delta$ = –11.48 ppm was assigned to the β-pyrrole protons 12,18-H by using the HMQC spectrum. Similarly, the signals at $\delta$ = –14.49, –0.66, and 3.72 ppm were assigned to the identical β-pyrrole protons, 13-H and 17-H, and the *meso* protons, γ-H and α-H, respectively.

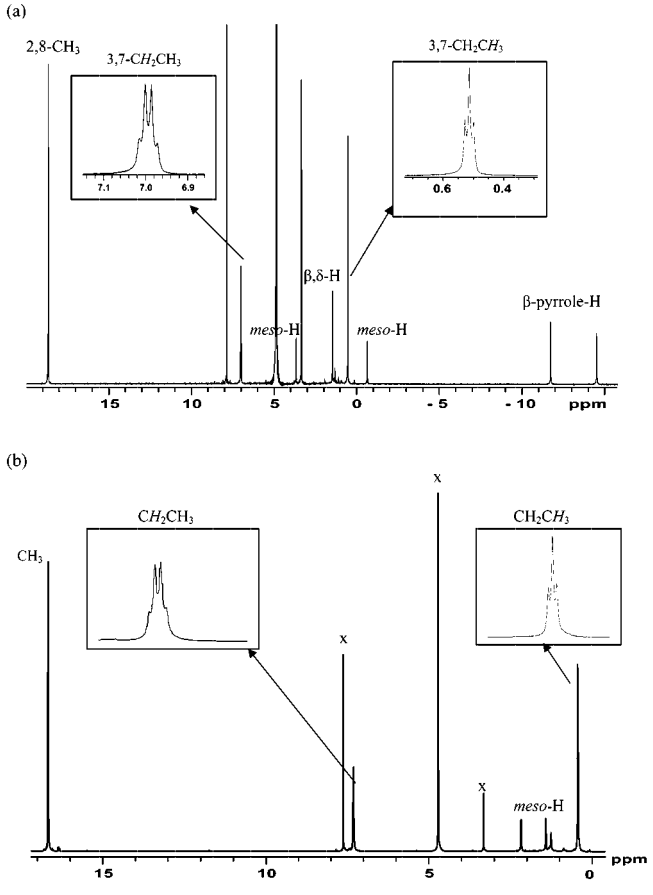


Figure 6. $^1$H NMR spectra at 298 K for (a) K[**2**·Fe(CN)$_2$] and (b) K[**3**·Fe(CN)$_2$] in $CDCl_3$/MeOD (60:40).

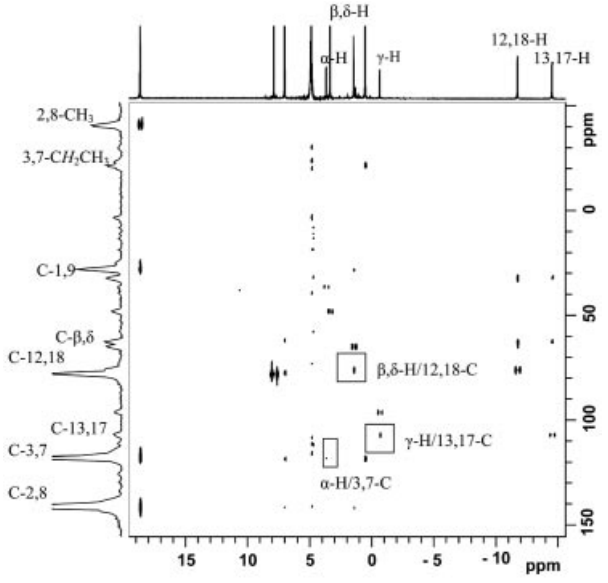


Figure 7. HMBC spectrum for K[**2**·Fe(CN)$_2$] at 298 K in $CDCl_3$/MeOD (60:40).

The $^1$H NMR spectrum of K[**3**·Fe(CN)$_2$] in methanol/chloroform at 298 K is shown in Figure 6b. As previously described for K[**2**·Fe(CN)$_2$], complete assignment of the protons and carbons was obtained by means of HMQC and HMBC spectroscopy as well as 2D COSY spectroscopy (not shown). Comparison of the *meso* proton and *meso* carbon chemical shifts of K[**3**·Fe(CN)$_2$] with K[**1**·Fe(CN)$_2$] and K[**2**·Fe(CN)$_2$] reveals that the former complex also shows mainly a $(d_{xy})^2(d_{xz},d_{yz})^3$ electronic ground state. The proton chemical shifts for K[**2**·Fe(CN)$_2$] and K[**3**·Fe(CN)$_2$] are also summarized in Table 2; all are compatible with a low-spin state, $S$ = 1/2.

Analysis of the curve in the Curie plot was made for K[**1**·Fe(CN)$_2$], K[**2**·Fe(CN)$_2$], and K[**3**·Fe(CN)$_2$]. As an example, the temperature dependences of the chemical shifts of the protons of K[**1**·Fe(CN)$_2$] in MeOD/$CDCl_3$ are shown in Figure 3c. The chemical shifts vary linearly with 1/$T$, but the extrapolated lines do not pass through the diamagnetic

 © 2007 Wiley-VCH Verlag GmbH & Co. KGaA, Weinheim 

value at $1/T = 0$. However, the intercepts at $1/T = 0$ for these signals were located between 0 and 15 ppm, and the chemical shift differences, if we consider the free-base porphyrin as a reference, do not vary to a great extent (less than 5 ppm). Similar results were obtained for the Curie plots of K[**2**·Fe(CN)$_2$] and K[**3**·Fe(CN)$_2$].

$^{13}$C NMR chemical shifts can also be a good probe to determine the electronic ground state, because they give the information on the spin distribution of any porphyrin carbons including *meso* and β-pyrrole carbons.[12,13] Table 3 shows the $^{13}$C NMR chemical shifts for K[**1**·Fe(CN)$_2$], K[**2**·Fe(CN)$_2$], and K[**3**·Fe(CN)$_2$] at 298 K. Signals were obtained and assigned on the basis of HMQC spectra. Examination of the data in Table 3 reveals that the *meso* carbons appear in a range of 35–97 ppm, and the β-pyrrole carbons appear in a range of 70–142 ppm.

Table 3. $^{13}$C chemical shifts [ppm] of low-spin bis(cyanido)iron porphyrins in $CDCl_3/CD_3OD$ (60:40) (298 K).

| Complex | β-pyrrole-C | *meso*-C | $CH_3$ | $CH_2CH_3$ | $CH_2CH_3$ |
|---|---|---|---|---|---|
| K[**1**·Fe(CN)$_2$] | 72.1 | 51.4 | –39.9 | –27.1 | 86.9 |
| | 74.1 | 53.8 | | | |
| | 94.6 | 83.1 | | | |
| | 94.8 | 83.3 | | | |
| | 102.0 | | | | |
| | 104.0 | | | | |
| K[**2**·Fe(CN)$_2$] | 76.18 | 35.8 | –42.2 | –22.7 | 77.8 |
| | 107.5 | 65.4 | | | |
| | 107.7 | 97.3 | | | |
| | 142.1 | | | | |
| K[**3**·Fe(CN)$_2$] | 127.4 | 57.1 | –37.46 | –22.5 | 77.7 |
| | 131.8 | 60.3 | | | |

### Electronic Ground State of Low-Spin Complexes

The spin density distribution at the pyrrole positions in low-spin iron(III) complexes of disymmetrically substituted tetraphenylporphyrins[14] and natural porphyrin derivatives[15] was previously reported. The results herein indicate that the introduction of only two alkyl substituents at the β-pyrrole positions of porphine can also produce significant changes in the spin density of the resulting iron(III) complexes to be detected by $^1$H NMR spectroscopy.

The ground electronic state of low-spin iron(III) porphyrins evolves between two extreme cases, i.e. $(d_{xy})^2(d_{xz},d_{yz})^3$ and $(d_{xz}d_{yz})^4(d_{xy})^1$[9] The $^1$H NMR spectra of the bis(cyanido) complexes of many artificial iron(III) porphyrins[16] and some naturally derived ferriheme[15] complexes were reported. The former studies generally indicated that the electronic ground state was $(d_{xy})^2(d_{xz},d_{yz})^3$ for these complexes. However, more recently, it was shown that the bis(cyanido) complexes of *meso*-substituted Fe$^{III}$ porphyrins having alkyl substituents of increasing size[17] and other iron(III) porphyrins having bulky substituents in the *meso* position[18–21] show a large shift in the pyrrole protons towards the diamagnetic region, which is indicative of a large contribution of the unusual $(d_{xz}d_{yz})^4(d_{xy})^1$ electronic configuration to the ground state. Furthermore, this situation is amplified when the NMR spectroscopic solvent is methanol because of a possible hydrogen bond between the axial ligand and the solvent.[6,13,22]

$^1$H NMR spectroscopic resonances for the β-pyrrole protons in K[**1**·Fe(CN)$_2$] and K[**2**·Fe(CN)$_2$] appear at very high magnetic field ($\delta$ = –10 to –20 ppm). This large upfield shift of the β-pyrrole protons indicates the existence of large spin densities on the β-pyrrole carbons, which is induced by the interactions between porphyrin $3e_g$ and iron $d_\pi$ orbitals. Because the $3e_g$ orbital places large electron densities on the β-pyrrole carbons, the spin transfer from porphyrin $3e_g$ to iron $d_\pi$ results in the large spin densities to these carbons, which would be translated as a large upfield shift of the β-pyrrole protons. This is a typical observation for a $(d_{xy})^2(d_{xz},d_{yz})^3$ electronic ground state.[10] By comparison with bis(cyanido)iron porphine,[23] (pyrrole –13.8 ppm, *meso* 1.8 ppm) it should be also noted that a large difference in the spin distribution of the pyrrole in K[**1**·Fe(CN)$_2$] is generated by adding only one methyl group and one ethyl group. In this particular case, all six β-pyrrole protons are detected separately, whereas a single peak at –13.8 ppm is observed for bis(cyanido)iron porphine.[23] It should also be noted that, generally, the $^1$H NMR spectra of dicyanohemin complexes are well-resolved, as the lines are quite narrow due to very rapid electron spin relaxation times and long proton relaxation times, $T_1$ and $T_2$, respectively.[9,24,25] This remarkable resolution was also detected with iron(III) geoporphyrins.[26]

It should be emphasized that the *meso* $^{13}$C chemical shift is also particularly useful to determine the electronic configuration.[27,28] Thus, the *meso* carbon signal in complexes with the $(d_{xy})^2(d_{xz},d_{yz})^3$ configuration appears more upfield than the corresponding signal in diamagnetic complexes because the $3e_g$ orbital, which interacts with the half-occupied $d_\pi$ orbital has a node at the *meso* carbon atom. By contrast, the complexes with a $(d_{xz},d_{yz})^4(d_{xy})^1$ ground state have large spin density at the *meso* carbon as a result of the $a_{2u}$–$d_{xy}$ interaction, exhibiting a *meso* carbon signal at a downfield position. Thus, it is quite obvious that the values summarized in Table 3 agree well with the $(d_{xy})^2(d_{xz},d_{yz})^3$ configuration and confirm the $^1$H NMR spectroscopic interpretation.

## Conclusions

$^1$H and $^{13}$C NMR spectroscopic analysis of β-alkyl-substituted iron porphyrins can be a very sensitive tool to probe the fine details of the electronic structure. This may be relevant to our protein studies with artificial hemes. Analysis of the pyrrole proton and *meso* carbon chemical shifts of K[**1**·Fe(CN)$_2$], K[**2**·Fe(CN)$_2$], and K[**3**·Fe(CN)$_2$] reveals that all complexes show mainly a low-spin $(d_{xy})^2(d_{xz},d_{yz})^3$ electronic ground state.

Thus, the spectroscopic observations are indicative of a metal-based electron in the $d_\pi$ orbitals of the iron(III) bis(cyano) complexes at any temperature. The change in ground state of low-spin Fe$^{III}$ from the usual

 © 2007 Wiley-VCH Verlag GmbH & Co. KGaA, Weinheim 

$(d_{xy})^2(d_{xz},>d_{yz})^3$ to the unusual $(d_{xz}d_{yz})^4(d_{xy})^1$ electronic configuration, which was previously suggested to occur from weak hydrogen bonding to the cyanido ligand in methanol solution with *ortho*-substituted tetraphenylporphyrins and even more with highly ruffled porphyrins,[21] is not observed with these *meso*-unsubstituted porphyrins that bear few substituents on the β-pyrrole positions. Accordingly, these results demonstrate the high energy barrier to ruffling, which seems to prevent ring deformation and, consequently, the interaction of the $d_{xy}$ orbital with the $a_{2u}(\pi)$ porphyrin orbital.

## Experimental Section

**General:** All reactions were performed under an atmosphere of argon. Solvents were distilled from appropriate drying agent prior to use: $Et_2O$ and THF from sodium and benzophenone, toluene from sodium, $CH_2Cl_2$ from $CaH_2$, $CHCl_3$ from $P_2O_5$, and all other solvents were HPLC grade. Commercially available reagents were used without further purification unless otherwise stated. All reactions were monitored by TLC with Merck precoated aluminium foil sheets (Silica gel 60 with fluorescent indicator $UV_{254}$). Compounds were visualized with UV light at 254 and 365 nm. Column chromatography was carried out by using silica gel from Merck (0.063–0.200 mm). High-resolution mass spectra were recorded with a ZabSpec TOF Micromass spectrometer in ESI positive mode at the CRMPO. Liquid UV/Vis spectra were recorded with a UVIKON XL from Biotech. $^1$H and $^{13}$C NMR in $CDCl_3$ were recorded with a Bruker Avance 500 operating at 500.15 MHz for $^1$H and 125.769 MHz for $^{13}$C with a 5 mm broadband probe equipped with a *z*-gradient coil. The spectral widths were adjusted depending on the spin state of the compounds, with 200 and 45 ppm for the proton spectra of high-spin and low-spin complexes, respectively. The $^{13}$C spectral width was 400 ppm for the low-spin complexes. Standard Bruker pulse programs were used for the acquisition of the 2D COSY, HSQC, and HMBC[29,30] spectra. Because of the paramagnetism of the derivatives, relatively short relaxation rates ($R_1$ and $R_2$) are expected. Consequently, recycling times of 0.5 and 0.8 s were used for the high-spin and the low-spin complexes. For the heteronuclear experiments, despite the large spectral width in the $^{13}$C dimension spectra, 2 K × 256 points were recorded. Some spectra were recorded with a Bruker Avance 300. The syntheses of β-pyrrole-substituted porphyrins **1**, **2**, and **3** were previously reported.[4,31]

### Preparation of Iron Porphyrins

**1·Fe$^{III}$Cl:** Iron was inserted following the procedure of Borovkov et al.[32] 3-Ethyl-2-methylporphyrin **1** (190 mg, 0.51 mmol) was dissolved in distilled chloroform (75 mL). $FeCl_2{\cdot}4H_2O$ (16 equiv.) dissolved in distilled methanol (50 mL) and two drops of 2,6-lutidine were then added. The reaction mixture was stirred at 50 °C and monitored by thin-layer chromatography (TLC) until completion. After evaporation of the solvent, the crude product was purified by column chromatography ($CH_2Cl_2$/MeOH, 3%). Before total evaporation, two drops of concentrated hydrochloric acid were added. Recrystallization from dichloromethane/pentane afforded 3-ethyl-2-methylporphyrin iron chloride **1·FeCl** as a black powder (100 mg, 0.24 mmol, 40%). $^1$H NMR (500 MHz, $CDCl_3$, 298 K): $\delta$ = –63.3 (s, 2 H, *meso*-H), –58.3 (s, 2 H, *meso*-H), 39.9 and 43.7 (s, 2 H, $CH_2CH_3$), 51.3 (s, 3 H, $CH_3$), 76.8, 77.7, and 78.6 (6 H, pyrrol-H) ppm. UV/Vis: $\lambda$ ($\varepsilon$, mM$^{-1}$ cm$^{-1}$) = 371 (110), 496 (10), 522 (10.7), 564 (3.2), 623 (5.8) nm. HRMS (LSIMS-MS): calcd. for $C_{23}H_{18}{}^{35}Cl^{56}FeN_4$ $[M]^{+\cdot}$ 441.0569; found 441.0574.

**2·FeCl:** Prepared as per **1·FeCl**. Yield: 75%. $^1$H NMR (500 MHz, $CDCl_3$, 298 K): $\delta$ = –63.3 (s, 1 H, α/γ-H), –59.3 (s, 2 H, β,δ-H), –53.8 (s, 1 H, α/γ-H), 40.4 and 43.3 (s, 4 H, $CH_2CH_3$), 54.0 (s, 6 H, $CH_3$), 76.8 and 79.06 (s, 4 H, pyrrol-H) ppm. UV/Vis ($CH_2Cl_2$): $\lambda$ ($\varepsilon$, mM$^{-1}$ cm$^{-1}$) = 375 (114.6), 499 (12.4), 525 (10.7), 570 (3.8), 627 (5.8) nm. HRMS (ESI-MS): calcd. for $C_{26}H_{24}{}^{56}FeN_4$ $[M – Cl]^+$ 448.1350; found 448.1355.

3·FeCl: Prepared as per **1·FeCl**. Yield: 55%. $^1$H NMR (500 MHz, $CDCl_3$, 298 K): $\delta$ = –56.6 (s, 2 H, *meso*-H), –54.9 (s, 2 H, *meso*-H), 40.5 and 43.9 (s, 8 H, $CH_2CH_3$), 52.5 (s, 12 H, $CH_3$) ppm. UV/Vis ($CH_2Cl_2$): $\lambda$ ($\varepsilon$, mM$^{-1}$ cm$^{-1}$) = 379 (98.9), 505 (8.4), 534 (8.5), 635 (4.4) nm. HRMS (ESI-MS): calcd. for $C_{32}H_{36}{}^{56}FeN_4$ $[M – Cl]^+$ 532.2289; found 532.2292.

**Preparation of the Dicyanido-Ligated Complexes:** Usually, these complexes were prepared in situ by dissolution of 2–3 mg of the respective high-spin complex in [$D_1$]chloroform/[$D_4$]MeOH solution (60:40) saturated with KCN. Under these experimental conditions, the black solution turned red, which is characteristic of the formation of the low-spin dicyano complex.

**K[1·Fe(CN)$_2$]:** $^1$H NMR (500 MHz; $CDCl_3$/MeOD, 60:40; 298 K): $\delta$ = –15.32 (s, 1 H, 8-H), –14.93 (s, 1 H, 17-H), –13.59 (s, 1 H, 12/13-H), –13.49 (s, 1 H, 12/13-H), –12.38 (s, 1 H, 18-H), –12.25 (s, 1 H, 7-H), 0.07 (s, 1 H, β/γ-H), 0.12 (s, 1 H, β/γ-H), 0.68 (t, $J$ = 5 Hz, 3 H, $CH_2CH_3$), 2.38 (s, 1 H, δ-H), 2.77 (s, 1 H, α-H), 8.62 (q, $J$ = 5 Hz, 2 H, $CH_2CH_3$), 18.89 (s, 3 H, $CH_3$) ppm. $^{13}$C NMR (125 MHz; $CDCl_3$/MeOD, 60:40): $\delta$ = –39.99 ($CH_3$), –27.10 ($CH_2CH_3$), 51.42 (C-α), 53.81 (C-δ), 72.14 (C-7), 74.14 (C-18), 83.10 (C-β), 83.30 (C-γ), 86.89 ($CH_2CH_3$), 94.66 (C-12/13), 94.86 (C-12/13), 102.04 (C-17), 104.03 (C-8) ppm.

**K[2·Fe(CN)$_2$]:** $^1$H NMR (500 MHz; $CDCl_3$/MeOD, 60:40; 298 K): $\delta$ = –14.43 (s, 2 H, 13,17-H), –11.48 (s, 2 H, 12,18-H), –0.98 (s, 1 H, γ-H), 0.50 (t, $J$ = 5 Hz, 6 H, $CH_2CH_3$), 1.29 (s, 2 H, β,δ-H), 3.72 (s, 1 H, α-H), 7.02 (q, $J$ = 5 Hz, 4 H, $CH_2CH_3$), 18.87 (s, 6 H, $CH_3$) ppm. $^{13}$C NMR (125 MHz; $CDCl_3$/MeOD, 60:40): $\delta$ = –42.2 ($CH_3$), –22.7 ($CH_3CH_2$), 28.3 (C-1,9), 32.19 (C-11,19), 35.83 (C-α), 62.14 (C-4,6), 62.96 (C-14,16), 65.4 (C-β,δ), 76.18 (C-12,18), 77.8 ($CH_2CH_3$), 97.26 (C-γ), 107.5 (C-13,17), 107.62 (C-3,7), 142.1 (C-2,8) ppm.

**K[3·Fe(CN)$_2$]:** $^1$H NMR (500 MHz; $CDCl_3$/MeOH, 60:40; 298 K): $\delta$ = 0.44 (t, $J$ = 5 Hz, 12 H, $CH_2CH_3$), 1.43 (s, 2 H, β,δ-H), 2.18 (s, 2 H, α,γ-H), 7.30 (q, $J$ = 5 Hz, 8 H, $CH_2CH_3$), 16.71 (s, 12 H, $CH_3$) ppm. $^{13}$C NMR (125 MHz; $CDCl_3$/MeOH, 60:40): $\delta$ = –37.46 ($CH_3$), –22.54 ($CH_2CH_3$), 39.85 (C-1,9,11,19), 47.22 (C-4,6,14,16), 57.06 (C-α,γ), 60.34 (C-β,δ), 77.72 ($CH_2CH_3$), 127.38 (C-2,8,12,18), 131.80 (C-3,7,13,17) ppm.


[1] Y. Lu, S. M. Berry, T. D. Pfister, *Chem. Rev.* **2001**, *101*, 3047–3080.
[2] T. Hayashi, Y. Hisaeda, *Acc. Chem. Res.* **2002**, *35*, 35–43.
[3] S. Neya, N. Fiunasaki, T. Sato, N. Igarashi, N. Tanaka, *J. Biol. Chem.* **1993**, *268*, 8935–8942.
[4] S. Juillard, G. Simonneaux, *Synlett* **2006**, *17*, 2818–2820.
[5] S. Juillard, A. Bondon, G. Simonneaux, *J. Inorg. Biochem.* **2006**, *100*, 1441–1448.
[6] G. N. La Mar, J. Del Gaudio, J. S. Frye, *Biochim. Biophys. Acta* **1977**, *498*, 422–435.
[7] I. Morishima, S. Kitagawa, E. Matsuki, T. Inubushi, *J. Am. Chem. Soc.* **1980**, *102*, 2429–2437.
[8] H. Kalish, J. E. Camp, M. Stepien, L. Latos-Grazynski, M. M. Olmstead, A. L. Balch, *Inorg. Chem.* **2002**, *41*, 989–997.


 © 2007 Wiley-VCH Verlag GmbH & Co. KGaA, Weinheim 

[9] F. A.Walker, "Proton NMR and EPR Spectroscopy of Paramagnetic Metalloporphyrins" in *The Porphyrin Handbook* (Eds.: K. M. Kadish, K. M. Smith, R. Guilard), Academic Press, San Diego, CA, **2000**, vol. 5, ch. 36, pp. 81–183.
[10] G. N. La Mar, F. A. Walker, *The Porphyrins* (Ed.: D. Dolphin), Academic Press, New York, **1979**, vol. 4, pp. 61–157.
[11] J. Wojaczynski, L. Latos-Grazynski, W. Hrycyk, E. Pacholska, K. Rachlewicz, L. Szterenberg, *Inorg. Chem.* **1996**, *35*, 6861–6872.
[12] M. Nakamura, *Coord. Chem. Rev.* **2006**, *250*, 2271–2294.
[13] A. Ikezaki, M. Nakamura, *Inorg. Chem.* **2002**, *41*, 2761–2768.
[14] H. Tan, U. Simonis, N. Shokhirev, F. A. Walker, *J. Am. Chem. Soc.* **1994**, *116*, 5784–5790.
[15] G. N. La Mar, D. B. Viscio, K. M. Smith, W. S. Caughey, M. L. Smith, *J. Am. Chem. Soc.* **1978**, *100*, 8085–8092.
[16] F. A. Walker, *Coord. Chem. Rev.* **1999**, *185–186*, 471–534.
[17] M. Nakamura, T. Ikeue, H. Fujii, T. Yoshimura, *J. Am. Chem. Soc.* **1997**, *119*, 6284–6291.
[18] S. Wolowiec, L. Latos-Grazynski, M. Mazzanti, J. C. Marchon, *Inorg. Chem.* **1997**, *36*, 5761–5771.
[19] J. Wojaczynski, L. Latos-Grazynski, T. Glowiak, *Inorg. Chem.* **1997**, *36*, 6299–6306.
[20] S. Wolowiec, L. Latos-Grazynski, M. Mazzanti, J. C. Marchon, *Inorg. Chem.* **1998**, *37*, 724–732.
[21] M. Nakamura, T. Ikeue, A. Ikezaki, Y. Ohgo, H. Fujii, *Inorg. Chem.* **1999**, *38*, 3857–3862.
[22] G. Simonneaux, F. Hindré, M. Le Plouzennec, *Inorg. Chem.* **1989**, *28*, 823–825.
[23] K. Wüthrich, *Struct. Bonding (Berlin)* **1970**, *8*, 53–121.
[24] S. W. Unger, T. Jue, G. N. La Mar, *J. Magn. Reson.* **1985**, *61*, 448–456.
[25] I. Bertini, P. Turano, A. Vila, *J. Chem. Rev.* **1993**, *93*, 2833–2932.
[26] S. Wolowiec, L. Latos-Grazynski, O. Serebrennikova, F. Czechowski, *Magn. Reson. Chem.* **1995**, *33*, 34–43.
[27] T. Ikeue, Y. Ohgo, T. Saitoh, M. Nakamura, H. Fujii, M. Yokoyama, *J. Am. Chem. Soc.* **2000**, *122*, 4068–4076.
[28] T. Ikeue, Y. Ohgo, T. Saitoh, T. Yamaguchi, M. Nakamura, *Inorg. Chem.* **2001**, *40*, 3423–3434.
[29] M. F. Summers, L. G. Marzilli, A. Bax, *J. Am. Chem. Soc.* **1986**, *108*, 4285–4294.
[30] A. Bax, D. Marion, *J. Magn. Reson.* **1988**, *78*, 186–191.
[31] S. Juillard, Y. Ferrand, G. Simonneaux, L. Toupet, *Tetrahedron* **2005**, *61*, 3489–3495.
[32] V. V. Borovkov, J. M. Lintuluoto, Y. Inoue, *Synlett* **1999**, *1*, 61–62.
[33] D. V. Behere, R. Birdy, S. Mitra, *Inorg. Chem.* **1982**, *21*, 386–390.

Received: May 9, 2007
Published Online: July 12, 2007

 © 2007 Wiley-VCH Verlag GmbH & Co. KGaA, Weinheim 

DOI: 10.1002/ejic.200700382

# New Single-Molecule Magnets by Site-Specific Substitution: Incorporation of "Alligator Clips" into $Fe_4$ Complexes

**Anne-Laure Barra,[a] Federica Bianchi,[b] Andrea Caneschi,[c] Andrea Cornia,*[d] Dante Gatteschi,[c] Lapo Gorini,[c] Luisa Gregoli,[d] Monica Maffini,[b] Francesca Parenti,[d] Roberta Sessoli,*[c] Lorenzo Sorace,[c] and Anna Maria Talarico[d]**

**Keywords:** Iron / Ligand design / Magnetic properties / EPR spectroscopy / Single molecule magnets

"Alligator clips" suitable for grafting on H-terminated silicon or gold surfaces have been incorporated into single-molecule magnets (SMMs) of the $Fe_4$ family. Tripodal ligands 2,2-bis-(hydroxymethyl)-10-undecen-1-ol ($H_3L^1$) and 11-(acetylthio)-2,2-bis(hydroxymethyl)undecan-1-ol ($H_3L^2$) have been used to replace the six methoxide bridges in $[Fe_4(OMe)_6(dpm)_6]$, affording new $Fe_4$ derivatives $[Fe_4(L^1)_2(dpm)_6]$ (**1**) and $[Fe_4(L^2)_2(dpm)_6]$ (**2**) in high yield (Hdpm = dipivaloylmethane). The molecular structures have been unambiguously established by XRD combined with ESI-MS and magnetic characterization techniques, including DC and AC magnetometry and high-frequency EPR spectroscopy. The two SMMs have an $S = 5$ ground state and an easy-axis magnetic anisotropy leading to slow relaxation of the magnetization at low temperature, with effective anisotropy barriers of 15.9(2) K in **1** and 15.1(2) K in **2**.
(© Wiley-VCH Verlag GmbH & Co. KGaA, 69451 Weinheim, Germany, 2007)

## Introduction

Single-molecule magnets (SMMs) are among the smallest magnetic structures that can be conceived, consisting of only a few magnetic atoms. The constituent magnetic units are d-block transition-metal or, more rarely, rare-earth ions.[1–3] The unique feature of SMMs is their large-spin ground state associated with a substantial easy-axis magnetic anisotropy. As a result, the "giant" total magnetic moment experiences a molecular anisotropy barrier $U_{eff}$, which governs relaxation. At sufficiently low temperatures the relaxation of the magnetic moment becomes so slow that hysteresis appears when the external field is cycled. In this respect, spin reversal occurs through a classical, thermally activated mechanism and is very similar to that observed in magnetic nanoparticles. However, because of the discreteness of the spin levels in SMMs, magnetic moment reversal may also occur through quantum tunneling (QT), giving rise to stepped hysteresis loops and making SMMs unique magnetic systems.[2]

In the last decade, SMM research has mainly focussed on large molecular assemblies such as single crystals, polycrystalline samples, solutions, and Langmuir–Blodgett films. The advances in nanotechnology nowadays enable the study of molecular magnetism in lower-dimensional systems.[4] For example, with scanning probe microscopy (sub)-monolayers of SMMs at surfaces are studied extensively.[5] Moreover, researchers have now reached the ultimate limit of electronic devices by connecting two wires to a single molecule, measuring the flow of electrons through it, and controlling this flow with a nearby gate electrode.[6] In this context, a key step is the development of strategies to introduce specific functionalities, like surface-binding sites, around the core of SMMs, without altering the magnetic behavior. As the grafting protocols usually involve liquid-phase operations, the complexes should additionally remain intact in solution and on surfaces. We are currently pursuing the functionalization of SMMs in order to realize molecular wires containing high-spin units that may be grafted on surfaces or linked to proximal electrodes. In a previous paper we demonstrated that four surface-binding groups can be linked to the core of $Mn_{12}$-type SMMs using proper ligand design.[7]

In this paper, we report the successful preparation of two novel iron(III)-based SMMs that exhibit a wire-like molecular geometry, **1** and **2** (Figure 1). The complexes feature long-chain alkyl tethers at opposite sides and terminal "alligator clips" of two different types: alkenyl (**1**) and thioacetyl (**2**) groups, which can be used for deposition on H-ter-

[a] Grenoble High Magnetic Field Laboratory – CNRS, 25 Avenue des Martyrs, 38042 Grenoble Cedex 9, France
[b] Department of General and Inorganic Chemistry, Analytical Chemistry, Physical Chemistry, Università degli Studi di Parma, Viale G. P. Usberti 17/A, 43100 Parma, Italy
[c] La. M. M., Department of Chemistry and INSTM Research Unit, Università degli Studi di Firenze, Via della Lastruccia 3, 50019 Sesto Fiorentino (FI), Italy
Fax: +39-55-4573372
E-mail: roberta.sessoli@unifi.it
[d] Department of Chemistry and INSTM Research Unit, Università degli Studi di Modena e Reggio Emilia, Via G. Campi 183, 41100 Modena, Italy
Fax: +39-59-373543
E-mail: acornia@unimore.it
Supporting information for this article is available on the WWW under http://www.eurjic.org or from the author.

 © 2007 Wiley-VCH Verlag GmbH & Co. KGaA, Weinheim 

minated silicon[8a] and gold[8b] substrates, respectively. Using DC and AC magnetometry and HF-EPR spectroscopy, we additionally show that the site-specific functionalization occurs with full retention of the magnetic properties.

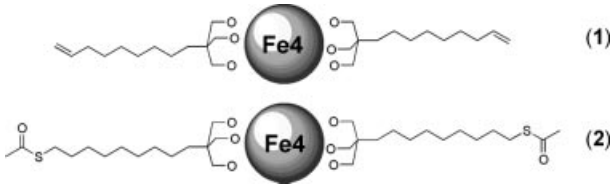


Figure 1. Approach to $Fe_4$-based SMMs with a wire-like geometry.

## Results and Discussion

### Synthesis

The derivatives of 2-(hydroxymethyl)propane-1,3-diol, $RC(CH_2OH)_3$, are widely used as versatile ligands in transition-metal chemistry because they can adopt a large variety of binding modes.[9] The $\eta^2,\eta^2,\eta^2,\mu_4$ mode is found in simple metal-centered $Fe^{III}$ triangles, commonly known as "ferric stars", which have an $S = 5$ ground state and behave as SMMs with energy barriers as high as 17 K.[10] The synthesis is very conveniently carried out starting from the archetypal $Fe_4$ compound $[Fe_4(OMe)_6(dpm)_6]$ (**3**) (Hdpm = dipivaloylmethane).[11] At variance with other "ferric stars",[5b,12] the bridging methoxide groups in **3** can be easily exchanged, leaving the bulky shell of terminal $dpm^-$ anions unchanged. The binding geometry of the tripods is such that the R groups lie on opposite sides of the flat $Fe_4$ moiety, thus providing access to molecular wire-like geometries (Figure 1).

In order to attach surface-binding functionalities to the $Fe_4$ core, we used the tripods 2,2-bis(hydroxymethyl)-10-undecen-1-ol ($H_3L^1$) and 11-(acetylthio)-2,2-bis(hydroxymethyl)undecan-1-ol ($H_3L^2$). The former was prepared from 10-undecenal and excess formaldehyde[13a] by Tollens condensation. The terminal double bond of $H_3L^1$ undergoes addition of thioacetic acid in the presence of 2,2′-azobis(2-methylpropionitrile) (AIBN) to afford the thioacetyl derivative $H_3L^2$ in moderate yield (Scheme 1).[13b]

The coordinating ability of the tripods $H_3L^1$ and $H_3L^2$ was first tested using $^2H$ NMR spectroscopy. Solutions of $[Fe_4(OMe)_6([D_{18}]dpm)_6]$ (**3D**) in dry $Et_2O$ are known[10a] to exhibit time-dependent spectra, which reveal progressive decomposition to afford monomeric Fe(dpm) species. By contrast, after the addition of excess tripodal ligands (R = Ph or Me), the spectra show persistent peaks at $\delta = 10.3$ and 12.7 ppm, arising from polynuclear iron(III) complexes ($Fe_4$ or structurally related species) and magnetically uncoupled Fe(dpm) complexes, respectively. From the same solutions, doubly substituted $Fe_4$ derivatives can be isolated in high yield.[10a,10b] Similar results were obtained with the two tripodal ligands prepared in this work. The spectra recorded several hours after the addition of $H_3L^1$ or $H_3L^2$ (2.7 equiv.) to a solution of **3D** in dry $Et_2O$ are characterized by peaks at $\delta = 10.3$ and 12.7 ppm in a 3:1 ratio (Figure 2a), suggesting that the coordinating ability of both $H_3L^1$ and $H_3L^2$ is comparable with that of simpler triols. The $Fe_4$ derivatives **1** and **2** could indeed be isolated in crystalline form (90–95% yield) by mixing **3** with an excess of

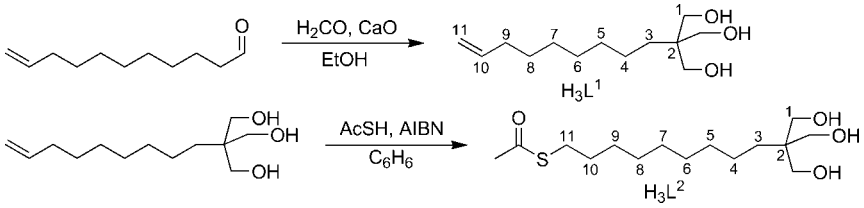


Scheme 1.

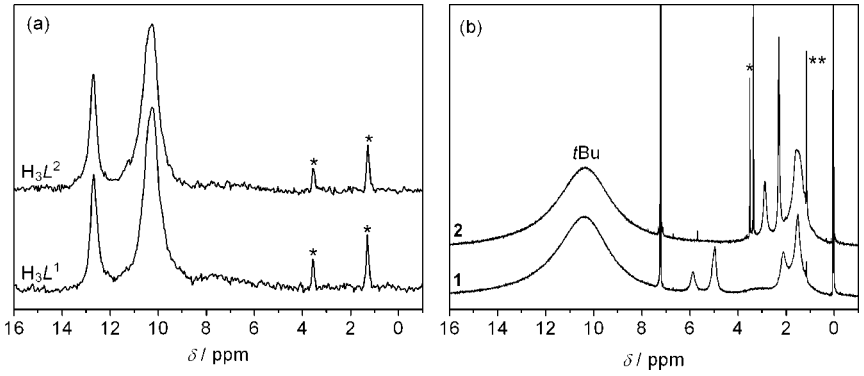


Figure 2. (a) $^2H$ NMR spectra of an $Et_2O$ solution of **3D** recorded 18 h after the addition of $H_3L^1$ or $H_3L^2$ (2.7 equiv.). The signals labeled with * are due to the solvent. (b) $^1H$ NMR spectra of **1** and **2** in $CDCl_3$. The sharp signals indicated with * and ** are due to traces of dimethoxyethane and free Hdpm, respectively.

 © 2007 Wiley-VCH Verlag GmbH & Co. KGaA, Weinheim 

the appropriate tripodal ligand in an organic solvent and by either slow diffusion of methanol vapors or slow concentration.

## Characterization

In spite of the presence of the long $C_9$ chains, compound $[Fe_4(L^1)_2(dpm)_6]$ (**1**) crystallizes in large X-ray-quality blocks that were investigated by X-ray diffraction methods at 120 K. The crystals belong to monoclinic space group *C*2/*c* and the lattice contains no crystallization solvent. The molecular structure has crystallographic $C_2$ symmetry, which has a twofold axis passing through Fe atoms Fe1 and Fe2 (Figures 3 and 4), but closely approaches $D_3$ symmetry. Selected interatomic distances and angles are gathered in Table 1.

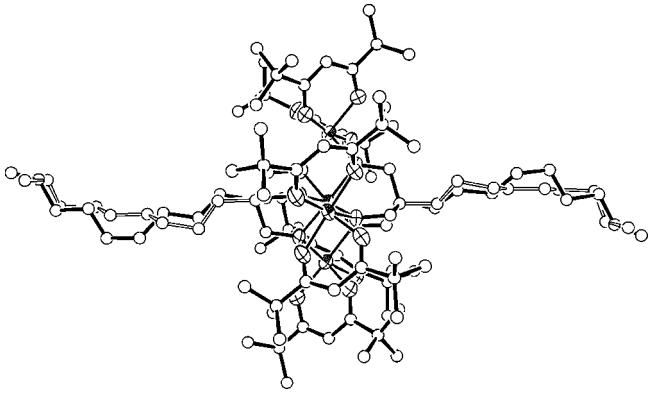

Figure 3. Molecular structure of **1** viewed approximately along the twofold axis. Iron and oxygen atoms are represented as 75%-probability ellipsoids, while carbon atoms are represented as spheres. H atoms have been omitted for clarity. The two positions occupied by the $C_9$ chain are drawn using solid and open bonds.

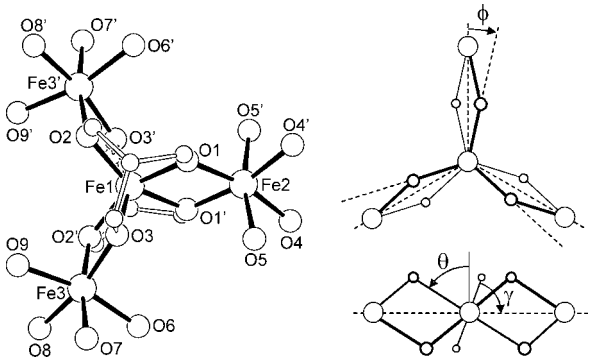


Figure 4. Left: structure of the Fe/O core in **1**, with four carbon atoms of the tripodal ligands and the atom-labeling scheme. Right: definition of the angles $\phi$, $\theta$, and $\gamma$. The dashed lines lie in the plane defined by the four metal centers.

The propeller-like structure of the precursor is retained, but replacement of the methoxide bridges with tripodal ligands leads to significant alterations of the core geometry (Figure 4). Assuming idealized $D_3$ symmetry, the angles $\theta$ and $\phi$, which define trigonal compression/elongation and trigonal rotation for Fe1, are 54.2° and 30.8°.[14] While $\theta$ differs from the octahedral value (54.74°) by less than 1°, $\phi$ departs from the value found in regular octahedral symmetry (60°) by almost 30°. Therefore, the dominant type of distortion for Fe1 is trigonal rotation, which is directly related to the propeller's pitch $\gamma$ (69.7°).[10a] Within the series of $Fe_4$ propellers so far synthesized, the structure of the Fe/O core in **1** is found to be intermediate between those observed for R = Me ($\theta$ = 54.1°, $\phi$ = 29.2°, $\gamma$ = 70.8°) and Ph ($\theta$ = 54.2°, $\phi$ = 32.3°, $\gamma$ = 68.8°), while it is very different from that of the precursor **3** ($\theta$ = 57.3°, $\phi$ = 37.7°, $\gamma$ = 63.2°).[10a,10b] As shown in Figure 3, the $C_9$ chains of the tripodal ligands are directed along the idealized threefold molecular axis and are disordered on two equally populated positions. The molecular size, evaluated from the distance between the two C11 carbon atoms (Scheme 1), is 2.5–2.6 nm.

Table 1. Selected interatomic distances [Å] and angles [°] for **1**.[a]

| | | | |
|---|---|---|---|
| Fe1···Fe2 | 3.0808(8) | Fe1···Fe3 | 3.0919(4) |
| Fe2···Fe3 | 5.2304(6) | Fe3···Fe3′ | 5.5652(6) |
| Fe1–O2 | 1.9774(17) | Fe1–O1′ | 1.9846(18) |
| Fe1–O3 | 1.9924(15) | Fe2–O1 | 1.9728(19) |
| Fe2–O5 | 1.9923(16) | Fe2–O4 | 2.0038(19) |
| Fe3–O3 | 1.9578(16) | Fe3–O7 | 1.9905(16) |
| Fe3–O2′ | 1.9944(16) | Fe3–O8 | 1.9972(17) |
| Fe3–O9 | 2.016(2) | Fe3–O6 | 2.0284(18) |
| Fe2···Fe1···Fe3 | 115.85(1) | Fe3···Fe1···Fe3′ | 128.30(2) |
| Fe3···Fe2···Fe3′ | 64.28(1) | Fe2···Fe3···Fe3′ | 57.86(1) |
| O1′–Fe1–O1 | 77.48(10) | O2–Fe1–O1′ | 155.54(7) |
| O2–Fe1–O1 | 88.67(7) | O2–Fe1–O2′ | 110.69(11) |
| O1′–Fe1–O3 | 108.75(7) | O1–Fe1–O3 | 88.40(7) |
| O2–Fe1–O3 | 90.66(7) | O2′–Fe1–O3 | 76.96(6) |
| O3–Fe1–O3′ | 158.31(11) | O1–Fe2–O1′ | 78.03(10) |
| O1–Fe2–O4 | 167.41(8) | O1′–Fe2–O4 | 92.01(7) |
| O4–Fe2–O4′ | 98.81(12) | O5–Fe2–O4 | 85.60(7) |
| O5′–Fe2–O4 | 85.92(7) | O1–Fe2–O5 | 88.81(8) |
| O1′–Fe2–O5 | 101.38(7) | O5–Fe2–O5′ | 166.95(13) |
| O3–Fe3–O2′ | 77.36(6) | O7–Fe3–O2′ | 170.01(8) |
| O3–Fe3–O6 | 102.04(8) | O7–Fe3–O6 | 85.22(7) |
| O2′–Fe3–O6 | 89.25(7) | O8–Fe3–O6 | 84.92(7) |
| O9–Fe3–O6 | 166.91(7) | O3–Fe3–O7 | 95.64(7) |
| O3–Fe3–O8 | 166.36(7) | O7–Fe3–O8 | 96.63(7) |
| O2′–Fe3–O8 | 91.15(7) | O3–Fe3–O9 | 89.09(7) |
| O7–Fe3–O9 | 86.86(7) | O2′–Fe3–O9 | 100.02(8) |
| O8–Fe3–O9 | 85.66(8) | Fe2–O1–Fe1 | 102.24(7) |
| Fe1–O2–Fe3′ | 102.24(7) | Fe1–O3–Fe3 | 103.02(7) |

[a] Symmetry transformations used to generate equivalent atoms: ′: $-x + 1$, $y$, $-z + 3/2$.

The second compound, $[Fe_4(L^2)_2(dpm)_6]$ (**2**), was isolated as weakly diffracting orange crystals, which turned out to be unsuitable for X-ray analysis. Structure elucidation was then based on elemental analysis, spectroscopic and spectrometric (ESI-MS) methods. The $^1H$ NMR spectra of **1** and **2** in $CDCl_3$ are compared in Figure 2b. In **1**, the very broad signal of paramagnetically shifted *t*Bu protons at $\delta$ = 10.4 ppm is accompanied by additional resonances at $\delta$ = 5.91 (2 H), 5.00 (4 H), and 2.16 (4 H) ppm due to C10, C11, and C9 hydrogen atoms, respectively, which undergo small paramagnetic shifts.[13a]

However, the signal from the $CH_2O$ hydrogen atoms of the tripod, which is observed as a sharp singlet at $\delta$ = 3.75 ppm in $H_3L^1$,[13a] is completely absent in the spectrum,

 © 2007 Wiley-VCH Verlag GmbH & Co. KGaA, Weinheim 

as expected because of the proximity of $CH_2O$ hydrogen atoms to the paramagnetic metal centers. Similarly, the broad peak at $\delta \approx 1.5$ ppm integrates to about 16 H per molecule, and does not account for the remaining 24 aliphatic protons. The four $CH_2$ groups closer to the metal core are presumably paramagnetically shifted and broadened beyond detection, as suggested by the very broad signal observed at $\delta \approx 3$ ppm. Therefore, spectroscopic data strongly indicate that the solid-state structure of **1** is fully retained in solution. The $^1H$ NMR spectrum of **2** in $CDCl_3$ shows, in addition to the broad *t*Bu signal, two resonances at $\delta = 2.89$ (4 H) and 2.31 (6 H) ppm due to C11 and acetyl hydrogen atoms, respectively, and no signal from $CH_2O$ protons. Again, the broad peak at $\delta \approx 1.5$ ppm integrates to about 24 H, as expected assuming that two $CH_2$ groups per tripodal ligand are not detectable. The UV/Vis absorption spectra of **1** and **2** in toluene solution are identical (Figure S1). They have two bands at 349 and 400 nm assigned to $t_{2g} \rightarrow \pi^*$ and $\pi \rightarrow t_{2g}$ charge transfer transitions, respectively, involving the β-diketonate ligands.[15] The solid-state IR spectra denote a strong similarity between the two structures, except for the presence of the characteristic absorptions due to the different terminal functionalities (Figure S2). In particular, in **1** the absorption bands typical of alkene groups are observed at 909, 994, and 1644 $cm^{-1}$, corresponding to –C=C–H in-plane and out-of-plane bending and C=C stretching modes, respectively. In **2** these bands are not present, but we find a new strong absorption at 1699 $cm^{-1}$ typical of the stretching vibration of the acetyl C=O group. We conclude that, according to $^1H$ NMR, UV/Vis, and IR spectroscopy, the structures of **1** and **2** in the solid state and in solution are strictly similar.

Electrospray ionization mass spectrometry (ESI-MS) was additionally used for the characterization of **1** and **2**. Owing to the capability of providing an accurate determination of the molecular mass of relatively large and labile molecules,[16] this soft ionization technique has been widely used for the characterization of cationic complexes as well as in the study of metal-ion-induced self-assembly processes and SMMs.[17] In this study, **1** and **2** were dissolved in dichloromethane/nitromethane (2:1) and directly infused into the electrospray mass spectrometer system. The experimental isotope clusters obtained are in agreement with the theoretical masses and reconstructed ESI isotope patterns, thus increasing the confidence in the identification.

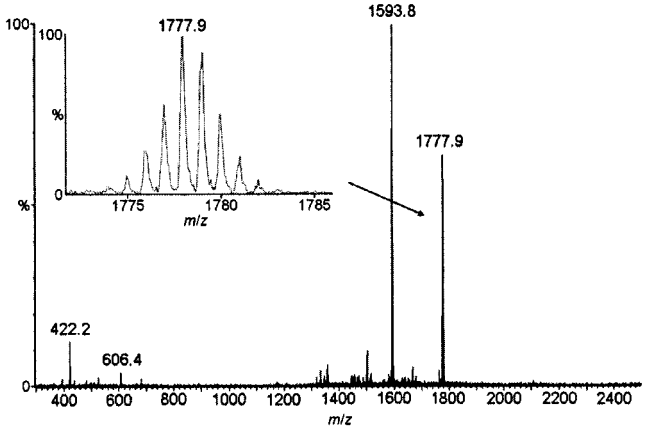


Figure 5. ESI(+)-MS full scan spectra of **1**. The inset shows a mass-scale-expanded segment of the ion signal at $m/z = 1777.9$ attributable to the $[\mathbf{1} + H]^+$ ion.

Both complexes appeared as ion distributions: more precisely, the ESI(+) spectra showed signals centered at $m/z = 1777.9$ and 1931.0, attributable to $[\mathbf{1} + H]^+$ and $[\mathbf{2} + H]^+$, respectively (Figures 5 and 6). As shown in the same figures, other signals were observed. The peaks occurring at $m/z = 1593.8$ and 1746.0 can be explained taking into account the loss of one $dpm^-$ group, thus being related to the presence of the ions $[\mathbf{1} - dpm]^+$ and $[\mathbf{2} - dpm]^+$, respectively. Other peaks, i.e., the signals at $m/z = 606.4$ and 422.2, observed in both **1** and **2**, were assigned to $[Fe(dpm)_3 + H]^+$ and $[Fe(dpm)_2]^+$, respectively.

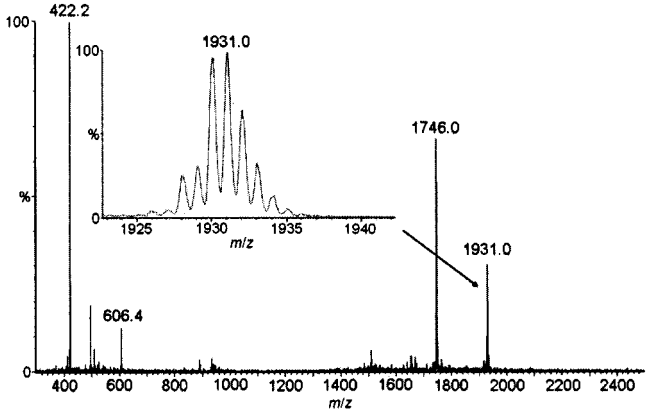


Figure 6. ESI(+)-MS full scan spectra of **2**. The inset shows a mass-scale-expanded segment of the ion signal at $m/z = 1931.0$ attributable to the $[\mathbf{2} + H]^+$ ion.

## Magnetic Properties

The incorporation of two tripodal ligands in the structure of **3** is known to preserve the ground $S = 5$ spin state of the parent compound, at the same time producing a more than twofold increase of magnetic anisotropy (from $D = -0.20$ $cm^{-1}$ in **3** to about $-0.45$ $cm^{-1}$).[10a,10b] The magnetic behavior of **1** and **2** was then compared in detail to support the proposed structural assignment. The molar magnetic susceptibility of **1** and **2**, reported in Figure 7 as a $\chi_m T$-versus-$T$ plot, is characteristic of "ferric stars", where the dominant antiferromagnetic interaction between the central and peripheral high-spin iron(III) centers generates an $S = 5$ ground state.[10,11] The $\chi_m T$ product first decreases upon cooling down from room temperature, goes through a minimum at around 100 K, and then reaches a maximum at 10–15 K. Further cooling results again in a decrease of the magnetic moment. The value at the maximum (14.1–14.6 emu K $mol^{-1}$) is close to the Curie constant for an $S = 5$ state (15.0 emu K $mol^{-1}$ for $g = 2.00$). The observation of a slightly lower magnetic moment, as well as the low-temperature decrease, is ascribed to saturation and/or anisotropy effects.

 © 2007 Wiley-VCH Verlag GmbH & Co. KGaA, Weinheim 

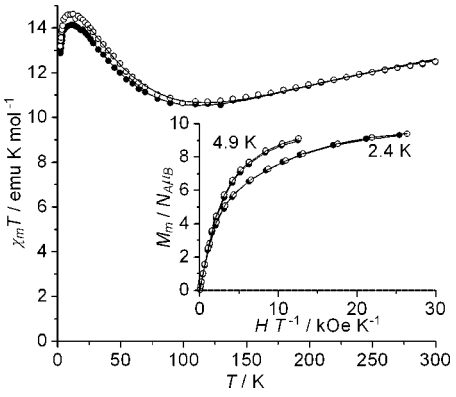


Figure 7. DC magnetic properties of **1** (open symbols) and **2** (solid symbols). The solid lines provide the best fit to the experimental data, as described in detail in the text.

Quantitative fitting of the data at $T > 20$ K using a Heisenberg spin-Hamiltonian with nearest-neighbor ($J_1$) and next-nearest-neighbor ($J_2$) coupling constants [Equation (1)] gives for **1**: $J_1 = 16.85(9)$ cm$^{-1}$, $J_2 = -0.07(9)$ cm$^{-1}$, and $g = 1.982(3)$; for **2**: $J_1 = 15.43(6)$ cm$^{-1}$, $J_2 = -0.54(5)$ cm$^{-1}$, and $g = 1.947(2)$.

$$\hat{\mathcal{H}}_0 = J_1(\hat{\mathbf{S}}_1\cdot\hat{\mathbf{S}}_2 + \hat{\mathbf{S}}_1\cdot\hat{\mathbf{S}}_3 + \hat{\mathbf{S}}_1\cdot\hat{\mathbf{S}}_4) + J_2(\hat{\mathbf{S}}_2\cdot\hat{\mathbf{S}}_3 + \hat{\mathbf{S}}_3\cdot\hat{\mathbf{S}}_4 + \hat{\mathbf{S}}_2\cdot\hat{\mathbf{S}}_4) + g\mu_B\hat{\mathbf{S}}\cdot\hat{\mathbf{H}} \quad (1)$$

As found in other $Fe_4$ complexes,[10a,10b] an accurate fit of magnetic data for **2** requires a small and ferromagnetic $J_2$ constant, though the real nature of next-nearest-neighbor interactions in this class of compounds remains to be fully ascertained. The isothermal molar magnetization measured at 4.9 and 2.4 K as a function of applied field (Figure 7, inset) approaches the appropriate value for an $S = 5$ state in high fields ($M_m/N_A\mu_B = 5g$). The fitting of experimental data with an axial zero-field splitting plus Zeeman Hamiltonian [Equation (2)] affords for **1**: $D = -0.450(5)$ cm$^{-1}$ and $g = 1.983(3)$; for **2**: $D = -0.437(7)$ cm$^{-1}$ and $g = 1.956(4)$.

$$\hat{\mathcal{H}}' = D[\hat{S}_z^2 - \tfrac{1}{3}S(S+1)] + g\mu_B\hat{\mathbf{S}}\cdot\hat{\mathbf{H}} \quad (2)$$

When imposing a positive $D$ parameter, the fit is much worse, thus clearly indicating the presence of Ising-type magnetic anisotropy in both compounds.

These findings were confirmed by HF-EPR spectra recorded at 190 GHz as a function of temperature (Figure 8). For both species the typical behavior of an $S = 5$ state with easy-axis type anisotropy ($D < 0$) was observed. Indeed, at the highest temperature five parallel and five perpendicular transitions are detected for magnetic fields lower and higher than that corresponding to $g = 2.0$ ($H_0 = 66.7$ kOe), respectively, thus confirming the $S = 5$ ground state. On lowering the temperature, the lowest-field parallel transition and the highest-field perpendicular one gain intensity, as expected for $D < 0$.[18] The line-to-line separations, which in the high-field limit correspond to $2|D|/g_{\parallel}\mu_B$ for parallel transitions and to $|D|/g_{\perp}\mu_B$ for perpendicular ones, are consistent with a $D$ value of about –0.43 cm$^{-1}$, which is characteristic of doubly substituted derivatives.[10a,10b] The spectra of **1** further evidence the presence of three isomers with slightly different zero-field splitting parameters. The relative intensity of the three signals is in the approximate ratio of 1:2:1, thus indicating that the three isomers are likely to arise from the disorder of the alkenyl chain. Indeed, given the two equally occupied positions (A and B) of the alkenyl chain observed in the X-ray structure, the three isomers should be AA (relative abundance = $0.5\times0.5 = 0.25$), AB = BA (relative abundance = $2\times0.5\times0.5 = 0.50$), and BB (relative abundance = $0.5\times0.5 = 0.25$).

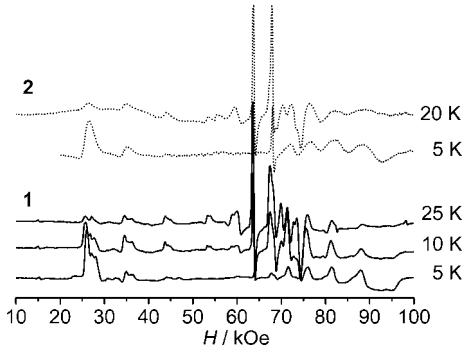


Figure 8. Temperature dependence of the HF-EPR spectra of **1** (continuous lines) and **2** (dotted lines) recorded at 190 GHz.

To obtain more detailed and precise information on the actual value of the zero-field splitting parameters, simulation of the spectra was undertaken. Given the monoclinic symmetry of derivative **1**, the following Hamiltonian was used for the simulation [Equation (3)].[19]

$$\hat{\mathcal{H}}_{EPR} = \mu_B\hat{\mathbf{S}}\cdot\mathbf{g}\cdot\hat{\mathbf{H}} + D\hat{\mathbf{S}}_z^2 + B_4^0\hat{\mathbf{O}}_4^0 + \frac{E}{2}\left(\hat{\mathbf{S}}_+^2 + \hat{\mathbf{S}}_-^2\right) \quad (3)$$

For both compounds $g$ was fixed at $2.000 \pm 0.005$, as expected for high-spin iron(III)-containing species.[20] For derivative **1** a satisfactory simulation (Figure 9, left) at both 10 and 25 K was obtained assuming a relative abundance 1:2:1 for the three isomers, with the following parameters: $D_1 = -0.431$ cm$^{-1}$, $E_1 = 0.010$ cm$^{-1}$; $D_2 = -0.442$ cm$^{-1}$, $E_2 = 0.024$ cm$^{-1}$; $D_3 = -0.420$ cm$^{-1}$, $E_3 = 0.021$ cm$^{-1}$; with $B_4^0 = 1.0\times10^{-5}$ cm$^{-1}$ for all isomers. The peculiar sharpness of the central lines of the spectrum has been accounted for by imposing different line widths for that group of resonances as well as by including the effect of a small distribution in the $D$ and $E$ values resulting from local strain-induced effects.

For compound **2**, the best simulations (Figure 9, right) were obtained with $D = -0.435$ cm$^{-1}$, $E = 0.018$ cm$^{-1}$, and $B_4^0 = 1.5\times10^{-5}$ cm$^{-1}$. The peculiar differences in line widths along the spectrum have been accounted for in the same way as for **1**. However, for this derivative strain effects are much more evident, especially for the $E$ parameter, as shown by the progressive broadening of the perpendicular transitions at higher fields.

 © 2007 Wiley-VCH Verlag GmbH & Co. KGaA, Weinheim 

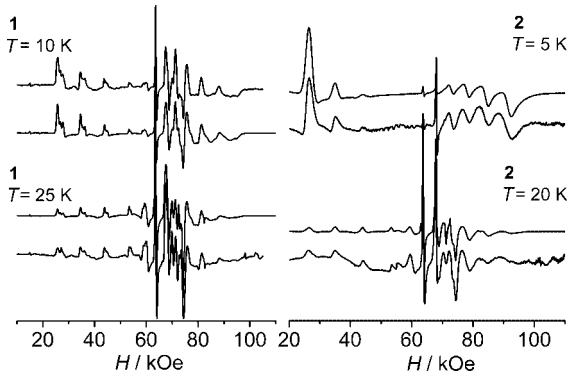


Figure 9. Best simulations (upper traces) of the experimental HF-EPR spectra recorded at 190 GHz (lower traces) at different temperatures for **1** (left) and **2** (right) obtained with the parameters reported in the text.

The zero-field splitting parameters obtained for **1** agree with the values expected on the basis of a recently proposed magnetostructural correlation between $D$, $B_4^0$, and the helical pitch $\gamma$.[10a] The presence of a small but non-negligible rhombic term ($E \neq 0$) confirms the deviation from ideal $D_3$ symmetry. The observation of slightly different $D$ values for the three isomers of **1** further indicates that a small modification in the structure, even when not directly involving the core of the molecule, might affect, in a measurable way, the zero-field splitting parameters. Finally, on the basis of the above-mentioned magnetostructural correlation,[10a] the results obtained for **2** unambiguously prove the strict structural similarity between **2** and **1**.

The spin ground state and the easy-axis magnetic anisotropy evidenced above suggest that **1** and **2** may behave as SMMs at low temperature, as indeed observed for **3** and other simpler $Fe_4$ compounds.[10,11] We have therefore measured the AC susceptibility in zero static field and we have found, below 6 K, a nonzero imaginary component that goes through a frequency-dependent maximum on lowering the temperature. The behaviors of **1** and **2** are very similar, as can be seen in Figure 10. From the same data, the temperature dependence of the relaxation time $\tau$ has been extracted, assuming that when $\chi''$ is maximum at a given frequency $\nu$, the condition $\tau = (2\pi\nu)^{-1}$ is satisfied. A linear behavior of $\ln(\tau)$ as a function of $1/T$ is observed over the investigated frequency range, confirming a thermally activated mechanism for the relaxation (Figure 11). The best-fit parameters using the Arrhenius law $\tau = \tau_0 \exp(U_{eff}/k_B T)$ are for **1**: $\tau_0 = 3.4(1) \times 10^{-8}$ s, $U_{eff}/k_B = 15.9(2)$ K; for **2**: $\tau_0 = 4.3(1) \times 10^{-8}$ s, $U_{eff}/k_B = 15.1(2)$ K. The $U_{eff}$ values are close to the anisotropy barriers predicted for integer spins by the formula $U = |D|S^2$, which neglects QT effects, as found in other doubly substituted $Fe_4$ derivatives.[10a,10b] The pre-exponential factors $\tau_0$ are also quite similar to those observed with simpler triols,[10a] suggesting that the bulkier and more flexible long aliphatic chains of **1** and **2** do not affect the spin-phonon coupling in a significant way.

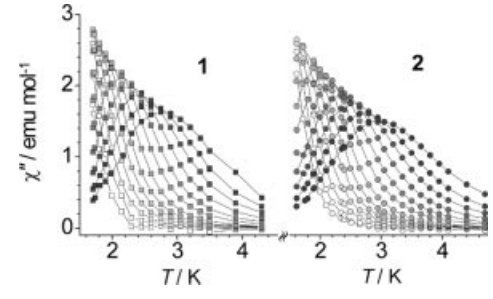


Figure 10. Imaginary component of the AC susceptibility measured for **1** (left) and **2** (right) in zero static field in the frequency range from 100 Hz (white) to 25 kHz (black).

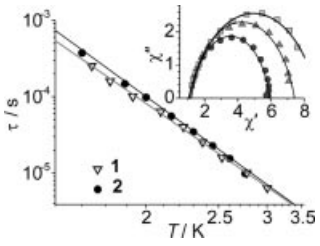


Figure 11. Temperature dependence of the relaxation time for **1** and **2**. The lines represent the best-fit curves using the Arrhenius law. The inset shows the Argand plot for **2** at 2.5 K (circles), 2.0 K (triangles), and 1.75 K (squares). The lines represent the best-fit curves using a modified Debye model. Susceptibilities are in emu mol$^{-1}$.

We have also investigated how the presence of different isomers, evidenced in **1**, or the sizeable strain effects in **2** influence the distribution of relaxation times. By plotting $\chi''$ versus $\chi'$ at a given temperature, a semicircumference centered on the $x$ axis should be observed in the absence of distribution, according to the Debye model.[21] The results are shown in the inset of Figure 11 for **2** and in Figure S3 of the Supporting Information for **1**. The presence of a distribution of relaxation times is accounted for by a parameter $\alpha$[1b,21] which has been evaluated for **1** and **2** and is found to increase on lowering the temperature to reach 0.26 at 1.75 K for both compounds. The closest-to-the-origin intercept of the semicircle with the $x$ axis represents the fraction of the magnetic susceptibility that relaxes much faster than the employed frequencies. Interestingly, both compounds show an almost temperature-independent fast relaxing component of the AC susceptibility of about 1 emu mol$^{-1}$. This value agrees well with the transverse component of the susceptibility of our randomly oriented powder samples evaluated by using the spin Hamiltonian parameters determined from HF-EPR experiments. The transverse component is not expected to experience any barrier when reversing its direction and thus is expected to relax much faster than the investigated frequency domain.

## Conclusions

Single-molecule magnets functionalized with terminal alkenyl and thioacetyl groups have been prepared by site-specific substitution on the complex $[Fe_4(OMe)_6(dpm)_6]$ (**3**) using derivatives of 2-(hydroxymethyl)propane-1,3-diol as incoming ligands. The two tripods are located along the

 © 2007 Wiley-VCH Verlag GmbH & Co. KGaA, Weinheim 

idealized threefold molecular axis, leading to wire-like molecular geometries, which are particularly well suited for the construction of metal-molecule-metal junctions. The complexes are found to be stable in solution and afford intense molecular peaks in the ESI-MS spectra. The magnetic properties, as revealed by DC and AC magnetometry and HF-EPR spectroscopy, indicate that the compounds have an $S = 5$ ground spin state. The easy-axis anisotropy is enhanced as compared with **3** and the effective energy barrier reaches up to 15–16 K, leading to slow relaxation of the magnetization at low temperature. We are currently investigating the formation of monolayers of **1** and **2** on H-terminated Si(100) (by hydrosilylation) and Au(111), respectively. The estimated distance between the thioacetyl "alligator clips" in **2** is 2.8–2.9 nm, and the molecule is then expected to fit into state-of-the-art metal nanogaps prepared using break junctions or electromigration.[6]

## Experimental Section

**Synthesis:** All chemicals were reagent-grade and used as received, unless otherwise noted. Diethyl ether, benzene, and toluene were distilled from sodium/benzophenone shortly before use. Benzene and toluene were stored over KOH pellets. Methanol was carefully dried by treatment with $Mg/I_2$ and distilled prior to use.[22] Dimethoxyethane (DME) was distilled from NaH. 2,2-Bis(hydroxymethyl)-10-undecen-1-ol ($H_3L^1$) was prepared by CaO-catalyzed Tollens reaction of 10-undecenal and formaldehyde in an EtOH/water mixture, according to a literature procedure.[13a] The precursor $[Fe_4(OMe)_6(dpm)_6]$ (**3**) and its deuterated variant, $[Fe_4(OMe)_6([D_{18}]dpm)_6]$ (**3D**), were prepared as described elsewhere.[10a]

**11-(Acetylthio)-2,2-bis(hydroxymethyl)undecan-1-ol ($H_3L^2$):** Thioacetic acid (0.660 g, 8.67 mmol) and 2,2′-azobis(2-methylpropionitrile) (0.713 g, 4.34 mmol) were added to a hot solution of $H_3L^1$ (1.00 g, 4.34 mmol) in dry benzene (10 mL). After stirring for 4 h at reflux temperature, the solution was cooled down and diethyl ether was added. The organic mixture was washed with saturated $NaHCO_3$ solution (3×) and brine. The solution was dried with $Na_2SO_4$ and filtered. After purification by column chromatography (eluent ethyl acetate/petroleum ether = 3:1), the product $H_3L^2$ was obtained as a white solid (0.745 g, 56%). $^1$H NMR (300 MHz, $CDCl_3$, 25 °C): $\delta$ = 3.74 [s, 6 H, C(1)$H_2$], 2.86 [t, $J$ = 2.0 Hz, 2 H, C(11)$H_2$], 2.47 (br. s, 3 H, OH), 2.32 (s, 3 H, $CH_3$), 1.62 [m, 2 H, C(10)$H_2$], 1.56 [m, 2 H, C(9)$H_2$], 1.40–1.10 (m, 12 H, Aliph) ppm. $C_{15}H_{30}O_4S_1$ (306.46): calcd. C 58.79, H 9.87, S 10.46; found C 58.58, H 9.96, S 10.32.

**$[Fe_4(L^1)_2(dpm)_6]$ (1):** Solid $H_3L^1$ (0.132 g, 0.573 mmol) and **3** (0.180 g, 0.119 mmol) were thoroughly mixed and heated to 70 °C under vacuum (0.1 Torr) for 15 min. The mixture was cooled down, powdered again, and reheated under the same conditions. After cooling, the solid was dissolved in dry toluene (12 mL) with gentle heating. Vapor diffusion of dry methanol (40 mL) into the filtered dark-orange solution afforded large dark-red blocks, which were washed with the external solvent mixture followed by pure methanol and then dried under vacuum (0.201 g, 95%). $C_{92}H_{160}Fe_4O_{18}$ (1777.60): calcd. C 62.16, H 9.07; found C 61.53, H 9.33. FTIR (KBr pellet): $\tilde{\nu}$ = 3080 (=C–H stretching), 1644 (C=C stretching), 994 (out-of-plane =C–H bending), 909 (in-plane =C–H bending) $cm^{-1}$.

**$[Fe_4(L^2)_2(dpm)_6]$ (2):** $H_3L^2$ (0.0658 g, 0.215 mmol) and **3** (0.120 g, 0.0795 mmol) were dissolved in dry DME/$Et_2O$ (1:1, v/v) (20 mL) with prolonged stirring. By slow concentration of the clear yellow-orange solution, a crystalline red-orange solid was obtained, which was washed with dry DME/MeOH (1:5, v/v) and dried under vacuum (0.1 Torr, 1 h) (0.138 g, 90%). $C_{96}H_{168}Fe_4O_{20}S_2$ (1929.89): calcd. C 59.75, H 8.77, S 3.32; found C 59.51, H 9.25, S 3.53. FTIR (KBr pellet): $\tilde{\nu}$ = 1699 (C=O stretching) $cm^{-1}$.

**X-ray Crystallography:** A single-crystal X-ray study was carried out on **1** with a four-circle Bruker X8APEX diffractometer equipped with a Kryo-Flex cryostat and controlled by Bruker-Nonius X8APEX software. Crystal structure data: $C_{92}H_{160}Fe_4O_{18}$, $M_r$ = 1777.60, crystal dimensions $0.42 \times 0.30 \times 0.24$ mm, monoclinic, space group $C2/c$ (no. 15), $a$ = 23.9416(3), $b$ = 15.6441(2), $c$ = 27.1433(4) Å, $\beta$ = 95.8450(10)°, $V$ = 10113.5(2) Å$^3$, $Z$ = 4, $\rho_{calcd.}$ = 1.167 g cm$^{-3}$, $2\theta_{max}$ = 52.02, Mo-$K_\alpha$ radiation, $\lambda$ = 0.71073 Å, $T$ = 120(2) K, $\mu$ = 0.621 mm$^{-1}$, collected/independent reflections 73989/9888 [$R$(int) = 0.0260]. The structure was solved by direct methods using the SIR92[23a] program. Full-matrix least-squares refinement on $F_o^2$ was performed using the SHELXL-97 program[23b] implemented in the WINGX suite[23c] on 9888 data points with 596 parameters and 43 restraints. All non-hydrogen atoms were refined anisotropically, and hydrogen atoms were added in idealized positions and assigned isotropic displacement parameters 50% and 20% larger than the $U_{eq}$ of the attached carbon atoms for aliphatic and methine hydrogen atoms, respectively. The alkyl chain of the tripodal ligand was found to be disordered over two equally populated positions. Final $R$ indices [$I > 2\sigma(I)$]: $R_1$ = 0.0425, $wR_2$ = 0.1113; $R$ indices (on all data): $R_1$ = 0.0593, $wR_2$ = 0.1298. Goodness-of-fit on $F^2$ = 1.031. Largest difference peak/hole 0.989/–0.667 e Å$^{-3}$. CCDC-646831 contains the supplementary crystallographic data for this paper. These data can be obtained free of charge from The Cambridge Crystallographic Data Centre via www.ccdc.cam.ac.uk/data_request/cif.

**Physical Techniques:** NMR spectra of the complexes were recorded at 302 K with a Bruker FT-DPX200 NMR spectrometer. Samples for $^1$H NMR spectroscopy were solutions of **1** and **2** in $CDCl_3$ (concentration about 13.5 mg/mL). Samples for $^2$H NMR spectroscopy were solutions of **3D** in dry $Et_2O$ (about 2.6 mg/mL), to which solid $H_3L^1$ or $H_3L^2$ (2.7 equiv.) was added. Chemical shifts were referenced to [$D_6$]acetone as external standard ($\delta$ =2.16 ppm). IR spectra were recorded with an FTIR Perkin–Elmer 1600 spectrometer. Samples were ground thoroughly with KBr at approximately 1% by weight and pressed into a pellet with a thickness of about 1 mm. UV/Vis spectra in the range 200–900 nm were recorded in toluene solution with a UV/Vis Perkin–Elmer λ650 spectrometer using quartz cuvettes with a 1-mm optical path. Electrospray mass spectra were acquired with a Micromass® Q-TOF micro™ mass spectrometer (Waters, UK) equipped with a Z-spray electrospray interface. Masslynx v. 3.5 software (Micromass) was used for data acquisition and processing. ESI-MS analyses were performed by operating the mass spectrometer in positive-ion (PI) mode acquiring mass spectra over the scan range $m/z$ = 300–2500, with a scan time of 1.2 s and an interscan delay of 0.1 s. The nebulizing gas (nitrogen, 99.999% purity) and the desolvation gas (nitrogen, 99.999% purity) were delivered at a flow rate of 150 and 600 l h$^{-1}$, respectively. The operating parameters of the interface were as follows: source temperature 90 °C, desolvation temperature 150 °C, cone voltage 30 V, ES (+) voltage 3.5 and 4.0 kV for the analysis of **1** and **2**, respectively. Q-TOF external calibration was performed using 0.1% (v/v) aqueous phosphoric acid solution. DC magnetic data were recorded using a Cryogenic S600 SQUID magnetometer. Susceptibility versus $T$ data from 2.2 to 300 K were collected on 22.75- and 31.80-mg microcrystalline samples of **1** and **2** with applied fields of 10 kOe (for $T > 30$ K) and 1 kOe (for $T <$

 © 2007 Wiley-VCH Verlag GmbH & Co. KGaA, Weinheim 

30 K) in order to reduce saturation effects. Isothermal magnetization versus $H$ curves were registered up to 60 kOe at about 2.4 and 4.9 K. Raw data were reduced with molecular weights equal to 1777.60 (**1**) and 1929.89 (**2**) and using diamagnetic corrections estimated from Pascal's constants $-1061.74 \times 10^{-6}$ and $-1146.72 \times 10^{-6}$ emu mol$^{-1}$ for **1** and **2**, respectively. The AC susceptibility of microcrystalline samples of **1** and **2** has been measured in the frequency range 100–25000 Hz with a home-made susceptometer[24] based on an Oxford Instruments MAGLAB2000 platform. High-frequency EPR (HF-EPR) spectra were recorded at the Grenoble High Magnetic Field Laboratory with a home-built spectrometer working in single-pass mode using a Gunn diode working at 95 GHz equipped with a frequency doubler as source excitation. Samples were pressed in pellets to avoid orientation effects.

**Spin Hamiltonian Calculations:** The NAG Fortran Library Routine E04FCF[25a] was used for fitting magnetic susceptibility and magnetization data with the aid of the ZHEEV routine (LAPACK Linear Algebra Package) for matrix diagonalization.[25b] Calculations were carried out with a Digital Alpha3000/800S computer.

**Supporting Information** (see footnote on the first page of this article): UV/Vis, IR, and fully labeled ESI-MS spectra for **1** and **2**, and Argand plot for **1**.

## Acknowledgments

This work was supported by the European Union through RTN "QUEMOLNA" (FP6-CT-2003-504880), NE "MAGMANET" (FP6-NMP3-CT-2005-515767), and NanoSci-ERA Project "SMMTRANS". Funding by Italian Ministero dell'Università e della Ricerca (MIUR) through FISR, FIRB, and PRIN projects is also acknowledged. We thank Rossella Gallesi (Department of Pharmaceutical Sciences, Università degli Studi di Modena e Reggio Emilia) for elemental analysis.

[1] a) R. Sessoli, D. Gatteschi, A. Caneschi, M. A. Novak, *Nature* **1993**, *365*, 141–143; b) D. Gatteschi, R. Sessoli, J. Villain, *Molecular Nanomagnets*, Oxford University Press, Oxford, **2006**.
[2] a) L. Thomas, F. Lionti, R. Ballou, D. Gatteschi, R. Sessoli, B. Barbara, *Nature* **1996**, *383*, 145–147; b) J. Friedman, M. P. Sarachick, J. Tejada, R. Ziolo, *Phys. Rev. Lett.* **1996**, *76*, 3830–3833; c) D. Gatteschi, R. Sessoli, *Angew. Chem. Int. Ed.* **2003**, *42*, 268–297.
[3] C. J. Milios, A. Vinslava, W. Wernsdorfer, S. Moggach, S. Parsons, S. P. Perlepes, G. Christou, E. K. Brechin, *J. Am. Chem. Soc.* **2007**, *129*, 2754–2755.
[4] A. Cornia, A. Fabretti Costantino, L. Zobbi, A. Caneschi, D. Gatteschi, M. Mannini, R. Sessoli, *Struct. Bond.* **2006**, *122*, 133–161.
[5] a) R. V. Martínez, F. García, R. García, E. Coronado, A. Forment-Aliaga, F. M. Romero, S. Tatay, *Adv. Mater.* **2007**, *19*, 291–295; b) R. W. Saalfrank, A. Scheurer, I. Bernt, F. W. Heinemann, A. V. Postnikov, V. Schünemann, A. X. Trautwein, M. S. Alam, H. Rupp, P. Müller, *Dalton Trans.* **2006**, 2865–2874; c) L. Zobbi, M. Mannini, M. Pacchioni, G. Chastanet, D. Bonacchi, C. Zanardi, R. Biagi, U. Del Pennino, D. Gatteschi, A. Cornia, R. Sessoli, *Chem. Commun.* **2005**, 1640–1642.
[6] a) H. B. Heersche, Z. de Groot, J. A. Folk, H. S. J. van der Zant, C. Romeike, M. R. Wegewijs, L. Zobbi, D. Barreca, E. Tondello, A. Cornia, *Phys. Rev. Lett.* **2006**, *96*, 206801/1–4; b) M.-H. Jo, J. Grose, K. Baheti, M. M. Deshmukh, J. J. Sokol, E. M. Rumberger, D. N. Hendrickson, J. R. Long, H. Park, D. C. Ralph, *Nano Lett.* **2006**, *6*, 2014–2020; c) J. J. Henderson, C. M. Ramsey, E. del Barco, A. Mishra, G. Christou, *J. Appl. Phys.* **2007**, *101*, O9E102/1-3.
[7] M. Pacchioni, A. Cornia, A. C. Fabretti, L. Zobbi, D. Bonacchi, A. Caneschi, G. Chastanet, D. Gatteschi, R. Sessoli, *Chem. Commun.* **2004**, 2604–2605.
[8] a) T. Strother, W. Cai, X. Zhao, R. J. Hamers, L. M. Smith, *J. Am. Chem. Soc.* **2000**, *122*, 1205–1209; b) Y. Kang, D.-J. Won, S. R. Kim, K. Seo, H.-S. Choi, G. Lee, Z. Noh, T. S. Lee, C. Lee, *Mater. Sci. Eng. C* **2004**, *24*, 43–46.
[9] E. K. Brechin, *Chem. Commun.* **2005**, 5141–5153.
[10] a) S. Accorsi, A. L. Barra, A. Caneschi, G. Chastanet, A. Cornia, A. C. Fabretti, D. Gatteschi, C. Mortalò, E. Olivieri, F. Parenti, P. Rosa, R. Sessoli, L. Sorace, W. Wernsdorfer, L. Zobbi, *J. Am. Chem. Soc.* **2006**, *128*, 4742–4755; b) A. Cornia, A. C. Fabretti, P. Garrisi, C. Mortalò, D. Bonacchi, D. Gatteschi, R. Sessoli, L. Sorace, W. Wernsdorfer, A.-L. Barra, *Angew. Chem. Int. Ed.* **2004**, *43*, 1136–1139; c) M. Moragues-Canovas, E. Riviere, L. Ricard, C. Paulsen, W. Wernsdorfer, G. Rajaraman, E. K. Brechin, T. Mallah, *Adv. Mater.* **2004**, *16*, 1101–1105.
[11] A. L. Barra, A. Caneschi, A. Cornia, F. Fabrizi de Biani, D. Gatteschi, C. Sangregorio, R. Sessoli, L. Sorace, *J. Am. Chem. Soc.* **1999**, *121*, 5302–5310.
[12] R. W. Saalfrank, I. Bernt, M. M. Chowdhry, F. Hampel, G. B. M. Vaughan, *Chem. Eur. J.* **2001**, *7*, 2765–2769.
[13] a) A. Muth, A. Asam, G. Huttner, A. Barth, L. Zsolnai, *Chem. Ber.* **1994**, *127*, 305–311; b) V. Gagnard, A. Leydet, A. Morère, J.-L. Montero, I. Lefèbvre, G. Gosselin, C. Pannecouque, E. De Clercq, *Bioorg. Med. Chem.* **2004**, *12*, 1393–1402.
[14] D. Gatteschi, L. Sorace, *J. Solid State Chem.* **2001**, *159*, 253–261.
[15] R. L. Lintvedt, L. K. Kernitsky, *Inorg. Chem.* **1970**, *9*, 491–494.
[16] a) J. B. Fenn, M. Mann, C. K. Meng, S. F. Wong, C. M. Whitehouse, *Science* **1989**, *246*, 64–71; b) I. Jardine, *Nature* **1990**, *345*, 747–748.
[17] a) V. Katta, S. K. Chowdhury, B. T. Chait, *J. Am. Chem. Soc.* **1990**, *112*, 5348–5349; b) T. G. Spence, T. D. Burns, G. B. Guckenberger, V. A. Posey, *J. Phys. Chem. A* **1997**, *101*, 1081–1092; c) E. Coronado, M. Feliz, A. Forment-Aliaga, C. J. Gomez-Garcia, R. Llusar, F. M. Romero, *Inorg. Chem.* **2001**, *40*, 6084–6085; d) H. Zhao, C. P. Berlinguette, J. Bacsa, A. V. Prosvirin, J. K. Bera, S. E. Tichy, E. J. Schelter, K. R. Dunbar, *Inorg. Chem.* **2004**, *43*, 1359–1369; e) P. Pelagatti, A. Bacchi, F. Calbiani, M. Carcelli, L. Elviri, C. Pelizzi, D. Rogolino, *J. Organomet. Chem.* **2005**, *690*, 4602–4610.
[18] A. L. Barra, L.-C. Brunel, D. Gatteschi, L. Pardi, R. Sessoli, *Acc. Chem. Res.* **1998**, *31*, 460–466.
[19] C. J. H. Jacobsen, E. Pedersen, J. Villadsen, H. Weihe, *Inorg. Chem.* **1993**, *32*, 1216–1221.
[20] J. R. Pilbrow, *Transition Ion Electron Paramagnetic Resonance*, Clarendon Press, Oxford, **1990**.
[21] a) K. S. Cole, R. H. Cole, *J. Chem. Phys.* **1941**, *9*, 341–351; b) C. Dekker, A. F. M. Arts, H. W. Wijn, A. J. van Duyneveldt, J. A. Mydosh, *Phys. Rev. B* **1989**, *40*, 11243–11251.
[22] A. I. Vogel, *Practical Organic Chemistry*, Longman, London, **1959**.
[23] a) A. Altomare, G. Cascarano, C. Giacovazzo, A. Guagliardi, *J. Appl. Crystallogr.* **1993**, *26*, 343–350; b) G. M. Sheldrick, *SHELX97, Programs for Crystal Structure Analysis (Release 97-2)*, University of Göttingen, Göttingen, **1997**; c) L. J. Farrugia, *J. Appl. Crystallogr.* **1999**, *32*, 837–838.
[24] S. Midollini, A. Orlandini, P. Rosa, L. Sorace, *Inorg. Chem.* **2005**, *44*, 2060–2066.
[25] a) *E04FCF, NAG Fortran Library Routine (Mark 17)*, NAG Ltd, Oxford, **1996**; b) *ZHEEV, LAPACK driver routine (Version 2.0)*, University of Tennessee, University of California Berkeley, NAG Ltd., Courant Institute, Argonne National Lab, Rice University, **1994**.

Received: April 5, 2007
Published Online: July 17, 2007

 © 2007 Wiley-VCH Verlag GmbH & Co. KGaA, Weinheim 

DOI: 10.1002/ejic.200700474

# Synthesis of Chiral, Monodentate Aminophosphane and Phosphoramidite Ligands Derived from Amino Acid Esters: Application in Rh-Catalysed Asymmetric Olefin Hydrogenation Reactions

**Luc Eberhardt,[a] Dominique Armspach,*[a] Dominique Matt,*[a] Loic Toupet,[b] and Benoît Oswald[c]**

**Keywords:** Phosphoramidites / Binol / Asymmetric catalysis / Rhodium / Olefin hydrogenation / Amino acid esters

Six chiral monodentate ligands combining a 1,3-dioxa-2-phosphacycloheptadinaphthyl moiety [(*R*)- or (*S*)-binoP] either with a phenylalanine- or with an alanine-derived fragment were synthesised. The new phosphoramidites are all relatively air stable. Related compounds in which the binoP moiety was replaced by a diphenylphosphanyl group were also prepared for comparison. The X-ray structures of two phosphoramidite complexes, *cis*-$PtCl_2$[(*R*)-binoP–NMeR]$_2$ [**5**, R = (*R*)-CH($CH_2$Ph)($CO_2$Me); **6**, R = (*S*)-CH($CH_2$Ph)-($CO_2$Me)], were determined by single X-ray analysis. In the solid state, both structures are nearly $C_2$ symmetric, and the nitrogen atoms lies out of the coordination plane. Owing to the particular orientation of the benzyl groups in **6**, the environment of the coordination sites occupied in this complex by the chlorine atoms is sterically more crowded than in **5**. In the hydrogenation of 2-(acetylamino)-3-(aryl)propenoic methyl esters (aryl = 4-X-$C_6H_4$, X = H, F, Cl; aryl = 3,4-$Cl_2$–$C_6H_3$), the alanine-derived phosphoramidites turned out to be ca. twice as active as the corresponding phenylalanine analogues. The highest *ee*'s were observed with the phenylalanine derivatives, for example 92 % in the hydrogenation of 2-(acetylamino)-3-(phenyl)propenoic methyl ester, by using (*R*)-binoP–NMe-(*R*)-CH($CH_2$Ph)($CO_2$Me).

(© Wiley-VCH Verlag GmbH & Co. KGaA, 69451 Weinheim, Germany, 2007)

## Introduction

In the last three decades natural amino acids and their derivatives have been often used as chiral backbones in the synthesis of optically active diphosphanes suitable for the enantioselective rhodium(I)-, ruthenium(II)- or iridium(I)-catalysed hydrogenation of prochiral unsaturated substrates.[1–4] For example, amino alcohols such as valinol, leucinol and prolinol gave access to a variety of mixed bidentate ligands, in particular aminophosphonite–phosphites,[5] aminophosphonite–phosphinites or aminophosphane–phosphinites[6–18] many of which turned out to give high enantiomeric excesses (*ee*'s) in enantioselective catalysis.

Recently, Feringa and Reetz found that monodentate, chiral phosphoramidite ligands, such as **A**, in which the phosphorus atom is part of a rigid, seven-membered ring involving a 1,1′-binaphthyl unit may lead to high conversions and enantiomeric excesses in metal-catalysed hydrogenations.[19–27] In their seminal works, they independently demonstrated that these readily accessible monodentate ligands give equivalent if not better results than conventional $P^{III}$ bidentate ligands.[28] The way these catalysts operate is still a matter of debate and a better understanding of their performance requires not only the synthesis and study of new variants of such ligands, but also solid-state studies that may establish particular structural features of their metal complexes.

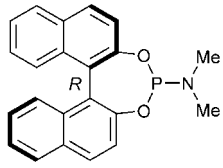


**A**

The present work describes the synthesis and structural characterisation of chiral *monodentate* ligands associating, for the first time, a phosphoramidite coordinating unit with the bulky and easily accessible *phenylalanine* backbone (Scheme 1). We also prepared ligands in which the latter was replaced by the less sterically demanding *alanine* fragment as well as some diphenylphosphanyl analogues of these phosphoramidites. A comparative study of their catalytic properties for the asymmetric rhodium-catalysed hydrogenation of α-*N*-acetaminoacrylic esters was carried out to assess the importance of the amino acid backbone on both catalyst selectivity and activity. In the following, the

[a] Laboratoire de Chimie Inorganique Moléculaire, Institut de Chimie UMR 7177 CNRS,
1 rue Blaise Pascal, 67008 Strasbourg Cedex, France
[b] Groupe Matière Condensée et Matériaux, UMR 6626, Université de Rennes 1,
Campus de Beaulieu, 35042 Rennes Cedex, France
[c] Genzyme Pharmaceuticals,
Eichenweg 1, 40410 Liestal, Switzerland

 © 2007 Wiley-VCH Verlag GmbH & Co. KGaA, Weinheim 

indexes "Bn", "Me" and "bin" refer to molecules containing –NMeCH($CH_2Ph$)($CO_2$Me), –NMeCH($Me$)($CO_2$Me) and *binaphthyl* groups, respectively. To date, monophosphoramidites that bear oxygen-containing pending groups have only been mentioned in two publications, one dealing with an ester[25] and the other with an ether[29] substituent.

(*R* or *S*)-*N*-methylphenylalanine methyl ester (*S*)-*N*-methylalanine methyl ester

Scheme 1. Phenylalanine and alanine derivatives used in this study as building blocks for the construction of chiral phosphanes.

## Results and Discussion

### Ligand Synthesis and Characterisation

We began this study by preparing aminophosphanes ($S_{Bn}$)-**2a** and ($R_{Bn}$)-**2b** (Scheme 2). These were obtained in ca. 85% yield by treating chlorodiphenylphosphane with (*S*)- and (*R*)-*N*-methylphenylalanine methyl ester, respectively, in the presence of 1 equiv. of diisopropylethylamine. We noted that the replacement of the latter amine by a less sterically hindered one, notably triethylamine, produced significant amounts of byproducts. The two aminophosphanes are relatively air stable and can be stored in air without particular care for months. Both products are characterised by a single peak at $\delta$ = 67.9 ppm in their $^{31}P\{^1H\}$ NMR spectra, a value that lies in the range found for similar ligands.[30]

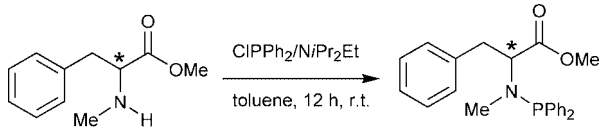


($S_{Bn}$)-**1a**
($R_{Bn}$)-**1b**

($S_{Bn}$)-**2a**
($R_{Bn}$)-**2b**

Scheme 2. Synthesis of aminophosphanes **2a** and **2b**.

To increase the chiral load of the molecules, we embarked on the synthesis of phosphoramidite ligands incorporating a 1,1′-binaphthyl unit in addition to a phenylalanine-derived fragment. Thus, the four stereoisomers ($S_{Bn}$,$S_{bin}$)-**3a**, ($R_{Bn}$,$R_{bin}$)-**3b**, ($R_{Bn}$,$S_{bin}$)-**3c** and ($S_{Bn}$,$R_{bin}$)-**3d**, all containing a –NMeCH($CH_2$Ph)($CO_2$Me) moiety, were synthesised (Scheme 3) from [(*R* or *S*)-(1,1′-binaphthalene-2,2′-diyl)] chlorophosphite (binoPCl[31]) and the appropriate amino acid ester according to the method described above. The two diastereoisomers ($S_{Me}$,$R_{bin}$)-**4a** and ($S_{Me}$,$S_{bin}$)-**4b**, containing the (*S*)-alanine-derived –NMeCH(Me)($CO_2$Me) fragment, were obtained by treatment of [($S_{Me}$)-**1c**]HCl with 2 equiv. of diisopropylethylamine and 1 equiv. of the corresponding chlorophosphite (Scheme 3). As expected for phosphoramidite ligands, all six compounds can be handled in air without noticeable oxidation, but they undergo P–N cleavage in the presence of water. The NMR spectra of the diastereoisomeric pairs of enantiomers ($S_{Bn}$,$S_{bin}$)-**3a**/($R_{Bn}$,$R_{bin}$)-**3b** and ($R_{Bn}$,$S_{bin}$)-**3c**/($S_{Bn}$,$R_{bin}$)-**3d**, in particular the $^{31}P\{^1H\}$ NMR spectra, which consist of single peaks at $\delta$ = 149.0 and 148.6 ppm,[32] are nearly identical. Similar small spectroscopic differences are observed between ($S_{Me}$,$R_{bin}$)-**4a** and ($S_{Me}$,$S_{bin}$)-**4b** [$\delta$($^{31}$P) = 148.5 and 148.2 ppm, respectively]. We note that whereas the H*C*(CO) carbon atom of ($S_{Bn}$)-**2a** is low-field shifted with respect to that of the parent amine, MeNHCHR($CO_2$Me), in the phosphoramidite ($S_{Bn}$,$S_{bin}$)-**3a** the corresponding carbon atom has undergone a high-field shift (Figure 1).

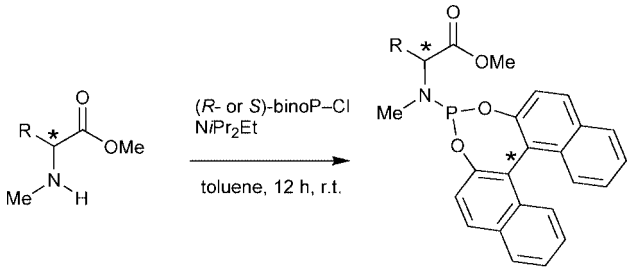


($S_{Bn}$)-**1a**; R = benzyl
($R_{Bn}$)-**1b**; R = benzyl
[($S_{Me}$)-**1c**]HCl; R = methyl

($S_{Bn}$,$S_{bin}$)-**3a**; R = benzyl
($R_{Bn}$,$R_{bin}$)-**3b**; R = benzyl
($R_{Bn}$,$S_{bin}$)-**3c**; R = benzyl
($S_{Bn}$,$R_{bin}$)-**3d**; R = benzyl
($S_{Me}$,$R_{bin}$)-**4a**; R = methyl
($S_{Me}$,$S_{bin}$)-**4b**; R = methyl

Scheme 3. Synthesis of the phosphoramidites **3** and **4**.

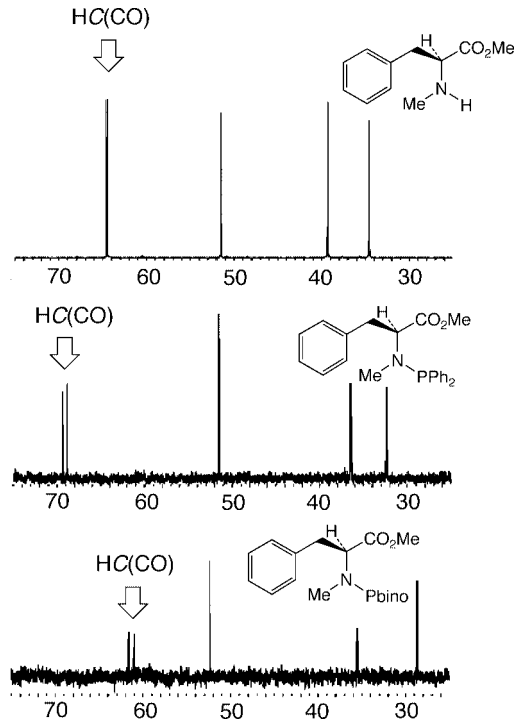


Figure 1. Part of the $^{13}$C NMR spectra ($CDCl_3$) of $S_{Bn}$-**1a**, $S_{Bn}$-**2a** and ($S_{Bn}$,$S_{bin}$)-**3a**. The arrows show the signals of the H*C*($CO_2$Me) carbon atoms.

 © 2007 Wiley-VCH Verlag GmbH & Co. KGaA, Weinheim 

To verify that the phosphoramidites described above are suitable to form square-planar complexes having two *cis* disposed phosphanes, which is the typical stereochemistry in most hydrogenation catalysts, we investigated the coordination properties of ($R_{Bn}$,$R_{bin}$)-**3b** and ($S_{Bn}$,$R_{bin}$)-**3d** towards platinum(II). The reaction of these ligands with [$PtCl_2$(cod)] (cod = 1,5-cyclooctadiene) or [$PtCl_2$(dcpd)] (dcpd = dicyclopentadiene) afforded complexes **5** and **6**, respectively (Scheme 4; see Experimental Section). The stereochemistry of the complexes was inferred from the corresponding $^{31}P$ NMR spectra, which both consist of a singlet flanked by two Pt satellites, with a $J_{P,Pt}$ coupling constant (5579 Hz for both complexes) in accord with the value reported by Hope et al. for another platinum phosphoramidite complex, namely *cis*-[$PtCl_2$(monophos)$_2$] (where monophos stands for ligand **A**).[33,34]

The stereochemistry of the complexes was further confirmed by single-crystal X-ray diffraction studies (Figure 2). The unit cell of **5** contains two inequivalent molecules (**5a** and **5b**), which structurally differ only a little, whereas that of **6** contains a single type of molecule. In both structures the molecules are nearly $C_2$ symmetric, and the nitrogen atoms are located out of the coordination plane [N to plane distances in **5a**: +1.31(1) and –1.31(1) Å; in **5b**: +1.32(1) and –1.31(1) Å; in **6**: +1.38(1) and –1.39(1) Å]. In all these molecules, the metal centre lies in an almost planar coordination environment, but the P–Pt–P angles are considerably larger than 90° [97.5(1)° and 97.6(1)° in **5**; 100.6(1)° in **6**], thus reflecting the steric bulk of the phosphane moieties. Similar deviations from an ideal square-planar coordination geometry were observed in the few structurally characterised binaphthyl-containing [$MX_2$(phosphoramidite)$_2$] complexes.[20,33] In both structures the nitrogen atoms are in a quasiplanar environment, and hence show that the electron-donating effect of the nitrogen atom onto the phosphorus atom is operating. The bond lengths about the metal centres are normal (see caption of Figure 2).

If the coordination plane is taken as a reference plane, the halide atoms of complex **5** may be viewed both as apically protected by a –$CO_2$Me moiety and a naphthyl group; these fragments belong to the same $P^{III}$ ligand and are located on either side of the plane. In complex **6**, the steric protection about each halide is markedly increased on one side of the plane, because here the benzyl groups occupy domains previously occupied by the smaller ester moieties.

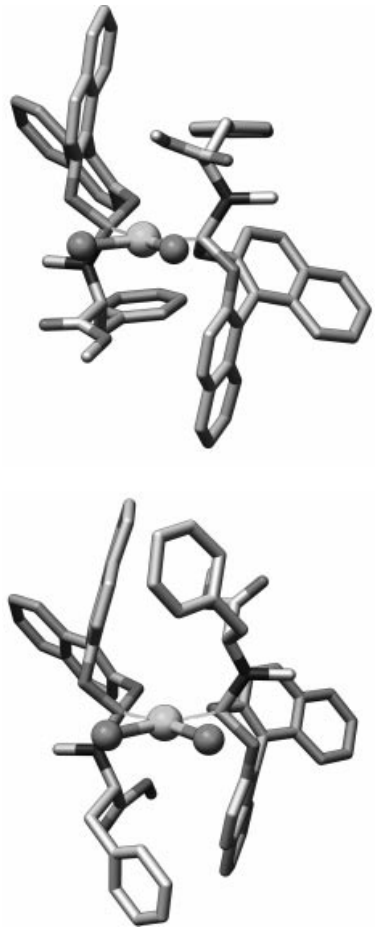

Figure 2. X-ray structures of compound **5a** (top) and compound **6** (bottom) showing the steric protection of the chloride atoms. Important bond lengths [Å]: **5a**: P(1)–Pt 2.207(3), P(2)–Pt 2.200(3), Pt–Cl(1) 2.336(3), Pt–Cl(2) 2.336(3), P(1)–N(1) 1.62(1), P(2)–N(2) 1.63(1); **6**: P(1)–Pt 2.222(2), P(2)–Pt 2.213(3), Pt–Cl(1) 2.349(3), Pt–Cl(2) 2.339(3), P(1)–N(1) 1.59(1), P(2)–N(2) 1.62(1). Dihedral angles [°] between the linked naphthyl units, in **5a**: 58.6 and 57.8; in **6**: 60.5 and 56.3.

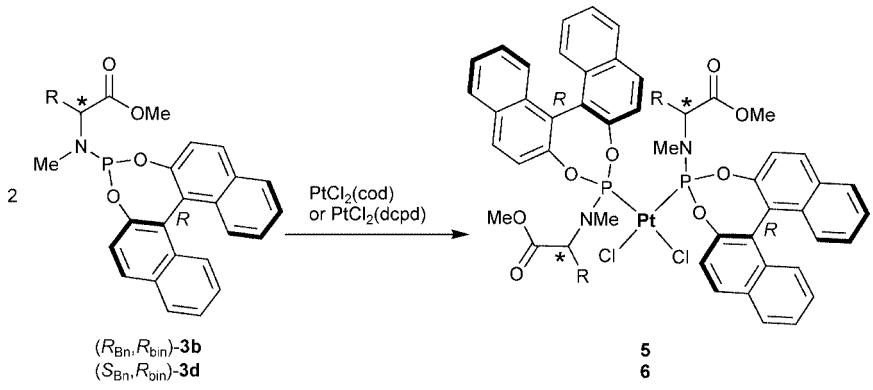


Scheme 4. Synthesis of platinum complexes **5** and **6**.

 © 2007 Wiley-VCH Verlag GmbH & Co. KGaA, Weinheim 

### Catalytic Studies

For the catalytic study, we focussed our attention on the reduction of 2-(acetylamino)-3-(4-fluorophenyl)propenoic methyl ester. A literature search revealed that this fluorinated amino acid has been relatively little studied. Some related compounds were also studied for comparison (Scheme 5).

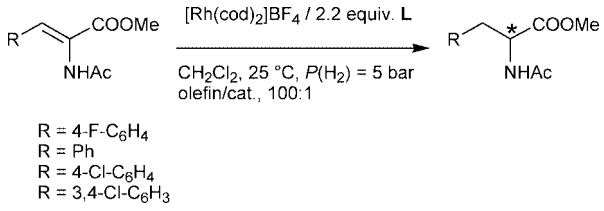


Scheme 5. Hydrogenation of 2-(acetylamino)-3-arylpropenoic methyl esters.

All catalytic runs (Table 1) were performed with in-situ-generated catalysts under 5 bar pressure by using an olefin/rhodium ratio of 100:1. It turned out that operating at r.t. afforded slightly higher yields than at 0 °C (Table 1, Entries 4 and 21). Further, among the solvents tested (thf, MeOH, AcOEt, $CH_2Cl_2$), dichloromethane gave the highest enantioselectivity (Table 1, Entries 1–3 and 21). In the following, we will therefore only discuss those runs performed at r.t. and in dichloromethane. As expected, we found that enantiomeric complexes (e.g. **3a** and **3b**) gave enantiomeric hydrogenation compounds; the *ee*'s were the same within experimental error.

As a general trend, and consistent with literature reports, the hydrogenation rates observed with the phosphoramidites were ca. 2–4 times better than those obtained with the aminophosphanes. We also found that aminophosphanes **2a** and **2b** resulted in very weak *ee*'s in the hydrogenation of 2-(acetylamino)-3-(phenyl)propenoic methyl ester and 2-(acetylamino)-3-(4-fluorophenyl)propenoic methyl ester (Table 1, Entries 5, 6, 19 and 20). This may be attributed to the fact that in the corresponding aminophosphane complexes the stereogenic centres are relatively far from the metal centre. We further observed that higher enantioselectivities were found for L/Rh ratios ≥ 2 (Table 1, compare Entry 8 with Entries 9–11, and compare Entry 12 with Entries 13–15) than for lower ratios. It is likely that L/Rh ratios below 2 result in part in the formation of [RhL(cod)]-$BF_4$ complexes in which the phosphoramidite behaves as a chelating ligand (possibly as a P,O rather than a P,N che-

Table 1. Enantioselective hydrogenation of α-dehydroamino esters by a Rh–monodentate phosphoramidite catalyst.[a]

| Entry | R | Ligand | Solvent | Time [h] | Conversion[b] [%] | *ee*[c] [%] | Configuration |
|---|---|---|---|---|---|---|---|
| 1 | (4-F)-Ph | **3a** | thf | 16 | 100 | 47 | *R* |
| 2 | (4-F)-Ph | **3a** | MeOH | 16 | 100 | 37 | *R* |
| 3 | (4-F)-Ph | **3a** | EtOAc | 16 | 100 | 35 | *R* |
| 4[d] | (4-F)-Ph | **3a** | $CH_2Cl_2$ | 16 | 75 | 86 | *R* |
| 5 | Ph | **2a** | $CH_2Cl_2$ | 24 | 93 | 2 | *R* |
| 6 | Ph | **2b** | $CH_2Cl_2$ | 24 | 90 | 2 | *S* |
| 7 | Ph | **3a** | $CH_2Cl_2$ | 24 | 100 | 90 | *R* |
| 8 | Ph | **3b** | $CH_2Cl_2$ | 24 | 100 | 92 | *S* |
| 9[e] | Ph | **3b** | $CH_2Cl_2$ | 24 | 100 | 69 | *S* |
| 10[f] | Ph | **3b** | $CH_2Cl_2$ | 24 | 100 | 83 | *S* |
| 11[g] | Ph | **3b** | $CH_2Cl_2$ | 24 | 100 | 90 | *S* |
| 12 | Ph | **3c** | $CH_2Cl_2$ | 24 | 93 | 87 | *R* |
| 13[e] | Ph | **3c** | $CH_2Cl_2$ | 24 | 86 | 79 | *R* |
| 14[f] | Ph | **3c** | $CH_2Cl_2$ | 24 | 85 | 81 | *R* |
| 15[g] | Ph | **3c** | $CH_2Cl_2$ | 24 | 86 | 85 | *R* |
| 16 | Ph | **3d** | $CH_2Cl_2$ | 24 | 93 | 90 | *S* |
| 17 | Ph | **4a** | $CH_2Cl_2$ | 18 | 100 | 81 | *S* |
| 18 | Ph | **4b** | $CH_2Cl_2$ | 18 | 100 | 78 | *R* |
| 19 | (4-F)-Ph | **2a** | $CH_2Cl_2$ | 65 | 94 | 8 | *R* |
| 20 | (4-F)-Ph | **2b** | $CH_2Cl_2$ | 65 | 93 | 7 | *S* |
| 21 | (4-F)-Ph | **3a** | $CH_2Cl_2$ | 24 | 90 | 85 | *R* |
| 22 | (4-F)-Ph | **3b** | $CH_2Cl_2$ | 24 | 94 | 88 | *S* |
| 23 | (4-F)-Ph | **3c** | $CH_2Cl_2$ | 24 | 12 | 67 | *R* |
| 24 | (4-F)-Ph | **3d** | $CH_2Cl_2$ | 24 | 14 | 68 | *S* |
| 25 | (4-F)-Ph | **4a** | $CH_2Cl_2$ | 18 | 100 | 78 | *S* |
| 26 | (4-F)-Ph | **4b** | $CH_2Cl_2$ | 18 | 100 | 76 | *R* |
| 27 | (3,4-Cl)-Ph | **3a** | $CH_2Cl_2$ | 24 | 98 | 85 | *R* |
| 28 | (3,4-Cl)-Ph | **3b** | $CH_2Cl_2$ | 24 | 96 | 84 | *S* |
| 29 | (4-Cl)-Ph | **3a** | $CH_2Cl_2$ | 24 | 98 | 89 | *R* |
| 30 | (4-Cl)-Ph | **3b** | $CH_2Cl_2$ | 24 | 99 | 92 | *S* |
| 31 | Ph | **3b+3d** | $CH_2Cl_2$ | 19 | 14 | 89 | *S* |
| 32 | Ph | **3d+4a** | $CH_2Cl_2$ | 19 | 32 | 92 | *S* |

[a] General conditions: $P(H_2)$ = 5 bar; $T$ = r.t.; substrate/Rh/ligand, 100:1:2.2. [b] Conversions were determined by means of $^1H$ NMR spectroscopic analysis. [c] Enantioselectivities were determined by chiral GC analysis by using a CHROMPAK chiral fused silica 25 m × 0.25 mm i.d. and/or specific rotation. Coating Chirasil-L-Val column. [d] Reaction carried out at 0 °C. [e] Substrate/Rh/ligand, 100:1:1. [f] Substrate/Rh/ligand, 100:1/1.5. [g] Substrate/Rh/ligand, 100:1:2.5.

 © 2007 Wiley-VCH Verlag GmbH & Co. KGaA, Weinheim 

late), which in turn give lower *ee*'s than the corresponding [Rh(phosphoramidite)$_2$(cod)]$BF_4$ complexes. Note that complexes of the latter type are generally formed when 2 equiv. of a monophosphoramidite are reacted with [Rh(cod)$_2$]$BF_4$.[20]

The highest *ee*'s, 92%, were obtained with phosphoramidite ($R_{Bn}$,$R_{bin}$)-**3b** (Table 1, Entries 8 and 30) in the hydrogenation of 2-(acetylamino)-3-(phenyl)propenoic methyl ester and 2-(acetylamino)-3-(4-chlorophenyl)propenoic methyl ester. The use of the same ligand for the hydrogenation of the fluorinated dehydroaminated ester (Table 1, Entry 22) gave an *ee* of 88%. It must be emphasised here that the performance of this ligand lies slightly below that of the reference ligand **A** [*ee*'s of ca. 95% for 2-(acetylamino)-3-(phenyl)propenoic methyl ester], which in contrast to **3b** contains an achiral amino substituent.[35] Interestingly, the number of binol-derived phosphoramidites in which the amino groups contains a stereogenic centre is limited. A literature survey revealed that, among this class of compounds, only Zheng's phosphoramidite **7**, which is derived from an expensive ferrocenyl–amine, gave better *ee*'s in the hydrogenation of cinammic acid esters than **A**.[36] Significantly lower enantioselectivities than those obtained for **3b** were obtained with proline derivative **8**[25] as well as with phosphoramidite **9**,[35] which contains two stereogenic centres in the amino group. Overall, these findings show that an improvement in the performances of **A** by using variants obtained from cheap, chiral amines remains a difficult task.

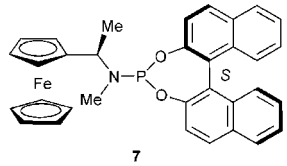


7

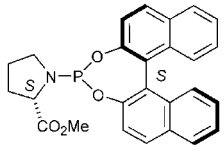


8

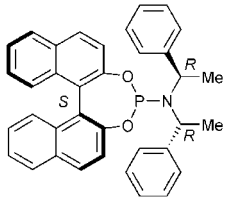


9

The most surprising result came from diastereomers ($R_{Bn}$,$S_{bin}$)-**3c** and ($R_{Bn}$,$R_{bin}$)-**3b**. Hydrogenation of the fluorinated olefin with ($R_{Bn}$,$S_{bin}$)-**3c** gave only 12% yield after 24 h (Table 1, Entries 23), whereas in the same time the reaction carried out with ($R_{Bn}$,$R_{bin}$)-**3b** was almost complete. Note that such a difference in activity was not observed with these ligands in the reduction of the slightly shorter 2-(acetylamino)-3-(phenyl)propenoic methyl ester (Table 1, Entries 12). Molecular models based on the X-ray structure of complex **6**, which contains ligand ($S_{Bn}$,$R_{bin}$)-**3d**, clearly show that in the hypothetical catalytic intermediates of type α and β (Figure 3), bidentate coordination of the fluorinated olefin results in considerable steric hindrance between the $Ar_{olefin}$ group and the benzyl groups. In the related **3b**-containing intermediates γ and δ, in which the amino acid ester moiety has a stereochemistry opposite to that of ($S_{Bn}$,$R_{bin}$)-**3d**, coordination of the olefin becomes much more favourable. The olefin–ligand interactions here mainly involve the smaller $CO_2Me$ group.

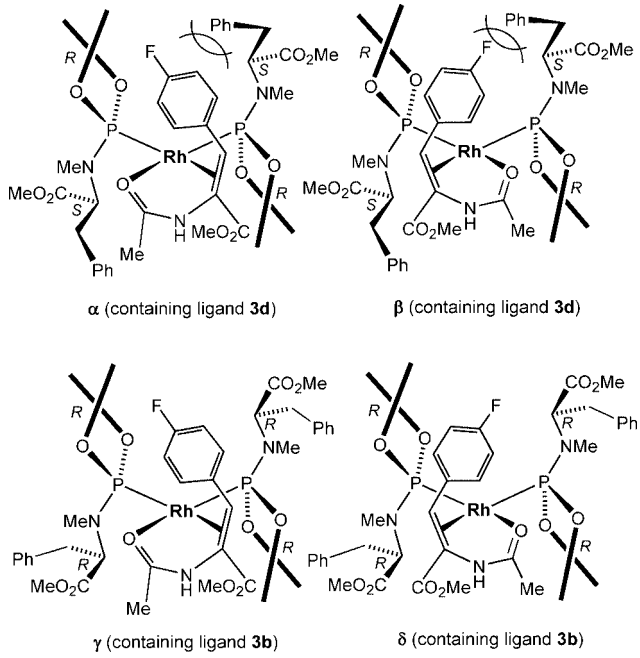


Figure 3. Possible coordination modes involving either complex **5** (α and β) or **6** (γ and δ) and 2-(acetylamino)-3-(4-fluorophenyl)-propenoic methyl ester.

To verify that these interactions have a determining impact on the catalyst activity, we tested ligands ($S_{Me}$,$R_{bin}$)-**4a** and ($S_{Me}$,$S_{bin}$)-**4b**, which contain a methyl group in place of a benzyl group. As anticipated, the hydrogenation reactions carried out with these ligands occurred much faster than those performed with their benzyl analogues (full substrate conversion within 18 h).

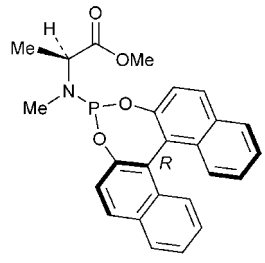


($S_{Me}$,$R_{bin}$)-**4a**

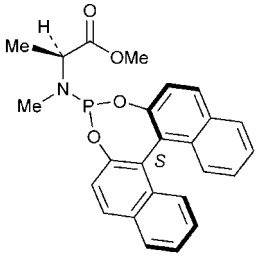


($S_{Me}$,$S_{bin}$)-**4b**

Furthermore, in the case of ($S_{Me}$,$S_{bin}$)-**4b**, a nonnegligible drop in the asymmetric induction was observed with respect to ($S_{Bn}$,$S_{bin}$)-**3a** in the catalytic reduction of 2-(acetylamino)-3-(phenyl)- and of 2-(acetylamino)-3-(4-fluorophenyl)propenoic methyl ester as well; the *ee*'s decrease by 12 and 9%, respectively (Table 1, Entries 18/7 and 26/21). The same trend was observed on going from ($S_{Bn}$,$R_{bin}$)-**3d** to ($S_{Me}$,$R_{bin}$)-**4a** in the hydrogenation of 2-(acetylamino)-3-(phenyl)propenoic methyl ester; *ee*'s decreased

 © 2007 Wiley-VCH Verlag GmbH & Co. KGaA, Weinheim 

by 9% (Table 1, Entries 17/16). Of course, we have to remain cautious in correlating the observed selectivities and activities, as the rate-determining steps are not known. Note that the hydrogenation of 2-(acetylamino)-3-(4-fluorophenyl)propenoic methyl ester with **3d** was too slow to allow comparison of the corresponding *ee* value with that obtained with the faster catalyst **4a**.

Finally, we found that by using equimolar mixtures of ($R_{Bn}$,$R_{bin}$)-**3b** and ($S_{Bn}$,$R_{bin}$)-**3d** in the hydrogenation of 2-(acetylamino)-3-(phenyl)propenoic methyl ester did not significantly modify the *ee* (Table 1, Entry 31), although in this experiment the activity unexpectedly dropped. Similar observations were made by using the ($S_{Bn}$,$R_{bin}$)-**3d**/($S_{Me}$,$R_{bin}$)-**4a** couple (Table 1, Entry 32). Thus, these results contrast the recent findings of Reetz et al. who showed that the combination of different phosphanes, in particular mixtures of chiral phosphites and *achiral* phosphanes, may produce a selectivity increase in hydrogenation experiments.[37]

## Conclusions

In the present study we described the first monodentate $P^{III}$ ligands combining a chiral 1,3-dioxa-2-phosphacycloheptadinaphthyl unit with a cost effective and readily available phenylalanine- or alanine-derived fragment. Despite their relative bulkiness, these ligands were found to readily form $[PtCl_2L_2]$ complexes adopting a *cis* stereochemistry. When used in the rhodium-catalysed hydrogenation of prochiral olefins, the alanine–phosphoramidites displayed considerably higher hydrogenation rates than the sterically more crowded phenylalanine analogues. The highest enantioselectivities, 92%, were found with ($R_{Bn}$,$R_{bin}$)-**3b**. These are higher than those obtained with related, cheap phosphoramidites in which the amino group contains at least one stereogenic centre, but remain slightly below the performances of the "Feringa–de Vries" ligand **A** when used under similar conditions. Overall, this study confirms previous studies that have already established that the bulky, binoP moiety has a major impact on the enantioselectivity of hydrogenation reactions, overwhelming that of other stereogenic centres present in the molecule.

## Experimental Section

**General Procedures:** All manipulations involving aminophosphanes and phosphoramidites were performed in Schlenk-type flasks under an atmosphere of dry nitrogen. Solvents were dried by conventional methods and distilled immediately prior to use. $CDCl_3$ was passed through a 5 cm-thick alumina column and stored under an atmosphere of nitrogen over molecular sieves (4 Å). Routine $^1H$, $^{13}C\{^1H\}$ and $^{31}P\{^1H\}$ spectra were recorded with Bruker FT Instruments (AC-200 and AC-300). $^1H$ NMR spectra were referenced to residual protonated solvents ($\delta$ = 7.26 ppm for $CDCl_3$ and 7.16 ppm for $C_6D_6$), $^{13}C$ chemical shifts are reported relative to deuterated solvents ($\delta$ = 77.16 ppm for $CDCl_3$ and 128.06 ppm for $C_6D_6$), and the $^{31}P$ NMR spectroscopic data are given relative to external $H_3PO_4$. Mass spectra were recorded with a Bruker MicroTOF spectrometer (ESI) and with $CH_2Cl_2$ as the solvent. Optical rotations were measured with a Perkin–Elmer 341 digital polarimeter with a 1 dm cell. The $^{13}C\{^1H\}$ NMR assignments for ($S_{Bn}$)-**2a** and ($R_{Bn}$)-**2b** are partially based on a literature reference.[38] The chlorophosphite binoPCl was prepared according to a procedure described in the literature.[31]

**Synthesis of Amino Esters**

**Methyl (*S*)-2-(Methylamino)-3-phenylpropionate [($S_{Bn}$)-1a]:** A solution of methyl (*S*)-2-(benzyloxycarbonylmethylamino)-3-phenylpropionate (3.196 g, 9.732 mmol), in MeOH (100 mL) was treated with 10% Pd/C (0.320 g, 10 wt.-% equiv.) and $H_2$ (1 atm) at 30 °C. After stirring for 2 h, the reaction mixture was filtered through Celite, and the solvent was evaporated under vacuum to afford a colourless oil. Yield: 1.891 g, 100%. $[\alpha]_D^{20}$ = +25.6 ($c$ = 0.30, $CHCl_3$) [ref.[38] $[\alpha]_D^{20}$ = +24.9 ($c$ = 0.30, $CHCl_3$)]. $^1H$ NMR (300 MHz, $CDCl_3$): $\delta$ = 7.27–7.11 (m, 5 H, arom. H), 3.60 (s, 3 H, $OCH_3$), 3.42 [t, $^3J_{H,H}$ = 6.8 Hz, 1 H, HC(CO)], 2.91 (d, $^3J_{H,H}$ = 6.8 Hz, 2 H, PhC$H_2$), 2.32 (s, 3 H, $NCH_3$), 1.76 (s, 1 H, N$H$CH$_3$) ppm. $^{13}C$ NMR (75 MHz, $CDCl_3$): $\delta$ = 174.49 (s, C=O), 137.04 (s, quat. C), 128.96 (s, arom. CH), 128.74 (s, arom. CH), 128.31 (s, arom. CH), 128.00 (s, arom. CH), 126.59 (s, arom. CH), 64.47 [s, H$C$(CO)], 51.42 (s, $OCH_3$), 39.26 (s, Ph$C$H$_2$), 34.52 (s, $NCH_3$) ppm. $C_{11}H_{15}NO_2$ (193.24): calcd. C 68.4, H 7.8, N 7.3; found C 68.6, H 7.8, N 7.3.

**Methyl (*R*)-2-(Methylamino)-3-phenylpropionate [($R_{Bn}$)-1b]:** ($R_{Bn}$)-**1b** was prepared according to the above procedure from methyl (*R*)-2-(benzyloxycarbonylmethylamino)-3-phenylpropionate (5.240 g, 15.96 mmol). Yield: 3.100 g, 100%. $[\alpha]_D^{20}$ = –25.5 ($c$ = 1.00, $CHCl_3$) [ref.[38] $[\alpha]_D^{20}$ = –25.1 ($c$ = 1.00, $CHCl_3$)]. $C_{11}H_{15}NO_2$ (193.24): calcd. C 68.4, H 7.8, N 7.3; found C 68.3, H, 7.9, N 7.4.

**Methyl (*S*)-2-(Methylamino)propionate Monohydrochloride {[($S_{Me}$)-1c]HCl}:** Thionyl chloride (1.300 g, 11.30 mmol, ca. 0.83 mL) was added dropwise to MeOH (15 mL) at 0 °C. To this mixture was added a solution of (*S*)-2-(methylamino)propionic acid (0.400 g, 3.80 mmol) in MeOH (10 mL). After stirring at r.t. for 4 d, the solvent was evaporated to dryness in vacuo to afford the product as a white solid. Yield: 0.600 g, 100%. $[\alpha]_D^{20}$ = +0.5 ($c$ = 2.00, EtOH) [ref.[39] $[\alpha]_D^{20}$ = +1.0 ($c$ = 2.00, EtOH)]. $^1H$ NMR (300 MHz, $CDCl_3$): $\delta$ = 10.06 (br., 1 H, N$H$), 3.94 [d, $^3J_{H,H}$ = 6.9 Hz, 1 H, HC(CO)], 3.84 (s, 3 H, OC$H_3$), 2.79 (s, 3 H, $NCH_3$), 1.73 (d, $^3J_{H,H}$ = 6.9 Hz, 3 H, CHC$H_3$) ppm. $^{13}C$ NMR (75 MHz, $CDCl_3$): $\delta$ = 169.09 (s, $C$=O), 56.20 [s, H$C$(CO)], 53.46 (s, $OCH_3$), 30.88 (s, $NCH_3$), 14.49 (s, CH$C$H$_3$) ppm. $C_5H_{12}ClNO_2$ (153.61): calcd. C 39.1, H 7.9, N 9.1; found C 39.2, H 7.8, N 9.1.

**Methyl (*S*)-2-(Methyldiphenylphosphanylamino)-3-phenylpropionate [($S_{Bn}$)-2a]:** To a solution of ($S_{Bn}$)-**1a** (2.110 g, 10.86 mmol) in toluene (30 mL) was added successively diisopropylethylamine (1.404 g, 13.90 mmol, ca. 1.88 mL) and chlorodiphenylphosphane (2.397 g, 10.86 mmol, ca. 1.95 mL). The mixture was stirred overnight at r.t., then filtered through $Al_2O_3$. The solvent was evaporated to dryness, after which the residue was purified by flash chromatography over silica (cyclohexane/ethyl acetate, 70:30). Product ($S_{Bn}$)-**2a** was obtained as a white solid. Yield: 3.510 g, 86%. M.p. 72–74 °C. $[\alpha]_D^{20}$ = –84.3 ($c$ = 1.00, toluene). $^1H$ NMR (300 MHz, $C_6D_6$): $\delta$ = 7.50–7.44 (m, 2 H, arom. H), 7.18–6.99 (m, 13 H, arom. H), 4.51 [ddd, $J_{H,H}$ = 6.2 Hz, $J_{H,H}$ = 9.8 Hz, $J_{H,P}$ = 11.6 Hz, 1 H, HC(CO)], 3.22 (s, 3 H, $OCH_3$), 3.23 and 3.02 (ABX spectrum, $^2J_{A,B}$ = 14.3 Hz, $^3J_{A,X}$ = 6.2 Hz, $^3J_{B,X}$ = 9.8 Hz, 2 H, PhC$H_2$), 2.43 (d, $^3J_{HP}$ = 2.6 Hz, 3 H, $NCH_3$) ppm. $^{13}C$ NMR (75 MHz, $C_6D_6$): $\delta$ = 172.74 (d, $^3J_{C,P}$ = 3.1 Hz, $C$=O), 139.44 (d, $^1J_{C,P}$ = 16.2 Hz, quat. C of $PPh_2$), 139.28 (d, $^1J_{C,P}$ = 11.8 Hz, quat. C of $PPh_2$), 138.46 (s, quat. C of benzyl), 132.76 (d, $J_{C,P}$ = 20.5 Hz, arom. CH of $PPh_2$), 132.65 (d, $J_{C,P}$ = 19.9 Hz, arom. CH of $PPh_2$), 129.65 (s, arom. CH of

 © 2007 Wiley-VCH Verlag GmbH & Co. KGaA, Weinheim 

benzyl), 128.83 (s, arom. CH of benzyl), 128.54 (d, $J_{C,P}$ = 11.8 Hz, arom. CH of $PPh_2$), 128.28 (s, arom. CH), 128.27 (d, $J_{C,P}$ = 8.8 Hz, arom. CH of $PPh_2$), 128.25 (s, arom. CH), 126.66 (s, arom. CH), 69.32 [d, $^2J_{C,P}$ = 40.3 Hz, *C*(CO)], 50.96 (s, $OCH_3$), 36.77 (d, $^3J_{C,P}$ = 9.3 Hz, Ph*C*$H_2$), 32.57 (d, $^2J_{C,P}$ = 8.7 Hz, $NCH_3$) ppm. $^{31}$P NMR (121 MHz, $C_6D_6$): $\delta$ = 67.9 (s) ppm. MS (ESI-TOF): *m*/*z* (%) = 378.18 (88) $[M + H]^+$. $C_{23}H_{24}NO_2P$ (377.42): calcd. C 73.2, H 6.4, N 3.7; found C 73.1, H 6.5, N 3.6.

**Methyl (*R*)-2-(Methyldiphenylphosphanylamino)-3-phenylpropionate [($R_{Bn}$)-2b]:** Compound ($R_{Bn}$)-**2b** was prepared according to the above procedure from ($R_{Bn}$)-**1b** (2.480 g, 12.77 mmol). Yield: 4.240 g, 88%. $[\alpha]_D^{20}$ = +85.2 (*c* = 1.00, toluene). MS (ESI-TOF): *m*/*z* (%) = 378.18 (100) $[M + H]^+$. $C_{23}H_{24}NO_2P$ (377.42): calcd. C 73.2, H 6.4, N 3.7; found C 73.1, H 6.5, N 3.6.

**General Procedure for the Synthesis of Phosphoramidites 3 and 4:** To a solution of $MeNHCHR(CO_2Me)$ (R = $CH_2Ph$, Me) in toluene (30 mL) was added diisopropylethylamine (1 equiv.) and chloro-(*S* or *R*)-2,2′-*O*,*O*′-(1,1′-binaphthyl)phosphite (1 equiv.). The mixture was stirred overnight at r.t. before being filtered through $Al_2O_3$. The solvent was removed in vacuo to afford the product as a white solid.

**Methyl (*S*)-2-{*N*,*N*-Methyl-[(*S*)-(dinaphtho[2,1-*d*:1′,2′-*f*][1,3,2]dioxaphosphepin-2-yl)]amino}-3-phenylpropionate [($S_{Bn}$,$S_{bin}$)-3a]:** Prepared according to the general procedure from ($S_{Bn}$)-**1a** (1.000 g, 5.15 mmol), diisopropylethylamine (0.665 g, 5.15 mmol, ca. 0.89 mL) and chloro-(*S*)-2,2′-*O*,*O*′-(1,1′-binaphthyl)phosphite (1.806 g, 5.15 mmol). Yield: 1.502 g, 58%. M.p. 70–71 °C. $[\alpha]_D^{20}$ = +281.2 (*c* = 0.26, toluene). $^1$H NMR (300 MHz, $CDCl_3$): $\delta$ = 7.95–7.73 (m, 4 H, arom. H), 7.48–7.15 (m, 12 H, arom. H), 6.66 (d, $J_{H,H}$ = 8.8 Hz, 1 H, arom. H), 4.53 [ddd, $^3J_{A,X}$ = 6.1 Hz, $^3J_{B,X}$ = 9.8 Hz, $^3J_{H,P}$ = 11.5 Hz, 1 H, HC(CO)], 3.76 (s, 3 H, OC*H*$_3$), 3.36 and 3.09 (ABX, $^2J_{A,B}$ = 14.4 Hz, $^3J_{A,X}$ = 6.1 Hz, $^3J_{B,X}$ = 9.8 Hz, 2 H, Ph$CH_2$), 2.23 (d, $^3J_{HP}$ = 4.0 Hz, 3 H, $NCH_3$) ppm. $^{13}$C NMR (75 MHz, $CDCl_3$): $\delta$ = 172.41 (d, $^3J_{C,P}$ = 6.2 Hz, C=O), 149.67–122.10 (arom. C′s), 61.27 [d, $J_{C,P}$ = 43.4 Hz, H*C*(CO)], 52.35 (s, $OCH_3$), 35.51 (d, $J_{C,P}$ = 6.2 Hz, Ph*C*$H_2$), 28.64 (s, $NCH_3$) ppm. $^{31}$P NMR (121 MHz, $CDCl_3$): $\delta$ = 149.0 (s) ppm. MS (ESI-TOF): *m*/*z* (%) = 530.16 (100) $[M + Na]^+$. $C_{31}H_{26}NO_4P$ (507.52): calcd. C 73.4, H 5.2, N 2.8; found C 73.5, H 5.3, N 2.6.

**Methyl (*R*)-2-{*N*,*N*-Methyl-[(*R*)-(dinaphtho[2,1-*d*:1′,2′-*f*][1,3,2]dioxaphosphepin-2-yl)]amino}-3-phenylpropionate [($R_{Bn}$,$R_{bin}$)-3b]:** Prepared according to the general procedure from ($R_{Bn}$)-**2b** (1.560 g, 8.03 mmol), diisopropylethylamine (1.047 g, 8.10 mmol, ca. 1.40 mL) and chloro-(*R*)-2,2′-*O*,*O*′-(1,1′-binaphthyl)phosphite (2.840 g, 8.10 mmol). Yield: 2.703 g, 66%. $[\alpha]_D^{20}$ = –285.3 (*c* = 1.00, toluene). NMR as for ($S_{Bn}$,$S_{bin}$)-**3a**. MS (ESI-TOF): *m*/*z* (%) = 530.16 (100) $[M + Na]^+$. $C_{31}H_{26}NO_4P$ (507.52): calcd. C 73.4, H 5.2, N 2.8; found C 73.4, H 5.4, N 2.6.

**Methyl (*R*)-2-{*N*,*N*-Methyl-[(*S*)-(dinaphtho[2,1-*d*:1′,2′-*f*][1,3,2]dioxaphosphepin-2-yl)]amino}-3-phenylpropionate [($R_{Bn}$,$S_{bin}$)-3c]:** Prepared according to the general procedure from ($R_{Bn}$)-**1b** (1.230 g, 6.33 mmol), diisopropylethylamine (0.818 g, 6.33 mmol, ca. 1.10 mL) and chloro-(*S*)-2,2′-*O*,*O*′-(1,1′-binaphthyl)phosphite (2.230 g, 6.33 mmol). Yield: 1.502 g, 58%. M.p. 70–71 °C. $[\alpha]_D^{20}$ = +542.6 (*c* = 1.00, toluene). $^1$H NMR (300 MHz, $CDCl_3$): $\delta$ = 7.95–7.89 (m, 4 H, arom. H), 7.46–7.19 (m, 13 H, arom. H), 4.48 [ddd, $J_{A,X}$ = 5.5 Hz, $J_{B,X}$ = 10.0 Hz, $J_{H,P}$ = 11.6 Hz, 1 H, HC(CO)], 3.90 (s, 3 H, $OCH_3$), 3.29 and 3.01 (ABX, $J_{A,B}$ = 14.3 Hz, $J_{A,X}$ = 5.5 Hz, $J_{B,X}$ = 10.0 Hz, 2 H, Ph$CH_2$), 2.26 (d, $J_{HP}$ = 3.2 Hz, 3 H, $NCH_3$) ppm. $^{13}$C NMR (75 MHz, $CDCl_3$): $\delta$ = 172.46 (d, $^3J_{C,P}$ = 5.0 Hz, *C*=O), 150.15 (d, $J_{C,P}$ = 5.6 Hz, quat. C), 149.32 (s, quat. C), 137.43 (s, quat. C), 132.85 (d, $J_{C,P}$ = 1.2 Hz, quat. C), 132.63 (s, quat. C), 131.48 (s, quat. C), 130.90 (s, quat. C), 130.29 (s, arom. CH), 130.15 (s, arom. CH), 129.52 (d, $J_{C,P}$ = 1.2 Hz, arom. CH), 128.60 (s, 2× arom. CH), 128.44 (s, arom. CH), 128.39 (s, arom. CH), 127.12 (s, arom. CH), 127.01 (s, arom. CH), 126.82 (s, arom. CH), 126.17 (s, 2× arom. CH), 124.90 (s, arom. CH), 124.73 (s, arom. CH), 123.97 (d, $J_{C,P}$ = 5.0 Hz, quat. C), 122.67 (d, $J_{C,P}$ = 1.9 Hz, quat. C), 122.21 (s, arom. CH), 122.04 (s, arom. CH), 122.02 (s, arom. CH), 61.99 [d, $^2J_{C,P}$ = 45.3 Hz, H*C*(CO)], 52.33 (s, $OCH_3$), 34.96 (d, $^3J_{C,P}$ = 6.2 Hz, Ph*C*$H_2$), 28.23 (d, $^2J_{C,P}$ = 3.7 Hz, $NCH_3$) ppm. $^{31}$P NMR (121 MHz, $CDCl_3$): $\delta$ = 148.6 (s) ppm. MS (ESI-TOF): *m*/*z* (%) = 530.16 (41) $[M + Na]^+$. $C_{31}H_{26}NO_4P$ (507.52): calcd. C 73.4, H 5.2, N 2.8; found C 73.3, H 5.2, N 2.6.

**Methyl (*S*)-2-{*N*,*N*-Methyl-[(*R*)-(dinaphtho[2,1-*d*:1′,2′-*f*][1,3,2]dioxaphosphepin-2-yl)]amino}-3-phenylpropionate [($S_{Bn}$,$R_{bin}$)-3d]:** Prepared according to the general procedure from ($S_{Bn}$)-**1a** (1.897 g, 9.77 mmol), diisopropylethylamine (1.262 g, 9.77 mmol, ca. 1.69 mL) and chloro-(*R*)-2,2′-*O*,*O*′-(1,1′-binaphthyl)phosphite (3.440 g, 9.81 mmol). Yield: 3.400 g, 69%. $[\alpha]_D^{20}$ = –533.5 (*c* = 1.00, toluene). NMR as for ($R_{Bn}$,$S_{bin}$)-**3c**. MS (ESI-TOF): *m*/*z* (%) = 530.16 (100) $[M + Na]^+$. $C_{31}H_{26}NO_4P$ (507.52): calcd. C 73.4, H 5.2, N 2.8; found C 73.4, H 5.2, N 2.6.

**Methyl (*S*)-2-{*N*,*N*-Methyl-[(*R*)-(dinaphtho[2,1-*d*:1′,2′-*f*][1,3,2]dioxaphosphepin-2-yl)]amino}propionate [($S_{Me}$,$R_{bin}$)-4a]:** Prepared according to the general procedure from [($S_{Me}$)-**1c**]HCl (0.300 g, 1.95 mmol), diisopropylethylamine (0.530 g, 4.10 mmol, ca. 0.69 mL) and chloro-(*R*)-2,2′-*O*,*O*′-(1,1′-binaphthyl)phosphite (0.720 g, 2.05 mmol). Yield: 0.767 g, 91%. M.p. 62–64 °C. $[\alpha]_D^{20}$ = –475.8 (*c* = 0.85, toluene). $^1$H NMR (300 MHz, $CDCl_3$): $\delta$ = 7.98–7.90 (m, 4 H, arom. H), 7.54 (d, $J_{H,H}$ = 8.8 Hz, 2 H, arom. H), 7.45–7.35 (m, 4 H, arom. H), 7.31–7.23 (m, 2 H, arom. H), 4.32 [dq, $^3J_{H,H}$ = 7.2 Hz, $^3J_{H,P}$ = 9.6 Hz, 1 H, HC(CO)], 3.84 (s, 3 H, $OCH_3$), 2.28 (d, $^3J_{H,P}$ = 4.8 Hz, 3 H, $NCH_3$), 1.42 (d, $^3J_{H,H}$ = 7.2 Hz, 3 H, $CCH_3$) ppm. $^{13}$C NMR (75 MHz, $CDCl_3$): $\delta$ = 173.43 (d, $^3J_{C,P}$ = 3.1 Hz, *C*=O), 150.08–122.04 (arom. C′s), 55.09 [d, $^2J_{C,P}$ = 42.2 Hz, H*C*(CO)], 52.22 (s, $OCH_3$), 28.10 (d, $^2J_{C,P}$ = 3.1 Hz, $NCH_3$), 16.08 (d, $^3J_{C,P}$ = 6.8 Hz, C*C*$H_3$) ppm. $^{31}$P NMR (121 MHz, $CDCl_3$): $\delta$ = 148.5 (s) ppm. MS (ESI-TOF): *m*/*z* (%) = 454.11 (91) $[M + Na]^+$. $C_{25}H_{22}NO_4P$ (431.42): calcd. C 69.6, H 5.1, N 3.3; found C 69.7, H 5.2, N 3.3.

**Methyl (*S*)-2-{*N*,*N*-Methyl-[(*S*)-(dinaphtho[2,1-*d*:1′,2′-*f*][1,3,2]dioxaphosphepin-2-yl)]amino}propionate [($S_{Me}$,$S_{bin}$)-4b]:** Prepared according to the general procedure from [($S_{Me}$)-**1c**]HCl (0.581 g, 3.78 mmol), diisopropylethylamine (1.026 g, 7.94 mmol, ca. 1.33 mL) and chloro-(*S*)-2,2′-*O*,*O*′-(1,1′-binaphthyl)phosphite (1.393 g, 3.97 mmol). Yield: 1.452 g, 89%. M.p. 61–63 °C. $[\alpha]_D^{20}$ = +481.2 (*c* = 0.85, toluene). $^1$H NMR (300 MHz, $CDCl_3$): $\delta$ = 7.97 (d, $J_{H,H}$ = 8.8 Hz, 1 H, arom. H), 7.93–7.87 (m, 3 H, arom. H), 7.53 (d, $J_{H,H}$ = 8.8 Hz, 1 H, arom. H), 7.44–7.38 (m, 4 H, arom. H), 7.34–7.21 (m, 3 H, arom. H), 4.24 [dq, $^3J_{H,H}$ = 7.2 Hz, $^3J_{H,P}$ = 9.9 Hz, 1 H, HC(CO)], 3.74 (s, 3 H, $OCH_3$), 2.33 (d, $^3J_{H,P}$ = 5.7 Hz, 3 H, NC*H*$_3$), 1.51 (d, $^3J_{H,H}$ = 7.2 Hz, 3 H, $CCH_3$) ppm. $^{13}$C NMR (75 MHz, $CDCl_3$): $\delta$ = 173.24 (d, $^3J_{CP}$ = 6.8 Hz, *C*=O), 149.80 (d, $J_{CP}$ = 5.6 Hz, quat. C), 149.42 (s, quat. C), 132.89 (d, $J_{C,P}$ = 1.2 Hz, quat. C), 132.69 (s, quat. C), 131.54 (s, quat. C), 130.87 (s, quat. C), 130.44 (s, arom. CH), 130.02 (s, arom. CH), 128.46 (s, arom. CH), 128.36 (s, arom. CH), 127.12 (s, arom. CH), 127.07 (s, arom. CH), 126.22 (s, arom. CH), 124.96 (s, arom. CH), 124.78 (s, arom. CH), 124.01 (d, $J_{C,P}$ = 5.0 Hz, quat. C), 122.69 (d, $J_{C,P}$ = 1.9 Hz, quat. C), 122.12 (s, arom. CH), 122.09 (s, arom. CH), 122.07 (s, arom. CH), 55.14 [d, $^2J_{C,P}$ = 37.2 Hz, H*C*(CO)], 52.19 (s, $OCH_3$), 28.79 (d, $^3J_{C,P}$ = 6.8 Hz, C*C*$H_3$), 16.54 (d, $^2J_{C,P}$ = 6.2 Hz, $NCH_3$) ppm. $^{31}$P NMR (121 MHz, $CDCl_3$): $\delta$ = 148.2 (s) ppm. MS (ESI-

 © 2007 Wiley-VCH Verlag GmbH & Co. KGaA, Weinheim 

TOF): *m/z* (%) = 454.14 (87) $[M + Na]^+$. $C_{25}H_{22}NO_4P$ (431.42): calcd. C 69.6, H 5.1, N 3.3; found C 69.7, H 5.3, N 3.1.

**Synthesis of Complexes**

***cis*-Dichloridobis[methyl (*R*)-2-{*N*,*N*-methyl-[(*R*)-(dinaphtho[2,1-*d*:1′,2′-*f*][1,3,2]dioxaphosphepin-2-yl)]amino}-3-phenylpropionate]-platinum(II) (5):** A solution of phosphoramidite ($R_{Bn}$,$R_{bin}$)-**3b** (0.250 g, 0.50 mmol) in $CH_2Cl_2$ (8 mL) was added to a solution of dichlorido(dicyclopentadienyl)platinum(II) (0.100 g, 0.25 mmol) in $CH_2Cl_2$ (10 mL). The solution was stirred at r.t. for 24 h. The solution was then concentrated to ca. 5 mL, after which *n*-pentane was added (30 mL). Cooling this solution down to –10 °C precipitated **5** as a white solid. Yield: 0.290 g, 91%. M.p. > 250 °C. $^1$H NMR (300 MHz, $CDCl_3$): $\delta$ = 8.35 (d, $J_{H,H}$ = 8.9 Hz, 1 H, arom. H), 8.12 (d, $J_{H,H}$ = 9.1 Hz, 1 H, arom. H), 7.98 (d, $J_{H,H}$ = 8.1 Hz, 1 H, arom. H), 7.91 (d, $J_{H,H}$ = 8.3 Hz, 1 H, arom. H), 7.71 (d, $J_{H,H}$ = 8.8 Hz, 1 H, arom. H), 7.52–7.42 (m, 3 H, arom. H), 7.36–7.32 (m, 2 H, arom. H), 7.03 (t, $J_{H,H}$ = 7.5 Hz, 1 H, arom. H), 6.74 (t, $J_{H,H}$ = 7.7 Hz, 2 H, arom. H), 6.63 (d, $J_{H,H}$ = 7.3 Hz, 2 H, arom. H), 6.36 (d, $J_{H,H}$ = 8.8 Hz, 1 H, arom. H), 4.12 [ddd, $^3J_{H,H}$ = 8.6 Hz, $^3J_{H,H}$ = 6.8 Hz, $^3J_{H,P}$ = 11.3 Hz, 1 H, HC(CO)], 3.41 (s, 3 H, $OCH_3$), 2.65 and 2.37 (ABX, $^2J_{A,B}$ = 14.3 Hz, $^3J_{A,X}$ = 8.6 Hz, $^3J_{B,X}$ = 6.8 Hz, 2 H, $PhCH_2$), 2.24 (d, $^3J_{H,P}$ = 10.4 Hz, 3 H, $NCH_3$) ppm. $^{13}$C NMR (75 MHz, $CDCl_3$): $\delta$ = 171.13 (s, *C*=O), 148.11 (virtual t, $^3J_{C,P}$ + $^5J_{C,P'}$ = 3.7 Hz, quat. C), 147.93 (d, $J_{C,P}$ = 6.2 Hz, quat. C), 136.13 (s, quat. C), 132.25 (s, quat. C), 131.90 (s, quat. C), 131.77 (s, quat. C), 131.46 (s, quat. C), 131.42 (s, arom. CH), 130.65 (s, arom. CH), 129.24 (s, arom. CH), 128.70 (s, arom. CH), 128.43 (s, arom. CH), 128.20 (s, arom. CH), 127.27 (s, arom. CH), 126.97 (s, arom. CH), 126.73 (s, arom. CH), 126.50 (s, arom. CH), 126.04 (s, arom. CH), 125.77 (s, arom. CH), 123.19 (s, arom. CH), 122.59 (s, quat. C), 122.19 (s, quat. C), 120.51 (s, arom. CH), 59.75 [virtual t, $^2J_{C,P}$ + $^4J_{C,P'}$ = 6.5 Hz, H*C*(CO)], 51.80 (s, $OCH_3$), 35.78 (s, Ph*C*$H_2$), 30.93 (virtual t, $^2J_{C,P}$ + $^4J_{C,P'}$ = 2.5 Hz, $NCH_3$) ppm. $^{31}$P NMR (121 MHz, $CDCl_3$): $\delta$ = 94.9 ($J_{Pt,P}$ = 5578 Hz) ppm MS (ESI-TOF): *m/z* (%) = 1244.17 (61) $[M - Cl]^+$. $C_{62}H_{52}Cl_2N_2O_8P_2Pt$ (1281.02): calcd. C 58.2, H 4.0, N 2.0; found C 58.0, H 4.2, N 2.0.

***cis*-Dichloridobis[methyl (*S*)-2-{*N*,*N*-methyl-[(*R*)-(dinaphtho[2,1-*d*:1′,2′-*f*][1,3,2]dioxaphosphepin-2-yl)]amino}-3-phenylpropionate]-platinum(II) (6):** A solution of phosphoramidite ($S_{Bn}$,$R_{bin}$)-**3d** (0.110 g, 0.22 mmol) in $CH_2Cl_2$ (8 mL) was added to a solution of [$PtCl_2$(cod)] (0.040 g, 0.11 mmol) in $CH_2Cl_2$ (10 mL). After stirring for 24 h, the solution was concentrated to 6 mL, after which *n*-pentane (30 mL) was added. Cooling the solution down to –10 °C afforded **6** as a white solid. Yield: 0.130 g, 95%. M.p. > 250 °C. $^1$H NMR (300 MHz, $CDCl_3$): $\delta$ = 8.34 (d, $J_{H,H}$ = 8.9 Hz, 1 H, arom. H), 8.12 (d, $J_{H,H}$ = 9.1 Hz, 1 H, arom. H), 7.98 (d, $J_{H,H}$ = 8.1 Hz, 1 H, arom. H), 7.89 (d, $J_{H,H}$ = 8.9 Hz, 1 H, arom. H), 7.69 (d, $J_{H,H}$ = 8.9 Hz, 1 H, arom. H), 7.47 (m, 3 H, arom. H), 7.35 (m, 2 H, arom. H), 7.17 (m, 1 H, arom. H), 7.01 (t, $J_{H,H}$ = 7.4 Hz, 1 H, arom. H), 6.73 (t, $J_{H,H}$ = 7.7 Hz, 2 H, arom. H), 6.62 (d, $J_{H,H}$ = 6.9 Hz, 2 H, arom. H), 6.36 (d, $J_{H,H}$ = 8.8 Hz, 1 H, arom. H), 4.11 [ddd, $^3J_{H,H}$ = 8.6 Hz, $^3J_{H,H}$ = 6.9 Hz, $^3J_{H,P}$ = 11.3 Hz, 1 H, HC(CO)], 3.39 (s, 3 H, $OCH_3$), 2.65 and 2.37 (ABX, $^2J_{A,B}$ = 14.2 Hz, $^3J_{A,X}$ = 8.6 Hz, $^3J_{B,X}$ = 6.9 Hz, 2 H, $CH_2Ph$), 2.22 (d, $^3J_{HP}$ = 10.9 Hz, 3 H, $NCH_3$) ppm. $^{13}$C NMR (75 MHz, $CDCl_3$): $\delta$ = 169.97 (virtual t, $^3J_{C,P}$ + $^5J_{C,P'}$ = 7.4 Hz, C=O), 148.37 (virtual t, $^3J_{C,P}$ + $^5J_{C,P'}$ = 12.4 Hz, quat. C), 147.82 (virtual t, $^3J_{C,P}$ + $^5J_{C,P'}$ = 6.8 Hz, quat. C), 137.38 (s, 2× quat. C), 132.41 (s, quat. C), 131.67 (d, $J_{C,P}$ = 0.6 Hz, quat. C), 131.60 (s, arom. CH), 130.96 (s, arom. CH), 130.44 (s, arom. CH), 129.23 (d, $J_{C,P}$ = 0.6 Hz, arom. CH), 128.53 (d, $J_{C,P}$ = 0.6 Hz, arom. CH), 128.39 (d, $J_{C,P}$ = 0.6 Hz, arom. CH), 127.47 (d, $J_{C,P}$ = 0.6 Hz, arom. CH), 127.06 (s, arom. CH), 126.55 (d, $J_{C,P}$ = 0.6 Hz, arom. CH), 126.48 (s, arom. CH), 126.30 (d, $J_{C,P}$ = 0.6 Hz, arom. CH), 126.11 (d, $J_{C,P}$ = 0.6 Hz, arom. CH), 125.36 (s, arom. CH), 122.88 (d, $J_{C,P}$ = 1.2 Hz, 2× quat. C), 122.19 (s, arom. CH), 122.01 (s, quat. C), 120.45 (s, arom. CH), 51.86 [virtual t, $^2J_{C,P}$ + $^4J_{C,P'}$ = 21 Hz, H*C*(CO)], 51.71 (s, $OCH_3$), 35.37 (d, $^3J_{C,P}$ = 1.9 Hz, Ph*C*$H_2$), 31.07 (s, $NCH_3$) ppm. $^{31}$P NMR (121 MHz, $CDCl_3$): $\delta$ = 95.0 ($J_{Pt,P}$ = 5579 Hz) ppm. MS (ESI-TOF): *m/z* (%) = 1244.25 (12) $[M - Cl]^+$. $C_{62}H_{52}Cl_2N_2O_8P_2Pt$ (1281.02): calcd. C 58.2, H 4.0, N 2.0; found C 58.0, H 4.2, N 2.0.

**X-ray Crystal Structure Determination of 5:** Crystals of **5** suitable for X-ray diffraction were obtained by slow diffusion of pentane into a chloroform solution of the complex. $2(C_{62}H_{52}Cl_2N_2O_8Pt)\cdot 2(0.5CHCl_3)\cdot 0.5C_5H_{12}$, $M$ = 2717.41, tetragonal, $P4_1$, $a$ = $b$ = 11.5731(2) Å, $c$ = 89.444(2) Å, $V$ = 11979.8(4) Å$^3$, $Z$ = 4, $D_{calcd.}$ = 1.507 g cm$^{-3}$, $\lambda$(Mo-$K_\alpha$) = 0.71073 Å, $\mu$ = 26.08 cm$^{-1}$, $F$(000) = 5468, $T$ = 100 K. The sample (0.25 × 0.20 × 0.20 mm) was studied with a Bruker AXS X8-APEX II diffractometer with graphite monochromatized Mo-$K_\alpha$ radiation. Data collection was carried out by using the Bruker collect suite.[40] 51864 Reflections were collected ($1.76 < \theta < 27.54°$), of which 20757 had $I > 2.0\sigma(I)$. The structure was solved with SIR-97,[41] which revealed the non-hydrogen atoms of the molecule. After anisotropic refinement, many hydrogen atoms could be localized on Fourier difference map. The whole structure was refined with SHELXL-97.[42] Hydrogen atoms were included and refined by using a riding mode in SHELX-97. Final results: $R_1$ = 0.065, $wR_2$ = 0.152, goodness of fit 1.135, 1465 parameters, residual electron density: min/max = –2.47/1.89. Flack parameter: 0.064(7).

**Crystal Data for 6:** Crystals of **6** suitable for X-ray diffraction were obtained by slow diffusion of pentane into a dichloromethane solution of the complex. $PtCl_2P_2C_{62}H_{52}O_8N_2\cdot 3H_2O$, $M$ = 1335.03, orthorhombic, space group $P2_12_12_1$, $a$ = 9.9546(3) Å, $b$ = 26.5366(9) Å, $c$ = 26.8868(9) Å, $V$ = 7102.5(4) Å$^3$, $Z$ = 4, $D_{calcd.}$ = 1.249 g cm$^{-3}$, $\lambda$(Mo-$K_\alpha$) = 0.71073 Å, $\mu$ = 21.47 cm$^{-1}$, $F$(000) = 2696, $T$ = 292(1) K. The sample (0.40 × 0.22 × 0.22 mm) was studied with an Oxford Diffraction Xcalibur Saphir 3 diffractometer with graphite monochromatized Mo-$K_\alpha$ radiation. The data collection was carried out by using CrysAlis RED.[43] 22955 Reflections collected ($1.76 < \theta < 27.54°$), 7763 observations with $I > 2.0\sigma(I)$. The structure was solved with SIR-97,[41] which revealed the non-hydrogen atoms of the molecule. After anisotropic refinement, many hydrogen atoms could be localized with a Fourier difference. The whole structure was refined with SHELXL97.[42] Hydrogen atoms were included and refined by using a riding mode in SHELX-97. Final results: $R_1$ = 0.060, $wR_2$ = 0.165, goodness of fit 0.917, 722 parameters, residual electron density: min/max = –0.957/1.526. Flack parameter: 0.069(10).

CCDC-613420 and -286303 contain the supplementary crystallographic data for this paper. These data can be obtained free of charge from The Cambridge Crystallographic Data Centre via www.ccdc.cam.ac.uk/data_request/cif.

**General Procedure for Asymmetric Hydrogenation and Determination of Enantiomeric Excesses:** To a solution of $[Rh(cod)_2]BF_4$ (0.010 g, 0.025 mmol) in $CH_2Cl_2$ (10 mL) was added a solution of the ligand (2.2 equiv.) in $CH_2Cl_2$ (10 mL), and the resulting mixture was stirred for 30 min. before being used in the catalytic run. For those runs carried out with another solvent, the previous solution was evaporated to dryness; the residue was then dissolved in the desired solvent (20 mL). The solution was introduced by syringe into a 100-mL glass-lined, stainless steel autoclave containing a magnetic stirring bar and the substrate (2.5 mmol); the autoclave was then placed under an atmosphere of hydrogen (5 bar). At the

 © 2007 Wiley-VCH Verlag GmbH & Co. KGaA, Weinheim 

end of the catalytic run, the autoclave was depressurized and the mixture was passed through a short silica column to remove the catalyst. Conversions were monitored by $^1$H NMR spectroscopy. Enantioselectivities were determined by chiral GC analysis by using a CHROMPAK chiral fused silica 25 m × 0.25 mm i.d. and/or specific rotation. Coating Chirasil-L-Val column.

## Acknowledgments

The authors gratefully acknowledge Genzyme Pharmaceuticals for financial support.

[1] E. Cesarotti, G. D'Alfonso, *Tetrahedron Lett.* **1982**, *23*, 2995–2996.
[2] E. Cesarotti, G. Ciani, A. Sironi, *J. Organomet. Chem.* **1983**, *251*, 79–91.
[3] G. Pracejus, H. Pracejus, *J. Mol. Catal.* **1984**, *24*, 227–230.
[4] E. Cesarotti, L. Prati, *Gazz. Chim. Ital.* **1987**, *117*, 129–133.
[5] E. Cesarotti, S. Araneo, I. Rimoldi, S. Tassi, *J. Mol. Catal. A* **2003**, *204–205*, 211–220.
[6] M. Petit, A. Mortreux, F. Petit, G. Buono, G. Peiffer, *New J. Chem.* **1983**, *7*, 593–596.
[7] A. Karim, A. Mortreux, F. Petit, G. Buono, G. Peiffer, C. Siv, *J. Organomet. Chem.* **1986**, *317*, 93–104.
[8] C. Hatat, A. Karim, N. Kokel, A. Mortreux, F. Petit, *New J. Chem.* **1990**, *14*, 141–152.
[9] F. Hapiot, F. Agbossou, A. Mortreux, *Tetrahedron: Asymmetry* **1995**, *6*, 11–14.
[10] C. Döbler, U. Schmidt, H. W. Krause, H. J. Kreuzfeld, M. Michalik, *Tetrahedron: Asymmetry* **1995**, *6*, 385–388.
[11] A. Roucoux, L. Thieffry, J. F. Carpentier, M. Devocelle, C. Méliet, F. Agbossou, A. Mortreux, *Organometallics* **1996**, *15*, 2440–2449.
[12] M. Devocelle, F. Agbossou, A. Mortreux, *Synlett* **1997**, 1306–1308.
[13] C. Pasquier, J. Eilers, I. Reiners, J. Martens, A. Mortreux, F. Agbossou, *Synlett* **1998**, 1162–1164.
[14] E. A. Broger, W. Burkart, M. Hennig, M. Scalone, R. Schmid, *Tetrahedron: Asymmetry* **1998**, *9*, 4043–4054.
[15] F. Agbossou, J.-F. Carpentier, F. Hapiot, I. Suisse, A. Mortreux, *Coord. Chem. Rev.* **1998**, *178–180*, 1615–1645.
[16] V. Turcry, C. Pasquier, F. Agbossou-Niedercorn, *C. R. Acad. Sci.* **2003**, *6*, 179–184.
[17] F. Agbossou-Niedercorn, I. Suisse, *Coord. Chem. Rev.* **2003**, *242*, 145–158.
[18] N. V. Dubrovina, V. I. Tararov, Z. Kadyrova, A. Monsees, A. Börner, *Synthesis* **2004**, *12*, 2047–2051.
[19] M. van den Berg, R. M. Haak, A. J. Minnaard, A. H. M. de Vries, J. G. de Vries, B. L. Feringa, *Adv. Synth. Catal.* **2002**, *344*, 1003–1007.
[20] A.-G. Hu, Y. Fu, J.-H. Xie, H. Zhou, L.-X. Wang, Q.-L. Zhou, *Angew. Chem. Int. Ed.* **2002**, *41*, 2348–2350.
[21] X. Jia, X. Li, L. Xu, Q. Shi, X. Yao, A. S. C. Chan, *J. Org. Chem.* **2003**, *68*, 4539–4541.
[22] D. Peña, A. J. Minnaard, J. A. F. Boogers, A. H. M. de Vries, J. G. de Vries, B. L. Feringa, *Org. Biomol. Chem.* **2003**, *1*, 1087–1089.
[23] L. Lefort, J. A. F. Boogers, A. H. M. de Vries, J. G. de Vries, *Org. Lett.* **2004**, *6*, 1733–1735.
[24] T. Jerphagnon, J. L. Renaud, C. Bruneau, *Tetrahedron: Asymmetry* **2004**, *15*, 2101–2111.
[25] H. Bernsmann, M. van den Berg, R. Hoen, A. J. Minnaard, G. Mehler, M. T. Reetz, J. G. de Vries, B. L. Feringa, *J. Org. Chem.* **2005**, *70*, 943–951.
[26] L. Panella, A. M. Aleixandre, G. J. Kruidhof, J. Robertus, B. L. Feringa, J. G. de Vries, A. J. Minnaard, *J. Org. Chem.* **2006**, *71*, 2026–2036.
[27] Q. H. Zeng, X. P. Hu, Z. C. Duan, X. M. Liang, Z. Zheng, *J. Org. Chem.* **2006**, *71*, 393–396.
[28] D. Peña, A. J. Minnaard, A. H. M. de Vries, J. G. de Vries, B. L. Feringa, *Org. Lett.* **2003**, *5*, 475–478.
[29] Q. H. Zeng, X. P. Ping Hu, X. M. Liang, Z. Zheng, *Chin. Chem. Lett.* **2005**, *16*, 1321–1323.
[30] A. M. Z. Slawin, J. D. Woollins, Q. Zhang, *Inorg. Chem. Commun.* **1999**, 386–388.
[31] R. Sablong, C. Newton, P. Dierkes, J. A. Osborn, *Tetrahedron Lett.* **1996**, *37*, 4933–4936.
[32] M. van den Berg, A. J. Minnaard, E. P. Schudde, J. van Esch, A. H. M. de Vries, J. G. de Vries, B. L. Feringa, *J. Am. Chem. Soc.* **2000**, *122*, 11539–11540.
[33] G. Francio, C. G. Arena, F. Faraone, C. Graiff, M. Lanfranchi, A. Tiripicchio, *Eur. J. Inorg. Chem.* **1999**, 1219–1227.
[34] J. Fawcett, E. G. Hope, A. M. Stuart, A. J. West, *Polyhedron* **2006**, *25*, 1182–1186.
[35] M. van den Berg, J. A. Minnaard, B. Feringa, G. J. de Vries, DE 601 23 093 T2 to DSM IP Assests, **2007**.
[36] Q.-H. Zeng, X.-P. Hu, Z.-C. Duan, X.-M. Liang, Z. Zheng, *J. Org. Chem.* **2006**, *71*, 393–396.
[37] M. T. Reetz, J.-A. Ma, R. Goddard, *Angew. Chem. Int. Ed.* **2005**, *44*, 412–415.
[38] J. D. Park, K. J. Lee, D. H. Kim, *Bioorg. Med. Chem.* **2001**, *9*, 237–243.
[39] J. Spengler, K. Burger, *Synthesis* **1998**, 67–70.
[40] *M. SMART Software* (Version 5.611) and *SAINT+* (Version 6.45), Bruker AXS, Wisconsin, USA.
[41] A. Altomare, M. C. Burla, M. Camalli, G. Cascarano, C. Giacovazzo, A. Guagliardi, A. G. G. Moliterni, G. Polidori, R. Spagna, *J. Appl. Crystallogr.* **1998**, *31*, 74–77.
[42] S. G. M. Sheldrick, *Program for the Refinement of Crystal Structures*, University of Göttingen, Germany, **1997**.
[43] *O.D.L. CrysAlis RED Software* (Version 1.171.29.9).

Received: May 2, 2007
Published Online: July 18, 2007

 © 2007 Wiley-VCH Verlag GmbH & Co. KGaA, Weinheim 

DOI: 10.1002/ejic.200700644

# Order-Disorder Phase Transition in Type-I Clathrate $Cs_8Sn_{44}\square_2$

**Andreas Kaltzoglou,[a] Stephan D. Hoffmann,[a] and Thomas F. Fässler*[a]**

*Dedicated to Prof. Dr. G. Huttner on the occasion of his 70th birthday*

**Keywords:** Clathrates / Order-disorder transitions / Single-crystal structure analysis / Thermoelectricity / Tin

The clathrate compound α-$Cs_8Sn_{44}\square_2$ has been synthesized from its elements under inert gas conditions and has been characterized by single-crystal and powder X-ray diffraction. At room temperature, it crystallizes with cubic symmetry [$a$ = 24.256(3) Å, space group $Ia\bar{3}d$, $Z$ = 8] and adopts a $2\times2\times2$ superstructure of the type-I clathrate and a high ordering of the vacancies (□) in the Sn framework. Single crystals of α-$Cs_8Sn_{44}\square_2$ reversibly transform at 90 °C to the high-temperature β form with primitive symmetry [$a$ = 12.135(1) Å, space group $Pm\bar{3}n$, $Z$ = 1] and a lower ordering of the defects. Differential thermal analysis corroborates the reversible character of the phase transition, which occurs with an enthalpy change of approximately 0.38 $J\,g^{-1}$. An atom-migration mechanism describing the order-disorder transition involving spiro-connected six-membered rings only (scsr mechanism) is proposed.
(© Wiley-VCH Verlag GmbH & Co. KGaA, 69451 Weinheim, Germany, 2007)

## Introduction

The discovery of clathrates as a distinct class of materials opened up a wide area of research involving specifically further synthesis and studies of their properties. The binary systems composed primarily of alkali or alkaline earth metals as guests and Group 14 elements (Si, Ge, Sn) as hosts of the three-dimensional framework are known as semiconducting clathrates and behave mostly like Zintl phases rather than typical intermetallic compounds.[1] The idea that clathrate compounds fulfill the criteria for the Phonon Glass Electron Crystal (PGEC) concept[2] and thus may qualify as thermoelectric materials has led to the rapid development of this compound family. Over the last decades, five clathrate structure types denoted with the Latin numbers I, II, III, VIII, IX have been established, with type I as the most common (Figure 1). In clathrate I, the tetravalent host atoms form interconnected polyhedra with shared pentagonal and hexagonal faces. The structure is further stabilized in the presence of the encaged metal cations. Even though much data on the composition, crystal structures, and physical properties are now available,[3–5] there is still a lack of understanding of the physics involved in the PGEC approach. A strong glass-like rattling of the guest atoms inside the cages of the three-dimensional network of host atoms is necessary for achieving high-quality thermoelectric materials. Therefore, a fine grasp of the lattice defects and phase transitions in clathrate-I compounds must play a decisive role in the understanding of the structure–property relationships in stannide clathrates.

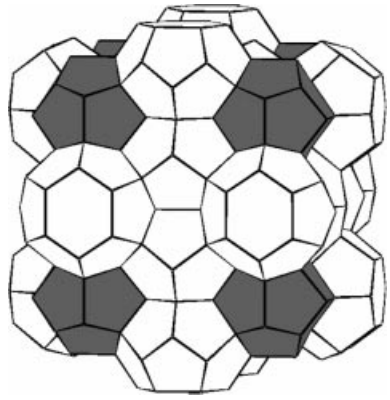

Figure 1. Structure of the type-I clathrate with pentagonal dodecahedra (grey [$5^{12}$]) and tetrakaidecahedra (white [$5^{12}6^2$]) in a 1:3 ratio.

A limited number of such compounds undergo phase transitions before melting. Interestingly, those temperature- or pressure-induced structural transformations can also affect certain physical properties. Recently, a magnetocaloric effect was reported for the doped $Eu_8Ga_{16}Ge_{30}$ resulting from the ferromagnetic transition from a type-I to a type-VIII structure.[6] Moreover, type-IX $Ba_6Ge_{25}$[7] tunes its electrical properties through a two-step phase transition, and phonon band structures of the non-defect type-I $K_8Si_{46}$ change drastically upon pressing.[8]

[a] Department of Chemistry, Technische Universität München, Lichtenbergstr. 4, 85747 Garching, Germany
E-mail: thomas.faessler@lrz.tum.de
Supporting information for this article is available on the WWW under http://www.eurjic.org or from the author.


© 2007 Wiley-VCH Verlag GmbH & Co. KGaA, Weinheim

Since the first report of the non-defect $K_8Sn_{46}$,[9] the exact composition and structure of the type-I tin clathrates was brought into question several times.[10,11] The discrepancies involve the presence of defects – a prerequisite for fulfilling the Zintl–Klemm concept – and their ordering in the crystal. A Mulliken population analysis[12] on the basis of topological charge stabilization for the stannides showed that the vacancies in the three-dimensional host lattice of Sn atoms are favored and that they are statistically distributed only at the framework sites that are part of six-membered rings and that do not belong to pentagonal dodecahedra (6 out of 46 sites); those possess the lowest electron density. These assumptions were indeed confirmed experimentally as the $A_8Sn_{44}\square_2$ compounds (A = K, Rb, Cs)[4,5,13] were found to crystallize in the $Pm\bar{3}n$ space group and the partially occupied positions were distributed along a $4_2$ screw axis. More recently, theoretical calculations for $Cs_8Sn_{44}$[14] and $K_8Sn_{44}$[15] indicated that one vacancy per six-membered ring is favored over two such vacancies per ring. A superstructure was experimentally established for $Rb_8Sn_{44}\square_2$, which was found to crystallize in the $Ia\bar{3}d$ space group and the $2\times2\times2$ unit cell with vacancies distributed along a $4_1$ axis instead of the $4_2$ axis (see also Figure 2).[16] However, the conditions under which the two modifications occur, or if they may co-exist, still remained unclear.

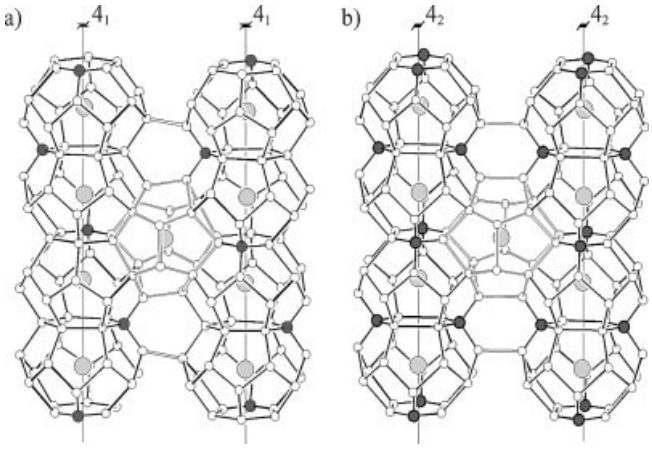


Figure 2. Partial view of the $Cs_8Sn_{44}\square_2$ structures composed of two chains of tetrakaidecahedra and one pentagonal dodecahedron. a) In the α form (space group $Ia\bar{3}d$), the partially occupied *24c* sites (dark grey Sn6 atoms, with an occupation factor of 0.339) are distributed along a $4_1$ helical axis. b) In the β form (space group $Pm\bar{3}n$), the partially occupied *6c* sites (dark grey Sn1 atoms, with an occupation factor of 0.687) are distributed along a $4_2$ axis. In both cases, only the Sn atoms of the split positions with closer contacts to the vacancy are shown.

Here we report on the discovery of a reversible phase transition of isostructural $Cs_8Sn_{44}\square_2$. The transformation sheds light on the structural trends of defect tin clathrates. Since we expect that most stannide clathrate-I compounds appear at low temperatures with a $2\times2\times2$ superstructure, the partial ordering of vacancies must be considered on the basis of property measurements and this might lead to a reinterpretation of several studies.[5,17]

## Results and Discussion

According to the room temperature powder X-ray analysis, $Cs_8Sn_{44}\square_2$ adopts the type-I clathrate structure with a superstructure as observed for $Rb_8Sn_{44}\square_2$.[16] The cell parameters and the space group [$a$ = 24.256(3) Å, space group $Ia\bar{3}d$] are confirmed by single-crystal analysis at room temperature. The single crystal of $Cs_8Sn_{44}\square_2$ was gradually heated on the diffractometer with steps of 20 °C. No significant changes in the reflection patterns occur until a temperature of 80 °C was reached. At 100 °C, the superstructure reflections of the low temperature form (α-$Cs_8Sn_{44}\square_2$) disappear (see Supporting Information) as the crystal transforms into the primitive lattice with smaller cell parameters. This has been observed previously for $Cs_8Sn_{44}$ (β form).[13] A full data set was collected at this temperature. The crystal was perfectly retained when cooled at a rate of 2 °C min$^{-1}$ to room temperature where a second set of data was collected, which confirmed the full reversibility of the phase transformation.

At 20 °C, the $Cs_8Sn_{44}\square_2$ clathrate crystallizes in the $Ia\bar{3}d$ centrosymmetric space group (Figure 2a). The partially occupied Sn6 sites of the polyanionic framework [Wyckoff position *24c*, occupation factor 0.339(6)] are distributed around a $4_1$ screw axis through the Cs atoms that reside in the tetrakaidecahedra. As a consequence, a split model for the adjacent *96h* site is adopted, which gives rise to Sn4a atoms [occupation factor 0.339(6)] and Sn5b atoms [occupation factor 0.661(6)] that correspond to occupied and vacant Sn6 sites, respectively. Further, the Sn3 atom has a relatively large $U_{eq}$ value [0.0263(3) Å$^2$], probably because three out of its four neighbors are the split Sn4a/Sn4b atoms (Table 1). Nevertheless, no split model could be applied for this position. Further, two crystallographically non-equivalent positions for the Cs atoms are observed: (i) The Cs1 atom located in the dodecahedra and (ii) The Cs2 atom located in the tetrakaidecahedra. In both cases the sites are fully occupied. The isotropic atomic displacement parameters are 0.0193(3) Å$^2$ and 0.0378(2) Å$^2$ for Cs1 and Cs2, respectively, proving the stronger "rattling" of the guest in the larger cavities. It is also worth mentioning that the Cs2 atoms do not reside exactly in the center of the cavities, but tend to the opposite site of the vacancy, namely closer to the Sn5 atom (*24d* Wyckoff position). Thus, a slight deviation from linearity (178.88°) is observed for the

Table 1. Atomic coordinates and equivalent isotropic displacement parameters for α-$Cs_8Sn_{44}\square_2$.

| Atom | Site | $x$ | $y$ | $z$ | Occupancy | $U_{eq}$ [Å$^2$] |
|---|---|---|---|---|---|---|
| Cs1 | *16a* | 0.5000 | 0.5000 | 0.0000 | 1 | 0.0193(3) |
| Cs2 | *48g* | 0.6250 | 0.24827(3) | 0.00173(3) | 1 | 0.0378(2) |
| Sn1 | *96h* | 0.50096(3) | 0.34668(2) | 0.05598(2) | 1 | 0.0170(2) |
| Sn2 | *96h* | 0.59456(3) | 0.40950(3) | 0.08969(3) | 1 | 0.0179(2) |
| Sn3 | *32e* | 0.59130(3) | 0.40870(3) | –0.09130(3) | 1 | 0.0263(3) |
| Sn4a | *96h* | 0.5029(2) | 0.3487(2) | –0.0599(2) | 0.339(6) | 0.0167(7) |
| Sn4b | *96h* | 0.5011(1) | 0.3275(1) | –0.06679(9) | 0.661(6) | 0.0185(4) |
| Sn5 | *24d* | 0.5000 | 0.2500 | 0.1250 | 1 | 0.0145(3) |
| Sn6 | *24c* | 0.5000 | 0.2500 | –0.1250 | 0.339(6) | 0.016(1) |

 © 2007 Wiley-VCH Verlag GmbH & Co. KGaA, Weinheim 

Cs2–Cs2–Cs2 chain parallel to the cubic axes, which is expressed in terms of displacement of 0.0593 Å from the center of the cage.

In the high temperature modification (space group $Pm\bar{3}n$), the *6c* Wyckoff site corresponds to the Sn1 atom with occupation factor 0.687(7) (Table 2). Within the standard deviation, this value is equivalent to the value of the I-centered crystals at room temperature and to the value of 2/3, anticipated for an electron precise Zintl phase. As expected, the adjacent *24k* site is better refined by means of a Sn3a/Sn3b model with occupancies 0.687(7) and 0.313(7), respectively. Once again, the Cs atoms that reside in the large framework cavities exhibit much higher atomic displacement parameters than those in the smaller cavities. The β modification exhibits larger ADPs (ADP = anisotropic displacement parameter) than the α modification and the values obtained from the room temperature data refinement in ref.[13], as expected from the temperature dependence in the Einstein's oscillator model.[5a] On the other hand, the Sn–Sn–Sn angles have very comparable values: 94.84(7)°–126.52(9)° for the I lattice and 94.68(1)°–125.2(1)° for the primitive lattice.

Table 2. Atomic coordinates and equivalent isotropic displacement parameters for β-$Cs_8Sn_{44}\square_2$.

| Atom | Site | *x* | *y* | *z* | Occupancy | $U_{eq}$ [Å$^2$] |
|---|---|---|---|---|---|---|
| Cs1 | *2a* | 0.0000 | 0.0000 | 0.0000 | 1 | 0.0223(5) |
| Cs2 | *6d* | 0.2500 | 0.5000 | 0.0000 | 1 | 0.0478(6) |
| Sn1 | *6c* | 0.2500 | 0.0000 | 0.5000 | 0.687(7) | 0.0197(9) |
| Sn2 | *16i* | 0.18314(4) | 0.18314(4) | 0.18314(4) | 1 | 0.0259(3) |
| Sn3a | *24k* | 0.0000 | 0.3064(2) | 0.1136(3) | 0.687(7) | 0.0233(5) |
| Sn3b | *24k* | 0.0000 | 0.3447(6) | 0.1344(6) | 0.313(7) | 0.025(1) |

The structure of α-$Cs_8Sn_{44}$ was verified by Rietveld refinement of the powder diffraction pattern. In this case as well, split models for the positions adjacent to the vacancies are applied.

The vacancy order–disorder transformation is also detectable by differential thermal analysis (DTA). At about 95 °C, a weak endothermic peak, which can be attributed to the $Ia\bar{3}d \rightarrow Pm\bar{3}n$ transition is observed (Figure 3). The reverse phenomenon takes place and is observed as an exothermic peak during cooling. The hysteresis of the peaks depends on the heating and cooling rate. From the average of the experimental maxima, one can define the transition temperature at $T_t$ = 89–90 °C. Further heating to 1000 °C at a rate of 10 °C min$^{-1}$ results in an endothermic peak at 580 °C (on set), which according to the phase diagram is attributed to peritectical decomposition of $Cs_8Sn_{44}$ into Sn and $CsSn_2$.[18] Finally, at 830 °C, a relatively weak and broad endothermic peak of the liquidus line is observed. On cooling, each peak has a corresponding exothermic phenomenon at 810 °C, 510 °C, and 215 °C, which corresponds to the solidification of Sn. Elemental Sn was initially not observed in the room temperature X-ray powder diffractogram. However, it has been shown by multitemperature diffraction experiments with synchrotron X-rays that the related compound $Rb_8Sn_{44}$ contains small amounts of impurities. The impurities are formed as a decomposition product already at 180 °C.[19] The X-ray powder diffraction pattern of the DTA residue after heating to 1000 °C was refined by the Rietveld method. It confirms the presence of α-$Cs_8Sn_{44}$ with a lower degree of crystallinity and also the formation of β-Sn, to approximately 6%.

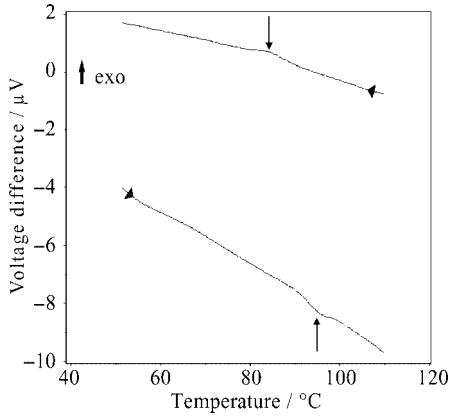


Figure 3. Section of the DTA diagram of $Cs_8Sn_{44}\square_2$ recorded in the range 25 °C–150 °C at a 1 °C min$^{-1}$ heating and cooling rate. Shown is the section between 50 °C and 110 °C. Vertical arrows show the endothermic and exothermic peaks.

The recent observation of a superstructure for clathrate-I $Rb_8Sn_{44}$[16] raises the question on the one hand if such an ordering of vacancies occurs in other stannides with clathrate-I structures and on the other hand why this superstructure has not been observed although many reports on those structures have been published. The detailed thermal analysis here shows that the phase transformation occurs at 89–90 °C with almost perfect reversibility. On the basis of the on set temperatures on heating and cooling the sample at 1 °C min$^{-1}$, the transition occurs with a hysteresis of approximately 2°. Even quenching of the reaction product from 100 °C or 700 °C into liquid nitrogen did not give rise to the high temperature β modification. During all transformations, no other impurity than small amounts of β-Sn was detected by X-ray powder diffraction, EDX, or DTA.

In general, superlattice formation can prevent under- or mixed occupancy of specific atomic sites, but can achieve vacancy formation and atom segregation. Four examples of superstructures have been discussed for doped and/or defect type-I clathrates: (a) $I_8[Sn_{14}In_{10}P_{21.2}\square_{0.8}]$ crystallizes in the tetragonal space group $P4_2/m$, exhibiting partial ordering of the defects;[20] (b) the orthorhombic (*Pbcn*) $Ba_8[Cu_{16}P_{30}]$ exhibits no disorder as P atoms exclusively occupy the *24k* and *6c* sites and Cu atoms the *16i* sites;[21] (c) more recently, the cubic ($Ia\bar{3}d$) $Rb_8Sn_{44}\square_2$ shows a partial ordering of the vacancies;[16] (d) $Ba_8Ge_{43}\square_3$ is characterized as a fully ordered superstructure when quenched quickly from 800 °C or as partially ordered when cooled slowly to ambient conditions.[22] In the present case as in $Rb_8Sn_{44}\square_2$ and $Ba_8Ge_{43}\square_3$, a "klassengleiche" symmetry reduction from

 © 2007 Wiley-VCH Verlag GmbH & Co. KGaA, Weinheim 

*Pm*$\bar{3}$*n* to *Ia*$\bar{3}$*d* takes places. However, the absence of a distinct transition temperature and the higher thermodynamic stability of the disordered modification for $Ba_8Ge_{43}\square_3$ are in contrast to our results here. For $Cs_8Sn_{44}\square_2$, as expected, the model with a lower degree of atom ordering represents the high temperature modification.

The full ordering of the defects in $Ba_8Ge_{43}\square_3$ is also reflected in the larger deviation of the position of the guest atom Ba from the ideal center of the tetrakaidecahedra. The larger displacement of the Ba atoms (0.0844 Å) originates from the presence of a full vacancy and not from the statistics of a partially filled position, as found in $Cs_8Sn_{44}\square_2$ with a displacement of 0.0593 Å for Cs.

According to DTA experiments, the phase transition occurs well below the melting temperature and involves an enthalpy change of about $\Delta H_t = -0.38\ J\,g^{-1}$ ($-2.390\ kJ\,mol^{-1}$) and is thus lower in energy than the first-order transition α-Sn → β-Sn at 13.2 °C ($\Delta H_t = -17.6\ J\,g^{-1}$ or $-2.089\ kJ\,mol^{-1}$).[23] Perfect preservation of the single crystal during the phase transition suggests a second-order transition. However, the enthalpy change at a distinct transition temperature shows that first-order contributions must also be considered.

We rationalize the different thermodynamic stability of the two modifications by studying the possible configurations of the hexagons in $[5^{12}6^2]$. In α-$Cs_8Sn_{44}\square_2$, each hexagon may either be defect-free or possess one defect. In the latter case the neighboring atomic positions are shifted towards the vacancy (Figure 4). In β-$Cs_8Sn_{44}\square_2$, in addition to the two configurations in Figure 4 with virtually identical structures, a third configuration with two vacancies per hexagon in the *para* positions may also occur (Figure 5). Consequently, the bonds between the remaining four atoms are even more elongated, i.e. 3.26(1) Å, which is about 0.3 Å longer than typical distances between three-bonded Sn atoms [see for example the tetrahedral $Sn_4$ clusters in $Cs_4Sn_4$ in which Sn–Sn = 2.939(2) Å].[24]

This next-nearest neighbor interaction of two vacancies significantly affects the stability of the system. Local density approximation studies on the hypothetical $Cs@Sn_{22}\square_2$ with isolated 24-atom cages show that the situation with the vacancies on two different six-membered rings is favored over that in which both vacancies are on the same ring.[14] These theoretical results reflect the trend obtained here experimentally, i.e. vacancy ordering is favored at room temperature. Despite the low enthalpy, no equilibrium is observed between the two modifications, as is also indicated by the first-order contribution to the phase transformation. On the other hand, β-$Cs_8Sn_{44}\square_2$ possesses higher symmetry than α-$Cs_8Sn_{44}\square_2$. For this reason and despite the thermodynamic instability, the disordered modification is favored at elevated temperatures by means of an entropy-driven phase transition.

The mechanism of this low-energy enantiotropic solid-state transformation can be rationalized as a continuous path rather than a nucleation-and-growth process that begins at the imperfections of the crystal.[25] Two ways of achieving the migration of certain Sn atoms are proposed

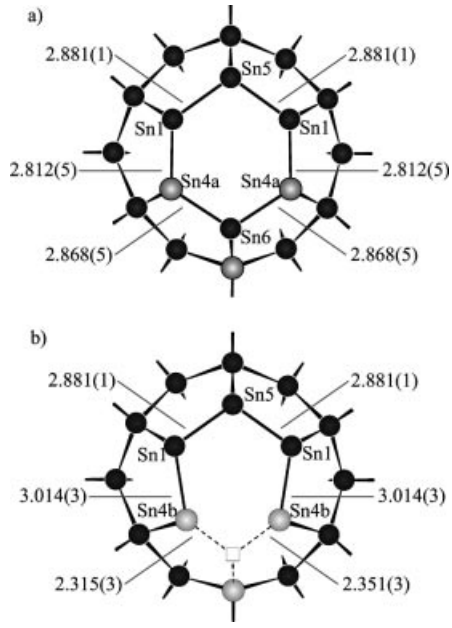


Figure 4. Perpendicular view of a hexagon in α-$Cs_8Sn_{44}\square_2$: a) no defects, b) one defect. All distances are given in Å.

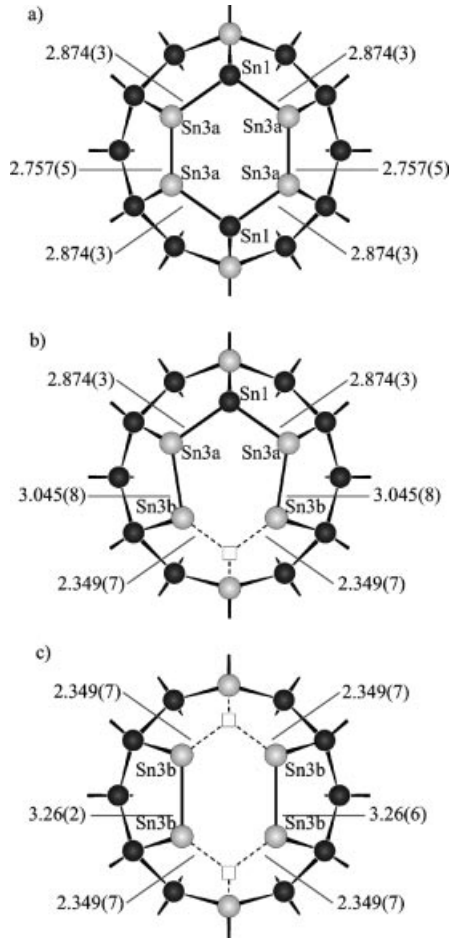


Figure 5. Perpendicular view of a hexagon in β-$Cs_8Sn_{44}\square_2$: a) no defects, b) one defect, c) two defects. All distances are given in Å.

 © 2007 Wiley-VCH Verlag GmbH & Co. KGaA, Weinheim 

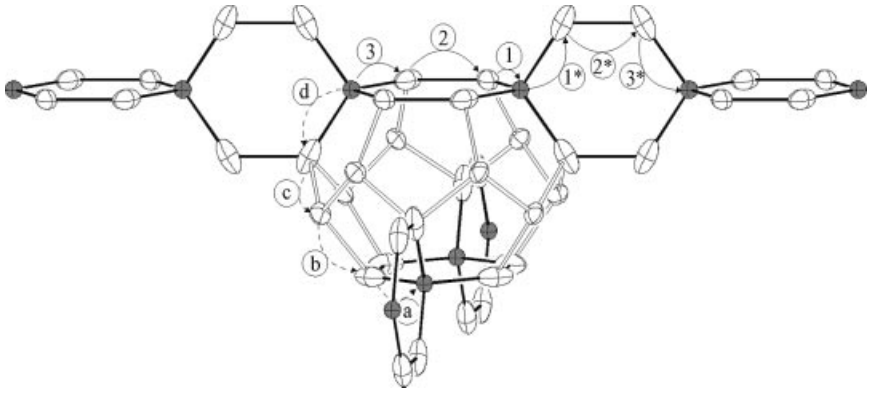


Figure 6. Two possible mechanisms of atom migration for the $Pm\bar{3}n$ to $Ia\bar{3}d$ phase transition. Fully and partially occupied Sn positions are drawn in white and grey, respectively, with thermal ellipsoids at the 80% probability level and without split positions for atoms adjacent to the vacancies.

(Figure 6): (a) A three-step mechanism including migration via two split positions within a six-membered ring is indicated as solid arrows. Migration occurs along spiro-connected six-membered rings (scsr) only. Because of the cubic symmetry, the spiro motive shown in Figure 6 appears in chains along all three directions and allows the rearrangement of the atoms in the three-dimensional framework. (b) A four-step mechanism with migration through two split and one non-split atomic positions, the latter being part of five-membered rings only, is indicated as dashed arrows. Large displacement vectors of the involved atoms favor the scsr mechanism.

## Conclusions

The present study establishes the temperature-dependent phase transition of $Cs_8Sn_{44}$ and sheds light on the controversial discussion of the properties of clathrate-I stannides. Still a question remains: could a fully ordered structure with the composition of an electron-precise Zintl phase $A_8Sn_{44}\square_2$ exist? The full ordering could occur in an enlarged $6\times6\times6$ unit cell with space group $Ia\bar{3}d$ or alternatively in a $3\times3\times3$ unit cell with $Pm\bar{3}n$ symmetry.[26] Nevertheless, no such superlattices were found by single-crystal analysis above –130 °C.

## Experimental Section

**Synthesis:** The $Cs_8Sn_{44}\square_2$ clathrate was prepared from the pure elements, which were handled in an Ar-filled glove box ($O_2$ and $H_2O$ levels <0.1 ppm). Stoichiometric amounts of Cs (ampoule, >98%, Riedel de Haën) and Sn (granules, 99.999%, Chempur) were weighted into Nb ampoules and sealed under reduced Ar pressure. The crucibles were subsequently closed in evacuated silica tubes (pressure ca. $3\times10^{-2}$ mbar), heated to 750 °C for 12 h (2 °C min$^{-1}$), slowly cooled to 500 °C (0.1 °C min$^{-1}$), held at this temperature for 10 d, and then air-quenched to ambient temperature. The title compound exhibits air and moisture stability and remains unchanged upon standing for months. Variation of the reactions conditions, such as reaction temperature between 700 °C and 950 °C, annealing steps, and cooling rates from 0.1 °C min$^{-1}$ to air-quenching, did not significantly affect the composition of the product; however, the quality of the crystals were affected and β-Sn disappeared by increasing the annealing times.

**X-ray Powder Diffraction:** The air-stable and metal-like products were identified on a STOE STADI powder diffractometer equipped with a linear position sensitive detector, using Cu-$K_\alpha$ radiation ($\lambda$ = 1.5406 Å, $10° \le 2\theta \le 90°$, step width = 0.01°) in transmission mode. Microcrystalline diamond was used as the internal standard. The patterns were indexed by using the software package WinXPOW (Stoe) and refined with the WinPLOTR program.[27]

**Single-Crystal X-ray Diffraction:** Reflection data sets were collected with a Stoe IPDS-IIT image plate diffractometer with graphite monochromated Mo-$K_\alpha$ radiation ($\lambda$ = 0.71073 Å) and an open-flow $N_2$ blower for the temperature range –180 °C to 100 °C (Oxford Cryostream Cooler). The temperature at the crystal was additionally checked at various heating steps by using an external thermocouple. Good quality single crystals were obtained by annealing the samples at 400–500 °C for several days. One plate-like crystal was transferred into a glass capillary (Hilgenberg, length = 80 mm, diameter = 0.3 mm) that were in turn mounted on the diffractometer. After checking the cell parameters and the space group ($a$ = 24.256 Å, $Ia\bar{3}d$), the crystal was subsequently heated to 100 °C. Data sets were collected at 100 °C with $a$ = 12.135 Å and the space group $Pm\bar{3}n$ and after cooling to 20 °C with $a$ = 24.256 Å and the space group $Ia\bar{3}d$ (Table 3). For structure solutions and refinements (direct methods, full-matrix least-squares on $F^2$, anisotropic atomic displacement parameters for all atoms, with numerical absorption corrections[28]), SHELXTL97 was used.[29] Note also that the occupation factors for defects and split positions were coupled through the PART command for disordered groups. Further details of the crystal structure investigations can be obtained from the Fachinformationszentrum Karlsruhe, 76344 Eggenstein-Leopoldshafen, Germany [Fax: (+49)7247-808-666; E-mail: crysdata@fiz-karlsruhe.de] on quoting the depository numbers CSD-417969 (α form) and 417970 (β form).

**Differential Thermal Analysis:** DTA was carried out on an annealed sample ($m$ = 370 mg) sealed in an Nb-crucible under an argon, protective atmosphere in the temperature range 25–1000 °C. The diagrams were obtained in two cycles using heating and cooling rates from 0.1 to 5 °C min$^{-1}$. The calibration was carried out by using known latent heats for the melting points of naphthalene ($T_m$ = 80.3 °C, $\Delta H_m$ = –147 J g$^{-1}$), In ($T_m$ = 156.6 °C, $\Delta H_m$ = –28.6 J g$^{-1}$), β-Sn ($T_m$ = 231.9 °C, $\Delta H_m$ = –60.5 J g$^{-1}$), and Al ($T_m$ = 660.3 °C, $\Delta H_m$ = –397 J g$^{-1}$) at a rate of ±2 K min$^{-1}$. The latent

 © 2007 Wiley-VCH Verlag GmbH & Co. KGaA, Weinheim 

Table 3. Crystal and structure refinement data for β-$Cs_8Sn_{44}\square_2$ (high temperature form) and α-$Cs_8Sn_{44}\square_2$ (low temperature form).

| | | |
|---|---|---|
| Chemical formula | β-$Cs_8Sn_{44.12(3)}$ | α-$Cs_8Sn_{44.02(1)}$[a] |
| Space group (No.) | $Pm\bar{3}n$ (223) | $Ia\bar{3}d$ (230) |
| Formula weight | 6299.88 | 6287.53 |
| Temperature, $T$ [°C] | 100 | 20 |
| Radiation, $\lambda$ [Å] | Mo-$K_\alpha$, 0.71073 | Mo-$K_\alpha$, 0.71073 |
| $Z$ | 1 | 8 |
| $\rho_{calcd.}$ [g cm$^{-3}$] | 5.840 | 5.851 |
| $A$ [Å] | 12.135(1) | 24.256(3) |
| $V$ [Å$^3$] | 1787.1(4) | 14272(3) |
| Absorption coeff., $\mu$ [mm$^{-1}$] | 19.06 | 19.10 |
| F (000) | 2640 | 21120 |
| $\theta$ range for data collection [°] | 4.11–25.24 | 2.06–25.25 |
| Index ranges | $0 \le h \le 8$, $0 \le k \le 10$, $2 \le l \le 14$ | $0 \le h \le 16$, $0 \le k \le 20$, $2 \le l \le 29$ |
| Reflections collected | 27209 | 85339 |
| Independent reflections | 317 ($R_{int}$ = 0.108) | 1083 ($R_{int}$ = 0.085) |
| Parameters | 23 | 53 |
| Goodness-of-fit on $F^2$ | 0.815[b] | 1.065[c] |
| Final $R$ indices [$I > 2\sigma(I)$] | $R_1$ = 0.020, $wR_2$ = 0.042 | $R_1$ = 0.035, $wR_2$ = 0.054 |
| $R$ indices (all data) | $R_1$ = 0.035, $wR_2$ = 0.043 | $R_1$ = 0.054, $wR_2$ = 0.058 |
| Largest diff. peak and hole [e Å$^{-3}$] | 0.678 and –1.308 | 0.775 and –1.185 |

[a] Data collection after heating the single crystal to 100 °C. [b] Final weighting scheme = $1/[\sigma^2(F_o^2) + (0.0232P)^2]$ where $P = (F_o^2 + 2F_c^2)/3$. [c] Final weighting scheme = $1/[\sigma^2(F_o^2) + (0.0244P)^2]$ where $P = (F_o^2 + 2F_c^2)/3$.

heat for the phase transition of $Cs_8Sn_{44}$ at 90 °C was determined by linear interpolation of the DTA data of the melting point of naphthalene and of indium.

**EDX Analyses:** These were performed with a JEOL 5900LV Scanning Electron Microscope.

**Supporting Information** (see footnote on the first page of this article): Selected image plate frames and Rietveld refinements are available.

## Acknowledgments

The authors wish to thank the RTN program of the European Union (EU-project Nr. HPRN-CT 2002–00193) for financial support. We also thank Dr. Annette Schier for reading the manuscript.

[1] a) J. S. Kasper, P. Hagenmuller, M. Pouchard, C. Cros, *Science* **1965**, *150*, 1713–1714; b) K. A. Kovnir, A. V. Shevelkov, *Russ. Chem. Rev.* **2004**, *73*, 923–938.
[2] a) G. Slack, *CRC Handbook of Thermoelectrics*, CRC Press, **1995**; b) B. Iversen, G. Nolas, G. Stucky, *J. Solid State Chem.* **2000**, *149*, 455–458.
[3] S. Bobev, S. Sevov, *J. Solid State Chem.* **2000**, *153*, 92–105.
[4] J. T. Zhao, J. Corbett, *Inorg. Chem.* **1994**, *33*, 5721–5726.
[5] a) G. S. Nolas, B. C. Chakoumakos, B. Mahieu, G. J. Long, T. J. R. Weakley, *Chem. Mater.* **2000**, *12*, 1947–1953; b) J. L. Cohn, G. Nolas, V. Fessatidis, T. H. Metcalf, G. Slack, *Phys. Rev. Lett.* **1999**, *82*, 779–782; c) F. Chen, K. L. Stokes, G. Nolas, *J. Phys. Chem. Solids* **2002**, *63*, 827–832.
[6] a) S. Srinath, J. Gass, D. J. Rebar, G. T. Woods, H. Srikanth, G. Nolas, *J. Appl. Phys.* **2006**, *99*, 08K902(3); b) S. Paschen, W. Carrillo-Carbera, A. Bentien, V. H. Tran, M. Baenitz, Yu. Grin, F. Steglich, *Phys. Rev. B* **2001**, *64*, 214404(11).
[7] a) H. Q. Yuan, F. M. Grosche, W. Carrillo-Carbera, V. Pacheco, G. Sparn, M. Baenitz, U. Schwarz, Yu. Grin, F. Steglich, *Phys. Rev. B* **2004**, *70*, 174512(6); b) S. Paschen, V. H. Tran, M. Baenitz, W. Carrillo-Carbera, Yu. Grin, F. Steglich, *Phys. Rev. B* **2002**, *65*, 134435(9).
[8] J. S. Tse, S. Desgreniers, Z. Li, M. R. Ferguson, Y. Kawazoe, *Phys. Rev. Lett.* **2002**, *89*, 195507(4).
[9] J. Gallmeier, H. Schäfer, A. Weiss, *Z. Naturforsch., Teil B* **1969**, *24*, 665–667.
[10] H.-G. von Schnering, *Nova Acta Leopoldina* **1985**, *59*, 168.
[11] Yu. Grin, L. Melekhov, K. Chuntonov, S. Yatsenko, *Kristallografiya* **1987**, *32*, 497–498.
[12] G. Miller in *Chemistry, Structure, and Bonding of Zintl Phases and Ions* (Eds.: S. Kauzlarich), VCH Publishers, **1996**.
[13] H.-G. von Schnering, R. Kröner, M. Baitinger, K. Peters, R. Nesper, Yu. Grin, *Z. Kristallogr. – New Cryst. Struct.* **2000**, *215*, 205–206.
[14] C. Myles, J. Dong, O. Sankey, *Phys. Rev. B* **2001**, *64*, 165202(11).
[15] L. Mollnitz, N. Blake, H. Metiu, *J. Chem. Phys.* **2002**, *117*, 1302–1312.
[16] F. Dubois, T. Fässler, *J. Am. Chem. Soc.* **2005**, *127*, 3264–3265.
[17] G. Frisch, C. Hoch, C. Röhr, P. Zönnchen, K. Becker, D. Niemeier, *Z. Anorg. Allg. Chem.* **2003**, *629*, 1661–1672.
[18] T. B. Massalski, H. Okamoto, P. R. Subramanian, L. Kacprzak, *Binary Alloy Phase Diagrams* 5th ed., ASM-International, Materials-Park, **2004**.
[19] unpublished results.
[20] M. M. Shatruk, K. A. Kovnir, M. Lindsjö, I. A. Presniakov, L. A. Kloo, A. Shevelkov, *J. Solid State Chem.* **2001**, *161*, 233–242.
[21] J. Duenner, A. Mewis, *Z. Anorg. Allg. Chem.* **1995**, *621*, 191–196.
[22] W. Carrilo-Carbera, S. Budnyk, Y. Prots, Yu. Grin, *Z. Anorg. Allg. Chem.* **2004**, *630*, 2267–2276.
[23] I. Barin, O. Knacke, *Thermochemical Properties of Inorganic Substances*, Springer-Verlag, Berlin, **1973**.
[24] M. Baitinger, Yu. Grin, H.-G. von Schnering, R. Kniep, *Z. Kristallogr. – New Cryst. Struct.* **1999**, *214*, 457–458.
[25] a) F. H. Herbstein, *Acta Crystallogr., Sect. B* **2006**, *62*, 341–383; b) A. R. West, *Solid State Chemistry and Its Applications*, John Wiley & Sons Ltd., **1984**.
[26] H. Wondratschek, U. Müller, *International Tables for Crystallography, Volume A1 (Symmetry Relations Between Space Groups)*, Kluwer Academic Publishers, **2004**.
[27] T. Roisnel, J. Rodriguez-Carvajal, *FULLPROF,* Version 3.20, France, **2005**.
[28] *X-Shape Program: Crystal Optimization for Numerical Absorption Corrections*, Version 2.04, STOE Darmstadt, **2004**.
[29] G. Sheldrick, *SHELX-97, Program for Crystal Structure Determination*, University of Göttingen, **1997**.

Received: April 16, 2007
Published Online: July 24, 2007

 © 2007 Wiley-VCH Verlag GmbH & Co. KGaA, Weinheim 

DOI: 10.1002/ejic.200700182

# Syntheses, Characterization, and Luminescent Properties of Monoethylzinc Complexes with Anilido–Imine Ligands

Qing Su,[a] Wei Gao,[a] Qiao-Lin Wu,[a] Ling Ye,[a] Guang-Hua Li,[b] and Ying Mu*[a]

**Keywords:** Luminescence / N ligands / Quinoline / Zinc

The syntheses of three anilido–imine ligands of the general formula *ortho*-$C_6H_4$(NHAr′)(CH=NAr′′ [Ar′ = 7-(2,4-$Me_2$)-$C_9H_4N$, Ar′′ = 2,6-$Me_2C_6H_3$ (**2a**); Ar′ = 7-(2,4-$Me_2$)$C_9H_4N$, Ar′′= 2,6-$Et_2C_6H_3$ (**2b**); Ar′ = 7-(2,4-$Me_2$)$C_9H_4N$, Ar′′= 2,6-*i*$Pr_2C_6H_3$ (**2c**)] and four zinc(II) complexes of the general formula [*ortho*-$C_6H_4$(NHAr′)(CH=NAr′′)]ZnEt [Ar′ = 7-(2,4-$Me_2$)$C_9H_4N$, Ar′′= 2,6-$Me_2C_6H_3$ (**3a**); Ar′ = 7-(2,4-$Me_2$)-$C_9H_4N$, Ar′′= 2,6-$Et_2C_6H_3$ (**3b**); Ar′ = 7-(2,4-$Me_2$)$C_9H_4N$, Ar′′ = 2,6-*i*$Pr_2C_6H_3$ (**3c**); Ar′′ = 2,6-$Me_2C_6H_3$, Ar′′ = 2,6-*i*$Pr_2C_6H_3$ (**3d**)] are described. The complexes were synthesized from the reaction of $ZnEt_2$ with corresponding ligands **2** by alkane elimination. All compounds were characterized by elemental analysis and $^1H$ and $^{13}C$ NMR spectroscopy. The molecular structures of compounds **2a**, **2b**, **3b**, and **3c** were determined by single-crystal X-ray crystallography. The X-ray analysis reveals that complexes **3b** and **3c** exist in the dimeric form with the N atom in the quinolyl ring coordinating to the other Zn atom to make the Zn atoms four coordinate. Luminescent properties of ligands **2a**–**2d** and complexes **3a**–**3d** in both solution and the solid state were studied.
(© Wiley-VCH Verlag GmbH & Co. KGaA, 69451 Weinheim, Germany, 2007)

## Introduction

Zinc(II) complexes as luminescent materials have been extensively studied in recent years.[1–9] Among these known luminescent Zn complexes, the ligands are mainly benzothiazolates,[1] quinolinolates,[2] salicylideneaminates,[3] dipyrrin,[6c] N-7-azaindolyl,[8] and 2,2′-dipyridylamino.[9] As $Zn^{II}$ with a closed shell is spectroscopically silent in essence, the luminescent properties of $Zn^{II}$ complexes can be easily tuned by the modification of the ligands. Meanwhile, $Zn^{II}$ complexes can have relatively flexible coordination numbers ranging from three-coordinate to six-coordinate depending on the structure of their ligands. Bis(8-hydroxyquinoline)-zinc(II) ($Znq_2$) was reported to be a good electroluminescent (EL) material that exists in the form of $(Znq_2)_4$.[2] Bis[2-(2-hydroxyphenyl)benzothiazolate]zinc $[Zn(BTZ)_2]_2$ was found to be an excellent white EL material.[1] Some polynuclear $Zn^{II}$ complexes[7,8] were also reported to have intriguing structural and photoluminescent properties. We reported a number of aluminum[10a,10b] and boron[10c] complexes with chelating anilido–imine ligands showing good luminescent properties. Similarly, zinc complexes with the anilido–imine ligands might also be efficient luminescent materials considering that the anilido–imine ligands and the salicylaldiminate ligands have similar structures. Recently, Lee et al. reported some dinuclear $Zn^{II}$ complexes with anilido–imine ligands.[11] As we are interested in tuning the luminescent properties of $Zn^{II}$ complexes by modification of the ligands and the coordination geometries of $Zn^{II}$ complexes, we synthesized three new anilido–imine ligands with a 7-amino-2,4-dimethylquinolyl chromophore, in which the nitrogen atom in the quinolyl ring might coordinate to the $Zn^{II}$ in another molecule to form dinuclear or polynuclear $Zn^{II}$ complexes. The results indicate that all three $Zn^{II}$ complexes with quinolyl exist in a novel dimeric form. Herein we report the syntheses, characterizations, and fluorescent properties of four new zinc complexes with anilido–imine ligands, *ortho*-$C_6H_4$(NHAr′)(CH=NAr′′)ZnEt [Ar′ = 7-(2,4-$Me_2$)$C_9H_4N$, Ar′′ = 2,6-$Me_2C_6H_3$ (**3a**); Ar′ = 7-(2,4-$Me_2$)$C_9H_4N$, Ar′′ = 2,6-$Et_2C_6H_3$ (**3b**); Ar′ = 7-(2,4-$Me_2$)-$C_9H_4N$, Ar′′ = 2,6-*i*$Pr_2C_6H_3$ (**3c**); Ar′ = 2,6-$Me_2C_6H_3$, Ar′′ = 2,6-*i*$Pr_2C_6H_3$ (**3d**)].

## Results and Discussion

### Syntheses of the Ligands

Preligands **1a**–**1c** *ortho*-$C_6H_4F$(CH=NAr′′) [Ar′′ = 2,6-$Me_2C_6H_3$ (**1a**), 2,6-$Et_2C_6H_3$ (**1b**), 2,6-*i*$Pr_2C_6H_3$ (**1c**)] were synthesized by a condensation reaction of *ortho*-fluorobenzaldehyde with 1 equiv. of the relevant amine in *n*-hexane in the presence of anhydrous $MgSO_4$ according to a modified literature method.[12] Among them, **1b** is a new compound and characterized by NMR spectroscopy along with ele-

[a] Key Laboratory for Supramolecular Structure and Materials of Ministry of Education, School of Chemistry, Jilin University, 2699 Qianjin Street, Changchun 130012, People's Republic of China
[b] State Key Laboratory of Inorganic Synthesis and Preparative Chemistry, School of Chemistry, Jilin University, 2699 Qianjin Street, Changchun 130012, People's Republic of China
Fax: +86-431-85193421
E-mail: ymu@mail.jlu.edu.cn

 © 2007 Wiley-VCH Verlag GmbH & Co. KGaA, Weinheim 

mental analysis. The imino CH proton of compound **1b** exhibits resonance at $\delta$ = 8.55 ppm and the corresponding imino CH carbon exhibits resonance at $\delta$ = 156.1 ppm. At room temperature, **1b** exists in the form of a yellow oil but as a yellow solid at lower temperatures. It can be purified by reduced-pressure distillation. Three new ligands, *ortho*-$C_6H_4(NHAr')(CH{=}NAr'')$ [Ar′ = 7-(2,4-$Me_2$)$C_9H_4N$, Ar″ = 2,6-$Me_2C_6H_3$ (**2a**); Ar′ = 7-(2,4-$Me_2$)$C_9H_4N$, Ar″ = 2,6-$Et_2C_6H_3$ (**2b**); Ar′ = 7-(2,4-$Me_2$)$C_9H_4N$, Ar″ = 2,6-*i*$Pr_2C_6H_3$ (**2c**)], were synthesized by nucleophilic aromatic substitution of fluoride in **1a**–**1c** by 7-amino-2,4-dimethylquinoline lithium salt according to a modified literature procedure[12] (Scheme 1) and characterized by $^1$H and $^{13}$C NMR spectroscopy along with elemental analysis. Ligands **2a** and **2b** were purified by chromatography on silica gel with ethyl acetate/petroleum ether as the eluent to give pure products as yellow crystals, whereas compound **2c** was purified by crystallization from methanol. For comparison, ligand **2d**[13] was synthesized according to a literature method and characterized by $^1$H NMR spectroscopy. The $^1$H NMR spectra of **2a**–**2c** exhibit resonances in the range of $\delta$ = 8.35–8.37 ppm for the imino CH proton, whereas the corresponding $^{13}$C NMR resonances are in the range of $\delta$ = 165.6–165.8 ppm. The NH proton resonance in **2a**–**2c** appears at relatively low field ($\delta$ = 11.64, 11.62, and 11.59 ppm, respectively) relative to those in compound **2d**[13] ($\delta$ =10.50 ppm) and other reported compounds of this type [$\delta$ =10.53 ppm for *ortho*-$C_6H_4${$NH(C_6H_3$*i*$Pr_2$-2,6)}-[$CH{=}NC_6H_3Me_2$-2,6],[10b] 10.60 ppm for *ortho*-$C_6H_4$-{$NH(C_6H_3Me_2$-2,6)}($CH{=}NC_6H_3Me_2$-2,6),[10a] 11.16 ppm for *ortho*-$C_6H_4${$NH(C_6H_4$Me-*p*)}($CH{=}NC_6H_3$*i*$Pr_2$-2,6),[10a] 11.24 ppm for *ortho*-$C_6H_4${$NH(C_6H_4$Me-*p*)}($CH{=}NC_6H_4$-Me-*p*)[10a]] as a result of the electron-withdrawing properties of the quinolyl group.

## Syntheses of the Complexes

Treatment of **2a**–**2d** with 1 equiv. of $ZnEt_2$ in toluene caused the elimination of ethane and afforded the corresponding monoethylzinc complexes **3a**–**3d** in good yields (78–85%). All complexes have good solubility in common solvents, such as toluene, dichloromethane, diethyl ether, THF, and *n*-hexane. All complexes were characterized by $^1$H and $^{13}$C NMR spectroscopy as well as elemental analysis, and satisfactory analytic results were obtained. The N–H proton signals of the free ligands disappear, and the new Zn–$CH_2$ proton signals appear at a higher field (0.55–0.02 ppm) in the $^1$H NMR spectra of complexes **3a**–**3d**, which is indicative of the formation of Zn–N bond in these compounds. The Zn–$CH_2$ carbon signals in the $^{13}$C NMR spectra are observed at –1.2 (for **3a**), –1.8 (for **3b**), –1.3 (for **3c**), and –2.9 (for **3d**) ppm. The two methyl groups of the isopropyl units in complex **3c** are inequivalent, for the coordination of the anilido–imine ligands to the zinc center causes the rotation about the N–aryl bond to become slow on the NMR timescale.[10a] All complexes have pretty good thermal stability and can be heated in boiling toluene for several hours without obvious decomposition. All complexes are air- and/or moisture-sensitive in solution and the solid state.

## Crystal Structures

The molecular structures of ligands **2a** and **2b** as well as complexes **3b** and **3c** were determined by X-ray crystallographic analysis. Crystals of ligands **2a** and **2b** suitable for X-ray crystal structure determination were grown from ethyl acetate/petroleum ether at room temp. Crystals of complexes **3b** and **3c** suitable for X-ray crystal structure de-

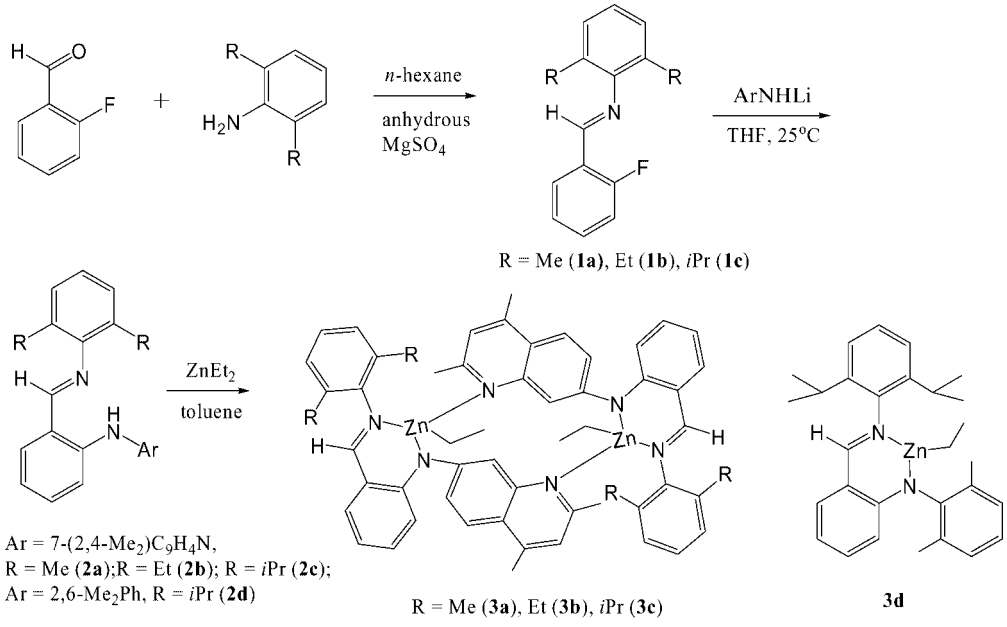


Scheme 1. Synthetic route for ligands **2a**–**2d** and complexes **3a**–**3d**.

 © 2007 Wiley-VCH Verlag GmbH & Co. KGaA, Weinheim 

termination were grown from *n*-hexane at room temp. The ORTEP drawings of the molecular structures of **2a**, **2b**, **3b**, and **3c** are shown in Figures 1 (top), 2, 3, and 4, respectively. Selected bond lengths and angles for **3b** and **3c** are given in Table 1. The crystal packing [Figure 1 (bottom)] of **2a** is consolidated by intramolecular N–H···N hydrogen bonds and weak intermolecular C–H···N interactions [3.496(2) Å, 170.2°, ($x$, 1.5 – $y$, 0.5 + $z$)] arising from the interactions between the nitrogen atom in the quinolyl ring and the hydrogen atom of the imino CH=N to form an infinite one-dimensional chain. There are no interactions between each adjacent chain. X-ray analysis revealed that the unit cell of **2b** contains two independent molecules, one of which is shown in Figure 2. There are intramolecular N–H···N hydrogen bonds but no intermolecular C–H···N interactions in the packing of **2b**. The C=N bond lengths in **2a** and **2b** [1.271(2) Å for **2a**, 1.267(4) and 1.275(4) Å for **2b**] are in the normal range.[11a] Complexes **3b** and **3c** belong to the monoclinic space group $C2/c$ and the triclinic space group $P\bar{1}$, respectively. There is an *n*-hexane solvent molecule in the unit cell of **3c**. Both **3b** and **3c** exist in the dimeric form with the nitrogen atom in the quinolyl ring coordinating to the zinc atom in another molecule. As seen in Figures 3 and 4, the zinc ions in both **3b** and **3c** adopt a distorted tetrahedral geometry with the metal center coordinated by an ethyl group, a quinolyl group, and the bidentate anilido–imine ligand. The anilido–imine ligand chelates to the zinc center to form a six-membered chelating ring that is nearly planar with the zinc atom lying 0.0371 Å (**3b**), 0.0327 Å, and 0.0926 Å (**3c**) out of the plane. The imino C=N bond [1.277(7) Å for **3b**] is slightly longer than that in the free ligand after coordination to $Zn^{II}$. The imino C=N bond in **3c** [1.290(5) Å] is longer than that in **3b** as a result of the increased steric hindrance of the isopropyl group rel-

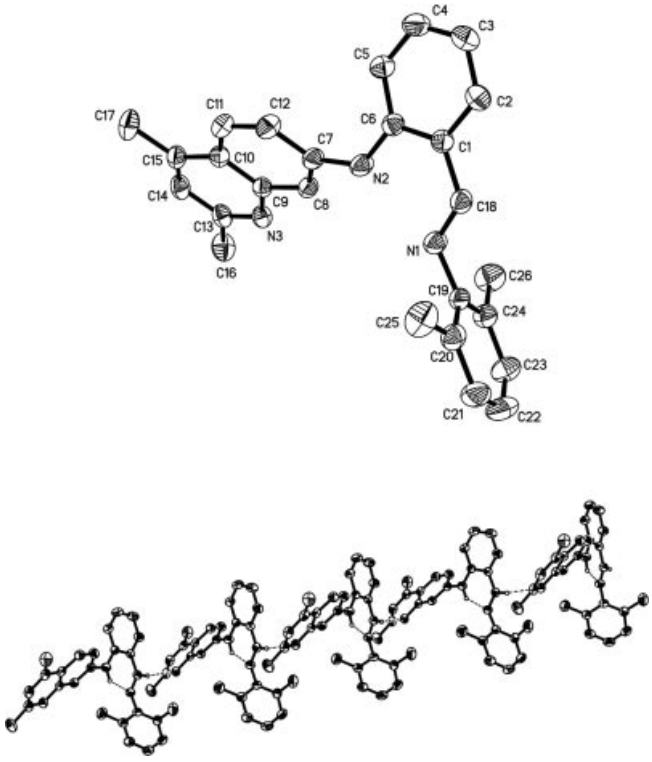


Figure 1. Top: Molecular structure of compound **2a**. Bottom: The packing of compound **2a** (hydrogen bonds are indicated by dashed lines and hydrogen atoms not involved in these interactions have been omitted for clarity, and the thermal ellipsoids are drawn at 30% probability levels).

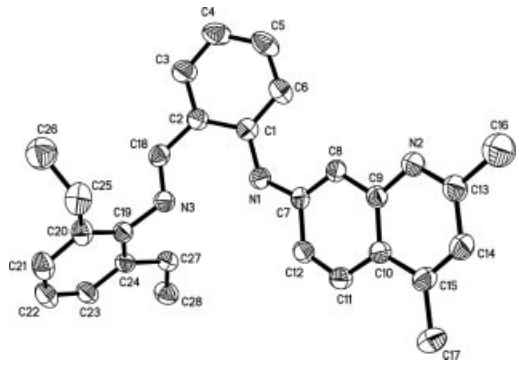


Figure 2. Molecular structure of compound **2b** (all hydrogen atoms and the other molecule have been omitted for clarity, and the thermal ellipsoids are drawn at 30% probability levels).

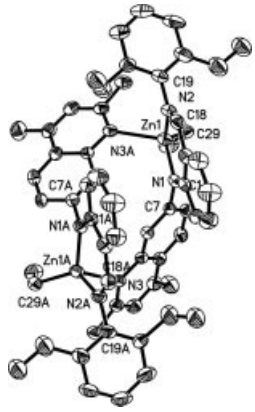


Figure 3. Molecular structure of complex **3b** (all hydrogen atoms have been omitted for clarity, and the thermal ellipsoids are drawn at 30% probability levels).

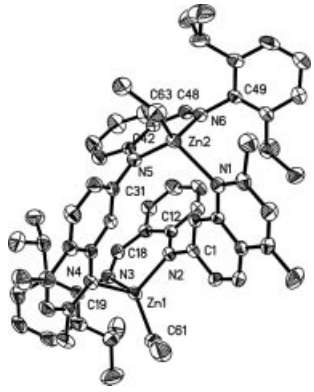


Figure 4. Molecular structure of complex **3c** (all hydrogen atoms and the *n*-hexane solvent molecule have been omitted for clarity, and the thermal ellipsoids are drawn at 30% probability levels).

 © 2007 Wiley-VCH Verlag GmbH & Co. KGaA, Weinheim 

ative to that of the ethyl group. The Zn–$N_{anilido}$ distances [2.014(4) Å in **3b**, 2.028(3) Å and 2.025(3) Å in **3c**] are shorter than the Zn–$N_{imine}$ distances [2.040(4) Å in **3b**, 2.055(4) Å and 2.063(3) Å in **3c**] owing to the formation of a polar (partially ionic) single bond from an electron-rich anilido nitrogen atom to the $Zn^{II}$ center as opposed to a coordination bond in the latter case. The Zn–$N_{quinolyl}$ distances [2.313(4) Å in **3b**, 2.290(4) Å and 2.266(3) Å in **3c**] are much longer than the Zn–$N_{imine}$ distances, indicating the weak coordination interaction between the zinc atom and the nitrogen atom in the quinolyl ring. The Zn–C lengths for complexes **3b** [2.012(6) Å] and **3c** [1.985(5) Å and 1.998(5) Å] are typical for such a bond[14] although slightly longer than that of similar [($C_6H_3iPr_2$)N=C(Me)CH=C(Me)N($C_6H_3iPr_2$)]ZnEt (1.96 Å).[15] The Zn–Zn separation distances are 6.625 Å in **3b** and 6.707 Å in **3c**, which is indicative of no metal–metal interaction. The $N_{imine}$–Zn–$N_{anilido}$ bite angles are 92.63(16)° (in **3b**), 92.33(14)° and 93.38(14)° (in **3c**), respectively. The dihedral angles between the six-membered chelating ring and the phenyl ring at the imine nitrogen are 80.7° (in **3b**), 77.7° and 85.6° (in **3c**), respectively. The dihedral angles between the six-membered chelating ring and the quinolyl ring are 58.7° (in **3b**), 59.9° and 122.3° (in **3c**), respectively.

Table 1. Selected bond lengths [Å] and angles [°] for **3b** and **3c**.[a]

| | | | |
|---|---|---|---|
| Complex **3b** | | | |
| Zn1–N1 | 2.014(4) | N1–Zn1–N2 | 92.63(16) |
| Zn1–N2 | 2.040(4) | C29–Zn1–N3#1 | 107.1(2) |
| Zn1–C29 | 2.012(6) | N1–Zn1–N3#1 | 112.90(16) |
| Zn1–N3#1 | 2.313(4) | N2–Zn1–N3#1 | 95.14(16) |
| N1–C1 | 1.366(6) | C7–N1–Zn1 | 114.0(3) |
| N2–C18 | 1.277(7) | C1–N1–Zn1 | 127.2(3) |
| C29–Zn1–N1 | 119.5(2) | C18–N2–Zn1 | 123.0(4) |
| C29–Zn1–N2 | 127.1(2) | C19–N2–Zn1 | 119.8(3) |
| Complex **3c** | | | |
| Zn1–N2 | 2.028(3) | Zn2–N5 | 2.025(3) |
| Zn1–N3 | 2.055(4) | Zn2–N6 | 2.063(3) |
| Zn1–N4 | 2.290(4) | Zn2–N1 | 2.266(3) |
| Zn1–C61 | 1.985(5) | Zn2–C63 | 1.998(5) |
| N2–C12 | 1.353(5) | N5–C42 | 1.361(5) |
| N3–C18 | 1.290(5) | N6–C48 | 1.290(5) |
| N2–Zn1–N3 | 92.33(14) | N5–Zn2–N6 | 93.38(14) |
| N2–Zn1–N4 | 112.36(13) | N5–Zn2–N1 | 110.00(13) |
| N2–Zn1–C61 | 118.2(2) | N5–Zn2–C63 | 117.21(19) |
| N3–Zn1–N4 | 96.08(14) | N6–Zn2–N1 | 95.95(13) |
| N3–Zn1–C61 | 127.9(2) | N6–Zn2–C63 | 121.79(18) |
| N4–Zn1–C61 | 107.7(2) | N1–Zn2–C63 | 114.99(18) |
| C1–N2–Zn1 | 113.3(2) | C31–N5–Zn2 | 114.7(3) |
| C12–N2–Zn1 | 127.5(3) | C42–N5–Zn2 | 125.6(3) |
| C18–N3–Zn1 | 122.6(3) | C48–N6–Zn2 | 121.5(3) |
| C19–N3–Zn1 | 119.7(3) | C49–N6–Zn2 | 121.7(3) |

[a] Symmetry transformations used to generate equivalent atoms: #1: $-x$, $y$, $-z + 0.5$.

## Fluorescent Properties

Table 2 summarizes the UV/Vis and fluorescent properties of compounds **2a**–**2d** and **3a**–**3d** determined in both solution and the solid state. In solution, free ligands **2a**–**2d** all have a weak emission band at $\lambda$ = 437, 437, 436, and 423 nm, respectively, whereas complexes **3a**–**3d** in solution show a stronger emission band (bandwidth at half-height = 77–79 nm) with $\lambda$ = 573, 565, 555, and 515 nm, respectively (Figure 5). The quantum yields of these complexes are relatively low in solution. According to the literature,[6a,6b,10] the observed luminescence of these complexes could be attributed to π*–π transitions of their conjugated ligands. The emission energies of these complexes are significantly red-shifted relative to those of the free ligands, which could be attributed to the fact that the coordination of the ligand to the metal center lowers the energy gap between π* and π of the ligand.[16] The emission energies of complexes **3a**–**3c** change in the order **3a** < **3b** < **3c**, depending on the size of the *ortho*-substituents of the rotatable aromatic ring attached to the imine N atom that might affect the dihedral angles between the aromatic ring and the six-membered chelating ring and thus the extent of conjugation in these complexes.[10a] The emission maxima of complexes **3a**–**3c**

Table 2. Optical properties of ligands **2a**–**2d** and complexes **3a**–**3d** in *n*-hexane and the solid state.

| Compound | Absorption [nm] ($\varepsilon$ [$dm^3 mol^{-1} cm^{-1}$]) | Emission $\lambda$ [nm] | Quantum yields[a] $\phi$ | Conditions (at $T$ = 298 K) |
|---|---|---|---|---|
| **2a** | 386 (14713) | 437 | 0.002 | *n*-hexane |
| | | 468 | | solid |
| **2b** | 383 (20480) | 437 | 0.002 | *n*-hexane |
| | | 468 | | solid |
| **2c** | 384 (23431) | 436 | 0.003 | *n*-hexane |
| | | 467 | | solid |
| **2d** | 372 (14253) | 423 | 0.015 | *n*-hexane |
| | | 436 | | solid |
| **3a** | 476 (11319) | 573 | 0.042 | *n*-hexane |
| | | 583 | | solid |
| **3b** | 472 (24198) | 565 | 0.048 | *n*-hexane |
| | | 561 | | solid |
| **3c** | 466 (22475) | 555 | 0.087 | *n*-hexane |
| | | 553 | | solid |
| **3d** | 454 (12176) | 515 | 0.070 | *n*-hexane |
| | | 523 | | solid |

[a] Determined by using quinine sulfate in 0.1 M sulfuric acid as a standard.

 © 2007 Wiley-VCH Verlag GmbH & Co. KGaA, Weinheim 

are redshifted by about 40–58 nm relative to the emission maximum of complex **3d** because of the larger conjugated quinolyl ring in **3a**–**3c**. All complexes **3a**–**3d** emit bright fluorescence in the solid state upon irradiation with an adequate excitation wavelength. The emission spectra of complexes **3a**–**3d** in the solid state are shown in Figure 6. Complexes **3a**–**3d** have a relatively narrow band (bandwidth at half-height = 72, 64, 55, and 60 nm) in the solid state with $\lambda$ = 583, 561, 553, and 523 nm, respectively. It seemed that the coordination number of zinc does not play a role in the fluorescence. The emission maxima of complexes **3b** and **3c** in the solid state are slightly blueshifted relative to their corresponding emission maxima in solution; this may be due to the reduced conjugation of the two complexes, as the free rotation of the aryl rings in these complexes is blocked in the solid state. The emission maxima of complexes **3a** and **3d** in the solid state show a redshift relative to their corresponding emission maximum in solution, which is normally observed for most fluorescent compounds in the solid state probably owing to π–π stacking of aromatic rings in the molecules.[6b]

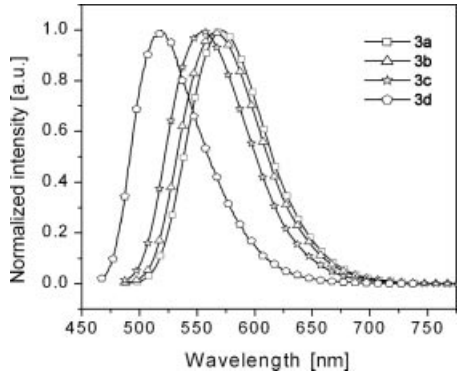


Figure 5. Emission spectra of complexes **3a**–**3d** in *n*-hexane.

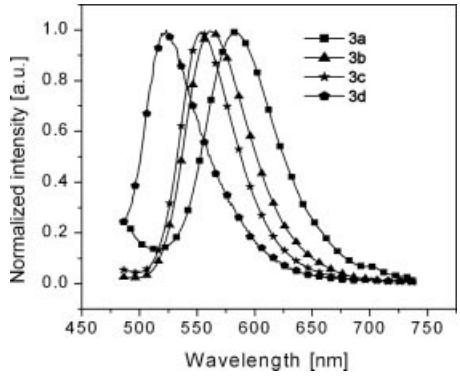


Figure 6. Emission spectra of complexes **3a**–**3d** in the solid state.

## Experimental Section

**General:** All organometallic reactions were performed by using standard Schlenk techniques under an atmosphere of high-purity argon or by using glove box techniques. Toluene, *n*-hexane, and THF were dried by refluxing over sodium and benzophenone and distilled under an atmosphere of argon prior to use. $C_6D_6$ was dried with activated 4 Å molecular sieves and vacuum-transferred to a sodium-mirrored air-free flask. $CDCl_3$ was dried with $CaH_2$ for 48 h and vacuum-transferred to an air-free flask. $ZnEt_2$ and *n*BuLi were purchased from Aldrich and used as received. *ortho*-$C_6H_4F(CH{=}NC_6H_3Me_2$-2,6) (**1a**) and *ortho*-$C_6H_4F(CH{=}NC_6H_3$-*i*$Pr_2$-2,6) (**1c**) were synthesized according to literature procedures.[11] 7-Amino-2,4-dimethylquinoline was synthesized according to a literature procedure.[17] The ligand *ortho*-$C_6H_4$-$(NHC_6H_3Me_2$-2,6)$(CH{=}NC_6H_3i Pr_2$-2,6) (**2d**) was synthesized according to a literature method.[12] $^1$H and $^{13}$C NMR spectra were measured with a Varian Mercury-300 or Bruker AVANCE-500 NMR spectrometer. Elemental analyses were performed with a Perkin–Elmer 2400 analyzer. UV/Vis absorption spectra were recorded with an UV-3100 spectrophotometer. Fluorescent measurements were carried out with an RF-5301PC.

***ortho*-$C_6H_4F(CH{=}NC_6H_3Et_2$-2,6) (1b):** A mixture of *ortho*-fluorobenzaldehyde (4.00 mL, 37.7 mmol), 2,6-diethylaniline (6.20 mL, 37.7 mmol), and anhydrous $MgSO_4$ (1 g) in *n*-hexane (40 mL) was stirred at room temp. for 2 h. The mixture was filtered, and the solvents were evaporated to dryness to give the product as salmon pink oil. The crude product was purified by reduced-pressure distillation. Yield: 6.0 g, 62%. $^1$H NMR (500 MHz, $CDCl_3$, 298 K): $\delta$ = 1.16 (t, $J$ = 7.5 Hz, 2×3 H, $CH_2CH_3$), 2.51 (q, $J$ = 7.5 Hz, 2×2 H, $CH_2CH_3$), 7.06 (d, $J$ = 6.5 Hz, 1 H), 7.11 (d, $J$ = 7.5 Hz, 2 H), 7.16 (t, $J$ = 9.5 Hz, 1 H), 7.29 (t, $J$ = 7.5 Hz, 1 H), 7.50 (q, $J$ = 7.5 Hz, 1 H), 8.25 (t, $J$ = 7.5 Hz, 1 H), 8.55 (s, 1 H, C*H*=N) ppm. $^{13}$C{$^1$H} NMR (125.1 MHz, $CDCl_3$, 298 K): $\delta$ = 15.1 ($CH_2CH_3$), 25.1 ($CH_2CH_3$), 116.3 (d, $^2J_{C,F}$ = 21 Hz), 124.2 (quaternary aromatic), 124.6, 124.9 (d, $^3J_{C,F}$ = 3.5 Hz), 126.7, 128.1 (d, $^4J_{C,F}$ = 2.6 Hz), 133.4 (d, $^3J_{C,F}$ = 8.5 Hz), 133.5 (quaternary aromatic), 150.8 (quaternary aromatic), 156.1 (d, $^3J_{C,F}$ = 4.8 Hz, *C*H=N), 163.2 (d, $^1J_{C,F}$ = 253.5 Hz, *C*F) ppm. $C_{17}H_{18}FN$ (255.33): calcd. C 79.97, H 7.11, N 5.49; found C 79.89, H 7.20, N 5.56.

***ortho*-$C_6H_4${7-NH(2,4-$Me_2$)$C_9H_4N$}$(CH{=}NC_6H_3Me_2$-2,6) (2a):** A solution of *n*BuLi (1.60 M, 22.5 mmol) in *n*-hexane was added to a solution of 7-amino-2,4-dimethylquinoline (3.89 g, 22.5 mmol) in THF (30 mL) at –78 °C. The mixture was warmed to room temp. and stirred overnight. The resulting solution was transferred into a solution of *ortho*-$C_6H_4F(CH{=}NC_6H_3Me_2$-2,6) (5.09 g, 22.5 mmol) in THF (30 mL) at 25 °C. After stirring for 2 d, the reaction was quenched with $H_2O$ (20 mL). The organic phase was evaporated to dryness to give the crude product as a brown oil that was purified by column chromatography on silica gel (ethyl acetate/petroleum ether, 1:5) to give the pure product as yellowish crystals (3.5 g, 41%). $^1$H NMR (300 MHz, $CDCl_3$, 298 K): $\delta$ = 2.21 (s, 2×3 H, $CH_3$), 2.65 (s, 3 H, quinolyl-$CH_3$), 2.72 (s, 3 H, quinolyl-$CH_3$), 6.93 (t, $J$ = 7.5 Hz, 1 H, Ph-*H*), 6.98–7.03 (m, 2 H, Ph-*H* and quinolyl-*H*), 7.11–7.13 (d, 2 H, Ph-*H*), 7.33–7.42 (m, 3 H, Ph-*H* and quinolyl-*H*), 7.81 (d, $J$ = 8.4 Hz, 1 H, Ph-*H*), 7.86 (d, $J$ = 9.3 Hz, 1 H, Ph-*H*), 8.03 (s, 1 H, quinolyl-*H*), 8.36 (s, 1 H, C*H*=NAr), 11.64 (s, 1 H, quinolyl-N*H*) ppm. $^{13}$C{$^1$H} NMR (75.4 MHz, $CDCl_3$, 298 K): $\delta$ = 18.5 ($CH_3$), 18.6 ($CH_3$), 24.9 (quinolyl-$CH_3$), 114.3, 114.9, 118.3, 119.0, 121.0, 121.2, 122.4, 124.1, 124.7, 127.8, 128.2, 132.1, 134.8, 142.4, 144.3, 144.8, 148.7, 150.1, 158.9, 165.8 (*C*H=N) ppm. $C_{26}H_{25}N_3$ (379.50): calcd. C 82.29, H 6.64, N 11.07; found C 82.21, H 6.70, N 11.02.

***ortho*-$C_6H_4${7-NH(2,4-$Me_2$)$C_9H_4N$}$(CH{=}NC_6H_3Et_2$-2,6) (2b):** A solution of *n*BuLi (1.60 M, 12.8 mmol) in *n*-hexane was added to a solution of 7-amino-2,4-dimethylquinoline (2.20 g, 12.8 mmol) in THF (20 mL) at –78 °C. The mixture was warmed to room temp. and stirred overnight. The resulting solution was transferred into a

 © 2007 Wiley-VCH Verlag GmbH & Co. KGaA, Weinheim 

solution of *ortho*-$C_6H_4F(CH{=}NC_6H_3Et_2$-2,6) (3.29 g, 12.8 mmol) in THF (30 mL) at 25 °C. After stirring for 2 d, the reaction was quenched with $H_2O$ (20 mL). The organic phase was evaporated to dryness to give the crude product as a dark brown oil that was purified by column chromatography on silica gel (ethyl acetate/petroleum ether, 1:3) to give the pure product as yellowish crystals (2.20 g, 43%). $^1$H NMR (300 MHz, $CDCl_3$, 298 K): $\delta$ = 1.16 (t, $J$ = 7.8 Hz, 2×3 H, $CH_3CH_2$), 2.57 (q, $J$ = 7.8 Hz, 2×2 H, $CH_3CH_2$), 2.64 (s, 3 H, quinolyl-$CH_3$), 2.70 (s, 3 H, quinolyl-$CH_3$), 6.92 (t, $J$ = 7.5 Hz, 1 H, Ph-*H*), 7.01 (s, 1 H, quinolyl-*H*), 7.06–7.16 (m, 3 H, Ph-*H*), 7.32 (dd, $J$ = 8.7, 2.4 Hz, 1 H, quinolyl-*H*), 7.38–7.43 (m, 2 H, Ph-*H* and quinolyl-*H*), 7.82 (d, $J$ = 9.0 Hz, 1 H, Ph-*H*), 7.87 (d, $J$ = 9.0 Hz, 1 H, Ph-*H*), 8.07 (s, 1 H, quinolyl-*H*), 8.37 (s, 1 H, C*H*=NAr), 11.62 (s, 1 H, quinolyl-N*H*) ppm. $^{13}$C{$^1$H} NMR (75.4 MHz, $CDCl_3$, 298 K): $\delta$ = 14.8 ($CH_2CH_3$), 18.4 (quinolyl-$CH_3$), 24.9 ($CH_3CH_2$), 25.0 (quinolyl-$CH_3$), 114.2, 115.0, 118.3, 118.9, 121.0, 121.3, 122.4, 124.4, 124.7, 126.4, 132.1, 133.7, 134.9, 142.3, 144.2, 144.8, 148.5, 149.4, 158.9, 165.6 (*C*H=N) ppm. $C_{28}H_{29}N_3$ (407.55): calcd. C 82.52, H 7.17, N 10.31; found C 82.59, H 7.21, N 10.20.

***ortho*-$C_6H_4${7-NH(2,4-$Me_2$)$C_9H_4N$}(CH=$NC_6H_3i Pr_2$-2,6) (2c):** A solution of *n*BuLi (1.60 M, 14.4 mmol) in *n*-hexane was added to a solution of 7-amino-2,4-dimethylquinoline (2.50 g, 14.4 mmol) in THF (30 mL) at –78 °C. The mixture was warmed to room temp. and stirred overnight. The resulting solution of LiNHAr [Ar = 7-(2,4-$Me_2$)$C_9H_4N$] was transferred into a solution of *ortho*-$C_6H_4F(CH{=}NC_6H_3iPr_2$-2,6) (4.10 g, 14.4 mmol) in THF (30 mL) at 25 °C. After stirring for 2 d, the reaction was quenched with $H_2O$ (20 mL). The organic phase was evaporated to dryness to give the crude product as a dark brown oil that was recrystallized from methanol to give the pure product as yellow solid (3.01 g, 48%). $^1$H NMR (300 MHz, $CDCl_3$, 298 K): $\delta$ = 1.19 [d, $J$ = 6.5 Hz, 12 H, $CH(CH_3)_2$], 2.63 (s, 3 H, quinolyl-$CH_3$), 2.68 (s, 3 H, quinolyl-$CH_3$), 3.05 [sept, $J$ = 6.5 Hz, 2 H, $CH(CH_3)_2$], 6.97 (t, $J$ = 7.5 Hz, 1 H, Ph-*H*), 7.01 (s, 1 H, quinolyl-*H*), 7.17–7.22 (m, 3 H, Ph-*H* and quinolyl-*H*), 7.31–7.43 (m, 3 H, Ph-*H* and quinolyl-*H*), 7.81–7.88 (m, 2 H, Ph-*H*), 8.04 (s, 1 H, quinolyl-*H*), 8.35 (s, 1 H, C*H*=NAr), 11.59 (s, 1 H, quinolyl-N*H*) ppm. $^{13}$C{$^1$H} NMR (75.4 MHz, $CDCl_3$, 298 K): $\delta$ = 18.5 (quinolyl-$CH_3$), 23.5 [$CH(CH_3)_2$], 25.0 (quinolyl-$CH_3$), 28.1 [$CH(CH_3)_2$], 114.3, 115.1, 118.3, 118.9, 121.0, 121.3, 122.5, 123.1, 124.6, 124.7, 132.2, 135.0, 138.1, 142.3, 144.2, 144.9, 148.3, 149.0, 159.0, 165.7 (*C*H=N) ppm. $C_{30}H_{33}N_3$ (435.60): calcd. C 82.72, H 7.64, N 9.65; found C 82.82, H 7.70, N 9.51.

***ortho*-$C_6H_4${7-N(2,4-$Me_2$)$C_9H_4N$}(CH=$NC_6H_3Me_2$-2,6)ZnEt (3a):** A solution of *ortho*-$C_6H_4${7-NH(2,4-$Me_2$)$C_9H_4N$}(CH=$NC_6H_3Me_2$-2,6) (0.19 g, 0.50 mmol) in toluene (20 mL) was slowly added to a solution of $ZnEt_2$ (0.50 mmol) in toluene (10 mL) at room temp. with stirring. The mixture was stirred at room temp. for 1 h and at 90 °C for an additional 3 h. The solvent was removed in vacuo, and the obtained orange-red residue was recrystallized from *n*-hexane (10 mL) to give an orange-red solid (0.18 g, 78%). $^1$H NMR (300 MHz, $C_6D_6$, 298 K): $\delta$ = 0.55 (q, $J$ = 7.8 Hz, 2 H, $ZnCH_2CH_3$), 1.16 (t, $J$ = 7.8 Hz, 3 H, $ZnCH_2CH_3$), 1.95 (s, 2×3 H, $CH_3$), 2.23 (s, 3 H, quinolyl-$CH_3$), 2.60 (s, 3 H, quinolyl-$CH_3$), 6.51 (t, $J$ = 7.8 Hz, 1 H, Ph-*H*), 6.63 (s, 1 H), 6.94–7.05 (m, 6 H), 7.49 (d, $J$ = 8.4 Hz, 1 H), 7.70 (s, 2 H), 8.40 (s, 1 H, C*H*=N) ppm. $^{13}$C{$^1$H} NMR (75.4 MHz, $C_6D_6$, 298 K): $\delta$ = –1.2 ($ZnCH_2CH_3$), 12.2 ($ZnCH_2CH_3$), 18.2 (quinolyl-$CH_3$), 18.5 ($CH_3$), 25.2 (quinolyl-$CH_3$), 114.4, 116.3, 117.5, 121.5, 124.6, 124.9, 125.7, 126.0, 128.7, 130.1, 134.7, 138.0, 143.2, 149.3, 150.6, 152.1, 157.5, 159.0, 170.2 (*C*H=N) ppm.$C_{56}H_{58}N_6Zn_2$ (945.88): calcd. C 71.11, H 6.18, N 8.88; found C 71.22, H 6.14, N 8.75.

***ortho*-$C_6H_4$[7-N(2,4-$Me_2$)$C_9H_4N$](CH=$NC_6H_3Et_2$-2,6)ZnEt (3b):** A solution of *ortho*-$C_6H_4${7-NH(2,4-$Me_2$)$C_9H_4N$}(CH=$NC_6H_3Et_2$-2,6) (0.19 g, 0.47 mmol) in toluene (20 mL) was slowly added to a solution of $ZnEt_2$ (0.47 mmol) in toluene (10 mL) at room temp. with stirring. The mixture was stirred at room temp. for 1 h and at 90 °C for an additional 3 h. The solvent was removed in vacuo, and the obtained orange-red residue was recrystallized from *n*-hexane (10 mL) to give orange-red crystals (0.19 g, 82%). $^1$H NMR (500 MHz, $C_6D_6$, 298 K): $\delta$ = 0.63 (q, $J$ = 8.0 Hz, 2 H, $ZnCH_2CH_3$), 1.09 (t, $J$ = 7.5 Hz, 2×3 H, $CH_2CH_3$), 1.22 (t, $J$ = 8.0 Hz, 3 H, $ZnCH_2CH_3$), 2.30 (s, 3 H, quinolyl-$CH_3$), 2.43–2.52 (m, 2×2 H, $CH_2CH_3$), 2.63 (s, 3 H, quinolyl-$CH_3$), 6.57 (t, $J$ = 7.5 Hz, 1 H, Ph-*H*), 6.70 (s, 1 H), 7.04–7.10 (m, 4 H), 7.15 (t, $J$ = 8.0 Hz, 1 H), 7.29 (t, $J$ = 9.0 Hz, 1 H), 7.57 (d, $J$ = 9.0 Hz, 1 H), 7.76 (d, $J$ = 9.0 Hz, 1 H), 7.92 (s, 1 H), 8.47 (s, 1 H, C*H*=N) ppm. $^{13}$C{$^1$H} NMR (125.1 MHz, $C_6D_6$, 298 K): $\delta$ = –1.8 ($ZnCH_2CH_3$), 12.0 ($ZnCH_2CH_3$), 14.5 ($CH_2CH_3$), 17.9 (quinolyl-$CH_3$), 25.0 (quinolyl-$CH_3$ and $CH_2CH_3$), 114.3, 115.9, 117.3, 121.3, 123.7, 124.5, 124.6, 125.5, 126.3, 126.6, 134.6, 135.9, 137.6, 142.9, 148.1, 150.5, 151.8, 157.4, 158.7, 170.0 (*C*H=N) ppm. $C_{60}H_{66}N_6Zn_2$ (1001.98): calcd. C 71.92, H 6.64, N 8.39; found C 71.85, H 6.58, N 8.50.

***ortho*-$C_6H_4${7-N(2,4-$Me_2$)$C_9H_4N$}(CH=$NC_6H_3iPr_2$-2,6)ZnEt (3c):** A solution of *ortho*-$C_6H_4${7-NH(2,4-$Me_2$)$C_9H_4N$}(CH=$NC_6H_3iPr_2$-2,6) (0.20 g, 0.55 mmol) in toluene (20 mL) was slowly added to a solution of $ZnEt_2$ (0.55 mmol) in toluene (10 mL) at room temp. with stirring. The mixture was stirred at room temp. for 1 h and at 90 °C for an additional 3 h. The solvent was removed in vacuo, and the obtained orange-red residue was recrystallized from *n*-hexane (10 mL) to give orange-red crystals (0.25 g, 84%). $^1$H NMR (300 MHz, $C_6D_6$, 298 K): $\delta$ = 0.56 (q, $J$ = 8.1 Hz, 2 H, $ZnCH_2CH_3$), 0.99 [d, $J$ = 6.6 Hz, 6 H, $CH(CH_3)_2$], 1.05 [dd, $J$ = 18.3, 6.9 Hz, 6 H, $CH(CH_3)_2$], 1.16 (t, $J$ = 8.1 Hz, 3 H, $ZnCH_2CH_3$), 2.15 (s, 3 H, quinolyl-$CH_3$), 2.49 (s, 3 H, quinolyl-$CH_3$), 2.97 [sept, $J$ = 6.9 Hz, 2×1 H, $CH(CH_3)_2$], 6.44 (t, $J$ = 8.1 Hz, 1 H, Ph-*H*), 6.55 (s, 1 H, quinolyl-*H*), 6.94–6.99 (m, 2×1 H, Ph-*H*), 7.03–7.10 (m, 3×1 H, Ph-*H*), 7.49 (dd, $J$ = 8.7, 2.1 Hz, 1 H, quinolyl-*H*), 7.62 (d, $J$ = 8.7 Hz, 1 H, quinolyl-*H*), 7.97 (s, 1 H, quinolyl-*H*), 8.41 (s, 1 H, C*H*=N) ppm. $^{13}$C{$^1$H} NMR (75.4 MHz, $C_6D_6$, 298 K): $\delta$ = –1.3 ($ZnCH_2CH_3$), 12.4 ($ZnCH_2CH_3$), 18.2 (quinolyl-$CH_3$), 24.4 [$CH(CH_3)_2$], 25.2 (quinolyl-$CH_3$), 28.8 [$CH(CH_3)_2$], 114.6, 116.1, 117.4, 121.6, 123.8, 123.9, 124.6, 124.9, 125.7, 127.0, 134.9, 138.0, 140.9, 143.3, 146.9, 150.6, 152.1, 157.6, 159.0, 170.2 (*C*H=N) ppm. $C_{64}H_{74}N_6Zn_2{\cdot}C_6H_{14}$ (1144.20): calcd. C 73.47, H 7.75, N 7.34; found C 73.36, H 7.81, N 7.16.

***ortho*-$C_6H_4$($NC_6H_3Me_2$-2,6)(CH=$NC_6H_3iPr_2$-2,6)ZnEt (3d):** A solution of *ortho*-$C_6H_4$($NHC_6H_3Me_2$-2,6)(CH=$NC_6H_3iPr_2$-2,6) (0.28 g, 0.72 mmol) in toluene (20 mL)was slowly added to a solution of $ZnEt_2$ (0.72 mmol) in toluene (10 mL) at room temp. with stirring. The mixture was stirred at room temp. for 1 h and at 90 °C for an additional 3 h. The solvent was removed in vacuo, and the obtained yellow-green residue was recrystallized from *n*-hexane (10 mL) to give a yellow solid (0.25 g, 85%). $^1$H NMR (300 MHz, $CDCl_3$, 298 K): $\delta$ = 0.02 (q, $J$ = 8.1 Hz, 2 H, $ZnCH_2CH_3$), 0.70 (t, $J$ = 8.1 Hz, 3 H, $ZnCH_2CH_3$), 1.27 [d, $J$ = 6.6 Hz, 4×3 H, $CH(CH_3)_2$], 2.23 (s, 2×3 H, $CH_3$), 3.10 [sept, $J$ = 6.6 Hz, 2×1 H, $CH(CH_3)_2$], 6.38 (d, $J$ = 9.0 Hz, 1 H), 6.56 (t, $J$ = 6.9 Hz, 1 H), 7.15–7.32 (m, 8 H), 8.29 (s, 1 H, C*H*=N) ppm. $^{13}$C{$^1$H} NMR (75.4 MHz, $CDCl_3$, 298 K): $\delta$ = –2.9 ($ZnCH_2CH_3$), 11.3 ($ZnCH_2CH_3$), 18.3 ($CH_3$), 24.1 [$CH(CH_3)_2$], 28.5 [$CH(CH_3)_2$], 113.0, 114.2, 115.1, 123.5, 124.2, 126.5, 128.5, 133.1, 134.7, 137.6, 140.5, 146.6, 147.3, 156.4, 169.5 (*C*H=N) ppm. $C_{29}H_{36}N_2Zn$ (478.00): calcd. C 72.87, H 7.59, N 5.86; found C 72.71, H 7.68, N 5.75.

 © 2007 Wiley-VCH Verlag GmbH & Co. KGaA, Weinheim 

**X-ray Structure Determinations of 2a, 2b, 3b, and 3c:** Single crystals of **2a** and **2b** suitable for X-ray structural analysis were obtained from ethyl acetate/petroleum ether at room temp. Single crystals of **3b** and **3c** suitable for X-ray structural analysis were obtained from *n*-hexane at room temp. Diffraction data were collected at 293 K with a Rigaku R-AXIS RAPID IP diffractometer equipped with graphite-monochromated Mo-$K_\alpha$ radiation ($\lambda$ = 0.71073 Å) for all compounds. The structures were solved by direct methods[18] and refined by full-matrix least-squares on $F^2$. All non-hydrogen atoms were refined anisotropically and the hydrogen atoms were included in idealized position. All calculations were performed by using the SHELXTL[19] crystallographic software packages. Details of the crystal data, data collections, and structure refinements are summarized in Tables 3 (**2a** and **2b**) and 4 (**3b** and **3c**). CCDC-636086 (for **2a**), -636087 (for **2b**), -636088 (for **3b**), and -636089 (for **3c**) contain the supplementary crystallographic data for this paper. These data can be obtained free of charge from The Cambridge Crystallographic Data Centre via www.ccdc.cam.ac.uk/data_request/cif.

Table 3. Crystal data and structural refinement details for **2a** and **2b**.

| | **2a** | **2b** |
|---|---|---|
| Empirical formula | $C_{26}H_{25}N_3$ | $C_{28}H_{29}N_3$ |
| Formula mass | 379.49 | 407.54 |
| Temperature [K] | 293(2) | 293(2) |
| Crystal system | monoclinic | triclinic |
| Space group | $P2_1/c$ | $P\bar{1}$ |
| $a$ [Å] | 17.371(4) | 9.989(2) |
| $b$ [Å] | 8.4558(17) | 13.204(3) |
| $c$ [Å] | 15.347(3) | 18.038(4) |
| $\alpha$ [°] | 90 | 75.85(3) |
| $\beta$ [°] | 107.62(3) | 87.79(3) |
| $\gamma$ [°] | 90 | 88.84(3) |
| Volume [Å$^3$] | 2148.5(7) | 2305.1(8) |
| Z | 4 | 4[a] |
| $D_{calcd.}$ [Mg m$^{-3}$] | 1.173 | 1.174 |
| $F(000)$ | 808 | 872 |
| $\theta$ range for data collection [°] | 3.11–27.48 | 3.01–27.48 |
| Limiting indices | $-22 \le h \le 20$ | $-12 \le h \le 12$ |
| | $-10 \le k \le 10$ | $-17 \le k \le 17$ |
| | $-19 \le l \le 19$ | $-23 \le l \le 23$ |
| Data/restraints/parameters | 4864/0/271 | 10002/30/568 |
| Goodness-of-fit on $F^2$ | 1.026 | 1.029 |
| Final $R$ indices [$I > 2\sigma(I)$] | $R_1$[b] = 0.0546 | $R_1$[b] = 0.0816 |
| | $wR_2$[c] = 0.1200 | $wR_2$[c] = 0.2028 |
| $R$ indices (all data) | $R_1$[b] = 0.1054 | $R_1$[b] = 0.1636 |
| | $wR_2$[c] = 0.1393 | $wR_2$[c] = 0.2450 |
| Largest diff. peak/hole [e Å$^{-3}$] | 0.152/–0.138 | 0.374/–0.315 |

[a] There are two crystallographically independent molecules in the asymmetric unit. [b] $R_1 = \Sigma||F_o| - |F_c||/\Sigma|F_o|$. [c] $wR_2 = \{\Sigma[w\,(F_o^2 - F_c^2)^2]/\Sigma[w\,(F_o^2)^2]\}^{1/2}$.

Table 4. Crystal data and structural refinement details for **3b** and **3c**.

| | **3b** | **3c** |
|---|---|---|
| Empirical formula | $C_{60}H_{66}N_6Zn_2$ | $C_{70}H_{88}N_6Zn_2$ |
| Formula mass | 1001.93 | 1144.20 |
| Temperature [K] | 293(2) | 293(2) |
| Crystal system | monoclinic | triclinic |
| Space group | $C2/c$ | $P\bar{1}$ |
| $a$ [Å] | 25.656(5) | 13.538(3) |
| $b$ [Å] | 17.437(4) | 15.539(3) |
| $c$ [Å] | 17.348(4) | 16.885(3) |
| $\alpha$ [°] | 90 | 105.85(3) |
| $\beta$ [°] | 129.37(3) | 108.94(3) |
| $\gamma$ [°] | 90 | 96.33(3) |
| Volume [Å$^3$] | 5999(2) | 3153.8(11) |
| Z | 4 | 2 |
| $D_{calcd.}$ [Mg m$^{-3}$] | 1.109 | 1.205 |
| $F(000)$ | 2112 | 1220 |
| $\theta$ range for data collection [°] | 3.04–27.48 | 3.03–27.48 |
| Limiting indices | $-33 \le h \le 33$ | $-17 \le h \le 16$ |
| | $-22 \le k \le 22$ | $-20 \le k \le 20$ |
| | $-18 \le l \le 22$ | $-21 \le l \le 21$ |
| Data/restraints/parameters | 6726/0/289 | 13686/5/719 |
| Goodness-of-fit on $F^2$ | 1.021 | 0.996 |
| Final $R$ indices [$I > 2\sigma(I)$] | $R_1$[a] = 0.0811 | $R_1$[a] = 0.0621 |
| | $wR_2$[b] = 0.1988 | $wR_2$[b] = 0.1668 |
| $R$ indices (all data) | $R_1$[a] = 0.1565 | $R_1$[a] = 0.1243 |
| | $wR_2$[b] = 0.2430 | $wR_2$[b] = 0.2109 |
| Largest diff. peak/hole [e Å$^{-3}$] | 0.981/–1.248 | 0.576/–0.436 |

[a] $R_1 = \Sigma||F_o| - |F_c||/\Sigma|F_o|$. [b] $wR_2 = \{\Sigma[w\,(F_o^2 - F_c^2)^2]/\Sigma[w\,(F_o^2)^2]\}^{1/2}$.

## Acknowledgments

This work was supported by the National Natural Science Foundation of China (No. 20674024) and Ministry of Science and Technology of China (No. 2002CB6134003).

[1] a) Y. Hamada, T. Sano, H. Fujii, Y. Nishino, K. Shibata, *Jpn. J. Appl. Phys.* **1996**, *35*, L1339–L1341; b) H. Tanaka, S. Tokito, Y. Taga, A. Okada, *J. Mater. Chem.* **1998**, *8*, 1999–2003 and references cited therein; c) G. Yu, S. W. Yin, Y. Q. Liu, Z. G. Shuai, D. B. Zhu, *J. Am. Chem. Soc.* **2003**, *125*, 14186–14824.

[2] a) Y. Hamada, T. Sano, M. Fujita, T. Fujii, Y. Nishino, K. Shibata, *Jpn. J. Appl. Phys.* **1993**, *32*, L514–L515; b) L. S. Sapachak, F. E. Benincasa, R. S. Schofield, J. L. Baker, K. K. C. Riccio, D. Fogarty, H. Kohlmann, K. F. Ferris, P. Burrows, *J. Am. Chem. Soc.* **2002**, *124*, 6119–6125; c) T. A. Hopkins, K. Meerholz, S. Shaheen, M. L. Anderson, A. Schmidt, B. Kippelen, A. B. Padias, H. K. Hall Jr, N. Peyghambarian, N. R. Armstrong, *Chem. Mater.* **1996**, *8*, 344–351; d) M. Ghedini, M. L. Deda, I. Aiello, A. Grisolia, *Inorg. Chim. Acta* **2004**, *357*, 33–40.

[3] a) Y. Hamada, T. Sano, M. Fujita, T. Fujii, Y. Nishino, K. Shibata, *Jpn. J. Appl. Phys.* **1993**, *32*, L511–L513; b) T. Sano, Y. Nishio, Y. Hamada, H. Takahashi, T. Usuki, K. Shibata, *J. Mater. Chem.* **2000**, *10*, 157–161; c) P. F. Wang, Z. R. Hong, Z. Y. Xie, S. W. Tong, O. Y. Wong, C.-S. Lee, N. B. Wong, L. S. Hung, S. T. Lee, *Chem. Commun.* **2003**, 1664–1665; d) K. H. Chang, C. C. Huang, Y. H. Liu, Y. H. Hu, P. T. Chou, Y. C. Lin, *Dalton Trans.* **2004**, 1731–1738.

[4] Y. Hamada, T. Sano, H. Fujii, Y. Nishino, H. Takahashi, K. Shibata, *Appl. Phys.* **1997**, *71*, 3338–3340.

[5] a) K. Y. Ho, W. Y. Yu, K. K. Cheung, C. M. Che, *Chem. Commun.* **1998**, 2101–2102; b) K. Y. Ho, W. Y. Yu, K. K. Cheung, C. M. Che, *J. Chem. Soc. Dalton Trans.* **1999**, 1581–1586.

[6] a) W. Y. Yang, H. Schmider, Q. D. Wu, Y. S. Zhang, S. N. Wang, *Inorg. Chem.* **2000**, *39*, 2397–2404; b) Q. G. Wu, J. A. Lavigue, Y. Tao, M. D'Iorio, S. Wang, *Inorg. Chem.* **2000**, *39*, 5248–5254; c) L. V. Sazanovich, C. Kirmarier, E. Hinclin, L. Yu, D. F. Bocian, J. S. Lindsey, D. Holten, *J. Am. Chem. Soc.* **2004**, *126*, 2664–2665; d) Y. J. Kang, C. Seward, D. T. Song, S. N. Wang, *Inorg. Chem.* **2003**, *42*, 2789–2797; e) W. Y. Wong, K. Y. Tsang, K. H. Tam, G. L. Lu, C. Sun, *J. Organomet. Chem.* **2000**, *601*, 237–245; f) M. R. Bermejo, M. Vazquez, J. Sanmartin, A. M. Carcía-Deilbe, M. Fondo, C. Lodeiro, *New J. Chem.* **2002**, *26*, 1365–1370; g) S. N. Wang, *Coord. Chem. Rev.* **2001**, *215*, 79–98.

[7] V. W.-W. Yam, Y.-L. Pui, K.-K. Cheung, *Inorg. Chem.* **2000**, *39*, 5741–5746.

[8] a) C.-F. Lee, K.-F. Chin, S.-M. Peng, C.-M. Che, *J. Chem. Soc. Dalton Trans.* **1993**, 467–470; b) Y. G. Ma, H.-Y. Chao, Y. Wu, S. T. Lee, W.-Y. Yu, C.-M. Che, *Chem. Commun.* **1998**, 2491–

 © 2007 Wiley-VCH Verlag GmbH & Co. KGaA, Weinheim 

2492; c) Y. G. Ma, T. S. Lai, Y. Wu, *Adv. Mater.* **2000**, *12*, 433–436.
[9] J. J. Klappa, S. A. Geers, S. J. Schmidtke, L. A. Macmanus-Spencer, K. McNeill, *Dalton Trans.* **2004**, 883–891.
[10] a) X. M. Liu, W. Gao, Y. Mu, G. H. Li, L. Ye, H. Xia, Y. Ren, S. H. Feng, *Organometallics* **2005**, *24*, 1614–1619; b) X. M. Liu, H. Xia, W. Gao, L. Ye, Y. Mu, Q. Su, Y. Ren, *Eur. J. Inorg. Chem.* **2006**, *6*, 1216–1222; c) Y. Ren, X. M. Liu, W. Gao, H. Xia, L. Ye, Y. Mu, *Eur. J. Inorg. Chem*. **2007**, *13*, 1808–1814.
[11] a) B. Y. Lee, H. Y. Kwon, S. Y. Lee, S. J. Na, S.-I. Han, H. Yun, H. Lee, Y.-W. Park, *J. Am. Chem. Soc.* **2005**, *127*, 3031–3037; b) T. Bok, H. Yun, B. Y. Lee, *Inorg. Chem.* **2006**, *45*, 4228–4237.
[12] P. G. Hayes, G. C. Welch, D. J. H. Emslie, C. L. Noack, W. E. Piers, M. Parvez, *Organometallics* **2003**, *22*, 1577–1579.
[13] H. Y. Gao, W. J. Guo, F. Bao, G. Q. Gui, J. K. Zhang, F. M. Zhu, Q. Wu, *Organometallics* **2004**, *23*, 6273–6280.
[14] A. Looney, R. Han, I. B. Gorrell, M. Comebise, K. Yoon, G. Parkin, A. L. Rheingold, *Organometallics* **1995**, *14*, 274–288.
[15] M. Cheng, D. R. Moore, J. J. Reczek, B. M. Chamberlain, E. B. Lobkovsky, G. W. Coates, *J. Am. Chem. Soc.* **2001**, *123*, 8738–8749.
[16] a) D. Rendell (Ed.), *Fluorescence and Phosphorescence*, Wiley, New York, **1987**; b) H. Yersin, A. Vogler (Eds.), *Photochemistry and Photophysics of Coordination Compounds*, Springer, Berlin, **1987**; c) A. W. Adamson, P. D. Fleischauer (Eds.), *Concepts of Inorganic Photochemistry*, Wiley, New York, **1975**; d) N. I. Nijegorodov, W. S. Downey, *J. Phys. Chem.* **1994**, *98*, 5639–5643.
[17] a) C. K. Bradsher, *Chem. Rev.* **1946**, *38*, 447–499; b) W. S. Johnson, F. J. Mathews, *J. Am. Chem. Soc.* **1944**, *66*, 210–215.
[18] G. M. Sheldrick, *SHELXTL*, PC Siemens Analytical X-ray Instruments, Madison WI, **1993**.
[19] G. M. Sheldrick, *SHELXTL: Structure Determination Programs*, Version 5.0, PC Siemens Analytical Systems, Madison, WI, **1994**.

Received: February 8, 2007
Published Online: July 12, 2007

 © 2007 Wiley-VCH Verlag GmbH & Co. KGaA, Weinheim 

DOI: 10.1002/ejic.200700185

# Introduction of Modified Electronic Parameters – Searching for a Unified Ligand Properties Scale through the Electrophilicity Index Concept

**Christodoulos Makedonas[a] and Christiana A. Mitsopoulou*[a]**

**Keywords:** Modified electronic parameters / Electrophilicity index / Diimine complexes / Reduction potential / Charge-transfer bands

In order to quantify the contribution of mainly, but not only, diimine ligands to the electronic properties of the corresponding complexes, two novel indices, namely modified electronic parameters (*ModEP*) and electrophilicity, $\omega$, are introduced and discussed in this report. First, we introduce the concept of *ModEP*, a novel scale relating to the electronic properties of diimine ligands. Mainly on the basis of well-characterized M(diimine)(dithiolato) complexes (M = Pt, Pd, or Ni), we derive the contribution of the diimine ligand to the reduction potentials of the complexes, and incorporating its contribution to the main charge-transfer band of the UV/Vis spectra, we obtain our *ModEP* values. The applicability of the introduced scale to several other classes of diimine compounds (W, Re, and Ru) is then tested. The performance of our scale in predicting the values of the reduction potentials and the position of the charge-transfer bands is very satisfactory. With this approach, some interesting aspects of ligand coordination were revealed. Next, we employ the recently introduced electrophilicity index $\omega$, in order to correlate our *ModEP* scale with various other empirical scales that are already known and extensively used. This permits us to unify most known scales, which were primarily derived for different types of ligands (e.g. *ModEP* for diimines, Tolman's for phosphanes). The proposed method of $\omega$ calculation (at the semiempirical AM1 level) avoids any experimental limitation and can be employed even for ligands that are not yet experimentally available, whereas its correlation to the known scales would immediately provide the properties of the compound. This supports the idea that the electrophilicity index could become a powerful tool in coordination and organometallic chemistry.

(© Wiley-VCH Verlag GmbH & Co. KGaA, 69451 Weinheim, Germany, 2007)

## Introduction

All the properties of inorganic and organometallic complexes and their potential applications, from the field of homogeneous catalysis to materials and from photochemistry to DNA binding and intercalation are determined by the combination of metal and ligand. However, for a given series of homologous compounds with the same metal, the role of the ligand in terms of both electronic and steric effects becomes dominant. For decades, coordination and organometallic chemists have been trying to find a way to predict the effect of a ligand change upon the properties of a complex,[1–7] trying to avoid the need for extensive synthetic work. This essential need for knowledge of ligand effects on a certain core or fragment is extended not only to different types of known ligands, but also to ones that have merely been considered for future work. In this sense, great effort has been put into the development of ligand parameters, on the basis of which properties of known compounds would be documented and properties of new ones could be predicted.

[a] Inorganic Chemistry Laboratory, Chemistry Department, National and Kapodistrian University of Athens, Panepistimiopolis, Zografou 157 71, Greece
E-mail: cmitsop@chem.uoa.gr

Of known importance is Tolman's electronic parameter (*TEP*) relating to phosphanes ($PR_3$).[1] It was derived on the basis of the $A_1$ $\nu$(CO) stretching vibration of $(R_3P)Ni(CO)_3$ complexes. As it is justified by backbonding theory, the greater the donor power of the phosphane the lower the stretching mode becomes. *TEP* has found wide usage over the years, but the expansion of the model is limited by the requirement that a new ligand L along with the corresponding $NiL(CO)_3$ complex should be synthesized and spectroscopically investigated, and this is not always an easy task.

This limitation is overcome by Crabtree's calculated electronic parameters (*CEP*).[2] In this approach, the $A_1$ $\nu$(CO) frequency is no longer experimentally derived, but it is calculated by means of density functional theory (DFT). The relative donor powers of a wide variety of cationic, neutral, and negatively charged ligands are reliably predicted; expanding the model, these parameters also correlate well with other empirically derived parameters. Even though the method avoids any experimental limitations, it incurs computational costs and provides no values for bidentate ligands, such as diimines.

Lever's electronic parameters (*LEP*)[3] are based on the electrochemical $E°$ value for various redox couples, notably $Ru^{III}/Ru^{II}$, in series of complexes containing the ligands of interest. *LEP* cover a much wider set of ligands than Tol-

 © 2007 Wiley-VCH Verlag GmbH & Co. KGaA, Weinheim 

man's scale, including anionic, O- and N-donor ligands. On the other hand, it has the disadvantage that an electrochemical apparatus for measurements is necessary, which is not always available. Another disadvantage of *LEP* is that electrochemical irreversibility can degrade the quality of the data for certain ligands, and solvation and ion-pairing effects could interfere to some extent.

Hammett substitution constants $\sigma$ have found wide usage both with organic and inorganic compounds.[5] These were defined by the ionization constants of the appropriately substituted benzoic acids. The most extensively employed are $\sigma_p$ and $\sigma_m$, relating to *para*- and *meta*- substituent effects, respectively. Hammett constants in most of the cases have only qualitative value, providing synthetic chemists with trends, but not with accurate properties of compounds under preparation. Moreover, they are limited by their own nature. They provide the trends that would arise by the substitution of a ligand in certain positions, but they can not show which effects would arise from a different ligand. Thus, in the case of the 2,2′-bipyridine ligand, for example, Hammett substitution constants might work if the substituents are added in the 4 and 4′ positions, but they will fail to predict what will happen if bipyridine is replaced by 1,10-phenanthroline or an aliphatic ligand, such as diiminosuccinonitrile.

Recently, Arca et al.[6] gave a quantitative description of the effect induced by both the metal and the ligands to the value of $\lambda_{max}$ in a series of dithiolene complexes of the M(R,R′timdt)$_2$ type and Poë et al.[7] presented an analysis of CO dissociative kinetics of Ru(CO)$_4$L (L = P-donor ligands).

Keeping all of the above in mind, herein we present our efforts to obtain a unified ligand properties scale. Our investigation for a quantitative analysis of ligand effects (QALE)[8–14] was carried out at two levels. In the first, we introduce the concept of modified electronic parameters (*ModEP*), a novel scale relating to the electronic properties of diimine ligands. Mainly on the basis of the well-characterized M(diimine)(dithiolato) complexes (M = Pt, Pd, or Ni), we derive the contribution of the diimines to the reduction potential of the complexes; in the next step, we incorporate their effect on the main charge-transfer band of the visible spectra of the complexes, and then we obtain our *ModEP* values. There are two reasons for choosing this class of complexes for our analysis. First of all, an extensive series of this type of compounds has been presented.[15–72] Furthermore, the interest toward mixed diimine–dithiolato complexes of d$^8$ metals is related to their unique properties, which include solution luminescence, solvatochromism, large molecular hyperpolarizabilities, and large excited-state oxidation potentials. Because of these properties, they are considered to be very promising candidates for nonlinear optical (NLO) materials, molecular photochemical devices (MPD), and photosensitizers for solar cells.

The electronic properties depend most likely on the existence in the same molecule of two different unsaturated chelating ligands, one of which is a good π*-donor (the dithiolato ligand) and the other a good π*-acceptor (the diimine). The possibility of applying mixed diimine–dithiolato complexes to any of the above-mentioned technologies mainly relies on the intense solvatochromic, visible absorption in the neutral state, $E_{MMLL'CT}$, caused by the mixed-metal–ligand-to-ligand-charge-transfer (MMLL′CT)[26] transition between the HOMO and LUMO, where the former is a mixture of metal and dithiolato ligand orbital and the latter a π* orbital of the diimine. This assignment has been confirmed by TD-DFT calculations,[69–72] and both experimental[16–34] and theoretical results[69–72] indicate that its frequency can be tuned from near-Vis to NIR by changing the substituents both at the diimine and dithiolate moieties. These complexes face a reversible, diimine-based, reduction process, which is well characterized.

Up to now, despite the extensive study of M(diimine)(dithiolato) complexes, only some general trends of the nature of the substituent groups on the main substrate of the diimine or dithiolato ligand have been revealed, but none of this data is in quantitative form. Between the two ligands, the one that is less studied from the point of view of its effect on the properties of a molecule is certainly the diimine.

The applicability of the introduced scale is then tested on several other types of W, Re, and Ru diimine compounds. The performance of our scale in predicting the value of the reduction potentials and the position of the charge-transfer bands is very satisfactory.

In the next level of investigation, we employ the recently introduced electrophilicity index $\omega$,[73] in order to correlate our *ModEP* scale with various other empirical scales that are already known and extensively used. This procedure gives us the chance to unify all these scales, which were derived by investigating different types of ligands (e.g. *ModEP* on diimines, Tolman's on phosphanes). This supports the idea that the electrophilicity index could become a powerful tool in coordination and organometallic chemistry.

## Computational Details

All the experimental data presented are taken from already published reports. In the following discussion, the abbreviations used for compounds are as follows: tdt = toluene-3,4-dithiolato, bpy = 2,2′-bipyridine, php = 1,10-phenanthrolinopyrrole, tmphen = 3,4,7,8-tetramethyl-1,10-phenanthroline, 3,5,6,8-tetramethyl-1,10-phenanthroline, *i*Pr-pya = *N*-isopropylpyridine-2-carbaldimine, dmphen = 4,7-dimethyl-1,10-phenanthroline, Bu-pya = *N*-butylpyridine-2-carbaldimine, 6,6′-dmbpy = 6,6′-dimethyl-2,2′-bipyridine, dbbpy = 4,4′-di-*tert*-butyl-2,2′-bipyridine, dmbpy = 4,4′-dimethyl-2,2′-bipyridine, 5,5′-dmbpy = 5,5′-dimethyl-2,2′-bipyridine, 2,9-dmphen = 2,9-dimethyl-1,10-phenanthroline, 5,6-dmphen = 5,6-dimethyl-1,10-phenanthroline, 2,9-dm-4,7-dpphen = 2,9-dimethyl-4,7-diphenyl-1,10-phenanthroline, mphen = 5-methyl-1,10-phenanthroline, dpphen = 4,7-diphenyl-1,10-phenanthroline, pphen = 4-phenyl-1,10-phenanthroline, phen = 1,10-phenanthroline, dpbpy = 4,4′-

 © 2007 Wiley-VCH Verlag GmbH & Co. KGaA, Weinheim 

diphenyl-2,2′-bipyridine, Cl-phen = 5-chloro-1,10-phenanthroline, Br-phen = 5-bromo-1,10-phenanthroline, $Br_2$-bpy = 4,4′-dibromo-2,2′-bipyridine, $Cl_2$-bpy = 4,4′-dichloro-2,2′-bipyridine, $NO_2$-phen = 5-nitro-1,10-phenanthroline, bipym = 2,2′-bipyrimidine, EHC-bpy = 4,4′-bis(2-ethylhexyloxycarbonyl)-2,2′-bipyridine, *t*Bu-DAB = *tert*-butyl-*N*,*N*′-bis(1,4-diazabutadiene), EC-bpy = 4,4′-bis(ethoxycarbonyl)-2,2′-bipyridine, dcphen = 4,7-dicarboxy-1,10-phenanthroline, dcbpy = 4,4′-dicarboxy-2,2′-bipyridine, BABA = biacetylbisaniline, dthdi = *N*,*N*′-ditolyl-3,4-hexanediimine, $(CF_3)_2$-bpy = 4,4′-ditrifluoromethyl-2,2′-bipyridine, $(NO_2)_2$-bpy = 4,4′-dinitro-2,2′-bipyridine, disn = diiminosuccinonitrile, bbqdi = *semi*-4-benzoylbenzoquinonediimine.

The calculation of the ground-state electronic structure of a Pt(bpy)(tdt) complex has been performed by using density functional theory[73,74] methods with the GAUSSIAN 1998 software package.[75] The functional used throughout this study is the B3LYP, consisting of a hybrid exchange functional as defined by Becke's three-parameter equation[76] and the Lee–Yang–Parr correlation functional.[77] The ground-state geometry was obtained in the gas phase by full geometry optimization, under no symmetry constraint. The VeryTight option was used, which demands tighter convergence criteria than the default ones, while numerical integration was performed with the UltraFine option, which requests a pruned (99,590) grid. The optimum structures located as stationary points on the potential energy surfaces were verified by the absence of imaginary frequencies. The derived wavefunctions were found to be free from internal instabilities. The basis set used for all nonmetal atoms was the well-known valence triple-zeta 6-311+G*.[78,79] The quasi-relativistic Stuttgart–Dresden effective core potential of the type ECP60MWB was used for Pt, and complemented by the corresponding valence basis sets.[80] Percentage compositions of molecular orbitals from the three contributing fragments were calculated with the AOMix program.[81,82]

Ground-state electronic structure calculations of all other compounds including the net ligands have been performed by using the AM1[83] and PM3[84,85] semiempirical techniques, with MOPAC2000[86] as implemented in the CAChe software package.[87] Structures have been preoptimized under the MM3 force field.[88] The ground-state geometries were obtained in the gas phase by full geometry optimization, under no symmetry constraint. Structures of the 2,2′-bipyridine derivatives and nonaromatic bidentate ligands have been considered under their planar arrangement (the binding N–C–C–N dihedral angle was set to zero). These geometries correspond to the first-order saddle point (transition state) that links the two energy minima at the potential energy surface through rotation of the C1–C1′ bond. We preferred to use this structure, because the compounds have this structure at the time of complex formation. For the rest of the compounds under study, the optimum structures were verified by the absence of imaginary frequencies. Frontier orbital contour plots presented herein were prepared with the aid of MOLEKEL.[89]

## Results and Discussion

### Deriving the Model – Modified Electronic Parameters

Our methodology for obtaining a structure-to-properties relation (SPR) will be based on Lever's arguments[3] and the general theory of ligand properties additivity,[90–93] starting from electrochemical data. According to the additivity theory, redox potentials of the complexes can be regarded as an additive property made up of the contributions of both the metals and the coordinated ligands. The weight of these contributions is defined by the percentage of each component of the LUMO orbital of the complex, since the relation between $E°$ and LUMO energy is well documented.[67,68] Our approach has five levels and provides the following equation [Equation (1)].

$$ModEP = -0.0001343\ E_{MMLL'CT} + 1.1671129\ (R^2 = 1) \quad (1)$$

(1) As we have already mentioned, we set the basis of our reasoning on the M(diimine)(dithiolato) complexes and especially on those with Pt, not only for their plethora, but also because they are more important candidates for potential applications.[17] In these compounds, the LUMO orbital is localized mainly on the diimine core as has been indicated both experimentally and theoretically.[69–72] Moreover, we needed a model compound, and Pt(bpy)(tdt) contains all the necessary prerequisites for this. First of all, platinum is coordinated to two bidentate ligands; both of them are good σ-donors, having medium π*-donating (the dithiolato)/π*-accepting (the diimine) ability. Secondly, there is a series of eight Pt(diimine)(tdt) complexes that are well characterized, with defined electrochemical and spectroscopic behavior (vide infra).[24]

(2) The origin of our model is based on reduction potentials. Pt(bpy)(tdt) has a reversible reduction wave at –1.339 V in a DMF solution.[24] This value arises from the contribution of both the diimine and the Pt/tdt fragment. In order to determine the contribution of diimine to this, we performed ground-state electronic calculations for the complex under investigation at the DFT level of theory. The frontier orbital energies along with the contributions from the two ligands and the metal are given in Table 1, while the HOMO and LUMO are presented in Figure 1.

The HOMO, a $b_1$ orbital in the local sense, is composed mainly of sulfur $3p_z$ orbitals on the chelating ring, while the LUMO is calculated to be located almost on the diimine with a limited contribution from the metal and dithiolato ligand. The calculated contribution of 2,2′-bipyridine to the LUMO orbital is 87%. Thus, we dissect the first reduction potential into two parts and *credit by definition* a value of $E_1 = -1.165$ V to the diimine, according to its contribution to the whole potential (87% of $E(Pt^{0/-})$. The remaining $E_2 = -0.174$ V is attributed to the system Pt/tdt. Once these values are well defined, we can obtain the corresponding values for all diimine ligands that are bound to the Pt(tdt) fragment, bearing in mind that the experimental conditions for the derivation of the corresponding potentials must be the same.

 © 2007 Wiley-VCH Verlag GmbH & Co. KGaA, Weinheim 

Table 1. Contribution of different fragments to Pt(bpy)(tdt) valence orbitals. The HOMO and LUMO are shown in bold.

| MO | *E* [eV] | Metal | Dithiolato | Diimine |
|---|---|---|---|---|
| Unoccupied | | | | |
| 95 | –0.64 | 38.7 | 2.4 | 58.9 |
| 94 | –1.02 | 44.9 | 47.4 | 7.7 |
| 93 | –1.78 | 1.4 | 0.5 | 98.2 |
| 92 | –2.02 | 1.4 | 0.5 | 98.1 |
| **91** | **–2.90** | **5.4** | **7.4** | **87.2** |
| Occupied | | | | |
| **90** | **–4.67** | **9.5** | **80.5** | **10.0** |
| 89 | –5.05 | 13.8 | 84.5 | 1.7 |
| 88 | –6.37 | 68.5 | 23.9 | 7.6 |
| 87 | –6.60 | 28.5 | 67.2 | 4.3 |
| 86 | –6.74 | 33.7 | 60.5 | 5.8 |
| 85 | –7.23 | 43.6 | 52.6 | 3.8 |

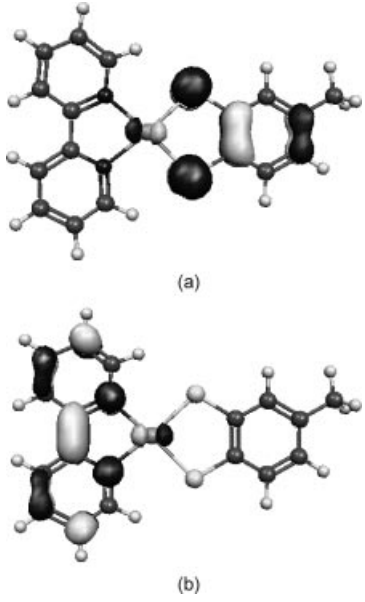


Figure 1. Contour plots of HOMO (a) and LUMO (b) orbitals of Pt(bpy)(tdt).

(3) Assuming that the $E_2$ value is kept constant along the series of eight Pt(diimine)(tdt) complexes,[24] we obtain the corresponding electronic parameters (*EP*) / contributions for the diimine ligands (taking the $E°$ values from Table 2) according to Equation (2).

$$EP = E_{\text{red (of each complex)}} - 0.13E_{\text{red/(dpy)Pt(tdt)}} \quad (2)$$

Thus, we get *EP* = –1.321 V for tmphen, –1.224 V for dbbpy, –1.197 V for dmbpy, –1.165 V for bpy, –1.145 V for phen, –1.083 V for Cl-phen, –0.869 V for $Cl_2$-bpy, and –0.788 V for EC-bpy.

On the basis of the well-documented interconnection of LUMO, $E_{red}$, and $E_{MML'CT}$, there should be a linear relation between the derived *EP* and the observed values of $E_{MML'CT}$ for the main low-energy solvatochromic band of these compounds. As a matter of fact, this is true, and an excellent correlation coefficient of 0.98 is derived (Figure 2).

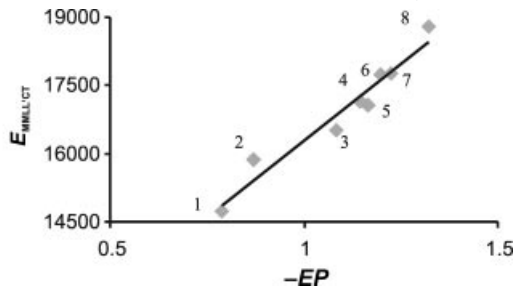


Figure 2. Graphic representation of the function $E_{MML'CT} = f(–EP)$ for M(diimine)(tdt) complexes. Spectra of Pt(EC-bpy(tdt) (1), Pt($Cl_2$-bpy)(tdt) (2), Pt(Cl-phen)(tdt) (3), Pt(bpy)(bdt) (4), Pt(phen)(tdt) (5), Pt(dmbpy)(tdt) (6), Pt(dbbpy)(tdt) (7), and Pt(tmphen)(tdt) (8) were recorded in $CH_2Cl_2$.

(4) Using the regression line derived from the original data, we recalculated *EP* values for any prespecified $E_{MML'CT}$. This recalculation was done in order to predict the *EP* values of the ligands not included in our primary data, on the basis of their $E_{MML'CT}$ values and also to reduce the error introduced by the assumption that the contribution of the Pt/tdt fragment to the reduction potential of the compound is the same.

So, *EP*s are reevaluated for these eight diimines, and the obtained values are called, for the needs of our discussion, modified electronic parameters (*ModEP*). Thus, *ModEP* becomes –1.359 V for tmphen, –1.220 V for dbbpy, –1.215 V for dmbpy, –1.126 V for bpy, –1.138 V for phen, –1.054 V for Cl-phen, –0.966 V for $Cl_2$-bpy, and –0.812 V for EC-bpy, according to Equation (1).

(5) Mainly on the basis of a large number of data for M(diimine)(dithiolato) compounds (Table 2) and the eight "starting" values derived in the previous paragraph, we have obtained the *ModEP* values for a satisfactory number of diimines (Table 3).

## Explanation and Physical Basis

Up to now, we have indicated the formulation employed in order to obtain *ModEP* values. In this section, we shall try to explain the properties of the new scale and the necessary prerequisites that a complex should satisfy in order for the additivity concept to be valid. First of all, *ModEP* values are given in V, but as soon as they are calculated they no longer depend on any experimental condition. This fact is justified, because *ModEP* values correspond to differences in reduction potentials and shifts in the energy of a charge-transfer band, measured under the same experimental conditions. So, for a series of compounds with different diimines, *ModEP* should correlate well with a ligand-based reduction potential and with the corresponding charge-transfer band as long as the experimental conditions are the same, no matter what these are. Subsequently, the *ModEP* values were calculated in order to provide the link between the ligands and the properties of the corresponding complexes. In this sense, diimines with large *ModEP* values when coordinated to a metal lead to easier reduction of the

 © 2007 Wiley-VCH Verlag GmbH & Co. KGaA, Weinheim 

Table 2. Electrochemical and spectroscopic results for M(diimine)(dithiolato) complexes. Please consult the original literature for the precision and the experimental conditions. The solvent provided refers to $\lambda_{max}$, since compounds under study are highly negatively solvatochromic.

| Complex | Solvent | $\lambda_{max}$ [nm] | $E_{MMLL'CT}$ [cm$^{-1}$] | $E_{redI}$ [V] | $E_{redII}$ [V] | $E_{ox}$ [V] | Ref. |
|---|---|---|---|---|---|---|---|
| Pt(bpy)(tdt)[a] | $CH_2Cl_2$ | 586 | 17065 | –1.339r | r[m] | +0.376qr | [24] |
| Pt(bpy)(bdt)[a] | $CHCl_3$ | 600 | 16667 | –1.31r[b] | –1.99ir | +0.40/0.70[b,c] | [68] |
| | | | | –1.775r[b,d] | – | +0.025[b,d] | [69] |
| Pt(bpy)(dpdt)[e] | $CH_2Cl_2$ | 614 | 16287 | – | – | +0.26r | [35] |
| Pt(bpy)(bbdt)[e] | $CH_2Cl_2$ | 590 | 16949 | – | – | +0.22r | [35] |
| Pt(phen)(mnt)[a] | $PhNO_2$ | 510 | 19608 | –1.21r | –1.75r | +1.15ir[m] | [33] |
| Pt(phen)(i-mnt)[a] | $PhNO_2$ | 423 | 23641 | –1.22r | –1.73r | +1.15ir | [33] |
| Pt(phen)(qdt)[a] | DMSO | 458 | 21834 | –1.06r | – | +0.95ir | [25,26] |
| Pt(phen)(tdt)[a] | $CH_2Cl_2$ | 583 | 17153 | –1.319r | r | +0.376qr[m] | [22,24,41] |
| Pt(phen)(dpdt)[e] | $CH_2Cl_2$ | 620 | 16129 | – | – | +0.30r | [35] |
| Pt(phen)(bbdt)[e] | $CH_2Cl_2$ | 627 | 15949 | – | – | +0.24r | [35] |
| Pt(bipym)(mnt)[e] | DMSO | 493 | 20284 | | | +1.32ir | [44] |
| Pt(bipym)(dmit)[e] | DMSO | 560 | 17857 | | | +0.80ir | [44] |
| Pt(BABA)(mnt)[e] | $CH_2Cl_2$ | 620 | 16129 | –0.70r | –1.50qr[f] | +0.8ir[f] | [43] |
| Pt(BABA)(tdt)[e] | $CH_2Cl_2$ | 682 | 14663 | –0.94r | –1.66qr[f] | +0.64ir[f] | [43] |
| Pt(dmbpy)(ecda)[e] | $CHCl_3$ | 450 | 22222 | –1.28r[g] | –1.77r | +0.83ir[g] | [34] |
| | | | | –1.21qr[g,h] | | +0.81ir[g,h] | [29] |
| Pt(dmbpy)(mnt)[h] | $CH_2Cl_2$ | 492 | 20325 | –1.17qr[g] | | +1.22qr[g] | [29] |
| | | | | –1.29r[g,a] | –1.78r | +1.07ir[g,a] | [33] |
| Pt(dmbpy)(i-mnt)[a] | $CH_2Cl_2$ | 417 | 23981 | –1.28r | –1.83r | +1.16ir | [33] |
| Pt(dmbpy)(tdt)[a] | $CH_2Cl_2$ | 563 | 17762 | –1.371r | r | +0.390ir | [22,24,41] |
| Pt(dpbpy)(mnt)[a] | $CH_2Cl_2$ | 513 | 19493 | –1.18r | –1.68r | +0.70 | [33] |
| Pt(dpbpy)(i-mnt)[a] | $CH_2Cl_2$ | 448 | 22321 | –1.11r | –1.71r | +0.72 | [33] |
| Pt(dbbpy)(tbcda)[a] | $CH_2Cl_2$ | 437 | 22883 | –1.302r | r | +0.963ir | [24] |
| Pt(dbbpy)(cpdt)[a] | $CH_2Cl_2$ | 434 | 23041 | –1.274r | r | +0.957ir | [24] |
| Pt(dbbpy)(endt)[a] | $CH_2Cl_2$ | 480 | 20833 | –1.484r | r | +0.431ir | [24] |
| Pt(dbbpy)(dmqdt)[a] | $CH_2Cl_2$ | 481 | 20790 | –1.334r | r | +0.814ir | [24] |
| Pt(dbbpy)(mnt)[a] | $CH_2Cl_2$ | 497 | 20121 | –1.266r | r | +0.944ir | [24] |
| Pt(dbbpy)(tdt)[a] | $CH_2Cl_2$ | 563 | 17762 | –1.398r | r | +0.389ir | [24] |
| Pt(dbbpy)(S-4-py)$_2$[e] | $CH_2Cl_2$ | 452 | 22124 | –1.73r | – | +0.66ir | [20] |
| Pt(Cl$_2$-bpy)(tdt)[a] | $CH_2Cl_2$ | 630 | 15873 | –1.043r | r | +0.380ir | [24] |
| Pt(EC-bpy)(tdt)[a] | $CH_2Cl_2$ | 679 | 14728 | –0.962r | r | +0.412ir | [24] |
| Pt(dcbpy)(ecda)[e] | EtOH/MeOH | 440 | 22727 | –1.1ir[i] | – | +0.95ir | [37,38] |
| Pt(dcbpy)(qdt)[e] | EtOH/MeOH | 460 | 21739 | –1.1ir[i] | – | +0.85ir | [37–39] |
| Pt(dcbpy)(tdt)[e] | EtOH/MeOH | 580 | 17241 | –1.2ir[i] | – | +0.45ir | [37–39] |
| Pt(dpphen)(ecda)[e] | $CHCl_3$ | 468 | 21368 | –1.12r[g] | –1.68r | +0.83ir[g] | [34] |
| | | | | –1.24qr[g,h] | | +0.81ir[g,h] | [29] |
| Pt(dpphen)(mnt)[j] | $CH_2Cl_2$ | 520 | 19231 | –1.17qr[g] | | +1.22qr[g] | [29,33] |
| | | | | –1.15r[a, g] | –1.72r | +0.72ir[a, g] | [33] |
| Pt(dpphen)(i-mnt)[a] | $CH_2Cl_2$ | 444 | 22523 | –1.18r | –1.73r | +0.75ir | [33] |
| Pt(tmphen)(tdt)[a] | $CH_2Cl_2$ | 532 | 18797 | –1.495r | r | +0347ir | [24] |
| Pt(Cl-phen)(tdt)[a] | $CH_2Cl_2$ | 605 | 16529 | –1.257r | r | +0.359qr | [24] |
| Pt(dcphen)(ecda)[e] | EtOH/MeOH | 436 | 22936 | –1.2ir[i] | – | +0.98ir | [37–39] |
| Pt(dcphen)(qdt)[e] | EtOH/MeOH | 480 | 20833 | –1.0ir[i] | – | +0.90ir | [37–40] |
| Pt(dcphen)(tdt)[e] | EtOH/MeOH | 568 | 17606 | –1.2ir[i] | – | +0.49ir | [37–39] |
| Pt(dcphen)(bdt)[e] | EtOH/MeOH | 565 | 17699 | –1.1ir[i] | – | +0.52ir | [37–39] |
| Pt(Et-pya)(dmit) | DMSO | 580 | 17241 | | | | [51] |
| Pt(*i*Pr-pya)(dmit) | DMSO | 570 | 17544 | | | | [51] |
| Pt(Bu-pya)($C_8H_4S_8$) | $CH_2Cl_2$ | 808 | 12376 | | | | [42,49] |
| Pt($C_{10}$-pya)(dmit)[j] | $CH_2Cl_2$ | 660 | 15152 | | | +0.36[k] | [53] |
| Pt($C_{10}$-pya)($C_8H_4S_8$)[j] | $CH_2Cl_2$ | 770 | 12987 | | | +0.26[k] | [53] |
| Pd(bpy)(bdt)[e] | $CHCl_3$ | 510 | 19608 | –1.846r | – | +0.165ir | [67] |
| Pd(BABA)(tdt)[e] | $CH_2Cl_2$ | 688 | 14535 | –0.98r | –1.66qr[f] | +0.58ir[f,l] | [62] |
| | | | | | | +1.20ir[f] | [62] |
| Pd(BABA)(mnt)[e] | $CH_2Cl_2$ | 600 | 16667 | –0.78r | –1.50qr[f] | +1.18ir[f] | [62] |
| Ni(bpy)(bdt) | $CHCl_3$ | 557 | 17953 | –1.828r | – | +0.084ir | [67] |
| Ni(BABA)(tdt)[e] | $CH_2Cl_2$ | 696 | 14368 | –1.00r | –1.66qr[f] | +0.48ir[f,l] | [62] |
| | | | | | | +1.20ir[f] | [62] |
| Ni(dpphen)(tbcda) | $CH_2Cl_2$ | 465 | 21505 | | | | [22] |
| Ni(dpphen)(tfd) | $CHCl_3$ | 543 | 18416 | | | | [43,50] |
| Ni(dthdi)(mnt) | $CHCl_3$ | 651 | 15361 | | | | [41,50] |
| Ni(dthdi)(tfd) | $CHCl_3$ | 671 | 14903 | | | | [41,50] |
| Ni(disn)(tfd) | $CHCl_3$ | 703 | 14225 | | | | [41,50] |
| Ni(EHC-bpy)(mnt) | $CHCl_3$ | 583 | 17153 | | | | [41,50] |
| Ni(EHC-bpy)(tfd) | $CHCl_3$ | 602 | 16611 | | | | [41,50] |
| Ni(bbqdi)(tfd) | $CHCl_3$ | 745 | 13423 | | | | [41,50] |
| Ni(NO$_2$-bpy)(tfd) | $CHCl_3$ | 742 | 13477 | | | | [41,50] |

[a] Observed potential vs. NHE. [b] The observed differences are quite substantial. [c] Two oxidations 1/2e$^-$. [d] Observed potential vs. $Fc^+/Fc$ (0.400 V vs. NHE). [e] Observed potential vs. SCE, $Hg/Hg_2Cl_2$ (KCl sat.) and $E^{25\,°C}$ = 0.2444 V. [f] Value for $E_{p/2}$. [g] There is a difference in the assignment of the wave. [h] Observed potential vs. SSCE, $Hg/Hg_2Cl_2$ (NaCl sat.). [i] Value for $E_p$. [j] Observed potential vs. Ag/AgCl ($a_{Cl^-}$ = 1 M) and $E^{25\,°C}$ = 0.22234 V. [k] Value for $E_0'$. [l] The wave corresponds to a two-electron procedure. [m] The symbols r, ir, and qr stand for reversible, irreversible, and quasi reversible waves, respectively.

 © 2007 Wiley-VCH Verlag GmbH & Co. KGaA, Weinheim 

Table 3. Modified electronic parameters (*ModEP*) for the most frequently used diimines in synthesis.

| Diimine | *ModEP* [V] |
|---|---|
| php | –1.408 |
| tmphen | –1.359 |
| 3,5,6,8-tmphen | –1.297 |
| *i*Pr-pya | –1.284 |
| dmphen | –1.270 |
| Bu-pya | –1.270 |
| 6,6′-dmbpy | –1.241 |
| dbbpy | –1.220 |
| dmbpy | –1.215 |
| 5,5′-dmbpy | –1.203 |
| 2,9-dmphen | –1.199 |
| 5,6-dmphen | –1.194 |
| 2,9-dm-4,7-dpphen | –1.188 |
| mphen | –1.172 |
| dpphen | –1.150 |
| pphen | –1.143 |
| phen | –1.138 |
| dpbpy | –1.132 |
| bpy | –1.126 |
| Cl-phen | –1.054 |
| Br-phen | –1.044 |
| $Br_2$-bpy | –0.980 |
| $Cl_2$-bpy | –0.966 |
| $NO_2$-phen | –0.963 |
| bipym | –0.956 |
| EHC-bpy | –0.926 |
| EC-bpy | –0.812 |
| dcphen | –0.799 |
| dcbpy | –0.787 |
| *t*Bu-DAB | –0.785 |
| BABA | –0.729 |
| dthdi | –0.703 |
| $(CF_3)_2$-bpy | –0.681 |
| $(NO_2)_2$-bpy | –0.582 |
| disn | –0.514 |
| bbqdi | –0.508 |

resultant complexes in a way that can be accurately predicted. Moreover, they stabilize the LUMO of the complexes. In other words, they cause a red shift of the main charge-transfer band, and its $\lambda_{max}$ is accurately predicted by correlations of the $E_{MMLL'CT} = f(ModEP)$ type.

Furthermore, *ModEP* values are indicative of the σ- and π- bonding ability of the diimines, covering a range of 1000 mV. In addition to this, when comparing diimines of the same core, such as 1,10-phenanthroline derivatives (e.g. dpphen and phen), *ModEP* values could be used as indices of only π-effects, provided that in these ligands the σ-donating ability is almost the same.

On the basis of the aforementioned discussion, we can set up the necessary arguments in order for the additivity concept to be valid and the expected accuracy of a prediction to be high. Thus, (i) reduction potentials under consideration must be reversible or at least quasi-reversible, (ii) the reduction process must be described by the scheme ML(diimine$^{-}$), (iii) the reduction must occur to the same unoccupied orbital (from an energetic and symmetry point of view). In the complexes under study, this is the diimine-based LUMO. Further, (iv) the charge-transfer band must be attributed to the same orbital, for example, in the case of M(diimine)(dithiolato) compounds, the main UV/Vis band arises from a singlet state well described by the HOMO → LUMO notion,[69–72] and (v) the effect of the solvent must be taken into account: comparison between either spectroscopic or electrochemical results is only possible if the same solvent is used. The reason for this is quite obvious. M(diimine)(dithiolato) complexes are greatly solvatochromic as a result of their polar ground state, and the nonpolar (or even polar in the opposite direction) excited state and this solvatochromism affects also their redox behavior.

Before testing the applicability of *ModEP*, we investigated its correlation to Hammett constants, since the latter meet a general acceptance and have found wide application. These were defined by the ionization constants of the appropriately substituted benzoic acids. In the case under study and in order to find out whether there are any correlations, we had to make a concession that had to do with the applicability of Hammett constants. Hammett constants can find application only in cases of ligands that have the same core, differing in terms of the substituting groups in exact positions, e.g. 4,4′-X,X-2,2′-bipyridines. In order to partly overcome this problem, we employed $\sigma_t$ values, as defined by Equation (3), where $\sigma_p$, $\sigma_m$, and $\sigma_o$, represent *para*-, *meta*-, and *ortho*- substituent effects, respectively.

$$\sigma_t = \Sigma\sigma_p + \Sigma\sigma_m + \Sigma\sigma_o \quad (3)$$

It is obvious that the *ModEP* scale surpasses Hammett constants in the sense that the former contains at the same time aromatic (e.g. 1,10-phenanthroline), "semi-aromatic" (e.g. *N*-butyl-pyridine-2-carbaldimine), and aliphatic (e.g. diiminosuccinonitrile) entries, while the latter gives the relation among ligands that are derivatives of the same parent compound. The Hammett constants employed are presented in Table 4 (vide infra). For 13 bipyridine derivatives, we obtain the relation in Equation (4) (Figure 3).

$$\sigma_t = 2.74\ ModEP + 3.10 \quad (4)$$

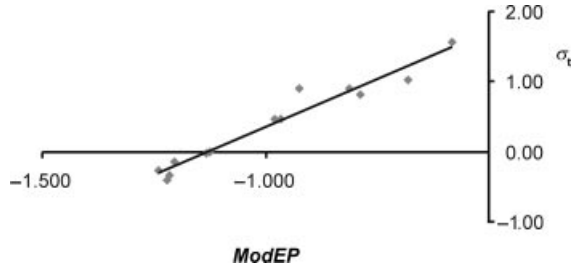


Figure 3. Graphic representation of the relation $\sigma_t = f(ModEP)$ for 13 2,2′-bipyridine derivatives ($R^2 = 0.96$).

The fit is excellent ($r = 0.96$). Moreover, in Figure 4, the corresponding correlation for 14 1,10-phenanthroline derivatives is depicted. A linear relation is also evident ($r = 0.93$) here [Equation (5)].

 © 2007 Wiley-VCH Verlag GmbH & Co. KGaA, Weinheim 

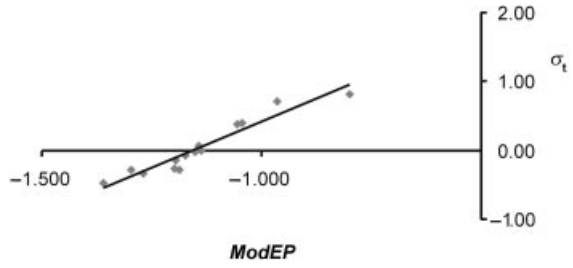


Figure 4. Graphic representation of the relation $\sigma_t = f(ModEP)$ for 14 1,10-phenanthroline derivatives ($R^2 = 0.93$).

$$\sigma_t = 2.68\ ModEP + 3.09 \quad (5)$$

Comparing Equations (4) and (5), we conclude that the same substituent groups on both aromatic ligands, namely phen and bpy, have a similar effect. Moreover, assuming that σ- donation is identical along the same series, this supports our belief that *ModEP* values are indicative of π- effects.

For an extensive series of M(diimine)(dithiolato) compounds, keeping the M(dithiolato) fragment constant and correlating *ModEP* with the experimentally derived reduction potentials and the charge-transfer energies, we conclude that our scale works fine with the compounds under consideration. The maximum error in the ligand-based reduction potential is 43 mV (the experimental error in most cases is around 10 mV) and a few nm in the case of the UV/Vis spectra. As a result, we are able to predict the properties of compounds that are not yet prepared. As an example, we employ again the series of Pt(diimine)(tdt) compounds mentioned earlier and three 1,10-phenanthroline derivatives, namely $NO_2$-phen (*ModEP* = –0.963 V), pphen (*ModEP* = –1.143 V), and 5,6-dmphen (*ModEP* = –1.194 V). Equation (6) gives the relation $E_{red} = f(ModEP)$ and Equation (7), the relation $E_{MMLL'CT} = f(ModEP)$.

$$E_{red} = 1.049\ ModEP - 0.107 \quad (6)$$

$$E_{MMLL'CT} = -7742\ ModEP + 8685 \quad (7)$$

$NO_2$-phen is anticipated to have a reduction potential of –1.117 V and a CT band at 631 nm, whereas the corresponding values for pphen and 5,6-dmphen should be –1.306 V and 582 nm, and –1.360 V and 569 nm, respectively. The standard deviation in all cases is around 39 mV and less than 1 nm (the low value for the latter comes also from the modification employed).

From all the experimental data available, we conclude that the *ModEP* scale finds application in M(diimine)(dithiolato) complexes. On the other hand this class of compounds was used in order for this scale to be extracted. So, the potential use of the *ModEP* scale must be tested on other classes of compounds. In the next two sections, several examples will be presented along with a discussion on the way in which the *ModEP* scale could be enriched and what its chemical meaning really is.

## Potential Applications

Trying to investigate the potential applications of the *ModEP* scale, we tested its response in several classes of compounds. In all cases, the rules i–v formulated in the previous section were observed to hold. The cases where the overall correlation was very good were employed to enrich the *ModEP* scale.

### *M(diimine)(CO)$_4$ (M = W, Mo, Cr)*

The first class of compounds on which we tested our model was M(diimine)$(CO)_4$. These compounds are known for their negative solvatochromism and luminescence in solution and find potential applications in material science.[94–101] They have a solvatochromic band that is attributed to a MLCT transition. On the basis of data from ref.[94–101] we obtain the correlation shown in Figure 5.

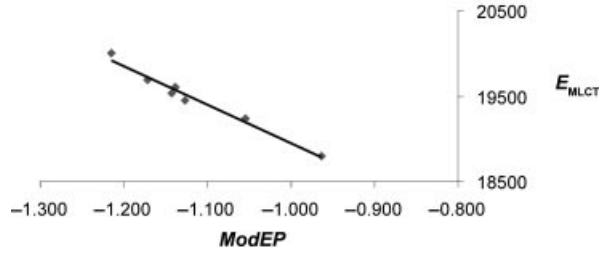


Figure 5. Graphic representation of the relation $E_{MLCT} = f(ModEP)$ for a series of W(diimine)$(CO)_4$ complexes ($R^2 = 0.98$). Transition energies were collected in benzene.

The relation $E_{MLCT} = f(ModEP)$ is linear and is described by Equation (8).

$$E_{MLCT} = -4502\ ModEP + 14449 \quad (8)$$

The maximum error anticipated for this range of transition energies is only 2 nm. Analogous relations hold also in the case of Mo and Cr, shown in Equations (9) ($R^2 = 0.97$) and (10) ($R^2 = 0.92$), respectively. Transition energies were collected in benzene.

$$E_{MLCT} = -5111\ ModEP + 14536 \quad (9)$$

$$E_{MLCT} = -4832\ ModEP + 13561 \quad (10)$$

The maximum errors in these cases are slightly larger, 3 and 5 nm, respectively, but they are certainly at a more than acceptable level. This fact supports the use of the *ModEP* scale for prediction purposes. For example, the charge-transfer band for the complex W(5,6-dmphen)$(CO)_4$, which, to the best of our knowledge, has not been prepared yet, is anticipated to be 504 ± 1 nm in benzene, on the basis of the *ModEP* value of the ligand (–1.194 V).

### *fac-[Re(CO)$_3$(CNx)(diimine)]$^+$*

Rhenium(I) tricarbonyl complexes containing bidentate heterocyclic ligands have been a source of interest for several years, largely because of their potential use in solar energy conversion.[95,102] These compounds display intense

 © 2007 Wiley-VCH Verlag GmbH & Co. KGaA, Weinheim 

luminescence in the visible region of the spectrum and have long emission lifetimes. Recently, Rillema et al. prepared a series of *fac*-[Re(CO)$_3$(CNx)(diimine)]$^+$ complexes.[103–106] These complexes have a diimine-based reversible reduction process. We tested the *ModEP* scale, searching for a correlation of the type $E_{red} = f(ModEP)$. In Figure 6, this correlation is schematically depicted, and Equation (11) gives the corresponding linear regression. The maximum deviation from linearity in this case is 42 mV.

$$E_{red} = 1.027\ ModEP - 0.035 \quad (11)$$

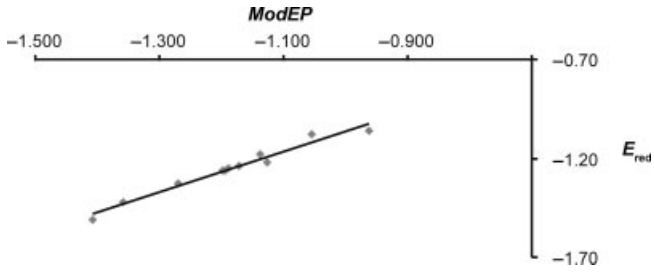


Figure 6. Graphic representation of the relation $E_{red} = f(ModEP)$ for a series of *fac*-[Re(CO)$_3$(CNx)(diimine)]$^+$ complexes ($R^2 = 0.98$). Potentials are reported vs. SSCE in $CH_3CN$ at room temperature, taken from ref.[103–106]

### *[{(diimine)Re(CO)$_3$}$_3$(μ-L)]$^+$*

The good correlation of $E_{red} = f(ModEP)$ obtained in the previous case, was tested also in a more demanding case. Sun and Lees prepared recently a series of trinuclear diimine Re$^I$ tricarbonyl complexes bridged by 1,3,5-tris-(4-ethenylpyridyl)benzene (L1) and 1,3,5-tris(4-ethynylpyridyl)benzene (L2).[107] These compounds have one or two reduction potentials, the first one representing the addition of one electron to the diimine ligands. Equations () and () give the corresponding correlations for the L1 and L2 bridges, respectively, and Figure 7 provides a graphic representation for the latter.

$$E_{red} = 2.638\ ModEP + 1.546 \quad (12)$$

$$E_{red} = 3.002\ ModEP + 1.902 \quad (13)$$

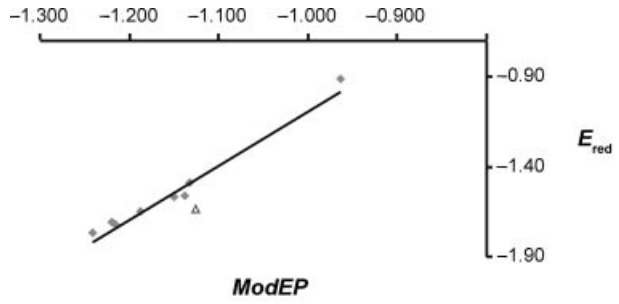


Figure 7. Graphic representation of the relation $E_{red} = f(ModEP)$ for a series of [{(diimine)Re(CO)$_3$}$_3$(μ-L2)]$^+$ complexes ($R^2 = 0.92$). The triangular point corresponds to bpy. Data taken from ref.[107]

For both cases very good correlations have been obtained. On the other hand, reduction potentials of the bpy complexes seem to deviate from linearity, but we can not provide a satisfactory explanation for that. Moreover, the slope of the linear relation is three times larger than the corresponding slope in *fac*-[Re(CO)$_3$(CNx)(dmbpy)]$^+$, which was previously described.

### *Cu$^{II}$ Uroporphyrin I Complexes*

In 1983, Shelnutt reported Raman shifts of copper uroporphyrin I induced by complex formation with phenanthroline derivatives.[108] We correlated these Raman shifts with our *ModEP* scale. A linear relation was obtained (Figure 8). Bulky derivatives have been excluded from the correlation. Shelnut observed an analogous relation to the Hammett constants and assigned this inconsistency to the fact that sterically hindered ligands can not lie flat on the porphyrin ring.

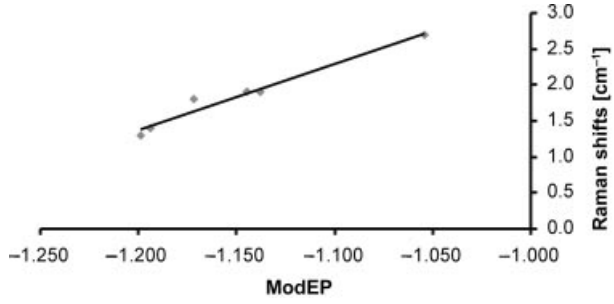


Figure 8. Graphic representation of the relation $\Delta\nu = f(ModEP)$ for the 1637 cm$^{-1}$ line for a series of 1,10-phenanthroline derivatives ($R^2 = 0.96$). Data taken from ref.[108] The experimental error is less than 1.0 cm$^{-1}$.

### *The Case of [Ru(diimine)$_3$]$^{2+}$*

[Ru(diimine)$_3$]$^{2+}$ complexes have proved to be one of the most important classes of photosensitizers ever synthesized.[109–113] Here, we shall investigate the applicability of the *ModEP* scale to these complexes and the way their properties could be predicted. First of all, this class of compounds is completely different in nature from those previously described. In their UV/Vis spectra, they have at least one MLCT band of a clear d → π* (diimine) type. This means that both the HOMO ($a_1$ and e with $D_3$ symmetry) and the LUMO ($a_2$ and e with $D_3$ symmetry) depend on the nature of the ligand. Thus, a correlation between $E_{MLCT}$ and *ModEP* or reduction potential is not expected. Moreover, more than one reversible reduction process is detected, but only one oxidation potential is present. The latter refers to the couple Ru$^{II}$/Ru$^{III}$ and can be assumed to involve the nonbonding or slightly π*-antibonding $t_{2g}$ ($a_1$ and e) metal-centered orbital.[3,82,109–115] Firstly, we tested the *ModEP* scale on the oxidation process, for which a large amount of data is available.[110] Although this process deviates from the rules previously established, it is evident that $E_{ox}$ is greatly dependent on the ligand. Thus, stronger σ-donors cause a lower oxidation potential of the Ru$^{II}$ complex, whereas more efficient π*-acceptors have the opposite ef-

 © 2007 Wiley-VCH Verlag GmbH & Co. KGaA, Weinheim 

fect.[110] Lever employed $E_{ox}$ also in order to derive his *LEP* parameters (vide infra). A graphic representation of the correlation $E_{ox} = f(ModEP)$ is provided in Figure 9. A regression coefficient of 0.92 is derived for this relation.

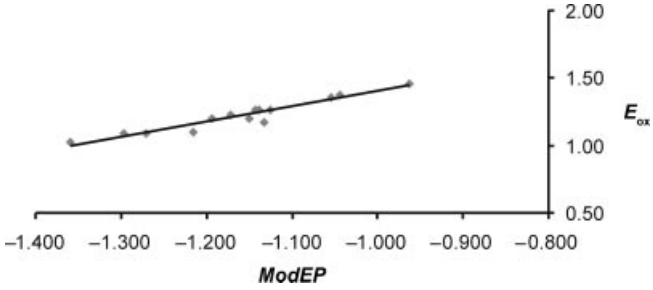


Figure 9. Graphic representation of the relation $E_{ox} = f(ModEP)$ for a series of $[Ru(diimine)_3]^{2+}$ complexes ($R^2 = 0.92$). Data taken from ref.[116]

A linear relation is obtained by employing data from ref.[116] Analogous results are extracted by employing data from ref.[110] [Equation (14)].

$$E_{red} = 1.133\ ModEP + 2.535 \quad (14)$$

Trying to find a net ligand process that could be correlated to the *ModEP* scale, we ended up with the excited-state oxidation potentials. $E_{ox}$* refers to an abstraction of an electron from the LUMO, and this process must certainly be dependent on the ligand, surpassing delocalization problems. An almost perfect correlation is observed (Figure 10).

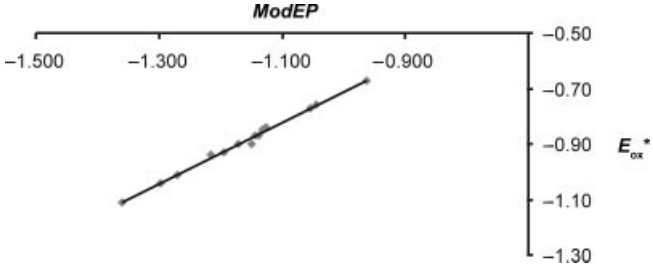


Figure 10. Graphic representation of the relation $E_{ox}^* = f(ModEP)$ for a series of $[Ru(diimine)_3]^{2+}$ complexes ($R^2 = 0.99$). Data taken from ref.[116]

The corresponding linear regression is given by Equation (15).

$$E_{ox}^* = 1.109\ ModEP + 0.397 \quad (15)$$

Equation (15) is of great importance since the excited-state oxidation potential of these complexes determines their ability to act as photosensitizers, and according to the best of our knowledge, it is presented for the first time.

The same trend is observed for M(diimine)(dithiolato) complexes, as given by Equation (16) ($r = 0.92$).

$$E_{ox}^* = 0.790\ ModEP - 0.561 \quad (16)$$

### *Interaction of $[Ru(NH_3)_4(diimine)]^{2+}$ with CT DNA*

In 2004, Mahesvari and Palaniandavar[112,113] reported the interaction of a series of mixed ligand complexes of the type $[Ru(NH_3)_4(diimine)]^{2+}$ with calf thymus DNA. Our *ModEP* scale correlates well with the oxidation and formal peak potentials of the complexes both with and without DNA. Moreover, a good correlation is obtained in the case of the reduction potentials of the complexes, but not with reduction potentials in the presence of DNA, a fact that is an indication that the nature of the reduction in the DNA-bound form is not the same. These correlations are provided in Equations (17), (18), (19), (20), and (21).

$$E_{ox} = 0.576\ ModEP + 1.044\ (R^2 = 0.94) \quad (17)$$

$$E_{red} = 0.452\ ModEP + 0.761\ (R^2 = 0.94) \quad (18)$$

$$E_{1/2} = 0.514\ ModEP + 0.883\ (R^2 = 0.99) \quad (19)$$

$$E_{ox} = 0.700\ ModEP + 1.135\ (R^2 = 0.95) \text{ (in the presence of CT DNA)} \quad (20)$$

$$E_{1/2} = 0.515\ ModEP + 0.853\ (R^2 = 0.97) \text{ (in the presence of CT DNA)} \quad (21)$$

The ligand 2,9-dmphen has been excluded from the regression analysis because of its deviation from linearity. This is in accord with its relatively high values for the ratio $i_{pa}/i_{pc}$ (1.39 in the case of DNA interaction) and $\Delta E_p$ (192 mV for the complex), which are strong indications of irreversible processes.

## The Role of the Coordinating Ligand – Expanding the Model

In the previous sections, we set up the basis of the *ModEP* scale and tested its applicability to several demanding cases. Moreover, we showed that *ModEP* finds potential application in the description of every ligand-based/determined process.

From all the examples mentioned above, covering a range of diimine compounds from material to biochemical science, we conclude that the role of the ligand in a complex can be predicted in a quantitative manner. In addition, the previously extracted correlations imply that the ligands act in a completely analogous way regardless of the metal fragment to which they are coordinated; this refers to all classes of ligands. Let's demonstrate a provocative example. From the previous discussion and the way *ModEP* is derived, we should expect that the energy of the *MMLL′CT* band in the M(diimine)(dithiolato) complexes correlates well with $[Ru(diimine)_3]^{2+}$ excited-state oxidation potentials. This argument has proved correct ($r = 0.998$). This idea is the result of a simple mathematical/numerical regression, but it also possesses an inherent chemical meaning. It denotes that ligands act in a fully predictable way upon coordination to a metal, and this is because of their electronic characteristics. Under this prism, the coordination of a metal to

 © 2007 Wiley-VCH Verlag GmbH & Co. KGaA, Weinheim 

a ligand determines a general property of a complex (e.g. luminescence) and causes the stabilization of ligands towards, for example, reduction, but it is the nature of the ligands that determines the extent of these properties. In other words, if we synthesize one or two compounds of a new family, we can predict with high accuracy their electronic properties with an extensive series of ligands, without the need to synthesize them individually.

In view of the above discussion, we conclude that a unified scale of ligand properties is what must become our main objective. In the Introduction, we mentioned some of the most widely accepted ligand scales. The major drawback of all of them is that they are oriented to certain types of ligands, e.g. diimines, phosphanes, and dithiolates. If we select one as the most appropriate, e.g. *CEP* or *TEP*, we must develop synthetic or computational routes in order to derive parameters for other types of ligands. In a different approach, for a large-scale comparison of data for different classes of compounds having different types of ligands, we could enrich the *ModEP* scale. However, both approaches are time consuming and constrained by experimental errors or different experimental conditions.

Herein, we suggest a different approach that can be employed for every type of ligand used or is under consideration for future work. This approach will be based on the electrophilicity index $\omega$.

### Electrophilicity Index $\omega$ – Application to Diimine Ligands

On the basis of an idea given by Maynard et.al.,[117] in 1999, Parr and co-workers defined the electrophilicity index, $\omega$, as a measure of the electrophilicity of a ligand[73] [Equation (22)].

$$\omega \equiv \mu^2/2\eta \tag{22}$$

where $\mu$ = chemical potential, defined by $\mu = [\partial E/\partial N]_v$ (and $\mu = -\chi$, $\chi$ = electronegativity) and $\eta$ = chemical hardness defined by $\eta = [\partial^2 E/\partial N^2]_v$.

Following Parr's arguments, Equation (23) is presented, where $\omega$ corresponds to the energy produced from the maximal flow of electrons between the donor and acceptor, where I is the compound's ionization potential and A is its electron affinity.

$$\omega = \frac{(I + A)^2}{8(I - A)} \tag{23}$$

Moreover, maximal electron flow is given by Equation (24).

$$\Delta N_{max} = \frac{I + A}{2(I - A)} \tag{24}$$

Both $\omega$ and electron affinity measure the capability of an agent to accept electrons. Nevertheless, the latter is by definition related strictly to a one-electron process, whereas the electrophilicity index measures the total energy lowering of a ligand due to maximal electron flow ($\Delta E = -\mu^2/2\eta$, $\Delta E < 0$, charge transfer being a spontaneous process), a value that could be different from unity.[73] The model was completed by Contreras et al., who introduced solvent effects,[118–121] and the importance of the electrophilicity index is well documented by Chattaraj et al.[122]

First of all, we tried to investigate the applicability of the electrophilicity index, $\omega$, to large molecules and, more precisely, in the detection of the behavior of the complexed diimines. To the best of our knowledge, this approach is employed for the first time.

We employed Koopmans' theorem, as given by the following relations [Equations (25) and (26)].

$$I \cong -E_{HOMO} \tag{25}$$

$$A \cong -E_{LUMO} \tag{26}$$

Equation (26) is not really part of the theorem. Nevertheless, it is usually used in the literature as a good approximation. In a first approach to the problem, the semiempirical AM1 model was employed (the PM3 model gave similar results). Although neither method matches the high precision of ab initio calculations, their main advantage is low computational cost and wide acceptance in the description of organic molecules. Some first calculations of diimine properties at the HF and MP2 level of theory gave similar results, but their application was not possible as soon as the structures became more complex.

In Table 4, the parameters for the diimines under study calculated at the AM1 level are presented. It is obvious that electron-accepting groups increase the electrophilicity and maximal electron flow of the diimine, whereas good σ-donors contribute to their reduction.

Both $\omega$ and *ModEP* give a measure of the maximal electron flow that a ligand can accept, and on the basis of this fact we anticipate the function $ModEP = f(\omega)$ to be linear. Figure 11 shows the linear correlation between *ModEP* and the computed $\omega$; a good correlation coefficient is found ($R^2 = 0.92$), and Equation (27) is obtained.

$$ModEP = 1.151\ \omega - 3.085 \tag{27}$$

Thus, both *ModEP* and $\omega$ can find application as quantitative indices of a ligand's electronic behavior. The great advantage of $\omega$ is that it can be easily calculated for a broad range of ligand types. Thus, by definition it must correlate satisfactorily with the electronic descriptors of all other ligands, either experimentally derived (*TEP* and *LEP*) or computed (*CEP*).

Employing data points from ref.[2] (Table 5), we derived the linear relations that are obtained for 17 molecules that are often used in synthesis as ligands. These relations are given by Equations (28), (29), (30), and (31). The majority of the entries are for phosphane ligands, because *TEP* and *CEP* have been derived for these types of compounds. The last column in Table 5 corresponds to *ModEP* values computed from Equation (27) for the given molecules.

 © 2007 Wiley-VCH Verlag GmbH & Co. KGaA, Weinheim 

Table 4. Ionization potentials, electron affinities, electrophilicity index, and maximal electron flow calculated with the AM1 model, along with Hammett's constants and modified electronic parameters for the diimines under study. Energy values are provided in eV.

| Diimine | *I* | *A* | $\omega$ | $\Delta N_{max}$ | $\sigma_t$ | *ModEP* |
|---|---|---|---|---|---|---|
| php | 10.691 | 0.491 | 1.532 | 0.548 | – | –1.408 |
| tmphen | 10.716 | 0.521 | 1.548 | 0.551 | –0.48 | –1.359 |
| 3,5,6,8-tmphen | 11.106 | 0.601 | 1.631 | 0.557 | –0.28 | –1.297 |
| *i*Pr-pya | 11.245 | 0.271 | 1.511 | 0.525 | – | –1.284 |
| dmphen | 11.044 | 0.658 | 1.648 | 0.563 | | –1.270 |
| Bu-pya | 11.256 | 0.293 | 1.521 | 0.527 | – | –1.270 |
| 6,6′-dmbpy | 11.180 | 0.481 | 1.589 | 0.545 | –0.26 | –1.241 |
| dbbpy | 11.126 | 0.449 | 1.569 | 0.542 | –0.40 | –1.220 |
| dmbpy | 11.202 | 0.508 | 1.603 | 0.548 | –0.34 | –1.215 |
| 5,5′-dmbpy | 11.260 | 0.566 | 1.635 | 0.553 | –0.14 | –1.203 |
| 2,9-dmphen | 11.040 | 0.662 | 1.649 | 0.564 | –0.26 | –1.199 |
| 5,6-dmphen | 11.173 | 0.692 | 1.679 | 0.566 | –0.14 | –1.194 |
| 2,9-dm-4,7-dpphen | 10.918 | 0.648 | 1.628 | 0.563 | –0.28 | –1.188 |
| 5-mphen | 11.175 | 0.706 | 1.685 | 0.567 | –0.07 | –1.172 |
| dpphen | 11.027 | 0.695 | 1.662 | 0.567 | –0.02 | –1.150 |
| pphen | 11.091 | 0.707 | 1.676 | 0.568 | 0.06 | –1.143 |
| phen | 11.158 | 0.719 | 1.689 | 0.569 | 0.00 | –1.138 |
| dpbpy | 11.120 | 0.560 | 1.615 | 0.553 | –0.02 | –1.132 |
| bpy | 11.271 | 0.585 | 1.644 | 0.555 | 0.00 | –1.126 |
| Cl-phen | 11.480 | 0.945 | 1.832 | 0.590 | 0.37 | –1.054 |
| Br-phen | 11.489 | 0.998 | 1.858 | 0.595 | 0.39 | –1.044 |
| $Br_2$-bpy | 11.741 | 0.989 | 1.884 | 0.592 | 0.46 | –0.980 |
| $Cl_2$-bpy | 11.743 | 0.952 | 1.867 | 0.588 | 0.46 | –0.966 |
| $NO_2$-phen | 11.331 | 1.136 | 1.906 | 0.611 | 0.71 | –0.963 |
| bipym | 11.524 | 0.942 | 1.836 | 0.589 | – | –0.956 |
| EHC-bpy | 11.699 | 1.059 | 1.912 | 0.600 | 0.90 | –0.926 |
| EC-bpy | 11.700 | 1.070 | 1.918 | 0.601 | 0.90 | –0.812 |
| dcphen | 11.508 | 1.503 | 2.115 | 0.650 | 0.82 | –0.799 |
| dcbpy | 11.822 | 1.203 | 1.997 | 0.613 | 0.82 | –0.787 |
| *t*Bu-DAB | 12.296 | 0.889 | 1.905 | 0.578 | –0.40 | –0.785 |
| BABA | 12.900 | 0.998 | 2.029 | 0.584 | –0.36 | –0.729 |
| dthdi | 12.889 | 0.957 | 2.008 | 0.580 | –0.40 | –0.703 |
| $(CF_3)_2$-bpy | 12.076 | 1.388 | 2.120 | 0.630 | 1.02 | –0.681 |
| $(NO_2)_2$-bpy | 10.411 | 1.853 | 2.197 | 0.717 | 1.56 | –0.582 |
| disn | 13.620 | 1.099 | 2.163 | 0.588 | 1.32 | –0.514 |
| bbqdi | 11.873 | 1.399 | 2.102 | 0.634 | – | –0.508 |

The majority of the ligands in Table 5 are strong or weak π-donors. Hence, *ModEP* values are more negative than the corresponding values for the diimines.

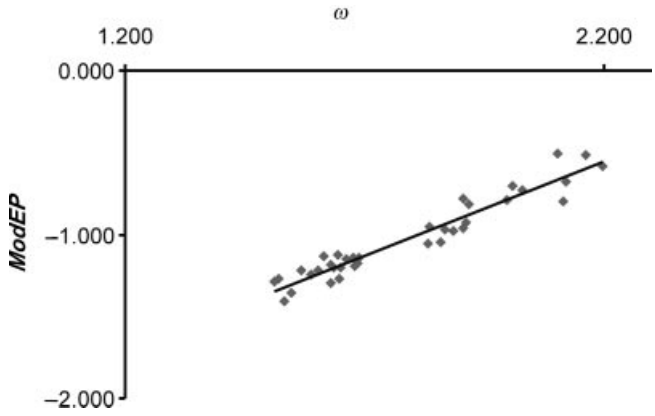


Figure 11. Graphic representation of the function $ModEP = f(\omega)$ for all compounds under study.

$$LEP_{(V)} = 0.9261\ \omega + 0.7124,\ R^2 = 0.90 \quad (28)$$

$$TEP_{(cm^{-1})} = 73.662\ \omega + 1989.2,\ R^2 = 0.95 \quad (29)$$

$$CEP_{(cm^{-1})} = 76.833\ \omega + 2074.3,\ R^2 = 0.94 \quad (30)$$

$$CEP^*_{(cm^{-1})} = 72.722\ \omega + 2077.1,\ R^2 = 0.93 \quad (31)$$

These relations enable us to express any experimental or computed parameter as a function of any other through the intermediacy of the easily computed $\omega$. In this way, existing empirical parameters like *ModEP* or *LEP* that express contrary properties of the ligands can be combined and enrich each other. This fact demonstrates that our attempt was successful and at the same time establishes the electrophilicity index as one of the most promising tools in the effort of synthesizing both inorganic and organometallic complexes with predefined properties. The combination of the above parameters would enrich not only the *ModEP* scale but also any other scale.

Table 5. Electrophilicity index $\omega$ and *ModEP* for the ligands studied. Values for *TEP* [$cm^{-1}$][1], *LEP* [V][3], *CEP* [$cm^{-1}$][2], and *CEP**[2] were taken from the corresponding references, while values in italics have been calculated from the corresponding linear regressions of the functions *TEP* = *f*(*CEP*) and *LEP* = *f*(*CEP*) as described in ref.[2]

| L | *I* | *A* | $\omega$ | $\Delta N$ *max* | *CEP* | *LEP* | *TEP* | *CEP** | *ModEP* |
|---|---|---|---|---|---|---|---|---|---|
| $Ph^-$ | 5.126 | –5.991 | 0.008 | –0.039 | 2085.8 | –0.62 | 2000.5 | 2085.5 | –3.075 |
| $MeS^-$ | 2.572 | –8.132 | 0.361 | –0.260 | 2097.1 | –0.48 | 2011.3 | 2097.0 | –2.670 |
| $CN^-$ | 3.150 | –10.096 | 0.455 | –0.262 | 2115.0 | 0.02 | 2028.5 | 2115.8 | –2.561 |
| $MeO^-$ | 3.573 | –10.894 | 0.463 | –0.253 | 2099.0 | –0.46 | 2013.2 | 2098.9 | –2.552 |
| $HS^-$ | 2.258 | –8.654 | 0.469 | –0.293 | 2102.5 | –0.42 | 2016.5 | 2102.5 | –2.546 |
| $P(NMe_2)_3$ | 11.953 | –1.618 | 0.984 | 0.381 | 2151.0 | 0.19 | 2061.9 | 2150.5 | –1.953 |
| $SbMe_3$ | 13.413 | –2.240 | 0.997 | 0.357 | 2155.9 | 0.25 | 2067.6 | 2155.7 | –1.938 |
| $PMe_3$ | 12.861 | –1.874 | 1.024 | 0.373 | 2152.4 | 0.33 | 2064.1 | 2152.0 | –1.907 |
| $NMe_3$ | 15.707 | –3.192 | 1.036 | 0.331 | 2155.9 | 0.25 | 2067.6 | 2155.9 | –1.893 |
| $P(OMe)_3$ | 13.311 | –1.758 | 1.107 | 0.383 | 2171.3 | 0.42 | 2079.5 | 2170.9 | –1.811 |
| $PHMe_2$ | 13.438 | –1.669 | 1.146 | 0.390 | 2158.1 | 0.28 | 2069.6 | 2157.9 | –1.766 |
| $AsMe_3$ | 13.790 | –1.404 | 1.262 | 0.408 | 2155.2 | 0.24 | 2067.0 | 2154.9 | –1.633 |
| $PH_2Me$ | 14.017 | –1.481 | 1.268 | 0.404 | 2164.3 | 0.35 | 2075.3 | 2164.2 | –1.626 |
| $PHF_2$ | 13.624 | –1.155 | 1.315 | 0.422 | 2190.0 | 0.67 | 2100.8 | 2189.9 | –1.572 |
| $PH_2F$ | 13.927 | –1.225 | 1.331 | 0.419 | 2179.6 | 0.54 | 2090.9 | 2179.6 | –1.553 |
| $PH_3$ | 14.387 | –1.320 | 1.359 | 0.416 | 2170.8 | 0.43 | 2083.2 | 2170.9 | –1.521 |
| CO | 16.302 | –0.942 | 1.710 | 0.445 | 2210.6 | 0.99 | 2120.0 | 2193.2 | –1.117 |

 © 2007 Wiley-VCH Verlag GmbH & Co. KGaA, Weinheim 

The main advantage of the electrophilicity index $\omega$ over the only other computed parameter, namely *CEP*, is on one hand the very low computational cost and on the other the fact that the information provided is not only for the ligand as a unit but also for the given complex.

## Conclusions

In this paper, we report the derivation of a new empirical scale, namely the modified electronic parameters, and provide the necessary criteria for its use. The basis for our analysis was the electrochemical and spectroscopic data for M(diimine)(dithiolato) complexes, which are known for their peculiar electronic structure and are possible candidates for use in the NLO materials industry and as photosensitizers. Modified electronic parameters provide, by definition, the contribution of the ligand to the reduction potential of the corresponding complexes and can be employed in order to predict those properties of the complexes that are ligand-based. *ModEP* values for homologous compounds correlate with Hammett's $\sigma_t$ constants. This correlation implies the same behavior in response to a change in the π-bonding properties of aromatic ligands as a result of changing their substituents.

*ModEP* was tested in several classes of compounds. Its high applicability denotes that ligands act in a fully predictable way upon coordination to a metal and this is due to their electronic characteristics. In other words, when a given series of ligands is coordinated to a metal fragment, it causes a fully predictable change in the ligand-based properties of the complex.

Trying to extrapolate our approach to other types of ligands, we introduced the relatively new concept of the electrophilicity index $\omega$ and proved its efficiency as a measure of the capability of a molecule to accept electrons. Thus, $\omega$ can become an important index for describing the behavior of the complexes, an approach that is referred to for the first time in this manuscript.

The general correlation between $\omega$ and all other electronic parameters such as *ModEP*, *LEP*, *TEP*, *CEP*, and Hammet's $\sigma_t$ provides us with a useful tool to enrich each one of the aforementioned scales in a quantitative manner. On the basis of this fact, we conclude that, in our effort to find a unified ligand scale, the electrophilicity index, $\omega$, should play a central role.

More contributions to these results will enrich and fully establish our study.

## Acknowledgments

The project is co-funded by the European Social Fund and National Resources – (EPEAEK II) PYTHAGORAS. The Special Research Account of NKUA is also acknowledged.

[1] C. A. Tolman, *Chem. Rev.* **1977**, *77*, 313–348.
[2] L. Perrin, E. Clot, O. Eisenstein, J. Loch, R. H. Crabtree, *Inorg. Chem.* **2001**, *40*, 5806–5811.
[3] a) A. B. P. Lever, *Inorg. Chem.* **1990**, *29*, 1271–1285; b) A. B. P. Lever, *Inorg. Chem.* **1991**, *30*, 1980–1985.
[4] R. S. Drago, S. Joerg, *J. Am. Chem. Soc.* **1996**, *118*, 2654–2663.
[5] K. Hansch, A. Leo, R. W. Taft, *Chem. Rev.* **1991**, *91*, 165–195.
[6] M. C. Aragoni, M. Arca, T. Cassano, C. Denotti, F. A. Devillanova, R. Frau, F. Isaia, F. Lejl, V. Lipolis, L. Nitti, P. Romaniello, R. Tomassi, G. Verani, *Eur. J. Inorg. Chem.* **2003**, 1939–1947.
[7] C. Chen, L. Koshevoy, I. O. Babij, A. J. Poë, *Dalton Trans.* **2004**, 833–838.
[8] K. D. Cooney, T. R. Cundari, N. W. Hoffman, K. A. Pittard, M. D. Temple, Y. Zhao, *J. Am. Chem. Soc.* **2003**, *125*, 4318–4324.
[9] M. R. Wilson, A. Prock, W. P. Giering, A. L. Fernandez, C. M. Haar, S. P. Nolan, B. M. Foxman, *Organometallics* **2002**, *21*, 2758–2763.
[10] M. Nakano, H. Fujita, M. Takahata, K. Yamaguchi, *J. Am. Chem. Soc.* **2002**, *124*, 9648–9655.
[11] S. Tobisch, T. Ziegler, *J. Am. Chem. Soc.* **2002**, *124*, 13290–13301.
[12] R. S. Drago, A. P. Dadmun, *J. Am. Chem. Soc.* **1993**, *115*, 8592–8602.
[13] R. S. Drago, *Inorg. Chem.* **1995**, *34*, 3543–3548.
[14] L. Gonsalvi, H. Adams, G. J. Sunley, E. Ditzel, A. Haynes, *J. Am. Chem. Soc.* **2002**, *124*, 13597–13612.
[15] T. R. Miller, I. G. Dance, *J. Am. Chem. Soc.* **1973**, *95*, 6970–6979.
[16] S. Huertas, M. Hissler, J. E. McGarrah, R. Eisenberg, R. J. Lachicotte, *Inorg. Chem.* **2001**, *40*, 1183–1188.
[17] M. Hissler, I. E. McGarrah, W. B. Connick, D. K. Geiger, S. D. Cummings, R. Eisenberg, *Coord. Chem. Rev.* **2000**, *208*, 115–137.
[18] W. B. Connick, D. Geiger, R. Eisenberg, *Inorg. Chem.* **1999**, *38*, 3264–3265.
[19] M. A. Mansour, R. J. Lachicotte, H. J. Gysling, R. Eisenberg, *Inorg. Chem.* **1998**, *37*, 4625–4632.
[20] W. Paw, R. J. Lachicotte, R. Eisenberg, *Inorg. Chem.* **1998**, *37*, 4139–4141.
[21] W. Paw, S. D. Cummings, M. A. Mansour, W. B. Connick, D. K. Geiger, R. Eisenberg, *Coord. Chem. Rev.* **1998**, *171*, 125–150.
[22] S. D. Cummings, L.-T. Cheng, R. Eisenberg, *Chem. Mater.* **1997**, *9*, 440–450.
[23] W. Paw, R. Eisenberg, *Inorg. Chem.* **1997**, *36*, 2287–2393.
[24] S. D. Cummings, R. Eisenberg, *J. Am. Chem. Soc.* **1996**, *118*, 1949–1960.
[25] S. D. Cummings, R. Eisenberg, *Inorg. Chem.* **1995**, *34*, 3396–3403.
[26] S. D. Cummings, R. Eisenberg, *Inorg. Chem.* **1995**, *34*, 2007–2014.
[27] J. M. Bevilacqua, R. Eisenberg, *Inorg. Chem.* **1994**, *33*, 1886–1890.
[28] J. M. Bevilacqua, R. Eisenberg, *Inorg. Chem.* **1994**, *33*, 2913–2923.
[29] J. A. Zuleta, J. M. Bevilacqua, D. M. Proserpio, P. D. Harvey, R. Eisenberg, *Inorg. Chem.* **1992**, *31*, 2396–2404.
[30] J. A. Zuleta, J. M. Bevilacqua, J. M. Rehm, R. Eisenberg, *Inorg. Chem.* **1992**, *31*, 1332–1337.
[31] J. A. Zuleta, J. M. Bevilacqua, R. Eisenberg, *Coord. Chem. Rev.* **1992**, *111*, 237–248.
[32] J. A. Zuleta, M. S. Burberry, R. Eisenberg, *Coord. Chem. Rev.* **1991**, *111*, 237–248.
[33] J. A. Zuleta, M. S. Burberry, R. Eisenberg, *Coord. Chem. Rev.* **1990**, *97*, 47–64.
[34] J. A. Zuleta, C. A. Chesta, R. Eisenberg, *J. Am. Chem. Soc.* **1989**, *111*, 89168917.
[35] K. Kubo, M. Nakano, H. Tamura, G.-E. Matsubayashi, *Inorg. Chim. Acta* **2002**, *336*, 120–124.
[36] G. Matsubayashi, M. Nakano, H. Tamura, *Coord. Chem. Rev.* **2002**, *226*, 143–151.

 © 2007 Wiley-VCH Verlag GmbH & Co. KGaA, Weinheim 

[37] A. Islam, H. Sugihara, K. Hara, L. P. Singh, R. Katoh, M. Yanakida, Y. Takahashi, S. Murata, H. Arakawa, *Inorg. Chem.* **2001**, *40*, 5371–5380.
[38] A. Islam, H. Sugihara, K. Hara, L. P. Singh, R. Katoh, M. Yanakida, Y. Takahashi, S. Murata, H. Arakawa, *J. Photochem. Photobiol. A: Chem.* **2001**, *145*, 135–141.
[39] A. Islam, H. Sugihara, K. Hara, L. P. Singh, R. Katoh, M. Yanakida, Y. Takahashi, S. Murata, H. Arakawa, *New J. Chem.* **2000**, *24*, 343–345.
[40] K. Natsuaki, M. Nakano, G.-E. Matsubayashi, R. Arakawa, *Inorg. Chim. Acta* **2000**, *299*, 112–117.
[41] C.-T. Chen, S.-Y. Liao, K.-J. Lin, C.-H. Chen, T.-Y. J. Lin, *Inorg. Chem.* **1999**, *38*, 2734–2741.
[42] C.-T. Chen, S.-Y. Liao, K.-J. Lin, L.-L. Lai, *Adv. Mater.* **1998**, *10*, 334–338.
[43] C.-T. Chen, T.-Y. J. Lin, C.-H. Chen, K.-J. Lin, *J. Chin. Chem. Soc.* **2000**, *47*, 197–201.
[44] G.-E. Matsubayashi, Y. Yamaguchi, T. Tanaka, *J. Chem. Soc. Dalton Trans.* **1988**, 2215–2219.
[45] B. W. Smucker, J. M. Hudson, M. A. Omary, K. R. Dunbar, *Inorg. Chem.* **2003**, *42*, 4714–4723.
[46] J. A. Weinstein, A. J. Blake, E. S. Davies, A. L. Davis, M. W. George, D. C. Grills, I. V. Lileev, A. M. Maksimov, P. Matousek, M. Y. Mel′nikov, A. W. Parker, V. E. Platonov, M. Towrie, C. Wilson, N. N. Zheligovskaya, *Inorg. Chem.* **2003**, *42*, 7077–7085.
[47] Y.-D. Chen, Y.-H. Qin, L.-Y. Zhang, L.-X. Shi, Z.-N. Chen, *Inorg. Chem.* **2004**, *43*, 1197–1205.
[48] Y.-D. Chen, L.-Y. Zhang, L.-X. Shi, Z.-N. Chen, *Inorg. Chem.* **2004**, *43*, 7493–7501.
[49] Z. Hao, Z. Tang, Q. Shi, *Inorg. Chim. Acta* **1999**, *284*, 112–115.
[50] C.-T. Chen, S.-Y. Liao, K.-J. Lin, T.-Y. J. Lin, L.-L. Lai, C.-H. Chen, *Nonlinear Optics* **1999**, *22*, 35.
[51] G.-E. Matsubayashi, M. Hirao, T. Tanaka, *Inorg. Chim. Acta* **1988**, *144*, 217–221.
[52] K. Kubo, M. Nakano, H. Tamura, G.-E. Matsubayashi, *Inorg. Chim. Acta* **2000**, *311*, 6–14.
[53] A. Nakahama, M. Nakano, G.-E. Matsubayashi, *Inorg. Chim. Acta* **1999**, *284*, 55–60.
[54] a) V. E. Kaasjager, E. Bouwman, S. Gorter, J. Reedijk, C. A. Grapperhaus, J. H. Reibenspies, J. J. Smee, M. Y. Darensbourg, A. Derecskei-Kovacs, L. M. Thomson, *Inorg. Chem.* **2002**, *41*, 1837–1844.
[55] K. H. Puthraya, T. S. Srivastava, *Tetrahedron* **1985**, *4*, 1579–1584.
[56] Y. Zhang, K. D. Ley, K. S. Schanze, *Inorg. Chem.* **1996**, *35*, 7102–7110.
[57] K. Base, M. T. Tierney, A. Fort, J. Muller, M. W. Grinstaff, *Inorg. Chem.* **1999**, *38*, 287–289.
[58] K. Base, M. W. Grinstaff, *Inorg. Chem.* **1998**, *37*, 1432–1433.
[59] J. Si, Q. Yang, Y. Wang, P. Ye, S. Wang, J. Qin, D. Lin, *Optics Commun.* **1996**, *132*, 311–315.
[60] R. Vicente, J. Ribas, P. Cassoux, C. Sourisseau, *Synth. Met.* **1986**, *15*, 79–89.
[61] A. Vogler, H. Kunkely, *Comments. Inorg. Chem.* **1990**, *9*, 201–220.
[62] A. Vogler, H. Kunkely, J. Hlavatsch, A. Merz, *Inorg. Chem.* **1984**, *23*, 506–509.
[63] A. Vogler, H. Kunkely, *J. Am. Chem. Soc.* **1981**, *103*, 1559–1560.
[64] C. Makedonas, C. Mitsopoulou, *J. Inorg. Biochem.* **2001**, *86*, 326.
[65] C. Makedonas, C. Mitsopoulou, *ICCC35*, Heidelberg, July **2002**.
[66] C. Makedonas, C. Mitsopoulou, *FIGIPS*7, Lisbon, June **2003**.
[67] T. M. Cocker, R. E. Bachman, *Inorg. Chem.* **2001**, *40*, 1550–1556.
[68] W. B. Connick, H. B. Gray, *J. Am. Chem. Soc.* **1997**, *119*, 11620–11627.
[69] C. Makedonas, C.-A. Mitsopoulou, F. J. Lahoz, A. I. Balana, *Inorg. Chem.* **2003**, *42*, 8853–8865.
[70] C. Makedonas, C.-A. Mitsopoulou, *Spectrochim. Acta A* **2006**, *64*, 918–930.
[71] C. Makedonas, C.-A. Mitsopoulou, *Eur. J. Inorg. Chem.* **2006**, 590–598.
[72] C. Makedonas, C.-A. Mitsopoulou, *Eur. J. Inorg. Chem.* **2006**, 2460–2468.
[73] R. G. Parr, L. V. Szentpály, S. Liu, *J. Am. Chem. Soc.* **1999**, *121*, 1922–1924.
[74] R. G. Parr, W. Yang, *Density Functional Theory of Atoms and Molecules*, Oxford University Press, Oxford, **1989**.
[75] M. J. Frisch, G. W. Trucks, H. B. Schlegel, G. E. Scuseria, M. A. Robb, J. R. Cheeseman, V. G. Zakrzewski, J. A. Montgomery Jr., R. E. Stratmann, J. C. Burant, S. Dapprich, J. M. Millam, A. D. Daniels, K. N. Kudin, M. C. Strain, O. Farkas, J. Tomasi, V. Barone, M. Cossi, R. Cammi, B. Mennucci, C. Pomelli, C. Adamo, S. Clifford, J. Ochterski, G. A. Petersson, P. Y. Ayala, Q. Cui, K. Morokuma, D. K. Malick, A. D. Rabuck, K. Raghavachari, J. B. Foresman, J. Cioslowski, J. V. Ortiz, A. G. Baboul, B. B. Stefanov, G. Liu, A. Liashenko, P. Piskorz, I. Komaromi, R. Gomperts, R. L. Martin, D. J. Fox, T. Keith, M. A. Al-Laham, C. Y. Peng, A. Nanayakkara, M. Challacombe, P. M. W. Gill, B. Johnson, W. Chen, M. W. Wong, J. L. Andres, C. Gonzalez, M. Head-Gordon, E. S. Replogle, J. A Pople, *Gaussian 98, Revision A.9*, Gaussian Inc., Pittsburgh, PA, **1998**.
[76] A. D. Becke, *J. Chem. Phys.* **1993**, *98*, 5648–5652.
[77] C. Lee, W. Yang, R. G. Parr, *Phys. Rev. B* **1988**, *37*, 785–789.
[78] A. D. McLean, G. S. Chandler, *J. Chem. Phys.* **1980**, *72*, 5639–5648.
[79] R. Krishnan, J. S. Binkley, R. Seeyer, J. A. Pople, *J. Chem. Phys.* **1980**, *72*, 650–654.
[80] D. Andrae, U. Haeussermann, M. Dolg, H. Stoll, H. Preuss, *Theor. Chim. Acta* **1990**, *77*, 123–141.
[81] S. I. Gorelsky, *AOMix*, *Program for Molecular Orbital Analysis, Revision 5.95*, http://www.sg-chem.net/aomix/, York University, Toronto, Canada, **1997**.
[82] S. I. Gorelsky, A. B. P. Lever, *J. Organomet. Chem.* **2001**, *635*, 187–196.
[83] M. J. S. Dewar, E. G. Zoebisch, E. F. Healy, *J. Am. Chem. Soc.* **1985**, *107*, 3902–3909.
[84] J. J. P. Stewart, *J. Comput. Chem.* **1989**, *10*, 209–220.
[85] J. J. P. Stewart, *J. Comput. Chem.* **1989**, *10*, 221–264.
[86] *MOPAC2000*, version 1.21, Fujitsu Limited, **2000**.
[87] *CAChe Worksystem 4.4*, Fujitsu Limited, **2000**.
[88] N. L. Allinger, *J. Am. Chem. Soc.* **1977**, *99*, 8127–8134.
[89] P. Flükiger, H. P. Lüthi, S. Portman, J. Weber, *MOLEKEL*, version 4.3, Swiss Center for Scientific Computing, Manno, Switzerland, **2000–2002**.
[90] C. J. Pickett, D. Pletchr, *J. Organomet. Chem.* **1975**, *102*, 327–333.
[91] J. Chatt, C. T. Kan, G. J. Leigh, C. J. Pickett, D. R. Stanley, *J. Chem. Soc. Dalton Trans.* **1980**, 2032–2038.
[92] B. E. Bursten, M. R. Green, *Progr. Inorg. Chem.* **1988**, *36*, 474–485.
[93] J. Chatt, *Coord. Chem. Rev.* **1982**, *43*, 337–347.
[94] D. J. Stufkens, *Coord. Chem. Rev.* **1990**, *104*, 39–112.
[95] A. J. Lees, *Coord. Chem. Rev.* **1998**, *177*, 3–35.
[96] A. Vlček Jr, *Coord. Chem. Rev.* **2002**, *230*, 225–242.
[97] D. M. Manuta, A. J. Lees, *Inorg. Chem.* **1986**, *25*, 1354–1359.
[98] D. M. Manuta, A. J. Lees, *Inorg. Chem.* **1986**, *25*, 3212–3218.
[99] S. Záliš, I. R. Farrel, A. Vlček Jr, *J. Am. Chem. Soc.* **2003**, *125*, 4580–4592.
[100] I. R. Farrel, F. Hartl, S. Záliš, T. Mahabiersing, A. Vlček Jr, *J. Chem. Soc., Dalton Trans.* **2000**, 4323–4331.
[101] I. R. Farrel, J. van Slageren, S. Záliš, A. Vlček Jr, *Inorg. Chim. Acta* **2001**, *315*, 44–52.
[102] T. J. Meyer, *Pure Appl. Chem.* **1986**, *58*, 1193–1206.

 © 2007 Wiley-VCH Verlag GmbH & Co. KGaA, Weinheim 

[103] J. M. Villegas, S. R. Stoyanov, W. Huang, D. P. Rillema, *Inorg. Chem.* **2005**, *44*, 2297–2309.
[104] J. M. Villegas, S. R. Stoyanov, W. Huang, D. P. Rillema, *Dalton Trans.* **2005**, 1042–1051.
[105] S. R. Stoyanov, J. M. Villegas, A. J. Cruz, L. L. Lockyear, J. H. Reibenspies, D. P. Rillema, *J. Chem. Theory Comput.* **2005**, *1*, 95–106.
[106] J. M. Villegas, S. R. Stoyanov, J. H. Reibenspies, D. P. Rillema, *Organometallics* **2005**, *24*, 395–404.
[107] S.-S. Sun, A. J. Lees, *Organometallics* **2002**, *21*, 39–49.
[108] J. A. Shelnutt, *J. Phys. Chem.* **1983**, *87*, 605–616.
[109] K. Kalyanasundaram, M. Grätzel, *Coord. Chem. Rev.* **1998**, *177*, 347–414.
[110] A. Juris, V. Balzani, F. Barigelletti, S. Campagna, P. Belser, A. von Zelewsky, *Coord. Chem. Rev.* **1988**, *84*, 85–277.
[111] K. Kalyanasundaram, *Coord. Chem. Rev.* **1982**, *46*, 159–244.
[112] P. U. Maheswari, M. Palaniandavar, *Inorg. Chim. Acta* **2004**, *357*, 901.
[113] P. U. Maheswari, M. Palaniandavar, *J. Inorg. Biochem.* **2004**, *98*, 219.
[114] A. B. P. Lever, S. I. Gorelsky, *Coord. Chem. Rev.* **2000**, *208*, 153–167.
[115] S. I. Gorelsky, A. B. P. Lever, *Can. J. Anal. Sci. Spect.* **2003**, *48*, 93–105.
[116] C.-T. Lin, W. Böttcher, M. Chou, C. Creutz, N. Sutin, *J. Am. Chem. Soc.* **1976**, *98*, 6536–6544.
[117] A. T. Maynard, M. Huang, W. G. Rice, D. G. Covel, *Proc. Natl. Acad. Sci. USA* **1998**, *95*, 11578–11583.
[118] P. Pérez, A. Toro-Labbé, R. Contreras, *J. Am. Chem. Soc.* **2001**, *123*, 5527–5531.
[119] P. K. Fuentealba, P. Chattaraj, B. Gómez, R. Contreras, *J. Am. Chem. Soc.* **2000**, *122*, 348–351.
[120] P. K. Chattaraj, B. Sarkar, U. Maiti, *J. Phys. Chem. A* **2003**, *107*, 4973–4975.
[121] E. Chamorro, P. K. Fuentealba, P. Chattaraj, *J. Phys. Chem. A* **2003**, *107*, 7068–7072.
[122] P. K. Chattaraj, U. Sarkar, D. R. Roy, *Chem. Rev.* **2006**, *106*, 2065–2091.

Received: February 8, 2007
Published Online: July 17, 2007

 © 2007 Wiley-VCH Verlag GmbH & Co. KGaA, Weinheim 

DOI: 10.1002/ejic.200700288

# Synthesis, Structure, Electrochemistry, and Mössbauer Effect Studies of the Ferraphosphadicarbollides $[(C_5R_5)Fe(PC_2B_8H_{10})]$ (R = H, Me)

**Alexander R. Kudinov,*[a] Rolfe H. Herber,*[b] Piero Zanello,*[c] Dmitry S. Perekalin,[a] Ivan V. Glukhov,[a] Israel Nowik,[b] Maddalena Corsini,[c] Serena Fedi,[c] and Franco Laschi[c]**

**Keywords:** Iron / Carboranes / Electrochemistry / X-ray diffraction / Mössbauer spectroscopy

Reaction of the phosphadicarbollide anion $[7,8,9\text{-}PC_2B_8H_{10}]^-$ (**4**) with $[CpFe(C_6H_6)]^+$ or $[Cp^*Fe(MeCN)_3]^+$ gives the expected 12-vertex ferraphosphadicarbollides $[1\text{-}C_5R_5\text{-}1,2,3,4\text{-}FePC_2B_8H_{10}]$ [R = H (**5a**), Me (**5b**); the metal atom is assigned number 1] in around 35 % yield. Compounds **5a**,**b** undergo selective polyhedral rearrangement at 150 °C to give the corresponding isomers $[1\text{-}C_5R_5\text{-}1,2,4,5\text{-}FePC_2B_8H_{10}]$ (**6a**,**b**). The structure of **5a** has been determined by X-ray diffraction. An electrochemical investigation has revealed that all the compounds obtained display the $Fe^{II}/Fe^{III}$ oxidation process with features of chemical reversibility on the cyclic voltammetric timescale. However, only cation $[\mathbf{6b}]^+$ is reasonably stable on the long timescales of electrolysis. Ferraphospadicarbollides **5a** and **6a** are more difficult to oxidize than the related dicarbollide and tricarbollide derivatives $[CpFe(C_2B_9H_{11})]^-$ and $[CpFe(C_3B_8H_{11})]$, respectively. Temperature-dependent Mössbauer effect studies show that the recoil-free fraction over the temperature interval 110–342 K for **5a** is well accounted for by a linear regression, and a calculation of the root-mean-square-amplitude-of-vibration (rmsav) of the iron atom, based on the Mössbauer effect (ME) data, is in reasonable agreement with the value calculated from the single-crystal X-ray study at 120 K. Similarly, the ME and X-ray rmsav data for **6a** at 293 K are in excellent agreement with each other, and the value at 120 K calculated for **6a** is in good agreement with that observed for **5a**. The metal atom motion is nearly isotropic with respect to the major symmetry axis running through the Cp ring and the Fe atom.
(© Wiley-VCH Verlag GmbH & Co. KGaA, 69451 Weinheim, Germany, 2007)

## Introduction

The ferracarborane anion $[CpFe(C_2B_9H_{11})]^-$ ($[\mathbf{1}]^-$)[1] can be considered as a ferrocene analog, although the different charges of the $[C_2B_9H_{11}]^{2-}$ and $Cp^-$ ligands lead to significant differences in the properties of $[\mathbf{1}]^-$ and $FeCp_2$. The use of monoanionic carborane ligands of two types, namely $[C_3B_8H_{11}]^-$ and $[9\text{-}L\text{-}7,8\text{-}C_2B_9H_{10}]^-$ (L = $SMe_2$, $NMe_3$, py), has allowed us to prepare closer analogs of ferrocene such as ferratricarbollides **2**, **3**[2] and charge-compensated ferradicarbollides $[CpFe(L\text{-}C_2B_9H_{10})]$ (for the meaning of the circles, see Scheme 1).[3]

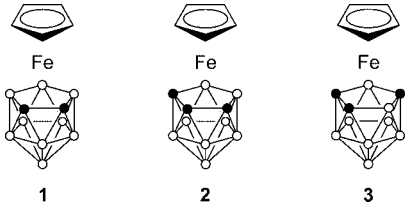


We have recently shown that combined structural, electrochemical, and Mössbauer effect (ME) studies can provide detailed information concerning the static and dynamic properties of cyclopentadienylferracarboranes and their monocations.[3a] In particular, we showed that the replacement of a boron atom by carbon results in an increase of the electron-withdrawing properties of the carborane ring. Herein we report the extension of these investigations to a number of cyclopentadienylferraphosphadicarbollides in order to elucidate the effect of a phosphorus atom on the chemical and physico-chemical characteristics of these unique compounds.

## Results and Discussion

### Synthesis

Štibr et al. have recently reported the synthesis of the first ferraphosphadicarbollide complex [1-Cp-1,2,3,5-

[a] A. N. Nesmeyanov Institute of Organoelement Compounds, Russian Academy of Science,
28 ul. Vavilova, 119991 Moscow, GSP-1, Russian Federation
Fax: +7-495-135-5085
E-mail: arkudinov@ineos.ac.ru
[b] Racah Institute of Physics, The Hebrew University,
91904 Jerusalem, Israel
E-mail: herber@vms.huji.ac.il
[c] Dipartimento di Chimica, Università di Siena,
Via Aldo Moro, 53100 Siena, Italy
E-mail: zanello@unisi.it
Supporting information for this article is available on the WWW under http://www.eurjic.org or from the author.

 © 2007 Wiley-VCH Verlag GmbH & Co. KGaA, Weinheim 

$FePC_2B_9H_{10}$] (**6a**) by interaction of 7,8,9-$PC_2B_8H_{11}$ with $[CpFe(CO)_2]_2$ in refluxing xylene.[4] However, owing to the drastic conditions, the reaction was accompanied by nonselective polyhedral rearrangements that gave a mixture of isomers.

We have found previously that room-temperature reactions of carborane anions with the $[CpFe]^+$ fragment (generated photochemically from $[CpFe(C_6H_6)]^+$) can be used for the synthesis of various ferracarboranes.[2,3,5] Employing this method with $[CpFe(C_6H_6)]^+$ and the phosphadicarbollide anion [7,8,9-$PC_2B_8H_{10}]^-$ (**4**) gave the unrearranged complex [1-Cp-1,2,3,4-$FePC_2B_9H_{10}$] (**5a**)[6] in 37% yield (Scheme 1). The pentamethylated derivative **5b** was obtained in 35% yield by reaction of **4** with the $[Cp^*Fe(MeCN)_3]^+$ cation. A significant amount (approx. 40%) of anion **4** remains unreacted in both cases, in accordance with the moderate yields, and this remains the same regardless of changes in reaction time/temperature. This may be due to σ-coordination of $[(C_5R_5)Fe]^+$ fragments to the phosphorus lone pair of anion **4**, which suppresses the formation of the π-complex.[7]

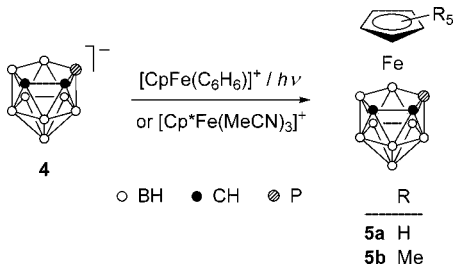


Scheme 1. Synthesis of complexes **5a**,**b**.

Complexes **5a**,**b** both undergo polyhedral rearrangement upon heating in refluxing nonane (150 °C) to give the 1,2,4,5-isomers **6a**,**b** (approx. 80% yield; Scheme 2). This rearrangement is highly selective, and no other isomers could be detected in the reaction mixture by means of $^{11}B$ and $^{31}P$ NMR spectroscopy. This observation is in sharp contrast to the nonselective isomerization of the analogous cobalt complex [1-($\eta^4$-$C_4Me_4$)-1,2,3,4-$CoPC_2B_9H_{10}$] at 110 °C[5] and the nonselective further rearrangement of **6a** in refluxing mesitylene.[8] The **5a** → **6a** isomerization process is exothermic by 12.8 kcal mol$^{-1}$, as estimated by DFT calculations at the B3LYP/6-31G* level.[9]

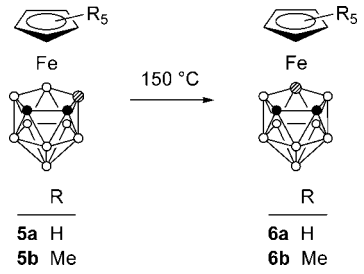


Scheme 2. Polyhedral rearrangement of complexes **5a**,**b**.

Compounds **5a**,**b** and **6a**,**b** were characterized by elemental analysis and $^1H$, $^{11}B$, and $^{31}P$ NMR spectroscopy. The $^{11}B$ signal assignment in **5a** and **6a** was performed with the help of DFT/GIAO calculations. The structure of **5a** was also investigated by X-ray diffraction (Figure 1).[10] The carbon atoms of the Cp ring as well as the P1 and B5 atoms were found to be disordered over two positions. The C3–C4 distance (1.609 Å) is notably longer than a typical C–C single bond but is in the usual range for *closo*-metallacarboranes.[11] The average Fe–$C_{cage}$ (2.020 Å) and Fe–P (2.237 Å) distances are close to those for isomer **6a** (2.018 and 2.251 Å).[4] The Fe···Cp distance in **5a** (1.683 Å) is also close to that in **6a** (1.681 Å), thus indicating similar coordinating properties of the isomeric phosphadicarbollide anions [7,8,9-$PC_2B_8H_{10}]^-$ and [7,9,10-$PC_2B_8H_{10}]^-$. The significantly longer Fe···Cp distances in **5a** and **6a** than in $FeCp_2$ (1.660 Å)[12] suggest a greater acceptor ability of the phosphadicarbollide ligands relative to $Cp^-$, in accordance with the electrochemical data (see below).

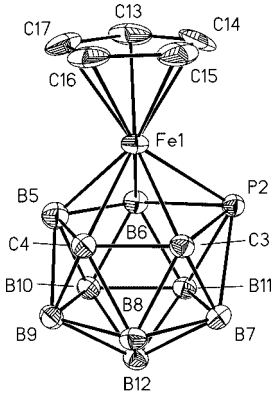


Figure 1. The molecular structure of **5a** (thermal ellipsoids at 50% probability). The hydrogen atoms and the second conformation of the Cp ring have been omitted for clarity. Selected interatomic distances [Å]: Fe1–P2 2.231(2), Fe1–C3 2.017(2), Fe1–C4 2.023(2), Fe1–B5 2.062(6), Fe1–B6 2.172(4), Fe1–C13 2.065(5), Fe1–C14 2.046(7), Fe1–C15 2.077(4), Fe1–C16 2.084(4), Fe1–C17 2.071(4), P2–B6 2.008(3), P2–C3 2.033(3), C3–C4 1.609(3).

## Mössbauer Effect (ME) Studies

As noted previously,[13] all diamagnetic iron compounds in which the sole metal atom does not occupy a cubic symmetry site give rise to doublet ME spectra which are characterized by their isomer shift (IS) and quadrupole splitting (QS) parameters. A typical ME spectrum (that of **6a** at 90 K) is shown in the bottom trace of Figure 2.

The ME parameters for compound **5a** are summarized in Table 1. The data for the $Fe^{III}$ complex [1-Cp-1,2,3-$FeC_2B_9H_{11}$] (**1**) are also included for comparison purposes. The temperature dependence of the IS of **5a** is well fitted by a linear regression in the range 110–342 K (correlation coefficient for 12 data points: 0.997) from which the effective vibrating mass $M_{eff}$ is calculated to be 94 ± 1 Da.[14] The difference between this value and the "bare" iron atom mass of 57 Da reflects the covalency of the metal–ligand

 © 2007 Wiley-VCH Verlag GmbH & Co. KGaA, Weinheim 

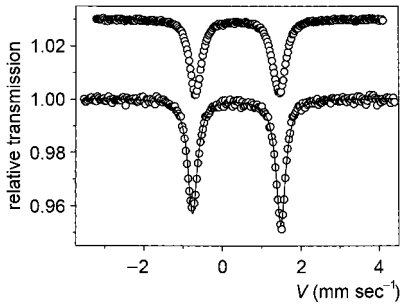


Figure 2. Mössbauer spectra of **6a** (bottom trace) and **6b** (top trace) at 90 K. The presence of a single Fe site is evident from the figure. The velocity scale is with reference to the centroid of an α-Fe absorber spectrum at room temperature.

interaction. It is worth noting that the IS of **5a** is significantly smaller than that of ferrocene itself ($0.536 \pm 1$ mm s$^{-1}$ at 90 K) and is slightly larger than that of **1** under the same conditions. The latter increase implies a decrease in the electron density at the metal atom center (since $\Delta r^2/r^2$ is negative for $^{57}$Fe), presumably due to an increase of the acceptor character of the ligand upon replacement of a B atom by P. The temperature dependence of the recoil-free fraction, extracted from the temperature dependence of ln $A$ (where $A$ is the area under the resonance curve for an optically thin absorber), is shown graphically in Figure 3 and is again well fitted by a linear regression.

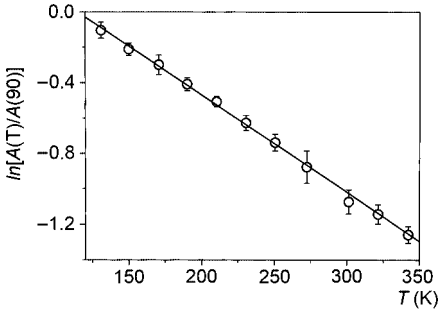


Figure 3. Temperature-dependence of the normalized logarithm of the area under the resonance curve for **5a**. The slope is $-(5.50 \pm 0.07) \times 10^{-3}$ K$^{-1}$ and the correlation coefficient for the 11 data points is 0.999.

As has been noted previously,[15] the recoil-free fraction data can be directly related to the $U_{ij}$ values for the iron atom determined from a single-crystal X-ray diffraction study. The average $U_{ij}$ value for **5a** at 120(2) K is 0.01740 Å$^2$. This translates into a root-mean-square-amplitude-of-vibration (rmsav) of the iron atom of 0.132 Å. The corresponding value extracted from the ME recoil-free fraction data is 0.111 Å, which is only a modest agreement. The analogous value for the dicarbollide complex **1** is $<x^2>^{1/2}_{ME} = 0.145$ Å, while $<x^2>^{1/2}_{X}$ is 0.151 Å at 120 K. The introduction of a P atom into the five-membered carborane face clearly leads to a small shortening of the rmsav of Fe. The area ratio, $R = [A(+)/A(-)]$ (where + and – indicate the position on the velocity scale of the resonance line with respect to the spectrum centroid), of the two QS components of the ME spectra shows only a very small temperature dependence, thereby indicating that the iron atom motion is nearly isotropic over the temperature range 91–341 K.

The ME spectroscopic results for **6a** are very similar to those observed for **5a** (see Table 1). Two points, however, must be made. First of all, the area ratio $R$ shows a significantly larger temperature dependence, which implies a larger anisotropy in the metal atom motion in **6a** compared to **5a** as a result of having the ring P atom flanked by two BH groups rather than flanked by a BH and a CH group as in **5a**. Secondly, the average $U_{ij}$ value reported for iron in the crystal structure of **6a** determined at 293(2) K[4] is 0.0344 Å$^2$, which translates into an rmsav of the iron atom of 0.183 Å. From the temperature dependence of the area under the resonance curve in the interval 135–303 K, the corresponding rmsav of the iron atom at 293 K is 0.180 Å, which is in good agreement (within 3.1%) with the X-ray value. Moreover, the rmsav value calculated from the ME data obtained at 120 K is 0.115 Å, which is in excellent agreement with the corresponding data reported for **5a** (see above) at the same temperature.

The ME spectroscopic parameters for the methylated compounds **5b** and **6b** are also given in Table 1. It should be noted that, while the IS parameters at 90 K are not sensitive to the replacement of Cp by Cp*, the QS parameters show a decrease of almost $0.123 \pm 0.009$ mm s$^{-1}$. Qualitatively, it may be surmised that the presence of the methyl groups increases the metal atom–ring distance and hence leads to a decrease in the electric field gradient at the metal center (see below). However, this increase is not sensitively reflected in the relative IS values as referred to above. The temperature dependence of ln[$A(T)$/$A$(90)] for both compounds is well accounted for by a linear regression. It should be noted, however, that the data for **6b** could only be extended over the range 90–272 K. At 272 K, the resonance

Table 1. Mössbauer parameters for the compounds discussed in the text.

| | **5a** | **6a** | **5b** | **6b** | **1**[a] |
|---|---|---|---|---|---|
| IS(90) [mm s$^{-1}$] | 0.384(4) | 0.370(1) | 0.358(5) | 0.374(6) | 0.337(3) |
| QS(90) [mm s$^{-1}$] | 2.147(4) | 2.248(1) | 2.069(5) | 2.082(6) | 0.525(3) |
| –d(IS)/d($T$) [$10^{-4}$ mm s$^{-1}$ K$^{-1}$] | 4.43(3)[b] | 5.12(22)[c] | 4.54(27)[d] | 4.27(14)[e] | 5.3(3) |
| –d(lnA)/d($T$) [$10^{-3}$ K$^{-1}$] | 5.50(7)[f] | 5.88(9)[g] | 6.90(28)[h] | 7.47(9)[i] | 7.9(1) |
| $M_{eff}$ [Da] | $94 \pm 1$ | $81 \pm 3$ | $92 \pm 5$ | $97 \pm 3$ | 78(4) |
| $\Theta_M$ [K] | 123 | 127 | 111 | 103 | 113 |

[a] Data taken from ref.[3a] [b] Ranges for determining "high temperature" slopes (see text): 110–342 K. [c] 150–342 K. [d] 150–322 K. [e] 170–272 K. [f] 110–342 K. [g] 130–302 K. [h] 90–320 K. [i] 111–272 K.

 © 2007 Wiley-VCH Verlag GmbH & Co. KGaA, Weinheim 

effect magnitude was found to be only around 1.3% and more than 6.6 million counts per channel were acquired to provide the necessary statistical accuracy.

Unfortunately, due to excessive crystalline disorder, it has not proved possible to acquire meaningful single X-ray data for these two compounds. However, it is possible to extract rmsav data for the iron atom at 120 K by assuming that the Mössbauer recoil-free fraction data are reasonably reliable over the cited temperature range. These vibrational amplitudes are 0.125 and 0.130 Å for **5b** and **6b**, respectively, and suggest an increase of this amplitude by about 0.014 Å on replacing Cp by Cp*, which agrees with the QS parameter results cited above. A comparison of the temperature dependence of $\ln[A(T)/A(90)]$ for **5a**, **5b**, and **1** is summarized in Figure 4.

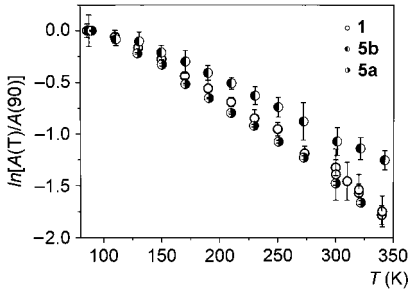


Figure 4. Temperature dependence of $\ln[A(T)/A(90)]$ for **5a** and **5b** showing the effect of substitution in the cyclopentadienido ring on the recoil-free fraction.

The slope difference between **5a** and **5b** provides evidence for lattice "softening" due to this interchange but is unexpected in view of the presumed increase in the metal atom–ring distance due to the presence of the methyl groups in the ring. A possible explanation for this observation lies in the assumption that replacing Cp with Cp* results in the presence of one or more low frequency vibrational modes that affect the dynamics of the whole molecule rather than just the metal atom center. In other words, both intra- and intermolecular motions must be considered to explain this observation. Note, however, that the Mössbauer lattice temperature,[15] $\Theta_M$, is smaller for **5b** and **6b** than for **5a** and **6a**.

Finally, it is worth noting that neither **5b** nor **6b** show a significant temperature dependence on R. The average value of this parameter for **5b** is $1.04 \pm 0.01$ over the range 90–322 K, which indicates an essentially isotropic motion of the metal atom parallel and perpendicular to the principal symmetry axis running through the metal atom.

## Electrochemistry

Figure 5 gives an overall picture of the $Fe^{II}/Fe^{III}$ electron-transfer process in the ferraphosphacarboranes **5a**,**b** and **6a**,**b**. The formal electrode potentials of the redox processes studied are compiled in Table 2, together with that of the classical dicarbollide [1-Cp-1,2,3-$FeC_2B_9H_{11}$] (**1**) and the ferratricarbollide isomers [1-Cp-1,2,3,4-$FeC_3B_8H_{11}$] (**2**) and [1-Cp-1,2,3,5-$FeC_3B_8H_{11}$] (**3**).

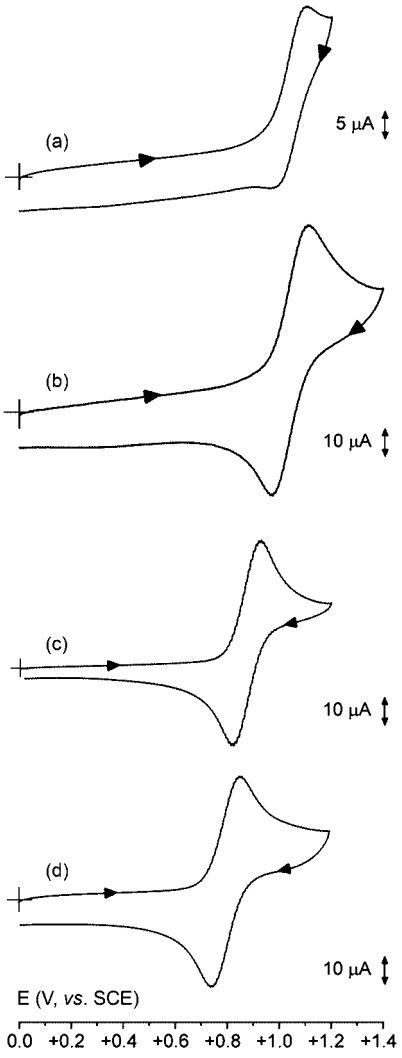


Figure 5. Comparison of the cyclic voltammetric responses given by ferraphosphacarboranes **5a**,**b** and **6a**,**b**: (a) **5a** ($0.7 \times 10^{-3}$ M); (b) **6a** ($1.2 \times 10^{-3}$ M); (c) **5b** ($1.0 \times 10^{-3}$ M); (d) **6b** ($0.7 \times 10^{-3}$ M). $CH_2Cl_2$ solutions contain $[Bu_4N][PF_6]$ (0.2 M) as supporting electrolyte. Gold working electrode. Scan rate: 0.5 $V s^{-1}$.

Table 2. Formal electrode potentials (V vs. SCE), peak-to-peak separation (mV), and current ratio for the redox changes exhibited by the compounds in $CH_2Cl_2$ solution.

| Compound | $E^{\circ\prime}_{Fe(II)/Fe(III)}$ | $\Delta E_p$[a] | $i_{pc}/i_{pa}$[b] | $E^{\circ\prime}_{Fe(II)/Fe(I)}$[a] |
|---|---|---|---|---|
| **5a** | +1.05 | 94[b] | 0.3 | –1.67[c] |
| **6a** | +1.05 | 104[b] | 0.7 | –1.85[c] |
| **5b** | +0.88 | 65 | 0.9 | –1.78[c] |
| **6b** | +0.79 | 74 | 1.0 | [d] |
| **1**[e] | –0.18 | 84 | 1.0 | – |
| **2**[e] | +0.74 | 72 | 0.8 | [d] |
| **3**[e] | +0.82 | 73 | 1.0 | [d] |

[a] Measured at 0.1 $V s^{-1}$. [b] Measured at 0.5 $V s^{-1}$. [c] Peak potential for irreversible processes. [d] Overlapped by the solvent discharge. [e] Data taken from ref.[3a]

The position of the phosphorus atom in the coordinating $PC_2B_2$ pentagonal face for the non-methylated compounds **5a** and **6a** seems to affect the kinetic rather than the thermodynamic parameters of the pertinent oxidation pro-

 © 2007 Wiley-VCH Verlag GmbH & Co. KGaA, Weinheim 

cesses. In fact, while both processes occur at the same formal electrode potential (see Table 2), there is a marked difference in the chemical stability of monocations $[\mathbf{5a}]^+$ and $[\mathbf{6a}]^+$, as measured by the current ratio $i_{pc}/i_{pa}$, which is equal to 0.4 s for **5a** and 0.9 s for **6a** at 2.0 $V s^{-1}$. As a consequence, assuming that a first-order chemical reaction accompanies the $Fe^{II}/Fe^{III}$ change, a lifetime of 0.2 and 6 s can be calculated for $[\mathbf{5a}]^+$ and $[\mathbf{6a}]^+$, respectively.

The opposite trend holds for the methylated derivatives **5b** and **6b**: their monocations seem to be stable on the cyclic voltammetric time scale ($i_{pc}/i_{pa}$ almost constantly equal to 1 with an increase of the scan rate), although their formal electrode potentials are somewhat different (see Table 2). In reality, the electrogenerated monocation $[\mathbf{5b}]^+$ proved to be unstable under exhaustive macroelectrolysis at room temperature (20 °C), whereas $[\mathbf{6b}]^+$ is reasonably stable (a minor trace of an unidentified species able to oxidize reversibly at $E°' = +1.1$ V appeared). Thus, the original pink-orange solution of **6b** ($\lambda_{max}$ = 482 nm) turns pale green upon exhaustive one-electron oxidation and displays a new band at 780 nm with a shoulder at 650 nm.

It should be also noted that all the ferraphosphacarboranes display an essentially irreversible $Fe^{II}/Fe^{I}$ reduction.

As previously pointed out,[3a] the replacement of a boron atom by a carbon atom in the coordinating pentagon of the dicarbollide ligand (i.e. passing from **1** to the isomeric species **2** and **3**) makes the $Fe^{II}/Fe^{III}$ oxidation dramatically more difficult (by about 1 V). We now find that the replacement of a carbon atom in the ferratricarbollides for a phosphorus atom (i.e. passing from **2** and **3** to **5a** and **6a**, respectively) further increases the oxidation potentials (by about 0.3 V). Unfortunately, we have not yet been able to find an unequivocal thermodynamic effect for the non-methylated complexes resulting from the position of the phosphorus atom in the cage, although it appears that the non-adjacent position in both series increases the kinetic stability of the monocations more than the adjacent position, with the $PC_2B_2$ assembly lowering it more severely than $C_3B_2$. Obviously, the $Fe^{II}/Fe^{I}$ reduction becomes more facile (in the order $PC_2B_2 > C_3B_2 > C_2B_3$) as a consequence of the shifts of the $Fe^{II}/Fe^{III}$ redox potential.

In light of the complete, or almost complete, chemical reversibility of cations $[\mathbf{6a}]^+$, $[\mathbf{5b}]^+$, and $[\mathbf{6b}]^+$ at room temperature, they were electrogenerated at 253 K and characterized by EPR spectroscopy. Figure 6 shows the first-derivative X-band EPR spectrum of a $CH_2Cl_2$ solution of $[\mathbf{6b}]^+$ at 105 K.

The line-shape analysis was performed by assuming a low-spin $Fe^{III}$ complex with a doublet state electron spin Hamiltonian in a strongly axial structure (Zeeman interaction).[16] The intense anisotropic signal displays two well separated [$\delta g_i = g_{\parallel} - g_{\perp}$ = 231(5) G] and unresolved absorptions (multiple derivative analysis). The $g_i$ values ($g_{\parallel} > g_{\perp} \neq g_{electron} = 2.0023$) are typical of metallic absorptions arising from effective $3d^5$ spin-orbit $\lambda$ ($S$ = 1/2) coupling.[16] No direct $^{57}Fe$ hyperfine ($I_{^{57}Fe}$ = 1/2, natural abundance = 2.2%) or $^{31}P$, $^{11}B$, $^{10}B$, $^{1}H$, or $^{13}C$ superhyperfine ($I_{^{31}P}$ = 1/2, natural abundance = 100%; $I_{^{11}B}$ = 1/2, natural abundance = 81.2%; $I_{^{10}B}$ = 3/2, natural abundance 18.8%; $I_{^{1}H}$ = 1/2, natural abundance = 99.99%; $I_{^{13}C}$ = 1/2, natural abundance = 1.1%) splitting is evident in the two spectral regions. The computed[17] anisotropic features are collected in Table 3.

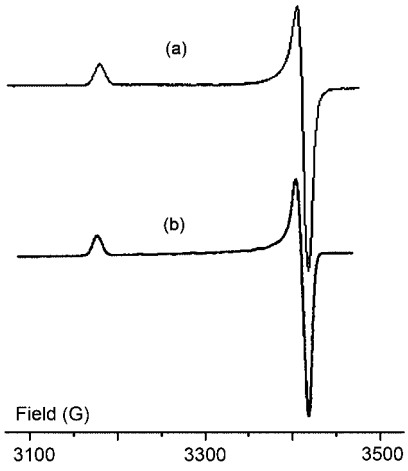


Figure 6. Experimental (a) and simulated (b) X-band EPR spectra of $[\mathbf{6b}]^+$ in $CH_2Cl_2$ solution containing $[Bu_4N][PF_6]$ (0.2 M). $T$ = 105 K. $\nu_o$ = 9.68 GHz.

Table 3. EPR parameters for the electrogenerated cations $[\mathbf{5b}]^+$, $[\mathbf{6a}]^+$, and $[\mathbf{6b}]^+$ in $CH_2Cl_2$ solution[a] [$<g> = 1/3(g_l + g_m + g_h) = 1/3(g_{\parallel} + 2g_{\perp})$; $\delta g_{l-h} = g_l - g_h$; error in $g_i$ and $\delta g_{l-h}$: ±0.005; error in $\Delta H_{iso}$: ±4 G].

| Complex | $g_l$ | $g_m$ | $g_h$ | $\delta g_{l-h}$ | $<g>$ | $g_{iso}$[b] | $\Delta H_{iso}$[b] |
|---|---|---|---|---|---|---|---|
| $[\mathbf{5b}]^+$ | 2.150 | 2.032 | 2.016 | 0.134 | 2.066 | 2.064 | 14 |
| $[\mathbf{6a}]^+$ | 2.183 | 2.029 | 2.029 | 0.154 | 2.080 | 2.066 | 10 |
| $[\mathbf{6b}]^+$ | 2.175 | 2.027 | 2.027 | 0.148 | 2.076 | – | – |

[a] $T$ = 105 K. [b] $T$ = 298 K.

Given the very low natural abundance of the magnetically active atoms present in the complex, particularly $^{57}Fe$ and $^{13}C$, the spectral features are expected to be significantly obscured by the experimental anisotropic linewidths [$\Delta H_{i(exp)}$]. The paramagnetic analysis strongly indicates that the actual SOMO is mainly constituted by the 3d atomic orbitals of the $Fe^{III}$ center, with minor contributions from the directly coordinating donor atoms.

Because of the effective speeding up of the electron paramagnetic relaxation mechanisms, raising the temperature to the glass/fluid transition causes the axial signals to disappear and the fluid solution becomes EPR-silent. Rapid refreezing restores the original anisotropic features. Such a temperature-dependent paramagnetic behavior is not unusual and is due to the effective speeding up of the electron paramagnetic relaxation mechanisms under fast motion conditions in the presence of active thermal effects.[16]

A substantially similar magnetic behavior is exhibited by the related non-methylated cation $[\mathbf{6a}]^+$, although the fluid solution ($T$ = 298 K) exhibits a broad signal with low intensity, the $g_{iso}$ value of which is slightly smaller than the $<g>$ value under glassy conditions because of the effective averaging of the original anisotropy.

 © 2007 Wiley-VCH Verlag GmbH & Co. KGaA, Weinheim 

Cation $[\mathbf{5b}]^+$ exhibits a different line-shape with a broader and unresolved rhombic pattern ($g_i \neq g_{electron}$) and a high field absorption that is partially split and overlapped. No hyperfine or superhyperfine resolution was visible in this case. In addition, a broad isotropic signal appears in the fluid solution at a $g_{iso}$ value that is essentially identical to the $<g>$ value in glassy solution. It should be noted that the paramagnetic features (see Table 3) suggest a slightly lower metallic character of the unpaired electron.

Since the EPR spectral symmetry (isotropic, axial, rhombic) reflects the local symmetry around the paramagnetic center, in other words the structure of the SOMO, the EPR evidence for different anisotropic line-shapes and linewidths must arise from significant differences in the geometrical coordinating frameworks.[16] In the present case, the fact that cation $[\mathbf{5b}]^+$ exhibits a less symmetrical ligand framework than cations $[\mathbf{6a}]^+$ and $[\mathbf{6b}]^+$ due to the adjacent vs. nonadjacent position of the heteroatoms could be responsible for the different spectral patterns.

We carried out a multiple derivatives analysis of the best-fit experimental anisotropic line-widths ($\Delta H_i$) in order to determine the upper limit for the unpaired electron couplings of cations $[\mathbf{5b}]^+$, $[\mathbf{6a}]^+$, and $[\mathbf{6b}]^+$ with the different magnetically active nuclei of the coordinating atoms (see Table S1 in the Supporting Information). This study clearly showed the metallic character of the X-band experimental spectra, although a significant interaction of the phosphorus nucleus seems to be involved in the magnetic interaction with the unpaired electron.

## Conclusions

Reaction of the phosphadicarbollide anion **4** with $[(C_5R_5)Fe]^+$ fragments under mild conditions leads to the non-rearranged ferraphosphacarboranes **5a**,**b**, whose thermal isomerization into **6a**,**b** correlates with an increase of the thermodynamic stability, as estimated by DFT calculations. The electrochemical data for these compounds suggest a greater acceptor character of the phosphadicarbollide ligands compared with their di- and tricarbollide analogues.

The isomer shifts of **5a**,**b** and **6a**,**b** at 90 K are significantly smaller than those for ferrocenes $Cp_2Fe$ and $Cp^*_2Fe$ (0.536 and 0.492 mm s$^{-1}$, respectively, at 90 K), which reflects a higher electron density at the metal atom in the former. This observation was somewhat unexpected, since the electrochemical data and electronegativity considerations would suggest the opposite. The quadrupole splitting parameter is not sensitive to the location (adjacent or not) of the two boron atoms facing the metal center in the carbollide structure. Temperature-dependent ME measurements of the rmsav of the metal atom in **6a** are in good agreement with the value extracted from single-crystal X-ray data at 293 K.

## Experimental Section

**General Remarks:** All reactions were carried out under argon in anhydrous solvents, which were purified and dried according to standard procedures. All products were isolated in air. The $^1$H, $^{11}$B, and $^{31}$P NMR spectra were recorded with a Bruker AMX-400 instrument at room temperature in $CDCl_3$. The salt $[Bu_4N][7,8,9\text{-}PC_2B_8H_{10}]$ ($[Bu_4N][\mathbf{4}]$) was prepared by mixing $7,8,9\text{-}PC_2B_8H_{11}$[18] and $Bu_4NBr$ in aqueous NaOH. Materials and apparatus for electrochemistry and joint EPR spectroscopy have been described elsewhere.[19] All the potential values are referred to the saturated calomel electrode (SCE). The one-electron oxidation of ferrocene occurs at $E^{\circ\prime}$ = +0.39 V under the present experimental conditions.

**[1-Cp-1,2,3,4-FePC$_2$B$_8$H$_{10}$] (5a):** A mixture of $[Bu_4N][\mathbf{4}]$ (230 mg, 0.6 mmol) and $[CpFe(C_6H_6)]PF_6$ (413 mg, 1.2 mmol) in $CH_2Cl_2$ (15 mL) was irradiated whilst stirring at room temperature for 4 h, during which time its color changed from yellow to bright-red. The reaction mixture was concentrated in vacuo and the residue eluted through a short (5 cm) silica gel column with a $CH_2Cl_2$/petroleum ether mixture (1:2) as eluent. Concentration of the red fraction by passing an argon stream over the solution gave red crystals of **5a** suitable for X-ray diffraction (60 mg, 37%). $^1$H NMR: $\delta$ = 5.03 (s, 5 H, Cp), 3.88 (s, 1 H, cage-CH), 3.55 (d, $J_{^{31}P,^1H}$ = 16 Hz, 1 H, cage-CH) ppm. $^{11}$B{$^1$H} NMR (exp./calcd.): $\delta$ = 1.9/3.1 (s, 1 B, B5), 0.3/–2.8 (s, 1 B, B12), –6.2/–5.0 (s, 1 B, B6), –6.4/–7.8 (s, 1 B, B10), –9.0/–10.3 (s, 1 B, B9 or B11), –10.8/–10.3 (s, 1 B, B9 or B11), –19.9/–21.4 (s, 1 B, B8), –27.0/–28.4 (s, 1 B, B7) ppm. $^{31}$P NMR: $\delta$ = 27.4 (s, 1 P, P2) ppm. $C_7H_{15}B_8FeP$ (272.50): calcd. C 30.87, H 5.51, B 31.75; found C 31.07, H 5.68, B 31.40.

**[1-Cp*-1,2,3,4-FePC$_2$B$_8$H$_{10}$] (5b):** A mixture of $[Bu_4N][\mathbf{4}]$ (157 mg, 0.4 mmol) and $[Cp^*Fe(MeCN)_3]PF_6$ (188 mg, 0.4 mmol) in thf (10 mL) was stirred at room temperature overnight, which resulted in a color change from dark- to bright-red. The reaction mixture was concentrated in vacuo and the residue eluted through a short (5 cm) silica gel column with a $CH_2Cl_2$/petroleum ether mixture (1:2) as eluent. Concentration of the red fraction gave red crystals of **5b** (47 mg, 35%). $^1$H NMR: $\delta$ = 2.88 (s, 1 H, cage-CH), 2.54 (d, $J_{^{31}P,^1H}$ = 13 Hz, 1 H, cage-CH), 1.84 (s, 15 H, Cp*) ppm. $^{11}$B{$^1$H} NMR: $\delta$ = 3.0 (s, 1 B), –3.3 (s, 1 B), –4.2 (s, 1 B), –8.9 (s, 1 B), –10.5 (s, 1 B), –11.9 (s, 1 B), –20.6 (s, 1 B), –28.5 (s, 1 B) ppm. $^{31}$P NMR: $\delta$ = 38.3 (s, 1 P, P2) ppm. $C_{12}H_{25}B_8FeP$ (342.63): calcd. C 42.07, H 7.35, B 25.24; found C 42.23, H 7.14, B 25.11.

**Thermal Isomerization of 5a,b:** Complex **5a** (100 mg) was refluxed in nonane (5 mL) for 6 h. The course of isomerization was checked every 2 h by recording the $^{11}$B and $^{31}$P NMR spectra. After the reaction was complete, the solution was slowly cooled to 0 °C to give bright red crystals of **6a**, which were washed with cold pentane and dried in vacuo (77 mg, 77%). Complex **6b** was obtained from **5b** in a similar manner in 83% yield. **6a:** $^1$H NMR: $\delta$ = 4.96 (s, 5 H, Cp), 4.37 (s, 2 H, cage-CH) ppm. $^{11}$B{$^1$H} NMR (exp/calc): $\delta$ = –2.1/–6.0 (s, 1 B, B12), –11.4/–11.0 (s, $J_{^{31}P,^{11}B}$ = 39 Hz, 2 B, B3,6), –13.1/–14.7 (s, 1 B, B9), –13.8/–13.1 (s, 2 B, B7,11), –21.1/–18.8 (s, 2 B, B8,10) ppm. $^{31}$P NMR: $\delta$ = –14.8 (s, 1 P, P2) ppm. **6b:** $^1$H NMR: $\delta$ = 3.40 (s, 2 H, cage-CH), 1.85 (s, 15 H, Cp*) ppm. $^{11}$B{$^1$H} NMR: $\delta$ = –5.0 (s, 1 B), –9.5 (s, $J_{^{31}P,^{11}B}$ = 38 Hz, 2 B), –13.6 (s, 1 B), –14.9 (s, 2 B), –19.6 (s, 2 B) ppm. $^{31}$P NMR: $\delta$ = –6.6 (s, 1 P, P2) ppm. $C_{12}H_{25}B_8FeP$ (342.63): calcd. C 42.07, H 7.35, B 25.24; found C 42.38, H 7.01, B 25.20.

**Mössbauer Spectroscopy:** The samples were transferred into plastic holders and mounted in a variable-temperature cryostat as described previously.[13] The methods for spectrometer calibration, data analysis, and temperature control monitoring have been detailed previously.[13] All isomer shifts (IS) are given with respect to a room-temperature α-Fe absorber spectrum which was also used for spectrometer calibration. The ME spectral line widths for the optically "thin" samples was 0.248 ± 0.013 mm s$^{-1}$.

 © 2007 Wiley-VCH Verlag GmbH & Co. KGaA, Weinheim 

**X-ray Crystallography for 5a:** $C_7H_{15}B_8FeP$, $M$ = 272.49, monoclinic, space group $P2_1/c$, 120 K, $a$ = 6.8292(12), $b$ = 9.811(2), $c$ = 18.015(3) Å, $\beta$ = 90.816(8)°, $V$ = 1206.9(4) Å$^3$, $Z$ = 4, $F(000)$ = 552, $d_{calcd.}$ = 1.500 g cm$^{-3}$, $\mu$ = 1.340 mm$^{-1}$. The unit cell parameters and intensities of 10973 reflections were measured with a Bruker SMART 1000 CCD area detector, using graphite-monochromated Mo-$K_\alpha$ radiation, ϕ- and $\omega$-scans, $\theta_{max}$ = 27°. The temperature of the crystal was maintained with a Cryostream (Oxford Cryosystems) open-flow nitrogen gas cryostat. Reflection intensities were integrated using SAINT software,[20] and absorption correction was applied semi-empirically using the SADABS program. The structure was solved by direct methods and refined by full-matrix least squares against $F^2$ in an anisotropic approximation for all non-hydrogen atoms except B5 and P2, which were found to be disordered over two sites with respect to the mirror plane passing through the center of the C3–C4 bond (3:2 occupancy), and the carbon atoms of the Cp ring, which were found to be disordered over two sites (4:1 occupancy). The disordered atoms were refined in an isotropic approximation. The polyhedron hydrogen atoms were located from the Fourier density synthesis and refined in an isotropic approximation. All calculations were performed using the SHELXTL software.[21] Final $R$ factors are equal to $R_1$ = 0.0349 for 2068 reflections with $I > 2\sigma(I)$ and $wR_2$ = 0.0834 for all 2585 independent reflections. CCDC-635642 contain the supplementary crystallographic data for this paper. These data can be obtained free of charge from The Cambridge Crystallographic Data Center via www.ccdc.cam.ac.uk/data_request/cif.

**Computational Details:** All calculations were performed using the Gaussian 98 (revision A.7) software[22] package at the B3LYP/6-31G* level. The structures of isomers **5a** and **6a** were optimized within $C_1$ and $C_s$ symmetry, respectively. The frequency calculations were performed to confirm the global minimum and include ZPE corrections to the energy. The $^{11}$B NMR shifts were calculated using the GIAO method by subtracting the calculated isotropic shielding values from that of $B_2H_6$ (93.50 at B3LYP/6-31G*). The experimental chemical shift of $B_2H_6$ was assigned to be $\delta$ = 16.6 ppm.[23]

**Supporting Information** (see footnote on the first page of this article): Computed upper limit values of the temperature-dependent hyperfine and superhyperfine couplings of cations **[5b]**$^+$, **[6a]**$^+$, and **[6b]**$^+$ in $CH_2Cl_2$ solution. Details of the DFT calculations of **5a** and **6a**, including the optimized coordinates, NBO charges, and NMR shielding tensors.

## Acknowledgments

This work was supported by the Division of Chemistry and Material Sciences of the Russian Academy of Sciences. P. Z. gratefully acknowledges the financial support of the University of Siena (PAR 2005).

[1] M. F. Hawthorne, R. L. Pilling, *J. Am. Chem. Soc.* **1965**, *87*, 3987–3988.
[2] D. S. Perekalin, J. Holub, D. G. Golovanov, K. A. Lyssenko, P. V. Petrovskii, B. Štíbr, A. R. Kudinov, *Organometallics* **2005**, *24*, 4387–4392.
[3] a) R. H. Herber, A. R. Kudinov, P. Zanello, I. Nowik, D. S. Perekalin, V. I. Meshcheryakov, K. A. Lyssenko, M. Corsini, S. Fedi, *Eur. J. Inorg. Chem.* **2006**, 1786–1795; b) A. R. Kudinov, V. I. Meshcheryakov, P. V. Petrovskii, M. I. Rybinskaya, *Izv. Akad. Nauk*, *Ser. Khim.* **1999**, 177–179; *Russ. Chem. Bull.* **1999**, *48*, 176–177.
[4] B. Štíbr, J. Holub, M. Bakardjiev, I. Pavlík, O. L. Tok, I. Císařova, B. Wrackmeyer, M. Herberhold, *Chem. Eur. J.* **2003**, 2239–2244.
[5] a) D. S. Perekalin, I. V. Glukhov, B. Štíbr, A. R. Kudinov, *Inorg. Chim. Acta* **2006**, *359*, 3264–3268; b) J. Holub, B. Grüner, D. S. Perekalin, D. G. Golovanov, K. A. Lyssenko, P. V. Petrovskii, A. R. Kudinov, B. Štíbr, *Inorg. Chem.* **2005**, *44*, 1655–1659.
[6] We use the numbering system in which the metal vertex bears number 1.
[7] A similar behavior has been observed for the reaction of the cation $[(C_4Me_4)Co(MeCN)_3]^+$ with $[9\text{-Cl-}7,8,11\text{-}PC_2B_8H_9]^-$, where formation of the σ-complex was confirmed by $^{31}$P and $^{11}$B NMR spectroscopy: E. V. Mutseneck, D. S. Perekalin, J. Holub, Z. A. Starikova, K. A. Lyssenko, P. V. Petrovskii, P. Zanello, M. Corsini, B. Štíbr, A. R. Kudinov, *Organometallics* **2006**, *25*, 2419–2426.
[8] B. Štíbr, J. Holub, M. Bakardjiev, I. Pavlík, O. L. Tok, B. Wrackmeyer, *Eur. J. Inorg. Chem.* **2003**, 2524–2528.
[9] This correlates with an energy difference of 12.2 kcal mol$^{-1}$ calculated at the B3LYP/6-311+G**//B3LYP/6-31G* level: F. A. Kiani, M. Hofmann, *Organometallics* **2006**, *25*, 485–490.
[10] Unfortunately, the X-ray structures of **5b** and **6b** were not solved because of severe disorder and libration even at 120 K.
[11] J. M. Oliva, N. L. Allan, P. v. R. Schleyer, C. Viñas, F. Teixidor, *J. Am. Chem. Soc.* **2005**, *127*, 13538–13547.
[12] A. Haaland, J. E. Nilsson, *Acta Chem. Scand.* **1968**, *23*, 2653–2656.
[13] G. Laus, H. Schottenberger, K. Wurst, R. H. Herber, U. Griesser, *J. Phys. Chem. B* **2004**, *108*, 5082–5087.
[14] R. H. Herber, in *Chemical Mössbauer Spectroscopy* (Ed.: R. H. Herber), Plenum Press, New York, **1984**.
[15] R. H. Herber, I. Nowik, V. Kahlenberg, H. Kopacka, H. Schottenberger, *Eur. J. Inorg. Chem.* **2006**, 3255–3260, and references cited therein.
[16] a) F. E. Mabbs, D. Collison, *Electron Paramagnetic Resonance of d Transition Metal Compounds*, in *Studies in Inorganic Chemistry*, Elsevier, New York, **1992**, vol. 16; b) J. R. Pilbrow, *Transition Ion Electron Paramagnetic Resonance*, Oxford Science Publications, Oxford, **1990**; c) R. S. Drago, *Physical Methods for Chemists*, Saunders College Publ., New York; **1992**.
[17] G. P. Lozos, B. M. Hoffman, C. G. Franz, *Quantum Chemistry Program Exchange* **1974**, *11*, 265.
[18] B. Štíbr, J. Holub, M. Bakardjiev, D. Hnyk, O. L. Tok, W. Milius, B. Wrackmeyer, *Eur. J. Inorg. Chem.* **2002**, 2320–2326.
[19] P. Zanello, F. Laschi, M. Fontani, C. Mealli, A. Ienco, K. Tang, X. Jin, L. Li, *J. Chem. Soc. Dalton Trans.* **1999**, 965–970.
[20] *SMART* (V5.051) and *SAINT* (V5.00), Area detector control and integration software, Bruker AXS Inc., Madison,WI 53719, USA, **1998**.
[21] G. M. Sheldrick, *SHELXTL-97* (V5.10), Bruker AXS Inc., Madison, WI 53719, USA, **1997**.
[22] M. J. Frisch, G. W. Trucks, H. B. Schlegel, G. E. Scuseria, M. A. Robb, J. R. Cheeseman, V. G. Zakrzewski, J. A. Montgomery Jr, R. E. Stratmann, J. C. Burant, S. Dapprich, J. M. Millam, A. D. Daniels, K. N. Kudin, M. C. Strain, O. Farkas, J. Tomasi, V. Barone, M. Cossi, R. Cammi, B. Mennucci, C. Pomelli, C. Adamo, S. Clifford, J. Ochterski, G. A. Petersson, P. Y. Ayala, Q. Cui, K. Morokuma, D. K. Malick, A. D. Rabuck, K. Raghavachari, J. B. Foresman, J. Cioslowski, J. V. Ortiz, B. B. Stefanov, G. Liu, A. Liashenko, P. Piskorz, I. Komaromi, R. Gomperts, R. L. Martin, D. J. Fox, T. Keith, M. A. Al-Laham, C. Y. Peng, A. Nanayakkara, C. Gonzalez, M. Challacombe, P. M. W. Gill, B. G. Johnson, W. Chen, M. W. Wong, J. L. Andres, M. Head-Gordon, E. S. Replogle, J. A. Pople, *Gaussian 98*, revision A.7, Gaussian, Inc., Pittsburgh, PA, **1998**.
[23] U. Dörfler, D. L. Ormsby, R. Greatrex, J. D. Kennedy, *Inorg. Chim. Acta* **2000**, *304*, 268–273.

Received: March 14, 2007
Published Online: July 17, 2007

 © 2007 Wiley-VCH Verlag GmbH & Co. KGaA, Weinheim 

DOI: 10.1002/ejic.200700424

# Pyrazole-Based Ligands for the [Copper–TEMPO]-Mediated Oxidation of Benzyl Alcohol to Benzaldehyde and Structures of the Cu Coordination Compounds

**Jorge Salinas Uber,[a] Yorick Vogels,[a] Dave van den Helder,[a] Ilpo Mutikainen,[b] Urho Turpeinen,[b] Wen Tian Fu,[a] Olivier Roubeau,[c] Patrick Gamez,[a] and Jan Reedijk*[a]**

**Keywords:** Copper(I) and copper(II) complexes / Catalysis / Oxidation / Luminescence / Bioinorganic chemistry

New pyrazole-based ligands have been designed, and the catalytic performances of their copper(II) complexes for the [copper/TEMPO]-mediated oxidation of benzyl alcohol to benzaldehyde have been examined. The pyridine-pyrazole ligands give efficient catalysts, while the use of naphthol-pyrazole ligands results in inactive catalytic systems. Single-crystals of four Cu coordination compounds obtained from pyridine-pyrazole ligands and a free ligand have been isolated and were characterized by X-ray diffraction. Thus, the solid-state structures of three copper(II) complexes are described, together with a copper(I) coordination chain, exhibiting luminescent properties.
(© Wiley-VCH Verlag GmbH & Co. KGaA, 69451 Weinheim, Germany, 2007)

## Introduction

The selective production of aldehydes from primary alcohols is a very important chemical transformation of organic synthesis, since a wide variety of fine chemicals possess this carbonyl function.[1,2] Various effective methods have been developed to perform this oxidation reaction.[3,4] For example, the synthesis of aldehydes may commonly be achieved by heating the primary alcohol in an acidified solution of potassium dichromate, which is reduced to $Cr^{3+}$ during the reaction,[5] or by the so-called "Swern oxidation" [$(CO)_2Cl_2$ + $(Me)_2SO$].[6] However, these oxidation procedures often involve the use of stoichiometric amounts of reagents, which leads to the formation of copious quantities of unfriendly waste for the environment. Hence, catalytic oxidations mediated by transition metal complexes represent a crucial and topical area of catalysis in term of green and sustainable chemistry.[7] Several efficient catalytic systems, including TEMPO-based ones have been reported;[8–16] nevertheless, severe limitations remain that are the chemo-, regio- and stereoselectivity of the catalytic oxidations. Recently, some of us have developed a bio-inspired copper-based catalyst able to selectively convert primary alcohols to the corresponding aldehydes in the presence of TEMPO as co-catalyst.[17,18] This catalytic system has been further developed by other research groups, showing its high potential and versatility for the production of a broad range of aldehydes.[19,20] In the present study, a number of related pyrazole-based ligands have been used for the [copper(II)/TEMPO]-catalysed oxidation of benzyl alcohol to benzaldehyde in order to obtain a better insight of its mechanism.

[a] Leiden Institute of Chemistry, Gorlaeus Laboratories, Leiden University,
P. O. Box 9502, 2300 RA Leiden, The Netherlands
Fax: +31-715274671
E-mail: reedijk@chem.leidenuniv.nl
[b] Department of Chemistry, Laboratory of Inorganic Chemistry, P. O. Box 55 (A. I. Virtasenaukio 1), 00014 University of Helsinki, Helsinki, Finland
[c] Université Bordeaux 1, Centre de Recherche Paul Pascal – CNRS UPR 8641,
115 avenue du dr. A. Schweitzer, 33600 Pessac, France
Supporting information for this article is available on the WWW under http://www.eurjic.org or from the author.

## Results and Discussion

### Preparation of the Ligands

A few years ago, an effective catalytic system for the conversion of primary alcohols to the corresponding aldehydes, under mild conditions, has been reported.[17] This catalytic oxidation reaction involves a copper complex, and it has been shown that the use of aromatic N-donor ligands leads to efficient catalysts.[21] The proposed catalytic cycle of this reaction brings in copper(II) and copper(I) species (Scheme 1).[21] 2,2′-Bipyridine (and derivatives) has been shown to be a prime ligand for this reaction.[21] The pyrazole ring is known to stabilize $Cu^{I}$ species. Thus, the use of mixed pyridine/pyrazole ligands is expected to generate active catalysts for the [Cu(ligand)-TEMPO]-mediated oxidation of primary alcohols, since both the $Cu^{I}$ and $Cu^{II}$ species may presumably be efficiently stabilised during the catalytic cycle. Therefore, a first series of new bidentate ligands have been designed and synthesized, which contain a pyridine unit connected to a less soft donor group, namely a pyrazole ring.

 © 2007 Wiley-VCH Verlag GmbH & Co. KGaA, Weinheim 

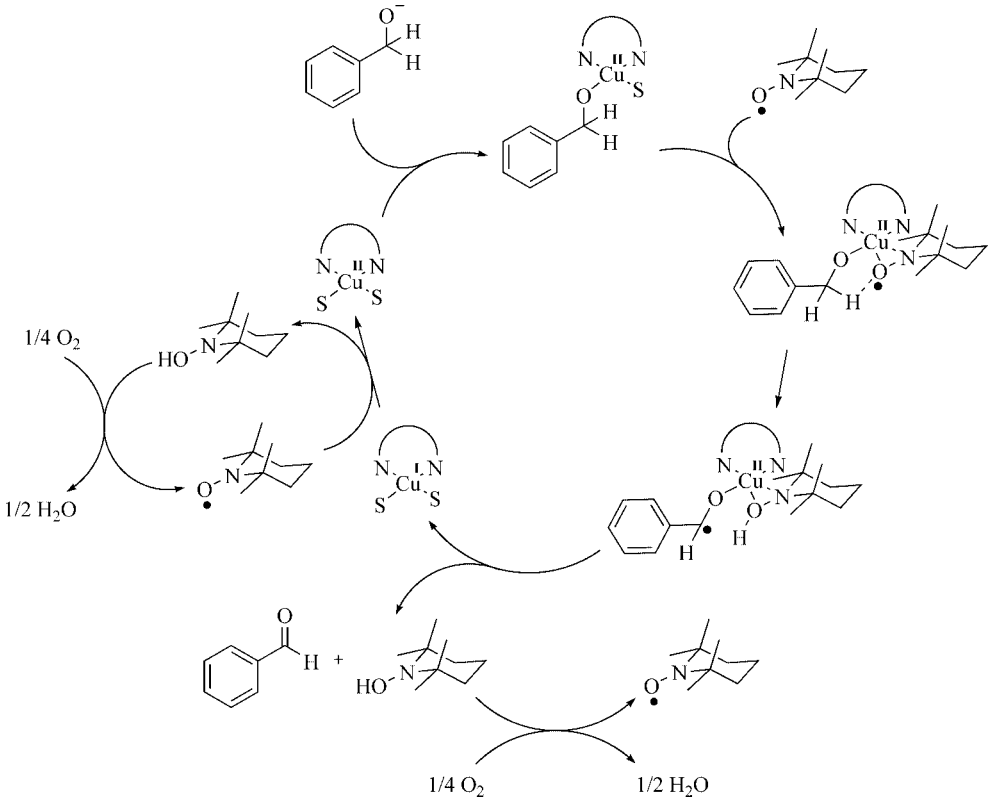


Scheme 1. Proposed catalytic cycle for the [copper/TEMPO]-catalyzed oxidation of benzyl alcohol to benzaldehyde.[21]

Moreover, the proposed catalytic cycle (Scheme 1)[21] of the [Cu(ligand)-TEMPO]-mediated oxidation is derived from the well-known mechanism of action of the copper enzyme galactose oxidase (GOase).[22] The active site of GOase contains a distorted square-pyramidal mononuclear copper(II) species, two of whose ligands are phenolic moieties (from tyrosinate side-chains).[22] A second series of pyrazole-based ligands possessing a naphthol group, have therefore been prepared to mimic the active site of GOase.

The synthetic procedure for the preparation of the pyrazole-containing ligands is based on an earlier reported method.[23] The first step of the synthesis is the reaction of an acyl derivative (**1**) with *N*,*N*-dimethylformamide dimethyl acetal (**2**) (Scheme 2). The resulting propenone (**3**) is treated with a hydrazine derivative to generate the pyrazole ring, via a ring-closure step (Scheme 2).

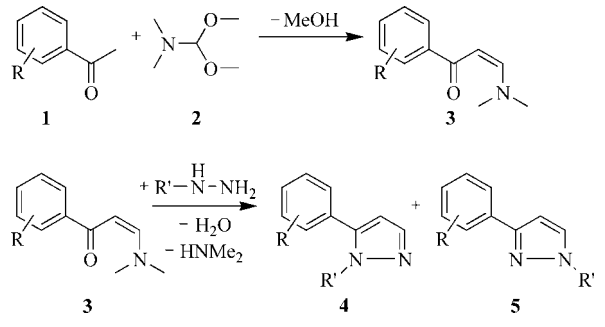


Scheme 2. Synthetic pathway for the preparation of the pyrazole-based ligands.

Using this straightforward synthetic route, the pyrazole-pyridine and the pyrazole-naphthol ligands depicted in Scheme 3 have been prepared in good yields (see Experimental section).

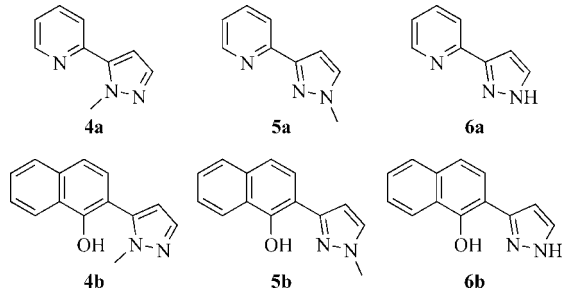


Scheme 3. Ligands used for the [copper–TEMPO]-catalysed oxidation of benzyl alcohol.

These pyrazole derivatives have been tested as ligands in the [copper–TEMPO]-catalysed oxidation of benzyl alcohol. Furthermore, various copper coordination compounds, whose crystal structures are described below, have been obtained by reaction of copper(II) bromide and some of these ligands.

## Description of the Structures

### *Crystal Structure of $[Cu_2(4a)_2Br_2]_n$ (7)*

Reaction of one equivalent of copper(II) bromide with one equivalent of ligand **4a** in methanol yields colourless

 © 2007 Wiley-VCH Verlag GmbH & Co. KGaA, Weinheim 

plates of **7** after one day. **7** crystallizes in the triclinic space group $P\bar{1}$. An ORTEP[24] view of compound **7** is depicted in Figure 1. Selected bond lengths and angles are given in Table 1, and details for the structure solution and refinement are summarized in Table S1 (see electronic supporting information). Compound **7** is constituted by tetracoordinate copper(I) ions exhibiting distorted tetrahedral coordination, with a $\tau_4$ value of 0.85.[25] Each copper centre is coordinated by a pyrazole N atom and a pyridine N atom, belonging to two different ligands. These two ligands coordinate to a crystallographically related copper(I) ion, generating a dimer (Figure 1). The coordination sphere of the metal centre is completed by two bromide anions. The Cu–N and Cu–Br bond lengths, as well as the bond angles are within normal ranges for such $Cu^I$ coordination geometry.[26,27] The $Cu_2(\mathbf{4a})_2Br_2$ dinuclear units are bridged by the bromine ions to form infinite one-dimensional chains (Figure S1). As evidenced in Figure S1, the crystal packing of **7** shows a two-dimensional arrangement of the chains along the *a* axis. Indeed, each 1D chain interacts with two adjacent chains by means of π–π contacts [the separation between the ring centroids amounts to 3.652(3) Å].

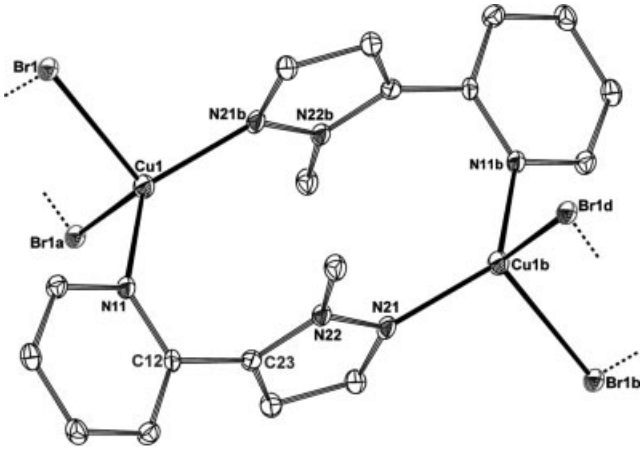


Figure 1. ORTEP drawing (30% probability level) of $[Cu_2(\mathbf{4a})_2Br_2]_n$ (**7**). Hydrogen atoms are omitted for clarity.

Table 1. Selected bond lengths [Å] and angles [°] for **7**–**10**.

| | | | |
|---|---|---|---|
| Compound **7** | | | |
| Cu1–Br1 | 2.590(1) | Cu1–Br1a | 2.517(1) |
| Cu1–N11 | 2.075(5) | Cu1–N21b | 2.032(4) |
| Br1–Cu1–Br1a | 108.1(1) | Br1–Cu1–N11 | 102.6(1) |
| Br1–Cu1–N21b | 99.7(1) | Br1a–Cu1–N11 | 103.6(1) |
| Br1a–Cu1–N21b | 118.3(2) | N11–Cu1–N21b | 122.5(2) |
| Compound **8** | | | |
| Cu1–Br1 | 2.372(1) | Cu1–Br2 | 2.394(1) |
| Cu1–Br3 | 2.371(1) | Cu1–N21 | 2.016(6) |
| Br1–Cu1–Br2 | 97.9(1) | Br1–Cu1–Br3 | 99.5(1) |
| Br1–Cu1–N21 | 138.4(2) | Br2–Cu1–Br3 | 134.6(1) |
| Br2–Cu1–N21 | 98.1(2) | Br3–Cu1–N21 | 96.1(2) |
| Compound **9** | | | |
| Cu1–Br1 | 2.345(1) | Cu1–Br2 | 2.354(2) |
| Cu1–N11 | 2.013(7) | Cu1–N21 | 2.003(7) |
| Br1–Cu1–Br2 | 100.2(1) | Br1–Cu1–N11 | 98.3(2) |
| Br1–Cu1–N21 | 146.7(2) | Br2–Cu1–N11 | 143.1(2) |
| Br2–Cu1–N21 | 99.8(2) | N11–Cu1–N21 | 80.9(3) |
| Cu2–Br3 | 2.385(1) | Cu2–Br4 | 2.416(2) |
| Cu2–Br3a | 2.932(2) | Cu2–N31 | 2.098(7) |
| Cu2–N41 | 1.985(7) | Cu2–Cu2a | 4.027(2) |
| Br3–Cu2–Br4 | 98.4(1) | Br4–Cu2–N41 | 96.1(2) |
| N41–Cu2–N31 | 79.2(3) | N31–Cu2–Br3 | 98.6(2) |
| Br3a–Cu2–Br4 | 132.0(1) | Br4–Cu2–N31 | 121.5(2) |
| N31–Cu2–Br3a | 105.6(2) | Br3–Cu2–N41 | 164.1(2) |
| Compound **10** | | | |
| Cu1–Br1 | 2.444(1) | Cu1–N1 | 2.076(6) |
| Cu1–N7 | 1.995(7) | Cu1–N12 | 2.088(7) |
| Cu1–N18 | 1.997(7) | | |
| Br1–Cu1–N1 | 123.3(2) | N1–Cu1–N12 | 114.8(3) |
| N12–Cu1–Br1 | 122.0(2) | N7–Cu1–N18 | 172.1(3) |

Complex **7** can be obtained by reaction of one equivalent of copper(I) bromide with one equivalent of **4a** in acetonitrile (see Exp. Sect. and Scheme 4).

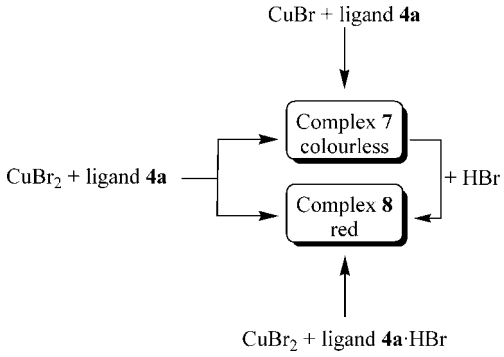


Scheme 4. Possible aerobic synthetic pathways for the preparation of complexes **7** and **8** (see Exp. Sect. for details).

As observed for other copper(I) complexes,[28,29] compound **7** possesses luminescence properties (see Figure S2). Indeed, under ambient conditions, solid **7** exhibits an intense blue-green emission centred at 490 nm, when excited at 365 nm.

### *Crystal Structure of [Cu(4aH)Br$_3$] (8)*

Red block-shaped single-crystals start to grow up, after three weeks, in the previous solution (from which compound **7** had rapidly crystallized). X-ray diffraction analysis of these crystals reveal them to be the mononuclear compound [Cu(**4a**H)$Br_3$] (**8**) (Figure 2), in which the Cu atoms are divalent and the pyridine N atoms are protonated. Similarly to **7**, **8** crystallizes in the triclinic space group $P\bar{1}$. Selected bond lengths and angles are listed in Table 1, and crystallographic data for the structural analysis are given in Table S1. The copper(II) ion is tetracoordinate and adopts a highly distorted tetrahedral arrangement ($\tau_4$ = 0.62),[25] as in previously observed for analogous $Cu^{II}Br_3N$ chromophores.[30,31] The Cu–Br as well as the Cu–N bond lengths are within normal ranges.[30] The coordination angles, ranging from 96.1(2) to 138.4(2)°, reflect the strong distortion, most likely due to the hydrogen bond involving the bromine atom Br1 (see Figure 3).

 © 2007 Wiley-VCH Verlag GmbH & Co. KGaA, Weinheim 

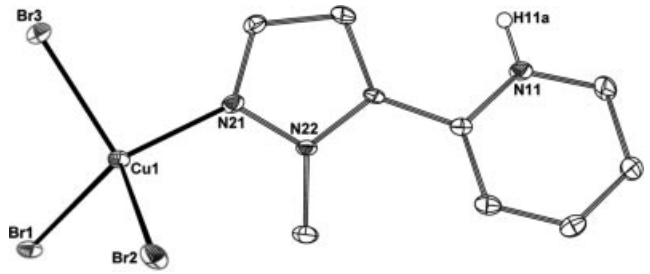


Figure 2. ORTEP drawing (30% probability level) of $[Cu(\mathbf{4a}H)_2Br_3]$ (**8**). Only the pyridinium hydrogen atom is shown.

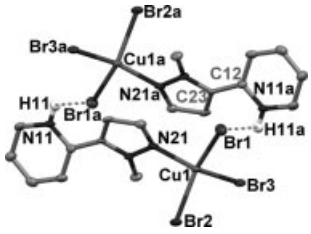


Figure 3. Representation of a dimer of complex **8**, assembled via double intermolecular hydrogen bonding interactions.

The crystal packing of **8** reveals interesting features (Figure 3 and S3). The bromide anion Br1 and the pyridinium hydrogen atom H11 are H-bonded to a neighbouring monocopper complex, producing a dimeric species resembling the dimer of **7** depicted in Figure 1. It thus appears that complex **8** is generated from the copper(I) complex **7** by addition of HBr, like reported by Haddad and Willett for the preparation of bis(dimethylaminopyridinium) tetrabromidocuprate(II).[32] HBr is most likely produced during the formation of complex **7** through decomposition of $CuBr_2$ to CuBr,[33] with concomitant oxidation of the solvent, i.e. methanol (see the section Catalytic Studies). The formal insertion of HBr between the atoms Cu1 and N11 of complex **7** under aerobic conditions (Figure 1) actually results in an increase of steric hindrance which prevents the generation of the 1D chains (observed in **7** and absent in **8**). In addition, the increased steric bulk owing to the additional bromine atom apparently forces the pyrazole ring to rotate around the C12–C23 bond (accordingly, the methyl groups are in opposite directions in Figure 1 and Figure 3).

The H-bonded dimer (Figure 3) is involved in multiple supramolecular interactions, generating a ladder-type framework (Figure S3). The pyrazole rings are π–π stacked with adjacent dimeric units [centroid-to-centroid distance of 3.647(4) Å]. Furthermore, the bromine atom Br3 is interacting with two pyridine rings, resulting in a π–anion–π motif [Figure S3, Br3···centroid $A$ = 3.796(3) Å, Br3···centroid $A'$ = 3.879(3) Å].[34]

To confirm the formation of **8** from **7**, via the addition of HBr under aerobic conditions (Scheme 4), the following experiment has been carried. As stated above, the reaction of $Cu^{I}Br$ with **4a** in acetonitrile produces complex **7**. The addition of HBr to this solution of **7** yields red crystals of **8** after one day, as confirmed by C, H, N, analyses and X-ray diffraction studies (see Exp. Sect.). Compound **8** can also be prepared by reaction of $Cu^{II}Br_2$ with the hydrobromic salt of **4a**, i.e **4a**·HBr (see Scheme 4 and Experimental Section).

### *Crystal Structure of $[Cu_3(5a)_3Br_6]$ (9)*

Reaction of one equivalent of copper(II) bromide with one equivalent of ligand **5a** in methanol produces red needle-shaped single crystals of **9** after one day. **9** crystallizes in the triclinic space group $P\bar{1}$. The important bond parameters and crystallographic data for the structural analysis are listed in Table 1 and S1, respectively. An ORTEP[24] view of compound **9** is depicted in Figure 4. The crystal lattice of this compound is composed of two different copper(II) ions identified as Cu1 and Cu2 (Figure 4). The coordination geometry around Cu1 is intermediate between square-plane and tetrahedral, with $\tau_4$ = 0.50.[25] The Cu–N and Cu–Br bond lengths can be considered as normal.[35,36] The coordination angles ranging from 96.1(2) to 146.7(2) reflect the strong distortion, most likely as a result of steric interactions between Br2 and the methyl substituent in the ligand (Figure S4). The geometry around the Cu2 atom is intermediate between the square-pyramid and the trigonal bipyramid ($\tau_5$ = 0.53).[37] The Cu–N and Cu–Br bond lengths are in normal ranges for this type of $CuBr_3N_2$ chromophore.[38] Cu2 is doubly bridged by two bromide anions to a crystallographically equivalent copper(II) ion, namely Cu2a, giving rise to a dinuclear moiety with a Cu2···Cu2a separation of 4.027(2) Å (Figure 4).

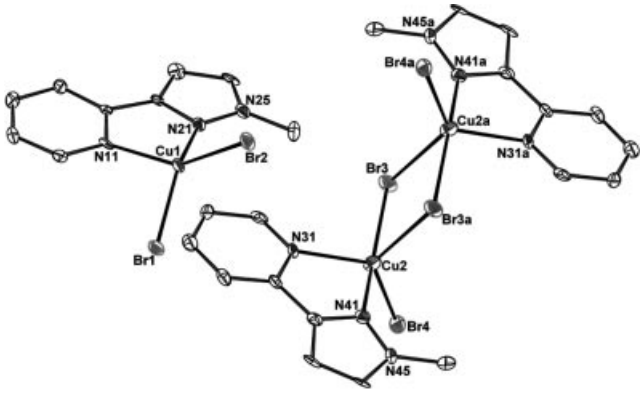


Figure 4. ORTEP drawing (30% probability level) of $[Cu_3(\mathbf{5a})_3Br_6]$ (**9**). Hydrogen atoms are omitted for clarity.

It has to be noted that, if the bromine atom Br3a, coordinated to Cu2 at a long distance of 2.932(2) Å, is omitted, the resulting tetracoordinate copper(II) centre (with $\tau_4$ = 0.53)[25] resembles the Cu1 ion (Figure S5). It thus appears that **9** is constituted by three $CuN_2Br_2$ units, two of them bridged via bromide anions. The crystal packing of **9** along the *a* axis reveals supramolecular interactions (Figure S6). The mononuclear units are π–π stacked in pairs [Figure S6; centroid-to-centroid distance of 3.654(5) Å], whereas the dinuclear units form a 1D chain by means of π–π interactions [see Figure S6: centroid-to-centroid distance of 3.605(5) Å].

 © 2007 Wiley-VCH Verlag GmbH & Co. KGaA, Weinheim 

### *Crystal Structure of [Cu(6a)$_2$Br]Br·H$_2$O·CH$_3$CN (10)*

Reaction of one equivalent of copper(II) bromide with one equivalent of ligand **6a** in acetonitrile yields green block-shaped single crystals of the mononuclear complex **10**. **10** crystallizes in the triclinic space group $P\bar{1}$. An ORTEP[24] view of compound **10** is depicted in Figure 5. Selected bond lengths and angles are given in Table 1, and details for the structure solution and refinement are summarized in Table S1. The copper(II) ion is pentacoordinate by two ligands **6a** and one bromide anion (Figure 5). The coordination geometry is best described as slightly distorted trigonal-bipyramidal with a $\tau_5$ value of 0.81.[37] The Cu–N and Cu–Br bond lengths are comparable to those of related $Cu^{II}N_4Br$ chromophores.[39,40] The lattice contains one water molecule and one acetonitrile of solvation as well as a bromide anion. The non-coordinating bromide ion and the water molecule are engaged in hydrogen bonding (Figure S7). Actually, the cationic part of **10**, namely [Cu(**6a**)$_2$-Br]$^+$, represents the building unit of a 1D supramolecular chain, assembled through π–π interactions [see Figure S7: centroid-to-centroid distances of 3.555(5) and 3.602(5) Å]. These chains are connected to two adjacent chains via H bonds between the bromine atom Br2, the water oxygen atom Ow, and the acidic pyrazolyl hydrogens H13A and H2A [see Figure S7: N13–H13A···Br2 3.286(7) Å, N2–H2A···Ow 2.801(9) Å].

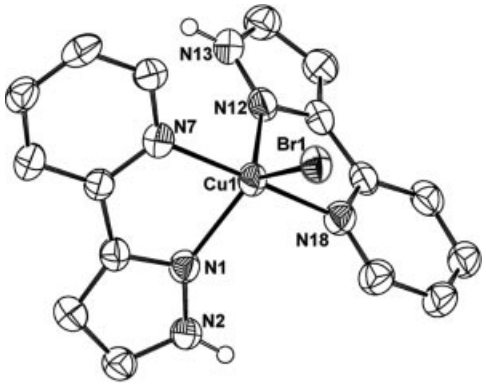


Figure 5. ORTEP drawing (30% probability level) of the cation [Cu(**6a**)$_2$Br]$^+$ of complex **10**. Only the N–H hydrogen atoms are shown for clarity.

## Catalytic Studies

All the ligands prepared have been tested in the [copper/TEMPO]-mediated oxidation of a model substrate, i.e. benzyl alcohol. The initial catalytic oxidations of benzyl alcohol to benzaldehyde were performed applying the experimental conditions reported earlier,[17,21] namely 5 mol-% $CuBr_2$/TEMPO in acetonitrile/water (2:1) with potassium *tert*-butoxide as basic co-catalyst (required to deprotonate the alcoholic substrate).[17,21] For comparison, the conversions achieved with the [$CuBr_2$(2,2′-bipyridine)]/TEMPO system, reported in earlier studies,[17] have been included (Table 2, entry 1). Thus, the use of **4a** as ligand only leads to a conversion of 8% after a reaction time of 1 h (Table 2, entry 2). This poor catalytic activity (1.6 catalytic cycles) is most likely due to the observed precipitation of copper species (green precipitate). Indeed, the insolubility of the copper catalyst obviously retards the rate of the chemical transformation. However, a good conversion of 89% to the exclusive benzaldehyde is reached after 24 h. A more homogeneous reaction system is obtained when acetonitrile is used as the sole solvent (Table 2, entry 3). In that case, a conversion of 31% to benzaldehyde is achieved after 1 h. As no immediate precipitation is observed in the present experiment, this result suggests that the presence of an excess of water (Table 2, entry 2) probably leads to the formation of (multi)copper hydroxide species, which are poorly soluble in the reaction medium. The use of tetrabutylammonium hydroxide (a base exhibiting a higher solubility in acetonitrile than potassium *tert*-butoxide) as basic co-catalyst results in an efficient catalytic system, able to fully and selectively convert benzyl alcohol, after a reaction time of 24 h (Table 2, entry 4). The best catalytic activity is obtained when triethylamine is used as co-catalyst, since more than 2 catalytic cycles are completed after 5 min, and about 40% of benzaldehyde is produced after 1 h (Table 2, entry 5). Interestingly, colourless crystals, exhibiting luminescent properties, start to appear in the reaction mixture after a reaction time of about 15 min. X-ray diffraction studies on these crystals reveals that their solid-state structure corresponds to complex **7**. Surprisingly, this copper(I) complex **7** is very stable in the oxidative conditions of the reaction. Indeed, the reaction is performed in air in the presence of TEMPO, which is believed to play a role in the re-oxidation of the $Cu^I$ species generated during the catalytic cycle (Scheme 1).[21,41] Thus, the lower catalytic activity achieved with this [copper/(pyrazole-pyridine)] system compared to the [copper/2,2′-bipyridine] one (Table 2, entry 1) may be justified by the gradual formation of **7** during the oxidation, resulting in a continuous decrease of active, homogeneous species in the reaction mixture. This high stability of **7** can be explained by the nature of the ligand **4a**. In fact, it has been lately established that a combination of hard/soft ligands appears to favour the stabilization of $Cu^I$ species.[42] **4a** has been purposely designed to contain both a pyridine ring and a pyrazole ring. Therefore, such ditopic ligands apparently can efficiently stabilise copper(I) centres. Thus, the use of dihydrogen peroxide to promote the re-oxidation of the $Cu^I$ ions to $Cu^{II}$ does not lead to an enhancement of the catalytic activity (Table 2, entries 5 and 7). Actually, less active species appear to be formed in the presence of dihydrogen peroxide, because the conversions to benzaldehyde are significantly decreased (Table 2, entries 5 and 7). No improvement in conversion rate is observed when the reaction is performed at 50 °C (see Table 2, entries 5 and 6). On the contrary, the catalyst seems to be less effective (27% conversion after 1 h, whereas 39% conversion can be reached at room temperature), most likely as a result of its partial degradation at a higher temperature. Finally, in contrast to the published catalytic system,[21] the presence of non-coordinating anions, i.e. tetrafluoridoborate and

 © 2007 Wiley-VCH Verlag GmbH & Co. KGaA, Weinheim 

Table 2. Room temperature [copper(ligand)]-catalysed oxidation of benzyl alcohol.[a]

| Entry | Ligand used | Cu(II) salt | Solvent | Basic co-catalyst | % Conv. after 5 min / 1 h / 24 h |
|---|---|---|---|---|---|
| 1 | **bipy** | $CuBr_2$ | MeCN/$H_2O$ | *t*BuOK | 10 / 55 / 99 |
| 2 | **4a** | $CuBr_2$ | MeCN/$H_2O$ | *t*BuOK | 3 / 8 / 89 |
| 3 | **4a** | $CuBr_2$ | MeCN | *t*BuOK | 5 / 31 / 97 |
| 4 | **4a** | $CuBr_2$ | MeCN | $Bu_4NOH$ | 8 / 20 / 99 |
| 5 | **4a** | $CuBr_2$ | MeCN | $Et_3N$ | 11 / 39 / 98 |
| 6 | **4a** | $CuBr_2$ | MeCN | $Et_3N$ (50 °C) | 7 / 27 / – |
| 7 | **4a** | $CuBr_2$ | MeCN | $Et_3N$ + $H_2O_2$ | 4 / 7 / 13 |
| 8 | **4a** | $Cu(BF_4)_2$ | MeCN/$H_2O$ | *t*BuOK | 3 / 7 / 25 |
| 9 | **4a** | $Cu(BF_4)_2$ | MeCN | *t*BuOK | 6 / 14 / – |
| 10 | **4a** | $Cu(ClO_4)_2$ | MeCN | $Bu_4NOH$ | 6 / 16 / – |
| 11 | **4a** | $Cu(ClO_4)_2$ | MeCN | $Et_3N$ | 5 / 14 / – |
| 12 | **5a** | $CuBr_2$ | MeCN/$H_2O$ | *t*BuOK | 10 / 29 / – |
| 13 | **5a** | $CuBr_2$ | MeCN | $Et_3N$ | 11 / 23 / 30 |
| 14 | **5a** | $CuBr_2$ | MeCN/$H_2O$ | *t*BuOK + $H_2O_2$ | 6 / 12 / – |
| 15 | **5a** | $CuBr_2$ | MeCN | *t*BuOK + $H_2O_2$ | 9 / 14 / – |
| 16 | **6a** | $CuBr_2$ | MeCN/$H_2O$ | *t*BuOK | 2 / 4 / 16 |
| 17 | **6a** | $CuBr_2$ | MeCN | $Et_3N$ | 5 / 31 / 33 |
| 18 | **6a** | $Cu(BF_4)_2$ | MeCN/$H_2O$ | *t*BuOK | 3 / 5 / 19 |
| 19 | **6a** | $Cu(BF_4)_2$ | MeCN | $Et_3N$ | 2 / 3 / – |
| 20 | **4b**[b] | $CuBr_2$ | MeCN/$H_2O$ | *t*BuOK | 0 / 1 / – |
| 21 | **5b** | $CuBr_2$ | MeCN/$H_2O$ | *t*BuOK | 0 / 2 / – |
| 22 | **6b** | $CuBr_2$ | MeCN/$H_2O$ | *t*BuOK | 0 / <1 / – |

[a] The catalytic oxidations of benzyl alcohol to benzaldehyde have been carried out using the procedure described in the Experimental Section. The ligand, copper(II) salt, solvent or solvent mixture, and basic co-catalyst used for each test reaction are mentioned in Table 2. [b] The use of 2 equiv. of *t*BuOK (instead of 1 equiv.) does not lead to a better catalytic activity (a conversion of 2% is achieved after a reaction time of 24 hours).

perchlorate, does not lead to an enhancement of the catalytic activity (see Table 2: entries 2 and 8, entries 3 and 9, entries 5 and 11, and entries 4 and 10). Presumably, coordinating anions, such as bromides, are required to complete the coordination sphere of the copper ion (see crystal structures of complexes **7** and **8**), giving rise to catalytically active species. Non-coordinating anions obviously leads to distinct coordination environments around the copper(II) centre, and actually to significantly less active species.

The use of **5a** (regioisomer of **4a**) as ligand in the copper-catalysed oxidation of benzyl alcohol gives less efficient catalysts (Table 2, entries 12–15). In fact, in all cases, a white precipitate rapidly develops in the reaction mixture which shows luminescent properties. This feature suggests the presence of copper(I) species (similarly to ligand **4a**, see above). Due to the fact that, contrary to **4a**, **5a** is a chelating ligand, its coordination probably induces an even better stabilisation of copper(I) entities. This hypothesis is corroborated by the interruption of the catalytic activity after about 1 h (only a conversion of 30% is achieved after a reaction time of 24 h, Table 2, entry 13), while the initial conversions (after a reaction time of 5 min) are comparable to those obtained with **4a** (see for instance Table 2, entries 5 and 12). Moreover, the addition of dihydrogen peroxide in the reaction medium does not favour the re-oxidation of the $Cu^{I}$ ions to $Cu^{II}$ (Table 2, entries 14 and 15), once again indicative of very stable copper(I) species.

The use of **6a** as a ligand generates poorly active catalysts (Table 2, entries 16–19). A maximum conversion of only 33% has been reached in pure acetonitrile, with triethylamine as co-catalyst, after a reaction time of 24 h (Table 2, entry 17). This lack of activity can be justified by the presence of the acidic N-pyrazolyl proton in the ligand. Indeed, under basic conditions, pyrazoles can be deprotonated, and the resulting pyrazolato ligands are known to promote the formation of cluster species.[43] In the present case, the addition of the base (to initiate the catalytic reaction, see experimental section) immediately results in the development of a green precipitate, which may originate from the deprotonation of the pyrazole ring, followed by the formation of insoluble (hence inactive) copper clusters.

Finally, the use of the naphthol-containing compounds **4b**–**6b** (Scheme 3) as ligands does not result in active catalytic systems (Table 2, entries 20–22). This lack of reactivity is obviously due to the presence of the naphtholic donor group in the ligands. In all cases, a dark brown-reddish solution is obtained while a light orange colour is observed with the first series of ligands (compounds **4a**–**6a**). Thus, the different coordination environment around the copper ions has a dramatic effect on the catalytic competence of the corresponding complex. In previous investigations, a bidentate donor, namely 2,2′-bipyridine (see also Table 2, entry 1), has been reported as an efficient ligand for the [copper/TEMPO]-catalysed oxidation of primary alcohols.[21] In the present study, bidentate pyridine/pyrazole donors (ligands **4a**–**6a**) and pyridine/phenol donors (ligands **4b**–**6b**) have been designed and tested in this copper-mediated reaction. It clearly appears that the use of pyridine/phenol bidentate ligands is not beneficial for this reaction, which should be considered for the design of new catalysts for this reaction.

 © 2007 Wiley-VCH Verlag GmbH & Co. KGaA, Weinheim 

## Conclusions

Two series of pyrazole-based bidentate ligands have been designed and used to coordinate copper ions. As expected and recently suggested by theoretical investigations,[42] the pyridine-pyrazole ligands are capable of stabilizing copper(I) species, so that an air-stable copper(I) coordination polymer could be isolated and characterized by X-ray diffraction. The copper complexes from these ligands show interesting catalytic behaviours. Indeed, high catalytic activities are observed at the beginning of the reaction, which start to significantly decrease after one hour reaction time. Actually, a colourless crystalline precipitate develops in the reaction medium after a reaction time of approximately 15 min. This luminescent solid material is ascribed to copper(I) species (in one case, the crystals obtained in the reaction mixture have been characterized by X-ray diffraction). Therefore, the amount of active species in solution decreases in time, resulting in the observed diminution of the catalytic activity. However, the total conversion of the substrate after a reaction time of 24 h suggests that the (very stable) copper(I) species are slowly re-oxidized by atmospheric oxygen, since the catalyst is not "dead". It appears that the use of naphthol-pyrazole ligands inhibits the catalytic abilities of the corresponding copper complexes, but more studies are required to appraise this ligand effect. For instance, the use of bis-pyrazole and pyridine-phenol ligands are now investigated to compare the catalytic activities of their copper(II) complexes with those reported in the previous[21] and present reports, and evaluate the influence of the phenol (naphthol) ring on the catalysis.

In summary, the results reported in this paper strongly indicate that the combination of well-chosen donors to design a bidentate ligand for this reaction would most likely lead to a very efficient copper catalyst. The mixed ligand should be able to stabilise both the $Cu^{I}$ and $Cu^{II}$ species occurring during the catalytic cycle, but also to allow an easy "switching" between the two oxidation states. Investigations are currently ongoing to find the right combination of donor groups.

## Experimental Section

**General Remarks:** All chemicals were of reagent grade and were used as commercially obtained. Elemental analyses for C, H, and N were performed with a Perkin–Elmer 2400 analyzer. FTIR spectra were recorded with a Perkin–Elmer Paragon 1000 FTIR spectrophotometer, equipped with a Golden Gate ATR device, using the reflectance technique (4000–300 $cm^{-1}$). $^1H$ NMR spectra were recorded on a Bruker DPX 300 (300 MHz) instrument. Chemical shifts are reported in $\delta$ (parts per million) relative to an internal standard of tetramethylsilane. ESI mass analyses were carried out on a Voyager Elite from PerSeptive Biosystems. The excitation and emission spectra were recorded with a Perkin–Elmer LS50B luminescence spectrometer. The intensity of the emission spectra was corrected for the sensitivity of the detector.

**Syntheses of the Ligands:** The preparation of the different ligands was based on an earlier published procedure.[44]

**Synthesis of 3-(Dimethylamino)-1-(pyridin-2-yl)prop-2-en-1-one (3a):**[45] 10 g (0.0825 mol) of 2-acetylpyridine (**1a**) were introduced in a round-bottomed flask. Then, 20 mL (17.9 g, 0.1504 mol) of *N*,*N*-dimethylformamide dimethyl acetal (**2**) were added, and the resulting reaction mixture was refluxed overnight. The dark brown solution obtained was evaporated to dryness. The resulting dark-brown crystalline material was washed with hexane (3 × 100 mL) and with diethyl ether (3 × 100 mL), yielding 10.6 g (yield 73%) of pure, bright yellow **3a**, as previously obtained by Balavoine et al.[45]

**Synthesis of 3-(Dimethylamino)-1-(1-hydroxynaphthalen-2-yl)prop-2-en-1-one (3b):**[46] **3b** was synthesized using the procedure described above for the preparation of **3a**, starting from 5 g (0.0269 mol) of 2-acetyl-1-naphthol. **3b** was obtained as a pure yellow powder,[46] with a yield of 75% (4.9 g).

**Synthesis of 2-(1-Methyl-1*H*-pyrazol-5-yl)pyridine (4a) and 2-(1-Methyl-1*H*-pyrazol-3-yl)pyridine (5a):** 3 g (0.0170 mol) of **3a** and 6 mL (0.1120 mol) of methylhydrazine were mixed in a 50 mL round-bottomed flask containing 10 mL of ethanol. The reaction mixture was heated at 60 °C and stirred for 30 min. After cooling to room temperature, 30 mL of distilled water were added, giving rise to the precipitation of a light yellow solid. This crude product containing both regioisomers, namely **4a** and **5a**, was purified by column chromatography ($SiO_2$, eluent ethyl acetate/hexane, 1:1 until the isolation of the first isomer **4a**; then an ethyl acetate/hexane mixture (8:2) was used as eluent to isolate pure **5a**). Yield 1.43 g of **4a** (53%) and 0.32 g of **5a** (17%).

**Isomer 4a:** $C_9H_9N_3$ (159.19): calcd. C 67.90, H 5.70, N 26.40; found C 68.20, H 5.32, N 25.95. ES(+)-MS: *m*/*z* = 160.04 [M + $H^+$], 181.99 [M + $Na^+$]. FT-IR (neat solid): $\tilde{\nu}$ = 2949, 1589, 1461, 1422, 1388, 1278, 1152, 996, 928, 765, 688, 648, 622, 403 $cm^{-1}$. $^1H$ NMR (300 MHz, $CDCl_3$, 20 °C): $\delta$ = 3.99 (s, 3 H, $CH_3$), 6.35 (d, $^3J_{H,H}$ = 1.9 Hz, 1 H, 4-H pz), 6.95 (dd, $^3J_{H,H}$ = 4.9, $^3J_{H,H}$ = 7.7 Hz, 1 H, 5-H py), 7.29 (d, $^3J_{H,H}$ = 1.9 Hz, 1 H, 3-H pz), 7.32 (d, $^3J_{H,H}$ = 2.0 Hz, 1 H, 3-H py), 7.42 (dd, $^3J_{H,H}$ = 2.0, $^3J_{H,H}$ = 7.7 Hz, 1 H, 4-H py), 8.41 (d, $^3J_{H,H}$ = 4.9 Hz, 1 H, 6-H pz) ppm.

**Isomer 5a:**[47] $C_9H_9N_3$ (159.19): calcd. C 67.90, H 5.70, N 26.40; found C 67.85, H 5.65, N 25.94. ES(+)-MS: *m*/*z* = 160.01 [M + $H^+$]. FT-IR (neat solid): $\tilde{\nu}$ = 2949, 1589, 1459, 1423, 1388, 1277, 1152, 996, 928, 764, 688, 648, 622, 402 $cm^{-1}$. $^1H$ NMR (300 MHz, $CDCl_3$, 20 °C): $\delta$ = 3.97 (s, 3 H, $CH_3$), 6.85 (d, $^3J_{H,H}$ = 2.2 Hz, 1 H, 4-H pz), 7.28 (dd, $^3J_{H,H}$ = 4.8, $^3J_{H,H}$ = 7.8 Hz, 1 H, 5-H py), 7.40 (d, $^3J_{H,H}$ = 2.2 Hz, 1 H, 3-H pz), 7.54 (dd, $^3J_{H,H}$ = 7.8, $^3J_{H,H}$ = 7.9 Hz, 1 H, 4-H py), (d, $^3J_{H,H}$ = 7.9 Hz, 1 H, 3-H py), 8.61 (d, $^3J_{H,H}$ = 4.8 Hz, 1 H, 6-H pz) ppm.

**Synthesis of 2-(1*H*-Pyrazol-3-yl)pyridine (6a):** 3 g (0.0170 mol) of **3a** and 6 mL (0.1235 mol) of hydrazine monohydrate were mixed in a 50 mL round-bottomed flask containing 10 mL of ethanol. The reaction mixture was heated at 60 °C and stirred for 30 min at this temperature. After cooling to room temperature, 30 mL of distilled water were added, producing a light yellow precipitate. This solid was washed on a glass filter with hexane (2 × 200 mL) and diethyl ether (2 × 200 mL). After drying at 100 °C for 4 h, the pure ligand **6a** is obtained. Yield 0.74 g (30%). $C_8H_7N_3$ (145.16): calcd. C 66.19, H 4.86, N 28.95; found C 65.89, H 4.82, N 29.12. ES(+)-MS: *m*/*z* = 146.07 [M + $H^+$], 167.99 [M + $Na^+$]. FT-IR (neat solid): $\tilde{\nu}$ = 3122, 2896, 1590, 1503, 1454, 1417, 1356, 1191, 1000, 876, 758, 615, 403 $cm^{-1}$. $^1H$ NMR (300 MHz, $CDCl_3$, 20 °C): $\delta$ = 6.84 (d, $^3J_{H,H}$ = 1.9 Hz, 1 H, 4-H pz), 7.28 (dd, $^3J_{H,H}$ = 3.6, $^3J_{H,H}$ = 4.9 Hz, 1 H, 5-H py), 7.69 (d, $^3J_{H,H}$ = 1.9 Hz, 1 H, 3-H pz), 7.78 (d, $^3J_{H,H}$ = 3.6 Hz, 1 H, 4-H py), 8.69 (d, $^3J_{H,H}$ = 4.9 Hz, 1 H, 6-H py), 12.11 (s, 1 H, N–H) ppm.

 © 2007 Wiley-VCH Verlag GmbH & Co. KGaA, Weinheim 

**Synthesis of 2-(1-Methyl-1*H*-pyrazol-5-yl)naphthalen-1-ol (4b) and 2-(1-Methyl-1*H*-pyrazol-3-yl)naphthalen-1-ol (5b):** 3 g (0.0124 mol) of **3b** and 6 mL (0.1120 mol) of methylhydrazine were mixed in a 50 mL round-bottomed flask containing 10 mL of ethanol. The reaction mixture was heated at 60 °C, and stirred for 30 min at this temperature. After cooling to room temperature, 30 mL of distilled water were added, resulting in a light brown emulsion. This solution was extracted with dichloromethane (3 × 50 mL). The pooled organic phase was dried with magnesium sulfate, filtered, and the solvent was evaporated under reduced pressure. The resulting brown viscous crude compound was purified by column chromatography ($SiO_2$, ethyl acetate/hexane, 1:1), yielding 1.6 g of **4b** (58%) and 0.78 g of **5b** (28%).

**Isomer 4b:**[48] $C_{14}H_{12}N_2O$ (224.26): calcd. C 74.98, H 5.39, N 12.49; found C 74.92, H 5.17, N 12.53. M.p. 85 °C. ES(+)-MS: *m*/*z* = 224.91 [M + H$^+$]. FT-IR (neat solid): $\tilde{\nu}$ = 2938, 1576, 1495, 1386, 1354, 1089, 805, 755, 745, 698, 659, 572, 486, 422 cm$^{-1}$. $^1$H NMR (300 MHz, $CDCl_3$, 20 °C): $\delta$ = 3.98 (s, 3 H, $CH_3$), 6.68 (d, $^3J_{H,H}$ = 2.3 Hz, 1 H, 4-H pz), 7.38 (d, $^3J_{H,H}$ = 8.6 Hz, 1 H, 4-H naphthol), 7.43 (d, $^3J_{H,H}$ = 2.3 Hz, 1 H, 3-H pz), 7.45 (dd, $^3J_{H,H}$ = 4.8 Hz, 1 H, 6-H naphthol), 7.49 (dd, $^3J_{H,H}$ = 3.9 Hz, 1 H, 7-H naphthol), 7.65 (d, $^3J_{H,H}$ = 8.6 Hz, 1 H, 3-H naphthol), 7.77 (d, $^3J_{H,H}$ = 4.8 Hz, 1 H, 5-H naphthol), 8.42 (d, $^3J_{H,H}$ = 3.9 Hz, 1 H, 8-H naphthol), 11.60 (br. s, 1 H, O–H) ppm. $^{13}$C NMR (75 MHz, $CDCl_3$, 20 °C): $\delta$ = 38.3, 101.9, 109.7, 118.5, 122.7, 123.6, 125.0, 125.3, 126.2, 127.2, 130.7, 133.8, 151.2, 151.4 ppm.

Single-crystals of **4b** were obtained, which were analysed by X-ray diffraction. An ORTEP view of ligand **4b** is depicted in Figure S8. The molecular structure is uneventful and as expected.

**Isomer 5b:**[48] $C_{14}H_{12}N_2O$ (224.26): calcd. C 74.98, H 5.39, N 12.49; found C 74.57, H 5.14, N 12.49. M.p. 142 °C. ES(+)-MS: *m*/*z* = 224.98 [M + H$^+$]. FT-IR (neat solid): $\tilde{\nu}$ = 2943, 1571, 1389, 1292, 1199, 1074, 809, 788, 739, 667, 570, 484, 436, 423 cm$^{-1}$. $^1$H NMR (300 MHz, $CDCl_3$, 20 °C): $\delta$ = 3.80 (s, 3 H, $CH_3$), 6.43 (d, $^3J_{H,H}$ = 1.8 Hz, 1 H, 4-H pz), 7.25 (d, $^3J_{H,H}$ = 8.2 Hz, 1 H, 4-H naphthol), 7.49 (d, $^3J_{H,H}$ = 8.2 Hz, 1 H, 3-H naphthol), 7.53–7.59 (m, 2 H, 6-H naphthol + 7-H naphthol), 7.61 (d, $^3J_{H,H}$ = 1.8 Hz, 1 H, 3-H pz), 7.84 (d, $^3J_{H,H}$ = 9.3 Hz, 1 H, 5-H naphthol), 8.33 (d, $^3J_{H,H}$ = 9.5 Hz, 1 H, 8-H naphthol), 11.72 (br. s, 1 H, O–H) ppm. $^{13}$C NMR (75 MHz, $CDCl_3$, 20 °C): $\delta$ = 36.8, 106.8, 110.3, 119.8, 122.8, 125.1, 125.6, 127.1, 127.2, 127.4, 134.8, 138.7, 139.6, 150.4 ppm.

**Synthesis of 2-(1*H*-Pyrazol-5-yl)naphthalen-1-ol (6b):**[48] 2.76 g (0.0114 mol) of **3b** and 6 mL (0.1235 mol) of hydrazine monohydrate were mixed in a 50 mL round-bottomed flask containing 9 mL of ethanol. The reaction mixture was heated at 60 °C and stirred for 30 min at this temperature. After cooling to room temperature, 30 mL of distilled water were added, producing a light brown crystalline product. This solid was filtered off, and washed with hexane (2 × 200 mL). After drying at 100 °C for 4 h, the pure ligand **6b** was obtained. Yield 1.8 g (75%). $C_{13}H_{10}N_2O$ (210.23): calcd. C 74.27, H 4.79, N 13.33; found C 74.16, H 4.99, N 13.18. ES(+)-MS: *m*/*z* = 210.92 [M$^+$], 232.92 [M + Na$^+$]. FT-IR (neat solid): $\tilde{\nu}$ = 3303, 3054, 1636, 1579, 1505, 1389, 1283, 1077, 976, 878, 759, 720, 656, 571, 484, 420 cm$^{-1}$. $^1$H NMR (300 MHz, $CDCl_3$, 20 °C): $\delta$ = 6.80 (d, $^3J_{H,H}$ = 2.6 Hz, 1 H, 4-H pz), 7.41 (d, $^3J_{H,H}$ = 8.6 Hz, 1 H, 4-H naphthol), 7.46–7.53 (m, 2 H, 3-H naphthol + 6-H naphthol), 7.67–7.70 (m, 2 H, 7-H naphthol + 3-H pz), 7.78 (d, $^3J_{H,H}$ = 9.4 Hz, 1 H, 5-H naphthol), 8.43 (d, $^3J_{H,H}$ = 9.7 Hz, 1 H, 8-H naphthol), 10.2–10.8 (v br. s, 2 H, O–H + N–H) ppm.

**Preparation of the Coordination Compounds**

**Synthesis of [$Cu_2$(4a)$_2Br_2$]$_n$ (7):** A solution of ligand **4a** (100 mg, 0.628 mmol) in methanol (10 mL) was added to a solution of copper(II) bromide (140 mg, 0.628 mmol) in methanol (10 mL). The resulting dark-green solution was filtered and the filtrate was left unperturbed for the slow evaporation of the solvent. After one day, colourless crystals of **7** were collected (yield 146 mg, 77%). $C_{18}H_{18}Br_2Cu_2N_6$ (605.28): calcd. C 35.72, H 3.00, N 13.88; found C 35.20, H 2.93, N 13.72. IR (neat): $\tilde{\nu}$ = 3119, 3051, 1599, 1465, 1420, 1390, 1284, 1225, 1009, 940, 808, 786, 755, 700, 645, 542, 414 cm$^{-1}$. Unit cell parameters: *a* = 7.668(2) Å, *b* = 8.492(2) Å, *c* = 9.174(2) Å, $\alpha$ = 96.90(3)°, $\beta$ = 114.06(3)°, $\gamma$ = 107.49(3)° (see Table S1).

The same coordination compound (as evidenced by single-crystal X-ray analysis) was obtained from an acetonitrile solution of the reactants (using the same concentration), but after one week (instead of one day in methanol).

Complex **7** has also been isolated during the catalysis reactions, and characterized by X-ray diffraction analysis.

Complex **7** is insoluble in common solvents such as methanol, acetonitrile, THF, chloroform and dichloromethane. Consequently, NMR studies of the solution structure of the diamagnetic complex are not possible.

Complex **7** can also be prepared directly from CuBr and the ligand **4a**, using the following reaction conditions: a solution of ligand **4a** (25 mg, 0.157 mmol) in acetonitrile (5 mL) was added to a solution of copper(I) bromide (23 mg, 0.157 mmol) in acetonitrile (5 mL). The resulting light-green solution was filtered and the filtrate was left unperturbed for the slow evaporation of the solvent. After two hours, colourless crystals of **7** started to grow. The crystals were collected after one day (yield 31 mg, 33%). $C_{18}H_{18}Br_2Cu_2N_6$ (605.28): calcd. C 35.72, H 3.00, N 13.88; found C 35.31, H 2.82, N 13.75. IR (neat): $\tilde{\nu}$ = 3119, 3054, 1560, 1464, 1418, 1392, 1284, 1225, 1010, 940, 808, 786, 755, 700, 645, 543, 414 cm$^{-1}$. The structure, corresponding to complex **7**, was confirmed by X-ray diffraction analysis. Unit cell parameters: *a* = 7.661(2) Å, *b* = 8.502(2) Å, *c* = 9.160(2) Å, $\alpha$ = 96.90(3)°, $\beta$ = 114.12(3)°, $\gamma$ = 107.39(3)°.

**Synthesis of [Cu(4aH)Br$_3$] (8):** Red crystals of **8** were obtained from the solution above. Since these few single-crystals were mixed with crystals of **7**, they were only characterised by X-ray diffraction (see Discussion). Unit cell parameters: *a* = 7.611(2) Å, *b* = 7.908(2) Å, *c* = 11.787(2) Å, $\alpha$ = 104.99(3)°, $\beta$ = 100.48(3)°, $\gamma$ = 94.75(3)° (see Table S1).

However, complex **8** could also be synthesized from $CuBr_2$ and **4a**·HBr according to the following procedure: 18 μL (0.157 mmol) of $HBr_{aq}$ 48% were added to a solution of ligand **4a** (25 mg, 0.157 mmol) in 5 mL of acetonitrile. The solution was stirred for 10 min, and 35 mg (0.157 mmol) of $CuBr_2$ were subsequently added. The resulting dark-green solution was filtered and the filtrate was left unperturbed for the slow evaporation of the solvent. After one day, red needle-shaped crystals were collected (yield 17 mg, 23%). $C_9H_{10}Br_3CuN_3$ (463.45): calcd. C 23.32, H 2.17, N 9.07; found C 23.10, H 2.63, N 9.12. IR (neat): $\tilde{\nu}$ = 2934, 2879, 1633, 1612, 1558, 1490, 1447, 1422, 1392, 1285, 1226, 1186, 1168, 1062, 1009, 914, 815, 764, 684, 640, 524, 469, 378 cm$^{-1}$. The structure, corresponding to complex **8**, was confirmed by X-ray diffraction analysis. Unit cell parameters: *a* = 7.598(2) Å, *b* = 7.892(2) Å, *c* = 11.785(2) Å, $\alpha$ = 105.12(3)°, $\beta$ = 100.39(3)°, $\gamma$ = 94.81(3)°.

Complex **8** could be obtained as well by addition of HBr to a solution of complex **7**. As for the preparation of complex **7** (from CuBr,

 © 2007 Wiley-VCH Verlag GmbH & Co. KGaA, Weinheim 

see above), a solution of one equivalent (25 mg, 0.157 mmol) of **4a** in 5 mL of acetonitrile was added to a solution of one equivalent of copper(I) bromide (23 mg, 0.157 mmol) in acetonitrile (5 mL). The resulting light-green solution was stirred for 15 min. Next, 18 μL (0.157 mmol) of $HBr_{aq}$ 48% were added, which resulted in an immediate change of the colour of the reaction mixture to dark-green. The solution was filtered and the filtrate was left unperturbed for the slow evaporation of the solvent. After one day, red needle-shaped crystals were collected (yield 10 mg, 14%). $C_9H_{10}Br_3CuN_3$ (463.45): calcd. C 23.32, H 2.17, N 9.07; found C 23.15, H 2.25, N 8.93. IR (neat): $\tilde{\nu}$ = 2934, 2878, 1633, 1612, 1558, 1490, 1447, 1423, 1393, 1285, 1226, 1186, 1168, 1063, 1010, 914, 815, 764, 684, 640, 524, 470, 379 $cm^{-1}$. The structure, corresponding to complex **8**, was confirmed by X-ray diffraction analysis. Unit cell parameters: $a$ = 7.605(2) Å, $b$ = 7.911(2) Å, $c$ = 11.792(2) Å, $\alpha$ = 104.96(3)°, $\beta$ = 100.45(3)°, $\gamma$ = 94.70(3)°.

**Synthesis of $[Cu_3(5a)_3Br_6]$ (9):** A solution of ligand **5a** (100 mg, 0.628 mmol) in acetonitrile (10 mL) was added to a solution of copper(II) bromide (140 mg, 0.628 mmol) in acetonitrile (10 mL). The resulting dark green-brown solution was filtered, and the filtrate was left unperturbed. After 10 min, red needle-shaped crystals of **9**, suitable for X-ray diffraction analysis, started to grow. After one day, the crystals were collected (yield 204 mg, 85%). $C_{27}H_{27}Br_6Cu_3N_9$ (1147.63): calcd. C 28.26, H 2.37, N 10.98; found C 28.29, H 1.95, N 11.19. IR (neat): $\tilde{\nu}$ = 3130, 1609, 1502, 1436, 1366, 1284, 1234, 1154, 1075, 1019, 896, 772, 719, 685, 643, 610, 417 $cm^{-1}$.

Complex **9** was also obtained (as evidenced by single-crystal X-ray analysis) from a methanolic solution of the reactants, exhibiting the same molar concentration.

**Synthesis of $[Cu(6a)_2Br]Br\cdot H_2O\cdot CH_3CN$ (10):** A solution of ligand **6a** (100 mg, 0.689 mmol) in acetonitrile (10 mL) was added to a solution of copper(II) bromide (154 mg, 0.689 mmol) in acetonitrile (10 mL). The resulting green solution was filtered, and the filtrate was left unperturbed for the slow evaporation of the solvent. After a few days, green block-shaped crystals of **10** were obtained (yield 142 mg, based on the ligand, 72%). $C_{18}H_{19}Br_2CuN_7O$ (572.74): calcd. C 37.75, H 3.34, N 17.12; found C 37.50, H 3.62, N 17.03. IR (neat): $\tilde{\nu}$ = 3301, 3113, 1610, 1454, 1442, 1432, 1375, 1290, 1187, 1090, 1060, 1016, 972, 768, 699, 642, 568, 487, 419 $cm^{-1}$.

**Typical Catalytic Experiment:** Benzyl alcohol (1.08 g, 10 mmol) was dissolved in 15 mL of acetonitrile. 112 mg (0.5 mmol) of copper(II) bromide were then added, followed by 0.5 mmol of ligand. Next, 78 mg (0.5 mmol) of TEMPO were added, resulting in a dark green solution. Finally, the oxidation reaction was initiated by the addition of 51 mg (0.5 mmol, 70 μL) of triethylamine, causing an instantaneous change of colour, from dark green to orange. The course of the reaction was monitored by gas chromatography (GC).

**X-Ray Crystal Structure Determinations:** Crystallographic data and refinement details are given in Tables S1 and S2. A crystal was selected for the X-ray measurements and mounted to the glass fiber using the oil drop method[49] and data were collected at 173 K (or 150 K for compound **10**) on a Nonius Kappa CCD diffractometer (Mo-$K_\alpha$ radiation, graphite monochromator, $\lambda$ = 0.71073). The intensity data were corrected for Lorentz and polarization effects, and for absorption. The programs collect,[50] SHELXS-97,[51] SHELXL-97[52] were used for data reduction, structure solution and structure refinement, respectively. The non-hydrogen atoms were refined anisotropically. The H atoms were introduced in calculated positions and refined with fixed geometry with respect to their carrier atoms.

CCDC-643549 to -643552 (for **4b**–**9**) and -643309 (for **10**) contain the supplementary crystallographic data for this paper. These data can be obtained free of charge from The Cambridge Crystallographic Data Centre via www.ccdc.cam.ac.uk/data_request/cif.

**Supporting Information** (see also the footnote on the first page of this article): Crystallographic data for compounds **4b** and **7**–**10**, crystal structure of **4b**, crystal packing diagrams for **7**–**10**, excitation and luminescent spectra of **7**.

## Acknowledgments

This work has been supported financially by the Graduate Research School Combination "Catalysis", a joint activity of the graduate research schools NIOK, HRSMC and PTN. Financial support from European Cooperation in the Field of Science and Technology (COST) Action D35/0011, Werkgroep Fundamenteel Materialen Onderzoek (WFMO) Nederlandse Organisatie voor Wetenschappelijk Onderzoek (NWO) – Foundation for the Chemical Sciences (Chemische Wetenschappen, CW), are gratefully acknowledged. Coordination by the FP6 Network of Excellence "Magmanet" (contract number 515767) is also kindly acknowledged. We would also like to thank Paul de Hoog for his help with the NMR studies.

[1] R. A. Sheldon, *J. Chem. Technol. Biotechnol.* **1997**, *68*, 381–388.
[2] R. A. Sheldon, *Chem. Tech.* **1991**, *21*, 566–576.
[3] G. Cainelli, G. Cardillo, in *Chromium Oxidations in Organic Chemistry*, Springer, Berlin, **1984**.
[4] W. S. Trahanovsky, in *Oxidation in Organic Chemistry*, Academic Press, New York, **1978**.
[5] E. J. Corey, G. Schmidt, *Tetrahedron Lett.* **1979**, *20*, 399–402.
[6] A. J. Mancuso, D. Swern, *Synthesis* **1981**, 165–185.
[7] R. A. Sheldon, I. Arends, G. J. Ten Brink, A. Dijksman, *Acc. Chem. Res.* **2002**, *35*, 774–781.
[8] P. Chaudhuri, M. Hess, J. Muller, K. Hildenbrand, E. Bill, T. Weyhermuller, K. Wieghardt, *J. Am. Chem. Soc.* **1999**, *121*, 9599–9610.
[9] P. Paraskevopoulou, N. Psaroudakis, S. Koinis, P. Stavropoulos, K. Mertis, *J. Mol. Catal. A* **2005**, *240*, 27–32.
[10] H. L. Wu, Q. H. Zhang, Y. Wang, *Adv. Synth. Catal.* **2005**, *347*, 1356–1360.
[11] M. J. Schultz, S. S. Hamilton, D. R. Jensen, M. S. Sigman, *J. Org. Chem.* **2005**, *70*, 3343–3352.
[12] E. Zueva, P. H. Walton, J. E. McGrady, *Dalton Trans.* **2006**, 159–167.
[13] K. Mori, T. Hara, T. Mizugaki, K. Ebitani, K. Kaneda, *J. Am. Chem. Soc.* **2004**, *126*, 10657–10666.
[14] W. Adam, C. R. Saha-Moller, P. A. Ganeshpure, *Chem. Rev.* **2001**, *101*, 3499–3548.
[15] A. E. J. de Nooy, A. C. Besemer, H. vanBekkum, *Synthesis* **1996**, 1153–1174.
[16] T. Inokuchi, S. Matsumoto, S. Torii, *J. Synth. Org. Chem. Jpn.* **1993**, *51*, 910–920.
[17] P. Gamez, I. W. C. E. Arends, J. Reedijk, R. A. Sheldon, *Chem. Commun.* **2003**, 2414–2415.
[18] R. A. Sheldon, I. W. C. E. Arends, *Adv. Synth. Catal.* **2004**, *346*, 1051–1071.
[19] D. Geisslmeier, W. G. Jary, H. Falk, *Monatsh. Chem.* **2005**, *136*, 1591–1599.
[20] N. Jiang, A. J. Ragauskas, *Org. Lett.* **2005**, *7*, 3689–3692.
[21] P. Gamez, I. W. C. E. Arends, R. A. Sheldon, J. Reedijk, *Adv. Synth. Catal.* **2004**, *346*, 805–811.
[22] P. Gamez, I. A. Koval, J. Reedijk, *Dalton Trans.* **2004**, 4079–4088.
[23] P. Gamez, J. von Harras, O. Roubeau, W. L. Driessen, J. Reedijk, *Inorg. Chim. Acta* **2001**, *324*, 27–34.

 © 2007 Wiley-VCH Verlag GmbH & Co. KGaA, Weinheim 

[24] A. L. Spek, *Platon, A Multipurpose Crystallographic Tool*, Utrecht University, The Netherlands, **2006**.
[25] L. Yang, D. R. Powell, R. P. Houser, *Dalton Trans.* **2007**, 955–964.
[26] J. C. Dyason, L. M. Engelhardt, P. C. Healy, C. Pakawatchai, A. H. White, *Inorg. Chem.* **1985**, *24*, 1950–1957.
[27] E. Bosch, C. L. Barnes, *J. Coord. Chem.* **2003**, *56*, 329–336.
[28] J. Wang, S. L. Zheng, S. Hu, Y. H. Zhang, M. L. Tong, *Inorg. Chem.* **2007**, *46*, 795–800.
[29] P. C. Ford, E. Cariati, J. Bourassa, *Chem. Rev.* **1999**, *99*, 3625–3647.
[30] A. Luque, J. Sertucha, L. Lezama, T. Rojo, P. Roman, *J. Chem. Soc. Dalton Trans.* **1997**, 847–854.
[31] M. M. Thackeray, L. R. Nassimbeni, *Acta Crystallogr., Sect. B* **1974**, *30*, 2469–2473.
[32] S. Haddad, R. D. Willett, *J. Chem. Crystallogr.* **2001**, *31*, 37–43.
[33] R. D. Willett, K. Halvorson, *Acta Crystallogr., Sect. B* **1988**, *44*, 2068–2071.
[34] T. J. Mooibroek, P. Gamez, *Inorg. Chim. Acta* **2007**, *360*, 381–404.
[35] A. M. Atria, R. F. Baggio, N. Espinosa, M. T. Garland, J. Manzur, Y. Moreno, E. Spodine, *Acta Crystallogr., Sect. C* **1994**, *50*, 1066–1069.
[36] M. B. Bushuev, V. P. Krivopalov, N. V. Semikolenova, E. V. Peresypkina, A. V. Virovets, L. A. Sheludyakova, L. G. Lavrenova, V. A. Zakharov, S. V. Larionov, *Russ. J. Coord. Chem.* **2006**, *32*, 199–207.
[37] A. W. Addison, T. N. Rao, J. Reedijk, J. van Rijn, G. C. Verschoor, *J. Chem. Soc. Dalton Trans.* **1984**, 1349–1356.
[38] M. T. Garland, D. Grandjean, *Acta Crystallogr., Sect. C* **1987**, *43*, 643–645.
[39] A. Morsali, A. Ramazani, M. Babaee, F. Jamali, F. Gouranlou, H. Arjmandfar, A. Yanovsky, *J. Coord. Chem.* **2003**, *56*, 455–461.
[40] C. M. Pask, K. D. Camm, N. J. Bullen, M. J. Carr, W. Clegg, C. A. Kilner, M. A. Halcrow, *Dalton Trans.* **2006**, 662–664.
[41] I. W. C. E. Arends, P. Gamez, R. A. Sheldon, *Adv. Inorg. Chem.* **2006**, *58*, 235–279.
[42] S. Sivasankar, N. Sadhukhan, J. K. Bera, A. G. Samuelson, *New J. Chem.* **2007**, *31*, 385–393.
[43] A. P. Sadimenko, S. S. Basson, *Coord. Chem. Rev.* **1996**, *147*, 247–297.
[44] L. D. Pachón, A. Golobic, B. Kozlevcar, P. Gamez, H. Kooijman, A. L. Spek, J. Reedijk, *Inorg. Chim. Acta* **2004**, *357*, 3697–3702.
[45] E. Bejan, H. A. Haddou, J. C. Daran, G. G. A. Balavoine, *Synthesis* **1996**, 1012–1015.
[46] Y. I. Lin, S. A. Lang, *J. Heterocycl. Chem.* **1977**, *14*, 345–347.
[47] W. R. Thiel, M. Angstl, T. Priermeier, *Chem. Ber.* **1994**, *127*, 2373–2379.
[48] J. Catalan, J. C. Delvalle, R. M. Claramunt, M. D. S. Maria, V. Bobosik, R. Mocelo, J. Elguero, *J. Org. Chem.* **1995**, *60*, 3427–3439.
[49] T. Kottke, D. Stalke, *J. Appl. Crystallogr.* **1993**, *26*, 615–619.
[50] Nonius, *COLLECT*, Nonius BV, Delft, The Netherlands, **2002**.
[51] G. M. Sheldrick, *SHELXS-97 Program for Crystal Structure Determination*, University of Göttingen, Germany, **1997**.
[52] G. M. Sheldrick, *SHELXL-97-2 Program for Crystal Structure Refinement*, University of Göttingen, Germany, **1997**.

Received: April 18, 2007
Published Online: July 17, 2007

 © 2007 Wiley-VCH Verlag GmbH & Co. KGaA, Weinheim 

DOI: 10.1002/ejic.200700275

# Organoiridium Quinolinolate Complexes: Synthesis, Structures, Thermal Stabilities and Photophysical Properties

**Stefan Kappaun,[a] Sabrina Eder,[b] Stefan Sax,[b] Kurt Mereiter,[c] Emil J. W. List,[b] and Christian Slugovc*[a]**

**Keywords:** Iridium / N,O ligands / Luminescence / Nitrogen heterocycles

The syntheses, solid-state structures, thermal properties and photophysics of a series of heteroleptic iridium(III) complexes with phenylpyridine as the cyclometalating ligands and quinolinolates are reported. The title compounds were formed by reaction of di-μ-chloro-tetrakis[$\kappa^2(C^2,N)$-2-phenylpyridine]-diiridium(III) with the corresponding 8-hydroxyquinolines in 56 to 86 % yield. The crystal structures of two of the complexes have been determined. Both complexes show the two carbon ligands in a *cis* disposition and the 2-phenylpyridine nitrogen atoms in a *trans* disposition. Assessment of the thermal stabilities of the compounds revealed huge differences depending on the substituents on the quinolinolato ligand. Most complexes are poor emitters in solution, in films and in OLEDs. Substitution of the quinolinolato ligand with electron-withdrawing functional groups in the 5-position caused additional absorption features in the visible region facilitating the finding of appropriate host materials for OLEDs and gave emission properties governed by the quinolinolato ligand.

(© Wiley-VCH Verlag GmbH & Co. KGaA, 69451 Weinheim, Germany, 2007)

## Introduction

The design, synthesis and characterisation of phosphorescent light-emitting materials have received considerable attention in the last couple of years due to a series of possible practical applications such as in organic light-emitting diodes (OLEDs),[1] light-emitting electrochemical cells (LECs)[2] or for sensing purposes.[3] Although tremendous improvements concerning device lifetimes, efficiencies, brightness and device structures[4] have been made for phosphorescent metal complexes containing platinum, osmium and iridium,[1,5] there is still a great demand for stable emitter materials that cover the entire visible spectrum.[6]

Among this class of materials, cyclometalated iridium(III) complexes have emerged as very promising candidates because of the powerful colour-tuning from blue to red brought about by variations in the cyclometalating ligands or extension of the corresponding conjugated ligand systems.[4] However, the drawbacks of this approach are the cumbersome synthesis of the μ-chloro-bridged precursor material. Harsh conditions are needed for the preparation of tris(cyclometallated) iridium(III) complexes and the formation of several by-products also occurs.[4,7] In contrast to the difficulties with the preparation of these homoleptic iridium(III) complexes, an alternative approach is based on the incorporation of ancillary ligands such as acetylacetonato, picolinato, triazolato or tetrazolato derivatives with clearly facilitated synthetic procedures.[4a] On the other hand, only a few examples of heteroleptic iridium(III) complexes with emission properties dominated by the third ligand have been reported[4,8] which is clearly disadvantageous for a fast and versatile approach to colour-tuneable phosphorescent emitter materials.

During the last two decades a large number of reports have been published concentrating on the design and characterisation of luminescent metal complexes bearing 8-hydroxyquinoline and its derivatives as ligands.[9] 8-Hydroxyquinolines are of particular interest because of the possibility of tuning the energy gap by the simple attachment of electron-donating or electron-withdrawing groups and the commercial availability of many 8-hydroxyquinoline derivatives.[6,9] Although considerable scientific efforts have been focused on studying luminescent metal complexes of aluminium, platinum, palladium or boron containing 8-hydroxyquinolines as ligands, corresponding investigations on the impact of ligand modifications on the materials properties of organoiridium quinolinolate complexes are rare.[10]

Recently we reported on heteroleptic iridium(III) complexes bearing 8-hydroxyquinolines as ligands for the preparation of white organic light-emitting diodes (WOLEDs)

[a] Institute of Chemistry and Technology of Organic Materials (ICTOS), Graz University of Technology,
Stremayrgasse 16, 8010 Graz, Austria
E-Mail: slugovc@tugraz.at
[b] Institute of Solid-State Physics and CD-Laboratory, Advanced Functional Materials, Graz University of Technology,
Petersgasse 16, 8010 Graz, Austria
[c] Institute of Chemical Technologies and Analytics, Vienna University of Technology, Getreidemarkt 9/164SC, 1060 Vienna, Austria

Supporting information for this article is available on the WWW under http://www.eurjic.org or from the author.

 © 2007 Wiley-VCH Verlag GmbH & Co. KGaA, Weinheim 

and communicated our first results on the colour-tuning of organoiridium quinolinolate complexes with emission properties controlled by the quinolinolato ligand.[11] In this work we wish to present the synthesis, structures, thermal and photophysical properties of a series of derivatives of bis[κ²(*C*²,*N*)-2-phenylpyridine][κ²(*N*,*O*)-8-quinolinolato]iridium(III). The presented systematic study on the influence of functional groups on materials properties corresponds to recent reports on iridium(III) complexes tailored towards particular needs[1c,11] and provides a step towards a general toolbox for realising low-cost and colour-tuneable iridium(III) compounds for, e.g., OLED applications. Parts of this work have been communicated briefly.[11b]

## Results and Discussion

The compounds under investigation were prepared as depicted in Scheme 1. According to a literature procedure starting from $IrCl_3 \cdot nH_2O$ (**1**) and 2-phenylpyridine (**2**),[12] the μ-chloro-bridged precursor material di-μ-chloro-tetrakis[κ²(*C*²,*N*)-2-phenylpyridine]diiridium(III) (**3**) could be obtained by heating the black coloured reaction mixture to reflux, in 2-ethoxyethanol and water, at 120 °C for 24 h. Purification of **3** was achieved by filtration of the greenish precipitate which formed during the reaction and repeated washing of the solid residue with hot MeOH. The various derivatives of bis[κ²(*C*²,*N*)-2-phenylpyridine][κ²(*N*,*O*)-8-quinolinolato]iridium(III) (**5a**–**5j**; for nomenclature see Exp. Sect.) were synthesised by treating **3** with 2.1 to 2.5 equiv. of the corresponding 8-hydroxyquinoline (**4a**–**4j**) in $CH_2Cl_2$, EtOH and $Et_3N$ at 80 °C for 20 h.[11] Work-up of the organoiridium(III) complexes **5a**–**5j** turned out to be straightforward and was achieved by filtration and subsequent washing of the yellow to deeply red solids with hot MeOH several times affording yields between 56 and 86% of the pure products. It is worth noting that with the exception of **4g** all 8-hydroxyquinoline derivatives were obtained from commercial sources. Compound **4g** was prepared by means of a Suzuki cross-coupling reaction of 8-benzyloxy-5,7-dibromoquinoline and phenylboronic acid in a solvent mixture of toluene, EtOH and water with $Na_2CO_3$ as a base and $[Pd(PPh_3)_4]$ as catalyst. Removal of the benzyloxy protecting group was achieved by treatment with $BF_3 \cdot Et_2O$ and KI in $CH_3CN$ as reported recently.[13]

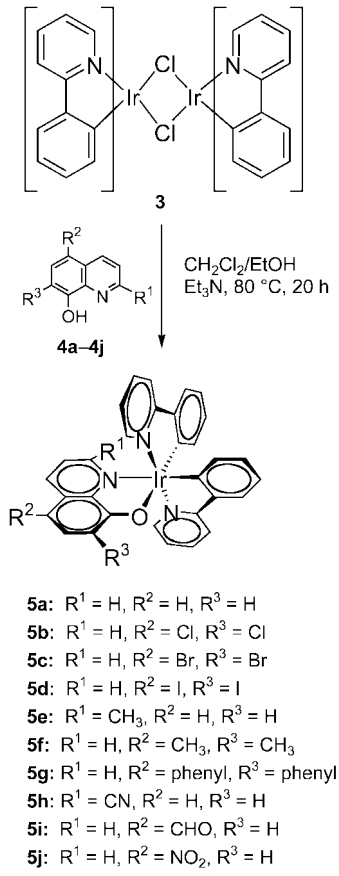


Scheme 1. Synthesis of bis[κ²(*C*²,*N*)-2-phenylpyridine][κ²(*N*,*O*)-8-quinolinolato]iridium(III) derivatives **5a**–**5j**.

Compounds **5a**–**5j** were characterised by $^1$H- and $^{13}$C-NMR spectroscopy, absorption and fluorescence measurements as well as matrix-assisted laser desorption ionisation time-of-flight (MALDI-TOF) MS. Furthermore, the thermal behaviour and the impact of ligand modifications on the thermal stability were probed by combined DSC/TGA measurements.

NMR spectroscopy has been shown to be a powerful tool for the characterisation of homo- and heteroleptic iridium(III) complexes.[14] Because organoiridium quinolinolate complexes have hitherto rarely been studied,[10,11] we herein present our interpretation and assignment of the proton NMR spectroscopic peaks of **5b** (Figure 1). Based on these results, the interpretation of the NMR spectra of the other studied compounds can also be easily performed as given in the Experimental Section.[11]

As shown in Figure 1 for **5b** in $[D_6]$DMSO, there are considerable differences in the shift values of the protons of the two phenylpyridine ligands resulting from the asymmetrical character of the quinolinolato ligand. Thus, different shifts especially for the protons of $Py^6$ ($\delta$ = 8.39 and 7.59–7.55 ppm), $Py^3$ (8.21 and 8.16 ppm) and $Py^5$ (7.30 and 7.10 ppm) can be observed. Less drastic differences may be found for the protons of the phenyl rings. While the peaks of $Ph^6$ are located at low-field around 7.91–7.80 ppm, the peaks for $Ph^5$ (6.93–6.87 ppm), $Ph^4$ (6.79 and 6.74 ppm) and $Ph^3$ (6.26 and 6.11 ppm) are shifted towards higher fields with an increased proximity to the metalation centre. For the quinolinolato ligand, the protons of $Q^4$, $Q^6$, $Q^2$ and $Q^3$ are located at 8.35, 7.74, 7.71 and 7.59–7.55 ppm, respectively. It is worth noting that for these complexes metalation causes a shift to higher-fields for $Q^2$, while for other metal complexes of quinolinolates, e.g. for organoboron quinolinolates, significantly higher shift-values are obtained.[9d]

For the corresponding carbon NMR spectra, similar results caused by the asymmetrical character of the quinolinolato ligand can be found for **5b** in $[D_6]$DMSO. Consequently, slightly different shift-values were obtained for all

 © 2007 Wiley-VCH Verlag GmbH & Co. KGaA, Weinheim 

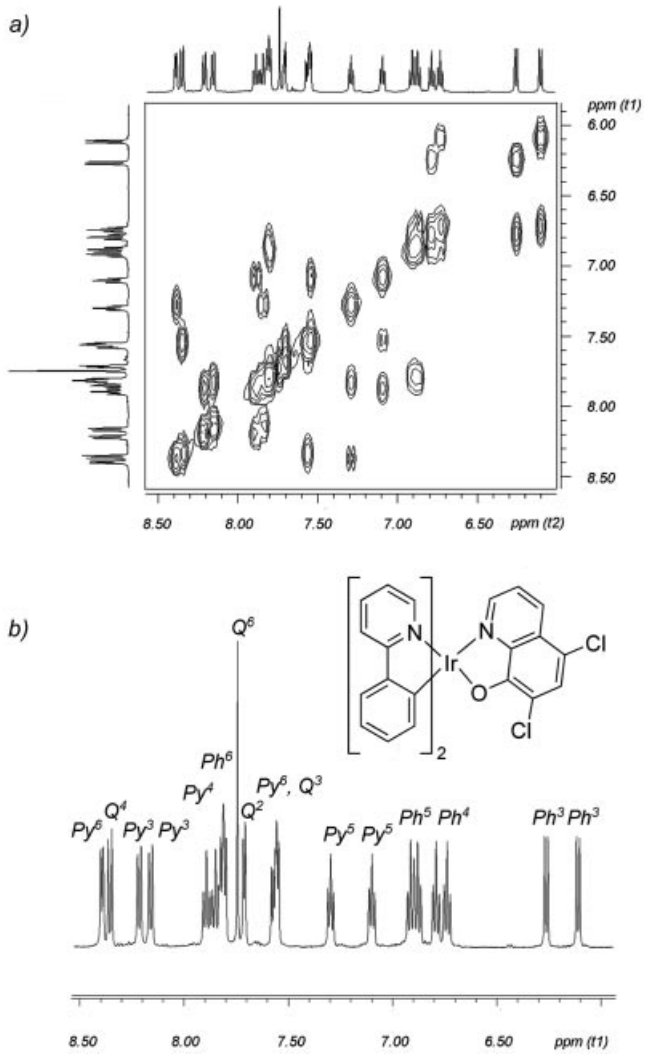


Figure 1. a) H,H-COSY NMR spectrum of **5b** and b) assignment of the $^1$H NMR spectroscopic peaks based on the proton-correlation experiment (spectra recorded in [D$_6$]DMSO).

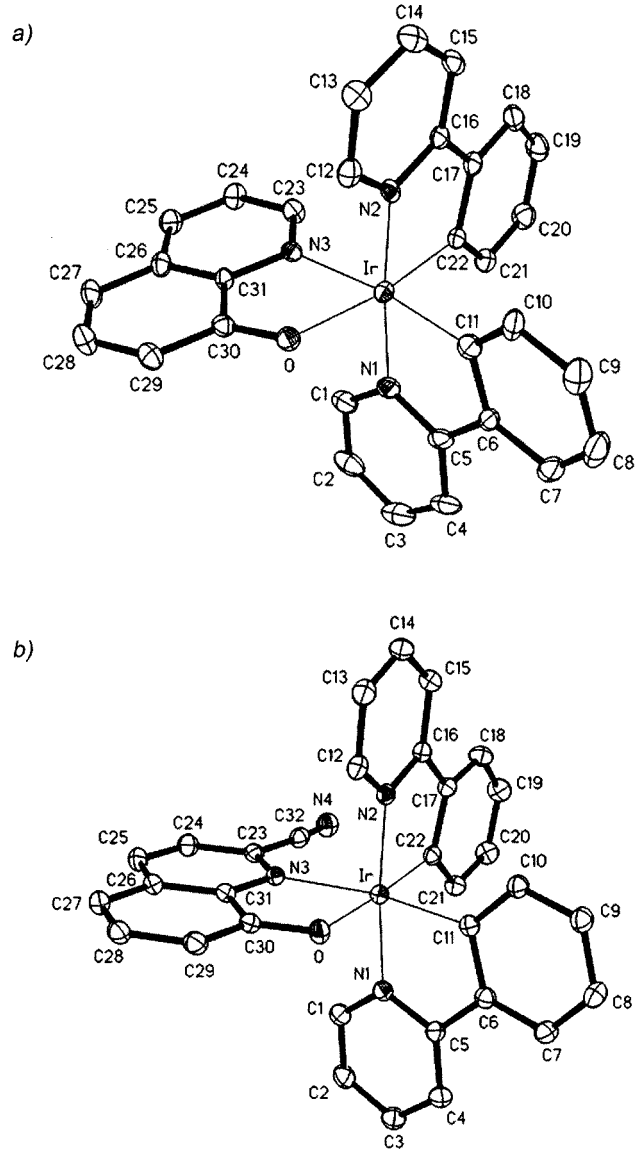


Figure 2. Structural views of a) **5a** and b) **5h** (40% ellipsoids, H atoms and cocrystallised diethyl ether in **5h** omitted). Key bond lengths and angles are given in Table 1.

carbon atoms of the phenylpyridine ligands as they are listed in the Experimental Section. For the other compounds under investigation, no unexpected NMR spectroscopic features were observed and all spectra are in accordance with the proposed structures.[11]

To further confirm the structural identities of the described organoiridium quinolinolate complexes, we tried to grow single-crystals from ether diffusion into saturated $CH_2Cl_2$ solutions and by layering $CH_2Cl_2$ solutions with *n*-pentane. Although all complexes could be crystallised by these methodologies, single-crystals suitable for X-ray diffraction were obtained only for **5a**, **5c**,[11a] **5g**,[11a] **5h** and **5j**.[11b] Structural views of the complexes **5a** and **5h** are shown in Figure 2. Key bond lengths and angles for all five complexes are shown for comparison in Table 1.

In all complexes the iridium exhibits a moderately distorted octahedral coordination environment with relatively uniform bond lengths and angles with mean bond lengths of 2.000(8) Å for the Ir–C distance, 2.037(8) Å for the Ir–

Table 1. Comparison of key bond lengths [Å] and angles [°] in the solid-state structures of **5a**, **5c**, **5g**, **5h** and **5j**.

| | **5a**[a] | **5c**[b,c] | **5g**[b] | **5h**[a] | **5j**[d] |
|---|---|---|---|---|---|
| Ir–N(1) | 2.038(5) | 2.046(2) | 2.045(2) | 2.040(3) | 2.044(5) |
| Ir–N(2) | 2.020(5) | 2.039(2) | 2.025(2) | 2.038(3) | 2.030(5) |
| Ir–N(3) | 2.127(5) | 2.137(2) | 2.143(2) | 2.189(3) | 2.131(5) |
| Ir–C(11) | 2.010(6) | 2.014(3) | 2.008(2) | 1.994(3) | 1.997(6) |
| Ir–C(22) | 1.996(5) | 2.000(3) | 1.988(2) | 2.005(3) | 1.989(6) |
| Ir–O | 2.151(4) | 2.163(2) | 2.152(2) | 2.130(2) | 2.181(5) |
| O–C(30) | 1.309(7) | 1.293(3) | 1.302(3) | 1.301(4) | 1.266(8) |
| N(1)–Ir–C(11) | 81.0(2) | 80.5(1) | 80.7(1) | 80.7(1) | 81.0(3) |
| N(2)–Ir–C(22) | 81.2(2) | 80.8(1) | 80.8(1) | 81.0(1) | 80.9(3) |
| N(3)–Ir–O | 78.3(2) | 77.5(1) | 77.1(1) | 77.7(1) | 76.8(2) |
| C(11)–Ir–C(22) | 91.9(2) | 88.9(1) | 85.9(1) | 88.7(1) | 88.0(2) |
| N(1)–Ir–N(2) | 174.4(2) | 175.1(1) | 174.3(1) | 174.4(1) | 174.5(2) |

[a] This work. [b] Data from the literature.[11a] [c] Mean values of two independent Ir complexes. [d] Data from the literature.[11b]

 © 2007 Wiley-VCH Verlag GmbH & Co. KGaA, Weinheim 

$N_{pyridine}$ distance, 2.145(22) Å for the Ir–$N_{quinoline}$ distance and 2.155(17) Å for the Ir–O distance. Characteristic for all complexes is that the two carbon ligands are in a *cis* disposition and that the 2-phenylpyridine nitrogen atoms are in a *trans* disposition. No indication for a reversal of this geometry was found and this is consistent with related bis(phenylpyridine)(acetylacetonato)iridium(III) [$ppy_2Ir(acac)$] complexes or similar compounds for which no bond breaking or spatial rearrangement of the phenylpyridine ligands was observed during complex formation from the precursor **3**.[4d,4e] Compared with the O–Ir–O bite angles of the acetylacetonato complexes, the N–Ir–O bite angles of the quinolinato complexes are systematically smaller by about 5°.

Whereas the quinolinato ligands are in all cases practically perfectly planar, the 2-phenylpyridine ligands occasionally show larger deviations from planarity by being either curved or twisted, e.g. in **5a** or **5g**,[11a] due to crystal packing effects. In the case of **5h** it is interesting to note that the 2-cyano group is in close intramolecular contact with the second 2-phenylpyridine ligand showing π-π interactions with comparatively short distances of C(32)–C(22) 3.112 Å and N(4)–C(21) 3.259 Å. This contact appears to be responsible for the slightly aberrant Ir–N(3) and Ir–O bond lengths of **5h** (Table 1).

To determine the thermal stabilities of **5a**–**5j**, heat flux DSC/TGA measurements were performed. For practical applications such as in OLEDs, materials with good thermal stabilities are very desirable due to the resultant improved device lifetimes.[15] For comparison of the compounds under investigation, a weight loss of 5% was chosen as a measure for the thermal stability. As depicted in Figure 3 and summarised in Table 2, a significant impact on the corresponding thermal stabilities can be observed as a result of ligand modifications.

While the unmodified organoiridium quinolinolate complex **5a** exhibits a 5% weight-loss at 136 °C,[11] the halogen-substituted derivatives **5b**–**5d** show noticeably increased thermal stabilities with temperature values of 380 °C, 347 °C and 328 °C, respectively.[11] Note that the thermal stabilities of the complexes **5b**–**5d** increase within the series I < Br < Cl which is presumably a result of steric effects of the halogen substituents. Also, for the alkyl and aryl-substituted derivatives **5e**–**5g**, a considerably higher thermal stability can be observed. While **5g** bearing phenyl rings at the 5 and 7 positions of the quinolinolato ligand shows only a slightly increased temperature value for a 5% weight loss at 211 °C, the 2-methyl- and 5,7-dimethyl-substituted derivatives **5e** and **5f** are thermally stable up to 380 and 357 °C, respectively. The most striking impact on the thermal properties is exhibited by **5h** with a weight loss of 5% at 422 °C. As reported recently,[11] significantly increased thermal stabilities compared with **5a** are also found for the formyl- and nitro-substituted derivatives **5i** and **5j** at 354 and 395 °C, respectively.

From these data, the significant influence of ligand modifications on the thermal stabilities of the organoiridium(III) complexes becomes evident. While electron-donating as well as electron-withdrawing groups improve the thermal properties of this class of materials, the cyano substituent in position 2 of the quinolinolato ligand causes the highest thermal stability.

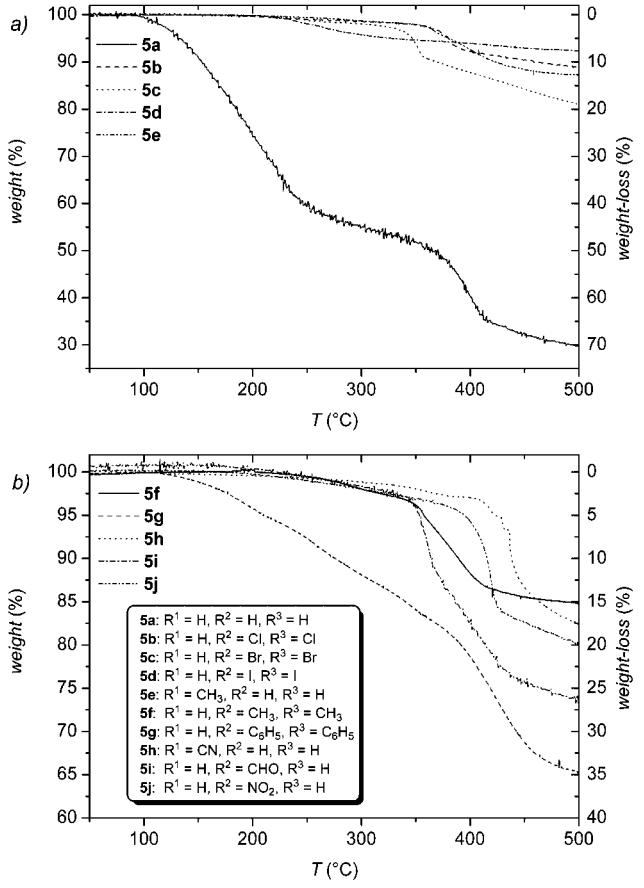


Figure 3. TGA runs of a) compounds **5a**–**5e** and b) **5f**–**5j** indicate increased thermal stability compared with **5a**.

Table 2. Temperatures at 5% weight loss $T_{5\%}$, absorption wavelengths $\lambda_{abs}$, molecular coefficients of extinction $\varepsilon$, emission wavelengths $\lambda_{em}$ in solution and emission wavelengths $\lambda_{77K}$ of films recorded at 77 K. Note that the spectra of **5a**, **5c**, **5g**, **5i** and **5j** have already been communicated elsewhere.[11]

| | $T_{5\%}$ /°C | $\lambda_{abs}$ ($\varepsilon$) /nm ($L\ mol^{-1}\ cm^{-1}$) | $\lambda_{em}$ ($\lambda_{77K}$) /nm |
|---|---|---|---|
| **5a** | 136 | 258.9 (53200) | – (640) |
| **5b** | 380 | 252.0 (52600) | – (664)[c] |
| **5c** | 347 | 254.0 (54070) | – (658)[c] |
| **5d** | 328 | 263.0 (42230)[a] | – (654)[c] |
| **5e** | 380 | 272.0 (22190)[a] | – (647) |
| **5f** | 357 | 270.0 (39070) | 521 (–) |
| **5g** | 211 | 264.0 (51030) | – (680) |
| | | 299.9 (43830)[a] | |
| **5h** | 422 | 263.9 (54670)[b] | – (–) |
| **5i** | 354 | 261.0 (52960) | 603, 645 (602, 655) |
| | | 427.0 (11750) | |
| **5j** | 39 | 266.0 (69060) | 670[d] (623, 678) |
| | 5 | 459.0 (34270) | |

[a] Broad absorption peak. [b] The onset of absorption is significantly red-shifted to approximately 615 nm. [c] The emission intensity is decreased presumably because of the heavy-atom effect. [d] Broad emission peak.

 © 2007 Wiley-VCH Verlag GmbH & Co. KGaA, Weinheim 

To investigate the photophysical properties of the studied compounds (see Table 2), UV/Vis absorption and photoluminescence (PL) spectra were recorded in dilute solutions of $CHCl_3$ at room temperature. In Figure 4 the UV/Vis absorption spectra of **5a**–**5j** are shown. The complexes **5a**–**5g** exhibit comparably weak absorption bands in the range of approximately 530 to 350 nm which can be assigned to spin-allowed and spin-forbidden metal–ligand charge transfer (MLCT) transitions. Significantly stronger absorption peaks resulting from π-π* transitions can be found in the higher energy region around 250 nm for all complexes.

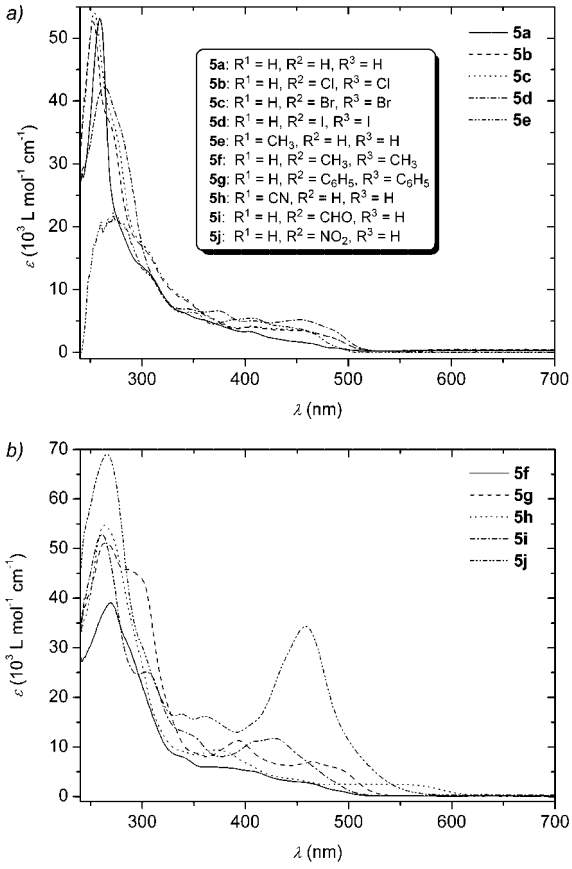


Figure 4. Absorption spectra of a) compounds **5a**–**5e** and b) **5f**–**5j** recorded in dilute $CHCl_3$ solutions.

Although the cyano, formyl and nitro modified compounds **5h**–**5j** exhibit, in general, the same spectroscopic features, the corresponding functional groups lead to additional absorption bands. Whereas for **5h** a shift of the onset of absorption towards longer wavelengths can be observed (i.e. approx. 615 nm), **5i** and **5j** feature distinct new absorption bands at 427 and 459 nm, respectively.

For practical applications, iridium(III) complexes with emission properties controlled by the "ancillary ligand" are desirable. Although this description can be frequently found in the literature, it is important to note that in such compounds this ligand is certainly not ancillary and therefore this term should be avoided. In any case, only a few successful examples of heteroleptic iridium(III) complexes with photophysical properties controlled by the third ligand have been reported.[4] Organoiridium quinolinolate complexes are known to be red phosphorescent emitter materials and thus the emission characteristics are dominated by the quinolinolato ligand.[10,11] From this point of view it is surprising that a systematic investigation of the impact of ligand modifications on the emission characteristics is missing since there is a significant demand for phosphorescent materials with easily tuneable photophysical properties.

To study the photoluminescence of the compounds under investigation, we tried to record the corresponding PL spectra of dilute $CHCl_3$ solutions at room temperature in aerated as well as degassed solutions (Figure 5). Among the studied complexes only **5f**, **5i** and **5j** gave weak photoluminescence with quantum yields ($\Phi$) smaller than 1% (apparent lifetimes at room temperature $\tau = 3 \pm 1$ μs for **5f** and $20 \pm 4$ μs for **5i** and **5j**)[11] while the other compounds were not found to be luminescent in solution (even in degassed solutions) indicating an unfavourable mixing of singlet and triplet excited states for these complexes when compared with, for example, $ppy_2Ir(acac)$ ($\Phi = 34\%$; $\tau = 1.6$ μs).[4]

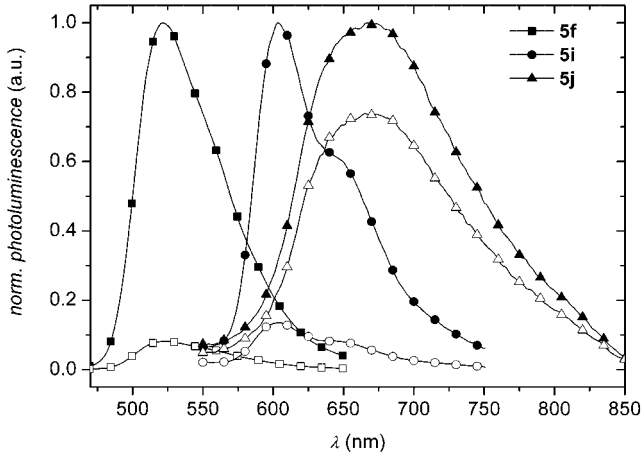


Figure 5. Photoluminescence spectra of **5f**, **5i** and **5j** in aerated (open symbols) and degassed (filled symbols) $CHCl_3$ solutions.

As depicted in Figure 5, significantly different emission wavelengths were achieved with these three luminescent compounds. While **5f** exhibits its emission maximum at 521 nm ($\lambda_{exc}$ = 390 nm), a structured PL spectrum with the maximum at 603 nm and a shoulder at 645 nm ($\lambda_{exc}$ = 400 nm) may be obtained for **5i**. Compound **5j** gave the most red-shifted spectrum displaying a broad and unstructured emission band peaking at 670 nm ($\lambda_{exc}$ = 450 nm). Although most of the studied materials were not luminescent in solution, film spectra of the organoiridium quinolinolate complexes blended into polystyrene were recorded at room temperature and also after cooling with liquid nitrogen to 77 K. With the exception of **5f** and **5h**, all compounds were found to be weakly luminescent in the red spectroscopic region at room temperature. However, cooling the samples gave slightly increased luminescence intensities (see Table 2 and Supporting Information).

From these data a striking impact of the ligand modifications on the emission properties becomes evident. While the

 © 2007 Wiley-VCH Verlag GmbH & Co. KGaA, Weinheim 

5-formyl- and 5-nitro-substituted complexes emit orange to red light dominated by the quinolinolato ligand in solution, the 5,7-dimethyl derivative gives greenish phosphorescence which is very similar to $ppy_2Ir(acac)$ suggesting a phenylpyridine governed emission in this case [for comparison, green-emitting $ppy_2Ir(acac)$ exhibits its emission maximum at 516 nm].[4c,4d] To further support this hypothesis, the photophysical properties of tris[$\kappa^2$(*N*,*O*)-5,7-dimethyl-8-quinolinolato]iridium(III) were investigated.[10b] From the corresponding emission spectrum peaking around 695 nm (see Supporting Information) a phenylpyridine-centred emission for **5f** can be concluded.

The luminescent compounds **5f**, **5i** and **5j** as well as **5a**, **5b**, **5c** and **5h** were tested as emitting materials in OLEDs using various host materials. As communicated recently, efficient light-emitting diodes were obtained from **5i** and **5j**. For example, a maximum luminance of 940 cd m$^{-2}$ was obtained at 13 V for diodes containing 1 wt.-% of **5i** in poly(vinylcarbazole) (PVK) as the host material.[11b] In contrast, attempts to prepare OLEDs from **5a**, **5b**, **5c**, **5f** and **5h** were unsuccessful. Similar to the above mentioned diodes built from **5i**, the herein studied complexes were investigated as the emitting guest using PVK as the host (1 wt.-% complex loading). OLEDs of the configuration ITO/PEDOT:PSS/host-guest emitting layer/Ca/Al gave weak electroluminescence at wavelengths similar to those listed in Table 2 for the 77 K measurements, with low luminescence intensities of 0.8–10 cd m$^{-2}$ at comparably high turn on voltages of more than 8 V (see Supporting Information). These findings distinctly underline the importance of introducing an electron-withdrawing group in the 5-position of the quinolinolato for obtaining efficient OLEDs. In these cases (i.e. **5i** and **5j**) the additional absorption bands with high extinction coefficients in the blue region are beneficial for providing efficient Förster energy transfer from the blue emitting host material. At the same time, the electron-withdrawing groups offer appropriate energy level tuning[11b] so that endothermic Dexter triplet energy back transfer from the phosphorescent iridium complex to the host material is prevented.[16]

## Conclusions

Herein we have reported the synthesis, structure, thermal stabilities and photophysical properties of a rarely studied class of materials, namely derivatives of bis[$\kappa^2$(*C*$^2$,*N*)-2-phenylpyridine][$\kappa^2$(*N*,*O*)-8-quinolinolato]iridium(III). Photophysical measurements revealed only minor changes in the absorption characteristics for most derivatives except that bearing electron-withdrawing groups in the 5-position of the quinolinolato ligand. These complexes exhibit absorption features with comparably high extinction coefficients in the visible suitable for finding appropriate host materials for OLED applications.[11] Only the 5-formyl, 5-nitro and 5,7-dimethyl derivatives were found to be luminescent in solution, whereas measurements at 77 K showed red photoluminescence in the solid state for most compounds under investigation. While in the case of **5f** the quinolinolate is rather a spectator ligand similar to acac and emission originates from the $ppy_2Ir$ fragment, the emissions of **5a**–**5e**, **5g**, **5i** and **5j** are quinolinolato-dominated. From the corresponding film measurements, PL spectra in degassed solutions and comparison with the photophysical properties of tris[$\kappa^2$(*N*,*O*)-8-quinolinolato]iridium(III) derivatives (see Supporting Information),[10b] an unfavourable mixing of singlet and triplet excited states of these complexes can be concluded rendering most of the described compounds insufficiently luminescent for typical OLED applications. With this information, the rational design of (electro-)luminescent iridium complexes bearing quinolinolato ligands has been revealed and further easily accessible iridium complexes based on 5-electron acceptor-substituted quinolinolato ligands can be foreseen to enter the stage of (electro)luminescent emitter materials.

## Experimental Section

**General:** Unless otherwise noted, materials were obtained from commercial sources (Aldrich, Fluka or Lancaster) and were used without further purification. Solvents for reactions were freshly distilled from appropriate drying agents prior to use (ee = ethyl acetate, cy = cyclohexane). Reactions were carried out under an inert atmosphere of Ar using standard Schlenk techniques. $^1$H NMR spectra were recorded on a Varian INOVA 500 MHz spectrometer at 500 MHz and $^{13}$C{$^1$H} NMR spectra were recorded at 125 MHz. Assignment of the peaks was carried out by DEPT and COSY NMR spectroscopy. Residual solvent peaks were used for referencing the NMR spectra to the corresponding values given in the literature.[17] UV/Vis absorption spectra were recorded on a Cary 50 Bio UV/Vis spectrophotometer and fluorescence spectra on a Perkin–Elmer luminescence spectrometer LS50B. MALDI-TOF mass spectra were recorded on a Micromass TofSpec 2E. The instrument was equipped with a nitrogen laser (337 nm wavelength, operated at a frequency of 5 Hz) and a time lag focusing unit. Spectra were taken in reflection mode at an accelerating voltage of +20 kV. Analysis of data was done with MassLynx 3.4 (Micromass, Manchester, UK). Samples were dissolved in THF (1 mg mL$^{-1}$). Dithranol or retinoic acid was used as the matrix (10 mg mL$^{-1}$ in THF). Solutions were mixed in the cap of a microtube in the ratio of 1 μL:10 μL. Then, 0.5 μL of the resultant mixture was spotted onto the target and air-dried. Combined DSC/TGA measurements were performed with a Netzsch STA 449C instrument equipped with a Quadrupole MS QMS 403C or with a Polymer Laboratories simultaneous thermal analyser STA 625 (crucibles: aluminium from Rheometric Scientific). The thermal properties were determined in aluminium pans with a heat rate of 10 °C min$^{-1}$ in a helium flow of approximately 50 mL min$^{-1}$ (Netzsch STA 449C) or a nitrogen flow of 20 mL min$^{-1}$ (Polymer Laboratories simultaneous thermal analyser STA 625).

**Di-μ-chloro-tetrakis[$\kappa^2$(*C*$^2$,*N*)-2-phenylpyridine]diiridium(III) (3):** $IrCl_3 \cdot nH_2O$ (**1**, 0.2123 g, 0.711 mmol) was suspended in a mixture of 2-ethoxyethanol (6 mL) and water (2 mL) under Ar. After the addition of 2-phenylpyridine (**2**, 270 μL, 1.889 mmol) the dark brown reaction mixture was stirred for 24 h at 120 °C. The greenish suspension formed was cooled to room temperature and the solvent was removed in vacuo. Washing the residue with hot methanol gave rise to 0.2025 g (53.1%) of a yellow-greenish powder of **3**. NMR spectra were found to be identical with that described in the literature.[11]

 © 2007 Wiley-VCH Verlag GmbH & Co. KGaA, Weinheim 

**General Procedure for the Preparation of Organoiridium Quinolinolate Complexes:** For the preparation of **5a**–**5j** 1 equiv. of **3** was suspended with 2.1 to 2.5 equiv. of the corresponding 8-hydroxyquinoline derivative **4a**–**4j** in a solvent mixture of degassed $CH_2Cl_2$/EtOH/$Et_3N$ under Ar and was heated to reflux at 80 °C for 20 h. The solvent was removed in vacuo and the residue was washed with hot methanol. Filtration of the precipitate gave the corresponding product in analytically pure form.

**Bis[κ²(C²,*N*)-2-phenylpyridine][κ²(*N*,*O*)-8-quinolinolato]iridium(III) (5a):** Compound **5a** was prepared starting from **3** (0.0403 g, 0.038 mmol) and **4a** (0.0126 g, 0.087 mmol) in $CH_2Cl_2$ (1 mL), EtOH (1 mL) and $Et_3N$ (300 μL) giving 0.0379 g (78.2%) of a yellow-orange powder. $R_f$(acetone) = 0.86. The recorded NMR and MALDI-TOF MS spectra are in accordance with literature data.[11]

**[κ²(*N*,*O*)-5,7-Dichloro-8-quinolinolato]bis[κ²(C²,*N*)-2-phenylpyridine]iridium(III) (5b):** Complex **5b** was obtained from **3** (0.0509 g, 0.047 mmol) and **4b** (0.0214 g, 0.100 mmol) in $CH_2Cl_2$ (2 mL), EtOH (1 mL) and $Et_3N$ (300 μL) yielding 0.0459 g (67.7%) of an orange solid. $R_f$(cy:ee = 3:1) = 0.27. $^1$H NMR ([D$_6$]DMSO, 500 MHz): $\delta$ = 8.39 (d, $J$ = 5.9 Hz, 1 H, *Py*$^6$), 8.35 (d, $J$ = 8.8 Hz, 1 H, *Q*$^4$), 8.21 (d, $J$ = 7.8 Hz, 1 H, *Py*$^3$), 8.16 (d, $J$ = 8.3 Hz, 1 H, *Py*$^3$), 7.91–7.80 (m, 4 H, *Py*$^4$, *Ph*$^6$), 7.74 (s, 1 H, *Q*$^6$), 7.71 (d, $J$ = 4.9 Hz, 1 H, *Q*$^2$), 7.59–7.55 (m, 2 H, *Py*$^6$, *Q*$^3$), 7.30 (t, $J$ = 7.3 Hz, 1 H, *Py*$^5$), 7.10 (t, $J$ = 7.3 Hz, 1 H, *Py*$^5$), 6.93–6.87 (2 t, $J$ = 7.3 Hz, 2 H, *Ph*$^5$), 6.79 (t, $J$ = 7.3 Hz, 1 H, *Ph*$^4$), 6.74 (t, $J$ = 7.3 Hz, 1 H, *Ph*$^4$), 6.26 (d, $J$ = 7.3 Hz, 1 H, *Ph*$^3$), 6.11 (d, $J$ = 7.3 Hz, 1 H, *Ph*$^3$) ppm. $^{13}$C NMR ([D$_6$]DMSO, 125 MHz): $\delta$ = 167.8, 167.0 (2 C, *Py*$^2$), 164.3 (1 C, *Q*$^8$), 150.7, 148.4 (2 C, *Ph*$^2$), 148.2, 147.4, 147.3 (3 C, *Py*$^6$, *Q*$^2$), 144.7, 144.3, 143.7 (3 C, *Ph*$^1$, *Q*$^{8a}$), 138.0, 134.0, 134.0, 132.0, 131.7, 129.7, 129.4, 129.0, 124.7, 124.3, 123.8, 123.3, 123.0, 121.1, 120.9, 119.4, 119.3 (17 C, *Ph*$^{3,4,5,6}$, *Py*$^{3,4,5}$, *Q*$^{3,4,6}$), 127.2 (1 C, *Q*$^{4a}$), 118.8 (1 C, *Q*$^5$), 110.7 (1 C, *Q*$^7$) ppm. HRMS: calcd. for $C_{31}H_{20}Cl_2IrN_3O$ 711.0590; found 711.0631.

**[κ²(*N*,*O*)-5,7-Dibromo-8-quinolinolato]bis[κ²(C²,*N*)-2-phenylpyridine]iridium(III) (5c):** The dibromo complex **5c** was synthesised from **3** (0.0520 g, 0.049 mmol) and **4c** (0.0293 g, 0.097 mmol) in $CH_2Cl_2$ (2 mL), EtOH (1 mL) and $Et_3N$ (300 μL). The product was obtained as orange powder in a yield of 0.0599 g (76.9%). $R_f$(cy:ee = 3:1) = 0.30. NMR and MALDI-TOF MS characterisation of this compound can be found in the literature.[11]

**[κ²(*N*,*O*)-5,7-Diiodo-8-quinolinolato]bis[κ²(C²,*N*)-2-phenylpyridine]iridium(III) (5d):** Compound **5d** resulted from the reaction of **3** (0.1000 g, 0.093 mmol) with **4d** (0.0820 g, 0.207 mmol) in $CH_2Cl_2$ (4 mL), EtOH (2 mL) and $Et_3N$ (600 μL). The complex was isolated in a yield of 0.1437 g (85.9%) as a yellow-brownish powder. $R_f$(cy:ee = 1:1) = 0.72. $^1$H NMR ([D$_6$]DMSO, 500 MHz): $\delta$ = 8.37 (d, $J$ = 5.8 Hz, 1 H, *Py*$^6$), 8.22 (s, 1 H, *Q*$^6$), 8.20 (d, $J$ = 8.3 Hz, 1 H, *Q*$^4$), 8.15–8.12 (2 d, each $J$ = 8.1 Hz, 2 H, *Py*$^3$), 7.88, 7.85–7.78 (dd, 2 × $J$ = 7.8 Hz, 1 H, m, 3 H, *Ph*$^6$, *Py*$^4$), 7.62 (d, $J$ = 4.6 Hz, 1 H, *Q*$^2$), 7.54–7.52 (m, 2 H, *Py*$^6$, *Q*$^3$), 7.29 (dd, 2 × $J$ = 6.6 Hz, 1 H, *Py*$^5$), 7.09 (dd, 2 × $J$ = 6.6 Hz, 1 H, *Py*$^5$), 6.92–6.86 (2 dd, each 2 x $J$ = 7.5 Hz, 2 H, *Ph*$^5$), 6.78 (dd, 2 × $J$ = 7.4 Hz, 1 H, *Ph*$^4$), 6.73 (dd, 2 × $J$ = 7.4 Hz, 1 H, *Ph*$^4$), 6.22 (d, $J$ = 7.5 Hz, 1 H, *Ph*$^3$), 6.11 (d, $J$ = 7.5 Hz, 1 H, *Ph*$^3$) ppm. $^{13}$C NMR ([D$_6$]DMSO, 125 MHz): $\delta$ = 169.4 (1 C, *Q*$^8$), 167.7, 167.0 (2 C, *Py*$^2$), 150.9, 148.5 (2 C, *Ph*$^2$), 148.1, 147.2, 147.2, 146.1 (4 C, *Py*$^6$, *Q*$^{2,6}$), 144.6, 144.2 (2 C, *Ph*$^1$), 142.1 (1 C, *Q*$^{8a}$), 140.9, 138.0, 137.9, 132.0, 131.6, 129.6, 129.1, 124.7, 124.6, 124.3, 123.2, 123.0, 121.0, 120.9, 119.4, 119.3 (16 C, *Ph*$^{3,4,5,6}$, *Py*$^{3,4,5}$, *Q*$^{3,4}$), 132.2 (1 C, *Q*$^{4a}$), 86.7 (1 C, *Q*$^5$), 74.3 (1 C, *Q*$^7$) ppm. HRMS: calcd. for $C_{31}H_{20}I_2IrN_3O$ 894.9302; found 894.9327.

**[κ²(*N*,*O*)-2-Methyl-8-quinolinolato]bis[κ²(C²,*N*)-2-phenylpyridine]iridium(III) (5e):** Complex **5e** was synthesised from **3** (0.0722 g, 0.067 mmol) and **4e** (0.0256 g, 0.161 mmol) in $CH_2Cl_2$ (4 mL), EtOH (2 mL) and $Et_3N$ (600 μL). The orange solid was isolated in a yield of 0.0669 g (75.4%). $R_f$(cy:ee = 1:1) = 0.23. $^1$H NMR ([D$_6$]-DMSO, 500 MHz): $\delta$ = 8.48 (d, $J$ = 5.6 Hz, 1 H, *Py*$^6$), 8.18 (d, $J$ = 8.1 Hz, 1 H, *Py*$^3$), 8.13 (d, $J$ = 8.1 Hz, 1 H, *Py*$^3$), 8.11 (d, $J$ = 8.5 Hz, 1 H, *Q*$^4$), 7.86, 7.83–7.81, 7.77, 7.74 (dd, 2 × $J$ = 7.9 Hz, 1 H, m, 2 H, d, $J$ = 7.8 Hz, 1 H, d, $J$ = 7.8 Hz, 1 H, *Ph*$^6$, *Py*$^{4,6}$), 7.25–7.19 (m, 3 H, *Py*$^5$, *Q*$^{3,6}$), 7.10 (dd, 2 × $J$ = 6.7 Hz, 1 H, *Py*$^5$), 6.83 (dd, 2 × $J$ = 7.3 Hz, 1 H, *Ph*$^5$), 6.79 (dd, 2 × $J$ = 7.3 Hz, 1 H, *Ph*$^5$), 6.74 (d, $J$ = 7.8 Hz, 1 H, *Q*$^5$), 6.68–6.65 (m, 3 H, *Ph*$^4$, *Q*$^7$), 6.25 (d, $J$ = 7.5 Hz, 1 H, *Ph*$^3$), 5.91 (d, $J$ = 7.5 Hz, 1 H, *Ph*$^3$), 2.00 (s, 3 H, *Q*-*CH*$_3$) ppm. $^{13}$C NMR ([D$_6$]DMSO, 125 MHz): $\delta$ = 169.6, 167.9, 167.5 (3 C, *Py*$^2$, *Q*$^8$), 158.1, 153.5, 149.2 (3 C, *Ph*$^2$, *Q*$^2$), 148.8, 147.5 (2 C, *Py*$^6$), 144.2, 143.7, 143.4 (3 C, *Ph*$^1$, *Q*$^{8a}$), 138.1, 137.4, 137.4, 132.4, 130.9, 129.3, 128.8, 128.7, 124.7, 123.9, 123.7, 123.1, 122.0, 120.9, 119.7, 119.3, 118.8, 116.2 (18 C, *Ph*$^{3,4,5,6}$, *Py*$^{3,4,5}$, *Q*$^{3,4,5,6}$), 129.8 (1 C, *Q*$^{4a}$), 110.1 (1 C, *Q*$^7$), 26.9 (1 C, *Q*-*CH*$_3$) ppm. HRMS: calcd. for $C_{32}H_{24}IrN_3O$ 657.1525; found 657.1474.

**[κ²(*N*,*O*)-5,7-Dimethyl-8-quinolinolato]bis[κ²(C²,*N*)-2-phenylpyridine]iridium(III) (5f):** The dimethyl complex **5f** was prepared starting from **3** (0.1006 g, 0.094 mmol) and **4f** (0.0362 g, 0.209 mmol) in $CH_2Cl_2$ (4 mL), EtOH (2 mL) and $Et_3N$ (600 μL). The product was obtained as dark orange solid in a yield of 0.1038 g (82.2%). $R_f$(cy:ee = 1:1) = 0.56. $^1$H NMR ([D$_6$]DMSO, 500 MHz): $\delta$ = 8.54 (d, $J$ = 5.6 Hz, 1 H, *Py*$^6$), 8.18–8.17 (2 d, each $J$ = 7.8 Hz, 2 H, *Py*$^3$), 8.10 (d, $J$ = 8.3 Hz, 1 H, *Q*$^4$), 7.86, 7.79–7.76 (dd, 2 × $J$ = 7.3 Hz, 1 H, m, 3 H, *Ph*$^6$, *Py*$^4$), 7.58 (d, $J$ = 4.4 Hz, 1 H, *Q*$^2$), 7.51 (d, $J$ = 5.6 Hz, 1 H, *Py*$^6$), 7.30–7.27 (dd, $J$ = 8.5 Hz, $J$ = 4.5 Hz, 1 H, *Q*$^3$), 7.22 (dd, 2 × $J$ = 6.5 Hz, 1 H, *Py*$^5$), 7.19 (s, 1 H, *Q*$^6$), 7.07 (dd, 2 × $J$ = 6.6 Hz, 1 H, *Py*$^5$), 6.89–6.83 (2 dd, each 2 × $J$ ≈ 7.3 Hz, 2 H, *Ph*$^5$), 6.77 (dd, 2 × $J$ ≈ 7.2 Hz, 1 H, *Ph*$^4$), 6.71 (dd, 2 × $J$ ≈ 7.2 Hz, 1 H, *Ph*$^4$), 6.28 (d, $J$ = 7.3 Hz, 1 H, *Ph*$^3$), 6.14 (d, $J$ = 7.3 Hz, 1 H, *Ph*$^3$), 2.46 (s, 3 H, *Q*$^5$-*CH*$_3$), 2.25 (s, 3 H, *Q*$^7$-*CH*$_3$) ppm. $^{13}$C NMR ([D$_6$]DMSO, 125 MHz): $\delta$ = 168.0, 167.3 (2 C, *Py*$^2$), 165.3 (1 C, *Q*$^8$), 152.8, 151.3 (2 C, *Ph*$^2$), 147.7, 147.4, 145.0 (3 C, *Py*$^6$, *Q*$^2$), 144.6, 144.4 (2 C, *Ph*$^1$), 142.6 (1 C, *Q*$^{8a}$), 137.5, 137.4, 134.0, 132.8, 132.1, 131.7, 129.5, 128.8, 124.5, 124.2, 122.9, 122.5, 120.6, 120.5, 120.4, 119.2, 118.9 (17 C, *Ph*$^{3,4,5,6}$, *Py*$^{3,4,5}$, *Q*$^{3,4,6}$), 128.0 (1 C, *Q*$^{4a}$), 123.8 (1 C, *Q*$^5$), 115.0 (1 C, *Q*$^7$), 16.9, 16.7 (2 C, *Q*$^5$-*CH*$_3$, *Q*$^7$-*CH*$_3$) ppm. HRMS: calcd. for $C_{33}H_{26}IrN_3O$ 671.1682; found 671.1752.

**[κ²(*N*,*O*)-5,7-Diphenyl-8-quinolinolato]bis[κ²(C²,*N*)-2-phenylpyridine]iridium(III) (5g):** The diphenyl-substituted compound **5g** was obtained from **3** (0.0930 g, 0.087 mmol) and **4g** (0.0500 g, 0.168 mmol) in $CH_2Cl_2$ (3 mL), EtOH (2 mL) and $Et_3N$ (300 μL) giving 0.0768 g (55.5%) of a yellow-orange powder. $R_f$(cy:ee = 1:1) = 0.77. NMR and MALDI-TOF MS spectra were found to be in accordance with literature.[11]

**[κ²(*N*,*O*)-2-Cyano-8-quinolinolato]bis[κ²(C²,*N*)-2-phenylpyridine]iridium(III) (5h):** Compound **5h** resulted from reacting **3** (0.0497 g, 0.046 mmol) with **4h** (0.0183 g, 0.108 mmol) in $CH_2Cl_2$ (2 mL), EtOH (1 mL) and $Et_3N$ (300 μL). From this complex 0.0468 g (75.4%) could be isolated as deeply red solid. $R_f$(acetone) = 0.9. $^1$H NMR ([D$_6$]DMSO, 500 MHz): $\delta$ = 8.39 (d, $J$ = 8.5 Hz, 1 H, *Q*$^4$), 8.31 (d, $J$ = 5.6 Hz, 1 H, *Py*$^6$), 8.19 (d, $J$ = 8.3 Hz, 1 H, *Py*$^3$), 8.15 (d, $J$ = 8.3 Hz, 1 H, *Py*$^3$), 7.90 (ddd, 2 × $J$ = ca. 7.8 Hz, $J$ = 1.2 Hz, 1 H, *Py*$^4$), 7.85–7.82 (m, 2 H, *Py*$^{4,6}$), 7.77 (d, $J$ = 7.8 Hz, 1 H, *Ph*$^6$), 7.74 (d, $J$ = 7.8 Hz, 1 H, *Ph*$^6$), 7.69 (d, $J$ = 8.5 Hz, 1 H, *Q*$^3$), 7.51 (dd, 2 × $J$ = 7.8 Hz, 1 H, *Q*$^6$), 7.21–7.18 (ddd, 2 × $J$ ≈

 © 2007 Wiley-VCH Verlag GmbH & Co. KGaA, Weinheim 

6.6 Hz, $J$ = 1.2 Hz, 1 H, $Py^5$), 7.12–7.10 (ddd, $2\times J \approx 6.6$ Hz, $J$ = 1.2 Hz, 1 H, $Py^5$), 6.90, 6.87–6.82 (dd, $J$ = 7.8 Hz, $J \approx 1$ Hz, 1 H, m, 2 H, $Ph^5$, $Q^{5,7}$), 6.80–6.77 (ddd, $2\times J$ = ca. 7.2 Hz, $J$ = 1.2 Hz, 1 H, $Ph^5$), 6.71–6.68 (ddd, $2\times J \approx 6.8$ Hz, $J$ = 1.2 Hz, 1 H, $Ph^4$), 6.64–6.61 (ddd, $2\times J \approx 6.8$ Hz, $J$ = 1.2 Hz, 1 H, $Ph^4$), 6.20 (d, $J$ = 7.6 Hz, 1 H, $Ph^3$), 5.93 (d, $J$ = 7.6 Hz, 1 H, $Ph^3$) ppm. $^{13}$C NMR ([D$_6$]DMSO, 125 MHz): $\delta$ = 170.6, 168.1, 167.1 (3 C, $Py^2$, $Q^8$), 150.5, 147.6 (2 C, $Ph^2$), 149.0, 147.4 (2 C, $Py^6$), 144.2, 144.0, 143.8 (3 C, $Ph^1$, $Q^{8a}$), 138.8, 138.0, 137.9, 132.7, 132.7, 131.2, 129.4, 128.9, 126.5, 124.7, 124.0, 123.4, 122.1, 121.3, 120.6, 119.5, 119.0, 118.2 (18 C, $Ph^{3,4,5,6}$, $Py^{3,4,5}$, $Q^{3,4,5,6}$), 132.1 (1 C, $Q^2$), 129.4 (1 C, $Q^{4a}$), 114.8 (1 C, *Q-CN*), 110.3 (1 C, $Q^7$) ppm. HRMS: calcd. for $C_{32}H_{21}IrN_4O$ 668.1321; found 668.1302.

**[κ²(*N*,*O*)-5-Formyl-8-quinolinolato]bis[κ²(C²,*N*)-2-phenylpyridine]-iridium(III) (5i):** The recently reported complex **5i** was synthesised from **3** (0.0500 g, 0.047 mmol) and **4i** (0.0184 g, 0.106 mmol) in $CH_2Cl_2$ (2 mL), EtOH (1 mL) and $Et_3N$ (300 μL) yielding 0.0474 g (75.5%) of an orange solid. $R_f$(acetone) = 0.88. NMR and MALDI-TOF MS characterisation can be found in the literature.[11]

**[κ²(*N*,*O*)-5-Nitro-8-quinolinolato]bis[κ²(C²,*N*)-2-phenylpyridine]-iridium(III) (5j):** The nitro complex **5j** was prepared from **3** (0.1010 g, 0.094 mmol) and **4j** (0.0446 g, 0.235 mmol) in $CH_2Cl_2$ (4 mL), EtOH (2 mL) and $Et_3N$ (600 μL). The deeply red product was isolated in a yield of 0.1091 g (84.0%). $R_f$(cy:ee = 1:1) = 0.57. NMR and MALDI-TOF MS spectra have been reported in the literature.[11]

**Crystal Structure Determinations of 5a and 5h:** X-ray data of **5a** and **5h** (in the form of the diethyl ether solvate **5h**·0.5 $C_4H_{10}O$) were collected on a Bruker Smart APEX CCD area detector diffractometer using graphite-monochromated Mo-$K_\alpha$ radiation ($\lambda$ = 0.71073 Å) and 0.3° $\omega$-scan frames. Corrections for absorption, $\lambda/2$ effects and crystal decay were applied.[18] After structure solution with SHELXS-97, refinement on $F^2$ was carried out with SHELXL-97.[19] Non-hydrogen atoms were refined anisotropically. All H atoms were placed in calculated positions and thereafter treated as riding. Salient crystallographic data are:

**5a:** $C_{31}H_{22}IrN_3O$, $M_r$ = 644.72, brown prism, 0.54 × 0.14 × 0.05 mm, monoclinic, space group $P2_1/n$ (no. 14), $a$ = 11.3945(7) Å, $b$ = 9.2935(6) Å, $c$ = 22.5274(15) Å, $\beta$ = 93.013(2)°, $V$ = 2382.2(3) Å$^3$, $Z$ = 4, $\mu$ = 5.635 mm$^{-1}$, $T$ = 100 K. 25068 reflections were collected up to $\theta_{max}$ = 30.05° and, after applying absorption corrections, merged to 5486 independent data ($R_{int}$ = 0.050). Final $R$ indices: $R_1$ = 0.0468 [6859 reflections with $I > 2\sigma(I)$], $wR_1$ = 0.0943 (all data), 325 parameters.

**5h·0.5 $C_4H_{10}O$:** $C_{32}H_{21}IrN_4O$·0.5 $C_4H_{10}O$, $M_r$ = 706.79, brown prism, 0.32 × 0.24 × 0.18 mm, monoclinic, space group $P2_1/n$ (no. 14), $a$ = 11.5085(8) Å, $b$ = 19.7715(14) Å, $c$ = 12.5921(9) Å, $\beta$ = 110.578(1)°, $V$ = 2682.4(3) Å$^3$, $Z$ = 4, $\mu$ = 5.016 mm$^{-1}$, $T$ = 100 K. 44953 reflections were collected up to $\theta_{max}$ = 30.07° and, after applying absorption corrections, merged to 7760 independent data ($R_{int}$ = 0.034). Final $R$ indices: $R_1$ = 0.0296 [6669 reflections with $I > 2\sigma(I)$], $wR_1$ = 0.0628 (all data), 371 parameters. A disorder of the solvent in was taken into account.

CCDC-634415 and -634416 contain the supplementary crystallographic data for this paper. These data can be obtained free of charge from The Cambridge Crystallographic Data Centre via www.ccdc.cam.ac.uk/data_request/cif.

**Supporting Information** (see also the footnote on the first page of this article): Film measurements, photophysical measurements of tris[κ²(*N*,*O*)-8-quinolinolato]iridium(III) derivatives and OLED characteristics.

## Acknowledgments

Financial support by the Austrian Science Fund in the framework of the Austrian Nano Initiative, RPC ISOTEC (RP 0701, RP 702) is gratefully acknowledged. The authors thank Prof. Robert Saf and Karin Bartl for MALDI TOF-MS measurements, Kerstin Waich for the lifetime measurement of **5h** and Gregor Trimmel for thermal analysis. Umicore's Precious Metals Chemistry division is acknowledged for a generous loan of $IrCl_3$.

[1] For examples see: a) R. H. Friend, R. W. Gymer, A. B. Holmes, J. H. Burroughes, R. N. Marks, C. Taliani, D. D. C. Bradley, D. A. Dos Santos, J. L. Bredas, M. Logdlund, W. R. Salaneck, *Nature* **1999**, *397*, 121–128; b) M. A. Baldo, M. E. Thompson, S. R. Forrest, *Nature* **2000**, *403*, 750–753; c) M. S. Lowry, S. Bernhard, *Chem. Eur. J.* **2006**, *12*, 7970–7977.

[2] For examples see: a) S.-J. Liu, Q. Zhao, R.-F. Chen, Y. Deng, Q.-L. Fan, F.-Y. Li, L.-H. Wang, C.-H. Huang, W. Huang, *Chem. Eur. J.* **2006**, *12*, 4351–4361; b) E. Holder, B. M. W. Langeveld, U. S. Schubert, *Adv. Mater.* **2005**, *17*, 1109–1121.

[3] a) M. C. DeRosa, D. J. Hodgson, G. D. Enright, B. Dawson, C. E. B. Evans, R. J. Crutchley, *J. Am. Chem. Soc.* **2004**, *126*, 7619–7626; b) S. W. Thomas III, S. Yagi, T. M. Swager, *J. Mater. Chem.* **2005**, *15*, 2829–2835.

[4] a) Y. You, S. Y. Park, *J. Am. Chem. Soc.* **2005**, *127*, 12438–12439; b) J. Li, P. I. Djurovich, B. D. Alleyne, M. Yousufuddin, N. N. Ho, J. C. Thomas, J. C. Peters, R. Bau, M. E. Thompson, *Inorg. Chem.* **2005**, *44*, 1713–1727; c) S. Lamansky, P. Djurovich, D. Murphy, F. Abdel-Razzaq, H.-E. Lee, C. Adachi, P. E. Burrows, S. R. Forrest, M. E. Thompson, *J. Am. Chem. Soc.* **2001**, *123*, 4304–4312; d) S. Lamansky, P. Djurovich, D. Murphy, F. Abdel-Razzaq, R. Kwong, I. Tsyba, M. Bortz, B. Mui, R. Bau, M. E. Thompson, *Inorg. Chem.* **2001**, *40*, 1704–1711; e) R. Ragni, E. A. Plummer, K. Brunner, J. W. Hofstraat, F. Babudri, G. M. Farinola, F. Naso, L. De Cola, *J. Mater. Chem.* **2006**, *16*, 1161–1170; f) C. S. K. Mak, A. Hayer, S. I. Pascu, S. E. Watkins, A. B. Holmes, A. Köhler, R. H. Friend, *Chem. Commun.* **2005**, 4708–4710.

[5] For examples see: a) R. C. Kwong, S. Sibley, T. Dubovoy, M. A. Baldo, S. R. Forrest, M. E. Thompson, *Chem. Mater.* **1999**, *11*, 3709–3713; b) W. Lu, B. X. Mi, M. C. W. Chan, Z. Hui, N. Zhu, S. T. Lee, C. M. Che, *Chem. Commun.* **2002**, 206–207; c) Y. G. Ma, H. Y. Zhang, J. C. Shen, C. M. Che, *Synth. Met.* **1998**, *94*, 245–246; d) J. H. Kim, M. S. Liu, A. K. Y. Jen, B. Carlson, L. R. Dalton, C. F. Shu, R. Dodda, *Appl. Phys. Lett.* **2003**, *83*, 776–778; e) P. Sun, C. Li, Y. Pan, Y. Tao, *Synth. Met.* **2006**, *156*, 525–528.

[6] V. A. Montes, R. Pohl, J. Shinar, P. Anzenbacher Jr, *Chem. Eur. J.* **2006**, *12*, 4523–4535.

[7] A. S. Ionkin, W. J. Marshall, D. C. Roe, Y. Wang, *Dalton Trans.* **2006**, 2468–2478.

[8] a) T. H. Kwon, H. S. Cho, M. K. Kim, J.-W. Kim, J.-J. Kim, K. H. Lee, S. J. Park, I.-S. Shin, H. Kim, D. M. Shin, Y. K. Chung, J.-I. Hong, *Organometallics* **2005**, *24*, 1578–1585; b) Q. Zhao, S. Liu, M. Shi, C. Wang, M. Yu, L. Li, F. Li, T. Yi, C. Huang, *Inorg. Chem.* **2006**, *45*, 6152–6160.

[9] a) C. W. Tang, S. A. VanSlyke, *Appl. Phys. Lett.* **1987**, *51*, 913–915; b) C. H. Chen, J. Shi, *Coord. Chem. Rev.* **1998**, *171*, 161–174; c) V. A. Montes, G. Li, R. Pohl, J. Shinar, P. Anzenbacher Jr, *Adv. Mater.* **2004**, *16*, 2001–2003; d) S. Kappaun, S. Rentenberger, A. Pogantsch, E. Zojer, K. Mereiter, G. Trimmel, R. Saf, K.-C. Möller, F. Stelzer, C. Slugovc, *Chem. Mater.* **2006**, *18*, 3539–3547; e) M. Ghedini, I. Aiello, M. La Deda, A. Grisolia, *Chem. Commun.* **2003**, 2198–2199; f) N. M. Shavaleev, H.

 © 2007 Wiley-VCH Verlag GmbH & Co. KGaA, Weinheim 

Adams, J. Best, R. Edge, S. Navaratnam, J. A. Weinstein, *Inorg. Chem.* **2006**, *45*, 9410–9415.
[10] a) A. Tsuboyama, H. Mizutani, S. Okada, T. Takiguchi, S. Miura, K. Noguchi, T. Moriyama, S. Igawa, J. Kamatani, M. Furugori, **2002**, *Eur. Pat. Appl.* 1211257 A2; b) R. Ballardini, G. Varani, M. T. Indelli, F. Scandola, *Inorg. Chem.* **1986**, *25*, 3858–3865.
[11] a) S. Kappaun, S. Eder, S. Sax, R. Saf, K. Mereiter, E. J. W. List, C. Slugovc, *J. Mater. Chem.* **2006**, *16*, 4389–4392; b) S. Kappaun, S. Sax, S. Eder, K. C. Möller, K. Waich, F. Niedermair, R. Saf, K. Mereiter, J. Jacob, K. Müllen, E. J. W. List, C. Slugovc, *Chem. Mater.* **2007**, *19*, 1209–1211.
[12] M. Nonoyama, *Bull. Chem. Soc. Jpn.* **1974**, *47*, 767–768.
[13] S. Kappaun, T. Sovic, F. Stelzer, A. Pogantsch, E. Zojer, C. Slugovc, *Org. Biomol. Chem.* **2006**, *4*, 1503–1511.
[14] F. O. Garces, K. A. King, R. J. Watts, *Inorg. Chem.* **1988**, *27*, 3464–3471.
[15] Y. H. Kim, J. H. Ahn, D. C. Shin, S. K. Kwon, *Polymer* **2004**, *45*, 2525–2532.
[16] N. R. Evans, L. S. Devi, C. S. K. Mak, S. E. Watkins, S. I. Pascu, A. Köhler, R. H. Friend, C. K. Williams, A. B. Holmes, *J. Am. Chem. Soc.* **2006**, *128*, 6647–6656.
[17] H. E. Gottlieb, V. Kotylar, A. Nudelman, *J. Org. Chem.* **1997**, *62*, 7512–7515.
[18] Bruker programs: SMART, version 5.629; SAINT+, version 6.45; SADABS, version 2.10; *SHELXTL*, version 6.14 (Bruker AXS Inc., Madison, WI, **2003**).
[19] G. M. Sheldrick, *SHELX-97: Program for Crystal Structure Determination*; University of Göttingen, Göttingen (Germany), **1997**.

Received: March 8, 2007
Published Online: July 18, 2007

 © 2007 Wiley-VCH Verlag GmbH & Co. KGaA, Weinheim 

DOI: 10.1002/ejic.200700328

# Synthesis and Structural Characterization of Tetra- and Pentanuclear Lanthanide Hydroxido Clusters

Simmi Datta,[a] Viswanathan Baskar,[a] Henan Li,[a] and Peter W. Roesky*[a]

**Keywords:** Cage compounds / Cluster compounds / Coordination modes / Bridging ligands / Lanthanides

Tetra- and pentanuclear lanthanide clusters having dibenzoylmethanido and *o*-nitrophenolato as ligands in the coordination sphere were prepared. Treating [$LnCl_3 \cdot 6H_2O$] (Ln = Er, Tm) with dibenzoylmethane and *o*-nitrophenol in the presence of triethylamine yielded the pentanuclear lanthanide clusters $HNEt_3^+[Ln_5(\mu_3\text{-}OH)_4(\mu_4\text{-}OH)(Ph_2acac)_7(o\text{-}O_2NC_6H_4\text{-}O)_3Cl]^-$ (Ln = Er, Tm). Under the same reaction conditions but using Yb and Lu as center metals, tetranuclear lanthanide clusters $[Ln_4(\mu_3\text{-}OH)_2(Ph_2acac)_8(o\text{-}O_2NC_6H_4O)_2]$ (Ln = Yb, Lu) were obtained. The structures of all new compounds were confirmed by single-crystal X-ray diffraction. The anions of the pentanuclear lanthanide cores are square pyramidal. Each triangular face of the square pyramid is capped by one $\mu_3$-O moiety. In the square base, four lanthanide atoms are linked by one $\mu_4$-O atom. The formation of the hydroxido bridges can be explained by deprotonation of the coordinated water molecules.

(© Wiley-VCH Verlag GmbH & Co. KGaA, 69451 Weinheim, Germany, 2007)

## Introduction

Inorganic clusters continue to attract considerable attention, as they represent the bridge linking molecular and solid-state chemistry, and also because they act as useful tools to understand the size-dependent physical properties of electronic materials.[1] While the cluster chemistry of the d-block transition metals is now firmly established, and huge clusters (especially of molybdenum,[2] copper,[3] silver,[4] and gold[5]) have been isolated, the analogous chemistry of the lanthanides is virtually undeveloped.[6,7] This is even more surprising, since oligomeric lanthanide structures are proposed to play a key role in some catalytic transformations.[8,9] It is well known that the most stable lanthanide clusters are oxido/hydroxido clusters.[10] Recently, we, along with others, synthesized new tetradeca- and pentadecanuclear lanthanide oxido/hydroxido clusters.[7,11] Basically, two different approaches towards the preparation of oxido/hydroxido clusters were investigated. One way to obtain these compounds is the hydrolysis of moisture-sensitive starting material,[11,12] whereas the other approach is a hydrolytic one in which the water molecules are deprotonated in a controlled way.[13–18] Most of the oxido/hydroxido clusters are stabilized by ligands such as alkoxides,[19,20] phenoxides,[21] diketones,[22,23] and more recently amino acids[7,24] and the *o*-nitrophenolato ligand.[11]

In a recent communication, we reported the synthesis and structure of a pentanuclear yttrium cluster, $H_5[Y_5(\mu_4\text{-}O)(\mu_3\text{-}O)_4(\mu\text{-}\eta^2\text{-}Ph_2acac)_4\eta^2\text{-}(Ph_2acac)_6]$. It was obtained by treating [$YCl_3 \cdot 6H_2O$] with dibenzoylmethane ($Ph_2acacH$) in the presence of triethylamine.[14] The cluster was found to catalyze the oxidation of aldehydes to the corresponding carboxylic acids in the presence of air. An isostructural cluster having europium as the center metal was reported.[13] In contrast, by using the larger lanthanides, tetranuclear clusters of composition $[Ln_4(\mu_3\text{-}OH)_2(Ph_2acac)_{10}]$ (Ln = Pr, Nd, and Sm) were obtained in a similar manner.[15] Single-crystal X-ray analysis of these compounds revealed that each cluster consists of four lanthanide atoms, two $\mu_3$-oxygen atoms, and ten $Ph_2acac$ ligands, which make up the peripheral part of the cluster. Three types of coordination modes [$\eta^2$-, ($\mu$-O)-$\eta^2$-, and ($\mu$-O)$_2$-$\eta^2$] are observed for the ligation of $Ph_2acac$ to the metal centers.

The second ligand that we successfully introduced in the synthesis of lanthanide clusters is *o*-nitrophenolato.[11] Infinite chains of composition $[(thf)_4\{K(o\text{-}O_2NC_6H_4O)_4\text{-}Ln\}_4]_n$ (Ln = Y, Er, Lu), infinite layers of composition $[\{K_2(o\text{-}O_2NC_6H_4O)_5Tb\}_n]$ and $[\{K_2(o\text{-}O_2NC_6H_4O)_5Ln)\}_n]$ (Ln = Sm, Eu), as well as tetradecanuclear clusters of composition $H_{18}[Ln_{14}(\mu\text{-}\eta^2\text{-}o\text{-}O_2NC_6H_4O)_8(\eta^2\text{-}o\text{-}O_2NC_6H_4O)_{16}(\mu_4\text{-}O)_2(\mu_3\text{-}O)_{16}]$ (Ln = Dy, Er, Tm, Yb), were obtained by using *o*-nitrophenolato as a ligand under different reaction conditions. Thus, *o*-nitrophenolato is a ligand that features different coordination modes and is thus able to stabilize different sorts of coordination polymers and oligomers.

We are now interested in synthesizing lanthanide clusters having both the dibenzoylmethanido and *o*-nitrophenolato ligands in the coordination sphere. Herein, we report on the synthesis and structure of a series of novel tetra- and

[a] Institut für Chemie und Biochemie, Freie Universität Berlin, Fabeckstraße 34–36, 14195 Berlin, Germany
E-mail: roesky@chemie.fu-berlin.de

 © 2007 Wiley-VCH Verlag GmbH & Co. KGaA, Weinheim 

pentanuclear clusters of composition $HNEt_3^+[Ln_5(\mu_3\text{-}OH)_4(\mu_4\text{-}OH)(Ph_2acac)_7(o\text{-}O_2NC_6H_4O)_3Cl]^-$ (Ln = Er, Tm), and $[Ln_4(\mu_3\text{-}OH)_2(Ph_2acac)_8(o\text{-}O_2NC_6H_4O)_2]$ (Ln = Yb, Lu).

## Results and Discussion

Reaction of $[LnCl_3{\cdot}6H_2O]$[25] with dibenzoylmethane and *o*-nitrophenol in methanol, in the presence of triethylamine as a base, yielded the pentanuclear lanthanide clusters $HNEt_3^+[Ln_5(\mu_3\text{-}OH)_4(\mu_4\text{-}OH)(Ph_2acac)_7(o\text{-}O_2NC_6H_4O)_3Cl]^-$ [Ln = Er (**1**), Tm (**2**)] (Scheme 1). As the clusters were soluble in methanol, we used toluene to extract them from the reaction mixture. The clusters have been characterized by standard analytical and spectroscopic techniques. The solid-state structures of compounds **1** and **2** were established by single-crystal X-ray diffraction. They crystallize in the monoclinic space group $P2_1/c$ and have four molecules in the unit cell. Crystals of compounds **1** and **2** that consist of an ion pair composed of a $HNEt_3^+$ cation and a $[Ln_5(\mu_3\text{-}OH)_4(\mu_4\text{-}OH)(Ph_2acac)_7(o\text{-}O_2NC_6H_4O)_3Cl]^-$ anion are isomorphous (Figure 1). The anions consist of pentanuclear lanthanide cores in a square pyramidal arrangement. This pentanuclear arrangement of the Ln core in compounds **1** and **2** is a common structural motif for lanthanide oxido/hydroxido clusters[13,14,26] and is observed in compounds such as $[Y_9O_2(OH)_8(aacac)_{16}]^-$[10] (aacac = allylacetoacetate), $[Ln_9O_2(OH)_8(ba)_{16}]^-$[12] (ba = benzoylacetone and Ln = Sm, Eu, Gd, Dy, Er), $H_{18}[Ln_{14}(\mu\text{-}\eta^2\text{-}o\text{-}O_2NC_6H_4O)_8(\eta^2\text{-}o\text{-}O_2NC_6H_4O)_{16}(\mu_4\text{-}O)_2(\mu_3\text{-}O)_{16}]$ (Ln = Dy, Er, Tm, Yb), and related compounds.[11,13] In contrast to these neutral clusters, compounds **1** and **2** contain anionic species. Each triangular face of the square pyramid is capped by one $\mu_3$-O moiety. In the square base, four lanthanide atoms are linked by one $\mu_4$-O atom. The pentanuclear Ln core is surrounded by ten peripheral ligands and a chlorine atom. A comparison with the pure dibenzoylmethanido clusters $[Ln_5(OH)_5(Ph_2acac)_{10}]$ is quite interesting. In $[Ln_5(OH)_5(Ph_2acac)_{10}]$, six ligands are terminal chelates and four are bridging chelates bonding to two metal ions that belong to the base of the polyhedron. In compounds **1** and **2**, three of the four bridging dibenzoylmethanido ligands are formally substituted by *o*-nitrophenolato ligands. The phenolate oxygen atoms always bridge two lanthanide atoms. Two of the three *o*-nitrophenolato ligands also bind a lanthanide atom through one oxygen atom of the $NO_2$ group, whereas the $NO_2$ group of the third *o*-nitrophenolato ligand, located between Ln1 and Ln5, is turned away from the cluster core. This generates a free coordination site on Ln5, which is occupied by a chlorine atom, and results in a negatively charged cluster core.

The formation of the hydroxido bridges can be explained by the presence of water in the solvents[27] and by the six water molecules coordinated to the metal center through the oxygen atom in the starting material $[LnCl_3{\cdot}6H_2O]$.[25] Addition of base leads only to the deprotonation of the coordinated water molecules. The bridging oxygen atoms in the core of the cluster are parts of hydroxy groups; this is confirmed by a broad peak around 3425 $cm^{-1}$ in the IR spectra. The Ln–O bond lengths to the dibenzoylmethanido and to the *o*-nitrophenolato ligands are in the expected range of 222.8(2) to 246.2(2) pm for compound **1** and 223.63(11) to 247.13(13) pm for compound **2**. Each triangular face of the square pyramid is capped by one $\mu_3$-O group,

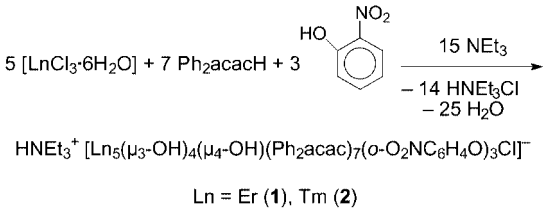


Scheme 1.

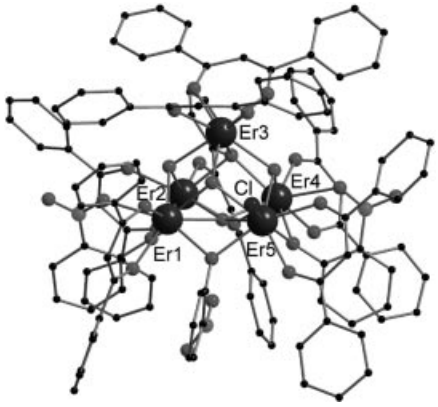


Figure 1. Solid-state structure of the anion of **1** showing the atom labeling scheme, with omission of hydrogen atoms. The small and larger dark spheres indicate carbon and oxygen atoms, respectively, and the lighter spheres stand for nitrogen atoms. Selected bond lengths [pm] (also given for the isostructural compound **2**): Er1–O1 222.8(2), Er1–O2 223.6(2), Er1–O3 229.2(2), Er1–O4 246.2(2), Er1–O21 228.9(2), Er1–O24 232.7(2), Er1–O25 250.0(3), Er1–O26 227.0(2), Er2–O3 230.6(2), Er2–O6 224.8(2), Er2–O7 222.1(2), Er2–O8 230.6(2), Er2–O9 230.5(2), Er2–O24 231.0(2), Er2–O25 250.6(2), Er2–O27 232.9(2), Er3–O10 227.1(2), Er3–O11 228.7(2), Er3–O12 227.8(2), Er3–O13 230.8(2), Er3–O24 235.6(2), Er3–O26 236.6(2), Er3–O28 237.4(2), Er3–O27 236.3(2), Er4–O9 234.3(2), Er4–O14 223.5(2), Er4–O15 224.1(2), Er4–O16 227.7(2), Er4–O17 244.2(2), Er4–O25 243.6(2), Er4–O27 227.8(2), Er4–O28 232.9(2), Er5–O16 234.5(3), Er5–O19 224.8(2), Er5–O20 222.8(2), Er5–O21 229.7(2), Er5–O25 263.7(2), Er5–O26 232.0(2), Er5–O28 230.3(2), Er5–Cl 272.2(4). **2**: Tm1–O1 225.31(11), Tm1–O2 223.63(11), Tm1–O3 229.00(13), Tm1–O4 247.13(13), Tm1–O21 230.68(14), Tm1–O24 232.59(13), Tm1–O26 226.34(12), Tm1–O25 248.56(10), Tm2–O3 232.16(13), Tm2–O6 226.65(12), Tm2–O7 223.77(13), Tm2–O8 230.99(12), Tm2–O9 230.17(13), Tm2–O24 229.68(12), Tm2–O25 250.59(12), Tm2–O27 231.60(12), Tm3–O10 228.69(12), Tm3–O11 232.36(13), Tm3–O12 228.49(11), Tm3–O13 230.87(12), Tm3–O24 235.50(12), Tm3–O26 235.79(13), Tm3–O27 235.37(12), Tm3–O28 236.22(12), Tm4–O9 234.68(13), Tm4–O14 225.27(13), Tm4–O15 224.96(10), Tm4–O16 228.58(14), Tm4–O17 245.18(12), Tm4–O25 242.31(10), Tm4–O27 228.14(13), Tm4–O28 231.56(12), Tm5–O16 234.86(13), Tm5–O19 226.76(13), Tm5–O20 226.54(13), Tm5–O21 229.54(14), Tm5–O25 262.70(11), Tm5–O26 230.26(13), Tm5–O28 230.37(13), Tm5–Cl 272.6(2).

 © 2007 Wiley-VCH Verlag GmbH & Co. KGaA, Weinheim 

whereas the square plane is capped by one $\mu_4$-bonded oxygen atom. The Ln–O bond lengths of the $\mu_4$-oxygen atoms are in the range of 243.6(2) to 263.7(2) pm in **1** and 242.31(10) to 262.70(11) pm in **2**. The Ln–Cl bond lengths are 272.2(4) pm in **1** and 272.6(2) pm in **2**. Selected metric parameters are given in the caption of Figure 1.

Since it is well known that dramatic changes in the microstructure of lanthanide clusters are observed by altering the ionic radius of the center metal, we were also interested in using smaller lanthanides. Under the same reaction conditions as those used to prepare compounds **1** and **2**, but using Yb and Lu as center metals, tetranuclear lanthanide clusters of composition $[Ln_4(\mu_3\text{-}OH)_2(Ph_2acac)_8(o\text{-}O_2NC_6H_4O)_2]$ [Ln = Yb (**3**), Lu (**4**)] were obtained (Scheme 2). The solid-state structures of compounds **3** and **4** were established by single-crystal X-ray diffraction, which revealed that they are tetranuclear (Figure 2). A comparable $Ln_4$ core was observed earlier in $[Nd_4(\mu_3\text{-}OH)_2(\mu_2\text{-},\mu_1\text{-}acac)_6(acac)_4]$ (acac = acetylacetonate)[28] and $[Ln_4(\mu_3\text{-}OH)_2(Ph_2acac)_{10}]$ (Ln = Pr, Nd, and Sm).[15] Compounds **3** and **4** are pseudopolymorphic to each other, because the amount of noncoordinated solvent (toluene) in the unit cell differs for each compound. Two types of coordination modes are observed for the ligation of $Ph_2acac$ to the metal centers in the clusters. Of the eight $Ph_2acac$ ligands, six chelate the metal centers in $\eta^2$ fashion, and two more both chelate and bridge two metal centers, thus they are $(\mu\text{-}O)_2\text{-}\eta^2$-coordinating. The *o*-nitrophenolato ligands chelate one metal atom and bridge another metal atom through one oxygen atom, thus they are $(\mu\text{-}O)\text{-}\eta^2$-coordinating. A comparison with the pure dibenzoylmethanido clusters $[Ln_4(\mu_3\text{-}OH)_2(Ph_2acac)_{10}]$ (Ln = Pr, Nd, and Sm)[15] shows the same interesting features as those observed for compounds **1** and **2**. The tetranuclear Ln core in $[Ln_4(\mu_3\text{-}OH)_2(Ph_2acac)_{10}]$ is similar to that in compounds **3** and **4**. Moreover, the $Ph_2acac$ ligands coordinate in a similar $\eta^2$- and $(\mu\text{-}O)_2\text{-}\eta^2$ fashion. The only difference between compounds **3** and **4** and $[Ln_4(\mu_3\text{-}OH)_2(Ph_2acac)_{10}]$ is the presence of the two *o*-nitrophenolato ligands. In $[Ln_4(\mu_3\text{-}OH)_2(Ph_2acac)_{10}]$, the positions of the *o*-nitrophenolato ligands are formally replaced by two more $Ph_2acac$ ligands, which bind in the same arrangement $[(\mu\text{-}O)\text{-}\eta^2$-coordination]. A significant difference arises with respect to the ionic radius of the center metal. Whereas in the pure $Ph_2acac$ clusters the cluster size decreases from penta- to tetranuclear by increasing the ionic radius, the opposite trend is observed for the mixed $Ph_2acac$/*o*-nitrophenolato compounds. In compounds **3** and **4**, the two $\mu_3$-oxygen atoms in the core of the cluster are parts of hydroxy groups, as revealed by a broad peak around 3430 $cm^{-1}$ in the IR spectra. This is supported by the Ln–O12–Ln bond angles, which are close to tetrahedral (e.g. for compound **4**: Lu1–O12–Lu1′ 108.20(6)°, Lu1–O12–Lu2 108.75(8)°, and Lu1–O12–Lu2′ 103.54(7)°). Each metal is coordinated to eight oxygen atoms in a square antiprismatic arrangement. The metal-to-oxygen distances of the coordinated ligands range from 230.1(5) to 240.7(6) pm (**3**) and from 234.5(2) to 243.6(2) pm (**4**) for the *o*-nitrophenolato ligands; for the $Ph_2acac$ ligands, the distances range from 223.1(5) to 257.6(7) pm in **3** and from 222.8(2) to 272.0(2) pm in **4**. Selected metric parameters are given in the caption of Figure 2.

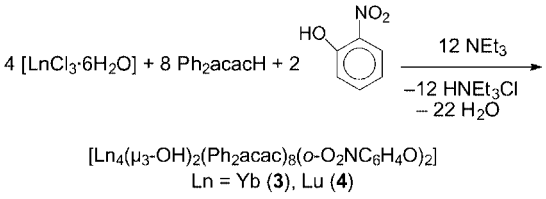


Scheme 2.

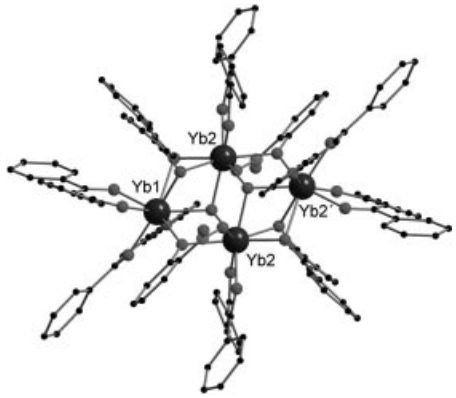


Figure 2. Solid-state structure of **3** showing the atom labeling scheme, with omission of hydrogen atoms. The small and larger dark spheres indicate carbon and oxygen atoms, respectively, and the lighter spheres stand for nitrogen atoms. Selected bond lengths [pm] (also given for the similar compound **4**): Yb1–O1 223.2(5), Yb1–O2 223.6(6), Yb1–O3 223.5(6), Yb1–O4 224.1(5), Yb1–O5 235.5(5), Yb1–O8 245.8(5), Yb1–O9 257.6(7), Yb1–O12 231.7(5), Yb2–O5′ 230.1(5), Yb2–O7 240.7(6), Yb2–O8 238.0(5), Yb2–O9 233.8(6), Yb2–O10 223.1(5), Yb2–O11 223.4(5), Yb2–O12 227.8(5), Yb2–O12′ 225.3(5). **4**: Lu1–O1 224.63(15), Lu1–O2 222.8(2), Lu1–O3 231.1(2), Lu1–O4 235.34(15), Lu1–O5 227.5(2), Lu1–O6 239.1(2), Lu1–O12 227.4(2), Lu1–O12′ 229.43(15), Lu2–O3 235.54(15), Lu2–O4 272.0(2), Lu2–O5′ 235.9(2), Lu2–O8 224.0(2), Lu2–O9 222.8(2), Lu2–O10 223.40(15), Lu2–O11 223.4(2), Lu2–O12′ 229.6(2), Lu3–O13 222.7(2), Lu3–O14 222.7(2), Lu3–O17 226.9(2), Lu3–O24 228.1(2), Lu3–O24′ 227.5(2), Lu3–O15 233.1(2), Lu3–O16 237.4(2), Lu3–O18 243.6(2), Lu4–O15 254.2(2), Lu4–O16 242.50(14), Lu4–O17′ 234.5(2), Lu4–O20 223.1(2), Lu4–O21 224.8(2), Lu4–O22 224.2(2), Lu4–O23 222.62(14), Lu4–O24 229.8(2).

## Conclusion

In summary, a series of tetra- and pentanuclear lanthanide clusters having dibenzoylmethanido and *o*-nitrophenolato as ligands in the coordination sphere were synthesized. By using the larger lanthanides as center metals, ionic clusters of composition $HNEt_3^+[Ln_5(\mu_3\text{-}OH)_4(\mu_4\text{-}OH)(Ph_2acac)_7(o\text{-}O_2NC_6H_4O)_3Cl]^-$ (Ln = Er, Tm) were obtained. In contrast, by using the smaller center metals Yb and Lu, clusters of composition $[Ln_4(\mu_3\text{-}OH)_2(Ph_2acac)_8(o\text{-}O_2NC_6H_4O)_2]$ were isolated. The formation of the hydroxido bridges can be explained by the six water molecules, which are coordinated through the oxygen atom to

 © 2007 Wiley-VCH Verlag GmbH & Co. KGaA, Weinheim 

the metal center of the starting material, $[LnCl_3 \cdot 6H_2O]$. Addition of base leads only to deprotonation of the coordinated water molecules. The bridging oxygen atoms in the cores of the clusters are parts of hydroxy groups, as revealed by the broad band in the IR spectra.

A comparison of the new mixed dibenzoylmethanido/*o*-nitrophenolato clusters with pure dibenzoylmethanido clusters shows the relationship between the two classes of clusters. Formally, the dibenzoylmethanide groups, which act in the pure dibenzoylmethanido clusters as tridentate ligands and bind in a (μ-O)-$\eta^2$ mode, are replaced by *o*-nitrophenolato ligands.

## Experimental Section

**General Considerations:** Deuterated solvents were obtained from Chemotrade or Euriso-Top GmbH (99% D atoms). NMR spectra were recorded with a Jeol JNM-LA 400 FT-NMR spectrometer. Chemical shifts are referenced to internal solvent resonances and are reported relative to tetramethylsilane. Raman spectra were recorded with a Bruker RFS 100. IR spectra were recorded with a Shimadzu FTIR-8400s. Elemental analyses were carried out with an Elementar vario EL. The lanthanide starting materials were synthesized from the corresponding oxides by neutralizing with concentrated hydrochloric acid, followed by concentration to dryness. Dibenzoylmethane, triethylamine, and the solvents were used as purchased from commercial sources without further purification.

**General Procedure for the Preparation of $HNEt_3^+[Ln_5(\mu_3\text{-}OH)_4(\mu_4\text{-}OH)(Ph_2acac)_7(o\text{-}O_2NC_6H_4O)_3Cl]^-$ [Ln = Er (1), Tm(2)] and $[Ln_4(\mu_3\text{-}OH)_2(Ph_2acac)_8(o\text{-}O_2NC_6H_4O)_2]$ [Ln = Yb (3), Lu (4)]:** $Ph_2$acacH (292 mg, 1.30 mmol) and *ortho*-nitrophenol (181 mg, 1.30 mmol) were combined in methanol (20 mL). Excess triethylamine (5.20 mmol) was slowly added to the resulting solution, and the reaction mixture was stirred for 1 h at room temp. To this was added a solution of the corresponding lanthanide trichloride hydrate (1.30 mmol) in methanol (20 mL), and the resulting yellow solution was stirred overnight at room temp. A crimson–yellow precipitate formed and was filtered off before the solvent was removed in vacuo. The residue was dissolved in toluene (5 mL) and stirred for 2 h, at which point the solution was filtered. Slow evaporation of toluene at room temp. yielded yellow crystals.

**$HNEt_3^+[Ln_5(\mu_3\text{-}OH)_4(\mu_4\text{-}OH)(Ph_2acac)_7(o\text{-}O_2NC_6H_4O)_3Cl]^-$ [Ln = Er (1), Tm (2)]**

**1:** Yield (single crystals): 100 mg (13%). IR (KBr): 3610 (m), 3525 (m), 3427 (m) (νOH), 3060 (m), 3026 (m), 1603 (s) (νCO), 1552 (s), 1521 (s) (νC⁼⁼C), 1479 (s), 1454 (s), 1441 (w), 1397 (s), 1341 (w), 1329 (w), 1315 (w), 1289 (w), 1253 (w), 1223 (w), 1180 (w), 1156 (w), 1137 (w), 1069 (w), 1023 (w), 1000 (w), 942 (w), 910 (w), 885 (w), 859 (w), 835 (w), 812 (w), 784 (w), 749 (m), 721 (m) (νC-H def), 687 (m), 618 (w), 610 (w), 526 (w) $cm^{-1}$. Raman (solid): 402 (w), 617 (w), 687 (w), 786 (w), 941 (m), 1000 (s), 1031 (w), 1062 (w), 1156 (w), 1181 (w), 1287 (s), 1315 (s), 1442 (w), 1490 (w), 1596 (s), 3064 (s) $cm^{-1}$. $C_{146.50}H_{130}ClEr_5N_4O_{28}$ (= **1**·2.5toluene) (3263.75): calcd. C 53.86, H 3.98, N 1.71; found C 53.75, H 3.52, N 1.75.

**2:** Yield (single crystals): 100 mg (13%). IR (KBr): 3601 (m), 3519 (m), 3426 (m) (νOH), 3060 (m), 3026 (m), 1603 (s) (νCO), 1553 (s), 1521 (s) (νC⁼⁼C), 1479 (s), 1454 (s), 1441 (w), 1399 (s), 1341 (w), 1329 (w), 1315 (w), 1289 (w), 1253 (w), 1224 (w), 1181 (w), 1157 (w), 1137 (w), 1070 (w), 1023 (w), 1000 (w), 942 (w), 885 (w), 859 (w), 836 (w), 812 (w), 784 (w), 750 (m), 721 (m) (νC–H def), 687 (m), 618 (w), 610 (w), 527 (w) $cm^{-1}$. Raman (solid): 402 (w), 579 (w), 617 (w), 688 (w), 785 (w), 942 (m), 1000 (s), 1033 (w), 1064 (w), 1157 (w), 1182 (w), 1224 (w), 1242 (w), 1289 (s), 1321 (s), 1442 (w), 1490 (m), 1596 (s), 3065 (s) $cm^{-1}$. $C_{146.50}H_{130}ClN_4O_{28}Tm_5$ (= **2**·2.5toluene) (3272.10): calcd. C 53.72, H 3.97, N 1.71; found C 53.09, H 3.65, N 1.67.

**$[Ln_4(\mu_3\text{-}OH)_2(Ph_2acac)_8(o\text{-}O_2NC_6H_4O)_2]$ [Ln = Yb (3), Lu (4)]**

**3:** Yield (single crystals): 220 mg (25%). IR (KBr): 3587 (m), 3429 (m) (νOH), 3058 (m), 3025 (m), 1597 (s) (νCO), 1553 (s), 1522 (s) (νC⁼⁼C), 1479 (s), 1455 (s), 1441 (w), 1404, 1341 (w), 1330 (w), 1316 (w), 1298 (w), 1290 (w), 1243 (w), 1223 (w), 1181 (w), 1156 (w), 1143 (w), 1069 (w), 1023 (w), 1000 (w), 942 (w), 925 (w), 885 (w), 862 (w), 836 (w), 819 (w), 812 (w), 785 (w), 750 (m), 721 (m) (νC–H def), 686 (m), 618 (w), 610 (w), 527 (w) $cm^{-1}$. Raman (solid): 525 (w), 617 (w), 688 (w), 705 (w), 749 (w), 790 (w), 810 (w), 842 (w), 942 (m), 1000 (s), 1024 (w), 1063 (w), 1126 (w), 1156 (w), 1181 (w), 1223 (w), 1284 (s), 1316 (s), 1377 (m), 1443 (w), 1490 (m), 1507 (w), 1552 (w), 1569 (w), 1596 (s), 3062 (s) $cm^{-1}$. $C_{132}H_{98}N_2O_{24}Yb_4$ (2786.16): calcd. C 56.85, H 3.51, N 1.00; found C 55.85, H 3.43, N 1.18.

**4:** Yield (single crystals): 100 mg (11.1%). $^1H$ NMR (400 MHz, $[D_8]$thf, 25 °C): $\delta$ = 2.29 (s), CH), 7.30–7.39 (m, 58 H, PhH), 8.07 (d, 30 H, PhH) ppm. IR (KBr): 3601 (m), 3430 (m) (νOH), 3059 (m), 3026 (m), 1598 (s) (νCO), 1554 (s), 1522 (s) (νC⁼⁼C), 1479 (s), 1455 (s), 1441 (m), 1405 (s), 1331 (m), 1316 (m), 1245 (m), 1224 (m), 1181 (w), 1156 (w), 1143 (w), 1069 (w), 1024 (w), 1000 (w), 988 (w), 971 (w), 942 (w), 926 (w), 885 (w), 868 (w), 837 (w), 812 (w), 785 (w), 750 (m), 720 (m) (νC–H def), 687 (m), 618 (w), 610 (w), 578 (w), 526 (w) $cm^{-1}$. Raman (solid): 402 (w), 578 (w), 617 (w), 688 (w), 789 (w), 836 (w), 886 (w), 942 (m), 1000 (s), 1026 (w), 1033 (w), 1065 (w), 1156 (w), 1182 (w), 1224 (w), 1243 (w), 1288 (s), 1319 (s), 1442 (w), 1490 (m), 1520 (w), 1561 (w), 1597 (s), 3066 (s) $cm^{-1}$. $C_{132}H_{98}Lu_4N_2O_{24}$ (2793.87): calcd. C 56.69, H 3.51, N 1.00; found C 56.16, H 3.42, N 1.43.

**X-ray Crystallographic Studies of 1–4:** Suitable crystals of **1**–**4** were covered in mineral oil (Aldrich) and mounted onto a glass fiber. The crystal was transferred directly to the cold (–73 °C or –100 °C) $N_2$ stream of a Stoe IPDS 2T or Bruker Smart 1000 CCD. Subsequent computations were carried out with an Intel Pentium IV PC.

**Data Collection and Refinement:** Data were processed with SHELXS-97[29] and SHELXL-97.[30]

**$HNEt_3^+[Er_5(\mu_3\text{-}OH)_4(\mu_4\text{-}OH)(Ph_2acac)_7(o\text{-}O_2NC_6H_4O)_3Cl]^-\cdot$ 2.5toluene (1):** Monoclinic, space group $P2_1/c$ (No. 14); lattice constants $a$ = 2165.5(9) pm, $b$ = 1976.2(6) pm, $c$ = 3312(3) pm, $\beta$ = 95.50(5)°, $V = 14109(13) \times 10^6$ pm$^3$, $Z$ = 4; $\mu$(Mo-$K_\alpha$) = 3.031 mm$^{-1}$; $2\theta_{max.}$ = 50.0°; 13128 ($R_{int}$ = 0.1037) independent reflections were measured, 13128 of which, observed with $I > 2\sigma(I)$, were considered; max. residual electron density 1.328 and –1.122 e/A$^{-3}$; 1385 parameters (all non-hydrogen atoms except those in the thf molecules were calculated anisotropically; for H atoms, the idealized positions were calculated) $R_1$ = 0.0592; $wR_2$ = 0.1637.

**$HNEt_3^+[Tm_5(\mu_3\text{-}OH)_4(\mu_4\text{-}OH)(Ph_2acac)_7(o\text{-}O_2NC_6H_4O)_3Cl]^-\cdot$ 2.5toluene (2):** Monoclinic, space group $P2_1/c$ (No. 14); lattice constants $a$ = 2166.89(7) pm, $b$ = 1989.77(5) pm, $c$ = 3308.94(10) pm, $\beta$ = 95.741(3)°, $V = 14195.3(7) \times 10^6$ pm$^3$, $Z$ = 4; $\mu$(Mo-$K_\alpha$) = 3.182 mm$^{-1}$; $2\theta_{max.}$ = 53.6°; 29856 ($R_{int}$ = 0.0703) independent reflections were measured, 20804 of which, observed with $I > 2\sigma(I)$, were considered; max. residual electron density 1.686 and –2.017 e/A$^{-3}$; 1384 parameters (all non-hydrogen atoms except those in

 © 2007 Wiley-VCH Verlag GmbH & Co. KGaA, Weinheim 

the thf molecules were calculated anisotropically; for H atoms, the idealized positions were calculated) $R_1 = 0.0548$; $wR_2 = 0.1551$.

**$[Yb_4(\mu_3\text{-}OH)_2(Ph_2acac)_8(o\text{-}O_2NC_6H_4O)_2]\cdot$6toluene (3):** Triclinic, space group $P\bar{1}$ (No. 2); lattice constants $a = 1392.42(8)$ pm, $b = 1613.72(10)$ pm, $c = 1820.81(10)$ pm, $\alpha = 84.901(5)°$, $\beta = 74.180(4)°$, $\gamma = 73.985(5)°$, $V = 3783.2(4) \times 10^6$ pm$^3$, $Z = 1$; $\mu$(Mo-$K_\alpha$) = 2.519 mm$^{-1}$; $2\theta_{max.} = 58.5°$; 19861 ($R_{int} = 0.0713$) independent reflections were measured, 14450 of which, observed with $I > 2\sigma(I)$, were considered; max. residual electron density 2.245 and –3.913 e/A$^{-3}$; 887 parameters (all non-hydrogen atoms except those in the thf molecules were calculated anisotropically; for H atoms, the idealized positions were calculated) $R_1 = 0.0731$; $wR_2 = 0.2427$.

**$[Lu_4(\mu_3\text{-}OH)_2(Ph_2acac)_8(o\text{-}O_2NC_6H_4O)_2]\cdot$2toluene (4):** Triclinic, space group $P\bar{1}$ (No. 2); lattice constants $a = 1419.7(5)$ pm, $b = 1440.7(5)$ pm, $c = 3090.1(5)$ pm, $\alpha = 83.974(5)°$, $\beta = 84.109(5)°$, $\gamma = 81.588(5)°$, $V = 6193(3) \times 10^6$ pm$^3$, $Z = 2$; $\mu$(Mo-$K_\alpha$) = 3.235 mm$^{-1}$; $2\theta_{max.} = 50.2°$; 21707 ($R_{int} = 0.0633$) independent reflections were measured, 14033 of which, observed with $I > 2\sigma(I)$, were considered; max. residual electron density 1.434 and –1.717 e/A$^{-3}$; 1356 parameters (all non-hydrogen atoms except those in the thf molecules were calculated anisotropically; for H atoms, the idealized positions were calculated) $R_1 = 0.0505$; $wR_2 = 0.1400$.

CCDC-641082 to CCDC-641085 contain the supplementary crystallographic data for this paper. These data can be obtained free of charge from The Cambridge Crystallographic Data Centre via www.ccdc.cam.ac.uk/data_request/cif.

## Acknowledgments

This work was supported by the Fonds der Chemischen Industrie and the Deutsche Forschungsgemeinschaft (DFG Schwerpunktprogramm (SPP 1166): Lanthanoidspezifische Funktionalitäten in Molekül und Material).

[1] a) G. Schmid (Ed.), *Clusters and Colloids. From Theory to Applications*, VCH, Weinheim, **1994**; b) L. J. de Jongh (Ed.), *Physics and Chemistry of Metal Cluster Compounds*, Kluwer, Dordrecht, **1994**.
[2] A. Müller, E. Krickmeyer, H. Bögge, M. Schmidtmann, F. Peters, *Angew. Chem.* **1998**, *110*, 3567–3571; *Angew. Chem. Int. Ed.* **1998**, *37*, 3360–3363.
[3] H. Krautscheid, D. Fenske, G. Baum, M. Semmelmann, *Angew. Chem.* **1993**, *105*, 1364–1367; *Angew. Chem. Int. Ed. Engl.* **1993**, *32*, 1303–1306.
[4] D. Fenske, N. Zhu, T. Langetepe, *Angew. Chem.* **1998**, *110*, 2784–2788; *Angew. Chem. Int. Ed.* **1998**, *37*, 2640–2644.
[5] P. Sevillano, O. Fuhr, M. Kattannek, P. Nava, O. Hampe, S. Lebedkin, R. Ahlrichs, D. Fenske, M. Kappes, *Angew. Chem.* **2006**, *118*, 3785–3791; *Angew. Chem. Int. Ed.* **2006**, *45*, 3702–3708.
[6] R. Anwander, *Angew. Chem.* **1998**, *110*, 619–622; *Angew. Chem. Int. Ed.* **1998**, *37*, 599–602.
[7] Z. Zheng, *Chem. Commun.* **2001**, 2521–2529.
[8] J. Gromada, A. Mortreux, T. Chenal, J. W. Ziller, F. Leising, J.-F. Carpentier, *Chem. Eur. J.* **2002**, *8*, 3773–3788.
[9] M. R. Bürgstein, H. Berberich, P. W. Roesky, *Chem. Eur. J.* **2001**, *7*, 3078–3085.
[10] a) M. K. Thompson, M. Vuchkov, I. A. Kahwa, *Inorg. Chem.* **2001**, *40,* 4332–4341; b) H.-X. Li, M.-L. Cheng, Z.-G. Ren, W.-H. Zhang, J.-P. Lang, Q. Shen, *Inorg. Chem.* **2006**, *45*, 1885–1887; c) L. Natrajan, J. Pécaut, M. Mazzanti, *Dalton Trans.* **2006**, 1002–1005.
[11] a) M. R. Bürgstein, P. W. Roesky, *Angew. Chem.* **2000**, *112*, 559–562; *Angew. Chem. Int. Ed.* **2000**, *39*, 549–551; b) M. R. Bürgstein, M. T. Gamer, P. W. Roesky, *J. Am. Chem. Soc.* **2004**, *126*, 5213–5218.
[12] R. Anwander, F. C. Munck, T. Priermeier, W. Scherer, O. Runte, W. A. Herrmann, *Inorg. Chem.* **1997**, *36*, 3545–3552.
[13] R.-G. Xiong, J.-L. Zuo, Z. Yu, X.-Z. You, W. Chen, *Inorg. Chem. Commun.* **1999**, *2*, 490–494.
[14] P. W. Roesky, G. Canseco-Melchor, A. Zulys, *Chem. Commun.* **2004**, 738–739.
[15] V. Baskar, P. W. Roesky, *Z. Anorg. Allg. Chem.* **2005**, *631*, 2782–2785.
[16] V. Baskar, P. W. Roesky, *Dalton Trans.* **2006**, 676–679.
[17] a) M.-B. Zhang, J. Zhang, S.-T. Zheng, G.-Y. Yang, *Angew. Chem.* **2005**, *117*, 1409–1412; *Angew. Chem. Int. Ed.* **2005**, *44*, 1385–1388; b) X. Fang, T. M. Anderson, C. Benelli, C. L. Hill, *Chem. Eur. J.* **2005**, *11*, 712–718.
[18] R. Wang, M. D. Carducci, Z. Zheng, *Inorg. Chem.* **2000**, *39*, 1836–1837.
[19] a) R. C. Mehrotra, A. Singh, U. M. Tripathi, *Chem. Rev.* **1991**, *91*, 1287–1303; b) L. G. Hubert-Pfalzgraf, *Coord. Chem. Rev.* **1998**, *178–180*, 967–997.
[20] J. Gromada, A. Mortreux, T. Chenal, J. W. Ziller, F. Leising, J.-F. Carpentier, *Chem. Eur. J.* **2002**, *8*, 3773–3788.
[21] W. J. Evans, M. A. Greci, J. W. Ziller, *Inorg. Chem.* **2000**, *39*, 3213–3220.
[22] L. G. Hubert-Pfalzgraf, N. M. Pajot, R. Papernik, J. Vaissermann, *J. Chem. Soc., Dalton Trans.* **1999**, 4127–4130.
[23] R. C. Mehrotra, R. Bohra, D. P. Gauer, *Metal β-Diketones and Allied Derivatives*, Academic Press, London, **1978**.
[24] a) R. Wang, Z. Zheng, T. Jin, R. J. Staples, *Angew. Chem.* **1999**, *111*, 1929–1931; *Angew. Chem. Int. Ed.* **1999**, *38*, 1813–1815; b) R. Wang, H. Liu, M. D. Carducci, T. Jin, C. Zheng, Z. Zheng, *Inorg. Chem.* **2001**, *40*, 2743–2750.
[25] E. J. Graeber, G. H. Conrad, S. F. Duliere, *Acta Crystallogr.* **1966**, *21*, 1012–1013.
[26] a) D. C. Bradley, H. Chudzynska, D. M. Frigo, M. E. Hammond, M. B. Hursthouse, M. A. Mazid, *Polyhedron* **1990**, *9*, 719–726; b) O. Poncelet, W. J. Sartain, L. G. Hubert-Pfalzgraf, K. Folting, K. G. Caulton, *Inorg. Chem.* **1989**, *28*, 263–267; c) R.-G. Xiong, J.-L. Zuo, Z. Yu, X.-Z. You, W. Chen, *Inorg. Chem. Commun.* **1999**, *2*, 490–494; d) W. J. Evans, M. A. Greci, J. W. Ziller, *Inorg. Chem.* **2000**, *39*, 3213–3220.
[27] L. Natrajan, J. Pécaut, M. Mazzanti, C. LeBrun, *Inorg. Chem.* **2005**, *44*, 4756–4765.
[28] O. Poncelet, L. G. Hubert-Pfalzgraf, *Polyhedron* **1989**, *8*, 2183-2188.
[29] G. M. Sheldrick, *SHELXS-97*, *Program of Crystal Structure Solution*, University of Göttingen, Germany, **1997**.
[30] G. M. Sheldrick, *SHELXL-97*, *Program of Crystal Structure Solution*, University of Göttingen, Germany, **1997**.

Received: March 23, 2007
Published Online: July 23, 2007

 © 2007 Wiley-VCH Verlag GmbH & Co. KGaA, Weinheim 

DOI: 10.1002/ejic.200700322

# Sterically Demanding Iminopyridine Ligands

**Torsten Irrgang,[a] Sandra Keller,[a] Heidi Maisel,[a] Winfried Kretschmer,[b] and Rhett Kempe*[a]**

**Keywords:** Ethylene polymerization / N ligands / Cobalt / Iron / Nickel / Palladium

Two sterically demanding iminopyridine ligands, (2,6-diisopropylphenyl)[6-(2,4,6-triisopropylphenyl)pyridin-2-ylmethylene]amine and (2,6-diisopropylphenyl)[6-(2,6-dimethylphenyl)pyridin-2-ylmethylene]amine, were prepared by a two-step process: first, condensation of 6-bromopyridine-2-carbaldehyde with an equimolecular amount of 2,6-diisopropylaniline, and second, Kumada-type coupling of in-situ-formed Grignard compounds of 1-bromo-2,6-dimethylphenyl and 1-bromo-2,4,6-triisopropylphenyl. Dichlorido complexes of the ligands were synthesized starting from $FeCl_2$, $[PdCl_2(cod)]$, $[NiCl_2(dme)]$, and $CoCl_2$ (cod = 1,5-cyclooctadiene, dme = dimethoxyethane). X-ray crystal structure analyses of a Fe, Pd, and Co complex were determined. Ethylene polymerization/oligomerization behavior of the dichlorido complexes after activation with methylaluminoxane or triethylaluminum was studied. Ethylene dimerization selectivity greater than 95 % was observed.

(© Wiley-VCH Verlag GmbH & Co. KGaA, 69451 Weinheim, Germany, 2007)

## Introduction

Olefin polymerization catalyzed by late-transition-metal complexes is an intensively explored area of research.[1] Out of the neutral N ligand environments studied so far, diimine group 10 (Scheme 1, left) and the pyridyl diimine Fe/Co catalysts (Scheme 1, right) have received most of the attention.[2] Remarkable changes in the polymerization behavior especially with regard to the obtained molecular weights of the polymers have been observed for these complexes if very bulky 2,6-diisopropylphenyl substituents were introduced.

Scheme 1. N-ligand-stabilized late-transition-metal olefin polymerization precatalysts (for instance: M = Ni, Pd; M′ = Fe, Co; X = Cl; R = H; $R^1 = CH_3$; Ar = 2,6-diisopropylphenyl).

Iminopyridine ligands (Scheme 2, right) might be considered to be structurally related to both of the above-mentioned ligand systems, and consequently, the olefin polymerization behavior of some of these complexes was investigated recently.[3–5] Sterically demanding examples bearing 2,6-diisopropylphenyl substituents in the pyridine ring are not known to the best of our knowledge.

[a] Lehrstuhl für Anorganische Chemie II, Universität Bayreuth, 95440 Bayreuth, Germany
E-mail: kempe@uni-bayreuth.de
[b] Stratingh Institut for Chemistry, Center for Catalytic Olefin Polymerization, University of Groningen, Nijenborgh 4, 9747 AG Groningen, The Netherlands

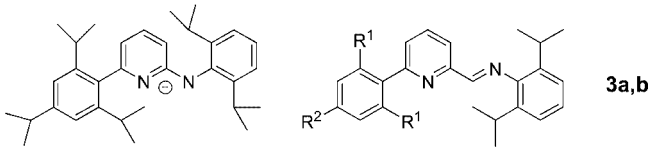

**3a,b**

Scheme 2. Sterically demanding aminopyridinato ligands (left) and iminopyridines [**3a**: $R^1 = CH_3$, $R^2$ = H; **3b**: $R^1 = R^2 = CH(CH_3)_2$].

Bianchini and coworkers for instance described phenyl and naphthalenyl substitution at the pyridine ring by Suzuki coupling.[4] It may not be possible to use such a protocol to cross couple sterically demanding phenyl derivatives like 2,6-diisopropylphenyl.[6] We recently described an efficient protocol to introduce 2,6-diisopropylphenyl substituents into pyridine rings by Kumada coupling. This chemistry was explored to synthesize sterically demanding aminopyridines[7] and to use them as aminopyridinato ligands (Scheme 2, left);[8] a class of ligands we investigated intensively in the past.[9]

Because of the importance of steric protection in late-metal-catalyzed olefin polymerization chemistry, as well as other areas of coordination chemistry, we became interested in the synthesis of bulky iminopyridines such as **3a**,**b** (Scheme 2, right). We felt that an approach we used to synthesize bulky aminopyridines might by suitable for the synthesis of ligands such as **3a**,**b** as well. The imine function that is usually sensitive towards the addition of Grignard reagents might be well enough protected due to the 2,6-diisopropylphenyl substituent at the imine N atom. Herein we report the synthesis of sterically demanding iminopyridine ligands, the syntheses and structures of Co, Ni, Fe,

 © 2007 Wiley-VCH Verlag GmbH & Co. KGaA, Weinheim 

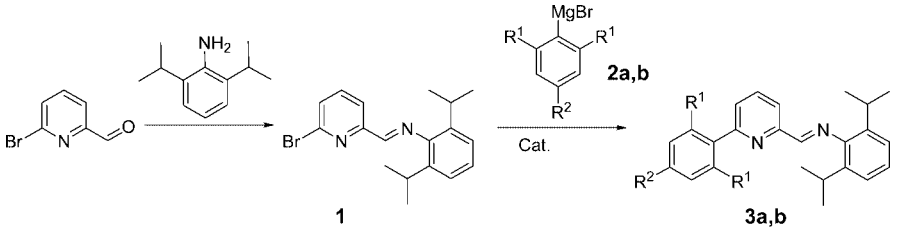


Scheme 3. Synthesis of **3** [$R^1$ = $CH_3$, $R^2$ = H (**2a/3a**); $R^1$ = $R^2$ = *i*Pr (**2b/3b**); cat for Kumada coupling is $FeCl_2$ or $MnCl_2$].

and Pd complexes stabilized by these ligands, and some aspects of the olefin polymerization/oligomerization behaviors of a few of these complexes.

## Results and Discussion

### Syntheses of the Ligands

The sterically demanding iminopyridine ligands **3a**,**b**[10] were prepared by the two-step process illustrated in Scheme 3. First, the convenient condensation of 6-bromopyridine-2-carbaldehyde with an equimolecular amount of 2,6-diisopropylaniline leads to **1**.[11] The reaction of in-situ-formed Grignard compounds **2a**,**b** of 1-bromo-2,6-dimethylphenyl and 1-bromo-2,4,6-triisopropylphenyl with **1** in the presence of a catalytic amount of $FeCl_2$ leads to iminopyridines **3a**,**b** (Scheme 3).[12] We observed similar results by using $MnCl_2$ as a catalyst. The catalyst was chosen on the basis of the results that were obtained from screening experiments with various transition-metal halogenides and N or P ligands. The 2,6-diisopropylphenyl group at the imine N atom protects the imine well enough if an efficient catalyst is added to accomplish biaryl formation.

Compounds **3a**,**b** were obtained as pale yellow crystalline materials. They differ in the steric demand ($R^1$ and $R^2$) of the phenyl substituent in the 6-position of the pyridine ring.

### Syntheses and Structures of the Complexes

Complexes **4**–**7** were obtained in high yields in the reaction of 1 equiv. of **3a** with anhydrous $FeCl_2$, [$PdCl_2$(cod)], [$NiCl_2$(dme)], and $CoCl_2$ (cod = 1,5-cyclooctadiene, dme = dimethoxyethane) in thf at 70 °C for 18 h (Scheme 4).

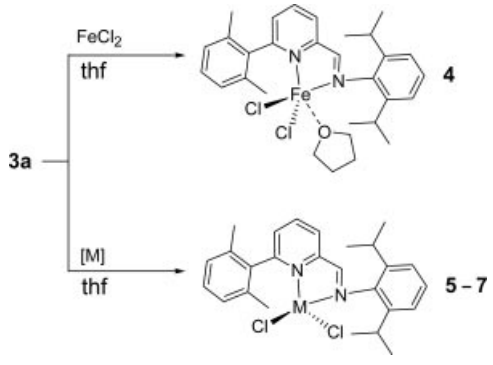


Scheme 4. Reaction of **3a** with late-transition-metal halogenides {[M] = [$PdCl_2$(cod)] (**5**); [$NiCl_2$(dme)] (**6**); $CoCl_2$ (**7**)}.

Single crystals of red paramagnetic complex **4** and yellow crystals of diamagnetic **5**[13] were grown from a concentrated thf solution at –25 °C. For both complexes, one uncoordinated thf molecule was found in the crystal lattice, and for **4**, one additional coordinated thf ligand was found. ORTEP drawings are reported in Figures 1 and 2 for **4** and **5**, respectively. Crystallographic details are summarized in Table 2. In **4**, the iron is five coordinate, and the coordination sphere is best described as distorted trigonal bipyramidal with the equatorial plane being occupied by the imino N atom and the two chlorine atoms. The axial positions are coordinated by the pyridine N atom and by the O atom of the coordinated thf ligand. A Cl–Fe–Cl angle of 131.81(6)° is observed within the equatorial plane and a "chelating" angle $N_{pyridine}$–Fe–$N_{imino}$ of 77.30(16)°. The Fe–O bond of the coordinated thf ligand is rather long [2.474(8) Å], which indicates a very weakly bound thf ligand. The Fe–O bond lengths of thf-coordinated iron chlorides range from 1.944 Å for [$FeCl_3$(thf)][14] to 2.181 Å for the [$Fe_2Cl_3$-$(thf)_6$]$^-$ anion.[15] The coordination of **5** is best described as square planar with a $N_{pyridine}$–Pd–$N_{imino}$ angle of 80.50(15)° and Cl–Pd–Cl angle of 88.84(5)°.

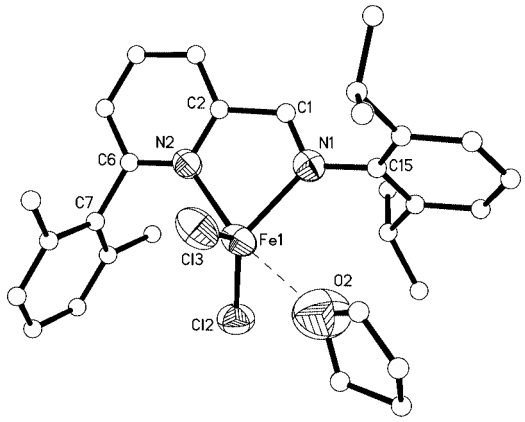


Figure 1. Molecular structure of **4**; selected bond lengths [Å] and angles [°]: C1–N1 1.271(6), C1–C2 1.486(7), C2–N2 1.357(6), C6–N2 1.353(6), C6–C7 1.490(7), C15–N1 1.441(6), N1–Fe1 2.140(4), N2–Fe1 2.201(4), Cl2–Fe1 2.2369(17), Cl3–Fe1 2.2586(17), O2–Fe1 2.473; N1–C1–C2 120.3(5), N2–C2–C1 115.4(5), N2–C6–C7 118.1(4), C1–N1–C15 118.4(4), C1–N1–Fe1 113.9(3), C15–N1–Fe1 126.9(3), C6–N2–C2 117.1(4), C6–N2–Fe1 131.0(3), C2–N2–Fe1 111.3(3), N1–Fe1–N2 77.30(16), N1–Fe1–Cl2 122.05(12), N2–Fe1–Cl2 105.29(12), N1–Fe1–Cl3 103.30(12), N2–Fe1–Cl3 99.34(12), Cl2–Fe1–Cl3 131.81(6).

 © 2007 Wiley-VCH Verlag GmbH & Co. KGaA, Weinheim 

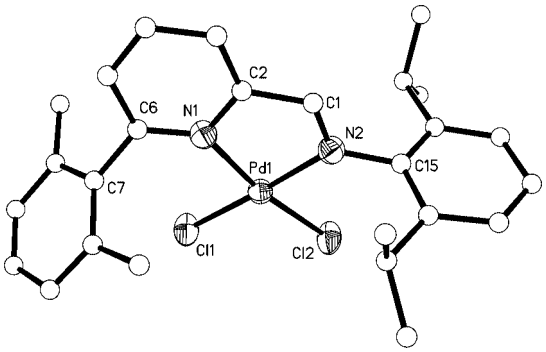


Figure 2. Molecular structure of **5**; selected bond lengths [Å] and angles [°]: Pd1–N2 2.012(4), Pd1–N1 2.090(4), Pd1–Cl1 2.273(13), Pd1–Cl2 2.2746(15), N2–C1 1.272(6), N2–C15 1.464(6), N1–C6 1.347(6), N1–C2 1.355(6), C1–C2 1.451(6), C6–C7 1.489(8); N2–Pd1–N1 80.50(15), N2–Pd1–Cl1 176.40(13), N1–Pd1–Cl1 99.43(10), N2–Pd1–Cl2 91.01(12), N1–Pd1–Cl2 170.89(11), Cl1–Pd1–Cl2 88.84(5), C1–N2–C15 117.9(4), C1–N2–Pd1 113.8(3), C15–N2–Pd1 128.2(3), C6–N1–C2 117.1(4), C6–N1–Pd1 132.8(3), C2–N1–Pd1 110.0(3), N2–C1–C2 119.1(4), N1–C2–C1 115.3(4), N1–C6–C7 121.2(4).

The reaction of sterically more demanding ligand **3b** with the anhydrous metal salts $FeCl_2$, $[PdCl_2(cod)]$, $[NiCl_2(dme)]$, and $CoCl_2$ leads to corresponding complexes **8**–**11** (Scheme 5). Compounds **8**, **10**, and **11** are paramagnetic.

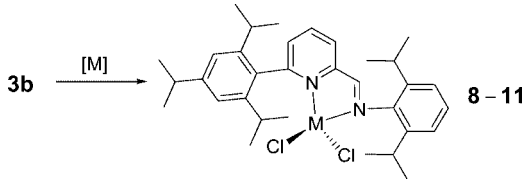


Scheme 5. Synthesis of **8** (M = Fe), **9** (M = Pd), **10** (M = Ni), and **11** (M = Co).

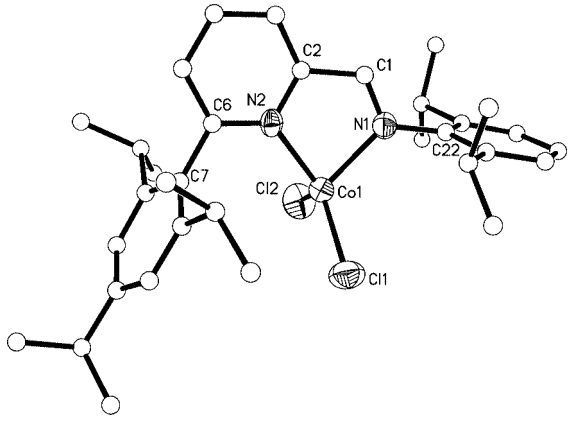


Figure 3. Molecular structure of **11**; selected bond lengths [Å] and angles [°]: Co1–N2 2.052(4), Co1–N1 2.057(4), Co1–Cl2 2.2023(16), Co1–Cl1 2.2007(15), N2–C2 1.346(6), N2–C6 1.353(6), N1–C1 1.267(6), N1–C22 1.453(6), C1–C2 1.477(7), C6–C7 1.479(7); N2–Co1–N1 80.23(16), N2–Co1–Cl2 111.01(11), N1–Co1–Cl2 109.89(12), N2–Co1–Cl1 125.20(12), N1–Co1–Cl1 113.17(22), Cl2–Co1–Cl1 112.60(7), C2–N2–C6 118.6(4), C2–N2–Co1 112.3(3), C6–N2–Co1 128.8(3), C1–N1–C22 120.1(4), C1–N1–Co1 113.2(3), C22–N1–Co1 126.7(3), N1–C1–C2 118.6(4), N2–C2–C1 114.7(4), N2–C6–C7 118.6(4).

The coordination of the cobalt centre of **11** is best described as slightly distorted tetrahedral. For the three structurally characterized metal complexes we observed three different coordination environments. The sterically demanding N ligands introduced here seem to be quite flexible with regard to the coordination they adopt with transition metals, and they do not force metals in energetically unfavored coordinations because of steric pressure. The chelating $N_{pyridine}$–Co–$N_{imino}$ angle of **11** is 80.24°. The bulky phenyl substituents in the 6-position of the pyridine and at the imino N atom are twisted relative to the pyridine ring with dihedral angles of 99.8° and 97.1°, respectively. The five-membered chelating $C_2CoN_2$ ring is nearly planar (0.0473 Å mean deviation). Details of the X-ray crystal structure analysis of **11** are summarized in Table 2. The molecular structure of **11** is shown in Figure 3.

## Olefin Polymerization/Oligomerization Behavior

Oligomerization results are summarized in Table 1. The investigated complexes mainly produce oligomeric materials. Nearly no activity is observed for the iron complexes. The highest activities are observed for the cobalt and nickel complexes. For both metals, Co and Ni, the changes in terms of activity and distribution of the oligomers are rather small. The sterically more demanding ligand shows essentially the same polymerization behavior, aside from a little enhanced activity. Noteworthy is that the selectivity for **6**, **7**, **10**, and **11** towards 1-butene is high. High ethylene dimerization selectivities were observed for iminopyridine complexes bearing sterically less-demanding substituents on the pyridine ring as well.[4] Activation with triethylaluminum (TEA), $Et_3Al$, instead of methylaluminoxane (MAO), leads to reduced activity but suppresses the formation of polymeric byproducts and increases the dimerization selectivity above 95%. The results obtained with our Co complexes are similar to (or nearly as good as) the results observed by Bianchini and coworkers.[4] They observed for iminopyridine Co complexes (activated with MAO) carrying a phenyl or naphthyl substituent on the pyridine ring the formation of oligomerization products and butenes, especially with conversions of 784 and 630 $kg_{product}mol_{cat}^{-1}h^{-1}bar^{-1}$, respectively. This comparison indicates that the introduction of steric bulk in the 6-position of the pyridine ring does not influence the nature of the products formed. It was recently demonstrated by these groups that their tetrahedral high-spin complexes react with MAO in toluene to give low-spin Co square-planar methyl complexes.[4e] This species, intercepted by EPR spectroscopy, inserts ethylene to form a cobalt–propyl intermediate that eliminates propene with the formation of a Co–H initiator. A similar mechanism is most likely in operation for our Co (and Ni) complexes; by ethylene insertion into a Co–H bond, an ethyl complex is formed. If this species undergoes β-H elimination/transfer we get back to the starting point (Co–H complex and ethylene). If a second insertion of ethylene takes place, a butyl complex is formed and

 © 2007 Wiley-VCH Verlag GmbH & Co. KGaA, Weinheim 

Table 1. Ethylene polymerization/oligomerization of metal complexes by using different activation protocols.[a] Products were analyzed by GC with the use of α-olefins as internal standards.

| Run | Complex[b] | Activator[c] | Conversion [$kg\,mol_{cat}^{-1}\,h^{-1}\,bar^{-1}$] | $m_{Pol.}$ [g] | C-4[d] [g] | C-6 [g] | C-8 [g] | Higher [g] |
|---|---|---|---|---|---|---|---|---|
| 1 | **4**, Fe | MAO | 2 | 0.05 | – | – | – | – |
| 2 | **4**, Fe[e] | TEA | 0 | – | – | – | – | – |
| 3 | **8**, Fe* | MAO | 2 | 0.06 | – | – | – | – |
| 4 | **8**, Fe*[e] | TEA | 0 | – | – | – | – | – |
| 5 | **7**, Co | MAO | 358 | 0.06 | 3.95 | 0.55 | – | – |
| 6 | **7**, Co[e] | TEA | 152 | – | 1.85 | 0.05 | – | – |
| 7 | **11**, Co* | MAO | 472 | 0.06 | 5.00 | 0.80 | – | – |
| 8 | **11**, Co*[e] | TEA | 172 | – | 2.10 | 0.05 | | |
| 9 | **6**, Ni | MAO | 150 | 0.06 | 1.16 | 0.35 | 0.23 | 0.11 |
| 10 | **6**, Ni | MMAO-3A | 136 | 0.06 | 1.10 | 0.15 | nd[f] | nd[f] |
| 11 | **10**, Ni* | MAO | 156 | 0.06 | 1.27 | 0.59 | 0.03 | – |
| 12 | **10**, Ni* | MMAO-3A | 140 | 0.06 | 1.21 | 0.34 | nd[f] | nd[f] |
| 13 | **5**, Pd | MAO | 12 | 0.3 | – | – | – | – |
| 14 | **5**, Pd | MMAO-3A | 8 | 0.2 | – | – | – | – |
| 15 | **9**, Pd* | MAO | 20 | 0.5 | – | – | – | – |
| 16 | **9**, Pd* | MMAO-3A | 12 | 0.3 | – | – | – | – |

[a] The general procedure and conditions as described in the Experimental Section were followed by using the catalyst (10 μmol), the activator (500 equiv.), and toluene (260 mL) at 30 °C, 5 bar ethylene with a 15 min run time. [b] * Indicates the sterically more-demanding ligand. [c] MMAO-3A: Modified MAO $\{[Me_{0.7}iBu_{0.3}AlO]_n\}$. [d] >95% 1-Butene. [e] M/Al, 1:200. [f] Not determined, isoparaffinic solvent (b.p. 118 °C).

subsequently butene can be eliminated. It looks as though β-H elimination/transfer is very fast with regard to chain growth for our Co complexes and thus we preferentially obtain butenes. If we activate with TEA, β-H elimination/transfer may become enhanced because butene selectivity is increased. Alternatively, TEA may reduce the Co dichloride complexes followed by oxidative coupling of two ethylene molecules including the formation of a cobaltacyclopentene followed by β-H elimination, forming a butenyl hydride that undergoes reductive elimination, and butene is formed. The stability of the transient cobaltacyclopropene against further ethylene insertion may lead to the exclusive formation of the dimerization product. Interestingly, we are able to dimerize selectively with relatively low cocatalyst loadings and MAO was not needed. Mapolie and coworkers studied the formation of polymeric materials for Pd complexes.[5] Conversions up to 15 $kg_{product}\,mol_{cat}^{-1}\,h^{-1}\,bar^{-1}$ were observed, which again is in accordance with the results obtained for our Pd complexes. Once more, no dramatic influence is seen due to the introduction of the very bulky substituents on the pyridine ring. It is surprising that the electronic situation that the iminopyridines provide dominate the polymerization chemistry and that the bulkiness of the ligands on the pyridine ring is of minor relevance despite the difference in shielding at the metal center. The shielding is visualized in Figure 4.

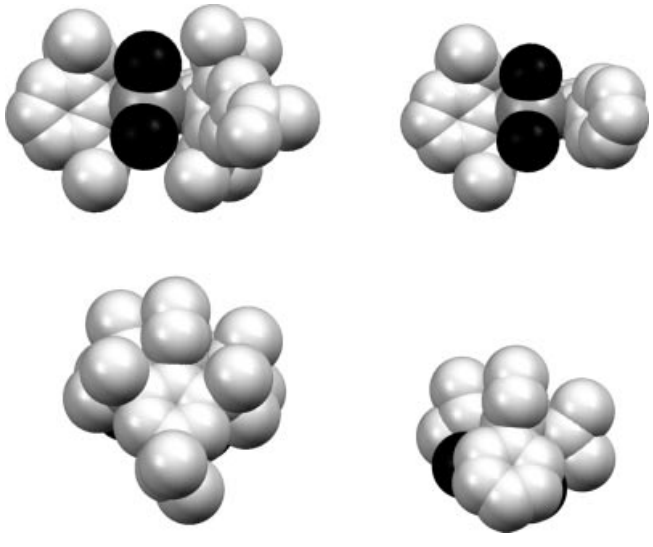

Figure 4. Visualization (space filling plot with C atoms light grey, Co atoms dark grey, Cl atoms black) of the steric protection of the 2,4,6-triisopropylphenyl substituent at the pyridine ring (right) versus shielding provided by a phenyl ring only (left).

## Conclusions

Four general conclusions can be drawn from the investigations discussed here. First, Kumada coupling is an efficient protocol to introduce sterically demanding substituents in the 6-position of the pyridyl ring of iminopyridines. Second, the sterically demanding ligands discussed here accomplish a variety of coordinations with late transition metals, such as trigonal bipyramidal, tetrahedral, and square planar. Third, the cobalt and nickel dichlorido complexes (if activated with MAO or TEA) dimerize ethylene rather than polymerize it and can show dimerization selectivities greater than 95%. Fourth, the introduction of the bulky 2,6-dialkylphenyl substituent in the pyridine moiety does not influence the polymerization behavior of the resulting late-transition-metal complexes (activation with MAO) tremendously relative to the significantly less bulky versions of those ligands.

 © 2007 Wiley-VCH Verlag GmbH & Co. KGaA, Weinheim 

## Experimental Section

### Polymerization Experiments

**General:** Toluene (Aldrich, anhydrous, 99.8%) was passed over columns of $Al_2O_3$ (Fluka), BASF R3–11 supported Cu oxygen scavenger and molecular sieves (Aldrich, 4 Å) prior to use. Ethylene (AGA polymer grade) was passed over BASF R3–11 supported Cu oxygen scavenger and molecular sieves (Aldrich, 4 Å) prior to use. TEA (1.6 M in toluene, Aldrich), PMAO (4.9 wt.-% in Al, toluene, Akzo), and MMAO-3A (2.1 wt.-% in Al; isoparaffinic solvent, b.p. 118 °C; Akzo) were used as received.

**Preparative Procedure:** The polymer samples were prepared by dissolving the polymer (15 mg) in $CD_2Cl_2$ (0.5 mL) at 100 °C for 3 h before measuring. Gel permeation chromatography (GPC) analysis was carried out with a Polymer Laboratories Ltd. (PL-GPC210) chromatograph, equipped with a capillary differential viscometer (Viscotek), a refractive index (RI) detector, and a two-angle (15 and 90°) light-scattering photometer at 150 °C by using 1,2,4-trichlorobenzene as the mobile phase. The samples were prepared by dissolving the polymer (0.1% weight/volume) in the mobile phase solvent in an external oven and were run without filtration. The molecular weight was referenced to polyethylene ($M_w$ = 50000 g mol$^{-1}$) and polystyrene ($M_w$ = 100000–500000 g mol$^{-1}$) standards. The reported values are the average of at least two independent determinations. GC analyses were performed with an HP 6890 instrument equipped with an HP-1 dimethylpolysiloxane column (19095 Z-123). GC–MS analyses were conducted with an HP 5973 mass-selective detector attached to an HP 6890 GC instrument.

**Polymethylaluminoxane (PMAO) Ethylene Conversion:** The catalytic ethylene conversion reactions were performed in a stainless steel 1-L autoclave (Medimex) in the semibatch mode (ethylene was added by replenishing flow to keep the pressure constant). The reactor was temperature, flow, and pressure controlled and equipped with separated toluene, catalyst, and cocatalyst injection systems and a sample outlet for continuous reaction monitoring. Up to 15 bar of ethylene pressure multiple injections of the catalyst with a pneumatically operated catalyst injection system were used. During a polymerization run, the pressure, the ethylene flow, the inner and the outer reactor temperature, and the stirrer speed were monitored continuously. In a typical semibatch experiment, the autoclave was evacuated and heated for 1 h at 125 °C prior to use. The reactor was then brought to the desired temperature, stirred at 600 rpm and charged with toluene (230 mL), PMAO (2.7 g of a toluene solution, 4.9 wt.-% Al, 5 mmol), and cyclohexane (10 g) as an internal standard. After pressurizing with ethylene to reach a total pressure of 5 bar, the autoclave was equilibrated for 5 min. Subsequently, the catalyst (10 μmol, M/Al, 1:500) suspended in toluene (30 mL) was injected to start the reaction. During the run the ethylene pressure was kept constant to within 0.2 bar of the initial pressure by replenishing flow. After a reaction time of 15 min, a sample of the reaction mixture was taken to analyze and quantify the soluble products before the reactor was vented and the residual aluminum alkyls were destroyed by the addition of ethanol (100 mL). The polymeric product was collected, stirred for 30 min in acidified ethanol, and rinsed with ethanol and acetone on a glass frit. The polymer was initially dried in air and subsequently in vacuo at 80 °C. The results are presented in Table 1.

**MMAO-3A Ethylene Conversion:** The general procedure and conditions as described above were followed with the use of MMAO-3A (6.4 g of an isoparaffinic solvent, b.p. 118 °C; 2.1 wt.-% Al, 5 mmol, M/Al, 1:500) instead of PMAO to charge the reactor. The results are presented in Table 1.

**TEA Ethylene Conversion:** The general procedure and conditions as described above were followed with the use of TEA (M/Al, 1:200) instead of PMAO to charge the reactor. The results are presented in Table 1.

### Syntheses and Structure Analyses

**General:** All reactions and manipulations with air-sensitive compounds were performed under an atmosphere of dry argon by using standard Schlenk and glove box techniques. Nonhalogenated solvents were distilled from sodium benzophenone ketyl and halogenated solvents from $P_2O_5$. Deuterated solvents were obtained from Cambridge Isotope Laboratories and were degassed, dried, and distilled prior to use. All other chemicals were purchased from commercial vendors and used without further purification. NMR spectra were obtained with a Bruker ARX 250 spectrometer. Chemical shifts are reported in ppm relative to the deuterated solvent. Elemental analyses were carried out with a Vario elementar EL III. Melting points were measured in sealed capillaries with a Stuart SMP3 apparatus. Magnetic moments were determined with a magnetic susceptibility balance Sherwood Mark 1 MSB at room temperature. X-ray crystal structure analyses were performed by with a STOE-IPDS II equipped with an Oxford Cryostream low-temperature unit. Structure solution and refinement were accomplished by using SIR97,[16] SHELXL-97,[17] and WinGX.[18] Crystallographic details are summarized in Table 2. CCDC-639686 (for **4**), -639684 (for **5**), and -639685 (for **11**) contain the supplementary crystallographic data for this publication. These data can be obtained free of charge from The Cambridge Crystallographic Data Centre via www.ccdc.cam.ac.uk/data_request/cif.

### Syntheses of the Ligands and Ligand Precursors

**1:** 6-Bromopyridine-2-carbaldehyde (2.0 g, 10.7 mmol) and 2,6-diisopropylaniline (2.03 mL, 1.91 g, 10.7 mmol) were dissolved in ethanol (30 mL), and the mixture was heated at reflux for 2 h. The solvent was removed under reduced pressure, and a pale yellow crystalline material was obtained and used without further purification. Yield: 3.59 (97%). M.p. 104 °C. $^1$H NMR (250.13 MHz, $CDCl_3$): $\delta$ = 8.26–8.25 (d, $J$ = 1.0 Hz, 1 H, CH), 8.23 (s, 1 H, N=CH), 7.73–7.66 (t, $J$ = 7.8 Hz, 1 H, CH), 7.61–7.57 (dd, $J$ = 7.9, 1.0 Hz, 1 H, CH), 7.24–7.08 (m, 3 H, CH), 3.08–2.92 [sept, $J$ = 6.9 Hz, 2 H, 2 × C$H$(CH$_3$)$_2$], 1.16–1.13 [d, $J$ = 6.9 Hz, 12 H, 2 × CH(C$H_3$)$_2$] ppm. $^{13}$C NMR (62.90 MHz, $CDCl_3$): $\delta$ = 161.44 (N=CH), 155.40, 147.85, 141.81, 138.99, 136.99, 129.79, 124.66, 123.03 (C$_m$, C$_6$H$_3$), 119.86, 27.91 [2 × $C$H(CH$_3$)$_2$], 23.37 [2 × CH($C$H$_3$)$_2$] ppm. $C_{18}H_{21}BrN_2$ (345.28): calcd. C 62.61, H 6.13, N 8.11; found C 62.66, H 6.05, N 8.01.

**2a:** A solution of 2-bromo-*m*-xylene (1.39 mL, 1.93 g, 10.4 mmol) in thf (30 mL) was added to magnesium turnings (0.30 g, 12.5 mmol), and the resulting suspension was stirred and activated by the addition of 1,2-bromoethane (0.2 mL). An exothermic reaction took place, and an ice bath was used to cool the reaction mixture when the reaction became too vigorous. The reaction mixture was stirred at r.t. for 2 h and then filtered, and the filtrate was directly used.

**2b:** To a suspension of magnesium turnings (0.21 g, 8.69 mmol) in thf (100 mL) was added by syringe 1-bromo-2,4,6-triisopropylbenzol (1.82 mL, 7.24 mmol). The resulting suspension was stirred and activated by the addition of 1,2-bromoethane (0.2 mL). A low exothermic reaction took place. The reaction mixture was stirred at r.t. for 2 h and then filtered, and the filtrate was directly used.

**3a:** To a solution of **1** (3.0 g, 8.69 mmol) in dioxane (30 mL) was added a suspension of $FeCl_2$ (0.11 g, 0.87 mmol) in thf (10 mL). The Grignard solution **2a** was then slowly added to the stirred sus-

 © 2007 Wiley-VCH Verlag GmbH & Co. KGaA, Weinheim 

Table 2. Details of the X-ray crystal structure analyses of **4**, **5**, and **11**.

| | **4** | **5** | **11** |
|---|---|---|---|
| Formula | $C_{34}H_{46}Cl_2FeN_2O_2$ | $C_{30}H_{38}Cl_2N_2OPd$ | $C_{45}H_{68}Cl_2CoN_2O_3$ |
| $M$ [g mol$^{-1}$] | 641.48 | 619.92 | 814.84 |
| Crystal system | monoclinic | monoclinic | hexagonal |
| Space group | $P2_1/c$ | $P2_1/c$ | $P6_1$ |
| $a$ [Å] | 17.386(1) | 9.428(1) | 13.013(1) |
| $b$ [Å] | 13.495(1) | 13.677(2) | 13.013(1) |
| $c$ [Å] | 14.802(1) | 23.309(2) | 47.354(4) |
| $\beta$ [°] | 96.69(1) | 93.82(1) | |
| $V$ [Å$^3$] | 3449.3(4) | 2999(1) | 6944.5(1) |
| $Z$ | 4 | 4 | 6 |
| Crystal size [mm] | $0.86 \times 0.10 \times 0.05$ | $0.33 \times 0.15 \times 0.05$ | $0.32 \times 0.12 \times 0.11$ |
| $\rho_{calcd.}$ [g cm$^{-3}$] | 1.235 | 1.373 | 1.169 |
| Absorption correction | numerical | no | no |
| $T$ [K] | 193(2) | 193(2) | 193(2) |
| $\theta$ range [°] | 1.92–26.27 | 1.73–25.64 | 1.81–21.86 |
| Reflections collected | 45992 | 12594 | 52889 |
| Independent reflections | 6890 | 5400 | 5542 |
| Observed reflections | 3082 | 3630 | 4716 |
| $R$ value [$I > 2\sigma(I)$] | 0.0695 | 0.0481 | 0.0475 |
| $wR_2$ (all data) | 0.2061 | 0.0951 | 0.1183 |

pension. The reaction mixture was heated to 70 °C for 48 h. Water (100 mL) and diethyl ether (80 mL) were added, and the resulting suspension was transferred to a 500-mL separatory funnel. The organic phase was collected, and the inorganic phase was washed twice with diethyl ether and extracted. The combined organic phases were washed with a saturated NaCl solution and dried with $Na_2SO_4$. The organic phase was concentrated to dryness under vacuum, resulting in a brown oily product. The oil was purified by silica chromatography (pentane) and then crystallized from pentane at –25 °C to afford a pale yellow crystalline material. Yield: 1.16 g (39%). M.p. 142.5 °C. $^1$H NMR (250.13 MHz, $CDCl_3$): $\delta$ = 8.36 (s, 1 H, N=CH), 8.29–8.25 (dd, $J$ = 7.9, 1.1 Hz, 1 H, pyridine), 7.95–7.89 (t, $J$ = 7.7 Hz, 1 H, $4_{pyridine\text{-}H}$), 7.37–7.34 (dd, $J$ = 7.6, 1.1 Hz, 1 H, pyridine), 7.25–7.04 (m, 6 H, $2 \times C_6H_3$), 3.08–2.92 [sept, $J$ = 6.9 Hz, 2 H, $2 \times CH(CH_3)_2$], 2.12 (s, 6 H, $2 \times CH_3$), 1.20–1.17 [d, $J$ = 6.9 Hz, 12 H, $2 \times CH(CH_3)_2$] ppm. $^{13}$C NMR (62.90 MHz, $CDCl_3$): $\delta$ = 163.29 (N=CH), 159.76 (C), 154.31 (C), 148.35 (C), 139.73 (C), 137.13 ($2 \times$ C), 137.01 (CH), 135.84 ($2 \times$ C), 128.17 (CH), 127.79 ($2 \times$ CH), 126.21 (CH), 124.35 (CH), 122.96 ($2 \times$ CH), 119.08 (CH), 27.90 [$2 \times CH(CH_3)_2$], 23.41 [$2 \times$ CH-$(CH_3)_2$], 20.34 ($2 \times CH_3$) ppm. $C_{26}H_{30}N_2$ (370.54): calcd. C 84.28, H 8.16, N 7.56; found C 83.74, H 8.15, N 7.47.

**3b:** To a solution of **1** (2.5 g, 7.24 mmol) in dioxane (30 mL) at 70 °C was added a suspension of $FeCl_2$ (0.092 g, 0.72 mmol) in thf (30 mL). The Grignard solution **2b** was then slowly added to the stirred suspension. The reaction mixture was stirred at 70 °C for 48 h. Water (100 mL) and hexane (80 mL) were added, and the resulting suspension was transferred to a 500-mL separatory funnel. The organic phase was collected, and the inorganic phase was washed twice with hexane and extracted. The combined organic phases were washed with a saturated NaCl solution and dried with $Na_2SO_4$. The organic phase was concentrated under vacuum, and at –25 °C pale yellow crystals were obtained. Yield: 2.14 g (86%). M.p. 193.5 °C. $^1$H NMR (250.13 MHz, $CDCl_3$): $\delta$ = 8.33 (s, 1 H, N=CH), 8.29–8.26 (dd, $J$ = 7.8, 0.9 Hz, 1 H, pyridine), 7.92–7.86 (t, $J$ = 7.7 Hz, 1 H, $4_{pyridine\text{-}H}$), 7.44–7.40 (dd, $J$ = 7.6, 0.9 Hz, 1 H, pyridine), 7.19–7.10 (m, 5 H, $C_6H_2/C_6H_3$), 3.07–2.90 [sept, $J$ = 6.8 Hz, 3 H, $3 \times (CH_3)_2CH\text{-}C_6H_2$], 2.63–2.46 [sept, $J$ = 6.8 Hz, 2 H, $2 \times (CH_3)_2CH\text{-}C_6H_3$], 1.28–1.26 [d, $J$ = 7.0 Hz, 12 H, $2 \times (CH_3)_2$-CH-$C_6H_3$], 1.18–1.12 [q, $J$ = 6.8 Hz, 18 H, $3 \times (CH_3)_2CH\text{-}C_6H_2$] ppm. $^{13}$C NMR (62.90 MHz, $CDCl_3$): $\delta$ = 163.61 (N=CH), 160.07 (C), 153.93 (C), 149.05 (C), 148.43 (C), 146.24 ($2 \times$ C), 137.22 ($2 \times$ C), 136.34 (CH), 135.71 (C), 126.60 (CH), 124.35 (CH), 122.99 ($2 \times$ CH), 120.96 ($2 \times$ CH), 118.87 (CH), 34.45 (CH), 30.48 (CH), 27.92 [$2 \times (CH_3)_2CH\text{-}C_6H_3$], 24.26 (CH), 24.09 (CH), 24.00 (CH), 23.49 [$2 \times (CH_3)_2CH\text{-}C_6H_3$] ppm. $C_{33}H_{44}N_2$ (468.72): calcd. C 84.56, H 9.46, N 5.46; found C 84.38, H 9.49, N 6.21.

**Syntheses of the Complexes**

**4:** A solution of **3a** (0.358 g, 0.97 mmol) and $FeCl_2$ (0.11 g, 0.86 mmol) in thf (30 mL) was heated at 70 °C whilst stirring for 18 h. The solvent was removed under vacuum, and the red residue was washed with hexane, dissolved in thf, and filtered through quartz. The filtrate was concentrated, and red crystals were grown at –25 °C. Yield: 0.434 g (90%). M.p. 240 °C. $\mu_{eff}$ = 4.44 BM (24.4 °C). $^1$H NMR (250.13 MHz, $CDCl_3$): $\delta$ = 34.50, 30.98, 8.23, 7.63, 7.14, 5.90, 3.97, 2.89, 2.03, 1.74, 1.23, 1.14, 0.86, 0.05, –2.57 ppm. $C_{26}H_{30}Cl_2FeN_2$ (497.25): calcd. C 62.80, H 6.08, N 5.63; found C 63.26, H 6.05, N 5.24.

**5:** A stirred solution of **3a** (0.229 g, 0.81 mmol) and [$PdCl_2$(cod)] (0.223 g, 0.79 mmol) in thf (30 mL) was heated at 70 °C for 18 h. The solvent was removed under vacuum, and the residue was washed with hexane, dissolved in dichloromethane (50 mL), and filtered through quartz. The resulting orange solution was concentrated, and yellow-orange crystals (needles) were grown at –25 °C. Yield: 76%. M.p. 255 °C. $^1$H NMR (250.13 MHz, $CD_2Cl_2$): $\delta$ = 8.23–8.16 (t, $J$ = 7.5 Hz, 1 H, $4_{pyridine\text{-}H}$), 8.19 (s, 1 H, N=CH), 7.97–7.94 (dd, $J$ = 7.7, 1.5 Hz, 1 H, pyridine), 7.59–7.55 (dd, $J$ = 8.3, 1.5 Hz, 1 H, pyridine), 7.40–7.09 (m, 6 H, $2 \times C_6H_3$), 3.44–3.31 [sept, $J$ = 6.8 Hz, 2 H, $2 \times CH(CH_3)_2$], 2.30 (s, 6 H, $2 \times CH_3$), 1.40–1.37 (d, $J$ = 6.8 Hz, 6 H, $2 \times CH_3$, isopropyl), 1.19–1.16 (d, $J$ = 6.9 Hz, 6 H, $2 \times CH_3$, isopropyl) ppm. $^{13}$C NMR (62.90 MHz, $CD_2Cl_2$): $\delta$ = 170.22 (N=CH), 166.21 (C), 154.87 (C), 143.30 (C), 140.98 (C), 140.11 (CH), 138.40 (C), 135.93 (CH), 133.78 (CH), 129.55 (CH), 128.76 (CH), 127.59 (CH), 123.49 (CH), 28.97 [$2 \times CH(CH_3)_2$], 24.27 ($2 \times CH_3$, isopropyl), 22.93 ($2 \times CH_3$, isopropyl), 20.68 [$(CH_3)_2CH\text{-}C_6H_4$] ppm. $C_{26}H_{30}Cl_2N_2Pd \cdot 0.5CH_2Cl_2$ (590.29): calcd. C 53.92, H 5.29, N 4.75; found C 53.52, H 5.35, N 4.41.

 © 2007 Wiley-VCH Verlag GmbH & Co. KGaA, Weinheim 

**6:** Compound **3a** (0.25 g, 0.67 mmol), [$NiCl_2$(dme)] (0.145 g, 0.66 mmol), and thf (50 mL) were added together in a Schlenk flask under an atmosphere of nitrogen. The reaction mixture was stirred at 70 °C for 18 h. The solvent was removed under vacuum, and the red residue was washed with hexane, dissolved in thf, and filtered through quartz. The filtrate was concentrated, and orange crystals were grown at –25 °C. Yield: 0.256 g (59%). $\mu_{eff}$ = 2.99 BM (25.9 °C). $^1$H NMR (250.13 MHz, $CDCl_3$): $\delta$ = 32.03, 24.09, 20.65, 10.74, 8.85, 8.34, 8.24, 7.92, 7.14, 5.48, 3.75, 2.99, 2.41, 2.10, 1.85, 1.18, 0.89, 0.06 ppm. $C_{26}H_{30}Cl_2N_2Ni{\cdot}2C_4H_8O$ (644.34): calcd. C 63.38, H 7.20, N 4.35; found C 63.04, H 7.57, N 4.54.

**7:** In a closed Schlenk flask, a stirred solution of **3a** (0.362 g, 0.98 mmol) and $CoCl_2$ (0.12 g, 0.92 mmol) in thf (30 mL) was heated at 70 °C for 18 h. The solvent was removed under vacuum, and the red residue was washed with hexane, dissolved in thf, and filtered through quartz. The filtrate was concentrated, and green needles were grown at –25 °C. Yield: 0.43 g (77%). M.p. 300 °C. $\mu_{eff}$ = 4.17 BM (25.9 °C). $^1$H NMR (250.13 MHz, $CDCl_3$): $\delta$ = 34.70, 32.45, 19.13, 7.16, 5.21, 3.75, 3.34, 2.33, 2.15, 2.09, 1.80, 1.43, 1.22, 1.17, 1.14, 1.10, 0.85, 0.82, 0.04, –2.40, –3.37, –8.80 ppm. $C_{26}H_{30}Cl_2CoN_2{\cdot}C_4H_8O$ (572.47): calcd. C 62.94, H 6.69, N 4.89; found C 63.23, H 6.22, N 5.18.

**8:** In a dry box, **3b** (0.243 g, 0.52 mmol), $FeCl_2$ (0.066 g, 0.52 mmol), and thf (50 mL) were combined in a Schlenk flask under an atmosphere of nitrogen. The resulting solution was stirred at 60 °C for 48 h. The solvent was removed, and the precipitate was washed with hexane, dissolved in thf, and filtered through quartz. The filtrate was concentrated to dryness under vacuum, resulting in a dark red solid product. Yield: 0.11 g (32%). $\mu_{eff}$ = 6.16 BM (25.1 °C). $^1$H NMR (250.13 MHz, $CDCl_3$): $\delta$ = 39.31, 8.23, 7.86, 7.09, 2.92, 2.50, 1.56, 1.13, 0.05 ppm. $C_{33}H_{44}Cl_2FeN_2{\cdot}C_4H_8O$ (667.57): calcd. C 66.57, H 7.85, N 4.20; found C 66.38, H 7.55, N 3.92.

**9:** A stirred solution of **3b** (0.252 g, 0.538 mmol) and [$PdCl_2$(cod)] (0.138 g, 0.483 mmol) in thf (50 mL) was heated at 60 °C for 72 h. The solvent was removed under vacuum, and the residue was washed with hexane, dissolved in toluene (50 mL), and filtered through quartz. The solvent was then removed, and the yellow product was dried under vacuum. Yield: 0.18 g (47%). M.p. 161 °C. $^1$H NMR (250.13 MHz, $CD_2Cl_2$): $\delta$ = 8.18 (s, 1 H, N=CH), 8.17–8.11 (t, $J$ = 8.0 Hz, 1 H, $4_{pyridine\text{-}H}$), 7.92–7.89 (d, $J$ = 7.5 Hz, 1 H, pyridine), 7.64–7.61 (d, $J$ = 7.9 Hz, 1 H, pyridine), 7.38–7.32 (t, $J$ = 7.2 Hz, 1 H, $p$-CH-$C_6H_3$), 7.22–7.18 (d, $J$ = 8.0 Hz, 2 H, 2 × $m$-CH-$C_6H_3$), 7.06 (s, 2 H, $C_6H_2$), 3.40–3.28 [sept, $J$ = 6.8 Hz, 2 H, 2 × C$H$($CH_3$)$_2$], 3.02–2.88 [sept, $J$ = 7.0 Hz, 1 H, $p$-C$H$($CH_3$)$_2$], 2.62–2.50 [sept, $J$ = 6.8 Hz, 2 H, 2 × C$H$($CH_3$)$_2$], 1.59–1.56 (d, $J$ = 6.8 Hz, 6 H, 2 × $CH_3$), 1.37–1.36 (d, $J$ = 6.8 Hz, 6 H, 2 × $CH_3$), 1.29–1.26 (d, $J$ = 6.9 Hz, 6 H, 2 × $CH_3$), 1.18–1.15 (d, $J$ = 6.9 Hz, 6 H, 2 × $CH_3$), 1.10–1.08 (d, $J$ = 6.8 Hz, 6 H, 2 × $CH_3$) ppm. $^{13}$C NMR (62.90 MHz, $CD_2Cl_2$): $\delta$ = 170.22 (N=CH), 166.71, 154.88, 151.11, 146.18, 143.42, 141.13, 139.20, 134.39, 134.16, 128.90, 127.70, 123.70, 121.24, 34.74, 31.72, 29.07, 25.18, 24.53, 24.18, 24.11, 23.18 ppm. $C_{33}H_{44}Cl_2N_2Pd{\cdot}C_4H_8O$ (718.15): calcd. C 61.88, H 7.30, N 3.90; found C 61.40, H 7.33, N 3.61.

**10:** Compound **3b** (0.24 g, 0.512 mmol), [$NiCl_2$(dme)] (0.113 g, 0.512 mmol), and thf (50 mL) were added together in a Schlenk flask under an atmosphere of nitrogen. The reaction mixture was stirred at 70 °C for 18 h. The solvent was removed, and the beige precipitate was washed with hexane, dissolved in thf, and filtered through quartz. After concentration, beige crystals were grown at –25 °C and dried under vacuum. Yield: 0.044 g (15%). $\mu_{eff}$ = 2.57 BM (26 °C). $^1$H NMR (250.13 MHz, $CDCl_3$): $\delta$ = 39.53, 24.43, 17.49, 11.24, 5.51, 3.46, 2.78, 2.53, 2.16, 1.25, 1.17, 1.14, 0.03, –4.63 ppm. $C_{33}H_{44}Cl_2N_2Ni$ (598.32): calcd. C 66.24, H 7.41, N 4.68; found C 65.94, H 7.22, N 4.44.

**11:** Compound **3b** (0.283 g, 0.604 mmol) and $CoCl_2$ (0.08 g, 0.604 mmol) were dissolved in thf (40 mL). The resulting dark green reaction mixture was stirred for 20 h at 60 °C. The solvent was removed under vacuum. The product was washed with hexane, dissolved in thf, filtered through quartz, and concentrated. Green crystals were collected at –25 °C. Yield: 0.21 g (58%). M.p. 272 °C. $\mu_{eff}$ = 4.38 BM (26 °C). $^1$H NMR (250.13 MHz, $CDCl_3$): $\delta$ = 28.16, 21.32, 8.29, 8.20, 7.86, 7.12, 7.07, 6.88, 5.05, 3.72, 3.11, 2.93, 2.50, 1.62, 1.39, 1.23, 1.12, 0.82, 0.70, 0.35, 0.04, –1.56, –4.38, –5.26, –5.43 ppm. $C_{33}H_{44}Cl_2CoN_2$ (598.56): calcd. C 66.22, H 7.41, N 4.68; found C 65.89, H 7.62, N 4.51.

## Acknowledgments

Financial support from the Fonds der Chemischen Industrie is gratefully acknowledged.

[1] S. Mecking, *Angew. Chem.* **2001**, *113*, 550–557; *Angew. Chem. Int. Ed.* **2001**, *40*, 534–540.

[2] a) G. J. P. Britovsek, V. C. Gibson, D. F. Wass, *Angew. Chem.* **1999**, *111*, 448–468; *Angew. Chem. Int. Ed.* **1999**, *38*, 428–447; b) S. D. Ittel, L. K. Johnson, M. Brookhart, *Chem. Rev.* **2000**, *100*, 1169–1203; c) C. Bianchini, G. Mantovani, A. Meli, F. Migliacci, F. Zanobini, F. Laschi, A. Sommazzi, *Eur. J. Inorg. Chem.* **2003**, 1620–1631.

[3] a) D. M. Haddleton, C. B. Jasieczek, M. J. Hannon, A. J. Shooter, *Macromolecules* **1997**, *30*, 2190–2193; b) P.-L. Bres, V. C. Gibson, C. D. F. Mabille, W. Reed, D. F. Wass, R. H. Weatherhead, *WO 98/49208* **1998**; c) D. M. Haddleton, D. J. Duncalf, D. Kukulj, M. C. Crossman, S. G. Jackson, S. A. F. Bon, A. J. Clark, A. J. Shooter, *Eur. J. Inorg. Chem.* **1998**, 1799–1806; d) G. M. DiRenzo, M. Messerschmidt, R. Mülhaupt, *Macromol. Rapid Commun.* **1998**, *19*, 381–384; e) A. J. Amass, C. A. Wyres, E. Colclough, I. M. Hohn, *Polymer* **2000**, *41*, 1697–1702; f) V. C. Gibson, R. K. O'Reilly, D. F. Wass, A. J. P. White, D. J. Williams, *Dalton Trans.* **2003**, 2824–2830.

[4] a) C. Bianchini, A. Sommazzi, G. Mantovani, R. Santi, F. Masi, *WO 02/34701 A1* **2002**; b) C. Bianchini, G. Mantovani, A. Meli, F. Migliacci, F. Laschi, *Organometallics* **2003**, *22*, 2545–2547; c) C. Bianchini, G. Giambastiani, G. Mantovani, A. Meli, D. Mimeau, *J. Organomet. Chem.* **2004**, *689*, 1356–1361; d) C. Bianchini, G. Giambastiani, A. Meli, A. Toti, *Organometallics* **2007**, *26*, 1303–1305; e) C. Bianchini, D. Gatteschi, G. Giambastiani, R. Guerrero Rios, A. Lenco, F. Laschi, C. Mealli, A. Meli, L. Sorace, A. Toti, F. Vizza, *Organometallics* **2007**, *26*, 726–739.

[5] a) R. Chen, S. F. Mapolie, *J. Mol. Catal. A* **2003**, *193*, 33–40; G. S. Smith, S. F. Mapolie, *J. Mol. Catal. A* **2004**, *213*, 187–192; R. Chen, J. Bacsa, S. F. Mapolie, *Polyhedron* **2003**, *22*, 2855–2861; J. Cloete, S. F. Mapolie, *J. Mol. Catal. A* **2006**, *243*, 221–225.

[6] Suzuki cross-coupling reactions involving sterically demanding substrates: a) N. G. Andersen, S. P. Maddaford, B. A. Keay, *J. Org. Chem.* **1996**, *61*, 9556–9559; b) M. G. Johnson, R. J. Foglesong, *Tetrahedron Lett.* **1997**, *38*, 7001–7002; c) J. Yin, S. L. Buchwald, *J. Am. Chem. Soc.* **2000**, *122*, 12051–12052; d) A. N. Cammidge, K. V. L. Crépy, *Chem. Commun.* **2000**, 1723–1724; e) A.-S. Castanet, F. Colobert, P.-E. Broutin, M. Obringer, *Tetrahedron: Asymmetry* **2002**, *13*, 659–665; f) R. B. Bedford, S. L. Hazelwood, M. E. Limmert, J. M. Brown, S. Ramdeehul, A. R. Cowley, S. J. Coles, M. B. Hursthouse, *Organometallics* **2003**, *22*, 1364–1371; g) R. B. Bedford, C. S. J. Cazin, M. B. Hursthouse, M. E. Light, V. J. M. Scordia, *Dalton Trans.* **2004**, 3864–3868; h) A. N. Cammidge, K. V. L. Crépy,

 © 2007 Wiley-VCH Verlag GmbH & Co. KGaA, Weinheim 

*Tetrahedron* **2004**, *60*, 4377–4386; i) P.-E. Broutin, F. Colobert, *Eur. J. Org. Chem.* **2005**, 1113–1128; j) H. Li, Y. Wu, W. Yan, *J. Organomet. Chem.* **2006**, *691*, 5688–5696.

[7] N. M. Scott, T. Schareina, O. Tok, R. Kempe, *Eur. J. Inorg. Chem.* **2004**, 3297–3304.

[8] a) N. M. Scott, R. Kempe, *Eur. J. Inorg. Chem.* **2005**, 1319–1324; b) W. P. Kretschmer, A. Meetsma, B. Hessen, T. Schmalz, S. Qayyum, R. Kempe, *Chem. Eur. J.* **2006**, *12*, 8969–8978; c) W. P. Kretschmer, A. Meetsma, B. Hessen, N. M. Scott, S. Qayyum, R. Kempe, *Z. Anorg. Allg. Chem.* **2006**, *632*, 1936–1938.

[9] For a review on aminopyridinato ligands, see: R. Kempe, *Eur. J. Inorg. Chem.* **2003**, 791–803.

[10] H. Maisel, S. Keller, T. Irrgang, R. Kempe, *Z. Kristallogr. New Cryst. Struct.* **2005**, *220*, 463–464.

[11] a) G. Bähr, H. Thämlitz, *Z. Anorg. Allg. Chem.* **1955**, *282*, 3; b) G. Bähr, H. G. Döge, *Z. Anorg. Allg. Chem.* **1957**, *292*, 19; c) G. Schmauss, P. Barth, *Z. Naturforsch. Teil B* **1970**, *25*, 789; d) M. E. Cucciolito, V. De Felice, A. Panunzi, A. Vitagliano, *Organometallics* **1989**, *8*, 1180–1187; e) S. Plentz Meneghetti, P. J. Lutz, J. Kress, *Organometallics* **1999**, *18*, 2734–2737; f) T. V. Laine, M. Klinga, M. Leskelä, *Eur. J. Inorg. Chem.* **1999**, 959–964; g) T. V. Laine, K. Lappalainen, J. Liimatta, E. Aitola, B. Löfgren, M. Leskelä, *Macromol. Rapid Commun.* **1999**, *20*, 487–491; h) T. V. Laine, M. Klinga, A. Maaninen, M. Leskelä, *Acta Chem. Scand.* **1999**, *53*, 968; i) T. V. Laine, U. Piironen, K. Lappalainen, M. Klinga, E. Aitola, M. Leskelä, *J. Organomet. Chem.* **2000**, *606*, 112–124; j) C. Bianchini, H. M. Lee, G. Mantovani, A. Meli, W. Oberhauser, *New J. Chem.* **2002**, *26*, 387–397.

[12] For selected examples of Grignard coupling reactions efficiently catalyzed by iron compounds, see: a) F. Babudri, A. D'Ettole, V. Fiandanese, G. Marchese, F. Naso, *J. Org. Chem.* **1991**, *405*, 53–58; b) A. Fürstner, A. Leitner, M. Méndez, H. Krause, *J. Am. Chem. Soc.* **2002**, *124*, 13856–13863; c) T. Nagano, T. Hayashi, *Org. Lett.* **2004**, *6*, 1297–1299; d) M. Nakamura, K. Matsuo, S. Ito, E. Nakamura, *J. Am. Chem. Soc.* **2004**, *126*, 3686–3687; e) B. Scheiper, M. Bonnekessel, H. Krause, A. Fürstner, *J. Org. Chem.* **2004**, *69*, 3943–3949; f) K. Itami, S. Higashi, M. Mineno, J.-I. Yoshida, *Org. Lett.* **2005**, *7*, 1219–1222; g) R. B. Bedford, M. Betham, D. W. Bruce, A. A. Danopoulos, R. M. Frost, M. Hird, *J. Org. Chem.* **2006**, *71*, 1104–1110.

[13] H. Maisel, S. Keller, T. Irrgang, R. Kempe, *Z. Kristallogr. New Cryst. Struct.* **2005**, *220*, 465–466.

[14] F. A. Cotton, R. L. Luck, Kyung-ae Son, *Acta Crystallogr. Sect. C: Cryst. Struct. Commun.* **1990**, *46*, 1424–1426.

[15] Z. Janas, P. Sobota, T. Lis, *J. Chem. Soc. Dalton Trans.* **1991**, 2429–2434.

[16] A. Altomare, M. C. Burla, M. Camalli, G. L. Cascarano, C. Giacovazzo, A. Guagliardi, A. G. G. Moliterni, G. Polidori, R. Spagna, *J. Appl. Crystallogr.* **1999**, *32*, 115–119.

[17] G. M. Sheldrick, *SHELXL-97: Program for Crystal Structure Analysis* (Release 97–2), Institut für Anorganische Chemie der Universität, Göttingen, Germany, **1998**.

[18] L. J. Farrugia, *J. Appl. Crystallogr.* **1999**, *32*, 837–838.

Received: April 12, 2007
Published Online: July 18, 2007

 © 2007 Wiley-VCH Verlag GmbH & Co. KGaA, Weinheim 

DOI: 10.1002/ejic.200700208

# Transition Metal(II)–Salen and –Salophen Macrocyclic Complexes for Rotaxane Formation: Syntheses and Crystal Structures

**Mamiko Narita,[a][‡] Il Yoon,[a][‡‡] Masaru Aoyagi,[a] Midori Goto,[a] Toshimi Shimizu,[a] and Masumi Asakawa*[a]**

*Dedicated to Professor J. Fraser Stoddart on the occasion of his 65th birthday*

**Keywords:** Rotaxanes / Ring opening / Ring closing / Transition metals / Porphyrinoids

We used a "threading-followed-by-shrinking" approach to prepare [2]rotaxanes possessing nickel(II)–salen and –salophen moieties. Reactions of macrocycles incorporating salen and salophen moieties with secondary dialkylammonium salts, followed by the addition of aqueous sodium sulfate, afforded the corresponding pseudorotaxanes; subsequent addition of nickel acetate shrank the effective size of the macrocycles to give the respective [2]rotaxanes. We obtained a [2]rotaxane possessing a salen unit in remarkably high yields − even in a polar solvent − indicating that the "threading-followed-by-shrinking" and "salen-ring-opening-and-closing" approaches occurred together. In addition, we expanded the "threading-followed-by-shrinking" approach to prepare a [2]rotaxane and a bis[2]rotaxane comprising two palladium(II)–salophen moieties linked in a bis-macrocycle and one and two secondary dialkylammonium salts, respectively. Furthermore, we prepared a tetraphenylporphyrin rhodium(III) chloride [Rh(TPP)Cl]-stoppered [2]rotaxane comprising a palladium(II)–salophen macrocycle and a pyridyl-terminated thread-like ion coordinated to the rhodium(III) center, which has potential as a next-generation molecular machine exhibiting catalytic function.
(© Wiley-VCH Verlag GmbH & Co. KGaA, 69451 Weinheim, Germany, 2007)

## Introduction

Interest in functionalized rotaxanes and their future potential as molecular machines in nanotechnology has increased in recent years.[1] Many template-directed methods for the preparation of rotaxanes have appeared in the literature; they generally involve clipping,[2] threading followed by stoppering,[3] and slipping[4] approaches. Functionalized rotaxanes can be immobilized onto solid surfaces through the use of self-assembled monolayers or Langmuir–Blodgett techniques.[5] We demonstrated − through molecularly resolved scanning tunneling microscopy (STM) images – that porphyrin and phthalocyanine derivatives self-assemble into ordered monolayer arrays on solid substrates.[6] Furthermore, we synthesized porphyrin-stoppered rotaxanes, explicitly pseudorotaxanes bound to the metal centers of metalloporphyrins through axial coordination, which suggest that such organic molecules can be immobilized onto two-dimensional arrays of metalloporphyrins on a solid substrate.[6a,6b,6d] Transition metals are often incorporated as templating or assembling centers for the formation of rotaxanes.[7] Previously, we demonstrated the synthesis of a [2]rotaxane incorporating a palladium(II)–salophen [*N*,*N*′-*o*-phenylenebis(salicylideneiminato) dianion] moiety by using a "threading-followed-by-shrinking" approach (Figure 1a) that involves threading a rod-like unit through a macrocycle and then shrinking the free space within the macrocycle through coordination of its salophen moiety to palladium metal; the rotaxane formation in this system occurs in a nonpolar solvent (dichloromethane) when a sodium(I)-complexed macrocycle possessing a salophen unit is used.[8] Furthermore, we reported the synthesis of monomeric and dimeric macrocycles incorporating salen [*N*,*N*′-ethylenebis(salicylideneiminato) dianion] moieties and a [2]-rotaxane formed by using a "ring-opening-and-closing" approach (Figure 1b) through the cleavage and formation of imino bonds of a salen moiety; the self-assembly of this macrocycle in the presence of a dumbbell-shaped rod-like component, followed by the addition of nickel acetate, af-

[a] Nanoarchitectonics Research Center, National Institute of Advanced Industrial Science and Technology (AIST),
Tsukuba Central 5, 1-1-1 Higashi, Tsukuba Ibaraki 305-8565, Japan
Fax: +81-29-861-4679
E-mail: masumi-asakawa@aist.go.jp
[‡] Current address: Toyota Central R&D Labs., Inc., 41-1, Aza Yokomichi, Oaza Nagakute, Nagakute-cho,
Aichi-gun, Aichi-Ken 480-1192, Japan
[‡‡] Current address: California NanoSystems Institute and Department of Chemistry and Biochemistry, University of California, Los Angeles,
405 Hilgard Avenue, Los Angeles, California 90095, USA
Supporting information for this article is available on the WWW under http://www.eurjic.org or from the author.

 © 2007 Wiley-VCH Verlag GmbH & Co. KGaA, Weinheim 

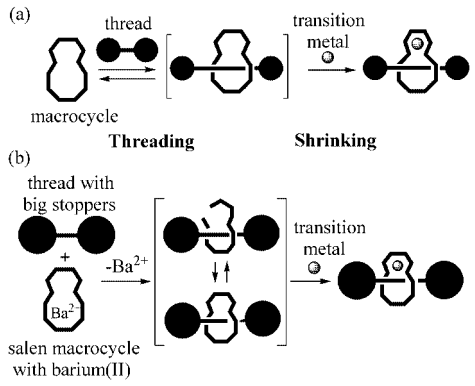


Figure 1. (a) "Threading-followed-by-shrinking" and (b) "ring-opening-and-closing" approaches toward [2]rotaxanes.

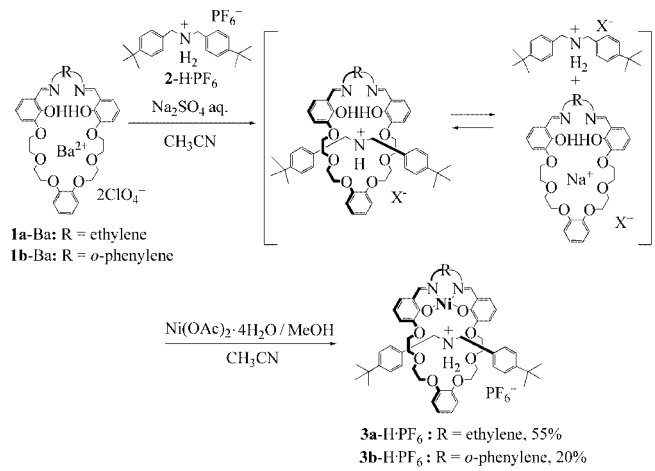


Scheme 1. Syntheses of [2]rotaxanes **3a**-H·$PF_6$ and **3b**-H·$PF_6$.

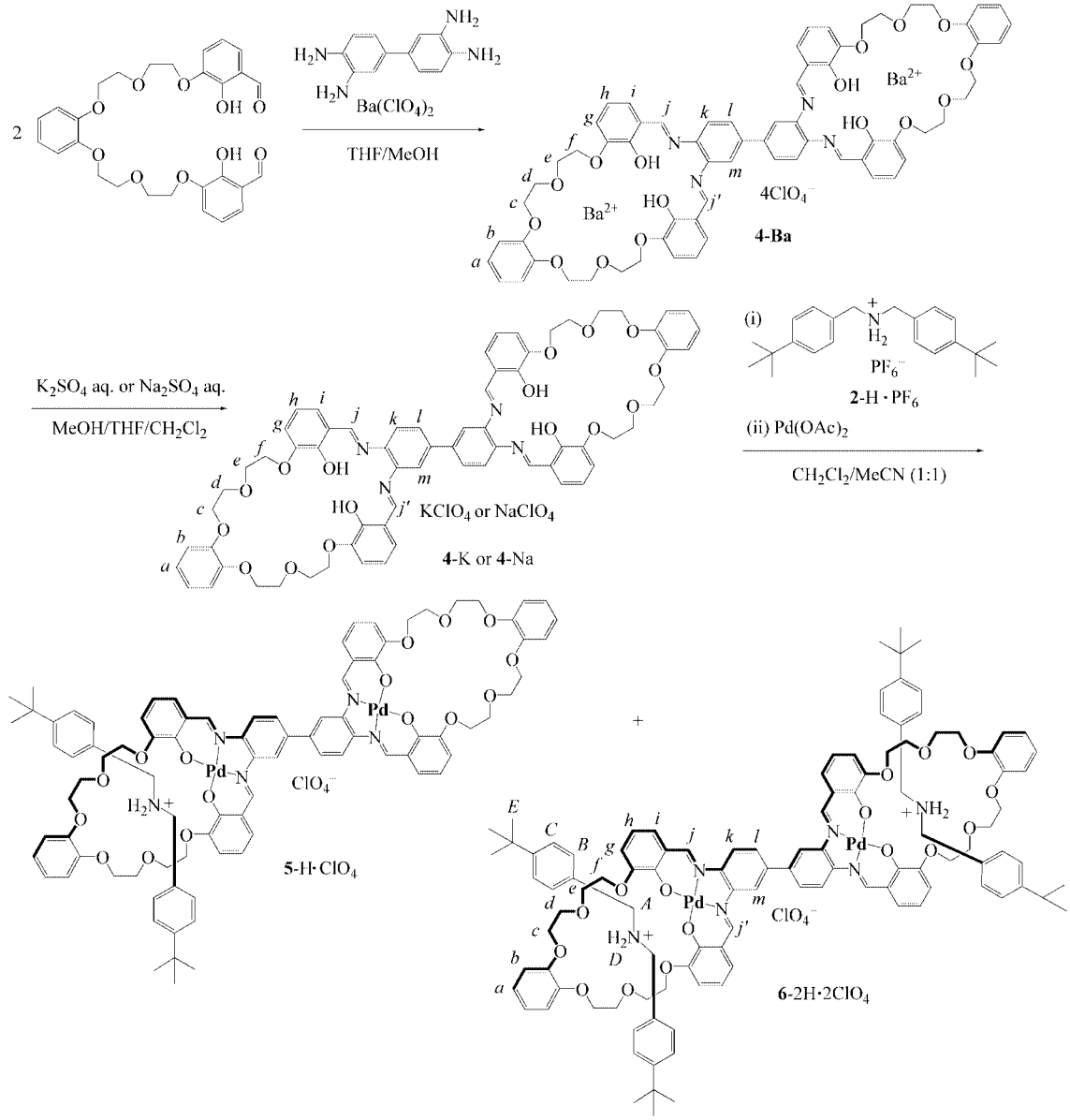


Scheme 2. Syntheses of macrocycles **4**-Ba, **4**-K, **4**-Na, and rotaxanes **5**-H·$ClO_4$ and **6**-2H·2$ClO_4$.

 © 2007 Wiley-VCH Verlag GmbH & Co. KGaA, Weinheim 

forded, after counterion exchange, a [2]rotaxane that was stabilized through coordination of the Ni ion to the macrocyclic salen moiety.[9]

In this paper, we describe a different synthetic system in which we combined both "threading-followed-by-shrinking"[8] and "ring-opening-and-closing"[9] approaches − and note the remarkably higher yield for the synthesis of a salen-based rotaxane relative to that of our previous approach[8] − for the formation of [2]rotaxanes **3a/b**-H·$PF_6$ (Scheme 1) from a precursor macrocycle [a barium(II)-complexed macrocycle possessing either a salen or salophen unit], a transition metal [nickel(II)], and a polar solvent (a mixture of water, methanol, and acetonitrile). Furthermore, we expanded the "threading-followed-by-shrinking" approach (Figure 2) to afford [2]rotaxane **5**-H·$ClO_4$ and bis[2]rotaxane **6**-2H·2$ClO_4$, which features two palladium(II)–salophen moieties linked in a bismacrocycle (Scheme 2). The transition metal(II)–salen or –salophen moiety, which behaves as the shrinking center, might also be of use for applications in areas related to, for example, metallocatalysis,[10] nonlinear optical response,[11] and electron transfer[12] when incorporated into rotaxane structures. In addition, we synthesized Rh(TPP)Cl-stoppered rotaxane **8**-H·Rh(TPP)Cl·$ClO_4$ (TPP = tetraphenylporphyrin; Scheme 3) by combining sequential "threading-followed-by-shrinking" and end-capping approaches, the latter through axial coordination of a pyridyl unit in the thread-like component and the rhodium(III) metal center. Such rotaxanes may allow the construction of catalytically active molecular machines on solid surfaces. We characterized rotaxanes **3a/b**-H·$PF_6$, **5**-H·$ClO_4$, **6**-2H·2$ClO_4$, and **8**-H·Rh(TPP)Cl·$ClO_4$ by using NMR and IR spectroscopy, mass spectrometry, elemental analysis, and X-ray crystallography (see the Supporting Information).

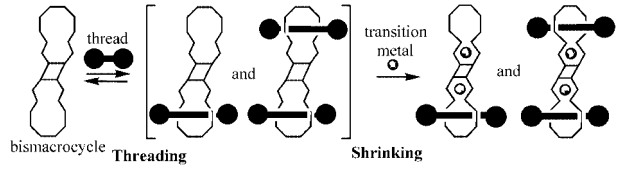


Figure 2. Graphical representation of the [2]rotaxane and bis[2]rotaxane when using the bismacrocycle and the "threading-followed-by-shrinking" approach.

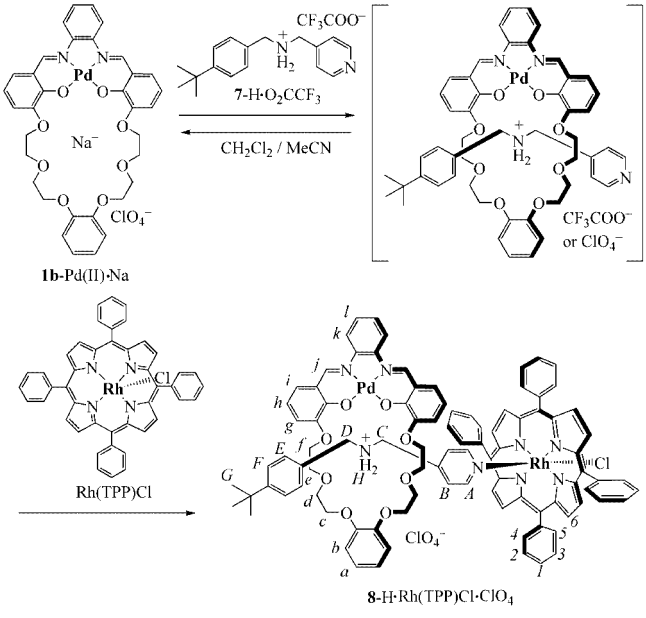


Scheme 3. Synthesis of tetraphenylporphyrin-stoppered [2]rotaxane **8**-H·Rh(TPP)Cl·$ClO_4$.

## Results and Discussion

As thread-like moieties, we used two types of the secondary dialkylammonium salt: **2**-H·$PF_6$,[4c] which contains two terminal *t*Bu groups, and **7**-H·$O_2CCF_3$,[13] which contains one *t*Bu group and one pyridyl unit as its termini. For the shrinking centers, we incorporated a salen moiety into macrocycle **1a**[9] and salophen moieties into macrocycle **1b**[12d] and bismacrocycle **4** (with each of these macrocycles prepared as a Ba complex). For end-capping, we used the rhodium(III) metal center of Rh(TPP)Cl. The reaction of **1a/b**-Ba and **2**-H·$PF_6$, followed by the addition of aqueous sodium sulfate, afforded the corresponding intermediate pseudorotaxanes, which could form free of macrocyclic and dumbbell components; the subsequent addition of nickel(II) acetate afforded [2]rotaxanes **3a/b**-H·$PF_6$ in yields of 55 and 20%, respectively (Scheme 1). The yield of rotaxane **3a**-H·$PF_6$, which incorporates the salen moiety, was remarkably high when considering that the use of polar solvents, which disrupt hydrogen bonding, was necessary because of the poor solubility of nickel(II) acetate in nonpolar solvents. Previously, we reported evidence for the "ring-opening-and-closing" approach occurring during the synthesis of a [2]rotaxane incorporating a salen moiety.[9] We believe that the unexpectedly high yield of **3a**-H·$PF_6$ relative to that of **3b**-H·$PF_6$ may be attributed to the different environments experienced by the salen and salophen moieties during their respective "ring-opening-and-closing" processes, which occurred through reactions at their imine bonds. The relatively low yield in the synthesis of **3b**-H·$PF_6$ may have arisen from the fact that ring opening and closing are very slow in the macrocycle incorporating the salophen moiety. In the case of salen rotaxane **3a**-H·$PF_6$, both "threading-followed-by-shrinking" and "ring-opening-and-closing" processes occurred together, whereas salophen rotaxane **3b**-H·$PF_6$ formed only through the "threading-followed-by-shrinking" process.

For the synthesis of an extended system, we used the "threading-followed-by-shrinking" approach[8] with bismacrocycle **4** possessing two macrocycle units linked through two salophen moieties (Figure 2). The reaction of two dialdehyde derivatives and 3,3′-diaminobenzidine afforded the barium(II)-complexed bismacrocycle possessing linked salophen moieties **4**-Ba (Scheme 2). The addition of aqueous potassium sulfate or aqueous sodium sulfate removed the coordinated barium(II) ions as precipitated

 © 2007 Wiley-VCH Verlag GmbH & Co. KGaA, Weinheim 

$BaSO_4$ to afford **4**-K or **4**-Na, respectively. The self-assembly of **4**-K or **4**-Na with **2**-H·$PF_6$, followed by the addition of palladium(II) acetate and counterion exchange, afforded a mixture of [2]rotaxane **5**-H·$ClO_4$ (i.e. possessing one thread-like moiety; 3% yield) and bis[2]rotaxane **6**-2H·2$ClO_4$ (i.e. possessing two thread-like moieties; 20% yield).

Toward our goal of immobilizing catalytically active rotaxanes as molecular machines on solid substrates, we synthesized the Rh(TPP)Cl-stoppered [2]rotaxane **8**-H·Rh(TPP)Cl·$ClO_4$. The reaction of **1b**-$Pd^{II}$·Na and **7**-H·$O_2CCF_3$, followed by the addition of Rh(TPP)Cl and counterion exchange, afforded the Rh(TPP)Cl-stoppered [2]rotaxane **8**-H·Rh(TPP)Cl·$ClO_4$ in 40% yield (Scheme 3). The yield of this [2]rotaxane is lower than the one we achieved previously (75%)[6b] when using dibenzo[24]-crown-8 as the macrocycle, possibly because of an increased steric clash between the larger salophen-containing macrocycle and the Rh(TPP)Cl unit or because of relatively weaker interactions between the components of this pseudorotaxane.

Figure 3 displays representative $^1$H NMR spectra of [2]-rotaxane **3a**-H·$PF_6$, the salen-incorporating macrocycle bound with nickel(II) [**1a**-$Ni^{II}$·Na],[9] and thread-like salt **2**-H·$PF_6$. The $^1$H NMR spectrum of **3a**-H·$PF_6$ (Figure 3c), together with its 2D ROESY and COSY NMR spectra (see Supporting Information) provides evidence for the successful formation of the [2]rotaxane. The signal of the $CH_2N^+$ protons (*A*) in the rotaxane has shifted downfield significantly relative to that in the free thread (Figure 3a) as a result of the formation of [C–H···O] hydrogen bonds[14] (Figure 6). In addition, these protons (*A*) resonate as a triplet in the rotaxane (Figure 3c), whereas they appear as a singlet in the free thread (Figure 3a), which might be a result of the reduced exchange rates of the ammonium protons in the rotaxane structure owing to the hydrogen bonds.

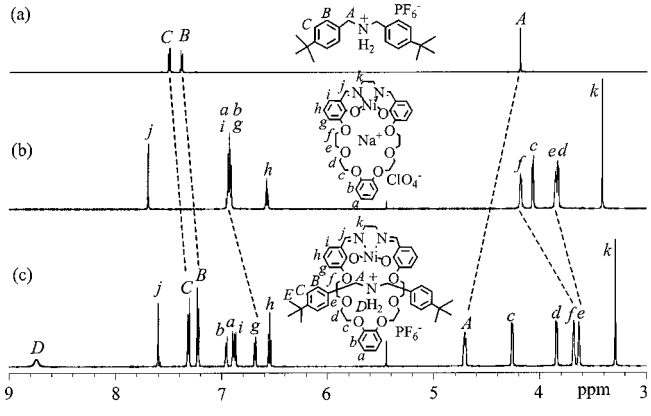


Figure 3. $^1$H NMR spectra (600 MHz, $CD_3CN$, 25 °C) of (a) **2**-H·$PF_6$, (b) **1a**-$Ni^{II}$·Na(I), and (c) **3a**-H·$PF_6$.

In contrast, two of the signals for the ether $CH_2O$ protons (*e* and *f*; Figure 3c) in the $Ni^{II}$-bound macrocycle of the rotaxane have shifted upfield relative to their location in the unthreaded $Ni^{II}$-complexed macrocycle (Figure 3b); we attribute this phenomenon to shielding by the aromatic units in the thread in bent conformations of the components (Figure 6). In addition, the signals of the protons of the aromatic groups in the salen moiety (*g*; Figure 3c) as well as in the thread (*B* and *C*; Figure 3c) have shifted upfield relative to their locations in the corresponding free components probably as a result of π–π stacking interactions.[15] As indicated in Figure 4, the $^1$H NMR spectrum of [2]rotaxane **3b**-H·$PF_6$ (Figure 4c) displays signals that are very similar to those observed for **3a**-H·$PF_6$, which provides good evidence of the successful formation of this rotaxane. Moreover, the ROESY NMR spectra (see Supporting Information) of both rotaxanes **3a/b**-H·$PF_6$ feature cross peaks between the signals of the protons of the ether units (*e* and *f*) in their respective macrocycles and the $CH_2N^+$ units (*A*) in their thread-like moieties.

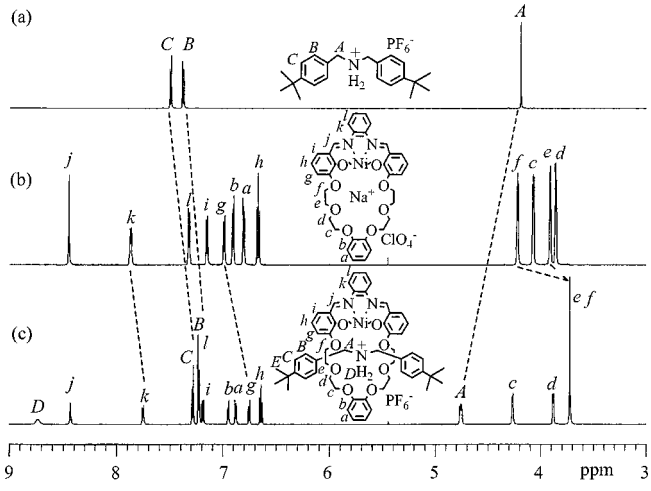


Figure 4. $^1$H NMR spectra (600 MHz, $CD_3CN$, 25 °C) of (a) **2**-H·$PF_6$, (b) **1b**-$Ni^{II}$·Na(I), and (c) **3b**-H·$PF_6$.

Figure 5 displays representative $^1$H NMR spectra of bis[2]rotaxane **6**-2H·2$ClO_4$, the salophen-incorporating bismacrocycle bound with palladium(II) [**4**-$Pd^{II}$·Na; for its synthesis, see the Supporting Information], and thread-like salt **2**-H·$PF_6$. Most of signals for the protons of bis[2]rotaxane **6**-2H·2$ClO_4$ (Figure 5c–e) are very similar to those observed for [2]rotaxanes **3a/b**-H·$PF_6$, which provides good evidence for the successful formation of this rotaxane and confirms its structure. At 25 °C (Figure 5c), the protons of the salophen and ether units in the bismacrocycle suggest that slow conformational changes occur on the $^1$H NMR spectroscopic timescale, which results in broadening and splitting (*e*, *h*, and *j*) of the signals for a few protons of the bismacrocycle. The spectrum became much simpler when the signals for these protons coalesced at higher temperatures (Figure 5d, e). In addition, the ROESY NMR spectrum (see Supporting Information) of this bis[2]rotaxane features cross peaks between the signals of the protons of the ether unit (*c* and *d*) in the bismacrocycle component and aromatic protons (*B* and *C*) in its two thread-like moieties.

The $^1$H NMR spectrum of the Rh(TPP)Cl-stoppered [2]-rotaxane **8**-H·Rh(TPP)Cl·$ClO_4$ (see Supporting Information) displays signals that are very similar to those that

 © 2007 Wiley-VCH Verlag GmbH & Co. KGaA, Weinheim 

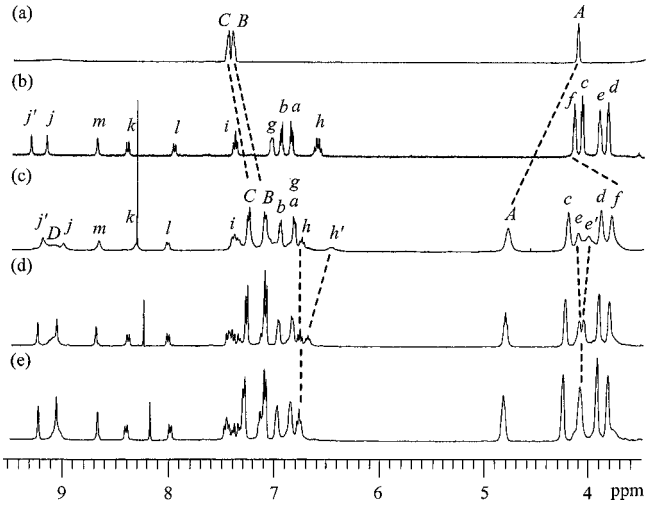


Figure 5. $^1$H NMR spectra (400 MHz, [$D_6$]DMSO) of (a) **2**-H·$PF_6$, (b) **4**-$Pd^{II}$·Na(I), and **6**-2H·2$ClO_4$ recorded at temperatures of (c) 298 K, (d) 323 K, and (e) 353 K.

we observed previously.[6a,6b,6d] In particular, the signal of the aromatic protons (*A*; Scheme 3) in the terminal pyridyl unit of the thread-like moiety is shifted upfield drastically relative to that in the free salt as a result of the shielding effect of the diamagnetic current of the porphyrin ring.[16]

We obtained dark-brown-colored single crystals of **3a**-H·$PF_6$ that were suitable for X-ray crystallographic analysis upon slow evaporation of a $CH_2Cl_2$/EtOAc solution of the [2]rotaxane; **3b**-H·$PF_6$ provided yellowish-brown-colored single crystals, also suitable for X-ray crystallographic analysis, upon vapor diffusion of diisopropyl ether into a $CH_2Cl_2$ solution of the [2]rotaxane. The crystal structures

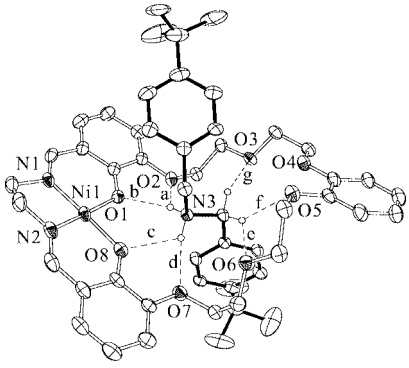


Figure 6. One molecular structure of **3a**-H·$PF_6$ that indicates the intercomponent [N+–H···O] and [C–H···O] hydrogen bonds. The other rotaxane molecule, the nonhydrogen-bonding hydrogen atoms, disordered carbon atoms, and the counter anion have been omitted for clarity. Hydrogen bonding geometries: [X···O], [H···O] distances [Å] and [X–H···O] angles [°] are (a) 3.067, 2.348, 136.8; (b) 2.840, 2.032, 148.6; (c) 2.737, 2.207, 117.1; (d) 2.892, 2.008, 166.8; (e) 3.264, 2.523, 134.0; (f) 3.429, 2.580, 147.6; (g) 3.185, 2.318, 149.9.

(Figures 6 and 7, respectively) confirm the proposed [2]rotaxane structures incorporating the nickel(II)–salen and –salophen moieties, respectively. Stabilization of these [2]-rotaxanes is achieved through a combination of (1) [$N^+$–H···O][17] and [C–H···O][17a,17c] hydrogen bonds involving $NH_2^+$ centers, their adjacent $CH_2$ groups, and the oxygen atoms in the macrocycles and (2) π–π stacking interactions[17] between aromatic rings (see Supporting Information). The packing arrays of both **3a/b**-H·$PF_6$ are stabilized by intra- and intermolecular [C–H···π] interactions.[17b,17d] The [$N^+$– H···O][17] and [C–H···O][17a,17c] hydrogen bonding distances (2.737–3.498 Å) are comparable to those found in a related [2]rotaxane incorporating a palladium(II)–salophen,[8] a nickel(II)–salen[9] moiety, and other[17] similar compounds. The nickel atom exists in a distorted square-planar array (see Supporting Information) that is very similar to the geometries we have observed previously for palladium atoms in related structures.[8,12d]

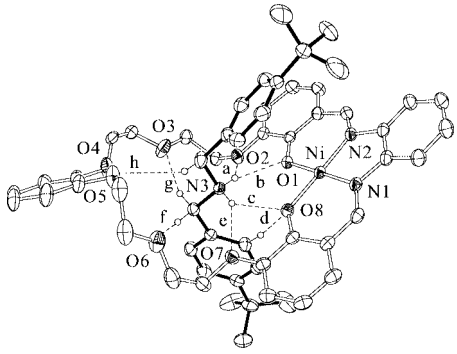


Figure 7. Molecular structure of **3b**-H·$PF_6$ that indicates the intercomponent [$N^+$–H···O] and [C–H···O] hydrogen bonds. The nonhydrogen-bonding hydrogen atoms, disordered carbon atoms, and the counter anion have been omitted for clarity. Hydrogen bonding geometries: [X···O], [H···O] distances [Å] and [X–H···O] angles [°] are (a) 2.906, 2.148, 141.5; (b) 2.829, 2.074, 140.7; (c) 2.858, 2.127, 137.8; (d) 3.498, 2.572, 162.1; (e) 2.920, 2.141, 144.4; (f) 3.408, 2.545, 149.7; (g) 3.259, 2.329, 162.8; (h) 3.323, 2.575, 134.9.

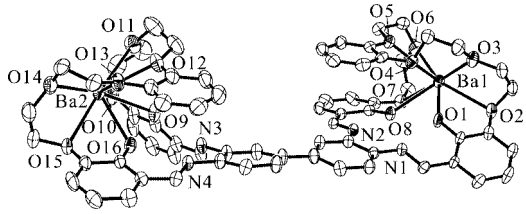


Figure 8. Molecular structure of **4**–Ba. Perchlorate anions, solvent molecules, and hydrogen atoms have been omitted for clarity. Selected bond lengths [Å] and angles [°]: Ba1–O1 2.745(5), Ba1–O2 3.001(5), Ba1–O3 2.975(5), Ba1–O4 2.934(5), Ba1–O5 3.010(5), Ba1–O6 2.965(5), Ba1–O7 2.903(5), Ba1–O8 2.786(5), Ba2–O9 2.828(5), Ba2–O10 3.046(6), Ba2–O11 2.945(6), Ba2–O12 2.932(6), Ba2–O13 2.956(5), Ba2–O14 2.984(6), Ba2–O15 2.995(6), Ba2–O16 2.816(5); O1–Ba1–O6 156.66(15), O8–Ba1–O3 116.71(14), O7–Ba1–O3 171.01(15), O4–Ba1–O2 98.17(14), O6–Ba1–O2 147.28(14), O2–Ba1–O5 149.92(14), O16–Ba2–O11 122.12(17), O9–Ba2–O14 154.50(16), O12–Ba2–O15 119.58(17), O11–Ba2–O15 175.73(17), O13–Ba2–O10 152.92(16), O14–Ba2–O10 150.05(16).

 © 2007 Wiley-VCH Verlag GmbH & Co. KGaA, Weinheim 

We obtained orange-colored single crystals of **4**-Ba suitable for X-ray crystallographic analysis upon the slow evaporation of a $CH_2Cl_2$/THF/MeOH solution of the $Ba^{II}$-coordinated bismacrocycle. The crystal structure (Figure 8) confirms that this bismacrocycle possesses two barium(II) ions; the two salophen macrocyclic units, which are attached through aromatic rings, are twisted at a dihedral angle of 14.8°. Each oligoether unit is folded completely to allow coordination of all of its oxygen atoms to the barium(II) ion.

## Conclusions

We synthesized [2]rotaxanes **3a**/**3b**-H·$PF_6$ that feature nickel(II)–salophen and –salen moieties, respectively. Both "ring-opening-and-closing" and "threading-followed-by-shrinking" processes occurred during the synthesis of the salen-based [2]rotaxane **3a**-H·$PF_6$, resulting in its remarkably higher yield than that of the salophen-based [2]rotaxane **3b**-H·$PF_6$, for which only a "threading-followed-by-shrinking" process occurs. During the formation of these [2]rotaxanes, the binding of nickel(II) ions to the salophen and salen moieties constitutes the shrinking event. Furthermore, we extended the synthetic system by using a "threading-followed-by-shrinking" approach to afforded [2]rotaxane **5**-H·$ClO_4$ and bis[2]rotaxane **6**-2H·2$ClO_4$, which both feature two palladium(II)–salophen moieties linked in a bismacrocycle. In addition, we synthesized the Rh(TPP)Cl-stoppered [2]rotaxane **8**-H·Rh(TPP)Cl·$ClO_4$ from salophen-based macrocycle **1b**-$Pd^{II}$·Na by using a combination of "threading-followed-by-shrinking" and end-capping through axial coordination between the pyridyl unit of the thread-like cationic component and the rhodium(III) center. We believe that these approaches will be useful for the construction of multifunctional rotaxanes and for the development of molecular devices as new tools. Such rotaxanes possessing salen and salophen moieties have the potential to behave as catalytically active molecular machines on solid surfaces.

## Experimental Section

**General Information:** Nickel(II) acetate tetrahydrate, 3,3′-diaminobenzidine, palladium(II) acetate, and tetracarbonyl-di-μ-chlororhodium(I) ($[Rh(CO)_2Cl]_2$) were purchased from Aldrich. Sodium sulfate, potassium sulfate, and barium perchlorate were purchased from Wako Pure Chemical Industries. **1a**-Ba[9] (Scheme 1), **1b**-Ba[12d] (Scheme 1), **1a**-$Ni^{II}$·Na,[9] **1b**-$Pd^{II}$·Na[12d] (Scheme 3), **2**-H·$PF_6$[4c] (Scheme 1), **7**-H·$CF_3COO$[13] (Scheme 3), and Rh(TPP)Cl[6b] (Scheme 3) were all prepared according to literature procedures. Solvents were purchased from commercial sources. Each reaction was performed under an anhydrous nitrogen atmosphere. Thin-layer chromatography (TLC) was performed by using aluminium sheets precoated with silica gel 60F (Merck 5554). The plates were inspected under UV light and developed in $I_2$ vapor. Column chromatography was conducted by using Wakogel C-400HG (Wako Pure Chemical Industries). $^1H$ and $^{13}C$ NMR spectra were recorded with a Bruker AVANCE 400 spectrometer (400 and 100 MHz for $^1H$ and $^{13}C$ NMR, respectively). All 2D NMR spectroscopy experiments were recorded by using 1 K data points and 256 time increments in phase-sensitive mode and were processed in a 1 K × 1 K matrix. The ROESY NMR spectroscopic experiment was performed with the use of a spin–lock mixing time of 200 ms and was processed using a forward linear prediction in the F1 dimension. Matrix-assisted laser-desorption/ionization time-off-light mass spectrometry (MALDI-TOF MS) was performed with a Shimazu Kratos Kompact-MALDI III with a 2,5-dihydroxybenzoic acid as the matrix. FAB mass spectra were recorded with an MS600H spectrometer. Infrared (IR) spectra were recorded by using a Jasco FTIR 620 spectrophotometer. Elemental analyses were performed with a CE Instruments EA1110. Gel permeation chromatography (GPC) separation was performed with an LC-918 (Japan Analytical Industry Co. Ltd.) equipped with JAIGL-1H and –2H columns; chloroform was used as the eluent.

**Macrocycle Coordinated to Both Nickel(II) and Sodium(I), 1b-$Ni^{II}$·Na:** A solution of sodium sulfate (2.00 g, 14.0 mmol) in water (20 mL) was added to a solution of **1b**-Ba (935 mg, 1.0 mmol) in MeCN (40 mL), and then the mixture was stirred at r.t. for 3 h. The reaction mixture was filtered to remove the precipitated barium sulfate. The filtrate was dried (anhydrous $Na_2SO_4$), the solvent was evaporated, and the residue was dried under high vacuum to yield **1b**-Na as an orange solid (801 mg, 95%). A solution of nickel(II) acetate tetrahydrate (274 mg, 1.1 mmol) in MeOH (12 mL) was added to a solution of **1b**-Na (616 mg, 0.73 mmol) in $CH_2Cl_2$ (40 mL), and then the mixture was stirred at r.t. for 2 h. The solvent was evaporated under reduced pressure. The residue was dissolved in a small amount of MeCN and purified by column chromatography ($SiO_2$; $CH_2Cl_2$/MeOH, 98:2). Fractions containing the product [$R_f$ = 0.42 for **1b**-$Ni^{II}$·Na; $CH_2Cl_2$/MeOH, 9:1] were combined, and the solvent was evaporated under reduced pressure to afford **1b**-$Ni^{II}$·Na (454 mg, 80%) as a brown solid. M.p. 141–142 °C. $^1H$ NMR (400 MHz, $CD_3CN$, 25 °C): $\delta$ = 8.00 (s, 2 H, *j*), 7.44 (br., 2 H, *k*), 6.89–6.86 (m, 2 H, *a*), 6.79–6.74 (m, 6 H, *b*, *i*, *l*), 6.61 (d, *J* = 7.8 Hz, 2 H, *g*), 6.40 (t, *J* = 7.8 Hz, 2 H, *h*), 4.13 (br., 4 H, *f*), 4.07 (br., 4 H, *c*), 3.86–3.85 (br., 8 H, *d*/*e*) ppm. $^{13}C$ NMR (100 MHz, $CD_3CN$, 25 °C): $\delta$ = 155.3, 154.1, 148.4, 147.3, 141.9, 127.4, 125.5, 121.7, 119.7, 115.4, 115.1, 114.7, 68.9, 68.2, 67.8, 67.0 ppm. IR (KBr): $\tilde{\nu}$ = 3504, 2920, 2874, 1707, 1610, 1543, 1503, 1450, 1254, 1202, 1100 ($ClO_4^-$), 936, 739 $cm^{-1}$. MS (MALDI-TOF): *m*/*z* = 678 (100) $[M + 1 - ClO_4]^+$. $C_{34}H_{32}ClN_2NaNiO_{12}$ (777.77): calcd. C 52.51, H 4.15, N 3.60; found C 52.58, H 4.28, N 3.51.

**3a/b-H·$PF_6$:** A solution of $Na_2SO_4$ (101 mg, 0.71 mmol) in $H_2O$ (2 mL) and MeCN (2 mL) was added to a solution of the relevant macrocycle–barium perchlorate complex (0.25 mmol; 222 mg for **1a**-Ba; 234 mg for **1b**-Ba) and **2**-H·$PF_6$ (229 mg, 0.50 mmol) in MeCN (20 mL), and then the mixture was stirred for 2 h. A solution of $Ni(OAc)_2·4H_2O$ (63.3 mg, 0.25 mmol) in MeOH (2 mL) and MeCN (2 mL) was added to the reaction mixture, which was stirred for 12 h. The solution was filtered, and then the solvent was evaporated under reduced pressure. The residue was dissolved in a small amount of MeCN and purified by column chromatography ($SiO_2$; $CH_2Cl_2$/MeOH, 9:1). Fractions containing the product ($R_f$ = 0.37 for **3a**-H·$PF_6$; $R_f$ = 0.33 for **3b**-H·$PF_6$; $CH_2Cl_2$/MeOH, 9:1) were combined, and the solvent was evaporated under reduced pressure to afford the [2]rotaxanes as either a yellow-green (**3a**-H·$PF_6$: 146 mg, 55%) or dark-brown solid (**3b**-H·$PF_6$: 56 mg, 20%). Selected data for **3a**-H·$PF_6$: M.p. 145–147 °C (decomp.). $^1H$ NMR (600 MHz, $CD_3CN$, 25 °C): $\delta$ = 8.74 (br., 2 H, *D*), 7.60 (s, 2 H, *j*), 7.31 (d, *J* = 8.4 Hz, 4 H, *C*), 7.23 (d, *J* = 8.4 Hz, 4 H, *B*), 6.95 (m, 2 H, *b*), 6.90 (m, 2 H, *a*), 6.88 (d, *J* = 7.8 Hz, 2 H, *i*), 6.68 (d, *J* = 7.8 Hz, 2 H, *g*), 6.55 (t, *J* = 7.8 Hz, 2 H, *h*), 4.71 (t, *J* = 6.6 Hz, 4 H, *A*), 4.25 (m, 4 H, *c*), 3.85 (m, 4 H, *d*), 3.68 (m, 4 H, *f*), 3.63 (m,

 © 2007 Wiley-VCH Verlag GmbH & Co. KGaA, Weinheim 

4 H, *e*), 3.29 (s, 4 H, *k*), 1.22 (s, 18 H, *E*) ppm. $^{13}$C NMR (150 MHz, $CD_3CN$, 25 °C): $\delta$ = 163.2, 152.7, 150.6, 147.9, 147.6, 130.2, 128.3, 124.8, 124.7, 120.5, 120.2, 114.8, 114.1, 111.9, 68.8, 68.3, 67.6, 67.1, 58.4, 50.4, 33.9, 30.3 ppm. IR (KBr): $\tilde{\nu}$ = 3436, 3094, 2958, 1629, 1607, 1549, 1504, 1450, 1304, 1228, 1132, 1089, 839 ($PF_6^-$), 741, 557 cm$^{-1}$. MS (FAB): *m*/*z* (%) = 916 (72) [M – $PF_6$]$^+$. $C_{52}H_{64}F_6N_3NiO_8P$ (1062.75): calcd. C 58.77, H 6.07, N 3.95; found C 59.07, H 6.27, N 3.61. Selected data for **3b**-H·$PF_6$: M.p. 314–315 °C. $^1$H NMR (600 MHz, $CD_3CN$, 25 °C): $\delta$ = 8.73 (br., 2 H, *D*), 8.44 (s, 2 H, *j*), 7.73 (m, 2 H, *k*), 7.28 (d, *J* = 8.4 Hz, 4 H, *C*), 7.24 (d, *J* = 8.4 Hz, 4 H, *B*), 7.21 (m, 2 H, *l*), 7.19 (d, *J* = 7.8 Hz, 2 H, *i*), 6.94 (m, 2 H, *b*), 6.89 (m, 2 H, *a*), 6.73 (d, *J* = 7.8 Hz, 2 H, *g*), 6.64 (t, *J* = 7.8 Hz, 2 H, *h*), 4.78 (t, *J* = 6.6 Hz, 4 H, *A*), 4.28 (m, 4 H, *c*), 3.88 (m, 4 H, *d*), 3.72 (s, 8 H, *e*/*f*), 1.09 (s, 18 H, *E*) ppm. $^{13}$C NMR (150 MHz, $CD_3CN$, 25 °C): $\delta$ = 156.9, 154.2, 150.9, 147.8, 147.5, 142.0, 130.1, 128.2, 127.9, 126.6, 124.6, 120.5, 120.3, 115.6, 115.5, 115.1, 111.9, 68.8, 68.0, 67.6, 67.0, 50.6, 33.7, 30.0 ppm. IR (KBr): $\tilde{\nu}$ = 3067, 2961, 1618, 1441, 1258, 1204, 1103, 840 ($PF_6^-$), 743, 556 cm$^{-1}$. MS (FAB): *m*/*z* (%) = 965 (90) [M + 1 – $PF_6$]$^+$. $C_{56}H_{64}F_6N_3NiO_8P$ (1110.79): calcd. C 60.55, H 5.81, N 3.78; found C 60.88, H 5.88, N 3.47.

**4-Ba:** A solution of the dialdehyde-functionalized crown ether derivative (526.5 mg, 1.0 mmol) and 3,3′-diaminobenzidine (107.2 mg, 0.5 mmol) in dry THF (20 mL) was added over 2 h to a solution of barium perchlorate (336.3 mg, 1.0 mmol) heated under reflux in dry MeOH (100 mL). The mixture was heated under reflux for an additional 24 h. During the reaction, an orange-colored solid precipitated out. This solid was filtered off and washed with $CH_2Cl_2$ to afford the barium perchlorate–bismacrocycle complex **4**-Ba as an orange solid (691 mg, 74%). M.p. 221–226 °C. $^1$H NMR (400 MHz, $CD_3CN$, 25 °C): $\delta$ = 14.89–14.67 (m, 4 H, *OH*), 9.42 (br., 2 H, *j*′), 9.04 (br., 2 H, *j*), 8.02 (s, 2 H, *m*), 7.95–7.90 (m, 2 H, *k*), 7.74–7.69 (m, 2 H, *l*), 7.24 (m, 4 H, *i*), 7.08 (m, 4 H, *g*), 6.93–6.85 (m, 8 H, *a*, *b*), 6.61 (m, 4 H, *h*), 4.47 (m, 8 H, *f*), 3.97–3.82 (m, 24 H, *c*–*e*) ppm. IR (KBr): $\tilde{\nu}$ = 1080 ($ClO_4^-$) cm$^{-1}$. MS (FAB): *m*/*z* (%) = 1431 (10) [M – Ba – 3$ClO_4$]$^+$. $C_{68}H_{66}Ba_2Cl_4N_4O_{32}\cdot 3H_2O$ (1921.80): calcd. C 42.50, H 3.78, N 2.92; found C 42.23, H 3.92, N 2.69.

**4-K and 4-Na:** A solution of potassium sulfate (1 g, 5.7 mmol) or sodium sulfate (0.81 g, 5.7 mmol) in $H_2O$ (50 mL) was added to a solution of **4**-Ba (1.06 g, 0.57 mmol) in a solution of MeOH/THF/MeCN/$Me_2CO$ (4:4:1:1, 200 mL), and then the mixture was stirred at r.t. for 3 h. The reaction mixture was filtered to remove the precipitated barium sulfate. The solvent was evaporated, and the residue was dried under high vacuum to yield **4**-K as an orange solid (684 mg, 90%) or **4**-Na as an orange solid (683 mg, 91%). Selected data for **4**-K: $^1$H NMR (400 MHz, [$D_6$]DMSO, 25 °C): $\delta$ = 13.59–13.56 (m, 4 H, *OH*), 9.11–9.02 (m, 4 H, *j*, *j*′), 8.55 (s, 2 H, *m*), 7.99 (m, 2 H, *k*), 7.67 (m, 2 H, *l*), 7.29–7.26 (m, 4 H, *i*), 7.15–7.14 (m, 4 H, *g*), 6.98–6.91 (m, 8 H, *a*, *b*), 6.89–6.86 (m, 4 H, *h*), 4.17 (m, 8 H, *f*), 4.11 (m, 8 H, *c*), 3.86 (m, 8 H, *e*), 3.83–3.82 (m, 8 H, *d*) ppm. $^{13}$C NMR (100 MHz, [$D_6$]DMSO, 25 °C): $\delta$ = 192.3, 192.2, 150.9, 150.8, 150.3, 148.1, 147.7, 147.6, 146.8, 146.3, 146.0, 143.9, 124.2, 121.8, 121.7, 120.8, 120.6, 118.7, 118.6, 118.0, 114.3, 113.7, 98.7, 54.3, 52.6, 48.0, 30.0 ppm. IR (KBr): $\tilde{\nu}$ = 1100 ($ClO_4^-$) cm$^{-1}$. MS (FAB): *m*/*z* (%) = 1233 (10) [M – $ClO_4$]$^+$.

**4-Pd$^{II}$·Na:** Solid palladium(II) acetate (384 mg, 1.71 mmol) was added to a $CH_2Cl_2$/THF/MeOH (6:2:2, 200 mL) solution of **4**-Na (751 mg, 0.57 mmol), and then the mixture was stirred at r.t. for 2 h. The solvent was evaporated under reduced pressure. The residue was dissolved in a small amount of MeCN and purified by column chromatography ($SiO_2$; $CH_2Cl_2$/MeOH, 98:2) to afford **4**-Pd$^{II}$·Na (752 mg, 80%) as a orange solid. $^1$H NMR (400 MHz, [$D_6$]-DMSO, 25 °C): $\delta$ = 9.37 (s, 2 H, *j*′), 9.22 (s, 2 H, *j*), 8.74 (s, 2 H, *m*), 8.45 (d, *J* = 9 Hz, 2 H, *k*), 8.02 (d, *J* = 9 Hz, 2 H, *l*), 7.43 (m, 4 H, *i*), 7.08 (br., 4 H, *g*), 6.98 (m, 4 H, *b*), 6.91 (m, 4 H, *a*), 6.66 (m, 4 H, *h*), 4.21 (br., 8 H, *f*), 4.14 (br., 8 H, *c*), 3.97 (br., 8 H, *e*), 3.89 (br., 8 H, *d*) ppm. IR (KBr): $\tilde{\nu}$ = 3003, 2391, 1853, 1630, 1481, 1346, 1163, 1053 ($ClO_4^-$), 976 cm$^{-1}$. MS (MALDI-TOF): *m*/*z* (%) = 1428 (100) [M + 1 – Na – 2$ClO_4$]$^+$, 1548 (4) [M – 1 – $ClO_4$]$^+$.

**5-H·$ClO_4$ and 6-2H·2$ClO_4$:** A solution of **2**-H·$PF_6$ (592 mg, 1.3 mmol) in MeCN (20 mL) was added to a solution of the bismacrocycle with potassium(I) perchlorate **4**-K (173 mg, 0.13 mmol) in $CH_2Cl_2$ (20 mL) and stirred for 16 h at r.t. Then, solid Pd(OAc)$_2$ (87 mg, 0.39 mmol) was added, and the reaction mixture was stirred for 4 h. The solvent was evaporated under reduced pressure, and the residue was dissolved in $CH_2Cl_2$ and filtered through a column ($SiO_2$; $CH_2Cl_2$/MeOH, 98:2). The crude material was purified by GPC ($CHCl_3$) to afford **6**-2H·2$ClO_4$ as a red-orange solid (58 mg, 20%). Selected data for **5**-H·$ClO_4$: IR (KBr): $\tilde{\nu}$ = 1100 ($ClO_4^-$) cm$^{-1}$. MS (FAB): *m*/*z* (%) = 1715 (18) [M – $ClO_4$]$^+$. Selected data for **6**-2H·2$ClO_4$: M.p. 184–187 °C. $^1$H NMR (400 MHz, [$D_6$]-DMSO, 25 °C): $\delta$ = 9.22 (s, 2 H, *j*′), 9.06 (m, 4 H, *D*), 8.68 (s, 2 H, *j*), 8.33 (m, 2 H, *m*), 8.32 (s, 2 H, *k*), 8.03 (m, 2 H, *l*), 7.36 (m, 4 H, *i*), 7.25 (m, 8 H, *C*), 7.11 (m, 8 H, *B*), 6.95 (m, 4 H, *b*), 6.83 (m, 8 H, *g*, *a*), 6.75 (t, *J* = 8 Hz, 2 H, *h*), 6.47 (br., 2 H, *h*′), 4.79 (br., 8 H, *A*), 4.22 (m, 8 H, *c*), 4.12 (m, 4 H, *e*), 4.02 (m, 4 H, *e*′), 3.91 (br., 8 H, *d*), 3.81 (br., 8 H, *f*) ppm. IR (KBr): $\tilde{\nu}$ = 3181, 2060, 1856, 1525, 1488, 1382, 1090 ($ClO_4^-$), 989, 687 cm$^{-1}$. MS (FAB): *m*/*z* (%) = 2023 (6) [M – 1 – $ClO_4$]$^+$, 1012 (13) [M – 2 $ClO_4$]$^{2+}$.

**8-H·Rh(TPP)Cl·$ClO_4$:** The thread-like salt **7**-H·$O_2CCF_3$ (44 mg, 0.12 mmol) was added to a $CH_2Cl_2$/MeCN (10:1, 50 mL) solution of the salophen macrocycle with palladium(II)-sodium(I) **1b**-Pd$^{II}$·Na(I) (100 mg, 0.12 mmol) and stirred for 1 h at r.t. Then, solid Rh(TPP)Cl (90 mg, 0.12 mmol) was added, and the reaction mixture was stirred for 60 h. The solvent was evaporated under reduced pressure. The residue was dissolved in $CH_2Cl_2$ and chromatographed ($SiO_2$; $CH_2Cl_2$/MeOH, 98:2) to afford the **8**-H·Rh(TPP)Cl·$ClO_4$ as a violet solid (86 mg, 40%). $^1$H NMR (400 MHz, $CDCl_3$, 25 °C): $\delta$ = 8.79 (s, 10 H, *j*, *6*), 8.35 (br., 2 H, *H*), 8.24 (m, 4 H, *5*), 8.04 (m, 2 H, *F*), 7.83 (d, *J* = 7 Hz, 4 H, *4*), 7.70 (m, 8 H, *1*, *3*), 7.52 (m, 4 H, *2*), 7.33 (m, 2 H, *k*), 7.11 (br., 2 H, *E*), 6.85 (m, 2 H, *b*), 6.70 (d, *J* = 8 Hz, 2 H, *g*), 6.65 (m, 2 H, *a*), 6.53 (d, *J* = 8 Hz, 2 H, *l*), 6.33 (m, 2 H, *i*), 6.17 (m, 2 H, *h*), 5.44 (m, 2 H, *B*), 4.13 (m, 4 H, *c*), 4.01 (m, 8 H, *f*, *e*), 3.95 (m, 4 H, *d*), 3.84 (m, 2 H, *C*), 3.75 (br., 2 H, *D*), 1.05 (d, *J* = 7 Hz, 2 H, *A*), 0.88 (s, 9 H, *G*) ppm. MS (MALDI-TOF): *m*/*z* (%) = 835 (4) [M – 1 – $ClO_4$ – Cl]$^{2+}$.

**X-ray Measurements**: X-ray data were obtained with a Bruker SMART-CCD diffractometer; structural determination and refinement were performed by using SAINT[18] and SHELXTL[19] software packages, and the empirical absorption correction was performed by using the SADABS[20] program. All structures were solved by direct methods and refined by a full-matrix least-squares method.

**Crystallographic Data**

**3a-H·$PF_6$:** [Ni($C_{30}H_{32}N_2O_8$)$C_{22}H_{32}N$]$_2$($PF_6$)$_2$·$CH_2Cl_2$·$C_4H_8O_2$, $C_{109}H_{138}Cl_2F_{12}N_6Ni_2O_{18}P_2$, *M* = 2298.51, monoclinic, space group *C*2/*c*, *a* = 67.469(4) Å, *b* = 13.7577(8) Å, *c* = 24.5387(14) Å, $\beta$ = 96.183(2)°, *V* = 22645(2) Å$^3$, *Z* = 8, $\rho_{calcd.}$ = 1.348 g cm$^{-3}$, $\mu$(Mo-$K_\alpha$) = 4.94 cm$^{-1}$, *T* = 183(2) K, yellow-brown plates, 0.20 × 0.15 × 0.10 mm, $R_1$ = 0.0819 [I > 2$\sigma$(*I*)], $wR_2$ = 0.2822 (all data), GOF = 0.940.

 © 2007 Wiley-VCH Verlag GmbH & Co. KGaA, Weinheim 

**3b-H·PF$_6$:** $[Ni(C_{34}H_{32}N_2O_8)C_{22}H_{32}N]PF_6$, $C_{56}H_{64}F_6N_3NiO_8P$, $M$ = 1110.78, triclinic, space group $P\bar{1}$, $a$ = 11.8973(12) Å, $b$ = 15.3612(16) Å, $c$ = 15.4538(16) Å, $\alpha$ = 104.457(2)°, $\beta$ = 97.949(2)°, $\gamma$ = 96.015(2)°, $V$ = 2679.8(5) Å$^3$, $Z$ = 2, $\rho_{calcd.}$ = 1.377 g cm$^{-3}$, $\mu$(Mo-$K_\alpha$) = 4.70 cm$^{-1}$, $T$ = 203(2) K, dark-brown plates, 0.40 × 0.30 × 0.20 mm, $R_1$ = 0.0538 [I > 2σ(I)], $wR_2$ = 0.1645 (all data), GOF = 1.055. **4-Ba:** $[Ba_2(C_{68}H_{66}N_4O_{16})(ClO_4)(MeOH)_3(H_2O)_2](ClO_4)_3(H_2O)_3$, $C_{71}H_{88}Ba_2Cl_4N_4O_{40}$, $M$ = 2053.93, triclinic, space group $P\bar{1}$, $a$ = 10.4086(9) Å, $b$ = 18.7294(16) Å, $c$ = 23.9428(20) Å, $\alpha$ = 107.823(2)°, $\beta$ = 99.645(2)°, $\gamma$ = 91.602(2)°, $V$ = 4365.1(6) Å$^3$, $Z$ = 2, $\rho_{calcd.}$ = 1.563 g cm$^{-3}$, $\mu$(Mo-$K_\alpha$) = 11.12 cm$^{-1}$, $T$ = 183 K, orange plates, 0.35 × 0.20 × 0.10 mm, $R_1$ = 0.0812 [I > 2σ(I)], $wR_2$ = 0.2670 (all data), GOF = 1.060.

CCDC-273373 (for **3a**-H·PF$_6$), -273372 (for **3b**-H·PF$_6$), and -622229 (for **4**-Ba) contain the supplementary crystallographic data for this paper. These data can be obtained free of charge from the Cambridge Crystallographic Data Centre via www.ccdc.cam.ac.uk/data_request/cif.

**Supporting Information** (see also the footnote on the first page of this article): NMR spectroscopic data of **3a/b**-H·PF$_6$ and **8**-H·Rh(TPP)ClClO$_4$, additional crystal structures of **3a/b**-H·PF$_6$ and **4**-Ba, and crystal data for **3a/b**-H·PF$_6$ and **4**-Ba.

## Acknowledgments

M. N. thanks the New Energy and Industrial Technology Development Organization (NEDO), Japan, for sponsoring an Industrial Technology Research Grant Program. I. Y. thanks the Japan Society for the Promotion of Science (JSPS) for a postdoctoral fellowship. We thank Dr. P. T. Glink (http://www.editchem.com) for valuable discussions.

[1] a) J.-M. Lehn, *Supramolecular Chemistry: Concepts and Perspectives*, Wiley-VCH, Weinheim, **1995**; b) M. Asakawa, P. R. Ashton, V. Balzani, A. Credi, C. Hamers, G. Mattersteig, M. Montalti, A. N. Shipway, N. Spencer, J. F. Stoddart, M. S. Tolley, M. Venturi, A. J. P. White, D. J. Williams, *Angew. Chem. Int. Ed.* **1998**, *37*, 333–337; c) S. I. Jun, J. W. Lee, S. Sakamoto, K. Yamaguchi, K. Kim, *Tetrahedron Lett.* **2000**, *41*, 471–475; d) B. L. Feringa (Ed.), *Molecular Switches*, Wiley-VCH, Weinheim, **2001**; e) C. A. Schalley, K. Beizai, F. Vögtle, *Acc. Chem. Res.* **2001**, *34*, 465–476; f) J.-P. Collin, C. Dietrich-Buchecker, P. Gaviña, M. C. Jimenez-Molero, J.-P. Sauvage, *Acc. Chem. Res.* **2001**, *34*, 477–487; g) V. Balzani, M. Venturi, A. Credi, *Molecular Devices and Machines*, Wiley-VCH, Weinheim, **2003**; h) D. A. Leigh, J. K. Y. Wong, F. Dehez, F. Zerbetto, *Nature* **2003**, *424*, 174–179; i) R. Hernandez, H.-R. Tseng, J. W. Wong, J. F. Stoddart, J. I. Zink, *J. Am. Chem. Soc.* **2004**, *126*, 3370–3371; j) J. D. Badjić, V. Balzani, A. Credi, S. Silvi, J. F. Stoddart, *Science* **2004**, *303*, 1845–1849.

[2] a) P. T. Glink, A. I. Oliva, J. F. Stoddart, A. J. P. White, D. J. Williams, *Angew. Chem. Int. Ed.* **2001**, *40*, 1870–1875; b) F. G. Gatti, D. A. Leigh, S. A. Nepogodiev, A. M. Z. Slawin, S. J. Teat, J. K. Y. Wong, *J. Am. Chem. Soc.* **2001**, *123*, 5983–5989; c) M. Asakawa, G. Brancato, M. Fanti, D. A. Leigh, T. Shimizu, A. M. Z. Slawin, J. K. Y. Wong, F. Zerbetto, S. J. Zhang, *J. Am. Chem. Soc.* **2002**, *124*, 2939–2950; d) J. A. Wisner, P. D. Beer, M. G. B. Drew, M. R. Sambrook, *J. Am. Chem. Soc.* **2002**, *124*, 12469–12476.

[3] a) S. J. Cantrill, D. A. Fulton, M. C. T. Fyfe, J. F. Stoddart, A. J. P. White, D. J. Williams, *Tetrahedron Lett.* **1999**, *40*, 3669–3672; b) J. Cao, M. C. T. Fyfe, J. F. Stoddart, G. R. L. Cousins, P. T. Glink, *J. Org. Chem.* **2000**, *65*, 1937–1946; c) Y. Tachibana, N. Kihara, Y. Ohga, T. Takata, *Chem. Lett.* **2000**, 806–807; d) S. J. Cantrill, D. A. Fulton, A. M. Heiss, A. R. Pease, J. F. Stoddart, A. J. P. White, D. J. Williams, *Chem. Eur. J.* **2000**, *6*, 2274–2287.

[4] a) M. Händel, M. Plevoets, S. Gestermann, F. Vögtle, *Angew. Chem. Int. Ed. Engl.* **1997**, *36*, 1199–1201; b) P. R. Ashton, M. C. T. Fyfe, C. Schiavo, J. F. Stoddart, A. J. P. White, D. J. Williams, *Tetrahedron Lett.* **1998**, *39*, 5455–5458; c) P. R. Ashton, I. Baxter, M. C. T. Fyfe, F. M. Raymo, N. Spencer, J. F. Stoddart, A. J. P. White, D. J. Williams, *J. Am. Chem. Soc.* **1998**, *120*, 2297–2307; d) S. J. Cantrill, J. A. Preece, J. F. Stoddart, Z.-H. Wang, A. J. P. White, D. J. Williams, *Tetrahedron* **2000**, *56*, 6675–6681.

[5] a) M. Asakawa, M. Higuchi, G. Mattersteig, T. Nakamura, A. R. Pease, F. M. Raymo, T. Shimizu, J. F. Stoddart, *Adv. Mater.* **2000**, *12*, 1099–1102; b) C. D. Nadai, C. M. Whelan, C. Perollier, G. Clarkson, D. A. Leigh, R. Caudano, P. Rudolf, *Surf. Sci.* **2000**, *454*, 112–117.

[6] a) M. Asakawa, T. Ikeda, N. Yui, T. Shimizu, *Chem. Lett.* **2002**, 174–175; b) T. Ikeda, M. Asakawa, M. Goto, Y. Nagawa, T. Shimizu, *Eur. J. Org. Chem.* **2003**, 3744–3751; c) T. Ikeda, M. Asakawa, M. Goto, K. Miyake, T. Ishida, T. Shimizu, *Langmuir* **2004**, *20*, 5454–5459; d) T. Ikeda, M. Asakawa, T. Shimizu, *New J. Chem.* **2004**, *28*, 870–873; e) T. Ikeda, M. Asakawa, K. Miyake, T. Shimizu, *Chem. Lett.* **2004**, *33*, 1418–1419; f) J. Otsuki, S. Kawaguchi, T. Yamakawa, M. Asakawa, K. Miyake, *Langmuir* **2006**, *22*, 5708–5715.

[7] a) M. C. Jiménez, C. Dietrich-Buchecker, J.-P. Sauvage, A. D. Cian, *Angew. Chem. Int. Ed.* **2000**, *39*, 1295–1298; b) M. Linke, J.-C. Chambron, V. Heitz, J.-P. Sauvage, S. Encinas, F. Barigelletti, L. Flamigni, *J. Am. Chem. Soc.* **2000**, *122*, 11834–11844; c) J.-P. Sauvage, *Science* **2001**, *291*, 2105–2106; d) M. Andersson, M. Linke, J.-C. Chambron, J. Davidsson, V. Heitz, L. Hammarström, J.-P. Sauvage, *J. Am. Chem. Soc.* **2002**, *124*, 4347–4362; e) C. Dietrich-Buchecker, B. Colasson, M. Fujita, A. Hori, N. Geum, S. Sakamoto, K. Yamaguchi, J.-P. Sauvage, *J. Am. Chem. Soc.* **2003**, *125*, 5717–5725; f) P. Mobian, J.-M. Kern, J.-P. Sauvage, *Angew. Chem. Int. Ed.* **2004**, *43*, 2392–2395.

[8] I. Yoon, M. Narita, T. Shimizu, M. Asakawa, *J. Am. Chem. Soc.* **2004**, *126*, 16740–16741.

[9] I. Yoon, M. Narita, M. Goto, T. Shimizu, M. Asakawa, *Org. Lett.* **2006**, *8*, 2341–2344.

[10] a) T. Katsuki, *Coord. Chem. Rev.* **1995**, *140*, 189–214; b) J. Wöltinger, J.-E. Bäckvall, Á. Zsigmond, *Chem. Eur. J.* **1999**, *5*, 1460–1467; c) V. v. A. Castelli, A. D. Cort, L. Mandolini, D. N. Reinhoudt, L. Schiaffino, *Eur. J. Org. Chem.* **2003**, 627–633.

[11] a) S. D. Bella, I. Fragalà, I. Ledoux, M. A. Diaz-Garcia, P. G. Lacroix, T. J. Marks, *Chem. Mater.* **1994**, *6*, 881–883; b) P. G. Lacroix, S. D. Bella, I. Ledoux, *Chem. Mater.* **1996**, *8*, 541–545; c) H.-C. Zhang, W.-S. Huang, L. Pu, *J. Org. Chem.* **2001**, *66*, 481–487.

[12] a) R. Foster, *Organic Charge Transfer Complexes*, Academic, London, **1969**; b) F. Franceschi, E. Solari, C. Floriani, M. Rosi, A. Chiesi-Villa, C. Rizzoli, *Chem. Eur. J.* **1999**, *5*, 708–721; c) F. Franceschi, E. Solari, R. Scopelliti, C. Floriani, *Angew. Chem. Int. Ed.* **2000**, *39*, 1685–1687; d) I. Yoon, M. Goto, T. Shimizu, S. S. Lee, M. Asakawa, *Dalton Trans.* **2004**, 1513–1515.

[13] M. Asakawa, T. Shimizu, manuscript in preparation.

[14] a) G. R. Desiraju, *Acc. Chem. Res.* **1991**, *24*, 290–296; b) F. M. Raymo, M. D. Bartberger, K. N. Houk, J. F. Stoddart, *J. Am. Chem. Soc.* **2001**, *123*, 9264–9267; c) T. Steiner, *Angew. Chem. Int. Ed.* **2002**, *41*, 48–76.

[15] a) C. A. Hunter, J. K. M. Sanders, *J. Am. Chem. Soc.* **1990**, *112*, 5525–5534; b) H. Adams, C. A. Hunter, K. R. Lawson, J. Perkins, S. E. Spey, C. J. Urch, J. M. Sanderson, *Chem. Eur. J.* **2001**, *7*, 4863–4877.

[16] H. Ogoshi, J. Setsume, T. Omura, Z. Yoshida, *J. Am. Chem. Soc.* **1975**, *97*, 6461–6466.

[17] a) P. R. Ashton, P. T. Glink, J. F. Stoddart, S. Menzer, P. A. Tasker, A. J. P. White, D. J. Williams, *Tetrahedron Lett.* **1996**,

 © 2007 Wiley-VCH Verlag GmbH & Co. KGaA, Weinheim 

*37*, 6217–6220; b) P. R. Ashton, R. Ballardini, V. Balzani, M. Gómez-López, S. E. Lawrence, M. V. Martínez-Díaz, M. Montalti, A. Piersanti, L. Prodi, J. F. Stoddart, D. J. Williams, *J. Am. Chem. Soc.* **1997**, *119*, 10641–10651; c) S. J. Cantrill, M. C. T. Fyfe, A. M. Heiss, J. F. Stoddart, A. J. P. White, D. J. Williams, *Chem. Commun.* **1999**, 1251–1252; d) S. J. Cantrill, M. C. T. Fyfe, A. M. Heiss, J. F. Stoddart, A. J. P. White, D. J. Williams, *Org. Lett.* **2000**, *2*, 61–64.

[18] *SAINTPLUS Version 6.22*, Bruker AXS, Madison, WI, USA.
[19] G. M. Sheldrick, *SHELXTL Version 6.12*, Bruker AXS, Madison, WI, USA, **2000**.
[20] G. M. Sheldrick, *SADABS: Program for Scaling and Correction of Area Detector Data*, University of Göttingen, Germany, **1998**.

Received: February 14, 2007
Published Online: July 18, 2007

 © 2007 Wiley-VCH Verlag GmbH & Co. KGaA, Weinheim 

DOI: 10.1002/ejic.200601213

# Synthesis, Characterisation and Luminescent Properties of Lanthanide-Organic Polymers with Picolinic and Glutaric Acids

**Penka I. Girginova,[a] Filipe A. Almeida Paz,[a] Paula C. R. Soares-Santos,[a] R. A. Sá Ferreira,[b] Luís D. Carlos,[b] Vítor S. Amaral,[b] Jacek Klinowski,[c] Helena I. S. Nogueira,[a] and Tito Trindade*[a]**

**Keywords:** Lanthanide complexes / Picolinic acid / Glutaric acid / Luminescence

Three new lanthanide(III) complexes (Ln = Sm, Tb and Eu) of picolinic and glutaric acid were prepared and characterised. The crystal structure of the complex [Sm(glu)(pic)-$(H_2O)_2$] (where Hpic and $H_2$glu stand for picolinic and glutaric acid, respectively) was determined by single-crystal X-ray diffraction. All the Ln complexes were characterised by elemental analysis, infrared spectroscopy, X-ray powder diffraction and thermoanalytical measurements. The combined data show that these Ln complexes are isostructural. The effect of both organic ligands on the photoluminescent behaviour of the $Sm^{3+}$, $Eu^{3+}$ and $Tb^{3+}$ complexes is discussed and we anticipate the possibility of controlling the photoluminescence of picolinic-containing lanthanide compounds by systematically varying the length of the bridging ligand.
(© Wiley-VCH Verlag GmbH & Co. KGaA, 69451 Weinheim, Germany, 2007)

## Introduction

The design of functional units from the molecular scale to macroscopic assemblies has emerged as a new paradigm in materials synthesis resulting in an interplay between conventional molecular chemistry and conventional solid-state science. This has been particularly clear in the development of functional materials using coordination compounds such as in the field of semiconductors technology, supramolecular machinery, microporous and hybrid materials and catalysis.[1] In some cases, the development of these functional materials is based on the chemistry of well-known coordination compounds as illustrated by the assembly of inorganic-organic extended lattices[2] and in the thermolysis of metal thiolato compounds to produce thin films or nanoparticles.[3]

Metals coordinated to aromatic ambidentate ligands form a class of compounds with a wide variety of coordination modes which has long attracted the attention of chemists.[4] Griffith and co-workers extended this type of chemistry to the second row transition metals and, in particular, to their applications in catalysis.[5] More recently, as part of our own studies of metal complexes with aromatic ambidentate ligands,[6] we began to exploit the coordination chemistry of 3-hydroxypicolinic acid and its derivatives in the synthesis of a series of lanthanide complexes and we investigated the role of this ligand in the photoluminescence of such complexes.[7] Picolinic acid complexes of lanthanides, particularly those of $Eu^{3+}$ and $Tb^{3+}$, show interesting photoluminescent behaviour because energy transfer from the aromatic groups close to the lanthanide ions may enhance the luminescent efficiency of the ion.[8] Even dispersed in solid matrices they can produce efficient luminescent materials, such as those in $SiO_2$ nanoparticles obtained by the sol-gel method.[7] Therefore, in principle, it should be possible to fine tune the luminescence of such nanocomposites by working out the coordination chemistry of the Ln complexes. Lanthanide coordination polymers, including those synthesised in the presence of dicarboxylato ligands have attracted considerable interest and many examples can be found in the literature.[9] However, we could not find examples of Ln-containing coordination compounds with this type of ligand or an aromatic antenna. Consequently, we report here a distinct approach which involves the simultaneous use of a highly flexible bridging ligand (glutaric acid) with a chelating aromatic ligand (picolinic acid) which, on the one hand, might function as an antenna, efficiently transferring energy to the Ln centre or, on the other hand, may remove available coordination sites thus controlling to some extent the dimensionality of the final product.

[a] Department of Chemistry, University of Aveiro, CICECO, 3810-193 Aveiro, Portugal
Fax: +351-234-370-084
E-mail: ttrindade@dq.ua.pt
[b] Department of Physics, University of Aveiro, CICECO, 3810-193 Aveiro, Portugal
[c] Department of Chemistry, University of Cambridge, Lensfield Road, CB2 1EW Cambridge, United Kingdom
Supporting information for this article is available on the WWW under http://www.eurjic.org or from the author.

 © 2007 Wiley-VCH Verlag GmbH & Co. KGaA, Weinheim 

## Results and Discussion

### Synthetic Aspects

Lanthanide-organic coordination polymers, with the general empirical formula [Ln(glu)(pic)($H_2O$)$_2$] (where $Ln^{3+}$ = $Sm^{3+}$, $Tb^{3+}$ and $Eu^{3+}$), have been prepared by reaction, in aqueous media, of the respective Ln nitrato salts with glutaric ($H_2$pic) and picolinic (Hpic) acids (see Exp. Sect.). Such a procedure invariably yielded microcrystalline powders. Thus, the reaction with $Sm^{3+}$ was allowed to proceed slowly in a silica gel matrix over a period of several months, leading to high-quality single-crystals suitable for a full structural determination using X-ray diffraction (see crystal description below). Phase identification of the $Tb^{3+}$ material was also performed using single-crystal X-ray diffraction whereas for the $Eu^{3+}$ complex only powder studies could be undertaken (see Exp. Sect. dedicated to X-ray crystallography and the Supporting Information). Crystal images of the $Sm^{3+}$ (SEM) and $Tb^{3+}$ (optical microscope) compounds are supplied as Supporting Information.

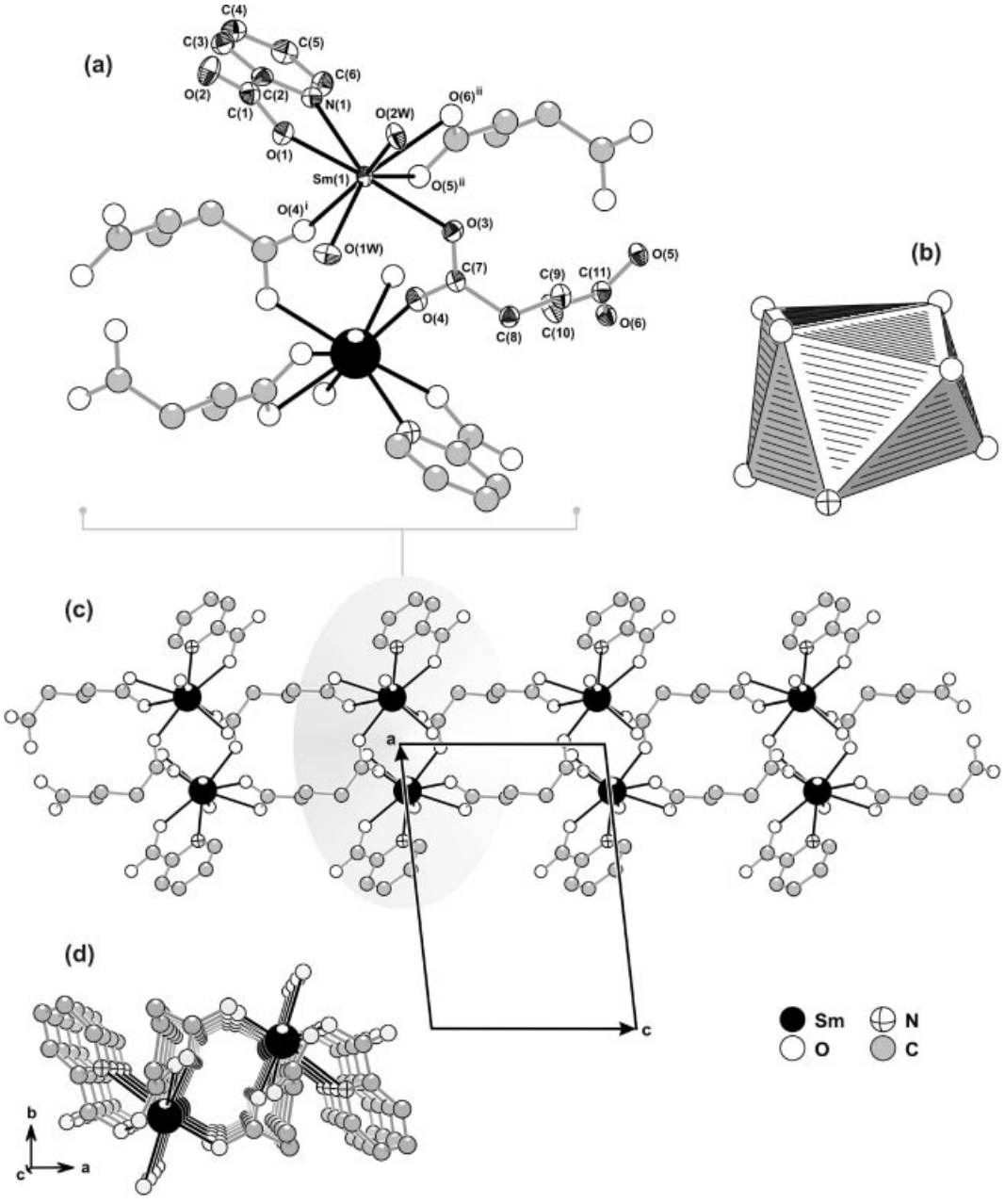


Figure 1. (a) Centrosymmetric binuclear secondary building unit of the coordination polymer, showing the labelling scheme for all non-hydrogen atoms belonging to the asymmetric unit. Thermal ellipsoids are shown at the 50% probability level. (b) Polyhedral representation of the coordination sphere of the $Sm^{3+}$ centre, {$SmNO_7$}, resembling a highly distorted dodecahedron. (c and d) Perspective views of the 1D $_\infty{}^1$[Sm(glu)(pic)($H_2O$)$_2$] molecular tape running parallel to the *c* axis of the unit cell. Hydrogen atoms have been omitted for clarity. For selected bond lengths and angles see Table 1. Symmetry transformations used to generate equivalent atoms: (i) 2 – *x*, 1 – *y*, – *z*; (ii) 2 – *x*, 1 – *y*, 1 – *z*.

 © 2007 Wiley-VCH Verlag GmbH & Co. KGaA, Weinheim 

### Crystal Structure Description of [Sm(glu)(pic)($H_2O$)$_2$]

When an aqueous solution containing $Sm^{3+}$ diffuses into a gel containing glutaric acid ($H_2glu$ = $C_5H_8O_4$) and picolinic acid (Hpic = $C_6H_5NO_2$) a crystalline material, which could be manually isolated in the form of large single-crystals, formed after a period of 4 months (see Exp. Sect.). The crystal structure of this material was elucidated by X-ray crystallography (see dedicated Exp. Sect.) and ultimately formulated as [Sm(glu)(pic)($H_2O$)$_2$]. The phase purity and homogeneity of the bulk sample were further confirmed using powder X-ray diffraction (not shown) and CHN elemental composition analyses.

The crystal structure contains a single crystallographically unique $Sm^{3+}$ metallic centre which appears coordinated to two water molecules, three glutarate anions ($glu^{2-}$) and one picolinic acid residue ($pic^-$) in a typical eight-coordination fashion (see part a of Figure 1, {$SmNO_7$}) best described as a highly distorted dodecahedron (Figure 1, b): while one trapezoid of this polyhedron is composed of two water molecules [O(1W) and O(2W)] and two oxygen atoms from distinct glutarato residues [O(4)$^{i}$ and O(6)$^{ii}$], the other is instead formed from the N,O-chelate of the picolinic acid moiety plus another two oxygen atoms from glutarate anions [O(3) and O(5)$^{ii}$] (Figure 1, a and b; symmetry codes: (i) 2 – *x*, 1 – *y*, –*z*; (ii) 2 – *x*, 1 – *y*, 1 – *z*). The Sm–O bond lengths for the coordinated water molecules and the carboxylato groups [found in the 2.407(3)–2.410(3) and 2.355(3)–2.508(3) Å ranges, respectively – see Table 1] are in good agreement with those typically found in related compounds, as revealed by a search of the Cambridge Structural Database (CSD, Version 5.27, November 2005),[10,11] while the typical Sm–$O_{water}$ distance can be found in the 2.32–2.89 Å range (from 41 entries with a median of 2.44 Å). The Sm–$O_{carboxylate}$ are instead in the 2.19–3.08 Å range (from 98 entries with a median of 2.41 Å). It is of considerable interest to mention that the lack of regularity in the dodecahedral coordination environment arises, mainly, because of the various binding modes of the ligands composing the first coordination sphere (details in the following paragraphs) which is directly reflected in the internal angles of the polyhedron (Table 1).

The compound contains a single crystallographically independent glutarato residue which appears with its two carboxylato groups having very distinct coordination modes (Scheme 1). On the one hand, the carboxylato group composed of O(5) and O(6) (Figure 1, a) coordinates to the $Sm^{3+}$ centre through a typical bidentate *syn*,*syn* chelating fashion with a bite angle of 52.33(9)° which is in good agreement with the values reported for analogous materials (from 35 entries in the CSD with a median of 51.2°). On the other hand, the opposite carboxylato group, composed of O(3) and O(4) (Figure 1, a), appears instead forming a *syn*,*anti* bridge with a neighbouring $Sm^{3+}$ cation, thus imposing a Sm(1)···Sm(1)$^{i}$ separation of 4.626(1) Å. This *syn*,*anti* bridge leads to the formation of a centrosymmetric binuclear moiety which can be further envisaged as the building block of the polymeric structure of the material (see below), a structural feature only found in a handful of other structures also containing lanthanide centres and glutarato anions, namely with $Nd^{3+}$,[12,13] $Ho^{3+}$ [13] and $Tb^{3+}$,[14] all of which are 1D materials. Interestingly, in those compounds, the glutarato anions exhibit markedly distinct coordination geometries compared with those recorded for our material. This is particularly notable for the bridging groups which appear as *syn*,*anti* bridges while in those related 1D compounds[12,13] one oxygen atom is simultaneously involved in a *syn*,*syn* chelate and in a *syn*,*anti* bridge. Moreover, this structural aspect exhibited by one carboxylato oxygen atom is repeatedly found in all the remaining known 2-[14] and 3D[15–21] lanthanide-organic materials containing glutaric acid residues, thus rendering the present compound the first example of a glutarato-lanthanide material in which an inter-lanthanide bridge via a carboxylato group is enforced by a *syn*,*anti* bridge. Apart from structurally creating the aforementioned bimetallic

Table 1. Selected bond lengths [Å] and angles [°] for the $Sm^{3+}$ coordination environment present in [Sm(glu)(pic)($H_2O$)$_2$].[a]

| | | | |
|---|---|---|---|
| Sm(1)–O(1) | 2.355(3) | Sm(1)–O(6)$^{ii}$ | 2.508(3) |
| Sm(1)–O(3) | 2.452(3) | Sm(1)–O(1W) | 2.407(3) |
| Sm(1)–O(4)$^{i}$ | 2.358(3) | Sm(1)–O(2W) | 2.410(3) |
| Sm(1)–O(5)$^{ii}$ | 2.461(3) | Sm(1)–N(1) | 2.624(3) |
| | | | |
| O(1)–Sm(1)–O(3) | 141.54(10) | O(4)$^{i}$–Sm(1)–O(1W) | 74.40(10) |
| O(1)–Sm(1)–O(4)$^{i}$ | 90.50(10) | O(4)$^{i}$–Sm(1)–O(2W) | 155.34(11) |
| O(1)–Sm(1)–O(5)$^{ii}$ | 140.99(10) | O(5)$^{ii}$ –Sm(1)–O(6)$^{ii}$ | 52.33(9) |
| O(1)–Sm(1)–O(6)$^{ii}$ | 120.16(10) | O(5)$^{ii}$–Sm(1)–N(1) | 76.10(10) |
| O(1)–Sm(1)–N(1) | 64.97(10) | O(6)$^{ii}$–Sm(1)–N(1) | 81.25(11) |
| O(1)–Sm(1)–O(1W) | 77.48(10) | O(1W)–Sm(1)–O(3) | 77.89(11) |
| O(1)–Sm(1)–O(2W) | 72.55(10) | O(1W)–Sm(1)–O(5)$^{ii}$ | 131.92(10) |
| O(3)–Sm(1)–O(5)$^{ii}$ | 76.61(10) | O(1W)–Sm(1)–O(6)$^{ii}$ | 146.77(10) |
| O(3)–Sm(1)–O(6)$^{ii}$ | 71.56(10) | O(1W)–Sm(1)–O(2W) | 84.31(11) |
| O(3)–Sm(1)–N(1) | 149.60(11) | O(1W)–Sm(1)–N(1) | 131.30(11) |
| O(4)$^{i}$–Sm(1)–O(3) | 110.58(10) | O(2W)–Sm(1)–O(3) | 76.03(10) |
| O(4)$^{i}$–Sm(1)–O(5)$^{ii}$ | 77.47(10) | O(2W)–Sm(1)–O(5)$^{ii}$ | 126.89(10) |
| O(4)$^{i}$–Sm(1)–O(6)$^{ii}$ | 128.57(10) | O(2W)–Sm(1)–O(6)$^{ii}$ | 76.05(10) |
| O(4)$^{i}$–Sm(1)–N(1) | 76.04(11) | O(2W)–Sm(1)–N(1) | 110.80(11) |

[a] Symmetry transformations used to generate equivalent atoms: (i) 2 – *x*, 1 – *y*, – *z*; (ii) 2 – *x*, 1 – *y*, 1 – *z*.

 © 2007 Wiley-VCH Verlag GmbH & Co. KGaA, Weinheim 

units, the glutarato anionic residues further establish physical links interconnecting the two $Sm^{3+}$ centres of one unit [Sm(1) plus $Sm(1)^{i}$ – Figure 1, a] with a third metallic centre of a neighbouring moiety [$Sm(1)^{iii}$], imposing Sm(1)···$Sm(1)^{iii}$ and $Sm(1)^{i}$···$Sm(1)^{iii}$ separations of 8.480(2) and 9.074(2) Å, respectively [symmetry code: (iii) $x$, $y$, $-1 + z$]. This leads to the formation of a 1D $_{\infty}^{1}$[Sm(glu)(pic)$(H_2O)_2$] molecular tape running parallel to the [001] direction of the unit cell (Figure 1, c and d).

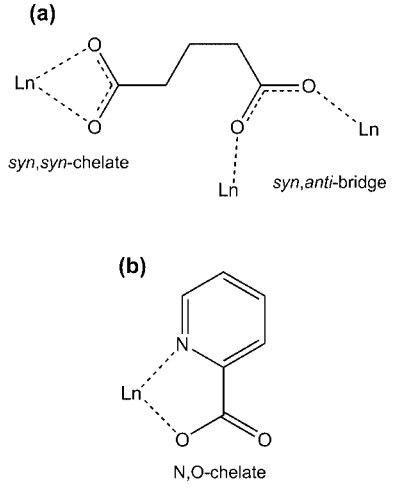


Scheme 1. Coordination modes of the ligands present in [Sm(glu)(pic)$(H_2O)_2$]: (a) glutaric acid; (b) picolinic acid.

As reported by Zhang et al.[13] for the 1D $_{\infty}^{1}$[Ln(glu)(phen)Cl] (where $Ln^{3+}$ = $Tb^{3+}$ and $Ho^{3+}$, phen = 1,10-phenanthroline) materials, the $_{\infty}^{1}$[Sm(glu)(pic)$(H_2O)_2$] molecular tape present in the crystal structure also contains, external to the glu/Sm core, chelating aromatic organic ligands (picolinato residues) which seem to prevent the growth of the hybrid polymer in more than one direction by removing available coordination sites in the metallic centres (Figure 1). Indeed for all known and related compounds, when these chelating moieties are not present, 2-[14] and 3D[15–22] materials are typically isolated. The picolinic acid residues appear coordinated to the $Sm^{3+}$ metallic centres in a typical N,O-chelating fashion (Scheme 1) with a bite angle of 64.97(10)°, a value consistent with those reported for similar compounds[23–26] (10 entries in the CSD, with values spanning from 60.5 to 67.6°; median of 64.0°).

Individual neutral 1D $_{\infty}^{1}$[Sm(glu)(pic)$(H_2O)_2$] molecular tapes close-pack in the solid state, mediated by weak interactions such as homonuclear O–H···O hydrogen bonds and π-π stacking to form a 3D supramolecular structure. On the one hand, strong and highly directional [all interaction angles <(DHA) are well above 150° – see Table 2] O–H···O hydrogen bonds involving the coordinated water molecules and the carboxylato groups interconnect neighbouring tapes in the *bc* plane of the unit cell leading to a 2D supramolecular framework (Figure 2, a). One of these interactions is particularly important for the structural integrity of the binuclear secondary building unit of the molecular tape, as represented in Figure 2 (b). The coordinated O(1W) water molecule donates one hydrogen atom in a strong hydrogen bonding interaction with a neighbouring carboxylato group [D···A of 2.753(4) Å with <(DHA) of 175(4)°]. In fact, for all other closely related compounds, connections between adjacent lanthanide centres are usually assured by four carboxylato groups, either belonging to the glutarato[12–14,16,18–21] or oxalato[15,17] anions in a pseudo-paddlewheel motif. For the $_{\infty}^{1}$[Sm(glu)(pic)$(H_2O)_2$] molecular tape, only two carboxylato groups bridge the metallic centres (Figure 2, b) with structural stability being achieved

Table 2. Hydrogen bonding geometry (distances in Å and angles in °) for [Sm(glu)(pic)$(H_2O)_2$].[a]

| D–H···A | *d*(D···A) | <(DHA) |
|---|---|---|
| O(1W)–H(1A)···O(5)$^{iii}$ | 2.753(4) | 175(4) |
| O(1W)–H(1B)···O(3)$^{iv}$ | 2.687(4) | 174(4) |
| O(2W)–H(2A)···O(6)$^{v}$ | 2.842(4) | 159(5) |
| O(2W)–H(2B)···O(1)$^{vi}$ | 2.764(4) | 172(4) |

[a] Symmetry transformations used to generate equivalent atoms: (iii) $x$, $y$, $-1 + z$; (iv) $x$, ½ – $y$, –½ + $z$; (v) 2 – $x$, – ½ + $y$, ½ – $z$; (vi) $x$, ½ – $y$, ½ + $z$.

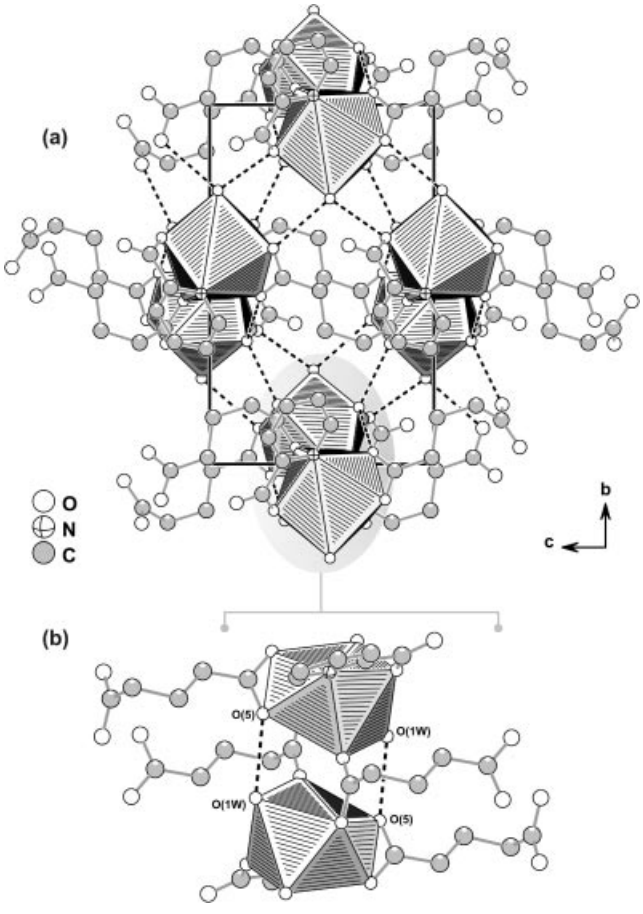


Figure 2. (a) Crystal packing of [Sm(glu)(pic)$(H_2O)_2$] viewed along the [100] direction of the unit cell. (b) Intra-dimer hydrogen bonds involving the coordinated O(1) water molecule and the *syn*,*syn* chelating carboxylato group. Hydrogen atoms and symmetry codes used to generate equivalent atoms have been omitted for clarity. Hydrogen bonds are represented as black-filled dashed lines. For hydrogen bonding geometric details see Table 2.

 © 2007 Wiley-VCH Verlag GmbH & Co. KGaA, Weinheim 

when the aforementioned hydrogen bonds are taken into account. Hydrogen-bonded supramolecular layers are in turn arranged in an orderly fashion along the [100] direction of the unit cell, mediated by offset π-π stacking interactions between neighbouring coordinated picolinic acid residues (Figure 3).

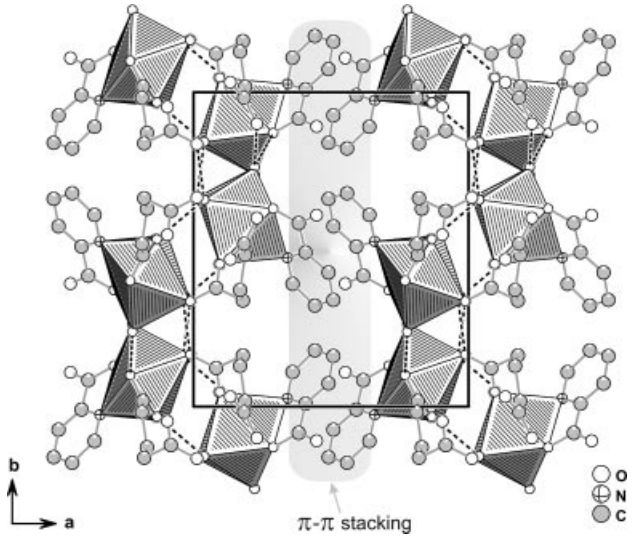


Figure 3. Mixed ball-and-stick and polyhedral (for the $\{SmNO_7\}$ coordination environments) representations of the crystal packing of $[Sm(glu)(pic)(H_2O)_2]$ viewed along [001] direction of the unit cell. Hydrogen atoms have been omitted for clarity and hydrogen bonds are represented as black-filled dashed lines.

## Spectroscopic and Thermoanalytical Results

The CHN elemental data for $[Ln(glu)(pic)(H_2O)_2]$ (where Ln = $Sm^{3+}$, $Tb^{3+}$ and $Eu^{3+}$) are summarised in Table 3 and agree well with the expected compositions based on the single-crystal X-ray studies performed (see above). Diagnostic FTIR and Raman spectroscopic data are also provided in Table 3. FTIR spectroscopy confirms the coordination of both ligands to the metal centres: $pic^-$ by means of the carboxylic group and the nitrogen atom from the aromatic ring and $glu^{2-}$ by its carboxylato groups. The asymmetric stretching $\nu_{asym}(-CO_2^-)$ mode shows shifts up to 33 $cm^{-1}$ (40 $cm^{-1}$ in the Raman spectra) to lower wavenumbers when compared with the values reported for the free picolinic acid. Furthermore, the measured values of $\Delta$ [$\nu_{asym}(-CO_2^-) - \nu_{sym}(-CO_2^-)$] for the Sm (281 $cm^{-1}$), Eu (283 $cm^{-1}$) and Tb (283 $cm^{-1}$) compounds are further evidence for the presence of carboxylato groups coordinated to the metal centres. The typical stretching $\nu$(C–N) vibrational mode of substituted pyridines appears for the uncoordinated picolinic acid at 1594 $cm^{-1}$ and shows small shifts (up to 13 $cm^{-1}$ in the FTIR spectra and up to 30 $cm^{-1}$ in the Raman spectra) for all compounds, in agreement with N,O-chelation involving the nitrogen atom of the $pic^-$ group. The typical stretching $\nu$(C–O) vibrational mode of the carboxylic group of glutaric acid at 1265 $cm^{-1}$ is shifted for all compounds by 26 $cm^{-1}$, confirming the bond formed between the deprotonated carboxylic group of glutaric acid and the lanthanide ion.

The thermal decomposition of $[Sm(glu)(pic)(H_2O)_2]$ occurs in a multi-step process from ambient temperature to 800 °C to yield $Sm_2O_3$ as the final residue (total weight loss: 57%; calculated: 60%). The first weight loss of ca. 8.4% occurs in the 57–230 °C temperature range (DTG peak at 182 °C) and can be attributed to the release of the two coordinated water molecules (calculated weight loss of 8.2%). Between 230 and 747 °C a total weight loss of ca. 49% corresponds to the thermal decomposition of the organic components (calculated 57%). The other Ln compounds exhibit similar thermal properties: for $[Tb(glu)(pic)(H_2O)_2]$ the total weight loss was 58% with a calculated value of 59% between 72 °C and 700 °C. For $[Eu(glu)(pic)(H_2O)_2]$ the total weight loss was 57% with a calculated value of 60% between 22 °C and 800 °C.

## Photoluminescence

The excitation spectra of the $Sm^{3+}$, $Eu^{3+}$ and $Tb^{3+}$ compounds represented in Figure 4 were monitored around the cation's more intense line which can be found at 597 nm for $Sm^{3+}$, 614 nm for $Eu^{3+}$ and 545 nm for $Tb^{3+}$. Each spectrum displays a large broad band in the range of 250–

Table 3. Analytical and spectroscopic data for $[Ln(glu)(pic)(H_2O)_2]$ (where Ln = $Sm^{3+}$, $Tb^{3+}$ and $Eu^{3+}$).

| Compound | Elemental composition (%)[a] | | | Vibrational data ($cm^{-1}$)[b] | | | | |
|---|---|---|---|---|---|---|---|---|
| | C | N | H | Picolinic acid | | | Glutaric acid | |
| | | | | $\nu_{as}$ ($CO_2$) | $\nu$(CC), $\nu$(CN) | $\nu_{sym}$($CO_2$) | $\nu$(CO) | $\nu$(C=O) |
| Picolinic acid (Hpic) | – | – | – | 1722<br>*1692* | 1608, 1594<br>*1620*, *1596* | 1344<br>*1358* | – | – |
| Glutaric acid ($H_2glu$) | – | – | – | – | – | – | 1250 | 1697 |
| $[Sm(glu)(pic)(H_2O)_2]$ | 29.20<br>(30.12) | 2.71<br>(3.19) | 3.23<br>(3.22) | 1689<br>*1652* | 1599, 1581<br>*1598*, *1566* | 1408<br>*1351* | 1276 | 1563 |
| $[Tb(glu)(pic)(H_2O)_2]$ | 29.58<br>(29.55) | 2.83<br>(3.16) | 3.15<br>(3.13) | 1691<br>*1654* | 1601, 1589<br>*1600*, *1568* | 1408<br>*1354* | 1276 | 1563 |
| $[Eu(glu)(pic)(H_2O)_2]$ | 29.99<br>(30.01) | 2.99<br>(3.18) | 3.19<br>(3.21) | 1690<br>*1653* | 1600, 1584<br>*1600*, *1567* | 1407<br>*1353* | 1276 | 1563 |

[a] Calculated values in parentheses. [b] Infrared and Raman (in italics) data.

 © 2007 Wiley-VCH Verlag GmbH & Co. KGaA, Weinheim 

340 nm and a series of sharp lines characteristic of the $Sm^{3+}$, $Eu^{3+}$ and $Tb^{3+}$ energy levels. The large broad bands can be ascribed to the excited levels of the ligands[24,26] and are mainly formed of two components, peaking around 275 and 295 nm, being most evident for the $Eu^{3+}$ and $Tb^{3+}$ compounds. The assignment of the intra-$4f^5$ transitions was based on the published literature.[27] Although the $^7F_1$ level of the $Eu^{3+}$ complex is populated at room-temperature, we have only explicitly assigned the $^7F_1 \rightarrow {}^5D_0$ transition. We also note that the intensity at lower wavelengths (250–260 nm) for the $Sm^{3+}$ complex is artificial due to the correction for the spectroscopic distribution of the lamp intensity (marked with an asterisk in Figure 4).

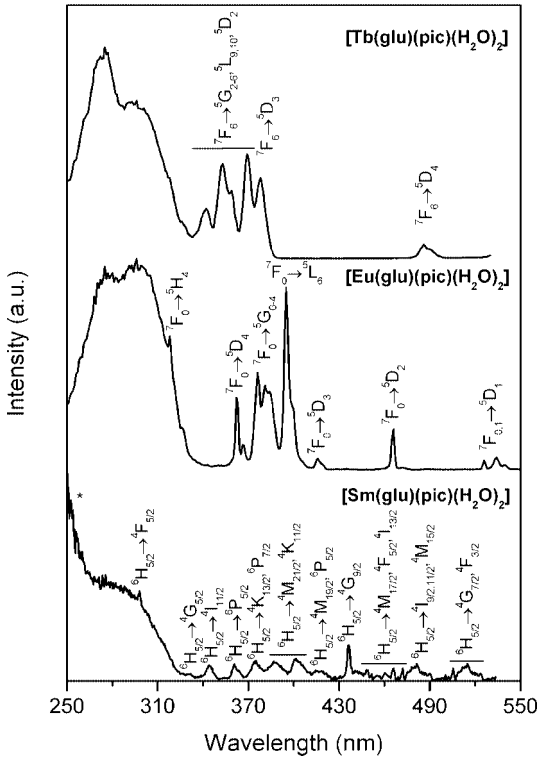


Figure 4. Excitation spectra of $[Ln(glu)(pic)(H_2O)_2]$ monitored at 597, 614, and 545 nm for the $Sm^{3+}$, $Eu^{3+}$ and $Tb^{3+}$ complexes, respectively.

Figure 5 shows the emission spectra of the $Sm^{3+}$, $Eu^{3+}$ and $Tb^{3+}$ compounds. No changes could be detected in the lines of the cations by varying the excitation wavelength, suggesting that the lanthanide centre has only one local environment. The emission spectra of the $Sm^{3+}$, $Eu^{3+}$ and $Tb^{3+}$ complexes are composed from the intra-$4f^5$ ($Sm^{3+}$), intra-$4f^6$ ($Eu^{3+}$) and intra-$4f^8$ ($Tb^{3+}$) transitions ($^4G_{5/2} \rightarrow {}^6H_{5/2,7/2,9/2}$, $^5D_0 \rightarrow {}^7F_{0-4}$, and $^5D_4 \rightarrow {}^7F_{6-3}$, respectively).

The $^5D_0$ ($Eu^{3+}$) and $^5D_4$ ($Tb^{3+}$) lifetimes were monitored within the more intense line of the $^5D_0 \rightarrow {}^7F_2$ and $^5D_4 \rightarrow {}^7F_5$ transitions, respectively, under the excitation which maximises the $Eu^{3+}$ and $Tb^{3+}$ emissions. The emission decay curves (not shown) reveal a single-exponential behaviour yielding lifetime values of $0.385 \pm 0.002$ ($^5D_0$) and $1.024 \pm 0.005$ ms ($^5D_4$). The quantum efficiency, $q$, of the emission arising from the $^5D_0$ level in the [Eu(glu)(pic)$(H_2O)_2$] complex has been estimated assuming that only nonradiative and radiative processes are essentially involved in the depopulation of the excited state, as already reported.[7,28] We obtained a $q$ value of ca. 10%, with a corresponding $k_r$ value of 0.253 $ms^{-1}$. These values, lifetimes and quantum efficiency values, although lower when compared with those obtained by Sendor et al. for the europium picolinato,[8] are of the same order of magnitude as those obtained for the $Eu^{3+}$ emission in the 3- hydroxypicolinato[7] and 2-hydroxynicotinato complexes.[29]

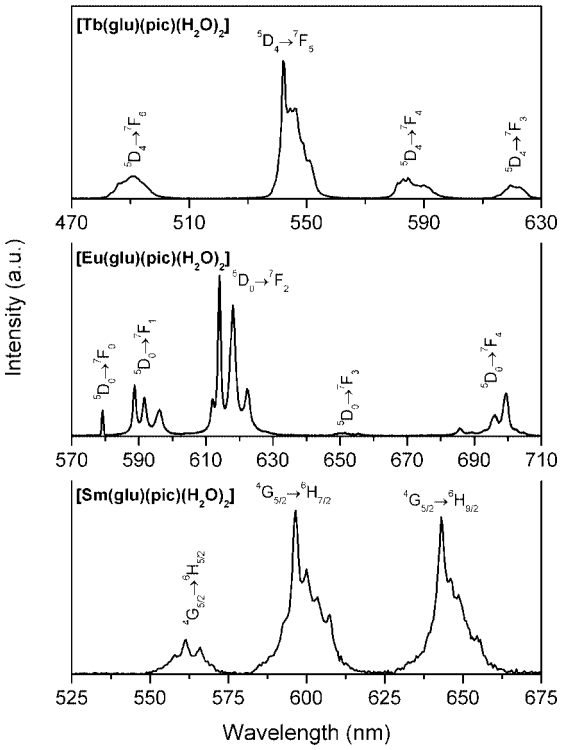


Figure 5. Emission spectra of $[Ln(glu)(pic)(H_2O)_2]$ (Ln = Sm, Eu, Tb), excited at 277, 305 and 277 nm for the $Sm^{3+}$, $Eu^{3+}$, and $Tb^{3+}$ complexes, respectively.

## Conclusions

A triad of isostructural lanthanide-organic 1D coordination polymers, $[Ln(glu)(pic)(H_2O)_2]$ (where Ln = $Sm^{3+}$, $Tb^{3+}$ and $Eu^{3+}$), were successfully isolated and characterised in the solid-state as homogeneous phase-pure materials. All these compounds share common structural features and show efficient intramolecular aromatic ligand-to-lanthanide energy transfer. These coordination polymers are composed of lanthanide dimers separated by long and flexible glutarato anions. The present results open up interesting prospects for future work concerning the investigation of the photoluminescent behaviour of other picolinic-containing lanthanide-organic polymers in which the length of the flexible ligand could be systematically varied.

 © 2007 Wiley-VCH Verlag GmbH & Co. KGaA, Weinheim 

## Experimental Section

**General Instrumentation:** Infrared spectra were recorded using KBr disks (Aldrich, 99%+, spectroscopic grade) with a Matson 7000 FTIR spectrometer. FT-Raman spectra were collected on a Bruker RFS 100 instrument with a Nd:YAG coherent laser ($\lambda$ = 1064 nm). Elemental analyses for C, H and N were performed using a CHNS-932 elemental analyser (at the Microanalysis Laboratory of the University of Aveiro) and also an Exeter Analytical CE 440 Elemental Analyser using helium as the purge gas (at the Department of Chemistry, University of Cambridge). Thermogravimetric analyses (TGA) were carried out using a Shimadzu TGA 50 instrument with a heating rate of 10 °C min$^{-1}$ under a continuous air stream with a flow rate of 10 cm$^3$ min$^{-1}$. Crystal photographs were taken using a Stemi 2000 stereomicroscope equipped with Carl Zeiss lenses and a high-resolution AxioCam MRc5 digital camera connected to a personal computer. Scanning Electron Microscopy (SEM) images were acquired using a Hitachi S-4100 field emission gun tungsten filament instrument working at 25 kV. Samples were prepared by deposition on aluminium sample holders and by carbon coating. The luminescence spectra were recorded at room temperature with a modular double grating excitation spectrofluorimeter with a TRIAX 320 emission monochromator (Fluorolog-3, Jobin Yvon-Spex) coupled to a R928 Hamamatsu photomultiplier by means of the front face acquisition mode. The excitation source was a 450 W Xe arc lamp. Excitation spectra were corrected from $\lambda$ = 240 to 600 nm for the spectral distribution of the lamp intensity using a photodiode reference detector. Emission spectra were also corrected for the spectral response of the monochromators and the detector by using typical correction spectra provided by the manufacturer. The lifetime measurements were acquired with the setup described for the luminescence spectra using a pulsed Xe-Hg lamp (6 μs pulse at half width and 20–30 μs tail).

**Syntheses:** Chemicals were obtained from commercial sources and used without further purification. Preparation of single crystals of [Sm(glu)(pic)($H_2O$)$_2$] of an appropriate size and stability for single-crystal X-ray diffraction studies was carried out in a gel formed from $Na_2SiO_3$·$H_2O$. A solution of $Na_2SiO_3$·5$H_2O$ (0.1 M, 5 mL) was added dropwise to an aqueous solution (10 mL, pH 4.3) containing glutaric acid and picolinic acid. The mixture was stirred and each test tube, with 5 mL of solution, was left for 24 h. Afterwards, $Sm(COO)_3$·$x$$H_2O$ (0.25 mmol) was added to the gel. White single crystals of [Sm(glu)(pic)($H_2O$)$_2$] were grown over a period of 4 months.

Isostructural materials, mainly isolated as microcrystalline powders, of picolinic acid and glutaric acid with $Tb^{3+}$ and $Eu^{3+}$ were synthesised by adding an aqueous solution of picolinic acid (1 mmol) to an aqueous solution containing glutaric acid (1 mmol) (pH 6.5, adjusted with KOH) and the corresponding lanthanide salt [Ln($NO_3$)$_3$·5$H_2O$, Ln = Tb and Eu] (0.25 mmol). For the compound [Tb(glu)(pic)($H_2O$)$_2$], small crystals could also be manually harvested which allowed unequivocal phase identification by means of the unit cell determination using single-crystal X-ray diffraction data. Phase identification of [Eu(glu)(pic)($H_2O$)$_2$] was performed by employing X-ray powder diffraction (see following sections).

**Single-Crystal X-ray Diffraction:** A suitable single-crystal of [Sm(glu)(pic)($H_2O$)$_2$] was mounted on a glass fibre using FOMBLIN Y perfluoropolyether vacuum oil (LVAC 25/6) purchased from Aldrich.[30] Data were collected at 180(2) K on a Nonius Kappa CCD area-detector diffractometer (Mo-$K_\alpha$ graphite-monochromated radiation, $\lambda$ = 0.7107 Å) equipped with an Oxford Cryosystems cryostream and controlled with the Collect software package.[31] Images were processed using the software packages Denzo and Scalepack[32] and data were corrected for absorption by the empirical method employed in Sortav.[33,34] The structure was solved by direct methods with SHELXS-97[35] and refined by full-matrix least-squares on $F^2$ using SHELXL-97.[36] All non-hydrogen atoms were directly located from difference Fourier maps and refined with anisotropic displacement parameters.

Even though the vast majority of the hydrogen atoms bound to carbon were markedly visible in the difference Fourier maps, they were instead located in their idealised positions using appropriate *HFIX* instructions in SHELXL (43 for the aromatic and 23 for the –$CH_2$– carbon atoms) and included in subsequent refinement cycles in riding-motion approximation with isotropic thermal displacements parameters ($U_{iso}$) fixed at 1.2 times $U_{eq}$ of the carbon atom to which they are each attached. Hydrogen atoms associated with the coordinated water molecules were directly located from difference Fourier maps and included in the final structural model with the O–H and H···H distances restrained to 0.95(1) Å and 1.55(1) Å, respectively (in order to ensure a chemically reasonable geometry for these molecules), and using a riding model with an isotropic displacement parameter fixed at *1.5* times $U_{eq}$ of the atom to which they are each attached. The last difference Fourier map synthesis showed the highest peak (0.892 e Å$^{-3}$) and deepest hole (–0.949 e Å$^{-3}$) located at 1.51 Å from C(5) and 0.82 Å from Sm(1), respectively.

A single-crystal of [Tb(glu)(pic)($H_2O$)$_2$] was also investigated using the same experimental conditions as for the $Sm^{3+}$ compound (see above). A full data set (data completeness 99.7%), collected in the 1.00° ≤ $\theta$ ≤ 32.03° range, consisted of 13480 integrated reflections ($R_{int}$ = 0.065 in $P2$ symmetry) of which 4800 are unique. A subset of 8701 reflections was used for unit cell refinement, with the final parameters converging to: $a$ = 8.4304(2) Å, $b$ = 13.3040(3) Å, $c$ =

Table 4. Crystal and structure refinement data for [Sm(glu)(pic)($H_2O$)$_2$].

| | |
|---|---|
| Formula | $C_{11}H_{14}NO_8Sm$ |
| Formula weight | 438.58 |
| Crystal system | monoclinic |
| Space group | $P2_1/c$ |
| $a$ [Å] | 11.855(2) |
| $b$ [Å] | 13.477(3) |
| $c$ [Å] | 8.4804(17) |
| $\beta$ [°] | 96.42(3) |
| Volume [Å$^3$] | 1346.4(5) |
| $Z$ | 4 |
| $D_c$ [g cm$^{-3}$] | 2.164 |
| $\mu$(Mo-$K_\alpha$) [mm$^{-1}$] | 4.401 |
| $F$(000) | 852 |
| Crystal size [mm] | 0.07 × 0.05 × 0.02 |
| Crystal type | colourless blocks |
| $\theta$ range [°] | 3.78 to 27.51 |
| Index ranges | –15 ≤ $h$ ≤ 15 |
| | –17 ≤ $k$ ≤ 16 |
| | –10 ≤ $l$ ≤ 10 |
| Reflections collected | 13389 |
| Independent reflections | 3076 ($R_{int}$ = 0.0630) |
| Final $R$ indices [$I > 2\sigma(I)$][a,b] | $R_1$ = 0.0307 |
| | $wR_2$ = 0.0660 |
| Final $R$ indices (all data)[a,b] | $R_1$ = 0.0409 |
| | $wR_2$ = 0.0705 |
| Weighting scheme[c] | $m$ = 0.0247 |
| | $n$ = 3.7121 |
| Largest diff. peak and hole [e Å$^{-3}$] | 0.892 and –0.949 |

[a] $R_1 = \Sigma||F_o| - |F_c||/\Sigma|F_o|$. [b] $wR_2 = \sqrt{\Sigma[w(F_o^2 - F_c^2)^2]/\Sigma[w(F_o^2)^2]}$. [c] $w = 1/[\sigma^2(F_o^2) + (mP) + nP]$ where $P = (F_o^2 + 2F_c^2)/3$.

 © 2007 Wiley-VCH Verlag GmbH & Co. KGaA, Weinheim 

11.9536(2) Å, $\beta$ = 96.4275(14)° and $V$ = 1332.27(5) Å$^3$ [crystal mosaicity of 0.500(2)°].

Information concerning crystallographic data collection and structure refinement details for [Sm(glu)(pic)$(H_2O)_2$] is summarised in Table 4. Selected bond lengths and angles for the $Sm^{3+}$ coordination environment are given in Table 1. Hydrogen bonding geometric details are provided in Table 2.

CCDC-611302 (for [Sm(glu)(pic)$(H_2O)_2$] contains the supplementary crystallographic data for this paper. These data can be obtained free of charge from The Cambridge Crystallographic Data Centre via www.ccdc.cam.ac.uk/data_request/cif.

**Powder X-ray Diffraction:** Powder X-ray diffraction data were collected on a X'Pert MPD Philips diffractometer (Cu-$K_\alpha$ X-radiation, $\lambda$ = 1.54060 Å) equipped with an X'Celerator detector, graphite-monochromated radiation and a flat-plate sample holder in a Bragg–Brentano para-focusing optics configuration (40 kV, 50 mA). Intensity data were collected in a continuous scanning mode in the ca. 3° ≤ 2$\theta$ ≤ 70° angular range.

The collected powder X-ray diffraction pattern for [Eu(glu)(pic)$(H_2O)_2$] was indexed by means of the routines provided with the software program DICVOL04[37] and by employing the first 20 well-resolved reflections (located using the derivative-based peak search algorithm provided with Fullprof.2k)[38,39] and a fixed absolute error on each line of 0.03° 2$\theta$. Preliminary unit cell metrics were calculated with high figures-of-merit: $M(20)$[40] = 44.4 and $F(20)$[41] = 97.6; zero shift of 0.0246°.

A Le Bail[42] whole-powder-diffraction-pattern profile fitting in the space group $P2_1/c$ (systematic absences unequivocally identified using CHECKCELL[43]) was performed with the FullProf.2k software package. The fit provided as in Figure S1 in the Supporting Information was obtained by using a typical pseudo-Voigt peak-shape function and, in the last stages of the fitting process the unit cell parameters and typical profile parameters, such as scale factor, zero shift, Caglioti function values and two asymmetry parameters were allowed to refine. Fixed background points were used. Refined unit cell parameters: $a$ = 12.025(1) Å, $b$ = 13.376(1) Å, $c$ = 8.480(1) Å, $\beta$ = 96.862(5)° ($R_{Bragg}$ = 1.54% and $\chi^2$ = 6.81).

**Supporting Information** (see also the footnote on the first page of this article): Le Bail whole-powder-diffraction-pattern profile fitting in the $P2_1/c$ space group for compound [Eu(glu)(pic)$(H_2O)_2$]. Optical and SEM images of crystals belonging to the compounds containing $Tb^{3+}$ and $Sm^{3+}$.

## Acknowledgments

We are grateful to Fundação para a Ciência e Tecnologia (FCT) for their general financial support (POCI/QUI/58377/2004), for support by FEDER and for the PhD and post-doctoral research grants SFRH/BD/17968/2004 (to P. G.) and SFRH/BPD/14954/2004 (to P. S.-S.), respectively.

[1] a) G. A. Ozin, A. C. Arsenault in *Nanochemistry*, RSC, Cambridge, **2005**; b) *Nanoparticles* (Ed.: G. Schmid), Wiley-VCH, Weinheim, **2004**; c) *The Chemistry of Nanomaterials* (Eds.: C. N. R. Rao, A. Müller, A. K. Cheetham), Wiley-VCH, Weinheim, **2003**; d) A. C. Jones, P. O'Brien in *CVD of Compound Semiconductors*, VCH, Weinheim, **1997**; e) C. Sanchez, B. Lebeau, F. Chaput, J. P. Boilot, *Adv. Mater.* **2003**, *15*, 1969–1994; f) F. A. Cotton, *J. Chem. Soc. Dalton Trans.* **2000**, 1961–1968; g) P. H. Dinolfo, J. T. Hupp, *Chem. Mater.* **2001**, *13*, 3113–3125.

[2] S. Kitagawa, R. Kitaura, S. Noro, *Angew. Chem. Int. Ed.* **2004**, *43*, 2334–2375.

[3] a) P. O'Brien, R. Nomura, *J. Mater. Chem.* **1995**, *5*, 1761–1773; b) M. Bochmann, *Chem. Vap. Deposition* **1996**, *2*, 88; c) T. Trindade, P. O'Brien, X. Zhang, *Chem. Mater.* **1997**, *9*, 523–530; d) O. C. Monteiro, H. I. S. Nogueira, T. Trindade, M. Motevalli, *Chem. Mater.* **2001**, *13*, 2103–2111; e) M. Green, P. Prince, M. Gardener, J. Steed, *Adv. Mater.* **2004**, *16*, 994–996.

[4] a) E. Kiss, A. Benyei, T. Kiss, *Polyhedron* **2003**, *22*, 27–33; b) S. Yano, M. Nakai, F. Sekiguchi, M. Obata, M. Kato, M. Shiro, I. Kinoshita, M. Mikuriya, H. Sakurai, C. Orvig, *Chem. Lett.* **2002**, *9*, 916–917; c) C. Y. Sun, X. J. Zheng, L. P. Jin, *J. Mol. Struct.* **2003**, *646*, 201–210; d) R. March, W. Clegg, R. A. Coxall, L. Cucurull-Sanchez, L. Lezama, T. Rojo, P. Gonzalez-Duarte, *Inorg. Chim. Acta* **2003**, *353*, 129–138; e) A. Shaver, J. B. NG, D. A. Hall, B. S. Lum, B. I. Posner, *Inorg. Chem.* **1993**, *32*, 3109–3113; f) S. Yano, M. Nakai, F. Sekiguchi, M. Obata, M. Kato, M. Shiro, I. Kinoshita, M. Mikuriya, H. Sakurai, C. Orvig, *Chem. Lett.* **2002**, *9*, 916–917; g) R. K. Barman, S. K. Singh, B. K. Das, *J. Chem. Crystallogr.* **2002**, *32*, 369–375; h) M. Palicova, P. Segl'a, D. Miklos, M. Kopcova, M. Melnik, B. Dudova, D. Hudecova, T. Glowiak, *Polyhedron* **2000**, *19*, 2689–2695.

[5] a) W. P. Griffith, H. I. S. Nogueira, A. J. P. White, D. J. Williams, *Polyhedron* **1997**, *16*, 1323–1329; b) W. P. Griffith, H. I. S. Nogueira, B. C. Parkin, R. N. Sheppard, A. J. P. White, D. J. Williams, *J. Chem. Soc. Dalton Trans.* **1995**, 1775–1781; c) W. P. Griffith, C. A. Pumphrey, J. T. Rainey, *J. Chem. Soc. Dalton Trans.* **1986**, 1125–1128.

[6] a) S. M. O. Quintal, H. I. S. Nogueira, V. Félix, M. G. B. Drew, *New J. Chem.* **2000**, *24*, 511–517; b) S. M. O. Quintal, H. I. S. Nogueira, V. Félix, M. G. B. Drew, *Polyhedron* **2002**, *21*, 2783–2791; c) P. I. Girginova, F. A. A. Paz, H. I. S. Nogueira, N. J. O. Silva, V. S. Amaral, J. Klinowski, T. Trindade, *J. Mol. Struct.* **2005**, *737*, 221–229; d) P. I. Girginova, F. A. A. Paz, H. I. S. Nogueira, N. J. O. Silva, V. S. Amaral, J. Klinowski, T. Trindade, *Polyhedron* **2005**, *24*, 563–569.

[7] P. C. R. Soares-Santos, H. I. S. Nogueira, V. Félix, M. G. B. Drew, R. A. Sá Ferreira, L. D. Carlos, T. Trindade, *Chem. Mater.* **2003**, *15*, 100–108.

[8] D. Sendor, M. Hilder, T. Juestel, P. Junk, U. Kynast, *New J. Chem.* **2003**, *27*, 1070–1077.

[9] O. Guillou, C. Daiguebonne, *Lanthanide-containing coordination polymers* in *Handbook on the Physics and Chemistry of Rare Earths* (Eds.: K. A. Gschneidner Jr, J.-C. G. Bünzli, V. K. Pecharsky), **2005**, *34*, p. 359.

[10] F. H. Allen, *Acta Crystallogr., Sect. B* **2002**, *58*, 380–388.

[11] F. H. Allen, W. D. S. Motherwell, *Acta Crystallogr., Sect. B* **2002**, *58*, 407–422.

[12] J. Legendziewicz, B. Keller, I. Turowska-Tyrk, W. Wojciechowski, *New J. Chem.* **1999**, *23*, 1097–1103.

[13] L. P. Zhang, Y. H. Wan, L. P. Jin, *J. Mol. Struct.* **2003**, *646*, 169–178.

[14] T. Glowiak, J. Legendziewicz, C. N. Dao, E. Huskowska, *J. Less-Common Met.* **1987**, *134*, 153–168.

[15] P. Thomas, J. C. Trombe, *J. Chem. Crystallogr.* **2000**, *30*, 633–639.

[16] B. Benmerad, A. Guehria-Laidoudi, S. Dahaoui, C. Lecomte, *Acta Crystallogr., Sect. C* **2004**, *60*, M119–M122.

[17] R. Vaidhyanathan, S. Natarajan, C. N. R. Rao, *J. Solid State Chem.* **2004**, *177*, 1444–1448.

[18] T. Glowiak, D. C. Ngoan, J. Legendziewicz, *Acta Crystallogr., Sect. C* **1986**, *42*, 1494–1496.

[19] F. Serpaggi, G. Ferey, *J. Mater. Chem.* **1998**, *8*, 2737–2741.

[20] F. Serpaggi, G. Ferey, *J. Mol. Struct.* **2003**, *656*, 201–206.

[21] B. Benmerad, A. Guehria-Laidoudi, F. Balegroune, H. Birkedal, G. Chapuis, *Acta Crystallogr., Sect. C* **2000**, *56*, 789–792.

[22] A. Dolbecq, P. Mialane, L. Lisnard, J. Marrot, F. Secheresse, *Chem. Eur. J.* **2003**, *9*, 2914–2920.

 © 2007 Wiley-VCH Verlag GmbH & Co. KGaA, Weinheim 

[23] P. C. R. Soares-Santos, H. I. S. Nogueira, V. Felix, M. G. B. Drew, R. A. S. Ferreira, L. D. Carlos, T. Trindade, *Inorg. Chem. Commun.* **2003**, *6*, 1234–1238.
[24] D. Sendor, M. Hilder, T. Juestel, P. C. Junk, U. H. Kynast, *New J. Chem.* **2003**, *27*, 1070–1077.
[25] J. F. Ma, N. H. Hu, J. Z. Ni, *Polyhedron* **1996**, *15*, 1797–1799.
[26] P. C. R. Soares-Santos, F. A. Almeida Paz, R. A. Sa Ferreira, J. Klinowski, L. D. Carlos, T. Trindade, H. I. S. Nogueira, *Polyhedron* **2006**, *25*, 2471–2482.
[27] a) M. D. Faucher, P. A. Tanner, *J. Phys. Condens. Matter.* **2006**, *18*, 8503–8522; b) J. B. Gruber, B. Zandi, M. F. Reid, *Phys. Rev. B* **1999**, *60*, 15643–15653; c) J.-P. R. Wells, M. Yamaga, T. P. J. Han, H. G. Gallagher, M. Honda, *Phys. Rev. B* **1999**, *60*, 3849–3855; d) A. R. Devi, C. K. Jayasankar, M. F. Reid, *Phys. Rev. B* **1994**, *49*, 12551–12555.
[28] J. A. Fernandes, R. A. Sá Ferreira, M. Pillinger, L. D. Carlos, J. Jepsen, A. Hazell, P. Ribeiro-Claro, I. S. Gonçalves, *J. Lumin.* **2005**, *113*, 50–63.
[29] P. C. R. Soares-Santos, H. I. S. Nogueira, J. Rocha, V. Félix, M. G. B. Drew, R. A. Sá Ferreira, L. D. Carlos, T. Trindade, *Polyhedron* **2003**, *22*, 3529–3539.
[30] T. Kottke, D. Stalke, *J. Appl. Crystallogr.* **1993**, *26*, 615–619.
[31] R. Hooft, *Collect: Data Collection Software*, Delft, The Netherlands, Nonius B. V., **1998**.
[32] Z. Otwinowski, W. Minor, in *Methods in Enzymology*, vol. 276 (Eds.: C. W. Carter Jr, R. M. Sweet), Academic Press, New York, **1997**, p. 307.
[33] R. H. Blessing, *Acta Crystallogr., Sect. A* **1995**, *51*, 33–38.
[34] R. H. Blessing, *J. Appl. Crystallogr.* **1997**, *30*, 421.
[35] G. M. Sheldrick, *SHELXS-97, Program for Crystal Structure Solution*, University of Göttingen (Germany), **1997**.
[36] G. M. Sheldrick, *SHELXL-97, Program for Crystal Structure Refinement*, University of Göttingen (Germany), **1997**.
[37] A. Boultif, D. Louer, *J. Appl. Crystallogr.* **2004**, *37*, 724–731.
[38] J. Rodriguez-Carvajal, *FULLPROF - A Program for Rietveld Refinement and Pattern Matching Analysis*, Abstract of the Satellite Meeting on Powder Diffraction of the XV Congress of the IUCR, Toulouse, France, **1990**, p. 127.
[39] T. Roisnel, J. Rodriguez-Carvajal, *WinPLOTR (rel. June* 2005) – *A Windows Tool for Powder Diffraction Pattern Analysis.* Materials Science Forum, Proceedings of the Seventh European Powder Diffraction Conference (EPDIC 7) (Eds.: R. Delhez, E. J. Mittenmeijer), **2000**, p. 118–123.
[40] A. Boultif, D. Louer, *J. Appl. Crystallogr.* **1991**, *24*, 987–993.
[41] D. Louer, in *Automatic Indexing: Procedures and Applications, Accuracy in Powder Diffraction II*, Gaithersburg, MD, USA, **1992**, pp. 92–104.
[42] A. Lebail, H. Duroy, J. L. Fourquet, *Mater. Res. Bull.* **1988**, *23*, 447–452.
[43] J. Laugier, B. Bochu, *CHECKCELL – A Software Performing Automatic Cell/Space Group Determination, Collaborative Computational Project Number 14 (CCP14)*, Laboratoire des Matériaux et du Génie Physique de l'Ecole Supérieure de Physique de Grenoble (INPG), France, **2000**.

Received: December 19, 2006
Published Online: July 18, 2007

 © 2007 Wiley-VCH Verlag GmbH & Co. KGaA, Weinheim 

DOI: 10.1002/ejic.200700754

# NMR Studies of Paramagnetic Metallocarbaporphyrinoids

**Ewa Pacholska-Dudziak[a] and Lechosław Latos-Grażyński*[a]**

**Keywords:** Carbaporphyrinoids / Porphyrinoids / NMR spectroscopy / Organometallic chemistry

*As a result of a technical error during the final stage of printing, the parts in color are missing in Scheme 2 on page 2596 of the original article.*[1] *The correct version in color is printed below. The electronic version is not affected by this error.*

*The Editors*

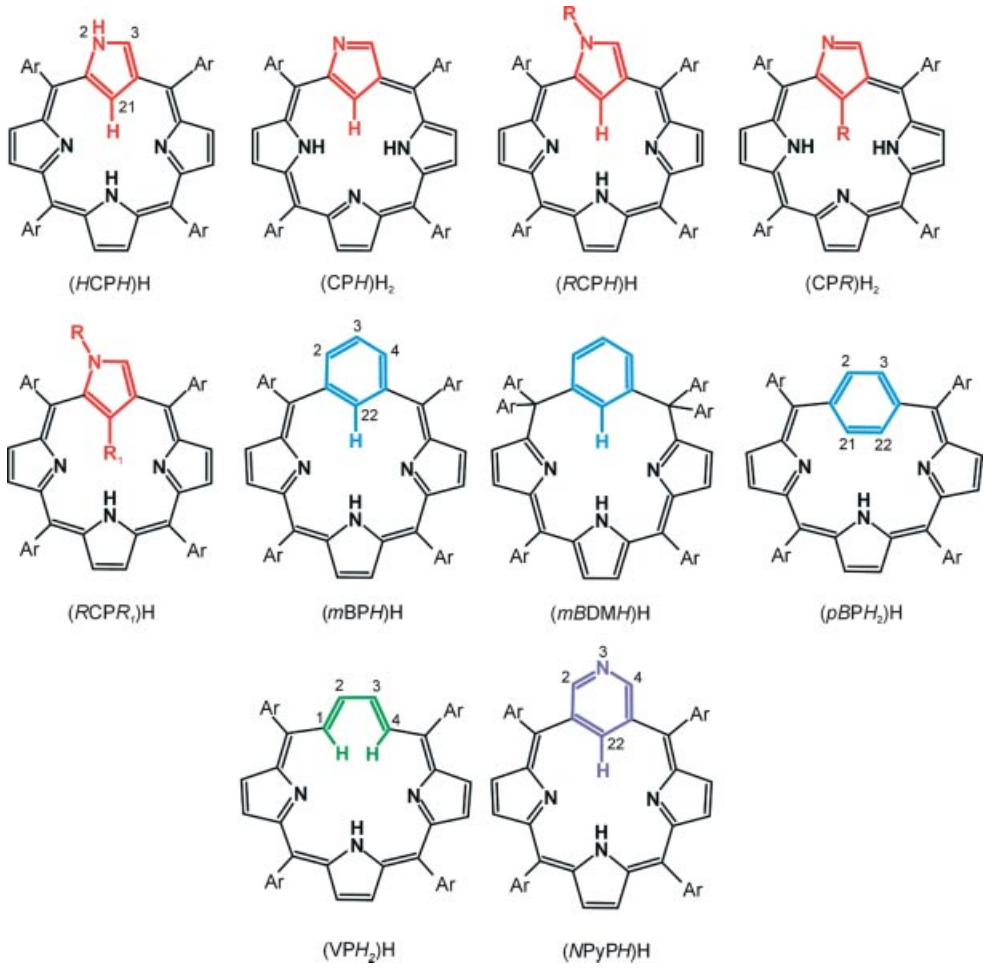


Scheme 2. Carbaporphyrinoids applied as ligands of paramagnetic complexes (partial numbering included).

[1] E. Pacholska-Dudziak, L. Latos-Grażyński, *Eur. J. Inorg. Chem.* **2007**, 2594–2608.

Received: July 11, 2007
Published Online: August 3, 2007

[a] Department of Chemistry, University of Wrocław,
14 F. Joliot-Curie St., Wrocław 50 383, Poland


© 2007 Wiley-VCH Verlag GmbH & Co. KGaA, Weinheim

**The EUChemSoc Societies have taken the significant step into the future by merging their traditional journals, to form two leading chemistry journals, the *European Journal of Inorganic Chemistry* and the *European Journal of Organic Chemistry.* Three further EUChemSoc Societies (Austria, Czech Republic and Sweden) are Associates of the two journals.**

## COVER PICTURE

**The cover picture shows** the reaction sequence of an $Ni^{II}$-assisted regiospecific *ortho*-aromatic hydroxylation. Sequential events of orthonickelation, oxygen insertion into the Ni−C bond induced by $H_2O_2$ and demetallation have been demonstrated to be involved in the aromatic hydroxylation in 2-(arylazo)aniline. The $H_2O_2$-induced O insertion into the Ni−C bond led to the formation of *metalloazosalophen* analogues of *metallosalophens* for the first time. Details are discussed in the article by S. Chattopadhyay et al. on p. 4263f.

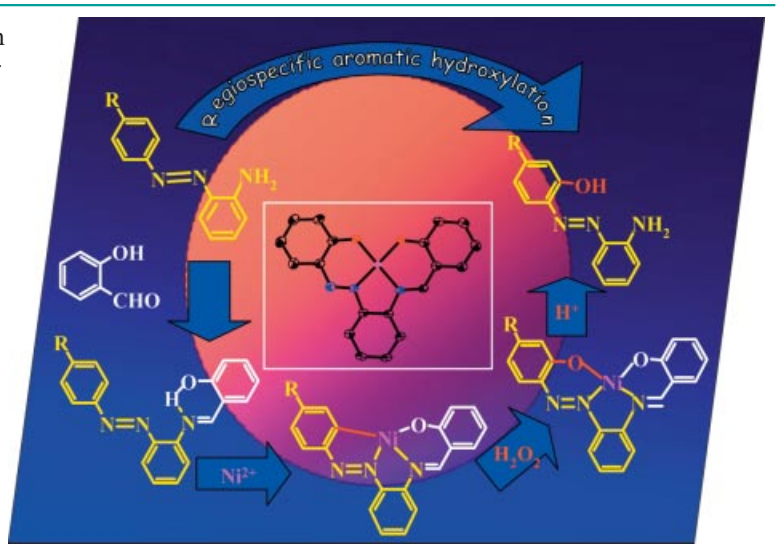


 © 2007 Wiley-VCH Verlag GmbH & Co. KGaA, Weinheim 

# CONTENTS

## FULL PAPERS

### Metal-Assisted Synthesis

**P. Pattanayak, J. Lal Pratihar, D. Patra, A. Burrows, M. Mohan, S. Chattopadhyay* ..... 4263–4271**

Regiospecific *ortho*-Aromatic Hydroxylation via Cyclonickelation Using Hydrogen Peroxide and Other Oxygen Donors: Synthesis of Metalloazosalophens

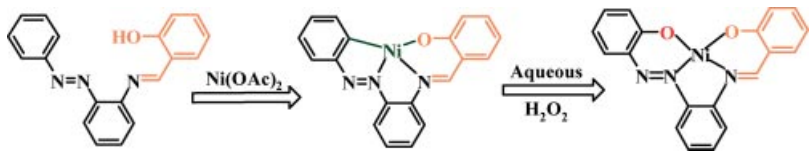


**Keywords:** Nickel / N,O ligands / Metallacycles / Oxygenation / Peroxo reagents / C–H activation

The first metalloazosalophen complexes, $(OL_{sal})Ni$, were prepared by a $Ni^{II}$-assisted route. Ni–C bond formation and subsequent facile oxygen insertion induced by peroxo reagents *m*CPBA, TBHP, or aqueous $H_2O_2$ were exploited for this purpose.

### $Pt^{II}$ and $Pd^{II}$ Chelates

**J. Lal Pratihar, B. Shee, P. Pattanayak, D. Patra, A. Bhattacharyya, V. G. Puranik, C. H. Hung, S. Chattopadhyay*..... 4272–4281**

Synthesis, Structure, and Reactivity of Diazoketiminato Complexes of Platinum(II) and Palladium(II): Cytotoxic Properties of a Platinum Complex

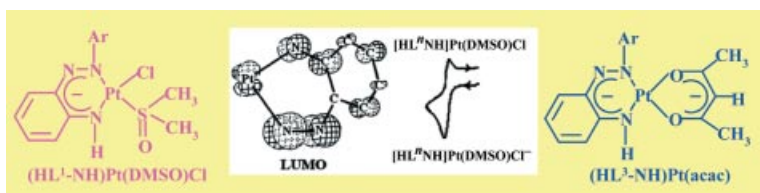


**Keywords:** Chelating ligands / Platinum / Palladium / Redox chemistry / Bioinorganic chemistry

New $Pt^{II}$ complexes incorporating delocalized diazoketimine ligands have been prepared and their chemical, electrochemical, and cytotoxic properties studied. A strategy to prepare an electroactive model $Pt^{II}$-based antitumor drug has emerged as a consequence.

### Phosphanes, Arsanes and Stibanes

**H. Nöth,* B. Gemünd, R. T. Paine ..... 4282–4297**

*N*-(2,4,6-Trimethylborazinyl)-Substituted Phosphanes, Arsanes, and Stibanes

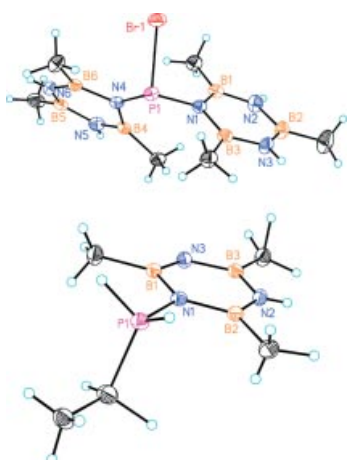

**Keywords:** Boron / Phosphanes / Arsenic / Antimony

*N*-Monolithio-*B*,*B*′,*B*′′-trimethylborazine reacts with $PX_3$, $AsX_3$, or $SbX_3$ (X = Cl, Br) to give the *N*-trimethylborazinyl-substituted phosphanes, arsanes, and stibanes $(Me_3B_3N_3H_2)_nEX_{3-n}$ (E = P, As, Sb; *n* = 1, 2, 3). Treatment of $(Me_3B_3N_3H_2)_2PCl$ with $LiAlH_4$ in diethyl ether gives the phosphane $(Me_3B_3N_3H_2)_2PH$, while $(Me_3B_3N_3H_2)PBr_2$ yields the zwitterionic compound $[Me_3B_3(NH)N(N^{-}\text{-}P^{+}H_2Et)]$. Dehalogenation of $(Me_3B_3N_3H_2)_2PBr$ with Na yields the corresponding diphosphane, and dehalogenation of $(Me_3B_3N_3H_2)PBr_2$ the corresponding cyclotetraphosphane.

### (Amino)(phosphanyl)alumane Chemistry

**T. Habereder, H. Nöth,* R. T. Paine* ..... 4298–4305**

Synthesis and Reactivity of New Bis(tetramethylpiperidino)(phosphanyl)alumanes

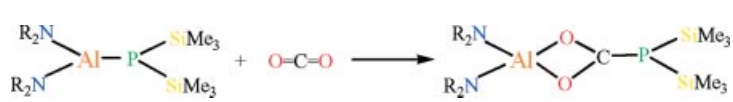


**Keywords:** Aminoalumanes / Phosphanylalumanes / Carbon dioxide insertion / Phosphanylcarbonate ligand / Structure elucidation

The bis(amino)(phosphanyl)alumane, $tmp_2AlP(SiMe_3)_2$, undergoes selective insertion in the Al–P bond, not the Al–N bonds, with $CO_2$, COS and $CS_2$.

 © 2007 Wiley-VCH Verlag GmbH & Co. KGaA, Weinheim 

## Aqueous Reduction of $[Cp^*_2W_2O_5]$

Two related triangular tungsten clusters, 3-electron $[Cp^*_3W_3O_4(OH)_2]^{2+}$ and 2-electron $[Cp^*_3W_3O_6]^{+}$ obtained by aqueous reduction of $[Cp^*_2W_2O_5]$, are described.

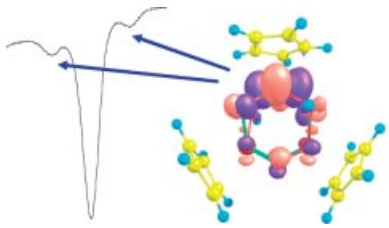

**C. Dinoi, P. Sözen, G. Taban, D. Demir, F. Demirhan,* P. Prikhodchenko, J. Gun, O. Lev, J.-C. Daran, R. Poli* ..... 4306–4316**

Aqueous Reduction of $[Cp^*_2W_2O_5]$: Characterization of the Triangular Clusters $[Cp^*_3W_3O_4(OH)_2]^{2+}$ and $[Cp^*_3W_3O_6]^{+}$ – Comparison with Molybdenum

**Keywords:** Tungsten / O ligands / Metal clusters / Density functional calculations

## Ferroexchange in Polyoxovanadates

DFT calculations suggest that the $V^{IV}/V^{V}$ mixed-valence alkoxo-polyoxovanadate $[4V^{IV} + 2V^{V}]$ is valence-trapped and characterized by ferromagnetic interactions between the vanadium(IV) centers.

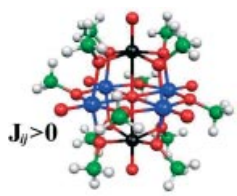


**E. M. Zueva,* S. A. Borshch,* M. M. Petrova, H. Chermette, A. M. Kuznetsov ..... 4317–4325**

Ferromagnetic Coupling in a Mixed-Valence Hexavanadate Core: Quantum-Chemical Forecast

**Keywords:** Mixed-valent compounds / Vanadates / Density functional calculations / Exchange interactions / Electron transfer

## $Fe^{II}$ Spin-Crossover Complexes

1-*N*-$R^2$-Imidazole-2-carboxaldehyde ($R^2$ = H, Me) was used as a carbonyl synthon for the synthesis of symmetrical and dissymmetrical tetradentate Schiff bases. In the symmetrical series the $NCS^-$ moieties are *trans* for $R^2$ = H and *cis* for $R^2$ = Me. In the dissymmetrical series the electronic behaviour evidences that the combination of pyridyl and imidazolyl rings allows the generation of an intermediate ligand field suitable for spin crossover.

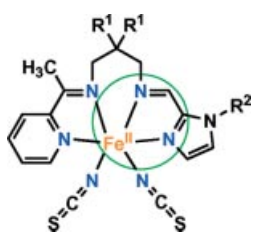


**N. Bréfuel,* S. Shova, J.-P. Tuchagues* ..... 4326–4334**

$Fe^{II}$ Bistable Materials with Dissymmetrical Ligands: Synthesis, Crystal Structure, Magnetic and Mössbauer Properties of $Fe^{II}$ Complexes Based on $N_4$ Schiff Bases Possessing 2-Pyridyl and 1-R-Imidazol-2-yl Rings

**Keywords:** Schiff bases / N ligands / Iron / Spin crossover / Magnetic properties / Mössbauer spectroscopy

## Oxoanionic Palladium Compounds

Elemental palladium can be oxidized by selenic acid at elevated temperatures to form $Pd(SeO_3)$, $Pd(SeO_4)$, or $Pd(Se_2O_5)$, depending on the reaction conditions. These compounds are the first oxoselenates of a platinum-group metal.

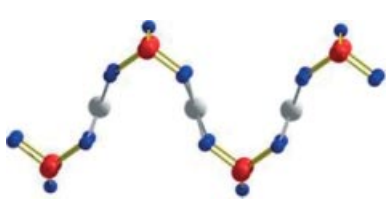

**A. Arndt, M. S. Wickleder* ... 4335–4339**

$Pd(SeO_3)$, $Pd(SeO_4)$, and $Pd(Se_2O_5)$: The First Palladium Oxoselenates

**Keywords:** Solid-state structures / Palladium / Selenium / Lone-pair effect / IR spectroscopy

 © 2007 Wiley-VCH Verlag GmbH & Co. KGaA, Weinheim 

# CONTENTS

## Ln−DOTA Complexes

**A. Pasha, G. Tircsó,* E. Tircsóné Benyó, E. Brücher, A. D. Sherry* ..... 4340−4349**

Synthesis and Characterization of DOTA-(amide)$_4$ Derivatives: Equilibrium and Kinetic Behavior of Their Lanthanide(III) Complexes

**Keywords:** Magnetic resonance imaging / Contrast agents / Protonation constants / Stability constants / Kinetics

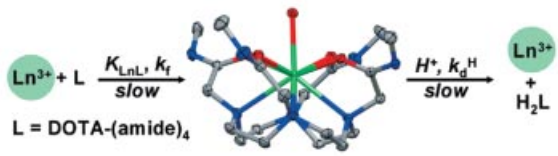


The stabilities of the lanthanide(III) DOTA-(amide)$_4$ complexes are several orders of magnitude lower than the stabilities of the corresponding $[Ln(DOTA)]^-$ complexes. The formation rates of the $[Ln\{DOTA\text{-}(MeAm)_4\}]^{3+}$ complexes proved to be slow, following second-order reaction kinetics. The rates of acid-catalyzed dissociation of $[Eu\{DOTA\text{-}(MeAm)_4\}]^{3+}$ complexes, however, are also quite slow, which suggests that these complexes may ultimately prove suitable for in vivo applications.

## Molybdenum Borylene Complexes

**H. Braunschweig,* K. Radacki, K. Uttinger ..... 4350−4356**

Synthesis and Characterisation of Semi-Bridging Molybdenum Borylene Complexes

**Keywords:** Boron / Borylene complexes / Molybdenum / Palladium / DFT calculations

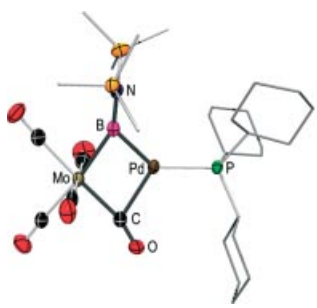


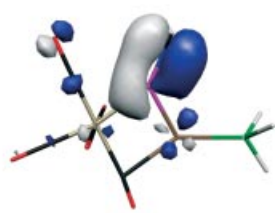

A variety of heterodinuclear borylene complexes was obtained from the reaction of $[(OC)_5Mo{=}B{=}N(SiMe_3)_2]$ with $[M(PCy_3)_2]$ (M = Pd, Pt). Structural studies and DFT computations revealed that the borylene ligand adopts a semi-bridging position.

## Functionalized Polyoxometalates

**F. Bannani, R. Thouvenot,* M. Debbabi* ..... 4357−4363**

Synthesis and Characterization of New Organosilyl Derivatives of Polyoxometalates $(n\text{Bu}_4\text{N})_2[\text{NbW}_5\text{O}_{19}\text{SiRR}'_2]$ (R = R′ = Et, *i*Pr, O*t*Bu, Ph; R = *t*Bu and R′ = Me) − The X-ray Crystal Structure of $(n\text{Bu}_4\text{N})_2[\text{NbW}_5\text{O}_{19}\text{SiPh}_3]$

**Keywords:** Polyoxometalates / Organic−inorganic hybrid / Multinuclear NMR spectroscopy

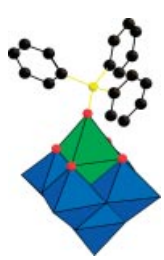

The selective coordination of electrophilic fragments $\{SiRR'_2\}^+$ to the terminal $O_t$(Nb) oxygen of the $NbW_5O_{19}^{3-}$ Lindqvist-type polyoxometalate leads to the formation of organic−inorganic hybrids. These species are characterized by multinuclear NMR, IR, and Raman spectroscopy. A single-crystal X-ray study of $(n\text{Bu}_4\text{N})_2[\text{NbW}_5\text{O}_{19}\text{SiPh}_2]$ supports the structure postulated on the basis of $^{183}$W NMR study.

## C=O Hydrogenation

**L. Dahlenburg,* R. Menzel, F. W. Heinemann ..... 4364−4374**

Synthesis and Catalytic Applications of Chiral Hydridoiridium(III) Complexes with Diamine/Bis(monophosphane) and Diamine/Diphosphane Coordination

**Keywords:** ridium / N ligands / P ligands / Asymmetric catalysis

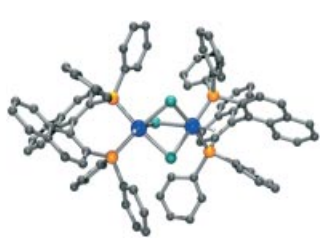

The triply chlorido-bridged cation $[\{(R)\text{-binap}\}_2Ir_2H_2(\mu\text{-Cl})_3]^+$ serves as a source of mixed-ligand compounds $[Ir(H)(Cl)(\text{diamine})\{(R)\text{-binap}\}]^+$ that are otherwise difficult to prepare. The use of such diamine/(*R*)-binap-containing $Ir^{III}$ complexes as (pre)catalysts for the enantioselective hydrogenation of acetophenone provides optical yields close to those of established $Ru^{II}$ catalysts bearing identical ligands.

 © 2007 Wiley-VCH Verlag GmbH & Co. KGaA, Weinheim 

## Tuning Coordination Polymers

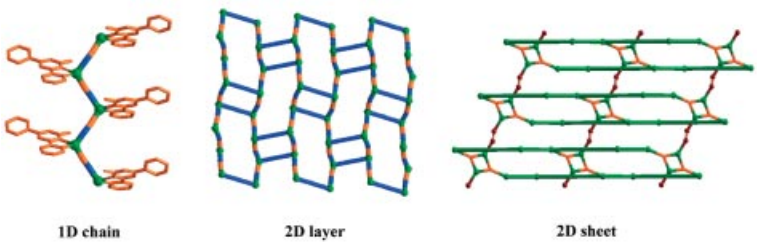


**Y.-N. Chi, F.-Y. Cui, Y.-Q. Xu, C.-W. Hu* ..... 4375–4384**

The Tuning Effect of 2-Amino-4,6-dipyridylpyrimidine Isomers on the Structural Dimensionalities and Motifs of Copper(I) Cyanide Complexes

Three ligand isomers, namely 2-amino-4,6-bis(2-pyridyl)pyrimidine ($L^1$), 2-amino-4-(2-pyridyl)-6-(4-pyridyl)pyrimidine ($L^2$), and 2-amino-4-(2-pyridyl)-6-(3-pyridyl)pyrimidine ($L^3$), are synthesized and employed in the copper(I) cyanide system. A novel 2D corrugated layer $[Cu_2(CN)_2L^1]_n$ (**1**), 1D zigzag chains $[CuCNL^2]_n$ (**2**) and $[CuCNL^3]_n$ (**4**), and a 2D sheet $[Cu_3(CN)_3L^3]_n$ (**3**) are successfully synthesized and their structures determined by single-crystal X-ray diffraction. These complexes demonstrate the tuning effect of the ligand isomerism upon the dimensionalities and motifs of the crystal structures.

**Keywords:** Copper / Chelating ligands / N ligands / Crystal engineering

## Sulfur–Nitrogen Bonds

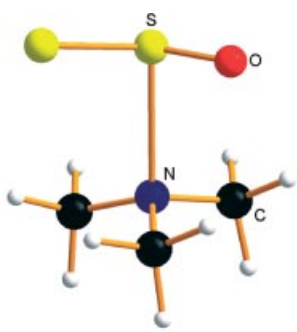


**R. Steudel,* Y. Steudel ..... 4385–4392**

Charge-Transfer Complexes between the Sulfur Molecules $SO_2$, $S_2O$, $S_3$, SONH, and $SOCl_2$ and the Amine Donors $NH_3$ and $NMe_3$ – A Theoretical Study

The acceptor molecules $SO_2$, $S_2O$, $S_3$, and $SOCl_2$ react with $NH_3$ and $NMe_3$ to form donor–acceptor complexes that are most stable in a polar environment with a high dielectric constant. The interaction enthalpy and the S–N bond length of the complexes are inversely related to each other.

**Keywords:** Ab initio calculations / Donor–acceptor systems / Thermodynamics / Sulfur / Solvent effects

**If not otherwise indicated in the article, papers in issue 26 were published online on August 23, 2007**

 © 2007 Wiley-VCH Verlag GmbH & Co. KGaA, Weinheim

**The EUChemSoc Societies have taken the significant step into the future by merging their traditional journals, to form two leading chemistry journals, the *European Journal of Inorganic Chemistry* and the *European Journal of Organic Chemistry.* Three further EUChemSoc Societies (Austria, Czech Republic and Sweden) are Associates of the two journals.**

## COVER PICTURE

**The cover picture shows** the reaction sequence of an $Ni^{II}$-assisted regiospecific *ortho*-aromatic hydroxylation. Sequential events of orthonickelation, oxygen insertion into the Ni−C bond induced by $H_2O_2$ and demetallation have been demonstrated to be involved in the aromatic hydroxylation in 2-(arylazo)aniline. The $H_2O_2$-induced O insertion into the Ni−C bond led to the formation of *metalloazosalophen* analogues of *metallosalophens* for the first time. Details are discussed in the article by S. Chattopadhyay et al. on p. 4263f.

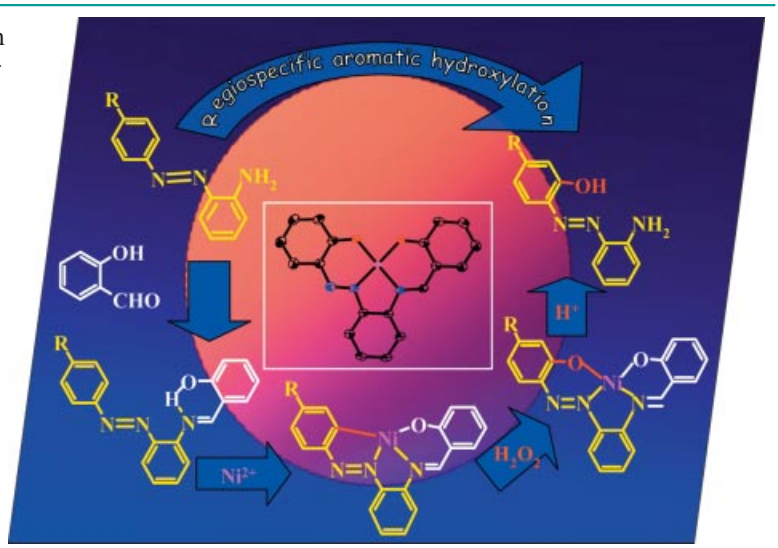


 © 2007 Wiley-VCH Verlag GmbH & Co. KGaA, Weinheim 

# SPOTLIGHTS …

## *Molecular Rotations*

S. Nishihara, T. Akutagawa,* D. Sato, S. Takeda, S.-i. Noro, T. Nakamura*

**Multirotations of (Anilinium)([18]Crown-6) Supramolecular Cation Structure in Magnetic Salt of $[Ni(dmit)_2]^-$**

*Chem. Asian J.*
DOI: **10.1002/asia.200700010**

**Round and round we go**: (Anilinium)-([18]crown-6) dynamic supramolecular cations undergo different modes of rotation in the solid state. The 180° flip-flop motion of anilinium and the rotation of [18]crown-6 were confirmed from solid-state NMR spectra. Multimolecular rotations of different motional freedoms were also observed simultaneously.

## *Enzyme Catalysis*

Y. Liu, C. Mihai, R. J. Kubiak, M. Rebecchi, K. S. Bruzik*

**Phosphorothiolate Analogues of Phosphatidylinositols as Assay Substrates for Phospholipase C**

*ChemBioChem*
DOI: **10.1002/cbic.200700061**

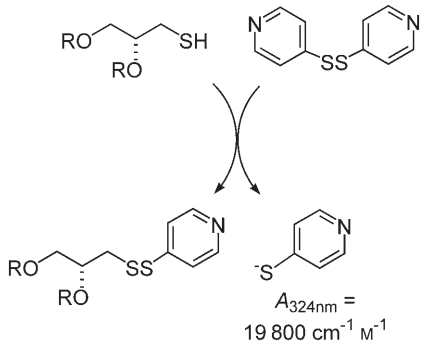


**Unnaturally superior**. Analogues of all naturally occurring phosphatidylinositols in which the scissile P–O bond is replaced by a P–S bond have been synthesized and shown to be useful assay substrates for the determination of phosphatidylinositol-specific phospholipase C activity.

## *Proton Transfer*

T. Majerus, T. Kottke, W. Laan, K. Hellingwerf, J. Heberle*

**Time-Resolved FT-IR Spectroscopy Traces Signal Relay within the Blue-Light Receptor AppA**

*ChemPhysChem*
DOI: **10.1002/cphc.200700248**

**Revealing intermediates:** Time-resolved step-scan FT-IR difference experiments (see figure) on flavin-containing photoreceptors reveal photocycle intermediates which have been spectrally silent in previous UV/Vis experiments on Appa–BLUF. The data indicate blue-light induced proton transfer or a change in H-bonding in the vicinity of a carboxylic side chain which represent an important step in signal transfer from the chromophore to the protein surface.

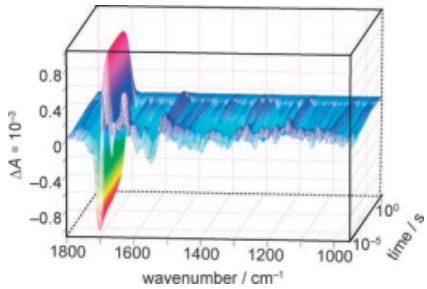


## *Virtual Screening*

C. Lamanna, A. Catalano, A. Carocci, A. Di Mola, C. Franchini,* V. Tortorella, P. M. L. Vanderheyden, M. S. Sinicropi, K. A. Watson, S. Sciabola

**$AT_1$ Receptor Ligands: Virtual-Screening-Based Design with TOPP Descriptors, Synthesis, and Biological Evaluation of Pyrrolidine Derivatives**

*ChemMedChem*
DOI: **10.1002/cmdc.200700082**

**A virtual approach** that uses TOPP 3D descriptors to explore the $AT_1$ receptor is presented. It features a new series of sartan analogues (shown), which were synthesized and biologically evaluated on CHO-h$AT_1$ cells stably expressing the human $AT_1$ receptor.

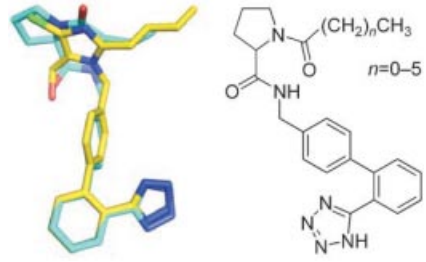


 © 2007 Wiley-VCH Verlag GmbH & Co. KGaA, Weinheim 

EurJIC European Journal of Inorganic Chemistry

## *Carbon Nanohorns*

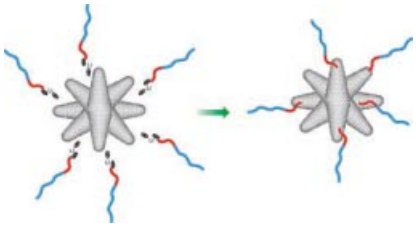

**Taking the nanotube by the horn!** The covalent functionalization of the newly discovered carbon nanohorns with well-defined homopolymers and block copolymers is described (see scheme). The synthesis and the properties of the above hybrid materials are elucidated using complementary techniques.

G. Mountrichas, S. Pispas,*
N. Tagmatarchis*

**Grafting Living Polymers onto Carbon Nanohorns**

*Chem. Eur. J.*
DOI: **10.1002/chem.200700770**

## *Pd-Catalyzed Cyclizations*

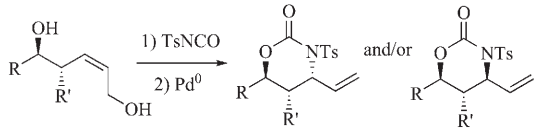


The Pd-catalyzed stereoselective cyclization of dicarbamates proceeded with 1,3-asymmetric induction under either thermodynamic or kinetic control to afford enantioselectively six-membered-ring cyclic carbamates. Calculations enabled us to rationalize the observed stereoselectivity.

G. Broustal, X. Ariza,
J.-M. Campagne,* J. Garcia,*
Y. Georges, A. Marinetti,
R. Robiette*

**A Stereoselective Approach to 1,3-Amino Alcohols Protected as Cyclic Carbamates: Kinetic vs. Thermodynamic Control**

*Eur. J. Org. Chem.*
DOI: **10.1002/ejoc.200700503**

## *Total Synthesis*

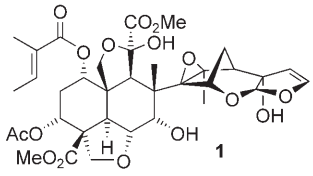


1

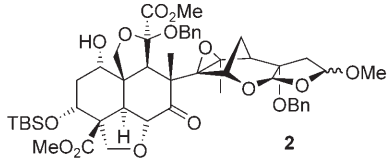


2

**22 Years in the making**: Azadirachtin (**1**) was synthesized for the first time by a highly convergent approach, utilizing a Claisen rearrangement and a radical cyclization as key steps. End-game strategies relied on intermediate **2**, which could be obtained by synthetic methods as well as by degradation of **1**. Bn = benzyl, TBS = *tert*-butyldimethylsilyl.

G. E. Veitch, E. Beckmann,
B. J. Burke, A. Boyer, S. L. Maslen,
S. V. Ley*

**Synthesis of Azadirachtin: A Long but Successful Journey**

*Angew. Chem. Int. Ed.*
DOI: **10.1002/anie.200703027**

On these pages, we feature a selection of the excellent work that has recently been published in our sister journals. If you are reading these pages on a computer, click on any of the items to read the full article. Otherwise please see the DOIs for easy online access through Wiley InterScience.

 © 2007 Wiley-VCH Verlag GmbH & Co. KGaA, Weinheim 

DOI: 10.1002/ejic.200700149

# Regiospecific *ortho*-Aromatic Hydroxylation via Cyclonickelation Using Hydrogen Peroxide and Other Oxygen Donors: Synthesis of Metalloazosalophens

**Poulami Pattanayak,[a] Jahar Lal Pratihar,[a] Debprasad Patra,[a] Andrew Burrows,[b] Mary Mohan,[b] and Surajit Chattopadhyay*[a]**

**Keywords:** Nickel / N,O ligands / Metallacycles / Oxygenation / Peroxo reagents / C–H activation

The new ligands *N*-[2-(arylazo)phenyl]salicylideneamine, $H_2L_{sal}$ [where H represents the dissociable protons upon complexation and aryl groups of $H_2L_{sal}$ are phenyl for $H_2L^1{}_{sal}$, *p*-methylphenyl for $H_2L^2{}_{sal}$, and *p*-chlorophenyl for $H_2L^3{}_{sal}$], were prepared by the reaction of 2-(arylazo)aniline, $H_2L$, with salicylaldehyde. $H_2L_{sal}$ ligands afforded stable ortho-metalated complexes, $(L_{sal})Ni$, upon treatment with $Ni(CH_3COO)_2{\cdot}4H_2O$. The dianionic $(L_{sal})^{2-}$ ligands bind $Ni^{II}$ in tetradentate (C,N,N,O) fashion in distorted square-planar geometry. Reaction of $(L_{sal})Ni$ with *meta*-chloroperbenzoic acid, *tert*-butyl hydroperoxide, or hydrogen peroxide furnished the metalloazosalophens, $(OL_{sal})Ni$, as a result of oxygen insertion into the Ni–C bond. The X-ray structures of $(L^1{}_{sal})Ni$ and $(OL^1{}_{sal})Ni$ were determined as representatives for unequivocal characterization. Treatment of $(OL^1{}_{sal})Ni$ with dilute $HClO_4$ liberated 2-(2-aminophenylazo)phenol, $H_2L^1OH$, which is an *ortho*-hydroxylated derivative of $H_2L^1$. The cyclic voltammograms of $(OL_{sal})Ni$ complexes display a reversible reductive response near –1.06 V vs. SCE.

(© Wiley-VCH Verlag GmbH & Co. KGaA, 69451 Weinheim, Germany, 2007)

## Introduction

The rich chemistry and usefulness of transition-metal complexes incorporating tetradentate (O,N,N,O) *salen* and its derivatives (also termed *metallosalens*, in general), **I**, have drawn interest in the areas of coordination chemistry,[1] catalysis,[2] and biochemistry research.[3] The challenge of the design and synthesis of new analogues of metallosalens prompted us to investigate the synthesis of azo-aldimine complexes as shown in **II**. These new complexes of type **II** are termed *metalloazosalophens* in this paper, in analogy to *metallosalophens*.

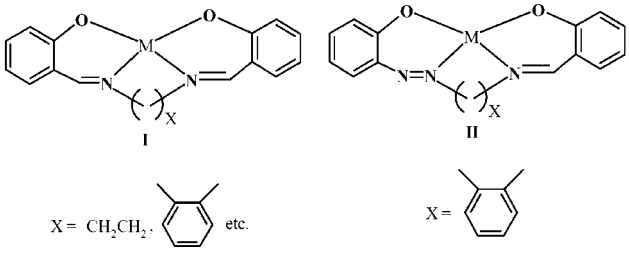


[a] Department of Chemistry, University of Kalyani, Kalyani, 741235, India
E-mail: scha8@rediffmail.com
[b] Department of Inorganic Chemistry, University of Bath, Claverton Down, Bath BA27AY, UK
Supporting information for this article is available on the WWW under http://www.eurjic.org or from the author.

The preparation of metalloazosalophen complexes was contemplated after successful preparation of the new ligand, *N*-[2-(arylazo)phenyl]salicylideneamine, $H_2L_{sal}$, **1**, which comprises of two types of N-donor ligands: azo (–N=N–) and aldimine (–CH=N–). The $H_2L_{sal}$ ligand is similar to 1,2-*N*,*N*-disalicylidene phenylamine, **2** (commonly known as "salophen"), as shown in **A**, where Z = H and Y = N for $H_2L_{sal}$ while Z = OH and Y = CH for "salophen" ligands.

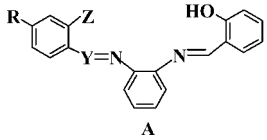


| No | Abbreviations of compounds | Y | Z |
|---|---|---|---|
| 1 | $H_2L_{sal}$ | N | H |
| 2 | salophen | CH | OH |
| 3 | $H_2OL_{sal}$ (azosalophen) | N | OH |

It was further realized that the substitution of Z (i.e., H) in $H_2L_{sal}$ by OH would afford the "azosalophen" analogue, $H_2OL_{sal}$, **3**, of "salophen" and the corresponding phenolato complex of this ligand would be the metalloazosalophens of type **II**.

Metal complexes incorporating azo ligands exhibited interesting electron-transfer properties, photophysical behavior, and biological activities.[4] Therefore, metalloazosalophens may not only possess the properties of enhanced performance compared with that of metallosalophens but also there are possibilities of new and interesting characteristics.

 © 2007 Wiley-VCH Verlag GmbH & Co. KGaA, Weinheim 

Metal-assisted chemical transformations have received attention in recent years because of their potential application in planned and directed organic synthesis for the preparation of target compounds which have not been prepared thus far by applying conventional synthetic protocols. Oxygenation (addition of an O atom in between a C–H bond) is highly desirable for functionalization of an aromatic ring. The regiospecificity of such an oxygenation has been appreciated for intended synthesis. One of the strategies towards regiospecific oxygenation is to activate a particular C–H bond through metal–carbon bond formation, followed by stoichiometric insertion of an oxygen atom within the metal–carbon bond. Therefore, the search for cheaper and easily available metal substrates and convenient reaction conditions to carry out such stoichiometric reactions, leading to the preparation of desired molecules, is important in terms of wide applicability and cost control. In this aspect it is worthwhile to mention that transition-metal-assisted aromatic hydroxylation has been recognized in essential biological reactions (e.g., oxygenase activity)[5] and in several complicated organic syntheses.[6]

Orthometalation is one of the processes of C–H bond cleavage (a precondition of C–H activation), which is reported amply in the cases of $Pd^{II}$ and $Pt^{II}$,[7] whereas it is scarce for $Ni^{II}$, the 3d congener of group 10 metals.[8] The usage of 3d metal ions in C–H activation has an edge over heavier members of group 10 metals in terms of cost effectiveness and availability.

Studies on orthopalladation and orthoplatination in azobenzene-related ligands were initiated after the discovery of the "Cope complex".[9] Later, stoichiometric regiospecific *ortho*-hydroxylation of azobenzene derivatives by cyclopalladation were reported.[7c,7d] In contrast, the preparative method based on oxygen insertion into nickel–aryl bonds to give new aryl oxide compounds was reported to occur either with $N_2O$ or $O_2$.[10,11] This background information on metal-assisted routes to the oxy-functionalization of aryl rings provides a stimulus to contemplate the preparation of new metalloazosalophen complexes of type **II**.

Herein, we report the syntheses of new cyclometalated $Ni^{II}$ complexes incorporating the dianion of deprotonated $H_2L_{sal}$ and its conversion to the corresponding aryloxy form (metalloazosalophen complex of type **II**) by oxidation with *meta*-chloroperbenzoic acid (*m*CPBA), *tert*-butyl hydroperoxide (TBHP), or hydrogen peroxide ($H_2O_2$) by oxygen insertion into the nickel–carbon bond. TBHP and *m*CPBA are non-atom-efficient reagents as oxidants, whereas $H_2O_2$ is an atom-efficient oxidant since water is the sole by-product and it can therefore be classified as a green oxidant.[12] Furthermore, oxidation with aqueous $H_2O_2$ is cheap, safe, and easy to handle.[13] Also, this report may provide valuable information concerning the issue of organonickel-intermediate formation during the oxygenation of hydrocarbons on the nickel surface.[14] The synthesis of the specifically *ortho*-hydroxylated derivative 2-(2-aminophenylazo)phenol is also described.

## Results and Discussion

### Synthesis and Reactions

The strategy of the preparation of the target metalloazosalophen complexes of type **II** is based on three major steps: (i) synthesis of the precursor ligand, $H_2L_{sal}$, **1**, (ii) nickel–carbon bond formation by orthonickelation in $H_2L_{sal}$, and (iii) regiospecific oxygenation by way of oxygen insertion into the nickel–carbon bond of new orthonickelated complexes.

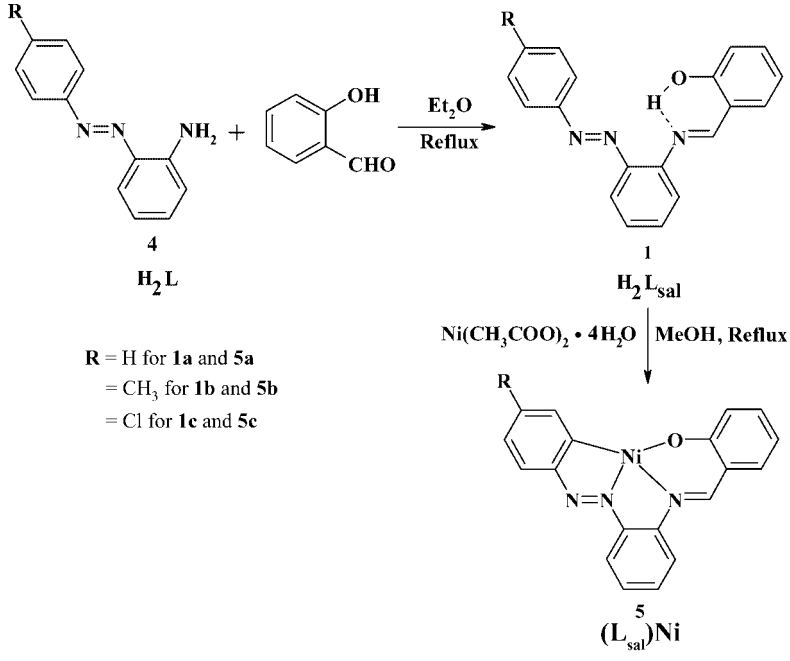


Scheme 1.

 © 2007 Wiley-VCH Verlag GmbH & Co. KGaA, Weinheim 

### *Syntheses of $H_2L_{sal}$ Ligands and Cyclonickelated ($L_{sal}$)Ni Complexes*

The azo-aldimine hybrid ligand *N*-[2-(arylazo)phenyl]salicylideneamine, $H_2L_{sal}$, **1**, was prepared by refluxing 2-(arylazo)aniline, $H_2L$, **4**, with salicylaldehyde in diethyl ether (Scheme 1). The solid, obtained upon evaporation of $Et_2O$, was used for further reactions without purification since the $^1$H NMR spectra (see later) exhibited good purity. The reaction of $H_2L_{sal}$ with nickel acetate tetrahydrate, $Ni(CH_3COO)_2{\cdot}4H_2O$, in refluxing methanol precipitated the orthonickelated green complex ($L_{sal}$)Ni, which was collected by filtration. The reaction is shown in Scheme 1. A further crop of product was isolated upon concentrating the filtrate. The total yield of ($L^1_{sal}$)Ni was 70%. Such a facile formation of cyclonickelated compounds upon treatment of $Ni(CH_3COO)_2{\cdot}4H_2O$ with tri- and bidentate azo ligands has not been reported so far.

### *Synthesis of ($OL_{sal}$)Ni from ($L_{sal}$)Ni*

The new metalloazosalophen complexes, ($OL_{sal}$)Ni, were prepared by the highly selective metaloxylation[15] of ($L_{sal}$)Ni with the oxidants *m*CPBA, TBHP, or $H_2O_2$. The oxygen insertion into the Ni–C bond of ($L_{sal}$)Ni occurred upon treatment with *m*CPBA or TBHP in either aprotic (dichloromethane) or protic (*tert*-butyl alcohol) solvent at room temperature to afford the diamagnetic and electroneutral $Ni^{II}$ complex, ($OL_{sal}$)Ni (Scheme 2). Furthermore, the reaction of ($L_{sal}$)Ni in $CH_2Cl_2$ with aqueous $H_2O_2$ (a better choice of oxidant) furnished ($OL_{sal}$)Ni after stirring for a period longer than that of the reactions of *m*CPBA or TBHP with ($L_{sal}$)Ni. The formation of ($OL_{sal}$)Ni complexes from ($L_{sal}$)Ni was monitored spectrophotometrically up to the extent of 85% conversion for all the reactions. Considerable delay in metaloxylation with aqueous $H_2O_2$ can be attributed to the heterogeneous solvent mixture ($CH_2Cl_2/H_2O$). The $^1$H NMR spectrum of the crude product, as obtained after oxidation, exhibited good purity of ($OL_{sal}$)Ni indicating the likelihood of quantitative transformation [the spectrum of crude ($OL^1_{sal}$)Ni is available as Supporting Information, Figure S24]. Nevertheless, after every reaction, pure ($OL_{sal}$)Ni complexes were isolated in ca. 65% yield by employing a conventional purification procedure using the silica gel preparative TLC plate. Pure product separated well, leaving an unidentified material at the bottom. Since the $^1$H NMR spectrum of crude ($OL_{sal}$)Ni exhibited good purity,[16] the unidentified material was assumed to be the decomposition product of ($OL_{sal}$)Ni on the silica plate.

Oxygen insertions into Pd–C σ bonds of arylpalladium(II) complexes, induced by *m*CPBA, have been reported.[7c–7e] These reactions followed a straightforward second-order rate law (first order in both organopalladium substrate and in *m*CPBA).[7c–7e] The probable mechanism was proposed to follow a concerted one-step process leading to O insertion into the Pd–C bond on the basis of kinetic results.[7c–7e] Reaction of *m*CPBA with ($L_{sal}$)Ni was so fast that it could not be monitored spectrophotometrically for kinetic studies. The reaction completed to the extent of 86% within one minute. However, by analogy with the proposed mechanism of O insertion into the Pd–C bond,[7c–7e] the oxygen insertion into the Ni–C bond of ($L_{sal}$)Ni with *m*CPBA has been assumed to follow a similar concerted one-step process via formation of intermediate **I-A** as shown in Scheme 3.

Realizing the fact that the Ni–C bond of ($L_{sal}$)Ni complexes is much more susceptible to metaloxylation compared with the Pd–C bond of orthopalladated complexes incorporating tridentate azo ligands,[7c–7e] oxidation was attempted with milder oxidizing agents such as TBHP or $H_2O_2$.

($L_{sal}$)Ni underwent oxygenation in the solvents *t*BuOH and $CH_2Cl_2$ with TBHP. The beneficial effect of protic solvents (*t*BuOH) in the metaloxylation of organopalladium complexes with TBHP has been reported.[17] Formation of alcohol oxide species (RHO–O) in protic solvents was believed to be the actual oxygen-donating agent in oxygen-transfer reactions by TBHP because the RHO–O species can provide an oxenoid oxygen atom and a neutral leaving group.[17] It is tempting to believe that TBHP reacts directly with ($L_{sal}$)Ni to afford ($OL_{sal}$)Ni, following a concerted one-step mechanism via formation of intermediate **I-B** as shown in Scheme 3. Nevertheless, formation of a ($L_{sal}$)$Ni^{IV}$=O intermediate[18] can not be excluded unequivocally though it is expected to be unstable for $Ni^{IV}$ ($d^n$ oxo system, $n > 4$),[19,7d] and a doubly bonded $Ni^{IV}$=O species is unlikely to be involved since it is better represented as either $Ni^{III}$–O· or $Ni^{IV}$–$O^-$.[18a]

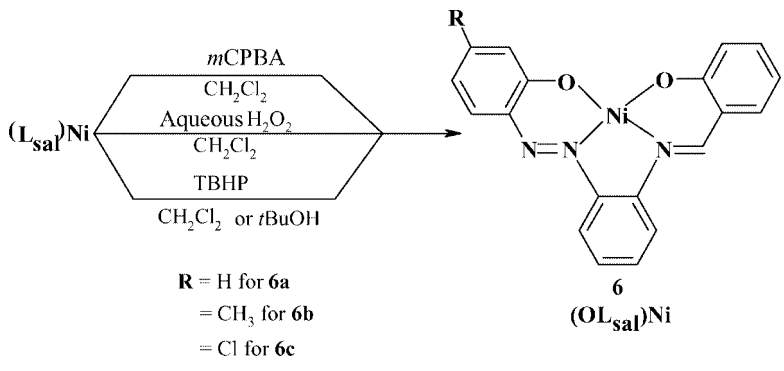


Scheme 2.

 © 2007 Wiley-VCH Verlag GmbH & Co. KGaA, Weinheim 

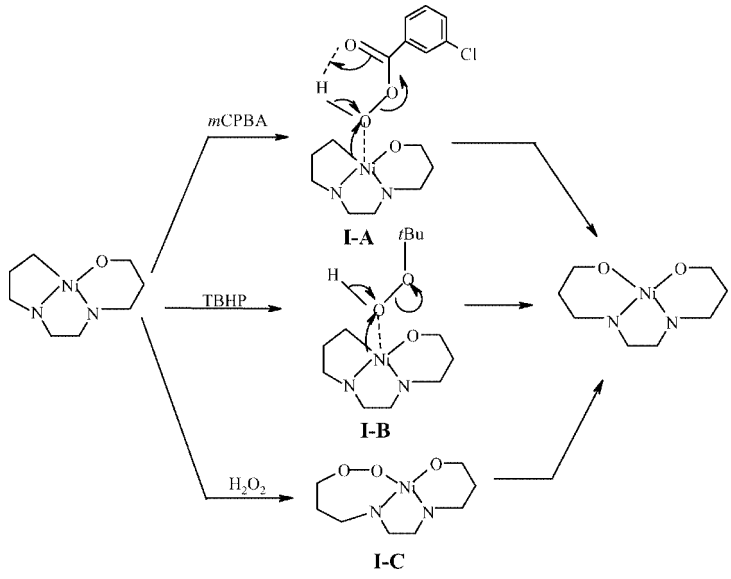


Scheme 3.

Interestingly, ($L_{sal}$)Ni could be oxidized to ($OL_{sal}$)Ni upon treatment with aqueous $H_2O_2$. Although there are studies on the formation of peroxo-bridged dinuclear nickel complexes upon treatment of square-planar $Ni^{II}$ with $H_2O_2$, to the best of our knowledge, there is no report on oxygen insertion into a Ni–aryl bond with $H_2O_2$.[20] It was demonstrated previously that the oxygen insertion into a Ni–aryl bond had taken place upon reaction with air (i.e., $O_2$), where formation of a peroxo–nickel(II) intermediate was postulated in the reaction trajectory.[10d] By analogy, a mechanism of O insertion into the Ni–aryl bond of ($L_{sal}$)-Ni with $H_2O_2$ has been proposed to proceed via formation of the peroxo–$Ni^{II}$ intermediate **I-C** as shown in Scheme 3. It is worthwhile to mention that the ($L_{sal}$)Ni did not undergo metaloxylation upon prolonged bubbling of air into an acetonitrile solution of the complex.

### *Synthesis of 2-(2-Aminophenylazo)phenol, $H_2L^1OH$*

The new organic substrate $H_2L^1OH$ [a specifically *ortho*-hydroxylated phenyl derivative of 2-(phenylazo)aniline, $H_2L^1$] was obtained upon treatment of ($OL^1_{sal}$)Ni with dilute $HClO_4$ in acetonitrile solution. Demetalation and hydrolysis of the aldimine bond[21] occurred in acid medium, liberating the free 2-(2-aminophenylazo)phenol, $H_2L^1OH$, in good yield. Therefore in general, the new hydroxylated derivative, $H_2L^1OH$, was obtained in four steps as a result of regiospecific hydroxylation of 2-(phenylazo)aniline (Scheme 4). It is important to mention that the synthesis of authentic $H_2L^1OH$ has not been reported so far, so we cannot compare the merits of different procedures. It seems that the conventional synthetic protocol for the preparation of $H_2L^1OH$ would require carrying out several nonspecific reactions followed by careful work-up and separation of products after each step. The present reaction sequence is not associated with the formation of side products, and the chemicals used are cheap and easy to use.

## Spectral Characterization

The new ligands and complexes were characterized by UV/Vis, IR, $^1H$ NMR, and mass spectral studies.

### *UV/Vis and IR Spectra*

Dichloromethane solutions of $H_2L_{sal}$ ligands display an intense broad absorption near 316 nm in the UV/Vis spectra, characteristic of the overlapping n → π* transitions of azo (N=N) and aldimine (N=CH) functionalities.[22] The UV/Vis spectra of the green solutions of ($L_{sal}$)Ni in $CH_2Cl_2$ feature a relatively weak absorption band near 630 nm for

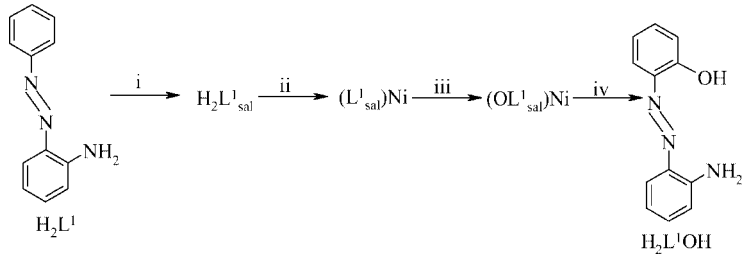


Scheme 4. (i) Salicylaldehyde in diethyl ether; (ii) $Ni(CH_3COO)_2{\cdot}4H_2O$ in refluxing methanol; (iii) *m*CPBA, TBHP, or $H_2O_2$ in $CH_2Cl_2$; (iv) dilute $HClO_4$ in $CH_3CN$.

 © 2007 Wiley-VCH Verlag GmbH & Co. KGaA, Weinheim 

the d–d transition,[23] while four absorption bands in the range 315 to 460 nm are assigned to MLCT transitions (N=N and C=N).[22] The absorption for the d–d transition in ($OL_{sal}$)Ni occurs at lower energy (640 nm) than that of the parent complex ($L_{sal}$)Ni. In addition, there are five MLCT absorptions in the range 340 to 520 nm in the UV/Vis spectra. Representative spectra of $H_2L^1_{sal}$, ($L^1_{sal}$)Ni, and ($OL^1_{sal}$)Ni are shown in Figure 1. The UV/Vis spectrum of $H_2L^1OH$ is different from that of either $H_2L^1_{sal}$ or $H_2L^1$ with an intense absorption at 450 nm in addition to the absorption at 318 nm due to the n → π* transition for the N=N functionality.

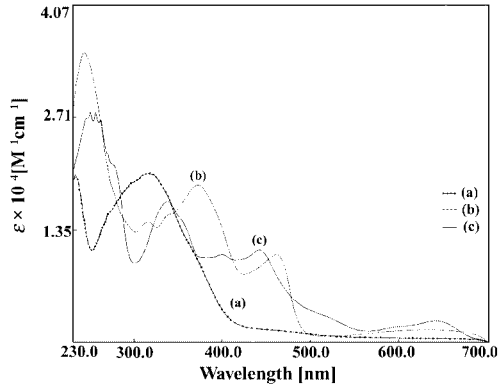


Figure 1. UV/Vis spectra of (a) $H_2L^1_{sal}$ ($C = 3.98 \times 10^{-5}$ M), (b) ($L^1_{sal}$)Ni ($C = 3.62 \times 10^{-5}$ M), and (c) ($OL^1_{sal}$)Ni ($C = 2.67 \times 10^{-5}$ M).

A sharp single band near 1614 $cm^{-1}$ in the IR spectra (KBr disc) of $H_2L_{sal}$ is characteristic of $\nu_{C=N}$.[22] The IR band near 1450 $cm^{-1}$ is assigned to $\nu_{N=N}$ by comparing the same band for other azo ligands and considering the extent of redshift upon coordination (see later).[23] The $\nu_{O-H}$ for the phenol OH of the salicylidene fragment is absent in conformity with the intramolecular hydrogen-bonded form of $H_2L_{sal}$. The $\nu_{C=N}$ and $\nu_{N=N}$ of ($L_{sal}$)Ni appear at slightly lower frequency (1605 and 1380 $cm^{-1}$, respectively) than those of the ligands, indicating coordination of aldimine (N=CH) and azo (N=N) nitrogen atoms. The $\nu_{C=N}$ and $\nu_{N=N}$ stretches of ($OL_{sal}$)Ni complexes appear near 1610 and 1375 $cm^{-1}$, respectively, consistent with azo (N=N) and aldimine (N=CH) coordination. The $\nu_{O-H}$ and $\nu_{NH_2}$ of $H_2L^1OH$ are observed at 3284 and 3407 $cm^{-1}$, respectively, in the IR spectrum while the $\nu_{N=N}$ appears at 1468 $cm^{-1}$.

### *$^1$H NMR Spectra*

The $H_2L_{sal}$ ligands display well-resolved $^1$H NMR spectra in $CDCl_3$, indicating good purity of products. The phenol OH of $H_2L_{sal}$ appears as a singlet near $\delta$ = 13.60 ppm which is absent in ($L_{sal}$)Ni and ($OL_{sal}$)Ni complexes, consistent with the phenolato coordination. The singlet resonance for the aldimine (N=CH) proton of the $H_2L_{sal}$ ligand near $\delta$ = 8.62 ppm is shifted marginally in the spectra of ($L_{sal}$)-Ni, observed in the range $\delta$ = 8.43 to 8.57 ppm. The resonance for the same aldimine proton of ($OL_{sal}$)Ni undergoes considerable upfield shift and appears within the range $\delta$ = 8.38 to 8.40 ppm. The $^1$H NMR spectral features for the aromatic protons of all the ligands and complexes are consistent with their structures. Data are collected in the Experimental Section.

The phenol OH proton and the $NH_2$ protons of $H_2L^1OH$ appear as singlets at $\delta$ = 12.84 and 6.19 ppm, respectively. Aromatic protons appear within the region $\delta$ = 6.75 to 7.76 ppm, in the sets of doublets at $\delta$ = 6.75, 7.67, and 7.76 ppm, triplets at $\delta$ = 6.83, 7.20, and 7.29 ppm, and a multiplet within the range $\delta$ = 6.99 to 7.04 ppm, with a total of eight equivalent protons. These spectral features are consistent with the structural formula. All the original $^1$H NMR spectra are given in the Supporting Information (Figures S18–S28).

### *Mass Spectra*

The electrospray mass spectrometry in $CH_2Cl_2$ solution (positive mode) was investigated for ($L^1_{sal}$)Ni and ($OL^1_{sal}$)-Ni as representatives. The mass spectra are consistent with the compositions and molecular masses. The major envelope, in each case, is satisfactorily simulated on the basis of formulae $C_{19}H_{13}N_3NiO$ and $C_{19}H_{13}N_3NiO_2$ for ($L^1_{sal}$)Ni and ($OL^1_{sal}$)Ni, respectively.

### X-ray Structures of ($L^1_{sal}$)Ni and ($OL^1_{sal}$)Ni

Unequivocal characterization of the cyclonickelated complex, ($L^1_{sal}$)Ni, and the corresponding oxygenated metalloazosalophen complex, ($OL^1_{sal}$)Ni, was performed by X-ray structure analysis. Figures 2 and 3 show the perspective views of ($L^1_{sal}$)Ni and ($OL^1_{sal}$)Ni molecules, respectively. Selected bond lengths and angles are collected in Tables 1 and 2. The dianions $(L^1_{sal})^{2-}$ and $(OL^1_{sal})^{2-}$ bind $Ni^{II}$ in distorted square-planar geometry in both complexes. The structure of the ($L^1_{sal}$)Ni crystal did not refine well ($R_w$ = 17%) because of bad quality but it could be characterized unequivocally (in combination with $^1$H NMR and mass spectral results, vide infra). The accuracy of bond lengths, angles, and anisotropic parameters were satisfactory after several full-matrix least-square refinements. The Ni($N_2OC$) and Ni($N_2O_2$) coordination spheres of ($L^1_{sal}$)Ni and ($OL^1_{sal}$)Ni are planar with mean deviations 0.006 and 0.003 Å, respectively. In the case of ($L^1_{sal}$)Ni, the Ni–C [1.984(10) Å] and Ni–O [1.820(6) Å] distances are comparable to reported values.[8d,22a]

The oxygen insertion into the nickel–carbon bond was confirmed as a result of the appearance of O2 in the molecular structure of ($OL^1_{sal}$)Ni. The Ni–N(azo) distance [Ni1–N2 1.8365(17) Å] of ($OL^1_{sal}$)Ni is shorter than the Ni–N-(aldimine) distance [Ni1–N3 1.8570(16) Å], indicating a stronger π-acidity of the azo (N=N) group relative to that of the aldimine (HC=N) group. Accordingly, the Ni1–O1 bond *trans* to N2 is longer [1.8420(15) Å] than the Ni1–O2 bond [1.8311(14) Å] *trans* to N1. However, the Ni–N and Ni–O distances are within the normal range.[22a] All the atoms in both the molecules ($L^1_{sal}$)Ni and ($OL^1_{sal}$)-Ni are coplanar with maximum deviations 0.08 and 0.75 Å, respectively, from the mean plane. Molecular stacking in

 © 2007 Wiley-VCH Verlag GmbH & Co. KGaA, Weinheim 

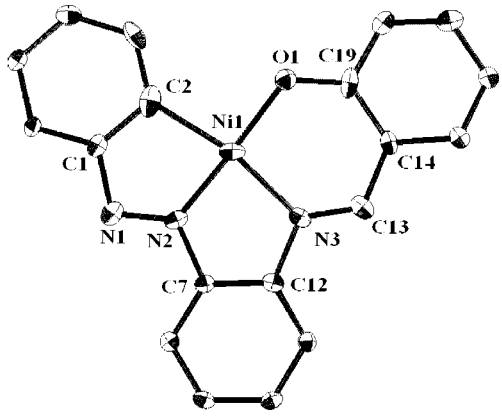


Figure 2. Perspective view (30% probability ellipsoids) of the molecular structure of $(L^1_{sal})Ni$ with atom numbering scheme. The hydrogen atoms have been omitted for clarity.

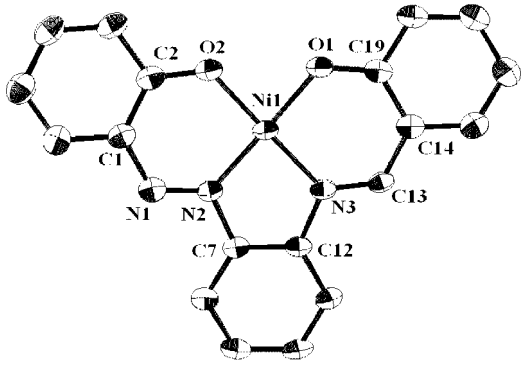


Figure 3. Perspective view (50% probability ellipsoids) of the molecular structure of $(OL^1_{sal})Ni$ with atom numbering scheme. The hydrogen atoms have been omitted for clarity.

Table 1. Selected bond lengths [Å] and angles [°] for compound $(L^1_{sal})Ni$.

| | | | |
|---|---|---|---|
| Ni1–O1 | 1.820(6) | N3–C12 | 1.426(11) |
| Ni1–N3 | 1.924(7) | N3–C13 | 1.291(12) |
| Ni1–N2 | 1.791(7) | C1–C2 | 1.374(13) |
| Ni1–C2 | 1.984(10) | C14–C19 | 1.449(13) |
| O1–C19 | 1.313(12) | C13–C14 | 1.411(13) |
| N1–N2 | 1.308(10) | C7–C12 | 1.405(12) |
| N1–C1 | 1.418(11) | | |
| N2–N1–C1 | 107.8(7) | Ni1–N3–C12 | 112.0(5) |
| O1–Ni1–N3 | 98.0(3) | N2–Ni1–C2 | 81.4(4) |
| O1–Ni1–C2 | 95.5(3) | N1–N2–C7 | 118.9(7) |
| N3–Ni1–C2 | 166.5(4) | N2–Ni1–N3 | 85.1(3) |

the crystal lattices exhibited that the planar molecules are held as *trans* pairs with Ni···Ni distances 3.199 and 3.136 Å in $(L^1_{sal})Ni$ and $(OL^1_{sal})Ni$, respectively. However, the crystal lattices feature slanted stacked arrangement of the *trans* pairs as shown in Figure 4 for $(L^1_{sal})Ni$. In contrast, the superposed molecules of Ni(salophen) are stacked infinitely in its crystal lattice,[24] unlike the Ni(azosalophen) analogue $(OL^1_{sal})Ni$.

Table 2. Selected bond lengths [Å] and angles [°] for compound $(OL^1_{sal})Ni$.

| | | | |
|---|---|---|---|
| Ni1–O1 | 1.8420(15) | N3–C12 | 1.421(3) |
| Ni1–N3 | 1.8570(16) | N3–C13 | 1.299(2) |
| Ni1–N2 | 1.8365(17) | C1–C2 | 1.432(3) |
| O1–C19 | 1.304(2) | C14–C19 | 1.424(3) |
| N1–N2 | 1.285(2) | C13–C14 | 1.410(3) |
| N1–C1 | 1.378(3) | C7–C12 | 1.393(3) |
| O2–C2 | 1.296(2) | Ni1–O2 | 1.8311(14) |
| N2–N1–C1 | 120.68(17) | Ni1–N3–C12 | 113.10(12) |
| O1–Ni1–N3 | 95.34(7) | N2–Ni1–O2 | 94.48(7) |
| O1–Ni1–O2 | 84.02(6) | N1–N2–C7 | 116.06(16) |
| N3–Ni1–O2 | 179.35(7) | N2–Ni1–N3 | 86.16(7) |
| Ni1–O2–C2 | 125.64(13) | | |

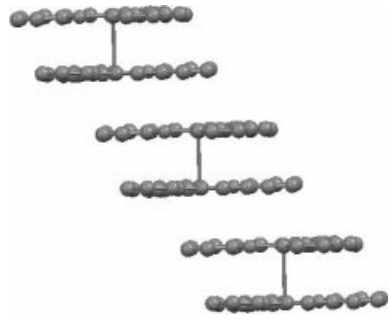

Figure 4. Partial packing of $(L^1_{sal})Ni$ showing the stairlike arrangement of planar molecules. The line between a pair indicates the weak Ni···Ni interaction at a distance of 3.199 Å.

## Electrochemistry

The cyclic voltammograms (Figure 5) of $(OL_{sal})Ni$ complexes display a reversible reductive response near –1.06 V vs. SCE in acetonitrile solution. This reductive response has been assigned to the $Ni^{II}/Ni^{I}$ couple according to Equation (1).

$$[(OL_{sal})Ni^{II}] + e^- \rightleftharpoons [(OL_{sal})Ni^{I}]^-$$

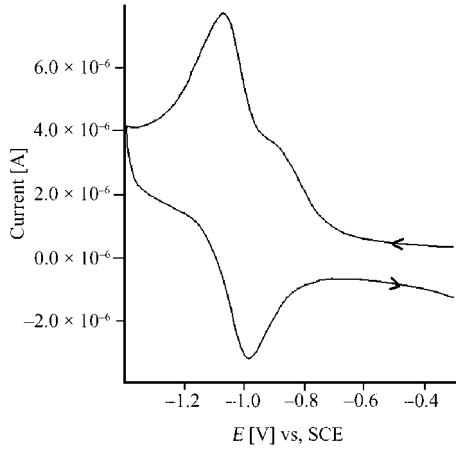


Figure 5. Cyclic voltammogram of $(OL^1_{sal})Ni$ in $CH_3CN$ and 0.1 M TEAP.

 © 2007 Wiley-VCH Verlag GmbH & Co. KGaA, Weinheim 

Similar reversible reduction for the [$Ni^{II}$(salen)] complex was reported to occur at –1.77 V vs. Ag/AgCl, and electrogenerated [Ni(salen)]$^-$ was demonstrated to be useful for the purpose of carrying out organic reactions.[25] Therefore, new electrogenerated [($OL_{sal}$)Ni]$^-$ may be active in a similar fashion as in the case of [Ni(salen)]$^-$.

## Conclusions

Unprecedented metalloazosalophen analogues of metallosalophens were prepared by way of oxygen insertion into the Ni–C bond of the precursor complex ($L_{sal}$)Ni. This facile Ni–C bond formation followed by oxygen insertion induced by peroxo reagents is a valuable report in terms of stoichiometric and catalytic oxo-functionalization of organic substrates. In addition to the synthesis of target metalloazosalophens, a synthetic procedure for the preparation of the regiospecifically hydroxylated derivative 2-(2-aminophenylazo)phenol, $H_2L^1OH$, has emerged to enhance the scope of further studies in this area. Although the O insertion into a Ni–C bond with $N_2O$[10a,10b] or $O_2$ (dioxygen)[10d] was documented previously, the use of peroxo reagents (especially $H_2O_2$) for O insertion into a Ni–C bond are described for the first time in this report. This information may provide important clues towards the design of appropriate organic substrates that are prone to form Ni–C σ bonds for oxygen insertion. The re-combination of $H_2L^1OH$ ($H_2LOH$, in general) with several other *ortho*-hydroxy aryl aldehydes are expected to afford a wide range of free azosalophen ligands. The metalloazosalophens derived from there may be useful for obtaining models of potential catalysts.

## Experimental Section

**Materials:** The solvents used in the reactions were of reagent grade obtained from E. Merck, Kolkata, India and were purified and dried by reported procedures.[26] Nickel acetate, salicylaldehyde, $HClO_4$, and $H_2O_2$ (6% in aqueous solution) were purchased from E. Merck, Kolkata, India. *m*CPBA (≈70%) and TBHP (≈70% in aqueous solution) were obtained from Aldrich, USA and were used as received (the activity of *m*CPBA was determined iodometrically before use). Silica gel G with binder was used for thin layer chromatography. 2-(Arylazo)aniline ligands were prepared according to the procedure described earlier.[23]

**Physical Measurements:** UV/Vis spectra were recorded with a Shimadzu UV-2401 PC spectrophotometer. IR spectra were obtained with a Perkin–Elmer L120–00A FTIR spectrophotometer (4000–225 $cm^{-1}$) using KBr pellets. Elemental analyses (C, H, N) were performed with a Perkin–Elmer 240C elemental analyzer. NMR spectra were recorded with Bruker Avance RPX 500 MHz and Bruker Avance DPX 300 spectrometers in $CDCl_3$ using TMS as the internal standard. Electrochemical measurements were made under dinitrogen using a PAR model VERSASTAT-II potentiostat. A glassy-carbon working electrode, platinum-wire auxiliary electrode, and standard saturated calomel electrode (SCE) were used in a three-electrode configuration. Tetraethyl perchlorate (0.1 M) was used as supporting electrolyte. All electrochemical data were collected at 298 K and are uncorrected for junction potentials. ESI mass spectra were recorded with a micromass Q-TOF mass spectrometer (serial no. YA 263).

**Syntheses of Ligands, $H_2L_{sal}$ (1)**

The three ligands $H_2L^1_{sal}$, $H_2L^2_{sal}$, and $H_2L^3_{sal}$ were prepared by a similar procedure. The detailed procedure for the preparation of $H_2L^1_{sal}$ is given.

***N*-[2-(Phenylazo)phenyl]salicylideneamine, $H_2L^1_{sal}$ (1a):** To a solution of 2-(phenylazo)aniline, $H_2L^1$, (100 mg, 0.50 mmol) in diethyl ether (40 mL) was added a little excess of salicylaldehyde (67 mg, 0.55 mmol). The resulting mixture was then heated to reflux for 8 h. The solvent was then evaporated in vacuo for 2 h to obtain the partially solid mass after removal of excess salicylaldehyde. It was further kept in a vacuum desiccator for 24 h to obtain the solid product of $H_2L_{sal}$. Isolated yield: 145 mg (95%). M.p.: 96 °C. $C_{19}H_{15}N_3O$ (301): calcd. C 75.74, H 4.98, N 13.95; found C 75.90, H 4.75, N 13.85. IR (KBr): $\tilde{\nu}$ = 1614 (C=N), 1450 (N=N) $cm^{-1}$. $^1H$ NMR ($CDCl_3$): $\delta$ = 6.91 (t, 1 H), 7.06 (d, 1 H), 7.33 (t, 1 H), 7.37 (d, 3 H), 7.46 (d, 1 H), 7.48–7.52 (m, 3 H), 7.78 (dd, 1 H), 7.92–7.95 (m, 2 H), 8.61 (s, 1 H), 13.59 (s, 1 H, OH) ppm. UV/Vis ($CH_2Cl_2$): $\lambda_{max}$ ($\varepsilon$, $M^{-1}cm^{-1}$) = 316 (18890), 232 (18750) nm.

***N*-[2-(*p*-Tolylazo)phenyl]salicylideneamine, $H_2L^2_{sal}$ (1b):** Isolated yield: 141 mg (95%). M.p.: 80 °C. $C_{20}H_{17}N_3O$ (315.37): calcd. C 76.19, H 5.39, N 13.33; found C 76.00, H 5.50, N 13.25. IR (KBr): $\tilde{\nu}$ = 1615 (C=N), 1452 (N=N) $cm^{-1}$. $^1H$ NMR ($CDCl_3$): $\delta$ = 2.42 (s, 3 H, *p*-$CH_3$), 6.93 (t, 1 H), 7.06 (d, 1 H), 7.31 (d, 2 H), 7.36 (t, 1 H), 7.46 (d, 1 H), 7.38–7.40 (m, 3 H), 7.51 (t, 1 H), 7.78 (d, 1 H), 7.85 (d, 2 H), 8.63 (s, 1 H), 13.59 (s, 1 H, OH) ppm. UV/Vis ($CH_2Cl_2$): $\lambda_{max}$ ($\varepsilon$, $M^{-1}cm^{-1}$) = 325 (26570), 233 (27114) nm.

***N*-[2-(*p*-Chlorophenylazo)phenyl]salicylideneamine, $H_2L^3_{sal}$ (1c):** Isolated yield: 137 mg (95%). M.p.: 92 °C. $C_{19}H_{14}ClN_3O$ (335.79): calcd. C 67.95, H 4.17, N 12.51; found C 67.80, H 4.15, N 13.90. IR (KBr): $\tilde{\nu}$ = 1617 (C=N), 1452 (N=N) $cm^{-1}$. $^1H$ NMR ($CDCl_3$): $\delta$ = 6.94 (t, 1 H), 7.07 (d, 1 H), 7.35 (t, 1 H), 7.40–7.42 (m, 3 H), 7.49 (d, 2 H), 7.57 (t, 1 H), 7.79 (d, 1 H), 7.90 (d, 2 H), 8.65 (s, 1 H), 13.58 (s, 1 H, OH) ppm. UV/Vis ($CH_2Cl_2$): $\lambda_{max}$ ($\varepsilon$, $M^{-1}cm^{-1}$) = 322 (24980), 233 (22250) nm.

**Syntheses of Complexes, ($L_{sal}$)Ni (5)**

All three complexes ($L^1_{sal}$)Ni, ($L^2_{sal}$)Ni, and ($L^3_{sal}$)Ni were prepared by a similar procedure. The detailed procedure for the preparation of ($L^1_{sal}$)Ni is given.

**($L^1_{sal}$)Ni (5a):** To $H_2L^1_{sal}$ (120 mg, 0.40 mmol) dissolved in methanol (40 mL) was added $Ni(OAc)_2{\cdot}4H_2O$ (100 mg, 0.40 mmol). The mixture was then heated to reflux for 12 h to obtain a green precipitate of ($L^1_{sal}$)Ni. The solid product was then filtered and washed with water and a little ethanol. The volume of the filtrate was reduced to ca. 20 mL and kept in a beaker covered with a watch glass. After 12 h a further crop of product was collected by filtration. All the product was taken together and recrystallized from dichloromethane/petroleum ether to obtain pure ($L^1_{sal}$)Ni. Yield: 99.82 mg (70%). $C_{19}H_{13}NiN_3O$ (358.04): calcd. C 63.74, H 3.63, N 11.74; found C 63.70, H 3.65, N 11.80. IR (KBr): $\tilde{\nu}$ = 1605 (C=N), 1389 (N=N) $cm^{-1}$. $^1H$ NMR ($CDCl_3$): $\delta$ = 6.57 (t, 1 H), 6.98 (d, 1 H), 7.12–7.14 (m, 1 H), 7.23–7.27 (m, 2 H), 7.39–7.43 (m, 3 H), 7.56 (d, 1 H), 7.67 (d, 1 H), 8.57 (s, 1 H) ppm. UV/Vis ($CH_2Cl_2$): $\lambda_{max}$ ($\varepsilon$, $M^{-1}cm^{-1}$) = 630 (1740), 460 (10867), 371 (19378), 341(15800), 315 (14820), 242 (35480) nm. ESI-MS: *m*/*z* = 358.

**($L^2_{sal}$)Ni (5b):** This complex was prepared by following a similar procedure as that described for ($L^1_{sal}$)Ni, using ligand $H_2L^2_{sal}$ in place of $H_2L^1_{sal}$. Yield: 89.91 mg (60%). $C_{20}H_{15}NiN_3O$ (372.07): calcd. C 64.59, H 4.03, N 11.29; found C 64.67, H 4.00, N 11.35.

 © 2007 Wiley-VCH Verlag GmbH & Co. KGaA, Weinheim 

IR (KBr): $\tilde{\nu}$ = 1605 (C=N), 1374 (N=N) $cm^{-1}$. $^1H$ NMR ($CDCl_3$): $\delta$ = 2.31 (s, 3 H, *p*-$CH_3$), 6.57 (t, 1 H), 6.90 (d, 1 H), 7.02 (d, 1 H), 7.14–7.19 (m, 3 H), 7.24–7.27 (m, 1 H), 7.38 (t, 1 H), 7.56 (d, 2 H), 7.65 (d, 1 H), 8.57 (s, 1 H) ppm. UV/Vis ($CH_2Cl_2$): $\lambda_{max}$ ($\varepsilon$, $M^{-1}cm^{-1}$) = 631 (2829), 460 (19244), 378 (30420), 340 (24340), 319 (20690), 243 (58351) nm.

**($L^3_{sal}$)Ni (5c):** This complex was prepared by following a similar procedure as that described for ($L^1_{sal}$)Ni, using ligand $H_2L^3_{sal}$ in place of $H_2L^1_{sal}$. Yield: 97.84 mg (62%). $C_{19}H_{12}ClNiN_3O$ (392.49): calcd. C 58.13, H 3.05, N 10.70; found C 58.18, H 3.00, N 10.75. IR (KBr): $\tilde{\nu}$ = 1606 (C=N), 1372 (N=N) $cm^{-1}$. $^1H$ NMR ($CDCl_3$): $\delta$ = 6.55 (t, 1 H), 6.93 (d, 1 H), 7.05 (d, 1 H), 7.12 (d, 1 H), 7.15 (t, 1 H), 7.22–7.29 (m, 2 H), 7.43 (t, 1 H), 7.51 (d, 2 H), 7.62 (d, 1 H), 8.43 (s, 1 H) ppm. UV/Vis ($CH_2Cl_2$): $\lambda_{max}$ ($\varepsilon$, $M^{-1}cm^{-1}$) = 634 (1990), 455 (13413), 372 (24432), 338 (18393), 314 (17445), 243 (44052) nm.

**Syntheses of Complexes, ($OL_{sal}$)Ni (6)**

All complexes were prepared by a similar procedure. The details for the preparation of ($OL^1_{sal}$)Ni are given.

**($OL^1_{sal}$)Ni (6a):** A solution of *m*CPBA (143 mg, 0.824 mmol) in dichloromethane (5 mL) was added dropwise to a stirred solution of ($L^1_{sal}$)Ni (100 mg, 0.279 mmol) in dichloromethane (25 mL). Immediately the color of the solution began to change from deep green to olive green. The stirring was continued for 10 min. Evaporation of the solvent in vacuo afforded a greenish solid mass. The solid mass was washed with diethyl ether (3 × 5 mL). The product was then purified by preparative TLC using a benzene/acetonitrile (19:1) mixture as eluent. Upon evaporation of the solvent, the pure target complex ($OL^1_{sal}$)Ni was obtained. Isolated yield: 67.90 mg (65%). $C_{19}H_{13}NiN_3O_2$ (374.04): calcd. C 61.01, H 3.47, N 11.23; found C 60.95, H 3.43, N 11.20. IR (KBr): $\tilde{\nu}$ = 1614 (C=N), 1376 (N=N) $cm^{-1}$. $^1H$ NMR ($CDCl_3$): $\delta$ = 6.68 (t, 1 H), 6.84 (t, 1 H), 7.15 (d, 1 H), 7.24–7.27 (m, 3 H), 7.33–7.40 (m, 4 H), 7.76–7.72 (m, 2 H), 8.17 (d, 1 H), 8.40 (s, 1 H) ppm. UV/Vis ($CH_2Cl_2$): $\lambda_{max}$ ($\varepsilon$, $M^{-1}cm^{-1}$) = 640 (3846), 442 (15468), 399 (14715), 356 (19842), 340 (23520), 255 (38277) nm. ESI-MS: *m*/*z* = 374.

**($OL^2_{sal}$)Ni (6b):** Complex ($OL^2_{sal}$)Ni was prepared using ($L^2_{sal}$)Ni in place of ($L^1_{sal}$)Ni. Isolated yield: 68 mg (65%). $C_{20}H_{15}NiN_3O_2$ (388.07): calcd. C 61.90, H 3.86, N 11.00; found C 61.46, H 3.92, N 10.91. IR (KBr): $\tilde{\nu}$ = 1611 (C=N), 1376 (N=N) $cm^{-1}$. $^1H$ NMR ($CDCl_3$): $\delta$ = 2.28 (s, 3 H), 6.67 (t, 2 H), 7.07 (s, 1 H), 7.14 (d, 1 H), 7.37 (t, 4 H), 7.62 (d, 1 H), 7.72 (d, 1 H), 8.17 (d, 1 H), 8.40 (s, 1 H) ppm. UV/Vis ($CH_2Cl_2$): $\lambda_{max}$ ($\varepsilon$, $M^{-1}cm^{-1}$) = 631 (3101), 441 (12902), 402 (12603), 356 (15848), 340 (17860), 261 (29455) nm.

**($OL^3_{sal}$)Ni (6c):** Complex ($OL^3_{sal}$)Ni was prepared using ($L^3_{sal}$)Ni in place of ($L^1_{sal}$)Ni. Isolated yield: 63 mg (60%). $C_{19}H_{12}ClNiN_3O_2$ (408.49): calcd. C 58.13, H 2.93, N 10.28; found C 57.91, H 2.82, N 10.32. IR (KBr): $\tilde{\nu}$ = 1611 (C=N), 1374 (N=N) $cm^{-1}$. $^1H$ NMR ($CDCl_3$): $\delta$ = 6.70 (t, 1 H), 6.83 (d, 2 H), 7.12 (d, 2 H), 7.33–7.42 (m, 4 H), 7.73 (t, 2 H), 8.15 (d, 1 H), 8.38 (s, 1 H) ppm. UV/Vis ($CH_2Cl_2$): $\lambda_{max}$ ($\varepsilon$, $M^{-1}cm^{-1}$) = 638 (4209), 441 (7795), 350 (9110), 339 (10340), 2276 (11872), 248 (14061) nm.

**Reaction of ($L_{sal}$)Ni with TBHP:** The reaction of ($L^1_{sal}$)Ni is given in detail. To a stirred solution of ($L^1_{sal}$)Ni (50 mg, 0.140 mmol) in dichloromethane or *tert*-butanol (25 mL) was added dropwise TBHP (0.30 mL, 2.76 mmol). Immediately the color of the solution began to turn from deep green to olive green. The stirring was continued for 30 min. Evaporation of the solvent in vacuo afforded a greenish solid mass. The solid mass was washed with water and diethyl ether. The product was then purified by preparative TLC using a benzene/acetonitrile (19:1) mixture as eluent. Upon evaporation of the solvent, the pure target complex ($OL^1_{sal}$)Ni was obtained. Isolated yield: 34.14 mg (65%).

**Reaction of ($L_{sal}$)Ni with $H_2O_2$:** The reaction of ($L^1_{sal}$)Ni is given in detail. To a stirred solution of ($L^1_{sal}$)Ni (30 mg, 0.083 mmol) in dichloromethane (15 mL) was added dropwise 6% $H_2O_2$ (10 mL). The color of the organic layer began to turn from deep green to olive green after 20 min. The stirring was continued for 1.5 h. Evaporation of the organic solvent, after separation from the aqueous layer, in vacuo afforded a greenish solid mass. The solid mass was washed with water. The product was then purified by preparative TLC using a benzene/acetonitrile (19:1) mixture as eluent. Upon evaporation of the solvent, the pure target complex ($OL^1_{sal}$)Ni was obtained. Isolated yield: 20.5 mg (65%).

**Preparation of 2-(2-Aminophenylazo)phenol, $H_2L^1OH$, from ($OL^1_{sal}$)Ni:** To an acetonitrile solution (20 mL) of ($OL^1_{sal}$)Ni (200 mg, 0.534 mmol) was added dropwise 0.1 M $HClO_4$ (5 mL) with continuous stirring. The color of the solution changed from olive green to yellow. Evaporation of the solvent in vacuo afforded a yellow solid mass. The solid mass was washed (3×) with water and extracted with dichloromethane and purified by preparative TLC using petroleum benzene as eluent. Upon evaporation of the solvent, the pure target compound $H_2L^1OH$ was obtained. Yield: 56.5 mg (50%). $C_{12}H_{11}N_3O$ (213.24): calcd. C 67.60, H 5.16, N 19.71; found C 67.65, H 5.06, N 19.65. IR (KBr): $\tilde{\nu}$ = 3407 ($NH_2$), 3284 (OH), 1468 (N=N) $cm^{-1}$. $^1H$ NMR ($CDCl_3$): $\delta$ = 6.19 (s, $NH_2$), 6.75 (d, 1 H), 6.83 (t, 1 H), 7.04–6.99 (m, 2 H), 7.20 (t, 1 H), 7.29 (t, 1 H), 7.67 (d, 1 H), 7.76 (d, 1 H), 12.84 (s, OH) ppm. UV/Vis ($CH_2Cl_2$): $\lambda_{max}$ ($\varepsilon$, $M^{-1}cm^{-1}$) = 450 (10566), 318 (13124), 230 (10646) nm.

**X-ray Crystallography:** Suitable X-ray-quality crystals of **5a** (0.08 × 0.23 × 0.25) and **6a** (0.13 × 0.13 × 0.20) for X-ray studies were grown by slow evaporation of a dichloromethane solution of **5a** and a dichloromethane/acetonitrile solution of **6a**. Data were collected with a Bruker SMART CCD diffractometer using a Mo-$K_\alpha$ monochromator ($\lambda$ = 0.71043). Structure solutions were performed using the SHELX-97 (PC version) program. The full-matrix least-square and anisotropic refinements were performed on all the atoms. Hydrogen atoms were included at calculated positions.

Table 3. Crystal data for complexes ($L^1_{sal}$)Ni and ($OL^1_{sal}$)Ni.

| Parameter | ($L^1_{sal}$)Ni | ($OL^1_{sal}$)Ni |
|---|---|---|
| Formula | $C_{19}H_{13}N_3ONi$ | $C_{19}H_{13}N_3NiO_2$ |
| *M* | 358.01 | 374.01 |
| Crystal system | monoclinic | monoclinic |
| Space group | $P2_1/n$ | $P2_1/n$ |
| *a* [Å] | 10.2834(4) | 10.8790(2) |
| *b* [Å] | 8.1049(4) | 7.8960(2) |
| *c* [Å] | 17.5313(7) | 18.0520(5) |
| $\alpha$ [°] | 90 | 90 |
| $\beta$ [°] | 98.465(2) | 103.4430(10) |
| $\gamma$ [°] | 90 | 90 |
| Wavelength [Å] | 0.71073 | 0.71073 |
| *V* [Å$^3$] | 1445.24(11) | 1508.19(6) |
| Cryst. dimens. [mm] | 0.08 × 0.23 × 0.25 | 0.13 × 0.13 × 0.20 |
| *Z* | 4 | 4 |
| *T* [K] | 250 | 150 |
| $D_{calcd.}$ [g cm$^{-3}$] | 1.645 | 1.647 |
| $\mu$ [mm$^{-1}$] | 1.353 | 1.305 |
| *R* (all data) | 0.0873 | 0.0303 |
| $wR_2$ [$I > 2\sigma(I)$] | 0.1901 | 0.0767 |
| $R_1$[a]/Gof | 1.05 | 1.015 |

[a] $R = \Sigma||F_o| - |F_c||/\Sigma|F_o|$.

 © 2007 Wiley-VCH Verlag GmbH & Co. KGaA, Weinheim 

The data collection parameters and relevant crystal data are collected in Table 3. CCDC-602075 and -617793 for ($L^1_{sal}$)Ni and ($OL^1_{sal}$)Ni complexes, respectively, contain the supplementary crystallographic data for this paper. These data can be obtained free of charge from The Cambridge Crystallographic Data Centre via www.ccdc.cam.ac.uk/data_request/cif.

**Supporting Information** (see footnote on the first page of this article): Figures S1–S7 (UV/Vis spectra), Figures S8–S17 (IR spectra), Figures S18–S28 ($^1$H NMR spectra), Figures S29 and S30 (cyclic voltammograms), and Figures S31 and S32 (ESI-MS spectra).

## Acknowledgments

We are thankful to the DST (New Delhi) for funding and a fellowship to J. L. P. under DST-SERC project (No. SR/S1/IC-09/2003). The necessary laboratory and infrastructural facility were provided by the Dept. of Chemistry, University of Kalyani. The support of DST under FIST program to the Department of Chemistry, University of Kalyani is acknowledged. We acknowledge Prof. Jui-Hsien Huang, National Changhua University of Education, Changhua, Taiwan for X-ray studies of ($L^1_{sal}$)Ni.

[1] a) H. Zhou, S. T. Nguyen, *Inorg. Chem.* **2004**, *43*, 4315; b) E. F. DiMauro, A. Mamai, M. C. Kozlowski, *Organometallics* **2003**, *22*, 850; c) K. J. Miller, J. H. Baag, M. M. Abu-Omar, *Inorg. Chem.* **1999**, *38*, 4510.

[2] a) E. M. McGarrile, D. G. Gilheany, *Chem. Rev.* **2005**, *105*, 1563; b) K. P. Bryliakov, E. P. Talsi, *Inorg. Chem.* **2003**, *42*, 7258.

[3] a) M. Costas, M. P. Mehn, M. P. Jensen Jr, L. Que, *Chem. Rev.* **2004**, *104*, 939; b) X. Zhou, J. Shearer, S. E. Rotika, *J. Am. Chem. Soc.* **2000**, *122*, 9046; c) J. E. Reed, A. A. Arnal, S. Neidle, R. Vilar, *J. Am. Chem. Soc.* **2006**, *128*, 5992.

[4] a) S. Karmakar, S. B. Choudhury, S. Ganguly, A. Chakravorty, *J. Chem. Soc. Dalton Trans.* **1997**, 585 and references cited therein; b) A. H. Velders, H. Kooijman, A. L. Spek, J. G. Haasnoot, D. de Vos, J. Reedijk, *Inorg. Chem.* **2000**, *39*, 2966; c) A. C. G. Hotze, E. P. L. van der Geer, S. E. Caspers, H. Kooijman, A. L. Spek, J. G. Haasnoot, J. Reedijk, *Inorg. Chem.* **2004**, *43*, 4935; d) T. Yitaka, M. Kurihara, K. Kubo, H. Nishihara, *Inorg. Chem.* **2000**, *39*, 3438; e) K. K. Kamar, S. Das, C.-H. Hung, A. Castineiras, M. D. Kuzmin, C. Rillo, J. Bartolome, S. Goswami, *Inorg. Chem.* **2003**, *42*, 5367; f) C. Das, S.-M. Peng, G.-H. Lee, S. Goswami, *New J. Chem.* **2002**, *26*, 222; g) T. K. Misra, T. K. Das, C. Sinha, P. Ghosh, C. K. Pal, *Inorg. Chem.* **1998**, *37*, 1672.

[5] J. L. Zhu, N. P. Grigoriadis, J. P. Lee, J. A. Porco, *J. Am. Chem. Soc.* **2005**, *127*, 9342.

[6] a) R. A. Johnson, K. B. Sharpless in *Catalytic Asymmetric Synthesis* (Ed.: I. Ojima), VCH, New York, **1993**, ch. 4.1; b) E. N. Jacobsen in *Catalytic Asymmetric Synthesis* (Ed.: I. Ojima), VCH, New York, **1993**, ch. 4.2; c) T. Katsuki, *Adv. Synth. Catal.* **2002**, *344*, 131; d) T. Katsuki, *Coord. Chem. Rev.* **1995**, *140*, 189; e) T. Katsuki, *J. Mol. Catal. A* **1996**, *113*, 87; f) C. T. Dalton, K. M. Ryan, V. M. Wall, C. Bousquet, D. G. Gilheany, *Top. Catal.* **1998**, *5*, 75; g) D. R. Kelly, S. M. Roberts, *Biopolymers* **2006**, *84*, 74; h) L. Canalai, D. C. Sherrington, *Chem. Soc. Rev.* **1999**, *28*, 85.

[7] a) M. Lersch, M. Tilset, *Chem. Rev.* **2005**, *105*, 2471 and references cited therein; b) J. Dupont, C. S. Consorti, J. Spencer, *Chem. Rev.* **2005**, *105*, 2527 and references cited therein; c) P. Bandyopadhyay, D. Bandyopadhyay, A. Chakravorty, F. A. Cotton, L. R. Fakvello, S. Han, *J. Am. Chem. Soc.* **1983**, *105*, 6327; d) S. Chattopadhyay, C. Sinha, P. Basu, A. Chakravorty, *Organometallics* **1991**, *10*, 1135; e) S. Chattopadhyay, C. Sinha, P. Basu, A. Chakravorty, *J. Organomet. Chem.* **1991**, *414*, 421; f) J. Pratihar, N. Maiti, P. Pattanayak, S. Chattopadhyay, *Polyhedron* **2005**, *24*, 1953.

[8] a) I. Omae, *Chem. Rev.* **1979**, *79*, 287; b) J. P. Kleiman, M. Dubeck, *J. Am. Chem. Soc.* **1963**, *85*, 1544; c) M. Ghedini, D. Pucci, A. Crispini, G. Barberio, *Organometallics* **1999**, *18*, 2116; d) T. Kawamoto, Y. Kushi, *Bull. Chem. Soc. Jpn.* **2004**, *77*, 289; e) G. K. Anderson, R. J. Cross, K. W. Muir, L. M. Muir, *J. Organomet. Chem.* **1989**, *362*, 225.

[9] A. C. Cope, R. W. Siekman, *J. Am. Chem. Soc.* **1965**, *87*, 3272.

[10] a) K. Koo, G. L. Hillhouse, *Organometallics* **1998**, *17*, 2924; b) P. T. Matsunaga, G. L. Hillhouse, *J. Am. Chem. Soc.* **1993**, *115*, 2075; c) P. T. Matsunaga, J. C. Mavropoulos, G. L. Hillhouse, *Polyhedron* **1995**, *14*, 175; d) M. A. Bennett, M. Glewis, D. C. R. Hockless, E. Wenger, *J. Chem. Soc. Dalton Trans.* **1997**, 3105.

[11] J. Cámpora, P. Palma, E. Carmona, *Coord. Chem. Rev.* **1999**, *193–195*, 207.

[12] I. W. C. E. Arends, *Angew. Chem. Int. Ed.* **2006**, *45*, 6250.

[13] I. W. C. E. Arends, R. A. Sheldon, *Top. Catal.* **2002**, *19*, 133.

[14] a) F. Zaera, J. M. Guevermont, N. R. Gleason, *J. Phys. Chem. B* **2001**, *105*, 2257; b) N. Gleason, J. Goevermont, F. Zaera, *J. Phys. Chem. B* **2003**, *107*, 11133 and references cited therein.

[15] The reaction M–C → M–OC has been termed metaloxylation.[7c,7d]

[16] The $^1$H NMR spectrum of crude ($OL^1_{sa\ l}$)Ni is available as Supporting Information (Figure S24).

[17] P. L. Alsters, H. T. Teunissen, J. Boersma, A. L. Spek, G. van Koten, *Organometallics* **1993**, *12*, 4691.

[18] a) J. F. Kinneary, J. S. Albert, C. J. Burrows, *J. Am. Chem. Soc.* **1988**, *110*, 6124; b) J. D. Koola, J. K. Kochi, *Inorg. Chem.* **1987**, *26*, 908.

[19] R. H. Holm, *Chem. Rev.* **1987**, *87*, 1401.

[20] M. Kujime, S. Hikichi, M. Akita, *Dalton Trans.* **2003**, 3506.

[21] M. Fieser, L. F. Fieser, *Reagents for Organic Synthesis*, Wiley-Interscience,New York, **1971**, vol. 3.

[22] a) T. Giaser, M. Heidemeier, T. Lügger, *Dalton Trans.* **2003**, 2381; b) B. Bosnich, *J. Am. Chem. Soc.* **1968**, *90*, 627.

[23] N. Maiti, S. Pal, S. Chattopadhyay, *Inorg. Chem.* **2001**, *40*, 2204.

[24] J. Wang, F. L. Bei, X. Y. Xu, X. J. Yang, X. Wang, *J. Chem. Crystallogr.* **2003**, *33*, 845.

[25] E. Dunach, A. P. Esteves, L. F. M. Leite, M. A. Lemos, M. J. Medeiros, S. Olivero, *Port. Electrochim. Acta* **2003**, *21*, 191.

[26] a) P. Chattopadhyay, M. K. Nayak, S. P. Bhattacharya, C. Sinha, *Polyhedron* **1997**, *16*, 1291; b) F. Basuli, P. Chattopadhyay, C. Sinha, *Polyhedron* **1996**, *15*, 2439.

Received: February 1, 2007
Published Online: June 27, 2007

 © 2007 Wiley-VCH Verlag GmbH & Co. KGaA, Weinheim 

DOI: 10.1002/ejic.200700350

# Synthesis, Structure, and Reactivity of Diazoketiminato Complexes of Platinum(II) and Palladium(II): Cytotoxic Properties of a Platinum Complex

**Jahar Lal Pratihar,[a] Biswaranjan Shee,[a] Poulami Pattanayak,[a] Debprasad Patra,[a] Arindam Bhattacharyya,[b] Vedavati G. Puranik,[c] C. H. Hung,[d] and Surajit Chattopadhyay*[a]**

**Keywords:** Chelating ligands / Platinum / Palladium / Redox chemistry / Bioinorganic chemistry

Reaction of the 2-(arylazo)anilines Ar-N=N-$C_6H_4NH_2$ [$HL^nNH_2$; Ar = $C_6H_5$ ($HL^1$), *p*-$CH_3C_6H_4$ ($HL^2$), *p*-$ClC_6H_4$ ($HL^3$)] with $K_2PtCl_4$ in dmso affords the new $Pt^{II}$ azoimine complexes [($HL^n$NH)Pt(dmso)Cl] where the chloride and dmso ligands are mutually *cis*. In contrast, treatment of $Na_2PdCl_4$ with $HL^nNH_2$ in dmso gives the chloro-bridged palladium dimer [{($HL^n$NH)$PdCl$}$_2$] as the major product along with [($HL^n$NH)$_2$Pd] as the minor product. Further, the reaction of $HL^n$NH$CH_2$Ph with $K_2PtCl_4$ in dmso also gives [($HL^n$NH)Pt(dmso)Cl] whereas $Na_2PdCl_4$ affords the ortho-palladated complexes [($L^n$NH$CH_2$Ph)PdCl]. This means that the N–C($CH_2$Ph) bond is selectively cleaved by $K_2PtCl_4$. The reaction of [($HL^n$NH)Pt(dmso)Cl] with acetylacetone (acacH) gives the heteroleptic complex [($HL^n$NH)Pt(acac)]. [($HL^n$NH)-Pt(dmso)Cl] and [($HL^n$NH)Pt(acac)] display a reversible reductive response at –1.20 and –1.46 V vs. SCE, respectively, in their cyclic voltammograms. The nature of the redox orbitals has been determined semi-empirically employing the EHMO method. The cytotoxicity of [($HL^1$NH)Pt(dmso)Cl] has been examined with HeLa cells and the sub-lethal dose (8 μM) determined by dose-dependence studies. The relative degree of apoptotic and necrotic cell death using a sub-lethal dose were measured by flow cytometry.

(© Wiley-VCH Verlag GmbH & Co. KGaA, 69451 Weinheim, Germany, 2007)

## Introduction

$Pt^{II}$ complexes have been known for a long time and their importance was enhanced with the discovery of cisplatin. Cisplatin and carboplatin are two widely used anticancer drugs although there are certain limitations in their therapeutic uses, therefore several appropriately designed models of $Pt^{II}$ complexes have been clinically tested in search of suitable alternatives.[1–9] One of the proposed models for $Pt^{II}$-based chemotherapeutic agents is [Pt(L)(dmso)Cl], where L is a bidentate anionic ligand and the anticipated labile ligands are dimethyl sulfoxide (dmso) and chloride.[10–13] These reports encouraged us to study the in vitro cytotoxic properties of our newly synthesized diazoketiminato complex [($HL^1$NH)Pt(dmso)Cl] in view of its importance as a potential model of anticancer agents.

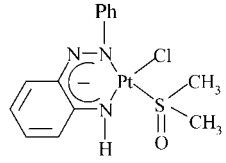


[($HL^1$NH)Pt(dmso)CL]

The work reported here stems from our interest in the coordination chemistry of platinum complexes incorporating bidentate (N,N), anionic, and delocalized diazoketimine ligands **1**. We have previously reported the bis-chelate complexes of $Pd^{II}$ and $Pt^{II}$ incorporating **1**,[14,15] and herein we report the reactions of $Na_2PdCl_4$ and $K_2PtCl_4$ with the ligand precursors Ar-N=N-$C_6H_4NH_2$ [$HL^nNH_2$; Ar = $C_6H_5$ ($HL^1$), *p*-$CH_3C_6H_4$ ($HL^2$), *p*-$ClC_6H_4$ ($HL^3$)] and $HL^n$NH$CH_2$Ph in dmso. Aspects related to N–C(alkyl) bond cleavage with $K_2PtCl_4$, the redox properties of the new platinum complexes formed, and a comparison of the reactivities of $Pt^{II}$ and $Pd^{II}$ substrates toward similar ligands are also described in this paper.

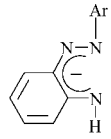


**1**

[a] Department of Chemistry, University of Kalyani, Kalyani 741235, India
E-mail: scha8@rediffmail.com
[b] Department of Environmental Science, University of Kalyani, Kalyani 741235, India
[c] Center for Materials Characterization, National Chemical Laboratory, Pune 411008, India
[d] National Changhua University of Education, Changhua 50058, Taiwan

Supporting information for this article is available on the WWW under http://www.eurjic.org or from the author.


© 2007 Wiley-VCH Verlag GmbH & Co. KGaA, Weinheim

Reaction of the 2-(arylazo)anilines $HL^nNH_2$ or their *N*-benzylated derivative $HL^nNHCH_2Ph$ with $K_2PtCl_4$ affords the electroactive complexes of the desired composition, namely [$(HL^nNH)Pt(dmso)Cl$]. Reaction of the same ligands with $Na_2PdCl_4$ was also performed to confirm that cleavage of the N–C(benzyl) bond only occurs with $K_2PtCl_4$. The reactions of [$(HL^nNH)Pt(dmso)Cl$] with the bidentate ligand acacH to give the new heteroleptic bis complexes of composition [$(HL^nNH)Pt(acac)$] show the feasibility of substituting the $Cl^-$ and dmso ligands in this complex. All new complexes have been characterized unequivocally and their structures confirmed by X-ray crystallography. The electron-transfer properties of the $Pt^{II}$ complexes have been examined electrochemically and the results rationalized by employing semi-empirical EHMO calculations. The dose dependence and nature of cell (HeLa) death (apoptotic or necrotic) have also been studied for [$Pt(HL^1NH)(dmso)Cl$].

## Results and Discussion

### Syntheses and Reactions

The reaction of $HL^nNH_2$ or $HL^nNHCH_2Ph$ with $K_2PtCl_4$ in warm dmso affords the pink complexes [$(HL^nNH)Pt(dmso)Cl$] in good yield (Scheme 1). Addition

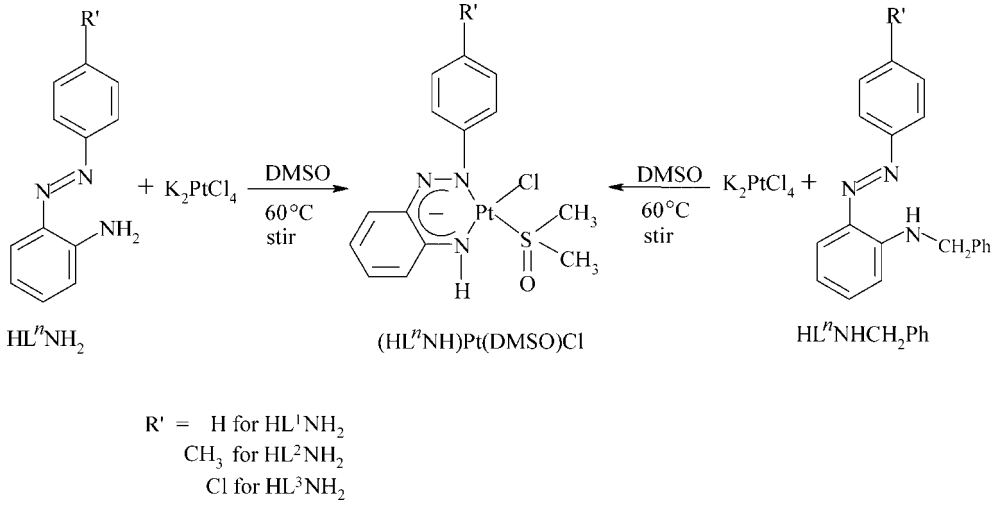


Scheme 1.

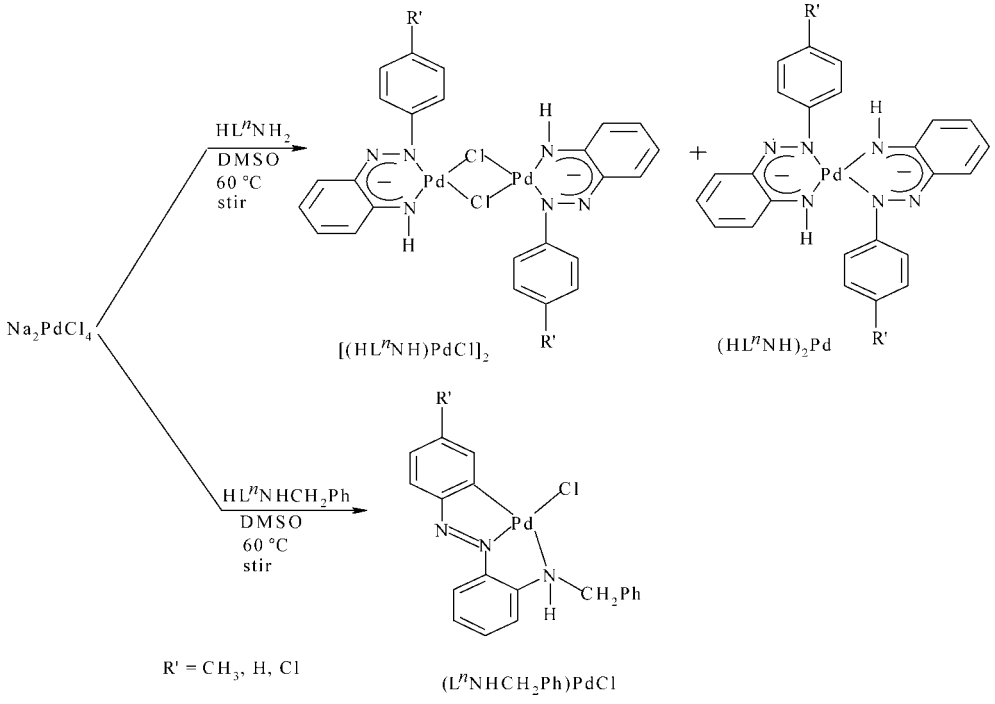


Scheme 2.

 © 2007 Wiley-VCH Verlag GmbH & Co. KGaA, Weinheim 

of $K_2PtCl_4$ to warm dmso is excepted to form the dmso-coordinated $Pt^{II}$ complex, which is likely to be the actual metal substrate that reacts with the ligands.

The formation of [(HL$^n$NH)Pt(dmso)Cl] prompted us to examine the reactions of the same ligands with $Na_2PdCl_4$ in warm dmso. The results of these reactions are summarized in Scheme 2.

The minor product [Pd(HL$^n$NH)$_2$] has been prepared in good yield previously,[14] while the major product, [{(HL$^n$NH)PdCl}$_2$], is isolated here for the first time. Its structure was confirmed by X-ray crystallography (see below). The orthopalladated complex [(L$^n$NHCH$_2$Ph)PdCl] was obtained, as expected,[16] upon treatment of HL$^n$NHCH$_2$Ph with $Na_2PdCl_4$, whereas the same reaction with $K_2PtCl_4$ gives [(HL$^n$NH)Pt(dmso)Cl] by cleavage of the N–C(benzyl) bond of HL$^n$NHCH$_2$Ph. Subtle difference in the properties of $Pt^{II}$ and $Pd^{II}$ are likely to be the origin of this mismatch in reactivity between $Na_2PdCl_4$ and $K_2PtCl_4$.

Reaction of [(HL$^n$NH)Pt(dmso)Cl] with the bidentate ligand acetylacetone (acacH) was performed in boiling methanol to give the blue neutral heteroleptic bis complex [(HL$^n$NH)Pt(acac)] (Scheme 3). Substitution of the mutually *cis* dmso and Cl$^-$ ligands of [(HL$^n$NH)Pt(dmso)Cl] by acetylacetonate indicates the possibility of coordination of this complex with the nucleoside bases of nucleic acids.

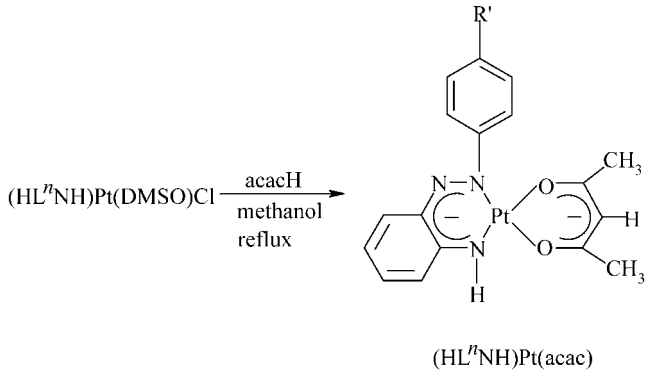


Scheme 3.

## Spectroscopic Characterization

The complexes [(HL$^n$NH)Pt(dmso)Cl] and [(HL$^n$NH)-Pt(acac)] dissolve in common organic solvents to give pink and blue solutions, respectively, consistent with the relative energies of absorptions in the visible region {approx. 560 nm for [(HL$^n$NH)Pt(dmso)Cl] and approx. 600 nm for [(HL$^n$NH)Pt(acac)]}. The positions of other higher energy absorption bands for all the complexes are alike with characteristic shifts. The relevant data are collected in Table 1 and representative spectra of [(HL$^1$NH)Pt(dmso)Cl] and [(HL$^1$NH)Pt(acac)] are shown in Figure 1.

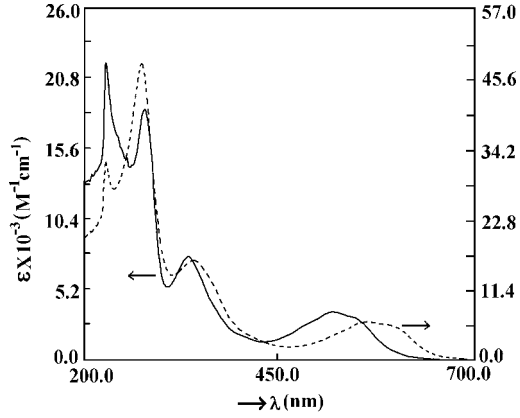


Figure 1. UV/Vis spectra of [(HL$^1$NH)Pt(dmso)Cl] (−) and [(HL$^1$NH)Pt(acac)] (---). The arrows indicate the scales of the corresponding spectrum.

The IR spectra of complexes [(HL$^n$NH)Pt(dmso)Cl] in solid KBr exhibit sharp $\nu_{N-H}$ absorptions in the range 3284–3291 cm$^{-1}$, thereby indicating the presence of one

Table 1. UV/Vis,[a] IR,[b] and cyclic voltammetric data for [(HL$^n$NH)Pt(dmso)Cl], [(HL$^n$NH)Pt(acac)], and [{(HL$^1$NH)PdCl}$_2$].

| Compound | $\lambda_{max}$ [nm] ($\varepsilon$ [M$^{-1}$ cm$^{-1}$]) | $\tilde{\nu}$ [cm$^{-1}$] | | | | | $E_{1/2}$ [V][c] ($\Delta E_p$ [mV]) |
|---|---|---|---|---|---|---|---|
| | | $\nu_{N-H}$ | $\nu_{C=N}$ | $\nu_{N=N}$ | $\nu_{S=O}$ | $\nu_{Pt-Cl}$ | |
| [(HL$^1$NH)Pt(dmso)Cl] | 555 (7300), 520 (8640)<br>330 (18400), 280 (44660) | 3284 | 1618 | 1341 | 1112 | 371 | –1.120 (80) |
| [(HL$^2$NH)Pt(dmso)Cl] | 560 (5180), 530 (5890)<br>340 (14500), 275(34600) | 3291 | 1615 | 1342 | 1118 | 374 | –1.246 (95) |
| [(HL$^3$NH)Pt(dmso)Cl] | 560 (11320), 530 (12270)<br>3400 (27350), 275 (71130) | 3289 | 1617 | 1342 | 1120 | 372 | –1.152 (95) |
| [(HL$^1$NH)Pt(acac)] | 600 (7430), 565 (6600)<br>340 (17150), 270 (51230) | 3330<br>3349 | 1615 | 1341 | – | – | –1.473 (110) |
| [(HL$^2$NH)Pt(acac)] | 600 (2800), 565 (3070)<br>350 (10800), 270 (25870) | 3321<br>3335 | 1616 | 1347 | – | – | –1.510 (115) |
| [(HL$^3$NH)Pt(acac)] | 600 (4800), 570 (5420)<br>345 (14120), 270 (37850) | 3320<br>3350 | 1617 | 1340 | – | – | –1.410 (100) |
| [{(HL$^1$NH)PdCl}$_2$] | 560 (5000), 525 (5150)<br>330 (17100) | 3338 | 1615 | 1333 | – | – | – |

[a] In dichloromethane. [b] In KBr disc. [c] vs. SCE in $CH_3CN$ as solvent; supporting electrolyte: $NBu_4ClO_4$.

 © 2007 Wiley-VCH Verlag GmbH & Co. KGaA, Weinheim 

amino proton. Surprisingly, the complexes [(HL$^n$NH)Pt(acac)] exhibit two overlapping $\nu_{N-H}$ absorptions in the range 3320–3350 cm$^{-1}$, which may be due to a site effect in the solid state.[17] The $\nu_{N=N}$ absorptions of both complexes are shifted to lower frequency (1340–1347 cm$^{-1}$) than in the free ligands HL$^n$NH$_2$ (approx. 1460 cm$^{-1}$).[14,15,18,19] The strong band observed at around 1617 cm$^{-1}$ which is absent in the free ligands can be assigned to the $\nu_{C=N}$ absorption.[14,15,18,19] The blue-shift of the $\nu_{S=O}$ absorption for complexes [(HL$^n$NH)Pt(dmso)Cl] (1112–1120 cm$^{-1}$) compared to free dmso (1050 cm$^{-1}$) indicates S-coordination. The $\nu_{Pt-Cl}$ absorption of [(HL$^n$NH)Pt(dmso)Cl] appears in the range 371–374 cm$^{-1}$. Relevant IR data are also collected in Table 1.

The $^1$H NMR spectra of complexes [(HL$^n$NH)Pt(dmso)Cl] display a resonance near $\delta$ = 3.5 ppm for coordinated dmso while the aromatic protons of the coordinated (HL$^n$NH)$^-$ ligands appear in the range $\delta$ = 6.58–7.75 ppm. The proton counts match well with the composition, thereby indicating no mismatch with the molecular structure in solution. The $^1$H NMR spectroscopic data are listed in Table 2. Although the spectrum of [(HL$^1$NH)Pt(dmso)Cl] is slightly more complicated in the aromatic region, the proton count is consistent with the composition. The spectra of [(HL$^2$NH)Pt(dmso)Cl] and [(HL$^3$NH)Pt(dmso)Cl] are well resolved in the aromatic region, where two doublets and two triplets, each integrating for one proton, appear for 2-H, 3-H, 4-H, and 5-H (the atom numbering scheme is shown in Figure 3, a). Two doublets, each integrating for two equivalent protons, are observed for 8,12-H and 9,11-H. A representative spectrum for [(HL$^2$NH)Pt(dmso)Cl] is shown in Figure 2. The N–H resonances for these complexes fall within the aromatic region and are overlapped by other resonances of the aromatic protons. However, the proton count matches the composition (HL$^n$NH)$^-$, thereby confirming the removal of one $NH_2$ proton upon complexation.

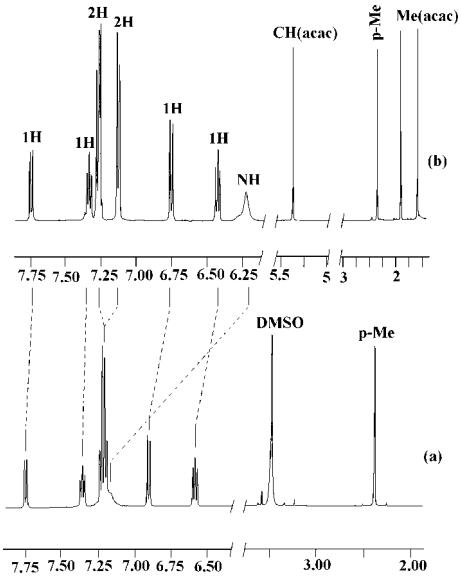


Figure 2. Correlation of aromatic proton resonances along with the proton count of [(HL$^2$NH)Pt(dmso)Cl] (a) and [(HL$^2$NH)Pt(acac)] (b).

The $^1$H NMR spectra of the [(HL$^n$NH)Pt(acac)] complexes exhibit the N–H resonance as a broad singlet in the range $\delta$ = 6.22–6.35 ppm, thereby confirming the (HL$^n$NH$_2$) → (HL$^n$NH)$^-$ transformation. The $^1$H NMR spectra of [(HL$^n$NH)Pt(acac)] are similar to those of [(HL$^n$NH)Pt(dmso)Cl] in the aromatic region but with slightly different chemical shift values. A one-to-one correlation of the aromatic protons is shown in Figure 2 for [(HL$^2$NH$_2$)Pt(acac)] and [(HL$^2$NH)Pt(dmso)Cl]. The coordinated acac ligand of [(HL$^n$NH)Pt(acac)] shows three sets of resonances, one for the methine proton ($\delta \approx$ 5.35 ppm) and two for the $CH_3$ groups ($\delta \approx$ 1.92 and 1.59 ppm),

Table 2. $^1$H NMR spectroscopic data for [(HL$^n$NH)Pt(dmso)Cl], [(HL$^n$NH)Pt(acac)], and [{(HL$^1$NH)PdCl}$_2$].

| Compound | $\delta$ [ppm][a] Aromatic H | Nonaromatic H | R ($CH_3$) | N–H |
|---|---|---|---|---|
| [(HL$^1$NH)Pt(dmso)Cl] | 7.75 (d, 1 H), 7.40 (t, 2 H), 7.38–7.25 (m, 4 H) 6.90 (d, 1 H), 6.59 (t, 1 H) | 3.50 (s, 6 H) | – | 7.17 (br., 1 H) |
| [(HL$^2$NH)Pt(dmso)Cl] | 7.74 (d, 1 H), 7.35 (t, 1 H), 7.24–7.18 (m, 4 H) 6.90 (d, 1 H), 6.58 (t, 1 H) | 3.50 (s, 6 H) | 2.40 (s, 3 H) | 7.17 (br., 1 H) |
| [(HL$^3$NH)Pt(dmso)Cl] | 7.71 (d, 1 H), 7.38–7.34 (m, 3 H), 7.28 (d, 2 H) 6.90 (d, 1 H), 6.60 (t, 1 H) | 3.51 (s, 6 H) | – | – |
| [(HL$^1$NH)Pt(acac)] | 7.74 (d, 1 H), 7.38 (d, 2 H), 7.36–7.32 (m, 3 H) 7.27 (d, 1 H), 6.76 (d, 1 H), 6.43 (t, 1 H) | 5.36 (s, 1 H), 1.92 (s, 3 H) 1.56 (s, 3 H) | – | 6.28 (br., 1 H) |
| [(HL$^2$NH)Pt(acac)] | 7.74 (d, 1 H), 7.38 (t, 1 H), 7.28–7.24 (m, 2 H) 7.13 (d, 2 H), 6.75 (d, 1 H), 6.42 (t, 1 H) | 5.37 (s, 1 H), 1.92 (s, 3 H) 1.58 (s, 3 H) | 2.37 (s, 3 H) | 6.22 (br., 1 H) |
| [(HL$^3$NH)Pt(acac)] | 7.72 (d, 1 H), 7.36–7.30 (m, 5 H), 6.75 (d, 1 H) 6.44 (t, 1 H) | 5.39 (s, 1 H), 1.93 (s, 3 H) 1.63 (s, 3 H) | – | 6.35 (br., 1 H) |
| [{(HL$^1$NH)PdCl}$_2$] | 8.08–8.00 (m, 1 H), 7.85 (t, 1 H), 7.57–7.36 (m, 2 H), 7.19 (t, 1 H), 6.88 (d, 1 H), 6.74–6.51 (m, 3 H) | – | – | 4.91 (br., 1 H) |

[a] In $CDCl_3$.

 © 2007 Wiley-VCH Verlag GmbH & Co. KGaA, Weinheim 

thereby indicating an unequal chemical environment about the two Me groups, consistent with the X-ray structure (see below).

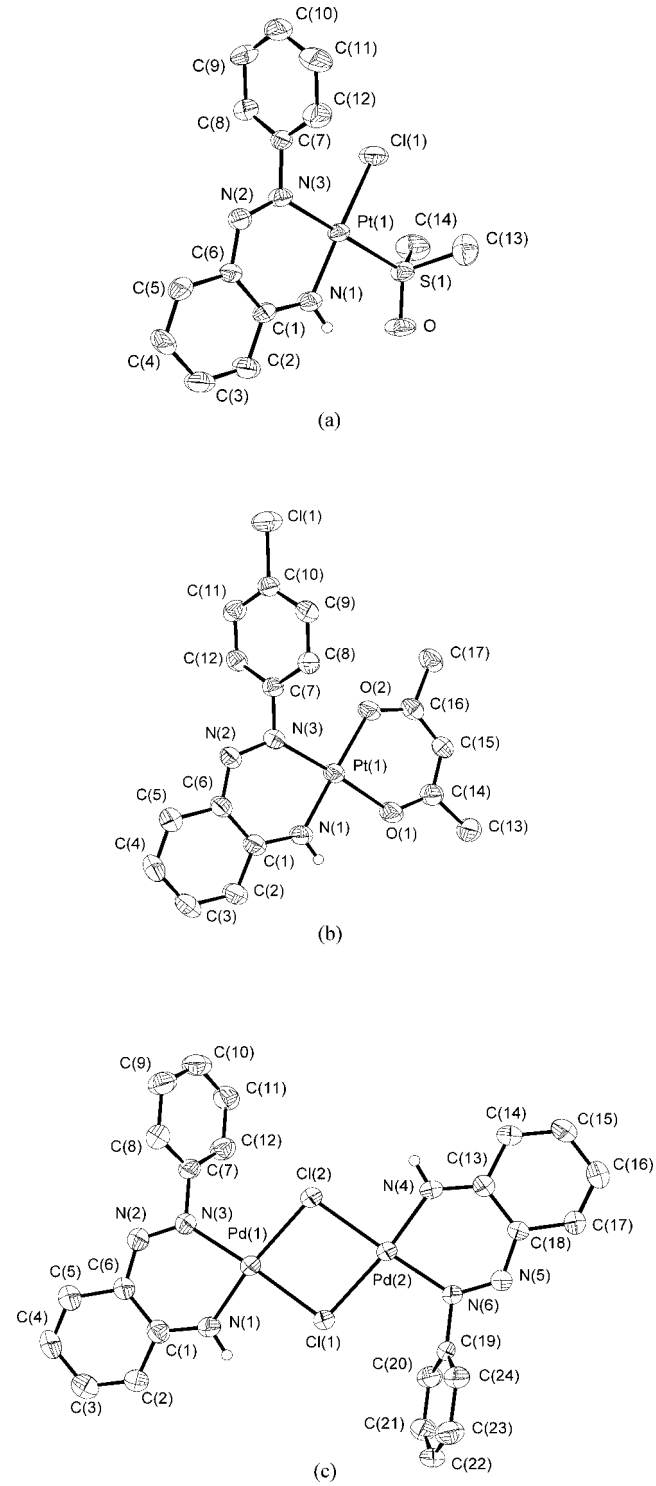


Figure 3. Perspective views of [(HL[1]NH)Pt(dmso)Cl] (a), [(HL[3]NH)Pt(acac)] (b), and [{(HL[1]NH)PdCl}$_2$] (c) with atom numbering scheme. Hydrogen atoms, except those on N1 in (a), (b), and (c) and N4 in (c), have been omitted for clarity.

## X-ray Structures

The crystal structures of [(HL[1]NH)Pt(dmso)Cl], [{(HL[1]NH)PdCl}$_2$], and [(HL[3]NH)Pt(acac)] were determined as representative examples of each type of complex. The (HL$^n$NH) ligands bind to the metals in an N,N-bidentate fashion in all three complexes. A chloride and a dmso ligand (coordinated to the Pt$^{II}$ through its S atom) are present in the coordination sphere of [(HL[1]NH)Pt(dmso)Cl], and the acac$^-$ ligand of [(HL[3]NH)Pt(acac)] binds Pt$^{II}$ in an O,O-bidentate fashion as expected. Two bridging chloride

Table 3. Selected bond lengths [Å] and angles [°] for [(HL[1]NH)Pt(dmso)Cl], [(HL[3]NH)Pt(acac)], and [{(HL[1]NH)PdCl}$_2$].

| [(HL[1]NH)Pt(dmso)Cl] | | | |
|---|---|---|---|
| Pt(1)–Cl(1) | 2.320(2) | N(1)–C(1) | 1.317(6) |
| Pt(1)–S(1) | 2.241(2) | N(2)–N(3) | 1.282(5) |
| Pt(1)–N(1) | 1.957(4) | N(2)–C(6) | 1.353(6) |
| Pt(1)–N(3) | 2.026(4) | N(3)–C(7) | 1.465(6) |
| S(1)–O | 1.466(4) | C(1)–C(6) | 1.445(6) |
| S(1)–C(13) | 1.779(5) | S(1)–C(14) | 1.775(5) |
| Cl(1)–Pt(1)–S(1) | 87.94(4) | C(13)–S(1)–C(14) | 101.5(2) |
| Cl(1)–Pt(1)–N(1) | 176.44(10) | O–S(1)–C(14) | 108.2(2) |
| Cl(1)–Pt(1)–N(3) | 93.66(11) | Pt(1)–N(1)–C(1) | 129.0(3) |
| S(1)–Pt(1)–N(1) | 89.50(10) | N(3)–N(2)–C(6) | 123.4(4) |
| S(1)–Pt(1)–N(3) | 175.30(9) | Pt(1)–N(3)–C(7) | 120.2(3) |
| N(1)–Pt(1)–N(3) | 89.08(14) | N(2)–N(3)–C(7) | 110.7(3) |
| Pt(1)–S(1)–O | 115.05(15) | O–S(1)–C(13) | 109.5(2) |
| Pt(1)–S(1)–C(13) | 108.42(15) | Pt(1)–S(1)–C(14) | 113.32(15) |
| [(HL[3]NH)Pt(acac)] | | | |
| Pt(1)–O(1) | 2.026(3) | N(2)–N(3) | 1.303(4) |
| Pt(1)–O(2) | 2.031(3) | N(2)–C(6) | 1.356(6) |
| Pt(1)–N(1) | 1.940(4) | N(3)–C(7) | 1.439(6) |
| Pt(1)–N(3) | 1.975(4) | C(1)–C(6) | 1.431(8) |
| O(1)–C(14) | 1.273(6) | C(14)–C(15) | 1.385(7) |
| O(2)–C(16) | 1.278(6) | C(15)–C(16) | 1.409(8) |
| N(1)–C(1) | 1.327(6) | | |
| O(1)–Pt(1)–O(2) | 93.41(12) | N(2)–C(6)–C(1) | 128.4(4) |
| Pt(1)–O(2)–C(16) | 122.5(3) | O(1)–Pt(1)–N(1) | 84.49(14) |
| O(1)–Pt(1)–N(3) | 175.19(13) | Pt(1)–N(1)–C(1) | 128.7(4) |
| O(2)–Pt(1)–N(3) | 91.28(13) | O(2)–Pt(1)–N(1) | 177.02(15) |
| N(1)–Pt(1)–N(3) | 90.87(15) | C(14)–C(15)–C(16) | 127.3(5) |
| Pt(1)–O(1)–C(14) | 123.6(3) | Pt(1)–N(3)–C(7) | 122.1(3) |
| O(1)–C(14)–C(15) | 126.2(5) | N(3)–N(2)–C(6) | 123.0(4) |
| N(2)–C(6)–C(5) | 113.3(5) | N(2)–N(3)–C(7) | 109.8(4) |
| Pt(1)–N(3)–N(2) | 128.1(3) | | |
| [{(HL[1]NH)PdCl}$_2$] | | | |
| Pd(1)–Cl(1) | 2.3596(11) | C(5)–C(6) | 1.425(5) |
| Pd(1)–Cl(2) | 2.3678(11) | C(4)–C(5) | 1.333(7) |
| Pd(1)–N(1) | 1.938(3) | C(3)–C(4) | 1.411(7) |
| Pd(1)–N(3) | 2.004(3) | C(2)–C(3) | 1.343(6) |
| N(1)–C(1) | 1.315(5) | C(1)–C(2) | 1.425(6) |
| N(2)–N(3) | 1.281(5) | N(3)–C(7) | 1.448(6) |
| N(2)–C(6) | 1.339(5) | C(1)–C(6) | 1.430(6) |
| Cl(2)–Pd(1)–N(3) | 98.61(10) | N(1)–C(1)–C(2) | 119.7(4) |
| Cl(2)–Pd(1)–N(1) | 172.14(10) | C(2)–C(1)–C(6) | 118.0(3) |
| Cl(1)–Pd(1)–N(3) | 175.96(10) | N(1)–C(1)–C(6) | 122.3(4) |
| Cl(1)–Pd(1)–N(1) | 87.45(10) | N(2)–C(6)–C(5) | 115.9(4) |
| N(2)–C(6)–C(1) | 126.3(3) | Cl(1)–Pd(1)–Cl(2) | 84.71(4) |
| N(2)–N(3)–C(7) | 112.2(3) | Pd(1)–N(3)–C(7) | 119.7(3) |
| Pd(1)–N(1)–C(1) | 129.1(3) | Pd(1)–N(3)–N(2) | 128.1(3) |
| N(1)–Pd(1)–N(3) | 89.20(14) | N(3)–N(2)–C(6) | 124.5(3) |
| C(3)–C(4)–C(5) | 119.5(4) | C(1)–C(6)–C(5) | 117.7(4) |
| C(1)–C(2)–C(3) | 121.0(4) | | |

 © 2007 Wiley-VCH Verlag GmbH & Co. KGaA, Weinheim 

ligands coordinate the $Pd^{II}$ apart from the bidentate $(HL^1NH)^-$ ligand in $[\{Pd(HL^1NH)Cl\}_2]$. The $(HL^1NH)^-$ ligands in this molecule are mutually *trans* with no substantial mismatch in the bond parameters. Perspective views of the molecules are shown in Figures 3 (a–c), and selected bond lengths and angles are collected in Table 3.

The geometries about the metal center are planar (mean deviations within 0.0216–0.0532 Å) for all three neutral molecules, thereby confirming the bivalent state of Pt and Pd and the formation of a mononegative anionic ligand $(HL^nNH)^-$ by dissociation of an amine proton from the precursor $HL^nNH_2$, consistent with the IR and $^1H$ NMR spectroscopic data (see above).[14,15,18,19] The equality in bond lengths within the chelate ring framework of coordinated acetylacetone of [(HL$^n$NH)Pt(acac)] signifies the expected delocalization upon deprotonation.[20] The C(1)–N(1) distances (approx. 1.324 Å) of all three molecules are much shorter than that of the C(7)–N(3) single bond (approx. 1.444 Å) in the same molecules. The C(1)–N(1) distances are, in fact, similar to that of an imine (approx. 1.34 Å).[14,15,18,19] The effect of delocalization within the chelate framework of $(HL^nNH)^-$ is further reflected by the adjacent phenyl ring [C(1)–C(6)], which has four long and two short bonds. The C(6)–N(2) bond length (approx. 1.35 Å) is shorter than the C(7)–N(3) single bond length as a consequence. These structural features allowed us to infer the formation of delocalized diazoketiminato chelates.[14,15,18,19]

The asymmetric unit of [(HL$^n$NH)Pt(acac)] contains two mutually *trans* molecules that are held together by a weak $Pt^{II}\cdots Pt^{II}$ interaction (3.898 Å). The stacking arrangement displayed by this weak dimer in the crystal lattice is shown in Figure 4 (inter dimer $Pt^{II}\cdots Pt^{II}$ distance is 4.320 Å). The $Pd^{II}\cdots Pd^{II}$ distance in the $[\{(HL^nNH)PdCl\}_2]$ dimer is 3.494 Å, which means that there is no Pd–Pd single bond formation and no possibility of forming a $Pd^I$–$Pd^I$ dimer.

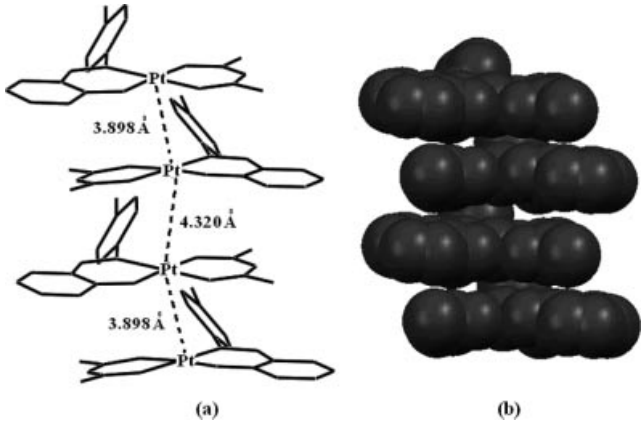


Figure 4. (a) Partial packing diagram and (b) stacking arrangement of [(HL$^3$NH)Pt(acac)].

## Electrochemistry

The cyclic voltammograms of complexes [(HL$^n$NH)Pt(dmso)Cl] display a quasi-reversible one-electron reduction (calibrated against the current height of the $Fc/Fc^+$ couple) in the range $E_{1/2} \approx -1.120$ to $-1.246$ V vs. SCE in acetonitrile. The voltammogram of [(HL$^1$NH)Pt(dmso)Cl] is shown in Figure 5 (a) as an example. The overall redox reactions are represented in Equation (1). The $E_{1/2}$ values vary systematically with R′ of the (HL$^n$NH) ligand, and a plot of $E_{1/2}$ vs. σ (the Hammett substituent constant) is linear (Figure 5, b).[21]

$$[(HL^nNH)Pt(DMSO)Cl]^- \xrightarrow[-e]{} [(HL^nNH)Pt(DMSO)Cl] \quad (1)$$

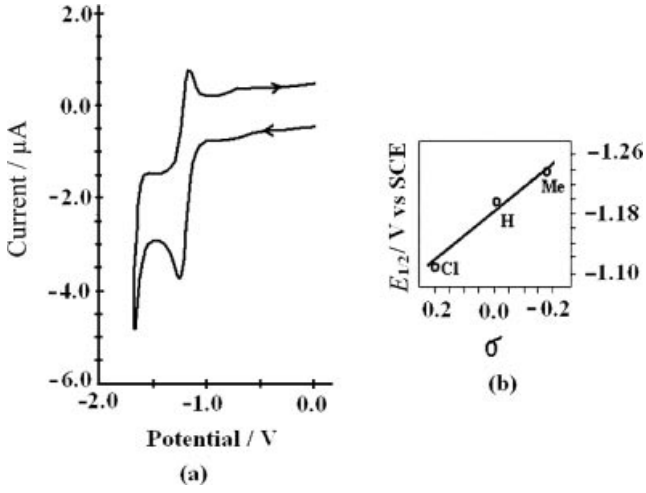


Figure 5. (a) Cyclic voltammogram of [(HL$^1$NH)Pt(dmso)Cl] in acetonitrile solution (0.1 M $NBu_4ClO_4$) vs. SCE. (b) A least-squares plot of $E_{1/2}$ values of [(HL$^n$NH)Pt(dmso)Cl] complexes vs. σ (Hammett substituent constant).

To gain an insight into the nature of the redox orbitals we performed EHMO calculations[22,23] using the crystallographic atomic coordinates of [(HL$^1$NH)Pt(dmso)Cl]. The energy level and interaction diagram was determined by FMO analysis, which showed that the LUMO is a nonbonding ligand group orbital (Figure 6). The contribution of an antibonding combination of azo (–N=N–) nitrogens to the LUMO is 50%, therefore the reductive response of [(HL$^n$NH)Pt(dmso)Cl] may be assigned to reduction of the azo function [Equation (2)].[24,25] The cyclic voltammogram of [(HL$^n$NH)Pt(acac)] is similar (see Figure S16) to that of the [(HL$^n$NH)Pt(dmso)Cl] complexes but with a characteristic shift of the $E_{1/2}$ values (–1.410 V to –1.510 V vs. SCE in acetonitrile). An EHMO calculation was also performed with the crystallographic atomic coordinates of [(HL$^3$NH)-Pt(acac)], and analysis of the LUMO showed a similar composition to that of [(HL$^n$NH)Pt(dmso)Cl], with a contribution from the azo-π* combination of also about 50%. The energy-level diagram with metal–ligand interactions and the orbital diagram of LUMO are given in Figure S1 (see Supporting Information).

$$—N{=}N— \xrightarrow{+e} —N\cdots N— \quad (2)$$

## Cytotoxicity

HeLa cells were treated with [(HL$^1$NH)Pt(dmso)Cl] in the concentration range 4.0–20.0 µM. A viability plot of the

 © 2007 Wiley-VCH Verlag GmbH & Co. KGaA, Weinheim 

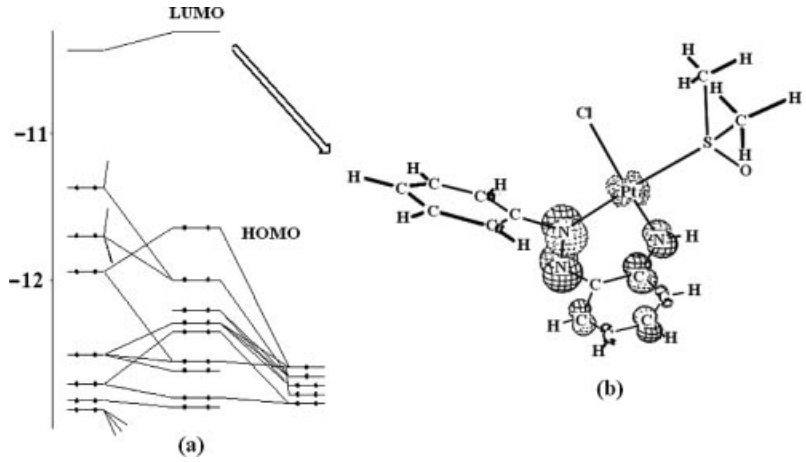


Figure 6. (a) Partial energy level and interaction diagram and (b) MO drawing of the LUMO of [(HL$^1$NH)Pt(dmso)Cl].

trypan blue dye exclusion assay is shown in Figure 7. The trypan blue assay showed that $ED_{75}$, which is the effective dose of [(HL$^1$NH)Pt(dmso)Cl] required to kill 75% of cells, is 12 μM for this complex. Around 50% of the cells were still viable after 5 h from the time of treatment of the cells with 8 μM [(HL$^1$NH)Pt(dmso)Cl], which is therefore the sub-lethal dose.[26] The pattern of cell death was studied by flow cytometric technique using appropriate dye stains. The apoptotic cell death was studied by the Annexin-V binding assay technique using a sub-lethal dose (8 μM) of [(HL$^1$NH)-Pt(dmso)Cl]. The cells were co-stained with propidium iodide (PI) in addition to Annexin V to distinguish between apoptotic and necrotic cell death.[27] Although the later stages of apoptosis cannot be distinguished from necrosis, the flipped-out phosphatidylserine residue selectively binds Annexin V-FITC on the cells' surface during the early stages of apoptosis. The results of the flow cytometric measurements are shown in Figure 8. Viable cells are negative to both dyes (PI and Annexin V-FITC), as shown in the bottom-left quadrant of Figure 8. The Annexin V conjugated cells appearing in the bottom-right quadrant of Figure 8 represent the apoptotic cells, and the upper-right quadrant represents the Annexin V and PI conjugated cells, which indicates late-stage apoptosis or necrosis.

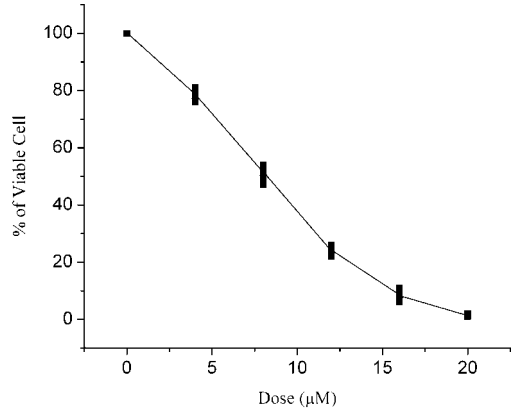


Figure 7. Plot of dose vs. viable cells to determine the sub-lethal dose.

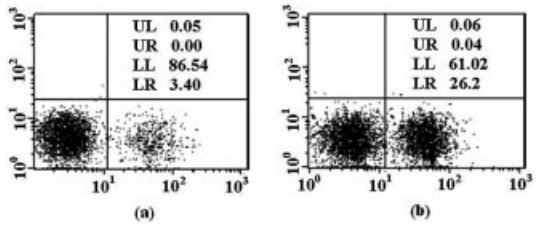


Figure 8. Flow cytometric measurements with HeLa cells using Annexin V-FITC/PI to distinguish between apoptosis and necrosis: (a) the plot for untreated cells; (b) the plot for cells treated with [(HL$^1$NH)Pt(dmso)Cl]. UL = upper left, UR = upper right, LL = lower left, LR = lower right.

These studies show the cytotoxic effects of this new class of platinum(II) chelate complexes [(HL$^1$NH)Pt(dmso)Cl] with mutually *cis*-coordinated dmso and chloride ligands. Although activation of apoptosis is a remarkable observation, a comparison of the results obtained with cisplatin is necessary and is currently underway.

## Concluding Remarks

The reactions of $K_2PtCl_4$ with HL$^n$NH$_2$ and HL$^n$NHCH$_2$Ph in refluxing dmso both afford the diazoketiminato complex [(HL$^n$NH)Pt(dmso)Cl] due to N–C(benzyl) bond cleavage in HL$^n$NHCH$_2$Ph. In contrast, $Na_2PdCl_4$ affords the orthopalladated complexes and chloro-bridged diazoketiminatodipalladium complexes upon reaction with HL$^n$NHCH$_2$Ph and HL$^n$NH$_2$, respectively. The reaction of [(HL$^n$NH)Pt(dmso)Cl] with acacH affords the new heteroleptic complex [(HL$^n$NH)Pt(acac)], thereby indicating the possibility of binding bioligands by substituting the chloride and/or dmso ligands of [(HL$^n$NH)Pt(dmso)Cl]. The crystal structure of [(HL$^n$NH)Pt(acac)] exhibits a stacked

 © 2007 Wiley-VCH Verlag GmbH & Co. KGaA, Weinheim 

arrangement with weak intermolecular interactions. Interestingly, the delocalized diazoketiminato chelates [(HL″NH)Pt(dmso)Cl] and [(HL″NH)Pt(acac)] exhibit reversible one-electron reductions in their cyclic voltammograms. This electron-transfer property has been attributed to a ligand-centered reversible azo (–N=N–) reduction by EHMO calculations. The results of an in vitro study of the cytotoxicity of [(HL$^1$NH)Pt(dmso)Cl] against the HeLa cell line are interesting in terms of dose dependence and apoptotic pattern of cell death. Further biological experiments are underway to compare the relative activities with cisplatin.

## Experimental Section

**Materials:** The solvents used in the reactions were of reagent grade (E. Merck, Kolkata, India) and were purified and dried by reported procedures.[14] Platinum chloride, dimethyl sulfoxide, and acetylacetone were purchased from the same company. Potassium tetrachloroplatinate and sodium tetrachloropalladate were prepared by a reported procedure. Trypan blue, propidium iodide, and Annexin V-FITC were obtained from Aldrich. HeLa cells were collected from NCCS, Pune, India. The ligands 2-(phenylazo)aniline (HL$^1$NH$_2$), 2-(*p*-tolylazo)aniline (HL$^2$NH$_2$), and 2-(*p*-chlorophenylazo)aniline (HL$^3$NH$_2$) were prepared following the reported procedures.[14,15,18]

**Physical Measurements:** Microanalysis (C,H,N) was performed using a Perkin–Elmer 240C elemental analyzer. Infrared spectra were recorded with a Perkin–Elmer L120-00A FT-IR spectrometer with the samples prepared as KBr pellets. Electronic spectra were recorded with a Shimadzu UV- 2401 PC spectrophotometer. $^1$H NMR spectra were obtained with Bruker 500 RPX and Bruker 300 DPX spectrometers in $CDCl_3$ using TMS as the internal standard. Electrochemical measurements were performed using a PAR Versastat II potentiostat with a platinum disk working electrode, a platinum wire auxiliary electrode, and an aqueous saturated calomel electrode (SCE) as reference, (0.1 M) $Bu_4NClO_4$ as supporting electrolyte, in acetonitrile. Electrochemical measurements were carried out under a dinitrogen atmosphere at 298 K and were uncorrected for junction potentials. Cytotoxicity was measured with a Fluorescence Microscope (Olympus BX40, Tokyo, Japan), FACS Calibur (BD Biosciences) and the Cell Quest (Bekton Dickinson) software package.

**Synthesis of [(HL$^1$NH)Pt(dmso)Cl]:** A solution of 2-(phenylazo)-aniline (HL$^1$NH$_2$; 100 mg, 0.5 mmol) in 5 mL of dmso was added to a solution of $K_2PtCl_4$ (207 mg, 0.5 mmol) in 5 mL of the same solvent. The mixture was stirred for 5 h at 60 °C and a dark pink solid was obtained upon evaporation of dmso. Pure [(HL$^1$NH)-Pt(dmso)Cl] was obtained from the pink solid by chromatography on a silica gel (60–120 mesh) column with toluene as the eluent. Solid [(HL$^1$NH)Pt(dmso)Cl] was obtained by evaporating the eluent. Yield: 115.25 mg (45%). $C_{14}H_{16}ClN_3OPtS$ (504.9): calcd. C 33.25, H 3.18, N 8.34; found C 33.27, H 3.16, N 8.31.

**[(HL$^2$NH)Pt(dmso)Cl] and [(HL$^3$NH)Pt(dmso)Cl]:** These complexes were prepared following the same procedure as for [(HL$^1$NH)Pt(dmso)Cl] but with HL$^2$NH$_2$ (106 mg, 0.5 mmol) and HL$^3$NH$_2$ (116 mg, 0.5 mmol). Yield: 104.27 mg (40%, for the HL$^2$NH$_2$ complex $C_{15}H_{18}ClN_3OPtS$) and 121.62 mg (45%, for the HL$^3$NH$_2$ complex $C_{14}H_{15}Cl_2N_3OPtS$). $C_{15}H_{18}ClN_3OPtS$ (518.9): calcd. C 34.71, H 3.41, N 8.12; found C 34.68, H 3.46, N 8.09. $C_{14}H_{15}Cl_2N_3OPtS$ (539.4): calcd. C 31.10, H 2.80, N 7.82; found C 31.14, H 2.78, N 7.78.

**[(HL$^1$NH)Pt(acac)]:** [(HL$^1$NH)Pt(dmso)Cl] (50 mg, 0.1 mmol) was dissolved in 40 mL of methanol and acetylacetone (10 mg, 0.38 mmol) was added. The mixture was then heated to reflux for 4 h to afford a blue solution. Evaporation of the solvent gave a dark blue residue, which was purified by chromatography on a silica gel (60–120 mesh) column with toluene as eluent. Evaporation of the solvent gave [(HL$^1$NH)Pt(acac)] as a dark blue solid. Yield: 32.10 mg (65%). $C_{17}H_{17}N_3O_2Pt$ (490.36): calcd. C 41.55, H 3.48, N 8.53; found C 41.60, H 3.46, N 8.56.

**[(HL$^2$NH)Pt(acac)] and [(HL$^3$NH)Pt(acac)]:** These compounds were prepared following the same procedure as for [(HL$^1$NH)Pt-(acac)] but with [(HL$^2$NH)Pt(dmso)Cl] (52 mg, 0.1 mmol) and [(HL$^3$NH)Pt(dmso)Cl] (54 mg, 0.1 mmol). Yield: 35.05 mg (70%, for the HL$^2$NH complex $C_{18}H_{19}N_3O_2Pt$) and 36.24 mg (70%, for the HL$^3$NH complex $C_{17}H_{16}ClN_3O_2Pt$).
$C_{18}H_{19}N_3O_2Pt$ (504.36): calcd. C 42.85, H 3.79, N 8.29; found C 42.82, H 3.76, N 8.32.
$C_{17}H_{16}ClN_3O_2Pt$ (524.86): calcd. C 38.83, H 3.08, N 8.05; found C 38.86, H 3.04, N 8.00.

**[(HL$^1$NH)PdCl]$_2$:** A solution of HL$^1$NH$_2$ (100 mg, 0.5 mmol) in 5 mL of dmso was added to a solution of $Na_2PdCl_4$ (150 mg, 0.5 mmol) in 5 mL of dmso. The mixture was stirred for 4 h at 60 °C and a dark pink solid was obtained upon evaporation of dmso. Pure [{(HL$^1$NH)PdCl}$_2$]was obtained from the pink solid by chromatography on a silica gel (60–120 mesh) column with toluene as the eluent. Solid [{(HL$^1$NH)PdCl}$_2$] was obtained upon evaporation of the eluent. Yield: 188.80 mg (55%). $C_{24}H_{20}Cl_2N_6Pd_2$ (1352.5): calcd. C 42.59, H 2.95, N 12.42; found C 42.54, H 3.01, N 12.38.

**Reaction of HL$^1$NHCH$_2$Ph with Na$_2$PdCl$_4$:** A solution of HL$^1$NHCH$_2$Ph (110 mg, 0.52 mmol) in 5 mL of dmso was added to a solution of $Na_2PdCl_4$ (150 mg, 0.52 mmol) in 5 mL of dmso. The mixture was stirred for 4 h at 60 °C and a dark brown solid was obtained upon evaporation of dmso. Pure [(HL$^1$NHCH$_2$Ph)-PdCl] was obtained from the brown solid by chromatography on a silica gel (60–120 mesh) column with a toluene/acetonitrile mixture (90:10 v/v) as eluent. Solid [(L$^1$NHCH$_2$Ph)PdCl] was obtained upon evaporation of the eluent. Yield: 119.99 (55%).

**Reaction of HL$^1$NHCH$_2$Ph with K$_2$PtCl$_4$:** A solution of HL$^1$NHCH$_2$Ph (110 mg, 0.52 mmol) in 5 mL of dmso was added to a solution of $K_2PtCl_4$ (215 mg, 0.52 mmol) in 5 mL of dmso. The mixture was stirred for 5 h at 60 °C and a dark pink solid was obtained upon evaporation of dmso. Pure [(HL$^1$NH)Pt(dmso)Cl] was isolated by chromatography on a silica gel (60–120 mesh) column with toluene as the eluent. Solid [(HL$^1$NH)Pt(dmso)Cl] was obtained upon evaporation of the eluent. Yield: 130.76 mg (50%).

**Viability Assay. Trypan Blue Exclusion Test:** HeLa cells were treated with 4, 8, 12, and 16 μM solutions of complex in dmso.[28] The cells (10 μL suspension) were then placed on cover slips at the required dilution and each cover slip was placed cell-side down onto a slide containing a drop of 0.125% Trypan Blue dye (wt/vol in sterile isotonic saline). The excess dye solution was removed by applying gentle pressure with gauze at the edges of the cover slip. The slides were viewed within ten minutes with a light microscope at a magnification of 40× and 50–100 cells counted. Viable cells remained unstained, while the nuclei of nonviable cells were stained blue.

**Differentiation Between Apoptosis and Necrosis by FACS:** To distinguish between apoptosis and necrosis treated or untreated cells ($1 \times 10^6$ in each case) were harvested, in a double labeling system, and PI and Annexin V Fluos (Boehringer Mannheim) added directly to the culture medium or to the cell suspension. The mixture

 © 2007 Wiley-VCH Verlag GmbH & Co. KGaA, Weinheim 

Table 4. Crystallographic data for [(HL$^1$NH)Pt(dmso)Cl], [(HL$^3$NH)Pt(acac)], and [{(HL$^1$NH)PdCl}$_2$].

| | [(HL$^1$H)Pt(dmso)Cl] | [(HL$^3$NH)Pt(acac)] | [{(HL$^1$NH)PdCl}$_2$] |
|---|---|---|---|
| Formula | $C_{14}H_{16}ClN_3OPtS$ | $C_{17}H_{16}ClN_3O_2Pt$ | $C_{24}H_{20}Cl_2N_6Pd_2$ |
| $M$ | 504.90 | 524.86 | 1352.4 |
| Space group | $Fdd2$ | $P\bar{1}$ | $P\bar{1}$ |
| Crystal system | orthorhombic | triclinic | triclinic |
| $a$ [Å] | 21.573(18) | 8.185(3) | 10.3262(10) |
| $b$ [Å] | 30.81(2) | 13.720(5) | 10.3626(10) |
| $c$ [Å] | 9.838(7) | 16.257(6) | 12.2239(12) |
| $\alpha$ [°] | 90 | 107.007(9) | 101.710(2) |
| $\beta$ [°] | 90 | 90.176(9) | 112.079(2) |
| $\gamma$ [°] | 90 | 91.980(10) | 92.665(2) |
| $\lambda$ [Å] | 0.71073 | 0.71073 | 0.71073 |
| $V$ [Å$^3$] | 6539(8) | 1744.6(11) | 1176.0(2) |
| $Z$ | 16 | 4 | 2 |
| $D_{calcd.}$ [g cm$^{-3}$] | 2.051 | 1.998 | 1.910 |
| $\mu$ [mm$^{-1}$] | 8.875 | 8.210 | 1.783 |
| $R_1$[a] | 0.0184 | 0.0322 | 0.0309 |
| $wR_2$[b] | 0.0340 | 0.0701 | 0.0648 |
| Unique reflections [$I > 2\sigma(I)$] | 21173/3886 | 28481/9547 | 7504/5218 |
| GOF[c] | 0.81 | 1.000 | 0.96 |

[a] $R_1 = \Sigma||F_o| - |F_c||/\Sigma|F_o|$. [b] $wR_2 = \Sigma[w(F_o^2 - F_c^2)^2]/\Sigma[w(F_o^2)^2]^{1/2}$ where $w = 1/\sigma^2(F_o^2) + (aP)^2 + bP$, $P = (F_o^2 + 2F_c^2)/3$. [c] GOF = $\Sigma[w(F_o^2 - F_c^2)^2]/(n - p)]^{1/2}$.

was then incubated for 15 min at 37 °C. Excess PI and Annexin V Fluos were washed off, and the cells were fixed and then analyzed with a FACS Calibur apparatus [quipped with a 488-nm argon laser light source, a 515-nm band pass filter (FL1-H), and a 623-nm band pass filter (FL2-H)] using the CellQuest program (Becton Dickinson). Electronic compensation of the instrument was done to exclude overlapping of the emission spectra. A total of 10,000 events were acquired, the cells were properly gated, and a dual parameter dot plot of FL1-H ($x$-axis; Fluos fluorescence) vs. FL2-H ($y$-axis; PI fluorescence) was produced in logarithmic fluorescence intensity.[29]

**X-ray Crystallography:** Crystals of [(HL$^1$NH)Pt(dmso)Cl], [(HL$^3$NH)Pt(acac)], and [{(HL$^1$NH)PdCl}$_2$] were grown by diffusion of hexane into a dichloromethane solution at 298 K. Data were collected with a Bruker SMART CCD diffractometer using Mo-$K_\alpha$-monochromated radiation ($\lambda$ = 0.71043 Å). Structure solutions were performed using the Shelx 97 program (PC version). Full-matrix least-squares and anisotropic refinements were performed on all the atoms. Hydrogen atoms were included at their calculated positions. The data collection parameters and relevant crystal data are collected in Table 4.

CCDC-283817 for [(HL$^1$NH)Pt(dmso)Cl], -283818 for [(HL$^3$NH)-Pt(acac)], and -283819 for [{(HL$^1$NH)PdCl}$_2$] contain the supplementary crystallographic data for this paper. These data can be obtained free of charge from The Cambridge Crystallographic Data Centre via www.ccdc.cam.ac.uk/data_request/cif.

**Supporting Information** (see also the footnote on the first page of this article): Figure S1 shows the EHMO diagrams for [(HL$^3$NH)-Pt(acac)]. Figures S2–S8 show the IR spectra and Figures S9–S15 the $^1$H NMR spectra of all the complexes; Figure S16 shows the cyclic voltammogram of [(HL$^1$NH)Pt(acac)].

## Acknowledgments

We are thankful to the Department of Science and Technology (DST), New Delhi for funding and a fellowship to J. P. under the DST-SERC project (no. SR/S1/IC-09/2003). We are also thankful to the Council of Scientific and Industrial Research for funding. The necessary laboratory and infrastructural facilities were provided by the Department of Chemistry, University of Kalyani. The support of DST under the FIST program to the Department of Chemistry, University of Kalyani is acknowledged. We acknowledge Prof. Jui-Hsien Huang, National Changhua University of Education, Changhua, Taiwan for performing the X-ray studies of [(HL$^3$NH)Pt(acac)].

[1] B. Rosenberg, L. V. Camp, *Nature* **1965**, *205*, 698–699.
[2] B. Rosenberg, L. V. Camp, J. E. Trosko, V. H. Mansour, *Nature* **1969**, *222*, 385–386.
[3] B. Rosenberg, L. V. Camp, *Cancer Res.* **1970**, *30*, 1799–1802.
[4] R. B. Weiss, M. C. Christian, *Drugs* **1993**, *46*, 360–377.
[5] J. Reedijk, *Inorg. Chim. Acta* **1992**, *198–200*, 873–881.
[6] C. F. J. Barnard, *Platinum Met. Rev.* **1989**, *33*, 162–167.
[7] T. W. Hambley, *Coord. Chem. Rev.* **1997**, *166*, 181–223.
[8] G. Natile, M. Coluccia, *Coord. Chem. Rev.* **2001**, *216–217*, 383–410.
[9] A. G. Quiroga, C. Navarro Ranninger, *Coord. Chem. Rev.* **2004**, *248*, 119–133.
[10] C. Sacht, M. S. Datt, S. Otto, A. Rood, *J. Chem. Soc. Dalton Trans.* **2000**, 727–733.
[11] C. Sacht, M. S. Datt, S. Otto, A. Rood, *J. Chem. Soc. Dalton Trans.* **2000**, 4579–4586.
[12] C. Sacht, M. Datt, *Polyhedron* **2000**, *19*, 1347–1354.
[13] A. Rodger, K. K. Patel, K. J. Sanders, M. Datt, C. Sacht, M. J. Hannon, *J. Chem. Soc. Dalton Trans.* **2002**, 3656–3663.
[14] N. Maiti, S. Pal, S. Chattopadhyay, *Inorg. Chem.* **2001**, *40*, 2204–2205 and references cited therein.
[15] N. Maiti, S. Chattopadhyay, *Indian. J. Chem. Sect. A* **2003**, *42*, 2327–2331.
[16] J. Pratihar, N. Maiti, P. Pattanayak, S. Chattopadhyay, *Polyhedron* **2005**, *24*, 1953–1960.
[17] J. Pratihar, N. Maiti, S. Chattopadhyay, *Inorg. Chem.* **2005**, *44*, 6111–6114.
[18] N. Maiti, B. K. Dirghangi, S. Chattopadhyay, *Polyhedron* **2003**, *22*, 3109–3113.
[19] J. Pratihar, D. Patra, S. Chattopadhyay, *J. Organomet. Chem.* **2005**, *690*, 4816–4821.
[20] M. Ghedini, D. Pucci, A. Crispini, G. Barberio, *Organometallics* **1999**, *18*, 2116–2124.
[21] L. P. Hammett, *Physical Organic Chemistry,* 2nd edn., McGraw Hill, New York, **1970**.

 © 2007 Wiley-VCH Verlag GmbH & Co. KGaA, Weinheim 

[22] C. Mealli, D. M. Proserpio, *CACAO* Version 4.0, Italy, **1994**.
[23] C. Mealli, D. M. Proserpio, *J. Chem. Educ.* **1990**, *67*, 399–403.
[24] P. K. Santra, D. Das, T. K. Misra, R. Roy, C. Sinha, S.-M. Peng, *Polyhedron* **1999**, *18*, 1909–1915.
[25] T. K. Misra, D. Das, C. Sinha, P. Ghosh, C. K. Pal, *Inorg. Chem.* **1998**, *37*, 1672–1678.
[26] L. Axanova, D. J. Morré, D. M. Morré, *Cancer Lett.* **2005**, *225*, 35–40.
[27] H. Ashush, L. A. Rozenszajn, M. Blass, M. Barda-Saad, D. Azimov, J. Radnay, D. Zipori, U. Rosenschein, *Cancer Res.* **2000**, *60*, 1014–1020.
[28] C. Gaiddon, P. Jeannequin, P. Bischoff, M. Pfeffer, C. Sirlin, J. P. Loeffler, *J. Pharmacol. Exp. Ther.* **2005**, *315*, 1403–1411.
[29] A. Bratasz, N. M. Wei, N. L. Parinandi, J. L. Zweier, R. Sridhar, L. J. Ignarro, P. Kuppusamy, *Pharmacology* **2006**, *103*, 3914–3919.

Received: March 28, 2007
Published Online: July 31, 2007

 © 2007 Wiley-VCH Verlag GmbH & Co. KGaA, Weinheim 

DOI: 10.1002/ejic.200601001

# *N*-(2,4,6-Trimethylborazinyl)-Substituted Phosphanes, Arsanes, and Stibanes[‡]

Heinrich Nöth,*[a] Birgit Gemünd,[a] and Robert T. Paine[b]

**Keywords:** Boron / Phosphanes / Arsenic / Antimony

Reaction of the *N*-lithioborazine $LiH_2N_3B_3Me_3{\cdot}OEt_2$ (**2**) in diethyl ether with $PCl_3$ or $PBr_3$ leads to the borazinylphosphanes $(Me_3B_3N_3H_2)PX_2$, $(Me_3B_3N_3H_2)_2PX$ (X = Cl, Br), and $(Me_3B_3N_3H_2)_3P$, depending on the initial stoichiometry. The analogous arsane and stibane derivatives were obtained in a similar manner. While $(Me_3B_3N_3H_2)_2PBr$ is reduced by $LiAlH_4$ in diethyl ether/hexane to give the monophosphane $(Me_3B_3N_3H_2)_2PH$ (**13**), the reaction of $(Me_3B_3N_3H_2)PBr_2$ (**5**) with $LiAlH_4$ in diethyl ether/hexane produces the zwitterionic compound $[Me_3B_3N_2(HN)]^-P^+H_2Et$ (**14**). Dehalogenation of $(Me_3B_3N_3H_2)_2PBr$ (**6**) with Na yields the diphosphane $(Me_3B_3N_3H_2)_2PP(H_2N_3B_3Me_3)_2$ (**18**), while the mixed diphosphane $(Me_3B_3N_3H)_2PPmes_2$ (**17**) is obtained from **6** and $LiPmes_2$. Dehalogenation of $Me_3B_3N_3H_2PBr_2$ with Na results in the exclusive formation of $(Me_3B_3N_3H_2)_4P_4$ (**19**), while the reaction of **5** with $Li_2Pmes$ leads to a mixture of cyclotetraphosphanes $(mes)_{4-n}(Me_3B_3N_3H_2)_nP_4$ (**A**–**F**) along with bicyclic $P_4mes_2$. The new compounds have been characterized by NMR and IR spectroscopy and partly by mass spectrometry. X-ray structures for compounds, **4**, **5**, **6**, **9**, **13**, **14**, **17**, **18**, **19**, and **E** have been determined. All show different B–N bond lengths within the borazine rings, and some have borazine rings in a half-chair conformation.

(© Wiley-VCH Verlag GmbH & Co. KGaA, 69451 Weinheim, Germany, 2007)

## Introduction

The deprotonation of borazines $R_3B_3N_3H_3$ by organolithium reagents was first described by Wagner and Bradford,[2] although none of the resulting *N*-lithioborazines were isolated and characterized − their formation was based on the observation that the products reacted with alkyl halides (R′X) to generate borazines of the type $R_3B_3N_3H_{3-n}R'_n$ ($n$ = 1–3), thereby indicating that the lithiation is not specific and yields a mixture of *N*-lithioborazines. Recently, we reported the isolation and structural characterization of ligand-stabilized *N*-monolithioborazines $R_3B_3N_3H_2Li{\cdot}L$ (e.g. R = Me, *i*Pr, *t*Bu, Ph; L = $Et_2O$, thf, tmeda, pmtda).[3,4] These proved to be versatile reagents for the preparation of hitherto unknown borazine derivatives of, for example, B, Al, Ge, or Ti.[5,6] Here, we describe borazinyl-substituted phosphanes, arsanes, and stibanes. Known P-containing borazines are derivatives of phosphorus esters in which either $(RO)_2P(O)_2$ groups are bonded to the B atoms[7] or an $(RO)PO_3$ group connects two borazine units through a B–O–B bond.[8] Other P-containing borazine derivatives include the interesting borazine cations $[Cl_{3-n}B_3(N{=}PPh_3)_3]^{+n}(Cl^-)_n$ ($n$ = 1, 2, 3).[9,10] However, no borazine derivatives have been reported to date where $R_2P$ groups are bonded to either B or N. These may be interesting ligands for transition metal complexes, particularly those which act as catalysts, because they will change the catalytic properties of triarylphosphane-based catalysts. Here, we describe the synthesis, structures, and reactivity of some of the heavier group 15 element 2,4,6-trimethylborazinyl compounds, with an emphasis on phosphane derivatives.

## Results and Discussion

### (2,4,6-Trimethylborazinyl)-halogeno-phosphanes, -arsanes, and -stibanes

#### *Synthesis*

2,4,6-Trimethylborazine (**1**) does not react with $PCl_3$ or $PBr_3$ in the presence of triethylamine to form borazinyl-halogeno-phosphanes $(Me_3B_3N_3H_2)_nPX_{3-n}$ ($n$ = 1, 2, 3; X = Cl, Br) as the ring N atoms are not sufficiently nucleophilic to attack the P atoms of the halogenophosphanes to allow $NEt_3$-assisted HX elimination. This contrasts with the reactivity of dialkylamines with phosphorus halides.[11,12] We therefore studied the reactions of phosphorus trichloride and tribromide, and their arsenic and antimony analogs, with the diethyl ether adduct of 1-lithio-2,4,6-trimethylborazine (**2**) in diethyl ether solution. Depending on the molar ratios employed, we obtained the borazinyldihalogenophosphanes **3** and **5**, as well as the bis(borazinyl)-halogenophosphanes **4** and **6** in acceptable yields (>75%). The tris(borazinyl)phosphane **11** could, however, not be prepared in pure state; it was always slightly contaminated with **4**. The borazinyl-arsanes **7**, **8** and borazinyl-stibanes **9**, **10** were prepared analogously. The formation of

[‡] Contribution to the Chemistry of Boron, 263. Contribution 262: Ref.[1]

[a] Department of Chemistry and Biochemistry, University of Munich,
Butenandtstr. 5–13, 81377 München, Germany
[b] Department of Chemistry, University of New Mexico, Albuquerque, New Mexico 87131, USA

 © 2007 Wiley-VCH Verlag GmbH & Co. KGaA, Weinheim 

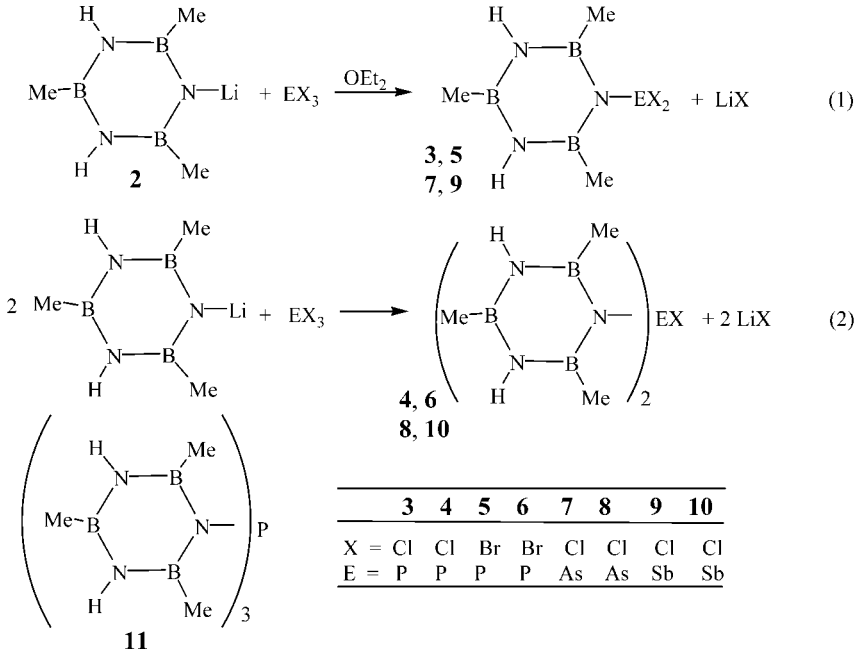


| | 3 | 4 | 5 | 6 | 7 | 8 | 9 | 10 |
|---|---|---|---|---|---|---|---|---|
| X = | Cl | Cl | Br | Br | Cl | Cl | Cl | Cl |
| E = | P | P | P | P | As | As | Sb | Sb |

$(Me_3B_3N_3H_2)_3E$ (E = As, Sb) was observed only by NMR spectroscopy, and these compounds could not be isolated in pure state. Compounds **4**, **5**, **6**, and **9** were obtained as single crystals.

### *Spectra*

Table 1 lists the NMR spectroscopic data of compounds **3**–**11**. Each of these compounds is characterized by two $^{11}B$ NMR signals in a 2:1 ratio. The signal at lower field results from the B atoms adjacent to the N1(4) atom(s) carrying the P, As, or Sb atoms (see Figures 1 and 3 for the numbering). The signals at higher field result from the *para* boron atoms B2(5). The shielding is practically unaffected by the number of halogen atoms at P, As, or Sb. The replacement of P by As or Sb leads to an exceptionally small low-field shift of 1–1.5 ppm, which is only a little bit larger for the bromides **5** and **6** (approx. 2.6 ppm). This shows that the charge distribution within the borazine ring is negligibly affected by the *N*-substitution. Even the replacement of the $Li(OEt_2)$ group by $EX_2$ or EX groups has little effect. The $^{11}B$ NMR shift of compound **2**, for example, is $\delta$ = 35.4 ppm[3] and that of the parent borazine **1** is $\delta$ = 32.3 ppm.[13]

There is a $^{31}P$ chemical shift difference of only 8.6 ppm between the borazinyl-chloro-phosphanes **3** and **4**, whereas this difference is 54.7 ppm for **3** and **11**. Similarly, $\Delta\delta^{31}P$ for the bromides **5** and **6** is only 1.5 ppm but 69.0 ppm for **5** and **11**. The corresponding $\Delta\delta^{31}P$ data for the series $Ph_{3-n}PCl_n$ ($n$ = 0, 1, 2) are 64 and 91.2 ppm and in the $(Me_2N)_{3-n}PCl_n$ series they are 6.3 and 37 ppm, respectively.[14] These latter data are similar to those of the borazinyl-chloro-phosphanes.

While the shielding of the boron nuclei is only slightly affected by the $EX_{2-n}$ groups, the methyl protons in the *para* position of the borazine rings show differences of 0.06 and 0.09 ppm for **3** and **4** and for **5** and **6**, respectively, in contrast to a difference of only 0.01 ppm for the *ortho* methyl groups. This trend is also observed for the arsenic and antimony compounds **7**–**10**.

The proton of the *o*-Me groups of compounds **3** to **6** couples with the $^{31}P$ nucleus. The resulting $^4J_{^{31}P,^1H}$ coupling constants cover the range 3.3–5.7 Hz, with those of the dihalides being larger than those of the monohalide species. A similar coupling has been observed in borylamino phosphanes.[15]

Table 2 contains a selection of the typical strong IR bands recorded in Hostaflon/Nujol mulls. There are two $\nu$(NH) bands for compounds **3** and **5**, while three $\nu$(NH) bands are observed for **4** and **6**, although either two or four are to be expected. The two borazinyl groups of **4** and **6** are obviously not equivalent in the solid state. All of these bands are comparatively sharp, and the bands at highest

Table 1. Chemical shifts of (trimethylborazinyl)-halogeno-phosphanes, -arsanes, and -stibanes (in ppm; solvent $C_6D_6$).

| | **2**·$OEt_2$ | **3** | **4** | **5** | **6** | **7** | **8** | **9** | **10** | **11** |
|---|---|---|---|---|---|---|---|---|---|---|
| $\delta_{^{11}B}$ | 35.4 | 34.6, 37.1 | 34.6, 37.2 | 36.1, 38.6 | 36.0, 38.8 | 35.7, 9.5 | 35.6, 37.9 | 36.0, 38.3 | 35.4, 37.8 | 35.5, 37.7 |
| $\delta_{^{31}P}$ | – | 183.6 | 175.0 | 189.3 | 190.9 | 120.3 | – | – | – | 120.3 |
| $\delta_{^1H}$ C$H_3$ | 0.47, 0.59 | 0.06, 0.66[a] | 0.12, 0.65[b] | –0.01, 0.69[c] | 0.10, 0.66[d] | 0.18, 0.64 | 0.15, 0.56 | 0.05, 0.52 | 0.11, 0.46 | 0.18, 0.50 |
| $\delta_{^1H}$ N*H* | 4.66 | 4.48 | 4.55 | 4.31 | 4.41 | 4.55 | 4.42 | 4.41 | 4.33 | 4.4 |

[a] $^4J_{^{31}P,^1H}$ = 3.6 Hz. [b] $^4J_{^{31}P,^1H}$ = 3.6 Hz. [c] $^4J_{^{31}P,^1H}$ = 5.7 Hz. [d] $^4J_{^{31}P,^1H}$ = 3.3 Hz.

 © 2007 Wiley-VCH Verlag GmbH & Co. KGaA, Weinheim 

wavenumbers are almost the same for all four compounds, whereas the others are lower for the bromides than for the chlorides. BN ring vibrations are found in the regions from 1500 to 1490 $cm^{-1}$ and 1430 to 1380 $cm^{-1}$ as strong bands. Those of the chlorides are observed at somewhat higher wavenumbers than those of the bromides, which suggests an inductive effect of the halides. Only one $\nu$(PN) band is observed for compounds **3** and **5**. As expected, there are two $PN_2$ bands ($\nu_{sym}PN_2$ and $\nu_{asym}PN_2$) for compounds **4** and **6** and their values suggest that the PN bonds of the chlorides are stronger than those of the bromides. This conclusion is also supported by the PN bonds lengths of these compounds (see below).

### *X-ray Structures*

Single crystals suitable for X-ray structure determinations were obtained for compounds **4**, **5**, **6**, and **9**. The dibromoborazinylphosphane **5** crystallizes in the orthorhombic space group *Pnma* with $Z = 8$, which means that there are two independent molecules in the unit cell (see Figure 1a). As expected, the structural parameters of the two molecules do not differ much, but they are nevertheless significantly different (see Table 3). Both molecules show $C_s$ symmetry, with the P, N, B, C, and some of the H atoms occupying special positions on a mirror plane. The symmetry-related bromine atoms are perpendicularly oriented with respect to the ring plane.

The P1–N1–B3 and P2–N4–B4 angles [119.8(6)° and 112.7(5)°, respectively] of compound **5** demonstrate that the $PBr_2$ groups lie closer to atoms C3 and C6, respectively. The P–N bond lengths of molecules **5A** and **5B** are equal within standard deviations. The B–N bond lengths of the borazine units show distortions relative to the parent molecule $Me_3B_3N_3H_3$.[16] For example, the P substituent induces a significant B–N bond lengthening for the B–N bonds involving the P-bonded atoms N1 and N4. The remaining B–N bonds are shorter than those observed for borazines of the type $(RB{=}NH)_3$ (1.42–1.44 Å).[17] The B–N–B angles at atoms N1 and N4 [119.8(6)° and 118.6(6)°, respectively] are more acute than all other B–N–B bond angles [125.5(6)–126.7(6)°] while all N–B–N bond angles are smaller than 120° (by an average of 4°).

Figure 1 (b) shows a plot of the packing of the two independent molecules in the unit cell. This packing leads to an identical orientation of the bromine atoms of **5A** and **5B** in the stacks of packed borazine rings along the *b*-axis. These stacks are formed by alternating **5A** and **5B** molecules. The closest interatomic distances between the stacks are: B4–B3A = 3.971, B6A–B2A = 3.802, N5A–N3A = 3.940, and N2A–N6A = 3.714 Å. This leads to an average centroid–centroid distance of 3.87 Å, which is larger than the distance between the BN planes of hexagonal boron nitride (3.33 Å). There are no NH···Br interactions and no close Br···Br contacts.

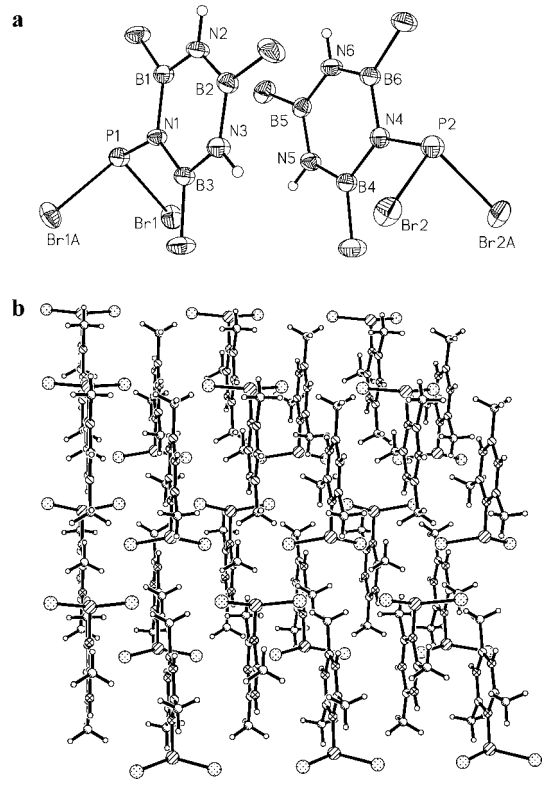


Figure 1. (a) Molecular structure of compound **5** showing the two independent molecules **5A** (left) and **5B** (right). CH hydrogen atoms have been omitted for clarity. The bonding parameters are listed in Table 3. (b) Packing of molecules **5A** and **5B**. These molecules are arranged in strings of alternating **5A** and **5B**.

The structure of **5** can best be compared with that of the dichlorostibane **9**, which crystallizes in the monoclinic system, space group $P2_1/n$, also with $Z = 8$. Relevant structural parameters are summarized in Table 3. The B–N bonds to the Sb-substituted atoms N1 and N4 are significantly longer than all other B–N bonds in the ring, and the B–N(1,4)–B bond angles are smaller (av. 120.95°) than all other B–N–B bond angles (av. 125.6°). The Cl–Sb–Cl bond angles of the two independent molecules differ by 4°, but the two pairs of Cl–Sb–N bond angles differ only by 2.7°.

Table 2. Selected IR data [$cm^{-1}$] for compounds **3**–**6**, **8**, **9**, and **10**.

| Compound | ν(NH) | ν(ring) | ν(EN) | ν(EX) |
|---|---|---|---|---|
| $(Me_3B_3N_3H_2)PCl_2$ | 3429, 3377 | 1499, 1402 | 1295 | 982, 960 |
| $(Me_3B_3N_3H_2)_2PCl$ | 3431, 3411, 3402 | 1487, 1435, 1396 | 1285 | 973 |
| $(Me_3B_3N_3H_2)PBr_2$ | 3423, 3414 | 1487, 1432, 1394 | 1290 | 975, 940 |
| $(Me_3B_3N_3H_2)_2PBr$ | 3430, 3401, 3391 | 1483, 1395 | 1282 | 962 |
| $(Me_3B_3N_3H_2)_2AsCl$ | 3419, 3411 | 1478, 1397 | 1285 | 920 |
| $(Me_3B_3N_3H_2)SbCl_2$ | 3421, 3406 | 1474, 1407, 1318 | 1262 | 889, 802 |
| $(Me_3B_3N_3H_2)_2SbCl$ | 3438, 3418 | 1473, 1449, 1400 | 1261 | 803 |

 © 2007 Wiley-VCH Verlag GmbH & Co. KGaA, Weinheim 

Table 3. Selected bond lengths [Å] and bond angles [°] for $Me_3B_3N_3H_2PBr_2$ (**5**) and $Me_3B_3N_3H_2SbCl_2$ (**8**).

| 5A | | 5B | | 9A | | 9B | |
|---|---|---|---|---|---|---|---|
| P1–Br1 | 2.261(1) | P2–Br2 | 2.307(2) | Sb1–Cl1 | 2.387(1) | Sb2–Cl3 | 2.365(1) |
| | | | | Sb1–Cl2 | 2.381(1) | Sb2–Cl4 | 2.375(1) |
| P1–N1 | 1.682(5) | P2–N4 | 1.674(5) | Sb1–N1 | 2.022(3) | Sb2–N4 | 2.027(3) |
| N1–B1 | 1.482(9) | N4–B4 | 1.506(9) | N1–B1 | 1.470(5) | N4–B4 | 1.455(5) |
| B1–N2 | 1.419(9) | B4–N5 | 1.411(9) | B1–N2 | 1.425(6) | B4–N5 | 1.429(5) |
| N2–B2 | 1.416(9) | N5–B5 | 1.406(9) | N2–B2 | 1.421(8) | N5–B5 | 1.425(6) |
| B2–N3 | 1.422(9) | B5–N6 | 1.416(9) | B2–N3 | 1.430(6) | B5–N6 | 1.412(6) |
| N3–B3 | 1.411(9) | N6–B6 | 1.386(9) | N3–B3 | 1.425(5) | N6–B6 | 1.424(6) |
| B3–N1 | 1.486(9) | B6–N4 | 1.495(9) | B3–N1 | 1.465(5) | B6–N4 | 1.465(5) |
| N1–P1–Br1 | 104.4(1) | N4–P2–Br2 | 105.89(1) | N1–Sb1–Cl1 | 97.50(9) | N4–Sb2–Cl3 | 99.73(9) |
| | | | | N1–Sb1–Cl2 | 100.27(9) | N4–Sb2–Cl4 | 97.52(9) |
| Br1–P1–Br1A | 99.86(8) | Br2–P2–Br2A | 98.99(8) | Cl1–Sb1–Cl2 | 91.63(4) | Cl3–Sb2–Cl4 | 95.40(4) |
| P1–N1–B1 | 113.2(4) | P2–N4–B4 | 118.8(6) | Sb1–N1–B1 | 126.0(3) | Sb2–N4–B4 | 126.5(2) |
| B1–N1–B3 | 119.8(6) | B4–N4–B6 | 118.8(6) | B1–N1–B3 | 120.9(3) | B4–N4–B6 | 121.0(3) |
| P1–N1–B3 | 119.8(6) | P2–N4–B6 | 112.7(5) | Sb1–N1–B3 | 113.1(2) | Sb2–N4–B6 | 112.4(3) |
| B1–N2–B2 | 125.5(6) | B4–N5–B5 | 126.7(6) | B1–N2–B2 | 126.6(4) | B4–N5–B5 | 121.0(3) |
| B2–N3–B3 | 126.5(6) | B4–N6–B6 | 126.6(6) | B2–N3–B3 | 125.4(4) | B4–N6–B6 | 125.3(4) |
| N1–B1–N2 | 117.0(6) | N4–B4–N5 | 115.8(7) | N1–B1–N2 | 115.9(4) | N4–B4–N5 | 116.5(3) |
| N2–B2–N3 | 115.0(6) | N5–B5–N6 | 115.0(6) | N2–B2–N3 | 114.3(4) | N5–B5–N6 | 115.2(4) |
| N3–B3–N1 | 116.1(6) | N6–B6–N4 | 117.0(6) | N3–B3–N11 | 116.8(3) | N6–B6–N4 | 116.9(4) |

The packing diagram of the molecules is depicted in part b of Figure 2, which reveals that the molecules are stacked on top of each other with the $SbCl_2$ groups oriented in opposite directions. The planar borazine rings are twisted against each other by 7° and are arranged perpendicularly to the respective $SbCl_2$ planes. Although the orientation of the Sb atoms with respect to the neighboring molecules suggests a higher coordination number than 3, the shortest intermolecular Sb–N distance is 3.693 Å, which is too long to be considered as a weak bond (sum of van der Waals radii: 3.8 Å). Even the intermolecular Sb–Cl interaction is weak because the respective Sb–Cl distance (3.310 Å) is only 0.05 Å shorter than the sum of the van der Waals radii.

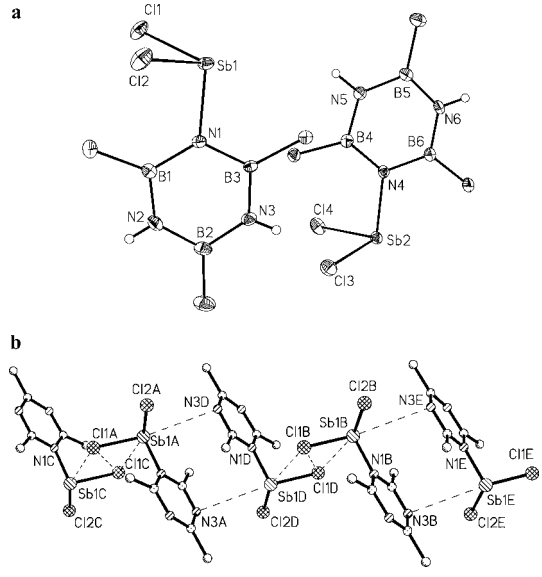


Figure 2. (a) The molecular structure of the two independent molecules in $(Me_3B_3N_3H_2)SbCl_2$ (**9**). Selected bonding parameters are listed in Table 3. CH hydrogen atoms have been omitted. (b) Interaction of one of the two independent molecules of **9**. Dotted lines represent the closests intermolecular interactions.

Figure 3 depicts the molecular structure of the bis(borazinyl)chlorophosphane **4**. This compound crystallizes with two molecules of toluene,[18] which are site disordered. The triclinic space group is $P\bar{1}$ with $Z = 2$. Relevant structural parameters are summarized in Table 4 together with the data for the corresponding bromide **6** (Figure 4). The configuration at the P atom is pyramidal (sum of bond angles: 303.5°). This represents partial $sp^3$ hybridization similar to that found in triaminophosphanes.[19] The P–Cl bond length [2.307(1) Å] of **4** is longer than that in $PCl_3$ [2.02(2) Å][20] and is also significantly longer than in most aminochlorophosphanes (2.109–2.197 Å).[21] The largest angle at the P1 atom is N1–P1–N4 (106.7°), while the angles N1–P1–Cl1 and N4–P1–Cl1 are only 100.3(1)° and 96.4(1)°, respectively. The opening of the N1–P1–N4 bond angle is most likely due to the steric demand of the trimethylborazinyl groups. The rings of these groups are not planar, as shown by the position of the atoms N1 and N4, which are bent out of the ring plane by 17° and 7°, respectively. The consequence of this ring distortion is that the methyl groups are also bent away from the ring plane in the opposite direction of the N1(4) atoms. Atoms C1 and C3 are more strongly affected, as shown by the value of 10° for

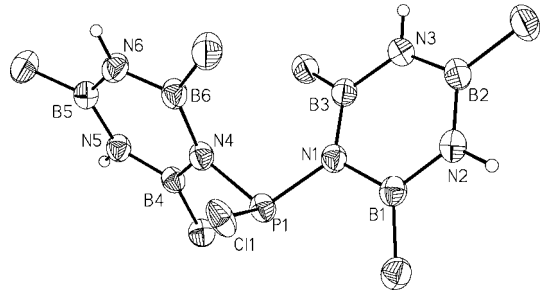


Figure 3. The molecular structure of compound $(Me_3P_3N_3H_2)_2PCl$ (**4**). Hydrogen atoms and the disordered toluene molecule have been omitted. See Table 4 for selected molecular parameters.

 © 2007 Wiley-VCH Verlag GmbH & Co. KGaA, Weinheim 

C1 and 13° for C3 (C4 and C6 are displaced only by 5° and 9°, respectively). Nevertheless, the sum of the bond angles at atoms N1 and N4 is 360°. It is also worthy to note that the B1–N1–P1 bond angle is 114.5(3)°, which contrasts with the value of 126.2° for the angle B3–N1–P1 [similarly B4–N3–P1 = 113.6(3)° and B6–N4–P1 = 125.7(3)°].

Table 4. Selected bonding parameters for the bis(trimethylborazinyl)halogenophosphanes **5** (X = Cl) and **6** (X = Br).

| | **4** | **6** | | **4** | **6** |
|---|---|---|---|---|---|
| P1–X | 2.307(2) | 2.334(1) | | | |
| P1–N1 | 1.702(4) | 1.704(3) | P1–N4 | 1.698(4) | 1.717(3) |
| B1–N1 | 1.474(7) | 1.475(5) | B4–N4 | 1.463(6) | 1.475(5) |
| B1–N2 | 1.423(6) | 1.410(6) | Be4–N5 | 1.422(7) | 1.419(5) |
| B2–N2 | 1.405(7) | 1.418(5) | B5–N5 | 1.422(7) | 1.420(6) |
| B2–N3 | 1.425(8) | 1.416(6) | B5–N6 | 1.424(7) | 1.425(6) |
| B3–N3 | 1.437(6) | 1.414(5) | B6–N6 | 1.425(7) | 1.415(5) |
| B3–N1 | 1.481(7) | 1.469(5) | B6–N4 | 1.481(6) | 1.469(5) |
| X–P1–N1 | 100.3(1) | 99.2(1) | X–P1–N4 | 96.4(1) | 101.1(1) |
| N1–P1–N4 | 106.7(2) | 106.2(1) | N1–P1–N4 | 108.7(4) | 106.2(2) |
| P1–N1–B1 | 114.5(3) | 126.5(2) | P1–N4–B4 | 125.7(3) | 126.6(2) |
| P1–N1–B3 | 126.2(3) | 112.9(2) | P1–N4–B6 | 120.6(4) | 114.0(2) |
| B1–N1–B3 | 119.1(4) | 120.5(3) | B4–N4–B6 | 126.1(4) | 118.9(3) |
| B1–N2–B2 | 125.9(5) | 126.9(4) | B4–N5–B5 | 125.8(4) | 115.6(3) |
| B2–N3–B3 | 125.6(5) | 126.5(4) | B5–N6–B6 | 126.1(4) | 126.3(4) |
| N1–B1–N2 | 116.6(5) | 115.8(3) | N5–B5–N6 | 114.5(4) | 113.0(4) |
| N3–B3–N1 | 115.2(5) | 116.3(3) | N6–B6–N4 | 116.0(4) | 116.6(3) |

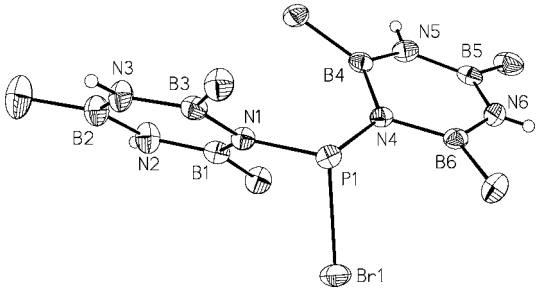


Figure 4. ORTEP plot of the molecular structure of $(Me_3B_3N_3H_2)_2$-PBr (**6**). Selected bonding parameters are listed in Table 4. CH hydrogen atoms have been omitted.

Amongst the B–N–B bond angles, those at atoms N1 and N4 are almost identical [119.1(4)° and 120.6(4)°, respectively]. The N–B–N bond angles to the B atoms opposite to N1 and N4 are only 114.7(4)° and 114.5(4)°, respectively, and are thus the smallest N–B–N bond angles of the two borazine moieties. In contrast, the B1–N2–B2 and B4–N5–B5 angles are quite wide [125.9(4)°]. The two borazine rings are twisted against each other by 56.6°.

Compound **6** crystallizes free of solvent molecules in the orthorhombic system, space group *Pbca*, with $Z = 8$. It is thus not isomorphous with **4** although the structural parameters of its trimethylborazinyl units are similar to those of **4**. This can readily be seen by comparing the data in Table 4. The sum of bond angles at the P1 atom is 306.4°, and, in analogy to **4**, the largest angle at the P atom is 106.2(1)° for N1–P1–N4.

The two borazine rings are twisted against each other by 51°. One of the borazine rings (N1 to B3) is planar, and the P1 atom is coplanar with this ring. The other borazine ring (N4 to B6) shows a half-chair conformation, with the plane B3–N4–B6 forming an angle of 15.9° with the B3–N5–B5–N6–B6 plane. Atoms C4 and C6 are placed below the plane of these five atoms. As observed in **4**, the N5–B4 and N6–B6 bonds are no longer parallel to one another, as would be expected for a planar borazine moiety, but are twisted against each other by 5°. This results in torsion angles of 7° for C6–B6–N5–P1 and 14° for C4–B4–N4–P1.

Once again, the B–N bonds to atoms N1 and N4 are longer [1.475(5) and 1.469(5)°] than all other B–N bonds in the rings. The shortest B–N bonds are B1–N2, B3–N3, B4–N5, and B6–N6, while those to the *p*-B atoms correspond best with those of symmetrically substituted borazines [1.418(6) Å].[17] The N–B–N bond angles vary from 113.9° to 115.8(3)°. While the bond angles B–N(1,4)–B are close to 120°, all other B–N–B bond angles are on average 126.7°. The P–Br bond length is 2.333(1) Å, which is 0.07 Å longer than in the dibromophosphane **5**.

### Reactions of the Bromo(trimethylborazinyl)phosphanes with Lithium Tetrahydridoaluminate

The reaction of the bromides **5** and **6** with $LiAlH_4$ should allow the synthesis of the corresponding phosphanes, $(Me_3B_3N_3H_2)PH_2$ and $(Me_3B_3N_3H_2)_2PH$, as shown in Equations (3) and (4), although it is known that aminophosphanes $(R_2N)_{2-n}PH_{n+1}$ are prone to undergo amine elimination.[22]

As shown in Equation (4), the reaction of **6** with $LiAlH_4$ in diethyl ether/hexane gives the compound bis(trimethylborazinyl)phosphane (**13**) in 75% yield. In contrast, the expected reaction [Equation (3)] between the dibromophosphane **5** and $LiAlH_4$ in the same solvents takes a different course. Thus, after removing the solid formed, the filtrate was found to be free of bromide. The crystals that separated from the concentrated filtrate within a week were found to exhibit three $^{11}B$ NMR signals at $\delta$ = 34.1, 35.3, and 36.8 ppm (in a ratio of about 1:1:1) but only a single $^{31}P$ NMR signal as a triplet at $\delta$ = 6.5 ppm ($^1J_{^{31}P,^1H}$ = 430 Hz) when dissolved in $C_6D_6$ (Figure 5, a). These data give evidence for the presence of a phosphonium $R(X)PH_2^+$ unit, and this was confirmed by the $^1H$ NMR spectrum, which shows two doublets (see Figure 5, b).

The signal of one of the doublets is further split into a triplet, while the other doublet is split into a quartet (see Figure 5, b). This gives convincing evidence that an ethyl group is attached to the P atom and that the solid is definitely not compound **12**, as would be expected from Equation (3). At this stage we assumed that the compound was most likely the zwitterionic phosphonium borazinate **14**. The $^1J_{^{31}P,^1H}$ coupling constant for the doublet of quartets is 380 Hz, while the $^1J_{^{31}P,^1H}$ coupling constant of the doublet of triplets is 370 Hz. Each of these resonances displays a further coupling of 7 Hz corresponding to $^3J_{^1H,^1H}$. Neither

 © 2007 Wiley-VCH Verlag GmbH & Co. KGaA, Weinheim 

$$2\,(Me_3B_3N_3H_2)PBr_2 + LiAlH_4 \rightarrow 2\,(Me_3B_3N_3H_2)PH_2 + LiAlBr_4 \quad (3)$$

**12**

$$4\,(Me_3B_3N_3H_2)_2PBr + LiAlH_4 \rightarrow 4\,(Me_3B_3N_3H_2)_2PH + LiAlBr_4 \quad (4)$$

**13**

$$Me_3B_3N_3H_2\text{-}PBr_2 + LiAlH_4 + OEt_2 \rightarrow Me_3B_3N_3H_2\text{-}PH_2 + LiBr + AlH_2Br{\cdot}OEt_2 \quad (5)$$

$$AlH_2Br{\cdot}OEt_2 \rightarrow AlH_2(OEt)] + EtBr \quad (6)$$

$$Me_3B_3N_3H_2\text{-}PH_2 + EtBr \rightarrow [(Me_3B_3N_3H_2)PH_2Et]Br \quad (7)$$

$$[(Mc_3B_3N_3H_2)PH_2Et]Br + AlH_2(OEt) \rightarrow (Me_3B_3(NH)(N^-)N)\text{-}P^+H_2Et + HAl(OEt)Br + H_2 \quad (8)$$

**14**

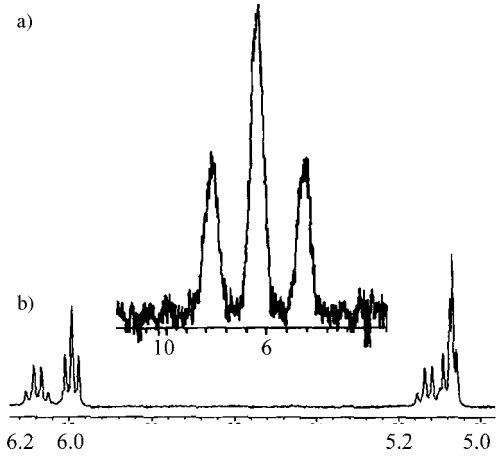


Figure 5. (a) $^{31}P$ NMR spectrum of **14**. (b) $^{1}H$ NMR spectrum of **14**.

of the signals shows a roof effect. This assignment was verified by recording a two dimensional $^{1}H$-$^{31}P$ spectrum.[5] The structure of **14** was finally confirmed by an X-ray structure determination. The $^{11}B$ NMR spectrum, with its three $^{11}B$ NMR signals, is also in line with these arguments.

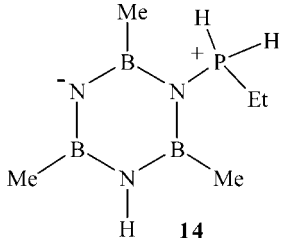


**14**

It is clear that the formation of **14** requires a number of steps. One hypothesis for its formation is summarized in Equations (5) to (8). The crucial step here is the formation of EtBr by an ether cleavage with $AlBr_3$, which is a well known process. EtBr is needed to form the phosphonium salt shown in Equation (7), which is the logical precursor to compound **14**. This reaction sequence is unique as no zwitterionic borazine is yet known and nor is a noncoordinated singly deprotonated borazine ring.

### *X-ray Structures*

The monophosphane **13** crystallizes from hexane as colorless needles (orthorhombic, space group *Pbca* with $Z = 8$). Its molecular structure is shown in Figure 6 and structural parameters are listed in Table 5. Its P–N bonds are significantly longer than those in compounds **4**, **5**, and **6**. The sum of bond angles at the P1 atom is 311°, which is a few degrees larger than in any of the borazinylphosphanes described previously. This results primarily from an N1–P1–H bond angle of 102.5(9)°. On the other hand, the N1–P1–N4 bond angle is 105.7(1)°, which corresponds with those found in **4** and **6**. The angles at the P1 atom are, in general, smaller than those found for aminophosphanes.[19]

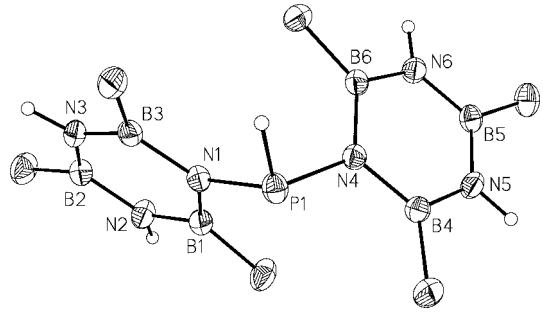


Figure 6. Molecular structure of the phosphane derivative **13**. Selected bonding parameters are listed in Table 5. CH hydrogen atoms have been omitted.

The two borazine units of **13** are almost planar and are twisted against each other by 84°, an angle that is significantly larger than in **4** or **6**, where the angle between the planes B1–N1–B3 and B1–B2–B3 is 5.2° and 8.0°, respectively. The exocyclic angles at N1 are 119.0(2)° for B1–N1–P1 and 120.0(2)° for B3–N1–P1, while the P1–N1–B2–C2 torsion angle is 177°. The B4–N4–P1 and B6–N4–P1 angles are 118.2(2)° and 121.7(2)°, respectively, whereas the P1–

 © 2007 Wiley-VCH Verlag GmbH & Co. KGaA, Weinheim 

Table 5. Selected bonding parameters for $(Me_3B_3N_3H_2)_2PH$ (**13**) and $(Me_3B_3N_3H)PH_2Et$ (**14**).

| | **13** | | | | **14** | | | |
|---|---|---|---|---|---|---|---|---|
| P1–N1 | 1.742(2) | P1–N4 | 1.734(2) | | P1–N1 | 1.694(2) | | |
| P1–H1 | 1.42(1) | | | | P1–C4 | 1.930(3) | | |
| N1–B1 | 1.435(4) | N4–B4 | 1.454(4) | | P1–H1 | 1.23(4) | | |
| B1–N2 | 1.429(4) | B4–N5 | 1.413(4) | | P1–H2 | 1.32(4) | | |
| N2–B2 | 1.427(4) | N5–B5 | 1.415(4) | | N1–B1 | 1.462(3) | | |
| B2–N3 | 1.407(5) | B5–N6 | 1.418(4) | | B1–N3 | 1.413(3) | | |
| N3–B3 | 1.433(4) | N6–B6 | 1.419(4) | | N2–B2 | 1.439(3) | | |
| B3–N1 | 1.464(4) | B6–N4 | 1.460(4) | | B2–N3 | 11.428(3) | | |
| N1–P1–N4 | 105.7(1) | N1–P1–H1 | 102.5(9) | | N3–B3 | 1.421(3) | | |
| N4–P1–H1 | 102.8(9) | | | | B3–N1 | 1.439(3) | | |
| B1–N1–P1 | 119.0(2) | B4–N4–P1 | 118.2(2) | | B1–N1–P1 | 119.5(2) | H1–P1–H2 | 103.4(9) |
| B3–N1–P1 | 120.0(2) | N6–N4–P1 | 121.8(2) | | B2–N1–P1 | 119.0(2) | H1–P1–C4 | 114.1(9) |
| B1–N1–B3 | 120.4(2) | B4–N4–B6 | 120.0(2) | | B1–N1–B3 | 121.3(2) | H2–P1–C4 | 113.6(4) |
| B1–N2–B2 | 124.8(3) | B4–N5–B5 | 125.5(2) | | B1–N2–B2 | 125.0(2) | H1–P1–N1 | 107.3(4) |
| B2–N3–B3 | 125.8(2) | B5–N6–B6 | 125.4(2) | | N2–N3–B3 | 125.3(2) | H2–P1–N1 | 102.6(4) |
| N1–B1–N2 | 117.3(3) | N4–B4–N5 | 117.0(2) | | N1–B1–N2 | 116.9(2) | N1–P1–C4 | 114.53(9) |
| N2–B2–N3 | 115.0(3) | N5–B5–N6 | 114.7(3) | | N2–B2–N3 | 114.9(2) | P1–C4–C5 | 112.2(3) |
| N3–B3–N1 | 116.4(3) | N6–B6–N4 | 116.9(2) | | N3–B3–N1 | 116.5(2) | | |

N4–B5–C5 torsion angle is only 33°, which deviates significantly from the corresponding P1–N1–B2–C2 torsion angle. Once again, the B–N bonds to N1 and N4 are longer [1.452(4), 1.464(4), 1.454(4), and 1.460(4) Å] than all other B–N bonds (av. 1.43 Å).

Compound **14** crystallizes in the orthorhombic space group $Pca2_1$ with $Z = 8$. Its molecular structure, depicted in Figure 7, demonstrates the presence of a phosphonium group. The bond angles at the P1 atom range from 102.6(4)° (N1–P1–H2) to 114.53(9)° (N1–P1–C4). The two P–H bonds seem to be significantly different [1.32(4) and 1.23(4) Å] and the bond angle between them is 103.4°. The P–C bond [1.930(3) Å] is much longer than in other organophosphonium salts [d(PC) = 1.674 to 1.849 Å],[23] and this bond is still 0.1 Å longer than the "normal" P–C single bond length when an electronegativity correction is applied.[24]

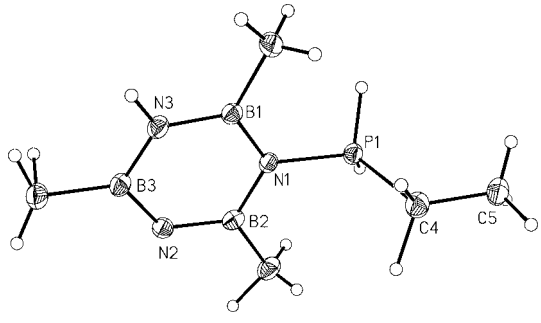


Figure 7. ORTEP plot of the molecular structure of the zwitterion **14**. Selected bonding parameters are listed in Table 5.

The borazine ring of **14** is planar and large B–N–B bond angles at atoms N2 and N3 [125.0(2)° and 125.3(2)°, respectively] are once again observed; the B1–N1–B2 bond angle is 121.3(2)°. The B1–N1–P1 and B2–N1–P1 bond angles are smaller than 120° [119.5(2)° and 119.0(2)°, respectively], and the N–B–N bond angles are also acute [114.9(2)–116.5(2)°]. Equivalent pairs of B–N bond lengths range from 1.462(3) and 1.459(3) Å (to N1) and include short [B1–N2 = 1.413(3), B3–N3 = 1.421(3) Å] and intermediate bond lengths [N2–B2 = 1.439(3), N3–B2 = 1.428(3) Å].

The difference Fourier analysis for NH hydrogen atoms revealed weak peaks on atoms N2 and N3. They refined best with a site occupation factor (SOF) of 0.5 as the $U_i$ values were not compatible with an SOF of 1. Figure 7 shows only one occupied NH position. The X-ray structure analysis excludes an Et/Me exchange between the P atom and a B atom.

### Trimethylborazinyldiphosphanes and Cyclotetraphosphanes

The trimethylborazinyl-halogeno-phosphanes appeared to be precursors for borazinyldiphosphanes and cyclophosphanes because it is well known that the dehalogenation of di- and monoorgano-halogeno-phosphanes leads to diphosphanes $P_2R_4$ and cyclophosphanes $(RP)_n$, respectively. Diphosphanes can also be prepared by the reaction of $R_2PX$ with $Me_3SiPR_2$. However, no reaction was observed on treating the bromide **6** with $Me_3SiPR_2$ [Equation (9)] even at reflux in toluene.

After replacement of $Me_3SiPR_2$ with $LiPmes_2$, however, good yields of the diphosphane **17** were obtained [Equation (10)]. The analogous reaction with $LiPPh_2$ generated **16**, although it could not be completely separated from accompanying $Ph_2PPPh_2$.

As the reaction shown in Equation (11) proceeded without problems, we also decided to treat the dibromide **5** with sodium in toluene. This reaction gave exclusively tetrakis(trimethylborazinyl)cyclotetraphosphane (**19**), as shown in Equation (12). This compound crystallized as strongly intergrown needles, which were also obtained by treating **5** with activated Mg or sodium naphthalide in thf.

While the crystal quality of **16** was insufficient for an X-ray structure determination, single crystals of **17** and **18** were obtained. However, those of **17** were quite small and did not diffract too well. Nevertheless, the refinement converged at $R_1 = 6.5\%$.

 © 2007 Wiley-VCH Verlag GmbH & Co. KGaA, Weinheim 

$$(Me_3B_3N_3H_2)_2PBr + Me_3SiPR_2 \not\rightarrow (Me_3B_3N_3H_2)_2P\text{-}PR_2 + Me_3SiBr \quad (9)$$

R = Et (**15**), Ph (**16**)

$$(Me_3B_3N_3H_2)_2PBr + LiPmes_2 \rightarrow (Me_3B_3N_3H_2)_2P\text{-}Pmes_2 + LiBr \quad (10)$$

**17**

$$2\,(Me_3B_3N_3H_2)_2PBr + 2\,Na \rightarrow (Me_3B_3N_3H_2)_2P\text{-}P(H_2N_2B_3Me_3)_2 + 2\,NaBr \quad (11)$$

**18**

$$4\,(Me_3B_3N_3H_2)PBr_2 + 4\,Na \rightarrow (Me_3B_3N_3H_2)_4P_4 + 4\,NaBr \quad (12)$$

**19**

$$2\,(Me_3B_3N_3I_2)PBr_2 + 2\,Li_2Pmes \rightarrow (Me_3B_3N_3I_2)_2P_4(mes)_2 + 4\,LiBr \quad (13)$$

**A** – **E**

We expected that the reaction of **5** with $Li_2Pmes$ might yield the 2,4-bis(mesityl)-1,3-bis(trimethylborazinyl)cyclotetraphosphane **D**. However, the $^{31}P$ NMR spectroscopic data of the solution showed that this ideal composition is not achieved. Rather, a mixture of the cyclotetraphosphanes **A**–**F** (Scheme 1) is formed, with no evidence for cyclotriphosphanes or cyclopentaphosphanes. Isolated single crystals turned out to be the isomer 2,3-bis(mesityl)-1,4-bis(trimethylborazinyl)cyclotetraphosphane (**E**).

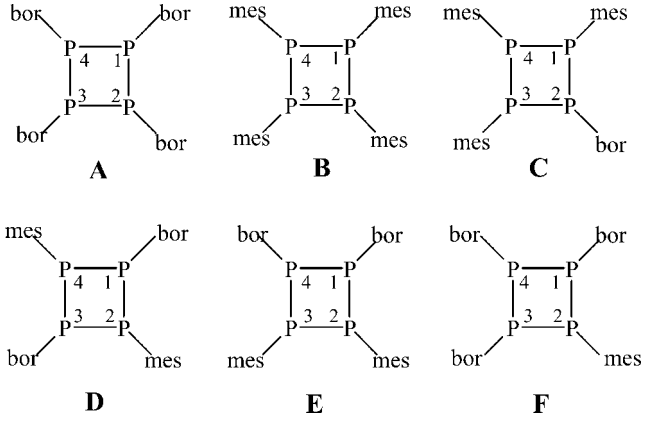


Scheme 1. Isomers of dimesitylbis(trimethylborazinyl)cyclotetraphosphane.

### *NMR Spectra*

Table 6 lists the chemical shifts and coupling constants of the nuclei $^1H$, $^{11}B$, and $^{31}P$ for the diphosphane derivatives. Surprisingly, both diphosphanes **17** and **18** show only a single but very broad $^{11}B$ resonance, which contrasts with the borazinyl-halogeno-phosphanes. As expected, **18** exhibits a single $^{31}P$ resonance signal at $\delta$ = 108.7 ppm, while there are two doublets at $\delta$ = 113.9 and –20.6 ppm for **17**, with a $^1J_{^{31}P,^{31}P}$ coupling constant of 223 Hz. Thus, the mesityl-bonded P nuclei are much better shielded than the P nuclei bearing borazine rings. Two sets of proton signals are observed for the BMe groups in **17** and **18**, with those of the *o*-BMe protons being better shielded than the *p*-BMe protons. The former appear as doublets due to $^4J_{^{31}P,^1H}$ coupling, whereas no such coupling is observed for the *o*-Me groups of the mesityl substituents.

The NMR spectra of compound **19** are rather simple, with only one signal appearing in each of the $^{11}B$ and $^{31}P$ NMR spectra. The $^{11}B$ NMR signal is rather broad. Since there are also single sets of $^1H$ NMR signals for the *o*-BMe and *p*-BMe groups, this suggests that the compound has an all-*trans* conformation. The *o*-BMe protons appear as doublets with a $^4J_{^{31}P,^1H}$ coupling constant of 5.2 Hz. These data also demonstrate that no cyclotriphosphane or cyclopentaphosphane is generated upon dehalogenation of **5**.

In contrast, the NMR spectra of the solution obtained by treating **5** with $Li_2Pmes$ are surprisingly complex. There are many $^{31}P$ NMR signals in the range from $\delta$ = –60 to –300 ppm, which indicates the presence of cyclotetraphosphanes. Most of these signals could be assigned. Thus, the weak triplets at $\delta$ = –171.2 and –299.0 ppm are due to the presence of *cis*-bis(mesityl)bicyclo[1.1.0]tetraphosphane,[24] which is also present as its *trans*-isomer ($\delta$ = –292.2 ppm (dd) and two triplets at $\delta$ = –155.7 and –161.2 ppm).[24]

Table 6. NMR spectroscopic data for compounds **17**, **18**, **19** and **E**. Half width (Hz) in parentheses.

| Compound | $\delta^{11}B$ | $\delta^{31}P$ | $\delta^1H$ *o*-BMe | $\delta^1H$ *p*-BMe | $\delta^1H$ NH | $\delta^1H$ *p*-CMe | $\delta^1H$ *o*-CMe | $\delta^1H$ CH |
|---|---|---|---|---|---|---|---|---|
| **17** | 36.4 (1250) | 113.9,[a] –20.6[a] | 0.87[b] | 0.13 | 4.39 | 2.03 | 2.56 | 6.67 |
| **18**[c] | 36.3 (1260) | 108.7 | 0.84 | 0.15 | 4.49 | – | – | – |
| **19** | 37.1 (1225) | 63.0 | 0.87[d] | 0.05 | 4.48 | | | |
| **E** | 36.8 (1300) | 60.9, –49.2 | 0.99[e] | 0.04 | | 2.80 | 2.71[f] | |

[a] $^1J_{^{31}P,^{31}P}$ = 223 Hz. [b] $^4J_{^{31}P,^1H}$ = 6.8 Hz. [c] bor = $Me_3B_3N_3H_2$. [d] $^4J_{^{31}P,^1H}$ = 5.2 Hz. [e] $^4J_{^{31}P,^1H}$ = 5.75 Hz. [f] $^4J_{^{31}P,^1H}$ = 3.57 Hz.

 © 2007 Wiley-VCH Verlag GmbH & Co. KGaA, Weinheim 

Fractional crystallization provided crystals of the isomer **E**. A solution of these crystals shows a single but rather broad $^{11}B$ NMR signal with $h_{1/2}$ = 1300 Hz. This may well result from two overlapping $^{11}B$ signals because the $^{1}H$ NMR spectra clearly show the presence of two types of BMe, NH, CMe, and CH signals in the expected intensity ratios. Both the *o*-BMe and *o*-CMe protons appear as doublets due to $^{4}J_{^{31}P,^{1}H}$ coupling.

A two-dimensional $^{31}P$ NMR spectrum[5] and high-resolution $^{31}P$ NMR spectra of the reaction solution give evidence for the presence of all isomers of the cyclotetraphosphanes **A**–**F**. The rings **A** and **B** should lead to an $A_4$ spin system ($^{31}P$ singlet for the all-*trans* conformer). The singlet at $\delta$ = 63.0 ppm demonstrates the presence of isomer **A**, and another singlet at $\delta$ = –43.2 ppm stems from compound **B**. Ring **E** should be represented by an AA′XX′ spin system and should therefore show a higher order spectrum, which, in a first approximation, could appear as a doublet of doublets. This doublet of doublets can indeed be observed at $\delta$ = 60.9 and –49.2 ppm and these signals show additional signals at higher resolution to give a spectrum of higher order. Ring **D** should give a first-order spectrum, as expected for an $A_2X_2$ spin system. This is indeed observed, with two triplets at $\delta$ = 36.9 and –7.8 ppm ($^{1}J_{^{31}P,^{31}P}$ = 170 Hz). The P2 atom of ring **C** should give an $A_2X$ type spectrum, in other words a triplet, which is found at $\delta$ = 77.3 ppm. Another triplet at $\delta$ = 32.5 ppm, with a coupling constant of 232 Hz, can be assigned to the atom P4. Finally, a doublet of doublets is observed at $\delta$ = –26.4 ppm representing atoms P1 and P3. The same signal types should result from the presence of isomer **F**. The respective chemical shifts are: a triplet at $\delta$ = –30.5 ppm for P2, a doublet of doublets at $\delta$ = 41.4 ppm for P1 and P3, and a triplet at $\delta$ = 74.9 ppm for P4. The coupling constant is 168 Hz. Examples of the observed and calculated $^{31}P$ NMR spectra are displayed in Figure 8. The program NUTS[36] was used to obtain the calculated spectra.

The mes and borazinyl substituents (or PX groups) therefore appear to have exchanged during the course of reaction to give a more or less random distribution of the cyclotetraphosphanes.

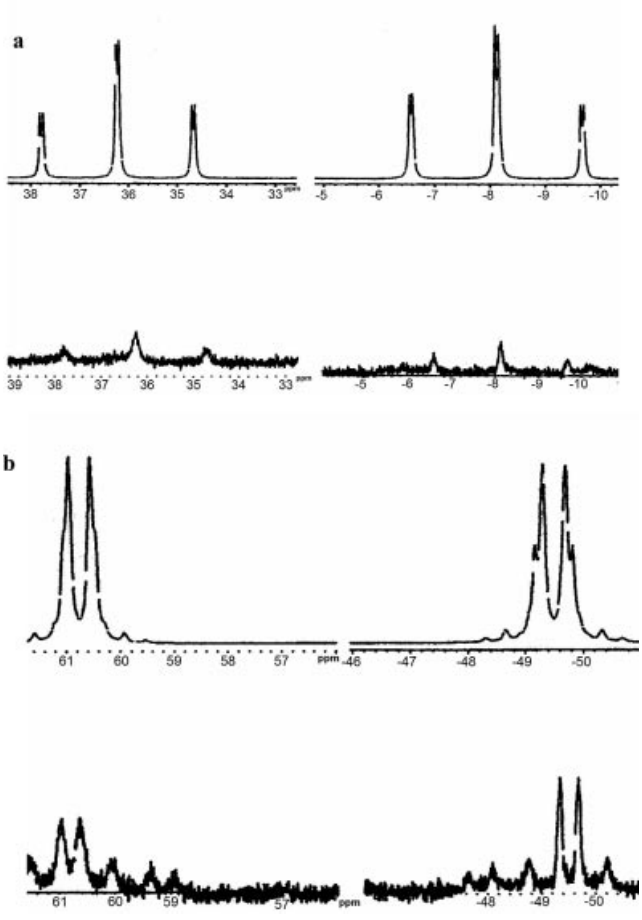


Figure 8. (a) Observed (bottom) and calculated (top) $^{31}P$ NMR spectra for the isomer 1,3-diborazinyl-2,4-dimesitylcyclotetraphosphane. (b) Observed (bottom) and calculated (top) $^{31}P$ NMR spectrum of the isomer 1,2-diborazinyl-3,4-dimesitylcyclotetraphosphane (**E**).

### *X-ray Structures*

The tetrakis(trimethylborazinyl)diphosphane **18** crystallizes from toluene as **18**$(C_6H_5Me)_2$ in the triclinic space group $P\bar{1}$; its molecular structure is depicted in Figure 9 and relevant bonding parameters are listed in Table 7. The borazinyl units in this compound are present in a staggered conformation. The dihedral angles of opposite rings are 164° for both ring pairs while the dihedral angles of adjacent rings differ by 30°. The N4–P1–P2 angle is 108.4(2)° while the N1–P1–P2 angle exceeds this angle by 7.8°. A twist of 32° is found for the borazinyl rings containing N1 and N7, and this value is even larger for N4 and N10 (97°). While the borazine rings containing N1 and N7 are planar, those including atoms N4 and N10 are slightly bent into a half-chair conformation, with N4 bent out of the plane by 11° and N10 by 9.2°. The BMe groups at the *ortho* positions are bent backwards, with the respective NBC angles ranging from 124.3(7)° to 127.4(7)°. Additional bonding parameters are listed in Table 7.

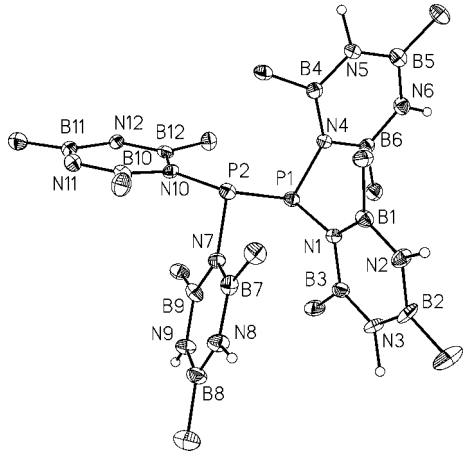


Figure 9. The molecular structure of tetrakis(trimethylborazinyl)diphosphane (**18**). The H atoms of the methyl groups are not shown. Selected bonding parameters are listed in Table 7.

 © 2007 Wiley-VCH Verlag GmbH & Co. KGaA, Weinheim 

Table 7. Selected bonding parameters for $P_2(H_2N_3B_3Me_3)_4$ (**18**).

| | | | | | | | |
|---|---|---|---|---|---|---|---|
| P1–P2 | 2.287(2) | | | | | | |
| P1–N1 | 1.735(6) | P1–N4 | 1.748(5) | P2–N7 | 1.755(6) | P2–N10 | 1.740(5) |
| B1–N1 | 1.44(1) | B4–N4 | 1.462(9) | B7–N7 | 1.472(9) | B10–N10 | 1.461(9) |
| B1–N2 | 1.44(1) | B4–N5 | 1.418(9) | B7–N8 | 1.42(1) | B10–N11 | 1.45(1) |
| N2–B2 | 1.42(1) | N5–B5 | 1.430(9) | N8–B8 | 1.42(1) | N11–B11 | 1.40(1) |
| B2–N3 | 1.45(1) | B5–N6 | 1.43(1) | B8–N9 | 1–40(1) | B11–N12 | 1.443(9) |
| N3–B3 | 1.41(1) | N6–B6 | 1.430(9) | N9–B9 | 1.42(1) | N12–B12 | 1.433(9) |
| B3–N1 | 1.49(1) | B6–N4 | 1.468(9) | B9–N7 | 1.452(9) | B12–N10 | 1.459(9) |
| P2–P1–N1 | 94.3(2) | P2–P1–N4 | 108.5(2) | P1–P2–N7 | 94.8(2) | P1–P2–N10 | 109.1(2) |
| N1–P1–N4 | 101.8(5) | | | N7–P2–N10 | 102.7(3) | | |
| P1–N1–B1 | 126.6(5) | P1–N4–B4 | 130.1(5) | P2–N7–B7 | 113.6(5) | P2–N10–B10 | 111.8(5) |
| P1–N1–B3 | 115.4(5) | P1–N4–B7 | 111.3(5) | P2–N7–B9 | 126.7(5) | P2–N10–B12 | 130.6(5) |
| B1–N1–B3 | 118.0(7) | B4–N4–B6 | 118.6(6) | B7–N7–B9 | 119.6(5) | B10–N10–B12 | 117.5(5) |
| B1–N2–B2 | 126.21(7) | B4–N5–B5 | 126.4(7) | B7–N8–B8 | 126.1(4) | B10–N11–B11 | 124.7(5) |
| B2–N3–B3 | 124.4(7) | B5–N6–B6 | 126.4(7) | B8–N9–B9 | 125.6(5) | B11–N12–B12 | 123.5(6) |
| N1–B1–N2 | 117.5(7) | N4–B4–N5 | 117.6(6) | N7–B7–N8 | 116.6(6) | N10–B10–N11 | 118.6(5) |
| N2–B2–N3 | 114.3(8) | N5–B5–N6 | 113.3(7) | N8–B8–N9 | 114.4(6) | N11–B11–N12 | 115.5(5) |
| N3–B3–N1 | 119.4(7) | N6–B6–N4 | 117.6(6) | N9–B9–N7 | 117.7(5) | N12–B12–N10 | 119.5(5) |

Figure 10 shows the molecular structure of the "mixed" diphosphane **17**, and Table 8 contains its bonding parameters. The P–P bond in **18** [2.287(1) Å] is longer than in **17** [2.268(1) Å], which may be a steric effect because the P–N bond in **18** is about 0.03 Å shorter than in **17**.

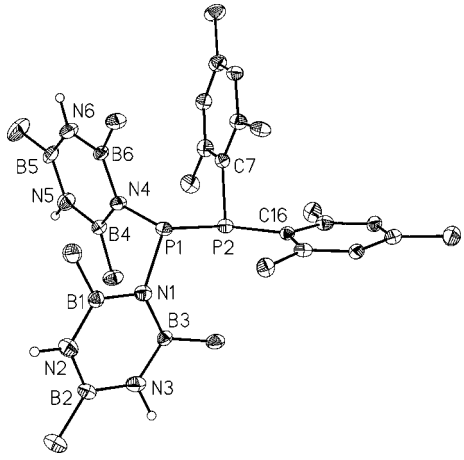


Figure 10. Molecular structure of *P*,*P*-dimesityl-*P'*,*P'*-bis(trimethylborazinyl)diphosphane (**17**). Hydrogen atoms, with the exception of the NH hydrogens, have been omitted. Selected bonding parameters are listed in Table 8.

The first fraction to crystallize from a hexane solution obtained by treating $Me_3B_3N_3H_2PBr_2$ with $Li_2Pmes$ proved to be uniform when inspected by microscopy. The crystals are monoclinic, space group $P\bar{1}$, with $Z = 2$. There is also one molecule of hexane in the unit cell. In a first attempt we solved the structure by assuming that the crystal might have the composition $P_4(H_2N_3B_3Me_3)_4$. The structure solution indeed revealed a cyclotetraphosphane ring, with each of the four P atoms carrying a six-membered ring. The structure refined to $R = 6.6\%$ with attached $B_3N_3$ rings. However, the thermal parameters and bond lengths clearly showed that this assumption was wrong as there are two long P–N bonds and two shorter ones, and the B–C bond lengths are also shorter for those rings with "long" P–N distances. This result suggests that these latter rings are mesityl rings rather than borazines. In this case the R value improved to $R_1 = 5.99\%$. The result of this latter refinement is shown in Figure 11, where it is clear that the crystal contains species **E**. Selected bonding parameters are summarized in Table 9.

Table 8. Selected bonding parameters for $(Me_3B_3N_3H_2)_2P\text{-}P(C_6H_2Me_3)_2$ (**17**).

| | | | | | | | |
|---|---|---|---|---|---|---|---|
| P1–P2 | 2.268(1) | | | | | | |
| P1–N1 | 1.778(2) | P1–N4 | 1.771(3) | P2–C7 | 1.831(3) | P2–C16 | 1.829(3) |
| N1–B1 | 1.451(5) | N4–B4 | 1.451(4) | C7–C8 | 1.422(4) | C16–C17 | 1.420(4) |
| B1–N2 | 1.415(4) | B4–N5 | 1.416t(5) | C8–C9 | 1.391(4) | C17–C18 | 1.388(5) |
| N2–B2 | 1.416(5) | N5–B5 | 1.412(5) | C9–C10 | 1.401(5) | C18–C19 | 1.391(4) |
| B2–N3 | 1.413(5) | B5–N6 | 1.420(5) | C10–C11 | 1.393(4) | C19–C20 | 1.394(5) |
| N3–B3 | 1.424(4) | N6–B6 | 1.409(5) | C11–C12 | 1.402(4) | C20 C21 | 1.393(5) |
| B3–N1 | 1.454(4) | B6–N4 | 1.456(4) | C12–C7 | 1.429(4) | C21–C16 | 1.426(4) |
| P2–P1–N1 | 108.7(1) | P2–P1–N4 | 102.4(1) | P1–P2–C7 | 96.3(1) | P1–P2–C16 | 110.9(9) |
| N1–P1–N4 | 102.4(1) | | | C7–P2–C16 | 102.1(1) | | |
| B1–N1–B3 | 118.4(3) | B4–N4–B6 | 119.(3) | C8–C7–C16 | 117.2(3) | C17–C16–C21 | 117.2(3) |
| B1–N2–B2 | 124.1(3) | B4–N5–B5 | 125.3(3) | C8–C9–C10 | 122.9(3) | C17–C18–C19 | 123.1(3) |
| B2–N3–B3 | 125.8(3) | B5–N6–B6 | 124.9(3) | C10–C11–C12 | 123.3(3) | C19–C20–C21 | 123.3(3) |
| N1–B1–N2 | 119.0(3) | N4–B4–N5 | 117.7(3) | C7–C8–C9 | 119.9(3) | C16–C17–C18 | 120.0(3) |
| N2–B2–N3 | 114.5(3) | N5–B5–N6 | 114.8(3) | C9–C10–C11 | 116.6(3) | C18–C19–C20 | 116.4(3) |
| N3–B3–N1 | 117.1(3) | N6–B6–N4 | 118.0(3) | C11–C12–C7 | 119.0(3) | C19–C20–C21 | 123.3(3) |

 © 2007 Wiley-VCH Verlag GmbH & Co. KGaA, Weinheim 

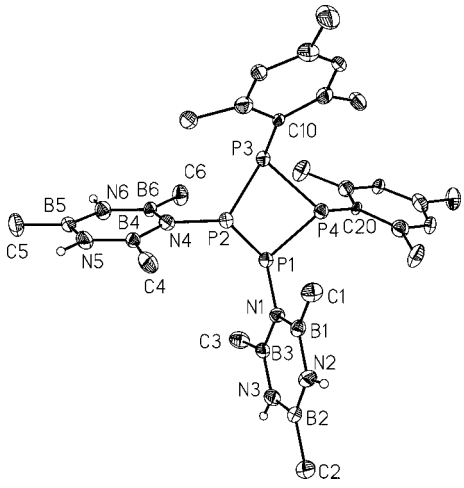


Figure 11. The molecular structure of 3,4-dimesityl-1,2-bis(trimethylborazinyl)cyclotetraphosphane (**E**). Hydrogen atoms at the methyl groups have been omitted. Selected bonding parameters are listed in Table 9.

The cyclotetraphosphane ring is folded, as expected, and it substituents are present in the *trans* orientation that is typical for other $P_4R_4$ rings.[25–28] The rings at atoms P1 and P3 are twisted against each other by 20° while those at atoms P2 and P4 make an angle of 93°. Amongst the P–P bonds, those to atom P4 are significantly longer than those to atom P2. The longer bonds match with those found for tetrakis(2,2,6,6-tetramethylpiperidino)cyclotetraphosphane or diphenylbis(tetramethylpiperidino)cyclotetraphosphane (2.245 Å).[26]

The endocyclic P–P–P angles span the range from 78.99(5)° (P4) to 84.35(5)° (P3) and are compatible with those of other cyclotetraphosphanes.[25–28] The four-membered ring is not uniformly bent, however, as the non-bonding P–P distances are 3.6 Å for P2–P4 and 2.8 Å for P1–P3.

## Discussion and Conclusion

The chemistry of borazines is well documented,[29–31] although neither *B*- nor *N*-phosphanylborazines have been reported. We now show that (2,4,6-trimethylborazinyl)-halogeno-phosphanes are readily available and may serve as starting materials for *N*-(diorganophosphanyl)borazines. *B*-Phosphanylborazines should also be accessible by treating *B*-haloborazines with alkali metal organophosphides.

Because halophosphanes do not react with borazines of the type $R_3B_3N_3H_3$, even in the presence of an HX acceptor, we have used the recently characterized *N*-monolithio-trimethylborazine (**2**) as a stronger nucleophile to bind the borazinyl unit to $P^{III}$, $As^{III}$, and $Sb^{III}$ centers. This gives access to all members of the series $(Me_3B_3N_3H_2)_n$-$EX_{3-n}$ (E = P, As, Sb), although the compounds with $n = 3$ were not obtained in pure state. We have also found that the borazinyl-halogeno-phosphanes are suitable reagents for preparing the corresponding bis(borazinyl)phosphane (**13**) as well as borazinyldiphosphanes or borazinylcyclotetraphosphanes. However, the reaction of $LiAlH_4$ with $Me_3B_3N_3H_2PBr_2$ in hexane/diethyl ether does not provide $Me_3B_3N_3H_2PH_2$; rather, this provides the zwitterionic phosphonium borazinate **14**, which shows that the P atom of $(Me_3B_3N_3H_2)PHEt$ is a stronger basic center than the ring N atoms because one of the NH atoms migrates to the P atom. This generates a new type of borazine derivative.[29–31] We are convinced that the reaction of $LiAlH_4$ with $Me_3B_3N_3H_2PBr_2$ in the absence of diethyl ether will lead to $Me_3B_3N_3H_2PH_2$, whose P atom should be less basic than that of the PHEt group.

The dehalogenation of organohalophosphanes with Na or other metals is often employed as a route to organodiphosphanes or organocyclophosphanes.[32] While the dehalogenation of **6** with Na or Mg produced the corresponding diphosphane derivative **18**, its reaction with $LiPmes_2$ gives access to the mixed substituted diphosphane **17**. However, in the case of $LiPPh_2$ the formation of $P_2Ph_4$ is also

Table 9. Selected bonding parameters for $(Me_3B_3N_3H_2)_2P_4mes_2$ (**E**).[a]

| | | | | | | | |
|---|---|---|---|---|---|---|---|
| P1–P4 | 2.215(2) | P1–P2 | 2.207(2) | P2–P3 | 2.251(2) | P3–P4 | 2.256(2) |
| P4–C20 | 1.804(4) | P1–N1 | 1.754(4) | P2–N4 | 1.769(4) | P3–C10 | 1.801(4) |
| C20–C21 | 1.428(7) | N1–B1 | 1.449(7) | N4–B4 | 1.451(6) | C10–C11 | 1.433(6) |
| C21–C22 | 1.379(7) | B1–N2 | 1.434(7) | B4–N5 | 1.402(7) | C11–C12 | 1.406(6) |
| C23–C24 | 1.395(7) | N2–B2 | 1.420(7) | N5–B5 | 1.411(8) | C13–C14 | 1.404(7) |
| C22–C23 | 1.407(7) | B2–N3 | 1.409(8) | B5–N6 | 1.396(7) | C12–C13 | 1.396(7) |
| C21–C22 | 1.379(7) | N3–B3 | 1.441(7) | N6–B6 | 1.410(8) | C11–C10 | 1.433(7) |
| C20–C21 | 1.428(7) | B3–N1 | 1.468(6) | B6–N4 | 1.450(7) | C10–C15 | 1.441(7) |
| P1–P4–P3 | 84.34(6) | P1–P2–P3 | 84.34(6) | P2–P1–P4 | 80.95(6) | P2–P3–P4 | 79.11(6) |
| P1–P4–C20 | 104.8(1) | P2–P3–N1 | 107.0(1) | P4–P3–N4 | 111.27(6) | P1–P4–C20 | 104.8(1) |
| P3–P4–C20 | 114.4(2) | P4–P2–N1 | 109.5(1) | P1–P2–N4 | 106.8(1) | P3–P4–C20 | 114.4(21) |
| P4–C20–C25 | 128.3(3) | P2–N1–B1 | 127.2(3) | P2–N4–B4 | 113.3(1) | P4–C20–C21 | 113.6(3) |
| P4–C20–C21 | 113.7(4) | P2–N1–B3 | 122.2(4) | P2–N4–B6 | 127.6(4) | P4–C20–C25 | 128.3(3) |
| C25–C20–C21 | 118.0(5) | B1–N1–B3 | 120.6(4) | B4–N4–B6 | 119.0(4) | C15–C10–C11 | 117.8(4) |
| C24–C25–C20 | 118.5(5) | N1–B1–N2 | 117.4(5) | N4–B4–N5 | 118.0(5) | C14–C15–C10 | 119.1(4) |
| C23–C24–C25 | 124.1(4) | B1–N2–B2 | 124.8(6) | B4–N5–B5 | 124.8(5) | C13–C14–C15 | 123.5(4) |
| C24–C23–C22 | 115.8(5) | N2–B2–N3 | 115.1(5) | N5–B5–N6 | 115.0(4) | C14–C13–C12 | 115.9(4) |
| C21–C22–C23 | 122.9(4) | B2–N3–B3 | 126.0(5) | B5–N6–B6 | 125.5(5) | C11–C12–C13 | 123.9(4) |

[a] Average B–C bond length: 1.557 Å; average C–C(*exo*) bond length: 1.529 Å.

 © 2007 Wiley-VCH Verlag GmbH & Co. KGaA, Weinheim 

observed along with $(Me_3B_3N_3H_2)_2PPPh_2$ (**16**). This indicates that a Li/Br exchange occurs during the reaction, and this also occurs during the reaction of $Li_2Pmes$ with **4**, as shown by the formation of compounds **A**–**F**, which is also accompanied by the formation of small amounts of bicylo[1.1.0]tetraphosphanes. The tetra(borazinyl)cyclotetraphosphane (**19**) shows only one $^{31}P$ signal ($\delta$ = 63 ppm),which fits nicely with the other $^{31}P$ data recorded for cyclotetraphosphanes of the type $(R_2NP)_4$.[26] As far as we are aware the exchange of organo substituents in organophosphorus chemistry is not common, although the borazinyl group, with its P–N bond, is a species with higher bond polarity and is therefore more likely to be more reactive, similar to the aminophosphanes.

This higher reactivity of the borazinylphosphanes with respect to the *N*-unsubstituted borazines seems to be a consequence of the changes in the structures of the new compounds. As shown by X-ray structure determinations, the P atom induces asymmetry in the borazine ring as shown by the comparatively long B–N bonds to the P-carrying N atom. This weakens the B1–N2 and B3–N4 bonds to the neighboring boron atoms. Atoms B1(3), on the other hand, usually form the shortest B–N bonds to atoms N2(5), while the B–N bonds to B2(5) (*para*-position) show B–N bond lengths that correspond to those found in symmetrically substituted borazines $(RB{=}NH)_3$.[30,31] In contrast, the lithium borazine **2**·$OEt_2$, which is dimeric, shows a different distortion. Here, the bonds N1–B1(3) are the shortest bonds in the borazine ring while the B1–N2 and N3–B3 bonds are the longest.[3] This demonstrates that the P substituents have an opposite effect on the B1(3)–N1 bonds, and therefore on the electron distribution in the P-substituted borazine rings, to the Li atom. Moreover, although most of the borazine rings in the new compounds are planar, several show a semi-chair distortion. The distortion is only weak but is nevertheless significant. We assume that this might be a packing effect. We will report shortly on new boron-, aluminum-, and titanium-substituted borazines, the latter of which show the strongest BN bond differences to date, and we are continuing to explore further aspects of this new field of borazine chemistry.

## Experimental Section

All experiments were performed using inert gas techniques. Solvents were dried by conventional methods and distilled under an $N_2$ atmosphere. Compounds **1** and **2** were prepared as described in the literature,[2] as were $LiPmes_2$, LiPmes, and $LiPPh_2$.[32] All other reagents were commercially available. NMR spectroscopic data were recorded in $C_6D_6$ solutions with TMS (int.), 85% $H_3PO_4$, or $BF_3$·$OEt_2$ (external) as standards with Bruker ACP 200 or Jeol FX 400 instruments. IR spectra were recorded as Nujol/Hostaflon mulls. Mass spectroscopy was performed with a Varian Atlas CH-7 instrument. A Siemens P4 four-circle diffractometer equipped with an area detector and a low temperature device was used for recording X-ray reflection data. Elemental analyses were performed by the analytical laboratory of the department. C/N values often deviate by more than 1%, particularly when the compounds contain aryl groups. This is due to incomplete combustion due to boron carbide or nitride formation or to partial hydrolysis.

**Dichloro(2,4,6-trimethylborazinyl)phosphane (3):** A solution of **2** (0.60 g, 2.96 mmol) in a mixture of hexane (10 mL) and diethyl ether (5 mL) was slowly added to a solution of $PCl_3$ (0.26 mL, 2.96 mmol) in hexane (30 mL). LiCl precipitated rapidly. After stirring overnight the solid was removed by filtration (yield 95% of LiCl) and the solvents were evaporated from the filtrate in vacuo. The oil which remained was distilled at 55 °C/1 Torr to give pure **3**. Yield 0.56 g (85%). $C_3H_{11}B_3Cl_2N_3P$ (223.45): calcd. C 16.12, H 4.96, N 18.80; found C 16.40, H 5.03, N 18.40. IR: $\tilde{\nu}$ = 3428 s, 3377 m, 3243 w, 2960 s, 2491 w, 2293 w, 2227 w, 2190 w, 2000 w, 1955 w, 1898 w, 1499 s, 1402 s, 1321 s, 1295 s, 1179 m, 1147 m, 1083 m, 1040 w, 1006 m, 982 s, 891 s, 811 m, 729 m, 626 w, 587 m, 532 w, 500 m. 459 m, 426 w, 362 w $cm^{-1}$.

**Chlorobis(2,4,6-trimethylborazinyl)phosphane (4):** Prepared in analogy to **3** from $PCl_3$ (0.18 mL, 2.02 mmol) in hexane (30 mL) and **2** (0.82 g, 4.05 mmol) in hexane/diethyl ether (10:5 mL). The filtrate was reduced to a fifth of its original volume in vacuo and then kept at –25 °C. Yellowish crystals of **4** separated within 5 d. After drying they melted at 110 °C (b.p. 140 °C/1 Torr). Yield 0.50 g (80%). $C_6H_{22}B_6ClN_6P$ (309.57): calcd. C 23.28, H 7.16, N 27.15; found C 22.95, H 6.96, N 26.43. IR: $\tilde{\nu}$ = 3441 s, 3411 s, 3402 s, 2988 m, 2956 m, 2941 m, 2911 m, 1487 s, 1435 s, 1396 s, 1302 s, 1285 s, 1193 m, 1176 m, 1159 s, 1145 s, 1080 m, 1010 w, 973 s, 960 s, 891 s, 808 m, 751 m, 735 m, 721 m, 704 m, 640 w, 591 m, 578 m, 566 m, 539 w, 503 w, 493 w, 468 w, 446 w, 431 w, 405 w, 366 w, 320 w, 296 w $cm^{-1}$.

**Dibromo(2,4,6-trimethylborazinyl)phosphane (5):** Prepared in analogy to **3** from $PBr_3$ (0.17 mL, 1.78 mmol) in hexane (30 mL) and **2** (360 mg, 1.78 mmol) in hexane/diethyl ether (10 mL each). LiBr precipitated rapidly and the solution turned yellow. After stirring overnight, filtration and evaporation of the solvents from the filtrate left a yellow oil (b.p. 95 °C/1 Torr). Within a month the liquid turned into yellow needles (m.p. 50 °C). Yield 0.5 g (85%). $C_3H_{11}B_3Br_2N_3P$ (312.35): calcd. C 11.54, H 3.55, N 13.45; found C 11.50, H 3.62, N 13.47. IR: $\tilde{\nu}$ = 3423 s, 3414 s, 2950 m, 2856 w, 2284 w, 2218 w, 1993 w, 1947 w, 1859 w, 1867 w, 1487 s, 1432 s, 1394 s, 1369 m, 1355 m, 1320 m, 1290 s, 1191 s, 1176 s, 1144 s, 1079 s, 975 s, 940 m, 889 s, 809 s, 731 s, 687 s, 569 s, 480 w, 465 w, 436 m, 389 s, 351 s, 286 w, 258 m $cm^{-1}$.

**Bromobis(2,4,6-trimethylborazinyl)phosphane (6):** Prepared in analogy to **4** from $PBr_3$ (0.18 mL, 1.63 mmol) dissolved in hexane (30 mL) and **2** (0.66 g, 3.26 mmol) in hexane/diethyl ether (10 mL each). After stirring overnight the precipitate (LiBr, 90%) was removed by filtration and two thirds of the solvent was removed in vacuo. Colorless crystals of **6** separated from the slightly yellow solution at 5 °C within a week. Yield 0.40 g (80%), m.p. 145 °C. $C_6H_{22}B_6BrN_6P$ (354.03): calcd. C 20.36, H 6.26, N 23.74; found C 19.27, H 6.19, N 23.23. IR: $\tilde{\nu}$ = 3430 s, 3401 s, 3391 s, 3314 m, 3142 m, 2989 s, 2859 m, 2808 m, 2459 w, 2296 w, 2224 w, 1993 w, 1945 w, 1747 w, 1682 w, 1483 s, 1395 s, 1282 s, 1224 m, 1192 m, 1174 m, 1158 s, 1142 s, 1037 w, 1006 w, 962 s, 889 s, 806 m, 759 m, 741 m, 704 m, 624 m, 596 m, 689 m, 567 m, 493 w, 454 w, 439 w, 423 w, 384 w, 362 w, 309 w, 284 w $cm^{-1}$. MS (70 eV): *m*/*z* (%) 354 (20) [$M^+$], 339 (15) [$M^+$ – Me], 309 (10) [$M^+$ – 3Me], 274 (100) [$M^+$ – Br], 259 (55), [$M^+$ – Br – Me], 244 (15) [$M^+$ – Br – 2Me], 121 (20) [$B_3N_3Me_3H_2^+$], 111 (65) [$PBr^+$].

**Dichloro(2,4,6-trimethylborazinyl)arsane (7):** A toluene solution of **2** (0.58 g, 2.86 mmol in 20 mL) was added dropwise to a solution of $AsCl_3$ (0.24 mL, 2.86 mmol) in hexane (30 mL). A white precipitate formed immediately. After stirring overnight the solid was removed

 © 2007 Wiley-VCH Verlag GmbH & Co. KGaA, Weinheim 

by filtration and the solvents evaporated in vacuo. A slightly yellow oil (0.5 g) remained as residue which decomposed on attempted distillation. Yield 500 mg (65%). $^1$H NMR: $\delta$ = 0.15 (s, 3 H, BMe), 0.56 (s, 6 H, BMe), 4.42 ppm (br. s, 2 H, NH). $^{11}$B NMR: $\delta$ = 35.6, 37.9 ppm (1:2).

**Chlorobis(2,4,6-trimethylborazinyl)arsane (8):** Prepared in analogy to **4** from $AsCl_3$ (0.30 mL, 3.58 mmol) in hexane (30 mL) and **2** (1.45 g, 7.16 mmol) in toluene (20 mL). LiCl was recovered in 95% yield. The filtrate was concentrated and the white amorphous precipitate that formed within a week was isolated. Yield 0.9 g (75%), m.p. 64 °C. No single crystals were obtained from toluene, diethyl ether, or thf solutions. $C_6H_{22}AsB_6ClN_6$ (353.49): calcd. C 20.38, H 6.27, N 23.37; found C 20.81, H 6.09, N 22.96. IR: $\tilde{\nu}$ = 3445 m, 3419 s, 3411 s, 2942 s, 2951 s, 2909 s, 2858 m, 1478 s, 1397 s, 1303 s, 1285 s, 1193 m, 1177 m, 1161 m, 1154 m, 1118 w, 1083 m, 1045 w, 1026 w, 920 s, 889 s, 805 m, 753 w, 734 m, 717 s, 573 s, 539 m, 505 w, 485 w, 458 w, 430 w, 416 w, 344 m, 322 w, 288 w, 282 w, 274 w cm$^{-1}$.

**Dichloro(2,4,6-trimethylborazinyl)stibane (9):** Freshly sublimed $SbCl_3$ (0.60 g, 2.62 mmol) was suspended in hexane (30 mL) and a solution of **2** (0.53 g, 1.57 mmol) in hexane (20 mL) was added. After keeping the suspension at reflux overnight the insoluble white material was removed by filtration. The solvent was evaporated from the filtrate in vacuo and the residue dissolved in a small quantity of hexane. Colorless crystals separated from this solution at –5 °C within a week. Yield 0.62 g (75%), m.p. 148–149 °C. $C_3H_{11}B_3Cl_2N_3Sb$ (314.23): calcd. C 11.47, H 3.53, Cl 22.56, N 13.37; found C 12.86, H 3.84, Cl 22.34, N 12.48. IR: $\tilde{\nu}$ = 3448 w, 3421 s, 3406 s, 2964 s, 2964 m, 2946 m, 2910 w, 1474 s, 1407 s, 1332 m, 1317 s, 1303 s, 1292 s, 1262 s, 1191 m, 1172 m, 1153 m, 1082 s, 1020 m, 889 s, 802 s, 757 m, 740 m, 715 s, 661 w, 569 s, 531 m, 400 w, 392 w, 342 s, 331 s, 318 st cm$^{-1}$. MS (50 eV): *m*/*z* (%) 314 (5) [$M^+$], 299 (45) [$M^+$ – Me], 207 (20) [$MeSbCl_2^+$], 192 (100) [$SbCl_2^+$], 156 (65) [$SbCl^+$], 122 (80) [$Me_3B_3N_3H_2^+$].

**Tris(2,4,6-trimethylborazinyl)arsane** was obtained from **2** (0.96 g, 4.69 mmol) in a solution of hexane (30 mL) and $AsCl_3$ (0.11 mL, 1.56 mmol) in 10 mL of hexane. After keeping the mixture at reflux for 3 d the solid was filtered off and the filtrate reduced to one third of its original volume. The solution still contained small amounts of chloride. The $^{11}$B NMR spectrum showed the formation of $(Me_3B_3N_3H_2)_3As$. $^1$H NMR ($C_6D_6$): $\delta$ = 0.07 (s, 3 H, BMe), 0.61 (s, 6 H, BMe), 4.42 ppm (br. s, 2 H, NH) with some weak signals from impurities. $^{11}$B NMR ($C_6D_6$): $\delta$ = 35.5, 36.9 ppm.

**Chlorobis(2,4,6-trimethylborazinyl)stibane (10):** A suspension of $SbCl_3$ (0.37 g, 1.62 mmol) in hexane (30 mL) was allowed to react with a solution of **2** (0.657 g, 3.24 mmol) in hexane (20 mL). After refluxing overnight the solid was removed by filtration and the filtrate reduced in volume by 3/4. From the solution settled a white powder at –25 °C. Yield 0.50 g of **10** (75%), dec. > 200 °C. $C_6H_{22}B_6ClN_6Sb$ (400.36): calcd. C 17.99, H 5.53, N 20.99; found C 20.47, H 5.38, N 21.79. IR: $\tilde{\nu}$ = 3438 s, 3418 s, 2963 s, 2932 m, 2861 m, 2791 w, 1473 s, 1449 m, 1429 m, 1300 s, 1370 m, 1360 w, 1321 m, 1282 w, 1261 s, 1193 w, 1170 w, 1095 s, 1021 w, 956 w, 893 w, 833 w, 803 w, 755 w, 700 m, 670 m, 658 m, 614 s, 533 w, 528 w, 477 w, 404 w cm$^{-1}$.

**Tris(2,4,6-trimethylborazinyl)phosphane (11):** $PBr_3$ (1.64 mmol) dissolved in toluene (10 mL) was added to a solution of **2** (1.00 g, 4.93 mmol) in toluene (30 mL). A white precipitate formed rapidly. After keeping the mixture at reflux for one day the solid was removed by filtration. A $^{31}$P NMR spectrum showed the formation of **11** ($\delta$ = 120.3 ppm) along with minor amounts of **6** ($\delta$ = 191 ppm). The latter could not totally be removed from **6** despite repeated crystallization from toluene/hexane at –20 °C. $^1$H NMR ($C_6D_6$): $\delta$ = 0.18 (s, 3 H, BMe), 0.64 (d, 6 H, BMe), 4.55 ppm (br. s, NH) ppm. $^{11}$B NMR ($C_6D_6$): $\delta$ = 35.7, 39.5 ppm (2:1). $^{31}$P NMR ($C_6D_6$): $\delta$ = 120.3 ppm.

**Tris(2,4,6-trimethylborazinyl)stibane** (impure) was obtained as a white powder upon treatment of a suspension of $SbCl_3$ (0.488 g, 2.13 mmol) in hexane (20 mL) with a solution of **2** (1.30 g, 6.24 mmol) in hexane (30 mL). After heating the mixture overnight to reflux and removing the insoluble material a white powder remained after evaporation of the solvent. The product was characterized only by NMR spectroscopy. $^1$H NMR: $\delta$ = 0.19 (s, 9 H, Me), 0.52 (s, 18 H, Me), 4.31 ppm (s, 6 H, Me) and some additional weak signals. $^{11}$B NMR: $\delta$ = 35.1, 37.3 ppm (1:2).

**Bis(2,4,6-trimethylborazinyl)phosphane (13):** Compound **6** (1.65 g, 4.67 mmol) was dissolved in hexane (30 mL) and a solution of $LiAlH_4$ in diethyl ether (0.83 mL of a 1.3 M solution) was added to this stirred solution to give a white precipitate. After stirring overnight the solid was removed by filtration and three quarters of the solvents were evaporated from the filtrate in vacuo. Storing the solution at +5 °C gave platelets of **13** within two weeks (m.p. 82 °C). Yield 0.95 g (75%). $C_6H_{23}B_6N_6P$ (275.12): calcd. C 26.19, H 8.43, N 30.54; found C 26.69, H 9.01, N 29.96. IR: $\tilde{\nu}$ = 3424 s, 3402 s, 2958 s, 2942 s, 2932 s, 2846 w, 2489 w. 2293 s, 2254 s, 2175 w, 2122 w, 2080 w, 1980 w, 1915 w, 1901 w, 1879 w, 1483 s, 1397 s, 1371 m, 1316 s, 1291 s, 1206 m, 1196 m, 1186 w, 1163 s, 1143 w, 1105 w, 1093 w, 1065 m, 1040 w, 1021 w, 991 m, 962 s, 895 s, 834 w, 912 m, 785 w, 748 s, 725 w, 636 w. 605 m, 592 m, 572 m, 492 w, 479 w, 440 w, 394 w. 371 m, 356 w cm$^{-1}$.

**Zwitterionic Ethylphosphonium 2,4,6-Trimethylborazinate 14:** A diethyl ether solution of $LiAlH_4$ (0.29 mmol, 1.4 M) was added to a hexane solution (30 mL) of **5** (0.52 g, 1.66 mmol) with stirring. The solid formed was removed by filtration after stirring the mixture overnight. The volume of the filtrate was then reduced to one fifth. Crystals separated within a week on storing this solution at –5 °C. Yield 0.20 g (65%). $C_5H_{17}B_3N_3P$ (182.59): calcd. C 32.89, H 9.37, N 23.01; found C 32.19, H 9.12, N 22.54. IR: $\tilde{\nu}$ = 3443 s, 3407 s, 2950 s, 2911 s, 2900 s, 2853 s, 2332 s, 1490 s, 1407 s, 1370 s, 1360 s, 1262 s, 1199 s, 1183 s, 1166 s, 1144 s, 1098 s, 1059 s, 1021 s, 997 s, 943 s, 888 s, 806 s, 748 s, 730 m, 715 m, 676 m, 667 m, 649 m, 642 m, 603 m, 567 m, 546 w, 397 w, 378 m cm$^{-1}$. $^1$H NMR: $\delta$ = 0.14 (s, 3 H, BMe), 0.30 (m, 5 H, Et). 0.35–0.47 (m, 5 H, P*Me*, P*CH*$_2$), 0.54 (d, $^4J_{^{31}P,^1H}$ = 1.9 Hz, 6 H, BMe), 5.52 (dt, $^1J_{^{31}P,^1H}$ = 370, $^3J_{^{31}P,^1H}$ = 7 Hz, 2 H, $PH_2$), 5.59 ppm (dq, $^1J_{^{31}P,^1H}$ = 379, $^3J_{^1H,^1H}$ = 7 Hz, 2 H, P*H*$_2$). $^{11}$B NMR: $\delta$ = 34.1, 35.3 ppm. $^{31}$P NMR: $\delta$ = 5.5 ppm (t, $^1J_{^{31}P,^1H}$ = 430 Hz).

**Bis(mesityl)bis(2,4,6-trimethylborazinyl)diphosphane (17):** A solution of **6** (0.88 g, 25 mmol) in hexane (20 mL) was added slowly to a stirred suspension of $LiPmes_2$ (0.69 g, 2.5 mmol) in hexane (50 mL) at –78 °C. The mixture was then kept at reflux for 14 h. Insoluble material was removed by filtration and about half of the solvent was removed in vacuo. The filtrate was kept at –25 °C and the microcrystalline material recrystallized from toluene at –30 °C as colorless prisms. Two crystals were selected for the X-ray structure determination and proved to contain toluene. The crystals became opaque in vacuo. After keeping them in vacuo for 3 h the yield was 1.15 g (85%), m.p. 182 °C. $C_{24}H_{44}B_6N_6P_2$ (542.47): calcd. 53.04, H 8.16, N 15.46; found C 51.71, H 8.66, N 14.74. IR: $\tilde{\nu}$ = 3424 m, 3414 m, 3403 w, 3100 w, 3089 m, 3025 m, 2965 s, 2924 s, 2864 m, 2731 w, 1667 w, 1601 m, 1549 w, 1478 s, 1432 s, 1396 m, 1298 s, 1277 s, 1188 m, 1178 m, 1152 m, 1083 m, 1031 w, 1016 w, 930 m, 896 m, 953 m, 861 m, 807 m, 787 w, 734 m, 699 w, 602 w,

 © 2007 Wiley-VCH Verlag GmbH & Co. KGaA, Weinheim 

581 s, 568 m, 559 m, 546 w, 521 w, 499 w, 453 w, 375 m, 365 m $cm^{-1}$.

**Tetrakis(2,4,6-trimethylborazinyl)diphosphane (18):** Freshly cut pieces of elemental Na (300 mg) were added to a solution of **6** (1.61 g, 5.0 mmol) in toluene (50 mL). There was no reaction at ambient temperature. The mixture was then kept at reflux (about 3 d) until the $^{31}P$ NMR signal of the **6** could no longer be observed. The solid material was then removed by filtration. The filtrate was free of bromide. Two thirds of the toluene was then evaporated in vacuo and the remaining solution kept at –25 °C. Crystals of **18** separated within 10 d. Yield 1.02 g (70%). $C_{12}H_{44}B_{12}N_{12}P_2$ (548.24): calcd. C 26.29, H 8.09, N 30.66; found C 28.34, H 8.36, N 29.86. IR: $\tilde{\nu}$ = 3432 s, 3413 s, 2956 m, 2943 m, 2855 m, 1483 s, 1399 s, 1293 s, 1280 s, 1200 m, 1190 s, 1177 s, 1153 s, 1084 m, 1041 w, 1030 w, 1019 w, 933 s, 889 s, 808 m, 736 s, 727 s, 715 m, 649 m, 683 s, 563 m, 518 w, 491 w 431 w, 374 m, 358 m $cm^{-1}$. $^1H$ NMR: $\delta$ = 0.15 (s, 12 H, BMe), 0.84 (s, 24 H, BMe), 4.49 ppm (s, 8 H, NH). $^{11}B$ NMR: = 36.3 ppm (br., $h_{1/2}$ = 1260 Hz). $^{31}P$ NMR: = 108.7 ppm (s).

**Tetrakis(2,4,6-trimethylborazinyl)cyclotetraphosphane (19):** A solution of **5** (0.33 g, 1.04 mmol) in hexane (50 mL) was treated with a suspension of finely cut sodium chips (ca. 0.5 g). The reaction started after heating the mixture to reflux. After 3 d the $^{31}P$ NMR signal of **5** could no longer be detected. The insoluble material was removed by filtration. No bromide was found in the filtrate. After reducing the volume of the filtrate by about 60% slightly yellowish crystals separated within two weeks at –50 °C. Attempts to obtain single crystals from hexane, toluene, or thf were unsuccessful. Yield 0.18 g (60%), m.p. 200 °C. $C_{12}H_{44}B_{12}N_{12}P_4$ (610.18): calcd. C 23.62, H 7.26, N 27.55; found C 24.12, H 7.34, N 24.89. IR: $\tilde{\nu}$ = 3437 w, 3422 w, 2969 m, 2890 w, 1483 s, 1397 s, 1380 m, 1364 w, 1282 s, 1261 m, 1193 m, 1178 m, 1150 m, 1131 w, 1082 m, 939 s, 878 s, 850 m, 808 m, 701 wm, 613 w, 574 w, 351 w, 343 w $cm^{-1}$.

**Dimesitylbis(2,4,6-trimethylborazinyl)cyclotetraphosphane (A–F):** A solution of **4** (0.33 g, 1.04 mmol) in toluene (20 mL) was slowly added at –78 °C to a suspension of $mesPLi_2$ (0.17 g, 1.04 mmol) in the same solvent (20 mL). The stirred mixture was allowed to reach room temperature and stirring was continued overnight. The insoluble material was then removed by filtration. The filtrate contained no bromide and was investigated by NMR spectroscopy. The volume of the filtrate was further reduced to one fifth. Colorless, prismatic crystals were isolated after two weeks which proved to be compound **E**. Yield 0.27 g (45%), m.p. 189 °C. Further fractional crystallizations yielded no other pure product. $C_{24}H_{44}B_6N_6P_4$ (605.35): calcd. C 42.55, H 7.37, N 14.61; found C 44.46, H 7.63, N 13. 84. IR: $\tilde{\nu}$ = 3437 w, 3428 w, 3409 w, 3400 m, 3025 w, 2959 m, 2860 w, 1602 m, 1481 s, 1399 s, 1370 m, 1361 w, 1285 s, 1263 m, 1201 m, 1191 m, 1178 m, 1150 m, 1130 w, 1084 m, 1028 w, 939 s, 888 s, 850 m, 733 m, 701 m, 607 w, 571 m, 467 w, 353 w $cm^{-1}$. $^1H$ NMR: $\delta$ = 0.043 (s, 6 H, BMe), 0.99 (d, $^4J_{^{31}P,^1H}$ = 5.75 Hz, 12 H, BMe), 2.80 (d, $^4J_{^{31}P,^1H}$ = 3.57 Hz, 12 H, CMe), 2.82 (s, 6 H, CMe), 4.47 (s, 4 H, NH), 6.68 ppm (s, 4 H, CMe). $^{31}P$ NMR: $\delta$ = 74.9 (t, $^1J_{^{31}P,^{31}P}$ = 168.3 Hz), –30.5 (t, $^1J_{^{31}P,^{31}P}$ = 168.4 Hz), 48.6 (dd, $^1J_{^{31}P,^{31}P}$ = 168.2 Hz), 63.4 (s), 60.7 (dd, $^1J_{^{31}P,^{31}P}$ = 57.0 Hz), –49.5 (dd, $^1J_{^{31}P,^{31}P}$ = 57.0 Hz), 36.2 (t, $^1J_{^{31}P,^{31}P}$ = 171.7 Hz), –8.1 (t, $^1J_{^{31}P,^{31}P}$ = 168.4 Hz), 77.3 (t, $^1J_{^{31}P,^{31}P}$ = 170.2 Hz), –26.4 (dd, $^1J_{^{31}P,^{31}P}$ = 170.2 Hz), –32 ppm (t, $^1J_{^{31}P,^{31}P}$ = 170.2 Hz).

**X-ray Structure Determinations:** Single crystals were covered with perfluoro ether oil under dinitrogen and a specimen selected. The selected crystal was mounted on the top of a glass fiber and placed

Table 10. Crystallographic data and data collection and structure solution parameters.

| Compound | **4** | **5** | **6** | **9** |
|---|---|---|---|---|
| Empirical formula | $C_{13}H_{26}B_6ClN_6P$ | $C_3H_{11}B_3Br_2N_3P$ | $C_6H_{22}B_6BrN_6P$ | $C_3H_{11}B_3Cl_2N_3Sb$ |
| Formula mass | 398.17 | 312.37 | 354.04 | 314.23 |
| Crystal size [mm] | 0.10 × 0.20 × 0.20 | 0.35 × 0.26 × 0.19 | 0.20 × 0.20 × 0.30 | 0.25 × 0.298 × 0.42 |
| Crystal system | triclinic | orthorhombic | orthorhombic | monoclinic |
| Space group | $P\bar{1}$ | *Pnma* (62) | *Pbca* | $P2_1/n$ |
| *a* [Å] | 8.0317(6) | 19.963(1) | 16.0349(4) | 8.1660(2) |
| *b* [Å] | 11.4558(9) | 7.4737(3) | 8.2488(2) | 9.7796(3) |
| *c* [Å] | 13.658(1) | 15.2362(8) | 27.1422(5) | 28.1685(8) |
| *α* [°] | 83.692(2) | 90 | 90 | 90 |
| *β* [°] | 74.337(2) | 90 | 90 | 90.5608(2) |
| *γ* [°] | 74.062(2) | 90 | 90 | 90 |
| *V* [Å$^3$] | 1162.6(2) | 2273.1(2) | 3590.1(1) | 2249.4(1) |
| *Z* | 2 | 8 | 8 | 8 |
| *ρ*(calcd.) [Mg m$^{-3}$] | 1.135 | 1.825 | 1.310 | 1.856 |
| *μ* [mm$^{-1}$] | 0.243 | 7.225 | 2.373 | 2.879 |
| *F*(000) | 415 | 1200 | 1440 | 1200 |
| Index ranges | $-10 \le h \le 8$, $14 \le k \le 14$, $-17 \le l \le 17$ | $-26 \le h \le 26$, $8 \le k \le 9$, $-20 \le l \le 17$ | $-19 \le h \le 19$, $10 \le k \le 10$, $-32 \le l \le 32$ | $-10 \le h \le 10$, $12 \le k \le 12$, $-32 \le l \le 35$ |
| 2*θ* [°] | 57.54 | 56.00 | 52.74 | 57.84 |
| Temp. [K] | 193(2) | 200(2) | 183 | 193 |
| Reflections collected | 6838 | 12290 | 18337 | 12381 |
| Reflections unique | 3581 | 2933 | 3515 | 4446 |
| Reflections observed (4σ) | 2646 | 1696 | 2337 | 4047 |
| *R* (int.) | 0.0195 | 0.0540 | 0.0624 | 0.0186 |
| Number of variables | 270 | 139 | 203 | 233 |
| Weighting scheme[a] *x*/*y* | 0.1907/0.612 | 0.0758/0.00 | 0.0297/3.5073 | 0.0339/3.4530 |
| GOOF | 1.118 | 0.926 | 1.104 | 1.140 |
| Final *R*(4σ) | 0.0881 | 0.0462 | 0.0519 | 0.0304 |
| Final *wR*2 | 0.2748 | 0.1184 | 0.0904 | 0.0719 |
| Largest residual peak [e/Å$^3$] | 1.270 | 1.277 | 0.319 | 0.696 |

[a] $w^{-1} = \sigma^2F_o^2 + (xP)^2 + yP$; $P = (F_o^2 + 2F_c^2)/3$.

 © 2007 Wiley-VCH Verlag GmbH & Co. KGaA, Weinheim 

Table 11. Crystallographic data and data collection and structure solution parameters.

| Compound | **13** | **14** | **17**·$2C_6H_8$ | **E** |
|---|---|---|---|---|
| Empirical formula | $C_6H_{23}B_6N_6P$ | $C_5H_{17}B_3N_3P$ | $C_{38}H_{56}B_6N_6P_2$ | $C_{24}H_{44}B_6N_6P_4$ |
| Formula mass | 275.13 | 182.62 | 723.69 | 605.80 |
| Crystal size [mm] | $0.05\times0.4\times0.5$ | $0.2\times0.3\times0.3$ | $0.2\times0.3\times0.4$ | $0.2\times0.23\times0.3$ |
| Crystal system | orthorhombic | orthorhombic | triclinic | triclinic |
| Space group | *Pbca* | $Pca2_1$ | $P\bar{1}$ | $P\bar{1}$ |
| *a* [Å] | 15.860(1) | 16.997(1) | 11.173(2) | 8.9312(7) |
| *b* [Å] | 8.0674(6) | 4.5201(3) | 11.495(3) | 11.2962(9) |
| *c* [Å] | 25.886(2) | 14.537(1) | 16.176(4) | 19.757(2) |
| *α* [°] | 90 | 90 | 77.833(9) | 81.619(2) |
| *β* [°] | 90 | 90 | 80.90(1) | 89.161(2) |
| *γ* [°] | 90 | 90 | 84.69(1) | 70.801(2) |
| *V* [Å$^3$] | 3312.2(4) | 1116.9(1) | 2001.6(8) | 1861.1(3) |
| *Z* | 8 | 4 | 2 | 2 |
| *ρ*(calcd.) [Mg m$^{-3}$] | 1.104 | 1.086 | 1.131 | 1.129 |
| *μ* [mm$^{-1}$] | 0.157 | 0.199 | 0.141 | 0.14 |
| *F*(000) | 1168 | 392 | 730 | 706 |
| Index ranges | $-16 \le h \le 19$, $10 \le k \le 10$, $-31 \le l \le 32$ | $-21 \le h \le 21$, $5 \le k \le 5$, $-18 \le l \le 18$ | $-11 \le h \le 15$, $14 \le k \le 14$, $-20 \le l \le 20$ | $-12 \le h \le 10$, $13 \le k \le 13$, $-25 \le l \le 25$ |
| 2*θ* [°] | 58.58 | 58.48 | 58.46 | 57.64 |
| Temp. [K] | 193(2) | 193(2) | 193(2) | 183(2) |
| Reflections collected | 17739 | 5956 | 11732 | 10765 |
| Reflections unique | 3361 | 2381 | 6286 | 5627 |
| Reflections observed (4σ) | 2060 | 2085 | 4531 | 3103 |
| *R* (int.) | 0.0621 | 0.0244 | 0.0251 | 0.0521 |
| Number of variables | 183 | 181 | 423 | 407 |
| Weighting scheme[a] *x*/*y* | 0.0772/1.4325 | 0.0806/0.0039 | 0.200/0.000 | 0.3621//0.000 |
| GOOF | 1.029 | 0.926 | 1.034 | 0.960 |
| Final *R*(4σ) | 0.0601 | 0.0393 | 0.0650 | 0 054 |
| Final *wR*2 | 0.1431 | 0.1100 | 0.1728 | 0.1144 |
| Largest residual peak [e/Å$^3$] | 0.229 | 0.214 | 0.604 | 0.245 |

[a] $w^{-1} = \sigma^2F_o^2 + (xP)^2 + yP$; $P = (F_o^2 + 2F_c^2)/3$.

on the goniometer head flushed with a cold stream of $N_2$. Data for the determination of the unit cell were colleted at –80 °C for a total of 75 frames. The unit cell was determined with the program SMART.[33] Data collection was performed in the hemisphere mode. After data reduction the model structure was determined with the program SAINT.[34] The structure determination package SHELXTL[35] was used to refine the data. Non-hydrogen atoms were refined anisotropically. Hydrogen atom positions were calculated and refined using a riding model. The NH hydrogen atoms were located in the difference Fourier map and their positions were refined with isotropic thermal parameters. The thermal ellipsoids in the figures are shown at the 25% probability level. Distances are given in Ångstroms and bond angles in degrees. Crystallographic data and data related to data collection and refinement are summarized in Tables 10 and 11.

CCDC-620997 to -621005 contain the supplementary crystallographic data for this paper. These data can be obtained free of charge from The Cambridge Crystallographic Data Centre via www.ccdc.cam.ac.uk/data_request/cif.

## Acknowledgments

This work was supported by the Fond der Chemischen Industrie and Chemetall GmbH, Frankfurt/Main. We thank Mr. P. Mayer and Mrs. D. Ewald for the recording many of the NMR, IR, and mass spectra. We are also grateful to Dr. M. Suter, Dr. T. Seifert, and Dr. M. Warchhold for collecting the data sets for the X-ray structure determination. Finally, we would also like to thank Prof. Dr. K. Karaghiosoff for interesting discussions.

[1] M. Fan, R. T. Paine, E. N. Duesler, H. Nöth, *Z. Anorg. Allg. Chem.* **2006**, *632*, 2443–2446.
[2] R. I. Wagner, J. L. Bradford, *Inorg. Chem.* **1962**, *1*, 93–98; R. I. Wagner, J. L. Bradford, *Inorg. Chem.* **1962**, *1*, 99–106.
[3] H. Nöth, S. Rojas-Lima, A. Troll, *Eur. J. Inorg. Chem.* **2005**, 1895–1906.
[4] H. Nöth, A. Troll, *Eur. J. Inorg. Chem.* **2005**, 3524–3535.
[5] B. Gemünd, PhD Thesis, University of Munich, **2000**.
[6] B. Gemünd, B. Ch. Günther, J. Huber, H. Nöth, unpublished results.
[7] W. Gerrard, E. F. Mooney, R. A. Rothenbury, *J. Appl. Chem.* **1962**, *12*, 373–375.
[8] K. Niedenzu, J. W. Dawson, *Angew. Chem.* **1960**, *72*, 920.
[9] M. Möhlen, B. Neumüller, A. Dashti-Mommertz, C. Müller, W. Massa, K. Dehnicke, *Z. Anorg. Allg. Chem.* **1999**, *625*, 1631–1637.
[10] M. Möhlen, B. Neumüller, K. Harms, H. Krautscheid, D. Fenske, M. Diedenhofen, G. Frenkin, K. Dehnicke, *Z. Anorg. Allg. Chem.* **1998**, *624*, 1105–1110.
[11] A. P. Lane, D. A. Morton, D. S. Payne, *J. Chem. Soc. A* **1967**, 1492–1498.
[12] Y. G. Trishin, V. N. Christokletov, A. A. Petrov, *Zh. Obsh. Khim.* **1979**, *49*, 39–44.
[13] H. Nöth, B. Wrackmeyer, *Nuclear Magnetic Resonance Spectroscopy of Boron Compounds* in *NMR: Basic Principles and Progress* (Eds.: P. Diehl, E. Fluck, R. Kosfeld), Springer Publishers, Berlin, Heidelberg, New York, **1978**.
[14] M. Crutchfield, C. H. Dungan, J. H. Letcher, V. Mark, J. F. R. van Wazer, *Top. Phosphorus Chem.* **1967**, *5*, 227–458.
[15] H. Nöth, W. Storch, *Chem. Ber.* **1977**, *110*, 2783–2789.
[16] K. Anzenhofer, *Mol. Phys.* **1966**, *11*, 495–497.

 © 2007 Wiley-VCH Verlag GmbH & Co. KGaA, Weinheim 

[17] T. Jaschke, M. Jansen, *Z. Anorg. Allg. Chem.* **2004**, *630*, 239–245; J. Haberecht, A. Krummland, F. Brehm, B. Gebhardt, H. Rueggen, R. Nesper, H. Grützmacher, *Dalton Trans.* **2003**, 2126–2132; A. H. Maulitz, P. Stollberg, R. Boese, *J. Mol. Struct. THEOCHEM* **1995**, *338*, 131–139.
[18] Both toluene molecules are disordered with an SOF of close to 0.5. This value was fixed to 0.5 in the refinement. One toluene looks like a xylene whereas the other is more differently disordered: the benzene rings are shifted so that the *p*-C atoms are centered in the middle of the other six-membered ring. However, the C–C distances are not equal. No H atoms have been added to these disordered molecules.
[19] B. Eichhorn, H. Nöth, *Z. Naturforsch., Teil B* **2000**, *55*, 352–360, and literature cited therein. See also C. Beddie, E. Hollink, P. Wei, S. Gould, D. W. Stephan, *Organometallics* **2004**, *23*, 5240–5251; J. M. Barendt, R. C. Haltiwanger, A. D. Norman, *J. Am. Chem. Soc.* **1986**, *108*, 3127–3128; T. Pfretzschner, L. Kleemann, B. Janza, K. Harms, *Chem. Eur. J.* **2004**, *10*, 6048–6057.
[20] J. R. van Wazer, *Phosphorus and its Compounds* **1958**, *1*, 222.
[21] J. P. Bezombes, K. B. Borisenko, P. B. Hitchcock, M. F. Lappert, J. E. Nye, D. W. H. Rankin, E. Robertson, *Dalton Trans.* **2004**, 1980–1985; K. W. Musir, *J. Chem. Soc. Dalton Trans.* **1975**, 259–262; R. Ullmann, H. Nöth, *Chem. Ber.* **1976**, *109*, 2581–2587; M. Nieger, E. Niecke, A. Dombrowski, *Z. Krist. New Cryst. Struct.* **1997**, *212*, 244–250.
[22] M. M. Olmstead, P. P. Power, G. A. Sigel, *Inorg. Chem.* **1988**, *27*, 2045–2049.
[23] E. C. Alyea, A. Costin, A. Ferguson, G. T. Frey, R. G. Goel, R. J. Restivo, *J. Chem. Soc. Dalton Trans.* **1975**, 1294–1298; L. D. Thorn, J. C. Calabrese, *J. Organomet. Chem.* **1984**, *272*, 283–293; F. A. Cotton, R. Poli, *Inorg. Chem.* **1986**, *25*, 3624–3629; L. Apostocolico, M. F. Mahon, K. C. Melloy, R. Binion, C. S. Blackman, C. J. Carmalt, I. P. Parkin, *Dalton Trans.* **2004**, 470–477; F. Dornhaus, H. W. Lerner, H. Bolte, *Acta Crystallogr., Sect. E* **2005**, *61*, 446–449; C. Aubauer, K. Daridge, T. M. Klapötke, P. Mayer, *Z. Anorg. Allg. Chem.* **2000**, *626*, 1783–1791.
[24] P. Maas, Diploma Thesis, University of Munich, **1994**.
[25] M. Scholz, H. W. Roesky, D. Stalke, K. Keller, F. T. Edelmann, *J. Organomet. Chem.* **1989**, *366*, 73–85.
[26] R. Appel, D. Gudat, E. Niecke, M. Nieger, C. Porz, H. Westermann, *Z. Naturforsch., Teil B* **1991**, *46*, 865–883.
[27] T. L. Breen, D. W. Stephan, *Organometallics* **1997**, *16*, 365–369.
[28] W. Weigand, A. W. Cordes, P. N. Swepston, *Acta Crystallogr., Sect. B* **1981**, *37*, 1631–1634.
[29] H. Steinberg, R. J. Brotherton, *Organoboron Chemistry*, vol. 2, John Wiley & Sons, New York, London, Sydney, **1966**.
[30] Gmelin, *Handbook of Inorganic Chemistry*, supplement to the 8th ed., **1975**, vol. 22 and **1978**, vol. 51; 1st supplement, **1980**, vol. 2; 4th supplement, **1991**, vol. 3a.
[31] M. F. Lappert, P. P. Power, A. R. Sanger, R. C. Srivastava, *Metal and Metalloid Amides*, Horwood Publishers, Chichester, **1980**.
[32] K. Issleib, M. Riemer, A. Zschunke, *Phosphorus Sulfur* **1985**, *22*, 349–352.
[33] *SMART*, Version 5.1, Bruker, Madison, **1995**.
[34] *SAINT*, Version, 5.2, Bruker, Madison, **1994**.
[35] *SHELXTL 93*, G. W. Sheldrick, University of Göttingen, Germany, **1993**.

Received: October 24, 2006
Published Online: August 8, 2007

 © 2007 Wiley-VCH Verlag GmbH & Co. KGaA, Weinheim 

DOI: 10.1002/ejic.200700415

# Synthesis and Reactivity of New Bis(tetramethylpiperidino)(phosphanyl)-alumanes

**Tassilo Habereder,[a,b] Heinrich Nöth,*[a] and Robert T. Paine*[b]**

*Dedicated in memory of Professor Robert W. Parry*

**Keywords:** Aminoalumanes / Phosphanylalumanes / Carbon dioxide insertion / Phosphanylcarbonate ligand / Structure elucidation

Syntheses for the new bis(2,2,6,6-tetramethylpiperidino)-(phosphanyl)alumanes, $tmp_2AlP(SiMe_3)_2$, $tmp_2AlP(SnMe_3)_2$ and $(tmp_2Al)_2PPh$ are described along with spectroscopic characterization and X-ray crystallographic structure determinations. In addition, the insertion reactions between $tmp_2AlP(SiMe_3)_2$ and $CO_2$, COS and $CS_2$ are described and compared with the outcomes for $CO_2$ insertion reactions with $tmp_2AlCl$ and $tmp_2AlMe$. In the case of the amino-phosphanyl-alumane, the Al–P bond undergoes the insertion chemistry in contrast to Al–N bond insertions observed with $tmp_2AlCl$ and $tmp_2AlMe$.

(© Wiley-VCH Verlag GmbH & Co. KGaA, 69451 Weinheim, Germany, 2007)

## Introduction

Since the initial report on the synthesis of $(tmp_2AlH)_2$ (tmp = 2,2,6,6-tetramethyl-piperidino)[1] steady development of the chemistry of the sterically congested $tmp_2Al$– fragment has led to the discovery of several structurally interesting compounds that are unique in comparison to other (alkylamido)alumanes as well as (alkylamido)boranes.[2–8] In particular, the bulky tmp group shows little tendency to participate in bridge bonding and the halide compounds, $tmp_2AlX$ [X = Cl (**1**), Br, I], are monomeric in the gas phase, in solutions and in the solid state.[2] The fluoride and hydride analogues, on the other hand, form dimers, $(tmp_2AlX)_2$ (X = F, H), through Al–F–Al and Al–H–Al bridge bonding. The halides undergo nucleophilic displacement forming a variety of $tmp_2AlX$ (X = OR, SR, $NR_2$, $PR_2$, $AsR_2$, $CR_3$ and $Si(SiMe_3)_3$) compounds all of which are monomeric.[5] Crystallographic structure studies and computational modelling indicate that these compounds develop little or no Al–N-pp(π) bonding interactions. Instead, the Al–N bonds can be considered to possess highly polar sigma-bond character.

As part of a continuing interest in the reactivity and utility of $tmp_2AlX$ reagents as synthons, we set out in this study to expand the available range of phosphanyl derivatives for this fragment. In the initial study mentioned above, only the formation of $tmp_2AlPPh_2$ was described.[5] As expected, this compound provides limited potential for use in, for example, N–Al–P ring or cage construction chemistry. In the current study, we directed attention to the synthesis of additional examples of (amino)(phosphanyl)alumanes and their reactivity.

[a] Department of Chemistry, University of Munich, Butenandtstr. 5–13, 81377, München, Germany
E-mail: H.Noeth@lrz.uni-muenchen.de
[b] Department of Chemistry, University of New Mexico, Albuquerque, NM 87131, USA
E-mail: rtpaine@unm.edu

### Synthesis and Reactions

Prior work in our group with (amino)(phosphanyl)boranes[9] suggested that the molecule $tmp_2AlPH_2$ might be an excellent building block for the construction of novel ring and cage compounds and this compound was the initial synthetic target. Numerous attempts to accomplish the 1:1 reaction of $tmp_2AlCl$ with $LiPH_2$·dme, as shown in Equation (1), were fruitless.

$$tmp_2AlCl + LiPH_2{\cdot}dme \xrightarrow[-LiCl]{hexane} tmp_2AlPH_2 \quad (1)$$

At 23 °C, the combination proved unreactive while under solvent reflux conditions tmpH formed along with insoluble solids some of which is LiCl. Efforts to employ $Me_3Si$-$PH_2$ directly in elimination chemistry with **1** or with strong base promotion also led to the formation of tmpH along with $(Me_3Si)_3P$ and slightly soluble, unidentified solids that may be oligomeric aminoalumane species. These results led to the subsequent studies of reactions between $tmp_2AlCl$ and $LiP(SiMe_3)_2$·$(thf)_2$, $LiP(SnMe_3)_2$ and $LiP(H)Ph$·$(thf)_n$.

 © 2007 Wiley-VCH Verlag GmbH & Co. KGaA, Weinheim 

Combination of one equivalent of **1** with one equivalent of $LiP(SiMe_3)_2{\cdot}(thf)_2$ or $LiP(SnMe_3)_2$ in hexane gave the respective (amino)(phosphanyl)alumanes **2** and **3** according to Equation (2). The substitution reactions are quantitative as evidenced by NMR analysis.

$$tmp_2AlCl + LiPR_2 \xrightarrow[-LiCl]{\text{hexane}} tmp_2AlPR_2$$

**2**: R = $SiMe_3$

**3**: R = $SnMe_3$ (2)

Following recrystallization from cold hexane, the compounds are isolated as analytically pure, colorless crystalline solids in 65–70% yield. The compounds are stable indefinitely at 23 °C in the absence of moisture and oxygen.

In a similar fashion, the 1:1 combination of **1** with $LiP(H)Ph{\cdot}(thf)_n$ unexpectedly gave the (amino)(phosphanyl)alumane **4**, which likely forms in two steps summarized in Equations (3) and (4).

$$tmp_2AlCl + LiP(H)Ph \xrightarrow[-LiCl]{\text{hexane}} tmp_2AlP(H)Ph \quad (3)$$

$$tmp_2AlP(H)Ph + tmp_2AlCl \xrightarrow[-HCl]{\text{hexane}} (tmp_2Al)_2PPh$$

**4** (4)

The initial combination of reagents at –78 °C produced no reaction; however, warming the mixture to 23 °C with stirring resulted in sluggish elimination of LiCl and formation, in low yield, of the anticipated product, $tmp_2AlP(H)Ph$, with a $^{31}P$ NMR resonance at $\delta$ = –112 ppm. Efforts to isolate this compound in pure form were not successful and attempts to complete the substitution by solvent reflux led to three additional $^{31}P$ NMR resonances, $\delta$ = –51, –72 and –96 ppm. The last corresponds to **4** obtained in about 45% yield in the crude reaction mixture. Following separation and recrystallization from cold hexane, **4** was isolated as colorless crystals in 33% yield. The species responsible for the $^{31}P$ resonances at $\delta$ = –51 and –72 ppm remain unidentified at this time.

Thwarted in our attempts to form $tmp_2Al–PH_2$ or $tmp_2Al–P(H)R$ reagents for systematic ring and/or cage construction chemistry, attention was turned to examinations of $Me_3SiCl$ and $Me_3SnCl$ elimination chemistry of **2** and **3** that might support ring/cage assembly processess. Such elimination chemistry routes have been used previously by us with (amino)(halo)boranes to form (amino)(phosphanyl)borane rings and cages.[9–15] In the present cases, the 1:1 combinations of $BCl_3$, $AlCl_3$ and $GaCl_3$ with **2** or **3** in hexane at 23 °C led to the formation of **1** identified by $^1H$ NMR ($\delta$ = 1.29, 1.40, 1.57) and very likely the respective $[MCl_2P(SiMe_3)_2]_n$ and $[MCl_2P(SnMe_3)_2]_n$ (M = B, Al, Ga) compounds. Attempts to obtain analytically pure samples and/or single crystals of the latter compounds were unsuccessful. These results indicate that alternative approaches will be required in the pursuit of systematic synthetic pathways for the construction of new ring and cage compounds containing multiple N–Al–P components.

Historically, another reactivity pathway of interest in our group is that involving insertion reactions into P–N,[16] B–N[17] and Al–N[18] bonds. In the current context, we have previously reported the reactions of $Al(NMe_2)_3$ and $Al(Cl)(NMe_2)_2$ with $CO_2$[19] and $CS_2$.[18] Each Al–N bond undergoes insertion with the formation of the corresponding carbamate or dithiocarbamate compounds, $Al(X_2CNMe_2)_3$ and $Al(Cl)(X_2CNMe_2)_2$ (X = O or S). A single-crystal X-ray structure determination for $Al(S_2CNMe_2)_3$ confirmed the formation of an unusual six coordinate aluminum center with bidentate dithiocarbamate chelation.[18] In close parallel to the present study, we have also previously observed $CO_2$ insertion in Al–N bonds in tmpAl fragments.[5,8] With the (amino)(phosphanyl)alumane, **2**, the question of interest was: will this reagent, with both Al–N and Al–P bonds, undergo selective insertion or insertion in all Al–N and Al–P bonds?

For comparison, the reaction of **1** with $CO_2$ was examined first. Slow diffusion of $CO_2$ gas into a hexane solution of **1** held first at –78 °C and then at 23 °C led over several days to the formation of a brown oil as summarized in Equation (5).

$$tmp_2AlCl + CO_2 \xrightarrow[23\ ^\circ C]{\text{hexane}} (tmp)(tmpCO_2)AlCl$$

**5** (5)

The oil was extracted with hexane and concentration led to the isolation of **5** as a crystalline solid. Although excess $CO_2$ was present, no evidence for double insertion was obtained. However, it cannot be ruled out that such a product is present in the brown oil that resists crystallization.

The combinations of **2** with excess $CO_2$, COS and $CS_2$ led to complete conversion of **2** to the insertion products **6**–**8** as summarized in Equation (6).

$$tmp_2AlP(SiMe_3)_2 + CXX' \longrightarrow tmp_2Al\begin{matrix}X'\\ \diagup\ \diagdown\\ X\end{matrix}CP(SiMe_3)_2$$

**2**

**6**: X = X' = O

**8**: X = X' = S

**7**: X = O; X' = S (6)

The compounds **6** and **7** are obtained in high yield (90–95%) as colorless and faintly yellow crystals, respectively. Compound **8** was isolated as a red oil along with small amounts of tmpH and $(Me_3Si)_3P$. All attempts to isolate a crystalline sample of **8** for X-ray analysis failed.

 © 2007 Wiley-VCH Verlag GmbH & Co. KGaA, Weinheim 

### NMR Characterization

The $^{1}H$, $^{13}C\{^{1}H\}$, $^{31}P$, $^{27}Al$ and $^{119}Sn$ NMR spectra were recorded as appropriate for **2**–**8**. The spectra for **2**–**4** can be compared with data for **1** and $tmp_2AlPPh_2$,[5] and the spectra for **5**–**8** can be examined against data for $[MeAl(O_2Ctmp)_2]_2$,[5] $[(tBuAl)_2(O_2Ctmp)_3]^+[tBu_3AlBrAltBu_3]^-$[8] and $Al(S_2CNMe_2)_3$.[18] In each of the new compounds **2**–**8**, the $^{1}H$ and $^{13}C\{^{1}H\}$ spectra are consistent with a single tmp group environment with free rotation about the Al–N bonds and rapid ring inversion. These spectra also show a single $Me_3Si$ or $Me_3Sn$ environment. The $^{31}P$ NMR spectra for **2** and **3** display high field resonances ($\delta$ = –238 and –282) significantly upfield from the value observed for $tmp_2AlPPh_2$ ($\delta$ =–42.9 ppm). This observation is typical of silyl- and stannylphosphanes and these shifts are similar to those in (amino)(phosphanyl)boranes reported previously.[9] The $^{31}P$ chemical shift for the bis-alumane **4** is downfield compared to **2** and **3**, and the shift ($\delta$ – 96) is comparable to related (phosphanyl)boranes.[9] The $^{31}P$ NMR shifts for **6**–**8** are successively shifted downfield from the starting material **2**: $\delta$ = –121.8 ($CO_2$), –57.8 (COS) and –16 ($CS_2$). This observation provides solid evidence that insertion of the small molecules occurs in the Al–P bond instead of the Al–N bond.

The $^{27}Al$ NMR spectra for **2** and **3** display a broad singlet at $\delta$ = 78 ($h_{1/2}$ = 3500 Hz) and 73 ($h_{1/2}$ = 3300 Hz) ppm, respectively. These are upfield of the reported shifts in $tmp_2AlPPh_2$, $\delta$ = 110 ppm, but similar to the shifts in $tmp_2AlX$ $\delta$ = 74 ppm ($AsPh_2$), 75 (OPh) and 85 (Odipp) ppm.[5] The line widths are somewhat lower than in other $tmp_2AlX$ compounds (ca. 8000–14,000 Hz), but in all cases they are characteristic of asymmetric, lower coordination environments on $^{27}Al$. The $^{27}Al$ NMR spectra for the insertion products **5**–**8** are very similar. Each displays a broad single resonance in the range $\delta$ = 75–81 ppm with $h_{1/2}$ = 3400–3600 Hz. These can be compared to the $^{27}Al$ NMR spectrum for $[(tBuAl)_2(O_2Ctmp)_3]^+[tBu_3AlBrAltBu_3]^-$ that shows a single broad resonance for the Al in the cation at $\delta$ = 53 ppm ($h_{1/2}$ = 3500 Hz). As discussed in the next section, this cation contains two four coordinate *t*BuAl units bridged by three carbamate ligands.[8]

### Crystal Structure Analyses

Single crystal X-ray diffraction structure determinations were completed for **2**–**7**. As found for **1**[2] and $tmp_2AlPPh_2$,[5] the compounds **2**–**4** are monomeric in the solid state and views of the molecules are shown in Figures 1, 2, and 3. In **2** and **3**, the tri-coordinate Al atom and tmp N atoms are planar while the phosphorus atom is pyramidal (sum of angles: **2**, 335.5°; **3**, 326.3°). The same atom geometries exist in $tmp_2AlPPh_2$ although the sum of angles at the P atom (316.2°) is smaller in $tmp_2AlPPh_2$. The Al–P bond lengths [**2**, 2.361(2) Å; **3**, 2.334(2) Å] are slightly shorter than that found in $tmp_2AlPPh_2$ [2.377(1) Å] but slightly longer than that reported for $trip_2Al$–P(Ada)($SiPh_3$) [2.342(2) Å] (trip = 2, 4, 6-*i*$Pr_3C_6H_2$; Ada = adamantyl).[20] The Al–N bond lengths [**2**, 1.846(4) Å and 1.848(4) Å; **3**, 1.832(4) Å and 1.818(4) Å] are slightly longer or identical to the distances in $tmp_2AlPPh_2$ [1.819(2) Å], while the Al–N distances in **1** are 1.785(4) Å and 1.810(4) Å.[2] These parameters are consistent with sigma-only Al–P bonding and highly polar sigma-only Al–N bonding. The molecular structure of **4** is similar (planar N and Al atom environments) to **2** and **3**, but different in that the P atom is also flat with C(37)–P(1)–Al(1) 109.1(2)°, C(37)–P(1)–Al(2) 109.4(2)° and Al(1)–P(1)–Al(2) 141.4(1)° (sum = 359.9°). The Al–P bond lengths [Al(1)–P(1), 2.287(3) Å; Al(2)–P(1), 2.292(3) Å] are slightly shorter than in **2**, **3** and $tmp_2AlPPh_2$ while the Al–N bond lengths [Al(1)–N(1) 1.826(5) Å, Al(1)–N(2) 1.825(5) Å, Al(2)–N(3) 1.819(5) Å, Al(2)–N(4) 1.812(5) Å] are comparable to those in **2**, **3** and $tmp_2AlPPh_2$. The flattened P atom environment is probably a result of steric constraints imposed by the tmp and phenyl substituent groups rather than the operation of Al–P pp–π bonding contributions. Furthermore, the N–Al–N angles in all three compounds fall in a narrow range, 121.8–132.4°, observed in other $tmp_2AlX$ compounds: 126.6(2)° for **2**, 127.2(2)° for **3**, and 126.8(2)° for **4**.[5] These parameters are consistent with the observation that N–Al–N bond angles offer a gauge of Al–N bond polarity and large angles (> 122°) appear in compounds containing weakly basic substituents X and highly polar Al–N bonds.[5]

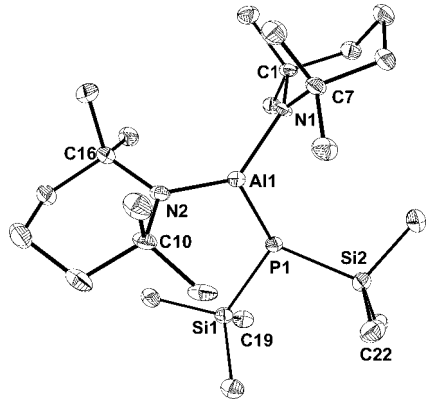


Figure 1. Molecular structure of **2**.

The core molecular structure for **5**, isolated from the reaction of **1** with $CO_2$, is shown in Figure 4 (tmp carbon atoms omitted for clarity). It is immediately apparent that **5** is dimeric. Furthermore, the structure reveals that $CO_2$ insertion takes place in only one of the two Al–N bonds and that the resulting carbamate acts as a bridging ligand toward a second Al(Cl)(tmp)(μ-$O_2$Ctmp) fragment. The resulting puckered eight-membered $[–Al–O–C–O–]_2$ ring has four coordinate Al atom environments with the terminal tmp groups and terminal Cl atoms in *cis* orientations across the ring. The terminal Al–Cl bond lengths [Al(1)–Cl(1) 2.164(2) Å and Al(2)–Cl(2) 2.159(1) Å] are slightly longer than the Al–Cl bond lengths in $tmp_2AlCl$, [2.144(2) Å] and in $(Me_2NAlCl_2)_2$ [2.088(3) Å and 2.123(3) Å].[21] The terminal Al–N bond lengths [Al(1)–N(2) 1.805(3) Å and Al(2)–N(4) 1.826(3) Å can be compared with the values in

 © 2007 Wiley-VCH Verlag GmbH & Co. KGaA, Weinheim 

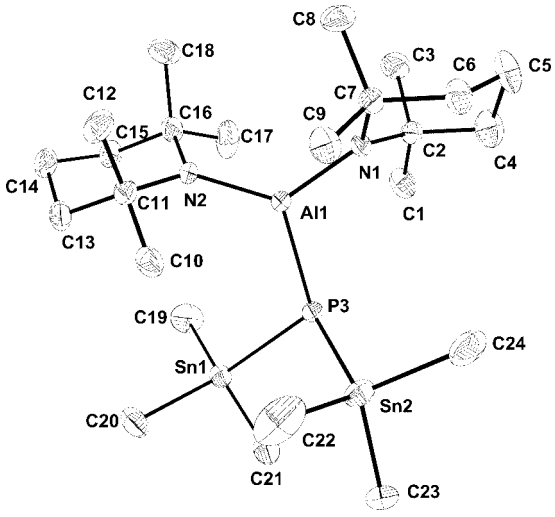


Figure 2. Molecular structure of **3**.

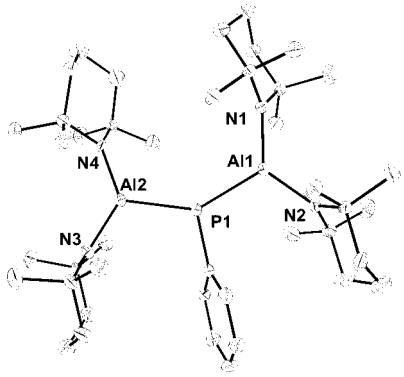


Figure 3. Molecular structure of **4**.

$tmp_2AlCl$ [1.785(4) and 1.810(4) Å]. The bonding parameters in the carbamate ligands are fairly symmetrical with N(1)–C(2) 1.328(4) Å, N(3)–C(1) 1.330(5) Å, O(1)–C(2) 1.289(4) Å O(4)–C(2) 1.275(4) Å, O(2)–C(1) 1.289(4) Å and O(3)–C(1) 1.271(4) Å. The carbamate bridging interactions with the two Al atoms are also relatively symmetrical with Al–O (avg) = 1.78(1) Å [Al(1)–O(1) 1.784(3) Å, Al(1)–O(2) 1.789(3) Å, Al(2)–O(3) 1.776(3) Å, Al(2)–O(4) 1.790(2) Å]. These Al–O bond lengths are significantly shorter than in the related but more fragile complex $[MeAl(O_2Ctmp)_2]_2$ whose four bridging bidentate carbamate ligands form a paddle-wheel structure with Al–O bond lengths in a range 1.863(3) to 1.880(3) Å.[5] On the other hand, the bonding parameters in **5** are similar to those in the cation $[(t\text{BuAl})_2(O_2Ctmp)_3]^+$: Al–O (avg) 1.763(4) Å, C–O (avg) 1.292(7) Å and C–N (avg) 1.308(6) Å.[8]

In direct contrast with **5**, the molecular structure determinations for **6** and **7** reveal that insertions of $CO_2$ and COS take place exclusively into the Al–P bond of **2** and the resulting compounds are monomeric in the solid state as shown in Figure 5 and Figure 6. The formal phosphanylcarbonate $(Me_3Si)_2PCO_2^{1-}$ and phosphanylthiocarbonate $(Me_3Si)_2PCOS^{1-}$ units are planar and they act as bidentate

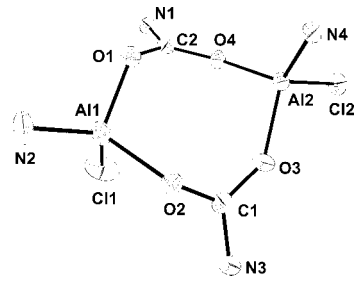


Figure 4. Molecular structure of **5** with tmp carbon atoms omitted for clarity.

chelating ligands toward tetrahedral Al centers in a formal $tmp_2Al$ cation. The Al–N bond lengths and internal N–Al–N bond angles in the two compounds are similar: **6**, Al(1)–N(1) 1.800(6) Å, Al(1)–N(2) 1.815(6) Å and N(1)–Al(1)–N(2) 129.8(3)°; **7**, Al(1)–N(1) 1.827(5) Å, Al(1)–N(2) 1.801(5) Å, and 128.2(2)°. In both compounds the N–Al–N angle is only slightly enlarged compared with the starting compound **2**. The phosphanylcarbonate, $(Me_3Si)_2PCO_2^{1-}$, unit is symmetrically bonded to the Al center in **6**: Al(1)–O(1) 1.921(5) Å, Al(1)–O(2) 1.918(4) Å, C(1)–O(1) 1.281(7) Å, C(1)–O(2) 1.285(7) Å and C(16)–P(1) 1.814(7) Å, with internal chelate ring angles O(1)–Al(1)–O(2) 68.4(2)°, Al(1)–O(1)–C(16) 88.1(4)°, Al(1)–O(2)–C(16) 88.2(4)° and O(1)–C(16)–O(2) 114.3(6)°. The $(Me_3Si)_2PCOS^{1-}$ unit of course forms a more asymmetric chelate ring in **7**: Al(1)–O(1) 1.887(3) Å, Al(1)–S(2) 2.422(2) Å, C(1)–O(1) 1.291(6) Å, C(1)–S(2) 1.708(5) Å and C(1)–P(1) 1.796(6) Å, with internal chelate ring angles O(1)–Al–S(2) 70.9(1)°, Al–O(1)–C(1) 101.6(3)°, Al–S(2)–C(1) 71.9(2)° and O(1)–C(1)–S(2) 114.8(4)°. It is notable that the Al–O bond lengths in **6** and **7** are significantly longer than in **5** [Al–O avg 1.78(1) Å] and in the cation $[(t\text{BuAl})_2(O_2Ctmp)_3]^+$ [Al–O (avg.) 1.763(7) Å]. The Al–O distances in **6** are, in fact, even significantly longer than the Al–O (avg.) in $[MeAl(O_2Ctmp)_3]_2$. Given these bonding parameters it is a little surprising that the complex is as stable as it appears to be where the carbonate ligands are bridging two Al atoms. It is also observed that the Al–S bond length in **7** is longer than the corresponding bond length in $Al(S_2CNMe_2)_3$ [Al–S avg 2.396(1) Å].[18]

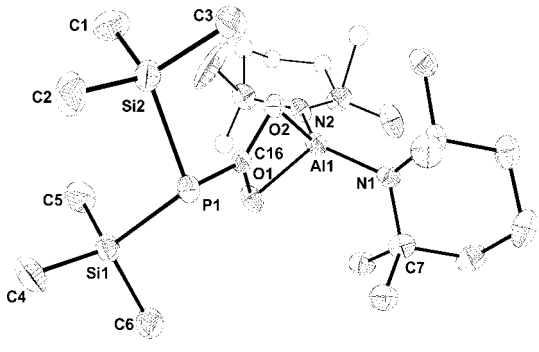


Figure 5. Molecular structure of **6**.

 © 2007 Wiley-VCH Verlag GmbH & Co. KGaA, Weinheim 

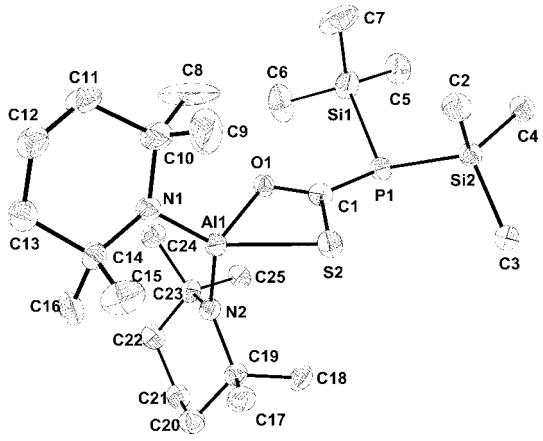


Figure 6. Molecular structure of **7**.

## Conclusions

The nucleophilic substitution chemistry on $tmp_2AlCl$ described in part in a previous report,[5] has been extended further in the present study. The initial intent was to prepare (amino)(phosphanyl)alumanes, $tmp_2AlPR_2$, that might find use for the construction of Al–P cage compounds related to those discovered in our prior work with (amino)-(phosphanyl)boranes.[9] Unfortunately, the principle target compound, $tmp_2AlPH_2$, either does not form or is unstable under forcing reaction conditions. However, three new (amino)(phosphanyl)alumanes, $tmp_2AlPR_2$, R = $SiMe_3$ (**2**), $SnMe_3$ (**3**) and $(tmp_2Al)_2PPh$ (**4**) were obtained and characterized.

It had been previously noted that the polar Al–N bond in (amino)alumanes is susceptible to $CO_2$ bond insertion.[5,8,19] In particular, both Al–N bonds in $tmp_2AlCH_3$ have been observed to undergo $CO_2$ insertion with formation of $[MeAl(tmpCO_2)_2]_2$ in which the two Al atoms are bridged by four carbamate ligands.[5] In the present study, it was expected that similar Al–N bond insertion would occur in both tmp–Al bonds of $tmp_2AlCl$, **1**. However, under the conditions explored, only one tmp–Al bond undergoes $CO_2$ insertion with resulting formation of $[Al(Cl)(tmp)(tmpCO_2)]_2$ **5**, a dimer with *two* bridging carbamate ligands and two terminal tmp groups. In a sense, this can be considered an intermediate product on the way to the formation of the compound $[MeAl(tmpCO_2)]_2$ that utilizes four bridging carbamate ligands to form a dimeric structure. Perhaps the electronic difference between Me and Cl is responsible for shutting down the reactivity of the second Al–N bond in **1**. It is also worth reviewing that $[MeAl(tmpCO_2)]_2$ is thermally unstable above –10 °C,[5] so perhaps the full insertion product from **1** is simply too unstable to allow isolation.

Molecule **2** presents the additional option that insertion might occur in the Al–P bond as well as the Al–N bonds. However, under the conditions utilized, reactions of **2** with $CO_2$, COS and $CS_2$ result *only* in Al–P bond insertion. Furthermore, crystal structure analyses indicate that the resulting phosphanylcarbonate $(Me_3Si)_2PCO_2^-$ and phosphanylthiocarbonate $(Me_3Si)_2PCOS^-$ fragments act as terminal, bidentate chelating ligands toward aluminum. Spectroscopic data, suggest that the same coordination condition results with $CS_2$ insertion that produces only $tmp_2Al[S_2CP(SiMe_3)_2]$.

## Experimental Section

Standard inert-atmosphere techniques were used for the manipulation of all reagents and solvents were rigorously dried and distilled before use. NMR spectra were recorded on Bruker WP-250 and JEOL GSX-400 NMR spectrometers from samples flame sealed in evacuated NMR tubes containing appropriate lock solvents. Spectra were referenced with external $Me_4Si$ ($^1H$ and $^{13}C$), 85% $H_3PO_4$ ($^{31}P$), 1 M aqueous LiCl ($^7Li$), 1 M aqueous $HAlCl_4$ ($^{27}Al$) and $Me_4Sn$ ($^{119}Sn$). Downfield shifts relative to the reference were assigned positive $\delta$ values. CHN-Analytical data obtained for these compounds are low in comparison to the calculated values and this is consistent with incomplete combustion and formation of aluminum carbide or silicide residues.[22–24] X-ray diffraction: Siemens P4 four-circle diffractometer with a CCD area detector and LT2 device, Mo-$K_\alpha$ radiation, graphite monochromator.

**Bis(trimethylsilyl)phosphanyl-bis(2,2,6,6-tetramethylpiperidino)alumane (2):** A suspension of $LiP(SiMe_3)_2\cdot(thf)_2$[25] (1.3 g, 4.3 mmol) in hexane (50 mL) was slowly treated (–78 °C) with $tmp_2AlCl$ (**1**) (1.5 g, 4.3 mmol) in hexane (50 mL). The mixture was warmed slowly with stirring and then held at 23 °C (1 h). Volatile components were vacuum-evaporated, the solid residue treated with fresh hexane (50 mL) and filtered. The filtrate was concentrated to ca. 10 mL and cooled (–78 °C). After several days colorless crystals were collected. Yield: 1.34 g (66%) of **2**, m.p. 87 °C (dec.). $^1H$ NMR ($C_6D_6$): $\delta$ = 0.46 [d, $J_{HP}$ = 4.8 Hz, 18 H, $Si(CH_3)_3$], 1.39 [m, 8 H, $CCH_2$], 1.55 [s, 24 H, $CCH_3$], 1.62 [m, 4 H, $CCH_2CH_2$] ppm. $^{13}C\{^1H\}$ NMR ($C_6D_6$): $\delta$ = 5.5 [d, $J_{CP}$ = 11.4 Hz, $SiCH_3$], 18.6 [$CCH_2CH_2$], 34.5 [$CH_3$], 40.7 [$CCH_2$], 52.7 [$C(CH_3)_2$] ppm. $^{27}Al$ NMR: $\delta$ = 78 ($h_{1/2}$ = 3500 Hz) ppm. $^{31}P\{^1H\}$ NMR: $\delta$ = –238 ppm. $C_{24}H_{54}AlN_2PSi_2$ (484.83): calcd. C 59.64, H 11.23, N 5.78; found C 57.70, H 9.42, N 6.80.

**Bis(trimethylstannyl)phosphanyl-bis(2,2,6,6-tetramethylpiperidino)-alumane (3):** A solution of $(Me_3Sn)_3P$[26] (2.91 g, 5.6 mmol) in THF (30 mL) was cooled (–78 °C) and *n*BuLi solution (3.5 mL, 5.6 mmol) in hexane was added with stirring. The mixture was warmed to 23 °C, stirred (1 h) and volatiles vacuum evaporated. The residue was treated with hexane (30 mL) and this suspension was cooled (–78 °C) and combined with $tmp_2AlCl$ (1.9 g, 5.5 mmol) in hexane (30 mL). The mixture was warmed to 23 °C and stirred (1 h). Volatile components were removed from the resulting mixture, the residue treated with hexane (50 mL) and filtered. The filtrate was concentrated (5 mL) and cooled (–20 °C). After several days, colorless crystals deposited. Yield: 1.84 g, 69% of **3**, m.p. 103–104 °C. $^1H$ NMR ($C_6D_6$): $\delta$ = 0.46 [m, $J_{HP}$ = 4.8, $J_{HSn}$ = 52 Hz, 18 H, $Sn(CH_3)$], 1.36 [m, 8 H, $CCH_2$], 1.52 [s, 24 H, $CCH_3$], 1.63 [m, 4 H, $CCH_2CH_2$] ppm. $^{13}C\{^1H\}$ NMR ($C_6D_6$): $\delta$ = –3.0 [m, $J_{CP}$ = 6.6, $J_{CSn}$ = 295 Hz, $SnCH_3$], 18.5 [$CCH_2CH_2$], 34.7 [$CH_3$], 41.0 [$CCH_2$], 52.6 [$C(CH_3)_2$] ppm. $^{27}Al$ NMR: $\delta$ = 73 [$h_{1/2}$ = 3300 Hz] ppm. $^{31}P\{^1H\}$ NMR: $\delta$ = –282 [m, $J_{PSn}$ = 754, 785 Hz] ppm. $^{119}Sn$ NMR: $\delta$ = 18.0 [d, $J_{SnP}$ = 785 Hz] ppm. $C_{24}H_{54}AlN_2PSn_2$ (666.04): calcd. C 43.28, H 8.17, N 4.21; found C 42.65, H 8.13, N 4.02.

**Phenyl-bis[bis(2,2,6,6-tetramethylpiperidino)alumanyl]phosphane (4):** A solution of $PhPH_2$ (0.55 g, 4.95 mmol) in THF (30 mL) was

 © 2007 Wiley-VCH Verlag GmbH & Co. KGaA, Weinheim 

cooled to –78 °C and combined with *n*BuLi/hexane solution (5.0 mmol). The mixture was stirred, warmed to 23 °C and stirred further (2 h) leaving an orange suspension. The volatiles were vacuum evaporated and the solid residue suspended in hexane (30 mL). The mixture was cooled (–78 °C) and combined with $tmp_2AlCl$ (1.7 g, 5.0 mmol) and then warmed, stirred (2 h) at 23 °C and then refluxed (2 d). The crude reaction mixture displayed $^{31}P$ NMR resonances at $\delta$ = –51, –72, –96 (broad) and –112. The mixture was filtered, the filtrate concentrated and cooled (–20 °C) and colorless crystals deposited which were collected and washed with cold hexane. Yield: 0.66 g, 33% of **4**, m.p. 200 °C (dec.). $^1H$ NMR ($C_6D_6$): $\delta$ = 1.25 (m, 24 H, $C(CH_2)_2$ and $CCH_2CH_2$), 1.61 (s, 48 H, $CCH_3$), 7.15 (m, 3 H Ph), 7.81 (t, $J_{HH}$ = 6.8 Hz, 2 H, Ph) ppm. $^{31}P\{^1H\}$ NMR: $\delta$ = –96 ppm. $C_{42}H_{77}Al_2N_4P$ (722.55): calcd. C 69.77, H 10.73, N 7.75; found C 66.40, H 9.93, N 6.48.

**Reaction of 1 with $CO_2$:** Carbon dioxide gas was allowed to slowly diffuse into a sample of **1** (0.5 g, 1.5 mmol) in hexane (10 mL) held at –78 °C. The resulting mixture was allowed to stand for several days and a brownish oil formed. The oil was crystallized from a minimum of hexane at 23 °C over several weeks and a few colorless crystals of **5** were isolated. The oil was examined by NMR spectroscopy. $^1H$ NMR ($C_6D_6$): $\delta$ = 1.23, 1.46, 1.52, 1.61 ppm. $^{27}Al$ NMR: $\delta$ = 81 ppm.

**Reaction of 2 with $CO_2$:** A sample of **2** (1.88 g, 4.0 mmol) in hexane (5 mL) was layered over dry-ice and allowed to stand at 23 °C for several days. Orange crystals deposited. Yield: 2.0 g, 95% of **6**, m.p. 109 °C (dec.). $^1H$ NMR ($C_6D_6$): $\delta$ = 0.46 [d, $J_{HP}$ = 5.5 Hz, 18 H, $SiCH_3$], 1.39 [m, 8 H, $CCH_2$], 1.51 [s, 24 H, $CCH_3$], 1.62 [m, 4 H, $CCH_2CH_2$] ppm. $^{13}C\{^1H\}$ NMR ($C_6D_6$): $\delta$ = 1.6 [d, $J_{CP}$ = 12.5 Hz, $SiCH_3$], 18.7 [$CCH_2CH_2$], 34.3 [$CH_3$], 41.5 [$CCH_2$], 52.3 [$C(CH_3)_2$] ppm. $^{27}Al$ NMR: $\delta$ = 75 [$h_{1/2}$ = 3500 Hz] ppm. $^{31}P\{^1H\}$ NMR: $\delta$ = –121.8 ppm. $C_{25}H_{54}AlN_2O_2PSi_2$ (528.84): calcd. C 56.78, H 10.29, N 5.30; found C 54.59, H 9.89, N 4.78.

**Reaction of 2 with COS:** A sample of **2** (1.0 g, 2.1 mmol) in hexane (40 mL) was frozen at –196 °C and COS gas (2.1 mmol) was measured volumetrically and condensed on the mixture. The combined mixture was warmed to –78 °C, stirred (2 h) and then warmed to 23 °C and stirred (12 h). The resulting cloudy orange solution was filtered and the filtrate concentrated (20 mL) and cooled (–20 °C). After several days, yellow crystals deposited. Yield: 0.95 g, 95% of **7**, m.p. 111–114 °C. $^1H$ NMR ($C_6D_6$): $\delta$ = 0.37 [d, $J_{HP}$ = 5.0 Hz, 18 H, $SiCH_3$], 1.46 [m, 8 H, $CCH_2$], 1.58 [s, 24 H, $CCH_3$], 1.67 [m, 4 H, $CCH_2CH_2$] ppm. $^{13}C\{^1H\}$ NMR ($C_6D_6$): $\delta$ = 1.7 [d, $J_{CP}$ = 12.1 Hz, $SiCH_3$], 18.6 [$CCH_2CH_2$], 34.5 [$CH_3$], 41.7 [$CCH_2$], 52.9 [$C(CH_3)_2$] ppm. $^{27}Al$ NMR: $\delta$ = 81 ppm [$h_{1/2}$ = 3400 Hz]. $^{31}P\{^1H\}$ NMR: $\delta$ = –57.8 ppm. $C_{25}H_{54}AlN_2OPSSi_2$ (544.90): calcd. C 55.64, H 9.99, N 5.14; found C 54.90, H 9.92, N 4.74.

**Reaction of 2 with $CS_2$:** A sample of **2** (0.85 g, 1.75 mmol) in hexane (20 mL) was treated with $CS_2$ (0.15 mL, 1.75 mmol). The reaction mixture was stirred at 23 °C and monitored by $^{31}P$ NMR spectroscopy. After 36 h, no resonance due to **2** was detected. The mixture was filtered leaving a bright red solution that was concentrated (10 mL) and cooled (–78 °C). A red oil, **8**, deposited. Efforts to purify **8** by crystallization were unsuccessful. The crude product contained small amounts of $P(SiMe_3)_3$ and tmpH that were not completely removed. $^1H$ NMR ($C_6D_6$): $\delta$ = 0.40 [d, $J_{HP}$ = 5.4 Hz, 9 H, $SiCH_3$], 0.50 [d, $J_{HP}$ = 4.8 Hz, 9 H, $SiCH_3$], 1.2–1.5 [m, 12 H, $CCH_2CH_2$], 1.54 [s, 12 H, $CCH_3$], 1.63 [s, 12 H, $CCH_3$] ppm. $^{13}C\{^1H\}$ NMR ($C_6D_6$): $\delta$ = 1.8 [d, $J_{CP}$ = 11.7 Hz, $SiCH_3$], 5.6 [d, $J_{CP}$ = 11.4 Hz, $SiCH_3$], 18.4 [$CCH_2CH_2$], 18.6 [$CCH_2CH_2$], 34.5

Table 1. Crystallographic data for **2**–**5**.

| | **2** | **3** | **4** | **5** |
|---|---|---|---|---|
| Code | Habe41 | Habe51 | Habe45 | Habe55a |
| Formula | $C_{24}H_{54}AlN_2PSi_2$ | $C_{24}H_{54}AlN_2PSn$ | $C_{42}H_{77}Al_2N_4P$ | $C_{38}H_{72}AlCl_2N_4O_4$ |
| Formula weight | 484.82 | 666.02 | 723.01 | 773.86 |
| Crystal size [mm] | 0.2 × 0.2 × 0.1 | 0.2 × 0.1 × 0.1 | 0.1 × 0.1 × 0.05 | 0.2 × 0.1 × 0.1 |
| Crystal system | monoclinic | monoclinic | monoclinic | monoclinic |
| Space group | $P2_1/c$ | $P2_1/n$ | $P2_1/n$ | $P2_1/c$ |
| $a$ [Å] | 12.65(1) | 12.1899(8) | 17.46(3) | 21.822(9) |
| $b$ [Å] | 11.95(1) | 18.734(1) | 11.14(1) | 11.358(4) |
| $c$ [Å] | 21.46(2) | 13.813(1) | 22.67(3) | 36.27(1) |
| $\alpha$ [°] | 90 | 90 | 90 | 90 |
| $\beta$ [°] | 105.68(2) | 93.729(2) | 101.65(2) | 106.814(6) |
| $\gamma$ [°] | 90 | 90 | 90 | 90 |
| $V$ [Å$^3$] | 3127(5) | 3147.9(4) | 4318(10) | 8604(6) |
| $Z$ | 4 | 4 | 4 | 8 |
| $P_{calcd.}$ [g cm$^{-3}$] | 1.030 | 1.405 | 1.112 | 1.195 |
| $\mu$ [mm$^{-1}$] | 0.206 | 1.678 | 0.137 | 0.233 |
| $F$(000) | 1072 | 1360 | 1592 | 3360 |
| Index range | $-13 \le h < 13$ | $-16 \le h \le 16$ | $-18 \le h \le 18$ | $-28 \le h \le 28$ |
| | $-12 \le k \le 12$ | $-23 \le k \le 23$ | $-11 \le k \le 11$ | $-15 \le k \le 15$ |
| | $-20 \le l \le 20$ | $-17 \le l \le 17$ | $-23 \le l < 23$ | $-45 \le l \le 45$ |
| 2$\theta$ [°] | 3.34–44.92 | 3.66–58.72 | 3.28–43.92 | 1.94–58.74 |
| $T$ [K] | 193 | 193 | 193 | 193 |
| Reflections collected | 12060 | 18257 | 16616 | 48953 |
| Reflections unique | 3630 | 5561 | 5201 | 17483 |
| Reflections observed (4σ) | 2190 | 3920 | 2354 | 9550 |
| $R_{int}$ | 0.0988 | 0.0459 | 0.2064 | 0.0703 |
| No. of variables | 285 | 285 | 458 | 933 |
| GooF | 0.927 | 1.019 | 0.969 | 1.029 |
| Final $R$ (4σ) | 0.0525 | 0.0396 | 0.0760 | 0.0729 |
| Final $wR_2$ | 0.1046 | 0.0864 | 0.1092 | 0.1723 |
| Largest residual peak [e/Å$^3$] | 0.214 | 0.811 | 0.262 | 0.715 |

 © 2007 Wiley-VCH Verlag GmbH & Co. KGaA, Weinheim 

Table 2. Crystallographic data for **6**, **7** and **9**.

| | **6** | **7** | **9** |
|---|---|---|---|
| Code | Habe39 | Habe42 | Habe54 |
| Formula | $C_{31}H_{126}AlN_2O_2PSi_2$ | $C_{25}H_{54}AlN_2OPSSi_2$ | $C_{14}H_{34}LiO_2PSn_2$ |
| Formula weight | 673.47 | 544.89 | 509.70 |
| Crystal size [mm] | $0.3\times0.2\times0.2$ | $0.2\times0.2\times0.1$ | $0.2\times0.1\times0.1$ |
| Crystal system | orthorhombic | triclinic | monoclinic |
| Space group | *P*2(1)2(1)2(1) | *P*1 | *C*2/*c* |
| *a* [Å] | 11.533(1) | 8.9907(8) | 18.441(3) |
| *b* [Å] | 12.140(1) | 12.327(1) | 13.746(2) |
| *c* [Å] | 23.126(1) | 16.489(1) | 19.074(3) |
| *α* [°] | 90 | 103.251(1) | 90 |
| *β* [°] | 90 | 96.195(2) | 107.519(2) |
| γ [°] | 90 | 109.0290(10) | 90 |
| *V* [Å$^3$] | 3237.8(6) | 1634.0(2) | 4610.6(11) |
| *Z* | 4 | 2 | 8 |
| $P_{calcd.}$ [g cm$^{-3}$] | 1.382 | 1.107 | 1.469 |
| $\mu$ [mm$^{-1}$] | 0.222 | 0.267 | 2.235 |
| *F*(000) | 1592 | 596 | 2016 |
| Index range | $-12\le h\le12$ | $-9\le h\le9$ | $-23\le h\le23$ |
| | $-13\le k\le13$ | $-12\le k\le12$ | $-16\le k\le16$ |
| | $-25\le l\le25$ | $-17\le l\le15$ | $-24\le l\le24$ |
| 2*θ* [°] | 3.52–46.50 | 3.66–43.94 | 3.76–58.24 |
| *T* [K] | 193 | 193 | 193 |
| Reflections collected | 14537 | 6490 | 12874 |
| Reflections unique | 4606 | 3316 | 4548 |
| Reflections observed (4σ) | 2211 | 2385 | 2726 |
| $R_{int}$ | 0.1340 | 0.0287 | 0.0298 |
| No. of variables | 310 | 313 | 187 |
| GooF | 0.876 | 1.091 | 1.024 |
| Final *R* (4σ) | 0.0679 | 0.0650 | 0.0483 |
| Final $wR_2$ | 0.1191 | 0.1755 | 0.1165 |
| Largest residual peak [e/Å$^3$] | 0.295 | 0.558 | 1.215 |

[C*C*H$_3$], 34.8 [C*C*H$_3$], 40.7 [C*C*H$_2$], 41.5 [C*C*H$_2$], 52.7 [*C*(CH$_3$)$_2$], 53.6 [*C*(CH$_3$)$_2$] ppm. $^{27}$Al NMR: $\delta$ = 75 ppm [$h_{1/2}$ = 3600 Hz]. $^{31}$P{$^1$H} NMR: $\delta$ = –16 ppm.

**X-Ray Structure Determinations:** Single crystals were covered with a polyfluoro ether oil and specimens mounted on the tip of glass fibers. After cooling the crystals on the goniometer head to –80 °C with the LT2 device, the unit cells were determined from reflections collected on 65 frames at five different settings of the $\omega$ and $\chi$ circles. Data collections were performed in the hemisphere mode (1200 frames) with programs implemented in SMART.[27] The program SAINT[28] was used for data reduction and absorption corrections were applied using SADABS.[29] The structures were solved by direct methods using SHELX97[30] and refined with the same package. Non-hydrogen atoms were refined with anisotropic thermal factors. Most hydrogen atoms were visible following anisotropic refinement but were placed in calculated positions and included in refinements by applying the riding model. Data related to the crystallography are summarized in Table 1 and Table 2.

CCDC-640019 to –640025 contain the supplementary crystallographic data for this paper. These data can be obtained free of charge from The Cambridge Crystallographic Data Centre via www.ccdc.cam.ac.uk/data_request/cif.

## Acknowledgments

We thank the National Science Foundation (CHE-9983205) and the Fonds der Chemischen Industrie for support of this research. We also thank M. Suter for X-ray data collection on one of the compounds.

[1] C. Klein, H. Nöth, M. Tacke, M. Thomann, *Angew. Chem.* **1993**, *105*, 923–925; *Angew. Chem. Int. Ed. Engl.* **1993**, *32*, 886–888.
[2] I. Krossing, H. Nöth, C. Tacke, M. Schmidt, H. Schwenk-Kircher, *Chem. Ber./Recueil* **1997**, *130*, 1047–1052.
[3] B. N. Anand, I. Krossing, H. Nöth, *Inorg. Chem.* **1997**, *36*, 1979–1981.
[4] I. Krossing, H. Nöth, H. Schwenk-Kircher, *Eur. J. Inorg. Chem.* **1998**, 927–939.
[5] K. Knabel, I. Krossing, H. Nöth, H. Schwenk-Kircher, M. Schmidt-Amelunxen, T. Seifert, *Eur. J. Inorg. Chem.* **1998**, 1095–1114.
[6] I. Krossing, H. Nöth, H. Schwenk-Kircher, T. Seifert, C. Tacke, *Eur. J. Inorg. Chem.* **1998**, 1925–1930.
[7] K. Knabel, H. Nöth, *Z. Naturforsch., Teil B* **2005**, *60*, 155–163.
[8] K. Knabel, H. Nöth, *Z. Naturforsch., Teil B* **2005**, *60*, 1027–1035.
[9] H. Nöth, R. T. Paine, *Chem. Rev.* **1995**, *95*, 343–379.
[10] G. L. Wood, D. Dou, C. K. Narula, E. N. Duesler, R. T. Paine, H. Nöth, *Chem. Ber.* **1990**, *123*, 1455–1459.
[11] G. L. Wood, C. K. Narula, E. N. Duesler, R. T. Paine, H. Nöth, *J. Chem. Soc. Chem. Commun.* **1987**, 496–498.
[12] H. Nöth, W. Schrägle, *Z. Naturforsch., Teil B* **1961**, *16*, 473–474.
[13] H. Nöth, W. Schrägle, *Chem. Ber.* **1965**, *98*, 352–362.
[14] M. S. Lube, R. L. Wells, P. S. White, *Inorg. Chem.* **1996**, *35*, 5007–5014.
[15] R. T. Paine, H. Nöth, T. Habereder, J. F. Janik, E. N. Duesler, D. Dreissig, *ACS Symp. Ser.* **2006**, *917*, 152–165.
[16] R. W. Light, L. D. Hutchins, R. T. Paine, C. F. Campana, *Inorg. Chem.* **1980**, *19*, 3597–3604.
[17] H. Nöth, P. Schweitzer, *Chem. Ber.* **1969**, *102*, 161–166.

 © 2007 Wiley-VCH Verlag GmbH & Co. KGaA, Weinheim 

[18] H. Nöth, P. Konrad, *Chem. Ber.* **1983**, *116*, 3552–3558.
[19] P. Konrad, Dissertation, Univ. Marburg, **1968**.
[20] R. J. Wehmschulte, K. Ruhlandt-Senge, P. P. Power, *Inorg. Chem.* **1994**, *33*, 3205–3207.
[21] A. Ahmed, W. Schwarz, H. Hess, *Acta Crystallogr., Sect. B* **1977**, *33*, 3574–3576.
[22] J. F. Janik, E. N. Duesler, R. T. Paine, *J. Organomet. Chem.* **1997**, *539*, 19–25.
[23] J. F. Janik, E. N. Duesler, R. T. Paine, *Chem. Ber.* **1993**, *126*, 2649–2651.
[24] J. F. Janik, E. N. Duesler, W. F. McNamara, M. Westerhausen, R. T. Paine, *Organometallics* **1989**, *8*, 506–514.
[25] G. Fritz, W. Hölderich, *Z. Anorg. Allgem. Chem.* **1976**, *422*, 1104–1114.
[26] J. P. von Linthoudt, E. V. von den Berghe, G. P. von der Kelen, *Spectrochim. Acta, Part A* **1980**, *36*, 17–21.
[27] *SMART*, Bruker Analytical Instruments, Madison, version 5.1.
[28] *SAINT*, Bruker Analytical Instruments, Madison, version 5.1.
[29] *SADABS*, Absorption corrections as implemented in *SHELXTL*, Bruker Analytical Instruments, Madison, version 5.1.
[30] *SHELXTL*, Bruker Analytical Instruments, Madison, version 5.1.

Received: April 16, 2007
Published Online: July 18, 2007

 © 2007 Wiley-VCH Verlag GmbH & Co. KGaA, Weinheim 

DOI: 10.1002/ejic.200700419

# Aqueous Reduction of $[Cp^*_2W_2O_5]$: Characterization of the Triangular Clusters $[Cp^*_3W_3O_4(OH)_2]^{2+}$ and $[Cp^*_3W_3O_6]^+$ – Comparison with Molybdenum

**Chiara Dinoi,[a] Pelin Sözen,[b] Gülnur Taban,[b] Deniz Demir,[b] Funda Demirhan,*[b] Petr Prikhodchenko,[c] Jenny Gun,[c] Ovadia Lev,[c] Jean-Claude Daran,[a] and Rinaldo Poli*[a]**

**Keywords:** Tungsten / O ligands / Metal clusters / Density functional calculations

Zinc reduction of $Cp^*_2W_2O_5$ in an acidified water–methanol medium affords the green 3-electron trinuclear cluster $[Cp^*_3W_3O_4(OH)_2]^{2+}$, isolated and crystallographically characterized as the triflate salt, **1**. Upon exposure to air, this complex is oxidized to a related 2-electron cluster, $[Cp^*_3W_3O_6]^+$, which was crystallized and characterized in three different salts, **2**–**4**. The 3-electron cluster exhibits a near-tetragonal frozen-glass EPR spectrum, and it shows evidence of coupling of the unpaired electron to only one of the three W atoms. The two-electron cluster is diamagnetic. An electrospray ionization $MS^n$ study revealed a stepwise expulsion of neutral $[Cp^*WO_2]$ units as the main fragmentation process. DFT calculations unveiled the intimate details of the electronic structures of these complexes and fully rationalized the structural and spectroscopic properties.

(© Wiley-VCH Verlag GmbH & Co. KGaA, 69451 Weinheim, Germany, 2007)

## Introduction

Aqueous organometallic chemistry is attracting growing interest because of its "green" impact[1–3] and because of its potential in catalytic[4,5] and biomedical applications.[6] Although this area is widely explored for low-valent systems, usually upon appending hydrophilic functionalities to the ligand periphery to increase solubility in an aqueous environment,[7–9] studies of high-oxidation organometallics are still rather scarce.[10–12] For redox-active metals, these studies are particularly interesting, as they may open the way to electrocatalytic applications.[12]

In a recent contribution,[13] we reported that the zinc reduction of $Cp^*_2Mo_2O_5$ in a strongly acidic ($CF_3COOH$ or $CF_3SO_3H$) mixed $H_2O$/MeOH medium affords the trinuclear mixed-valence ($Mo_3^{13+}$) cluster $[Cp^*_3Mo_3O_2(OH)_4]^{2+}$. The ion adopts a nearly equilateral triangular shape; each edge is bridged by two ligands. The distortion of the triangle is caused by one edge that is bridged by two OH groups, whereas the other two edges are bridged by one O atom and one OH group. As a consequence, the former edge is slightly longer than the latter ones. Although the number of bridging OH versus O groups was not revealed directly by the X-ray structural analysis, it was suggested indirectly by the same technique through the existence of short hydrogen-bonding contacts (or lack thereof) between the $Mo_3O_6$ core and the two $CF_3CO_2$ and $CF_3SO_3$ anions, and this was confirmed by comparison with a DFT geometry-optimized model, by EPR spectrometry, and by magnetic susceptibility measurements.

In this contribution, we examine the parallel behavior of the pentamethylcyclopentadienyltungsten system and report the isolation and characterization of two new redox-related tritungsten oxido clusters, $[Cp^*_3W_3O_6]^+$ and $[Cp^*_3W_3O_4(OH)_2]^{2+}$.

[a] Laboratoire de Chimie de Coordination, UPR CNRS 8241 liée par convention à l'Université Paul Sabatier et à l'Institut National Polytechnique de Toulouse,
205 Route de Narbonne, 31077 Toulouse Cedex, France
Fax: +33-561553003
E-mail: Rinaldo.Poli@lcc-toulouse.fr
[b] Celal Bayar University, Faculty of Sciences & Liberal Arts, Department of Chemistry,
45030 Muradiye-Manisa, Turkey
[c] Laboratory of Environmental Chemistry, The Casali Institute of Applied Chemistry, The Hebrew University of Jerusalem,
Jerusalem 91904, Israel

Supporting information for this article is available on the WWW under http://www.eurjic.org or from the author.

## Results and Discussion

### The $[Cp^*_3W_3O_4(OH)_2]^{2+}$ Cluster

The reduction of $[Cp^*_2W_2O_5]$ was carried out under the same conditions previously used for the reduction of $[Cp^*_2Mo_2O_5]$, namely by metallic zinc in an acidic $H_2O$/MeOH mixed solvent. MeOH is necessary to increase the solubility of the starting material. The reaction was carried out in the presence of two different acids, trifluoroacetic acid and trifluoromethylsulfonic (triflic) acid. As for the

Mo analogue, a series of color changes was observed over a period of three days, yielding a final green solution through an intermediate orange-red color. Crystallization of the final green product was successful in the case of the triflic acid reaction, revealing the nature of the compound as $[Cp^*_3W_3O_4(OH)_2](CF_3SO_3)_2{\cdot}2H_2O$ (**1**). Thus, the reaction stoichiometry is as shown in Equation (1). The oxidation state of tungsten in the final product is +5, yielding a 3-electron $W_3^{15+}$ cluster. Compound **1** is quite soluble in $CH_2Cl_2$ and its solutions are air sensitive, and they turn rapidly to orange when exposed to the atmosphere. The nature of the orange product is shown in the next section.

$$3[Cp^*_2W_2O_5] + 3Zn + 10H^+ \rightarrow 2[Cp^*_3W_3O_4(OH)_2]^{2+} + 3H_2O + 3Zn^{2+} \quad (1)$$

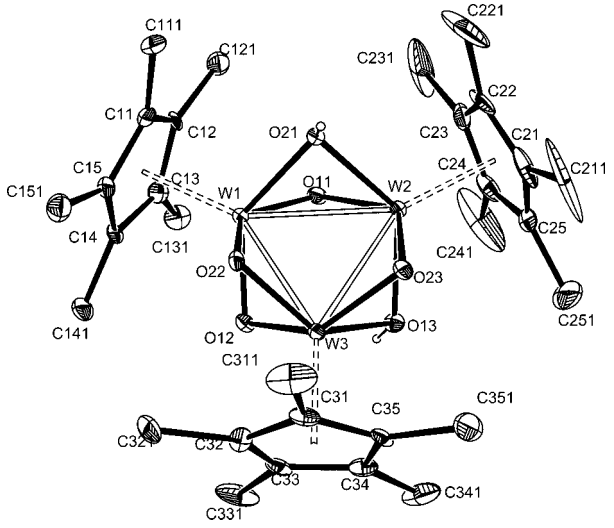


Figure 1. An ORTEP view of the dication in compound $[Cp^*_3W_3O_4(OH)_2](CF_3SO_3)_2{\cdot}2H_2O$ (**1**).

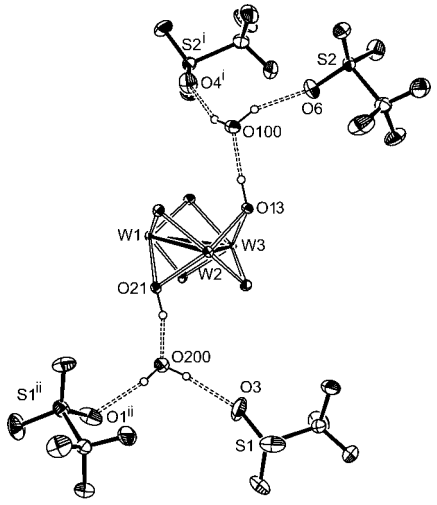


Figure 2. An ORTEP view of compound **1** that highlights the H-bonding interactions between dication, anions, and interstitial water molecules. The Cp* ligands bonded to the $W_3$ cluster are omitted for clarity [symmetry codes: (i) 3/2 – *x*, *y* – 1/2, 1 – *z*; (ii) 1/2 – *x*, *y* – 1/2, –*z*].

Table 1. Selected bond lengths and angles for the trinuclear clusters in all compounds.[a]

| Bond lengths [Å] | | | | |
|---|---|---|---|---|
| | **1** | **2**[b] | **3** | **4** |
| W1–W2 | 2.7416(3) | 2.6565(4) | 2.6685(5) | 2.6637(8) |
| W1–W3 | 2.6545(3) | 2.6505(5) | 2.6657(5) | 2.6614(9) |
| W2–W3 | 2.7485(3) | | 2.6849(5) | 2.6606(8) |
| W1–O11 | 1.882(4) | 1.958(5) | 1.980(6) | 1.917(8) |
| W1–O12 | 1.905(4) | 1.975(4) | 1.967(6) | 1.931(8) |
| W1–O21 | 2.076(3) | 1.967(4) | 1.949(6) | 1.958(8) |
| W1–O22 | 2.009(3) | 1.952(4) | 1.955(5) | 1.973(8) |
| W1–CG1 | 2.034(2) | 2.0507(3) | 2.054(4) | 2.0555(6) |
| W2–O11 | 1.979(4) | 1.948(5) | 1.937(6) | 1.935(8) |
| W2–O13 | 2.038(4) | | 1.968(5) | 1.944(8) |
| W2–O21 | 2.045(3) | 1.960(4) | 1.954(5) | 1.966(8) |
| W2–O23 | 2.001(4) | | 1.977(5) | 1.967(8) |
| W2–CG2 | 2.003(2) | 2.0400(4) | 2.068(7) | 2.0549(6) |
| W3–O12 | 2.003(4) | | 1.960(6) | 1.955(8) |
| W3–O13 | 2.080(4) | | 1.998(5) | 1.936(8) |
| W3–O23 | 1.872(3) | | 1.962(6) | 1.945(8) |
| W3–O22 | 1.899(3) | | 1.963(6) | 1.952(8) |
| W3–CG3 | 2.050(2) | | 2.053(8) | 2.0510(6) |
| **Bond angles [°]** | | | | |
| W2–W1–W3 | 61.216(8) | 60.075(7) | 60.443(14) | 59.95(2) |
| W1–W3–W2 | 60.955(7) | | 59.828(13) | 60.07(2) |
| W1–W2–W3 | 57.829(7) | 59.843(7) | 59.728(13) | 59.98(2) |
| CG1–W1–O11 | 111.29(11) | 113.53(13) | 113.2(3) | 112.5(2) |
| CG1–W1–O12 | 112.01(11) | 113.00(13) | 112.7(3) | 110.3(2) |
| CG1–W1–O21 | 114.19(10) | 112.67(13) | 113.6(3) | 115.7(2) |
| CG1–W1–O22 | 113.22(10) | 112.96(13) | 113.2(3) | 114.0(2) |
| O11–W1–O12 | 93.18(15) | 84.6(2) | 85.1(2) | 87.2(3) |
| O11–W1–O22 | 134.61(16) | 134.02(18) | 133.6(2) | 133.4(3) |
| O12–W1–O22 | 78.29(14) | 76.75(19) | 76.8(2) | 74.9(3) |
| O11–W1–O21 | 73.59(14) | 77.6(2) | 75.7(2) | 76.5(3) |
| O12–W1–O21 | 133.66(15) | 133.80(19) | 133.6(2) | 134.0(3) |
| O22–W1–O21 | 80.67(14) | 85.72(19) | 86.6(2) | 85.8(3) |
| CG2–W2–O11 | 114.72(10) | 113.40(14) | 112.0(3) | 114.0(2) |
| CG2–W2–O23 | 113.47(10) | | 114.0(3) | 113.2(2) |
| CG2–W2–O13 | 114.14(10) | 112.61(13) | 111.5(2) | 112.9(2) |
| CG2–W2–O21 | 115.30(10) | | 114.1(2) | 113.9(2) |
| O11–W2–O23 | 131.80(14) | 85.23(19) | 133.9(2) | 132.8(3) |
| O11–W2–O13 | 87.65(15) | | 86.2(2) | 87.0(3) |
| O23–W2–O13 | 72.14(14) | 77.16(19) | 76.0(2) | 75.4(3) |
| O11–W2–O21 | 72.32(15) | | 76.6(2) | 75.9(3) |
| O23–W2–O21 | 88.19(14) | | 86.2(2) | 84.9(3) |
| O13–W2–O21 | 130.57(14) | 133.2(3) | 134.4(2) | 133.2(3) |
| CG3–W3–O23 | 111.55(11) | | 114.9(3) | 114.5(2) |
| CG3–W3–O22 | 112.91(10) | | 112.07(18) | 113.7(2) |
| CG3–W3–O12 | 112.40(10) | | 111.4(3) | 111.6(2) |
| CG3–W3–O13 | 113.53(10) | | 114.06(18) | 111.5(2) |
| O23–W3–O22 | 93.60(15) | | 86.4(2) | 86.6(3) |
| O23–W3–O12 | 134.86(15) | 134.8(3) | 133.7(2) | 133.9(3) |
| O22–W3–O12 | 78.58(15) | | 75.6(2) | 75.0(3) |
| O23–W3–O13 | 73.76(15) | | 76.8(2) | 75.9(3) |
| O22–W3–O13 | 133.32(15) | | 133.7(2) | 134.8(3) |
| O12–W3–O13 | 79.89(15) | | 85.6(2) | 87.7(3) |
| W1–O11–W2 | 90.44(15) | 85.70(18) | 86.3(2) | 87.5(3) |
| W1–O12–W3 | 85.55(14) | 85.12(17) | 85.9(2) | 86.5(3) |
| W2–O13–W3 | 83.74(13) | 84.91(17) | 85.8(2) | 86.6(3) |
| W2–O21–W1 | 83.39(13) | | 85.5(2) | 85.5(3) |
| W3–O22–W1 | 85.53(14) | | 85.9(2) | 85.6(3) |
| W3–O23–W2 | 90.36(15) | | 85.2(2) | 85.5(3) |

[a] CGn is the center of gravity of the Cp* ligand bonded to atom Wn. [b] This structure has a symmetry imposed $C_2$ axis passing through atoms W2 and the midpoint of the W1–W1$^i$ bond. Numbering scheme correspondence: W3=W1$^i$; O12 = O22$^i$; symmetry code: (i) –*x*, *y*, –*z* + 3/2.

 © 2007 Wiley-VCH Verlag GmbH & Co. KGaA, Weinheim 

The structure of the dication is shown in Figure 1, whereas Figure 2 illustrates the arrangement of the anions and the interstitial $H_2O$ molecules relative to the trimetallic cluster. Relevant bonding parameters are collected in Table 1. The H atoms on the bridging OH groups could not be directly located from the diffraction data, but their presence is clearly demonstrated by the H-bonding network. Hydrogen bond contacts for compound **1** are available in the Supporting Information. As shown in Figure 2, the bridging atoms O13 and O21 establish short contacts with atoms O100 and O200 of the interstitial water molecules. The latter, in turn, establish short contacts with two different atoms of triflate anions: O100 with O6 but also with O4 of a second asymmetric unit; O200 with O3 but also with O1 of a third asymmetric unit. Close inspection of the difference Fourier map obtained after refinement of all heavy atoms revealed in fact the position of the H atoms on the interstitial $H_2O$ molecules. This observation excludes the alternative formulation as a neutral $[Cp^*_3W_3O_6]$ complex with two interstitial $CF_3SO_3H$ molecules, because in the latter case only one of the two $H_2O$ protons would point towards an oxygen atom of the trifluoromethylsulfonate group, whereas the other one would point towards the bridging oxido group of the $W_3$ cluster. Although these considerations establish the presence of H atoms on O13 and O21, they provide no information on the absence or presence of H atoms on the other bridging O atoms, O11, O12, O22, and O23. This point will be addressed in further detail later by inspection of the spectroscopic properties and by comparison of the experimental (X-ray diffraction) and computed (DFT) bonding parameters.

A most informative structural feature is the variation of the W–W distances: the two bonds bridged by one O atom and one OH group, W1–W2 [2.7416(3) Å] and W2–W3 [2.7485(3) Å], are almost 0.1 Å longer than the bond bridged by two O groups, W1–W3 [2.6545(3) Å]. In addition, the W–OH distances [in the range 2.038–2.080 Å; average 2.06(2) Å] are statistically longer than the W–O distances [in the range 1.872–2.009 Å; average 1.94(6) Å]. Furthermore, the W–(μ–OH)–W angles [83.39(13) and 83.73(13)°] are smaller than the W–(μ-O)–W angles in the $W(\mu\text{-}O)_2W$ moiety [average 85.54(14)°]. The W–(μ-O)–W angles in the W(μ-O)(μ-OH)W moiety are even larger [average 90.40(15)°]. This is certainly a secondary effect related to the longer W–W distance.

## The $[Cp^*_3W_3O_6]^+$ Cluster

### *The Triflate Structure – Compound 2*

As stated above, exposure of solutions of compound **1** to air rapidly yields orange-red solutions. Crystallization from this oxidized solution yielded red crystals of compound **2**, which was shown by X-ray analysis to correspond to $[Cp^*_3W_3O_6](CF_3SO_3)$. This formulation is consistent with the spectroscopic properties and with a comparison between the experimental (X-ray diffraction) and computed (DFT) structural parameters, as shown in a later section. The cation is a mixed-valence $W_3^{V,V,VI}$ cluster, namely a 2-electron cluster. Thus, the transformation generating this cluster can be described as in Equation (2).

$$[Cp^*_3W_3O_4(OH)_2]^{2+} + [ox] \rightarrow [Cp^*_3W_3O_6]^+ + 2H^+ + [red] \quad (2)$$

Like compound **1**, compound **2** is soluble in $CH_2Cl_2$, but it is also fairly soluble in $MeOH/H_2O$ solvent mixtures. These solutions are relatively stable in air, but not indefinitely so, to ultimately yield colorless solutions, which apparently occurs faster at high pH values. $^1H$ NMR spectroscopic monitoring in $MeOD/D_2O$ reveals the formation of a single resonance ($\delta$ = 2.05 ppm) attributed to $[Cp^*WO_3]^-$[14] at neutral or basic pH, whereas several other products, yet to be identified, are obtained under strongly acidic conditions (pH 2: resonances at $\delta$ = 2.22, 2.19, 2.15).

The structure of **2** contains a simple anion and no interstitial solvent molecules, which firmly establishes the +1 charge of the cluster. However, the cation exhibits a symmetry-imposed disorder because of a twofold axis that

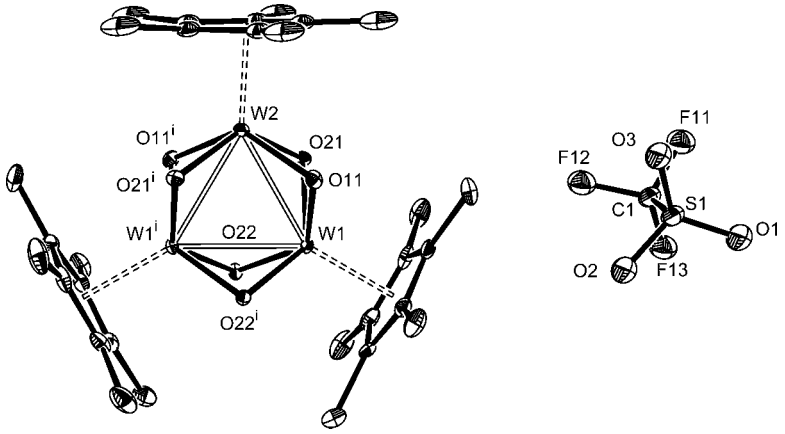


Figure 3. A view of the relative orientation of the cation and anion in the structure of $[Cp^*_3W_3O_6](CF_3SO_3)$ (**2**). Only one of the two symmetry-related orientations of the trifluoromethylsulfonate anion and of the Cp*(2) ligand are shown for the sake of clarity.

 © 2007 Wiley-VCH Verlag GmbH & Co. KGaA, Weinheim 

passes through atom W2 and through the midpoint of the W1–W1$^{i}$ bond. Therefore, there is a 50:50 distribution of two symmetry-related orientations of the Cp* ligand bonded to atom W2. In addition, the triflate anion is also located on a special position (another $C_2$ axis, orthogonally cutting through the C–S bond), yielding again a 50:50 distribution of two symmetry-related orientations. In spite of this problem, the structural model refined to quite acceptable final residuals, yielding relatively precise bond lengths and angles.

The crucial question concerns the absence of H atoms on the bridging O atoms. No residual electron density that could be assigned to such atoms was visible from the final difference Fourier map. However, even more convincing is the absence of close contacts between the two ions. The anion is located on the same plane as the $W_3$ triangle, separated from it by one of the Cp* ligands, see Figure 3. Two of the Cp* methyl H atoms are in close contact with the anion: H11B···O2 2.448, H11B···F11 2.506, H12C···O11 2.428, H12C···F12 2.540 Å. It may be reasonably argued that, if any OH group was present on the triangular $W_3$ cluster, this would establish H-bonding contacts with the triflate anion, as observed for the reduced analogue **1** (see above). Rather, the space above and below the $W_3$ triangle, in close contact with the bridging O atoms, is occupied by $CH_3$ groups of the $[Cp^*_3W_3O_6]^+$ ions located in other asymmetric units.

### *Two Trifluoroacetate Structures – Compounds 3 and 4*

Before discussing the structural parameters within the $[Cp^*_3W_3O_6]^+$ ion in more detail, we introduce two additional compounds related to **2**. These were obtained from the same synthetic procedure shown above but by using $CF_3COOH$ in place of triflic acid. Although the green product could not be obtained in single crystalline form, red crystals of the oxidation product were obtained after exposure to air. From two batches, crystallized under slightly different conditions, two different crystals containing the same $[Cp^*_3W_3O_6]^+$ ion were obtained: $[Cp^*_3W_3O_6][Zn_3(\mu_3\text{-}O)(\mu\text{-}CF_3COO)_4(CF_3COO)(CF_3COOH)(H_2O)_3]\cdot CF_3COOH$ (**3**) and $[Cp^*_3W_3O_6]_2[Zn(H_2O)_6](CF_3COO)_2(CF_3COOHOOCCF_3)_2\cdot 4H_2O$ (**4**). The bonding parameters for the tritungsten cluster of each compound are collected in Table 1, together with those of compounds **1** and **2**.

Compound **3** contains a complex, apparently unprecedented trinuclear zinc anion, as well as an interstitial $CF_3COOH$ molecule as shown in Figure 4. The closest relatives appear to be $Zn_3(\mu_3\text{-}O)(\mu\text{-}CF_3COO)_x$ clusters with $x = 5$[15] or 6,[16] and with similar frameworks and geometries. The anion in compound **3** contains one four-coordinate (Zn2) and two six-coordinate (Zn1, Zn3) zinc ions joined together by a triply bridging ligand O4. One carboxylate ligand bridges atoms Zn1 and Zn2, a second one bridges atoms Zn2 and Zn3, two additional ones bridge atoms Zn2 and Zn3, and a fifth one is terminally bonded to the four-coordinate Zn2 atom. The latter one is disordered among two different positions, one of which features a H-bond to the aqua ligand identified by atom O2 [O71a···O2 = 2.70(2) Å]. The other position features two weaker H-bonding interactions, the first one with the same aqua ligand [O71···O2 = 3.11(3) Å] and the second one (not shown in Figure 4) with atom O92 of a coordinated acid ligand [O71···O92 = 3.02(2) Å]. The latter ligand is terminally bonded to atom Zn3 through the carbonyl oxygen atom O91, whereas the OH functionality of this ligand (O92) is engaged as a proton donor in H-bonding with the triply bridging oxygen atom O4. The most relevant H-bonding contacts in compound **3** are supplied in the Supporting Information. The coordination sphere of six-coordinate Zn1 is completed by two water molecules (O1 and O2), whereas that of six-coordinate Zn3 is completed by a third water molecule (O3). The interstitial acid is a proton donor to the OH group of the coordinated acid (O92) and an acceptor from one of the aqua ligands (O2). The anion also establishes H-bonding interactions, as a proton donor, with the $W_3$ cation: three stronger ones through the aqua ligands O1 and O3 (with atoms O21, O23, and O13$^{i}$), plus two weaker ones through the aqua ligands O3 (with atom O12$^{i}$) and O2 (with atom O22), see Figure 5. H-bonding interactions are established on both opposite sides of the triangular $W_3$ face, which results in zig–zag 1D H-bonded chains (see Figure S1, Supporting Information). The most significant bonding parameters of the $[Zn_3(\mu_3\text{-}O)(\mu\text{-}CF_3COO)_4(CF_3COO)(CF_3COOH)(H_2O)_3]^-$ anion are collected in Table 2.

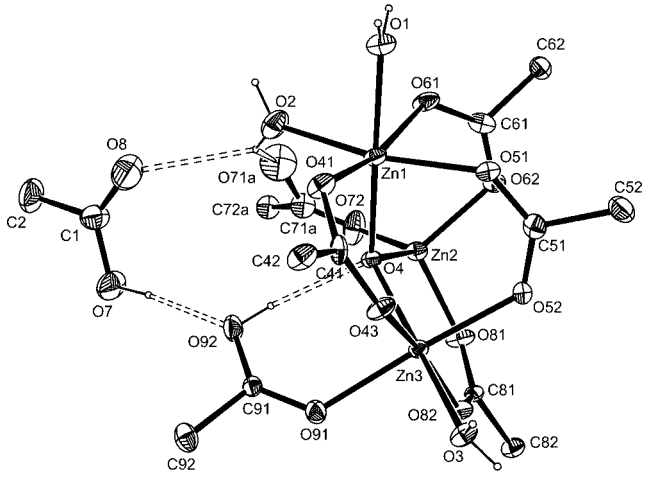


Figure 4. A view of the $[Zn_3(\mu_3\text{-}O)(\mu\text{-}CF_3COO)_4(CF_3COO)(CF_3COOH)(H_2O)_3]^-$ anion and the interstitial $CF_3COOH$ molecule in compound **3**. Only one component (C71a, C72a, and O71a) of the disordered $CF_3COO$ group is shown for the sake of clarity.

Compound **4** features a $[Zn(H_2O)_6]^{2+}$ ion sitting on an inversion center, plus an isolated $CF_3COO^-$ ion, a homoconjugate $CF_3COO\cdots H\cdots OOCCF_3^-$ ion, and two water molecules in general positions, in addition to the $[Cp^*W_3O_6]^+$ ion, also located in a general position. The three bridging O atoms on one face of the $W_3$ triangle (O21, O22, and O23) are acceptors for H-bonds with the aqua ligands of the $[Zn(H_2O)_6]^{2+}$ cation, see Figure 6. The opposite face of the $W_3$ triangle (atoms O11, O12, and O13) does not establish H-bonds. In addition, the aqua ligands of the

 © 2007 Wiley-VCH Verlag GmbH & Co. KGaA, Weinheim 

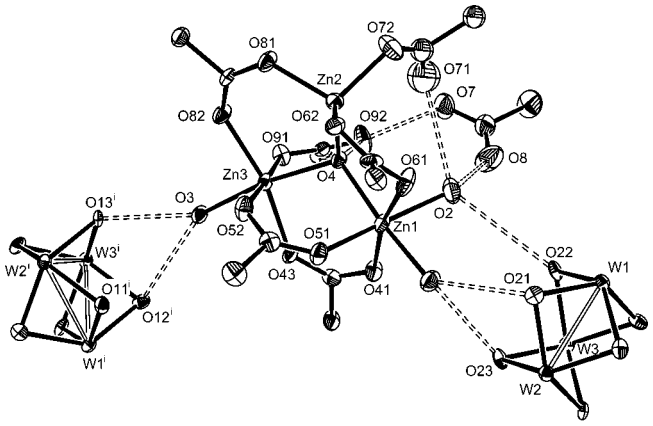


Figure 5. A view of the arrangement between the $[Zn_3(\mu_3\text{-}O)(\mu\text{-}CF_3COO)_4(CF_3COO)(CF_3COOH)(H_2O)_3]^-$ anion, the interstitial $CF_3COOH$ molecule, and the $[Cp^*_3W_3O_6]^+$ cation in compound **3**. The cation Cp* ligands and the aqua H atoms have been removed and only the coordination spheres of the Zn atoms are shown for clarity [symmetry code: (i) 1/2 + *x*, 3/2 – *y*, *z* – 1/2].

Table 2. Relevant bond lengths and angles for the $[Zn_3(\mu_3\text{-}O)(\mu\text{-}CF_3COO)_4(CF_3COO)(CF_3COOH)(H_2O)_3]^-$ anion of compound **3**.

| Bond lengths [Å] | | | |
|---|---|---|---|
| Zn1–O1 | 2.047(6) | Zn2–O81 | 1.966(7) |
| Zn1–O41 | 2.050(6) | Zn2–O62 | 1.970(6) |
| Zn1–O51 | 2.065(7) | Zn3–O3 | 2.068(6) |
| Zn1–O4 | 2.076(6) | Zn3–O52 | 2.070(6) |
| Zn1–O12 | 2.098(7) | Zn3–O4 | 2.092(6) |
| Zn1–O61 | 2.229(6) | Zn3–O82 | 2.108(6) |
| Zn2–O72 | 1.953(7) | Zn3–O91 | 2.122(6) |
| Zn2–O4 | 1.954(5) | Zn3–O43 | 2.132(6) |
| **Bond angles [°]** | | | |
| O4–Zn1–O1 | 172.8(2) | O4–Zn3–O31 | 170.9(2) |
| O4–Zn1–O2 | 91.6(3) | O4–Zn3–O43 | 94.4(2) |
| O4–Zn1–O41 | 99.5(2) | O4–Zn3–O52 | 90.6(2) |
| O4–Zn1–O51 | 93.4(2) | O4–Zn3–O82 | 100.6(2) |
| O4–Zn1–O61 | 93.7(2) | O4–Zn3–O91 | 92.0(2) |
| O1–Zn1–O2 | 85.7(3) | O3–Zn3–O43 | 76.6(2) |
| O1–Zn1–O41 | 87.3(3) | O3–Zn3–O52 | 89.0(3) |
| O1–Zn1–O51 | 88.0(3) | O3–Zn3–O82 | 88.4(2) |
| O1–Zn1–O61 | 79.4(3) | O3–Zn3–O91 | 88.8(3) |
| O2–Zn1–O41 | 92.8(3) | O43–Zn3–O52 | 94.5(3) |
| O2–Zn1–O51 | 168.1(3) | O43–Zn3–O82 | 164.8(3) |
| O2–Zn1–O61 | 84.7(3) | O43–Zn3–O91 | 87.2(3) |
| O41–Zn1–O51 | 97.0(3) | O52–Zn3–O82 | 87.7(3) |
| O41–Zn1–O61 | 166.7(3) | O52–Zn3–O91 | 176.8(3) |
| O51–Zn1–O61 | 84.2(3) | O82–Zn3–O91 | 89.9(3) |
| O4–Zn2–O62 | 112.7(2) | Zn1–O4–Zn2 | 111.2(3) |
| O4–Zn2–O72 | 115.0(3) | Zn1–O4–Zn3 | 112.1(2) |
| O4–Zn2–O81 | 112.3(3) | Zn2–O4–Zn3 | 111.0(3) |
| O62–Zn2–O72 | 107.4(3) | | |
| O62–Zn2–O81 | 103.6(3) | | |
| O72–Zn2–O81 | 105.0(3) | | |

$[Zn(H_2O)_6]^{2+}$ cation are H-bond donors towards the interstitial water molecules ($O111^i$ to O2W and $O113^i$ to O1W) and to the free $CF_3COO^-$ ion (O112 to O51). The other O atom of the latter (O52) is a H-bond acceptor from O1W. The homoconjugate anion, $CF_3COOHOOCCF_3^-$, also establishes H-bonds as acceptor with both interstitial water molecules. The relevant H-bonding parameters are provided in the Supporting Information. The H-bonding network yields an arrangement of the structure in 2D layers (see Figure S2, Supporting Information).

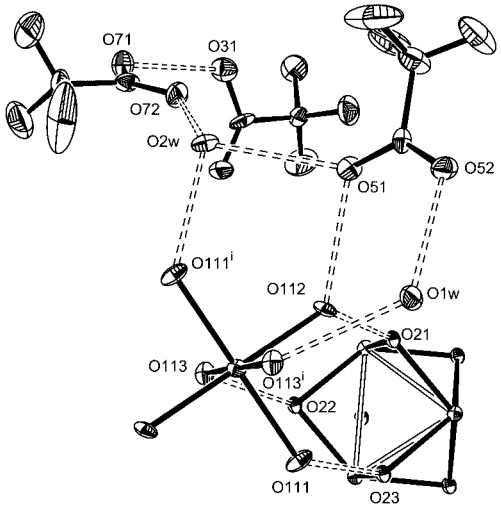


Figure 6. A view of the arrangement between the $[Cp^*_3W_3O_6]^+$, $[Zn(H_2O)_6]^{2+}$, $CF_3COO^-$, and $CF_3COO\cdots H\cdots OOCCF_3^-$ ions, and the two interstitial $H_2O$ molecules, in the structure of compound **4**. The cation Cp* ligands and all H atoms have been removed for clarity [symmetry code: (i) –*x*, –*y*, –*z*].

### *Description of the $[Cp^*_3W_3O_6]^+$ Structure*

The $[Cp^*_3W_3O_6]^+$ cluster has identical bonding parameters, within experimental error, in the structures of compounds **2**, **3**, and **4**, see Table 1. A representative view is shown in Figure 7. These parameters are significantly different from those of the dication of compound **1**. In particular, the three W–W distances are essentially equivalent, and they are placed in the narrow range 2.650–2.685 Å, with averages of 2.655(3) Å for **2**, 2.673(10) Å for **3**, and 2.662(2) Å for **4** or 2.663(10) Å for the entire set. This value is very close to the distance of the W–W bond bridged by

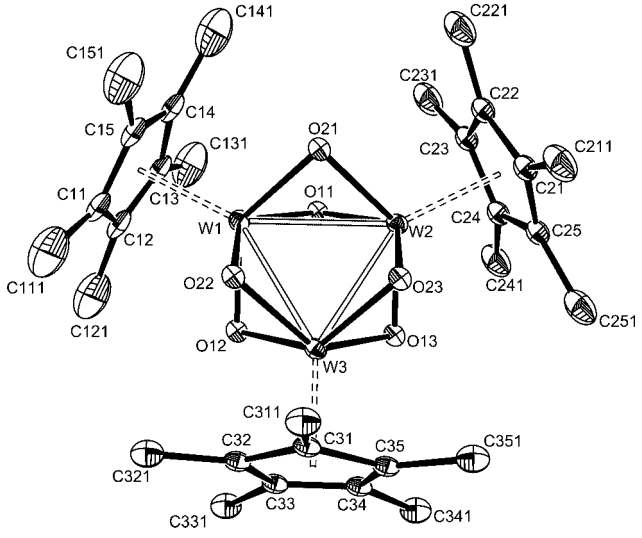


Figure 7. An ORTEP view of the $[Cp^*_3W_3O_6]^+$ ion from the structure of compound **3**.

 © 2007 Wiley-VCH Verlag GmbH & Co. KGaA, Weinheim 

two O ligands in compound **1**. The higher symmetry of the $Cp^*_3W_3O_6$ scaffold in the monocation, approaching ideal $D_{3h}$ symmetry, is also revealed by the small spread of the W–O distances [range 1.918–1.998 Å; averages 1.960(10) Å for **2**, 1.964(16) Å for **3**, 1.948(17) Å for **4**; global average 1.957(16) Å] and W–O–W angles [range 84.9–87.5°; averages 85.2(4)° for **2**, 85.8(4)° for **3**, 86.2(8)° for **4**; global average 85.7(7)°]. These values are also close to those of the $W(\mu\text{-}O)_2W$ moiety in compound **1**.

### Spectroscopic Identification

According to the formulation of the two clusters, derived from the X-ray analyses shown above, as $[Cp^*_3W_3O_4(OH)_2]^{2+}$ for the green derivative and $[Cp^*_3W_3O_6]^+$ for the red-orange derivatives, the first cluster has three metal electrons and should therefore be paramagnetic, whereas the second one has only two, which should be located in a symmetric metal–metal bonding combination,[13] and should therefore be diamagnetic. These expectations are in agreement with the experiment.

Compound **1** does not exhibit any strong $^1H$ NMR spectroscopic signal. In contrast, it has an EPR resonance, although this is clearly visible only at low temperatures (<200 K). The frozen glass spectrum in $CH_2Cl_2$ solution is shown in Figure 8. The overall shape is close to that expected for tetragonal symmetry, though a slight splitting of the perpendicular component is clearly visible. This is in nice agreement with the asymmetry of the bridge system, which introduces a slight perturbation to the threefold symmetry of the $W_3$ triangle as also indicated by the W–W distances. The perpendicular component does not have sufficient resolution to reveal the $^{183}W$ satellites. The parallel component, conversely, shows them quite clearly (see enlargement in Figure 8b). This feature was satisfactorily simulated as the sum of three Lorentzians, plus a quadratic function to account for the baseline drift. The satellites correspond to ca. 15% of the total intensity, in agreement with coupling of the unpaired electron with only one of the three cluster W atoms (theoretical values of 14.4, 24.7, and 31.6% are expected for coupling to 1, 2, or 3 equiv. W atoms, respectively). This observation will be fully rationalized on the basis of the computational results (vide infra).

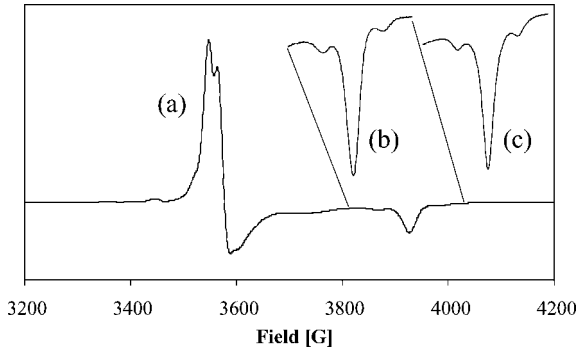


Figure 8. EPR spectrum of a frozen $CH_2Cl_2$ solution of compound **1** at 120 K: (a) experimental spectrum; (b) enlargement of the 3800–4050 G range; (c) simulation of (b), see text.

Contrary to compound **1**, compounds **2**–**4** do not show any EPR signal. They exhibit instead an NMR resonance at $\delta$ = 2.28 ppm in $CDCl_3$, consistent with the equivalence of the three Cp* ligands. Because this single $^1H$ NMR spectroscopic resonance is not conclusively proving the chemical constitution of the isolated bulk material, further characterization was sought by mass spectrometry (MS).

An electrospray ionization (ESI) MS study of compound **4** in $CH_2Cl_2$ gives a very clean isotopic cluster, which agrees with the theoretical isotopic distribution of $[Cp^*_3W_3O_6]^+$, see Figure 9. The same pattern is also observed in MeOH and in $MeOH/H_2O$ mixtures. Note the absence of fragmentation peaks, which reflects the robustness of the molecular

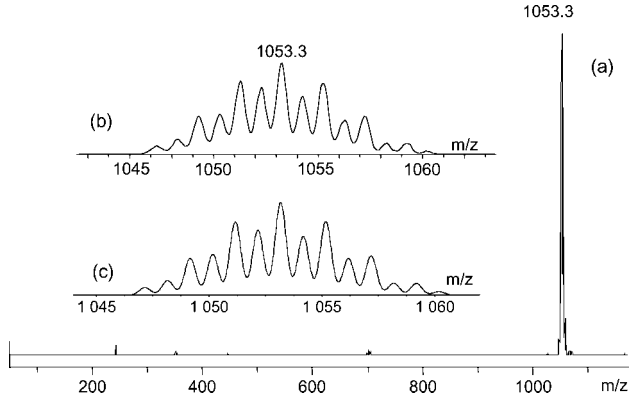


Figure 9. MS (ESI) of a $CH_2Cl_2$ solution of compound **4**. An expansion of the molecular ion isotopic cluster is shown in part (b) and the theoretical simulation in part (c).

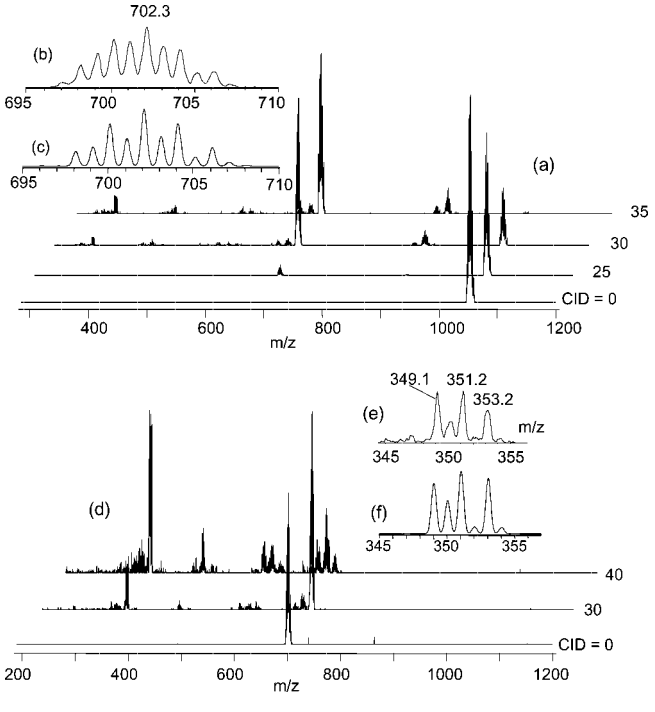


Figure 10. $MS^n$ studies of the $[Cp^*_3W_3O_6]^+$ ion: (a) MS–MS(1053) at increasing collision energies; (b) expansion; and (c) simulation of the product ion; (d) MS–MS(1053)–MS(702) at increasing collision energies; (e) expansion; and (f) simulation of the product ion.

 © 2007 Wiley-VCH Verlag GmbH & Co. KGaA, Weinheim 

scaffold. To learn about the fragmentation pattern, the collision-induced decay (CID) of this ion was investigated by $MS^n$. As shown in Figure 10(a), the ion displays a major decay pathway by expulsion of a $[Cp^*WO_2]$ fragment with transformation into $[Cp^*_2W_2O_4]^+$ (isotope cluster centered at $m/z$ = 702). However, the isotope pattern [Figure 10(b) with simulation in Figure 10(c)] reveals the presence of a second species one mass unit lighter. Therefore, elimination of a $[Cp^*WO_2H]$ unit, with the presumed involvement of a $CH_3$ group and generation of a tetramethylfulvene ligand, constitutes a competitive fragmentation pathway. Further trapping of these species and new CID in an $MS^3$ experiment, see Figure 10(d), is less selective but the major decay pathway is once again expulsion of a $[Cp^*WO_2]$ fragment from $[Cp^*_2W_2O_4]^+$, yielding $[Cp^*WO_2]^+$ (isotope cluster centered at $m/z$ = 351). The latter ion is not produced in a major pathway by direct expulsion of $[Cp^*_2W_2O_4]$ from the trinuclear species.

## DFT Calculations

Model compounds of the triangular $W_3$ clusters, obtained by replacing the Cp* ligands with the simpler Cp ring, i.e. $[Cp_3W_3O_4(OH)_2]^{2+}$ (**5**) for compound **1** and $[Cp_3W_3O_6]^+$ (**6**) for compounds **2**–**4**, were subjected to geometry optimization to find further supporting evidence for their stoichiometry (notably the number of OH vs. O groups) and to investigate their electronic structure. The calculations were run with no symmetry restrictions. Both calculations converged smoothly, giving final geometries in remarkably good agreement with the corresponding experimental ones for the Cp* derivatives (see Table 3). The only slight discrepancy consists of slightly longer bond lengths from the calculations relative to the experiment (W–O distances by 0.02–0.05 Å; W–W distances by 0.06–0.10 Å), as is typically observed for DFT calculations.

The geometrical trends for the less symmetric dihydroxido cluster **5** (see Scheme 1) are perfectly reproduced. Particularly notable is the difference between the W–W and W–W′ distances. The dioxido-bridged (W–W) bond is shorter than the two oxidohydroxido-bridged (W–W′) bonds by about 0.1 Å, like in the experimental structure. The lengths of different types of W–O bonds also have the same trend in the calculated and experimental structures (b > d > a > c, for the labeling, refer to Scheme 1), as do the different types of W–OH bonds (e > f). Finally, the two W–CG distances are longer than the W′–CG′ distance.

Excellent agreement is also found between the optimized geometry for the $[Cp_3W_3O_6]^+$ cluster and the experimentally observed structure for the Cp* analogue. In particular, the geometry is now close to the ideal $D_{3h}$ symmetry, with three very similar W–W distances. Note that the average optimized W–W distance in **6** is essentially identical to the shorter W–W distance for the dioxido-bridged bond in **5**. The same phenomenon is observed in the experimental structures. The three W–CG distances are also essentially equivalent.

Table 3. Comparison of the DFT optimized geometries (distances [Å], angles [°]) for the model $[Cp_3W_3O_4(OH)_2]^{2+}$ (**5**) and $[Cp_3W_3O_6]^+$ (**6**) complexes with the X-ray structures of the Cp* analogues.[a]

| Parameter[b,c] | $[(C_5R_5)_3W_3O_4(OH)_2]^{2+}$ | |
|---|---|---|
| | R = H (DFT) (**5**) | R = Me (X-ray)[d] |
| W–W | 2.723 | 2.6545(3) |
| W–W′ | 2.839, 2.853 | 2.745(6) |
| W–(μ-O) (a) | 1.920, 1.914 | 1.902(4) |
| W–(μ-O) (b) | 2.049, 2.054 | 2.005(4) |
| W–(μ-O) (c) | 1.894, 1.896 | 1.877(5) |
| W′–(μ-O) (d) | 2.012, 2.018 | 1.990(11) |
| W–(μ-OH) (e) | 2.148, 2.152 | 2.078(4) |
| W′–(μ-OH) (f) | 2.091, 2.091 | 2.042(7) |
| W–CG | 2.096, 2.099 | 2.043(14) |
| W′–CG′ | 2.060 | 2.003(2) |
| W′–W–W′ | 57.17 | 57.829(7) |
| W–W′–W′ | 61.66, 61.17 | 61.08(13) |
| W–(μ-O)–W (a–b) | 86.60, 86.60 | 85.54(14) |
| W–(μ-O)–W′ (c–d) | 93.16, 93.60 | 90.40(15) |
| W–(μ-OH)–W′ (e–f) | 84.09, 84.49 | 83.6(3) |
| CG-W–(μ–O) (a) | 112.28, 113.29 | 112.5(4) |
| CG–W–(μ-O) (b) | 113.86, 115.23 | 112.8(4) |
| CG–W–(μ-O) (c) | 110.54, 111.46 | 111.4(3) |
| CG–W′–(μ-O) (d) | 113.85, 115.97 | 114.1(12) |
| CG–W–(μ-OH) (e) | 115.33, 116.00 | 113.9(7) |
| CG′–W′–(μ-OH) (f) | 116.11, 116.37 | 114.7(12) |
| Parameter | $[(C_5R_5)_3W_3O_6]^+$ | |
| | R = H (DFT) (**6**) | R = Me (X-ray)[e] |
| W–W | 2.725, 2.732, 2.717 | 2.663(10) |
| W-(μ-O) | 1.946, 2.014, 1.932, 2.038, 1.919, 2.047, 1.919, 2.054, 1.918, 2.047, 1.937, 2.037 | 1.957(16) |
| W–CG | 2.108, 2.109, 2.110 | 2.053(7) |
| W–W–W | 59.71, 60.01, 60.28 | 60.0(2) |
| W-(μ-O)–W | 86.99, 85.95, 86.63, 87.03, 87.05, 86.24 | 85.7(7) |
| CG–W-(μ-O) | 114.55, 113.05, 112.90, 114.23, 112.56, 114.42, 114.56, 112.92, 113.39, 114.48, 112.47, 113.93 | 113(1) |

[a] The experimental parameters (X-ray structures) that are chemically and geometrically equivalent are averaged; for the individual parameters, see Table 1. [b] Label W refers to the two geometrically equivalent W atoms; W′ refers to the unique atom sitting on the ideal $C_2$ symmetry axis; CG and CG′ are the centers of gravity of the rings bonded to atoms W and W′, respectively. [c] For the labels assigned to geometrically different W–O and W–OH bonds (a–f), refer to Scheme 1. [d] From the structure of compound **1**. [e] Averaged values from the structures of compounds **2**–**4**.

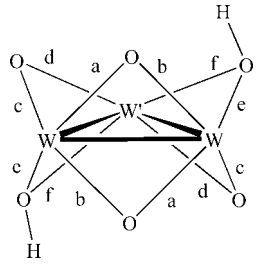


Scheme 1. Labeling of geometrically different W–O bonds in the structure of $[Cp_3W_3O_4(OH)_2]^{2+}$. The ideal $C_2$ symmetry axis passes through atom W′ and through the midpoint of the W–W vector. The Cp ligands are not drawn for the sake of clarity.

 © 2007 Wiley-VCH Verlag GmbH & Co. KGaA, Weinheim 

The electronic structure analysis is particularly interesting. The qualitative interaction diagram for the metal-based orbitals in this type of molecular scaffold was previously discussed[17,18] and is reproduced in Scheme 2 for convenience. The relevant metal-based molecular orbitals calculated for the two systems are shown in Figure 11, whereas more extensive data are available in the Supporting Information. For system **6** – a 2-electron $W_3^{V,V,VI}$ cluster – the two metal electrons are located in the $a(z^2)$ orbital, as expected. This orbital interaction insures the metal–metal attractive force. The additional electron in system **5** – a 3-electron $W_3^{V,V,V}$ cluster – is located in one of the two orbitals derived from the $e(xy)$ set. Because the ideal symmetry is reduced from $D_{3h}$ to $C_2$ by the addition of the two protons, the $e(xy)$ set splits ($e_1$ of $a$ type + $e_2$ of $b$ type) and the unpaired electron is located in the symmetric $a$ component. Note that, whereas the antisymmetric ($b$) component must be nil on the unique tungsten atom (W′) (see Supporting Information), there is no symmetry restriction for the composition of the $a$-type orbital. However, the composition of this orbital is such that the contribution from the two symmetry-equivalent W atoms is negligible, whereas atom W′ contributes greatly. Thus, the spin density is very much localized on the W′ atom (0.911), whereas it is negligible on the two W atoms (0.028 and 0.036), in perfect agreement with the measured relative intensity of the satellites in the EPR spectrum (vide supra). In this respect, it should be noted that the related molybdenum complex $[Cp^*_3Mo_3O_2(OH)_4]^{2+}$ – a 5-electron $Mo_3^{IV,IV,V}$ cluster – was shown to have the same ordering for the metal-based molecular orbitals.[13] Therefore, the unpaired electron for that complex is located in the antisymmetric $b$ orbital and couples to only two Mo nuclei, again consistent with the experimental evidence from EPR spectroscopy.

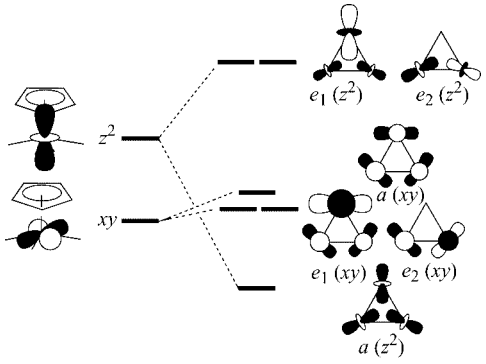


Scheme 2. Qualitative metal–metal orbital interactions for a $Cp_3M_3L_6$ molecule of ideal $D_{3h}$ symmetry.

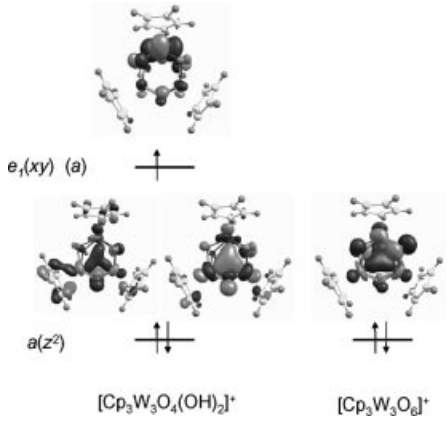


Figure 11. Filled metal-based molecular orbitals for systems **5** (left) and **6** (right). For the former, both spin orbitals resulting from the spin unrestricted calculation are shown.

## Comparison with Molybdenum and Redox Considerations

The reduction process reported here parallels that reported recently for the reduction of $Cp^*_2Mo_2O_5$.[13] However, the Mo system leads to a deeper reduction with generation of a 5-electron cluster, the trinuclear $Mo_3^{IV,IV,V}$ $[Cp^*_3Mo_3O_2(OH)_4]^{2+}$ complex. This product has the same molecular architecture as the two trinuclear W clusters described here, differing only by the number of protons and electrons. This difference agrees with the general trend of greater stability for higher oxidation states upon descending the same group of transition metals. It may be predicted that, by treatment with suitable oxidizing agents (or at a suitable electrochemical potential in an electrochemical experiment) the 5-electron Mo cluster could produce a 3-electron or a 2-electron cluster with the same structure found in the present study for the W system. Conversely, suitable reductive treatment of the W system could afford a 5-electron system such as the previously reported Mo cluster. Other electronic configurations such as 4-electron $M^{IV,V,V}$ could also exist. Given that proton gains/losses are associated with these transformations (at least between the two types of W clusters reported in the present contribution), it may also be expected that the redox potential is pH dependent in a protic environment. A detailed analysis of the electrochemical behavior of these clusters is beyond the scope of the present investigation and may be carried out at a later time.

Previous studies of the $Cp^*_2Mo_2O_5$ system by a coupled electrochemical–electrospray mass spectrometry methodology, by using a flow-through electrochemical cell,[19,20] revealed a very rich redox behavior, including the formation of trinuclear clusters that are related to the isolated cluster. We have now attempted to carry out a similar investigation for $Cp^*_2W_2O_5$, but no sufficient quantities of soluble products were revealed by the mass spectrometric analysis. At the potential at which the Mo system started to yield reductive processes, the W system showed no activity, whereas the rapid formation of a film on the surface of the electrode, which blocked any further electrochemical transformation, was observed at lower potentials. Therefore, it seems that the $Cp^*_2W_2O_5$ is more difficult to reduce than the Mo analogue and the primary reduction products (perhaps including the isolated trinuclear clusters described here) are unstable under these highly reducing conditions and proceed further to yield insoluble products.

 © 2007 Wiley-VCH Verlag GmbH & Co. KGaA, Weinheim 

## Conclusions

Like its Mo analogue,[13] the compound $[Cp^*_2W_2O_5]$ can be reduced in an aqueous medium to a triangular metal–metal bonded cluster. However, only 2- and 3-electron clusters are obtained for W, whereas the Mo system undergoes a deeper reduction to yield a 5-electron cluster. Like for the Mo cluster, the oxido/hydroxido asymmetry in the bridge system splits the degeneracy of the "*e*"-type frontier orbitals, as indicated by the EPR spectrum of the 3-electron cluster and confirmed by the DFT calculations. The variability of the cluster electrons for this system will be further explored for applications in organometallic chemistry and catalysis.

## Experimental Section

**General Procedures:** All preparations and manipulations were carried out with Schlenk techniques under an oxygen-free argon atmosphere. All glassware was oven-dried at 120 °C. Solvents were dried by standard procedures and distilled under nitrogen prior to use. $^1$H NMR spectra were recorded with a Bruker AM 250. Chemical shifts are expressed in ppm downfield from $Me_4Si$. Coupling constants are given in Hertz. Mass spectra were recorded with a Finnigan (San Francisco, USA) LCQ quadrupole ion-trap mass spectrometer equipped with an electrospray-ionization (ESI) interface. The ESI was operated in the positive ion mode with a spray voltage of 4.5 kV. The capillary voltage was 20 V and the source temperature was 100 °C. Mass spectra were obtained by scanning the mass analyzer from *m*/*z* 100 to 2000 with 5 total microscans. Maximum inject time was 400 ms. The analyzer was operated at a background pressure of $2 \times 10^{-5}$ Torr. In all experiments, helium was introduced at an estimated pressure of 1 mTorr to improve the ion-trapping efficiency and as collision gas for the collision-induced dissociation events. The compounds were isolated in the ion trap with an isolation width of 12 *m*/*z* units and activated by using increased collision energy to obtain collision-energy-dissociation profiles. EPR measurements were carried out at the X-band microwave frequency with a Bruker ESP300 spectrometer. The spectrometer frequency was calibrated with diphenylpicrylhydrazyl (DPPH, $g = 2.0037$). The starting compound, $[Cp^*_2W_2O_5]$, was prepared as described in the literature.[14]

**Synthesis and Crystallization of $[Cp^*_3W_3O_4(OH)_2](CF_3SO_3)_2 \cdot 2H_2O$ (1):** Metallic zinc (20 mesh, 0.415 g, 6.34 mmol) was added to a solution of $[Cp^*_2W_2O_5]$ (50 mg, 0.070 mmol) in MeOH/$H_2O$ (1:1, 6 mL). The mixture was acidified with $CF_3SO_3H$ (10 drops) and stirred under an atmosphere of argon at r.t. for 3 d, during which time it changed from a yellow solution to a green suspension. The mixture was filtered, and the solid was extracted with THF (0.5 mL). The addition of $Et_2O$ (1.5 mL) to the filtrate yielded the product as a green precipitate (0.047 g, 72%). A single crystal for X-ray analysis was obtained by diffusion of an $Et_2O$ layer into a THF solution at r.t. EPR (X-band, $CH_2Cl_2$, 120 K): $g_\perp = 1.89$; $g_\parallel = 1.72$ ($a_{W\parallel} = 114$ G).

**Synthesis and Crystallization of $[Cp^*_3W_3O_6](CF_3SO_3)$ (2):** A sample of compound **1** (61 mg, 0.044 mmol) was dissolved in $CH_2Cl_2$ and stirred for 1 h at r.t. in open air. The color of the green solution turned orange. The solvent was evaporated to dryness to afford an orange power, which was recrystallized from $CH_2Cl_2$/pentane to give red crystals (25 mg, 47% yield). $^1$H NMR (250 MHz, $CDCl_3$): $\delta = 2.28$ ppm.

**Reduction of $[Cp^*_2W_2O_5]$ by Zinc in the Presence of $CF_3COOH$ – Formation of Compounds 3 and 4:** Metallic zinc (20 mesh, 0.415 g, 6.34 mmol) was added to a solution of $[Cp^*_2W_2O_5]$ (50 mg, 0.070 mmol) in MeOH/$H_2O$ (1:1, 6 mL). The mixture was acidified with $CF_3COOH$ (10 drops) and stirred under an atmosphere of argon at r.t. for 5 d during which time it changed from a yellow solution to a green suspension. The mixture was filtered, and the solid was dried under vacuum (31 mg). Attempts to produce single crystals from this material failed as only powdery precipitates were obtained. Red single crystals of compound **3** were eventually obtained from $CH_2Cl_2$/hexane after exposure of the solution to air. $^1$H NMR (250 MHz, $CD_2Cl_2$): $\delta = 2.26$ ppm.

In a parallel identical procedure, from one of the numerous attempts to crystallize the green solid, the yellow mother solution of the green powdery precipitate was recovered, dried, and the yellow-orange residue was set again for crystallization from THF/hexane to yield single crystals of compound **4**. $^1$H NMR (250 MHz, $CDCl_3$): $\delta = 2.28$ ppm. MS (ESI, $CH_2Cl_2$): $m/z = 1053$ (envelope) $[M]^+$ (see Results and Discussion section).

**X-Ray Diffraction Studies:** A single crystal of each compound was mounted under inert perfluoropolyether at the tip of a glass fiber and cooled in the cryostream of an Oxford-Diffraction XCALIBUR CCD diffractometer. Data were collected by using the monochromatic Mo$K_\alpha$ radiation ($\lambda = 0.71073$). The structures were solved by direct methods (SIR97)[21] and refined by least-squares procedures on $F^2$ by using SHELXL-97.[22] All H atoms attached to carbon were introduced at idealized positions and treated with the riding model. All H atoms attached to oxygen were either located on difference Fourier syntheses or their coordinates were calculated on the basis of hydrogen bonding geometry and energy considerations.[23] They were then treated as riding on their parent O atoms. In compound $Cp^*_3W_3O_6(CF_3SO_3)$, the cation, $Cp^*_3W_3O_6$, is arranged around a twofold axis resulting in one of the Cp* to be disordered over two positions. The $CF_3SO_3$ anion is also disordered and arranged around another twofold axis. For both the disordered parts, the atomic positions and anisotropic thermal parameters were restrained to reasonable values using the tools available within SHELXL-97.[22] The drawing of the molecules was realized with the help of ORTEP3.[24] Crystal data and refinement parameters are shown in Table 4. CCDC-643997 to -644000 contain the supplementary crystallographic data for this paper. These data can be obtained free of charge from the Cambridge Crystallographic Data Centre via www.ccdc.cam.ac.uk/data_request/cif.

**Computational Details:** The DFT calculations were carried out on model systems where the Cp* ligands were replaced on the simpler Cp rings. The starting geometries were based on the crystallographically determined structures and no symmetry restrictions were imposed. The geometries were fully optimized and the resulting minima of the potential energy surface (PES) were verified by the positive value of all second derivatives of the energy. The calculations were performed by using the B3LYP three-parameter hybrid density functional method of Becke[25] and the standard LANL2DZ basis set, which included the Hay and Wadt effective core potentials (ECP) for the tungsten atoms,[26] as implemented in the Gaussian03 suite of programs.[27] The calculation on the open-shell system **5** was carried out by using the spin-unrestricted formulation. The value of $<S^2>$ resulting from the calculation is 0.7575, indicating negligible spin contamination.

**Supporting Information** (see footnote on the first page of this article): Packing diagrams for compounds **3** and **4**, energy diagrams

 © 2007 Wiley-VCH Verlag GmbH & Co. KGaA, Weinheim 

Table 4. Selected crystallographic and refinement parameters for all compounds.

| Compound | **1** | **2** | **3** | **4** |
|---|---|---|---|---|
| Empirical formula | $C_{32}H_{49}F_6O_{14}S_2W_3$ | $C_{31}H_{45}F_3O_9SW_3$ | $C_{44}H_{53}F_{21}O_{24}W_3Zn_3$ | $C_{36}H_{53}F_9O_{17}W_3Zn_{0.5}$ |
| Formula weight | 1387.38 | 1202.28 | 2112.52 | 1513.02 |
| Temperature [K] | 180(2) | 180(2) | 180(2) | 180(2) |
| Wavelength [Å] | 0.71073 | 0.71073 | 0.71073 | 0.71073 |
| Crystal system | monoclinic | monoclinic | monoclinic | triclinic |
| Space group | $P2_1/a$ | $C2/c$ | $Cc$ | $P\bar{1}$ |
| $a$ [Å] | 19.6490(7) | 16.7981(11) | 12.9884(12) | 12.8993(12) |
| $b$ [Å] | 11.1968(4) | 15.1424(7) | 21.8922(15) | 13.2879(13) Å |
| $c$ [Å] | 19.7744(8) | 14.9343(8) | 22.862(2) | 16.6848(18) Å |
| $\alpha$ [°] | 90 | 90 | 90 | 96.016(8) |
| $\beta$ [°] | 106.433(3) | 113.172(5) | 90.493(7) | 104.993(9) |
| $\gamma$ [°] | 90 | 90 | 90 | 116.737(9) |
| Volume [Å$^3$] | 4172.8(3) | 3492.3(3) | 6500.5(9) | 2384.7(4) |
| $Z$ | 4 | 4 | 4 | 2 |
| Density (calculated) [mg m$^{-3}$] | 2.208 | 2.287 | 2.159 | 2.107 |
| Absorption coefficient [mm$^{-1}$] | 8.438 | 9.984 | 6.509 | 7.564 |
| $F$(000) | 2644 | 2272 | 4040 | 1446 |
| Crystal size [mm] | 0.27 × 0.14 × 0.09 | 0.26 × 0.205 × 0.043 | 0.32 × 0.2 × 0.126 | 0.34 × 0.15 × 0.034 |
| $\theta$ range [°] | 2.79 to 26.37 | 3.65 to 30.03 | 3.20 to 28.28 | 2.61 to 25.03 |
| $h$, $k$, $l$ ranges | –24 to 24 | –23 to 16 | –16 to 17 | –15 to 15 |
| | –13 to 13 | –21 to 21 | –29 to 29 | –15 to 14 |
| | –23 to 24 | –19 to 21 | –30 to 29 | –19 to 18 |
| Reflections collected | 29412 | 17199 | 28767 | 14697 |
| Independent reflections | 8524 [$R$(int) = 0.0348] | 5088 [$R$(int) = 0.0369] | 11663 [$R$(int) = 0.0547] | 8107 [$R$(int) = 0.0691] |
| Completeness to $\theta$ = 25.00° [%] | 99.8 | 99.7 | 99.9 | 96.3 |
| Absorption correction | multi-scan | multi-scan | multi-scan | multi-scan |
| Max. and min. transmission | 0.3589 and 0.1896 | 0.3236 and 0.1509 | 1.0 and 0.2368 | |
| Refinement method | full-matr. least-sq. ($F^2$) | full-matr. least-sq. ($F^2$) | full-matr. least-sq. ($F^2$) | full-matr. least-sq. ($F^2$) |
| Data/restraints/parameters | 8524/8/547 | 5088/32/226 | 11663/32/857 | 8107/0/436 |
| Goodness-of-fit on F$^2$ | 1.124 | 1.182 | 0.923 | 0.867 |
| $R1$, $wR2$ [$I > 2\sigma(I)$] | 0.0324, 0.0738 | 0.0417, 0.0883 | 0.0382, 0.0619 | 0.0502, 0.0921 |
| $R1$, $wR2$ (all data) | 0.0413, 0.0772 | 0.0484, 0.0909 | 0.0502, 0.0649 | 0.1356, 0.1097 |
| Absolute structure parameter | | | 0.007(6) | |
| Largest diff. peak and hole [e Å$^{-3}$] | 3.747 and –1.748 | 2.455 and –3.030 | 1.489 and –1.302 | 4.859 and –1.751 |

and representative molecular orbitals for systems **5** and **6** (5 pages), H-bonding parameters of **1**, **3**, and **4**.

## Acknowledgments

We are grateful to the European Commission for funding of this work through the AQUACHEM Research Training Network (Project no. MRTN-CT-2003-503864). We also thank CINES and CICT (project CALMIP) for a grant of free computer time. Supplemental travel support was provided by a Bosphorus bilateral Program of Integrated Actions, co-sponsored by the French Ministry of Foreign Affairs in France and by TUBITAK in Turkey [TBAG-U/142(105T256)].

[1] T. Chan, L. Li, Y. Yang, W. Lu, *ACS Symp. Ser.* **2002**, *819*, 166–177.
[2] F. Joó, *Acc. Chem. Res.* **2002**, *35*, 738–745.
[3] I. T. Horvath, *Acc. Chem. Res.* **2002**, *35*, 685.
[4] D. Sinou, *Top. Curr. Chem.* **1999**, *206*, 41–59.
[5] D. Sinou, *Adv. Synth. Catal.* **2002**, *344*, 221–237.
[6] G. E. Jaouen, *J. Organomet. Chem.* **1999**, *589* (special issue: bioorganometallic chemistry).
[7] P. Kalck, F. Monteil, *Adv. Organomet. Chem.* **1992**, *34*, 219–284.
[8] B. E. Hanson, *Coord. Chem. Rev.* **1999**, *186*, 795–807.
[9] C. Muller, D. Vos, P. Jutzi, *J. Organomet. Chem.* **2000**, *600*, 127–143.
[10] A. Bino, F. A. Cotton, Z. Dori, *J. Am. Chem. Soc.* **1981**, *103*, 243–244.
[11] A. Bino, M. Ardon, E. Shirman, *Science* **2005**, *308*, 234–235.
[12] R. Poli, *Chem. Eur. J.* **2004**, *10*, 332–341.
[13] F. Demirhan, B. Çagatay, D. Demir, M. Baya, J.-C. Daran, R. Poli, *Eur. J. Inorg. Chem.* **2006**, 757–764.
[14] C. Dinoi, G. Taban, P. Sözen, F. Demirhan, J.-C. Daran, R. Poli, *J. Organomet. Chem.* **2007**, *692*, 3743–3749.
[15] A. L. Grzesiak, F. J. Uribe, N. W. Ockwig, O. M. Yaghi, A. J. Matzger, *Angew. Chem. Int. Ed.* **2006**, *45*, 2553–2556.
[16] J. S. Seo, D. Whang, H. Lee, S. I. Jun, J. Oh, Y. J. Jeon, K. Kim, *Nature* **2000**, *404*, 982–986.
[17] P. Kubácek, R. Hoffmann, Z. Havlas, *Organometallics* **1982**, *1*, 180–188.
[18] T. A. Albright, J. K. Burdett, M. H. Whangbo, *Orbital Interactions in Chemistry*, John Wiley & Sons, New York, **1985**.
[19] J. Gun, A. Modestov, O. Lev, D. Saurenz, M. A. Vorotyntsev, R. Poli, *Eur. J. Inorg. Chem.* **2003**, 482–492.
[20] J. Gun, A. Modestov, O. Lev, R. Poli, *Eur. J. Inorg. Chem.* **2003**, 2264–2272.
[21] A. Altomare, M. Burla, M. Camalli, G. Cascarano, C. Giacovazzo, A. Guagliardi, A. Moliterni, G. Polidori, R. Spagna, *J. Appl. Crystallogr.* **1999**, *32*, 115–119.
[22] G. M. Sheldrick, *SHELXL97: Program for Crystal Structure Refinement*, University of Göttingen, Göttingen, Germany, **1997**.
[23] M. Nardelli, *J. Appl. Crystallogr.* **1999**, *32*, 563–571.
[24] L. J. Farrugia, *J. Appl. Crystallogr.* **1997**, *32*, 565.
[25] A. D. Becke, *J. Chem. Phys.* **1993**, *98*, 5648–5652.
[26] P. J. Hay, W. R. Wadt, *J. Chem. Phys.* **1985**, *82*, 270–283.

 © 2007 Wiley-VCH Verlag GmbH & Co. KGaA, Weinheim 

[27] M. J. Frisch, G. W. Trucks, H. B. Schlegel, G. E. Scuseria, M. A. Robb, J. R. Cheeseman, J. Montgomery, J. A., T. Vreven, K. N. Kudin, J. C. Burant, J. M. Millam, S. S. Iyengar, J. Tomasi, V. Barone, B. Mennucci, M. Cossi, G. Scalmani, N. Rega, G. A. Petersson, H. Nakatsuji, M. Hada, M. Ehara, K. Toyota, R. Fukuda, J. Hasegawa, M. Ishida, T. Nakajima, Y. Honda, O. Kitao, H. Nakai, M. Klene, X. Li, J. E. Knox, H. P. Hratchian, J. B. Cross, C. Adamo, J. Jaramillo, R. Gomperts, R. E. Stratmann, O. Yazyev, A. J. Austin, R. Cammi, C. Pomelli, J. W. Ochterski, P. Y. Ayala, K. Morokuma, G. A. Voth, P. Salvador, J. J. Dannenberg, V. G. Zakrzewski, S. Dapprich, A. D. Daniels, M. C. Strain, O. Farkas, D. K. Malick, A. D. Rabuck, K. Raghavachari, J. B. Foresman, J. V. Ortiz, Q. Cui, A. G. Baboul, S. Clifford, J. Cioslowski, B. B. Stefanov, G. Liu, A. Liashenko, P. Piskorz, I. Komaromi, R. L. Martin, D. J. Fox, T. Keith, M. A. Al-Laham, C. Y. Peng, A. Nanayakkara, M. Challacombe, P. M. W. Gill, B. Johnson, W. Chen, M. W. Wong, C. Gonzalez, J. A. Pople, *Gaussian 03, Revision B.04*, Gaussian, Inc., Pittsburgh PA, **2003**.

Received: April 17, 2007
Published Online: July 24, 2007

 © 2007 Wiley-VCH Verlag GmbH & Co. KGaA, Weinheim 

DOI: 10.1002/ejic.200700421

# Ferromagnetic Coupling in a Mixed-Valence Hexavanadate Core: Quantum-Chemical Forecast

**Ekaterina M. Zueva,*[a] Serguei A. Borshch,*[b] Maria M. Petrova,[a] Henry Chermette,[c] and Andrey M. Kuznetsov[a]**

**Keywords:** Mixed-valent compounds / Vanadates / Density functional calculations / Exchange interactions / Electron transfer

The electronic structure and magnetic properties of the recently synthesized $V^{IV}/V^{V}$ mixed-valence alkoxo-polyoxovanadate comprising a hexanuclear vanadium core with four unpaired electrons have been studied within the DFT framework. The results of calculations suggest that the d electrons are completely trapped within the hexavanadate core, in agreement with the experimental observations. The exchange coupling constants computed using the broken symmetry formalism appeared to be of a ferromagnetic nature. Such interactions are very rare in oxovanadium complexes and are a consequence of a specific core geometry imposed by the polyoxometalate architecture. It has been shown that the earlier proposed intramolecular electron transfer cannot change the ground spin-state multiplicity irrespective of the sign of the exchange parameters.

(© Wiley-VCH Verlag GmbH & Co. KGaA, 69451 Weinheim, Germany, 2007)

## Introduction

Polyoxometalates (POMs) constitute a large group of polynuclear metal–oxygen anionic species possessing interesting and potentially valuable physical, chemical, and electrochemical properties. The ability of some transition metals (e.g., V, Mo, W, etc.) in their high oxidation states (+5, +6) to form POMs in solution has inspired many studies on POMs, giving rise to a variety of POM derivatives with intriguing architectures. Because of their unique properties, these species have multiple applications in different disciplines, such as catalysis (both heterogeneous and homogeneous), medicine, and materials science.[1–4] It has been found that unstable POM architectures can be stabilized by the introduction of alkoxo ligands because of the charge compensation associated with formal substitution of peripheral oxo ligands.[5] Among many other alkoxo-polyoxometalates, the fully alkylated polyoxovanadate derivatives $[V^{IV}_{n}V^{V}_{6-n}O_7(OR)_{12}]^{(4-n)}$ (R = $CH_3$, $C_2H_5$) of the classical (Lindqvist) POM structure $[M_6O_{19}]^{n-}$, which as an entity is not known for vanadium, have been reported by Hartl et al.[6,7] In these complexes, the hexavanadate core contains an $OV_6$ unit in which the vanadium ions are arranged in an octahedral fashion; six oxo groups act as terminal ligands and twelve alkoxo groups act as bridging ligands. The chemical synthesis and crystal structures of such alkoxo-polyoxovanadium compounds differing in their $V^{IV}$ content ($n$ = 2, 3, 4, 5, 6) have been described (see Figure 1). Interestingly, the complexes with two, three, and four vanadium(IV) centers give rare examples of cationic and neutral POM species. With the exception of the isovalent systems comprising six unpaired electrons ($n$ = 6), the reported complexes are mixed-valent and, as such, are of great interest for studying the interplay between exchange coupling and electron transfer in the hexanuclear framework. For the neutral and positively charged redox isomers of the methoxo and ethoxo series, experimental studies (X-ray structural, IR spectroscopic, cyclovoltammetric) of electron delocalization between vanadium centers have been performed.[7] The results obtained from these investigations suggest that the hexavanadate core can display either trapped metal valences or partly and fully delocalized d electrons, depending on the state of the compound (solid or solution), the $V^{IV}/V^{V}$ ratio, the nature of the μ-bridging alkoxo ligands, and the temperature. The neutral methoxo and ethoxo species ($n$ = 4) seem to contain trapped vanadium valences in the solid state, the four vanadium(IV) centers being located in a planar $V_4O_4$ ring. This result has been obtained from valence sum calculations conducted on the X-ray structural data collected at 173 K. The same conclusion has been drawn from the IR spectra (KBr pellet, room

[a] Department of Inorganic Chemistry, Kazan State Technological University,
68 K. Marx Street, 420015 Kazan, Russia
[b] Laboratoire de Chimie, UMR 5182 CNRS – Ecole Normale Supérieure de Lyon,
46 allée d'Italie, 69364 Lyon Cedex 07, France
[c] Chimie Physique Théorique, Bât. Paul Dirac (210), Université Lyon1 and CNRS UMR 5180 Sciences Analytiques,
43 Boulevard du 11 Novembre 1918, 69622 Villeurbanne Cedex, France

 © 2007 Wiley-VCH Verlag GmbH & Co. KGaA, Weinheim 

temperature), where the shape of the $O_b$–R absorption band is supposed to reflect the extent of trapped valence on the IR timescale. It should be mentioned, however, that the X-ray structure analysis conducted at room temperature yields, in the case of the ethoxo derivative, a structure displaying complete d-electron delocalization within the hexavanadate core. The phase transition[8] of the neutral ethoxo compound to the structure with completely detrapped vanadium valences is accompanied by disorder of the ethyl chains. It has been supposed that the latter is responsible for the delocalization of the unpaired electrons because it causes motion of the μ-bridging oxygen atoms. The event of valence detrapping at room temperature, which is revealed by valence sum calculations from crystallographic data, is not, however, manifested in the IR spectrum of the ethoxo derivative. As for the neutral methoxo species, the valence sums for its ambient-temperature X-ray structure still show the trapped vanadium valences, and differential scanning calorimetry measurements indicate no detectable phase transition in the temperature range 153–323 K. At the same time, the EPR-spectroscopic studies carried out for the $[V^{IV}_4V^{V}_2O_7(OCH_3)_{12}]$ single crystals[9] display the presence of an EPR signal, which has been attributed to a triplet ground state. As this observation does not agree with the expected antiferromagnetic interactions, active between four unpaired electrons, the results have been explained by introducing an internal dynamical process, namely, the intramolecular electron transfer. However, the attribution of the low-temperature signal to a triplet spin state is not unambiguous and, unfortunately, is not accompanied by thorough magnetic susceptibility measurements. Moreover, an abrupt transformation of the EPR spectrum discovered on cooling at about 190 K has been interpreted as a first-order phase transition. In the case of monocationic methoxo and ethoxo species containing three unpaired electrons ($n$ = 3), the X-ray structures obtained from hexachloroantimonate salts at 173 K comprise a highly symmetrical hexavanadate core, for which the valence sums indicate that all three d electrons are equally delocalized over the vanadium centers. In the dicationic ethoxo species ($n$ = 2), obtained again from its hexachloroantimonate salt, valence sum calculations conducted on the X-ray structure at 173 K indicate that the two unpaired electrons are located in a planar $V_4O_4$ ring, however it is not clear whether they are trapped or delocalized within the ring. The IR spectroscopic data (KBr pellet, room temperature) suggest that the monocationic derivatives exhibit a smaller degree of trapped valence than the neutral species, as well as the dicationic derivative in the ethoxo series, and are, therefore, in agreement with the solid-state results obtained by the X-ray structural analysis. We would also like to note that the earlier reported X-ray structural data for the methoxo compound series at 193 K[6] suggest that the monocationic derivative, if coupled with other counterions (e.g., polyhalide, $VOCl_4^-$), displays a distorted core and, apparently, a certain degree of trapped valence. Unfortunately, none of the mixed-valence alkoxo-polyoxovanadates have been studied using magnetic susceptibility measurements.

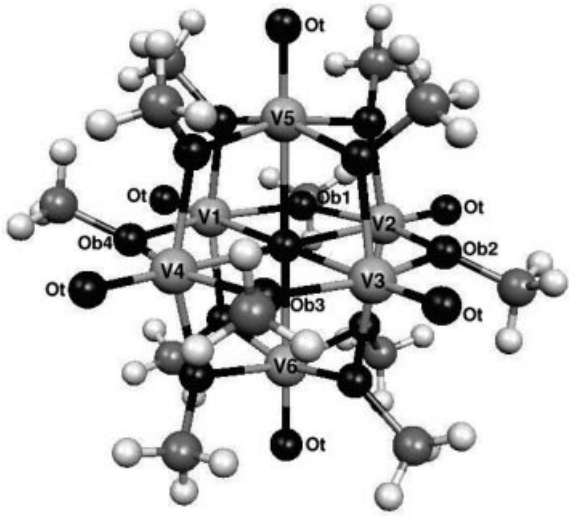


Figure 1. Crystal structure of the uncharged methoxo-bridged complex $[V^{IV}_4V^{V}_2O_7(OCH_3)_{12}]$ (ref.[6]).

The results of the cyclovoltammetric experiment carried out for the methoxo and ethoxo compound series are attributed to the solvated state of the redox isomers. Large potential separations $\Delta E^{o/}$ between successive one-electron redox processes have been observed in the cyclic voltammograms. Supposing that the stabilization energy imparted to the mixed-valence species by d-electron delocalization is the major factor influencing the splitting of the redox potentials, Hartl et al. have concluded that the unpaired electrons in redox isomers are significantly delocalized in the solvated state.[7] Interestingly, within any series of compounds (methoxo or ethoxo), the monocationic isomer displays a greater $\Delta E^{o/}$ value than the neutral complex (the $\Delta E^{o/}$ values for dicationic systems have not been determined yet).

On the basis of the obtained data, the given alkoxo-polyoxovanadium complexes have been classified as class II mixed-valence compounds. It has been assumed that the valence trapping found in the solid state is specifically linked to the cooperative effects encountered in the crystalline phase. However, the experimental results available to date are quite conflicting, especially for the $n$ = 4 member of the series, and are not conclusive for the reported compounds. Hartl et al. have pointed out that investigations by UV/Vis and NIR spectroscopy are imperative to the further understanding of these series of compounds, as well as EPR-spectroscopic studies and magnetic measurements. Herein, we present the results of a density functional theory (DFT) investigation carried out for the neutral species $[V^{IV}_4V^{V}_2O_7(OR)_{12}]$. Such a study provides an insight into mixed valency in the individual molecule or allows assessment of the electronic properties of the compound in its solid state (if calculations are performed on the X-ray molecular structure). On the basis of the results obtained from the quantum-chemical investigation, strong dynamical vibronic coupling has been assumed to be effective in a given species. The DFT calculations allowed evaluation of the

 © 2007 Wiley-VCH Verlag GmbH & Co. KGaA, Weinheim 

magnetic exchange constants which, contrary to widespread opinion, appeared to be of a ferromagnetic nature. Such interactions result in the magnetic ground state, whereas, as will be shown below, the intramolecular electron transfer, assumed in a previous publication,[9] cannot change the ground spin-state multiplicity and, consequently, cannot lead to a magnetic ground state in the presence of antiferromagnetic exchange.

## Computational Methodology

All DFT calculations reported in this paper were performed by means of the GAUSSIAN03 package[10] using the hybrid B3LYP exchange-correlation functional.[11–13] In some cases (see below), to simplify the calculations, we used hydroxo groups as μ-bridging ligands. In order to determine the extent of d-electron delocalization, we computed the electronic state with the highest total spin (S = 2) using the spin-unrestricted formalism. For both hydroxo- and methoxo-bridged complexes (**I** and **II** vide infra), the unrestricted high-spin (HS) solution obtained either on the optimized molecular structure or X-ray geometry (if available) is a good representation of the quintet state (the computed $<\mathbf{S}^2>$ values are close to 6.000, the expectation value for the pure S = 2 state, see Tables S1 and S2 in the electronic supporting information). The electronic states with lower spin multiplicity (three triplet and two singlet states) are not represented by a single-determinant wave function and can be described using sophisticated post-Hartree–Fock methods that take into account electron correlation effects (either only nondynamical correlation or both nondynamical and dynamical effects). However, such multideterminant approaches are very computationally demanding and have been applied so far only for small model systems.

As will be shown below, the unrestricted SCF calculations of the HS state resulted in the localization of four unpaired electrons on four vanadium centers. The magnetic properties of systems containing localized spins are generally interpreted using the Heisenberg–Dirac–van Vleck (HDVV) spin Hamiltonian

$$H = -\Sigma_{i>j} J_{ij} \mathbf{S}_i \cdot \mathbf{S}_j,$$

which introduces an isotropic interaction between the paramagnetic centers $i$ and $j$ described through the exchange coupling constant $J_{ij}$. In the above notation, the $J_{ij}$ value is positive if the spins $S_i$ and $S_j$ are coupled ferromagnetically; the negative $J_{ij}$ value means antiferromagnetic coupling. The eigenfunctions of the HDVV spin Hamiltonian are simply spin functions of the system $|S,M>$, constructed as linear combinations of the products of single-center spin functions $|S_1,M_1>|S_2,M_2>...|S_n,M_n>$ ($|S_i,M_i>$ vide infra). The eigenvalues of the above Hamiltonian represent the energies of the total spin states expressed as functions of $J_{ij}$. In isotropic systems, the energies of the electronic states with different total spin are related to the eigenvalues of the HDVV spin Hamiltonian. For a simple system, the energies of electronic states can be accurately computed at a high level of theory (i.e., within a multiconfigurational approach) and they can be used to obtain the $J_{ij}$ values. These values are directly comparable to those obtained by fitting the magnetic susceptibility data to the expression derived using the HDVV model Hamiltonian. For a system of chemical complexity, an accurate CI calculation becomes intractable. However, the exchange parameters can be estimated in the framework of a single-determinant method using the broken symmetry (BS) approach developed by Noodleman et al.,[14–17] as already described in the literature.[18–22] This method establishes the one-to-one matching between a diagonal element of the exact nonrelativistic Hamiltonian matrix computed in a basis set of single determinants (HS and so-called BS states) and the corresponding diagonal element of the HDVV spin Hamiltonian matrix computed in a basis set of products of single-center spin functions. It should be emphasized that the one-to-one matching is achieved provided that one deals with the orthogonal set of single determinants constructed from the same set of orthogonal space orbitals comprising doubly occupied closed-shell orbitals and singly occupied magnetic orbitals localized (not strictly) on the different spin centers. The set of $n$ different $J_{ij}$ values can be determined from the computed $n + 1$ single-determinant energies corresponding to different (nonequivalent) spin configurations. As these energies are related to the diagonal elements of the HDVV spin Hamiltonian matrix, the $J_{ij}$ values are obtained from a system of $n$ equations expressing the differences in energy between two single determinants as functions of $J_{ij}$. It is important to note that the HS and BS single determinants represent the wave functions related to one (ground) electronic configuration and, therefore, the BS approach neglects the dynamical correlation contribution to $J_{ij}$ (see Figure 2 illustrating the simplest case of two unpaired electrons on two centers A and B, where a and b are magnetic orbitals mainly localized on A and B, respectively).

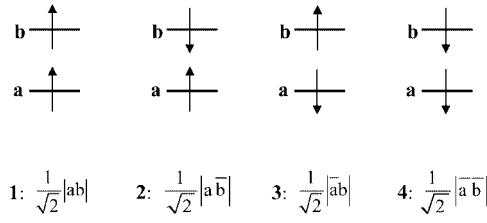


Figure 2. HS (**1** and **4**) and BS (**2** and **3**) single determinants for a dinuclear system with two unpaired electrons. **1** and **4** (S = 1, $M_S = \pm 1$) represent the equivalent spin configurations (degenerate states) and are related to $|\alpha\alpha>$ and $|\beta\beta>$ products of single-center spin functions; **2** and **3** ($M_S = 0$) also represent the equivalent spin configurations and are related to $|\alpha\beta>$ and $|\beta\alpha>$ products of single-center spin functions.

All SCF calculations presented here were carried out within the spin-unrestricted formalism using the tight SCF convergence criteria[10] to ensure sufficiently well converged values for the HS- and BS-state energies. The stability of all unrestricted SCF solutions was confirmed by means of the

 © 2007 Wiley-VCH Verlag GmbH & Co. KGaA, Weinheim 

stability analysis of Seeger and Pople.[23] Full geometry optimizations were carried out without imposing symmetry constraints; tight convergence criteria[10] were employed. The contracted Gaussian basis sets reported by Ahlrichs et al.[24,25] were used throughout the calculations. These all-electron basis sets are commonly applied[19,21,26–33] in the framework of the UB3LYP-BS computational procedure. On the vanadium and oxygen atoms, the triple-ζ valence basis sets extended by one polarization function (p-function for V, d-function for O) were used (TZVP). The carbon and hydrogen atoms were described by slightly smaller basis sets (SVP) that are of double-ζ quality in the valence region and contain one polarization function (d-function for C, p-function for H).

## Results and Discussion

### Exchange Interactions between Localized Electrons

In all systems studied, the spin-density distribution computed from the unrestricted HS solution clearly indicates that all four d electrons are completely trapped (see Tables S1 and S2) and our next task was the evaluation of exchange interactions between localized electrons. Before presenting the results of the DFT calculations of the exchange parameters in complexes **I** and **II**, we would like to mention the two problems arising when the BS approach is employed using a standard quantum-chemical program package. In this case, the HS and BS single determinants and their energies are obtained by performing unrestricted SCF calculations. One of the problems associated with this computational procedure is that the single determinants are constructed from the spatially nonorthogonal α and β orbitals. Another problem is that the spin-polarized orbitals are determined for each single determinant from a separate SCF calculation and, strictly speaking, the orbital sets obtained for different single determinants are not equivalent to each other. As a result, the computed single determinants have nonzero overlap integrals. In such a case, the energies of single determinants are not directly related to the diagonal elements of the HDVV spin Hamiltonian matrix and the effect of nonorthogonality should be taken into account to derive the relationships between the computed single-determinant energies and the $J_{ij}$ values. Such a complex problem has been solved only for dinuclear systems, provided that all single determinants are built from the equivalent orbital sets, which causes the $M_S$ components of the total spin state (constructed from these single determinants) to be degenerate.[18–20] For more complex systems, the effect of nonorthogonality of the computed single determinants can hardly be explicitly considered and it is simply ignored. Herein, we judge the performance of the UB3LYP-BS computational procedure to describe the magnetic structure of a given species by using the following two criteria. The first one establishes whether the nonorthogonality problem affects the single-determinant $<\mathbf{S}^2>$ values. Comparison of the computed $<\mathbf{S}^2>_{HS}$ and $<\mathbf{S}^2>_{BS}$ values with those derived using the Clebsch–Gordan algebra answers this question.[34] The second criterion is the compatibility of the equations for $J_{ij}$ derived for the orthogonal single-determinant basis set with the computed HS- and BS-state energies. Apparently, this criterion can be employed if the number of $J_{ij}$ is less than the number of the nonequivalent BS states that could be generated for a system. In these cases, any set of equations should have the same solution if the influence of the nonorthogonality on the $J_{ij}$ values is negligible. The necessity of considering a complete set of BS single determinants has also been pointed out by Bencini et al.[22] However, in this work it was implicitly assumed that the computed $J_{ij}$ values are not affected by the nonorthogonality problem and the consistency of equations for $J_{ij}$ was tested to check the validity of the nearest-neighbors approximation.

For complex **I**, the UB3LYP-BS calculations were performed on the HS-state geometry. For complex **II**, besides its HS-state geometry, the X-ray molecular structure[6] was also used (see Figure 1). All three systems were found to possess $C_i$ symmetry; the structural parameters are collected in Table 1. In each system, the hexavanadate core has a significantly distorted geometry: for the equatorial metal centers ($V^{IV}$ sites, see the HS-state atomic spin densities in Tables S1 and S2), the $V–O_c$ bonds are significantly elongated, whereas the same bonds for the remaining axial metal ions ($V^V$ sites) appear to be relatively short. In other words, the hexavanadate core has a "short" $O_t–V^V–O_c–V^V–O_t$ axis and two "long" $O_t–V^{IV}–O_c–V^{IV}–O_t$ axes. These results suggest that electron transfer is suppressed in the individual and solid-state molecules of **I** and **II** and their magnetic properties can be analyzed using the HDVV spin Hamiltonian. For the given systems, this Hamiltonian contains four exchange parameters ($C_i$ symmetry) and reads

$$H(4) = -[J_{12}(\mathbf{S}_1\cdot\mathbf{S}_2 + \mathbf{S}_3\cdot\mathbf{S}_4) + J_{14}(\mathbf{S}_1\cdot\mathbf{S}_4 + \mathbf{S}_2\cdot\mathbf{S}_3) + J_{13}\mathbf{S}_1\cdot\mathbf{S}_3 + J_{24}\mathbf{S}_2\cdot\mathbf{S}_4] \quad (1)$$

where $S_i = 1/2$. Spins are indexed according to the numbering shown in Figure 1.

Table 1. Structural parameters for complexes **I** and **II** (bond lengths in Å, bond angles in °).

| Parameter | **I** (S = 2)[a] | **II** (S = 2)[a] | **II** (X-ray)[b] |
|---|---|---|---|
| $V_1–O_c$ | 2.37 | 2.33 | 2.280 |
| $V_2–O_c$ | 2.38 | 2.33 | 2.296 |
| $V_5–O_c$ | 2.32 | 2.31 | 2.266 |
| $V_1–V_2$ | 3.36 | 3.30 | 3.247 |
| $V_1–V_4$ | 3.36 | 3.30 | 3.224 |
| $V_1–O_{b1}$ | 2.01 | 2.01 | 1.955 |
| $V_1–O_{b4}$ | 2.01 | 2.00 | 1.965 |
| $V_2–O_{b1}$ | 2.01 | 2.00 | 1.991 |
| $V_2–O_{b2}$ | 2.01 | 2.01 | 1.979 |
| $V_1–O_{b1}–V_2$ | 113.4 | 110.6 | 110.8 |
| $V_1–O_{b4}–V_4$ | 113.0 | 110.5 | 109.7 |
| $V_1–O_c–V_2$ | 90.0 | 90.0 | 90.4 |
| $V_1–O_c–V_4$ | 90.0 | 90.0 | 89.6 |
| $V–O_t$ | <1.58> | <1.59> | <1.588> |

[a] The geometry of a given complex optimized for the HS state. [b] The X-ray structural data collected at 193 K (ref.[6]).

 © 2007 Wiley-VCH Verlag GmbH & Co. KGaA, Weinheim 

The eight SCF single determinants computed for **I** and **II** are reported in Tables S1 and S2, respectively. The products of single-center spin functions associated with the computed single determinants representing different spin configurations are shown in Table 2. For any system, the remaining eight microstates are simply spin-reversed analogues of those listed in the table. In order to check whether the SCF convergence criteria were strong enough, such spin-reversed counterparts were computed for BS1, BS2, and BS3 states. In all cases, the degeneracy of the single determinants representing the equivalent spin configurations was found. As can be expected for $C_i$ symmetry, BS4 and BS6 states, as well as BS5 and BS7 states, appear to be equivalent to each other (see Tables S1 and S2). From these tables it can also be seen that the single-determinant $<\mathbf{S}^2>$ values are not significantly affected by the nonorthogonality problem inherent in the computational procedure. The computed $<\mathbf{S}^2>_{BS}$ values are close to 2.000 and 3.000 expected for the pure BS states (which are eigenfunctions of $\mathbf{S}_z$) with $M_S = 0$ and $M_S = 1$, respectively; the computed $<\mathbf{S}^2>_{HS}$ values approach 6.000, the expectation value for the pure S = 2 state.

Table 2. Diagonal matrix elements of the model spin Hamiltonian H(4) [Equation (1)] associated with SCF energies corresponding to different spin configurations of the systems studied.

| SD: $\|S_i,M_i>$ | $E_{SD}$: $<S_i,M_i\|H(4)\|S_i,M_i>$ |
|---|---|
| HS: $\|\alpha\alpha\alpha\alpha>$, $M_S = 2$ | $E_{HS}$: $-\frac{J_{12}}{2} - \frac{J_{14}}{2} - \frac{J_{13}}{4} - \frac{J_{24}}{4}$ |
| BS1: $\|\alpha\beta\alpha\beta>$, $M_S = 0$ | $E_{BS1}$: $\frac{J_{12}}{2} + \frac{J_{14}}{2} - \frac{J_{13}}{4} - \frac{J_{24}}{4}$ |
| BS2: $\|\alpha\alpha\beta\beta>$, $M_S = 0$ | $E_{BS2}$: $-\frac{J_{12}}{2} + \frac{J_{14}}{2} + \frac{J_{13}}{4} + \frac{J_{24}}{4}$ |
| BS3: $\|\alpha\beta\beta\alpha>$, $M_S = 0$ | $E_{BS3}$: $\frac{J_{12}}{2} - \frac{J_{14}}{2} + \frac{J_{13}}{4} + \frac{J_{24}}{4}$ |
| BS4 (BS6): $\|\alpha\alpha\alpha\beta>$ ($\|\alpha\beta\alpha\alpha>$), $M_S = 1$ | $E_{BS4(BS6)}$: $-\frac{J_{13}}{4} + \frac{J_{24}}{4}$ |
| BS5 (BS7): $\|\alpha\alpha\beta\alpha>$ ($\|\beta\alpha\alpha\alpha>$), $M_S = 1$ | $E_{BS5(BS7)}$: $\frac{J_{13}}{4} - \frac{J_{24}}{4}$ |

The diagonal matrix elements of the model spin Hamiltonian H(4) [Equation (1)] associated with the computed single-determinant energies are listed in the second column of Table 2. From Table 2, 15 equations for $J_{ij}$ can be obtained (see Table S3 of supporting information). The consistency of these equations with the computed HS- and BS-state energies was tested by considering all possible sets of four equations. For any system, five noncoincident values were found for $J_{12}$ and $J_{14}$, and seven for $J_{13}$ and $J_{24}$. The average values and their standard deviations are reported in Table 3. According to these results, the influence of the single-determinant nonorthogonality on the $J_{ij}$ values can be considered negligible for the given systems. The energies of the total spin states (one quintet, three triplet, and two singlet levels) computed using the obtained $J_{ij}$ values are (in $cm^{-1}$):

Table 3. $J_{ij}$ means and their standard deviations (in parentheses) obtained for complexes **I** and **II** using the model spin Hamiltonians H(4) and H(2) containing four and two exchange parameters, respectively (in $cm^{-1}$).

| | $J_{ij}$ | Sample size | **I** (S = 2)[a] | **II** (S = 2)[a] | **II** (X-ray)[b] |
|---|---|---|---|---|---|
| H(4) | $J_{12}$ | $n = 5$ | 67.6 (0.3) | 10.9 (1.8) | 196.9 (1.6) |
| | $J_{14}$ | $n = 5$ | 51.4 (0.3) | 12.2 (1.8) | 193.2 (1.6) |
| | $J_{13}$ | $n = 7$ | 31.2 (0.7) | 21.6 (4.7) | 73.3 (4.1) |
| | $J_{24}$ | $n = 7$ | 16.7 (0.7) | 22.5 (4.7) | 55.3 (4.1) |
| H(2) | $J_{12}$ | $n = 5$ | 59.5 (0.3) | 11.5 (1.8) | 195.1 (1.6) |
| | $J_{13}$ | $n = 4$ | 24.0 (0.3) | 22.3 (2.0) | 64.1 (1.7) |

[a] The values computed on the HS-state geometry of a given complex. [b] The values computed for the X-ray structure (ref.[6]).

**I** (HS-state geometry): –71.5 (S = 2); 1.1, 22.8, 47.5 (S = 1); 33.2, 109.7 (S = 0);
**II** (HS-state geometry): –22.6 (S = 2); 0.5, 10.2, 11.8 (S = 1); 12.0, 33.1 (S = 0);
**II** (X-ray geometry): –227.2 (S = 2); 23.0, 41.3, 162.9 (S = 1); 96.4, 358.0 (S = 0).

Interestingly, reasonable $J_{ij}$ values can be obtained if the model spin Hamiltonian containing two $J_{ij}$ parameters [Equation (1) with $J_{14} = J_{12}$ and $J_{24} = J_{13}$] is used:

$$H(2) = -[J_{12}(\mathbf{S}_1\cdot\mathbf{S}_2 + \mathbf{S}_1\cdot\mathbf{S}_4 + \mathbf{S}_2\cdot\mathbf{S}_3 + \mathbf{S}_3\cdot\mathbf{S}_4) + J_{13}(\mathbf{S}_1\cdot\mathbf{S}_3 + \mathbf{S}_2\cdot\mathbf{S}_4)] \quad (2)$$

where $S_i = 1/2$. This Hamiltonian describes the total spin levels of a highly symmetrical system comprising the square $S_i = 1/2$ unit with the equivalent $|\alpha\alpha\beta\beta>$ and $|\alpha\beta\beta\alpha>$ states, as well as $|\alpha\alpha\alpha\beta>$ and $|\alpha\alpha\beta\alpha>$ ones. The diagonal matrix elements of such a Hamiltonian are equal to those listed in Table 2 provided that $J_{14} = J_{12}$ and $J_{24} = J_{13}$. From these expressions the following equations for $J_{ij}$ can be obtained:

$$E_{HS} - E_{BS1} = -2J_{12}$$
$$E_{HS} - E_{BS2} = -J_{12} - J_{13}$$
$$E_{HS} - E_{BS4} = -J_{12} - \frac{J_{13}}{2}$$
$$E_{BS1} - E_{BS2} = J_{12} - J_{13}$$
$$E_{BS1} - E_{BS4} = J_{12} - \frac{J_{13}}{2}$$
$$E_{BS2} - E_{BS4} = \frac{J_{13}}{2}$$

The systems studied have only $C_i$ symmetry and, thus, the computed BS2 and BS3 states, as well as BS4 and BS5 states, are not equivalent to each other (see Tables S1 and S2). From the above equations we obtained (for each system) the sets of noncoincident values for $J_{12}$ and $J_{13}$ using the average of BS2 and BS3 state energies for $E_{BS2}$ and the average of BS4 and BS5 state energies for $E_{BS4}$. The $J_{12}$ and $J_{13}$ means and their standard deviations are reported in Table 3. For each system, the obtained $J_{12}$ value coincides with the average of $J_{12}$ and $J_{14}$ values obtained using the model spin Hamiltonian H(4). Similarly, the $J_{13}$ value [for H(2)] is equal to the average of $J_{13}$ and $J_{24}$ values [for H(4)].

 © 2007 Wiley-VCH Verlag GmbH & Co. KGaA, Weinheim 

We would like to stress that the one-to-one matching between the matrix elements of the electronic and spin Hamiltonians, being the basis of the BS approach, exists if all single-determinant states are constructed by assuming the same molecular geometry. Therefore, for the systems studied, we used the same structure (the HS-state or X-ray one) throughout the single-determinant calculations. We also did a series of test SCF calculations using the geometries optimized for all single-determinant states. As expected, the equations for $J_{ij}$ became inconsistent. The $J_{ij}$ values obtained from different sets of equations dramatically differ; the standard deviations were found to be twice as much as the mean values.

In the literature, the so-called nonprojected scheme[19] is often used for the estimation of the exchange coupling constant in dinuclear transition-metal complexes in the DFT framework.[19,26–29,32] Within this scheme, the single-determinant BS solution (associated with $|S_1,M_1 = S_1\rangle|S_2,M_2 = -S_2\rangle$ or $|S_1,M_1 = -S_1\rangle|S_2,M_2 = S_2\rangle$) is assumed to describe the electronic state with the lowest total spin $S = |S_1 - S_2|$, that is, the energy of the BS state is used as the energy of the pure $S = S_{min}$ state. Thus, the equation for J is obtained from the expressions for the eigenvalues of the HDVV spin Hamiltonian: $E(S_{max})$ and $E(S_{min})$. This scheme was found to give a better agreement between the computed and experimental exchange coupling constants in a number of dimers (especially when used with the B3LYP functional).[19,26,35] The success of the nonprojected approach was recently explained by a partial account of the nondynamical electron correlation in the DFT-BS solutions through the self-interaction error.[35] This statement was, however, questioned in the literature.[36] Such a technique may be adopted for a more complex system if its total spin states are described by the HDVV model Hamiltonian having the analytical solution. However, the use of this scheme in general cases of polynuclear systems is less straightforward. For example, in the case of the systems studied, the analytical expression for the energies of the total spin states is available only for the model spin Hamiltonian containing two $J_{ij}$ parameters [Equation (2)]. The solution of this Hamiltonian reads

$$E(S,S_{13},S_{24}) = -\frac{J_{13}}{2}[S_{13}(S_{13} + 1) + S_{24}(S_{24} + 1) - 3] - \frac{J_{12}}{2}[S(S + 1) - S_{13}(S_{13} + 1) - S_{24}(S_{24} + 1)],$$ where

$$S_{13} = S_1 + S_3, ..., |S_1 - S_3|$$
$$S_{24} = S_2 + S_4, ..., |S_2 - S_4|$$
$$S = S_{13} + S_{24}, ..., |S_{13} - S_{24}|.$$

The eigenvalues $E(S,S_{13},S_{24})$ and eigenfunctions $|S,S_{13},S_{24}\rangle$ of the Hamiltonian (2) when $S_i = 1/2$ can be easily obtained and they are presented in Table S4 of the electronic supporting information. The given total spin levels are associated to a highly symmetrical system comprising the square $S_i = 1/2$ unit with the equivalent $|\alpha\alpha\beta\beta\rangle$ (BS2) and $|\alpha\beta\beta\alpha\rangle$ (BS3) states, as well as $|\alpha\alpha\alpha\beta\rangle$ (BS4), $|\alpha\alpha\beta\alpha\rangle$ (BS5), $|\alpha\beta\alpha\alpha\rangle$ (BS6), and $|\beta\alpha\alpha\alpha\rangle$ (BS7) ones. The systems studied were found to possess $C_i$ symmetry and, therefore, the average of the computed BS-state energies may be used for the energy of the single-determinant states that should be degenerate in the idealized system having the square vanadium(IV) unit. Thus, there are three single-determinant energies, $E_1$ (for BS1), $E_2$ (for BS2 and BS3), and $E_3$ (for BS4, BS5, BS6, and BS7), to be associated with four pure-spin state energies, E(0,0,0), E(0,1,1), E(1,1,1), and E(1,1,0) = E(1,0,1). In the case of the singlet states, even if we suppose that E(0,0,0) can be approximated by $E_2$, the use of $E_1$ as E(0,1,1) is questionable (see the expressions for $|0,0,0\rangle$ and $|0,1,1\rangle$ in Table S4). As for the triplet states, it is not evident which of the two energies, E(1,1,1) or E(1,1,0) = E(1,0,1), can be approximated by $E_3$.

Table 3 shows that all $J_{ij}$ values obtained for **I** and **II** are positive, that is, paramagnetic centers are coupled ferromagnetically. The HS state was found to be the ground state of the systems. This implies that complexes **I** and **II** considered as individual molecules should possess ferromagnetic properties, as well as complex **II** in the solid state. This result is very intriguing, as most of the oxovanadium(IV) compounds reported so far display antiferromagnetic coupling in the vanadium pairs.[32,37] From the results obtained for the individual molecules of **I** and **II**, it is seen that the introduction of the methyl groups weakens the ferromagnetic coupling within the dimeric units comprising the μ-OR bridges. The coupling between the diagonal vanadium(IV) ions bridged by the central oxygen atom is not significantly affected. In the case of the methoxo-bridged complex, the two geometries studied display a sizeable difference in the strength of exchange. In the solid-state structure, because of the crystalline effects, the hexavanadate core is compressed along the $O_t$–V–$O_c$–V–$O_t$ axes. This results in smaller V–V distances (see Table 1). The decrease of the intermetal separations enhances the ferromagnetic interactions between the vanadium(IV) ions, especially within the dimeric units comprising the μ-methoxo bridges (the distance between the vanadium centers within the unit is reduced by 0.08 Å). In the diagonal vanadium(IV) pairs, where metal centers are separated by more than 4.5 Å, the coupling is not so sensitive to variations of the V–V distances.

The presence of ferromagnetic coupling in the alkoxo(hydroxo)-bridged dimeric units can be rationalized within the Kahn–Briat model, which relates the antiferromagnetic contribution of the exchange coupling constant between two paramagnetic centers (A and B) with the overlap between "magnetic orbitals", that is, the orbitals of the two localized A–X and X–B fragments (if a simple A–X–B system is considered) bearing the unpaired electrons.[38,39] In the systems studied, the V–$O_t$ bonds are directed along the mutually orthogonal axes (the V–$O_c$–V angles are equal to 90°), that is, the $d_{xy}$ orbitals[40] on the vanadium centers within an alkoxo(hydroxo)-bridged dimeric unit are orthogonal to each other (see Figure S1 in the supporting information presenting the HS-state spin density for the crystal structure of **II** as an example). Thus, the ferromagnetic coupling in the $V_1$–$V_2$ ($V_3$–$V_4$) and $V_1$–$V_4$ ($V_2$–$V_3$) pairs can

 © 2007 Wiley-VCH Verlag GmbH & Co. KGaA, Weinheim 

be expected as the antiferromagnetic term in the expression for $J_{ij}$ vanishes because of the orthogonality of the "magnetic orbitals" imposed by the POM architecture.

The given dimeric unit has syncoplanar configuration according to the classification proposed by Plass.[41] A DFT study of exchange coupling in alkoxo(hydroxo)-bridged dinuclear oxovanadium(IV) compounds with different core arrangements has been carried out by Ruiz et al.[32] In syncoplanar complexes, the antiferromagnetic interactions were found to be active between vanadium centers. It was shown that the coupling decreases from –94 to –43 $cm^{-1}$ (for hydroxo-bridged model structures) when the V–O–V angle becomes smaller (angle values between 108 and 100° were considered). However, the situation when the V–O–V angle is 90°, encountered in the systems studied here, was not examined. Only a few examples of ferromagnetic coupling between the vanadium(IV) sites in oxovanadium complexes are known in the literature.[41–43] Among them, the octanuclear vanadium complex with the ligand 1,3,5-triamino-1,3,5-trideoxy-*cis*-inositol (taci) is the most exciting one.[43] The peculiar chelating properties of the ligand enforce a mutually orthogonal orientation of the V–$O_t$ bonds favoring ferromagnetic coupling between the vanadium(IV) centers.

### Possible Effects of d-Electron Delocalization

Until now we have considered the energy spectrum of magnetic levels resulting from the exchange interactions between localized magnetic electrons. Let us now consider what effects can be expected on the energy spectrum from the electron hopping between vanadium centers. For the sake of simplicity, we consider an idealized system of six V centers forming an octahedron and four magnetic electrons, which can be transferred between orbitals localized on these centers. There are two types of distribution of four electrons between six octahedron vertices: in one type four paramagnetic centers form a square and in another type they are arranged in a rhombic butterfly structure. Three square distributions and twelve butterfly distributions can be formed. The magnetic interactions in the first case are described by the Hamiltonian (2). For the rhombic distribution, a very similar Hamiltonian can be written

$$H_b = -[J_{12}(\mathbf{S}_1\cdot\mathbf{S}_2 + \mathbf{S}_1\cdot\mathbf{S}_4 + \mathbf{S}_2\cdot\mathbf{S}_3 + \mathbf{S}_3\cdot\mathbf{S}_4 + \mathbf{S}_2\cdot\mathbf{S}_4) + J_{13}\mathbf{S}_1\cdot\mathbf{S}_3]$$

with the following eigenvalues:

$$E(S,S_{13},S_{24}) = -\frac{J_{12}}{2}[S(S+1) - S_{13}(S_{13}+1) - \frac{3}{2}] - \frac{J_{13}}{2}[S_{13}(S_{13}+1) - \frac{3}{2}] \quad (3)$$

The eigenvalues of both Hamiltonians are characterized by the values of the total spin S and the intermediate spin $S_{13}$, but for the Hamiltonian (2) the energies also depend on $S_{24}$, whereas the eigenenergies of (3) are degenerate over this quantum number.

The electron transfer between different vanadium sites can be taken into account by the same procedure that has been used before for two-electron mixed-valence polyoxometalates.[44,45] We consider that the eigenfunctions of the Hamiltonians (2) and (3) are linear combinations of the Slater four-electron determinants composed from orthogonal s-type orbitals localized on different centers. If we take into account only the possibility of the electron transfer between nearest neighbors and suppose that the matrix element of the transfer operator on a one-electron localized wave function is equal to t, the total matrix of the electron Hamiltonian can be built on the multielectron wave functions, characterized by spin quantum numbers and different positions of magnetic electrons, using the common Clebsch–Gordan algebra. The analysis of these matrices shows that only the states characterized by the same spin quantum numbers are mixed through the electron transfer. For each set of spin quantum numbers, the electron transfer Hamiltonian can be represented as a $15 \times 15$ matrix, where the diagonal elements are the energies resulting from the Hamiltonians (2) and (3) and the nondiagonal elements are obtained from the electron transfer operator. It can be seen that the nondiagonal parts of all matrices are similar. If we neglect the difference between the two exchange Hamiltonians (2) and (3) (i.e., supposing $J_{12} = J_{13}$), the electron transfer leads to 15 repeated energy spectra of the unique exchange Hamiltonian, with the center of gravity at 4t (1), 2t (6), 0 (3), –2t (2), and –4t (3), where the numbers in parentheses give the degeneracy of transfer levels. However, if the difference between the two exchange Hamiltonians is taken into account, the electron energy spectrum will consist of

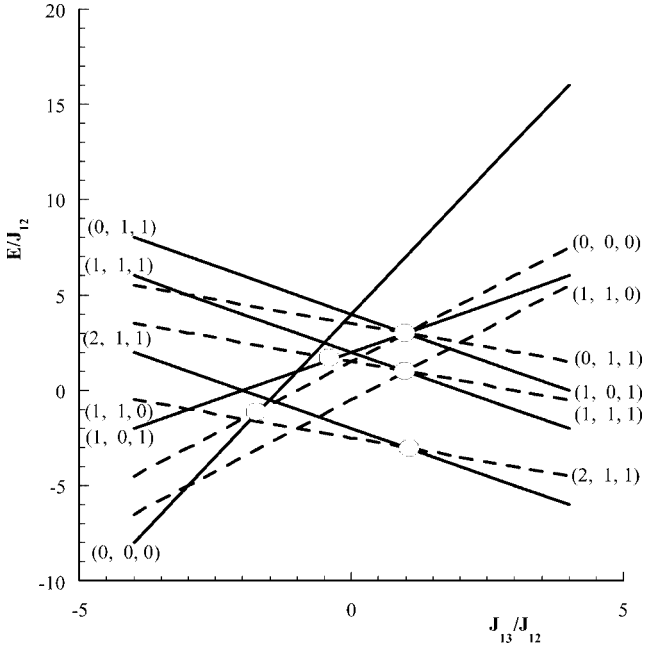


Figure 3. Spin levels of square (full lines) and rhombic four-nuclear complexes. The corresponding spin states (S, $S_{13}$, $S_{24}$) are indicated left and right for the square and rhombic configurations, respectively. The circles show the positions of avoided crossings resulting from the electron transfer.

 © 2007 Wiley-VCH Verlag GmbH & Co. KGaA, Weinheim 

15 similar groups presenting the superposition of the energy spectra of the two exchange Hamiltonians. Within each group, the electron transfer results in avoided crossings in the crossing points of energy levels belonging to different Hamiltonians but characterized by the same total and intermediate spins (see Figure 3). Although these effects will modify the energies in the vicinity of the crossing point, they are not able to change the multiplicity of the ground state imposed by the "static" exchange interaction.

## Conclusions

The DFT results obtained for the neutral representative of the $[V^{IV}_{n}V^{V}_{6-n}O_7(OR)_{12}]^{(4-n)}$ series indicate that its individual molecule (because of internal vibronic interactions) does not possess octahedral symmetry within the hexavanadate core and comprises a slightly distorted square-bipyramidal $OV_6$ unit, which is characterized by localized spin-density distribution; the four vanadium(IV) centers are involved in ferromagnetic coupling. According to the available experimental data mentioned in the Introduction, the complex retains its structural features to a large extent in the crystal lattice and displays the trapped vanadium valences at least at low temperature. In solution, the experimental observations have been interpreted as arising from delocalization of the unpaired electrons, which has been associated with the intervalence electron transfer. However, it is improbable that interaction of the neutral species with the solvation sphere can result in significant changes in the core geometry enabling d-electron delocalization.

The results of the experimental studies could be explained without introducing the electron transfer process if the existence of strong dynamical vibronic coupling in a given species is proposed. Such coupling produces the three valence-trapped structures (states), which can be obtained from each other by changing the "short" axis, that is, the "short" and "long" axes in one structure change into the "long" and "short" axes in another structure, respectively. Apparently, one of these states is frozen (i.e., the transitions between the states are suppressed or their rates are very low) in the crystal lattice because of cooperative solid-state effects. Upon temperature increase, the rates of transitions increase and, on the timescale of the X-ray structural analysis, an averaged structure displaying a symmetrical octahedral vanadium framework and fully delocalized d electrons can be obtained. Such a structure has been obtained, for example, in the case of species with ethylated bridges, where the disorder of the ethyl groups apparently has a pronounced effect on the rates of transitions. Extensive d-electron delocalization detected by the cyclovoltammetric experiment implies the reduction of the barriers between the states in solution, that is, the electronic and molecular structure of the neutral complex in its solvated state can be assessed by taking a superposition of the three valence-trapped forms.

The most interesting feature of the systems studied is the ferromagnetic coupling in the vanadium(IV) pairs – a result obtained from the DFT calculations. Ferromagnetic interactions are very rare in oxovanadium complexes and are a consequence of a specific core geometry imposed by the POM architecture. The results described here present a step toward understanding the properties of a given alkoxo-polyoxovanadium compound series, however, magnetic susceptibility measurements and EPR-spectroscopic studies carried out on the freshly prepared samples are required to make final conclusions.

**Supporting Information** (see also the footnote on the first page of this article): Tables S1 and S2 deal with the SCF single determinants and present atomic spin densities, expectation values of $\mathbf{S}^2$, and energies (in a.u.) computed for complexes **I** and **II**. Table S3 shows the energy differences between the single-determinant states as functions of $J_{ij}$ obtained with the model spin Hamiltonian H(4) [Equation (1)]. Table S4 contains the eigenvalues and eigenfunctions of the model spin Hamiltonian H(2) with $S_i = 1/2$. Figure S1 presents the plot of the HS-state spin density for the crystal structure of complex **II**.

## Acknowledgments

We thank Prof. Yu. V. Yablokov for attracting our attention to the problem of magnetic states in mixed-valence hexavanadates. E. M. Z. thanks the US Civilian Research & Development Foundation and RF Ministry of Education and Science for financial support (BRHE program, grant Y2-C-07-11).

[1] M. T. Pope, A. Muller (Eds.), *Polyoxometalates: From Platonic Solids to Anti-Retroviral Activity*, Kluwer Academic Publishers, Dordrecht, **1994**.
[2] *Chem. Rev.* **1998**, *98*, Special Issue on Polyoxometalates (Ed.: C. L. Hill).
[3] M. T. Pope, A. Muller (Eds.), *Polyoxometalate Chemistry: From Topology via Self-Assembly to Applications*, Kluwer Academic Publishers, Dordrecht, **2001**.
[4] J. J. Borras-Almenar, E. Coronado, A. Muller (Eds.), *Polyoxometalate Molecular Science*, Kluwer Academic Publishers, Dordrecht, **2003**.
[5] P. Gouzerh, A. Proust, *Chem. Rev.* **1998**, *98*, 77–111.
[6] J. Spandl, C. Daniel, I. Brudgam, H. Hartl, *Angew. Chem. Int. Ed.* **2003**, *42*, 1163–1166.
[7] C. Daniel, H. Hartl, *J. Am. Chem. Soc.* **2005**, *127*, 13978–13987.
[8] Differential scanning calorimetry measurements conducted on the neutral ethoxo derivative show a barely detectable phase transition at about 220 K.
[9] M. A. Augustyniak-Jablokow, S. A. Borshch, C. Daniel, H. Hartl, Yu. V. Yablokov, *New J. Chem.* **2005**, *29*, 1064–1071.
[10] M. J. Frisch, G. W. Trucks, H. B. Schlegel, G. E. Scuseria, M. A. Robb, J. R. Cheeseman, J. A. Montgomery Jr, T. Vreven, K. N. Kudin, J. C. Burant, J. M. Millam, S. S. Iyengar, J. Tomasi, V. Barone, B. Mennucci, M. Cossi, G. Scalmani, N. Rega, G. A. Petersson, H. Nakatsuji, M. Hada, M. Ehara, K. Toyota, R. Fukuda, J. Hasegawa, M. Ishida, T. Nakajima, Y. Honda, O. Kitao, H. Nakai, M. Klene, X. Li, J. E. Knox, H. P. Hratchian, J. B. Cross, V. Bakken, C. Adamo, J. Jaramillo, R. Gomperts, R. E. Stratmann, O. Yazyev, A. J. Austin, R. Cammi, C. Pomelli, J. W. Ochterski, P. Y. Ayala, K. Morokuma, G. A. Voth, P. Salvador, J. J. Dannenberg, V. G. Zakrzewski, S. Dapprich, A. D. Daniels, M. C. Strain, O. Farkas, D. K. Malick, A. D. Rabuck, K. Raghavachari, J. B. Foresman, J. V. Ortiz, Q. Cui, A. G. Baboul, S. Clifford, J. Cioslowski, B. B. Stefanov, G. Liu, A. Liashenko, P. Piskorz, I. Komaromi, R. L. Martin, D. J. Fox, T. Keith, M. A. Al-Laham, C. Y. Peng, A. Nanayak-

 © 2007 Wiley-VCH Verlag GmbH & Co. KGaA, Weinheim 

kara, M. Challacombe, P. M. W. Gill, B. Johnson, W. Chen, M. W. Wong, C. Gonzalez, J. A. Pople, *Gaussian 03*, Revision D.01, Gaussian, Inc., Wallingford, CT, **2004**.
[11] A. D. Becke, *J. Chem. Phys.* **1993**, *98*, 5648.
[12] A. D. Becke, *Phys. Rev. A: At. Mol. Opt. Phys.* **1988**, *38*, 3098.
[13] C. Lee, W. Yang, R. G. Parr, *Phys. Rev. B: Condens. Matter* **1988**, *37*, 785.
[14] L. Noodleman, J. G. Norman Jr, *J. Chem. Phys.* **1979**, *70*, 4903.
[15] L. Noodleman, *J. Chem. Phys.* **1981**, *74*, 5737.
[16] L. Noodleman, E. R. Davidson, *Chem. Phys.* **1986**, *109*, 131.
[17] L. Noodleman, D. A. Case, *Adv. Inorg. Chem.* **1992**, *38*, 423.
[18] R. Caballol, O. Castell, F. Illas, P. R. Moreira, J. P. Malrieu, *J. Phys. Chem. A* **1997**, *101*, 7860–7866.
[19] E. Ruiz, J. Cano, S. Alvarez, P. Alemany, *J. Comput. Chem.* **1999**, *20*, 1391–1400.
[20] T. Soda, Y. Kitagawa, T. Onishi, Y. Takano, Y. Shigeta, H. Nagao, Y. Yoshioka, K. Yamaguchi, *Chem. Phys. Lett.* **2000**, *319*, 223–230, and references therein.
[21] E. Ruiz, A. Rodriguez-Fortea, J. Cano, S. Alvarez, P. Alemany, *J. Comput. Chem.* **2003**, *24*, 982–989.
[22] A. Bencini, F. Totti, *Int. J. Quantum Chem.* **2005**, *101*, 819–825.
[23] R. Seeger, J. A. Pople, *J. Chem. Phys.* **1977**, *66*, 3045.
[24] A. Schafer, C. Huber, R. Ahlrichs, *J. Chem. Phys.* **1994**, *100*, 5829–5835.
[25] A. Schafer, H. Horn, R. Ahlrichs, *J. Chem. Phys.* **1992**, *97*, 2571–2577.
[26] E. Ruiz, P. Alemany, S. Alvarez, J. Cano, *J. Am. Chem. Soc.* **1997**, *119*, 1297–1303.
[27] E. Ruiz, P. Alemany, S. Alvarez, J. Cano, *Inorg. Chem.* **1997**, *36*, 3683–3688.
[28] E. Ruiz, J. Cano, S. Alvarez, P. Alemany, *J. Am. Chem. Soc.* **1998**, *120*, 11122–11129.
[29] E. Ruiz, C. Graaf, P. Alemany, S. Alvarez, *J. Phys. Chem. A* **2002**, *106*, 4938–4941.
[30] E. Ruiz, A. Rodriguez-Fortea, P. Alemany, S. Alvarez, *Polyhedron* **2001**, *20*, 1323–1327.
[31] E. Ruiz, J. Cano, S. Alvarez, A. Caneschi, D. Gatteschi, *J. Am. Chem. Soc.* **2003**, *125*, 6791–6794.
[32] A. Rodriguez-Fortea, P. Alemany, S. Alvarez, E. Ruiz, *Eur. J. Inorg. Chem.* **2004**, 143–153.
[33] P. Ghosh, E. Bill, T. Weyhermuller, F. Neese, K. Wieghardt, *J. Am. Chem. Soc.* **2003**, *125*, 1293–1308.
[34] In the absence of the nonorthogonality problem, the BS state is an eigenfunction of $\mathbf{S}_z$ and can be expressed as a linear combination of the corresponding $M_S$ components of the pure-spin states, the coefficients being computed using the Clebsch–Gordan algebra; the HS state is obviously the pure-spin state with $M_S = S$.
[35] E. Ruiz, S. Alvarez, J. Cano, V. Polo, *J. Chem. Phys.* **2005**, *123*, 164110.
[36] C. Adamo, V. Barone, A. Bencini, R. Broer, M. Filatov, N. M. Harrison, F. Illas, J. P. Malrieu, I. de P. R. Moreira, *J. Chem. Phys.* **2006**, *124*, 107101.
[37] A. Muller, F. Peters, M. T. Pope, D. Gatteschi, *Chem. Rev.* **1998**, *98*, 239–271.
[38] O. Kahn, B. Briat, *J. Chem. Soc. Trans.* **1976**, *72*, 268.
[39] O. Kahn, B. Briat, *J. Chem. Soc. Trans.* **1976**, *72*, 1441.
[40] A local coordinate frame with the *x* and *y* axes pointing towards the bridging oxygen atoms, and the *z* axis directed along the V–$O_t$ bond is considered.
[41] W. Plass, *Angew. Chem. Int. Ed. Engl.* **1996**, *35*, 627.
[42] M. J. Manos, A. J. Tasiopoulos, E. J. Tolis, N. Lalioti, J. D. Woolins, A. M. Z. Slawin, M. P. Sigalas, T. A. Kabanos, *Chem. Eur. J.* **2003**, *9*, 695.
[43] K. Hegetschweiler, B. Morgenstern, J. Zubieta, P. J. Hagrman, N. Lima, R. Sessoli, F. Totti, *Angew. Chem. Int. Ed.* **2004**, *43*, 3436–3439.
[44] S. A. Borshch, B. Bigot, *Chem. Phys. Lett.* **1993**, *212*, 398.
[45] S. A. Borshch, *Inorg. Chem.* **1998**, *37*, 3116.

Received: April 18, 2007
Published Online: July 24, 2007

 © 2007 Wiley-VCH Verlag GmbH & Co. KGaA, Weinheim 

DOI: 10.1002/ejic.200700320

# $Fe^{II}$ Bistable Materials with Dissymmetrical Ligands: Synthesis, Crystal Structure, Magnetic and Mössbauer Properties of $Fe^{II}$ Complexes Based on $N_4$ Schiff Bases Possessing 2-Pyridyl and 1-R-Imidazol-2-yl Rings[‡]

**Nicolas Bréfuel,*[a] and Sergiu Shova,[a][‡‡] and Jean-Pierre Tuchagues*[a]**

**Keywords:** Schiff bases / N ligands / Iron / Spin crossover / Magnetic properties / Mössbauer spectroscopy

The synthesis and characterization of two symmetrical $Fe^{II}$ complexes, $[FeL^{B4}(NCS)_2]$, **1**, and $[FeL^{B5}(NCS)_2]$, **2** {$L^{Bx}$ = *N*,*N*′-bis[(2-*N*-R-imidazol-1-yl)methylene]-2,2-dimethylpropane-1,3-diamine ligands; **1**: *x* = 4, R = H; **2**: *x* = 5, R = Me} are reported. Whereas the tetradentate ligand $L^{B4}$ is planar in **1**, the X-ray structure of **2** illustrates the folded conformation of $L^{B5}$. Ferrous $[FeL^{Ex}(NCS)_2]$ complexes were synthesized {$L^{Ex}$ = *N*-[(1-*N*-$R^2$-imidazol-2-yl)methylene]-*N*′-(1-pyridin-2-yl-ethylidene)-2,2-$R^1$-propane-1,3-diamine; **3**: *x* = 1, $R^1$ = H, $R^2$ = H; **4**: *x* = 2, $R^1$ = H, $R^2$ = Me; **5**: *x* = 3, $R^1$ = Me, $R^2$ = H; **6**: *x* = 4, $R^1$ = Me, $R^2$ = Me}. These dissymmetrical Schiff bases, possessing pyridine and imidazole rings, are obtained through the reaction of 2-methyl-2-pyridin-2-yl-hexahydropyrimidine ($R^1$ = H; **3**, **4**) or 2,5,5-trimethyl-2-pyridin-2-yl-hexahydropyrimidine ($R^1$ = Me; **5**, **6**) aminals with imidazole-2-carboxaldehyde ($R^2$ = H: **3**, **5**) or 1-*N*-methylimidazole-2-carboxaldehyde ($R^2$ = Me: **4**, **6**) and iron(II) thiocyanate. Single-crystal X-ray structures were determined for $[FeL^{E1}(NCS)_2]$ **3** $[FeL^{E3}(NCS)_2]$ **5** and $[FeL^{E4}(NCS)_2]$ **6**; these complexes are in the low-spin state at 180 K. Magnetic susceptibility and Mössbauer measurements showed a smooth and incomplete spin crossover involving ca. 50 % of the iron centres between 200 and 400 K for **5** and **6**; **3** and **4** remain low spin up to 350 K; the slight $\chi_M T$ increase between 350 and 400 K results from the onset of spin crossover for **3** and **4**. The spin crossover properties in the $[FeL^{Ex}(NCS)_2]$ series may thus be tuned by the ligand substituents: by changing $R^1$ from H (for **3**, **4**) to Me (for **5**, **6**) the spin crossover is lowered from above 400 K to ca. 350 K; the effect of the imidazolyl substituent is weaker: by changing $R^2$ from H (for **5**) to Me (for **6**) the spin crossover temperature is lowered by ca. 35 K. The electronic effect of the highly conjugated Fe–N=C–C=N– imidazolyl fragment overpasses and qualitatively and quantitatively modifies the effects of $R^1$ and $R^2$.
(© Wiley-VCH Verlag GmbH & Co. KGaA, 69451 Weinheim, Germany, 2007)

## Introduction

Most iron(II) complexes have octahedral geometry, and depending on the strength of the ligand field, either the low-spin (LS) or the high-spin (HS) electronic configuration is observed. For some $Fe^{II}$ complexes, mainly those characterized by an $[FeN_6]$ core, the ligand field is intermediate and allows a LS ($S$ = 0, $^1A_{1g}$) ↔ HS ($S$ = 2, $^5T_{2g}$) spin crossover (SC) that may be induced by a variation in temperature, pressure or light irradiation.[1] Slight modifications to the ligand(s) may provide conditions that do or do not favour SC, depending on the balance between the ligand field and the mean spin-pairing energy. Whereas the phenomenon is mainly molecular in solution, intermolecular interactions, such as π–π staking or hydrogen bonds between complex molecules, are the key for observing cooperative transition in the solid state, as a result of the supramolecular structure.[2] Such a behaviour, evidenced by thermal hysteresis of the magnetic properties, is attractive owing to the potential technological applications of these materials in molecular electronics and memory devices.[3]

In previous studies, we showed that a rational approach for the design of SC materials allows tuning of the ligand field by combination, in a same tetradentate Schiff base ligand, of both the "strong ligand field" pyridine moiety and the "weak ligand field" imidazole ring.[4] Reaction between the isolated aminal-type ligands 2-methyl-2-pyridin-2-yl-hexahydropyrimidine ($R^1$ = H) or 2,5,5-trimethyl-2-pyridin-2-yl-hexahydropyrimidine ($R^1$ = Me) and 2-$R^2$-imidazole-4-carboxaldehyde, in the presence of iron(II) thiocyanate, led to the $[FeL^{Cx}(NCS)_2]$ complexes {$L^{Cx}$ = *N*-[(2-$R^2$-1H-imidazol-4-yl)methylene]-*N*′-(1-pyridin-2-ylethylidene)-2,2-$R^1$-propane-1,3-diamine ($R^1$ = H, Me; $R^2$ = H, Me, Ph)}.[4a] Because the complexes in the $[FeL^{Cx}(NCS)_2]$ family exhibit only partial SC in the 60–400 K temperature range, we explored the $[FeL^{Dx}(NCX)_2]$ (X = S, Se) series

[‡] $Fe^{II}$ Bistable Materials with Dissymmetrical Ligands, 3. Part 1, ref.[4a]; part 2, ref.[4b]

[a] Laboratoire de Chimie de Coordination du CNRS, UPR 8241
205 route de Narbonne, 31077 Toulouse Cedex, France
Fax: +33-561-553003
E-mail: brefuel@lcc-toulouse.fr
jean-pierre.tuchagues@lcc-toulouse.fr
[‡‡]On leave from the Institute of Applied Physics, Academy of Sciences of Moldova,
Academiei str. 3. 2028 Chisinau, Moldova

Supporting information for this article is available on the WWW under http://www.eurjic.org or from the author.


© 2007 Wiley-VCH Verlag GmbH & Co. KGaA, Weinheim

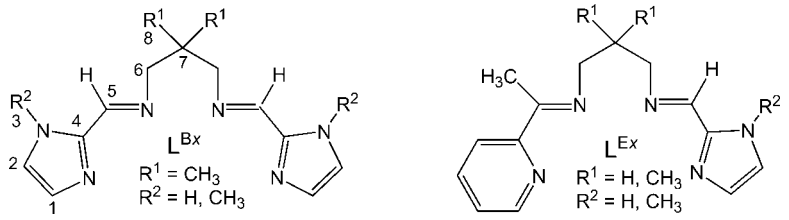


Figure 1. Schematic drawing of the $L^{Bx}$ and $L^{Ex}$ ligands ($R^1$ = H, Me; $R^2$ = H, Me).

where the terminal imidazolyl fragment of $L^{Dx}$ originates from 5-methyl-4-formylimidazole.[4b] The complexes in the corresponding $[FeL^{Dx}(NCX)_2]$ series exhibit steeper SC, with hysteresis or with two steps, depending on the pseudohalide ligands (NCS or NCSe) and on the $R^1$ substituent of the propyl chain. Detailed structural studies revealed the prominent role of the hydrogen bond network in the occurrence of steep SC, as underlined by the hysteresis evidenced through their magnetic study.[4b]

In this paper, we report the synthesis and characterization of six ferrous materials including: (1) two HS complexes of general formula $[FeL^{Bx}(NCS)_2]$ {$L^{Bx}$ = *N*,*N*′-bis-[(2-*N*-R-imidazol-1-yl)methylene]-2,2-dimethylpropane-1,3-diamine ligands (Figure 1); **1**: $x$ = 4, R = H; **2**: $x$ = 5, R = Me} and (2) a series of ferrous complexes $[FeL^{Ex}(NCS)_2]$ {$L^{Ex}$ = *N*-[(1-*N*-$R^2$-imidazol-2-yl)methylene]-*N*′-(1-pyridin-2-ylethylidene)-2,2-$R^1$-propane-1,3-diamine ligands (Figure 1); **3**: $x$ = 1, $R^1$ = H, $R^2$ = H; **4**: $x$ = 2, $R^1$ = H, $R^2$ = Me; **5**: $x$ = 3, $R^1$ = Me, $R^2$ = H; **6**: $x$ = 4, $R^1$ = Me, $R^2$ = Me}. The molecular structure of these materials was investigated by single-crystal X-ray diffraction, and their electronic properties were explored by variable-temperature magnetic susceptibility and Mössbauer studies.

## Results

### Description of the Structures

The molecular structures along with the main geometric characteristics of complexes **2**, **3**, **5** and **6** are presented in Figures 2, 4, 6 and 8, respectively.

The X-ray structural study of **2** reveals a highly distorted octahedral geometry with the thiocyanato ligands *cis* to each other and a folded conformation of the $L^{B5}$ tetradentate ligand (Figure 2). This strong deviation of the coordination site from the regular octahedron, suggested by the Fe–N distances and N–Fe–N angles, is associated with the HS electronic configuration.

The crystal packing of **2** is characterized by isolated dimeric units (Figure 3) formed through π–π stacking interactions between centrosymmetrically related $[FeL^{B5}(NCS)_2]$ molecules ($1-x$, $2-y$, $2-z$) with a centroid-to-centroid distance of 3.50 Å. Other intermolecular separations equal or exceed the sum of van der Waal radii.

The $Fe^{2+}$ ion in complex **3** (Figure 4) presents a slightly distorted $N_6$ octahedral environment constituted by four nitrogen atoms from the $L^{E1}$ tetradentate ligand (two $N_{imino}$, one $N_{pyridyl}$ and one $N_{imidazolyl}$) and two N donors from the *trans*-coordinated $NCS^-$ anions. The values of the Fe–N bond lengths are in the range 1.932–2.028 Å, and they are indicative of a LS state of $Fe^{II}$ in complex **3** at 180 K.

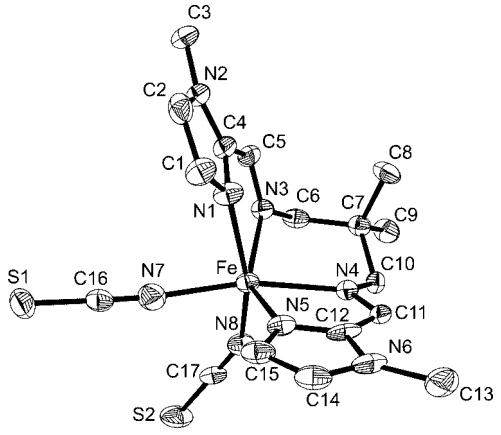


Figure 2. Molecular structure of $[FeL^{B5}(NCS)_2]$ (**2**). Thermal ellipsoids are drawn at the 40% probability level. H atoms have been omitted for clarity. Selected bond lengths [Å] and angles [°]: Fe–N1 2.235(4), Fe–N3 2.185(4), Fe–N4 2.212(7), Fe–N5 2.144(5), Fe–N7 2.122(10), Fe–N8 2.119(5); N1–Fe–N3 73.49(16), N1–Fe–N4 107.9(2), N1–Fe–N5 87.79(18), N1–Fe–N7 81.7(3), N1–Fe–N8 158.2(2), N3–Fe–N4 79.8(2), N3–Fe–N5 142.8(3), N3–Fe–N7 112.1(2), N3–Fe–N8 93.15(16), N4–Fe–N5 75.8(3), N4–Fe–N7 166.86(16), N4–Fe–N8 85.9(2), N5–Fe–N7 96.0(3), N5–Fe–N8 112.37(16), N7–Fe–N8 87.9(3).

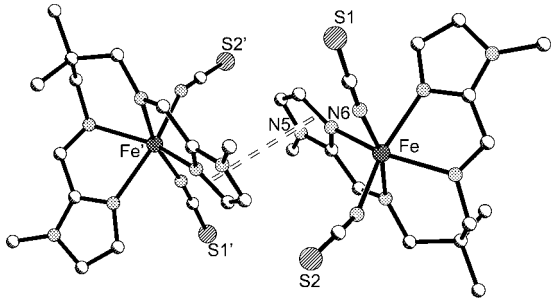


Figure 3. π–π stacking interactions in the crystal structure of $[FeL^{B5}(NCS)_2]$ (**2**).

Both H-bonds and π–π stacking interactions are responsible for the crystal packing of **3**. $[FeL^{E1}(NCS)_2]$ molecules are alternately associated into infinite chains through two N–H···S hydrogen bonds with the following parameters: N2···S1′ ($x$, $1-y$, $1+z$) = 3.330(2) Å, N2–H = 0.86 Å, ∠N2–H···S1′ = 160.0°. Interactions of the π–π type be-

 © 2007 Wiley-VCH Verlag GmbH & Co. KGaA, Weinheim 

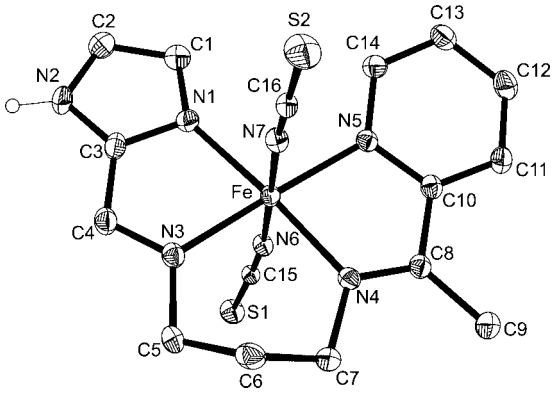


Figure 4. Molecular structure of $[FeL^{E1}(NCS)_2]$ (**3**). Thermal ellipsoids are drawn at the 40% probability level. H atoms have been omitted for clarity. Selected bond lengths [Å] and angles [°]: Fe–N1 2.0277(17), Fe–N3 1.9618(17), Fe–N4 1.9493(17), Fe–N5 1.9692(17), Fe–N6 1.9391(18), Fe–N7 1.9324(18); N1–Fe–N3 80.67(7), N1–Fe–N4 174.76(7), N1–Fe–N5 101.71(7), N1–Fe–N6 87.95(7), N1–Fe–N7 91.52(7), N3–Fe–N4 96.80(7), N3–Fe–N5 177.25(7), N3–Fe–N6 88.82(7), N3–Fe–N7 90.45(7), N4–Fe–N5 80.94(7), N4–Fe–N6 87.41(7), N4–Fe–N7 93.09(7), N5–Fe–N6 92.62(7), N5–Fe–N7 88.13(7), N6–Fe–N7 179.15(7).

tween centrosymmetrically related $(1-x, -y, 1+z)$ pyridine rings with a centroid-to-centroid distance of 3.62 Å organize the chains into 2D layers, a fragment of which is shown in Figure 5.

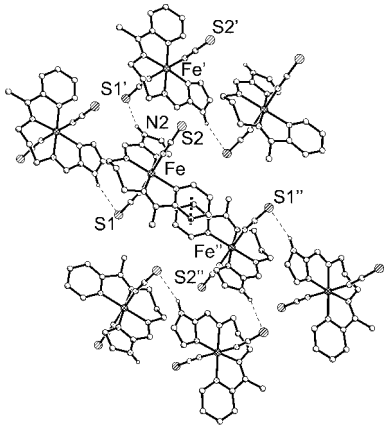


Figure 5. Fragment of a 2D layer of $[FeL^{E1}(NCS)_2]$ (**3**) that shows the H-bonds and π–π stacking interactions responsible for the crystal packing.

Solution and further refinement of the crystal structure of complex **5**, $[FeL^{E3}(NCS)_2]$, showed the presence of a statistical disorder of the external parts of the ligand. As a result, $L^{E3}$ occupies two distinct positions around Fe (Figure 6), related by C2 rotation through the Fe···C6 axis. The refined values of the site occupancy factors are equal to 0.74 and 0.26 for the major and minor (*) components, respectively. The average value of the Fe–N bond lengths, 1.969 Å, evidences the LS state of $Fe^{II}$ in **5** at 180 K.

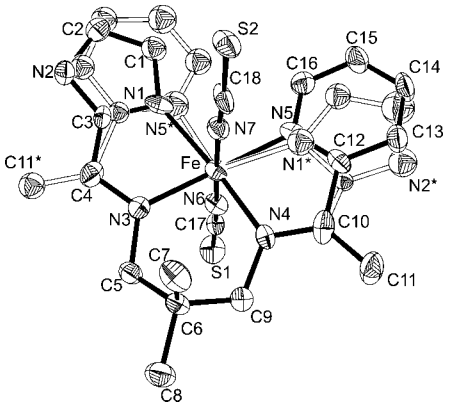


Figure 6. Molecular structure of $[FeL^{E3}(NCS)_2]$ (**5**). Thermal ellipsoids are drawn at the 40% probability level. H-atoms have been omitted for clarity. The minor location of $L^{E3}$ is drawn with thin lines. Selected bond lengths [Å] and angles [°]: Fe–N1 2.061(6), Fe–N1* 2.028(14), Fe–N3 1.946(4), Fe–N4, 1.939(4), Fe–N5 1.962(6), Fe–N5* 1.957(13), Fe–N6 1.928(4), Fe–N7 1.931(4); N1–Fe–N3 78.6(2), N1*–Fe–N3 171.7(7), N1–Fe–N4 173.0(3), N1*–Fe–N4 76.1(7), N1–Fe–N5 102.1(4), N1*–Fe–N5* 99.8(8), N1–Fe–N6 93.4(2), N1*–Fe–N6 90.8(8), N1–Fe–N7 85.2(2), N1*–Fe–N7 87.1(8), N3–Fe–N4 95.65(15), N3–Fe–N5 177.5(3), N3–Fe1–N5* 88.5(5), N3–Fe–N6 90.17(15), N3–Fe–N7 92.17(15), N4–Fe–N5 83.5(3), N4–Fe–N5* 174.6(5), N4–Fe–N6 90.56(16), N4–Fe–N7 91.11(15), N5–Fe–N6 92.1(3), N5*–Fe–N6 86.0(5), N5–Fe–N7 85.6(3), N5*–Fe–N7 92.2(5), N6–Fe–N7 176.98(16).

The crystal packing of **5** is essentially determined by the only possible N–H···S hydrogen bond [N2H···S2′ $(1+x, y, z)$ = 3.37 Å, H(N2)···S2′ = 2.52(4) Å, ∠N2HS2′ = 168.5°], which leads to the formation of infinite chains, as depicted in Figure 7. Further association of the components occurs through the short S2···S1′$(x-0.5, 0.5-y, 0.5+z)$ interchain contacts (3.38 Å), which result in 2D layers parallel to the [010] plane.

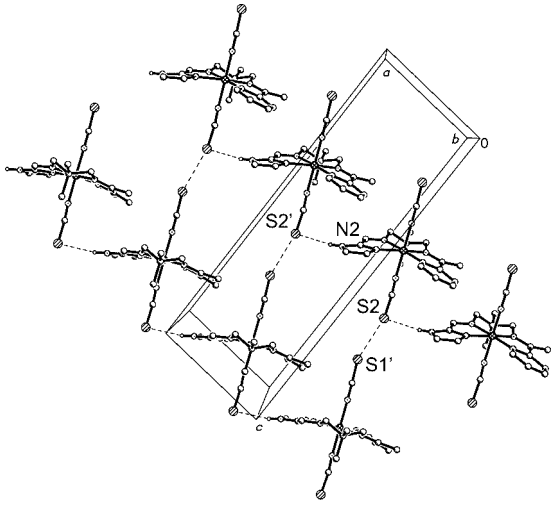


Figure 7. Fragment of a 1D chain of $[FeL^{E3}(NCS)_2]$ **5** that shows the H-bonds responsible for the crystal packing.

Complex **6** has a molecular structure that consists of neutral $[FeL^{E4}(NCS)_2]$ complex molecules as depicted in Figure 8. Geometrical parameters (Fe–N distances and N–

 © 2007 Wiley-VCH Verlag GmbH & Co. KGaA, Weinheim 

Fe–N angles) of the Fe $–N_6$ core at 180 K, close to those of a regular octahedron, indicate a LS electronic configuration of the $Fe^{2+}$ ions.

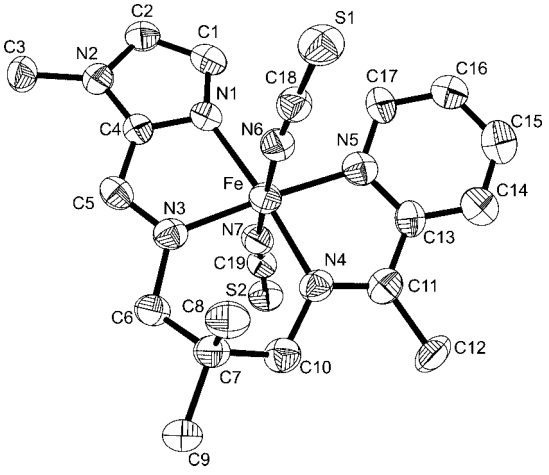


Figure 8. Molecular structure of $[FeL^{E4}(NCS)_2]$, the complex molecule of **6**. Thermal ellipsoids are drawn at the 40% probability level. H-atoms have been omitted for clarity. Selected bond lengths [Å] and angles [°]: Fe–N1 2.048(6), Fe–N3 1.945(6), Fe–N4 1.948(6), Fe–N5 1.946(7), Fe–N6 1.948(7), Fe–N7 1.944(7); N1–Fe–N3 81.4(3), N1–Fe–N4 174.0(2), N1–Fe–N5 102.7(3), N1–Fe–N6 88.0(3), N1–Fe–N7 89.6(3), N3–Fe–N4 94.8(3), N3–Fe–N5 175.8(3), N3–Fe–N6 92.0(3), N3–Fe–N7 91.6(3), N4–Fe–N5 81.2(3), N4–Fe–N6 96.8(3), N4–Fe–N7 85.8(3), N5–Fe–N6 87.1(3), N5–Fe–N7 89.5(3), N6–Fe–N7 175.3(3).

MeOH solvate molecules are associated to the $[FeL^{E4}(NCS)_2]$ complex molecules in the 1:1 ratio through O–H···S hydrogen bonds with distances O1–H = 1.03 Å, O1···S2 = 3.227(7) Å and O1–H···S2 = 2.30 Å and ∠O1HS2 = 149.9° (Figure 9). In addition, π–π stacking interactions between centrosymmetrically related ($–x$, $2–y$, $1–z$) imidazolyl rings are evidenced by the short interplanar (3.49 Å) and centroid-to-centroid (3.88 Å) distances. Centrosymmetric $\{[FeL^{E4}(NCS)_2]\cdot CH_3OH\}_2$ pairs are quite separated in the crystal space as a result of this π–π stacking interaction. In this respect, the crystal packing motif of **6** resembles that of **2**.

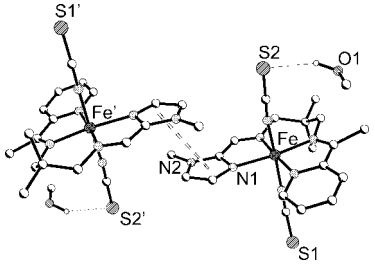


Figure 9. The dimeric association in $[FeL^{E4}(NCS)_2]\cdot CH_3OH$ (**6**) that shows the H-bonds and π–π stacking interactions responsible for the crystal packing.

## Magnetic Studies

The thermal variation of the magnetic susceptibility $\chi_M$ was explored for complexes **1** and **3**–**6**: the $\chi_M T$ data for selected temperatures ($T$) are collated in Table S1 (Supporting Information). The $\chi_M T$ vs. $T$ data are shown in Figure 10 for complexes **1** and **3**–**6**. It was not possible to study the magnetic properties of **2**, because this sample was obtained in very poor yield as a mixture with complex **6** (see Experimental Section).

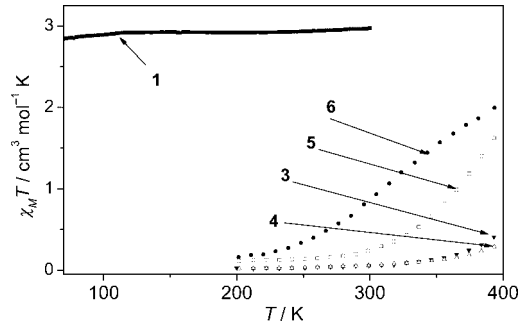


Figure 10. Thermal variation of the $\chi_M T$ product for complexes **1** and **3**–**6**.

The magnetic study of **1** shows that this complex is in the HS state between 70 and 300 K, with a $\chi_M T$ value close to 3 $cm^3 mol^{-1} K$. The $\chi_M T$ product for complexes $[FeL^{E1}(NCS)_2]$ (**3**; $R^1$ = H, $R^2$ = H) and $[FeL^{E2}(NCS)_2]$ (**4**; $R^1$ = H, $R^2$ = Me) is practically constant over the 200–350 K range and characteristic of LS $Fe^{II}$ $\chi_M T \approx 0$ $cm^3 mol^{-1} K$). The slight increase in $\chi_M T$ above 350 K ($\chi_M T$ = 0.4 $cm^3 mol^{-1} K$ at 400 K) may be considered as the onset of SC, with ca. 10% of HS sites at 400 K. Similarly, the $\chi_M T$ product for **5** ($R^1$ = Me, $R^2$ = H) is practically constant from 200 to 300 K and characteristic of LS $Fe^{II}$. Then, $\chi_M T$ increases from 0.2 $cm^3 mol^{-1} K$ at 300 K to 1.6 $cm^3 mol^{-1} K$ at 400 K, indicating LS→HS SC of ca. 50% $Fe^{II}$ centres at 400 K. Complex **6** ($R^1$ = Me, $R^2$ = Me) is essentially LS at 200 K ($\chi_M T$ = 0.4 $cm^3 mol^{-1} K$) and exhibits a smooth and incomplete SC upon heating with ca. 60% $Fe^{II}$ sites in the HS state at 400 K. Relative to that of complex **5**, the SC is smoother for **6**. The same behaviour is observed in the cooling mode, indicating the absence of hysteresis for these compounds.

## Mössbauer Spectroscopy

### *$[FeL^{Bx}(NCS)_2]$ Complexes*

Mössbauer spectra were recorded at selected temperatures in the 80–250 K range for complexes **1** and **2**. Values of the Mössbauer parameters (isomer shift $\delta$, quadrupole splitting $\Delta E_Q$ and line width $\Gamma/2$) resulting from fitting the spectra are collated in Table S2 (Supporting Information). The isomer shift values decrease slightly with increasing temperature, indicating the operation of second-order Doppler effect.[5]

The Mössbauer spectra of **1** evidence two HS doublets characteristic of slightly inequivalent Fe centres, $Fe^{II}$(A) and $Fe^{II}$(B) sites, as previously observed in related complexes.[4a] These doublets were fitted with similar isomer shift

 © 2007 Wiley-VCH Verlag GmbH & Co. KGaA, Weinheim 

values [1.098(2) and 1.120(2) mm s$^{-1}$ at 80 K, Table S2] as expected for identical $N_6$ donor sets around $Fe^{II}$(A) and $Fe^{II}$(B) and different $\Delta E_Q$ values [2.582(8) and 2.982(8) mm s$^{-1}$ at 80 K for $Fe^{II}$(A) and $Fe^{II}$(B), respectively], suggesting different low symmetry environments (Figure 11).[5]

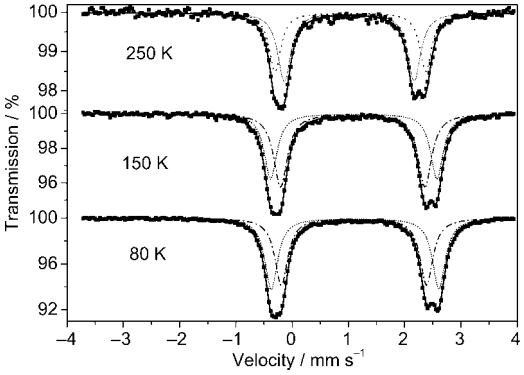


Figure 11. Representative least-squares-fitted Mössbauer spectra of [FeL$^{B4}$(NCS)$_2$] **1**. The solid line represents the fit of the data to two subspectra, the dash–dot line corresponds to site A and the dotted line to site B with the parameters given in the text and in Table S2.

In contrast, **2** is characterized by a unique quadrupole-split doublet [$\delta$ = 1.17(2) and $\Delta E_Q$ = 2.66(4) mm s$^{-1}$ at 80 K] typical of HS iron(II). The Mössbauer spectra of **2** were obtained from a sample resulting from the synthetic procedure described in the Experimental Section of **6**: this sample was the first solid obtained, specifically a mixture of **2** (red crystals) and **6** (dark-blue powder), because it was not possible to isolate enough red crystals of **2** in order to carry out Mössbauer measurements. The second solid (pure single crystals of **6**) were obtained in good yield through slow evaporation of the resulting filtrate; it was then possible to carry out Mössbauer measurements of **6** (pure) and thus to ascertain that the major doublet in the Mössbauer spectrum of the mixture was indeed that of **6**, and moreover to evaluate the relative ratio of **2** [11(2)%] in its mixture with **6**.

### *[FeL$^{Ex}$(NCS)$_2$] Complexes*

The Mössbauer spectra of complexes **3**–**6** confirm the spin states deduced from the magnetic data for these materials (Table S2, Supporting Information); however, as a result of poor counting statistics, high-temperature spectra (350–400 K) of complexes **3**, **4** and **5** could not be obtained in good quality. As an example for the materials in this series, we describe the study of complex **6** for which representative Mössbauer spectra recorded in the heating mode are shown in Figure 12. These spectra, measured in the 200–400 K range, confirm the partial SC deduced from the magnetic measurements. At 200 K, a unique LS doublet [$\delta$ = 0.417(4) and $\Delta E_Q$ = 0.787(8) mm s$^{-1}$] is observed;[4–7] at and above 300 K, the asymmetry of this doublet results from the presence of a growing HS component that is difficult to fit owing to the poor counting statistics. This Mössbauer behaviour confirms the SC observed by magnetic measurements. It is also worth mentioning that these high temperature spectra are very broad [$\Gamma_{1/2}$(LS) = 0.22 mm s$^{-1}$, $\Gamma_{1/2}$(HS) = 0.23 mm s$^{-1}$]. In the case of SC materials, observation of broadened Mössbauer spectra is usually related to dynamic phenomena: the interstate conversion rates $K_{LH}$ (LS→HS) and $K_{HL}$ (HS→LS) are comparable to the hyperfine frequency ($10^8$ s$^{-1}$).[8,9]

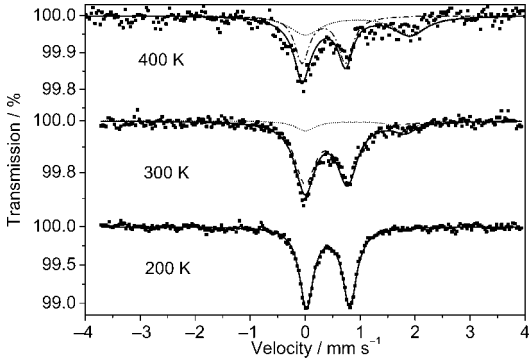


Figure 12. Representative least-squares-fitted Mössbauer spectra of [FeL$^{E4}$(NCS)$_2$] (**6**). The solid line represents the fit of the data to two subspectra, the dash–dot line corresponds to the LS site and the dotted line to the HS site with the parameters given in the text and in Table S2.

Mössbauer spectra of complexes **3**, **4** and **5** were recorded between 77 and 300 K. In agreement with the magnetic studies, all spectra show a unique doublet with parameters characteristic of the LS iron(II) state [$\delta$ = 0.376(1), $\Delta E_Q$ = 0.719(2) mm s$^{-1}$ for **3** at 293 K; $\delta$ = 0.357(4), $\Delta E_Q$ = 0.663(7) mm s$^{-1}$ for **4** at 293 K; $\delta$ = 0.377(4), $\Delta E_Q$ = 0.634(8) mm s$^{-1}$ for **5** at 300 K; Table S2).

### IR Spectroscopy

The IR spectroscopic study was focused on the NCS stretching absorptions (2000–2100 cm$^{-1}$ range), which serves as a good sensor for the *cis* or *trans* conformation of the coordinated thiocyanate anions. Usually, *trans* isomers exhibit a single absorption, whereas *cis* isomers are characterized by a splitting of the $\nu_{CN}$ absorption.[10] However, this criterion must be considered with much caution because the splitting of this band is very sensitive to slight deformations of the coordination sphere (in particular the N–M–N angle between the two thiocyanate ligands coordinated to the metal centre). The IR spectrum of [FeL$^{B4}$(NCS)$_2$] (**1**) shows two doublets (2081, 2070 and 2052, 2036 cm$^{-1}$), and this is similar to that of [FeL$^{B1}$(NCS)$_2$],[4a] which shows one doublet (2097, 2095 cm$^{-1}$) and one singlet (2025 cm$^{-1}$; Figure S1). The X-ray structure of [FeL$^{B1}$(NCS)$_2$] evidences two independent *trans* NCS molecules with strongly and differently distorted octahedral symmetries and its Mössbauer spectra confirm the presence of two HS $Fe^{II}$ sites.[4a] The presence of two HS $Fe^{II}$ sites {with $\delta$ and $\Delta E_Q$ parameters similar to those of [FeL$^{B1}$(NCS)$_2$]} in the Mössbauer spectra of **1**, together with the similarity of its IR spectrum to that of [FeL$^{B1}$(NCS)$_2$], strongly advocates to the similarity of their molecular structures with two independent *trans* NCS molecules with strongly and differently distorted octahedral

 © 2007 Wiley-VCH Verlag GmbH & Co. KGaA, Weinheim 

symmetry. As mentioned above, the splitting (or broadening) of the $\nu_{CN}$ absorptions is characteristic of a strong distortion of the octahedral symmetry. In contrast, the X-ray structure of $[FeL^{B2}(NCS)_2]$ evidences only one *trans* molecule with strongly distorted octahedral symmetry and the Mössbauer spectra of $[FeL^{B2}(NCS)_2]$ and $[FeL^{B3}(NCS)_2]$ show the presence of one HS $Fe^{II}$ site.[4a] The IR spectra of $[FeL^{B2}(NCS)_2]$ and $[FeL^{B3}(NCS)_2]$ show one doublet (2093, 2065 and 2082, 2018 $cm^{-1}$, respectively; Figure S1), and they are in agreement with the strong distortion of their unique *trans* NCS molecule. Consequently, the four bands between 2081 and 2036 $cm^{-1}$ observed for **1** confirm the presence of two distinct *trans* isomers as observed through Mössbauer spectroscopy, and in accordance with previous studies.[4]

## Discussion

As part of our systematic approach to generate new ferrous materials of the general formula $[FeL(NCS)_2]$ with predictable magnetic properties, in this contribution we report the results obtained when 1-*N*-$R^2$-imidazole-2-carboxaldehyde ($R^2$ = H, Me) is used as a carbonyl synthon in combination with 1,3-diaminopropane and 2,2-dimethyl-1,3-diaminopropane as diamino synthons for the synthesis of symmetrical $L^{Bx}$ and dissymmetrical $L^{Ex}$ tetradentate Schiff base ligands (Figures 1 and 13).

The change in carbonyl synthon from 2-$R^2$-imidazole-4-carboxaldehyde ($R^2$ = H, $CH_3$, $C_6H_5$)[4a] or 5-methylimidazole-4-carboxaldehyde[4b] to 1-*N*-$R^2$-imidazole-2-carboxaldehyde ($R^2$ = H, $CH_3$) involves minor structural modifications in the case of $[FeL^{B4}(NCS)_2]$ (**1**; $R^2$ = H), which is characterized by a *trans* coordination of the thiocyanato ligands and a planar conformation of $L^{B4}$, as suggested by comparison of the IR spectra and X-ray data of $[FeL^{B1}(NCS)_2]$, $[FeL^{B2}(NCS)_2]$ and **1**. These three complexes have the same coordination sphere and a very similar geometry around the metal centre with a planar conformation of $L^{Bx}$ (see above and ref.[4a]). However, in $[FeL^{B5}(NCS)_2]$ (**2**; $R^2$ = $CH_3$), which is characterized by a *cis* coordination of the thiocyanato ligands, $L^{B5}$ has a folded conformation, as demonstrated by X-ray analysis (see above). One plausible explanation for obtaining different isomers is the absence/presence of a methyl substituent at the 1-*N*-imidazole, which would allow/prevent the involvement of N–H hydrogen bonds as observed in the previous studies[4a,4b] and also for $[FeL^{Ex}(NCS)_2]$ complexes described in the present report. In the crystal structure of **2**, the *cis* arrangement of the thiocyanato anions associated to the folded conformation of the tetradentate ligand allows π–π stacking interactions between adjacent imidazolyl rings, which result in a crystal packing made of isolated dimeric associates. Although no structural data is available for **1**, the *trans* NCS coordination is likely to be promoted by N–H···S and/or N–H···N hydrogen bonds as observed in $[FeL^{B1}(NCS)_2]$,[4a] $[FeL^{B2}(NCS)_2]$,[4a] $[FeL^{D2}(NCS)_2]$,[4b] **3** and **5** (this work).

With regard to the series based on the disymmetrical $L^{Ex}$ ligands, we may establish a parallelism between the statistical disorder of $L^{E3}$ observed in **5**, which implies the presence of two configurations of the propylene fragment and the statistical disorder of the propylene fragment of $L^{D2}$ in $[FeL^{D2}(NCS)_2]$ at and below 300 K.[4b] Two conformers similarly distinguished by the configuration of one of the propylene fragments of $H_2L^{2-Me}$ were also observed in the crystal structure of $[FeH_2L^{2-Me}](ClO_4)_2$ ($H_2L^{2-Me}$ = bis{[(2-methylimidazol-4-yl)methylidene]-3-aminopropyl}ethylene diamine) at low temperature.[2k] Although no molecular structure is available, it is thus likely that the two-step SC of $[FeL^{D1}(NCS)_2]$, which is also characterized by two quadrupole-split LS doublets at low temperature,[4b] originates from the presence of two conformers distinguished by the configuration of the propylene fragment of $L^{D1}$.

Similar to the previously reported $[FeL^{Cx}(NCS)_2]$[4a] and $[FeL^{Dx}(NCS)_2]$[4b] series (Figure 14), the electronic behaviours of **3**–**6** evidences that a combination of pyridyl and imidazolyl rings to yield $Fe^{II}$ complexes that are based on a dissymmetrical tetradentate $L^{Ex}$ ligand allows the generation of an intermediate ligand field suitable for SC. In the absence of substituents on the central carbon atom of the propylene bridge of $L^{Ex}$ ($R^1$ = H, **3** and **4**), the onset of SC is above 350 K, regardless of the 1-*N*-$R^2$-imidazolyl substit-

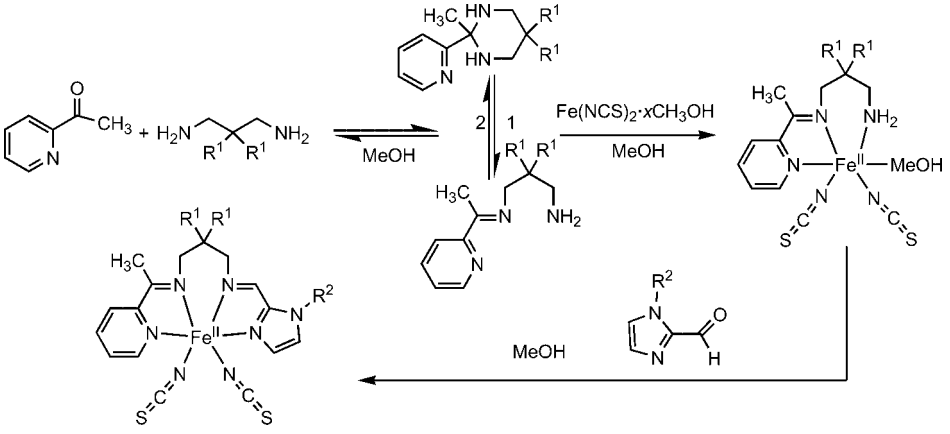


Figure 13. Synthetic pathway for the $[FeL^{Ex}(NCS)_2]$ ($R^1$ = H, Me; $R^2$ = H, Me).

 © 2007 Wiley-VCH Verlag GmbH & Co. KGaA, Weinheim 

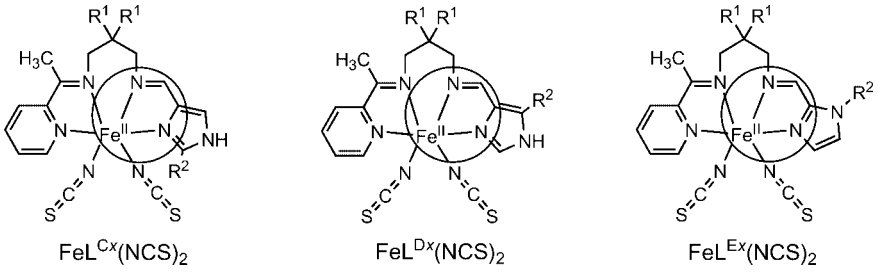


Figure 14. Compared schematic drawings of the $[FeL^{Cx}(NCS)_2]$,[4a] $[FeL^{Dx}(NCS)_2]$[4b] and $[FeL^{Ex}(NCS)_2]$ complexes (this work).

uent. Because the electronic properties of these materials cannot be evaluated above ca. 400 K, the effect of the 1-*N*-$R^2$-imidazolyl substituent on the compared SC behaviours of **3** and **4** cannot be appreciated. In the presence of substituents on the central carbon atom of the propylene bridge of $L^{Ex}$ ($R^1$ = Me, **5** and **6**), the SC is shifted towards lower temperatures. This down shift is modulated by the effect of the 1-*N*-$R^2$-imidazolyl substituent in two ways: (1) $T_{1/2}$ is higher for **5** ($R^2$ = H) than for **6** ($R^2$ = Me), ca. 390 vs. ca. 360 K and (2) the SC is much steeper for **5** than for **6**, indicating a more cooperative behaviour of **5** in line with the presence of extended intermolecular interactions in **5** versus isolated dimeric associates in **6**. The higher $T_{1/2}$ for **5** ($R^2$ = H) relative to that of **6** ($R^2$ = Me) is in line with our previous studies showing that the ligand fields exerted by $L^{C1}$ and $L^{C4}$ ($R^2$ = H) are weaker (higher $T_{1/2}$) than those exerted by the remaining $L^{Cx}$ ligands ($R^2$ = Me or Ph).[4a] However, the $R^2$ substituent is at the C2 imidazolyl in the $L^{Cx}$ series, whereas it is at the 1-*N*-imidazolyl in the present $L^{Ex}$ series (Figure 14); thus both the steric and inductive effects of $R^2$ are significantly different from one series to the other one, which prevents a more detailed comparison.

From our previous studies,[4a,4b] the role of $R^1$ in tuning the ligand field, as estimated through approximated $T_{1/2}$ values, was considered as more limited than that of $R^2$ and opposite in trend (lower $T_{1/2}$ associated with $R^1$ = H). It may thus seem striking to observe the opposite situation for the present series where the role of $R^1$ in tuning the ligand field is larger than (and similar in trend to) that of $R^2$. However, it must be underlined that the change in carbonyl synthon from 2-$R^2$-imidazole-4-carboxaldehyde[4a] or 5-methylimidazole-4-carboxaldehyde[4b] to 1-*N*-$R^2$-imidazole-2-carboxaldehyde (this work) moves the connection of the imidazolyl fragment (to the propyl chain) from the 4- to the 2-imidazolyl position: this change switches the orientation of the coordinated imidazolyl and the position of the imine imidazolyl nitrogen with respect to the adjacent Schiff base imine function (Figure 14). As a result, in the present $[FeL^{Ex}(NCS)_2]$ series the metallacycle involving the imidazolyl fragment is highly conjugated (Fe–N=C–C=N–) at variance with the corresponding metallacycle in the $[FeL^{Cx}(NCS)_2]$[4a] and $[FeL^{Dx}(NCS)_2]$[4b] series (Fe–N–C–C=N–), see Figure 14. It is then clear that this electronic effect not only largely overpasses but also qualitatively and quantitatively modifies the effects of $R^1$ and $R^2$.

As a final comment, we would like to stress the role of hydrogen bonds in the SC behaviour within this series of compounds: involvement of 1-*N*-Me-imidazole-2-carboxaldehyde for the synthesis of dissymmetrical ligands **4** and **6** prevents $NH_{imidazole}$···SCN interactions. Indeed, no weak interactions of this type are found in **6**, yielding isolated dimeric associates through π–π stacking interactions. As a consequence, **6** exhibits a very smooth SC that spreads over 200 K because of the lack of intermolecular interactions/cooperativity relative to its chemical isomer $[FeL^{D1}(NCS)_2]$ (including the 5-methyl-4-imidazolyl fragment), which exhibits a steep SC with a 5 K hysteresis.[4b]

## Experimental Section

**General:** All reagents and solvents are commercially available (Aldrich, Wako), and they were used without further purification. Elemental analyses were carried with a Perkin–Elmer 2400 series II device (C, H, N) at the Microanalytical Laboratory of the Laboratoire de Chimie de Coordination in Toulouse, and with a Maxim Thermoelectron device (S, Fe) at the Service Central de Microanalyses du CNRS in Vernaison, France. 1D $^1$H and 1D $^{13}$C NMR spectra were obtained with an AC 250 FT spectrometer (Bruker). Chemical shifts are given relative to tetramethylsilane by using $CDCl_3$ as the solvent. IR spectra were measured in the 400–4000 $cm^{-1}$ range with a 9800 FTIR spectrometer (Perkin–Elmer). Mössbauer spectra were recorded with a constant-acceleration conventional spectrometer with a 50 mCi source of $^{57}$Co (Rh matrix). The absorber was a powdered sample enclosed in a 20-mm diameter cylindrical plastic sample holder, the size of which was determined to optimize the absorption. Spectra were obtained in the 80–400 K range by using a MD306 Oxford cryostat (4–293 K) or an homemade vacuum oven (300–500 K), the thermal scanning being monitored by an Oxford ITC4 servo control device (± 0.1 K accuracy). A least square computer program[12] was used to fit the Mössbauer parameters and to determine their standard deviations of statistical origin (given in parentheses). Isomer shift values ($\delta$) are relative to iron foil at 293 K. Variable temperature magnetic susceptibility data were collected from powdered samples with a MPMS-55 Quantum design SQUID magnetometer or a Faraday type susceptometer under applied magnetic fields lower than 0.5 T. Diamagnetic corrections were applied by using Pascal's constants.[13]

### *Synthesis of Ligands*

**Symmetrical Ligands $L^{Bx}$:** 2,2-Dimethyl-1,3-diaminopropane (0.102 g, $10^{-3}$ mol) and imidazole-2-carboxaldehyde (0.192 g,

 © 2007 Wiley-VCH Verlag GmbH & Co. KGaA, Weinheim 

$2 \times 10^{-3}$ mol, for $L^{B4}$) or 1-methylimidazole-2-carboxaldehyde (0.220 g, $2 \times 10^{-3}$ mol, for $L^{B5}$) in methanol (20 mL) were stirred for 2 h at r.t. Slow evaporation of the solvent yielded brown-yellow oils. Yield: 0.190 g (74%) and 0.234 g (82%) for $L^{B4}$ and $L^{B5}$, respectively. Data for $L^{B4}$: $^1$H NMR (250 MHz, $CDCl_3$): $\delta$ = 8.16 (s, 2 H, 4-H), 7.14 (s, 2 H + 2 H, 1-H + 2-H, NH proton exchange did not allow distinguishing the two types of protons), 3.43 (s, 4 H, 5-H5), 0.90 (s, 6 H, 7-H) ppm. Data for $L^{B5}$: $^1$H NMR (250 MHz, $CDCl_3$): $\delta$ = 8.26 (s, 2 H, 4-H), 7.05–6.88 (2s, 2 H + 2 H, 1-H + 2-H), 3.956 (s, 6 H, 3-H), 3.42 (s, 4 H, 5-H), 0.97 (s, 6 H, 7-H).

**Synthesis of the Half-Units L and L′:** The synthetic pathway was adapted from ref.[4b]: 2-acetylpyridine and 1,3-diaminopropane (for L) or 2,2-dimethyl-1,3-diaminopropane (for L′) were mixed for 30 min in a 1:1 ratio (1 equiv. = $10^{-3}$ mol) in methanol (10 mL). The resulting pale yellow solution was used immediately for the preparation of complexes **3**–**6**.

***Synthesis of Complexes***

All complexation reactions and sample preparations for physical measurements were carried out under a purified nitrogen atmosphere within a glove box (Vacuum Atmospheres H.E.43.2) equipped with a dry train (Jahan EVAC 7).

**$Fe(NCS)_2 \cdot x$MeOH:** Prepared through the 1:2 reaction of $Fe(ClO_4)_2 \cdot xH_2O$ with potassium thiocyanate in MeOH.[11] After removal of potassium perchlorate through filtration, the freshly prepared $Fe(NCS)_2 \cdot x$MeOH was used immediately for the preparation of complexes **1**–**6**.

*Caution: Although no such behaviour was observed during the present work, perchlorate salts are potentially explosive and should be handled in small quantities and with much care.*

**General Procedure for 1 and 2:** A methanolic solution ($10^{-3}$ mol in 10 mL) of $[Fe(NCS)_2] \cdot x$MeOH was added slowly to a methanolic solution ($10^{-3}$ mol in 10 mL) of the ligand. The solution immediately changed from pale yellow to orange-yellow and was stirred for 30 min.

**$[FeL^{B4}(NCS)_2]$ (1):** Yield: 0.28 g, 65%, microcrystalline powder. IR: 2081, 2070, 2052, 2036 (NCS, 4 bands), 1619 (imine) $cm^{-1}$. $C_{15}H_{18}FeN_8S_2$ (430.3): calcd. C 41.87, H 4.22, N 26.04, S 14.90, Fe 12.98; found C 41.68, H 3.91, N 25.36, S 14.23, Fe 12.67.

**$[FeL^{B5}(NCS)_2]$ (2):** Could not be obtained as a pure species through the general method described above. However, during the synthesis of **6** with the dissymmetrical ligand $L^{E4}$, see below, we observed the systematic (and reproducible) formation of single crystals of red complex **2** in a poor yield, mixed with the desired dark-blue complex **6**. The amount of **2** in this mixture was evaluated by Mössbauer spectroscopy to 11(2)% (Table S2). The red single-crystal selected for X-ray data collection was picked from the mixture of **2** and **6**, see synthetic details for **6**, below.

**General Procedure for 3–6:** The synthetic pathway was adapted from the method previously described[4] (Figure 13). To a pale-yellow solution ($10^{-3}$ mol, 10 mL of methanol) of aminal L, **3** or **4**, or L′, **5** or **6**, was slowly added the freshly prepared $Fe(NCS)_2$ solution ($10^{-3}$ mol, 10 mL of methanol). The colour of the reaction mixture immediately turned to dark blue, and the mixture was stirred for 5 min. The appropriate 1-*N*-$R^1$-imidazole-2-carboxaldehyde ($10^{-3}$ mol, 10 mL of methanol) was then added (imidazole-2-carboxaldehyde for **3** and **5**, and 1-*N*-methyl-imidazole-2-carboxaldehyde for **4** and **6**). No further colour change was observed; the solution was stirred for another 30 min and then left undisturbed until a microcrystalline powder or crystals formed quantitatively.

**$[FeL^{E1}(NCS)_2]$ (3):** Yield: 0.32 g, 75%, dark-blue single crystals. IR (KBr): 2125, 2113 (NCS); 1645 (imine) $cm^{-1}$. $C_{16}H_{17}FeN_7S_2$ (427.3): calcd. C 44.97, H 4.01, N 22.94, S 15.01, Fe 13.07; found C 45.29, H 3.72, N 22.75, S 14.68, Fe 12.72.

**$[FeL^{E2}(NCS)_2]$ (4):** Yield: 0.32 g, 73%, dark-blue microcrystalline powder. IR (KBr): 2109, 2080 (NCS), 1647 (imine) $cm^{-1}$. $C_{17}H_{19}FeN_7S_2$ (441.4): calcd. C 46.26, H 4.34, N 22.22, S 14.53, Fe 12.65; found C 46.15, H 4.18, N 21.86, S 13.96, Fe 11.96.

**$[FeL^{E3}(NCS)_2]$ (5):** Yield: 0.31 g, 68%, dark-blue single crystals. IR (KBr): 2127, 2111 (NCS), 1656 (imine) $cm^{-1}$. $C_{18}H_{21}FeN_7S_2$ (455.4): calcd. C 47.48, H 4.65, N 21.53, S 14.08, Fe 12.26; found C 48.02, H 4.43, N 21.34, S 13.68, Fe 11.88.

**$[FeL^{E4}(NCS)_2] \cdot CH_3OH$ (6):** After removal of a small amount of a mixture of **2** and **6** by filtration, **6** was obtained from the resulting filtrate 2 d later. Yield: 0.36 g, 72%, dark-blue single crystals. IR (KBr): 2113, 2070 (NCS), 1635 (imine) $cm^{-1}$. $C_{20}H_{27}FeN_7OS_2$ (501.4): calcd. C 47.91, H 5.42, N 19.55, S 12.79, Fe 11.14; found C 47.69, H 4.92, N 20.13, S 12.43, Fe 10.86.

Table 1. Crystallographic data collection and structure determination for complexes **2**, **3**, **5** and **6**.

| Compound | $[FeL^{B5}(NCS)_2]$ (**2**) | $[FeL^{E1}(NCS)_2]$ (**3**) | $[FeL^{E3}(NCS)_2]$ (**5**) | $[FeL^{E4}(NCS)_2]$ $CH_3OH$ (**6**) |
|---|---|---|---|---|
| Formula | $C_{17}H_{22}FeN_8S_2$ | $C_{16}H_{17}FeN_7S_2$ | $C_{18}H_{21}FeN_7S_2$ | $C_{20}H_{27}FeN_7OS_2$ |
| Formula weight | 458.40 | 427.34 | 455.39 | 501.43 |
| Crystal system | monoclinic | monoclinic | monoclinic | monoclinic |
| Space group | $P2_1/n$ | $P2_1/c$ | $P2_1/n$ | $P2_1/c$ |
| $a$ / Å | 9.966(2) | 8.8108(5) | 8.114(3) | 8.1657(11) |
| $b$ / Å | 8.4072(17) | 24.3767(14) | 11.208(5) | 19.007(2) |
| $c$ / Å | 25.953(5) | 8.6855(5) | 23.067(19) | 15.3398(19) |
| $\alpha$ / ° | 90 | 90 | 90 | 90 |
| $\beta$ / ° | 93.61(3) | 90.076(5) | 95.83(4) | 100.787(15) |
| $\gamma$ / ° | 90 | 90 | 90 | 90 |
| $V$ / Å$^3$ | 2170.2(8) | 1865.45(18) | 2087(2) | 2338.7(5) |
| $Z$ | 4 | 4 | 4 | 4 |
| $\rho_{calcd.}$ / g cm$^{-3}$ | 1.403 | 1.522 | 1.449 | 1.416 |
| $\lambda$ / Å | 0.71073 | 0.71073 | 0.71073 | 0.71073 |
| $T$ / K | 180 | 180 | 180 | 180 |
| $\mu$(Mo-$K_\alpha$) / cm$^{-1}$ | 0.907 | 1.048 | 0.941 | 0.850 |
| $R$[a] [$I > 2\sigma(I)$] | 0.0600 | 0.0327 | 0.0579 | 0.0845 |
| $wR$[b] | 0.1219 | 0.0846 | 0.1232 | 0.1887 |

[a] $R = \Sigma F_o - F_c / \Sigma F_o$. [b] $wR = [\Sigma w(F_o^2 - F_c^2)^2 / \Sigma w F_o^{22}]^{1/2}$.

 © 2007 Wiley-VCH Verlag GmbH & Co. KGaA, Weinheim 

**Crystallographic Data Collection and Structure Determination for 2, 3, 5 and 6:** The X-ray data for compounds **2** and **6** were collected at 180 K with a Stoe Imaging Plate Diffractometer System (IPDS) equipped with an Oxford Cryosystems cooler device by using a graphite monochromator ($\lambda$ = 0.71073 Å). Data were collected[14] by using $f$ rotation movement with the crystal-to-detector distance equal to 80 mm (**2**), 70 (**6**) and $f$ = 0.0–250°, $\Delta f$ = 1.5° (**2**), $f$ = 0.0–200°, $\Delta f$ = 2.0° (**6**). Crystallographic measurements for **3** and **5** were carried out at 180 K with an Oxford-Diffraction XCALIBUR CCD diffractometer by using graphite-monochromated Mo-$K_\alpha$ radiation. The crystals were placed 50 mm from the CCD detector. More than the hemisphere of reciprocal space was covered by combination of four sets of exposures; each set had a different $f$-angle (0, 90, 180, 270°). The unit cell determination and data integration were carried out using the CrysAlis package of Oxford Diffraction.[15] All structures were solved by direct methods by using SHELXS-97[16] and refined by full-matrix least-squares on $F_o^2$ with SHELXL-97[17] with anisotropic displacement parameters for non-hydrogen atoms. All H atoms attached to carbon were introduced in idealized positions ($d_{CH}$ = 0.96 Å) by using the riding model with their isotropic displacement parameters fixed at 120% of their riding atom. Because of statistical disorder of the tetradentate ligand around Fe, the structure of **5** was refined by using a disordered approach in combination with the tools available from the SHELXL97 program package, yielding conformations with respective occupancy factors of 0.74(1) and 0.26(1)*. The molecular plots were obtained using the ZORTEP program.[18] The main crystallographic data together with refinement details are summarized in Table 1. CCDC-639917 for **2**, -639919 for **3**, -639918 for **5** and -639916 for **6**, contain the supplementary crystallographic data for this paper. These data can be obtained free of charge from The Cambridge Crystallographic Data Centre via www.ccdc.cam.ac.uk/data_request/cif.

**Supporting Information** (see footnote on the first page of this article): Table of the $\chi_M T$ data vs. temperature ($T$) for complexes **1** and **3**–**6**, Table of the Mössbauer parameters (isomer shift $\delta$, quadrupole splitting $\Delta E_Q$ and line width $\Gamma/2$) resulting from fitting the spectra of complexes **1**–**6** and the IR spectra of **1** and the three related complexes.

## Acknowledgments

Financial support by the French Ministry for Education, Research, and Technology through a doctoral grant to N. B. and by the CNRS-DFG collaborative programme through a postdoctoral grant to S. S. are gratefully acknowledged.

[1] P. Gütlich, H. A. Goodwin (Eds.), *Topics in Current Chemistry Vol. 233: Spin Crossover in Transition Metal Compounds I*, Springer, Berlin, **2004**, pp. 1–47, and references cited therein.

[2] a) L. J. Wilson, D. Georges, M. A. Hoselton, *Inorg. Chem.* **1975**, *14*, 2968–2975; b) H. Toftlund, S. Yde-Andersen, *Acta Chem. Scand.* **1981**, *A35*, 575–585; c) L. L. Martin, K. S. Hagen, A. Hauser, R. L. Martin, A. M. Sargeson, *J. Chem. Soc. Chem. Commun.* **1988**, *19*, 1313–1315; d) A. H. R. Obaidi, J. J. McGarvey, K. P. Taylor, S. E. J. Bell, K. B. Jensen, H. Toftlund, *J. Chem. Soc. Chem. Commun.* **1993**, *6*, 536–538; e) A. H. R. Al-Obaidi, K. B. Jensen, J. J. McGarvey, H. Toftlund, B. Jensen, S. E. J. Bell, J. G. Carroll, *Inorg. Chem.* **1996**, *35*, 5055–5060; f) Y. Sunatsuki, Y. Ikuta, N. Matsumoto, H. Ohta, M. Kojima, S. Iijima, S. Hayami, Y. Maeda, S. Kaizaki, F. Dahan, J.-P. Tuchagues, *Angew. Chem. Int. Ed.* **2003**, *42*, 1614–1618; g) Y. Ikuta, M. Ooidemizu, Y. Yamahata, M. Yamada, S. Osa, N. Matsumoto, S. Iijima, Y. Sunatsuki, M. Kojima, F. Dahan, J.-P. Tuchagues, *Inorg. Chem.* **2003**, *42*, 7001–7017; h) M. Yamada, M. Ooidemizu, Y. Ikuta, S. Osa, N. Matsumoto, S. Iijima, M. Kojima, F. Dahan, J.-P. Tuchagues, *Inorg. Chem.* **2003**, *42*, 8406–8416; i) Y. Sunatsuki, H. Ohta, M. Kojima, Y. Ikuta, Y. Goto, N. Matsumoto, S. Iijima, H. Akashi, S. Kaizaki, F. Dahan, J.-P. Tuchagues, *Inorg. Chem.* **2004**, *43*, 4154–4171; j) S. Arata, H. Torigoe, T. Iihoshi, N. Matsumoto, F. Dahan, J.-P. Tuchagues, *Inorg. Chem.* **2005**, *44*, 9288–9292; k) N. Bréfuel, S. Imatomi, H. Torigoe, H. Hagiwara, S. Shova, J.-F. Meunier, S. Bonhommeau, J.-P. Tuchagues, N. Matsumoto, *Inorg. Chem.* **2006**, *45*, 8126–8135.

[3] a) O. Kahn, J.-P. Launay, *Chemtronics* **1988**, *3*, 140–151; b) O. Kahn, J. Krober, C. Jay, *Adv. Mater.* **1992**, *4*, 718–728; c) O. Kahn, C. Jay-Martinez, *Science* **1998**, *279*, 44–48.

[4] a) N. Bréfuel, I. Vang, S. Shova, F. Dahan, J.-P. Costes, J.-P. Tuchagues, *Polyhedron* **2007**, *26*, 1745–1757; b) N. Bréfuel, S. Shova, J. Lipkowski, J.-P. Tuchagues, *Chem. Mater.* **2006**, *18*, 5467–5479.

[5] N. N. Greenwood, T. C. Gibbs in *Mössbauer Spectroscopy*, Chapman and Hall, New York, **1971**, pp. 9–11, 50–53.

[6] N. Bréfuel, C. Lepetit, S. Shova, F. Dahan, J.-P. Tuchagues, *Inorg. Chem.* **2005**, *44*, 8916–8928.

[7] P. Gütlich, H. A. Goodwin (Eds.), *Topics in Current Chemistry Vols. 233–235: Spin Crossover in Transition Metal Compounds I–III*, Springer, Berlin, **2004**, and references cited therein.

[8] a) F. Hartmann-Boutron, *Ann. Phys.* **1975**, *9*, 285–356; b) P. Adler, A. Hauser, A. Vef, H. Spiering, P. Gütlich, *Hyperfine Interact.* **1989**, *47*, 343–356; c) P. Adler, H. Spiering, P. Gütlich, *J. Chem. Phys.* **1989**, *50*, 587–597.

[9] a) G. Lemercier, A. Bousseksou, M. Verelst, J.-P. Tuchagues, F. Varret, *J. Magn. Magn. Mater.* **1995**, *150*, 227–230; b) A. Thiel, A. Bousseksou, M. Verelst, F. Varret, J.-P. Tuchagues, *Chem. Phys. Lett.* **1999**, *302*, 549–554.

[10] K. Nakamoto, *Infrared and Raman Spectra of Inorganic and Coordination Compounds*, 4th ed., John Wiley & Sons, New York, **1986**.

[11] N. E. Erikson, N. Sutin, *Inorg. Chem.* **1966**, *5*, 1834–1835.

[12] K. Lagarec, *Recoil, Mössbauer Analysis Software for Windows*, http://www.physics.uottawa.ca/~recoil.

[13] P. Pascal, *Ann. Chim. Phys.* **1910**, *19*, 5–70.

[14] STOE, *IPDS Manual* (Version 2.93), Stoe & Cie, Darmstadt, Germany, **1997**.

[15] *CrysAlis RED* (Version 1.170.32), Oxford Diffraction Ltd., Oxford, U. K., **2003**.

[16] G. M. Sheldrick, *SHELXS-97: Program for Crystal Structure Solution*, University of Göttingen, Göttingen, Germany, **1990**.

[17] G. M. Sheldrick, *SHELXL-97: Program for the Refinement of Crystal Structures from Diffraction Data*, University of Göttingen, Göttingen, Germany, **1997**.

[18] L. Zsolnai, H. Pritzkow, G. Huttner, *ZORTEP – Ortep for PC: Program for Molecular Graphics*, University of Heidelberg, Heidelberg, Germany, **1996**.

Received: March 22, 2007
Published Online: July 30, 2007

 © 2007 Wiley-VCH Verlag GmbH & Co. KGaA, Weinheim 

DOI: 10.1002/ejic.200700321

# $Pd(SeO_3)$, $Pd(SeO_4)$, and $Pd(Se_2O_5)$: The First Palladium Oxoselenates

**Annika Arndt[a] and Mathias S. Wickleder*[a]**

**Keywords:** Solid-state structures / Palladium / Selenium / Lone-pair effect / IR spectroscopy

Depending on the reaction conditions, the reaction of elemental palladium with $H_2SeO_4$ in sealed glass tubes at 350 °C leads to red single crystals of $Pd(SeO_3)$ [$C2/m$, $Z = 4$, $a = 6.788(2)$, $b = 7.030(2)$, $c = 7.008(2)$ Å, $\beta = 118.09(3)°$] or to yellow-orange single crystals of $Pd(SeO_4)$ [$C2/c$, $Z = 4$, $a = 8.171(1)$, $b = 5.286(1)$, $c = 8.115(1)$ Å, $\beta = 94.54(1)°$]. Yellow-orange single crystals of $Pd(Se_2O_5)$ [$I2/a$, $Z = 4$, $a = 7.212(1)$, $b = 5.569(1)$, $c = 12.177(3)$ Å, $\beta = 106.84(2)°$] are obtained when $SeO_3$ is added to the reaction mixture. X-ray single-crystal diffraction shows that $Pd(SeO_3)$ consists of layers that are formed by square-planar coordinated $Pd^{2+}$ ions and pyramidal $SeO_3^{2-}$ groups. These layers are held together by weak interactions involving the lone electron pairs of the selenium atoms. The Se–O distances within the selenite ion are different (1.69 and 1.76 Å), in accordance with the different attachment of the oxygen atoms to the $Pd^{2+}$ ions. The square-planar $[PdO_4]$ units in the crystal structure of $Pd(SeO_4)$ are linked by tetrahedral $SeO_4^{2-}$ ions into a three-dimensional network. These anions act as monodentate ligands towards the $Pd^{2+}$ ions, with Se–O distances of around 1.65 Å. The $Pd^{2+}$ ions in the crystal structure of $Pd(Se_2O_5)$ are coordinated by two chelating diselenite ions. The $Se_2O_5^{2-}$ ions link the palladium ions into corrugated chains, which are held together by weak interactions only. The IR spectra of these compounds display the typical bands for oxoselenate anions.

(© Wiley-VCH Verlag GmbH & Co. KGaA, 69451 Weinheim, Germany, 2007)

## Introduction

Despite the vital importance of platinum group metals in various fields, complete classes of compounds of these elements are almost essentially unexplored. This is particularly true for those compounds containing complex oxo anions. To some degree this is astonishing as these compounds play a crucial role in various applications: the separation of platinum metals involves reactions with sulfuric acid, for example, and the rhodium sulfate $Rh_2(SO_4)_3 \cdot 12H_2O$ is used as a homogeneous catalyst, although its structure is not known.[1] Such compounds might also be important as precursors for the preparation of metal nanoparticles by thermolysis.[2] The investigation, and especially the structure elucidations, of these compounds are often difficult because single crystals are hard to obtain. Recently, we started to investigate compounds of precious metals with complex oxo anions in a systematic way and were able to develop suitable preparative routes for compounds of the elements gold and platinum. We found that the oxidation of gold with concentrated selenic acid and of platinum with sulfuric acid leads to gold selenites and platinum sulfates, respectively.[3,4] Surprisingly, in the case of platinum only platinum(III) sulfates were obtained. The extension of this chemistry to further platinum group metals has now afforded the selenite $Pd(SeO_3)$ by oxidation of elemental palladium with $H_2SeO_4$. Furthermore, the selenate $Pd(SeO_4)$ has been obtained by using $H_2SeO_4$ in excess, and $Pd(Se_2O_5)$ is formed when $SeO_3$ is added to the reaction mixture. $Pd(SeO_3)$, $Pd(SeO_4)$, and $Pd(Se_2O_5)$ are the first binary oxoselenates of a platinum group metal. Only two other structurally characterized palladium compounds with complex oxo anions have been reported to date, namely $Pd(SO_4)$, which has been prepared in a single crystalline form,[5] and $Pd(NO_3)_2 \cdot 2H_2O$, which has been characterized by powder diffraction data.[6] IR data are presented for a number of perchlorate salts.[7]

[a] Universität Oldenburg, Institut für Reine und Angewandte Chemie,
Postfach 2503, 26129 Oldenburg, Germany
Fax: +49-441-798-3660
E-mail: mathias.wickleder@uni-oldenburg.de

## Results and Discussion

### Crystal Structures

$Pd(SeO_3)$ crystallizes in the monoclinic space group $C2/m$. In the crystal structure the $Pd^{2+}$ ion is located at the special site 4*e* (site symmetry: $C_i$) and the selenium atom of the $SeO_3^{2-}$ group is placed at the position 4*i* (site symmetry: $C_s$) of that space group (Table 1). The $Pd^{2+}$ ion in square-planar coordination of four oxygen atoms ($2 \times O1$ and $2 \times O2$) from four monodentate selenite ions. The Pd–O distances are 2.01 and 2.02 Å, respectively, and a slight distortion of the square-planar coordination is found, with O1–Pd–O2 angles of 85.3° and 94.7° (Table 2). Two remarkably different distances are found within the $SeO_3^{2-}$ group, namely 1.69 Å for Se–O1 and 1.76 Å for Se–O2. The differ-

 © 2007 Wiley-VCH Verlag GmbH & Co. KGaA, Weinheim 

ence between these two can be attributed to the different coordination of the oxygen atoms by $Pd^{2+}$ ions: O1 is bonded to only one palladium ion while O2 has two neighbors. In this way the $SeO_3^{2-}$ ion is surrounded by four $Pd^{2+}$ ions, and this linkage leads to electronically neutral $^2_\infty[Pd(SeO_3)_{4/4}]$ layers that are stacked in the [102] direction of the monoclinic unit cell. The square-planar $[PdO_4]$ units within these layers join two *trans* vertices to each other to yield infinite $^1_\infty[PdO(1)_{2/1}O(2)_{2/2}]^{4+}$ chains (Figure 1). The $Pd^{2+}$–$Pd^{2+}$ distances are 3.52 Å within the chains and 3.39 Å between adjacent chains. The most remarkable feature of the crystal structure of $Pd(SeO_3)$ is that the neutral $^2_\infty[Pd(SeO_3)_{4/4}]$ layers are held together only by weak Van der Waals interactions with respect to the observed distances between the atoms of adjacent sheets (Figure 2). The selenium atoms of one layer and the oxygen atoms of the neighboring layer are separated by 3.15 Å, and the selenium atoms show a shortest distance of 3.70 Å from layer to layer. Thus, there is a large gap between the layers, which obviously contains the lone electron pairs of the selenium atoms. The layer type structure and the presence of only weak forces between the layers weakens the single crystals, which results in severe problems in finding a suitable single crystal for X-ray diffraction, as reflected by the rather high residual values (Table 4).

Table 1. Atomic positions and equivalent displacement parameters for $Pd(SeO_3)$, $Pd(SeO_4)$, and $Pd(Se_2O_5)$.[a]

| Atom | Wyckoff | *x*/*a* | *y*/*b* | *z*/*c* | $U_{eq}$/Å$^2$ |
|---|---|---|---|---|---|
| | | | $Pd(SeO_3)$ | | |
| Pd | 4*e* | 1/4 | 1/4 | 0 | 0.0123(8) |
| Se | 4*i* | 0.1658(5) | 1/2 | 0.3527 | 0.0153(3) |
| O1 | 8*j* | 0.268(2) | 0.304(2) | 0.290(2) | 0.019(4) |
| O2 | 4*i* | 0.894(4) | 1/2 | 0.132(4) | 0.018(3) |
| | | | $Pd(SeO_4)$ | | |
| Pd | 4*c* | 3/4 | 1/4 | 1/2 | 0.0048(2) |
| Se | 4*e* | 0 | 0.0684 | 1/4 | 0.0044(2) |
| O1 | 8*f* | 0.9776(4) | 0.2479(69 | 0.4144(4) | 0.0092(7) |
| O2 | 8*f* | 0.1679(3) | 0.8943(6) | 0.2788(4) | 0.0094(6) |
| | | | $Pd(Se_2O_5)$ | | |
| Pd | 4*a* | 0 | 0 | 0 | 0.0100(3) |
| Se | 8*f* | 0.1819(2) | 0.9114(1) | 0.36149(8) | 0.0091(3) |
| O1 | 4*e* | 1/4 | 0.052(1) | 1/2 | 0.020(2) |
| O2 | 8*f* | 0.375(1) | 0.730(1) | 0.3699(7) | 0.015(2) |
| O3 | 8*f* | 0.001(1) | 0.730(1) | 0.3704(7) | 0.013(2) |

[a] $U_{eq} = 1/3[U_{22} + 1/\sin^2\beta(U_{11} + U_{33} + 2U_{13}\cos\beta)]$.

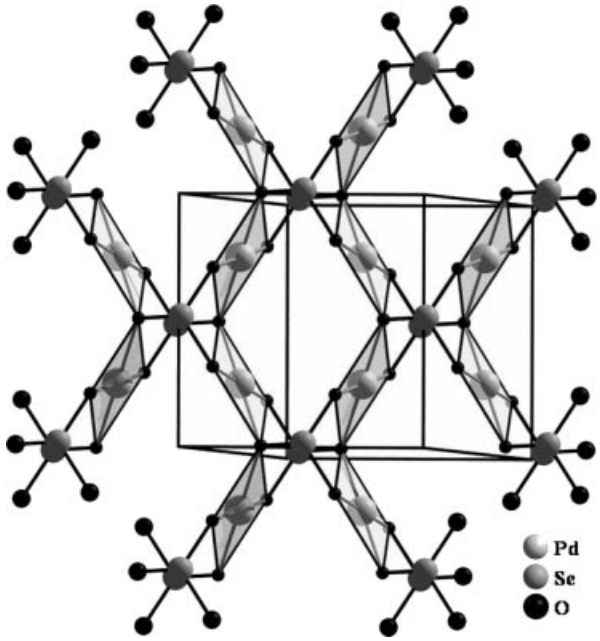


Figure 1. Linkage of the $[PdO_4]$ units according to $^1_\infty[PdO(1)_{2/1}O(2)_{2/2}]^{4+}$. The metal ions lie in a square plane of oxygen atoms and are connected via *trans* vertices into chains.

$Pd(SeO_4)$ also crystallizes monoclinically with a face centered unit cell (space group *C*2/*c*) and is isotypic with the recently reported $Pd(SO_4)$.[5] The palladium atoms are surrounded in a square-planar manner by oxygen atoms, and the selenium atoms are tetrahedrally coordinated by oxygen atoms. Both the palladium and the selenium atoms are located on special sites (4*c* and 4*e*, respectively), which implies $C_i$ symmetry for the $[PdO_4]$ units and $C_2$ symmetry for the $SeO_4^{2-}$ anions (Table 1). The Pd–O distances are in the same range as found for $Pd(SeO_3)$ and show values of 2.04 (O1) and 2.02 Å (O2; Table 2). This is also in good agreement with the findings reported for $Pd(SO_4)$.[5] Similarly to $Pd(SeO_3)$, a distortion of the $[PdO_4]$ unit has to be taken into account, with O1–Pd–O2 angles of 87.0 and 93.0°,

Table 2. Selected bond distances [Å] and angles [°] in $Pd(SeO_3)$, $Pd(SeO_4)$, and $Pd(Se_2O_5)$.

| $Pd(SeO_3)$ | | | $Pd(SeO_4)$ | | | $Pd(Se_2O_5)$ | | |
|---|---|---|---|---|---|---|---|---|
| Pd–O1 | (2x) | 2.02(1) | Pd–O1 | (2x) | 2.036(3) | Pd–O2 | (2x) | 2.035(8) |
| Pd–O2 | (2x) | 2.01(1) | Pd–O2 | (2x) | 2.015(3) | Pd–O3 | (2x) | 2.036(8) |
| O1–Pd–O1 | | 180 | O1–Pd–O1 | | 180 | O2–Pd–O2 | | 180 |
| O1–Pd–O2 | (2x) | 85.3(8) | O1–Pd–O2 | (2x) | 87.0(1) | O2–Pd–O3 | (2x) | 96.0(2) |
| O2–Pd–O1 | (2x) | 94.7(8) | O2–Pd–O1 | (2x) | 93.0(1) | O2–Pd–O1 | (2x) | 84.0(2) |
| O2–Pd–O2 | | 180 | O2–Pd–O2 | | 180 | O3–Pd–O3 | | 180 |
| Se–O1 | (2x) | 1.69(1) | Se–O1 | (2x) | 1.659(3) | Se–O1 | | 1.793(3) |
| Se–O2 | | 1.76(2) | Se–O2 | (2x) | 1.653(3) | Se–O2 | | 1.69(1) |
| | | | | | | Se–O3 | | 1.678(9) |
| O1–Se–O1 | | 109.1(9) | O1–Se–O1 | | 110.3(2) | O1–Se–O3 | | 101.9(3) |
| O1–Se–O2 | (2x) | 99.3(6) | O1–Se–O2 | (2x) | 106.8(1) | O1–Se–O2 | | 101.8(3) |
| | | | O2–Se–O1 | (2x) | 110.4(2) | O2–Se–O3 | | 106.2(3) |
| | | | O2–Se–O2 | | 112.3(2) | Se–O1–Se | | 131.0(2) |

 © 2007 Wiley-VCH Verlag GmbH & Co. KGaA, Weinheim 

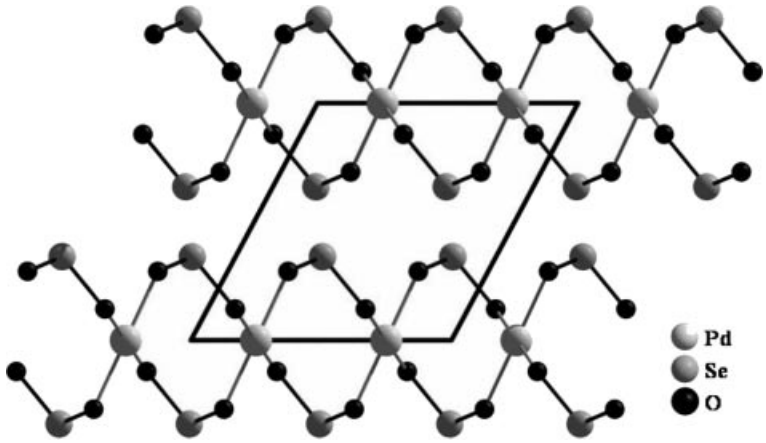


Figure 2. Stacking of electronically neutral $^{2}_{\infty}[Pd(SeO_3)_{4/4}]$ layers along the [102] direction of the unit cell.

respectively. The oxygen atoms of the $[PdO_4]$ groups ($2\times$O1, $2\times$O2) come from four monodentate $SeO_4^{2-}$ ions. Each of the latter must be connected to four $Pd^{2+}$ ions to achieve the composition $Pd(SeO_4)$. Thus, each of the oxygen atoms is connected to a $Pd^{2+}$ ion, which leads to uniform Se–O distances of about 1.65 Å within the anions. Judging from the O–Se–O angles within the anion (106.8–112.3°) a slight deviation of the ideal tetrahedral symmetry is observed. The connectivity of $Pd^{2+}$ and $SeO_4^{2-}$ ions leads to a three-dimensional network, as expressed by the Niggli formula $^{3}_{\infty}[Pd(SeO_4)_{4/4}]$ (Figure 3). The crystal structure of $Pd(SeO_4)$ is related to that of PdSe if the complex $SeO_4^{2-}$ ions are regarded as spheres.[8] The $Se^{2-}$ ions in PdSe have the same coordination as the $SeO_4^{2-}$ groups in $Pd(SeO_4)$.

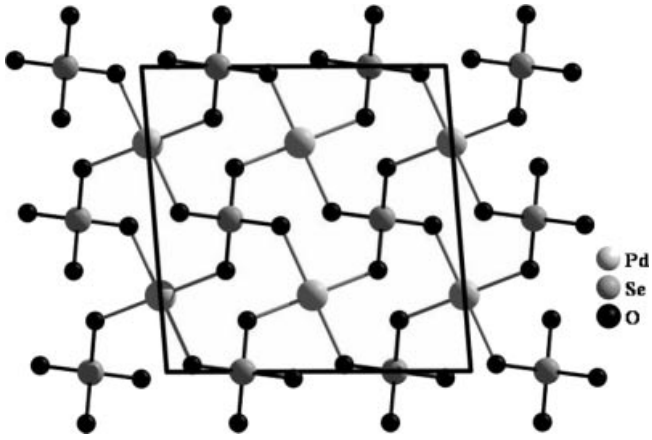


Figure 3. Perspective view of the crystal structure of $Pd(SeO_4)$ along the [010] direction of the unit cell.

The monoclinic structure of $Pd(Se_2O_5)$ (*I*2/*a*) contains the $Pd^{2+}$ ion (Wyckoff site 4*e*; site symmetry: $C_i$) in a square-planar environment of oxygen atoms ($2\times$O2 and $2\times$O3) with the Pd–O distances being essentially equal at 2.03 Å. The deviation of the $[PdO_4]$ unit from ideal $D_{4h}$ symmetry is again significant (Table 2). The four oxygen atoms belong to two $Se_2O_5^{2-}$ ions that act as chelating ligands (Figure 4). The distance between the bridging oxygen atom (O1) and the crystallographically equivalent selenium atoms is 1.793(3) Å, which matches the value that has been reported for other diselenites.[9] Furthermore, the Se–O1–Se angle of 131° lies within the range reported so far.[9] The oxygen atom O1 is located at the 4*e* site of space group

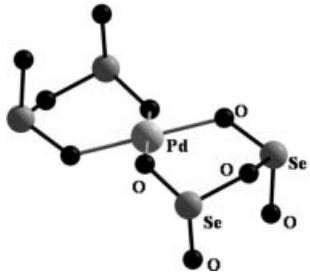


Figure 4.Coodination of the $Pd^{2+}$ ion by two chelating $Se_2O_5^{2-}$ groups in the crystal structure of $Pd(Se_2O_5)$.

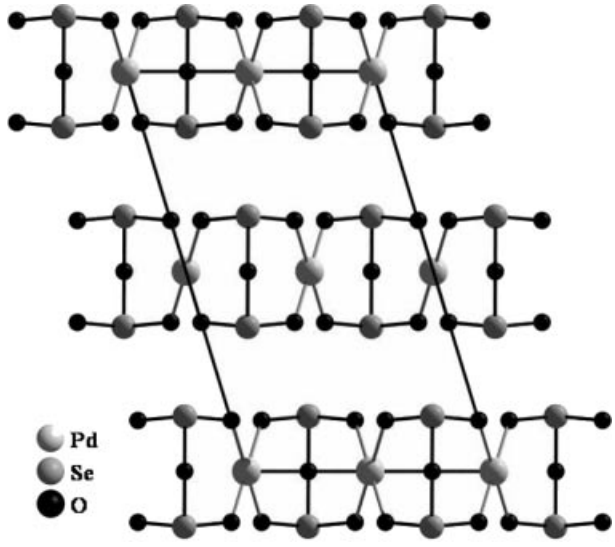


Figure 5. Perspective view of the crystal structure of $Pd(Se_2O_5)$ along the [010] direction of the unit cell.

 © 2007 Wiley-VCH Verlag GmbH & Co. KGaA, Weinheim 

*I*2/*a*, which yields $C_2$ symmetry for the $Se_2O_5^{2-}$ ion. According to the formulation $^1_\infty[Pd(Se_2O_5)_{2/2}]$, each $Se_2O_5^{2-}$ ion is coordinated to two $Pd^{2+}$ ions, which leads to the formation of infinite chains (Figure 5). These chains are strongly corrugated, as shown in Figure 6, and are stacked in the [010] direction. The Pd–Pd distance between adjacent $[PdO_4]$ units is 3.60 Å. The $^1_\infty[Pd(Se_2O_5)_{2/2}]$ chains are only held together by weak interactions and therefore, similarly to $Pd(SeO_3)$, single crystals of $Pd(Se_2O_5)$ suitable for X-ray diffraction were hard to obtain.

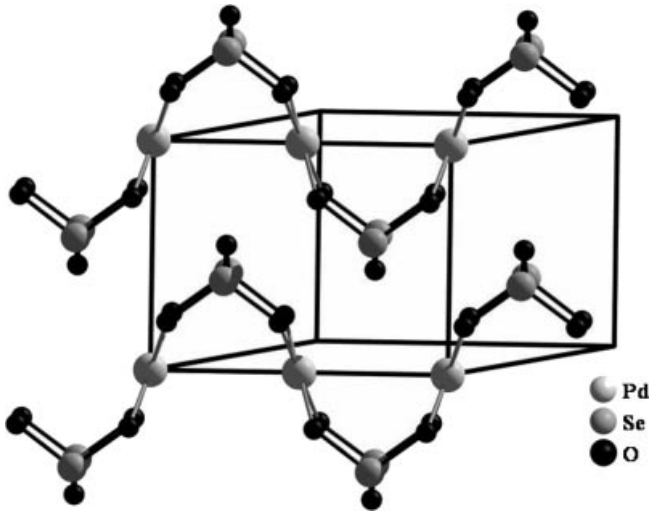


Figure 6. Stacking of the electronically neutral $^1_\infty[Pd(Se_2O_5)_{2/2}]$ chains in the crystal structure of $Pd(Se_2O_5)$.

### Vibrational Spectroscopy

The symmetry of the $SeO_3^{2-}$, $SeO_4^{2-}$, and $Se_2O_5^{2-}$ ions is remarkably lower in the compounds under discussion than in the free anions. Thus, the anion in $Pd(SeO_3)$ has $C_s$ symmetry, $SeO_4^{2-}$ shows $C_2$ symmetry in $Pd(SeO_4)$, and $C_2$ symmetry is also found for the $Se_2O_5^{2-}$ ion in $Pd(Se_2O_5)$. A number of bands are observed in the IR spectra between 400 and 4000 $cm^{-1}$. These are summarized in Table 3 and their assignment is straightforward by comparison with literature data.[9,10]

Table 3. IR data [$cm^{-1}$] for $Pd(SeO_3)$, $Pd(SeO_4)$, and $Pd(Se_2O_5)$.[a]

| Assignment | Wavenumber |
|---|---|
| | $Pd(SeO_3)$ |
| $\nu_s$ ($SeO_2$) | 863 (s), 829 (s) |
| $\delta_s$ ($SeO_3$) | 530 (s), 413 (s) |
| $\nu_{as}$ ($SeO_2$) | 744 (s), 700 (sh) 663 (s) 640 (s) |
| $\delta_{as}$ ($SeO_3$) | –[b] |
| | $Pd(SeO_4)$ |
| $\nu_s$ ($SeO_2$) | 823 (s), 910 (s), 709 (s), 739 (s) |
| $\delta_s$ ($SeO_4$) | –[b] |
| $\nu_{as}$ ($SeO_2$) | 956 (s), 1160(w) 1247 (s) |
| $\delta_{as}$ ($SeO_4$) | 422 (m), 470(m) |
| | $Pd(Se_2O_5)$ |
| $\nu_s$ ($SeO_2$) | 862 (s) 822 (s) |
| $\nu_{as}$ ($SeO_2$) | 732 (m), 702 (sh) 664 (s) |
| $\nu_s$ (SeOSe) | 473 (w) |
| $\nu_{as}$ (SeOSe) | 525 (w) |
| $\delta_s$ ($SeO_3$) | 410 (m) |
| $\delta_{as}$ ($SeO_3$) | –[b] |

[a] s = strong, m = medium, sh = shoulder, w = weak. [b] Out of measuring range.

## Conclusions

As an extension of our work on direct oxidation of precious metals by mineral acids, we have shown in this paper that elemetal palladium can be oxidized by selenic acid under solvothermal conditions, which leads to $Pd(SeO_3)$ or $Pd(SeO_4)$, depending on the metal/acid ratio. Furthermore, the diselenite $Pd(Se_2O_5)$ is obtained if $SeO_3$ is added to the reaction mixture. The compounds were characterized by single-crystal X-ray diffraction and IR spectroscopy.

## Experimental Section

**Synthesis:** For the preparation of $Pd(SeO_3)$, 30 mg of palladium powder and 1 mL of $H_2SeO_4$, which was prepared from $H_2O_2$ and $SeO_2$ according to the literature procedure,[11] were sealed in a glass ampoule (length: 100 mm; width: 6 mm). This ampoule was heated to 350 °C for 72 h and then cooled slowly (3 °C/h). Plate-shaped and easily cleavable red crystals of $Pd(SeO_3)$ were recovered from the ampoule. Following the same procedure, lath-shaped yellow single crystals of $Pd(SeO_4)$ were obtained when only 15 mg of palladium powder was used in the reaction. Orange-yellow slightly needle shaped and cleavable single crystals of $Pd(Se_2O_5)$ were obtained upon treating 8 mg of palladium powder with 1 mL of $H_2SeO_4$ and 50 mg of $SeO_3$. This mixture was sealed in a glass ampoule, heated to 250 °C, and then slowly cooled (3 °C/h). The yields of the reactions were almost quantitative, and the samples were found to be single phase within the accuracy of X-ray powder diffraction.

**Caution:** All selenium-containing compounds are potentially poisonous. The glass ampoules are under considerable pressure after the reaction and should be handled with care and appropriate protection.

**X-ray Crystallography:** Crystals of $Pd(SeO_3)$, $Pd(SeO_4)$, or $Pd(Se_2O_5)$ were transferred into protecting oil and several specimens were glued on glass fibers and checked with the help of an image plate diffractometer (STOE IPDS). Reflection intensities for the best crystals were collected with the same diffractometer at 153 K. The crystal structures were solved by direct methods with the help of the program SHELXS97[12] assuming the space groups *C*2/*m* ($PdSeO_3$), *C*2/*c* ($PdSeO_4$), and *I*2/*a* $Pd(Se_2O_5)$. The latter setting of space group no. 15 was chosen in order to obtain a smaller monoclinic angle. Full-matrix least-squares refinements on $F^2$ were performed for all compounds using SHELXL97.[12] All atoms were refined anisotropically after applying numerical absorption corrections.[13] Details of the data collection are given in Table 4. Crystallographic and structural data are summarized in Tables 1 and 2, respectively. The final residuals for $Pd(SeO_3)$ and $Pd(Se_2O_5)$ are significantly higher than those for $Pd(SeO_4)$ due to the structural features of the former two compounds (extremely fragile crystals). Crystallographic data (excluding structure factors) for the structures in this paper have been deposited with the Fachinformationzentrum Karlsruhe, 76344 Eggenstein-Leopoldshafen. These data

 © 2007 Wiley-VCH Verlag GmbH & Co. KGaA, Weinheim 

Table 4. Crystallographic data and structure determination parameters for $Pd(SeO_3)$, $Pd(SeO_4)$, and $Pd(Se_2O_5)$.

| | $Pd(SeO_3)$ | $Pd(SeO_4)$ | $Pd(Se_2O_5)$ |
|---|---|---|---|
| $a$ [Å] | 6.788(2) | 8.171(1) | 7.212(1) |
| $b$ [Å] | 7.030(2) | 5.286(1) | 5.569(1) |
| $c$ [Å] | 7.008(2) | 8.115(1) | 12.177(3) |
| $\beta$ [°] | 118.09(3) | 94.54(1) | 106.84(2) |
| $V$ [Å$^3$] | 295.0(1) | 349.37(9) | 468.1(2) |
| $Z$ | 4 | 4 | 4 |
| Crystal system | monoclinic | monoclinic | monoclinic |
| Space group | *C*2/*m* (no. 12) | *C*2/*c* (no. 15) | *I*2/*a* (no. 15) |
| Measuring device | | Stoe IPDS I | |
| Radiation | | Mo-$K_\alpha$ (graphite monochromated, $\lambda$ = 71.07 pm) | |
| $T$ [K] | 153 | 153 | 153 |
| Theta range [°] | $3.3 < 2\theta < 52.3$ | $3.3 < 2\theta < 52.1$ | $3.3 < 2\theta < 52.1$ |
| Index range | $-8 \le h \le 8$ | $-10 \le h \le 10$ | $-8 \le h \le 8$ |
| | $-8 \le k \le 8$ | $-6 \le k \le 6$ | $-6 \le k \le 6$ |
| | $-8 \le l \le 8$ | $-9 \le l \le 9$ | $-15 \le l \le 14$ |
| Rotation angle [°]; $\phi$ increment [°] | $0 < \phi < 270$; 3 | $0 < \phi < 240$; 1 | $0 < \phi < 250.2$; 1.8 |
| No. of exposures | 90 | 160 | 139 |
| Exposure time | 7 min | 6 min | 6 min |
| Detector distance | 70 mm | 70 mm | 70 mm |
| Data correction | | Polarization and Lorentz factors | |
| Absorption correction | | numerical | |
| $\mu$ [cm$^{-1}$] | 184.1 | 155.7 | 194.35 |
| Measured reflections | 1537 | 1530 | 2313 |
| Unique reflections | 290 | 333 | 2313 |
| with $I_o > 2\sigma(I)$ | 317 | 317 | 1445 |
| No. of variables | 29 | 23 | 25 |
| $R_{int}$ | 0.0958 | 0.0379 | 0.0821 |
| Structure determination | | SHELXS-97 and SHELXL-97 | |
| Scattering factors | | International Tables, vol. C | |
| Extinction coefficient | 0.002(2) | 0.0016(4) | 0.0006(4) |
| Goodness of fit | 1.374 | 1.054 | 1.038 |
| $R_1/wR_2$ [$I_o > 2\sigma(I)$] | 0.0614/0.1496 | 0.0191/0.0401 | 0.0498/0.1343 |
| $R_1/wR_2$ (all data) | 0.0757/0.1717 | 0.0203/0.0402 | 0.0804/0.1520 |
| Depository number | 415955 | 416646 | 417900 |

can be obtained on quoting the depository number given in Table 4.

**Vibrational Spectroscopy:** The IR data were collected with a Vector 22 spectrometer (Bruker) in the range 400–4000 cm$^{-1}$. Some crystals of $Pd(SeO_3)$ and $Pd(Se_2O_5)$ were prepared in a KBr pellet while CsCl was used as mulling agent for $Pd(SeO_4)$. The data obtained are given in Table 3.

## Acknowledgments

The authors would like to thank Mr. Wolfgang Saak for collecting the X-ray data. Financial support from the Deutsche Forschungsgemeinschaft is gratefully acknowledged.

[1] J. A. Abys, C. A. Dullaghan, P. Epstein, J. J. Maisano, US Patent **2001**, US 6,241,870 B.
[2] a) H. H. Lamb, X. Wang, S. Sigmon, J. J. Spivey, *Catal. Today* **2004**, *96*, 11; b) C. Chen, M. Akashi, *Langmuir* **1997**, *13*, 6465.
[3] M. S. Wickleder, O. Büchner, C. Wickleder, S. El Sheik, G. Brunklaus, H. Eckert, *Inorg. Chem.* **2004**, *43*, 5860.
[4] a) M. Pley, M. S. Wickleder, *Z. Anorg. Allg. Chem.* **2004**, *630*, 1036; b) M. Pley, M. S. Wickleder, *Z. Anorg. Allg. Chem.* **2004**, *630*, 1753; c) M. Pley, M. S. Wickleder, *Eur. J. Inorg. Chem.* **2005**, *631*, 529; d) M. Pley, M. S. Wickleder, *Z. Anorg. Allg. Chem.* **2005**, *631*, 592; e) M. Pley, M. S. Wickleder, *Angew. Chem.* **2004**, *116*, 4262; *Angew. Chem. Int. Ed.* **2004**, *43*, 4168.
[5] T. Dahmen, P. Rittner, S. Boeger-Seidl, R. Gruehn, *J. Alloys Compd.* **1994**, *216*, 11.
[6] Y. Laligant, G. Ferey, A. Le Bail, *Mater. Res. Bull.* **1991**, *26*, 269.
[7] F. Cunin, F. Favier, J.-L. Pascal, *Can. J. Chem.* **2000**, *78*, 1544.
[8] I. Ijjaali, J. A. Ibers, *Z. Kristallogr.* **2001**, *216*, 485.
[9] V. P. Verma, *Thermochim. Acta* **1999**, *327*, 63 and references cited therein.
[10] a) J. Weidlein, U. Müller, K. Dehnicke, *Schwingungsspektroskopie*, Thieme, Stuttgart, New York, **1988**; b) H. Siebert, *Anwendung der Schwingungsspektroskopie in der Anorganischen Chemie*, Springer, Berlin, Heidelberg, New York, **1966**; c) K. Sathianandan, L. D. McCory, J. L. Margrave, *Spectrochim. Acta* **1964**, *20*, 957; H. Miulu, J. Valkonen, *Acta Chem. Scand., Sect. A* **1987**, *41*, 183.
[11] G. Brauer, *Handbuch der Präparativen Anorganischen Chemie*, F. Enke, Stuttgart, **1975**, p. 1750–1751.
[12] a) G. M. Sheldrick, *SHELXS-97, Program for the Solution of Crystal Structures*, University of Göttingen, Germany, **1997**; b) G. M. Sheldrick, *SHELXL-97, Program for the Refinement of Crystal Structures*, University of Göttingen, Germany, **1997**.
[13] a) *X-SHAPE 1.01, Crystal Optimization for Numerical Absorption Correction*, Stoe & Cie, Darmstadt, Germany, **1996**; b) *X-RED 1.07, Data Reduction for STADI4 and IPDS*, Stoe & Cie, Darmstadt, Germany, **1996**.

Received: March 22, 2007
Published Online: July 24, 2007

 © 2007 Wiley-VCH Verlag GmbH & Co. KGaA, Weinheim 

DOI: 10.1002/ejic.200700354

# Synthesis and Characterization of DOTA-(amide)$_4$ Derivatives: Equilibrium and Kinetic Behavior of Their Lanthanide(III) Complexes

**Azhar Pasha,[a] Gyula Tircsó,*[a] Enikő Tircsóné Benyó,[a] Ernő Brücher,[b] and A. Dean Sherry*[a,c]**

**Keywords:** Magnetic resonance imaging / Contrast agents / Protonation constants / Stability constants / Kinetics

Lanthanide complexes of tetraamide derivatives of DOTA are of interest today because of their application as chemical exchange saturation transfer (CEST) agents for magnetic resonance imaging (MRI). The protonation constants of some simple tetraamide derivatives of DOTA and the stability constants of the complexes formed with some endogenous metal ions, namely $Mg^{2+}$, $Ca^{2+}$, $Cu^{2+}$, $Zn^{2+}$, and lanthanide(III) ions, have been studied. These complexes were found to be considerably less stable than the corresponding $[M(DOTA)]^{2-}$ complexes, largely due to the lower basicity of the tetraamide ligands. The $Mg^{2+}$ and $Ca^{2+}$ complexes are well described by formation of only ML species at equilibrium while the $Zn^{2+}$ and $Cu^{2+}$ complexes exhibit one and two additional deprotonation steps above a pH of around 6, respectively. The extra deprotonation that occurs at high pH for the $[Zn\{DOTA\text{-}(amide)_4\}]^{2+}$ complexes has been assigned to an amide deprotonation by $^1H$ NMR spectroscopy. The first deprotonation step for the $Cu^{2+}$ complexes was traced to formation of the ternary hydroxo complexes ML(OH) (by UV/Vis spectrophotometry) while the second step corresponds to deprotonation of an amide group to form $ML(OH)H_{-1}$-type complexes. The trends in the stability constants of the $[Ln\{DOTA\text{-}(amide)_4\}]^{3+}$ complexes follow similar trends with respect to ion size as those reported previously for the corresponding $[Ln(DOTA)]^-$ complexes, but again, the stability constants are about 10–11 orders of magnitude lower. A kinetic analysis of complex formation has shown that complexes are directly formed between a $Ln^{3+}$ cation and fully deprotonated L without formation of a protonated intermediate. $[Ln\{DOTA\text{-}(MeAm)_4\}]^{3+}$ complex formation occurs at a rate that is two to three orders of magnitude slower than those of the corresponding $[Ln(DOTA)]^-$ complexes, while the variation in complex formation rates with $Ln^{3+}$ ion size is opposite to that observed for the corresponding $[Ln(DOTA)]^-$ complexes. The $Ce^{3+}$ and $Eu^{3+}$ complexes of DOTA-$(MeAm)_4$ are kinetically inert with respect to acid-catalyzed dissociation, which suggests that these complexes may potentially be safe for use in vivo.

(© Wiley-VCH Verlag GmbH & Co. KGaA, 69451 Weinheim, Germany, 2007)

## Introduction

Magnetic resonance imaging (MRI) is one of the most powerful and versatile techniques in modern medical diagnostics. Contrast agents (CA) are used to enhance MR contrast in 40–50% of all clinical MRI applications. The most common CAs are $Gd^{3+}$ complexes due to the high spin state (seven unpaired electrons) and favorable relaxation properties of the $Gd^{3+}$ ion.[1] The first contrast agent used in medical diagnosis was the $Gd^{3+}$ complex of diethylenetriamine-*N*,*N*,*N*′,*N*′′,*N*′′-pentaacetic acid ($H_5$DTPA), followed shortly thereafter by the $Gd^{3+}$ complex of 1,4,7,10-tetraazacyclododecane-1,4,7,10-tetraacetic acid ($H_4$DOTA). These complexes are negatively charged and therefore must be formulated as salts. The next two approved agents, [Gd(DTPA-BMA)] and [Gd(HP-DO3A)], derived from an open-chain DTPA ligand and a macrocyclic DOTA ligand, respectively, are both neutral complexes.[2–4] All four of these systems are nonadentate, with one $Gd^{3+}$ coordination site occupied by a water molecule. Rapid relaxation of this inner-sphere water molecule by the paramagnetic $Gd^{3+}$ results in a shortening of the bulk water proton relaxation time ($T_1$) through the rapid exchange of an inner-sphere bound water molecule with tissue water. Lanthanide(III) complexes of some tetraamide derivatives of DOTA have been known for many years but were neglected as possible contrast agents due to the slow water-exchange rates exhibited by the $Ln^{III}$ complexes of these ligands and their less than favorable thermodynamic stablility.[5] However, a recent report by Balaban et al. describing the chemical exchange saturation transfer (CEST) mechanism for generating a negative image con-

[a] Department of Chemistry, University of Texas at Dallas, 2601 N. Floyd Road, P. O. Box 830668, Richardson, TX 75083, USA
Fax: +1-972-883-2925
E-mail (A. D. S.): sherry@utdallas.edu
E-mail (G. T.): gyulat@gmail.com
[b] Department of Inorganic and Analytical Chemistry, University of Debrecen, P. O. Box 21, Egyetem tér 1, Debrecen, 4010, Hungary
Fax: +36-52-489-667
E-mail: ebrucher@delfin.unideb.hu
[c] Advanced Imaging Research Center, University of Texas Southwestern Medical Center, 5323 Harry Hines Boulevard, Dallas, Texas 75390

Supporting information for this article is available on the WWW under http://www.eurjic.org or from the author.

 © 2007 Wiley-VCH Verlag GmbH & Co. KGaA, Weinheim 

trast has renewed interest in these complexes.[6] CEST contrast begins with application of a presaturation RF pulse applied at the resonance freqnency of an exchangeable OH or NH proton on a CEST agent and this partially saturated spin then exchanges with the protons of bulk water. Given proper exchange kinetics and relaxation times, this results in a reduction in the bulk water signal intensity and negative contrast in an image. More recently, Sherry and co-workers discovered the CEST effect in [Eu{DOTA-(gly-OEt)$_4$}]$^{3+}$ (Scheme 1) and showed that a particularly useful exchange site for CEST activation is provided by the highly shifted (approx. 50 ppm), slow-exchanging water protons bound to a paramagnetic $Eu^{3+}$ ion in this complex.[7] Paramagnetic CEST (PARACEST) agents that contain a highly shifted CEST activation site offer some advantages over the diamagnetic agents proposed originally; most importantly, the large chemical-shift difference between the exchanging protons on the agent and the bulk water reduces the possibility of off-resonance saturation of the bulk water signal. This observation has catalyzed interest in the synthesis and design of new tetraamide derivatives of DOTA as potential CEST systems, and this potential new application makes it especially important to evaluate the thermodynamic and kinetic stability of these complexes in solution and in the presence of adventitious ions.

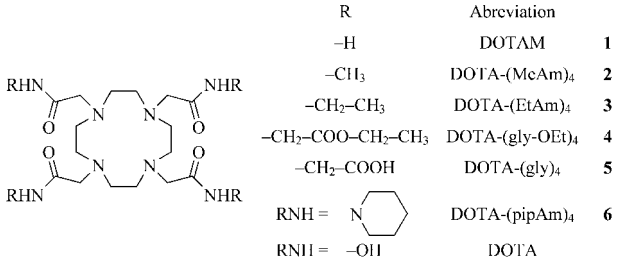


Scheme 1. Ligands investigated in this work.

Lanthanide(III) complexes of DOTA are among the most thermodynamically stable and kinetically inert complexes known to date.[8–10] A recently published report on the thermodynamic stability and kinetics of [Ln{DOTA-(gly)$_4$}]$^-$ complex formation demonstrated that both the basicity of the amide ligands and the stability of the complexes are several orders of magnitude lower than for their [Ln(DOTA)]$^-$ analogues.[11] It was also shown that spontaneous dissociation of [Eu{DOTA-(gly)$_4$}]$^-$ occurs somewhat faster than [Eu(DOTA)]$^-$, but that acid-catalyzed dissociation of the protonated intermediate [Eu{H$_4$DOTA-(gly)$_4$}]$^{3+}$ seems to occur more slowly than for its protonated [Eu(H$_2$DOTA)]$^+$ analog.[9,11] This suggests that these systems may in fact be suitable for in vivo imaging applications.

The stability constants of the $Ca^{2+}$, $Sr^{2+}$, $Ba^{2+}$, $Cu^{2+}$, $Zn^{2+}$, $Hg^{2+}$, $La^{3+}$, and $Gd^{3+}$ complexes of DOTAM have been reported by Maumela et al.[12] The authors also provided the lower limit for the stability constants of the $Cd^{2+}$ and $Pb^{2+}$ complexes ($\log K_{min}$ = 19.0), because these stabilities are too high to be measured experimentally.[12] A more detailed study involving eleven $Ln^{III}$ ions was published recently by Voss et al., who used competition reactions between various $Ln^{III}$ ions and $Eu^{III}$ and followed the competition by the measurement of the luminescence intensity to calculate the ratio of the stability constants $K_{Ln}^{III}/K_{Eu}^{III}$.[13] No information about possible hydroxo complex formation (or amide dissociation) for $Cu^{2+}$, $Zn^{2+}$, and $Ln^{III}$ complexes are available in these papers. The protonation constants of the ligand DOTA-(MeAm)$_4$ and the stability of the $Eu^{3+}$ and $Gd^{3+}$ complexes have also been reported by Virtuani and co-workers,[14] and the formation of MHL and ML [M(OH)L and M(OH)$_2$ for $Cu^{2+}$ and $Zn^{2+}$ ions] species in solution was subsequently reported.[15] The stability constants of metal ion complexes of DOTA-(EtAm)$_4$ and DOTA-(gly-OEt)$_4$ have not been reported previously.

These earlier reports leave the impression that these structurally similar ligand systems behave quite differently in solution, which led to the present investigation of detailed thermodynamic studies of the divalent ions $Mg^{2+}$, $Ca^{2+}$, $Cu^{2+}$, and $Zn^{2+}$ and the trivalent lanthanide(III) ions with the ligands shown in Scheme 1. The rates of complex formation and acid-catalyzed dissociation of some [Ln{DOTA-(MeAm)$_4$}]$^{3+}$ complexes (where $Ln^{3+}$ = $Ce^{3+}$, $Eu^{3+}$, and $Lu^{3+}$ in the complex formation studies and $Ln^{3+}$ = $Ce^{3+}$ and $Eu^{3+}$ in the acid-catalyzed dissociation studies) have also been studied.

## Results and Discussion

The simple tetraamide ligands DOTAM (**1**), its *N*-methyl analog DOTA-(MeAm)$_4$ (**2**), the *N*-ethyl analog DOTA-(EtAm)$_4$ (**3**), and the glycinate ethyl ester analog DOTA-(gly-OEt)$_4$ (**4**) were prepared following established procedures by alkylation of 1,4,7,10-tetraazacyclododecane with the appropriate α-halo amide derivative.[12,15–18] The characteristics of these ligands were in a good agreement with those reported previously.

### Equilibrium Studies

The protonation constants of the ligands and stability constants of the complexes formed with the DOTA-(amide)$_4$ ligands were determined by pH-potentiometry. The protonation constants ($\log K_i^H$) of these tetraamide ligands are listed and compared to the literature values for DOTA and DOTA-(gly)$_4$ in Table 1 (the values shown in parentheses are the standard deviations).[11,19] Our data agree well with the published values except for the variation in the first p$K_a$ of the ligand DOTAM, where the difference is larger than one order of magnitude. This variation can be attributed to the different ionic strength used in the present study. The protonation constants of DOTAM have been determined in 0.1 M NaCl at 25 °C by Maumela et al.[12] The $Na^+$ ion is known to form more stable complexes with most of the ligands than the $K^+$ ion. For instance, the stability of [Na(DOTA)]$^{3-}$ is $\log K_{NaL}$ = 4.2 in contrast to

 © 2007 Wiley-VCH Verlag GmbH & Co. KGaA, Weinheim 

Table 1. Protonation constants of several DOTA-(amide)$_4$ ligands ($I$ = 1.0 M KCl, $T$ = 25 °C, values given in parentheses are standard deviations).

| | DOTAM | DOTA-(MeAm)$_4$ | DOTA-(EtAm)$_4$ | DOTA-(gly-OEt)$_4$ | DOTA-(gly)$_4$[a] | DOTA[b] |
|---|---|---|---|---|---|---|
| $\log K_1^H$ | 9.08(1)<br>7.70[c] | 9.56(1)<br>9.27[d] | 9.33(2) | 9.18(3) | 9.19 | 12.60 |
| $\log K_2^H$ | 6.44(1)<br>6.21[c] | 5.95(1)<br>5.55[d] | 6.39(3) | 5.47(4) | 6.25 | 9.70 |
| $\log K_3^H$ | – | 1.56[d] | – | 1.82(6) | 4.08 | 4.50 |
| $\log K_4^H$ | – | – | – | – | 3.45 | 4.14 |
| $\log K_5^H$ | – | – | – | – | 3.20 | 2.32 |
| $\log K_6^H$ | – | – | – | – | 1.40 | – |
| $\Sigma \log K_i^H$ | 15.52 | 15.51 | 15.72 | 16.47 | 27.57 | 33.26 |

[a] Ref.[11] [b] Ref.[20] [c] Ref.[12] [d] Refs.[14,15]

[K(DOTA)]$^{3-}$, which is $\log K_{KL}$ = 1.6.[20] The stability of the $Na^+$ and $K^+$ complexes with DOTAM differ considerably from those reported for DOTA, so one can argue that measurements in a KCl background give more realistic p$K_a$ values than those measured in an NaCl background. Only two protonations were found for these ligands above a pH of about 1.8. The highest protonation constant was typically in the range 9.0–9.6, while the second protonation constant was in the range 5.4–6.5. The sum of these protonation constants (reflecting the total ligand basicity) is in the range 15.5–16.5 log $K$ units (Table 1). These values are around 50% of the total ligand basicity of DOTA, thus demonstrating the importance of the negatively charged acetate sidechains in DOTA in stabilizing the protonated ring nitrogen atoms of DOTA through hydrogen-bonding interactions. Similar variations in p$K_a$ values of DOTA-(MeAm)$_4$ to those reported by Virtuani and co-workers were found.[14,15]

The reaction between these ligands and different divalent endogenous metal ions was rapid enough to allow direct potentiometric titrations for stability determinations. However, under acidic conditions, where complex formation is slow, the interval between base additions was maintained at 30 minutes to ensure complete equilibrium complexation at each titration step. The time needed for the $Cu^{2+}$ complexes to reach equilibrium was verified by UV/Vis spectrophotometry. These stability constants are summarized and compared with previous literature values in Table 2.

The equilibria involving these ligands with $Mg^{2+}$ and $Ca^{2+}$ ions can be described by formation of ML-type complexes only; no protonated complexes or terniary hydroxo complexes [ML(OH)] were detected. The stability of the MgL complexes is so low that competition by hydrolysis of $Mg^{2+}$ at higher pH values was significant. Hydrolysis of $Ca^{2+}$, however, occurs at much higher pH values [$\log K_a(Ca^{2+})$ = 12.8] so formation of ML(OH)-type complexes was neither anticipated nor observed.[21] The titration curves measured for the CuL complexes show two extra deprotonation steps above the pH at which the complexes were fully formed. The absorption spectra of [Cu(DOTAM)]$^{2+}$ and [Cu{DOTA-(MeAm)$_4$}]$^{2+}$ are identical and addition of the first equivalent of base to form a CuL(OH) species resulted in no apparent change in the visible spectra of these complexes. However, addition of a second equivalent of base resulted in a significant blue shift in their

Table 2. Stability constants ($\log K$) of DOTA-(amide)$_4$ complexes with selected divalent metal ions ($I$ = 1.0 M KCl, $T$ = 25 °C).

| Ligand | Species | $Mg^{2+}$ | $Ca^{2+}$ | $Cu^{2+}$ | $Zn^{2+}$ |
|---|---|---|---|---|---|
| DOTAM | ML | 4.65(4) | 10.32(1)<br>7.54[a] | 14.50(1)<br>16.31[a] | 13.77(1)<br>10.47[a] |
| | $MLH_{-1}$ | – | – | 8.41(4) | 10.57(6) |
| | $MLH_{-2}$ | – | – | 8.82(2) | – |
| DOTA-(MeAm)$_4$ | ML | 4.33(2) | 10.11(1)<br>9.47[b] | 14.61(4)<br>14.12[b] | 13.66(2)<br>13.00[b] |
| | $MLH_{-1}$ | – | – | 8.78(7) | 10.71(3) |
| | $MLH_{-2}$ | – | – | 10.31(6) | – |
| DOTA-(EtAm)$_4$ | ML | 4.49(1) | 10.74(2) | 16.40(8) | 16.55(10) |
| | $MLH_{-1}$ | – | – | 8.96(9) | 10.86(10) |
| | $MLH_{-2}$ | – | – | 11.27(9) | – |
| DOTA-(gly-OEt)$_4$[c] | ML | 3.97(7) | 9.09(5) | 17.18(9) | 11.44(5) |
| DOTA[d] | ML | 11.15 | 16.37 | 22.72 | 18.17 |
| | MHL | 4.09 | 3.54 | 3.78 | 4.18 |
| | $MLH_{-1}$ | – | – | 10.54 | 10.62 |
| DOTA-(gly)$_4$[e] | ML | 4.34 | 10.39 | 13.39 | – |
| | MHL | – | 4.23[f] | 4.38[f] | – |

[a] Ref.[12] [b] Ref.[14,15] [c] The constant $MLH_{-1}$ cannot be evaluated for any of the metal ions studied due to slow hydrolysis of the ester bonds. [d] Ref.[20] [e] Ref.[11] [f] Three and two more protonated species are known for the $Ca^{2+}$ and $Cu^{2+}$ complexes, respectively (protonation of the acetate pendant arms).

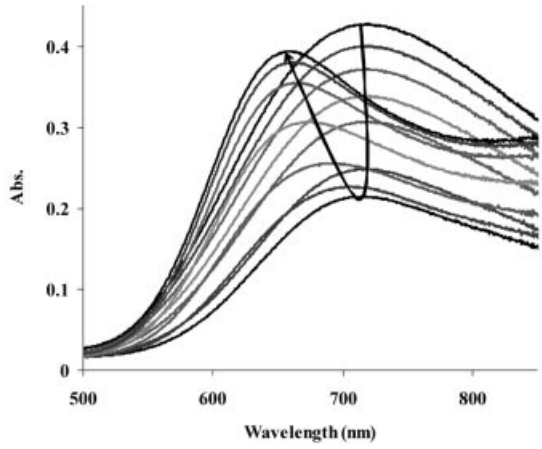


Figure 1. Visible spectra of [Cu{DOTA-(MeAm)$_4$}]$^{2+}$ ($C_{Cu}$ = $C_L$ = $2.5 \times 10^{-3}$ M) as a function of sample pH. The pH of the samples following the arrow are: 6.43, 7.39, 7.76, 8.00, 8.26, 8.72, 9.33, 9.90 10.26, 10.67, 11.05, 11.34, and 11.89.

 © 2007 Wiley-VCH Verlag GmbH & Co. KGaA, Weinheim 

absorption maxima from 715 nm to about 650 nm (Figure 1). Such spectral changes are known to occur for $Cu^{2+}$-oligopeptide complexes, where deprotonation and coordination of an amide group to the $Cu^{2+}$ ion is known to occur. However, the terminal $NH_2$ group (anchor nitrogen atom) plays a critical role in the deprotonation and coordination of the adjacent amide moiety in the $Cu^{2+}$-polypeptide systems.[20]

The peptide hydrogen deprotonation in $Zn^{2+}$-oligopeptide systems is known to occur only above a pH of 10.[22] The titration curve of $[Zn\{DOTA\text{-}(amide)_4\}]^{2+}$ systems also reflects an extra deprotonation step after the protons associated with the ligand are neutralized (above pH > 10). Furthermore, the X-ray structure of $[Zn(DOTAM)]^{2+}$ shows a $Zn^{2+}$ ion coordinated by four nitrogen atoms of the cyclen ring and two oxygen atoms of the amide pendant arms, with no inner-sphere water molecule, so the extra deprotonation likely reflects an amide proton.[12] $^1$H NMR titrations of $[Zn(DOTAM)]^{2+}$ and $[Zn\{DOTA\text{-}(MeAm)_4\}]^{2+}$ complexes (Figure S2 in the Supporting Information and Figure 2) over the pH range 7–12 were consistent with this assignment.

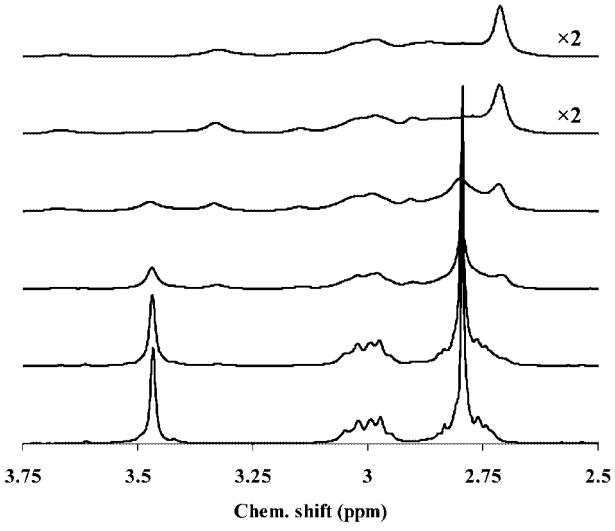


Figure 2. $^1$H NMR titration of the $[Zn\{DOTA\text{-}(MeAm)_4\}]^{2+}$ complex ($C_{Zn} = C_L = 3.0 \times 10^{-2}$ M). The pD of the samples are as follows (from top to bottom): 12.04 (the intensity of the spectra is doubled), 11.44 (the intensity of the spectra is doubled), 10.94, 10.49, 9.84 and 6.95.

Aqueous solutions of DOTA-(gly-OEt)$_4$ are unstable toward hydrolysis of the ester above a pH of around 5. When dissolved in 0.01 M acid, the ligand is stable enough to allow estimates of the stabilities of its $Mg^{2+}$, $Ca^{2+}$, $Cu^{2+}$, and $Zn^{2+}$ complexes (Table 2) using titration data up to pH 5. With further increases in pH, hydrolysis of the ester bonds was evident so this precluded an examination of whether $MLH_{-1}$ type complexes are formed with this ligand. Similarly, it was not possible to calculate the stabilities of the LnL complexes with this ligand because slow kinetics of complex formation dictated that the "out-of-cell" technique be used and this requires sample heating for an extended period to reach equilibrium; this favors ester hydrolysis which, in turn, distorts the pH-potentiometric data.

The stability constants of the complexes formed between several DOTA-(amide)$_4$ ligands and numerous $Ln^{3+}$ ions are summarized in Table 3. The values increase with a decrease in $Ln^{3+}$ ion size near the beginning of the lanthanide series, then remain relatively constant for the heavier ions until the very end of the series, where a decrease is noted. A similar trend has been noted by Voss et al. for the $[Ln(DOTAM)]^{3+}$ complexes, although the changes with lanthanide size differed somewhat.[13] The stability constants of the $[Ln\{DOTA\text{-}(EtAm)_4\}]^{3+}$ and $[Ln\{DOTA\text{-}(gly)_4\}]^{-}$ complexes are nearly identical for most lanthanides, as one would expect for systems with similar structures and ligand basicities.[11] The data also show that the stabilities are not influenced by the overall charge on these complexes and that the extended glycinate groups do not coordinate to the central metal ions in ML complexes.

The stabilities of $[Eu\{DOTA\text{-}(MeAm)_4\}]^{3+}$ and $[Gd\{DOTA\text{-}(MeAm)_4\}]^{3+}$ previously reported by Virtuani et al. are in good agreement with the current results; the deviation of about 0.5 log$K$ units in these two studies can be traced to differences in the $\log K_i^H$ values of the ligands themselves.[14,15] A noticeable difference in the equilibrium model is that we could find no evidence for formation of protonated (LnHL) complexes (either from "out-of-cell" data or from the titration data obtained for fully formed LnL complexes with HCl), while Virtuani et al. included protonated species in their model.[14,15]

An extra deprotonation was evident for all three $[Ln\{DOTA\text{-}(amide)_4\}]^{3+}$ complexes at pH values above 10.5. Virtuani, et al. have also reported formation of ternary hydroxo complexes $[Ln(OH)L^{2+}]$, although the pH

Table 3. Stability constants (log$K$) of DOTA-(amide)$_4$ ML-type complexes formed with several trivalent lanthanide ions $Ln^{3+}$ ($I$ = 1.0 M KCl, $T$ = 25 °C).

| $Ln^{3+}$ | DOTAM | DOTA-(MeAm)$_4$ | DOTA-(AmEt)$_4$ | DOTA-(gly)$_4$[a] | DOTA[b] |
|---|---|---|---|---|---|
| $Ce^{3+}$ | 11.93(7) | 12.68(1) | 13.00(8) | 13.02 | 23.4 |
| $Nd^{3+}$ | 12.40(5) | 13.08(6) | 14.37(2) | 14.45 | 23.0 |
| $Eu^{3+}$ | 13.80(2) | 13.67(8)[c] | 15.09(6) | 14.84 | 23.5 |
| $Gd^{3+}$ | 13.12(4)[d] | 13.54(4)[e] | 14.83(25) | 14.54 | 24.7 |
| $Dy^{3+}$ | 13.57(14) | 13.84(5) | 15.09(2) | 14.37 | 24.8 |
| $Tm^{3+}$ | 13.46(2) | 14.08(5) | 14.74(3) | – | 24.4 |
| $Lu^{3+}$ | 13.53(5) | 13.91(3) | 14.62(3) | 14.25[f] | 25.4 |

[a] Ref.[11] [b] Ref.[20] [c] $\log K_{EuL}$ = 13.17 from Refs.[14,15] [d] $\log K_{GdL}$ = 10.05 from ref.[12] [e] $\log K_{GdL}$ = 12.80 from refs.[14,15] [f] This value corresponds to the nearest neighbour (YbL) complex.

 © 2007 Wiley-VCH Verlag GmbH & Co. KGaA, Weinheim 

range for this deprotonation was much lower in their study (in the range pH 7–9).[14,15] These differences may be due to the presence of excess free metal ions in their study since our titration curves resemble the titration curve of a strong acid with a strong base (no buffering region is observed below pH 10.5, Figure S3). So, if one accepts that a deprotonated species does form in these complexes, does the site of deprotonation correspond to an amide deprotonation or does deprotonation of the coordinated water molecule occur in these complexes? To answer this question, several additional experiments were performed. First, high resolution $^1$H NMR spectra of the diamagnetic $Lu^{3+}$ complexes of DOTAM and DOTA-$(MeAm)_4$ showed no change in the chemical shift of the $CH_2$ protons of the amide side-arms (AB coupling pattern) upon addition of up to 2.5 equivalents of base (Figures S4 and S5 show the $^1$H NMR titrations of the $[Lu(DOTAM)]^{3+}$ and $[Lu(DOTA\text{-}(MeAm)_4\})]^{3+}$ complexes, respectively). This result is inconsistent with dissociation of an amide proton. The most convincing evidence that deprotonation occurs at the coordinated water molecule was obtained by luminescence studies with the $Eu^{3+}$ complexes. It is known from the literature that both $[Eu(DOTAM)]^{3+}$ and $[Eu\{DOTA\text{-}(MeAm)_4\}]^{3+}$ contain one inner-sphere coordinated water molecule ($q$ = 1).[23] This was verified by measuring the luminescence rate constants for depopulation of the $Eu^{3+}$ excited states in $H_2O$ vs. $D_2O$. At pH 7 and 25 °C, these lifetimes are 1.79 ($H_2O$)/0.44 $ms^{-1}$ ($D_2O$) and 1.96 ($H_2O$)/0.46 $ms^{-1}$ ($D_2O$) for $[Eu(DOTAM)]^{3+}$ and $[Eu\{DOTA\text{-}(MeAm)_4\}]^{3+}$, respectively. These values give an estimated $q$ of 1.02 and 1.20 for the two complexes.[23] With an increase in pH (pD) to 11.8, the measured $q$ values decrease to 0.47 and 0.52 for $[Eu(DOTAM)]^{3+}$ and $[Eu\{DOTA\text{-}(MeAm)_4\}]^{3+}$, respectively, consistent with deprotonation of the coordinated water molecule and a decrease in OH (OD) oscillators of about 50%. These data do not, however, rule out the possibility of amide deprotonation in these complexes at even higher pH values (>11.8) but it is not likely that amide deprotonation would lead to a change in the coordination environment around the chelated $Ln^{3+}$ ion. This is in good agreement with the results published previously by Aime et al.[24]

### Formation Kinetics of Some $[Ln\{DOTA\text{-}(MeAm)_4\}]^{3+}$ Complexes

The complexation reaction involving macrocyclic ligands is usually several orders of magnitude slower than that with linear polyamino-polycarboxylate type ligands.[25] It is now generally accepted that complex formation in LnDOTA-type systems takes place in several discrete steps.[26] First, an unusually stable intermediate where the $Ln^{3+}$ ion is positioned "out of cage" and one or two of the macrocyclic amino groups remain protonated, which has been detected by several spectroscopic techniques, is formed quickly. Subseqnent slow base-catalyzed deprotonation of those amines and rearrangement leads to the formation of a final $[Ln(DOTA)]^-$ complex where the $Ln^{3+}$ ion is trapped "in cage".[8–10,27] Evidence for a similar stable intermediate has been reported during formation of the $[Ln\{DOTA\text{-}(gly)_4\}]^-$ complexes as well.[11] Furthermore, an interesting structure that is thought to be the reactive intermediate in the formation of $[Ln(DOTAM)]^{3+}$ complexes was characterized recently by X-ray diffraction.[28]

The visible spectra of solutions recorded after mixing DOTA-$(MeAm)_4$ with $CeCl_3$ (both reagents were present at $5\times10^{-4}$ M) at pH 5.26 are shown in Figure 3. At this pH, the ligand is distributed between the forms $H_2L$ (80%) and HL (20%), both of which are favorable for formation of such an intermediate. With time, two new absorption bands, with $\lambda_{max}$ = 269 and 323 nm, respectively, appear in the spectra, the intensities of which increase with time as the "in cage" complex forms. The rate constants calculated from each absorption band agree with each other to within 3%, thereby indicating that both bands characterize the same reaction process. These changes are similar to those described for formation of $[Ce(DOTA)]^-$ except that the $\lambda_{max}$ of the $[Ce(H_2DOTA)]^+$ kinetic intermediate occurs at 297 nm. Another major difference is that the $[Ce\{DOTA\text{-}(MeAm)_4\}]^{3+}$ reaction requires about 8 hours to reach equilibrium at pH 5.26, which is considerably more than the time required for $[Ce(DOTA)]^-$ complexation to reach equilibrium at pH 4.45.[8] The presence of one isosbestic point at $\lambda$ = 260 nm indicates that only two absorbing components are present – the reactant ($Ce^{3+}$) and the product $[Ce\{DOTA\text{-}(MeAm)_4\}]^{3+}$.

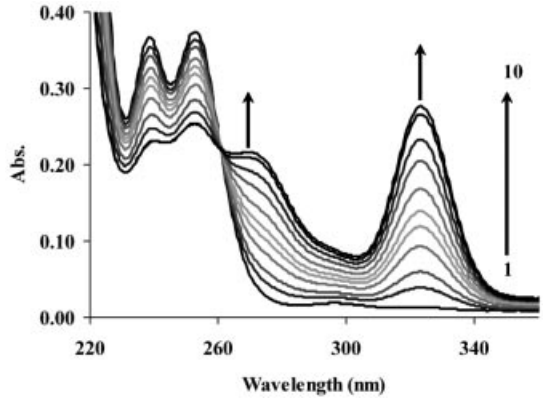


Figure 3. Formation of $[Ce\{DOTA\text{-}(MeAm)_4\}]^{3+}$ as a function of time. Absorption spectra were recorded (150 nm/min) at 1 (1), 9 (2), 17 (3), 33 (4), 49 (5), 65 (6), 97 (7), 161 (8), 241 (9), and 401 (10) minutes after the reaction was started and at equilibrium [$C_{Ce} = C_L = 5\times10^{-4}$ M in NMP buffer ($C_{NMP} = 2.5\times10^{-2}$ M) with pH 5.26].

It is also possible to follow the rate of $[Eu\{DOTA\text{-}(MeAm)_4\}]^{3+}$ complex formation by following changes in the $Eu^{3+}$ charge-transfer (CT) bands (broad "shoulder" between 240 and 305 nm, Figure S6). A wavelength of 255 nm was selected for these studies since the absorbance of $Eu^{3+}$ and ligand are not significant at this wavelength and $[Eu\{DOTA\text{-}(MeAm)_4\}]^{3+}$ is the only absorbing species (Figure S6).

Kasprzyk et al. have reported that the reaction between metal and ligand can proceed by three possible mechanisms,[29] one of which is a simple second-order reaction

 © 2007 Wiley-VCH Verlag GmbH & Co. KGaA, Weinheim 

where saturation kinetics is not observed and the rate constant is a linear function of the metal ion concentration. The linear variation of pseudo-first-order rate constants ($k_{obs}$) with analytical concentration of $Ln^{3+}$ at different pH values is displayed graphically in Figure 4 for $Ce^{3+}$ (similar data were also observed for $Eu^{3+}$ and $Lu^{3+}$, see Figures S7 and S8, respectively, in the Supporting Information). $k_{obs}$ was found to vary linearly with $Ln^{3+}$ concentration for all systems, and since [L] ≤ 10[M], these data may be described by Equation (1).

$$v = \frac{d[LnL]_t}{dt} = k_{obs}[L]_t \quad (1)$$

The rates of complex formation are pH-dependent, slowing considerably with increasing the acid concentrations. Based on this, one can assume that some protonated species may be involved in the formation reaction. Taking into account all possible pathways, the rate of complex formation may be described by Equation (2), where $k_0$, $k_1$, and $k_2$ are rate constants characterizing the reaction of the nonprotonated (L), monoprotonated ($HL^+$), and diprotonated ($H_2L^{2+}$) forms of the ligand, respectively.

$$v = k_0[M][L] + k_1[M][HL] + k_2[M][H_2L] \quad (2)$$

Given that the analytical concentration of the ligand is $[L]_t = [L] + [HL^+] + [H_2L^{2+}]$, and substituting the appropriate concentrations from the definition of the protonation constants of the ligand ($K_1^H = [HL^+]/[H^+][L]$ and $K_2^H = [H_2L^{2+}]/[H^+][HL^+]$), rearranging Equation (2) yields Equation (3).

$$k_{obs} = \frac{[M]\cdot(k_0 + k_1K_1^H[H^+] + k_2\cdot K_1^H\cdot K_2^H[H^+]^2)}{1 + K_1^H[H^+] + K_1^H\cdot K_2^H[H^+]^2} \quad (3)$$

The $k_{obs}$ values obtained at different metal concentrations for each pH were fitted to Equation (3) using the ligand protonation constants ($K_1^H$ and $K_2^H$, Table 1) to obtain $k_0$, $k_1$, and $k_2$ (Figure 4). The $k_2$ values were either negligible or negative for all metal ions examined here, and hence were ultimately omitted during final data refinement. This indicates that a diprotonated form of the ligand is not involved in this reaction. The fitting yielded positive $k_1$ values, although the errors in these values were about an order of magnitude higher than the rate constants themselves (for [Ce{DOTA-(MeAm)$_4$}]$^{3+}$ $k_1 = 0.0026 \pm 0.0146$ M$^{-1}$ s$^{-1}$; for [Eu{DOTA-(MeAm)$_4$}]$^{3+}$ $k_1 = 0.0025 \pm 0.0227$ M$^{-1}$ s$^{-1}$; for [Lu{DOTA-(MeAm)$_4$}]$^{3+}$ $k_1 = 0.081 \pm 0.184$ M$^{-1}$ s$^{-1}$). This result suggests that although the monoprotonated ligand may contribute somewhat to the reaction, the fully deprotonated ligand is clearly the most reactive species. This is a surprising conclusion because, over the pH range investigated, the concentration of HL is about four to five orders of magnitude higher than the concentration of L (the ratio [HL]/[L] decreases from $9 \times 10^5$ to $7 \times 10^4$). These combined data suggest that the pathway involving the monoprotonated ligand can also be ignored in the overall reaction and that formation of the [Ln{DOTA-(MeAm)$_4$}]$^{3+}$ complexes occurs due to the direct encounter between the $Ln^{3+}$ ions and the fully deprotonated ligand. Thus, Equation (3) can be simplified to Equation (4).

$$k_{obs} = \frac{k_0[M]}{1 + K_1^H[H^+] + K_1^H\cdot K_2^H[H^+]^2} \quad (4)$$

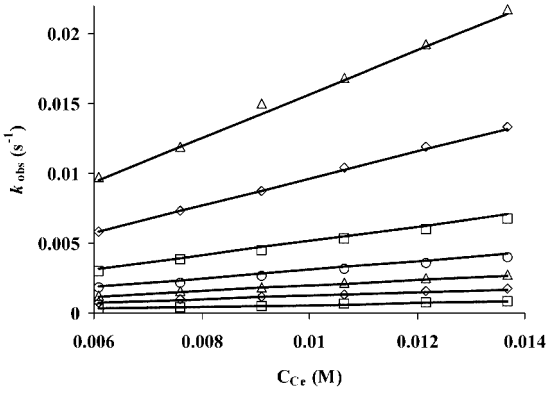


Figure 4. Dependence of $k_{obs}$ on metal concentration for formation of [Ce{DOTA-(MeAm)$_4$}]$^{3+}$ at different pH values (5.71, 5.59, 5.43, 5.31, 5.20, 5.09, and 4.92 from top to bottom).

The rate constants $k_0$ determined here for three [Ln{DOTA-(MeAm)$_4$}]$^{3+}$ complexes and the rate constants characterizing the formation of the corresponding [Ln(DOTA)]$^-$ and [Ln(DOTAM)]$^{3+}$ complexes are compared in Table 4. These data show that formation of [Ln{DOTA-(MeAm)$_4$}]$^{3+}$ occurs about two to three orders of magnitude slower than for the corresponding [Ln(DOTA)]$^-$ complexes. This may be partially attributed to differences in ligand charge since DOTA, in its active from, is negatively charged ([$H_2$DOTA]$^{2-}$ is the primary species in most cases) while the tetraamide ligand is neutral. Interestingly, the rates of [Ln{DOTA-(MeAm)$_4$}]$^{3+}$ complex formation are somewhat slower than for formation of the [Ln(DOTAM)]$^{3+}$ complexes, likely due to the presence of the methyl group on the amide pendant arm.[30] The rates of complex formation can be altered further by increasing the bulkiness of the substituent on the amide pendant arms

Table 4. Comparison of the formation rate constants for [Ln{DOTA-(MeAm)$_4$}]$^{3+}$ ($k_0$, M$^{-1}$ s$^{-1}$), [Ln(DOTAM)]$^{3+}$, and [Ln(DOTA)]$^-$ complexes.

| $Ln^{3+}$ | $Ce^{3+}$ | $Eu^{3+}$ | $Lu^{3+}$ |
|---|---|---|---|
| DOTAM[a] | $7.7 \times 10^3$ | $2.7 \times 10^4$ | $6.6 \times 10^3$ [d] |
| DOTA-(AmMe)$_4$ | $(3.0 \pm 0.1) \times 10^4$ | $(4.8 \pm 0.1) \times 10^4$ | $(6.5 \pm 0.7) \times 10^3$ |
| DOTA | $3.5 \times 10^6$ [b] | $1.1 \times 10^7$ | $4.1 \times 10^7$ [b,d] |
| | $2.7 \times 10^6$ [c] | | $9.3 \times 10^7$ [c,d] |

[a] Ref.[30] [b] Ref.[9] [c] Ref.[10] [d] Refers to the $Yb^{3+}$ complex.

 © 2007 Wiley-VCH Verlag GmbH & Co. KGaA, Weinheim 

(formation of $[Ln\{DOTA\text{-}(pipAm)_4\}]^{3+}$ complexes).[31] The trends in formation rates across the lanthanide series follow a similar trend to that observed for $[Ln(DOTAM)]^{3+}$ complexes recently and opposite to that observed for $[Ln(DOTA)]^-$ complexes.[9,30] The water-exchange rates of $[Ln\{DOTA\text{-}(amide)_4\}]^{3+}$ complexes have been found to behave identically when they are plotted against the size of the $Ln^{3+}$ ions (maximum at $Eu^{3+}$).[32,33] This indicates that the water-exchange rates may influence the rates of complex formation of $[Ln\{DOTA\text{-}(amide)_4\}]^{3+}$ complexes and can be used to interpret the trends in the rates of complex formation. Similar phenomena have often been observed for the formation of lanthanide complexes of with mono- and multidentate ligands.[34]

### Acid-Catalyzed Dissociation of $[Ln\{DOTA\text{-}(MeAm)_4\}]^{3+}$ Complexes

Lanthanide complexes used for medical diagnosis must be kinetically stable because neither product of dissociation (the $Ln^{3+}$ aqua ions or the ligands) is well tolerated in vivo. Several groups have demonstrated that dissociation of $[Ln(DOTA)]^-$ and Ln(DOTA) derivatives takes place by a proton-assisted pathway and that endogenous metal ions such as $Cu^{2+}$ or $Zn^{2+}$ have little affect on the dissociation rates.[8–10,35] As the structures of the complexes examined here do not differ substantially from those of the $[Ln(DOTA)]^-$ complexes, one could anticipate a similar kinetic dissociation behavior for the LnDOTA-tetraamides. Acid-catalyzed dissociation of $[Ce\{DOTA\text{-}(MeAm)_4\}]^{3+}$ and $[Eu\{DOTA\text{-}(MeAm)_4\}]^{3+}$ was examined at a pH below 2, where one would predict complete dissociation of the complexes based upon the thermodynamic measurements. At pH 2, the complexes dissociate so slowly that it was difficult to collect kinetic data over a reasonable period of time. Ultimately, it was found that the kinetic measurements could be performed over the range $0.5 < [HClO_4] < 3.0$ M and by maintaining a constant ionic strength with addition of $NaClO_4$ when necessary $[(H^+ + Na^+)ClO_4^-$ constant at 3.0 M]. As the total acid concentration was more than two orders of magnitude greater than the complex concentration in all cases, the dissociation rates follow pseudo-first-order kinetics ($k_{obs} = k_d$) and can be described by Equation (5), where $[LnL]_t$ is the total complex concentration.

$$-\frac{d[LnL]_t}{dt} = k_d \cdot [LnL]_t \quad (5)$$

Plots of first-order dissociation rates vs. acid concentration were found to be similar for both complexes (Figure 5). Similar results have been obtained in a study of the dissociation rates of $[Gd(DOTA)]^-$ and $[Eu\{DOTA\text{-}(gly)_4\}]^-$.[10,11] It has been shown previously that dissociation of $[Ce(DOTA)]^-$ is second order with respect to $[H^+]$ while dissociation of $[Eu(DOTA)]^-$ shows saturation behaviour.[8,9] Like other complexes, dissociation of $[Ln\{DOTA\text{-}(MeAm)_4\}]^{3+}$ is initiated by protonation, probably at an amide pendant arm. This is in agreement with the observation that there is no change in the absorption spectrum of either complex immediately after mixing the complex with a strong acid. The proton must therefore be transferred to the ring nitrogen atom, after which the metal ion moves out from the "coordination cage" (rearrangement), since the "in cage" complexes cannot dissociate directly. A protonation constant of $K^H_{[Eu(DOTA)]^-} = 14$, which corresponds to the protonation of the acetate arm coordinated to the $Eu^{3+}$ in the complex, was found for $[Eu(DOTA)]^-$.[9] Complexes formed with extended phosphonate or glycinate pendant arms have even higher $\log K_i^H$ values. For example, three to four protonation steps can be measured for the $Ln^{III}$ complexes of DOTA-$(gly)_4$ ($\log K_i^H$ = 2–4) and four steps for the $[Ln(DOTP)]^{5-}$ complexes ($\log K_i^H$ = 4–8).[11,36] The protonation constants of the $[Ln\{DOTA\text{-}(MeAm)_4\}]^{3+}$ complexes are very low and no protonation constant can be obtained from the titration data of 0.01 M complex solutions with 0.1 M HCl. This can be explained by the large difference in basicity of the donor atoms in the pendant arms of the amides compared to acetates or phosphonates. This is easily understood if one compares $\log K^H$ values for aminomethanephosphonic acid, glycine, and glycine amide. The protonation constant of aminomethanephosphonic acid falls in the range 5.32–5.40 and the protonation constant of glycine is in the range 2.33–2.79, while the protonation of the amide nitrogen of glycine amide occurs only at high acid concentrations and $\log K^H$ can not be determined by pH-potentiometry.[20,37]

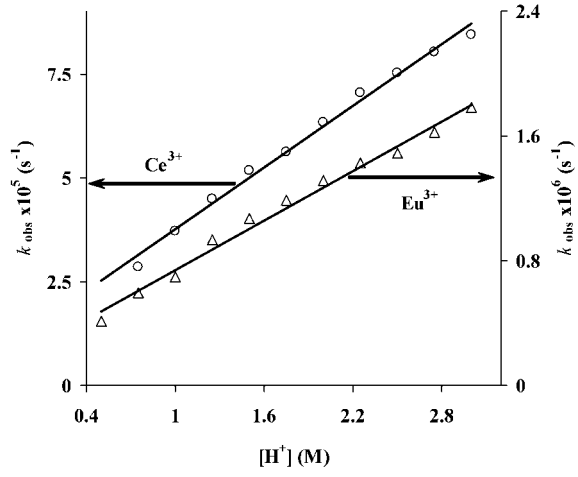


Figure 5. Rates of dissociation of $[Ln\{DOTA\text{-}(MeAm)_4\}]^{3+}$ {$Ln^{3+}$ = $Ce^{3+}$ (circles) and $Eu^{3+}$ (triangles)}. The solid line represents the fitted curves while the points are the measured values.

The data in Figure 5 demonstrate that the rates of dissociation of the complexes are linearly proportional to the acid concentration and are hence described by Equation (6), where $k_0$ corresponds to dissociation of the complex (most likely spontaneous) while $k_1$ corresponds to acid-catalyzed dissociation of the monoprotonated LnLH complex.

$$k_d = k_0 + k_1 \cdot [H^+] \quad (6)$$

The rate constants calculated from these data are listed in Table 5 along with comparative values for $[Ce(DOTA)]^-$ and $[Eu(DOTA)]^-$.

 © 2007 Wiley-VCH Verlag GmbH & Co. KGaA, Weinheim 

Table 5. Proton-assisted dissociation rates for two [Ln{DOTA-(MeAm)$_4$}]$^{3+}$ complexes.

| $Ln^{3+}$ | $k$ | DOTA | DOTA-(MeAm)$_4$ | DOTA-(gly)$_4$[a] |
|---|---|---|---|---|
| $Ce^{3+}$ | $k_0$ $s^{-1}$ | not observed | $(1.1 \pm 0.1) \times 10^{-5}$ | not studied |
| | $k_1$ $M^{-1} s^{-1}$ | $8 \times 10^{-4}$ [b] | $(2.6 \pm 0.1) \times 10^{-5}$ | not studied |
| $Eu^{3+}$ | $k_0$ $s^{-1}$ | not observed[c] | $(1.5 \pm 0.2) \times 10^{-7}$ | $7.3 \times 10^{-7}$ |
| | $k_1$ $M^{-1} s^{-1}$ | $1.4 \times 10^{-5}$ [d] | $(5.6 \pm 0.2) \times 10^{-7}$ | $8.1 \times 10^{-6}$ |

[a] Ref.[11] [b] Ref.[8], second-order dependence on $H^+$ ion concentration with a third-order rate constant of $2.0 \times 10^{-3}$ $M^{-2} s^{-1}$ was also observed. [c] For [Gd(DOTA)]$^-$, $k_0 = 5 \times 10^{-8}$ $s^{-1}$ and $k_1 = 5 \times 10^{-6}$ $M^{-1} s^{-1}$ from ref.[10] [d] Ref.[9]

Spontaneous dissociation of [Ln{DOTA-(MeAm)$_4$}]$^{3+}$ ($k_0$) is somewhat faster than [Gd(DOTA)]$^-$ but the corresponding data ($k_0$) for [Ce(DOTA)]$^-$ and [Eu(DOTA)]$^-$ are not available. However, the acid-catalyzed rates of dissociation ($k_1$) are about 25–30-fold slower than the corresponding rates for the [Ln(DOTA)]$^-$ complexes, perhaps reflecting the ease of protonation of a charged carboxylate side-arm in [Ln(DOTA)]$^-$ compared to the difficulty of protonating a neutral amide side-arm in [Ln{DOTA-(MeAm)$_4$}]$^{3+}$. There is also a noticeable difference in the rates of acid-catalyzed dissociation of [Eu{DOTA-(MeAm)$_4$}]$^{3+}$ vs. [Eu{DOTA-(gly)$_4$}]$^-$ (both tetraamide complexes) − the latter complex dissociates about 15-fold faster than the former.[11] This likely reflects the greater overall positive charge on [Eu{DOTA-(MeAm)$_4$}]$^{3+}$ compared to [Eu{DOTA-(gly)$_4$}]$^-$. Thus, even though the LnDOTA-tetraamide complexes are thermodynamically considerably less stable than the corresponding [Ln(DOTA)]$^-$ complexes, it appears to be more difficult to protonate the neutral amide side-chains in these complexes and this ultimately limits their rates of acid-catalyzed dissociation. Similar conclusions have been reported previously for some phosphinate and phosphonate ester derivatives of DOTA.[38,39] This suggests that the kinetic inertness of the LnDOTA-tetraamide complexes may ultimately allow for their use as imaging agents in vivo.

## Conclusions

The protonation constants of several tetraamide derivatives of DOTA show similar $\log K_i^H$, values with the highest protonation constant falling in the range 9.0–9.6 and the lowest in the range 5.5–6.5. In comparison to DOTA, the basicity ($\Sigma \log K_i^H$) of the tetraamide ligands is about 15–16 orders of magnitude less than that of DOTA. This indicates that the DOTA-tetraamide ligands have a greatly reduced ability to bind $H^+$ and metal ions. Only ML type complexes are formed between these ligands and $Mg^{2+}$ or $Ca^{2+}$ ions while complexes formed with $Zn^{2+}$ and $Cu^{2+}$ undergo additional deprotonation steps either at a bound water molecule (first deprotonation step) or an amide side-chain (first deprotonation step for $Zn^{2+}$ and second deprotonation step for $Cu^{2+}$ complexes). The thermodynamic stability constants of several LnL complexes determined using the "out-of-cell" technique show an unusual trend in that they increase between $Sm^{3+}$ and $Eu^{3+}$ then remain relatively constant with further decreases in $Ln^{3+}$ size until the very end of the lanthanide series. The thermodynamic constants are about 10–11 orders of magnitude lower than the corresponding [Ln(DOTA)]$^-$ complexes. The [Ln{DOTA-(amide)$_4$}]$^{3+}$ complexes also undergo an additional deprotonation above pH 10.5 which is accompanied by formation of the ternary Ln(OH)L complex, with the deprotonation likely occurring at the coordinated water molecule in these systems.

The rates of [Ln{DOTA-(MeAm)$_4$}]$^{3+}$ complex formation are about two to three orders of magnitude slower than those of the corresponding [Ln(DOTA)]$^-$ complexes. The variation of the formation rates with $Ln^{3+}$ ion size is the opposite of that observed for the [Ln(DOTA)]$^-$ complexes. This is most likely due to the higher positive charge density of the heavier $Ln^{3+}$ ions resulting in greater repulsion between the positively charged $Ln^{3+}$ ions and the ligand. [Ce{DOTA-(MeAm)$_4$}]$^{3+}$ and [Eu{DOTA-(MeAm)$_4$}]$^{3+}$ are kinetically inert toward acid-catalyzed dissociation due to the unfavorable acid-base properties of the uncharged amide pendant arms in these complexes. Based on the slow rates of acid-catalyzed dissociation, LnDOTA-(amide)$_4$ systems may prove safe for in vivo imaging applications.

## Experimental Section

**Synthesis of the Ligands:** The tetraamide ligands DOTAM (**1**),[12] DOTA-(MeAm)$_4$ (**2**)[15,16] DOTA-(EtAm)$_4$ (**3**),[16,17] and DOTA-(gly-OEt)$_4$ (**4**)[18] were prepared by established procedures and their purity established by $^1H$ and $^{13}C$ NMR spectroscopy, EI mass spectrometry, elemental analysis, and melting point determinations for all solids.

**Potentiometric Measurements:** The pH-potentiometric titrations were carried out with a Thermo Orion expandable ion analyzer EA940 pH meter using Thermo Orion semi-micro combination electrode 8103BN in a mixing vessel thermostatted at 25.0 °C. A Metrohm DOSIMATE 665 autoburette (5 mL capacity) was used for base additions and 1.0 M KCl was used to maintain the ionic strength. All equilibrium measurements (direct titrations) were carried out in 10.00 mL sample volumes with magnetic stirring. Argon was passed over the top of the sample during the titrations to maintain the cell free of $CO_2$. Standard buffers (Borax: 0.01 M, pH 9.180 and KH-phthalate 0.05 M, pH 4.005) were used to calibrate the electrode. The titrant, a carbonate-free KOH solution, was standardized against 0.05 M KH-phthalate solution by pH-potentiometry. A standard solution of hydrochloric acid was prepared using doubly distilled water and the concentration was determined by pH-potentiometry with standard KOH solution. A method proposed by Irving et al. was used to obtain $H^+$ ion concentrations from the measured pH values.[40] The $pK_w$ of water was also calculated from these titration data and was found to be 13.845. The protonation constants ($\log K_i^H$) and stability constants were evaluated from the potentiometric data by using the PSEQUAD computer program.[41]

 © 2007 Wiley-VCH Verlag GmbH & Co. KGaA, Weinheim 

**Stock Solutions:** Stock solutions of metal ions (prepared from chloride salts) at about 0.02–0.06 M were calibrated by complexometric titration against standardized [$Na_2(H_2EDTA)$] using the appropriate end-point indicator.[42] [$Na_2(H_2EDTA)$] was purchased from Alfa-Aesar and standardized by a pH-potentiometric titration using standardized KOH. Stock solutions of the ligands synthesized in this work (0.02–0.05 M) were prepared in deionized water maintaining the pH in the range 3–4 with acid (HCl). It was found important to maintain the stock solution of DOTA-(gly-OEt)$_4$ somewhat acidic (pH ≤ 3) due to slow hydrolysis of the ester bonds. The concentrations of stock solutions of these ligands were determined by pH-potentiometry from the titration data obtained in the absence and in the presence of an approximately 50-fold excess of $CaCl_2$.

**Protonation and Metal Binding (Stability) Constants:** The protonation constants of the ligands were calculated from the data obtained by titrating 2 and 5 mM samples (180–268 data points) with standardized KOH solution (0.18 M) in the absence of $Ca^{2+}$ over the pH range 1.8–12.0. The protonation constants of the ligand ($\log K_i^H$) are defined according to Equation (7), where $i$ = 1, 2, and 3 and [$H_{i-1}L$] and [$H^+$] are the equilibrium concentrations of the ligand ($i$ = 1), protonated forms of the ligand ($i$ = 2 or 3) and hydrogen ions, respectively.

$$K_i^H = \frac{[H_iL]}{[H_{i-1}L][H^+]} \quad (7)$$

Relatively rapid equilibrium was observed in the systems containing $Mg^{2+}$, $Ca^{2+}$, $Zn^{2+}$, or $Cu^{2+}$. This proved fast enough to be able to use a direct titration method for stability constant determinations. In these measurements, a time period of 900–1200 seconds was allowed between each addition of KOH to ensure equilibrium before the sample pH was read. The next addition of base was made only when four consecutive pH readings collected over 60 seconds were identical within ±0.0006 pH units. The titrations were carried out at 1:1 and 2:1 metal to ligand concentration ratios and the concentration of the ligands was maintained at around 2 mM. These combined titration data were fitted simultaneously and the thermodynamic stability constants ($K_{ML}$) were evaluated and reported based on Equations (8) and (9).

$$K_{ML} = \frac{[ML]}{[M][L]} \quad (8)$$

$$K_{MLH_{-1}} = \frac{[MLH_{-1}][H^+]}{[ML]} \text{ and } K_{MLH_{-2}} = \frac{[MLH_{-2}][H^+]}{[MLH_{-1}]} \quad (9)$$

The complexation of lanthanide(III) ions with macrocyclic ligands is very slow (about four to five weeks are required to achieve equilibrium at room temperature), so "out-of-cell" experiments (also known as the batch method) were performed instead of direct titrations. Typically, 25.0 mL of a mixture of $Ln^{3+}$ and ligand each at 2–2.5 mM was prepared and divided into 16 individual solutions (1.5 mL each). The pH of the samples was adjusted with HCl or KOH to span the range pH 2.5–4.5 (where complex formation is ongoing but not complete). The samples were sealed and placed in a 45 °C incubator for 21 days followed by an additional 28 days at room temperature to re-equilibrate the mixtures. The pH of each individual sample was then measured. Acid/base titrations were also performed under identical conditions before and after measuring the pH of the samples. The average of these measurements was used to correct the pH of the samples for the difference between the measured and calculated pH by following the method proposed by Irving et al.[40] This difference was usually greater than the one obtained in the stirred samples and can be attributed to the difference in the diffusion of the ions in the samples not being stirred.

**Formation and Dissociation Kinetics of the [Ln{DOTA-(MeAm)$_4$}]$^{3+}$ Complexes:** The formation rates of [Ce{DOTA-(MeAm)$_4$}]$^{3+}$ ($\lambda_{max}$ = 323 nm) and [Eu{DOTA-(MeAm)$_4$}]$^{3+}$ ($\lambda_{max}$ = 255 nm) were studied at 25 °C and 1.0 M KCl ionic strength by spectrophotometry using a Cary 300 Bio UV/Vis spectrophotometer equipped with thermostatted cell holders and semi-micro quartz cells (Starna, optical path length 1 cm). All the reactions were performed under pseudo-first-order conditions where the metal ions were in 10–25-fold excess. The concentration of the ligand in the formation reactions of $Ce^{3+}$, $Eu^{3+}$,and $Lu^{3+}$ complexes was set to $5.62 \times 10^{-4}$, $9.83 \times 10^{-4}$, and $1.12 \times 10^{-3}$ M, respectively. Since $Lu^{3+}$ ions do not absorb in the UV/Vis region, the indicator method proposed by Kasprzyk et al. using indicators bromocresol green (pH 4.0–5.6) and bromocresol purple (pH 5.2–6.8) was used to record the absorbance change at a wavelength of 615 nm.[29] An appropriate concentration of indicator and buffer at different pH values was established experimentally to allow slight pH change in these systems (ΔpH ≤ 0.1). The pH of each sample was re-measured after the equilibrium was reached (usually the next day) and any samples with a pH change greater than 0.1 pH units were either excluded from the calculations or the process was repeated at a higher buffer concentration. Formation kinetic studies were carried out with the non-coordinating buffers *N*-methylpiperazine (NMP, $\log K_2^H$ = 4.83) at a concentration of 0.05 M for $Ce^{3+}$ and $Eu^{3+}$ and dimethylpiperazine (DMP, $\log K_2^H$ = 4.18) at 0.025–0.05 M for $Lu^{3+}$ to maintain constant pH.[20]

Absorbance data recorded as a function of time were fitted to Equation (10) to evaluate the first-order rate constants, where $A_0$, $A_e$, and $A_t$ are the absorbance values measured at the start of the reaction ($t$ = 0), at equilibrium, and at time $t$, respectively. These data were fitted to Equation (10) with the Scientist® (Micromath) software using a standard least-squares procedure.[43]

$$A_t = A_e + (A_0 - A_e)\cdot e^{(-k_{obs}\cdot t)} \quad (10)$$

Proton-assisted dissociation of the complexes takes place slowly after addition of excess strong acid. The dissociation kinetics were studied in 0.5–3.0 M $HClO_4$ acidic solutions at 25 °C and 3.0 M ionic strength provided by ($Na^+ + H^+$)$ClO_4$ in samples where the concentration of complexes was 1 mM. The decrease in absorbance was measured periodically at 323 nm for [Ce{DOTA-(MeAm)$_4$}]$^{3+}$ and at 255 nm for [Eu{DOTA-(MeAm)$_4$}]$^{3+}$. The complete kinetics curve was registered for the $Ce^{3+}$ complex and used for the fitting procedure, whereas the dissociation curves for the $Eu^{3+}$ complex were followed until 60–70% conversion was reached.

**Supporting Information** (see also the footnote on the first page of this article): Visible spectra of the [Cu(DOTAM)]$^{2+}$ complex as a function of pH (Figure S1); $^1$H NMR titration of the [Zn(DOTAM)]$^{2+}$ complex (Figure S2); titration curves obtained for some [Ln{DOTA-(MeAm)$_4$}]$^{3+}$ complexes ($Ln^{3+}$ = $Ce^{3+}$, $Eu^{3+}$, and $Lu^{3+}$; Figure S3); $^1$H NMR titration of the [Lu(DOTAM)]$^{3+}$ complex (Figure S4); $^1$H NMR titration of the [Lu{DOTA-(MeAm)$_4$}]$^{3+}$ complex (Figure S5); formation of [Eu{DOTA-(MeAm)$_4$}]$^{3+}$ with time (Figure S6); dependence of $k_{obs}$ on the $Eu^{3+}$ concentration for the formation of [Eu{DOTA-(MeAm)$_4$}]$^{3+}$ at different pH values (Figure S7); dependence of $k_{obs}$ on the $Lu^{3+}$ concentration for the formation of [Lu{DOTA-(MeAm)$_4$}]$^{3+}$ at different pH.

 © 2007 Wiley-VCH Verlag GmbH & Co. KGaA, Weinheim 

## Acknowledgments

The authors thank the National Institutes of Health (NIH) (RR-02584, CA-115531 and EB-004582 A. D. S.), the Robert A. Welch Foundation (AT-584 A. D. S.) and the EMIL Project funded by the EC FP6 Framework Program (LSCH-2004-503569 E. B.) for financial assistance.

[1] R. B. Lauffer, *Chem. Rev.* **1987**, *87*, 901–927.
[2] D. H. Carr, J. Brown, G. M. Bydder, H. J. Weinmann, U. Speck, D. J. Thomas, I. R. Young, *Lancet* **1984**, *1*, 484–486.
[3] P. M. Parizel, H. R. Degryse, J. Gheuens, J. J. Martin, M. Vanvyve, C. Delaporte, P. Selosse, P. Vandeheyning, A. M. Deschepper, *J. Comp. Assisted Tomography* **1989**, *13*, 378–385.
[4] D. Meyer, M. Schaefer, B. Bonnemain, *Invest. Radiol.* **1988**, *23*, S232–S235.
[5] S. Aime, A. Barge, M. Botta, D. Parker, A. S. DeSousa, *J. Am. Chem. Soc.* **1997**, *119*, 4767–4768.
[6] K. M. Ward, A. H. Aletras, R. S. Balaban, *J. Magn. Reson.* **2000**, *143*, 79–87.
[7] S. R. Zhang, P. Winter, K. C. Wu, A. D. Sherry, *J. Am. Chem. Soc.* **2001**, *123*, 1517–1518.
[8] E. Brucher, G. Laurenczy, Z. Makra, *Inorg. Chim. Acta* **1987**, *139*, 141–142.
[9] E. Toth, E. Brucher, I. Lazar, I. Toth, *Inorg. Chem.* **1994**, *33*, 4070–4076.
[10] X. Y. Wang, T. Z. Jin, V. Comblin, A. Lopezmut, E. Merciny, J. F. Desreux, *Inorg. Chem.* **1992**, *31*, 1095–1099.
[11] Z. Baranyai, E. Brucher, T. Ivanyi, R. Kiraly, I. Lazar, L. Zekany, *Helv. Chim. Acta* **2005**, *88*, 604–617.
[12] H. Maumela, R. D. Hancock, L. Carlton, J. H. Reibenspies, K. P. Wainwright, *J. Am. Chem. Soc.* **1995**, *117*, 6698–6707.
[13] D. A. Voss, E. R. Farquhar, W. D. Horrocks, J. R. Morrow, *Inorg. Chim. Acta* **2004**, *357*, 859–863.
[14] L. Alderighi, A. Bianchi, L. Calabi, P. Dapporto, C. Giorgi, P. Losi, L. Paleari, P. Paoli, P. Rossi, B. Valtancoli, M. Virtuani, *Eur. J. Inorg. Chem.* **1998**, 1581–1584.
[15] A. Bianchi, L. Calabi, C. Giorgi, P. Losi, P. Mariani, P. Paoli, P. Rossi, B. Valtancoli, M. Virtuani, *J. Chem. Soc. Dalton Trans.* **2000**, 697–705.
[16] W. E. Weaver, W. M. Whaley, *J. Am. Chem. Soc.* **1947**, *69*, 515–516.
[17] S. Shinoda, T. Nishimura, M. Tadokoro, H. Tsukube, *J. Org. Chem.* **2001**, *66*, 6104–6108.
[18] S. R. Zhang, K. C. Wu, M. C. Biewer, A. D. Sherry, *Inorg. Chem.* **2001**, *40*, 4284–4290.
[19] L. Burai, I. Fabian, R. Kiraly, E. Szilagyi, E. Brucher, *J. Chem. Soc. Dalton Trans.* **1998**, 243–248.
[20] A. E. Martell, R. M. Smith, R. J. Motekaitis, *Critically Selected Stability Constants of Metal Complexes*, Database Version 8.0, Texas A&M University, **2004**.
[21] C. F. J. Baes, R. E. Mesmer, *The Hydrolysis of Cations*, John Wiley & Sons Inc., New York, **1976**.
[22] H. Sigel, R. B. Martin, *Chem. Rev.* **1982**, *82*, 385–426.
[23] A. Beeby, I. M. Clarkson, R. S. Dickins, S. Faulkner, D. Parker, L. Royle, A. S. de Sousa, J. A. G. Williams, M. Woods, *J. Chem. Soc. Perkin Trans. 2* **1999**, 493–503.
[24] S. Aime, A. Barge, J. I. Bruce, M. Botta, J. A. K. Howard, J. M. Moloney, D. Parker, A. S. de Sousa, M. Woods, *J. Am. Chem. Soc.* **1999**, *121*, 5762–5771.
[25] E. Brucher, *Top. Curr. Chem.* **2002**, *221*, 103–122.
[26] E. Csajbok, I. Banyai, E. Brucher, *Dalton Trans.* **2004**, 2152–2156.
[27] S. L. Wu, W. D. Horrocks, *Inorg. Chem.* **1995**, *34*, 3724–3732.
[28] P. A. Stenson, A. L. Thompson, D. Parker, *Dalton Trans.* **2006**, 3291–3293.
[29] S. P. Kasprzyk, R. G. Wilkins, *Inorg. Chem.* **1982**, *21*, 3349–3352.
[30] Z. Baranyai, I. Bányai, E. Brücher, R. Király, E. Terreno, *Eur. J. Inorg. Chem.* DOI: 10.1002/ejic.200700178.
[31] G. Tircsó, E. Tircsóné Benyó, A. D. Sherry, unpublished results **2007**.
[32] S. R. Zhang, M. Merritt, D. E. Woessner, R. E. Lenkinski, A. D. Sherry, *Acc. Chem. Res.* **2003**, *36*, 783–790.
[33] S. R. Zhang, K. C. Wu, A. D. Sherry, *J. Am. Chem. Soc.* **2002**, *124*, 4226–4227.
[34] S. F. Lincoln, A. E. Merbach, *Advances in Inorganic Chemistry*, Academic Press, New York, **1995**, p. 1–87.
[35] K. Kumar, M. F. Tweedle, *Inorg. Chem.* **1993**, *32*, 4193–4199.
[36] A. D. Sherry, J. Ren, J. Huskens, E. Brucher, E. Toth, C. F. C. G. Geraldes, M. M. C. A. Castro, W. P. Cacheris, *Inorg. Chem.* **1996**, *35*, 4604–4612.
[37] M. Liler, *J. Chem. Soc. Perkin Trans. 2* **1971**, 334–338.
[38] K. P. Pulukkody, T. J. Norman, D. Parker, L. Royle, C. J. Broan, *J. Chem. Soc. Perkin Trans. 2* **1993**, 605–620.
[39] L. Burai, R. Kiraly, I. Lazar, E. Brucher, *Eur. J. Inorg. Chem.* **2001**, 813–820.
[40] H. M. Irving, M. G. Miles, L. D. Pettit, *Analytica Chim. Acta* **1967**, *38*, 475–488.
[41] L. Zekany, I. Nagypal, in *Computational Methods for the Determination of Formation Constants* (Ed.: D. J. Leggett), Plenum Press, New York, **1985**, p. 291.
[42] G. Schwarzenbach, H. Flaschka, in *Complexometric Titrations*, 2nd ed. in English, Barnes and Noble, New York, **1969**, p. 490.
[43] http://www.micromath.com/products.php?p=scientist.

Received: March 30, 2007
Published Online: July 31, 2007

 © 2007 Wiley-VCH Verlag GmbH & Co. KGaA, Weinheim 

DOI: 10.1002/ejic.200700356

# Synthesis and Characterisation of Semi-Bridging Molybdenum Borylene Complexes

**Holger Braunschweig,*[a] Krzysztof Radacki,[a] and Katharina Uttinger[a]**

**Keywords:** Boron / Borylene complexes / Molybdenum / Palladium / DFT calculations

Investigation of the reactivity of the molybdenum borylene complex $[(OC)_5Mo{=}B{=}N(SiMe_3)_2]$ towards the late transition metal complexes $[M(PCy_3)_2]$ (M = Pd, Pt) indicated the formation of $[(OC)_4Mo(\mu\text{-}CO)\{\mu\text{-}BN(SiMe_3)_2\}Pd(PCy_3)]$ and $[(Cy_3P)(OC)_3Mo(\mu\text{-}CO)\{\mu\text{-}BN(SiMe_3)_2\}Pt(PCy_3)]$, respectively, as the first Mo-based semi-bridging borylene complexes. The new complexes were fully characterised spectroscopically and analysed by X-ray diffraction. The conclusions drawn from the experimental data for the ligand-metal interactions for this particular coordination mode of a borylene group were supported by DFT computations.

(© Wiley-VCH Verlag GmbH & Co. KGaA, 69451 Weinheim, Germany, 2007)

Transition metal boryl complexes have attracted significant interest due to their role as key intermediates in catalysed hydro-[1] and diboration reactions[2] as well as in C–H bond activation of organic compounds.[3] Borylene complexes as another type of metal-boron compound are also in the focus of research[4] because of their close relationship to carbonyl complexes and due to their propensity to effectively stabilise[4g,5] elusive borylenes[6] in the coordination sphere of a metal. In particular, group 6 transition metal carbonyl fragments have been shown to possess good stabilising properties resulting in the formation, by means of a salt elimination reaction, of $[(OC)_5M{=}B{=}N(SiMe_3)_2]$ (M = Cr, **1**; W, **2**) which are the first two-coordinate borylene complexes.[7] Unfortunately, this method of preparation is limited in scope and, hence, the borylene transfer under thermal[8] or photochemical conditions[9] has become established as a highly useful alternative for the synthesis of borylene complexes and borylene functionalised main group element substrates.[10]

Very recently, it was demonstrated that borylene ligands (Figure 1) can adopt rather unusual coordination modes beyond the common scope of mononuclear neutral (e.g. **1**, **2** and **3**)[7,9,11] and cationic (e.g. **4**)[12] or symmetrically bridged homodinuclear species (e.g. **5** and **6**).[9a,13] Important examples include heterodinuclear borylene complexes (e.g. **7**),[14] metalloborylenes (e.g. **8**)[8d,15] (Figure 1) and dinuclear compounds with semi-bridging borylene ligands.[8a,8b]

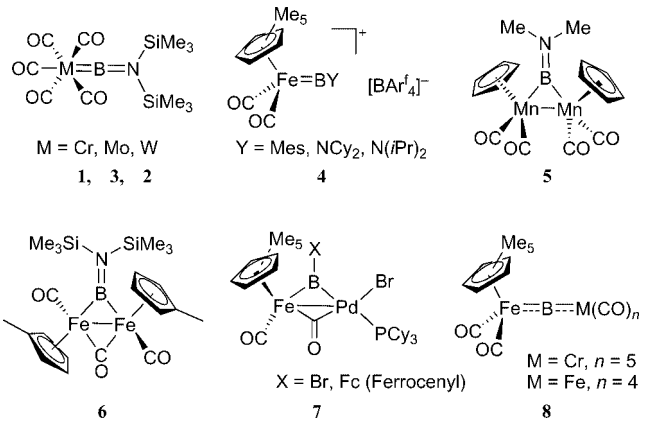


Figure 1. Different coordination modes for borylene ligands: terminal **1**,[7,9a] **2**[7] and **3**,[11b] cationic **4**,[12a,12b,12c] symmetrically bridging homodinuclear **5**[13a] and **6**,[13b] symmetrically bridging heterdionuclear **7**[14] and metalloborylene **8**.[15]

In the case of the group 6 transition metals, several boryl and borylene complexes of tungsten are known for example $[L(OC)_4W{=}B{=}N(SiMe_3)_2]$ (L = CO, **2**; $PCy_3$)[7,11b] and $[(\eta^5\text{-}C_5H_5)_2WXBR_2]$ (X = H, $R_2$ = $Ph_2$, 1,2-$O_2$-$C_6H_4$; X = Cl, $R_2$ = 1,2-$O_2$-$C_6H_4$),[16] $[(\eta^5\text{-}C_5H_5)_2W(BR_2)_2]$ [$R_2$ = (1,2-$O_2$-4-*t*Bu$C_6H_3$), (1,2-$O_2$-3,5-*t*$Bu_2C_6H_2$)][16b,17] or $[(\eta^5\text{-}C_5H_5)\text{-}W(CO)_3\{B(NMe_2)B(NMe_2)X\}]$ (X = Cl, Br, I),[18] most of them being fully characterised including crystallographic data. Likewise, a variety of chromium borylene complexes were reported, e.g. $[L(OC)_4Cr{=}B{=}N(SiMe_3)_2]$ (L = CO, **1**; $PCy_3$, **10**),[7,8a,9a,11b] $[(OC)_5Cr{=}B{-}Si(SiMe_3)_3]$[11a] and $[(OC)_5\text{-}Cr{=}B{-}Fe(\eta^5\text{-}C_5H_5)(CO)_2]$ (**8**)[15] and in addition, one boryl complex $[Cr(\eta^6\text{-}C_6H_6)(CO)_2(\eta^2\text{-}tmp'BCR_2)]$ [$tmp'BCR_2$ = ($\eta^2$-9-fluorenylidene)(2,2,6,6-tertramethylpiperidino)-borane].[19] In the case of molybdenum, however, only few boryl complexes of molybdenum are known, e.g.

[a] Institut für Anorganische Chemie, Julius-Maximilians-Universität Würzburg,
Am Hubland, 97074 Würzburg, Germany
Fax: +49-931-888-4623
E-mail: h.braunschweig@mail.uni-wuerzburg.de

Supporting information for this article is available on the WWW under http://www.eurjic.org or from the author.


© 2007 Wiley-VCH Verlag GmbH & Co. KGaA, Weinheim

[Mo(tpb′)(CO)$_2${B(Et)CH$_2$-*p*-tolyl}] [tpb′ = tris(3,5-dimethylpyrazol-1-yl)hydroborate][20] or the diborane(4)yl complex [($\eta^5$-C$_5$H$_5$)Mo(CO)$_3${B(NMe$_2$)B(NMe$_2$)X}] (X = Br, I)[18b,18c,18d] and only very recently we contributed the first Mo borylene complex [(OC)$_5$Mo=B=N(SiMe$_3$)$_2$] (**3**) and reported its conversion to *trans*-[(Cy$_3$P)(OC)$_4$-Mo=B=N(SiMe$_3$)$_2$] (**11**).[11b] Presumably, the relative scarcity of Mo–boron complexes can be attributed to the enhanced lability of 4d transition metal complexes with respect to their corresponding 3d and 5d analogues.[21]

Recent studies have shown that metal coordinated borylene and, albeit to a lesser extent, boryl ligands[22] are highly susceptible to the addition of transition metal bases, leading in the case of the former to novel heterodi- and trinuclear borylene species.[8c,8d]

In this paper we report on the reactivity of [(OC)$_5$-Mo=B=N(SiMe$_3$)$_2$] (**3**)[11b] towards the late transition metal complexes [M(PCy$_3$)$_2$] (M = Pd, **12**; Pt, **13**)[23] which leads to the first Mo-species comprised of a semi-bridging borylene ligand. In addition, we provide detailed results of DFT studies which have elucidated the electronic structures of the title compounds.

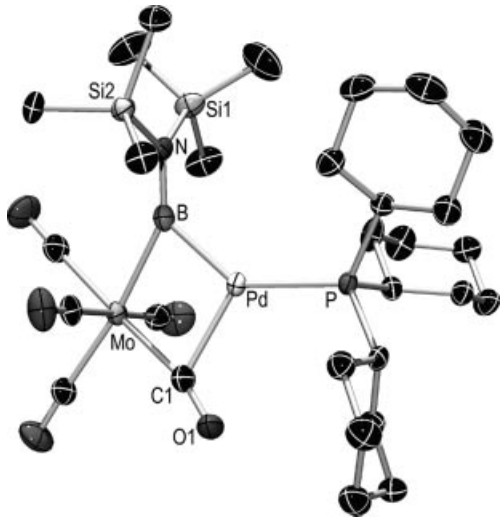


Figure 2. Molecular structure of [(OC)$_4$Mo(μ-CO){μ-BN(SiMe$_3$)$_2$}Pd(PCy$_3$)] (**16**). Thermal ellipsoids are set at the 50% probability level. Selected bond lengths [Å] and angles [°]: Mo–B 2.235(4), Pd–B 2.065(4), B–N 1.376(5), Pd–P 2.3764(9), Pd–Mo–C1 51.74(10), Mo–C1–O1 164.3(3), Pd–Mo–B 47.59(10), Mo–B–N 150.7(3), Si1–N–B–Pd 86.1(3).

## Results and Discussion

Equimolar amounts of [(OC)$_5$Mo=B=N(SiMe$_3$)$_2$] (**3**) and [Pd(PCy$_3$)$_2$] (**12**) were mixed in C$_6$D$_6$ at room temperature. The progress of the reaction was monitored by multinuclear NMR spectroscopy and, after 30 min, complete conversion of the starting materials, formation of a new compound and liberation of PCy$_3$ [$\delta$ ($^{31}$P) = 10.0 ppm] was observed. The product was isolated as orange crystals in 53% yield by layering a toluene solution with hexane and storing at –35 °C overnight. The $^{11}$B{$^1$H} NMR spectrum shows a broad signal at $\delta$ = 99 ppm which is downfield shifted with respect to that in the precursor **3** ($\delta$ = 89.7 ppm).[11b] A sharp resonance at $\delta$ = 35.1 ppm in the $^{31}$P{$^1$H} NMR spectrum can be observed for the metal coordinated phosphane ligand indicating the presence of only one tricyclohexylphosphane unit in the molecule. The $^1$H NMR spectrum features one singlet for both trimethylsilyl groups at $\delta$ = 0.41 ppm which is deshielded with respect to that of the borylene precursor **3** ($\delta$ = 0.15 ppm)[11b] but comparable to those of the Cr and W analogues ([(OC)$_4$-M(μ-CO){μ-BN(SiMe$_3$)$_2$}Pd(PCy$_3$)], M = Cr, **14**; M = W, **15**; $\delta$ = 0.42 ppm).[10a]

The result of a single-crystal X-ray diffraction study of [(OC)$_4$Mo(μ-CO){μ-BN(SiMe$_3$)$_2$}Pd(PCy$_3$)] (**16**) is shown in Figure 2.

Compound **16** crystallises in the orthorhombic space group *Pna*2$_1$ with the two metal fragments [Mo(CO)$_4$] and [Pd(PCy$_3$)] linked by a bridging CO and a –BN(SiMe$_3$)$_2$ group. The latter is oriented almost perpendicular with respect to the plane containing Mo, B and Pd as indicated by the dihedral angle Si1–N–B–Pd of 86.1(3)°. The Mo–B bond [2.235(4) Å] is elongated by 8 pm when compared with the terminal Mo-borylene complex **3** [2.1519(15) Å][11b] and this is due to the increased coordination number of the boron centre in the former. However, it is still shorter (10 pm) than the distance in the only structurally characterised complex with a Mo–B–bond [($\eta^5$-C$_5$H$_5$)Mo(CO)$_2$-COB(NMe$_2$)B(NMe$_2$)Mo(CO)$_3$] [Mo–B 2.348(4) Å].[18b,18c] Likewise, the Pd–B bond length [2.065(4) Å] lies within the expected range for three-coordinate boron linked to a palladium centre [2.006(9)–2.077(6) Å].[24] The relatively short B–N distance of 1.376(5) Å, which is only marginally longer than in the corresponding borylene complex **3** [1.3549(18) Å], indicates significant double bond character in the B–N linkage.[11b] In contrast, the homodinuclear bridged aminoborylene species [{($\eta^5$-C$_5$H$_5$)Mn(CO)$_2$}$_2${μ-BNMe$_2$}] (**5**)[13a] and [{($\eta^5$-C$_5$H$_4$Me)Fe(CO)}$_2$(μ-CO){μ-BN(SiMe$_3$)$_2$}] (**6**),[13b] in which the boron centres possess formal sp$^2$ hybridisation, display a different arrangement. In **5** the B–N distance of 1.39(1) Å is also in agreement with the formulation of a B=N double bond, the plane of the BNMe$_2$ substituent, however, is arranged almost coplanar [8(3)°] with respect to the Mn$_2$B plane[13a] whereas in **6** the BN(SiMe$_3$)$_2$ plane is twisted by 53(1)° with respect to the Fe$_2$B plane resulting in less effective N–B π bonding and, hence, an elongation of the B–N bond [1.412(4) Å].[13b] The perpendicular disposition of the two respective planes in **16** in combination with a typical B–N double bond length disagrees with the description of a formally sp$^2$ hybridised boron centre. More appropriate is the description of the overall bonding situation in terms of a terminal borylene centre being stabilised by a metal base. The Lewis-basic [(Cy$_3$P)Pd] fragment releases electron density into the empty orbitals of CO and the borylene moiety (vide infra). Thus, the π acceptor fragments CO and BN(SiMe$_3$)$_2$ form a pair of two noncompensating, semi-bridging ligands. The classification scheme for semi-bridging carbonyl ligands de-

 © 2007 Wiley-VCH Verlag GmbH & Co. KGaA, Weinheim 

veloped by Crabtree[25] is applicable to the relevant bond angles [Pd–Mo–C1 51.74(10)°; Mo–C1–O1 164.3(3)°]. The corresponding angles for the semi-bridging B–R moiety [Pd–Mo–B 47.59(10)°; Mo–B–N 150.7(3)°] lie clearly between those typically found for terminal and symmetrically bridging ligands and are similar to their semi-bridging Cr and W analogues **14** and **15**.[10a]

For the synthesis of **16**, it is important to restrict the reaction time to a minimum since liberated phosphane tends to substitute a carbonyl group at Mo which subsequently leads to formation of a variety of degradation products as indicated by $^{31}P\{^1H\}$ NMR spectroscopic data: $[(Cy_3P)(OC)_3Mo(\mu\text{-}CO)\{\mu\text{-}BN(SiMe_3)_2\}Pd(PCy_3)]$ (**17**) [$\delta$ ($^{31}P$) = 50.7 ppm (d, $^4J_{P,P}$ = 12 Hz, $P_{Mo}$), 33.9 ppm (d, $^4J_{P,P}$ = 12 Hz, $P_{Pd}$); $\delta$ ($^1H$) = 0.63 ppm (s, $SiMe_3$)], *trans*-$[(Cy_3P)(OC)_4Mo{=}BN(SiMe_3)_2]$ (**11**) [$\delta$ ($^{31}P$) = 51.2 ppm (s); $\delta$ ($^1H$) = 0.37 ppm (s, $SiMe_3$)],[11b] and $[(OC)_5Mo(PCy_3)]$ (**18**) [$\delta$ ($^{31}P$) = 47.8 ppm(s)]. In a typical experiment, a ratio of 9:1 for $[(OC)_4Mo(\mu\text{-}CO)\{\mu\text{-}BN(SiMe_3)_2\}Pd(PCy_3)]$ (**16**) to $[(Cy_3P)(OC)_3Mo(\mu\text{-}CO)\{\mu\text{-}BN(SiMe_3)_2\}Pd(PCy_3)]$ (**17**) was observed after 30 min which decreased after 1 d to 3:1 and, in addition, *trans*-$[(Cy_3P)(OC)_4Mo{=}BN(SiMe_3)_2]$ (**11**) started to be formed. Finally, after 4 d the ratio was approximately 4:3:3 according to the $^1H$ NMR spectra.

In order to study whether *trans*-$[(Cy_3P)(OC)_4Mo{=}BN(SiMe_3)_2]$ (**11**) is available in an analogous manner to the Cr complex **10** by irradiation of the heterodinuclear complex **14**,[10a] $[(OC)_4Mo(\mu\text{-}CO)\{\mu\text{-}BN(SiMe_3)_2\}Pd(PCy_3)]$ (**16**) was photolysed. According to the $^{31}P\{^1H\}$ NMR spectra, however, the aforementioned product mixture of **16**, **17**, **11** and **18** was already obtained after 30 min but now with a ratio of 5:4:6:14.

In order to complete the series of semi-bridging group 6 borylene complexes with Pd- and Pt-base stabilisation, $[(OC)_5Mo = BN(SiMe_3)_2]$ (**3**) was treated with $[Pt(PCy_3)_2]$ (**13**) in $C_6D_6$ under identical conditions. The reaction mixture showed several compounds, from which $[(Cy_3P)(OC)_3Mo(\mu\text{-}CO)\{\mu\text{-}BN(SiMe_3)_2\}Pt(PCy_3)]$ (**19**), *trans*-$[(Cy_3P)(OC)_4Mo{=}BN(SiMe_3)_2$ (**11**), $[(OC)_5Mo(PCy_3)]$ (**18**) and $PCy_3$ could be identified by $^{31}P\{^1H\}$ NMR spectroscopy. The dinuclear complex **19** was isolated by layering a toluene solution with hexane and slow evaporation of the solvent.

The $^{31}P\{^1H\}$ NMR spectrum of the isolated compound **19** showed two doublets [$\delta$ = 70 ppm (d, $^4J_{P,P}$ = 11 Hz, $^1J_{P,Pt}$ = 5002 Hz, $P_{Pt}$), 49.9 (d, $^4J_{P,P}$ = 11 Hz, $^3J_{P,Pt}$ = 73 Hz, $P_{Mo}$)], indicating the presence of two nonequivalent phosphane ligands. A singlet for the $-SiMe_3$ groups ($\delta$ = 0.63 ppm) in the $^1H$ NMR spectrum as well as a broad resonance in the $^{11}B\{^1H\}$ NMR spectrum ($\delta$ = 100 ppm) were observed downfield shifted with respect to the signals of the starting material **3**.[11b] The reaction with $[Pt(PCy_3)_2]$ (**13**) proceeds even faster than that with $[Pd(PCy_3)_2]$ (**12**), or the one of **13** with the W-borylene **2**.[10b] Therefore, very fast work-up is required, since the NMR spectroscopic data recorded 1 h after mixing the reactants already indicated a 2:2:1 mixture of the subsequently isolated product $[(Cy_3P)(OC)_3Mo(\mu\text{-}CO)\{\mu\text{-}BN(SiMe_3)_2\}Pt(PCy_3)]$ (**19**), the borylene complex *trans*-$[(Cy_3P)(OC)_4Mo{=}BN(SiMe_3)_2]$ (**11**)[11b] and $[(Cy_3P)Mo(CO)_5]$ (**18**) (Scheme 1). After one week, the ratio has changed to 1:2:2, thus explaining the low yield of 12%.

The molecular constitution of **19** was determined by a single-crystal X-ray diffraction study (see Figure 3). The complex crystallises in the triclinic space group $P\bar{1}$ and

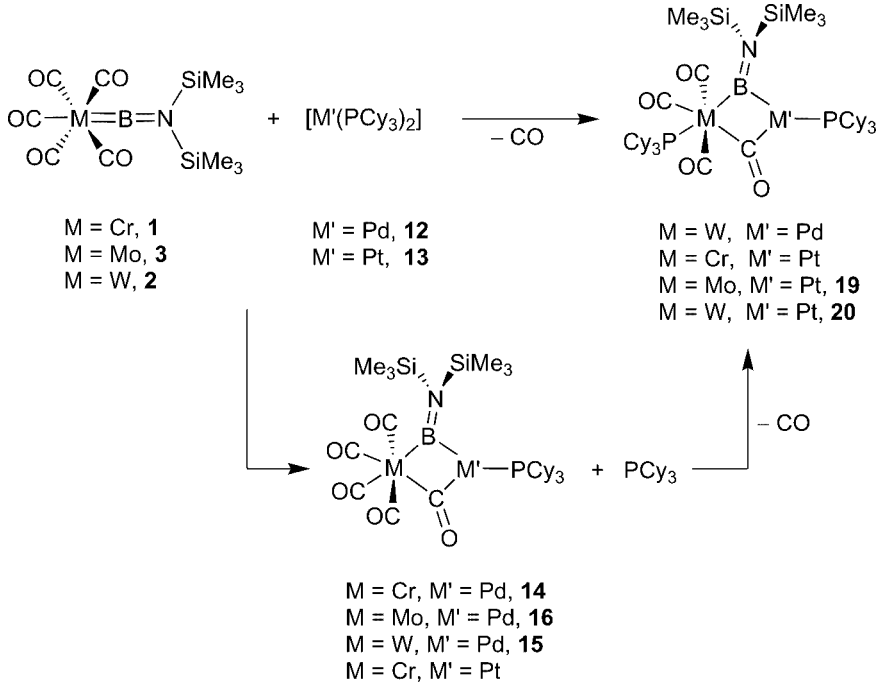


Scheme 1. Survey for the reaction mechanism of the formation of different semi-bridging borylene complexes.

 © 2007 Wiley-VCH Verlag GmbH & Co. KGaA, Weinheim 

shows similar structural features to the W analogue **20**[10b] or the Mo–Pd compound **16** particularly with respect to the geometries of the CO [Pt–Mo–C1 51.38(14)°; Mo–C1–O1 165.7(4)°] and borylene ligands [Pt–Mo–B 49.34(15)°; Mo–B–N 153.2(4)°]. These data together with the short B=N double bond [1.408(7) Å] and the orthogonal orientation of the aminoborylene group with respect to the M–B–Pt plane [Si2–N–B–Mo 91.2(9)°] demonstrate the presence of semi-bridging borylene and CO ligands, respectively. Comparison of the Mo–B bond lengths in the mono- and diphosphane complexes **16** and **19**, however, reveals distinct differences. In the case of **19**, the Mo–B separation of 2.138(6) Å is significantly smaller than that in **16** [2.235(4) Å] but falls barely below the Mo–B distance in **3** [2.1519(15) Å][11b] despite the higher coordination number of the boron atom in the diphosphane complex **19**. The same effect has already been observed in the corresponding complexes of W (**15** and **20** in comparison with **2**).[10b] Clearly, the presence of the $PCy_3$ group in a *trans* position to the borylene leads to a decreased M–B separation due to the reduced π acceptor abilities of the phosphane when compared with CO, thus inducing a stronger M–B $d_\pi$–$p_\pi$ back donation. A similar observation was made in the case of terminal borylene complexes **1**–**3**, substituted with a phosphane ligand in *trans* position to the boron atom [*trans*-[$(Cy_3P)(OC)_4$M=BN$(SiMe_3)_2$] (M = Cr, **9**; Mo, **11**; W, **10**)].[10b,11b]

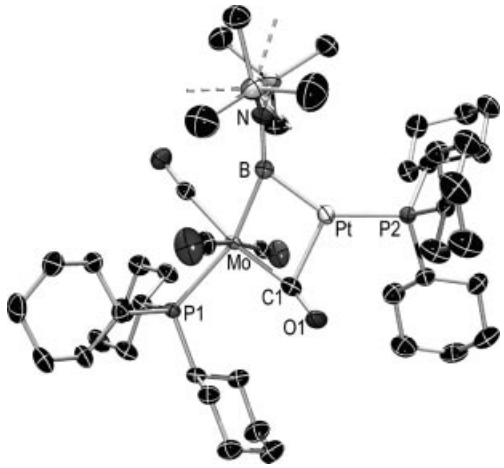


Figure 3. Molecular structure of [$(Cy_3P)(OC)_3$Mo(μ-CO){μ-BN$(SiMe_3)_2$}Pt$(PCy_3)$] (**19**). Thermal ellipsoids are set at the 50% probability level Selected bond lengths [Å] and angles [°]: B–N 1.408(7), Mo–B 2.138(6), Pt–P2 2.2912(13), Mo–P1 2.5587(12), Pt–Mo–C1 51.38(14), Mo–C1–O1 165.7(4), Pt–Mo–B 49.34(15), Mo–B–N 153.2(4), Si2–N–B–Mo 91.2(9).

## Calculations

To gain some deeper insight into the electronic structures of semi-bridging borylene complexes, we performed DFT computations on model systems of the complexes **16**, **17** and **19**.[26] Since no significant difference was observed between the Pd and Pt analogues, only the results for the Pd complexes are presented. To reduce computation time $PMe_3$ was used instead of $PCy_3$ and $N(SiMe_3)_2$ was replaced by $N(SiH_3)_2$.

To our surprise, the optimised geometry of the model compound [$(OC)_4$Mo(μ-CO){μ-BN$(SiH_3)_2$}Pd$(PMe_3)$] (**16a**) displays a Si–N–B–Mo torsion angle of ca. 41°. Reoptimisation with the smaller $NH_2$ group (**16b**$_{Min}$) led to the coplanar system $C_\mu M_2B{=}NH_2$, thus allowing π interaction between the electron lone pair on the nitrogen and the empty p orbital of the boron atom to extend to both metal atoms, thus providing evidence that the mutual orthogonal orientation of the amino-group and the four-membered ring $C_\mu M_2B$ is caused by steric effects. The molecule with an orthogonal disposition of the two respective planes was found to be a transition state (**16b**$_{TS}$) on the PES which is 34.4 kJ mol$^{-1}$ higher in energy than the coplanar minimum structure **16b**$_{Min}$.

As mentioned before, the B–N bond in **16** is only negligibly longer than that in the terminal borylene **3** (137.6 vs. 135.5 pm). The DFT computations for **16b**$_{Min}$ and **16b**$_{TS}$ result in very similar B–N distances (138.5 and 139.9 pm respectively) thus mirroring the short experimental B–N bond despite the orthogonal orientation of the amino-group to the $BM_2$ plane. The arguments against $sp^2$ hybridisation of boron were already raised in the crystal structure discussion and are supported by theory. Even for **16b**$_{TS}$ with its orthogonally orientated amino-group, one can identify an orbital clearly describing the B=N π interaction (HOMO–8), thus backing up the relative high s character of the hybrid orbital at the boron atom (see Figure 4).

We analysed the canonical orbitals of the parent compound **16b**$_{TS}$ with regards to interaction between the Mo borylene moiety [$(OC)_5MoBNH_2$] and the metal base [$Pd(PH_3)$]. For this analysis the transition state geometry **16b**$_{TS}$ rather than the minimum **16b**$_{Min}$ was employed since it displays the same orientation for the amino group as that found experimentally for **16**. Selected orbitals for **16b**$_{TS}$ are depicted in Figure 4.

The HOMO-9 and HOMO-10 are characterised mainly by σ interaction between the lone pair of the formal borylene $BNH_2$ and d orbitals of palladium. The HOMO-7 is primarily composed of a palladium $d_{xz}$ + $d_{yz}$ hybrid (ca. 2:1) orbital with some admixture of the boron $p_z$ orbital and thus describes the Pd→B π backbonding interaction. Inspection of the orbitals revealed, that in spite of similarities between borylenes and carbonyls, there is a difference in their interaction with metal bases. Marder et al. employed the Fragment Orbital Analysis for [($\eta^5$-$C_5H_5$)(OC)Rh(μ-CO)$_2$Cr(CO)($C_6H_6$)] and found that the dominant interaction between the metal-base [($\eta^5$-$C_5H_5$)(OC)Rh] and the metal-carbonyl fragment [$(OC)_3$Cr($\eta^6$-$C_6H_6$)] is that of occupied d orbitals of rhodium with unoccupied π* orbitals on the carbonyl groups. In the case of the borylene, however, the HOMO-3 shows no bonding character between the boron and metal centre because the hybrid orbital on boron is a mixture of $p_y$ and $p_x$ with s orbitals. Mixing of both p functions adjusts the direction of the hybrid towards molybdenum and subtraction of the s function removes a lobe pointing toward palladium and leads to further polari-

 © 2007 Wiley-VCH Verlag GmbH & Co. KGaA, Weinheim 

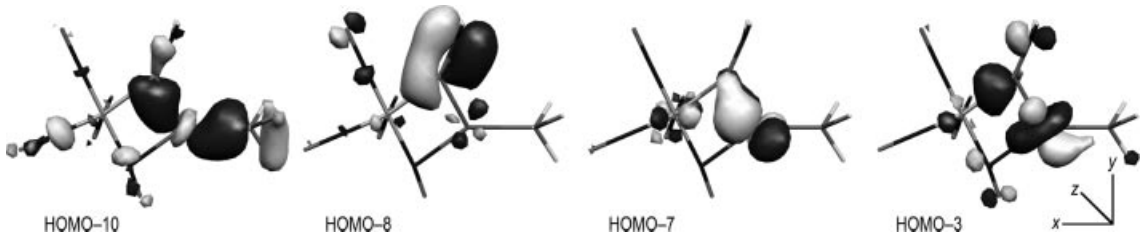


Figure 4. Kohn–Sham orbitals of $[(OC)_4Mo(\mu\text{-}CO)(\mu\text{-}BNH_2)Pd(PH_3)]$ **16b**$_{TS}$.

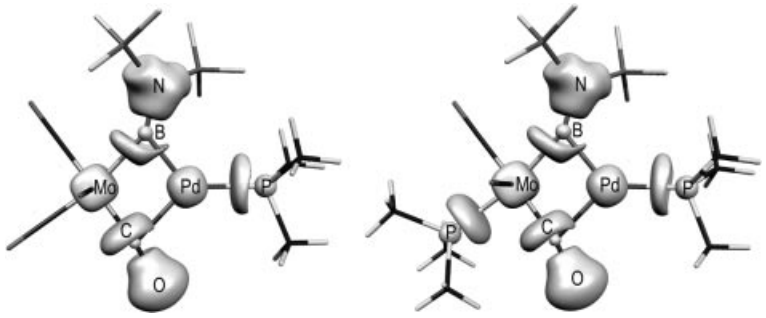


Figure 5. Plot of the ELF (isosurface: 0.70) of $[(OC)_4Mo(\mu\text{-}CO)\{\mu\text{-}BN(SiH_3)_2\}Pd(PMe_3)]$ **16a** and $[(Me_3P)(OC)_3Mo(\mu\text{-}CO)\{\mu\text{-}BN(SiH_3)_2\}Pd(PMe_3)]$ **17a**. The ELF surface around the ligands has been omitted for clarity.

sation towards Mo. The interaction of the Pd-fragment with the unoccupied orbital of the carbonyl group plays only a minor role as also indicated by the experimental data, i.e. the Pd–$C_\mu$ distance is significantly greater than the Pd–B separation.

Analysis of the Electron Localisation Function (ELF) can provide insight into the topology of valence electron pairs. Similar to $[(\mu_3\text{-}BMe)\{[(\eta^5\text{-}C_5H_5)Mn(CO)_2][Pd(PMe_3)]_2\}]$,[8c–8d] ELF computations located, in all computed molecules, three-synaptic basins representing (3c,2e)–Mo–B–Pd bonds, with their attractors localised on the boron-metal side. The situation of the bridging carbonyls resembles that of the borylenes. The ELF attractors of the Mo–C–Pd basins are also placed between Mo and the bridging atom (see Figure 5). In all cases the highest atomic contribution to the three-synaptic basins is provided by the central atom (ca. 50%).

The shape of the ELF basins of **16a** is very similar to that of $[(Me_3P)(OC)_3Mo(\mu\text{-}CO)\{\mu\text{-}BN(SiH_3)_2\}Pd(PMe_3)]$ (**17a**). There is, however, a distinct discrepancy in the population of the B–N disynaptic basins which illustrates the difference in the *trans* effect of carbonyl vs. the phosphane groups. Formal exchange of CO in **17a** by a phosphane leads to a stronger Mo–B interaction, thus resulting in weaker B=N and B–Pd bonds. This phenomenon is reflected in the values of the Wiberg Bond Index (WBI). The WBI of the B–Mo bonds increases from 0.59 to 0.76 while at the same time it decreases for the B–Pd bonds from 0.61 to 0.53 when compared **16a** with **17a**. It should be mentioned, that despite short interatomic distances, neither ELF attractors nor the WBI indicates a distinct Mo–Pd interaction (see Table 1).

Table 1. Analysis of bonding in $[(OC)_4Mo(\mu\text{-}CO)(\mu\text{-}BNH_2)Pd(PH_3)]$ (**16b**$_{Min}$ and **16b**$_{TS}$) $[(OC)_4Mo(\mu\text{-}CO)\{\mu\text{-}BN(SiH_3)_2\}Pd(PMe_3)]$ (**16a**), and $[(Me_3P)(OC)_3Mo(\mu\text{-}CO)\{\mu\text{-}BN(SiH_3)_2\}Pd(PMe_3)]$ (**17a**).

| | **16b**$_{Min}$ | **16b**$_{TS}$ | **16a** | **17a** |
|---|---|---|---|---|
| **Bond lengths [pm] and angles [°]** | | | | |
| $\angle(M_2BC)(R_2NB)$ | 0.0 | 90.0 | 41.0 | 39.2 |
| B–Mo | 224.5 | 224.2 | 226.4 | 217.4 |
| B–Pd | 204.3 | 203.8 | 204.8 | 210.0 |
| $C_\mu$–Mo | 207.2 | 208.2 | 207.8 | 207.6 |
| $C_\mu$–Pd | 236.4 | 236.0 | 233.4 | 227.5 |
| B=N | 138.5 | 139.9 | 139.9 | 140.9 |
| N–B–Mo | 146.3 | 150.2 | 149.2 | 153.1 |
| Mo–B–Pd | 82.2 | 82.1 | 81.5 | 81.8 |
| **Wiberg Bond Indices** | | | | |
| B–Mo | 0.61 | 0.63 | 0.59 | 0.76 |
| B–Pd | 0.62 | 0.58 | 0.61 | 0.53 |
| $C_\mu$–Mo | 0.76 | 0.74 | 0.74 | 0.75 |
| $C_\mu$–Pd | 0.21 | 0.22 | 0.24 | 0.28 |
| B=N | 1.13 | 1.03 | 1.01 | 0.98 |
| Mo–Pd | 0.11 | 0.11 | 0.11 | 0.12 |
| **Natural charges** | | | | |
| B | 0.54 | 0.62 | 0.61 | 0.64 |
| Mo | –1.17 | –1.20 | –1.17 | –1.20 |
| Pd | 0.06 | 0.02 | 0.01 | 0.01 |
| $C_\mu$ | 0.51 | 0.51 | 0.51 | 0.49 |
| **ELF basin population** | | | | |
| B=N | 3.92 | 3.97 | 3.47 | 2.67 |
| Mo–B–Pd | 3.13 | 3.13 | 3.23 | 3.22 |
| Mo–C–Pd | 3.08 | 3.15 | 3.15 | 3.20 |

## Conclusions

The first Mo-based semi-bridging borylene complexes $[(OC)_4Mo(\mu\text{-}CO)\{\mu\text{-}BN(SiMe_3)_2\}Pd(PCy_3)]$ (**16**) and $[(Cy_3P)(OC)_3Mo(\mu\text{-}CO)\{\mu\text{-}BN(SiMe_3)_2\}Pt(PCy_3)]$ (**19**) were ob-

 © 2007 Wiley-VCH Verlag GmbH & Co. KGaA, Weinheim 

tained from the reaction of $[(OC)_5Mo{=}B{=}N(SiMe_3)_2]$ (**3**) with the late transition metal complexes $[M(PCy_3)_2]$ (M = Pd, **12**; Pt, **13**) and fully characterised in solution and in the crystalline state. As indicated by multinuclear NMR spectroscopy, the formation of these heterodinuclear species is induced by cleavage of $PCy_3$ from the Pd and Pt precursors and subsequent addition of the Lewis-basic metal fragments $[M(PCy_3)]$ to the borylene moiety, thus representing a rare case of reactivity of terminal aminoborylene complexes under thermal (i.e. nonphotolytic) conditions. The generally increased lability of Mo organometallics with respect to their Cr and W counterparts is reflected by the rapid formation of the borylene species reported here and, in particular, by their enhanced reactivity, thus leading to the formation of a variety of side and degradation products. This, above all, is true for the instantaneous generation of the diphosphane complex **19** which is supposedly formed via a monophosphane intermediate $[(OC)_4M(\mu\text{-}CO)\{\mu\text{-}BN(SiMe_3)_2\}Pt(PCy_3)]$ analogous to **16** and which is known for M = Cr and W but could not be detected here in the case of M = Mo. Besides, this facile substitution of CO by $PCy_3$ provides further evidence of the strong *trans* influence of boron centred ligands.

The particular coordination mode of the aminoborylene ligand in the title compounds was elucidated for the first time by detailed DFT and ELF studies which demonstrated, in agreement with the structural data, that the $(Me_3Si)_2NB$ moiety adopts a semi-bridging position which is well known for related carbonyl complexes but has only very recently started to appear for borylenes. From the computational data it can be concluded that the $(Me_3Si)_2NB$ ligand is characterised by a pronounced B=N double bond and a predominantly sp hybridised boron atom and donates σ electron density from its formal lone pair to both metal centres and receives in return π back donation into a $p_z$ orbital. In addition, structural and computational data indicate that a phosphane group *trans* to the semi-bridging borylene (e.g. **19**) increases the Mo–B bond strength with respect to a *trans* CO ligand, due to the higher π acceptor abilities of the latter.

## Experimental Section

All manipulations were performed either under an atmosphere of dry argon or in vacuo using standard Schlenk line and glove-box techniques. Solvents were dried by standard methods and were distilled and stored over molecular sieves prior to use. Deuterated solvents ($C_6D_6$) were degassed by three freeze-pump-thaw cycles and stored over molecular sieves in the glove-box. The irradiation experiments were carried out using a Heraeus TQ 150 high-pressure Hg lamp. IR spectra were recorded as toluene solutions between NaCl plates on a Bruker Vector 22 FTIR spectrometer. NMR spectra were acquired either on a Bruker AMX 400 or a Bruker Avance 500 NMR spectrometer. Reaction mixtures were monitored on a Bruker Avance 200 NMR spectrometer. $^1H$ and $^{13}C\{^1H\}$ NMR spectra were referenced to external TMS by the residual proton resonances of the solvent ($^1H$) or the solvent itself ($^{13}C$). $^{11}B\{^1H\}$ NMR spectra were referenced to external $BF_3{\cdot}OEt_2$ and $^{31}P\{^1H\}$ NMR spectra to 85% $H_3PO_4$. Microanalyses for C, H and N were performed on a Leco CHNS-932 elemental analyser.

**$[(OC)_4Mo(\mu\text{-}CO)\{\mu\text{-}BN(SiMe_3)_2\}Pd(PCy_3)]$ (16):** Solid $[(OC)_5Mo{=}B{=}N(SiMe_3)_2]$ (**3**) (0.060 g, 0.147 mmol) was added to a pale yellow solution of $[Pd(PCy_3)_2]$ (**12**) (0.098 g, 0.147 mmol) in $C_6D_6$ (0.5 mL). After 5 min the reaction mixture was layered with hexane (2 mL) and stored at –35 °C. Over night orange crystals of $[(OC)_4Mo(\mu\text{-}CO)\{\mu\text{-}BN(SiMe_3)_2\}Pd(PCy_3)]$ (**16**) had formed (0.062 g, 53%). $^1H$ NMR (400 MHz, $C_6D_6$, 21 °C): $\delta$ = 1.97–1.14 (m, 33 H, Cy), 0.41 (s, 18 H, $SiMe_3$) ppm. $^{13}C\{^1H\}$ NMR (101 MHz, $C_6D_6$, 21 °C): $\delta$ = 213.0 (d, $J_{C,P}$ = 2 Hz, CO), 210.8 (d, $J_{C,P}$ = 4 Hz, CO), 34.0 (d, $^1J_{C,P}$ = 13 Hz, $C^1$, Cy), 31.5 (d, $^3J_{C,P}$ = 5 Hz, $C^{3,5}$, Cy), 27.8 (d, $^2J_{C,P}$ = 11 Hz, $C^{2,6}$, Cy), 26.5 (d, $^4J_{C,P}$ = 1 Hz, $C^4$, Cy), 3.8 (s, $SiMe_3$) ppm. $^{11}B\{^1H\}$ NMR (64 MHz, $C_6D_6$, 23 °C): $\delta$ = 99 (br. s, $\omega_{1/2}$ = 810 Hz) ppm. $^{31}P\{^1H\}$ NMR (162 MHz, $C_6D_6$, 21 °C): $\delta$ = 35.1 (s) ppm. IR (toluene): $\tilde{\nu}$ = 2043, 1962, 1939, 1876 [ν(C=O)] $cm^{-1}$. $C_{29}H_{51}BMoNO_5PPdSi_2$ (794.03): calcd. C 43.87, H 6.47, N 1.76; found C 43.77, H 6.47, N 1.72.

**$[(Cy_3P)(OC)_3Mo(\mu\text{-}CO)\{\mu\text{-}BN(SiMe_3)_2\}Pt(PCy_3)]$ (19):** Solid $[(OC)_5Mo{=}B{=}N(SiMe_3)_2]$ (**3**) (0.045 g, 0.110 mmol) was added to a pale yellow solution of $[Pt(PCy_3)_2]$ (**13**) (0.084 g, 0.110 mmol) in toluene (0.5 mL). The solution turned brown and then red. After 5 min the reaction mixture was layered with hexane (2 mL) and the solvent was allowed to slowly evaporate in the glovebox. The solid was extracted with $C_6D_6$, the red solution was layered with hexane (1.5 mL) and the solvent was allowed to evaporate. After 4 d pale red-brown crystals formed which were recrystallised from toluene/hexane yielding 15 mg (12%) of $[(Cy_3P)(OC)_3Mo(\mu\text{-}CO)\{\mu\text{-}BN(SiMe_3)_2\}Pt(PCy_3)]$ (**19**). $^1H$ NMR (500 MHz, $C_6D_6$, 27 °C): $\delta$ = 2.20–2.05 (m, 18 H, Cy), 1.80–1.58 (m, 30 H, Cy), 1.28–1.20 (m, 18 H, Cy), 0.63 (s, 18 H, $SiMe_3$) ppm. $^{13}C\{^1H\}$ NMR (126 MHz, $C_6D_6$, 27 °C): $\delta$ = 220.4 (d, $^2J_{C,P}$ = 2 Hz, CO), 220.3 (d, $^2J_{C,P}$ = 2 Hz, CO), 37.1 (d, $^1J_{C,P}$ = 13 Hz, $C^1$, $Cy^{Mo}$), 36.4 (d, $^1J_{C,P}$ = 22 Hz, $C^1$, $Cy^{Pt}$), 31.1 (d, $^3J_{C,P}$ = 2 Hz, $C^{3,5}$, $Cy^{Pt}$), 30.4 (s, $C^{3,5}$, $Cy^{Mo}$), 28.1 (d, $^2J_{C,P}$ = 10 Hz, $C^{2,6}$, $Cy^{Mo}$), 27.9 (d, $^2J_{C,P}$ = 11 Hz, $C^{2,6}$, $Cy^{Pt}$), 26.8 (s, $C^4$, $Cy^{Mo}$), 26.7 (s, $C^4$, $Cy^{Pt}$), 4.2 (s, $SiMe_3$) ppm. $^{11}B\{^1H\}$ NMR (160 MHz, $C_6D_6$, 27 °C): $\delta$ = 100 (br. s, $\omega_{1/2}$ = 1557 Hz) ppm; $^{31}P\{^1H\}$ NMR (202 MHz, $C_6D_6$, 27 °C): $\delta$ = 70.6 (d, $^4J_{P,P}$ = 11 Hz, $^1J_{P,Pt}$ = 5002 Hz, $P^{Pt}$), 49.9 (d, $^4J_{P,P}$ = 11 Hz, $^3J_{P,Pt}$ = 73 Hz, $P^{Mo}$) ppm. IR (toluene): $\tilde{\nu}$ = 1985, 1889, 1796, 1766 [ν(C=O)] $cm^{-1}$. $C_{46}H_{84}BMoNO_4P_2PtSi_2$ (1135.11): calcd. C 48.67, H 7.46, N 1.23; found C 48.54, H 7.11, N 1.20.

**Crystal Structure Determination:** The crystal data of **16** and **19** were collected on a Bruker X8APEX diffractometer with a CCD area detector and Mo-$K_\alpha$ radiation monochromated by using a multilayer mirror. The structures were solved by direct methods, refined with the Shelx software package (G. Sheldrick, University of Göttingen, 1997) and expanded using Fourier techniques. All non-hydrogen atoms were refined anisotropically. Hydrogen atoms were assigned to idealised positions and were included in structure factor calculations.

**Crystal Data for 16:** $C_{29}H_{51}BMoNO_5PPdSi_2$, $M_r$ = 794.01, orange bar, 0.23 × 0.21 × 0.13 mm, orthorhombic space group $Pna2_1$, $a$ = 17.7385(13) Å, $b$ = 9.5613(7) Å, $c$ = 21.3089(15) Å, $V$ = 3614.1(5) $Å^3$, $Z$ = 4, $\rho_{calcd}$ = 1.459 $g\,cm^{-3}$, $\mu$ = 0.990 $mm^{-1}$, $F(000)$ = 1632, $T$ = 173(2) K, $R_1$ = 0.0307, $wR_2$ = 0.0649, 7134 independent reflections [$2\theta \leq 52.24°$] and 370 parameters.

**Crystal Data for 19:** $C_{46}H_{84}BMoNO_4P_2PtSi_2$, $M_r$ = 1135.10, yellow block, 0.19 × 0.10 × 0.07 mm, triclinic space group $P\bar{1}$, $a$ = 12.2522(7) Å, $b$ = 13.4914(8) Å, $c$ = 16.2482(10) Å, $\alpha$ = 96.7280(10)°, $\beta$ = 101.2180(10)°, $\gamma$ = 96.7180(10)°, $V$ = 2589.3(3) $Å^3$, $Z$ = 2, $\rho_{calcd}$ = 1.456 $g\,cm^{-3}$, $\mu$ = 3.088 $mm^{-1}$, $F(000)$ =

 © 2007 Wiley-VCH Verlag GmbH & Co. KGaA, Weinheim 

1164, $T$ = 173(2) K, $R_1$ = 0.0462, $wR_2$ = 0.1017, 10261 independent reflections [$2\theta \leq 52.28°$] and 551 parameters.

CCDC-645809 and -645810 contain the crystallographic data for this article. These data can be obtained free of charge from the Cambridge Crystallographic Data Centre via www.ccdc.cam.ac.uk/data_request/cif

**Supporting Information** (see also the footnote on the first page of this article): Results of DFT calculations.

## Acknowledgments

This work was supported by the Deutsche Forschungsgemeinschaft (DFG). The authors thank Dr. F. Seeler for performing the X-ray diffraction study of compound **19**.

[1] a) K. Burgess, M. J. Ohlmeyer, *Chem. Rev.* **1991**, *91*, 1179–1191; b) I. Beletskaya, A. Pelter, *Tetrahedron* **1997**, *53*, 4957–5026.
[2] T. B. Marder, N. C. Norman, *Top. Catal.* **1998**, *5*, 63–73.
[3] a) J.-Y. Cho, M. K. Tse, D. Holmes, R. E. Maleczka Jr, M. R. Smith III, *Science* **2002**, *295*, 305–308; b) T. Ishiyama, N. Miyaura, *J. Organomet. Chem.* **2003**, *680*, 3–11; c) T. Ishiyama, Y. Nobuta, J. F. Hartwig, N. Miyaura, *Chem. Commun.* **2003**, 2924–2925; d) D. N. Coventry, A. S. Batsanov, A. E. Goeta, J. A. K. Howard, T. B. Marder, R. N. Perutz, *Chem. Commun.* **2005**, 2172–2174; e) J. F. Hartwig, K. S. Cook, M. Hapke, C. D. Incarvito, Y. Fan, C. E. Webster, M. B. Hall, *J. Am. Chem. Soc.* **2005**, *127*, 2538–2552, and references therein.
[4] a) H. Braunschweig, *Angew. Chem.* **1998**, *110*, 1882–1898; *Angew. Chem. Int. Ed.* **1998**, *37*, 1786–1801; b) H. Braunschweig, M. Colling, *Coord. Chem. Rev.* **2001**, *223*, 1–51; c) H. Braunschweig, M. Colling, *Eur. J. Inorg. Chem.* **2003**, 393–403; d) H. Braunschweig, *Adv. Organomet. Chem.* **2004**, *51*, 163–192; e) H. Braunschweig, C. Kollann, D. Rais, *Angew. Chem.* **2006**, *118*, 5380–5400; *Angew. Chem. Int. Ed.* **2006**, *45*, 5254–5274; f) J. Uddin, C. Boehme, G. Frenking, *Organometallics* **2000**, *19*, 571–582; g) J. Uddin, C. Boehme, G. Frenking, *Coord. Chem. Rev.* **2000**, *197*, 249–276; h) J. Uddin, G. Frenking, *J. Am. Chem. Soc.* **2001**, *123*, 1683–1693.
[5] a) A. W. Ehlers, E. J. Baerends, F. M. Bickelhaupt, U. Radius, *Chem. Eur. J.* **1998**, *4*, 210–221; b) U. Radius, F. M. Bickelhaupt, A. W. Ehlers, N. Goldberg, R. Hoffmann, *Inorg. Chem.* **1998**, *37*, 1080–1090.
[6] a) P. L. Timms, *J. Am. Chem. Soc.* **1967**, *89*, 1629–1632; b) P. L. Timms, *Acc. Chem. Res.* **1973**, *6*, 118–123.
[7] H. Braunschweig, C. Kollann, U. Englert, *Angew. Chem.* **1998**, *110*, 3355–3357; *Angew. Chem. Int. Ed.* **1998**, *37*, 3179–3180.
[8] a) H. Braunschweig, D. Rais, K. Uttinger, *Angew. Chem.* **2005**, *117*, 3829–3832; *Angew. Chem. Int. Ed.* **2005**, *44*, 3763–3766; b) H. Braunschweig, K. Radacki, D. Rais, K. Uttinger, *Organometallics* **2006**, *25*, 5159–5164; c) H. Braunschweig, C. Burschka, M. Burzler, S. Metz, K. Radacki, *Angew. Chem.* **2006**, *118*, 4458–4461; *Angew. Chem. Int. Ed.* **2006**, *45*, 4352–4355; d) H. Braunschweig, K. Radacki, D. Rais, F. Seeler, *Angew. Chem.* **2006**, *118*, 1087–1090; *Angew. Chem. Int. Ed.* **2006**, *45*, 1066–1069; e) H. Braunschweig, M. Forster, K. Radacki, *Angew. Chem.* **2006**, *118*, 2187–2189; *Angew. Chem. Int. Ed.* **2006**, *45*, 2132–2134.
[9] a) H. Braunschweig, M. Colling, C. Kollann, H. G. Stammler, B. Neumann, *Angew. Chem.* **2001**, *113*, 2359–2361; *Angew. Chem. Int. Ed.* **2001**, *40*, 2298–2300; b) H. Braunschweig, M. Colling, C. Hu, K. Radacki, *Angew. Chem.* **2003**, *115*, 215–218; *Angew. Chem. Int. Ed.* **2003**, *42*, 205–208.
[10] a) H. Braunschweig, T. Herbst, D. Rais, F. Seeler, *Angew. Chem.* **2005**, *117*, 7627–7629; *Angew. Chem. Int. Ed.* **2005**, *44*, 7461–7463.
[11] a) H. Braunschweig, M. Colling, C. Kollann, K. Merz, K. Radacki, *Angew. Chem.* **2001**, *113*, 4327–4329; *Angew. Chem. Int. Ed.* **2001**, *40*, 4198–4200; b) B. Blank, H. Braunschweig, M. Colling-Hendelkens, C. Kollann, K. Radacki, D. Rais, K. Uttinger, G. R. Whittell, *Chem. Eur. J.* **2007**, *13*, 4770–4781.
[12] a) D. L. Coombs, S. Aldridge, C. Jones, D. J. Willock, *J. Am. Chem. Soc.* **2003**, *125*, 6356–6357; b) D. L. Kays (née Coombs), J. K. Day, L.-L. Ooi, S. Aldridge, *Angew. Chem.* **2005**, *117*, 7623–7626; *Angew. Chem. Int. Ed.* **2005**, *44*, 7457–7460; c) S. Aldridge, C. Jones, T. Gans-Eichler, A. Stasch, D. L. Kays (née Coombs), N. D. Coombs, D. J. Willock, *Angew. Chem.* **2006**, *118*, 6264–6268; *Angew. Chem. Int. Ed.* **2006**, *45*, 6118–6122; d) H. Braunschweig, K. Radacki, D. Rais, D. Scheschkewitz, *Angew. Chem.* **2005**, *117*, 5796–5799; *Angew. Chem. Int. Ed.* **2005**, *44*, 5651–5654 ; e) H. Braunschweig, K. Radacki, K. Uttinger, *Angew. Chem.* **2007**, *119*, 4054–4057; *Angew. Chem. Int. Ed.* **2007**, *46*, 3979–3982.
[13] a) H. Braunschweig, T. Wagner, *Angew. Chem.* **1995**, *107*, 904–905; *Angew. Chem. Int. Ed. Engl.* **1995**, *34*, 825–826; b) H. Braunschweig, C. Kollann, U. Englert, *Eur. J. Inorg. Chem.* **1998**, 465–468; c) H. Braunschweig, C. Kollann, K. W. Klinkhammer, *Eur. J. Inorg. Chem.* **1999**, 1523–1529.
[14] H. Braunschweig, K. Radacki, D. Rais, F. Seeler, K. Uttinger, *J. Am. Chem. Soc.* **2005**, *127*, 1386–1387.
[15] H. Braunschweig, K. Radacki, D. Scheschkewitz, G. R. Whittell, *Angew. Chem.* **2005**, *117*, 1685–1688; *Angew. Chem. Int. Ed.* **2005**, *44*, 1658–1660.
[16] a) J. F. Hartwig, S. R. DeGala, *J. Am. Chem. Soc.* **1994**, *116*, 3661–3662; b) J. F. Hartwig, X. He, *Organometallics* **1996**, *15*, 5350–5358.
[17] J. F. Hartwig, X. He, *Angew. Chem.* **1996**, *108*, 352–354; *Angew. Chem. Int. Ed. Engl.* **1996**, *35*, 315–317.
[18] a) H. Braunschweig, B. Ganter, M. Koster, T. Wagner, *Chem. Ber.* **1996**, *129*, 1099–1101; b) H. Braunschweig, K. W. Klinkhammer, M. Koster, K. Radacki, *Chem. Eur. J.* **2003**, *9*, 1303–1309 ; c) . H. Braunschweig, K. W. Klinkhammer, M. Koster, *Angew. Chem.* **1999**, *111*, 2368–2370; *Angew. Chem. Int. Ed.* **1999**, *38*, 2229–2231; d) H. Braunschweig, M. Koster, R. Wang, *Inorg. Chem.* **1999**, *38*, 415–416.
[19] S. W. Helm, G. Linti, H. Nöth, S. Channareddy, P. Hofmann, *Chem. Ber.* **1992**, *125*, 73–86.
[20] H. Wadepohl, U. Arnold, H. Pritzkow, *Angew. Chem.* **1997**, *109*, 1009–1011; *Angew. Chem. Int. Ed. Engl.* **1997**, *36*, 974–976.
[21] J. R. Graham, R. J. Angelici, *Inorg. Chem.* **1967**, *6*, 2082–2085.
[22] H. Braunschweig, K. Radacki, D. Rais, G. R. Whittell, *Angew. Chem.* **2005**, *117*, 1217–1219; *Angew. Chem. Int. Ed.* **2005**, *44*, 1192–1194.
[23] a) W. Kuran, A. Musco, *Inorg. Chim. Acta* **1975**, *12*, 187–193; b) S. Otsuka, T. Yoshida, M. Matsumoto, K. Nakatsu, *J. Am. Chem. Soc.* **1976**, *98*, 5850–5858.
[24] a) S.-Y. Onozawa, Y. Hatanaka, T. Sakakura, S. Shimada, M. Tanaka, *Organometallics* **1996**, *15*, 5450–5452; b) S.-Y. Onozawa, M. Tanaka, *Organometallics* **2001**, *20*, 2956–2958.
[25] R. H. Crabtree, M. Lavin, *Inorg. Chem.* **1986**, *25*, 805–812.
[26] Electronic structure calculations reported in this work were performed with *Gaussian 03, Revision B.04*, Gaussian, Inc., Pittsburgh PA, **2003**; The Electron Localisation Function and its properties were computed with the TopMoD package of S. Noury, X. Krokidis, F. Fuster, B. Silvi, **1997**; the charges and the Wiberg Bond Indices were calculated with the NBO 5 program of E. D. Glendening, J. K. Badenhoop, A. E. Reed, J. E. Carpenter, J. A. Bohmann, C. M. Morales, **2001**. See electronic supporting information for details on the computations.

Received: March 30, 2007
Published Online: July 27, 2007

 © 2007 Wiley-VCH Verlag GmbH & Co. KGaA, Weinheim 

DOI: 10.1002/ejic.200700357

# Synthesis and Characterization of New Organosilyl Derivatives of Polyoxometalates ($n$Bu$_4$N)$_2$[NbW$_5$O$_{19}$SiRR′$_2$] (R = R′ = Et, $i$Pr, O$t$Bu, Ph; R = $t$Bu and R′ = Me) – X-ray Crystal Structure of ($n$Bu$_4$N)$_2$[NbW$_5$O$_{19}$SiPh$_3$]

**Fatma Bannani,[a,b] René Thouvenot,*[b] and Mongi Debbabi*[a]**

**Keywords:** Polyoxometalates / Organic–inorganic hybrid / Multinuclear NMR spectroscopy

Reactions of ($n$Bu$_4$N)$_4$[(NbW$_5$O$_{18}$)$_2$O] with trialkyl/arylsilanols in dichloromethane and/or acetonitrile forms respectively ($n$Bu$_4$N)$_2$[NbW$_5$O$_{19}$SiRR′$_2$] [R = R′ = Et (**1**), $i$Pr (**3**), O$t$Bu (**4**), Ph (**5**); R = $t$Bu and R′ = Me (**2**)] in ca. 90–64 % isolated yields. The compounds have been characterized by elemental analysis, IR, Raman, multinuclear NMR in solution ($^1$H, $^{13}$C, $^{29}$Si, $^{183}$W) and in the solid-state by $^{29}$Si CP-MAS NMR spectroscopy. Multinuclear NMR and IR spectroscopic data suggest that the SiRR′$_2^+$ electrophilic fragment binds selectively to the terminal NbO oxygen atom which appears the most reactive site in ($n$Bu$_4$N)$_3$[NbW$_5$O$_{19}$]. This is supported by X-ray crystallographic analysis of ($n$Bu$_4$N)$_2$[NbW$_5$O$_{19}$SiPh$_3$] (**5**) which crystallizes in the monoclinic system, space group $P2_1/a$ with lattice parameters $a$ = 19.884(5), $b$ = 16.801(2), $c$ = 20.644(3) Å, $\beta$ = 112.050(12)°, $V$ = 6392(2) Å$^3$, and $Z$ = 4. Hydrolysis of the alkyl/arylsilyloxide derivatives leads to the back formation of the (NbW$_5$O$_{18}$)$_2$O$^{4-}$ dimer by the cleavage of the Si–O bond.
(© Wiley-VCH Verlag GmbH & Co. KGaA, 69451 Weinheim, Germany, 2007)

## Introduction

Polyoxometalates (POMs) form a class of inorganic metal-oxygen cluster compounds having a rising popularity in diverse fields ranging from catalysis to pharmacology.[1] These interesting properties have increased studies to modify polyoxometalates and prepare new compounds in order to well understand polyoxometalates reactivities.[2,3] One of the classical methods to obtain derivatized polyoxometalates is the reaction between the nucleophilic oxygen atom in d$^0$ transition metal oxocomplexes and electrophilic species[4–6] such as organic and organometallic groups. With organic groups bearing reactive moieties, these hybrid species may be further functionalized to be ultimately grafted onto surfaces for obtaining photo- or electrochemical materials. While monosubstituted niobotungstates are relatively poorly reactive,[7] dimeric species with connecting Nb–O–Nb bridge(s) are excellent starting materials for the preparation of organic and organometallic derivatized polyoxoanions.[8–11] Herein, we report the preparation and characterization by IR, Raman, and multinuclear NMR spectroscopy of the $n$Bu$_4$N$^+$ (TBA) salts of alkyl/arylsilylated Nb$^V$-monosubstituted Lindqvist POMs and the X-ray structural determination of ($n$Bu$_4$N)$_2$[NbW$_5$O$_{19}$SiPh$_3$] (**5**). In addition the reaction of these anions with respect to hydrolysis has been investigated.

[a] Laboratoire de Physico-Chimie des Matériaux, Faculté des Sciences de Monastir,
5019 Monastir, Tunisie
Fax: +216-73-500-514
E-mail: mongi.debbabi@enim.rnu.tn
[b] Laboratoire de Chimie Inorganique et Matériaux Moléculaires, UMR CNRS 7071, Université Pierre et Marie Curie – Paris 6, Institut de Chimie Moléculaire FR 2769,
Case Courrier 42, 4, Place Jussieu, 75252 Paris Cedex 05, France
Fax: +33-1-44-27-38-41
E-mail: rth@ccr.jussieu.fr

## Results and Discussion

### Synthesis and Reactivity

The substitution of Nb$^V$ for W$^{VI}$ in the inert hexatungstate results in the increase of the overall charge of the polyoxometalate and in partial localization of the supplementary charge on the terminal oxygen atoms bound to the Nb atom.[17,18] Moreover, the oxygen–niobium bond in NbW$_5$O$_{19}$ is known to be labile with respect to $^{17}$O exchange.[8,19] Although the terminal ONb oxygen atoms are not the most basic among the oxygen atoms bound to Nb atoms both the lability and steric interaction allow reactions with electrophilic species to occur selectively at this oxygen site.[8] Actually in the case of the substituted Keggin anion PW$_{11}$NbO$_{40}$ the reaction of Me$_3$SiSO$_3$CF$_3$ leads directly to the trimethylsilyl derivatives PW$_{11}$O$_{39}$NbOSiMe$_3$.[20] In our case the reaction of R$_3$SiSO$_3$CF$_3$ (R = Me, Et) and $t$BuMe$_2$SiSO$_3$CF$_3$ with NbW$_5$O$_{19}^{3-}$ leads invariably to complex mixtures. By reacting alcohols and silanols with the dimeric form (Nb$_2$W$_4$O$_{18}$)$_2$O$^{6-}$ instead of the monomer Klemperer described the clean synthesis of

 © 2007 Wiley-VCH Verlag GmbH & Co. KGaA, Weinheim 

terminal alkoxide and organosilyl-Lindqvist derivatives.[21] Later Beer[8] applied the same strategy to prepare terminal alkoxide Lindqvist derivatives by reacting the dimeric form of $NbW_5O_{19}^{3-}$ with alcohols. In light of the reactivities of the dimers it was expected that $(NbW_5O_{18})_2O^{4-}$ could also react under controlled conditions with silanols to give $NbW_5O_{19}SiRR'_2{}^{2-}$ according to Equation (1).

$$(NbW_5O_{18})_2O^{4-} + 2SiRR'_2OH \rightarrow 2NbW_5O_{19}SiRR'_2 + H_2O \quad (1)$$

The reaction of $(n\mathrm{Bu}_4\mathrm{N})_4[(NbW_5O_{18})_2O]$ with a stoichiometric amount of $RR'_2SiOH$ at room temperature, under argon, in freshly distilled dichloromethane (R = R′ = Et, *i*Pr; R = *t*Bu, R′ = Me) or in acetonitrile (R = R′ = Ph, O*t*Bu) yields $NbW_5O_{19}SiRR'_2{}^{2-}$ [R = R′ = Et (**1**), *i*Pr (**3**); R = *t*Bu, R′ = Me (**2**)] in satisfactory yields. For R = Ph (**5**) or O*t*Bu (**4**) the low yields (ca. 25%) in $CH_2Cl_2$ were increased by using acetonitrile as the solvent.

As shown by the solution studies the hybrid anions are relatively stable in $CH_2Cl_2$ and $CH_3CN$ but they are progressively hydrolyzed by atmospheric moisture to give $(NbW_5O_{18})_2O^{4-}$ which crystallizes from these solutions.

The formation of the dimer is described by Equation (2); the dimeric anion is in equilibrium with the protonated monomer according to Equation (3).

$$2NbW_5O_{19}SiRR'_2 + H_2O \rightarrow (NbW_5O_{18})_2O^{4-} + 2SiRR'_2OH \quad (2)$$

$$(NbW_5O_{18})_2O^{4-} + H_2O \rightleftarrows 2HNbW_5O_{19}^{2-} \quad (3)$$

This behavior is similar to that observed by Klemperer on $(Nb_2W_4O_{18})_2O^{6-}$ and by Beer on α-$\{PW_{11}O_{39}\}$-$NbOEMe_3^{3-}$[20,21] where (E = C, Si). Beer demonstrated using $^{17}O$ NMR that the primary hydrolysis product of the hybrid species is the dimer $(\alpha\text{-}\{PNbW_{11}O_{39}\})_2O^{6-}$ which hydrolyzes further to the monomer $\alpha\text{-}PNbW_{11}O_{40}^{4-}$.

In our case the reaction stops at the dimer because of its insolubility in dichloromethane and in acetonitrile.

Moreover, in more polar solvents such as DMSO the species are not stable and completely decompose into nonidentified species as shown by both IR and $^{183}W$ NMR spectroscopy.

## Vibrational Spectroscopy

### *IR Characterization*

Infrared spectroscopy analysis gives preliminary structural information in the solid state. Characteristic bands of the parent anion are present at nearly the same positions as in $(n\mathrm{Bu}_4\mathrm{N})_3[NbW_5O_{19}]$ namely at 810 $cm^{-1}$ ($\nu_{as}$ M–$O_b$), 584 $cm^{-1}$ ($\nu_s$ M–$O_b$), 446 $cm^{-1}$ (δ M–$O_b$) indicating that the Lindqvist structure is kept in the organic–inorganic hybrid. Nevertheless the strong band assigned to ($\nu_{as}$ W–$O_t$) shifts from 958 $cm^{-1}$ in $NbW_5O_{19}^{3-}$ to 971 $cm^{-1}$ in $(NbW_5O_{18})_2O^{4-}$ and the organosilyl species. Such a high frequency shift has already been observed for Keggin silyl derivatives[22] as a consequence of the grafting of organosilyl moieties on the POM framework. In the low-wave number region (from 300 to 1000 $cm^{-1}$) characteristic of the metal oxygen framework vibration, all compounds exhibit nearly identical spectra (Figure 1). The absence of the bands at 692 $cm^{-1}$ characteristic of the Nb–O–Nb bridge of the $(NbW_5O_{18})_2O^{4-}$ shows that the hybrid species is built up from the monomeric anion while the lack of the Nb–$O_t$ (915 $cm^{-1}$) in the $NbW_5O_{19}^{3-}$[23] pleads in favor of derivatization at this terminal ONb oxygen atom.

### *Raman Characterization*

Raman spectra of the dimer and of all hybrid derivatives are very similar in the low-wavenumber part ($\tilde{\nu}$ <1050 $cm^{-1}$)

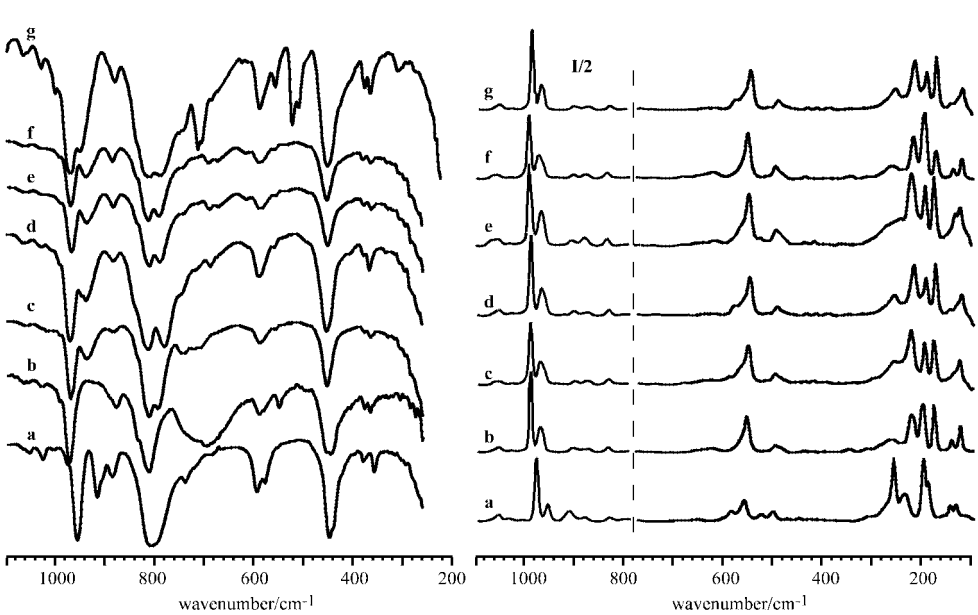


Figure 1. Infrared (left) and Raman (right) spectra of tetrabutylammonium salts of (a) $NbW_5O_{19}^{3-}$, (b) $(NbW_5O_{18})_2O^{4-}$, (c) $NbW_5O_{19}SiEt_3^{2-}$ (**1**), (d) $NbW_5O_{19}Si\mathit{t}BuMe_2^{2-}$ (**2**), (e) $NbW_5O_{19}Si\mathit{i}Pr_3^{2-}$ (**3**), (f) $NbW_5O_{19}Si(O\mathit{t}Bu)_3^{2-}$ (**4**), (g) $NbW_5O_{19}SiPh_3^{2-}$ (**5**). The high frequency part (>800 $cm^{-1}$) of the Raman spectra is scaled by half.

 © 2007 Wiley-VCH Verlag GmbH & Co. KGaA, Weinheim 

(Figure 1). They differ markedly from the spectrum of $NbW_5O_{19}^{3-}$ in the low frequency region $<300\ cm^{-1}$ and also in the high frequency region (900–1000 $cm^{-1}$); in particular as for IR the $\nu_s(W–O_t)$ and $\nu_{as}(W–O_t)$ are shifted by ca. 13 $cm^{-1}$ to a higher frequency in the dimer and in the hybrid species.

### *Multinuclear NMR Characterization*

The presence of several NMR active nuclei allows the structural characterization of POMs by multinuclear NMR spectroscopy.[24–28] Moreover, the high solubility of the TBA salt of POMs in some polar organic solvent permits us to prepare the concentrated solutions required for $^{183}W$ and $^{29}Si$ NMR spectroscopy. Multinuclear NMR ($^1H$, $^{13}C$, $^{29}Si$, and $^{183}W$) measurements have been performed in dichloromethane and acetonitrile solutions. Because of the presence of the organic moieties, $NbW_5O_{19}SiRR'_2$ hybrids are soluble in the less polar organic solvents such as $CH_2Cl_2$.

The $^1H$ and $^{13}C$ spectra of the hybrid species present the signals characteristic of the organosilyl part along with those of the TBA cations (see experimental part). The relative integration of the signals agrees with two TBA for one $SiRR'_2$ group according to the formula $(n-Bu_4N)_2[NbW_5O_{19}SiRR'_2]$.

Room-temperature solid-state $^{29}Si$ CP-MAS spectra were obtained for compounds **1**, **2**, **3**, and **5** (Table 1). They all present only one isotropic signal; while for **3** the signal is relatively narrow ($\Delta\nu_{1/2}$ ca. 100 Hz, 1.3 ppm), it appears broader for the three other compounds ($\Delta\nu_{1/2}$ 300 to 500 Hz, see Table 1); this differential behavior is likely due to more or less rapid rotation around the Si–O bond, leading to different motional narrowing of the $^{29}Si$ resonances. No significant signal could, however, be obtained for compound **4**, even with a large contact time, likely because of inefficient transfer between the silicium nucleus and the more remote protons. The $^{29}Si$ solution spectra present also a single line; contrary to the $^{29}Si$ spectra of the silyl derivatives of Keggin polyoxometallates,[22,27] no $^{183}W$ satellites could be detected for the $NbW_5$ hybrids; this is again in favor of the $SiRR'_2$ group grafted on $O_t$–Nb. The observed chemical shifts are as expected for the M ($SiOC_3$) group in the case of **1**, **2**, **3**, and **5** and for a Q ($SiO_4$) group for **4** (see Table 1). The close values of the isotropic chemical shifts in solution and in the solid-state indicate that hybrid anions keep their structures in solution; at variance with the solid-state case, the line in the solution spectra are, however, very narrow, which agrees with rapid reorientation of the organosilyl part in solution.

The $^{183}W$ NMR spectra of all compounds exhibit two narrow signals around 28–35 ppm (4 W) and 75–79 ppm (1 W) assigned to four equatorial and one axial tungsten atoms, respectively (Figure 2). Each signal presents a pair of satellites due to homonuclear tungsten–tungsten coupling with a coupling constant value (9 Hz) in the classical range characteristic of an "edge-sharing-junction" in iso- and heteropolyanions.[24,26,28] This is again consistent with an effective $C_{4v}$ symmetry of the hybrid anions in solution, with rapid reorientation of the organosilyl group grafted onto the terminal $O_t$–Nb oxygen atom.

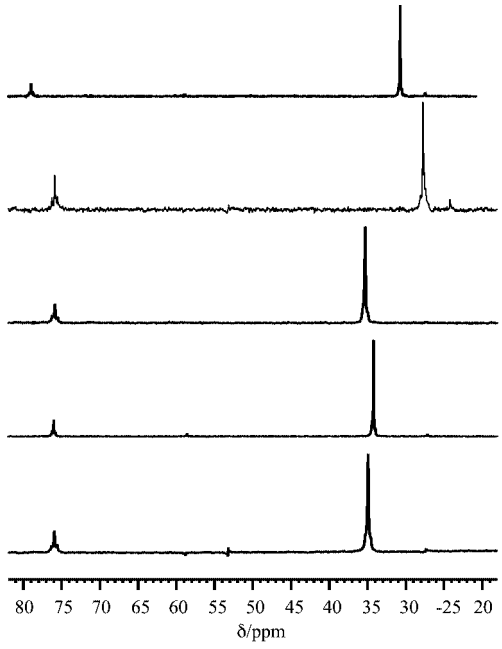


Figure 2. $^{183}W$ NMR solution spectra of the siloxide derivatives: from top to bottom, $NbW_5O_{19}SiPh_3^{2-}$ (**5**), $NbW_5O_{19}Si(O\mathit{t}Bu)_3^{2-}$ (**4**), $NbW_5O_{19}Si\mathit{i}Pr_3^{2-}$ (**3**), $NbW_5O_{19}Si\mathit{t}BuMe_2^{2-}$ (**2**), and $NbW_5O_{19}SiEt_3^{2-}$ (**1**).

The $^{183}W$ chemical shifts are known to be extremely sensitive to subtle structural changes.

In the present case changing the substituent on the Si atom induces chemical shift variations of ca. 7 and 4 ppm

Table 1. $^{183}W$ and $^{29}Si$ NMR spectroscopic data for $Nb^V$-monosubstituted Lindqvist polyoxometalates.

| Compound | $^{183}W$ $\delta(W_{ax})$[a] | $\Delta(W_{eq})$[a] | $\Delta\delta$[b] | $^{29}Si$ $\delta$[c] | $\delta_{iso}$[d] | $\Delta\nu_{1/2}$[e] |
|---|---|---|---|---|---|---|
| $NbW_5O_{19}SiEt_3^{2-}$ (**1**) | 75.9 | 34.9 | +41 | 25.8 | 26.8 | 400 (5) |
| $NbW_5O_{19}Si\mathit{t}BuMe_2^{2-}$ (**2**) | 76.3 | 34.5 | +41.8 | 25.6 | 25.5 | 500 (6.3) |
| $NbW_5O_{19}Si\mathit{i}Pr_3^{2-}$ (**3**) | 75.9 | 35.3 | +40.5 | 24.8 | 22 | 100 (1.3) |
| $NbW_5O_{19}Si(O\mathit{t}Bu)_3^{2-}$ (**4**) | 75.9 | 27.7 | +48.2 | –100.7 | | |
| $NbW_5O_{19}SiPh_3^{2-}$ (**5**) | 79.0 | 30.7 | +48.3 | –15 | –15.1 | 300 (3.7) |
| $(NbW_5O_{18})_2O^{4-}$ | 75.0 | 24.5 | +50.5 | | | |
| $NbW_5O_{19}^{3-}$ | 30.5 | 74.1 | –43.6 | | | |

[a] δ values, ppm. [b] $\Delta\delta = \delta(W_{ax}) - \delta(W_{eq})$. [c] δ values, ppm; solution spectra. [d] δ values, ppm; solid-state CP-MAS spectra. [e] Full width at half maximum of the isotropic signal; in Hz and ppm (in brackets).

 © 2007 Wiley-VCH Verlag GmbH & Co. KGaA, Weinheim 

for equatorial and axial W nuclei, respectively. These small variations are nevertheless relatively important if we consider that these W atoms are five- and seven-bond remote from the substituting atom. Moreover, by comparison with the monomeric nonderivatized anion, the signals of the two types of W nuclei exchange their position and shift to the opposite direction in $(NbW_5O_{18})_2O^{4-}$ and in the silicon derivatives, i.e. the equatorial Ws are shielded by ca. 40 ppm in the organosilyl derivatives and by ca. 50 ppm in the dimer while the axial Ws are deshielded by about 45 ppm (Figure 3). This behavior has been already noticed by Finke on niobium derivatives of the Keggin anion: dimerization of $SiNb_3W_9$ by formation of three Nb–O–Nb bridges induces the shielding of the proximal W by ca. 30 ppm.[9]

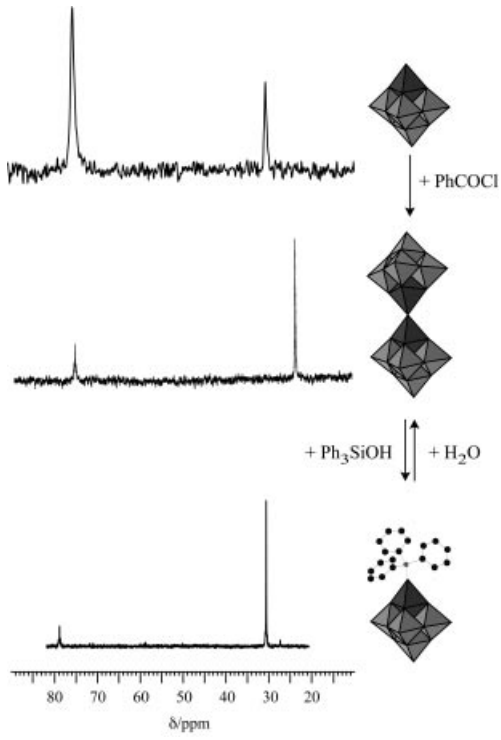


Figure 3. Comparison of the $^{183}W$ NMR spectra of: from top to bottom, $NbW_5O_{19}^{3-}$, $(NbW_5O_{18})_2O^{4-}$, and $NbW_5O_{19}SiPh_3^{2-}$ (left) and schematic representation of the formation and cleavage of $NbW_5O_{19}SiPh_3^{2-}$.

$^{93}Nb$ NMR was registered for two compounds namely **2** and **4**; as was observed by Beer et al. for the dimeric form, the $^{93}Nb$ resonances of the silyl derivatives are very broad compared with that of underivatized monomeric $NbW_5O_{19}$. While the line width for a concentrated viscous solution of $NbW_5O_{19}^{3-}$ in DMSO does not exceed 5 kHz, it amounts to 12 and 25 kHz for **4** and **2** in diluted solution in the low-viscosity solvents acetonitrile and dichloromethane, respectively. This large $^{93}Nb$ line width originates from very rapid quadrupolar relaxation of the $^{93}Nb$ nucleus ($I = 9/2$); such a rapid relaxation ($T_2 < 3$ μs) explains the narrow $^{183}W$ resonance due to an effective self-decoupling of the $^{93}Nb$ nucleus.

### X-ray Diffraction Analysis of $(n-Bu_4N)_2[NbW_5O_{19}SiPh_3]$ (5)

Whatever the nature of the solvents, attempts to grow crystals of hybrids suitable for X-ray crystallographic study were unsuccessful. Actually in all cases the crystals which formed were proved to contain the poorly soluble μ-oxo-bridged dimer $(NbW_5O_{18})_2O^{4-}$ which was formed by hydrolysis of the organosilyl $NbW_5O_{19}SiR_3^{2-}$ compounds (see above). Nevertheless, good quality crystals of $(n-Bu_4N)_2$-$[NbW_5O_{19}SiPh_3]$ were formed slowly at room temperature on the bottom of the firmly taped NMR tube containing the concentrated acetonitrile solution. The molecular structure of the anion **5** is shown in Figure 4. The X-ray single crystal study confirmed the monomeric structure of **5**, in fact the structure of the hybrid anion is built up from the monosubstituted Lindqvist anion $NbW_5O_{19}$ on which is grafted the $\{Si(C_6H_5)_3\}$ fragment through the terminal $O_t$–Nb oxygen atom. The asymmetric unit contains one $NbW_5O_{19}SiPh_3^{2-}$ anion and two TBA cations. The hybrid anion $NbW_5O_{19}SiPh_3^{2-}$ does not possess any crystallographic symmetry element in the solid state. However, in solution, because of rapid reorientation of the organosilyl fragment, the symmetry of the hybrid anion is consistent with $C_{4v}$ as shown by $^{183}W$ NMR spectroscopy. Moreover, the grafting of this fragment to the Lindqvist anion hinders the random orientational disorder of the $NbW_5O_{19}$ unit[12] and allows differentiation of the Nb from the W atoms and access to precise metrical data for these anions (Table 2).

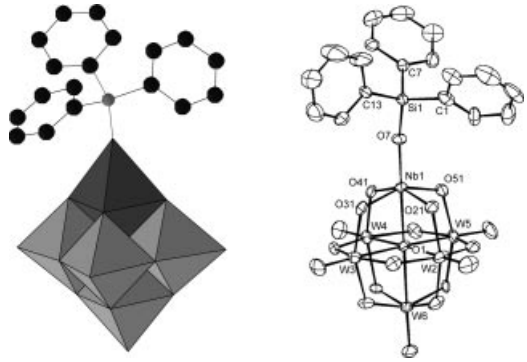


Figure 4. Representations of the molecular structure of $NbW_5O_{19}SiPh_3^{2-}$. Left: combined polyhedral and ball and stick model; right: Cameron representation with ellipsoids drawn at the 30% probability level.

The Nb–O bond length of 1.871(9) Å in the Nb–O–Si bridge compares well with similar bonds in $(n-Bu_4N)_3$-$[Nb_2W_4O_{19}\{Si(Me)_2(CMe_3)\}]$ [1.86(2) Å], while the Nb–O–Si bridge is more open (167°) in **5** than in the $Nb_2W_4O_{19}$ derivative (154°). The mean terminal and bridging W–O (1.70 and 1.92 Å, respectively) are also similar to those observed in $W_6O_{19}^{2-}$ (1.69 and 1.92 Å).[29]

Concerning the metal–central oxygen distances, Nb–$O_1$ (2.262 Å) is significantly shorter than the W–O mean value for the equatorial bonds W–$O_1$ (2.32 Å) and than the axial $W_6$–$O_1$ (2.373 Å); the relatively short Nb–$O_c$ distance is a consequence of the reduced *trans* influence of $O_7$ in the Nb–O–Si bridge. Analogous contractions have been observed in

 © 2007 Wiley-VCH Verlag GmbH & Co. KGaA, Weinheim 

Table 2. Selected bond lengths [Å] and angles [°] for $(n\mathrm{Bu_4N})_2[\mathrm{NbW_5O_{19}SiPh_3}]$ (**5**).

| | | | |
|---|---|---|---|
| Nb1–O7 | 1.871(9) | Nb1–O21–W2 | 117.51(50) |
| Nb1–O1 | 2.262(9) | Nb1–O31–W3 | 116.09(46) |
| Nb1–O21 | 1.945(9) | Nb1–O41–W4 | 116.25(50) |
| Nb1–O31 | 1.968(12) | Nb1–O51–W5 | 117.33(45) |
| Nb1–O41 | 1.951(11) | Nb1–O7–Si1 | 167.15(56) |
| Nb1–O51 | 1.952(12) | O7–Si1–C1 | 110.58(51) |
| W2–O1 | 2.318(9) | O7–Si1–C7 | 108.48(51) |
| W3–O1 | 2.318(11) | O7–Si1–C13 | 106.51(64) |
| W4–O1 | 2.318(11) | C1–Si1–C7 | 111.22(75) |
| W5–O1 | 2.341(11) | C1–Si1–C13 | 111.76(81) |
| Si1–O7 | 1.638(9) | C7–Si1–C13 | 108.11(67) |
| Si1–C1 | 1.838(16) | | |
| Si1–C7 | 1.871(17) | | |

monofunctionalized Lindqvist-type polyoxometallates such as $\mathrm{Nb_2W_4O_{19}Si(Me)_2(CMe_3)^{3-}}$ where Nb–$O_c$ and $W_{ax}$–$O_c$ amount to 2.27 and 2.37 Å, respectively. The remaining geometrical parameters of the $\mathrm{NbW_5O_{19}}$ core are very similar; for example Nb–O–W bridge angles (between 116.09 and 117.51°) are only slightly smaller than the W–O–W ones (between 117.09 and 118.93°).

The tetrahedral Si atom displays a slight distortion from ideal geometry toward the terminal O–Nb bond with C–Si–C and O–Si–C angles on average 110.0° and 108.3°, respectively. The Si–C distances, which range from 1.823(19) to 1.871(19) Å, are longer than Si–O [1.633(11) Å].

## Conclusions

In this work we report a valuable method for the clean preparation of organosilyl derivatives of monosubstituted hexaniobotungstate in good yields. Equation (1) features this functionalization which consists of a selective coordination of an electrophilic fragment $\{\mathrm{SiRR'}_2\}^+$ [R = R′ = Et (**1**), *i*Pr (**3**), O*t*Bu (**4**), Ph (**5**); R = *t*Bu and R′ = Me (**2**)] to the terminal Nb–$O_t$ oxygen atom which leads to the formation of a terminal organosilyloxide-derivatized monosubstituted niobotungstate. This organic–inorganic hybrid has a good solubility in a variety of polar organic solvents that makes it easily studied and characterized in solution by multinuclear NMR spectroscopy. Spectroscopic studies, along with an X-ray study of $\mathrm{NbW_5O_{19}SiPh_3^{2-}}$ show that derivatization of $\mathrm{NbW_5O_{19}^{3-}}$ occurs selectively at the terminal Nb–$O_t$ rather than the bridging Nb–$O_b$–W oxygen atoms. Grafting of $\mathrm{R_3Si^+}$ permits the resolution of the disorder problem in crystal structure. Hydrolysis of the siloxide derivative occurs at the Si–O bond and leads to the back formation of the starting material $\mathrm{(NbW_5O_{18})_2O^{4-}}$.

## Experimental Section

**Reagents and Methods:** Solvents (analytical grade) and the following reagents were purchased from commercial sources and used without further purification: triphenylsilanol, triethylsilanol, triisopropylsilanol, *tert*-butyldimethylsilanol, tri-*tert*-butoxysilanol, diethyl ether. Acetonitrile and dichloromethane were distilled under argon from $CaH_2$. Syntheses of $(n\mathrm{Bu_4N})_4[(\mathrm{NbW_5O_{18}})_2\mathrm{O}]$ and $(n\mathrm{Bu_4N})_3[\mathrm{NbW_5O_{19}}]$ followed literature procedures described.[8,12] All subsequent reactions were performed under an inert atmosphere of argon in a Schlenk line to avoid the polymerization of the silanols by the air moisture. The $^1$H and $^{13}$C spectra were obtained at 300 K from $CD_2Cl_2$ and $CD_3CN$ solutions in 5-mm o.d. tubes at 300 and 75.5 MHz, respectively, with Bruker AC300 or Bruker AvanceII spectrometers. $^{29}$Si and $^{183}$W spectra were recorded at 300 K from $CH_2Cl_2/CD_2Cl_2$ solution in a 10-mm o.d. tube with the Bruker AC300 (59.6 and 12.5 MHz) and Bruker DRX 500 (99.3 and 20.8 MHz) spectrometers. Chemical shift values for $^1$H, $^{13}$C, and $^{29}$Si were internally referenced to tetramethylsilane (TMS) using the solvent peak as secondary standard and for $^{183}$W are given with respect to an external 2 M $Na_2WO_4$ solution in alkaline $D_2O$, using a saturated solution of dodecatungstosilicic acid ($\mathrm{SiW_{12}O_{40}H_4}$) as a secondary standard ($\delta$ = –103.8 ppm). The solid-state $^{29}$Si NMR CP-MAS spectra were obtained at room temperature with a Bruker Avance 400 spectrometer operating at 79.5 MHz; spinning rates of 5 kHz, contact times of 3 to 10 ms, and a recycling delay of 5 s were used for obtaining spinning-sideband-free spectra in ca. 10 h. Chemical shifts of the isotropic line are reported with respect to TMS. FTIR spectra were recorded from KBr pellets with a Bio-rad FTS 165 IR-FT spectrometer with a resolution of 4 $cm^{-1}$. Raman spectra were collected with a Kaiser Optical Systems HL5R Raman spectrometer equipped with a near-IR laser diode working at 785 nm. The laser power was adjusted to 10–15 mW at the sample position for all spectra. The average resolution is equal to 3 $cm^{-1}$. Elemental analyses were performed by the Laboratoire Central d′Analyses du CNRS (Vernaison, France).

**Crystal-Structure Analysis:** Crystal structure data are summarized in Table 3. A colorless parallelepiped crystal (0.08 × 0.10 × 0.25 mm) of $(n\mathrm{Bu_4N})_2[\mathrm{NbW_5O_{19}Si}P\mathrm{h_3}]$ was glued to a glass fiber, covered with a thin layer of epoxy cement, and examined by X-ray crystallography. Data were collected with a Kappa-CCD Bruker AXS diffractometer at 300 K using graphite-monochromated Mo-$K_\alpha$ radiation ($\lambda$ = 0.71073 Å). Lattice parameters were obtained by

Table 3. Crystal data and structure refinement for $(n\mathrm{Bu_4N})_2[\mathrm{NbW_5O_{19}SiPh_3}]$ (**5**).[a]

| | |
|---|---|
| Empirical formula | $\mathrm{C_{50}H_{87}N_2NbO_{19}SiW_5}$ |
| Formula mass [g mol$^{-1}$] | 3762.25 |
| Crystal system | monoclinic |
| Space group | $P2_1/a$ |
| $a$ [Å] | 19.884(5) |
| $b$ [Å] | 16.801(2) |
| $c$ [Å] | 20.644(3) |
| $\beta$ [°] | 112.050(12) |
| $V$ [Å$^3$] | 6329(2) |
| $Z$ | 4 |
| $\mu$ [cm$^{-1}$] | 9.219 |
| $\rho_{\mathrm{calcd.}}$ [g cm$^{-1}$] | 2.141 |
| $\theta$ range [°] | 4–22 |
| Index range | $-27 \le h \le 20$, $-23 \le k \le 22$, $-29 \le l \le 29$ |
| Reflections collected | 63469 |
| Independent reflections | 18157 |
| Reflections with $I > 3\sigma(I)$ | 6674 |
| Parameters refined | 533 |
| Goodness of fit, $S$ | 1.09 |
| $R$ | 0.0434 |
| $R_w$* | 0.0517 |
| $\Delta\rho$ (max/min) [e·Å$^{-3}$] | 2.54/–1.82 |

[a] Weighting scheme of the form $w = w'\{1 - [(||F_o| - |F_c||)/6\sigma(F_o)]^2\}^2$ with $w' = 1/\Sigma_r A_r T_r(X)$ with coefficients 2.56, 0.00658, 2.13 for a Chebyshev series for which $X = F_c/F_c(\mathrm{max})$.

 © 2007 Wiley-VCH Verlag GmbH & Co. KGaA, Weinheim 

least-squares refinement of the diffraction data of 151 reflections within the range of $4° < 2\theta < 22°$. The index ranges of data collection were $-27 \le h \le 20$, $-23 \le k \le 22$, $-29 \le l \le 29$. Intensity data were collected using 6674 reflections with $I \ge 3\sigma(I)$. The structure was solved by direct methods and refined with full-matrix least-squares technique on $F$ using the SHELXS86[13] and CRYSTALS[14] programs. Hybrid anion atom parameters were refined anisotropically and TBA cations were refined isotropically. The values of the discrepancy indices $R_1$ ($R_{w2}$) for all data were 0.0434 (0.0517). The molecular structure was drawn with Diamond and Cameron programs[15,16] and reported in Figure 4.

CCDC-635634 contains the supplementary crystallographic data for this paper. These data can be obtained free of charge from The Cambridge Crystallographic Data Centre via www.ccdc.cam.ac.uk/data_request/cif.

**($n$Bu$_4$N)$_2$[NbW$_5$O$_{19}$SiEt$_3$] (1):** To a suspension of ($n$Bu$_4$N)$_4$[(NbW$_5$O$_{18}$)$_2$O] (1 g, 0.28 mmol) in 30 mL of dry dichloromethane was added $(C_2H_5)_3SiOH$ (0.086 mL, 0.56 mmol). The resulting solution was stirred vigorously at ambient temperature under a static argon atmosphere for 24 h, then centrifuged at 4000 rpm for 15 min. The supernatant was added with diethyl ether, whilst stirring, precipitation of the hybrid has generally to be initiated by scraping the beaker walls with a glass spatula; the white precipitate was filtered and washed three times with 100 mL of diethyl ether and dried under vacuum to give 788 mg of crude product (73% yield). $C_{38}H_{87}N_2NbO_{19}SiW_5$ (1916.23): calcd. C 23.79, H 4.57, N 1.46, Nb 4.84, W 47.99; found C 23.73, H 4.57, N 1.33, Nb 4.16, W 47.35. IR (1300–400): $\tilde{\nu}$ = 446 (s), 583 (m), 706 (m), 718 (m), 742 (m), 792 (vs), 809 (vs), 884 (w), 938 (m), 971 (vs), 1239 (w) cm$^{-1}$. $^1$H NMR ($CD_2Cl_2$): $\delta$ = 3.28 (t, 16 H, N–C$H_2$–CH$_2$–CH$_2$–CH$_3$), 1.71 (q, 16 H, N–CH$_2$–C$H_2$–CH$_2$–CH$_3$), 1.49 (m, 16 H, N–CH$_2$–CH$_2$–C$H_2$–CH$_3$), 1.08 (m, 33 H, N–CH$_2$–CH$_2$–CH$_2$–C$H_3$), 0.75 (q, 6 H, Si–C$H_2$–CH$_3$) ppm. $^{13}$C NMR ($CD_2Cl_2$): $\delta$ = 59.06 (N–*C*H$_2$–CH$_2$–CH$_2$–CH$_3$), 24.34 (N–CH$_2$–*C*H$_2$–CH$_2$–CH$_3$), 20.09 (N–CH$_2$–CH$_2$–*C*H$_2$–CH$_3$), 13.89 (N–CH$_2$–CH$_2$–CH$_2$–*C*H$_3$), 6.61 (Si–*C*H$_2$–CH$_3$), 7.47 (Si–CH$_2$–*C*H$_3$) ppm. $^{29}$Si NMR (0.06 M, $CH_2Cl_2/CD_2Cl_2$): $\delta$ = 25.8 ppm. $^{183}$W NMR (0.06 M, $CH_2Cl_2/CD_2Cl_2$): $\delta$ = 34.9 ($J_{W-W}$ = 8.8 Hz, 4 W, $W_{eq}$), 75.9 ($J_{W-W}$ = 8.8 Hz, 1 W, $W_{ax}$) ppm.

**($n$Bu$_4$N)$_2$[NbW$_5$O$_{19}$Si$t$BuMe$_2$] (2):** This compound was prepared by the same procedure as for **1** using $[C(CH_3)_3(CH_3)_2]SiOH$ (0.16 mL, 0.56 mmol) instead of $(C_2H_5)_3SiOH$ (yield of crude product: 977 mg, 91%). $C_{38}H_{87}N_2NbO_{19}SiW_5$ (1916.23): calcd. C 23.79, H 4.57, N 1.46, Nb 4.84, W 47.99; found C 23.62, H 4.53, N 1.33, Nb 4.43, W 47.5. IR (1300–400): $\tilde{\nu}$ = 446 (s), 583 (m), 683 (w), 738 (sh), 777 (vs), 810 (vs), 881 (w), 938 (m), 970 (vs), 1029 (w), 1066 (w), 1108 (w), 1152 (w), 1253 (m) cm$^{-1}$. $^1$H NMR ($CD_2Cl_2$): $\delta$ = 3.28 (t, 16 H, N–C$H_2$–CH$_2$–CH$_2$–CH$_3$), 1.72 (q, 16 H, N–CH$_2$–C$H_2$–CH$_2$–CH$_3$), 1.49 (m, 16 H, N–CH$_2$–CH$_2$–C$H_2$–CH$_3$), 1.08 (m, 33 H, N–CH$_2$–CH$_2$–CH$_2$–C$H_3$), 0.24 [s, 6 H, Si(C$H_3$)$_2$C(CH$_3$)$_3$] ppm. $^{13}$C NMR ($CD_2Cl_2$): $\delta$ = 58.57 (N–*C*H$_2$–CH$_2$–CH$_2$–CH$_3$), 25.31 [Si(CH$_3$)$_2$C(*C*H$_3$)$_3$], 23.98 (N–CH$_2$–*C*H$_2$–CH$_2$–CH$_3$), 19.67 (N–CH$_2$–CH$_2$–*C*H$_2$–CH$_3$), 19 [Si(CH$_3$)$_2$*C*(CH$_3$)$_3$], 13.54 (N–CH$_2$–CH$_2$–CH$_2$–*C*H$_3$), –3.85 [Si(*C*H$_3$)$_2$C(CH$_3$)$_3$] ppm. $^{29}$Si NMR (0.06 M, $CH_2Cl_2/CD_2Cl_2$): $\delta$ = 25.7 ppm. $^{183}$W NMR (0.06 M, $CH_2Cl_2/CD_2Cl_2$): $\delta$ = 34.5 ($J_{W-W}$ = 8.8 Hz, 4 W, $W_{eq}$), 76.3 ($J_{W-W}$ = 8.8 Hz, 1 W, $W_{ax}$) ppm.

**($n$Bu$_4$N)$_2$[NbW$_5$O$_{19}$Si$i$Pr$_3$] (3):** This compound was prepared by the same procedure as for **1** using $[CH(CH_3)_2]_3SiOH$ (0.11 mL, 0.56 mmol) instead of $(C_2H_5)_3SiOH$ (yield of crude product: 923 mg, 84%). $C_{41}H_{93}N_2NbO_{19}SiW_5$ (1958.27): calcd. C 25.12, H 4.78, N 1.43, Si 1.43, W 46.96; found C 24.87, H 4.74, N 1.23, W 46.12. IR (1300–400): $\tilde{\nu}$ = 445 (vs), 583 (m), 611 (w), 668 (sh), 687 (w), 739 (sh), 788 (vs), 809 (vs), 883 (m), 969 (vs), 1062 (w), 1107 (w), 1152 (w), 1247 (w) cm$^{-1}$. $^{13}$C NMR ($CD_2Cl_2$): $\delta$ = 58.42 (N–*C*H$_2$–CH$_2$–CH$_2$–CH$_3$), 23.59 (N–CH$_2$–*C*H$_2$–CH$_2$–CH$_3$), 19.46 (N–CH$_2$–CH$_2$–*C*H$_2$–CH$_3$), 17.1 [SiCH(*C*H$_3$)$_2$], 13.06 (N–CH$_2$–CH$_2$–CH$_2$–*C*H$_3$), 0.81 [Si*C*H(CH$_3$)$_2$] ppm. $^{29}$Si NMR (0.06 M, $CH_2Cl_2/CD_2Cl_2$): $\delta$ = 24.8 ppm. $^{183}$W NMR (0.06 M, $CH_2Cl_2/CD_2Cl_2$): $\delta$ = 35.3 ($J_{W-W}$ = 9 Hz, 4 W, $W_{eq}$), 75.9 ($J_{W-W}$ = 9 Hz, 1 W, $W_{ax}$) ppm.

**($n$Bu$_4$N)$_2$[NbW$_5$O$_{19}$Si(O$t$Bu)$_3$] (4):** To a suspension of ($n$Bu$_4$N)$_4$[(NbW$_5$O$_{18}$)$_2$O] (1 g, 0.28 mmol) in 30 mL of dry acetonitrile was added, under argon, $[OC(CH_3)_3]_3SiOH$ (148 mg, 0.56 mmol). The resulting clear colorless solution was stirred vigorously at room temperature for 24 h. This solution was centrifuged at 4000 rpm for 15 min and then diethyl ether was added to the supernatant from which a white powder was precipitated under vigorous stirring. It was washed twice with diethyl ether and dried under vacuum to give 1013 mg in 88% yield. IR (1400–400): $\tilde{\nu}$ = 447 (s), 511 (w), 540 (w), 584 (m), 651 (m), 705 (m), 741 (m), 791 (vs), 811 (vs), 880 (m), 938 (m), 968 (vs), 996 (m), 1031 (m), 1077 (vs), 1189 (s), 1244 (s), 1367 (s), 1390 (m) cm$^{-1}$. $^{13}$C NMR ($CD_2Cl_2$): $\delta$ = 59.31 (N–*C*H$_2$–CH$_2$–CH$_2$–CH$_3$), 31.43 [SiOC(*C*H$_3$)$_3$], 24.37 (N–CH$_2$–*C*H$_2$–CH$_2$–CH$_3$), 20.32 (N–CH$_2$–CH$_2$–*C*H$_2$–CH$_3$), 13.89 (N–CH$_2$–CH$_2$–CH$_2$–*C*H$_3$) ppm. $^{29}$Si NMR (0.06 M, $CH_2Cl_2/CD_2Cl_2$): $\delta$ = –100.7 ppm. $^{183}$W NMR (0.05 M, $CH_2Cl_2/CD_2Cl_2$): $\delta$ = 27.7 ($J_{W-W}$ = 9 Hz, 4 W, $W_{eq}$), 75.9 ($J_{W-W}$ = 9 Hz, 1 W, $W_{ax}$) ppm.

**($n$Bu$_4$N)$_2$[NbW$_5$O$_{19}$SiPh$_3$] (5):** To a mixture of ($n$Bu$_4$N)$_4$[(NbW$_5$O$_{18}$)$_2$O] (1 g, 0.28 mmol) and $(C_6H_5)_3SiOH$ (0.155 g, 0.56 mmol) was added with stirring 30 mL of dry acetonitrile. The resulting slightly cloudy solution was stirred vigorously at room temperature for 48 h under a static argon atmosphere. This solution was centrifuged for 15 min and then diethyl ether was added to the supernatant from which a white powder was precipitated under vigorous stirring. It was washed twice with diethyl ether and dried under vacuum to give 745 mg of air- and moisture-stable microcrystalline white powder, in 64% yield. $C_{50}H_{87}N_2NbO_{19}SiW_5$ (2060.23): calcd. C 29.12, H 4.25, N 1.36, Si 1.36, Nb 4.5, W 44.64; found C 29.15, H 4.26, N 1.32, Si 1.65, Nb 3.48, W 43.65. IR (1450–400): $\tilde{\nu}$ = 445 (vs), 504 (m), 517 (m), 552 (w), 584 (m), 703 (m), 710 (m), 787 (vs), 810 (vs), 879 (w), 951 (m), 971 (vs), 1002 (sh), 1030 (w), 1066 (w), 1106 (sh), 1117 (s), 1162 (w), 1190 (w), 1262 (w), 1430 (m) cm$^{-1}$. $^1$H NMR ($CD_2Cl_2$): $\delta$ = 3.42 (t, 16 H, N–C$H_2$–CH$_2$–CH$_2$–CH$_3$), 1.8 (q, 16 H, N–CH$_2$–C$H_2$–CH$_2$–CH$_3$), 1.45 (m, 16 H, N–CH$_2$–CH$_2$–C$H_2$–CH$_3$), 1 (t, 24 H, N–CH$_2$–CH$_2$–CH$_2$–C$H_3$), 7.46 (m, 6 H, *meta*), 7.5 (dd, 3 H, *para*), 7.75 (dd, 6 H, *ortho*) ppm. $^{13}$C NMR ($CD_2Cl_2$): $\delta$ = 137.5, 142.3, 141.6, 135.2 (Ph), 59.1 (N–*C*H$_2$–CH$_2$–CH$_2$–CH$_3$), 24.24 (N–CH$_2$–*C*H$_2$–CH$_2$–CH$_3$), 20.09 (N–CH$_2$–CH$_2$–*C*H$_2$–CH$_3$), 13.66 (N–CH$_2$–CH$_2$–CH$_2$–*C*H$_3$) ppm. $^{29}$Si NMR (0.06 M, $CH_2Cl_2/CD_2Cl_2$): $\delta$ = –12.8 ppm. $^{183}$W NMR (0.04 M, $CH_2Cl_2/CD_2Cl_2$): $\delta$ = 30.7 ($J_{W-W}$ = 8.7 Hz, 4 W, $W_{eq}$), 79.0 ($J_{W-W}$ = 9.2 Hz, 1 W, $W_{ax}$) ppm. The product is contaminated by a very small amount of hexatungstate $W_6O_{19}^{2-}$ as shown by $^{183}$W NMR spectroscopy.

## Acknowledgments

This work is supported by the Centre National de Recherche Scientifique (CNRS), France and the Direction Générale de la Recherche Scientifique (DGRST), Tunisia in the frame of a bilateral joint project. We gratefully acknowledge the Comité Mixte pour la Coopération Universitaire (CMCU) (program 05G1211). We are also grateful to Patrick Herson (UPMC) for crystal data collection and for his assistance in structure resolution, and to Jocelyne Maquet for her help in recording the $^{29}$Si solid-state CP-MAS spectra on the Bruker Avance 400 spectrometer (S.I.A.R.E. UPMC).

 © 2007 Wiley-VCH Verlag GmbH & Co. KGaA, Weinheim 

[1] M. T. Pope, *Heteropoly and Isopoly Oxometalates*, Springer Verlag, Heidelberg, Germany, **1983**.
[2] P. Gouzerh, A. Proust, *Chem. Rev.* **1998**, *98*, 77 and references cited therein.
[3] V. W. Day, W. G. Klemperer, *Science* **1985**, *228*, 533.
[4] D. A. Robert, G. L. Geoffrey in *Comprehensive Organometallic Chemistry* (Eds.: G. Wilkinson, F. G. A. Stone, E. W. Abel), Pergamon, Oxford, **1982**, chapter 40.
[5] W. A. Nugent, J. M. Mayer, *Metal-Ligand Multiple Bonds*, Wiley, New York, **1988**, p. 28 and chapter 6.
[6] B. O. West, *Polyhedron* **1989**, *8*, 219.
[7] E. V. Radkov, V. G. Young, R. H. Beer, *J. Am. Chem. Soc.* **1999**, *121*, 8953.
[8] Y. J. Lu, R. Lalancette, R. H. Beer, *Inorg. Chem.* **1996**, *35*, 2524–2529.
[9] R. G. Finke, M. W. Droege, *J. Am. Chem. Soc.* **1984**, *106*, 7274.
[10] D. J. Edlund, R. J. Saxton, D. K. Lyon, R. G. Finke, *Organometallics* **1988**, *7*, 1692.
[11] R. G. Finke, K. Nomiya, C. A. Green, M. W. Droege, *Inorg. Synth.* **1992**, *29*, 239.
[12] F. Bannani, H. Driss, R. Thouvenot, M. Debbabi, *J. Chem. Crystallogr.* **2007**, *37*, 37.
[13] G. M. Sheldrick, *SHELXS86*, program for the solution of crystal structure, University of Göttingen, Germany, **1986**.
[14] D. J. Watkin, C. K. Prout, J. R. Carruthers, P. W. Betteridge, R. I. Cooper, *CRYSTALS*, Chemical Crystallography Laboratory, University of Oxford, **2001**.
[15] K. Brandenburg, *DIAMOND*, version 2.0, Gerhard-Domagk-Straβe 1, 53121 Bonn, Germany, **1998**.
[16] L. J. Pearce, D. J. Watkin, *CAMERON*, Chemical Crystallography Laboratory, University of Oxford, **1996**.
[17] P. J. Hay, W. R. Wadt, *J. Chem. Phys.* **1985**, *82*, 270.
[18] J. M. Maestre, J. P. Sarasa, C. Bo, J. M. Poblet, *Inorg. Chem.* **1998**, *37*, 3071–3077.
[19] C. J. Besecker, W. G. Klemperer, D. J. Maltbie, D. A. Wright, *Inorg. Chem.* **1985**, *24*, 1027.
[20] E. V. Radkov, Y. J. Lu, R. H. Beer, *Inorg. Chem.* **2000**, *297*, 191–198.
[21] V. W. Day, W. G. Klemperer, C. Schwartz, *J. Am. Chem. Soc.* **1987**, *109*, 6030–6034.
[22] A. Mazeaud, N. Ammari, F. Robert, R. Thouvenot, *Angew. Chem. Int. Ed. Engl.* **1996**, *35*, 1961.
[23] C. Rocchiccioli-Deltcheff, R. Thouvenot, M. Dabbabi, *Spectrochim. Acta, Ser. A* **1977**, *33*, 143.
[24] N. Ammari, G. Hervé, R. Thouvenot, *New J. Chem.* **1991**, *15*, 607.
[25] C. R. Mayer, R. Thouvenot, *J. Chem. Soc. Dalton Trans.* **1998**, 7–13.
[26] C. R. Mayer, I. Fournier, R. Thouvenot, *Eur. J. Inorg. Chem.* **2000**, *6*, 205.
[27] D. Agustin, J. Dallery, C. Coelho, A. Proust, R. Thouvenot, *J. Organomet. Chem.* **2007**, *692*, 746.
[28] E. Cadot, R. Thouvenot, A. Tézé, G. Hervé, *Inorg. Chem.* **1992**, *31*, 4128–4133.
[29] J. Fuchs, W. Freiwald, H. Hartl, *Acta Crystallogr., Sect. B* **1987**, *34*, 1764.

Received: March 30, 2007
Published Online: July 24, 2007

 © 2007 Wiley-VCH Verlag GmbH & Co. KGaA, Weinheim 

DOI: 10.1002/ejic.200700380

# Synthesis and Catalytic Applications of Chiral Hydridoiridium(III) Complexes with Diamine/Bis(monophosphane) and Diamine/Diphosphane Coordination

**Lutz Dahlenburg,*[a] Ralf Menzel,[a] and Frank W. Heinemann[a]**

*Dedicated to Professor Gottfried Huttner on the occasion of his 70th birthday*

**Keywords:** Iridium / N ligands / P ligands / Asymmetric catalysis

The $P_2/N_2$-coordinated *cis*-dihydridoiridium(III) chelate complexes (*OC*-6-13)-[$IrH_2(H_2N\cap NH_2)(PR_3)_2$]$BF_4$ [$PR_3$ = $PPh_3$, $H_2N\cap NH_2$ = 1,2-$(H_2N)_2C_6H_4$ (**1a**); (1*R*,2*R*)-$(H_2N)_2C_6H_{10}$ {(*R*,*R*)-dach} (**1b**); (*R*)-2,2′-diamino-1,1′-binaphthyl {(*R*)-dabin} (**1c**); $PR_3$ = P*i*Pr$_3$, $H_2N\cap NH_2$ = (*R*,*R*)-dach (**2a**), (*R*)-dabin (**2b**); $PR_3$ = $PCy_3$, $H_2N\cap NH_2$ = (*R*)-dabin (**3**)] were obtained by treating the respective diamine ligands with labile precursors such as [$IrH_2(OCMe_2)_2(PPh_3)_2$]$BF_4$, [($\eta^4$-1,5-$C_8H_{12}$)Ir($PPh_3$)$_2$]$BF_4$, or [$IrH_5(PR_3)_2$]/$HBF_4$ (R = *i*Pr, Cy). While oxidative addition of HCl to [($\eta^4$-1,5-$C_8H_{12}$)Ir{(*S*,*S*)-bdpcp}]$BF_4$ [(*S*,*S*)-bdpcp = (1*S*,2*S*)-$(Ph_2P)_2C_5H_8$] yields the usual mononuclear adduct [($\eta^4$-1,5-$C_8H_{12}$)Ir(H)(Cl){(*S*,*S*)-bdpcp}]$BF_4$ (**4**), similar treatment of [($\eta^4$-1,5-$C_8H_{12}$)Ir{(*R*)-binap}]$BF_4$ furnishes the triply chlorido-bridged diiridium complex [{(*R*)-binap}$_2$$Ir_2H_2(\mu$-Cl)$_3$]$BF_4$ (**5**). Opening of the μ-Cl bridges of **5** by N,N nucleophiles was used to synthesise the three diamine/(*R*)-binap complexes [Ir(H)(Cl)-($H_2N\cap NH_2$){(*R*)-binap}]$BF_4$ [$H_2N\cap NH_2$ = (1*R*,2*R*)-$H_2NCH(Ph)CH(Ph)NH_2$ {(*R*,*R*)-dpen} (**6a**), (*R*,*R*)-dach (**6b**), and $H_2NCMe_2CMe_2NH_2$ {tmen} (**6c**). Whereas the dihydrides [$IrH_2${(*R*,*R*)-dach}$(PR_3)_2$]$BF_4$ and [$IrH_2${(*R*)-dabin}-$(PR_3)_2$]$BF_4$ (R = *i*Pr, Ph) are only poor (pre)catalysts for the enantioselective hydrogenation of acetophenone, complexes **6a**–**c** catalyze the formation of 1-phenylethanol in good enantiomeric excess [$ee_{max}$ = 82–84 % (*S*)] in the presence of base. The crystal structures of **1a**, **4**, and **5** have been determined. (© Wiley-VCH Verlag GmbH & Co. KGaA, 69451 Weinheim, Germany, 2007)

## Introduction

We recently[1] described some 2,2′-bis(diphenylphosphanyl)-1,1′-binaphthyl-coordinated diamine(diphosphane)-rhodium(I) complexes such as [Rh{(*R*,*R*)-$H_2NCH(Ph)CH(Ph)NH_2$}{(*R*)-binap}]$BF_4$ and the like, which were made without difficulty by treating [($\eta^4$-1,5-$C_8H_{12}$)Rh{(*R*)-binap}]$BF_4$ with N,N-chelate ligands under hydrogen. Oxidative addition of HCl led to the rhodium(III) derivative (*OC*-6-43)-[Rh(H)(Cl){(*R*,*R*)-$H_2NCH(Ph)CH(Ph)NH_2$}{(*R*)-binap}]$BF_4$. From a structural point of view, this latter complex can be regarded as an analog of the neutral ruthenium(II) compound (*OC*-6-43)-[Ru(H)(Cl){(*R*,*R*)-$H_2NCH(Ph)CH(Ph)NH_2$}{(*R*)-binap}], which is well known to be an excellent (pre)catalyst for the stereoselective hydrogenation of ketones and imines.[2a]

If activated by a strong base in 2-propanol, the diamine-(diphosphane)rhodium complexes were also found to act as enantioselective catalysts for the reduction of acetophenone, although both their activity and selectivity ($ee_{max.}$ = 71 %)[1] were inferior to those of the established $Ru^{II}$-based systems.[3]

In our search for complexes of the Group 9 transition metals with possibly improved catalytic properties we set out to synthesize and investigate some cationic hydrido compounds of iridium(III) with coordination spheres dominated by (preferentially chiral) diamine and (di)phosphane ligands, namely [$IrH_2(H_2N\cap NH_2)(PR_3)_2$]$BF_4$ (R = Ph, *i*Pr, Cy) and [Ir(H)(X)($H_2N\cap NH_2$)($Ph_2P\cap PPh_2$)]$BF_4$ (X = H or Cl).

## Results and Discussion

### Complexes

Either of the cationic $Ir^I$ or $Ir^{III}$ complexes [($\eta^4$-1,5-$C_8H_{12}$)Ir$(PR_3)_2$]$^+$ and [$IrH_2(OCMe_2)_2(PR_3)_2$]$^+$ (R = Ph),[4] respectively, or the pentahydrides [$IrH_5(PR_3)_2$] (R = *i*Pr, Cy)[5] could be used as starting material for the preparation of the target compounds [$IrH_2(H_2N\cap NH_2)(PR_3)_2$]$^+$. Thus, stoichiometric 1:1 reactions of the solvento complex [Ir-$H_2(OCMe_2)_2(PPh_3)_2$]$BF_4$ with 1,2-phenylenediamine (1,2-phdn) or (1*R*,2*R*)-1,2-diaminocyclohexane [(*R*,*R*)-dach] resulted in smooth replacement of the loosely bound acetone

[a] Institut für Anorganische Chemie der Friedrich-Alexander-Universität Erlangen-Nürnberg,
Egerlandstrasse 1, 91058 Erlangen, Germany
Fax: +49-9131-85-27387
E-mail: Lutz.Dahlenburg@chemie.uni-erlangen.de

 © 2007 Wiley-VCH Verlag GmbH & Co. KGaA, Weinheim 

ligands by the two diamines to give $[IrH_2(1,2\text{-phdn})(PPh_3)_2]BF_4$ (**1a**)[6] and $[IrH_2\{(R,R)\text{-dach}\}(PPh_3)_2]BF_4$ (**1b**), as expected (Scheme 1). Since the weakly solvated dihydrides $[IrH_2(solv)_2(PR_3)_2]^+$ are formed in the presence of a coordinating solvent, either by hydrogenation of $[(\eta^4\text{-}1,5\text{-}C_8H_{12})Ir(PR_3)_2]^+$[4] or by protonation of $[IrH_5(PR_3)_2]$ with a strong acid,[4c,5b] both the dieneiridium(I) complexes and the pentahydrides could be employed as precursors as well. For example, treatment of $[(\eta^4\text{-}1,5\text{-}C_8H_{12})Ir(PPh_3)_2]BF_4$ with an equimolar amount of (*R*)-2,2′-diamino-1,1′-binaphthyl [(*R*)-dabin] in $CH_2Cl_2$ under hydrogen gave $[IrH_2\{(R)\text{-dabin}\}(PPh_3)_2]BF_4$ (**1c**) as an additional diamine-containing bis(triphenylphosphane) complex, whereas the triisopropyl- and tricyclohexylphosphane analogues $[IrH_2\{(R,R)\text{-dach}\}(PiPr_3)_2]BF_4$ (**2a**), $[IrH_2\{(R)\text{-dabin}\}(PiPr_3)_2]BF_4$ (**2b**), and $[IrH_2\{(R)\text{-dabin}\}(PCy_3)_2]BF_4$ (**3**) were obtained from $[IrH_5(PiPr_3)_2]$ or $[IrH_5(PCy_3)_2]$ by acidolysis with $HBF_4$ (54% in $Et_2O$) and subsequent reaction with the required diamine in a 1:1 molar ratio (Scheme 1).

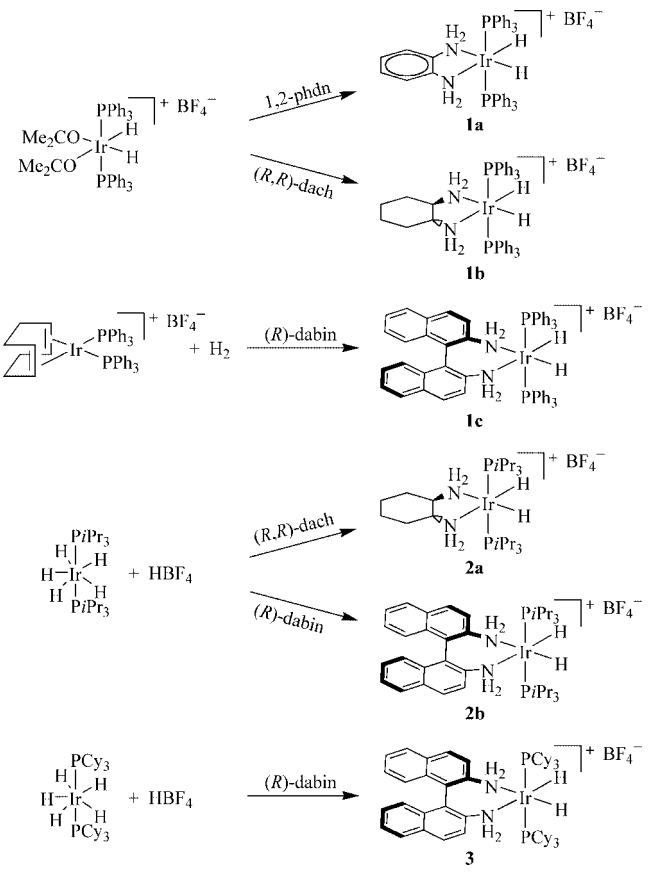


Scheme 1. Synthesis of complexes **1**–**3**.

The *OC*-6-13 stereochemistry of compounds **1**–**3** (Scheme 1) follows from the observation of their IrH resonances between $\delta$ = –21 and –27 ppm, which is typical for hydridoiridium(III) complexes with hard donor ligands *trans* to H.[4b] Further confirmation of the coordination geometry depicted in Scheme 1 came from the *cis*-$^2J_{P,H}$ coupling constants of 16–18 Hz found in all cases.

Crystals of $[IrH_2(1,2\text{-phdn})(PPh_3)_2]BF_4$ (**1a**) suitable for an X-ray diffraction study were grown from dichloromethane. As anticipated, the structure determination revealed the presence of N–H···F hydrogen-bonded ion-pairs with the iridium atom in the close to octahedral coordination environment inferred from the NMR spectroscopic data above (Figure 1). The hydride ligands could not be located from the final density maps in any of the structures reported in this paper but were placed, with *d*(Ir–H) restrained to 1.6 Å, at the positions calculated by Orpen's HYDEX energy-minimizing procedure.[7,8] The metal-to-phosphane distances of 2.292(1) and 2.302(1) Å are slightly shorter than, but still comparable to, the Ir–P bond lengths previously reported by Crabtree for the structurally related acetone complex $[IrH_2(OCMe_2)_2(PPh_3)_2]BF_4$ [*d*(Ir–P) = 2.313 and 2.321 Å].[4c] A feature of interest is the coordination of the *ortho*-phenylenediamine ligand, with the two Ir–$NH_2$ distances amounting to 2.163(4) and 2.202(5) Å. The Ir–$NH_2$ linkages of **1a** tend to be longer than the iridium–amine bond lengths of, for example, (*OC*-6-12)-$[IrCl_2\{Me_2P(CH_2)_2NH_2\}_2]PF_6$ [*d*(Ir–$NH_2$) *trans* to Ir–N: 2.090 Å),[9a] (*OC*-6-43)-[Ir(H)(Cl)$\{Ph_2P(CH_2)_2NH_2\}_2$]Cl [*d*(Ir–N) *trans* to Ir–P: 2.136 and 2.137 Å),[10a] and (*OC*-6-13)-$[IrCl_2\{Ph_2P(CH_2)_2NH_2\}_2]BF_4$ [*d*(Ir–N) *trans* to Ir–P: 2.142 and 2.152 Å),[9b] which reflects the high *trans*-bond-weakening influence of the two hydrides opposite to the amine donors.

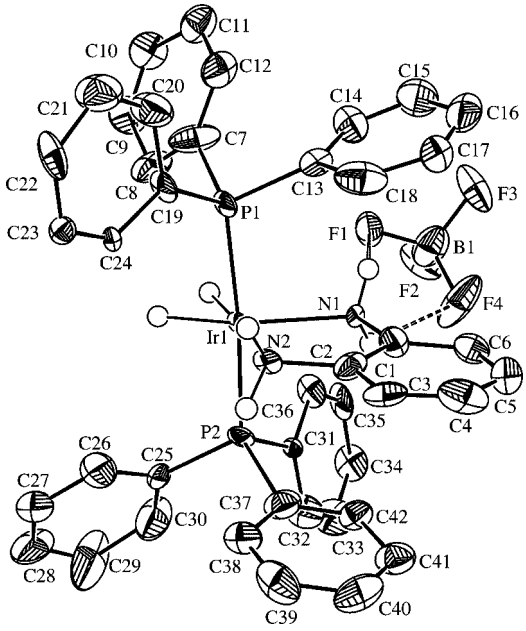


Figure 1. Structure of the ion-pair $[IrH_2(1,2\text{-phdn})(PPh_3)_2]BF_4$ (**1a**); phenyl H atoms have been omitted for clarity. Selected bond lengths [Å] and angles [°]: Ir1–P1 2.302(1), Ir–P2 2.292(1), Ir–N1 2.163(4), Ir–N2 2.202(5); P1–Ir–P2 174.37(6), P1–Ir–N1 93.5(1), P1–Ir–N2 90.8(1); hydrogen-bonding interactions (D–H, H···A, D···A [Å], D–H···A [°]): N1–H···F1 0.92, 2.27, 2.854(5), 121.1; N1–H···F4 0.92, 2.42, 2.997(6), 120.5; N2–H···F2_#1 0.92, 2.17, 2.863(7), 131.2; N2–H···F3_#1 0.92, 2.37, 3.001(6), 125.3. Symmetry transformation used to generate equivalent atoms: #1 = $x$ + 1/2, $y$ + 1/2, $z$.

 © 2007 Wiley-VCH Verlag GmbH & Co. KGaA, Weinheim 

In exploratory studies aimed at synthesizing the $P_2/N_2$-coordinated hydride complexes $[Ir(H)(X)(H_2N\cap NH_2)(Ph_2P\cap PPh_2)]BF_4$ (X = H, Cl), which have one chiral bidentate rather than two achiral monodentate phosphorus ligands, two diene(diphosphane) complexes $[(\eta^4\text{-}1,5\text{-}C_8H_{12})Ir(Ph_2P\cap PPh_2)]BF_4$ {$Ph_2P\cap PPh_2$ = (*R*)-binap[11] and (1*S*,2*S*)-1,2-bis(diphenylphosphanyl)cyclopentane [(*S*,*S*)-bdpcp]} were selected as potential starting materials. As mentioned by way of introduction, related rhodium chemistry has shown that the bis(chelates) $[Rh(H_2N\cap NH_2)\{(R)\text{-binap}\}]BF_4$ {$H_2N\cap NH_2$ = $H_2NCMe_2CMe_2NH_2$ (tmen), (1*R*,2*R*)-$H_2NCH(Ph)CH(Ph)NH_2$ [(*R*,*R*)-dpen], or (1*R*,2*R*)-1,2-$(H_2N)_2C_6H_{10}$ [(*R*,*R*)-dach]} are smoothly formed when $[(\eta^4\text{-}1,5\text{-}C_8H_{12})Rh\{(R)\text{-binap}\}]BF_4$ is hydrogenated in the presence of the required diamine ligand.[1] In view of the greater stability of the Ir–H bond than the Rh–H bond, we expected that similar treatment of the diene(diphosphane) iridium precursors $[(\eta^4\text{-}1,5\text{-}C_8H_{12})Ir(Ph_2P\cap PPh_2)]BF_4$ would result in the formation of mixed-ligand complexes $[IrH_2(H_2N\cap NH_2)(Ph_2P\cap PPh_2)]BF_4$ by oxidative addition of dihydrogen to initially formed $[Ir(H_2N\cap NH_2)(Ph_2P\cap PPh_2)]BF_4$ intermediates. However, only mixtures of various hydride-containing complexes were produced, from which none of the hoped-for compounds could be isolated.

Expecting that it might be easier to substitute the hard nitrogen donors for the σ,π-bonded diolefin ligand at the $Ir^{III}$ rather than the $Ir^{I}$ oxidation stage, we prepared the complex $[(\eta^4\text{-}1,5\text{-}C_8H_{12})Ir(H)(Cl)\{(S,S)\text{-bdpcp}\}]BF_4$ (**4**) by oxidative addition of hydrogen chloride to its $[(\eta^4\text{-}1,5\text{-}C_8H_{12})Ir\{(S,S)\text{-bdpcp}\}]BF_4$ precursor. Compound **4** was shown by NMR spectroscopy, together with an X-ray structure analysis, to bear *trans*-bonded chlorido and hydrido ligands. The structure consists of discrete $[(\eta^4\text{-}1,5\text{-}C_8H_{12})Ir(H)(Cl)\{(S,S)\text{-bdpcp}\}]^+$ cations (Figure 2) and $BF_4^-$ anions. The Ir–Cl bond *trans* to the hydride is long at 2.490(4) Å,[12] which is entirely consistent with the strong *trans* influence of hydrido ligands.

In contrast to the "normal" oxidative addition of HCl to $[(\eta^4\text{-}1,5\text{-}C_8H_{12})Ir\{(S,S)\text{-bdpcp}\}]BF_4$, the reaction of hydrogen chloride with $[(\eta^4\text{-}1,5\text{-}C_8H_{12})Ir\{(R)\text{-binap}\}]BF_4$ did not lead to a mononuclear $Ir^{III}$ complex but instead gave the triply chlorido-bridged binuclear product $[\{(R)\text{-binap}\}_2Ir_2H_2(\mu\text{-}Cl)_3]BF_4$ (**5**) (Scheme 2). It is well known that $Ir^{III}$ has a pronounced tendency to form cationic[13] confacial-bioctahedral structures held together by three connecting mononegative donors such as halide, hydride, alkoxide, amide, and the like. Reported examples include the (*R*)-binap-coordinated complexes $[\{(R)\text{-binap}\}_2Ir_2H_2(\mu\text{-}OR)_2(\mu\text{-}Cl)]Cl$ (R = H, $CH_3$), which were obtained by oxidative addition of the O–H bonds of water and methanol

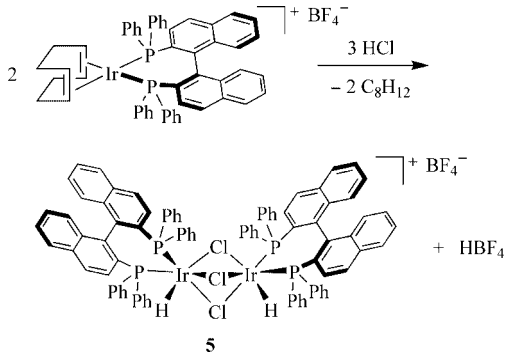


Scheme 2. Formation of diiridium complex **5**.

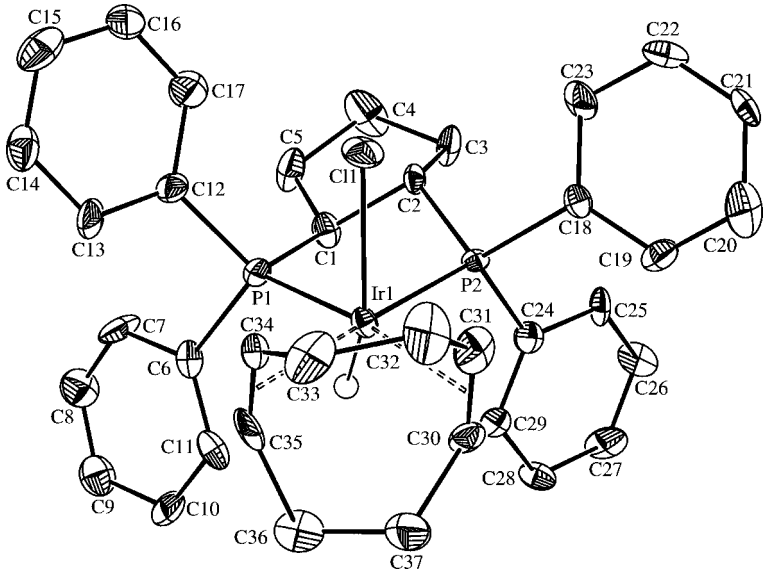


Figure 2. Structure of the cation of $[(\eta^4\text{-}1,5\text{-}C_8H_{12})Ir(H)(Cl)\{(S,S)\text{-bdpcp}\}]BF_4$ (**4**); carbon-bonded H atoms have been omitted for clarity. Selected bond lengths [Å] and angles [°]: Ir–Cl1 2.490(4), Ir–P1 2.332(4), Ir–P2 2.319(4); Cl1–Ir–P1 88.8(1), Cl1–Ir–P2 84.0(1), P1–Ir–P2 85.5(1).

 © 2007 Wiley-VCH Verlag GmbH & Co. KGaA, Weinheim 

to [{(*R*)-binap}$_2$Ir$_2$(μ-Cl)$_2$],[13h] as well as the recently described halide salts [{(*S*)-binap}$_2$Ir$_2$H$_2$(μ-X)$_3$]X (X = Cl, Br, I), which were formed by sequential treatment of [(η$^2$-C$_8$H$_{14}$)$_4$Ir$_2$(μ-Cl)$_2$] first with the chelate phosphane and then with aqueous HX.[13p]

We propose that [(η$^4$-1,5-C$_8$H$_{12}$)Ir{(*R*)-binap}]BF$_4$ reacts with hydrogen chloride to initially give an HCl adduct similar to **4**, where the greater bulkiness of the two "Ph$_2$Pnaphthyl" binap building blocks than that of the two "Ph$_2$Palkyl" halves of the chelate ring in the mononuclear complex

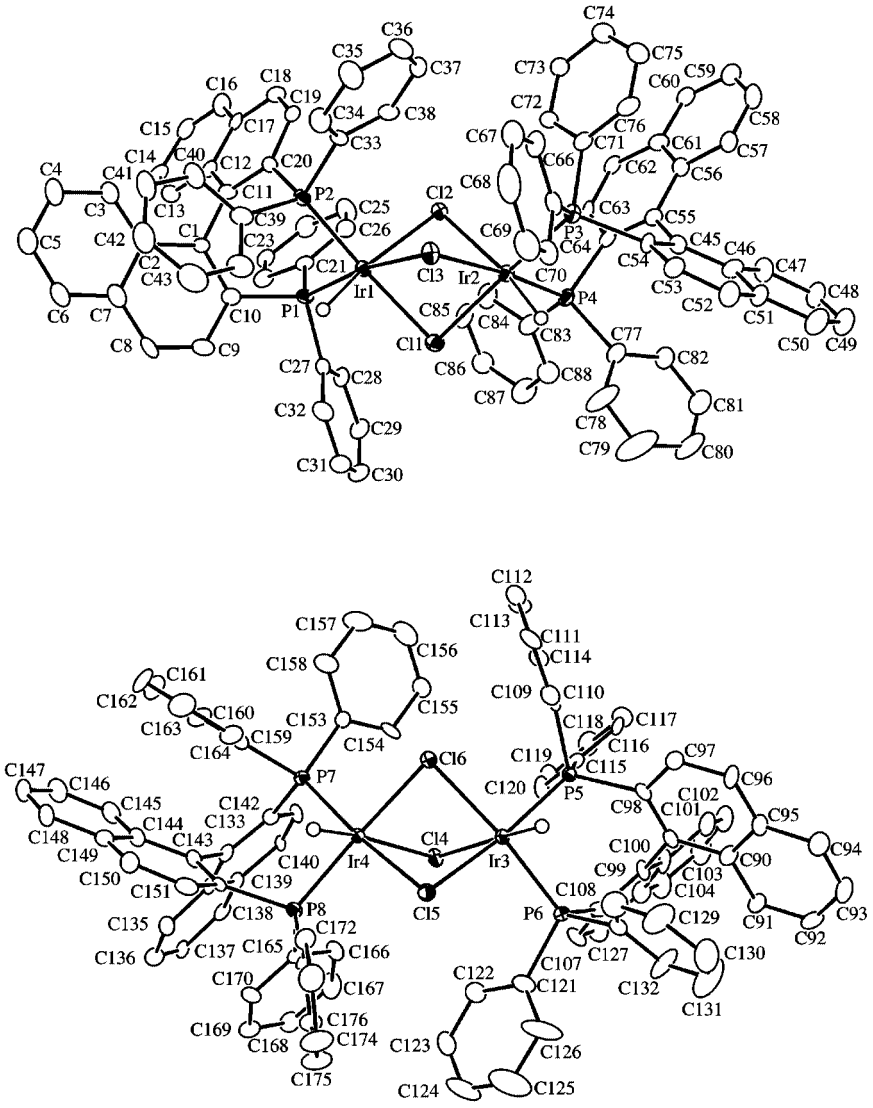


Figure 3. Structures of the two crystallographically independent cations of [{(*R*)-binap}$_2$Ir$_2$H$_2$(μ-Cl)$_3$]BF$_4$ (**5**); aryl H atoms have been omitted for clarity. Selected bond lengths [Å] and angles [°] for cation I: Ir1–Cl1 2.470(1), Ir1–Cl2 2.534(1), Ir1–Cl3 2.428(1), Ir1–P1 2.251(1), Ir1–P2 2.257(1), Ir2–Cl1 2.436(1), Ir2–Cl2 2.532(1), Ir2–Cl3 2.458(1), Ir2–P3 2.252(1), Ir2–P4 2.245(1); Cl1–Ir1–Cl2 78.99(4), Cl1–Ir1–Cl3 79.37(5), Cl1–Ir1–P1 94.37(5), Cl1–Ir1–P2 173.17(5), Cl2–Ir1–Cl3 79.27(4), Cl2–Ir1–P1 106.40(5), Cl2–Ir1–P2 100.72(5), Cl3–Ir1–P1 170.74(5), Cl3–Ir1–P2 93.85(5), P1–Ir1–P2 92.26(5), Cl1–Ir2–Cl2 79.65(4), Cl1–Ir2–Cl3 79.45(5), Cl1–Ir2–P3 170.01(5), Cl1–Ir2–P4 94.66(5), Cl2–Ir2–Cl3 78.77(4), Cl2–Ir2–P3 106.54(5), Cl2–Ir2–P4 100.37(5), Cl3–Ir2–P3 93.89(5), Cl3–Ir2–P4 174.11(5), P3–Ir2–P4 91.94(5), Ir1–Cl1–Ir2 86.10(1), Ir1–Cl2–Ir2 82.76(1), Ir1–Cl3–Ir2 86.52(1). Selected dihedral angles, given as (plane)/(plane) [°]: (Ir1,Cl1,Cl2)/(Ir2,Cl1,Cl2) 58.43(4), (Ir1,Cl1,Cl3)/(Ir2,Cl1,Cl3) 54.49(5), (Ir1,Cl2,Cl3)/(Ir2,Cl2,Cl3) 58.44(4), (Ir1,Cl1,Ir2)/(Ir1,Cl2,Ir2) 61.00(1), (Ir1,Cl1,Ir2)/(Ir1,Cl3,Ir2) 57.72(1), (Ir1,Cl2,Ir2)/(Ir1,Cl3,Ir2) 61.28(1), (naphthyl C1–C10)/(naphthyl C11–C20), 76.1(1); (naphthyl C45–C54)/(naphthyl C55–C64), 67.7(1). Corresponding parameters for cation II: Ir3–Cl4 2.530(1), Ir3–Cl5 2.426(1), Ir3–Cl6 2.463(1), Ir3–P5 2.259(1), Ir3–P6 2.250(1), Ir4–Cl4 2.542(1), Ir4–Cl5 2.452(1), Ir4–Cl6 2.440(1), Ir4–P7 2.260(1), Ir4–P8 2.257(1); Cl4–Ir3–Cl5 79.80(4), Cl4–Ir3–Cl6 79.03(4), Cl4–Ir3–P5 107.61(5), Cl4–Ir3–P6 98.80(5), Cl5–Ir3–Cl6 79.83(4), Cl5–Ir3–P5 168.85(5), Cl5–Ir3–P6 93.89(5), Cl6–Ir3–P5 93.21(5), Cl6–Ir3–P6 173.61(5), P5–Ir3–P6 93.18(5), Cl4–Ir4–Cl5 79.10(4), Cl4–Ir4–Cl6 79.23(4), Cl4–Ir4–P7 100.53(5), Cl4–Ir4–P8 105.97(5), Cl5–Ir4–Cl6 79.78(5), Cl5–Ir4–P8 92.68(5), Cl5–Ir4–P7 174.44(5), Cl6–Ir4–P7 94.69(5), Cl6–Ir4–P8 170.00(5), P7–Ir4–P8 92.74(5), Ir3–Cl4–Ir4 82.33(1), Ir3–Cl5–Ir4 86.38(1), Ir3–Cl6–Ir4 85.83(1); (Ir3,Cl4,Cl5)/(Ir4,Cl4,Cl5) 58.37(5), (Ir3,Cl4,Cl6)/(Ir4,Cl4,Cl6) 59.38(5), (Ir3,Cl5,Cl6)/(Ir4,Cl5,Cl6) 54.29(3), (Ir3,Cl4,Ir4)/(Ir3,Cl5,Ir4) 60.85(1), (Ir3,Cl4,Ir4)/(Ir3,Cl6,Ir4) 61.92(1), (Ir3,Cl5,Ir4)/(Ir3,Cl6,Ir4) 57.23(1), (naphthyl C89–C98)/(naphthyl C99–C108), 73.0(1); (naphthyl C133–C142)/(naphthyl C143–C152), 72.0(1).

 © 2007 Wiley-VCH Verlag GmbH & Co. KGaA, Weinheim 

facilitates the decoordination of the cyclooctadiene ligand through "steric pressure".[14a,14b] Bridge-closing combination of the remaining "[{(*R*)-binap}Ir(H)(Cl)]$^+$ fragments would then form [{(*R*)-binap}$_2$Ir$_2$H$_2$(μ-Cl)$_2$]$^{2+}$, which stabilizes to **5** by the addition of an extra chloride ion provided by the excess of HCl.[14c]

The bimetallic structure of **5** was confirmed by X-ray analysis. Single crystals grown from an acetone/diethyl ether solvent mixture were found to have the idealized composition [{(*R*)-binap}$_2$Ir$_2$H$_2$(μ-Cl)$_3$]BF$_4$·Me$_2$CO·1/2 H$_2$O·1/4 Et$_2$O and to contain, in addition to the different solvent molecules, two crystallographically independent ion pairs in the asymmetric unit. Perspective views of the molecular models that resulted for the cationic parts are presented in Figure 3. The structures of the two cations are very close to $C_2$-symmetric, with the twofold rotation axes passing through the midpoints of the Ir···Ir vectors and the chlorido ligands Cl2 and Cl4 *trans* to the Ir–H bonds. In solution, this molecular $C_2$ symmetry is mirrored by a deceptively simple AA′BB′ $^{31}$P{$^1$H} NMR pattern arising from the two chiral diphosphane ligands (pairs of "doublets", where only $|^2J_{P,P} + {}^4J_{P,P}|$ = 20.0 Hz is resolved). The pair-wise shared coordination planes spanned by one metal center and two bridging chlorido ligands are inclined to each other at angles between 120.62° and 125.71°, with the interplanar angles of the Ir(μCl)Ir bridges varying from 118.08(1)° to 122.77(1)° (ranges of the supplementary dihedral angles given in the legend to Figure 3: 59.38(5)–54.29(3)° and 61.92(1)–57.23(1)°, respectively). The angles between the normals to the four pairs of naphthyl least squares planes amount to 67.7(1)° and 76.1(1)° in cation I and 72.0(1)° and 73.0(1)° in cation II. Though much less than the dihedral angle of 81.4° displayed by the pairs of naphthalene rings in the related [{(*R*)-binap}$_2$Ir$_2$H$_2$(μ-OCH$_3$)$_2$(μ-Cl)]$^+$ cation,[13h] these values clearly fall within the limits of about 65–77° that have previously been reported for several mono- and binuclear binap compounds of Ru$^{II}$, Rh$^{I}$, Ir$^{I}$, and Ir$^{III}$.[13p,15] As anticipated, the Ir–Cl bonds *trans* to Ir–H [2.530(1)–2.534(1) Å] are significantly longer than those opposite to the Ir–P bonds [2.426(1)–2.470(1) Å] and are amongst the longest Ir$^{III}$–μ–Cl distances reported to date.[16] The Ir–P bond lengths of **7** vary between 2.246(1) and 2.260(1) Å and thus compare favorably with the metal-to-phosphorus distances of 2.248 and 2.262 Å measured for the aforementioned chlorido/methoxido-bridged diiridium(III) complex.[13h] The obtuse P–Ir–P angles of 91.94(5)–93.18(5)° likewise closely resemble those of other structurally characterized iridium complexes bearing (*R*)- or (*S*)-binap ligands.[13h,13p,15g,15h]

Completely unexpectedly, the reaction of [(η$^4$-1,5-C$_8$H$_{12}$)-Ir(H)(Cl){(*S*,*S*)-bdpcp}]BF$_4$ (**4**) with different H$_2$N∩NH$_2$ chelate ligands did not result in diene/diamine exchange. Depending on the reaction conditions, the less basic aromatic or aliphatic amines 2,2′-diamino-1,1′-binaphthyl and 1,2-diphenylethylenediamine either left the compound unchanged or furnished mixtures with the dehydrochlorinated iridium(I) precursor [(η$^4$-1,5-C$_8$H$_{12}$)Ir{(*S*,*S*)-bdpcp}]BF$_4$. Complete removal of hydrogen chloride from the Ir$^{III}$ center was observed in the reaction of the HCl adduct with the stronger basic aliphatic diamine 1,2-(H$_2$N)$_2$C$_6$H$_{10}$. Brønsted base-assisted dehydrohalogenations, as observed between **4** and diamines, are the infrequently encountered reverse reaction of HX oxidative addition; they are comparatively common with Ir$^{III}$.[17] In fact, similar amine-induced eliminations of HCl have recently been reported for some triply chlorido-bridged binuclear hydrides of iridium(III) bearing trimethylene-linked N-heterocyclic carbenes (NHCs) as terminal ligands.[13o] Whereas those [{(NHC)(CH$_2$)$_3$(NHC)}$_2$Ir$_2$H$_2$(μ-Cl)$_3$]PF$_6$ dimers underwent complete degradation in the presence of nitrogen bases, binap-chelated diiridium complex **5** reacts with several diamines to smoothly produce the diamine(diphosphane) target compounds [Ir(H)(Cl)(H$_2$N∩NH$_2$){(*R*)-binap}]BF$_4$ [H$_2$N∩NH$_2$ = (*R*,*R*)-dpen (**6a**), (*R*,*R*)-dach (**6b**), and tmen (**6c**)] by nucleophilic opening of the chlorido bridges. In order to favor the formation of these three cationic species (Scheme 3), the liberated chloride was removed by precipitation with AgBF$_4$, although the addition of Ag$^+$ is not imperative with the completely aliphatic and, hence, more electron-rich diamines tmen and dach. Diiridium complex **5** does not undergo the bridge-opening reaction upon combination with (*R*)-2,2′-diamino-1,1′-binaphthyl, either because of too much steric pressure in the resulting [Ir(H)(Cl){(*R*)-dabin)}{(*R*)-binap}]$^+$ cation or because of a too low nucleophilicity of the aromatic (*R*)-dabin ligand.

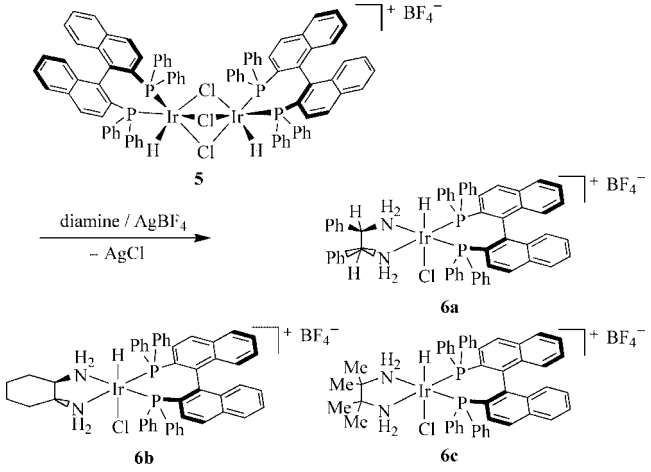


Scheme 3. Synthesis of mixed-ligand complexes **6a**–**c**.

Complexes **6a**–**c** proved difficult to crystallize and therefore could only be characterized spectroscopically. Their $^1$H NMR spectra were found to display hydride signals at around $\delta$ = –20 ppm as doublets of doublets. Two $^2J_{P,H}$ coupling constants amounting to around 16 and 18 Hz place these hydrido ligands in a position *cis* to two chemically inequivalent binap P atoms which, accordingly, give rise to two $^{31}$P{$^1$H} doublets ($\delta$ = –13 to –10 and –1 ppm; *cis*-$^2J_{P,P} \approx$ 22 Hz). These data indicate that the stereochemistry of **6a**–**c** is either *OC*-6-43 with the hydride trans to Cl, as proposed for [Rh(H)(Cl){(*R*,*R*)-dpen}{(*R*)-binap}]-BF$_4$,[1] or *OC*-6-23, where the Ir–H bond is opposite to one

 © 2007 Wiley-VCH Verlag GmbH & Co. KGaA, Weinheim 

of the $NH_2$ functionalities. Although we could not corroborate the actual structure by X-ray analysis, the geometry with the hydride *trans* to chloride shown in Scheme 3 is favored over the *trans*-H–Ir–N alternative by comparison with the IrH NMR spectroscopic data of some [Ir(H)(Cl)(aminophosphane)$_2$]X chelate complexes having crystallographically established *OC*-6-43 stereochemistry, for example [Ir(H)(Cl)($H_2N(CH_2)_2PPh_2)_2$]Cl[10a] and [Ir(H)(Cl){*o*-HN(R)$C_6H_4PPh_2$}$_2$]X (R = Et, $CH_2Ph$; $X^-$ = $Cl^-$, $OH^-$, $MeCO_2^-$).[18] Similar to **6a**–**c**, all of these compounds display $\delta$(IrH) in the range –22 to –20 ppm with *cis*-$^2J$(P,H) ≈ 18 Hz.[19]

## Catalytic Hydrogenation of Acetophenone

Both the chiral chlorido-hydrido complexes [Ir(H)(Cl)($H_2N\cap NH_2$){(*R*)-binap}]$BF_4$ [$H_2N\cap NH_2$ = (*R*,*R*)-dpen (**6a**), (*R*,*R*)-dach (**6b**), or tmen (**6c**)] and the dihydrides [$IrH_2${$H_2N\cap NH_2$}$(PR_3)_2$]$BF_4$ [$H_2N\cap NH_2/PR_3$ = (*R*,*R*)-dach/$PPh_3$ (**1b**), (*R*)-dabin/$PPh_3$ (**1c**), (*R*,*R*)-dach/P*i*$Pr_3$ (**2a**), or (*R*)-dabin/P*i*$Pr_3$ (**2b**)] were investigated for their ability to form stereoselective >C=O hydrogenation catalysts. In fact, all of them catalyzed the asymmetric hydrogenation of acetophenone to (*S*)-1-phenylethanol at substrate-to-catalyst (*s*:*c*) ratios ranging from 200:1 to 5000:1 in the presence of a strong base (typically 50 equiv. of KOH) in alcoholic solution under $H_2$ (20 bar) at 40–60 °C (Table 1). The success of these hydrogenation reactions depends critically on the presence of extra base in the catalytic system and the use of a protic reaction medium. Thus, virtually no catalytic >C=O reduction occurred in alcohols in the absence of base or in an aprotic solvent such as benzene containing a basic additive. Methanol proved to be the solvent of choice, as reactions in ethanol and 2-propanol proceeded slower and resulted in reduced enantioselectivity (Table 1, entries 2–4).

The likelihood of the ketone reduction proceeding by direct metal-assisted transfer of $H^{\delta-}/H^{\delta+}$ equivalents from the $H_2$ molecule to the carbonyl dipole was substantiated by ruling out the alternative pathway involving $H^{\delta-}/H^{\delta+}$ transfer from the solvent. Thus, when a solution of acetophenone in $CH_3OH$ was hydrogenated with $D_2$ (10 bar) employing the combined **6b**/KOH catalyst, α-deuterated $PhCD(OH)CH_3$ was formed as the main alcohol product, which was demonstrated by NMR spectroscopy as described previously.[10b] The observation of minor amounts of $PhCH(OH)CH_3$ as a by-product of the deuteration reaction cannot be attributed to the methanol molecule serving as a hydrogen source because no formation of $PhCH(OH)CH_3$ or $PhCD(OH)CH_3$ was observed when the reaction was carried out in the absence of hydrogen gas in $CH_3OH$ or $CD_3OH$. The formation of the non-deuterated isotopomer rather points to "$D_2 + CH_3OH = CH_3OD + HD$" and "$HD + CH_3OH = CH_3OD + H_2$" exchange processes accompanying the catalysis. We have shown in previous work[10b] that the exchange of isotopes between a protic solvent and the hydrogen atmosphere, which is typical of heterolytic activation of the hydrogen molecule during reaction,[20] is a characteristic feature of iridium-based >C=O hydrogenation catalysts bearing ligands that, like the diamines used in the present study, have acidic primary or secondary amine ends.

Table 1. Enantioselective hydrogenation of acetophenone in the presence of base-modified iridium(III) precatalysts; $p(H_2)$ = 20 bar.

| No. | Precatalyst | *t* [h] | PhCH(OH)Me [%] | *ee* [%] (config.) |
|---|---|---|---|---|
| 1 | **6a**[a] | 1.5 | 100 | 82 (*S*) |
| 2 | **6b**[a] | 1.5 | 100 | 75 (*S*) |
| 3 | **6b**[b] | 2 | 61 | 59 (*S*) |
| 4 | **6b**[c] | 4 | 42 | 38 (*S*) |
| 5 | **6c**[a] | 1.5 | 100 | 73 (*S*) |
| 6 | **1b**[a] | 2 | 51 | 24(*S*) |
| 7 | **1c**[a] | 1 | 37 | <2 (*S*) |
| 8 | **2a**[a] | 2 | 69 | <2 (*S*) |
| 9 | **2b**[a] | 2 | 37 | 9 (*S*) |
| 10 | **6a**[d] | 3 | 11 | 80 (*S*) |
| 11 | **6b**[d] | 3 | 62 | 66 (*S*) |
| 12 | **5**/(*R*,*R*)-dpen[e] | 2 | 100 | 84 (*S*) |
| 13 | **5**/(*R*,*R*)-dach[e] | 2 | 100 | 71 (*S*) |

[a] Acetophenone (5.0 mmol), 0.01 mmol of $Ir^{III}$ complex, KOH (50 equiv.), methanol (3 mL); *T* = 50 °C. [b] In ethanol at *s*:*c* = 500:1; *T* = 40 °C. [c] In 2-propanol at *s*:*c* = 200:1; *T* = 60 °C. [d] 33.0 mmol of acetophenone, $6.6\times10^{-3}$ mmol of $Ir^{III}$ complex, and 0.33 mmol of KOH in methanol (4 mL); *T* = 50 °C. [e] In situ catalysts activated with 25 equiv. of KOH in methanol; *s*:*c* = 250:1, *T* = 50 °C.

As compared to complexes **1b**/**1c** and **2a**/**2b**, where only the diamine ligands can contribute to the (poor) stereoselective outcome of the catalytic runs (Table 1, entries 6–9), compounds **6a**–**c**, which possess an additional (*R*)-binap ligand, form much more enantioselective systems, as expected. Best results of 82–84% *ee* were obtained with the preformed complex [Ir(H)(Cl){(*R*,*R*)-dpen}{(*R*)-binap}]$BF_4$ (**6a**) and its in situ generated equivalent [{(*R*)-binap}$_2Ir_2H_2(\mu\text{-}Cl)_3$]$BF_4$/(*R*,*R*)-dpen [**5**/(*R*,*R*)-dpen; Table 1, entries 1 and 12).[21] With (*R*,*R*)-dach as the diamine co-ligand, the *ee* achieved with both the preformed and the in situ catalysts **6b** and **5**/(*R*,*R*)-dach was seen to drop to 71–75% (Table 1, entries 2 and 13). Further replacement of the (*R*,*R*)-dach chelate by the achiral diamine $H_2NCMe_2CMe_2NH_2$ in precatalyst **6c** left the optical yield of the (*S*) isomer (73%; Table 1, no. 5) essentially unchanged, thus suggesting that it is preferentially the diphosphane which determines the asymmetric induction. Comparison of these results with those obtained with isoelectronic $Ru^{II}$-based catalysts reveals some interesting trends.

At first glance, the combined system [Ir(H)(Cl)(tmen){(*R*)-binap}]$BF_4$/KOH/MeOH appears to be superior in selectivity [73% for (*S*)-PhCH(OH)Me] to the [Ru(H)(Cl)(tmen){(*R*)-binap}]-derived dihydride [Ru(H)$_2$(tmen){(*R*)-binap}], which produced the (*S*) isomer of 1-phenylethanol in only 6–14% yield when used in 2-propanol without added base.[2b,2c] However, the seemingly poor performance of this ruthenium complex results from catalyst deactivation by formation of diastereomeric alkoxides such as [Ru(H){(*S*)-OCH(Me)Ph}(tmen){(*R*)-binap}] and [Ru(H)-

 © 2007 Wiley-VCH Verlag GmbH & Co. KGaA, Weinheim 

{(*R*)-OCH(Me)Ph}(tmen){(*R*)-binap}] during the build up of the acidic product alcohol. This unwanted side reaction can be prevented by the addition of base or by lowering the polarity of the solvent. Running the Ru-catalyzed reaction in 2-propanol in the presence of base or in benzene (where Ir complex **6c** remains completely inactive) thus established an inherent enantioselectivity of 51–68% (*R*) for the ruthenium-based (*R*)-binap/tmen system,[2b,2c] which is therefore comparable to **6c** with respect to the *ee* values that can be attained but yields the opposite enantiomer. In the presence of base, the $Ru^{II}$ complex [Ru(H)(Cl){(*R*,*R*)-dach}{(*R*)-binap}] catalyzes the hydrogenation of acetophenone (neat or dissolved in benzene) to afford (*S*)-PhCH(OH)Me in 88% *ee*,[2a,2c] which makes it a somewhat more selective catalyst than [Ir(H)(Cl){(*R*,*R*)-dach}{(*R*)-binap}]$BF_4$ (**6b**), which gives the (*S*) form of the alcohol in only around 75% *ee*. With base-modified [Ru(H)(Cl){(*R*,*R*)-dpen}{(*R*)-binap}], the Morris group has achieved 73% *ee* for the formation of (*S*)-PhCH(OH)Me,[2a] while the catalytic species generated in basic media from the dichlorido precursor [$RuCl_2$\{(*S*,*S*)-dpen\}{(*S*)-tolbinap}] (tolbinap is the di-*p*-tolyl analogue of binap) afforded the (*R*) enantiomer in 78–83% yield, as reported independently by Noyori and coworkers[22] and Rautenstrauch and Morris et al.[2d] Hence, the selectivity of the corresponding iridium-based system [Ir(H)(Cl){(*R*,*R*)-dpen}{(*R*)-binap}]$BF_4$/KOH/MeOH [82% *ee* for the (*S*) isomeric alcohol] compares favorably with that observed for the two established ruthenium catalysts possessing the same ligands. However, the $Ru^{II}$ complexes, which work very fast at substrate-to-catalyst ratios as high as $10^5$–$10^6$, form much more active systems: the most active $Ir^{III}$ catalyst studied in this work is formed from the only moderately selective complex **6b** in the presence of 50 equiv. of KOH. This system furnished 62% of 1-phenylethanol within 3 h at *s*:*c* = 5000, albeit with a reduced selectivity of 66% *ee* for the (*S*) isomer (Table 1, entry 11). Under identical conditions, the most selective precatalyst **6a** maintains an optical yield of 80% *ee* (*S*) but shows poor activity, transforming only 11% of the ketone to the product alcohol (Table 1, entry 10).

## Conclusions

This work has shown that cationic dihydridoiridium(III) complexes with two monodentate phosphanes and one chelating diamine can easily be made by treating different $H_2N\cap NH_2$ ligands with a number of readily accessible substitutionally labile precursors. The preparation of the mixed-ligand bis(chelates) [Ir(H)(Cl)($H_2N\cap NH_2$){(*R*)-binap}]$BF_4$ [$H_2N\cap NH_2$ = (*R*,*R*)-dpen (**6a**), (*R*,*R*)-dach (**6b**), or tmen (**6c**)] is more involved and requires dinuclear [{(*R*)-binap}$_2$$Ir_2H_2(\mu\text{-}Cl)_3$]$BF_4$ as a synthetic intermediate. While *cis*-dihydrides such as [$IrH_2$\{(*R*,*R*)-dach\}$(PR_3)_2$]$BF_4$ and [$IrH_2$\{(*R*)-dabin\}$(PR_3)_2$]$BF_4$ (R = *i*Pr, Ph) are only poor (pre)catalysts for the enantioselective hydrogenation of acetophenone to 1-phenylethanol, the combined systems (**6a**–**c**)/KOH/MeOH catalyze the formation of the product alcohol with a degree of enantioselectivity which, in the most favorable cases, closely matches that of established isoelectronic $Ru^{II}$-based catalysts containing identical phosphorus and nitrogen donor ligands.

## Experimental Section

**General:** All manipulations were performed under nitrogen or argon, unless stated otherwise. Solvents were distilled from the appropriate drying agents prior to use. NMR: Bruker DPX 300 (300.1 MHz for $^1H$, 75.5 MHz for $^{13}C$, and 121.5 MHz for $^{31}P$) with $SiMe_4$ as internal or $H_3PO_4$ as external standard (downfield positive) at ambient temperature ("m" = deceptively simple multiplet). GC: Shimadzu GC-17A (FID). Silver tetrafluoroborate, $HBF_4$ (54% in $Et_2O$), and the diphosphane and diamine ligands (*R*)-2,2′-bis(diphenylphosphanyl)-1,1′-binaphthyl [(*R*)-binap], 1,2-phenylenediamine (1,2-phdn), (*R*)-2,2′-diamino-1,1′-binaphthyl [(*R*)-dabin], (1*R*,2*R*)- and (1*S*,2*S*)-1,2-diphenylethylenediamine [(*R*,*R*)-, (*S*,*S*)-dpen], and (1*R*,2*R*)-1,2-diaminocyclohexane [(*R*,*R*)-dach] were used as purchased. 1,1′,2,2′-Tetramethylethylenediamine (tmen),[23] (1*S*,2*S*)-1,2-bis(diphenylphosphanyl)cyclopentane [(*S*,*S*)-bdpcp],[24] [$(\eta^4\text{-}1,5\text{-}C_8H_{12})_2Ir_2(\mu\text{-}Cl)_2$],[25] [$(\eta^4\text{-}1,5\text{-}C_8H_{12})$-$Ir(PPh_3)_2$]$BF_4$,[4d,4e] [$IrH_2(OCMe_2)_2(PPh_3)_2$]$BF_4$,[4d,4e] [$IrH_5$(P-*i*$Pr_3)_2$],[5d] and [$IrH_5(PCy_3)_2$][5e] were prepared according to published procedures or slight modifications thereof. The complex [$(\eta^4$-1,5-$C_8H_{12})$Ir\{(*R*)-binap\}]$BF_4$ was previously made from [$(\eta^4$-1,5-$C_8H_{12})$$Ir(NCMe)_2$]$BF_4$ which, in turn, was synthesized from [$(\eta^4$-1,5-$C_8H_{12})_2Ir_2(\mu\text{-}Cl)_2$] via [$(\eta^4$-1,5-$C_8H_{12})_2Ir$]$BF_4$ as a further intermediate.[11] A more direct route is given here: A 1:2:2 molar mixture of [$(\eta^4$-1,5-$C_8H_{12})_2Ir_2(\mu\text{-}Cl)_2$] (425 mg, 0.63 mmol), (*R*)-binap (785 mg, 1.26 mmol), and $AgBF_4$ (245 mg, 1.26 mmol) in 30 mL of methanol was stirred for 24 h at ambient conditions with the exclusion of light. Precipitated silver chloride was then removed by filtration through diatomaceous earth (Celite® 521), which was washed with small portions of $CH_2Cl_2$ until the residue on the filter was colorless. Evaporation of the filtrate to a final volume of about 2 mL followed by dilution with 30 mL of diethyl ether gave the product as a raspberry-colored solid, which was filtered off, washed with diethyl ether (3 × 5 mL), and dried under vacuum; yield: 950 mg (75%). $^1H$ NMR ($CD_2Cl_2$): $\delta$ = 1.84–2.30 (m, 8 H, $CH_2$), 4.15, 4.40 (both m, 2 H each, both CH), 6.39–7.78 (m, 32 H, aryl H) ppm. $^{31}P\{^1H\}$ NMR ($CD_2Cl_2$): $\delta$ = 16.05 (s) ppm [ref.[11] $\delta$ = 15.1 ppm in $CDCl_3$]. $C_{52}H_{44}BF_4IrP_2$ (1008.9): calcd. C 61.85, H 4.39; found C 62.08, H 4.54.

[$(\eta^4$-1,5-$C_8H_{12})$Ir\{(*S*,*S*)-bdpcp\}]$BF_4$ was isolated in 60% yield from a similar 1:2:2 reaction of [$(\eta^4$-1,5-$C_8H_{12})_2Ir_2(\mu\text{-}Cl)_2$] with $AgBF_4$ and the diphosphane in methanol: $^1H$ NMR ($CD_2Cl_2$): $\delta$ = 1.16, 1.70–2.36 (both m, 2 + 12 H, both $CH_2$), 2.74 (m, 2 H, PCH), 4.00, 4.73 (both m, 2 H each, both diene CH), 7.31–7.89 (m, 20 H, aryl H) ppm. $^{31}P\{^1H\}$ NMR ($CD_2Cl_2$): $\delta$ = 20.70 (s) ppm. $C_{37}H_{40}BF_4IrP_2$ (825.70): calcd. C 53.82, H 4.88; found C 53.61, H 4.71.

**[$IrH_2$(1,2-phdn)($PPh_3)_2$]$BF_4$ (1a):** A solution of [$IrH_2(OCMe_2)_2$-$(PPh_3)_2$]$BF_4$ (440 mg, 0.49 mmol) in 15 mL of thf was stirred with 1,2-phenylenediamine (55 mg, 0.50 mmol) at room temperature. After a short while the product separated from the reaction mixture as a colorless solid, which was filtered off, washed with diethyl ether (2 × 3 mL), and dried under vacuum. Yield: 198 mg (44%). $^1H$ NMR ($CD_2Cl_2$): $\delta$ = –20.84 (t, $^2J_{P,H}$ = 16.7 Hz, 2 H, $IrH_2$), 4.04 (br., 4 H, $NH_2$), 6.77, 7.03 (AA′BB′-type m, 4 H, phenylene H), 7.30–7.51 (m, 30 H, phenyl H) ppm. $^{13}C\{^1H\}$ NMR ($CD_2Cl_2$): $\delta$ = 128.58, 129.66 (both s, phenylene C-3,6 and C-4,5), 129.88 (t, $^3J_{P,C}$

 © 2007 Wiley-VCH Verlag GmbH & Co. KGaA, Weinheim 

= 20.2 Hz, phenyl C-3,5), 131.70 (s, phenyl C-4), 132.26 (t, $^1J_{P,C}$ = 103.9 Hz, phenyl C-1), 133.99 (t, $^2J_{P,C}$ = 24.5 Hz, phenyl C-2,6), 139.81 (phenylene C-1,2) ppm. $^{31}P\{^1H\}$ NMR ($CD_2Cl_2$): $\delta$ = 24.49 (s) ppm. $C_{42}H_{40}BF_4IrN_2P_2$ (913.71): calcd. C 55.21, H 4.41, N 3.07; found C 54.71, H 4.25, N 2.72.

**$[IrH_2\{(R,R)$-dach$\}(PPh_3)_2]BF_4$ (1b):** This complex was prepared as described for **1a** from $[IrH_2(OCMe_2)_2(PPh_3)_2]BF_4$ (200 mg, 0.22 mmol) and the diamine ligand (25 mg, 0.22 mmol) in 10 mL of thf. Yield: 121 mg (60%) of a colorless solid. $^1H$ NMR ($CD_2Cl_2$): $\delta$ = –21.07 (t, $^2J_{P,H}$ = 17.6 Hz, 2 H, $IrH_2$), 0.33, 0.71, 1.20–1.33, 1.39, 1.75 (all m, 2 + 2 + 4 + 2 + 2 H, $CH_2$ and $NH_2$), 2.79 (m, 2 H, CH), 7.4–7.7 (m, 30 H, $C_6H_5$) ppm. $^{13}C\{^1H\}$ NMR: $\delta$ = 25.13 (s, $C_6H_{10}$ C-4,5), 36.28 (s, $C_6H_{10}$ C-3,6), 60.96 (s, $C_6H_{10}$ C-1,2), 129.96 (t, $^3J_{P,C}$ = 20.2 Hz, phenyl C-3,5), 131.62 (s, phenyl C-4), 133.66 (t, $^1J_{P,C}$ = 104.0 Hz, phenyl C-1), 134.10 (t, $^2J_{P,C}$ = 24.6 Hz, phenyl C-2,6) ppm. $^{31}P\{^1H\}$ NMR ($CD_2Cl_2$): $\delta$ = 21.92 (s) ppm. $C_{42}H_{46}BF_4IrN_2P_2$ (919.81): calcd. C 54.84, H 5.04, N 3.05; found C 54.45, H 5.49, N 2.91.

**$[IrH_2\{(R)$-dabin$\}(PPh_3)_2]BF_4$ (1c):** A solution of $[(\eta^4$-1,5-$C_8H_{12})$-$Ir(PPh_3)_2]BF_4$ (106 mg, 0.12 mmol) and an equimolar quantity of (*R*)-dabin (34 mg) in 10 mL of $CH_2Cl_2$ was stirred for 20 min under an atmosphere of hydrogen, which caused the mixture to change color from red to pale yellow. The off-white product was isolated by adding diethyl ether (80 mL), then washed with $Et_2O$ and dried under vacuum. Yield: 109 mg (83%). $^1H$ NMR ([D$_6$]acetone): $\delta$ = –23.48 (t, $^2J_{P,H}$ = 18.1 Hz, 2 H, $IrH_2$), 3.62 (br., 4 H, $NH_2$), 5.90, 6.05, 6.44 (all d, $^3J_{H,H}$ = 8.8, 10.4, and 8.2 Hz, 2 H each, all aryl H), 7.17, 7.28, 7.37, 7.91 (all m, 44 H, aryl H) ppm. $^{31}P\{^1H\}$ NMR ([D$_6$]acetone): $\delta$ = 24.33 (s) ppm. Complex **1c** as well as its analogues **2a**, **2b**, and **3** were found to retain varying amounts of residual $CH_2Cl_2$ solvent so that no satisfactory elemental analyses could be obtained: $C_{56}H_{48}BF_4IrN_2P_2$ (1090.0): calcd. C 61.71, H 4.44, N 2.57; found C 59.45, H 4.38, N 2.31; calcd. for $C_{56}H_{48}BF_4IrN_2P_2{\cdot}CH_2Cl_2$ (1162.9): calcd. C 57.84, H 4.33, N 2.41.

**$[IrH_2\{(R,R)$-dach$\}(P\mathit{i}Pr_3)_2]BF_4$ (2a):** Tetrafluoroboric acid (54% in $Et_2O$) was added dropwise to a solution of $[IrH_5(P\mathit{i}Pr_3)_2]$ (525 mg, 1.02 mmol) in 15 mL of benzene until no further evolution of hydrogen was observed. The diamine ligand (116 mg, 1.02 mmol) was then added and the resulting mixture stirred for 1 h at room temperature. The residue remaining after evaporation to dryness was redissolved in 5 mL of $CH_2Cl_2$ and the product was isolated as an off-white solid by adding 50 mL of diethyl ether. Yield: 418 mg (57%). $^1H$ NMR ($C_6D_6$): $\delta$ = –23.28 (t, $^2J_{P,H}$ = 18.0 Hz, 2 H, $IrH_2$), 0.58 (m, 4 H, $CH_2$), 1.19 (dd, $^3J_{H,H}$ = 7.1, $^3J_{P,H}$ = 15.4 Hz, 36 H, $CH_3$), 1.37 (m, 4 H, $CH_2$), 2.17 (m, 6 H, PCH), 2.46, 2.60 (both br., 2 H each, both $NH_2$), 3.88 (m, 2 H, NCH) ppm. $^{31}P\{^1H\}$ NMR ($C_6D_6$): $\delta$ = 44.02 (s) ppm. $C_{24}H_{58}BF_4IrN_2P_2$ (715.71): calcd. C 40.28, H 8.17, N 3.91; found C 39.13, H 7.90, N 3.78; calcd. for $C_{24}H_{58}BF_4IrN_2P_2{\cdot}CH_2Cl_2$ (800.64): calcd. C 37.50, H 7.55, N 3.50. Compounds **2b** and **3** were obtained analogously:

**$[IrH_2\{(R)$-dabin$\}(P\mathit{i}Pr_3)_2]BF_4$ (2b):** Synthesized from $[IrH_5(P\mathit{i}Pr_3)_2]$ (228 mg, 0.44 mmol), treated with $HBF_4$ as described above, and (*R*)-dabin (125 mg, 0.44 mmol) in 15 mL of benzene in 82% yield (320 mg). $^1H$ NMR ($CD_2Cl_2$): $\delta$ = –26.56 (t, $^2J_{P,H}$ = 18.3 Hz, 2 H, $IrH_2$), 0.86 (dd, $^3J_{H,H}$ = 6.6, $^3J_{P,H}$ = 14.8 Hz, 36 H, $CH_3$), 2.06 (m, 6 H, PCH), 4.98, 5.10 (both br., 2 H each, both $NH_2$), 6.69 (d, $^3J_{H,H}$ = 8.8 Hz, 2 H, aryl 3-H), 7.15 ("t", $\Sigma^3J_{H,H}$ = 15.0 Hz, 2 H, aryl 6-H), 7.35 (m, 4 H, aryl 7,8-H), 7.82 (d, $^3J_{H,H}$ = 8.2 Hz, 2 H, aryl 5-H), 7.98 (d, $^3J_{H,H}$ = 8.8 Hz, 2 H, aryl 4-H) ppm. $^{31}P\{^1H\}$ NMR ($C_6D_6$): $\delta$ = 44.35 (s) ppm. $C_{38}H_{60}BF_4IrN_2P_2$ (885.87): calcd. C 51.52, H 6.83, N 3.16; found C 49.73, H 6.60, N 3.08; calcd. for $C_{38}H_{60}BF_4IrN_2P_2{\cdot}CH_2Cl_2$ (970.81): calcd. C 48.25, H 6.44, N 2.89.

**$[IrH_2\{(R)$-dabin$\}(PCy_3)_2]BF_4$ (3):** Synthesized from $[IrH_5(PCy_3)_2]$ (115 mg, 0.15 mmol), treated with $HBF_4$ as outlined for **2a**, and the diamine (43 mg, 0.15 mmol) in 10 mL of benzene in 80% yield (135 mg). $^1H$ NMR ($CD_2Cl_2$): $\delta$ = –26.57 (t, $^2J_{P,H}$ = 18.1 Hz, 2 H, $IrH_2$), 1.15–1.87 (m, 66 H, cyclohexyl H), 2.06 (m, 6 H, PCH), 4.99, 5.21 (both br., 2 H each, both $NH_2$), 6.82 (d, $^3J_{H,H}$ = 8.8 Hz, 2 H, aryl 3-H), 7.15 ("t", $\Sigma^3J_{H,H}$ = 15.0 Hz, 2 H, aryl 6-H), 7.42 (m, 4 H, aryl 7,8-H), 7.98 (d, $^3J_{H,H}$ = 8.2 Hz, 2 H, aryl 5-H), 8.10 (d, $^3J_{H,H}$ = 8.8 Hz, 2 H, aryl 4-H) ppm. $^{31}P\{^1H\}$ NMR ($CD_2Cl_2$): $\delta$ = 20.92 (s) ppm. $C_{56}H_{84}BF_4IrN_2P_2$ (1126.27): calcd. C 59.72, H 7.52, N 2.49; found C 58.66, H 7.14, N 2.32; calcd. for $C_{56}H_{84}BF_4IrN_2P_2{\cdot}CH_2Cl_2$ (1211.2): calcd. C 56.52, H 7.16, N 2.31.

**$[(\eta^4$-1,5-$C_8H_{12})Ir(H)(Cl)\{(S,S)$-bdpcp$\}]BF_4$ (4):** Dropwise addition of a saturated solution of hydrogen chloride in diethyl ether to a suspension of $[(\eta^4$-1,5-$C_8H_{12})Ir\{(S,S)$-bdpcp$\}]BF_4$ (204 mg, 0.25 mmol) in 20 mL of thf gave a clear yellow solution, from which the product separated within 1 h as pale-yellow microcrystals. Yield (after washing three times with 2 mL of $Et_2O$ and drying): 190 mg (89%). $^1H$ NMR ($CD_2Cl_2$): $\delta$ = –14.05 (dd, *cis*-$^2J_{P,H}$ = 7.1 and 11.5 Hz, 1 H, IrH), 0.96, 1.47 (both m, 1 H each, both $CH_2$), 1.85–2.86 (m, 14 H, $CH_2$ and phosphane CH), 3.89, 4.27, 5.32 (all m, 1 + 2 + 1 H, diene CH), 7.21–7.82 (m, 20 H, aryl H) ppm. $^{31}P\{^1H\}$ NMR ($CD_2Cl_2$): $\delta$ = 6.03, 15.30 (both d, $J_{P,P}$ = 15.6 Hz) ppm. $C_{37}H_{41}BClF_4IrP_2$ (862.16): calcd. C 51.55, H 4.79; found C 50.98, H 4.66.

**$[\{(R)$-binap$\}_2Ir_2H_2(\mu$-Cl$)_3]BF_4$ (5):** A solution of dry HCl gas in diethyl ether was added dropwise to a stirring solution of $[(\eta^4$-1,5-$C_8H_{12})Ir\{(R)$-binap$\}]BF_4$ (205 mg, 0.20 mmol) in 10 mL of thf under ambient conditions. The red mixture gradually became yellow and the addition of $HCl{\cdot}Et_2O$ was stopped when no further color change was discernible. The product was precipitated after stirring for an additional 10 min and concentration of the solution to about 1 mL by adding 20 mL of diethyl ether. It was then washed twice with 2 mL of $Et_2O$ and dried under vacuum. Yield: 172 mg (94%). $^1H$ NMR ($CD_2Cl_2$): $\delta$ = –22.73 (dd, $^2J_{P,H}$ = 15.6 and 21.5 Hz, 2 H, IrH), 6.30–8.03 (m, 64 H, aryl H) ppm. $^{31}P\{^1H\}$ NMR ($CD_2Cl_2$): $\delta$ = –6.54, 1.59 (both AA′BB′-type "d", $|^2J_{P,P} + {}^4J_{P,P}|$ = 20.0 Hz) ppm. $C_{88}H_{66}BCl_3F_4Ir_2P_4$ (1825.0): calcd. C 57.89, H 3.65; found C 57.83, H 3.50.

**$[Ir(H)(Cl)\{(R,R)$-dpen$\}\{(R)$-binap$\}]BF_4$ (6a):** A mixture of (*R*,*R*)-dpen (44 mg, 0.21 mmol) and $AgBF_4$ (20 mg, 0.10 mmol) in 5 mL of thf was added to a solution of **5** (185 mg, 0.10 mmol) in 5 mL of thf. After stirring for 30 min under ambient conditions, the precipitate of AgCl was filtered off and the filtrate was concentrated to about 1 mL. Precipitation with 20 mL of diethyl ether, followed by filtration and washing with $Et_2O$ (2 × 3 mL) gave 108 mg (47%) of the product as a yellowish white solid. $^1H$ NMR ($CD_2Cl_2$): $\delta$ = –19.81 (dd, $^2J_{P,H}$ = 15.9 and 18.0 Hz, 1 H, IrH), 2.91, 3.00, 3.29, 3.89 (all br., 1 H each, $NH_2$), 4.39 (m, 2 H, CH), 6.18–8.12 (m, 42 H, aryl H) ppm. $^{31}P\{^1H\}$ NMR ($CD_2Cl_2$): $\delta$ = –9.99, –0.64 (both d, $J_{P,P}$ = 22.3 Hz) ppm. $C_{58}H_{49}BClF_4IrN_2P_2$ (1150.5): calcd. C 60.55, H 4.29, N 2.43; found C 61.15, H 4.53, N 2.38. Similar procedures were used for the preparation of complexes **6b** and **6c**.

**$[Ir(H)(Cl)\{(R,R)$-dach$\}\{(R)$-binap$\}]BF_4$ (6b):** Synthesized from **5** (100 mg, 0.05 mmol) and the diamine (13 mg, 0.11 mmol) in 10 mL of thf. Yield: 84 mg (73%). $^1H$ NMR ($CD_2Cl_2$): $\delta$ = –20.35 (dd, $^2J_{P,H}$ = 15.5 and 18.2 Hz, 1 H, IrH), 1.19–2.09 (m, 8 H, $CH_2$), 2.85 (br., 4 H, $NH_2$), 3.01, 4.81 (both m, 1 H each, both CH), 6.28–8.15 (m, 32 H, aryl H) ppm. $^{31}P\{^1H\}$ NMR ($CD_2Cl_2$): $\delta$ = –10.69, –1.10 (both d, $J_{P,P}$ = 22.3 Hz) ppm. $C_{50}H_{47}BClF_4IrN_2P_2$ (1052.4): calcd. C 57.07, H 4.50, N 2.66; found C 56.96, H 4.32, N 2.43.

 © 2007 Wiley-VCH Verlag GmbH & Co. KGaA, Weinheim 

**[Ir(H)(Cl)(tmen){(*R*)-binap}]$BF_4$ (6c):** Synthesized from **5** (120 mg, 0.07 mmol) and the diamine ligand (16 mg, 0.14 mmol) in thf (10 mL). Yield: 64 mg (48%). $^1$H NMR ($CD_2Cl_2$): $\delta$ = –20.00 (dd, $^2J_{P,H}$ = 15.6 and 17.4 Hz, 1 H, IrH), 1.02, 1.08, 1.12, 1.20 (all s, 3 H each, all $CH_3$), 2.06, 2.37, 3.96, 4.85 (all br., 1 H each, all $NH_2$), 6.23–8.12 (m, 32 H, aryl H) ppm. $^{31}$P{$^1$H} NMR ($CD_2Cl_2$): $\delta$ = –12.92, –1.10 (both d, $J_{P,P}$ = 22.4 Hz) ppm. $C_{50}H_{49}BClF_4IrN_2P_2$ (1054.4): calcd. C 56.96, H 4.68, N 2.66; found C 56.83, H 4.58, N 2.34.

**General Procedure for Catalytic >C=O Hydrogenation:** A 10-mL Schlenk tube equipped with a small magnetic stirring bar was charged with an alcoholic solution of the catalyst complex (typically 0.01 mmol in 3.0 mL of methanol). The required amounts of potassium hydroxide and acetophenone (see Table 1) were then added, the mixture was stirred for 10 min under ambient conditions, and the tube was inserted into an argon-filled stainless steel autoclave. The autoclave was sealed and vented several times with $H_2$ (Messer–Griesheim; 99.999%), subsequently pressurized to 20 bar, and the contents stirred at 40–60 °C. At the end of the reaction, the pressure was vented, the solvent removed under vacuum, and the residue was diluted with diethyl ether to precipitate the catalyst as a brownish black solid. The solution was decanted and chromatographed on a silica gel column using diethyl ether as the eluent. Volatile material was distilled off and the mixture of products was analyzed by $^1$H NMR spectroscopy. Conversions and product compositions were determined on the basis of the integrations of the PhC(O)C$H_3$ and PhCH(OH)C$H_3$ signals. Enantiomeric excesses were measured by GC using a Chrompack Chirasil-Dex CB column.

**X-ray Structure Determinations:** The crystal used for the structure analysis of **1a** was grown from dichloromethane. Recrystallization of **4** and **5** from acetone/diethyl ether mixtures afforded single crystals of solvent-containing addition compounds identified as [($\eta^4$-1,5-$C_8H_{12}$)Ir(H)(Cl){(*S*,*S*)-bdpcp}]$BF_4$·$Me_2CO$ and [{(*R*)-binap}$_2$-$Ir_2H_2(\mu$-Cl)$_3$]$BF_4$·$Me_2CO$·1/2 $H_2O$·1/4 $Et_2O$ ("**4·Me$_2$CO**" and "**5·solv**" hereafter). Diffraction measurements were made at –173(2) °C with a Bruker-Nonius Kappa CCD instrument for compounds **1a** and **5·solv** and at –160(2) °C with an Enraf–Nonius CAD4 MACH3 diffractometer for **4·Me$_2$CO**, both of which used Mo-$K_\alpha$ radiation ($\lambda$ = 0.71073 Å); diffraction data were corrected for absorption by appropriate numerical[26] (**1a**: $T_{min}$ = 0.277, $T_{max}$ = 0.801), refined[27] (**4·Me$_2$CO**: $T_{min}$ = 0.227, $T_{max}$ = 0.621), or empirical[28] (**5·solv**: $T_{min}$ = 0.738, $T_{max}$ = 1.000) methods. The structures were solved by direct methods and subsequently refined by full-matrix (**1a**, **4·Me$_2$CO**) or, in view of the large dimensions of **5·solv**, by block-matrix least-squares procedures on $F^2$ with allowance for anisotropic thermal motion of all non-hydrogen atoms employing both the SHELXTL NT 6.12[29] and the WinGX[30a] package with some of the relevant programs (SIR-97,[31] SHELXL-97,[32] XHYDEX,[7] ORTEP-3[30b]) implemented therein. The crystal of **1a** under study proved to be a pseudomerohedral twin. The twin law used during the refinement was –1 0 0 0 –1 0 0 0 –1 and resulted in a twin component ratio of approximately 5:1 (BASF 0.2122).

**1a:** 0.40 × 0.40 × 0.06 mm$^3$, $C_{42}H_{40}IrN_2P_2$·$BF_4$ (913.71); monoclinic, $C_2$, $a$ = 9.1624(9), $b$ = 17.197(2), $c$ = 24.204(2) Å, $\beta$ = 99.947(7)°, $V$ = 3756.3(9) Å$^3$, $Z$ = 4, $d_{calcd.}$ = 1.616 g cm$^{-3}$, $\mu$(Mo-$K_\alpha$) = 3.693 mm$^{-1}$; 3.33° ≤ $\Theta$ ≤ 28.01°, 30833 reflections collected (–11 ≤ $h$ ≤ +12, –21 ≤ $k$ ≤ +22, –31 ≤ $l$ ≤ +31), 8279 unique ($R_{int}$ = 0.0643); $wR_2$ = 0.1270 for all data and 475 parameters, $R_1$ = 0.0572 for 6804 intensities $I > 2\sigma(I)$; absolute structure parameter $x$ = –0.02(2).[33]

**4·Me$_2$CO:** 0.38 × 0.30 × 0.13 mm$^3$, $C_{37}H_{41}ClIrP_2$·$BF_4$·$C_3H_6O$ (920.18); orthorhombic, $P2_12_12_1$, $a$ = 10.431(1), $b$ = 19.128(3), $c$ = 19.438(7) Å, $V$ = 3878(2) Å$^3$, $Z$ = 4, $d_{calcd.}$ = 1.576 g cm$^{-3}$, $\mu$(Mo-$K_\alpha$) = 3.644 mm$^{-1}$; 2.10° ≤ $\Theta$ ≤ 25.17°, 4928 reflections collected (–3 ≤ $h$ ≤ +12, –3 ≤ $k$ ≤ +22, –3 ≤ $l$ ≤ +23), 4652 unique ($R_{int}$ = 0.0471); $wR_2$ = 0.1373 for all data and 454 parameters, $R_1$ = 0.0578 for 3712 intensities $I > 2\sigma(I)$; absolute structure parameter $x$ = –0.010(17).[33]

**5·solv:** 0.26 × 0.18 × 0.16 mm$^3$, $C_{88}H_{66}Cl_3Ir_2P_4$·$BF_4$·$C_3H_6O$·$HO_{0.5}$·$CH_{2.5}O_{0.25}$ (1910.5); orthorhombic, $P2_12_12_1$, $a$ = 21.205(2), $b$ = 24.821(4), $c$ = 32.830(3) Å, $V$ = 17279(4) Å$^3$, $Z$ = 8, $d_{calcd.}$ = 1.469 g cm$^{-3}$, $\mu$(Mo-$K_\alpha$) = 3.299 mm$^{-1}$; 2.67° ≤ $\Theta$ ≤ 28.00°, 172715 reflections collected (–20 ≤ $h$ ≤ +28, –32 ≤ $k$ ≤ +32, –42 ≤ $l$ ≤ +43), 39510 unique ($R_{int}$ = 0.0462); $wR_2$ = 0.1264 for all data and 1943 parameters, $R_1$ = 0.0427 for 32060 intensities $I > 2\sigma(I)$; absolute structure parameter $x$ = 0.010(4).[33]

CCDC-640544 (for **1a**), -640546 (for **4·Me$_2$CO**), and -640545 (for **5·solv**) contain the supplementary crystallographic data for this paper. These data can be obtained free of charge from The Cambridge Crystallographic Data Center via www.ccdc.cam.ac.uk/data_request/cif.

## Acknowledgments

Support of this work by the Deutsche Forschungsgemeinschaft (SFB 583) is gratefully acknowledged. We are also indebted to Mrs. S. Hoffmann and Mr. P. Bakatselos for their skilful assistance.

[1] L. Dahlenburg, H. Treffert, Ch. Farr, F. W. Heinemann, A. Zahl, *Eur. J. Inorg. Chem.* **2007**, 1738–1751.

[2] a) K. Abdur-Rashid, A. J. Lough, R. H. Morris, *Organometallics* **2001**, *20*, 1047–1049; b) K. Abdur-Rashid, M. Faatz, A. J. Lough, R. H. Morris, *J. Am. Chem. Soc.* **2001**, *123*, 7473–7474; c) K. Abdur-Rashid, S. E. Clapham, A. Hadzovic, J. N. Harvey, A. J. Lough, R. H. Morris, *J. Am. Chem. Soc.* **2002**, *124*, 15104–15118; d) V. Rautenstrauch, X. Hoang-Cong, R. Churlaud, K. Abdur-Rashid, R. H. Morris, *Chem. Eur. J.* **2003**, *9*, 4954–4967.

[3] For leading overviews, see: a) R. Noyori, S. Hashiguchi, *Acc. Chem. Res.* **1997**, *30*, 97–102; b) M. J. Palmer, M. Wills, *Tetrahedron: Asymmetry* **1999**, *10*, 2045–2061; c) M. Wills, M. Gamble, M. Palmer, A. Smith, J. Studley, J. Kenny, *J. Mol. Catal. A* **1999**, *146*, 139–148; d) T. Ohkuma, R. Noyori, in *Comprehensive Asymmetric Catalysis* (Eds.: E. N. Jacobs, A. Pfaltz, H. Yamamoto), Springer, Berlin, **1999**, vol. 1, chapter 6.1; e) R. Noyori, T. Ohkuma, *Pure Appl. Chem.* **1999**, *71*, 1493–1501; f) R. Noyori, T. Ohkuma, *Angew. Chem.* **2001**, *113*, 40–75; *Angew. Chem. Int. Ed.* **2001**, *40*, 40–73; g) R. Noyori, M. Koizumi, D. Ishii, T. Ohkuma, *Pure Appl. Chem.* **2001**, *73*, 227–232; h) R. Noyori, *Angew. Chem.* **2002**, *114*, 2108–2123; *Angew. Chem. Int. Ed.* **2002**, *41*, 2008–2022 (2001 Nobel Lecture in Chemistry; i) S. E. Clapham, A. Hadzovic, R. H. Morris, *Coord. Chem. Rev.* **2004**, *248*, 2201–2237; j) T. Ohkuma, R. Noyori, in *Transition Metals for Organic Synthesis*, 2nd ed. (Eds.: M. Beller, C. Bolm), Wiley-VCH, Weinheim, **2004**, vol. 2, pp. 29–113; k) M. Kitamura, R. Noyori, in *Ruthenium in Organic Synthesis* (Ed.: S.-I. Murahashi), Wiley-VCH, Weinheim, **2004**, pp. 3–52; l) R. Noyori, *Org. Biomol. Chem.* **2006**, *4*, 393–406; m) S. Gladiali, E. Alberico, *Chem. Soc. Rev.* **2006**, *35*, 226–236.

[4] a) J. R. Shapley, R. R. Schrock, J. A. Osborn, *J. Am. Chem. Soc.* **1969**, *91*, 2816–2817; b) R. H. Crabtree, P. C. Demou, D. Eden, J. M. Mihelcic, C. A. Parnell, J. M. Quirk, G. E. Morris, *J. Am. Chem. Soc.* **1982**, *104*, 6994–7001; c) R. H. Crabtree, G. G. Hlatky, C. P. Parnell, B. E. Segmüller, R. J. Uriarte, *Inorg. Chem.* **1984**, *23*, 354–358; d) R. H. Crabtree, M. F. Mellea,

 © 2007 Wiley-VCH Verlag GmbH & Co. KGaA, Weinheim 

J. M. Mihelcic, *Inorg. Synth.* **1989**, *26*, 122–126; e) R. H. Crabtree, M. F. Mellea, J. M. Mihelcic, *Inorg. Synth.* **1990**, *28*, 56–60.

[5] a) M. G. Clerici, S. Di Gioacchino, F. Maspero, E. Perrotti, A. Zanobi, *J. Organomet. Chem.* **1975**, *84*, 379–388; b) R. H. Crabtree, H. Felkin, G. E. Morris, *J. Organomet. Chem.* **1977**, *141*, 205–215; c) L. Garlaschelli, S. I. Khan, R. Bau, *J. Am. Chem. Soc.* **1985**, *107*, 7212–7213; d) S. E. Landau, K. E. Groh, A. J. Lough, R. H. Morris, *Inorg. Chem.* **2002**, *41*, 2995–3007; e) S. Brinkmann, R. H. Morris, R. Ramachandran, S.-H. Park, *Inorg. Synth.* **1998**, *32*, 303–308.

[6] A survey in SciFinder revealed that the triflate salt of the $[IrH_2(1,2\text{-phdn})(PPh_3)_2]^+$ cation has previously been obtained from the substitutionally labile sulfonato complex $[IrH_2(O\text{-}SO_2CF_3)(PPh_3)_3]$ and the diamine in refluxing benzene: P. A. Harding, S. D. Robinson, *J. Chem. Soc. Dalton Trans.* **1987**, 947–952.

[7] A. G. Orpen, *J. Chem. Soc. Dalton Trans.* **1980**, 2509–2516.

[8] Albeit frequently used in the absence of neutron diffraction data, the HYDEX procedure is not an infallible method and may result in inaccurate hydride positions due to the lack of suitable potentials for the different metal atoms. See, for example: a) A. Albinati, S. Chaloupka, A. Currao, W. T. Klooster, Th. F. Koetzle, R. Nesper, L. M. Venanzi, *Inorg. Chim. Acta* **2000**, *300–302*, 903–911; b) A. Albinati, L. M. Venanzi, *Coord. Chem. Rev.* **2000**, *200–202*, 687–715.

[9] a) H. Uekusa, S. Ohba, K. P. Simonsen, M. Kojima, J. Fujita, *Acta Crystallogr., Sect. C* **1992**, *48*, 1111–1112; b) T. Suzuki, M. Rude, K. P. Simonsen, M. Morooka, H. Tanaka, S. Ohba, F. Galsboel, J. Fujita, *Bull. Chem. Soc. Jpn.* **1994**, *67*, 1013–1023.

[10] a) L. Dahlenburg, R. Götz, *Inorg. Chim. Acta* **2004**, *357*, 2875–2880; b) L. Dahlenburg, R. Götz, *Eur. J. Inorg. Chem.* **2004**, 888–905.

[11] K. Mashima, T. Akutagawa, X. Zhang, H. Takaya, T. Taketomi, H. Kumobayashi, S. Akutagawa, *J. Organomet. Chem.* **1992**, *428*, 213–222.

[12] For a collection of Ir–Cl distances opposite to ligands purported to exert respectively weak, intermediate, or strong *trans* influences, see, for example: M. J. Auburn, R. D. Holmes-Smith, S. R. Stobart, P. K. Bakshi, T. S. Cameron, *Organometallics* **1996**, *15*, 3032–3036.

[13] For examples with terminal phosphane, carbonyl, carbene, and other two-electron donor ligands, see ref.[5b] and: a) P. J. Roberts, G. Ferguson, *Acta Crystallogr., Sect. B* **1976**, *32*, 1513–1517; b) M. J. Nolte, E. Singleton, E. van der Stok, *Acta Crystallogr., Sect. B Chem.* **1978**, *34*, 1684–1687; c) H. H. Wang, L. H. Pignolet, *Inorg. Chem.* **1980**, *19*, 1470–1480; d) A. L. Casalnuovo, J. C. Calabrese, D. Milstein, *J. Am. Chem. Soc.* **1988**, *110*, 6738–6744; e) A. M. Mueting, W. Bos, B. D. Alexander, P. D. Boyle, J. A. Casalnuovo, S. Balaban, L. N. Ito, S. M. Johnson, L. H. Pignolet, *New J. Chem.* **1988**, *12*, 505–527; f) A. M. Mueting, P. D. Boyle, R. Wagner, L. H. Pignolet, *Inorg. Chem.* **1988**, *27*, 271–279; g) H. H. Wang, A. M. Mueting, J. A. Casalnuovo, S. Yan, J. K. H. Barthelmes, L. H. Pignolet, *Inorg. Synth.* **1990**, *27*, 22–26; h) K. Tani, A. Iseki, T. Yamagata, *Angew. Chem.* **1998**, *110*, 3590–3592; *Angew. Chem. Int. Ed.* **1998**, *37*, 3381–3383; i) M. V. Jiménez, E. Sola, J. A. López, F. J. Lahoz, L. A. Oro, *Chem. Eur. J.* **1998**, *4*, 1398–1410; j) J. R. Bleeke, P. V. Hinkle, N. P. Rath, *Organometallics* **2001**, *20*, 1939–1951; k) M. V. Jiménez, E. Sola, J. Caballero, J. J. Lahoz, L. A. Oro, *Angew. Chem.* **2002**, *114*, 1256–1259; *Angew. Chem. Int. Ed.* **2002**, *41*, 1208–1259; l) R. Dorta, H. Rozenberg, L. J. W. Shimon, D. Milstein, *J. Am. Chem. Soc.* **2002**, *124*, 188–189; m) R. Dorta, H. Rozenberg, L. J. W. Shimon, D. Milstein, *Chem. Eur. J.* **2003**, *9*, 5237–5249; n) R. Dorta, D. Broggini, R. Stoop, H. Rüegger, F. Spindler, A. Togni, *Chem. Eur. J.* **2004**, *10*, 267–278; o) M. Viciano, M. Poyatos, M. Sanaú, E. Peris, A. Rossin, G. Ujaque, A. Lledós, *Organometallics* **2006**, *25*, 1120–1134; p) T. Yamagata, H. Tadaoka, M. Nagata, T. Hirao, Y. Kataoka, V. Ratovelomanana-Vidal, J. P. Genet, K. Mashima, *Organometallics* **2006**, *25*, 2505–2513.

[14] For the concept of "steric pressure", see: a) W. C. Kaska, H. A. Mayer, *Chem. Rev.* **1994**, *94*, 1239–1272; b) R. T. Boré, Y. Zhang, *J. Organomet. Chem.* **2005**, *690*, 2651–2657. c) The formation of some triply chlorido-bridged binuclear N-heterocyclic carbene complexes $[\{(NHC)(CH_2)_3(NHC)\}_2Ir_2H_2(\mu\text{-}Cl)_3]PF_6$ from $[(\eta^4\text{-}1,5\text{-}C_8H_{12})Ir\{(NHC)(CH_2)_3(NHC)\}]PF_6$ and HCl has been explained similarly.[13o]

[15] a) A. Miyashita, A. Yasuda, H. Takaya, K. Toriumi, T. Ito, T. Souchi, R. Noyori, *J. Am. Chem. Soc.* **1980**, *102*, 7932–7934; b) K. Toriumi, T. Ito, H. Takaya, T. Souchi, R. Noyori, *Acta Crystallogr., Sect. B* **1982**, *38*, 807–812; c) K. Tani, T. Yamagata, Y. Tatsuno, Y. Yamagata, K.-I. Tomita, S. Akutagawa, H. Kumobayashi, S. Otsuka, *Angew. Chem.* **1985**, *97*, 232–234; *Angew. Chem. Int. Ed. Engl.* **1985**, *24*, 217–219; d) T. Ohta, H. Takaya, R. Noyori, *Inorg. Chem.* **1988**, *27*, 566–569; e) K. Mashima, K. Kusano, T. Ohta, R. Noyori, *J. Chem. Soc. Chem. Commun.* **1989**, 1208–1210; f) R. Noyori, H. Takaya, *Acc. Chem. Res.* **1990**, *23*, 345–350; g) T. Yamagata, A. Iseki, K. Tani, *Chem. Lett.* **1997**, *12*, 1215–1216; h) R. Dorta, P. Egli, F. Zürcher, A. Togni, *J. Am. Chem. Soc.* **1997**, *119*, 10857–10858.

[16] The Cambridge Structural Database System, version CSD V5.28, **2007** (403790 entries): a) F. H. Allen, O. Kennard, *Chem. Des. Autom. News* **1993**, *8*, 32–37; b) F. H. Allen, *Acta Crystallogr., Sect B* **2002**, *58*, 380–388; c) I. J. Bruno, J. C. Cole, P. R. Edgington, M. Kessler, C. F. Macrae, P. McCabe, J. Pearsom, R. Taylor, *Acta Crystallogr., Sect B* **2002**, *58*, 389–397.

[17] a) J. F. Harrod, D. F. R. Gilson, R. Charles, *Can. J. Chem.* **1969**, *47*, 1431–1433; b) W. R. Roper, K. G. Town, *J. Organomet. Chem.* **1983**, *252*, C97–C100; c) C. E. Johnson, R. Eisenberg, *J. Am. Chem. Soc.* **1985**, *107*, 3148–3160; d) V. V. Grushin, V. I. Bakhmutov, I. S. Akhrem, M. E. Vol'pin, *Izv. Akad. Nauk SSSR, Ser. Khim.* **1988**, 494–495; e) V. V. Grushin, A. B. Vymenits, M. E. Vol'pin, *J. Organomet. Chem.* **1990**, *382*, 185–189.

[18] S. Park, M. P. Johnson, D. M. Roundhill, *Organometallics* **1989**, *8*, 1700–1707.

[19] Some remaining ambiguity about the assignment of *OC*-6-43 stereochemistry to compounds **6a**–**c** arises from the recently reported characterization of the bis(chelate)complexes $[Ir(H)(X)(O_2CMe)\{(S)\text{-binap}\}]$ (X = Cl, Br, I) as *OC*-6-43 and *OC*-6-23 stereoisomers, where the IrH chemical shifts of the two forms ($\delta \approx -25$ ppm) differ, at best, by around 2 ppm.[13p]

[20] For pertinent reviews on heterolytic $H_2$ activation, see: a) P. J. Bothers, *Prog. Inorg. Chem.* **1981**, *28*, 1–61; b) G. J. Kubas, *Acc. Chem. Res.* **1988**, *21*, 120–128; c) P. G. Jessop, R. H. Morris, *Coord. Chem. Rev.* **1992**, *121*, 121–284; d) D. M. Heinekey, W. J. Oldham Jr, *Chem. Rev.* **1993**, *93*, 913–926; e) R. H. Crabtree, *Angew. Chem.* **1993**, *105*, 828–845; *Angew. Chem. Int. Ed. Engl.* **1993**, *32*, 789–805; f) M. A. Esteruelas, L. A. Oro, *Chem. Rev.* **1998**, *98*, 577–588; g) G. Jia, C.-P. Lau, *Coord. Chem. Rev.* **1999**, *190–192*, 83–108; h) D. Sellmann, A. Fürsattel, J. Sutter, *Coord. Chem. Rev.* **2000**, *200–202*, 545–561; i) G. J. Kubas, *Metal Dihydrogen and σ-Bond Complexes*, Kluver Academic/Plenum Publishers, New York, **2001**, chapters 9 and 10.

[21] Recently described iridium(I)-based catalysts with chiral planar (diphenylphosphanylferrocenyl)thioether ligands give enantioselectivities of up to 87% for the same acetophenone substrate: E. Le Roux, R. Malacea, E. Manoury, R. Poli, L. Gonsalvi, M. Peruzzini, *Adv. Synth. Catal.* **2007**, *349*, 309–313.

[22] a) H. Doucet, T. Ohkuma, K. Murata, T. Yokozawa, M. Kozawa, E. Katayama, A. F. England, T. Ikariya, R. Noyori, *Angew. Chem.* **1998**, *110*, 1792–1796; *Angew. Chem. Int. Ed.* **1998**, *37*, 1703–1707; b) Ch. A. Sandoval, T. Ohkuma, K. Muñiz, R. Noyori, *J. Am. Chem. Soc.* **2003**, *125*, 13490–13503.

[23] a) M. F. Asaro, I. Nakayama, R. B. Wilson Jr, *J. Org. Chem.* **1992**, *57*, 778–782; b) C. Hirel, K. E. Vostrikova, J. Pécaut, V. I. Ovcharenko, O. Rey, *Chem. Eur. J.* **2001**, *7*, 2007–2014.

 © 2007 Wiley-VCH Verlag GmbH & Co. KGaA, Weinheim 

[24] L. Dahlenburg, *Coord. Chem. Rev.* **2005**, *249*, 2962–2992, and references cited therein.
[25] J. L. Herde, J. C. Lambert, C. V. Senoff, *Inorg. Synth.* **1974**, *15*, 18–20.
[26] a) P. Coppens, L. Leiserowitz, D. Rabinovich, *Acta Crystallogr.* **1965**, *21*, 1035–1038; b) P. Coppens, *Crystallogr. Comput., Proc. Int. Summer Sch.* **1970**, 255–270.
[27] N. Walker, D. Stuart, *Acta Crystallogr., Sect. A* **1983**, *39*, 159–166.
[28] *SADABS*, Program for Absorption Correction for Area Detectors, version 2.06; Bruker-AXS, Inc., Madison, WI, **2002**.
[29] *SHELXTL NT*, Program Library for Structure Solution and Molecular Graphics, version 6.12; Bruker AXS, Inc., Madison, WI, **2002**.
[30] a) L. J. Farrugia, *J. Appl. Crystallogr.* **1999**, *32*, 837–838; b) L. J. Farrugia, *J. Appl. Crystallogr.* **1997**, *30*, 565.
[31] A. Altomare, M. C. Burla, M. Camalli, G. L. Cascarano, C. Giacovazzo, A. Guagliardi, A. G. G. Moliterni, G. Polidori, R. Spagna, *J. Appl. Crystallogr.* **1999**, *32*, 115–119.
[32] G. M. Sheldrick, *SHELXL-97*, Program for the Refinement of Crystal Structures (release 97-2), University of Göttingen, Germany, **1998**.
[33] H. D. Flack, *Acta Cystallogr., Sect. A* **1983**, *39*, 876–881.
Received: April 5, 2007
Published Online: July 27, 2007

 © 2007 Wiley-VCH Verlag GmbH & Co. KGaA, Weinheim 

DOI: 10.1002/ejic.200700387

# The Tuning Effect of 2-Amino-4,6-dipyridylpyrimidine Isomers on the Structural Dimensionalities and Motifs of Copper(I) Cyanide Complexes

**Ying-Nan Chi,[a,b] Feng-Yun Cui,[a,b] Yan-Qing Xu,[a,b] and Chang-Wen Hu*[a,b]**

**Keywords:** Copper / Chelating ligands / N ligands / Crystal engineering

Four novel copper(I) cyanide complexes of three isomeric oligopyridine ligands, namely 2-amino-4,6-bis(2-pyridyl)pyrimidine ($L^1$), 2-amino-4-(2-pyridyl)-6-(4-pyridyl)pyrimidine ($L^2$), 2-amino-4-(2-pyridyl)-6-(3-pyridyl)pyrimidine ($L^3$) have been hydrothermally synthesized. These complexes have one- and two-dimensional structures, as determined by single-crystal X-ray diffraction. The structural dimensionalities and motifs of complexes **1**–**4** are directed by the coordination modes of the ligands. Thus, $L^1$ acts as a bis-chelating ligand in complex **1** to join the adjacent 1D $\{CuCN\}_n$ chains into a two-dimensional corrugated layer. Complexes **2** and **4** both consist of one-dimensional zigzag chains where the ligands ($L^2$ for complex **2** and $L^3$ for complex **4**) occupy the terminal positions and N···$NH_2$ hydrogen bonds play an important role in the assembly of the supramolecular network. Complex **3** (another product isolated from the $L^3$-Cu-CN reaction system) is a two-dimensional network in which $L^3$ acts as a bridging ligand and the cyanide groups exhibit both $\mu_2$ and $\mu_3$ linking modes. Further investigation shows that the thermal stability of complexes **1**–**4** is in the order **1** > **3** > **2** > **4**. (© Wiley-VCH Verlag GmbH & Co. KGaA, 69451 Weinheim, Germany, 2007)

## Introduction

Considerable attention has recently been paid to the crystal engineering of coordination polymers due to their structural and topological novelty[1] and their potential applications in the fields of catalysis, molecular recognition, separation, and nonlinear optics.[2] Although a wide variety of coordination complexes with interesting structures and properties have been reported, it is still a great challenge to control the motifs and dimensionalities of coordination polymers as the formation of these complexes is influenced by many factors, including the coordination behavior of the organic ligand, the solvent system, the metal-to-ligand ratio, the template, and the counteranion.[3] Amongst these factors, the coordination geometry of the organic ligand is very important as, under suitable conditions, the structural information stored in the organic ligand can be read out by the metal ion.[4] This allows the construction of desired architectures by the judicious choice of metal ion and ligand. In this regard, ligand isomers play an important role and sometimes have a tuning effect on the structural dimensionality and motif.[5] A typical case is the bipyridine system, where 4,4′-bipyridine usually acts as a bridging unit to form extended coordination structures with high dimensionalities[6] while 2,2′-bipyridine generally acts as a terminal ligand to form discrete or 1D complexes.[7]

This paper concerns three isomers of 2-amino-4,6-dipyridylpyrimidine, namely 2-amino-4,6-bis(2-pyridyl)pyrimidine ($L^1$), 2-amino-4-(2-pyridyl)-6-(4-pyridyl)pyrimidine ($L^2$), and 2-amino-4-(2-pyridyl)-6-(3-pyridyl)pyrimidine ($L^3$; Scheme 1), and $Cu^{II}$ and $CN^-$ ions for the construction of coordination polymers. The Cu-CN system was selected based on the following considerations. A great deal of attention has been focused on copper cyanide complexes[8] recently because the coordination flexibility of copper ions and the versatile bridging modes of the cyanide ligand make copper cyanide complexes structurally varied.[9] A successful approach employed to develop new metal cyanides is to incorporate bidentate/multidentate organic ligands such as 2,2′-bipyridine or ethylenediamine into the metal-cyanide framework.[10] The structural motifs and dimensionalities of the resultant coordination polymers are often highly influenced by the incorporated ligand.[11] For example, the steric constraints of the introduced ligands and the spatial distances between imine donor groups of the ligands have been shown to have an obvious effect on the structures of Cu-CN complexes.[11a,11c] To the best of our knowledge, however, there is no report of the influence of isomeric ligands on the structure of copper cyanide complexes. Our aim is to understand how the structural motifs and dimensionalities of the Cu-CN coordination polymers can be manipulated by the ligand isomers.

Ligands $L^1$–$L^3$ are pentadentate, multifunctional ligands. The coordination chemistry of these ligands has not been

[a] The Institute for Chemical Physics, and Department of Chemistry, Beijing Institute of Technology,
Beijing 100081, P. R. China
[b] State Key Labarotory of Explosion Science and Technology, Beijing Institute of Technology,
Beijing, 100081, P. R. China
Fax: +86-10-68914780
E-mail: cwhu@bit.edu.cn

Supporting information for this article is available on the WWW under http://www.eurjic.org or from the author.

 © 2007 Wiley-VCH Verlag GmbH & Co. KGaA, Weinheim 

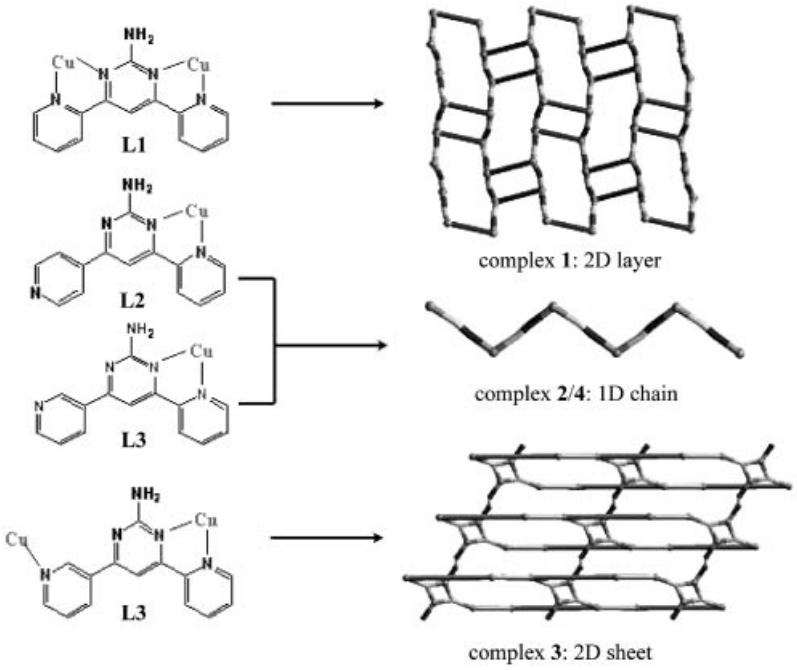


Scheme 1. The coordination modes of the three ligand isomers $L^1$–$L^3$ in complexes **1**–**4** and their resultant structural motifs.

explored widely to date, except for a few silver(I) and copper(I/II) complexes reported by us recently.[12] We found that the structures of these complexes are directed by the counteranions and ligand isomerism. Every isomer has a bidentate binding site that is capable of chelating one metal center, but the different pyridine substituent groups at the 6-position of the pyrimidine ring make them exhibit different coordination modes, which probably have a large influence on the resultant structures. In addition, the three isomers possess hydrogen-bond donor (amino group) and acceptor (aromatic N atoms) groups, which could be available for the formation of an H-bond network.

Herein we report four new copper-cyanide coordination polymers, namely $[Cu_2(CN)_2L^1]_n$ (**1**), $[CuCNL^2]_n$ (**2**), $[Cu_3(CN)_3L^3]_n$ (**3**), and $[CuCNL^3]_n$ (**4**), in all of which $Cu^{II}$ has been reduced to $Cu^{I}$ under the hydrothermal conditions used. The dimensionalities of complexes **1**–**4** vary with the coordination modes of the ligands (Scheme 1) and complexes **2** and **4** have the same molecular formula and different structures. These complexes not only enrich the structural database of copper(I) cyanide complexes but also demonstrate the tuning effect of ligand isomerism upon the dimensionalities and motifs of the resultant crystal structures.

## Results and Discussion

### Synthesis

Solvothermal reactions have recently been demonstrated to be a versatile technique for the construction of coordination polymers, and a large number of cyanide complexes have been synthesized by this method. We chose $K_3[Fe(CN)_6]$ as the source of cyanide anions because cyanide ions are slowly released from this complex under hydrothermal condition. Several kinds of $Cu^{II}$ salts [$CuCl_2{\cdot}2H_2O$, $CuBr_2$, $Cu(NO_3)_2{\cdot}3H_2O$, $Cu(OOCCH_3)_2{\cdot}H_2O$] were investigated but they were found to only act as a copper source and the counteranions are not involved in the crystal structures. Moreover, the $Cu^{II}$ ions are reduced to $Cu^{I}$ in all four complexes. This observation is consistent with the fact that copper(I) cyanide species are more stable than copper(II) complexes at elevated temperatures and pressures.[13] The cyanide groups obtained from the dissociation of $[Fe(CN)_6]^{3-}$ are probably responsible for the reduction process, yielding cyanogen as the oxidation product.

To investigate the influence of the reaction conditions we varied the metal/ligand ratio, reaction time, and temperature. Formation of complexes **1** and **2** is not obviously affected by the metal/ligand ratio ($CuCl_2/K_3[Fe(CN)_6]/L$ = 1:1:1, 1:2:1, 2:1:1, and 2:1:2), reaction time (24, 48, and 72 h), or temperature (120, 140, 160, 180 °C), although the yields did vary somewhat. However, the reaction conditions have a tuning effect on the final product obtained from the reaction between $L^3$, $Cu^{II}$, and $K_3[Fe(CN)_6]$. Thus, when the reaction was run with a molar ratio of 1:2:1 at 160 °C for 72 h the dominant product was complex **4**, whereas complex **3** was isolated in high yield with a 2:1:1 ratio. Similarly, when the same reaction with a 1:1:1 molar ratio was carried out at 160 °C for 24 h **4** was the only product, whereas after 48 or 72 h both complexes **3** and **4** both were obtained with different yields. When reactions with a 1:1:1 molar ratio were performed at 120 °C for 72 h only complex **4** was formed, whereas at 180 °C complex **3** was isolated as a pure phase and at 140 and 160 °C both complexes **3** and **4** were formed. On the basis of the above results we can conclude

 © 2007 Wiley-VCH Verlag GmbH & Co. KGaA, Weinheim 

that increasing the temperature or extending the reaction time is beneficial to the formation of **3**, therefore careful control of the reaction conditions allows us to obtain the desired product.

The coordination modes of ligands $L^1$–$L^3$ and the structural motifs of complexes **1**–**4** are summarized in Scheme 1. The structure of complex **1** consists of a wave-like layer in which CN groups link the $Cu^I$ ions to form a 1D $\{CuCN\}_n$ chain and $L^1$ acts as a bis-chelating ligand to bridge adjacent chains. Complexes **2** and **4** contain a zigzag chain that is unable to propagate to higher dimensionality, probably due to the terminal coordination mode of $L^2$/$L^3$. The structure of complex **3** is a 2D sheet in which the CN groups exhibit both $\mu_2$ and $\mu_3$ bridging modes and $L^3$ binds two metal centers, one through the N atoms in a chelating mode and the other through the N atom on the 3-pyridine ring. We suppose that the different coordination modes adopted by the ligand isomers, in combination with the versatile linking behavior of the cyanide groups, is responsible for the diversity of the structures reported.

## IR Spectroscopy

The IR bands corresponding to the CN stretching vibrations for complexes **1**–**4** appear in the range 2099–2123 $cm^{-1}$, which is typical for bridging cyanide groups and higher than that of terminal cyanide groups (approx. 2050 $cm^{-1}$).[14] The IR spectra of complexes **2** and **4** exhibit one ν(CN) stretching band at 2107 (for **2**) and 2099 (for **4**) $cm^{-1}$, which is in agreement with the presence of only one type of cyanide, while complexes **1** and **3** exhibit two stretching bands, thus indicating the existence of two types of cyanide bridges in the structure. The cyanide groups in the crystal structure of complex **3** exhibit $\mu_2$ and $\mu_3$ bridging modes but for complex **1** there is only one type of $\mu_2$-CN group, therefore the presence of two stretching bands for the latter might originate from the subtle difference of the $Cu^I$–N bond lengths [1.981(4) and 1.952(3) Å]. A similar phenomenon has been observed in other cyanide complexes.[11d,15] The absorption peaks between 3460 and 3280 $cm^{-1}$ are assigned to the asymmetric and symmetric stretching vibrations of the $NH_2$ group, and the absorption peaks below 1700 $cm^{-1}$ are mainly attributed to the vibrations of the aromatic rings.

## X-ray Crystal Structures

### *Complex 1*

The structure of complex **1** can be described as a neutral non-interpenetrating corrugated sheet containing two different types of copper(I) centers (Figure 1), both of which coordinate to two N atoms from $L^1$ and two cyanide groups and exhibit distorted tetrahedron geometries. $L^1$ acts as a bis-chelating ligand bridging two metal centers, as observed previously in silver(I) complexes of $L^1$.[12] The Cu–$N_{aryl}$ bond lengths fall in a narrow range [2.082(3)–2.112(3) Å] and the Cu–$C_{cyanide}$ bond lengths [Cu1–C16 = 1.886(4), Cu2–C15A = 1.885(4) Å] are very similar. The Cu–$N_{cyanide}$ distances [Cu1–N6 = 1.981(4), Cu2–N7A = 1.952(3) Å], however, are different. The acute angles at the chelating sites of $L^1$ [77.20(11)° for N1–Cu1–N4 and 77.23(10)° for N2–Cu2–N5] are responsible for the distorted tetrahedral geometries of the copper centers. In this case, the dihedral angles between the pyrimidine ring and two pyridine rings are 2.0° and 5.2°, respectively, and that between the two pyridine rings is 6.5°. All the dihedral angles in complex **1** are clearly smaller than those observed in $Ag^IL^1$ complexes.[12]

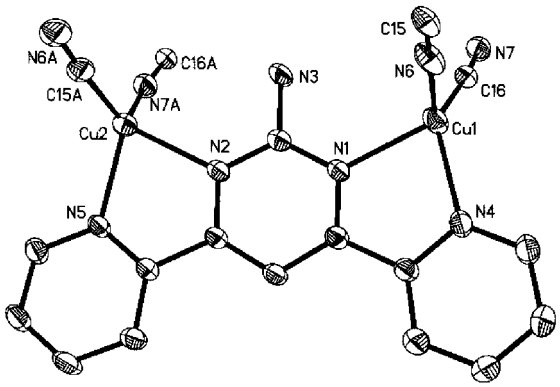


Figure 1. Coordination environments of the Cu ions in complex **1**. All H atoms have been omitted for clarity. Symmetry codes: (A) 5/2 – *x*, –1/2 + *y*, 3/2 – *z*; (B) 2 – *x*, –*y*, 2 – *z*.

As shown in Figure 2, the structure of **1** is constructed from zigzag $\{CuCN\}_n$ chains running along the *c*-axis that are linked together by the $L^1$ ligands to generate a 4.8(2) network (Figure S1 in the Supporting Information). Interestingly, the sheet contains two kinds of rings: a 16-membered $Cu_4(CN)_2(L^1)_2$ ring A and a 26-membered $Cu_8(CN)_6(L^1)_2$ ring B. This means that the structure can also be described as a layer composed of A and B rings. In ring A, the distance between two Cu atoms chelated by the same $L^1$ ligand is 6.154 Å, and two Cu atoms separated by a cyanide group are 4.930 Å apart. In general, 2D networks

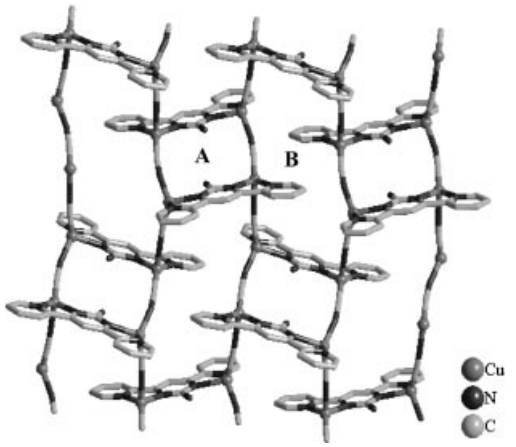


Figure 2. A view of the 2D layer in complex **1**.

 © 2007 Wiley-VCH Verlag GmbH & Co. KGaA, Weinheim 

in the Cu-CN system are generated by the linking of 1D $\{CuCN\}_n$ chains by linear dipodal ligands such as 4,4′-bipyridine, 2,2′-bipyrimidine, pyrazine, etc., and these networks usually only include one kind of ring unit.[7a,10c,11c] The 2D net observed in **1**, however, consists of two types of rings (A and B), and we believe that the non-linear bridging mode of $L^1$ is responsible for this special motif. The 2D sheets are stacked in an ABAB pattern and are assembled into a 3D supramolecular structure by π–π interactions between the $L^1$ ligands, with a plane-to-plane distance of about 3.55 Å (Figure S2).

### *Complex 2*

The cyanide groups in **2** connect the copper(I) anions to form a neutral zigzag chain along the *b*-axis with the $L^2$ ligands hanging from the metal centers (Figure 3). The asymmetric unit in **2** contains one copper center, one cyanide group, and one $L^2$ ligand. The copper ion is coordinated by two cyanide groups and two nitrogen atoms from $L^2$ with a distorted tetrahedral geometry. Ligand $L^2$ does not adopt the bridging mode previously found in $Ag^IL^2$ and $Cu^IL^2$ complexes but acts as a terminal ligand that binds through the chelating N atoms. The N5 atom on the 4-pyr-

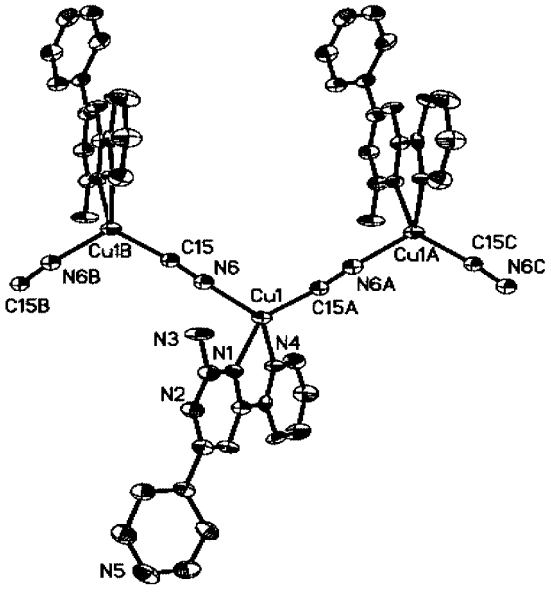


Figure 3. The 1D zigzag chain of complex **2**. All H atoms have been omitted for clarity. Symmetry codes: (A) *x*, –1/2 + *y*, 1/2 – *z*; (B) *x*, 1/2 + *y*, 1/2 – *z*; (C) *x*, –1 + *y*, *z*.

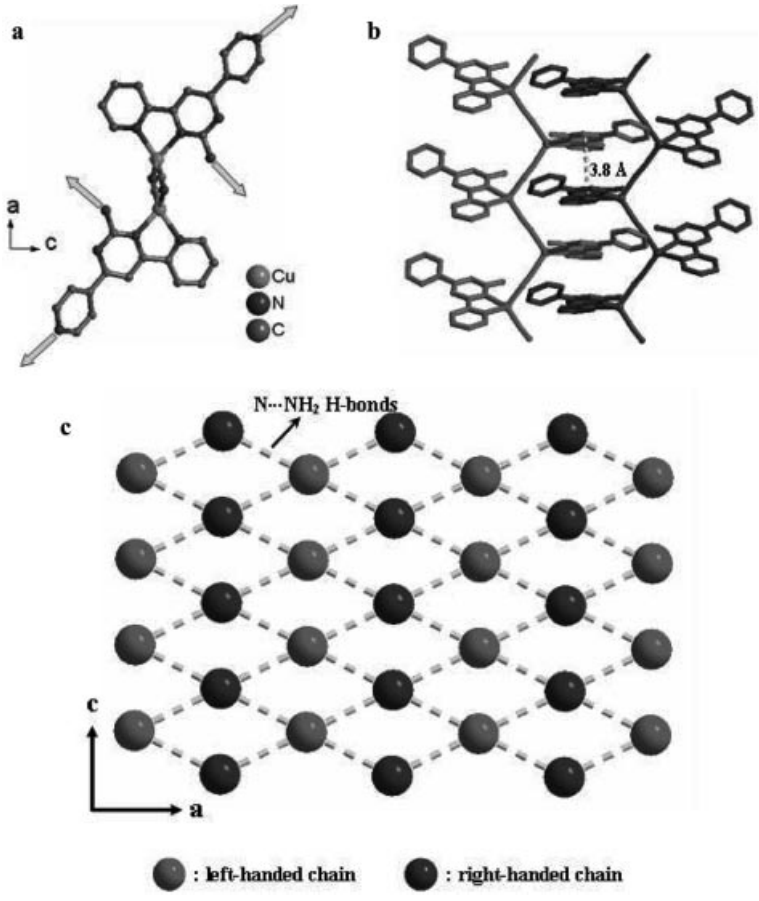


Figure 4. (a) A side view of the zigzag chain of complex **2** projected along the *b*-axis. The arrows represent the directions along which the 1D chain forms H-bonds with four neighboring chains. (b) Two differently orientated chains with π–π interactions in complex **2**. (c) A schematic presentation of the 3D supramolecular structure of complex **2**.

 © 2007 Wiley-VCH Verlag GmbH & Co. KGaA, Weinheim 

idine ring does not participate in coordination and points away from the zigzag chain. The Cu–$N_{py}$ [2.094(4) Å] and Cu–$N_{pym}$ [2.090(3) Å] bond lengths are rather similar and the acute angle at the chelating site of $L^2$ [78.2(3)° for N1–Cu1–N4] accounts for the obviously distorted geometry of the copper ion. The bond lengths involving the cyanide group [Cu1–C6 = 1.874(5), Cu1–N15A = 1.965(4), C15–N6 = 1.148(5) Å] are similar to those found in other copper cyanide complexes.[16] The shortest Cu···Cu distance within the chain is 4.949 Å and the shortest interchain Cu···Cu distance is 6.814 Å. The pyrimidine and 2-pyridine rings are nearly coplanar (dihedral angle of 2.4°) while the 4-pyridine ring lies outside of this plane. The dihedral angle between the 4-pyridine and pyrimidine rings is 23.5° and that between the 4-pyridine and 2-pyridine rings is 24.2°.

Neighboring chains in this structure have different orientations (Figure 4, b) and the $L^2$ ligands from two adjacent chains are stacked in an offset fashion with a plane-to-plane distance of 3.8 Å, thus indicating weak π–π interactions. For clarity, one is referred to as the left-handed chain and the other the right-handed chain. A projected view of the zigzag chain shows that the N atoms of the 4-pyridine and amino groups point in four different directions (Figure 2, a), and every chain forms H-bonds (N···$NH_2$ = 3.041 Å; H–N···N = 150.17°) with four neighboring chains along these four directions. The more interesting observation is that each left-handed chain connects to four adjacent right-handed chains, and vice versa (Figure 4, c and Figure S3, Supporting Information). The isolated zigzag chains are therefore assembled into a 3D supramolecular structure by H-bonds. The H-bond interaction is an important element in the construction of supramolecular structure, but seldom appears in Cu CN complexes.[9c,16] In this case, the successful formation of H-bonds is due to the $L^2$ ligand containing both an H-bond acceptor (N5) and donor ($NH_2$).

### *Complex 3*

The presence of ligand $L^3$ results in a 2D sheet in **3**. As shown in Figure 5 (a), there are three different metal centers (Cu1, Cu2, Cu3) in the asymmetric unit of **3**, all of which are three-coordinate with distorted trigonal geometries. The detailed coordination environments of the three Cu atoms are different. Cu1 is coordinated to three N atoms from two cyanide groups and one $L^3$ ligand with N–Cu–N bond angles varying from 102.6(5)° to 148.2(5)°, Cu2 is ligated to two N atoms from the chelating site of $L^3$ and one cyanide group, with the bond angles around $Cu^I$ ranging from 80.5(3)° to 145.8(4)°, while Cu3 is coordinated by three cyanide groups, with bond angles in the range 107.6(6)°–131.6(7)°. The Cu–$N_{aryl}$ bond lengths range from 2.052(11)

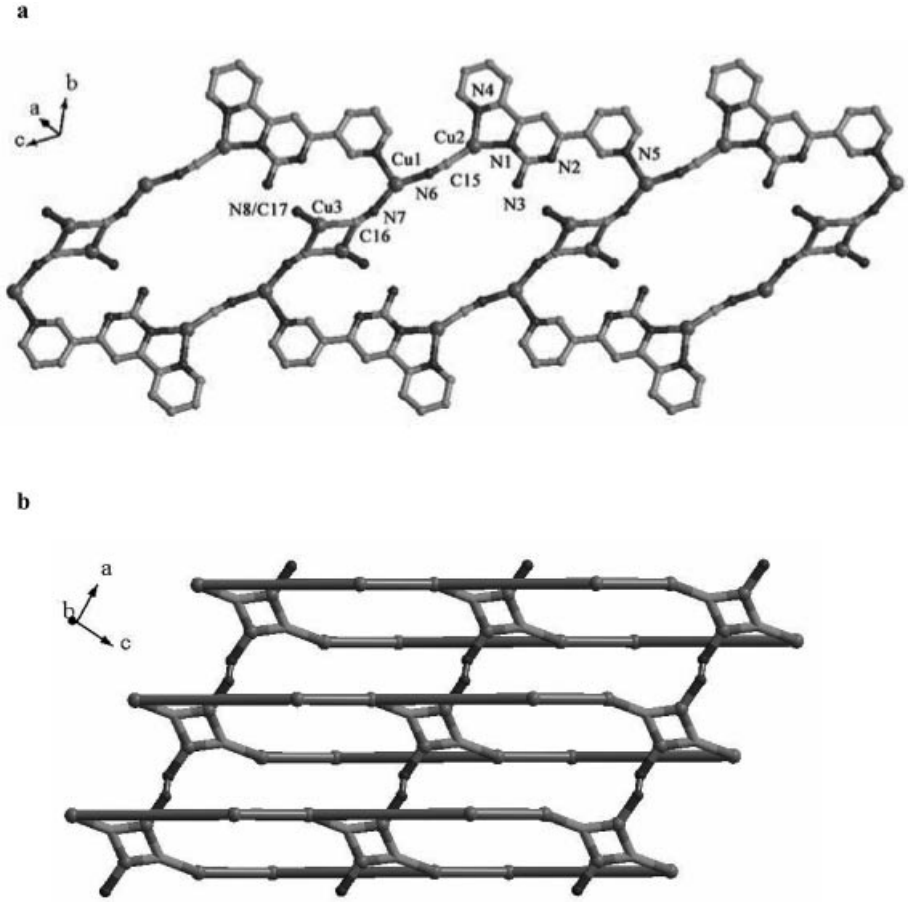


Figure 5. (a) The staggered ladder in complex **3**. All H atoms have been omitted for clarity. (b) A schematic presentation of the 2D sheet of complex **3**.

 © 2007 Wiley-VCH Verlag GmbH & Co. KGaA, Weinheim 

to 2.158(12) Å and the Cu–N/$C_{cyano}$ bond lengths are in the range 1.930(13)–2.210(19) Å. $L^3$ acts as a bridging ligand linking two copper centers. The three aromatic rings of $L^3$ are nearly in the same plane, with dihedral angles ranging from 2.3° to 3.6°. All the dihedral angles observed in complex **3** are smaller that those in complexes **1** and **2**.

The cyanide groups in **3** exhibit both $\mu_2$- and $\mu_3$-bridging modes. Two $\mu_3$-cyanide groups bond link two Cu3 centers through their carbon atoms to form a $Cu_2(CN)_2$ unit that includes a $Cu_2C_2$ rhombic ring with a Cu···Cu distance of 2.532 Å. The $Cu_2(CN)_2$ unit is a familiar motif in complexes containing $\mu_3$-cyanide and reported cases almost all have a short $Cu^I$···$Cu^I$ distance of between 2.42 and 2.66 Å.[8c,11c,11d,17] As shown in Figure 5 (a), two $Cu_2(CN)_2$ units, two $\mu_2$-cyanide groups, two $L^3$ ligands, and six copper ions are assembled into a 40-membered ring in which the largest Cu···Cu distance is 22.006 Å, the distance between two Cu atoms chelated by the same $L^3$ ligand is 9.865 Å, and two Cu atoms separated by a $Cu_2(CN)_2$ unit are 9.430 Å apart. Two ligands lie parallel to each other in the macrocycle with the amino groups pointing towards the center of the ring. Adjacent rings are fused along the edges containing the $Cu_2(CN)_2$ unit to form a ribbon. Alternatively, the ribbon may be described as a staggered ladder with $\{CuL^3(CN)\}_n$ chains as the side-rails and $Cu_2(CN)_2$ units as the rungs. For clarity, the staggered ladder can be simplified with the Cu atoms as nodes and $L^3$ ligands and $\mu_2$-cyanide groups as linkers (Figure S4). The rhombic rings of $Cu_2(CN)_2$ units are almost perpendicular to the ladder and the Cu3 atoms point to opposite sides. The disordered $\mu_2$-cyanide groups link the Cu3 centers from adjacent 1D ladders to generate a 2D sheet along the *a*-axis (Figure 5, b). The shortest Cu···Cu distance between adjacent sheets is 3.084 Å.

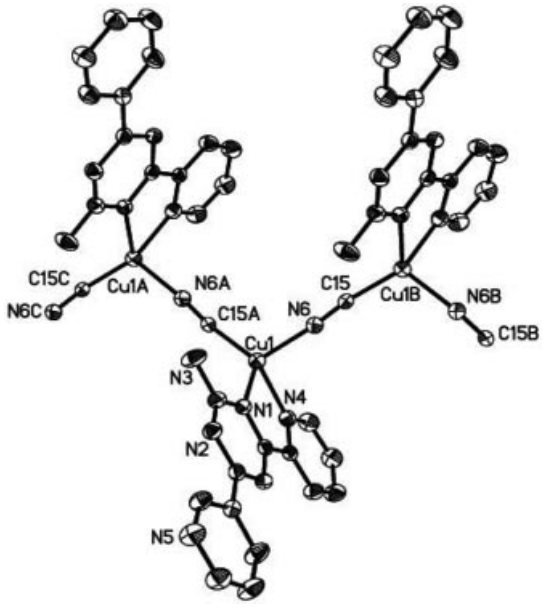


Figure 6. The 1D zigzag chain of complex **4**. All H atoms have been omitted for clarity. Symmetry codes: (A) *x*, 1/2 – *y*, –1/2 + *z*; (B) *x*, 1/2 – *y*, 1/2 + *z*; (C) *x*, *y*, –1 + *z*.

### *Complex 4*

Complex **4** is a 1D zigzag chain extending along the *c*-axis. As shown in Figure 6, there is only one kind of copper center in **4**, which is four-coordinated by two N atoms from $L^3$ and two cyanide groups and adopts a distorted tetrahedron geometry. The bond lengths around $Cu^I$ range from 1.884(3) to 2.099(2) Å and the bond angles are in the range 77.84(9)–119.76(11)°. Ligand $L^3$ does not adopt the bridging mode observed in **3** in this complex but acts as a terminal ligand. The pyrimidine and 2-pyridine rings are almost in the same plane, with a dihedral angle of about 0.8°, and the dihedral angles between pyrimidine and the 2-pyridine and 3-pyridine rings are about 3.1° and 3.9°, respectively. The dihedral angles observed in this crystal are obviously smaller than those in complex **2**. The shortest intrachain Cu···Cu distance is 5.011 Å and the shortest interchain Cu···Cu distance is 5.494 Å.

Complexes **2** and **4** have the same molecular formula and their structures are also very similar. However, a side view

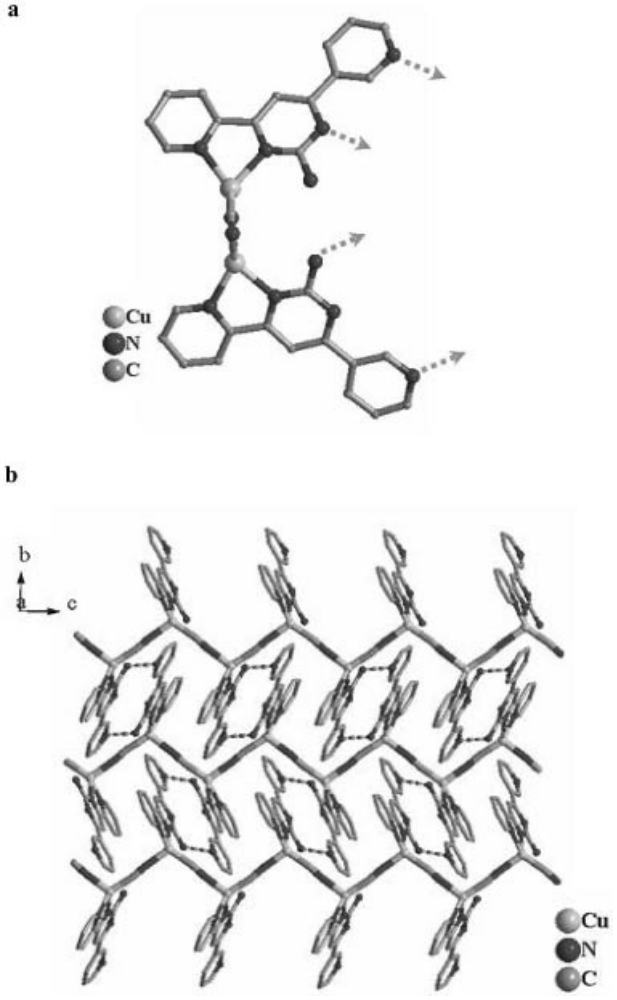


Figure 7. (a) A side view of the zigzag chain in complex **4** projected along the *c*-axis. The dashed arrows represent the directions along which the 1D chain forms H-bonds with two neighboring chains. (b) The 2D supramolecular network in complex **4** assembled by H-bonds. The dashed lines represent the H-bond interactions.

 © 2007 Wiley-VCH Verlag GmbH & Co. KGaA, Weinheim 

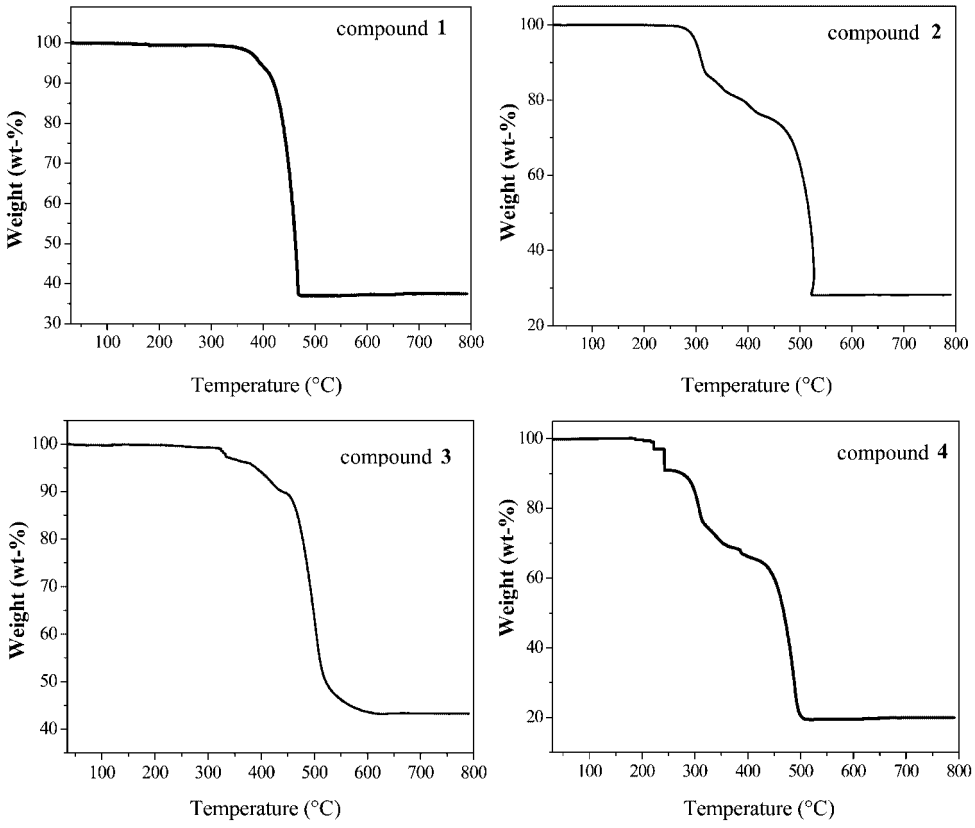


Figure 8. The TG curves of complexes **1**–**4**.

(see parts a in Figures 4 and 7) shows clearly that the orientation of the ligands in the two structures is different. Thus, the $L^2$ ligands are located on the two sides of the chain with the amino groups and the N atoms of the 4-pyridine rings pointing in four different directions in complex **2**, whereas in complex **4** the $L^3$ ligands are nearly oriented on the same side and the amino groups and the uncoordinated N atoms on the 3-pyridine rings point in only two different directions. As in complex **2**, the neighboring chains of **4** have different orientations and are linked together by H-bonds (N···N 2.980 Å; N–H···N 158.53°) between the $NH_2$ and N5 atoms to form a 2D supramolecular network (Figure 7, b). These 2D layers are assembled into a 3D supramolecular framework by π–π interactions between the pyrimidine and 2-pyridine rings (plane-to-plane distance of approx. 3.5 Å).

Interestingly, complexes **3** and **4**, which have distinct structural motifs and dimensionalities, were isolated from the same reaction system. We think that the structural diversity of the Cu/CN/$L^3$ system originates from the flexible and adjustable coordination modes of ligand $L^3$. To the best of our knowledge, this case represents the first example where two Cu-CN coordination polymers are obtained from the same reaction system.

### Thermal Stability

The thermal stability of complexes **1**–**4** was determined by TG analysis (Figure 8). Complex **1** is stable from room temperature up to 350 °C. It then undergoes a total weight loss of 63.02% (calculated value: 64.01%), corresponding to one $L^1$ ligand and one cyanide group, in the range 350–570 °C. Complex **2** shows a two-step weight loss between 275 and 500 °C. The total weight loss of **2** is 72.14% (calculated value: 73.41%), which corresponds to one ligand $L^2$. The weight loss for complex **3** between 320 and 600 °C is 57.99% (calculated value: 56.67%), which corresponds to one $L^3$ ligand and one cyanide group. The total weight loss for complex **4** between 200 and 500 °C is 80.56% (calculated value: 81.12%), which corresponds to one $L^3$ ligand and one cyanide group. The thermal stability of complexes **1**–**4** follows the order **1** (350 °C) > **3** (320 °C) > **2** (275 °C) > **4** (200 °C). These results are consistent with the above structural analysis and confirm that the high-dimensional networks (**1** and **3**) are more stable than the low-dimensional chains (**2** and **4**), and, for the 1D polymers, that the 3D H-bonded supramolecular structure (**2**) is more stable than the 2D supramolecular structure (**4**).

## Conclusions

Four novel copper(I) complexes, **1**–**4**, have been successfully prepared under hydrothermal condition by using three isomeric ligands $L^1$, $L^2$, and $L^3$ in combination with cyanide groups. $L^3$ is a new compound and, to the best of our knowledge, ligands $L^1$, $L^2$, and $L^3$ are employed here in the copper cyanide system for the first time. Ligands $L^2$ and $L^3$

 © 2007 Wiley-VCH Verlag GmbH & Co. KGaA, Weinheim 

in complexes **2** and **4** act as terminal ligands to form a 1D structure, while the two-dimensional networks of **1** and **3** are constructed from $L^1$ and $L^3$ exhibiting different bridging modes. The above results indicate that the coordination modes adopted by ligand isomers $L^1$, $L^2$, and $L^3$ have a tuning effect on the structural motifs and dimensionalities of the coordination polymers. Further investigation of the role of these three isomeric ligands in other transition metal systems is in progress.

## Experimental Section

**General Remarks:** All copper(II) salts were purchased from commercial sources and used without further purification. Organic solvents with analytical purity were supplied by commercial sources and used as received. Infrared spectra were recorded (as KBr pressed pellets) with a Nicolet 170SXFT/IR spectrometer. $^1$H NMR spectra (for $L^3$) were recorded with a Bruker DPX 500 spectrometer. X-ray powder diffraction (XPRD) patterns were collected with a Japan Rigaku D/max $\gamma$A X-ray diffractometer equipped with graphite-monochromated Cu-$K_\alpha$ radiation ($\lambda$ = 0.154060 nm). Elemental analyses were performed with a Perkin–Elmer 2400 CHN elemental analyzer. TG analyses were carried out in air between 30 and 800 °C at a heating rate of 10 °C min$^{-1}$ with a 2960 SDT simultaneous thermal analyzer.

**Synthesis of $L^1$, $L^2$, and $L^3$:** The ligands $L^1$, $L^2$, and $L^3$ were prepared according to previously reported synthetic procedures.[18] The synthesis of $L^3$ was similar to that of ligands $L^1$[18] and $L^2$.[12a] Data for $L^3$: Yield: 63%; m.p. 182–184 °C. $^1$H NMR ($CDCl_3$, 500 MHz, 25 °C): $\delta$ = 9.35 (s, 1 H, 2-pyridyl), 8.74–8.71 (m, 2 H, pyridyl), 8.43–8.39 (m, 2 H, pyridyl), 8.17 (s, 1 H, pyrimidyl), 7.88–7.86 (m, 1 H, pyridyl), 7.44–7.40 (m, 2 H, pyridyl), 5.24 (s, 2 H, amino group) ppm. IR (KBr): $\tilde{\nu}$ = 3329 (m), 3197 (m), 3055 (w), 2991 (w), 1650 (s), 1575 (s), 1564 (s), 1478 (s), 1433 (w), 1365 (s), 1238 (m), 1133 (w), 1092 (w), 994 (w), 845 (w), 781 (s), 743 (w), 706 (m), 661 (w), 623 (w) cm$^{-1}$.

**Synthesis of $[Cu_2(CN)_2L^1]_n$ (1):** A mixture of $L^1$ (24.9 mg, 0.1 mmol), $CuCl_2{\cdot}2H_2O$ (16.9 mg, 0.1 mmol), $K_3[Fe(CN)_6]$ (32.8 mg, 0.1 mmol), and $H_2O$ (8 mL) was transferred and sealed in a 15-mL Teflon-lined stainless steel autoclave, which was heated to 160 °C for 72 h and then cooled to room temperature. Red-brown cubic crystals were collected for X-ray analysis. Yield: 39.1 mg (91%, based on $L^1$). $C_{16}H_{11}Cu_2N_7$ (428.4): calcd. C 44.86, H 2.59, N 22.89; found C 44.92, H 2.67, N 22.78. IR (KBr): $\tilde{\nu}$ = 3460 (s), 3349 (s), 3096 (w), 3059 (w), 2112 (s), 2101 (s), 1732 (w), 1596 (s), 1583 (s), 1540 (s), 1456 (m), 1421 (m), 1370 (m), 1305 (m), 1240 (s), 1169 (w), 1156 (w), 1055 (w), 1007 (w), 852 (m), 791 (s), 772 (s), 737 (m), 664 (m) cm$^{-1}$.

**Synthesis of $[CuCNL^2]_n$ (2):** Complex **2** was synthesized in a manner similar to that used to obtain complex **1**, but with $L^2$ as ligand. Red-brown stick crystals were collected for X-ray analysis. Yield: 28.8 mg (85%, based on $L^2$). $C_{15}H_{11}CuN_6$ (338.8): calcd. C 53.17, H 3.27, N 24.80; found C 53.11, H 3.36, N 24.89. IR (KBr): $\tilde{\nu}$ = 3422 (m), 3298 (m), 3182 (w), 3066 (w), 2107 (s), 1624 (s), 1583 (s), 1547 (s), 1500 (w), 1470 (m), 1414 (m), 1373 (s), 1257 (w), 1230 (m), 1066 (w), 998 (w), 830 (s), 785 (s), 743 (w), 650 (m), 631 (m) cm$^{-1}$.

**Synthesis of $[Cu_3(CN)_3L^3]_n$ (3):** Complex **3** was synthesized at 180 °C in a manner similar to that used to obtain complex **1**, but with $L^3$ as ligand. Dark red crystals were collected for X-ray analysis. Yield: 19.4 mg (41%, based on $L^3$). $C_{16.5}H_{11}Cu_{2.5}N_{7.5}$ (473.2): calcd. C 41.88, H 2.34, N 22.20; found C 41.94, H 2.42, N 22.29. IR (KBr): $\tilde{\nu}$ = 3615 (w), 3443 (w), 3358 (m), 3059 (w), 2924 (w), 2123 (s), 2101 (s), 1592 (s), 1539 (s), 1478 (s), 1449 (s), 1420 (m), 1367 (s), 1257 (w), 1232 (m), 1200 (w), 1143 (w), 1049 (w), 1028 (w), 1016 (w), 778 (s), 701 (m), 660 (m), 640 (w) cm$^{-1}$.

**Synthesis of $[CuCNL^3]_n$ (4):** A mixture of $L^3$ (24.9 mg, 0.1 mmol), $CuCl_2$ (16.9 mg, 0.1 mmol), $K_3[Fe(CN)_6]$ (65.6 mg, 0.2 mmol), and $H_2O$ (8 mL) was transferred and sealed in a 15-mL Teflon-lined stainless steel autoclave, which was heated to 160 °C for 72 h and then cooled to room temperature. Brown cubic crystals were collected for X-ray analysis. Yield: 30.2 mg (89%, based on $L^3$). $C_{15}H_{11}CuN_6$ (338.8): calcd. C 53.17, H 3.27, N 24.80; found C

Table 1. Crystallographic data for complexes **1**–**4**.

| | **1** | **2** | **3** | **4** |
|---|---|---|---|---|
| Formula | $C_{16}H_{11}Cu_2N_7$ | $C_{15}H_{11}CuN_6$ | $C_{16.5}H_{11}Cu_{2.5}N_{7.5}$ | $C_{15}H_{11}CuN_6$ |
| *Fw* | 428.40 | 338.84 | 473.18 | 338.84 |
| *a* [Å] | 11.127(2) | 16.528(15) | 7.72(4) | 11.743(3) |
| *b* [Å] | 12.274(2) | 8.168(8) | 9.76(5) | 15.539(4) |
| *c* [Å] | 12.334(2) | 21.62(2) | 12.21(6) | 8.085(2) |
| *α* [°] | 90 | 90 | 97.85(7) | 90 |
| *β* [°] | 92.299(3) | 90 | 94.85(6) | 98.038(3) |
| *γ* [°] | 90 | 90 | 90.85(6) | 90 |
| Space group | $P2_1/n$ | *Pbca* | $P\bar{1}$ | $P2_1/c$ |
| $D_{calc}$ [Mg m$^{-3}$] | 1.691 | 1.542 | 1.731 | 1.541 |
| *Z* | 4 | 8 | 2 | 4 |
| Crystal system | monoclinic | orthorhombic | triclinic | monoclinic |
| Volume [Å$^3$] | 1683.1(6) | 2910(2) | 908(8) | 1460.8(7) |
| *F*(000) | 856 | 1376 | 470 | 688 |
| Crystal size [mm] | 0.33 × 0.21 × 0.14 | 0.65 × 0.21 × 0.04 | 0.43 × 0.21 × 0.19 | 0.37 × 0.34 × 0.25 |
| Reflections collected | 8620 | 14078 | 4125 | 7380 |
| Unique reflections | 2966 | 2576 | 2903 | 2572 |
| Goof | 1.048 | 0.948 | 0.981 | 1.074 |
| $R1$ [$I > 2\sigma(I)$][a] | 0.0325 | 0.0492 | 0.0762 | 0.0330 |
| $\omega R2$ [$I > 2\sigma(I)$] | 0.0734 | 0.0953 | 0.1990 | 0.0802 |
| $R1$ (all data) | 0.0520 | 0.1102 | 0.1524 | 0.0562 |
| $\omega R2$ (all data) | 0.0840 | 0.1152 | 0.2628 | 0.0982 |

[a] $R_1 = \Sigma||F_o| - |F_c||/\Sigma|F_o|$; $wR_2 = \Sigma[w(F_o^2 - F_c^2)^2]/\Sigma[w(F_o^2)^2]^{1/2}$.

 © 2007 Wiley-VCH Verlag GmbH & Co. KGaA, Weinheim 

53.23, H 3.34, N 24.72. IR (KBr): $\tilde{\nu}$ = 3398 (m), 3284 (w), 3108 (m), 2099 (s), 1633 (s), 1588 (s), 1547 (s), 1461 (s), 1420 (m), 1363 (s), 1232 (m), 1192 (w), 1143 (w), 1057 (w), 1024 (m), 844 (w), 824 (m), 779 (s), 742 (m), 705 (m), 664 (m), 551 (m), 431 (w) $cm^{-1}$.

**X-ray Crystallographic Analysis:** Suitable single crystals of complexes **1**–**4** were mounted on a Bruker-AXS CCD diffractometer equipped with a graphite-monochromated Mo-$K_\alpha$ radiation source ($\lambda$ = 0.07103 Å) at 298 K. All absorption corrections were performed with the SADABS program. All the structures were solved by direct methods and expanded using Fourier techniques. The non-hydrogen atoms were refined anisotropically. Hydrogen atoms were located in the calculated positions. All calculations were performed using the SHELXTL-97 program.[19] The crystallographic details of complexes **1**–**4** are summarized in Table 1. Selected bond lengths and angles of complexes **1**–**4** are listed in Table 2.

Table 2. Selected bond lengths [Å], angles [°], and other distances for **1**–**4**.[a]

| | | | |
|---|---|---|---|
| Complex **1** | | | |
| Cu(1)–C(16) | 1.886(4) | N(4)–Cu(1)–N(1) | 77.20(11) |
| Cu(1)–N(6) | 1.981(4) | C(16)–Cu(1)–N(6) | 115.02(14) |
| Cu(1)–N(4) | 2.088(3) | N(6)–Cu(1)–N(4) | 108.42(13) |
| Cu(1)–N(1) | 2.107(3) | C(16)–Cu(1)–N(1) | 121.29(13) |
| Cu(2)–C(15)#1 | 1.885(4) | C(15)#1–Cu(2)–N(7)#2 | 119.78(14) |
| Cu(2)–N(7)#2 | 1.952(3) | N(5)–Cu(2)–N(2) | 77.23(10) |
| Cu(2)–N(5) | 2.082(3) | N(7)#2–Cu(2)–N(2) | 102.21(11) |
| Cu(2)–N(2) | 2.112(3) | C(15)#1–Cu(2)–N(2) | 115.64(14) |
| N(6)–C(15) | 1.150(5) | C(15)–N(6)–Cu(1) | 176.5(3) |
| N(7)–C(16) | 1.148(4) | N(7)–C(16)–Cu(1) | 173.8(3) |
| Complex **2** | | | |
| Cu(1)–N(1) | 2.090(3) | N(1)–Cu(1)–N(4) | 78.2(3) |
| Cu(1)–N(4) | 2.094(4) | C(15)#1–Cu(1)–N(6) | 113.8(3) |
| Cu(1)–N(6) | 1.965(4) | N(6)–Cu(1)–N(4) | 119.5(3) |
| Cu(1)–C(15)#1 | 1.874(5) | C(15)#1–Cu(1)–N(1) | 122.2(4) |
| N(6)–C(15) | 1.148(5) | C(15)–N(6)–Cu(1) | 166.0(9) |
| Cu(1)–Cu(1)#1 | 4.953(3) | N(6)–C(15)–Cu(1)#2 | 174.2(8) |
| Complex **3** | | | |
| Cu(1)–N(7) | 1.930(13) | N(7)–Cu(1)–N(6) | 148.2(5) |
| Cu(1)–N(6) | 1.948(11) | N(7)–Cu(1)–N(5)#1 | 108.5(6) |
| Cu(1)–N(5)#1 | 2.158(12) | N(6)–Cu(1)–N(5)#1 | 102.6(5) |
| Cu(2)–C(15) | 1.872(12) | C(15)–Cu(2)–N(1) | 145.8(4) |
| Cu(2)–N(1) | 2.052(11) | C(15)–Cu(2)–N(4) | 132.5(4) |
| Cu(2)–N(4) | 2.080(14) | N(1)–Cu(2)–N(4) | 80.5(3) |
| Cu(2)···Cu(2)#2 | 3.046(12) | N(8)–Cu(3)–C(16) | 131.6(7) |
| Cu(3)–N(8) | 2.055(17) | N(8)–Cu(3)–C(16)#3 | 119.7(6) |
| Cu(3)–C(16) | 2.072(14) | C(16)–Cu(3)–C(16)#3 | 107.6(6) |
| Cu(3)–C(16)#3 | 2.210(19) | C(16)–N(7)–Cu(1) | 161.6(13) |
| Cu(3)···Cu(3)#3 | 2.532(16) | C(15)–N(6)–Cu(1) | 162.3(8) |
| Complex **4** | | | |
| Cu(1)–C(15)#1 | 1.884(3) | N(1)–Cu(1)–N(4) | 77.84(9) |
| Cu(1)–N(6) | 1.994(3) | C(15)#1–Cu(1)–N(1) | 119.76(11) |
| Cu(1)–N(1) | 2.084(2) | C(15)#1–Cu(1)–N(6) | 110.76(12) |
| Cu(1)–N(4) | 2.099(2) | N(6)–Cu(1)–N(4) | 101.90(11) |

[a] Symmetry codes for **1**: #1 $-x + 5/2$, $y - 1/2$, $-z + 3/2$; #2 $-x + 2$, $-y$, $-z + 2$; **2**: #1 $-x$, $y - 1/2$, $-z + 1/2$; #2 $-x$, $y + 1/2$, $-z + 1/2$; **3**: #1 $x - 1$, $y$, $z - 1$; #2 $-x + 1$, $-y$, $-z$; #3 $-x$, $-y + 1$, $-z - 1$; **4**: #1 $x$, $-y + 1/2$, $z - 1/2$.

CCDC-635075 to -635078 contain the crystallographic data for for **1**–**4**. These data can be obtained free of charge from The Cambridge Crystallographic Data Centre via www.ccdc.cam.ac.uk/data_request/cif.

**Supporting Information** (see also the footnote on the first page of this article): A schematic presentation of the 2D net in **1** (Figure S1), the 3D supramolecular structure of **1** projected along the *b*-axis (Figure S2), H-bond interactions in **2** (Figure S3), a schematic presentation of the staggered ladder chain in **3** (Figure S4), solid-state excitation and emission spectra of ligand L3 at room temperature (Figure S5), and XPRD patterns of **1**−**4** (Figure S6).

## Acknowledgments

The ligands were synthesized with the help of Prof. Q. Liu at Northeast Normal University. This project was supported by the Natural Science Fund Council of China (NSFC) (grant nos. 20671011, 20331010, 90406002, and 90406024), the 111 Project (B07012), and the Key Laboratory of Structural Chemistry Foundation (KLSCF) (grant no. 060017).

[1] a) F.-C. Liu, Y.-F. Zeng, J.-R. Li, X.-H. Bu, H.-J. Zhang, J. Ribas, *Inorg. Chem.* **2005**, *44*, 7298; b) Y.-F. Zhou, F.-L. Jiang, D.-Q. Yuan, B.-L. Wu, R.-H. Wang, Z.-Z. Lin, M.-C. Hong, *Angew. Chem. Int. Ed.* **2004**, *43*, 5665; c) M. Fujita, M. Tominaga, K. Suzuki, M. Kawano, T. Kusukawa, *Angew. Chem. Int. Ed.* **2004**, *43*, 5621.

[2] a) M. Fujita, Y. J. Kwon, S. Washizu, K. Ogura, *J. Am. Chem. Soc.* **1994**, *116*, 1151; b) O. R. Evans, W. Lin, *Acc. Chem. Res.* **2002**, *35*, 511; c) K. Kasai, M. Aoyagi, M. Fujita, *J. Am. Chem. Soc.* **2000**, *122*, 2140; d) S. Kitagawa, R. Kitaura, S.-I. Noro, *Angew. Chem. Int. Ed.* **2004**, *43*, 2334.

[3] a) X.-H. Bu, W. Chen, W.-F. Hou, M. Du, R.-H. Zhang, F. Brisse, *Inorg. Chem.* **2002**, *41*, 3477; b) B. Hasenknopf, J. M. Lehn, N. Boumediene, A. Dupont-Gervais, B. O. Kneisel, D. Fenske, *J. Am. Chem. Soc.* **1997**, *119*, 10956; c) R. P. Feazell, C. E. Carson, K. K. Klausmeyer, *Inorg. Chem.* **2006**, *45*, 2635; d) X.-C. Huang, J.-P. Zhang, X.-M. Chen, *J. Am. Chem. Soc.* **2004**, *126*, 13218; e) X.-H. Bu, Y.-B. Xie, J.-R. Li, R.-H. Zhang, *Inorg. Chem.* **2003**, *42*, 7422.

[4] J. M. Lehn, *Supramolecular Chemistry – Concepts and Perspectives*, VCH, Weinheim, **1995**.

[5] a) Z. He, Z.-M. Wang, C.-H. Yan, *CrystEngComm* **2005**, *7*, 143; b) J. Seo, M. R. Song, S. S. Lee, *Inorg. Chem.* **2006**, *45*, 952; c) L. Hou, D. Li, *Inorg. Chem.* **2005**, *44*, 7825.

[6] a) J. D. Woodward, R. Backov, K. A. Abboud, H. Ohnuki, M. W. Meisel, D. R. Talham, *Polyhedron* **2003**, *22*, 2821; b) J. L. Manson, J. G. Lecher, J. Gu, U. Geiser, J. A. Schlueter, R. Henning, X.-P. Wang, A. J. Schultz, H.-J. Koo, M.-H. Whangbo, *Dalton Trans.* **2003**, 2905.

[7] a) E. Colacio, J. M. Domínguez-Vera, F. Lloret, J. M. Moreno Sánchez, R. Kivekäs, A. Rodríguez, R. Sillanpää, *Inorg. Chem.* **2003**, *42*, 4209; b) Z.-M. Sun, J.-G. Mao, Y.-Q. Sun, H.-Y. Zeng, A. Clearfield, *Inorg. Chem.* **2004**, *43*, 336; c) A.-Q. Wu, F.-K. Zheng, W.-T. Chen, L.-Z. Cai, G.-C. Guo, J.-S. Huang, Z.-C. Dong, Y. Takano, *Inorg. Chem.* **2004**, *43*, 4839.

[8] a) T. Korzeniak, K. Stadnicka, R. Pelka, M. Balanda, K. Tomala, K. Kowalski, B. Sieklucka, *Chem. Commun.* **2005**, 2939; b) L. Yi, B. Ding, B. Zhao, P. Cheng, D.-Z. Liao, S.-P. Yan, Z.-H. Jiang, *Inorg. Chem.* **2004**, *43*, 33; c) J.-M. Zheng, S.-R. Batten, M. Du, *Inorg. Chem.* **2005**, *44*, 3371; d) P. V. Bernhardt, F. Bozoglian, B. P. Macpherson, *Coord. Chem. Rev.* **2005**, *249*, 1902; e) J. Černák, M. Orendáč, *Coord. Chem. Rev.* **2002**, *224*, 51.

[9] a) E. Colacio, F. Lloret, M. Navarrete, *New J. Chem.* **2005**, *29*, 1189; b) D.-H. Kim, J.-E. Koo, C. S. Hong, S. Oh, Y. Do, *Inorg.*

 © 2007 Wiley-VCH Verlag GmbH & Co. KGaA, Weinheim 

*Chem.* **2005**, *44*, 4383; c) J.-D. Lin, S.-W. Du, *Inorg. Chem. Commun.* **2006**, *9*, 675.
[10] a) F. B. Stocker, T. P. Staeva, *Inorg. Chem.* **1999**, *38*, 984; b) X.-Y. Chen, P. Cheng, W. Shi, J. Xia, *Inorg. Chem.* **2005**, *44*, 4263; c) E. Colacio, A. Debdoubi, R. Kibekäs, A. Rodríguez, *Eur. J. Inorg. Chem.* **2005**, 2860; d) O. Teichert, W. S. Z. Sheldrick, *Z. Anorg. Allg. Chem.* **2000**, *626*, 1509.
[11] a) E. Colacio, R. Kivekäs, F. Lloret, M. Sunberg, *Inorg. Chem.* **2002**, *41*, 5141; b) D. J. Chesnut, A. Kusnetzow, J. Zubieta, *Inorg. Chem.* **1999**, *38*, 5484; c) D. J. Chesnut, D. Plewak, J. Zubieta, *J. Chem. Soc. Dalton Trans.* **2001**, 2567; d) X. He, C.-Z. Lu, C.-D. Wu, L.-J. Chen, *Eur. J. Inorg. Chem.* **2006**, 2491.
[12] a) Y.-N. Chi, K.-L. Huang, F.-Y. Cui, Y.-Q. Xu, C.-W. Hu, *Inorg. Chem.* **2006**, *45*, 10605; b) Y.-N. Chi, F.-Y. Cui, Y.-Q. Xu, C.-W. Hu, *Inorg. Chem. Commun.* **2007**, *10*, 695.
[13] A. G. Sharp, *The Chemistry of Cyano Complexes of the Transition Metals*, Academic Press, New York, **1976**, pp. 226–271.
[14] K. Nakamoto, *Infrared and Roman Spectra of Inorganic Coordination Compounds*, Wiley, New York, **1986**, pp. 272.
[15] D. J. Chesnut, A. Kusnetzow, J. Zubieta, *J. Chem. Soc. Dalton Trans.* **2001**, 2581.
[16] B. Yan, V. O. Golub, A. Lachgar, *Inorg. Chim. Acta* **2006**, *359*, 118.
[17] a) J. Kildea, B. Skelton, A. White, *Aust. J. Chem.* **1985**, *38*, 1329; b) M. Schwarten, J. Chomic, J. Cernak, D. Babel, *Z. Anorg. Allg. Chem.* **1996**, *622*, 1449.
[18] S. Takagi, T. Sahashi, K. Sako, K. Mizuno, M. Kurihara, H. Nishihara, *Chem. Lett.* **2002**, 628.
[19] a) G. M. Sheldrick, SHELXS 97, *Program for Crystal Structure Solution*; University of Göttingen, Germany, **1997**; b) G. M. Sheldrick, SHELXL 97, *Program for Crystal Structure Refinement*; University of Göttingen, Germany, **1997**.

Received: April 9, 2007
Published Online: July 31, 2007

 © 2007 Wiley-VCH Verlag GmbH & Co. KGaA, Weinheim 

DOI: 10.1002/ejic.200700399

# Charge-Transfer Complexes between the Sulfur Molecules $SO_2$, $S_2O$, $S_3$, SONH, and $SOCl_2$ and the Amine Donors $NH_3$ and $NMe_3$ – A Theoretical Study

**Ralf Steudel*[a] and Yana Steudel[a]**

**Keywords:** Ab initio calculations / Donor–acceptor systems / Thermodynamics / Sulfur / Solvent effects

The formation of adducts between the acceptor molecules $SO_2$, $S_2O$, $S_3$, and $SOCl_2$ and the donor molecules ammonia and trimethylamine has been studied by high-level G3X(MP2) theory, in most cases for the first time. Minimum energy structures with a 1:1 composition and with sulfur–nitrogen bonds have been located for all complexes. The thermodynamic properties, vibrational spectra, and atomic charges of these molecules have been calculated. Of the 10 investigated complexes, only $SO_2{\cdot}NMe_3$ (**2**) and $S_2O{\cdot}NMe_3$ (**4**) are predicted to be thermodynamically stable in the gas phase under standard conditions ($\Delta G°_{298} < 0$). However, all adducts except $S_3{\cdot}NH_3$ (**5**), $SOCl_2{\cdot}NH_3$ (**7**), and $SOCl_2{\cdot}NMe_3$ (**8**) are stable thermodynamically at 77 K. In a polar continuum with a dielectric constant ($\varepsilon$) of 40, complexes **2**, **4**, and $S_3{\cdot}NMe_3$ (**6**) are stable even at 25 °C. However, if the adducts are formed in the polar continuum from the gaseous components, all adducts except $S_3{\cdot}NH_3$ are formed not only exothermally but also exergonically. Complexes **2**, **4**, and **8** are the only species known in the solid state so far. The charge transfer from donor to acceptor in the various complexes in the gas phase ranges from 0.08 to 0.39 electrostatic units and correlates inversely with the S–N bond length, which ranges from 198 to 295 pm. In general, the charge transfer weakens the bonds within the acceptor molecule, which therefore may be considered to become activated. The formation of thionyl imide (SONH) from $SOCl_2$ and $NH_3$ is exergonic in the gas phase and the interaction between SONH and $NH_3$ is very weak. In the case of $SO_2$, the 1:2 complexes $SO_2{\cdot}2NH_3$ (**1a**) and $SO_2{\cdot}2NMe_3$ (**2a**), which contain two S–N bonds, are unstable with respect to their three-component molecules both in the gas phase and in a polar medium at 25 °C, but they are stable in the polar phase with respect to the gaseous components.

(© Wiley-VCH Verlag GmbH & Co. KGaA, 69451 Weinheim, Germany, 2007)

## Introduction

Sulfur dioxide forms well-known charge-transfer complexes with both ammonia and trimethylamine and with the two stoichiometries 1:1 and 1:2. The ammonia complexes $SO_2{\cdot}NH_3$ (**1**) and $SO_2{\cdot}2NH_3$ (**1a**) were first discovered by equilibrium vapor pressure measurements on $SO_2/NH_3$ mixtures[1] and were subsequently characterized by matrix infrared spectroscopy[2] and quantum chemical calculations.[3,4] Both molecules have $C_s$ symmetry with sulfur–nitrogen bonds approximately perpendicular to the plane of the $SO_2$ unit.[3] The enthalpies of formation of the two solid compounds **1** and **1a** from the gaseous components were estimated from the above-mentioned vapor pressure measurements as being $-40 \pm 4$ and $-96 \pm 19$ kJ mol$^{-1}$, respectively.[1] On the other hand, ab initio calculations at the MP3/6-31+G(2d,p) level of theory have predicted that the enthalpies of formation from the separated components in the gas phase at 25 °C are only –18.8 for **1** and –31.3 kJ mol$^{-1}$ for **1a**. After correction for the basis set superposition error (BSSE), the (absolute) interaction energy between $SO_2$ and $NH_3$ in **1** was found to be smaller by 6 kJ mol$^{-1}$, at –12.8 kJ mol$^{-1}$.[3] Both **1** and **1a** are unstable at room temperature and ambient pressure.

The related adduct $SO_2{\cdot}NMe_3$ (**2**) is much more stable than **1** and was first prepared in 1943 as a colorless solid.[5] Subsequently, this compound has been extensively studied by X-ray crystallography of single crystals,[6,7] microwave spectroscopy in the vapor phase,[7] UV/Vis spectroscopy in solution,[8] vapor density measurements,[9] and ab initio MO calculations.[3,10–12] The most recent and most sophisticated theoretical study applying the MP2/6-31G* level of theory predicted S–N distances of 235.9 pm for **2** and 270.7 pm for $SO_2{\cdot}2NMe_3$ (**2a**).[3]

The preparation of the adducts $S_2O{\cdot}NMe_3$ (yellow crystals) and $SOCl_2{\cdot}NMe_3$ (colorless crystals) was reported in 1963.[13] Both compounds can be sublimed in a vacuum, probably with complete dissociation in the gas phase. However, neither spectra nor structural determinations or theoretical calculations are known for these complexes. To elucidate the structures, thermodynamics, and bonding of these

[a] Institut für Chemie, Technische Universität Berlin, Sekr. C2
10623 Berlin, Germany
Fax: +49-30-3142-6519
E-mail: steudel@sulfur-research.de

Supporting information for this article is available on the WWW under http://www.eurjic.org or from the author.

 © 2007 Wiley-VCH Verlag GmbH & Co. KGaA, Weinheim 

interesting adducts and of a number of related species we have carried out extensive quantum chemical calculations at the G3X(MP2) level of theory not only for **1**, **1a**, **2**, and **2a**, but also for the first time for the related complexes $S_2O{\cdot}NH_3$ (**3**), $S_2O{\cdot}NMe_3$ (**4**), $S_3{\cdot}NH_3$ (**5**), $S_3{\cdot}NMe_3$ (**6**), $SOCl_2{\cdot}NH_3$ (**7**), $SOCl_2{\cdot}NMe_3$ (**8**), and $SONH{\cdot}NH_3$ (**9**). The Gibbs energies of formation from the separated components have also been calculated for the species **1**–**8** for the first time, both in the vapor phase and in a polar medium, to predict the thermodynamic stability of these compounds under standard and nonstandard conditions. All relative energies and enthalpies reported in the text for gas-phase species correspond to the G3X(MP2) level, while all reported structural parameters as well as the energies of solvated species correspond to the B3LYP/6-31G(2df,p) level of theory.

## Results and Discussion

### Adducts in the Gas Phase

#### *Adducts of $SO_2$*

The molecular structure of the complex $SO_2{\cdot}NH_3$ (**1**) was confirmed to be of $C_s$ symmetry with a relatively long S–N bond of 266.3 pm. Other bond lengths are given in Figure 1 and bond angles are listed in Table S1 in the Supporting Information. The binding energy of **1** (–18.1 kJ mol$^{-1}$) is approximately one third that of $SO_2{\cdot}NMe_3$ (see below), and the Gibbs energy for the formation reaction of **1** is even positive at 298 K (14.6 kJ mol$^{-1}$; Table 1). In other words, the gaseous complex **1** is not stable under standard conditions with respect to dissociation into the two components. However, at liquid nitrogen temperature (77 K) the Gibbs energy is negative (–10.9 kJ mol$^{-1}$), and even after a BSSE correction of +4.9 kJ mol$^{-1}$ has been applied the Gibbs energy is still –6.0 kJ mol$^{-1}$ (Table 1, last column).

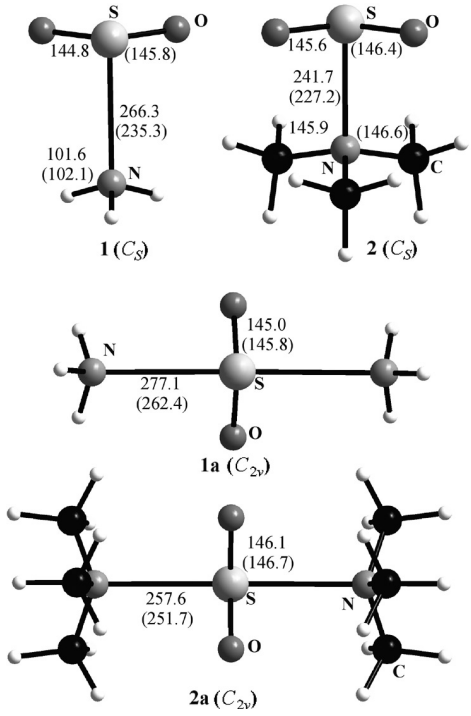


Figure 1. Structures, bond lengths (in pm), and symmetry of the complexes $SO_2{\cdot}NH_3$ (**1**), $SO_2{\cdot}2NH_3$ (**1a**), $SO_2{\cdot}NMe_3$ (**2**), and $SO_2{\cdot}2NMe_3$ (**2a**) in the gas phase. The bond lengths in a polar continuum of dielectric constant $\varepsilon = 40$ are given in parentheses. All data calculated at the B3LYP/6-31G(2df,p) level of theory. See Table S1 (Supporting Information) for bond angles.

The S–O bonds of **1** (144.8 pm) are slightly longer than those calculated for $SO_2$ (144.3 pm). In line with this finding is the fact that the two S–O stretching vibrations are calculated to have somewhat lower wavenumbers (1162 and 1356 cm$^{-1}$) than predicted for free $SO_2$ at the same level of theory (1171 and 1381 cm$^{-1}$). The experimental values for the asymmetric SO stretching vibration of matrix-isolated **1** and of free $SO_2$ are 1338 and 1350 cm$^{-1}$,[2] respectively, in

Table 1. Reaction energies ($\Delta E_o$), enthalpies ($\Delta H°$), and Gibbs energies ($\Delta G°$) [uncorrected G3X(MP2) data in kJ mol$^{-1}$] for the formation of the gaseous donor–acceptor complexes **1**–**8** from their donor and acceptor components, as well as S–N bond lengths ($d_{SN}$) of the adducts along with the dipole moments ($\mu$, in Debye) of the sulfur component (acceptor) and of the complex, calculated at the B3LYP/6-31G(2df,p) level of theory. $\Delta e$ is the charge (in electrostatic units) transferred from the donor(s) to the acceptor on adduct formation, based on the NBO atomic charges. The BSSE correction to the reaction energy [kJ mol$^{-1}$] is given in the last-but-one column and is applied to the Gibbs energy at 77 K in the last column.

| Complex | $\Delta E_o$ | $\Delta H°_{298}$ | $\Delta G°_{298}$ | $\Delta H°_{77}$ | $\Delta G°_{77}$ | $d_{SN}$ | $\mu$ (acceptor) | $\mu$ (complex) | $\Delta e$ | BSSE correction | $\Delta G°_{77}$ corrected |
|---|---|---|---|---|---|---|---|---|---|---|---|
| $SO_2{\cdot}NH_3$ (**1**) | –18.1 | –18.1 | +14.6 | –19.7 | –10.9 | 266.3 | 1.55 | 3.83 | 0.08 | +4.9 | –6.0 |
| $SO_2{\cdot}2NH_3$ (**1a**) | –34.0 | –32.3 | +30.3 | –36.5 | –19.1 | 277.1 | 1.55 | 1.20 | 0.10 | +9.3 | –9.8 |
| $SO_2{\cdot}NMe_3$ (**2**) | –51.5 | –50.9 | –7.3 | –53.0 | –41.1 | 241.7 | 1.55 | 4.34[a] | 0.16 | +11.8 | –29.3 |
| $SO_2{\cdot}2NMe_3$ (**2a**) | –86.3 | –82.7 | +0.7 | –88.2 | –64.5 | 257.6 | 1.55 | 2.47 | 0.21 | +20.8 | –43.7 |
| $S_2O{\cdot}NH_3$ (**3**) | –12.2 | –11.6 | +21.0 | –13.6 | –4.5 | 275.5 | 1.30 | 3.78 | 0.08 | +4.9 | +0.4 |
| $S_2O{\cdot}NMe_3$ (**4**) | –48.4 | –47.5 | –1.3 | –49.8 | –37.1 | 246.1 | 1.30 | 4.78 | 0.20 | +12.2 | –24.9 |
| $S_3{\cdot}NH_3$ (**5**) | –7.9 | –6.2 | +21.1 | –8.8 | –0.8 | 295.1 | 0.61 | 3.44 | 0.05 | +4.2 | +3.4 |
| $S_3{\cdot}NMe_3$ (**6**) | –38.4 | –36.5 | +6.9 | –39.5 | –27.1 | 260.7 | 0.61 | 4.67 | 0.22 | +10.9 | –16.2 |
| $SOCl_2{\cdot}NH_3$ (**7**) | +45.1 | +43.1 | +85.0 | +43.3 | +53.7 | 198.0 | 1.35 | 4.71 | 0.39 | +13.6 | +67.3 |
| $SOCl_2{\cdot}NMe_3$ (**8**) | –4.8 | –3.5 | +44.8 | –5.7 | +7.0 | 214.9 | 1.35 | 6.87 | 0.39 | +19.7 | +26.7 |
| $SONH{\cdot}NH_3$ (**9**) | –11.5 | –10.4 | +20.4 | – | – | 293.4 | 1.07 | 2.28 | – | – | – |

[a] Experimental value in the gas phase: 4.800(5) D;[7] estimated experimental value in benzene solution: 4.95 D.[29]

 © 2007 Wiley-VCH Verlag GmbH & Co. KGaA, Weinheim 

good agreement with our calculated data. As expected, the calculated O–S–O bond angle of **1** (117.7°) is slightly smaller than that calculated for $SO_2$ (119.2°) as a result of the higher coordination number at the sulfur atom. Our geometrical data are significantly different from the best previous theoretical results obtained at the MP2/6-31G* level.[3] The S–N bond, for example, is shorter (by 5.8 pm), although the overall conformation is identical. Surprisingly, the binding enthalpy calculated here is practically the same as that reported by Wong and Wiberg.[3] The absolute energies and enthalpies of complexes **1**–**9** and their components are given in Table S2.

The structure of the trimethylamine adduct **2** (Figure 1) is in agreement with previous theoretical calculations. The plane defined by the $SO_2$ unit is almost perpendicular to the $C_3$ axis of the donor $NMe_3$ (angle: 83.5°) and the shortest O···H contact is 266.4 pm. The calculated S–O bond length of 145.8 pm agrees very well with the value derived by Kuczkowski et al. from the microwave spectrum of gaseous **2** [144(1) pm] if the uncertainty of the experimental data is taken into account. These authors reported three S–N distances, depending on the type of data analysis with varying simplifications (232.8, 228.5, and 226.0 pm). The larger S–N bond length of 232.8 pm was derived from a least-squares fit of all isotopic data, although the smallest value [226(3) pm] was eventually recommended.[7] Thus, the "estimated uncertainty" of 3 pm reported by Kuczkowski et al. for the S–N distance may be just a lower limit. We obtained an S–N bond length of 239.6 pm by performing DFT calculations at the higher B3LYP/6-31+G(2df,p) level.

The agreement of the gas-phase structure of **2** with the solid-state structure is rather limited and most of the bond lengths differ considerably. In particular, our calculated S–N bond length of 241.7 pm is much larger than the reported solid state value of 204.6(4) pm.[7] This latter value may, however, be affected by packing forces and by the polar environment (see below) due to the large dipole moment (4.34 D) of this complex (Table 1). The charge transfer from the amine to the $SO_2$ unit can be calculated from the NBO atomic charges as being 0.16 electrostatic units. This value is in line with the upper limit of the charge transfer of 0.2–0.3 electrons estimated by Kuczkowski et al.[7] from the experimental dipole moment (4.80 D) and the nitrogen nuclear quadrupole coupling constants. The NBO charges on the sulfur atom (+1.64) and on the nitrogen atom (–0.50) remain practically constant during the formation of this complex, while the oxygen atoms become more negative, changing from –0.82 in $SO_2$ to –0.90 in **2**. In compensation, the nine hydrogen atoms become slightly more positively charged, changing from an average of +0.22 units in $NMe_3$ to +0.24 in **2**. Thus, the electron density moves essentially from the least electronegative atoms (H) to the most electronegative atoms (O) even though these atoms are far apart from each other. The same situation was found for the other adducts discussed below. It can be concluded from the geometry of complexes **1**–**6** that the charge transfer takes place into the π* molecular orbitals of the acceptor molecule. The binding energy is expected to result from charge delocalization as well as from mutual polarization.

The interaction energy between $SO_2$ and $NMe_3$ in the 1:1 complex **2** was first estimated by Grundnes and Christian in 1968 using the concentration- and temperature-dependence of the optical absorption of this charge-transfer complex near 275 nm in the temperature range 39–60 °C.[14] On the assumption that only a 1:1 complex is formed, even with the large excess of $NMe_3$ used in these experiments, the reaction enthalpy in the gas phase was determined as $-40.6 \pm 1.7$ kJ mol$^{-1}$. Our calculations, which include a BSSE correction, gave a $\Delta H°_{298}$ value of –50.9 + 11.8 = –39.1 kJ mol$^{-1}$ for complex **2** and –61.9 kJ mol$^{-1}$ for the formation of the 1:2 complex **2a** from the three components (Table 1). The agreement between experiment and theory is therefore excellent.

In principle, the structures of **1**, **1a**, **2**, and **2a** are models not only for the nucleophilic attack of an amine on an $SO_2$ molecule but also more generally for the solvation of $SO_2$ by Lewis bases in solution and in the solid state. The calculated structures of the 1:2 adducts $SO_2{\cdot}2NH_3$ (**1a**) and $SO_2{\cdot}2NMe_3$ (**2a**) are shown in Figure 1, and bond angles are given in Table S1. These structures are in agreement with previous predictions.[3] No experimental structures of these species are known. The structure of **1a** ($C_{2v}$ symmetry) is characterized by two rather long S–N bonds (277.1 pm). The coordination sphere at the sulfur atom is pseudo-trigonal-bipyramidal, with the oxygen atoms and the assumed lone pair in the equatorial positions. The two axial S–N bonds are bent slightly towards the formal lone pair position with an N–S–N angle of 174.8°. An analogous structure is predicted for the related complex $SO_2{\cdot}2NMe_3$ (**2a**), which is also of $C_{2v}$ symmetry (Figure 1 and Table S1). The thermodynamic data of **1a** and **2a** are given in Table 1. The corrected Gibbs energies of formation of **1a** and **2a** from the components at 298 K are positive (39.6 and 21.5 kJ mol$^{-1}$, respectively), but the corresponding values at 77 K are negative (–9.8 and –43.7 kJ mol$^{-1}$, respectively). Both complexes are therefore predicted to be stable species in the gas phase only at temperatures well below 0 °C or in the presence of a large excess of the amine donor. The dipole moments of these two species are much smaller than those of the corresponding 1:1 complexes (Table 1).

### *Adducts of $S_2O$*

In the gas phase, disulfur monoxide is most conveniently prepared from thionyl chloride and silver sulfide at low pressures [Equation (1)]:[15]

$$SOCl_2 + Ag_2S \rightarrow S{=}S{=}O + 2\,AgCl \quad (1)$$

This molecule was the first example of a compound containing a formal double bond between heavier main group elements to be isolated in a pure form at 20 °C. Gaseous $S_2O$ is stable for a few days at room temperature at pressures of less than 1 mbar.[16] On condensation, even at liquid nitrogen temperatures, immediate exothermic dispro-

 © 2007 Wiley-VCH Verlag GmbH & Co. KGaA, Weinheim 

portionation and polymerization takes place, with the primary decomposition products being $S_3$ and $SO_2$ [Equation (2)]:[17]

$$2\ S_2O \rightarrow SO_2 + S_3 \quad (2)$$

$\Delta H°_{298} = -49.5\ kJ\,mol^{-1}$, $\Delta G°_{298} = -47.8\ kJ\,mol^{-1}$

We have investigated the structure and properties of the hypothetical adduct $S_2O{\cdot}NH_3$ (**3**), which is predicted to be $C_1$-symmetric with a structure analogous to that of $SO_2{\cdot}NH_3$ (**1**; see Figure 2). Due to the lower positive NBO charge on the central sulfur atom of $S_2O$ (+1.01) compared to $SO_2$ (+1.64), the interaction with Lewis bases is expected to be weaker. Thus, it is not surprising that the S–N bond of **3** is longer (275.5 pm) than that of **1** (266.3 pm). Interestingly, the length of the rather polar S=S bond of free $S_2O$ (190.8 pm) changes only slightly on complex formation with $NH_3$ (by +1.1 pm). The (uncorrected) dissociation enthalpy of **3** is only 11.6 kJ mol$^{-1}$ (Table 1). As a consequence of this weak interaction, the standard Gibbs energy of formation from the two components is positive (21.0 kJ mol$^{-1}$), which means that gaseous **3** is not a stable compound at room temperature.

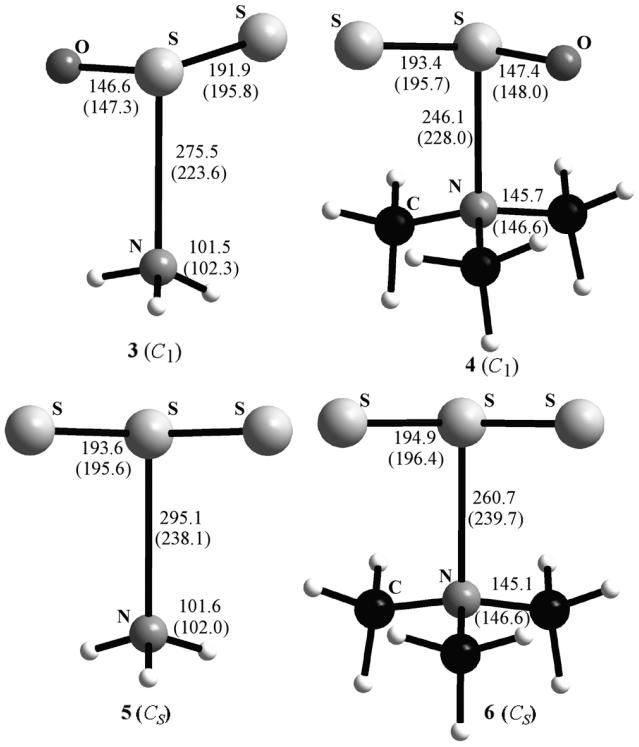


Figure 2. Structures, bond lengths (in pm), and symmetry of the complexes $S_2O{\cdot}NH_3$ (**3**), $S_2O{\cdot}NMe_3$ (**4**), $S_3{\cdot}NH_3$ (**5**), and $S_3{\cdot}NMe_3$ (**6**) in the gas phase. The bond lengths in a polar continuum of dielectric constant $\varepsilon = 40$ are given in parentheses. All data calculated at the B3LYP/6-31G(2df,p) level of theory. See Table S1 (Supporting Information) for bond angles.

The adduct $S_2O{\cdot}NMe_3$ (**4**) was prepared as yellow crystals that are stable only below –30 °C by co-condensation of $S_2O$ and $NMe_3$; its structure is unknown.[15] The calculated structure of **4** is shown in Figure 2 and bond angles are given in Table S1. The S–N bond (246.1 pm) is almost as short as that in $SO_2{\cdot}NMe_3$ (241.7 pm), therefore the interaction is clearly stronger than in the corresponding ammonia complex **3**. As a consequence, the S–S bond length increases by 2.6 pm compared to free $S_2O$ while the S–O bond length increases by only 0.9 pm. Interestingly, the S–N bond dissociation enthalpy of **4** (47.5 kJ mol$^{-1}$) is almost as large as that of the corresponding $SO_2$ adduct **2** (50.9 kJ mol$^{-1}$), whereas the standard Gibbs energy of the dissociation reaction is close to zero (–1.3 kJ mol$^{-1}$) and even becomes positive if a BSSE correction is applied (10.9 kJ mol$^{-1}$). This result explains the reported dissociation of **4** on sublimation in a vacuum. However, the Gibbs energy at 77 K is negative and **4** is expected to be a stable gas-phase species (Table 1).

### *Adducts of $S_3$*

The highly reactive molecule $S_3$ is a component of high-temperature sulfur vapors,[18] although $S_3$ has been isolated in inert matrices at low temperatures and characterized by vibrational and UV/Vis spectroscopy.[19] The structure of $S_3$ has been determined by microwave spectroscopy.[20] As mentioned above, $S_3$ is the primary disproportionation product of $S_2O$. Due to the small positive charge on the central atom of $S_3$ (NBO value: +0.33), adduct formation with $NH_3$ and $NMe_3$ is expected to be relatively weak. However, the structures of the corresponding complexes are analogous to those discussed above. Accordingly, the S–N bond of $S_3{\cdot}NH_3$ (**5**) is much longer (295.1 pm) than in any other adduct investigated in this work (see Table 1 and Figure 2). With the stronger base $NMe_3$, the S–N bond length decreases to 260.7 pm in $S_3{\cdot}NMe_3$ (**6**) (Figure 2). These structural properties are also reflected in the BSSE-corrected S–N bond-dissociation enthalpies, which are only 2.0 kJ mol$^{-1}$ for **5** and 25.6 kJ mol$^{-1}$ for **6** (Table 1). The Gibbs reaction energies for both **5** and **6** are positive at 298 K but negative for **6** at 77 K. In other words, $S_3$ may be stabilized by complex formation with $NMe_3$ at 77 K, in analogy to $S_2O$ (see above). One way to make **6** may be by disproportionation of **4**, in analogy to the reaction shown in Equation (3):

$$2\,S_2O{\cdot}NMe_3\ (\mathbf{4}) \rightarrow SO_2{\cdot}NMe_3\ (\mathbf{2}) + S_3{\cdot}NMe_3\ (\mathbf{6}) \quad (3)$$

This reaction is predicted to be exothermic in the gas-phase by $\Delta H°_{298} = -41.9\ kJ\,mol^{-1}$ ($\Delta G°_{298} = -45.7\ kJ\,mol^{-1}$). It will be shown below that complex **6** is even more stable than in the gas phase at 77 K in a polar continuum.

### *Adducts of $SOCl_2$*

Thionyl chloride vapor reacts violently with gaseous ammonia with elimination of HCl and formation of thionyl imide [OSNH; Equation (4)]:[21]

$$SOCl_2 + 3\,NH_3 \rightarrow O{=}S{=}NH + 2\,NH_4Cl \quad (4)$$

The reaction of $SOCl_2$ with $NH_3$ in solution produces $NH_4Cl$, $S_4N_4$, $NH_4(S_4N_4O)$, and other products.[22] The formation of the adduct $SOCl_2{\cdot}NH_3$ (**7**; Figure 3) may be the first step in these reactions. According to our calcula-

 © 2007 Wiley-VCH Verlag GmbH & Co. KGaA, Weinheim 

tions, this hypothetical molecule adopts an unusual pseudo-trigonal-bipyramidal structure with the chlorine atoms in axial positions. The S–N bond (198.0 pm) is shorter than in any of the other adducts studied in this work. Most remarkable, however, is the fact that the two chlorine atoms are bent towards the two nearest hydrogen atoms with a non-bonding Cl···H contact of just 254.7 pm and a Cl–S–Cl bond angle of 154.0° compared to 98.0° in free $SOCl_2$. Thus, the elimination of two molecules of HCl and formation of OSNH is already pre-organized in the structure of **7**, which has $C_s$ symmetry. Unexpectedly, the S–O bond of **7** is slightly shorter (143.8 pm) than calculated for free $SOCl_2$ (144.3 pm), and the SO stretching wavenumber of **7** is predicted to be larger (1285 $cm^{-1}$) than calculated for $SOCl_2$ (1271 $cm^{-1}$). The shortest O···H contact is 290.7 pm. Evidently, the considerable positive charge on the sulfur atom of $SOCl_2$ (+1.28) and the large negative charge on the nitrogen atom of $NH_3$ (–1.13) are responsible for the formation of a very short and very polar covalent S–N bond.

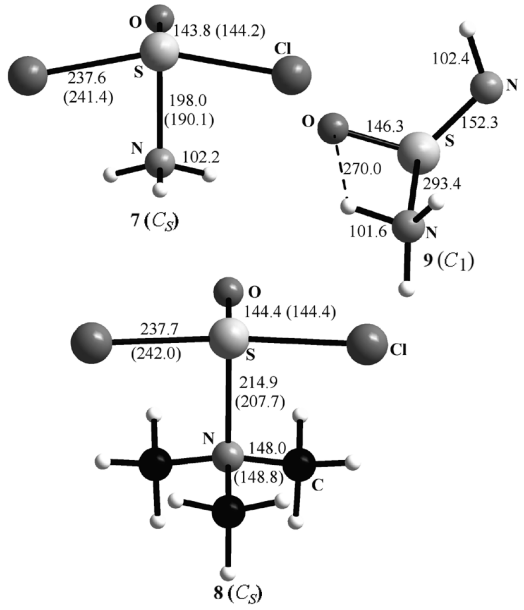


Figure 3. Structures, bond lengths (in pm), and symmetry of the complexes $SOCl_2{\cdot}NH_3$ (**7**), $SOCl_2{\cdot}NMe_3$ (**8**), and $SONH{\cdot}NH_3$ (**9**) in the gas phase. The bond lengths of **7** and **8** in a polar continuum of dielectric constant $\varepsilon = 40$ are given in parentheses. All structures calculated at the B3LYP/6-31G(2df,p) level of theory. See Table S3 (Supporting Information) for bond angles.

However, **7** is not a stable species in the gas phase at 298 K since the binding energy is positive, as is the Gibbs energy of formation from the two components. The energy gained on S–N bond formation is evidently overcompensated by the simultaneous weakening of the two S–Cl bonds, which increase dramatically in length from 212.2 pm in $SOCl_2$ to 237.6 pm in **7**. On the other hand, the NH bond lengths increase by only 0.5 pm. The bond angles of **7** are listed in Table S2.

The formation of gaseous SONH via the hypothetical intermediate Cl–SO–$NH_2$ is exergonic, as shown by the data in Equations (5), (6), and (7):

$$SOCl_2 + NH_3 \rightarrow Cl\text{–}SO\text{–}NH_2 + HCl \quad (5)$$
$$\Delta H°_{298} = -10.2\ kJ\,mol^{-1},\ \Delta G°_{298} = -4.7\ kJ\,mol^{-1}$$

$$Cl\text{–}SO\text{–}NH_2 \rightarrow O{=}S{=}NH + HCl \quad (6)$$
$$\Delta H°_{298} = +20.1\ kJ\,mol^{-1},\ \Delta G°_{298} = -21.2\ kJ\,mol^{-1}$$

$$SOCl_2 + NH_3 \rightarrow O{=}S{=}NH + 2\ HCl \quad (7)$$
$$\Delta H°_{298} = +9.9\ kJ\,mol^{-1},\ \Delta G°_{298} = -25.9\ kJ\,mol^{-1}$$

For comparison, the formation of SONH from $SO_2$ is predicted to be strongly endothermic and endergonic [Equation (8)]:

$$SO_2 + NH_3 \rightarrow O{=}S{=}NH + H_2O \quad (8)$$
$$\Delta H°_{298} = +50.5\ kJ\,mol^{-1},\ \Delta G°_{298} = +51.6\ kJ\,mol^{-1}$$

In contrast to the hypothetical $SOCl_2{\cdot}NH_3$, a compound of composition $SOCl_2{\cdot}NMe_3$ (**8**) has been prepared[15] but its structure is unknown. The predicted structure of gaseous **8** is similar to that of **7** and is also of $C_s$ symmetry (Figure 3; see Table S3 for bond angles). The S–Cl bonds are again quite long (237.7 pm) but the S–N bond (214.9 pm) is considerably longer than in **7** (198.0 pm). The charge difference between N (–0.43) and S (+1.40) is 1.83 units in **8**, which results in a large dipole moment of 6.87 D (Table 1). One can therefore expect this structure to change considerably in a polar environment (see below). All fundamental vibrations of **8** are strongly coupled with other modes. The wavenumber of the S–O stretching mode is predicted to be 1262 $cm^{-1}$, compared to 1271 $cm^{-1}$ calculated for free $SOCl_2$.

Gaseous $SOCl_2{\cdot}NMe_3$ seems to be unstable under standard conditions since the Gibbs energy of the formation reaction is positive. This also holds for a temperature of 77 K if the BSSE correction is taken into account (Table 1). We will show below, however, that the formation of **8** is more favorable in a polar medium.

### *Adduct of SONH*

We have also investigated the structure of a 1:1 adduct of thionyl imide with ammonia, namely $SONH{\cdot}NH_3$ (**9**; see Figure 3). The very long S–N bond (293.4 pm) and the rather small (uncorrected) dissociation enthalpy of 10.4 $kJ\,mol^{-1}$ are surprising since there is an additional O···H bonding interaction between the sulfinyl group and one of the hydrogen atoms of $NH_3$, as can be deduced from the close contact distance of 270.0 pm. This additional interaction can be interpreted as a Coulomb attraction between the positively charged H atom and the π electrons of the almost planar OSNH molecule (O=S=N–H torsion angle: 3.5°) with an H–N–S=O torsion angle of 2.5°. On the other hand, this type of interaction is also known as hyperconjugation between the π electrons of the sulfinyl group and the antibonding σ orbital of the NH bond. The $NH_3$ group is tilted with respect to the S–N single bond as a consequence of this O···H attraction but the N–H bond lengths within the ammonia molecule are all identical (101.6 pm). Because of the small interaction energy of **9** we

 © 2007 Wiley-VCH Verlag GmbH & Co. KGaA, Weinheim 

did not analyze this species any further (see Tables 1 and S2 for more details). Compound **9** may exist as $[NH_4][SON]$ in the solid state.

### *General Considerations*

Analysis of the data in Table 1 reveals that there is an inverse relationship between the formation enthalpies ($\Delta H°_{298}$) of adducts **1**–**8** and the S–N bond lengths, although there is a considerable scattering of the data. No such relationship exists between $\Delta H°_{298}$ and the dipole moments of the acceptors. This is not surprising since the dipole moment vectors of donor and acceptor are almost perpendicular to each other in adducts **1**–**6**. In other words, the dipole–dipole attraction can only be a minor contribution to the interaction energy in these complexes. On the other hand, the charge transfer, $\Delta e$, from donor to acceptor is clearly related to the dissociation enthalpy − a higher $\Delta e$ gives a more negative $\Delta H°_{298}$ (Table 1).

Adduct formation becomes more favorable at low temperatures due to a decrease of the reaction entropy. To study this effect we chose a temperature of 77 K as liquid nitrogen is normally used for cold traps in preparative experiments. The Gibbs energies for the adduct-formation reactions are provided for this temperature in Table 1, assuming all reactants and products still to be gaseous. The data corrected for the BSSE indicate that all adducts except $S_3{\cdot}NH_3$, $SOCl_2{\cdot}NH_3$, and $SOCl_2{\cdot}NMe_3$ are stable at this temperature in the gas phase ($\Delta G°_{77} < 0$).

### Adducts in a Polar Continuum

As outlined above, the transfer of the highly polar adducts **1**–**8** into a polar continuum is expected to result in their stabilization and considerable structural changes, although the polar components are also stabilized in this kind of continuum. Our thermodynamic data calculated at the B3LYP/6-31G(2df,p) level of theory using the polar continuum model (PCM) are summarized in Table 2. The results reveal that all ammonia complexes, with the exception of $SOCl_2{\cdot}NH_3$ (**7**), are expected to be less stable at $\varepsilon = 40$ while all the trimethylamine complexes are predicted to be more stable than in the gas phase. Definitely negative Gibbs energies of formation are predicted at 298 K only for $SO_2{\cdot}NMe_3$ and $S_2O{\cdot}NMe_3$, and these two species do in fact exist as crystalline solids. The reported compound of composition $SOCl_2{\cdot}NMe_3$[15] may therefore have a different structure than assumed in this work. An alternative to the donor–acceptor adduct would be an ionic solid $[Me_3NSOCl]^+Cl^-$ containing a pyramidal coordinated sulfur atom as in $SOCl_2$.

The standard Gibbs energy of formation in the case of $S_3{\cdot}NMe_3$ is close to zero (–0.8 kJ mol$^{-1}$), which means that this adduct may exist at temperatures considerably lower than 25 °C. This prediction is more convincing if one uses the energies of formation of the complexes in the polar continuum but with respect to the *gaseous* components. The corresponding data are presented in Table 3. All complexes except $S_2O{\cdot}NH_3$ and $S_3{\cdot}NH_3$ are thermodynamically stable under standard conditions and with respect to their components, even $SOCl_2{\cdot}NMe_3$. Experimental data are available for the two ammonia complexes of $SO_2$. The reaction enthalpies of the solid adducts from the gaseous components have been determined as $-40 \pm 4$ kJ mol$^{-1}$ for **1** and $-96 \pm 19$ kJ mol$^{-1}$ for **1a** from equilibrium vapor measurements.[1] Our calculations of the reaction enthalpies in the polar continuum but from the gaseous components resulted in enthalpy values of –57.1 and –81.7 kJ mol$^{-1}$, respectively (Table 3), in fair agreement with experiment, especially if the BBSE correction is applied qualitatively.

Table 3. Reaction energies ($\Delta E_o$), enthalpies ($\Delta H°_{298}$), and Gibbs energies ($\Delta G°_{298}$) [G3X(MP2) in kJ mol$^{-1}$] for the formation of the solvated donor–acceptor complexes **1**–**8** in a polar continuum of dielectric constant $\varepsilon = 40$, but from the gaseous components.

| Complex | $\Delta E_o$ (solv-gas) | $\Delta H°_{298}$ (solv-gas) | $\Delta G°_{298}$ (solv-gas) |
|---|---|---|---|
| $SO_2{\cdot}NH_3$ (**1**) | –55.7 | –57.1 | –21.3 |
| $SO_2{\cdot}2NH_3$ (**1a**) | –82.5 | –81.7 | –23.3 |
| $SO_2{\cdot}NMe_3$ (**2**) | –85.6 | –85.5 | –40.0 |
| $SO_2{\cdot}2NMe_3$ (**2a**) | –114.9 | –111.6 | –26.6 |
| $S_2O{\cdot}NH_3$ (**3**) | –37.4 | –39.2 | +2.1 |
| $S_2O{\cdot}NMe_3$ (**4**) | –79.7 | –79.2 | –30.9 |
| $S_3{\cdot}NH_3$ (**5**) | –16.5 | –17.3 | +21.5 |
| $S_3{\cdot}NMe_3$ (**6**) | –62.5 | –61.0 | –15.0 |
| $SOCl_2{\cdot}NH_3$ (**7**) | –44.4 | –46.2 | –4.3 |
| $SOCl_2{\cdot}NMe_3$ (**8**) | –54.0 | –51.6 | –10.6 |

Table 2. Reaction energies, enthalpies, and Gibbs energies [kJ mol$^{-1}$] for the formation of the solvated donor–acceptor complexes **1**–**8** from their components in the gas phase ($\Delta E_o$ only) and in a polar continuum of dielectric constant $\varepsilon = 40$, as well as S–N bond lengths [pm] and dipole moments [D] of the solvated adducts, all calculated at the B3LYP/6-31G(2df,p) level of theory.

| Complex | $\Delta E_o$ (gas) | $\Delta E_o$ (solv) | $\Delta H°_{298}$ (solv) | $\Delta G°_{298}$ (solv) | $d_{SN}$ (solv) | $\mu$ (solv) |
|---|---|---|---|---|---|---|
| $SO_2{\cdot}NH_3$ (**1**) | –31.2 | –15.0 | –16.5 | +21.2 | 235.3 | 6.28 |
| $SO_2{\cdot}2NH_3$ (**1a**) | –50.7 | –21.7 | –20.9 | +39.2 | 262.4 | 3.71 |
| $SO_2{\cdot}NMe_3$ (**2**) | –47.9 | –56.8 | –56.5 | –9.5 | 227.2 | 6.54 |
| $SO_2{\cdot}2NMe_3$ (**2a**) | –73.3 | –77.8 | –74.3 | +12.0 | 251.7 | 3.46 |
| $S_2O{\cdot}NH_3$ (**3**) | –24.1 | –5.2 | –5.3 | +36.1 | 223.6 | 7.71 |
| $S_2O{\cdot}NMe_3$ (**4**) | –42.8 | –57.5 | –57.0 | –8.9 | 228.0 | 7.81 |
| $S_3{\cdot}NH_3$ (**5**) | –15.7 | +9.5 | +8.7 | +47.6 | 238.3 | 7.10 |
| $S_3{\cdot}NMe_3$ (**6**) | –32.0 | –48.2 | –46.8 | –0.8 | 239.7 | 7.90 |
| $SOCl_2{\cdot}NH_3$ (**7**) | +18.3 | –11.8 | –13.9 | +28.5 | 190.1 | 7.20 |
| $SOCl_2{\cdot}NMe_3$ (**8**) | +7.7 | –33.3 | –31.1 | +10.2 | 207.5 | 9.66 |

 © 2007 Wiley-VCH Verlag GmbH & Co. KGaA, Weinheim 

Table 4. Selected fundamental modes of the gaseous adducts **1**–**4** and **6** (wavenumbers in $cm^{-1}$), calculated at the B3LYP/6-31G(2df,p) level of theory (X, Y, Z = O, S). Wavenumbers for the polar continuum of dielectric constant 40 are given in parentheses (ν: stretching mode; δ: bending mode).

| Mode | $SO_2{\cdot}NH_3$ (**1**) | $SO_2{\cdot}NMe_3$ (**2**) | $S_2O{\cdot}NH_3$ (**3**) | $S_2O{\cdot}NMe_3$ (**4**) | $S_3{\cdot}NMe_3$ (**6**) |
|---|---|---|---|---|---|
| $\nu_{SO}$ | 1166/1356 (1134/1275) | 1137/1319 (1099/1249) | 1194 (1149) | 1160 (1118) | – |
| $\nu_{SS}$ | – | – | 671 (630) | 652 (607) | 582/655 (562/599) |
| $\nu_{SN}$ | 131 (165) | 128 (149) | 161 (174) | 133/283[a](155/317)[a] | 97 (121) |
| $\nu_{NC}$ (symm.) | – | 819 (809) | – | 817 (805) | 819 (806) |
| $\delta_{XYZ}$ | 528 (551) | 529 (533) | 385 (365) | 381 (379) | 267 (280) |

[a] Splitting due to coupling with other modes.

The structural changes on transfer of the gaseous complexes into a medium of dielectric constant $\varepsilon = 40$ mainly concern the S–N bonds, which shorten dramatically in adducts **1**–**6** but much less so in the $SOCl_2$ complexes **7** and **8**. Accordingly, the calculated structure of $SO_2{\cdot}NMe_3$ (**2**) at $\varepsilon = 40$ is in much better agreement with the X-ray structure of this complex than the structure predicted for the gas phase. For instance, the calculated S–N bond length decreases from 241.7 pm in the gas phase to 227.2 pm at $\varepsilon = 40$ (a value of 204.6 pm has been derived crystallographically).[7] The O–S–O, O–S–S, and S–S–S bond angles of species **2** all decrease by about 2° in the polar medium (Table S1), and the symmetry of some complexes (e.g., **1**, **1a**, and **8**) is lower in the polar medium ($C_1$) than in the gas phase.

The vibrational spectra also reflect the structural changes of the adducts between the gas phase and the polar continuum. In general, the fundamental modes are strongly coupled due to the low symmetry of the complexes, although a few assignments can be made. The most important vibrations of the acceptor parts of the molecules are given for both phases in Table 4. Thus, while the S–O and S–S stretching vibrations are shifted to lower wavenumbers in the polar continuum, the S–N stretching modes are predicted to appear at higher wavenumbers in the polar phase. For example, the two S–O stretching vibrations of $SO_2$ vary from 1171/1381 $cm^{-1}$ for gaseous $SO_2$, via 1166/1356 $cm^{-1}$ for gaseous $SO_2{\cdot}NH_3$ and 1137/1319 $cm^{-1}$ for gaseous $SO_2{\cdot}NMe_3$, to 1099/1249 $cm^{-1}$ for $SO_2{\cdot}NMe_3$ in the polar continuum. The vibrations of the $NMe_3$ units in complexes **2**, **4**, and **6**, however, are much less affected. For example, the symmetrical stretching mode of the $NC_3$ skeleton always occurs at $818 \pm 1$ $cm^{-1}$ in the gas phase and at $807 \pm 2$ $cm^{-1}$ in the polar continuum, whereas the bending modes of the acceptors do not show any uniform shift on transfer of the gaseous complexes into the polar continuum.

## Conclusions

According to our G3X(MP2) calculations, the structures of the adducts $SO_2{\cdot}NH_3$ (**1**), $SO_2{\cdot}2NH_3$ (**1a**), $SO_2{\cdot}NMe_3$ (**2**), $SO_2{\cdot}2NMe_3$ (**2a**), $S_2O{\cdot}NH_3$ (**3**), $S_2O{\cdot}NMe_3$ (**4**), $S_3{\cdot}NH_3$ (**5**), $S_3{\cdot}NMe_3$ (**6**), $SOCl_2{\cdot}NH_3$ (**7**), $SOCl_2{\cdot}NMe_3$ (**8**), and $SONH{\cdot}NH_3$ (**9**) correspond to energy minima on the corresponding potential hypersurfaces. However, only **2** and **4** are thermodynamically stable in the gas phase under standard conditions with respect to their acceptor and donor components ($\Delta G°_{298} < 0$). The latter two complexes have, in fact, been prepared as solid materials. Species **2**, **4**, and **6** are predicted to be stable in a polar continuum of dielectric constant $\varepsilon = 40$. Thus, the preparation of $S_3{\cdot}NMe_3$ can be expected in the future. All species except **3** and **5** are thermodynamically stable if the equilibrium between the gaseous components and the adduct in the polar continuum is analyzed. The structures of complexes **3**–**9** have been calculated for the first time. The structural changes on complex formation as well as the vibrational spectra indicate a weakening of the bonds in the acceptor molecule, in particular in the polar continuum. On the other hand, the donor–acceptor interaction is stronger in the polar environment than in the gas phase and, as a consequence, the S–N bond lengths are shorter under such circumstances.

## Computational Details

The structures and energies of the various complexes were examined according to G3X(MP2) theory[23] using the GAUSSIAN 03[24] program package. This composite method corresponds effectively to QCISD(T)/G3XL//B3LYP/6-31G(2df,p) energy calculations together with zero-point vibrational and isogyric corrections. The G3X(MP2) theory represents a modification of the G3(MP2)[25] theory with three important changes: (1) B3LYP/6-31G(2df,p) geometry, (2) B3LYP/6-31G(2df,p) zero-point energy, and (3) addition of a *g* polarization function to the G3Large basis set for the second-row atoms at the Hartree–Fock level. All three features are particularly important for the correct description of the sulfur-containing species examined in this work. Harmonic fundamental vibrations were calculated at the B3LYP/6-31G(2df,p) level to characterize stationary points as equilibrium structures, with all frequencies real. A charge density analysis was performed for all investigated species using the natural bond orbital (NBO) approach based on the B3LYP/6-31G(2df,p) wavefunction.[26] NBO atomic charges of small molecules have recently been demonstrated to agree well with experimental values obtained from X-ray diffraction data.[27] As far as gas-phase species are concerned, all relative energies and enthalpies reported in the text correspond to the G3X(MP2) level, while all reported structural parameters correspond to the B3LYP/6-31G(2df,p) level. The correction to the basis set superposition error (BSSE) was calculated at the MP2/GTMP2Large level using the counterpoise method of the GAUSSIAN 03 program. Since this correction is calculated with fixed monomer geometries, taken from the complexes, the obtained data must be considered as upper limits, especially if there is a strong deformation, as is the case for the thionyl chloride complexes.

 © 2007 Wiley-VCH Verlag GmbH & Co. KGaA, Weinheim 

The investigated complexes are characterized by large dipole moments, therefore it is to be expected that the thermodynamics of formation of such species in the solid state and in polar solvents will be quite different from that in the gas phase. Calculations according to Tomasi's polar continuum model (PCM)[28] were carried out at the B3LYP/6-31G(2df,p) level to study the influence of a polar environment. This method of studying the electrostatic solute/solvent interaction has proven to be very successful in reproducing solvent effects as the solvent is represented by a continuous dielectric, characterized by a given dielectric constant ($\varepsilon$), and the solute is assumed to be embedded in a cavity in the medium. The permanent dipole of the solute induces a dipole in the medium, which in turn interacts with the molecular dipole leading to stabilization. A dielectric constant of 40.0 was used for the PCM calculations to represent the polar medium. No such calculations on complexes **1**–**8** have been reported so far.

**Supporting Information** (see footnote on the first page of this article): Absolute energies, bond angles, and atomic coordinates of compounds **1**–**8**.

## Acknowledgments

We appreciate invaluable advice from Prof. Ming Wah Wong (Richard), Singapore, and support from the Norddeutscher Verbund für Hoch- und Höchstleistungsrechnen (HLRN).

[1] R. Landreth, R. G. de Pena, J. Heicklen, *J. Phys. Chem.* **1974**, *78*, 1378. Earlier work (W. D. Scott, D. Lamb, *J. Am. Chem. Soc.* **1970**, *92*, 3943) seems to be in error since the derived enthalpies of dissociation are much too large.
[2] C. S. Cass, B. S. Ault, *J. Phys. Chem.* **1984**, *88*, 432.
[3] M. W. Wong, K. B. Wiberg, *J. Am. Chem. Soc.* **1992**, *114*, 7527.
[4] For older theoretical calculations, see: a) R. R. Lucchese, K. Haber, H. F. Schaefer, *J. Am. Chem. Soc.* **1976**, *98*, 7617; b) J. E. Douglas, P. A. Kollman, *J. Am. Chem. Soc.* **1978**, *100*, 5226. The theoretical levels in these investigations are much lower and in some cases rigid geometries based on experimental data were used for the components of the complexes.
[5] A. B. Burg, *J. Am. Chem. Soc.* **1943**, *65*, 1629.
[6] D. van der Helm, J. D. Childs, S. D. Christian, *J. Chem. Soc. C* **1969**, 887.
[7] J. J. Oh, M. S. LaBarge, J. Matos, J. W. Kampf, K. W. Hillig, R. L. Kuczkowski, *J. Am. Chem. Soc.* **1991**, *113*, 4732.
[8] J. Grundnes, S. D. Christian, *J. Am. Chem. Soc.* **1968**, *90*, 2239.
[9] J. Grundnes, S. C. Christian, V. Cheam, S. B. Farnham, *J. Am. Chem. Soc.* **1971**, *93*, 20.
[10] R. R. Lucchese, K. Haber, H. F. Schaefer, *J. Am. Chem. Soc.* **1976**, *98*, 7617.
[11] J. E. Douglas, P. A. Kollman, *J. Am. Chem. Soc.* **1978**, *100*, 5226.
[12] S. Sakaki, H. Sato, Y. Imai, K. Morokuma, K. Ohkubo, *Inorg. Chem.* **1985**, *24*, 4538.
[13] a) P. W. Schenk, R. Steudel, *Z. Anorg. Allg. Chem.* **1966**, *342*, 265; b) P. W. Schenk, R. Steudel, *Angew. Chem.* **1963**, *75*, 793; *Angew. Chem. Int. Ed. Engl.* **1963**, *2*, 685.
[14] J. Grundnes, S. D. Christian, *J. Am. Chem. Soc.* **1968**, *90*, 2239.
[15] a) P. W. Schenk, R. Steudel, *Z. Anorg. Allg. Chem.* **1966**, *342*, 253; b) P. W. Schenk, R. Steudel, *Angew. Chem.* **1964**, *76*, 97; *Angew. Chem. Int. Ed. Engl.* **1964**, *3*, 61.
[16] Review: R. Steudel, *Top. Curr. Chem.* **2003**, *231*, 203.
[17] a) R. Steudel, *Eur. J. Inorg. Chem.* **2004**, 3513; b) J. Nakayama, S. Aoki, J. Takayama, A. Sakamoto, Y. Sugihara, A. Ishi, *J. Am. Chem. Soc.* **2004**, *126*, 9085.
[18] Review: R. Steudel, Y. Steudel, M. W. Wong, *Top. Curr. Chem.* **2003**, *230*, 117.
[19] Review: B. Eckert, R. Steudel, *Top. Curr. Chem.* **2003**, *231*, 31.
[20] M. C. McCarthy, S. Thorwirth, C. A. Gottlieb, P. Thaddeus, *J. Am. Chem. Soc.* **2004**, *126*, 4096.
[21] P. W. Schenk, *Ber. Detsch. Chem. Ges.* **1942**, *75B*, 94.
[22] a) R. Steudel, *Z. Naturforsch. Teil B* **1969**, *24*, 934; b) R. Steudel, P. Luger, H. Bradaczek, *Angew. Chem.* **1973**, *85*, 307; *Angew. Chem. Int. Ed. Engl.* **1973**, *12*, 316.
[23] L. A. Curtiss, P. C. Redfern, K. Raghavachari, J. A. Pople, *J. Chem. Phys.* **2001**, *114*, 108.
[24] M. J. Frisch, G. W. Trucks, H. B. Schlegel, G. E. Scuseria, M. A. Robb, J. R. Cheeseman, V. G. Zakrzewski, J. A. Montgomery Jr, R. E. Stratmann, J. C. Burant, S. Dapprich, J. M. Millam, A. D. Daniels, K. N. Kudin, M. C. Strain, O. Farkas, J. Tomasi, V. Barone, M. Cossi, R. Cammi, B. Mennucci, C. Pomelli, C. Adamo, S. Clifford, J. Ochterski, G. A. Petersson, P. Y. Ayala, Q. Cui, K. Morokuma, D. K. Malick, A. D. Rabuck, K. Raghavachari, J. B. Foresman, J. Cioslowski, J. V. Ortiz, A. G. Baboul, B. B. Stefanov, G. Liu, A. Liashenko, P. Piskorz, I. Komaromi, R. Gomperts, R. L. Martin, D. J. Fox, T. Keith, M. A. Al-Laham, C. Y. Peng, A. Nanayakkara, C. Gonzalez, M. Challacombe, P. M. W. Gill, B. Johnson, W. Chen, M. W. Wong, J. L. Andres, C. Gonzalez, M. Head-Gordon, E. S. Replogle, J. A. Pople, *GAUSSIAN 98*, Gaussian Inc., Pittsburgh, PA, **1998**.
[25] L. A. Curtiss, P. C. Redfern, K. Raghavachari, V. Rassolov, J. A. Pople, *J. Chem. Phys.* **1999**, *110*, 4703.
[26] A. E. Reed, L. A. Curtiss, F. Weinhold, *Chem. Rev.* **1988**, *88*, 899.
[27] M. Messerschmidt, A. Wagner, M. W. Wong, P. Luger, *J. Am. Chem. Soc.* **2002**, *124*, 732.
[28] a) S. Miertus, E. Scrocco, J. Tomasi, *Chem. Phys.* **1981**, *55*, 117; b) S. Miertus, J. Tomasi, *Chem. Phys.* **1982**, *65*, 239; c) M. Cossi, V. Barone, R. Cammi, J. Tomasi, *Chem. Phys. Lett.* **1996**, *255*, 327.
[29] J. A. Moede, C. Curran, *J. Am. Chem. Soc.* **1949**, *71*, 852.

Received: April 11, 2007
Published Online: July 31, 2007

 © 2007 Wiley-VCH Verlag GmbH & Co. KGaA, Weinheim

**The EUChemSoc Societies have taken the significant step into the future by merging their traditional journals, to form two leading chemistry journals, the *European Journal of Inorganic Chemistry* and the *European Journal of Organic Chemistry*. Three further EUChemSoc Societies (Austria, Czech Republic and Sweden) are Associates of the two journals.**

## COVER PICTURE

**The cover picture shows** the shearing-like distortion, which was found to play a dominant role in the control of magnetic properties of $Cu^{II}$ azido complexes. From ab initio calculations, it was demonstrated that the smaller the shearing amplitude, the larger the antiferromgnetic character. A practical route to enhance ferromagnetism is suggested in the light of this theoretical analysis. Details are discussed in the article by D. Luneau, V. Robert et al. on p. 4434ff.

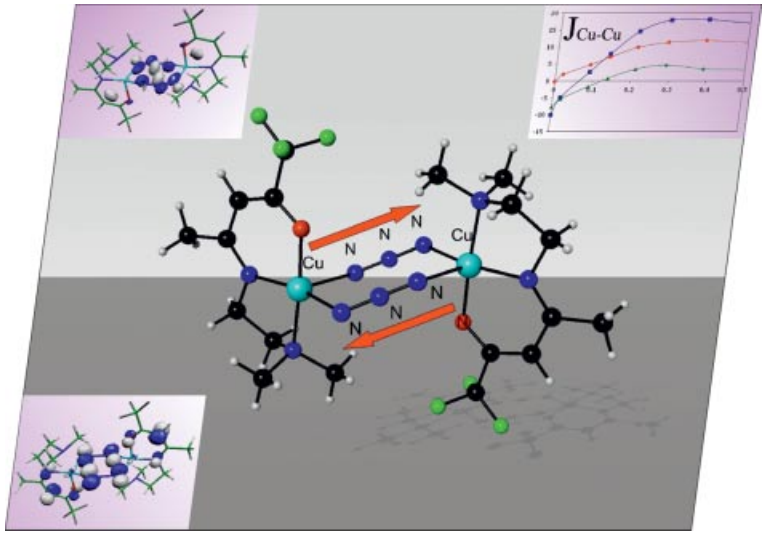


 © 2007 Wiley-VCH Verlag GmbH & Co. KGaA, Weinheim

**The EUChemSoc Societies have taken the significant step into the future by merging their traditional journals, to form two leading chemistry journals, the *European Journal of Inorganic Chemistry* and the *European Journal of Organic Chemistry*. Three further EUChemSoc Societies (Austria, Czech Republic and Sweden) are Associates of the two journals.**

## COVER PICTURE

**The cover picture shows** the shearing-like distortion, which was found to play a dominant role in the control of magnetic properties of $Cu^{II}$ azido complexes. From ab initio calculations, it was demonstrated that the smaller the shearing amplitude, the larger the antiferromgnetic character. A practical route to enhance ferromagnetism is suggested in the light of this theoretical analysis. Details are discussed in the article by D. Luneau, V. Robert et al. on p. 4434ff.

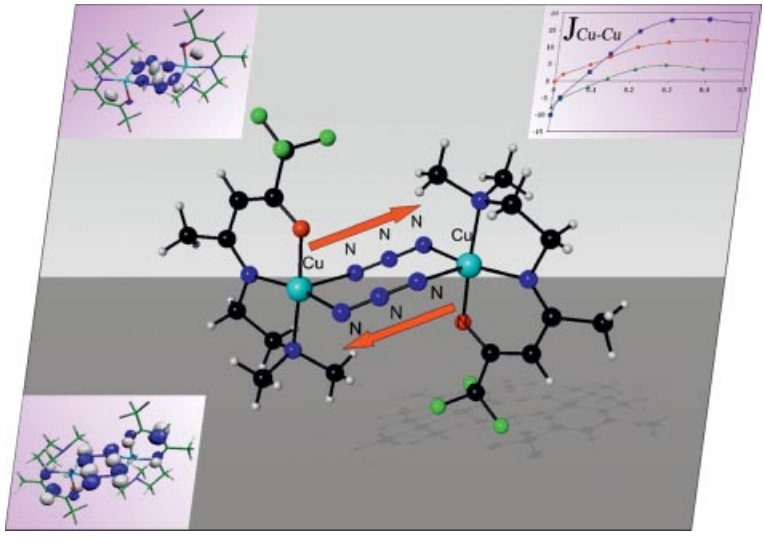


 © 2007 Wiley-VCH Verlag GmbH & Co. KGaA, Weinheim 

# CONTENTS

## MICROREVIEW


### Hydrogen on Metal Clusters

**A. S. Weller,* J. S. McIndoe* ... 4411–4423**

Reversible Binding of Dihydrogen in Multimetallic Complexes

**Keywords:** Hydrides / Homogeneous catalysis / Heterogeneous catalysis / Cluster compounds / Hydrogen


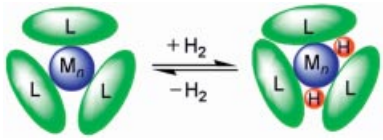


The reversible attachment of hydrogen to metal complexes, especially multimetallic systems, constitutes a technologically and academically important area ranging from commodity chemical synthesis (catalysis) through to the storage of hydrogen. In this contribution, the binding of dihydrogen in multimetallic cluster complexes is reviewed.

## SHORT COMMUNICATION


### Halogen-Bridged $Ni^{III}$ Nanowires

**H. Ohtsu,* S. Takaishi, K. Imamura, A. Ishii, K. Tanaka, M. Hasegawa, M. Yamashita* ..... 4425–4428**

Remarkable Functions of Long-Chain Alkyl Groups in Halogen-Bridged Nickel(III) Nanowire Complexes

**Keywords:** Nickel / Nanostructures / Long-chain alkyl groups / Average-valent compounds / Thin films


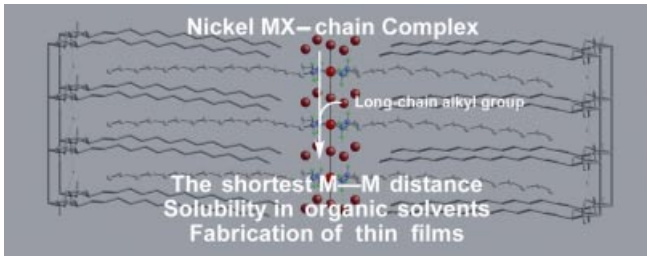


The long-chain alkyl groups of new bidentate ligands make it possible to generate nickel MX–chain complexes exhibiting the shortest $Ni^{III}$–$Ni^{III}$ distance among all MX–chain compounds reported. Dissolution in organic solvents occurs without dissociation of the MX–chain units, and the successful fabrication of thin films is reported.

## FULL PAPERS


### Tellurostannates

**E. Ruzin, W. Massa, S. Dehnen* ..... 4429–4433**

Treating $[K_4(H_2O)_{0.5}][SnTe_4]$ with $PPh_4^+$ or $AsPh_4^+$: Formation of a Highly Air-Stable Tellurostannate Salt, a Tellurolate with One-Coordinate Te Atoms, and a Polytelluride Salt with $^{\infty}_{1}[Te_4(H_2O)_2]^{2-}$ Chains

**Keywords:** Arsonium salts / Phosphonium salts / Tellurolate / Tellurostannate / Polytelluride / X-ray diffraction


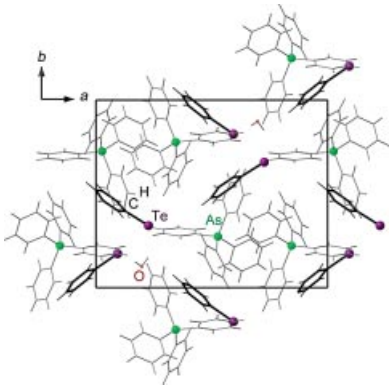


Beyond a simple cation exchange! By treating orthotellurostannates with $EPh_4Cl$ (E = P, As), one obtains air-stable tellurodistannate **1** by partial replacement of the strongly interacting $K^+$ by the much more weakly interacting $[PPh_4]^+$ cations, or telluropheno late **2** (see figure) with a one-coordinate Te atom upon As–C bond cleavage. Oxidation of the air-sensitive $[Sn_2Te_6]^{4-}$ and $Te^{2-}$ anions in solution produces tetratelluride salt **3** with strands of $H_2O$-bridged $[Te_4]^{2-}$ units.

## Molecular Magnetism

Prediction of the magnetic properties of binuclear $Cu^{II}$ compounds containing asymmetric azide bridges remains a challenge. A combination of correlated ab initio calculations and the analysis of the experimental data shows that the asymmetry of the coordination of the azido bridge is a determining factor in the tuning of the coupling constant value.

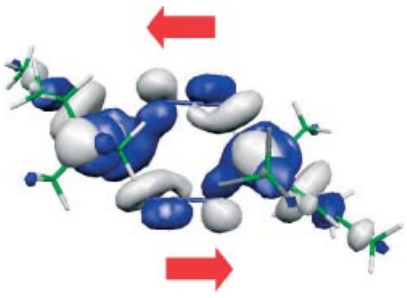

**M. Angels Carvajal, C. Aronica, D. Luneau,* V. Robert* ..... 4434–4437**

Shearing-Like Distortion in Binuclear End-to-End $Cu^{II}$ Azido Compounds: An Ab Initio Study of the Magnetic Interactions

**Keywords:** Magnetic properties / Azido bridge / Ab initio calculations

## Selenium Microwires

The formation of Se microwire networks by hydrothermal treatment in tungstosilicic acid solution is described. The kinetics of crystallization of the Se assembly is studied as a function of reaction time.

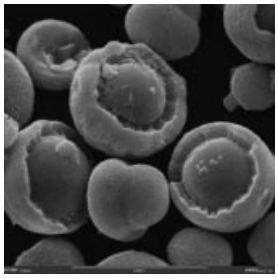

**L. Yang, Y. Shen,* A. Xie, J. Liang ..... 4438–4444**

Oriented Attachment Growth of Three-Dimensionally Packed Trigonal Selenium Microspheres into Large-Area Wire Networks

**Keywords:** Nanostructures / Self-assembly / Selenium

## Zirconocene Complexes

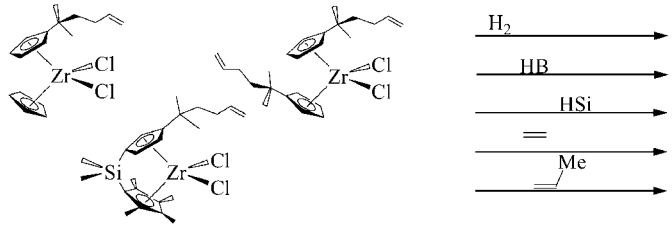


New zirconocene and *ansa*-zirconocene complexes containing pendant alkenyl substituents and their respective hydrogenation, hydroboration and hydrosilylation products have been studied as catalysts for ethylene and propylene polymerisation.

**S. Gómez-Ruiz, D. Polo-Cerón, S. Prashar,* M. Fajardo, A. Antiñolo, A. Otero ..... 4445–4455**

Synthesis and Reactivity of Alkenyl-Substituted Zirconocene Complexes and Their Application as Olefin Polymerisation Catalysts

**Keywords:** Zirconium / Metallocenes / Polymerisation / Homogeneous catalysis / Cyclopentadienyl ligands

## Inorganic Reaction Mechanisms

The kinetics of the process $AuCl_3(am) + Cl^- \rightarrow AuCl_4^- + am$ (am = pyridines with different π systems and $sp^3$ amines) have been studied in methanol at 25 °C. The reactivity of the considered N-donors is different and follows the order $sp^3$ N-donors > "normal" pyridines > "π-extended" pyridines. This result, with the support of ground-state DFT calculations on the $AuCl_3(am)$ derivatives, is explained on the basis of an Au–N bond enforcement due to an increased π-back-donation contribution.

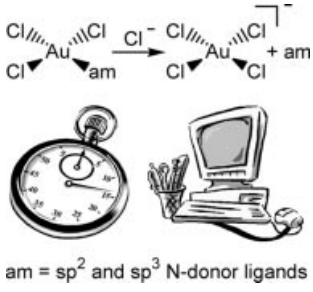


**B. Pitteri,* M. Bortoluzzi ..... 4456–4461**

Displacement of Neutral Nitrogen Donors by Chloride in $AuCl_3(am)$ (am= Pyridines and Amines): Kinetics and DFT Calculations Show the Effects of Basicity and π-Acceptor Ability

**Keywords:** Gold / Kinetics / Nitrogen donors / Reaction mechanisms / DFT

 © 2007 Wiley-VCH Verlag GmbH & Co. KGaA, Weinheim 

# CONTENTS


## [Fe-only] Hydrogenase Models

**J. Windhager, H. Görls, H. Petzold, G. Mloston, G. Linti,* W. Weigand* ..... 4462–4471**

Reactions of 1,2,4-Trithiolanes with Nonacarbonyldiiron: Sulfurdithiolatodiiron and -tetrairon Complexes as Mimics for the Active Site of [Fe-only] Hydrogenase

**Keywords:** Iron / Cluster compounds / S ligands / Hydrogenases / Density functional calculations

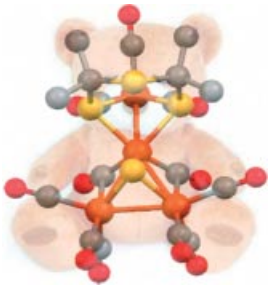

The synthesis of novel structural models for the active site of [Fe-only] hydrogenase is described starting from 1,2,4-trithiolane and its derivatives. The products are characterised by spectroscopic methods and X-ray structure analyses. Density functional calculations are reported for a representative example of the unusual tetranuclear iron clusters formed.

## SOD Mimics

**F. Cisnetti, A.-S. Lefèvre, R. Guillot, F. Lambert, G. Blain, E. Anxolabéhère-Mallart, C. Policar* ..... 4472–4480**

A New Pentadentate Ligand Forms Both a Di- and a Mononuclear $Mn^{II}$ Complex: Electrochemical, Spectroscopic and Superoxide Dismutase Activity Studies

**Keywords:** Manganese(II) / Enzyme models / SOD mimic / N,O ligands / Bioinorganic chemistry

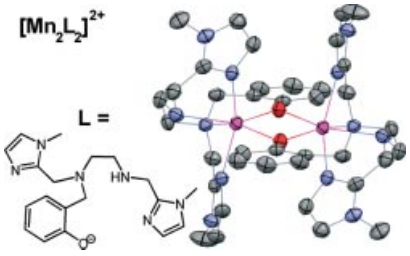


A new 1,2-ethanediamine-centered pentadentate ligand that contains imidazole and phenol moieties is presented and a dinuclear $Mn^{II}-Mn^{II}$ complex of this ligand characterized (X-ray diffraction, electrochemistry, EPR spectroscopy). This complex forms a mononuclear complex, whose SOD-like activity has been evaluated, in aqueous solution.

## Spin-Crossover in $Fe^{II}$ Complexes

**M. Seredyuk, A. B. Gaspar,* M. C. Muñoz, M. Verdaguer, F. Villain, P. Gütlich* ..... 4481–4491**

Cooperative Spin-Crossover Behaviour in Polymeric 1D $Fe^{II}$ Coordination Compounds: $[\{Fe(tba)_3\}X_2]\cdot nH_2O$

**Keywords:** Spin crossover / Bistability / Cooperative effects / Iron(II) complexes / Substituted triazoles

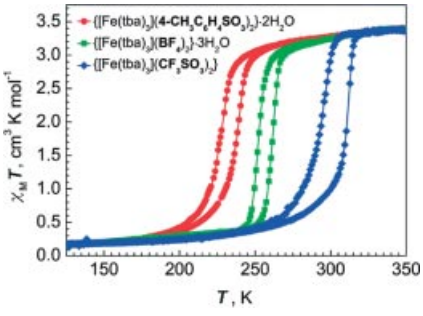


The synthesis and physical characterisation of new 1D cooperative spin-crossover polymers with general formula $[\{Fe(tba)_3\}X_2]\cdot nH_2O$ [tba = *N*-(4*H*-1,2,4-triazol-4-yl)benzamide; X = $CF_3SO_3^-$, $BF_4^-$ and $4\text{-}CH_3C_6H_4SO_3^-$] is reported.

## C–C Coupling

**Z.-X. Wang,* Z.-Y. Chai ..... 4492–4499**

Palladium(II) and Nickel(II) Complexes Bearing N,N,O-Chelate Ligands: Syntheses, Characterization and Catalysis in Heck and Kumada Coupling Reactions

**Keywords:** N,N,O ligands / Palladium / Nickel / Chelates / Homogeneous catalysis / C–C coupling

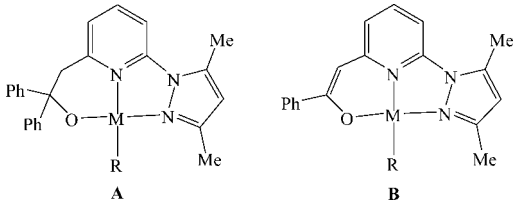


Novel N,N,O-tridentate ligands and their nickel and palladium complexes **A** and **B** are synthesized and characterized, and the catalytic behavior of these complexes in the Heck and Kumada reactions is evaluated.


 © 2007 Wiley-VCH Verlag GmbH & Co. KGaA, Weinheim 

## Proton-Coupled Electron Transfer

**S. Das, S. Mukhopadhyay* ... 4500–4507**

Oxidation of $N^{III}$ and $N^{-I}$ by an $\{Mn_4O_6\}^{4+}$ Core in Aqueous Media: Proton-Coupled Electron Transfer

**Keywords:** Kinetics / Mechanisms / Manganese / Oxidation / Nitrogen

$[Mn_4(\mu\text{-}O)_6(bipy)_6]^{4+}$ ($\mathbf{1}^{4+}$) and the oxo-bridged protonated species $\mathbf{1}H^{5+}$ quantitatively oxidise nitrite and hydroxylamine to nitrate and nitrous oxide, respectively, with $\mathbf{1}H^{5+}$ reacting much faster. A hydrogen atom transfer (HAT) mechanism (1e, $1H^+$; electroprotic) seems feasible ($R_{Red}$ = $N^{III}$ or $N^{-I}$, $R_{Ox}$ = $N^{V}$ or $N^{I}$, bipy = 2,2′-bipyridine).

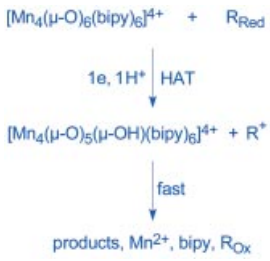


## Indium Oxyhydroxides

**L. Chen, X. Ma, Y. Liu, Y. Zhang, W. Wang, Y. Liang, Z. Zhang* ..... 4508–4513**

3D Architectures of InOOH: Ultrasonic-Assisted Synthesis, Growth Mechanism, and Optical Properties

**Keywords:** Indium / Mechanism / UV/Vis spectroscopy / Solvothermal synthesis

InOOH with a hierarchical 3D architecture assembled from uniform single-crystalline nanowires was synthesized by an ultrasonic-assisted solvothermal route.

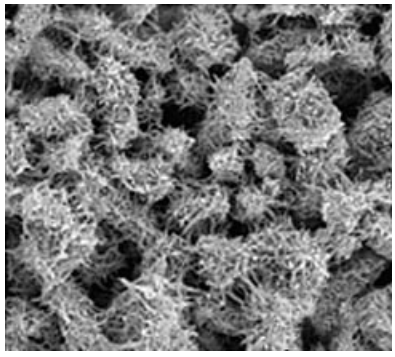

## Dichalcogens

**L. Du, L. Yao, M. Ge* ..... 4514–4519**

Two Novel Species, (Methoxycarbonyl)-sulfenyl Thiocyanate and (Methoxycarbonyl)sulfenyl Selenocyanate: Spectroscopic Characterization by Photoelectron Spectroscopy, and Quantum Chemical Investigation

**Keywords:** Ab initio calculations / Dichalcogens / Electronic structure / Photoelectron spectroscopy

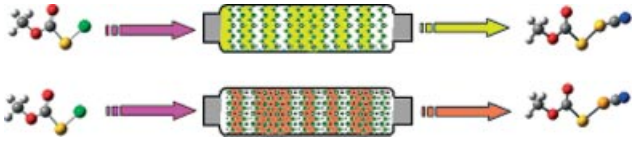

Two novel dichalcogens, $CH_3OC(O)SSCN$ and $CH_3OC(O)SSeCN$, have been generated in a convenient way by gas–solid reactions between $CH_3OC(O)SCl$ and AgSCN or AgSeCN. Photoelectron spectroscopy and theoretical calculations have been performed to investigate their electronic and geometrical structure. Their HOMOs correspond to the electron mainly localized on the S 3p or Se 4p lone pair MOs: $\{38a(n_{S(SCN)})\}^{-1}$ and $\{47a(n_{Se})\}^{-1}$, respectively.

## Metal Phosphonates

**Z.-Y. Du, H.-B. Xu, X.-L. Li, J.-G. Mao* ..... 4520–4529**

A New Approach to Novel Cluster Compounds of Lead(II) Phosphonates

**Keywords:** Lead / Sulfonate-phosphonates / Solvothermal synthesis / Cluster compounds

Five new lead(II) sulfonate-phosphonates, namely $[Pb_3(L)_2(H_2O)_2]\cdot 4H_2O$ (**1**), $[Pb(HL)(phen)]\cdot H_2O$ (**2**), $[Pb_6(L)_4(phen)_8]\cdot 3H_2O$ (**3**), $[Pb_6(L)_4(phen)_{10}]\cdot 2H_2O$ (**4**), and $[Pb_6(L)_4(4,4'\text{-bipy})(H_2O)_2]\cdot 2H_2O$ (**5**; $H_3L$ = *m*-$HO_3S$-$C_6H_4$-$PO_3H_2$), have been prepared and structurally characterized. They exhibit novel 0D, 2D, or 3D structures. Compounds **3** and **4** are the first cage compounds of $Pb^{II}$ phosphonates.

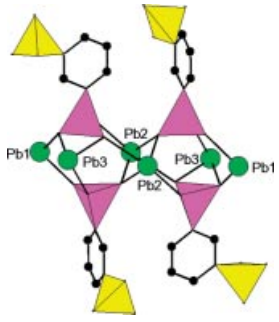


 © 2007 Wiley-VCH Verlag GmbH & Co. KGaA, Weinheim 

# CONTENTS

## Boron Hydrides

**O. Ciobanu, P. Roquette, S. Leingang, H. Wadepohl, J. Mautz, H.-J. Himmel* ..... 4530–4534**

Synthesis and Characterization of a New Guanidine–Borane Complex and a Dinuclear Boron(II) Hydride with Bridging Guanidinate Ligands

**Keywords:** Hydrides / Boron / Low oxidation states / Hydrogen elimination

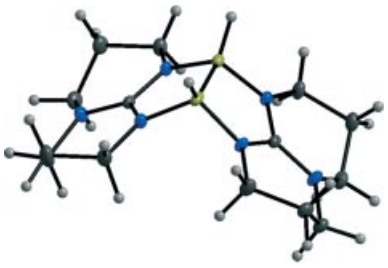

Dihydrogen elimination from a guanidine–borane complex followed by dimerization and further $H_2$ elimination leads to the formation of a new dinuclear $B^{II}$ hydride.

## Isolated $LiO_2$ Cation

**E. Barnea, C. Averbuj, M. Kapon, M. Botoshansky, M. S. Eisen* ..... 4535–4540**

Synthesis and Crystal Structure of New Early-Lanthanide Organometallic Clusters

**Keywords:** Organolanthanide halide clusters / Lithium / Bridging ligands

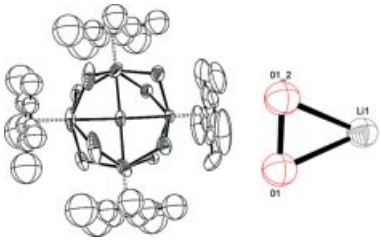


Lanthanide clusters are formed when catecholborane reacts with the corresponding $Cp^*_2LnCl{\cdot}LiCl$ (Ln = Nd, Sm). For Nd, in the presence of oxygen, a tetranuclear anion containing the isolated $LiO_2$ cationic motif is formed.

**If not otherwise indicated in the article, papers in issue 27 were published online on September 10, 2007**

 © 2007 Wiley-VCH Verlag GmbH & Co. KGaA, Weinheim 

# SPOTLIGHTS …

## *Reaction Mechanisms*

X. Lin, C. Zhao, C.-M. Che,* Z. Ke, D. L. Phillips

**A DFT Study on the Mechanism of $Rh_2^{II,II}$-Catalyzed Intramolecular Amidation of Carbamates**

*Chem. Asian J.*
DOI: **10.1002/asia.200700068**

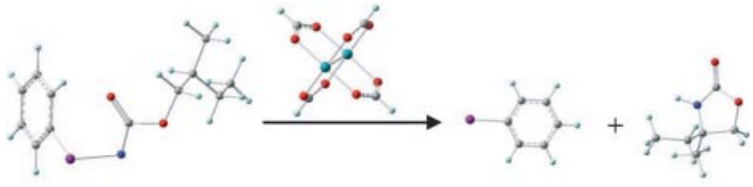

**Alone yet together**: DFT calculations elucidate the catalytic process of a dirhodium tetracarboxylate catalyzed intramolecular C–H bond-amidation reaction. Out of six reaction pathways that involve a metal–nitrene complex, the singlet concerted pathway that produces the product with retention of chirality at C is predicted to be the predominant one.

## *Biomineralization*

S. Matsunaga, R. Sakai,* M. Jimbo, H. Kamiya

**Long-Chain Polyamines (LCPAs) from Marine Sponge: Possible Implication in Spicule Formation**

*ChemBioChem*
DOI: **10.1002/cbic.200700305**

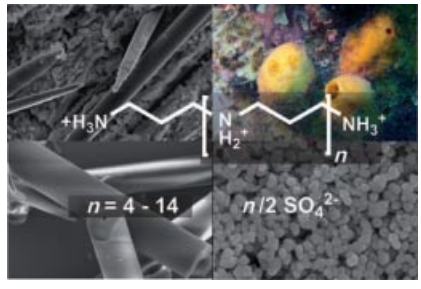


**LCPAs in sponge spicules** relate two distinct marine organisms, diatoms and sponges, by "silica deposition". LCPA-directed silica deposition has been proposed for the formation of silica walls in diatoms, while other chemical factors have been suggested for sponges. Here we show that LCPAs can be an additional factor involved in spiculogenesis in the sponge.

## *Dielectrophoretic Trapping*

M. Kumemura,* D. Collard,* C. Yamahata, N. Sakaki, G. Hashiguchi, H. Fujita

**Single DNA Molecule Isolation and Trapping in a Microfluidic Device**

*ChemPhysChem*
DOI: **10.1002/cphc.200700268**

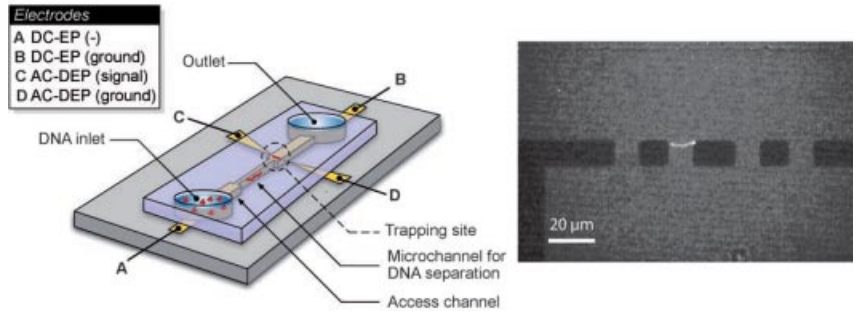


**DNA bridges:** A double stranded $\lambda$-DNA molecule is isolated by dc electrophoresis and trapped by ac dielectrophoresis between aluminium electrodes in a microfluidic chip [see device (left) in figure and DNA bridge between electrodes (right)]. This single-molecule trapping technique is highly effective, allowing long DNA fragments to be instantly captured in stretched formation.

## *Inhibitor Design*

A. Thiry,* B. Masereel, J.-M. Dogné, C. T. Supuran, J. Wouters, C. Michaux

**Exploration of the Binding Mode of Indanesulfonamides as Selective Inhibitors of Human Carbonic Anhydrase Type VII by Targeting Lys91**

*ChemMedChem*
DOI: **10.1002/cmdc.200700057**

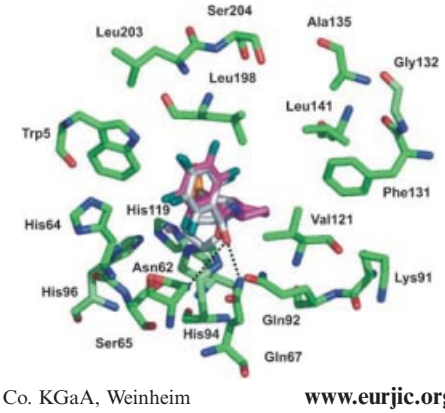


**The binding mode** of (*R*)- (magenta) and (*S*)-1-pentafluorophenylamido-5-sulfonamide (light gray) inside the human carbonic anhydrase VII active site is shown. A shared hydrogen bond between the carbonyl group of each compound and Gln67 and Asn62 is observed. To increase hCA VII selectivity, structural modifications of these compounds are proposed in order to design new anticonvulsant agents.

 © 2007 Wiley-VCH Verlag GmbH & Co. KGaA, Weinheim 

# … ON OUR SISTER JOURNALS

EurJIC European Journal of Inorganic Chemistry

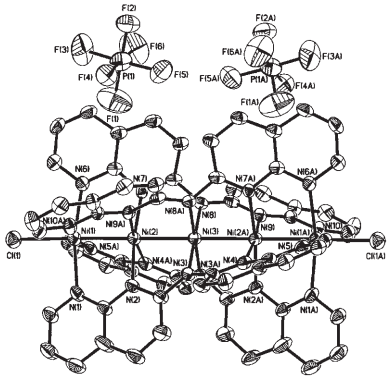

**Metal string!** The first linear nickel framework in which the usual sequence of $Ni^{II}$ atoms has been reduced by two electrons is presented. The electronic structure of the metal framework appears intermediate between a localized picture corresponding to $Ni^{II}$-$Ni^{I}$-$Ni^{II}$-$Ni^{I}$-$Ni^{II}$ and a fully delocalized model represented as $(Ni_2)^{3+}$-$Ni^{II}$-$(Ni_2)^{3+}$.

## *Mixed-Valent Compounds*

I. P.-C. Liu, M. Bénard,* H. Hasanov, I.-W. P. Chen, W.-H. Tseng, M.-D. Fu, M.-M. Rohmer, C.-h. Chen, G.-H. Lee, S.-M. Peng*

**A New Generation of Metal String Complexes: Structure, Magnetism, Spectroscopy, Theoretical Analysis, and Single Molecular Conductance of an Unusual Mixed-Valence Linear $[Ni_5]^{8+}$ Complex**

*Chem. Eur. J.*
DOI: **10.1002/chem.200700750**

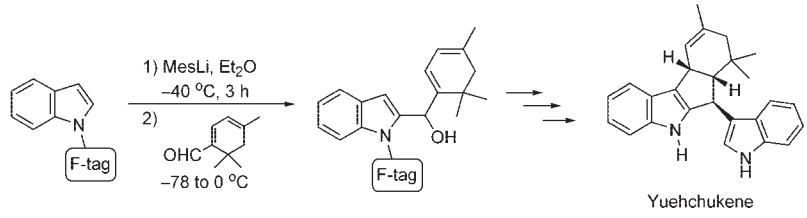


Mesityllithium was found to be a suitable reagent for the α-lithiation of perfluoroalkyl-tagged 1-(arylsulfonyl)-indole, and the fluorous synthesis of yuehchukene was accomplished efficiently using this method as a key step.

## *Lithiation of Fluorous-Tagged Indole*

H. Naka, Y. Akagi, K. Yamada, T. Imahori, T. Kasahara, Y. Kondo*

**Fluorous Synthesis of Yuehchukene by α-Lithiation of Perfluoroalkyl-Tagged 1-(Arylsulfonyl)indole with Mesityllithium**

*Eur. J. Org. Chem.*
DOI: **10.1002/ejoc.200700525**

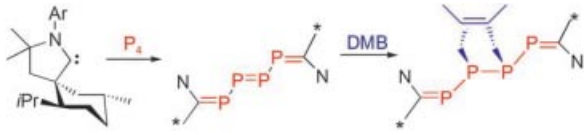


**Broken down and added onto**: An enantiomerically pure cyclic (alkyl)-(amino)carbene cleanly activates $P_4$, affording highly reactive products that can be further used for the diastereoselective construction of $P_4$-containing molecules that feature phosphorus–carbon bonds (see scheme; DMB = 2,3-dimethylbutadiene; portions of the products have been omitted, * denotes stereogenic carbon center).

## *$P_4$ Activation*

J. D. Masuda, W. W. Schoeller, B. Donnadieu, G. Bertrand*

**Carbene Activation of $P_4$ and Subsequent Derivatization**

*Angew. Chem. Int. Ed.*
DOI: **10.1002/anie.200703055**

On these pages, we feature a selection of the excellent work that has recently been published in our sister journals. If you are reading these pages on a computer, click on any of the items to read the full article. Otherwise please see the DOIs for easy online access through Wiley InterScience.

 © 2007 Wiley-VCH Verlag GmbH & Co. KGaA, Weinheim 

DOI: 10.1002/ejic.200700661

# Reversible Binding of Dihydrogen in Multimetallic Complexes

**Andrew S. Weller*[a][‡] and J. Scott McIndoe*[b]**

**Keywords:** Hydrides / Homogeneous catalysis / Heterogeneous catalysis / Cluster compounds / Hydrogen

The interaction of hydrogen with metal surfaces is one of the most important and fundamental processes in the chemical industry. Hydrogen is also strongly tipped to play a central role in new challenges that are emerging in terms of climate change and energy supply, and the reversible binding of $H_2$ to suitable materials will play a keystone role in the realisation of the hydrogen economy. The reversible interaction of hydrogen with multimetallic centres is also an important theme in biological processes; the role of hydrogenases in the metabolism of $H_2$ is an example. Thus the reversible interaction of $H_2$ with multimetallic metal complexes is an area that spans considerable breadth. This review is concerned with the reversible interaction of $H_2$ with soluble multimetallic complexes, defined broadly as clusters, in which there are no other ligands lost or gained in the process. The review is organised under the subheadings: equilibrium reversible ($H_2$ is lost upon removal of the $H_2$ atmosphere), thermally reversible or reversible when placed under vacuum, photochemically reversible and electrochemically reversible interactions; a brief outline of reversible $H_2$ binding in systems of biological interest; giant metal clusters that display reversible $H_2$ binding.
(© Wiley-VCH Verlag GmbH & Co. KGaA, 69451 Weinheim, Germany, 2007)

## Introduction

The interaction of hydrogen with metal surfaces is one of the most important and fundamental processes in the chemical industry. Catalytic hydrogenations are the largest chemical reactions by volume, as all crude oil is treated with $H_2$ in desulfurisation, while ammonia production from $N_2$ and $H_2$ over an iron oxide catalyst produces ammonia fertiliser on a multimillion tonne scale per year. Both of these processes involve heterogeneous metal catalysts and accordingly the interaction of hydrogen with a metal surface. Hydrogen is also strongly tipped to play a central role in new challenges that are emerging in terms of climate change and energy supply, in that it is a valuable future fuel that when burnt (either in a combustion engine or a fuel cell) releases only water. It is widely accepted that the realisation of the

[a] Department of Chemistry, University of Bath, Bath, BA2 7AY, UK
[b] Department of Chemistry, University of Victoria, P. O. Box 3065, Victoria, BC V8W 3V6, Canada
E-mail: mcindoe@uvic.ca
[‡] New address (from September 2007): Department of Chemistry, Chemistry Research Laboratory, University of Oxford, Mansfield Road, Oxford OX1 3TA, UK
E-mail: andrew.weller@chem.ox.ac.uk

*Andrew Weller completed his first degree at the University of Warwick and his PhD at the University of Bristol (1994) under the supervision of Dr John Jeffery. After postdoctoral positions with Professor Alan Welch (Heriot-Watt University) and Professor Thomas Fehlner (University of Notre Dame) he returned to the UK and took up a Royal Society University Research Fellowship at the University of Bath in 1999. He was promoted to Reader in 2004. In September 2007 he moved to the Department of Chemistry University of Oxford. His research broadly covers synthetic organometallic chemistry, catalysis and structure and bonding. Major research themes in his group are: (i) the synthesis of high-hydride-content rhodium clusters (and their precursors) and (ii) the transition-metal chemistry of low-coordinate cationic late-transition-metal complexes, especially those incorporating weakly coordinating anions, for use in catalysis and C–H/C–C activation processes.*

*Scott McIndoe was born and educated in New Zealand. He completed his DPhil in synthetic (in)organometallic chemistry at the University of Waikato under the supervision of Professor Brian Nicholson. In 1998, he won a New Zealand Foundation for Research, Science & Technology Postdoctoral Fellowship and joined the group of Professor Brian Johnson FRS at the University of Cambridge (UK). In 2000, he took up a college lectureship, teaching at Trinity and Newnham Colleges, Cambridge, and continued his research in the Department of Chemistry. Three years later he moved to his current position, as assistant professor in the Department of Chemistry at the University of Victoria, where his research group uses mass spectrometry as a rapid discovery tool in organometallic chemistry and catalysis.*

 © 2007 Wiley-VCH Verlag GmbH & Co. KGaA, Weinheim 

"hydrogen economy"[1] will require breakthroughs in the crucial area of efficient storage of hydrogen accompanied with favourable charge/discharge kinetics and operating temperatures.[2] Although they are not the only possible solution, metal complexes of hydrogen could well make important contributions to the realisation of this goal; even though it is highly unlikely that a practicable solution to store $H_2$ would involve metal complexes from the second or third rows with attached ligands – a consequence of the combined factors of very low %H content and cost. The study of the reversible interaction of hydrogen with metal surfaces and other materials is an area that has been occupying molecular and solid-state chemists, surface scientists and physicists for many years, and the level of interest in this field remains high.

This review is concerned with the reversible interaction of $H_2$ with well-defined multimetallic soluble complexes, defined broadly as clusters. Reversibility in this context suggests that there is no other change in formulation to the cluster material on addition or removal of $H_2$, meaning that there must be no other ligands lost or gained in the process. The consequence of this stipulation is that reversible uptake of $H_2$ in multimetallic systems without ligand displacement must occur on a molecule that has available low lying orbitals to take up the bonding pairs of $H_2$ – in other words the system must be formally electronically (and most likely coordinatively) unsaturated or have access to such a state by ligand or metal-core rearrangement. The review limits itself to well-defined molecular systems, venturing briefly into nearly monodisperse nanoclusters but avoiding larger metal particles, surfaces and bulk metals except for the purpose of comparison.

## Hydrogen–Transition-Metal Bonding

Hydrogen may either chemisorb on a metal surface as atomic hydrogen or physisorb as an intact $H_2$ molecule. Both have parallels in molecular cluster chemistry: metal hydrides and metal dihydrogen complexes, respectively. Detecting hydrogen bound to a metal surface is not straightforward and requires the use of a limited set of high-vacuum techniques, such as electron energy loss spectroscopy (EELS) or scanning tunnelling microscopy (STM).[3] Information obtained from such experiments shows that on a metal(111) surface atomic hydrogen adsorbs to form a monolayer of hydrogen at 37 K, and the H atoms are chemisorbed on threefold face-centred cubic sites, positioned in the hollows between the metal atoms. Binding of intact $H_2$ to nanoclusters and metal surfaces is rare because of the preferential formation of hydrides,[4,5] although there is evidence for dihydrogen bound to a Ni(510) surface.[6] In the molecular realm, the interaction of atomic hydrogen with metal clusters (hydride ligands) is very well documented, and there are literally thousands of examples of metal hydride cluster species.[7] By contrast, the coordination of molecular hydrogen in complexes with multimetallic systems is considerably less common, and to the best of our knowledge only a handful of examples exist in which a relatively reliable indicator such as a short $T_1$ relaxation time associated with the bound dihydrogen has been reported.[8–12]

The exemplar for dihydrogen coordination to soluble metal complexes remains the original Kubas complex $W(PR_3)_2(CO)_3$ (R = Cy, *i*Pr), in which an agostic C–H–M interaction from a bulky cyclohexyl group provides light stabilisation of the metal centre, allowing for an operationally unsaturated 16-electron complex. Addition of $H_2$ displaces this interaction to form the, now classic, complex $W(PR_3)_2(CO)_3(\eta^2\text{-}H_2)$ (R = Cy, *i*Pr) (Scheme 1). Placing this compound under a non-hydrogen atmosphere or vacuum removes the bound $H_2$ and re-establishes the agostic C–H bond.[5,13] These dihydrogen complexes are also in equilibrium in solution with the tautomeric dihydride forms (the dihydrogen complexes are favoured), and the $\Delta G^{\ddagger}$ for this oxidative addition of $H_2$ has been estimated to be 60 kJ mol$^{-1}$. The equilibrium demonstrates an important point in that even though a dihydride is observed as the major (or often the only) species by NMR spectroscopy and X-ray crystallography, a low-energy pathway to a coordinated dihydrogen ligand can allow for the loss of $H_2$. If the resulting complex is stabilised in the absence of $H_2$ by either steric bulk and/or agostic interactions, then the molecule is available to take up $H_2$ again without decomposition. Examples of $H_2$ loss in mononuclear complexes where the resulting molecule is unstable and dimerises to relieve the unsaturation are known, but we do not focus on these here.[10]

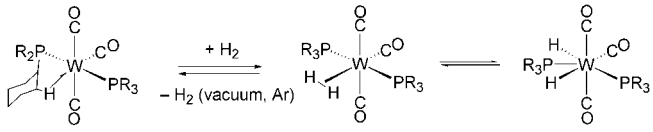


Scheme 1. R = Cy.

Although examples of multimetallic complexes where dihydride and dihydrogen complexes are in slow equilibrium with one another are not known, computational and experimental studies indicate that such a transformation is likely to have a comparable barrier to those determined for mononuclear complexes. For example, the rapid H/D exchange in $CpRu(\mu\text{-}H)_4RuCp$ on addition of $D_2$ is calculated as passing through a dihydrogen transition state with a rate-determining barrier of less than 80 kJ mol$^{-1}$.[14] The dihydride complex $Re_2H(\mu\text{-}H)(CO)_9$ irreversibly loses $H_2$ above 253 K and is a highly fluxional molecule, exchanging hydride sites through a low-energy process (Scheme 2).[15] NMR spectroscopic data ($T_1$ measurements) suggest a dihydride structure; however, experimental and theoretical studies are in close agreement and show that the barrier for exchange through a dihydrogen intermediate is only 23 and 27 kJ mol$^{-1}$, respectively. $(\eta^2\text{-}H_2)$(isoPFA)$Ru(\mu\text{-}Cl)_2(\mu\text{-}H)$-$RuH(PPh_3)_2$ undergoes rapid exchange between dihydrogen and bridging dihydride ligands at 20 °C (barrier 53 kJ mol$^{-1}$)[8,16] as do related chelated phosphane complexes[12] and the cluster $[Ru_4(\eta^6\text{-}C_6H_6)_4H_6]^{2+}$,[11] both of which have a mixture of dihydrogen and dihydride ligands

 © 2007 Wiley-VCH Verlag GmbH & Co. KGaA, Weinheim 

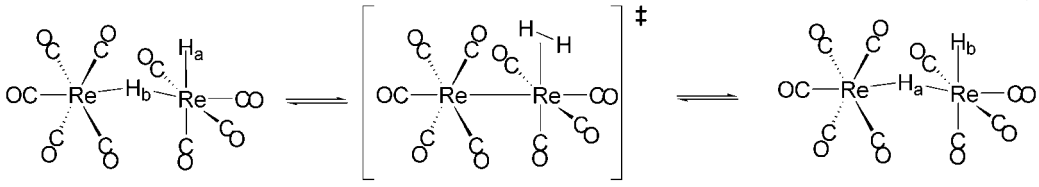

Scheme 2.

as characterised by $T_1$ relaxation time measurements by NMR spectroscopy at low temperature. The iridium dimer $Ir_2(PiPr_3)_2(pz)_2(H)_2(\mu\text{-}H)(\eta^2\text{-}H_2)$ is suggested to have a dihydrogen ligand that undergoes rapid exchange with a terminal hydride, with a barrier of 32 kJ mol$^{-1}$.[17] Mechanisms for hydride/dihydrogen exchange have recently been reviewed in the more general sense of exchange mechanisms in sigma complexes.[18]

In mononuclear complexes hydrogen is found either as a hydride ligand (H) or as dihydrogen ($\eta^2$-$H_2$). The H–H distance defines the difference between a true $H_2$ complex (0.8–1.0 Å) and a dihydride (> 1.6 Å),[5] with intermediate H–H lengths described as elongated $H_2$ complexes or compressed dihydrides.[19] In polynuclear metal clusters, however, hydrogen may occupy a variety of different positions with respect to the metal centres that are not available to mononuclear complexes, including bridging, face-bridging and interstitial locations (Figure 1).

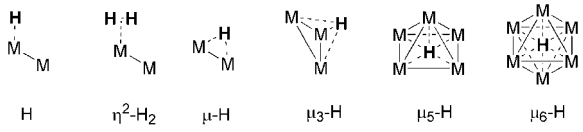


Figure 1. Hydrogen bonding modes observed in cluster complexes; terminal hydride (H), dihydrogen complex ($\eta^2$-$H_2$), bridging hydride (μ-H), face-bridging hydride ($\mu_3$-H) and interstitial hydrides ($\mu_5$- and $\mu_6$-H).

Neutron diffraction studies are the definitive structural answer to the exact mode of hydrogen coordination, and all of the cluster-only ($\mu_n$-) binding modes have been unambiguously characterised by this method; examples include (**μ-H**)$Ru_3(CO)_9(\mu_3\text{-}\eta^2\text{-}CCCMe_3)$,[20] (**$\mu_3$-H**)$_4Co_4(\eta^5\text{-}C_5Me_4Et)_4$,[21] [(**$\mu_5$-H**)$_2Rh_{13}(CO)_{24}$]$^{3-}$[22] and [(**$\mu_6$-H**)$Ru_6(CO)_{18}$]$^-$.[23] However, terminal hydride and dihydrogen ligands are sufficiently rare in cluster chemistry, and they remain uncharacterised by neutron diffraction. An unusually well-characterised example of a bimetallic species with a dihydrogen ligand is ($\eta^2$-$H_2$)(isoPFA)Ru(μ-Cl)$_2$(μ-H)RuH($PPh_3$)$_2$ (isoPFA = {$\eta^5$-$C_5H_5$}Fe($\eta^5$-$C_5H_3$($CHMeNMe_2$)-$PiPr_2$}), which was investigated by X-ray crystallography and variable-temperature $^1$H- and $^{31}$P-NMR spectroscopy.[8] The structure (Figure 2) is notable for having three different binding modes of H present in one structure. The NMR spectroscopic data for this compound revealed fast exchange between the $\eta^2$-$H_2$ and the μ-H at 20 °C and a slower exchange of these three hydrogen atoms with the terminal hydride.

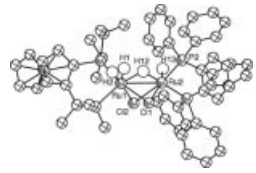

Figure 2. X-ray crystal structure of ($\eta^2$-$H_2$)(isoPFA)Ru(μ-Cl)$_2$(μ-H)RuH($PPh_3$)$_2$.[8]

In almost all instances, addition of hydrogen to a metal cluster is preceded or accompanied by ligand dissociation to generate a coordinatively and electronically unsaturated[24] cluster to which $H_2$ can be added. For example, addition of $H_2$ to $Os_3(CO)_{12-n}(NCMe)_n$ ($n$ = 1,2) occurs by NCMe dissociation and addition of $H_2$ to form $Os_3(CO)_{10}$-(μ-H)$_2$.[25] For unsaturated metal clusters, often decorated with bulky phosphane ligands such as $PtBu_3$, $PCy_3$ and $PiPr_3$, ligand dissociation is not a prerequisite for addition of $H_2$. These ligands provide a steric shield around the metal centre that prevents ligands other than the smallest molecules, such as $H_2$, from easily entering the coordination sphere of the cluster (see Figure 3). Thus these clusters are *kinetically* stabilised with respect to addition of further ligands. As will be shown, these unsaturated complexes often have low-lying unoccupied molecular orbitals that show small HOMO–LUMO gaps and are well set up for uptake of electrons from the $H_2$ bonding pairs.

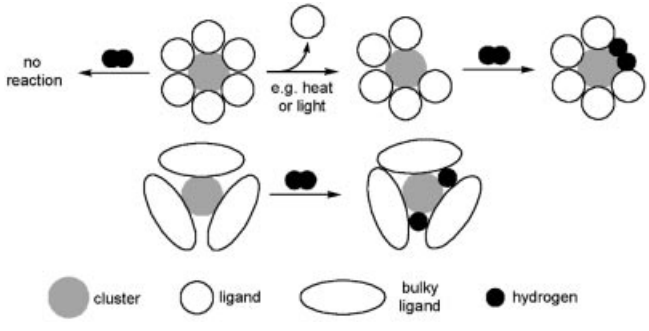


Figure 3. Cartoon showing (top) how most multimetallic compounds require ligand loss prior to hydrogen binding and (bottom) how electronically unsaturated compounds with bulky ligands escape this requirement and can frequently bind hydrogen reversibly without significant structural change.

 © 2007 Wiley-VCH Verlag GmbH & Co. KGaA, Weinheim 

## Equilibrium Reversible ($H_2$ Is Lost upon Removal of the $H_2$ Atmosphere)

Many unsaturated multimetallic complexes add $H_2$ to give hydride species, but often this is a reversible process, and removal of the $H_2$ atmosphere regenerates the starting material. Given that hydrogen addition and loss are clearly low-energy processes, in these examples it is not surprising to find that many of these complexes also undergo rapid H/D exchange when placed under a $D_2$ atmosphere.

Muetterties, and later Fryzuk, reported that addition of $H_2$ to the unsaturated (28 electrons) dimeric complexes $[L_2Rh_2(\mu\text{-}H)_2]$ (**1a**–**e**) (L = $i$Pr$_2$P(CH$_2$)$_n$P$i$Pr$_2$ $n$ = 2 **1a**; 3 **1b**; 4 **1c**;[26] L = P$i$OPr$_3$ **1d**, L = POMe **1e**[27]) results in the complexes $[L_2Rh_2(\mu\text{-}H)_3H]$ (**2a**–**e**), which are best formulated as having $Rh^{III}/Rh^{I}$ metal centres and have been characterised spectroscopically.[26] For the chelating ligand **2c** with the largest bite angle, the extra hydrides are held quite firmly – even under vacuum – and require an acceptor (1-hexene) to remove $H_2$. For the ligands **2a** and **2b** with smaller bite angles, the hydrogen is lost on removal of the $H_2$ atmosphere. The ligand in **2c** presumably shields the metal centres more effectively and kinetically blocks $H_2$ loss. This reasoning we will return to later, and steric blocking seems important in both the generation and stabilisation of hydrogen-rich complexes. Large ligands block the approach of additional large ligands that would satisfy the metal cluster electronically, resulting in unsaturation at the metal centre, and only the smallest molecule, $H_2$, is allowed access to the metal centre. Accordingly, for the monodentate phosphite species **2d** and **2e** that show less shielding of the metal centres, hydrogen addition is reversible on application of vacuum.[27] Iridium dimers, with stronger M–H bonds, are stable with four hydrides, e.g. $L_2Ir_2(\mu\text{-}H)_3H$ L = $(C_2F_5)_2PCH_2CH_2P(C_2F_5)_2$ ("dfepe") (**3**), but reversibly take up an extra equivalent of $H_2$ to afford $[(dfepe)Ir(H)_2(\mu\text{-}H)]_2$ (**4**), which has two terminal and one bridging hydride ligands per metal centre. The $H_2$ is lost rapidly when the $H_2$ atmosphere is removed to regenerate **3**.[28]

Addition of $H_2$ to 30-electron $Ir_2(t\text{Bu}_2\text{PH})_2(CO)_2(H)(\mu\text{-P}t\text{Bu}_2)$ (**5**) results in the generation of the 32-electron dimetallic complex $Ir_2(t\text{Bu}_2\text{PH})_2(CO)_2(H)_3(\mu\text{-P}t\text{Bu}_2)$ (**6**), in which two hydrides bridge the Ir–Ir connectivity. $T_1$ values from NMR spectroscopy indicated a dihydride, rather than a dihydrogen, structure. This addition is reversible, both in solution and in the solid state, and **6** loses $H_2$ when placed under vacuum or exposed to a $N_2$ purge.[29] The unsaturated, thiol-bridged bimetallic rhodium complex $[Rh(triphos)(\mu\text{-}S)]_2[BPh_4]_2$ (**7**) [triphos = MeC(CH$_2$PPh$_2$)$_3$] reacts with $H_2$ to give $[Rh(triphos)H(\mu\text{-}SH)]_2[BPh_4]_2$ (**8**), in which $H_2$ has undergone heterolytic $H_2$ cleavage[30] to form a Rh-hydride and a {μ-SH} group, presumably via a coordinated dihydrogen intermediate. Removing the $H_2$ under a stream of argon regenerates **7**.[31] Although a dihydrogen intermediate has not been isolated, NMR spectroscopic studies indicate stepwise addition of $H_2$, sequentially at each Rh centre. DFT calculations support this, with a calculated barrier to reversible $H_2$ loss of 35.1 kcal mol$^{-1}$.[32] These complexes also model the reversible, heterolytic cleavage of $H_2$ in hydrogenase enzymes.

Reversible $H_2$ gain and loss is reported for the heterometallic, 58-electron, formally unsaturated cluster, $Os_3Pt(\mu\text{-}H)_2(CO)_{10}(PCy_3)$ (**9**), which adds $H_2$ at high pressure (200 atm) to give the electron-precise, 60-electron cluster $Os_3Pt(\mu\text{-}H)_4(CO)_{10}(PCy_3)$ (**10**). Purging with $N_2$ reforms the starting material.[33]

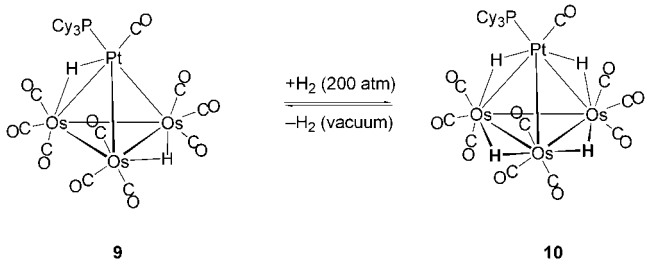


**9** **10**

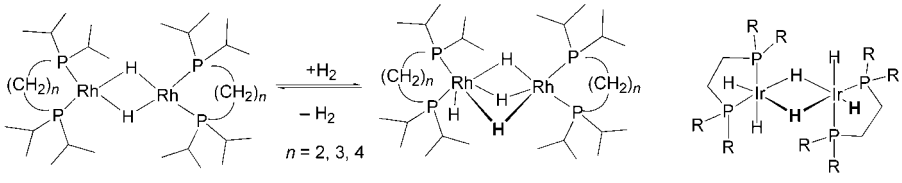


**1a,b,c** **2a,b,c** **4**

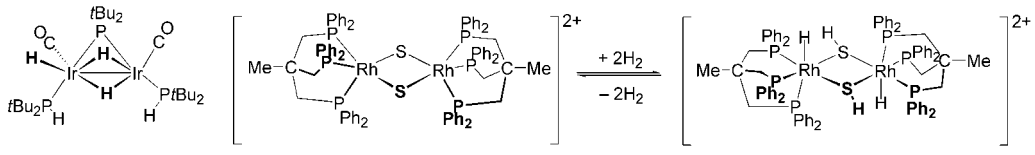


**6** **7** **8**

 © 2007 Wiley-VCH Verlag GmbH & Co. KGaA, Weinheim 

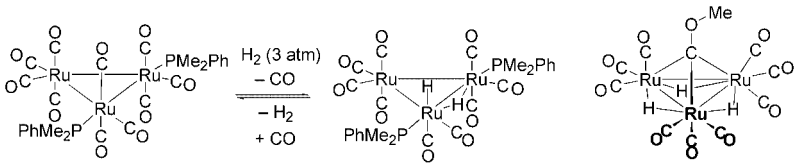


**11** **12** **14**

Duckett, Dyson and Johnson have reported the reversible addition of $H_2$ to a triruthenium cluster $Ru_3(CO)_{10}(PMe_2Ph)_2$ (**11**), which gives a mixture of two exchanging isomers of the product of $H_2$ addition, both of which have a terminal and a bridging hydride (e.g. **12**). On removal of the $H_2$ atmosphere these complexes disappear, suggesting that the $H_2$ binding is reversible. Varying the $H_2$ concentration affords thermochemical data for this process and shows that an equilibrium is established for $H_2$ addition. Interestingly, the mechanism of $H_2$ addition, as well as the exchange of the isomers, invokes a heterolysis of a Ru–Ru bond and an $\eta^2$-$H_2$ ligand bound at a coordinatively unsaturated Ru centre.[34] Reversible addition of $H_2$ to ruthenium carbonyl clusters, $Ru_3H(\mu\text{-}COMe)(CO)_{10}$ (**13**) by displacement of CO to form $Ru_3H_3(\mu\text{-}COMe)(CO)_{10}$ (**14**) has been reported by Keister. Kinetic experiments suggest that the rate-determining step is oxidative addition of $H_2$ at one of the metal centres after CO loss.[35] Reversible addition of $H_2$/CO (at 6.2 bar, 60 °C) to the $Rh^I$ complex *rac*-$[Rh_2(CO)_4(L)][BF_4]_2$, which does not have a Rh–Rh bond, affords the spectroscopically characterised $[Rh^{II}]_2$ dimer *rac*-$[Rh_2H_2(\mu\text{-}CO)_2(CO)_2(L)][BF_4]_2$ [L = $(Et_2PCH_2CH_2)P(Ph)CH_2P(Ph)CH_2CH_2PEt_2$].[36]

Platinum- and palladium-gold clusters such as $[Pt(AuPPh_3)_8][NO_3]_2$ (**15**) have been shown to be excellent catalysts for $H_2/D_2$ equilibration to form HD. The mechanism proposed invokes reversible addition of both $H_2$ and $D_2$ to the metal cluster to afford metal hydride species,[37] which have been observed experimentally to form reversibly on addition of $H_2$.[38] A theoretical analysis suggests that activation occurs at the platinum centre, with dihydrogen and dihydride tautomers being close in energy – consistent with the rapid HD exchange observed experimentally.[39] The unsaturated, 46-electron triosmium dihydride cluster $Os_3(CO)_{10}(\mu\text{-}H)_2$ similarly catalyses $H_2/D_2$ equilibration, but the presumed saturated intermediate $HOs_3(CO)_{10}(\mu\text{-}H)(\eta^2\text{-}H_2)$ has never been isolated or spectroscopically observed.[40] Computational studies have demonstrated that the H/D exchange mechanism in the binuclear polyhydride complex $Cp^*Ru(\mu\text{-}H)_4RuCp^*$[41] on addition of $D_2$ proceeds by an associative mechanism via a number of $\eta^2$-$H_2$, $\eta^2$-HD and $\eta^2$-$D_2$ intermediates that are not experimentally observed.[14]

$H_2$ addition to the *saturated* 48-electron triangular cluster $(\mu\text{-}H)_2Ru_3(CO)_8(\mu\text{-}PtBu_2)_2$ (**16**) results in the opening up of the cluster to form a linear, also electron-precise, $Ru_3$ trimetallic species $(\mu\text{-}H)H_2Ru_3(CO)_8(\mu\text{-}PtBu_2)_2$ (**17**), with no overall loss of CO. Purging a solution with $N_2$ reforms the starting cluster **16**, although in the solid state the cluster is stable to $H_2$ loss.[42] Detailed kinetic studies demonstrated that the mechanism involves CO loss (thus forming an unsaturated cluster) that precedes $H_2$ addition to a single-metal centre with concomitant breaking of a Ru–Ru bond. Addition of CO affords the product that has made a net gain of $H_2$. Interestingly, this reaction does not occur with other bridging phosphido complexes (such a $PPh_2$ or $PCy_2$), and steric arguments are invoked that involve weakening of the Ru–Ru bonding and promotion of CO loss by the bulky $PtBu_2$ groups.[43] Hydrogen addition is suggested to occur at the unsaturated metal centre and not across a metal–metal bond, consistent with orbital symmetry arguments.[44]

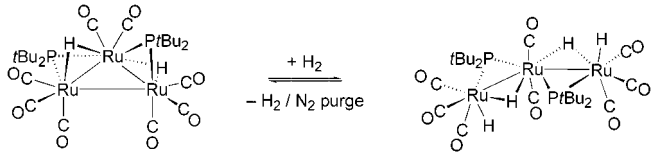


**16** **17**

Nocera has reported that the mixed-valence, unsaturated, 32-electron, $Ir_2$ dimer **18** reversibly adds $H_2$ across the Ir–Ir bond to form saturated dihydride **19**.[45] Purging with $N_2$ recovers **18**. The mechanism is suggested to proceed by addition of $H_2$ to one metal centre and then hydride migration rather than the symmetry-forbidden concerted 1,2 addition. Subsequent DFT calculations support this mechanism and show that addition of $H_2$ occurs at one metal centre (to give a dihydrogen complex) and passes through a transition structure with a terminal and bridging hydride, finally to rest at a terminal hydride on each Ir centre.[46] Interestingly, experimentally the reversible hydrogen addition is solvent-dependant. Removal of the $H_2$ atmosphere from a $CH_2Cl_2$ solution of **19** regenerates **18**, but in $CH_3CN$ solutions the solvent has to be evaporated for $H_2$ loss to occur. It is suggested, from crystallographic evidence, that H-bonding interactions with acetonitrile impose a kinetic barrier to $H_2$ loss.

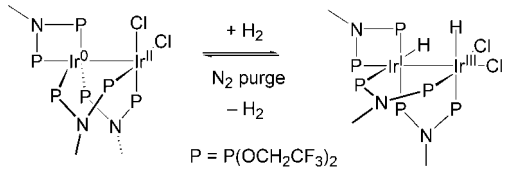


**18** **19**

 © 2007 Wiley-VCH Verlag GmbH & Co. KGaA, Weinheim 

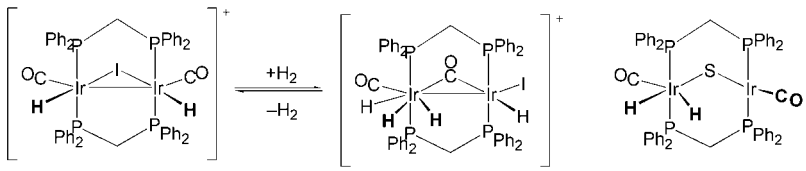


20 21 25

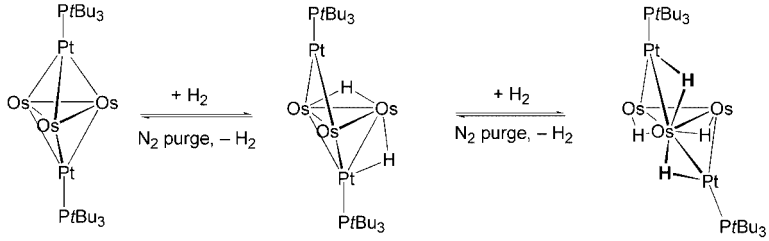


26 27 28

carbonyl groups not shown for clarity

Cowie and Vaartstra reported that addition of $H_2$ to the A-frame iridium dimer, $[Ir_2(dppm)_2H_2(CO)_2I][BF_4]$ (**20**), gives the fluxional tetrahydride, $[Ir_2(dppm)_2H_4(CO)_2I][BF_4]$ (**21**), for which $T_1$ measurements indicate that all the metal-bound hydrogen ligands are hydride-like. Removing the $H_2$ atmosphere regenerates **20** on gentle warming. The neutral, diiodido complex $Ir_2(dppm)_2(CO)_2I_2$ (**22**) also reversibly adds $H_2$ to give a dihydride, $Ir_2H_2(dppm)_2(CO)_2I_2$ (**23**), which loses $H_2$ upon being purged with $N_2$.[47] Although **20** is a 34-electron cluster, and thus would not be expected to add further $H_2$ without rupturing the Ir–Ir bond, the bridging iodine moves to a terminal position in the product **21** (3 $e^-$ to 1 $e^-$), allowing for overall $H_2$ addition. Duckett and co-workers have studied a related compound, $Ir_2(dppm)_2(CO)_2(\mu\text{-}S)_2$ (**24**), by using parahydrogen-induced polarisation NMR spectroscopy, and they also showed that the product of addition of $H_2$, $Ir_2(dppm)_2(CO)_2(H)_2(\mu\text{-}S)_2$ (**25**), also loses $H_2$ upon being purged with $N_2$.[48] In this case, $H_2$ addition transforms a square planar $Ir^I$ centre into an octahedral $Ir^{III}$ centre.

Trigonal bipyramidal, 68-electron $Pt_2Os_3(CO)_{10}(PtBu_3)_2$ (**26**) takes up two molecules of $H_2$ reversibly in a stepwise manner to eventually give $Pt_2Os_3(CO)_{10}(PtBu_3)_2H_4$ (**28**) through the (isolated) intermediate **27**. Purging with $N_2$ removes the bound $H_2$ to reform **26**, although this reaction only gives 28% of the starting material back. The low reverse-conversion is attributed to the open structure of **28** that is more prone to decomposition. On addition of $H_2$, **26** undergoes successive Os–Pt cleavages to give an $Os_3$ triangle with two edge bridging {Pt(CO)P*t*Bu$_3$}groups. This behaviour is in contrast to other, closely related, clusters such as **40** and **41** in which addition of $H_2$ results in no significant core cluster change.[49]

## Thermally Reversible or Reversible When Placed Under Vacuum

Oxidative addition of $H_2$ to the formal triple bond of $[(\eta^5\text{-}C_5H_4i\text{Pr})WCl_2]_2$ (**29**) gives complex **30**, $[(\eta^5\text{-}C_5H_4i\text{Pr})\text{-}W(\mu\text{-}H)Cl_2]_2$, which has bridging dihydrides clearly identified by using NMR spectroscopy by very long $T_1$ times of approximately 1.2 seconds. Gentle heating of **30** results in the reversible (quantitative by NMR spectroscopy) loss of $H_2$ to reform **29**.[50]

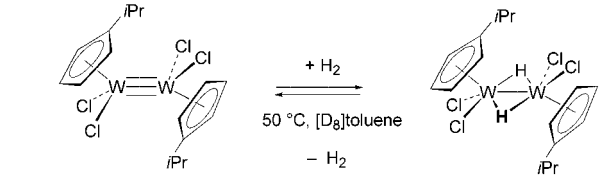


29 30

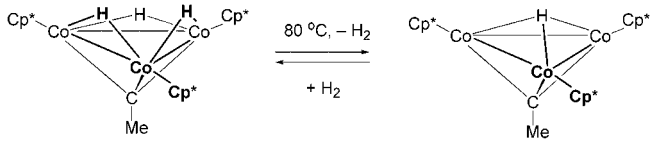


31 32

The 48-electron, cluster $(Cp^*Co)_3(\mu_2\text{-}H)_3(\mu_3\text{-}CMe)$ (**31**) reversibly loses $H_2$ when heated to 80 °C, to afford the para-

 © 2007 Wiley-VCH Verlag GmbH & Co. KGaA, Weinheim 

magnetic, 46-electron cluster $(Cp^*Co)_3(\mu_3\text{-}H)(\mu_3\text{-}CMe)$ (**32**). $\Delta G^{\ddagger}$ for this process is calculated as 23.8 kcal mol$^{-1}$.[51] Related chemistry involving reversible addition of $H_2$ to the unsaturated cluster $Cp^*_3Co_3(\mu_3\text{-}CO)_2$ (**33**) yields similar activation parameters.[52] The valence isoelectronic clusters $Cp^*_3Rh_2M(\mu_3\text{-}CO)_2$ (**34**) (M = Co, Ir) also add $H_2$ reversibly to form $Cp_3Rh_2M(\mu_3\text{-}CO)_2(\mu\text{-}H)_2$ (**35**). Warming (to an unspecified temperature, M = Rh) releases the $H_2$ to reform the unsaturated trimetallic cluster.[53]

The 56-electron platinum cluster $[Pt_4H_7(PtBu_3)_4][BPh_4]$ (**36**), reported by Spencer in 1984, loses $H_2$ by "atmospheric oxidation" to afford the C–H activated complex $[Pt_4(PtBu_3)_3\{PtBu_2(CMe_2CH_2)\}][BPh_4]$ (**37**), which formally has 50 electrons (this complex was not crystallographically characterised). Cluster **36** can be regenerated by adding $H_2$ (1 atm, 293 K) to **37**.[54] The conversion of **36** to **37** represents a remarkable net loss of 8 hydrogen atoms. Again, the bulky *tert*-butyl groups on the phosphanes no doubt stabilise the cluster towards $H_2$ loss. Although this transformation is described as an oxidation, it might also better be described as initial stepwise loss of $3H_2$, oxidative addition of C–H and loss of $H_2$. Interestingly, the isoelectronic *neutral* cluster $Pt_4H_8(PtBu_3)_4$ is not reported to lose $H_2$,[55] but whether this is a simple consequence of the fact that this complex was never left on the open bench is not clear! Whatever the reason, these unsaturated platinum complexes are fascinating, given the reversible addition of a large amount of $H_2$, and surely warrant further investigation some twenty years after they were reported. A related "oxidative" transformation to **36** → **37** occurs upon addition of $O_2$ to the tetrametallic ruthenium cluster $[Ru_4(\eta^6\text{-}C_6H_6)_4H_6]^{2+}$, **38**,[56] which initially was formulated as a hexahydride but later suggested (on the basis of $T_1$ measurements and DFT calculations) to be a dihydrogen/tetrahydride complex,[11] to form $[Ru_4(\eta^6\text{-}C_6H_6)_4H_4]^{2+}$ (**39**). The tetrahydride cluster adds $H_2$ again (60 atm) to reform **38**.

Adams and co-workers have recently reported a set of unsaturated platinum-rhenium complexes with bulky $tBu_3P$ ligands that allow for electronically unsaturated clusters to be synthesised in a systematic manner. $Pt_2Re_2(CO)_7(PtBu_3)_2\text{-}H_2$ (**40**), an unsaturated 54-electron tetrahedral cluster (tetrahedral $Pt_2M_2$ often have an electron count of 58, especially when decorated with bulky ligands, e.g. $Pt_2Mo_2(\eta^5\text{-}C_5H_4Me)_2(CO)_6(PCy_3)_2$[57]), takes up $H_2$ to form $Pt_2Re_2(CO)_7(PtBu_3)_2H_4$ (**41**), which has 4 hydride ligands. Cluster **41** eliminates $H_2$ nearly quantitatively on heating to 97 °C or on irradiation (UV/Vis). The mechanism for $H_2$ addition (and by the principle of microscopic reversibility, that for $H_2$ loss) has been studied by DFT methods and involves end-on $\eta^1$-attack of $H_2$ on one of the Pt atoms (where the LUMO is centred), moving through an $\eta^2\text{-}H_2$ intermediate, which oxidatively adds to the same Pt atom to give the observed product.[58] Addition of hydrogen results in no gross structural change to the cluster (i.e. metal–metal bond scission or rearrangement of the polyhedral core), consistent with the addition of electron pairs to an unsaturated cluster.

The clusters $[Rh_6(PR_3)_6H_{12}][BAr^F{}_4]_2$ (**42**) (R = *i*Pr **42a**, Cy **42b**) reversibly take up two equivalents of $H_2$ to give the sixteen-hydride clusters $[Rh_6(PR_3)_6H_{16}][BAr^F{}_4]_2$ (**43a**,**b**).[59] This uptake is rapid (less than 5 min). Placing **43a** or **43b**

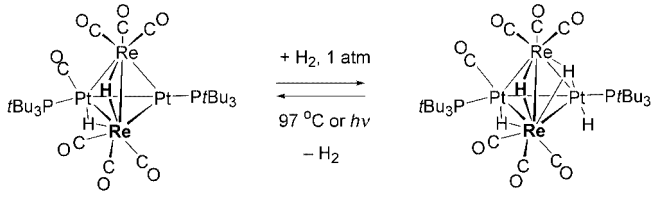


**40** **41**

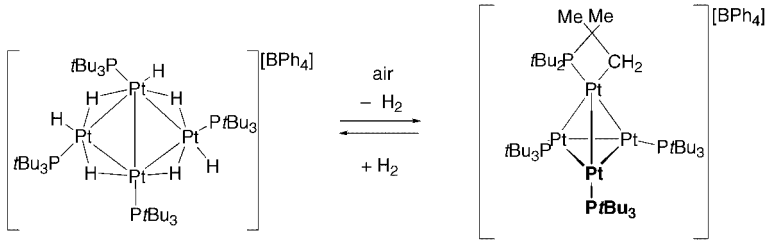


**36** **37**

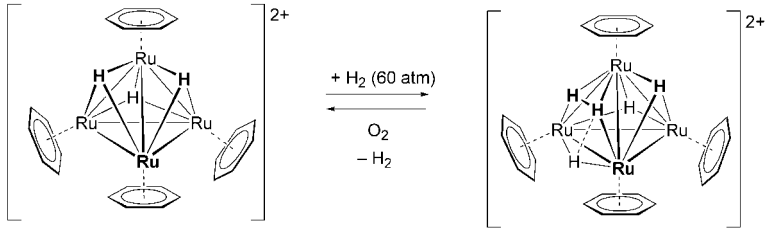


**39** **38**

 © 2007 Wiley-VCH Verlag GmbH & Co. KGaA, Weinheim 

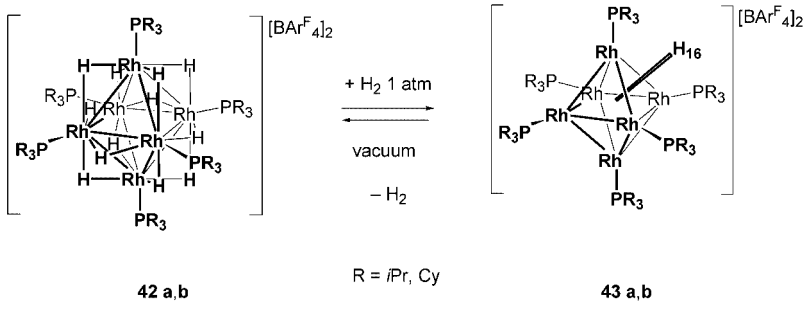


under vacuum removes the $H_2$ and regenerates **42a**,**b**, both in solution and the solid state. As for **40**, these clusters can be considered as being unsaturated (76-electrons) and DFT calculations show that there are two low-lying empty orbitals available for the take-up of two $H_2$ bonding pairs.[60] Again, it is the bulky alkylphosphane ligands that shield the metal core from decomposition and allow the low electron count to be maintained. DFT calculations also indicate that the sixteen-hydride cluster contains an interstitial hydride and two dihydrogen-like $H_2$ molecules, which have an average binding energy to the cluster of 60 kJ mol$^{-1}$, consistent with that reported for mononuclear dihydrogen complexes (Figure 4).[5] Although these dihydrogen ligands are not observed either by X-ray crystallography or NMR spectroscopy, indirect evidence comes from H/D exchange experiments with $D_2$ and the observation of HD(g). The reversible $H_2$ loss can be modulated by the phosphane. With P*i*Pr$_3$, $H_2$ loss from **43a** when placed under vacuum is relatively quick (12 hours), but for **43b** with $PCy_3$ ligands, $H_2$ loss under vacuum takes 1 week. This difference is accounted for by the tighter interdigitation of the cyclohexyl groups that kinetically stabilise the cluster towards $H_2$ loss.

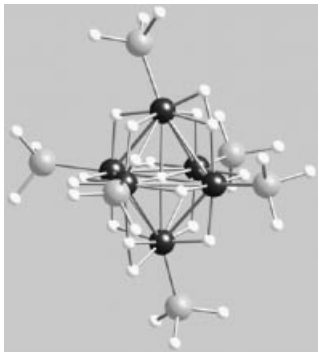

Figure 4. The DFT calculated structure of $[Rh_6(PH_3)_6H_{16}]^{2+}$, showing the two dihydrogen-like ligands.

Reduction of clusters **42** affords $[Rh_6(PR_3)_6H_{12}]^{n+}$ ($n$ = 1 **44**, 0 **45**).[61] Inspection of the frontier molecular orbitals suggests that these clusters should also take up one equivalent of $H_2$. The cluster $[Rh_6(PR_3)_6H_{12}]^+$ (**44**) adds one $H_2$ to give $[Rh_6(PR_3)_6H_{14}]^+$ (**46**), as characterised by ESI-MS. Removing the $H_2$ atmosphere regenerates **44**. By contrast, neutral $[Rh_6(PR_3)_6H_{12}]$ (**45**), which is a paramagnetic species having a triplet ground state ($S$ = 1), takes up $H_2$ to give the diamagnetic cluster $[Rh_6(PR_3)_6H_{14}]$ (**47**) ($S$ = 0, R = *i*Pr only). This reaction is much slower than for the other clusters (16 hours), attributed to "spin blocking" – a significant barrier along the reaction coordinate induced by a spin change that results in a significantly slower reaction when there is a spin-state change.[62] Consistent with microscopic reversibility arguments, **45** does not lose $H_2$ readily.

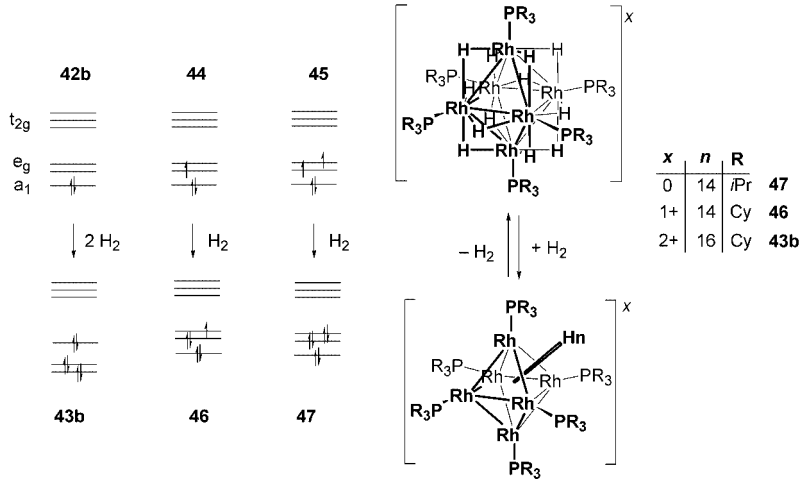


 © 2007 Wiley-VCH Verlag GmbH & Co. KGaA, Weinheim 

## Electrochemically Reversible

Inspection of the MO diagram for **43a**,**b** suggests that addition of one extra electron would result in the population of a high-lying orbital, and this could destabilise the cluster, resulting in $H_2$ loss to re-establish a large HOMO–LUMO gap. If coupled with a sequential oxidation of the cluster, this potentially could lead to the reversible binding and release of $H_2$, triggered by a single-electron redox event. This prediction was borne out experimentally.[60,61,63] The cyclic voltammogram of **43b** shows an irreversible loss of $H_2$ on reduction, presumably from an unstable, putative species $[Rh_6(PCy_3)_6H_{16}]^+$ (Scheme 3). The formation of $[Rh_6(PCy_3)_6H_{12}]^+$ (**44**) results, which can be oxidised to form $[Rh_6(PCy_3)_6H_{12}]^{2+}$ (**42b**) and subsequently recharged with $H_2$ to reform $[Rh_6(PCy_3)_6H_{16}]^{2+}$ (**43b**), completing a complete hydrogen-store cycle. The loss of $H_2$ is kinetically fast ($t_{1/2}$ as measured electrochemically is 170 ms). The redox cycle can be duplicated by using chemical reductants/oxidants and followed by ESI-MS. This facile, reusable gain and loss of two equivalents of $H_2$ by using a simple one-electron redox switch represents a new method of hydrogen storage. Although the overall storage capacity is very low (0.1% by weight), the attractive conditions of room temperature and pressure, actuation by the addition of a single electron and rapid desorption kinetics makes the concept of interest for future $H_2$ storage applications.

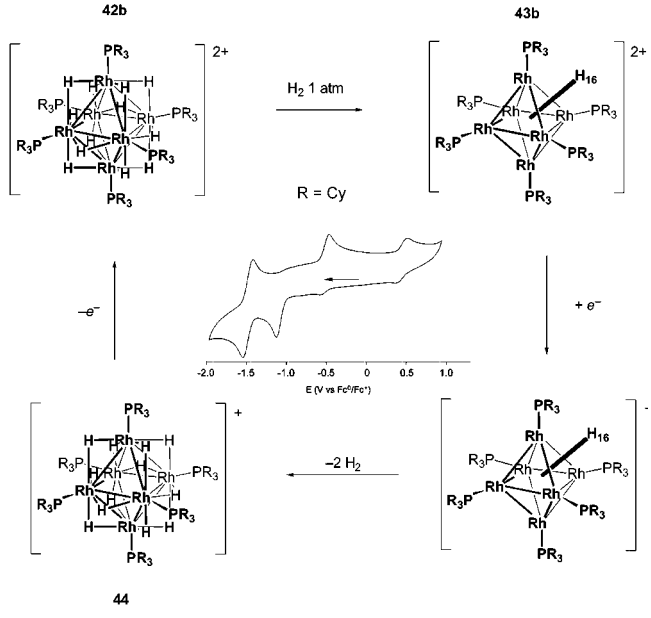


Scheme 3. Insert shows the cyclic voltammogram; the irreversible reductions are attributed to $H_2$ loss at ≈ 1.0 V.

Redox-induced loss of hydrogen or protons is known to occur in mononuclear systems. Irreversible oxidation of the complex $[Co\{P(CH_2CH_2PPh_2)_3\}(H_2)][PF_6]$[64] (originally suggested to be a dihydrogen complex, but later reformulated by Heinekey as a dihydride[65]) results in the loss of a proton, while reduction of vinylidene complex $[Rh(=C=CHPh)\{N(CH_2CH_2PPh_2\}_3][BF_4]$ results in $H_2$ loss, to form an acetylide.[66] Redox-promoted oxidation of $H_2$ to afford protons (or the reverse reaction – electrocatalytic generation of $H_2$) is, of course, also very well documented in the study of hydrogenase chemistry.[67] However, none of these processes involves the reversible binding of $H_2$ as found for **43b**.

## Photochemically Reversible

An early (1983) report of the photolysis of $(\eta^5\text{-}C_5H_5)W(CO)_3H$ suggested that it proceeded by $CO/H_2$ expulsion to afford a putative dimeric species $[(\eta^5\text{-}C_5H_5)W(CO)_2]_2$ (**48**) that reversibly added $H_2$ under photochemical conditions to give $[(\eta^5\text{-}C_5H_5)W(\mu\text{-}H)(CO)_2]_2$, (**49**), which is related to **30**.[68] Aspects of the dimerisation mechanism have been subsequently questioned.[69]

The rhodium analogue of **19**, complex **51**, can be formed by addition of $H_2$ to **50**. Interestingly, complex **51** does not lose $H_2$ readily on standing, nor does it exchange with $D_2$ appreciably after one week. However, $H_2$ loss is fast upon photochemical irradiation to afford **50**.[70] These complexes provide insight into the photocycle for hydrogen production from HX solutions. $[Pt_2H_3(dppm)_2][PF_6]$ (**52**) loses $H_2$ in solution and the solid state on irradiation to give a complex of formula $[Pt_2H(dppm)_2][PF_6]$ (**53**), which reacts back slowly with $H_2$ to give **52**.[71]

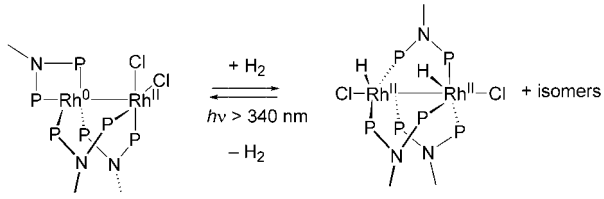


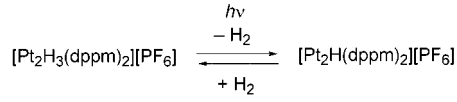


The electronically unsaturated, 62-electron trigonal bipyramidal cluster $Pt_3Re_2(PtBu_3)_3(CO)_6$ (**53**) adds three molecules of $H_2$ in a stepwise manner to eventually afford $Pt_3Re_2(PtBu_3)_3(CO)_6H_6$ (**56**). This reaction is reversible under photolytic conditions, and irradiating **56** eliminates dihydrogen, ultimately to afford the dihydride complex $Pt_3Re_2(PtBu_3)_3(CO)_6H_2$ (**54**). The last elimination of $H_2$ is presumably a high-energy process and does not occur under the conditions used.[72] Cluster **53** is unsaturated by 10 electrons for a trigonal bipyramid (albeit platinum clusters often count lower than expected), and the bulky $tBu_3P$ groups no doubt have a role to play in this – stabilising the unsaturated core by providing a steric shield against addition of further, large, metal fragments. Space-filling diagrams nonetheless indicate that there is sufficient room for the approach of a $H_2$ molecule. The molecular orbital structure shows five low-lying unoccupied molecular orbitals,

 © 2007 Wiley-VCH Verlag GmbH & Co. KGaA, Weinheim 

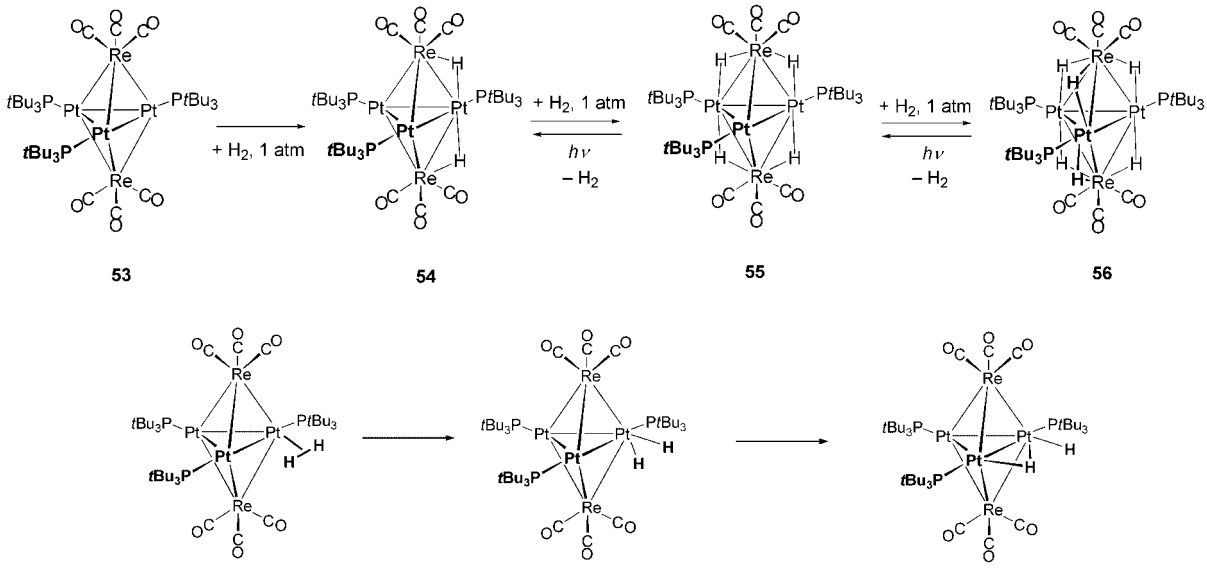


Scheme 4.

three of which are suitably aligned along the Pt–Re bonds to accept electron density from an incoming $H_2$ molecule. Detailed theoretical analysis of the mechanism of $H_2$ addition indicates a possible pathway that starts with hydrogen addition at Pt to give a dihydrogen intermediate, followed by $H_2$ cleavage and the formation of a complex with a terminal hydride and a hydride bridging a Pt–Pt bond. This configuration rearranges to give the observed product with hydrides bridging the Pt–Re bonds (Scheme 4). The related tetranuclear cluster $Pt_2Re_2(CO)_7(tBu_3P)_2H_4$ (**41**) also eliminates one equivalent of $H_2$ on irradiation.[58,73] The addition of $H_2$ to a single metal centre is consistent with qualitative molecular orbital arguments by Hoffman, who showed that intramolecular reductive elimination (and the microscopic reverse: oxidative addition) would be symmetry-forbidden for 1,2-elimination (or 1,2-addition) and have a large barrier for a concerted least-motion pathway.[44]

## Reversible Biological Systems

Hydrogenases regulate the metabolism of hydrogen in microorganisms, and these enzymes have attracted an enormous amount of attention in the hope of developing electrochemically active, bio-inspired catalytic systems employing hydrogen.[74] The active site of one class of these enzymes have been shown crystallographically to contain a dinuclear NiFe cluster with bridging sulfur ligands. The reversible binding of hydrogen at the active site is a key stage in the proposed mechanism of action, and the presence of the biologically unusual, strong-*trans*-influence CO ligand favours this process (by reducing the ability of the metal to back-donate into the σ* orbital of $H_2$). Heterolytic cleavage of $H_2$ follows the binding event, generating a bridging hydride ligand and releasing a proton. The salient part of the enzymatic cycle is shown in Scheme 5.

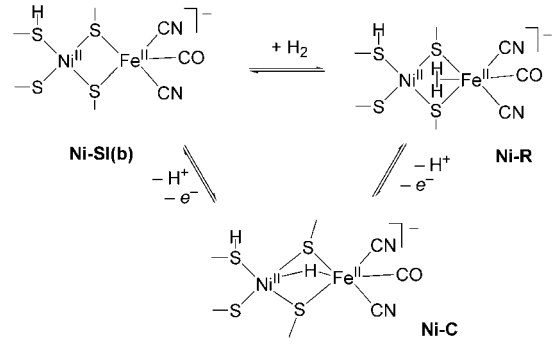


Scheme 5.

**Ni-SI(b)** (the mechanism has its own shorthand) reacts with $H_2$ to generate **Ni-R**, in which the hydrogen is suggested to be present as a dihydrogen ligand bound to $Fe^{II}$. One-electron oxidation of **Ni-R** liberates a proton to generate **Ni-C**, thought to possess a bridging hydride ligand, which, upon further one-electron oxidation, is released as a proton, and **Ni-SI(b)** is regenerated. The involvement of the hydride and dihydrogen intermediates is implicated by the fact that during catalyst turnover under a $D_2$ atmosphere, HD and/or HDO is formed, despite the lack of spectroscopic evidence for the existence of metal–hydride or metal–dihydrogen species. Catalysis of H/D exchange reactions is characteristic of the hydrogenases.[75]

Iron-only hydrogenases also exist, containing a $\{Fe_4S_4\}$ cubane cluster linked to a $\{Fe_2S_3\}$ subsite through a bridging cysteinyl ligand. The fact that both the NiFe and $Fe_2$ units have thiolate, $CN^-$ and CO ligands – all common in coordination chemistry – means that a huge range of dinuclear complexes have been synthesised with the aim of modelling the geometry, connectivity, metals, ligand sets and chemistry displayed by the hydrogenases.[76] This topic has

 © 2007 Wiley-VCH Verlag GmbH & Co. KGaA, Weinheim 

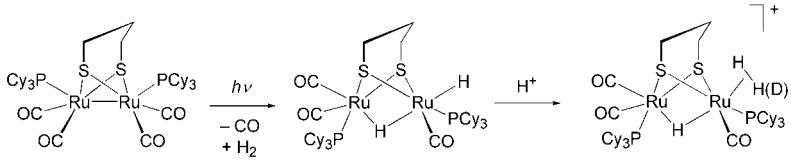


57

been heavily reviewed, so only a few examples with particular relevance to reversible hydrogen binding will be mentioned herein.

Many complexes designed to model the hydrogenases react *irreversibly* with $H_2$, such as the recent example of a water-soluble NiRu complex that takes up $H_2$ under ambient conditions, resulting in heterolytic cleavage of $H_2$ to form $H^+$ and a bridging hydride.[77] Less common are dinuclear complexes that react reversibly with hydrogen; a notable example is from Rauchfuss, who characterised the first dihydrogen complex of a hydrogenase active site model.[78]

$[Ru_2(\mu\text{-}H)(H_2)(\mu\text{-}SCH_2CH_2CH_2S)(PCy_3)_2(CO)_3]^+$ (**57**) was shown to catalyse $H_2/D_2$ equilibration. Related complexes also catalyse H/D scrambling via what is assumed to be an ($\eta^2$-$H_2$)-containing intermediate; examples of compounds displaying this chemistry include $[Fe_2(\mu\text{-}H)(\mu\text{-}SCH_2CH_2CH_2S)(PMe_3)_2(CO)_4]^+$ (**58**)[79] and $[Fe_2(\mu\text{-}H)(\mu\text{-}SCH_2CH_2CH_2S)(CN\textit{t}Bu)_2(CO)_4]^+$ (**59**).[80] A vacant coordination site must first be created, and, consistent with this requirement, the H/D scrambling reaction is often promoted by irradiation with UV light but inhibited by the presence of CO.

## Giant Clusters Displaying Reversible $H_2$ Binding

Palladium metal has an unusually high affinity for hydrogen, absorbing up to 935 times its own volume (an approximate composition of $Pd_4H_3$), and Pd/Ag membranes are used on an industrial scale to produce ultrapure hydrogen.[81] Various models of the hydrogen-rich lattice have been reported, most notably Dahl's cluster $H_{12}Pd_{28}(PtPMe_3)(PtPPh_3)_{12}(CO)_{27}$ (**60**) (Figure 5).[82] The cluster was treated with $D_2$, which resulted in an 80% decrease in the hydride signal by $^1H$ NMR spectroscopy, suggesting that hydrogen is readily exchanged. However, no attempt seems to have been made to add $H_2$ under pressure or to remove it by vacuum, heat or light, so regrettably little is known about the hydrogen storage capabilities of this material.

Giant, ligand-stabilised palladium clusters can be readily synthesised by reduction of palladium acetate with hydrogen gas.[83] With careful control of conditions, the size distribution is nearly monodisperse (see Figure 6) and centred on particular "magic numbers" corresponding to different numbers of concentric shells ($n$) of Pd atoms around a central atom, where each shell contains ($10n^2 + 2$) atoms.[84]

The behaviour of the series $Pd_{55}(phen)_{36}O_{30}$ (2 shells, diameter ≈ 1 nm; phen = phenanthroline), $Pd_{561}(phen)_{36}O_{200}$ (5 shells, diameter ≈ 2.6 nm), $Pd_{1415}(phen)_{60}O_{1100}$ (7 shells, diameter ≈ 3.7 nm) and Pd powder (diameter ≈ 50 μm) towards hydrogen has been investigated in detail by

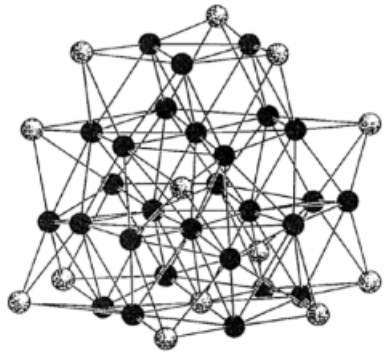

Figure 5. Crystallographically determined metal core (Pd black, Pt grey) structure of $H_{12}Pd_{28}(PtPMe_3)(PtPPh_3)_{12}(CO)_{27}$ (**60**). Hydrogen atoms were not located. Figure reproduced courtesy of the American Chemical Society from ref.[83]

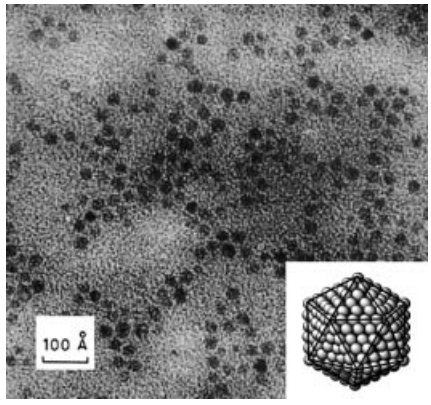


Figure 6. Electron micrograph of palladium nanoparticles deposited on a carbon support. Reproduced courtesy of the Royal Society of Chemistry from ref.[84] Inset: idealised icosahedral structure of $Pd_{561}$ core, approximate diameter 26 Å.

Züttel and co-workers. They found that Pd clusters of all size ranges reversibly absorbed and desorbed hydrogen,[85] but that the reversible hydrogen storage capacity (H/Pd ratio) decreased with decreasing cluster size.[86] This effect was attributed to the fact that the smaller clusters had a greater proportion of surface atoms and that only the interstitial sites in the Pd lattice were available for reversible hydrogen storage. The reasoning here was that the binding energy of the surface hydrides was greater than the interstitial hydrogen, and the surface hydrides could therefore not be easily removed simply by application of vacuum. The cluster samples had dramatically improved discharge kinetics relative to bulk Pd, and X-ray diffraction revealed that the crystallographic structure of the clusters was not altered by absorption and desorption cycles.[87] However, others have shown that 5-nm Pd clusters do undergo structural change

 © 2007 Wiley-VCH Verlag GmbH & Co. KGaA, Weinheim 

upon hydrogen absorption, probably from a cubic lattice to an icosahedral one.[88]

Pd clusters loaded on carbon have been shown to absorb more hydrogen per Pd atom than does bulk Pd,[89] an effect attributed to spillover (a process whereby hydrogen spreads from a metal particle to its support).[90] The absorption was shown to be reversible but a significant fraction of the stored hydrogen required pressures of less than 5 Torr or high temperatures in order to be released.

## Conclusions

Multimetallic compounds that reversibly bind hydrogen without experiencing dramatic structural changes have several features in common:

(i) Bulky ligands (especially phosphanes) are often a feature of the coordination sphere. Such ligands provide kinetically controlled steric blocking of coordination sites, favouring electronic unsaturation. However the smallest of molecules, $H_2$, is often able to penetrate the coordination sphere and binds to the metal to (sometimes only partially) relieve the electronic unsaturation at the metal centre.

(ii) The metals involved are generally late-transition metals, especially Rh, Pd and the surrounding elements, in relatively low oxidation states. Such metals form strong bonds with soft ligands such as the bulky phosphanes that appear to be crucial for successful reversible hydrogen bonding; they also have sufficient d electrons for back-donation to the σ* orbital on H as well as suitable empty acceptor orbitals.

(iii) The hydrogen does not have to be bound side-on as $\eta^2$-$H_2$ in order for reversible binding behaviour to be observed; the rapid exchange between the wide variety of binding modes (including bridging and interstitial) and the low energy differences between them facilitates the ready distribution of H ligands around the cluster core (hence making definitive characterisation of H location often problematic).

Approaches to multimetallic complexes that reversibly bind hydrogen have historically resulted from serendipity as much as from an avowed intention to make compounds with this useful and interesting property (with the notable exception of the efforts to model the hydrogenases). However, a few simple design rules outlined above seem to apply quite generally and it is reasonable to expect that the field will develop by further exploitation of the structural variety and rich redox properties offered by polynuclear metal cores and the kinetic blocking of coordination sites by bulky ligands. Firm establishment of the structure–property relationships inherent to systems that efficiently and reversibly bind hydrogen should allow the application of these concepts to other (cheaper!) metals and materials.

[1] See, for example, the dedicated website of the U. S. Department of Energy, at: http://www.hydrogen.energy.gov/storage.html.

[2] J. L. C. Rowsell, O. M. Yaghi, *Angew. Chem. Int. Ed.* **2005**, *44*, 4670–4679; L. Schlapbach, A. Züttel, *Nature* **2001**, *414*, 353–358.
[3] T. Mitsui, M. K. Rose, E. Fomin, D. F. Ogletree, M. Salmeron, *Surf. Sci.* **2003**, *540*, 5–11; T. Mitsui, M. K. Rose, E. Fomin, D. F. Ogletree, M. Salmeron, *Nature* **2003**, *422*, 705–707.
[4] G. J. Kubas, *Proc. Natl. Acad. Sci.* **2007**, *104*, 6901–6907.
[5] G. J. Kubas, *Metal Dihydrogen and σ-Bond Complexes*, Kluwer Academic/Plenum Publishers, New York, **2001**.
[6] A. S. Martensson, C. Nyberg, S. Andersson, *Surf. Sci.* **1988**, *205*, 12–24.
[7] P. Braunstein, L. A. Oro, P. R. Raithby (Eds.), *Metal Clusters in Chemistry*, Wiley-VCH Weinheim, **1999**.
[8] C. Hampton, W. R. Cullen, B. R. James, J. P. Charland, *J. Am. Chem. Soc.* **1988**, *110*, 6918–6919.
[9] B. Chaudret, J. Devillers, R. Poilblanc, *Organometallics* **1985**, *4*, 1727–1732.
[10] T. Arliguie, B. Chaudret, R. H. Morris, A. Sella, *Inorg. Chem.* **1988**, *27*, 598–599; K. Abdur-Rashid, D. G. Gusev, A. J. Lough, R. H. Morris, *Organometallics* **2000**, *19*, 1652–1660.
[11] G. Süss-Fink, L. Plasseraud, A. Maisse-François, H. Stoeckli-Evans, H. Berke, T. Fox, R. Gautier, J. Y. Saillard, *J. Organomet. Chem.* **2000**, *609*, 196–203.
[12] D. Amoroso, G. P. A. Yap, D. E. Fogg, *Organometallics* **2002**, *21*, 3335–3343.
[13] G. J. Kubas, R. R. Ryan, B. I. Swanson, P. J. Vergamini, H. J. Wasserman, *J. Am. Chem. Soc.* **1984**, *106*, 451–452; G. J. Kubas, C. J. Unkefer, B. I. Swanson, E. Fukushima, *J. Am. Chem. Soc.* **1986**, *108*, 7000–7009.
[14] S. Tussupbayev, S. F. Vyboishchikov, *Organometallics* **2007**, *26*, 56–64.
[15] M. Bergamo, T. Beringhelli, G. D'Alfonso, P. Mercandelli, A. Sironi, *J. Am. Chem. Soc.* **2002**, *124*, 5117–5126.
[16] C. Hampton, I. R. Butler, W. R. Cullen, B. R. James, J. P. Charland, J. Simpson, *Inorg. Chem.* **1992**, *31*, 5509–5520.
[17] E. Sola, V. I. Bakhmutov, F. Torres, A. Elduque, J. A. Lopez, F. J. Lahoz, H. Werner, L. A. Oro, *Organometallics* **1998**, *17*, 683–696.
[18] R. N. Perutz, S. Sabo-Etienne, *Angew. Chem. Int. Ed.* **2007**, *46*, 2578–2592.
[19] D. M. Heinekey, A. Lledos, J. M. Lluch, *Chem. Soc. Rev.* **2004**, *33*, 175–182.
[20] M. Catti, G. Gervasio, S. A. Mason, *J. Chem. Soc., Dalton Trans.* **1977**, 2260–2264.
[21] R. Bau, N. N. Ho, J. J. Schneider, S. A. Mason, G. J. McIntyre, *Inorg. Chem.* **2004**, *43*, 555–558.
[22] R. Bau, M. H. Drabnis, L. Garlaschelli, W. T. Klooster, Z. W. Xie, T. F. Koetzle, S. Martinengo, *Science* **1997**, *275*, 1099–1102.
[23] P. F. Jackson, B. F. G. Johnson, J. Lewis, P. R. Raithby, M. McPartlin, W. J. H. Nelson, K. D. Rouse, J. Allibon, S. A. Mason, *J. Chem. Soc., Chem. Commun.* **1980**, 295–297.
[24] D. M. P. Mingos, *Acc. Chem. Res.* **1984**, *17*, 311–319.
[25] R. H. E. Hudson, A. J. Poe, C. N. Sampson, A. Siegel, *J. Chem. Soc., Dalton Trans.* **1989**, 2235–2240.
[26] M. D. Fryzuk, W. E. Piers, F. W. B. Einstein, T. Jones, *Can. J. Chem.* **1989**, *67*, 883–896.
[27] A. J. Sivak, E. L. Muetterties, *J. Am. Chem. Soc.* **1979**, *101*, 4878–4887.
[28] R. C. Schnabel, P. S. Carroll, D. M. Roddick, *Organometallics* **1996**, *15*, 655–662.
[29] A. M. Arif, D. E. Heaton, R. A. Jones, K. B. Kidd, T. C. Wright, B. R. Whittlesey, J. L. Atwood, W. E. Hunter, H. Zhang, *Inorg. Chem.* **1987**, *26*, 4065–4073.
[30] G. J. Kubas, *Adv. Inorg. Chem.* **2004**, *56*, 127–177.
[31] C. Bianchini, C. Mealli, A. Meli, M. Sabat, *Inorg. Chem.* **1986**, *25*, 4617–4618.
[32] A. Ienco, M. J. Calhorda, J. Reinhold, F. Reineri, C. Bianchini, M. Peruzzini, F. Vizza, C. Mealli, *J. Am. Chem. Soc.* **2004**, *126*, 11954–11965.
[33] L. J. Farrugia, M. Green, D. R. Hankey, A. G. Orpen, F. G. A. Stone, *J. Chem. Soc., Chem. Commun.* **1983**, 310–312.

 © 2007 Wiley-VCH Verlag GmbH & Co. KGaA, Weinheim 

[34] D. Blazina, S. B. Duckett, P. J. Dyson, B. F. G. Johnson, J. A. B. Lohman, C. J. Sleigh, *J. Am. Chem. Soc.* **2001**, *123*, 9760–9768.
[35] L. M. Bavaro, P. Montangero, J. B. Keister, *J. Am. Chem. Soc.* **1983**, *105*, 4977–4981.
[36] R. C. Matthews, D. K. Howell, W. J. Peng, S. G. Train, W. D. Treleaven, G. G. Stanley, *Angew. Chem. Int. Ed. Engl.* **1996**, *35*, 2253–2256.
[37] M. A. Aubart, L. H. Pignolet, *J. Am. Chem. Soc.* **1992**, *114*, 7901–7903; M. A. Aubart, B. D. Chandler, R. A. T. Gould, D. A. Krogstad, M. F. J. Schoondergang, L. H. Pignolet, *Inorg. Chem.* **1994**, *33*, 3724–3734.
[38] T. Kappen, J. J. Bour, P. P. J. Schlebos, A. M. Roelofsen, J. G. M. Vanderlinden, J. J. Steggerda, M. A. Aubart, D. A. Krogstad, M. F. J. Schoondergang, L. H. Pignolet, *Inorg. Chem.* **1993**, *32*, 1074–1075.
[39] X. Xu, Y. Z. Yuan, K. Asakura, Y. Iwasawa, H. L. Wan, K. R. Tsai, *Chem. Phys. Lett.* **1998**, *286*, 163–170.
[40] S. Aime, W. Dastru, R. Gobetto, J. Krause, L. Matas, A. Viale, *Organometallics* **1996**, *15*, 4967–4970.
[41] H. Suzuki, H. Omori, D. H. Lee, Y. Yoshida, M. Fukushima, M. Tanaka, Y. Morooka, *Organometallics* **1994**, *13*, 1129–1146.
[42] A. M. Arif, T. A. Bright, R. A. Jones, C. M. Nunn, *J. Am. Chem. Soc.* **1988**, *110*, 6894–6895.
[43] F. J. Safarowic, D. J. Bierdeman, J. B. Keister, *J. Am. Chem. Soc.* **1996**, *118*, 11805–11812.
[44] G. Trinquier, R. Hoffmann, *Organometallics* **1984**, *3*, 370–380.
[45] A. F. Heyduk, D. G. Nocera, *J. Am. Chem. Soc.* **2000**, *122*, 9415–9426.
[46] T. G. Gray, A. S. Veige, D. G. Nocera, *J. Am. Chem. Soc.* **2004**, *126*, 9760–9768.
[47] B. A. Vaartstra, M. Cowie, *Inorg. Chem.* **1989**, *28*, 3138–3147.
[48] S. M. Oldham, J. F. Houlis, C. J. Sleigh, S. B. Duckett, R. Eisenberg, *Organometallics* **2000**, *19*, 2985–2993.
[49] R. D. Adams, B. Captain, L. Zhu, *J. Am. Chem. Soc.* **2007**, *129*, 2454–2455.
[50] M. L. H. Green, P. Mountford, *J. Chem. Soc., Chem. Commun.* **1989**, 732–734; F. Qian, M. Ferrer, M. L. H. Green, P. Mountford, V. S. B. Mtetwa, K. Prout, *J. Chem. Soc., Dalton Trans.* **1991**, 1397–1406.
[51] C. P. Casey, S. L. Hallenbeck, R. A. Widenhoefer, *J. Am. Chem. Soc.* **1995**, *117*, 4607–4622.
[52] C. P. Casey, R. A. Widenhoefer, S. L. Hallenbeck, R. K. Hayashi, J. A. Gavney, *Organometallics* **1994**, *13*, 4720–4731.
[53] A. C. Bray, M. Green, D. R. Hankey, J. A. K. Howard, O. Johnson, F. G. A. Stone, *J. Organomet. Chem.* **1985**, *281*, C12–C16.
[54] R. J. Goodfellow, E. M. Hamon, J. A. K. Howard, J. L. Spencer, D. G. Turner, *J. Chem. Soc., Chem. Commun.* **1984**, 1604–1606.
[55] D. Gregson, J. A. K. Howard, M. Murray, J. L. Spencer, *J. Chem. Soc., Chem. Commun.* **1981**, 716–717.
[56] G. Meister, G. Rheinwald, H. Stoeckli-Evans, G. Süss-Fink, *J. Chem. Soc., Dalton Trans.* **1994**, 3215–3223.
[57] P. Braunstein, C. D. Debellefon, S. E. Bouaoud, D. Grandjean, J. F. Halet, J. Y. Saillard, *J. Am. Chem. Soc.* **1991**, *113*, 5282–5292.
[58] R. D. Adams, B. Captain, M. D. Smith, C. Beddie, M. B. Hall, *J. Am. Chem. Soc.* **2007**, *129*, 5981–5991.
[59] a) S. K. Brayshaw, M. J. Ingleson, J. C. Green, J. S. McIndoe, P. R. Raithby, G. Kociok-Kohn, A. S. Weller, *J. Am. Chem. Soc.* **2006**, *128*, 6247–6263; b) S. K. Brayshaw, M. J. Ingleson, J. C. Green, P. R. Raithby, G. Kociok-Kohn, J. S. McIndoe, A. S. Weller, *Angew. Chem. Int. Ed.* **2005**, *44*, 6875–6878.
[60] S. K. Brayshaw, J. C. Green, N. Hazari, A. S. Weller, *Dalton Trans.* **2007**, 1781–1792.
[61] S. K. Brayshaw, A. Harrison, J. S. McIndoe, F. Marken, P. R. Raithby, J. E. Warren, A. S. Weller, *J. Am. Chem. Soc.* **2007**, *129*, 1793–1804.
[62] J. L. Carreon-Macedo, J. N. Harvey, *J. Am. Chem. Soc.* **2004**, *126*, 5789–5797.
[63] S. K. Brayshaw, J. C. Green, N. Hazari, J. S. McIndoe, F. Marken, P. R. Raithby, A. S. Weller, *Angew. Chem. Int. Ed.* **2006**, *45*, 6005–6008.
[64] C. Bianchini, F. Laschi, M. Peruzzini, F. M. Ottaviani, A. Vacca, P. Zanello, *Inorg. Chem.* **1990**, *29*, 3394–3402.
[65] D. M. Heinekey, A. Liegeois, M. van Roon, *J. Am. Chem. Soc.* **1994**, *116*, 8388–8389.
[66] C. Bianchini, A. Meli, M. Peruzzini, F. Zanobini, P. Zanello, *Organometallics* **1990**, *9*, 241.
[67] a) C. Tard, X. M. Liu, S. K. Ibrahim, M. Bruschi, L. De Gioia, S. C. Davies, X. Yang, L. S. Wang, G. Sawers, C. J. Pickett, *Nature* **2005**, *433*, 610–613; b) R. Mejia-Rodriguez, D. Chong, J. H. Reibenspies, M. P. Soriaga, M. Y. Darensbourg, *J. Am. Chem. Soc.* **2004**, *126*, 12004–12014.
[68] H. G. Alt, K. A. Mahmoud, A. J. Rest, *Angew. Chem. Int. Ed. Engl.* **1983**, *22*, 544–545.
[69] T. E. Bitterwolf, J. C. Linehan, J. E. Shade, *Organometallics* **2000**, *19*, 4915–4917.
[70] A. J. Esswein, A. S. Veige, D. G. Nocera, *J. Am. Chem. Soc.* **2005**, *127*, 16641–16651.
[71] H. C. Foley, R. H. Morris, T. S. Targos, G. L. Geoffroy, *J. Am. Chem. Soc.* **1981**, *103*, 7337–7339.
[72] R. D. Adams, B. Captain, *Angew. Chem. Int. Ed.* **2005**, *44*, 2531–2533; R. D. Adams, B. Captain, C. Beddie, M. B. Hall, *J. Am. Chem. Soc.* **2007**, *129*, 986–1000.
[73] R. D. Adams, B. Captain, M. D. Smith, *Angew. Chem. Int. Ed.* **2006**, *45*, 1109–1112.
[74] D. J. Evans, C. J. Pickett, *Chem. Soc. Rev.* **2003**, *32*, 268–275.
[75] P. M. Vignais, *Coord. Chem. Rev.* **2005**, *249*, 1677–1690.
[76] A. C. Marr, D. J. E. Spencer, M. Schröder, *Coord. Chem. Rev.* **2001**, *219*, 1055–1074.
[77] S. Ogo, R. Kabe, K. Uehara, B. Kure, T. Nishimura, S. C. Menon, R. Harada, S. Fukuzumi, Y. Higuchi, T. Ohhara, T. Tamada, R. Kuroki, *Science* **2007**, *316*, 585–587.
[78] A. K. Justice, R. C. Linck, T. B. Rauchfuss, S. R. Wilson, *J. Am. Chem. Soc.* **2004**, *126*, 13214–13215.
[79] X. Zhao, I. P. Georgakaki, M. L. Miller, R. Mejia-Rodriguez, C. Y. Chiang, M. Y. Darensbourg, *Inorg. Chem.* **2002**, *41*, 3917–3928.
[80] J. L. Nehring, D. M. Heinekey, *Inorg. Chem.* **2003**, *42*, 4288–4292.
[81] N. N. Greenwood and A. Earnshaw, *Chemistry of the Elements*, Butterworth-Heinemann, Oxford, **1997**.
[82] J. M. Bemis, L. F. Dahl, *J. Am. Chem. Soc.* **1997**, *119*, 4545–4546.
[83] M. N. Vargaftik, V. P. Zagorodnikov, I. P. Stolyarov, I. I. Moiseev, V. A. Likholobov, D. I. Kochubey, A. L. Chuvilin, V. I. Zaikovsky, K. I. Zamaraev, G. I. Timofeeva, *J. Chem. Soc., Chem. Commun.* **1985**, 937–939.
[84] G. Schmid, M. Harms, J. O. Malm, J. O. Bovin, J. Vanruitenbeck, H. W. Zandbergen, W. T. Fu, *J. Am. Chem. Soc.* **1993**, *115*, 2046–2048.
[85] A. Züttel, C. Nutzenadel, G. Schmid, D. Chartouni, L. Schlapbach, *J. Alloys Compd.* **1999**, *295*, 472–475.
[86] A. Züttel, C. Nutzenadel, G. Schmid, C. Emmenegger, P. Sudan, L. Schlapbach, *Appl. Surf. Sci.* **2000**, *162*, 571–575.
[87] C. Nutzenadel, A. Züttell, D. Chartouni, G. Schmid, L. Schlapbach, *Eur. Phys. J. D* **2000**, *8*, 245–250.
[88] A. Pundt, M. Suleiman, C. Bahtz, M. T. Reetz, R. Kirchheim, N. M. Jisrawi, *Mater. Sci. Eng. B* **2004**, *108*, 19–23.
[89] A. Anson, E. Lafuente, E. Urriolabeitia, R. Navarro, A. M. Benito, W. K. Maser, M. T. Martinez, *J. Phys. Chem. B* **2006**, *110*, 6643–6648.
[90] W. C. Conner, J. L. Falconer, *Chem. Rev.* **1995**, *95*, 759–788.

Received: June 27, 2007
Published Online: September 5, 2007

 © 2007 Wiley-VCH Verlag GmbH & Co. KGaA, Weinheim 

DOI: 10.1002/ejic.200700768

# Remarkable Functions of Long-Chain Alkyl Groups in Halogen-Bridged Nickel(III) Nanowire Complexes

**Hideki Ohtsu,*[a] Shinya Takaishi,[b] Keita Imamura,[b] Ayumi Ishii,[a] Koji Tanaka,[c] Miki Hasegawa,[a] and Masahiro Yamashita*[b]**

**Keywords:** Nickel / Nanostructures / Long-chain alkyl groups / Average-valent compounds / Thin films

The long-chain alkyl groups of new bidentate ligands make it possible to generate nickel MX–chain complexes exhibiting the shortest $Ni^{III}$–$Ni^{III}$ distance among all MX–chain compounds reported. Dissolution in organic solvents occurs without dissociation of the MX–chain units, and the successful fabrication of thin films is reported.
(© Wiley-VCH Verlag GmbH & Co. KGaA, 69451 Weinheim, Germany, 2007)

## Introduction

Much attention has been paid to quasi-one-dimensional assembled electronic systems in the fields of chemistry and physics because these compounds exhibit novel phenomena such as the generation of solitons and polarons in π-conjugated polymers,[1,2] metallic-[3] and super-conductivity,[4] and slow magnetic relaxation in several ferromagnetic and ferrimagnetic complexes.[5] Among such one-dimensional compounds, halogen-bridged quasi-one-dimensional transition-metal complexes (MX–chain complexes) have been one of the most important and attractive research objectives, as they exhibit various electronic states and many noticeable physical properties such as intense charge-transfer bands,[6] overtone progressions of the resonance Raman spectra,[7] intense luminescence spectra with large Stokes shifts,[8] photogeneration[9] and long-range migration[10] of solitons and polarons, and gigantic third-order optical nonlinearity,[11] etc.

The electronic structures of MX–chain compounds have been regarded as extended Peierls–Hubbard models,[12] where the electron–phonon interaction ($S$), electron transfer ($T$), and intra- and intersite Coulomb repulsion energies ($U$ and $V$, respectively) compete or cooperate with each other. Pt and Pd compounds indicate charge-density-wave (CDW) states caused by the strong $S$, where the bridging halide ions are displaced from the midpoints between the neighboring two metal ions (···$M^{II}$···$X^-$–$M^{IV}$–$X^-$···$M^{II}$···$X^-$–$M^{IV}$–$X^-$···).[13,14] On the other hand, Ni compounds are Mott–Hubbard-type MX–chain complexes induced by the strong $U$, where the bridging halide ions are located at the midpoints between the neighboring two metal ions (–$M^{III}$–$X^-$–$M^{III}$–$X^-$–$M^{III}$–$X^-$–$M^{III}$–$X^-$–).[13,15]

A number of MX–chain complexes have so far been synthesized and characterized to provide further valuable insight into the characteristic electronic structures and unique physical properties. In particular, the MX–chain complex $[Ni^{III}(chxn)_2Br]Br_2$[16] has been attracting much attention because it shows the largest gigantic third-order optical nonlinearity [$\chi^{(3)}$ = ca. $10^{-4}$ esu].[11] The special feature of this compound, however, appears only in the solid state, as MX–chain units are disrupted in solution. The inherent instability of the complex in solution has precluded further development into useful molecular devices such as thin films.

Reported herein is the synthesis and characterization of nickel MX–chain complexes supported by new bidentate ligands with long-chain alkyl groups (Figure 1) that not only impart solubility to the MX–chain compounds but these groups also cause the shortening of the M–M distances, which can result in increased $\chi^{(3)}$ values.[11] Moreover, we attained the successful fabrication of thin films consisting of the MX–chain complexes, which can be promising candidates for optical switching devices.

[a] Department of Chemistry and Biological Science, College of Science and Engineering, Aoyama Gakuin University
5-10-1 Fuchinobe, Sagamihara 229-8558, Japan
Fax: +81-42-759-6493
E-mail: ohtsu@chem.aoyama.ac.jp
[b] Department of Chemistry, Graduate School of Science, Tohoku University and CREST (JST)
6-3 Aramaki Aza-Aoba, Aoba-ku, Sendai 980-8578, Japan
Fax: +81-22-795-6544
E-mail: yamasita@agnus.chem.tohoku.ac.jp
[c] Institute for Molecular Science
5-1, Higashiyama, Myodaiji, Okazaki 444-8787, Japan
Supporting information for this article is available on the WWW under http://www.eurjic.org or from the author.

 © 2007 Wiley-VCH Verlag GmbH & Co. KGaA, Weinheim 

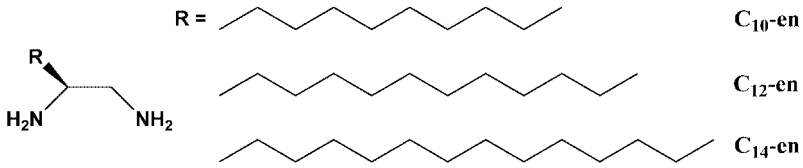


Figure 1. Structures of bidentate ligands having long-chain alkyl groups.

## Results and Discussion

The nickel MX–chain complexes, represented as $[Ni^{III}(C_n\text{-en})_2Br]Br_2$ [$n$ = 10 (**1**), 12 (**2**), and 14 (**3**)], were obtained as black microcrystals by puffing $Br_2$ gas into the corresponding nickel(II) complexes in ethanol, and the compositions of **1**, **2**, and **3** were determined by elemental analysis. The syntheses of these complexes afforded no well-shaped single crystals; however, we successfully obtained accurate powder X-ray diffraction (XRD) data for **1**, **2**, and **3** by synchrotron powder diffraction with a large Debye–Scherrer camera at 100 K and are able to image the XRD data for **3** by the Rietveld method as shown in Figure 2.[17,18]

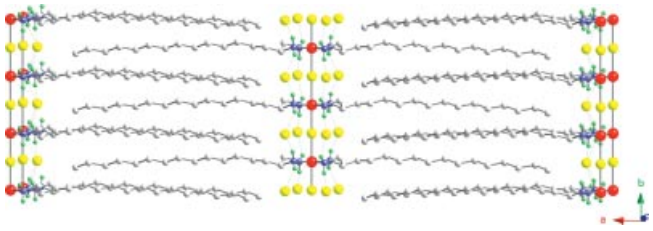

Figure 2. Representation of the molecular structure of **3** on the basis of the results of synchrotron XRD, IR, and EPR measurements (Ni red, Br yellow, C gray, H green, N blue).

$Ni^{III}$ ions and bromide ions are arranged alternately along the *b* axis to form the linear MX–chain structures. The linear chains are connected by hydrogen bonds between the hydrogen atoms of the amino group of the $C_{14}$-en ligand and the counter bromide ions, which is consistent with an IR spectrum exhibiting a signal due to the hydrogen-bonded N–H stretching mode of the ligand at 3005 $cm^{-1}$ (Figure S2).[19] The bridging bromide ions are placed at the midpoints between the neighboring two nickel ions, a fact that indicates the electronic structure of **3** is a Mott–Hubbard state, and the assignment of which is harmonious with the results of IR spectroscopy (Figure S2)[20] and temperature-dependent EPR measurements (Figure S3).[21] In the case of **1** and **2**, these molecular structures and electronic configurations are essentially the same as those of **3** except for the length of the alkyl chain of the bidentate ligands, and the structures are strongly supported by synchrotron XRD, IR, and EPR studies. It should be noted that the $Ni^{III}$–$Ni^{III}$ distance (5.06 Å) in all the complexes is the shortest among all of the MX–chain complexes reported so far {$[Ni^{III}(chxn)_2Br]Br_2$ 5.157(1) Å,[15,16] $[Ni^{III}(bn)_2Br]Br_2$ 5.136(6) Å,[22,23] $[Ni^{III}(pn)_2Br]Br_2$ 5.110(7) Å[22,24]}. Such a drastic shortening in the $Ni^{III}$–$Ni^{III}$ distance may be ascribed to the chemical pressure effect induced by the hydrophobic interaction between the long-chain alkyl groups of the bidentate ligands.

The function of the long-chain alkyl groups *cannot* confine itself to leading the chemical pressure effect. These groups of the ligands enable us to disperse the nickel MX–chain complexes in organic solvents without the decomposition of MX–chain cores and to fabricate thin films containing the MX–chain compounds. Figure 3 displays the absorption spectrum of **3** in chloroform solution and as a thin film together with that in the solid state at 298 K. The intense absorption band centered at 1.33 eV is observed in solution and as a thin film and is quite the same as that in the solid state.[25] This characteristic absorption band can be assigned to the charge-transfer band from the bridging bromide ion to the upper Hubbard band of the nickel $3d_{z^2}$ orbital along the MX–chain direction.[12] In addition, it should be noted that no absorption spectral disturbance caused by light scatterings is observed even in the higher energy region. In fact, the size of **3** (0.1–0.7 μm) as determined by scanning electron microscopy (SEM) is much smaller than the wavelength in the visible light region (Figure S5); the morphology and height distributions of the thin films characterized by using atomic force microscopy (AFM) analysis are quite smooth and $1.54 \pm 0.03$ μm in thickness (Figure S6). The lack of interruption due to light scatterings can thus be the reason why nickel MX–chain complex **3** is dispersed uniformly in solution and as a thin film with the help of the long-chain alkyl groups.[26]

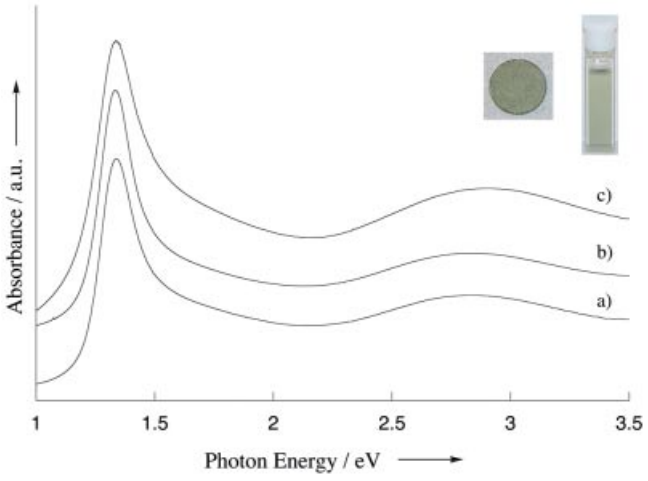


Figure 3. Absorption spectra of **3** in (a) chloroform solution, (b) film state, and (c) solid state at 298 K. Inset: Photographs of **3** (right) in solution and (left) as a thin film.

 © 2007 Wiley-VCH Verlag GmbH & Co. KGaA, Weinheim 

## Conclusions

We successfully synthesized nickel MX–chain complexes exhibiting not only the shortest $Ni^{III}$–$Ni^{III}$ distance among all MX–chain compounds reported. The solubility of these compounds in organic solvents occurs without dissociation of the MX–chain units bearing new bidentate ligands containing the long-chain alkyl groups. Moreover, the successful fabrication of thin films consisting of the nickel nanowire complex has been accomplished by the spin-coating method. These results provide valuable information for the further development of MX–chain complexes having many interesting physical properties derived from one-dimensional electronic systems and shed light on the applications of functional transition-metal complexes.

## Experimental Section

**Materials:** All chemicals used for the synthesis of the ligands and complexes were commercial products of the highest available purity and were further purified by standard methods.[27] Solvents were also purified by standard methods before use.[27]

**Synthesis:** All ligands and complexes used in this study were prepared according to the following procedures, and the structures of the products were confirmed by analytical data (vide infra).

**(*S*)-Dodecane-1,2-diamine ($C_{10}$-en), (*S*)-Tetradecane-1,2-diamine ($C_{12}$-en), and (*S*)-Hexadecane-1,2-diamine ($C_{14}$-en):** These ligands were synthesized by a literature procedure.[28,29]

**$[Ni^{II}(C_{10}\text{-en})_2Br_2]$:** To a methanol solution of $C_{10}$-en (1.002 g, 5.0 mmol) was added $NiBr_2{\cdot}3H_2O$ (0.681 g, 2.5 mmol) in methanol. Addition of ether to the resulting solution gradually gave pale violet powder that was collected by filtration and recrystallized from ethanol. Yield: 0.628 g (40.5%). $C_{24}H_{56}Br_2N_4Ni$ (619.25): calcd. C 46.55, H 9.11, N 9.04; found C 46.25, H 9.05, N 9.17.

**$[Ni^{II}(C_{12}\text{-en})_2Br_2]$:** This complex was prepared in the same manner as that for the synthesis of $[Ni^{II}(C_{10}\text{-en})_2Br_2]$ by using the $C_{12}$-en ligand instead of $C_{10}$-en. Yield: 1.016 g (60.2%). $C_{28}H_{64}Br_2N_4Ni$ (675.36): calcd. C 49.79, H 9.55, N 8.29; found C 49.34, H 9.02, N 8.28.

**$[Ni^{II}(C_{14}\text{-en})_2Br_2]$:** This complex was prepared in the same manner as that for the synthesis of $[Ni^{II}(C_{10}\text{-en})_2Br_2]$ by using the $C_{14}$-en ligand instead of $C_{10}$-en. Yield: 1.245 g (68.1%). $C_{32}H_{72}Br_2N_4Ni$ (731.47): calcd. C 52.54, H 9.92, N 7.65; found C 52.12, H 9.62, N 7.62.

**$[Ni^{III}(C_{10}\text{-en})_2Br]Br_2$ (1):** $Br_2$ gas was puffed in a ethanol suspension of $[Ni^{II}(C_{10}\text{-en})_2Br_2]$ (0.062 g, 0.1 mmol). Black powder immediately precipitated and was separated by filtration. Yield: 0.056 g (80.7%). $C_{24}H_{57}Br_3N_4NiO_{0.5}$ (708.16): calcd. C 40.70, H 8.11, N 7.91; found C 40.79, H 7.94, N 7.96.

**$[Ni^{III}(C_{12}\text{-en})_2Br]Br_2$ (2):** This complex was prepared in the same manner as that for the synthesis of $[Ni^{III}(C_{10}\text{-en})_2Br]Br_2$ by using $[Ni^{II}(C_{12}\text{-en})_2Br_2]$ instead of $[Ni^{II}(C_{10}\text{-en})_2Br_2]$. Yield: 0.073 g (96.0%). $C_{28}H_{66}Br_3N_4NiO$ (773.28): calcd. C 43.49, H 8.60, N 7.24; found C 43.32, H 8.25, N 7.25.

**$[Ni^{III}(C_{14}\text{-en})_2Br]Br_2$ (3):** This complex was prepared in the same manner as that for the synthesis of $[Ni^{III}(C_{10}\text{-en})_2Br]Br_2$ by using $[Ni^{II}(C_{14}\text{-en})_2Br_2]$ instead of $[Ni^{II}(C_{10}\text{-en})_2Br_2]$. Yield: 0.081 g (99.6%). $C_{24}H_{56}Br_2N_4Ni$ (619.25): calcd. C 46.34, H 8.99, N 6.75; found C 46.00, H 8.55, N 6.75.

**Fabrication of the Thin Films of 3:** Compound **3** (10.0 mg) was dispersed in chloroform (0.5 mL) containing PMMA (36.5 mg) with ultrasonication, and the resulting dispersion was filtered though a 1.0-μm membrane filter. The thin films were prepared from the blend solution by spin-coating on quartz substrates ($\phi$ = 10 mm).

**Measurements:** Synchrotron XRD measurements were carried out with a SPring-8 BL02B2 beam line to obtain XRD data with high angular resolution ($2\theta$ = 1–75°) at 100 K. The sample powders were sufficiently fine and gave a homogeneous intensity distribution in the Debye–Scherrer powder ring. The powder samples were enclosed in silica glass capillaries (0.3 mm internal diameter). The exposure time was 40 min, and reflections were collected on an imaging plate installed on a large Debye–Scherrer camera. The wavelength of the incident X-rays was ≈ 1.0 Å, which was calibrated by using standard $CeO_2$ powder. The structure was solved by the Rietveld technique, and the hydrogen atoms of the $NH_2$ group were located at the calculated positions. Infrared spectra were measured as KBr disks with a JASCO FTIR-620 spectrophotometer. EPR spectra were taken with a JEOL JES-FA200 equipped with an attached VT (Variable Temperature) apparatus and were recorded under nonsaturating microwave power conditions. The magnitude of the modulation was chosen to optimize the resolution and the signal-to-noise ratio of the observed spectra. The *g* values were calibrated with a $Mn^{II}$ marker used as a reference. Electronic absorption spectra were recorded with a Shimadzu UV-3100PC spectrophotometer with the samples prepared as KBr pellets in the case of the solid states. SEM measurements were performed with a JEOL JSM-6390LA operated at an accelerating voltage of 1.5 kV. Samples for SEM studies were prepared by placing a drop of the chloroform dispersion of the nanowire complexes on a piece of Pt plate under ambient conditions; the sample was then dried and stored in vacuo for SEM characterization. AFM imaging was carried out in noncontact mode with a JEOL JSPM-5200. Elemental analyses were carried out at the Research and Analytical Center for Giant Molecules, Graduate School of Science, Tohoku University.

**Supporting Information** (see footnote on the first page of this article): XRD, IR, EPR, absorption spectra, SEM, and AFM data.

## Acknowledgments

The synchrotron radiation X-ray powder diffraction experiments were performed at Spring-8 BL02B2 with the approval of the Japan Synchrotron Radiation Research Institute (JASRI) (proposal no. 2006A1646). We are grateful to Dr. Keiichi Osaka, Dr. Kenichi Kato, and Prof. Masaki Takata for helpful experiments at JASRI and to Dr. Eiji Nishibori, Prof. Masaki Takata, and Prof. Makoto Sakata for permitting the use of their Rietveld program. We also thank JEOL Ltd. for SEM measurements. This work was partly supported by a grant from the Aoyama Gakuin 21st Century COE Program and supported in part by a Grant-in-Aid for Scientific Research on Priority Areas (Chemistry of Coordination Space) from the Ministry of Education, Culture, Sports, Science, and Technology.

[1] I. B. Goldberg, H. R. Crowe, P. R. Newman, A. J. Heeger, A. G. MacDiarmid, *J. Chem. Phys.* **1979**, *70*, 1132–1136.
[2] W. P. Su, J. R. Schrieffer, A. J. Heeger, *Phys. Rev. B* **1980**, *22*, 2099–2111.
[3] a) H. Yersin, G. Gliemann, *Ann. N. Y. Acad. Sci.* **1978**, *313*, 539–559; b) J. S. Miller (Ed.), *Extended Linear Chain Compounds, Vols. 1–3*, Plenum, New York, **1982**.
[4] a) J. G. Bednorz, K. A. Mueller, *Z. Phys.* **1986**, *64*, 189–193; b) M. K. Wu, J. R. Ashburn, C. J. Torng, P. H. Hor, R. L. Meng,

 © 2007 Wiley-VCH Verlag GmbH & Co. KGaA, Weinheim 

L. Gao, Z. J. Huang, Y. Q. Wanag, C. W. Chu, *Phys. Rev. Lett.* **1987**, *58*, 908–910.
[5] a) A. Caneschi, D. Gatteschi, N. Lalioti, C. Sangregorio, R. Sessoli, G. Venturi, A. Vindigni, A. Rettori, M. G. Pini, M. A. Novak, *Angew. Chem.* **2001**, *113*, 1810–1813; *Angew. Chem. Int. Ed.* **2001**, *40*, 1760–1763; b) R. Clérac, H. Miyasaka, M. Yamashita, C. Coulon, *J. Am. Chem. Soc.* **2002**, *124*, 12837–12844; c) R. Lescouëzec, J. Vaissermann, C. Ruiz-Pérez, F. Lloret, R. Carrasco, M. Julve, M. Verdaguer, Y. Dromzee, D. Gatteschi, W. Wernsdorfer, *Angew. Chem.* **2003**, *115*, 1521–1524; *Angew. Chem. Int. Ed.* **2003**, *42*, 1483–1486.
[6] a) M. Tanaka, S. Kurita, T. Kojima, Y. Yamada, *Chem. Phys.* **1984**, *91*, 257–265; b) Y. Wada, T. Mitani, M. Yamashita, T. Koda, *J. Phys. Soc. Jpn.* **1985**, *54*, 3143–3153.
[7] a) R. J. H. Clark, M. L. Franks, W. R. Trumble, *Chem. Phys. Lett.* **1976**, *41*, 287–292; b) R. J. H. Clark, M. Kurmoo, D. N. Mountney, H. Toftlund, *J. Chem. Soc. Dalton Trans.* **1982**, 1851–1860; c) R. J. H. Clark, *Adv. Infrared Raman Spectrosc.* **1983**, *11*, 95–130.
[8] H. Tanino, K. Kobayashi, *J. Phys. Soc. Jpn.* **1983**, *52*, 1446–1456.
[9] H. Okamoto, T. Mitani, K. Toriumi, M. Yamashita, *Phys. Rev. Lett.* **1992**, *69*, 2248–2251.
[10] N. Kimura, S. Ishimaru, R. Ikeda, M. Yamashita, *J. Chem. Soc. Faraday Trans.* **1998**, *94*, 3659–3663.
[11] H. Kishida, H. Matsuzaki, H. Okamoto, T. Manabe, M. Yamashita, Y. Taguchi, Y. Tokura, *Nature* **2000**, *405*, 929–932.
[12] H. Okamoto, Y. Shimada, Y. Oka, A. Chainani, T. Takahashi, H. Kitagawa, T. Mitani, K. Toriumi, K. Inoue, T. Manabe, M. Yamashita, *Phys. Rev. B* **1996**, *54*, 8438–8445.
[13] M. B. Robin, P. Day, *Adv. Inorg. Chem. Radiochem.* **1967**, *10*, 247–422.
[14] A. Hazell, *Acta Crystallogr., Sect. C* **1991**, *47*, 962–966.
[15] K. Toriumi, Y. Wada, T. Mitani, S. Bandow, M. Yamashita, Y. Fujii, *J. Am. Chem. Soc.* **1989**, *111*, 2341–2342.
[16] chxn = (1*R*,2*R*)-diaminocyclohexane.
[17] The reliability factors based on the powder pattern ($R_{wp}$) and the Bragg integrated intensities ($R_I$) were 8.78 and 11.7%, respectively. Observed and calculated synchrotron X-ray powder diffraction patterns and the determined unit cell parameters are given in Figure S1 and Table S1, respectively.
[18] Only one orientation of the disordered long-chain alkyl group is shown for the sake of clarity.
[19] IR measurements around 3000 $cm^{-1}$ are good probes for elucidating the electronic states of the MX–chain complexes. A Mott–Hubbard state shows a singlet $\nu$(N–H) signal, whereas a CDW state exhibits a double $\nu$(N–H) signal; see ref.[20]
[20] K. Okaniwa, H. Okamoto, T. Mitani, K. Toriumi, M. Yamashita, *J. Phys. Soc. Jpn.* **1991**, *60*, 997–1004.
[21] H. Okamoto, K. Toriumi, T. Mitani, M. Yamashita, *Phys. Rev. B* **1990**, *42*, 10381–10387.
[22] M. Sasaki, S. Takaishi, H. Miyasaka, K. Sugiura, M. Yamashita, *J. Am. Chem. Soc.* **2005**, *127*, 14958–14959.
[23] bn = (2*R*,3*R*)-diaminobutane.
[24] pn = (*R*)-1,2-diaminopropane.
[25] The same absorption bands are observed in the case of **1** (1.33 eV) and **2** (1.33 eV); see Figure S4.
[26] a) N. Kimizuka, N. Oda, T. Kunitake, *Inorg. Chem.* **2000**, *39*, 2684–2689; b) N. Kimizuka, S. H. Lee, T. Kunitake, *Angew. Chem.* **2000**, *112*, 402–404; *Angew. Chem. Int. Ed.* **2000**, *39*, 389–391; c) N. Kimizuka, *Adv. Mater.* **2000**, *12*, 1461–1463.
[27] D. D. Perrin, W. L. F. Armarego, *Purification of Laboratory Chemicals*, Butterworth–Heinemann, Oxford, **1988**.
[28] L. He, H.-S. Byun, R. Bittman, *J. Org. Chem.* **2000**, *65*, 7618–7626.
[29] S. G. Gouin, J. F. Gestin, K. Joly, A. Loussouarn, A. Reliquet, J. C. Meslin, D. Deniaud, *Tetrahedron* **2002**, *58*, 1131–1136.

Received: July 19, 2007
Published Online: August 28, 2007

 © 2007 Wiley-VCH Verlag GmbH & Co. KGaA, Weinheim 

DOI: 10.1002/ejic.200700726

# Treating $[K_4(H_2O)_{0.5}][SnTe_4]$ with $PPh_4^+$ or $AsPh_4^+$: Formation of a Highly Air-Stable Tellurostannate Salt, a Tellurolate with One-Coordinate Te Atoms, and a Polytelluride Salt with $^1_\infty[Te_4(H_2O)_2]^{2-}$ Chains

**Eugen Ruzin,[a] Werner Massa,[a] and Stefanie Dehnen*[a]**

*Dedicated to Professor Dieter Fenske on the occasion of his 65th birthday*

**Keywords:** Arsonium salts / Phosphonium salts / Tellurolate / Tellurostannate / Polytelluride / X-ray diffraction

In reactions of potassium orthotellurostannates with $EPh_4Cl$ (E = P, As), different single-crystalline products are obtained. An air-stable dimeric tellurostannate forms by partial replacement of strongly interacting $K^+$ cations by weakly interacting or noninteracting $[PPh_4]^+$ ions. For E = As, an equally air-stable tellurophenolate, in which Te has the rare coordination number 1, results upon As–C bond cleavage at a tetraphenylarsonium cation. Oxidation of the air-sensitive $[Sn_2Te_6]^{4-}$ anion and $Te^{2-}$ by $O_2$ (air) affords a tetratelluride salt with strands of $H_2O$-bridged $[Te_4]^{2-}$ anions.
(© Wiley-VCH Verlag GmbH & Co. KGaA, 69451 Weinheim, Germany, 2007)

## Introduction

The influence of counterions on both structure and reactivity of complex anions and anionic networks is subtle and therefore actively investigated.[1] Ion-exchange reactions in solution may lead to either crystallization of the anionic structure with another cation or the crystallization of another anionic species than originally used due to a lower solubility of further co-existing components of the equilibrium in solution, or even upon a chemical reaction. Being interested in the effect of bulky cations on the properties of chalcogenostannate anions, we have performed reactions of the highly reactive potassium salt of $[SnTe_4]^{4-}$ with $EPh_4Cl$ (E = P, As). For E = P, the phosphonium salt of dimeric $[Sn_2Te_6]^{4-}$ crystallized – similar to observations that have been made in the presence of $NR_4^+$ cations.[2] However, this salt shows an unexpected air-stability which is unique for tellurostannate compounds. A completely different behavior was observed for E = As, where the only crystalline product evinced to be a tellurolate salt with Te in its rare coordination number 1. If air is allowed to diffuse into the reaction mixture, the tellurolate salt remains unaffected, whereas unreacted telluride species are oxidized to form a novel tetratelluride compound.

## Results and Discussion

$[K_2(MeOH)_6][PPh_4]_2[Sn_2Te_6]$ (**1**), $[AsPh_4][TePh(H_2O)_{0.5}]$ (**2**), and $[AsPh_4]_2[Te_4(H_2O)_2]$ (**3**) were obtained by reactions of $[K_4(H_2O)_{0.5}][SnTe_4]$[3] with $PPh_4Cl$ or $AsPh_4Cl$ (Scheme 1). All compounds have been structurally characterized by means of single-crystal X-ray diffraction.[4,5] Table 1 summarizes the crystallographic data. The anion of compound **1** is the product of a dimerization reaction [Equation (1)] that is based on an aggregation equilibrium [Equation (2)], which is known to occur in protic solutions of $[SnQ_4]^{4-}$ anions (Q = S, Se, Te).[6] However, the reported shift of the respective equilibrium when decreasing the pH value upon addition of acid or dilution of the solution cannot be the reason for the crystallization of the dimeric anion here, since the addition of $PPh_4Cl$ does not affect the pH value. Thus, the observation is rather the result of better crystallization due to better matching sizes of cations and anions when the anionic diameter is increased. Figure 1 shows fragments of the crystal packing in **1**.

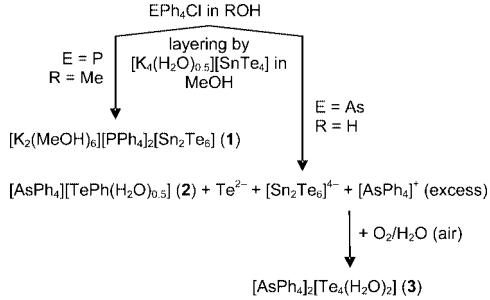


Scheme 1. Syntheses of compounds **1**, **2**, and **3**.

The asymmetric unit in **1** comprises half a formula unit, i.e. one half of the hexatellurostannate dimer, "$SnTe_3$", one potassium cation, one tetraphenylphosphonium cation, and

[a] Philipps-Universität Marburg, Fachbereich Chemie, Hans-Meerwein-Strasse, 35043 Marburg, Germany
E-mail: dehnen@chemie.uni-marburg.de

 © 2007 Wiley-VCH Verlag GmbH & Co. KGaA, Weinheim 

$$2\,[SnTe_4]^{4-} + 2\,[PPh_4]^{+} + 6\,MeOH \rightarrow [K_2(MeOH)_6][PPh_4]_2[Sn_2Te_6]\,(\mathbf{1}) + 2\,Te^{2-} \quad (1)$$

$$2\,[SnQ_4]^{4-} \rightleftarrows [Sn_2Q_6]^{4-} + 2\,Q^{2-}\ (Q = S, Se, Te) \quad (2)$$

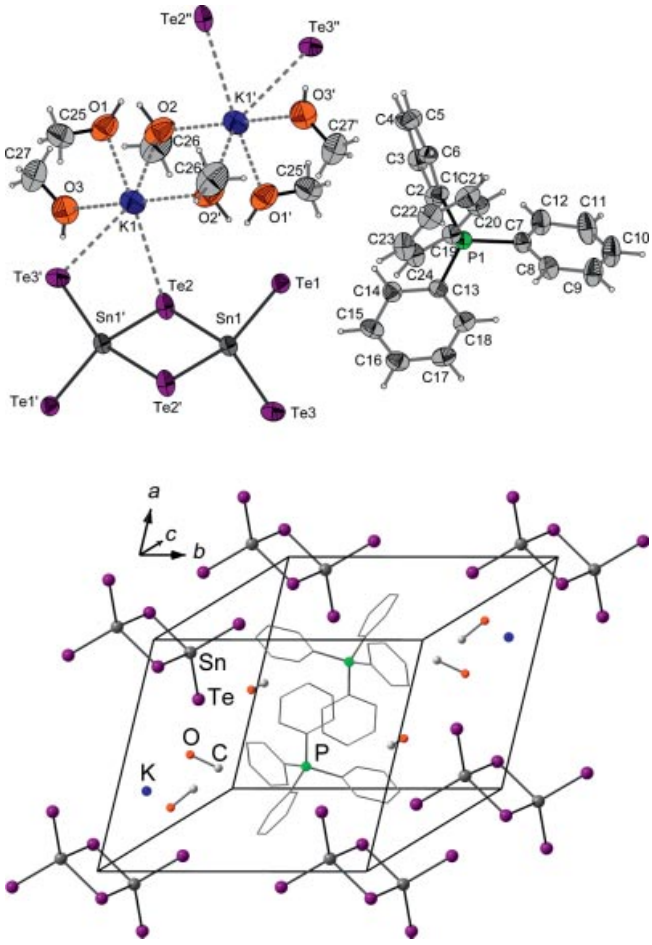


Figure 1. Top: relative orientation of the tetraphenylphosphonium cation, potassium cations within their coordination sphere, and an $[Sn_2Te_6]^{4-}$ anion in **1**. Thermal ellipsoids are drawn to 50% probability. Selected interatomic distances [Å] and angles [°]: Sn–$Te_t$ 2.682(1)–2.806(1), Sn–(μ-Te) 2.794(8)–2.806(1), Sn1···Sn1′ 3.799(1), P–C 1.783(8)–1.793(9), Te···(H–)O 3.481(6)–3.578(10), Te···K 3.383(4)–3.766(4), Te···H(–C) 3.147(5)–3.577(2) K···$O_t$ 2.753(11)–2.789(11), K···(μ-O) 2.670(13)–2.728(11); $Te_t$–Sn–μ-Te 108.41(3)–115.05(3), Te1–Sn–Te3 114.37(3), Te2–Sn–Te2 94.55(3), C–P–C 109.5(3). The subscript "t" denotes terminal atoms. Bottom: fragment of the crystal packing in **1**. H atoms are omitted for clarity.

three MeOH molecules. The latter coordinate to $K^+$ ions to form a coordination aggregate of two edge-sharing octahedra, $[(MeOH)_2Te_2K(\mu\text{-}MeOH)]_2$, the Te donor atoms arising from two adjacent $[Sn_2Te_6]^{4-}$ anions that are linked this way. In addition, all MeOH molecules form hydrogen bonds to terminal tellurium atoms. $PPh_4^+$ cations do not seem to interact significantly with any of the further components. The shortest interatomic distance Te···H–C around the phosphonium group is 3.147(5) Å. Compound **1** is unexpectedly air-stable: although the starting compound, $[K_4(H_2O)_{0.5}][SnTe_4]$, decomposes within seconds upon contact with air, **1** remains unchanged for several days at room temperature. This is in contrast to the air-sensitivity of recently reported $[Mn(en)_3]_2[Sn_2Te_6]{\cdot}nH_2O$[7–9] and $[K_2(2,2,2\text{-crypt-}K)_2][Sn_2Te_6]$.[10] Although all of these salts contain bulky cations, the noninteracting $PPh_4^+$ ion seems to protect the $[Sn_2Te_6]^{4-}$ groups most effectively. This might be due to its own distinct indifference toward air, i.e. its insensitivity toward hydration or oxidation.

The synthesis of compound **2** provides feasible access to the very rare tellurophenolate anion, that could so far only be obtained by using a multistage synthesis in liquid ammonia:[11] free telluride anions, which were obtained according to Equation (2), combine with a phenyl rest of a tetraphenylarsonium cation [Equation (3)]. This observation is in agreement with similar bond strengths of As–C bonds ($E_{Diss}$ = 252 kJ/mol)[12a] and Te–C bonds ($E_{Diss}$ ≈ 250 kJ/mol)[12b,c] in comparison with somewhat stronger P–C bonds ($E_{Diss}$ = 264 kJ/mol)[12d] that are less likely to break.

Compound **2** contains two crystallographically independent cations, two crystallographically independent anions, and one water molecule per asymmetric unit. The latter is situated between two tellurium atoms, forming two hydrogen bonds (Figure 2). Most of the crystal structures of known compounds containing $RTe^-$ exhibit direct Te···A interactions involving the metal counterion $A^+$. For instance, even in the structures of mesitylene analogs with large counterions $[Na(tmeda)_2]^+$ or $[K(18\text{-crown-}6)]^+$, one observes direct Te···A contacts (Te···Na 3.494 Å, Te···K 3.499 Å).[13] Compound **2** is thus one of the very few examples in which Te exhibits the rare coordination number 1. To the best of our knowledge, these are up to now the tellurocyanate $[Ph_3P{=}N{=}PPh_3][TeCN]$,[14] two 2-thienyl analogs, $[PPh_4][C_4H_3STe]$ and its 5-methyl derivative, tetraphenylphosphonium 2-tellurido-5-methylthiophene,[15] and $[Li(THF)_4][(PhMe_2Si)_3C\text{–}Te]$,[16] all four with bulky, weakly interacting cations. However, the low coordination number does not seem to affect the Te–C distances: in **2**, the Te–C distances (2.130 Å on average) range between the extremely short value in the tellurocyanate (2.020 Å) and that in the tris(phenyldimethyl)silyl tellurolate (2.270 Å), all of which do not differ significantly from the Te–C distances of the metal coordinating tellurolates [2.135(5) or 2.150(3) Å].[13]

$$2\,[SnTe_4]^{4-} + 2\,[AsPh_4]^{+} + 0.5H_2O \rightarrow [AsPh_4][TePh(H_2O)_{0.5}]\,(\mathbf{2}) + AsPh_3 + Te^{2-} + [Sn_2Te_6]^{4-} \quad (3)$$

 © 2007 Wiley-VCH Verlag GmbH & Co. KGaA, Weinheim 

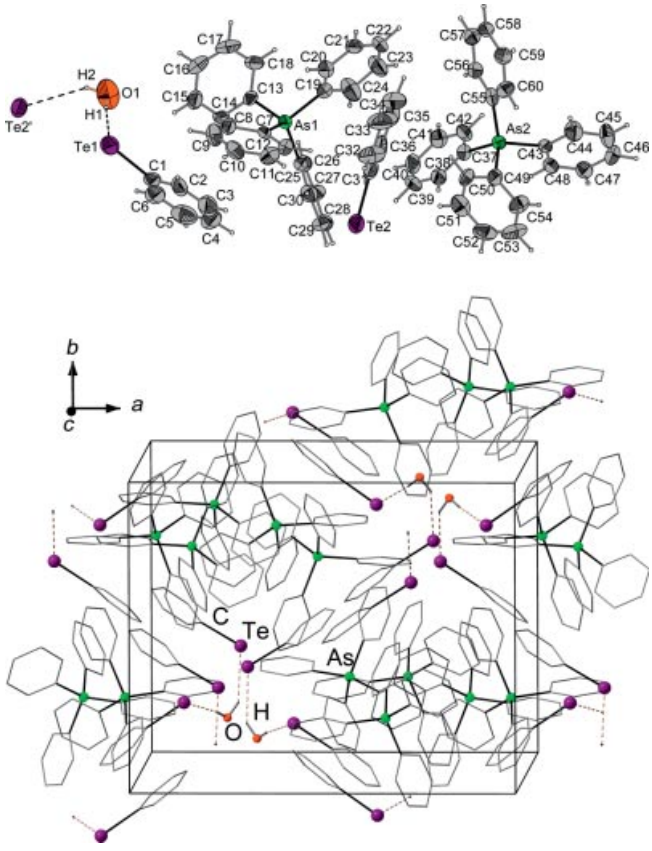


Figure 2. Top: relative orientation of independent cations, anions, and one water molecule in **2**, showing the two independent formula units within one asymmetric unit. Adjacent Te···H distances are indicated by dashed lines. Thermal ellipsoids are drawn to 50% probability. Selected interatomic distances [Å] and angles [°]: As–C 1.899(9)–1.941(8), Te–C 2.123(9)–2.136(10), Te···(H–)O 3.654(9)–3.736(8), Te···H(–C) 3.469(1)–3.553(1); C–As–C 109.3(1). Bottom: fragment of the crystal packing in **2**, viewed down the crystallographic *a* axis. H atoms at C are omitted for clarity.

Being interested in the air-stability of **2** within the mother liquor, we allowed air to enter into the reaction mixture for a second. After three months, compound **3** was obtained in addition to unchanged **2**. Upon slow oxidation of the $[Sn_2Te_6]^{4-}$ and $Te^{2-}$ ions [cf. Equation (3)] by air according to Equation (4), the reaction solution turned from red to transparent – an unambiguous hint that oxidation has taken place [Equation (4)].

By the same reaction that led to the synthesis of **1** here [cf. Equation (1)], Haushalter and co-workers obtained a mixture of $[PPh_4]_2[Te_4(MeOH)_2]$ and another, not further specified, tin-containing product.[17] Similar to the process observed here [Equation (4)], intrusion of air caused the formation of the polytelluride. The crystal structure of **3** comprises isolated tetraphenylarsonium cations and water-bridged tetratelluride anions. The relative orientation of the ions are shown as fragments of the crystal packing in **3** (Figure 3). Te1 and Te4 lie one on top of each other in the direction of the crystallographic *a* axis. Thus, the anionic substructure resembles the arrangement of the infinite chains $^1_\infty Te_n$ in elemental α-tellurium,[18] which have been formally cleaved by addition of two extra electrons after every fourth atom, thereby enlarging the Te–Te–Te angles [109.24(1)° and 109.01(1)° in **3**, 103.2° in α-Te]. The dihedral angle Te1–Te2–Te3–Te4 [103.94(1)°] is slightly larger than those in other tetratellurides, such as $[PPh_4]_2[Te_4(MeOH)_2]$ [99.85(12)°] or $[Sr(15\text{-crown-}5)_2][Te_4(H_2O)]$ [102.47(1)°].[19] A significant structural difference between **3**

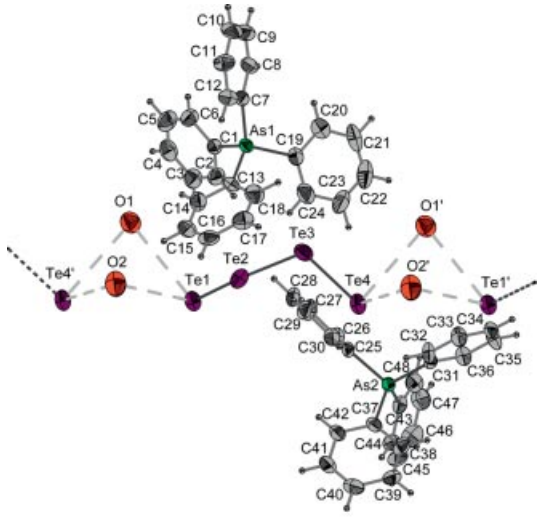


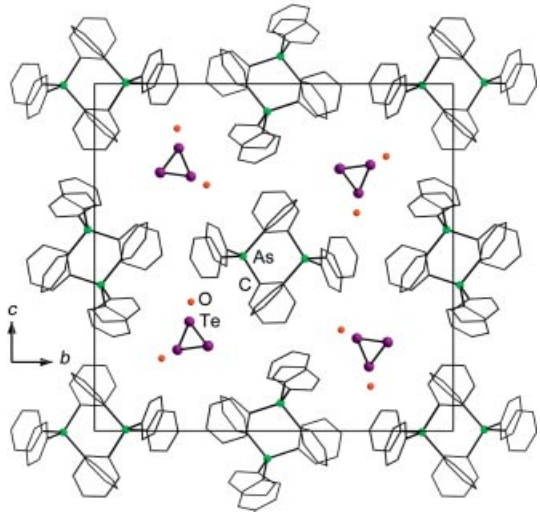


Figure 3. Top: relative orientation of the two independent cations, one tetratelluride anion and bridging water molecules in **3**. Adjacent Te···(H–)O distances are indicated by dashed lines. Thermal ellipsoids are drawn to 50% probability. Selected interatomic distances [Å] and angles [°]: As–C 1.882(10)–1.930(4), Te···(H–)O 3.628(47)–3.703(14), Te1–Te2 2.690(34), Te2–Te3 2.731(36), Te3–Te4 2.718(5), Te1···Te4′ 4.749(1), Te···H(–C) 3.103(1)–3.406(11); C–As–C 109.7(7), Te1–Te2–Te3 109.24(1), Te2–Te3–Te4 109.01(1). Bottom: fragment of the crystal packing in **3**. H atoms are omitted for clarity.

$$[Sn_2Te_6]^{4-} + 2\ Te^{2-} + 3\ O_2 + 8\ H_2O + 4\ [AsPh_4]^+ \rightarrow 2\ [AsPh_4]_2[Te_4(H_2O)_2]\ (\mathbf{3}) + 2\ [Sn(OH)_6]^{2-} \quad (4)$$

 © 2007 Wiley-VCH Verlag GmbH & Co. KGaA, Weinheim 

and known $[Te_4]^{2-}$ compounds is the coordination sphere around the polytelluride anion: while two methanol molecules each form one hydrogen bond to the terminal tellurium atoms of one polytelluride anion in $[PPh_4]_2[Te_4(MeOH)_2]$,[17] two bridging water molecules lead to the formation of a one-dimensional coordination polymer $^1_\infty[Te_4(H_2O)_2]^{2-}$ in **3**. In other known hydrates of alkali(ne earth) metal polytellurides, $H_2O$ molecules either coordinate to the metal counterion, like in $\{[BaCl(18\text{-crown-}6)(dmf)_2]_2[BaCl(18\text{-crown-}6)(dmf)(H_2O)]_2[Te_4]_2\}$,[16] or one molecule is connected to both ends of one $Te_4^{2-}$ unit through hydrogen bonds, like in $[Sr(15\text{-crown-}5)_2][Te_4(H_2O)]$. Te···(H–)O hydrogen bonds to water {e.g. in **2**, **3**, and $[Sr(15\text{-crown-}5)_2][Te_4(H_2O)]$} are by 11.1 pm longer on average than Te···(H–)O contacts to methanol molecules {e.g. in **1** or $(PPh_4)_2[Te_4(MeOH)_2]$}. Beside the supramolecular arrangement, the structural parameters [see Figure 3 (bottom)] are very similar to those in the cited tetratellurides and show the same characteristic distribution of bond lengths along the polytelluride chain as reported for all structurally characterized polychalcogenides.[20]

## Conclusions

An uncommon synthesis route into a single-crystalline, surprisingly air-stable tellurostannate salt (**1**), a tellurolate salt (**2**), and a tetratelluride salt (**3**) provided high-yield access to these homologues of silicate, thiophenolate, or polysulfide compounds. The presented crystal structures extend the yet limited number of structural reports of $[Sn_2Te_6]^{4-}$, $[TePh]^-$, and $[Te_n]^{2-}$ salts. The synthesis of compound **2** represents a remarkably simple alternative to known syntheses of chalcogenophenolate compounds under drastic conditions. The investigations showed that the nature of cations (and solvent molecules) significantly affect the nature of the stabilized anion and the resulting crystal packing.

## Experimental Section

**General:** All synthesis steps were performed under exclusion of air and external moisture (Ar atmosphere at a high-vacuum, double-manifold Schlenk line or $N_2$ atmosphere in a glove box), unless otherwise noted. MeOH was dried and freshly distilled prior to use; water was degassed by applying dynamic vacuum ($10^{-3}$ Torr) for 1 h.

**$[K_2(MeOH)_6][PPh_4]_2[Sn_2Te_6]$ (1):** $PPh_4Cl$ (375 mg, 1 mmol) was drained in MeOH (5 mL). The solution was layered by a solution of $[K_4(H_2O)_{0.5}][SnTe_4]$ (159 mg, 0.2 mmol) in MeOH (5 mL). Dark red blocks of **1** crystallized after two days. Yield: 275 mg [0.161 mmol, 80.5% according to Equation (1)]. $C_{54}H_{58}K_2O_6P_2Sn_2Te_6$ (1946.20): calcd. C 33.33, H 3.00; found C 33.62, H 2.98.

**$[AsPh_4][TePh(H_2O)_{0.5}]$ (2):** $AsPh_4Cl$ (419 mg, 1 mmol) was drained in $H_2O$ (5 mL). The solution was layered by a solution of $[K_4(H_2O)_{0.5}][SnTe_4]$ (159 mg, 0.2 mmol) in MeOH (5 mL). Large orange parallelepipeds of **2** crystallized after one hour. Yield: 49 mg [0.084 mmol, 83.3% according to Equation (3)]. $C_{30}H_{26}AsO_{0.5}Te$ (597.03): calcd. C 60.35, H 4.39; found C 59.99, H 4.42.

**$[AsPh_4]_2[Te_4(H_2O)_2]$ (3):** Big black blocks of **3** crystallized after three months from the same solution as **2** upon opening the Schlenk tube for one second. Yield: 171 mg [0.130 mmol, 80.7% according to Equation (4)]. $C_{48}H_{44}As_2O_2Te_4$ (1313.07): calcd. C 43.91, H 3.38; found C 44.19, H 3.29.

Table 1. Crystal data and experimental details of the single-crystal X-ray analyses of compounds **1**, **2**, and **3**.

| | **1** | **2** | **3** |
|---|---|---|---|
| Empirical formula | $C_{54}H_{58}O_6K_2P_2Sn_2Te_6$ | $C_{30}H_{26}O_{0.5}AsTe$ | $C_{48}H_{44}O_2As_2Te_4$ |
| Formula weight [g mol$^{-1}$] | 1946.20 | 597.03 | 1313.07 |
| Crystal color and shape | dark red block | orange parallelepiped | black block |
| Crystal size [mm$^3$] | $0.30\times0.14\times0.14$ | $0.41\times0.15\times0.11$ | $0.26\times0.18\times0.11$ |
| Diffractometer | Stoe IPDS | Stoe IPDS | Stoe IPDS |
| Radiation ($\lambda$ [Å]) | Mo-$K_\alpha$ (0.71073) | Mo-$K_\alpha$ (0.71073) | Mo-$K_\alpha$ (0.71073) |
| Temperature [K] | 120 | 193 | 193 |
| Crystal system | triclinic | orthorhombic | monoclinic |
| Space group | $P\bar{1}$ (no. 2) | $Pca2_1$ (no. 29) | $P2_1/c$ (no. 14) |
| $a$ [Å] | 11.0590(7) | 17.5966(11) | 10.790(2) |
| $b$ [Å] | 12.7370(7) | 14.2255(14) | 21.173(4) |
| $c$ [Å] | 13.3224(7) | 20.5170(17) | 20.521(4) |
| $\alpha$ [°] | 75.252(4) | 90 | 90 |
| $\beta$ [°] | 67.782(5) | 90 | 93.48(3) |
| $\gamma$ [°] | 76.021(5) | 90 | 90 |
| $V$ [Å$^3$] | 1657.73(16) | 5135.8(7) | 4679.4(16) |
| $Z$ | 1 | 8 | 4 |
| $\rho_{calc}$ [g cm$^{-3}$] | 1.955 | 1.544 | 1.864 |
| $\mu$(Mo-$K_\alpha$) [mm$^{-1}$] | 3.556 | 2.45 | 3.909 |
| Reflections measured | 24634 | 29441 | 34351 |
| Unique reflections | 9072 | 9526 | 8572 |
| No. of parameters | 325 | 590 | 506 |
| $wR_2$ (all data) | 0.2183 | 0.0885 | 0.1458 |
| $R_1$ [$F_o > 4\sigma(F_o)$] | 0.0772 | 0.0425 | 0.0572 |
| $S$ (all data) | 1.008 | 0.858 | 1.042 |
| Largest diff. peak/hole [e$^-$ $10^{-6}$ pm$^{-3}$] | 4.548/–3.238 | 1.086/–0.757 | 1.12/–1.74 |
| Flack parameter[5] | – | 0.008(15) | – |

 © 2007 Wiley-VCH Verlag GmbH & Co. KGaA, Weinheim 

**Optical Absorption Spectrum of 1:** For the investigation of the optical absorption behavior of compound **1**, a UV/vis spectrum of the single crystalline material was recorded. As expected and in accordance with the visible color of the crystals, the onset of absorption – i.e. the lowest electronic excitation energy $E_g$ – of compound **1** (1.4 eV) is small. It is even smaller than that in $[Mn(en)_3]_2[Sn_2Te_6]\cdot 4H_2O$ (1.6 eV).[5]

**NMR Spectroscopy of 1:** The $^{125}$Te-NMR and $^{119}$Sn-NMR spectra of **1** served to prove the purity of this compound in $D_2O$ solution, according to the known value for $[SnTe_4]^{4-}$.[3] $^{125}$Te: two strong signals at $\delta$ = –199.9 ppm (terminal) and 553.0 ppm (bridged) and a very weak signal at –372.7 ppm arising from the $[SnTe_4]^{4-}$ monomer. $^{119}$Sn: $\delta$ = –1680.5 ppm; slight shift in comparison to the signal of the monomer at –1670.2 ppm, which was not observed here.

**Crystal Structure Analyses:** All X-ray diffraction measurements were performed with Stoe Imaging Plate Systems (IPDS). The crystal data and experimental conditions are summarized in Table 1. For the data sets of **1** and **2** a numerical, for that of **3** a semiempirical absorption correction has been applied. The structures were solved by direct methods of SHELXS-97[4] and refined by full-matrix least-squares methods of SHELXL-97[4] with use of anisotropic displacement parameters for all non-hydrogen atoms. The H-atoms were treated as riding on idealized positions with isotropic displacement parameters set 1.2 $U_{eq}$ (1.5 $U_{eq}$ for methyl groups) of their bonding partners. For **1**, only crystals of poor quality could be quarried out of conglomerates. Thus, the precision of the results is reduced. In the structure of **2**, the H atomic positions of the water molecule were calculated for the orientation of possible H bonds toward the neighboring Te1 and Te2 atoms. The subsequent refinement as rigid groups with free rotation and free common isotropic displacement parameters for the H atoms converged well. The refined Flack parameter of 0.008(15) confirms the correct absolute structure. In the structure of **3**, the crystal showed a small contribution of a (001) reflection twinning. The 24 most affected reflections 4*kl* and 5*kl* were therefore eliminated. The hydrogen atoms of the two water molecules could not be localized.

CCDC 652251 (**1**), -652252 (**2**), and -652253 (**3**) contain the supplementary crystallographic data for this paper. These data can be obtained free of charge from The Cambridge Crystallographic Data Centre via www.ccdc.cam.ac.uk/data_request/cif.


[1] Reviews: a) P. Feng, X. Bu, N. Zheng, *Acc. Chem. Res.* **2005**, *38*, 293–303; b) X. Bu, N. Zheng, P. Feng, *Chem. Eur. J.* **2004**, *10*, 3356–3362; c) M. G. Kanatzidis, A. C. Sutorik, *Progr. Inorg. Chem.* **1995**, *43*, 151–265; d) S. Dehnen, M. Melullis, *Coord. Chem. Rev.* **2006**, *251*, 1259–1280.

[2] a) J. C. Huffman, J. P. Haushalter, A. M. Umarji, G. K. Shenoy, R. C. Haushalter, *Inorg. Chem.* **1984**, *23*, 2312–2315; b) E. Ruzin, E. Zent, S. Dehnen, manuscript in preparation.

[3] E. Ruzin, A. Kracke, S. Dehnen, *Z. Anorg. Allg. Chem.* **2006**, *632*, 1018–1026.

[4] G. W. Sheldrick, *SHELXS-97 and SHELXL-97*, *Programs for the Solution and Refinement of Crystal Structures*, Göttingen **1997**.

[5] H. D. Flack, *Acta Crystallogr., Sect. A* **1983**, *39*, 876–881.

[6] B. Krebs, *Angew. Chem.* **1983**, *95*, 113–134; *Angew. Chem. Int. Ed. Engl.* **1983**, *22*, 113–134.

[7] E. Ruzin, C. Zimmermann, P. Hillebrecht, S. Dehnen, *Z. Anorg. Allg. Chem.* **2007**, *633*, 820–829.

[8] A. Kromm, W. S. Sheldrick, *Acta Crystallogr., Sect. E* **2005**, *61*, m2234–2236.

[9] J. Li, Z. Chen, T. J. Emge, T. Yuen, D. M. Proserpio, *Inorg. Chim. Acta* **1998**, *273*, 310–315.

[10] J. Campbell, L. A. Devereux, M. Gerken, H. P. A. Mercier, A. M. Pirani, G. J. Schrobilgen, *Inorg. Chem.* **1996**, *35*, 2945–2962.

[11] J. Liesk, P. Schulz, G. Klar, *Z. Anorg. Allg. Chem.* **1977**, *435*, 98–102.

[12] a) C. T. Mortimer, P. W. Sellers, *J. Chem. Soc.* **1964**, 1965–1970; b) T. McAllister, *J. Cryst. Growth* **1989**, *96*, 552–560; c) J. Connor, G. Grieg, O. P. Strausz, *J. Am. Chem. Soc.* **1969**, *91*, 5695–5696; d) A. F. Holleman, E. Wiberg, *Lehrbuch der Anorganischen Chemie*, 102nd ed., deGruyter, Berlin, New York, **1995**, p. 143.

[13] P. J. Bonasia, J. Arnold, *J. Chem. Soc. Chem. Commun.* **1990**, 1299–1301.

[14] A. S. Foust, *J. Chem. Soc. Chem. Commun.* **1979**, 414–415.

[15] a) J. Zhao, D. Adcock, W. T. Pennington, J. W. Kolis, *Inorg. Chem.* **1990**, *29*, 4358–4360; b) J. Zhao, J. W. Kolis, W. T. Pennington, *Acta Crystallogr., Sect. C* **1993**, *49*, 1753–1756.

[16] T. M. Klapötke, B. Krumm, H. Nöth, J. C. Galvez-Ruiz, K. Polborn, I. Schwab, M. Suter, *Inorg. Chem.* **2005**, *44*, 5254–5265.

[17] J. C. Huffman, R. C. Haushalter, *Z. Anorg. Allg. Chem.* **1984**, *518*, 203–209 and references cited therein.

[18] C. Ardenis, V. Langer, O. Lindqvist, *Acta Crystallogr., Sect. C* **1989**, *45*, 941–942.

[19] D. Fenske, G. Baum, H. Wolkers, B. Schreiner, F. Weller, K. Dehnicke, *Z. Anorg. Allg. Chem.* **1984**, *518*, 203–209 and references cited therein.

[20] R. G. Teller, L. J. Krause, R. C. Haushalter, *Inorg. Chem.* **1983**, *22*, 1809–1812 and references cited therein.


Received: July 10, 2007
Published Online: September 5, 2007

 © 2007 Wiley-VCH Verlag GmbH & Co. KGaA, Weinheim 

DOI: 10.1002/ejic.200700456

# Shearing-Like Distortion in Binuclear End-to-End $Cu^{II}$ Azido Compounds: An Ab Initio Study of the Magnetic Interactions

**Maria Angels Carvajal,[a] Christophe Aronica,[b] Dominique Luneau,*[b] and Vincent Robert*[a]**

**Keywords:** Magnetic properties / Azido bridge / Ab initio calculations

The direct control of magnetic interactions in $Cu^{II}$ azido-bridged binuclear complexes is investigated by means of explicitly correlated ab initio calculations. It is shown that in the end-to-end series, the shearing-like asymmetry parameter $\delta = d_{long}(Cu–N) – d_{short}(Cu–N)$ should be considered as an important parameter in the control of the coupling constant. A practical route that could be used to enhance the ferromagnetism of the compound is suggested in light of our calculations.

(© Wiley-VCH Verlag GmbH & Co. KGaA, 69451 Weinheim, Germany, 2007)

## Introduction

The synthesis and characterization of magnetic systems such as fascinating single-molecule magnets (SMMs)[1] are of continuous interest. This particular activity stems from a simultaneous need for microscopic interpretations and the design of original materials. In particular, the demand for efficient information storage devices has stimulated the use of various metal centre types ranging from 3d to 4f ions.[1e] Meanwhile, the development of an effective magnetic coupler in binuclear systems has grown since the use of acetate groups.[2] In the $Cu^{II}$ series, the magnetic interactions result from the presence of two unpaired electrons that give rise to the triplet (T) and singlet (S) states of energy difference $J = E_T – E_S$, where $J$ is the traditional magnetic exchange coupling constant in a spin-only Heisenberg-type Hamiltonian $\hat{H} = –2J\hat{S}_1\hat{S}_2$. The intimate participation of the bridging moieties in the magnetic properties has been much investigated in the literature; an important manifestation is the so-called "noninnocent" ligands.[3] In this respect, the prediction of the magnetic properties in binuclear $Cu^{II}$ compounds containing azide bridges remains a challenging issue. It is well-established that the azido group can bridge metal ions in two ways: the so-called end-on (EO) and end-to-end (EE) families (Figure 1). Nevertheless, the determination of the structural parameters that may control the magnetic interaction nature of the compounds is still much debated in the literature.[4,5] The general trend is that the EE mode affords antiferromagnetic interactions, whereas the EO mode favours ferromagnetic behaviour. However, the alternation of short and long Cu–N distances (so-called asymmetric coordination mode, see Figure 1) may result in either ferromagnetic or antiferromagnetic interactions whatever the coordination mode.[4] For symmetrically bridged compounds, theoretical investigations have rationalized the unequivocal distinction between the EO and EE families. Interestingly though, antiferromagnetic behaviour has been predicted in the EO series as soon as the Cu–N–Cu valence angle is sufficiently large (>104°),[6] which has also been experimentally confirmed.[7]

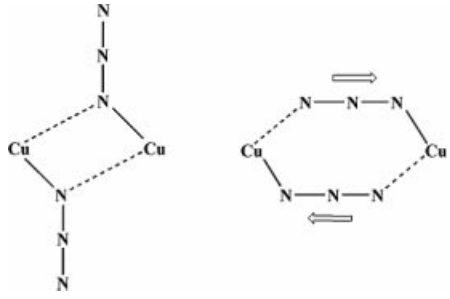


Figure 1. Asymmetric coordination modes of the azide bridge: EO (left) and EE (right). The arrows indicate the shearing distortion which is analyzed in this communication.

Magnetostructural correlations dedicated to EE compounds have pointed out that the symmetry of the coordination sphere measured by the Addison parameter ($\tau$)[8] and the N–Cu···Cu–N torsion angle ($\Delta$) are likely to govern the nature and strength of the magnetic interaction. Regarding the symmetry of the coordination sphere, it was proposed that in the square pyramid (sp) coordination limit ($\tau = 0$) magnetic orbitals are mainly $d_{x^2-y^2}$ and weak ferromagnetic

[a] Laboratoire de Chimie de Lyon (UMR5182), Ecole Normale Supérieure de Lyon,
46, allée d'Italie, 69364 Lyon Cedex 07, France
Fax: +33-472-72-80-80
E-mail: Vincent.robert@ens-lyon.fr
[b] Laboratoire des Multimatériaux et Interfaces (UMR 5615), Université Claude Bernard Lyon 1,
69622 Villeurbanne Cedex, France
Supporting information for this article is available on the WWW under http://www.eurjic.org or from the author.


© 2007 Wiley-VCH Verlag GmbH & Co. KGaA, Weinheim

interactions should result.[4c] Additionally, it was observed that large torsion angles $\Delta$ enhance ferromagnetic behaviour.[4c] Thus, considering the importance of azido-based clusters in the design of magnetic objects, we felt that the role of the coordination mode symmetry should be clarified. With the use of ab initio calculations, the contributions of spin polarization and dynamical correlation effects were analyzed in a series of EE complexes. The present works sheds light on another important structural parameter; the Cu–N bond length alternation. This particular shearing distortion mode acts as an electron-localizing factor in the eight-membered Cu–N rings of EE complexes. To clarify the role of the so-called shearing-mode, we used the crystal structure of a recently reported $Cu^{II}$ azido complex.[9] We carried out the synthesis, structure and magnetic, polarized neutron of an asymmetric EE $Cu^{II}$ azido complex $[Cu(L)(N_3)_2]_2$ [L = 7-(dimethylamino)-1,1,1-trifluoro-4-methyl-5-aza-3-hepten-2-onato] (**1**, Figure 2) that exhibits ferromagnetic interactions ($J$ = 16 $cm^{-1}$) in contrast with most EE systems.[4] The strategy we developed consists of the systematic ab initio evaluation of the exchange coupling constant in a series of fictitious analogues of **1**. Therefore, starting from the experimental geometry for which ferromagnetism has been theoretically elucidated in our previous paper,[9] the Cu–N distances were modified whilst the rest of the complex was kept frozen ($\tau$ = 0.19 and $\Delta$ = 44.3). This particular approach differs from a previous study that focused on the long Cu–N distance;[5] here, we concentrated on the difference between the long and short Cu–N distances. This parameter we shall refer to as $\delta = \delta_{long}$(Cu–N) – $\delta_{short}$(Cu–N) measures the amplitude of this shearing-like distortion away from a perfectly symmetric bridging mode. Let us mention that for $\delta$ = 0 Å, the Cu–N distances all equal 2.155 Å. Along this scheme, the Cu–Cu distance remains unchanged (5.1 Å). We then investigated the sensitivity of $J$ with respect to $\delta$ in EE compounds reported in the literature.

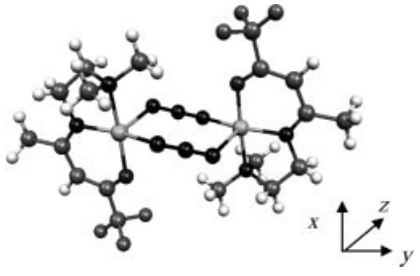


Figure 2. Structure of the EE $[Cu(N_3)L]_2$ compound with L = 7-(dimethylamino)-1,1,1-trifluoro-4-methyl-5-aza-3-hepten-2-onato.[9]

### Theoretical Details

State-of-the-art ab initio, as well as density functional theory (DFT) calculations, proved to reach very satisfactory agreement with experimental measurements in both the EE and EO series. Nevertheless, correlated ab initio calculations were preferred here, as the information extracted from a multiconfigurational wavefunction is very insightful into the mechanism of magnetic interactions. First, complete active space self-consistent field calculations (CASSCF) including two electrons in two orbitals [CAS(2,2)] were performed by using the Molcas5.0 Package[10] to qualitatively incorporate the leading physical configurations. Because the local environments of the $Cu^{2+}$ ions ($d^9$) are roughly $ML_5$, the singly occupied d-type orbitals are perpendicular to the missing ligand direction, which shall be referred to as $z$ (see Figure 2). At this level, the low-lying triplet reads $|gu|$ where $g$ and $u$ are mainly the in-phase and out-of-phase linear combinations of the $d_{x^2-y^2}$ atomic orbitals, respectively (i.e. $g = \frac{a+b}{\sqrt{2}}$, $u = \frac{a-b}{\sqrt{2}}$, where $a$ and $b$ are the $d_{x^2-y^2}$AOs). Along this multiconfigurational scheme, the contributions of the so-called ionic forms $|a\bar{a}|$ and $|b\bar{b}|$in the ground-state singlet $\lambda|g\bar{g}| - \mu|u\bar{u}|$ may be underestimated. Thus, one has to incorporate dynamical correlation effects to fully account for the intimate mechanisms responsible for the singlet-triplet energy gap. By using the triplet molecular orbitals (MOs), dynamic correlation contributions were included with the difference dedicated configuration interaction (DDCI) method[11] implemented in the CASDI code[12] (see the Supporting Information for a detailed description of the computational procedure). This particular framework has provided very accurate results for these types of compounds and solid-state magnetic materials.[9,13]

## Results and Discussion

Detailed analysis of the different contributions to the exchange magnetic coupling constant was given previously.[14] Therefore, we concentrated on: (1) the spin polarization (SP) effects, which are dominated by excitations involving the bridging-ligand orbitals and (2) the dynamical correlation (DC) effects that arise from the instantaneous polarization of the copper ions environments. By allowing specific excitations in the CI treatment, one can grasp selectively those effects and clarify the exchange coupling character. The variations in the $J$, SP and DC contributions as a function of $\delta$ are plotted in Figure 3.

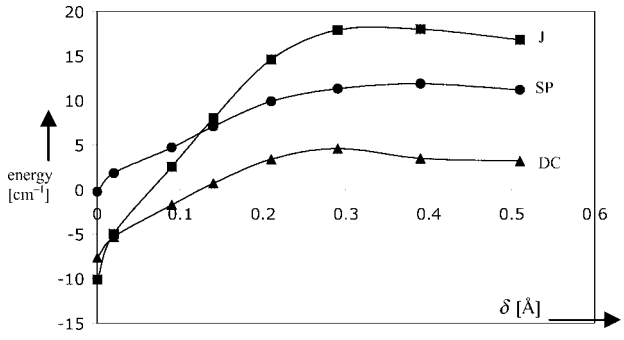


Figure 3. Calculated $J$ (■), SP (●) and DC (▲) energies [$cm^{-1}$] in a series of **1** hypothetical analogues as a function of $\delta$ [Å].

 © 2007 Wiley-VCH Verlag GmbH & Co. KGaA, Weinheim 

As the asymmetry $\delta$ is increased (i.e. the Cu–N distances become significantly different), our calculated $J$ values steadily increase to finally plateau close to 18 $cm^{-1}$ for $\delta$ ca. 0.3 Å. This is in contrast to the dependence upon the long Cu–N distance for which no monotonic behaviour is observed (Supporting Information, Figure S1).

As previously reported,[14] the SP effects arise mainly from the polarization of the closed shells that are localized on the bridging units. As a result of the exchange operators $\hat{K}_a$ and $\hat{K}_b$, the closed shells $h$ become polarized through $\langle p|K_a|h\rangle$ and $\langle p|K_b|h\rangle$ matrix elements involving virtual MOs $p$. The presence of a reflection plane makes the frontier MOs of the azido part $h$ and $p$ symmetric and antisymmetric, respectively (see Figure 4).

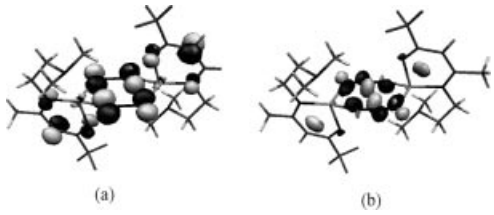


Figure 4. Frontier MOs (a) occupied $h$; (b) virtual $p$.

Thus, one can expect the SP contribution to be negligible, because the matrix elements are vanishingly small in the low-$\delta$ regime. As $\delta$ increases, a competition between the simultaneous shortening and lengthening of the Cu–N bond lengths results. Thus, the different copper–azido overlaps compete to reach a maximum, which fixes the SP contribution, which in turn favours the triplet state. Clearly, given the large Cu–Cu distance in the complex (≈ 5 Å), the contribution of the direct exchange is expected to be negligible.[13] A very similar behaviour for the DC effects is to be noticed. The DC contributions increase regularly with respect to the bridge shearing. The modification of the kinetic exchange only affects the singlet state because the ionic determinants are pure singlet and do not contribute to the triplet wavefunction. A detailed analysis of the wavefunction shows that the weights of these ionic forms is maximum, and still small, in the symmetric complex, i.e. for small $\delta$ values (Supporting Information, Table S1). Therefore, the singlet state is stabilized over the triplet and antiferromagnetic character results. One can intuitively expect the electron delocalization to be less efficient as the Cu–N bond lengths in the eight-membered ring alternate.

To investigate the role of the chemical environment of the copper atoms, we transformed the $CF_3$ electron-withdrawing groups into methyl groups. From our calculations performed at the same level, the magnetic coupling constant is 18 $cm^{-1}$, which is almost identical to the experimental and theoretical values reported for **1**.[9] Thus, one can take advantage of the structuring role of the $CF_3$ groups without greatly affecting the magnetic properties.

From this prospective analysis based on ab initio calculations, we finally examined whether magnetic behaviours could be anticipated in reported EE analogues. Table 1 summarizes the main structural parameters and experimentally determined coupling constants for some EE asymmetric azido-bridged complexes that are available in the literature.

We focused on pentacoordinate Cu compounds with only one exchange pathway. Figure 5 shows the variation of $J$ with respect to both the dihedral angle $\Delta$ and shearing parameter $\delta$. Even though the trend is not monotonous (see Figure 5), complexes with small $\delta$ values exhibit antiferromagnetic character (lower block in Figure 5), whereas ferromagnetic behaviour is exhibited as the shearing deformation increases (upper block in Figure 5). Strikingly though, complex **8** for which $\delta$ is relatively large displays antiferromagnetism. However, this compound presents a very asymmetric structure, with four different Cu–N distances. Moreover, the Cu–Cu distance as well as the $\tau$ value is significantly larger than that in all the other reported

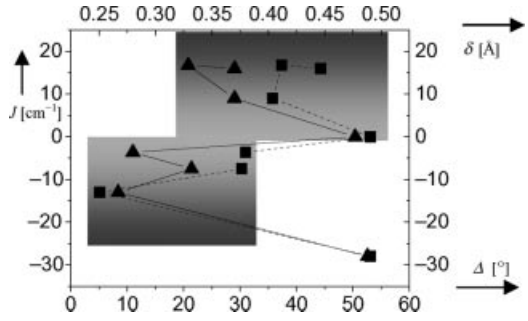


Figure 5. Variations of $J$ with respect to $\Delta$ (■ dashed line) and $\delta$ (▲solid line).

Table 1. Structural and magnetic parameters for asymmetric Cu azido-bridged compounds.

| Compound[a] | Cu–Cu [Å] | $\tau$ | $\Delta$ [°] | $\delta$ [Å] | $J$ [$cm^{-1}$] | Ref. |
|---|---|---|---|---|---|---|
| **1** $[Cu(L)(N_3)_2]_2$ | 5.073 | 0.19 | 44.3 | 0.370 | 16 | [9] |
| **2** $[Cu_2(bben)_2(N_3)_4]_n$ | 5.281 | 0.18 | 37.4 | 0.329 | 16.8 | [4b] |
| **3** $[Cu(Et_3dien)(N_3)_2]_2(ClO_4)_2$ | 5.407 | 0.20 | 35.8 | 0.370 | 9 | [4c] |
| **4** $[Cu(bp)(N_3)_2]_2(ClO_4)_2$ | 5.004 | 0.20 | 53.1 | 0.477 | 0 | [4d] |
| **5** $[Cu(EtMe_4dien)(N_3)_2]_2$ | 5.289 | 0.28 | 31.0 | 0.280 | –3.6 | [4e] |
| **6** $[Cu(Me_5dien)(N_3)_2]_2(ClO_4)_2$ | 5.294 | 0.23 | 30.3 | 0.332 | –7.5 | [4e] |
| **7** $[Cu(Me_5dien)(N_3)_2]_2(BPh_4)_2$ | 5.228 | 0.29 | 5.15 | 0.267 | –13 | [4f] |
| **8** $[Cu(Et_5dien)(N_3)_2]_2(ClO_4)_2$[b] | 5.464 | 0.43 | 53.1 | 0.488 | –28 | [4e] |

[a] L = 7-(dimethylamino)-1,1,1-trifluoro-4-methyl-5-aza-3-hepten-2-onato, bben = 1,2-bis(benzylamino)ethane, $Et_3dien$ = triethyldiethylenetriamine, bp = 2,2′-bipyridine, $EtMe_4dien$ = 4-ethyl-1,1,7,7-tetramethyldiethylenetriamine, $Me_5dien$ = 1,1,4,7,7- pentamethyldiethylenetriamine, $Et_5dien$ = 1,1,4,7,7-pentaethyldiethylenetriamine, Medpt = methyldipropylenetriamine. [b] Parameters calculated with average angles and bond lengths, as this compound exhibits two nonequivalent dimers.

 © 2007 Wiley-VCH Verlag GmbH & Co. KGaA, Weinheim 

compounds. Thus, from previous calculations one may expect a simultaneous reduction, though small, of the direct exchange contribution and an enhancement in the superexchange effects. The comparison of **8** with compound **4** is very instructive as the sets of parameters $\Delta$ and $\delta$ are very comparable. Therefore, the unexpected behaviour of **8** is completely attributable to the large $\tau$ value. Clearly, the magnetic behaviour is not strictly governed by a single structural parameter because important variations are observed around $\delta \approx 0.33$ Å (see compounds **4** and **6**).

Finally we looked into the variation of $J$ with respect to $\Delta$ and our shearing parameter $\delta$. Interestingly, these variations are similar (see Figure 5).

Whereas $\Delta$ concentrates on angular distortion, it is rather puzzling that $\delta$, which takes into account the asymmetry of the coordination mode, can describe in a similar way the magnetic behaviour of such a system. This observation clearly deserves further investigation. One may suggest that in synthetic compounds any change in the torsion angle $\Delta$ can be a consequence of a variation of the shear $\delta$ value. From a structural analysis, these parameters cannot be completely independent. Therefore, one may expect a strong correlation between the variations of $\delta$ and $\Delta$. The rationalization we have provided for the influence of this new parameter will call for more magnetostructural data, in particular in the field of single-chain magnets. However, our calculations in which we kept $\Delta$ frozen on purpose indicate that $\delta$ has a direct influence on the $J$ value.

## Conclusions

The $\delta$ parameter, which measures the shearing between the two azido bridges, strongly influences the magnetic behaviour of EE $Cu^{II}$ compounds. The different leading contributions were analyzed by means of explicitly correlated calculations. We believe that magnetostructural correlations should include this particular parameter that turns out to be predictive. This work also suggests that specific magnetic properties can be tuned by varying $\delta$ on copper–azido magnetic prototype compounds. Undoubtedly, the versatility of the azide magnetic coupler arises from its ability to bind paramagnetic centres in various geometries.

**Supporting Information** (see footnote on the first page of this article): The theoretical framework that was used for the ab initio calculations, the xyz files (Angström) of the generated structures and the corresponding variations in the ionic over neutral forms in the singlet wavefunction. Variations in the $J$ values in the reported systems are plotted as a function of the Cu–N long distance as proposed in ref.[5]

## Acknowledgments

The "Région Rhône-Alpes" is gratefully acknowledged for financial support and postdoctoral fellowship to M. A. C. Dr. Daniel Maynau is acknowledged for kindly providing the ab initio CASDI code. The authors are grateful to the referees for enlightening suggestions with respect to the discussion regarding the parameters influence.

[1] See, for example: a) S. K. Ritter, *Chem. Eng. News* **2004**, *82*, 29–35; b) A. J. Tasiopoulos, A. Vinslava, W. Wernsdorfer, K. A. Abboud, G. Christou, *Angew. Chem. Int. Ed.* **2004**, *43*, 2117–2121; c) D. Gatteschi, R. Sessoli, *Angew. Chem. Int. Ed.* **2003**, *42*, 268–297; d) W. Wernsdorfer, N. Aliaga-Alcalde, D. N. Hendrickson, G. Christou, *Nature* **2002**, *416*, 406–409; e) C. Aronica, G. Pilet, G. Chastanet, W. Wernsdorfer, J.-F. Jacquot, D. Luneau, *Angew. Chem. Int. Ed.* **2006**, *45*, *4659*–4662.

[2] a) B. C. Guha, *Proc. R. Soc. London, Ser. A* **1951**, *206*, 353–364; b) B. Bleaney, K. D. Bowers, *Proc. R. Soc. London, Ser A* **1952**, *214*, 451–459.

[3] See, for example: a) J. F. Berry, E. Bill, E. Bothe, F. Neese, K. Wieghardt, *J. Am. Chem. Soc.* **2006**, *128*, 13515–13528; b) U. Beckmann, E. Bill, T. Weyhermüller, K. Wieghardt, *Inorg. Chem.* **2003**, *42*, 1045–1056; c) D. Herebian, E. Bothe, E. Bill, T. Weyhermüller, K. Wieghardt, *J. Am. Chem. Soc.* **2003**, *125*, 10997–11005; d) X. Sun, H. Chun, K. Hildenbrand, E. Bothe, T. Weyhermüller, F. Neese, K. Wieghardt, *Inorg. Chem.* **2002**, *41*, 4295–4303.

[4] a) M. A. Aebersold, B. Gillon, O. Plantevin, L. Pardi, O. Kahn, P. Bergerat, I. von Seggern, F. Tuczek, L. Örström, A. Grand, E. Lelièvre-Berna, *J. Am. Chem. Soc.* **1998**, *120*, 5238–5245; b) Y. Xie, Q. Liu, H. Jiang, C. Du, X. Xu, M. Yu, Y. Zhu, *New J. Chem.* **2002**, *26*, 176–179; c) C. Escuer, M. Font-Bardia, S. S. Massoud, F. A. Mautner, E. Peñalba, X. Solans, R. Vicente, *New J. Chem.* **2004**, *28*, 681–686; d) I. Bkouche-Waksman, S. Sikorav, O. Kahn, *J. Crystallogr. Spectrosc. Res.* **1983**, *13*, 303–311; e) A. Escuer, M. Font-Bardia, E. Peñalba, X. Solans, R. Vicente, *Inorg. Chim. Acta* **2000**, *298*, 195–201; f) T. R. Felthouse, D. N. Hendrickson, *Inorg. Chem.* **1978**, *17*, 444–456; g) L. Li, D. Liao, Z. Jiang, J. M. Mouesca, P. Rey, *Inorg. Chem.* **2006**, *45*, 7665–7670.

[5] S. Triki, C. J. Gomez-Garcia, E. Ruiz, J. Sala-Pala, *Inorg. Chem.* **2005**, *44*, 5501–5508.

[6] F. Fabrizi de Biani, E. Ruiz, J. Cano, J. J. Novoa, S. Alvarez, *Inorg. Chem.* **2000**, *39*, 3221–3229.

[7] L. K. Thompson, S. S. Tandon, M. E. Manuel, *Inorg. Chem.* **1995**, *34*, 2356–2366.

[8] A. W. Addison, T. N. Rao, J. Reedijk, G. C. Verschoor, *J. Chem. Soc. Dalton Trans.* **1984**, 1349–1356.

[9] C. Aronica, E. Jeanneau, H. El Moll, D. Luneau, B. Gillon, A. Goujon, A. Cousson, M. A. Carvajal, V. Robert, *Chem. Eur. J.* **2007**, *13*, 3666–3674.

[10] K. Anderson, M. P. Fülscher, G. Karlström, R. Lindh, P. A. Malqvist, J. Olsen, B. Roos, A. J. Sadlej, M. R. A. Blomberg, P. E. M. Siegbahn, V. Kello, J. Noga, M. Urban, P. O. Widmark, *MOLCAS, Version 5.4*, University of Lund, Lund, Sweden, **1998**.

[11] DDCI: J. Miralles, O. Castell, R. Caballol, J. P. Malrieu, *Chem. Phys.* **1993**, *172*, 33–43.

[12] *CASDI Suite of Programs.* N. Ben Amor, D. Maynau, *Chem. Phys. Lett.* **1998**, *286*, 211–220.

[13] J. Cabrero, C. de Graaf, E. Bordas, R. Caballol, J.-P. Malrieu, *Chem. Eur. J.* **2003**, *9*, 2307–2315.

[14] a) C. J. Calzado, J. Cabrero, J.-P. Malrieu, R. Caballol, *J. Chem. Phys.* **2002**, *116*, 2728–2746; b) J. C. Calzado, J. Cabrero, J.-P. Malrieu, R. Caballol, *J. Chem. Phys.* **2002**, *116*, 3985–4000; c) P. de Loth, P. Cassoux, J. P. Daudey, J.-P. Malrieu, *J. Am. Chem. Soc.* **1981**, *103*, 4007–4016.

Received: April 26, 2007
Published Online: July 6, 2007

 © 2007 Wiley-VCH Verlag GmbH & Co. KGaA, Weinheim 

DOI: 10.1002/ejic.200601135

# Oriented Attachment Growth of Three-Dimensionally Packed Trigonal Selenium Microspheres into Large-Area Wire Networks

Liangbao Yang,[a] Yuhua Shen,*[a] Anjian Xie,[a] and Jianjun Liang[b]

**Keywords:** Nanostructures / Self-assembly / Selenium

The formation of Se microwire networks by hydrothermal treatment in tungstosilicic acid solution is described. The kinetics of crystallization of the Se assembly is studied as a function of reaction time. During the formation process, single-crystal Se rods can direct the self-aggregation of the amorphous nanoparticles derived from a supersaturation precipitation reaction and promote their crystallization and transformation under mild hydrothermal conditions. In this system, the rod-directed epitaxial aggregation of Se was clearly observed in addition to the traditional Ostwald ripening process.

(© Wiley-VCH Verlag GmbH & Co. KGaA, 69451 Weinheim, Germany, 2007)

## Introduction

Solution synthesis has been an important route to nanoparticles with specific shape, size, orientation, etc., which play key roles in tailoring the properties of nanomaterials. Traditional solution-synthetic methods have been widely used for the controlled synthesis of various colloidal nanoparticles.[1] There are different opinions on the mechanisms of morphological synthesis of inorganic nanoparticles. One basic crystal-growth mechanism in solution systems is the well-known "Ostwald ripening process".[2] In the Ostwald ripening process, the formation of tiny crystalline nuclei in a supersaturated medium occurs first. This is followed by crystal growth, in which the larger particles will grow at the cost of the smaller ones, because the smaller ones have a higher solubility on the basis of the Gibbs–Thompson law.[3] Another growth mechanism mainly involving oriented particle aggregation,[4–7] which was conceptually termed "oriented attachment" by Penn and Banfield et al.,[8–12] has emerged recently.[13] In this theory, the bigger particles grow from small primary nanoparticles through an orientated attachment process in which the adjacent nanoparticles self-assemble by sharing a common crystallographic orientation and by docking themselves at a planar interface.[9]

More and more evidence has been observed in several systems for either directed or undirected particle aggregation. A growth mode of this kind can lead to the formation of faceted particles or anisotropic growth if it occurs near equilibrium and if there is sufficient difference in the surface energies of different crystallographic faces.[11] Very recently, Shu-Hong Yu et al. reported evidence for the oriented attachment mechanism in which the nanorods obviously act as epitaxial "substrates" or guide the directional aggregation process for the formation of nanorod-based aggregated structures.[14]

Tungstosilicic acid ($H_4SiW_{12}O_{40}$, TSA) ions form a subset of the polyoxometalates that have Keggin structure. Polyoxometalates with Keggin structure have the general formula $(XM_{12}O_{40})^{(8-n)-}$, where "M" stands for the element W or Mo, "X" stands for heteroatoms such as P, Si, Ge, and $n$ is the valency of X.[15] It is well known that Keggin ions undergo stepwise multielectron redox processes without structural change.[15] They may be reduced electrolytically, photochemically, and chemically (with suitable reducing agents). They are a large category of metal–oxygen cluster anions with well-defined structures and properties, with diverse applications in the fields of analytical chemistry, biochemistry, and solid-state devices, and have been used as antiviral and antitumor reagents. Their redox chemistry is characterized by their ability to accept and release a certain number of electrons, in distinct steps, without decomposition.[16]

Selenium is a material suitable for a self-organization studies, because of the excellent ability of trigonal selenium (t-Se) to grow preferentially along the *c* axis and the possibility of controlling the one-dimensional growth of selenium by diverse approaches.[17–21] If its three-dimensionally packed precursor is obtained, it is possible to transform it to a crossed nanowire array by choosing proper experimental conditions. Due to its photoconductivity with a spectral sensitivity that covers almost the entire visible range, selenium is also important in a wide variety of applications that

[a] School of Chemistry and Chemical Engineering, Anhui University,
Hefei 230039, P. R. China
Fax: +86-551-5107342
E-mail: s_yuhua@163.com
[b] Chuzhou Vocational Technology College,
Chuzhou 239000, P. R. China

Supporting information for this article is available on the WWW under http://www.eurjic.org or from the author.

 © 2007 Wiley-VCH Verlag GmbH & Co. KGaA, Weinheim 

range from photocells, photographic exposure meters, and solar cells to semiconductor rectifiers. In this study, we have designed a hydrothermal synthesis for the selenium microcrystal. To the best of our knowledge, a hydrothermal synthesis of a Se single crystal with this novel structure has not been achieved previously in TSA solution.

## Results and Discussion

Figure 1A presents the Raman spectrum of the synthesized sample. The resonance peak at 233 $cm^{-1}$ is a characteristic signature of trigonal selenium, which can be assigned to the vibration of the Se helical chain.[14] A peak around 142 $cm^{-1}$ results from the transverse optical photon mode. For comparison, the characteristic Raman peaks for monoclinic selenium and α-Se are at 256 $cm^{-1}$ and 264 $cm^{-1}$, respectively.[22] The XRD pattern recorded from a drop-coated film of the sample on a glass substrate is shown in Figure 1B, curve a. All of the strong and sharp reflection peaks can be readily indexed to a single phase of trigonal-structured selenium [t-Se, space group $P3_121$ (152)] containing infinite, helical chains of selenium atoms packed parallel to each other along the *c* axis, with cell parameters $a = 0.4367$ nm and $c = 0.4959$ nm. These values are in agreement with the values reported in the literature.[23] For comparison, the XRD spectrum of bulk t-Se is shown in Figure 1B, curve b; it is similar to the spectra recorded by the Xie group.[24,25] These results, obtained from Raman spectroscopy and XRD, indicate that the product is crystalline.

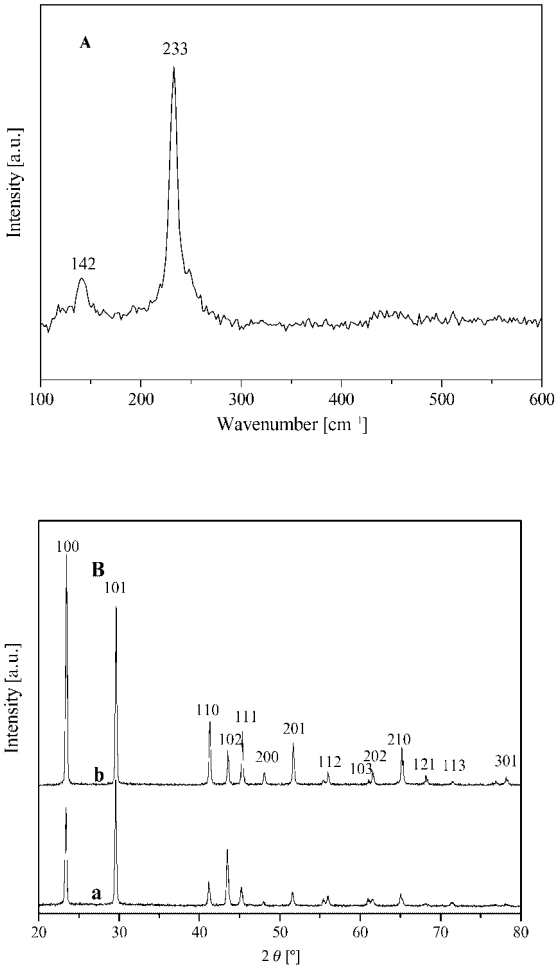


Figure 1. Raman spectrum of the synthesized sample (A) and XRD pattern (B) of a sample of the precipitates obtained as a result of hydrothermal treatment (curve a) and a sample of the bulk t-Se (curve b).

The product was characterized by using scanning electron microscopy (SEM), and a typical image is shown in Figure 2. The image shown in Figure 2A clearly reveals that a large-area microwire network was successfully fabricated. The units for the build-up of the network are uniform microwires with an average diameter of about 1.5 μm and lengths of up to hundreds of micrometers. The aspect ratio of the wire is in the range of several hundreds, which may be a useful feature in some applications. The structure and morphology of the microwires was further characterized by transmission electron microscopy (TEM) and selected-area electron diffraction (SAED). Figure 2B shows a typical TEM image of the microwires, revealing their high aspect ratio, good crystallinity, and uniformity. Figure 2C shows

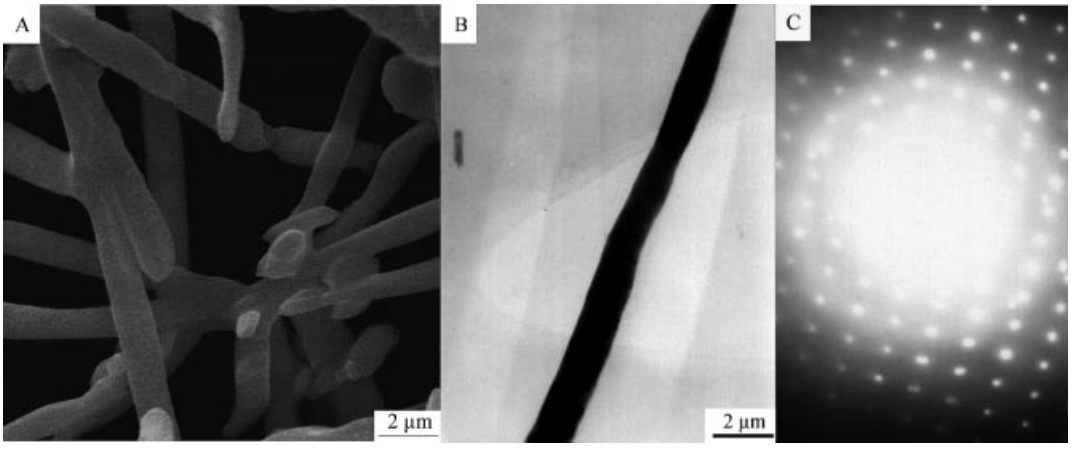


Figure 2. A representative SEM image (A), the TEM image (B), and the associated SAED pattern of the t-Se microcrystal (C).

 © 2007 Wiley-VCH Verlag GmbH & Co. KGaA, Weinheim 

the associated SEAD pattern recorded by focusing the incident electron beam on an individual microwire and exhibits the single-crystalline nature of the wire. The twofold rotational symmetry associated with this pattern indicates that these t-Se wires have predominately grown along the [001] direction (*c* axis), with the helical *c* chains of the Se atoms parallel to the longitudinal axis.[26] We have also carried out extensive investigations on more individual wires by using electron diffraction (ED), the results of which demonstrate that the as-synthesized sample is single-crystalline.[26]

To ensure that the TSA present in the system has an important effect on the synthesis of the Se particles, a control experiment was performed under the the same conditions, but only without TSA. A lot of irregular microparticles were obtained (see the SEM image in the Supporting Information, FigureS1). On the basis of the above analyses, we conclude that TSA significantly affects the shapes of the particles.

To study the formation mechanism of the network of t-Se microwires, various growth stages of the t-Se microwire network were investigated. Figure 3 shows a set of SEM images corresponding to samples obtained at different growth stages of the microwire. After 1 h of hydrothermal treatment, spherical α-Se was obtained (Figure 3A), and no ED pattern was detected. The image shows highly uniform colloidal particles of predominantly spherical morphology. An analysis of 100 such particles from several SEM micrographs resulted in determination of the average particle size of $64 \pm 14$ nm. When the solution was treated for 3 h, spherical t-Se particles were formed, and some of the spheres were broken (Figure 3B). The size of t-Se spherical particles was about $3.5 \pm 1.4$ μm. In Figure 3C, it is clearly seen that most of the spheres are broken, and an interesting core–shell structure is revealed. The structural characteristics of the crystal were further elucidated by the TEM and ED techniques (inset in Figure 3C). The SAED patterns for the shell and core areas are identical. A further investigation of such a complex growth process is ongoing. The Se rods formed at the initial stage from the seeds of spherical t-Se were observed at a hydrothermal treatment time of 6 h (Figure 3D). It can be seen that some rods and a lot of spheres coexist. The Se microrods grew as the hydrothermal treatment time was prolonged to 12 h. The number of rods increased, the rods became longer, and the spheres tailed off. Most of the spheres grew alongside the rods (Figure 3E). After 24 h of treatment, the t-Se microwires grew into a well-organized, shaped network (Figure 3F), and any longer treatment made no difference in the morphology.

According to the Stranski rule, in crystals that may exhibit various allotropes, the least stable and most soluble phase, which is favored kinetically, usually precipitates first, and then this metastable phase is transformed during the aging process into a more thermodynamically stable phase.[27] In order to understand the growth process of the Se microwires on the basis of the results obtained, a feasible route is presented as shown in Figure 4. First, the unstable spherical α-Se particles are formed (a). Second, α-Se transforms into the more stable t-Se. Under hydrothermal treatment, the Se rods begin to grow on the surface of the spherical t-Se (c–f); then the Se microrods are formed after continuous growth, and at last, the microrods are transformed into the microwire network by the Ostwald ripening process (g). We believe that the aggregated growth along the circumference of the gap in the broken sphere resulting from the hydrothermal treatment leads to the formation of microrods, which is similar to the conclusion reached by Yang et al.[28] It seems that the situation is almost the same in this study. The long-term hydrothermal treatment somehow breaks the selenium sphere and forms a crater on the sphere. The edge of the crater acts as the initiation spot, and further directional growth of the selenium crystal along this crater yields the rod product. The transition of microrods into the microwire network indicates that the wires are thermodynamically stable.

The conventional hydrothermal crystallization or transformation process with amorphous nanoparticles as precursors is a typical Ostwald ripening process, in which a highly supersaturated solution is adopted, and amorphous fine particulates act as the precursors. In this mechanism, the formation of tiny crystalline nuclei in a supersaturated medium occurs at first and is then followed by crystal growth. The larger particles (Figure 3B) will grow at the expense of the small ones (Figure 3A) because of the difference in solubility between large and smaller particles according to the well-known Gibbs–Thomson law. In the early stage, the examination of intermediate products (Figure 3D) shows the coexistence of the short rods and microspherical particles. As the reaction goes on, the microspheres decrease in number, and longer microrods form (Figure 3E), suggesting that the longer rods obviously grow at the expense of the microspheres. On the other hand, we think that the growth mode for rods in our work is similar to the seed-mediated growth mechanism of metals.[29–31] The so-called rod-directed self-aggregation process in our case is the directional aggregation of the tiny spherelike particles on the backbone of the rods. Crystalline microrods with rough surface structures then transform into the microwire network.

We performed an additional experiment to determine whether the growth process was a "ripening" or an "oriented attachment". A fresh mixture of $H_2SeO_3$ and TSA was added to the solutions in the presence of a suitable amount of single-crystal Se wires (0.1 mmol), and the mixture was heated at 160 °C for 3 h. The pure Se wire networks with a typical shape are shown in Figure 5. In general, Se nanospheres transform into networks in 24 h. In this experiment, this process only needed 3 h. The results indicated that all small particles tend to attach onto the backbone of the nanowires and then form micronetworks. It is interesting that no individual dispersed nanoparticles were found in the solution.

A control experiment was performed wherein microspheres were autoclaved for 12 h at 160 °C. At first, the wires and the spheres coexisted (Figure 6A), and then the wire networks were formed (shown in Figure 6B). There is little difference in morphology between Figure 6B and Fig-

 © 2007 Wiley-VCH Verlag GmbH & Co. KGaA, Weinheim 

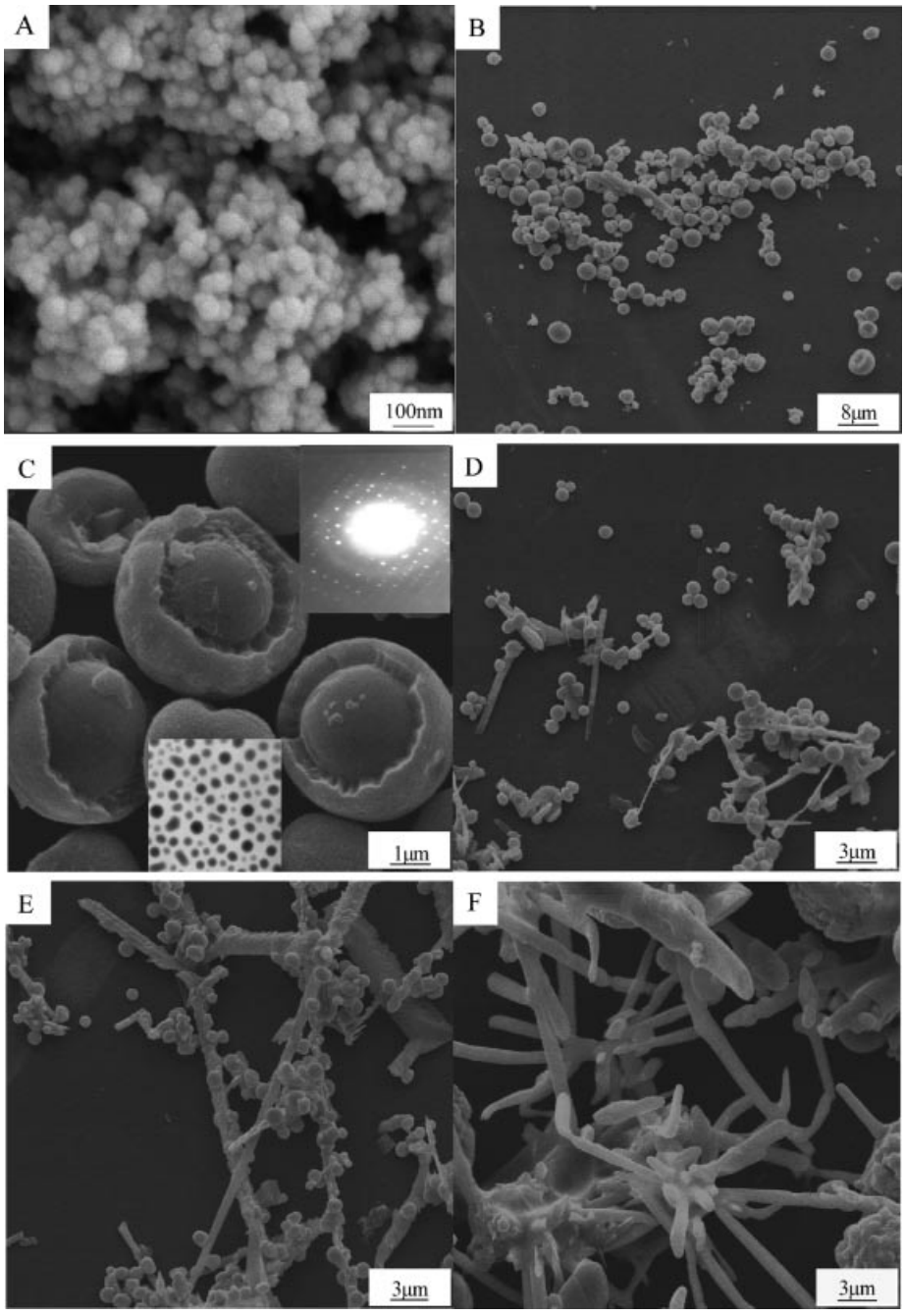


Figure 3. A set of SEM images corresponding to samples at different stages of growth of the microwire network obtained by hydrothermal treatment: after 1 h (A); low (B) and high magnifications of the rough microspheres after 3 h (C), 6 h (D), 12 h (E), and 24 h (F). The insets of (C) are the TEM and ED patterns.

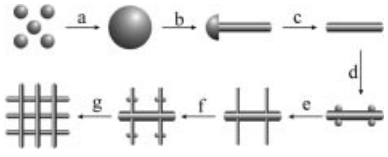


Figure 4. Formation of the wire networks by hydrothermal crystallization. In the early stage, there are a plenty of spheres (a,b); later the short rods and small nanospheres coexist (c–f); at last, the networks of Se form (g).

ure 5. These results indicated that the obvious Se-wire-directed oriented attachment mechanism and its promotion of further crystallization and transformation of the nanoparticulates are undoubtedly the mechanisms involved.

Such spontaneous "landing" of the small spherical particles on the backbone of the rods (Figure 3E) followed by the self-aggregation of these combinations of spheres and rods instead of aggregation among the small particles only could be related with one mechanism: the so-called "contact epitaxy" proposed by Averback et al.[32,33] The driving

 © 2007 Wiley-VCH Verlag GmbH & Co. KGaA, Weinheim 

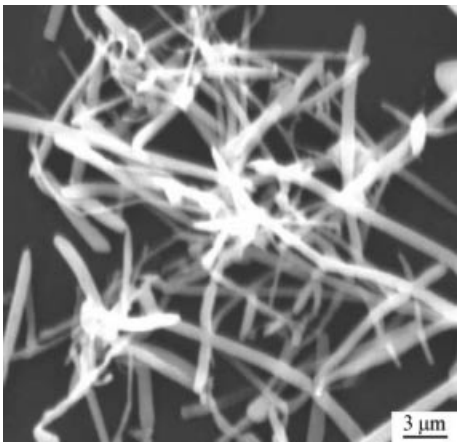


Figure 5. Typical SEM image of the sample which was obtained after adding a fresh mixture of $H_2SeO_3$ and TSA solutions to a 20-mL solution containing 0.1-mmol Se wires and heating the mixture for 3 hours.

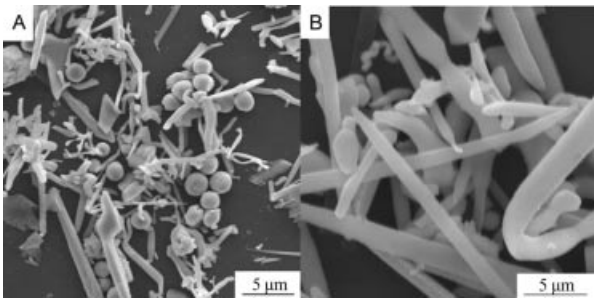


Figure 6. Typical SEM images of the samples which were obtained after heating the microspheres in an autoclave for 2 h (A) and 12 h (B).

force for this spontaneous oriented attachment is that the elimination of the pairs of high energy surfaces will lead to a substantial reduction in the surface free energy from the thermodynamic viewpoint.[10,13] The initial randomly oriented crystals can align epitaxially with the substrate (which are the rods here). This alignment is explained as the rotation of the particles within the aggregates driven by short-range interactions between adjacent surfaces.[32,33]

The surfactants were found to significantly affect the shape of the particles. The shape of the particles obtained in the presence of surfactants was completely different from that observed without surfactants. The surfactant (CTAB or SDB) plays an important role in controlling the mor-

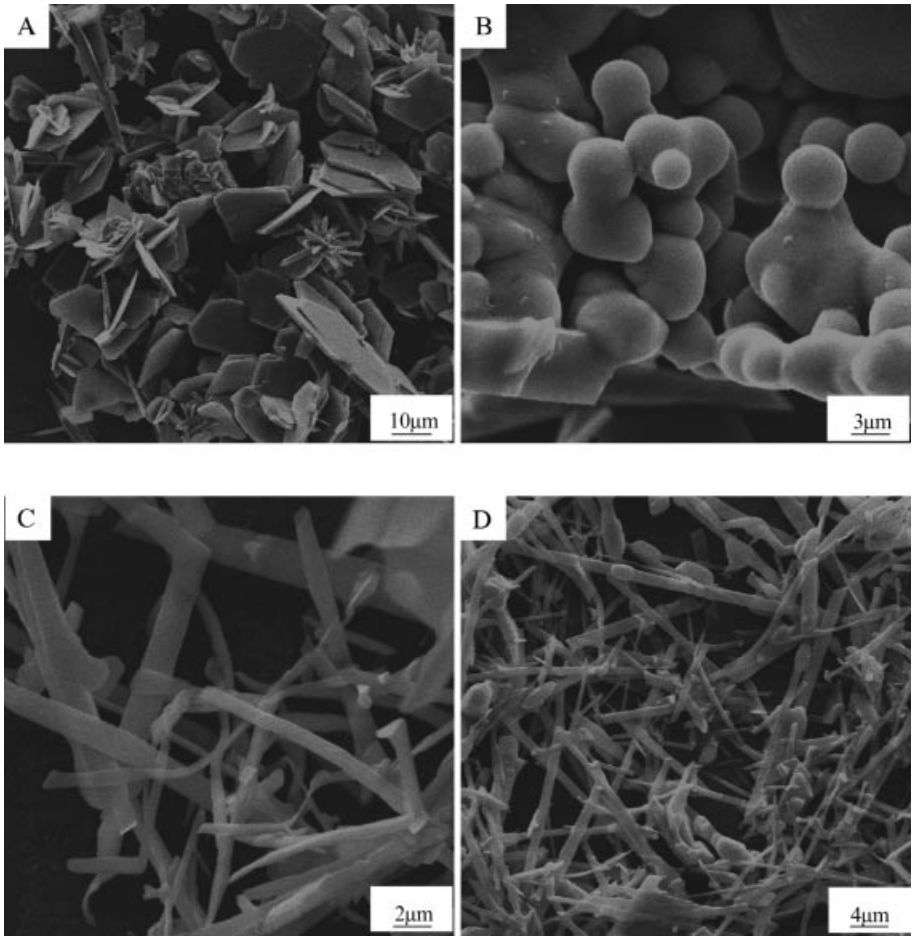


Figure 7. The SEM images of the Se particles synthesized by hydrothermal treatment for 6 h in the presence of CTAB/SDB: CTAB 0.1 M (A); CTAB 0.01 M (B); SDB 0.1 M (C); SDB 0.01 M (D).

 © 2007 Wiley-VCH Verlag GmbH & Co. KGaA, Weinheim 

phology of Se. When the other conditions are kept the same but CTAB (0.1 M) is added, plenty of flakes are obtained (Figure 7A). When the concentration of CTAB decreases to 0.01 M, there is some effect on the morphology of the Se crystals (Figure 7B). When SDB is added instead of CTAB, a lot of microrods and microbands are obtained at higher concentrations (Figure 7C, 0.1 M) and at lower concentrations (Figure 7D, 0.01 M). This observation can be explained by the fact that CTAB or SDB is adsorbed on specific facets of the Se crystal and changes the surface energy if the amount of CTAB or SDB is appropriate. In contrast, the nonadsorbed facets will grow rapidly. This behavior is similar to that observed in the synthesis of other crystals controlled by a surfactant.[34] When the concentration of CTAB is too low, there will not be enough surfactant adsorbed on all of the facets, and the surfactant loses the ability to control the morphology of the growing crystals (see Figure 7B).

## Conclusion

In summary, on the basis of the structure and surface analysis data, we conclude that the formation of wire networks in our work is based on the Ostwald ripening process and the oriented attachment mechanism. Such spontaneous self-aggregation and crystallization induced by the well-crystallized rods could provide a unique route for improving the properties of an anisotropic material. We believe that this finding could be extended to various oxide systems or even to non-oxide rod systems.

## Experimental Section

**Chemicals:** TSA, selenious acid ($H_2SeO_3$), propan-2-ol [$CH_3CH(OH)CH_3$], cetyltrimethylammonium bromide (CTAB), and sodium dodecyl sulfonate (SDS), were all A.R. grade and obtained from Shanghai Reagent Co. All the reagents in the experiments were used as received. Double-distilled water was used to prepare the solutions.

**Preparation of Se Nanoparticles:** In a typical experiment, an aqueous deaerated solution of TSA (30 mL, 1 mM) was taken in a test tube along with an aqueous deaerated solution of $H_2SeO_3$ (30 mL, 1 mM) and propan-2-ol (2 mL). About 20 mL of the solution was transferred into a 25-mL stainless-steel, Teflon-lined autoclave. The autoclave was sealed, maintained at 160 °C for the corresponding time, and then cooled to room temperature naturally. The precipitates obtained were centrifuged, washed several times with distilled water and absolute ethanol, and dried in vacuo at 60 °C for 6 h. The procedure of the corresponding control experiments with addition of different surfactants to the reaction solution is similar to the above experiments.

**Analysis:** FTIR spectroscopy measurements were carried out with a Nexus 870 FTIR spectrophotometer having a resolution of 4 $cm^{-1}$ (America Nicolet Co.). SEM measurements were performed with a Leica Stereoscan-440 scanning electron microscope. The Raman spectra were recorded with a Jobin Yvon HR800 (Horiba group) instrument by using 514.5 nm as the excitation line. The products were characterized by their X-ray diffraction (XRD) patterns, which were recorded with an MXP 18 AHF X-ray diffractometer (MAC Science Co. Ltd.) with monochromatized Cu-$K_\alpha$ radiation ($\lambda$ = 1.54056 Å). XPS measurements of Se nanoparticles were carried out with a VG ESCALAB MKII instrument at a pressure less than $10^{-6}$ Pa. The general scan and Se core-level spectra were recorded with non-monochromatized Mg-$K_\alpha$ radiation (photon energy = 1253.6 eV). The core-level binding energies (BEs) were aligned with respect to the $C_{1s}$ binding energy (BE) of 285 eV. Samples for TEM analysis were prepared by drop-coating films of the Se solution on carbon-coated copper TEM grids, allowing the grid to stand for 2 min, and then removing the extra solution with blotting paper. The TEM measurements mentioned above were carried out with a JEM model 100SX electron microscope (Japan Electron Co.) operated at an accelerating voltage of 80 kV.

**Supporting Information** (see footnote on the first page of this article): SEM image of the Se particles synthesized without TSA.

## Acknowledgments

This work is supported by the National Science Foundation of China (20471001, 20371001), the Specific Project for Talents of Science and Technology of Universities of Anhui Province (2005hbz03), the Key Laboratory of Environment-Friendly Polymer Materials of Anhui Province, and Science Foundation of Anhui Province (2006KJ155B).

[1] E. Matijevic, *Curr. Opin. Colloid Interface Sci.* **1996**, *1*, 176–183.
[2] T. Sugimoto, *Adv. Colloid Interface Sci.* **1987**, *28*, 65–108.
[3] J. W. Mullin, *Crystallization*, 3rd ed., Butterworth-Heinemann, Oxford, **1997**.
[4] J. K. Bailey, C. J. Brinker, M. L. Mecartney, *J. Colloid Interface Sci.* **1993**, *157*, 1–13.
[5] M. Ocana, M. P. Morales, C. J. Serna, *J. Colloid Interface Sci.* **1995**, *171*, 85–91.
[6] V. Privman, D. V. Goia, J. Park, E. Matijevic, *J. Colloid Interface Sci.* **1999**, *213*, 36–45.
[7] A. Chemseddine, T. Moritz, *Eur. J. Inorg. Chem.* **1999**, 235–245.
[8] R. L. Penn, J. F. Banfield, *Geochim. Cosmochim. Acta* **1999**, *63*, 1549–1557.
[9] R. L. Penn, J. F. Banfield, *Science* **1998**, *281*, 969–971.
[10] F. Banfield, S. A. Welch, H. Zhang, T. T. Ebert, R. L. Penn, *Science* **2000**, *289*, 751–754.
[11] R. L. Penn, G. Oskam, T. J. Strathmann, P. C. Searson, A. T. Stone, D. R. Veblen, *J. Phys. Chem. B* **2001**, *105*, 2177–2182.
[12] R. L. Penn, A. T. Stone, D. R. Veblen, *J. Phys. Chem. B* **2001**, *105*, 4690–4697.
[13] A. P. Alivisatos, *Science* **2000**, *289*, 736–737.
[14] B. Liu, S.-H. Yu, F. Zhang, L. J. Li, Q. Zhang, L. Ren, K. Jiang, *J. Phys. Chem. B* **2004**, *108*, 2788–2792.
[15] a) M. T. Pope, A. Muller, *Angew. Chem. Int. Ed. Engl.* **1991**, *30*, 34–48; b) V. Kogan, Z. Izenshtat, R. Neumann, *Angew. Chem. Int. Ed.* **1999**, *38*, 3331–3334.
[16] M. T. Pope in *Inorganic Chemistry Concepts* (Eds.: C. K. Jorgensen, M. F. Lappert, S. J. Lippard, J. L. Margrave, K. Niedenzu, H. Nobh, R. W. Parry, H. Yamatera), Springer Verlag, West Berlin, **1983**, vol. 8, p. 101.
[17] B. Gates, Y. Yin, Y. Xia, *J. Am. Chem. Soc.* **2000**, *122*, 12582–12583.
[18] B. Gates, B. Mayers, A. Grossman, Y. Xia, *Adv. Mater.* **2002**, *14*, 1749–1752.
[19] X. Zhang, Y. Xie, F. Xu, X. H. Liu, *Chin. J. Inorg. Chem.* **2003**, *19*, 77–81.
[20] Y. Ding, Q. Li, Y. B. Jia, L. Chen, J. Y. Xing, Y. T. Qian, *J. Cryst. Growth* **2002**, *241*, 489–497.

 © 2007 Wiley-VCH Verlag GmbH & Co. KGaA, Weinheim 

[21] A. Abdelousa, W. L. Gong, W. Lutze, J. A. Shelnutt, R. Franco, J. Moura, *Chem. Mater.* **2000**, *12*, 1250–1256.
[22] B. Gates, B. Mayers, B. Cattle, Y. Xia, *Adv. Funct. Mater.* **2002**, *12*, 219–227.
[23] C. H. An, K. B. Tang, X. M. Liu, Y. T. Qian, *Eur. J. Inorg. Chem.* **2003**, 3250–3255.
[24] B. Zhang, X. Ye, Y. Xie, *Nanotechnology* **2006**, *17*, 385–390.
[25] X. B. Cao, Y. Xie, L. Y. Li, *Adv. Mater.* **2003**, *15*, 1914–1918.
[26] L. Stuke in *Selenium* (Eds: R. A.Zingaro, W. C. Cooper), van Nostrand Reinhold, New York, **1994**.
[27] J. P. Jolivet, M. Henry, J. Livage, *Metal Oxide Chemistry and Synthesis - from Solution to Solid State*, John Wiley and Sons, Chichester, U. K. **2000**, p. 47.
[28] H. Zhang, D. Yang, Y. Ji, X. Ma, D. Que, *J. Phys. Chem. B* **2004**, *108*, 1179–1182.
[29] H. Liao, J. H. Hafner, *J. Phys. Chem. B* **2004**, *108*, 19276–19280.
[30] a) Z. Wei, A. J. Mieszawska, F. P. Zamborini, *Langmuir* **2004**, *20*, 4322–4326; b) Z. Wei, F. P. Zamborini, *Langmuir* **2004**, *20*, 11301–11304.
[31] N. Taub, O. Krichevski, G. Markovich, *J. Phys. Chem. B* **2003**, *107*, 11579–11582.
[32] H. L. Zhu, R. S. Averback, *Philos. Mag. Lett.* **1996**, *73*, 27–33.
[33] M. Yeadon, M. Ghaly, J. C. Yang, R. S. Averback, J. M. Gibson, *Appl. Phys. Lett.* **1998**, *73*, 3208–3210.
[34] Y. W. Jun, M. F. Casula, J. H. Sim, S. Y. Kim, J. Cheon, A. P. Alivisatos, *J. Am. Chem. Soc.* **2003**, *125*, 15981–15985.

Received: November 30, 2006
Published Online: August 9, 2007

 © 2007 Wiley-VCH Verlag GmbH & Co. KGaA, Weinheim 

DOI: 10.1002/ejic.200700394

# Synthesis and Reactivity of Alkenyl-Substituted Zirconocene Complexes and Their Application as Olefin Polymerisation Catalysts

**Santiago Gómez-Ruiz,[a] Dorian Polo-Cerón,[a] Sanjiv Prashar,*[a] Mariano Fajardo,[a] Antonio Antiñolo,[b] and Antonio Otero[b]**

**Keywords:** Zirconium / Metallocenes / Polymerisation / Homogeneous catalysis / Cyclopentadienyl ligands

The zirconocene complexes [Zr($\eta^5$-$C_5H_5$){$\eta^5$-$C_5H_4$-($CMe_2CH_2CH_2CH{=}CH_2$)}$Cl_2$] (**4**) and [Zr{$\eta^5$-$C_5H_4$($CMe_2$-$CH_2CH_2CH{=}CH_2$)}$_2Cl_2$] (**5**) were synthesised from the reaction of the lithium derivative [Li{$C_5H_4$($CMe_2CH_2$-$CH_2CH{=}CH_2$)}] (**1**) with [Zr($\eta^5$-$C_5H_5$)$Cl_3$] or $ZrCl_4$, respectively. The *ansa*-zirconocene complex [Zr{$Me_2Si$($\eta^5$-$C_5Me_4$)-($\eta^5$-$C_5H_3${$CMe_2CH_2CH_2CH{=}CH_2$})}$Cl_2$] (**6**) was obtained from the reaction of the lithium precursor [$Li_2${$Me_2Si$($\eta^5$-$C_5Me_4$)($\eta^5$-$C_5H_3${$CMe_2CH_2CH_2CH{=}CH_2$})}] (**3**) with zirconium tetrachloride. Catalytic hydrogenation of **4**–**6** gave the zirconocene complexes [Zr($\eta^5$-$C_5H_5$){$\eta^5$-$C_5H_4$($CMe_2CH_2$-$CH_2CH_2CH_3$)}$Cl_2$] (**7**), [Zr{$\eta^5$-$C_5H_4$($CMe_2CH_2CH_2CH_2$-$CH_3$)}$_2Cl_2$] (**8**) and [Zr{$Me_2Si$($\eta^5$-$C_5Me_4$)($\eta^5$-$C_5H_3${$CMe_2CH_2$-$CH_2CH_2CH_3$})}$Cl_2$] (**9**), respectively. Hydroboration of **4**–**6** with 9-BBN (9-borabicyclo[3.3.1]nonane) yielded [Zr($\eta^5$-$C_5H_5$){$\eta^5$-$C_5H_4$($CMe_2CH_2CH_2CH_2CH_2BC_8H_{14}$)}$Cl_2$] (**10**), [Zr{$\eta^5$-$C_5H_4$($CMe_2CH_2CH_2CH_2CH_2BC_8H_{14}$)}$_2Cl_2$] (**11**) and [Zr{$Me_2Si$($\eta^5$-$C_5Me_4$)($\eta^5$-$C_5H_3${$CMe_2CH_2CH_2CH_2CH_2BC_8$-$H_{14}$})}$Cl_2$] (**12**), respectively, and the catalytic hydrosilylation of **4**–**6** with $SiHMe_2Cl$ gave [Zr($\eta^5$-$C_5H_5$){$\eta^5$-$C_5H_4$($CMe_2$-$CH_2CH_2CH_2CH_2SiMe_2Cl$)}$Cl_2$] (**13**), [Zr{$\eta^5$-$C_5H_4$($CMe_2$-$CH_2CH_2CH_2CH_2SiMe_2Cl$)}$_2Cl_2$] (**14**) and [Zr{$Me_2Si$($\eta^5$-$C_5Me_4$)($\eta^5$-$C_5H_3${$CMe_2CH_2CH_2CH_2CH_2SiMe_2Cl$})}$Cl_2$] (**15**), respectively. The dinuclear complex [$Cl_2$Zr{$Me_2Si$($\eta^5$-$C_5$-$Me_4$)($\eta^5$-$C_5H_3${$CMe_2(CH_2)_4SiMe_2OSiMe_2(CH_2)_4Me_2C$}$\eta^5$-$C_5$-$H_3$)($\eta^5$-$C_5Me_4$)$SiMe_2$}$ZrCl_2$] (**16**) was obtained upon controlled hydrolysis of **15**. The zirconocene compounds were tested as catalysts in the polymerisation of ethylene and propylene. Isotactic polypropylene with [mmmm] pentads of the order of 75 % were obtained with the *ansa*-zirconocene catalysts, whereas the unbridged metallocene catalysts produced atactic polypropylene. The molecular structures of **4** and **5** were determined by single-crystal X-ray diffraction studies.

(© Wiley-VCH Verlag GmbH & Co. KGaA, 69451 Weinheim, Germany, 2007)

## Introduction

Metallocene dichloride complexes of group 4 metals have received a large amount of attention in the past few decades because they are excellent catalysts for the polymerisation of α-olefins[1] and for other processes in organic synthesis such as carbometallation, hydrometallation, carbonylation, acylation, isomerisation, hydrogenation, hydroamination, dehydrosilylation and hydrosilylation.[2]

The current goal in the field of olefin polymerisation with metallocene catalysts is moving towards supported catalysts that allow homogeneous single-site selectivity in a heterogeneous medium.[3] A variety of routes have been developed for supporting metallocene complexes on silica, including the direct reaction of silica with a metallocene complex followed by activation with a co-catalyst, such as MAO, reaction of MAO-modified silica with a metallocene complex, or similar approaches where other co-catalysts are supported on silica.[4] Recently, considerable attention has been focused on the anchoring of metallocene complexes on silica through either metallocene synthesis on the support or reaction of a suitably functionalised metallocene complex with silica.[4,5] One of the most common routes for the immobilisation of metallocene complexes is the reactivity of the C=C double bond of an alkenyl substituent on the cyclopentadienido ring or at the *ansa*-bridge atom.[6]

In contrast to their late transition metal analogues,[7] the use and transformation of functional groups at the cyclopentadienido rings of early transition metal compounds has been rather limited.[8] The reactivity of such alkenyl-functionalised metallocene complexes has been mainly studied in olefin metathesis reactions[9,10] and hydrometallation.[10]

As a continuation of our work on the synthesis and catalytic reactivity of group 4 metallocene complexes,[11] we report here the synthesis of new alkenyl-substituted zirconocene and *ansa*-zirconocene complexes and their reactivity in hydrogenation, hydroboration and hydrosilylation processes. We also describe the catalytic behaviour of the zirconocene complexes in the polymerisation of ethylene and propylene.

[a] Departamento de Química Inorgánica y Analítica, E.S.C.E.T., Universidad Rey Juan Carlos,
28933 Móstoles (Madrid), Spain
Fax: +34-91-488-8143
E-mail: sanjiv.prashar@urjc.es
[b] Departamento de Química Inorgánica, Orgánica y Bioquímica, Universidad de Castilla-La Mancha, Facultad de Químicas, Campus Universitario,
13071 Ciudad Real, Spain

 © 2007 Wiley-VCH Verlag GmbH & Co. KGaA, Weinheim 

## Results and Discussion

Methyllithium reacts with 6-(4-buten-1-yl)-6-methylfulvene by nucleophilic addition at the exocyclic double bond to give the cyclopentadienidolithium compound [Li{$C_5H_4(CMe_2CH_2CH_2CH{=}CH_2)$}] (**1**) [Equation (1)].

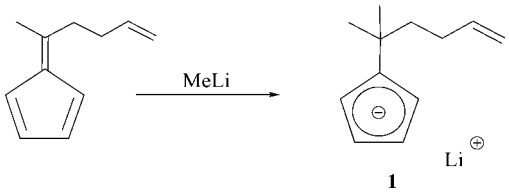


**1** (1)

Complex **1** was characterised by $^1H$ and $^{13}C$ NMR spectroscopy (see Experimental Section). Two multiplets at $\delta$ = 5.46 and 5.48 ppm in the $^1H$ NMR spectrum of **1** can be assigned to the cyclopentadienido ring protons, with a singlet due to the two methyl groups substituting the carbon atom bonded to the cyclopentadienido ring at $\delta$ = 1.19 ppm. The alkenyl fragment exhibits four sets of signals, two corresponding to the $CH_2$ protons (two multiplets at $\delta$ = 1.50 and 1.91 ppm), one corresponding to the proton at C-$\gamma$ (a multiplet at $\delta$ = 5.73 ppm) and two for the terminal olefinic protons (multiplets at $\delta$ = 4.74 and 4.87 ppm). The $^{13}C\{^1H\}$ NMR spectrum of **1** shows the expected signals (one signal at $\delta$ = 46.5 ppm for the carbon atom bonded to the cyclopentadienido ring, one signal at $\delta$ = 35.4 ppm for the two methyl groups, four signals at $\delta$ = 31.0, 31.1, 112.8 and 128.8 ppm for the alkenyl fragment, and three signals at $\delta$ = 100.9, 101.8, and 141.6 ppm for the cyclopentadienido moiety).

The asymmetrically substituted *ansa* ligand precursor $Me_2Si(C_5HMe_4)\{C_5H_4(CMe_2CH_2CH_2CH{=}CH_2)\}$ (**2**) was prepared by treating **1** with $Me_2Si(C_5HMe_4)Cl$ according to previously reported synthetic protocols [Equation (2)].[11a,11b,11f] Compound **2** was isolated as a mixture of the double bond positional isomers, with one isomer being predominant as confirmed by $^1H$ NMR spectroscopy. This compound was also characterised by electron impact mass spectrometry (see Experimental Section). The dilithium derivative, [$Li_2\{Me_2Si(C_5Me_4)(C_5H_3\{CMe_2CH_2CH_2CH{=}CH_2\})\}$] (**3**) was obtained in the traditional manner by treating **2** with *n*-butyllithium. It was isolated as a highly moisture- and oxygen-sensitive white solid and characterised by elemental analysis (carbon and hydrogen; see Experimental Section).

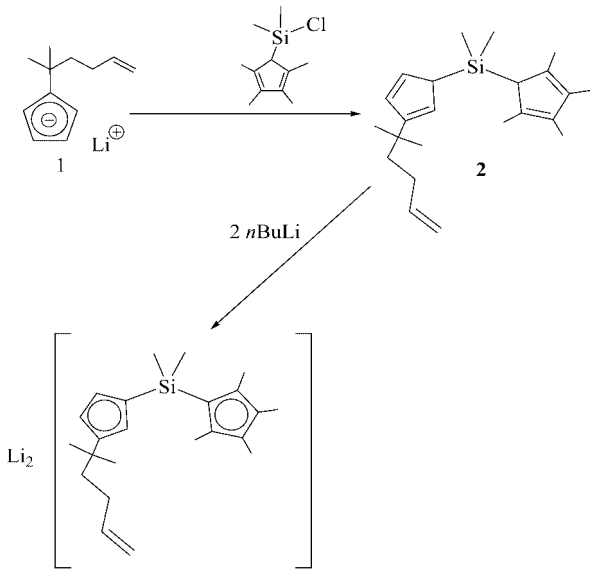


(2)

Treatment of **1** with either [$Zr(\eta^5\text{-}C_5H_5)Cl_3$] or $ZrCl_4$ yielded the corresponding zirconocene(IV) dichloride complexes [$Zr(\eta^5\text{-}C_5H_5)\{\eta^5\text{-}C_5H_4(CMe_2CH_2CH_2CH{=}CH_2)\}Cl_2$] (**4**) and [$Zr\{\eta^5\text{-}C_5H_4(CMe_2CH_2CH_2CH{=}CH_2)\}_2Cl_2$] (**5**), respectively [Equation (3)], which were isolated as crystalline solids and characterised spectroscopically. The $^1H$ NMR spectrum of **4** shows one singlet for the unsubstituted cyclopentadienido ring protons at $\delta$ = 6.48 ppm, two multiplets at $\delta$ = 6.36 and 6.45 ppm for the substituted cyclopentadienido ring protons, and a singlet at $\delta$ = 1.39 ppm corresponding to the two methyl groups. The alkenyl fragment exhibits four sets of signals, two corresponding to the $CH_2$ protons (two multiplets at $\delta$ = 1.56 and 1.75 ppm), one for the proton at C-$\gamma$ (a multiplet at $\delta$ = 5.71 ppm) and two corresponding to the terminal olefinic protons (multiplets at $\delta$ = 4.89 and 4.96 ppm). A similar spectral pattern was also observed for the alkenyl fragment in the $^1H$ NMR spectrum of **5** along with a singlet at $\delta$ = 1.41 ppm (assigned to the two methyl groups) and two multiplets at $\delta$ = 6.32 and 6.41 ppm for the cyclopentadienido protons. The $^{13}C\{^1H\}$ NMR spectrum of **4** shows one signal at $\delta$ = 115.9 ppm assigned to the unsubstituted $C_5$ ring and three signals at $\delta$ = 112.2, 113.0 and 143.3 ppm for the substituted $C_5$ ring. The carbon atom bonded to the cyclopentadienido ring appears in the spectrum as one signal at $\delta$ = 46.1 ppm, and the carbon atoms of the two methyl groups are observed as one signal at $\delta$ = 36.4 ppm. The four signals at $\delta$ = 27.2, 29.0, 114.1 and 138.5 ppm were assigned to the alk-

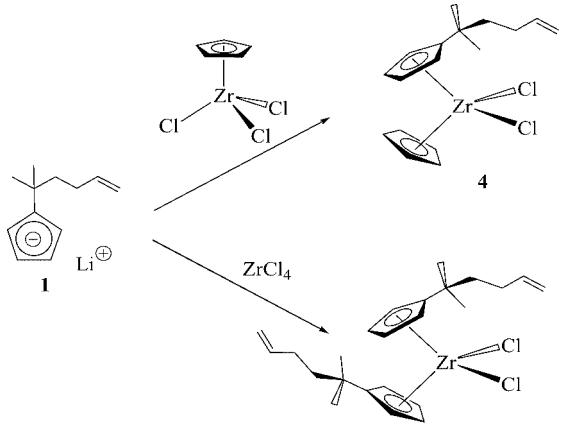


(3)

 © 2007 Wiley-VCH Verlag GmbH & Co. KGaA, Weinheim 

enyl moiety. The expected signals were observed in the $^{13}C\{^1H\}$ NMR spectrum of **5** (see Experimental Section).

The molecular structures of **4** and **5** were determined by single-crystal X-ray diffraction studies. The molecular structures and atomic numbering schemes are shown in Figures 1 and 2, respectively, and selected bond lengths and angles for **4** and **5** are given in Table 1.

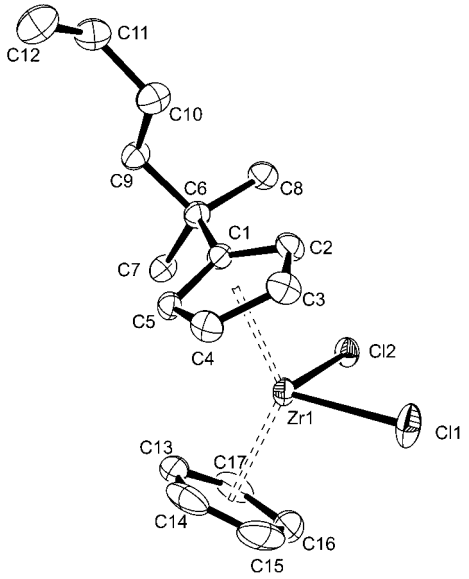


Figure 1. Molecular structure and atom-labelling scheme for $[Zr(\eta^5\text{-}C_5H_5)\{\eta^5\text{-}C_5H_4(CMe_2CH_2CH_2CH{=}CH_2)\}Cl_2]$ (**4**), with thermal ellipsoids at 50% probability.

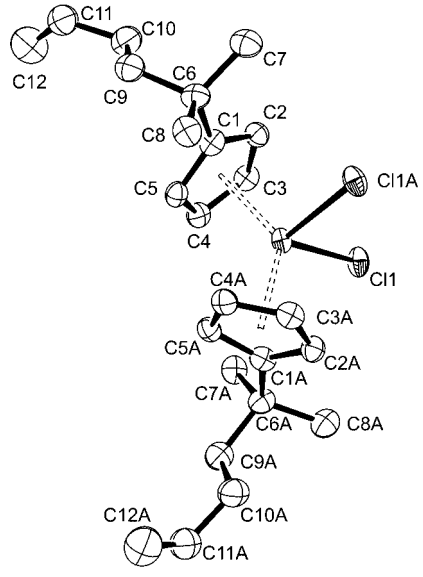


Figure 2. Molecular structure and atom-labelling scheme for $[Zr\{\eta^5\text{-}C_5H_4(CMe_2CH_2CH_2CH{=}CH_2)\}_2Cl_2]$ (**5**), with thermal ellipsoids at 50% probability.

Complex **4** crystallises in the triclinic space group $P\bar{1}$ with four molecules in the unit cell and two in the asymmetric unit that are structurally almost identical. Complex **5**, on the other hand, crystallises in the centrosymmetric monoclinic space group *C*2/*c* with four molecules in the unit cell and only half of the molecule in the asymmetric unit; the other half is generated by symmetry operations. The molecular structures of **4** and **5** reveal that the zirconium atoms have a distorted tetrahedral geometry with both $C_5$ rings bound to the metal atom in an $\eta^5$ mode. The centroids of the cyclopentadienido rings form an angle with the zirconium atom of 129.98° and 130.10° for **4** and 129.22° for **5**, which are typical for zirconocene dichloride complexes. The Zr–Cl distances (approx. 2.45 Å) and Cl–Zr–Cl angle (approx. 95°) for **4** and **5** are in the expected range.[1e] The bond lengths in the butenyl moiety are also normal [C(9)–C(10) 1.541(5) and 1.531(5) Å for **4** and 1.532(5) Å for **5**; C(10)–C(11) 1.496(6) and 1.491(6) Å for **4** and 1.494(5) Å for **5**; C(11)–C(12) 1.294(7) and 1.304(7) Å for **4** and 1.288(6) Å for **5**]. The C(11)–C(12) distances are typical for terminal C–C double bonds[10c,10e] and the C(10)–C(11)–C(12) angle [125.7(4) and 125.4(4)° for **4** and 126.1(4)° for **5**] confirms the $sp^2$ hybridisation of C(12) in both cases. Selected structural data for **4** and **5** are compared with those of similar zirconocene complexes in Table 2.

Table 1. Selected bond lengths [Å] and angles [°] for **4** and **5**.

| | **4** | **4a** | **5** |
|---|---|---|---|
| Zr(1)–Cent(1) | 2.211 | 2.216 | 2.211 |
| Zr(1)–Cent(2) | 2.200 | 2.197 | |
| Zr(1)–Cl(1) | 2.451(1) | 2.450(1) | 2.4533(8) |
| Zr(1)–Cl(2) | 2.447(1) | 2.458(1) | |
| C(9)–C(10) | 1.541(5) | 1.531(5) | 1.532(5) |
| C(10)–C(11) | 1.496(6) | 1.491(6) | 1.494(5) |
| C(11)–C(12) | 1.294(7) | 1.304(7) | 1.288(6) |
| Cent(1)–Zr(1)–Cent(2)[a] | 129.98 | 130.10 | 129.22 |
| Cl(1)–Zr(1)–Cent(1) | 106.91 | 108.59 | 107.20 |
| Cl(1)–Zr(1)–Cent(2) | 105.47 | 105.31 | |
| Cl(2)–Zr(1)–Cent(1) | 106.36 | 106.14 | |
| Cl(2)–Zr(1)–Cent(2) | 106.36 | 106.30 | |
| Cl(1)–Zr(1)–Cl(2) | 94.58(3) | 94.83(3) | |
| Cl(1)–Zr(1)–Cl(1A) | | | 94.92(9) |
| C(9)–C(10)–C(11) | 112.0(3) | 111.8(3) | 112.0(3) |
| C(10)–C(11)–C(12) | 125.7(4) | 125.4(4) | 126.1(4) |

[a] Cent(1) and Cent(2) are the centroids of C(1)–C(5) and C(13)–C(17) for **4** and C(1)–C(5) and C(1A)–C(5A) for **5**, respectively.

Treatment of the dilithium derivative **3** with $ZrCl_4$ gave the corresponding *ansa*-metallocene dichloride complex $[Zr\{Me_2Si(\eta^5\text{-}C_5Me_4)(\eta^5\text{-}C_5H_3\{CMe_2CH_2CH_2CH{=}CH_2\})\}Cl_2]$ (**6**) [Equation (4)], which was isolated as a crystalline solid and characterised spectroscopically. The $^1H$ NMR spectrum for **6** shows three multiplets for the protons of the alkenyl-substituted $C_5$ ring (between $\delta$ = 5.5 and 7.0 ppm), four singlets for the methyl groups of the tetramethyl-substituted $C_5$ ring (between $\delta$ = 1.9 and 2.1 ppm), and two singlets corresponding to the methyl groups of the $SiMe_2$ bridging unit ($\delta$ = 0.83 and 0.87 ppm).

The signals for the alkenyl fragment have similar chemical shifts and identical spectral patterns to those observed in the zirconocene complexes **4** and **5**. However, the methyl groups substituting the carbon atom bonded to the cyclopentadienido ring are diastereotopic in **6** due to the planar

 © 2007 Wiley-VCH Verlag GmbH & Co. KGaA, Weinheim 

Table 2. Selected structural data of some zirconocene complexes.

| Complex | Zr–Cl [Å] | Cp–Zr–Cp[a] [°] | Cl–Zr–Cl [°] | C=C [Å] | C–C=C [°] | Ref. |
|---|---|---|---|---|---|---|
| $[Zr(\eta^5\text{-}C_5H_5)\{\eta^5\text{-}C_5H_4(CMe_2CH_2CH_2CH{=}CH_2)\}Cl_2]$ (**4**) | 2.451(1)<br>2.447(1) | 130.0<br>130.1 | 94.6(1) | 1.298(6) | 125.7(4) | this work |
| $[Zr(\eta^5\text{-}C_5H_4\{CMe_2CH_2CH_2CH{=}CH_2\})_2Cl_2]$ (**5**) | 2.453(1) | 129.2 | 94.9(1) | 1.288(6) | 126.1(4) | this work |
| $[Zr(\eta^5\text{-}C_5H_4\{CCH_3(=CH_2)\})_2Cl_2]$ | 2.446(1) | 129.8 | 96.2(1) | 1.34(2) | 123.3(11) | [9g] |
| $[Zr(\eta^5\text{-}C_5H_3t\text{Bu}\{CCH_3(=CH_2)\})_2Cl_2]$ | 2.433(1)<br>2.442(1) | 130.5 | 96.1(1) | 1.345(4)<br>1.374(5) | 120.5(3)<br>119.9(3) | [9g] |
| $[Zr\{Me_2Si(\eta^5\text{-}C_5Me_4)(\eta^5\text{-}C_5H_3\{CH_2CH{=}CH_2\})\}Cl_2]$ | 2.429(1)<br>2.429(1) | 126.0 | 98.7(1) | 1.304(4) | 125.9(3) | [9c] |
| $[Zr\{Me(CH_2CH{=}CH_2)Si(\eta^5\text{-}C_5H_4)_2\}Cl_2]$ | 2.444(2)<br>2.431(2) | 125.4 | 98.1(1) | 1.26(5) | 124(5) | [11c] |
| $[Zr\{Me(CH_2CH{=}CH_2)Si(\eta^5\text{-}C_5Me_4)(\eta^5\text{-}C_5H_4)\}Cl_2]$ | 2.428(2)<br>2.429(2) | 126.7 | 100.9(1) | 1.320(10) | 123.0(10) | [11c] |
| $[Zr\{CH_2{=}CHCH_2(H)Si(\eta^5\text{-}C_5Me_4)_2\}Cl_2]$ | 2.425(3)<br>2.413(3) | 128.5 | 97.5(1) | 1.330(10) | 124.8(9) | [11e] |

[a] Cp refers to the $C_5H_5$, $C_5H_4$ or $C_5Me_4$ moiety.

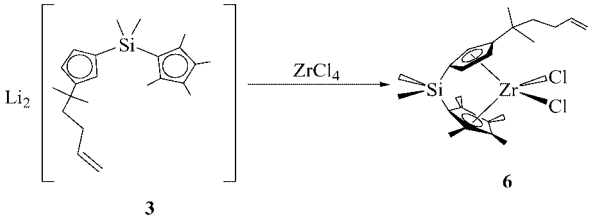


(4)

chirality present in the molecule and thus appear as two singlets ($\delta$ = 1.42 and 1.51 ppm) in the $^1$H NMR spectrum.

We next attempted to hydrogenate the C=C double bond of the alkenyl fragment in complexes **4**–**6**. These complexes react with $H_2$ in a Pd/C-catalysed hydrogenation to give the saturated metallocene compounds $[Zr(\eta^5\text{-}C_5H_5)\{\eta^5\text{-}C_5H_4(CMe_2CH_2CH_2CH_2CH_3)\}Cl_2]$ (**7**), $[Zr\{\eta^5\text{-}C_5H_4(CMe_2CH_2CH_2CH_2CH_3)\}_2Cl_2]$ (**8**) and $[Zr\{Me_2Si(\eta^5\text{-}C_5Me_4)(\eta^5\text{-}C_5H_3\{CMe_2CH_2CH_2CH_2CH_3\})\}Cl_2]$ (**9**), respectively, as the only products [Equation (5)]. The $^1$H NMR spectra of these complexes show four multiplets about $\delta \approx$ 0.8, 0.9, 1.2 and 1.4 ppm due to the newly formed alkyl moiety, with four signals in the alkyl carbon region between $\delta$ = 23 and 28 ppm in the $^{13}C\{^1H\}$ NMR spectra.

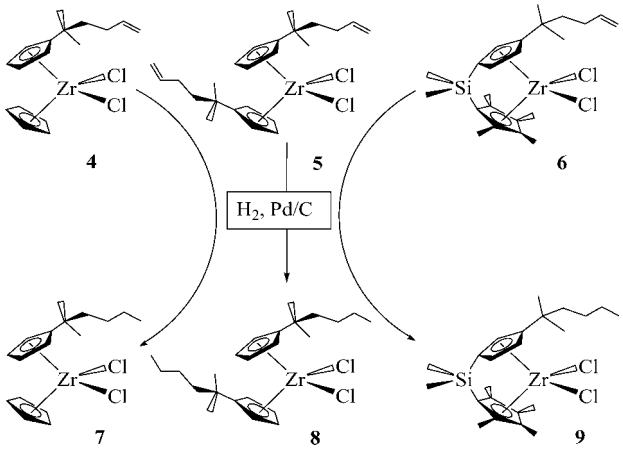


(5)

The alkenyl substituent in complexes **4**–**6** should also be suitable for the introduction of borane groups by hydroboration. Since previous studies have shown that a further functionalisation of the alkenyl side-chain and the isolation of the respective product is rather difficult,[10a–10d,11c,12] highly selective 9-borabicyclo[3.3.1]nonane (9-BBN) was chosen as the hydroboration agent. Reaction of complexes **4**–**6** with 9-BBN gave the product resulting from anti-Markovnikoff addition, namely $[Zr(\eta^5\text{-}C_5H_5)\{\eta^5\text{-}C_5H_4(CMe_2CH_2CH_2CH_2CH_2BC_8H_{14})\}Cl_2]$ (**10**), $[Zr\{\eta^5\text{-}C_5H_4(CMe_2CH_2CH_2CH_2CH_2BC_8H_{14})\}_2Cl_2]$ (**11**) and $[Zr\{Me_2Si(\eta^5\text{-}C_5Me_4)(\eta^5\text{-}C_5H_3\{CMe_2CH_2CH_2CH_2CH_2BC_8H_{14}\})\}Cl_2]$ (**12**), respectively [Equation (6)]. Complexes **10**–**12** were characterised by standard spectroscopic techniques. The $^1$H NMR spectra of **10**–**12** show four multiplets between $\delta$ = 1.2 and 1.9 ppm for the boranyl moiety, corresponding to the four distinct proton environments (see Experimental Section). In these cases a change in the signals previously attributed to the alkenyl moiety in **4**–**6** to four multiplets at $\delta \approx$ 0.9, 1.0, 1.2 and 1.4 ppm was observed.

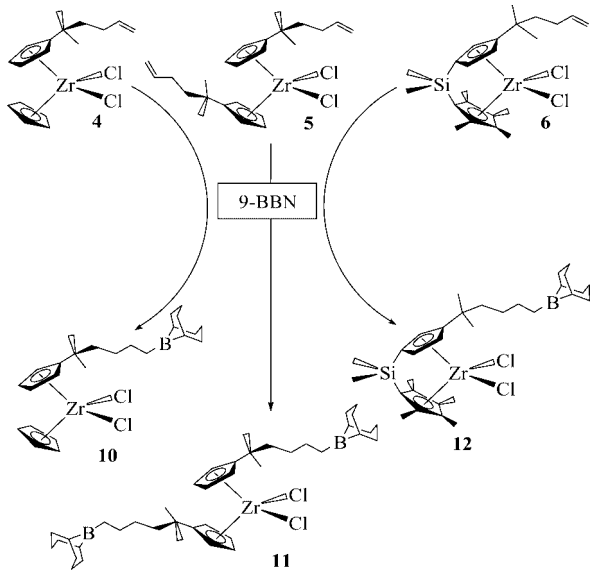


(6)

 © 2007 Wiley-VCH Verlag GmbH & Co. KGaA, Weinheim 

Catalytic hydrosilylation reactions are an excellent method for constructing different structures containing metallocene complexes.[6,11d,11e,13] With this in mind, we carried out the hydrosilylation reaction of **4**–**6** with an excess of chlorodimethylsilane in the presence of Karstedt's catalyst to give the β-hydrosilylation products [Zr($\eta^5$-$C_5H_5$){$\eta^5$-$C_5H_4$($CMe_2CH_2CH_2CH_2CH_2SiMe_2Cl$)}$Cl_2$] (**13**), [Zr{$\eta^5$-$C_5H_4$($CMe_2CH_2CH_2CH_2CH_2SiMe_2Cl$)}$_2Cl_2$] (**14**) and [Zr{$Me_2Si$($\eta^5$-$C_5Me_4$)($\eta^5$-$C_5H_3${$CMe_2CH_2CH_2CH_2CH_2$-$SiMe_2Cl$})}$Cl_2$] (**15**), respectively [Equation (7)]. Complexes **13**–**15** were characterised by $^1H$, $^{13}C\{^1H\}$, and $^{29}Si\{^1H\}$ NMR and IR spectroscopy and also by mass spectrometry. Completion of the hydrosilylation reaction was monitored by $^1H$ NMR spectroscopy, where the spectra recorded showed the absence of the olefinic proton signals of the alkenyl moiety and the appearance of four multiplets corresponding to the $–CH_2CH_2CH_2CH_2Si–$ fragment in the region $\delta$ = 0.7–1.6 ppm. Additional signals due to the methyl groups attached to the silicon atom are present at $\delta \approx$ 0.4 ppm. The $^{13}C\{^1H\}$, and $^{29}Si\{^1H\}$ NMR spectroscopic data confirmed the proposed structures (see Experimental Section), with a resonance being observed in the $^{29}Si\{^1H\}$ NMR spectra at $\delta \approx$ 30 ppm due to the silicon atom of the new silyl fragment. Mass spectrometric analysis showed the molecular ion peak in all the cases (see Experimental Section).

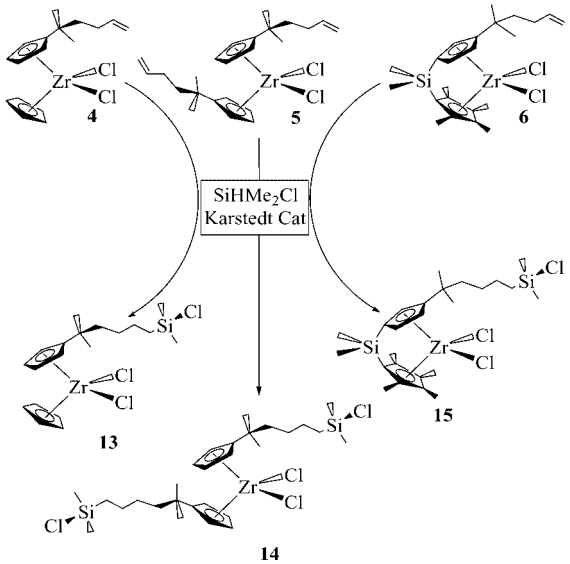


(7)

The dinuclear, Si–O–Si-bridged complex [$Cl_2Zr${$Me_2Si$-($\eta^5$-$C_5Me_4$)($\eta^5$-$C_5H_3${$CMe_2(CH_2)_4SiMe_2OSiMe_2(CH_2)_4$-$Me_2C$}$\eta^5$-$C_5H_3$)($\eta^5$-$C_5Me_4$)$SiMe_2$}$ZrCl_2$] (**16**) was obtained upon addition of a stoichiometric amount of $H_2O$ to a toluene solution of complex **15** [Equation (8)]. Selective hydrolysis of the Si–Cl bond and formation of an Si–O–Si bridge was confirmed by multinuclear NMR and IR spectroscopy. Complex **15** contains an element of planar chirality, therefore coupling of two such units should lead to the formation of two diastereoisomers (*rac* and *meso*). However, only one set of signals was observed in the NMR spectra of **16**. This is most probably due to the fact that the two chiral metallocene subunits are sufficiently separated in space that the signals corresponding to the respective *rac* and *meso* isomers coincide.

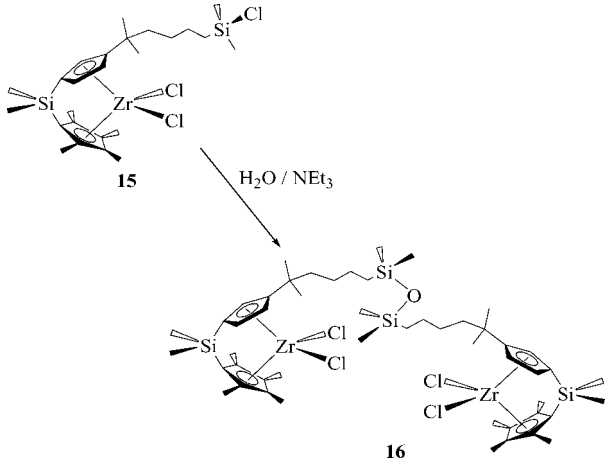


(8)

The signal for the methyl groups attached to the siloxane silicon atoms in the $^1H$ NMR spectrum of **16** is displaced from $\delta$ = 0.39 (in **15**) to 0.00 ppm. The $^{29}Si\{^1H\}$ NMR spectrum shows a new signal at $\delta$ = 7.1 ppm due to the silicon atoms of the Si–O–Si fragment as well as the signal corresponding to the silicon atoms of the *ansa* bridge ($\delta$ = –14.2 ppm). This chemical shift is in agreement with those reported in other studies.[14] It should be noted that similar reactions for early transition metals have been reported recently.[15]

We also examined the polymerisation of ethylene using the zirconocene derivatives described in this paper as catalyst. The polymerisation experiments were conducted with an MAO/metal catalyst ratio of 1000:1 at 20 °C and an olefin pressure of 2 bar during 15 min. Polymerisation was also carried out with the reference compound [Zr($\eta^5$-$C_5H_5$)$_2Cl_2$] under the same experimental conditions. The catalytic activities and polymer molecular weights and molecular weight distributions are given in Table 3.

The symmetrical metallocene systems **5**, **8**, **11** and **14** show lower catalytic activities than the asymmetric or *ansa* complexes. Indeed, **11** is not catalytically active in the polymerisation of ethylene. The asymmetric metallocene catalysts, on the other hand, are active to different degrees, with **13** proving to be the most active catalyst of the series tested, **10** one of the least and **4** giving a value comparable to that of the reference catalyst [Zr($\eta^5$-$C_5H_5$)$_2Cl_2$]. The catalytic activity of the *ansa*-metallocene complexes **6**, **9** and **12** is relatively high, although lower activities were observed for **15** and the dinuclear complex **16**.

In order to explain the zero activity of **11** in polymerisation we prepared the dimethyl/borane derivatives, [$ZrCp'_2Me$][$MeB(C_6F_5)_3$], of **10**–**12** on an NMR scale. According to Horton and co-workers, the chemical shift difference between the *meta*- and *para*-fluorine atoms in the $^{19}F$ NMR spectra provides information about the possible in-

 © 2007 Wiley-VCH Verlag GmbH & Co. KGaA, Weinheim 

Table 3. Ethylene polymerisation results for **4**–**16** and $[Zr(\eta^5\text{-}C_5H_5)_2Cl_2]$.[a]

| Catalyst | Activity[b] | $M_w$ | $M_w/M_n$ |
|---|---|---|---|
| $[Zr(\eta^5\text{-}C_5H_5)_2Cl_2]$ | 11650 | 169000 | 2.3 |
| **4** | 9717 | 881000 | 9.6 |
| **5** | 3070 | 978000 | 5.7 |
| **6** | 8170 | 62000 | 3.8 |
| **7** | 6925 | 742000 | 8.8 |
| **8** | 1435 | 576000 | 6.5 |
| **9** | 10231 | 42000 | 4.0 |
| **10** | 3400 | 938000 | 8.6 |
| **11** | 0 | – | – |
| **12** | 9100 | 62000 | 5.9 |
| **13** | 15867 | 168000 | 10.6 |
| **14** | 4067 | 157000 | 3.3 |
| **15** | 4867 | 224000 | 4.0 |
| **16** | 2800 | 664000 | 7.5 |

[a] At 20 °C, 2 bar monomer pressure, 200 mL of toluene, [Al] = $3\times10^{-2}$ M, [Zr] = $3\times10^{-5}$ M, $t$ = 15 min. [b] In kg polymer (mol Zr h bar)$^{-1}$.

teraction between the anion and the metal centre.[16] A difference of less than 3 ppm indicates the absence of anion coordination to the metal centre, whilst a value between 3 and 6 ppm suggests coordination. We observed that the dimethyl/borane derivatives of **10** and **12** gave values of about 2.1 ppm, thus indicating that anion coordination does not take place and permitting the formation of a vacant site at the metal centre which allows polymerisation. This value is 3.3 ppm for the derivative of the inactive catalyst **11**, and using the above argument one can reason that the anion is coordinated to the metal centre, therefore a vacant site cannot be readily formed at the metal atom for polymerisation.

With the exception of **15** and **16**, the *ansa*-metallocene catalysts gave polyethylene with lower molecular weights (approx. 60000) than that produced with the other catalysts employed in this study. High molecular weight polyethylene was produced with catalysts **4**, **5**, **7** and **10**. The unbridged metallocene complexes **4**, **5**, **7**, **8**, **10** and **13** produced broad polymer molecular weight distributions with polydispersity values between 6 and 10. This phenomenon has previously been explained by considering the rotation of the $C_5$ ring to be slower than the propagation of the polymer chain, which creates different rotamers of the catalyst that act as distinct active centres.[8g,17] One can thus envisage the formation of multi-site catalysts generated by the rotation of the substituted cyclopentadienido ligands. The *ansa*-metallocene catalysts **6**, **9**, **12** and **15** generally gave lower polydispersity values than their analogous unbridged complexes.

The polymerisation of propylene using the zirconocene derivatives **5**, **6**, **8**, **9**, **11**, **12**, **14**, **15** and **16** as catalyst was also examined. The polymerisation experiments were conducted with an MAO/metal catalyst ratio of 3000:1 at 0 °C and an olefin pressure of 2.5 bar during 60 min. Polymerisation was also carried out with the reference compound $[Zr(\eta^5\text{-}C_5H_5)_2Cl_2]$ under the same experimental conditions. The catalytic activities, polymer molecular weights, molecular weight distributions and isotacticities are given in Table 4.

Table 4. Propylene polymerisation results for **5**, **6**, **8**, **9**, **11**, **12**, **14**, **15**, **16** and $[Zr(\eta^5\text{-}C_5H_5)_2Cl_2]$.[a]

| Catalyst | Activity[b] | $M_w$ | $M_w/M_n$ | [mmmm] [%] |
|---|---|---|---|---|
| $[Zr(\eta^5\text{-}C_5H_5)_2Cl_2]$ | 48 | 2000 | 1.8 | 4.0 |
| **5** | 76 | 2300 | 2.0 | 12.1 |
| **6** | 123 | 18100 | 3.0 | 75.2 |
| **8** | 156 | 2200 | 1.9 | 12.3 |
| **9** | 192 | 13700 | 3.1 | 79.0 |
| **11** | 0 | – | – | – |
| **12** | 85 | 13100 | 2.4 | 77.1 |
| **14** | 94 | 2500 | 1.8 | 12.0 |
| **15** | 109 | 2800 | 1.9 | 78.6 |
| **16** | 85 | 2000 | 1.8 | 75.9 |

[a] At 0 °C, 2.5 bar monomer pressure, 200 mL of toluene, [Al] = $2.25\times10^{-1}$ M, [Zr] = $7.5\times10^{-5}$ M, $t$ = 60 min. [b] In kg polymer (mol Zr h bar)$^{-1}$.

All the catalysts tested gave higher activities than the reference catalyst $[Zr(\eta^5\text{-}C_5H_5)_2Cl_2]$, although no polymerisation was observed with **11**. The *ansa*-metallocene catalysts **6**, **9** and **12** produced polypropylene with molecular weights significantly higher than that produced with the other catalysts. The polydispersity values observed were between 1.8 and 3.1 and are typical for single-site catalysts. It appears that rotation of the $C_5$ ring is restricted in the low-temperature polymerisation of propylene, thus preventing the formation of multiple active sites like those proposed in the polymerisation of ethylene.

The isotacticity of the polymers was measured by $^{13}C\{^1H\}$ NMR spectroscopy using the pentad method. The [mmmm] pentad values for the *ansa*-metallocene catalysts **6**, **9**, **12**, **15** and **16** were of the order of 75% and are comparable with those reported previously for similar $C_1$-symmetric complexes.[11b,11f,18] The stereoselectivity exhibited in the polymerisation can be explained by either a Cossee–Arlman site control[11f] or a back-skip mechanism.[11f,18b,19]

The unbridged metallocene catalysts **5**, **8** and **14** produced atactic polypropylene with [mmmm] pentads of 12%. We have previously observed that rotation of the cyclopentadienido ring in similar metallocene systems can be restricted by the introduction of bulky substituents and this translates into the formation of stereoselective active sites and polypropylene with low to medium isotacticity.[11g] However, this is not the case for **5**, **8** and **14**, where one can envisage that the alkenyl or alkyl chain substituents are flexible enough to position themselves so as not to restrict rotation of the cyclopentadienido rings.

## Conclusions

We have reported the synthesis and catalytic activity of new alkenyl-substituted zirconocene complexes along with their structural characterisation. The reactivity of these complexes in hydrogenation, hydroboration and hydrosilylation processes has been studied and opens up not only the possibility of ligand design and modification but also the potential of supporting the catalysts on distinct substrates.

 © 2007 Wiley-VCH Verlag GmbH & Co. KGaA, Weinheim 

We have also studied the catalytic activity of the zirconocene and *ansa*-zirconocene complexes in the polymerisation of ethylene and propylene. The polymerisation of propylene using the $C_1$-symmetric *ansa*-metallocene complexes as catalysts gave polymers with relatively high isotacticity.

## Experimental Section

**General Remarks:** All reactions were performed using standard Schlenk tube techniques under dry nitrogen. Solvents were distilled from the appropriate drying agents and degassed before use. $C_5H_2Me_4$, $ZrCl_4$, $HSiMe_2Cl$, $SiMe_3Cl$, *n*BuLi (1.6 M in hexane), MeLi (1.6 M in $Et_2O$), MAO (10 wt.-% in toluene), 9-BBN (0.5 M in thf) and $CH_3COCH_2CH_2CH{=}CH_2$ were purchased from Aldrich and the Karstedt catalyst from ABCR. All commercial reagents were used directly. 6-(4-Buten-1-yl)-6-methylfulvene was prepared according to the methodology described by Little and coworkers.[20] IR spectra were recorded with a Thermo Nicolet Avatar 330 FT-IR spectrophotometer. $^1H$, $^{13}C$ and $^{29}Si$ NMR spectra were recorded with a Varian Mercury FT-400 spectrometer. Microanalyses were carried out with a Perkin–Elmer 2400 or LECO CHNS-932 microanalyzer. Mass spectrometric analyses were performed with a Hewlett–Packard 5988A instrument (*m*/*z* = 50–1000). Polymer molecular weights and distributions were determined by GPC (Waters 150C Plus or Alliance GPC-2000) in 1,2,4-trichlorobenzene at 150 °C. Polymer isotacticity was calculated from the $^{13}C\{^1H\}$ NMR spectra of polymer samples dissolved in 1,2,4-trichlorobenzene/$C_6D_6$ (1:1).

**Preparation of [Li{$C_5H_4(CMe_2CH_2CH_2CH{=}CH_2)$}] (1):** MeLi (12.8 mL, 20.51 mmol) was added dropwise to a solution of 6-(4-buten-1-yl)-6-methylfulvene (3.00 g, 20.51 mmol) in $Et_2O$ (75 mL) at –78 °C. The reaction mixture was warmed to room temperature and stirred for 3 h. The solvent was then removed in vacuo to give a white solid, which was washed with hexane (2 × 50 mL) and dried under vacuum to yield the title complex as a free flowing white solid. Yield: 2.48 g (72%). $^1H$ NMR (400 MHz, [D$_8$]THF, 25 °C): $\delta$ = 1.19 (s, 6 H, C$Me_2$), 1.50 and 1.91 (2 m, each 2 H, C$H_2$C$H_2$), 4.74 (*cis*) and 4.85 (*trans*) (2 dd, $^3J_{cis}$ = 10.0, $^3J_{trans}$ = 16.8 Hz, each 1 H, $CH_2$-CH=C$H_2$), 5.73 (m, 1 H, $CH_2$-C$H$=$CH_2$), 5.46 and 5.48 (2 m, each 2 H, $C_5H_4$) ppm. $^{13}C\{^1H\}$ NMR (100 MHz, [D$_8$]THF, 25 °C): $\delta$ = 31.0 and 31.1 (*C*$H_2$*C*$H_2$), 35.4 (C$Me_2$), 46.5 (Cp*C*), 100.9, 101.8 and 141.6 ($C_5H_4$), 112.8 ($CH_2$-CH=*C*$H_2$), 128.8 ($CH_2$*C*H=$CH_2$) ppm. $C_{12}H_{17}Li$ (168.2): calcd. C 85.69, H 10.19; found C 85.33, H 10.17.

**Preparation of $Me_2Si(C_5HMe_4)\{C_5H_4(CMe_2CH_2CH_2CH{=}CH_2)\}$ (2):** $Me_2Si(C_5HMe_4)Cl$ (2.55 g, 11.89 mmol) in thf (50 mL) was added to a solution of **1** (2.00 g, 11.89 mmol) in thf (50 mL) at –78 °C. The reaction mixture was warmed to room temperature and stirred for 6 h. The solvent was then removed in vacuo and hexane (150 mL) was added to the resulting dark orange oil. The mixture was filtered and the solvent removed from the filtrate under reduced pressure to yield the title compound as a dark yellow oil. Yield: 3.96 g (98%). $^1H$ NMR (400 MHz, $CDCl_3$, 25 °C; for the predominant isomer): $\delta$ = –0.11 (s, 6 H, Si$Me_2$), 1.19 (s, 6 H, C$Me_2$), 1.59 and 1.83 (2 m, each 2 H, C$H_2$C$H_2$), 1.88 and 2.01 (2 s, each 6 H, $C_5Me_4$), 2.96 and 3.23 (2 m, each 1 H, 2 × *H*$C_5$), 4.90 (*cis*) and 4.97 (*trans*) (2 dd, $^3J_{cis}$ = 10.2, $^3J_{trans}$ = 16.9 Hz, each 1 H, $CH_2$CH=C$H_2$), 5.81 (m, 1 H, $CH_2$C$H$=$CH_2$), 5.92, 6.33 and 6.57 (3 m, each 1 H, $C_5H_3$) ppm. EI MS: *m*/*z* (%) = 340 (28) [M$^+$], 285 (46) [M$^+$ – $CH_2CH_2CH{=}CH_2$], 243 (100) [M$^+$ – $CMe_2CH_2CH_2CH{=}CH_2$]. $C_{23}H_{36}Si$ (340.6): calcd. C 81.10, H 10.65; found C 81.00, H 10.61.

**Preparation of $[Li_2\{Me_2Si(C_5Me_4)(C_5H_3\{CMe_2CH_2CH_2CH{=}CH_2\})\}]$ (3):** *n*BuLi (11.0 mL, 17.62 mmol) was added dropwise to a solution of **4** (3.00 g, 8.81 mmol) in $Et_2O$ (100 mL) at –78 °C. The mixture was warmed to 25 °C and stirred for 15 h. The solvent was then removed in vacuo to give a white solid, which was washed with hexane (2 × 50 mL) and dried under vacuum to yield the title complex as a white solid (2.54 g, 82%). $C_{23}H_{34}Li_2Si$ (352.5): calcd. C 78.37, H 9.72; found C 77.97, H 9.75.

**Preparation of $[Zr(\eta^5\text{-}C_5H_5)\{\eta^5\text{-}C_5H_4(CMe_2CH_2CH_2CH{=}CH_2)\}Cl_2]$ (4):** A solution of **1** (1.00 g, 5.94 mmol) in thf (50 mL) was added dropwise during 15 min to a solution of $[Zr(\eta^5\text{-}C_5H_5)Cl_3]$ (1.56 g, 5.94 mmol) in thf (50 mL) at 0 °C. The reaction mixture was warmed to room temperature and stirred for 2 h. The solvent was then removed in vacuo and hexane (125 mL) added to the resulting solid. The mixture was filtered and the filtrate concentrated (20 mL) and cooled to –30 °C to yield crystals of the title complex. Yield: 1.43 g (62%). IR (ZnSe): $\tilde{\nu}$ = 3100 ($\nu_{CH}$), 1640 ($\nu_{C=C}$) cm$^{-1}$. $^1H$ NMR (400 MHz, $CDCl_3$, 25 °C): $\delta$ = 1.39 (s, 6 H, C$Me_2$), 1.56 and 1.75 (2 m, C$H_2$C$H_2$), 4.89 (*cis*) and 4.96 (*trans*) (2 dd, $^3J_{cis}$ = 10.6, $^3J_{trans}$ = 17.2 Hz, each 1 H, $CH_2$CH=C$H_2$), 5.71 (m, 1 H, $CH_2$C$H$=$CH_2$), 6.36 and 6.45 (2 m, each 2 H, $C_5H_4$), 6.48 (s, 5 H, $C_5H_5$) ppm. $^{13}C\{^1H\}$ NMR (100 MHz, $CDCl_3$, 25 °C): $\delta$ = 27.2 and 29.0 (*C*$H_2$*C*$H_2$), 36.4 (C$Me_2$), 46.1 (Cp*C*), 112.2, 113.0 and 143.3 ($C_5H_4$), 115.9 ($C_5H_5$), 114.1 ($CH_2$-CH=*C*$H_2$), 138.5 ($CH_2$-*C*H=$CH_2$) ppm. EI MS: *m*/*z* (%) = 386 (20) [M$^+$], 331 (36) [M$^+$ – $CH_2CH_2CH{=}CH_2$], 225 (100) [M$^+$ – $C_5H_4(CMe_2CH_2CH_2$-$CH{=}CH_2)$]. $C_{17}H_{22}Cl_2Zr$ (388.5): calcd. C 52.56, H 5.71; found C 52.51, H 5.69.

**Preparation of $[Zr\{\eta^5\text{-}C_5H_4(CMe_2CH_2CH_2CH{=}CH_2)\}_2Cl_2]$ (5):** The synthesis of **5** was carried out in an identical manner to **4** from **1** (1.00 g, 5.94 mmol) and $ZrCl_4$ (0.69 g, 2.97 mmol). Yield: 0.83 g (58%). IR (ZnSe): $\tilde{\nu}$ = 3103 ($\nu_{CH}$), 1637 ($\nu_{C=C}$) cm$^{-1}$. $^1H$ NMR (400 MHz, $CDCl_3$, 25 °C): $\delta$ = 1.41 (s, 12 H, 2 × C$Me_2$), 1.56 (4 H) and 1.77 (4 H) (2 m, each 4 H, 2 × C$H_2$C$H_2$), 4.88 (*cis*) and 4.95 (*trans*) (2 dd, $^3J_{cis}$ = 10.2, $^3J_{trans}$ = 16.9 Hz, each 2 H, 2 × $CH_2$CH=C$H_2$), 5.71 (m, 2 H, 2 × $CH_2$C$H$=$CH_2$), 6.32 and 6.41 (2 m, each 4 H, 2 × $C_5H_4$) ppm. $^{13}C\{^1H\}$ NMR (100 MHz, $CDCl_3$, 25 °C): $\delta$ = 27.1 and 29.0 (*C*$H_2$*C*$H_2$), 36.5 (C$Me_2$), 46.2 (Cp*C*), 112.2, 116.2 and 142.8 ($C_5H_4$), 114.0 ($CH_2$CH=*C*$H_2$), 138.7 ($CH_2$*C*H=$CH_2$) ppm. EI MS: *m*/*z* (%) = 484 (1) [M$^+$], 321 (100) [M$^+$ – $C_5H_4(CMe_2CH_2CH_2CH{=}CH_2)$], 266 (34) [M$^+$ – $C_5H_4(CMe_2CH_2CH_2CH{=}CH_2)$ – $CH_2CH_2CH{=}CH_2$], 231 (41) [M$^+$ – $C_5H_4(CMe_2CH_2CH_2CH{=}CH_2)$ – $CH_2CH_2CH{=}CH_2$ – Cl]. $C_{24}H_{34}Cl_2Zr$ (484.7): calcd. C 59.48, H 7.07; found C 59.39, H 7.02.

**Preparation of $[Zr\{Me_2Si(\eta^5\text{-}C_5Me_4)(\eta^5\text{-}C_5H_3\{CMe_2CH_2CH_2$-$CH{=}CH_2\})\}Cl_2]$ (6):** The synthesis of **6** was carried out in an identical manner to **4** from **5** (1.50 g, 4.25 mmol) and $ZrCl_4$ (0.99 g, 4.25 mmol). Yield: 1.00 g (47%). IR (ZnSe): $\tilde{\nu}$ = 3099 ($\nu_{CH}$), 1632 ($\nu_{C=C}$) cm$^{-1}$. $^1H$ NMR (400 MHz, $CDCl_3$, 25 °C): $\delta$ = 0.83 and 0.87 (2 s, each 3 H, Si$Me_2$), 1.42 and 1.51 (2 s, each 3 H, C$Me_2$), 1.56 and 1.69 (2 m, each 2 H, C$H_2$C$H_2$), 1.92, 2.01, 2.03 and 2.06 (4 s, each 3 H, $C_5Me_4$), 4.88 (*cis*) and 4.95 (*trans*) (2 dd, $^3J_{cis}$ = 10.3, $^3J_{trans}$ = 16.9 Hz, each 1 H, $CH_2$CH=C$H_2$), 5.73 (m, 1 H, $CH_2$C$H$=$CH_2$), 5.57, 5.71 and 6.85 (3 m, each 1 H, $C_5H_3$) ppm. $^{13}C\{^1H\}$ NMR (100 MHz, $CDCl_3$, 25 °C): $\delta$ = –0.4 and 0.4 (Si$Me_2$), 12.3, 12.5, 15.3 and 15.4 ($C_5Me_4$), 27.4 and 29.0 (*C*$H_2$*C*$H_2$), 36.5 (C$Me_2$), 46.2 (Cp*C*), 97.5 and 104.2 (*C*$^1$-Cp), 113.9 ($CH_2$CH=*C*$H_2$), 138.9 ($CH_2$*C*H=$CH_2$), 111.2, 123.9, 135.0 and 149.9 ($C_5H_3$), 113.5, 126.6, 127.2 and 136.2 ($C_5Me_4$) ppm. $^{29}Si\{^1H\}$

 © 2007 Wiley-VCH Verlag GmbH & Co. KGaA, Weinheim 

NMR (79.5 MHz, $CDCl_3$, 25 °C): $\delta$ = –22.0 (*Si*$Me_2$) ppm. EI MS: *m/z* (%) = 498 (11) [$M^+$], 443 (38) [$M^+ - CH_2CH_2CH{=}CH_2$], 407 (100) [$M^+ - CH_2CH_2CH{=}CH_2 - Cl$]. $C_{23}H_{34}Cl_2SiZr$ (500.7): calcd. C 55.17, H 6.84; found C 54.93, H 6.79.

**Preparation of [Zr(η⁵-$C_5H_5$){η⁵-$C_5H_4$($CMe_2CH_2CH_2CH_2CH_3$)}$Cl_2$] (7):** Compound **4** (0.15 g, 0.39 mmol) was dissolved in $CH_2Cl_2$ (50 mL) and the Pd/C (10% palladium) catalyst was added (8 mg). Hydrogen was passed through the solution at 1 bar with stirring for 2 h. The resulting suspension was filtered and the solvent removed from the filtrate under reduced pressure to give the title complex as a crystalline solid. Yield: 0.14 g (97%). $^1$H NMR (400 MHz, $CDCl_3$, 25 °C): $\delta$ = 0.91 (m, 3 H, $CH_2CH_2CH_2CH_3$), 0.98, 1.19 and 1.44 (3 m, each 2 H, $CH_2CH_2CH_2CH_3$), 1.39 (s, 6 H, C$Me_2$), 6.35 and 6.44 (2 m, each 2 H, $C_5H_4$), 6.47 (s, 5 H, $C_5H_5$) ppm. $^{13}$C{$^1$H} NMR (100 MHz, $CDCl_3$, 25 °C): $\delta$ = 14.0, 23.1, 26.6 and 27.1 ($CH_2CH_2CH_2CH_3$), 36.3 (C$Me_2$), 46.7 (Cp*C*), 113.3, 115.5 and 144.1 ($C_5H_4$), 115.9 ($C_5H_5$) ppm. EI MS: *m/z* (%) = 388 (14) [$M^+$], 331 (55) [$M^+ - CH_2CH_2CH_2CH_3$], 225 (100) [$M^+ - C_5H_4(CMe_2CH_2CH_2CH_2CH_3)$]. $C_{17}H_{24}Cl_2Zr$ (390.5): calcd. C 52.29, H 6.19; found C 52.01, H 6.23.

**Preparation of [Zr{η⁵-$C_5H_4$($CMe_2CH_2CH_2CH_2CH_3$)}$_2Cl_2$] (8):** The synthesis of **8** from **5** (0.15 g, 0.31 mmol) was carried out in an identical manner to **7**. Yield: 0.14 g (92%). $^1$H NMR (400 MHz, $CDCl_3$, 25 °C): $\delta$ = 0.82 (m, 6 H, 2× $CH_2CH_2CH_2CH_3$), 0.96, 1.18 and 1.43 (3 m, each 4 H, 2× $CH_2CH_2CH_2CH_3$), 1.36 (s, 12 H, 2× C$Me_2$), 6.32 and 6.40 (2 m, each 4 H, 2× $C_5H_4$) ppm. $^{13}$C{$^1$H} NMR (100 MHz, $CDCl_3$, 25 °C): $\delta$ = 14.0, 23.2, 26.6 and 27.0 ($CH_2CH_2CH_2CH_3$), 36.4 (C$Me_2$), 46.8 (Cp*C*), 112.4, 116.1 and 143.5 ($C_5H_4$) ppm. EI MS: *m/z* (%) = 486 (4) [$M^+$], 429 (72) [$M^+ - CH_2CH_2CH_2CH_3$], 387 (100) [$M^+ - C_5H_4(CMe_2CH_2CH_2CH_2CH_3)$]. $C_{24}H_{38}Cl_2Zr$ (488.7): calcd. C 58.99, H 7.84; found C 58.66, H 7.86.

**Preparation of [Zr{$Me_2Si$(η⁵-$C_5Me_4$)(η⁵-$C_5H_3${$CMe_2CH_2CH_2CH_2CH_3$}}$Cl_2$] (9):** The synthesis of **9** from **6** (0.15 g, 0.30 mmol) was carried out in an identical manner to **7**. Yield: 0.12 g (81%). $^1$H NMR (400 MHz, $CDCl_3$, 25 °C): $\delta$ = 0.81 and 0.85 (3 H) (2 s, each 3 H, Si$Me_2$), 0.83 (m, 3 H, $CH_2CH_2CH_2CH_3$), 0.95, 1.17 and 1.42 (3 m, each 2 H, $CH_2CH_2CH_2CH_3$), 1.37 and 1.46 (2 s, each 3 H, C$Me_2$), 1.90, 1.99, 2.01 and 2.04 (4 s, each 3 H, $C_5Me_4$), 5.55, 5.67 and 6.84 (3 m, each 1 H, $C_5H_3$) ppm. $^{13}$C{$^1$H} NMR (100 MHz, $CDCl_3$, 25 °C): $\delta$ = –0.5 and 0.2 (Si$Me_2$), 12.1, 12.3, 14.1 and 15.1 ($C_5Me_4$), 23.2, 24.5 26.6 and 27.2 ($CH_2CH_2CH_2CH_3$), 36.4 (C$Me_2$), 46.9 (Cp*C*), 97.5 and 104.1 (*C*$^1$-Cp), 111.3, 123.9, 127.3 and 150.9 ($C_5H_3$), 113.6, 126.7, 135.1 and 136.4 ($C_5Me_4$) ppm. $^{29}$Si{$^1$H} NMR (79.5 MHz, $CDCl_3$, 25 °C): $\delta$ = –14.2 (*Si*$Me_2$) ppm. EI MS: *m/z* (%) = 502 (11) [$M^+$], 443 (38) [$M^+ - CH_2CH_2CH_2CH_3$], 407 (100) [$M^+ - CH_2CH_2CH_2CH_3 - Cl$]. $C_{23}H_{36}Cl_2SiZr$ (502.8): calcd. C 54.95, H 7.22; found C 54.93, H 7.27.

**Preparation of [Zr(η⁵-$C_5H_5$){η⁵-$C_5H_4$($CMe_2CH_2CH_2CH_2CH_2BC_8H_{14}$)}$Cl_2$] (10):** Complex **4** (0.15 g, 0.39 mmol) was dissolved in thf (50 mL), and 9-BBN (0.5 M in thf; 0.78 mL, 0.39 mmol) was added dropwise at room temperature during 5 min. The solution was then stirred for 15 h. The solvent was removed under reduced pressure to give the title compound as a crystalline solid (0.20 g, 100%). $^1$H NMR (400 MHz, $CDCl_3$, 25 °C): $\delta$ = 0.96, 1.02, 1.19 and 1.44 (4 m, each 2 H, $CH_2CH_2CH_2CH_2B$), 1.35 and 1.84 (2 m, each 2 H, γ-H of 9-BBN), 1.63 and 1.84 (2 m, each 4 H, β- and δ-H of 9-BBN), 1.80 (m, 2 H, α-H of 9-BBN), 1.35 (s, 6 H, C$Me_2$), 6.34 and 6.45 (2 m, each 2 H, $C_5H_4$), 6.48 (s, 5 H, $C_5H_5$) ppm. $^{11}$B{$^1$H} NMR (85.6 MHz, $CDCl_3$, 25 °C): $\delta$ = 86 ppm. $^{13}$C{$^1$H} NMR (100 MHz, $CDCl_3$, 25 °C): $\delta$ = 24.9, 25.6, 27.6and 28.9 ($CH_2CH_2CH_2CH_2B$), 23.2, 27.0, 27.1 and 33.1 (9-BBN), 36.4 (C$Me_2$), 47.2 (Cp*C*), 113.3, 115.6 and 144.0 ($C_5H_4$), 115.9 ($C_5H_5$) ppm. EI MS: *m/z* (%) = 508 (2) [$M^+$], 331 (74) [$M^+ - CH_2CH_2CH_2CH_2BC_8H_{14}$], 255 (100) [$M^+ - CH_2CH_2CH_2CH_2BC_8H_{14} - Cl$]. $C_{25}H_{37}BCl_2Zr$ (510.5): calcd. C 58.82, H 7.31; found C 58.47, H 7.30.

**Preparation of [Zr{η⁵-$C_5H_4$($CMe_2CH_2CH_2CH_2CH_2BC_8H_{14}$)}$_2Cl_2$] (11):** The synthesis of **11** from **5** (0.15 g, 0.31 mmol) and 9-BBN (0.5 M in thf; 1.24 mL, 0.62 mmol) was carried out in an identical manner to **10**. Yield: 0.21 g (100%). $^1$H NMR (400 MHz, $CDCl_3$, 25 °C): $\delta$ = 0.97, 1.01, 1.21 and 1.46 (4 m, each 4 H, 2× $CH_2CH_2CH_2CH_2B$), 1.32 and 1.83 (2 m, each 4 H, 2× γ-H of 9-BBN), 1.64 and 1.88 (m, each 8 H, 2× β- and δ-H of 9-BBN), 1.81 (m, 4 H, 2× α-H of 9-BBN), 1.38 (s, 12 H, 2× C$Me_2$), 6.31 and 6.40 (2 m, each 4 H, 2× $C_5H_4$) ppm. $^{11}$B{$^1$H} NMR (85.6 MHz, $CDCl_3$, 25 °C): $\delta$ = 86 ppm. $^{13}$C{$^1$H} NMR (100 MHz, $CDCl_3$, 25 °C): $\delta$ = 25.1, 25.7, 27.7 and 31.0 ($CH_2CH_2CH_2CH_2B$), 23.3, 27.1, 27.2 and 33.2 (9-BBN), 36.6 (C$Me_2$), 47.4 (Cp*C*), 112.3, 116.1 and 143.2 ($C_5H_4$) ppm. EI MS: *m/z* (%) = 726 (7) [$M^+$], 549 (21) [$M^+ - CH_2CH_2CH_2CH_2BC_8H_{14}$], 373 (100) [$M^+ - 2\ CH_2CH_2CH_2CH_2BC_8H_{14}$]. $C_{40}H_{64}B_2Cl_2Zr$ (728.7): calcd. C 65.93, H 8.85; found C 65.50, H 8.81.

**Preparation of [Zr{$Me_2Si$(η⁵-$C_5Me_4$)(η⁵-$C_5H_3${$CMe_2CH_2CH_2CH_2CH_2BC_8H_{14}$}}$Cl_2$] (12):** The synthesis of **12** from **6** (0.15 g, 0.30 mmol) and 9-BBN (0.5 M in thf; 0.60 mL, 0.30 mmol) was carried out in an identical manner to **10**. Yield: 0.18 g (100%). $^1$H NMR (400 MHz, $CDCl_3$, 25 °C): $\delta$ = 0.83 and 0.86 (2 s, each 3 H, Si$Me_2$), 0.97, 1.17, 1.21 and 1.45 (4 m, each 2 H, $CH_2CH_2CH_2CH_2B$), 1.33 and 1.83 (2 m, each 2 H, γ-H of 9-BBN), 1.65 and 1.85 (2 m, each 4 H, β and δ-H of 9-BBN), 1.78 (m, 2 H, α-H of 9-BBN), 1.39 and 1.49 (2 s, each 3 H, C$Me_2$), 1.91, 2.00, 2.03 and 2.05 (4 s, each 3 H,$C_5Me_4$), 5.55, 5.66 and 6.83 (3 m, each 1 H,$C_5H_3$) ppm. $^{11}$B{$^1$H} NMR (85.6 MHz, $CDCl_3$, 25 °C): $\delta$ = 86 ppm. $^{13}$C{$^1$H} NMR (100 MHz, $CDCl_3$, 25 °C): $\delta$ = –0.4 and 0.4 (Si$Me_2$), 12.2, 12.4, 14.3 and 15.2 ($C_5Me_4$), 19.1, 24.4, 25.1 and 27.7 ($CH_2CH_2CH_2CH_2B$), 23.3, 27.5, 33.2 and 33.3 (9-BBN), 36.6 (C$Me_2$), 47.6 (Cp*C*), 97.8 and 104.0 (*C*$^1$-Cp), 111.3, 123.8, 127.1 and 150.7 ($C_5H_3$), 113.5, 126.4, 135.0 and 136.1 ($C_5Me_4$) ppm. $^{29}$Si{$^1$H} NMR (79.5 MHz, $CDCl_3$, 25 °C): $\delta$ = –14.2 (*Si*$Me_2$) ppm. EI MS: *m/z* (%) = 620 (9) [$M^+$], 443 (27) [$M^+ - CH_2CH_2CH_2CH_2BC_8H_{14}$], 409 (100) [$M^+ - CH_2CH_2CH_2CH_2BC_8H_{14} - Cl$], 374 (66) [$M^+ - CH_2CH_2CH_2CH_2BC_8H_{14} - 2\ Cl$]. $C_{31}H_{49}BCl_2SiZr$ (622.8): calcd. C 59.79, H 7.93; found C 59.67, H 7.88.

**Preparation of [Zr(η⁵-$C_5H_5$){η⁵-$C_5H_4$($CMe_2CH_2CH_2CH_2CH_2SiMe_2Cl$)}$Cl_2$] (13):** Two drops of the Karstedt catalyst [divinyltetramethylsiloxaneplatinum(0) in xylene (3–3.5%)] were added to a solution of **4** (0.15 g, 0.39 mmol) in toluene (25 mL) and the mixture was stirred at room temperature for 10 min. An excess of $SiHMe_2Cl$ (0.15 g, 1.56 mmol) was then added to this solution dropwise and the reaction mixture stirred for 6 h. The mixture was filtered, and volatiles were removed from the filtrate under reduced pressure to give the title product as a light brown solid. Yield: 0.18 g (99%). $^1$H NMR (400 MHz, $CDCl_3$, 25 °C): $\delta$ = 0.39 (s, 6 H, Si$Me_2$Cl), 0.76, 1.05, 1.32 and 1.47 (4 m, each 2 H, $CH_2CH_2CH_2CH_2Si$), 1.36 (s, 6 H, C$Me_2$), 6.35 and 6.43 (2 m, each 2 H, $C_5H_4$), 6.48 (s, 5 H, $C_5H_5$) ppm. $^{13}$C{$^1$H} NMR (100 MHz, $CDCl_3$, 25 °C): $\delta$ = 1.8 (Si$Me_2$Cl), 19.1, 23.6, 27.2 and 27.9 ($CH_2CH_2CH_2CH_2$-Si), 36.4 (C$Me_2$), 46.7 (Cp*C*), 113.1, 115.5 and 143.7 ($C_5H_4$), 115.8 ($C_5H_5$) ppm. $^{29}$Si{$^1$H} NMR (79.5 MHz, $CDCl_3$, 25 °C): $\delta$ = 31.7 (*Si*$Me_2$Cl) ppm. EI MS: *m/z* (%) = 480 (100) [$M^+$], 331 (41) [$M^+ - CH_2CH_2CH_2CH_2SiMe_2Cl$], 255 (23) [$M^+ - CH_2CH_2CH_2CH_2SiMe_2Cl - Cl$]. $C_{19}H_{29}Cl_3SiZr$ (483.1): calcd. C 47.24, H 6.05; found C 47.47, H 6.07.

 © 2007 Wiley-VCH Verlag GmbH & Co. KGaA, Weinheim 

**Preparation of [Zr{η⁵-C₅H₄(CMe₂CH₂CH₂CH₂CH₂SiMe₂Cl)}₂Cl₂] (14):** The synthesis of **14** from **5** (0.15 g, 0.31 mmol) and $SiHMe_2Cl$ (0.15 g, 1.56 mmol) was carried out in an identical manner to **13**. Yield: 0.21 g (98%). $^1$H NMR (400 MHz, $CDCl_3$, 25 °C): $\delta$ = 0.37 (s, 12 H, 2 × Si*Me*$_2$Cl), 0.74, 1.04, 1.33 and 1.44 (4 m, each 4 H, 2 × C*H*$_2$C*H*$_2$C*H*$_2$C*H*$_2$Si), 1.36 (s, 12 H, 2 × C*Me*$_2$), 6.32 and 6.40 (2 m, each 4 H, 2 × C$_5$*H*$_4$) ppm. $^{13}$C{$^1$H} NMR (100 MHz, $CDCl_3$, 25 °C): $\delta$ = 1.8 (Si*Me*$_2$Cl), 19.3, 23.6, 27.1 and 27.8 (*C*H$_2$*C*H$_2$-*C*H$_2$*C*H$_2$Si), 36.5 (C*Me*$_2$), 46.3 (Cp*C*), 112.2, 116.1 and 143.1 (*C*$_5$H$_4$) ppm. $^{29}$Si{$^1$H} NMR (79.5 MHz, $CDCl_3$, 25 °C): $\delta$ = 31.8 (*Si*Me$_2$Cl) ppm. EI MS: *m*/*z* (%) = 670 (97) [M$^+$], 635 (100) [M$^+$ – Cl], 521 (44) [M$^+$ – $CH_2CH_2CH_2CH_2SiMe_2Cl$]. $C_{28}H_{48}Cl_4Si_2Zr$ (673.9): calcd. C 49.90, H 7.18; found C 50.12, H 7.21.

**Preparation of [Zr{Me₂Si(η⁵-C₅Me₄)(η⁵-C₅H₃{CMe₂CH₂CH₂CH₂-CH₂SiMe₂Cl})}Cl₂] (15):** The synthesis of **15** from **6** (0.15 g, 0.30 mmol) and $SiHMe_2Cl$ (0.15 g, 1.56 mmol) was carried out in an identical manner to **13**. Yield: 0.18 g (100%). $^1$H NMR (400 MHz, $CDCl_3$, 25 °C): $\delta$ = 0.39 (s, 6 H, Si*Me*$_2$Cl), 0.83 and 0.87 (2 s, each 3 H, Si*Me*$_2$ *ansa* bridge), 0.79, 0.99, 1.28 and 1.45 (4 m, each 2 H, C*H*$_2$C*H*$_2$C*H*$_2$C*H*$_2$Si), 1.39 and 1.49 (2 s, each 3 H, C*Me*$_2$), 1.92, 2.01, 2.03 and 2.05 (4 s, each 3 H, C$_5$*Me*$_4$), 5.56, 5.68 and 6.84 (3 m, each 1 H, C$_5$*H*$_3$) ppm. $^{13}$C{$^1$H} NMR (100 MHz, $CDCl_3$, 25 °C): $\delta$ = –0.4 and 0.3 (Si*Me*$_2$ *ansa* bridge) 1.8 (Si*Me*$_2$Cl), 12.2, 12.5, 15.2 and 19.1 (C$_5$*Me*$_4$), 23.4, 23.6, 24.7 and 27.9 (*C*H$_2$*C*H$_2$*C*H$_2$*C*H$_2$Si), 36.5 (C*Me*$_2$), 46.8 (Cp*C*), 97.5 and 104.2 (*C*$^1$-Cp), 111.2, 123.9, 127.2 and 150.5 (*C*$_5$H$_3$), 113.5, 126.4, 135.1 and 136.2 (*C*$_5$Me$_4$) ppm. $^{29}$Si{$^1$H} NMR (79.5 MHz, $CDCl_3$, 25 °C): $\delta$ = –14.2 (*Si*Me$_2$ *ansa* bridge), 31.8 (Si*Me*$_2$Cl) ppm. EI MS: *m*/*z* (%) = 595 (63) [M$^+$], 557 (21) [M$^+$ – Cl], 443 (100) [M$^+$ – $CH_2CH_2CH_2CH_2SiMe_2Cl$], 409 (72) [M$^+$ – $CH_2CH_2CH_2CH_2SiMe_2Cl$ – Cl]. $C_{25}H_{41}BCl_3Si_2Zr$ (595.4): calcd. C 50.44, H 6.94; found C 50.67, H 6.88.

**Preparation of [Cl₂Zr{Me₂Si(η⁵-C₅Me₄)(η⁵-C₅H₃{CMe₂(CH₂)₄Si-Me₂OSiMe₂(CH₂)₄Me₂C}η⁵-C₅H₃)(η⁵-C₅Me₄)SiMe₂}ZrCl₂] (16):** Degassed distilled water (4.5 μL, 0.25 mmol) was added to a mixture of **15** (0.30 g, 0.50 mmol) and $NEt_3$ (70.2 μL, 0.50 mmol) in toluene (15 mL). After stirring at room temperature for 2 h, the solution was filtered, and the volatiles were removed under vacuum to give **16** as a brown solid. Yield: 0.14 g (51%). $^1$H NMR (400 MHz, $CDCl_3$, 25 °C): $\delta$ = 0.00 (s, 12 H, 2 × Si*Me*$_2$O), 0.84 (6 H), 0.87 (6 H) (2 s, each 6 H, 2 × Si*Me*$_2$ *ansa* bridge), 0.45, 0.97, 1.19 and 1.44 (4 m, each 4 H, 2 × C*H*$_2$C*H*$_2$C*H*$_2$C*H*$_2$Si), 1.40 and 1.49 (2 s, each 6 H, 2 × C*Me*$_2$), 1.93, 2.01, 2.03 and 2.06 (4 s, each 6 H, 2 × C$_5$*Me*$_4$), 5.56, 5.67 and 6.84 (3 m, each 2 H, 2 × C$_5$*H*$_3$) ppm. $^{13}$C{$^1$H} NMR (100 MHz, $CDCl_3$, 25 °C): $\delta$ = –0.4 and 0.4 (Si*Me*$_2$ *ansa* bridge), 0.6 (Si*Me*$_2$O), 12.2, 12.5, 15.2 and 18.6 (C$_5$*Me*$_4$), 21.6, 24.0, 27.4 and 28.3 (*C*H$_2$*C*H$_2$*C*H$_2$*C*H$_2$Si), 36.5 (C*Me*$_2$), 47.2 (Cp*C*), 97.5 and 104.1 (*C*$^1$-Cp), 111.2, 123.9, 127.1 and 150.7 (*C*$_5$H$_3$), 113.5, 126.4, 135.0 and 136.1 (*C*$_5$Me$_4$) ppm. $^{29}$Si{$^1$H} NMR (79.5 MHz, $CDCl_3$, 25 °C): $\delta$ = –14.2 (*Si*Me$_2$ *ansa* bridge), 7.2 (Si*Me*$_2$O) ppm. EI MS: *m*/*z* (%) 631 (22) [M$^+$ – Zr{Me$_2$Si(η$^5$-C$_5$Me$_4$)(η$^5$-C$_5$H$_3$-{CMe$_2$CH$_2$CH$_2$CH$_2$CH$_2$})}Cl$_2$], 557 (8) [M$^+$ – Zr{Me$_2$Si(η$^5$-C$_5$Me$_4$)(η$^5$-C$_5$H$_3$-{CMe$_2$CH$_2$CH$_2$CH$_2$CH$_2$CH$_2$-SiMe$_2$O})}Cl$_2$], 443 (50) [M$^+$ – Zr{Me$_2$Si(η$^5$-C$_5$Me$_4$)(η$^5$-C$_5$H$_3$-{CMe$_2$CH$_2$CH$_2$CH$_2$CH$_2$SiMe$_2$OSiMe$_2$CH$_2$CH$_2$CH$_2$CH$_2$})}Cl$_2$], 409 (100) [M$^+$ – Zr{Me$_2$Si(η$^5$-C$_5$Me$_4$)(η$^5$-C$_5$H$_3$-{CMe$_2$CH$_2$CH$_2$-CH$_2$CH$_2$SiMe$_2$OSiMe$_2$CH$_2$CH$_2$CH$_2$CH$_2$})}Cl$_2$ – Cl]. $C_{50}H_{82}Cl_4O$-$Si_4Zr_2$ (1135.8): calcd. C 52.87, H 7.28; found C 52.69, H 7.29.

**Polymerisation of Ethylene:** The zirconocene catalyst (6 μmol), MAO (10% in toluene) (6000 μmol) and toluene (200 mL) were mixed together for 15 min in a 1 L glass autoclave. The $N_2$ pressure inside the autoclave was reduced under vacuum, an ethylene pressure of 2 bar was applied and maintained and stirring of the mixture commenced (1000 rpm). Stirring was halted after exactly 15 min and the ethylene pressure released. Excess MAO was then destroyed by cautiously adding a mixture of methanol/HCl (90:10). The polymer was isolated by filtration, washed with ethanol and dried under vacuum at 90 °C for 16 h.

**Polymerisation of Propylene:** The zirconocene catalyst (15 μmol), MAO (10% in toluene) (45000 μmol) and toluene (200 mL) were mixed together for 15 min in a 1 L glass autoclave. The $N_2$ pressure inside the autoclave was reduced under vacuum, a propylene pressure of 2.5 bar was then applied and maintained and stirring of the mixture commenced (1000 rpm). Stirring was halted after exactly 60 min and the propylene pressure released. Excess MAO was then destroyed by cautiously adding a mixture of methanol/HCl (90:10). The solvent was then removed under reduced pressure and a mixture of acetone/methanol (50:50; 200 mL) added. The mixture was stirred for 16 h and then filtered to isolate the polymer, which was washed with ethanol and dried under vacuum at 25 °C for 16 h.

**X-ray Structure Determination of [Zr(η⁵-C₅H₅){η⁵-C₅H₄(CMe₂-CH₂CH₂CH=CH₂)}Cl₂] (4) and [Zr{η⁵-C₅H₄(CMe₂CH₂CH₂-CH=CH₂)}₂Cl₂] (5):** Data for **4** and **5** were collected with a Siemens SMART CCD diffractometer [$\lambda$(Cu-$K_\alpha$) = 1.54178 Å] in the $\omega$- and $\phi$-scans modes. Semiempirical absorption corrections were carried out with SADABS.[21] The structures were solved by direct methods.[22] Structure refinement was carried out with SHELXL-97,[23] which is included in the software package WINGX.[24] All non-hydrogen atoms were refined anisotropically, and the H atoms of the cyclopentadienido rings and the hydrogen atoms of the terminal double bonds were located by difference maps and refined isotropically. Weights were optimised in the final cycles. Crystallographic data are given in Table 5. CCDC-642241 (**4**) and -642240 (**5**) contain the supplementary crystallographic data for this paper.

Table 5. Crystal and structure refinement data for **4** and **5**.[a]

| | **4** | **5** |
|---|---|---|
| Empirical formula | $C_{17}H_{22}Cl_2Zr$ | $C_{24}H_{34}Cl_2Zr$ |
| Formula mass | 388.47 | 484.63 |
| $T$ [K] | 100(2) | 100(2) |
| Crystal system | triclinic | monoclinic |
| Space group | $P\bar{1}$ | $C2/c$ |
| $a$ [Å] | 12.4708(2) | 26.5942(5) |
| $b$ [Å] | 12.7217(2) | 6.62880(10) |
| $c$ [Å] | 13.0835(2) | 13.9555(2) |
| $\alpha$ [°] | 116.2580(10) | 90 |
| $\beta$ [°] | 99.5690(10) | 106.3420(10) |
| $\gamma$ [°] | 105.5060(10) | 90 |
| $V$ [Å$^3$] | 1693.75(5) | 2360.79(7) |
| $Z$ | 4 | 4 |
| $D_{calcd.}$ [g cm$^{-3}$] | 1.523 | 1.364 |
| $\mu$ [mm$^{-1}$] | 8.106 | 5.923 |
| $F$(000) | 792 | 1008 |
| Crystal size [mm] | 0.12 × 0.09 × 0.04 | 0.07 × 0.06 × 0.03 |
| $\theta$ range [°] | 3.90–67.11 | 3.46–71.18 |
| $hkl$ range | $-14 \le h \le 14$, $-15 \le k \le 14$, $-15 \le l \le 15$ | $-31 \le h \le 32$, $-8 \le k \le 8$, $-16 \le l \le 17$ |
| Data/parameters | 5693/461 | 2183/125 |
| Goodness-of-fit on $F^2$ | 1.006 | 1.011 |
| Final $R$ indices [$I > 2\sigma(I)$] | $R_1$ = 0.0351, $wR_2$ = 0.0842 | $R_1$ = 0.0345, $wR_2$ = 0.0831 |
| $R$ indices (all data) | $R_1$ = 0.0466, $wR_2$ = 0.0913 | $R_1$ = 0.0461, $wR_2$ = 0.0892 |
| Largest diff. peak/hole [e Å$^{-3}$] | 1.335/–0.444 | 0.779/–0.366 |

[a] $R_1 = \Sigma||F_o| - |F_c||/\Sigma|F_o|$; $wR_2 = \{\Sigma[w(F_o^2 - F_c^2)^2]/\Sigma[w(F_o^2)^2]\}^{0.5}$.

 © 2007 Wiley-VCH Verlag GmbH & Co. KGaA, Weinheim 

These data can be obtained free of charge from the Cambridge Crystallographic Data Centre via www.ccdc.cam.ac.uk/data_request/cif.

## Acknowledgments

We gratefully acknowledge financial support from the Ministerio de Educación y Ciencia, Spain (grant nos. CTQ2005-07918-C02-02/BQU and CTQ2006-11845/BQU), the Comunidad de Madrid (S-0505/PPQ-0328) and the Universidad Rey Juan Carlos (graduate fellowship for D. P.-C.). We would also like to thank Repsol YPF and LATEP (Universidad Rey Juan Carlos) for their assistance in polymer analysis, Dr. Cesar Pastor (Universidad Autónoma de Madrid) for his aid in the structural resolution of **4** and **5** and Manuel L. Reyes (Repsol-YPF) for valuable discussions.

[1] See for example: a) H. G. Alt, A. Köppl, *Chem. Rev.* **2000**, *100*, 1205–1222; b) G. W. Coates, *Chem. Rev.* **2000**, *100*, 1223–1252; c) L. Resconi, L. Cavallo, A. Fait, F. Piemontesi, *Chem. Rev.* **2000**, *100*, 1253–1346; d) H. H. Brintzinger, D. Fischer, R. Mülhaupt, B. Rieger, R. M. Waymouth, *Angew. Chem. Int. Ed. Engl.* **1995**, *34*, 1143–1170; e) S. Prashar, A. Antiñolo, A. Otero, *Coord. Chem. Rev.* **2006**, *250*, 133–154.

[2] a) E. Negishi, T. Takahashi, *Aldrichim. Acta* **1985**, *18*, 31–47; b) E. Negishi, T. Takahashi, *Synthesis* **1988**, 1–19; c) C. L. Buchwald, R. B. Nielsen, *Chem. Rev.* **1988**, *88*, 1047–1058; d) R. L. Halterman, *Chem. Rev.* **1992**, *92*, 965–994; e) E. Negishi, T. Takahashi, *Acc. Chem. Res.* **1994**, *27*, 124–130; f) A. H. Hoveyda, J. P. Morken, *Angew. Chem. Int. Ed. Engl.* **1996**, *35*, 1262–1284; g) P. Wipf, H. Jahn, *Tetrahedron* **1996**, *52*, 12853–12910; h) A. H. Hoveyda, J. P. Morken, *Metallocenes* (Eds.: A. Togni, R. L. Halterman), Wiley-VCH, Weinheim, **1998**; i) E. Negishi, T. Takahashi, *Bull. Chem. Soc. Jpn.* **1998**, *71*, 755–769; j) P. Wipf, C. Kendall, *Org. Lett.* **2001**, *3*, 2773–2776; k) P. Wipf, C. Kendall, *Chem. Eur. J.* **2002**, *8*, 1778–1784; l) R. Wartchow, S. Doyle, *J. Organomet. Chem.* **1998**, *566*, 287–291; m) T. Imori, T. D. Tilley, *Polyhedron* **1994**, *13*, 2231–2243; n) V. K. Dioumaev, J. F. Harrod, *Organometallics* **1994**, *13*, 1548–1550; o) R. M. Shaltout, J. Y. Corey, *Tetrahedron* **1995**, *51*, 4309–4320; p) T. Takahashi, M. Hasegawa, N. Suzuki, M. Saburi, C. J. Rousset, P. E. Fanwick, E.-I. Negishi, *J. Am. Chem. Soc.* **1991**, *113*, 8564–8566; q) J. Y. Corey, X.-H. Zhu, *Organometallics* **1992**, *11*, 672–683; r) M. R. Kesti, R. M. Waymouth, *Organometallics* **1992**, *11*, 1095–1103; s) J. Terao, K. Torii, K. Saito, N. Kambe, A. Baba, N. Sonoda, *Angew. Chem. Int. Ed.* **1998**, *37*, 2653–2656; t) Y. Ura, R. Hara, T. Takahashi, *Chem. Lett.* **1998**, 195–196.

[3] G. G. Hlatky, *Chem. Rev.* **2000**, *100*, 1347–1376.

[4] a) K. Kageyama, J. Tamazawa, T. Aida, *Science* **1999**, *285*, 2113–2115; b) H. C. L. Abbenhuis, *Angew. Chem. Int. Ed.* **1999**, *38*, 1058–1060; c) T. Sano, K. Doi, H. Hagimoto, Z. Wang, T. Uozumi, K. Soga, *Chem. Commun.* **1999**, 733–734; d) S. B. Roscoe, J. M. J. Frechet, J. F. Walzer, A. J. Dias, *Science* **1998**, *280*, 270–273; e) T. Kamfjord, T. S. Wester, E. Rytter, *Macromol. Rapid Commun.* **1998**, *19*, 505–509; f) H. G. Alt, P. Schertl, A. Koppl, *J. Organomet. Chem.* **1998**, *568*, 263–269.

[5] a) B. Y. Lee, J. S. Oh, *Macromolecules* **2000**, *33*, 3194–3196; b) M. Galan-Fereres, T. Koch, E. Hey-Hawkins, M. S. Eisen, *J. Organomet. Chem.* **1999**, *580*, 145–155; c) B. Y. Lee, J. S. Oh, *PCT/Kr* 99/00169, **1999**; d) J. Sancho Royo, G. Hidalgo Llinas, A. Muñoz-Escalona Lafuente, F. Martinez Nunez, C. Martin Marcos, P. Lafuente Canas, B. Peña Garcia, *Eur. Pat. Appl.* 839836, **1998**; e) B. Y. Lee, J. S. Oh, *J. Organomet. Chem.* **1998**, *552*, 313–317; f) M. Antberg, H. Luker, L. Bohm, *Eur. Pat.* 293815, **1988**; g) J. Tian, Y. Soo-Ko, R. Metcalfe, Y. Feng, S. Collins, *Macromolecules* **2001**, *34*, 3120–3122; h) C. Alonso, A. Antiñolo, F. Carrillo-Hermosilla, P. Carrion, A. Otero, J. Sancho, E. Villaseñor, *J. Mol. Catal. A* **2004**, *220*, 285–295; i) L. K. Van Looveren, D. F. Geysen, K. A. Vercruysse, B. H. Wouters, P. J. Grobet, P. A. Jacobs, *Angew. Chem. Int. Ed.* **1998**, *37*, 517–520; j) J. Tudor, D. O'Hare, *Chem. Commun.* **1997**, 603–604; k) C. Alonso-Moreno, A. Antiñolo, F. Carrillo-Hermosilla, P. Carrión, I. López-Solera, A. Otero, S. Prashar, J. Sancho, *Eur. J. Inorg. Chem.* **2005**, 2924–2934.

[6] a) Y. Yamaguchi, N. Suzuki, T. Mise, Y. Wakatsuki, *Organometallics* **1999**, *18*, 996–1001; b) H. Zhu, G.-X. Jin, N. Hu, *J. Organomet. Chem.* **2002**, *655*, 167–171; c) C. Takayama, Y. Yamaguchi, T. Mise, N. Suzuki, *J. Chem. Soc. Dalton Trans.* **2001**, 948–953; d) T. Huhn, N. Suzuki, Y. Yamaguchi, T. Mise, T. Chihara, Y. Wakatsuki, *Chem. Lett.* **1997**, 1201–1202; e) D. Seyferth, R. Wyrwa, *US Pat.* 5969073, **1999**; f) C. J. Miller, D. O'Hare, *Chem. Commun.* **2004**, 1710–1711; g) J. Zhang, X. Wang, G.-X. Jin, *Coord. Chem. Rev.* **2006**, *250*, 95–109.

[7] a) M. Rosenblum, R. B. Woodward, *J. Am. Chem. Soc.* **1958**, *80*, 5443–5449; b) A. Togni, T. Hayashi, *Ferrocenes: Homogeneous Catalysis, Organic Synthesis, Materials Science* (Eds.: A. Togni, T. Hayashi), VCH, Weinheim, **1995**.

[8] a) B. Pfeifer, W. Milius, H. G. Alt, *J. Organomet. Chem.* **1998**, *553*, 205–220; b) L. Duda, G. Erker, R. Fröhlich, *Eur. J. Inorg. Chem.* **1998**, 1153–1162; c) S. Knüppel, G. Erker, R. Fröhlich, *Angew. Chem. Int. Ed.* **1999**, *38*, 1923–1926; d) S.-D. Bai, X.-H. Wei, J.-P. Guo, D.-S. Liu, Z.-Y. Zhou, *Angew. Chem. Int. Ed.* **1999**, *38*, 1926–1928; e) J. Wonnemann, M. Oberhoff, G. Erker, R. Fröhlich, K. Bergander, *Eur. J. Inorg. Chem.* **1999**, 1111–1120; f) K. Klass, L. Duda, N. Kleigrewe, G. Erker, R. Fröhlich, E. Wegelius, *Eur. J. Inorg. Chem.* **1999**, 11–19; g) A. Reb, H. G. Alt, *J. Mol. Catal. A* **2001**, *174*, 35–49; h) L. Lukesova, P. Stepnicka, K. Fejfarova, R. Gyepes, I. Cisarova, M. Horacek, J. Kubista, K. Mach, *Organometallics* **2002**, *21*, 2639–2653; i) J. Cano, P. Gómez-Sal, G. Heinz, G. Martínez, P. Royo, *Inorg. Chim. Acta* **2003**, *345*, 15–26; j) A. I. Licht, H. G. Alt, *J. Organomet. Chem.* **2002**, *648*, 134–148; k) A. I. Licht, H. G. Alt, *J. Organomet. Chem.* **2003**, *687*, 142–152; l) S. Venne-Dunker, G. Kehr, R. Fröhlich, G. Erker, *Organometallics* **2003**, *22*, 948–958.

[9] a) G. Erker, G. Kehr, R. Fröhlich, *J. Organomet. Chem.* **2004**, *689*, 1402–1412; b) M. Ogasawara, T. Nagano, T. Hayashi, *J. Am. Chem. Soc.* **2002**, *124*, 9068–9069; c) J. C. Sierra, D. Hüerländer, M. Hill, G. Kehr, G. Erker, R. Fröhlich, *Chem. Eur. J.* **2003**, *9*, 3618–3622; d) G. Erker, G. Kehr, R. Fröhlich, *J. Organomet. Chem.* **2004**, *689*, 1402–1412; e) G. Erker, *Polyhedron* **2005**, *24*, 1289–1297; f) G. Erker, G. Kehr, R. Fröhlich, *Coord. Chem. Rev.* **2006**, *250*, 36–46; g) J. Paradies, G. Kehr, R. Fröhlich, G. Erker, *Proc. Natl. Acad. Sci. USA* **2006**, *103*, 15333–15337.

[10] a) D. Kunz, G. Erker, R. Fröhlich, G. Kehr, *Eur. J. Inorg. Chem.* **2000**, 409–416; b) D. Harmsen, G. Erker, R. Fröhlich, G. Kehr, *Eur. J. Inorg. Chem.* **2002**, 3156–3171; c) H. Schumann, A. Heim, J. Demtschuk, S. H. Mühle, *Organometallics* **2003**, *22*, 118–128; d) M. Hill, G. Kehr, G. Erker, O. Kataeva, R. Fröhlich, *Chem. Commun.* **2004**, 1020–1021; e) G. Erker, R. Nolte, R. Aul, S. Wilker, C. Krüger, R. Noe, *J. Am. Chem. Soc.* **1991**, *113*, 7594–7602.

[11] a) A. Antiñolo, I. López-Solera, I. Orive, A. Otero, S. Prashar, A. M. Rodríguez, E. Villaseñor, *Organometallics* **2001**, *20*, 71–78; b) A. Antiñolo, I. López-Solera, A. Otero, S. Prashar, A. M. Rodríguez, E. Villaseñor, *Organometallics* **2002**, *21*, 2460–2467; c) A. Antiñolo, M. Fajardo, S. Gómez-Ruiz, I. López-Solera, A. Otero, S. Prashar, A. M. Rodríguez, *J. Organomet. Chem.* **2003**, *683*, 11–22; d) A. Antiñolo, M. Fajardo, S. Gómez-Ruiz, I. López-Solera, A. Otero, S. Prashar, *Organometallics* **2004**, *23*, 4062–4069; e) S. Gómez-Ruiz, S. Prashar, M. Fajardo, A. Antiñolo, A. Otero, M. A. Maestro, V. Volkis, M. S. Eisen, C. J. Pastor, *Polyhedron* **2005**, *24*, 1298–1313; f) S. Gómez-Ruiz, S. Prashar, L. F. Sánchez-Barba, D. Polo-Cerón, M. Fajardo, A. Antiñolo, A. Otero, M. A. Maestro, C. J. Pas-

 © 2007 Wiley-VCH Verlag GmbH & Co. KGaA, Weinheim 

tor, *J. Mol. Catal. A* **2007**, *264*, 260–269; g) D. Polo-Cerón, S. Gómez-Ruiz, S. Prashar, M. Fajardo, A. Antiñolo, A. Otero, I. López-Solera, M. L. Reyes, *J. Mol. Catal. A* **2007**, *268*, 264–276.
[12] J. E. Soderquist, G. León, *Tetrahedron Lett.* **1998**, *39*, 2511–2514.
[13] a) H. G. Alt, R. Ernst, I. Böhmer, *J. Mol. Catal. A* **2003**, *191*, 177–185; b) H. G. Alt, R. Ernst, I. K. Böhmer, *J. Organomet. Chem.* **2002**, *658*, 259–265; c) H. G. Alt, R. Ernst, *Inorg. Chim. Acta* **2003**, *350*, 1–11; d) H. G. Alt, R. Ernst, *J. Mol. Catal. A* **2003**, *195*, 11–27; e) R. Andrés, E. de Jesús, F. J. de la Mata, J. C. Flores, R. Gómez, *Eur. J. Inorg. Chem.* **2002**, 2281–2286; f) E. de Jesús, R. Andrés, S. Arévalo, J. M. Benito, F. J. de la Mata, J. C. Flores, R. Gómez, *Polym. Mater. Sci. Eng.* **2001**, *84*, 1027–1028; g) R. Duchateau, *Chem. Rev.* **2002**, *102*, 3525–3542; h) O. Rossell, M. Seco, I. Angurell, *C. R. Chim.* **2003**, *6*, 803–817.
[14] G. Tsantes, N. Auner, T. Müller, *Organosilicon Chemistry V* (Eds.: N. Auner, J. Weis), VCH, Weinheim, **2003**.
[15] R. Arteaga-Müller, J. Sánchez-Nieves, P. Royo, M. E. G. Mosquera, *Polyhedron* **2005**, *24*, 1274–1279.
[16] a) A. D. Horton, J. de With, *Chem. Commun.* **1996**, 1375–1376; b) A. D. Horton, J. de With, A. J. van der Linden, H. Van der Weg, *Organometallics* **1996**, *15*, 2672–2674.
[17] a) Y. Zhang, J. Huang, X. Yang, J. Zhang, Y. Qian, *J. Polym. Sci., Part A: Polym. Chem.* **2005**, *43*, 1261–1269; b) I. Lee, W. J. Gauthier, J. M. Ball, B. Iyengar, S. Collins, *Organometallics* **1992**, *11*, 2115–2122; c) R. Schmidt, M. Deppner, H. G. Alt, *J. Mol. Catal. A* **2001**, *172*, 43–65.
[18] a) M. A. Giardello, M. S. Eisen, C. L. Stern, T. J. Marks, *J. Am. Chem. Soc.* **1993**, *115*, 3326–3327; b) M. A. Giardello, M. S. Eisen, C. L. Stern, T. J. Marks, *J. Am. Chem. Soc.* **1995**, *117*, 12114–12129.
[19] a) J. Kukral, P. Lehmus, T. Feifel, C. Troll, B. Rieger, *Organometallics* **2000**, *19*, 3767–3775; b) M. H. Lee, Y. Han, D.-H. Kim, J.-W. Hwang, Y. Do, *Organometallics* **2003**, *22*, 2790–2796; c) A. Razavi, L. Peters, L. Nafpliotis, D. Vereecke, D. Daw, J. L. Atwood, U. Thewald, *Macromol. Symp.* **1995**, *89*, 345–367.
[20] K. J. Stone, R. D. Little, *J. Org. Chem.* **1984**, *49*, 1849–1853.
[21] G. M. Sheldrick, *SADABS, Program for Empirical Absorption Correction*, University of Göttingen, Germany, **1998**.
[22] G. M. Sheldrick, *SHELXS-97, Program for Crystal Structure Solution*, University of Göttingen, Germany, **1997**.
[23] G. M. Sheldrick, *SHELXL-97, Program for the Refinement of Crystal Structures*, University of Göttingen, Germany, **1997**.
[24] L. J. Farrugia, *J. Appl. Crystallogr.* **1999**, *32*, 837–838.

Received: April 10, 2007
Published Online: August 3, 2007

 © 2007 Wiley-VCH Verlag GmbH & Co. KGaA, Weinheim 

DOI: 10.1002/ejic.200700457

# Displacement of Neutral Nitrogen Donors by Chloride in $AuCl_3$(am) (am = Pyridines and Amines): Kinetics and DFT Calculations Show the Effects of Basicity and π-Acceptor Ability

**Bruno Pitteri*[a] and Marco Bortoluzzi[a]**

**Keywords:** Gold / Kinetics / Nitrogen donors / Reaction mechanisms / DFT

The kinetics of the process $AuCl_3(am) + Cl^- \rightarrow AuCl_4^- + am$ (am = $sp^2$ N-donor isosteric pyridines with different π systems and $sp^3$ amines; they cover a wide range of basicity) have been studied in methanol at 25 °C. The reactions obey the usual two-term rate law observed in substitutions on square-planar complexes. The second-order rate constants, $k_2$, are very sensitive to the nature of the leaving group, and plots of $\log k_2$ against the $pK_a$ of the conjugate acids are linear, with the same slope, –0.68, for both "normal" pyridines and pyridines with a more extended π system, such as 4-cyanopyridine, isonicotinic acid, methyl isonicotinate and 4-acetylpyridine. The reactivity of the considered N-donors is different and follows the order $sp^3$ N-donors > "normal" pyridines > "π-extended" pyridines. This result, with the support of ground-state DFT calculations on the $AuCl_3$(am) derivatives, is explained on the basis of an Au–N bond enforcement due to an increased π-back-donation contribution.

(© Wiley-VCH Verlag GmbH & Co. KGaA, 69451 Weinheim, Germany, 2007)

## Introduction

The reactivity of gold(III) derivatives with nitrogen-donor bases has been widely studied, mainly involving pyridine and substituted pyridines (am) as entering nucleophiles or leaving groups.[1–3] Substitution reactions of the type (1) take place with an associative mechanism, whose rate constants, in the forward as well as in the reverse reaction, obey the general relationship $k_{obs} = k_1 + k_2$[nucleophile], which is usual for nucleophilic substitutions at planar four-coordinate $d^8$ metal complexes.[4]

$$AuCl_4^- + am \rightleftarrows AuCl_3(am) + Cl^- \quad (1)$$

The first-order rate constant, $k_1$, and the second-order rate constant, $k_2$, refer to the nucleophilic attack on the substrate by, respectively, the solvent and the nucleophile. The second-order rate constants, $k_2$, are markedly influenced by the nature of am, indicating that the discriminating ability of gold(III) complexes is good. A linear free-energy relationship, $\log k_2 = a pK_a$ + constant, occurs between the rate constant and the basicity of am, measured as the $pK_a$ of its conjugated acid $Ham^+$. Moreover, steric retardation is observed for pyridines containing one or two *ortho* groups.

Recently, we studied the kinetics of the reverse reaction of process (1) using five-membered N-donor heterocycles (thiazoles, oxazoles, imidazoles and their derivatives) as leaving groups[5] and the results were compared with those in a paper[3] where am = pyridines. It was observed that the reactivity depends not only upon the ligand basicity but also upon the nature of the ligand in the order: pyridines > five-membered heterocycles and this behaviour was attributed to different π interactions in the ground state between the metal centre and the N-donor ligands.

In this work we tried to improve the knowledge about the role of π interactions between N-donors and $Au^{III}$ in the kinetics of displacement by chloride of these ligands from $AuCl_3$(am). As for $Pt^{II}$ substrates,[6] on considering the second-order rate constants $k_2$, the displaced nitrogen donors can be divided into three groups: (i) "normal" pyridines, (ii) pyridines having a more extended π system and (iii) $sp^3$ nitrogen-donor bases; and the reactivity towards ligand substitution is in the order: $sp^3$ nitrogen-donor bases > "normal" pyridines > pyridines with a more extended π system. These differences, which were mainly attributed to a ground-state stabilization due to the π-back-donation from the filled orbitals of the metal to the antibonding orbitals of the pyridine ligands, have been correlated in this paper with the calculated Au–N bond lengths of the $AuCl_3$(am) complexes, obtained by performing ground-state DFT B3PW91 calculations. By plotting the $r_{Au-N}$ values of the $AuCl_3$(am) complexes versus the corresponding $pK_a$ values, linear relationships comparable to those derived from the kinetic measurements were obtained. Furthermore, a

[a] Dipartimento di Chimica, Università "Cà Foscari" di Venezia, Calle Larga S. Marta 2137, 30123 Venezia, Italy
E-mail: pitteri@unive.it

Supporting information for this article is available on the WWW under http://www.eurjic.org or from the author.

 © 2007 Wiley-VCH Verlag GmbH & Co. KGaA, Weinheim 

systematic shortening of the Au–N bond length was observed for pyridines having an extended π system.

## Result and Discussion

When a methanolic solution of the neutral $AuCl_3$(am) substrate is allowed to react with an appropriate excess of chloride, repetitive scanning of the spectrum in the region 240–360 nm shows that the reaction evolves in a first-order fashion leading to the substitution of the neutral base with a chloride ion. The presence of well-maintained isosbestic points, whose positions depend only upon the spectrum of the starting compound, and the comparison of the final spectrum with that of original samples of the substituted products at the same concentration, clearly indicate a single reaction stage. The addition of $LiClO_4$ indicates that primary salt effects are absent and secondary effects are negligible, thus no further attempt has been made to maintain constant ionic strength. The reactions have been studied in the presence of 0.1 mol dm$^{-3}$ $CH_3SO_3H$. Preliminary experiments have shown that, at constant chloride concentration, the rate of reaction is independent of the concentration of acid over the range 0.02–0.2 mol dm$^{-3}$. The acid simply serves to protonate the released N-donor ligand, thus preventing the reverse reaction and forcing the reaction to completion. Moreover, the presence of acid helps to avoid a slow reduction of the gold(III) derivatives of the most basic amines. The rate constants have been determined in the usual way from the change in absorbance as a function of time at convenient wavelength. All the reactions have been studied in the presence of a sufficient excess of chloride over the substrate to provide pseudo-first-order conditions and the observed rate constants, $k_{obs}$, collected in Table 1, obey the general relationship $k_{obs} = k_1 + k_2[Cl^-]$, which is usual for nucleophilic substitutions on gold(III) complexes.

The $k_1$ terms, referring to the pathway in which the rate-determining step is the nucleophilic attack of the solvent, followed by the rapid entry of chloride into the solvento complex,[7] are quite small and thus this reaction pathway makes a small contribution to the whole process. The $k_2$ terms are the second-order rate constants for the direct at-

Table 1. First-order rate constant, $k_{obs}$, for the reaction $AuCl_3$(am) + $Cl^- \rightarrow AuCl_4^-$ + am in methanol at 25 °C (0.1 mol dm$^{-3}$ $CH_3SO_3H$).

| am | [Cl$^-$] /mol dm$^{-3}$ | $10^3k_{obs}$/s$^{-1}$ | am | [Cl$^-$] /mol dm$^{-3}$ | $10^3k_{obs}$/s$^{-1}$ |
|---|---|---|---|---|---|
| 4-Methoxypyridine | 0.01 | 0.69 ± 0.01 | pyridine | 0.01 | 4.17 ± 0.02 |
| | 0.02 | 1.27 ± 0.01 | | 0.02 | 7.54 ± 0.01 |
| | 0.03 | 1.78 ± 0.01 | | 0.03 | 10.7 ± 0.04 |
| | 0.04 | 2.40 ± 0.02 | | 0.04 | 13.9 ± 0.03 |
| | 0.05 | 2.95 ± 0.01 | | 0.05 | 18.1 ± 0.02 |
| Methyl isonicotinate | 0.001 | 9.6 ± 0.1 | 4-cyanopyridine | 0.0005 | 48.0 ± 0.1 |
| | 0.002 | 12.2 ± 0.1 | | 0.0010 | 62.7 ± 0.7 |
| | 0.003 | 14.3 ± 0.1 | | 0.0015 | 71.0 ± 0.1 |
| | 0.004 | 18.0 ± 0.2 | | 0.0020 | 83.6 ± 0.3 |
| | 0.005 | 20.2 ± 0.1 | | 0.0025 | 93.0 ± 0.2 |
| 4-Acetylpyridine | 0.001 | 4.0 ± 0.2 | 3,5-dimethylpyridine | 0.01 | 0.76 ± 0.01 |
| | 0.002 | 5.6 ± 0.1 | | 0.02 | 1.58 ± 0.02 |
| | 0.003 | 7.1 ± 0.1 | | 0.03 | 2.21 ± 0.03 |
| | 0.004 | 9.0 ± 0.2 | | 0.04 | 3.11 ± 0.07 |
| | 0.005 | 10.3 ± 0.1 | | 0.05 | 3.84 ± 0.03 |
| 4-Chloropyridine | 0.001 | 7.58 ± 0.01 | piperidine | 0.1 | 0.15 ± 0.01 |
| | 0.002 | 10.16 ± 0.02 | | 0.2 | 0.29 ± 0.01 |
| | 0.003 | 12.63 ± 0.01 | | 0.3 | 0.41 ± 0.02 |
| | 0.004 | 15.80 ± 0.02 | | 0.4 | 0.53 ± 0.01 |
| | 0.005 | 18.38 ± 0.01 | | 0.5 | 0.64 ± 0.01 |
| 4-Methylpyridine | 0.01 | 1.38 ± 0.01 | isonicotinic acid | 0.001 | 2.51 ± 0.06 |
| | 0.02 | 2.48 ± 0.02 | | 0.002 | 5.01 ± 0.06 |
| | 0.03 | 3.44 ± 0.03 | | 0.003 | 7.71 ± 0.07 |
| | 0.04 | 4.48 ± 0.03 | | 0.004 | 9.93 ± 0.06 |
| | 0.05 | 5.51 ± 0.01 | | 0.005 | 12.61 ± 0.03 |
| 4-Aminopyridine | 0.02 | 0.016 ± 0.001 | 4-bromopyridine | 0.0005 | 5.29 ± 0.04 |
| | 0.04 | 0.03 ± 0.02 | | 0.0010 | 6.44 ± 0.03 |
| | 0.07 | 0.05 ± 0.01 | | 0.0015 | 7.78 ± 0.04 |
| | 0.10 | 0.07 ± 0.01 | | 0.0020 | 8.98 ± 0.02 |
| | 0.15 | 0.10 ± 0.01 | | 0.0025 | 10.02 ± 0.03 |
| 4-(Dimethylamino)pyridine | 0.1 | 0.05 ± 0.01 | cyclohexylamine | 0.1 | 1.2 ± 0.1 |
| | 0.2 | 0.10 ± 0.02 | | 0.2 | 1.9 ± 0.2 |
| | 0.3 | 0.16 ± 0.01 | | 0.3 | 3.0 ± 0.2 |
| | 0.4 | 0.21 ± 0.01 | | 0.4 | 4.0 ± 0.3 |
| | 0.5 | 0.26 ± 0.02 | | 0.5 | 4.9 ± 0.1 |
| Morpholine | 0.002 | 0.04 ± 0.01 | | | |
| | 0.01 | 0.14 ± 0.03 | | | |
| | 0.02 | 0.28 ± 0.01 | | | |
| | 0.03 | 0.38 ± 0.06 | | | |
| | 0.04 | 0.51 ± 0.09 | | | |

 © 2007 Wiley-VCH Verlag GmbH & Co. KGaA, Weinheim 

tack of $Cl^-$ at the substrate and are summarized in Table 2. For a better comparison of the different reactivity of the groups of amines, we have again examined some of the reactions in ref.[3], in the same experimental conditions, increasing both the number of pyridines and the p$K_a$ range.

Table 2. Second-order rate constants, $k_2$,[a] and p$K_a$ of $Ham^+$ for the reaction $AuCl_3(am) + Cl^- \rightarrow AuCl_4^- + am$ in methanol at 25 °C (0.1 mol dm$^{-3}$, $CH_3SO_3H$).

| am | $k_2$/dm$^3$ mol s$^{-1}$ | p$K_a$ of $Ham^+$[b] |
|---|---|---|
| 4-Methoxypyridine | 0.0565 ± 0.0008 | 6.47 |
| Methyl isonicotinate | 2.7 ± 0.1 | 3.26 |
| 4-Acetylpyridine | 1.60 ± 0.04 | 3.52 |
| 4-Chloropyridine | 2.73 ± 0.06 | 3.84 |
| 4-Methylpyridine | 0.103 ± 0.001 | 6.02 |
| 4-Aminopyridine | 0.00065 ± 0.00001 | 9.12 |
| 4-Bromopyridine | 2.40 ± 0.06 | 3.84 |
| Pyridine | 0.34 ± 0.01 | 5.25 |
| 4-Cyanopyridine | 22 ± 1 | 1.90 |
| 3,5-Dimethylpyridine | 0.078 ± 0.002 | 6.34 |
| Piperidine | 0.00122 ± 0.00003 | 11.1 |
| Isonicotinic acid | 2.51 ± 0.04 | 3.26 |
| 4-(Dimethylamino)pyridine | 0.000537 ± 0.000007 | 9.37 |
| Morpholine | 0.0122 ± 0.0003 | 8.33 |
| Cyclohexylamine | 0.0095 ± 0.0003 | 10.66 |

[a] Determined by linear regression of $k_{obs}$ values vs. chloride concentration. [b] p$K_a$ values were taken from ref.[8]

The reacting species can be divided into three groups, as depicted in the plot of $\log k_2$ versus p$K_a$ of $Ham^+$ (Figure 1):

*i*: "normal" pyridines;
*ii*: pyridines with a more extended π system;
*iii*: $sp^3$ nitrogen-donor bases.

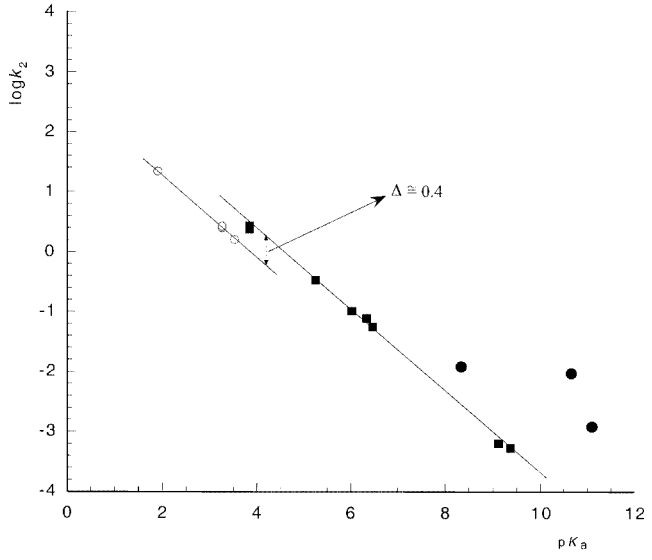


Figure 1. Plots of $\log k_2$ for the reaction $AuCl_3(am) + Cl^- \rightarrow AuCl_4^- + am$ against p$K_a$ of $Ham^+$: (■) pyridine, 4-chloropyridine, 4-methoxypyridine, 4-methylpyridine, 4-bromopyridine, 3,5-dimethylpyridine, 4-aminopyridine, 4-(dimethylamino)pyridine; (○) 4-cyanopyridine, 4-acetylpyridine, methyl isonicotinate, isonicotinic acid; (●) morpholine, cyclohexylamine, piperidine.

The first group includes the complexes with pyridine: 4-bromopyridine, 4-chloropyridine, 4-methylpyridine, 4-methoxypyridine, 4-aminopyridine, 4-(dimethylamino)pyridine and 3,5-dimethylpyridine, while the second group includes the derivatives of 4-cyanopyridine: isonicotinic acid, methyl isonicotinate and 4-acetylpyridine. The lability of pyridines is considerably lower than that of the third group of derivatives, that is, the complexes of the $sp^3$-ligands piperidine, cyclohexylamine and morpholine. Unfortunately, the different steric hindrance around the N atom of these $sp^3$ N-donors avoids a direct relationship between $\log k_2$ and the corresponding p$K_a$ values.

Both "normal" (■ in Figure 1) and "π extended" (○ in Figure 1) pyridines obey the linear relationship $\log k_2 = \alpha pK_a$ + constant, with $\alpha = -0.68$. For the entry of pyridines on $AuCl_4^-$ in the same experimental conditions, a similar free-energy relationship was found,[1] with $\alpha = 0.16$. The parameter $\alpha$ is a measure of the ability of a substrate to discriminate among isosteric nitrogen donors and can be assumed to be a relative measure of its electrophilicity. The asynchronous substitution, characteristic of planar-tetracoordinate gold(III) complexes, offers the opportunity to describe separately the energetic contributions of bond formation and bond rupture to the free energy of activation.[7] The relatively low discrimination among nitrogen donors in the entry reaction ($\alpha = 0.16$), together with the relatively high dependence of reactivity upon the basicity of the leaving nitrogen bases in the reverse processes ($\alpha = -0.68$, this work), strongly suggests a transition state for all these substitutions in which the Au–N bond is only partially formed in the rate-determining transition state, whereas the Au–Cl bond is practically formed to the same extent in the ground and transition states.

The lower lability of pyridine ligands, as compared with the $sp^3$ N-donors, allows the assumption that the Au–N bond in the case of pyridine derivatives may be reinforced by π bonding, that is, by the π-back-donation from the filled orbitals of the metal to the antibonding orbitals of the ligand, leading to a relative stabilization of the corresponding ground state. Moreover, π interactions of this type can also be invoked to explain the small but significant difference between the reactivity of "normal" and "π-extended" pyridines, which is $\Delta\log k_2 \approx 0.4$ (Δ in Figure 1), corresponding to about 2.3 kJ mol$^{-1}$. To support this hypothesis, ground-state DFT calculations on the $AuCl_3(am)$ (am = pyridines) have been performed and the $r_{Au-N}$ bond lengths, collected in Table 3, have been measured.

By plotting the $r_{Au-N}$ values of the $AuCl_3(am)$ complexes versus the corresponding p$K_a$ values, linear relationships comparable to those derived from the kinetic measurements have been obtained, as depicted in Figure 2. "Normal" pyridines (■ in Figure 2) respond to the equation $r_{Au-N} = (-0.0027 \pm 0.0001)pK_a + (2.1119 \pm 0.0005)$, while the equation for "π-extended" pyridines (○ in Figure 2) is $r_{Au-N} = (-0.0027 \pm 0.0001)pK_a + (2.1077 \pm 0.0004)$. The increase of electron density on the N atom, quite well represented by the p$K_a$ values of the free ligands, appears to lead to an enforcement of the Au–N σ bond. The effect of growing

 © 2007 Wiley-VCH Verlag GmbH & Co. KGaA, Weinheim 

Table 3. Calculated $r_{Au-N}$ bond lengths of $AuCl_3$(am) derivatives (am = pyridines) and $pK_a$ of $Ham^+$.[a]

| am | $r_{Au-N}$ /Å | $pK_a$ of $Ham^+$ |
|---|---|---|
| 4-Methoxypyridine | 2.09397 | 6.47 |
| Methyl isonicotinate | 2.09899 | 3.26 |
| 4-Acetylpyridine | 2.09800 | 3.52 |
| 4-Chloropyridine | 2.10118 | 3.84 |
| 4-Methylpyridine | 2.09490 | 6.02 |
| 4-Aminopyridine | 2.08734 | 9.12 |
| 4-Bromopyridine | 2.10175 | 3.84 |
| Pyridine | 2.09816 | 5.25 |
| 4-Cyanopyridine | 2.10250 | 1.90 |
| 3,5-Dimethylpyridine | 2.09429 | 6.34 |
| Isonicotinic acid | 2.09871 | 3.26 |
| 4-(Dimethylamino)pyridine | 2.08601 | 9.37 |

[a] More details on the geometries and energies of the optimized systems are available in the electronic supporting information.

$pK_a$ on the metal–pyridine bond shortening was, however, already partly observed in a paper regarding $Pt^{II}$-pyridines derivatives, where it was confirmed on the basis of NMR measurements.[10]

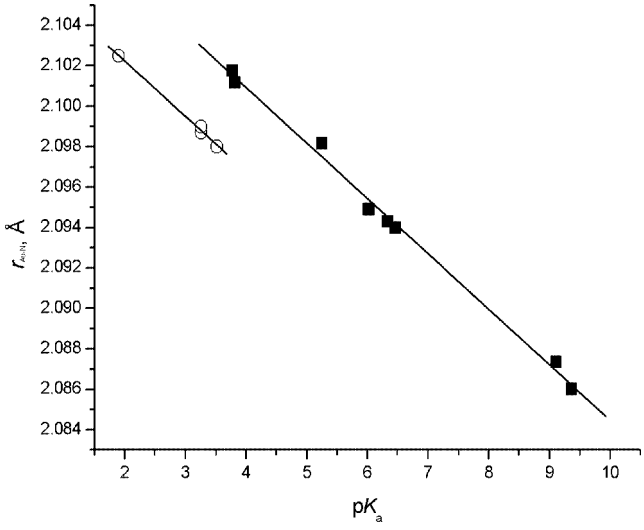


Figure 2. Plots of $r_{Au-N}$ bond lengths against $pK_a$ of $Ham^+$: (■) pyridine, 4-chloropyridine, 4-methoxypyridine, 4-methylpyridine, 4-bromopyridine, 3,5-dimethylpyridine, 4-aminopyridine, 4-(dimethylamino)pyridine; (○) 4-cyanopyridine, 4-acetylpyridine, methyl isonicotinate, isonicotinic acid.

The small difference between the reactivity of the "normal" and "p-extended" groups of pyridines appears to be correlated to a small difference between the corresponding ground-state $r_{Au-N}$ bond lengths, which is about 0.004 Å. As all the considered pyridines are isosteric, it seems reasonable to conclude that this difference could be ascribed to an enforcement of the Au–N bond because of a greater π-back-donation contribution for the second group of ligands, as supposed from the results of the kinetic measurements.

## Conclusion

In summary, the results of kinetic measurements on the process $AuCl_3$(am) + $Cl^- \rightarrow AuCl_4^-$ + am (am = $sp^2$ N-donor isosteric pyridines with different π systems and $sp^3$ amines) reported in this paper highlight the role of π-back-donation from the gold centre to the N-donor ligands in the stabilization of the $AuCl_3$(am) complexes and in the reactivity of these species towards substitution reactions. Besides the great difference between $sp^2$ and $sp^3$ N-donors, the small but significant difference observed between "normal" and "π-extended" pyridines, which has found a nice correlation with the calculated $r_{Au-N}$ bond lengths, should be noted.

## Experimental Section

**Materials:** The compound $KAuCl_4 \cdot 2H_2O$ was prepared from pure gold foil (99.99%). Pure reagent-grade LiCl, $LiClO_4$ and $CH_3SO_3H$ (Aldrich) were used without further purification. Pyridines and amines were recrystallized or distilled before use when necessary. Anhydrous MeOH was obtained by distillation over Mg wires, but traces of water did not appear to have any appreciable effect upon the reactions. Acetone and dimethylformamide were pure reagent-grade products (Aldrich and BDH).

**Instruments:** Electronic spectra and kinetic measurements were obtained on a Perkin–Elmer Lambda 15 spectrophotometer. $^1H$ NMR spectra were taken on Bruker Avance 300 and/or Bruker AC 200 spectrometers at 298 K and are referred to internal tetramethylsilane. The conductivity of $1 \times 10^{-3}$ mol dm$^{-3}$ solutions of the complexes in dimethylformamide at 25 °C was measured with a Radiometer CDM 83 instrument. Elemental analyses were performed by the Microanalytical Laboratory of the Faculty of Pharmaceutical Sciences of the University of Padua.

**Preparation of the Complexes:** Trichloro(pyridine)gold(III) was first characterized by Renz,[9] trichloro(3,5-dimethylpyridine)gold(III) and trichloro(4-methylpyridine)gold(III) by Cattalini and Tobe[3] and trichloro(4-cyanopyridine)gold(III) by Cattalini et al.,[1] but the other derivatives of the type $AuCl_3$(am) are described here for the first time. All the complexes were prepared by the following method: $KAuCl_4 \cdot 2H_2O$ (0.415 g, 1.0 mmol) was dissolved in water (20 mL) and a stoichiometric amount of the nitrogen-donor base, dissolved in a small volume of water (2–3 mL), was added dropwise whilst stirring. The yellow precipitate, formed almost immediately, was filtered off, washed three times with water (10 mL) and dried in vacuo. For the most basic ligands, piperidine, cyclohexylamine, 4-aminopyridine, 4-(dimethylamino)pyridine and morpholine, it was necessary to keep them at 0 °C and in the dark to prevent a possible reduction of gold(III). All the complexes were nonconductive in organic solvents. Yields were in any case nearly quantitative (>95%). Analytical and $^1H$ NMR spectra are collected in Tables 4 and 5, respectively.

**Kinetics:** The reactions were initiated by adding a 0.015 mol dm$^{-3}$ acetone solution (10–20 μL) of the substrate complex, $AuCl_3$(am), to a methanolic solution of chloride ion, previously brought to the reaction temperature (25 °C) in a thermostatted cell in the spectrophotometer. The concentration of the entering group was always large enough to provide pseudo-first-order conditions. After preliminary repetitive scan experiments in the range 240–360 nm to search for isosbestic points and spectral changes, the kinetics were studied by measuring the changing absorbance at suitable wave-

 © 2007 Wiley-VCH Verlag GmbH & Co. KGaA, Weinheim 

Table 4. Analytical data for the complexes (calculated values in parentheses).

| Complex | Formula | C | H | N | Cl |
|---|---|---|---|---|---|
| (pyridine)$AuCl_3$ | $C_5H_5AuCl_3N$ | 15.9 (15.7) | 1.67 (1.32) | 3.71 (3.66) | 27.5 (27.8) |
| (4-methylpyridine)$AuCl_3$ | $C_6H_7AuCl_3N$ | 18.3 (18.2) | 1.65 (1.78) | 3.49 (3.53) | 26.7 (26.8) |
| (3,5-dimethylpyridine)$AuCl_3$ | $C_7H_9AuCl_3N$ | 20.4 (20.5) | 2.18 (2.21) | 3.33 (3.41) | 25.7 (25.9) |
| (4-chloropyridine)$AuCl_3$ | $C_5H_4AuCl_4N$ | 14.2 (14.4) | 1.27 (0.97) | 3.32 (3.36) | 34.1 (34.0) |
| (4-bromopyridine)$AuCl_3$ | $C_5H_4AuBrCl_3N$ | 12.9 (13.0) | 1.04 (0.87) | 3.12 (3.04) | 23.0 (23.1) |
| (4-methoxypyridine)$AuCl_3$ | $C_6H_7AuCl_3NO$ | 17.5 (17.5) | 1.62 (1.71) | 3.31 (3.40) | 25.6 (25.8) |
| (4-aminopyridine)$AuCl_3$ | $C_5H_6AuCl_3N_2$ | 15.1 (15.1) | 1.39 (1.52) | 7.13 (7.05) | 26.9 (26.8) |
| [4-(dimethylamino)pyridine]$AuCl_3$ | $C_7H_{10}AuCl_3N_2$ | 19.6 (19.8) | 2.21 (2.37) | 6.47 (6.58) | 24.8 (25.0) |
| (4-cyanopyridine)$AuCl_3$ | $C_6H_4AuCl_3N_2$ | 17.6 (17.7) | 1.23 (0.99) | 6.72 (6.88) | 17.6 (17.7) |
| (4-acetylpyridine)$AuCl_3$ | $C_7H_7AuCl_3NO$ | 19.7 (19.8) | 1.49 (1.66) | 3.34 (3.30) | 25.0 (25.1) |
| (methyl isonicotinate)$AuCl_3$ | $C_7H_7AuCl_3NO_2$ | 19.3 (19.1) | 1.61 (1.60) | 3.24 (3.18) | 24.3 (24.1) |
| (isonicotinic acid)$AuCl_3$ | $C_6H_5AuCl_3NO_2$ | 16.7 (16.9) | 0.99 (1.18) | 3.37 (3.28) | 25.0 (24.9) |
| (piperidine)$AuCl_3$ | $C_5H_{11}AuCl_3N$ | 15.3 (15.5) | 2.76 (2.85) | 3.71 (3.61) | 27.2 (27.4) |
| (morpholine)$AuCl_3$ | $C_4H_9AuCl_3NO$ | 12.3 (12.3) | 2.54 (2.32) | 3.32 (3.59) | 27.1 (27.2) |
| (cyclohexylamine)$AuCl_3$ | $C_6H_{13}AuCl_3N$ | 18.0 (17.9) | 3.27 (3.26) | 3.46 (3.48) | 26.3 (26.4) |

Table 5. $^1H$ NMR spectroscopic data for the complexes.

| Complex | $^1H$ NMR, $(CD_3)_2CO$, 298 K |
|---|---|
| (pyridine)$AuCl_3$[a] | 8.89 (dd, 2 H, $^3J_{HH}$ = 6.5, $^4J_{HH}$ = 1.5 Hz, $H_\alpha$); 8.33 (tt, 1 H, $^3J_{HH}$ = 7.8, $^4J_{HH}$ = 1.5 Hz, $H_\gamma$); 7.89 (dd, 2 H, $^3J_{HH}$ = 6.5, $^3J$ = 7.8 Hz, $H_\beta$) |
| (4-methylpyridine)$AuCl_3$ | 8.90 (d, 2 H, $^3J_{HH}$ = 6.2 Hz, $H_\alpha$); 7.80 (d, 2 H, $^3J_{HH}$ = 6.2 Hz, $H_\beta$); 2.62 (s, 3 H, $CH_3$) |
| (3,5-dimethylpyridine)$AuCl_3$ | 8.74 (s, 2 H, $H_\alpha$); 8.05 (s, 1 H, $H_\gamma$); 2.52 (s, 6 H, $CH_3$) |
| (4-chloropyridine)$AuCl_3$ | 9.14 (d, 2 H, $^3J_{HH}$ = 7.0 Hz, $H_\alpha$); 8.13 (d, 2 H, $^3J_{HH}$ = 7.0 Hz, $H_\beta$) |
| (4-bromopyridine)$AuCl_3$ | 9.04 (d, 2 H, $^3J_{HH}$ = 6.8 Hz, $H_\alpha$); 8.27 (d, 2 H, $^3J_{HH}$ = 6.8 Hz, $H_\beta$) |
| (4-methoxypyridine)$AuCl_3$ | 8.85 (d, 2 H, $^3J_{HH}$ = 7.3 Hz, $H_\alpha$); 7.46 (d, 2 H, $^3J_{HH}$ = 7.3 Hz, $H_\beta$); 4.16 (s, 3 H, $CH_3$) |
| (4-aminopyridine)$AuCl_3$ | 8.25 (d, 2 H, $^3J_{HH}$ = 7.1 Hz, $H_a$); 6.91 (d, 2 H, $^3J_{HH}$ = 7.1 Hz, $H_b$); 7.06 (br. s, 2 H, $NH_2$) |
| [4-(dimethylamino)pyridine]$AuCl_3$ | 8.28 (d, 2 H, $^3J_{HH}$ = 7.8 Hz, $H_\alpha$); 6.91 (d, 2 H, $^3J_{HH}$ = 7.8 Hz, $H_\beta$); 3.26 (s, 6 H, $NMe_2$) |
| (4-cyanopyridine)$AuCl_3$ | 9.47, 8.46 (AA′BB′ spin system, 4 H, $^3J_{AB} = {}^3J_{A'B'}$ = 6.5, $^4J_{AA'} = {}^4J_{BB'}$ = 2.0 Hz, *aromatic protons*) |
| (4-acetylpyridine)$AuCl_3$ | 9.33, 8.37 (AA′BB′ spin system, 4 H, $^3J_{AB} = {}^3J_{A'B'}$ = 7.0, $^4J_{AA'} = {}^4J_{BB'}$ = 2.0 Hz, *aromatic protons*); 2.80 (s, 3 H, $CH_3$) |
| (isonicotinic acid)$AuCl_3$ | 9.36, 8.43 (AA′BB′ spin system, 4 H, $^3J_{AB} = {}^3J_{A'B'}$ = 6.9, $^4J_{AA'} = {}^4J_{BB'}$ = 1.5 Hz, *aromatic protons*) |
| (methyl isonicotinate)$AuCl_3$ | 9.36, 8.42 (AA′BB′ spin system, 4 H, $^3J_{AB} = {}^3J_{A'B'}$ = 7.3, $^4J_{AA'} = {}^4J_{BB'}$ = 1.0 Hz, *aromatic protons*); 4.05 (s, 3 H, $CH_3$) |
| (piperidine)$AuCl_3$ | 3.63 (br. s, 1 H, *NH*); 3.56 (m, 4 H, $CH_2$-*N*); 2.00–1.50 (m, 6 H, $CH_2$) |
| (morpholine)$AuCl_3$ | 4.03 (m, 4 H, $CH_2$-*O*); 3.56 (m, 4 H, $CH_2$-*N*); 3.80 (br. m, 1 H, *NH*) |
| (cyclohexylamine)$AuCl_3$ | 3.92 (s, very br., 2 H, $NH_2$); 2.48 (br. m, 1 H, *CH*-*N*); 1.62 (m, 4 H, $CH_2$); 1.39 (m, 4 H, $CH_2$); 1.19 (m, 2 H, $CH_2$) |

[a] $CD_3NO_2$, 298 K.

lengths as a function of time. Pseudo-first-order rate constants ($k_{obs}$, $s^{-1}$) were obtained either from the gradient of plots of $\log(D_t - D_\infty)$ versus time or from a nonlinear least-squares fit of experimental data to $D_t = D_\infty + (D_0 - D_\infty)\exp(-k_{obs}t)$ with $D_0$, $D_\infty$ and $k_{obs}$ as the parameters to be optimized ($D_0$ is absorbance after mixing the reactants, $D_\infty$ is absorbance at completion of reaction).

**Computational Details:** The computational geometry optimizations of the $AuCl_3$(am) complexes were performed in vacuo using the hybrid DFT B3PW91 method[11] without symmetry constraints, in combination with the polarized, single-ζ core, triple-ζ valence 6-311G** basis set on the elements of the first rows of the periodic table and the ECP-based SDD basis set on Au.[12] The "restricted" formalism was applied in all calculations, together with tight convergence criteria. All the resultant stationary points were characterized as true minima (i.e., no imaginary frequencies). All calculations were carried out at CINECA (Centro Italiano di Supercalcolo, Bologna, Italy) using IBM p5-575 computers with 64-bit IBM Power5 processors, which operated at 1.9 GHz frequency. The software used was the Gaussian '03.[13] The Natural Bond Orbitals analysis[14] was performed during our studies, using the NBO version 3.1 implemented in Gaussian 03. Unfortunately, the software separated all our complexes into three different fragments, $[AuCl_2]^{x+}$, $[Cl]^{y-}$ and $[pyridine]^{(y-x)+}$, leading to uncorrected results; for example the apparent $d^{10}$ configuration of the gold centres. For this reason, no discussion based on the NBO analysis was helpful for this work.

**Supporting Information** (see also the footnote on the first page of this article): Selected geometry data and energies for the prepared gold(III) complexes.

## Acknowledgments

We sincerely thank the Ca' Foscari University of Venice for financial support (Ateneo fund 2005).

[1] L. Cattalini, M. Nicolini, A. Orio, *Inorg. Chem.* **1966**, *5*, 1674.
[2] L. Cattalini, A. Orio, A. Doni, *Inorg. Chem.* **1967**, *6*, 280.
[3] L. Cattalini, M. L. Tobe, *Inorg. Chem.* **1966**, *5*, 1145.
[4] F. Basolo, R. G. Pearson, *Mechanism of Inorganic Reactions*, 2nd ed., Wiley, New York, **1967**.
[5] B. Pitteri, M. Bortoluzzi, *Transition Met. Chem.* **2006**, *31*, 1028.
[6] a) B. Pitteri, G. Marangoni, L. Cattalini, *J. Chem. Soc. Dalton Trans.* **1994**, 3539; b) M. Bellicini, L. Cattalini, G. Marangoni, B. Pitteri, *J. Chem. Soc. Dalton Trans.* **1994**, 1805; c) B. Pitteri,

 © 2007 Wiley-VCH Verlag GmbH & Co. KGaA, Weinheim 

G. Marangoni, L. Cattalini, *Polyhedron* **1995**, *14*, 2331; d) B. Pitteri, G. Marangoni, F. Visentin, L. Cattalini, T. Bobbo, *Polyhedron* **1998**, *17*, 475; e) G. Annibale, L. Cattalini, L. Maresca, G. Michelon, G. Natile, *Inorg. Chim. Acta* **1974**, *10*, 211; f) B. Pitteri, M. Bortoluzzi, *Polyhedron* **2006**, *25*, 2698.

[7] M. L. Tobe in *Comprehensive Coordination Chemistry* (Eds.: G. Wilkinson, R. D. McCleverty), Pergamon, Oxford, **1987**, vol. 1.

[8] a) D. D. Perrin, *Dissociation Constants of Organic Bases in Aqueous Solutions*, Butterworths, London, **1965**; b) R. M. Smith, A. E. Martell, *Critical Stability Constants*, Second Printing, Plenum Press, New York, **1990**, vol. 2; c) H. K. Hall, *J. Phys. Chem.* **1956**, *60*, 63.

[9] C. Renz, *Z. Anorg. Chem.* **1903**, *36*, 100.

[10] M. Bortoluzzi, G. Annibale, G. Marangoni, G. Paolucci, B. Pitteri, *Polyhedron* **2006**, *25*, 1979.

[11] a) R. G. Parr, W. Yang, *Density-functional Theory of Atoms and Molecules*, Oxford University Press, Oxford, **1989**; b) J. K. Labanowski, J. Andzelm, *Density Functional Methods in Chemistry*, Springer-Verlag, New York, **1991**; c) P. Geerlings, F. De Proft, W. Langenaker, *Chem. Rev.* **2003**, *103*, 1793; d) T. Ziegler, *Chem. Rev.* **1991**, *91*, 651; e) A. D. Becke, *J. Chem. Phys.* **1993**, *98*, 5648; f) K. Burke, J. P. Perdew, Y. Wang in *Electronic Density Functional Theory: Recent Progress and New Directions* (Eds.: J. F. Dobson, G. Vignale, M. P. Das), Plenum, New York, **1998**.

[12] a) A. D. McLean, G. S. Chandler, *J. Chem. Phys.* **1980**, *72*, 5639; b) R. Krishnan, J. S. Binkley, R. Seeger, J. A. Pople, *J. Chem. Phys.* **1980**, *72*, 650; c) E. R. Davidson, D. Feller, *Chem. Rev.* **1986**, *86*, 681; d) M. Dolg in *Modern Methods and Algorithms of Quantum Chemistry* (Ed.: J. Grotendorst), John Neumann Institute for Computing, NIC series, Jülich, **2000**, vol. 1, pp. 479–508.

[13] M. J. Frish, G. W. Trucks, H. B. Schlegel, G. E. Scuseria, M. A. Robb, J. R. Cheeseman, J. A. Montgomery Jr, T. Vreven, K. N. Kudin, J. C. Burant, J. M. Millam, S. S. Ivengar, J. Tomasi, V. Barone, B. Mennucci, M. Cossi, G. Scalmani, N. Rega, G. A. Petersson, H. Nakatsuji, M. Hada, M. Ehara, K. Toyota, R. Fukuda, J. Hasegawa, M. Ishida, T. Nakajima, Y. Honda, O. Kitao, H. Nakai, M. Klene, X. Li, J. E. Knox, H. P. Hratchian, J. B. Cross, V. Bakken, C. Adamo, J. Jaramillo, R. Gomperts, R. E. Stratmann, O. Yazyev, A. J. Austin, R. Cammi, C. Pomelli, J. W. Ochterski, P. Y. Ayala, R. Morokuma, G. A. Voth, P. Salvador, J. J. Dannenberg, V. G. Zakrewski, S. Dapprich, A. D. Daniels, M. C. Strain, O. Farkas, D. K. Malick, A. D. Rabuck, K. Raghavachari, J. B. Foresman, J. V. Ortiz, Q. Cui, A. G. Baboul, S. Clifford, J. Cioslowski, B. B. Stefanov, G. Liu, A. Liashenko, P.Piskorz, I. Komaromi, R. L. Martin, D. J. Fox, T. Keith, M. A. Al-Laham, C. Y. Peng, A. Nanayakkara, M. Challacombe, P. M. W. Gill, B. Johnson, W. Chen, M. W. Wong, C. Gonzales, J. A. Pople, *Gaussian 03*, Revision D.02, Gaussian Inc., Wallingford, CT, **2004**.

[14] A. E. Reed, L. A. Curtiss, F. Weinhold, *Chem. Rev.* **1988**, *88*, 899.

Received: April 26, 2007
Published Online: July 31, 2007

Please note: Minor changes have been made to this manuscript since its publication in the *European Journal of Inorganic Chemistry* Early View. The Editor.

 © 2007 Wiley-VCH Verlag GmbH & Co. KGaA, Weinheim 

DOI: 10.1002/ejic.200700465

# Reactions of 1,2,4-Trithiolanes with Nonacarbonyldiiron: Sulfurdithiolatodiiron and -tetrairon Complexes as Mimics for the Active Site of [Fe-only] Hydrogenase

**Jochen Windhager,[a] Helmar Görls,[a] Holm Petzold,[a] Grzegorz Mloston,[b] Gerald Linti,*[c] and Wolfgang Weigand*[a]**

*Dedicated to Prof. Dieter Seebach on the occasion of his 70th birthday*

**Keywords:** Iron / Cluster compounds / S ligands / Hydrogenases / Density functional calculations

The reactions of 1,2,4-trithiolane (**1a**), 3,3,5,5-tetramethyl-1,2,4-trithiolane (**1b**), 3,3,5,5-tetraethyl-1,2,4-trithiolane (**1c**), 3,3,5,5-bis(pentamethylene)-1,2,4-trithiolane (**1d**) and dispiro{tricyclo[3.3.1.1]decane-2,3′′-(1,2,4)-trithiolane-5′,2′-tricyclo[3.3.1.1]decane} (**1e**) with nonacarbonyldiiron (**2**) have been investigated. The sulfurdithiolatodiiron complexes **3a–e**, which can be considered as novel model complexes of the active site of the [Fe-only] hydrogenase, were isolated as the main products of these reactions. X-ray structure analyses were performed on compounds **3b–e**. The carbon dithiolato ($SCR_2S$)-bridged diiron side-products **4a–e** and the tetranuclear clusters **6b–d** were also obtained and characterised by X-ray diffraction analysis (**4b–e** and **6b–d**). In contrast, the reaction of **1e** with **2** affords the trinuclear complex **7**, which contains a side-on bonded adamantanethione, besides **3e** and **4e**. Finally, the reaction of **3a** with two equivalents of $(Et_4N)CN$ gives the monocyanide complex **8** in good yield. Density functional calculations have been performed to evaluate the bonding situation in the di- and tetranuclear clusters.

(© Wiley-VCH Verlag GmbH & Co. KGaA, 69451 Weinheim, Germany, 2007)

## Introduction

The oxidative addition of platinum(0) complexes to cyclic disulfides has received significant attention during the last few years.[1] We have recently investigated reactions of 1,2,4-trithiolanes with platinum(0) complexes, which lead to the insertion of the platinum(0) complex fragment into the S–S bond,[2] and have also shown that 1,2,4-trithiolane (**1a**) can be added oxidatively to $[Fe_2(CO)_9]$ (**2**) to give the sulfurdithiolatodiiron (SDT) complex $[Fe_2(\mu\text{-}SCH_2SCH_2S\text{-}\mu)(CO)_6]$ (**3a**) as well as $[Fe_2(\mu\text{-}SCH_2S\text{-}\mu)(CO)_6]$ (**4a**).[3,4] Similar reactions involving $[Fe_3(CO)_{12}]$ and **1a**, which lead to complex **3a**, have been reported recently.[3c]

Since publication of the first X-ray structure determination of the [Fe-only] hydrogenase,[6] numerous model compounds for the active site of the enzyme, such as propanedithiolato- (PDT),[7a–7d] azadithiolato- (ADT)[7e–7g] and oxadithiolatodiiron (ODT) derivatives, have been described (Scheme 1).[7f,7i,7l]

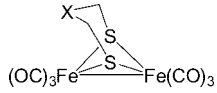


Scheme 1. Model complexes for the active site of [Fe-only] hydrogenase with X = $CH_2$, NH, O and S.

In the light of recent results, reactions of iron carbonyls with sulfur-rich heterocycles such as 1,2,4-trithiolanes could offer a new approach to the synthesis of products related to [Fe-only] hydrogenase. To the best of our knowledge, reactions of 1,2,4-trithiolane derivatives with iron carbonyls have seldom been described.[3c,3d]

Here we describe the reactions of tetrasubstituted 1,2,4-trithiolanes **1a–e** (Scheme 2) with $[Fe_2(CO)_9]$ (**2**) as a systematic investigation of the influence of the substituents' size on the molecular structure of the products. Density functional calculations for one complex are also reported.

[a] Institut für Anorganische und Analytische Chemie, Friedrich-Schiller-Universität Jena,
August-Bebel-Strasse 2, 07743 Jena, Germany
Fax: +49-3641-948-102
E-Mail: c8wewo@uni-jena.de
[b] Section of Heteroorganic Compounds, University of Lodz,
Narutowicza 68, 90–136 Lodz, Poland
Fax: +48-42-678-1609
E-mail: gmloston@uni.lodz.pl
[c] Anorganisch-Chemisches Institut, Ruprecht-Karls-Universität Heidelberg,
Im Neuenheimer Feld 270, 69120 Heidelberg, Germany
Fax: +49-6221-54-66-17
E-mail: gerald.linti@aci.uni-heidelberg.de

Supporting information for this article is available on the WWW under http://www.eurjic.org or from the author.

 WILEY InterScience DISCOVER SOMETHING GREAT © 2007 Wiley-VCH Verlag GmbH & Co. KGaA, Weinheim 

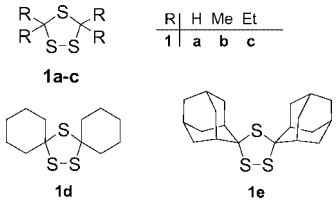


Scheme 2. 1,2,4-Trithiolanes **1a**–**e**.

## Results and Discussion

### Reactions of 1,2,4-Trithiolanes (1a–d) with [$Fe_2(CO)_9$] (2)

Three equivalents of nonacarbonyldiiron (**2**) were treated with one equivalent of the corresponding 1,2,4-trithiolane **1a**–**d** (Scheme 2) for five hours at room temperature in thf to afford a mixture of four compounds of type **3**, **4**, **5** and **6** (Scheme 3), which were isolated by column chromatography. Compounds **3a**,[3] **4a**[4] and **5**[5] have already been described. Complex **6a** was formed at room temperature exclusively but not in the reaction performed at 65 °C.

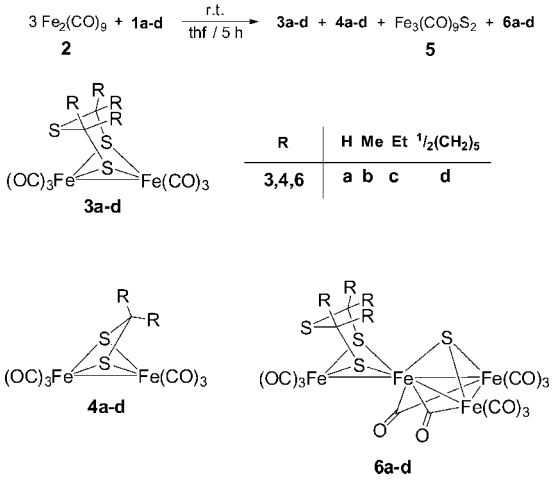


Scheme 3. Reactions of 1,2,4-trithiolanes **1a**–**d** with [$Fe_2(CO)_9$].

The $^1$H NMR spectra of **3b**,**c** and **4b**,**c** show that the corresponding alkyl groups (R = Me, Et) are chemically equivalent. Furthermore, the $^{13}C\{^1H\}$ NMR spectra display one signal for four methyl groups in **3b** and two signals for four ethyl groups in **3c**. The $^{13}C\{^1H\}$ NMR spectrum of complex **3d** contains three resonance signals at $\delta$ = 22.80, 25.23 and 43.22 ppm, respectively, which were attributed to the pentamethylene moiety. The $^1$H and $^{13}C\{^1H\}$ NMR spectra of **4b**–**d** indicate that the R groups bonded to the bridging carbon atoms ($SCR_2S$) are equivalent. The mass spectra of **3b**–**d** and **4b**–**d** show the molecular peaks (see Experimental Section) and stepwise fragmentation of six CO groups similar to **3a** and **4a**. Finally, X-ray diffraction analysis confirmed the formation of the dithiolatodiiron complexes **3b**–**d** (Figures 1, 2 and 3, respectively) and **4b**–**d** (see Figures S1–S3 in the electronic supporting information).

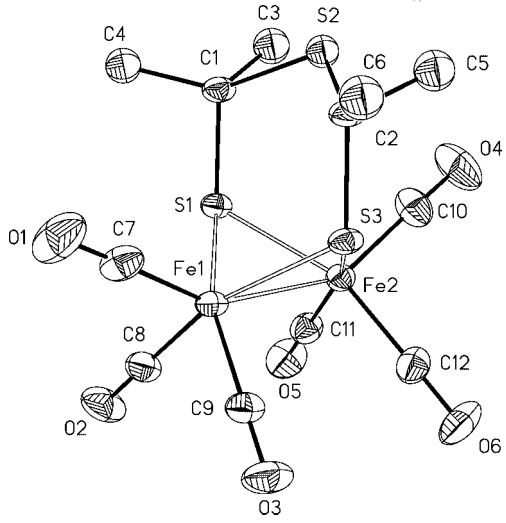


Figure 1. Structure of [$Fe_2\{SC(CH_3)_2SC(CH_3)_2S\}(CO)_6$] (**3b**) showing thermal ellipsoids at the 50% probability level (hydrogen atoms have been omitted for clarity). Selected distances [Å] and angles [°]: Fe(1)–Fe(2) 2.5219(6), Fe(2)–C(7) 1.792(4), Fe(2)–C(8) 1.793(3), Fe(2)–C(9) 1.799(3), Fe(1)–S(1) 2.2495(8), Fe(1)–S(3) 2.2480(9); Fe(1)–S(1)–Fe(2) 68.12(3), Fe(1)–S(3)–Fe(2) 68.18(3).

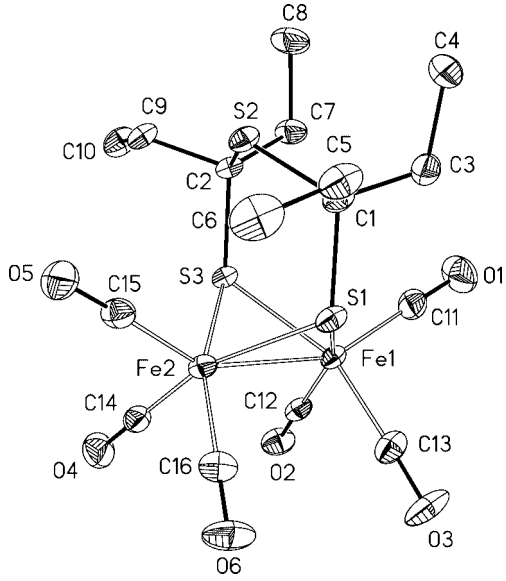


Figure 2. Structure of [$Fe_2\{SC(CH_2CH_3)_2SC(CH_2CH_3)_2S\}(CO)_6$] (**3c**) showing thermal ellipsoids at the 50% probability level (hydrogen atoms have been omitted for clarity). Selected distances [Å] and angles [°]: Fe(1)–Fe(2) 2.5151(4), Fe(1)–C(11) 1.804(2), Fe(1)–C(12) 1.7960(19), Fe(1)–C(13) 1.793(2), Fe(1)–S(1) 2.2648(5), Fe(1)–S(3) 2.2481(5); Fe(1)–S(1)–Fe(2) 67.469(15), Fe(1)–S(3)–Fe(2) 68.055(16).

The iron coordination geometry in **3b**–**d** is rather similar to the sulfurdithiolato (SDT) analogue [$Fe_2(\mu$-$SCH_2SCH_2S$-$\mu)(CO)_6$] (**3a**).[3] The Fe–Fe bond lengths found in **3b**–**d** are between 2.5151 and 2.5288 Å, slightly longer than those in the corresponding PDT [2.5103(11) Å],[7a–7d] ODT [2.5113(13) Å],[7f,7i,7l] ADT [2.4924(7) Å][7e–7g] and SDT analogs [2.5120(5) Å].[3] Simi-

 © 2007 Wiley-VCH Verlag GmbH & Co. KGaA, Weinheim 

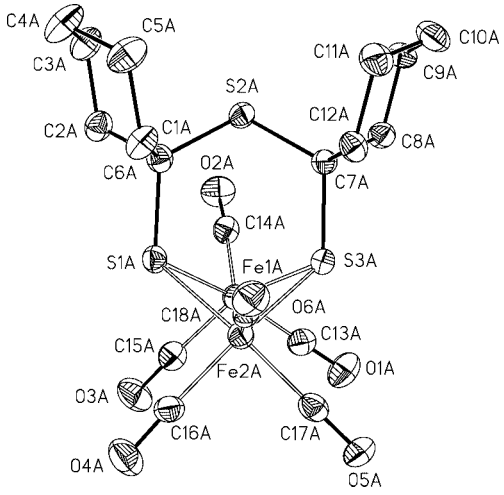


Figure 3. Structure of $[Fe_2\{SC(CH_2)_5SC(CH_2)_5S\}(CO)_6]$ (**3d**) showing thermal ellipsoids at the 50% probability level (hydrogen atoms have been omitted for clarity). Selected distances [Å] and angles [°]: Fe(1A)–Fe(2A) 2.5288(13), Fe(1A)–C(A13) 1.787(8), Fe(A1)–C(A14) 1.819(6), Fe(A1)–C(A15) 1.790(7), Fe(1A)–S(1A) 2.2505(19), Fe(1A)–S(3A) 2.2483(17); Fe(1A)–S(1A)–Fe(2A) 68.31(5), Fe(1A)–S(3A)–Fe(2A) 68.60(5).

larly to the ODT and SDT complexes, the bridgehead sulfur atoms in **3b** and **3d** are disordered (50%).

In contrast to the above-described NMR spectra for complexes **3b**–**d**, the $^1H$ and $^{13}C\{^1H\}$ NMR spectra of **6a**–**d** show that the R groups connected to the bridging carbon atoms ($SCR_2SCR_2S$) are chemically non-equivalent. For example, the $^1H$ NMR spectrum of **6a** contains the splitting pattern of an AA′BB′ system which was assigned to the protons of the two methylene groups, and the IR spectrum displays a characteristic vibration band at 1898 $cm^{-1}$ assigned to the bridging CO ligands. Compound **6b** also shows two singlets attributed to two pairs of non-equivalent methyl groups. Similar observations were made for **6c** and **6d**. The desorption electron ionization (DEI) mass spectra for **6b**, **6c** and **6d** reveal the presence of $[M]^+$ ions at *m*/*z* 744, 800 and 824, respectively, and a stepwise fragmentation of eleven CO groups. Additionally, the IR spectroscopic measurements prove the presence of bridging CO ligands [ν(CO) = 1910 (for **6b**) and 1923, 1901 $cm^{-1}$ (for **6c**)].

Complexes **6b**–**d** were characterised as tetranuclear iron clusters based on the X-ray diffraction analysis (Figure 4 and Figures S5 and S6 in the electronic supporting information). Compounds **6b**–**d** contain an $(OC)_3Fe(\mu\text{-}SCR_2SCR_2S\text{-}\mu)Fe$ fragment [**6b**: R = Me, **6c**: R = Et, **6d**: R = 1/2 $(CH_2)_5$] coordinated to an $Fe_2(CO)_6(\mu\text{-}CO)_2S$ unit which is likely to be formed in the reaction of $Fe_2(CO)_9$ with the sulfur originating from the decomposition of the in situ generated thiosulfinates (see below). The $Fe_2(CO)_6(\mu\text{-}CO)_2S$ moiety acts as a six-electron donor ligand that formally substitutes three CO ligands from the complex of type **3** to finally give an eight-coordinate Fe(2) atom. A similar cluster has been synthesised by the reaction of the sulfur with $Fe_3(CO)_{12}$ in 1-hexene to give $[Fe_4(CO)_{11}(\mu^3\text{-}S)(\mu\text{-}L)]$ (L = 1,2-hexylenedithiolate).[8a,b] In contrast to our results, very unusual triiron clusters with seven coordinated CO ligands were obtained when $[Fe_3(CO)_{12}]$ was treated with 1,2- and 1,3-dithioles in toluene at 70 °C.[8c] The Fe(1) and Fe(2) centres are $\mu^2$-bridged by the alkyl-substituted SDT ligands and the Fe(2), Fe(3), Fe(4) and S(4) atoms form a tetrahedron. The Fe(1)–Fe(2) distances are about 0.04 Å longer than the corresponding bond lengths in **3b**–**d**, and the Fe(2)–Fe(3)/Fe(4) bond lengths in the tetrahedron are remarkably longer than the Fe(1)–Fe(2) distances [e.g. **6b**: 2.6419(9)/2.6365(10) Å].

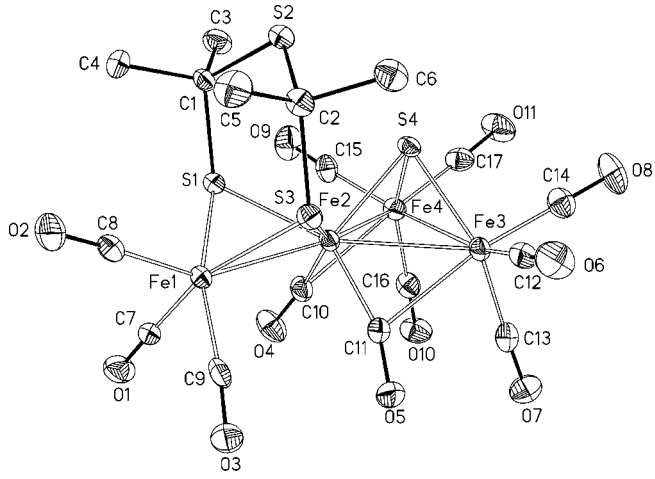


Figure 4. Structure of $[Fe_4(\mu\text{-}SCR_2SCR_2S\text{-}\mu)(CO)_9(\mu\text{-}CO)_2S]$ (**6b**; R = Me) showing thermal ellipsoids at the 50% probability level (hydrogen atoms have been omitted for clarity). Selected distances [Å] and angles [°]: Fe(1)–Fe(2) 2.5672(9), Fe(2)–Fe(3) 2.6419(9), Fe(2)–Fe(4) 2.6365(10), Fe(3)–Fe(4) 2.5855(10), Fe(1)–C(8) 1.804(6), Fe(1)–C(9) 1.806(6), Fe(2)–C(10) 1.813(6), Fe(2)–C(11) 1.827(6), Fe(3)–C(11) 2.381(5), Fe(1)–S(1) 2.2366, Fe(1)–S(3) 2.2329, Fe(2)–S(4) 2.2017(13); Fe(1)–S(1)–Fe(2) 69.65(4), Fe(1)–S(3)–Fe(2) 69.73(4), Fe(3)–Fe(2)–S(4) 52.72(4), Fe(4)–Fe(2)–S(4) 52.39(4), Fe(3)–Fe(2)–Fe(4) 58.66(3), Fe(3)–Fe(4)–Fe(2) 60.78(3).

### Reaction of 1,2,4-Trithiolane 1e with $[Fe_2(CO)_9]$ (2)

The reaction of 1,2,4-trithiolane **1e** with three equivalents of **2** at room temperature in thf gave complexes **3e**, **4e** and **7** (Figures 5 and 6 and Figures S4 in the supporting information) which were separated by column chromatography (Scheme 4). Compound **4e** has already been isolated by Alper et al. from the reaction of adamantanethione with **2** in benzene.[3d] The single-crystal diffraction analysis of **3e** showed that the Fe–Fe distance [2.5525(13) Å] is about 0.045 Å longer than that in **3a** (Figure 5). The Fe–Fe distance in **3e** is very similar to that found in the reduced state diiron subsite of the enzyme structure (2.55 Å).[6a]

Due to the sterically demanding influence of the adamantyl substituents, the average Fe–S–Fe angle of 69.3° is slightly larger than that in **3a** (67.7°). The large C(1)–S(3)–C(11) angle of 111.4(3)° in **3e** differs significantly from that in complex **3a** [102.77(9)°].

Unlike the reactions of **1a**–**d** with **2**, the formation of a tetranuclear iron cluster similar to **6a**–**d** was not observed, although we were able to isolate complex **7**. The DEI mass

 © 2007 Wiley-VCH Verlag GmbH & Co. KGaA, Weinheim 

spectrum of **7** shows the [M$^+$] ion at *m*/*z* 586 and stepwise fragmentation of nine CO groups. This indicates that three $Fe(CO)_3$ moieties are coordinated to adamantanethione, a result which was also confirmed by X-ray structure analysis (Figure 6).

As a tentative mechanism we propose that the interaction of 1,2,4-trithiolanes **1a**–**e** with an $Fe_2(CO)_6$ complex fragment initially results in its insertion into the S–S bond to form complexes **3a**–**e**. But how can we explain the formation of complexes **4a**–**e**, **6a**–**d** and **7**? The insertion of iron carbonyl into the S–S bond, which results in the formation of **3** (Scheme 5, pathway a), competes with decomposition of the intermediate zwitterion to form **4** (Scheme 5, pathway b), which can be considered as a formal complex of $Fe_2(CO)_6$ with dithiirane, and the corresponding thioketone. In contrast to the enolisable aliphatic and cycloaliphatic thioketones, adamantanethione is a relatively stable compound,[9] which cannot undergo this undesired side reaction and is trapped in situ with the $Fe_3(CO)_9$ fragment to yield **7** (Scheme 5). Less stable aliphatic thioketones or products of their secondary transformations act as sulfur donors in the multistep reaction leading to clusters of type **6**.

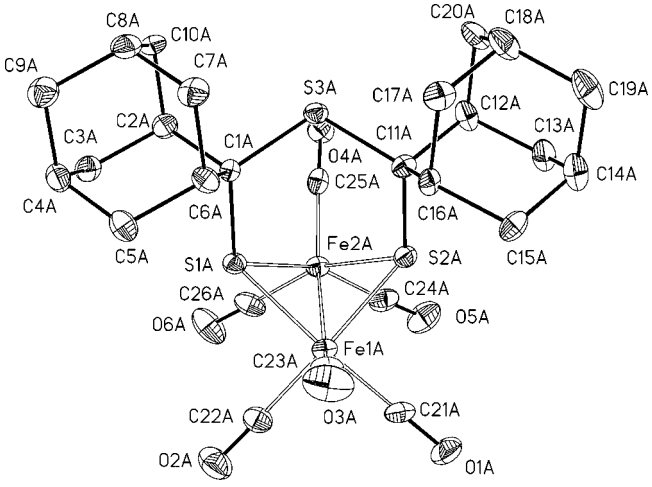


Figure 5. Structure of [$Fe_2${SC(ad)SC(ad)S}$(CO)_6$] (ad = adamantyl) **3e** with thermal ellipsoids set at the 50% probability level (hydrogen atoms have been omitted for clarity). Selected distances [Å] and angles [°]: Fe(1A)–Fe(2A) 2.5525(13), Fe(1A)–C(A21) 1.803(8), Fe(A1)–C(A22) 1.785(8), Fe(A1)–C(A23) 1.807(8), Fe(1A)–S(1A) 2.247(2), Fe(1A)–S(2A) 2.2407(19); Fe(1A)–S(1A)–Fe(2A) 69.18(6), Fe(1A)–S(2A)–Fe(2A) 69.49(6).

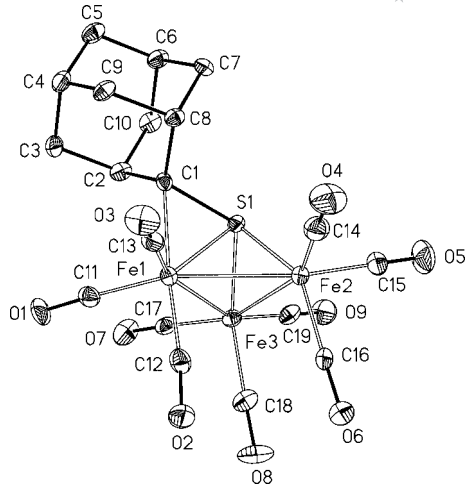


Figure 6. Structure of [$Fe_3$(ad)S$(CO)_9$] (**7**; ad = adamantyl) showing thermal ellipsoids at the 50% probability level (hydrogen atoms have been omitted for clarity). Selected distances [Å] and angles [°]: Fe(1)–Fe(2) 2.6256(11), Fe(2)–Fe(3) 2.6704(12), Fe(3)–Fe(1) 2.6272(12), Fe(1)–C(1) 2.122(6), Fe(1)–S(1) 2.2068(16), S(1)–C(1) 1.781(6); Fe(1)–C(1)–S(1) 68.2(2), Fe(1)–Fe(3)–Fe(2) 59.42(3), Fe(2)–Fe(1)–Fe(3) 61.11(3), Fe(1)–S(1)–Fe(2) 74.34(5), Fe(2)–S(1)–Fe(3) 77.28(6).

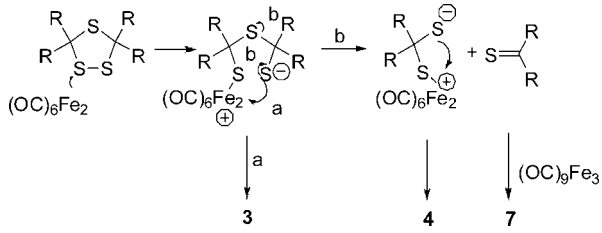


Scheme 5. Proposed mechanism for the formation of **3**, **4** and **7**.

In order to exclude the formation of complexes **4a**–**e** from **3a**–**e** we treated **3b** with an excess of **2** in thf at room temperature for 5 h. Complex **3b** does not react further under these conditions.

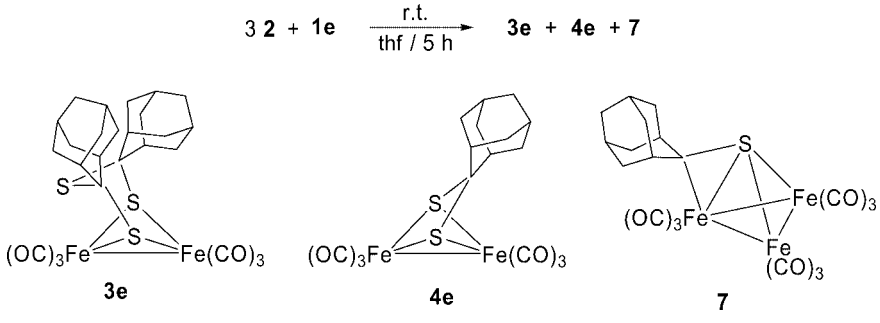


Scheme 4. Reaction of 1,2,4-trithiolane **1e** with [$Fe_2(CO)_9$].

 © 2007 Wiley-VCH Verlag GmbH & Co. KGaA, Weinheim 

Figure 6 shows that the adamantanethione molecule is bonded side-on to a three-iron triangle where Fe(1)–Fe(3) and S(1) form a tetrahedron. The C(1)–S(1) distance [1.781(6) Å] is significantly longer than that in a corresponding organic compound such as thiobenzoephenone due to this side-on coordination.[10]

### Substitution Reaction of 3a with $(Et_4N)CN$

The displacement of one CO ligand with one equivalent of $CN^-$ anion leads to the formation of complex **8**, which was successfully isolated from reaction mixture. This product is formed by the addition of $(Et_4N)CN$ to **3a**. The same reaction has been applied very recently to substitute two CO ligands by $CN^-$ ions to yield $(Et_4N)_2[Fe_2(SDT)(CO)_4(CN)_2]$.[3c]

The $^1H$ NMR spectrum of **8** shows one broad singlet for the $SCH_2S$ groups at $\delta = 2.59$ ppm, which is different to the corresponding resonances in $(Et_4N)_2[Fe_2(SDT)(CO)_4(CN)_2]$ ($\delta = 3.30$ ppm)[3c] and $(Et_4N)[Fe_2(ODT)(CO)_5(CN)]$ ($\delta = 4.09$ ppm).[7] Although both methylene groups in **8** and in $(Et_4N)[Fe_2(ODT)(CO)_5(CN)]$ are diastereotopic, the four protons appear as a broad singlet, which indicates a dynamic process in the complexes. The ESI mass spectrum of **8** reveals the anion at *m*/*z* 401.9 and the cation at *m*/*z* 130.2. All ν(CO) bands in the IR spectra are shifted, as expected, towards lower energies than in **3a** due to the negative charge of the complex. The isotopic pattern for the anion confirmed the postulated monocyanide complex **8** (see Figure S7 in the Supporting Information). The structure of **8** was confirmed by single-crystal X-ray diffraction (Figure 7), which unequivocally confirmed the formation of complex **8**. The Fe–Fe bond length [2.5240(12) Å] is slightly longer than that in **3a** and very similar to that in $(Et_4N)[Fe_2(PDT)(CN)(CO)_5]$ [2.5291(6) Å].[6b] In analogy to $(Et_4N)[Fe_2(PDT)(CN)(CO)_5]$, the five Fe–CO distances (1.77 Å) are shorter than the Fe–CN distance [1.940(6) Å]. In contrast to $(Et_4N)[Fe_2(ODT)(CN)(CO)_5]$, however, where the bridgehead oxygen atom is fixed completely opposite the Fe atom attached to the CN ligand, the bridgehead sulfur atom in complex **8** is orientated towards the Fe atom attached to the cyanide ligand.

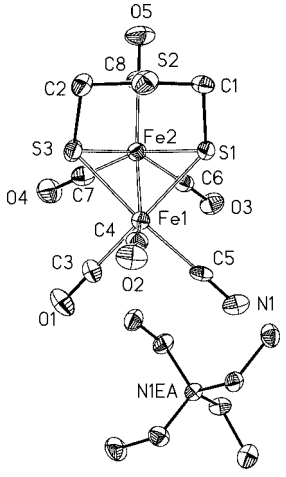


Figure 7. Structure of $(Et_4N)[Fe_2(SDT)(CN)(CO)_5]$ (**8**) showing thermal ellipsoids at the 50% probability level (hydrogen atoms have been omitted for clarity). Selected distances [Å] and angles [°]: Fe(1)–Fe(2) 2.5240(12), Fe(1)–C(3) 1.786(6), Fe(1)–C(4) 1.761(7), Fe(2)–C(5) 1.940(6), Fe(1)–S(1) 2.2488(16), Fe(1)–S(3) 2.2499(17); Fe(1)–S(1)–Fe(2) 67.93(5), Fe(1)–S(3)–Fe(2) 67.92(5).

### Quantum Chemical Calculations

Geometry optimisation was performed at the RI-DFT and DFT levels with BP86 and B3LYP functionals and LANL2DZ, def-SV(P) basis sets using the TURBOMOLE[11–13] and Gaussian 03[14] software packages. The structure calculated for **9** (Figure 8), which differs from **6b** only in the substitution of the methyl groups for hydrogen, has main structural features that are very similar to those of **6b** and are in line with this complex being built up from an $Fe_2(CO)_6S$ (**10**; Figure 9) and an $Fe_2(CO)_5(SCH_2)_2S$ (**12**) unit. Complex **11** is the CO adduct of this latter fragment (Figure 10) and its structural data are similar to those of **3b**.

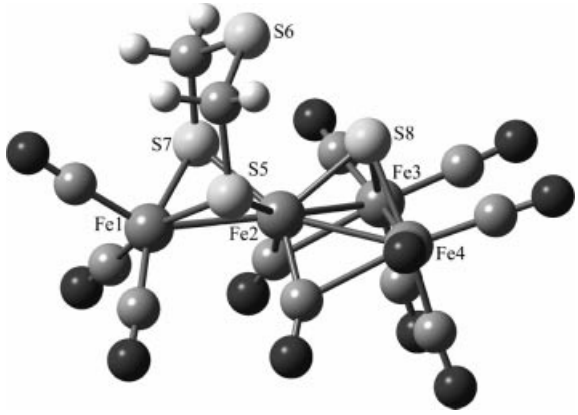


Figure 8. Structure of **9** obtained from the density functional calculations [BP86/def-SV(P)]. Selected distances [Å]: Fe(1)–Fe(2) 2.579, Fe(2)–Fe(3) 2.604, Fe(2)–Fe(4) 2.607, Fe(3)–Fe(4) 2.584, Fe(1)–C 1.775–1.799, Fe(2)–C 1.818, Fe(3)–C 1.785, 2.309, Fe(1)–S(5,7) 2.279, Fe(2)–S(5,7) 2.286, Fe(2)–S(8) 2.208, Fe(3)–S(8) 2.223.

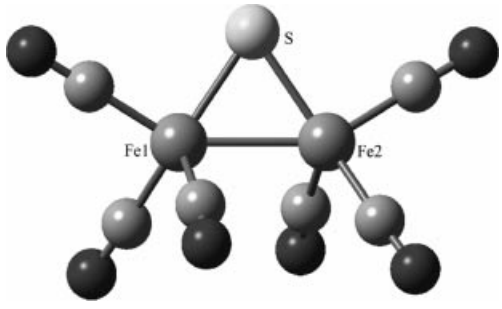


Figure 9. Structure of **10** obtained from the density functional calculations [BP86/def-SV(P)]. Selected distances [Å]: Fe(1)–Fe(2) 2.453, Fe–S 2.159, Fe–C 1.745–1.778.

 © 2007 Wiley-VCH Verlag GmbH & Co. KGaA, Weinheim 

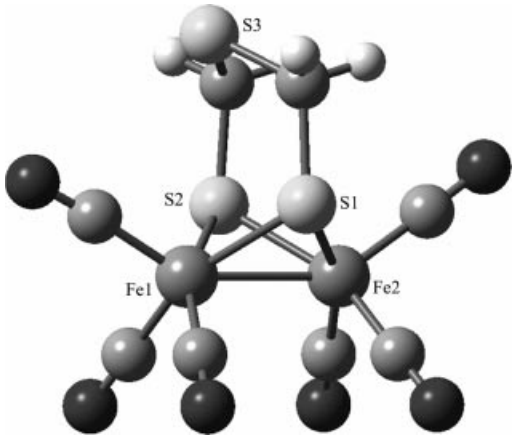


Figure 10. Structure of **11** obtained from the density functional calculations [BP86/def-SV(P)]. Selected distances [Å]: Fe(1)–Fe(2) 2.531, Fe–S 2.295–2.300, Fe–C 1.775–1.783.

Substitution of a CO ligand in **11** for **10** leaves the core of **11** essentially unaffected, whilst **10** is changed more drastically (the Fe–Fe and Fe–S distances are elongated by 0.1 Å). This is also shown by the shared electron numbers (SEN),[15] which indicate shorter Fe–Fe contacts in **10** ($SEN_{Fe–Fe}$ = 1.2) than in **11** ($SEN_{Fe–Fe}$ = 0.88). This is also the case for the Fe–S contacts [$SEN_{Fe–S}$ = 1.47 (**10**), 1.08 (**11**)].

Inspection of the frontier orbitals (Figure 11) shows that the **10** and **11** can be viewed in a first approximation as separate units that are linked mainly by an Fe–S interaction. The pseudo-bridging CO ligands on the Fe(2)–Fe(3,4) edges are only weakly bonded to Fe(3,4).

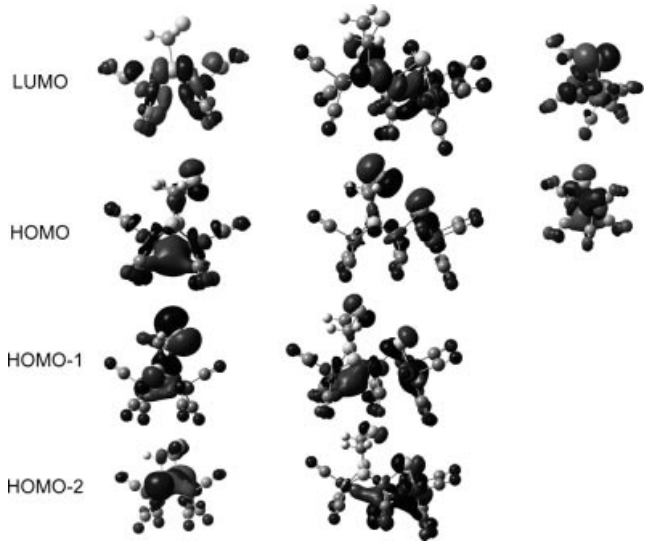


Figure 11. Kohn–Sham frontier orbitals for **9**–**11**.

An alternative description of **9** as a $Fe_3S$ clusters with a $Fe(CO)_3$ ligand attached to two S atoms, as depicted in Scheme 3, might also be possible. Complex **12** would be balanced as a cluster with six skeletal electron pairs, which would fit a Wade-type[16,17] *nido* cluster isolobal with $P_4$. The results of the calculations on **9** and **11**, however, show that this interpretation is less valid.

## Conclusions

We have shown that the 1,2,4-trithiolanes **1a**–**e** react with $[Fe_2(CO)_9]$ (**2**) by insertion into the S–S bond to provide novel mimics (**3a**–**e**) of [Fe-only] hydrogenase. We also succeeded in isolating the carbondithiolato ($SCR_2S$)-bridged diiron products **4a**–**e** and the tetranuclear clusters **6b**–**d** as side products. Interestingly, the reaction of **1e** with **2** yielded the adamantanethione complex **7** as well as **3e** and **4e**; no tetranuclear cluster of type **6** was observed. These reaction pathways can be explained by an interaction of the $Fe_2(CO)_6$ complex fragment with the disulfide moiety in the 1,2,4-trithiolanes **1a**–**e**, which induces ring opening. Reaction of the resulting zwitterionic intermediate competes with its decomposition to **4**, which can be considered as a formal complex of $Fe_2(CO)_6$ with dithiirane, and the corresponding thioketone. In the case of **7**, the eliminated adamantanethione, which is a relatively stable compound,[9] is trapped in situ by an $Fe_3(CO)_9$ fragment (Scheme 5). Less stable aliphatic thioketones or products of their secondary transformations act as sulfur donors in the multistep reaction leading to clusters of type **6**. Density functionl calculations have shown that tetrairon clusters of type **6** are built from two dinuclear subunits linked by iron–sulfur contacts.

## Experimental Section

**General:** The $^1H$ and $^{13}C\{^1H\}$ NMR spectra were recorded with a Bruker DRX 200 or DRX 400 spectrometer using the solvent as reference. The 2D NMR measurements were done on the DRX 400 spectrometer. The mass spectra were recorded with a FINNIGAN MAT SSQ 710 instrument. The IR spectra were recorded with a Thermoelectron Nicolet AVATAR 30070 DTGS by using KBr pellets, with a Biorad FTF 25 in ATR cuvettetes when measuring neat substance and with a Perkin–Elmer 2000 FT-IR spectrometer when measuring solutions. 1,2,4-Trithiolane (**1a**), 3,3,5,5-tetramethyl-1,2,4-trithiolane (**1b**), 3,3,5,5-tetraethyl-1,2,4-trithiolane (**1c**), 3,3,5,5-bis(pentamethylene)-1,2,4-trithiolane (**1d**) and dispiro{tricyclo[3.3.1.1]decane-2,3′′-(1,2,4)-trithiolane-5′,2′-tricyclo[3.3.1.1]decane} (**1e**) were prepared according to literature protocols.[18–20] Elemental analyses were performed with LECO CHNS-932. Solvents and $[Fe_2(CO)_9]$ (**2**) were purchased from Sigma–Aldrich. Thf was dried with sodium/benzoephenone before use. Reported yields refer to the amount of purified products. Merck Silica gel 60 (0.015–0.040 mm) was used for column chromatography. TLC was performed on Merck TLC aluminium sheets (slica gel 60 $F_{254}$).

**Preparation of Complexes 3a–e, 4a–e, 6a–d and 7. General Procedure:** Nonacarbonyldiiron (**2**; 4.5 mmol) and 1,2,4-trithiolane **1a**–**e** (1.5 mmol) were dissolved in thf (20 mL) and stirred at room temperature for five hours under argon. The light-orange solution turned deep red and a brown solid (mixture of inorganic iron sulfides) precipitated. The solvent was removed under reduced pressure and the crude product was purified by column chromatography using hexane as eluent. A yellow fraction representing the

 © 2007 Wiley-VCH Verlag GmbH & Co. KGaA, Weinheim 

side products **4a**–**e**, the orange main fraction containing complexes **3a**–**e**, and the third, red-brown and brown fractions containing **6a** and **6b**–**d** and **7**, respectively, were collected and the solvent removed in vacuo. The products were obtained as red-orange (for **3a**–**e** and **4a**–**e**), dark-red (for **6a**) or brown solids (for **6b**–**d** and **7**).

Crystals suitable for X-ray diffraction analysis were obtained by slow evaporation of hexane into a concentrated pentane solution at 0 °C (for **3a**–**e**). Products **3a**–**e**, **4a**–**e**, **6b**–**d** and **7** were crystallised from a solution of hexane at –25 °C.

**[Fe$_2$(SDT)(CO)$_6$] (3a):**[3] $R_f$ = 0.5 (hexane): Yield 234 mg (0.58 mmol, 38.6%). $C_8H_4Fe_2O_6S_3$ (403.79): calcd. C 23.78, H 0.99, S 23.81; found C 23.81, H 1.26, S 23.48. $^1$H NMR (200 MHz, $CDCl_3$, 25 °C): $\delta$ = 3.21 (s, 4 H, C$H_2$) ppm. $^{13}$C{$^1$H} NMR (100 MHz, $CDCl_3$): $\delta$ = 27.7 (*C*H$_2$), 206.8 (*C*O) ppm. FT-IR (KBr disc): $\tilde{\nu}$ = 2075 (s), 2027 (s), 1999 [vs ($\nu$CO, terminal)] cm$^{-1}$. MS (DEI, 70 eV): *m*/*z* 404 (16) [M$^+$], 376 (100) [M$^+$ – CO], 348 (70) [M$^+$ – 2CO], 320 (46) [M$^+$ – 3CO], 292 (17) [M$^+$ – 4CO], 264 (42) [M$^+$ – 5CO], 236 (58) [M$^+$ – 6CO], 208 (58) [M$^+$ – 5CO – Fe], 176 (26) [M$^+$ – 5CO – Fe – S], 144 (68) [M$^+$ – 5CO – Fe – 2S], 122 (12) [M$^+$ – 5CO – Fe – 3S], 78 (8) [$CH_2S_2$], 56 (26), 45 (12) [CHS].

**[Fe$_2${SC(CH$_3$)$_2$SC(CH$_3$)$_2$S}(CO)$_6$] (3b):** $R_f$ = 0.49 (hexane). Yield 251.8 mg (0.548 mmol, 36.5%). $C_{12}H_{12}Fe_2O_6S_3$ (460.11): calcd. C 31.33, H 2.63, S 20.91; found C 31.24, H 2.89, S 20.72. $^1$H NMR (200 MHz, $CDCl_3$, 25 °C): $\delta$ = 1.61 (s, 12 H, C$H_3$) ppm. $^{13}$C{$^1$H} NMR (100 MHz, $CDCl_3$, 25 °C): $\delta$ = 35.3 (*C*H$_3$), 46.0 ($C_q$), 207.3 (*C*O) ppm. FT-IR (KBr disc): $\tilde{\nu}$ = 2073 (s), 2029 (s), 2002 (vs), 1970 [s ($\nu$CO, terminal)] cm$^{-1}$. MS (DEI, 70 eV): *m*/*z* (%) 460 (2) [M$^+$], 432 (30) [M$^+$ – CO], 404 (38) [M$^+$ – 2CO], 376 (36) [M$^+$ – 3CO], 348 (26) [M$^+$ – 4CO], 320 (60) [M$^+$ – 5CO], 292 (56) [M$^+$ – 6CO].

**[Fe$_2${SC(CH$_2$CH$_3$)$_2$SC(CH$_2$CH$_3$)$_2$S}(CO)$_6$] (3c):** $R_f$ = 0.48 (hexane). Yield 309.6 mg (0.6 mmol, 40%). $C_{16}H_{20}Fe_2O_6S_3$ (516.21): calcd. C 37.23, H 3.91, S 18.63; found C 37.21, H 3.86, S 18.64. $^1$H NMR (200 MHz, $CDCl_3$, 25 °C): $\delta$ = 0.98 (t, $^3J$ = 7.2 Hz, 12 H, C$H_3$), 1.76 (q, $^3J$ = 7.6 Hz, 4 H, C$H_2$), 1.77 (q, $^3J$ = 7.6 Hz, 4 H, C$H_2$) ppm. $^{13}$C{$^1$H} NMR (100 MHz, $CDCl_3$, 25 °C): $\delta$ = 9.3 (*C*H$_3$), 23.4 (*C*H$_2$), 54.3 ($C_q$), 207.5 (*C*O) ppm. FT-IR (KBr disc): $\tilde{\nu}$ = 2073 (s), 2028 (s), 2013 (s), 1985 (s), 1973 [s ($\nu$CO, terminal)] cm$^{-1}$. MS (DEI, 70 eV): *m*/*z* (%) 516 (29) [M$^+$], 488 (100) [M$^+$ – CO], 460 (67) [M$^+$ – 2CO], 432 (86) [M$^+$ – 3CO], 404 (52) [M$^+$ – 4CO], 376 (84) [M$^+$ – 5CO], 248 (63) [M$^+$ – 6CO].

**[Fe$_2${SC[(CH$_2$)$_5$]SC[(CH$_2$)$_5$]S}(CO)$_6$] (3d):** $R_f$ = 0.57 (hexane). Yield 332.1 mg (0.615 mmol, 41%). $C_{18}H_{20}Fe_2O_6S_3$ (540.23): calcd. C 40.02, H 3.73, S 17.81; found C 40.04, H 3.90, S 17.59. $^1$H NMR (200 MHz, $CDCl_3$, 25 °C): $\delta$ = 1.84 (m, 8 H, CC$H_2$CH$_2$), 1.65 (m, 8 H, CCH$_2$C$H_2$), 1.47 and 1.33 (m, 4 H, CCH$_2$CH$_2$C$H_2$) ppm. $^{13}$C{$^1$H} NMR (100 MHz, $CDCl_3$): $\delta$ = 22.8 (CCH$_2$*C*H$_2$), 25.2 (CCH$_2$CH$_2$*C*H$_2$), 43.2 (C*C*H$_2$CH$_2$), 50.8 ($C_q$), 207.6 (*C*O) ppm. FT-IR (KBr disc): $\tilde{\nu}$ = 2072 (s), 2035 (vs), 2014 (s), 1985 [s ($\nu$CO, terminal)] cm$^{-1}$. MS (DEI, 70 eV): *m*/*z* (%) 540 (3) [M$^+$], 512 (34) [M$^+$ – CO], 484 (30) [M$^+$ – 2CO], 456 (44) [M$^+$ – 3CO], 428 (40) [M$^+$ – 4CO], 400 (64) [M$^+$ – 5CO], 372 (100) [M$^+$ – 6CO].

**[Fe$_t$SC(ad)SC(ad)S}(CO)$_6$] (3e):** $R_f$ = 0.6 (hexane). Yield 328.4 mg (0.51 mmol, 34%). $C_{26}H_{28}Fe_2O_6S_3$ (644.38): calcd. C 48.46, H 4.38, S 14.90; found C 48.18, H 4.37, S 14.39. $^1$H NMR (200 MHz, $CDCl_3$): $\delta$ = 1.41–1.69 (m, 16 H), 1.88 (s, 4 H), 2.52 (m, 4 H), 2.72 (m, 4 H) ppm. $^{13}$C{$^1$H} NMR (100 MHz, $CDCl_3$): $\delta$ = 26.7, 26.9 (4*C*H), 33.6, 34.4 (2 and 4 *C*H$_2$), 38.6 (4 *C*H), 41.6 (4 *C*H$_2$), 60.2 (2 $C_q$), 207.5 (*C*O) ppm. FT-IR (KBr disc): $\tilde{\nu}$ = 2070 (s), 2033 (s), 1994 (s), 1980 [s ($\nu$CO, terminal)] cm$^{-1}$. MS (DEI, 70 eV): *m*/*z* (%) 644 (2) [M$^+$], 616 (6) [M$^+$ – CO], 588 (4) [M$^+$ – 2CO], 560 (26) [M$^+$ – 3CO], 532 (28) [M$^+$ – 4CO], 504 (44) [M$^+$ – 5CO], 476 (100) [M$^+$ – 6CO].

**[Fe$_2${SC(CH$_2$)S}(CO)$_6$] (4a):**[4] $R_f$ = 0.52 (hexane). This product obtained by column chromatography was partially contaminated with **5**,[5] therefore the corresponding yield could not be determined exactly. Yield approx. 46.5 mg (approx. 0.13 mmol, 8.6%). $^1$H NMR (200 MHz, $CDCl_3$, 25 °C): $\delta$ = 4.60 (s, 2 H, C$H_2$) ppm.

**[Fe$_2${SC(CH$_3$)$_2$S}(CO)$_6$] (4b):** $R_f$ = 0.54 (hexane). Yield 85.7 mg (0.22 mmol, 14.8%). HR-MS (ESI) calcd. for $C_9H_6Fe_2O_6S_3$: 385.8305; found 385.8305. $^1$H NMR (200 MHz, $CDCl_3$, 25 °C): $\delta$ = 1.76 (s, 4 H, C$H_2$) ppm. $^{13}$C{$^1$H} NMR (100 MHz, $CDCl_3$): $\delta$ = 40.9 (*C*H$_3$), 83.4 ($C_q$), 208.6 (*C*O) ppm. FT-IR (KBr disc): $\tilde{\nu}$ = 2072 (s), 2025 (s), 2006 (s), 1983 (m), 1963 [m ($\nu$CO, terminal)] cm$^{-1}$. MS (DEI, 70 eV): *m*/*z* (%) 386 (26) [M$^+$], 358 (16) [M$^+$ – CO], 330 (20) [M$^+$ – 2CO], 302 (14) [M$^+$ – 3CO], 274 (24) [M$^+$ – 4CO], 246 (32) [M$^+$ – 5CO], 218 (74) [M$^+$ – 6CO], 176 (100) [$Fe_2S_2$].

**[Fe$_2${SC(CH$_2$CH$_3$)$_2$S}(CO)$_6$] (4c):** $R_f$ = 0.55 (hexane). Yield 40.4 mg (0.1 mmol, 6.5%). $^1$H NMR (200 MHz, $CDCl_3$, 25 °C): $\delta$ = 0.79 (t, $^3J$ = 7.4 Hz, 12 H, C$H_3$), 2.05 (q, $^3J$ = 7.4 Hz, 8 H, C$H_2$) ppm. $^{13}$C{$^1$H} NMR (100 MHz, $CDCl_3$, 25 °C): $\delta$ = 7.1 (*C*H$_3$), 40.6 (*C*H$_2$), 93.3 ($C_q$), 208.6 (*C*O) ppm. MS (DEI, 70 eV): *m*/*z* (%) 414 (100) [M$^+$], 386 (82) [M$^+$ – CO], 358 (61) [M$^+$ – 2CO], 330 (67) [M$^+$ – 3CO], 302 (37) [M$^+$ – 4CO], 274 (54) [M$^+$ – 5CO], 246 (21) [M$^+$ – 6CO].

**[Fe$_2${SC[(CH$_2$)$_5$]S}(CO)$_6$] (4d):** $R_f$ = 0.73 (hexane). Yield 56.9 mg (0.13 mmol, 8.9%). $C_{12}H_{10}Fe_2O_6S_2$ (426.02): calcd. C 33.83, H 2.37, S 15.05; found C 33.89, H 2.64, S 15.33. $^1$H NMR (200 MHz, $CDCl_3$, 25 °C): $\delta$ = 2.09 (m, 4 H, CC$H_2$CH$_2$), 1.43 (m, 4 H, CCH$_2$C$H_2$), 1.38 (m, 2 H, CCH$_2$CH$_2$C$H_2$) ppm. $^{13}$C{$^1$H} NMR (100 MHz, $CDCl_3$): $\delta$ = 22.0 (CCH$_2$*C*H$_2$), 26.1 (CCH$_2$CH$_2$*C*H$_2$), 49.8 (C*C*H$_2$CH$_2$), 89.9 ($C_q$), 208.6 (*C*O) ppm. FT-IR (KBr disc): $\tilde{\nu}$ = 2074 (s), 2032 (s), 2002 (s), 1969 [s ($\nu$CO, terminal)] cm$^{-1}$. MS (DEI, 70 eV): *m*/*z* (%) 426 (100) [M$^+$], 398 (82) [M$^+$ – CO], 370 (64) [M$^+$ – 2CO], 342 (47) [M$^+$ – 3CO], 314 (43) [M$^+$ – 4CO], 286 (25) [M$^+$ – 5CO], 258 (60) [M$^+$ – 6CO].

**[Fe$_2${SC(ad)S}(CO)$_6$] (4e):** $R_f$ = 0.62 (hexane). Yield 117.6 mg (0.25 mmol, 16.4%). $C_{16}H_{14}Fe_2O_6S_2$ (478.1): calcd. C 40.19, H 2.95, S 13.41; found C 40.21, H 2.92, S 13.18. $^1$H NMR (200 MHz, $CDCl_3$, 25 °C): $\delta$ = 2.57 (br. s, 2 H, 2C*H*), 1.87 and 1.56 (d, $^2J$ = 12.4 Hz, 8 H, 4C$H_2$), 1.77 (br. s, 2 H, 2C*H*), 1.67 (br. s, 2 H, C$H_2$) ppm. $^{13}$C{$^1$H} NMR (100 MHz, $CDCl_3$): $\delta$ = 27.6 (2*C*H), 31.9 (4 *C*H$_2$), 37.0 (*C*H$_2$), 49.1 (2 *C*H), 98.3 ($C_q$), 208.6 (CO) ppm. FT-IR (KBr disc): $\tilde{\nu}$ = 2070 (s), 2026 (s), 2000 (s), 1983 [s ($\nu$CO, terminal)] cm$^{-1}$. MS (DEI, 70 eV): *m*/*z* (%) 478 (54) [M$^+$], 450 (30) [M$^+$ – CO], 422 (24) [M$^+$ – 2CO], 394 (28) [M$^+$ – 3CO], 366 (47) [M$^+$ – 4CO], 338 (35) [M$^+$ – 5CO], 310 (100) [M$^+$ – 6CO].

**[Fe$_4$(μ-SCH$_2$SCH$_2$S-μ)(CO)$_9$(μ-CO)$_2$S] (6a):** Yield 31 mg (0.045 mmol, 3%). $^1$H NMR (200 MHz, $CDCl_3$, 25 °C): $\delta$ = 3.1 (m, AA′BB′ spin system, 4 H, 2C$H_2$) ppm. $^{13}$C{$^1$H} NMR (100 MHz, $CDCl_3$): $\delta$ = 26.8 (*C*H$_2$), 26.9 (*C*H$_2$), 203.5 and 206.8 (*C*O) ppm. FT-IR (KBr disc): $\tilde{\nu}$ = 2068 (s), 2034 (s), 1997 (s), 1975 [s ($\nu$CO, terminal)], 1898 [m ($\nu$($\mu^2$-CO)] cm$^{-1}$.

**[Fe$_4$(μ-SCMe$_2$SCMe$_2$S-μ)(CO)$_9$(μ-CO)$_2$S] (6b):** Yield 24.6 mg (0.033 mmol, 2.2%). $C_{17}H_{12}Fe_4O_{11}S_4$ (743.91): calcd. C 27.45, H 1.63, S 17.24; found C 27.53, H 2.15, S 16.90. $^1$H NMR (200 MHz, $CDCl_3$, 25 °C): $\delta$ = 1.6 (s, 6 H, C$H_3$), 1.87 (s, 6 H, C$H_3$) ppm. $^{13}$C{$^1$H} NMR (100 MHz, $CDCl_3$): $\delta$ = 34.1 and 35.0 (*C*H$_3$), 49.4 ($C_q$) ppm. FT-IR (ATR cuvette): $\tilde{\nu}$ = 2079 (w), 2056 (m), 2026 (m), 2009 (s), 1978 [s ($\nu$CO, terminal)], 1923, 1910 [$\nu$($\mu^2$-CO)] cm$^{-1}$. MS (DEI, 70 eV): *m*/*z* (%) 744 (0.1) [M$^+$], 716 (1) [M$^+$ – CO], 688 (1.2) [M$^+$ – 2CO], 660 (2.7) [M$^+$ – 3CO], 632 (0.4) [M$^+$ – 4CO], 604 (3.2)

 © 2007 Wiley-VCH Verlag GmbH & Co. KGaA, Weinheim 

[M⁺ – 5CO], 576 (4.4) [M⁺ – 6CO], 548 (3.7) [M⁺ – 7CO], 520 (100) [M⁺ – 8CO], 492 (5) [M⁺ – 9CO].

**[$Fe_4$(μ-$SCEt_2SCEt_2S$-μ)(CO)$_9$(μ-$CO)_2$S] (6c):** Yield 24 mg (0.03 mmol, 2%). $^1$H NMR (400 MHz, $CDCl_3$, 25 °C): $\delta$ = 0.95 (m, 12 H, C$H_3$), 1.73 (m, 4 H, C$H_2$), 1.87 and 2.21 (m, 4 H, C$H_2$) ppm. $^{13}$C{$^1$H} NMR (100 MHz, $CDCl_3$): $\delta$ = 8.9 and 9.7 (*C*$H_3$), 33.2 and 34.4 (*C*$H_2$), 57.7 ($C_q$) ppm. FT-IR (KBr disc): $\tilde{\nu}$ = 2084 (m), 2058 (s), 2015 (s), 1993 (s), 1969 [m (νCO, terminal)], 1924, 1902 [ν(μ²-CO)] cm$^{-1}$. MS (DEI, 70 eV): *m*/*z* (%) 800 (0.1) [M⁺], 772 (0.3) [M⁺ – CO], 744 (0.9) [M⁺ – 2CO], 716 (4.6) [M⁺ – 3CO], 688 (0.1) [M⁺ – 4CO], 660 (3) [M⁺ – 5CO], 632 (3.9) [M⁺ – 6CO], 604 (2.3) [M⁺ – 7CO], 576 (9.2) [M⁺ – 8CO], 548 (2.3) [M⁺ – 9CO], 520 (4.6) [M⁺ – 10CO], 492 (17.7) [M⁺ – 11CO].

**[$Fe_4$(μ-$SCR_2SCR_2S$-μ)(CO)$_9$(μ-$CO)_2$S] (6d) [R = 1/2($CH_2$)$_5$]:** Yield 28.4 mg (0.035 mmol, 2.3%). $C_{23}H_{20}Fe_4O_{11}S_4$ (824.04): calcd. C 33.52, H 2.45, S 15.56; found C 33.34, H 2.94, S 14.67. $^1$H NMR (400 MHz, $CDCl_3$, 25 °C): $\delta$ = 1.25 and 1.51 (m, 4 H, $CCH_2CH_2CH_2$), 1.66 (m, 8 H, $CCH_2CH_2$), 1.84 and 2.37 (m, 4 H, $CCH_2CH_2$), 1.84 and 1.89 (m, 4 H, $CCH_2CH_2$) ppm. $^{13}$C{$^1$H} NMR (100 MHz, $CDCl_3$): $\delta$ = 23.2 and 23.3 ($CCH_2CH_2$), 25.0 ($CCH_2CH_2CH_2$), 41.6 and 43.6 ($CCH_2CH_2$), 54.1 ($C_q$), 222.8 (*C*O) ppm. FT-IR (ATR cuvette): $\tilde{\nu}$ = 2077 (m), 2054 (m), 2028 (m), 2005 (s), 1969 [m (νCO, terminal)], 1913, 1897 [ν(μ²-CO)] cm$^{-1}$. MS (DEI, 70 eV): *m*/*z* (%) 824 (0.1) [M⁺], 796 (0.2) [M⁺ – CO], 768 (0.4) [M⁺ – 2CO], 740 (1) [M⁺ – 3CO], 712 (0.1) [M⁺ – 4CO], 684 (0.1) [M⁺ – 5CO], 656 (0.1) [M⁺ – 6CO], 628 (0.1) [M⁺ – 7CO], 600 (0.4) [M⁺ – 8CO], 572 (0.1) [M⁺ – 9CO], 544 (0.3) [M⁺ – 10CO], 516 (1) [M⁺ – 11CO].

**[$Fe_3$(CO)$_9$S(ad)] (7; ad = adamantyl):** Yield 7 mg (4.3%). $^1$H NMR (400 MHz, $CDCl_3$, 25 °C): $\delta$ = 2.00–2.40 (m, 14 H) ppm. $^{13}$C{$^1$H} NMR (100 MHz, $CDCl_3$): $\delta$ = 37.7, 37.6, 49.9, 56.8 (4CH and 5*C*$H_2$), 211.3 (*C*O) ppm; $C_q$ not observed. FT-IR (ATR cuvette): $\tilde{\nu}$ = 2071 (m), 2005 (s), 1978 (s), 1965 [m (νCO, terminal)] cm$^{-1}$. MS (DEI, 70 eV): *m*/*z* (%) 586 (12) [M⁺], 558 (13) [M⁺ – CO], 530 (5) [M⁺ – 2CO], 502 (30) [M⁺ – 3CO], 474 (46) [M⁺ – 4CO], 446 (57) [M⁺ – 5CO], 418 (98) [M⁺ – 6CO], 390 (100) [M⁺ – 7CO], 362 (65) [M⁺ – 8CO], 334 (92) [M⁺ – 9CO]

**Preparation of the Monocyanide Complex ($Et_4N$)[$Fe_2$(SDT)(CO)$_5$-(CN)] (8):** A solution of **3a** (100 mg, 0.25 mmol) in MeCN (15 mL) at 0 °C was treated with a solution of $Et_4NCN$ (80 mg, 0.50 mmol) in MeCN (15 mL). After warming the reaction mixture to room temperature, it was stirred for an additional 1.5 h. The solvent was then removed in vacuo and the residue washed thoroughly with diethyl ether and hexane. The washed residue was again evaporated to dryness to give a red solid. Single crystals suitable for X-ray diffraction analysis were obtained by diffusion of pentane into its MeCN solution. Yield 120 mg (90%). $^1$H NMR (200 MHz, $CD_3CN$): $\delta$ = 3.18 (br. s, 8 H, $CH_2CH_3$), 2.43 (br. s, 4 H, $SCH_2$), 1.10 (br. s, 12 H, $CH_2CH_3$) ppm. $^{13}$C{$^1$H} NMR (100 MHz, $CD_3CN$): $\delta$ = 8.0 ($CH_2CH_3$), 27.3 ($SCH_2$), 53.3 ($CH_2CH_3$), 150.7 (*C*N), 219.7 (*C*O) ppm. FT-IR (thf solution): $\tilde{\nu}$ = 2052 [s (νCN)], 2033 (s), 1981 (s), 1953 (m), 1921 [w (νCO, terminal)] cm$^{-1}$. MS (ESI pos., 70 eV): *m*/*z* (%) 130.2 (100) [M⁺, $C_8H_{20}N$]. MS (ESI neg., 70 eV): *m*/*z* (%) 401.9 (100) [M⁻, $C_8H_4Fe_2NO_5S_3$].

**Supporting Information** (see also the footnote on the first page of this article): Figures S1, S3 and S4 display the X-ray structures of compounds **4b**, **4d** and **4e**. The structure of **4c** is available as Figure S2. Figures S5 and S6 present the X-ray structures of **6c** and **6d**, respectively. Figure S7 shows the experimental and theoretical isotopic pattern of **8**⁻ (anion of **8**).

**X-ray Structure Determination of 3b, 3c, 3d, 3e, 4b, 4c, 4d, 4e, 6b, 6c, 6d, 7 and 8:**[21] Intensity data were collected with a Nonius Kappa CCD diffractometer using graphite-monochromated Mo-$K_\alpha$ radiation. Data were corrected for Lorentz polarisation, but not for absorption effects.[22,23] Crystallographic data as well as structure solution and refinement details are summarised in Tables 1 and 2.

The structures were solved by direct methods (SHELXS[24]) and refined by full-matrix least-squares techniques against $F_o^2$ (SHELXL-97[25]). The hydrogen atoms were included at calculated

Table 1. Crystal data and refinement details for the X-ray structure determinations.

| | **3b** | **3c** | **3d** | **3e** | **4b** | **4c** | **4d** |
|---|---|---|---|---|---|---|---|
| Formula | $C_{12}H_{12}Fe_2O_6S_3$ | $C_{16}H_{20}Fe_2O_6S_3$ | $C_{18}H_{20}Fe_2O_6S_3$ | $C_{26}H_{28}Fe_2O_6S_3$ | $C_9H_6Fe_2O_6S_2$ | $C_{11}H_{10}Fe_2O_6S_2$ | $C_{12}H_{10}Fe_2O_6S_2$ |
| *Fw* [g mol$^{-1}$] | 460.10 | 516.20 | 540.22 | 644.36 | 385.96 | 414.01 | 426.02 |
| *T* [°C] | –90(2) | –90(2) | –90(2) | –90(2) | –90(2) | –90(2) | –90(2) |
| Crystal system | triclinic | monoclinic | triclinic | monoclinic | triclinic | monoclinic | triclinic |
| Space group | $P\bar{1}$ | $P2_1/c$ | $P\bar{1}$ | $C2/c$ | $P\bar{1}$ | $C2/c$ | $P\bar{1}$ |
| *a* [Å] | 8.1108(3) | 8.9271(2) | 9.7862(9) | 30.2126(11) | 8.6954(3) | 31.268(2) | 11.6020(4) |
| *b* [Å] | 10.3222(4) | 11.0165(3) | 14.9104(18) | 10.0703(4) | 11.5723(4) | 18.3625(13) | 12.7499(5) |
| *c* [Å] | 11.1169(4) | 21.7868(4) | 16.824(2) | 47.6223(17) | 14.9455(5) | 43.754(4) | 17.2305(4) |
| *α* [°] | 76.155(2) | 90 | 64.218(5) | 90 | 110.606(2) | 90 | 105.944(2) |
| *β* [°] | 81.608(2) | 96.496(1) | 83.966(8) | 100.493(1) | 94.740(2) | 95.507(3) | 101.834(2) |
| *γ* [°] | 82.637(2) | 90 | 81.145(8) | 90 | 97.143(2) | 90 | 93.938(2) |
| *V* [Å$^3$] | 889.78(6) | 2128.88(8) | 2182.1(4) | 14246.8(9) | 1383.77(8) | 25006(3) | 2377.41(14) |
| *Z* | 2 | 4 | 4 | 20 | 4 | 64 | 6 |
| *ρ* [g cm$^{-3}$] | 1.717 | 1.611 | 1.644 | 1.502 | 1.853 | 1.760 | 1.785 |
| *μ* [cm$^{-1}$] | 20.04 | 16.85 | 16.48 | 12.76 | 24.13 | 21.43 | 21.16 |
| Measured data | 6370 | 14854 | 12537 | 32291 | 9476 | 35222 | 16087 |
| Data with $I > 2\sigma(I)$ | 3486 | 4005 | 5206 | 9270 | 3803 | 10112 | 7799 |
| Unique data | 4037 | 4866 | 9001 | 14543 | 6204 | 21331 | 10540 |
| $wR_2$ (all data, on $F^2$)[a] | 0.1069 | 0.0710 | 0.1611 | 0.2018 | 0.2849 | | 0.0884 |
| $R_1$ [$I > 2\sigma(I)$][a] | 0.0411 | 0.0279 | 0.0650 | 0.0709 | 0.0834 | | 0.0355 |
| *s*[b] | 1.012 | 1.010 | 1.032 | 1.024 | 1.050 | | 0.980 |
| Resid. dens. [e Å$^{-3}$] | 1.577/–1.256 | 0.279/–0.400 | 0.530/–0.774 | 0.970/–0.572 | 1.839/–0.746 | | 0.569/–0.536 |
| Absorption correction | none | none | none | none | none | none | none |

[a] $R_1 = (\Sigma||F_o| - |F_c||)/\Sigma|F_o||$, $wR_2 = \{\Sigma[w(F_o^2 - F_c^2)^2]/\Sigma[w(F_o^2)^2]\}^{1/2}$ with $w^{-1} = \sigma^2(F_o^2) + (aP)^2$. [b] $s = \{\Sigma[w(F_o^2 - F_c^2)^2]/(N_o - N_p)\}^{1/2}$.

 © 2007 Wiley-VCH Verlag GmbH & Co. KGaA, Weinheim 

Table 2. Crystal data and refinement details for the X-ray structure determinations.

| | **4e** | **6b** | **6c** | **6d** | **7** | **8** |
|---|---|---|---|---|---|---|
| Formula | $C_{16}H_{14}Fe_2O_6S_2$ | $C_{17}H_{12}Fe_4O_{11}S_4$ | $C_{21}H_{20}Fe_4O_{11}S_4$ | $C_{23}H_{20}Fe_4O_{11}S_4$ | $C_{19}H_{14}Fe_3O_9S$ | $C_8H_4Fe_2NO_5S_3{\cdot}C_8H_{20}N$ |
| *Fw* [g mol$^{-1}$] | 478.09 | 743.91 | 800.01 | 824.03 | 585.91 | 532.25 |
| *T* [°C] | –90(2) | –90(2) | –90(2) | –90(2) | –90(2) | –90(2) |
| Crystal system | monoclinic | triclinic | triclinic | triclinic | monoclinic | monoclinic |
| Space group | $P2_1/n$ | $P\bar{1}$ | $P\bar{1}$ | $P\bar{1}$ | $P2/c$ | $P2_1$ |
| *a* [Å] | 9.3431(3) | 9.9870(6) | 9.8115(5) | 11.3477(13) | 13.1719(5) | 7.4131(6) |
| *b* [Å] | 14.0459(3) | 11.4368(6) | 11.7948(5) | 11.9251(17) | 7.9576(2) | 12.6401(13) |
| *c* [Å] | 14.5478(5) | 12.9150(8) | 13.0075(6) | 12.4537(18) | 20.7565(8) | 12.1092(10) |
| *α* [°] | 90 | 73.088(3) | 105.078(3) | 83.751(6) | 90 | 90 |
| *β* [°] | 106.955(2) | 82.212(3) | 94.819(2) | 73.305(8) | 99.768(2) | 101.290(6) |
| *γ* [°] | 90 | 64.417(3) | 93.969(3) | 66.080(8) | 90 | 90 |
| *V* [Å$^3$] | 1826.16(9) | 1272.90(13) | 1441.82(12) | 1475.5(3) | 2144.09(13) | 1112.70(17) |
| *Z* | 4 | 2 | 2 | 2 | 4 | 2 |
| *ρ* [g cm$^{-3}$] | 1.739 | 1.941 | 1.843 | 1.855 | 1.815 | 1.589 |
| *μ* [cm$^{-1}$] | 18.47 | 26.16 | 23.16 | 22.67 | 21.49 | 16.13 |
| Measured data | 12112 | 9105 | 9971 | 9388 | 14777 | 7420 |
| Data with $I > 2\sigma(I)$ | 3526 | 3897 | 4765 | 4034 | 3853 | 3212 |
| Unique data | 4151 | 5765 | 6538 | 6474 | 4897 | 4771 |
| $wR_2$ (all data, on $F^2$)[a] | 0.0679 | 0.1356 | 0.1015 | 0.1831 | 0.1613 | 0.1014 |
| $R_1$ [$I > 2\sigma(I)$][a] | 0.0265 | 0.0515 | 0.0433 | 0.0658 | 0.0635 | 0.0517 |
| *s*[b] | 1.016 | 0.986 | 1.027 | 1.054 | 1.136 | 0.955 |
| Resid. dens. [e Å$^{-3}$] | 0.343/–0.525 | 1.139/–0.723 | 0.681/–0.531 | 0.830/–1.129 | 1.431/–0.696 | 0.442/–0.471 |
| Flack parameter | – | – | – | – | – | –0.01(2) |
| Absorption correction | none | none | none | none | none | none |

[a] $R_1 = (\Sigma||F_o| - |F_c||/\Sigma|F_o|$, $wR_2 = \{\Sigma[w(F_o^2 - F_c^2)^2]/\Sigma[w(F_o^2)^2]\}^{1/2}$ with $w^{-1} = \sigma^2(F_o^2) + (aP)^2$. [b] $s = \{\Sigma[w(F_o^2 - F_c^2)^2]/(N_o - N_p)\}^{1/2}$.

positions with fixed thermal parameters. All non-hydrogen atoms except for the disordered part of molecules were refined anisotropically.[25] The quality of the data of compound **4c** was poor therefore we will only publish the conformation of the molecule and the crystallographic data. The data have no been deposited in the Cambridge Crystallographic Data Centre.

## Acknowledgments

Financial support for this work was provided by the Freistaat Thüringen (Landesgraduiertenstipendium for J. W.). We are grateful to Ulf-Peter Apfel for experimental assistance.

[1] a) S. M. Aucott, H. L. Milton, S. D. Robertson, A. M. Z. Slawin, G. B. Walker, J. D. Woollins, *Chem. Eur. J.* **2004**, *10*, 1666–1676; b) S. M. Aucott, P. Kilian, S. D. Robertson, A. M. Z. Slawin, J. D. Woollins, *Chem. Eur. J.* **2006**, *12*, 895–902; c) S. M. Aucott, P. Kilian, H. L. Milton, S. D. Robertson, A. M. Z. Slawin, J. D. Woollins, *Inorg. Chem.* **2005**, *44*, 2710–2718; d) A. Ishii, M. Saito, M. Murata, J. Nakayama, *Eur. J. Org. Chem.* **2002**, 979–982; e) A. Ishii, T. Kawai, M. Noji, J. Nakayama, *Tetrahedron Lett.* **2005**, *61*, 6693–6699; f) A. Ishii, M. Murata, H. Oshida, K. Matsumoto, J. Nakayama, *Eur. J. Inorg. Chem.* **2003**, 3716–3721.

[2] W. Weigand, S. Bräutigam, G. Mloston, *Coord. Chem. Rev.* **2003**, *245*, 167–175 and references cited therein.

[3] a) H. Petzold, S. Bräutigam, J. Windhager, W. Weigand, A. Majchrzak, G. Mloston, in *11th International Symposium on Inorganic Ring Systems* (Eds.: R. S. Laitinen, R. Oilunkaniemi), *Reports Series in Chemistry* **2006**, Oulu University Press, vol. 70, p. 62 (ISBN 9514281535); b) J. Windhager, M. Rudolph, S. Bräutigam, H. Görls, W. Weigand, *Eur. J. Inorg. Chem.* **2007**, 2748–2760; c) L. C. Song, Z. Y. Yang, Y. J. Hua, H. T. Wang, Y. Liu, Q.-M. Hu, *Organometallics* **2007**, *26*, 2106–2110; d) H. Alper, A. S. K. Chan, *Inorg. Chem.* **1974**, *13*, 232–263.

[4] a) A. Shaver, P. J. Fitzpatrick, K. Steliou, J. S. Butler, *J. Am. Chem. Soc.* **1979**, *101*, 1313–1315; b) C. Alvarez-Toledano, E. Delgardo, B. Donnadieu, E. Hernandez, G. Martin, F. Zamora, *Inorg. Chim. Acta* **2003**, *351*, 119–122.

[5] R. Seidel, B. Schautz, G. Henkel, *Angew. Chem. Int. Ed. Engl.* **1996**, *35*, 1710–1714.

[6] a) Y. Nicolet, A. L. de Lacey, X. Vernède, V. M. Fernandez, E. C. Hatchikian, J. C. Fontecilla-Camps, *J. Am. Chem. Soc.* **2001**, *123*, 1596–1601; b) Y. Nicolet, B. J. Lemon, J. C. Fontecilla-Camps, J. W. Peters, *Trends Biochem. Sci.* **2000**, *25*, 138–143; c) Y. Nicolet, C. Piras, P. Legrand, C. E. Hatchikian, J. C. Fontecilla-Camps, *Structure* **1999**, *7*, 13–23.

[7] a) X. Zhao, I. P. Georgakaki, M. L. Miller, J. C. Yarbrough, M. Y. Darensbourg, *J. Am. Chem. Soc.* **2001**, *123*, 9710–9711; b) F. Gloaguen, J. D. Lawrence, M. Schmidt, S. R. Wilson, T. B. Rauchfuss, *J. Am. Chem. Soc.* **2001**, *123*, 12518–12527; c) E. J. Lyon, I. P. Georgakaki, J. H. Reibenspies, M. Y. Darensbourg, *J. Am. Chem. Soc.* **2001**, *123*, 3268 –3278; d) M. Razavet, S. C. Davies, D. L. Hughes, J. E. Barclay, D. J. Evans, S. A. Fairhurst, X. Liu, C. J. Pickett, *Dalton Trans.* **2003**, 586 –595; e) J. D. Lawrence, H. Li, T. B. Rauchfuss, M. Benard, M.-M. Rohmer, *Angew. Chem. Int. Ed.* **2001**, *40*, 1768–1771; f) H. Li, T. B. Rauchfuss, *J. Am. Chem. Soc.* **2002**, *124*, 726–727; g) S. Ott, M. Kritikos, B. Åkermark, L. Sun, *Angew. Chem. Int. Ed.* **2003**, *42*, 3285–3288; h) C. Tard, X. Liu, S. K. Ibrahim, M. Bruschi, L. De Gioia, S. C. Davies, X. Yang, L.-S. Wang, G. Sawers, C. J. Pickett, *Nature* **2005**, *433*, 610–613; i) L.-C. Song, Z.-Y. Yang, H.-Z. Bian, Q.-M. Hu, *Organometallics* **2004**, *23*, 3082–3084; j) D. Seyferth, R. S. Henderson, L.-C. Song, *Organometallics* **1982**, *1*, 125–133; k) D. Seyferth, R. S. Henderson, L.-C. Song, *J. Organomet. Chem.* **1980**, *192*, C1; l) L.-C. Song, Z.-Y. Yang, H.-Z. Bian, Y. Liu, H.-T. Wang, X.-F. Liu, Q.-M. Hu, *Organometallics* **2005**, *24*, 6126–6135; m) M. Y. Darensbourg, E. J. Lyon, J. J. Smee, *Coord. Chem. Rev.* **2000**, *206–207*, 533–561; n) R. C. Linck, T. B. Rauchfuss, in *Bioorganometallics* (Ed.: D. Jaouen), Wiley-VCH, **2006**, 403–435; o) X. Zhang, C. Y. Chiang, M. L. Miller, M. V. Rampersad, M. Y. Darensbourg, *J. Am. Chem. Soc.* **2003**, *125*, 518–524; p) J. D.

 © 2007 Wiley-VCH Verlag GmbH & Co. KGaA, Weinheim 

Lawrence, H. Li, T. B. Rauchfuss, *Chem. Commun.* **2001**, 1482–1483; q) L. C. Song, J. Gao, H. T. Wang, Y. J. Hua, H. T. Fan, X. G. Zhang, Q. M. Hu, *Organometallics* **2006**, *25*, 5724–5729.
[8] a) , B. I. Kolobkov, A. I. Nekhaev, G. G. Aleksandrov, M. T. Tashev, Kh. B. Dustov, N. A. Parpiev, *Koord. Khim. Koord. Khim.* **1988**, *14*, 558–562; b) B. I. Kolobkov, A. I. Nekhaev, G. G. Aleksandrov, M. T. Tashev, Kh. B. Dustov, A. Ya. Sideridu, A. Ya. Seriya, *Khimicheskaya* **1987**, *4*, 953–954; c) A. Winter, L. Zsolnai, G. Huttner, *Z. Naturforsch., Teil B* **1982**, *37*, 1430–1436.
[9] H. Heimgartner, G. Mloston, J. Romanski, *Adamantanethione. Electronic Encyclopedia of Reagents for Organic Synthesis* (Ed.: L. A. Paquette), Article – RN 00504, John Wiley & Sons, New York, **2005**.
[10] G. Rindorf, L. Carlsen, *Acta Crystallogr., Sect. B* **1979**, *35*, 1179–1182.
[11] K. Eichkorn, O. Treutler, H. Oehm, M. Haeser, R. Ahlrichs, *Chem. Phys. Lett.* **1995**, *242*, 652–660.
[12] O. Treutler, R. Ahlrichs, *J. Chem. Phys.* **1995**, *102*, 346–354.
[13] K. Eichkorn, F. Weigend, O. Treutler, R. Ahlrichs, *Theor. Chem. Acc.* **1997**, *97*, 119–124.
[14] M. J. Frisch, G. W. Trucks, H. B. Schlegel, G. E. Scuseria, M. A. Robb, J. R. Cheeseman, J. A. Montgomery Jr, T. Vreven, K. N. Kudin, J. C. Burant, J. M. Millam, S. S. Iyengar, J. Tomasi, V. Barone, B. Mennucci, M. Cossi, G. Scalmani, N. Rega, G. A. Petersson, H. Nakatsuji, M. Hada, M. Ehara, K. Toyota, R. Fukuda, J. Hasegawa, M. Ishida, T. Nakajima, Y. Honda, O. Kitao, H. Nakai, M. Klene, X. Li, J. E. Knox, H. P. Hratchian, J. B. Cross, C. Adamo, J. Jaramillo, R. Gomperts, R. E. Stratmann, O. Yazyev, A. J. Austin, R. Cammi, C. Pomelli, J. W. Ochterski, P. Y. Ayala, K. Morokuma, G. A. Voth, P. Salvador, J. J. Dannenberg, V. G. Zakrzewski, S. Dapprich, A. D. Daniels, M. C. Strain, O. Farkas, D. K. Malick, A. D. Rabuck, K. Raghavachari, J. B. Foresman, J. V. Ortiz, Q. Cui, A. G. Baboul, S. Clifford, J. Cioslowski, B. B. Stefanov, G. Liu, A. Liashenko, P. Piskorz, I. Komaromi, R. L. Martin, D. J. Fox, T. Keith, M. A. Al-Laham, C. Y. Peng, A. Nanayakkara, M. Challacombe, P. M. W. Gill, B. Johnson, W. Chen, M. W. Wong, C. Gonzalez, J. A. Pople, *Gaussian 03*, Gaussian, Inc., Pittsburgh PA, **2003**.
[15] R. Heinzmann, R. Ahlrichs, *Theor. Chim. Acta* **1976**, *42*, 33–45.
[16] R. W. Rudolph, *Acc. Chem. Res.* **1976**, *9*, 446.
[17] D. M. P. Mingos, *Acc. Chem. Res.* **1984**, *17*, 311.
[18] F. Asinger, M. Thiel, G. Lipfert, *Justus Liebigs Ann. Chem.* **1959**, *627*, 195–212.
[19] H. Petzold, Diplomarbeit, FSU Jena, **2003**.
[20] G. Mloston, J. Romanski, H. Heimgartner, *Pol. J. Chem.* **1996**, *70*, 437–445.
[21] CCDC-640951 (for **3b**), -640952 (for **3c**), -640953 (for **3d**), -640954 (for **3e**), -640955 (for **4b**), -640956 (for **4d**), -640957 (for **4e**), -640958 (for **6b**), -640959 (for **6c**), -640960 (for **6d**), -640961 (for **7**) and -640962 (for **8**) contain the supplementary crystallographic data excluding structure factors. These data can be obtained free of charge from The Cambridge Crystallographic Data Centre via www.ccdc.cam.ac.uk/data_request/cif.
[22] *COLLECT*, Data Collection Software, Nonius B. V., Netherlands, **1998**.
[23] Z. Otwinowski, W. Minor, *Processing of X-ray Diffraction Data Collected in Oscillation Mode*, in *Methods in Enzymology*, vol. 276, Macromolecular Crystallography, Part A (Eds.: C. W. Carter, R. M. Sweet), Academic Press, New York, **1997**, pp. 307–326.
[24] G. M. Sheldrick, *Acta Crystallogr., Sect. A* **1990**, *46*, 467–473.
[25] G. M. Sheldrick, *SHELXL-97 (Release 97–2)*, University of Göttingen, Germany, **1997**.

Received: April 27, 2007
Published Online: August 10, 2007

 © 2007 Wiley-VCH Verlag GmbH & Co. KGaA, Weinheim 

DOI: 10.1002/ejic.200601236

# A New Pentadentate Ligand Forms Both a Di- and a Mononuclear $Mn^{II}$ Complex: Electrochemical, Spectroscopic and Superoxide Dismutase Activity Studies

**Federico Cisnetti,[a,b] Anne-Sophie Lefèvre,[a,b] Régis Guillot,[b,c] François Lambert,[a,b] Guillaume Blain,[b,c] Elodie Anxolabéhère-Mallart,[b,d] and Clotilde Policar*[a,b]**

**Keywords:** Manganese(II) / Enzyme models / SOD mimic / N,O ligands / Bioinorganic chemistry

The X-ray crystal structure of the dinuclear complex [**1**$(PF_6)_2$] derived from a new ligand bearing both imidazole and phenolato moieties, namely *N*-(2-hydroxybenzyl)-*N*,*N*′-bis[2-(*N*-methylimidazolyl)methyl]ethane-1,2-diamine (LH), is described and its properties in organic solvent ($CH_3CN$) investigated (EPR, electrochemistry). [**1**$(PF_6)_2$] is shown to be a mononuclear $Mn^{II}$ species in aqueous solution and displays an efficient SOD-like activity, as measured by the McCord–Fridovich assay performed both in conventional phosphate buffer and in a noncoordinating buffer (PIPES).
(© Wiley-VCH Verlag GmbH & Co. KGaA, 69451 Weinheim, Germany, 2007)

## Introduction

Superoxide is known to be a toxic reactive oxygen species (ROS) involved in oxidative stress[1–4] and is considered to be responsible for several pathologic situations. Under normal conditions, its concentration is kept low (8–40 pM)[5,6] by metalloenzymes, known as superoxide dismutases (SODs), that catalyze its dismutation. As the therapeutic use of purified enzymes has major drawbacks,[3] different low molecular weight complexes have been synthesized for this purpose using either copper, iron, manganese, or cobalt ions. As Mn derivatives do not lead to Fenton chemistry, special interest has been devoted to Mn complexes (oxidation states II, III, or IV) as antisuperoxide agents for possible therapeutic use.[2–4] Free $Mn^{II}$[7–9] or Mn coordinated to salen derivatives,[8,10–12] cyclic polyamines,[3,13–19] tri- or dipodal ligands,[20–28] 1,2-ethanediamine-based ligands,[29–32] desferrioxamine derivatives[13,33,34] polyaminocarboxylato[35–37] or polycarboxylato ligands,[38] peptides,[39–41] as well as $Mn^{III}$ porphyrins,[42–47] or dinuclear biliverdin manganese complexes[48] have been reported to react with superoxide either as a true SOD mimetic or as a scavenger.

One of the goals of our research is the synthesis of bioactive complexes of therapeutic interest in the case of oxidative stress.[2–4] In the past few years we have synthesized a series of Mn complexes containing tripodal amines as tetradentate ligands that show an SOD-like activity, according to the results of the indirect McCord–Fridovich assay[24,27,28] and pulsed radiolysis experiments.[26,27] These complexes were designed as bio-inspired functional SOD mimics bearing in mind that the active site of Mn-based SODs has a trigonal-bipyramidal $N_3O_2$ core with three histidines, a monodentate aspartate, and an aqua or hydroxido ligand.[49]

Pentadentate ligands based on a 1,2-ethanediamine moiety are interesting alternatives to the previous tetradentate N-tripod series because they offer a larger number of possible variations.[50–52] We report here the synthesis of a complex with a new pentadentate ligand L [LH = *N*-(2-hydroxybenzyl)-*N*,*N*′-bis[2-(*N*-methylimidazolyl)methyl]ethane-1,2-diamine], which contains a 1,2-ethanediamine backbone bearing one phenol (mimicking the monodentate carboxylate present at the Mn-SOD active site) and two 1-methylimidazole groups (mimicking the histidine side-chains) as coordinating groups (Scheme 1). We describe the structure and solution characterization (EPR and UV/Vis spectroscopy, electrochemistry) of the dinuclear complex [(L)MnMn(L)]$(PF_6)_2$ [**1**$(PF_6)_2$] in organic solution and show that in aqueous solution this complex is in the monometallic form $[(L)Mn]^+$ (EPR, cyclic voltammetry). The SOD-like activity of the $[(L)Mn]^+$ species has been measured in aqueous solution using the conventional McCord–

[a] Equipe de Chimie Biorganique et Bioinorganique, Institut de Chimie Moléculaire et des Matériaux d'Orsay, Univ. Paris-Sud, UMR 8182,
91405 Orsay, France
E-mail: cpolicar@icmo.u-psud.fr
[b] Institut de Chimie Moléculaire et des Matériaux d'Orsay, CNRS, UMR 8182,
91405 Orsay, France
[c] Institut de Chimie Moléculaire et des Matériaux d'Orsay, Univ. Paris-Sud, UMR 8182,
91405 Orsay, France
[d] Equipe de Chimie Inorganique, Institut de Chimie Moléculaire et des Matériaux d'Orsay, Univ. Paris-Sud, UMR 8182,
91405 Orsay, France
Supporting information for this article is available on the WWW under http://www.eurjic.org or from the author.

 InterScience © 2007 Wiley-VCH Verlag GmbH & Co. KGaA, Weinheim 

Fridovich test under noncoordinating conditions. The good activity found is consistent with the redox potential of the $[(L)Mn]^+$ species measured by CV.

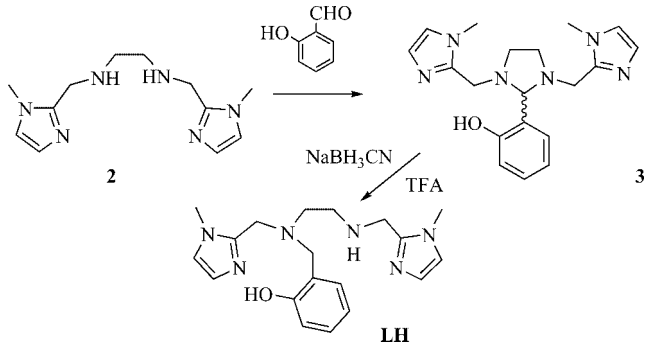


Scheme 1. Synthetic route to LH.

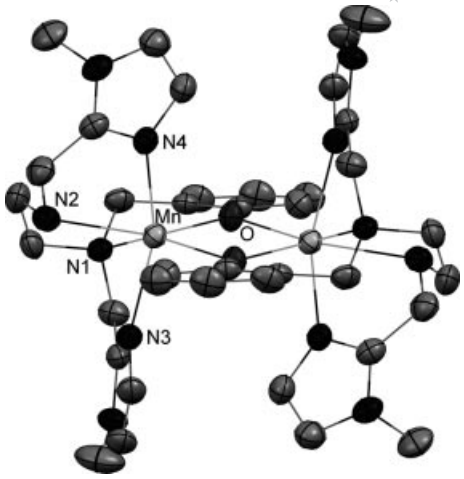


Figure 1. Ellipsoid plot of the centrosymmetric cationic moiety **1**, produced with Mercury 1.4.2.[56] Ellipsoids are drawn at 50% probability level. $PF_6^-$ and H atoms have been omitted for clarity.

## Results and Discussion

The synthesis of LH is straightforward. *N*,*N*′-Bis[2-(*N*-methylimidazolyl)methyl]ethane-1,2-diamine (**2**) was obtained by a conventional two-step reductive amination procedure starting from 1-methyl-2-imidazolecarboxaldehyde[53] and 1,2-ethanediamine, as published elsewhere.[54] The dissymmetric pentadentate ligand containing a phenolic group was then obtained by treating **2** with salicylaldehyde to obtain the aminal **3** (Scheme 1), which was reductively opened with $NaBH_3CN$ in the presence of an acid.[55] The whole synthesis proceeded with high yields. The reaction of crude LH with $MnBr_2$ in warm methanolic solution led to the formation of a $Mn^{II}$ complex. Crystals suitable for X-ray diffraction were grown by cooling this solution to room temperature under argon in the presence of hexafluorophosphate anion.

Table 1. Selected bond distances [Å] and angles [°] in the cationic complex **1**. The uncertainties correspond to 2σ (σ is given in the cif file).

| | | | | | |
|---|---|---|---|---|---|
| N4–Mn | 2.205(8) | O–Mn–O | 79.2(2) | O–Mn–N2 | 128.5(2) |
| N2–Mn | 2.420(8) | O–Mn–N4 | 94.2(3) | N1–Mn–N2 | 76.8(3) |
| N1–Mn | 2.354(8) | N4–Mn–N2 | 71.0(3) | N4–Mn–N1 | 113.7(3) |
| O–Mn | 2.111(6) | N1–Mn–O | 83.1(1) | N3–Mn–O | 109.9(3) |
| O′–Mn | 2.172(6) | N1–Mn–N3 | 72.8(2) | N3–Mn–N2 | 86.0(3) |
| N3–Mn | 2.226(8) | N3–Mn–O | 89.0(2) | N4–Mn–O | 97.1(3) |

### Description of the Structure

The X-ray crystal structure of this complex revealed it to be dinuclear with the formula $[(L)MnMn(L)](PF_6)_2$ [**1**$(PF_6)_2$]. A view of cation **1** is presented in Figure 1. This cation is dinuclear and centrosymmetric with a central di-μ-phenolato $Mn_2O_2$ diamond core. Selected bond lengths and angles are reported in Table 1.

Each $Mn^{II}$ ion is hexacoordinate, with four nitrogen atoms of the anionic form $L^-$ of the ligand and two oxygen atoms from the phenolato groups, the first one from the same ligand and the other one from the ligand chelating the second $Mn^{II}$ ion. The Mn environment departs from that of a regular octahedron (see Table 1). The longest coordination bond is that to the secondary amine N2, and the N2–Mn–O angle is much larger than the ideal value for an octahedron. These distances and deformations are similar to those reported for similar $Mn^{II}$ dinuclear compounds,[50,51] in particular to the dinuclear phenolate-bridged dication $[(mL')Mn^{II}Mn^{II}(mL')]^{2+}$ [mL′H = *N*-(2-hydroxybenzyl)-*N*′-methyl-*N*,*N*′-bis(2-pyridylmethyl)-ethane-1,2-diamine].[51] Such a dinuclear structure in which manganese atoms show a distorted octahedral geometry is in line with the fact that $Mn^{II}$ complexes, due to their half-filled $d^5$ shell, have no electronic coordination preference.[57]

### EPR Spectroscopy

The X-band EPR spectrum of a 1.1 mM acetonitrile solution of **1**$(PF_6)_2$ in the presence of 0.1 M tetrabutylammonium perchlorate was recorded at 7 K in both the perpendicular and parallel modes. The spectrum recorded in the perpendicular mode exhibits features extending from 0 to 800 mT (Figure 2), which arise from the superimposition of the signal of the five paramagnetic spin states $S$= 1 to 5 and is characteristic of dinuclear $Mn^{II}$ complexes.[51,52,58–63] The band at around 260 mT (B) shows a nice hyperfine structure with a field separation between two lines of about 41 G (see insert Figure 2), which is typical of dinuclear $Mn^{II}Mn^{II}$ complexes. Increasing the temperature induced only slight modifications in the spectral profile [the band at around 204 mT (A) and the intensity of the signal at 330 mT (C)]. Unlike previous observations with a dinuclear bis-μ-phenolato $Mn^{II}Mn^{II}$ complex with a $J$-value of $-1.5\ cm^{-1}$,[50] the intensities do not reach a maximum but decrease on increasing the temperature from 7 to 30 K (see Figure 2). This thermal behavior is consistent with the very

 © 2007 Wiley-VCH Verlag GmbH & Co. KGaA, Weinheim 

weak *J*-value estimated from the measurement of the magnetic susceptibility as a function of temperature (see Experimental Section).

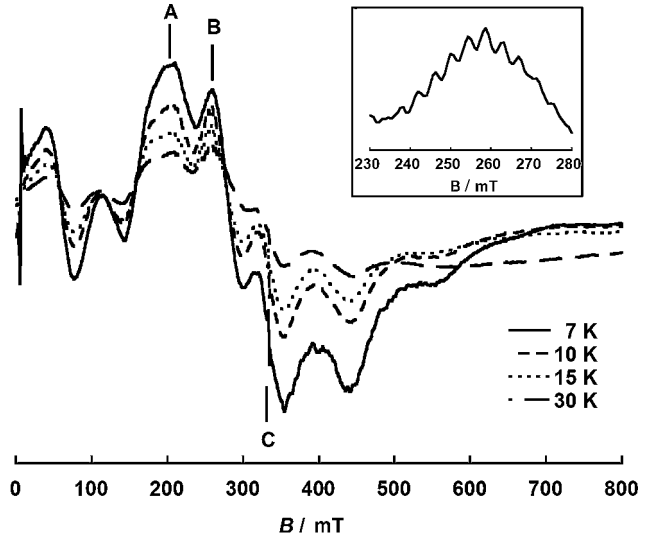


Figure 2. X-band EPR spectrum of $\mathbf{1}(PF_6)_2$ (1.1 mM in $CH_3CN$ containing 0.1 M tetrabutylammonium perchlorate) at 7 K. Microwave frequency: 9.63 GHz; microwave power: 2 mW; modulation amplitude: 0.5 mT; modulation frequency: 100 kHz; gain: 40 dB.

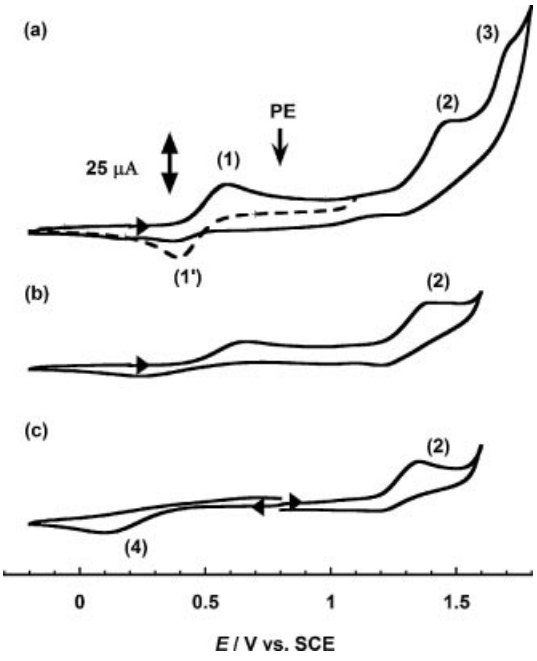


Figure 3. Cyclic voltammograms of $\mathbf{1}(PF_6)_2$ (1.1 mM in $CH_3CN$ with 0.1 M tetrabutylammonium perchlorate) under argon (v = 0.1 $V s^{-1}$; working electrode: glassy carbon; counter electrode: Pt wire; reference electrode: $Ag/AgClO_4$) at 20 (a) –25 (b), and –25 °C after electrolysis at $E$ = +0.8 V vs. SCE (c). PE = potential of the preparative electrolysis.

### Electrochemical Access to $Mn^{III}$

The cyclic voltammogram of a 1.1 mM acetonitrile solution of $\mathbf{1}(PF_6)_2$ is shown in Figure 3. The CV trace shows a well-defined anodic wave (wave 1 in Figure 3a) at $E_p^a$ = 0.58 V vs. SCE and a well-defined cathodic wave on the reverse scan at $E_p^c$ = 0.39 V vs. SCE (wave 1′). The difference between these two values ($\Delta E_p = E_p^a - E_p^c$) of 190 mV is indicative of a slow electron transfer. A similar behavior has previously been reported for related dinuclear $Mn^{II}Mn^{II}$ complexes with pyridine instead of imidazole moieties.[50] Controlled potential coulometry performed at +0.8 V vs. SCE indicated a one electron per Mn process for the first oxidation. Thus, the first anodic wave (1/1′; $E_{1/2}$ = 0.485 V vs. SCE)[64] can be attributed to a two-electron $Mn^{II}Mn^{II} \rightarrow Mn^{III}Mn^{III}$ process. This oxidation occurs at lower potential than that reported for the pyridine-containing ligand mL′[51] as the imidazole group has a higher electron-donating effect than pyridine, which leads to greater stabilization of the $Mn^{III}$ oxidation state.

Two other anodic peaks (labeled 2 and 3 in Figure 3, a) are observed at $E_p^a$ = 1.4 and 1.7 V vs. SCE respectively. These second and third oxidation processes are tentatively attributed to $Mn^{III}$ to $Mn^{IV}$ and phenolato oxidation processes.[50,65]

In an effort to determine the exact nature of the resulting $Mn^{III}$ species, a controlled potential electrolysis was performed at +0.8 V vs. SCE at –25 °C. Aliquots of the electrolyzed solution were collected during the course of the electrolysis and their UV/Vis absorption (Figure 4) and EPR spectra recorded. Figure 3 shows the cyclic voltammograms recorded at –25 °C before (Figure 3, b) and after (Figure 3, c) complete electrolysis at +0.8 V vs. SCE. After electrolysis one anodic process was detected at $E_p^a$ = +1.35 V vs. SCE

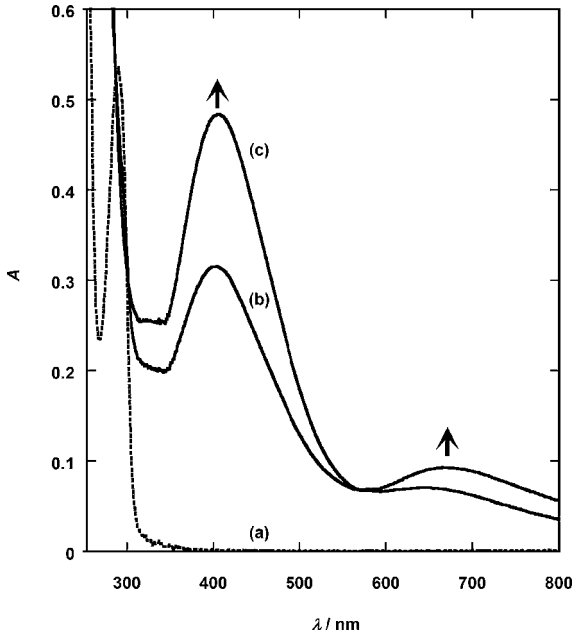


Figure 4. Evolution of the UV/Vis spectrum of $\mathbf{1}(PF_6)_2$ (1.1 mM acetonitrile solution) during bulk electrolysis at $E$ = 0.8 V vs. SCE before electrolysis (a), after 0.5 electron/Mn (b), and after 1 electron/Mn (c) at room temperature. Path length = 0.1 cm.

 © 2007 Wiley-VCH Verlag GmbH & Co. KGaA, Weinheim 

and one irreversible cathodic process at $E_p^c$ = +0.1 V vs. SCE when scanning towards low potential (labeled 4 in Figure 3, c).

As expected for a $Mn^{II}$ oxidation state, the UV/Vis spectrum of **1** (Figure 4) only shows features in the UV region ($\lambda_1$ = 287 nm, $\varepsilon_1$ = 4909 $M^{-1}cm^{-1}$) associated with π–π* transitions of the ligand. The colorless solution turns pink upon oxidation at 0.8 V and two new absorption bands appear at $\lambda_2$ = 403 and $\lambda_3$ = 672 nm. Based on a complete conversion of the initial $Mn^{II}$ into $Mn^{III}$, the extinction coefficients calculated per Mn ion are $\varepsilon_2$ = 2181 and $\varepsilon_3$ = 432 $M^{-1}cm^{-1}$. Similar bands have been reported in the literature for mononuclear $Mn^{III}$ complexes[66] or dinuclear $Mn^{III}Mn^{III}$ complexes with phenolato/pyridine ligands.[65] The band at 403 nm can therefore be attributed to a phenolato to $Mn^{III}$ LMCT transition. Due to the lower value of its extinction coefficient, and previous reports in the literature, the band at 672 nm can be attributed to a d-d transition.[67,68]

The intensity of the X-band perpendicular mode EPR spectrum of the initial $Mn^{II}Mn^{II}$ complex decreased during the course of the electrolysis. After completion of the electrolysis (1 electron/1 Mn), the pink solution was EPR-silent in the perpendicular mode (data not shown), as expected for a $Mn^{III}$ complex. Unfortunately, no signal was detected when a parallel mode EPR spectrum was recorded for the pink solution.

The above-mentioned experimental data confirm the $Mn^{III}$ oxidation state of the oxidized species, although the exact nature of the $Mn^{III}$ species remains uncertain as a dinuclear bis-μ-phenolato $Mn^{III}Mn^{III}$ complex is likely to be unstable in solution. As reported previously in the literature, the bis-μ-phenolato bridge can easily break and generate two mononuclear $[(L)Mn^{III}(S)]^{2+}$ complexes, where S can either be a water molecule or a solvent molecule.[51] It should be noted that wave 2 disappeared upon addition of 2,6-lutidine[69] and a new anodic wave appeared at 1.02 V vs. SCE. Based on these results (see Figure S1 in the electronic supporting information), wave 2 can be assigned to the $[(L)Mn^{III}(OH_2)]^{2+}/[(L)Mn^{IV}(OH_2)]^{3+}$ oxidation process and the wave at 1.02 V to the $[(L)Mn^{III}(OH)]^{+}/[(L)Mn^{IV}(OH)]^{2+}$ oxidation process as deprotonation of the aqua complex lowers the $Mn^{IV}/Mn^{III}$ redox potential. Wave 4 can tentatively be assigned to reduction of the mononuclear $[(L)Mn^{III}(OH_2)]^{2+}$ species into $[(L)Mn^{II}(OH_2)]^{+}$.

## Nature of the Complex in Water

Cyclic voltammetry and the EPR spectrum recorded in $CH_3CN$ are consistent with a dinuclear $[(L)MnMn(L)]^{2+}$ species (**1**; see above). In order to investigate the behavior of the complex in aqueous solution, electrochemistry and EPR spectra were recorded in a noncoordinating buffer, namely piperazine-*N*,*N*′-bis(2-ethanesulfonic acid) (PIPES; 50 mM, pH 7.5).[38,70]

The EPR spectra of a 1 mM solution in PIPES (Figure 5) displays a large six-line signal at $g$ = 2 ($\Delta B_{av}$ = 96 G) characteristic of a mononuclear $Mn^{II}$ center. The low-intensity signal at $g \approx 3.94$ is typical for distorted $Mn^{II}$ environ-

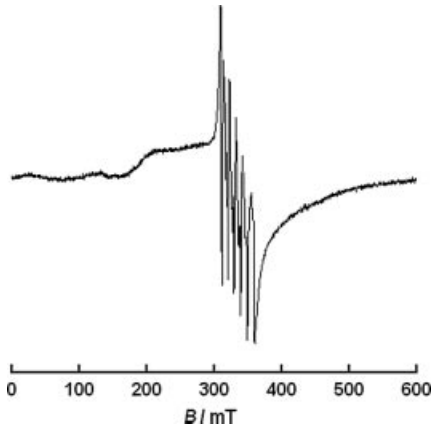


Figure 5. X-band EPR spectra of $\mathbf{1}(PF_6)_2$ ($10^{-3}$ M in 50 mM aqueous PIPES buffer, pH 7.5). Microwave frequency: 9.38 GHz; microwave power: 2.0 mW; modulation amplitude: 0.5 mT; modulation frequency: 100 kHz; gain: 20 dB.

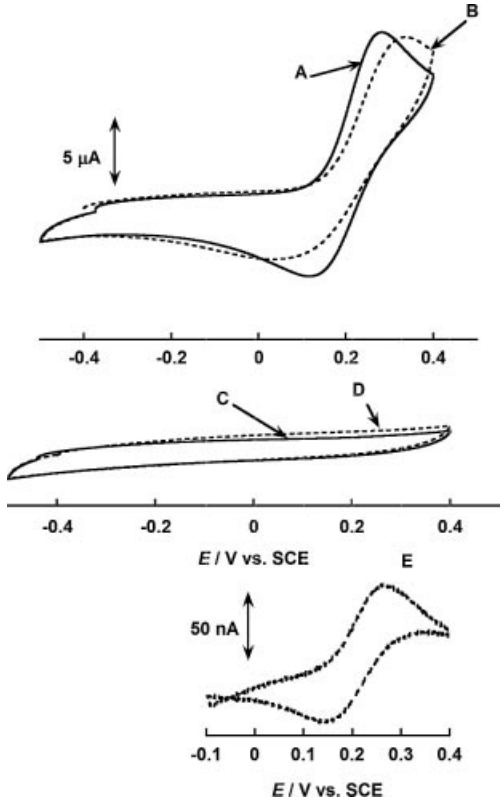


Figure 6. Cyclic voltammograms in aqueous solution: (A) $\mathbf{1}(PF_6)_2$ ($10^{-3}$ M) in aqueous PIPES buffer (pH 7.5, 50 mM) and (B) in aqueous phosphate buffer (pH 7.8, 50 mM); (**C**) $MnCl_2$ ($10^{-3}$ M) in aqueous PIPES buffer (pH 7.5, 50 mM) and (D) in aqueous phosphate buffer (pH 7.8, 50 mM); (E) $\mathbf{1}(PF_6)_2$ ($10^{-5}$ M) in aqueous PIPES buffer (pH 7.5, 50 mM; the signal recorded for pure PIPES buffer has been subtracted). Working electrode: glassy carbon; counter electrode: Pt wire; reference electrode: SCE.

 © 2007 Wiley-VCH Verlag GmbH & Co. KGaA, Weinheim 

ments.[71–74] This species will be labeled $[(L)Mn]^+$ in the following discussion, although there is probably a water molecule coordinated to the metal center.

Figure 6 shows the cyclic voltammogram of $[\mathbf{1}(PF_6)_2]$ dissolved in PIPES (1 mM; trace A). Trace A displays a well-defined anodic wave at $E_p^a = 0.282$ V vs. SCE and a well-defined cathodic wave on the reverse scan at $E_p^c = 0.116$ V vs. SCE ($E_{1/2} = 0.199$ V vs. *SCE* and $\Delta E_p = 165$ mV). Neither $MnCl_2$ (trace C in Figure 6) nor $Mn(ClO_4)_2$ (not shown) dissolved in PIPES show any wave at these potentials. A similar voltammogram, although less reversible, was recorded for $\mathbf{1}(PF_6)_2$ dissolved in pH 7.8 phosphate buffer (see Figure 6 trace B, $E_{1/2} = 0.184$ V vs. SCE; $E_p^a = 0.334$ V, $E_p^c = 0.037$ V vs. SCE; $\Delta E_p = 331$ mV).

Taken together, the EPR spectra and cyclic voltammograms unambiguously indicate that in aqueous solution the metal-containing species is therefore mononuclear $Mn^{II}$ (EPR) coordinated to L (the CV signature is different from that of uncoordinated $Mn^{2+}$).

The nature of this species was also investigated at $10^{-5}$ M both by CV and EPR spectroscopy. The electrochemical signature of the mononuclear $[(L)Mn]^+$ complex was still observed, with an intensity two orders of magnitude smaller, as expected for a concentration that is two orders of magnitude smaller. This indicates that no de-coordination occurs at this low concentration and is also consistent with the electrospray mass spectrometry analysis of a $10^{-5}$ M aqueous solution of $\mathbf{1}(PF_6)_2$, which shows a peak assigned to the mononuclear $[(L)Mn]^+$ cation (with spacings in the *M* multiplet equal to 1) and no peaks assignable to either **1** (at $M_{dinuclear}/2$, with expected spacings of 1/2) or to monocationic adducts.

## SOD-Like Activity in Aqueous Buffer

The mononuclear $[(L)Mn]^+$ cation was tested for its superoxide dismutase like activity using the McCord–Fridovich assay,[34,75] as published previously,[24,27] with ferricytochrome c as the detector. Two different buffers, namely phosphate buffer (pH 7.8, 50 mM) and the noncoordinating buffer PIPES (pH 7.5, 50 mM), were used, as in a previous study by Fridovich et al.[38] To the best of our knowledge, the PIPES buffer has only been used in the original publication by Fridovich et al.[38] even though these conditions appear to be a good alternative to phosphate buffer conditions.

The complex $[(L)Mn]^+$ displays very similar SOD-like activity under both sets of conditions, as shown by the inhibition of the reduction of ferricytochrome c. As shown in Figure 7, the activity of the complex is different from that of $Mn^{2+}_{aq}$ (see insert in Figure 7 and Table 2), which is consistent with the fact that the complex remains coordinated in dilute aqueous solution, as evidenced by the CV and ES-MS experiments at $10^{-5}$ M (see above).

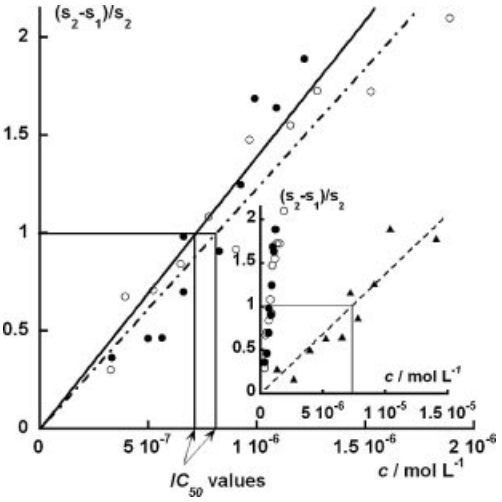


Figure 7. Determination of the $IC_{50}$ value for $[(L)Mn]^+$ in PIPES buffer (50 mM, pH 7.5; exp. points: filled circles; linear curve fit: solid line) and phosphate buffer (50 mM, pH 7.8; exp. points: open circles; linear curve fit: dot-dashed line). Inset: comparison with $MnCl_2$ in 50 mM PIPES (exp. points: triangles; linear fit: dashed line). The assay was performed by recording the reduction of ferricytochrome c at 550 nm as a function of time. The slope of the line $A_{550nm} = f(t)$ before addition of the SOD mimic is $s_1$ and $s_2$ is the slope after addition of the SOD mimic. $(s_1 - s_2)/s_2$ was plotted against the complex concentration to provide a line, and the $IC_{50}$ was then obtained for $(s_1 - s_2)/s_2 = 1$.[79]

Table 2. $IC_{50}$ values.

| | $IC_{50\ buffer}$[a,b] | $k_{McCF}$ [$M^{-1}\,s^{-1}$][c] |
|---|---|---|
| $Mn^{2+}_{aq}$ ($MnCl_2$) | $IC_{50\ PIPES} = (7.3 \pm 0.5) \times 10^{-6}$ M | –[d] |
| $[(L)Mn]^+$ | $IC_{50\ PIPES} = (7.2 \pm 0.4) \times 10^{-7}$ M | – |
| | $IC_{50\ Phosphate} = (8.1 \pm 0.3) \times 10^{-7}$ M | $(7.0 \pm 0.3) \times 10^6$ |

[a] 50% Inhibition concentration. [b] Uncertainties were obtained from the fitting linearization procedure. [c] $k_{McCF}$ values were recalculated from the $IC_{50}$ value. [d] $k_{McCF}$ was not recalculated as free $Mn^{II}$ is known to be catalytically inactive.[2] See ref.[4] for a comparison with similar $N_4O$ complexes.

$IC_{50}$ values are dependent on the concentration of the detector, therefore in order to determine the activity we recalculated the apparent kinetic constant $k_{McCF}$.[27] At the $IC_{50}$ value, the kinetics of the reduction of ferricytochrome c by superoxide is reduced by 50% as 50% of the superoxide is consumed by the ferricytochrome c and 50% by the complex (auto-dismutation being negligible in comparison). The apparent kinetic constant can thus be defined as $k_{McCF} = k_{detector} \times [detector]/IC_{50}$[27,76] and can be derived in the case of the phosphate buffer, for which the kinetic constant $k_{cytC}$ has been measured [$k_{cytC}$ (pH 7.8, 50 mM phosphate, 21 °C) = $2.6 \times 10^5$ $M^{-1}\,s^{-1}$].[77,78] The complex $[(L)Mn]^+$ therefore displays an apparent catalytic rate $k_{McCF}$ of $(7.0 \pm 0.3) \times 10^6$ $M^{-1}\,s^{-1}$.

The activity reported here is one of the best reported for the series of $Mn^{II}$ complexes with a similar coordination sphere (N/O coordination sphere with N from imidazole or pyridine and O from carboxylato or phenolato) reported by us and others,[23–25,27,28,80] which makes sense in light of the redox potential for the mononuclear $[(L)Mn]^+$ species mea-

 © 2007 Wiley-VCH Verlag GmbH & Co. KGaA, Weinheim 

sured in aqueous buffer. As the catalysis of the dismutation of superoxide is a redox process involving both $Mn^{II}$ and $Mn^{III}$ oxidation states, the potential of the $Mn^{II}/Mn^{III}$ couple is a key parameter.[27] It should lie between the potential of the two couples $O_2/O_2^-$ and $O_2^-/H_2O_2$ with the optimum being the midpoint, that is 0.12 V vs. SCE (at pH 7), which is the case for all SODs.[27,81,82] The mononuclear complex $[(L)Mn]^+$ ($E_{1/2}$ = 0.199 V vs. SCE) fulfills this requirement.

## Conclusions

The dinuclear bis-μ-phenolato complex $[(L)Mn^{II}Mn^{II}(L)](PF_6)_2$ [**1**$(PF_6)_2$], which contains a new amino/imidazole pentadentate $N_4O$ ligand, has been synthesized and its structure resolved by X-ray diffraction. An X-band EPR spectroscopy investigation has confirmed the dinuclear nature of the compound in acetonitrile solution. The cyclic voltammogram of **1** in acetonitrile solution displays a quasi-reversible anodic process at $E_{1/2}$ = 0.485 V vs. SCE assigned to the two-electron oxidation of the $Mn^{II}Mn^{II}$ species into the $Mn^{III}Mn^{III}$ species. The electrochemical formation of a $Mn^{III}$ species has been followed by UV/Vis and EPR spectroscopy. In aqueous solution, the dinuclear complex has been shown to be converted into a cationic mononuclear complex $[(L)Mn]^+$ with a redox potential of +0.199 V vs. SCE. Its superoxide dismutase-like (SOD-like) activity has been evaluated by the means of the McCord–Fridovich assay. The complex has a potent SOD-like activity, with an apparent catalytic rate, $k_{McCF}$, of $(7.0 \pm 0.3) \times 10^6$ $M^{-1}s^{-1}$. The development of manganese complexes based on 1,2-ethanediamine is of interest for the synthesis of efficient SOD mimics.

## Experimental Section

All reagents were bought from Acros Organics and used without further purification. 1-Methyl-imidazole carboxaldehyde was synthesized according to Iberson et al.[53] *N*,*N*′-Bis[2-(*N*-methylimidazolyl)methyl]ethane-1,2-diamine was synthesized according to Laronde et al.[54] NMR spectra were recorded with a Bruker AV360 or DRX300 spectrometer. IR spectra (KBr pellets) were recorded with a Bruker IFS 66 FT-IR spectrometer. Microanalysis was performed by the Service de Microanalyse de l'ICSN (Gif-sur-Yvette, France) for C,H,N, and by the Service Central d'Analyse du CNRS (Vernaison, France) for other elements.

Electrospray-ionization mass spectra were recorded with a Finnigan Mat 95S in the BE configuration at low resolution. X-band EPR spectra were recorded with a Bruker ELEXSYS 500 spectrometer fitted with an Oxford Instrument continuous-flow liquid helium or nitrogen cryostat and a temperature control system. UV/Vis spectra were recorded with a Cary 300 Bio Spectrophotometer with a 0.1-cm optical path quartz cuvette. The McCord–Fridovich assay was performed on the same apparatus at 25 °C and with a 1-cm optical path quartz cuvette. All electrochemical experiments were performed under argon. Cyclic voltammetry and coulometry were performed with a M273 EGG PAR potentiostat. The counter electrode for cyclic voltammetry was a Pt wire and the working electrode a glassy carbon disk, which was carefully polished before each voltammogram with a 1-μm diamond paste, sonicated in an ethanol bath, and then washed carefully with ethanol and dried. The counter electrode for bulk electrolysis was a piece of Pt separated from the rest of the solution with a fritted bridge. The working electrode was a Pt gauze (about 20 $cm^2$). The solvent used was (a) distilled acetonitrile with tetrabutylammonium perchlorate added to obtain a 0.1 M supporting electrolyte or (b) doubly distilled water with either phosphate or PIPES buffer (50 mM). The reference electrode was (a) an $Ag/AgClO_4$ electrode (0.3 V vs. SCE) for experiments in $CH_3CN$ and (b) an SCE electrode for experiments in water. In both cases, the reference electrode was isolated from the rest of the solution with a fritted bridge. Temperature regulation (20 °C) was ensured by a Julabo circulation cryostat.

**2-(2-Hydroxybenzyl)-*N*,*N*′-bis[2-(*N*-methylimidazolyl)methyl]imidazolidine (3):** A solution of compound **2**[54] (0.500 g, 2.01 mmol, 1 equiv.) in absolute ethanol (10 mL) was mixed with salicylaldehyde (0.246 g, 215 μL, 2.01 mmol, 1 equiv.). After stirring the reaction mixture for 24 h at ambient temperature, anhydrous sodium sulfate (0.5 g) was added to eliminate water. After stirring for a further 30 min the reaction mixture was filtered and the solvent evaporated to give the crude product as a yellow oil (0.700 g, quantitative yield). $^1$H NMR (360 MHz, $CDCl_3$, 23 °C): $\delta$ = = 7.22 (t, $J$ = 7.8 Hz, 1 H, $CH_{PhOH}$), 7.06 (d, $J$ = 7.3 Hz, 1 H, $CH_{PhOH}$), 6.8 (m, 4 H, $H_{Ar}$), 6.70 (s, 2 H, $CH_{Im}$), 3.91 (s, 1 H, $CH_{aminal}$), 3.78 (d, $J$ = 13.3 Hz, 2 H, $CH_2$-Im), 3.51 (d, $J$ = 13.3 Hz, 2 H, $CH_2$-Im), 3.35 (s, 6 H, $CH_3$), 3.05 (m, 2 H, $NCH_2CH_2N$), 2.79 (m, 2 H, $NCH_2CH_2N$) ppm. $^{13}$C NMR (90.6 MHz, $CDCl_3$, 23 °C): $\delta$ = 157.8 ($C_{Ar}$-OH), 144.0 ($C_{quatIm}$), 131.2, 130.4, 119.0, and 116.6 ($C_{PhOH}H$), 127.1 and 121.7 ($C_{Im}H$), 120.6 ($C_{quatPhOH}$), 88.1 ($CH_{aminal}$), 49.6 and 48.0 ($CH_2C_{Im}$, N-$CH_2$-$CH_2$-N), 32.4 (Me) ppm. ES-MS: *m*/*z* (%) 353.4 (100) $[M + H]^+$.

***N*-(2-Hydroxybenzyl)-*N*,*N*′-bis[2-(*N*-methylimidazolyl)methyl]ethane-1,2-diamine (LH):** $NaBH_3CN$ (0.107 g, 1.70 mmol, 1 equiv.) and then $CF_3COOH$ (0.390 g, 340 mL, 3.40 mmol, 2 equiv.) were added to a solution of **3** (0.600 g, 1.70 mmol, 1 equiv.) in absolute ethanol (30 mL). After stirring for 2 h, 1 M NaOH (10 mL) was added and the ethanol was evaporated. $CH_2Cl_2$ (20 mL) was then added and the pH adjusted to 9 by addition of 1 M HCl. The organic phase was decanted and the aqueous phase extracted with $3 \times 20$ mL of $CH_2Cl_2$. The combined organic fractions were concentrated to obtain the product as a yellow oil (0.600 g, quantitative yield). $^1$H NMR (300 MHz,$CDCl_3$, 23 °C): $\delta$ = 7.18 (t, $J$ = 7.5 Hz, 1 H, $H_{Ar}$), 6.92 (d, $J$ = 7.5 Hz, 1 H, $H_{Ar}$), 6.8 (m, 6 H, $H_{Ar}$), 3.74 (s, 2 H, N-$CH_2$-$C_{Ar}$), 3.71, (s, 2 H, N-$CH_2$-$C_{Ar}$), 3.70 (s, 2 H, N-$CH_2$-$C_{Ar}$), 3.58 (s, 3 H, N-$CH_3$), 3.40 (s, 3 H, N-$CH_3$), 2.78 (m, 4 H, $CH_2$-$CH_2$) ppm. $^{13}$C NMR (75.5 MHz, $CDCl_3$, 23 °C): $\delta$ = 157.0 ($C_{Ar}$-OH), 145.1 and 144.7 ($C_{quatIm}$), 130.1, 128.6, 126.3, 122.7, 121.0, 120.7, 118.4, and 116.1 ($C_{Ar}$-H), 123.1 ($C_{quatPhOH}$), 56.1, 51.6, 49.3, 45.4, and 43.4 ($CH_2$), 32.8 and 32.3 (N-$CH_3$) ppm. ES-MS: *m*/*z* (%) 355.3 $[M + H]^+$ (100). IR (KBr pellet): $\tilde{\nu}_{max}$ = 757 ($\delta_{imidazol}$), 1282 ($\nu_{C-O}$), 1454 and 1487 $cm^{-1}$ ($\nu_{C=N}$).

**$[Mn_2(L)_2](PF_6)_2$:** $NEt_3$ (16 mg, 21 μL, 0.155 mmol, 0.5 equiv.) was added to a solution of LH (0.110 g, 0.310 mmol, 1 equiv.) in MeOH (40 mL) and argon was bubbled into the solution to remove $O_2$. A deoxygenated solution of $MnBr_2$ (67 mg, 0.310 mmol, 1 equiv.) in MeOH (10 mL) was added to this mixture and the solution heated at 50 °C for 30 min. A deoxygenated solution of $NH_4PF_6$ (101 mg, 0.621 mmol, 2 equiv.) in methanol (1 mL) was then added and the resulting solution allowed to cool overnight. The complex started to crystallize out of solution, and 92 mg (40% yield) of nearly colorless crystals were isolated by filtration. ES-MS [dilute aqueous solution ($5 \times 10^{-5}$ M and $5 \times 10^{-6}$ M)]: *m*/*z* (%) 408.6 $[(L)Mn]^+$ (100), 353.3 $[LH + H]^+$ (23). The peak separation within the 408.6 mul-

 © 2007 Wiley-VCH Verlag GmbH & Co. KGaA, Weinheim 

tiplet is +1, which indicates a +1 charge and is consistent with the monometallic species $[(L)Mn]^+$. IR (KBr pellet): $\tilde{\nu}_{max}$ = 760 ($\delta_{imidazol}$), 837 ($PF_6$), 1290 ($\nu_{C-O}$), 1447 and 1484 $cm^{-1}$ ($\nu_{C=N}$). $C_{38}H_{50}F_{12}Mn_2N_{12}O_2P_2$ (1106.7): calcd. C 41.24, H 4.55, Mn 9.93, N 15.19, P 5.60; found C 40.99, H 4.61, Mn 9.36, N 14.98, P 5.48.

**Magnetic Measurements and Fitting Procedures:** Magnetization data were collected for ground crystals with a Quantum Design MPMS5 magnetometer in the 2–300 K temperature region (applied field: 10 kG). The data were corrected for the diamagnetism contributions of the sample and of the cell. At 300 K, $\chi T$ = 8.01 $cm^3 K mol^{-1}$. This value remained constant down to about 50 K upon lowering the temperature and then decreased abruptly to a value of 0.65 $cm^3 K mol^{-1}$ at 2 K. This behavior is indicative of an antiferromagnetic coupling between the two $Mn^{II}$ ions. The experimental data were fitted to the expression for a dinuclear $Mn^{II}$ ($S_1$ = 5/2)–$Mn^{II}$ ($S_2$ = 5/2) complex using the Hamiltonian $H = -JS_1S_2$ (Marquardt algorithm from KaleidaGraph). A $g$-value of 1.94 was obtained from the fitting of $\chi T = f(T)$ at high temperatures. A $J$-value of –0.9 $cm^{-1}$ was obtained by fitting $\chi = f(T)$ using $g$ = 1.94. As shown in Figure 8, a good agreement was obtained for $\mathbf{1}(PF_6)_2$ in the whole temperature range for both $\chi T$ and $\chi$.

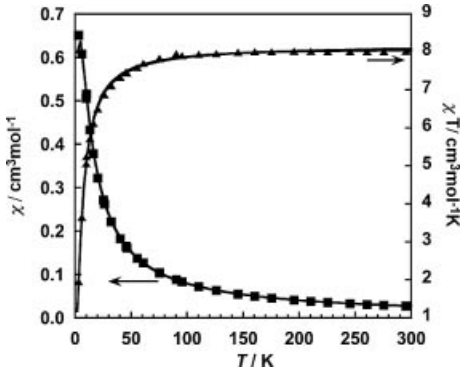


Figure 8. Thermal variation of $\chi T$ (triangles) and $\chi$ (squares) vs. temperature for $\mathbf{1}(PF_6)_2$. For clarity, only 30% of the recorded data are shown. The solid lines correspond to the data calculated with the parameters $g$ = 1.94 and $J$ = –0.9 $cm^{-1}$ with $H = -JS_1S_2$.

**X-ray Crystallography:** X-ray diffraction data for $\mathbf{1}(PF_6)_2$ were collected with a Kappa X8 APPEX II Bruker diffractometer with graphite-monochromated Mo-$K_\alpha$ radiation ($\lambda$ = 0.71073 Å) and corrected for Lorentz, polarization, and absorption effects. The structures were solved by direct methods using SHELXS-97[83] and refined against $F^2$ by full-matrix least-squares techniques using SHELXL-97[84] with anisotropic displacement parameters for all non-hydrogen atoms. Hydrogen atoms were located on a difference Fourier map and introduced into the calculations as a riding model with isotropic thermal parameters. All calculations were performed with the crystallographic software package WINGX.[85] The crystal data collection and refinement parameters are given in Table 3.

CCDC-622751 contains the supplementary crystallographic data for this paper. These data can be obtained free of charge from the Cambridge Crystallographic Data Centre via www.ccdc.cam.ac.uk/data_request/cif.

**SOD Activity Measurements:** The assay and controls to ensure reliability were performed as described previously.[24,27] The standard conditions used were: $T$ = 25 °C (potassium phosphate buffer, 50 mM, pH 7.8 or PIPES, 50 mM, pH 7.5),[38] [xanthine] = 200 μM and a quantity of xanthine oxidase ensuring a $\Delta A$ of at least 0.025 $min^{-1}$. The reduction of ferricytochrome c at 550 nm was monitored first in the absence of any putative SOD mimic and then after addition of the mimic. The slope of the line $A_{550nm} = f(t)$ before addition of the SOD mimic is $s_1$ and $s_2$ is the slope after addition of the SOD mimic. $(s_1 - s_2)/s_2$ was plotted against the complex concentration to provide a line and the $IC_{50}$ was then obtained for $(s_1 - s_2)/s_2 = 1$. Experiments were performed in duplicate for each buffer.

Table 3. Crystallographic data for $\mathbf{1}(PF_6)_2$.

| | |
|---|---|
| Formula | $C_{38}H_{50}Mn_2N_{12}O_2 \cdot 2(PF_6)$ |
| $Fw$ | 1106.72 |
| Crystal system | triclinic |
| Space group | $P\bar{1}$ |
| $a$ [Å] | 9.2677(12) |
| $b$ [Å] | 11.0617(14) |
| $c$ [Å] | 13.2606(16) |
| $\alpha$ [°] | 107.965(2) |
| $\beta$ [°] | 107.114(3) |
| $\gamma$ [°] | 92.810(3) |
| $V$ [Å$^3$] | 1221.2(3) |
| $Z$ | 1 |
| $F$(000) | 566 |
| $\lambda$ [Å] | 0.71073 |
| $T$ [K] | 273(2) |
| $\rho_{calcd.}$ [$Mg m^{-3}$] | 1.505 |
| $\mu$(Mo-$K_\alpha$) [$mm^{-1}$] | 0.675 |
| Crystal size [$mm^3$] | $0.20 \times 0.14 \times 0.06$ |
| $\theta$ range [°] | 3.00–26.19 |
| Number of data collected | 6141 |
| Number of unique data | 3291 |
| $R$(int) | 0.0252 |
| Absorption correction | SADABS |
| Number of variable parameters | 307 |
| Number of observed reflections[a] | 2639 |
| $R$[b] obsd., all | 0.0565, 0.0702 |
| $R_w$[c] obsd., all | 0.1671, 0.1795 |
| $S$ | 1.075 |
| Largest diff. peak and hole [e Å$^{-3}$] | 0.805, –0.450 |

[a] Data with $F_o > 4\sigma(F_o)$. [b] $R = \Sigma||F_o|-|F_c||/\Sigma|F_o|$. [c] $R_w = [\Sigma w(|F_o^2|-|F_c^2|)^2/\Sigma w|F_o^2|^2]^{1/2}$.

**Supporting Information** (see footnote on the first page of this article): Figure S1, Evolution of the cyclic voltammogram of $[\mathbf{1}(PF_6)_2]$ upon addition of base (2,6-lutidine).

## Acknowledgments

We thank Eric Rivière for recording the magnetic measurements and Geneviève Blondin for useful discussions on the EPR spectroscopy. This work was supported by the French government (grant no. ACI-2004 JC2044 to C. P.).

[1] B. Halliwell, J. M. C. Gutteridge, *Free Radicals in Biology and Medicine*, Oxford University Press, New York, **1999**.
[2] D. P. Riley, *Chem. Rev.* **1999**, *99*, 2573–2587.
[3] D. Salvemini, C. Muscoli, D. P. Riley, S. Cuzzocrea, *Pulm. Pharmacol. Ther.* **2002**, *15*, 439–447.
[4] J. M. McCord, M. A. Edeas, *Biomed. Pharmacother.* **2005**, *59*, 139–142.
[5] P. R. Gardner, I. Raineri, L. B. Epstein, C. W. White, *J. Biol. Chem.* **1995**, *270*, 13399–13405.
[6] P. R. Gardner, I. Fridovich, *J. Biol. Chem.* **1992**, *267*, 8757–8763.
[7] F. S. Archibald, I. Fridovich, *J. Bacteriol.* **1981**, *145*, 442–451.

 © 2007 Wiley-VCH Verlag GmbH & Co. KGaA, Weinheim 

[8] R. J. Sanchez, C. Srinivasan, W. H. Munroe, M. A. Wallace, J. Martins, T. Y. Kao, K. Le, E. B. Gralla, J. S. Valentine, *J. Biol. Inorg. Chem.* **2005**, *10*, 913–923.
[9] M. Al-Maghrebi, I. Fridovich, L. Benov, *Arch. Biochem. Biophys.* **2002**, *402*, 104–109.
[10] M. Baudry, S. Etienne, A. Bruce, M. Palucki, E. Jacobsen, B. Malfroy, *Biochem. Biophys. Res. Commun.* **1993**, *192*, 964–968.
[11] A. Puglisi, G. Tabb, G. Vecchio, *J. Inorg. Biochem.* **2004**, *98*, 969–976.
[12] T. Magwere, M. West, K. Riyahi, M. P. Murphy, R. A. J. Smith, L. Partridge, *Mech. Ageing Dev.* **2006**, *127*, 356–370.
[13] J. D. Rush, Z. Maskos, W. H. Koppenol, *Arch. Biochem. Biophys.* **1991**, *289*, 97–102.
[14] D. P. Riley, R. H. Weiss, *J. Am. Chem. Soc.* **1994**, *116*, 387–388.
[15] D. P. Riley, S. L. Henke, P. J. Lennon, R. H. Weiss, W. L. Neumann, W. J. J. Rivers, K. W. Aston, K. R. Sample, H. Rahman, C.-S. Ling, J.-J. Shieh, D. H. Busch, W. Szulbinski, *Inorg. Chem.* **1996**, *35*, 5213–5231.
[16] D. P. Riley, S. L. Henke, P. J. Lennon, K. Aston, *Inorg. Chem.* **1999**, *38*, 1908–1917.
[17] D. Salvemini, Z.-Q. Wang, J. L. Zweier, A. Samouilov, H. Macarthur, T. P. Misko, M. G. Currie, S. Cuzzocrea, J. A. Sikorski, D. P. Riley, *Science* **1999**, *286*, 304–305.
[18] R. D'Agata, G. Grasso, G. Iacono, G. Spoto, G. Vecchio, *Org. Biomol. Chem.* **2006**, *4*, 610–612.
[19] A. Dees, A. Zahl, R. Puchta, N. J. R. Van Eikema Hommes, F. W. Heinemann, I. Ivanovic-Burmazovic, *Inorg. Chem.* **2007**, *46*, 2459–2470.
[20] N. Kitajima, M. Osawa, N. Tamura, Y. Moro-Oka, T. Hirano, M. Hirobe, T. Nagano, *Inorg. Chem.* **1993**, *32*, 1879–1880.
[21] A. Deroche, I. Morgenstern-Badarau, M. Cesario, J. Guilhem, B. Keita, L. Nadjo, C. Houée-Levin, *J. Am. Chem. Soc.* **1996**, *118*, 4567–4573.
[22] D. F. Xiang, X. S. Tan, Q. W. Hang, W. X. Tang, B.-M. Wu, T. C. W. Mak, *Inorg. Chim. Acta* **1998**, *277*, 21–25.
[23] K. Yamato, I. Miyahara, A. Ichimura, K. Hirotsu, Y. Kojima, H. Sakurai, D. Shiomi, K. Sato, T. Takui, *Chem. Lett.* **1999**, 295–296.
[24] C. Policar, S. Durot, F. Lambert, M. Cesario, F. Ramiandrasoa, I. Morgenstern-Badarau, *Eur. J. Inorg. Chem.* **2001**, 1807–1818.
[25] E. A. Lewis, H. H. Khodr, R. C. Hider, J. R. Lindsay-Smith, P. H. Walton, *Dalton Trans.* **2004**, 187–188.
[26] S. Durot, F. Lambert, J.-P. Renault, C. Policar, *Eur. J. Inorg. Chem.* **2005**, 2789–2793.
[27] S. Durot, C. Policar, F. Cisnetti, F. Lambert, J.-P. Renault, G. Pelosi, G. Blain, H. Korri-Youssoufi, J.-P. Mahy, *Eur. J. Inorg. Chem.* **2005**, 3513–3523.
[28] F. Cisnetti, G. Pelosi, C. Policar, *Inorg. Chim. Acta* **2007**, *360*, 557–562.
[29] Z.-R. Liao, X.-F. Zheng, B.-S. Luo, L.-R. Shen, D.-F. Li, H.-L. Liu, W. Zhao, *Polyhedron* **2001**, *20*, 2813–2821.
[30] J. Alexandre, C. Nicco, C. Chéreau, A. Laurent, B. Weill, F. Goldwasser, F. Batteux, *J. Natl. Cancer Inst.* **2006**, *98*, 236–244.
[31] H. Brurok, J. H. Ardenkjaer-Larsen, G. Hansson, S. Skarra, K. Berg, J. O. G. Karlsson, I. Laursen, P. Jynge, *Biochem. Biophys. Res. Commun.* **2006**, *254*, 768–772.
[32] S. Groni, G. Blain, R. Guillot, C. Policar, E. Anxolabéhère-Mallart, *Inorg. Chem.* **2007**, *46*, 1951–1953.
[33] W. F. Beyer, I. Fridovich, *Arch. Biochem. Biophys.* **1989**, *271*, 149–156.
[34] K. M. Faulkner, R. D. Stevens, I. Fridovich, *Arch. Biochem. Biophys.* **1994**, *310*, 341–346.
[35] J. Lati, D. Meyerstein, *J. Chem. Soc. Dalton Trans.* **1978**, 1105–1118.
[36] J. Stein, J. P. Fackler, G. J. McClune, J. A. Fee, L. T. Chan, *Inorg. Chem.* **1979**, *18*, 3511–3518.
[37] W. H. Koppenol, F. Levine, T. L. Hatmaker, J. Epp, J. D. Rush, *Arch. Biochem. Biophys.* **1986**, *251*, 594–599.
[38] F. S. Archibald, I. Fridovich, *Arch. Biochem. Biophys.* **1982**, *214*, 452–463.
[39] M. A. Bailey, M. J. Ingram, D. P. Naughton, *Biochem. Biophys. Res. Commun.* **2004**, *317*, 1155–1158.
[40] A. E. O. Fisher, D. P. Naughton, *Biomed. Pharmacother.* **2005**, *59*, 158–162.
[41] T. Piacham, C. Isarankura-Na-Ayudhya, C. Nantasenamat, S. Yainoy, L. Ye, L. Bülow, N. Prachayasittihul, *Biochem. Biophys. Res. Commun.* **2006**, *341*, 925–930.
[42] J. S. Valentine, A. E. Quinn, *Inorg. Chem.* **1976**, *15*, 1997–1999.
[43] K. M. Faulkner, S. I. Liochev, I. Fridovich, *J. Biol. Chem.* **1994**, *269*, 23471–23476.
[44] I. Batinic-Haberle, S. I. Liochev, I. Spasojevic, I. Fridovich, *Arch. Biochem. Biophys.* **1997**, *343*, 225–233.
[45] I. Batinic-Haberle, L. Benov, I. Spasojevic, I. Fridovich, *J. Biol. Chem.* **1998**, *273*, 24521–24528.
[46] P. J. F. Gauuan, M. P. Trova, L. Gregor-Boros, S. B. Bocckino, J. D. Crapo, B. J. Day, *Bioorg. Med. Chem.* **2002**, *10*, 3013–3021.
[47] I. Batinic-Haberle, I. Spasojevic, R. D. Stevens, B. Bondurant, A. Okado-Matsumoto, I. Fridovich, Z. Vujaskovic, M. W. Dewhirsta, *Dalton Trans.* **2006**, 617–624.
[48] I. Spasojevic, I. Batinic-Haberle, R. D. Stevens, P. Hambright, A. N. Thorpe, J. Grodkowski, P. Neta, I. Fridovich, *Inorg. Chem.* **2001**, *40*, 726–739.
[49] G. O. E. Borgstahl, H. E. Parge, M. J. Hickey, W. F. Beyer, R. A. Hallewell, J. A. Tainer, *Cell* **1992**, *71*, 107–118.
[50] C. Hureau, E. Anxolabéhère-Mallart, M. Nierlich, F. Gonnet, E. Rivière, G. Blondin, *Eur. J. Inorg. Chem.* **2002**, 2710–2719.
[51] C. Hureau, L. Sabater, E. Anxolabéhère-Mallart, M. Nierlich, M.-F. Charlot, F. Gonnet, E. Rivière, G. Blondin, *Chem. Eur. J.* **2004**, *10*, 1998–2010.
[52] C. Baffert, M.-N. Collomb, A. Deronzier, S. Kjærgaard-Knudsen, J.-M. Latour, C. H. Lund, C. J. McKenzie, M. Mortensen, L. P. Nielsen, N. Thorup, *Dalton Trans.* **2003**, 1765–1772.
[53] P. E. Iberson, H. Lund, *Acta Chem. Scand.* **1966**, *20*, 2649.
[54] F. J. Laronde, M. A. Brooks, *Inorg. Chim. Acta* **1999**, *296*, 208–221.
[55] J. Brinskma, M. T. Rispens, R. Hage, B. L. Feringa, *Inorg. Chim. Acta* **2002**, 75–82.
[56] C. F. Macrae, P. R. Edington, P. R. McCabe, E. Pidcock, G. P. Shields, R. Taylor, M. Towler, J. Van De Streek, *J. Appl. Crystallogr.* **2006**, *39*, 453–457.
[57] M. G. B. Drew, C. J. Harding, V. McKee, G. G. Morgan, J. Nelson, *J. Chem. Soc. Chem. Commun.* **1995**, 1035–1038.
[58] D. P. Kessissoglou, W. M. Butler, V. L. Pecoraro, *Inorg. Chem.* **1987**, *26*, 195–203.
[59] H. Adams, N. A. Bailey, N. A. Debaecker, D. E. Fenton, W. Kanda, J.-M. Latour, H. Okawa, H. Sakiyama, *Angew. Chem. Int. Ed. Engl.* **1995**, *34*, 2535–2537.
[60] B. E. Schultz, B.-H. Ye, X.-Y. Li, S. I. Chan, *Inorg. Chem.* **1997**, *36*, 2617–2622.
[61] T. Howard, J. Tesler, V. J. Derose, *Inorg. Chem.* **2000**, *39*, 3379–3385.
[62] S. Blanchard, G. Blain, E. Rivière, M. Nierlich, G. Blondin, *Chem. Eur. J.* **2003**, *9*, 4260–4268.
[63] S. Blanchard, G. Blondin, E. Rivière, M. Nierlich, J. J. Girerd, *Inorg. Chem.* **2003**, *42*, 4568–4578.
[64] $E_{1/2} = 1/2[E_p^a + E_p^c]$.
[65] L. Sabater, C. Hureau, G. Blain, R. Guillot, P. Thuery, E. Rivière, A. Aukaulo, *Eur. J. Inorg. Chem.* **2006**, 4324–4337.
[66] A. Neves, S. M. D. Erthal, I. Vencato, A. S. Ceccato, Y. P. Mascarenhas, O. R. Nascimento, M. Horner, A. A. Batista, *Inorg. Chem.* **1992**, *31*, 4749–4755.
[67] H. Diril, H.-R. Chang, M. J. Nilges, X. Zhang, J. A. Potenza, H. J. Schugar, S. S. Isied, D. N. Hendrickson, *J. Am. Chem. Soc.* **1989**, *111*, 5102–5114.
[68] J. A. Bonadies, M. J. Maroney, V. L. Pecoraro, *Inorg. Chem.* **1989**, *28*, 2044–2797.


 © 2007 Wiley-VCH Verlag GmbH & Co. KGaA, Weinheim 

[69] 2,6-Lutidine was chosen based on previous reports by Hureau et al.[50,51].
[70] N. E. Good, G. D. Winget, W. Winter, T. N. Connolly, S. Izawa, R. M. M. Singh, *Biochemistry* **1966**, *5*, 467–477.
[71] C. Policar, I. Artaud, D. Mansuy, *Inorg. Chem.* **1996**, *35*, 210–216.
[72] R. D. Dowsing, J. F. Gibson, D. M. L. Goodgame, M. Goodgame, P. J. Hayward, *Nature* **1968**, *219*, 1037–1038.
[73] R. D. Dowsing, J. F. Gibson, M. Goodgame, P. J. Hayward, *J. Chem. Soc. C* **1969**, 187–193.
[74] E. J. Laskowski, D. N. Hendrickson, *Inorg. Chem.* **1978**, *17*, 457–470.
[75] J. M. McCord, I. Fridovich, *J. Biol. Chem.* **1969**, *244*, 6049–6055.
[76] R. F. Pasternack, B. Halliwell, *J. Am. Chem. Soc.* **1979**, *101*, 1026–1031.
[77] J. Butler, W. H. Koppenol, E. Margoliash, *J. Biol. Chem.* **1982**, *257*, 10747–10750.
[78] It should be noted that the kinetic constant for the reaction between ferricytochrome c in PIPES at pH 7.5 has not been measured, but the fact that the $IC_{50}$ values are very close in PIPES at pH 7.5 and phosphate buffer at pH 7.8 suggests that the $k_{cytC}$ (pH 7.5, PIPES 50 mM, 21 °C) should be very close to that reported in phosphate buffer.
[79] Y. Sawada, I. Yamazaki, *Biochem. Biophys. Acta* **1973**, *327*, 257–265.
[80] For a more exhaustive comparison with the Mn complexes from the literature, see ref.[27]
[81] W. C. J. Barrette, D. T. Sawyer, J. A. Fee, K. Asada, *Biochemistry* **1983**, *22*, 624–627.
[82] I. Batinic-Haberle, I. Spasojevic, R. D. Stevens, P. Hambright, P. Neta, A. Okado-Matsumoto, I. Fridovich, *Dalton Trans.* **2004**, 1696–1702.
[83] G. M. Sheldrick, *SHELXS-97, Program for Crystal Structure Solution*, University of Göttingen, Germany, **1990**.
[84] G. M. Sheldrick, *SHELXL 97, Program for the refinement of crystal structures from diffraction data*, University of Göttingen, Germany, **1997**.
[85] L. J. Farrugia, *J. Appl. Crystallogr.* **1999**, *32*, 837–838.

Received: December 22, 2006
Published Online: August 9, 2007

 © 2007 Wiley-VCH Verlag GmbH & Co. KGaA, Weinheim 

DOI: 10.1002/ejic.200700293

# Cooperative Spin-Crossover Behaviour in Polymeric 1D $Fe^{II}$ Coordination Compounds: $[\{Fe(tba)_3\}X_2]\cdot nH_2O$

**Maksym Seredyuk,[a] Ana B. Gaspar,*[b] M. Carmen Muñoz,[c] Michel Verdaguer,[d] Françoise Villain,[d] and Philipp Gütlich*[a]**

**Keywords:** Spin crossover / Bistability / Cooperative effects / Iron(II) complexes / Substituted triazoles

A new family of 1D cooperative spin-crossover polymers with general formula $[\{Fe(tba)_3\}X_2]\cdot nH_2O$ [tba = *N*-(4*H*-1,2,4-triazol-4-yl)benzamide; X = $CF_3SO_3^-$, *n* = 2 (**1**), *n* = 0 (**4**); $BF_4^-$, *n* = 3 (**2**), *n* = 0 (**5**); 4-$CH_3C_6H_4SO_3^-$, *n* = 3 (**3**), *n* = 0 (**6**)] has been synthesised and characterised using a series of spectroscopic methods, X-ray powder diffraction, magnetic susceptibility measurements and differential scanning calorimetry. The copper analogue of **1**, $[\{Cu(tba)_3\}(CF_3SO_3)_2]\cdot 3H_2O$ (**7**), has also been synthesised and its crystal structure solved at 293 K. Compound **7** crystallises in the $P\bar{1}$ space group. The bidentate *N*-(4*H*-1,2,4-triazol-4-yl)benzamide ligand bridges the copper ions through the 1,2-nitrogen positions leading to a one-dimensional infinite polymer. The EXAFS data collected at 80 K for **1** agree perfectly with a linear chain structure, as observed for **7**, with $[Fe(tba)_3]$ chromophores linked to each other through the adjacent nitrogen atoms of three *N*-(4*H*-1,2,4-triazole-4-yl)benzamide ligands. IR spectroscopic studies confirm the retention of the $C_{2v}$ symmetry for the triazole rings in **2** and **3**, thereby suggesting a similar chainlike arrangement in these compounds. Compound **1** is low spin (LS) at room temperature while **2** and **3** are high spin (HS). The latter two complexes undergo cooperative thermal spin transition at $T_c\downarrow$ = 250 and $T_c\uparrow$ = 258 K in **2** and $T_c\downarrow$ = 226 and $T_c\uparrow$ = 238 K in **3**. The spin transition in **2** and **3** is accompanied by a change of colour from white in the HS state to violet in the LS state. The thermodynamic parameters associated with the spin transition estimated from DSC measurements are $\Delta H$ = 17.8 (**2**) and 14.6 kJ mol$^{-1}$ (**3**), and $\Delta S$ = 67.2 (**2**) and 63.5 J K$^{-1}$ mol$^{-1}$ (**3**). In contrast, the dehydrated compounds **4**, **5** and **6** show very different spin-transition behaviour. Complex **4** exhibits an abrupt spin transition centred at room temperature and is accompanied by a relatively large hysteresis loop with a width of 25 K ($\Delta H$ = 19.7 kJ mol$^{-1}$ and $\Delta S$ = 65.6 J K$^{-1}$ mol$^{-1}$). Like **2** and **3**, **4** shows a dramatic colour change upon the spin transition. Complex **5** shows a continuous and incomplete spin transition, and **6** is HS over the whole temperature range investigated (10–400 K).
(© Wiley-VCH Verlag GmbH & Co. KGaA, 69451 Weinheim, Germany, 2007)

## Introduction

Spin crossover (SCO) has turned out to be a particularly appealing phenomenon as it offers one of the best examples of molecular bistability. This reversible change between low-spin (LS) and high-spin (HS) states driven by variation of temperature and/or pressure or also by light irradiation is mainly observed in pseudo-octahedral iron(II) coordination complexes. SCO compounds have distinct magnetic and optical properties, dielectric constant, colour and structure in the HS and LS states. These properties may be altered drastically in a narrow temperature range for cooperative transitions.[1–4] Furthermore, hysteresis accompanies a first-order spin transition (ST) when the structural changes are transmitted cooperatively throughout the whole solid.

SCO materials are potentially useful for rewritable optical, thermal or pressure memories at a nanometric scale due to their switching properties.[5–7] The necessary conditions that an SCO material must fulfil for the construction of devices for thermal displays or recording data include abruptness of spin transition with hysteresis, room-temperature operation, change of colour and chemical stability. Prototypes of thermal displays based on the 1D SCO polymeric systems $[Fe(4\text{-}Rtrz)_3](ClO_4)_2$, $[Fe(4\text{-}R^1trz)_{3-3x}(4\text{-}R^2trz)_{3x}](A)_2\cdot nH_2O$ and $[Fe(4\text{-}Rtrz)_3](A^1{}_{1-x}A^2{}_x)_2\cdot nH_2O$ (4-Rtrz = 4-substituted-1,2,4-triazole), where $x \leq 1$ and $n \geq 0$, have been described.[6,7] These salts, and their closely related

[a] Institut für Anorganische und Analytische Chemie, Johannes-Gutenberg-Universität,
Staudinger-Weg 9, 55099 Mainz, Germany
[b] Institut de Ciència Molecular/Departament de Química Inorgànica, Universitat de València, Edifici de Instituts de Paterna, Apartat de Correus 22085,
46071 València, Spain
[c] Departament de Física Aplicada, Universitat Politécnica de València,
Camí de Vera s/n, 46022, València, Spain
[d] Laboratoire de Chimie Inorganique et Matériaux Moléculaires, UMR-CNRS 7071, FR-CNRS 2769, Université Pierre et Marie Curie,
4 place Jussieu, case courrier 42, 75252 Paris Cedex 05, France
Supporting information for this article is available on the WWW under http://www.eurjic.org or from the author.

 © 2007 Wiley-VCH Verlag GmbH & Co. KGaA, Weinheim 

analogs $[Fe(Htrz)_3](A)_2$, have been subjected to intense studies because of their interesting properties.[8] Similarly, 4-substituted triazole ligands like 4-amino-1,2,4-triazole,[9] 4-(2′-hydroxyethyl)-1,2,4-triazole (hyetrz),[10] 4-*n*-alkyl-1,2,4-triazoles[11] and 4-(3′-hydroxypropyl)-1,2,4-triazole (hyptrz)[12] have also afforded interesting 1D SCO polymers. This family of polymeric compounds has recently been reviewed.[13] Several of the polymers belonging to this family undergo cooperative SCO at close to room temperature with large hysteresis loops. Furthermore, these materials display dramatic changes in colour from purple to white upon spin transition LS↔HS, which makes them particularly attractive for memory and sensor devices.[6,7] Other groups linked to the 4-substituted triazole ligands have yielded 1D SCO polymers exhibiting liquid-crystal properties,[14] Langmuir–Blodgett films showing spin transition and SCO gels.[15b,15c] Two more kinds of one-dimensional (1D) $Fe^{II}$ SCO compounds can be distinguished depending on the nature of the N-donating groups involved in the bridges, namely those bearing tetrazole[13,16,17] or pyridine groups.[18–21]

In our search for new SCO systems, and in light of the suitability of triazole-based ligands for achieving cooperative spin transitions, we chose the ligand *N*-(4*H*-1,2,4-triazol-4-yl)benzamide (tba). Herein we present the synthesis and physical characterisation by means of magnetic susceptibility measurements, Mössbauer spectroscopy, differential scanning calorimetry, EXAFS and XRD analysis of a new family of 1D spin crossover polymers with general formula $[\{Fe(tba)_3\}X_2]\cdot nH_2O$ [Scheme 1; X = $CF_3SO_3^-$, $n$ = 2 (**1**), $n$ = 0 (**4**); $BF_4^-$, $n$ = 3 (**2**), $n$ = 0 (**5**); 4-$CH_3C_6H_4SO_3^-$, $n$ = 3 (**3**), $n$ = 0 (**6**)]. The copper analogue $[\{Cu(tba)_3\}(CF_3SO_3)_2]\cdot 3H_2O$ (**7**) has also been synthesised and its crystal structure solved at 293 K.

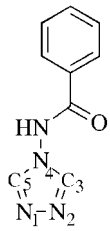


Scheme 1. Ligand *N*-(4*H*-1,2,4-triazol-4-yl)benzamide (tba).

## Results and Discussion

### Crystal Structure of $[\{Cu(tba)_3\}(CF_3SO_3)_2]\cdot 3H_2O$ (7)

As discussed in the Experimental Section, all attempts to obtain single crystals of the $[\{Fe(tba)_3\}X_2]\cdot nH_2O$ compounds were unsuccessful. However, it proved possible to obtain single crystals of the copper analog $[\{Cu(tba)_3\}(CF_3SO_3)_2]\cdot 3H_2O$ (**7**). X-ray diffraction data were collected at 293 K and the structure was solved by direct methods using SHELXS-97[22] and refined by full-matrix least squares on $F^2$ using SHELXL-97. Due to the medium quality of the single crystals it was not possible to decrease the *R* factor of the structure below 0.1749. The powder diffraction pattern of **7** was collected at 293 K, where it matches exactly that calculated from the single crystal data (Figure S1, Supporting Information). Compound **7** crystallises in the triclinic space group $P\bar{1}$. The crystallographic data are provided in the Experimental Section and a selection of bond lengths and angles is given in Table 1. Figure 1 displays a fragment of the 1D polymer **7** together with the corresponding atom-numbering scheme. The unit cell contains four crystallographically independent copper ions with an occupancy factor of 0.5 for Cu1 and Cu4, nine tba

Table 1. Selected bond length [Å] and angles [°] for **7** at 293 K.

| | | | | | |
|---|---|---|---|---|---|
| Cu1–N14 | 2.011(9) | Cu3–N18 | 2.016(9) | Cu4–N30 | 2.008(10) |
| Cu1–N71 | 2.151(10) | Cu3–N19 | 2.029(10) | Cu4–N17 | 2.036(10) |
| Cu1–N24 | 2.242(10) | Cu3–N15 | 2.043(11) | Cu4–N25 | 2.035(11) |
| Cu2–N16 | 2.044(10) | Cu3–N21 | 2.080(10) | Cu4–N8 | 2.053(9) |
| Cu2–N11 | 2.159(10) | Cu3–N22 | 2.329(10) | Cu4–N23 | 2.329(10) |
| Cu2–N13 | 2.259(10) | Cu3–N7 | 2.365(10) | Cu4–N20 | 2.351(10) |
| N14–Cu1–N14[a] | 180.0(5) | N18–Cu3–N19 | 176.7(4) | N30–Cu4–N17 | 177.7(4) |
| N14–Cu1–N24 | 91.0(4) | N18–Cu3–N15 | 89.1(4) | N30–Cu4–N25 | 88.9(4) |
| N14–Cu1–N24[a] | 89.0(4) | N19–Cu3–N15 | 92.3(4) | N17–Cu4–N25 | 91.4(4) |
| N24–Cu1–N24[a] | 180.0(5) | N18–Cu3–N21 | 90.5(4) | N30–Cu4–N8 | 91.3(4) |
| N14–Cu1–N71 | 90.0(4) | N19–Cu3–N21 | 88.0(4) | N17–Cu4–N8 | 88.4(4) |
| N71–Cu1–N71[a] | 180.0(4) | N15–Cu3–N21 | 179.6(4) | N25–Cu4–N8 | 179.5(4) |
| N71–Cu1–N24 | 93.5(4) | N18–Cu3–N22 | 92.1(4) | N30–Cu4–N23 | 90.7(4) |
| N71[a]–Cu1–N24 | 86.5(4) | N19–Cu3–N22 | 90.8(4) | N17–Cu4–N23 | 91.6(4) |
| N16–Cu2–N16[a] | 180.0(4) | N15–Cu3–N22 | 92.8(4) | N25–Cu4–N23 | 91.9(4) |
| N16–Cu2–N11 | 88.3(4) | N21–Cu3–N22 | 87.0(4) | N8–Cu4–N23 | 87.7(4) |
| N16–Cu2–N11[a] | 91.7(4) | N18–Cu3–N7 | 90.2(4) | N30–Cu4–N20 | 90.1(4) |
| N11–Cu2–N11[a] | 180.0(0) | N19–Cu3–N7 | 86.9(4) | N17–Cu4–N20 | 87.6(4) |
| N16–Cu2–N13 | 90.4(4) | N15–Cu3–N7 | 89.3(4) | N25–Cu4–N20 | 89.1(4) |
| N16–Cu2–N13[a] | 89.6(4) | N21–Cu3–N7 | 90.9(4) | N8–Cu4–N20 | 91.3(3) |
| N11–Cu2–N13 | 93.1(4) | N22–Cu3–N7 | 176.9(3) | N23–Cu4–N20 | 178.7(4) |
| N11–Cu2–N13[a] | 86.9(4) | | | | |
| N13–Cu2–N13[a] | 180.0(0) | | | | |

[a] $i = 1 - x, 1 - y, -z$

 © 2007 Wiley-VCH Verlag GmbH & Co. KGaA, Weinheim 

ligands, six $CF_3SO_3^-$ anions and nine water molecules. The bidentate *N*-(4*H*-1,2,4-triazol-4-yl)benzamide ligand bridges the copper ions through the 1- and 2-nitrogen atoms to form a one-dimensional infinite polymer. Each $Cu^{II}$ ion is coordinated to six N atoms belonging to six tba ligands with pseudo-octahedral symmetry, as indicated by the bond lengths and angles (Table 1). The axial bond lengths are notably larger than the equatorial ones due to the Jahn–Teller distortion, which are in the range 2.242(10)–2.351(10) Å for the four $Cu^{II}$ ions. The average $Cu^{II}$–N bond length is 2.134, 2.154, 2.143 and 2.135 Å for Cu1, Cu2, Cu3 and Cu4, respectively. The Cu–Cu distance through the tba bridge is 3.8915(12) Å. These structural parameters are similar to those observed previously for other $Cu^{II}$-triazole systems.[23]

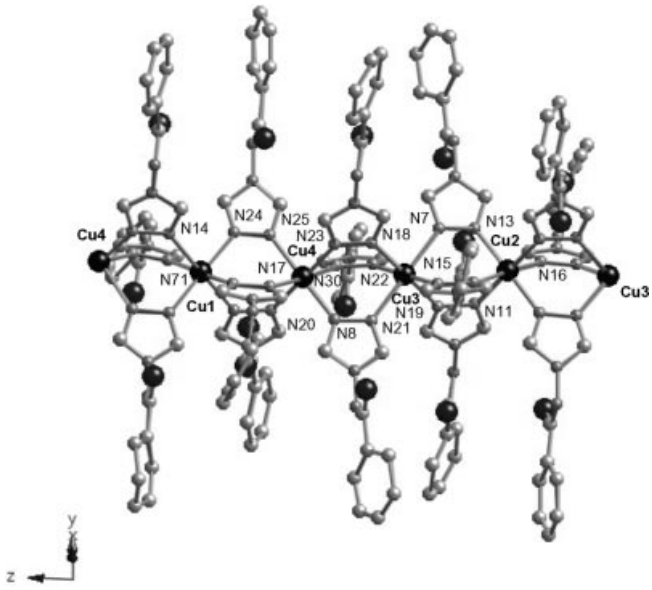


Figure 1. Fragment of the 1D polymer **7** together with the corresponding atom numbering scheme.

Figure 2 illustrates the crystal packing of **7** in the *xy* plane. The molecular crystal packing of **7** can be described as an infinite hexagonal array of $[Cu(tba)_3]^{2+}$ linear chains along the *z* direction, with water molecules and $CF_3SO_3^-$ counterions in the vacancies. The distance between the $Cu^{II}$ linear chains is 17.816(2) Å. There are no intermolecular interactions between the chains through the phenyl group of the tba ligands or between the counterions, the water molecules and the tba ligands. The shortest distance between the carbon atoms of two phenyl groups belonging to adjacent chains is 5.219(2) Å. The water molecules are located around the $Cu^{II}$ linear chain at a distance to the $Cu^{II}$ ion between 4.509(2) and 4.951(2) Å.

## X-ray Powder Diffraction of Compounds 1–3 and 7

X-ray powder patterns of **1**–**3** and **7** were recorded at 293 K (Figure 3). Only two compounds have similar profiles, namely compounds **1** and **7**, where small discrepancies between weak peaks can be interpreted as being due to the hydration numbers of both compounds. The profiles of compounds **2** and **3** are not similar and therefore they are not isostructural with **1**. Only two intense peaks located at about the same values (5–6° and 23–24°) were found to be common to all the patterns. This, together with the fact that similar patterns are only found for the triflate complexes of iron(II) and copper(II), shows that, although a chain structure seems to be present in all of these compounds, the dif-

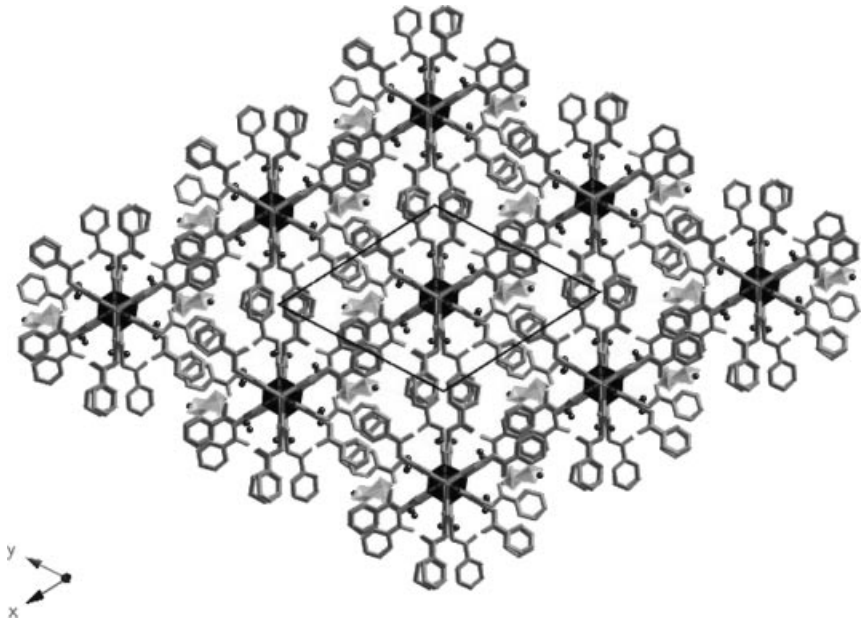


Figure 2. View of the crystal packing of compound **7** in the *xy* plane depicting the packing of the $CF_3SO_3^-$ anions (light grey polyhedra) and water molecules (black spheres) between the cationic linear chains.

 © 2007 Wiley-VCH Verlag GmbH & Co. KGaA, Weinheim 

ferent packing and lattice arrangements caused by the different nature of the anions yield completely different crystallographic patterns.[24]

### IR Spectroscopic Studies of 1–3 and 7

Information about the coordination modes of tba in complexes **1**–**3** and **7** can be derived directly from the room-temperature IR spectra. The intense peaks located at 627, 625, 625 and 628 $cm^{-1}$ for **1**–**3** and **7**, respectively, correspond to torsion vibrations of the triazole rings coordinated in a bridging fashion through N(1) and N(2) (Scheme 1) to neighbouring $Fe^{II}$ or $Cu^{II}$ ions.[25a] The band at 1207 $cm^{-1}$ assigned to the exocyclic N–N bond stretching in uncoordinated tba ligand should be shifted to higher frequency upon bidentate coordination. Indeed, the value of this band in the linear coordination polymers is typically 15–30 $cm^{-1}$ higher than in the free ligand[25b] (1228, 1222, 1223 and 1227 $cm^{-1}$ for compounds **1**–**3** and **7**, respectively). These findings confirm the one-dimensional polymeric organisation of **1** and **7** and strongly suggest the same for compounds **2** and **3**.

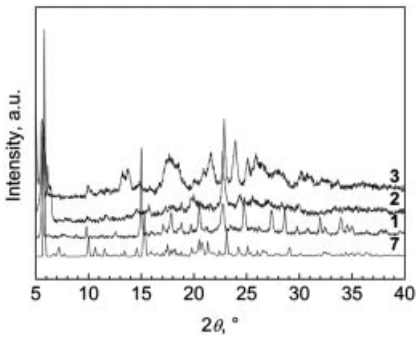


Figure 3. XRD powder diffraction patterns of complexes **1**–**3** and **7** at 293 K.

### EXAFS and XANES Characterisation of Compound 1

The normalised XANES spectrum of **1** recorded at 80 K is typical for an octahedral complex of iron(II) (Figure 4a). It includes absorption in the pre-edge region P assigned to the symmetry-forbidden electronic dipolar 1s→3d transition.[26] The first strong absorption (peak A) is located at 7130 eV and can be attributed to a metal 1s→4p dipole-allowed transition.[26] Further intense shoulders B and M with energies of 7142 and 7154 eV, respectively, are caused by multiple electron-scattering processes.[27] Finally, absorp-

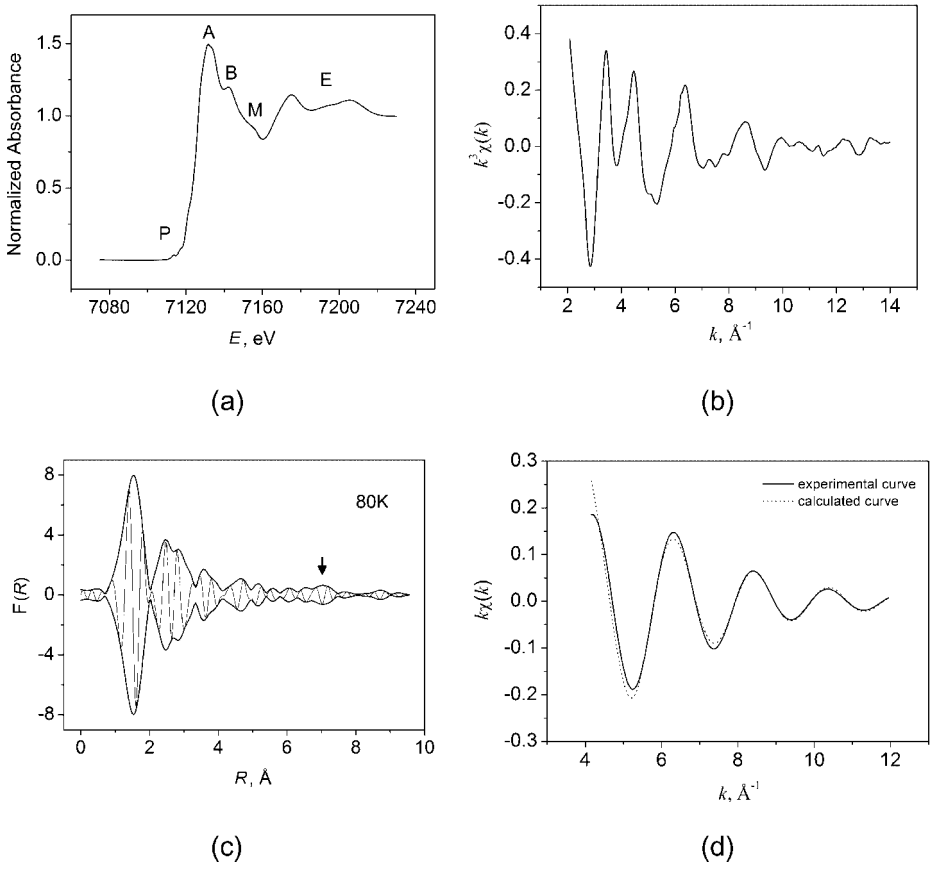


Figure 4. (a) XANES spectrum of complex **1** at 80 K. P: pre-edge; A: top of the edge; B and M: shoulders; E: EXAFS oscillations. (b) $k^3\chi(k)$ spectrum of complex **1**. (c) Fourier transforms of the EXAFS spectrum of complex **1** at 80 K including the modulus and imaginary parts. The arrow indicates the peak at about 7 Å that corresponds to the multiple scattering path Fe–Fe–Fe. (d) Comparison of the experimental and calculated $k\chi(k)$ values for the first filtered shell of complex **1** (solid line: experimental; dashed line: fitting curve).

 © 2007 Wiley-VCH Verlag GmbH & Co. KGaA, Weinheim 

tion E is at the frontier of the XANES and EXAFS regions and, for such molecular systems, is mainly determined by scattering processes inside the first coordination shell. The EXAFS oscillation positioned at relatively high energy (7205 eV) confirms the low-spin character of the iron centre.

The EXAFS spectrum of **1** measured at 80 K is shown in Figure 4b, with its Fourier transform displayed in Figure 4c. The EXAFS signal provides direct information about the radial distribution of the backscattering atoms around the absorbing atom. Similar materials have been investigated by means of EXAFS analysis in previous studies and their linear local structure deduced.[28–30] The complex shown in Scheme 2 is composed of triazole moieties and iron(II) ions arranged in a one-dimensional fashion, with the N–N groups of the triazoles bridging adjacent metal centres. The spectrum at 80 K consists of five main peaks (Figure 4c). The first intense peak at 1.53 Å can be attributed to the first coordination shell $N_6(1)$ of the iron ion. The peak value is located at a short distance, thus clearly indicating the LS state. Several peaks are distinguishable in the region between 2 and 4 Å. These correspond to several kinds of distances such as Fe–N(2), C(5), Fe–N(3), C(4) (Scheme 1), and Fe with its two nearest Fe neighbours.[28] According to a previous study,[29] the peak at about 7.0 Å for the LS triazole-based complexes is ascribed to the Fe–Fe–Fe alignment, the intensity of which is strongly enhanced due to the multiple-scattering focusing effect of the collinearly arranged Fe chains.[28] The presence of this peak provides confirmation of the polymeric structure of **1**.

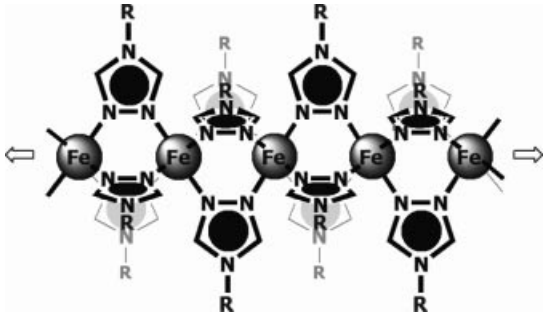


Scheme 2. Drawing of the linear chain structure of $[Fe(R\text{-}trz)_3]^{2+}{}_\infty$.

A curve-fitting analysis was performed for the first coordination sphere of iron (Figure 4d). The fitting variables were the Fe–N distance $R$, the edge energy shift $\Delta E_0$ and the Debye–Waller factor $\sigma$; the coordination number $N$ was fixed to 6. The obtained values were $R$ = 1.96 Å, $\Delta E_0$ = 1.8 eV, $\sigma$ = 0.068 Å with goodness of fit $\rho$ = 1.2%. The value of the Fe–N contact distance is in good agreement with previously reported data for the same type of compounds.[28,30]

## Magnetic Properties of Compounds 1–6

The magnetic data expressed in the form of $\chi_M T$ vs. $T$ plots, where $\chi_M$ is the molar magnetic susceptibility and $T$ the temperature, are shown in Figure 5 for compounds **1**–**6**. The temperature dependence of the magnetic susceptibility was recorded at a rate of 2 K min$^{-1}$. Compound **1** is in the LS configuration at 290 K, as shown by the low $\chi_M T$ value. Upon heating, $\chi_M T$ increases abruptly, reaching a value of 3.29 cm$^3$ K mol$^{-1}$ at 400 K. TGA experiments have shown that dehydration takes place in the same temperature region where the change of spin state occurs (Figure S2, Supporting Information). The dehydration and change of spin state take place in two distinct steps. A synergy between dehydration and spin-state change, as observed in this material, has been reported in several other cases.[1,6,14]

The $\chi_M T$ value for compound **2** at 330 K is 3.41 cm$^3$ K mol$^{-1}$, which falls into the range of values expected for an $Fe^{II}$ compound in the high-spin configuration. This value decreases abruptly at around 260 K as a conse-

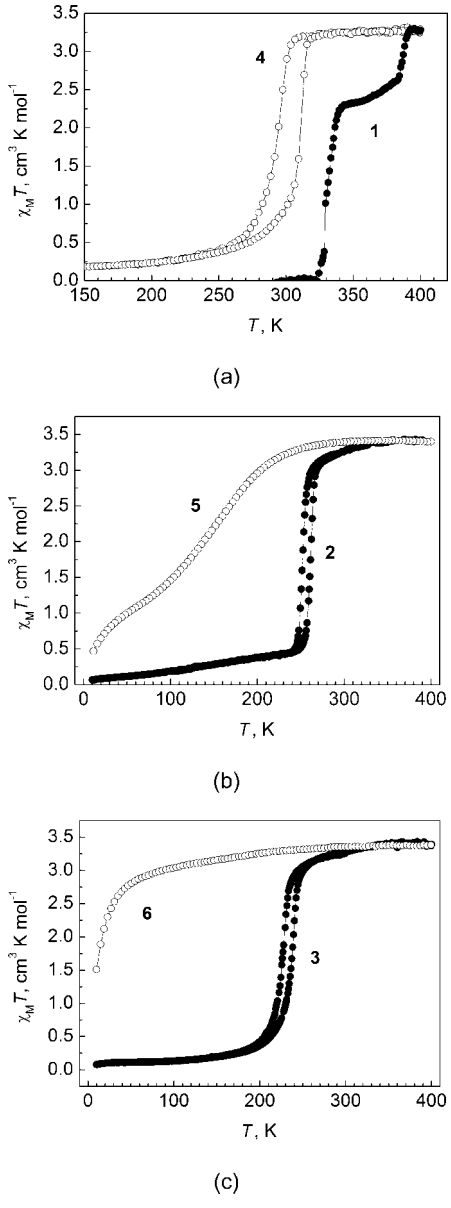


Figure 5. Magnetic properties of compounds **1**–**6** in the form of $\chi_M T$ vs. $T$ plots.

 © 2007 Wiley-VCH Verlag GmbH & Co. KGaA, Weinheim 

quence of a spin transition, reaching a value of 0.43 $cm^3 K mol^{-1}$ at 230 K ($T_c\downarrow$ = 250 K). The transition is complete at this temperature as the magnetic susceptibility decreases only very gradually down to 0.07 $cm^3 K mol^{-1}$ at 10 K, thus indicating that almost all the $Fe^{II}$ ions are in the LS state. In the warming mode, the measurement reveals a hysteresis width of 8 K ($T_c\uparrow$ = 258 K).

Like **2**, compound **3** undergoes an abrupt spin transition, although at lower temperatures ($T_c\downarrow$ = 226 and $T_c\uparrow$ = 238 K). The $\chi_M T$ value for **3** at 290 K is 3.30 $cm^3 K mol^{-1}$, which diminishes slightly on lowering the temperature to 250 K (3.07 $cm^3 K mol^{-1}$). $\chi_M T$ falls to 0.65 $cm^3 K mol^{-1}$ upon further cooling as a consequence of a change of spin state of approximately 90% of the $Fe^{II}$ ions. The $\chi_M T$ value at 145 K is 0.19 $cm^3 K mol^{-1}$, which corresponds to about 95% LS $Fe^{II}$.

The magnetic properties of the dehydrated complexes **4**–**6** were also investigated (Figure 5). Dehydration of these complexes is complete at 400 K (Figure S2, Supporting Information). The samples were therefore heated from 300 to 400 K and then kept at this temperature for 15 min in the SQUID magnetometer. Subsequently, the magnetic susceptibility of the dehydrated samples was recorded from 400 K down to 10 K and again up to 400 K. Compound **4** exhibits an abrupt spin transition centred at room temperature. The $\chi_M T$ value at 400 K is 3.28 $cm^3 K mol^{-1}$, which remains practically constant down to the vicinity of $T_c\downarrow$. $\chi_M T$ diminishes suddenly at 300 K, reaching a value of 0.39 $cm^3 K mol^{-1}$ at 250 K and 0.090 $cm^3 K mol^{-1}$ at 10 K. The critical temperatures in the cooling and warming mode ($T_c\downarrow$ and $T_c\uparrow$) are 284 and 309 K, respectively. It is worthwhile mentioning the relatively large hysteresis width of 25 K that accompanies the spin transition in **4**. The reproducibility of the thermal hysteresis loops in **2**–**4** was confirmed, and they are perfectly reproducible after two or three cooling/warming cycles. Moreover, the spin transition in **2**–**4** is accompanied by a change of colour from white (HS state) to violet (LS state).

Compound **5** exhibits a very gradual and incomplete spin transition. The $\chi_M T$ value at around 400 K shows that all molecules are in the HS state (3.41 $cm^3 K mol^{-1}$). This value remains practically constant down to 250 K, where the HS→LS transition sets in. A further decrease of the temperature gives rise to a progressive decrease of the magnetic susceptibility due to a spin transition of approximately 50% of the $Fe^{II}$ ions. This spin transition is kinetically blocked below 70 K, and the decrease of $\chi_M T$ below this temperature is due most probably to zero-field splitting (ZFS) of the 50% of $Fe^{II}$ ions that remain in the HS state ($S$ = 2). The temperature dependence of the magnetic susceptibility of compound **6** shows a high spin behaviour over the whole temperature range under study (10–400 K). The $\chi_M T$ value at 400 K is 3.38 $cm^3 K mol^{-1}$ and remains constant down to 100 K, where it diminishes most probably due to ZFS.

A weak antiferromagnetic coupling between high-spin iron(II) ions for **5** and **6** cannot be excluded from this explanation. This could, in part, also be responsible for the decrease of the susceptibility on lowering the temperature since a similar behaviour has been found in the triazole-based copper analogue **7** (Figure S3, Supporting Information) as well as in another copper-based triazole polymer.[23a]

### Mössbauer Spectroscopy of Compounds 1–4

Table 2 collects the Mössbauer parameter values and percentages of populations in the HS and LS states for compounds **1**–**4** recorded at different temperatures. The Mössbauer spectrum of compound **1** was recorded at 80 K (Figure 6a). This spectrum clearly indicates the presence of only one slightly asymmetrical doublet characterised by an isomer shift and a quadrupole splitting typical of LS iron(II), which matches the data from the magnetic measurements of **1**. The Mössbauer spectrum of **4** recorded at 80 K shows a doublet with parameters typical for HS iron(II) (Table 2), the intensity of which increases dramatically upon heating up to 330 K. The spectrum also reveals the presence of LS $Fe^{II}$ ions, thereby confirming the incomplete character of the spin transition.

Table 2. Mössbauer parameters ($IS$ and $\Delta E_Q$) for **1**–**4** at different temperatures.

| | $T$ [K] | Spin state | $IS$ [mm $s^{-1}$] | $\Delta E_Q$ [mm $s^{-1}$] | $A$ [%] |
|---|---|---|---|---|---|
| **1** | 80 | d, LS | 0.49(0) | 0.23(1) | 100 |
| **2** | 80 | d, LS | 0.51(0) | 0.27(0) | 97 |
| | | d, HS | 1.22(0) | 3.40(0) | 3 |
| | 290 | d, LS | 0.29(0) | 0.15(0) | 3 |
| | | d, HS | 1.04(0) | 2.80(1) | 97 |
| **3** | 145 | d, LS | 0.52(1) | 0.28(1) | 95 |
| | | d, HS | 1.15(1) | 3.35(0) | 5 |
| | 290 | d, LS | 0.40(1) | 0.14(0) | 8 |
| | | d, HS | 1.05(0) | 2.85(1) | 92 |
| **4** | 80 | d, LS | 0.51(0) | 0.25(1) | 95 |
| | | d, HS | 1.17(1) | 3.29(0) | 5 |
| | 330 | d, LS | 0.32(0) | 0.20(0) | 14 |
| | | d, HS | 1.02(0) | 2.71(1) | 86 |

The Mössbauer spectra of **2** were recorded above and below $T_c$ (Figure 7a). The spectrum at 290 K shows mainly a doublet characteristic of the HS state of $Fe^{II}$. The Mössbauer spectrum recorded at 80 K clearly evidences the change of spin state. After cooling, the HS doublet almost disappears and the LS fraction increases significantly. Like the magnetic measurements, the Mössbauer analysis proves that almost 100% of the $Fe^{II}$ ions undergo a spin transition in **2**.

The Mössbauer spectra of **3** were recorded at 290 and 145 K (Figure 7b). Two doublets are observed at 290 K corresponding to the HS and LS states of the $Fe^{II}$ ions. The analysed spectrum at 290 K yields a relative population of 95% HS and 5% LS states. There is a clear inversion of the population distribution at 145 K due to spin transition: practically all the $Fe^{II}$ ions are in the LS state at this temperature (92%). The Mössbauer spectral analyses of **1**–**4** agree well with the above reported magnetic properties.

 © 2007 Wiley-VCH Verlag GmbH & Co. KGaA, Weinheim 

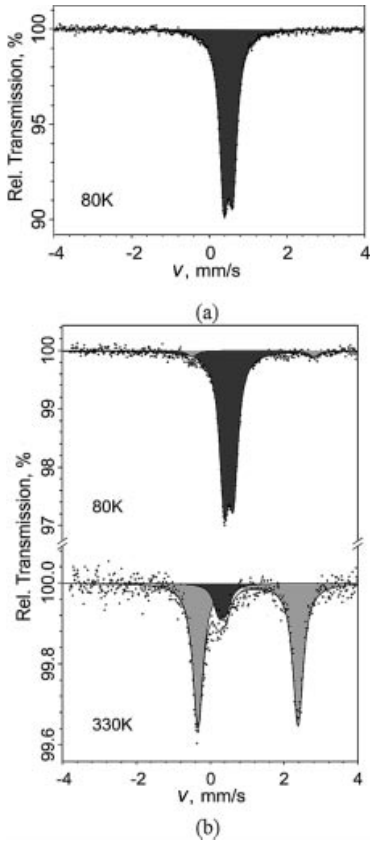


Figure 6. (a) Mössbauer spectrum of **1** at 80 K. (b) Mössbauer spectra of **4** recorded at 80 and 330 K. Dark grey corresponds to the LS doublet; light grey corresponds to the HS doublet.

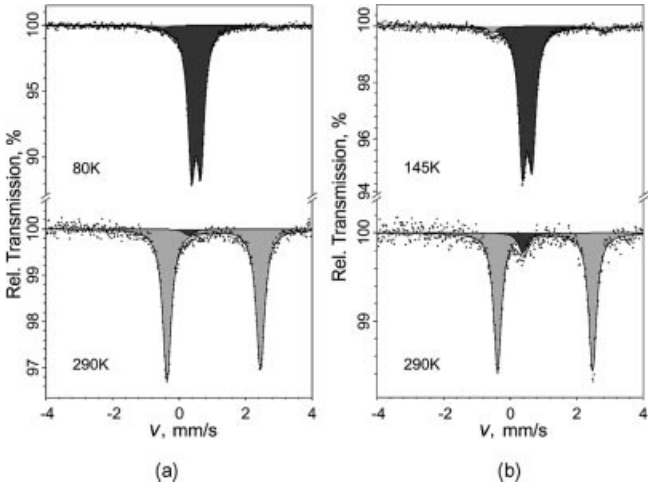


Figure 7. (a) Mössbauer spectra of **2** at 80 and 290 K. (b) Mössbauer spectra of **3** recorded at 145 and 290 K. Dark grey corresponds to the LS doublet; light grey corresponds to the HS doublet.

## Differential Scanning Calorimetry of Compounds 2–4

The differential scanning calorimetric measurements were carried out in the 175–400 K temperature range at a rate of 7 K min$^{-1}$. The temperature dependence of the heat flow in the heating and cooling modes for **2**–**4** is shown in Figure 8. The anomalies in the heat flow for compound **2** appear in the cooling mode at $T_c\downarrow$ = 240 and $T_c\uparrow$ = 252 K in the warming mode, thus indicating the occurrence of a hysteresis with a width of 12 K. These values agree reasonably well with those observed from the $\chi_M T$ vs. $T$ plot. Compounds **3** and **4** exhibit anomalies in the heat flow at $T_c\downarrow$ = 226 and $T_c\uparrow$ = 238 K and $T_c\downarrow$ = 290 and $T_c\uparrow$ = 310 K, respectively, which match reasonably well with the reported magnetic data. The small differences in critical temperatures between the DSC and magnetic data are due to the different heating/cooling rates used in the experiments. Table 3 summarises the derived thermodynamic pa-

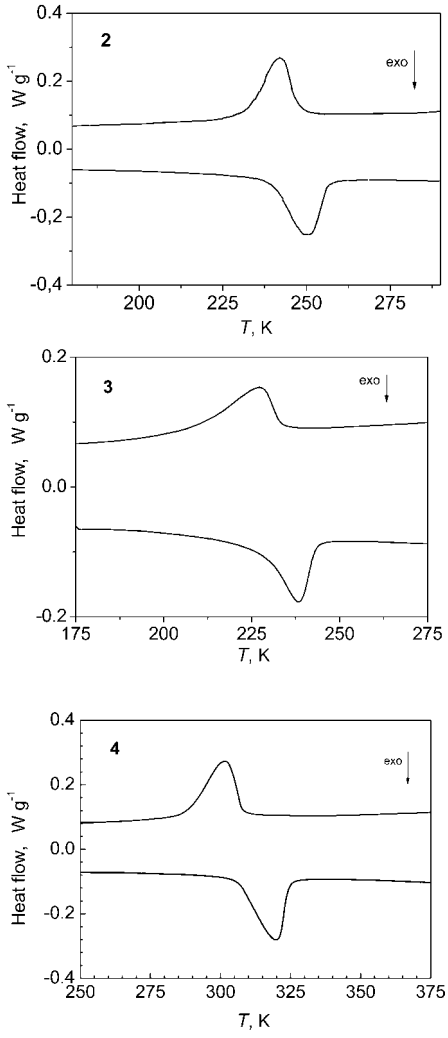


Figure 8. DSC data of complexes **2**–**4** in the warming and cooling modes recorded at a rate of 7 K min$^{-1}$.

Table 3. Thermodynamic parameters ($\Delta H$ and $\Delta S$) for compounds **2**–**4**.

| | $\Delta H$ [kJ mol$^{-1}$] | $\Delta S$ [J K$^{-1}$ mol$^{-1}$] |
|---|---|---|
| **2** | 17.8 | 67.2 |
| **3** | 14.6 | 63.5 |
| **4** | 19.7 | 65.6 |

 © 2007 Wiley-VCH Verlag GmbH & Co. KGaA, Weinheim 

rameters $\Delta H_{SCO}$ and $\Delta S_{SCO}$ for the compounds **2**–**4**; the values obtained are in the range of values expected for $Fe^{II}$ SCO compounds.[1,31,32]

## Discussion

The linear chain structure of compound **1** has been convincingly derived from EXAFS data, thereby confirming the collinear alignment of the metal ions within the polymeric aggregates formed by alternating triazole bridges. Moreover, the crystal structure of the analog $[\{Cu(tba)_3\}(CF_3SO_3)_2]\cdot 3H_2O$ (**7**) confirms the structural features of **1** due to the almost identical powder XRD profiles of these two complexes. The fact that the powder X-ray patterns of **2** and **3** are not similar to those of **1** and **7** does not rule out a similar structure for these complexes as different packing and lattice arrangements would yield different crystallographic patterns even for similar linear chain structures. The final evidence for the similar structural organisation in **1**–**3** and **7** is provided by IR spectroscopy, namely by the absorption bands assigned to the vibrations of the bridging triazole rings featuring $C_{2v}$ symmetry.

The new family of chainlike 4-substituted-1,2,4-triazole $Fe^{II}$ compounds $[\{Fe(tba)_3\}X_2]\cdot nH_2O$ presents similar SCO characteristics to other complexes reported previously.[6–13] Three main influences have been reported to play a crucial role in the spin transition and its characteristics in these compounds: (i) the water content in the crystal lattice,[4,10] (ii) the chemical nature and size of the 4-R substituents[11] and the counterions,[12] and (iii) the length of the polymeric chains.[24a] Stabilisation of the low-spin state by interaction with lattice water molecules has frequently been observed for $Fe^{II}$ SCO compounds, particularly for polymers based on a triazole bridge.[1,13] This is also the case for compound **1**, which loses its lattice water upon heating and undergoes an abrupt change from the LS to the HS state. When the dehydrated material **4** is cooled, an abrupt HS→LS transition occurs at $T_c\downarrow$ = 284 K ($T_c\uparrow$ = 309 K). Subsequent reheating reveals a hysteresis loop of 25 K width centred at room temperature. The length of the chains has been found to be critical for the observation of cooperative and complete spin transition in such triazole polymers.[6–13] The longer the chains are the lower is the residual HS fraction. The Mössbauer spectrum of compound **4** at 80 K clearly denotes the completeness of the spin transition in this complex, with almost all iron(II) ions in the LS state. For compound **1**, the Mössbauer spectrum recorded at 80 K shows that all iron(II) ions are in the LS state. These facts, together with the observation that all water molecules are removed below 400 K (lattice water), allow us to rule out the possibility of having water coordinated to the outer iron(II) ions of the polymeric chains in **1** and **4**. It is therefore likely that the end groups are monocoordinated tba ligands. Taking into account that the spin-transition properties and thermodynamic parameters of **4** are similar to those observed in $[Fe(Htrz)trz](BF_4)$, one could suggest a similar average chain size for both compounds (around 13 nm).[24a]

Compounds **2** and **3** undergo abrupt spin transitions at 258 and 238 K, respectively, both with a hysteresis width of about 10 K. A similar cooperative spin transition has also been observed for $[Fe(fatrz)_3](X)_2\cdot nH_2O$[24a] and $[Fe(4\text{-}n\text{-alkyl-trz})_3](X)_2\cdot nH_2O$.[11] The estimated average chain size in these compounds is 7 nm.[24] Mössbauer spectra recorded for compounds **2** and **3** at liquid-nitrogen temperature indicate that almost all $Fe^{II}$ ions are in the LS state, with a small residual HS fraction. A very different temperature-dependent magnetic behaviour is observed for the corresponding dehydrated compounds **5** and **6**. Thus, complex **5** presents a continuous and incomplete spin transition at $T_{1/2} \approx 100$ K, while **6** shows a paramagnetic behaviour over the whole temperature range studied (10–400 K). These results demonstrate that the water contained in the lattices of these compounds plays a dominant role in the SCO behaviour.

## Conclusion

The present family of polymeric 4-R-substituted triazole $Fe^{II}$ compounds adds new examples to the richness of spin-transition properties of triazole-based polymers. These materials have been suggested to have possible applications as optical sensors by virtue of their thermochromic properties. Indeed, compound **1** represents a new example of a material with potential applications as a temperature threshold optical indicator. As compound **4** is stable at ambient conditions, however, **1** can only be used as a "single-shot" indicator. On the other hand, compound **4** could be used for thermal displays or recording data as it fulfils the necessary conditions (abruptness, hysteresis, room-temperature operation, change of colour and chemical stability). Compounds **2** and **3** could be useful in another temperature range of operation, namely the freezing-water region.

## Experimental Section

**Synthesis of Materials:** Starting reagents and solvents were obtained commercially from Aldrich and used as received.

**Measurements:** FTIR spectra (KBr pellets) were recorded with a Bruker Tensor 27 spectrometer in the range of 400–4000 $cm^{-1}$. Elemental analyses were performed with a Vario EL Mikro Elementaranalysator. NMR spectroscopic measurements were performed with a Bruker DRX 400 spectrometer.

***N*-(4*H*-1,2,4-Triazol-4-yl)benzamide (tba):** A suspension of 4-amino-4*H*-1,2,4-triazole (4.2 g, 50 mmol) and benzoyl chloride (7.0 g, 50 mmol) in dry pyridine (100 mL) was refluxed for 24 h. The solvents were then removed in vacuo to provide a cream-coloured solid, which was dissolved in hot water (100 mL) and neutralised with sodium hydrogen carbonate until no further effervescence was observed. The white precipitate obtained on cooling was filtered, washed with water and finally recrystallised from ethanol to give 6.48 g of tba (69%). $^1H$ NMR (400 MHz, [D$_6$]DMSO): $\delta$ = 12.1 (br. s, 1 H, N*H*), 8.73 (s, 2 H, CH of trz), 7.89 (dd, $J$ = 1.36, 7.20 Hz, 2 H, ph*H*), 7.61 (tt, $J$ = 1.36, 7.20 Hz, 1 H, ph*H*), 7.52 (t, $J$ = 7.2 Hz, 2 H, ph*H*) ppm. FT-IR (KBr): $\tilde{\nu}$ = 3113 [$\nu$(CH of trz)], 2000–1750 [$\nu$(Ph)], 1674 [$\nu$(C=O)] $cm^{-1}$. $C_9H_8N_4O$ (188.19): calcd.

 © 2007 Wiley-VCH Verlag GmbH & Co. KGaA, Weinheim 

C 57.44, H 4.28, N 29.77; found C 57.41, H 4.24, N 29.81. EI MS: *m*/*z* (%) = 188.2 (2) $[M]^+$, 105.0 (100) $[M - trzNH]^+$.

**$Cu(CF_3SO_3)_2·6H_2O$:** Copper(II) hydroxide, obtained by the metathesis reaction of copper(II) sulfate with sodium hydroxide, was dissolved in a hot aqueous solution of trifluoromethanesulfonic acid. The blue crystals that formed upon cooling were filtered off and air-dried to provide the analytically pure salt in quantitative yield. FT-IR (KBr): $\tilde{\nu}$ = 3473 [br., ν(O–H)], 1255 [s, $\nu_a(SO_3^-)$], 1032 [s, ν(C–F)] $cm^{-1}$. $C_2H_{12}CuF_6O_{12}S_2$ (469.76): calcd. C 5.11, H 2.57, S 13.65; found C 5.07, H 2.67, S 13.92.

**General Procedure for the Synthesis of the Iron(II) Salts:** Iron powder was dissolved in an aqueous solution containing a stoichiometric amount of the corresponding acid by heating. The greenish crystalline precipitate that formed upon cooling was filtered off and air-dried to provide the analytically pure salt in quantitative yield.

**$[Fe(CF_3SO_3)_2]·6H_2O$:** FT-IR (KBr): $\tilde{\nu}$ = 3473 [br., ν(O–H)], 1188 [$\nu_a(SO_3^-)$], 1035 [s, ν(C–F)] $cm^{-1}$. $C_2H_{12}F_6FeO_{12}S_2$ (462.06): calcd. C 5.20, H 2.62, S 13.88; found C 5.25, H 2.60, S 13.89.

**$[Fe\{4\text{-}CH_3(C_6H_4)SO_3\}_2]·6H_2O$:** FT-IR (KBr): $\tilde{\nu}$ = 3407 [br., ν(O–H)], 1669 (s), 1496 (s), 813 [s, ν(Ph)], 1190 [s, $\nu_a(SO_3^-)$], 3407 [br., ν(O–H)] $cm^{-1}$. $C_{14}H_{26}FeO_{12}S_2$ (506.32): calcd. C 33.21, H 5.18, S 12.67; found C 33.24, H 4.93, S 13.05.

**General Procedure for the Synthesis of Compounds 1–3 and 7:** A methanolic solution of the $MA_2$ salt (0.53 mmol; M = Cu or Fe; A = 4-$CH_3C_6H_4SO_3^-$, $CF_3SO_3^-$, $BF_4^-$) was added to a hot methanolic solution of *N*-(4*H*-1,2,4-triazol-4-yl)benzamide (0.3 g, 1.6 mmol). The mixture was refluxed for 5 min, then concentrated by concentrating and cooled to room temperature. The resulting precipitate was filtered off and dried in air. The yields of complexes varied in the range 70–85%.

**$[\{Fe(tba)_3\}(CF_3SO_3)_2]·2H_2O$ (1):** FT-IR (KBr): $\tilde{\nu}$ = 3483 [br., ν(O–H)], 2000–1750 [ν(Ph)], 1694 [ν(C=O)], 1269 [$\nu_{as}(SO_3^-)$] $cm^{-1}$. $C_{29}H_{28}F_6FeN_{12}O_{11}S_2$ (954.57): calcd. C 36.49, H 2.96, N 17.61, S 6.72; found C 36.10, H 2.93, N 17.21, S 6.95.

**$[\{Fe(tba)_3\}(BF_4)_2]·3H_2O$ (2):** FT-IR (KBr): $\tilde{\nu}$ = 3491 [br., ν(O–H)], 3127 [$\nu_{as}$(C–H)], 2000–1750 [ν(Ph)], 1688 [ν(C=O)], 1093 [ν(B–F)]. $C_{27}H_{30}B_2F_8FeN_{12}O_6$ (848.06): calcd. C 38.24, H 3.57, N 19.82; found C 38.02, H 3.56, N 19.87.

**$[\{Fe(tba)_3\}(4\text{-}CH_3C_6H_4SO_3)_2]·3H_2O$ (3):** FT-IR (KBr): $\tilde{\nu}$ = 3483 [br., ν(O–H)], 2000–1750 [ν(Ph)], 1694 [ν(C=O)], 1168 [$\nu_{as}(SO_3^-)$] $cm^{-1}$. $C_{41}H_{44}FeN_{12}O_{12}S_2$ (1016.84): calcd. C 48.43, H 4.36, N 16.53, S 6.31; found C 47.61, H 4.50, N 16.20, S 6.65.

**$[Fe(tba)_3](CF_3SO_3)_2$ (4), $[Fe(tba)_3][BF_4]_2$ (5) and $[Fe(tba)_3](4\text{-}CH_3C_6H_4SO_3)_2$ (6):** Compounds **4**–**6** were obtained by heating the hydrated compounds **1**–**3** in an oven at 400 K for 30 min.

**$[\{Cu(tba)_3\}(CF_3SO_3)_2]·3H_2O$ (7):** This complex was recrystallised from hot water by slow cooling in a thermostat overnight to provide blue, needle-like crystals. FT-IR (KBr): $\tilde{\nu}$ = 3480 [br., ν(O–H)], 2000–1750 [ν(Ph)], 1697 [ν(C=O)], 1267 [$\nu_{as}(SO_3^-)$] $cm^{-1}$. $C_{29}H_{32}CuF_6N_{12}O_{13}S_2$ (998.30): calcd. C 34.89, H 3.23, N 16.84, S 6.42; found C 35.03, H 3.11, N 16.55, S 6.24.

**Thermogravimetric Analysis:** TGA measurements were performed with a Mettler Toledo TGA/SDTA 851 in tandem with a mass spectrometer in the 300–680 K temperature range under nitrogen with a heating rate of 10 K $min^{-1}$.

**Differential Scanning Calorimetry:** DSC measurements were performed with a Mettler model DSC 822e calibrated with metallic indium and zinc. The samples were located in sealed sample pans. DSC profiles were recorded at the rate of 7 K $min^{-1}$ and analysed with the Netzsch Proteus software (NETZSCH-Geraetebau GMBH; http://www.e-thermal.com/proteus.htm).

**Magnetic Susceptibility Measurements:** The variable-temperature magnetic susceptibility measurements were performed with a Quantum Design MPMS2 SQUID susceptometer equipped with a 5.5 T magnet at 1 T and 1.8–400 K. Experimental data were corrected for diamagnetism using Pascal's constants.[33]

**Mössbauer Spectroscopy:** Mössbauer spectra were recorded in transmission geometry with a $^{57}Co/Rh$ source kept at room temperature and a conventional spectrometer operating in the constant-acceleration mode. The samples were sealed in a Plexiglass sample holder and mounted in a nitrogen-bath cryostat. The Recoil 1.03a Mössbauer Analysis Software (Dr. E. Lagarec; http://www.isapps.ca/recoil/) was used to fit the experimental spectra.

**X-ray Single-Crystal Crystallographic Study:** Diffraction data for complex **7** were collected with a Nonius Kappa-CCD single crystal diffractometer using Mo-$K_\alpha$ radiation ($\lambda$ = 0.71073 Å). A multiscan absorption correction was found to have no significant effect on the refinement results. The structure was solved by direct methods using SHELXS-97 and refined by full-matrix least squares on $F^2$ using SHELXL-97.[22] All non-hydrogen atoms were refined anisotropically. Further details can be found in Table 4. CCDC-636097 contains the supplementary crystallographic data for compound **7**. These data can be obtained free of charge from The Cambridge Crystallographic Data Centre via www.ccdc.cam.ac.uk/data_request/cif.

Table 4. Crystal data for **7** at 293 K.

| | |
|---|---|
| Empirical formula | $C_{29}H_{30}CuF_6N_{12}O_{12}S_2$ |
| Formula mass | 980.31 |
| Space group | $P\bar{1}$ |
| *a* [Å] | 17.8020(3) |
| *b* [Å] | 17.8160(4) |
| *c* [Å] | 23.2650(5) |
| *α* [°] | 89.2120(10) |
| *γ* [°] | 60.3130(10) |
| *V* [$Å^3$] | 6371.8(2) |
| *Z* | 6 |
| $D_{calcd.}$ [mg $cm^{-3}$] | 1.533 |
| *F*(000) | 2994 |
| *μ* (Mo-$K_\alpha$) [$mm^{-1}$] | 0.709 |
| Crystal size [mm] | 0.02 × 0.02 × 0.05 |
| Temperature [K] | 293(2) |
| Total reflections | 16963 |
| Reflections [$I > 2\sigma(I)$] | 10839 |
| $R_1$[a] [$I > 2\sigma(I)$] | 0.1749 |
| *wR* | 0.4591 |
| *S* | 1.396 |

[a] $R_1 = \Sigma||F_o| - |F_c||/\Sigma|F_o|$; $wR = \{\Sigma[w(F_o^2 - F_c^2)^2]/\Sigma[w(F_o^2)^2]\}^{1/2}$; $w = 1/[\sigma^2(F_o^2) + (mP)^2 + nP]$ where $P = (F_o^2 + 2F_c^2)/3$, $m$ = 0.2000 and $n$ = 0.0000.

**X-ray Powder Diffraction:** X-ray measurements were obtained with a STOE STADI 2 diffractometer equipped with a linear position-sensitive detector (STOE mini PSD). Monochromatic Cu-$K_\alpha$ radiation was obtained by using a curved germanium detector (111 plane).

**X-ray Absorption Data Recording and Processing:** The Fe K-edge XANES (X-ray absorption near-edge structures) and EXAFS (extended X-ray absorption fine structures) data were taken in the conventional transmission mode on beamline A1 at the German Electron Synchrotron (DESY), Hamburg. The spectrum was recorded from 6970 to 7997 eV. The energy scale at the iron K-edge

 © 2007 Wiley-VCH Verlag GmbH & Co. KGaA, Weinheim 

was calibrated with reference to the strong absorption peak of elemental iron at 7111.2 eV. A water-cooled Si(111) channel-cut crystal was employed as a monochromator. The intensities of the incident and transmitted X-rays were recorded using ionisation chambers. The mass of the sample was calculated to obtain a product $a \times d$ of about 2.5 for energies just above the absorption K-edge of iron ($a$ is the linear absorption coefficient and $d$ is the thickness of the pellet). The calculated amount of sample was ground, then mixed with crystalline cellulose and pressed into a pellet of 13 mm diameter and about 1 mm thickness. The temperature of the experiment was 80 K, which was maintained with a closed-cycle He cryostat. The temperature was measured with an Si diode placed close to the sample. The acquisition time for each data point was 1 s. EXAFS data analysis was performed with the program EXAFS98.[34] This standard analysis includes linear pre-edge background removal, a smoothing spline atomic absorption energy-dependent procedure, called Lengeler–Eisenberg EXAFS spectrum normalisation, and reduction from the absorption data $\mu(E)$ to the EXAFS spectrum $\chi(k)$ with

$$k = \sqrt{\frac{2m_e}{(\hbar)^2}(E - E_0)}$$

where $E_0$ is the energy threshold taken at the absorption maximum ($7130 \pm 1$ eV). The radial distribution function $F(R)$ was calculated by Fourier transformation of $k^3 w(k)\chi(k)$ in the 2–14 Å$^{-1}$ range; $w(k)$ is a Kaiser–Bessel apodisation window with smoothness coefficient $\tau = 3$. After Fourier filtering, the first single-shell Fe–$N_6$ was fitted in the 4–12 Å$^{-1}$ range to the standard EXAFS formula, without multiple scattering:

$$k_\chi(k) = -S_0^2 \sum_{i=1,5} \left[ \frac{N_i}{R_i^2} \cdot (F\pi, k) \,|\, e^{-2\sigma^2 k^2} e^{-\frac{2R_i}{\lambda(k)}} \sin(2kR_i + 2\partial_1(k) + \Psi(k)) \right]$$

where $S_0^2$ is the inelastic reduction factor, $N$ is the number of nitrogen atoms at a distance $R$ from the iron centre, $\lambda$ is the mean free path of the photoelectron, $\sigma$ is the Debye–Waller coefficient, characteristic of the width of the Fe–N distance distribution, $\partial_1(k)$ is the central atom phase shift, and $|(F\pi,k)|$ and $\psi(k)$ the amplitude and phase of the nitrogen back-scattering factor, respectively. The curve-fitting analysis for the first coordination sphere of the iron atom was performed with the Round Midnight[35] code after Fourier filtering in the 0.7–2.0 Å range of the EXAFS spectrum with spherical-wave theoretical amplitudes and phase shifts calculated by the McKale[36] code. Since theoretical phase shifts were used, it was necessary to fit the energy threshold $E_0$ by adding an extra fitting parameter, $\Delta E_0$. The goodness of fit was given by:

$$\rho(\%) = \frac{\Sigma[k\chi_{exp}(k) - k\chi_{th}(k)]^2}{\Sigma[k\chi_{exp}(k)]^2}$$

**Supporting Information** (see footnote on the first page of this article): XRD diffraction patterns of **7**, both experimental and calculated from the single crystal data (Figure S1), TGA plots of compounds **1**–**3** (Figure S2), and magnetic properties of compound **7** in the form of a $\chi_M T$ vs. $T$ plot (Figure S3).

## Acknowledgments

We acknowledge financial help from the Deutsche Forschungsgemeinschaft (Priority Program 1137 "Molecular Magnetism"), the Fonds der Chemischen Industrie and the Materialwissenschaftliches Forschungszentrum der Universität Mainz. A. B. G. thanks the Spanish MEC for a Ramón y Cajal research contract and the Alexander von Humboldt Foundation for a fellowship. A. B. G. and M. C. M. thank the Spanish MEC (project CTQ2004-03456-BQU) and the Generalitat Valenciana (ACOMP07/110). We thank Dr. V. Ksenofontov for helpful discussions. We also acknowledge the support of Dr. E. Welter from HASYLab, Dr. H. Ehrenberg and Dominic Stürmer from TU Darmstadt for the EXAFS measurements at beamline A1, the technicians E. Muth and P. Räder from MPI Polymerforschung Mainz for DSC and TGA measurements and A. Michalowicz for providing us with his XAS analysis package.[35]

[1] *Spin Crossover in Transition Metal Compounds* (Eds.: P. Gütlich, H. A. Goodwin), in *Topics in Current Chemistry*, Springer-Verlag, Berlin, Heidelberg, **2004**, vols. 233, 234, 235.
[2] a) J. A. Real, A. B. Gaspar, M. C. Muñoz, *Dalton Trans.* **2005**, 2062; b) A. B. Gaspar, V. Ksenofontov, M. Seredyuk, P. Gütlich, *Coord. Chem. Rev.* **2005**, 249, 2661.
[3] J. A. Real, A. B. Gaspar, V. Niel, M. C. Muñoz, *Coord. Chem. Rev.* **2003**, *236*, 121.
[4] P. Gütlich, A. Hauser, H. Spiering, *Angew. Chem. Int. Ed. Engl.* **1994**, *33*, 2024.
[5] A. Galet, A. B. Gaspar, M. C. Muñoz, G. V. Bukin, G. Levchenko, J. A. Real, *Adv. Mater.* **2005**, *17*, 2949.
[6] a) O. Kahn, C. J. Martinez, *Science* **1998**, *279*, 44; b) O. Kahn, J. Kröber, C. Jay, *Adv. Mater.* **1992**, *4*, 718.
[7] Y. García, V. Ksenofontov, P. Gütlich, *Hyperfine Interact.* **2002**, *139*, 543.
[8] a) L. G. Lavrenova, V. N. Ikorski, V. A. Varnek, G. A. Berezovskii, V. G. Bessergenev, N. V. Bausk, S. B. Erenburg, S. V. Larionov, *Koord. Khim.* **1996**, *22*, 357; b) J. Kröber, R. Audière, R. Claude, E. Codjovi, O. Kahn, J. G. Haasnoot, F. Grolière, C. Jay, A. Bousseksou, J. Linares, F. Varret, A. Gonthier-Vassal, *Chem. Mater.* **1994**, *6*, 1404.
[9] L. G. Lavrenova, V. N. Ikorski, V. A. Varnek, I. M. Oglezneva, S. V. Larionov, *Koord. Khim.* **1986**, *12*, 207.
[10] Y. Garcia, P. J. van Koningsbruggen, R. Lapouyade, L. Fournès, L. L. Rabardel, O. Kahn, V. Ksenofontov, G. Levchenko, P. Gütlich, *Chem. Mater.* **1998**, *10*, 2426.
[11] O. Roubeau, J. M. Alcazar-Gómez, E. Balskus, J. J. A. Kolnaar, J. G. Haasnoot, J. Reedijk, *New J. Chem.* **2001**, *25*, 144.
[12] Y. Garcia, P. J. van Koningsbruggen, P. Lapouyade, L. Rabardel, O. Kahn, M. Wierczorek, R. Bronisz, Z. Ciunik, M. F. Rudolf, *C. R. Acad.. Sci.. Paris IIc* **1998**, *1*, 523.
[13] a) P. J. van Koningsbruggen, *Top. Curr. Chem.* **2004**, *233*, 123; b) J. G. Haasnoot, *Coord. Chem. Rev.* **2000**, *200–202*, 131.
[14] a) T. Fujigaya, D.-L. Jiang, T. Aida, *J. Am. Chem. Soc.* **2003**, *125*, 14690; b) T. Fujigaya, D.-L. Jiang, T. Aida, *J. Am. Chem. Soc.* **2005**, *127*, 5584; c) M. Seredyuk, A. B. Gaspar, V. Ksenofontov, S. Reiman, Y. Galyametdinov, W. Haase, E. Rentschler, P. Gütlich, *Chem. Mater.* **2006**, *18*, 2513; d) M. Seredyuk, A. B. Gaspar, V. Ksenofontov, S. Reiman, Y. Galyametdinov, W. Haase, E. Rentschler, P. Gütlich, *Hyperfine Interact.* **2006**, *166*, 385.
[15] a) O. Roubeau, B. Agricole, R. Clèrac, S. Ravaine, *J. Phys. Chem. B* **2004**, *108*, 15110; b) O. Roubeau, A. Colin, V. Schmitt, R. Clérac, *Angew. Chem. Int. Ed.* **2004**, *43*, 3883; T. Fujigaya, D.-L. Jiang, T. Aida, *Chem. Asian J.* **2007**, *2*, 106; c) O. Roubeau, E. Natividad, B. Agricole, S. Ravaine, *Langmuir* **2007**, *23*, 3110.
[16] P. J. van Koningsbruggen, Y. Garcia, O. Kahn, L. Fournès, H. Kooijman, J. G. Haasnoot, J. Moscovici, K. Provost, A. Michalowicz, F. Renz, P. Gütlich, *Inorg. Chem.* **2000**, *39*, 891.
[17] J. Schweifer, P. Weinberger, K. Mereiter, M. Boca, C. Reichl, G. Wiesinger, G. Hilscher, P. J. van Koningsbruggen, H. Kooijman, M. Grunert, W. Linert, *Inorg. Chim. Acta* **2002**, *339*, 297.
[18] N. Moliner, M. C. Muñoz, S. Létard, L. Salmon, J. P. Tuchagues, A. Bousseksou, J. A. Real, *Inorg. Chem.* **2002**, *41*, 6997.

 © 2007 Wiley-VCH Verlag GmbH & Co. KGaA, Weinheim 

[19] G. S. Matouzenko, G. Molnar, N. Bréfuel, M. Perrin, A. Bousseksou, S. A. Borshch, *Chem. Mater.* **2003**, *15*, 550.
[20] S. Hayami, K. Hashiguchi, G. Juhász, M. Ohba, H. Ohkawa, Y. Maeda, K. Kato, K. Osaka, M. Takata, K. Inoue, *Inorg. Chem.* **2004**, *43*, 4124.
[21] A. Galet, M. C. Muñoz, J. A. Real, *Inorg. Chem.* **2006**, *45*, 4583.
[22] G. M. Sheldrick, *SHELX97, Program for Crystal Structure Determination*, University of Göttingen, Germany, **1997**.
[23] a) Y. Garcia, P. J. van Koningsbruggen, G. Bravic, P. Guionneau, D. Chasseau, G. L. Cascarano, J. Moscovici, K. Lambert, A. Michalowicz, O. Kahn, *Inorg. Chem.* **1997**, *36*, 6357; b) K. Drabent, Z. Ciunik, *Chem. Commun.* **2001**, 1254; c) Y. Garcia, P. J. van Koningsbruggen, G. Bravic, D. Chasseau, O. Kahn, *Eur. J. Inorg. Chem.* **2003**, 356.
[24] a) O. Roubeau, J. G. Haasnoot, E. Codjovi, F. Varret, J. Reedijk, *Chem. Mater.* **2002**, *14*, 2559; b) K. Sugiyarto, H. A. Goodwin, *Aust. J. Chem.* **1994**, *47*, 263.
[25] a) J. G. Haasnoot, G. Vos, W. L. Groeneveld, *Z. Naturforsch., Teil B* **1977**, *32*, 1421; b) V. P. Sinditsky, V. I. Sokol, A. E. Fogelzang, M. D. Dutov, V. V. Serushkin, M. A. Porai-Koshits, B. S. Svetlov, *Russ. J. Inorg. Chem.* **1987**, *32*, 1950.
[26] J. A. Real, I. Castro, A. Bousseksou, M. Verdaguer, R. Burriel, M. Castro, J. Linares, F. Varret, *Inorg. Chem.* **1997**, *36*, 455.
[27] C. Hannay, M.-J. Hubin-Franskin, F. Grandjean, V. Briois, J.-P. Itie, A. Polian, S. Trofimenko, G. J. Long, *Inorg. Chem.* **1997**, *36*, 5580.
[28] T. Yokoyama, Y. Murakami, M. Kiguchi, T. Komatsu, N. Kojima, *Phys. Rev. B* **1998**, *58*, 14238.
[29] A. Michalowicz, J. Moscovici, B. Ducourant, D. Cracco, O. Kahn, *Chem. Mater.* **1995**, *7*, 1833.
[30] a) S. B. Erenburg, N. V. Bausk, V. A. Varnek, L. G. Lavrenova, *J. Magn. Magn. Mater.* **1996**, *157–158*, 595; b) S. B. Erenburg, N. V. Bausk, L. G. Lavrenova, L. N. Mazalov, *Nucl. Instrum Methods Phys. Res., Sect. A* **2000**, *448*, 351; c) S. B. Erenburg, N. V. Bausk, L. G. Lavrenova, L. N. Mazalov, *J. Magn. Magn. Mater.* **2001**, *226–230*, 1967.
[31] a) V. Ksenofontov, A. B. Gaspar, G. Levchenko, B. Fitzsimmons, P. Gütlich, *J. Phys. Chem. B* **2004**, *108*, 7723; b) V. Niel, J. M. Martinez-Agudo, M. C. Muñoz, A. B. Gaspar, J. A. Real, *Inorg. Chem.* **2001**, *40*, 3838; c) N. Moliner, A. B. Gaspar, M. C. Muñoz, V. Niel, J. Cano, J. A. Real, *Inorg. Chem.* **2001**, *40*, 3986; d) A. Galet, A. B. Gaspar, M. C. Muñoz, G. Levchenko, J. A. Real, *Inorg. Chem.* **2006**, *45*, 9670.
[32] M. Sorai, M. Nakano, Y. Miyazaki, *Chem. Rev.* **2006**, *106*, 976.
[33] O. Kahn, *Molecular Magnetism*, VCH, New York, **1993**.
[34] a) A. Michalowicz in *Logiciels pour la Chimie*, Société Française de Chimie, Paris, **1991**, p. 102; b) A. Michalowicz, *J. Phys. IV* **1997**, *7*, 235.
[35] a) A. Michalowicz in *Logiciels pour la Chimie*, Société Française de Chimie, Paris, **1991**, p. 116.
[36] a) A. G. McKale, G. S. Knapp, S.-K. Chan, *Phys. Rev. B* **1986**, *33*, 841; b) A. G. McKale, B. W. Veal, A. P. Paulikas, S.-K. Chan, G. S. Knapp, *J. Am. Chem. Soc.* **1988**, *110*, 3763.

Received: March 15, 2007
Published Online: August 8, 2007

 © 2007 Wiley-VCH Verlag GmbH & Co. KGaA, Weinheim 

DOI: 10.1002/ejic.200700347

# Palladium(II) and Nickel(II) Complexes Bearing N,N,O-Chelate Ligands: Syntheses, Characterization and Catalysis in Heck and Kumada Coupling Reactions

**Zhong-Xia Wang*[a] and Zuo-Yun Chai[a]**

**Keywords:** N,N,O ligands / Palladium / Nickel / Chelates / Homogeneous catalysis / C–C coupling

Two new anionic ligands, namely [2-{$OC(Ph)_2CH_2$}-6-(3,5-$Me_2C_3HN_2$)$C_5H_3N$]$^-$ ($L1^-$) and [2-{OC(Ph)=CH}-6-(3,5-$Me_2C_3HN_2$)$C_5H_3N$]$^-$ ($L2^-$), and their palladium and nickel complexes, were synthesized and characterized. 6-(3,5-Dimethyl-1*H*-pyrazol-1-yl)-2-methylpyridine was lithiated with *n*BuLi and the lithiated product treated with benzophenone to give Li(L1) (**2**), whereas treatment of 2-[6-(3,5-dimethyl-1*H*-pyrazol-1-yl)pyridin-2-yl]-1-phenylethanone with NaH afforded Na(L2) (**6**). The palladium and nickel complexes [(L1)PdCl] (**3**), [(L1)NiAr] [Ar = *o*-$MeC_6H_4$ (**4a**), 1-$C_{10}H_7$ (**4b**)], [(L2)PdCl] (**7**) and [(L2)NiAr] [Ar = *o*-$MeC_6H_4$ (**8a**), 1-$C_{10}H_7$ (**8b**)] were obtained by ligand-transfer reactions between Li(L1) or Na(L2) and [$PdCl_2$(PhCN)$_2$] or [$(Ph_3P)_2$Ni(Ar)Cl] (Ar = *o*-$MeC_6H_4$ and 1-$C_{10}H_7$, respectively). These complexes are diamagnetic and were characterized by NMR spectroscopy and elemental analyses. The structures of complexes **4b** and **8a** were determined by single-crystal X-ray diffraction techniques. The catalytic activity of the nickel and palladium complexes in the Heck and Kumada cross-coupling reactions were investigated.
(© Wiley-VCH Verlag GmbH & Co. KGaA, 69451 Weinheim, Germany, 2007)

## Introduction

Group 10 metal catalyzed C–C coupling has been recognized as one of the most useful methods for C–C bond formation in organic synthesis and has been well developed over the past decades.[1] The most frequently used cross-coupling reactions include the reactions of alkyl halides or pseudohalides with olefins (Heck reaction) and with nucleophilic organometallic reagents such as Grignard reagents (Kumada reaction), organozinc reagents (Negishi reaction), and organotin (Stille reaction), organoboron (Suzuki reaction), and organosilicon (Hiyama reaction) derivatives.[1] The Heck reaction, which is mainly catalyzed by palladium complexes, is one of the simplest ways to obtain variously substituted olefins, dienes, and other unsaturated compounds.[2] Other transition metals can also catalyze this reaction but they normally exhibit lower catalytic activity. The Kumada reaction, which was the first reported cross-coupling (early 1970s),[3] is still attracting attention over 30 years later. Current investigation focuses mainly on the development of new catalyst systems and extension of this reaction to substrates such as organic chlorides.[4] Complexes of Ni, Pd, Fe, Co, and other transition metals have been used to catalyze this reaction,[1,4,5] although nickel and palladium complexes are the most attractive and intensively studied.

[a] Department of Chemistry, University of Science and Technology of China,
Hefei, Anhui 230026, China
Fax: +86-551-360-1592
E-mail: zxwang@ustc.edu.cn

The choice of supporting ligands on the central metal atoms is crucial to the catalytic behavior of the complexes. The most often used ligands, which have achieved great success in catalysts for the Heck and Kumada reactions, are tertiary phosphanes. However, phosphane ligands are often expensive, poisonous, air-sensitive, and prone to degrade at elevated temperatures;[6] therefore the development of phosphane-free ligands is a topic of current interest in this area. A number of phosphane-free ligands have been examined for palladium- and nickel-catalyzed Heck and Kumada couplings, some of which have exhibited excellent behavior.[7] Herein we report the syntheses and characterization of new N,N,O-chelate ligands and their nickel and palladium complexes as well as the catalytic behavior of these complexes in the Heck and Kumada coupling reactions.

## Results and Discussion

### Syntheses and Characterization of Compounds 2–8b

The syntheses of the compounds discussed in this paper are shown in Scheme 1. 2-(3,5-Dimethyl-1*H*-pyrazol-1-yl)-6-methylpyridine (**1**) was prepared by treatment of 2-hydrazino-6-methylpyridine with pentane-2,4-dione in acetic acid according to our previously reported method.[8] Compound **1** was readily lithiated by treatment with LDA and the lithiated product treated with benzophenone to afford [Li{2-[$OC(Ph)_2CH_2$]-6-(3,5-$Me_2C_3HN_2$)$C_5H_3N$}] (**2**) in good yield. Complex **2** proved to be a good ligand-transfer reagent in reactions with [$PdCl_2$(PhCN)$_2$] and [$(Ph_3P)_2$Ni-

 © 2007 Wiley-VCH Verlag GmbH & Co. KGaA, Weinheim 

(Ar)Cl] (Ar = *o*-$MeC_6H_4$, 1-$C_{10}H_7$), yielding the corresponding complexes **3**, **4a** and **4b**, respectively. Lithiated **1** was treated with PhCN and subsequently dilute $H_2SO_4$ to afford 2-[6-(3,5-dimethyl-1*H*-pyrazol-1-yl)pyridin-2-yl]-1-phenylethanone (**5**). Treatment of **5** with *n*BuLi or LDA gave a mixture of the lithiated product and unreacted **5**. However, the reaction with NaH in thf formed [Na{2-[OC(Ph)=CH]-6-(3,5-$Me_2C_3HN_2$)$C_5H_3N$}] (**6**) cleanly.

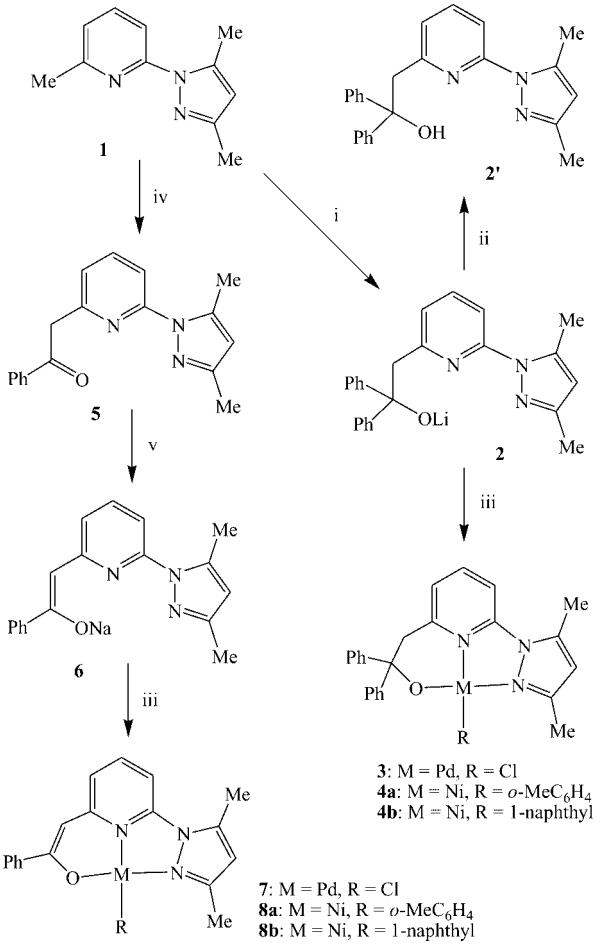


Scheme 1. Ligand and complex syntheses. Reagents and conditions: (i) LDA, thf, –60 to –20 °C, 20 min, then $Ph_2CO$, –80 °C to room temp., 12 h; (ii) 2 M aqueous solution of HCl, room temp., 1 h; (iii) [$PdCl_2(PhCN)_2$] or [$(Ph_3P)_2Ni(Ar)Br$] (Ar = *o*-$MeC_6H_4$ or 1-$C_{10}H_7$), thf, –80 °C to room temp., 10–30 h; (iv) LDA, thf, –60 to –20 °C, 20 min, then PhCN, –80 to –20 °C, 30 min, room temp., 10 h, then 2 M aqueous $H_2SO_4$, 0 °C to room temp., 10 h; (v) NaH, thf, refluxing, 12 h.

Treatment of **6** with [$PdCl_2(PhCN)_2$] afforded the palladium complex [PdCl{2-[OC(Ph)=CH]-6-(3,5-$Me_2C_3HN_2$)-$C_5H_3N$}] (**7**), while treatment of **6** with [$(Ph_3P)_2Ni(Ar)Cl$] (Ar = *o*-$MeC_6H_4$, 1-$C_{10}H_7$) afforded complexes **8a** and **8b**, respectively. Attempts to synthesize [Ni(X){2-[OC(Ph)$_2$-$CH_2$]-6-(3,5-$Me_2C_3HN_2$)$C_5H_3N$}] and [Ni(X){2-[OC(Ph)=CH]-6-(3,5-$Me_2C_3HN_2$)$C_5H_3N$}] (X = Cl, Br) by treating **2** and **6**, respectively, with various nickel compounds such as [(dme)$NiCl_2$], [$(R_3P)NiCl_2$] (R = Ph, Et), [$(Ph_3P)NiBr_2$], and $NiBr_2$ were unsuccessful. Each reaction produced an unidentified white precipitate. The neutral compound **5** is a pale-yellow solid and was characterized by $^1H$ and $^{13}C$ NMR spectroscopy and elemental analysis. Complexes **2** and **6** are air-sensitive colorless (**2**) or pale-yellow (**6**) crystals. The palladium and nickel complexes are pale-yellow (**3**), brown (**8a**), or red (**4a**, **4b**, **7** and **8b**) crystals and are air-stable in the solid state. The nickel complexes are soluble in $CHCl_3$, $CH_2Cl_2$, and thf, but only slightly soluble in toluene. The palladium complexes are soluble in $CH_2Cl_2$, partly soluble in thf, and almost insoluble in toluene and $Et_2O$. Each of the complexes was characterized by NMR spectroscopy and elemental analyses and the data were found to be consistent with their respective structures. In addition, the diamagnetism of the four-coordinate palladium and nickel complexes revealed that these complexes have a square-planar geometry at the respective central metal atom, which means that the ligand coordinates to the central metal atom as an N,N,O-tridentate chelate. This was confirmed by single-crystal X-ray diffraction analyses of complexes **4b** and **8a**.

An ORTEP drawing of complex **4b** is presented in Figure 1 along with selected bond lengths and bond angles. This complex shows a distorted square-planar geometry around the nickel atom. The fact that the N1–Ni1–O1 bond angle [95.73(10)°] is wider than N1–Ni1–N3 [82.54(11)°] is consistent with the corresponding chelate ring size. Similarly, the Ni1–N1–C15 angle [126.3(2)°] is also wider than Ni1–N1–C19 [113.6(2)°]. The Ni1–N3 distance of 1.893(2) Å is shorter than that of Ni1–N1 [1.959(2) Å] and is also much shorter than the distances between the pyrazolyl nitrogen atoms and the nickel atom in [$NiCl_2${$NCH_2CH_2(N_2C_3HMe_2$-3,5)}]·$H_2O$ [2.0334(19) and 2.069(2) Å, respectively],[9] but similar to the Ni–N dis-

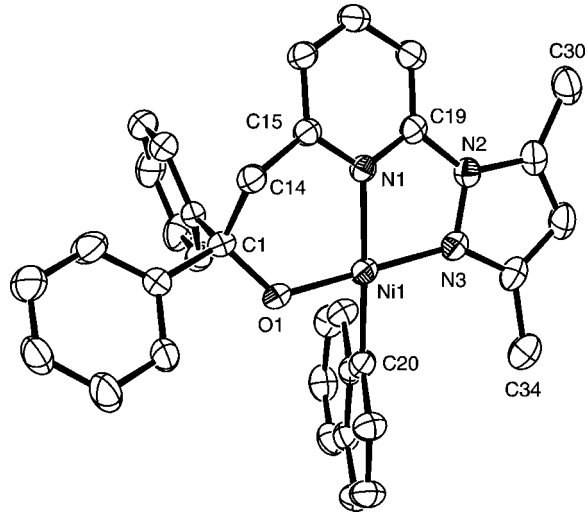


Figure 1. ORTEP drawing of complex **4b** with thermal ellipsoids drawn at the 30% probability level. Selected bond lengths [Å] and angles [°]: Ni1–O1 1.840(2), Ni1–N1 1.959(2), Ni1–N3 1.893(3), Ni1–C20 1.900(3), C1–O1 1.397(3), C1–C14 1.553(4), C14–C15 1.486(4), N2–N3 1.395(3), N2–C19 1.406(4), N1–Ni1–O1 95.73(10), N3–Ni1–O1 175.05(10), C20–Ni1–O1 86.30(11), N1–Ni1–N3 82.54(11), N1–Ni1–C20 172.68(12), N3–Ni1–C20 95.98(12), Ni1–N1–C19 113.6(2), Ni1–N3–N2 112.69(18), Ni1–O1–C1 122.03(18), Ni1–N1–C15 126.3(2).

 © 2007 Wiley-VCH Verlag GmbH & Co. KGaA, Weinheim 

tances in $[Ni_2\{(NSiMe_3)_2CPh\}_2]$ [1.868(5)–1.876(5) Å][10] and $[Ni\{(2,6\text{-}Me_2C_6H_3)NC(Me)C(H)C(Ph)O\}_2]$ [Ni1–N2 = 1.901(3) Å].[11] The Ni–O and Ni–C distances are within the normal range.

An ORTEP drawing of complex **8a** is presented in Figure 2 along with selected bond lengths and angles. Complex **8a** also shows a distorted square-planar geometry at the nickel atom and its structural skeleton is similar to that of complex **4b**, although with some differences in the bond lengths and angles. For example, the Ni1–N1, Ni1–N3, and Ni1–C19 distances in **8a** are shorter than the corresponding ones in **4b**, while the N1–Ni1–C19 and N3–Ni1–O2 angles in **8a** are wider than the corresponding ones in **4a**. The C6–C7 distance of 1.370(8) Å in **8a** is typical of a C–C double bond. The C5, C6, C7, and O2 atoms are almost coplanar, with a torsion angle of 0.5°.

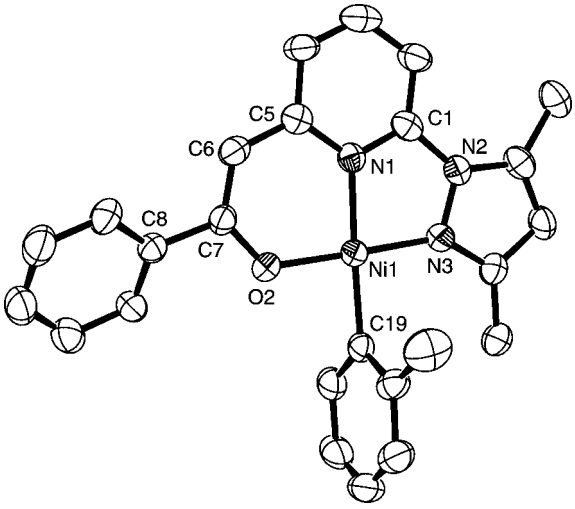


Figure 2. ORTEP drawing of complex **8a** with thermal ellipsoids drawn at the 30% probability level. Selected bond lengths [Å] and angles [°]: Ni1–O2 1.840(4), Ni1–N1 1.908(5), Ni1–N3 1.888(5), Ni1–C19 1.886(6), C5–C6 1.423(8), C6–C7 1.370(8), C7–O2 1.300(6), N2–C1 1.410(7), N2–N3 1.408(6), O2–Ni1–C19 85.1(2), O2–Ni1–N3 177.2(2), C19–Ni1–N3 96.0(2), O2–Ni1–N1 95.88(18), C19–Ni1–N1 174.9(2), N1–Ni1–N3 83.2(2).

### Catalytic Activity of Complexes 3, 4, 7, and 8 in the Heck and Kumada Reactions

We first examined the catalytic activity of complexes **3**, **4**, **7**, and **8** in the Heck reaction. The palladium complexes **3** and **7** catalyze the coupling of aryl iodides and bromides with butyl acrylate in the presence of a base, whereas under similar reaction conditions the nickel complexes only catalyze the reactions of aryl iodides with butyl acrylate. Complex **3** exhibits a higher catalytic activity than complex **7** in most cases, especially for substrates *p*-$MeC(O)C_6H_4Br$ and *p*-$MeOC_6H_4Br$. For example, 0.1 mol-% of **3** catalyzes the coupling of *p*-$MeOC_6H_4Br$ with butyl acrylate at 120 °C in NMP in the presence of $K_2CO_3$ to give the coupling product *trans*-*p*-$MeOC_6H_4CH{=}CHCOO$*n*Bu in 86% yield (Table 1, Entry 7), while the reaction of the same substrates catalyzed by 0.1 mol-% of **7** under the same conditions afforded the coupling product in only 15% yield (Table 1, Entry 22). The iodides were found to be more reactive than the bromides, and aryl chlorides were completely inert. The electronic effects of the substituents on the aryl ring of the halides obviously affect the coupling reactions catalyzed by **7** as both electron-withdrawing and electron-donating groups lead to a large decrease of the reactivity of the aryl bromides (Table 1, Entries 15, 18, 22, 36, 38, and 40). However, the electronic effects of the substituents on the aryl ring of the halides is much smaller in the reactions catalyzed by **3** than in the same reactions catalyzed by **7** (Table 1, Entries 2, 4, 7, 29, 31, and 33). The type of base used also affects the reaction. Thus, $K_2CO_3$ gave excellent results in the catalyst systems tested, while $Et_3N$ led to relatively poor results in most cases.

Complexes **4a**, **4b**, **8a**, and **8b** showed similar catalytic activity, with 0.5 mol-% of catalyst being sufficient to drive the reaction between PhI and butyl acrylate to completion with a quantitative yield of coupling product.

The couplings of aryl iodides or bromides with $PhCH{=}CH_2$ were also investigated. The nickel complexes were found to be almost inactive to the coupling reactions, although the palladium complexes **3** and **7** exhibited catalytic activity. These reactions showed a similar trend with respect to the reactions between aryl halides and butyl acrylate. Between 0.5 and 2 mol-% of the catalysts was required to drive these reactions to completion, depending on the aryl bromides employed. In addition, each coupling reaction gave only the *trans* product (by $^1H$ NMR spectroscopy); no *cis* isomer was observed.

de Vries and other researchers have recently reported that most of the palladium catalysts used for the Heck reaction decompose to form soluble palladium(0) colloids or nanoparticles at high temperature (higher than 120 °C), and that this colloidal palladium reacts further with aryl halides to form anionic intermediates.[12] The reaction temperature is as high as 120 °C in our reaction system, and thus it seems that the palladium complexes might have decomposed during reaction. However, we did observe different catalytic activity between complexes **3** and **7**. For comparison, we also tested the Heck reaction catalyzed by $PdCl_2$ and $PdCl_2$ together with neutral ligand **2′** using the same substrates and reaction conditions as those for **3**. The results showed that $PdCl_2$ alone exhibits very low catalytic activity (Table 1, Entries 42 and 44), while $PdCl_2$+**2′** shows good catalytic activity (Table 1, Entries 43 and 45), although a little lower than that of **3**. This could be because the ligand stabilizes the colloids and prevents their aggregation, as suggested by de Vries.[12a] The ligand probably also stabilizes the anionic palladium species formed by reaction of colloidal palladium with aryl bromides.

The catalytic behavior of complexes **3**, **4**, **7**, and **8** in the Kumada cross-coupling reaction was also evaluated. Palladium complexes **3** and **7** were found to catalyze the coupling of both aryl iodides and aryl bromides with *p*-$MeC_6H_4MgBr$ to give the cross-coupling products (Table 2). Complex **7** exhibits a slightly better catalytic ac-

 © 2007 Wiley-VCH Verlag GmbH & Co. KGaA, Weinheim 

Table 1. Coupling of $RCH{=}CH_2$ (R = COO*n*Bu or Ph) and aryl bromides or iodides catalyzed by complexes **3**, **4**, **7**, and **8**.[a]

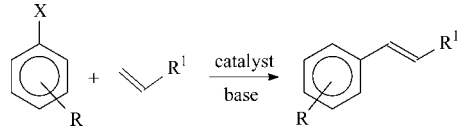


| Entry | R | X | $R^1$ | Catalyst (mol-%) | Solvent | Time [h] | *T* [°C][b] | Base | Yield [%][c] |
|---|---|---|---|---|---|---|---|---|---|
| 1 | H | Br | $CO_2n$Bu | **3** (0.05) | NMP | 32 | 120 | $K_2CO_3$ | 62 |
| 2 | H | Br | $CO_2n$Bu | **3** (0.1) | NMP | 32 | 120 | $K_2CO_3$ | 98 |
| 3 | H | Br | $CO_2n$Bu | **3** (0.5) | DMF | 20 | 120 | $K_2CO_3$ | 98 |
| 4 | *p*-MeCO | Br | $CO_2n$Bu | **3** (0.1) | NMP | 32 | 120 | $K_2CO_3$ | 93 |
| 5 | *p*-MeCO | Br | $CO_2n$Bu | **3** (1) | NMP | 12 | 120 | $NEt_3$ | 82 |
| 6 | *p*-MeCO | Br | $CO_2n$Bu | **3** (1) | NMP | 3 | 100 | $K_2CO_3$ | 98 |
| 7 | *p*-MeO | Br | $CO_2n$Bu | **3** (0.1) | NMP | 32 | 120 | $K_2CO_3$ | 86 |
| 8 | *p*-MeO | Br | $CO_2n$Bu | **3** (1.3) | NMP | 3 | 100 | $K_2CO_3$ | 98 |
| 9 | *o*-Me | Br | $CO_2n$Bu | **3** (0.1) | NMP | 32 | 120 | $K_2CO_3$ | 78 |
| 10 | *o*-Me | Br | $CO_2n$Bu | **3** (1) | NMP | 12 | 120 | $K_2CO_3$ | 97 |
| 11 | H | I | $CO_2n$Bu | **4a** (0.5) | DMF | 12 | 120 | $K_2CO_3$ | 99 |
| 12 | H | I | $CO_2n$Bu | **4b** (0.5) | DMF | 12 | 120 | $K_2CO_3$ | 99 |
| 13 | H | I | $CO_2n$Bu | **7** (0.001) | DMF | 10 | 110 | $K_2CO_3$ | 99 |
| 14 | H | Br | $CO_2n$Bu | **7** (0.05) | NMP | 32 | 120 | $K_2CO_3$ | 52 |
| 15 | H | Br | $CO_2n$Bu | **7** (0.1) | NMP | 32 | 120 | $K_2CO_3$ | 95 |
| 16 | H | Br | $CO_2n$Bu | **7** (0.1) | DMF | 24 | 120 | $K_2CO_3$ | 78 |
| 17 | H | Br | $CO_2n$Bu | **7** (0.2) | DMF | 32 | 120 | $K_2CO_3$ | 93 |
| 18 | *p*-MeCO | Br | $CO_2n$Bu | **7** (0.1) | NMP | 32 | 120 | $K_2CO_3$ | 22 |
| 19 | *p*-MeCO | Br | $CO_2n$Bu | **7** (0.2) | NMP | 20 | 120 | $K_2CO_3$ | 46 |
| 20 | *p*-MeCO | Br | $CO_2n$Bu | **7** (0.2) | DMF | 20 | 120 | $NEt_3$ | 62 |
| 21 | *p*-MeCO | Br | $CO_2n$Bu | **7** (0.5) | NMP | 12 | 100 | $NEt_3$ | 98 |
| 22 | *p*-MeO | Br | $CO_2n$Bu | **7** (0.1) | NMP | 32 | 120 | $K_2CO_3$ | 15 |
| 23 | *p*-MeO | Br | $CO_2n$Bu | **7** (1) | NMP | 3 | 100 | $K_2CO_3$ | 98 |
| 24 | *p*-MeO | Br | $CO_2n$Bu | **7** (1) | NMP | 12 | 120 | $NEt_3$ | 75 |
| 25 | *o*-Me | Br | $CO_2n$Bu | **7** (0.1) | NMP | 32 | 120 | $K_2CO_3$ | 18 |
| 26 | *o*-Me | Br | $CO_2n$Bu | **7** (0.5) | NMP | 12 | 120 | $K_2CO_3$ | 99 |
| 27 | H | I | $CO_2n$Bu | **8a** (0.5) | DMF | 12 | 120 | $K_2CO_3$ | 99 |
| 28 | H | I | $CO_2n$Bu | **8b** (0.5) | DMF | 12 | 120 | $K_2CO_3$ | 99 |
| 29 | H | Br | Ph | **3** (0.1) | NMP | 32 | 120 | $K_2CO_3$ | 89 |
| 30 | *p*-Me | Br | Ph | **3** (0.8) | NMP | 15 | 120 | $K_2CO_3$ | 99 |
| 31 | *p*-MeCO | Br | Ph | **3** (0.1) | NMP | 32 | 120 | $K_2CO_3$ | 93 |
| 32 | *p*-MeCO | Br | Ph | **3** (1.5) | NMP | 15 | 120 | $K_2CO_3$ | 93 |
| 33 | *p*-MeO | Br | Ph | **3** (0.1) | NMP | 32 | 120 | $K_2CO_3$ | 88 |
| 34 | *p*-MeO | Br | Ph | **3** (2) | NMP | 24 | 120 | $K_2CO_3$ | 94 |
| 35 | H | I | Ph | **4a** (2) | NMP | 48 | 120 | $K_2CO_3$ | trace |
| 36 | H | Br | Ph | **7** (0.1) | NMP | 32 | 120 | $K_2CO_3$ | 94 |
| 37 | *p*-Me | Br | Ph | **7** (0.5) | NMP | 12 | 120 | $K_2CO_3$ | 98 |
| 38 | *p*-MeCO | Br | Ph | **7** (0.1) | NMP | 32 | 120 | $K_2CO_3$ | 22 |
| 39 | *p*-MeCO | Br | Ph | **7** (1.5) | NMP | 24 | 120 | $K_2CO_3$ | 97 |
| 40 | *p*-MeO | Br | Ph | **7** (0.1) | NMP | 32 | 120 | $K_2CO_3$ | 16 |
| 41 | *p*-MeO | Br | Ph | **7** (2) | NMP | 24 | 120 | $K_2CO_3$ | 97 |
| 42 | H | Br | $CO_2n$Bu | $PdCl_2$ (0.1) | NMP | 32 | 120 | $K_2CO_3$ | 24 |
| 43 | H | Br | $CO_2n$Bu | $PdCl_2$ (0.1) + **2′** (0.1) | NMP | 32 | 120 | $K_2CO_3$ | 88 |
| 44 | H | Br | Ph | $PdCl_2$ (0.5) | NMP | 32 | 120 | $K_2CO_3$ | 64 |
| 45 | H | Br | Ph | $PdCl_2$ (0.5) + **2′** (0.5) | NMP | 32 | 120 | $K_2CO_3$ | 95 |

[a] Reaction conditions: ArX: 2 mmol; olefin: 3 mmol; solvent: 6 mL; base: 3 mmol. [b] Bath temperature. [c] Yields of isolated products.

tivity than complex **3**. For example, 1 mol-% of **7** gave a 99% yield of the coupling product of PhBr and *p*-$MeC_6H_4MgBr$, while 1 mol-% of **3** under the same conditions gave only 93% of the coupling product. The nickel complexes also catalyze the coupling of aryl iodides with *p*-$MeC_6H_4MgBr$ efficiently. However, the coupling of aryl bromides gave very low product yields. Complexes **4a**, **4b**, **8a**, and **8b** show very similar catalytic activity in the reactions tested, and 2 mol-% of catalyst was sufficient to drive the reactions to completion. These nickel complexes also proved to be good catalysts for deactivated aryl iodides. For example, 2 mol-% of **4b** or **8b** can catalyze the coupling of *p*-$MeOC_6H_4I$ with *p*-$MeC_6H_4MgBr$ to give the cross-coupling product in excellent yield (Table 2, Entries 10 and 19). We also found that increased steric hindrance of the reaction substrates led to a decrease of the product yields. For

 © 2007 Wiley-VCH Verlag GmbH & Co. KGaA, Weinheim 

Table 2. Coupling of $R^1C_6H_4MgBr$ and aryl bromides or iodides catalyzed by complexes **3**, **4**, **7**, and **8**.[a]

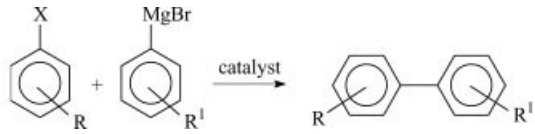


| Entry | R | $R^1$ | X | Catalyst (mol-%) | *T* [°C][b] | Time [h] | Yield [%][c] |
|---|---|---|---|---|---|---|---|
| 1 | H | *p*-Me | I | **3** (0.8) | 100 | 12 | 98 |
| 2 | H | *p*-Me | Br | **3** (1) | 100 | 6 | 93 |
| 3 | *o*-Me | *o*-Me | Br | **3** (1) | 100 | 24 | 96 |
| 4 | *o*-Me | 2,4,6-trimethyl | Br | **3** (2) | 100 | 24 | 74 |
| 5 | 2,4,6-trimethyl | 2,4,6-trimethyl | Br | **3** (2) | 100 | 24 | 72 |
| 6 | H | *p*-Me | I | **4a** (2) | 100 | 12 | 99 |
| 7[d] | H | *p*-Me | I | **4a** (2) | 60 | 12 | 81 |
| 8 | *o*-Me | *o*-Me | I | **4a** (2) | 100 | 20 | 81 |
| 9 | H | *p*-Me | I | **4b** (2) | 100 | 12 | 99 |
| 10 | *p*-MeO | *p*-Me | I | **4b** (2) | 100 | 12 | 91 |
| 11 | H | *p*-Me | I | **7** (0.5) | 100 | 12 | 99 |
| 12 | H | *p*-Me | Br | **7** (1) | 100 | 6 | 99 |
| 13 | *o*-Me | *o*-Me | Br | **7** (1) | 100 | 24 | 93 |
| 14 | *o*-Me | 2,4,6-trimethyl | Br | **7** (2) | 100 | 24 | 46 |
| 15 | 2,4,6-trimethyl | 2,4,6-trimethyl | Br | **7** (2) | 100 | 24 | 42 |
| 16 | H | *p*-Me | I | **8a** (2) | 100 | 12 | 99 |
| 17 | *o*-Me | *o*-Me | I | **8a** (2) | 100 | 20 | 80 |
| 18 | H | *p*-Me | I | **8b** (2) | 100 | 12 | 99 |
| 19 | *p*-MeO | *p*-Me | I | **8b** (2) | 100 | 12 | 95 |

[a] Reactions were carried out in a 1:1 mixture of thf/toluene unless otherwise indicated. [b] Bath temperature. [c] Yields of isolated products. [d] Reaction was carried out in thf.

example, the reactions of 2,4,6-$Me_3C_6H_2MgBr$ with 2,4,6-$Me_3C_6H_2Br$ or *o*-$MeC_6H_4Br$ catalyzed by either **3** or **7** gave relatively low yields of coupling products (Table 2, Entries 4, 5, 14 and 15). The reaction between *o*-$MeC_6H_4MgBr$ and *o*-$MeC_6H_4I$ catalyzed by the nickel catalysts **4a** or **8a** also gave lower yields of coupling product than the reaction between *p*-$MeC_6H_4MgBr$ and $C_6H_5I$ (Table 2, Entries 8 and 17), whereas the reaction of *o*-$MeC_6H_4MgBr$ and *o*-$MeC_6H_4Br$ catalyzed by **3** or **7** seems to be unaffected (Table 2, Entries 3 and 13).

## Conclusion

We have synthesized and characterized nickel and palladium complexes of the novel ligands [2-{$OC(Ph)_2CH_2$}-6-(3,5-$Me_2C_3HN_2$)$C_5H_3N$]$^-$ and [2-{OC(Ph)=CH}-6-(3,5-$Me_2C_3HN_2$)$C_5H_3N$]$^-$. These complexes have square-planar coordination geometries around the metal centers, as shown by their diamagnetism and single-crystal X-ray diffraction results (for complexes **4b** and **8a**). The palladium complexes exhibit good catalytic activity in the Heck and Kumada reactions. The nickel complexes also catalyze the coupling reaction between aryl iodides and butyl acrylate or *p*-$MeC_6H_4MgBr$.

## Experimental Section

**General Procedure:** All experiments were performed under nitrogen using standard Schlenk and vacuum-line techniques. Solvents were distilled under nitrogen from sodium (toluene), sodium/benzophenone (thf, $Et_2O$ and *n*-hexane), or $CaH_2$ ($CH_2Cl_2$) and degassed prior to use; dmf and dmp were dried with activated molecular sieves, distilled under nitrogen, and degassed prior to use. $CDCl_3$, $C_5D_5N$, and $C_6D_6$ (Acros Organics) were degassed and stored over either activated molecular sieves ($CDCl_3$ and $C_5D_5N$) or Na/K alloy ($C_6D_6$). 2-Hydrazino-6-methylpyridine,[13] [$(Ph_3P)_2Ni(Ar)Br$],[14] and [$PdCl_2(PhCN)_2$][15] were prepared according to literature methods. Diisopropylamine was dried with NaOH, distilled under nitrogen, and degassed prior to use. The aryl bromides used for preparation of Grignard reagents, including *p*-$MeC_6H_4Br$, *o*-$MeC_6H_4Br$, and α-bromonaphthalene, were distilled and degassed prior to use. All other chemicals were obtained commercially and used as received. NMR spectra were recorded with a Bruker av300 spectrometer at ambient temperature. $^1H$ and $^{13}C$ NMR chemical shifts are referenced to TMS or internal solvent resonances. Elemental analyses were performed by the Analytical Center of the University of Science and Technology of China.

### Preparations

**2-(3,5-Dimethyl-1*H*-pyrazol-1-yl)-6-methylpyridine (1):**[8] Pentane-2,4-dione (0.48 g, 48 mmol) was added dropwise to a stirred solution of 2-hydrazino-6-methylpyridine (0.50 g, 40.6 mmol) in acetic acid (10 mL) at room temperature and the resultant mixture refluxed for 12 h. The acetic acid was then removed under reduced pressure and the residue dissolved in $CH_2Cl_2$ (20 mL). This $CH_2Cl_2$ solution was washed twice with 10% $Na_2CO_3$ solution and then dried with $Na_2SO_4$. The $Na_2SO_4$ was removed by filtration and the solvent removed from the filtrate by rotary evaporation. The residue was distilled under reduced pressure to give a colorless oil (0.71 g, 93%), b.p. 78–80 °C/0.1 Torr. $^1H$ NMR ($CDCl_3$): $\delta$ = 2.24 (s, 3 H, Me), 2.46 (s, 3 H, Me), 2.55 (s, 3 H, Me), 5.90 (s, 1 H, pyrazolyl), 6.93 (dd, $J$ = 0.9, 7.4 Hz, 1 H, Py), 7.52–7.61 (m, 2 H, Py) ppm.

 © 2007 Wiley-VCH Verlag GmbH & Co. KGaA, Weinheim 

**[Li{2-[OC(Ph)$_2$CH$_2$]-6-(3,5-Me$_2$C$_3$HN$_2$)C$_5$H$_3$N}] (2):** A solution of 2-(3,5-dimethyl-1*H*-pyrazol-1-yl)-6-methylpyridine (0.48 g, 2.57 mmol) in thf (10 mL) was cooled to about –60 °C and a solution of LDA in $Et_2O$ [prepared from diisopropylamine (0.29 g, 2.8 mmol) and *n*BuLi (1.2 mL of a 2.5 M solution in hexane, 3 mmol) in $Et_2O$] was added with stirring. After stirring at –20 °C for 20 min, the mixture was added dropwise to a solution of benzophenone (0.50 g, 2.75 mmol) in thf (5 mL) at about –80 °C. The resultant mixture was warmed to room temperature and stirred for 12 h. The solvent was then removed under vacuum and the residue dissolved in toluene (10 mL). The solution was filtered and the filtrate was concentrated to about 2 mL. Diethyl ether (2 mL) was added to the solution to give compound **2** (0.54 g, 56%) as colorless crystals, m.p. 227–228 °C. $^1$H NMR ($C_6D_6$): $\delta$ = 1.79 (s, 3 H, Me), 2.20 (s, 3 H, Me), 3.86 (s, 2 H, $CH_2$), 5.41 (s, 1 H, pyrazolyl), 6.12 (d, $J$ = 8.1 Hz, 1 H, Py), 6.23 (d, $J$ = 7.5 Hz, 1 H, Py) 6.68 (t, $J$ = 7.8 Hz, 1 H, Py), 6.84–6.87 (m, 2 H, Ph), 6.98 (br., 4 H, Ph), 7.65 (d, $J$ = 7.2 Hz, 4 H, Ph) ppm. $^{13}$C NMR ($C_6D_6$): $\delta$ = 13.03, 14.01, 53.27, 81.62, 109.45, 122.48, 124.31, 126.84, 137.06, 138.04, 148.64, 151.04, 162.25 ppm. $C_{24}H_{22}LiN_3O$ (375.39): calcd. C 76.79, H 5.91, N 11.19; found C 76.90, H 5.90, N 11.11.

**2-[OC(Ph)$_2$CH$_2$]-6-(3,5-Me$_2$C$_3$HN$_2$)C$_5$H$_3$N (2′):** Hydrochloric acid (2 M, 20 mL) was added to a solution of **2** [prepared from **1** (0.72 g, 3.85 mmol), LDA, and $Ph_2CO$ according to the above procedure] in thf (15 mL). The mixture was stirred for 1 h and then neutralized with 2 M NaOH. The aqueous layer was extracted twice with $CH_2Cl_2$ (20 mL each time), and the combined organic layers were dried with $MgSO_4$. After concentration in vacuo, the product was recrystallized from $CH_2Cl_2$/$Et_2O$ to give a white solid (1.0 g, 70.4% based on the amount of **1**), m.p. 156–157 °C. $^1$H NMR ($CDCl_3$): $\delta$ = 2.28 (s, 3 H, Me), 2.43 (s, 3 H, Me), 3.74 (s, 2 H, $CH_2$), 5.98 (s, 1 H, pyrazolyl), 6.91 (dd, $J$ = 2.4, 6 Hz, 1 H, Py), 7.12–7.27 (m, 7 H, Ph), 7.41–7.44 7.12–7.27 (m, 3 H, Ph), 7.50–7.66 (m, 2 H, Py) ppm. $^{13}$C NMR ($CDCl_3$): $\delta$ = 13.70, 14.22, 47.50, 78.36, 109.33, 114.74, 122.11, 126.32, 126.78, 128.13, 139.28, 141.11, 146.89, 150.26, 152.30, 157.22 ppm. $C_{24}H_{23}N_3O$ (369.46): calcd. C 78.02, H 6.27, N 11.37; found C 77.79, H 6.24, N 11.22.

**[Pd(Cl){2-[OC(Ph)$_2$CH$_2$]-6-(3,5-Me$_2$C$_3$HN$_2$)C$_5$H$_3$N}] (3):** A solution of **2** (0.11 g, 0.29 mmol) in thf (5 mL) was added to a stirred solution of [$PdCl_2(PhCN)_2$] (0.105 g, 0.27 mmol) in thf (10 mL) at about –80 °C. The mixture was warmed to room temperature and stirred for 10 h, then the solvent was removed under vacuum. The residue was dissolved in $CH_2Cl_2$ and then filtered. Concentration of the filtrate afforded pale-yellow crystals (0.11 g, 80%), m.p. 293–295 °C. $^1$H NMR ($CDCl_3$): $\delta$ = 2.54 (s, 3 H, Me), 2.59 (s, 3 H, Me), 3.97 (s, 2 H, $CH_2$), 6.01 (s, 1 H, pyrazolyl), 7.03 (d, $J$ = 7.8 Hz, 1 H, Py), 7.12–7.25 (m, 7 H, Ph+Py), 7.62 (d, $J$ = 8.1 Hz, 4 H, Ph), 7.80 (t, $J$ = 8.4 Hz, 1 H, Py) ppm. $C_{24}H_{22}ClN_3OPd$ (510.32): calcd. C 56.49, H 4.35, N 8.23; found C 56.89, H 4.23, N 8.28.

**[Ni(*o*-MeC$_6$H$_4$){2-{OC(Ph)$_2$CH$_2$}-6-(3,5-Me$_2$C$_3$HN$_2$)C$_5$H$_3$N}] (4a):** A solution of **2** (0.22 g, 0.59 mmol) in thf (5 mL) was added to a stirred solution of [$(Ph_3P)_2$Ni(*o*-$MeC_6H_4$)Br] (0.44 g, 0.58 mmol) in thf (10 mL) at about –80 °C. The resultant solution was warmed to room temperature and stirred for 30 h, then the solvent was removed under vacuum and the residue was extracted with $CH_2Cl_2$. The solvent was removed from the extract under reduced pressure and the residual solid was recrystallized from thf to give red crystals (0.28 g, 92%), m.p. 203–204 °C. $^1$H NMR ($CDCl_3$): $\delta$ = 1.16 (s, 3 H, Me), 2.39 (s, 3 H, Me), 2.78 (s, 3 H, Me), 3.49 (d, $J$ = 14.4 Hz, 1 H, CH), 3.68 (d, $J$ = 14.4 Hz, 1 H, CH), 5.74 (s, 1 H, pyrazolyl), 6.68–7.10 (m, 11 H, Ar), 7.37 (d, $J$ = 6.3 Hz, 2 H, Ar), 7.61–7.70 (m, 4 H, Ar) ppm. $^{13}$C NMR ($CDCl_3$): $\delta$ = 13.50, 21.32, 24.97, 49.05, 77.27, 113.98, 122.05, 122.38, 124.83, 125.14, 125.36, 126.40, 126.59, 126.87, 127.08, 128.08, 128.27, 128.88, 136.72, 137.72, 147.52, 155.62, 159.87 ppm. $C_{31}H_{29}N_3NiO$ (518.28): calcd. C 71.84, H 5.64, N 8.11; found C 71.76, H 5.51, N 8.19. Single crystals of complex **4a** suitable for an X-ray diffraction analysis were obtained by recrystallization of the sample from a mixture of thf and toluene.

**[Ni(1-C$_{10}$H$_7$){2-{OC(Ph)$_2$CH$_2$}-6-(3,5-Me$_2$C$_3$HN$_2$)C$_5$H$_3$N}] (4b):** A solution of **2** (0.08 g, 0.21 mmol) in thf (5 mL) was added to a stirred solution of [$(Ph_3P)_2$Ni(naphthyl)Br] (0.17 g, 0.22 mmol) in thf (10 mL) at about –80 °C. The mixture was warmed to room temperature and stirred for 30 h, then the solvent was removed under vacuum and the residue extracted with $CH_2Cl_2$. The extract was filtered and then concentrated to dryness to give a red solid, which was recrystallized from a mixture of $CH_2Cl_2$/hexane (1:1) to afford red crystals (0.11 g, 83%), m.p. 171–173 °C. $^1$H NMR ($CDCl_3$): $\delta$ = 0.72 (s, 3 H, Me), 2.32 (s, *Me*$C_6H_5$), 2.38 (s, 3 H, Me), 3.54 (d, $J$ = 15.3 Hz, 1 H, CH), 3.81 (d, $J$ = 15.3 Hz, 1 H, CH), 5.63 (s, 1 H, pyrazolyl), 6.90–6.98 (m, 4 H, Ar), 7.06–7.15 (m, 6 H, Ar), 7.20–7.31 (m, 5 H, Ar), 7.37 (d, $J$ = 7.2 Hz, 3 H, Ar), 7.60 (d, $J$ = 7.2 Hz, 3 H, Ar), 7.70 (t, $J$ = 8.1 Hz, 1 H, Ar), 8.00 (d, $J$ = 6.9 Hz, 1 H, Ar), 9.29–9.32 (m, 1 H, Ar) ppm. $^{13}$C NMR ($CDCl_3$): $\delta$ = 13.86, 21.58, 49.32, 77.27, 107.16, 114.41, 122.19, 122.74, 123.70, 123.79, 123.92, 125.08, 125.24, 125.43, 125.96, 126.72, 127.42, 127.61, 128.02, 128.36, 129.17, 132.75, 133.54, 133.89, 138.02, 139.14, 140.23, 141.68, 151.77, 151.82, 156.11, 156.97, 160.38 ppm. $C_{34}H_{29}N_3NiO{\cdot}0.8C_7H_8$ (628.02): calcd. C 75.73, H 5.68, N 6.69; found C 75.75, H 5.75, N 6.67.

**2-[6-(3,5-Dimethyl-1*H*-pyrazol-1-yl)pyridin-2-yl]-1-phenylethanone (5):** A solution of 2-(3,5-dimethyl-1*H*-pyrazol-1-yl)-6-methylpyridine (0.48 g, 2.57 mmol) in thf (10 mL) was cooled to about –60 °C and a solution of LDA in $Et_2O$ [prepared from diisopropylamine (0.29 g, 2.8 mmol) and *n*BuLi (1.2 mL of a 2.5 M solution in hexane, 3 mmol) in $Et_2O$] was added with stirring. The mixture was stirred at –20 °C for 20 min and was then added dropwise to PhCN (0.30 g, 2.91 mmol) at about –80 °C. The resultant solution was stirred at –20 °C for 30 min and at room temperature for 10 h. A 2 M aqueous solution of $H_2SO_4$ (10 mL) was then added at 0 °C. The mixture was stirred at room temperature for 10 h and then neutralized with NaOH solution. The organic layer was separated and the aqueous layer was extracted twice with diethyl ether (20 mL each time). The combined ether solutions were dried with $Na_2SO_4$, then the $Na_2SO_4$ was removed by filtration and the filtrate was concentrated to give pale-yellow crystals (0.49 g, 66%), m.p. 80–81 °C. $^1$H NMR ($CDCl_3$): $\delta$ = 2.19 (s, 3 H, Me), 2.41 (s, 3 H, Me), 4.37 (s, 2 H, $CH_2$), 5.86 (s, 1 H, pyrazolyl), 7.07 (t, $J$ = 4.2 Hz, 1 H, Ar), 7.32–7.50 (m, 3 H, Ar), 7.65 (d, $J$ = 4.2 Hz, 2 H, Ar), 7.94–7.97 (m, 2 H, Ar) ppm. $^{13}$C NMR ($CDCl_3$): $\delta$ = 13.67, 14.64, 47.89, 109.05, 113.66, 120.71, 125.44, 128.43, 128.66, 128.85, 133.31, 136.59, 138.90, 141.68, 149.81, 153.28, 153.68, 196.73 ppm. $C_{18}H_{17}N_3O$ (291.35): calcd. C 74.20, H 5.88, N 14.42; found C 74.28, H 5.58, N 14.26.

**[Na{2-[OC(Ph)=CH]-6-(3,5-Me$_2$C$_3$HN$_2$)C$_5$H$_3$N}] (6):** A mixture of **5** (0.60 g, 2.06 mmol) and NaH (0.08 g, 3.3 mmol) in thf (20 mL) was refluxed for 12 h, then the mixture was filtered and the solvent removed from the filtrate under vacuum. The residue was recrystallized from a mixture of thf/hexane (1:1) to give pale-yellow crystals (0.50 g, 77%), m.p. 245–247 °C. $^1$H NMR ($C_6D_6$): $\delta$ = 1.76 (s, 3 H, Me), 1.86 (s, 3 H, Me), 5.30 (s, 1 H, pyrazolyl), 5.67 (s, 1 H, CH), 5.92 (d, $J$ = 7.5 Hz, 1 H, Py), 6.42–6.45 (m, 1 H, Py), 6.82–7.16 (m, 4 H, Ph + Py), 7.99 (t, $J$ = 7.8 Hz, 1 H, Py), 6.62–6.67 (m, 4 H, Ph), 7.79 (d, $J$ = 7.2 Hz, 2 H, Ph) ppm. $^{13}$C NMR ($C_6D_6$): $\delta$ = 13.57, 13.70, 95.16, 106.15, 108.68, 119.64, 127.02, 127.60,

 © 2007 Wiley-VCH Verlag GmbH & Co. KGaA, Weinheim 

128.23, 135.73, 139.06, 147.35, 150.19, 150.37, 161.98, 173.33 ppm. $C_{18}H_{16}N_3NaO$ (313.33): calcd. C 69.00, H 5.15, N 13.41; found C 69.32, H 5.11, N 13.75.

**[Pd(Cl){2-{OC(Ph)=CH}-6-(3,5-Me$_2$C$_3$HN$_2$)C$_5$H$_3$N}] (7):** A solution of **6** (0.13 g, 0.42 mmol) in thf (5 mL) was added to a stirred solution of $[PdCl_2(PhCN)_2]$ (0.13 g, 0.34 mmol) in thf (10 mL) at about –80 °C. The mixture was stirred at room temperature overnight, then the solvent was removed under vacuum. The residue was dissolved in $CH_2Cl_2$ and then filtered. Concentration of the filtrate afforded red crystals of **7** (0.10 g, 68%), m.p. 293–295 °C. $^1$H NMR ($CDCl_3$): $\delta$ = 2.58 (s, 3 H, Me), 2.62 (s, 3 H, Me), 5.93 (s, 1 H, CH), 6.04 (s, 1 H, pyrazolyl), 6.86 (d, $J$ = 8.1 Hz, 1 H, Py), 6.91 (d, $J$ = 8.1 Hz, 1 H, Py), 7.27–7.32 (m, 3 H, Ph), 7.53 (t, $J$ = 8.1 Hz, 1 H, Py), 7.80–7.83 (m, 2 H, Ph) ppm. $^{13}$C NMR ($CDCl_3$+$C_5D_5N$): $\delta$ = 14.19, 14.35, 77.37, 112.15, 118.83, 119.16, 119.48, 121.46, 122.84, 124.39, 126.02, 127.26, 127.29, 128.07, 134.95, 147.42, 147.78, 157.20 ppm. $C_{18}H_{16}ClN_3OPd$ (432.21): calcd. C 50.02, H 3.73, N 9.72; found C 50.00, H 3.64, N 9.64.

**[Ni(*o*-MeC$_6$H$_4$){2-[OC(Ph)=CH]-6-(3,5-Me$_2$C$_3$HN$_2$)C$_5$H$_3$N}] (8a):** A solution of **6** (0.15 g, 0.48 mmol) in thf (5 mL) was added to a stirred solution of $[(PPh_3)_2Ni(o\text{-}MeC_6H_4)Br]$ (0.33 g, 0.43 mmol) in thf (10 mL) at about –80 °C. The solution was warmed to room temperature and stirred for 30 h, then the solvent was removed under vacuum and the residue extracted with $CH_2Cl_2$. The solvent was removed from the extract under vacuum and the residual solid was recrystallized from a 1:1 mixture of thf/toluene to afford brown crystals of **8a** (0.16 g, 85%), m.p. 247–248 °C. $^1$H NMR ($CDCl_3$): $\delta$ = 1.17 (s, 3 H, Me), 2.37 (s, 3 H, Me), 3.00 (s, 3 H, Me), 5.75 (s, 1 H, pyrazolyl), 5.98 (s, 1 H, CH), 6.63 (d, $J$ = 7.8 Hz, Py), 6.73–6.75 (m, 4 H, $C_6H_4$+Py), 7.11–7.15 (m, 3 H, Ph), 7.45 (t, $J$ = 8.1 Hz, 1 H, Py), 7.51–7.54 (m, 2 H, Ph), 7.67–7.71 (m, 1 H, $C_6H_4$) ppm. $^{13}$C NMR ($CDCl_3$): $\delta$ = 14.13, 15.19, 25.16, 92.96, 99.66, 113.76, 119.46, 122.67, 122.74, 122.47, 126.47, 127.89, 128.64, 136.05, 136.46, 139.93, 140.12, 144.27, 146.15, 152.67, 153.56, 155.04, 169.88 ppm. $C_{25}H_{23}N_3NiO$ (440.16): calcd. C 68.22, H 5.27, N 9.55; found C 68.42, H 5.42, N 9.49. Single crystals for X-ray diffraction analysis were obtained by recrystallization of the sample from a mixture of thf and benzene.

**[Ni(1-C$_{10}$H$_7$){2-[OC(Ph)=CH]-6-(3,5-Me$_2$C$_3$HN$_2$)C$_5$H$_3$N}] (8b):** A solution of **5** (0.17 g, 0.54 mmol) in thf (5 mL) was added to a stirred solution of $[(PPh_3)_2Ni(naphthyl)Br]$ (0.40 g, 0.51 mmol) in thf (10 mL) at about –80 °C. The resultant solution was warmed to room temperature and stirred for 30 h, then the solvent was removed under vacuum and the residue dissolved in $CH_2Cl_2$. The mixture was filtered and the filtrate was concentrated to give red crystals of **8b** (0.17 g, 71%), m.p. 239–240 °C. $^1$H NMR ($CDCl_3$): $\delta$ = 0.84 (s, 3 H, Me), 2.48 (s, 3 H, Me), 5.76 (s, 1 H, pyrazolyl), 6.08 (s, 1 H, CH), 6.75 (d, $J$ = 7.8 Hz, 1 H, Py), 6.84 (d, $J$ = 8.1 Hz, 1 H, Py), 7.01–7.15 (m, 5 H, Ar), 7.27–7.43 (m, 5 H, Ar), 7.53 (t, $J$ = 8.1 Hz, 1 H, Py), 7.58–7.62 (m, 1 H, Ar), 7.89 (d, $J$ = 6.6 Hz, 1 H, Ar), 9.66 (d, $J$ = 7.8 Hz, 1 H, Ar) ppm. $^{13}$C NMR ($CDCl_3$): $\delta$ = 14.39, 15.27, 93.11, 99.56, 113.89, 119.66, 122.72, 123.56, 123.77, 124.23, 126.59, 127.82, 127.86, 128.38, 128.70, 129.19, 132.86, 133.16, 133.88, 136.17, 139.77, 140.18, 141.97, 146.45, 153.84, 155.16, 155.32, 170.23 ppm. $C_{28}H_{23}N_3NiO$ (476.20): calcd. C 70.62, H 4.87, N 8.82; found C 70.46, H 4.81, N 9.07.

**Crystal Structure Determination:** Single crystals were mounted in Lindemann capillaries under nitrogen. Diffraction data were collected with a Siemens CCD area detector with graphite-monochromated Mo-$K_\alpha$ radiation ($\lambda$ = 0.71073 Å). The structure was solved by direct methods using SHELXS-97[16] and refined against $F^2$ by full-matrix least squares using SHELXL-97.[17] Hydrogen atoms were placed in calculated positions. Crystal data and experimental details of the structure determinations are listed in Table 3. CCDC-641763 and -641764 (for **4b**·$C_7H_8$ and **8a**·0.5$C_6H_6$, respectively) contain the supplementary crystallographic data for this paper. These data can be obtained free of charge from The Cambridge Crystallographic Data Centre via www.ccdc.cam.ac.uk/data_request/cif.

Table 3. Summary of crystal data for complexes **4b** and **8a**.

| | **4b**·$C_7H_8$ | **8a**·0.5$C_6H_6$ |
|---|---|---|
| Empirical formula | $C_{41}H_{37}N_3NiO$ | $C_{28}H_{26}N_3NiO$ |
| Formula mass | 646.45 | 479.23 |
| Crystal system | monoclinic | monoclinic |
| Space group | $P2_1/n$ | $C2/c$ |
| $a$ [Å] | 15.609(2) | 20.171(3) |
| $b$ [Å] | 11.1736(15) | 13.841(2) |
| $c$ [Å] | 19.144(3) | 18.560(3) |
| $\beta$ [°] | 95.792(2) | 96.873(2) |
| $V$ [Å$^3$] | 3321.7(8) | 5144.5(14) |
| $Z$ | 4 | 8 |
| $T$ [K] | 294(2) | 298(2) |
| $D_{calcd.}$ [g cm$^{-3}$] | 1.293 | 1.237 |
| $F$(000) | 1360 | 2008 |
| $\mu$ [mm$^{-1}$] | 0.621 | 0.777 |
| $\theta$ range for data collection [°] | 1.77–26.40 | 2.03–25.01 |
| Absorption correction | semiempirical from equivalents | semiempirical from equivalents |
| No. of reflections collected | 18266 | 12474 |
| No. of independent reflections ($R_{int}$) | 6767 ($R_{int}$ = 0.0493) | 4477 ($R_{int}$ = 0.0531) |
| No. of data/restraints/parameters | 6767/92/457 | 4477/102/325 |
| Goodness of fit on $F^2$ | 1.000 | 1.001 |
| Final $R$ indices[a] [$I > 2\sigma(I)$] | $R_1$ = 0.0464, $wR_2$ = 0.0962 | $R_1$ = 0.0695, $wR_2$ = 0.1775 |
| $R$ indices (all data) | $R_1$ = 0.1007, $wR_2$ = 0.1202 | $R_1$ = 0.1352, $wR_2$ = 0.2258 |
| Largest diff peak/hole [e Å$^{-3}$] | 0.328/–0.239 | 0.571/–0.589 |

[a] $R_1 = \Sigma||F_o| - |F_c||/\Sigma|F_o|$; $wR_2 = [\Sigma w(F_o^2 - F_c^2)^2/\Sigma w(F_o^4)]^{1/2}$.

 © 2007 Wiley-VCH Verlag GmbH & Co. KGaA, Weinheim 

**General Procedure for the Heck Reactions:** A Schlenk tube was charged with aryl halide (2 mmol), butyl acrylate or styrene (3 mmol), a base (3 mmol), the pre-catalyst, and solvent (6 mL) and the mixture was stirred at the appropriate temperature for the specified period of time. The mixture was then cooled to room temperature and quenched with a 1 M aqueous solution of hydrochloric acid (3 mL). The aqueous phase was extracted with $CH_2Cl_2$ ($3 \times 5$ mL), then the combined organic layers were washed with water (10 mL) and dried with $Na_2SO_4$. The $NaSO_4$ was removed by filtration and the filtrate was concentrated. The residue was purified by column chromatography.

**General Procedure for the Kumada Reactions:** A Schlenk tube was charged with aryl halide (2 mmol), pre-catalyst, solvent (4 mL), and a magnetic stir bar, then a thf solution of *p*-$MeC_6H_4MgBr$ (prepared from 2.4 mmol of *p*-$MeC_6H_4Br$ and 3 mmol of Mg in thf) was added dropwise at room temperature with stirring. The reaction mixture was stirred at the appropriate temperature for the specified period of time. After the mixture had been cooled to room temperature, the reaction was quenched with water. The aqueous phase was extracted with $CH_2Cl_2$ ($3 \times 5$ mL) and the combined organic layers were dried with $MgSO_4$. The $MgSO_4$ was removed by filtration and the filtrate was concentrated. The residue was purified by column chromatography.

## Acknowledgments

We thank the Natural Science Foundation of Anhui Province (project code: 070416238) for support.

[1] a) E. Negishi, *Handbook of Organopalladium Chemistry for Organic Synthesis*, Wiley, New York, **2002**, vol. 1; b) J. Tsuji, *Palladium Reagents and Catalysis: New Perspectives for the 21st Century*, Wiley, Chichester, **2004**; c) Y. Tamaru, *Modern Organonickel Chemistry*, Wiley-VCH, Weinheim, **2005**; d) R. B. Bedford, C. S. J. Cazin, D. Holder, *Coord. Chem. Rev.* **2004**, *248*, 2283–2321; e) J.-P. Corbet, G. Mignani, *Chem. Rev.* **2006**, *106*, 2651–2710; f) H.-U. Blaser, A. Indolese, F. Naud, U. Nettekoven, A. Schnyder, *Adv. Synth. Catal.* **2004**, *346*, 1583–1598; g) I. J. S. Fairlamb, R. J. K. Taylor, J. L. Serrano, G. Sanchez, *New J. Chem.* **2006**, *30*, 1695–1704.

[2] I. P. Beletskaya, A. V. Cheprakov, *Chem. Rev.* **2000**, *100*, 3009–3066.

[3] a) K. Tamao, K. Sumitani, M. Kumada, *J. Am. Chem. Soc.* **1972**, *94*, 4374–4376; b) R. J. P. Corriu, J. P. Masse, *J. Chem. Soc. Chem. Commun.* **1972**, 144; c) S. Schröter, C. Stock, T. Bach, *Tetrahedron* **2005**, *61*, 2245–2267.

[4] a) A. F. Littke, G. C. Fu, *Angew. Chem. Int. Ed.* **2002**, *41*, 4176–4211; b) J. Huang, S. P. Nolan, *J. Am. Chem. Soc.* **1999**, *121*, 9889–9890; c) V. P. W. Böhm, T. Weskamp, C. W. K. Gstöttmayer, W. A. Herrmann, *Angew. Chem. Int. Ed.* **2000**, *39*, 1602–1604.

[5] a) H. Shinokubo, K. Oshima, *Eur. J. Org. Chem.* **2004**, 2081–2091; b) A. Furstner, R. Martin, *Chem. Lett.* **2005**, *34*, 624–629; c) M. Nakamura, K. Matsuo, S. Ito, E. Nakamura, *J. Am. Chem. Soc.* **2004**, *126*, 3686–3687; d) R. B. Bedford, M. Betham, D. W. Bruce, A. A. Danopoulos, R. M. Frost, M. Hird, *J. Org. Chem.* **2006**, *71*, 1104–1110; e) K. Bica, P. Gaertner, *Org. Lett.* **2006**, *8*, 733–735; f) H. Ohmiya, K. Wakabayashi, H. Yorimitsu, K. Oshima, *Tetrahedron* **2006**, *62*, 2207–2213; g) R. Martin, A. Fürstner, *Angew. Chem. Int. Ed.* **2004**, *43*, 3955–3957; h) A. Fürstner, H. Krause, C. W. Lehmann, R. Martin, A. Furstner, *Angew. Chem. Int. Ed.* **2006**, *45*, 440–444; i) R. B. Bedford, D. W. Bruce, R. M. Frost, J. W. Goodby, M. Hird, *Chem. Commun.* **2004**, 2822–2823; j) R. B. Bedford, D. W. Bruce, R. M. Frost, M. Hird, *Chem. Commun.* **2005**, 4161–4163; k) H. Ohmiya, H. Yorimitsu, K. Oshima, *J. Am. Chem. Soc.* **2006**, *128*, 1886–1889; l) H. Ohmiya, T. Tsuji, H. Yorimitsu, K. Oshima, *Chem. Eur. J.* **2004**, *10*, 5640–5648; m) T. Tsuji, H. Yorimitsu, K. Oshima, *Angew. Chem. Int. Ed.* **2002**, *41*, 4137–4139.

[6] a) X. Cui, Y. Zhou, N. Wang, L. Liu, Q.-X. Guo, *Tetrahedron Lett.* **2007**, *48*, 163–167; b) V. Farina, *Adv. Synth. Catal.* **2004**, *346*, 1553–1582.

[7] a) A. C. Hillier, G. A. Grasa, M. S. Viciu, H. M. Lee, C. Yang, S. P. Nolan, *J. Organomet. Chem.* **2002**, *653*, 69–82; b) A. Dallas, H. Kuhtz, A. Farrell, B. Quilty, K. Nolan, *Tetrahedron Lett.* **2007**, *48*, 1017–1021; c) A. C. Frisch, M. Belle, *Angew. Chem. Int. Ed.* **2005**, *44*, 674–688; d) J. Terao, H. Todo, H. Watanabe, A. Ikumi, N. Kambe, *Angew. Chem. Int. Ed.* **2004**, *43*, 6180–6182; e) M.-T. Chen, C.-A. Huang, C.-T. Chen, *Eur. J. Inorg. Chem.* **2006**, 4642–4648; f) N. T. S. Phan, D. H. Brown, H. Adams, S. E. Spey, P. Styring, *Dalton Trans.* **2004**, 1348–1357; g) I. Özdemir, S. Demir, B. Çetinkaya, *Tetrahedron* **2005**, *61*, 9791–9798; h) K. Inamoto, J.-I. Kuroda, K. Hiroya, Y. Noda, M. Watanabe, T. Sakamoto, *Organometallics* **2006**, *25*, 3095–3098; i) D. Yang, Y. C. Chen, N. Y. Zhu, *Org. Lett.* **2004**, *6*, 1577–1580; j) X. Cui, Z. Li, C.-Z. Tao, Y. Xu, J. Li, L. Liu, Q.-X. Guo, *Org. Lett.* **2006**, *8*, 2467–2470; k) J. C. Xiao, B. Twamley, J. M. Shreeve, *Org. Lett.* **2004**, *6*, 3845–3847; l) S. B. Park, H. Alper, *Org. Lett.* **2003**, *5*, 3209–3212; m) A. K. Gupta, C. H. Song, C. H. Oh, *Tetrahedron Lett.* **2004**, *45*, 4113–4116; n) D. Kovala-Demertzi, P. N. Yadav, M. A. Demertzis, J. P. Jasiski, F. J. Andreadaki, I. D. Kostas, *Tetrahedron Lett.* **2004**, *45*, 2923–2926; o) S. Iyer, G. M. Kulkarni, C. Ramesh, *Tetrahedron* **2004**, *60*, 2163–2172; p) C. Najera, J. Gil-Moito, S. Karlstrum, L. R. Falvello, *Org. Lett.* **2003**, *5*, 1451–1454; q) T. Kawano, T. Shinomaru, I. Ueda, *Org. Lett.* **2002**, *4*, 2545–2547; r) K.-M. Wu, C.-A. Huang, K.-F. Peng, C.-T. Chen, *Tetrahedron* **2005**, *61*, 9679–9687; s) P. A. Gossage, H. A. Jenkins, P. N. Yadav, *Tetrahedron Lett.* **2004**, *45*, 7689–7691.

[8] Z.-G. Zhao, Z.-X. Wang, *Synth. Commun.* **2007**, *37*, 137–147.

[9] N. Ajellal, M. C. A. Kuhn, A. D. G. Boff, M. Hörner, C. M. Thomas, J.-F. Carpentier, O. L. Casagrande, *Organometallics* **2006**, *25*, 1213–1216.

[10] E. Nelkenbaum, M. Kapon, M. S. Eisen, *Organometallics* **2005**, *24*, 2645–2659.

[11] Y.-Z. Zhu, J.-Y. Liu, Y.-S. Li, Y.-J. Tong, *J. Organomet. Chem.* **2004**, *689*, 1295–1303.

[12] a) J. G. de Vries, *Dalton Trans.* **2006**, 421–429; b) D. Astruc, *Inorg. Chem.* **2007**, *46*, 1884–1894; c) N. T. S. Phan, M. Van Der Sluys, C. W. Jones, *Adv. Synth. Catal.* **2006**, *348*, 609–679.

[13] D. S. Tarbell, C. W. Todd, M. C. Paulson, E. G. Lindstrom, V. P. Wystrach, *J. Am. Chem. Soc.* **1948**, *70*, 1382–1385.

[14] A. Klein, *Z. Anorg. Allg. Chem.* **2001**, *627*, 645–650.

[15] N. M. Colquhoun, J. Holton, D. J. Thompson, M. V. Twigg, *New Pathways for Organic Synthesis: Practical Applications of Transition Metals*, Plenum Press, New York, **1984**, pp. 382.

[16] G. M. Sheldrick, *Acta Crystallogr., Sect. A* **1990**, *46*, 467–473.

[17] G. M. Sheldrick, *SHELXL97, Programs for structure refinement*, University of Göttingen, Germany, **1997**.

Received: March 28, 2007
Published Online: July 31, 2007

 © 2007 Wiley-VCH Verlag GmbH & Co. KGaA, Weinheim 

DOI: 10.1002/ejic.200700363

# Oxidation of $N^{III}$ and $N^{-I}$ by an $\{Mn_4O_6\}^{4+}$ Core in Aqueous Media: Proton-Coupled Electron Transfer

**Suranjana Das[a] and Subrata Mukhopadhyay*[a]**

**Keywords:** Kinetics / Mechanisms / Manganese / Oxidation / Nitrogen

$[Mn_4(\mu\text{-}O)_6(bipy)_6]^{4+}$ ($\mathbf{1}^{4+}$; bipy = 2,2′-bipyridine) and its conjugate acid $[Mn_4(\mu\text{-}O)_5(\mu\text{-}OH)(bipy)_6]^{5+}$ ($\mathbf{1}H^{5+}$) quantitatively oxidise $N^{III}$ ($HNO_2$ and $NO_2^-$) and $N^{-I}$ ($NH_3OH^+$ and $NH_2OH$) to $N^V$ (nitrate) and $N^I$ (nitrous oxide), respectively, in aqueous solution (pH 2.0–6.0), with $\mathbf{1}H^{5+}$ reacting much faster than $\mathbf{1}^{4+}$. An uncommon feature of these reactions is the kinetic superiority of $HNO_2$ over its conjugate base $NO_2^-$. $NH_2OH$, however, behaves normally – the conjugate acid $NH_3OH^+$ is less reactive than $NH_2OH$. These reactions show remarkable kinetic isotope effects: the observed rate of $N^{III}$ oxidation increases in $D_2O$ media whereas the $N^{-I}$ oxidation rate slows down in media enriched with $D_2O$. A search of the available data on the redox kinetics of multinuclear oxidants suggests that the title $\{Mn_4O_6\}^{4+}$ reduction by $N^{III}$, the rate of which is accelerated in $D_2O$, is the only one established so far. A hydrogen atom transfer (HAT) mechanism (1e, $1H^+$; electroprotic) is proposed.

(© Wiley-VCH Verlag GmbH & Co. KGaA, 69451 Weinheim, Germany, 2007)

## Introduction

The oxygen-evolving complex (OEC)[1–5] oxidises water to molecular dioxygen in photosystem II (PS II) at the redox catalytic centre on the lumenal side of PS II, which includes four manganese ions, a calcium ion and a chloride ion.[6,7] The OEC cycles over five redox states $S_0$–$S_4$, where the index refers to the number of oxidising equivalents stored;[8,9] dioxygen is evolved in the $S_4 \rightarrow S_0$ transition.

Successive changes in the redox states of the Mn atoms in the OEC during this cycle are associated with protonation/deprotonation of the oxo bridges[10] and of the nearby amino acid residues as well as the simultaneous movements of proton and electrons within the OEC.[11]

The acid/base chemistry resulting from oxo-bridge protonations in synthetic multinuclear Mn complexes has been studied mostly in non-aqueous media.[12] It has also been demonstrated that oxo-bridge protonation sometimes increases the reactivity of a binuclear Mn oxidant[12d,12e] and completely quenches the catalase activity of an $Mn^{IV}$ dimer.[12c] How such protonations affect the chemical behaviour of higher-valent synthetic Mn complexes is not known, despite the relevance of such knowledge to PS II. This is particularly true in water, the medium where PS II acts.

The title complex $[Mn_4(\mu\text{-}O)_6(bipy)_6]^{4+}$ ($\mathbf{1}^{4+}$; Figure 1) formally corresponds to the fully oxidised $S_3$ or $S_4$ state of OEC[2] [although involvement of an even higher state ($Mn^V$) is feasible in the water oxidation process],[13] which is stable in aqueous solution over a wide acidity range (pH 2.0–6.0). Its one-electron-reduced, mixed-valent $Mn^{IV}{}_3Mn^{III}$ form is an EPR spectroscopic model for the $S_2$ state,[14] which means that the electron-transfer reactivity of the title Mn tetramer will thus be instructive.

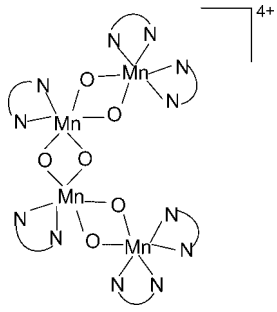


Figure 1. Schematic drawing of $[Mn_4(\mu\text{-}O)_6(bipy)_6]^{4+}$. N-N = 2,2′-bipyridine.

We demonstrated recently that $\mathbf{1}^{4+}$ oxidises glyoxylic and pyruvic acid through an electroprotic mechanism and that the oxo-bridged protonated species $\mathbf{1}H^{5+}$ is a kinetically superior oxidant to $\mathbf{1}^{4+}$.[15] It therefore seemed worthwhile to investigate whether the relative acidities of the reducing agents influence the proton-coupled electron transfer mechanism as well as the reactivity of the oxo-bridged protonated oxidant. The present investigation was thus planned with two selected reducing agents, namely $HNO_2$ and $NH_3OH^+$ (and their conjugate bases), which have a sufficient separation in their $pK_a$ values.[16,17] We further note that hydroxylamine[18] reduces the Mn ions in PS II whereas nitrite does not.[19]

[a] Department of Chemistry, Jadavpur University, Calcutta 700 032, India
E-mail: smukhopadhyay@chemistry.jdvu.ac.in

Supporting information for this article is available on the WWW under http://www.eurjic.org or from the author.

 © 2007 Wiley-VCH Verlag GmbH & Co. KGaA, Weinheim 

## Results and Discussion

### Equilibrium Measurements

The measured p$K_a$ values of these reducing acids in a 95% $D_2O$ medium are $3.80 \pm 0.10$[20,21] and $6.40 \pm 0.10$ for nitrous acid and hydroxylammonium cation respectively. The reported p$K_a$ values used in this investigation for $HNO_2$ and $NH_3OH^+$ in an $H_2O$ medium are 3.00[16] and 6.00,[17] respectively. All the p$K_a$ values are at 25.0 °C, $I$ = 1.0 M ($NaNO_3$). The pH-metric titration of the title tetranuclear Mn oxidant, however, did not result in any ionisation constant in the pH interval 2.0–7.0.

### Stoichiometric Analyses

Nitrate ($NO_3^-$) was detected as the oxidation product of nitrite whereas no red colouration was observed when the product solutions of the redox reaction of hydroxylamine were tested for nitrite or nitrate. The results of several stoichiometric experiments, under both kinetic ($T_R > 4[Mn^{IV}_4]$) and non-kinetic conditions ($T_R < 4[Mn^{IV}_4]$), are summarised in Table 1, which establishes a 1:4 stoichiometry (oxidant:reductant) for both the redox reactions, where $T_R$ is the analytical concentration of the reducing agent defined as $T_R = [HNO_2] + [NO_2^-]$ for $[N^{III}]_T$ and $T_R = [NH_3OH^+] + [NH_2OH]$ for $[N^{-I}]_T$. The title Mn tetramer is not a powerful oxidant (see below) and it is clear from the ratio $\Delta[Mn^{IV}_4]/\Delta[T_R]$ (Table 1) that $N_2O$ is the sole oxidation product of hydroxylamine − no further oxidation of $N_2O$ to nitrite or nitrate was observed. The results of EDTA titrations of the product solutions revealed quantitative formation of $Mn^{II}$ as the sole reduction product of $Mn^{IV}$. The likely $Mn^{II}$ species under these reaction conditions is an $Mn^{II}$-bipy complex.[22] Optical spectra for the product solutions were superimposable on those of mixtures of $Mn(NO_3)_2$ and 2,2′-bipyridine under similar experimental conditions. Equations (1) and (2) are thus closest to our above observations.

$$[Mn_4O_6(bipy)_6]^{4+} + 4\,NO_2^- + 4\,H^+ \longrightarrow 4\,Mn^{2+} + 4\,NO_3^- + 6\,bipy + 2\,H_2O \quad (1)$$

$$[Mn_4O_6(bipy)_6]^{4+} + 4\,NH_2OH + 4\,H^+ \longrightarrow 4\,Mn^{2+} + 2\,N_2O + 6\,bipy + 8\,H_2O \quad (2)$$

### Kinetics

The decay in absorbance vs. time plots could be fitted with standard first-order decay curves at least up to three half-lives. The observed first-order rate constants ($k_0$) do not depend on the wavelength chosen for the measurements (380–500 nm) where only the oxidant absorbs sufficiently, the presence or absence of dissolved oxygen in the reaction medium or on the concentration of the Mn oxidant (0.05–0.30 mM). Averages of $k_0$ values from at least three measurements were taken and the average coefficients of variation (CV)[23] for these measurements were within 3%. The observed proton-dependences of $k_0$ in these two redox reactions is interesting (Table 2). For nitrite oxidation, $k_0$ values increase with an increase in acidity of the reaction medium whereas they decrease with increasing acidity for hydroxylamine oxidation until the very low pH region, where $k_0$ increases with a decrease in pH. We can suppose a superior kinetic reactivity of $HNO_2$ over $NO_2^-$ from these trends whereas $NH_2OH$ is superior to $NH_3OH^+$. However, the title complex ($\mathbf{1}^{4+}$) may suffer protonation at very low pH, as was evident from its reaction with α-keto acids.[15] The species formed ($\mathbf{1}H^{5+}$) may act as an additional oxidant in the low pH region despite being present in only a low concentration. Protonated oxidants always react quicker than their conjugate bases[24] within a system, and thus $\mathbf{1}H^{5+}$ is expected to react faster than $\mathbf{1}^{4+}$. We measured several $k_0$ values in the presence of varying amounts of added bipy over the entire pH range for both the redox reactions. The lack of influence of added bipy on the observed rate of either reaction at any acidity rules out the possibility of bipy dissociation from the parent Mn complex in solution. We observed a linear variation of $k_0$ with $T_R$ in the entire pH range studied and found no indication of rate saturation even at the highest $T_R$ studied. Table 2 collects some representative $k_0$ values.

A strong pre-equilibrium ($K$) binding of the reducing species with the title oxidant followed by reaction of the intermediate thus formed with a second reducing species would lead to the observed kinetics (linear dependence of $k_0$ on $T_R$) provided that $KT_R$ is much greater than 1, which requires a $K$ value as high as $10^4$ (lowest $T_R = 5.0 \times 10^{-3}$ M). However, the tetranuclear Mn oxidant is coordinatively saturated at each Mn centre and an inner-sphere attachment of reducing species seems unlikely. Moreover, $d^3$ $Mn^{IV}$ is substitution inert and the oxidant retains its bipy ligands in aqueous solution in the entire pH range studied (see above), which means there is no scope for the formation of the aqua species that could lead to an inner-sphere mechanism in solution. We thus disregard this kind of pathway in the kinetics of the title redox reaction. The observed proton-

Table 1. Stoichiometry of reduction of the $Mn^{IV}_4$ complex by $N^{III}$ and $N^{-I}$ ($T$ = 25.0 °C, $C_{bipy}$ = [Hbipy$^+$] + [bipy] = 3.0 mM).

| $[Mn^{IV}_4]$ [mM] | pH | $[N^{III}]_T$ (= $T_R$) [mM] | $[N^{-I}]_T$ (= $T_R$) [mM] | $\Delta[Mn^{IV}_4]/\Delta[T_R]$ |
|---|---|---|---|---|
| 0.20 | 3.3 | 1.50 | | 0.27 |
| 0.40 | 3.6 | 2.00 | | 0.26 |
| 0.60 | 5.6 | 3.50 | | 0.23 |
| 1.50 | 5.5 | 10.0 | | 0.26 |
| 0.10 | 3.5 | 0.20 | | 0.24 |
| | | | | average = 0.25 ± 0.02 |
| 0.20 | 2.5 | | 2.00 | 0.23 |
| 0.50 | 4.5 | | 4.00 | 0.24 |
| 0.80 | 5.0 | | 6.00 | 0.27 |
| 1.30 | 5.3 | | 10.0 | 0.23 |
| 0.20 | 5.1 | | 0.60 | 0.23 |
| | | | | average = 0.24 ± 0.02 |

 © 2007 Wiley-VCH Verlag GmbH & Co. KGaA, Weinheim 

Table 2. Some representative first-order rate constants for the oxidation of nitrite and hydroxylamine by the title complex (0.10 mM) at $T$ = 25.0 °C, $I$ = 1.0 M ($NaNO_3$). The values in parentheses are calculated from Equation (9) using the rate constants reported in Table 3.

| pH Nitrite | $T_R$ [M] | $C_{bipy}$ [mM] | $10^4 k_0$ [$s^{-1}$] |
|---|---|---|---|
| 2.50 | 0.05 | 3.0 | 491 (500) |
| 2.82 | 0.05 | 3.0 | 197 (202) |
| 3.14 | 0.05 | 3.0 | 74.0 (76.6) |
| 3.78 | 0.05 | 3.0 | 11.2 (10.4) |
| 4.18 | 0.05 | 3.0 | 3.44 (3.34) |
| 4.75 | 0.05 | 3.0 | 0.74 (0.78) |
| 5.15 | 0.05 | 3.0 | 0.28 (0.30) |
| 5.56 | 0.05 | 3.0 | 0.11 (0.11) |
| 4.69 | 0.025 | 3.0 | 0.43 (0.45) |
| 4.69 | 0.075 | 3.0 | 1.39 (1.35) |
| 4.67 | 0.10 | 3.0 | 1.81(1.89) |
| 4.15 | 0.05 | 20 | 3.66 (3.62) |
| 4.13 | 0.05 | 50 | 3.81 (3.82) |
| 4.13 | 0.05 | 80 | 4.03 (3.82) |
| 3.22 | 0.05 | 20 | 57.8 (59.6) |
| 3.24 | 0.05 | 50 | 58.9 (56.0) |
| 3.23 | 0.05 | 80 | 59.2 (57.8) |
| 4.71 | 0.05 | 3.0 | 1.06[a] |
| 4.70 | 0.05 | 3.0 | 1.39[b] |
| 2.51 | 0.05 | 3.0 | 496 [a] |
| 2.53 | 0.05 | 3.0 | 499 [b] |
| Hydroxylamine | | | |
| 2.04 | 0.01 | 5.0 | 3.60 (3.58) |
| 2.37 | 0.01 | 5.0 | 1.95 (1.92) |
| 3.02 | 0.01 | 5.0 | 0.79 (0.84) |
| 3.20 | 0.01 | 5.0 | 0.73 (0.76) |
| 3.42 | 0.01 | 5.0 | 0.74 (0.74) |
| 4.00 | 0.01 | 5.0 | 1.19 (1.12) |
| 4.41 | 0.01 | 5.0 | 1.98 (2.10) |
| 4.84 | 0.01 | 5.0 | 4.52 (4.69) |
| 5.35 | 0.01 | 5.0 | 12.2 (12.4) |
| 6.00 | 0.01 | 5.0 | 32.0 (32.2) |
| 3.61 | 0.02 | 5.0 | 1.51 (1.58) |
| 3.62 | 0.04 | 5.0 | 3.23 (3.18) |
| 3.61 | 0.10 | 5.0 | 7.79 (7.90) |
| 4.11 | 0.01 | 1.0 | 1.21 (1.30) |
| 4.10 | 0.01 | 10 | 1.23 (1.28) |
| 4.13 | 0.01 | 20 | 1.29 (1.34) |
| 4.12 | 0.01 | 40 | 1.37 (1.32) |
| 4.12 | 0.01 | 60 | 1.42 (1.32) |
| 5.95 | 0.01 | 5.0 | 30.1[a] |
| 5.93 | 0.01 | 5.0 | 30.5[b] |
| 2.11 | 0.01 | 5.0 | 2.61[a] |
| 2.12 | 0.01 | 5.0 | 2.08[b] |
| 3.60 | 0.01 | 5.0 | 1.22[a] |
| 3.62 | 0.01 | 5.0 | 1.05[b] |

[a] $I$ = 0.5 M ($NaNO_3$). [b] $I$ = 0.1 M ($NaNO_3$).

dependence of $k_0$ on [$H^+$] could not be fitted to any type of reaction scheme with only one protic equilibrium, which means that Equations (3) and (4) need to be considered simultaneously, as shown in Scheme 1 for both the reactions under investigation.

Scheme 1 leads to the rate law in Equation (9), assuming that $K_1$[$H^+$] is much less than 1. This scheme does not take into account any protonation equilibrium of $HNO_2$[25] to generate $NO^+$ [Equation (10)] or a disproportionation equilibrium of $HNO_2$[26] to generate NO and $NO_2$ [Equation (11)]. A reaction path involving NO would require an $[HNO_2]^2$ term in the rate law and $NO^+$ requires a third-order term $[Mn^{IV}_4][HNO_2][H^+]$. The equilibrium constants of these reactions are small, which might be the main reason for not obtaining the reactivities, if any, of these species. We therefore used $[N^{III}]_T = [HNO_2] + [NO_2^-]$. Except for $NH_2OH$ and $NH_3OH^+$, no other pH-dependent $N^{-I}$ species are known.

$$1^{4+} + H^+ \overset{K_1}{\rightleftharpoons} 1H^{5+} \quad (3)$$

$$RH \overset{K_a}{\rightleftharpoons} R^- + H^+ \quad (4)$$

$$1H^{5+} + RH \xrightarrow{k_1} \text{products} \quad (5)$$

$$1H^{5+} + R^- \xrightarrow{k_2} \text{products} \quad (6)$$

$$1^{4+} + RH \xrightarrow{k_3} \text{products} \quad (7)$$

$$1^{4+} + R^- \xrightarrow{k_4} \text{products} \quad (8)$$

Scheme 1. (RH = $HNO_2$ or $NH_3OH^+$).

$$k_0(K_a + [H^+])/T_R = k_1K_1[H^+]^2 + (k_2K_1K_a + k_3)[H^+] + k_4K_a \quad (9)$$

$$HNO_2 + H^+ \rightleftharpoons NO^+ + H_2O \qquad K = 3.0 \times 10^{-7} \quad (10)$$

$$2\,HNO_2 \rightleftharpoons NO + NO_2 + H_2O \qquad K = 6.0 \times 10^{-6} \quad (11)$$

Plots of the left-hand side of Equation (9) resulted in a good polynomial fit of [$H^+$] for both redox reactions (Figure 2, $r > 0.98$), from which we obtain $k_1K_1$, $(k_2K_1K_a + k_3)$

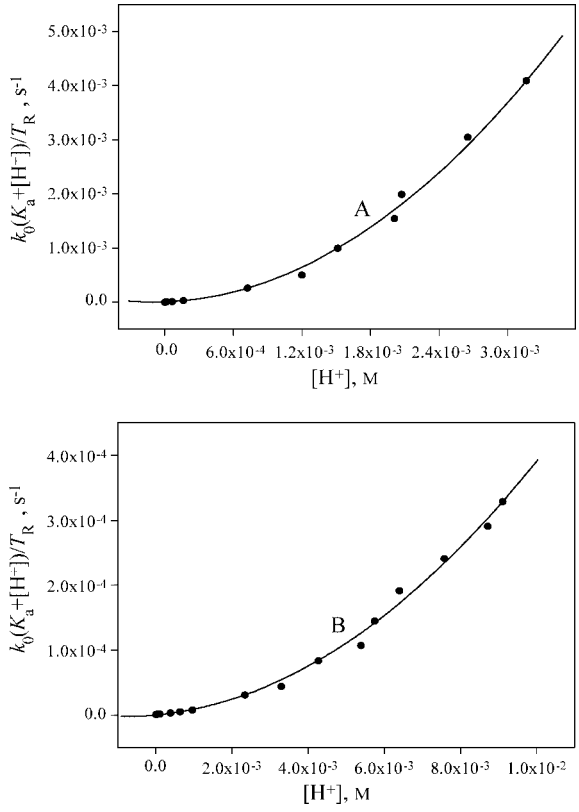


Figure 2. Plot of the left-hand side of Equation (9) vs. [$H^+$]. [complex] = 0.10 mM, $T$ = 25.0 °C, $I$ = 1.0 M. A: $N^{III}$, $C_{bipy}$ = 3.0 mM; B: $N^{-I}$, $C_{bipy}$ = 5.0 mM.

 © 2007 Wiley-VCH Verlag GmbH & Co. KGaA, Weinheim 

Table 3. Rate constants for the reduction of $\mathbf{1}^{4+}$ by nitrite and hydroxylamine at $T$ = 25.0 °C, $I$ = 1.0 M ($NaNO_3$).

| | $k_1K_1$ [$M^{-2}s^{-1}$] | $k_2K_1K_a + k_3$ [$M^{-1}s^{-1}$] | $k_4$ [$M^{-1}s^{-1}$] |
|---|---|---|---|
| $H_2O$ medium $N^{III}$ | $390 \pm 20$ | $(8.2 \pm 0.5) \times 10^{-2}$ | 0 |
| $H_2O$ medium $N^{-I}$ | $3.43 \pm 0.20$ | $(4.4 \pm 0.3) \times 10^{-3}$ | $(6.6 \pm 0.4) \times 10^{-1}$ |
| 95% $D_2O$ medium $N^{III}$ | $760 \pm 45$ | $(5.0 \pm 0.3) \times 10^{-2}$ | 0 |
| 95% $D_2O$ medium $N^{-I}$ | $0.65 \pm 0.04$ | $(1.9 \pm 0.1) \times 10^{-4}$ | $(5.5 \pm 0.3) \times 10^{-2}$ |

and $k_4$ (see Table 3). The non-existence of the $k_4$ path for the nitrite redox reaction, as determined by the above second-order polynomial, was further confirmed by plotting $k_0(K_a + [H^+])/(T_R[H^+])$ against $[H^+]$ (see electronic supporting information), which resulted in a good straight line ($r > 0.98$) with slope $k_1K_1$ and intercept ($k_2K_1K_a + k_3$), in close agreement (within 5%) with the values reported in Table 3. On the other hand, the $k_4$ path was found to be significant for hydroxylamine redox above a pH of about 4, and a plot of $T_R/k_0$ against $[H^+]$ yielded a good straight line with slope $1/k_4$ and intercept $1/(k_4K_a)$ at pH $\geq$ 5.3 (see electronic supporting information). The value of $k_4$ determined in this way matches well with the values reported in Table 3.

It cannot be concluded, however, that, as $\mathbf{1}^{4+}$ does not react with $NO_2^-$ (the $k_4$ path does not contribute to the overall rate), $\mathbf{1}H^{5+}$ would not oxidise $NO_2^-$. Protonated metal complexes are superior oxidants than their deprotonated analogues[20,24] and a finite contribution of $k_2$ path may therefore be anticipated, although kinetic resolution of the proton-ambiguous $k_2$ and $k_3$ paths is not possible. We also note that the $k_1$ path starts contributing towards the observed rate at pH $\leq$ 5.0 for the $N^{III}$ redox reaction whereas for the $N^{-I}$ redox reaction a more acidic environment is needed to ensure a finite contribution of the $k_1$ path (pH $\leq$ 4.0), as judged by the values of $k_1K_1[H^+]^2$ and $(k_2K_1K_a + k_3)[H^+]$ for both redox reactions at these pHs. Below pH 3.0, hydroxylamine is almost quantitatively present as cationic $NH_3OH^+$, whose oxidation by $\mathbf{1}H^{5+}$ is electrostatically more unfavourable than the oxidation of $NH_2OH$. Oxidation of cationic $NH_3OH^+$ requires higher concentrations of $\mathbf{1}H^{5+}$, which are produced at much lower pH than that required for the oxidation of neutral $HNO_2$ purely on charge grounds.

It should be noted here that a scheme comprising only $HNO_2$ as the active reducing species reacting with $\mathbf{1}H^{5+}$ ($k_1$) and $\mathbf{1}^{4+}$ ($k_1'$) is an alternative to Scheme 1 and results in $k_1K_1$ and $k_1'$ values identical to those reported in Table 3 ($k_1'$ is similar to $k_3$ in Scheme 1, assuming the $k_2$ path is absent). However, this alternative cannot confirm the absence of the $k_2$ path in the nitrite redox reaction. The rate constants measured in presence of varying amounts of added $NaNO_3$ might be instructive here. At pH 4.7 (where $[NO_2^-] >> [HNO_2]$), $k_0$ increases substantially with a decrease in ionic strength of the reaction medium (Table 2), which indicates a reaction between opposite charges, therefore a finite contribution of the $k_2$ path may thus be anticipated ($\mathbf{1}H^{5+}$ is a stronger oxidant than $\mathbf{1}^{4+}$ and the $k_4$ path is absent in $N^{III}$ oxidation), while at pH 5–6 the value of $k_0$ remains unaltered in the range $I$ = 1.0–0.1 M ($NaNO_3$) for the $N^{-I}$ redox reaction (Table 2), in line with the maximum contribution of the uncharged $NH_2OH$ path ($k_4$) towards the overall rate at the highest pH extreme. Around pH 2.5, where $[HNO_2]$ is much greater than $[NO_2^-]$, the rate of the nitrite redox reaction was found to be independent of any variation in the ionic strength of the medium (Table 2), whereas at pH 2.1 or 3.6, where $[NH_3OH^+]$ is much greater than $[NH_2OH]$, the rate of hydroxylamine oxidation decreases significantly with decreasing ionic strength of the medium (Table 2). These observations qualitatively support the involvement of neutral $HNO_2$ and cationic $NH_3OH^+$ as reactive species with cationic $\mathbf{1}^{4+}$ or $\mathbf{1}H^{5+}$.

We can estimate $K_1$ to be between $10^{-9}$ and 10 from the fact that $K_1[H^+]$ is much less than 1 and the $k_1K_1$ values listed in Table 3. The fact that $K_1[H^+]$ is much less than 1 sets an upper limit for the pre-equilibrium binding of nearly 10 as the maximum $[H^+]$ used in this study is $10^{-2}$ M. Assuming the diffusion-controlled limit is $10^{11}$ $M^{-1}s^{-1}$, the lower limit of $K_1$ derived from the $k_1K_1$ values in Table 3 is around $10^{-9}$. For comparison, we note that the reported p$K_a$ of the analogous complex $[Mn^{IV}_4(\mu\text{-}O)_5(\mu\text{-}OH)(bpea)_4]^{5+}$ [bpea = *N*,*N*′-bis(2-pyridylmethyl)ethylamine] is –6,[12h] which shows that the bridging oxo group is much less basic. The strong acidity of the protonated oxo-bridge may thus be inferred. The Mn tetramer used here does not undergo any spectral change in the pH range 2.0–6.0 therefore spectral evaluation of its basicity was not possible.

It appears from Table 3 that the maximum value of $k_3$ is $4.4 \times 10^{-3}$ $M^{-1}s^{-1}$ for $N^{-I}$ oxidation while it is $8.2 \times 10^{-2}$ $M^{-1}s^{-1}$ for $N^{III}$ oxidation. The reactivity of $NH_2OH$ is higher than $NH_3OH^+$ as the rate increases with pH while it decreases with an increase in pH for the $N^{III}$ redox reaction. The maximum value of $k_2K_1$ for this latter reaction is 82 (much lower than $k_1K_1$), which clearly indicates that $HNO_2$ reacts much quicker with $\mathbf{1}H^{5+}$ or $\mathbf{1}^{4+}$ than $NO_2^-$. The overwhelming dominance of the reactivity of $\mathbf{1}H^{5+}$ is clear in both redox reactions.

## Mechanism

The electrochemistry of $[Mn_4(\mu\text{-}O)_6(bipy)_6]^{4+}$ has been extensively studied by Dunand-Sauthier et al.[27] The cyclic voltammogram of $[Mn_4(\mu\text{-}O)_6(bipy)_6]^{4+}$ in bipy/Hbipy$^+$

 © 2007 Wiley-VCH Verlag GmbH & Co. KGaA, Weinheim 

buffer shows only an irreversible reduction peak near 0.40 V (vs. Ag/AgCl) which leads to the formation of $[Mn(bipy)_3]^{2+}$ species.[27] Attempts at electrolytic reduction resulted in decomposition of the tetranuclear complex into four $Mn^{II}$ ions. Standard chemical reduction in solution also failed to achieve the monoreduced form $[Mn^{IV}{}_3Mn^{III}(\mu\text{-}O)_6(bipy)_6]^{3+}$.[14] Exhaustive reduction of $[Mn_4(\mu\text{-}O)_6(bipy)_6]^{4+}$ at 0.20 V (vs. Ag/AgCl) consumes almost eight equivalent of electrons per mole of the tetranuclear oxidant and leads to $Mn^{II}$.[27a] These authors have also shown an intermediate generation of the mixed-valent $[Mn^{III,IV}(\mu\text{-}O)_2(bipy)_4]^{3+}$ species during the conversion to $Mn^{II}$. This mixed-valent species could not, however, be generated selectively and quantitatively as the reduction of the tetranuclear and the mixed-valent species occurs at a very similar potential (approx. 0.4 V vs. Ag/AgCl).[27] We did not observe formation of any such spectrally characterisable binuclear intermediate during the chemical reduction of the title oxidant when reducing agents were used in either excess, deficit or stoichiometric amounts, see Equations (1) and (2).

We can conclude from the known electrochemical behaviour of the title tetranuclear Mn comlex that this species is not a powerful oxidant. The one-electron oxidation of $NO_2^-$ or $HNO_2$ and $NH_2OH$ or $NH_3OH^+$ is, however, highly endothermic. The one-electron oxidation potentials for $NO_2^-/NO_2$, $HNO_2/NO_2$, $H^+$, $NH_2OH/NH_2OH^+$ and $NH_3OH^+/NH_2OH^+$, $H^+$ couples are –1.04,[26] –1.22,[28] –0.91[29] and –1.30 V respectively.[28] An initial one-electron exchange between $[Mn_4(\mu\text{-}O)_6(bipy)_6]^{4+}$ and these reducing species is thus energetically unfavourable although we observe that these reducing agents smoothly reduce the $Mn^{IV}$ oxidant to $Mn^{II}$. An inner-sphere attachment of the reducing species to the $Mn^{IV}$ centres that could provide an alternative pathway is not likely as the $d^3$ $Mn^{IV}$ atoms in the coordinatively saturated oxidant are substitution inert. However, it can be concluded from the known electrochemical behaviour of the tetranuclear Mn oxidant that the intermediate mixed-valent forms are too reactive. In fact, the very high reactivity of the most likely one-electron reduced species produced by cryogenic radiolytic reduction of $\mathbf{1}^{4+}$, namely $[Mn^{IV}{}_3Mn^{III}(\mu\text{-}O)_6(bipy)_6]^{3+}$, has been documented.[30] This species is very unstable even at low temperature (190 K).[30]

In order to further explore the electron-transfer mechanism we measured $k_0$ values in media enriched with $D_2O$ and computed the second-order rate constants or their composites (Table 3) in the same way as in pure $H_2O$ media; they showed kinetic isotope effects. Interestingly, we also note that the $k_1K_1$ path in $N^{III}$ oxidation increases substantially in $D_2O$ media whereas all the other rate constants or their composites decrease. A lowering of the rate in $D_2O$ media is clearly indicative of an electroprotic mechanism.[31] Notably, we also found that the rate enhancement and rate decrease in $H_2O/D_2O$ mixtures for $N^{III}$ and $N^{-I}$ oxidations, respectively, are linearly related ($r > 0.98$) to the $D_2O$ content (Figure 3), which suggests transfer of a single proton in the slow steps.[32]

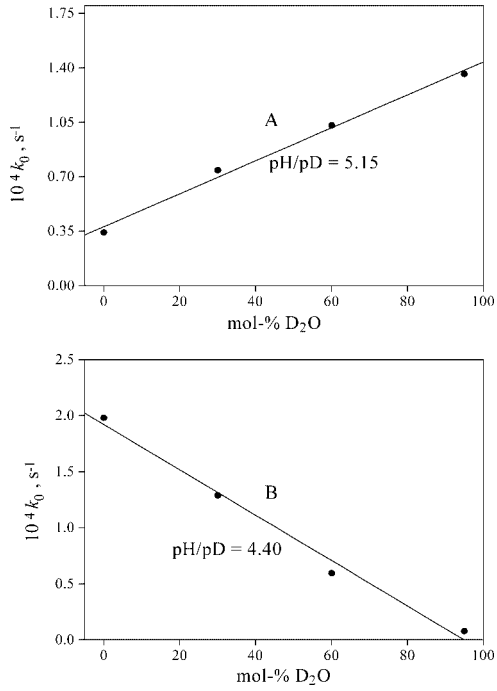


Figure 3. Effect of the amount of $D_2O$ (mol-%) on $k_0$. [complex] = 0.10 mM, $T$ = 25.0 °C, $I$ = 1.0 M. A: $N^{III}$, $[N^{III}]_T$ = 0.05 M, $C_{bipy}$ = 3.0 mM; B: $N^{-I}$, $[N^{-I}]_T$ = 0.01 M, $C_{bipy}$ = 5.0 mM.

An initial one-electron transfer rate-limiting step in the overall eight electron transactions [Equations (5)–(8)] is proposed to result in the intermediate mixed-valent Mn species $Mn^{IV}{}_3Mn^{III}$, which is likely to be reduced quickly in the following steps by the excess reducing agents or the radicals generated at the rate-determining step. We did not observe any polymerisation in either redox reaction when the reactions were carried out in 6% v/v acrylonitrile, although this does not rule out the production of radicals as they may react faster with the one-electron reduced mixed-valent Mn species, which is itself very reactive.[30] The one-electron reduced species of $\mathbf{1}^{4+}$ or $\mathbf{1}H^{5+}$ would have much more basic oxo bridges that immediately accept a proton from the reaction medium, which could remove thermodynamic or kinetics barriers to further reduction.[33] A large increase in the basicity of oxo bridges after one-electron reduction of the bridge carrying higher valent Mn atoms in di- or polynuclear Mn complexes is well documented[34] and is a key feature in the redox steps of the Kok cycle in PS II.[1c,35] Radicals produced from one-electron oxidation of nitrite and hydroxylamine, namely $NO_2$ and $NH_2OH^+$, are well-documented in the literature and pathways leading to the formation of nitrate[16b,36] and nitrous oxide[37] are well-established facets of nitrogen chemistry.

It has been known for a long time that rate increases significantly with $D_2O$ content in an $H_2O/D_2O$ mixture if acid/base pre-equilibrium steps are involved prior to the rate-determining step.[38a–38c] $D_2O$ has a smaller autoprotolysis constant than $H_2O$ by a factor of about 5 and thus it is less basic than water,[38a] which means that the oxo bridges in the title oxidant will be able to compete with the

 © 2007 Wiley-VCH Verlag GmbH & Co. KGaA, Weinheim 

solvent for the deuteron in $D_2O$ more effectively than for the proton in $H_2O$. An increase in the $K_1$ value in $D_2O$ is thus expected. In general, weak acids in $H_2O$ become much weaker in $D_2O$,[38] and we found that reducing acids like glyoxylic, pyruvic, nitrous and hydroxylammonium cation have considerably higher p$K_a$'s in $D_2O$.[15,20,21] We can thus reasonably expect a higher concentration of $\mathbf{1}H^{5+}$ in $D_2O$ and the observed reversal in the rate constants $k_1K_1$ in the two redox reactions might be a result of competitive increase in the $K_1$ value and a decrease in the $k_1$ value (electroprotic mechanism).

It has been shown recently[39] that an inverse deuterium isotope effect ($k_H < k_D$) is observed during charge recombination between the fully reduced $FADH^-$ anion (FAD = flavin adenine dinucleotide) and the neutral (deprotonated) radical of the solvent-exposed tryptophan W306. This can be interpreted by a model of fast protonation equilibrium for the W306 radical that involves an increase in the p$K_a$ of the radical in $D_2O$, which is 0.56-times that in $H_2O$ buffer. The authors were able to kinetically separate the rate constants, and the rate constant for recombination via deprotonated radical was found to be higher in $H_2O$ than in $D_2O$ (1.4 times).

It seems likely that the second-order rate constants decrease to such a great extent that this overcompensates the effect of an increase in the $K_1$ value in $D_2O$ for the $N^{-I}$ redox reaction whereas it is unable to slow down the $N^{III}$ redox reaction. The rate retardations in $D_2O$ for the oxidation of glyoxylic and pyruvic acid by the title Mn oxidant are much smaller[15] than those observed in the oxidation of $N^{-I}$, which might indicate that the effect of an increase in $K_1$ is almost cancelled out by the decrease in rate constants in $D_2O$ for the oxidations of these α-keto acids. A substantial decrease of $K_a$ in $D_2O$ (compared to that in $H_2O$) also contributes significantly to a remarkable decrease of the composite ($k_2K_1K_a + k_3$) for the $N^{III}$ redox reaction in $D_2O$.

The contribution of reaction (8) in Scheme 1 (for $R^- = NO_2^-$) towards the overall rate is statistically insignificant (Table 3). Moreover, $(k_2K_1)_{max}$ is much lower than $k_1K_1$ for $N^{III}$ oxidation, therefore we may reasonably expect that the $k_3$ path contributes significantly to the measured rate of $N^{III}$ oxidation. The superior reactivity of $HNO_2$ over $NO_2^-$ in reducing $\mathbf{1}^{4+}$ or $\mathbf{1}H^{5+}$ is thus clearly established. Both $NH_2OH$ and $NH_3OH^+$, on the other hand, react with the tetrameric Mn oxidant. It appears that the presence of an H-atom in both these reducing agents is responsible for the observed reactivity and thus a hydrogen atom transfer (HAT) from the reducing acids may be mechanistically conceived to produce the radicals $NO_2^{\cdot}$ or $NHOH^{\cdot}$ along with the protonated oxo bridge in the mixed-valent $Mn^{IV}_3Mn^{III}$ species. The kinetic superiority of $\mathbf{1}H^{5+}$ may be due, at least in part, to its more oxidising nature than $\mathbf{1}^{4+}$ as well as a more facile movement of hydrogen or hydrogen ion through the H-bonding framework formed from the oxo bridges of $\mathbf{1}H^{5+}$ and the oxygen and hydrogens of the reducing species. The molecular mechanics computed structure of the OEC reveals a network of organised hydrogen-bonded species around the OEC[13a,13b,40] cluster, thereby providing an insight into the movement of protons and water in the site.

## Experimental Section

**Materials:** The complex salt hydrate $[Mn_4(\mu\text{-}O)_6(bipy)_6][ClO_4]_4 \cdot 2H_2O$ was synthesised following the literature procedure.[14] One of its water molecules is easily lost[14] therefore the elemental analyses of the material closely resemble the values expected for the monohydrate. The tetramer used here thus appears to be the monohydrate. $C_{60}H_{50}Cl_4Mn_4N_{12}O_{23}$: calcd. C 43.16, H 2.99, N 10.07; found C 43.39, H 3.03, N 10.00.

The preparation, standardisation and storage of sodium nitrite, hydroxylamine nitrate and sodium nitrate have been described previously.[20,41] 2,2′-Bipyridine was used as received from Sigma. $D_2O$ (99.9 atom-% D) and $DNO_3$ (99+ atom-% D) were also purchased from Sigma. All other chemicals were of reagent grade and used as received. Doubly distilled, deionised and then freshly boiled water was used throughout.

**Equilibrium Measurements:** The acid dissociation constants of the reducing acids $HNO_2$ and $NH_3OH^+$ cation in 95% $D_2O$ medium were determined by pH-metric titration using a Metrohm (736 GP Titrino) autotitrator at 25.0(±0.1) °C, $I$ = 1.0 M ($NaNO_3$), as described previously.[20,41,42] To avoid nitrous acid decomposition in acidic media, solutions of $NaNO_2$ were titrated with $DNO_3$ while aliquots of hydroxylamine solutions (initially at pH 2 made by adding $HNO_3$) were titrated with carbonate-free NaOH. The reported values[16,17] of these ionisation constants in $H_2O$ media were used. A similar pH-metric titration of $[Mn_4(\mu\text{-}O)_6(bipy)_6]^{4+}$ was performed in the pH range 2.0–7.0 to examine the basicity of its oxo bridges.

**Stoichiometry Measurements:** The stoichiometries of the reactions were measured with both an excess and a deficit of reducing agent. Reaction mixtures containing 6–15-times $N^{III}$ over the Mn oxidant (0.05–1.50 mM) were allowed to react until the solutions became colourless (absorbance of less than 0.01 at 420 nm). Unreacted $N^{III}$ in these product mixtures was determined colourimetrically. After appropriate dilution, the product solutions were treated with α-naphthylamine and sulfanilic acid. The red dye thus formed was estimated at 520 nm ($\varepsilon = 4.0 \times 10^4$ $M^{-1}cm^{-1}$).[43] We verified that bipyridine, $Mn^{II}$ and $ClO_4^-$ do not interfere in this coupling reaction. $NO_3^-$ as the $N^{III}$ oxidation product was qualitatively detected by the above-mentioned coupling reaction after adding Zn dust. For this purpose reaction mixtures were prepared with complex:$N^{III}$ ratios of between 1:2 and 1:4. The Mn tetramer did not interfere in this colour reaction. Unreacted hydroxylamine was determined by titrating with standard $KBrO_3$ in the usual manner[44] when $Mn^{IV}_4$ (0.5–1.50 mM) was treated with (5–10 mM) $N^{-I}$. Formation of $NO_2^-$ or $NO_3^-$ as the $N^{-I}$ oxidation product was also tested by the coupling reaction described above. Under non-kinetic conditions, 0.10–0.50 mM of the $Mn^{IV}_4$ complex was treated with a less than stoichiometric amount of the reducing agents. Unreacted $Mn^{IV}_4$ complex was measured at 420 nm ($\varepsilon = 7.5 \times 10^3$ $M^{-1}cm^{-1}$) when the reactions reached equilibrium. $Mn^{II}$ in the product solutions was estimated by EDTA titrations using EBT as indicator.[45] For this purpose, excess reducing agent was treated with the Mn oxidant until the absorbance at 420 nm became less than 0.01 and then $Mn^{II}$ was estimated. We verified that $NO_2^-$, $NO_3^-$, $NH_2OH$ or bipy do not interfere in this complexometric titration.

**Physical Measurements and Kinetics:** Absorbance and electronic spectra were recorded with a Shimadzu (1601 PC) spectrophotome-

 © 2007 Wiley-VCH Verlag GmbH & Co. KGaA, Weinheim 

ter using 1.00-cm quartz cells. The kinetics was monitored in situ with the instrument in "kinetic mode" at 420 nm in an electrically controlled thermostatted 25.0(±0.1) °C cell housing (CPS-240A). Reactions with $t_{1/2}$ less than 30 seconds were monitored using a Biologic SFM-03/QS stopped-flow spectrophotometer with DT-2801 data transmission system. The ionic strength was normally maintained at 1.0 M with $NaNO_3$. The excess 2,2′-bipyridine concentration, $C_{bipy}$ = [(Hbipy$^+$) + (bipy)] was in the range 1–80 mM and acted as a good buffer in the pH range studied (2.0–6.0), which was measured with an Orion-Ross Combined electrode system (Model 81–02) before and after the reaction. Excess bipyridine present in the reaction medium buffers the reaction within 0.05 pH units in the entire pH range studied for nitrite oxidation while for hydroxylamine oxidation a maximum pH increase of 0.15 units was seen when working at a pH below 3.0 but above pH 3.0 the pH drift was around 0.05 pH units. It is possible that $HNO_2$ in the low pH range and both bipyridine and hydroxylamine in the higher pH range act as good buffers.

The electrode calibration was described earlier to read $-\log_{10}[H^+]$ directly from a calibration curve constructed by plotting the pH-meter reading against $-\log_{10}[H^+]$.[46] For reactions in $D_2O$, pD was calculated as $pH_{measured} + 0.40$.[47] An excess of reducing agent was maintained in all the kinetic runs. The $\log_{10}$(absorbance) vs. time plots were found to be good straight lines for up to at least 90% completion of reactions and the observed rate constants ($k_0$) were calculated in the usual way.

**Supporting Information** (see also the footnote on the first page of this article): Linearisation of Equation (9) for the $N^{III}$ redox reaction and evaluation of $k_4$ for the $N^{-I}$ redox reaction from a linear plot at pH ≥ 5.3.

## Acknowledgments

The award of a Senior Research Fellowship (SRF) to Suranjana Das by the Council of Scientific and Industrial Research, New Delhi, India is gratefully acknowledged. We also thank Professor Soumen Basak, Head, Chemical Sciences Division, Saha Institute of Nuclear Physics (SINP), Salt Lake, Calcutta 700 064 and Dr. Kalyan Giri of SINP for permitting us to use the stopped-flow spectrophotometer at SINP and providing kind help.

[1] a) J. P. McEvoy, G. W. Brudvig, *Chem. Rev.* **2006**, *106*, 4455–4483; b) J. Yano, J. Kern, K. Sauer, M. J. Latimer, Y. Pushkar, J. Biesiadka, B. Loll, W. Saenger, J. Messinger, A. Zouni, V. K. Yachandra, *Science* **2006**, *314*, 821; c) S. Mukhopadhyay, S. K. Mandal, S. Bhaduri, W. H. Armstrong, *Chem. Rev.* **2004**, *104*, 3981–4026.

[2] J. W. Murray, J. Barber, *Biochemistry* **2006**, *45*, 4128–4130.

[3] Photosynthetic water oxidation: J. Nugent, *Biochim. Biophys. Acta* **2001**, *1503*, 1 (special dedicated issue).

[4] *Manganese Red-Ox Enzymes* (Ed: V. L. Pecoraro), VCH Publishers, New York, **1992**.

[5] J. Yano, Y. Pushkar, P. Glatzel, A. Lewis, K. Sauer, J. Messinger, U. Bergmann, V. Yachandra, *J. Am. Chem. Soc.* **2005**, *127*, 14974–14975.

[6] K. N. Ferreira, T. M. Iverson, K. Maghlaoui, J. Barber, S. Iwata, *Science* **2004**, *303*, 1831–1838; this work shows that the OEC of PS II contains a cubane-like $Mn_3CaO_4$ cluster linked to a fourth, distinct Mn by a mono μ-oxo bridge. However, the conditions used for the structure determination by X-ray crystallography may cause serious damage specifically to the metal site structure. See, for example:J. Yano, J. Kern, K.-D. Irrgang, M. K. Latimer, U. Bergmann, P. Glatzel, Y. Pushkar, J. Biesiadka, B. Loll, K. Sauer, J. Messinger, A. Zouni, V. Yachandra, *Proc. Natl. Acad. Sci. USA* **2005**, *102*, 12047–12052.

[7] E. M. Sproviero, J. A. Gascón, J. P. McEvoy, G. W. Brudvig, V. S. Batista, *J. Chem. Theory Comput.* **2006**, *2*, 1119–1134.

[8] P. Joliot, G. Barbieri, R. Chabaud, *Photochem. Photobiol.* **1969**, *10*, 309–315.

[9] B. Kok, B. Forbush, M. McGloin, *Photochem. Photobiol.* **1970**, *11*, 457–475. For a recent description of structure and oxidation state changes of PS II Mn complexes in these states, see: M. Haumann, C. Müller, P. Liebisch, L. Iuzzolino, J. Dittmer, M. Grabolle, T. Neisius, W. Meyer-Klaucke, H. Dau, *Biochemistry* **2005**, *44*, 1894–1908.

[10] a) J. B. Vincent, G. Christou, *Inorg. Chim. Acta* **1987**, *136*, L41–L43; b) C. Meinke, V. A. Solé, P. Pospisil, H. Dau, *Biochemistry* **2000**, *39*, 7033–7040; c) P. E. M. Siegbahn, *Inorg. Chem.* **2000**, *39*, 2923–2935.

[11] a) J. P. McEvoy, J. A. Gascon, V. S. Batista, G. W. Brudvig, *Photochem. Photobiol. Sci.* **2005**, *4*, 40–949; b) L. I. Krishtalik, *Biochim. Biophys. Acta* **1986**, *849*, 162–171; c) C. W. Hoganson, N. Lydakis-Simantiris, X. S. Tang, C. Tommos, K. Warncke, G. T. Babcock, B. A. Diner, J. McCracken, S. Styring, *Photosynth. Res.* **1995**, *46*, 177–184; d) C. W. Hoganson, G. T. Babcock, *Science* **1997**, *277*, 1953–1956.

[12] a) M. J. Baldwin, T. M. Stemmler, P. J. Riggs-Gelasco, M. L. Kirk, J. E. Penner-Hahn, V. L. Pecoraro, *J. Am. Chem. Soc.* **1994**, *116*, 11349–11356; b) K. S. Hagen, T. D. Westmoreland, M. J. Scott, W. H. Armstrong, *J. Am. Chem. Soc.* **1989**, *111*, 1907–1909; c) E. J. Larson, P. J. Riggs, M. L. Kirk, J. E. Penner-Hahn, V. L. Pecoraro, *J. Chem. Soc. Chem. Commun.* **1992**, 102–103; d) K. Wieghardt, U. Bossek, B. Nuber, J. Weiss, J. Bonvoisin, M. Corbella, S. E. Vitols, J. J. Girerd, *J. Am. Chem. Soc.* **1988**, *110*, 7398–7411; e) H. Chen, J. W. Faller, R. H. Crabtree, G. W. Brudvig, *J. Am. Chem. Soc.* **2004**, *126*, 7345–7349; f) C. E. Dubé, D. W. Wright, W. H. Armstrong, *J. Am. Chem. Soc.* **1996**, *118*, 10910–10911; g) J. M. Carroll, J. R. Norton, *J. Am. Chem. Soc.* **1993**, *115*, 12639; h) C. E. Dubé, D. W. Wright, S. Pal, P. J. Bonitatebus Jr, W. H. Armstrong, *J. Am. Chem. Soc.* **1998**, *120*, 3704–3716; i) S. Mahapatra, T. K. Lal, R. Mukherjee, *Inorg. Chem.* **1994**, *33*, 1579–1980; j) T. K. Lal, R. Mukherjee, *Inorg. Chem.* **1998**, *37*, 2373–2382.

[13] Several authors have proposed the involvement of a unique, highly oxidised $Mn^V$=O species (in $S_4$ state) in the O–O bond-formation step ($S_4 \rightarrow S_0$). See, for example: a) J. Limburg, V. A. Szalai, G. W. Brudvig, *J. Chem. Soc. Dalton Trans.* **1999**, 1353–1362; b) J. P. McEvoy, G. W. Brudvig, *Phys. Chem. Chem. Phys.* **2004**, *6*, 4754–4763; c) V. L. Pecoraro, M. J. Baldwin, M. T. Candle, W. Y. Hsieh, N. A. Law, *Pure Appl. Chem.* **1998**, *70*, 925–929; d) P. E. M. Siegbahn, R. H. Crabtree, *J. Am. Chem. Soc.* **1999**, *121*, 117–127; e) P. E. M. Siegbahn, *Curr. Opin. Struct. Biol.* **2002**, *6*, 227–235; f) V. K. Yachandra, K. Sauer, M. P. Klein, *Chem. Rev.* **1996**, *96*, 2927–2950.

[14] C. Philouze, G. Blondin, J.-J. Girerd, J. Guilhem, C. Pascard, D. Lexa, *J. Am. Chem. Soc.* **1994**, *116*, 8557–8565.

[15] S. Das, J. Bhattacharyya, S. Mukhopadhyay, *Helv. Chim. Acta* **2006**, *89*, 1947–1958.

[16] a) P. Lumme, J. Tummavuori, *Acta Chem. Scand.* **1965**, *19*, 617–621; b) V. Zang, R. van Eldik, *Inorg. Chem.* **1990**, *29*, 4462–4468; c) S. Mukhopadhyay, R. Banerjee, *J. Chem. Soc. Dalton Trans.* **1994**, 1349–1353.

[17] P. Lumme, P. Lahermo, J. Tummavuori, *Acta Chem. Scand.* **1965**, *19*, 2175–2188.

[18] a) W. F. Beck, G. W. Brudvig, *Biochemistry* **1987**, *26*, 8285–8295; b) R. D. Guiles, V. K. Yachandra, A. E. McDermott, J. L. Cole, S. L. Dexheimer, R. D. Britt, K. Sauer, M. P. Klein, *Biochemistry* **1990**, *27*, 486–496; c) W. F. Beck, G. W. Brudvig, *J. Am. Chem. Soc.* **1988**, *110*, 1517–1523.

[19] a) A. Sahay, A. Jajoo, S. Bharti, *Luminescence* **2006**, *21*, 143–147; b) H. Spiller, P. Boger, *Photochem. Photobiol.* **1971**, *26*, 397–402; c) A. Stemler, J. B. Murphy, *Plant Physiol.* **1985**, *77*, 974–977.

 © 2007 Wiley-VCH Verlag GmbH & Co. KGaA, Weinheim 

[20] J. Bhattacharyya, S. Mukhopadhyay, *Helv. Chim. Acta* **2005**, *88*, 2661–2674.
[21] A. Das, S. Mukhopadhyay, *Helv. Chim. Acta* **2005**, *88*, 2561–2572.
[22] R. M. Smith, A. E. Martell, in *Critical Stability Constants*, Plenum, New York, **1976**, vol. 2, p. 235.
[23] CV was measured using the relation: CV = sd × 100/$x$, where sd is the standard deviation of the measurements of $k_0$ and $x$ is the average $k_0$. See: G. H. Jeffery, J. Bassett, J. Mendham and R. C. Denney, in *Vogel's Textbook of Quantitative Chemical Analysis*, Longman Scientific and Technical, England, 5th ed., **1989**, p. 135.
[24] a) P. Bandyopadhyay, B. B. Dhar, J. Bhattacharyya, S. Mukhopadhyay, *Eur. J. Inorg. Chem.* **2003**, 4308–4312; b) K. Lemma, A. M. Sargeson, L. I. Elding, *J. Chem. Soc. Dalton Trans.* **2000**, 2267–2272; c) A. Das, S. Mukhopadhyay, *Polyhedron* **2004**, *23*, 895–901.
[25] N. S. Bayliss, R. Dingle, D. W. Watts, R. J. Wilkie, *Aust. J. Chem.* **1963**, *16*, 933–942.
[26] M. S. Ram, D. M. Stanbury, *Inorg. Chem.* **1985**, *24*, 2954–2962.
[27] a) M.-N. C. Dunand-Sauthier, A. Deronzier, A. Piron, X. Pradon, S. Ménage, *J. Am. Chem. Soc.* **1998**, *120*, 5373–5380; b) M.-N. C. Dunand-Sauthier, A. Deronzier, A. Piron, *J. Electroanal. Chem.* **1999**, *463*, 119–122; c) M.-N. C. Dunand-Sauthier, A. Deronzier, A. Piron, X. Pradon, *J. Am. Chem. Soc.* **1997**, *119*, 3173–3174; d) C. Baffert, S. Romain, A. Richardot, J.-C. Lepretre, B. Lefebvre, A. Deronzier, M.-N. C. Dunand-Sauthier, *J. Am. Chem. Soc.* **2005**, *127*, 13694–13704.
[28] The oxidation potentials for $HNO_2 \rightarrow NO_2 + H^+ + e^-$ and for $NH_3OH^+ \rightarrow NH_2OH^+ + H^+ + e^-$ were calculated from the respective potentials for the $NO_2^-/NO_2$ and $NH_2OH/NH_2OH^+$ couples and the p$K_a$ values of $HNO_2$ and $NH_3OH^+$.
[29] M.-L. Hung, M. L. McKee, D. M. Stanbury, *Inorg. Chem.* **2001**, *40*, 2206.
[30] G. Blondin, R. Davydov, C. Philouze, M. F. Charlot, S. Styring, B. Åkermark, J. J. Girerd, A. Boussac, *J. Chem. Soc. Dalton Trans.* **1997**, 4069–4074.
[31] a) W. H. Albery, in *Proton Transfer Reactions* (Eds.: E. Caldin, V. Gold), Wiley, New York, **1975**, ch. 9; b) J. A. Gilbert, S. W. Gersten, T. J. Meyer, *J. Am. Chem. Soc.* **1982**, *104*, 6872–6873; c) R. A. Binstead, M. E. McGuire, A. Dovletoglou, W. K. Seok, L. E. Roecker, T. J. Meyer, *J. Am. Chem. Soc.* **1992**, *114*, 173–186; d) I. J. Rhile, J. M. Mayer, *J. Am. Chem. Soc.* **2004**, *126*, 12718–12719; e) M. Sjödin, S. Styring, H. Wolpher, Y. Xu, L. Sun, L. Hammarström, *J. Am. Chem. Soc.* **2005**, *127*, 3855–3863.
[32] W. H. Albery, M. H. Davis, *J. Chem. Soc. Faraday Trans.* **1972**, *68*, 167–181.
[33] D. M. Kurtz Jr, *Chem. Rev.* **1990**, *90*, 585–606.
[34] a) M. J. Baldwin, V. L. Pecoraro, *J. Am. Chem. Soc.* **1996**, *118*, 11325–11326; b) J. S. Vrettos, J. Limburg, G. W. Brudvig, *Biochim. Biophys. Acta* **2001**, *1503*, 229–245.
[35] G. Renger, *Biochim. Biophys. Acta* **2004**, *1655*, 195–204.
[36] a) G. Davies, K. Kustin, *Inorg. Chem.* **1969**, *8*, 484–490; b) S. K. Ghosh, R. N. Bose, E. S. Gould, *Inorg. Chem.* **1987**, *26*, 2684–2687; c) D. W. Margerum, L. M. Schurter, J. Hobson, E. E. Moore, *Environ. Sci. Technol.* **1994**, *28*, 331–337; d) D. W. Johnson, D. W. Margerum, *Inorg. Chem.* **1991**, *30*, 4845–4851.
[37] a) M. Simic, E. Hayon, *J. Am. Chem. Soc.* **1971**, *93*, 5982–5986; b) J. N. Coopert, D. W. Margerum, *Inorg. Chem.* **1993**, *32*, 5905–5910; c) R. M. Liu, M. R. McDonald, D. W. Margerum, *Inorg. Chem.* **1995**, *34*, 6093–6099.
[38] a) K. B. Wiberg, *Chem. Rev.* **1955**, *55*, 713–743; b) D. Ghosh, A. D. Shukla, R. Banerjee, A. Das, *J. Chem. Soc. Dalton Trans.* **2002**, 1220–1225; c) E. L. Purlee, *J. Am. Chem. Soc.* **1959**, *81*, 263–272; d) R. P. Bell, in *Acid-Base Catalysis*, Oxford University Press, London, **1941**, p. 145; e) R. P. Bell, in *The Proton in Chemistry*, Chapman and Hall, London, **1973**; f) D. M. Quinn, L. D. Sutton, in *Enzyme Mechanism from Isotope Effects* (Ed.: P. F. Cook), CRC Press, Boca Raton, **1991**, chapter 3, pp. 73–126; g) K. B. Schowen, R. L. Schowen, in *Methods in Enzymology* (Ed.: D. L. Purich), Academic Press, Inc., New York, **1982**, vol. 87, pp. 551– 606.
[39] M. Byrdin, V. Sartora, A. P. M. Eker, M. H. Vos, C. Aubert, K. Brettel, P. Mathis, *Biochim. Biophys. Acta* **2004**, *1655*, 64–70.
[40] a) B. A. Diner, D. A. Force, D. W. Randall, R. D. Britt, *Biochemistry* **1998**, *37*, 17931–17934; b) C. Jeans, M. J. Schilstra, N. Ray, S. Husain, J. Minagawa, J. H. A. Nugent, D. R. Klug, *Biochemistry* **2002**, *41*, 15754–15761; c) M. Haumann, A. Mulkidjanian, W. Junge, *Biochemistry* **1999**, *38*, 1258–1267; d) C. Berthomieu, R. Hienerwadel, A. Boussac, J. Breton, B. A. Diner, *Biochemistry* **1998**, *37*, 10547–10554.
[41] S. Banerjee, U. Roy Choudhury, R. Banerjee, S. Mukhopadhyay, *J. Chem. Soc. Dalton Trans.* **2002**, 2047–2052.
[42] J. Bhattacharyya, K. Dutta, S. Mukhopadhyay, *Dalton Trans.* **2004**, 2910–2917.
[43] a) G. Charlot, in *Colorimetric Determination of Elements: Principles and Methods*, Elsevier Publishing Company, New York, **1964**, p. 324; b) N. G. Bunton, N. T. Crosey, S. J. Patterson, *Analyst* **1969**, *94*, 585–588.
[44] G. H. Jeffery, J. Bassett, J. Mendham and R. C. Denney, in *Vogel's Textbook of Quantitative Chemical Analysis*, Longman Scientific and Technical, England, 5th edn., **1989**, p. 408.
[45] Reference 44, p. 334.
[46] a) S. Banerjee, U. Roy Choudhury, B. C. Ray, R. Banerjee, S. Mukhopadhyay, *Anal. Lett.* **2001**, *34*, 2797–2815; b) H. N. Irving, M. G. Miles, L. D. Pettit, *Anal. Chim. Acta* **1967**, *38*, 475–488.
[47] a) P. K. Glasoe, F. A. Long, *J. Phys. Chem.* **1960**, *64*, 188–190; b) P. Salomaa, L. L. Schaleger, F. A. Long, *J. Am. Chem. Soc.* **1964**, *86*, 1–7; c) A. K. Covington, R. A. Robinson, R. G. Bates, *J. Phys. Chem.* **1966**, *70*, 3820–3824.

Received: April 2, 2007
Published Online: August 10, 2007

 © 2007 Wiley-VCH Verlag GmbH & Co. KGaA, Weinheim 

DOI: 10.1002/ejic.200700364

# 3D Architectures of InOOH: Ultrasonic-Assisted Synthesis, Growth Mechanism, and Optical Properties

Liyong Chen,[a] Xuchu Ma,[a] Yankuan Liu,[a] Yan'ge Zhang,[a] Weizhi Wang,[a] Yi Liang,[a] and Zude Zhang*[a]

**Keywords:** Indium / Mechanism / UV/Vis spectroscopy / Solvothermal synthesis

An ultrasonic-assisted solvothermal route based on the hydrolysis of $In^{3+}$ was utilized to synthesize InOOH with a hierarchic three-dimensional (3D) architecture, which was assembled by single-crystalline nanowires with diameters of about 10 nm and lengths up to several hundred nanometers. X-ray powder diffraction (XRD), field emission scanning electron microscopy (FE-SEM), transmission electron microscopy (TEM), and FTIR spectra were used to characterize the obtained products. Alkaline media and solvent play crucial roles in influencing the phase and the morphology of the products. A possible mechanism was proposed to explain the formation process of the InOOH 3D nanostructure. The optical properties of InOOH was also investigated by ultraviolet and visible (UV/Vis) spectroscopy, which indicated that InOOH is a wide band-gap semiconductor.

(© Wiley-VCH Verlag GmbH & Co. KGaA, 69451 Weinheim, Germany, 2007)

## Introduction

In the past few years the synthesis of materials has essentially focused on size and shape and dimensionality control.[1] To date, challenges in the synthesis of nanomaterials include the control of morphology and the assemblage of ensembles of nanostructures. Because hierarchical structures may provide new forms with extremely high surface-to-volume ratios with potential applications as new catalysts or as a scaffolding support, nanoscale units used to build complex and hierarchical nanoarchitectures have attracted significant interest in material synthesis and device fabrication; some of these architectures include hierarchical three-dimensional (3D) MnS[2] and $TiO_2$,[3] flower-like iron oxide[4] and AlOOH,[5] dandelion-like CuO[6] and ZnO,[7] and urchin-like NiS[8] and $WO_3$.[9] Previously, several synthetic strategies were developed to fabricate 3D architectures assembled from nanowires, where polymers or solid templates were required to control the highly oriented growth of the nanowires.[10] However, the use of additives (i.e. polymers, templates) would increase the production cost and also introduce heterogeneous impurities. Thus, it is still a significant project to develop facile, additive-free, and easily controlled synthetic methods for the construction of 3D architectures of anisotropic materials.

Nanometer-scale indium oxyhydroxide (InOOH) and indium sesquioxide ($In_2O_3$) have found applications in the fields of semiconductors and optical materials.[11] InOOH, the hydrate of $In_2O_3$,[12] can be directly formed by the dehydration of $In(OH)_3$. Further calcination of InOOH at ambient pressure will produce metastable corundrum-type $In_2O_3$, an important n-type semiconductor with a direct bandgap of ca. 3.6 eV.[11b,13] To the best of our knowledge, many efforts have been made to synthesize micro- and/or nanostructured InOOH with different morphologies, such as nanofibers,[13a] nanotubes,[13b] and hollow spheres.[11c] However, hierarchical InOOH architectures consisting of nanoscale units have seldom been reported. Recently, sonochemical methods were proposed to synthesize nanomaterials with various structures,[14] because ultrasonic sound waves can provide energy by radiating through a solution and causing alternative high and low pressures in the liquid medium. The energy released from sonication can lead to enhanced chemical reactivity and accelerated reaction rates. Herein, we address our recent work on the synthesis of hierarchically 3D InOOH architectures composed of uniform nanowires, which involves an additives-free ultrasonic-assisted solvothermal route. This method uses the reaction among ethylenediamine (En), water, and $In^{3+}$. On the basis of investigations on the effect of En, we find that it might server as the structure-directing agent in the formation of InOOH nanowires, similar to the role of En as a structure-directing coordination template in previous studies.[15] Moreover, the UV/Vis spectrum showed that InOOH with a hierarchical 3D architecture is a typical wide band-gap semiconductor with $E_g$ of ca. 4.44 eV, which suggests that InOOH has the potential to be used in optical devices.

[a] Department of Chemistry, University of Science and Technology of China,
Hefei, Anhui 230026, P. R. China
Fax: +86-551-3601592
E-mail: zzd@ustc.edu.cn

 InterScience © 2007 Wiley-VCH Verlag GmbH & Co. KGaA, Weinheim 

## Results and Discussion

Figure 1 shows the XRD pattern of the products prepared at 210 °C for 24 h. All the diffraction peaks can be indexed to orthorhombic InOOH with cell parameters $a$ = 5.23 Å, $b$ = 4.55 Å, and $c$ = 3.26 Å, which are in good agreement with values from the standard card (JCPDS No. 71-2277). The XRD pattern confirms a highly crystalline nature of InOOH. Note that the diffraction peaks become broad, indicating that the size of the domain may be small.

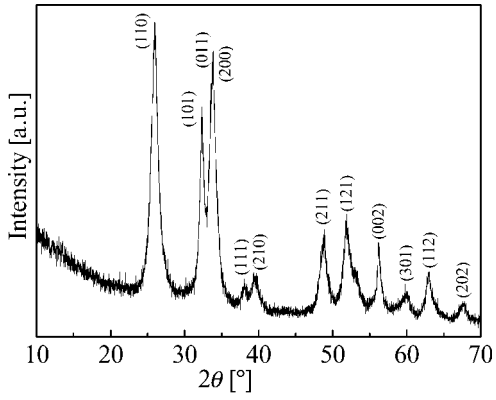


Figure 1. XRD pattern of InOOH prepared at 210 °C for 24 h.

The morphology and structure of the products obtained at 210 °C for 24 h were determined by FE-SEM and TEM. Figure 2a shows a panoramic FE-SEM image that shows that the samples have hierarchical 3D architectures with sizes in the range of several hundred nanometers to 1 μm. Figure 2b is a high-magnification FE-SEM image and Figures 2c–e are TEM images. Through careful observation (Figure 2b, d), we find that the architectures consist of nanowires with uniform diameters of ca. 10 nm and lengths up to several hundred nanometers. The nanowires were also investigated by the selected area electron diffraction (SAED) pattern and high-resolution transmission electron microscopy (HR-TEM). In the SAED pattern (Figure 2e, inset), the first diffraction ring corresponds to the (110) plane reflection of the orthorhombic InOOH structure. Owing to the fact that the atomic plane spacings of (101), (011), and (200) are very close, and that these three reflection rings look like one, the second diffraction ring cannot be distinguished well. Figure 2f is a HRTEM image, taken from a randomly chosen nanowire, where the average value of the plane spacing along the vertical direction is ca. 0.265 nm, and the value of the plane spacing along the inclined direction is about 0.279 nm. These two series of interplanar spacings correspond to the d spacing of the (101) and (200) planes of orthorhombic InOOH, respectively. These results further confirm the single-crystal nature of the samples.

In this strategy, we explored the influencing factors and optimized the reaction conditions; we coupled this with the appropriate choice of alkaline media and solvent to control the phase and the morphology of the obtained products. Sonication was extensively used for the generation of zero-

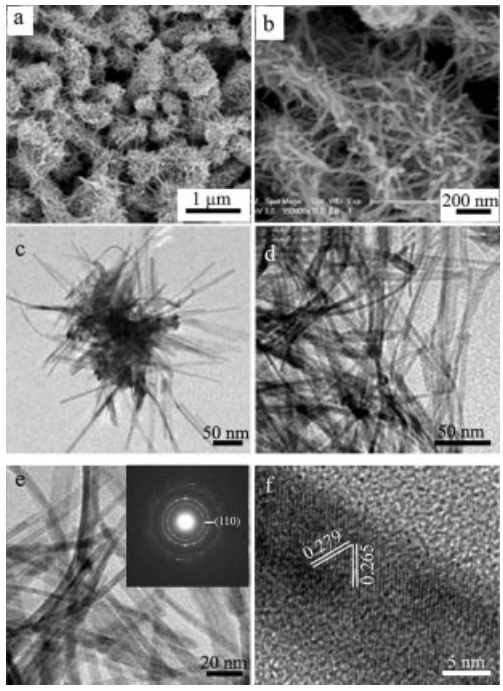


Figure 2. (a) Panoramic and (b) high-magnification FE-SEM images of InOOH with 3D architectures; (c) low-magnification TEM image of InOOH with 3D architectures; (d) high-magnification TEM image taken from their edge; (e) TEM image of InOOH nanowires (inset is SAED pattern); (f) HRTEM image of a single InOOH nanowire.

dimensional (0D) and one-dimensional (1D) nanostructures, as sonication is generally used as the driving force for nucleation. Here, we utilized the energy from the sonication process to induce the formation of uniform seeds,[14c] which favored the formation of nanowires with uniform diameters under solvothermal conditions. The TEM image (Figure 3a) reveals that the morphology of the products prepared without presonication have 3D structures composed of nonuniform nanowires. Figure 3b presents a high-magnification TEM image taken from their edge, which further testifies to the fact that the diameter of these nanowires are not uniform.

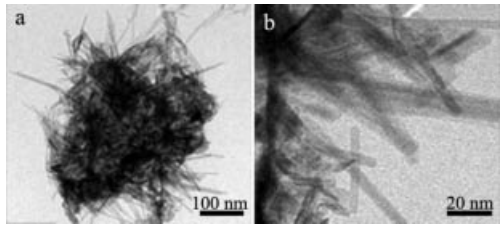


Figure 3. (a) Low-magnification TEM image of 3D InOOH architectures; (b) high-magnification TEM image recorded at the edge of the InOOH 3D architectures that shows nanowires with nonuniform diameters. These InOOH products were prepared without sonication.

As far as the alkaline media was concerned, En was found to be important in determining the phase and the morphology of the products. En acts as a structure-direct-

 © 2007 Wiley-VCH Verlag GmbH & Co. KGaA, Weinheim 

ing coordination agent to obtain InOOH nanowires as a result of it being a good ligand. En also provides the basicity for the system and facilitates the hydrolysis reaction of $In^{3+}$ and the formation of the orthorhomic InOOH phase. To better understand the role of En in this synthetic process, different organic amines such as hexamethylene diamine or diethylamine were used as a substitute for En in controlled experiments. Figures 4a, b show TEM images of the products prepared in both parallel experiments; both products are solid quasispherical structures composed of nanoparticles. Their phases are characterized by XRD patterns (Figure 4c), where all diffraction peaks can be indexed to cubic $In_2O_3$ (JCPDS No. 76-0152). Obviously, En may play a crucial factor in determining the phase and morphology of InOOH. To further explore the function of En, the intermediate products prepared in the initial 1, 2, 6, and 24 h were studied by FTIR as shown in Figure 4d, Curves 1–4, respectively. Figure 4d, Curve 1 clearly displays peaks at 3220 and 3097 $cm^{-1}$ for the –NH stretching vibration; it is shifted to lower wavenumbers than that of free En, whereas peaks at 2936 and 2890 $cm^{-1}$ for the $–CH_2$ stretching vibration and the peak at 1580 $cm^{-1}$ for the –NH bending vibration are shifted to higher wavenumbers relative to free En.[15c,16] These data confirm that the coordinative effect of En mostly exists in our experiments. Curves 3 and 4 (Figure 4d) exhibit two peaks at 3425 and 1980 $cm^{-1}$ together with a broad band at 2700 $cm^{-1}$ for the –OH vibration of InOOH and another peak at 445 $cm^{-1}$ for the In–O vibration absorption,[11c,17] which reveals that InOOH has already formed after the initial 6 h. On the contrary, the intensity of the characteristic absorption peaks of En gradually decreases, whereas those of InOOH gradually increase with prolonged reaction times. These experimental results reveal that En is the optimum alkaline medium and has a great influence on the growth of InOOH with 3D architectures.

To further investigate the mechanism of formation of InOOH with a hierarchical 3D architecture, time-dependent experiments involved in growth processes were conducted. The products prepared at various stages were followed by TEM imaging. Figure 5 shows TEM images of the intermediate samples obtained at 1, 2, 6, 8, 12, and 36 h. At the initial stage there are many nanoparticles formed with small sizes (Figure 5a, b). With prolonged reaction times, some short nanorods are developed at the expense of these small nanoparticles (Figure 5c). After longer reaction times, the nanoparticles gradually disappear and nanorods slowly grow into long nanowires (Figure 5d, e). These images clearly show the transformation process of the products from nanoparticles to nanorods and then to nanowires. However, the obtained sample has a 3D architecture composed of nonuniform nanowires (Figure 5f) when the reaction time is prolonged to 36 h, which reveals that an increase in the reaction time to greater than 24 h is unfavorable for the formation of uniform nanowires. The evolution of the products was also tracked by XRD (Figure 6a–f). As shown in Figure 6a, the product formed in the initial first hour is amorphous. From Figure 6b, it is found that there

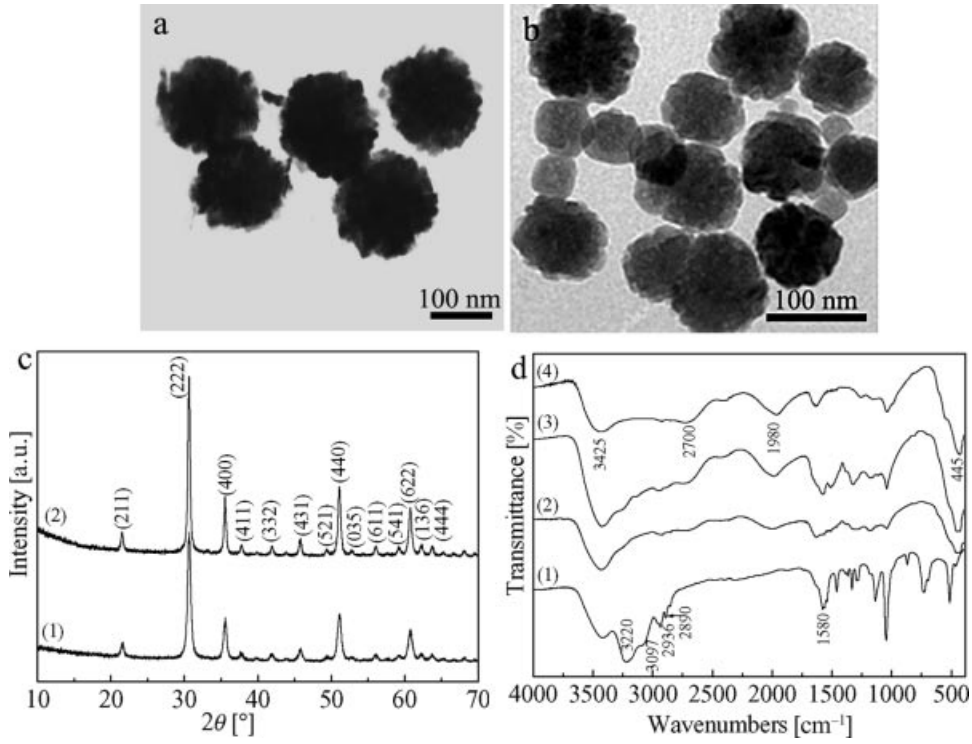


Figure 4. TEM images of samples obtained in alkaline media of (a) hexamethylene diamine; (b) diethylamine; (c) XRD patterns of samples obtained in (1) hexamethylene diamine and (2) diethylamine; (d) FTIR spectra of intermediate samples prepared in alkaline media of ethylenediamine and at 210 °C for (1) 1 h, (2) 2 h, (3) 6 h, and (4) 24 h.

 © 2007 Wiley-VCH Verlag GmbH & Co. KGaA, Weinheim 

is a diffraction peak at 22.4°, which corresponds to the diffraction of (200) lattice plane of cubic $In(OH)_3$ (JCPDS No. 85-1338) and indicates that the products already exist as cubic $In(OH)_3$ phases in the initial 2 h. By increasing the reaction time to 6 h and then 8 h, the diffraction peak of the (200) lattice plane increases firstly (Figure 6c), but then gradually decreases (Figure 6d). When the reaction time reaches 12 h, the diffraction peak completely disappears (Figure 6e). The orthorhombic InOOH diffraction peaks are also observed in the initial 2 h, and they progressively become sharper and stronger with longer reaction times. When the reaction time is increased to 36 h, a highly crystalline InOOH phase is obtained (Figure 6f). On the basis of these XRD patterns there is evidence to support a "dissolution–recrystallization" process. The $In(OH)_3$, nanoparticles are first formed and then slowly dissolved together with the gradual formation of InOOH nanocrystals owing to the fact that the solubility of $In(OH)_3$ is larger than that of InOOH. Hence, the phase transformation from $In(OH)_3$ to InOOH exists in this strategy, and the reactions can be simply expressed in Equations (1) and (2).

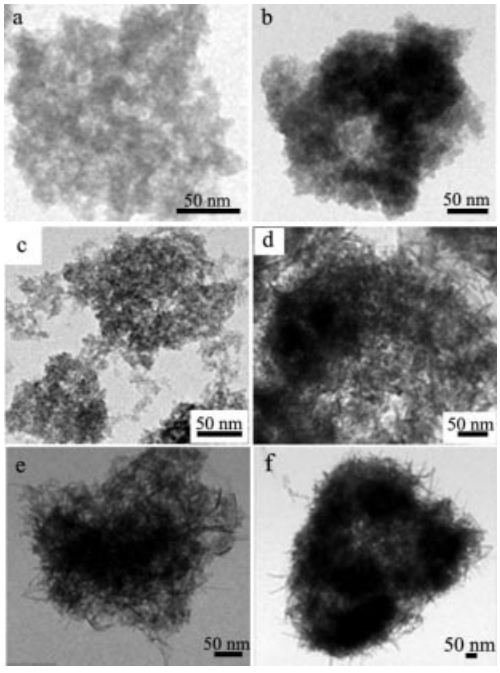


Figure 5. TEM images of intermediate products obtained in the presence of ethylenediamine and at 210 °C for (a) 1 h; (b) 2 h; (c) 6 h; (d) 8 h; (e) 12 h; and (f) 36 h.

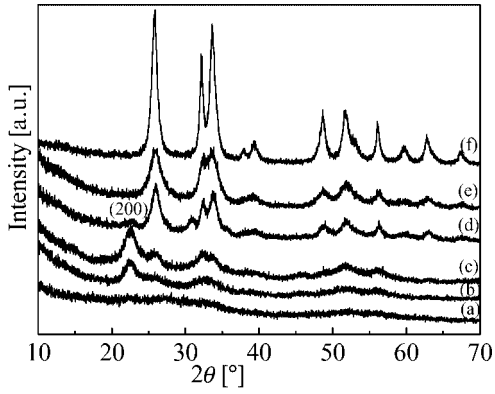


Figure 6. XRD patterns of the products obtained in the presence of ethylenediamine and at 210 °C with different heating time of (a) 1 h; (b) 2 h; (c) 6 h; (d) 8 h; (e) 12 h; and (f) 36 h.

$$In^{3+} + 3H_2O \rightarrow In(OH)_3 + 3H^+ \quad (1)$$

$$In(OH)_3 \rightarrow InOOH + H_2O \quad (2)$$

Additionally, it is found that the morphology and the phase of the products also depend on the solvents used in the synthesis process. A mixture of dimethyl formamide (DMF) and water as the solvent results in the growth of uniform InOOH nanowires rather than 3D structures. If dimethyl acetamide (DMA) is used as the solvent instead of DMF while all other conditions are kept unchanged, only aggregated InOOH nanorods are obtained (Figure 7a), which indicates that InOOH nanowires could not form in DMA medium. The experimental result reveals that DMF is favorable for the exhibition of the coordination template effect from En. Also, when varying the volume of deionized water, the formation of the products prepared is seriously affected. Figure 7b shows the TEM image of a sample obtained in the presence of 1 mL of deionized water; it indicates that the increase in water facilitates the formation of aggregated InOOH short nanorods. Moreover, if the amount of water is less than 0.25 mL or more than 5 mL, we cannot obtain pure InOOH, which denotes that the amount of water is a crucial factor in controlling the phase of the orthorhombic InOOH. This is possibly due to small amounts of water inhibiting the hydrolysis of $In^{3+}$ and the abundant amount of water restraining dehydration of $In(OH)_3$ [Equations (1) and (2)]. These control experiments revealed that 3D InOOH architectures consisting of nanowires can be obtained when using a mixture of DMF (15 mL) and water with a volume between 0.25 and 0.4 mL.

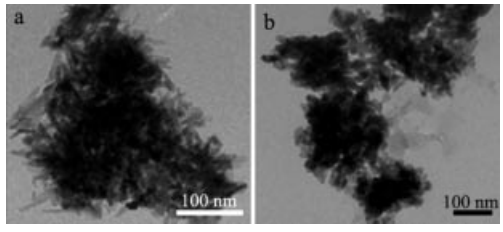


Figure 7. TEM images of samples: (a) when dimethyl acetamide was used as the solvent; (b) in the presence of deionized water (1 mL).

Combined with the above-mentioned discussion, a structure-directing coordination template mechanism under the ultrasonic-assisted conditions is proposed. The growth process of InOOH with hierarchical 3D architecture undergoes four distinctive stages: (1) Sonication induces the nucleation from the reaction of water, En, and $In^{3+}$. (2) Subsequently, many nanoparticles with small sizes are formed under the

 © 2007 Wiley-VCH Verlag GmbH & Co. KGaA, Weinheim 

solvothermal conditions and aggregate loosely due to the presence of the amido groups on the surface of the nanoparticles. Here, the phase of products formed in the stage is cubic $In(OH)_3$, which results from the hydrolysis of amorphous precursors. (3) Owing to the difference in solubilities of $In(OH)_3$ and InOOH, $In(OH)_3$ progressively dehydrolyzes to form InOOH. Simultaneously, InOOH nanorods are gradually obtained in the "dissolution–recrystallization" process of the particles of the precipitate as a result of the anisotropic crystal structure and the structure-directing coordination template effect from En, because En selectively adsorbs onto the lateral surfaces of the InOOH nanorods and restrains the lateral growth of the nanorods.[18] (4) With longer reaction times, all of the $In(OH)_3$ is eventually transformed into InOOH. Moreover, the nanorods would develop continuously into long nanowires and these nanowires could assemble into a 3D architecture because of the presence of hydrogen bonding between the hydroxy[5] and amido groups on the surface of the nanowires.

Finally, a UV/Vis spectrum was recorded with ethanol used as a reference to investigate the optical properties of the synthesized InOOH with a hierarchical 3D architecture. Figure 8 shows a typical UV/Vis spectrum; there is a broad absorption peak located at 279 nm (ca. 4.44 eV). Relative to the literature data of 3.5 eV,[11c] an obvious blueshift is observed, which can be attributed to the smaller diameters and larger aspect ratios of the nanowires.[19] The result from the UV/Vis spectrum indicates that InOOH is a wide band-gap semiconductor.

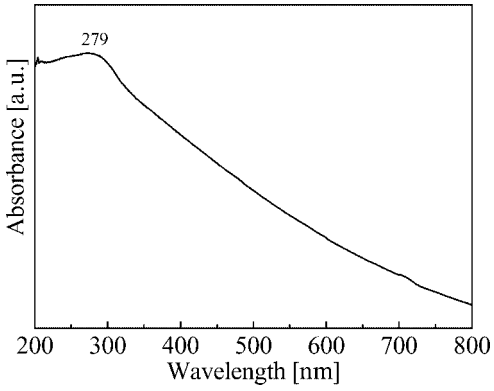


Figure 8. UV/Vis absorbance spectrum of InOOH with 3D architectures.

## Conclusions

InOOH with a hierarchical 3D architecture was synthesized by a facile solvothermal route under the assistance of ultrasonic conditions. The phase and the morphology of the products were controlled by the choice of alkaline media and also the solvent. Sonication can help to form nucleation of uniform nanowires that assemble into 3D nanostructures. A possible structure-directing coordination template mechanism is proposed to explain the formation of InOOH with 3D hierarchical architectures. On the basis of a UV/Vis spectrum, InOOH is an important wide band-gap semiconductor. The present method is simple, and it can be extended to the preparation of other 3D nanostructured materials.

## Experimental Section

**Preparation of InOOH with a Hierarchical 3D Architecture:** All reagents were of analytical grade, purchased from Shanghai Chemical Company, and used without further purification. In a typical procedure, $InCl_3{\cdot}4H_2O$ (0.5 mmol) and deionized water (0.25–0.40 mL) were mixed in a conical flask. After $InCl_3$ dissolution, dimethylformamide (15 mL) and ethylenediamine (5 mL) were added into the flask, and then the mixture was sonicated for about 1 h. The resulting solution was transferred to a 22-mL Teflon-lined autoclave, which was sealed and maintained between 210–220 °C for 24 h in a digital-temperature-controlled oven. The autoclave was cooled to room temperature naturally, and a white precipitate was collected by centrifugation and washed with distilled water and absolute ethanol several times, and dried in vacuo at 50 °C for 4 h.

**Sample Characterization:** The XRD patterns of the sample were recorded with a Philips X′pert X-ray diffractometer with Cu-$k_\alpha$ radiation ($\lambda$ = 1.54187 Å). The morphology of the sample was observed with a JOEL JSM-6700 field emission scanning electron microscopy (FE-SEM). The nanostructures of the sample were analyzed with a JEOL-2010 transmission electron microscopy (TEM) at an acceleration voltage of 200 kV. The FTIR spectra were obtained with a PerkinElmer FTIR spectrometer. The ultraviolet and visible (UV/Vis) spectrum was recorded with a Shimadzu DUV-3700 spectrophotometer.

## Acknowledgments

The financial support from the National Nature Science Research Foundation of China is gratefully acknowledged.

[1] a) C. N. R. Rao, A. K. Cheetham, *J. Mater. Chem.* **2001**, *11*, 2887–2894; b) C. N. R. Rao, A. MRller, A. K. Cheetham, *The Chemistry of Nanomaterials*, Wiley-VCH, Weinheim, **2004**; c) Y. N. Xia, P. D. Yang, Y. G. Sun, Y. Y. Wu, B. Mayers, B. Gates, Y. D. Yin, F. Kim, H. Q. Yan, *Adv. Mater.* **2003**, *15*, 353–389.
[2] Y. Cheng, Y. S. Wang, C. Jia, F. Bao, *J. Phys. Chem. B* **2006**, *110*, 24399–24402.
[3] X. X. Li, Y. J. Xiong, Z. Q. Li, Y. Xie, *Inorg. Chem.* **2006**, *45*, 3493–3495.
[4] L. S. Zhong, J. S. Hu, H. P. Liang, A. M. Cao, W. G. Song, L. J. Wan, *Adv. Mater.* **2006**, *18*, 2426–2431.
[5] J. Zhang, S. J. Liu, J. Lin, H. S. Song, J. J. Luo, E. M. Elssfah, E. Ammar, Y. Huang, X. X. Ding, J. M. Gao, S. R. Qi, C. C. Tang, *J. Phys. Chem. B* **2006**, *110*, 14249–14252.
[6] B. Liu, H. C. Zeng, *J. Am. Chem. Soc.* **2004**, *126*, 8124–8125.
[7] B. Liu, H. C. Zeng, *J. Am. Chem. Soc.* **2004**, *126*, 16744–16746.
[8] W. Q. Zhang, L. Q. Xu, K. B. Tang, F. Q. Li, Y. T. Qian, *Eur. J. Inorg. Chem.* **2005**, 653–656.
[9] Z. J. Gu, T. Y. Zhai, B. F. Gao, X. H. Sheng, Y. B. Wang, H. B. Fu, Y. Ma, J. N. Yao, *J. Phys. Chem. B* **2006**, *110*, 23829–23836.
[10] a) D. Routkevitch, T. Bigioni, M. Moskovits, J. M. Xu, *J. Phys. Chem.* **1996**, *100*, 14037–14047; b) H. Q. Cao, Z. Xu, H. Sang, D. Sheng, C. Y. Tie, *Adv. Mater.* **2001**, *13*, 121–123; c) M. H. Huang, S. Mao, H. Feich, H. Q. Yan, Y. Y. Wu, H. Kind, E. Weber, R. Russo, P. D. Yang, *Science* **2001**, *292*, 1897–1899; d) C. Z. Wu, Y. Xie, D. Wang, J. Yang, T. W. Li, *J. Phys. Chem. B* **2003**, *107*, 13583–13587; e) D. H. Wang, H. M. Luo, R. Kou,

 © 2007 Wiley-VCH Verlag GmbH & Co. KGaA, Weinheim 

M. P. Gil, S. G. Xiao, V. O. Golub, Z. Z. Yang, C. J. Brinker, Y. F. Lu, *Angew. Chem. Int. Ed.* **2004**, *43*, 6169–6173.
[11] a) W. S. Seo, H. H. Jo, K. Lee, J. T. Park, *Adv. Mater.* **2003**, *15*, 795–797; b) C. H. Lee, M. Kim, T. Kim, A. Kim, J. Paek, J. W. Lee, S. Y. Choi, K. Kim, J. B. Park, K. Lee, *J. Am. Chem. Soc.* **2006**, *128*, 9326–9327; c) H. L. Zhu, K. H. Yao, H. Zhang, D. R. Yang, *J. Phys. Chem. B* **2005**, *109*, 20676–20679.
[12] R. Roy, M. W. Shafer, *J. Phys. Chem.* **1954**, *58*, 372–375.
[13] a) D. B. Yu, S. H. Yu, S. Y. Zhang, J. Zuo, D. B. Wang, Y. T. Qian, *Adv. Funct. Mater.* **2003**, *13*, 497–501; b) C. L. Chen, D. R. Chen, X. L. Jiao, C. Q. Wang, *Chem. Commun.* **2006**, *44*, 4632–4634; c) M. Epifani, P. Siciliano, A. Gurlo, N. Barsan, U. Weimar, *J. Am. Chem. Soc.* **2004**, *126*, 4078–4079.
[14] a) K. S. Suslick, *Science* **1990**, *247*, 1439–1445; b) B. Gates, B. Mayers, A. Grossman, Y. N. Xia, *Adv. Mater.* **2002**, *14*, 1749–1752; c) B. T. Mayers, K. Liu, D. Sunderland, Y. N. Xia, *Chem. Mater.* **2003**, *15*, 3852–3858.
[15] a) Y. D. Li, H. W. Liao, Y. Ding, Y. T. Qian, L. Yang, G. E. Zhou, *Chem. Mater.* **1998**, *10*, 2301–2303; b) Y. D. Li, H. W. Liao, Y. Ding, Y. Fan, Y. Zhang, Y. T. Qian, *Inorg. Chem.* **1999**, *38*, 1382–1387; c) Z. X. Deng, C. Wang, X. M. Sun, Y. D. Li, *Inorg. Chem.* **2002**, *41*, 869–873; d) F. Gao, Q. Y. Lu, S. H. Xie, D. Y. Zhao, *Adv. Mater.* **2002**, *14*, 1537–1540.
[16] S. Gorai, D. Ganguli, S. Chaudhuri, *Cryst. Growth Des.* **2005**, *5*, 875–877.
[17] V. C. Farmer, *The Infrared Spectra of Minerals* (Translated into Chinese by: C. G. Li, Z. Li, Y. P. Ying, S. S. Wang, X. L. Han, Y. Q. Li), Science Press, Beijing, **1982**, p. 119.
[18] D. Xu, Z. P. Liu, J. B. Liang, Y. T. Qian, *J. Phys. Chem. B* **2005**, *109*, 14344–14349.
[19] a) B. M. I. Van der Zande, L. Pagès, R. A. M. Hikmet, A. van Blaaderen, *J. Phys. Chem. B* **1999**, *103*, 5761–5767; b) Y. F. Liu, J. B. Cao, J. H. Zeng, C. Li, Y. T. Qian, S. Y. Zhang, *Eur. J. Inorg. Chem.* **2003**, 644–647.

Received: April 3, 2007
Published Online: July 31, 2007

 © 2007 Wiley-VCH Verlag GmbH & Co. KGaA, Weinheim 

DOI: 10.1002/ejic.200700455

# Two Novel Species, (Methoxycarbonyl)sulfenyl Thiocyanate and (Methoxycarbonyl)sulfenyl Selenocyanate: Spectroscopic Characterization by Photoelectron Spectroscopy and Quantum Chemical Investigation

**Lin Du,[a,b] Li Yao,[a,b] and Maofa Ge*[a]**

**Keywords:** Ab initio calculations / Dichalcogens / Electronic structure / Photoelectron spectroscopy

Two novel dichalcogens, (methoxycarbonyl)sulfenyl thiocyanate, $CH_3OC(O)SSCN$, and (methoxycarbonyl)sulfenyl selenocyanate, $CH_3OC(O)SSeCN$ have been generated in a convenient way by gas-solid reactions between $CH_3OC(O)SCl$ and AgSCN or AgSeCN. Photoelectron spectroscopy and theoretical calculations have been performed to investigate their electronic and geometrical structures. Both compounds are theoretically predicted to prefer *gauche* structure as the most stable conformation. In $CH_3OC(O)SSCN$, the S–S bond length and the dihedral angle around the S–S bond for the most stable conformer are 2.075 Å and 80.5°, respectively. And the S–Se bond length and the dihedral angle around the S–Se bond in $CH_3OC(O)SSeCN$ are predicted to be 2.210 Å and 80.4°, respectively. The first vertical ionization energies of $CH_3OC(O)SSCN$ and $CH_3OC(O)SSeCN$ are determined to be 10.19 and 9.84 eV, respectively. The HOMOs correspond to the electron mainly localized on the S 3p or Se 4p lone pair MOs: $\{38a(n_{S(SCN)})\}^{-1}$ and $\{47a(n_{Se})\}^{-1}$, respectively.
(© Wiley-VCH Verlag GmbH & Co. KGaA, 69451 Weinheim, Germany, 2007)

## 1. Introduction

In recent years, it has been found that chalcogen–chalcogen interactions play a crucial role in the structure and reactivity of a great variety of chalcogen-containing compounds.[1,2] The chalcogen–chalcogen bonds in bivalent compounds (REE′R′, E, E′ = O, S, Se) are known to prefer *gauche* conformations, which is usually attributed to lone-pair interactions.[3] These interactions favor a dihedral angle of about 90°, and steric interactions between the substituents (R, R′) tend to increase this angle. There are many experimental studies about the structural and conformational properties of homonuclear dichalcogens ROOR′,[4,5] RSSR′,[6,7] and RSeSeR′.[8,9]

In 1977, Snyder et al.[10] discussed the lone pair interactions in RSSR vs. RSOR by means of semiempirical MO calculations. Particular attention was paid to the α-lone pair interactions, and the study concluded that the two species were predicted to exhibit comparable equilibrium geometries. Because of the instability of thioperoxides RSOR′, until recently, only a few experimental studies were performed to investigate their structural and conformational properties.[11–13] Very recently, the parent compound of thioperoxides, HSOH was studied by microwave spectroscopy and high-level ab initio calculations [CCSD(T)/cc-pCVQZ],[14] which demonstrated its structure in detail. As for the experimental studies of the electronic structure of thioperoxides, dimethoxysulfane $[(CH_3O)_2S]$ and dimethoxydisulfane $[(CH_3O)_2S_2]$ were discussed according to their photoelectron spectra.[15] In 2006, Zeng et al.[16] investigated bis(trifluoroaceto) disulfide, $CF_3C(O)OSSOC(O)CF_3$, by Raman, photoelectron spectroscopy (PES), and theoretical calculations.

The electronegativity of selenium is close to that of sulfur. Therefore, similar structural and spectroscopic characteristics are expected in the selenium and sulfur derivatives.[17] As for the studies of sulfenoselenates with the general formula RSSeR′, there were some theoretical investigations about HSSeH,[18–20] and the crystal structure of NCSSeSCN[21] was also reported. In 2003, Sanz et al.[22] investigated the gas-phase acidity of 1,8-chalcogen-bridged naphthalenes, which also possess the S–Se bond, by means of high-level density functional theory computations.

However, there is no experimental work reported of RSSeR′, and no electronic structure information is currently available. They are quite unstable and difficult to obtain for experimental detection. In the present work, a simple dichalcogen hydride, (methoxycarbonyl)sulfenyl selenocyanate $[CH_3OC(O)SSeCN]$, was generated and characterized by photoelectron spectroscopy. With the help of quantum chemical calculations, its geometric structure was theoretically predicted and its electronic structure was discussed. The first vertical ionization energy of $CH_3OC(O)$-

[a] Beijing National Laboratory for Molecular Sciences (BNLMS), State Key Laboratory for Structural Chemistry of Unstable and Stable Species, Institute of Chemistry, Chinese Academy of Sciences,
100080 Beijing, P. R. China
Fax: +86-10-62559373
E-mail: gemaofa@iccas.ac.cn
[b] Graduate University of Chinese Academy of Sciences,
100039 Beijing, P. R. China
Supporting information for this article is available on the WWW under http://www.eurjic.org/ or from the author.

 © 2007 Wiley-VCH Verlag GmbH & Co. KGaA, Weinheim 

SSeCN was determined for the first time by means of PES. In addition, a novel disulfide, (methoxycarbonyl)sulfenyl thiocyanate [$CH_3OC(O)SSCN$], which has a similar structure to $CH_3OC(O)SSeCN$, was generated and characterized with the same method for comparison.

## 2. Results and Discussion

### 2.1 Molecular Structure

For both compounds, stable conformers with synperiplanar (sp) or antiperiplanar (ap) orientation of the C=O bond with respect to the S–S or S–Se bond are expected. Preliminary structure optimizations at the B3LYP/6-31G* level resulted in *gauche* structures around the S–S or S–Se bond. The potential functions for internal rotation around the S–S bond in $CH_3OC(O)SSCN$ were derived by structure optimizations at fixed dihedral angles between 30° and 330° using the HF and B3LYP method with the basis set of 6-31G* (Figure 1). There is no other minimum except the expected minima for the *gauche* structures with the dihedral angle around 80° (HF/6-31G*) or 90° (B3LYP/6-31G*). And the energy barrier for the S–S rotation is calculated to be 4.42 (HF/6-31G*) and 3.84 (B3LYP/6-31G*) kcal/mol, respectively. This is caused by the S–S lone pair repulsion and steric interactions between $CH_3OC(O)$ and CN moieties. Because of the structural similarity between the title compounds, the situation for $CH_3OC(O)SSeCN$ is probably the same, that is to say, conformers with *gauche* structure around the S–Se bond should be stable. Furthermore, according to the relative orientation of the $CH_3O$ moiety with respect to the C=O bond, which also can be synperiplanar (sp) or antiperiplanar (ap), four possible conformers exist for each of $CH_3OC(O)SSCN$ and $CH_3OC(O)SSeCN$. After structural optimization and vibrational analysis, three conformers of each compound are found to be stable, except the conformers with the C=O bond *anti* to the S–S or S–Se bond and $CH_3O$ *anti* to the C=O bond. The three stable conformers of $CH_3OC(O)SSeCN$ are presented in Figure 2.

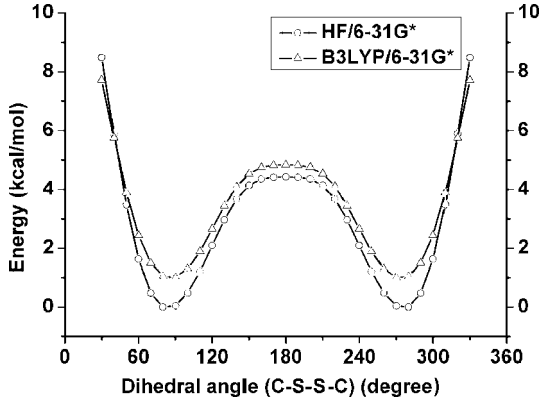


Figure 1. Calculated potential curves for internal rotation around the S–S bond in $CH_3OC(O)SSCN$. The curve of B3LYP/6-31G* is shifted by 1 kcal/mol.

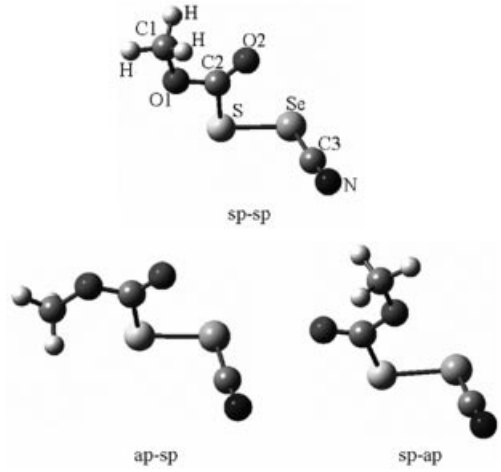


Figure 2. Schematic representation of the three stable conformers of $CH_3OC(O)SSeCN$.

Relative Gibbs free energies ($\Delta G$) calculated at 298 K for all the stable conformers of $CH_3OC(O)SSCN$ and $CH_3OC(O)SSeCN$ are summarized in Table 1. According to these relative Gibbs free energies, the *gauche* (sp-sp) and the *gauche* (sp-ap) conformers are expected to be more stable. All the calculations predict the lowest energy for the *gauche* (sp-sp) conformer. Similar to their parent compound, $CH_3OC(O)SCl$, the structures of $CH_3OC(O)SSCN$ and $CH_3OC(O)SSeCN$ can be rationalized by the aromaticity and the anomeric effect.[23] The stabilization of the *gauche* (sp-sp) conformers are accounted for by the attractive π nonbonded interactions in those conformations. Moreover, the instability of the *anti* conformers in these two molecules can be understood on the basis of the aromaticity. Besides, if one of the central atoms in an A–B–C–D chain, e.g., B, possesses one or more lone pairs, the generalized anomeric effect may have a large influence on the conformational properties.[24] This effect contributes to the preference for the *syn* form for the conformation of –C(O)-S–containing compounds.[25] Our discussion of the geometrical and electronic structures of these two compounds will mainly focus on the theoretically most stable conformers.

Table 1. Calculated relative Gibbs free energies ($\Delta G$, kcal/mol, $T$ = 298 K) for different conformers of $CH_3OC(O)SSCN$ and $CH_3OC(O)SSeCN$.

| | HF/6-31+G* | B3PW91/6-31+G* | B3LYP/6-311G* |
|---|---|---|---|
| $CH_3OC(O)SSCN$ | | | |
| *gauche* (sp-sp)[a] | 0 | 0 | 0 |
| *gauche* (ap-sp) | 8.93 | 6.32 | 6.93 |
| *gauche* (sp-ap) | 1.09 | 0.62 | 0.81 |
| $CH_3OC(O)SSeCN$ | | | |
| *gauche* (sp-sp) | 0 | 0 | 0 |
| *gauche* (ap-sp) | 8.42 | 5.91 | 6.94 |
| *gauche* (sp-ap) | 0.60 | 0.19 | 0.77 |

[a] *gauche* refers to the configuration around the S–S or S–Se bond. The first orientation (sp or ap) refers to $CH_3O$ with respect to the C=O bond, and the second orientation (sp or ap) refers to the C=O bond with respect to the S–S or S–Se bond.

 © 2007 Wiley-VCH Verlag GmbH & Co. KGaA, Weinheim 

The optimized geometrical parameters for the *gauche* (sp-sp) conformer of $CH_3OC(O)SSCN$ and $CH_3OC(O)SSeCN$ at different levels are listed in Table 2.

Table 2. Optimized geometrical parameters for the *gauche* (sp-sp) conformer of $CH_3OC(O)SSCN$ and $CH_3OC(O)SSeCN$.[a]

| Parameters | $CH_3OC(O)SSCN$ | | | $CH_3OC(O)SSeCN$ | | |
|---|---|---|---|---|---|---|
| | B3PW91 | B3LYP | MP2 | B3PW91 | B3LYP | MP2 |
| $r_{C1O1}$ | 1.442 | 1.451 | 1.445 | 1.441 | 1.451 | 1.445 |
| $r_{O1C2}$ | 1.328 | 1.332 | 1.337 | 1.329 | 1.334 | 1.339 |
| $r_{C2O2}$ | 1.192 | 1.193 | 1.201 | 1.193 | 1.194 | 1.202 |
| $r_{C2S}$ | 1.818 | 1.829 | 1.802 | 1.819 | 1.830 | 1.806 |
| $r_{SSe}$[b] | 2.081 | 2.102 | 2.075 | 2.208 | 2.231 | 2.210 |
| $r_{SeC3}$[b] | 1.695 | 1.703 | 1.697 | 1.846 | 1.856 | 1.849 |
| $r_{C3N}$ | 1.159 | 1.159 | 1.181 | 1.159 | 1.159 | 1.182 |
| $a_{C1O1C2}$ | 115.7 | 116.1 | 114.1 | 115.6 | 116.0 | 113.9 |
| $a_{O1C2O2}$ | 127.7 | 127.7 | 127.3 | 127.4 | 127.4 | 127.1 |
| $a_{O1C2S}$ | 105.7 | 105.7 | 105.9 | 105.7 | 105.8 | 105.8 |
| $a_{C2SSe}$[b] | 100.4 | 100.6 | 99.3 | 101.0 | 101.3 | 100.0 |
| $a_{SSeC3}$[b] | 101.6 | 101.8 | 99.7 | 99.5 | 99.7 | 98.0 |
| $\delta_{C1O1C2O2}$ | –0.6 | –0.6 | –0.8 | –0.5 | –0.6 | –1.3 |
| $\delta_{O1C2SSe}$[b] | 177.6 | 177.6 | 176.7 | 178.7 | 178.8 | 176.2 |
| $\delta_{C2SSeC3}$[b] | 87.6 | 87.3 | 80.5 | 88.6 | 88.2 | 80.4 |

[a] Distances in Å, angles in degrees. All the calculations were performed with the basis set of 6-311++G(d,p). As for the atom numbering of $CH_3OC(O)SSeCN$, see Figure 2. [b] For $CH_3OC(O)SSCN$, Se atoms should be replaced by the corresponding S atoms.

The electronegativity of selenium and sulfur are close to each other. Therefore, the structures of $CH_3OC(O)SSCN$ and $CH_3OC(O)SSeCN$ are similar (Table 2). It is well known that the B3LYP method doesn't do well in modeling relatively weak polar bonds. The MP2 method is believed to be more accurate to obtain the geometry. When optimized with the three methods (Table 2), polarization and diffusion functions were added to assure the calculations were more accurate. The optimized structures with B3LYP and B3PW91 methods, both of which are DFT methods, are nearly identical. Our discussion of the geometry is based on the structures optimized with the MP2 method.

A study on the structural and conformational properties of disulfanes has been reported recently.[7] The conformation of dichalcogens (REE′R′) is mainly determined by the geometry of the EE′ moiety. According to theoretical calculations, the S–S or S–Se bond lengths of $CH_3OC(O)SSCN$ and $CH_3OC(O)SSeCN$ are 2.075 Å and 2.210 Å [MP2/6-311++G(d,p)], respectively. The S–S bond length in $CH_3OC(O)SSCN$ is slightly larger than that of its parent compound, HSSH [2.0610(3) Å].[26] However, there is no experimental work reported about HSSeH. The S–Se bond length in HSSeH was predicted to be 2.269 Å according to ab initio calculations.[19] As determined by X-ray diffraction, the S–Se bond length in NCSSeSCN is 2.214 Å,[21] which is quite close to the predicted value of $CH_3OC(O)SSeCN$.

Besides the E–E′ bond length, another important structural parameter for dichalcogens is the torsional angle $\delta_{REE'R'}$, which greatly influenced the whole structure of the molecules. Gas-phase structures of noncyclic dichalcogens are characterized by the dihedral angle $\delta_{REE'R'}$ close to 90°: for example, HOOH (112°),[27] HSSH [90.76(6)°],[26] and $CH_3SeSeCH_3$ (87.5°).[8] The torsional angle in HSOH was 91.3°, as determined by high-level ab initio calculations [CCSD(T)/cc-pCVQZ].[14] In $CH_3OC(O)SSCN$ and $CH_3OC(O)SSeCN$, the dihedral angles around the S–S or S–Se bond are 80.5° and 80.4° [MP2/6-311++G(d,p)], respectively. The interpretation of the population analysis[28] is consistent with two qualitative arguments about the preference of about 90° of the RSSR′ dihedral angle. A plausible interpretation of the population analysis is related to the resulting barrier formed by the repulsion of 3pπ AO lone pairs. The repulsion is minimized, if these AOs are oriented orthogonal to each other. The second argument[29] is based on a hyperconjugative mechanism, whereby the π-character of the S–S bond is enhanced when, for example in HSSH, the S–H bonds are aligned for maximum transfer of electron density through the 3pπ AOs to the H atom. This feature is consistent with the anomeric effect, that is, the electron donation from the sulfur lone pair into the empty σ* orbitals of the opposite S–H bonds.[24] In other dichalcogens, a similar feature may also exist.

### 2.2 Photoelectron Spectroscopy

Photoelectron spectroscopy with a HeI resonance source (58.4 nm) is an effective method to investigate electronic structures of unstable compounds and free radicals in combination with ab initio calculations.[30,31] The valence shell structure of molecular vapors can be readily obtained by HeI photoelectron energy analysis, especially for studying similar molecules.[32] The HeI photoelectron spectra of $CH_3OC(O)SSCN$ and $CH_3OC(O)SSeCN$ are shown in Figure 3 and Figure 4, respectively. Before assigning the spec-

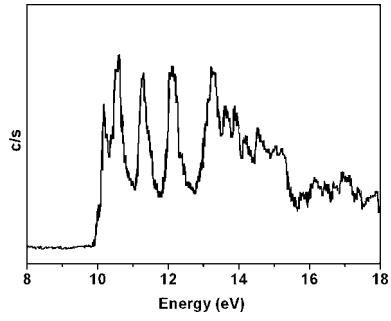


Figure 3. HeI photoelectron spectrum of $CH_3OC(O)SSCN$.

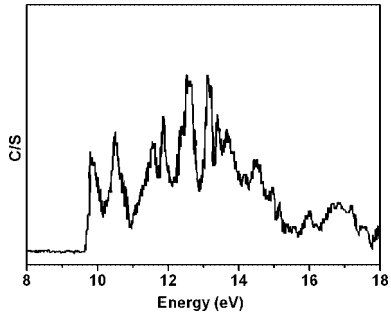


Figure 4. HeI photoelectron spectrum of $CH_3OC(O)SSeCN$.

 © 2007 Wiley-VCH Verlag GmbH & Co. KGaA, Weinheim 

tra, ROVGF[33] calculations were carried out to obtain the ionization energies for $CH_3OC(O)SSCN$ and $CH_3OC(O)SSeCN$. No noticeable difference can be found between the orbital energies of the two stable conformers of *gauche* (sp-sp) and *gauche* (sp-ap), therefore our discussion is reduced to the analysis of the slightly more stable conformer *gauche* (sp-sp). The experimental vertical ionization potentials, theoretical vertical ionization energies, molecular orbitals, and corresponding characters of outer valence shells for the *gauche* (sp-sp) conformers of $CH_3OC(O)SSCN$ and $CH_3OC(O)SSeCN$ are listed in Table 3. The ROVGF results are in general in agreement with the experimental data. Drawings of nine MOs for $CH_3OC(O)SSCN$ and $CH_3OC(O)SSeCN$ are given in the supporting information.

Table 3. Experimental vertical ionization energies (IP in eV), computed vertical ionization energies [ROVGF/6-311++G(d,p), $E_v$ in eV], and molecular orbital characters for $CH_3OC(O)SSCN$ and $CH_3OC(O)SSeCN$.

| Molecule | Exp. IP | Calcd. $E_v$ | MO | Character |
|---|---|---|---|---|
| $CH_3OC(O)SSCN$ | | | | |
| | 10.19 | 10.27 | 38 | $n_{S(SCN)}$ |
| | 10.60 | 10.64 | 37 | $n_{S(COS)}$ |
| | 11.32 | 11.60 | 36 | $n_{O(C=O)}$ |
| | 12.08 | 12.09 | 35 | $\sigma_{SS}$, $\pi_{C\equiv N}$ |
| | | 12.13 | 34 | $n_{O(CH3O)}$, $n_{O(C=O)}$ |
| | 13.26 | 13.41 | 33 | $\pi_{SCN}$ |
| | 13.61 | 13.66 | 32 | $\sigma_{CN}$ |
| | 13.87 | 13.93 | 31 | $\pi_{CH3}$, $n_{O(CH3O)}$ |
| | 14.17 | 14.19 | 30 | $\pi_{SCN}$ |
| $CH_3OC(O)SSeCN$ | | | | |
| | 9.84 | 9.85 | 47 | $n_{Se}$ |
| | 10.56 | 10.48 | 46 | $n_S$ |
| | 11.54 | 11.57 | 45 | $n_{O(C=O)}$ |
| | 11.84 | 11.80 | 44 | $\sigma_{SSe}$, $\pi_{C\equiv N}$ |
| | 12.50 | 12.05 | 43 | $n_{O(CH3O)}$, $n_{O(C=O)}$ |
| | 13.11 | 13.11 | 42 | $\pi_{C\equiv N}$ |
| | 13.41 | 13.54 | 41 | $\sigma_{CN}$ |
| | 13.65 | 13.68 | 40 | $\pi_{CH3}$, $n_{O(CH3O)}$ |
| | | 13.70 | 39 | $\pi_{SeCN}$ |

As pointed out by Baker et al.,[34] for disulfides, peroxides, and diselenides, the first two bands in the photoelectron spectra correspond to the symmetric and antisymmetric linear combinations of the outermost *p*-atomic orbitals. The first two peaks in the photoelectron spectrum of $CH_3OC(O)SSCN$ are centered at 10.19 and 10.60 eV. The main characters for the first two outmost orbitals are $\{38a(n_{S(SCN)})\}^{-1}$ and $\{37a(n_{S(COS)})\}^{-1}$, and the theoretically predicted first two vertical ionization energies are 10.27 and 10.64 eV, respectively, in good agreement with the experimentally observed values. The energy difference $\Delta E$ between the first two bands in $CH_3OC(O)SSCN$ ($\delta_{CSSC}$ = 80.5°) is 0.41 eV, which is bigger than that of $FC(O)SSCH_3$ [$\Delta E$ = 0.3 eV, $\delta_{CSSC}$ = 83.5(15)°].[35] This difference is originated by the interaction of the two lone pairs at the adjacent S atoms showing a clear dependence on the dihedral angle. Generally, it is to be expected that as the dihedral angle $\delta$ deviates from 90°, the energy difference $\Delta E$ will increase, i.e., the 3p orbitals in parallel configuration ($\delta$ = 0°, 180°) interact more strongly than in an orthogonal configuration ($\delta$ = 90°).[28]

The most peculiar aspects of the photoelectron spectra of the dichalcogens (REE′R′) concern the pattern of the n ionization energies, whose ordering and splitting have been rationalized in terms of the popular concepts of mediated interplay of through-bond and through-space interactions between semilocalized orbitals.[20] In general, the pattern of the splitting is predicted to be $\Delta(OO) > \Delta(SS) \approx \Delta(SeSe)$ for the homonuclear systems and $\Delta(SO) > \Delta(SeS)$ for the heteronuclear; the differences in heteronuclear systems are much larger than those in homonuclear systems.[20] The successive replacement of O by S and Se causes only a progressively minor perturbation of the electronic structure, as is expected from the electronegativity sequence of the chalcogens, O (3.5 on Pauling's scale), S (2.5), and Se (2.4).[20] For sulfenoselenates with the general formula RSSeR′, the splitting of the bands also exists in the photoelectron spectra. The first two peaks in the photoelectron spectrum of $CH_3OC(O)SSeCN$ is centered at 9.84 and 10.56 eV, respectively, which are lower than the corresponding ionization energies of $CH_3OC(O)SSCN$. The energy difference $\Delta E$ in $CH_3OC(O)SSeCN$ is 0.72 eV. This difference is larger than that of $CH_3OC(O)SSCN$, but close to its parent compound HSSeH (0.66 eV),[20] as clearly seen from Figure 5.

The third band (11.32 eV) in the photoelectron spectrum of $CH_3OC(O)SSCN$ can be attributed to the $n_O$ electron of the C=O bond, which is similar to the corresponding orbital of the third band (11.54 eV) in that of $CH_3OC(O)SSeCN$. In comparison to the first band of $CH_3OC(O)H$[32] at 10.99 eV $\{13a'(n_{O(C=O)})\}^{-1}$, the inductive effect of the SSCN or SSeCN moiety has raised the ionization energy of the carbonyl oxygen lone pair orbital $n_O$ by 0.33 and 0.55 eV, respectively. The third band in the photoelectron spectrum of $FC(O)SSCH_3$ (11.3 eV),[35] also caused by the ionization of the $n_O$ lone pair, is nearly equal to the corresponding ionization energy of $CH_3OC(O)SSCN$. The ionization from the orbital mainly localized at the $\sigma$ bond of the SS or SSe moiety and the $\pi$ orbital on the C≡N moiety causes the energies of 12.08 and 11.84 eV in $CH_3OC(O)SSCN$ and $CH_3OC(O)SSeCN$, respectively. Both are smaller than the ionization energies from $\sigma_{EE'}$ orbitals of their corresponding parent compounds (Figure 5). The differences are caused by the effect of the different substituents on the E–E′ bonds.

The vertical ionization energies from the ionization process of $\{4a''(n_{O(CH3O)}, n_{O(C=O)})\}^{-1}$ in $CH_3OC(O)Cl$ and $CH_3OC(O)CN$ are 12.21 and 12.01 eV, respectively.[32] While in $CH_3OC(O)SSCN$ and $CH_3OC(O)SSeCN$, the corresponding ionization energies are 12.08 and 12.50 eV, respectively. The ionization energies from 13.26 eV to 14.17 eV in $CH_3OC(O)SSCN$ correspond to different orbitals on the SCN moiety. The situation in $CH_3OC(O)SSeCN$ is similar. The electronic structure of the SeCN moiety can be explained in two ways.[17] We can assume a single Se–C bond and a triple C≡N bond, so two bands from the C≡N $\pi$ bond are expected in the low-energy region of the spectrum. Another interpretation is when the SeCN unit is con-

 © 2007 Wiley-VCH Verlag GmbH & Co. KGaA, Weinheim 

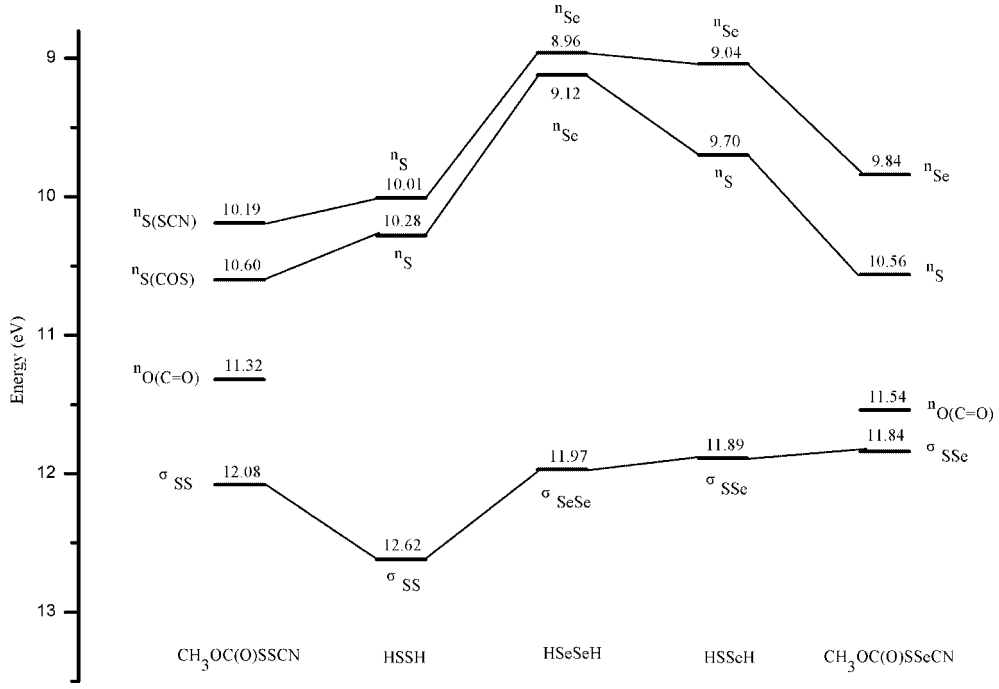


Figure 5. Correlation between selected dichalcogens (REE′R′). The ionization energies of HSSH are taken from ref.,[36] and those of HSeSeH and HSSeH are taken from ref.[20]

sidered as two perpendicular four-electron three-center π systems, which suggests four new bands in the spectrum (the high-energy $\pi_1$ and $\pi_{1\perp}$ and the low-energy $\pi_2$ and $\pi_{2\perp}$). If the molecular skeleton is linear, the perpendicular MO pairs are degenerate. In the case of the *gauche* $CH_3OC(O)SSeCN$, all four bands are expected theoretically. However, the Se lone pair in the SeCN moiety is part of a π system and the $\sigma_{SSe}$ orbital is also part of the perpendicular π system. In a word, only two additional bands from the π orbitals of the SeCN moiety are expected in the low-energy region. The assignments for the bands of $CH_3OC(O)SSCN$ and $CH_3OC(O)SSeCN$ agree with this explanation, as summarized in Table 3. The remaining bands in the high-ionization region (>14.5 eV) arising from inner molecular orbitals can not be assigned with certainty.

## 3. Conclusion

(Methoxycarbonyl)sulfenyl thiocyanate, $CH_3OC(O)SSCN$, and (methoxycarbonyl)sulfenyl selenocyanate, $CH_3OC(O)SSeCN$ are generated and characterized by photoelectron spectroscopy. With the help of quantum chemical calculations, the geometry of the two molecules are investigated and the electronic structure analyzed. Both compounds prefer a *gauche* conformation as predicted by structural optimization and vibrational analysis. The first vertical ionization energies of $CH_3OC(O)SSCN$ and $CH_3OC(O)SSeCN$ are determined to be 10.19 and 9.84 eV, respectively. The HOMOs are mainly localized at the lone pair of the S and Se atom, respectively.

## Experimental Section

$CH_3OC(O)SSCN$ and $CH_3OC(O)SSeCN$ were heterogeneously generated at a room temperature of 20 °C by passing $CH_3OC(O)SCl$ vapor over finely powdered AgSCN or AgSeCN, respectively, and the photoelectron spectrum was recorded subsequently after generation. Simultaneously, the product was checked by photoionization mass spectrometry. In the mass spectrum of $CH_3OC(O)SSCN$, there is no signal of the parent ion of the precursor [$CH_3OC(O)SCl^{+}$, $m/z$ = 126], which indicates that $CH_3OC(O)SCl$ reacts with AgSCN completely. However, there are characteristic signals of the product $CH_3OC(O)SSCN$: $CH_3OC(O)SSCN^{+}$ ($m/z$ = 149), $NCSSC(O)^{+}$ ($m/z$ = 118), and $NCSS^{+}$ ($m/z$ = 90). Similarly, in the mass spectrum of $CH_3OC(O)SSeCN$, there are analogously characteristic signals, $CH_3OC(O)SSeCN^{+}$ ($m/z$ = 197), $NCSeSC(O)^{+}$ ($m/z$ = 166), and $NCSeS^{+}$ ($m/z$ = 138), which can confirm the generation of $CH_3OC(O)SSeCN$. The reaction route is illustrated below:

$$CH_3OC(O)SCl\,(g) + AgSCN\,(s) \rightarrow CH_3OC(O)SSCN\,(g) + AgCl\,(s)$$
$$CH_3OC(O)SCl\,(g) + AgSeCN\,(s) \rightarrow CH_3OC(O)SSeCN\,(g) + AgCl\,(s)$$

The precursor $CH_3OC(O)SCl$ was purchased from Alfa Aesar, and used without further purification after confirmation of its identity by obtaining its photoionization mass spectrum. AgSCN was purchased from Alfa Aesar. AgSeCN was prepared according to the previous report[37] by adding a solution of KSeCN to a solution of $AgNO_3$ in stoichiometric amounts. The precipitate formed was collected by filtration, washed with water, and dried in a desiccator under dynamic vacuum. Care should be taken to avoid exposure to light. Before reaction, both silver salts were dried in vacuo ($1 \times 10^{-4}$ Torr) for 2 h.

The photoelectron spectrum was recorded on a double-chamber UPS-II instrument,[16,30] which was specially designed for detecting unstable species. The spectral resolution of the HeI spectrum is

 © 2007 Wiley-VCH Verlag GmbH & Co. KGaA, Weinheim 

about 30 meV, when measured as the full width at half-maximum (FWHM) of the $3p^{-1}\ ^2P_{2/3}\ Ar^+ \leftarrow Ar\ (^1S_0)$ line. During the experiments, small amounts of Ar gas and $CH_3I$ were added to the sample flow, which were used to calibrate the experimental vertical ionization potentials.

Quantum chemical calculations were performed for the investigated molecules by the Gaussian 03 program package.[38] The structures of all the stable conformers were optimized with ab initio and DFT methods. Higher levels of theory were used to optimize the theoretically most-stable conformers. To interpret the photoelectron spectra, ROVGF[33] calculations with the basis set of 6-311++G(d,p) were performed to obtain the theoretical vertical ionization energies.

**Supporting Information** (see also the footnote on the first page of this article): Drawings of nine MOs for the *gauche* (sp-sp) conformer of $CH_3OC(O)SSCN$, and drawings of nine MOs for the *gauche* (sp-sp) conformer of $CH_3OC(O)SSeCN$.

## Acknowledgments

This project was supported by the Knowledge Innovation Program of the Chinese Academy of Sciences (grant number KZCX2-YW-205) and by the Ministry of Science and Technology of China, Hundred Talents Fund, program 973 (number 2006CB403701), and the National Natural Science Foundation of China (contract numbers 20577052, 20673123, 20473094, 20503035).

[1] C. Bleiholder, D. B. Werz, H. Köppel, R. Gleiter, *J. Am. Chem. Soc.* **2006**, *128*, 2666–2674.
[2] C. Bleiholder, R. Gleiter, D. B. Werz, H. Köppel, *Inorg. Chem.* **2007**, *46*, 2249–2260.
[3] R. Steudel, H. Schmidt, E. Baumeister, H. Oberhammer, T. Koritsanszky, *J. Phys. Chem.* **1995**, *99*, 8987.
[4] H.-G. Mack, C. O. Della Védova, H. Oberhammer, *Angew. Chem. Int. Ed. Engl.* **1991**, *30*, 1145.
[5] A. Hermann, J. Niemeyer, H.-G. Mack, R. Kopitzky, M. Beuleke, H. Willner, D. Christen, M. Schäfer, A. Bauder, H. Oberhammer, *Inorg. Chem.* **2001**, *40*, 1672.
[6] H.-G. Mack, C. O. Della Védova, H. Oberhammer, *J. Phys. Chem.* **1992**, *96*, 9215.
[7] J. G. Breitzer, A. I. Smirnov, L. F. Szczepura, S. R. Wilson, T. B. Rauchfuss, *Inorg. Chem.* **2001**, *40*, 1421–1429.
[8] P. D'Antonio, C. George, A. H. Lowrey, J. Karle, *J. Chem. Phys.* **1971**, *55*, 1071–1075.
[9] J. E. Anderson, L. Henriksen, *J. Chem. Soc. Chem. Commun.* **1985**, 1397–1398.
[10] J. P. Snyder, L. Carlsen, *J. Am. Chem. Soc.* **1977**, *99*, 2931–2942.
[11] S. E. Ulic, C. O. Della Védova, A. Hermann, H.-G. Mack, H. Oberhammer, *Inorg. Chem.* **2002**, *41*, 5699–5705.
[12] S. E. Ulic, A. Kosma, C. Leibold, C. O. Della Védova, H. Willner, H. Oberhammer, *J. Phys. Chem. A* **2005**, *109*, 3739–3744.
[13] S. E. Ulic, A. Kosma, C. O. Della Védova, H. Willner, H. Oberhammer, *J. Phys. Chem. A* **2006**, *110*, 10201–10205.
[14] G. Winnewisser, F. Lewen, S. Thorwirth, M. Behnke, J. Hahn, J. Gauss, E. Herbst, *Chem. Eur. J.* **2003**, *9*, 5501–5510.
[15] R. Gleiter, I. Hyla-Kryspin, H. Schmidt, R. Steudel, *Chem. Ber.* **1993**, *126*, 2363–2365.
[16] X. Zeng, M. Ge, Z. Sun, D. Wang, *J. Phys. Chem. A* **2006**, *110*, 5685–5691.
[17] G. Bajor, T. Veszprémi, E. H. Riague, J.-C. Guillemin, *Chem. Eur. J.* **2004**, *10*, 3649–3656.
[18] R. Laitinen, T. Pakkanen, *J. Mol. Struct. (Theochem)* **1983**, *91*, 337–352.
[19] R. Laitinen, T. Pakkanen, *J. Mol. Struct. (Theochem)* **1985**, *124*, 293–305.
[20] V. Galasso, *J. Electron Spectrosc. Relat. Phenom.* **1984**, *34*, 283–289.
[21] S. Hauge, *Acta Chem. Scand., Ser. A* **1979**, *33*, 313.
[22] P. Sanz, M. Yáñez, O. Mó, *CHEMPHYSCHEM* **2003**, *4*, 830–837.
[23] M. F. Erben, C. O. Della Védova, R. M. Romano, R. Boese, H. Oberhammer, H. Willner, O. Sala, *Inorg. Chem.* **2002**, *41*, 1064–1071.
[24] A. J. Kirby, *The Anomeric Effect and Related Stereoelectronic Effects at Oxygen*, Springer, Berlin, **1983**.
[25] J. R. Larson, N. D. Epiotis, F. Bernardi, *J. Am. Chem. Soc.* **1978**, *100*, 5713–5716.
[26] C. J. Marsden, B. J. Smith, *J. Phys. Chem.* **1988**, *92*, 347–353.
[27] A. M. Halpern, E. D. Glendening, *J. Chem. Phys.* **2007**, *121*, 273.
[28] B. Boyd, *J. Am. Chem. Soc.* **1972**, *94*, 8799.
[29] G. Winnewisser, N. Winnewisser, W. Gordy, *J. Chem. Phys.* **1968**, *49*, 3465.
[30] L. Yao, M. Ge, W. Wang, X. Zeng, Z. Sun, D. Wang, *Inorg. Chem.* **2006**, *45*, 5971–5975.
[31] Z. Sun, S. Zheng, J. Wang, M. Ge, D. Wang, *Chem. Eur. J.* **2001**, *7*, 2995–2999.
[32] X. Zeng, M. Ge, L. Du, Z. Sun, D. Wang, *J. Mol. Struct.* **2006**, *800*, 62–68.
[33] W. von Niessen, J. Schirmer, L. S. Cederbaum, *Comput. Phys. Rep.* **1984**, *1*, 57–125.
[34] A. D. Baker, M. Brisk, M. Gellender, *J. Electron Spectrosc. Relat. Phenom.* **1974**, *3*, 227.
[35] M. F. Erben, C. O. Della Védova, *Inorg. Chem.* **2002**, *41*, 3740–3748.
[36] B. Solouki, H. Bock, *Inorg. Chem.* **1977**, *16*, 665–669.
[37] F. Cataldo, *Polyhedron* **2000**, *19*, 681–688.
[38] M. J. Frisch, G. W. Trucks, H. B. Schlegel, G. E. Scuseria, M. A. Robb, J. R. Cheeseman, J. A. Montgomery Jr, T. Vreven, K. N. Kudin, J. C. Burant, J. M. Millam, S. S. Iyengar, J. Tomasi, V. Barone, B. Mennucci, M. Cossi, G. Scalmani, N. Rega, G. A. Petersson, H. Nakatsuji, M. Hada, M. Ehara, K. Toyota, R. Fukuda, J. Hasegawa, M. Ishida, T. Nakajima, Y. Honda, O. Kitao, H. Nakai, M. Klene, X. Li, J. E. Knox, H. P. Hratchian, J. B. Cross, C. Adamo, J. Jaramillo, R. Gomperts, R. E. Stratmann, O. Yazyev, A. J. Austin, R. Cammi, C. Pomelli, J. W. Ochterski, P. Y. Ayala, K. Morokuma, G. A. Voth, P. Salvador, J. J. Dannenberg, V. G. Zakrzewski, S. Dapprich, A. D. Daniels, M. C. Strain, O. Farkas, D. K. Malick, A. D. Rabuck, K. Raghavachari, J. B. Foresman, J. V. Ortiz, Q. Cui, A. G. Baboul, S. Clifford, J. Cioslowski, B. B. Stefanov, G. Liu, A. Liashenko, P. Piskorz, I. Komaromi, R. L. Martin, D. J. Fox, T. Keith, M. A. Al-Laham, C. Y. Peng, A. Nanayakkara, M. Challacombe, P. M. W. Gill, B. Johnson, W. Chen, M. W. Wong, C. Gonzalez, J. A. Pople, *Gaussian 03 (Revision B.01)*, Gaussian, Inc., Pittsburgh PA, **2003**.

Received: April 26, 2007
Published Online: August 3, 2007

 © 2007 Wiley-VCH Verlag GmbH & Co. KGaA, Weinheim 

DOI: 10.1002/ejic.200700463

# A New Approach to Novel Cluster Compounds of Lead(II) Phosphonates

Zi-Yi Du,[a] Hai-Bing Xu,[a] Xiu-Ling Li,[a] and Jiang-Gao Mao*[a]

**Keywords:** Lead / Sulfonate-phosphonates / Solvothermal synthesis / Cluster compounds

Five new lead(II) sulfonate-phosphonates, namely $[Pb_3(L)_2(H_2O)_2]\cdot 4H_2O$ (**1**), $[Pb(HL)(phen)]\cdot H_2O$ (**2**), $[Pb_6(L)_4(phen)_8]\cdot 3H_2O$ (**3**), $[Pb_6(L)_4(phen)_{10}]\cdot 2H_2O$ (**4**), and $[Pb_6(L)_4(4,4'\text{-bipy})(H_2O)_2]\cdot 2H_2O$ (**5**; $H_3L$ = *m*-$HO_3S$-$C_6H_4$-$PO_3H_2$, phen = 1,10-phenanthroline, 4,4′-bipy = 4,4′-bipyridine) have been prepared and structurally characterized. Compound **1** features a novel 3D framework in which 1D chains of $Pb_3O_4$ cluster units are further bridged by sulfonate-phosphonate ligands, whereas compound **2** features a layer structure in which 1D chains of $Pb_2O_4$ clusters are further bridged by sulfonate-phosphonate ligands. Compounds **3** and **4** represent the first zero-dimensional lead(II) phosphonates and feature novel isolated hexanuclear lead(II) clusters in which six $Pb^{II}$ ions are bridged by two tetradentate and two pentadentate phosphonate groups. Compound **5** features a 3D framework that is similar to that in compound **1** despite the different coordination modes for some sulfonate groups of the ligands. The main difference is that an aqua ligand in compound **1** is replaced by a nitrogen atom of the 4,4′-bipy ligand, which results in the splitting of the large cavities in compound **1** into two small apertures in compound **5**. Compounds **1** and **5** exhibit strong broad blue fluorescent emission bands at 398 and 420 nm, respectively.

(© Wiley-VCH Verlag GmbH & Co. KGaA, 69451 Weinheim, Germany, 2007)

## Introduction

The chemistry of metal phosphonates has been expanding rapidly in recent years, mainly due to their potential application in the areas of catalysis, ion exchange, proton conductivity, intercalation chemistry, photochemistry, and material chemistry.[1] Similarly, the surface modification of inorganic surfaces with phosphonic acids is of growing importance since it opens the way to a large variety of novel functional materials.[1c,1d] Most investigations have been concentrated on the divalent transition and trivalent lanthanide elements.[2–6] Lead(II), however, has a lone pair of electrons and could therefore lead to interesting topological arrangements or to materials with redox as well as catalytic properties.[7–11] A wide variety of lead(II) phosphonates have been reported to date.[7–11] The strategy of using bisfunctional or multifunctional anionic units, such as diphosphonates, aminophosphonates, or phosphonocarboxylates, has led to a number of new lead phosphonates with microporous or open-framework structures.[7–10] Another useful way of building new types of phosphonate hybrids is by introducing a second metal linker, and we have used an acidic metal linker such as carboxylic acid or carboxylic-sulfonic acid to prepare a series of lead phosphonate hybrids with different architectures.[11] The carboxylic or carboxylic-sulfonic acid acts either as a multidentate bridging ligand or pendant group on the lead(II) phosphonate layer or intercalates between two layers.[11] These materials mostly exhibit layered structures, although 3D networks with micropores and 1D chains have also been reported.[7–11] Surprisingly, no discrete lead phosphonates have been reported thus far.

Three zinc(II) phosphonates based on tetranuclear or hexanuclear cluster units and four lanthanide(III) phosphonates based on tetranuclear cluster units have been isolated by our group by using *m*-sulfophenylphosphonic acid and a basic second metal linker such as 4,4′-bipy or phen.[12] The weak coordination ability of the sulfonate group and the bidentate chelating nature of the second ligand such as phen facilitate the formation of cage compounds with discrete cluster units. We therefore hoped that such an approach might be extended to the field of $Pb^{II}$ phosphonates, where the isolation of cluster compounds is very difficult. The combination of $Pb^{II}$ and *m*-sulfophenylphosphonic acid with a basic second metal linker led to five novel, discrete, 2D or 3D lead(II) sulfonate-phosphonates based on cluster units, namely $[Pb_3(L)_2(H_2O_2)]\cdot 4H_2O$ (**1**), $[Pb(HL)(phen)]\cdot H_2O$ (**2**), $[Pb_6(L)_4(phen)_8]\cdot 3H_2O$ (**3**), $[Pb_6(L)_4(phen)_{10}]\cdot 2H_2O$ (**4**), and $[Pb_6(L)_4(4,4'\text{-bipy})(H_2O)_2]\cdot 2H_2O$ (**5**). Herein we report their syntheses, crystal structures, and characterization.

## Results and Discussion

Compounds **1**–**5** represent the first series of lead(II) compounds based on sulfonate-phosphonate ligands. Com-

[a] State Key Laboratory of Structural Chemistry, Fujian Institute of Research on the Structure of Matter, Chinese Academy of Sciences,
Fuzhou, Fujian 350002, P. R. China
E-mail: mjg@fjirsm.ac.cn

Supporting information for this article is available on the WWW under http://www.eurjic.org or from the author.

 © 2007 Wiley-VCH Verlag GmbH & Co. KGaA, Weinheim 

pounds **3** and **4** also represent the first discrete $Pb^{II}$ polynuclear clusters based on phosphonate ligands. They exhibit novel, discrete, hexanuclear, 2D or 3D structures.

## Synthesis

Compounds **1**–**5** were obtained during our systematic investigation of the Pb/L/phen (or bipy) systems with different Pb/L/phen ratios and pH values. We successfully prepared single-phase products for all five compounds except compound **4**. The preparations of compounds **1**–**5** rely on well-established hydrothermal methods. In general, a mixture of $Pb(OAc)_2$ and $H_3L$, with or without a second ligand such as phen or 4,4′-bipy, was treated hydrothermally for four days at 150 °C to produce crystalline products. The type of second ligand used has a strong influence on the final structure of these lead(II) sulfonate-phosphonates as compounds **2**–**5** were obtained instead of compound **1** when phen or 4,4′-bipy was employed as the second ligand. The molar ratio of reactants as well as the reaction pH also play important roles. Thus, compounds **2**–**4** were obtained from the $Pb(OAc)_2/H_3L$/phen system when the amount of phen and the reaction pH increased. We still do not fully understand why these compounds form under different reaction conditions, but it seems likely that the nature and amount of the second ligand play an important role by changing the coordination environment around the metal ions and the connectivities between the metal ions. Furthermore, the reaction medium becomes less acidic when more phen is used, and this can affect the coordination mode that the phosphonate ligand adopts.

## Structure of $[Pb_3(L)_2(H_2O)_2]\cdot 4H_2O$ (1)

The structure of compound **1** features a novel porous 3D network with three unique lead(II) ions in the asymmetric unit (Figure 1). Pb(1) is six-coordinate with four phosphonate oxygen atoms from four $L^{3-}$ anions as well as two sulfonate oxygen atoms from another two $L^{3-}$ anions. Its coordination geometry can be described as a severely distorted $PbO_6$ octahedron. Pb(2) ion is five-coordinate with three phosphonate oxygen atoms from three $L^{3-}$ anions and one sulfonate oxygen atom from another $L^{3-}$ anion as well as an aqua ligand. The coordination geometry around Pb(2) can be described as a severely distorted ψ-$PbO_5$ octahedron with one site occupied by the lone pair of the $Pb^{II}$ ion. The coordination environment of Pb(3) ion is similar to that of Pb(2) ion. The Pb–O distances [2.311(5)–2.833(7) Å] are similar to those reported for other lead(II) phosphonates and sulfonates.[7–11]

There are two unique $L^{3-}$ ligands in compound **1**. The first, containing atoms P(1) and S(1), is hexadentate and bridges six lead(II) ions through its three phosphonate oxygen atoms and one sulfonate oxygen atom. Two phosphonate oxygen atoms [O(1) and O(3)] act as a $\mu^2$-bridging ligand. The second sulfonate-phosphonate containing P(2) and S(2) is octadentate, with all three phosphonate oxygen atoms and three sulfonate oxygen atoms involved in metal coordination. Two phosphonate oxygen atoms [O(7) and O(8)] act as a $\mu^2$-bridging ligand (Scheme 1).

The interconnection of the $Pb^{II}$ ions via the bridging phosphonate groups leads to a 1D lead(II) phosphonate chain based on "$Pb_3O_4$" cluster units. Each pair of $Pb^{II}$ ions within a $Pb_3O_4$ cluster unit is bridged by a pair of

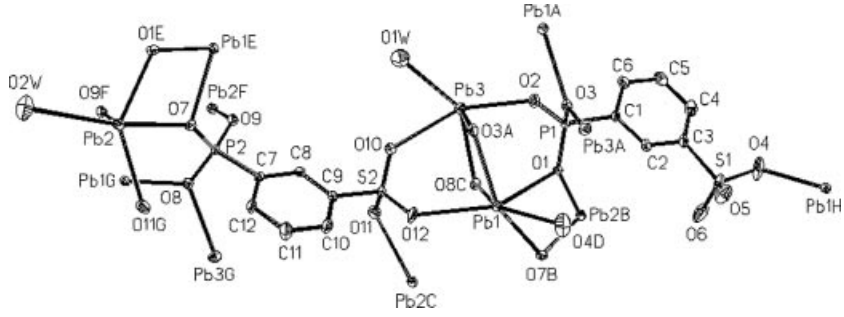


Figure 1. ORTEP representation of the selected unit of **1**. The thermal ellipsoids are drawn at 30% probability. Lattice water molecules have been omitted for clarity. Symmetry codes for the generated atoms: A) 1 – *x*, 1 – *y*, 1 – *z*; B) 1/2 + *x*, 1/2 – *y*, 1/2 + *z*; C) 3/2 – *x*, 1/2 + *y*, 1/2 – *z*; D) 3/2 – *x*, –1/2 + *y*, 3/2 – *z*; E) 1/2 + *x*, 1/2 – *y*, 3/2 – *z*; F) 1 – *x*, –*y*, –*z*; G) 3/2 – *x*, –1/2 + *y*, 1/2 – *z*; H) 3/2 – *x*, 1/2 + *y*, 3/2 – *z*.

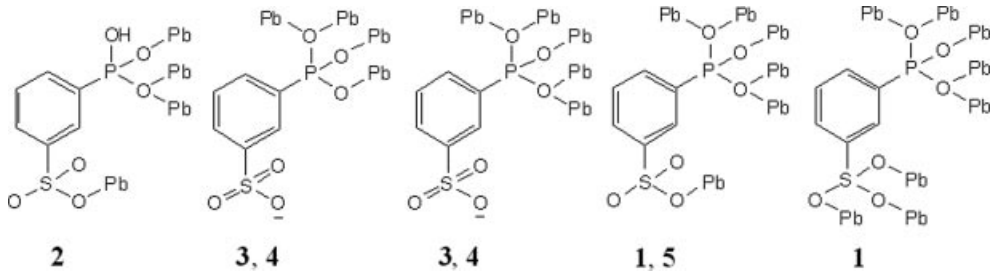


Scheme 1. The coordination modes of *m*-sulfophenylphosphonic acid in compounds **1**–**5**.

 © 2007 Wiley-VCH Verlag GmbH & Co. KGaA, Weinheim 

phosphonate oxygen atoms, and neighboring cluster units are further interconnected by bridging phosphonate and sulfonate groups into a 1D hybrid chain (Figure 2, a). These 1D chains are further cross-linked by the bridging $L^{3-}$ ligands into a 3D network with long, narrow apertures along *a*-axis (Figure 3). The total solvent accessible space is about 24.3% of the cell volume according to our calculations.[13] The lattice water molecules are located in the above apertures and there are a number of hydrogen bonds between sulfonate oxygen atom O(11), the aqua ligands, and lattice water molecules (Table 1), with O···O contacts ranging from 2.71(1) to 3.03(1) Å. It is interesting to note that the hydrogen bonds between water molecules lead to the formation of a 1D water chain along the *a*-axis (Figure 2, b).

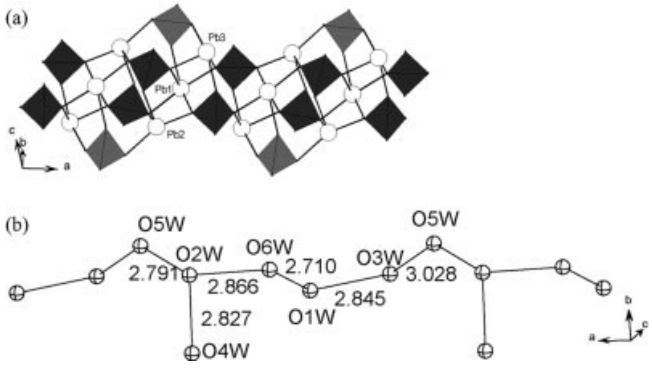


Figure 2. A 1D lead sulfonate-phosphonate chain based on $Pb_3O_4$ cluster units (a) and a 1D hydrogen-bonded water chain (b) in compound **1**. The $CPO_3$ and $CSO_3$ groups are shaded in dark and medium gray, respectively. Pb, O, and C atoms are drawn as white, crossed and black circles, respectively.

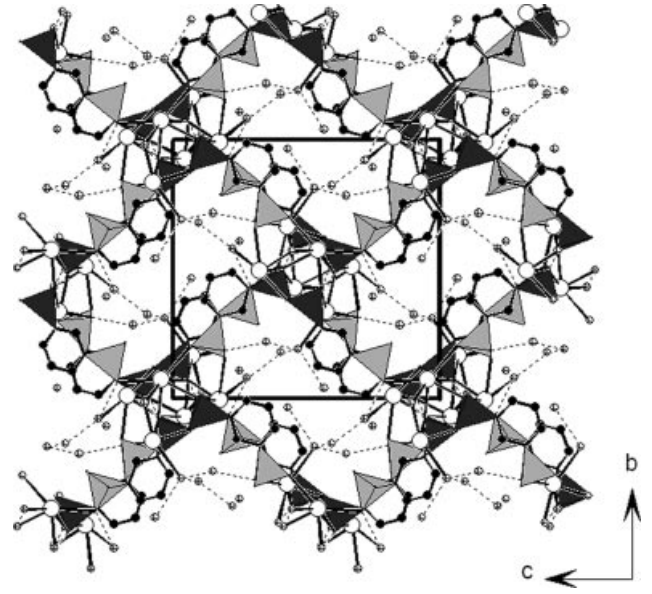


Figure 3. View of the structure of compound **1** along the *a*-axis. The $CPO_3$ and $CSO_3$ groups are shaded in dark and medium grey, respectively. Pb, O, and C atoms are drawn as open, crossed and black circles, respectively. Hydrogen bonds are drawn as dashed lines.

Table 1. Selected bond lengths [Å] for compounds **1**–**5**.[a]

| | | | |
|---|---|---|---|
| **1** | | | |
| Pb(1)–O(8)#1 | 2.440(4) | Pb(1)–O(1) | 2.486(4) |
| Pb(1)–O(3)#2 | 2.556(5) | Pb(1)–O(7)#3 | 2.584(4) |
| Pb(1)–O(12) | 2.723(5) | Pb(1)–O(4)#4 | 2.781(6) |
| Pb(2)–O(9)#5 | 2.362(4) | Pb(2)–O(7) | 2.370(4) |
| Pb(2)–O(1)#6 | 2.528(4) | Pb(2)–O(11)#7 | 2.659(5) |
| Pb(2)–O(2W) | 2.833(7) | Pb(3)–O(3)#2 | 2.311(5) |
| Pb(3)–O(2) | 2.445(5) | Pb(3)–O(8)#1 | 2.592(4) |
| Pb(3)–O(1W) | 2.634(7) | Pb(3)–O(10) | 2.797(5) |
| *Hydrogen bonds* | | | |
| O(11)···O(5W) | 2.764(8) | O(1W)···O(6W) | 2.71(1) |
| O(1W)···O(3W) | 2.85(1) | O(2W)···O(5W)#5 | 2.79(1) |
| O(2W)···O(4W)#5 | 2.83(1) | O(2W)···O(6W)#5 | 2.87(1) |
| O(3W)···O(5W)#8 | 3.03(1) | | |
| **2** | | | |
| Pb(1)–N(2) | 2.446(6) | Pb(1)–N(1) | 2.499(5) |
| Pb(1)–O(2)#1 | 2.531(5) | Pb(1)–O(1)#2 | 2.550(5) |
| Pb(1)–O(1) | 2.727(5) | Pb(1)–O(5)#3 | 2.820(5) |
| P(1)–O(2) | 1.496(5) | P(1)–O(1) | 1.512(5) |
| P(1)–O(3) | 1.579(5) | | |
| *Hydrogen bonds* | | | |
| O(3)···O(4)#4 | 2.650(8) | O(1W)···O(2)#1 | 2.848(8) |
| **3** | | | |
| Pb(1)–O(3) | 2.320(6) | Pb(1)–O(8)#1 | 2.353(5) |
| Pb(1)–N(2) | 2.544(7) | Pb(1)–N(1) | 2.595(7) |
| Pb(2)–O(7) | 2.291(5) | Pb(2)–O(2)#1 | 2.468(5) |
| Pb(2)–O(7)#1 | 2.657(5) | Pb(2)–N(6) | 2.669(6) |
| Pb(2)–O(1) | 2.697(5) | Pb(2)–N(5) | 2.766(7) |
| Pb(3)–O(9)#1 | 2.463(7) | Pb(3)–O(1) | 2.482(6) |
| Pb(3)–O(3) | 2.614(8) | Pb(3)–N(4) | 2.66(1) |
| Pb(3)–N(3) | 2.73(1) | Pb(3)–N(7) | 2.84(1) |
| Pb(3)–N(8) | 3.00(1) | | |
| *Hydrogen bonds* | | | |
| O(6)···O(2W) | 2.78(3) | | |
| **4** | | | |
| Pb(1)–O(8)#1 | 2.386(6) | Pb(1)–O(1) | 2.494(6) |
| Pb(1)–N(8) | 2.502(8) | Pb(1)–N(7) | 2.697(9) |
| Pb(1)–N(10) | 2.853(8) | Pb(1)–N(9) | 2.95(1) |
| Pb(2)–O(7) | 2.294(5) | Pb(2)–O(2)#1 | 2.431(6) |
| Pb(2)–N(2) | 2.614(8) | Pb(2)–O(3) | 2.625(5) |
| Pb(2)–N(1) | 2.708(8) | Pb(2)–O(7)#1 | 2.750(5) |
| Pb(3)–O(9)#1 | 2.286(6) | Pb(3)–O(1) | 2.572(6) |
| Pb(3)–O(3) | 2.597(5) | Pb(3)–N(6) | 2.778(8) |
| Pb(3)–N(5) | 2.814(9) | Pb(3)–N(3) | 2.821(8) |
| Pb(3)–N(4) | 2.880(8) | | |
| *Hydrogen bonds* | | | |
| O(12)···O(1W) | 3.04(1) | | |
| **5** | | | |
| Pb(1)–O(1) | 2.367(6) | Pb(1)–O(12)#1 | 2.475(6) |
| Pb(1)–O(11)#2 | 2.535(6) | Pb(1)–O(3)#3 | 2.597(6) |
| Pb(1)–O(5)#4 | 2.882(9) | Pb(2)–O(10)#1 | 2.283(6) |
| Pb(2)–O(11)#2 | 2.441(6) | Pb(2)–O(8) | 2.531(7) |
| Pb(2)–N(1) | 2.631(9) | Pb(2)–O(1) | 2.713(6) |
| Pb(3)–O(3)#3 | 2.270(6) | Pb(3)–O(2) | 2.334(6) |
| Pb(3)–O(12)#1 | 2.496(6) | Pb(3)–O(1W) | 2.81(1) |
| *Hydrogen bonds* | | | |
| O(7)···O(2W) | 2.90(1) | O(9)···O(1W)#5 | 2.93(1) |
| O(1W)···O(2W)#3 | 2.84(2) | | |

[a] Symmetry codes: for **1**: #1 $-x + 3/2$, $y + 1/2$, $-z + 1/2$; #2 $-x + 1$, $-y + 1$, $-z + 1$; #3 $x + 1/2$, $-y + 1/2$, $z + 1/2$; #4 $-x + 3/2$, $y - 1/2$, $-z + 3/2$; #5 $-x + 1$, $-y$, $-z$; #6 $x - 1/2$, $-y + 1/2$, $z - 1/2$; #7 $-x + 3/2$, $y - 1/2$, $-z + 1/2$; #8 $x - 1$, $y$, $z$. For **2**: #1 $-x + 1$, $-y + 2$, $-z + 2$; #2 $-x$, $-y + 2$, $-z + 2$; #3 $x$, $y - 1$, $z$; #4 $-x$, $3 - y$, $2 - z$. For **3**: #1 $-x + 1$, $-y + 1$, $-z + 1$. For **4**: #1 $-x + 1$, $-y$, $-z + 1$. For **5**: #1 $x - 1/2$, $-y - 1/2$, $z - 1/2$; #2 $-x - 3/2$, $y - 1/2$, $-z + 1/2$; #3 $-x - 3$, $-y - 1$, $-z$; #4 $-x - 5/2$, $y - 1/2$, $-z + 1/2$; #5 $-x - 2$, $-y - 1$, $-z$.

 © 2007 Wiley-VCH Verlag GmbH & Co. KGaA, Weinheim 

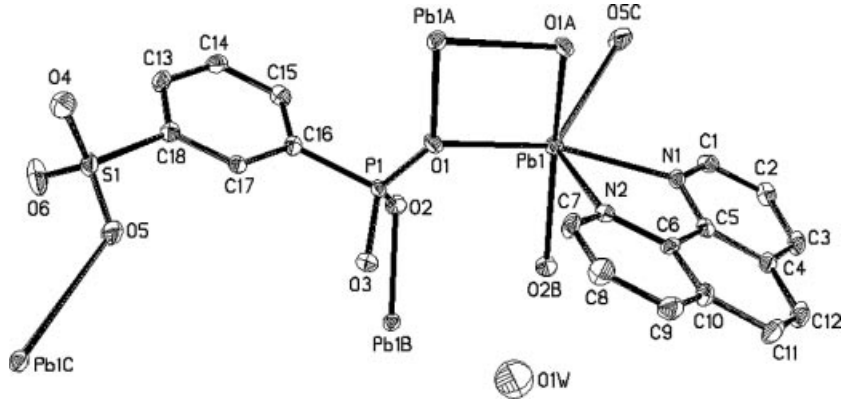


Figure 4. ORTEP representation of the selected unit of **2**. The thermal ellipsoids are drawn at 30% probability. Symmetry codes for the generated atoms: A) $-x$, $2-y$, $2-z$; B) $1-x$, $2-y$, $2-z$; C) $x$, $-1+y$, $z$.

The open framework of compound **1** remains intact after heating at 180 °C for 3 h based on X-ray powder diffraction studies (see Supporting Information).

### Structure of $[Pb(HL)(phen)]\cdot H_2O$ (2)

The structure of compound **2** features a layered architecture. The Pb(1) ion is six-coordinate with three phosphonate oxygen atoms from three $HL^{2-}$ anions, one sulfonate oxygen atom from another $HL^{2-}$ anion, and one bidentate chelating phen ligand (Figure 4). The coordination geometry around Pb(1) can be described as a severely distorted $PbO_4N_2$ octahedron, with Pb–O [2.531(5)–2.820(5) Å] and Pb–N [2.446(6)–2.499(5) Å] distances similar to those reported for other lead(II) phosphonates and sulfonates.[7–11]

There is one unique $HL^{2-}$ ligand in compound **2**. The phosphonate group of this ligand is singly protonated, as indicated by the much longer P(1)–O(3) bond [1.579(5) Å] than those of the other two P–O bonds [P(1)–O(2) 1.496(5), P(1)–O(1) 1.512(5) Å]. The $HL^{2-}$ ligand is tetradentate and bridges four lead(II) ions via its two phosphonate oxygen atoms and one sulfonate oxygen atom (Scheme 1). O(1) acts as a $\mu^2$-metal linker. Each pair of $Pb^{II}$ ions is bridged by a pair of phosphonate oxygen atoms into a $Pb_2O_2$ dimer. These $Pb_2O_2$ dimeric units are further interconnected by bridging phosphonate groups into a 1D chain along the *a* axis, and these chains are further connected by the bridging $HL^{2-}$ ligands into a layered structure (Figure 5). Strong hydrogen bonds are formed between noncoordinated phosphonate and sulfonate oxygen atoms [O(3)···O(4) 2.650(8) Å; symmetry code: $-x$, $3-y$, $2-z$) within the 2D layer. The 2D layers in compound **2** are assembled into a three dimensional structure through van der Waals forces (Figure 6). The lattice water molecules are located at the cavities of the structure and are involved in hydrogen bonding with coordinated phosphonate oxygen atom O(2) (Table 1).

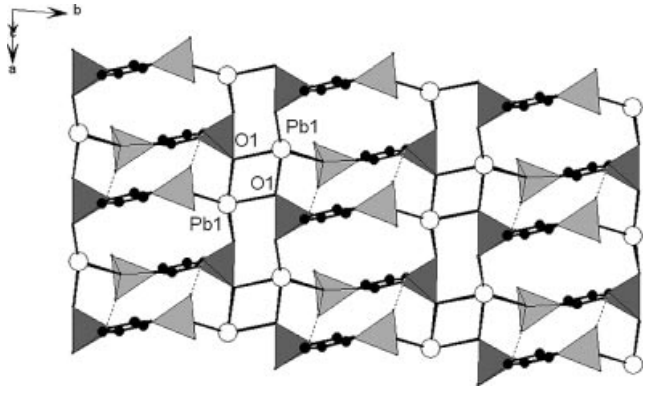


Figure 5. A lead(II) sulfonate-phosphonate layer in compound **2**. The $CPO_3$ and $CSO_3$ groups are shaded in medium and light grey, respectively. The phen ligands have been omitted for clarity. Hydrogen bonds are drawn as dashed lines.

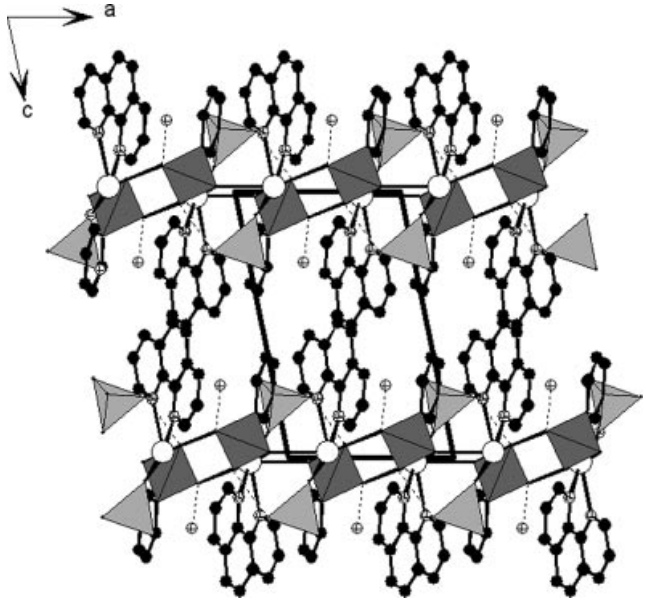


Figure 6. View of the structure of compound **2** down the *a*-axis. The $CPO_3$ and $CSO_3$ groups are shaded in medium and light gray, respectively. Pb, O, N and C atoms are drawn as open, crossed, octanded, and black circles, respectively. Hydrogen bonds are drawn as dashed lines.

 © 2007 Wiley-VCH Verlag GmbH & Co. KGaA, Weinheim 

### Structure of $[Pb_6(L)_4(phen)_8]\cdot 3H_2O$ (3)

The structure of compound **3** features an isolated hexanuclear lead(II) cluster unit. There are three crystallographically independent lead(II) ions in the structure (Figure 7). The Pb(1) ion is four-coordinate with two phosphonate oxygen atoms from two $L^{3-}$ anions as well as one bidentate chelating phen ligand. The coordination geometry around Pb(1) can best be described as a slightly distorted ψ-$PbO_4$ square-pyramid. The Pb(2) ion is six-coordinate with four phosphonate oxygen atoms from four $L^{3-}$ anions as well as one bidentate chelating phen ligand. The coordination geometry around Pb(2) can be described as a slightly distorted ψ-$PbO_4N_2$ pentagonal pyramid with the lone pair occupying the open site of the pyramid. Pb(3) is seven-coordinate with three phosphonate oxygen atoms from two $L^{3-}$ anions as well as two bidentate chelating phen ligands. The coordination geometry around Pb(3) can best be described as an irregular $PbO_4N_2$ polyhedron. The Pb–O [2.291(5)–2.697(5) Å] and Pb–N [2.544(7)–3.00(1) Å] distances are similar to those reported for other lead(II) phosphonates and sulfonates.[7–11]

There are two unique $L^{3-}$ anions in compound **3**. The first, which contains P(1) and S(1), is pentadentate and bridges four $Pb^{II}$ ions by using its three phosphonate oxygen atoms, whereas the other $L^{3-}$ anion, which contains P(2) and S(2), is tetradentate and bridges four $Pb^{II}$ ions through its three phosphonate oxygen atoms. O(1), O(3), and O(7) act as a $\mu^2$-bridging ligand (Figure 7, Scheme 1). The interconnection of six $Pb^{II}$ ions by the above two types of $L^{3-}$ anions results in a novel hexanuclear cluster unit (Figure 8, a) which can be viewed as a double-cage structure. This "double-cage" hexanuclear cluster unit is different from our previously reported "chair-like" hexanuclear cluster units in zinc(II) sulfonate-phosphonates[8] owing to the different coordination modes of the sulfonate-phosphonate ligands. Thus, the two independent $L^{3-}$ ligands in $[Zn_6L_4(phen)_8]\cdot 11H_2O$ connect three and four $Zn^{II}$ ions, respectively, whereas each $L^{3-}$ ligand in $[Zn_6L_4(bipy)_6(H_2O)_4]\cdot 18H_2O$ bridges three $Zn^{II}$ ions.

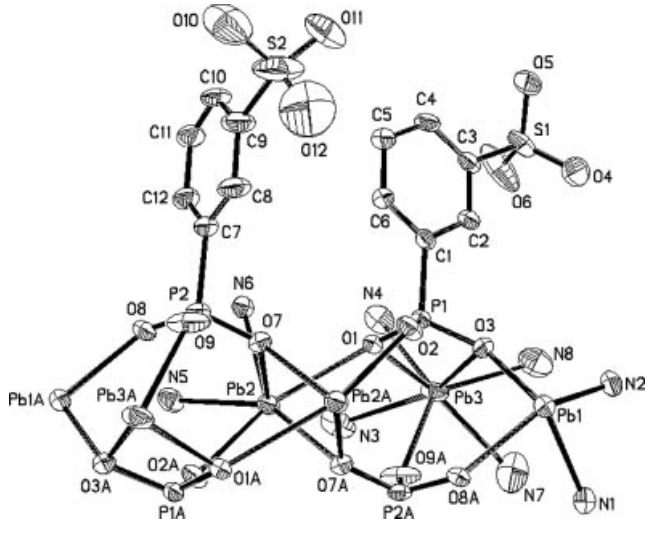


Figure 7. ORTEP representation of the selected unit of **3**. The thermal ellipsoids are drawn at 30% probability. Lattice water molecules and the carbon atoms of the phen ligands have been omitted for clarity. Only one orientation is shown for the disordered Pb(3) atom for the sake of clarity. Symmetry codes for the generated atoms: A) $1-x$, $1-y$, $1-z$.

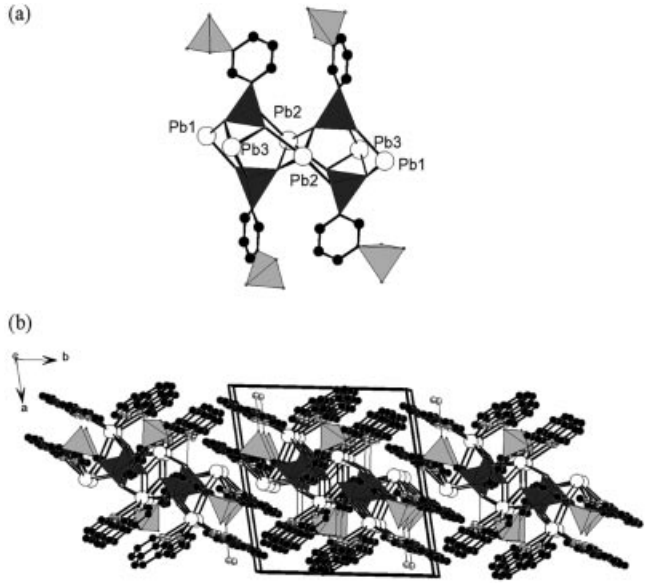


Figure 8. A $\{Pb_6L_4\}$ cluster unit in compound **3** (a) and a view of the structure of compound **3** down the *c*-axis (b). The $CPO_3$ and $CSO_3$ groups are shaded in dark and light gray, respectively. Pb, O, N and C atoms are drawn as open, crossed, octanded, and black circles, respectively. Hydrogen bonds are drawn as dashed lines.

The discrete clusters in compound **3** are assembled into a three dimensional structure through van der Waals forces (Figure 8, b). The lattice water molecules are located in the cavities of the structure, and O(2w) forms a hydrogen bond with the noncoordinating sulfonate oxygen atom O(6) (Table 1).

### Structure of $[Pb_6(L)_4(phen)_{10}]\cdot 2H_2O$ (4)

Compound **4** contains two more phen ligands than compound **3**. Its structure also features an isolated hexanuclear $Pb^{II}$ cluster similar to that in compound **3**. There are three crystallographically independent lead(II) ions in the asymmetric unit (Figure 9). Pb(1) is six-coordinate with two phosphonate oxygen atoms from two $L^{3-}$ anions as well as two bidentate chelating phen ligands. The coordination geometry around Pb(1) can be described as a distorted ψ-$PbO_2N_4$ pentagonal pyramid. Pb(2) is six-coordinate with four phosphonate oxygen atoms from four $L^{3-}$ anions as well as a bidentate chelating phen ligand. Pb(3) is seven-coordinate with three phosphonate oxygen atoms from two $L^{3-}$ anions as well as two bidentate chelating phen ligands. The coordination environments around Pb(2) and Pb(3) are same as those in compound **3**. The Pb–O [2.286(6)–2.750(5) Å] and Pb–N [2.502(8)–2.95(1) Å] distances are similar to those reported for other lead(II) phosphonates and sulfonates.[7–11]

 © 2007 Wiley-VCH Verlag GmbH & Co. KGaA, Weinheim 

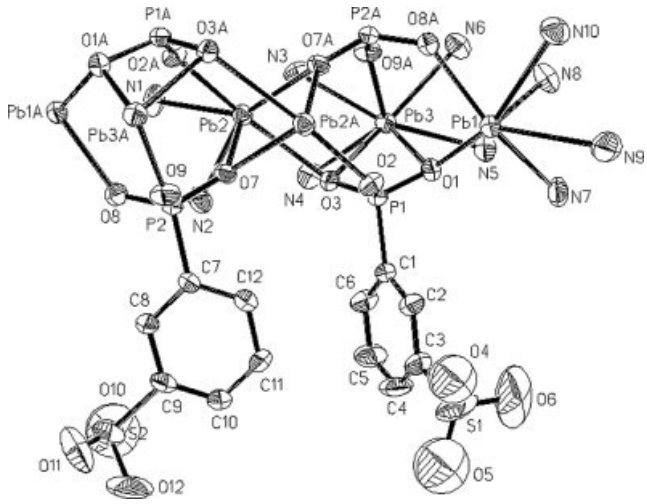


Figure 9. ORTEP representation of the selected unit of **4**. The thermal ellipsoids are drawn at 30% probability. Lattice water molecules and carbon atoms of the phen ligands have been omitted for clarity. Only one orientation is shown for the disordered O(11) atom for the sake of clarity. Symmetry codes for the generated atoms: A) $1 - x, -y, 1 - z$.

The coordination modes of the two unique $L^{3-}$ anions in compound **4** are the same as those in compound **3** which means that the cluster unit of compound **4** is similar to that of compound **3**, the only difference being that Pb(1) in compound **4** has a higher coordination number due to the coordination of an additional phen ligand.

The discrete clusters in compound **4** are also assembled into a three-dimensional structure through van der Waals forces as well as a π···π packing interaction between the phen ligands (Figure 10). The lattice water molecules [O(1w)] are located in the cavities and form weak hydrogen bonds with the noncoordinating sulfonate oxygen atoms O(12) (Table 1).

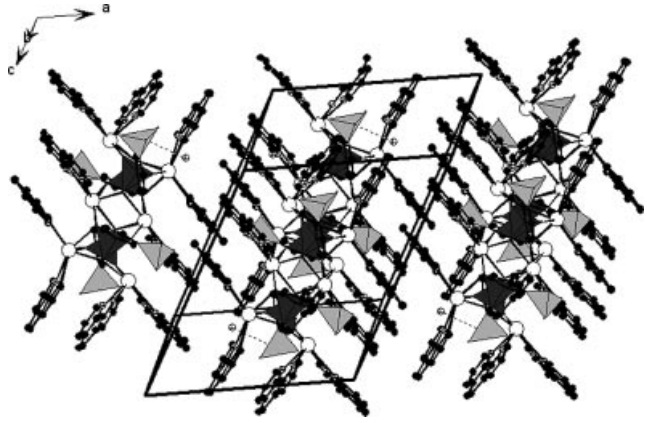


Figure 10. View of the structure of compound **4** down the *b*-axis. The $CPO_3$ and $CSO_3$ groups are shaded in dark and light gray, respectively. Pb, O, N, and C atoms are drawn as open, crossed, octanded, and black circles, respectively. Hydrogen bonds are drawn as dashed lines.

### Structure of $[Pb_6(L)_4(4,4'\text{-bipy})(H_2O)_2]\cdot 2H_2O$ (5)

The structure of compound **5** features a complex 3D network. There are three unique $Pb^{II}$ ions in the asymmetric unit of compound **5** (Figure 11). Pb(1) is five-coordinate with four phosphonate oxygen atoms from four $L^{3-}$ anions and one sulfonate oxygen atom from another $L^{3-}$ anion. The coordination geometry around Pb(1) can be described as a distorted ψ-$PbO_5$ octahedron with one axial site occupied by the lone pair of the $Pb^{II}$ ion. Pb(2) is five-coordinate with three phosphonate oxygen atoms from three $L^{3-}$ anions, one sulfonate oxygen atom from another $L^{3-}$ anion, and a nitrogen atom from a 4,4′-bipy ligand. The coordination geometry around Pb(2) can be described as a severely distorted ψ-$PbO_4N$ octahedron with one site occupied by the lone pair of the $Pb^{II}$ ion. Pb(3) is four-coordinate with three phosphonate oxygen atoms from three $L^{3-}$ anions and one aqua ligand. The coordination geometry around Pb(3) can be described as a distorted ψ-$PbO_4$ trigonal bipyramid with one pyramidal site occupied by the lone pair of the $Pb^{II}$ ion. The Pb–O [2.270(6)–2.882(9) Å] and Pb–N [2.631(9) Å] distances are similar to those reported for other lead(II) phosphonates and sulfonates.[7–11]

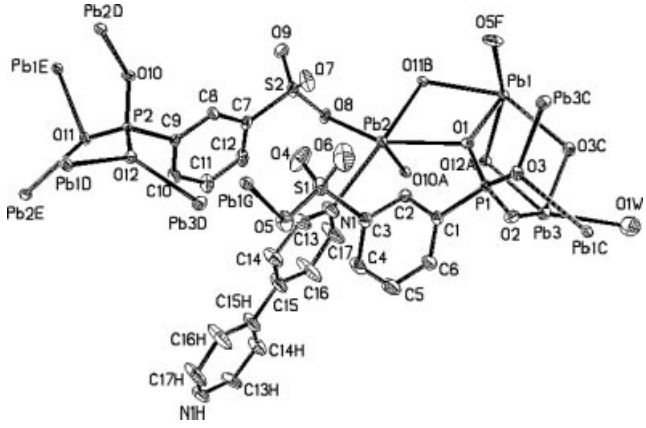


Figure 11. ORTEP representation of the selected unit of **5**. The thermal ellipsoids are drawn at 30% probability. Lattice water molecules have been omitted for clarity. Symmetry codes for the generated atoms: A) $-1/2 + x, -1/2 - y, -1/2 + z$; B) $-3/2 - x, -1/2 + y, 1/2 - z$; C) $-3 - x, -1 - y, -z$; D) $1/2 + x, -1/2 - y, 1/2 + z$; E) $-3/2 - x, 1/2 + y, 1/2 - z$; F) $-5/2 - x, -1/2 + y, 1/2 - z$; G) $-5/2 - x, 1/2 + y, 1/2 - z$; H) $-2 - x, -y, -z$.

There are two unique $L^{3-}$ ligands in compound **5**, both of which are hexadentate and bridge six lead(II) ions through three phosphonate oxygen atoms and one sulfonate oxygen atom. Four phosphonate oxygen atoms [O(1), O(3), O(11), and O(12)] act as a $\mu^2$-bridging ligand. A similar type of coordination mode has also been observed in compound **1**. Interconnection of the $Pb^{II}$ ions through the bridging phosphonate groups leads to a 1D chain based on $Pb_3O_4$ cluster units (Figure 12, a). In contrast to the 1D chain in compound **1**, neighboring $Pb_3O_4$ cluster units within the chain are interconnected solely by the bridging phosphonate groups. These 1D chains are further cross-linked by the bridging $L^{3-}$ and 4,4′-bipy ligands into a 3D network with small apertures along the *a*-axis (Figure 12,

 © 2007 Wiley-VCH Verlag GmbH & Co. KGaA, Weinheim 

b). Although fewer sulfonate oxygen atoms are involved in metal coordination in compound **5** than in compound **1**, the framework of compound **5** is still somewhat similar to that in compound **1**. The replacement of one aqua ligand in compound **1** by a nitrogen atom from a 4,4′-bipy ligand in compound **5** results in the splitting of the large cavities in compound **1** into two smaller parts (Figure 12). Due to the occupation of the cavities by the 4,4′-bipy ligands, compound **5** contains only a few lattice water molecules. A number of hydrogen bonds are formed among non-coordinating sulfonate oxygen atoms [O(7), O(9)], aqua ligands, and lattice water molecules (Table 1), with O···O contacts ranging from 2.84(2) to 2.93(1) Å.

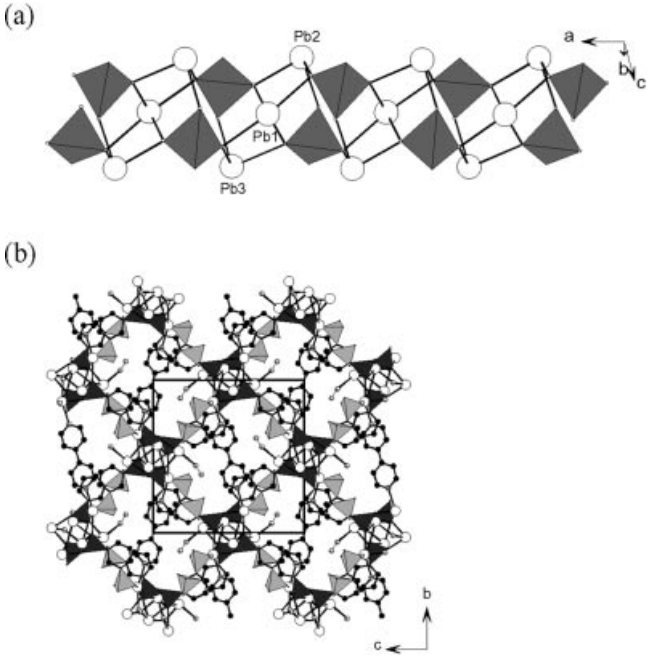


Figure 12. A 1D lead(II) phosphonate chain based on $Pb_3O_4$ units (a) and a view of the structure of compound **5** along the *a*-axis (b). The $CPO_3$ and $CSO_3$ groups are shaded in dark and medium grey, respectively. Pb, O, N, and C atoms are drawn as white, crossed, octanded, and black circles, respectively.

## Luminescent Properties

The solid-state luminescent properties of compounds **1**, **2**, **3**, and **5** as well as the free phosphonate ligand were investigated at room temperature. The free ligand exhibits only a fluorescent emission band at $\lambda_{max}$ = 370 nm upon excitation at 308 nm. The phen ligand displays a fluorescent emission band at $\lambda_{max}$ = 381 nm with a shoulder at 364 nm upon excitation at 339 nm. Compound **1** displays a strong fluorescent emission band at $\lambda_{max}$ = 398 nm ($\lambda_{ex}$ = 330 nm; Figure 13) upon complexion of the $L^{3-}$ ligands with the $Pb^{II}$ ions, whereas compounds **2** and **3** display a weak broad emission band in the range 350–600 nm upon complexion of both sulfonate-phosphonate and phen ligands with the lead(II) ions. The bipy ligand displays a broad fluorescent emission band at $\lambda_{max}$ = 423 nm ($\lambda_{ex}$ = 345 nm), and upon complexion of both $L^{3-}$ and bipy ligands with the $Pb^{II}$ ions compound **5** displays a fluorescent emission band at $\lambda_{max}$ = 420 nm ($\lambda_{ex}$ = 330 nm; Figure 13). These emission bands are neither metal-to-ligand charge transfer (MLCT) nor ligand-to-metal charge transfer (LMCT) in nature, but rather can be attributed to an intraligand emission state.

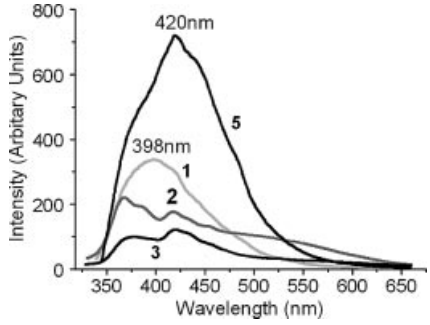


Figure 13. Solid-state emission spectra of compounds **1**, **2**, **3**, and **5**.

## TGA Studies

The TGA curves of compounds **1**, **2**, **3**, and **5** all exhibit three main weight loss steps (Figure 14). The onset and final temperatures of these three steps as well as the weight

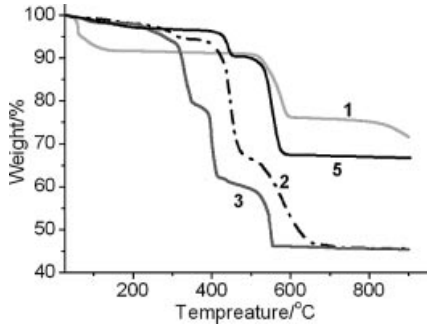


Figure 14. TGA curves for compounds **1**, **2**, **3**, and **5**.

Table 2. TGA data of compounds **1**, **2**, **3**, and **5**.

| | First step | | Second step | Third step | Total weight loss |
|---|---|---|---|---|---|
| | Temperature (onset/end) [°C] | Weight loss of $H_2O$ (exp./calcd.) [%] | Temperature (onset/end) [°C] | Temperature (onset/end) [°C] | [%] |
| **1** | 40/180 | 8.6/9.0 | 492/605 | 780/>900 | 28.4 |
| **2** | 45/205 | 2.5/2.8 | 240/336 | 370/735 | 54.1 |
| **3** | 40/115 | 1.7/1.5 | 182/415 | 415/556 | 54.6 |
| **5** | 40/209 | 2.9/3.0 | 360/455 | 486/600 | 32.6 |

 © 2007 Wiley-VCH Verlag GmbH & Co. KGaA, Weinheim 

losses are given in Table 2, where it can be seen that the observed weight losses of water molecules are close to the calculated values. The final residues were not characterized. The thermal stability of compound **4** was not studied due to our failure to obtain it as a single-phase product.

## Conclusions

In summary, we have reported the hydrothermal synthesis, crystal structures, and characterization of five new lead(II) sulfonate-phosphonates, namely $[Pb_3(L)_2(H_2O)_2]\cdot 4H_2O$ (**1**), $[Pb(HL)(phen)]\cdot H_2O$ (**2**), $[Pb_6(L)_4(phen)_8]\cdot 3H_2O$ (**3**), $[Pb_6(L)_4(phen)_{10}]\cdot 2H_2O$ (**4**), and $[Pb_6(L)_4(4,4'\text{-bipy})(H_2O)_2]\cdot 2H_2O$ (**5**; $H_3L$ = *m*-$HO_3S$-$C_6H_4$-$PO_3H_2$). The diverse structural frameworks of these five compounds depend on the flexible coordination ability of $Pb^{II}$ as well as the mediation of an auxiliary ligand such as phen or 4,4′-bipy. *m*-Sulfophenylphosphonic acid is a versatile ligand that can adopt various coordination modes. In the absence of the second ligand or with 4,4′-bipy, which usually binds in a bidentate bridging mode, two types of 3D networks (compounds **1** and **5**) are obtained. The dimensionality of the structure is reduced when the bidentate chelating ligand phen is added as the second metal linker. Compound **2**, which has a layered structure, is obtained with a Pb/phen ratio close to 1:1. Further increase of the amount of phen and the pH leads to two types of discrete clusters (compounds **3** and **4**) which have the same skeleton but differ in the coordination numbers of the lead(II) ions. The results of our study indicate that by using *m*-sulfophenylphosphonic acid with phen as the auxiliary ligand we should be able to synthesize cluster compounds of not only d-block and f-block metals but also main group metals. Future research effects will be devoted to the designing of new types of cluster compounds containing other metal phosphonates.

## Experimental Section

**Materials and Methods:** *m*-Sulfophenylphosphonic acid (*m*-$HO_3S$-$C_6H_4$-$PO_3H_2$, $H_3L$) was synthesized according to the procedures previously described by Montoneri.[14] All other chemicals were obtained from commercial sources and used without further purification. Elemental analyses were performed with an Elementary Vario EL III instrument. The FT-IR spectra were recorded with a Nicolet Magna 750 FT-IR spectrometer using KBr pellets in the range of 4000–400 $cm^{-1}$. Photoluminescence analyses were performed with a Perkin–Elmer LS55 fluorescence spectrometer. Thermogravimetric analyses were carried out with a NETZSCH STA 449C unit at a heating rate of 10 °C $min^{-1}$ under an oxygen atmosphere. X-ray powder diffraction (XRD) patterns (Cu-$K_\alpha$) were collected with a XPERT-MPD θ–2θ diffractometer.

**Synthesis of $[Pb_3(L)_2(H_2O)_2]\cdot 4H_2O$ (1):** The pH of a mixture of $Pb(OAc)_2$ (0.32 mmol) and $H_3L$ (0.3 mmol) in 10 mL of distilled water was adjusted to about 4.8 with 1 M NaOH solution and the mixture was then sealed into a Parr Teflon-lined autoclave (23 mL) and heated at 150 °C for 4 d. The final pH was 4.6. Colorless brick-shaped crystals of **1** were collected in approx. 62% yield (0.079 g) based on Pb. The purity of this compound was confirmed by powder XRD (see Supporting Information). $C_{12}H_{20}O_{18}P_2S_2Pb_3$ (1199.9): calcd. C 12.01, H 1.68; found C 11.95, H 1.57. IR (KBr): $\tilde{\nu}$ = 3436 (s), 3059 (m), 2924 (m), 2852 (w), 1631 (m), 1402 (m), 1102 (s), 1022 (vs), 995 (vs), 962 (s), 800 (m), 669 (m), 618 (m), 557 (s) $cm^{-1}$.

**Synthesis of $[Pb(HL)(phen)]\cdot H_2O$ (2):** A mixture of $Pb(OAc)_2$ (0.3 mmol), $H_3L$ (0.3 mmol), and phen (0.32 mmol) in 10 mL of distilled water, with an initial pH of 3.6, was sealed into a Parr Teflon-lined autoclave (23 mL) and heated at 150 °C for 4 d. The final pH remained unchanged. Colorless pillar-shaped crystals of **2** were collected in approx. 85% yield (0.16 g) based on Pb. The purity of this compound was confirmed by powder XRD (see Supporting Information). $C_{18}H_{15}N_2O_7PPbS$ (641.54): calcd. C 33.70, H 2.36, N 4.37; found C 33.75, H 2.68, N 4.29. IR (KBr): $\tilde{\nu}$ = 3582 (m), 3423 (m), 3062 (m), 2833 (m), 1624 (m), 1593 (m), 1520 (m), 1495 (m), 1428 (m), 1400 (m), 1188 (s), 1147 (s), 1106 (vs), 1025 (vs), 915 (s), 850 (s), 803 (m), 792 (m), 727 (m), 694 (m), 681 (m), 617 (m), 555 (s), 528 (m) $cm^{-1}$.

**Synthesis of $[Pb_6(L)_4(phen)_8]\cdot 3H_2O$ (3):** A mixture of $Pb(OAc)_2$ (0.36 mmol), $H_3L$ (0.3 mmol), and phen (0.48 mmol) in 10 mL of distilled water, with its pH adjusted to about 4.0 with 1 M NaOH solution, was sealed into a Parr Teflon-lined autoclave (23 mL) and heated at 150 °C for 4 d. The final pH was 3.9. Colorless brick-shaped crystals of **3** were collected in approx. 77% yield (0.17 g) based on Pb. The purity of this compound was confirmed by powder XRD (see Supporting Information). $C_{120}H_{86}N_{16}O_{27}P_4Pb_6S_4$ (3679.3): calcd. C 39.17, H 2.36, N 6.09; found C 39.01, H 2.49, N 5.91. IR data (KBr): $\tilde{\nu}$ = 3435 (s), 3055 (m), 2923 (m), 2852 (m), 1621 (m), 1588 (m), 1512 (m), 1424 (m), 1343 (m), 1189 (s), 1097 (vs), 1029 (vs), 996 (s), 956 (m), 845 (m), 795 (m), 728 (m), 700 (m), 686 (m), 617 (m), 549 (m) $cm^{-1}$.

**Synthesis of $[Pb_6(L)_4(Phen)_{10}]\cdot 2H_2O$ (4):** A mixture of $Pb(OAc)_2$ (0.3 mmol), $H_3L$ (0.27 mmol), and phen (0.5 mmol) in 10 mL of distilled water, with its pH adjusted to about 6.0 with 1 M NaOH solution, was sealed into a Parr Teflon™-lined autoclave (23 mL) and heated at 150 °C for 4 d. The final pH was 5.8. Colorless crystals of compound **4** were collected with some unidentified impurities. Although many experiments were performed under different reaction conditions, compound **4** could not be obtained as a single phase.

**Synthesis of $[Pb_6(L)_4(4,4'\text{-Bipy})(H_2O)_2]\cdot 2H_2O$ (5):** A mixture of $Pb(OAc)_2$ (0.36 mmol), $H_3L$ (0.3 mmol), and 4,4′-bipy (0.25 mmol) in 10 mL of distilled water, with its pH adjusted to about 4.6 with 1 M NaOH solution, was sealed into a Parr Teflon-lined autoclave (23 mL) and heated at 150 °C for 4 d. The final pH was 4.7. Colorless brick-shaped crystals of **5** were collected in apprx. 64% yield (0.093 g) based on Pb. The purity of this compound was confirmed by powder XRD (see Supporting Information). $C_{34}H_{32}N_2O_{28}P_4Pb_6S_4$ (2411.9): calcd. C 16.93, H 1.34, N 1.16; found C 16.62, H 1.47, N 1.10. IR (KBr): 3435 (s), 3053 (m), 2924 (m), 2846 (w), 1604 (m), 1400 (m), 1220 (s), 1165 (s), 1101 (vs), 1059 (s), 1019 (vs), 995 (vs), 967 (vs), 796 (m), 686 (m), 623 (m), 552 (s) $cm^{-1}$.

**Single-Crystal Structure Determination:** Data collection for compounds **1**, **2**, and **5** was performed with a Siemens Smart CCD diffractometer, data collection for compound **3** was performed with a Mercury CCD diffractometer, and that for compound **4** with a Saturn 70 CCD diffractometer. All diffractometers were equipped with a graphite-monochromated Mo-$K_\alpha$ radiation source ($\lambda$ = 0.71073 Å). Intensity data for all compounds were collected by the narrow frame method at 293 K. The data sets were corrected for Lorentz and polarization factors as well as for absorption with SADABS or by the multi-scan method.[15a,15b] All structures were

 © 2007 Wiley-VCH Verlag GmbH & Co. KGaA, Weinheim 

Table 3. Summary of crystal data and structural refinements for **1**–**5**.

| | **1** | **2** | **3** | **4** | **5** |
|---|---|---|---|---|---|
| Empirical formula | $C_{12}H_{20}O_{18}P_2S_2Pb_3$ | $C_{18}H_{15}N_2O_7PPbS$ | $C_{120}H_{86}N_{16}O_{27}P_4S_4Pb_6$ | $C_{144}H_{100}N_{20}O_{26}P_4S_4Pb_6$ | $C_{34}H_{32}N_2O_{28}P_4S_4Pb_6$ |
| Formula weight | 1199.91 | 641.54 | 3679.30 | 4021.70 | 2411.88 |
| Space group | $P2_1/n$ | $P\bar{1}$ | $P\bar{1}$ | $P\bar{1}$ | $P2_1/n$ |
| $a$ [Å] | 10.3642(1) | 7.2187(2) | 14.963(4) | 14.790(6) | 10.2544(1) |
| $b$ [Å] | 15.5661(3) | 11.0945(3) | 15.141(4) | 15.479(6) | 16.3825(2) |
| $c$ [Å] | 16.4630(2) | 11.7759(3) | 15.471(4) | 19.444(7) | 16.6409(3) |
| $\alpha$ [°] | 90.00 | 89.527(1) | 68.069(7) | 97.196(2) | 90.000 |
| $\beta$ [°] | 102.965(1) | 78.516(1) | 81.46(1) | 106.154(2) | 103.783(1) |
| $\gamma$ [°] | 90.00 | 84.841(1) | 77.416(9) | 111.849(4) | 90.000 |
| $V$ [Å$^3$] | 2588.27(6) | 920.44(4) | 3165(2) | 3835(2) | 2715.05(6) |
| $Z$ | 4 | 2 | 1 | 1 | 2 |
| $D_{calcd.}$ [g cm$^{-3}$] | 3.079 | 2.315 | 1.931 | 1.741 | 2.950 |
| $\mu$ [mm$^{-1}$] | 19.831 | 9.414 | 8.146 | 6.730 | 18.897 |
| GOF on $F_2$ | 1.142 | 1.195 | 0.995 | 0.999 | 1.158 |
| $R_1$,[a] $wR_2$[b] [$I > 2\sigma(I)$] | 0.0264, 0.0524 | 0.0345, 0.0749 | 0.0493, 0.1255 | 0.0534, 0.1425 | 0.0357, 0.0666 |
| $R_1$,[a] $wR_2$[b] (all data) | 0.0368, 0.0558 | 0.0388, 0.0782 | 0.0766, 0.1436 | 0.0760, 0.1612 | 0.0484, 0.0711 |

[a] $R_1 = \Sigma||F_o| - |F_c||/\Sigma|F_o|$. [b] $wR_2 = \{\Sigma w[(F_o)^2 - (F_c)^2]^2/\Sigma w[(F_o)^2]^2\}^{1/2}$.

solved by direct methods and refined by full-matrix least-squares fitting on $F^2$ with SHELX-97.[15c] All non-hydrogen atoms, except O(2w) in compound **3**, were refined with anisotropic thermal parameters. All hydrogen atoms were generated geometrically and refined isotropically. The hydrogen atoms for the water molecules are not included in the refinements. Pb(3) in compound **3** is severely disordered and displays two orientations with 50% occupancy for each site. One sulfonate group in compound **2** is also severely disordered with O(11) exhibiting two orientations with 50% occupancy each. The occupancy factor of O(2w) in compound **3** was reduced to 50% due to its large thermal parameter. Important bond lengths are listed in Table 1. Crystallographic data and structural refinements for compounds **1**–**5** are summarized in Table 3.

CCDC-632076–632080 (for **1**–**5**) contain the supplementary crystallographic data for this paper. These data can be obtained free of charge from The Cambridge Crystallographic Data Center via www.ccdc.cam.ac.uk/data_request/cif.

**Supporting Information** (see also the footnote on the first page of this article): Figure S1. Simulated and experimental XRD powder patterns for compounds **1**, **2**, **3**, and **5** (Figure S1).

## Acknowledgments

This work is supported by the National Natural Science Foundation of China (20521101), a Key Project of the Chinese Academy of Sciences (KJCX2-YW-H01), and the Natural Science Foundation of Fujian Province (E0420003, E0610034).

[1] a) A. Clearfield, *Metal Phosphonate Chemistry* in *Progress in Inorganic Chemistry* (Ed.: K. D. Karlin), John Wiley & Sons, New York, **1998**, vol. 47, pp. 371–510 and references cited therein; b) K. Maeda, *Microporous Mesoporous Mater.* **2004**, *73*, 47 and references cited therein; c) G. Nonglaton, I. O. Benitez, I. Guisle, M. Pipelier, J. Leger, D. Dubreuil, C. Tellier, D. R. Talham, B. Bujoli, *J. Am. Chem. Soc.* **2004**, *126*, 1497–1502; d) T. L. Schull, L. Henley, J. R. Deschamps, R. J. Butcher, D. P. Maher, C. A. Klug, K. Swider-Lyons, W. J. Dressick, B. Bujoli, A. E. Greenwood, L. K. B. Congiardo, D. A. Knight, *Organometallics* **2007**, *26*, 2272–2276.

[2] a) A. K. Cheetham, G. Férey, T. Loiseau, *Angew. Chem. Int. Ed.* **1999**, *38*, 3269–3292; b) J. Zhu, X. Bu, P. Feng, G. D. Stucky, *J. Am. Chem. Soc.* **2000**, *122*, 11563–11564; c) F. Fredoueil, M. Evain, D. Massiot, M. Bujoli-Doeuff, P. Janvier, A. Clearfield, B. Bujoli, *J. Chem. Soc. Dalton Trans.* **2002**, 1508–1512; d) P. Rabu, P. Janvier, B. Bujoli, *J. Mater. Chem.* **1999**, *9*, 1323–1326; e) N. Stock, S. A. Frey, G. D. Stucky, A. K. Cheetham, *J. Chem. Soc. Dalton Trans.* **2000**, 4292–4296.

[3] a) S. J. Hartman, E. Todorov, C. Cruz, S. C. Sevov, *Chem. Commun.* **2000**, 1213–1214; b) J.-G. Mao, Z. Wang, A. Clearfield, *Inorg. Chem.* **2002**, *41*, 2334–2340; c) J.-G. Mao, Z. Wang, A. Clearfield, *Inorg. Chem.* **2002**, *41*, 3713–3720.

[4] a) P. Yin, L.-M. Zheng, S. Gao, X.-Q. Xin, *Chem. Commun.* **2001**, 2346–2347; b) L.-M. Zheng, S. Gao, H.-H. Song, S. Decurtins, A. J. Jacobson, X.-Q. Xin, *Chem. Mater.* **2002**, *14*, 3143–3147; c) L.-M. Zheng, P. Yin, X.-Q. Xin, *Inorg. Chem.* **2002**, *41*, 4084–4086.

[5] a) E. Burkholder, V. Golub, C. J. O'Connor, J. Zubieta, *Chem. Commun.* **2003**, 2128–2129; b) R. C. Finn, E. Burkholder, J. Zubieta, *Chem. Commun.* **2001**, 1852–1853; c) R. C. Finn, J. Zubieta, *Inorg. Chem.* **2001**, *40*, 2466–2467; d) R. C. Finn, E. Burkholder, J. Zubieta, *Inorg. Chem.* **2001**, *40*, 3745–3754.

[6] a) C. Lei, J.-G. Mao, Y.-Q. Sun, H.-Y. Zeng, A. Clearfield, *Inorg. Chem.* **2003**, *42*, 6157–6159; b) J.-L. Song, H.-H. Zhao, J.-G. Mao, K. R. Dunbar, *Chem. Mater.* **2004**, *16*, 1884–1889; c) B.-P. Yang, J.-G. Mao, *Inorg. Chem.* **2005**, *44*, 566–571; d) J.-L. Song, J.-G. Mao, *Chem. Eur. J.* **2005**, *11*, 1417–1424; e) J.-L. Song, C. Lei, J.-G. Mao, *Inorg. Chem.* **2004**, *43*, 5630–5634.

[7] a) D. M. Poojary, B. Zhang, A. Cabeza, M. A. G. Aranda, S. Bruque, A. Clearfield, *J. Mater. Chem.* **1996**, *6*, 639–644; b) J.-G. Mao, Z. Wang, A. Clearfield, *Inorg. Chem.* **2002**, *41*, 6106–6111; c) J.-G. Mao, Z. Wang, A. Clearfield, *J. Chem. Soc. Dalton Trans.* **2002**, 4541–4546; d) M. M. Gomez-Alcantara, A. Cabeza, M. A. G. Aranda, A. Guagliardi, J.-G. Mao, A. Clearfield, *Solid State Sci.* **2004**, *6*, 479–487.

[8] a) S. Ayyappan, G. D. Delgado, A. K. Cheetham, G. Ferey, C. N. R. Rao, *J. Chem. Soc. Dalton Trans.* **1999**, 2905–2907; b) N. Stock, *Solid State Sci.* **2002**, *4*, 1089–1094; c) D. T. Tran, Y. S. Kam, P. Y. Zavalij, S. R. J. Oliver, *Inorg. Chem.* **2003**, *42*, 2165–2172; d) E. Irran, T. Bein, N. Stock, *J. Solid State Chem.* **2003**, *173*, 293–298.

[9] a) Z.-M. Sun, J.-G. Mao, Y.-Q. Sun, H.-Y. Zeng, A. Clearfield, *New J. Chem.* **2003**, *27*, 1326–1330; b) B.-P. Yang, J.-G. Mao, Y.-Q. Sun, H.-H. Zhao, A. Clearfield, *Eur. J. Inorg. Chem.* **2003**, 4211–4217; c) S.-M. Ying, J.-G. Mao, B.-P. Yang, Z.-M. Sun, *Inorg. Chem. Commun.* **2003**, *6*, 1319–1322; d) B.-P. Yang, Z.-M. Sun, J.-G. Mao, *Inorg. Chim. Acta* **2004**, *357*, 1583–1588.

[10] a) J.-L. Song, J.-G. Mao, Y.-Q. Sun, H.-Y. Zeng, R. K. Kremer, A. Clearfield, *J. Solid State Chem.* **2004**, *177*, 633–641; b) C. Lei, J.-G. Mao, Y.-Q. Sun, *J. Solid State Chem.* **2004**, *177*,

 © 2007 Wiley-VCH Verlag GmbH & Co. KGaA, Weinheim 

2449–2455; c) J.-L. Song, J.-G. Mao, *J. Mol. Struct.* **2005**, *740*, 181–186.
[11] a) J.-L. Song, J.-G. Mao, Y.-Q. Sun, A. Clearfield, *Eur. J. Inorg. Chem.* **2003**, 4218–4226; b) S.-M. Ying, J.-G. Mao, *Eur. J. Inorg. Chem.* **2004**, 1270–1276; c) Z.-M. Sun, J.-G. Mao, B.-P. Yang, S.-M. Ying, *Solid State Sci.* **2004**, *6*, 295–300; d) J.-L. Song, C. Lei, Y.-Q. Sun, J.-G. Mao, *J. Solid State Chem.* **2004**, *177*, 2557–2564; e) S.-M. Ying, J.-G. Mao, *J. Mol. Struct.* **2005**, *748*, 63–70; f) Z.-Y. Du, S.-M. Ying, J.-G. Mao, *J. Mol. Struct.* **2006**, *788*, 218–223.
[12] a) Z.-Y. Du, H.-B. Xu, J.-G. Mao, *Inorg. Chem.* **2006**, *45*, 6424–6430; b) Z.-Y. Du, H.-B. Xu, J.-G. Mao, *Inorg. Chem.* **2006**, *45*, 9780–9788.
[13] A. L. Spek, *Platon: A Multi-purpose Crystallographic Tool*, Utrecht University, The Netherlands, **2001**.
[14] a) E. Montoneri, *Phosphorus Sulfur Silicon Relat. Elem.* **1991**, *55*, 201–204; b) E. Montoneri, M. C. Gallazzi, *J. Chem. Soc. Dalton Trans.* **1989**, 1819–1823.
[15] a) G. M. Sheldrick, *Program SADABS*, University of Göttingen, Germany, **1995**; b) CrystalClear, version 1.3.5 Rigaku Corp., Woodlands, TX, **1999**; c) G. M. Sheldrick, *SHELX-96 Program for Crystal Structure Determination*, University of Göttingen, Germany, **1996**.

Received: April 27, 2007
Published Online: August 7, 2007

 © 2007 Wiley-VCH Verlag GmbH & Co. KGaA, Weinheim 

DOI: 10.1002/ejic.200700507

# Synthesis and Characterization of a New Guanidine–Borane Complex and a Dinuclear Boron(II) Hydride with Bridging Guanidinate Ligands

**Oxana Ciobanu,[a] Pascal Roquette,[a] Simone Leingang,[a] Hubert Wadepohl,[a] Jürgen Mautz,[a] and Hans-Jörg Himmel*[a]**

**Keywords:** Hydrides / Boron / Low oxidation states / Hydrogen elimination

We report the synthesis and structural characterization of the new monomeric borane complex $H_3B$·hppH (hppH = 1,3,4,6,7,8-hexahydro-2*H*-pyrimido[1,2-*a*]pyrimidine), which represents the first example of a structurally characterized 1:1 complex between hppH and a group 13 element hydride. Significant intramolecular and, in the crystalline phase, intermolecular H···H contacts are established in this complex. It is shown that the complex can be used as a precursor to new dinuclear boron(II) compounds featuring a B–B single bond. Thus $H_2$ elimination followed by dimerization of $H_3B$·hppH leads to $[(hpp)BH]_2$ with two bridging hpp units. The structural details derived from X-ray diffraction measurements are reported.

(© Wiley-VCH Verlag GmbH & Co. KGaA, 69451 Weinheim, Germany, 2007)

## Introduction

In Linus Pauling's concept of electronegativity, the dissociation energy of a compound A–B is comparable to half of the sum of the dissociation energies of $A_2$ and $B_2$, if A and B have similar electronegativities. This implies that reactions of the type E–E + $H_2 \rightarrow$ 2EH (where E represents any element in the periodic table) should be associated with a small reaction enthalpy at standard conditions if the electronegativity of E is close to that of H. If the reaction barrier can be controlled to remain low, the chances of reversibility of such a reaction under mild conditions are increased, and E–E might be regarded as a molecular hydrogen storage material. An inspection of the periodic table shows that the (Pauling) electronegativities of main-group elements E such as B (2.0), P (2.1), As (2.0), Sb (1.9), Bi (1.9) and Te (2.1) are close to that of H (2.1). Of these elements, boron stands out as by far the lightest and therefore most interesting element with regard to applications in the field of hydrogen storage.[1] That group 13 element compounds are in principle interesting in this context has been shown by our group with a very simple example, namely the diatomic $Ga_2$ (Ga being the heavier "sister" of B). The $Ga_2$ dimer, which can be stabilized with the help of the matrix isolation technique, readily takes up dihydrogen to form a cyclic $Ga(\mu\text{-}H)_2Ga$ molecule [see Equation (1)].[2] The reaction barrier, estimated on the basis of the IR spectra recorded in experiments with mixtures of $H_2$ and $D_2$, amounts to ca. 40 kJ mol$^{-1}$, a value which is in good agreement with the results of quantum chemical calculations.[3]

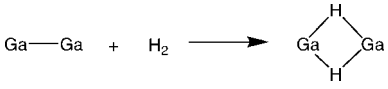


(1)

These experiments therefore demonstrated that low reaction barriers are indeed possible. However, $Ga_2$ is not stable under normal conditions and therefore not directly relevant for application purposes. It would also be more interesting to find B compounds, which are lighter than their Ga counterparts. Therefore we searched for suitable dinuclear B compounds in low oxidation states in which the two B atoms can establish a direct B–B bond. In general, this can be achieved by bridging the two B atoms with one or more suitable ligands. If the two bridging ligands coordinate, the general reaction sequence (2) describes the possible uptake or release of $H_2$ for these molecular compounds (E being preferably B).

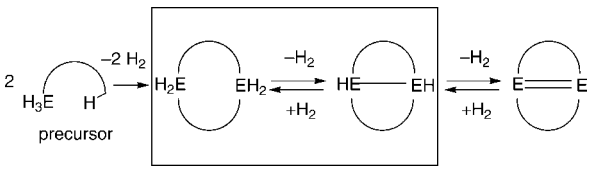


(2)

In the hpp ligand, which is obtained after H abstraction from hppH (1,3,4,6,7,8-hexahydro-2*H*-pyrimido[1,2-*a*]pyrimidine), we have now found a first example of a ligand where this concept might work. This ligand has been used extensively to bring together two transition-metal atoms in dinuclear compounds and engage them in direct and sometimes multiple metal–metal bonding. Examples of this in-

[a] Anorganisch-Chemisches Institut, Ruprecht-Karls-Universität Heidelberg,
Im Neuenheimer Feld 270, 69120 Heidelberg, Germany
E-mail: hans-jorg.himmel@aci.uni-heidelberg.de


© 2007 Wiley-VCH Verlag GmbH & Co. KGaA, Weinheim

clude the complexes $Nb_2(hpp)_4$[4] and $M_2(hpp)_4Cl_2$ (where, for example, M = Ru,[5] W, Os and Pt[6]). Reaction sequence (2) then describes the conversion of a mononuclear $E^{III}$ compound into a dinuclear $E^{III}$ compound, which then eliminates dihydrogen to form a dinuclear $E^{II}$ and finally a dinuclear $E^{I}$ compound, the latter two featuring direct E–E bonding. It has also been shown recently that activation of hydrogen by subvalent compounds featuring direct E–E bonds is possible for the dinuclear compound Ar′GeGeAr′ [Ar′ = $C_6H_3$-2,6($C_6H_3$-2,6-*i*$Pr_2$)$_2$], which can add one, two or three equivalents of $H_2$ to give first Ar′(H)GeGe(H)Ar′, then Ar′$H_2$GeGe$H_2$Ar′ and finally Ar′$GeH_3$.[7] It should also be noted that catalytic $H_2$ elimination from amine–borane adducts such as $H_3BNMe_2H$ has been extensively studied recently.[8]

## Results and Discussion

First we prepared the monomeric compound $H_3B$·hppH [see Equation (3)]. It is the first example of a structurally characterized 1:1 adduct of hppH to a group 13 element hydride, and it can be used as a precursor to the desired dinuclear hydrides. $H_3B$·hppH was synthesized by heating a solution containing equimolar quantities of $H_3B$·$NMe_3$ and hppH for a period of 18 h at 60 °C. The analogous reaction between $H_3Ga$·$NMe_3$ and hppH resulted in the direct formation of the dinuclear compound $[H_2Ga(hpp)]_2$,[9] even at 0 °C, and it proved impossible to isolate this adduct. In the crystal structure of $H_3B$·hppH illustrated in Figure 1[10] are featured two intramolecular as well as two intermolecular H···H contacts that are established between positively and negatively polarized H atoms.

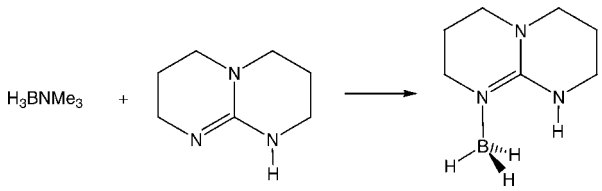


(3)

These contacts are important, since they lower the barrier for $H_2$ elimination (vide infra). The intramolecular H···H contacts between two of the H atoms attached to the B atom and the H atom attached to the N atom of the same molecule are 223 and 224 pm (217 and 218 pm when normalized E–H distances are used[11]), respectively, and the corresponding intermolecular contacts measure 228 and 236 pm (220 and 228 pm). The B–N bond length is 157.5 pm. This value is shorter than the B–N bonds of borane–amine adducts. To name two recently reported examples, the B–N bond distances in the $BH_3$ adducts of $PhCH_2N(CH_3)_2$[12] and $HC(CH_2CH_2)_3N$[13] have been determined to be 162.0(2) and 160.8(5) pm, respectively. The distance is also shorter than that reported for imine adducts such as the *N*-benzyl (Bn) imine adduct $Ph_2C{=}N(Bn)$·$B(C_6F_5)_3$ featuring a B–N bond length of 164.2(8) pm.[14] The B–H bond lengths measure 110(2) (no H···H contacts),

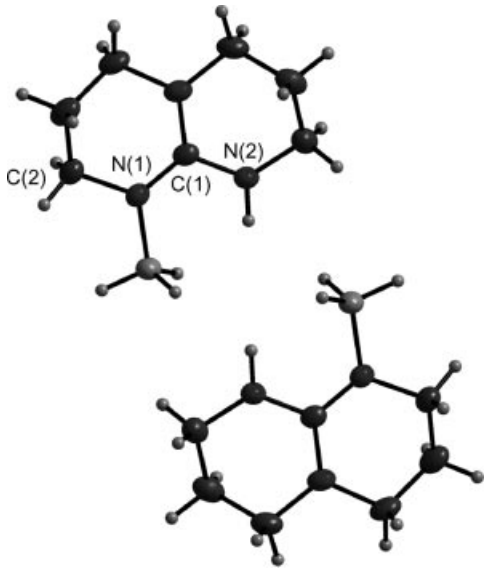


Figure 1. Molecular structure of $H_3B$·hppH in the crystalline phase showing the arrangement of two symmetrically equivalent molecules. The thermal ellipsoids are drawn at the 50% probability level. Selected bond parameters (distances in pm, bond angles in degrees): B–H 110(2), 112(1), 112(2); B–N(1) 157.5(2); N(2)/N(1)–C(1) 134.8(2)/132.1(2); N(2)–H 89(2); B–N(1)–C(1) 122.3(1); B–N(1)–C(2) 117.8(1); N(1)–C(1)–N(2) 118.0(1).

112(1) and 112(2) pm, and the N–H bond is 89(2) pm long. Calculations were carried out to determine whether the inter- or intramolecular H···H contacts are responsible for the conformation of the $BH_3$ group. Calculations for an isolated molecule returned a conformation very close to that observed, and thus the intramolecular H···H contacts determine the geometry. This is also in line with the smaller observed values for the intramolecular H···H distances. In Figure 2 the relative energy is plotted as a function of the dihedral angle between the C–N–B and the N–B–H planes as calculated by using MP2/SVP.[15] It can be seen that the barrier for rotation around the B–N axis is no more than 4.5 kJ mol$^{-1}$.

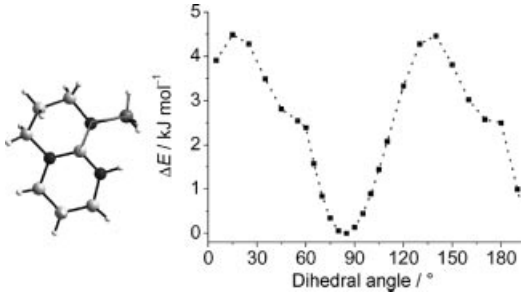


Figure 2. Relative energy as a function of the dihedral angle C–N–B–H as calculated with MP2/SVP.

Hydrogen is eliminated if a solution of the precursor $H_3B$·hppH is heated in toluene to 110 °C for 20 h. Interestingly, we did not obtain $[H_2B(hpp)]_2$ as the product of this reaction, as in the reaction of the corresponding Ga homologue,[9] but rather $[HB(hpp)]_2$ was produced directly [see

 © 2007 Wiley-VCH Verlag GmbH & Co. KGaA, Weinheim 

Equation (4)]. The barrier for $H_2$ elimination from $[H_2B(hpp)]_2$ is so small that this process occurs at temperatures below 110 °C. $[HB(hpp)]_2$ is the product of a redox reaction and features two B atoms in the formal oxidation state +2. In the case of $[H_2Ga(hpp)]_2$, we observed $H_2$ elimination even at 25 °C, and all signs indicated that $[HGa(hpp)]_2$ was the product.[9] However, we have so far been unable to structurally characterize this species. In the case of the boron compound, we have obtained good-quality crystals from toluene solutions, and Figure 3 illustrates the crystal structure derived from our X-ray diffraction data.[10] $[HB(hpp)]_2$ features a B–B single bond measuring 177.2(3) pm and a *cis*-bent arrangement of the H–B–B–H fragment [with B–H distances of 115(3) and 106(4) pm]. The value of the B–B bond length is in a range typical for B–B single bonds. For example, gas-phase electron diffraction measurements of $B_2(NMe_2)_4$ and $B_2(OMe)_4$ indicated B–B bond lengths of 176.2(1.1) and 172.0(6) pm.[16] The four B–N bond lengths are almost equal: 158.2(3), 156.3(3), 157.2(3) and 157.1(3) pm. The two five-membered BBNCN rings are almost planar, and the dihedral angle between them is 67.80(8)°. The IR spectrum contains absorptions in a region typical for terminal B–H stretches (2398–2230 $cm^{-1}$).

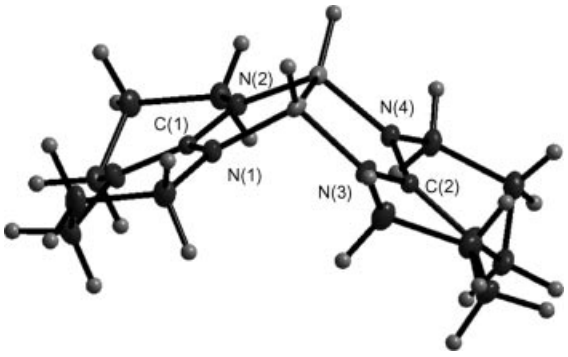


Figure 3. Molecular structure of $[HB(hpp)]_2$ in the crystalline phase. The thermal ellipsoids are drawn at the 50% probability level. Selected bond parameters (distances in pm, bond angles in degrees): B–H 115(3), 106(4); B–B 177.2(3); B–N 157.1(2), 157.2(3), 156.3(3), 158.2(3); N(1)/N(2)–C(1) 133.1(2), 134.3(2); N(3)/N(4)–C(2) 133.8(2), 133.4(2); N(1)–C(1)–N(2) 115.6(2); N(3)–C(2)–N(4) 115.3(2); N(1)/N(2)–B–N(3)/N(4) 111.0(2), 110.8(2).

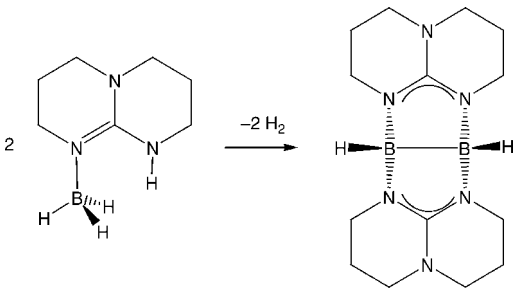


(4)

The reaction pathway proposed on the basis of quantum chemical calculations leading from $H_3B{\cdot}hppH$ to $[HB(hpp)]_2$ is illustrated in reaction sequence (5) (generalized to guanidine derivatives). Intramolecular $H_2$ elimination from $H_3B{\cdot}hppH$ is facilitated by intramolecular H···H contacts and leads to a diene-type intermediate. The reaction energy and the standard Gibbs free energy for this first step are +74 (+46 with zero-point vibrational energy corrections) and +17 kJ $mol^{-1}$, respectively.[14] This diene-type intermediate is in equilibrium with a four-membered ring structure

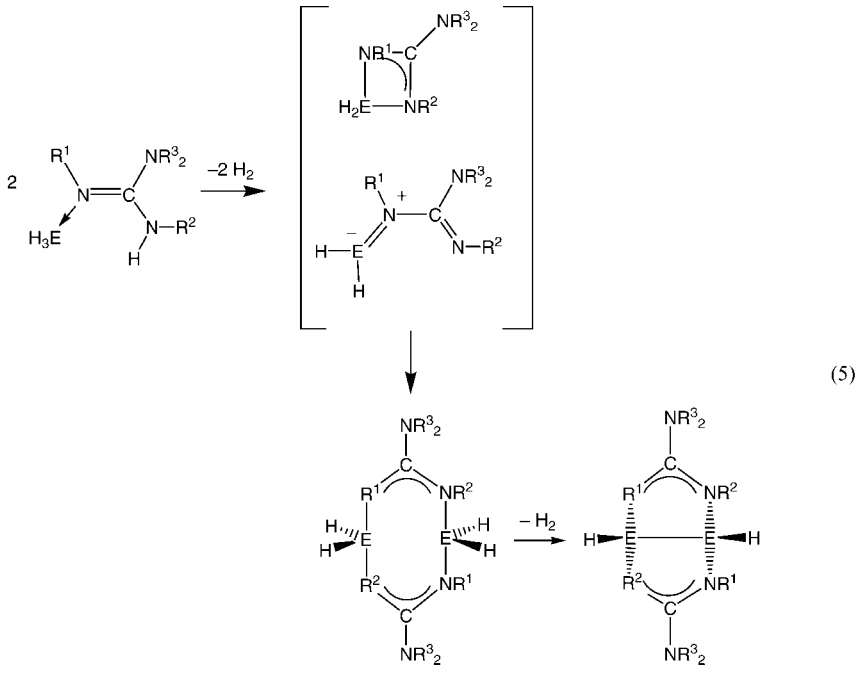


(5)

 © 2007 Wiley-VCH Verlag GmbH & Co. KGaA, Weinheim 

in which the guanidinate ligand adopts a chelating binding mode. The standard Gibbs free energy change between the diene and the four-membered ring is calculated to be no more than 3 kJ mol$^{-1}$ (in favour of the four-membered ring). The diene subsequently undergoes a [4+4] cycloaddition to give $[H_2B(hpp)]_2$. This second step is associated with an energy change of –109 (–118 including zero-point vibrational energy corrections) kJ mol$^{-1}$ and a standard Gibbs free energy change of –87 kJ mol$^{-1}$. Finally, and most importantly, the reaction energy and standard Gibbs free energy for the formation of $[HB(hpp)]_2$ by $H_2$ elimination from $[H_2B(hpp)]_2$ come out to be +32 (+1 including zero-point vibrational energy corrections) and –30 kJ mol$^{-1}$, respectively. Solvation effects for this particular reaction were estimated by using the COSMO method[17] with $\varepsilon_r$ = 2.38 for toluene. As expected, the effects are very small ($\Delta E$ decreases to +30 kJ mol$^{-1}$, and $\Delta G^0$ increases slightly to –27 kJ mol$^{-1}$). Figure 4 shows $\Delta G$ for the decomposition reaction of $[H_2B(hpp)]_2$ to give $[HB(hpp)]_2$ and $H_2$ as a function of temperature at a pressure of 1 bar. Experiments will be undertaken to analyze whether the $H_2$ elimination can be accomplished reversibly. We are also extending our work to related compounds featuring two B atoms connected by one or two bridging guanidinate or amidinate ligands.

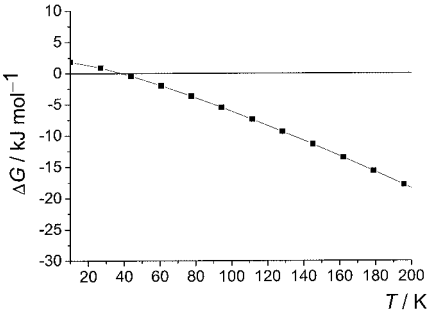


Figure 4. $\Delta G$ for the reaction $[H_2B(hpp)]_2 \rightarrow [HB(hpp)]_2 + H_2$ as a function of temperature at a constant pressure of 1 bar.

## Conclusion

The base exchange reaction between $H_3B{\cdot}NMe_3$ and the guanidine derivative hppH affords the new borane adduct $H_3B{\cdot}$hppH . Intramolecular BH···HN contacts are established therein, facilitating $H_2$ elimination, which was observed around 110 °C. Dimerization and repeated $H_2$ elimination leads directly to the new diborane (4) derivative $[HB(hpp)]_2$. X-ray diffraction measurements reveal the presence of a trigonal prismatic central $B_2N_4$ unit in this hydride. Quantum chemical calculations were carried out to analyse the reaction pathway. These calculations suggest the formation of a diene-type intermediate upon intramolecular $H_2$ elimination followed by cycloaddition and elimination of a second $H_2$ molecule to give the observed product. Future experiments concentrate on the synthesis of other derivatives of this class of compounds, which might also be interesting for $H_2$ activation, and on the synthesis of the intermediate $[HB(hpp)]_2$ by catalytic dehydrocoupling reactions.

## Experimental Section

All reactions were carried out under a dry argon atmosphere by using standard Schlenk techniques. All solvents were dried by using standard methods followed by distillation. $H_3B{\cdot}NMe_3$ and hppH were purchased from Aldrich and used as received.

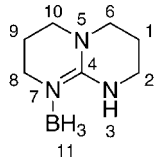


**$H_3B{\cdot}$hppH:** A solution of $H_3B{\cdot}NMe_3$ (0.524 g, 7.18 mmol) in toluene (20 mL) was added to a solution of hppH (1.00 g, 7.18 mmol) in toluene (20 mL) by syringe, and the reaction mixture was stirred for 18 h at 60 °C. The colourless solution was concentrated, and *n*-pentane (ca. 10 mL) was added to obtain a white precipitate in 70% yield (0.70 g, 5.03 mmol). Crystals suitable for X-ray diffraction were grown from a hexane/toluene (2:1) mixture at –20 °C. $C_7H_{16}BN_3$ (153.03): calcd. C 54.94, H 10.54, N 27.46; found C 54.36, H 10.38, N 26.91. $^1$H NMR (400 MHz, $C_6D_6$): $\delta$ = 6.29 (s, 1 H, NH), 3.34 (t, $^3J$ = 5.9 Hz, 2 H, 8-H), 2.83 (br. q, $^1J$ = 93 Hz, 3 H, $BH_3$), 2.27 (t, $^3J$ = 5.9 Hz, 2 H, 6-H), 2.13 (t, $^3J$ = 6.0 Hz, 2 H, 10-H), 2.03 (t, $^3J$ = 6.0 Hz, 2 H, 2-H), 1.17 (quint, $^3J$ = 6.0 Hz, 2 H, 9-H), 0.91 (quint, $^3J$ = 6.0 Hz, 2 H, 1-H) ppm. $^{13}$C{$^1$H} NMR (100.55 MHz, $C_6D_6$): $\delta$ = 150.69 (C-4), 47.47 (C-8), 47.27 (C-10), 46.82 (C-2), 38.38 (C-6), 21.80 (C-9), 21.57 (C-1) ppm. $^{11}$B NMR (128.30 MHz, $C_6D_6$): $\delta$ = –19.15 (q, $^1J$ = 93 Hz, $BH_3$) ppm. HRMS (EI+): *m*/*z* (%) = 152.14 (100.0) $[M - H]^+$, 138.10 (28.2) $[hpp]^+$, 122.09 (5.6) $[M - CH_3NH_2]^+$, 113.00 (5.1) $[M - CH_3NB]^+$, 95.07 (2.8) $[M - C_2H_9NB]^+$. IR (solid CsI): $\tilde{\nu}$ = 3352 (s) (N–H val), 2960 (m) (C–H val), 2872 (m) (C–H val), 2363 (m) (B–H), 2301 (m) (B–H), 2253 (m) (B–H), 1625 (s) (C=N val.), 1570 (s) (N–H def.), 1447 (w) (C–H def.), 1322 (m), 1174 (m) (B–N), 1148 (m) cm$^{-1}$.

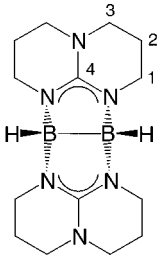


**$[HB(hpp)]_2$:** A solution of $H_3B{\cdot}NMe_3$ (0.21 g, 2.9 mmol) in toluene (15 mL) was slowly added to a solution of hppH (0.4 g, 2.9 mmol) in toluene (15 mL). The reaction mixture was heated under reflux for 20 h at 110 °C. The solution was concentrated, and colourless crystals of the toluene solvate were obtained from these solutions after storage for several days at –20 °C. $^1$H NMR (600 MHz, [D$_8$]toluene): $\delta$ = 3.23 (t, $^3J$ = 5.8 Hz, 2 H, 1-H), 2.57 (t, $^3J$ = 6.6 Hz, 2 H, 3-H), 1.56 (quint, 2 H, 2-H) ppm. $^{13}$C{$^1$H} NMR (150.9 MHz, [D$_8$]toluene): $\delta$ = 47.96 (C-3), 47.19 (C-1), 24.21 (C-2) ppm. $^{11}$B{$^1$H} NMR (192.5 MHz, [D$_8$]toluene): $\delta$ = –2.39 (BH) ppm. MS (EI+): *m*/*z* = 299.4 $[C_{14}H_{26}B_2N_6]^+$, 138.2 $[hpp]^+$. IR (solid CsI): $\tilde{\nu}$

 © 2007 Wiley-VCH Verlag GmbH & Co. KGaA, Weinheim 

= 2964 (m) (C–H), 2852 (m) (C–H), 2398–2230 (m) (B–H), 1565 (s) (C–N), 1321 (m) (B–N) $cm^{-1}$. It should be noted that the NMR spectra provided evidence for a second species in very small quantities. This might be the isomer of $[HB(hpp)]_2$ featuring hpp ligands which are coordinated to only one B atom. This second species is characterized by the following NMR spectra: $^1H$ NMR (600 MHz, [D$_8$]toluene): $\delta$ = 3.48 (m, 1 H, $C_AH_2$), 3.39 (m, 1 H, $C_AH_2$), 2.52 (m, 1 H, $C_CH_2$), 2.42 (m, 1 H, $C_CH_2$), 1.59 (m, 1 H, $C_AH_2$), 1.49 (m, 1 H, $C_AH_2$) ppm. $^{13}C\{^1H\}$ NMR (150.9 MHz, [D$_8$]toluene): $\delta$ = 47.59 ($C_C$), 45.81 ($C_A$), 23.37 ($C_B$) ppm. $^{11}B\{^1H\}$ NMR (192.5 MHz, [D$_8$]toluene): $\delta$ = –1.12 (BH) ppm.

## Acknowledgments

The authors gratefully acknowledge continuous financial support from the *Deutsche Forschungsgemeinschaft* (DFG) and the *Fonds der Chemischen Industrie*.

[1] Boron compounds have been shown previously to be of interest for hydrogen storage. For very recent examples, see: a) F. H. Stephens, R. T. Baker, M. H. Matus, D. J. Grant, D. A. Dixon, *Angew. Chem.* **2007**, *119*, 760; *Angew. Chem. Int. Ed.* **2007**, *46*, 746; b) T. J. Clark, C. A. Russell, I. Manners, *J. Am. Chem. Soc.* **2006**, *128*, 9582; c) G. C. Welch, R. R. San Juan, J. D. Masuda, D. W. Stephan, *Science* **2006**, *314*, 1124.

[2] a) H.-J. Himmel, L. Manceron, A. J. Downs, P. Pullumbi, *Angew. Chem.* **2002**, *114*, 829; *Angew. Chem. Int. Ed.* **2002**, *41*, 796; b) H.-J. Himmel, L. Manceron, A. J. Downs, P. Pullumbi, *J. Am. Chem. Soc.* **2002**, *124*, 4448.

[3] A. Köhn, H.-J. Himmel, B. Gaertner, *Chem. Eur. J.* **2003**, *9*, 3909.

[4] F. A. Cotton, J. H. Matonic, C. A. Murillo, *J. Am. Chem. Soc.* **1997**, *119*, 7889.

[5] J. L. Bear, Y. Li, B. Han, K. M. Kadish, *Inorg. Chem.* **1996**, *35*, 1395.

[6] a) R. Clérac, F. A. Cotton, L. M. Daniels, J. P. Donahue, C. A. Murillo, D. J. Timmons, *Inorg. Chem.* **2000**, *39*, 2581; b) F. A. Cotton, C. A. Murillo, X. Wang, C. C. Wilkinson, *Inorg. Chim. Acta* **2003**, *351*, 191.

[7] G. H. Spikes, J. C. Fettinger, P. P. Power, *J. Am. Chem. Soc.* **2005**, *127*, 12232.

[8] a) C. A. Jaska, I. Manners, *J. Am. Chem. Soc.* **2004**, *126*, 9776–9785; b) T. J. Clark, C. A. Russell, I. Manners, *J. Am. Chem. Soc.* **2006**, *128*, 9582–9583.

[9] G. Robinson, C. Y. Tang, R. Köppe, A. R. Cowley, H.-J. Himmel, *Chem. Eur. J.* **2007**, *13*, 2648.

[10] $H_3B{\cdot}$hppH: $C_7H_{16}BN_3$, $M_r$ = 153.04; 0.30 × 0.30 × 0.20 $mm^3$, orthorhombic, space group *Pbca*; $a$ = 8.459(2) Å, $b$ = 13.534(3) Å, $c$ = 15.111(3) Å, $V$ = 1730.0(6) $Å^3$, $Z$ = 8, $d_{calc}$ = 1.175 $Mg\,m^{-3}$, Mo-$K_\alpha$ radiation (graphite monochromated, $\lambda$ = 0.71073 Å), $T$ = 173(2) K, $\theta$ range 3.1 to 27.5°. Reflections measured: 3671, independent: 1977, $R_{int}$ = 0.033, empirical absorption correction. Final $R$ indices [$I > 2\sigma(I)$]: $R_1$ = 0.044, $wR_2$ = 0.1148, maximum residual electron density 0.16 e $Å^{-3}$. All non-hydrogen atoms were given anisotropic displacement parameters. The hydrogen atom positions on the N and B atoms were taken from difference Fourier syntheses and refined with individual isotropic displacement parameters. All other hydrogen atoms were input in calculated positions. $[HB(hpp)]_2$: $C_{14}H_{26}B_2N_6{\cdot}C_7H_8$, $M_r$ = 392.16; 0.30 × 0.15 × 0.15 $mm^3$, monoclinic, space group *Pn*; $a$ = 8.1843(5) Å, $b$ = 8.3965(6) Å, $c$ = 15.5586(10) Å, $\beta$ = 100.9340(10)°, $V$ = 1049.77(12) $Å^3$, $Z$ = 2, $d_{calc}$ = 1.241 $Mg\,m^{-3}$, Mo-$K_\alpha$ radiation (graphite monochromated, $\lambda$ = 0.71073 Å), $T$ = 100(2) K, $\theta$ range 2.4 to 32.1°. Reflections measured: 25932, independent: 3513, $R_{int}$ = 0.050, semiempirical absorption correction.[18] Final $R$ indices [$I > 2\sigma(I)$]: $R_1$ = 0.0457, $wR_2$ = 0.1161. All non-hydrogen atoms were given anisotropic displacement parameters. All hydrogen atom positions (except those of the methyl group, which was refined as a variable metric rigid group with hydrogen atoms input at calculated positions) were taken from difference Fourier syntheses and refined with individual isotropic displacement parameters. A maximum residual electron density of 0.80 e $Å^{-3}$ was found above the centre of and attributed to the boron–boron bond. Structure solution by using direct methods: SHELXS-97,[19] refinement by full-matrix least-squares on $F^2$: SHELXL-97.[20] CCDC-642232 ($H_3B{\cdot}$hppH) and CCDC-642233 {$[HB(hpp)]_2$} contain the supplementary crystallographic data for this paper. These data can be obtained free of charge from The Cambridge Crystallographic Data Centre via www.ccdc.cam.ac.uk/data_request/cif.

[11] Corrections which take into account thermal elongations and the effect of high-electron-density gradients generally leading to too short E–H bond lengths in the X-ray structures.

[12] A. Shibli, H. A. Ali, I. Goldberg, M. Srebnik, *J. Organomet. Chem.* **2005**, *690*, 2180.

[13] F. Blockhuys, D. A. Wann, C. Van Alsenoy, H. E. Robertson, H.-J. Himmel, C. Y. Tang, A. R. Cowley, A. J. Downs, D. W. H. Rankin, *Dalton Trans.* **2007**, 1687.

[14] J. M. Blackwell, W. E. Piers, M. Parvez, R. McDonald, *Organometallics* **2002**, *21*, 1400.

[15] Calculations were carried out with the TURBOMOLE program package. See: a) R. Ahlrichs, M. Bär, M. Häser, H. Horn, C. Kölmel, *Chem. Phys. Lett.* **1989**, *162*, 165; b) K. Eichkorn, O. Treutler, H. Öhm, M. Häser, R. Ahlrichs, *Chem. Phys. Lett.* **1995**, *240*, 283; c) K. Eichkorn, O. Treutler, H. Öhm, M. Häser, R. Ahlrichs, *Chem. Phys. Lett.* **1995**, *242*, 652; d) K. Eichkorn, F. Weigend, O. Treutler, R. Ahlrichs, *Theor. Chem. Acc.* **1997**, *97*, 119; e) F. Weigend, M. Häser, *Theor. Chem. Acc.* **1997**, *97*, 331; f) F. Weigend, M. Häser, H. Patzelt, R. Ahlrichs, *Chem. Phys. Lett.* **1998**, *294*, 143. If not stated otherwise, the BP86 method in combination with a TZVPP basis set has been applied (A. Schäfer, H. Horn, R. Ahlrichs, *J. Chem. Phys.* **1992**, *97*, 2571).

[16] P. T. Brain, A. J. Downs, P. Maccallum, D. W. H. Rankin, H. E. Robertson, G. A. Forsyth, *J. Chem. Soc. Dalton Trans.* **1991**, 1195.

[17] A. Klamt, G. Schürmann, *J. Chem. Soc. Perkin Trans. 2* **1993**, 799.

[18] G. M. Sheldrick, *SADABS-2004/1*, Bruker AXS, **2004**.

[19] G. M. Sheldrick, *SHELXS-97*, University of Göttingen, **1997**.

[20] G. M. Sheldrick, *SHELXL-97*, University of Göttingen, **1997**.

Received: May 10, 2007
Published Online: August 13, 2007

 © 2007 Wiley-VCH Verlag GmbH & Co. KGaA, Weinheim 

DOI: 10.1002/ejic.200601167

# Synthesis and Crystal Structure of New Early-Lanthanide Organometallic Clusters

Eyal Barnea,[a] Claudia Averbuj,[a] Moshe Kapon,[a] Mark Botoshansky,[a] and Moris S. Eisen*[a]

**Keywords:** Organolanthanide halide clusters / Lithium / Bridging ligands

Reaction of $Cp^*_2NdCl{\cdot}LiCl{\cdot}2thf$ (**1**) with excess catecholborane affords the hexameric cluster $(Cp^*NdCl_2)_6(LiCl)_3(thf)_3$ (**2**) bearing three types of bridging chloride ions. Heating the reaction mixture affords the tetrameric cluster $[(Cp^*NdCl_2)_4(\mu_4\text{-}Cl)]_2[LiO_2][LiO_2{}^*Li_2O^*O_2]$ (**3**), which has the first crystal structure with the $LiO_2^+$ motif. Reaction of complex **1** or the analogous Sm complex, **4**, with pinacolborane affords clusters **5a** (Nd) or **5b** (Sm), respectively, a second type of hexameric cluster built from two $CpNd_3Cl_5(thf)$ units bonded by two $\mu_2$-Cl atoms.
(© Wiley-VCH Verlag GmbH & Co. KGaA, 69451 Weinheim, Germany, 2007)

## Introduction

Organometallic rare-earth complexes bearing one Cp* ligand and a heteroatom have received considerable attention in recent years due to their potential use in homogeneous catalysis, especially in the polymerization of olefins.[1] However, the synthesis of mono(Cp) complexes of lanthanides is still a challenging task, because of the relative ease of the synthesis of bis(Cp) complexes and/or their rearrangement into the more thermodynamically stable homoleptic tris(Cp) derivatives.[2] In addition, these metals are also known to form organometallic heteroatom clusters.[3] Recently, Visseaux et al.[4] reported the synthesis and crystal structure of new monocyclopentadienyl lanthanide clusters bearing chlorido or borohydride bridges and up to six Nd or Sm atoms in the metallic backbone. Higher-order lanthanide–halide clusters bearing up to 12 metal atoms in the backbone were reported by Kretschmer et al.[5] In this contribution, we present the crystal structures of four new organolanthanide chlorido clusters as well as the unique counterion $LiO_2^+$.

## Results and Discussion

We recently reported the synthesis of inclusion complexes of organic ligands with f-elements in which the metal is encapsulated by trianionic triborate–tribenzo crown ethers.[6a] When we attempted to prepare such a macrocyclic complex bearing Nd as the metal center by the reaction of catecholborane (HBcat) with complex **1**, $Cp^*_2NdCl{\cdot}LiCl{\cdot}2thf$ [Equation (1a)], we found that the presence of HBcat (neat, no solvent) induced a selective clustering reaction, yielding cubelike blue crystals of cluster **2**, which were analyzed by X-ray crystallography. Cluster **2** crystallizes in the cubic space group $I\bar{4}3d$ (see Table 1 for complete crystallographic data and Figure 1 for selective bond lengths and angles). The X-ray diffraction analysis (Figure 1) revealed a hexameric cluster structure bearing six Nd atoms bridged by 14 chloride ions. In addition, three groups of four chloride ions are bridged by a Li–thf moiety. Each Nd atom is also bonded to one Cp* ligand outside the cluster. The six Nd atoms describe a trigonal prism, which has a central isolated chloride ion (Cl7). The bonds between the Nd atoms and the central Cl atom are considerably longer (3.388 Å) than other Nd–Cl bonds in the cluster (2.92 Å in average, similar to those observed in the literature[4,5]). Each Nd atom has nine coordination sites. Interestingly, the presence of a $\mu^6$-heteroatom in the center of a cluster has been already observed for oxygen,[7] halogen,[8] and selenium.[9]

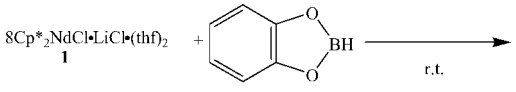


$$\underset{\mathbf{2}}{Cp^*_6Nd_6Cl_{15}Li_3(thf)_3} + 4Cp^*Li + 2NdCp^*_3 + LiCl + 13thf \qquad (1a)$$

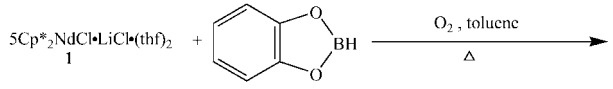


$$\underset{\mathbf{3}}{Cp^*_4Nd_4Cl_9LiO_2} + 3Cp^*Li + NdCp^*_3 + LiCl + 10thf \qquad (1b)$$

[a] Schulich Faculty of Chemistry and Institute of Catalysis Science and Technology, Technion-Israel Institute of Technology, Haifa, 32000, Israel

 © 2007 Wiley-VCH Verlag GmbH & Co. KGaA, Weinheim 

Table 1. Crystallographic data for complexes **2** and **3**.

| | **2** | **3** |
|---|---|---|
| Color | blue | pale blue |
| Size [mm$^3$] | $0.42\times0.36\times0.24$ | $0.40\times0.24\times0.21$ |
| Chemical formula | $C_{75}H_{114}Cl_{15}Li_3Nd_6O_{4.5}$ | $C_{42}H_{62}Cl_9Li_{1.33}Nd_4O_{2.5}$ |
| Fw | 2505.67 | 1512.18 |
| Crystal system | cubic | monoclinic |
| Space group | $I\bar{4}3d$ | $C2/m$ |
| $T$ [K] | 240.0(1) | 230.0(1) |
| $a$ [Å] | 34.407(7) | 32.8430(6) |
| $b$ [Å] | 34.407(7) | 21.1480(4) |
| $c$ [Å] | 34.407(7) | 14.6670(4) |
| $\alpha$ [°] | 90 | 90 |
| $\beta$ [°] | 90 | 113.8510(8) |
| $\gamma$ [°] | 90 | 90 |
| $V$ [Å$^3$] | 40732(14) | 9317.2(4) |
| $Z$, $D_{calc}$ [g cm$^{-3}$] | 48, 1.634 | 6, 1.617 |
| $\mu$ (Mo-$K_\alpha$) [mm$^{-1}$] | 3.435 | 3.703 |
| $\theta$ range [°] | 1.387–27.48 | 1.18–25.05 |
| Limiting indices | $-44 \le h \le 29$; $-37 \le k \le 44$; $-22 \le l \le 35$ | $-39 \le h \le 39$; $-23 \le k \le 25$; $-17 \le l \le 17$ |
| Collected refIns./unique | 38574/4085 | 15080/8487 |
| $R$(int) | 0.0870 | 0.0323 |
| Parameters | 324 | 293 |
| GOF on $F^2$ | 1.054 | 1.067 |
| Final $R$ indices | $R_1 = 0.0426$, | $R_1 = 0.0771$, |
| $[I>2\sigma(I)]$ | $wR_2 = 0.1210$ | $wR_2 = 0.2218$ |
| $\rho_{min}$, $\rho_{max}$ [e Å$^{-3}$] | –0.884, 1.359 | –2.576, 1.400 |

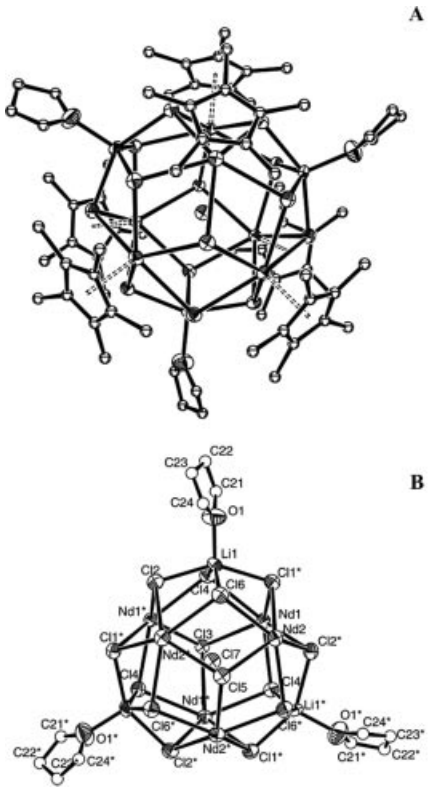


Figure 1. ORTEP representation (50% probability) of the molecular structure of complex **2**. (A) Full structure and (B) with removal of hydrogen atoms and Cp* ligands for clarity. Selected bond lengths [Å] and angles [°]: Nd1–Cl1* 2.898(3), Nd–Cp*(CNT) 2.341(10), Nd1–Cl2 2.882(3), Nd1–Cl5 2.972(4), Nd1–Cl7 3.388(5), Cl–Li 2.488(5), Li1–O1 1.931(6), Nd1–Nd2 4.427(10); Nd1–Cl7–Nd2 80.08(9), Nd1–Cl7–Nd1* 82.63(9), Nd1–Cl1*–Nd2 98.26(9).

The formation of **2** is accompanied by the formation of LiCp*, NdCp*$_3$,[10] and LiCl, as presented in Equation (1a); in contrast, a very small amount of product forms when the reaction is carried out in only a slight excess of the borane. It is important to point out that our attempts to perform the same reaction in the absence of the borane or by adding a strong Lewis acid ($Me_3Al$) resulted in decomposition products only.

When the same reaction was performed at higher temperatures (in the expectation of lowering the clustering effect) a different cluster was formed [Equation (1b)]. The crystal structure of cluster **3** (Figure 2 and Figure 3) revealed a tetrameric cluster with four Cp*Nd units bridged by eight $\mu_2$-Cl ions. In addition, in the center of the square described by the four Nd atoms lies an isolated $\mu_4$-Cl ion.[11] The unit cell contains two clusters, each with a –1 charge. These charges are counterbalanced by two microstructures of $LiO_2^+$ ion outside the cluster. In the first structure, the $Li^+$ ion is bonded to $O_2$ in a triangular fashion to form the ordered $[LiO_2]^+$. To the best of our knowledge, this is the first solid-state characterization of this motif. The O–Li–O angle is 46.5 °, which is the same as the calculated angle of the $LiO_2$ radical of 46.5 °.[12] However, the Li–O bond length (1.922 Å) differs significantly from the calculated length (1.76 Å),[12] which is reasonable if it is taken into account that the calculations were done for the $LiO_2$ radical and not the cationic $[LiO_2]^+$. We believe that the oxygen comes from contamination of the reaction mixture with traces of molecular oxygen in the glove box, where there is

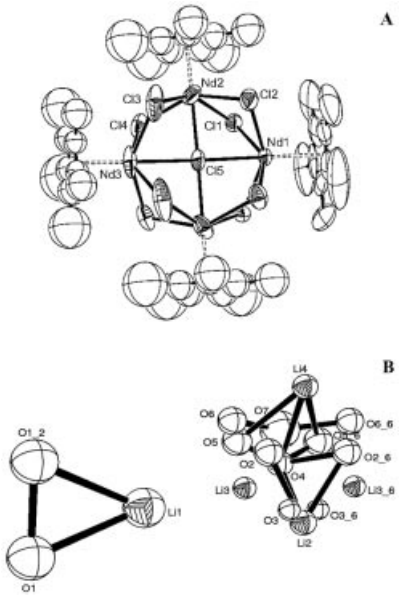


Figure 2. ORTEP representation (30% probability) of the molecular structure of compound **3**. (A) Side view of the anionic cluster; hydrogen atoms were removed for clarity. (B) Top view of both cationic microstructures: the ordered $LiO_2^+$ (left) and the disordered $LiO_2^+/Li_2O/O_2$ cluster fragment. Selected bond lengths [Å] and angles [°]: Nd1–Cl1 2.877, Nd–Cp*(CNT) 2.414, Nd1–Cl2 2.825, Nd1–Cl5 2.875, O1–Li1 1.943, Nd1–Nd2 4.090, O1–O1_2 1.534; Nd1–Cl5–Nd2 90.75, Nd2–Cl5–Nd3 89.17, Nd1–Cl1–Nd2 91.03, Nd1–Cl2–Nd2 92.32, O1–Li1–O1_2 46.87.

 © 2007 Wiley-VCH Verlag GmbH & Co. KGaA, Weinheim 

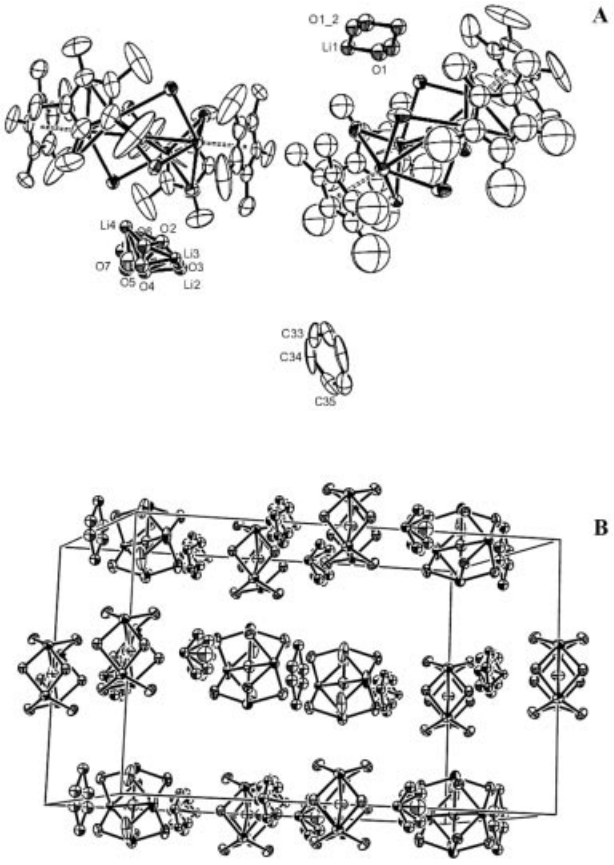


Figure 3. ORTEP representation (30% probability) of (A) the two different cluster units of complex **3**, along with the solvent molecule and the two microstructures of $LiO_2^+$ and (B) the unit cell of complex **3**. Cp* methyl groups and hydrogen atoms were removed for clarity.

no humidity and hence no hydrolysis products were observed. The presence of molecular oxygen can also be inferred from the second cationic microstructure, which shows a highly disordered $Li_3O_5^+$ fragment. This results from the combination of the following motifs: $LiO_2^+$, $Li_2O$, and $O_2$. The formulation of these fragments is postulated according to the occupancies of the different atoms, bond length, angles, and total charge of the unit cell.[13]

Addition of dry oxygen to the reaction mixture allowed us to synthesize complex **3**, although the yield was not predictable. It seems that the most important factor is the concentration of the oxygen dissolved in the solution and not its total amount in the Schlenk tube.

As we have reported,[6] the reaction of the analogous complex **4**, $Cp^*_2SmCl{\cdot}MgCl_2{\cdot}2thf$ with HBcat yields a macrocyclic inclusion complex. To exclude the option of macrocycle formation, we turned our attention to pinacolborane (HBpin), which was found to be inactive in the macrocycle formation reaction.[6a] The reaction of complexes **1** or **4** with excess HBpin at room temperature afforded crystals of the isostructural clusters **5a** (Ln = Nd) or **5b** (Ln = Sm), respectively [Equations (2a) and (2b)], which were characterized by X-ray crystallography. Both clusters crystallize in the monoclinic space group *C*2/*c* with almost

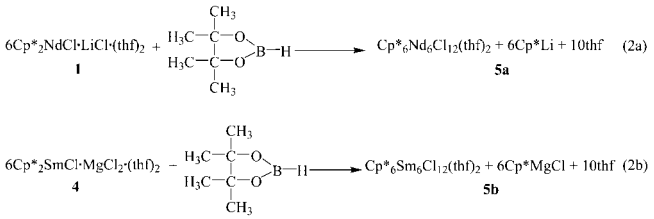


Table 2. Crystallographic data for complexes **5a** and **5b**.

| | **5a** | **5b** |
|---|---|---|
| Color | pale blue | pale red |
| Size [mm$^3$] | $0.12\times0.12\times0.08$ | $0.12\times0.12\times0.08$ |
| Chemical formula | $C_{68}H_{106}Cl_{12}Nd_6O_2$ | $C_{68}H_{106}Cl_{12}O_2Sm_6$ |
| Fw | 2246.37 | 2283.09 |
| Crystal system | monoclinic | monoclinic |
| Space group | *C*2/*c* | *C*2/*c* |
| *T* [K] | 230.0(1) | 240.0(1) |
| *a* [Å] | 25.9700(8) | 25.8930(11) |
| *b* [Å] | 20.1800(6) | 20.1770(10) |
| *c* [Å] | 17.2250(7) | 17.2360(9) |
| *α* [°] | 90 | 90 |
| *β* [°] | 114.213(14) | 114.135(3) |
| *γ* [°] | 90 | 90 |
| *V* [Å$^3$] | 8233.0(5) | 8217.7(7) |
| *Z*, $D_{calc}$ [g cm$^{-3}$] | 4, 1.812 | 4, 1.845 |
| *μ* (Mo-$K_α$) [mm$^{-1}$] | 4.142 | 4.646 |
| *θ* range [°] | 1.33–21.11 | 1.59–25.04 |
| Limiting indices | $-26 \le h \le 26$; | $-30 \le h \le 29$; |
| | $-18 \le k \le 20$; | $-22 \le k \le 24$; |
| | $-17 \le l \le 17$ | $-20 \le l \le 20$ |
| Collected reflns./unique | 8114/4465 | 25676/7259 |
| *R*(int) | 0.0452 | 0.2122 |
| Parameters | 412 | 398 |
| GOF on $F^2$ | 0.932 | 0.794 |
| Final *R* indices | $R_1 = 0.0343$, | $R_1 = 0.0567$, |
| $[I > 2\sigma(I)]$ | $wR_2 = 0.0637$ | $wR_2 = 0.0959$ |
| $\rho_{min}$, $\rho_{max}$ [e Å$^{-3}$] | –0.415, 0.528 | –1.174, 1.333 |

identical unit cells (see Table 2 for complete crystallographic data and Figure 4 for selective bond lengths and angles). As depicted in Figure 4, compound **5** is a hexameric cluster built from two symmetric units, which are bonded by two $\mu_2$-Cl ions (Cl6 and Cl6*). Each unit is built from three Ln atoms, two of which are bonded to the two $\mu_2$-Cl ligands, while the third Ln atom has a coordinated thf ligand, maintaining the stereoelectronic saturation of the cluster. In each $(Cp^*Ln)_3Cl_5$ unit, there are two $\mu_3$ (Cl1 and Cl4) and three $\mu_2$ (Cl2, Cl3, and Cl5) bridging chlorido ligands. The structure of the fragment can be regarded as a hexagonal plane of alternating Ln and Cl atoms and two apical Cl ligands bonded to the metal. In the overall structure of the cluster, the six Ln centers adopt a chairlike geometry with Cp*Ln(thf) ends, similar to that of the mixed chlorido/borohydride clusters presented by Visseaux et al.[4] As can be expected from the smaller ionic radii of Sm relative to Nd, the bond lengths in **5b** are slightly shorter than those in **5a**.[14] Regarding the role of borane in the formation of the clusters, we suggest that the thf ligands of complexes **1** and **4** are removed by the borane in order to coordinate

 © 2007 Wiley-VCH Verlag GmbH & Co. KGaA, Weinheim 

the boron atom instead of the Li or Mg salt. Attempts to determine the fate of the Cp* ligation were unsuccessful. The removal of LiCl/$MgCl_2$ and solvent from the starting complex by the strong Lewis acidic borane induces the coordinative unsaturation of the resulting complex. In addition, we propose that the borane fragment has a role in trapping one of the Cp* ligands of the starting complex. These two factors increase the tendency of the remaining Cp*LnCl fragments to form clusters. Attempts to perform the reaction without a borane did not lead to products but rather resulted in decomposition.

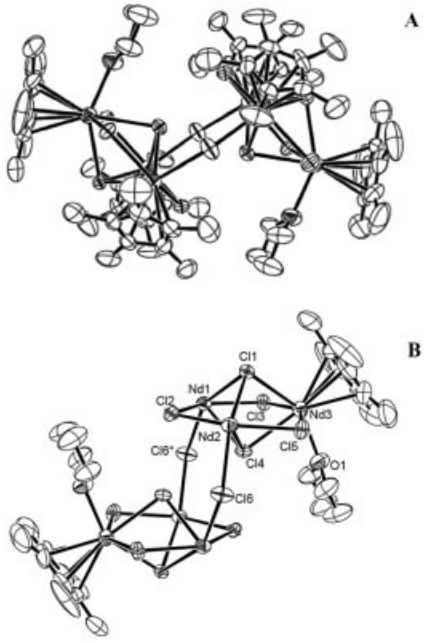


Figure 4. ORTEP representation (50% probability) of the molecular structure of complex **5a**: (A) full structure and (B) with removal of hydrogen atoms and Cp* ligands (bonded to Nd1 and Nd2) for clarity. Selected bond lengths [Å] and angles [°]: Nd–Cl1 2.932, Nd–Cp*(CNT) 2.414(9), Nd–Cl4 2.898(2), Nd1–Cl2 2.795(2), Nd1–Cl3 2.834(2), Nd1–Cl6* 2.758(2), Nd2–Cl6 2.772(2), Nd3–Cl3 2.784(2), Nd3–O1 2.458(6), Nd–Nd 4.122(5); Nd1–Cl1–Nd2 88.58(12), Nd1–Cl4–Nd2 91.59(6), Nd1–Cl2–Nd2 95.81(6), Nd2–Cl6–Nd1* 136.60(9). Complex **5b** shows an isostructural cluster. Selected bond lengths [Å] and angles [°] for complex **5b**: Sm–Cl1 2.884, Sm–Cp*(CNT) 2.361(15), Sm–Cl4 2.912(4), Sm1–Cl2 2.789(3), Sm1–Cl3 2.825(4), Sm1–Cl6* 2.743(3), Sm2–Cl6 2.769(4), Sm3–Cl3 2.771(4), Sm3–O1 2.435(10), Sm–Sm 4.101(7); Sm1–Cl1–Sm2 88.66(9), Sm1–Cl4–Sm2 91.63(9), Sm1–Cl2–Sm2 95.63(9), Sm3–Cl6–Sm1* 137.05(14).

## Conclusion

In conclusion, we have presented four new mono-Cp* lanthanide clusters, composed of tetramers or hexamers with chloride ions as the bridging units of the cluster. These complexes are formed by the reaction of a borane with the complexes containing chlorido ligands. In addition, the crystal structure of the unique and unusual $LiO_2^+$ counterion was presented.

## Experimental Section

**Instruments and Methods:** All manipulations of air-sensitive materials were performed with the rigorous exclusion of oxygen and moisture in flamed Schlenk-type glassware on a dual-manifold Schlenk line, in a Schlenk line interfaced with a high-vacuum ($10^{-5}$ Torr) line, or in a nitrogen-filled Vacuum Atmospheres glovebox with a medium-capacity recirculator (1–2 ppm $O_2$). Argon and nitrogen were purified by passage through a MnO oxygen removal column and a Davison 4 Å molecular sieves column. NMR spectra were recorded with Avance 300 and Avance 500 spectrometers. Chemical shifts for $^1$H NMR and $^{13}$C NMR are referenced to internal solvent resonances and are reported relative to tetramethylsilane. The NMR experiments were conducted in Teflon valve-sealed tubes (J. Young) after vacuum transfer of the liquids in a high vacuum line.

**Reagents and Standards:** Hydrocarbon solvents [$D_8$]thf, [$D_6$]benzene, and [$D_8$]toluene (Aldrich) were distilled under nitrogen from over a Na/K alloy. All solvents for vacuum line manipulations were stored in vacuo over Na/K alloy in resealable bulbs. $NdCl_3$ (Aldrich) was degassed and stored under argon. Catecholborane (HBcat) and pinacolborane (Hbcat) (Aldrich) were used without purification. Cp*$_2$NdCl·LiCl·2thf[15] and Cp*$_2$SmCl·$MgCl_2$·2thf[6c] were prepared according to published procedures.

**Crystal Structure Determination – General Procedure:** Single crystals immersed in Parathone-N oil were quickly removed with a glass rod and mounted on a KappaCCD diffractometer under a cold stream of nitrogen at 230 K. Data collection was carried out with monochromatized Mo-$K_\alpha$ radiation by using omega and phi scans to cover the Ewald sphere.[16] Accurate cell parameters were obtained with complete collections of intensities and these were corrected in the usual way.[17,18] The structures were solved by direct methods and completed by using successive Fourier difference maps.[19] Refinements were performed anisotropically with respect to the non-hydrogen atoms.[20] Hydrogen atoms were placed at calculated positions and refined by using the riding model until convergence was reached. Figures were prepared with ORTEP.[21]

**Syntheses**

**Cp*$_6$Nd$_6$Cl$_{15}$Li$_3$(thf)$_3$ (2):** A Schlenk tube was charged in the glovebox with Cp*$_2$NdCl·LiCl·2thf (35 mg, 0.056 mmol) and HBcat (80 mg, 0.67 mmol). After 24 h at room temperature, the large, cubelike, blue crystalline precipitate was isolated (15 mg, 86%) and characterized by single-crystal X-ray diffraction. $^1$H NMR (500 MHz, [$D_8$]thf, 298 K): $\delta$ = 8.23 (s, 15 H, $C_5Me_5$) ppm. $^{13}$C NMR (125 MHz, [$D_8$]thf, 298 K): $\delta$ = 243.6 (s, $C_5$Me$_5$), –14.7 (s, $C_5Me_5$) ppm. $C_{72}H_{114}Cl_{15}Li_3Nd_6O_4$ (2483.5): calcd. C 34.79, H 4.59, Cl 21.44; found C 35.02, H 4.12, Cl 21.21.

**[Cp*$_4$Nd$_4$Cl$_9$]$_2$[$LiO_2$]$_2$·$Li_2O$·$O_2$·3$C_6H_6$ (3):** A Schlenk tube was charged in the glovebox with Cp*$_2$NdCl·LiCl·2thf (35 mg, 0.056 mmol), HBcat (80 mg, 0.67 mmol), and toluene (1 mL) and then heated to 110 °C for a few days. After the heating period, the white precipitate was removed by filtration to leave behind a clear blue solution. The solvent was removed by vacuum, and benzene was added to the tube by vacuum transfer. The tube was allowed to stand at high temperature for 24 h, affording a few pale blue crystals, which were isolated (10 mg, 44%) and characterized by single-crystal X-ray diffraction. $^1$H NMR (500 MHz, [$D_8$]thf, 298 K): $\delta$ = 8.55 (s, 15 H, $C_5Me_5$) ppm. Attempts to introduce measured amounts of dry oxygen resulted in the same product but in lower yields. When a measured amount or regular-moisture air was introduced into the reaction mixture, no product was observed.

 © 2007 Wiley-VCH Verlag GmbH & Co. KGaA, Weinheim 

$C_{98}H_{138}Cl_{18}Li_4Nd_8O_7$ (3245.6): calcd. C 36.24, H 4.25, Cl 19.68; found C 35.02, H 4.09, Cl 20.67.

**[Cp*$_3$Nd$_3$Cl$_5$(thf)]$_2$(μ$_2$-Cl)$_2$ (5a):** A Schlenk tube was charged in the glovebox with Cp*$_2$NdCl·LiCl·2thf (35 mg, 0.056 mmol) and HBpin (80 mg, 0.62 mmol). After 72 h at room temperature, the blue crystalline precipitate was isolated (18 mg, 86%) and characterized by single-crystal X-ray diffraction. $^1$H NMR (500 MHz, [D$_8$]thf, 298 K): $\delta$ = 7.89 (s, 15 H, C$_5$*Me*$_5$) ppm. $^{13}$C NMR (125 MHz, [D$_8$]thf, 298 K): $\delta$ = 240.5 (s, *C*$_5$Me$_5$), –13.2 (s, C$_5$*Me*$_5$) ppm. $C_{68}H_{106}Cl_{12}Nd_6O_2$ (2246.37): calcd. C 36.32, H 4.71, Cl 18.96; found C 35.94, H 4.47, Cl 19.11.

**[Cp*$_3$Sm$_3$Cl$_5$(thf)]$_2$(μ$_2$-Cl)$_2$ (5b):** A Schlenk tube was charged in the glovebox with Cp*$_2$SmCl·MgCl$_2$·2thf (35 mg, 0.054 mmol) and HBpin (80 mg, 0.62 mmol). After 72 h, the colorless crystalline precipitate was isolated (18 mg, 87.8%) and characterized by single-crystal X-ray diffraction. $^1$H NMR (500 MHz, [D$_8$]thf, 298 K): $\delta$ = 2.45 (s, 15 H, C$_5$*Me*$_5$) ppm. $^{13}$C NMR (125 MHz, [D$_8$]thf, 298 K): $\delta$ = 113.8 (s, *C*$_5$Me$_5$), 16.3 (s, C$_5$*Me*$_5$) ppm. $C_{68}H_{106}Cl_{12}O_2Sm_6$ (2283.09): calcd. C 35.74, H 4.64, Cl 18.65; found C 36.01, H 4.35, Cl 18.11.

**Crystal Structure Analysis of Complex 3:** A single pale blue crystal was removed from Parathone oil and mounted on the KappaCCD diffractometer under a cold stream of nitrogen at 230 K. Unit cell parameters were determined with 9306 reflections by using Mo-$K_\alpha$ radiation. The complete set of 15080 reflections were collected and processed in the usual way. The structure was solved by direct methods with the program package 'maXus'. After the correct space group *C*2/*m* was established, Fourier maps revealed the positions of the heavy atoms as follows: Nd1, Nd3, and Cl5 on the mirror plane at $y$ = 0 site *i*, Cl6 and Cl7 on the mirror plane at $y$ = 0.5 site *i*, Cl9 on site 2/*m* (*b*) and Nd2, Nd4, Cl1, Cl2, Cl3, Cl4, and Cl8 in general positions. The positions of these heavy atoms were refined anisotropically by using the SHELXL97 program package. The carbon atoms of the Cp* groups found from Fourier difference maps were refined anisotropically, whereas the positions of the methyl hydrogen atoms were calculated and shifted by using the riding model.

At this stage it was clear that the unit cell contains six cluster units of $Nd_4Cl_9Cp^*_4$ bearing a charge of –1 by assuming a valence of +3 for the Nd cation. One cluster unit defined by Nd1–Nd3 is located on a mirror plane at $y$ = 0, whereas a second cluster defined by Nd4 occupies a 2/*m* site (*b*), and the overall number of clusters is (½ + ¼)·8 = 6. Careful examination of the difference maps revealed numerous small peaks which could not be assigned easily as $Li^+$ counterions. Three peaks with occupancies of ½ were identified as half benzene rings located on the mirror plane at $y$ = 0. The remaining peaks were found to be grouped into two regions, and they were analyzed by considering the interaction of disordered $Li^+$ ions with oxygen molecules and charged oxygen species. After tedious attempts, the following occupancies were given to the Li and oxygen atoms by constraining the total charge, keeping reasonable geometries for the Li–O species, and meaningful $U_{iso}$ values for the various atomic positions (Table 3).

This model fulfils the following formula per unit cell: $6LiO_2{\cdot}Li_2O{\cdot}O_2$ or $LiO_2{\cdot}Li_2O{\cdot}O_2$ per cluster unit. The $LiO_2$ unit grouped separately is located on a mirror plane and is attributed to the interaction of $Li^+$ with neutral $O_2$. The second region of grouped peaks contains $Li_2O$ composed of $Li^+$ and $O^{-2}$. There is also $O_2$ as a neutral species. In this model only one $Li^+$ neutralizes the charge of one cluster unit.

CCDC-643835, 643836, 643843, 643844 contain the supplementary crystallographic data for this paper. These data can be obtained free of charge from The Cambridge Crystallographic Data Center via http://www.ccdc.cam.ac.uk/data_request/cif.

Table 3. List of atoms and occupancies in one of the counterions for complex **3**.

| Atom | Occupancy | $U_{iso}$ | Number of atoms in the unit cell |
|---|---|---|---|
| Li1 | 0.25 | 0.072 | 2 |
| Li2 | 0.25 | 0.056 | 2 |
| Li3 | 0.25 | 0.044 | 2 |
| Li4 | 0.25 | 0.055 | 2 |
| O1 | 0.50 | 0.087 | 4 |
| O2 | 0.50 | 0.069 | 4 |
| O3 | 0.125 | 0.038 | 1 |
| O4 | 0.25 | 0.062 | 2 |
| O5 | 0.25 | 0.077 | 2 |
| O6 | 0.125 | 0.0751 | – |
| O7 | 0.125 | 0.141 | – |

## Acknowledgments

This research was supported by the Israel Science Foundation Administered by the Israel Academy of Science and Humanities under Contract 1069/05.

[1] a) F. Bonnet, M. Visseaux, A. Pereira, D. Barbier-Baudry, *Macromolecules* **2005**, *38*, 3162–3169; b) F. Bonnet, M. Visseaux, D. Barbier-Baudry, E. Vigier, M. M. Kubicki, *Chem. Eur. J.* **2004**, *10*, 2428–2434 and references cited therein; c) R. D. Miotti, M. De-Souza, P. Alessandra, S. Icaro, U. Schuchardt, W. De-Oliveira, *J. Alloys Compd.* **2002**, *344*, 92–95; d) Z. Hou, Y. Wakatsuki, *Coord. Chem. Rev.* **2002**, *231*, 1–22.

[2] S. Arndt, J. Okuda, *Chem. Rev.* **2002**, *102*, 1953–1976 and references therein.

[3] For a review on self-assembly in organolanthanide chemistry and the formation of rings and clusters see: R. Anwander, *Angew. Chem. Int. Ed.* **1998**, *37*, 599–602.

[4] F. Bonnet, M. Visseaux, D. Barbier-Baudry, A. Hafid, E. Vigier, M. M. Kubicki, *Inorg. Chem.* **2004**, *43*, 3682–3690.

[5] W. P. Kretschmer, J. H. Teuben, S. I. Troyanov, *Angew. Chem. Int. Ed.* **1998**, *37*, 88–90.

[6] a) E. Barnea, T. Andrea, M. Kapon, M. S. Eisen, *J. Am. Chem. Soc.* **2004**, *126*, 5066–5067; b) E. Barnea, T. Andrea, M. Kapon, M. Botoshansky, C. Averbuj, I. Goldberg, M. S. Eisen, *From Boron Containing Macrocyclic Complexes to Organometallic Clusters. Proceedings of the 71st Annual Meeting*, Israel Chem. Soc., Tel Aviv, Israel, February 27–28, **2006**, p.155. For the synthesis of Cp*$_2$SmCl·MgCl$_2$·2thf see: c) W. J. Evans, D. K. Drummond, J. W. Grate, H. Zhang, J. L. Atwood, *J. Am. Chem. Soc.* **1987**, *109*, 3928–3936. This complex was prepared by using Cp*MgCl instead of Cp*Li and by the procedure reported in ref.[6b] with similar yields and spectral properties.

[7] a) N. Mahe, O. Guillou, C. Daiguebonne, Y. Gerault, A. Caneschi, C. Sangregorio, J. Y. Chane-Ching, P. E. Car, T. Roisnel, *Inorg. Chem.* **2005**, *44*, 7743–7750; b) G. Helgesson, S. Jagner, O. Poncelet, L. G. Hubert-Pfalzgraf, *Polyhedron* **1991**, *10*, 1559–1564.

[8] See ref.[5] and R. A. Anderson, D. H. Templeton, A. Zalkin, *Inorg. Chem.* **1978**, *17*, 1962–1965.

[9] a) G. X. Jin, Y. Cheng, Y. Lin, *Organometallics* **1999**, *18*, 947–949; b) G. X. Jin, Y. Cheng, Y. Lin, *Organometallics* **1999**, *18*, 5735; c) W. J. Evans, G. W. Rabe, M. A. Ansari, J. W. Ziller, *Angew. Chem. Int. Ed. Engl.* **1994**, *33*, 2110–2111.

[10] W. J. Evans, C. A. Seibel, J. W. Ziller, *J. Am. Chem. Soc.* **1998**, *120*, 6745–6752.

 © 2007 Wiley-VCH Verlag GmbH & Co. KGaA, Weinheim 

[11] For examples of tetrameric lanthanide clusters bearing a central $\mu_4$-heteroatom see: a) R. Wang, Z. Zheng, Q. D. Liu, S. Wand, *Inorg. Synth.* **2004**, *34*, 184–187; b) Z. Xie, S. Wang, Q. Yang, T. C. W. Mak, *Organometallics* **1999**, *18*, 1578–1579; c) S. Gao, L. Li, G. Xu, *Zhongguo Xitu Xuebao* **1993**, *11*, 8–12; d) J. Guan, Q. Shen, J. Hu, Y. Lin, *Jiegou Huaxue* **1990**, *9*, 184–187; e) J. Guan, Q. Shen, J. Hu, Y. Lin, *Jiegou Huaxue* **1992**, *11*, 77; f) X. Li, J. Liu, S. Jin, Y. Lin, G. Liu, *Jiegou Huaxue* **1991**, *10*, 60–66; g) P. L. Watson, T. H. Tulip, I. Williams, *Organometallics* **1990**, *9*, 1999–2009. Central $\mu_5$-heteroatom clusters are also known. See: h) S. Banerjee, L. Huebner, M. D. Romanelli, G. A. Kumar, R. E. Riman, T. J. Emge, J. G. Brennan, *J. Am. Chem. Soc.* **2005**, *127*, 15900–15906; i) R. Wang, H. D. Selby, H. Liu, M. D. Carducci, T. Jin, Z. Zheng, J. W. Anthis, R. J. Staples, *Inorg. Chem.* **2002**, *41*, 278–286; j) M. Kritikos, M. Moustiakimov, M. Wijk, G. D. Westin, *Dalton Trans.* **2003**, 1931–1938; k) R. Wang, H. Liu, M. D. Carducci, T. Jin, C. Zheng, Z. Zheng, *Inorg. Chem.* **2001**, *40*, 2743–2750 and references therein.

[12] S. V. O'Neil, H. F. Schaefer III, C. F. Bender, *J. Chem. Phys.* **1973**, *59*, 3608–3611.

[13] See the Experimental Section for the complete crystallographic analysis of complex **3**.

[14] R. D. Shannon, *Acta Crystallogr., Sect. A* **1976**, *32*, 751–767.

[15] G. Jeske, H. Lauke, H. Mauermann, P. N. Swepston, H. Schumann, T. J. Marks, *J. Am. Chem. Soc.* **1985**, *107*, 8091–8103.

[16] Data collection: *Collect*, Nonius KappaCCD Server Software, Nonius BV, Delft, the Netherlands, **1997**.

[17] Cell refinement: *DENZO-SMN*, Z. Otwinowski, W. Minor, *Methods Enzymol.* **1997**, *276*, 307–326.

[18] Data reduction: Z. Otwinowski, W. Minor, *HKL Denzo and Scalepack*, **1997**.

[19] S. Mckay, C. J. Gilmore, C. Edwards, M. Tremayne, N. Stuart, K. Shankland, *"maXus": A Computer Program for the Solution and Refinement of Crystal Structures from Diffraction Data*, University of Glasgow, Scotland, UK, Nonius BV, Delft, The Netherlands and McScience Co. Ltd., Yokohama, Japan, **1998**.

[20] G. M. Sheldrick, *SHELXL97*, Program for the refinement of crystal structures, University of Göttingen, Germany, **1997**.

[21] *ORTEP: TEXRAY Structure Analysis Package*, Molecular Structure Corporation, MSC, 3200 Research Forest Drive, The Woodlands, TX 77381, USA, **1999**.

Received: December 10, 2006
Published Online: August 9, 2007

 © 2007 Wiley-VCH Verlag GmbH & Co. KGaA, Weinheim

**The EUChemSoc Societies have taken the significant step into the future by merging their traditional journals, to form two leading chemistry journals, the *European Journal of Inorganic Chemistry* and the *European Journal of Organic Chemistry.* Three further EUChemSoc Societies (Austria, Czech Republic and Sweden) are Associates of the two journals.**

## COVER PICTURE

**The cover picture shows** unique examples of homo- and heterochiral, dimeric metal capsules resulting from the self-assembly of two helical, bowl-shaped tetranuclear copper(II) complexes that encapsulate different anions in the solid state, like pearls in an oyster (shown as the background). This kind of self-assembled, coordination-bonded motifs are a major topic in metallosupramolecular chemistry because of their binding capabilities and associated host–guest chemistry. However, their magnetic properties are largely unexplored, and here we provide one of the rare magnetic studies on these host–guest systems. For more details on the combined structural and magnetic investigations of this class of synthetic "oyster" molecules, see the article by F. Lloret, Y. Journaux et al. on p. 4569ff.

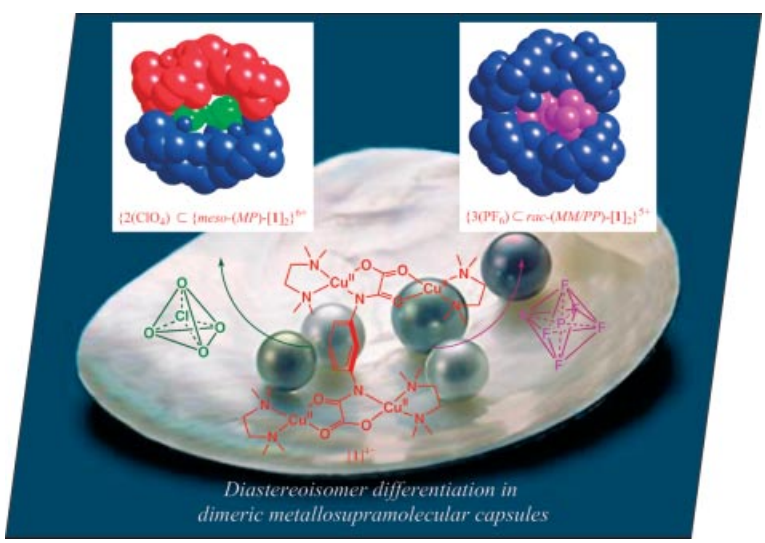


 © 2007 Wiley-VCH Verlag GmbH & Co. KGaA, Weinheim 

# CONTENTS

## MICROREVIEW


### Controlled Solid-State Reactivity

**D.-K. Bučar, G. S. Papaefstathiou, T. D. Hamilton, Q. L. Chu, I. G. Georgiev, L. R. MacGillivray* ..... 4559–4568**

Template-Controlled Reactivity in the Organic Solid State by Principles of Coordination-Driven Self-Assembly

**Keywords:** Self-assembly / Dimerization / Solid-state reactivity / Hydrogen bonds

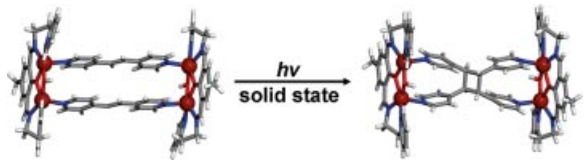


Principles and applications of solid-state reactivity by coordination-driven self-assembly are described. How the products obtained from templated solid-state reactions are used as organic building units of metal–organic frameworks and coordination capsules is also addressed.


## SHORT COMMUNICATIONS


### Crystal Engineering

**E. Pardo, K. Bernot, F. Lloret,* M. Julve, R. Ruiz-García, J. Pasán, C. Ruiz-Pérez, D. Cangussu, V. Costa, R. Lescouëzec, Y. Journaux* ..... 4569–4573**

Solid-State Anion–Guest Encapsulation by Metallosupramolecular Capsules Made from Two Tetranuclear Copper(II) Complexes

**Keywords:** Copper / Host–guest systems / Magnetic properties / Polynuclear complexes / Structure elucidation

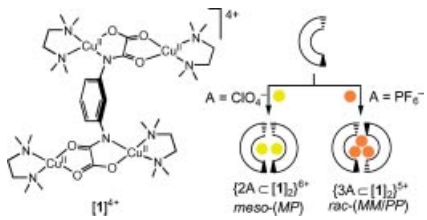


Like pearls within an oyster: a bowl-shaped cationic tetranuclear copper(II) oxamato complex with a helical conformation self-assembles in the solid state to form dimeric molecular capsules, either hetero- (*MP*) or homochiral (*MM*/*PP*), where two perchlorate or three hexafluorophosphate anions are hosted.

### Tetranuclear Copper Cubane

**B. Abarca,* R. Ballesteros, M. Chadlaoui, C. R. de Arellano, J. A. Real* ..... 4574–4578**

[(Pyridylcarbonyl)pyridyl]triazolopyridines, Useful Ligands for the Construction of Polynuclear Coordination Compounds – Synthesis, Crystal Structure and Magnetic Properties of a Novel Tetranuclear Copper(II) Cubane

**Keywords:** Polydentate ligands / Triazolopyridine ligands / Copper(II) complexes / Tetranuclear complexes / Molecular magnetism

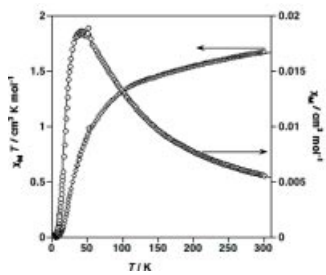


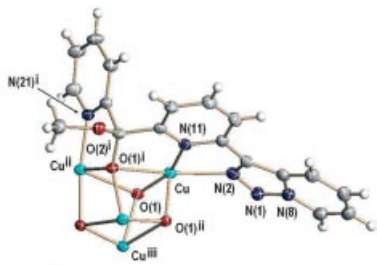


A new tetranuclear cubane $Cu_4O_4$ complex with $S_4$ symmetry has been synthesised from assembly of $Cu^{II}$ ions and the polydentate ligand (pyridin-2-yl){6-([1,2,3]triazolo[1,5-*a*]pyridin-3-yl)pyridin-2-yl}methanone. Its crystal structure and magnetic properties have been analysed.


 © 2007 Wiley-VCH Verlag GmbH & Co. KGaA, Weinheim 

## Chromium Mixed Chalcogenide

Chromium oxyselenide was synthesised by chemical vapor synthesis.

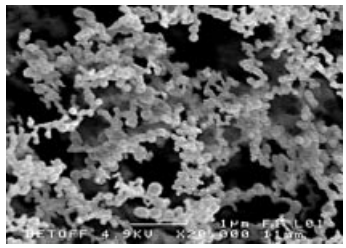

**N. D. Boscher, C. J. Carmalt, A. G. Prieto, Q. A. Pankhurst, R. G. Palgrave, I. P. Parkin* ..... 4579–4582**

Synthesis and Charaterisation of Chromium Oxyselenide ($Cr_2Se_{0.7}O_{2.3}$) Formed from Chemical Vapour Synthesis: A New Antiferromagnet

**Keywords:** Chemical vapour synthesis / Chromium oxyselenide / Antiferromagnet

## f-Block Element Spin–Spin Coupling

An f-block-element–f-block-element NMR spin–spin coupling pattern is observed for the first time, and the relevance of such investigations in understanding dimer equilibria and rearrangement chemistry of rather bulky structural ensembles is discussed.

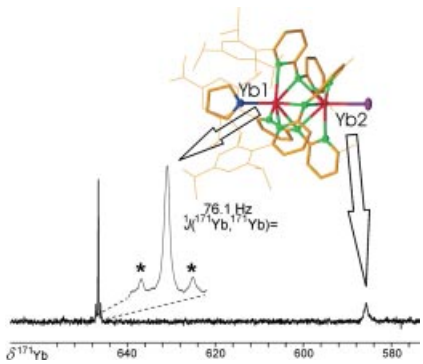


**A. M. Dietel, O. Tok, R. Kempe* ..... 4583–4586**

f-Block-Element–f-Block-Element NMR Spin–Spin Coupling

**Keywords:** Amido ligands / Bimetallic complexes / Dynamic N ligands / NMR spectroscopy / Ytterbium

## The Chiral Grail

Chiral calixarene-based diphosphite ligands **3a**–**d** have been obtained via lower-rim functionalisation of the *p*-*tert*-butylcalix[4]-arene core. High enantiomeric excesses (up to 94 %) and good activities were obtained in the rhodium-catalyzed asymmetric hydrogenation of prochiral olefins with TADDOL-containing diphosphites **3c**,**d**.

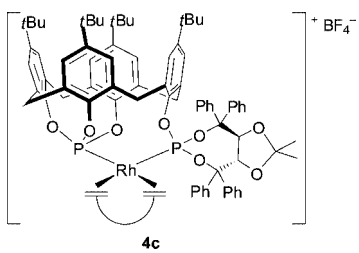


**4c**

**A. Marson, Z. Freixa, P. C. J. Kamer,* P. W. N. M. van Leeuwen* ..... 4587–4591**

Chiral Calix[4]arene-Based Diphosphites as Ligands in the Asymmetric Hydrogenation of Prochiral Olefins

**Keywords:** Homogeneous catalysis / Stereoselective catalysis / Asymmetric hydrogenation / Calixarenes / Diphosphites

## 1D Water Cluster

$\{[Co(tart)(phen)]\cdot 6H_2O\}_n$ (**1**) (tart, tartrate dianion; phen, 1,10-phenanthroline) forms a 3D supramolecular network through π-π and H-bonding interactions. A variable-temperature magnetic study **1** has been carried out and the interpretation of the already reported $\{[Co(tart)(bpy)]\cdot 5H_2O\}_n$ (**2**) has been re-visited: both **1** and **2** show weak antiferromagnetic interaction.

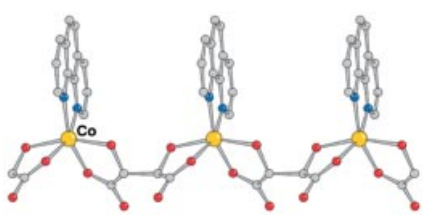


**S. C. Manna, E. Zangrando, J. Ribas,* N. Ray Chaudhuri* ..... 4592–4595**

Self-Assembled 1D Water Cluster in a Supramolecular Architecture of $Co^{II}$-(Tartrate)(Phenanthroline/Bipyridine): An Assessment of Magnetic Property

**Keywords:** Cobalt(II) / Tartrate / Magnetic properties / Water cluster

 © 2007 Wiley-VCH Verlag GmbH & Co. KGaA, Weinheim 

# CONTENTS

## FULL PAPERS


### Bi-1,2,3-triazole Ligand Properties

**U. Monkowius,* S. Ritter, B. König,* M. Zabel, H. Yersin ..... 4597–4606**

Synthesis, Characterisation and Ligand Properties of Novel Bi-1,2,3-triazole Ligands

**Keywords:** N ligands / Ligand design / Nitrogen heterocycles / Click reaction / 1,2,3-Triazole

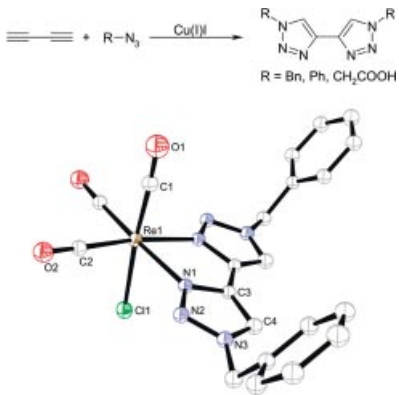


Three bi-1,2,3-triazoles (R-bta; R = Bn, Ph, $CH_2COOH$) were synthesised by a $Cu^I$-catalysed "click" reaction to act as potential bidentate, nitrogen-based ligands. The ligand properties were probed by the preparation of $Ru^{II}$, $Cu^I$, and $Re^I$ complexes. X-ray crystallographic data are presented for the ligands and complexes as well as the results of electronic absorption spectroscopy.

### Tetrahedral Cobalt Complexes

**M. C. Aragoni, M. Arca, M. B. Carrea, A. Garau, F. A. Devillanova, F. Isaia,* V. Lippolis, G. L. Abbati, F. Demartin, C. Silvestru, S. Demeshko, F. Meyer ..... 4607–4614**

Tetrahedral $Co^{II}$ Complexes with $CoI_2O_2$ and $CoO_2S_2$ Cores – Crystal Structures of $[Co\{HN(OPPh_2)(SPPh_2)\text{-}O\}_2I_2]$ and $[Co\{N(OPPh_2)(SPPh_2)\text{-}O,S\}_2]$

**Keywords:** Cobalt / O,S ligands / Phosphanes / Sulfides / Density functional calculations / Magnetic properties

Two $Co^{II}$ complexes were synthesised with the ligand $HN(OPPh_2)(SPPh_2)$, which contains mixed hard (O) and soft (S) donor atoms. The X-ray crystal structures of these compounds show the presence of a $CoI_2O_2$ and a $CoO_2S_2$ core. The mutual conversion of the complexes is driven by the protonation/deprotonation of the imido nitrogen atoms.

### Phthalocyanine–Porphyrin Arrays

**X. Leng, D. K. P. Ng* ..... 4615–4620**

Axial Coordination of Porphyrinatocobalt(II) Complexes with Bis(pyridinolato)-silicon(IV) Phthalocyanines

**Keywords:** Phthalocyanines / Porphyrins / Axial coordination / UV/Vis spectroscopy

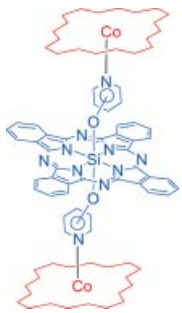


Bis(pyridinolato)silicon(IV) phthalocyanins axially bind to porphyrinatocobalt(II) complexes forming the novel hetero phthalocyanine–porphyrin dyads and triads. The binary complexes are stable and can thus be isolated and spectroscopically characterized.

### Water–Chloride Clusters

**M. N. Kopylovich,* E. A. Tronova, M. Haukka, A. M. Kirillov, V. Yu. Kukushkin,* J. J. R. Fraústo da Silva, A. J. L. Pombeiro* ..... 4621–4627**

Identification of Hexameric Water and Hybrid Water–Chloride Clusters Intercalated in the Crystal Hosts of (Imidoylamidine)-nickel(II) Complexes

**Keywords:** Crystal engineering / Hydrogen bonds / Imidoylamidine complexes / Water clusters / X-ray diffraction

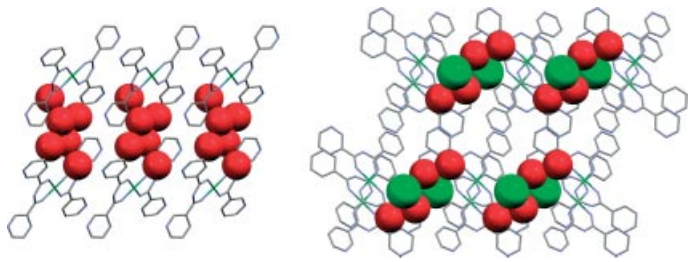

Bis(imidoylamidine)nickel(II) compounds reveal the presence, in the solid state, of geometrically similar, but distinct in composition, discrete $(H_2O)_6$ and $[(H_2O)_4(Cl)_2]^{2-}$ clusters. They occupy voids in the crystal cells and display extensive H-bonding interactions with monomeric metal–organic units, thus playing a key role in the formation of 3D H-bonded supramolecular assemblies.


 © 2007 Wiley-VCH Verlag GmbH & Co. KGaA, Weinheim 

## Pentacoordinate $Ni^{II}$ Complexes

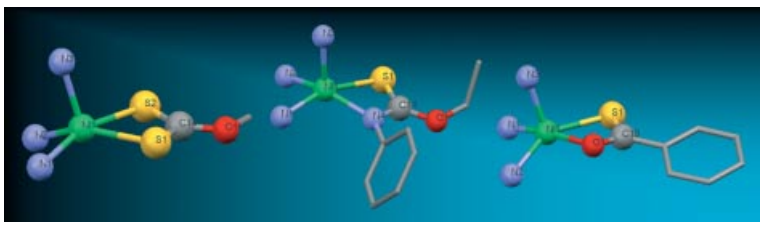

**M. D. Santana,* M. Sáez-Ayala, L. García, J. Pérez, G. García ..... 4628–4636**

Preparation of Thiocarboxylate, Thiocarbamate and Xanthate Complexes of Pentacoordinate Nickel(II): Insertion of Heterocumulenes Into Nickel(II) Hydroxido Complexes

**Keywords:** Nickel / Macrocyclic ligands / S ligands / Insertion / NMR spectroscopy / X-ray diffraction

The reactivity of hydroxido Ni complexes with $CS_2$ or PhCNS, in the presence of alcohols, to form *O*-alkyl dithiocarbonate (xanthate) or *O*-alkyl *N*-phenylthiocarbamate pentacoordinate $Ni^{II}$ complexes, respectively, was investigated. The thiocarboxylate complexes were also prepared by the acid–base reaction of these hydroxido complexes with the corresponding thioacid.

## C–N Bond Activation

**A. M. Arnaiz, A. Carbayo, J. V. Cuevas,* V. Diez, G. García-Herbosa, R. González, A. Martínez, A. Muñoz ..... 4637–4644**

Methylation of a Terdentate Schiff Base Ligand *NNO*-Coordinated to Palladium with Nitromethane

**Keywords:** Palladium / Henry reaction / Nucleophilic attack / Nitroaldol / Schiff bases

The reaction of the complex [Pd(κ$^3$-NN′O)-$CH_3$] [NN′O = 2-Py-CH=N-(*o*-$C_6H_4$)$O^-$] (**1a**) with nitromethane affords a mixture of two compounds in which methylation of the ligand can be observed. The methylation reaction is proposed to occur through nucleophilic attack of the nitronate anion on the iminic carbon atom. DFT calculations are presented in order to support a part of the mechanism of the reaction.

## Cross-Coupling Mechanisms

**N. Taccardi, R. Paolillo, V. Gallo, P. Mastrorilli,* C. F. Nobile, M. Räisänen, T. Repo ..... 4645–4652**

On the Mechanism of Palladium-Catalyzed Cross-Coupling of Diazonium Salts with Aryltrifluoroborates: A Combined ESI-MS/NMR Study

**Keywords:** Homogeneous catalysis / Metallacycles / Mass spectrometry / Cross-coupling / Diazo compounds

This mechanistic study on the palladium-catalysed cross-coupling reaction between aryldiazonium salts and aryltrifluoroborates combines the results obtained from $^{19}F$ NMR and ESI-MS studies.

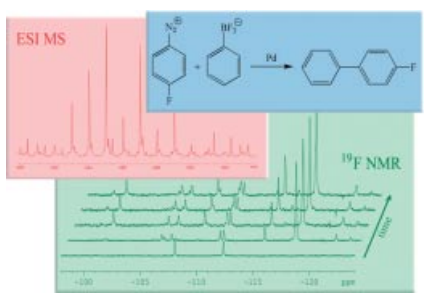


## Supramolecular Catalysis

**V. F. Slagt, P. Kaiser, A. Berkessel, M. Kuil, A. M. Kluwer, P. W. N. M. van Leeuwen, J. N. H. Reek* ..... 4653–4662**

Fine-Tuning Ligands for Catalysis Using Supramolecular Strategies

**Keywords:** Supramolecular catalysts / Self-assembly / Ligand effects / Phosphorus ligands / Porphyrinoids

Coordination chemistry has been used to prepare supramolecular ligands. The construction of these ligands is based on selective metal–ligand interactions, leading to well-defined catalyst assemblies. Important catalyst properties such as activity and (enantio)selectivity are fine-tuned by the building blocks used for the assembly formation.

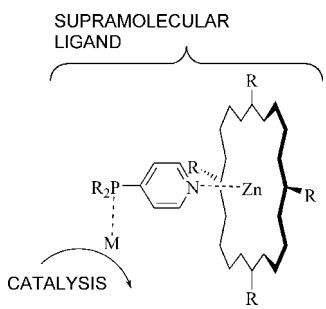


 © 2007 Wiley-VCH Verlag GmbH & Co. KGaA, Weinheim 

# CONTENTS


## Coupled Electron−Proton Transfer

**H. Sugimoto,* M. Tarumizu, H. Miyake, H. Tsukube ..... 4663−4668**

Synthesis and Characterization of Bis(dithiolene) Tungsten(VI), -(V), and -(IV) Complexes and Their Reactivities in Coupled Electron−Proton Transfer: A New Series of Active Site Models of Tungstoenzymes

**Keywords:** Bioinorganic chemistry / Enzyme models / Molybdenum / S ligands / Tungsten

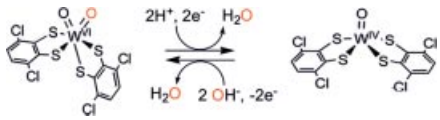


3,6-Dichloro-1,2-benzenedithiolate ($bdtCl_2$), $(Et_4N)_2[W^{VI}O_2(bdtCl_2)_2]$ {$(Et_4N)_2$[**1**]}, $(Et_4N)[W^{V}O(bdtCl_2)_2]$ {$(Et_4N)$[**2**]}, and $(Et_4N)_2[W^{IV}O(bdtCl_2)_2]$ {$(Et_4N)_2$[**3**]} were synthesized and characterized. The isomerization between the octahedral structures (Δ and Λ forms) of $(Bu_4N)_2$[**1**] was characterized by variable-temperature $^1H$ NMR spectroscopy. $(Et_4N)_2$[**1**] underwent an irreversible reduction at −2.1 V vs. SCEin $CH_3CN$ by coupled electron−proton transfer (CEPT) to yield $(Et_4N)_2$[**3**], while $(Et_4N)_2$[**3**] underwent an irreversible oxidation by the CEPT process at −0.27 V in the presence of 2 equiv. $Et_4NOH$ in $CH_3CN$ to yield $(Et_4N)_2$[**1**]. $(Et_4N)$[**2**] disproportionated into 0.5 equiv. $(Et_4N)_2$[**1**] and 0.5 equiv. $(Et_4N)_2$[**3**] when treated with 1 equiv. $Et_4NOH$ in $CH_3CN$.

## Ring-Expansion Reactions

**H. Helten, C. Neumann, A. Espinosa, P. G. Jones, M. Nieger, R. Streubel* ..... 4669−4678**

Evidence for Ligand-Centered Reactivity of a 17e Radical Cationic 2*H*-Azaphosphirene Complex

**Keywords:** Ligand-centered reactivity / Phosphorus heterocycles / Electron transfer

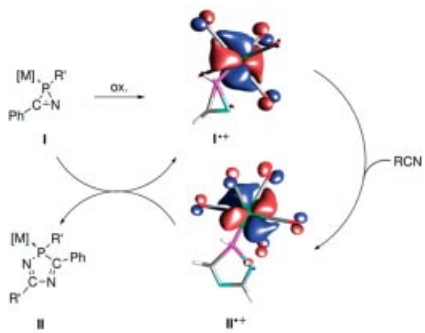


Experimental and theoretical investigations on the selective ring-expansion reactions of 2*H*-azaphosphirene complexes with nitriles are presented. The dependence on the minimum amount of single-electron transfer reagent and the selectivity on the donor abilities of the employed nitriles were also examined. The ligand-centered reactivity of a 17e radical cationic complex was elucidated.

## Heterobimetallic Complexes

**H. Zhang, S. Dechert, M. Linseis, R. F. Winter, F. Meyer* ..... 4679−4686**

Organometallic and Classical Coordination Sites in Highly Preorganized Pyrazolate-Based Hybrid Systems: The Mn/Ni Case

**Keywords:** Bridging ligands / Cyclopentadienyl ligands / Manganese / Nickel / Heterometallic complexes

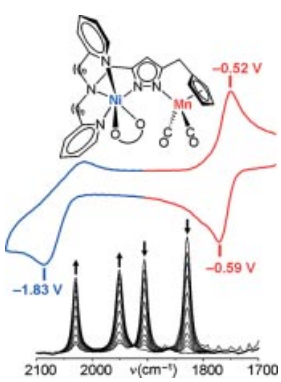


Ligand asymmetry in pyrazolate-bridged heterobimetallic complexes induces strict confinement of redox processes to either the organometallic Mn site or the Werner-type Ni site.

## KCl Flux Growth of Metal Oxides

**K. Teshima,* Y. Niina, K. Yubuta, T. Suzuki, N. Ishizawa, T. Shishido, S. Oishi ..... 4687−4692**

Environmentally Friendly Growth of Layered $K_4Nb_6O_{17}$ Crystals from a KCl Flux

**Keywords:** Flux growth / Environmental chemistry / Layered compounds / Photocatalyst

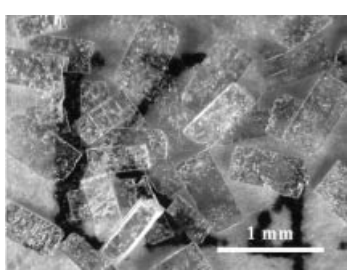


Environmentally friendly, high-quality, transparent, and colorless plate-like crystals of $K_4Nb_6O_{17}$ were successfully grown by the evaporation and cooling of a KCl flux.


 © 2007 Wiley-VCH Verlag GmbH & Co. KGaA, Weinheim 

EurJIC European Journal of Inorganic Chemistry

# CORRECTION

**Keywords:** Phosphane selenide dibromides / Heteronuclear NMR / Raman spectroscopy / X-ray structures / Bromine exchange / Ab initio calculations

The Bromination of Bulky Trialkylphosphane Selenides $R_2R'PSe$ (R, R′ = *i*Pr and/or *t*Bu) Studied by Physical and Computational Methods

**C. G. Hrib, F. Ruthe, E. Seppälä, M. Bätcher, C. Druckenbrodt, C. Wismach, P. G. Jones, W.-W. du Mont,* V. Lippolis, F. A. Devillanova, M. Bühl ..... 4693**

**If not otherwise indicated in the article, papers in issue 28 were published online on September 18, 2007**

 © 2007 Wiley-VCH Verlag GmbH & Co. KGaA, Weinheim

**The EUChemSoc Societies have taken the significant step into the future by merging their traditional journals, to form two leading chemistry journals, the *European Journal of Inorganic Chemistry* and the *European Journal of Organic Chemistry.* Three further EUChemSoc Societies (Austria, Czech Republic and Sweden) are Associates of the two journals.**

## COVER PICTURE

**The cover picture shows** unique examples of homo- and heterochiral, dimeric metal capsules resulting from the self-assembly of two helical, bowl-shaped tetranuclear copper(II) complexes that encapsulate different anions in the solid state, like pearls in an oyster (shown as the background). This kind of self-assembled, coordination-bonded motifs are a major topic in metallosupramolecular chemistry because of their binding capabilities and associated host–guest chemistry. However, their magnetic properties are largely unexplored, and here we provide one of the rare magnetic studies on these host–guest systems. For more details on the combined structural and magnetic investigations of this class of synthetic "oyster" molecules, see the article by F. Lloret, Y. Journaux et al. on p. 4569ff.

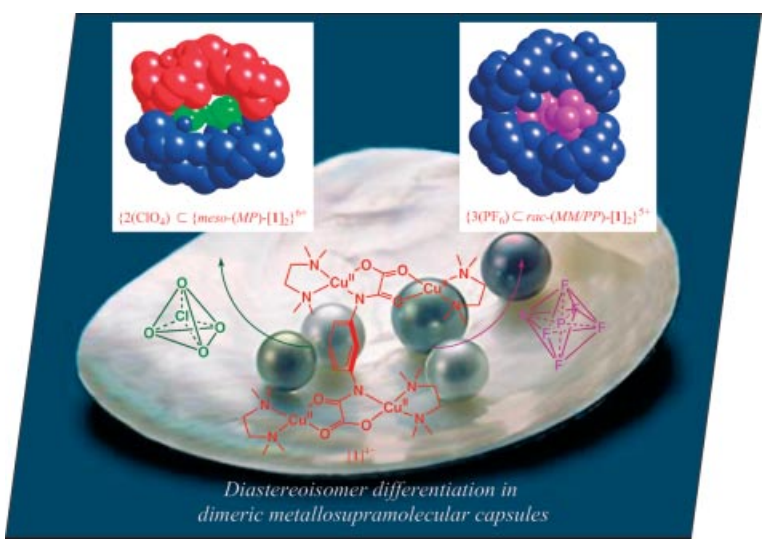


 © 2007 Wiley-VCH Verlag GmbH & Co. KGaA, Weinheim 

# SPOTLIGHTS …

## *Helical Structures*

M. Ikeda, S. Haraguchi, M. Numata, S. Shinkai*

**Controlled Stability of the Triple-Stranded Helical Structure of a β-1,3-Glucan with a Chromophoric Aromatic Moiety at a Peripheral Position**

*Chem. Asian J.*
DOI: **10.1002/asia.200700150**

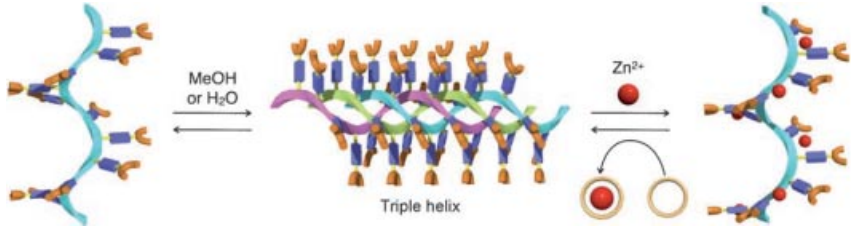


**Twisted nature**: A semiartificial β-1,3-glucan that bears chromophoric aromatic groups at its peripheral positions adopts a triple-stranded helical configuration in water- and methanol-rich dimethyl sulfoxide. The stability of this structure can be controlled by solvent composition and metal-ion binding.

## *Aptamers*

E. Friedrichs, F. C. Simmel*

**Controlling DNA Polymerization with a Switchable Aptamer**

*ChemBioChem*
DOI: **10.1002/cbic.200700296**

**Controllable biochemical reactions**. DNA polymerization by Taq polymerase can be controlled by switching an aptamer for Taq Pol between a binding and a nonbinding form.

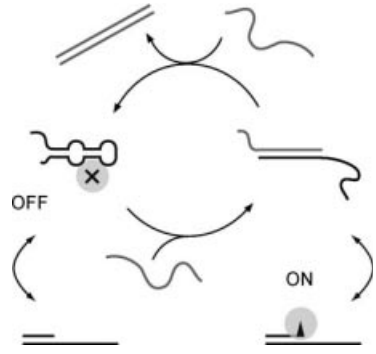


## *Semiconducting Nanocrystals*

A. Hofmann, C. Graf,* C. Boeglin, E. Rühl

**Magnetic and Structural Investigation of $Mn^{2+}$-Doped ZnSe Semiconductor Nanoparticles**

*ChemPhysChem*
DOI: **10.1002/cphc.200700050**

**Single manganese ions** are located in the bulk interior of Mn-doped ZnSe (ZnSe:Mn) nanoparticles, according to studies by X-ray magnetic circular dichroism (XMCD). This method is a powerful tool for exploring the local electronic environment of transition-metal ions and for the quantitative investigation of their magnetic properties. The picture shows the XMCD spectrum and a schematic of a single particle with stabilizing organic ligands (green).

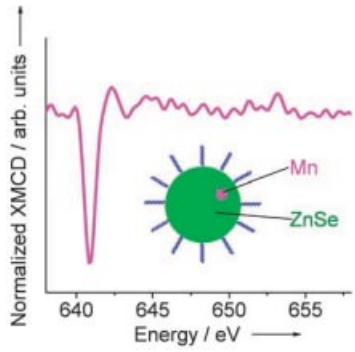


## *Antiviral Agents*

K. F. Adebambo, S. Zanoli, M. G. Thomas, R. Cancio, N. M. Howarth,* G. Maga*

***N*$^2$-Benzyloxycarbonylguan-9-yl Acetic Acid Derivatives as HIV-1 Reverse Transcriptase Non-Nucleoside Inhibitors with Decreased Loss of Potency Against Common Drug-Resistance Mutations.**

*ChemMedChem*
DOI: **10.1002/cmdc.200700045**

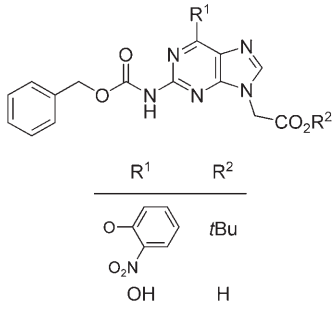


**Beating the RT mutants**: A novel class of *N*$^2$-Cbz-guan-9-yl acetic acid derivatives is endowed with anti-HIV-1 reverse transcriptase (RT) activity in the low micromolar range. These compounds have improved efficacy towards drug-resistant RT mutants relative to nevirapine and efavirenz. Their unique scaffold and interesting resistance profiles warrant further development.


© 2007 Wiley-VCH Verlag GmbH & Co. KGaA, Weinheim

# … ON OUR SISTER JOURNALS

EurJIC European Journal of Inorganic Chemistry

## *Single-Molecule Magnets*

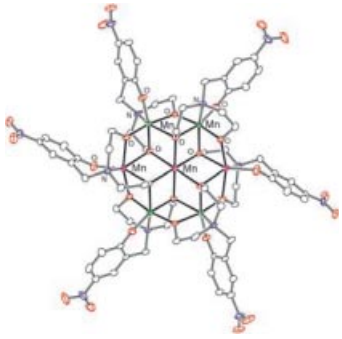

**Wheel of magnets**: A heptanuclear $Mn^{II,III}$ wheel-shaped single molecule magnet (see figure) has an $S = 19/2$ spin ground state with an easy-axis-type magnetic anisotropy of $D = -0.283$ K. Magnetization experiments using static and pulse field magnets showed different magnetic hysteresis loops due to quantum tunneling of the magnetization.

S. Koizumi, M. Nihei, T. Shiga, M. Nakano, H. Nojiri, R. Bircher, O. Waldmann, S. T. Ochsenbein, H. U. Güdel, F. Fernandez-Alonso, H. Oshio*

**A Wheel-Shaped Single-Molecule Magnet of $[Mn^{II}_3Mn^{III}_4]$: Quantum Tunneling of Magnetization under Static and Pulse Magnetic Fields**

*Chem. Eur. J.*
DOI: **10.1002/chem.200700714**

## *Molecular Wires*

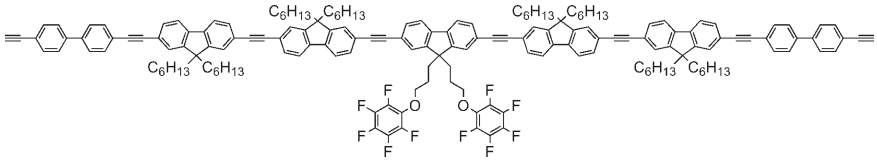

An aryleneethynylene derivative of ca. 8 nm molecular length with terminal alkyne substituents and 9,9-dihexylfluorene units in the backbone has been synthesized.

X. Zeng, C. Wang, M. R. Bryce,* A. S. Batsanov, S. Sirichantaropass, V. M. García-Suárez, C. J. Lambert, I. Sage

**Functionalized 8 nm Long Aryleneethynylene Molecular Wire with Alkyne Termini**

*Eur. J. Org. Chem.*
DOI: **10.1002/ejoc.200700507**

## *Carbenes*

**At last**, two general types of radical adducts have been obtained by the addition of radicals to a stable N-heterocyclic carbene. Addition products were obtained with $(i\text{PrO})_2(O)P^{\bullet}$ and $[(CO)_5Re^{\bullet}]$, while with $[(CO)_5Mn^{\bullet}]$ and $[(CO)_3CpMo^{\bullet}]$ (Cp = $\eta^5$-cyclopentadienyl) substitution of one carbonyl ligand and coordination to the metal center occurred to give novel metal-centered radicals (see scheme).

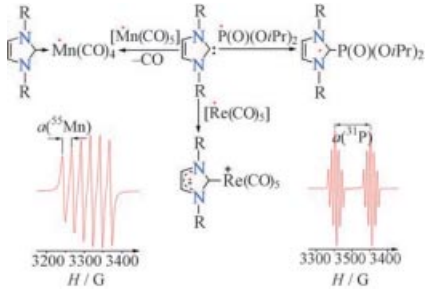


B. Tumanskii,* D. Sheberla, G. Molev, Y. Apeloig*

**Dual Character of Arduengo Carbene–Radical Adducts: Addition versus Coordination Product**

*Angew. Chem. Int. Ed.*
DOI: **10.1002/anie.200702297**

On these pages, we feature a selection of the excellent work that has recently been published in our sister journals. If you are reading these pages on a computer, click on any of the items to read the full article. Otherwise please see the DOIs for easy online access through Wiley InterScience.

 © 2007 Wiley-VCH Verlag GmbH & Co. KGaA, Weinheim 

DOI: 10.1002/ejic.200700442

# Template-Controlled Reactivity in the Organic Solid State by Principles of Coordination-Driven Self-Assembly

**Dejan-Krešimir Bučar,[a] Giannis S. Papaefstathiou,[b] Tamara D. Hamilton,[a] Qianli L. Chu,[a] Ivan G. Georgiev,[a] and Leonard R. MacGillivray*[a]**

**Keywords:** Self-assembly / Dimerization / Solid-state reactivity / Hydrogen bonds

In this microreview, we show how principles of coordination-driven self-assembly can be used to direct chemical reactivity in the organic solid state. We also show how products obtained from the templated solid-state reactions can be used as organic building units of metal–organic frameworks and coordination capsules. Self-assembled structures based on dinuclear $Zn^{II}$ and $Ag^{I}$ complexes are used to direct stereocontrolled [2+2] photodimerizations of vinylpyridines in the solid state in up to quantitative yield. The products are used as bi- and polytopic ligands of self-assembled coordination capsules and metal–organic frameworks. We also describe emerging metal-based approaches to conduct mechanochemical reactions in organic solids. In addition to the field of supramolecular coordination chemistry, these observations impact the field of green chemistry.

(© Wiley-VCH Verlag GmbH & Co. KGaA, 69451 Weinheim, Germany, 2007)

## Introduction

Reactions that occur in the organic solid state bear widespread relevance to organic synthesis and materials science. The homogeneous, confined and surprisingly flexible nature[1] of a molecular lattice means that molecules can react in solids with perfect control of stereochemistry and in a quantitative yield. That such reactions can occur in the absence of solvent also means that reactions in the organic solid state bear relevance to the field of green chemistry.[2] Green chemistry has emerged owing to the accepted need to reduce and prevent pollution from the use and production of hazardous chemicals in synthetic chemistry. Thus, the development of strategies that employ reduced amounts of solvent, as well as other chemical auxiliaries, in chemical synthesis is a central goal of green chemistry.[2]

Photoinduced reactions in the organic solid state were first discovered near the beginning of the last century. In the early 1900s, Riiber discovered that cynnamylidineacetic acid and cynnamylidinemalonic acid could photoreact in the solid state to give cyclobutanes.[3] Two decades later, Stobbe and de Jong discovered that the α- and β-forms of *trans*-cinnamic acid undergo solid-state [2+2] photodimerizations to give α-truxillic and β-truxinic acid, respectively. It was proposed that the reactions were a consequence of the packing of the monomer units;[4] however, the mechanistic details of the reactions were not well understood. This was largely a result of a lack of efficient methods to characterize the structures of organic solids. Consequently, it was difficult, at the time, to foresee practical uses of reactions in organic solids. This contrasts reactivity in the liquid phase, which was being systematically studied and becoming reasonably well understood.

On the basis of X-ray crystal structure analyses of a wide range of cinnamic acids, Schmidt and coworkers identified, during the 1960s, structural requirements for two C=C bonds to undergo a [2+2] photodimerization in the solid state.[5] The requirements, collectively known as the topochemical[6] postulate, state that a [2+2] photodimerization can be expected to occur if the C=C bonds lie parallel to each other and with a centre-to-centre distance <4.2 Å. Thus, of the three known polymorphs of *o*-ethoxy-*trans*-cinnamic acid, namely α-, β- and γ-, the α- and β-forms are photoactive (Figure 1).[7] In all three solids, the alkenes

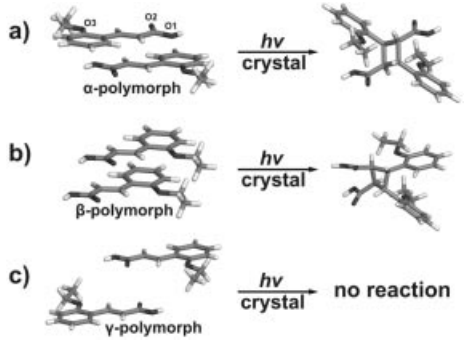


Figure 1. Solid-state reactivity of *o*-ethoxy-*trans*-cinnamic acid: (a) α-, (b) β- and (c) γ-polymorphs.

[a] Department of Chemistry, University of Iowa, Iowa City, Iowa 52242-1294, USA
Fax: +1-319-335-1270,
E-mail: len-macgillivray@uiowa.edu
[b] Laboratory of Inorganic Chemistry, Department of Chemistry, National and Kapodistrian University of Athens Panepostimiopolis, Zografou 15771, Greece

 © 2007 Wiley-VCH Verlag GmbH & Co. KGaA, Weinheim 

pack parallel in one-dimensional (1D) slipped stacks. In the cases of the α- and β-forms, C=C bonds of neighbouring monomers lie parallel to each other and are separated by approximately 4 Å. Adjacent monomers of the α-polymorph adopt an antiparallel orientation, and they are related by a crystallographic centre of inversion. This geometry leads to the formation of the "head-to-tail" α-truxillic acid dimer upon photoreaction. Adjacent monomers of the

*Dejan-Krešimir Bučar was born in Zagreb, Croatia in 1975. He obtained a BSc in chemistry from the University of Zagreb in 2004. In 2005 he joined the research group of Professor Leonard R. MacGillivray at the University of Iowa as a graduate student. His principal research interests concern various aspects of organic solid-state chemistry with particular focus on template-directed solid-state synthesis and pharmaceutical cocrystals. He is also interested in synthetic organic chemistry, single-crystal X-ray crystallography and coordination-driven self-assembly.*

*Giannis S. Papaefstathiou obtained his BA in 1998 and his PhD in 2002 from the University of Patras, Greece, while working with Professor Spyros P. Perlepes. He moved to the University of Iowa in 2002 to work with Professor Leonard R. MacGillivray as a postdoctoral fellow for two years. He then moved back to Greece to work as a temporary Lecturer at the University of Patras and as an Associate Instructional Personnel at the Hellenic Open University. He joined the faculty at the Department of Chemistry of the National and Kapodistrian University of Athens in 2006 as a Lecturer. His current research interests are in aspects of coordination chemistry and supramolecular chemistry.*

*Tamara D. Hamilton was born in Nova Scotia, Canada in 1979. In 2001, she graduated from Acadia University with a BSc (Honours). In 2005, she obtained her PhD from the University of Iowa for studies on the coordination chemistry of products from template-directed synthesis in the solid state with Professor Leonard R. MacGillivray. Currently, she is a Natural Sciences and Engineering Research Council of Canada (NSERC) postdoctoral researcher in the group of Professor James D. Wuest at l'Université de Montréal. Her research involves engineering crystals built from molecular tectons with pyrogallol functionalities.*

*Qianli Chu was born in 1975. He performed his undergraduate studies in organic chemistry at Shanghai University, P. R. China (1993–1997). He then spent four years at the Shanghai Institute of Organic Chemistry (SIOC) as a Research Assistant with Professor Shizheng Zhu. He joined the research group of Professor Leonard R. MacGillivray at the University of Iowa where he obtained his PhD in supramolecular chemistry in 2005. He is currently working as a postdoctoral fellow under the guidance of Professor Dennis P. Curran at the University of Pittsburgh with research efforts that mainly focus on fluorous organocatalysis and molecular recognition. His research interests are concentrated at the interface of organic chemistry and supramolecular chemistry.*

*Ivan G. Georgiev was born in Bulgaria in 1973. He received his BA in chemistry from Missouri State University in 2002 and then graduated with a MA degree from the same university conducting research under the supervision of Professor Eric Bosch on the design and synthesis of supramolecular complexes. He is currently a fourth year graduate student at the University of Iowa and working in the laboratory of Professor Leonard R. MacGillivray. His research interest lies in the areas of supramolecular chemistry and organic solid-state reactivity.*

*Len MacGillivray was born in Nova Scotia, Canada, where he received a BSc in chemistry (honours) from Saint Mary's University in 1994. After receiving a PhD from the University of Missouri-Columbia in 1998 while working in the lab of Professor Jerry L. Atwood, he joined the Functional Materials Program at the Steacie Institute of Molecular Science, National Research Council of Canada, Ottawa, where he was a Research Associate and Adjunct Research Professor with the Carleton-Ottawa Chemistry Institute from 1998 to 2000. In 2000, he joined the Department of Chemistry at the University of Iowa as an Assistant Professor and was promoted to his current rank of Associate Professor in 2005. His research focuses upon the field of supramolecular chemistry, particularly as it relates to the design and construction of organic solids.*

 © 2007 Wiley-VCH Verlag GmbH & Co. KGaA, Weinheim 

β-polymorph adopt a parallel orientation, and they are related by a translation axis. Photodimerization of the β-polymorph produces a "head-to-head" β-truxinic acid. The γ-polymorph is photostable, and the C=C bonds are too far apart to react.

In recent years, we introduced a method to direct [2+2] photodimerizations in the solid state by using principles of molecular recognition and self-assembly.[8] The method exploits the strength and directionality of hydrogen bonds to construct target molecules such as cyclophanes[9] and ladderanes[10] by using small molecules in the form of templates. In this microreview, we will outline how the template approach can be expanded to the principles of coordination-driven self-assembly.[11] We will also demonstrate how molecules constructed with the use of the template method can be used as building blocks of finite and infinite coordination assemblies.[12] We will then discuss how the area of mechanochemistry[13] can be applied to eliminate solvents associated with reactions mediated by metal ions in organic solids.

## Template-Controlled Photodimerizations by Using Organic Molecules

In 2000, we introduced a method to control chemical reactivity in the organic solid state by using small organic molecules that function as linear templates.[8] The templates assemble olefins for [2+2] photodimerizations within multi-component supramolecular assemblies. In particular, we demonstrated that resorcinol (res) can be used as a linear template to assemble and juxtapose *trans*-1,2-bis(4-pyridyl)-ethylene (4,4′-bpe) for photoreaction. Cocrystallization of res with 4,4′-bpe produced the four-component assembly 2(res)·2(4,4′-bpe) held together by four O–H···N hydrogen bonds. The two olefins were oriented by res in a parallel fashion and at a distance of 3.65 Å (Figure 2). This placed the C=C bonds of 4,4′-bpe in a geometry that conformed to the topochemical postulate of Schmidt for the reaction. UV irradiation of crystalline 2(res)·2(4,4′-bpe) produced the corresponding photodimer, *rctt*-tetrakis(4-pyridyl)cyclobutane (4,4′-tpcb), regiospecifically and in 100% yield.[14]

In addition to 4,4′-tpcb, we showed that the method can be used to construct relatively complex molecules such as a [2.2]paracyclophane and [*n*]ladderanes (where: $n$ = 3 or 5).[9,10] Templates based on res were used to organize di- and triolefins, similar to 2(res)·2(4,4′-bpe), within four-component hydrogen-bonded assemblies. UV irradiation of the solids produced the targeted cyclophane and ladderanes regiospecifically and in quantitative yield (Figure 3).

## Template-Controlled Photodimerizations by Using Metal Ions

Inspired by work in the field of coordination-driven self-assembly,[15] we recently addressed whether transition-metal-ion complexes can be used as linear templates to di-

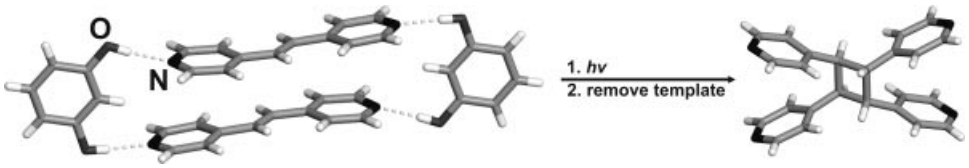


Figure 2. Solid-state synthesis of 4,4′-tpcb by using resorcinol as a template.

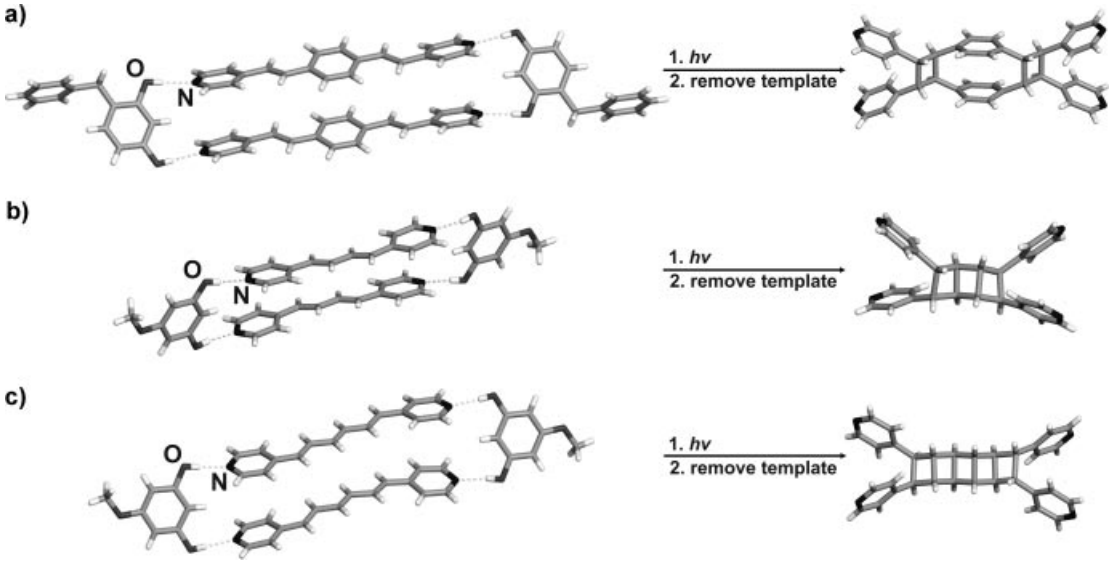


Figure 3. Solid-state synthesis of: (a) [2.2]paracyclophane, (b) [3]ladderane and (c) [5]ladderane.

 © 2007 Wiley-VCH Verlag GmbH & Co. KGaA, Weinheim 

rect [2+2] photodimerizations in the solid state. The field of coordination-driven self-assembly, which has experienced tremendous growth during the last decade,[15,16] involves reactions of metal ions with bi- and polytopic ligands. The metal and organic components are used to form finite (e.g. metallomacrocycle) and/or infinite [e.g. metal–organic framework (MOF)] self-assembled frameworks. The frameworks are designed to exhibit properties (e.g. host–guest, magnetic) typically not encountered in the individual components. We wondered whether coordination bonds could be used to effectively replace the hydrogen bonds of a resorcinol-based template. In such a design, a dinuclear metal complex would assemble and preorganize two olefins to react in a solid. The ensuing solid-state reaction could also be used to affect bulk physical properties[11a] conferred by the metals in a solid.

Prior to our work, there were two examples in which a metal-ion complex facilitated a [2+2] photodimerization in the solid state (Figure 4).[17–19] In particular, Praetorius and Korn reported the ability of a mononuclear complex of uranyl chloride and *trans,trans*-dibenzylideneacetone (dba) to undergo a stereospecific photodimerization to give the truxillic-type dimer *rctt*-1,3-bis(3-phenylprop-2-enoloxo)-2,4-bis(phenyl)cyclobutane (Figure 4a).[17] X-ray crystal structures of both the unsolvated and solvated forms, $[(UO_2)Cl_2(dba)_2]$ and $[(UO_2)Cl_2(dba)_2]\cdot 2CH_3CO_2H$, showed that the metal ions adopted an octahedral geometry surrounded by two chlorine atoms, two oxygen atoms of the uranyl group and two keto-oxygen atoms of the dba ligand (Figure 4a).[18] The complexes assembled in the solid such that the distances between the alkenes of adjacent dba ligands were 4.09 and 3.51 Å in the unsolvated and solvated forms, respectively. The reactivity was, thus, largely the result of the packing of the complexes. Later, Lewis and coworkers demonstrated [2+2] photoreactivity in a series of crystalline cinnamic esters mediated by Lewis acids (e.g. $SnCl_4$).[19] The cinnamic esters formed 1:1 complexes with $BF_3$ and 2:1 complexes with $SnCl_4$. UV irradiation of the solids produced truxillic-type dimers (Figure 4b). A structure analysis of the ethyl cinnamate–$SnCl_4$ complex revealed an octahedral coordination environment around the $Sn^{IV}$ ion (Figure 4b). The photoreaction occurred between neighbouring cinnamate ligands. Adjacent ligands were stacked in a head-to-tail fashion and were separated by 4.12 Å.

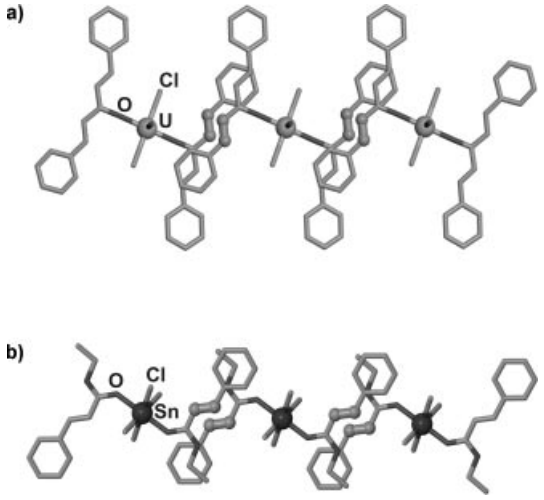


Figure 4. Crystal structures of the photoactive: (a) dba–$UO_2Cl_2$ complex and (b) ethyl cinnamate–$SnCl_4$ complex. Reactive alkene groups highlighted.

Our first study pertaining to a dinuclear complex involved the Schiff base complex $[Zn_2\mathbf{L}(OH)]^{2+}$ {where: **L** = 2,6-bis[*N*-(2-pyridylethyl)formimidoyl]-4-methylphenol} as a template (Figure 5).[11a] The Schiff base ligand was originally introduced by Robson and Okawa as a model of enzymatic processes (Figure 5a.).[20] An analysis of the Cam-

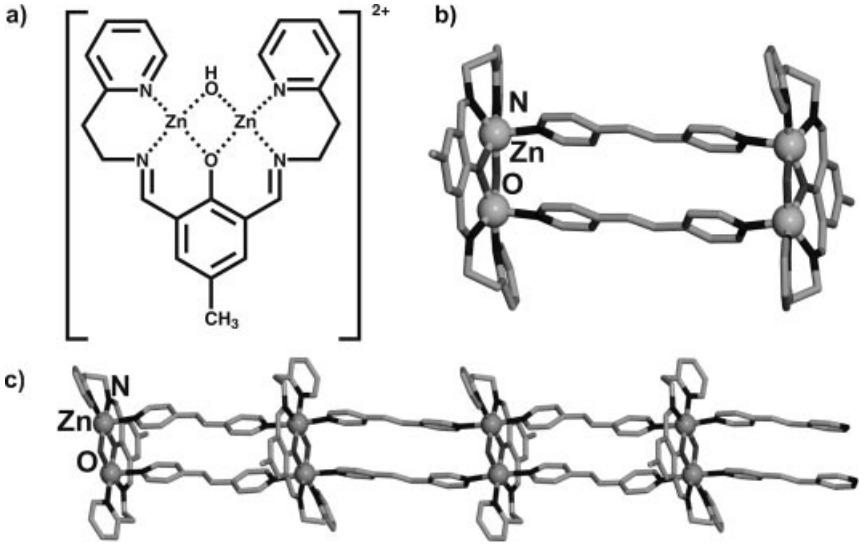


Figure 5. (a) Schematic representation of the dinuclear template first reported by Robson and Okawa and the wireframe models of (b) a discrete photoactive assembly and (c) a photoactive linear polymer.

 © 2007 Wiley-VCH Verlag GmbH & Co. KGaA, Weinheim 

bridge Structural Database revealed that the metal atoms of such complexes are separated on the order of 3.10 to 3.15 Å. This range was well within the distance criterion of Schmidt for photodimerization in a solid. We showed that reaction of $[Zn_2\mathbf{L}(OH)](ClO_4)_2$ with 4,4′-bpe produces the tetranuclear assembly $[Zn_4\mathbf{L}(OH)_2(4,4'\text{-bpe})_2](ClO_4)_2$ (Figure 5b). The metal atoms of the assembly adopted a square-pyramidal coordination environment and the two stacked pyridine moieties were located in the apical positions. The C=C bonds of the olefins were arranged parallel and separated by 3.64 Å. UV irradiation of the solid produced 4,4′-tpcb in quantitative yield. We later showed that stacked molecules of 4,4′-bpe could be achieved within the 1D MOF $\{[Zn_2\mathbf{L}(OH)(4,4'\text{-bpe})_2](ClO_4)_2\}_\infty$.[11b] In this case, each metal ion adopted an octahedral coordination environment. The solid reacted to give 4,4′-tpcb in 95% yield (Figure 5c).[21]

During the course of our studies involving tetranuclear $[Zn_4\mathbf{L}(OH)_2(4,4'\text{-bpe})_2](ClO_4)_2$, we determined that the photoreaction proceeded by a rare single-crystal-to-single-crystal (SCSC) transformation (Figure 6).[22] We also discovered that the single crystals displayed different fluorescence emissions before and after the photoreaction.[11a] Specifically, excitation of the crystals with 290 nm light prior to the photoreaction produced a blue emission at 464 nm, whereas the fully reacted solid produced a green emission at 520 nm. That the change in emission was a consequence of the solid-state reaction was supported by laser-scanning confocal fluorescence microscopy, which revealed a difference in the fluorescence between the unreacted and reacted solid. To the best of our knowledge, the tetranuclear assembly represented the first example of a SCSC reaction that exhibited photocontrolled fluorescence. The reaction involving the 1D framework $[Zn_2\mathbf{L}(OH)(4,4'\text{-bpe})_2](ClO_4)_2$ did not occur through a SCSC transformation.

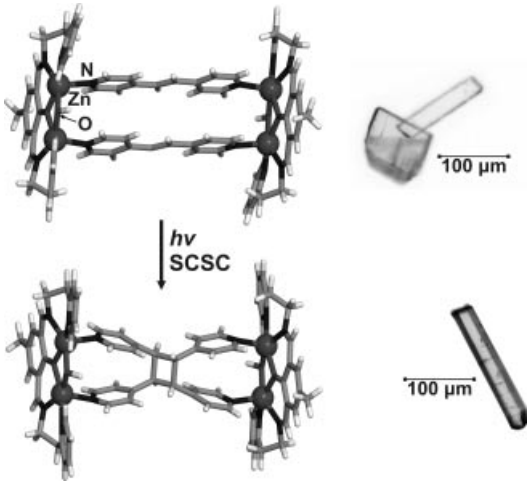


Figure 6. Photocontrolled fluorescence in single-crystalline $[Zn_4L_2(OH)_2(4,4'\text{-tpcb})](ClO_4)_4{\cdot}4H_2O$.

To expand the template method to an additional dinuclear unit, we turned to the $Ag^I$ ion.[11c] It is well established that $Ag^I$ exhibits linear coordination while also participating in $Ag^I\cdots Ag^I$ or argentophilic forces.[23] $Ag^I$ ions engaged in argentophilic forces are separated on the order of 3.40 Å, which falls within the distance criterion of Schmidt. These observations encouraged us to investigate the ability of $Ag^I$ ions, in a T-shaped geometry, to steer *trans*-coordinated olefins towards a [2+2] photodimerization. In this design, the argentophilic forces would stack two pairs of olefins for reaction in a solid. We determined the ability of the $Ag^I$ ions to assemble *trans*-1-(4-pyridyl)-2-(phenyl)ethylene (4-stilbz) in crystalline $[Ag_2(4\text{-stilbz})_4][CO_2CF_3]_2$ for a regiocontrolled head-to-head photodimerization to give *rctt*-1,2-bis(4-pyridyl)-3,4-bis(phenyl)cyclobutane (4-pyr-ph-cb) in quantitative yield (Figure 7). The metal ions were separated by 3.41 Å, whereas the C=C bonds of the stacked olefins exhibited a disordered criss-cross arrangement with a separation of 3.82 Å. That the photoreaction was able to proceed, despite the C=C bonds being crossed, was attributed to the olefins undergoing a pedal-like rotation.[11c] Similar to $[Zn_4\mathbf{L}(OH)_2(4,4'\text{-bpe})_2](ClO_4)_2$, the photoreaction proceeded through a SCSC transformation.[22]

Figure 7. Alignment of 4-stilbz molecules within the dinuclear complex $[Ag_2(4\text{-stilbz})_4]^{2+}$.

The photoreaction involving $[Ag_2(4\text{-stilbz})_4][CO_2CF_3]_2$ also converted the dinuclear complex into a 1D coordination network (Figure 8). In particular, the generation of the photoproduct involved major movements of the metal and organic components. The $Ag^I$ ions moved away from each other by approximately 1.16 Å ($Ag^I\cdots Ag^I$ distance 5.73 Å), which broke the argentophilic forces. This movement was accompanied by an approximate 90° rotation of the carboxylate ions. As a result of these movements, $Ag^I\cdots C$(phenyl) forces ($Ag^I\cdots C$ distance 2.63 Å) formed between each repositioned $Ag^I$ ion and the *para* carbon atom of the phenyl group of a neighbouring assembly. These new forces served,

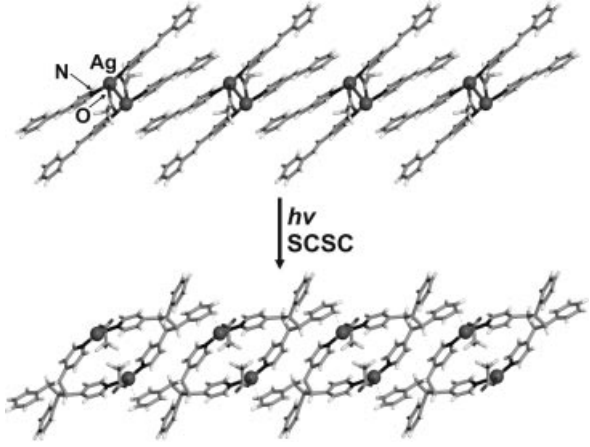


Figure 8. SCSC conversion of $[Ag_2(4\text{-stilbz})_4]^{2+}$ into 1D $[Ag_2(4\text{-py-ph-cb})_2]^{2+}_\infty$.

 © 2007 Wiley-VCH Verlag GmbH & Co. KGaA, Weinheim 

in effect, to link adjacent complexes to produce a linear coordination network. The photoconversion of $[Ag_2(4\text{-stilbz})_4]^{2+}$ into $[Ag_2(4\text{-py-ph-cb})_2]^{2+}$ was, to the best of our knowledge, the first case in which a metal complex was transformed into an infinite coordination network by a photoreaction. In related and earlier work, Foxman had revealed the ability of the $Ni^{II}$ complex $[NiBr_2(PCH_2CH_2CN)_3]$ to undergo a highly stereocontrolled thermal polymerization in a solid that involved the formation of Ni–N coordination bonds.[24]

## Applications of the Products

The products of the [2+2] photodimerizations that we conducted in the solid state are functionalized with, in a minimal case, two pyridyl groups. The products also typically form in quantitative yield, gram amounts and in the absence of byproducts.[8] For us, these features made the products attractive for studies in coordination-driven self-assembly. We hypothesized that the products, once removed from the template, could serve as bi- and polytopic linkers of MOFs and related materials.[12,25–28] A cyclobutane ring could serve as a hub[29] providing both acute and obtuse angles to propagate the coordination geometry of a metal in an assembly process. Importantly, whereas molecules synthesized in the liquid phase routinely encounter practical applications in areas ranging from pharmaceutical chemistry to materials science, the products of molecules synthesized in the solid state had experienced virtually none.[30] This can be attributed to difficulties in engineering solid-state structures such that the molecules can undergo reactions "at will" to synthesize molecules by design.[31]

### 1D MOF

In 2002, we set out to determine whether the products obtained from linear templates in the solid state could be used as ligands to form MOFs. The major driving force behind the synthesis of MOFs is a promise to generate materials with tailorable electronic,[32] magnetic,[33] optical[34] and/or host–guest properties.[35] Thus, MOFs with cavities and pores are expected to exhibit properties akin to zeolites and mesoporous materials and, thereby, have applications in areas such separations,[36] gas storage[37] and catalysis.[38]

One of our first reactions involved 2,2′-tpcb with $CuSO_4{\cdot}5H_2O$. We generated 2,2′-tpcb by using a hydrogen-bond-mediated synthesis.[39] In particular, we showed that the components assembled in the solid state to give a 1D MOF in which 2,2′-tpcb served as a bis-chelating ligand in $[Cu_2(\mu\text{-}2\text{-}SO_4)_2(\mu\text{-}2,2'\text{-tpcb})(H_2O)_2]_\infty$ (Figure 9).[25] Each $Cu^{II}$ ion exhibited a square-pyramidal coordination environment with two N atoms of two 2-pyridyl groups, one O atom of a sulfate ion and one O atom of a water molecule in the basal plane. The apical site was occupied by an O atom of a second sulfate ion. The 1D polymer assembled in parallel and offset strands, with interstices occupied by solvent water molecules. In the same report, we showed that the self-assembly process was sensitive to changes to the counterion.

Specifically, reaction of 2,2′-tpcb with $Cu(NO_3)_2{\cdot}2.5H_2O$ produced the dinuclear complex $[Cu_2(NO_3)_4(\mu\text{-}2,2'\text{-tpcb})]$. Similar to the 1D framework, 2,2′-tpcb served as a bis-chelating ligand. Two chelating nitrate ions completed a distorted octahedral coordination sphere.

### 2D MOFs

That same year, we determined that 4,4′-tpcb could be used as a 4-connected node of a porous 2D MOF. Specifically, reaction of 4,4′-tpcb with the copper paddle-wheel complex $[Cu_2(O_2CCH_3)_4(H_2O)_2]$ produced the 2D MOF $[Cu_4(O_2CCH_3)_8(4,4'\text{-tpcb})]_\infty$ (Figure 10).[12a] The cyclobutane and dicopper complex produced a 2D grid with identical rhombic cavities of approximate dimensions 17.2 Å × 17.2 Å and corner angles 75° and 104° (Figure 10a). The 2D grids stacked to form a 3D framework with isolated 1D channels of approximate dimensions 10 Å × 12 Å (Figure 10b). The channels were occupied by benzene solvent molecules, which assembled in an edge-to-face manner. We showed that the solvent molecules could be removed from the framework by a SCSC transformation.[22] We also revealed that the methyl groups of the paddle-wheel complex were directed into the cavities. In doing so, the methyl groups segregated the space of the cavities into smaller compartments. These observations suggested that further functionalization of the cavities could be achieved by modifying the R group of the paddle-wheel complex. We termed the framework an inverted MOF (IMOF), as the metal complex acted as a linear bridge and

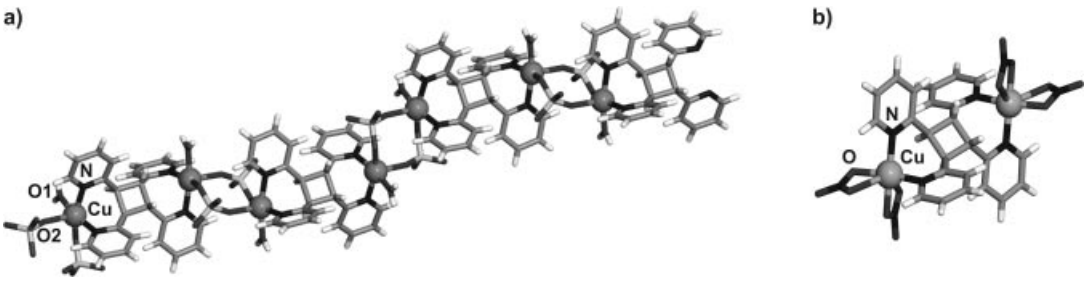


Figure 9. View of: (a) 1D polymer $[Cu_2(\mu\text{-}2\text{-}SO_4)_2(\mu\text{-}2,2'\text{-tpcb})(H_2O)_2]_\infty$ and (b) dinuclear complex $[Cu_2(NO_3)_4(\mu\text{-}2,2'\text{-tpcb})]$.

 © 2007 Wiley-VCH Verlag GmbH & Co. KGaA, Weinheim 

the organic spacer served as a node; thus, the roles of the metal and organic components, relative to a more conventional MOF,[15,16] were inverted or reversed. Moreover, that the metal component served as a linear bridge meant that the terminal carboxylates were available to decorate the cavities of the framework.

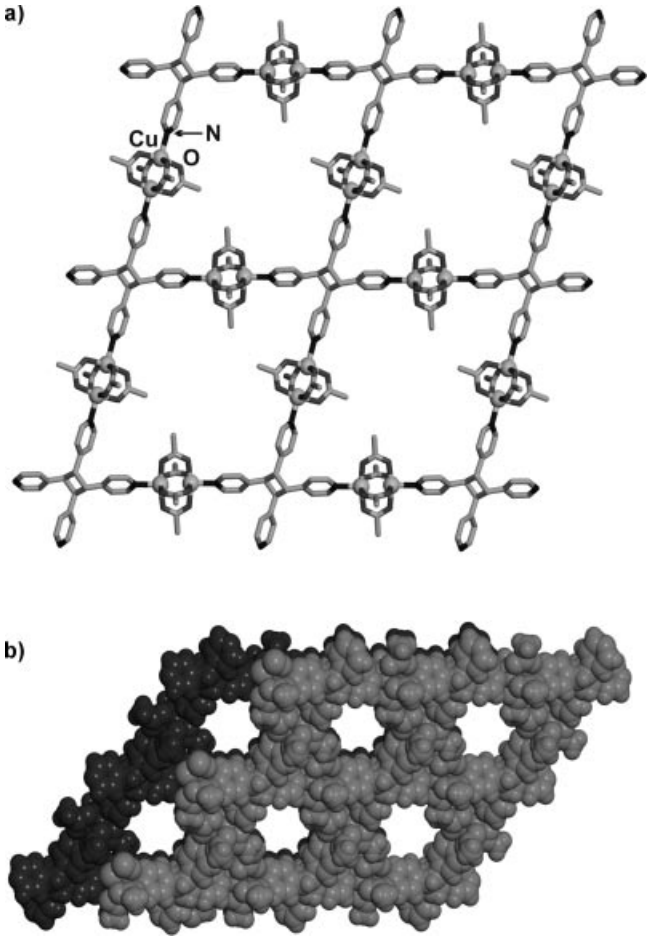


Figure 10. Perspective views of $[Cu_4(O_2CCH_3)_8(4,4'\text{-tpcb})]_\infty$: (a) ball-and-stick model and (b) space-filling model of the stacking of two layers.

In a later report, we described a 2D MOF based on 4,4′-tpcb that involved metal and cyclobutane components that served as 4-connected nodes.[40] In particular, reaction of 4,4′-tpcb with $[Co(O_2CCH_3)_2(H_2O)_4]$ produced the 2D MOF $[Co(O_2CCH_3)_2(4,4'\text{-tpcb})]_\infty$. The framework, similar to $[Cu_4(O_2CCH_3)_8(4,4'\text{-tpcb})]_\infty$, possessed rhombic cavities with edge lengths of 7.3 Å. In contrast to $[Cu_4(O_2CCH_3)_8(4,4'\text{-tpcb})]_\infty$, however, the framework was made up of two different rhombic cavities (Figure 11). That the framework possessed two different cavities was a result of the stereochemistry of the cyclobutane ring, which provided two different angles (75 and 104°) for cavities within the network. The cavities stacked in an ABAB manner producing small interstices occupied by solvent methanol molecules. We also demonstrated that the crystallinity of the solid was maintained upon removing the guests by heating.

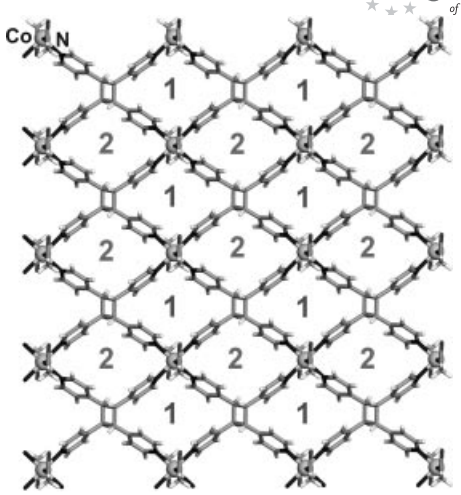


Figure 11. Perspective view of $[Co(O_2CCH_3)_2(4,4'\text{-tpcb})]_\infty$ that illustrates the different cavities of the 2D MOF.

More recently, we demonstrated that a product of a template-directed solid-state synthesis forms a 2D MOF with a topology that conforms to a nonregular net (Figure 12). Most 2D MOFs exhibit topologies of regular (i.e. tiling of regular polygons with identical nodes) or semiregular (i.e. tiling of different regular polygons with identical vertices) nets. In the minimal case, a MOF with a topology of a nonregular net will possess two different polygonal cavities and two nodes of different connectivity. It was recently argued that the self-assembly process that produces a MOF is predisposed to generate high-symmetry frameworks

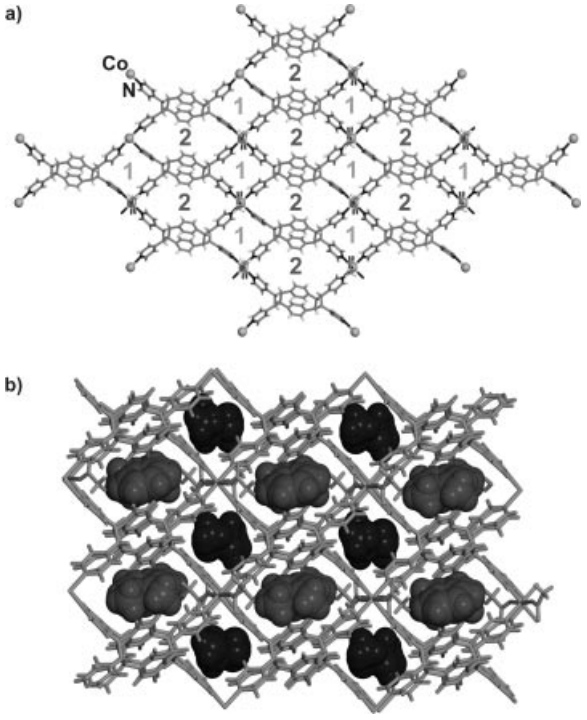


Figure 12. Perspective view of $[Co(O_2CCH_3)_2(4,4'\text{-tppcp})]_\infty$: (a) different cavities of the 2D framework and (b) space-filling model of the included solvent molecules.

 © 2007 Wiley-VCH Verlag GmbH & Co. KGaA, Weinheim 

based on identical nodes (i.e. regular and semiregular nets).[41] To design a MOF that conforms to a nonregular net, we treated the [2.2]paracyclophane 4,4′-tppcp with $Co(O_2CCH_3)_2{\cdot}4H_2O$, which afforded the 2D MOF $[Co(O_2CCH_3)_2(4,4'\text{-tppcp})]_\infty$ (Figure 12a).[28] The components self-assembled to give a 2D MOF with both square and hexagonal cavities in which 4,4′-tppcp and the $Co^{II}$ ion served as 3- and 4-connected nodes, respectively. The paracyclophane effectively served as two covalently fused 3-connected nodes in which the stacked rings of the cyclophane provided the covalent connection. Moreover, that the cyclophane acted as two fused 3-connected nodes meant that the formation of higher-symmetry MOFs with structures solely based on linkages between 3- and 4-connected nodes (i.e. with no linkages between two 3-connected nodes) was prohibited. The two different cavities hosted two different solvent molecules as guests. Specifically, a methanol molecule filled hydrophilic square cavities, whereas toluene molecules filled hydrophobic hexagon cavities (Figure 12b).

## Metal–Organic Polyhedra and Polygons

In addition to MOFs, we discovered that products of linear templates in the solid state can generate metal–organic polyhedra and polygons.[12b,26,27] The internal cavities of such self-assembled frameworks have, in recent years, gained much attention as materials with applications in areas such as logical gates,[42] reaction vessels[43] and catalysis.[44]

Our first report described the self-assembly of the unsymmetrical tetrapyridine 2,4′-tpcb (Figure 13) with $Cu^{II}$ ions to form a polyhedron. Reaction of 2,4′-tpcb with $Cu(ClO_4)_2{\cdot}6H_2O$ produced a hexanuclear polyhedron in $[Cu_6(2,4\text{-tpcb})_6(H_2O)_6][ClO_4]_{12}$ with a structure that conformed to a trigonal antiprism (Figure 13).[12b] Each metal ion adopted a square-pyramidal coordination environment and occupied a vertex of the polyhedron. The coordination environment consisted of two chelating 2-pyridyl groups and two monodentate 4-pyridyl groups that formed the base and a water molecule that formed the apex. Thus, the 4-pyridyl groups corresponded to the edges of the polyhedron whereas the 2-pyridyl groups corresponded to the corners. The coordination behaviour of the 2- and 4-pyridyl groups was consistent with the MOFs involving 4,4′- and 2,2′-tpcb.[12] The assembly process produced a central cavity that hosted two $ClO_4^-$ anions as guests.

Very recently, we showed that an unsymmetrical isomer of the 2,4′-tpcb ligand, namely 2,3′-tpcb, assembles with $Cu^{II}$ ions to form a polyhedron with a structure that conforms to a tetrahedron (Figure 14).[26] We anticipated that changing the 4-pyridyl group to a 3-pyridyl group would result in a smaller polyhedron owing to a decrease in the angle of the coordination vector (Figure 15). We employed a hydrogen-bond-directed synthesis to generate 2,3′-tpcb. As expected, 2,3′-tpcb assembled with the metal ions to form a smaller polyhedron. To our surprise, the polyhedron $[Cu_4(2,3'\text{-tpcb})_4(H_2O)_4]^{8+}$ adopted a topology of a tetrahedron and exhibited a chiral $D_2$ topology. The structure was a rare example of a chiral self-assembled polyhedron composed of achiral components. The chirality of the tetrahedral capsule was attributed to a geometric fit of the metal and organic components, which prohibited the formation of mirror planes in the structure. As in the case of the trigonal antiprism, the $Cu^{II}$ ions occupied the corners of the tetrahedron and exhibited a square-pyramidal coordination environment. The tetrahedron also possessed a central cavity that hosted a $NO_3^-$ ion as a guest.

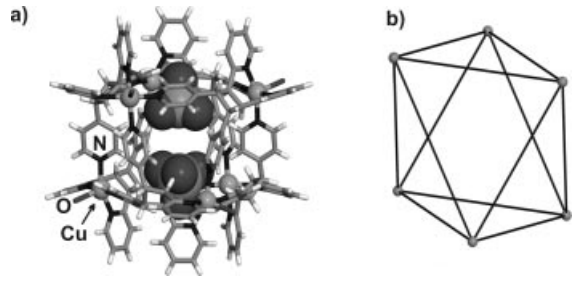


Figure 13. Perspective view of $[Cu_6(2,4\text{-tpcb})_6(H_2O)_6]^{12+}$: (a) space-filling model of two encapsulated $ClO_4^-$ ions and (b) the trigonal antiprism formed by the $Cu^{II}$ ions.

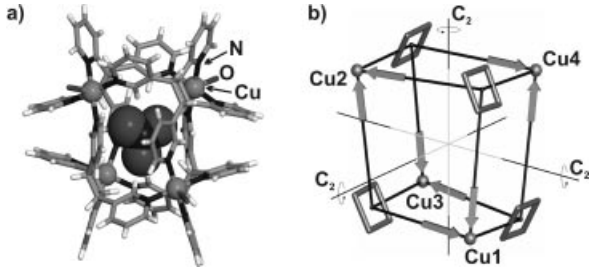


Figure 14. Perspective view of $[Cu_4(2,3'\text{-tpcb})_4(H_2O)_4]^{8+}$: (a) space-filling model of the encapsulated $NO_3^-$ ion and (b) the tetrahedron topology.

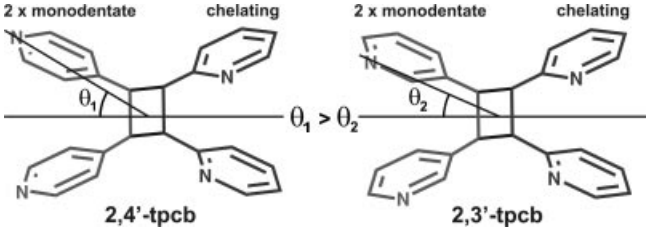


Figure 15. Polydentate 2,3′-tpcb and 2,4′-tpcb ligands (θ – angle of the coordination vector).

In addition to a polyhedron, we demonstrated that 2,4′-tpcb can form a polygon.[27] By changing from a noncoordinating (i.e. $ClO_4^-$) to chelating counter anion, in the form of the hexafluoroacetylacetonate anion (hfacac), we described the formation of the tetranuclear metal–organic rhomboid $[Cu_4(2,4\text{-tpcb})_2(hfacac)_8]$ (Figure 16a). In particular, two molecules of 2,4′-tpcb assembled with the $Cu^{II}$ ions to give a dinuclear cavity of approximate dimensions 4.0 Å × 4.2 Å and corner angles of 79 and 101°. Mono-

 © 2007 Wiley-VCH Verlag GmbH & Co. KGaA, Weinheim 

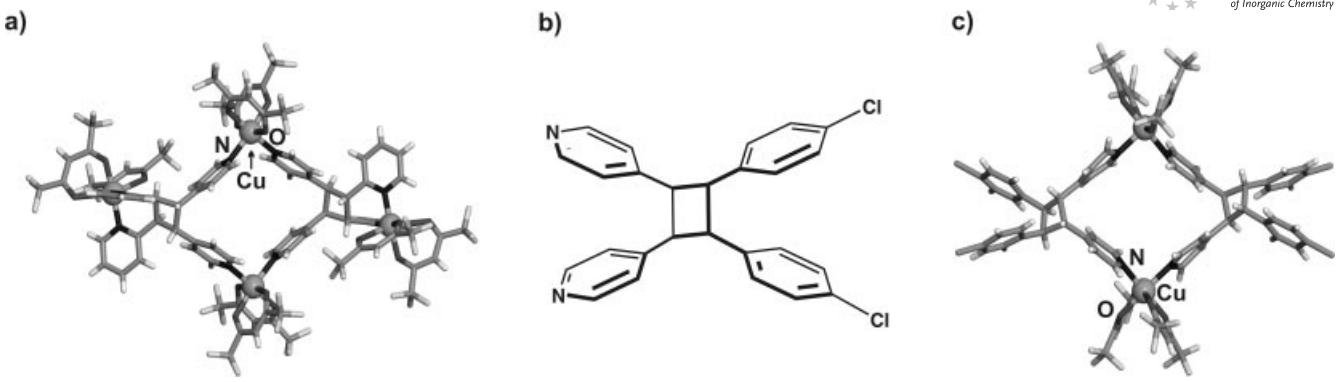


Figure 16. Perspective views of: (a) $[Cu_4(2,4\text{-tpcb})_2(hfacac)_8]$, (b) schematic representation of 4-py-4-Cl-p-cb and (c) $[Cu_2(4\text{-py-4-Cl-p-cb})_2(hfacac)_4]$.

dentate 4-pyridyl groups defined the edges of the polygon. Each $Cu^{II}$ ion exhibited octahedral coordination with two 4-pyridyl units and two hfacac anions in a *cis* arrangement. Chelating 2-pyridyl groups were located along the periphery of the assembly and were being coordinated to two $Cu^{II}$ ions. We also showed that the bifunctional cyclobutane *rctt*-1,2-bis(4-pyridyl)-3,4-bis(chlorophenyl)cyclobutane (4-py-4-Cl-p-cb; Figure 16b) supports the formation of a dinuclear polygon by, similar to $[Cu_4(2,4\text{-tpcb})_2(hfacac)_8]$, the 4-pyridyl groups (Figure 16c).[27]

## Emergence of Mechanochemical Preparation of Coordination Materials

The coordination solids described above were prepared by using crystallizations that involve an organic solvent. To increase the relevance of the template approach to the field of green chemistry,[2] it would be desirable to further reduce the organic solvents employed in the syntheses. In recent years, the field of coordination chemistry has witnessed a rapid surge of interest in the development of solvent-free, or mechanochemical, methods[45] to synthesize self-assembled coordination materials. The approach relies on simple grinding of metal and organic components to induce the formation of metal complexes and self-assembled materials.

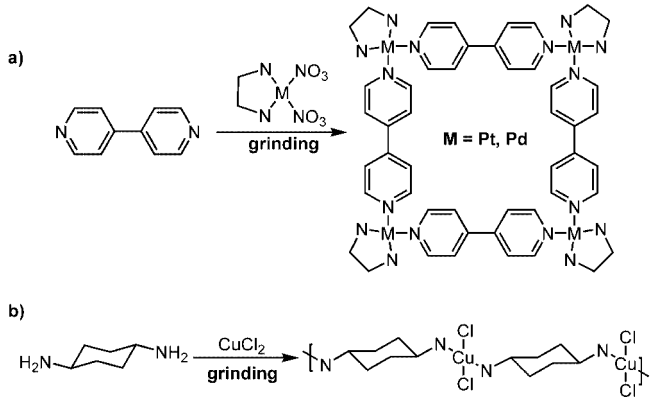


Figure 17. Coordination solids based on both (a) finite and (b) infinite self-assembled architectures constructed by mechanochemical methods.

Coordination solids based on both finite and infinite self-assembled architectures have been constructed by this approach (Figure 17).[46,47] We are now addressing whether mechanochemical methods can be applied to construct reactive, self-assembled solids, as well as the applications of the molecules synthesized in the solid state.

## Summary and Outlook

Linear templates allow chemists to organize reactive molecules within finite supramolecular assemblies constructed by coordination-driven self-assembly. In such assemblies, olefins are preorganized to conform to Schmidt's topochemical postulates for a [2+2] photodimerization in a solid. The strategy has been, thus far, used to synthesize mono- and polyfunctional pyridyls in solids. Here, we have also presented the diversity of products obtained in studies that apply the ligands in metallosupramolecular chemistry. We have revealed that the template method provides access to molecules that can be used as organic building units of self-assembled polygons and polyhedra, as well as MOFs. We are now moving to develop this approach for the application in more mainstream synthetic chemistry and with an increasing relevance to green chemistry.

[1] J. L. Atwood, L. J. Barbour, A. Jerga, B. L. Schottel, *Science* **2002**, *298*, 1000–1002.
[2] P. T. Anatas, J. C. Warner in *Green Chemistry: Theory and Practice*, Oxford University Press, New York, **1998**.
[3] a) C. N. Riiber, *Ber. Dtsch. Chem. Ges.* **1902**, *35*, 2411–2415; b) C. N. Riiber, *Ber. Dtsch. Chem. Ges.* **1913**, *46*, 335–338.
[4] a) H. Stobbe, F. K. Steinberger, *Ber. Dtsch. Chem. Ges.* **1922**, *55B*, 2225–2245; b) H. Stobbe, A. Lehfeldt, *Ber. Dtsch. Chem. Ges.* **1925**, *58B*, 2415–2427; c) A. W. K. de Jong, *Ber. Dtsch. Chem. Ges.* **1923**, *56B*, 818–832; d) A. W. K. de Jong, *Ber. Dtsch. Chem. Ges.* **1922**, *55B*, 463–474.
[5] G. M. J. Schmidt, *Pure Appl. Chem.* **1971**, *27*, 647–678.
[6] V. Kohlschütter, *Z. Anorg. Allg. Chem.* **1918**, *105*, 1–25.
[7] a) G. M. J. Schmidt, *J. Chem. Soc.* **1964**, *385*, 2014–2021; b) M. A. Fernandes, D. C. Levendis, C. B. De Koning, *Cryst. Eng.* **2001**, *4*, 215–231.
[8] L. R. MacGillivray, G. S. Papaefstathiou, T. Friščić, D. B. Varshney, T. D. Hamilton, *Top. Curr. Chem.* **2004**, *248*, 201–221.
[9] T. Friščić, L. R. MacGillivray, *Chem. Commun.* **2003**, 1306–1307.

 © 2007 Wiley-VCH Verlag GmbH & Co. KGaA, Weinheim 

[10] X. Gao, T. Friščić, L. R. MacGillivray, *Angew. Chem. Int. Ed.* **2004**, *43*, 232–236.
[11] a) G. S. Papaefstathiou, Z. Zhong, L. Geng, L. R. MacGillivray, *J. Am. Chem. Soc.* **2004**, *126*, 9158–9159; b) G. S. Papaefstathiou, I. G. Georgiev, T. Friščić, L. R. MacGillivray, *Chem. Commun.* **2005**, 3974–3976; c) Q. Chu, D. C. Swenson, L. R. MacGillivray, *Angew. Chem. Int. Ed.* **2005**, *44*, 3569–3572.
[12] a) G. S. Papaefstathiou, L. R. MacGillivray, *Angew. Chem. Int. Ed.* **2002**, *41*, 2070–2073; b) T. D. Hamilton, G. S. Papaefstathiou, L. R. MacGillivray, *J. Am. Chem. Soc.* **2002**, *124*, 11606–11607.
[13] a) J. J. Gilman, *Science* **1996**, *274*, 65; b) V. V. Boldyrev, K. Tkacova, *J. Mater. Synth. Process.* **2000**, *8*, 121–132.
[14] L. R. MacGillivray, J. L. Reid, J. A. Ripmeester, *J. Am. Chem. Soc.* **2000**, *122*, 7817–7818.
[15] a) S. R. Seidel, P. J. Stang, *Acc. Chem. Res.* **2002**, *35*, 972–983; b) M. Fujita, M. Tominaga, A. Hori, B. Therrien, *Acc. Chem. Res.* **2005**, *38*, 371–380; c) D. L. Dana, K. N. Raymond, *Acc. Chem. Res.* **1999**, *32*, 975–982; d) N. C. Gianneschi, M. S. Masar III, C. A. Mirkin, *Acc. Chem. Res.* **2005**, *38*, 825–837.
[16] a) S. Kitagawa, S. Noro, T. Nakamura, *Chem. Commun.* **2006**, 701–707; b) R. Custelcean, M. G. Gorbunova, *J. Am. Chem. Soc.* **2005**, *127*, 16362–16363; c) C.-D. Wu, A. Hu, L. Zhang, W. Lin, *J. Am. Chem. Soc.* **2005**, *127*, 8940–8941; d) M. Eddaoudi, J. Kim, N. Rosi, D. Vodak, J. Wachter, M. O'Keeffe, O. M. Yaghi, *Science* **2002**, *295*, 469–472.
[17] P. Praetorius, F. Korn, *Ber. Dtsch. Chem. Ges.* **1910**, *43*, 2744–2746.
[18] N. Alcock, P. de Meester, T. J. Kemp, *J. Chem. Soc. Perkin Trans. 2* **1979**, 921–926.
[19] F. D. Lewis, J. D. Oxman, J. C. Huffman, *J. Am. Chem. Soc.* **1984**, *106*, 466–468.
[20] a) R. Robson, *Inorg. Nucl. Chem. Lett.* **1970**, *6*, 125–128; b) H. Okawa, *Bull. Chem. Soc. Jpn.* **1970**, *43*, 3019.
[21] For recent developments, see: M. Nagarathinam, J. J. Vittal, *Macromol. Rapid Commun.* **2006**, *27*, 1091–1099.
[22] a) G. J. Halder, C. J. Kepert, *Aust. J. Chem.* **2006**, *59*, 597–604; b) T. Friščić, R. MacGillivray, *Z. Kristallogr.* **2005**, *220*, 351–363.
[23] a) M. Jansen, *Angew. Chem. Int. Ed. Engl.* **1987**, *26*, 1098–1110; b) P. Pyykkö, *Chem. Rev.* **1997**, *97*, 597–636.
[24] K. Cheng, B. M. Foxman, *J. Am. Chem. Soc.* **1977**, *99*, 8102–8203.
[25] T. D. Hamilton, G. S. Papaefstathiou, L. R. MacGillivray, *CrystEngComm* **2002**, *4*, 223–226.
[26] T. D. Hamilton, D.-K. Bučar, L. R. MacGillivray, *Chem. Commun.* **2007**, 1603–1604.
[27] G. S. Papaefstathiou, T. D. Hamilton, T. Friščić, L. R. MacGillivray, *Chem. Commun.* **2004**, 270–271.
[28] G. S. Papaefstathiou, T. Friščić, L. M. MacGillivray, *J. Am. Chem. Soc.* **2005**, *127*, 14160–14161.
[29] A. J. Blake, N. R. Champness, S. M. Chung, W.-S. Li, M. Schröder, *Chem. Commun.* **1997**, 1675–1676.
[30] a) L. Siman-Seveyrat, A. Hajjaji, E. Emziane, B. Guiffard, D. Guyomar, *Ceram. Int.* **2007**, *33*, 35–40; b) J. Lu, S. Yang, K. M. Ng, C.-H. Su, C.-S. Yeh, Y.-N. Wu, D.-B. Shieh, *Nanotechnology* **2006**, *17*, 5812–5820.
[31] G. R. Desiraju, *Angew. Chem. Int. Ed. Engl.* **1995**, *34*, 2311–2327.
[32] D. B. Mitzi, C. A. Field, W. T. A. Harrison, A. M. Guloy, *Nature* **1994**, *369*, 467–469.
[33] O. Kahn, *Acc. Chem. Res.* **2000**, *33*, 647–657.
[34] W. Lin, Z. Wang, L. Ma, *J. Am. Chem. Soc.* **1999**, *121*, 11249–11250.
[35] a) M. Fujita, D. Oguro, M. Miyazawa, H. Oka, K. Yamaguchi, K. Ogura, *Nature* **1995**, *378*, 469–471; b) P. J. Stang, D. H. Cao, K. Chen, G. M. Gray, D. C. Muddimann, R. D. Smith, *J. Am. Chem. Soc.* **1997**, *119*, 5163–5168; c) M. Tominaga, K. Suzuki, M. Kawano, T. Kusukawa, T. Ozeki, S. Sakamoto, K. Yamaguchi, M. Fujita, *Angew. Chem. Int. Ed.* **2004**, *43*, 5621–5625; d) S. Kitagawa, R. Kitaura, S. Noro, *Angew. Chem. Int. Ed.* **2004**, *43*, 2334–2375.
[36] a) J. S. Seo, D. Whang, H. Lee, S. I. Jun, J. Oh, Y. J. Jeon, K. Kim, *Nature* **2000**, *404*, 982–986; b) J. Yoshida, K. Itami, *Chem. Rev.* **2002**, *102*, 3693–3716.
[37] a) J. L. Atwood, L. J. Barbour, A. Jerga, *Science* **2002**, *296*, 2367–2369; J. L. C. Rowsell, E. C. Spencer, J. Eckert, J. A. K. Howard, O. M. Yaghi, *Science* **2005**, *309*, 1350–1354.
[38] M. Fujita, Y. J. Kwon, S. Washizu, K. Ogura, *J. Am. Chem. Soc.* **1994**, *116*, 1151–1152.
[39] G. S. Papaefstathiou, A. J. Kipp, L. R. MacGillivray, *Chem. Commun.* **2001**, 2462–2463.
[40] G. S. Papaefstathiou, C. Milios, L. R. MacGillivray, *Microporous Mesoporous Mater.* **2004**, *71*, 11–15.
[41] N. W. Ockwig, O. Delgado-Friedrichs, M. O'Keeffe, O. M. Yaghi, *Acc. Chem. Res.* **2005**, *38*, 176–182.
[42] M. Yoshizawa, M. Tamura, M. Fujita, *J. Am. Chem. Soc.* **2004**, *126*, 6846–6847.
[43] a) M. Yoshizawa, S. Miyagi, M. Kawano, K. Ishiguro, M. Fujita, *J. Am. Chem. Soc.* **2004**, *126*, 9172–9173; b) K. Takaoka, M. Kawano, T. Ozeki, M. Fujita, *Chem. Commun.* **2006**, 1625–1627.
[44] M. D. Pluth, R. G. Bergmann, K. N. Raymond, *Science* **2007**, *316*, 85–88.
[45] D. Braga, S. L. Giaffreda, F. Grepioni, A. Pettersen, L. Maini, M. Curzi, M. Polito, *Dalton Trans.* **2006**, 1249–1263.
[46] A. Orita, L. Jiang, T. Nakano, N. Ma, J. Otera, *Chem. Commun.* **2002**, 1362–1363.
[47] D. Braga, M. Curzi, A. Johansson, M. Polito, F. Grepioni, *Angew. Chem. Int. Ed.* **2006**, *45*, 142–146.

Received: April 23, 2007
Published Online: September 14, 2007

 © 2007 Wiley-VCH Verlag GmbH & Co. KGaA, Weinheim 

DOI: 10.1002/ejic.200700794

# Solid-State Anion–Guest Encapsulation by Metallosupramolecular Capsules Made from Two Tetranuclear Copper(II) Complexes

**Emilio Pardo,[a] Kevin Bernot,[a] Francesc Lloret,*[a] Miguel Julve,[a] Rafael Ruiz-García,[b,c] Jorge Pasán,[d] Catalina Ruiz-Pérez,[d] Danielle Cangussu,[e] Valeria Costa,[e] Rodrigue Lescouëzec,[e] and Yves Journaux*[e]**

**Keywords:** Copper / Host–guest systems / Magnetic properties / Polynuclear complexes / Structure elucidation

A new cationic tetranuclear copper(II) complex self-assembles from one 1,3-phenylenebis(oxamato) (mpba) bridging ligand and four $Cu^{II}$ ions partially blocked with *N*,*N*,*N*′,*N*′-tetramethylethylenediamine (tmen) terminal ligands. In the solid state, two of these tetracopper(II) oxamato complexes of bowl-like shape and helical conformation then serve as a building block for the generation of either hetero- (*MP*) or homochiral (*MM*/*PP*) dimeric capsules depending on the nature of the encapsulated anion guest, perchlorate or hexafluorophosphate. The overall magnetic behaviour of these metallosupramolecular capsules does not depend on the nature of the encapsulated anion guest, but it is consistent with the dimer-of-dimer structure of the tetracopper(II) cation host, where the interdimer magnetic coupling through the *meta*-phenylenediamidate bridge is negligibly small relative to the reasonably strong intradimer one across the oxamato bridge.

(© Wiley-VCH Verlag GmbH & Co. KGaA, 69451 Weinheim, Germany, 2007)

## Introduction

Coordination chemistry offers many possibilities for the construction of a seemingly limitless range of metallosupramolecular species based on metal–ligand coordinative interactions.[1] These include a great variety of metal cages formed by the self-assembly of rigid organic ligands and transition metal ions.[2–10] Some of them are formed with the use of templates and counterions, either cations[3] or anions,[4–7] that are hosted within the confined space of the charged metal cage and held through ionic interactions and/or weak coordination bonds. Others are even able to reversibly bind or stabilise neutral guest molecules through hydrophobic interactions and/or hydrogen bonds.[8] In contrast to their purely organic analogues prepared from covalent synthesis[9] and/or hydrogen-bond-directed self-assembly,[10] these metallosupramolecular capsules may possess other interesting properties ligated to the presence of the transition metal ions. Thus, the combination of the encapsulation ability with other metal-based electronic properties (redox, optical or magnetic) would render these assemblies suitable for applications as molecular sensors or switches.

In the search for self-assembling metallosupramolecular complexes with aromatic dioxamato ligands,[11a] we recently prepared double- and triple-stranded binuclear copper(II) complexes of the metallacyclophane- and metallacryptand-type from the self-assembly of two $Cu^{II}$ ions and either two or three 1,3-phenylenebis(oxamato) (mpba) ligands, respectively, which then served as building blocks for discrete hexa- and octanuclear copper(II) complexes.[11b–11d] In this communication, we report the syntheses, X-ray crystal structures and magnetic properties of two new tetranuclear oxamato copper(II) complexes of formula $[Cu_4(mpba)(tmen)_4(H_2O)_4](ClO_4)_4{\cdot}3H_2O$ (**1a**) and $[Cu_4(mpba)(tmen)_4(H_2O)_4](PF_6)_4{\cdot}2H_2O$ (**1b**) (tmen = *N*,*N*,*N*′,*N*′-tetramethylethylenediamine), which constitute unique examples of anion guest encapsulation in the solid state.

## Results and Discussion

Complexes **1a** and **1b** were synthesised in one step by a stoichiometric reaction (1:4) in water of the diethyl ester derivative of 1,3-phenylenebis(oxamic acid)-($H_2Et_2mpba$),[11a] previously treated with 4 equiv. of NaOH

[a] Departament de Química Inorgànica, Instituto de Ciencia Molecular (ICMOL), Universitat de València,
Paterna, Valencia, Spain
Fax: +34-963544328
E-mail: francisco.lloret@uv.es
[b] Departament de Química Orgànica, Instituto de Ciencia Molecular (ICMOL), Universitat de València,
Paterna, Valencia, Spain
[c] Fundació General de la Universitat de València (FGUV)
Valencia, Spain
[d] Laboratorio de Rayos X y Materiales Moleculares, Departamento de Fisica Fundamental II, Universidad de La Laguna,
Tenerife, Spain
[e] Laboratoire de Chimie Inorganique et Matériaux Moléculaires, Université Pierre et Marie Curie-Paris 6, UMR 7071,
Paris, France
Fax: +33-144273841
E-mail: jour@ccr.jussieu.fr

 © 2007 Wiley-VCH Verlag GmbH & Co. KGaA, Weinheim 

that serve to deprotonate and hydrolyse the amide and ester groups, respectively, and the perchlorate or nitrate salts of the cationic mononuclear copper(II) complex $[Cu(tmen)]^{2+}$, which were prepared in situ from a mixture of either $Cu(ClO_4)_2 \cdot 6H_2O$ or $Cu(NO_3)_2 \cdot 3H_2O$ and tmen in a 1:1 relation. They were isolated as either the perchlorate (**1a**) or the hexafluorophosphate (**1b**) salts by addition of $KPF_6$ at the end of the reaction in the latter case.

The structures of **1a** and **1b** consist of tetranuclear copper(II) cations, $[Cu_4(mpba)(tmen)_4(H_2O)_4]^{4+}$ (Figure 1), crystallisation water molecules and either perchlorate or hexafluorophosphate anions, respectively. The tetracopper(II) cations are formed by four $[Cu(tmen)(H_2O)]^{2+}$ subunits connected by the tetrakis(bidentate) mpba ligand, which adopts a helical conformation with the two oxamato bridging groups tilted up and down with respect to the plane of the *m*-phenylene spacer. The values of the torsion angle around the N(amide)–C(phenylene) bonds ($\phi$) are 91.0(3) and 108.8(4)° for **1a** and 90.7(5) and 112.7(6)° for **1b**, values which are greater than that of $H_2Et_2$mpba [$\phi$ = 32.6(5)°].[11a] This gives rise to chiral bisbinuclear entities of pseudo-twofold symmetry, either *M* or *P* helical conformers, which are made up of two oxamato-bridged $Cu^{II}_2$ units connected through a *meta*-phenylenediamidate bridge between one of the two copper atoms of each binuclear unit (Figure 1, left). The intramolecular distances between the copper atoms through the oxamato bridge average 5.190(2) (**1a**) and 5.224(2) Å (**1b**), whereas those through the *meta*-phenylenediamidate bridge are 7.762(2) (**1a**) and 7.571(2) Å (**1b**).

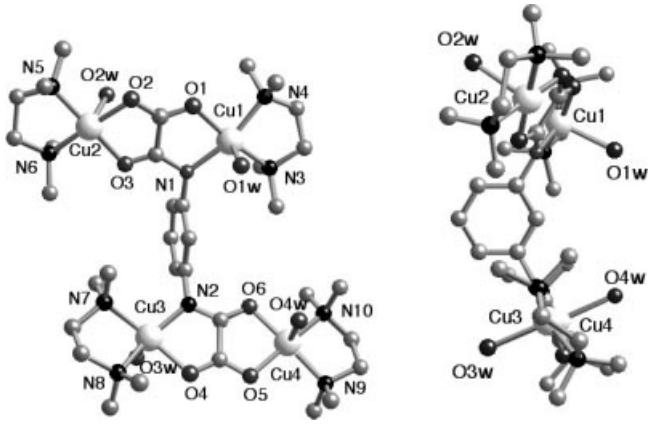


Figure 1. Front and side views of the cationic tetracopper unit of **1a** with the atom numbering scheme for the metal coordination environments (hydrogen atoms are omitted for clarity). Selected intermetallic distances [Å] with standard deviations in parentheses: Cu1–Cu2 5.199(2), Cu1–Cu3 7.762(2), Cu1–Cu4 7.989(2), Cu2–Cu3 7.796(2), Cu2–Cu4 10.844(2) and Cu3–Cu4 5.180(2) for **1a**; Cu1–Cu2 5.229(2), Cu1–Cu3 7.571(2), Cu1–Cu4 8.122(2), Cu2–Cu3 7.654(2), Cu2–Cu4 10.934(2) and Cu3–Cu4 5.218(2) for **1b**.

The four crystallographically independent copper atoms of **1a** and **1b** exhibit five-coordinate square pyramidal geometries, $CuN_3O_2$ for Cu1 and Cu3 and $CuN_2O_3$ for Cu2 and Cu4, with axially coordinated water molecules [Cu–Ow 2.283(8)–2.521(9) for **1a** and 2.365(7)–2.460(6) Å for **1b**], which are arranged in a *trans* position within each binuclear unit (Figure 1, right). The values of the geometric $\tau$ parameter are in the range 0.02–0.20 (for **1a**) and 0.01–0.12 (for **1b**) ($\tau$ = 0 and 1 for ideal square pyramidal and trigonal bipyramidal geometries, respectively).[11d] The two oxamato groups of the mpba ligand coordinate through the amidate nitrogen and carboxylate oxygen atoms to the Cu1 and Cu3 atoms [Cu–N 1.997(6)–2.012(7) (**1a**) and 2.002(6)–2.004(6) Å (**1b**); Cu–O 1.979(5)–2.004(7) (**1a**) and 1.984(5)–2.003(6) Å (**1b**)] and through the carbonyl oxygen atoms to the Cu2 and Cu4 atoms [Cu–O 1.948(5)–1.965(9) (**1a**) and 1.951(5)–1.996(5)(**1b**)], whereas the remaining positions of the equatorial plane are occupied by two amine nitrogen atoms from the tmen ligands [Cu–N 1.994(7)–2.048(7) (**1a**) and 2.000(7)–2.036(8) Å (**1b**)]. The copper basal planes and the oxamato plane of each binuclear unit are quite coplanar [dihedral angles in the range 3.8(2)–17.7(2) (**1a**) and 6.7(2)–11.2(2)° (**1b**)], whereas they are almost perpendicular to the phenylene plane [dihedral angles in the range 70.4(3)–89.3(2) (**1a**) and 75.4(2)–84.1(2)° (**1b**)]. Because of the *meta* topology of the ligand spacer, the two mean planes of the two oxamato bridging groups form a dihedral "bite" angle of 54.5(2) (**1a**) and 53.9(1)° (**1b**), which thus confers a global bowl-like shape to the tetracopper(II) cations (Figure 1, right).

Interestingly, two symmetry-related, bowl-shaped tetranuclear copper(II) cations of opposite (**1a**) or identical (**1b**) chirality encapsulate two perchlorate and three hexafluorophosphate anions, respectively, to yield either a centrosymmetric heterochiral (*MP* mesomer) or a racemic mixture of twofold homochiral (*MM* and *PP* enantiomers) dimeric capsules (Figure 2a and Figure 2b, respectively). The diastereoisomer differentiation that occurs in these 2:2 and 2:3 host–guest complexes, $\{2(ClO_4)\grave{I}meso\text{-}(MP)\text{-}[Cu_4(mpba)(tmen)_4(H_2O)_4]_2\}^{6+}$ and $\{3(PF_6)\grave{I}rac\text{-}(MM/PP)\text{-}[Cu_4(mpba)(tmen)_4(H_2O)_4]_2\}^{5+}$, respectively, would be likely related to the different size and geometry of the tetrahedral perchlorate and octahedral hexafluorophosphate anions. The intermolecular distances between the equivalent copper atoms from each tetranuclear cation are in the range 9.988(2)–14.626(2) (**1a**) and 7.031(2)–14.135(2) Å (**1b**), values which can be taken as the approximate dimensions of these nanometre-sized metallosupramolecular capsules.

The encapsulated $ClO_4^-$ and $PF_6^-$ anions establish weak dative interactions with the coordinatively unsaturated copper atoms [Cu–O 2.894(2) Å (**1a**) and Cu–F 3.044(8)–3.221(8) Å (**1b**)], together with hydrogen bonds with the axially coordinated water molecules pointing toward the inner side of the capsule [Ow–O 2.977(9) Å (**1a**) and Ow–F 2.858(8)–2.933(8) Å (**1b**)]. These coordinative and hydrogen-bonding interactions between the cationic hosts and the anionic guests contribute to stabilise the resulting noncovalent capsules, together with the host–guest Coulombic attractions. The two encapsulated $ClO_4^-$ anions in **1a** occupy equivalent positions within the confined space of the capsule [Cl3–Cl3$^{I}$ 5.247(4) Å] (Figure 2a), whereas the three encapsulated $PF_6^-$ anions in **1b** are disposed in a triangular

 © 2007 Wiley-VCH Verlag GmbH & Co. KGaA, Weinheim 

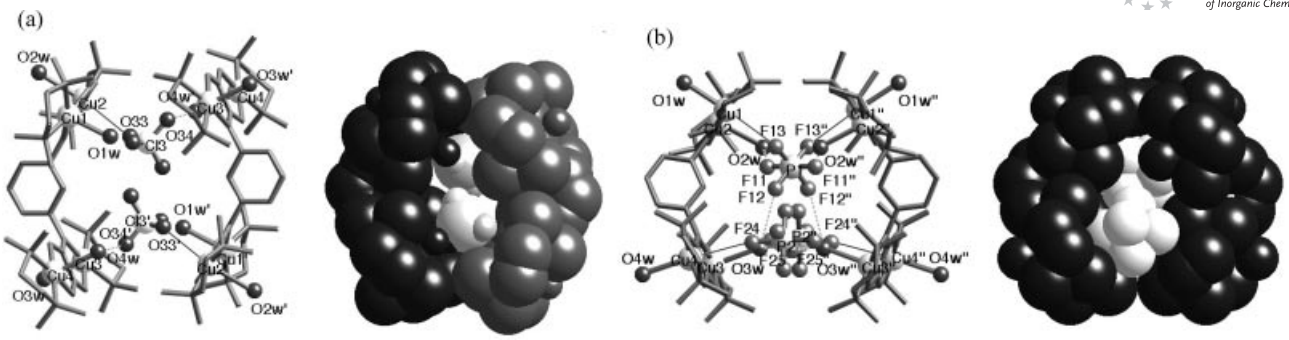


Figure 2. Perspective views of the dimeric capsule of **1a** (a) and **1b** (b) with two and three encapsulated perchlorate and hexafluorophosphate anions, respectively (hydrogen atoms are omitted for clarity). Coordinative and hydrogen bonds with the encapsulated anions are drawn as solid and dashed lines, respectively, in the ball-and-stick model (left). Atoms from each tetracopper helical unit are represented by black (*M* conformer) and grey (*P* conformer) spheres, whereas those of the encapsulated perchlorate and hexafluorophosphate anions are white in the space-filling model (right). Selected intermetallic distances [Å] with standard deviations in parentheses: Cu1–Cu1$^{I}$ 9.988(2), Cu2–Cu2$^{I}$ 14.626(2), Cu3–Cu3$^{I}$ 10.718(2) and Cu4–Cu4$^{I}$ 11.674(2) for **1a**; Cu1–Cu1$^{II}$ 7.031(2), Cu2–Cu2$^{II}$ 10.094(2), Cu3–Cu3$^{II}$ 7.485(2) and Cu4–Cu4$^{II}$ 14.135(2) for **1b** (I = –*x*, – *y*, – *z*; II = –*x*, *y*, 1/2 – *z*).

arrangement [P1–P2 5.632(6) Å and P2–P2$^{II}$ 8.898(7) Å] (Figure 2b).

In the crystal lattice, some of the unencapsulated $ClO_4^-$ and $PF_6^-$ anions also establish weak coordinative bonds with the copper atoms [Cu–O 2.874(8) Å (**1a**) and Cu–F 3.411(8) Å (**1b**)] and hydrogen bonds with the axially coordinated water molecules pointing toward the outer side of the capsule [Ow–O 2.563(8)–2.918(8) Å (**1a**) and Ow–F 2.951(8)–2.959(8) Å (**1b**)]. This situation gives rise to a rather close packing of the spherical-shaped capsules for **1a** and **1b** (Figure 3a and Figure 3b, respectively). Certainly, these intermolecular interactions can play a nonnegligible role in the different metallosupramolecular structural motifs of **1a** and **1b**.

The magnetic properties of **1a** and **1b** in the form of both $\chi_M$ and $\chi_M T$ versus $T$ plots ($\chi_M$ being the magnetic susceptibility per $Cu_4$ unit and $T$ the temperature) indicate an overall antiferromagnetic interaction with a singlet spin ($S$ = 0) ground state (Figure 4). At 315 K, $\chi_M T$ is 0.82 (**1a**) and 0.88 $cm^3 K mol^{-1}$ (**1b**), values which are well below that expected for four magnetically isolated Cu$^{II}$ ions ($\chi_M T$ = 1.65 $cm^3 mol^{-1} K$ with $g$ = 2.1). Upon cooling, $\chi_M T$ decreases continuously and vanishes around 60 (**1a**) and 50 K (**1b**), whereas $\chi_M$ shows a rounded maximum at 310 (**1a**) and 295 K (**1b**).

The temperature dependence of the magnetic susceptibility data of **1a** and **1b** were fitted according to the spin Hamiltonian for a "dimer-of-dimers" model, $\mathbf{H} = -J(\mathbf{S}_1 \cdot \mathbf{S}_2 + \mathbf{S}_3 \cdot \mathbf{S}_4) - J'(\mathbf{S}_1 \cdot \mathbf{S}_3) + g\beta(\mathbf{S}_1 + \mathbf{S}_2 + \mathbf{S}_3 + \mathbf{S}_4) \cdot B$ [Equation (1), with $S_1 = S_2 = S_3 = S_4 = S_{Cu} = 1/2$], where $J$ ($J = J_{12} = J_{34}$) and $J'$ ($J' = J_{13}$) are the intra- and interdimer coupling constants, respectively, and $g$ is the Zeeman factor of the Cu$^{II}$ ions.[12] In this model, the interdimer interactions given by $J''$ ($J'' = J_{14} = J_{23}$) and $J'''$ ($J''' = J_{24}$) were ignored because they involve longer exchange pathways. The quality of the fit according to this model does not depend on the sign and magnitude of the $J'$ value, which can be varied from zero to a few tens of $cm^{-1}$, either positive or negative, with a relatively small variation in the $J$ value.[13]

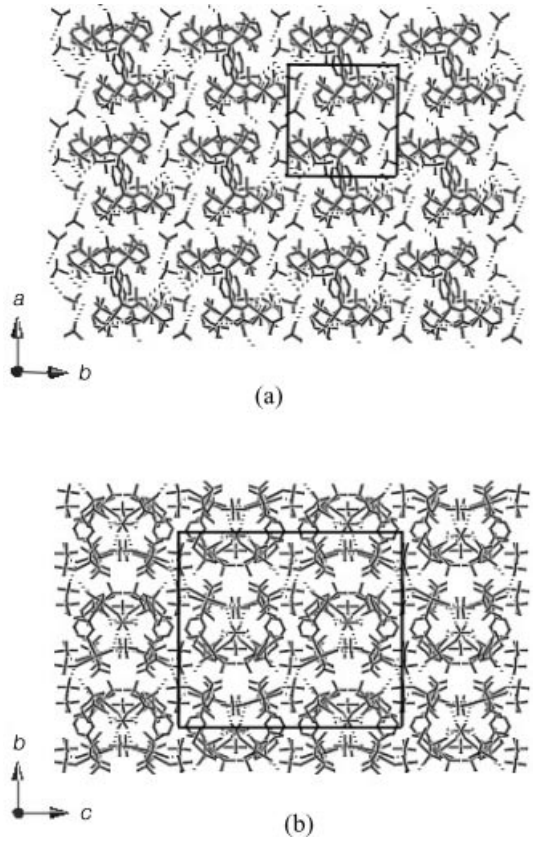


Figure 3. View of the crystal packing of the dimeric capsules of **1a** (a) and **1b** (b) with both encapsulated and unencapsulated perchlorate and hexafluorophosphate anions, respectively, and crystallisation water molecules (hydrogen atoms are omitted for clarity). Coordinative and hydrogen bonds with the anions are drawn as solid and dashed lines, respectively.

This fact suggests that the interdimer magnetic coupling through the *meta*-phenylenediamidate bridge is negligible relative to the intradimer one across the oxamato bridge. Least-squares fit of the experimental data through the Bleaney–Bowers equation for a dimer model ($J'$ = 0) gave

 © 2007 Wiley-VCH Verlag GmbH & Co. KGaA, Weinheim 

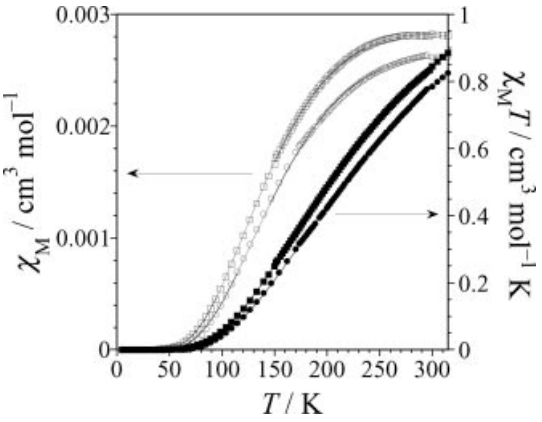


Figure 4. Temperature dependence of $\chi_M$ and $\chi_M T$ for **1a** (○,●) and **1b** (□,■). The solid lines are the best fit curves (see text).

$J = -350$ cm$^{-1}$, $g = 2.09$ and $R = 3.4 \times 10^{-8}$ for **1a**, and $J = -330$ cm$^{-1}$, $g = 2.10$ and $R = 3.0 \times 10^{-8}$ for **1b** {$R$ is the agreement factor defined as $R = \Sigma[(\chi_M T)_{exp} - (\chi_M T)_{calcd}]^2 / \Sigma[(\chi_M T)_{exp}]^2$}. The theoretical curves reproduce very well the experimental data over the whole temperature range (solid lines in Figure 4). The calculated $-J$ values for **1a** and **1b** agree with those reported for related strong antiferromagnetically coupled oxamato-bridged dicopper(II) complexes ($-J$ = 366–425 cm$^{-1}$).[14]

## Conclusions

Discrete cationic tetranuclear copper(II) complexes possessing a helical conformation and a bowl-like shape were self-assembled through metal–ligand coordinative interactions from a *m*-phenylenedioxamato acting as a tetrakis(bidentate) bridging ligand toward four $Cu^{II}$ ions with a diamine as a blocking ligand. Importantly, two of these tetracopper(II) cations further self-assemble in the solid state through noncovalent host–guest interactions (Coulombic attractions, weak coordination and hydrogen bonds) with anions of different size and geometry to yield unusual examples of homo- and heterochiral metallosupramolecular capsules. Current efforts are devoted to analyse the influence of the nature of the ligand spacer (size, rigidity and substitution pattern) of related tetranuclear copper(II) oxamato complexes on their anion encapsulation ability in the solid state.

## Experimental Section

**Preparation of the Complexes:** A solution of $H_2Et_2$mpba (0.077 g, 0.25 mmol) in water (10 mL) and NaOH (0.040 g, 1.0 mmol) was added dropwise to a solution of $Cu(ClO_4)_2 \cdot 6H_2O$ (0.37 g, 1.0 mmol) and tmen (0.150 mL, 1.0 mmol) in water (10 mL). The obtained deep-green solution was filtered and allowed to evaporate in air at room temperature. X-ray quality green prisms of **1a** were obtained after several days on standing. Yield: 0.36 g (75%). IR (KBr): $\tilde{\nu}$ = 3419 (OH), 2986 and 2909 (CH), 1636 (CO), 1144, 1113, and 1089 (ClO) cm$^{-1}$. $C_{34}H_{82}Cl_4Cu_4N_{10}O_{29}$ (1491.06): calcd. C 27.36, H 5.50, N 9.39; found C 27.06, H 5.45, N 9.45.

Complex **1b** was prepared in a similar way as described for **1a**, but with the use of $Cu(NO_3)_2 \cdot 3H_2O$ (0.24 g, 1.0 mmol), and solid $KPF_6$ (0.19 g, 1.0 mmol) was added at the end of the reaction. X-ray quality green prisms of **1b** were obtained by slow evaporation at room temperature of the deep-green filtered solution after 1 d. Yield: 0.31 g (80%). IR (KBr): $\tilde{\nu}$ = 3428 (OH), 2991 and 2930 (CH), 1633 (CO), 841 (PF) cm$^{-1}$. $C_{34}H_{80}Cu_4F_{24}N_{10}O_{12}P_4$ (1655.12): calcd. C 24.65, H 4.83, N 8.46; found C 24.34, H 4.72, N, 8.68.

**X-ray Crystallographic Data:** $C_{34}H_{82}Cl_4Cu_4N_{10}O_{29}$ (**1a**), $M$ = 1491.06, triclinic, space group $P\bar{1}$, $a$ = 14.3494(9) Å, $b$ = 14.8957(15) Å, $c$ = 15.1787(19) Å, $\alpha$ = 70.862(8)°, $\beta$ = 86.966(6)°, $\gamma$ = 88.797(6)°, $V$ = 3060.7(5) Å$^3$, $T$ = 100(2) K, $Z$ = 2, $\rho_{calcd.}$ = 1.618 g cm$^{-3}$, $\mu$(Mo-$K_\alpha$) = 1.634 mm$^{-1}$. $C_{34}H_{80}Cu_4F_{24}N_{10}O_{12}P_4$ (**1b**), $M$ = 1655.12, monoclinic, space group $C2/c$, $a$ = 16.045(2) Å, $b$ = 26.659(2) Å, $c$ = 30.758(3) Å, $\beta$ = 96.187(10)°, $V$ = 13080(3) Å$^3$, $T$ = 293(2) K, $Z$ = 8, $\rho_{calcd.}$ = 1.681 g cm$^{-3}$, $\mu$(Mo-$K_\alpha$) = 1.506 mm$^{-1}$. 13164 (**1a**) and 14223 (**1b**) unique reflections, and 11057 (**1a**) and 6115 (**1b**) observed with $I > 2\sigma(I)$. All the measured independent reflections were used in the analysis. The structures were solved by direct methods and refined with full-matrix least-squares technique on $F^2$ by using the SHELXS-97 and SHELXL-97 programs. The hydrogen atoms from the organic ligands were calculated and refined with isotropic thermal parameters, whereas those from the water molecules were neither found nor calculated. Refinement of 730 (**1a**) and 790 (**1b**) variables with anisotropic thermal parameters for all non-hydrogen atoms gave $R$ = 0.0743 (**1a**) and 0.0854 (**1b**), and $R_w$ = 0.1920 (**1a**) and 0.1379 (**1b**), with $S$ = 1.058 (**1a**) and 1.013 (**1b**) (observed data).

CCDC-650175 (**1a**) and -650176 (**1b**) contain the supplementary crystallographic data for this paper. These data can be obtained free of charge from The Cambridge Crystallographic Data Centre via www.ccdc.cam.ac.uk/data_request/cif.

**Magnetic Measurements:** Variable-temperature (2.0–315 K) magnetic susceptibility measurements were carried out on powdered samples of **1a** and **1b** with a Quantum Design SQUID magnetometer. The magnetic data were corrected for diamagnetism of the sample holder and the constituent atoms and for the temperature-independent paramagnetism of the copper atoms ($60 \times 10^{-6}$ cm$^3$ per $Cu^{II}$ ion) as well.

## Acknowledgments

This work was supported by the Ministerio de Educación y Ciencia (MEC, Spain) (Projects CTQU2004-03633, MAT2004-03112 and "Factoria de Cristalización, CONSOLIDER INGENIO-2010"), the Centre National de la Recherche Scientifique (CNRS, France), the Coordenação de Aperfeiçoamento de Pessoal de Nível Superior (CAPES, Brazil), the European Union through the Network QuEMOLNA (Project MRTN-CT-2003-504880) and the Gobierno Autónomo de Canarias (PI2002/175). E. P., D. C. and V. C. thank the MEC and the CAPES for grants.

[1] a) S. Leininger, B. Olenyuk, P. J. Stang, *Chem. Rev.* **2000**, *100*, 853; b) G. F. Swiegers, T. J. Malefetse, *Chem. Rev.* **2000**, *100*, 3483.

[2] a) O. D. Fox, N. K. Dalley, R. G. Harrison, *J. Am. Chem. Soc.* **1998**, *120*, 7111; b) O. D. Fox, J. F. Y. Leung, J. M. Hunter, N. K. Dalley, R. G. Harrison, *Inorg. Chem.* **2000**, *39*, 783.

[3] a) D. L. Caulder, R. E. Powers, T. N. Parac, K. N. Raymond, *Angew. Chem. Int. Ed.* **1998**, *37*, 1840; b) T. N. Parac, D. L. Caulder, K. N. Raymond, *J. Am. Chem. Soc.* **1998**, *120*, 8003; c) M. Ziegler, J. L. Brumaghin, K. N. Raymond, *Angew. Chem. Int. Ed.* **2000**, *39*, 4119.

 © 2007 Wiley-VCH Verlag GmbH & Co. KGaA, Weinheim 

[4] a) H. Amouri, M. N. Rager, F. Cagnol, J. Vaissermann, *Angew. Chem. Int. Ed.* **2001**, *40*, 3636; b) H. Amouri, L. Mimassi, M. N. Rager, B. E. Mann, C. Guyard-Duhayon, L. Raehm, *Angew. Chem. Int. Ed.* **2005**, *44*, 4543.
[5] a) J. S. Fleming, K. L. V. Mann, C.-A. Carraz, E. Psillakis, J. C. Jeffery, J. A. McCleverty, M. D. Ward, *Angew. Chem. Int. Ed.* **1998**, *37*, 1279; b) R. L. Paul, S. P. Argent, J. C. Jeffery, J. P. Harding, J. M. Lynam, M. D. Ward, *Dalton Trans.* **2004**, 3453.
[6] a) R.-D. Schnebeck, E. Freisinger, B. Lippert, *Angew. Chem. Int. Ed.* **1999**, *38*, 168; b) R.-D. Schnebeck, E. Freisinger, F. Glahé, B. Lippert, *J. Am. Chem. Soc.* **2000**, *122*, 1381.
[7] a) S. Manne, G. Huttner, L. Zsolnai, K. Heinze, *Angew. Chem. Int. Ed. Engl.* **1996**, *35*, 2808; b) D. A. McMorran, P. J. Steel, *Angew. Chem. Int. Ed.* **1998**, *37*, 3295; c) C.-Y. Su, Y.-P. Cai, C.-L. Chen, F. Lissner, B.-S. Kang, W. Kaim, *Angew. Chem. Int. Ed.* **2002**, *41*, 3371.
[8] a) M. Fujita, S.-Y. Yu, T. Kusukawa, H. Funaki, K. Ogura, Y. Yamaguchi, *Angew. Chem. Int. Ed.* **1998**, *37*, 2082; b) N. Takeda, K. Umemoto, M. Yamaguchi, M. Fujita, *Nature* **1999**, *398*, 794; c) S.-Y. Yu, T. Kusukawa, K. Biradha, M. Fujita, *J. Am. Chem. Soc.* **2000**, *122*, 2665; d) K. Umemoto, H. Tsukui, T. Kusukawa, K. Biradha, M. Fujita, *Angew. Chem. Int. Ed.* **2001**, *40*, 2620.
[9] a) D. J. Cram, S. Karvach, Y. H. Kim, L. Baczynskyj, G. W. Kalleymeyn, *J. Am. Chem. Soc.* **1985**, *107*, 2575; b) J. Gabard, A. Collect, *J. Chem. Soc. Chem. Commun.* **1981**, 1137; c) N. Chopra, J. C. Sherman, *Angew. Chem. Int. Ed.* **1999**, *38*, 1955.
[10] a) R. Wayler, J. Mendoza, J. Rebek Jr, *Angew. Chem. Int. Ed. Engl.* **1993**, *32*, 1699; b) M. M. Conn, J. Rebek Jr, *Chem. Rev.* **1997**, *97*, 1647; c) J. Rebek Jr, *Chem. Commun.* **2000**, 637; d) A. Shivanyuk, J. Rebek Jr, *Chem. Commun.* **2001**, 2374.
[11] a) G. Blay, I. Fernández, J. R. Pedro, R. Ruiz-García, M. C. Muñoz, J. Cano, R. Carrrasco, *Eur. J. Org. Chem.* **2003**, *9*, 1627; b) E. Pardo, K. Bernot, M. Julve, F. Lloret, J. Cano, R. Ruiz-García, F. S. Delgado, C. Ruiz-Pérez, X. Ottenwaelder, Y. Journaux, *Inorg. Chem.* **2004**, *43*, 2768; c) E. Pardo, K. Bernot, M. Julve, F. Lloret, J. Cano, R. Ruiz-García, J. Pasán, C. Ruiz-Pérez, X. Ottenwaelder, Y. Journaux, *Chem. Commun.* **2004**, 920; d) E. Pardo, R. Ruiz-García, F. Lloret, M. Julve, J. Cano, J. Pasán, C. Ruiz-Pérez, Y. Filali, L. M. Chamoreau, Y. Journaux, *Inorg. Chem.* **2007**, *46*, 4504.
[12] R. Ruiz, F. Lloret, M. Julve, J. Faus, M. C. Muñoz, X. Solans, *Inorg. Chim. Acta* **1998**, *268*, 263.
[13] Least-squares fit of the magnetic susceptibility data of **1a** and **1b** by full-matrix diagonalisation of the appropriate spin Hamiltonian for a tetranuclear model, $\mathbf{H} = -J(\mathbf{S}_1\cdot\mathbf{S}_2 + \mathbf{S}_3\cdot\mathbf{S}_4) - J'(\mathbf{S}_1\cdot\mathbf{S}_3) - J''(\mathbf{S}_1\cdot\mathbf{S}_4 + \mathbf{S}_2\cdot\mathbf{S}_3) - J'''(\mathbf{S}_2\cdot\mathbf{S}_4) + g\beta(\mathbf{S}_1 + \mathbf{S}_2 + \mathbf{S}_3 + \mathbf{S}_4)\cdot B$ [Equation (2), with $S_1 = S_2 = S_3 = S_4 = S_{Cu} = 1/2$], leads to the same conclusions than those derived from the dimer-of-dimers model.
[14] a) M. Verdaguer, O. Kahn, M. Julve, A. Gleizes, *Nouv. J. Chim.* **1985**, *9*, 325; b) S. Emori, K. Todoko, *Bull. Chem. Soc. Jpn.* **1993**, *66*, 3513.

Received: July 26, 2007
Published Online: September 4, 2007

 © 2007 Wiley-VCH Verlag GmbH & Co. KGaA, Weinheim 

DOI: 10.1002/ejic.200700640

# [(Pyridylcarbonyl)pyridyl]triazolopyridines, Useful Ligands for the Construction of Polynuclear Coordination Compounds – Synthesis, Crystal Structure and Magnetic Properties of a Novel Tetranuclear Copper(II) Cubane

**Belén Abarca,*[a] Rafael Ballesteros,[a] Mimoun Chadlaoui,[a] Carmen Ramirez de Arellano,[a] and José A. Real*[b]**

*Dedicated to Professor Ramón Mestres on the occasion of his retirement*

**Keywords:** Polydentate ligands / Triazolopyridine ligands / Copper(II) complexes / Tetranuclear complexes / Molecular magnetism

A new tetranuclear cubane $Cu_4O_4$ complex has been synthesised from assembly of $Cu^{II}$ ions and the polydentate ligand (pyridin-2-yl){6-([1,2,3]triazolo[1,5-*a*]pyridin-3-yl)pyridin-2-yl}methanone. Crystallographic analysis indicates that the $Cu_4O_4$ unit has an $S_4$ symmetry. The magnetic properties have been analysed using the $H = -2\sum_{i,j} J_{ij} S_i S_j$ spin Hamiltonian. Two distinct coupling constants, $2J_{1,3} = -37.4$ cm$^{-1}$ and $2J_{1,2} = -2.6$ cm$^{-1}$, obtained from the fitting of the experimental data have been rationalised on the basis of a density functional study of magnetostructural correlations in cubane complexes containing the $Cu_4O_4$ core.

(© Wiley-VCH Verlag GmbH & Co. KGaA, 69451 Weinheim, Germany, 2007)

## Introduction

High-nuclearity transition-metal complexes are of importance as new magnetic materials,[1] single molecular magnets (SMM),[2–5] in the emerging science of nanomaterials,[6] and as models for the multimetal active sites of metal storage proteins.[7]

Despite the interest in the properties of such systems, synthetic methods have to reach the level of efficiency attained with mononuclear complexes, and the term "serendipity" is frequently used to explain why one polynuclear complex is obtained rather than another.

Copper(II) complexes are particularly popular since the ion is paramagnetic and polynuclear clusters are easily accessible. Copper(II) forms many dinuclear complexes in which it shows a basically square-planar coordination with two bridging ligands, very frequently hydroxide or alkoxide groups, linking the two metals (Scheme 1, **I**). Copper(II) readily accepts a fifth ligand above the plane, and this offers a means of association of two dimeric units to give either the so-called cubane unit (Scheme 1, **II**) or the stepped cubane (Scheme 1, **III**).[8]

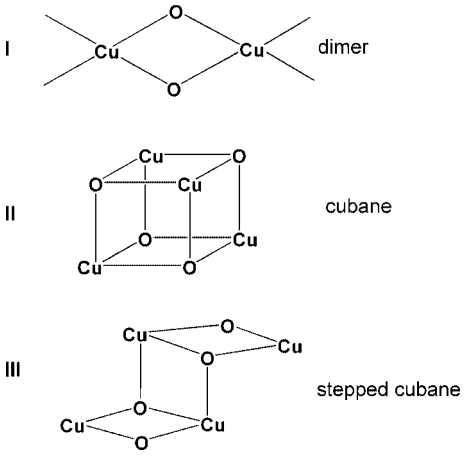


Scheme 1. Di- and tetranuclear copper(II) species.

During our research on the chemistry of [1,2,3]triazolo[1,5-*a*]pyridines, we had synthesized (pyridin-2-yl)([1,2,3]triazolo[1,5-*a*]pyridin-7-yl)methanones of type **1**,[9,10] as starting materials to prepare poly(pyridylcarbonyl)pyridines of type **2**, polydentate ligands able to make high-nuclearity clusters (Scheme 2).[11] In this context we had found an interesting structural feature for the precursor **3A** (**1**, R =

[a] Departamento de Química Orgánica, Facultad de Farmacia, Universidad de Valencia,
Avda. Vicente Andrés Estellés s/n, 46100 Burjassot (Valencia), Spain
Fax: +34-963544939
E-mail: Belen.Abarca@uv.es
[b] Instituto de Ciencia Molecular / Departamento de Química Inorgánica, Universidad de Valencia, Edificios de Institutos de Paterna,
P. O. Box 22085, 46071, Valencia, Spain
E-mail: jose.a.real@uv.es

 © 2007 Wiley-VCH Verlag GmbH & Co. KGaA, Weinheim 

pyridin-2-yl) (Scheme 3). The $^1$H NMR spectrum demonstrates that this compound exists almost entirely as its isomer **3B** (R = 2-PyCO).[10] To account for this structure we assumed that, in solution, the first formed compound **3A** (R = 2-PyCO) {3-(pyridin-2-yl)[1,2,3]triazolo[1,5-*a*]pyridin-7-yl derivative} is in equilibrium with the diazo form, an intermediate which may undergo a new ring-chain isomerisation,[12,13] giving **3B** {6-{[1,2,3]triazolo[1,5-*a*]pyridin-3-yl}pyridin-2-yl derivative} (see Scheme 3). By a $^1$H NMR study and DFT/B3LYP/6-31G* calculations of a series of 7-substituted 3-(pyridin-2-yl)triazolopyridines, we had proved that the **A/B** ratio depends on the electronic properties of the substituent R. Electron-donating substituents [$SiMe_3$, $B(OR)_2$] favour the **A** form, electron-withdrawing substituents [COMe, Br, Cl, I, *p*-MeOPh] favour the **B** form, and only in the case R = Me, both forms are present (75% of **A**, 25% of **B**).[14]

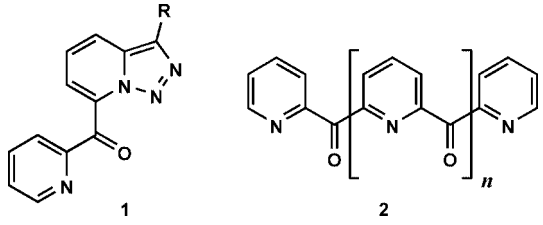


Scheme 2.

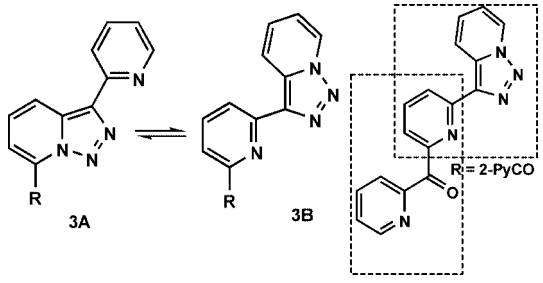


Scheme 3.

The structure **3B** (R = 2-PyCO) has two interesting features as a potential ligand to form high-nuclearity transition-metal complexes (Scheme 3). On one hand, a part of the structure is analogue to that of the 3-(pyridin-2-yl)-triazolopyridines, which coordinates through the N2 and N11 atoms, i. e. to $Cu^{II}$, and $Fe^{II}$ ions.[15,16] In particular, the $Fe^{II}$ derivatives with $NCS^-$ and $NCSe^-$ coordinating anions undergo spin crossover behaviour. On the other hand, the 2,2′-dipyridyl ketone moiety is also present. This moiety can undergo metal-assisted nucleophilic attack by solvent molecules on its carbonyl function, thus yielding its *gem*-diol or hemiacetal form, depending on the solvent. Subsequent deprotonations of the hydroxyl groups can yield the mono- or dianion (in the case of the *gem*-diol form), which can adopt a large number of coordination modes, bridging up to five metal ions. The latter coordinating motive has been extensively studied by Perlepes et al.[17–20] and have important magnetic properties.

In this context, we have been investigating **3B** as a suitable candidate to have similar solvolysis, deprotonation, and coordination properties. Here we report the synthesis, crystal structure and magnetic behaviour of the tetranuclear cubane compound $[Cu(\mathbf{3B^*})]_4(NO_3)_4{\cdot}8H_2O$ where the ligand **3B*** is the hemiacetal of the (pyridin-2-yl){6-([1,2,3]triazolo[1,5-*a*]pyridin-3-yl)pyridin-2-yl}methanone.

## Results and Discussion

The molecular structure of a representative fragment of the cationic unit $[Cu(\mathbf{3B^*})]_4^{4+}$ is shown in Figure 1. The cubane shows an $S_4$ symmetry with the $Cu^{II}$ ion in the middle of a strongly distorted $[CuO_3N_3]$ octahedron. Two nitrogen atoms belong to the [N(2) and N(11)] atoms of one ligand **3B*** while the remaining nitrogen atom belongs to the isolate pyridine group [$N(21)^i$] of a second **3B***. The three oxygen atoms correspond to the O(1) site, one belongs to the same ligand that the two nitrogen (N2 and N11) while the other two corresponds to two adjacent ligands. There are four short distances Cu–N(11) 2.0243(23), Cu–N(21) 1.9923(23), Cu–O(1) 1.9519(18), and Cu–$O(1)^{ii}$ = 1.9984(18) Å and two elongated distances Cu–N(2)

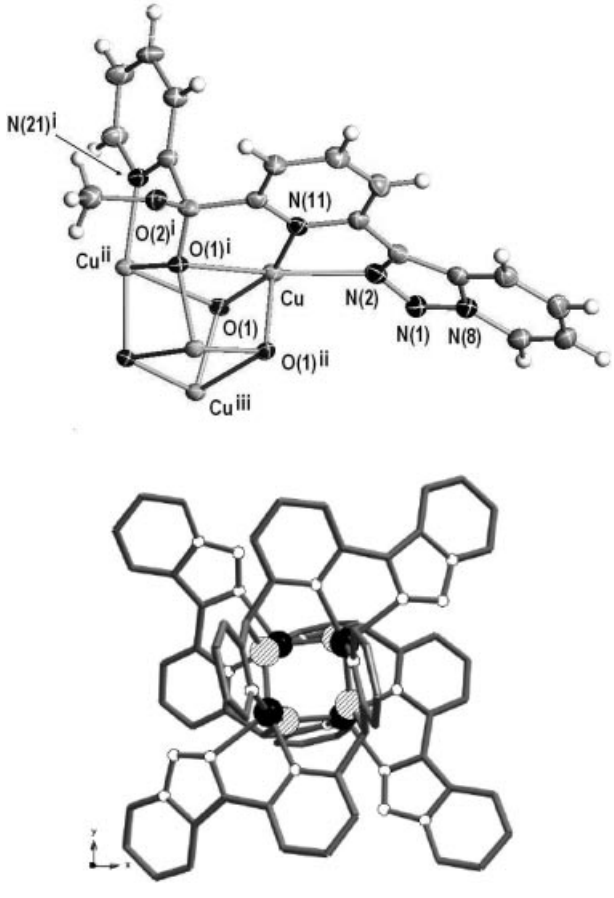


Figure 1. Ellipsoid plot of a representative fragment of the $[Cu(\mathbf{3B^*})]_4^{4+}$ cation with the representative atom numbering (left). Thermal ellipsoids are represented at 50% probability level. View of a complete $[Cu(\mathbf{3B^*})]_4^{4+}$ cation seen along 001 direction [copper (black spheres), oxygen (striped spheres), nitrogen (white spheres)].

 © 2007 Wiley-VCH Verlag GmbH & Co. KGaA, Weinheim 

2.250(2), and Cu–O(1)$^{i}$ = 2.5775(19) Å [i: $-x + 2$, $-y + 1/2$, $+z$; ii: $-y + 5/4$, $+x - 3/4$, $-z + 5/4$].

The O(1) atom connects three $Cu^{II}$ ions which in addition are coordinated to three O(1) atoms in an approximately orthogonal fashion defining a distorted cube in which the oxygen and copper atoms are arranged in an alternate way. The angles defined by these atoms in the distorted cube are Cu–O(1)–Cu$^{i}$ 89.20(7), Cu$^{i}$–O(1)–Cu$^{iii}$ 89.15(7), Cu–O(1)–Cu$^{iii}$ 110.10(9)° and O(1)–Cu–O(1)$^{i}$ 87.83(7), O(1)–Cu–O(1)$^{ii}$ 88.16(7) and O(1)$^{i}$–Cu–O(1)$^{ii}$ 72.58(7)°. The N(11)-pyridine ring forms dihedral angles of 22.00(7)° and 87.02(10)° with the triazolopyridine and the N(21)-pyridine rings, respectively. The $NO_3^-$ anions and the $H_2O$ molecules interact via hydrogen bonding defining a 3D supramolecular framework with large dodecagon-like section channels where the cationic cubane $[Cu(\mathbf{3B^*})]_4^{4+}$ complexes are intalled (see Figures 2 and 3).

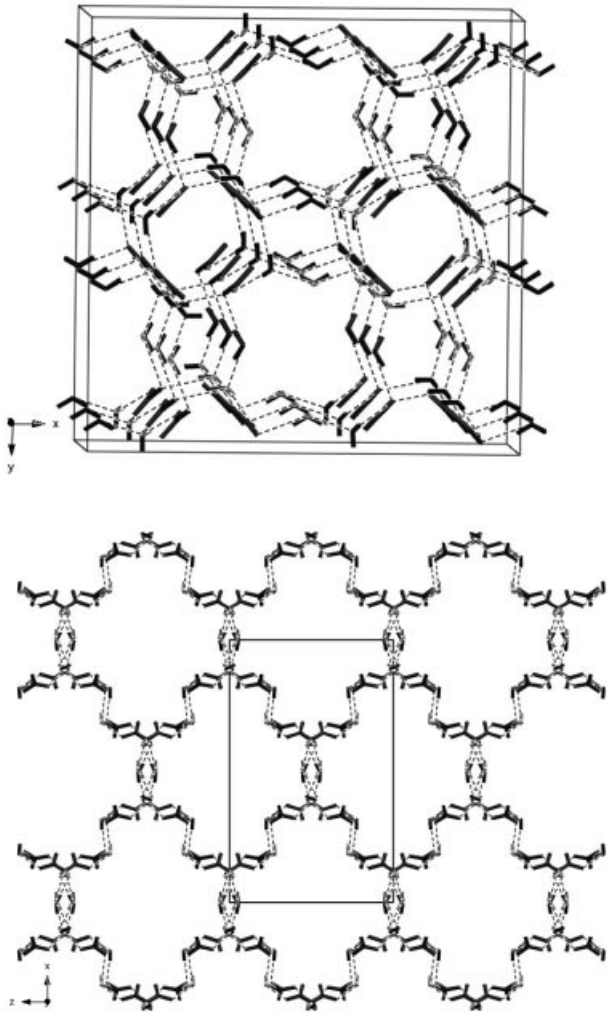

Figure 2. Supramolecular 3D framework defined by hydrogen bond interactions between $NO_3^-$ and $H_2O$. View of the unit cell along $z$ direction (left) and perspective view along $y$ direction (right). The tetranuclear cations, which fill the dodecagonal motives, have been eliminated for simplicity. Doted lines represent the hydrogen bonds.

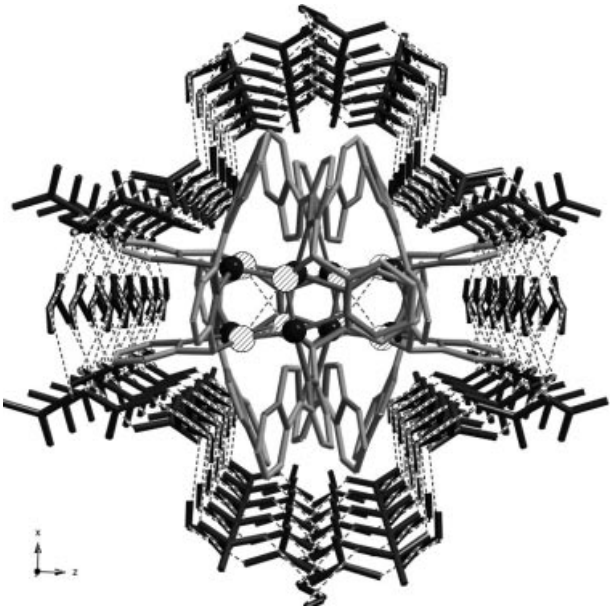

Figure 3. View of a dodecagonal channel loaded with two adjacent $[Cu(\mathbf{3B^*})]_4^{4+}$ cations. Dotted lines represent the hydrogen bonds. Hatched and black spheres correspond to the oxygen atoms of the cubane and the copper ions, respectively.

The hydrogen bond lengths [Å] and angles [°] are: $H_2O(21)\cdots O(11)NO_2$: H(1A)···O(11) 2.10(3), O(21)···O(11) 2.950(4), O(21)–H(1A)···O(11) 159(5); $H_2O(21)$–H(1B)··· O(22)$^{iv}$: H(1B)···O(22)$^{iv}$ 1.85(2), O(21)···O(22)$^{iv}$ 2.740(5), O(21)–H(1B)···O(22)$^{iv}$ 166(6); $H_2O(22)\cdots O(13)^{v}NO_2$: H(2A)···O(13)$^{v}$ 2.12(3), O(22)···O(13)$^{v}$ 2.893(4), O(22)–H(2A)···O(13)$^{v}$ 152(4); $H_2O(22)\cdots O(11)NO_2$: H(2B)···O(11) 2.03(2), O(22)···O(11) 2.853(4), O(22)–H(2B)···O(11) 165(4); $H_2O(22)\cdots O(12)^{v}NO_2$: H(2A)···O(12) 2.58(3), O(22)··· O(12) 3.351(4), O(22)–H(2A)···O(12) 152(4) and $H_2O(22)\cdots O(12)^{v}NO_2$: H(1A)···O(12)$^{v}$ 2.59(5), O(22)···O(12)$^{v}$ 3.262(5), O(22)–H(1A)···O(12)$^{v}$ 132(5) [iv: $-x + 3/2$, $-y + 3/2$, $-z + 3/2$ and v: $-y + 5/4$, $x - 1/4$, $z - 1/4$].

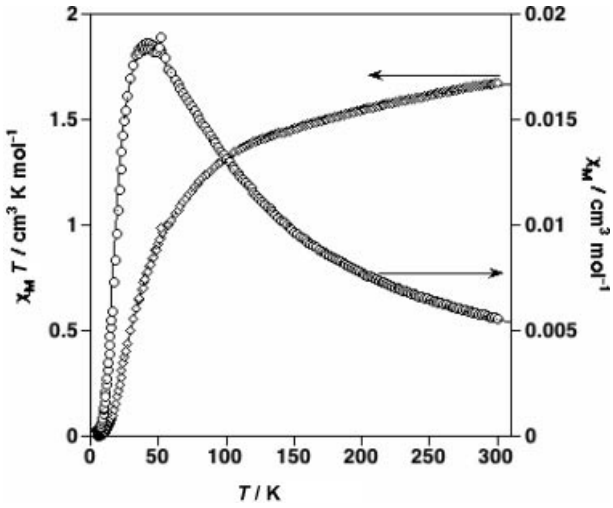


Figure 4. $\chi_M$ and $\chi_M T$ product vs. $T$ plots of $[Cu(\mathbf{3B^*})]_4(NO_3)_4 \cdot 8H_2O$.

 © 2007 Wiley-VCH Verlag GmbH & Co. KGaA, Weinheim 

The magnetic properties of the title compound are displayed in Figure 4 in the form of $\chi_M$ and $\chi_M T$ vs. $T$, where $\chi_M$ represents the magnetic susceptibility per mol of compound and $T$ the temperature. The $\chi_M T$ product is equal to 1.67 $cm^3 K mol^{-1}$, which corresponds quite well to the expected value for four weakly or uncoupled S = ½ centres. This value decreases continuously up to reach a value close to cero below 10 K. In contrast the $\chi_M$ value increases continuously from $5.50 \times 10^{-3}$ $cm^3 mol^{-1}$ at 300 K until $1.86 \times 10^{-2}$ $cm^3 mol^{-1}$ at ca 43 K where the $\chi_M$ vs. $T$ curve passes through a maximum and then decreases to reach values close to cero below 10 K. This behaviour corresponds to intramolecular antiferromagnetic coupling. This magnetic behaviour can be explained in terms of the isotropic Heisenberg–Dirac–van Vleck Hamiltonian (1).

$$H = -2\sum_{i,j} J_{ij} S_i S_j \quad (1)$$

which in the case of a tetranuclear $Cu_4O_4$ core with $S_4$ symmetry becomes Equation (2) (see also Figure 5, a).

$$H = -2J_{1,2}(S_1S_2 + S_3S_4) - -2J_{1,3}(S_1S_3 + S_2S_3 + S_2S_4 + S_1S_4) \quad (2)$$

The analytical of $\chi_M$ vs. $T$ curve deduced from Equation (2) can be expressed as follows in Equation (3).

$$\chi_M = \frac{2N\beta^2 g^2}{kT} \cdot \frac{A}{B} + N\alpha \quad (3)$$

where

$$A = 2\exp(2J_{1,2}/kT) + \exp[(4J_{1,2} - 2J_{1,3})7kT] + 5\exp[(4J_{1,2} + 2J_{1,3})/kT]$$

$$B = 1 + 6\exp[(2J_{1,2})7kT] + \exp[(4J_{1,2} - 4J_{1,3})7kT] + 3\exp[(4J_{1,2} - 2J_{1,3})7kT] + 5\exp[(4J_{1,2} + 2J_{1,3})/kT]$$

The relevant parameters have been obtained by least-squares fitting of Equation (3) to the experimental data. The parameter $N\alpha$ has been fixed at $240 \times 10^{-6}$ $cm^3 mol^{-1}$. The best fit for calculated and experimental $\chi_M$ values has been found for $2J_{13}$ = –37.4 $cm^{-1}$, $2J_{12}$ = –2.6 $cm^{-1}$, $g$ = 2.16 and $R = 1 \times 10^{-4}$. $R$ is the agreement factor defined as $\Sigma_i\{(\chi_M)_i^{exp} - [(\chi_M)_i^{calc}]^2/[(\chi_M)_i^{exp}]^2\}$. The solid line in Figure 4 corresponds to the calculated curve showing that an excellent agreement between the experimental and theoretical $\chi_M$ data is achieved. The magnitude and sign of $J_{12}$ and $J_{13}$ is determined by the angle Cu–O–Cu, Cu–O distances ($d_1$, $d_2$) and the orientation of the orbitals bearing the unpaired electrons (ie $d_{x^2-y^2}$) (see Figure 5, b–d). The exchange pathway determining the $J_{1,2}$ value involves two short and two long Cu–O distances (Figure 5, d), consequently direct overlap between the $d_{x^2-y^2} - d_{z^2}$ orbitals instead of the $d_{x^2-y^2} - d_{x^2-y^2}$ orbitals is observed. Hence, $J_{1,2}$ is expected to be very small and in general positive (ferromagnetic) due to the small participation of the $d_{z^2}$ orbital in the ground state of the $Cu^{II}$ [$\alpha$(Cu–O–Cu) = 89.15°, $d_2$ = 2.578 Å]. Although the exchange pathway $J_{1,3}$ is not appropriate for strong magnetic coupling it is expected to be significantly stronger than $J_{1,2}$ and antiferromagnetic in nature, given that the occurrence of a short Cu–O distance ($d_1$ = 1.998 Å) and a $\beta$(Cu–O–Cu) angle equal to 110.10° facilitates partial overlap between the $d_{x^2-y^2}$ orbitals.

Álvarez and co-workers have recently performed magnetostructural correlations in polynuclear complexes containing $Cu_4O_4$ cubane structure employing theoretical calculations based on DFT.[21] For $S_4$, also referred 4+2, cubanes their theoretical calculations predict that $J_{1,2}$ is small in magnitude, ferromagnetic and little dependent on the geometrical parameters. On the contrary, $J_{1,3}$ displays larger influence of the geometry and changes from ferro- to antiferromagnetic in nature for $\beta$ angles larger than 104°. These predictions clearly justify the results obtained for the title compound. The negative sign of $J_{12}$ may be a consequence of its very small magnitude together with some correlation in the evaluation of the $J_{13}$ parameter.

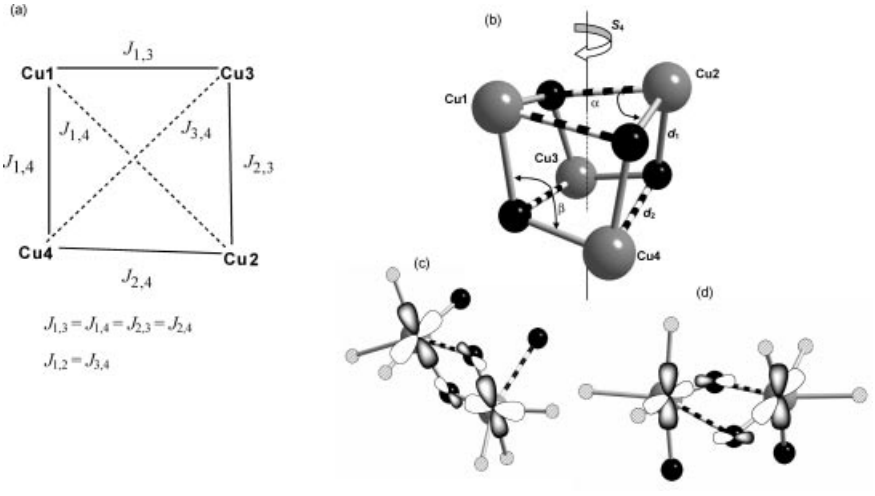


Figure 5. Scheme of the spin-coupling model used for the analysis of the magnetic data (a). Arrangement of the copper atoms in the cubane (b). Magnetic exchange pathways (c) and (d), see text.

 © 2007 Wiley-VCH Verlag GmbH & Co. KGaA, Weinheim 

## Conclusions

In summary we have demonstrated the capability of the polydentate ligand (pyridin-2-yl){6-([1,2,3]triazolo[1,5-*a*]-pyridin-3-yl)pyridin-2-yl}methanone to afford tetranuclear $Cu^{II}$ complexes. A next step in this research will require the synthesis of novel tetranuclear complexes with other divalent and trivalent first row transition metal ions.

## Experimental Section

**Synthesis:** To a solution of (pyridin-2-yl){6-([1,2,3]triazolo[1,5-*a*]-pyridin-3-yl)pyridin-2-yl}methanone (**3B**) (48 mg, 0.15 mmol) in ethanol (30 mL), a solution of $Cu(NO_3)_2{\cdot}3H_2O$ (40 mg, 0.16 mmol) in water (10 mL) was added. A green solution was formed. It was leaved covered at room temperature till the formation of green crystals, which were filtered and recrystallized from methanol (31.48 mg, 40% yield). $C_{72}H_{72}Cu_4N_{24}O_{28}$ (1975.7): calcd. C 43.76, H 3.65, N 17.02; found C 43.41, H 3.72, N 16.75.

**Magnetic Susceptibility Measurements:** The variable-temperature magnetic susceptibility measurements were performed on small single crystals by using a Quantum Design MPMS2 SQUID susceptometer equipped with a 5.5 T magnet and operating at 1 T and 1.8–375 K. Experimental data were corrected for diamagnetism using Pascal's constants.

**Crystal Data:** Green needle, $0.42 \times 0.12 \times 0.10$ mm size, tetragonal, $I4_1/a$, $a = 23.089(3)$, $c = 14.463(3)$ Å, $V = 7710(2)$ Å$^3$, $Z = 4$, $\rho_{calcd.} = 1.702$ g cm$^{-3}$, $\theta_{max} = 28.29$, Mo-$K_\alpha$, $\lambda = 0.71073$ Å, ω-scan, diffractometer Nonius Kappa CCD, $T = 120(2)$ K, 27774 reflections collected of which 4765 were independent ($R_{int} = 0.077$), direct primary solution and refinement on $F^2$ (SHELXS-97 and SHELXL-97, G. M. Sheldrick, University of Göttingen, 1997), 304 refined parameters, $OH_2$ hydrogen atoms were located in a difference Fourier synthesis, other hydrogen atoms were included using a riding model or as rigid methyl groups, $R_1[I > 2\sigma(I)] = 0.0441$, $wR_2$(all data) = 0.1132.

CCDC-641246 contains the supplementary crystallographic data for this paper. These data can be obtained free of charge from the Cambridge Crystallographic Data Centre via www.ccdc.cam.ac.uk/data_request/cif.

## Acknowledgments

Financial support is acknowledged from the Spanish Ministerio de Educación y Ciencia (MEC) through Projects CTQ 2004-03456 and CTQ2006-15672-C05-03.

[1] E. Coronado, D. Gatteschi, *J. Mater. Chem.* **2006**, *16*, 2513.
[2] a) D. Gatteschi, R. Sessoli, *Angew. Chem. Int. Ed.* **2003**, *42*, 268; b) G. Christou, D. Gatteschi, D. N. Hendrickson, R. Sessoli, *MRS Bull.* **2000**, *25*, 66.
[3] W. Wernsdorfer, N. Aliaga-Alcalde, D. N. Hendrickson, G. Christou, *Nature* **2002**, *416*, 408.
[4] a) R. Sessoli, H. L. Tsai, A. R. Schake, S. Wang, J. B. Vincent, K. Folting, D. Gatteschi, G. Christou, D. N. Hendrickson, *J. Am. Chem. Soc.* **1993**, *115*, 1804; b) R. Sessoli, D. Gatteschi, A. Caneschi, M. A. Novak, *Nature* **1993**, *365*, 141.
[5] A. K. Boudalis, B. Donnadieu, V. Nastopoulos, J. M. Clemente-Juan, A. Mari, Y. Sanakis, J. P. Tuchagues, S. P. Perlepes, *Angew. Chem. Int. Ed.* **2004**, *43*, 2266.
[6] a) R. E. P. Winpenny, *Adv. Inorg. Chem.* **2001**, *52*, 1; b) V. G. Makhankova, O. Y. Vassilyeva, V. N. Kokozay, B. W. Skelton, J. Reedijk, G. A. Vanalbada, L. Sorace, D. Gatteschi, *New J. Chem.* **2001**, *25*, 685.
[7] a) H. Oshio, N. Hoshino, T. Ito, M. Nakano, F. Renz, P. Gütlich, *Angew. Chem. Int. Ed.* **2003**, *42*, 223; b) A. Caneschi, A. Cornia, S. J. Lippard, *Angew. Chem. Int. Ed. Engl.* **1995**, *34*, 467.
[8] a) K. Isele, P. Franz, C. Ambrus, G. Bernardini, S. Decurtins, A. F. Williams, *Inorg. Chem.* **2005**, *44*, 3896; b) A. Mukherjee, R. Raghunathan, M. K. Saha, M. Nethaji, S. Ramasesha, A. R. Chakravarty, *Chem. Eur. J.* **2005**, *11*, 3087; c) R. Wegner, M. Gottschaldt, H. Görls, E.-G. Jäger, D. Klemm, *Chem. Eur. J.* **2001**, *7*, 2143; d) S. G. Ang, B. W. Sun, S. Gao, *Inorg. Chem. Commun.* **2004**, *7*, 795; e) W.-H. Gu, X.-Y. Chen, L.-H. Yin, A. Yu, X.-Q. Fu, P. Cheng, *Inorg. Chim. Acta* **2004**, *357*, 4085; f) E. A. Buvaylo, V. N. Kokozay, O. Yu. Vassilyeva, B. W. Skelton, J. Jezierska, L. C. Brunel, A. Ozarowski, *Inorg. Chem.* **2005**, *44*, 206; g) X. S. Tan, Y. Fujii, R. Nukada, M. Mikuriya, Y. Nakano, *J. Chem. Soc. Dalton Trans.* **1999**, 2415; h) H. Astheimer, F. Nepveu, L. Walz, W. Haase, *J. Chem. Soc. Dalton Trans.* **1985**, 315; i) J. P. Laurent, J. J. Bonnet, F. Nepveu, H. Astheimer, L. Walz, W. Haase, *J. Chem. Soc. Dalton Trans.* **1982**, 2433.
[9] B. Abarca, R. Ballesteros, M. Elmasnaoui, *Tetrahedron* **1998**, *54*, 15287.
[10] B. Abarca, R. Ballesteros, M. Chadlaoui, *Tetrahedron* **2004**, *60*, 5785.
[11] A. K. Boudalis, C. P. Raptopoulou, B. Abarca, R. Ballesteros, M. Chadlaoui, J. P. Tuchages, A. Terzis, *Angew. Chem. Int. Ed.* **2006**, *45*, 432.
[12] J. H. Boyer, R. Borgers, L. T. Wolford, *J. Am. Chem. Soc.* **1957**, *79*, 678.
[13] B. Abarca, R. Ballesteros, M. Elmasnaouy, *Tetrahedron* **1999**, *55*, 12881.
[14] B. Abarca, I. Alkorta, R. Ballesteros, F. Blanco, M. Chadlaoui, J. Elguero, F. Mojarrad, *Org. Biomol. Chem.* **2005**, *3*, 3905.
[15] L. P. Battaglia, M. Carcelli, F. Ferraro, L. Mavilla, C. Pillizi, *J. Chem. Soc. Dalton Trans.* **1994**, 2651.
[16] V. Niel, A. B. Gaspar, M. C. Muñoz, B. Abarca, R. Ballesteros, J. A. Real, *Inorg. Chem.* **2003**, *42*, 4782.
[17] G. S. Papaefstathiou, S. P. Perlepes, *Comments Inorg. Chem.* **2002**, *23*, 249.
[18] A. Tsohos, S. Dionyssopoulou, C. P. Raptopoulou, A. Terzis, E. Bakalbassis, S. P. Perlepes, *Angew. Chem. Int. Ed.* **1999**, *38*, 983.
[19] G. S. Papaefstathiou, S. P. Perlepes, A. Escuer, R. Vicente, M. Font-Bardía, X. Solans, *Angew. Chem. Int. Ed.* **2001**, *40*, 884.
[20] N. Lalioti, C. P. Rattopoulou, A. Terzis, A. E. Aliev, I. P. Gerothanassis, E. Manessizoupa, S. P. Perlepes, *Angew. Chem. Int. Ed.* **2001**, *40*, 3211.
[21] J. Tercero, E. Ruiz, S. Álvarez, A. Rodriguez-Fortea, P. Alemany, *J. Mater. Chem.* **2006**, *16*, 2729.

Received: June 20, 2007
Published Online: September 7, 2007

 © 2007 Wiley-VCH Verlag GmbH & Co. KGaA, Weinheim 

DOI: 10.1002/ejic.200700789

# Synthesis and Charaterisation of Chromium Oxyselenide ($Cr_2Se_{0.7}O_{2.3}$) Formed from Chemical Vapour Synthesis: A New Antiferromagnet

**Nicolas D. Boscher,[a] Claire J. Carmalt,[a] A. Garcia Prieto,[b] Quentin A. Pankhurst,[b] Robert G. Palgrave,[a] and Ivan P. Parkin*[a]**

**Keywords:** Chemical vapour synthesis / Chromium oxyselenide / Antiferromagnet

Chromium oxyselenide $Cr_2Se_{0.71}O_{2.30}$ was synthesised by chemical vapor synthesis of chromium oxychloride and diethyl selenide. The material adopts the $Cr_2Se_3$ structure type with $a$ = 6.26(3) Å and $c$ = 17.45(3) Å. The Raman spectrum shows bands at 225 and 550 $cm^{-1}$. X-ray photoelectron spectroscopy and wavelength dispersive analysis by X-rays confirmed the material was homogeneous and of uniform composition $Cr_2Se_{0.71}O_{2.30}$. The material is an antiferromagnet with a Neel temperature of 43 K. This is the first solid-state chromium oxyselenide reported and shows that the hard oxygen and soft selenium can co-exist in the same lattice if formed under the kinetic product conditions of a rapid gas-phase reaction.

(© Wiley-VCH Verlag GmbH & Co. KGaA, 69451 Weinheim, Germany, 2007)

## Introduction

Chromium mixed chalcogenides have been thoroughly investigated by various workers over many years because of their interesting magnetic properties. The synthesis and magnetic properties of chromium sulfoselenide,[1] chromium sulfotelluride[2–4] and chromium selenotelluride[5,6] have been widely reported for a range of different compositions.[7,8] In contrast, only one paper reports the existence of a chromium oxysulfide, $Cr_2S_2O$,[9] neither chromium oxyselenide or oxytelluride phases are known. Indeed this is often a common pattern in solid-state transition metal chemistry where in polarisability terms the "hard" oxygen and "soft" selenium find it difficult to coexist in a solid solution without phase segregation or formation of layered materials in which the oxide and selenide blocks are separated. This is not to say that metal oxide-selenide solid solutions cannot exist, rather that by the conventional synthesis they invariably produce the thermodynamic product. A large number of phases have been reported in the chromium-selenium system and include $Cr_5Se_8$,[10] $CrSe_2$,[11,12] $CrSe_3$[13] and a series of compounds CrSe,[14,15] $Cr_7Se_8$,[16] $Cr_5Se_6$,[17] $Cr_3Se_4$,[18] and $Cr_2Se_3$ with the NiAs-type crystal structure, in which chromium vacancies are ordered. $Cr_2Se_3$ has a rhombohedral-type superstructure, which leads to complex antiferromagnetic arrangements below the Néel temperature $T_N$ = 43 K.[19] An order-order magnetic transition is also known to occur at $T_t$ = 38 K. The chromium-oxygen system is simpler than the chromium-selenium one, the most common phase being $Cr_2O_3$.[20] This phase is also an antiferromagnet with $T_N$ = 307 K. Chromium(III) selenide has found applications such as protective films, black matrix films in liquid crystal displays, solar thermal energy collectors, in catalysis and in tunnel junction barriers.[21,22] Here we present the first report of the existence of a chromium oxyselenide phase formed from a rapid gas phase synthesis route, we hypothesise that the reason we can obtain an oxyselenide in this case is that the reaction is a fast and that we effectively "trap-out" the kinetic product.

## Results and Discussion

Chromium oxyselenide was prepared from the atmospheric pressure chemical vapour deposition (APCVD) reaction of chromyl chloride and diethylselenide. Synthesis was accomplished under a dinitrogen atmosphere (99.99%) in a horizontal-bed cold-wall APCVD reactor heated to 600 °C. $Et_2Se$ and $CrO_2Cl_2$ were preheated to 70 °C and 75 °C in their respective bubblers before being introduced into gas stream of hot $N_2$. They were then passed through a mixing chamber heated to 200 °C and were introduced into the reactor chamber. Chromyl chloride reacts in the gas phase with diethyl selenide to form a black fine powder that collects on the glass substrate. This can be readily removed by brushing with a fine hair-brush. Notably the same reaction at lower substrate temperatures of 400–550 °C forms a green adherent crystalline chromium oxide film and not the black chromium oxy-selenide powder.

[a] Materials Chemistry Research Centre, Department of Chemistry, University College London,
20 Gordon Street, London WC1H 04J, UK
Fax: +44-20-7679-7463
E-mail: i.p.parkin@ucl.ac.uk
[b] London Centre for Nanotechnology, University College London,
17–19 Gordon Street, London WC1H 04J, UK

 © 2007 Wiley-VCH Verlag GmbH & Co. KGaA, Weinheim 

Scanning electron microscopy (SEM) images show a single morphological type of spherical nanoparticles with a mean size of 100 nm (Figure 1). Energy and wavelength-dispersive X-ray analysis (EDX/WDX) show that the powder contains chromium, oxygen and selenium. The elemental stoichiometry of the particles was determined to be $Cr_2Se_{0.71}O_{2.30}$ and the chlorine and carbon levels within the powder were found to be below the detection limit of the instrument (less than 0.5 atom-%). The sample was homogeneous by spot EDX analysis.

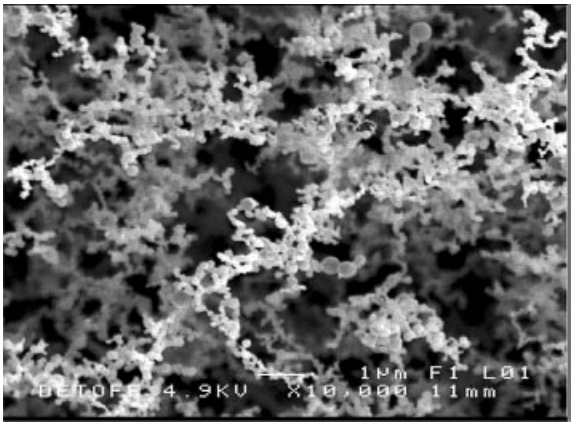


Figure 1. Scanning electron micrograph of the powder produced from the gas phase reaction of $CrO_2Cl_2$ and $Et_2Se$ at 600 °C.

Powder X-ray diffraction (Figure 2) confirmed that the product from the gas-phase reaction is single-phase, crystalline and matches the reported pattern for rhombohedral $Cr_2Se_3$ (JCPDS File No. 040-1403).[19] The lattice parameters were calculated as $a$ = 6.26(3) Å and $c$ = 17.45(3) Å. Notably no chromium oxide was detected by powder diffraction. It has been shown previously that APCVD of chromyl chloride produces crystalline chromium oxide films at the same temperature of deposition (ca. 600 °C).[22–24]

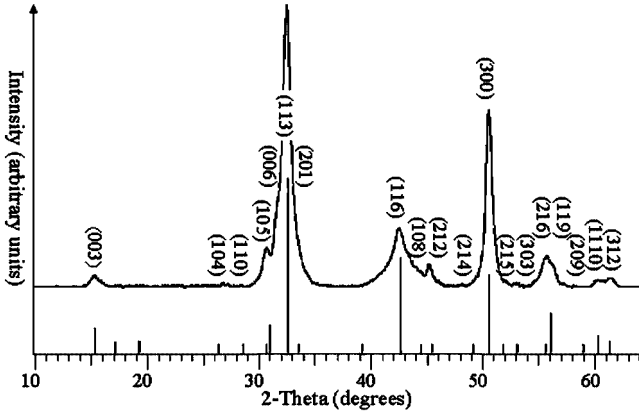


Figure 2. XRD pattern obtained for the powder formed from the APCVD reaction of $CrO_2Cl_2$ and $Et_2Se$ at 600 °C. Literature stick pattern for rh-$Cr_2Se_3$ powder (JCPDS file No. 040-1403) is shown.

X-ray photoelectron spectroscopy of the as-prepared powder (Figure 3) shows the presence of three elements – chromium, oxygen and selenium in the same ratio as found from EDX analysis ($Cr_2Se_{0.7}O_{2.3}$). A single environment can be seen for each element; Cr $2p_{1/2}$ = 583.3 eV, Cr $2p_{3/2}$ = 576.2 eV; O 1s = 531.5 eV; Se $3d_{3/2}$ = 55.1 eV and Se 3d = 54.0 eV. The chromium environment for the $2p_{3/2}$ peak is intermediate between that of $Cr_2O_3$ at 576.6 eV and $Cr_2Se_3$ at 574.6 eV and indicative of $Cr^{III}$.[25,26] The oxygen 1s environment shows a narrow full width half maximum peak at 1.7 eV – indicative of a single environment with a binding energy shift consistent with an oxide and 0.7 eV close to that in chromium oxide 530.8 eV.[27] The selenium $3d_{3/2}$ peak matches that found in $Cr_2Se_3$ at 54.0 eV.[25]

Raman analysis of the powder (Figure 4) reveals broad bands at 225 $cm^{-1}$ and 550 $cm^{-1}$. The absence of the distinctive (relatively intense) $Cr_2O_3$ Raman bands at 307, 350, 524, 551 and 610 $cm^{-1}$ or $CrO_2$ bands at 458, 570 and

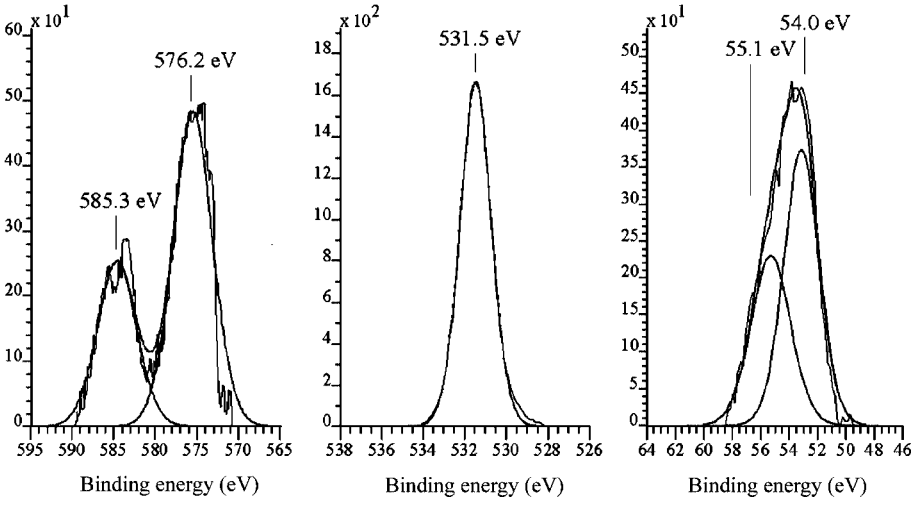


Figure 3. Selected area XPS spectra of the chromium oxyselenide powder produced at 600 °C from the gas phase reaction of $CrO_2Cl_2$ and $Et_2Se$. Left, Cr 2p region; middle, O 1s region; right, Se 3d region. Darker lines are the best fit and lighter lines the actual experimental data.

 © 2007 Wiley-VCH Verlag GmbH & Co. KGaA, Weinheim 

682 $cm^{-1}$ (or indeed $CrO_3$) confirms that no chromium oxide was formed and co-doped during the gas-phase reaction of $CrO_2Cl_2$ and $Et_2Se$.[28,29]

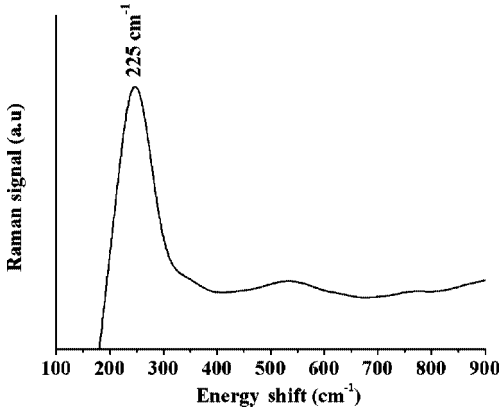


Figure 4. Raman pattern obtained for the powder formed from the gas phase reaction of $CrO_2Cl_2$ and $Et_2Se$ at 600 °C.

The thermogravimetric analysis of $Cr_2Se_{0.7}O_{2.3}$ in air shows a gradual increase in weight of +24% between 60 °C and 420 °C. This is attributed to the oxidation of the selenium in the material to a selenate. A weight loss of –8% is observed from 420 °C to 550 °C corresponding to the decomposition of the selenate to form $Cr_2O_3$ and $SeO_2$ by loss of $O_2$. The second weight loss corresponding to –36% is seen from 600–800 °C and corresponds to the sublimation of all selenium in the form of $SeO_2$.[30]

The dc magnetic susceptibility ($\chi$) as a function of temperature (Figure 5) shows a peak at 11 K. The large particle size (100 nm) precludes the possibility of this being due to a superparamagnetic blocking transition, and the substitution of oxygen with selenium is unlikely to generate any frustrated magnetic states. We therefore attribute the peak to an antiferromagnetic ordering transition. The Néel temperature at $T_N$ = 11 K in $Cr_2Se_{0.7}O_{2.3}$ is less than that of $Cr_2Se_3$ ($T_N$ = 43 K),[19] and much less that that of $Cr_2O_3$ ($T_N$ = 307 K),[31] implying that the new material has somewhat different magnetic properties compared to its parent compounds.

The characterization data are all consistent with the formation of a hitherto unknown solid solution of $Cr_2Se_{0.7}O_{2.3}$ rather than the formation of two intimately mixed phases of $Cr_2O_3$ and $Cr_2Se_3$. SEM analysis shows a single type of particle morphology – spherical and agglomerated together – consistent with a gas-phase reaction, rather than two types of crystallite. WDX and EDX analysis show that the material is homogeneous to spot analysis with the same elemental formulation across the surface. The X-ray diffraction pattern shows a single-phase material of the $Cr_2Se_3$ structural type but with a larger unit cell. Previously we have shown that $Cr_2O_3$ is crystalline when prepared by CVD at 400 °C and adopts an adhesive film with angular crystallites.[22–24] Furthermore, we showed in this work at deposition temperatures from 450–600 °C a green chromium oxide film formed from reaction of $Et_2Se$ and $CrO_2Cl_2$. It was only at 600 °C and above that a chromium

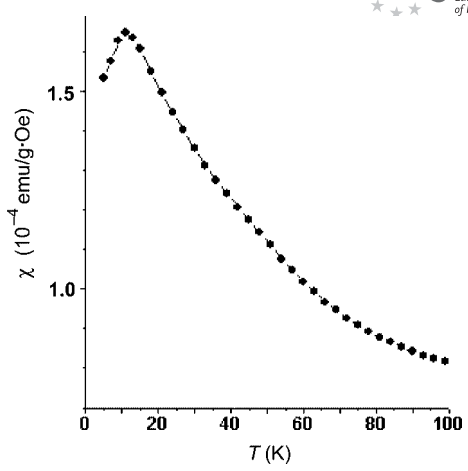


Figure 5. DC magnetic susceptibility (in a measurement field of 10 Oe) as a function of temperature for $Cr_2Se_{0.7}O_{2.3}$.

oxyselenide phase formed, by gas-phase nucleation that "snowed" onto the surface to form a poorly adherent film that could be readily collected. The XPS analysis for the chromium oxyselenide showed only a single chromium environment rather than two well separated peaks for the oxide and selenide, furthermore the quantification of the element abundances matched the WDX analysis. The thermal gravimetric analysis results also correlate well with the elemental formula. The Raman pattern does not show any chromium oxide (corundum) in the powder but is consistent with a layered metal-selenide type structure. Furthermore the magnetic properties of the new material are unlike either – $Cr_2Se_3$ or $Cr_2O_3$ – which although both are antiferromagnets and have Néel temperatures of 43 and 307 K respectively. Hence there is strong evidence for the formation of a new chromium oxyselenide phase. We have yet to account for why the Néel temperature is depressed for the new oxyselenide phase compared to the end members of the series – however the magnetic structure of $Cr_2Se_3$ is extraordinarily complicated.[19] We are hopeful that by varying the reaction conditions it will be possible to make other compositions within the solid solution series $CrO_xSe_y$ ($x + y = 3$). This work has shown that the "hard" oxygen and "soft" selenium can marry in the same chromium solid-state material without phase segregation. It also indicates that a fast gas-phase kinetic route could be the way forward for making a range of hitherto unknown oxyselenide phases.

## Experimental Section

Synthesis of the chromium oxyselenide nanoparticles was carried out under a dinitrogen atmosphere (99.99%) on glass substrates using a conventional horizontal bed cold-wall atmospheric pressure CVD reactor. The glass substrate was $SiO_2$ coated standard float glass (Pilkington, UK). The substrate was heated to 600 °C by a graphite block and the nitrogen carrier gas was preheated to 150 °C by being passed along 2 m lengths of coiled stainless steel tubing inside a tube furnace. The gases in the reaction were made to pass over the heated substrate and confined in position by a top plate that was ca. 4 mm above the substrate. After passage through the

 © 2007 Wiley-VCH Verlag GmbH & Co. KGaA, Weinheim 

reaction chamber the gas stream was treated with bleach to destroy the possible presence of $H_2Se$ and vented inside a fume cupboard.

Chromyl chloride was obtained form Strem and diethyl selenide was supplied by Aldrich. They were both used without further purification. The chromyl chloride and diethyl selenide were placed into two different stainless steel bubblers, which were respectively heated to 75 °C and 70 °C by an external jacket. They were both introduced into gas streams by passing hot $N_2$ through the bubblers. Flow rates of nitrogen through the $CrO_2Cl_2$ bubbler and $Et_2Se$ were respectively 0.2 L min$^{-1}$ (3 mmol min$^{-1}$) and 2.0 L min$^{-1}$ (30 mmol min$^{-1}$) and the flow rate through the mixing chamber was kept constant to 3.0 L min$^{-1}$. Deposition time for the experiment was one minute. At the end of the deposition, the bubbler line was closed and the substrate was cooled under nitrogen in the reactor. Then the samples were collected on the substrate and handled briefly in air before storage in a dry oxygen-free nitrogen atmosphere in a glove box. It was subsequently found that the samples were air and water stable, so this procedure was not necessary.

X-ray diffraction patterns were measured on a Bruker AX5 B8 instrument using monochromated Cu-$K_{\alpha 1}$ radiation ($K_{\alpha 1}$ = 1.5406 Å). The diffractometer used glancing incident radiation (5°). The samples were indexed using Unit cell and compared to database standards. Wavelength dispersive X-ray and Energy dispersive X-ray analysis were obtained on a Philips XL30ESEM instrument and SEM was obtained on a JEOL 6301 instrument. Raman spectra were acquired on a Renishaw Raman System 1000 using a helium–neon laser of wavelength 632.8 nm. The Raman system was calibrated against the emission lines of neon. X-ray photoelectron spectroscopy was undertaken using a VG ESCALAB 220I XL instrument with focused (300 mm spot) monochromatic Al-$K_\alpha$ radiation at a pass energy of 20 eV. Scans were acquired with steps of 50 meV. A flood gun was used to control charging. Binding energies were referenced to an adventitious C 1s peak at 284.6 eV (this peak is due to residual pump oil used in the XPS high vacuum system, but is removed on the first argon ion etching). Argon sputtering was used for approximately 1 min in a rastering mode in order to remove surface contamination. Thermal gravimetric analysis (TGA) was performed with a heating rate of 10 °C min$^{-1}$ and on a Netzsch STA 449C instrument. Direct-current magnetic susceptibility measurements were performed using a commercial SQUID magnetometer (Quantum Design MPMS-XL) in a magnetic field of 10 Oe.

## Acknowledgments

Dr. G. Reid, Prof. W. Levason and Dr. A. Hector are thanked for useful discussions on related projects. The Engineering and Physical Sciences Research Council (EPSRC) is thanked for financial support.

[1] a) L. M. Doronina, V. S. Filatkina, S. S. Batsanov, *Neorg. Mater.* **1967**, *3*, 1696; b) V. N. Ikorskii, L. M. Doronina, S. S. Batsanov, *Zh. Struk. Khim.* **1968**, *9*, 143.
[2] S. S. Batsanov, L. M. Doronina, *Neorg. Mater.* **1966**, *2*, 491.
[3] V. N. Ikorskii, *Neorg. Mater.* **1973**, *9*, 938.
[4] a) M. Yuzuri, T. Yusuki, *J. Magn. Magn. Mater.* **1986**, *54*, 923; b) Y. Adachi, M. Yuzuri, T. Kaneko, S. Abe, *J. Magn. Magn. Mater.* **1990**, *90*, 153; c) Y. Adachi, M. Yuzuri, T. Kaneko, S. Abe, *J. Magn. Magn. Mater.* **1992**, *104*, 887; d) M. Yuzuri, Y. Adachi, T. Kaneko, H. Yoshida, S. Abe, *J. Magn. Magn. Mater.* **1995**, *140*, 151.
[5] M. Yuzuri, K. Segi, *Phys. B+C: Phys. Condens. Matt. + Atom., Mol. Plasma Phys.* **1977**, *86*, 891.
[6] S. Ohta, Y. Narui, Y. Sakayori, *J. Magn. Magn. Mater.* **1997**, *170*, 168.
[7] S. S. Batsanov, L. M. Doronina, *Ser. Khim.* **1968**, *9*, 2155.
[8] V. N. Ikorskii, S. S. Batsanov, *Neorg. Mater.* **1972**, *8*, 1858.
[9] S. S. Batsanov, L. M. Doronina, N. V. Podberezskaya, *Zh. Struk. Khim.* **1964**, *154*, 624.
[10] A. W. Sleight, T. A. Bither, *Inorg. Chem.* **1969**, *8*, 566.
[11] C. M. Fang, C. F. van Bruggen, R. A. de Groot, G. A. Wiegers, C. Haas, *J. Phys.: Condens. Matter.* **1997**, *9*, 10173.
[12] Y. Yoshida, K. Motizuki, *J. Phys. Soc. Jpn.* **1982**, *51*, 2107.
[13] a) S. J. Hibble, D. A. Rice, M. J. Almond, K. A. Hassan Mohammad, S. P. Pearse, J. R. Sagar, *J. Mater. Chem.* **1992**, *2*, 1237–1240; b) S. J. Hibble, R. I. Walton, D. M. Pickup, *J. Chem. Soc., Dalton Trans.* **1996**, *11*, 2245.
[14] M. Koyama, N. Happo, M. Tamura, J. Harada, T. Mihara, A. Furuta, M. Nakatake, H. Sato, M. Taniguchi, Y. Ueda, *J. Electron Spectrosc. Relat. Phenom.* **1996**, *78*, 83.
[15] L. M. Corliss, N. Elliott, J. M. Hastings, R. L. Sass, *Phys. Rev.* **1961**, *5*, 1402.
[16] T. Kaneko, J. Sugawara, K. Kamigaki, S. Abe, H. Yoshida, *J. Appl. Phys.* **1982**, *53*, 2223.
[17] H. Sato, M. Koyama, K. Takada, H. Okuda, K. Shimada, Y. Ueda, J. Ghijsen, M. Taniguchi, *J. Electron Spectrosc. Relat. Phenom.* **1998**, *88*, 333.
[18] M. Behrens, R. Kiebach, W. Bensch, D. Haeussler, W. Jaeger, *Inorg. Chem.* **2006**, *45*, 2704.
[19] a) Y. Adachi, M. Yuzuri, T. Kaneko, S. Abe, H. Yoshida, *J. Phys. Soc. Jpn.* **1994**, *63*, 369; b) Y. Adachi, M. Ohashi, T. Kaneko, M. Yuzuri, Y. Yamaguchi, S. Funahashi, Y. Morii, *J. Phys. Soc. Jpn.* **1994**, *63*, 1548; c) S. Ohta, Y. Adachi, T. Kaneko, M. Yuzuri, H. Yoshida, *J. Phys. Soc. Jpn.* **1994**, *6*, 2225.
[20] K. P. Lillerud, P. Kofstad, *J. Electrochem. Soc.* **1980**, *127*, 2397.
[21] P. M. Sousa, A. J. Silvestre, N. Popovici, O. Conde, *Appl. Surf. Sci.* **2005**, *247*, 423.
[22] a) A. Anguelouch, A. Gupta, G. Xiao, D. W. Abraham, Y. Ji, S. Ingvarsson, C. L. Chien, *Phys. Rev. B: Condens. Matt. Mater. Phys.* **2001**, *64*, 180408/1; b) A. Anguelouch, A. Gupta, G. Xiao, G. X. Miao, D. W. Abraham, S. Ingvarsson, Y. Ji, C. L. Chien, *J. Appl. Phys.* **2002**, *10*, 7140.
[23] I. P. Parkin, M. N. Field, *J. Phys. IV: Proceedings of the Twelfth Eur. Conf. on Chem. Vap. Dep.* **1999**, *1*, 387.
[24] a) W. J. DeSisto, P. R. Broussard, T. F. Ambrose, B. E. Nadgorny, M. S. Osofsky, *Appl. Phys. Lett.* **2000**, *76*, 3789; b) Y.-N. Cho, W. J. DeSisto, *Chem. Vap. Dep.* **2003**, *9*, 121.
[25] E. Agostinelli, C. Battistoni, D. Fiorani, G. Mattogno, M. Nogues, *J. Phys. Chem. Solids* **1989**, *50*, 269.
[26] C. D. Wagner, in *Pratical Surface Analysis Second Edition* (Eds.: D.Briggs, M. P.Seah), Wiley, Salle-Sauerlander, **1990**, vol. 1, p. 606–610.
[27] I. Ikemoto, K. Ishii, S. Kinoshita, H. Kuroda, M. A. A. Franco, J. M. J. Thomas, *J. Solid State Chem.* **1976**, *17*, 425.
[28] S. Kikuchi, K. Kawauchi, M. Kurosawa, H. Honjho, T. Yagishita, *Anal. Sci.* **2005**, *21*, 197.
[29] J. Mougin, T. Le Bihan, G. Lucazeau, *J. Phys. Chem. Solids* **2001**, *62*, 553.
[30] S. M. Grigorovich, A. V. Novoselova, Y. M. Ukrainskii, *Neorg. Mater.* **1975**, *11*, 2125.
[31] B. N. Brockhouse, *J. Chem. Phys.* **1953**, *21*, 961.

Received: July 25, 2007
Published Online: September 7, 2007

 © 2007 Wiley-VCH Verlag GmbH & Co. KGaA, Weinheim 

DOI: 10.1002/ejic.200700679

# f-Block-Element–f-Block-Element NMR Spin–Spin Coupling

**Anna M. Dietel,[a] Oleg Tok,[a] and Rhett Kempe*[a]**

*Dedicated to Professor Bernd Wrackmeyer on the occasion of his 60th birthday*

**Keywords:** Amido ligands / Bimetallic complexes / Dynamic N ligands / NMR spectroscopy / Ytterbium

This is a report on the synthesis and structure of novel dinuclear $Yb^{II}$ complexes. In one of the described compounds, the two $Yb^{II}$ centres are in close proximity and chemically different. Thus, an f-block-element–f-block-element coupling pattern was observed. The low-field $^{171}Yb$ signal consists of a central singlet and two satellites with integral intensities of about 7 % each. This 14 % approximately corresponds to the natural abundance of the $^{171}Yb$ isotope and was assigned as a doublet arising from $^{1}J(^{171}Yb, ^{171}Yb)$ spin–spin coupling with a magnitude of 76.1 Hz. Furthermore, the relevance of such studies in understanding dimer equilibria and the rearrangement chemistry of rather bulky structural ensembles is discussed.

(© Wiley-VCH Verlag GmbH & Co. KGaA, 69451 Weinheim, Germany, 2007)

## Introduction

The last decade has seen a dramatic increase in the importance of the organometallic chemistry of lanthanide elements. Solution-state NMR, one of the organometallic chemist's most informative tools, has been applied infrequently to the direct observation of compounds of f-block elements. This omission is probably because the majority of the complexes (except those of $La^{III}$, $Yb^{II}$ and $Lu^{III}$) are paramagnetic, and many of the NMR-active f-block nuclei have large quadrupole moments. $^{171}Yb$ is a spin-1/2 nucleus, with a natural abundance of 14.31 % and a moderately sized, positive gyromagnetic ratio ($4.735 \times 10^7$ rad $T^{-1}$ $s^{-1}$); these features combine to give a receptivity about 4.5 times greater than that of $^{13}C$.[1] The first direct high-resolution NMR observation of an f-block element was reported by Lawless, Lappert, et al.[2] In principle, $^{171}Yb$–$^{171}Yb$ coupling should be observable as well. Dinuclear and polynuclear Yb complexes are a well-documented class of compounds. The metal centres in many of these complexes are close enough (3.5 Å was used as the upper limit)[3] to observe f-block-element–f-block-element spin–spin coupling. Complexes that meet this requirement can consist of $Yb^{III}$,[4] exhibit mixed oxidation states (II/III)[5] or might be diamagnetic due to the presence of $Yb^{II}$[6,7] ions only. Nonsymmetrical polynuclear $Yb^{II}$ complexes are rare,[6] and metal centres in different chemical environments are a prerequisite to observe $^{1}J(^{171}Yb,^{171}Yb)$ coupling. Furthermore, in systems undergoing dynamic processes such as bridge–terminal exchange or monomer–dimer equilibria, coupling constants will be time-averaged and thus may be unobservable.[1] On the other hand, $^{1}J(^{171}Yb,^{171}Yb)$ coupling patterns, if observed, could be a highly sensitive probe on the dynamic aspect of f-block-element–f-block-element interactions in solution, an area of chemistry difficult to access by other methods. We started recently a research program in which we used very bulky aminopyridinato ligands[8] in order to avoid ligand redistribution in low-valent and organolanthanide chemistry.[9] We report here on the synthesis and structure of a novel dinuclear $Yb^{II}$ complex in which the two $Yb^{II}$ centres are in close proximity and chemically different within the NMR time scale, as well as the $^{171}Yb$ NMR spectroscopy of this species.

## Results and Discussion

Bimetallic $Yb^{II}$ complexes should be accessible by the introduction of a sterically encumbered extension at an aminopyridinato ligand, which leads to bipyridylamide ligands, and the nonsymmetrical bulk could lead to homobimetallic complexes having $Yb^{II}$ in different chemical environments. The "simple" bipyridylamide ligand was already used successfully by Müller-Buschbaum to stabilise, for instance, multinuclear $Yb^{III}$ complexes.[10] The sterically demanding dipyridylamide ligand precursor **1** was synthesised by Pd-catalysed aryl amination (Scheme 1) in good yield.

[a] Lehrstuhl für Anorganische Chemie II, Universität Bayreuth, 95440 Bayreuth, Germany
E-mail: kempe@uni-bayreuth.de

Supporting information for this article is available on the WWW under http://www.eurjic.org or from the author.

 © 2007 Wiley-VCH Verlag GmbH & Co. KGaA, Weinheim 

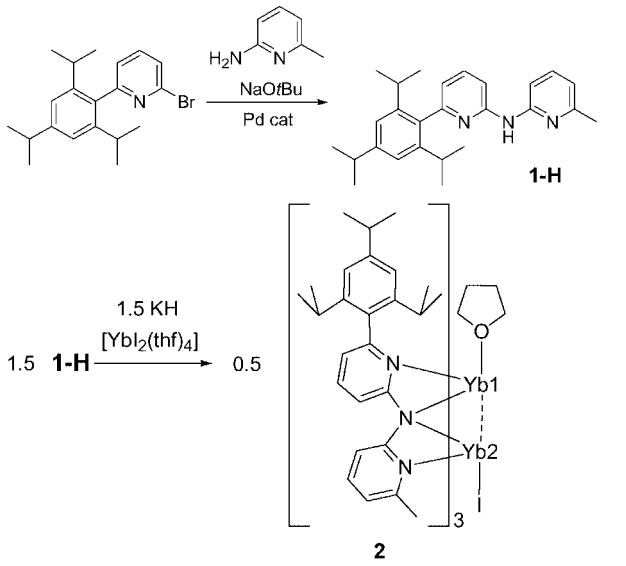


Scheme 1. Synthesis of **1** and **2**.

The reaction of **1-H** with KH and subsequent treatment with $[YbI_2(thf)_4]$[11] leads to the bimetallic complex **2** with a residual iodido ligand to guarantee asymmetry. The molecular structure of complex **2** (Figure 1) was investigated by X-ray crystal structure analysis[12] and NMR spectroscopy.

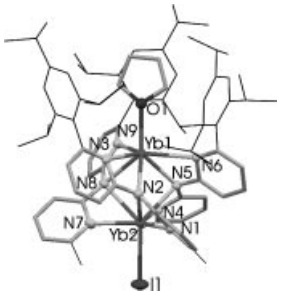


Figure 1. Molecular structure of **2** (ORTEP plot for all non-C,H-atoms). Substituents at the pyridine rings are plotted in wire frame style for clarity. Selected bond lengths [Å] and angles [°]: Yb1–Yb2 3.4200(3), N1–Yb2 2.469(3), N2–Yb1 2.538(3), N2–Yb2 2.640(3), N3–Yb1 2.611(3), N4–Yb2 2.476(3), N5–Yb1 2.568(3), N5–Yb2 2.578(3), N6–Yb1 2.681(3), N7–Yb2 2.451(4), N8–Yb1 2.604(3), N8–Yb2 2.622(3), N9–Yb1 2.613(3), O1–Yb1 2.431(3), I1–Yb2 3.0714(4); N5–Yb1–N6 52.19(10), N2–Yb1–N3 53.32(10), N8–Yb1–N9 52.55(10), N4–Yb2–N5 53.61(10), N7–Yb2–N8 53.58(10), N1–Yb2–N2 53.28(10).

The two $Yb^{II}$ ions in complex **2** are triply bridged by the amido N atoms of **1**, which results in a short metal–metal distance [3.4200(3) Å]. Shorter $Yb^{II}$–$Yb^{II}$ distances have been observed for carbon- and oxygen-bridged dimers.[5,6] The Yb–$N_{amido}$ bond lengths are indicative of two symmetric bridges (N5 and N8) and one nonsymmetrical (via N2) bridge. N2 seems to provide the anionic function of the amido ligand dominantly to Yb1, which is perfectly in accordance with the facts that the additional neutral ligand (thf) coordinates Yb1 and the anionic iodido ligand binds Yb2.

The bimetallic nature of complex **2** in solution was confirmed by $^{171}Yb$ NMR spectroscopy. In $C_6D_6$ there are two signals at 585.6 (broad, $\nu_{1/2}$ = 92.0 Hz) and 646.6 (sharp, $\nu_{1/2}$ = 8.5 Hz) ppm. The broad signal belongs to the Yb atom bonded directly to iodine, and the broadening arises from unresolved $^{171}Yb$–$^{127}I$ scalar coupling. The low-field signal consists of a central singlet and two satellites with an integral intensity of about 7% each. This 14% approximately corresponds to the natural abundance of the $^{171}Yb$ isotope and was assigned as a doublet arising from $^1J(^{171}Yb, ^{171}Yb)$ spin–spin coupling with a magnitude of 76.1 Hz. The chemical shift for $Yb^{II}$ amides ranges from $\delta(^{171}Yb)$ = 614 ppm to $\delta(^{171}Yb)$ = 1228 ppm, and the line width associated with $^{171}Yb$ resonances of these compounds ranges from $\Delta\nu_{1/2}$ = 70 Hz to $\Delta\nu_{1/2}$ = 550 Hz.[2] $^nJ(^{171}Yb,X)$ couplings have been observed for a variety of nuclei. Coupling constants usually cover a large range, for instance from 8627–9479 Hz (X = $^{119}Sn$) and 8254–9058 Hz (X = $^{117}Sn$),[13] 758 Hz (X = $^{125}Te$),[14] 233–265 Hz (X = $^{13}C$; resulting from alkyl carbon atoms)[15] up to 73 Hz (X = $^{31}P$).[16] Well-resolved $^3J(^{171}Yb,^{19}F)$ and $^4J(^{171}Yb,^{19}F)$ couplings have been recorded for perfluorophenyl ytterbium complexes. Coupling constants range from 13 to 48 Hz.[17]

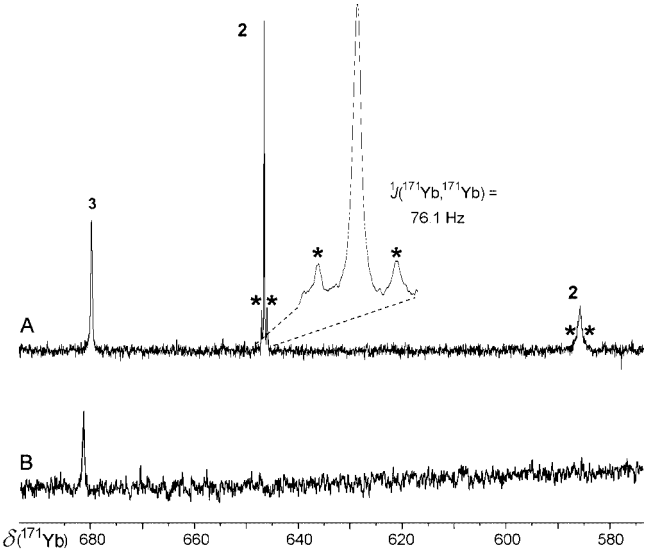


Figure 2. $^{171}Yb\{^1H\}$ NMR spectra (69.96 MHz, $[D_8]$thf) of complex **2** (A) and complex **3** (B).

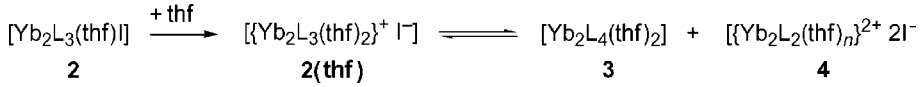


Scheme 2. Observed rearrangement reactions of **2** in thf (L = **1**).

 © 2007 Wiley-VCH Verlag GmbH & Co. KGaA, Weinheim 

Although complex **2** is stable in $C_6D_6$ for days, the $^{171}$Yb NMR spectrum in [$D_8$]thf solution consists of two already noted resonances ($\delta$ = 585.6 and 646.6 ppm) together with a third signal at $\delta$ = 679.8 ppm ($\nu_{1/2}$ = 25.5 Hz). In the $^1$H NMR spectrum at room temperature there is an additional set of broad signals. At low temperature (from 0 °C and lower), the signal set which belongs to the monoiodido complex **2** did not change, but the broad lines were more narrow and gave two sets (in a ratio of ca. 1:3) where the chemical shifts of the major set were completely identical to the $^1$H NMR spectrum of binuclear complex **3** (Scheme 2). In the $^{171}$Yb NMR spectrum of **3** in [$D_8$]thf, the signal at $\delta$ = 681.9 ppm was observed (Figure 2B). This value is very close to the chemical shift of the third signal in the spectrum presented in Figure 2A. Both $^1$H and $^{171}$Yb NMR spectroscopic data suggest that in thf solution complex **2** can dissociate to give cationic compound **2**(thf), where one coordination position is occupied by thf instead of iodine (Scheme 2). Complex **2**(thf) seems not to be stable and rearranges with the formation of neutral compound **3** and (most likely) dicationic **4**. The signal for complex **4** was not observed because of the low solubility of the complex (precipitation was observed).

In order to confirm the identity of complex **3**, it was independently synthesised by the reaction of **2** with the potassium salt of **1-H**, generated by treatment of **1-H** with KH (Scheme 3).

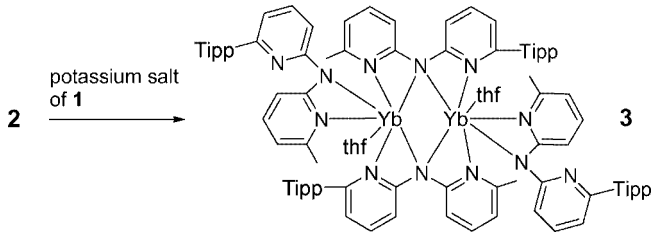


Scheme 3. Synthesis of **3** [Tipp = tri(isopropyl)phenyl].

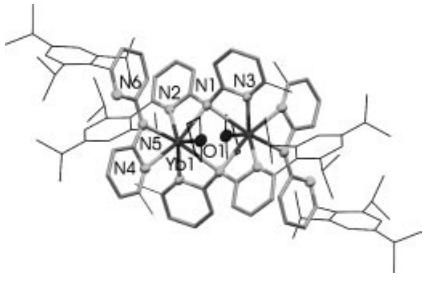


Figure 3. Molecular structure of **3** (ORTEP plot for all non-C,H-atoms). Substituents at the pyridine rings are plotted in wire frame style for clarity. Selected bond lengths [Å] and angles [°]: Yb1–O1 2.457(6); Yb1–N3 2.462(7), Yb1–N5 2.488(7), Yb1–N1 2.517(8), Yb1–N4 2.586(8), Yb1–N2 2.607(8), Yb1–N1′ 2.681(7), Yb1–Yb1′ 3.8685(11); N1–Yb1–N2 53.6(2), N3–Yb1–N1 53.0(2), N5–Yb1–N4 52.7(2).

The X-ray crystal structure analysis of **3** revealed[11] it to be a bimetallic complex in which two deprotonated bipyridylamide ligands act as tridentate bridging ligands and two of them as terminal bidentate aminopyridinates (Figure 3).

## Conclusion

We observed the first f-block-element–f-block-element coupling pattern in solution and have shown the relevance of such investigations in understanding dimer equilibria and rearrangement chemistry of rather bulky structural ensembles. Chemical transformations of low-valent lanthanide species has hitherto been difficult to follow.

## Experimental Section

**NMR Investigations:** The $^{171}$Yb NMR spectra were recorded by using a single-pulse sequence with pulse: approx. 30°, relaxation delay: 1 s, digital FID resolution: 0.3–0.5 Hz before zero filling and with proton decoupling during acquisition. The suitable signal-to-noise ratio was reached after 2–4 h. The chemical shifts are given relative to 0.171 M [Yb($\eta^5$-$C_5Me_5$)(thf)$_2$] in thf [$\delta$ ($^{171}$Yb) = 0 ppm for $\Xi$ ($^{171}$Yb) = 17.499306 MHz].

**Synthesis of Complex 2:**

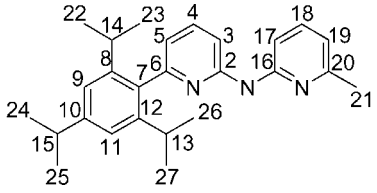

In a glove box, [$YbI_2(thf)_4$][18] (2.13 g, 2.98 mmol) and 1.90 g (3.82 mmol) of **1-K** were combined in a flask and thf (100 mL) was added at 0 °C. The resulting dark red reaction mixture was stirred at room temperature for 16 h. After separation of the solution from the precipitated potassium iodide by filtration, the solvent was removed under reduced pressure. The resulting solid was dissolved in toluene (100 mL) and filtered. The filtrate was reduced to dryness, and a dark red-black product was obtained. Crystals of **2** were grown from a concentrated toluene solution. Yield 2.06 g (72%). M.p. 190 °C. $C_{82}H_{104}IN_9OYb_2{\cdot}3C_4H_8O$ (1921.06): calcd. C 58.77, H 6.72, N 6.56; found C 58.77, H 6.67, N 6.93. $^1$H NMR (250 MHz, $C_6D_6$, 323 K): $\delta$ = 0.67–1.24 (m, $^3J$ = 6.7 Hz, 54 H, 22-H, 23-H, 24-H, 25-H, 26-H, 27-H), 1.43 (br., 4 H, β-C$H_2$, thf), 2.38 (sept, $^3J$ = 6.9 Hz, 3 H, 15-H), 2.60 (sept, $^3J$ = 7.0 Hz, 3 H, 14-H), 2.66 (s, 9 H, 21-H), 2.78 (sept, $^3J$ = 6.7 Hz, 3 H, 13-H), 3.53 (br., 4 H, α-C$H_2$, thf), 6.00 (d, $^3J$ = 6.7 Hz, 3 H, 19-H), 6.16 (d, $^3J$ = 6.6 Hz, 3 H, H$^5$), 6.83–7.16 (m, 18 H, 3-H, 4-H, 9-H, 11-H, 17-H, 18-H) ppm. $^{13}$C NMR (62.9 MHz, $C_6D_6$, 298 K): $\delta$ = 24.0 (s, C-22, C-23, C-26, C-27), 24.1 (s, C-22, C-23, C-26, C-27), 24.2 (s, C-22, C-23, C-26, C-27), 24.3 (s, C-22, C-23, C-26, C-27), 26.1 (s, β-*C*H$_2$, thf), 26.8 (s, C-24, C-25), 27.1 (s, C-24, C-25), 29.8 (s, C-13, C-14), 30.0 (s, C-13, C-14), 34.6 (s, C-15), 67.7 (s, α-*C*H$_2$, thf), 109.5 (s, C-19), 113.4 (s, C-17), 114.5 (s, C-5), 116.2 (s, C-3), 121.0 (s, C-9, C-11), 135.8 (s, C-4), 137.5 (s, C-7, C-18), 137.6 (s, C-7, C-18), 146.9 (s, C-8, C-12), 147.1 (s, C-8, C-12), 148.5 (s, C-10), 156.8 (s, C-2, C-16), 157.4 (s, C-2, C-16), 164.2 (s, C-20), 169.1 (s, C-6) ppm. $^{171}$Yb NMR (70 MHz, $C_4H_8O$, 298 K): $\delta$ = 646.6 [s, $^1J$($^{171}$Yb, $^{171}$Yb) = 76.1 Hz, *Yb*-thf], 585.6 (br., *Yb*-I) ppm.

 © 2007 Wiley-VCH Verlag GmbH & Co. KGaA, Weinheim 

**Supporting Information** (see footnote on the first page of this article): Details of the synthesis of the other compounds (ligand and complexes) reported for the first time within this publication can be found in the supporting information.

## Acknowledgments

We thank the DFG (SPP 1166 "Lanthanide Specific Functionalities in Molecules and Materials") and the Fonds der Chemischen Industrie for financial support, as well as Germund Glatz and Christian Döring for their support in the X-ray lab.

[1] J. M. Keates, G. A. Lawless, *Advanced Applications of NMR to Organometallic Chemistry* (Eds.: M. Gielen, R. Willem, B. Wrackmeyer), John Wiley and Sons, Chichester, **1996**.

[2] A. G. Avent, M. A. Edelman, M. F. Lappert, G. A. Lawless, *J. Am. Chem. Soc.* **1989**, *111*, 3423–3425.

[3] We chose this criterion because we expected the metal centres to be close enough to observe NMR coupling.

[4] a) O. Tardif, M. Nishiura, Z. Hou, *Tetrahedron* **2003**, *59*, 10525–10539; b) H.-S. Chan, H.-W. Li, Z. Xie, *Chem. Commun.* **2002**, 652–653; c) J. Holton, M. F. Lappert, D. G. H. Ballard, R. Pearce, J. L. Atwood, W. E. Hunter, *J. Chem. Soc. Dalton Trans.* **1979**, 54–61; d) P. L. Watson, T. H. Tulip, I. Williams, *Organometallics* **1990**, *9*, 1999–2009; e) W. J. Evans, D. K. Drummond, L. R. Chamberlain, R. J. Doedens, S. G. Bott, H. Zhang, J. L. Atwood, *J. Am. Chem. Soc.* **1988**, *110*, 4983–4994; f) M. Niemeyer, *Z. Anorg. Allg. Chem.* **2002**, *628*, 647–657; g) S. Anfang, T. Grob, K. Harms, G. Seybert, W. Massa, A. Greiner, K. Dehnicke, *Z. Anorg. Allg. Chem.* **1999**, *625*, 1853–1859; h) T. Gröb, G. Seybert, W. Massa, F. Weller, R. Palaniswami, A. Greiner, K. Dehnicke, *Angew. Chem.* **2000**, *112*, 4542–4544; *Angew. Chem. Int. Ed.* **2000**, *39*, 4373–4375; i) D. C. Bradley, H. Chudzynska, D. M. Frigo, M. E. Hammond, M. B. Hursthouse, M. A. Mazid, *Polyhedron* **1990**, *9*, 719–726; j) D. J. Duncalf, P. B. Hitchcock, G. A. Lawless, *Chem. Commun.* **1996**, 269–271; k) Z. Wu, Z. Xu, X. You, X. Zhou, X. Huang, *J. Organomet. Chem.* **1994**, *483*, 107–113; l) Z.-Z. Wu, Z.-E. Huang, R.-F. Cai, Z. Xu, X.-Z. You, X.-Y. Huang, *Polyhedron* **1996**, *15*, 13–22; m) A. A. Trifonov, M. N. Bochkarev, H. Schumann, J. Loebel, *Angew. Chem.* **1991**, *103*, 1170–1172; *Angew. Chem. Int. Ed. Engl.* **1991**, *30*, 1149–1151; n) M. Geissinger, J. Magull, *Z. Anorg. Allg. Chem.* **1995**, *621*, 2043–2048; o) E. Silina, Yu. Bankovsky, V. Belsky, J. Lejejs, L. Pech, *Latv. Kim. Z.* **1997**, *4*, 89–90; p) M. R. Bürgstein, P. W. Roesky, *Angew. Chem.* **2000**, *112*, 559–562; *Angew. Chem. Int. Ed.* **2000**, *39*, 549–551.

[5] a) A. G. Avent, P. B. Hitchcock, A. V. Khvostov, M. F. Lappert, A. V. Protchenko, *Dalton Trans.* **2004**, 2272–2280; b) D. M. M. Freckmann, T. Dube, C. D. Berube, S. Gambarotta, G. P. A. Yap, *Organometallics* **2002**, *21*, 1240–1246; c) T. Grob, G. Seybert, W. Massa, K. Dehnicke, *Z. Anorg. Allg. Chem.* **2000**, *626*, 349–353; d) M. N. Bochkarev, V. V. Khramenkov, Yu. F. Rad′kov, L. N. Zakharov, Yu. T. Struchkov, *J. Organomet. Chem.* **1992**, *429*, 27–39; e) G. B. Deacon, C. M. Forsyth, P. C. Junk, B. W. Skelton, A. H. White, *Chem. Eur. J.* **1999**, *5*, 1452–1459; f) O. Eisenstein, P. B. Hitchcock, A. V. Khvostov, M. F. Lappert, L. Maron, L. Perrin, A. V. Protchenko, *J. Am. Chem. Soc.* **2003**, *125*, 10790–10791.

[6] a) J. R. van den Hende, P. B. Hitchcock, M. F. Lappert, *J. Chem. Soc. Dalton Trans.* **1995**, 2251–2258; b) J. R. van den Hende, P. B. Hitchcock, M. F. Lappert, *J. Chem. Soc. Chem. Commun.* **1994**, 1413–1414.

[7] For metal–metal distances less than 3.5 Å only one example is known: M. N. Bochkarev, V. V. Khramenkov, Yu. F. Rad′kov, L. N. Zakharov, Yu. T. Struchkov, *J. Organomet. Chem.* **1991**, *421*, 29–38.

[8] Review articles on aminopyridinato ligands: R. Kempe, *Eur. J. Inorg. Chem.* **2003**, 791–803.

[9] a) N. M. Scott, T. Schareina, O. Tok, R. Kempe, *Eur. J. Inorg. Chem.* **2004**, 3297–3304; b) N. M. Scott, R. Kempe, *Eur. J. Inorg. Chem.* **2005**, 1319–1324; c) W. P. Kretschmer, A. Meetsma, B. Hessen, T. Schmalz, S. Qayyum, R. Kempe, *Chem. Eur. J.* **2006**, *12*, 8969–8978.

[10] a) K. Müller-Buschbaum, *Z. Anorg. Allg. Chem.* **2003**, *629*, 2127–2132; b) C. C. Quitmann, K. Müller-Buschbaum, *Angew. Chem.* **2004**, *116*, 6120–6122; *Angew. Chem. Int. Ed.* **2004**, *43*, 5994–5996; c) K. Müller-Buschbaum, *Z. Anorg. Allg. Chem.* **2005**, *631*, 811–828; d) K. Müller-Buschbaum, C. C. Quitmann, *Inorg. Chem.* **2006**, *45*, 2678–2687.

[11] J. R. van den Hende, P. B. Hitchcock, S. A. Holmes, M. F. Lappert, W.-P. Leung, T. C. W. Mak, S. Prashar, *J. Chem. Soc. Dalton Trans.* **1995**, 1427–1433.

[12] Selected details of the X-ray crystal structure analyses: **2**·2thf/$C_6D_6$: space group: $P\bar{1}$, $a$ = 13.3350(5) Å, $b$ = 15.8580(6) Å, $c$ = 22.9500(9) Å, $\alpha$ = 102.371(3) °, $\beta$ = 91.499(3) °, $\gamma$ = 107.584(3) °, $V$ = 4497.4(3) Å$^3$, $z$ = 2, reflections collected/unique/observed [$I > 2\sigma(I)$] = 58816/16943/13427, parameters = 933, $R$ (obs.) = 0.0336, $wR^2$ (all data) = 0.0825, $wR^2$ (obs.) = 0.0785; **3**·2$C_6D_6$ space group: $P\bar{1}$, $a$ = 14.2870(12) Å, $b$ = 14.3730(10) Å, $c$ = 16.8380(14) Å, $\alpha$ = 114.563(6) °, $\beta$ = 93.070(6) °, $\gamma$ = 109.525(6) °, $V$ = 2888.2(4) Å$^3$, $z$ = 1, reflections collected/unique/observed [$I > 2\sigma(I)$] = 37338/10918/5889, parameters = 672, $R$ (obs.) = 0.0654, $wR^2$ (all data) = 0.1385, $wR^2$ (obs.) = 0.1201; X-ray crystal structure analysis was carried out with a STOE IPDS II diffractometer equipped with an Oxford Cryostream low-temperature unit. CCDC-642879 (**2**) and CCDC-642880 (**3**) contain the supplementary crystallographic data for this paper. These data can be obtained free of charge from The Cambridge Crystallographic Data Centre via www.ccdc.cam.ac.uk/data_request/cif.

[13] F. G. N. Cloke, C. I. Dalby, P. Hitchcock, H. Karamallakis, G. A. Lawless, *J. Chem. Soc. Chem. Commun.* **1991**, 779–781.

[14] A. R. Strzelecki, C. L. Likar, B. A. Hesel, T. Utz, M. C. Lin, P. A. Bianconi, *Inorg. Chem.* **1994**, *33*, 5188–5194.

[15] a) P. B. Hitchcock, S. A. Holmes, M. F. Lappert, S. Tian, *J. Chem. Soc. Chem. Commun.* **1994**, 2691–2692; b) G. B. Deacon, P. B. Hitchcock, S. A. Holmes, M. F. Lappert, P. MacKinnon, R. H. Newnham, *J. Chem. Soc. Chem. Commun.* **1989**, 935–937.

[16] M. L. Green, A. K. Huges, D. M. Michaelidou, P. J. Mountford, *J. Chem. Soc. Chem. Commun.* **1993**, 591–593.

[17] G. B. Deacon, C. M. Forsyth, *Chem. Eur. J.* **2004**, *10*, 1798–1804.

[18] F. T. Edelmann, *Lanthanoids and Actinides: Synthetic Methods of Organometallic and Inorganic Chemistry* (Ed.: W. A. Hermann), Thieme Medical Publishers, New York, **1997**.

Received: June 29, 2007
Published Online: September 7, 2007

 © 2007 Wiley-VCH Verlag GmbH & Co. KGaA, Weinheim 

DOI: 10.1002/ejic.200700764

# Chiral Calix[4]arene-Based Diphosphites as Ligands in the Asymmetric Hydrogenation of Prochiral Olefins

**Angelica Marson,[a] Zoraida Freixa,[b] Paul C. J. Kamer,*[c] and Piet W. N. M. van Leeuwen*[a]**

**Keywords:** Homogeneous catalysis / Stereoselective catalysis / Asymmetric hydrogenation / Calixarenes / Diphosphites

Chiral calixarene-based diphosphite ligands **3a**–**d** have been obtained via lower-rim functionalisation of the *p*-*tert*-butylcalix[4]arene core. High enantiomeric excesses (up to 94 %) and good activities were obtained in the rhodium-catalyzed asymmetric hydrogenation of prochiral olefins with TADDOL-containing diphosphites **3c**,**d**. This is the first example of chiral calix[4]arene-modified ligands that induce high enantioselectivity in metal-catalysed asymmetric reactions.

(© Wiley-VCH Verlag GmbH & Co. KGaA, 69451 Weinheim, Germany, 2007)

## Introduction

Asymmetric reactions catalysed by transition metals are among the most efficient methods for preparing a wide range of enantiomerically pure compounds.[1] The tremendous achievements in organometallic chemistry have resulted in fundamental understanding of elementary steps and consequently in many examples of rational ligand design.[2] Still, the rates and selectivity of enzymatic catalysis are seldom equalled by transition metal catalysis. Chemical transformations catalyzed by enzymes often operate via complicated mechanisms and require large and sophisticated protein structures that have been obtained after millions of years of evolution. Although nowadays enzymes are applied successfully in many chemical conversions, their substrate specificity can be too high in certain cases and the biological reaction conditions might be not wanted. This is why the majority of industrial processes is based on man-made catalysts. Many attempts are being made to obtain efficient catalysts that can compete with enzymes in substrate-selectivity and activity, such as incorporation of transition metal complexes in proteins and antibodies.[3] To bridge the gap between enzyme and transition metal catalysts it is important to develop new catalyst systems that, mimicking enzymes, impose steric confinement on metal and substrates in addition to the well-explored ligand effects.

Calixarenes form a suitable scaffold for the development of new bulky and structurally well-defined ligands.[4] The combination of calixarene cavities with catalytic centres might lead to shape-selective catalysts, adding this successfully exploited feature of biological systems to transition metal catalysis. Although the number of successful applications of the shape selectivity of calixarene-based catalysts is growing,[5] high selectivities in asymmetric catalysis have not been achieved so far.[6]

From the different functionalities that one can consider, phosphite ligands proved their adequacy in many transition metal-catalysed reactions such as hydrogenation, hydroformylation, hydrocyanation and allylic alkylation.[2]

## Results and Discussion

Here we report on the asymmetric hydrogenation of prochiral olefins, as model reaction, using enantiopure calix[4],BINOL- and calix[4],TADDOL-containing diphosphites. The effective formation of a shape defined active site is achieved by directly attaching three of the hydroxy groups of the calix[4]arene through $\mu_3$-bridging phosphorus atom. In this way, these new C1-symmetric bidentate ligands, which combine the intrinsic steric bulk of the calix[4]arene scaffold with a stereocentre located on a phosphite pendent arm linked to the lower rim of the calix[4]-cavity, represent the first class of chiral calix[4]arene-modified ligands to be reported in literature and successfully applied in metal-catalysed asymmetric reactions. In order to gain information about the potential of such type of ligands, we carried out some preliminary investigations on two different types of

[a] Van't Hoff Institute for Molecular Sciences, University of Amsterdam,
Nieuwe Achtergracht 166, 1018 WV Amsterdam, The Netherlands
Fax: +31-20-525-5604
E-mail: pwnm@science.uva.nl
[b] Institute of Chemical Research of Catalonia (ICIQ),
Av. Països Catalans 16, 43007 Tarragona, Spain
[c] School of Chemistry, University of St Andrews,
St. Andrews, Fife, KY16 9ST, United Kingdom
Fax: +44-1334-467285
E-mail: pcjk@st-and.ac.uk

Supporting information for this article is available on the WWW under http://www.eurjic.org or from the author.

 © 2007 Wiley-VCH Verlag GmbH & Co. KGaA, Weinheim 

chiral moieties and by comparing the role of the stereocentre, we evaluated the efficacy of the ligand systems and their catalytic performances.

Chiral diphosphite ligands **3a**–**d** were prepared through a two-step synthesis according to reported calixarenes-phosphorylation procedures (Scheme 1).[5g] Since the sequence in which the two steps are followed is crucial in order to obtain diphosphites in the appropriate *cone* conformation,[5d,7] *p*-*tert*-butylcalix[4]arene **1** was firstly treated with one equivalent of *n*BuLi in THF at room temperature and then reacted with one equivalent of chiral phosphorochloridites (**a**–**d**),[8,9] affording the monofunctionalised calix[4]arene intermediates **2a**–**d**. In the present study, we focused our attention on chiral units derived from commercially available diols such as (*R*)- and (*S*)-BINOL [(*R*)-, (*S*)-2,2′-dihydroxy-1,1′-binaphthyl] and (*R*,*R*)- and (*S*,*S*)-TADDOL [(*R*,*R*)-, (*S*,*S*)-2,2-dimethyl-α,α,α′,α′-tetraphenyldioxolane-4,5-dimethanol] which allow an economically attractive preparative method of bidentate ligands and a fast and efficient preliminary investigation of the catalytic performances of the corresponding metal complexes.

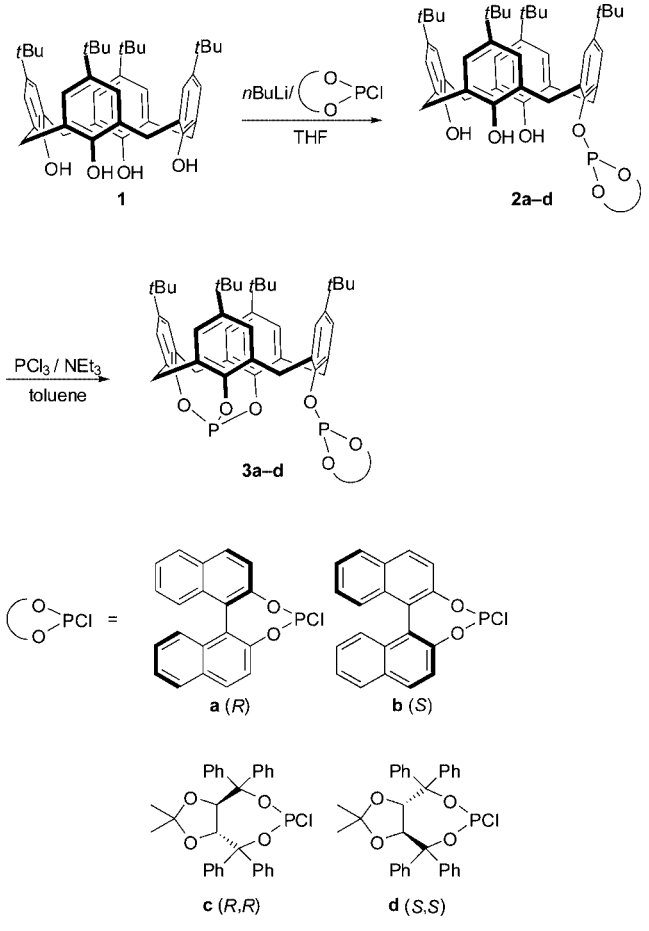


Scheme 1. Synthesis of chiral calix[4]arene-based diphosphites **3a**–**d**.

The first reaction step is not very selective towards monofunctionalisation and gives rise to the formation of by-products, like 1,3-disubstituted calix[4]arenes. We observed that the steric bulk of the phosphorochloridites strongly affects the product distribution. As expected, the more sterically hindered fragments (i.e. TADDOL-PCl **c**,**d**) afford mainly monofunctionalised products, while with the bare BINOL derivatives **a**,**b** the two fractions are obtained in a 1:1 ratio. Nevertheless, no further purification was carried out on the isolated crude products, which were treated in the second step with an excess of $PCl_3/NEt_3$ to give, after chromatographic separation, the pure chiral diphosphite products **3a**–**d**. Thus, the resulting calix[4],BINOL- (**3a**,**b**) and calix[4],TADDOL-based diphosphites **3c**,**d** are characterised by the presence of one phosphorus atom, acting as a triple $\mu_3$-*O*,*O*,*O* bridge, at the lower rim of the calix[4]-cavity and a second phosphorus atom on a pendent chiral unit.

The $^{31}P$ NMR spectra show in all cases two distinctive singlets for the two non-equivalent phosphite moieties of each ligand: one at $\delta$ = 104 ppm for the $\mu_3$-bridging phosphorus atom and one for the chiral fragment-containing phosphite ($\delta$ = 147 ppm for BINOL derivatives **3a**,**b**; $\delta$ = 140 ppm for TADDOL derivatives **3c**,**d** respectively). Both chemical shifts fall into the expected ranges for calix[4]-based $\mu_3$-bridging phosphites,[5d,5g] and for TADDOL- or BINOL-based phosphite ligands.[10] Also in the corresponding $^1H$ NMR spectra, ligands **3a**–**d** show similar spectroscopic features. The four *tert*-butyl signals and the four AB patterns for the bridging methylene units (Ar$CH_2$Ar), with AB separations larger than 1 ppm, clearly prove the $C_1$ symmetry of these structures and the overall *cone* conformation of the calix[4]arene backbone This geometry was further confirmed by the $^{13}C$ NMR spectra in which some of the signals for the Ar$CH_2$Ar fall into the expected range for *syn*-oriented phenolic neighbours (ca. 35–36 ppm), while others fall in an intermediate range of values (ca. 36–37 ppm).[5g,11] It should be recalled that, due to the strain imposed by the very short $\mu_3$-bridging phosphite unit, the observation of signals with an intermediate chemical shift might be interpreted in terms of partial flattening of the calixarene core.

Investigations have been carried out to define the coordination chemistry of diphosphites **3a**,**d** and assess their chelating abilities towards square planar $Rh^I$ precursors. The complexation reaction of ligands **3a**,**c** with one equivalent of $[Rh(nbd)_2BF_4]$ (nbd = 2,5-norbornadiene) in dichloromethane solution proceeds rapidly. Displacement of one molecule of 2,5-norbornadiene occurs after 30 minutes at room temperature whilst stirring, affording complexes $[Rh(nbd)(P^1 \cap P^2)][BF_4]$ (**4a**,**c**). The corresponding $^{31}P$ NMR spectra showed two distinctive double doublets as a result of phosphorus–rhodium and phosphorus–phosphorus couplings [$^1J(Rh,P^1)$ = 274 Hz, $^1J(Rh,P^2)$ = 265 Hz and $^2J(P^1,P^2)$ = 83 Hz (**4a**); $^1J(Rh,P^1)$ = 265 Hz, $^1J(Rh,P^2)$ = 249 Hz and $^2J(P^1,P^2)$ = 81 (**4c**)].

The observed rhodium–phosphorus coupling constants are very similar to those reported for $[Rh(diolefin)(P^1 \cap P^2)]^+$ rhodium complexes with coordinated diphosphite ligands, while the coupling constants between the two non-equivalent phosphorus atoms are larger than expected.[12] Coupling constants between 27 and 50 Hz are generally observed

 © 2007 Wiley-VCH Verlag GmbH & Co. KGaA, Weinheim 

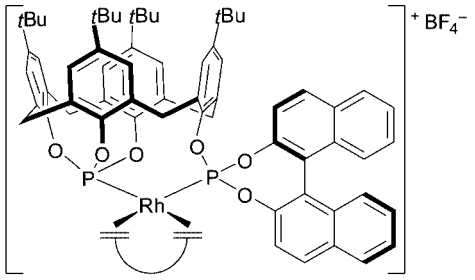


**4a**

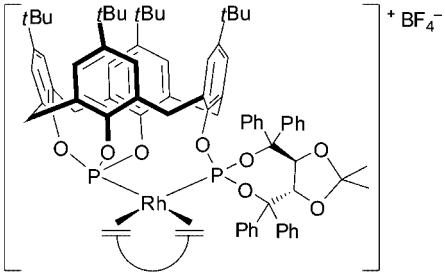


**4c**

between the two non-equivalent phosphorus atoms in relative *cis* positions. Lowering the temperature to 193 K did not result in any additional splitting of the $^{31}P$ NMR signals, which indicates that, for both rhodium complexes **4a**,**c**, only one isomer is present in solution. Clearly, this might represent an advantage in terms of enantioselectivity when these complexes are employed as catalysts in asymmetric transformations.

Chiral diphosphites **3a**–**d** were tested as ligands in the asymmetric rhodium-catalysed hydrogenation and of prochiral olefins using $[Rh(nbd)_2BF_4]$ as metal precursor. Catalytic experiments were run in a parallel manner using an autoclave equipped with 5, 8, or 15 mini-reactors (see Supporting Information for details). The catalyst precursors were formed in situ by mixing metal complexes with ligands **3a**–**d** under inert atmosphere. The autoclave was purged four times with hydrogen and then charged with the appropriate gas pressure.

The rhodium-catalysed hydrogenation, carried out under mild conditions (25 °C, 5 bar $H_2$), was examined as model reaction employing dimethyl itaconate (**A**) and α-(acylamino)acrylate (**B**) as representative substrates. Parallel experiments were run employing a standard substrate/rhodium ratio of 100 and using catalyst precursors formed in situ by mixing ligands **3a**,**c** with $[Rh(nbd)_2BF_4]$. The formation of the active species $[Rh(P^1 \cap P^2)(solvent)_2][BF_4]$, generated by removal of the diolefin, is generally faster when it involves the hydrogenation of the more reactive norbornadiene rather than that of cyclooctadiene.[13] Different outcomes have been observed, regarding both the activity and the selectivity of the catalytic process, depending on the nature of the substrate and of the diphosphite used.

The hydrogenation of dimethyl itaconate providing dimethyl methylsuccinate [**A**; Equation (1)], in dichloromethane, was chosen as the test reaction and the activity and the enantioselectivity of the catalyst precursors evaluated at different reaction conditions (Table 1). Initially the ligand to rhodium ratio was kept constant at 1.5 (entries 1 and 6), then the reaction time and the substrate/rhodium ratios were changed from 20 h to 4 h (entries 2 and 7) and from 100 to 1000 (entries 3 and 8), respectively.

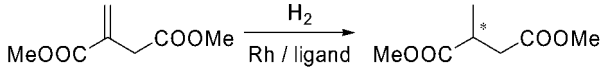


**A** (1)

Table 1. Asymmetric hydrogenation of prochiral olefins with $[Rh(nbd)_2BF_4]$ and ligands **3a**–**d**.[a]

| Entry | Ligand | Substrate | % Conv. (*t* [h])[b] | % *ee* (config.)[c] |
|---|---|---|---|---|
| 1 | **3a** | **A** | 100 (20) | 74 (*R*) |
| 2 | **3a** | **A** | 100 (4) | 74 (*R*) |
| 3[d] | **3a** | **A** | 100 (4) | 76 (*R*) |
| 4[e] | **3a** | **A** | 60 (20) | 20 (*S*) |
| 5 | **3a** | **B** | 100 (20) | 32 (*R*) |
| 6 | **3c** | **A** | 100 (20) | 92 (*R*) |
| 7 | **3c** | **A** | 100 (4) | 92 (*R*) |
| 8[d] | **3c** | **A** | 100 (4) | 94 (*R*) |
| 9[f] | **3c** | **A** | 100 (20) | 92 (*R*) |
| 10 | **3c** | **B** | 100 (20) | 94 (*R*) |
| 11 | **3b** | **A** | 100 (20) | 75 (*S*) |
| 12 | **3d** | **A** | 100 (20) | 92 (*S*) |

[a] Standard conditions: [Rh] = 1 mM; [ligand]/[Rh] = 1.5; [substrate]/[Rh] = 100; solvent = $CH_2Cl_2$ (2.0 mL); $p$ = 5 bar; $T$ = 25 °C; catalyst precursors prepared in situ. [b] Percent conversion measured by GC. [c] Percent enantiomeric excess measured by chiral GC. [d] [substrate]/[Rh] = 1000. [e] Solvent: $CH_2Cl_2$/toluene, 1:3. [f] [ligand]/[Rh] = 5.

The results summarised in Table 1 show that the catalytic systems obtained with diphosphites **3a**,**c** are very active in the hydrogenation of dimethyl itaconate (**A**) and, although a standard reaction time of 20 h was chosen, complete conversion was already reached after 4 h. The increase of the ligand to rhodium ratio or the substrate to rhodium ratio does not have a negative effect on the activity of the reported catalytic systems, which still afford high enantioselectivities (*ee* up to 94%) and full conversions after 4 h reaction time. In one case (entry 4) the solvent of the reaction was changed to a mixture of dichloromethane/toluene (1:3) showing that the efficiency of the process depends strongly on the nature of solvent employed, and that the catalyst performance, both in terms of activity and enantioselectivity, was best when pure dichloromethane was used. Interestingly, opposite stereoinduction was observed in this case. It should be noted that rhodium-catalysed asymmetric hydrogenation reactions are commonly performed in methanol, but since phosphite ligands are known to decompose in protic solvents,[14] further hydrogenation reactions were studied using dichloromethane.

Ligand **3c**, which contains the bulky TADDOL moiety, affords the best catalyst, reaching enantioselectivities around 92% in all experiments. The results obtained with

 © 2007 Wiley-VCH Verlag GmbH & Co. KGaA, Weinheim 

ligand **3a** follow the same trend as observed for ligand **3c**, but the enantioselectivities are somewhat lower. As it would be expected by less bulky ligands, the asymmetric inductions with precursors containing ligand **3a** are lower than those with ligand **3c**. Besides ligands **3a**,**c**, which were used extensively in these catalytic investigations, their enantiomers, namely ligands **3b**,**d**, were also employed in analogous hydrogenation experiments showing, as expected, identical results but with opposite stereoinduction (entries 11,12).

We also studied the hydrogenation of α-(acylamino)acrylates [Equation (2)] under standard reaction conditions. Hydrogenation of methyl α-acetamidoacrylate [**B**; Equation (2)] giving the alanine derivative afforded high enantioselectivity (*ee* = 94%) with ligand **3c**, while a low value of 32% was obtained with ligand **3a**. In both cases complete conversion was reached after 20 h reaction time (entries 5,10).

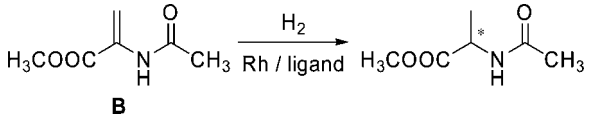


(2)

In general, the catalytic systems obtained with calix[4]-arene-based diphosphites **3a**–**d** were found to be comparable, in terms of performances, to the diphosphites previously reported in literature by Reetz et al. and by Claver et al., leading to excellent activities and high enantioselectivities in the hydrogenation of dimethyl itaconate and methyl α-acetamidoacrylate.[10a,12,15]

## Conclusions

We have synthesized novel chiral diphosphite ligands built up on calix[4]arene backbones and characterised by a $C_1$ symmetry. We employed these ligands in the rhodium-catalysed hydrogenation of prochiral olefins, reaching excellent activities and enantioselectivities in the hydrogenation of dimethyl itaconate and methyl α-acetamidoacrylate. The best enantioselectivities have been obtained for both substrates with the same, most bulky, ligand. These preliminary investigations demonstrated for the first time that calix[4]-arene-based $C_1$-symmetric diphosphites can be successfully applied in metal-catalysed asymmetric transformations. Due to their ease of preparation, different classes of chiral bidentates can be generated, for example, by systematic variation of the steric and electronic properties of the stereocentre linked to the lower rim of the calix[4]-cavity. Thus, the results reported herein have to be considered as an important starting point and further study of this promising type of ligands in homogeneous catalysis is in progress.

## Experimental Section

Experimental details for all compounds and procedures are given in the Supporting Information.

**Supporting Information** (see also the footnote on the first page of this article): Catalyst preparation, synthetic and catalytic procedures.

## Acknowledgments

This research was financed by the Division of Chemical Sciences of the Netherlands Organization for Scientific Research (NWO-CW).

[1] *Handbook of Chiral Chemicals*, 2nd ed. (Ed.: D. J. Ager), Marcel Dekker, New York, **2005**.
[2] P. W. N. M. van Leeuwen, *Homogeneous Catalysis, Understanding the art*, Kluwer Academic Publisher, **2004**, and references herein.
[3] a) E. T. Kaiser, D. S. Lawrence, *Science* **1984**, *226*, 505–511; b) M. E. Wilson, G. M. Whitesides, *J. Am. Chem. Soc.* **1978**, *100*, 306–307; c) D. Qi, C. M. Tann, D. Haring, M. D. Distefano, *Chem. Rev.* **2001**, *101*, 3081–3111; d) M. T. Reetz, *Proc. Natl. Acad. Sci. USA* **2004**, *101*, 5716–5722; e) C. Letondor, N. Humbert, T. R. Ward, *Proc. Natl. Acad. Sci. USA* **2005**, *102*, 4683–4687; f) L. Panella, J. Broos, J. Jin, M. W. Fraaije, D. B. Janssen, M. Jeronimus-Stratingh, B. L. Feringa, A. J. Minnaard, J. G. de Vries, *Chem. Commun.* **2005**, 5656–5658; g) H. Yamaguchi, T. Hirano, H. Kiminami, D. Taura, A. Harada, *Org. Biomol. Chem.* **2006**, *4*, 3571–3573.
[4] a) C. Wieser, C. B. Dieleman, D. Matt, *Coord. Chem. Rev.* **1997**, *165*, 93–161; b) C. Jeunesse, D. Armspach, D. Matt, *Chem. Commun.* **2005**, 5603–5614.
[5] a) F. J. Parlevliet, M. A. Zuideveld, C. Kiener, H. Kooijman, A. L. Spek, P. C. J. Kamer, P. W. N. M. van Leeuwen, *Organometallics* **1999**, *18*, 3394–3405; b) R. Paciello, L. Siggel, M. Röper, *Angew. Chem.* **1999**, *111*, 2045–2048; R. Paciello, L. Siggel, M. Röper, *Angew. Chem. Int. Ed.* **1999**, *38*, 1920–1923; c) C. J. Cobley, D. D. Ellis, A. G. Orpen, P. G. Pringle, *J. Chem. Soc. Dalton Trans.* **2000**, 1109–1112; d) F. J. Parlevliet, C. Kiener, J. Fraanje, K. Goubitz, M. Lutz, A. L. Spek, P. C. J. Kamer, P. W. N. M. van Leeuwen, *J. Chem. Soc. Dalton Trans.* **2000**, 1113–1122; e) C. Kunze, D. Selent, R. Schmutzler, A. Spannenberg, A. Börner, *Heteroat. Chem.* **2001**, *12*, 577–585; f) C. Kunze, D. Selent, I. Neda, M. Freytag, P. G. Jones, R. Schmutzler, W. Baumann, A. Börner, *Z. Anorg. Allg. Chem.* **2002**, *628*, 779–787; g) S. Steyer, C. Jeunesse, D. Matt, R. Welter, M. Wesolek, *J. Chem. Soc. Dalton Trans.* **2002**, 4264–4274; h) D. Sémeril, C. Jeunesse, D. Matt, L. Toupet, *Angew. Chem.* **2006**, *118*, 5942–5945; D. C. Jeunesse, D. Matt, L. Toupet, *Angew. Chem. Int. Ed.* **2006**, *45*, 5810–5814.
[6] a) C. Dieleman, S. Steyer, C. Jeunesse, D. Matt, *J. Chem. Soc. Dalton Trans.* **2001**, 2508–2517; b) C. Gaeta, M. De Rosa, M. Fruilo, A. Soriente, P. Neri, *Tetrahedron: Asymmetry* **2005**, *16*, 2333–2340.
[7] A. Marson, *Phosphorus-Functionalised Calixarenes*, Ph. D. Thesis, van't Hoff Institute for Molecular Sciences, University of Amsterdam, The Netherlands, **2006**.
[8] A. van Rooy, D. Burgers, P. C. J. Kamer, P. W. N. M. van Leeuwen, *Recl. Trav. Chim. Pays-Bas* **1996**, *115*, 492–498.
[9] G. J. H. Buisman, L. A. van der Veen, A. Klootwijk, W. G. J. de Lange, P. C. J. Kamer, P. W. N. M. van Leeuwen, D. Vogt, *Organometallics* **1997**, *16*, 2929–2939.
[10] a) M. Diéguez, A. Ruiz, C. Claver, *J. Org. Chem.* **2002**, *67*, 3796–3801; b) G. J. H. Buisman, L. A. van der Veen, P. C. J. Kamer, P. W. N. M. van Leeuwen, *Organometallics* **1997**, *16*, 5681–5687; c) M. T. Reetz, G. Mehler, *Angew. Chem.* **2000**, *112*, 4047–4049; M. T. Reetz, G. Mehler, *Angew. Chem. Int. Ed.* **2000**, *39*, 3889–3890; d) D. Seebach, M. Hayakawa, J. I. Sakaki, W. B. Schweizer, *Tetrahedron* **1993**, *49*, 1711–1724; e) A. Alexakis, J. Vastra, J. Burton, C. Benhaim, P. Mangeney, *Tetrahedron Lett.* **1998**, *39*, 7869–7872; f) R. Hilgraf, A. Pfaltz, *Adv. Synth. Catal.* **2005**, *347*, 61–77.

 © 2007 Wiley-VCH Verlag GmbH & Co. KGaA, Weinheim 

[11] C. Jaime, J. de Mendoza, P. Prados, P. M. Nieto, C. Sánchez, *J. Org. Chem.* **1991**, *56*, 3372–3376.
[12] a) R. Kadyrov, D. Heller, R. Selke, *Tetrahedron: Asymmetry* **1998**, *9*, 329–340; b) O. Pàmies, G. Net, A. Ruiz, C. Claver, *Tetrahedron: Asymmetry* **2000**, *11*, 1097; c) O. Pàmies, G. Net, A. Ruiz, C. Claver, *Eur. J. Inorg. Chem.* **2000**, 1287–1294.
[13] a) A. Börner, D. Heller, *Tetrahedron Lett.* **2001**, *42*, 223–225; b) H. J. Drexler, W. Baumann, A. Spannenberg, C. Fischer, D. Heller, *J. Organomet. Chem.* **2001**, *621*, 89–102; c) C. J. Cobley, I. C. Lennon, R. McCague, J. A. Ramsden, A. Zanotti Gerosa, *Tetrahedron Lett.* **2001**, *42*, 7481–7483.
[14] a) M. J. Baker, K. N. Harrison, A. G. Orpen, G. Shaw, P. G. J. Pringle, *J. Chem. Soc. Chem. Commun.* **1991**, 803–804; b) P. C. Nirchio, D. J. Wink, *Organometallics* **1991**, *10*, 336–340.
[15] M. T. Reetz, T. Neugebauer, *Angew. Chem.* **1999**, *111*, 134–137; M. T. Reetz, T. Neugebauer, *Angew. Chem. Int. Ed.* **1999**, *38*, 179–181.

Received: July 19, 2007
Published Online: September 4, 2007

 © 2007 Wiley-VCH Verlag GmbH & Co. KGaA, Weinheim 

DOI: 10.1002/ejic.200700574

# Self-Assembled 1D Water Cluster in a Supramolecular Architecture of $Co^{II}$(Tartrate)(Phenanthroline/Bipyridine): An Assessment of Magnetic Property

**Subal Chandra Manna,[a] Ennio Zangrando,[b] Joan Ribas,*[c] and Nirmalendu Ray Chaudhuri*[a]**

**Keywords:** Cobalt(II) / Tartrate / Magnetic properties / Water cluster

The coordination polymer, $\{[Co(tart)(phen)]\cdot 6H_2O\}_n$ (**1**) (tart, tartrate dianion; phen, 1,10-phenanthroline) has been synthesized and characterized by single-crystal X-ray structure determination, magnetic measurement and thermal analysis. The structural analyses reveal two adjacent parallel 1D –[Co(phen)-tart-Co(phen)]– coordination polymers zipped through π-π interactions. The lattice water molecules, forming a 1D water cluster, function as glue to form a 3D supramolecular network through an extended hydrogen bonding. A comparison highlighting the structural differences with the corresponding 2,2′-bipyridine (bpy) derivative, $\{[Co(tart)(bpy)]\cdot 5H_2O\}_n$ (**2**) containing a less amount of lattice water molecules is discussed. The variable-temperature magnetic study of **1** has been carried out and interpretation of the already reported complex **2** has been re-visited: both polymers **1** and **2** show weak antiferromagnetic interaction.
(© Wiley-VCH Verlag GmbH & Co. KGaA, 69451 Weinheim, Germany, 2007)

## Introduction

For the unusual properties and fundamental importance manifested in many biological and physico-chemical processes, water and hydrogen bonds have received considerable attention in current research.[1] The environment designed by the crystal host stabilizes various topologies of water clusters and plays an important role in the formation of different water morphology.[2] The structural study sometimes supported by theoretical and experimental research on such "discrete" water clusters is of great importance for the understanding of the behavior of bulk water or ice.[3] Recently, a number of papers describing the cooperative association of water molecules to form a variety of oligomers and clusters,[4,5] sometimes connected to form one dimensional,[6] layered aggregates,[7] and 3D "ice-like" open frameworks,[8] have been published. However, the study of larger water aggregates, which represent the bridge between cluster and bulk water, is still a challenging scientific endeavor.[9]

Here we report on the synthesis, X-ray crystal structure, and thermal study of a 3D supramolecular architecture, $\{[Co(tart)(phen)]\cdot 6H_2O\}_n$ (**1**) (tart, tartrate dianion; phen, 1,10-phenanthroline). The structural data are compared with analogous 2,2′-bipyridine (bpy) derivative, $\{[Co(tart)(bpy)]\cdot 5H_2O\}_n$ (**2**).[10] The magnetic behavior of **1** is also reported which questions the reliability of the corresponding data of **2**, demanding the re-magnetic measurement of **2**.

## Results and Discussion

X-ray crystal structure analysis reveals that complex **1** consists of 1D polymeric chains, elongated along axis *a*, having Co(phen) units doubly chelated by tartrate dianion. The dianion acts as $\eta^4\mu$-tetradentate ligand through hydroxyl and carboxyl oxygen atoms and assumes a conformation as indicated by the torsion angle in the carbon atom skeleton of –151.13(18)°. The octahedral cobalt ligand arrangement is severely distorted with bond angles considerably deviating from ideal values (Table 1). The Co–N bond lengths average to 2.124(2) Å, and the Co–O(carboxylate) bond lengths, located in *trans* position to nitrogen atoms [2.058(2) and 2.047(2) Å], are slightly shorter than the others involving hydroxyl groups, of 2.163(2) and 2.172(2) Å. The polymers are arranged in pairs zipped by π-π interactions between phen aromatic rings with distances between ring centroids of 3.623(2) and 3.547(2) Å (Figure 1). The complex **1** is isomorphous and isostructural with the $Mn^{II}$ and $Cu^{II}$ derivatives.[11,12]

[a] Department of Inorganic Chemistry, Indian Association for the Cultivation of Science,
Kolkata 700032, India
Fax: +91-33-2473-2805
E-mail: icnrc@iacs.res.in
[b] Dipartimento di Scienze Chimiche, University of Trieste,
34127 Trieste, Italy
[c] Departament de Química Inorgànica, Universitat de Barcelona,
Diagonal, 647, 08028 Barcelona, Spain
E-mail: joan.ribas@qi.ub.es
Supporting information for this article is available on the WWW under http://www.eurjic.org or from the author.

 © 2007 Wiley-VCH Verlag GmbH & Co. KGaA, Weinheim 

Table 1. Selected bond length [Å] and angles [°] of **1**.

| | | | |
|---|---|---|---|
| Co–N(1) | 2.1232(19) | Co–O(3) | 2.0472(18) |
| Co–N(2) | 2.1258(17) | Co–O(5) | 2.1630(17) |
| Co–O(1) | 2.0579(17) | Co–O(6) | 2.1722(17) |
| N(1)–Co–N(2) | 77.84(7) | N(2)–Co–O(6) | 89.70(7) |
| N(1)–Co–O(1) | 159.51(8) | O(1)–Co–O(3) | 101.26(8) |
| N(1)–Co–O(3) | 92.18(8) | O(1)–Co–O(5) | 75.81(6) |
| N(1)–Co–O(5) | 88.63(7) | O(1)–Co–O(6) | 92.59(7) |
| N(1)–Co–O(6) | 105.61(7) | O(3)–Co–O(5) | 91.27(7) |
| N(2)–Co–O(1) | 93.22(7) | O(3)–Co–O(6) | 76.71(6) |
| N(2)–Co–O(3) | 160.46(7) | O(5)–Co–O(6) | 161.50(6) |
| N(2)–Co–O(5) | 105.07(7) | | |

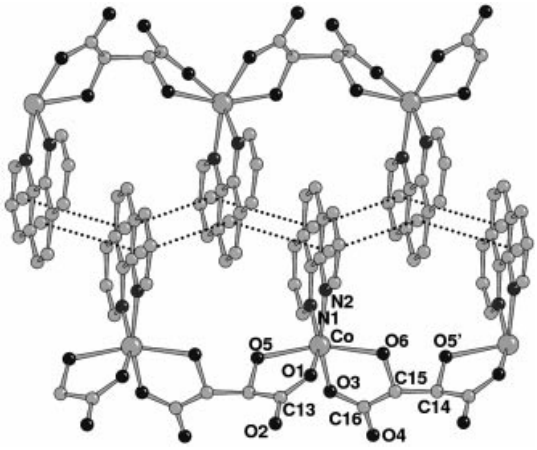


Figure 1. Coordination polymeric chains zipped by π-π interactions in **1**.

The complex {[Co(tart)(bpy)]·5H$_2$O}$_n$ (**2**), containing a smaller amount of guest water molecules, is isostructural to **1** and has been reported recently.[10] However, subtle differences are apparent between the two structures. The intrachain Co–Co distances in **1** and **2** are comparable within 2–3σ [6.617(3) vs. 6.629(1) Å, respectively], but the shortest metal–metal separation between coupled chains in **1** is 8.870 Å, significantly larger than the value of 7.507 Å measured in the bpy analogue (**2**).[10] This feature is ascribed due to the less bulky bpy which lacks the ethylene bridge and allows a better interdigitation between adjacent 1D chains.

The six crystallographically independent lattice water molecules, held together by hydrogen bonds with an ordered proton arrangement form a cluster sitting between the pairs of 1D coordination chains (Figure 2).

The water network consists of tetramers [O(3w–6w)] connected through the O(6w)–H···O(3w) hydrogen bond. In addition, two water molecules [O(2w) and O(1w)] are appended in sequence to the rhomboid structural motif at O(6w). The ΔFourier map allows to detect all the water hydrogen atoms and O(2w), O(3w), and O(6w) show a tetrahedral environment, as these behave as double donors and acceptors. This feature is evident for O(6w) from Figure 2, while the tetrahedral geometry about molecules O(2w) and O(3w) is completed, respectively, through the donor properties towards O(1), O(3), and O(2) of the tartrate dianion (Table 1S). The dicarboxylate provides potential hydrogen bonding intermolecular interactions, beside its coordination ability towards metal ions.

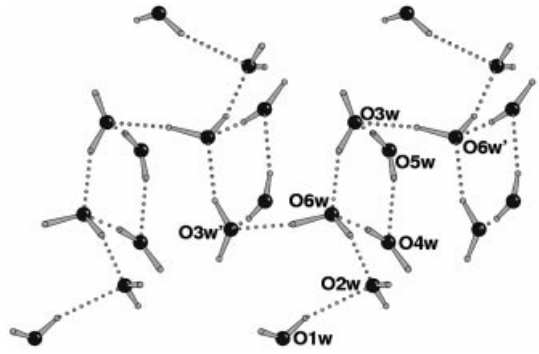


Figure 2. View of the hydrogen-bonding motif of the water molecules in **1**.

The H-bonds between the water cluster and the tartrate oxygen atoms build up a supramolecular 3D network. The O···O distances of hydrogen bonds engaging water molecules as H donor average to 2.79 Å, while those involving the hydroxyl tartrate oxygen (mean 2.62 Å) indicate slightly stronger interactions.

On the other hand, it is worth to note that the water molecules in {[Co(tart)(bpy)]·5H$_2$O}$_n$ (**2**) form a totally different 1D sequence containing cyclic pentamers sharing a side with an appended dimer.[10] Thus, in complex **1** the water molecules are structured by the cobalt polymers and the crystal structure may simulate the interactions occurring between the polymer and the water in a ca. 9 M frozen concentrated solution. Interestingly, among the numerous water networks reported in the literature,[4–8] complex **1** as well as **2**,[10] Mn$^{II}$ and Cu$^{II}$ derivatives[11–12] represent examples where the structured water molecules are not involved in any weak or strong direct interaction with the metal ion.

Thermal analysis reveals that complexes start dehydration at about 35 °C and lose all the lattice water molecules in a number of steps overlapping to each other. The deaquated species collapses immediately upon deaquation at about 150 °C.

The temperature-dependent magnetic susceptibility measurement[13] for **1** has been carried out on a polycrystalline sample in the temperature range 2–300 K. The $\chi_M T$ vs. $T$ plot for **1** ($\chi_M$ is the molar magnetic susceptibility for one Co$^{II}$ ion) is shown in Figure 3. $\chi_M T$ value at 300 K is 3.6 cm$^3$ mol$^{-1}$ K which progressively decreases up to 2.05 cm$^3$ mol$^{-1}$ K at 2 K.

Based on the reasoning already reported by us[14] relating to the calculation of an estimated $J$ value, we have used the two-exponential Rueff expression,[15,16] $\chi_M T = A \exp(-E_1/kT) + B \exp(-E_2/kT)$ {$A + B$ equals the Curie constant [about 2.8–3.4 cm$^3$ mol$^{-1}$ K for octahedral cobalt(II) ions], and $E_1$, $E_2$ represent the "activation energies" corresponding to the spin-orbit coupling and the antiferromagnetic exchange interaction}, which is suitable for any temperature greater than the possible $T_c$. The best-fit values obtained

 © 2007 Wiley-VCH Verlag GmbH & Co. KGaA, Weinheim 

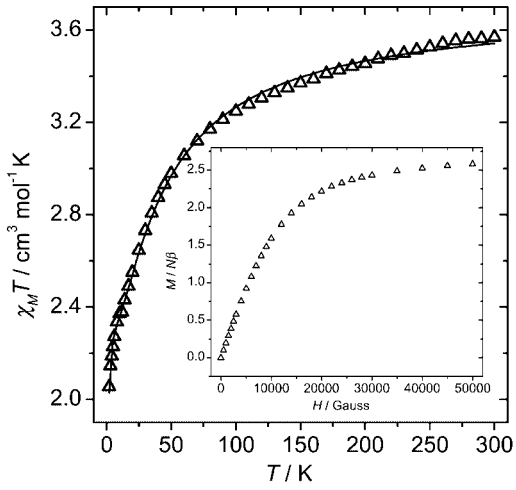


Figure 3. Top: $\chi_M T$ vs. $T$ plot for complex **1** (solid line represents the best fit). Inset: plot of the reduced magnetization ($M/N\beta$) vs. $H$ at 2 K for **1**.

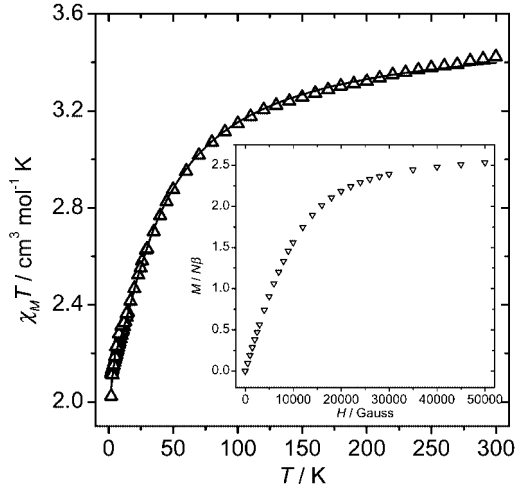


Figure 4. $\chi_M T$ vs. $T$ plot for complex **2** (solid line represents the best fit). Inset: plot of the reduced magnetization ($M/N\beta$) vs. $H$ at 2 K for **2**.

with this procedure are: $A + B = 3.41$ cm$^3$ mol$^{-1}$ K, in perfect agreement with those given in the literature for the Curie constant ($C \approx 2.8$–$3.4$ cm$^3$ mol$^{-1}$ K),[15,16] $E_1/k = 42.32$ K which is of the same magnitude to those reported by Rueff *et al* for several one- and two-dimensional cobalt(II) complexes.[16] As far as the antiferromagnetic exchange interaction, the value found is very weak ($E_2/k = 0.35$ K), corresponding to $J = -0.70$ K ($= -0.50$ cm$^{-1}$), according to the Ising chain approximation, $\chi_M T \propto \exp(J/2kT)$. The small $J$ value is compatible with the two possible exchange pathways between Co atoms. One is across the saturated dicarboxylate {with the long bridging spacer [O(6)–O(5) distance of 2.76 Å, O(6)–C(15)–C(14)–O(5′) torsion angle of –38.8°]} which should be a very weak exchange interaction. The other exchange pathway is through the π-π stacking of the phenanthroline ring, which is very weak in this system. The small $J$ value agrees with those reported by Coronado et al. for a series of Co$^{II}$ (as well as Mn$^{II}$, Fe$^{II}$, and Ni$^{II}$) complexes with tartrate as ligand.[17] The reduced magnetization curve, $M/N\beta$, at 2 K tends to $2.5N\beta$ at 5 T (Figure 3, inset) in perfect agreement with the values reported for isolated or quasi-isolated cobalt(II) ions.[15] Interestingly, Lu et al. reported a ferromagnetic interaction for the bpy derivative **2**.[10]

After going through the magnetic result we have identified a wrong interpretation in fitting the magnetic data of **2** (assuming that there is no spin-orbit coupling). Thereby we have repeated the synthesis and structural characterization of complex **2**. The structural results match those already reported,[10] but the magnetic results (Figure 4) follow those of complex **1**. Corresponding fitting parameters are $A + B = 3.43$, $E_1/k = 36.97$ K, $E_2/k = 0.21$ K, $J = -0.42$ K ($= -0.30$ cm$^{-1}$). The $J$ value for **1** and **2** are almost equal based on the accuracy of the fitting method. Thus the $J$ value is weak and equally antiferromagnetic for the two complexes as expected.

## Conclusions

We have presented here the synthesis, crystal structure, magnetic behavior and thermal study of Co$^{II}$(tart)(phen/bpy) complexes having a well resolved water chain, which acts as glue in stabilizing the host chains and gives origin to a 3D supramolecular architecture. In phen derivative the water chain consists of cyclic tetramers with appended water dimers whereas in bpy derivative there is totally different 1D sequence containing cyclic pentamer sharing a side with an appended dimer. Thus, the study provides an example of a differently structured water cluster realized by modulating the size of the metal-organic framework. Both complexes show similar weak antiferromagnetic interaction, in agreement with structures.

## Experimental Section

**Complex 1:** Single crystals of **1** were obtained by diffusing an aqueous solution (5 mL) of cobalt nitrate hexahydrate (0.291 g, 1 mmol) on a water/methanol (1:2) layer (15 mL) of disodium tartrate (0.150 g, 1 mmol) and phen (0.198 g, 1 mmol) mixture in a corked tube. The red colored single crystals were deposited at the junction of the two solutions after a few weeks, yield 74%, 0.366 g. $C_{16}H_{24}CoN_2O_{12}$ (495.30): calcd. C 38.76, H 4.84, N 5.65; found C 39.23, H 4.51, N 5.92. IR: $\tilde{\nu}$ = 3480–3030 (vs), 2868 (s), 2720 (s), 1618 (vs), 1518 (s), 1426 (s), 1361 (vs), 1294 (s), 1224 (w), 1126 (s), 1069 (w), 997 (vw), 924 (vw), 850 (s), 820 (s), 726 (vs), 642 (vw), 526 (vw) cm$^{-1}$.

**Complex 2:** Preparation by adopting the same procedure as described for **1**; bpy (0.156 g, 1 mmol) instead of phen, yield 70%, 0.317 g. $C_{14}H_{22}CoN_2O_{11}$ (453.27): calcd. C 37.06, H 4.85, N 6.18; found C 37.62, H 4.66, N 6.34. IR: $\tilde{\nu}$ = 3470–3050 (vs), 1640 (vs), 1605 (vs), 1474 (s), 1447 (s), 1363 (vs), 1313 (s), 1232 (w), 1176 (w), 1129 (s), 1057 (s), 1025 (w), 885 (w), 825 (w), 775 (w), 729 (w), 648 (vw) 532 (vs) cm$^{-1}$.

**X-ray Diffraction Studies:** Diffraction data of **1** were collected at room temperature on a Nonius DIP-1030H system, equipped with

 © 2007 Wiley-VCH Verlag GmbH & Co. KGaA, Weinheim 

Mo-$K_\alpha$ radiation ($\lambda$ = 0.71073 Å) graphite-monochromatized. Cell refinement, indexing and scaling of the data set were carried out using programs Denzo[18] and Scalepack[18] The structure was solved by Patterson and Fourier analyses[19] and refined by the full-matrix least-squares method based on $F_2$ with all observed reflections.[19] The H atoms of water molecules were located on the ΔFourier map, others at geometrically calculated positions. All the calculations were carried out using program WinGX system, Ver 1.70.01.[20]

CCDC-632709 contains the supplementary crystallographic data for **1**. These data can be obtained free of charge from The Cambridge Crystallographic Data Centre via www.ccdc.cam.ac.uk/data_request/cif.

**Crystal Data for 1:** $C_{16}H_{24}CoN_2O_{12}$, $M$ = 495.30, orthorhombic, space group $P2_12_12_1$, $a$ = 6.617(3), $b$ = 15.313(3), $c$ = 20.110(4) Å, $V$ = 2037.7(11) Å$^3$, $Z$ = 4, $D_c$ = 1.615 g/cm$^3$, $\mu$(Mo-$K_\alpha$) = 0.910 mm$^{-1}$, $F$(000) = 1028, $\theta$ range = 2.66–29.65°. Final $R1$ = 0.0344, $wR2$ = 0.0871, $S$ = 0.970 for 323 parameters and 22937 collected reflections, 5526 unique [$R$(int.) = 0.0400], of which 4614 with $I > 2\sigma(I)$, absolute structure parameter = 0.002(14), max. positive and negative peaks in the $\Delta F$ map: 0.299 and –0.326 e Å$^{-3}$.

**Supporting Information** (see also the footnote on the first page of this article): ORTEP drawing and a Table containing H-bonding parameters of **1**.


[1] a) G. A. Jeffrey, *An Introduction to Hydrogen Bonding*, Oxford University Press, Oxford, **1997**; b) P. Ball, *$H_2O$: A Biography of Water*, Weidenfeld & Nicolson, London, **1999**; c) M. Henry, *ChemPhysChem* **2002**, *3*, 607; d) R. Ludwig, *Angew. Chem. Int. Ed.* **2001**, *40*, 1808; e) J. M. Ugalde, I. Alkorta, J. Elguero, *Angew. Chem. Int. Ed.* **2000**, *39*, 717.

[2] a) Q.-Y. Liu, L. Xu, *CrystEngComm* **2005**, *7*, 87; b) P. S. Lakshminarayanan, D. K. Krishna, P. Ghosh, *Inorg. Chem.* **2005**, *44*, 7540; c) G. Beobide, O. Castillo, A. Luque, U. Garcıa-Couceiro, J. P. Garcıa-Teran, P. Roman, *Inorg. Chem.* **2006**, *45*, 5367; d) S. Das, P. K. Bharadwaj, *Cryst. Growth Des.* **2006**, *6*, 187 and references cited therein; e) P. S. Lakshminarayanan, E. Suresh, P. Ghosh, *J. Am. Chem. Soc.* **2005**, *127*, 13132.

[3] A. Muller, E. Krickemeyer, H. Bogge, M. Schmidtmann, B. Botar, M. O. Talismanova, *Angew. Chem. Int. Ed.* **2003**, *42*, 2085.

[4] a) S. K. Ghosh, P. K. Bharadwaj, *Inorg. Chem.* **2005**, *44*, 5553, and references cited therein; b) R. J. Doedens, E. Yohannes, M. I. Khan, *Chem. Commun.* **2002**, 62; c) J. N. Moorthy, R. Natarajan, P. Venugopalan, *Angew. Chem. Int. Ed.* **2002**, *41*, 3417.

[5] a) L. J. Barbour, G. W. Orr, J. L. Atwood, *Chem. Commun.* **2000**, 859; b) L. J. Barbour, G. W. Orr, J. L. Atwood, *Nature* **1998**, *393*, 671; c) J. L. Atwood, L. J. Barbour, T. J. Ness, C. L. Raston, P. L. Raston, *J. Am. Chem. Soc.* **2001**, *123*, 7192; d) S. K. Ghosh, P. K. Bharadwaj, *Angew. Chem. Int. Ed.* **2004**, *43*, 3577.

[6] a) S. Pal, N. B. Sankaran, A. Samanta, *Angew. Chem. Int. Ed.* **2003**, *42*, 1741; b) J.-M. Zheng, S. R. Batten, M. Du, *Inorg. Chem.* **2005**, *44*, 3371; c) B.-H. Ye, B.-B. Ding, Y.-Q. Weng, X.-M. Chen, *Inorg. Chem.* **2004**, *43*, 6866.

[7] a) L. Randaccio, E. Zangrando, A. Cesàro, D. Holthenrich, B. Lippert, *J. Mol. Struct.* **1998**, *440*, 221; b) Y. Yorkovsky, M. Kapon, Z. Dori, *Inorg. Chim. Acta* **1986**, *124*, 149; c) B.-Q. Ma, H.-L. Sun, S. Gao, *Angew. Chem. Int. Ed.* **2004**, *43*, 1374; d) J.-H. Yu, J. Lu, Y. Xu, X. Zhang, J.-Q. Xu, *Inorg. Chim. Acta* **2006**, *359*, 3205; e) R. P. Doyle, M. Nieuwenhuyzen, P. E. Kruger, *Dalton Trans.* **2005**, 3745.

[8] R. Carballo, B. Covelo, C. Lodeiro, E. M. Vázquez-López, *CrystEngComm* **2005**, *7*, 294, and refs. cited therein.

[9] a) N. S. Oxtoby, A. J. Blake, N. R. Champness, C. Wilson, *Chem. Eur. J.* **2005**, *11*, 1; b) K. Liu, J. D. Cruzan, R. J. Saykally, *Science* **1996**, *271*, 929; c) U. Buck, F. Huisken, *Chem. Rev.* **2000**, *100*, 3863; d) T. Head-Gordon, G. Hura, *Chem. Rev.* **2002**, *102*, 2651.

[10] J. Lu, J.-H. Yu, X.-Y. Chen, P. Cheng, X. Zhang, J.-Q. Xu, *Inorg. Chem.* **2005**, *44*, 5978.

[11] X. Zhang, D. Huang, C. Feng, C. Chen, Q. Liu, L. Sun, *Acta Crystallogr., Sect. C* **2003**, *59*, m402.

[12] M. McCaan, F. Humphreys, V. McKee, *Polyhedron* **1997**, *16*, 3655.

[13] Magnetic measurements were carried out in the Servei de Magnetoquímica (Universitat de Barcelona) on polycrystalline samples (30 mg) with a Quantum Design SQUID MPMS-XL magnetometer working in the 2–300 K range at 0.1 T. The diamagnetic corrections were evaluated from Pascal's constants.

[14] S. C. Manna, S. Konar, E. Zangrando, K. Okamoto, J. Ribas, N. Ray Chaudhuri, *Eur. J. Inorg. Chem.* **2005**, 4646.

[15] J.-M. Rueff, N. Masciocchi, P. Rabu, A. Sironi, A. Skoulios, *Eur. J. Inorg. Chem.* **2001**, 2843.

[16] J.-M. Rueff, N. Masciocchi, P. Rabu, A. Sironi, A. Skoulios, *Chem. Eur. J.* **2002**, *8*, 1813, and references cited therein.

[17] E. Coronado, J. R. Galán-Mascarós, C. J. Gómez-García, A. Murcia-Martínez, *Chem. Eur. J.* **2006**, *12*, 3484 and references cited therein.

[18] Z. Otwinowski, W. Minor, *Processing of X-ray Diffraction Data Collected in Oscillation Mode*, *Methods in Enzymology*, vol. 276: *Macromolecular Crystallography*, part A, 307–326 (Eds.: C. W. Carter Jr, R. M. Sweet), Academic Press, New York, **1997**.

[19] *SHELX 97 Programs for Crystal Structure Analysis (Release 97-2)*. G. M. Sheldrick,University of Göttingen, Germany, **1998**.

[20] L. J. Farrugia, *J. Appl. Crystallogr.* **1999**, *32*, 837.


Received: June 1, 2007
Published Online: September 7, 2007

 © 2007 Wiley-VCH Verlag GmbH & Co. KGaA, Weinheim 

DOI: 10.1002/ejic.200700479

# Synthesis, Characterisation and Ligand Properties of Novel Bi-1,2,3-triazole Ligands

**Uwe Monkowius,*[a] Stefan Ritter,[b] Burkhard König,*[b] Manfred Zabel,[b] and Hartmut Yersin[c]**

**Keywords:** N ligands / Ligand design / Nitrogen heterocycles / Click reaction / 1,2,3-Triazole

Three 1,1′-disubstituted 4,4′-bi-1*H*-1,2,3-triazols [R-bta; R = Bn (**1**), Ph (**2**), $CH_2COOH$ (**3**)] have been synthesised as bidentate, nitrogen-based ligands by a $Cu^I$-catalysed "click" reaction between 1,3-butadiyne and organic azides. Their ligand properties were investigated by preparation of the complexes $[Ru^{II}(R\text{-bta})_3]Cl_2$ [R = Bn (**4**), Ph (**5**), $CH_2COOH$ (**6**)], $[(Bn\text{-bta})Cu^I(DPEPhos)]$ (**7**) [DPEPhos = bis{2-(diphenylphosphanyl)phenyl} ether] and $[(Bn\text{-bta})Re^I(CO)_3Cl]$ (**8**) following standard reaction procedures. All compounds were analysed by elemental analysis, mass spectrometry and NMR, IR, UV/Vis and luminescence spectroscopy. In addition, the molecular structures of **1**–**4**, **7**, and **8** have been determined by X-ray crystallography. In all complexes the Bn-bta acts as a bidentate ligand with structural features comparable to the analogous 2,2′-bipyridine complexes. In their electronic absorption spectra the $Ru^{II}$ and $Re^I$ complexes exhibit a lowest energy band at around 300 nm, which is substantially higher in energy than in analogous complexes with bpy ligands. All R-bta ligands yield complexes that are not luminescent in solution or in the solid state, which makes these ligands particularly suited for use as spectator ligands.

(© Wiley-VCH Verlag GmbH & Co. KGaA, 69451 Weinheim, Germany, 2007)

## Introduction

A large number of transition metal complexes based on the 2,2′-bipyridine (bpy) ligand and its derivatives have been investigated in different fields of chemistry due to their high stability and remarkable (electro)chemical and photophysical properties. More than 4200 entries were found in the Cambridge Structural Database when searching for complexes with byp (February 2007). There have been many reports about the application of these metal complexes in opto-electronic devices, as redox- and photo-catalysts, as building blocks of supramolecular structures and for medical and analytical purposes.[1–4] Prominent examples are $[Ru(bpy)_3]^{2+}$ and related octahedral $d^6$ transition metal complexes, which are frequently employed in studies that take advantage of the properties of their excited state, such as in photochemistry, chemoluminescence, electro-chemoluminescence and electron-transfer chemistry.[5–8]

New chromophoric ligands that are capable of generating emissions in the blue region of the spectrum are in demand due to the rapid development of OLED (organic light emitting device) technology. It has been shown that the emission energy increases with decreasing size of the chromophoric π-system, and this strategy has been successfully applied by Thompson et al. in the case of cyclometallated $Ir^{III}$ complexes, where replacement of the pyridine moiety by the five-membered ring of a pyrazolyl group led to a hypsochromic shift of the emission wavelength.[9] Chelating ligands with high energy electronic states are also useful as auxiliary, ancillary, spectator or innocent ligands in light-emitting complexes.[10] De Cola et al. recently reported a blue light emitting heteroleptic $Ir^{III}$ complex ($\lambda_{max}$ = 461 nm), where the anionic 1,2,4-triazolyl ligand (Figure 1) does not participate directly in the electronic transition.[11–13]

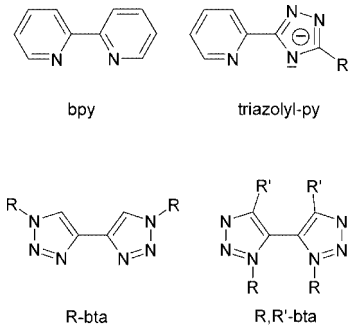


Figure 1. Bpy and triazolyl-py, R-bta and R,R′-bta ligands.

1,1′-$R_2$-4,4′-Bi(1,2,3-triazole) ligands (R-bta, R = organic group) seem to be promising alternatives to bipyr-

[a] Institut für Anorganische Chemie, Johannes Kepler Universität Linz,
4040 Linz, Austria
E-Mail: Uwe.Monkowius@jku.at
[b] Institut für Organische Chemie, Universität Regensburg,
93040 Regensburg, Germany
E-Mail: Burkhard.Koenig@chemie.uni-regensburg.de
[c] Institut für Physikalische Chemie, Universität Regensburg,
93040 Regensburg, Germany

Supporting information for this article is available on the WWW under http://www.eurjic.org or from the author.

 © 2007 Wiley-VCH Verlag GmbH & Co. KGaA, Weinheim 

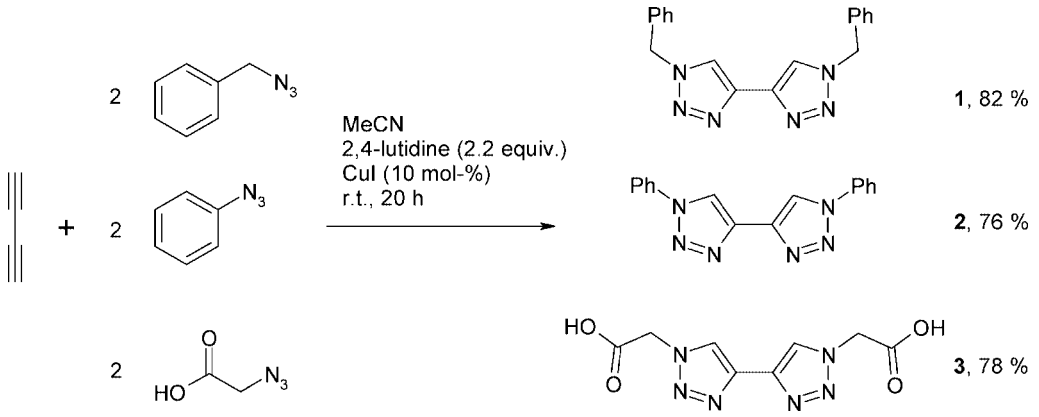


Scheme 1. Synthesis of the bitriazoles **1**–**3**.

idine ligands in transition metal complexes (Figure 1). In addition, functionalisation with a wide range of different substituents is possible using the "click chemistry" approach for the preparation of novel R-bta ligands.[14] Compared to bpy, where substitution with certain organic groups is usually cumbersome,[4,15] this may facilitate ligand preparation significantly. CuAAC (copper-catalysed azide-alkyne cycloaddition) has been used recently to synthesise 1,4-disubstituted 1,2,3-triazole ligands,[16] and the oxidative coupling products R,R′-bta (Figure 1) have been observed as major products under basic conditions in the CuAAC.[17]

Complexes of $Ru^{II}$, $Re^{I}$ and $Cu^{I}$ have been synthesised to evaluate the ligand properties of R-bta and the spectroscopic behaviour of these ligands and complexes investigated by UV/Vis and luminescence spectroscopy.

## Results and Discussion

### Synthesis of Triazole Ligands

The desired R-bta ligands **1**–**3** were synthesised by a $Cu^{I}$-catalysed cycloaddition between 1,3-butadiyne and the organic azides (benzyl azide, phenyl azide[14] and β-azidoacetic acid). The 1,3-butadiyne was freshly prepared from 1,4-dichlorobutyne[18] and treated immediately with the azide compound in basic acetonitrile solution in the presence of a catalytic amount of copper iodide (Scheme 1). Workup with aqueous $H_2O_2$ (3%) and saturated aqueous EDTA was necessary to remove the $Cu^{I}$ salt as it could form a complex with the synthesised R-bta ligands. Compounds **1**–**3** were obtained in acceptable yields as colourless powders after purification. All compounds are sparingly soluble in most organic solvents and insoluble in water.

### Spectroscopic Characterisation

The spectroscopic properties of compounds **1**–**3** were investigated by UV/Vis and luminescence spectroscopy. The compounds absorb in the UV region between 220 and 260 nm (Figure 11, Figures S3 and S4 in the Supporting Information). Compound **3** shows a very weak emission signal at 414 nm ($\lambda_{ex}$ = 267 nm) in the luminescence spectrum.

### Structural Studies

All free ligands were structurally characterised by single-crystal X-ray experiments. Ligand **1** crystallises in two different modifications, namely prisms (monoclinic space group $P2_1/c$, with two molecules in the unit cell) and needles (monoclinic space group *Cc*, with four molecules in the unit cell). Whereas the prisms crystallise as the more stable form from most organic solvents used (e.g. $CH_2Cl_2$, $CHCl_3$, MeCN), needles are obtained as the major fraction only by slow crystallisation from methanol. Because each of the equivalent molecules in crystals of the first modification of **1** has an inversion centre, the asymmetric unit contains only one half of the formula unit (Figure 2). The individual molecules in the latter modification show no crystallographically imposed symmetry, but they approach closely the symmetry of the molecules in the prismatic crystal (Figure 3).

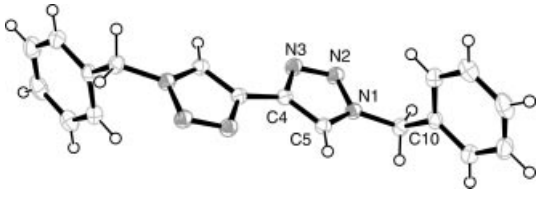


Figure 2. ORTEP drawing of the molecular structure of compound **1** (prismatic crystals) with 50% probability ellipsoids. Selected bond lengths [Å], angles [°] and torsion angles [°]: N1–N2 1.3476(15), N2–N3 1.3195(15), N3–C4 1.3643(17), N1–C5 1.3522(15), C4–C4′ 1.4666(16), C4–C5 1.3764(17); N1–N2–N3 107.26(10), N2–N3–C4 108.71(10), N3–C4–C5 108.54(10), C4–C5–N1 104.45(11), N2–N1–C5 111.05(10), C4′–C4–C5 129.85(11); N3–C4–C4′–N3′ 180.00(11).

Compounds **2** and **3** were obtained as colourless needles. Compound **2** crystallises in the triclinic space group $P\bar{1}$ with three molecules in the unit cell and 1.5 formula units

 © 2007 Wiley-VCH Verlag GmbH & Co. KGaA, Weinheim 

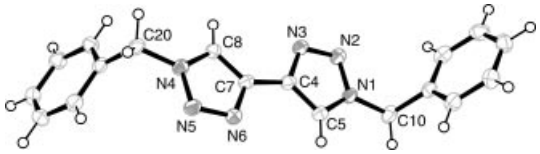


Figure 3. Molecular structure of compound **1** (needles). Selected bond lengths [Å], angles [°] and torsion angles [°]: N1–N2 1.344(4), N2–N3 1.328(4), N3–C4 1.368(4), C4–C5 1.374(4), N1–C5 1.356(4), N4–N5 1.353(4), N5–N6 1.331(4), N6–C7 1.371(4), C7–C8 1.372(4), C8–N4 1.354(4), C4–C7 1.463(3); N2–N1–C5 111.6(2), N1–N2–N3 107.0(2), N2–N3–C4 108.4(3), N3–C4–C5 108.9(3), C4–C5–N1 104.1(3), C5–C4–C7 130.6(3), N5–N4–C8 11.6(2), N4–N5–N6 106.7(2), N5–N6–N7 108.4(2), N6–C7–C8 109.0(2), C7–C8–N4 104.3(2), C4–C7–C8 129.2(3); N3–C4–C7–N6 174.9(3).

per asymmetric unit. This means that there are two independent molecules present, one of which is centrosymmetric and the other roughly $C_2$-symmetric (Figure 4). Crystals of compound **3** are monoclinic (space group $P2_1/c$ with two molecules in the unit cell). Again, the molecules in crystals of compound **3** are centrosymmetric and the asymmetric unit consists of one half of the formula unit (Figure 5). The carboxylate proton exhibits an intermolecular hydrogen bond with the N3 atom of a neighbouring molecule to form helices [*d*(O1–H) 0.80(6), *d*(H–N3) 1.88(6), *d*(O1–N3) 2.670(4) Å; ∠(O1–H–N3) 171(4)°; Figure 6]. Each discrete helical subunit is connected to two others by the second carboxylate group of the molecule to yield a layered structure of interconnected helices (Figure S1).

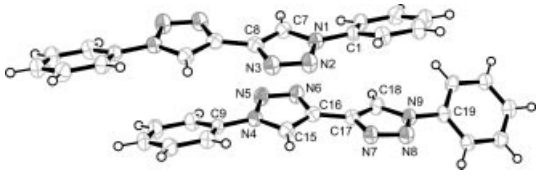


Figure 4. Structure of the two independent molecules in crystals of compound **2**. Selected bond lengths [Å], angles [°] and torsion angles [°]: C8–C8′ 1.452(2), N1–N2 1.357(3), N2–N3 1.310(3), N3–C8 1.365(4), C7–C8 1.372(4), N4–N5 1.358(3), N5–N6 1.312(3), N6–C16 1.368(4), C15–C16 1.372(4), C16–C17 1.449(4), C17–C18 1.374(4), C17–N7 1.368(4), N7–N8 1.310(3), N8–N9 1.362(3); N2–N1–C7 110.5(2), N1–N2–N3 107.4(2), N2–N3–C8 108.7(2), N1–C7–C8 105.1(2), N3–C8–C7 108.3(2), C7–C8–C8′ 129.6(2), N5–N4–C15 110.6(2), N4–N5–N6 107.3(2), N5–N6–C16 108.9(2), N4–C15–C16 105.0(2), N6–C16–C15 108.3(2), N8–N7–C17 108.9(2), N7–N8–N9 107.3(2), N8–N9–C18 110.4(2), N7–C17–C18 108.1(2), C15–C16–C17 130.5(2), C16–C17–C18 129.7(2), C17–C18–N9 105.3(2); N3–C8–C8′–N3′ 180.0(2), N6–C16–C17–N7 173.3(2).

The bitriazole units of molecules **1**–**3** are planar with an (*E*)-configuration of the 3,3′-N atoms. This configuration is also found in all solid-state structures of the free ligand 2,2′-bipyridine.[19] All bond lengths and angles of the triazole moiety lie in a very narrow range and are comparable to those of previously published structures of 1,2,3-triazole compounds.[20] The C–C bonds between the triazole groups have lengths of between 1.449 and 1.466 Å and are therefore shorter than the analogous bond in 2,2′-bipyridine [1.4881(13) Å] (Table 1).[19]

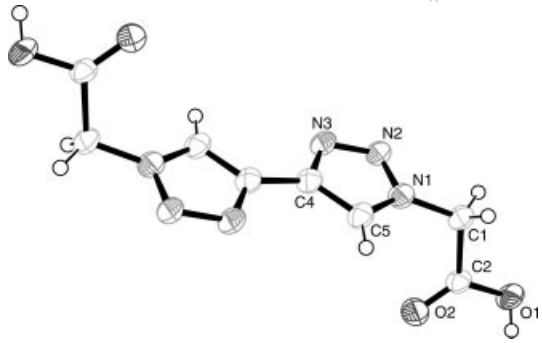


Figure 5. Molecular structure of compound **3**. Selected bond lengths [Å], angles [°] and torsion angles [°]: N1–N2 1.339(4), N2–N3 1.328(5), N3–C4 1.359(5), N1–C5 1.345(5), C4–C4′ 1.446(5), C4–C5 1.377(5); N1–N2–N3 106.1(3), N2–N3–C4 109.5(3), N3–C4–C5 107.9(3), C4–C5–N1 104.6(3), N2–N1–C5 112.0(3), C4′–C4–C5 130.0(3); N3–C4–C4′–N3′ 180.0(4).

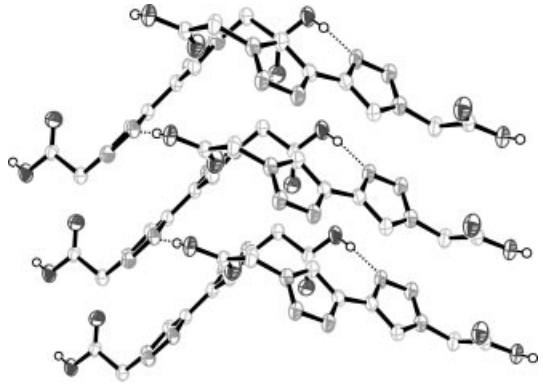

Figure 6. Excerpt from a cell plot of the crystalline phase of compound **3** depicting the helix formed by the intermolecular hydrogen bonds (dotted lines) between the carboxylate protons and the N3 atoms of the neighbouring molecules. Only the participating H atoms are shown for clarity.

## Synthesis of Complexes

The synthesis of homoleptic $Ru^{II}$ complexes of ligands **1**–**3** was carried out with $RuCl_3 \cdot 4H_2O$ in boiling ethylene glycol solution. Precipitation of complexes **4**–**6** was provoked by addition of ethanol or diethyl ether (Scheme 2).

The synthesis of a heteroleptic $Cu^{I}$ complex (**7**) was performed with ligand **1**, bis[2-(diphenylphosphanyl)phenyl] ether (DPEPhos) and $[Cu^{I}(NCMe)_4]PF_6$ (Scheme 3). The DPEPhos ligand was chosen as related heteroleptic $Cu^{I}$ complexes with a 1,10-phenanthroline (phen) ligand show high quantum yields.[21] The colourless crystals of this complex are only modestly soluble in polar organic solvents. Complex **7** is perfectly stable in solution and the solid state in air at room temperature; no oxidation to $Cu^{II}$ occurs.

The heteroleptic carbonylrhenium(I) complex **8** was obtained from ligand **1** and $[Re^{I}(CO)_5]Cl$, after reaction in toluene and recrystallisation from $MeCN/Et_2O$, as colourless crystals in almost quantitative yield (Scheme 4). This complex is modestly soluble in hot MeCN and, as is the case for its bpy and phen analogs, it is stable in solution and the solid state in air.

 © 2007 Wiley-VCH Verlag GmbH & Co. KGaA, Weinheim 

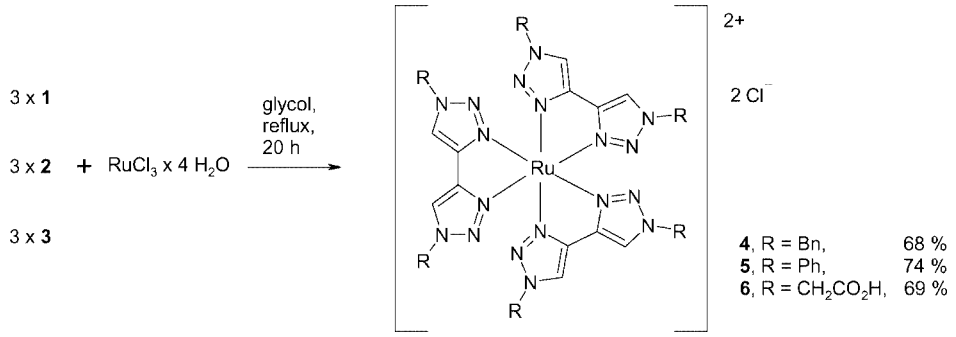


Scheme 2. Synthesis of the homoleptic complexes **4**–**6**.

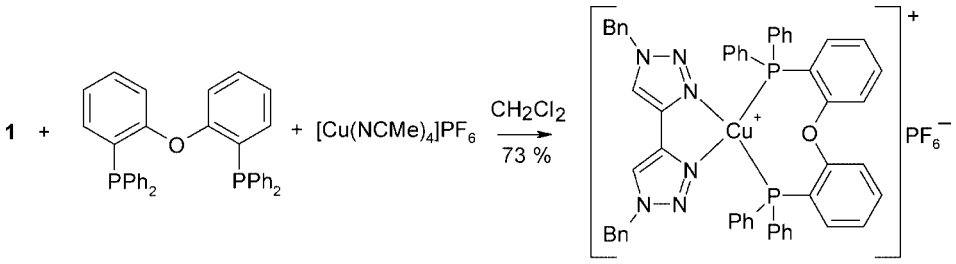


**7**

Scheme 3. Synthesis of heteroleptic copper(I) complex **7**.

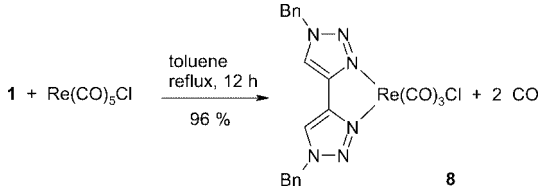


**8**

Scheme 4. Synthesis of heteroleptic rhenium(I) complex **8**.

## Structural Studies

Recrystallisation from ethylene glycol/ethanol or MeCN/$Et_2O$ yielded complexes **4**–**6** as light yellow crystals, although only the crystals of complex **4** were of sufficient, though still low, quality for an X-ray structure refinement (Figure 7). The quality of the structural data is less accurate because crystals of **4** contain an unspecified number and type of solvent molecules (Figure S2 in the Supporting Information). Complex **4** crystallises in the monoclinic space group $P2_1/a$ with four molecules in the unit cell. The $Ru^{II}$ atom shows a distorted octahedral coordination geometry with both the Λ and Δ enantiomers present in the unit cell. The benzyl substituents have a random orientation and do not approach a symmetrical pattern. The average Ru–N distances of the cations in **4** [*d*(Ru–N) 2.05(3) Å] and $[Ru(bpy)_3]^{2+}$ [*d*(Ru–N) 2.056(2) Å] are roughly the same within experimental error. The average bite angles of the bpy ligand in $[Ru(bpy)_3]^{2+}$ are 79° compared to 77.7(12)° and 77.9(11)° (N7–Ru1–N10 and N13–Ru1–N16, respectively) for the bta ligand in complex **4**.[22] A further discussion of the structural data and a comparison with the free ligand **1** is not meaningful due to the inaccuracy of the experimental data.

The crystals of **7** obtained upon cooling of a dichloromethane solution to –35 °C are triclinic (space group $P\bar{1}$ with four molecules in the unit cell). The asymmetric unit contains two independent complexes with both copper atoms coordinated by **1** and DPEPhos in a distorted tetrahedral environment (Figures 8 and 9). There are no sub van der Waals contacts between the oxygen of the phosphane ligands and the copper centres. Both cations differ in their geometrical parameters, with one benzyl group being disordered over two positions in the cation containing Cu2 (occupation 55:45). Furthermore, the bta ligand deviates significantly from planarity in the case of the cation containing Cu1 [Cu1: ∠(N3–C45–C46–N4) 14.9(8)°; Cu2: ∠(N10–C106–C107–N9) 3.0(6)°]. There is a high degree of asymmetry in the bitriazole coordination [Cu1–N3 2.118(4), Cu1–N4 2.201(5), Cu2–N9 2.233(5), Cu2–N10 2.075(6) Å], as was also found, although less pronounced, for bpy in the crystal structure of the complex $[(bpy)Cu(PPh_3)_2]ClO_4$.[23] The bite angle of bpy in the latter complex and of the bi-triazoles in **7** are comparable [78.53(18)/78.7(2)° vs. 79.6(4)°].[23] The asymmetric coordination of the copper atoms in the crystal structure of **7** arises due to the steric restraints of the bta and DPEPhos ligand, and the differences between the two cations are caused by the disordered benzyl group and packing forces.

Crystals of **8** were obtained from MeCN/$Et_2O$. The compound crystallises in the orthorhombic space group *Pnma* with four molecules in the unit cell. The complexes in the crystals possess a mirror plane including Re1, Cl1 and C1, thus the asymmetric unit contains only one half of the formula unit. The $Re^{I}$ atom exists in a distorted octahedral

 © 2007 Wiley-VCH Verlag GmbH & Co. KGaA, Weinheim 

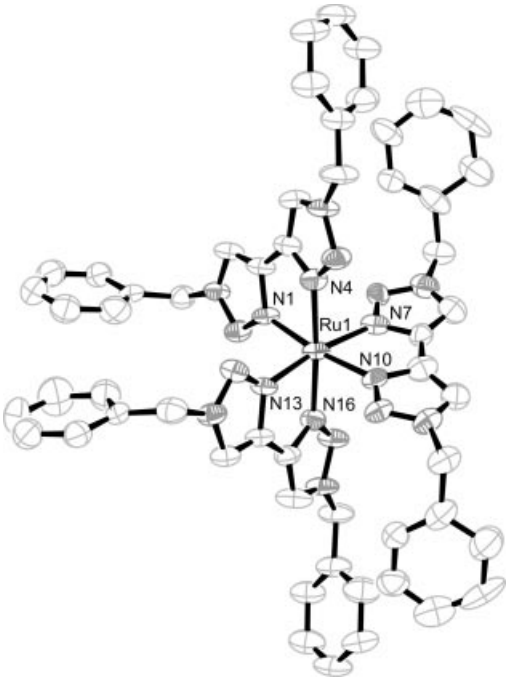


Figure 7. Crystal structure of the homoleptic $Ru^{II}$ complex cation of **4** (H atoms, chloride anions and solvent molecules have been omitted for clarity). Because of the low quality of the structure no atom distances or torsion angles are discussed (see text and Supporting Information). Bond angles [°]: N1–Ru1–N4 74.9(12), N7–Ru1–N10 77.7(12), N13–Ru1–N16 77.9(11), N4–Ru1–N10 100.7(11), N7–Ru1–N16 98.7(12), N1–Ru1–N10 167.5(10), N4–Ru1–N16 172.5(12), N7–Ru1–N13 172.1(11).

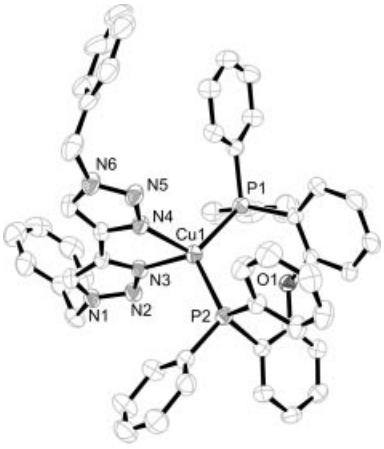


Figure 8. ORTEP drawing (30% probability ellipsoids) of the structure of the cation containing Cu1 in the crystals of **7**. Selected bond lengths [Å], angles [°] and torsion angles [°]: Cu1–P1 2.2631(17), Cu1–P2 2.3016(19), Cu1–N3 2.118(4), Cu1–N4 2.201(5); P1–Cu1–P2 115.44(7), P1–Cu1–N3 119.68(15), P2–Cu1–N4 113.05(13), N3–Cu1–N4 78.53(18); N3–C45–C46–N4 14.9(8).

environment defined by a *fac* arrangement of the three carbonyl groups, the chloride atom and the two nitrogen atoms of the bta ligand (Figure 10). The distortion from octahedral symmetry essentially arises from the steric demands of the chelating bta ligand. Again, the bite angle of the bitriazole [∠(N1–Re–N1′) 73.4(2)°] is very similar to the bite

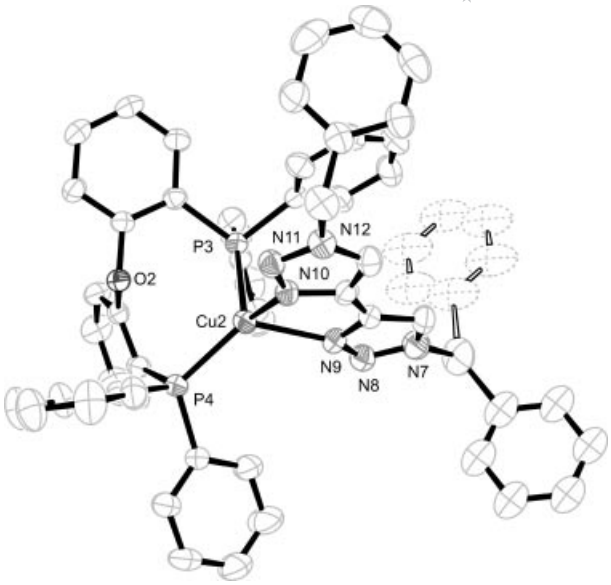


Figure 9. ORTEP drawing (30% probability ellipsoids) of the structure of the cation containing Cu2 in the crystals of **7**. Selected bond lengths [Å], angles [°] and torsion angles [°]: Cu2–P3 2.3079(18), Cu2–P4 2.2292(16), Cu2–N9 2.233(5), Cu2–N10 2.075(6); P3–Cu2–P4 114.39(7), P3–Cu2–N9 97.32(14), P4–Cu2–N10 130.61(14), N9–Cu2–N10 78.7(2); N10–C105–C106–N9 3.0(6). As indicated in the text, one benzyl group is disordered.

angles of several complexes of the type [(s-bpy)$Re^{I}(CO)_3X$] (X = anionic or neutral ligand) containing a substituted bpy ligand [∠(N1–Re–N1′) ca. 74°].[24] The bitriazole ligand is perfectly planar as a result of the mirror symmetry. The characteristic bond lengths and angles are normal and are similar to previously reported values in analogous bpy complexes.[24]

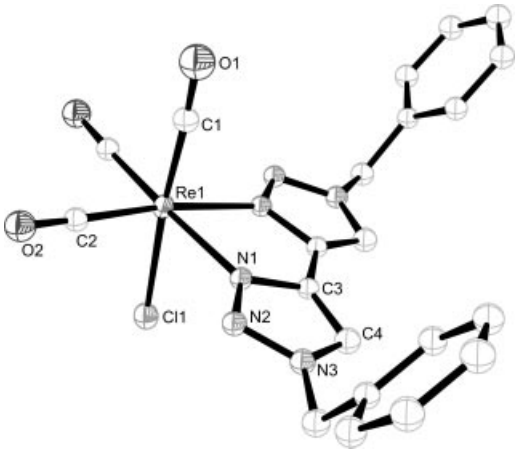


Figure 10. Crystal structure of **8** (H atoms have been omitted for clarity). Selected bond lengths [Å], angles [°] and torsion angles [°]: Re1–N1 2.176(6), Re1–Cl1 2.494(2), Re1–C1 1.890(12), Re1–C2 1.907(8), C1–O1 1.175(15), C2–O2 1.161(10); N1–Re1–N1 73.4(2), Cl1–Re1–N1 81.26(18), Cl1–Re1–C1 175.3(4), N1–Re1–C1 95.0(3), N1–Re1–C2 99.1(3), C1–Re1–C2 88.1(4), Re1–C2–O2 177.7(6), Re1–C1–O1 176.9(11); N1–C3–C3′–N1′ 0.0(9).

The present crystal structures display the strong similarities of the ligand properties of 2,2′-bipyridines and bi-1,2,3-triazoles in terms of steric features.

 © 2007 Wiley-VCH Verlag GmbH & Co. KGaA, Weinheim 

### Spectroscopic Characterisation

All compounds were analysed by NMR, IR and UV/Vis spectroscopy (see Experimental Section). No $^{13}C$ NMR spectra could be recorded for complexes **4**, **7** or **8** due to their low solubility. The proton and carbon signals in the NMR spectra are in the usual regions, and the IR spectrum of **8** shows three intense signals at $\tilde{\nu}$ = 2018, 1906 and 1866 $cm^{-1}$, as expected for the vibrations of carbonyl groups in a facial conformation.[25]

The electronic absorption spectra of ligand **1** and its complexes with $Ru^{II}$, $Re^{I}$ and $Cu^{I}$ are depicted in Figure 11. Each complex exhibits a low-energy band at $\lambda_{max}$ = 302 (**4**, log $\varepsilon$ = 4.549), 272 (**7**, log $\varepsilon$ = 3.883) and 302 (**8**, log $\varepsilon$ = 3.918), and complexes **4** and **7** also exhibit a transition near the band of the free ligand absorption. The lowest energy band of complexes **5** and **6** appears at $\lambda$ = 307 (log $\varepsilon$ = 4.517) and 299 nm (log $\varepsilon$ = 4.169), respectively (see Figures S3 and S4 in the Supporting Information). The complexes show absorption peaks between 270 and 370 nm, a region where no corresponding ligand absorption is found. We therefore tentatively assign these absorptions to MLCT bands. It is noteworthy that the maxima of the lowest absorptions in $[(bpy)Re^{I}(CO)_3Cl]$ ($\lambda_{max}$ = 386 nm)[26] and $[(bpy)_3Ru]^{2+}$ ($\lambda_{max}$ = 451 nm)[27] are substantially lower in energy than in the complexes of ligands **1**–**3**. Poor solubility in non-polar solvents precludes a more detailed study. None of the complexes is an emitter in solution or the solid state.

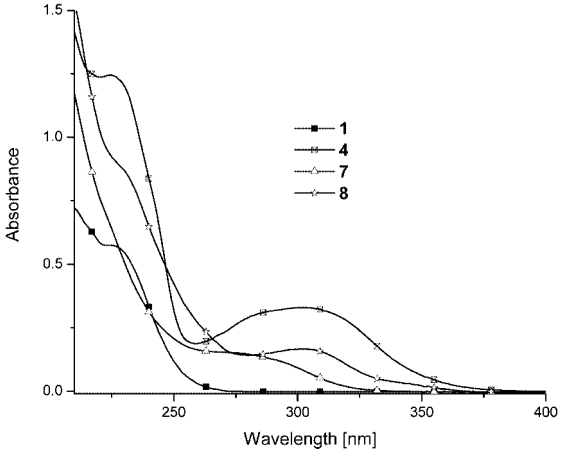


Figure 11. Electronic absorption spectra of compounds **1**, **4**, **7**, and **8** in acetonitrile ($c$ = 20 μM).

### Summary

New 1,1′-disubstituted 4,4′-bi-1,2,3-triazole compounds have been synthesised by a $Cu^{I}$-catalysed cycloaddition between 1,4-butadiyne and various alkyl and aryl azides. These compounds have been employed as ligands for transition metal complexes. Three homoleptic $Ru^{II}$ complexes of the obtained ligands as well as one $Cu^{I}$ and $Re^{I}$ complex with one of the ligands have been synthesised. All of them are readily accessible by standard reactions and are perfectly stable. The steric properties of the ligands are similar to those of 2,2′-bipyridine, although the photophysical properties are not. The complexes show no luminescence. Application of these new compounds as bidentate and easy-to-modify "innocent" ligands may be envisaged. The ligand properties may be varied using established synthetic routes. For example, monosubstituted 4,4′-bitriazoles could be obtained from 1,4-butadiyne and a mixture of alkyl azide and trimethylsilyl azide.[28] This would allow the formation of a triazolyl anion after deprotonation of the unsubstituted triazole and asymmetric functionalisation. The use of 2,6-diethynylpyridine instead of 1,4-butadiyne would give access to terpyridine analogues, and substitution of the triazole-CH would allow introduction of further functionality at the ring carbon atom.[29]

## Experimental Section

**General Information:** All reactions were performed under an inert atmosphere of $N_2$ using standard Schlenk techniques, unless otherwise stated. Melting points were determined on a Tottoli micro melting point apparatus and are uncorrected. TLC analyses were performed on silica gel 60 F-254 with a 0.2-mm layer thickness. Detection was by UV light at 254/366 nm or by discolouration with ninhydrin in EtOH. Merck Geduran SI 60 silica gel was used for preparative column chromatography. Commercially available solvents of standard quality were used. Unless otherwise stated, purification and drying was done according to accepted general procedures.[30] Elemental analyses were carried out by the Centre for Chemical Analysis of the Faculty of Natural Sciences of the University of Regensburg.

**Safety Note:** *Sodium azide is toxic and can generate the extremely hazardous hydrazoic acid (volatile, toxic, explosive) if it comes into contact with acids. Organic azides with a saturated carbon:azide ratio of less than 6 may be heat- and shock-sensitive and should be handled with care.*

Absorption spectra were recorded with a Varian Cary BIO 50 UV/Vis/NIR Spectrometer with a 1-cm quartz cell (Hellma) and Uvasol solvents (Merck or Baker). NMR spectra were recorded with a Bruker Avance 300 spectrometer ($^1H$: 300.1 MHz; $^{13}C$: 75.5 MHz; $T$ = 300 K). The chemical shifts are reported in ppm relative to external standards (solvent residual peak) and coupling constants are given in Hertz. The spectra were analysed as being first order. Assignment of signals in the $^{13}C$ NMR spectra was performed with the DEPT technique (pulse angle: 135°) and given as (+) for $CH_3$ or CH, (–) for $CH_2$ and ($C_{quat}$) for quaternary C. Error of reported values: chemical shift: 0.01 ppm for $^1H$ NMR, 0.1 ppm for $^{13}C$ NMR and 0.1 Hz for coupling constants. The solvent used is reported for each spectrum. Mass spectra were recorded with a Varian CH-5 (EI), Finnigan MAT 95 (CI, FAB and FD) or Finnigan MAT TSQ 7000 (ESI) spectrometer with xenon as the ionisation gas for FAB. IR spectra were recorded with a Bio-Rad FTS 2000 MX FT-IR or Bio-Rad FT-IR FTS 155 spectrometer.

**Synthesis of Triazole Ligands and Complexes. General Procedures:**

**GP 1: Twofold "Click Reaction" with 1,3-Butadiyne:** The freshly prepared butadiyne was condensed into 5 mL of acetonitrile at –40 °C and a solution of the azide (2.0 equiv.), 2,4-lutidine (2.2 equiv.) and CuI (10 mol-%) in 10 mL of acetonitrile was cooled to –40 °C and added. The reaction mixture was then warmed to room temperature. The reaction vessel was stored in a closed autoclave to prevent evaporation of the butadiyne. After stirring for

 © 2007 Wiley-VCH Verlag GmbH & Co. KGaA, Weinheim 

20 h, the mixture was poured into 50 mL of an aqueous solution of $H_2O_2$ (3%). The mixture was stirred until the generation of gas ceased, then 50 mL of a saturated aqueous solution of EDTA was added and the mixture was stirred for 30 min. Further purification was different for each compound.

**GP 2: Synthesis of Homoleptic $Ru^{II}$ Complexes:** The bitriazole ligand (3 equiv.) and $RuCl_3·4H_2O$ were suspended in ethylene glycol (10 mL) in a round-bottomed flask (25 mL). The mixture was heated (oil bath temperature: 200 °C) to yield a dark-red solution, which slowly turned to brownish orange over 20 h. The solution was concentrated in vacuo with heating to 3 mL, then boiling ethanol was added to the solution at 80 °C until a white precipitate appeared. The mixture was stored at –20 °C overnight to complete precipitation, then the solid was separated by centrifugation and dried in vacuo.

**1,1′-Dibenzyl-4,4′-bi-1*H*-1,2,3-triazolyl (1):** Synthesised following GP 1 from butadiyne (563 mg, 11.3 mmol), benzyl azide (3.00 g, 22.5 mmol, 2 equiv.), 2,4-lutidine (2.65 g, 2.86 mL, 24.8 mmol, 2.2 equiv.) and CuI (214 mg, 1.13 mmol, 10 mol-%). After workup, the aqueous solution was extracted with $CHCl_3$ (3 × 100 mL) and the organic phase was dried with $Na_2SO_4$, filtered and concentrated at reduced pressure. The crude product was purified by column chromatography with a dichloromethane/MeOH gradient from 99:1 to 96:4. This yielded 2.93 g of **4** as colourless crystals (82%). M.p. 228 °C. $^1$H NMR (300 MHz, [D$_6$]DMSO): $\delta$ = 5.67 (s, 4 H, $CH_2$), 7.31–7.40 (m, 10 H, CH), 8.58 (s, 2 H, triazole) ppm. $^{13}$C NMR (75.5 MHz, [D$_6$]DMSO): $\delta$ = 52.8 (–, 2 C), 121.7 (+, 2 C, triazole), 127.9 (+, 4 C), 128.1 (+, 2 C), 128.7 (+, 4 C), 139.2 (1 C, $C_{quat}$), 142.2 (1 C, $C_{quat}$) ppm. MS (ESI, DCM/MeOH): *m*/*z* (%) 317.1 (100) [$MH^+$]. $C_{18}H_{16}N_6$ (316.37): calcd. C 68.34, H 5.10, N 26.56; found C 68.21, H 5.21, N 26.42. UV/Vis (MeCN): $\lambda$ (log $\varepsilon$) = 225 nm (4.458). IR (KBr): $\tilde{\nu}$ = 3133, 3101, 3031, 2984, 2946, 2858, 1673, 1494, 1439, 1410, 1364, 1293, 1231, 1076, 1058, 949, 836, 722 cm$^{-1}$.

**1,1′-Diphenyl-4,4′-bi-1*H*-1,2,3-triazolyl (2):** Synthesised following GP 1 from butadiyne (335 mg, 6.7 mmol), phenyl azide (1.60 g, 13.4 mmol, 2 equiv.), 2,4-lutidine (1.58 g, 1.70 mL, 14.8 mmol, 2.2 equiv.) and CuI (127 mg, 0.67 mmol, 10 mol-%). After workup, the aqueous solution was heated to 40 °C and extracted with warm $CHCl_3$ (40 °C, 8 × 80 mL). The organic phase was dried with $Na_2SO_4$, filtered, concentrated at reduced pressure and dried in vacuo. The residue was dissolved in boiling $CHCl_3$, filtered through charcoal and Celite and concentrated again. The crude product was purified by recrystallisation from $CHCl_3$/petroleum ether. This yielded 1.47 g of **2** as colourless crystals (76%). M.p. 236 °C. $^1$H NMR (300 MHz, $CHCl_3$): $\delta$ = 7.49 (t, $^3J$ = 7.7 Hz, 2 H, CH), 7.53–7.59 (m, 4 H, CH), 7.82 (d, $^3J$ = 7.6 Hz, 4 H, CH), 8.59 (s, 2 H, triazole) ppm. $^{13}$C NMR (75.5 MHz, $CHCl_3$): $\delta$ = 118.9 (+, 2 C, triazole), 120.6 (+, 4 C), 129.0 (+, 2 C), 129.9 (+, 4 C), 136.9 (1 C, $C_{quat}$), 140.5 (1 C, $C_{quat}$) ppm. MS (ESI, DCM/MeOH): *m*/*z* (%) 289.1 (100) [$MH^+$]. $C_{16}H_{12}N_6$ (288.31): calcd. C 66.66, H 4.20, N 29.15; found C 66.57, H 4.31, N 29.01. UV/Vis ($CH_3CN$): $\lambda$ (log $\varepsilon$) = 232 (4.480), 257 nm (4.366). IR (KBr): $\tilde{\nu}$ = 3132, 3093, 3065, 1654, 1597, 1504, 1464, 1396, 1257, 1234, 1034, 825, 756 cm$^{-1}$.

**1,1′-Bis(carboxymethyl)-4,4′-bi-1*H*-1,2,3-triazolyl (3):** Synthesised following GP 1 from butadiyne (541 mg, 10.8 mmol), β-azidoacetic acid (2.18 g, 21.6 mmol, 2 equiv.), 2,4-lutidine (2.55 g, 2.75 mL, 23.8 mmol, 2.2 equiv.) and CuI (206 mg, 1.08 mmol, 10 mol-%). After workup, the aqueous solution was acidified to pH 2 with 6 N aqueous HCl. The precipitate was filtered, washed with water and suspended in 10 mL of water. A 0.1 N aqueous solution of NaOH was then added dropwise until the solid dissolved completely. The solution was lyophilized to yield the sodium salt of **3** (2.50 g, 8.4 mmol, 78%). NMR, mass and UV spectra were recorded for this salt. The solid was dissolved in water (20 mL), the solution was heated to reflux and 0.5 N aqueous HCl was added dropwise until a precipitate appeared. After cooling to room temperature, 2 N aqueous HCl was added until no further product precipitated. The solid was filtered, washed with water and dried in vacuo. This yielded 2.12 g of **3** as colourless crystals (78%). M.p. > 215 °C (decomp.). $^1$H NMR (300 MHz, $D_2O$): $\delta$ = 5.05 (s, 4 H, $CH_2$), 8.20 (s, 2 H, triazole) ppm. $^{13}$C NMR (75.5 MHz, $D_2O$): $\delta$ = 53.3 (–, 2 C), 123.9 (+, 2 C, triazole), 138.6 (2 C, $C_{quat}$), 173.1 (2 C, $C_{quat}$) ppm. MS (ESI, $H_2O$/MeCN): *m*/*z* (%) 253.1 (100) [$MH^+$]. $C_8H_8N_6O_4$ (252.16): calcd. C 38.10, H 3.20, N 33.32; found C 37.97, H 3.32, N 33.17. UV/Vis ($H_2O$): $\lambda$ (log $\varepsilon$) = 225 nm (4.092). IR (KBr): $\tilde{\nu}$ = 3435, 3151, 3117, 3013, 2947, 2792, 2708, 2594, 2511, 1930, 1794, 1724, 1496, 1420, 1347, 1295, 1257, 1223, 1151, 1109, 1064, 1011, 976, 896, 795 cm$^{-1}$.

**Ru Complex 4:** Ligand **1** (100 mg, 0.32 mmol) and $RuCl_3·3H_2O$ (28 mg, 0.11 mmol) were suspended in 20 mL of ethylene glycol in a round-bottomed flask fitted with a reflux condenser and the mixture was heated (oil bath temperature: 200 °C). This yielded a dark-red solution which slowly turned to brownish orange over 20 h. The solvent was removed in vacuo by heating. The remaining solid was dissolved in boiling MeCN and filtered. $Et_2O$ was then added to the solution to precipitate the product. This yielded a light yellow powder, which was recrystallised from MeCN/$Et_2O$ to give 84 mg of **7** as yellowish crystals (0.07 mmol, 68%). M.p. > 210 °C (decomp.). $^1$H NMR (300 MHz, $CD_3CN$): $\delta$ = 5.55 (s, 12 H, $CH_2$), 7.12–7.18 (m, 12 H, CH), 7.28–7.36 (m, 18 H, CH), 8.54 (s, 6 H, triazole) ppm. MS (ESI, $H_2O$/MeCN): *m*/*z* (%) 525.4 (100) [$(L_3Ru^{2+})^{2+}$], 1185.5 (1) [$(L_3Ru^{2+} + Cl^-)^+$]. $C_{54}H_{48}Cl_2N_{18}Ru·4H_2O$ (1193.1): calcd. C 54.36, H 4.73, N 21.13; found C 54.46, H 4.62, N 20.47. UV/Vis ($H_2O$): $\lambda$ (log $\varepsilon$) = 302 (4.549), 222 nm (5.143). IR (ATR): $\tilde{\nu}$ = 3116, 3032, 1446, 1456, 1426, 1356, 1340, 1276, 1112, 1078, 1042, 720, 694, 654 cm$^{-1}$.

**Ru Complex 5:** Synthesised following GP 2 from **2** (250 mg, 0.87 mmol) and $RuCl_3·4H_2O$ (78 mg, 0.29 mmol). This yielded 665 mg of **5** as colourless crystals (74%). M.p. > 210 °C (decomp.); $^1$H NMR (300 MHz, [D$_6$]DMSO): $\delta$ = 7.54–7.66 (m, 18 H, CH), 7.89 (d, $^3J$ = 7.1 Hz, 12 H, CH), 9.76 (s, 6 H, triazole) ppm. $^{13}$C NMR (75.5 MHz, [D$_6$]DMSO): $\delta$ = 120.1 (+, 2 C, triazole), 120.5 (+, 4 C), 129.9 (+, 2 C), 130.0 (+, 4 C), 135.6 (1 C, $C_{quat}$), 140.9 (1 C, $C_{quat}$) ppm. MS (ESI, $H_2O$/MeCN): *m*/*z* (%) 483.2 (100) [$(L_3Ru^{2+})^{2+}$], 1115.4 (5) [$(L_3Ru^{2+} + TfO^-)^+$]. UV/Vis ($H_2O$): $\lambda$ (log $\varepsilon$) = 307 (4.517), 239 nm (5.012). IR (KBr): $\tilde{\nu}$ = 3102, 3062, 1595, 1499, 1464, 1422, 1313, 1271, 1065, 999, 760 cm$^{-1}$.

**Ru Complex 6:** Synthesised following GP 2 from **3** (250 mg, 0.99 mmol) and $RuCl_3·4H_2O$ (90 mg, 0.33 mmol). This yielded 634 mg of **6** as colourless crystals (69%). M.p. > 205 °C (decomp.). $^1$H NMR (300 MHz, $D_2O$): $\delta$ = 5.22 (s, 12 H, $CH_2$), 8.50 (s, 6 H, triazole) ppm. $^{13}$C NMR (75.5 MHz, $D_2O$): $\delta$ = 51.5 (–, 6 C), 122.0 (+, 6 C, triazole), 138.2 (6 C, $C_{quat}$), 171.0 (6 C, $C_{quat}$) ppm. MS (ESI, $H_2O$/MeCN): *m*/*z* (%) 478.2 (100), 507.2 (100), 521.3 (100), 955.3 (65). UV/Vis ($H_2O$): $\lambda$ (log $\varepsilon$) = 299 (4.169), 225 nm (4.721). IR (KBr): $\tilde{\nu}$ = 3429. 3136, 2925, 1746, 1629, 1454, 1377, 1288, 1221, 1021 cm$^{-1}$.

**$Cu^I$ Complex 7:** Ligand **1** (50 mg, 0.16 mmol), $[Cu^I(NCMe)_4]PF_6$ (59 mg, 0.16 mmol) and bis[2-(diphenylphosphanyl)phenyl] ether (85 mg, 0.16 mmol) were dissolved in degassed dichloromethane and heated to reflux for 3 h. The solution was concentrated and diethyl ether was added to precipitate the product. The suspension was filtered and the filtrate cooled to – 35 °C. This gave colourless

 © 2007 Wiley-VCH Verlag GmbH & Co. KGaA, Weinheim 

crystals of **7** suitable for X-ray crystallography. Complex **7** was obtained in an overall yield of 73% (123 mg). $^1$H NMR (300 MHz, $CD_3CN$): $\delta$ = 5.59 (s, 4 H, $CH_2$), 6.66–6.75 (m, 2 H, CH), 6.90–7.02 (m, 4 H, CH), 7.25–7.47 (m, 32 H, CH), 8.12 (s, 2 H, triazole) ppm. $^{31}$P NMR (162 MHz, $CDCl_3$): $\delta$ = –13.38 ppm. MS (ESI): *m*/*z* (%) 317.1 (8) [**1**$^+$], 601.2 (28) [(DPEPhos)Cu$^+$], 642.2 (100) [{(DPEPhos)Cu + MeCN}$^+$], 917.4 (51) [(DPEPhos)(**1**)Cu$^+$]. $C_{54}H_{44}CuN_6OP_2{\cdot}PF_6$ (1063.4): calcd. C 60.99, H 4.17, N 7.90;

Table 1. Crystal data, data collection and structure refinement for compounds **1**–**3**.

| | **1** (prisms) | **1** (needles) | **2** | **3** |
|---|---|---|---|---|
| Formula | $C_{18}H_{16}N_6$ | $C_{18}H_{16}N_6$ | $C_{16}H_{12}N_6$ | $C_8H_8N_6O_4$ |
| $M_w$ | 316.37 | 316.37 | 288.32 | 252.20 |
| Crystal size [mm] | 0.32 × 0.22 × 0.18 | 0.48 × 0.28 × 0.02 | 0.42 × 0.06 × 0.04 | 0.44 × 0.02 × 0.01 |
| Crystal system | monoclinic | monoclinic | triclinic | monoclinic |
| Space group | $P2_1/c$ | $Cc$ | $P\bar{1}$ | $P2_1/c$ |
| $a$ [Å] | 8.1669(10) | 34.414(3) | 5.729(4) | 7.4088(4) |
| $b$ [Å] | 9.4871(13) | 5.5439(5) | 11.019(18) | 4.5388(3) |
| $c$ [Å] | 10.3595(12) | 8.4506(7) | 16.744(14) | 14.5860(9) |
| $\alpha$ [°] | 90 | 90 | 101.38(11) | 90 |
| $\beta$ [°] | 94.135(14) | 102.466(10) | 93.17(7) | 95.767(5) |
| $\gamma$ [°] | 90 | 90 | 102.51(11) | 90 |
| $V$ [Å$^3$] | 800.57(17) | 1574.3(2) | 1006(2) | 488.00(5) |
| $\rho_{calc}$ [g cm$^{-3}$] | 1.311 | 1.335 | 1.428 | 1.716 |
| $Z$ | 2 | 4 | 3 | 2 |
| $\mu$ [mm$^{-1}$] | 0.083 | 0.085 | 0.741 | 1.221 |
| $T$ [K] | 123 | 123 | 150 | 123 |
| $\Theta$ range [°] | 2.50–26.80 | 2.42–26.80 | 2.71–50.31 | 6.10–62.10 |
| Reflections collected | 5365 | 6381 | 5716 | 1756 |
| Unique reflections | 1589 [$R$(int) = 0.0337] | 3264 [$R$(int) = 0.0854] | 2062 [$R$(int) = 0.0298] | 748 [$R$(int) = 0.0298] |
| Observed reflections [$I > 2\sigma(I)$] | 1166 | 2516 | 1411 | 558 |
| Parameters refined/restraints | 109/0 | 217/2 | 298/0 | 85/0 |
| Absorption correction | none | none | semi-empirical from equivalents | semi-empirical from equivalents |
| $T_{max}$, $T_{min}$ | | | 0.6559, 1.0 | 0.4862, 1.0 |
| $\sigma_{fin}$ (max./min.) [e Å$^{-3}$] | 0.238/–0.137 | 0.294/–0.248 | 0.146/–0.213 | 1.021/–0.299 |
| $R_1$ [$I \geq 2\sigma(I)$] | 0.0333 | 0.0565 | 0.0338 | 0.0773 |
| $wR_2$ | 0.0805 | 0.1401 | 0.0754 | 0.2273 |
| CCDC number | 645041 | 645040 | 645044 | 645045 |

Table 2. Crystal data, data collection and structure refinement for compounds **4**, **7** and **8**.

| | **4** | **7** | **8** |
|---|---|---|---|
| Formula | $C_{54}H_{48}Cl_2N_{18}RuS$[a] | $2(C_{54}H_{44}CuN_6OP_2)\ 2(PF_6)$ | $C_{21}H_{16}ClN_6O_3Re$ |
| $M_w$ | –[a] | 2124.87 | 622.06 |
| Crystal size [mm] | 0.36 × 0.11 × 0.06 | 0.34 × 0.22 × 0.14 | 0.11 × 0.026 × 0.015 |
| Crystal system | monoclinic | triclinic | orthorhombic |
| Space group | $P2_1/a$ | $P\bar{1}$ | $Pnma$ |
| $a$ [Å] | 16.3417(3) | 13.742(1) | 10.475(4) |
| $b$ [Å] | 23.1347(4) | 14.425(1) | 18.574(7) |
| $c$ [Å] | 18.0784(5) | 29.195(2) | 10.584(4) |
| $\alpha$ [°] | 90 | 83.511(9) | 90 |
| $\beta$ [°] | 107.787(3) | 86.160(9) | 90 |
| $\gamma$ [°] | 90 | 71.812(8) | 90 |
| $V$ [Å$^3$] | 6508.0(3) | 5459.8(7) | 2059.3(14) |
| $\rho_{calc}$ [g cm$^{-3}$] | –[a] | 1.294 | 2.006 |
| $Z$ | 4 | 4 | 4 |
| $\mu$ [mm$^{-1}$] | –[a] | 0.551 | 13.070 |
| $T$ [K] | 123 | 123 | 150 |
| $\Theta$ range [°] | 3.20–51.54 | 2.00–25.00 | 5.94–51.16 |
| Reflections collected | 32311 | 54865 | 4576 |
| Unique reflections | 6840 [$R$(int) = 0.0455] | 18094 [$R$(int) = 0.0969] | 1081 [$R$(int) = 0.0935] |
| Observed reflections [$I > 2\sigma(I)$] | 4589 | 6873 | 889 |
| Parameters refined/restraints | 677/0 | 1252/0 | 75/0 |
| Absorption correction | semi-empirical from equivalents | analytical from crystal shape | semi-empirical from equivalents |
| $T_{min}$, $T_{max}$ | 0.63090, 1.0 | 0.8458, 0.9441 | 0.25246, 1.0 |
| $\sigma_{fin}$ (max/min) [e Å$^{-3}$] | 1.916/–0.698 | 0.796/–0.259 | 1.713/–1.067 |
| $R_1$ [$I \geq 2\sigma(I)$] | 0.0817 | 0.0562 | 0.0449 |
| $wR_2$ | 0.2567 | 0.1461 | 0.1104 |
| CCDC number | 645042 | 645043 | 645046 |

[a] Crystals of **4** contain an unspecified number of solvents, which are highly disordered, thus no formula and no reliable values for the parameters or formula can be given.

 © 2007 Wiley-VCH Verlag GmbH & Co. KGaA, Weinheim 

found C 60.54, H 4.23, N 7.74; UV/Vis (MeCN): $\lambda$ (log $\varepsilon$) = 272 nm (3.883). IR (ATR): $\tilde{\nu}$ = 3138, 2944, 2884, 2364, 2328, 2210, 2162, 2048, 1976, 1498, 1458, 1288, 1260, 1046, 814, 716 cm$^{-1}$.

**Re$^{I}$ Complex 8:** Ligand **1** (50 mg, 0.16 mmol) and [Re$^{I}$(CO)$_5$]Cl (57 mg, 0.16 mmol) were dissolved in degassed toluene and heated to reflux for 12 h. After cooling to room temperature, the colourless precipitate was filtered and dried in vacuo. Recrystallisation from MeCN/Et$_2$O yielded **8** as colourless crystals (94 mg, 96%). $^1$H NMR (300 MHz, CD$_3$CN): $\delta$ = 5.72 (s, 4 H, CH$_2$), 7.39–7.46 (m, 10 H, CH), 8.28 (s, 2 H, triazole) ppm. MS (ESI): *m/z* (%) 91.1 (100) [Bn$^+$], 503.0 (10) [(**1**)Re$^+$], 538.0 (1) [(M – 3CO + H)$^+$], 566.0 (2) [(M – 2CO + H)$^+$], 593.3 (2) [M – CO$^+$], 621.9 (1) [M$^+$]. IR (ATR): $\tilde{\nu}$ = 3136, 2944, 2886, 2018, 1906, 1866, 1494, 1448, 1422, 1292, 1266, 1178, 1158, 1108, 1082, 1050, 818, 744, 698, 660 cm$^{-1}$. UV/Vis (MeCN): $\lambda$ (log $\varepsilon$) = 350 (sh), 302 (3.918), 228 nm (sh). $C_{21}H_{16}ClN_6O_3Re$ (622.05): calcd. C 40.55, H 2.59, N 13.51; found C 40.47, H 2.59, N 13.55.

**Crystal Structure Determination:** Diffraction data for crystals of compound **1** (needles and prisms) and complex **7** were collected with a STOE-IPDS diffractometer[31] with graphite-monochromated Mo-$K_\alpha$ radiation ($\lambda$ = 0.71073 Å), whereas data for crystals of **2**, **3**, **4** and **8** were collected with an Oxford Diffraction Gemini Ultra CCD diffractometer[32] with multilayer optics and Cu-$K_\alpha$ radiation ($\lambda$ = 1.5418 Å). Further crystallographic and refinement data can be found in Tables 1 and 2. The structures were solved by direct methods (SIR-97)[33] and refined by full-matrix least-squares on $F^2$ (SHELXL-97).[34] The H atoms were calculated geometrically and a riding model was applied during the refinement process. The structure solution of **4** and **8** was handicapped by poor crystal quality. For **4**, the obviously present solvent molecules could not be identified and were included in the refinement steps as C atoms (C100–C112) or as Cl atoms. For **8** only the heavy atoms could be refined with anisotropic displacement factors.

CCDC-645040–645046 contain the supplementary crystallographic data for this paper. These data can be obtained free of charge from The Cambridge Crystallographic Data Centre via www.ccdc.cam.ac.uk/data_request/cif.

**Supporting Information** (see also the footnote on the first page of this article): Cell plot of compound **3** (Figure S1), complete asymmetric unit of complex **4** (Figure S2), electronic absorption spectra of compounds **2**/**5** (Figure S3) and **3**/**6** (Figure S4).

## Acknowledgments

Parts of this work were supported by the Bundesministerium für Bildung und Forschung (BMBF). We also acknowledge financial support from the DFG (SPP 1118). S.R. thanks the Elitenetzwerk Bayern for a graduate fellowship.

[1] K. Kalyanasundaram, *Photochemistry of Polypyridine and Porphyrin Complexes*, Academic Press, London, **1992**.

[2] A. Juris, V. Balzani, F. Barigeletti, S. Campagna, P. Belser, A. von Zelewsky, *Coord. Chem. Rev.* **1988**, *84*, 85; K. P. Balashev, M. V. Puzyk, V. S. Kotlyar, M. V. Kulikova, *Coord. Chem. Rev.* **1997**, *159*, 109; C. E. Housecroft, *Compr. Coord. Chem. II* **2004**, *5*, 555; O. S. Wolfbeis, L. J. Weis, M. J. P. Leiner, W. E. Ziegler, *Anal. Chem.* **1988**, *60*, 2028; M. Maestri, D. Sandrini, V. Balzani, L. Chassot, P. Jolliet, A. von Zelewsky, *Chem. Phys. Lett.* **1985**, *122*, 375.

[3] J. K. Hurst, *Coord. Chem. Rev.* **2005**, *249*, 313; K. Szaciłowski, W. Macyk, A. Drzewiecka-Matuszek, M. Brindell, G. Stochel, *Chem. Rev.* **2005**, *105*, 2647; L.-N. Ji, X.-H. Zou, J.-G. Liu, *Coord. Chem. Rev.* **2001**, *216–217*, 513; D. B. Rorabacher, *Chem. Rev.* **2004**, *104*, 651; S. Welter, N. Salluce, P. Belser, M. Groeneveld, L. De Cola, *Coord. Chem. Rev.* **2005**, *249*, 1327; R. T. F. Jukes, V. Adamo, F. Hartl, P. Belser, L. De Cola, *Coord. Chem. Rev.* **2005**, *249*, 1327; V. Balzani, F. Scandola, *Supramolecular Photochemistry*, E. Horwood, Chichester, **1991**; R. Hage, *Coord. Chem. Rev.* **1991**, *111*, 161; M. Ruben, S. Rau, A. Skirl, K. Krause, H. Gorls, D. Walther, J. G. Vos, *Inorg. Chim. Acta* **2000**, *303*, 206; V. J. Catalano, T. J. Craig, *Inorg. Chem.* **2003**, *42*, 321; D. M. D'Alessandro, P. H. Dinolfo, J. T. Hupp, P. C. Junk, F. R. Keene, *Eur. J. Org. Chem.* **2006**, *4*, 772; H. Yersin, C. Kratzer, *Coord. Chem. Rev.* **2002**, *229*, 75.

[4] U. S. Schubert, C. Eschbaumer, *Angew. Chem. Int. Ed.* **2002**, *41*, 2892.

[5] H. Yersin, *Top. Curr. Chem.* **2004**, *241*, 1; K. W. Lee, J. D. Slinker, A. A. Gorodetsky, S. Flores-Torres, H. D. Abruna, P. L. Housten, G. G. Malliaras, *Phys. Chem. Chem. Phys.* **2003**, *5*, 2706; L. J. Stoltzberg, J. D. Slinker, S. Flores-Torres, A. D. Bernards, G. G. Malliaras, H. D. Abruna, J.-S. Kim, R. H. Friend, M. D. Kaplan, V. Goldberg, *J. Am. Chem. Soc.* **2006**, *128*, 7761; C. Zhen, Y. Chuai, C. Lao, L. Huang, D. Zou, D. N. Lee, B. H. Kim, *Appl. Phys. Lett.* **2005**, *87*, 093508/1; F. W. Vergeer, X. Chen, F. Lafolet, L. De Cola, H. Fuchs, L. Chi, *Adv. Funct. Mater.* **2006**, *16*, 625.

[6] L. De Cola, P. Belser, A. von Zelewsky, F. Vögtle, *Inorg. Chim. Acta* **2007**, *360*, 775; R. T. F. Jukes, B. Bozic, F. Hartl, P. Belser, L. De Cola, *Inorg. Chem.* **2006**, *45*, 8326; S. Welter, F. Lafolet, E. Cecchetto, F. Vergeer, L. De Cola, *ChemPhysChem.* **2005**, *6*, 2417; W. J. Finkenzeller, P. Stoessel, H. Yersin, *Chem. Phys. Lett.* **2004**, *397*, 289; C. A. Bignozzi, R. Argazzi, C. Chiorboli, S. Roffia, F. Scandola, *Coord. Chem. Rev.* **1991**, *111*, 261; D. M. D'Alessandro, F. R. Keene, *Chem. Rev.* **2006**, *106*, 2270; S. Ranjan, S. K. Dikshit, *Transition Met. Chem.* **2002**, *27*, 668; E. Tfouni, *Coord. Chem. Rev.* **2000**, *196*, 281; D. W. Thompson, J. R. Schoonover, T. J. Meyer, R. Argazzi, C. A. Bignozzi, *J. Chem. Soc. Dalton Trans.* **1999**, *21*, 3729; A. B. Tamayo, S. Garon, T. Sajoto, P. I. Djurovich, I. M. Tsyba, R. Bau, M. E. Thompson, *Inorg. Chem.* **2005**, *44*, 8723.

[7] P. McCord, A. J. Bard, *J. Electroanal. Chem.* **1991**, *318*, 91.

[8] H. Yersin, W. Humbs, J. Strasser, *Top. Curr. Chem.* **1997**, *191*, 153.

[9] T. Sajoto, P. I. Djurovich, A. Tamayo, M. Yousufuddin, R. Bau, M. E. Thompson, *Inorg. Chem.* **2005**, *44*, 7992.

[10] J. Li, P. I. Djurovich, B. D. Alleyne, I. Tsyba, N. N. Ho, R. Bau, M. E. Thompson, *Polyhedron* **2004**, *23*, 419; J. Li, P. I. Djurovich, B. D. Alleyne, M. Yousufuddin, N. N. Ho, J. C. Thomas, J. C. Peters, R. Bau, M. E. Thompson, *Inorg. Chem.* **2005**, *44*, 1713.

[11] P. Coppo, E. A. Plummer, L. De Cola, *Chem. Commun.* **2004**, 1774.

[12] P. Coppo, M. Duati, V. N. Kozhevnikov, J. W. Hofstraat, L. De Cola, *Angew. Chem. Int. Ed.* **2005**, *44*, 1806.

[13] B. W. D'Andrade, J. Brooks, V. Adamovich, M. E. Thompsom, S. R. Forrest, *Adv. Mater.* **2002**, *14*, 1032; B. W. D'Andrade, S. R. Forrest, *Adv. Mater.* **2004**, *16*, 1585; J. Slinker, A. D. Bernards, P. L. Houston, H. D. Abruna, S. Bernhard, G. G. Malliaras, *Chem. Commun.* **2003**, 2392.

[14] The synthesis of a phenyl-substituted 1,2,3-bitriazole by a thermal cycloaddition has been reported in the literature, although a mixture of different products was obtained and no analytical data for this compound are available: L. V. Sokolyanska, A. N. Volkov, B. A. Trofimov, *Khim. Geterotsikl. Soedin.* **1979**, *6*, 849.

[15] F. H. Westheimer, O. T. Benfey, *J. Am. Chem. Soc.* **1956**, *78*, 5309; I. Antonini, F. Claudi, G. Cristalli, P. Fianchetti, M. Grifantini, S. Martelli, *J. Med. Chem.* **1981**, *24*, 1181; F. Kröhnke, *Synthesis* **1976**, 1; J. Uenishi, T. Tanaka, K. Nishiwaki, S. Wakabayashi, S. Oae, H. Tsukube, *J. Org. Chem.* **1993**, *58*, 4382; C. L. Fraser, N. R. Inastasi, J. J. S. Lamba, *J. Org. Chem.* **1997**, *62*, 9314; R.-A. Fallahpour, *Eur. J. Inorg. Chem.* **1998**, 1205; S. Dholakia, R. D. Gillard, F. L. Wimmer, *Polyhedron* **1985**, *5*, 791.

 © 2007 Wiley-VCH Verlag GmbH & Co. KGaA, Weinheim 

[16] T. L. Mindt, H. Struthers, L. Brans, T. Anguelov, C. Schweinsberg, V. Maes, D. Tourwé, R. Schibli, *J. Am. Chem. Soc.* **2006**, *128*, 15096; B. M. J. M. Suijkerbuijk, B. N. H. Aerts, H. P. Dijkstra, M. Lutz, A. L. Spek, G. van Koten, J. M. Klein Gebbink, *Dalton Trans.* **2007**, 1273; P. Wu, V. V. Fokin, *Aldrichimica Acta* **2007**, *40*, 7; V. D. Bock, H. Hiemstra, J. H. van Maarseveen, *Eur. J. Org. Chem.* **2006**, 51; T. R. Chan, R. Hilgraf, K. B. Sharpless, V. V. Fokin, *Org. Lett.* **2004**, *6*, 2853.
[17] Y. Angell, K. Burgess, *Angew. Chem. Int. Ed.* **2007**, *46*, 3649.
[18] H. D. Verkruijsse, L. Brandsma, *Synth. Commun.* **1991**, *21*, 657.
[19] F. J. Cagle Jr., *Acta Crystallogr.* **1948**, *1*, 158; L. L. Merritt, E. D. Schroeder, *Acta Crystallogr.* **1956**, *9*, 801; K. Nakatsu, H. Yoshioka, M. Matsui, S. Kosa, S. Ooi, *Acta Crystallogr., Sect. A* **1972**, *28*, S24; M. H. Chrisholm, J. C. Huffman, I. P. Rothwell, P. G. Bradley, N. Kress, W. H. Woodruff, *J. Am. Chem. Soc.* **1981**, *103*, 4945; F. E. Kuhn, M. Groarke, E. Bencze, E. Hardtweck, A. Prazeres, A. M. Santos, M. J. Calhorda, C. C. Romao, I. S. Goncalves, A. D. Lopes, M. Pillinger, *Chem. Eur. J.* **2002**, *8*, 2370.
[20] M. A. Sridhar, N. K. Lokanath, J. S. Prasad, K. S. Rangappa, N. V. A. Kumar, D. G. B. Gowda, *Mol. Cryst. Liq. Cryst. Sci. Technol., Sect. A* **1998**, *319*, 137; Y.-M. Wu, J. Deng, X. Fang, Q.-Y. Chen, *J. Fluorine Chem.* **2004**, *125*, 1415; K. Harju, M. Vahermo, I. Mutikainen, J. Yli-Kauhaluoma, *J. Comb. Chem.* **2003**, *5*, 826.
[21] Q. Zhang, Q. Zhou, Y. Cheng, L. Wang, D. Ma, X. Jing, F. Wang, *Adv. Mater.* **2004**, *16*, 432; T. McCormick, J. Wen-Li, S. Wang, *Inorg. Chem.* **2006**, *45*, 147.
[22] D. P. Rillema, D. S. Jones, C. Woods, H. A. Levy, *Inorg. Chem.* **1992**, *31*, 2935; M. Biner, H.-B. Bürgi, A. Ludi, C. Röhr, *J. Am. Chem. Soc.* **1992**, *114*, 5197.
[23] L. M. Engelhardt, C. Pakawatchai, A. H. White, P. C. Healy, *J. Chem. Soc. Dalton Trans.* **1985**, 125.
[24] S. Trammell, P. A. Goodson, B. P. Sullivan, *Inorg. Chem.* **1996**, *35*, 1421; P. A. Anderson, F. R. Keene, E. Horn, R. T. Tiekink, *Appl. Organomet. Chem.* **1990**, *4*, 523; V. W.-W. Yam, V. C.-Y. Lau, K.-K. Cheung, *Organometallics* **1995**, *14*, 2749; O. O. Gerlits, P. Coppens, *Acta Crystallogr., Sect. E* **2001**, *57*, m164.
[25] L. H. Staal, A. Oskam, V. Vrieze, *J. Organomet. Chem.* **1979**, *170*, 235.
[26] J. V. Caspar, T. J. Meyer, *J. Phys. Chem.* **1983**, *87*, 952.
[27] E. M. Kober, B. P. Sullivan, T. J. Meyer, *Inorg. Chem.* **1984**, *23*, 2098.
[28] T. Jin, S. Kamijo, Y. Yamamoto, *Eur. J. Org. Chem.* **2004**, *18*, 3789.
[29] Y.-M. Wu, J. Deng, Q.-Y. Chen, *Synthesis* **2005**, *8*, 1314.
[30] S. Hünig, G. Märkl, J. Sauer, *Einführung in die apparativen Methoden in der Organischen Chemie*, 2nd ed., Würzburg, Regensburg, **1994**; Author collective, *Organikum*, 17th ed., VEB Deutscher Verlag der Wissenschaften, Berlin, **1988**.
[31] STOE (**1998**) IPDS software, Version 2.89, STOE & CIE GmbH, Darmstadt, Germany.
[32] *CrysAlis CCD*, Oxford Diffraction Ltd., Version 1.171.30.3 (release 12-05-2006 CrysAlis171.NET).
[33] A. Altomare, G. Cascarano, C. Giacovazzo, A. Guagliardi, *J. Appl. Crystallogr.* **1993**, *26*, 343.
[34] G. M. Sheldrick, *SHELXL-97. Program for crystal structure refinement*, University of Göttingen, Germany, **1997**.

Received: May 2, 2007
Published Online: August 20, 2007

 © 2007 Wiley-VCH Verlag GmbH & Co. KGaA, Weinheim 

DOI: 10.1002/ejic.200700441

# Tetrahedral $Co^{II}$ Complexes with $CoI_2O_2$ and $CoO_2S_2$ Cores – Crystal Structures of $[Co\{HN(OPPh_2)(SPPh_2)\text{-}O\}_2I_2]$ and $[Co\{N(OPPh_2)(SPPh_2)\text{-}O,S\}_2]$

**M. Carla Aragoni,[a] Massimiliano Arca,[a] M. Bonaria Carrea,[a] Alessandra Garau,[a] Francesco A. Devillanova,[a] Francesco Isaia,*[a] Vito Lippolis,[a] Gian Luca Abbati,[b] Francesco Demartin,[c] Cristian Silvestru,[d] Serhiy Demeshko,[e] and Franc Meyer[e]**

**Keywords:** Cobalt / O,S ligands / Phosphanes / Sulfides / Density functional calculations / Magnetic properties

The compound $[Co^{II}\{HN(OPPh_2)(SPPh_2)\text{-}O\}_2I_2]$ (**1**) was synthesised by the reaction of cobalt in powder with the iodine adduct of tetraphenylthiooxoimidodiphosphinic acid, $HN(OPPh_2)(SPPh_2)$, in $Et_2O$; treatment of compound **1** with NaOH resulted in deprotonation of the ligands bound to the metal ion and a separation of $[Co^{II}\{N(OPPh_2)(SPPh_2)\text{-}O,S\}_2]$ (**2**). Molecular structures of complexes **1** and **2** were elucidated by X-ray diffraction analysis, which revealed a $CoI_2O_2$ tetrahedral core for compound **1** in which two neutral ligands bind through the oxygen atoms the $Co^{II}$ ion, and a tetrahedral $CoO_2S_2$ core for compound **2** with the oxygen and sulfur atoms of each anionic ligand chelating a $Co^{II}$ centre. Variable-temperature magnetic susceptibility measurements are consistent with tetrahedral high-spin ($S = 3/2$) $Co^{II}$ that possesses a $^4A_2$ ground state with best fit parameters $g = 2.25$, $|D| = 12.0\ cm^{-1}$ and $g = 2.37$, $|D| = 11.9\ cm^{-1}$ for complexes **1** and **2**, respectively. The compounds were further characterised by UV/Vis and IR spectroscopy. DFT calculations were performed on model complexes $[Co^{II}\{N(OPH_2)(SPH_2)\text{-}O,S\}_2]$ (**3**) and $[Co^{II}\{N(SPH_2)_2\text{-}S,S'\}_2]$ (**4**) to compare the electronic properties of the $CoO_2S_2$ and $CoS_4$ cores.

(© Wiley-VCH Verlag GmbH & Co. KGaA, 69451 Weinheim, Germany, 2007)

## Introduction

The use of iodine or interhalogen charge-transfer adducts of chalcogen donor molecules as oxidising/complexing agents towards zero-valent metals has been attracting some interest in recent years because of their applications both in the recovery of precious metals from waste industrial materials and in the recovery of toxic metals for the environment.[1] Because a great number of iodine adducts with ligands containing sulfur donor atoms have been synthesised, a wide choice of "reagents" is to be considered potentially available for the oxidation/complexation of metals.[2] However, only a few of them have really proved successful to date. Previous studies led us to consider that the overall oxidation/complexation reaction was composed of two distinct processes in which the adduct was accountable for the oxidation of the metal and the ligand/donor for the complexation of the formed metal ion.[3] On the basis of these considerations, the formation of the $I_2$ adduct of tetraphenyldithioimidodiphosphinic acid, $HN(SPPh_2)_2$, $HL_{(SS)}$, represents a successful attempt to join together the donor ability of the phosphane sulfide group and $I_2$. The result is a "robust" adduct, and the intrinsic ability of $HL_{(SS)}$ and its deprotonated form $[N(SPPh_2)_2]^-$, $L_{(SS)}$, to adapt well to the preferred coordination geometries of the metal ion results in a variety of coordination patterns mainly involving S,S′ sulfur chelation. In this respect, the reaction in diethyl ether of the $HL_{(SS)}\cdot I_2$ adduct with a variety of metal powders − Au, Co, Cu, In, Pd and Sb − and liquid Hg allowed their oxidation and the formation of complexes of the resulting metal ions with the ligand in its anionic form.[1c–1e,4] In the reaction with Hg and Cu, it was also possible to separate solid compounds whose crystal structures showed the unusual presence of $HL_{(SS)}$ in a S,S′-isobidentate coordinated fashion, i.e. complexes $[Hg\{HL_{(SS)}\}I_2]$ and $[Cu\{HL_{(SS)}\}_2]I_3$.[1d,5]

As a natural development of this synthetic route, we selected the adduct $HN(OPPh_2)(SPPh_2)\cdot I_2$, $HL_{(OS)}\cdot I_2$, as the oxidising agent on the basis of the ligand containing mixed

[a] Dipartimento di Chimica Inorganica ed Analitica, Università degli Studi di Cagliari,
S.S. 554 Bivio per Sestu, 09042 Cagliari, Italy
[b] Dipartimento di Chimica, Università di Modena e Reggio Emilia,
Via G. Campi 183, 41100 Modena, Italy
[c] Dipartimento di Chimica Strutturale e Stereochimica Inorganica, Università di Milano,
Via G. Venezian 21, 20133 Milano, Italy
[d] Facultatea de Chimie si Inginerie Chimica, Universitatea Babes-Bolyai,
400028 Cluj-Napoca, Romania
[e] Institut für Anorganische Chemie, Georg-August-Universität Göttingen,
Tammannstrasse 4, 37077 Göttingen, Germany
Supporting information for this article is available on the WWW under http://www.eurjic.org or from the author.

 © 2007 Wiley-VCH Verlag GmbH & Co. KGaA, Weinheim 

hard (O) and soft (S) donor atoms for better ion-complexing adaptability. The chemistry of this ligand has been studied far less than that of $HL_{(SS)}$; according to the complexes reported in the literature, chelation as an O,S-bidentate anionic ligand [$L_{(OS)}$; Scheme 1, structure I] is dominant, but not exclusive, with the S-monodentate coordination mode (Scheme 1, structure II) being adopted in a variety of complexes.[6] To date, no complexes of $HL_{(OS)}$ have been characterised by X-ray crystallographic analysis.

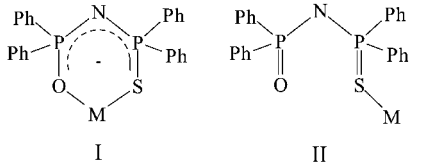


Scheme 1.

This manuscript reports the reactivity of $HL_{(OS)}$ with cobalt powder by using $I_2$ as the activating agent; the structures of complexes $[Co^{II}\{HN(OPPh_2)(SPPh_2)\text{-}O\}_2I_2]$ (**1**) and $[Co^{II}\{N(OPPh_2)(SPPh_2)\text{-}O,S\}_2]$ (**2**), the latter obtained by imido deprotonation of the ligands in **1**, were determined by single-crystal X-ray diffraction analysis. Magnetic parameters were also determined for both complexes. The reactivity of complex **1** towards a few soft metal ions was studied in an attempt to synthesise heterobinuclear complexes; moreover, the protonation reaction of **2** by aqueous hydroiodic acid is reported. In addition, the electronic nature of the $CoO_2S_2$ and $CoS_4$ cores was investigated by DFT calculations on model compounds $[Co^{II}\{N(OPH_2)(SPH_2)\text{-}O,S\}_2]$ and $[Co^{II}\{N(SPH_2)_2\text{-}S,S'\}_2]$.

## Results and Discussion

### Synthesis and Crystal Structure Determination of $[Co^{II}\{HN(OPPh_2)(SPPh_2)\text{-}O\}_2I_2]$ (1)

The reaction between equimolar amounts of the adduct $HL_{(OS)}\cdot I_2$ and Co powder was carried out under a nitrogen atmosphere in anhydrous diethyl ether. After three days of stirring, $^{31}P$ NMR spectroscopic resonances of the $HL_{(OS)}\cdot I_2$ species were not detectable any longer in the mixture. In the course of the reaction, the initial dark-red colour of the solution, typical of the charge-transfer adduct $HL_{(OS)}\cdot I_2$ bearing the S–I–I group, turned to light emerald green, and gradually, a light greenish powder separated from the solution. Elemental analyses of the separated powder agrees with the formed complex having stoichiometry $[Co^{II}\{HL_{(OS)}\}_2I_2]$ (**1**), and both ligand molecules are coordinated, unprecedentedly, in their neutral form, in accordance with the overall reaction in Equation (1).

$$\underset{HL_{(OS)}}{2\ HN(OPPh_2)(SPPh_2)} + I_2 + Co \xrightarrow{Et_2O} \underset{\mathbf{1}}{[CoI_2\{HN(OPPh_2)(SPPh_2)\}_2]} \quad (1)$$

Because of the different bonding modes that are inherently possible for $HL_{(OS)}$, and the unusual formulation of complex **1**, X-ray diffraction analysis was undertaken to firmly establish the coordination pattern at the cobalt centre.

The molecular structure of **1** is reported in Figure 1; selected bond lengths and angles are given in Table 1. The complex contains a tetrahedral $Co^{2+}$ ion surrounded by two iodide anions and by two $HL_{(OS)}$ monodentate ligands coordinated to the metal atom through the oxygen atom. The tetrahedral $CoO_2I_2$ core is slightly distorted with a Co(1)–I(1)–I(1)/Co(1)–O(1)–O(2) dihedral angle of 84.21(7)°; the X–Co–Y (X, Y = I, O) angles are in the range 100.94(11)–

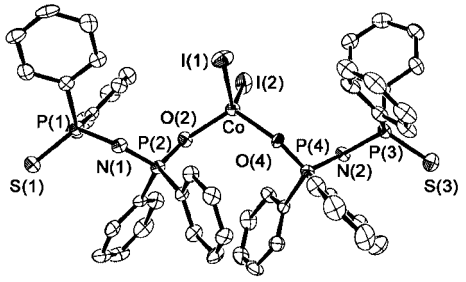


Figure 1. ORTEP drawing and atom-labelling scheme for $[Co^{II}\{HN(OPPh_2)(SPPh_2)\text{-}O\}_2I_2]$ (**1**). Thermal ellipsoids are drawn at 30% probability.

Table 1. Selected bond lengths [Å] and angles [°] for compounds **1** and **2**.

| | | | |
|---|---|---|---|
| Compound **1** | | | |
| Co–O(2) | 1.957(4) | Co–O(4) | 1.975(4) |
| Co–I(1) | 2.5720(8) | Co–I(2) | 2.5704(8) |
| S(1)–P(1) | 1.941(2) | S(3)–P(3) | 1.934(2) |
| O(2)–P(2) | 1.496(4) | O(4)–P(4) | 1.510(4) |
| P(1)–N(1) | 1.693(4) | P(2)–N(1) | 1.642(5) |
| P(3)–N(2) | 1.686(4) | P(4)–N(2) | 1.657(5) |
| I(1)–Co–I(2) | 118.93(3) | I(1)–Co–O(2) | 108.35(11) |
| I(1)–Co–O(4) | 100.94(11) | O(2)–Co–O(4) | 113.19(15) |
| I(2)–Co–O(2) | 102.76(11) | I(2)–Co–O(4) | 113.01(11) |
| Co–O(2)–P(2) | 141.3(2) | Co–O(4)–P(4) | 144.4(2) |
| S(1)–P(1)–N(1) | 115.6(2) | S(3)–P(3)–N(2) | 114.2(2) |
| O(2)–P(2)–N(1) | 113.8(2) | O(4)–P(4)–N(2) | 114.4(2) |
| P(1)–N(1)–P(2) | 131.2(3) | P(3)–N(2)–P(4) | 129.9(3) |
| Compound **2** | | | |
| Co(1)–O(1) | 2.003(4) | Co(1)–O(2) | 1.956(4) |
| Co(1)–S(1) | 2.3199(19) | Co(1)–S(2) | 2.3426(19) |
| S(1)–P(1) | 2.012(2) | S(2)–P(3) | 2.024(2) |
| O(1)–P(2) | 1.598(4) | O(2)–P(4) | 1.526(4) |
| P(1)–N(1) | 1.584(5) | P(3)–N(2) | 1.568(5) |
| P(2)–N(1) | 1.574(5) | P(4)–N(2) | 1.591(5) |
| S(1)···O(1) | 3.553(5) | S(2)···O(2) | 3.439(4) |
| S(1)···S(2) | 3.798(3) | O(1)···O(2) | 3.159(5) |
| S(1)···O(2) | 3.612(4) | O(1)···S(2) | 3.575(4) |
| O(1)–Co(1)–S(1) | 110.34(14) | O(2)–Co(1)–S(2) | 105.93(13) |
| O(2)–Co(1)–S(1) | 115.03(14) | O(1)–Co(1)–S(2) | 110.46(13) |
| O(2)–Co(1)–O(1) | 105.86(17) | S(1)–Co(1)–S(2) | 109.09(7) |
| Co(1)–S(1)–P(1) | 98.67(8) | Co(1)–S(2)–P(3) | 95.82(8) |
| Co(1)–O(1)–P(2) | 122.0(3) | Co(1)–O(2)–P(4) | 125.4(2) |
| S(1)–P(1)–N(1) | 118.0(2) | S(2)–P(3)–N(2) | 117.10(19) |
| O(1)–P(2)–N(1) | 118.9(2) | O(2)–P(4)–N(2) | 116.8(2) |
| P(1)–N(1)–P(2) | 133.2(3) | P(3)–N(2)–P(4) | 135.5(3) |

 © 2007 Wiley-VCH Verlag GmbH & Co. KGaA, Weinheim 

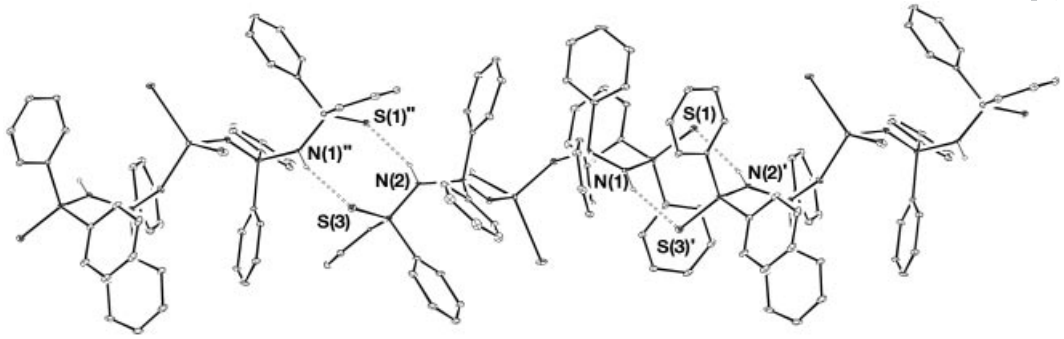


Figure 2. View of the hydrogen bonding pattern for the molecules of compound **1**.

118.93(3)°, and the Co–I and Co–O average distances are 2.5712(8) and 1.966(4) Å, respectively, (Table 1), which are very close to those reported for several monomeric $Co^{II}$ complexes displaying tetracoordination.[7] The O and S atoms of each $HL_{(OS)}$ ligand are on opposite sides with respect to the P–N–P plane and are arranged so that the sulfur atoms are involved in S···H–N hydrogen bonding with adjacent complex molecules to form a polymeric array as shown in Figure 2; the S(1)···N(2)′ (′ = *x*, 3/2 – *y*, 1/2 + *z*) interaction is 3.365(5) Å and the N(1)···S(3)′ is 3.306(4) Å; the S1···H′–N(2)′ and N(1)–H–S(3)′ angles are 161.7 and 155.8°, respectively.

### Reactivity of Complex 1 and Crystal Structure of $[Co^{II}\{N(OPPh_2)(SPPh_2)\text{-}O,S\}_2]$ (2)

The X-ray crystal structure of **1** highlights two interesting features not yet reported: (1) the neutral $HL_{(OS)}$ ligands form units within the complex and (2) the O-monodentate coordination mode at the $Co^{II}$ centre, which leaves the $-PPh_2(S)$ groups in a dangling position. These aspects make compound **1** attractive, as further coordination towards the soft metal centre through the S donor atoms to form heterobinuclear complexes is, in principle, feasible. Moreover, the mono- or dideprotonation of the coordinated ligands in **1** may increase the nucleophilicity of the sulfur donor atoms as a consequence of the delocalisation of the negative charge(s) over the complex. First, the reactivity of **1** was tested towards a soft acceptor species such as molecular iodine, as the formation/separation of 1:1 or 1:2 neutral adducts between **1** and $I_2$ molecules would provide useful information for the bonding ability of the sulfur atoms. The reaction of **1** with increasing amounts of molecular iodine was carried out in MeCN and in the less polar solvent $CH_2Cl_2$. In both cases, the formation of red oils, which failed to crystallise on long standing, was observed. The FT-Raman spectra recorded in the ν(I–I) region at **1**/$I_2$ molar ratios of 1:1 and 1:2 showed an intense peak at 113 $cm^{-1}$ in MeCN and at 110 $cm^{-1}$ in $CH_2Cl_2$ solution, which are indicative of the formation/presence of the $I_3^-$ species. A further addition of $I_2$, according to Raman peaks at 113, 146 and 169 $cm^{-1}$ (MeCN) and 113, 146 and 169 $cm^{-1}$ ($CH_2Cl_2$), led to the formation of complex mixtures.[8]

The reaction of **1** with an equimolar amount of mercury(II) perchlorate or lead(II) nitrate, carried out in MeCN at room temperature, quickly led to the decolouration of the solution with the formation of a mixture of white and brown sticky powders. Conversely, in the reaction with palladium(II) chloride the colour change was not observed, and complex **1** was recovered unreacted when the solution was slowly concentrated in air. Interestingly, when the above reactions were carried out in the presence of aqueous NaOH to obtain a **1**/M/NaOH [M = $Hg^{II}$, $Pb^{II}$ and $Pd^{II}$ ions] reaction molar ratio of 1:1:2, sticky oils including a thin blue powder were observed in all cases. The addition of aqueous NaOH to a solution of complex **1** (**1**/NaOH, 1:2) in $CH_3CN$ readily afforded a deep-blue solution along with a very thin brown powder.[9] From the concentration of the solution a blue powder was obtained, and subsequent crystallisation from $CH_3CN$/hexane yielded well-shaped blue crystals with elemental analyses corresponding to the formulation $[Co\{L_{(OS)}\}_2]$ (**2**).

Solid complexes **1** and **2** and their MeCN solutions are easily recognisable because of their green and blue colour, respectively. Visible absorption spectra of these complexes in the range 500–800 nm are reported in Figure 3; in both compounds, the molar intensities of the d–d electronic transition bands [compound **1**: UV/Vis ($CH_3CN$): $\lambda_{max}$ (ε, $dm^3\,mol^{-1}\,cm^{-1}$) = 661 (172), 696 (346), 734 (432) nm; com-

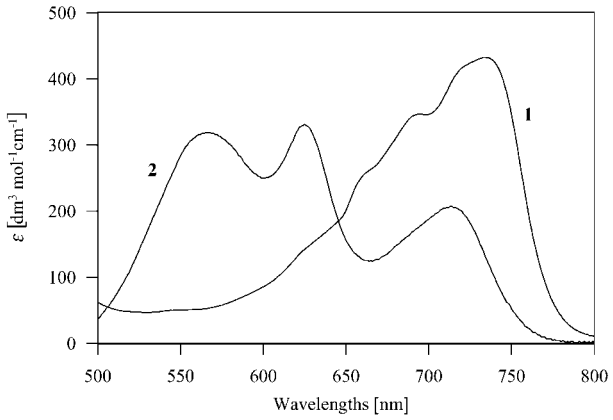


Figure 3. Visible absorption spectra in MeCN of complexes **1** [$\lambda_{max}$ = 734, 696, 661 (sh) nm] and **2** ($\lambda_{max}$ = 715, 625, 566 nm).

 © 2007 Wiley-VCH Verlag GmbH & Co. KGaA, Weinheim 

pound **2**: UV/Vis ($CH_3CN$): $\lambda_{max}$ ($\varepsilon$, $dm^3 mol^{-1} cm^{-1}$) 566 (319), 625 (331), 715 (205) nm] are consistent with $Co^{II}$ bound in a tetrahedral or distorted tetrahedral coordination geometry.[10] The absorption spectra in the visible region, taken after the addition of increasing amounts of aqueous NaOH to a solution of **1** in MeCN are reported in Figure 4; from the analysis of the bands at 734 and 566 nm, related to complexes **1** and **2**, respectively, it results that only a partial conversion of **1** into **2** occurs because of the observed concomitant formation of a thin brown powder.[9] The inset to Figure 4 gives evidence of this fact and shows that a near sixfold excess of NaOH over the amount of **1** is necessary to obtain a 55% yield of **2**.

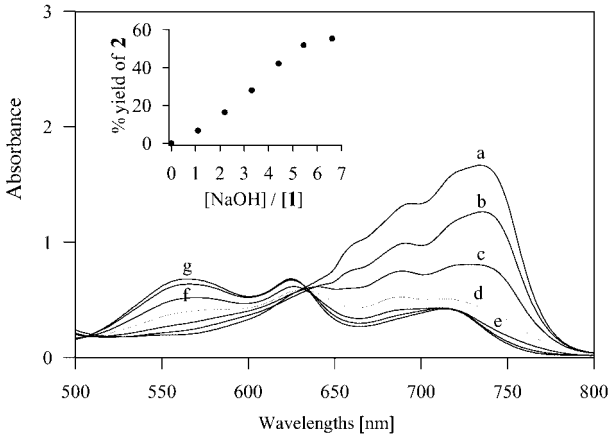


Figure 4. Base-induced conversion of complex **1** into **2**, as monitored by Visible absorption spectroscopy. (a) [Co{$HL_{(OS)}$}$_2I_2$] (**1**), $3.85 \times 10^{-3}$ M in MeCN, 21 °C; and after the addition of NaOH (1.0 M in water) to realise a NaOH/[**1**] molar ratio of (b) 1.1; (c) 2.2; (d) 3.3; (e) 4.4; (f) 5.5 and (g) 6.6. Inset: percent yield of complex **2**, which results from analysis of the bands at 566 and 734 nm, plotted vs. [NaOH]/[**1**] molar ratios.

The molecular structure of **2** (Figure 5 and Table 1) features a $Co^{II}$ ion in a tetrahedral coordination geometry linked through oxygen and sulfur atoms to two bidentate anionic ligands [$N(OPPh_2)(SPPh_2)$]$^-$. As a result, the metal ion is surrounded by a spirobicyclic {$NP_2(S)O$}Co{$O(S)P_2N$} system, with endocyclic S···O bites of 3.439(4)/3.553(5) Å (see Table 1). The tetrahedral $CoO_2S_2$ core is slightly distorted and shows X–Co–Y (X, Y = S, O) angles in the range 105.86(17)–115.03(14)°, Co–O/Co–S average distances of 1.980(6)/2.331(3) Å (Table 1) and a Co(1)–S(1)–O(1)/Co(1)–S(2)–O(2) dihedral angle of 86.28(10)°. The Co–X (X = S, O) bond lengths are very close to those reported for various monomeric $Co^{II}$ complexes with tetra- or octahedral coordination geometry,[11] such as [Co{$N(SPPh_2)_2$}$_2$][4b] [av. Co–S 2.335(2) Å], [$Co(OAc)_2$(etu)$_2$],[12a] [Co–S 2.328(3) Å, av. Co–O 1.957(7) Å; etu = ethylenthiourea] and [$Co(acac)_2(py)_2$][12b] [Co–O 2.034(3) Å; acac = acethylacetonate]. As similarly observed in complexes [Mn{$N(OPPh_2)(SPPh_2)$}$_2$][13a] and [Ni{$N(OPR_2)(SPPh_2)$}$_2$] (R = Ph, Me),[13b] no static disorder effects[13c] in the metal-bonded donor-atom sites are present. Close inspection of the structure shows that the two chemically equivalent, nonplanar $CoO(S)P_2N$ rings exhibit different geometries. The Co(1)–S(2)–P(3)–N(2)–P(4)–O(2) ring in fact, is arranged in a pseudochair conformation with P(4) and S(2) in the apices and dihedral angles between the nearly planar Co(1)–P(3)–N(2)–O(2) array [max. dev. from mean plane ±0.040(2) Å] and Co(1)–S(2)–P(3) and O(2)–P(4)–N(2) planes of 42.08(9) and 13.0(3)°, respectively. Co(1)–S(1)–P(1)–N(1)–P(2)–O(1) indeed shows a highly distorted pseudoboat geometry where S(1) and P(2) act as "bow" and "stern" in comparison to the slightly twisted Co(1)–P(1)–N(1)–P(2) plane [max. dev. ±0.119(2) Å], with P(1)–S(1)–Co(1)–N(1)–P(1)–Co(1)–O(1) and N(1)–P(2)–O(1)–N(1)–P(1)–Co(1)–O(1) dihedral angles of 30.92(15) and 17.7(4)°, respectively. As already observed in the related complex [Co{$N(SPPh_2)$}$_2$], some degree of π-electron delocalisation is present on the $CoO(S)P_2N$ rings, as shown by the P–X (X = S, O) average bond lengths, which increase with respect to [$HN(OPPh_2)(SPPh_2)$][14] by 0.071 Å (P–O) and 0.083 Å (P–S), whereas the average N–P distances decrease by 0.104 Å.

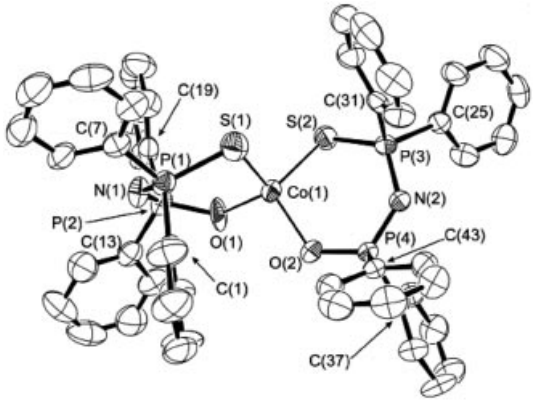


Figure 5. ORTEP drawing and atom-labelling scheme for [$Co^{II}${$N(OPPh_2)(SPPh_2)$-*O*,*S*}$_2$] (**2**). Thermal ellipsoids are drawn at 50% probability.

## Reactivity of Complex 2

In previous papers it was demonstrated that in complexes of the formula M{$L_{(SS)}$}$_2$ (M = Pd, Cu)[4c,5] it was possible to protonate the metal-bound ligands to form the corresponding cationic complexes in which the S,S′ chelation of the ligands was preserved. As a result of the different set of donor atoms in complex **2**, the protonation of the metal-bound ligands may induce different coordination modes at the metal centre: complexes with $CoO_2X_2$ or $CoS_2X_2$ cores and with X being a cobalt-coordinating anion. The formation of the cationic complex [Co{$HL_{(OS)}$}$_2$]$^{2+}$ in which the $CoO_2S_2$ core is preserved cannot be excluded either. In this study the reactivity of **2** was only tested towards HI to verify the feasibility of this synthetic procedure and the nature of the formed complex. The reaction of **2** in MeCN with increasing amounts of hydroiodic acid (55 wt.-% in water) to reach a **2**/HI molar ratio of 1:4 results in the complete disappearance of the visible band at 566 nm, which is characteristic of complex **2**, and the formation of the pattern of

 © 2007 Wiley-VCH Verlag GmbH & Co. KGaA, Weinheim 

bands related to the formation of complex **1**. The diagram reporting the conversion of **2** into complex **1** vs. the molar ratios of HI/**2** shows that such a conversion is almost stoichiometric (ca. 92%) when starting with a HI/**2** molar ratio of 2 (Figure 6).

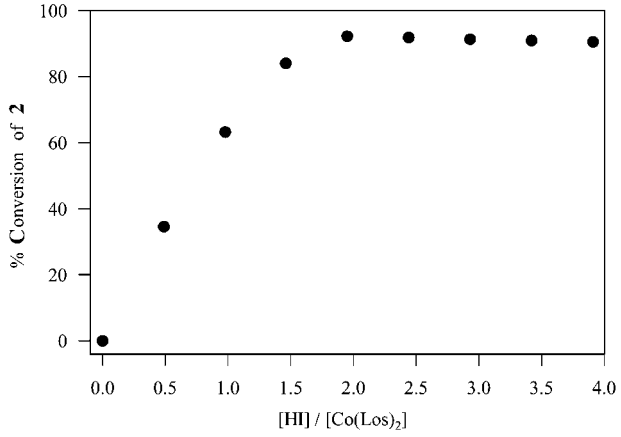


Figure 6. Percent conversion of compound **2** into **1** vs. [HI]/[**2**] molar ratios, which results from analysis of the bands at 566 and 734 nm. $[Co\{L_{(OS)}\}_2]$ (**2**), $7.25 \times 10^{-4}$ M in MeCN, HI (55% in water), 21 °C. HI/[**2**] molar ratios: 0.00, 0.48, 0.97, 1.46, 1.95, 2.44, 2.93, 3.42, 3.91.

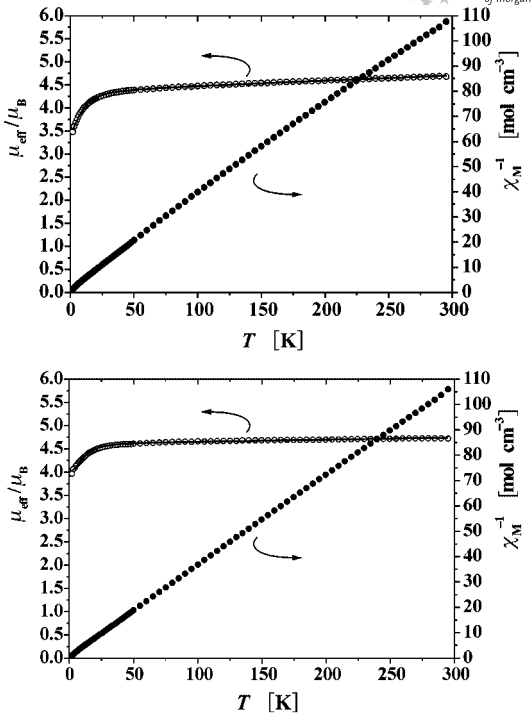


Figure 7. Plots of $\mu_{eff}$ (○) and $\chi_M^{-1}$(●) vs. temperature for **1** (top) and **2** (bottom) at 5000 G; the solid lines represent the fitted calculated curve (see text).

## Magnetic Studies and Theoretical Calculations

Electronic structures of the new complexes were probed by SQUID measurements and DFT calculations. Magnetic susceptibility measurements were carried out for both complexes at two different magnetic fields in a temperature range from 2.0 to 295 K. No significant field dependence was observed for either of the complexes. The temperature dependence of $\chi_M^{-1}$ and the effective magnetic moment $\mu_{eff}$ are shown in Figure 7. The value of $\mu_{eff}$ is around 4.70 or 4.75 $\mu_B$ for **1** or **2**, respectively, at room temperature, which is in the range expected for high-spin ($S$ = 3/2) $Co^{II}$ ions that reside in a tetrahedral environment.[15] The value of $\mu_{eff}$ remains almost constant over a large temperature range but drops to around 3.5 $\mu_B$ at very low temperatures. This may be attributed to zero-field splitting (ZFS) of the $^4A_2$ ground state, which can be quite large for tetrahedral $Co^{II}$ (although smaller than for five- or six-coordinate $Co^{II}$ ions).[15–18] Magnetic parameters were determined by using a fitting procedure to the spin Hamiltonian for axial ZFS and Zeeman interaction as shown in Equation (2).[19]

$$H = D[S_z^2 - 1/3\,S(S+1)] + g\mu_B \vec{S}\cdot\vec{B} \quad (2)$$

Temperature-independent paramagnetism (*TIP*) was included according to $\chi_{calcd.} = \chi + TIP$. For both complexes slightly better agreement with experimental data was obtained when intermolecular interactions were considered in a mean field approach by using a Weiss temperature $\Theta$.[20,21] Best simulation parameters are $g$ = 2.25, $|D|$ = 12.0 $cm^{-1}$, $TIP = 1310 \times 10^{-6}$ $cm^3 mol^{-1}$ and $\Theta$ = 0.11 K for **1** and $g$ = 2.37, $|D|$ = 11.9 $cm^{-1}$, $TIP = 541 \times 10^{-6}$ $cm^3 mol^{-1}$ and $\Theta$ = 0.66 K for **2**. The $|D|$ parameters for **1** and **2** are almost identical and lie in the upper range of typical values for many tetrahedral $Co^{II}$ compounds (7–12 $cm^{-1}$).[15,17] ZFS values around –9.5 $cm^{-1}$ were recently found for two other compounds with a tetrahedral $[CoI_2O_2]$ core, whereas larger values $D$ = –12.4 $cm^{-1}$ and $D$ = –16.7 $cm^{-1}$ were reported for $[CoCl_2(PPh_3)_2]$ and $[CoBr_2(PPh_3)_2]$, respectively.[21] The Weiss temperature $\Theta$ relates to intermolecular interactions $zJ$ of 0.03 $cm^{-1}$ for **1** and 0.18 $cm^{-1}$ for **2**, where $J$ is the interaction parameter between two nearest neighbour magnetic centres and $z$ is the number of nearest neighbours.[22] Intermolecular interactions are apparently very weak if not negligible for both complexes, and they appear to be even smaller for **1** than for **2**. This confirms that no significant coupling occurs through the H-bonding linkages that constitutes the 1D polymeric array in **1**.

DFT calculations (see Experimental Section) were performed on the anionic model ligands $[N(OPH_2)(SPH_2)]^-$, $L'_{(OS)}$, and $[N(SPH_2)_2]^-$, $L'_{(SS)}$, and on the corresponding neutral $Co^{II}$ complexes $[Co\{N(OPH_2)(SPH_2)\text{-}O,S\}_2]$ (**3**) and $[Co\{N(SPH_2)_2\text{-}S,S'\}_2]$ (**4**). The geometry optimisation of these complexes in their quartet electron configuration with the use of the UB3LYP hybrid functional yields bond lengths and angles very close to the structural ones (Tables S1 and S2, Supporting Information). As regards $L'_{(SS)}$, the optimised bond lengths and angles are reproduced well relative to those previously reported with

 © 2007 Wiley-VCH Verlag GmbH & Co. KGaA, Weinheim 

Gaussian 94 at the same level of theory.[4b] In Figure 8, the HOMO and LUMO computed for $L'_{(OS)}$ and $L'_{(SS)}$ are depicted. In both compounds, the HOMO is mainly built of the in-plane p atomic orbitals of the sulfur donor atoms, which are negatively charged; the calculated Mulliken charge for $L'_{(OS)}$ are $Q_S$ = –0.582 e, $Q_O$ = –0.578 e and for $L'_{(SS)}$ the calculated charge $Q_S$ = –0.561 e. It is noteworthy that the calculated $Q_S$ charges show similar values, which suggests a similar bonding ability for the P–S groups in the related anionic ligands; the acidity constant values determined experimentally for the $HL_{(OS)}$ and $HL_{(SS)}$ ligands ($pK_a$ = 5.42 and 5.61, respectively) further support this view. The Mulliken charge calculated on the metal centre at the fully relaxed geometry (Figure 9) shows a marked difference in the $Co^{II}O_2S_2$ and $Co^{II}S_4$ cores ($Q_{Co}$ = 0.436 and 0.023 e in **3** and **4**, respectively), which might be the basis for the different reactivities of the two complexes. This is reflected in a different charge distribution on the S–P–N–P–O and S–P–N–P–S elements that constitute the backbones of complexes **3** and **4**, which show markedly different values, mostly related to the P=O and P=S groups.

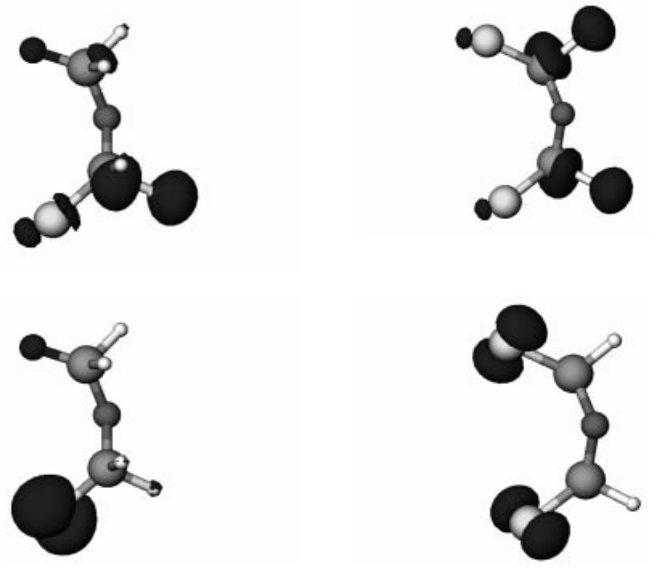

Figure 8. HOMO (bottom row) and LUMO (top row) drawings in $L'_{(OS)}$ (left) and $L'_{(SS)}$ (right). Optimised selected bond lengths and angles: $L'_{(OS)}$: P–S 1.984, P–O 1.504, N–P(O) 1.621, N–P(S) 1.619 Å; P–N–P 128.14°;·$L'_{(SS)}$: P–S 1.980, P–N 1.623 Å; P–N–P 128.20°.

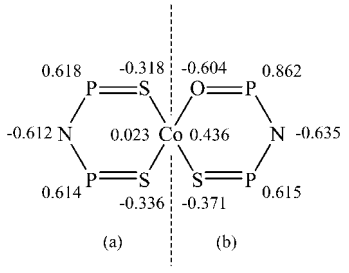


Figure 9. Mulliken charge distribution (e) in model complexes **4** (a) and **3** (b). Hydrogen atoms are omitted for clarity.

## Conclusions

The $Co^{II}$ complex $[Co\{[HN(OPPh_2)(SPPh_2)\text{-}O]_2\}I_2]$ (**1**) was synthesised in a single step from the oxidation of cobalt powder by the adduct $HL_{(OS)}{\cdot}I_2$ in $Et_2O$ prepared in situ. The X-ray crystal structure of this complex shows a $Co^{II}$ ion in a tetrahedral coordination environment with the ligands in a neutral form, which has not been previously observed, and the metal ion is bound through the oxygen atoms and two iodide ions, which completes the $CoI_2O_2$ core. This mode of ligation leaves the $–PPh_2(S)$ groups in a dangling position, which we were unsuccessful in involving in further coordination activity towards "soft" centres. The treatment of **1**, dissolved in MeCN, with NaOH caused the deprotonation of the imido group in the ligands and the formation of $[Co\{[N(OPPh_2)(SPPh_2)\text{-}O,S]_2\}]$ (**2**), in which the $Co^{II}$ ion is found to occupy a tetrahedral coordination environment with a $CoO_2S_2$ core. The magnetic behaviour of **1** and **2** is consistent with tetrahedral high-spin ($S$ = 3/2) $Co^{II}$ possessing a $^4A_2$ ground state with appreciable ZFS ($|D| \approx 12\ cm^{-1}$). When complex **2** is treated with hydroiodic acid, complex **1** is almost quantitatively reobtained. Comparison of the Mulliken charges at the $Co^{II}$ centres in the $CoO_2S_2$ and $CoS_4$ cores reveals that the metal in the latter core is markedly less electropositive (0.437 and 0.023 e, respectively) than the former, which instills different intrinsic reactivity towards nucleophilic agents.

## Experimental Section

**Materials and instrumentation:** Reagents were used as purchased from Aldrich. Diethyl ether was distilled from $LiAlH_4$ shortly before use. IR spectra were measured as KBr (4000–400 $cm^{-1}$) pellets with a Bruker Equinox 55 FTIR spectrometer. FT-Raman spectra were recorded with a Bruker FRS 100/S Fourier transform Raman spectrometer operating with a diode-pumped Nd:YAG exciting laser emitting at 1064 nm. $^{31}P$ NMR spectra were recorded with a Varian Unity 300 MHz spectrometer. The $pK_a$ values of the $HL_{(OS)}$ and $HL_{(SS)}$ ligands were determined by NMR spectroscopic measurements according to the guidelines reported in the IUPAC Technical Report.[23] The $^{31}P$ NMR spectra of 19 different solutions in MeCN/$H_2O$, 4:1 ($5.12 \times 10^{-3}$ M) and 0.1 M $[(Bu)_4N(NO_3)]$, as supporting electrolyte, at (25.0 ± 0.2) °C were recorded in the pH range 2.5–12.0. The pH values were adjusted by the addition of HCl or NaOH (0.1 or 0.5 M). Peak positions are reported relative to $H_3PO_4$ (85%) at $\delta$ = 0.00 ppm used as external reference in a sealed coaxial tube. pH values were measured with a glass electrode. The experimental data were fitted by a sigmoidal equation with the SigmaPlot software (see Supporting Information, section S3). Visible absorption spectra were measured with a Nicolet Evolution 300 spectrophotometer. Susceptibility measurements were carried out with a Quantum-Design MPMS-5S SQUID magnetometer equipped with a 5 T magnet in the range from 295 to 2 K. The powdered samples were contained in a gel bucket and fixed in a nonmagnetic sample holder. Each raw data file for the measured magnetic moment was corrected for the diamagnetic contribution of the sample holder and the gel bucket. Experimental data were corrected for the underlying diamagnetism by using tabulated Pascal constants (incremental method). Simulations of the experimental magnetic data were performed with full-matrix diagonalisation of zero-field splitting

 © 2007 Wiley-VCH Verlag GmbH & Co. KGaA, Weinheim 

and Zeeman interaction according to the appropriate Hamiltonian (see text) and including temperature-independent paramagnetism (*TIP*).[24] The ligand $HN(OPPh_2)(SPPh_2)$, $HL_{(OS)}$, was prepared according to ref.[25] Quantum chemical calculations were carried out at the density functional theory (DFT) level by using the NWChem. 4.7 program[26,27] and ECCE 3.2.5.[28] DFT calculations were attempted on $[Co\{[HN(OPh_2)(SPh_2)\text{-}O]_2\}I_2]$, $[Co\{[HN(SPh_2)(OPh_2)\text{-}S]_2\}I_2]$, $[Co\{N(OPh_2)(SPh_2)\text{-}O,S\}_2]$ (**3**) and $[Co\{N(SPh_2)_2\text{-}S,S'\}_2]$ (**4**) by adopting different functionals and basis sets. Unfortunately, notwithstanding the numerous attempts and different types of SCF convergence methods, a combination of functional and basis set capable to allow SCF convergence for all compounds was not found. We report here the results obtained for **3** and **4** by using Schafer, Horn and Ahlrichs all-electron double-ζ basis sets with polarisation function[29] for the ligand atoms, the LanL2DZ basis set along with effective core potentials[30] for Co,[31] with the three-parameter[32] hybrid B3LYP functional (based on the gradient corrected Becke exchange functional[33] along with the Lee, Yang and Parr correlation functional[34]). All calculations were performed on a Pentium 4 workstation running on a Linux Mandriva One 2006 operating system.

**$[Co\{HN(OPPh_2)(SPPh_2)\text{-}O\}_2I_2]$ (1).** A mixture of $HL_{(OS)}$ (0.100 g, 0.230 mmol) and $I_2$ (0.058 g, 0.230 mmol) in diethyl ether (200 mL) was stirred at 25 °C under an atmosphere of $N_2$ until the reagents were completely dissolved. Cobalt metal powder (< 2 μ; 0.014 g, 0.237 mmol) was added while stirring. This was continued at room temperature for ca. 4 d. The resulting emerald green solid was collected by suction filtration, washed with a mixture of $CH_2Cl_2$/*n*-hexane (1:5) and dried in vacuo. Yield: 0.074 g (26.4%). M.p. > 250 °C. IR (KBr): $\tilde{\nu}$ = 2632 (w), 1436 (vs), 1328 (m), 1312 (s), 1172 (s), 1151 (s), 1129 (s), 1099 (s), 1026 (w), 998 (w), 998 (s), 944 (s), 789 (s), 747 (s), 728 (s), 688 (s), 646 (s), 614 (w), 569 (m), 523 (m), 487 (m) $cm^{-1}$. UV/Vis ($CH_3CN$): $\lambda_{max}$ ($\varepsilon$, $dm^3\,mol^{-1}\,cm^{-1}$) = 661 (172), 696 (346), 734 (432) nm. $C_{48}H_{42}CoI_2N_2O_2P_4S_2$ (1179.57): calcd. C 48.87, H 3.59, N 2.37, S 5.44; found C 49.1, H 3.7, N 2.4, S 5.2.

**$[Co\{N(OPPh_2)(SPPh_2)\text{-}O,S\}_2]$ (2)**. To a stirred solution of compound **1** (0,100 g, 0.084 mmol) dissolved in $CH_3CN$ (25 mL) was slowly added NaOH (1 M, 180 μL, 0.180 mmol). The deep-blue solution was concentrated to separate well-shaped blue crystals that were washed with $CH_2Cl_2$/*n*-hexane (1:5) and dried in vacuo. Yield: 0.064 g (83%). M.p. 176 °C. IR (KBr): $\tilde{\nu}$ = 3054 (w), 1636 (m), 1482 (w), 1436 (s), 1236 (vs), 1233 (vs), 1178 (s), 1121 (s), 1045 (vs), 1025 (s), 998 (m), 799 (w), 745 (s), 725 (vs), 692 (vs), 618 (w), 575 (vs), 548 (vs), 419 (s), 506 (s) $cm^{-1}$. UV/Vis ($CH_3CN$): $\lambda_{max}$ ($\varepsilon$, $dm^3\,mol^{-1}\,cm^{-1}$) = 566 (319), 625 (331), 715 (205) nm. $C_{48}H_{40}CoN_2O_2P_4S_2$ (923.75): calcd. C 62.41, H 4.36, N 3.03, S 6.94; found C 63.0, H 4.4, N 3.0, S 7.1.

**X-ray Crystallography:** Intensities were corrected for Lorentz-polarisation effects and absorption effects by employing multiscan SADABS for compound **1**,[35] and $\psi$-scan[36a] for compound **2**. Both structures were solved by direct methods (SIR-97)[36b] and refined on $F_o^2$ with the SHELXL-97[36c] program (WINGX suite[36d]). All non-hydrogen atoms were refined with anisotropic displacement parameters. All H atoms, seen on the $\Delta F$ maps, were introduced in the structure model. For compound **1** they were allowed to ride on the corresponding C atoms, whereas for compound **2** they were refined with isotropic displacement parameters. Alternative element type assignments to the donor atoms of the chelating ligands were carefully tested, but led to unphysical variation of displacement parameters across the ligand and discarded. The maximum and minimum residual electron density on the final $\Delta F$ map are 1.344 and –1.050 e $Å^{-3}$, respectively for compound **1** and 0.527 and –0.447 e $Å^{-3}$ for compound **2**.

CCDC-641240 and -641241 contain the supplementary crystallographic data for this paper. These data can be obtained free of charge from The Cambridge Crystallographic Data Centre via www.ccdc.cam.ac.uk/data_request/cif.

**Crystal data for 1:** $C_{48}H_{42}CoI_2N_2O_2P_4S_2$, $M$ = 1179.57, orthorhombic, $a$ = 21.892(2) Å, $b$ = 18.590(2) Å, $c$ = 24.046(2) Å, $U$ = 9786.1(16) $Å^3$, $T$ = 294(2) K, space group *P*bca (no. 61), $Z$ = 8, $\mu$ = (Mo-$K_\alpha$) 1.868 $mm^{-1}$. 85740 reflections (9660 unique) were collected at room temperature in the range $3.22 \le 2\theta \le 52.20°$ by employing a 0.10 × 0.10 × 0.05 mm crystal mounted on a Siemens SMART CCD diffractometer. 5768 reflections ($R_{int}$ = 0.0807), final $R_1$ [$wR_2$] values of 0.0506 [0.1306] on $I > 2\sigma(I)$ [all data], with GoF = 0.954 for 550 parameters.

**Crystal data for 2:** $C_{48}H_{40}CoN_2O_2P_4S_2$, $M$ = 923.75, monoclinic, $a$ = 12.511(2) Å, $b$ = 18.272(5) Å, $c$ = 19.599(3) Å, $\beta$ = 100.495(10)°, $U$ = 4405.3(16) $Å^3$, $T$ = 298(2) K, space group $P2_1/c$ (no. 14), $Z$ = 4, $\mu$ = (Mo-$K_\alpha$) 0.671 $mm^{-1}$. 7551 reflections (6064 unique) were collected at room temperature in the range $4.22 \le 2\theta \le 46.00°$ by employing a 0.26 × 0.22 × 0.08 mm crystal mounted on a P4RA Siemens automatic diffractometer. 7548 reflections ($R_{int}$ = 0.0563), final $R_1$ [$wR_2$] values of 0.0606 [0.1471] on $I > 2\sigma(I)$ [all data], with GoF = 1.020 for 692 parameters and 4 restraints.

**Supporting Information** (see footnote on the first page of this article): Optimised geometries of complexes **3** and **4** in Cartesian orthogonal coordinate format, as derived from DFT calculations, and $pK_a$ determination of $HN(OPPh_2)(SPPh_2)$ and $HN(SPPh_2)(SPPh_2)$.

## Acknowledgments

Thanks are expressed to Prof. Antonio C. Fabretti (Dipartimento di Chimica, Università di Modena) for helpful discussions and to the "Centro Interdipartimentale Grandi Strumenti (C.I.G.S.)" of the University of Reggio Emilia for providing P4-RA Siemens X-ray equipment. Financial support from the National University Research Council (CNCSIS, Romania; Research project No. A-1456/2007) is greatly appreciated.

[1] a) F. Bigoli, P. Deplano, M. L. Mercuri, M. A. Pellinghelli, G. Pintus, A. Serpe, E. F. Trogu, *Chem. Commun.* **1998**, 2351–2352; b) F. Bigoli, M. C. Cabras, P. Deplano, M. L. Mercuri, L. Marchiò, A. Serpe, E. F. Trogu, *Eur. J. Inorg. Chem.* **2004**, *5*, 960–963; c) G. L. Abbati, M. C. Aragoni, M. Arca, F. A. Devillanova, C. Fabretti, A. Garau, F. Isaia, V. Lippolis, G. Verani, *Dalton Trans.* **2003**, 1515–1519; d) M. C. Aragoni, M. Arca, M. B. Carrea, F. Demartin, F. A. Devillanova, A. Garau, F. Isaia, V. Lippolis, G. Verani, *Eur. J. Inorg. Chem.* **2004**, 4660–4668; e) M. C. Aragoni, M. Arca, M. B. Carrea, F. Demartin, F. A. Devillanova, A. Garau, F. Isaia, V. Lippolis, M. Marcelli, C. Silvestru, G. Verani, *Eur. J. Inorg. Chem.* **2005**, 589–596.

[2] a) M. C. Aragoni, M. Arca, F. A. Devillanova, A. Garau, F. Isaia, V. Lippolis, G. Verani, *Coord. Chem. Rev.* **1999**, *184*, 271–290; b) M. C. Aragoni, M. Arca, F. Demartin, F. A. Devillanova, A. Garau, F. Isaia, V. Lippolis, G. Verani, *Trends in Inorg. Chem.* **1999**, *6*, 1–18.

[3] V. Lippolis, F. Isaia, *Handbook of Chalcogen Chemistry* (Ed.: F. A. Devillanova), RSC, Cambridge, UK, **2007**, ch. 8.2, pp. 477–496.

[4] a) M. Arca, F. A. Devillanova, A. Garau, F. Isaia, V. Lippolis, G. Verani, G. L. Abbati, A. Cornia, *Z. Anorg. Allg. Chem.* **1999**, *625*, 517–520; b) M. C. Aragoni, M. Arca, A. Garau, F. Isaia, V. Lippolis, G. Abbati, C. Fabretti, *Z. Anorg. Allg. Chem.*

 © 2007 Wiley-VCH Verlag GmbH & Co. KGaA, Weinheim 

**2000**, *626*, 1454–1459; c) G. L. Abbati, M. C. Aragoni, M. Arca, C. Fabretti, F. A. Devillanova, A. Garau, F. Isaia, V. Lippolis, G. Verani, *J. Chem. Soc. Dalton Trans.* **2001**, 1105–1110.
[5] M. C. Aragoni, M. Arca, M. B. Carrea, F. Demartin, F. A. Devillanova, A. Garau, M. B. Hursthouse, F. Isaia, V. Lippolis, G. Verani, *Eur. J. Inorg. Chem.* **2006**, *1*, 200–206.
[6] I. Haiduc, *Comprehensive Co-ordination Chemistry II: From Biology to Nanotechnology* (Ed.: A. B. P. Lever), Elsevier, Amsterdam **2003**, vol. 1, pp. 323–347.
[7] a) P. T. Ndifon, C. A. McAuliffe, A. G. Mackie, R. G. Pritchard, *Inorg. Chim. Acta* **1998**, *282*, 25–29; b) S. K. Bauer, C. J. Wilis, N. C. Payne, *Acta Crystallogr., Sect. C: Cryst. Struct. Commun.* **1995**, *51*, 586–588; c) S. A. Cotton, V. Franckevicius, J. Fawcett, *Transition Met. Chem.* **2002**, *27*, 38–41.
[8] A. J. Blake, F. A. Devillanova, R. O. Gould, W.-S. Lee, V. Lippolis, S. Parsons, C. Radek, M. Schroder, *Chem. Soc. Rev.* **1998**, *27*, 195–216.
[9] This solid was insoluble in most common organic solvents and in water. Elemental analyses: C 9.4, H 2.1.
[10] F. A. Cotton, D. M. L. Goodgame, M. Goodgame, *J. Am. Chem. Soc.* **1961**, *83*, 4690–4699.
[11] a) L. M. Gilby, B. Piggott, *Polyhedron* **1999**, *18*, 1077–1082; b) C. Silvestru, R. Rosler, J. E. Drake, J. Yang, G. Espinosa-Perez, I. Haiduc, *J. Chem. Soc. Dalton Trans.* **1998**, 73–78; c) C. Silvestru, R. Rosler, I. Haiduc, R. Cea-Olivares, G. Espinosa-Perez, *Inorg. Chem.* **1995**, *34*, 3352–3354.
[12] a) E. M. Holt, S. L. Holt, K. J. Watson, *J. Am. Chem. Soc.* **1970**, *92*, 2721–2724; b) R. C. Elder, *Inorg. Chem.* **1968**, *7*, 1117–1123.
[13] a) I. Szekely, C. Silvestru, J. E. Drake, G. Balasz, S. I. Farcas, I. Haiduc, *Inorg. Chim. Acta* **2000**, *299*, 247–252; b) A. Silvestru, D. Bîlc, R. Rösler, J. E. Drake, I. Haiduc, *Inorg. Chim. Acta* **2000**, *305*, 106–110; c) M. B. Robin, P. Day, *Adv. Inorg. Chem. Radiochem.* **1967**, *10*, 247–422.
[14] J. Yang, J. E. Drake, S. Hernandez-Ortega, R. Rösler, C. Silvestru, *Polyhedron* **1997**, *16*, 4061–4071.
[15] R. L. Carlin, *Magnetochemistry*, Springer, Berlin, Heidelberg, **1986**.
[16] R. L. Carlin, *Science* **1985**, *227*, 1291–1295.
[17] M. W. Makkinen, M. B. Yim, *Proc. Natl. Acad. Sci. USA* **1981**, *78*, 6221–6225.
[18] Because of strong paramagnetic anisotropy, orientation effects were observed when higher external magnetic fields were applied or when a nonpowdered crystalline material was used (partial alignment of the crystals with the applied field because of a dominance of the parallel susceptibility over the perpendicular component).
[19] $D$ is the axial ZFS parameter, $\mu_B$ is the Bohr magneton and $g$ is the Landé factor. Inclusion of a rhombic $E$ term in the ZFS leads to very low values for the rhombic distortion ($E/D < 0.01$).
[20] O. Kahn, *Molecular Magnetism*, VCH, Weinheim, **1993**.
[21] T. Avilés, A. Dinis, J. O. Gonçalves, V. Félix, M. J. Calhorda, A. Prazeres, M. G. B. Drew, H. Alves, R. T. Henriques, V. Da Gama, P. Zanello, M. Fontani, *J. Chem. Soc. Dalton Trans.* **2002**, 4595–4602.
[22] Weiss temperature defined as $\Theta = zJS(S + 1)/3k$.
[23] K. Popov, H. Rönkkömäki, L. H. J. Lajunen, *Pure Appl. Chem.* **2006**, *78*, 663–675.
[24] E. Bill, *julX Program*, Max-Planck Institute for Bioinorganic Chemistry, Mülheim, Ruhr, Germany.
[25] A. Schmidpeter, H. Groeger, *Chem. Ber.* **1967**, *100*, 3979–3991.
[26] E. Aprà, T. L. Windus, T. P. Straatsma, E. J. Bylaska, W. de Jong, S. Hirata, M. Valiev, M. Hackler, L. Pollack, K. Kowalski, R. Harrison, M. Dupuis, D. M. A. Smith, J. Nieplocha, V. Tipparaju, M. Krishnan, A. A. Auer, E. Brown, G. Cisneros, G. Fann, H. Fruchtl, J. Garza, K. Hirao, R. Kendall, J. Nichols, K. Tsemekhman, K. Wolinski, J. Anchell, D. Bernholdt, P. Borowski, T. Clark, D. Clerc, H. Dachsel, M. Deegan, K. Dyall, D. Elwood, E. Glendening, M. Gutowski, A. Hess, J. Jaffe, B. Johnson, J. Ju, R. Kobayashi, R. Kutteh, Z. Lin, R. Littlefield, R. X. Long, B. Meng, T. Nakajima, S. Niu, M. Rosing, G. Sandrone, M. Stave, H. Taylor, G. Thomas, J. van Lenthe, A. Wong, Z. Zhang, *NWChem: A Computational Chemistry Package for Parallel Computers (version 4.7)*, Pacific Northwest National Laboratory, Richland, Washington, **2005**.
[27] R. A. Kendall, R. E. Aprà, D. E. Bernholdt, E. J. Bylaska, M. Dupuis, G. I. Fann, R. J. Harrison, J. Ju, J. A. Nichols, J. Nieplocha, T. P. Straatsma, T. L. Windus, A. T. Wong, *Comput. Phys. Commun.* **2000**, *128*, 260–283.
[28] G. Black, B. Didier, T. Elsethagen, D. Feller, D. Gracio, M. Hackler, S. Havre, D. Jones, E. Jurrus, T. Keller, C. Lansing, S. Matsumoto, B. Palmer, M. Peterson, K. Schuchardt, E. Stephan, L. Sun, H. Taylor, G. Thomas, E. Vorpagel, T. Windus, C. Winters, *Ecce: A Problem Solving Environment for Computational Chemistry (version 3.2.5)*, Pacific Northwest National Laboratory, Richland, Washington, **2006**.
[29] A. Schafer, H. Horn, R. Ahlrichs, *J. Chem. Phys.* **1992**, *97*, 2571–2576.
[30] P. J. Hay, W. R. Wadt, *J. Chem. Phys.* **1985**, *82*, 284–298.
[31] Basis sets were obtained from the Extensible Computational Chemistry Environment Basis Set Database (version 02/25/04), as developed and distributed by the Molecular Science Computing Facility, Environmental and Molecular Sciences Laboratory, which is part of the Pacific Northwest Laboratory, P. O. Box 999, Richland, Washington 99352, USA, and funded by the U. S. Department of Energy. The Pacific Northwest Laboratory is a multiprogram laboratory operated by Battelle Memorial Institute for the U. S. Department of Energy under contract DE–AC06–76RLO 1830.
[32] A. D. Becke, *J. Chem. Phys.* **1993**, *98*, 5648–5652.
[33] A. D. Becke, *Phys. Rev. A* **1988**, *38*, 3098–3100.
[34] C. Lee, W. Yang, R. G. Parr, *Phys. Rev. B* **1988**, *37*, 785–789.
[35] *SADABS: Area–Detector Absorption Correction*, Siemens Industrial Automation, Inc., Madison, WI, **1996**.
[36] a) A. C. T. North, D. C. Phillips, F. S. Mathews, *Acta Crystallogr., Sect. A* **1968**, *24*, 351–359; b) A. Altomare, M. C. Burla, M. Camalli, G. L. Cascarano, C. Giacovazzo, A. Guagliardi, A. G. G. Moliterni, G. Polidori, R. Spagna, *J. Appl. Crystallogr.* **1999**, *32*, 115–119; c) G. M. Sheldrick, *SHELX97: Programs for Crystal Structure Analysis (Release 97–2)*, University of Göttingen, Germany, **1998**; d) L. J. Farrugia, *J. Appl. Crystallogr.* **1999**, *32*, 837–838.

Received: April 23, 2007
Published Online: August 20, 2007

 © 2007 Wiley-VCH Verlag GmbH & Co. KGaA, Weinheim 

DOI: 10.1002/ejic.200700451

# Axial Coordination of Porphyrinatocobalt(II) Complexes with Bis(pyridinolato)silicon(IV) Phthalocyanines

**Xuebing Leng[a] and Dennis K. P. Ng*[a]**

**Keywords:** Phthalocyanines / Porphyrins / Axial coordination / UV/Vis spectroscopy

Treatment of dichlorosilicon(IV) phthalocyanine with 3- or 4-hydroxypyridine in the presence of pyridine in toluene gave the corresponding bis(pyridinolato)silicon(IV) phthalocyanine complexes SiPc(3-OPy)$_2$ (**1**) or SiPc(4-OPy)$_2$ (**2**), respectively, which were spectroscopically and structurally characterized. As shown by electronic absorption spectroscopy, these compounds axially bind to *meso*-tetraphenylporphyrinatocobalt(II) [Co(TPP) (**3**)] and *meso*-tetrakis(3,5-di-*tert*-butylphenyl)porphyrinatocobalt(II) [Co(TBPP) (**4**)] with the two pyridyl ligands forming the corresponding mixed phthalocyanine–porphyrin triads. The binding constants $K_1$ between the 4-pyridyl phthalocyanine **2** and the porphyrinatocobalt(II) complexes ($1.1–1.2 \times 10^4$ M$^{-1}$) are about threefold higher than those for the 3-pyridyl counterpart **1**. The heterodyads **2**·**3** and **2**·**4** were isolated by column chromatography and characterized by mass and absorption spectroscopy.
(© Wiley-VCH Verlag GmbH & Co. KGaA, 69451 Weinheim, Germany, 2007)

## Introduction

Phthalocyanines and porphyrins are two important classes of functional dyes. Owing to their unique and intriguing properties, these macrocycles have found widespread applications in various disciplines ranging from materials science, catalysis, nanotechnology to medicine.[1] Despite their structural similarities, these two classes of π systems exhibit very different optical and electronic properties making them useful in different areas. A hybrid system containing both of these macrocycles may combine their advantageous properties and improve the overall performance. One obvious example is the complementary major absorptions of phthalocyanines (650–700 nm) and porphyrins (400–450 nm) in the visible region. Mixed phthalocyanine–porphyrin assemblies can absorb strongly over a large part of the solar spectrum, which can facilitate various light-induced processes. This property is important in applications such as light harvesting, photovoltaics, and molecular photonics.[2] A substantial number of mixed phthalocyanine–porphyrin arrays have been reported.[3] Apart from a covalent linkage the two types of macrocycles can also be linked by a metal center in the form of sandwich-type complexes,[4] by a bridging nitrido, oxo, chloro, or hydroxo ligand to form cofacial complexes[5] or by electrostatic interactions to form face-to-face aggregates.[3,6] The use of host-guest interactions to assemble these macrocycles has also been reported recently.[7] Although axial coordination has been widely used to construct various multiporphyrin systems,[8] the use of this strategy to build mixed phthalocyanine–porphyrin scaffolds remains little studied.[9] We have recently prepared the bis(4-pyridinolato)silicon(IV) phthalocyanine (**2**), which can axially bind to various tetrapyrrolatozinc(II) derivatives forming the corresponding 1:2 or 1:1 molecular assemblies.[9b] We describe herein an extension of this work using **2** as well as the 3-pyridyl analogue **1** as the cores to complex with porphyrinatocobalt(II) complexes. The relatively strong cobalt–pyridine binding interactions allow the isolation of the heterodyads.

## Results and Discussion

The preparation of bis(3-pyridinolato)silicon(IV) phthalocyanine complex **1** was similar to that of the 4-pyridyl analogue **2** (Figure 1).[9b] It involved a ligand-substitution reaction of dichlorosilicon(IV) phthalocyanine with 3-hydroxypyridine in the presence of pyridine in toluene. Both **1** and **2** were soluble in common organic solvents and could be purified readily by column chromatography giving a comparable yield (75% and 72%, respectively). The porphyrinatocobalt(II) complexes Co(TPP) (**3**) and Co(TBPP) (**4**) (Figure 1) were prepared by cobaltation of the corresponding metal-free porphyrins.[10]

Both compounds **1** and **2** were fully characterized by using various spectroscopic methods and X-ray diffraction analyses. Single crystals of **1** were grown by slow diffusion of nitrobenzene into a $CHCl_3$ solution of **1**. The compound cocrystallized with two molecules of nitrobenzene in the triclinic system. As shown in part a of Figure 2, the structure contains an inversion center at the silicon center relating

[a] Department of Chemistry and Center of Novel Functional Molecules, The Chinese University of Hong Kong, Shatin, N.T., Hong Kong, China
Fax: +852-2603-5057
E-mail: dkpn@cuhk.edu.hk
Supporting information for this article is available on the WWW under http://www.eurjic.org or from the author.

 © 2007 Wiley-VCH Verlag GmbH & Co. KGaA, Weinheim 

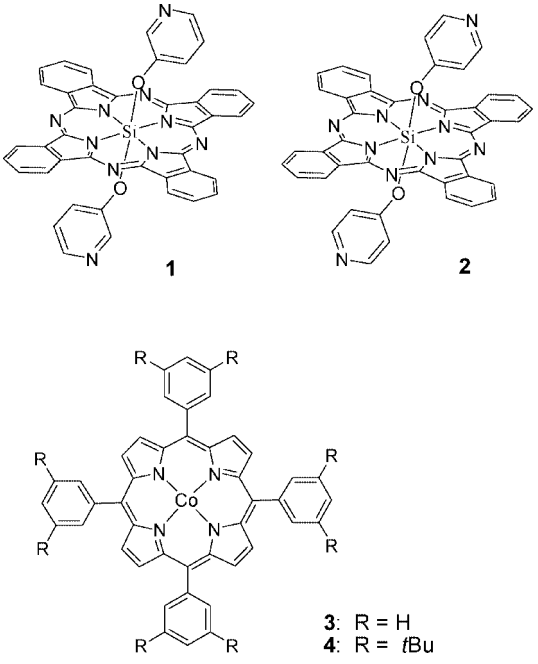


Figure 1. Structures of the bis(pyridyl) phthalocyanines **1** and **2**, and the porphyrinatocobalt(II) complexes **3** and **4**.

the two halves of the molecule. The silicon center is hexacoordinate with four isoindole nitrogen atoms of the phthalocyanine ring and two oxygen atoms of the pyridinolato ligands. The Si–O [1.740(2) Å] and average Si–N [1.912(4) Å] bond lengths as well as the other structural parameters are unexceptional.

Single crystals of **2** were grown by slow diffusion of MeOH into a $CHCl_3$ solution of **2**. The compound crystallized in the monoclinic system. The molecular structure of **2** (Figure 2, b) also contains an inversion center. The Si–O [1.715(2) Å] and average Si–N [1.910(4) Å] bond lengths are comparable with those of **1**. The phthalocyanine rings of **1** and **2** are essentially planar with a dihedral angle of 42.5° and 57.5°, respectively, between the phthalocyanine N(isoindole)$_4$ plane and the pyridyl ring. In both structures, particularly for **2**, the pyridyl-nitrogen atoms point outward favoring the complexation process.

The complexation of SiPc(4-OPy)$_2$ (**2**) and Co(TPP) (**3**) was first studied by electronic absorption spectroscopy. Figure 3 shows the UV/Vis spectra of mixtures of these two compounds in different ratios in $CHCl_3$, where the total concentration was fixed at 5.0 μM. It can be seen that as the mole fraction of SiPc(4-OPy)$_2$ (**2**) increases, the phthalocyanine B band at 354 nm, Q band at 684 nm, and vibronic band at 614 nm all increase in intensity. The porphyrin Soret band at 410 nm becomes attenuated and a new band at

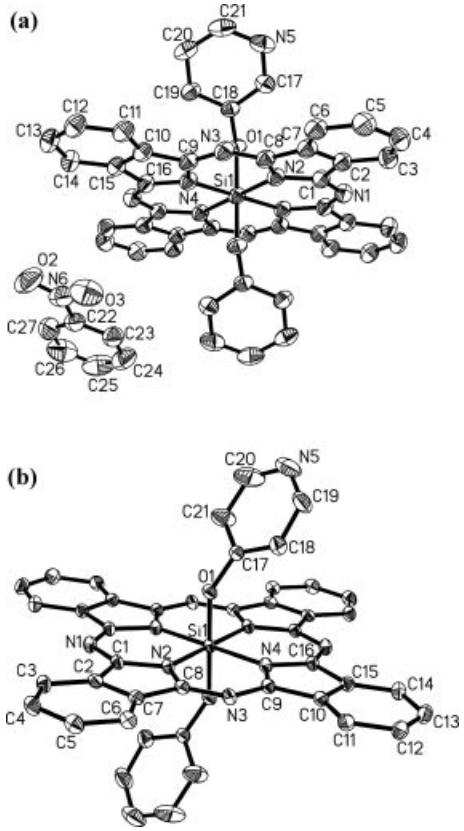


Figure 2. Molecular structures of (a) SiPc(3-OPy)$_2$ (**1**) and (b) SiPc(4-OPy)$_2$ (**2**) showing the 30% probability thermal ellipsoids for all non-hydrogen atoms.

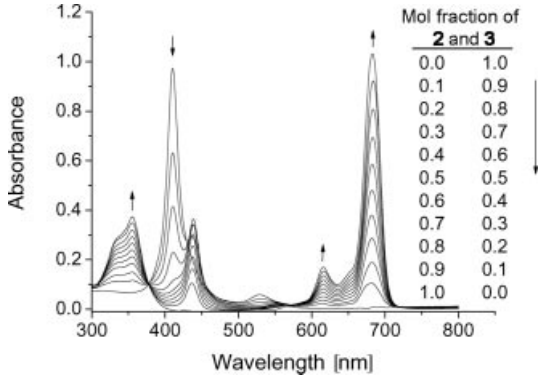


Figure 3. Absorption spectra of mixtures of SiPc(4-OPy)$_2$ (**2**) and Co(TPP) (**3**) in $CHCl_3$. The total concentration of the two compounds was fixed at 5.0 μM.

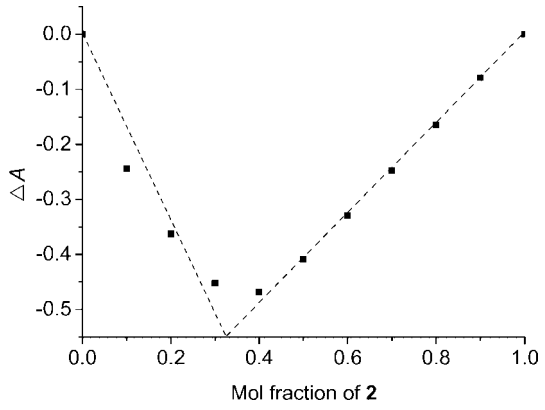


Figure 4. Job's plot for the complexation of SiPc(4-OPy)$_2$ (**2**) and Co(TPP) (**3**) in $CHCl_3$ obtained by monitoring the band at 410 nm.

 © 2007 Wiley-VCH Verlag GmbH & Co. KGaA, Weinheim 

435 nm appears, which can be attributed to the axially bound species. The corresponding Job's plot[11] (Figure 4), obtained by monitoring the band at 410 nm, shows a minimum when the mole fraction of **2** is about 0.34. This suggests a 1:2 stoichiometry for **2** and **3**, and the formation of the heterotriad **2**·(**3**)$_2$.

Figure 5 shows the changes of the Soret band of Co(TPP) (**3**), fixed at a concentration of 4.5 μM, upon titration with SiPc(4-OPy)$_2$ (**2**) (from 75 to 260 μM) in $CHCl_3$. The corresponding solution of **2** with the same concentration was used as the reference in recording the spectra. Under these conditions the phthalocyanine SiPc(4-OPy)$_2$ (**2**) was in great excess. Therefore, the 1:1 complex was predominantly formed and the Benesi–Hildebrand equation [Equation (1)] could be applied to determine the binding constant $K_1$.[12]

$$\frac{b}{\Delta A} = \frac{1}{S_t K_1 \Delta\varepsilon[L]} + \frac{1}{S_t \Delta\varepsilon} \quad (1)$$

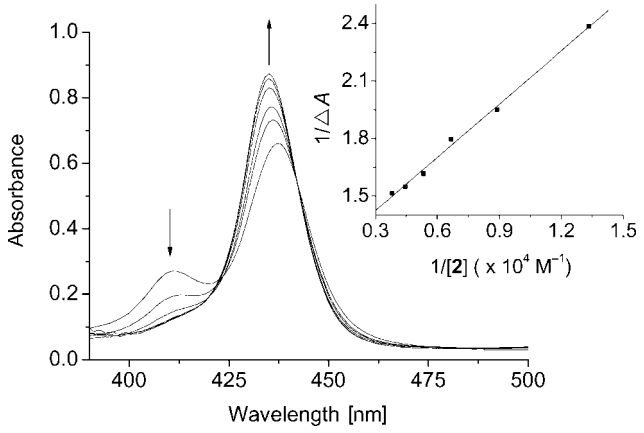


Figure 5. Changes in the UV/Vis spectrum of Co(TPP) (**3**) (4.5 μM) upon titration with SiPc(4-OPy)$_2$ (**2**) (from 75 to 260 μM) in $CHCl_3$. The inset shows the corresponding Benesi–Hildebrand plot obtained by monitoring the change in absorbance at 435 nm.

where $b$ is the optical path length (1 cm); $\Delta A$ is the change in absorbance at 435 nm, where the largest change was observed; $S_t$ is the total concentration of substrate (i.e. **3**); [L] is the concentration of ligand [i.e. **2**, which can be approximated as $L_t$ (the total concentration of ligand) where $L_t >> S_t$]; and $\Delta\varepsilon = \varepsilon_{11} - \varepsilon_S - \varepsilon_L$, where $\varepsilon_{11}$, $\varepsilon_S$, and $\varepsilon_L$ are the molar absorptivities of the 1:1 complex, **3**, and **2** at 435 nm, respectively. A plot of $1/\Delta A$ vs. 1/[**2**] (inset of Figure 5) gave a straight line from which the value of $K_1$ was determined to be $(1.2 \pm 0.1) \times 10^4$ M$^{-1}$. Similarly, a linear relationship was also found in the Scott or Scatchard plot giving virtually the same $K_1$ value.[12]

The complexation of other systems including SiPc(4-OPy)$_2$ (**2**) with Co(TBPP) (**4**), as well as the 3-pyridyl analogue **1** with these two porphyrinatocobalt(II) complexes, was investigated by the same approach. All the systems gave very similar spectral changes except the complexation of SiPc(3-OPy)$_2$ (**1**) with Co(TBPP) (**4**), for which the band ascribed to the axially bound species appeared as a shoulder at ca. 440 nm instead of a distinct signal (see Figure S1 in the Supporting Information). The results showed that both phthalocyanines **1** and **2** bind to porphyrinatocobalt(II) complexes **3** and **4** in a 1:2 manner proceeding in a stepwise fashion as shown in Figure 6.

Table 1 summarizes the binding constants ($K_1$) for these systems determined by absorption spectroscopy. The corresponding data for the complexation of 3- and 4-hydroxypyridine (3-OHPy and 4-OHPy) with Co(TPP) (**3**) were also determined by the same method and are included for comparison. It can be seen that the values for the 4-pyridinolato complex **2** are about three times larger than those of the 3-pyridinolato counterpart **1**. The addition of *tert*-butyl groups on the *meso*-phenyl substituents of porphyrin does not have a significant influence on the binding constants. The stronger binding for **2** compared with that of **1** can be attributed to the fact that the 4-pyridinolato ligand is a better σ donor than the 3-pyridinlolato analogue (because of the presence of the resonance form A as shown in Figure S2 in the Supporting Information). In addition, the 4-pyridin-

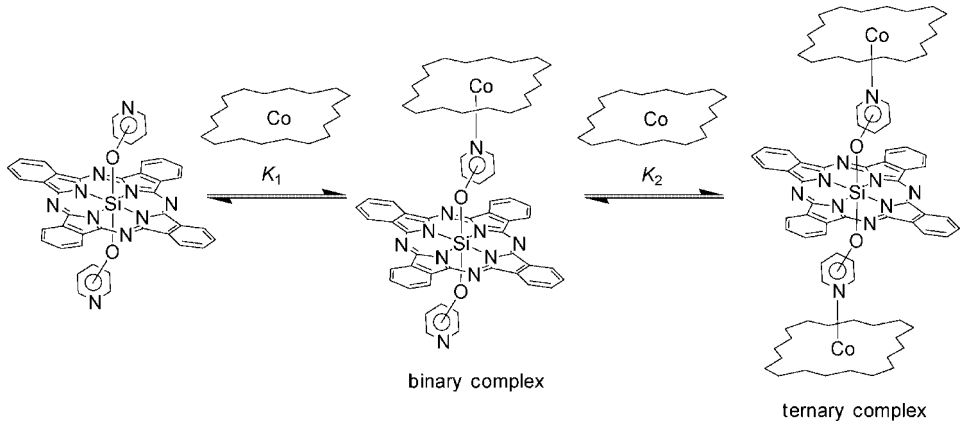


Figure 6. A schematic diagram showing the axial coordination porphyrinatocobalt(II) complexes **3** and **4** with bis(pyridyl) phthalocyanines **1** and **2**.

 © 2007 Wiley-VCH Verlag GmbH & Co. KGaA, Weinheim 

olato ligand can readily complex with the cobalt center, but for the 3-pyridinolato analogue complexation can only occur when the nitrogen atom is pointing away from the phthalocyanine plane (conformation B rather than C as shown in Figure S3 in the supporting information). However, since the $K_1$ value for 4-OHPy is also almost three times larger than that for 3-OHPy it seems that the electronic factor plays a dominant role. The binding constants determined for these systems are comparable with those reported for other porphyrinatocobalt(II) complexes and pyridine-type donor ligands.[13]

Table 1. Comparison of the binding constants.[a]

| Ligand | Porphyrin | $K_1$ [M$^{-1}$] |
|---|---|---|
| SiPc(3-OPy)$_2$ (**1**) | Co(TPP) (**3**) | $(3.9 \pm 1.2) \times 10^3$ |
| SiPc(3-OPy)$_2$ (**1**) | Co(TBPP) (**4**) | $(4.3 \pm 0.3) \times 10^3$ |
| SiPc(4-OPy)$_2$ (**2**) | Co(TPP) (**3**) | $(1.2 \pm 0.1) \times 10^4$ |
| SiPc(4-OPy)$_2$ (**2**) | Co(TBPP) (**4**) | $(1.1 \pm 0.2) \times 10^4$ |
| 3-OHPy | Co(TPP) (**3**) | $(3.6 \pm 0.4) \times 10^3$ |
| 4-OHPy | Co(TPP) (**3**) | $(1.4 \pm 0.1) \times 10^4$ |

[a] Determined by absorption spectroscopy in $CHCl_3$.

Because of the relatively large binding constants attempts were made to isolate the complexed species. By stirring a 1:2 (in mole) mixture of SiPc(4-OPy)$_2$ (**2**) and Co(TPP) (**3**) or Co(TBPP) (**4**) in $CHCl_3$ a new TLC spot with an $R_f$ value of ca. 0.3 in $CHCl_3$/MeOH (v/v, 5:1) appeared. The new products could be isolated as a blue solid by silica-gel column chromatography using $CHCl_3$/MeOH (v/v, 9:1) as eluent. Mass and UV/Vis spectroscopic methods showed that they were the binary complexes **2·3** and **2·4**. The corresponding ternary complexes **2·(3)**$_2$ and **2·(4)**$_2$ could not be isolated, which is probably because of their small quantity (the binary complexes could only be isolated in ca. 5% yield). The MALDI-TOF mass spectra of the dyads showed an envelope peaking at $m/z$ = 1399.0 or 1847.7, assignable to the corresponding molecular ion. For both signals, the isotopic pattern was in good agreement with the simulated spectrum. The identity of these complexes was further confirmed by accurate mass measurements (using ESI mass spectrometry).

Figure 7 compares the UV/Vis spectrum of the dyad **2·3** in $CHCl_3$ and the sum of the spectra of **2** and **3**, all at the same concentration. It can be seen that the porphyrin Soret band is redshifted from 410 nm to 435 nm upon complexation, while the absorptions of the phthalocyanine component are essentially unchanged. Similar results were obtained for the binary complex **2·4** (see Figure S4 in the Supporting Information). These observations supported the findings that the binary complexes were stable enough to be isolated, which is in contrast to the porphyrinatozinc(II) counterparts.[9b] Under the same conditions, the binary complexes of the 3-pyridyl analogue **1** and the porphyrinatocobalt(II) complexes **3** and **4** could not be isolated, which is in accord with their weaker binding interactions.

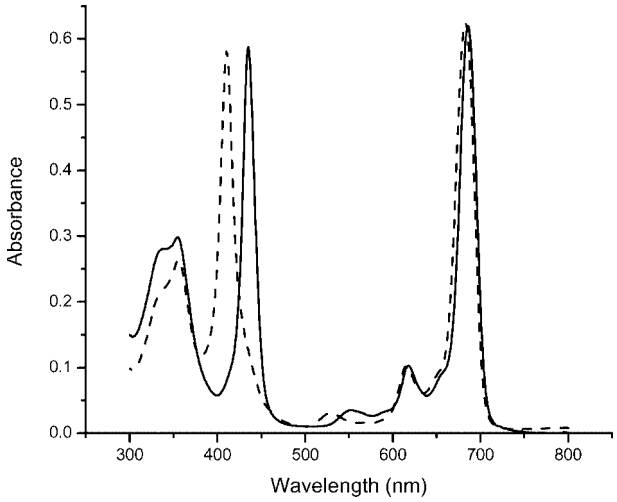


Figure 7. UV/Vis spectrum of the binary complex **2·3** (———) and the addition spectrum of **2** and **3** (-----) in $CHCl_3$. The concentrations of all the species were fixed at 3.2 μM.

## Conclusions

In summary, the bis(pyridyl) phthalocyanines **1** and **2** serve as good building blocks for hetero phthalocyanine–porphyrin arrays. As shown by absorption spectroscopy, they formed 1:2 complexes with porphyrinatocobalt(II) **3** and **4** with binding constants $K_1$ in the range of $3.9 \times 10^3$ to $1.2 \times 10^4$ M$^{-1}$. The heterodyads **2·3** and **2·4** could also be isolated and spectroscopically characterized. It is envisaged that this axial coordination approach can be extended to construct larger mixed phthalocyanine–porphyrin arrays. This work is in progress.

## Experimental Section

**General:** Reactions were performed under nitrogen. Toluene was distilled from sodium prior to use. *N*,*N*-Dimethylformamide (DMF) was predried with barium oxide and distilled under reduced pressure. The chloroform used in the UV/Vis studies was freshly distilled from $CaH_2$ under nitrogen. All other solvents and reagents were used as received. Chromatographic purifications were performed with silica gel (Macherey–Nagel, 70–230 mesh) columns with the indicated eluents. Compounds **2**,[9b] **3**,[10a] and the metal-free *meso*-tetrakis(3,5-di-*tert*-butylphenyl)porphyrin [$H_2$(TBPP)][10b] were prepared by previously described methods. $^1$H and $^{13}$C{$^1$H} NMR spectra were recorded with a Bruker DPX 300 spectrometer ($^1$H NMR, 300; $^{13}$C NMR, 75.4 MHz) in $CDCl_3$. Spectra were referenced internally using the residual solvent ($^1$H NMR: $\delta$ = 7.26 ppm) or solvent ($^{13}$C NMR: $\delta$ = 77.0 ppm) resonances relative to $SiMe_4$. MALDI-TOF mass spectra were recorded with a Bruker bench TOF mass spectrometer equipped with a standard UV-laser desorption source, using α-cyano-4-hydroxycinnamic acid as the matrix. FAB and ESI mass spectra were measured with a Thermo Finnigan MAT 95 XL mass spectrometer. UV/Vis spectra were recorded with a Cary 5G spectrophotometer. Elemental analyses were performed by the Shanghai Institute of Organic Chemistry, Chinese Academy of Sciences, China.

**SiPc(3-OPy)$_2$ (1):** A mixture of dichlorosilicon(IV) phthalocyanine (1.0 g, 1.64 mmol), 3-hydroxypyridine (0.32 g, 3.36 mmol), and pyr-

 © 2007 Wiley-VCH Verlag GmbH & Co. KGaA, Weinheim 

idine (2 mL) in toluene (50 mL) was heated at reflux overnight. The volatiles were then removed under reduced pressure and the residue was chromatographed on a silica gel column using $CHCl_3$/MeOH (v/v, 9:1) as eluent to give the product as a blue solid (0.89 g, 75%). $^1$H NMR: $\delta$ = 9.64–9.67 (m, 8 H, Pc-$H_\alpha$), 8.40–8.43 (m, 8 H, Pc-$H_\beta$), 6.98 (dd, $J$ = 1.6, 4.8 Hz, 2 H, Py-*H*), 5.63 (dd, $J$ = 4.8, 8.4 Hz, 2 H, Py-*H*), 3.92 (d, $J$ = 1.6 Hz, 2 H, Py-*H*), 2.87 (d, $J$ = 8.4 Hz, 2 H, Py-*H*) ppm. $^{13}$C{$^1$H} NMR: $\delta$ = 149.7, 146.2, 139.2, 138.5, 135.2, 131.7, 125.6, 124.1, 122.0 ppm. UV/Vis ($CHCl_3$) [$\lambda_{max}$ (log $\varepsilon$)]: 354 (4.89), 614 (4.59), 654 (4.53), 684 (5.36) nm. HRMS (FAB): calcd. for $C_{42}H_{25}N_{10}O_2Si$ [$MH^+$] 729.1931; found 729.1928. $C_{42}H_{24}N_{10}O_2Si$·MeOH (760.85): calcd. C 67.88, H 3.71, N 18.41; found C 67.81, H 4.01, N 18.54.

**Co(TBPP) (4):** A mixture of $H_2$(TBPP) (100 mg, 0.09 mmol) and anhydrous cobalt(II) chloride (20 mg, 0.15 mmol) in DMF (10 mL) was stirred at 120 °C for 8 h. The cooled dark red solution was then poured into MeOH (100 mL), and the precipitate was filtered off and washed with MeOH. The crude product was purified by column chromatography using $CHCl_3$ as eluent (92 mg, 87%). UV/Vis ($CHCl_3$) [$\lambda_{max}$ (log $\varepsilon$)]: 411 (5.18), 528 (4.11) nm. HRMS (FAB): calcd. for $C_{76}H_{92}CoN_4$ [$M^+$] 1119.6653; found 1119.6638.

**Heterodyad 2·3:** A mixture of SiPc(4-OPy)$_2$ (**2**) (20 mg, 0.03 mmol) and Co(TPP) (**3**) (37 mg, 0.06 mmol) in $CHCl_3$ (50 mL) was stirred at room temp. overnight. After removing the solvent in vacuo the residue was chromatographed with $CHCl_3$/MeOH (v/v, 9:1) as eluent. The third blue band was collected and evaporated to give the product (2 mg, 5%). UV/Vis ($CHCl_3$) [$\lambda_{max}$ (log $\varepsilon$)]: 355 (4.96), 435 (5.26), 553 (4.04), 618 (4.51), 686 (5.29) nm. MS (MALDI-TOF): an isotopic cluster peaking at $m/z$ = 1399.0 [$M^+$]. HRMS (ESI): calcd. for $C_{86}H_{53}CoN_{14}O_2Si$ [$MH^+$] 1400.3577; found 1400.3574.

**Heterodyad 2·4:** According to the above procedure, SiPc(4-OPy)$_2$ (**2**) (20 mg, 0.03 mmol) complexed with Co(TBPP) (**4**) (66 mg, 0.06 mmol) in $CHCl_3$ (50 mL) to give the dyad **2·4** (3 mg, 6%). UV/Vis ($CHCl_3$) [$\lambda_{max}$ (log $\varepsilon$)]: 351 (4.95), 437 (5.33), 551 (4.13), 619 (4.52), 688 (5.28) nm. MS (MALDI-TOF): an isotopic cluster peaking at $m/z$ = 1847.7 [$M^+$]. HRMS (ESI): calcd. for $C_{118}H_{117}CoN_{14}O_2Si$ [$MH^+$] 1848.8584; found 1848.8052.

**X-ray Crystallographic Analysis of 1 and 2:** Crystal data and details of data collection and structure refinement are given in Table 2. For **1**, data were collected at 293 K with an MSC/Rigaku RAXIS IIc imaging-plate system using Mo-$K_\alpha$ radiation ($\lambda$ = 0.71073 Å) from a Rigaku RU-200 rotating-anode generator operating at 50 kV and 90 mA ($2\theta_{min}$ = 3°, $2\theta_{max}$ = 55°, 2–5° oscillation frames in the range 0–180°, exposure 12 min per frame).[14] A self-consistent semi-empirical absorption correction based on a Fourier coefficient fitting of symmetry-equivalent reflections was applied by using the ABSCOR program.[15] Crystallographic data of **2** were collected with a Bruker SMART CCD diffractometer with a Mo-$K_\alpha$ sealed tube ($\lambda$ = 0.71073 Å) at 293 K, using a $\omega$ scan mode with an increment of 0.3°. Preliminary unit-cell parameters were obtained from 45 frames. Final unit-cell parameters were obtained by global refinements of reflections obtained from integration of all the frame data. The collected frames were integrated using the preliminary cell-orientation matrix. The SMART software was used for collecting frames of data, indexing reflections, and determination of lattice constants; SAINT-PLUS for the integration of the intensity of reflections and scaling;[16] SADABS for absorption corrections;[17] and SHELXL for space group and structure determination, refinements, graphics, and structure reporting.[18]

CCDC-644806 and CCDC-644807 contain the supplementary crystallographic data for this paper. These data can be obtained free of charge from The Cambridge Crystallographic Data Centre via www.ccdc.cam.ac.uk/data_request/cif.

**Supporting Information** (see also the footnote on the first page of this article): Absorption spectra of mixtures of SiPc(3-OPy)$_2$ (**1**) and Co(TBPP) (**4**) in $CHCl_3$; different resonance structures of the 3- and 4-pyridinolato ligands; schematic diagrams showing the complexation of SiPc(3-OPy)$_2$ (**1**) with porphyrinatocobalt(II) complexes. UV/Vis spectrum of the binary complex **2·4** and the addition spectrum of **2** and **4** in $CHCl_3$.

Table 2. Crystallographic data for **1** and **2**.

| | **1**·2$C_6H_5NO_2$ | **2** |
|---|---|---|
| Empirical formula | $C_{54}H_{34}N_{12}O_6Si$ | $C_{42}H_{24}N_{10}O_2Si$ |
| Formula mass [g mol$^{-1}$] | 975.02 | 728.80 |
| Crystal size [mm] | 0.50 × 0.40 × 0.20 | 0.25 × 0.20 × 0.10 |
| Crystal system | triclinic | monoclinic |
| Space group | $P\bar{1}$ | $P2_1/c$ |
| $a$ [Å] | 8.6413(17) | 9.613(3) |
| $b$ [Å] | 11.060(2) | 19.394(5) |
| $c$ [Å] | 13.297(3) | 9.945(3) |
| $\alpha$ [°] | 94.96(3) | 90 |
| $\beta$ [°] | 101.70(3) | 118.599(4) |
| $\gamma$ [°] | 110.34(3) | 90 |
| $V$ [Å$^3$] | 1149.6(4) | 1627.8(8) |
| $Z$ | 1 | 2 |
| $F$(000) | 504 | 752 |
| $D_{calcd.}$ [mg m$^{-3}$] | 1.408 | 1.487 |
| $\mu$ [mm$^{-1}$] | 0.120 | 0.131 |
| $\theta$ range [°] | 2.33–25.53 | 2.10–25.02 |
| Reflections collected | 3613 | 7044 |
| Independent reflections | 3613 | 2867 |
| Parameters | 331 | 250 |
| $R_1$ [$I > 2\sigma(I)$] | 0.0556 | 0.0531 |
| $wR_2$ [$I > 2\sigma(I)$] | 0.1541 | 0.1138 |
| Goodness-of-fit on $F^2$ | 1.067 | 1.038 |
| Largest diff. peak and hole [e Å$^{-3}$] | 0.350 and –0.229 | 0.318 and –0.284 |

 © 2007 Wiley-VCH Verlag GmbH & Co. KGaA, Weinheim 

## Acknowledgments

This work was supported by a strategic investments scheme administered by The Chinese University of Hong Kong.

[1] *The Porphyrin Handbook* (Eds.: K. M. Kadish, K. M. Smith, R. Guilard), Academic Press, San Diego, **2000**, vol. 6; **2003**, vol. 14 and 19.
[2] D. Holten, D. F. Bocian, J. S. Lindsey, *Acc. Chem. Res.* **2002**, *35*, 57–69.
[3] P.-C. Lo, X. Leng, D. K. P. Ng, *Coord. Chem. Rev.* **2007**, doi:10.1016/j.ccr.2007.03.007.
[4] a) D. K. P. Ng, J. Jiang, *Chem. Soc. Rev.* **1997**, *26*, 433–442; b) J. W. Buchler, D. K. P. Ng, in *The Porphyrin Handbook* (Eds.: K. M. Kadish, K. M. Smith, R. Guilard), Academic Press, San Diego, **2000**, vol. 3, pp. 245–294.
[5] a) B. Floris, M. P. Donzello, C. Ercolani, in *The Porphyrin Handbook* (Eds.: K. M. Kadish, K. M. Smith, R. Guilard), Academic Press, San Diego, **2003**, vol. 18, pp. 1–62; b) G. Kwag, E. Park, S. Kim, *Bull. Korean Chem. Soc.* **2004**, *25*, 298–300; c) M. P. Donzello, L. Bartolino, C. Ercolani, C. Rizzoli, *Inorg. Chem.* **2006**, *45*, 6988–6995.
[6] T.-H. Tran-Thi, *Coord. Chem. Rev.* **1997**, *160*, 53–91.
[7] X. Leng, C.-F. Choi, P.-C. Lo, D. K. P. Ng, *Org. Lett.* **2007**, *9*, 231–234.
[8] Y. Kobuke, *Eur. J. Inorg. Chem.* **2006**, 2333–2351.
[9] a) X.-y. Li, D. K. P. Ng, *Eur. J. Inorg. Chem.* **2000**, 1845–1848; b) M. T. M. Choi, C.-F. Choi, D. K. P. Ng, *Tetrahedron* **2004**, *60*, 6889–6894; c) A. N. Cammidge, G. Berber, I. Chambrier, P. W. Hough, M. J. Cook, *Tetrahedron* **2005**, *61*, 4067–4074.
[10] a) W. Mikolaiski, G. Baum, W. Massa, R. W. Hoffmann, *J. Organomet. Chem.* **1989**, *376*, 397–405; b) S. Takagi, T. K. Miyamoto, Y. Sasaki, *Bull. Chem. Soc. Jpn.* **1986**, *59*, 2371–2373.
[11] K. Hirose, *J. Inclusion Phenom. Macrocycl. Chem.* **2001**, *39*, 193–209.
[12] K. A. Connors, *Binding Constants*, Wiley, New York, **1987**, pp. 141–160.
[13] a) F. A. Walker, *J. Am. Chem. Soc.* **1973**, *95*, 1150–1153; b) J. S. Summers, A. M. Stolzenberg, *J. Am. Chem. Soc.* **1993**, *115*, 10559–10567.
[14] a) J. Tanner, K. Krause, *Rigaku J.* **1994**, *11*, 4–7; b) J. Tanner, K. Krause, *Rigaku J.* **1990**, *7*, 28–32; c) K. Krause, G. N. Phillips Jr, *J. Appl. Crystallogr.* **1992**, *25*, 146–154; d) M. Sato, M. Yamamoto, K. Imada, Y. Katsube, N. Tanaka, T. Higashi, *J. Appl. Crystallogr.* **1992**, *25*, 348–357.
[15] T. Higashi, *ABSCOR – An Empirical Absorption Correction Based on Fourier Coefficient Fitting*, Rigaku Corporation, Tokyo, **1995**.
[16] *SMART and SAINT for Windows NT Software Reference Manuals, Version 5.0*, Bruker Analytical X-ray Systems, Madison, WI, **1997**.
[17] G. M. Sheldrick, *SADABS – A Software for Empirical Absorption Correction*, University of Göttingen, Germany, **1997**.
[18] *SHELXL Reference Manual, Version 5.1*, Bruker Analytical X-ray Systems, Madison, WI, **1997**.

Received: April 25, 2007
Published Online: August 13, 2007

 © 2007 Wiley-VCH Verlag GmbH & Co. KGaA, Weinheim 

DOI: 10.1002/ejic.200700462

# Identification of Hexameric Water and Hybrid Water–Chloride Clusters Intercalated in the Crystal Hosts of (Imidoylamidine)nickel(II) Complexes

**Maximilian N. Kopylovich,*[a] Ekaterina A. Tronova,[a,b] Matti Haukka,[c] Alexander M. Kirillov,[a] Vadim Yu. Kukushkin,*[b] João J. R. Fraústo da Silva,[a] and Armando J. L. Pombeiro*[a]**

**Keywords:** Crystal engineering / Hydrogen bonds / Imidoylamidine complexes / Water clusters / X-ray diffraction

Two structurally related bis(imidoylamidine or 1,3,5-triazapentadiene)nickel(II) compounds {Ni[HN=C(3-py)NC(3-py)=NH]$_2$}·$H_2O$·MeOH (**1**) and [Ni{HN=C(3-py)N(H)C(3-py)=NH}$_2$]$Cl_2$ (**2**) with symmetrical 3-pyridyl (3-py) substituents have been prepared by direct 2-butanone oxime mediated transformation of 3-cyanopyridine in the presence of Ni(MeCO$_2$)$_2$·$4H_2O$ or $NiCl_2$·$2H_2O$, respectively. Compounds **1** and **2** have been characterized by elemental analyses, IR, $^1$H and $^{13}$C{$^1$H} NMR spectroscopy, and FAB$^+$ mass spectrometry, while their slow recrystallization in air from organic solvents revealed a high affinity for water and resulted in the formation of the derived compounds [Ni{HN=C(3-py)NC(3-py)=NH}$_2$]·$6H_2O$ (**1′**) and [Ni{HN=C(3-py)N(H)$_{0.5}$C(3-py)=NH}$_2$]Cl·$2H_2O$ (**2′**). Single-crystal X-ray diffraction analyses allowed the identification of discrete hexameric water or hybrid water–chloride clusters hosted by the crystal matrixes of **1′** and **2′**, respectively. Both the $(H_2O)_6$ and $[(H_2O)_4(Cl)_2]^{2-}$ clusters possess similar geometries and consist of cyclic planar tetranuclear $(H_2O)_4$ or $[(H_2O)_2(Cl)_2]^{2-}$ cores with two dangling water molecules. These water associates occupy voids in the crystal cells and display extensive H-bonding interactions with monomeric nickel–organic units, thus playing a key role in the formation of 3D hydrogen-bonded supramolecular assemblies.
(© Wiley-VCH Verlag GmbH & Co. KGaA, 69451 Weinheim, Germany, 2007)

## Introduction

The identification, characterization, and classification of various water assemblies in different crystalline materials has recently become a popular research field, namely towards understanding the properties of bulk water in its liquid and solid phases as well as interpretation of water–water interactions in various environments including, for example, inorganic materials, supramolecular systems, and biomolecules.[1–3] In contrast, the investigation of hybrid $H_2O$ clusters composed of hydrogen-bonded water associates with other solvents, counterions, or small molecules has received less attention.[1b,4] In particular, there are only a few reports focused on the experimental identification and analysis of discrete water–chloride clusters[5a,5g] or H-bonded networks between water of crystallization and chloride counterions[1b,5b–5f,5h] in crystalline materials, in spite of the substantial theoretical studies[6] on such objects, and the importance of the latter in, for example, natural environments, biochemistry, materials chemistry, drug design, catalysis, and atmospheric research.[5,6]

Within our ongoing studies on the self-assembly synthesis of various transition-metal complexes,[7] we have recently reported the new Cu/Na[3a] and Ni[3b] coordination compounds and shown that their metal–organic matrixes host different types of decameric water clusters with unusual geometries. Thus, in pursuit of these and other studies, namely focusing on the new synthetic methods for phthalocyanines[8a] and analogous imidoylamidine (imam) compounds,[8b,8c] we report herein the preparation and full characterization of two structurally related bis(imidoylamidine)nickel(II) complexes **1** and **2**, which upon recrystallization lead to the derived compounds **1′** and **2′** that act in the solid state as crystal hosts for water-containing clusters. We also show how a slight modification of the synthetic and crystallization procedures may result in the incorporation of geometrically related, but in their composition distinctly different, hexameric $(H_2O)_6$ or $[(H_2O)_4(Cl)_2]^{2-}$ clusters.

[a] Centro de Química Estrutural, Complexo I, Instituto Superior Técnico, Universidade Técnica de Lisboa,
Av. Rovisco Pais, 1049-001 Lisbon, Portugal
Fax: +351-21-846-4455
E-mail: pombeiro@ist.utl.pt
kopylovich@popsrv.ist.utl.pt
[b] Department of Chemistry, St. Petersburg State University, 198504 Stary Petergof, Russian Federation
E-mail: kukushkin@VK2100.spb.edu
[c] University of Joensuu, Department of Chemistry, P. O. Box 111, 80101, Joensuu, Finland

## Results and Discussion

### Synthesis and Spectroscopic Characterization

The bis(imidoylamidine or 1,3,5-triazapentadiene) compounds [Ni{HN=C(3-py)NC(3-py)=NH}$_2$]·$H_2O$·MeOH (**1**)

 © 2007 Wiley-VCH Verlag GmbH & Co. KGaA, Weinheim 

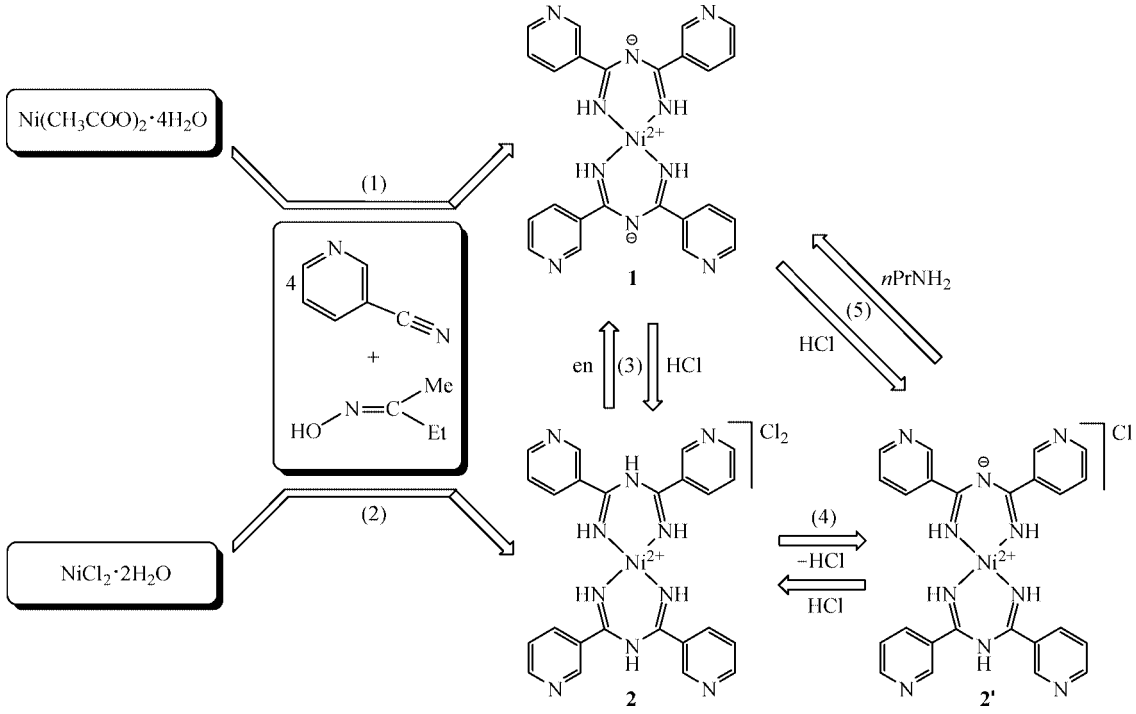


Scheme 1. Synthesis of bis(imidoylamidine)nickel(II) complexes (solvent molecules of crystallization are omitted for the sake of clarity); en = $H_2NCH_2CH_2NH_2$.

and [Ni{HN=C(3-py)N(H)C(3-py)=NH}$_2$]$Cl_2$ (**2**) with symmetrical 3-pyridyl (3-py) substituents were easily synthesized by modifying our previously reported[8c] (ketoxime)nickel(II)-mediated procedure for a variety of related bis(imidoylamidine) complexes. Hence, treatment of nickel(II) acetate tetrahydrate with 4 equiv. of 3-cyanopyridine in solution of 2-butanone oxime at 70 °C resulted in a single-pot formation of the neutral $Ni(imam)_2$ complex **1** [Scheme 1, reaction (1)]. It was isolated as a bright yellow crystalline solid in the form of a methanol/water solvate upon recrystallization from hot methanol in the presence of ethylenediamine.

However, the repetition of this synthetic procedure using nickel(II) chloride dihydrate as the nickel salt led to the formation of the cationic (+2) complex **2** isolated as a yellow powder from the reaction mixture [Scheme 1, reaction (2)]. The interconversion of compounds **1** and **2** can be achieved by treatment with HCl (**1**→**2**) or ethylenediamine (**2**→**1**) [Scheme 1, reactions (3)]. It should be mentioned that related bis(imidoylamidine)nickel(II) and -copper(II) complexes with various aromatic substituents have been previously reported,[9] but their synthetic procedures are different and more complicated than those now reported for compounds **1** and **2**, usually involving several reaction steps or rather harsh reaction conditions (e.g. solvothermal synthesis).

The presence of 2-butanone oxime (another oxime can also be applied) is essential for the synthesis of **1** and **2**, since the respective reactions between the nickel(II) salts and 3-cyanopyridine do not proceed in the absence of the oxime. In fact, this reagent, namely upon nucleophilic addition to the nitrile (NCR), can promote its hydrolytic conversion into ammonia and amidine $RC(=NH)NH_2$ (the latter upon coupling of $NH_3$ to NCR) which, on further nucleophilic addition to a ligated nitrile, leads to the imidoylamidine products. The reaction can proceed via an intermediate complex derived from double addition of the oxime to the nitrile ligand, as proposed for the oxime-mediated conversion of phthalonitriles into phthalocyanines and for related (ketoxime)nickel(II)-promoted processes.[8] The compounds **1** and **2** have been characterized by IR, $^1H$ and $^{13}C\{^1H\}$ NMR spectroscopy, $FAB^+$ mass spectrometry, elemental and single-crystal X-ray diffraction (for products **1′** and **2′** derived upon recrystallization) analysis.

The IR spectra of **1** and **2** show typical bands for bis(imidoylamidine)nickel(II) complexes[8b,8c] due to ν(NH), ν(C=N), and δ(NH) vibrations with absorbance maxima in the ranges of 3292–3169, 1655–1642, and 1548–1547 $cm^{-1}$, respectively. The overall identical $[M + H]^+$ (for **1**) and $[M - H]^+$ (for **2**) ions are observed at *m*/*z* = 507, with the expected isotopic distribution patterns, in the $FAB^+$ mass spectra. The $^1H$ and $^{13}C\{^1H\}$ NMR spectra reveal the expected resonances at typical chemical shifts for the corresponding imam ligands[8b,8c,9b–9d,10] (and solvents of crystallization in the case of **1**), while the elemental analyses are consistent with the proposed formulations. Complexes **1** and **2** are insoluble in water, but during the crystal growth experiments in organic medium, they appear to show a high affinity for water, absorbing its traces from organic solvents and/or air, and resulting in the formation of the derived compounds [Ni{HN=C(3-py)NC(3-py)=NH}$_2$]·$6H_2O$ (**1′**) and [Ni{HN=C(3-py)N(H)$_{0.5}$C(3-py)=NH}$_2$]Cl·$2H_2O$ (**2′**),

 © 2007 Wiley-VCH Verlag GmbH & Co. KGaA, Weinheim 

whose crystal cells according to the X-ray analyses contain 6 or 2 strongly associated water molecules of crystallization, respectively, as discussed below. Compound **2′** resulted from deprotonation of **2** upon recrystallization in air from a methanol/chloroform solution, and regenerated **2** on reaction with HCl [Scheme 1, reactions (4)]. It is also obtained by single protonation (by HCl) of **1** and conversely yielded the latter upon reaction with *n*$PrNH_2$ [Scheme 1, reactions (5)].

### X-ray Crystal Structure of [Ni{HN=C(3-py)NC-(3-py)=$NH\}_2$]·$6H_2O$ (1′)

Compound **1′** crystallizes in the triclinic space group $P\bar{1}$, and consists of the neutral bis(imidoylamidine) [Ni{H*N*=C(3-py)NC(3-py)=*N*H}$_2$] unit (Figure 1a) and six water molecules of crystallization. The nearly square-planar coordination environment around the centrosymmetric tetracoordinate Ni(1) center is filled by two imam ligands. They act as *N*,*N*-chelators through equivalent Ni(1)–N(1) [1.847(1) Å] and Ni(1)–N(3) [1.848(1) Å] bonds, forming the six-membered Ni(1)–N(1)–C(1)–N(2)–C(14)–N(3) rings with N(1)–Ni(1)–N(3) bite angles of 89.48(6)° (Figure 1a). Within the Ni(imam)$_2$ core the N(1)–C(1) [1.310(2) Å] and N(3)–C(14) [1.315(2) Å] bonds are only slightly shorter (by ca. 0.03 Å) than N(2)–C(1) [1.357(2) Å] and N(2)–C(14) [1.353(2) Å], thus potentially indicating a delocalized character of Ni–imam rings, as reported previously for related compounds.[9b] Although the Ni(imam)$_2$ core is almost planar, the 3-pyridyl substituents are significantly bent out of its plane. Most of the bonding parameters in **1′** are comparable to those reported previously for related bis(imidoylamidine)nickel complexes.[8b,8c,9b–9d,10]

The most interesting feature of the solid-state structure of **1′** is the hydrogen-bonding interactions of all six water molecules of crystallization (Table 1), providing the formation of finite hexameric water clusters intercalated in the crystal host of the (imidoylamidine)nickel complex (Figure 2a). Hence, two symmetry-generated water trimers [O(1)···O(2)···O(3)] are doubly interconnected through the O(2)–H(2OA)···O(3)$^{ii}$ [2.901(2) Å] hydrogen bonds generating the $(H_2O)_6$ clusters composed of a cyclic tetrameric core [O(2)···O(3)···O(2)···O(3)] and two pendent water molecules O(1). According to the systematization introduced by Infantes et al.,[1a,1b] such $(H_2O)_6$ clusters can be classified within the *R*4 type. The $(H_2O)_4$ core possesses a planar geometry with the O(2)···O(3)···O(2) and O(3)···O(2)···O(3) angles of ca. 76.89 and 103.11°, respectively (Figure 2a). Within the hexameric water associate the average O···O contact of ca. 2.82 Å (Table 1) is comparable to one found in liquid water (i.e. 2.85 Å)[1d] and in other discrete $(H_2O)_6$ clusters,[1a–1c,2] which are trapped by various metal–organic matrixes and composed of (i) a cyclic hexameric core of diverse conformations,[2a,2b,2d] (ii) a hexameric chain,[3b] or (iii) a cyclic tetrameric core with two pendent water molecules.[2c]

The $(H_2O)_6$ clusters occupy voids in the crystal cell of **1′** (Figure 3a) and extensively interact through multiple O–H···O or N–H···O hydrogen bonds [avg. 2.902(2) Å] with the host metal–organic matrix (Table 1). Hence, each dangling O(1) water molecule interacts with three imam nitrogen atoms [N(1), N(2), and N(5)] and each O(3) water contacts with one N(4) nitrogen atom (Figure 2a, Table 1), leading to the simultaneous multidimensional binding of every $(H_2O)_6$ cluster to eight different Ni(imam)$_2$ units in total. These multiple interactions play a key role in the

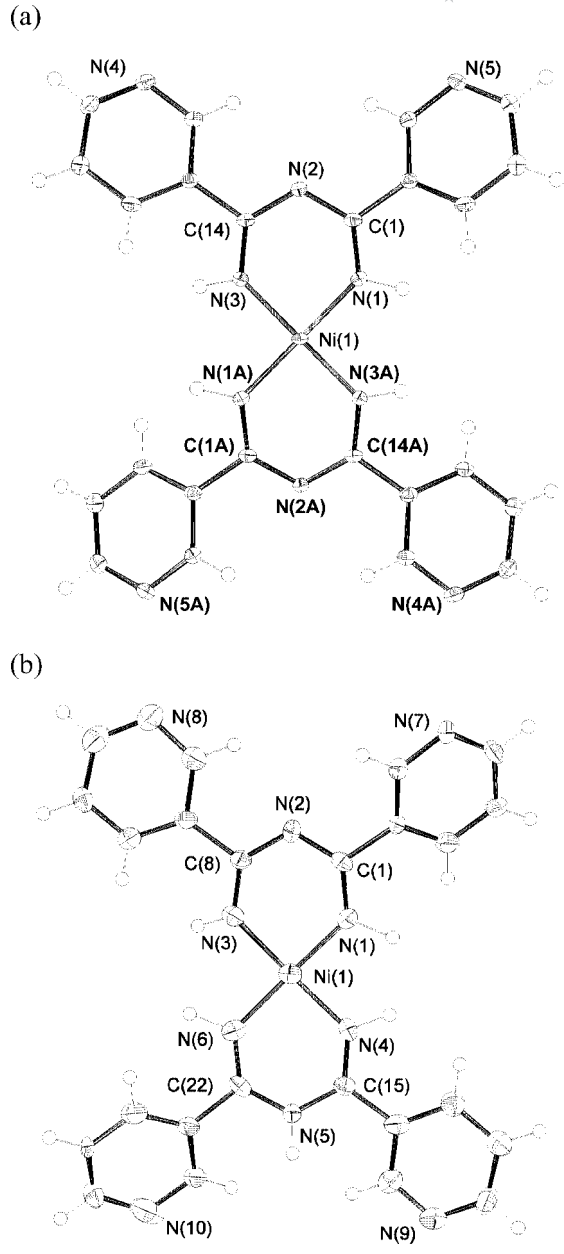


Figure 1. Thermal ellipsoid views of **1′** (a) and **2′** (b) with partial atomic numbering scheme. Thermal ellipsoids are drawn at 50% probability. Water molecules of crystallization and counterions are omitted for clarity. Symmetry transformations used to generate the equivalent atoms in **1′**: (A) $-x + 1, -y, -z + 1$. Selected bond lengths [Å] and angles [°] in **1′**: Ni(1)–N(1) 1.847(1), Ni(1)–N(3) 1.848(1), N(1)–C(1) 1.310(2), N(3)–C(14) 1.315(2), N(2)–C(1) 1.357(2), N(2)–C(14) 1.353(2); N(1)–Ni(1)–N(1A) 180.0, N(1)–Ni(1)–N(3) 89.48(6), N(3)–Ni(1)–N(3A) 179.999(2).

 © 2007 Wiley-VCH Verlag GmbH & Co. KGaA, Weinheim 

Table 1. Hydrogen bonds [Å] in **1′**.[a]

| D–H···A | *d*(D···A) |
|---|---|
| Within hexameric water cluster | |
| O(2)–H(2OB)···O(1)$^{i}$ | 2.757(2) |
| O(2)–H(2OA)···O(3)$^{ii}$ | 2.901(2) |
| O(3)–H(3OA)···O(2)$^{iii}$ | 2.788(2) |
| Between water cluster and metal–organic matrix | |
| O(1)–H(1OA)···N(5)$^{iii}$ | 2.8030(19) |
| O(1)–H(1OB)···N(2)$^{iv}$ | 2.8320(18) |
| O(3)–H(3OB)···N(4) | 2.9149(19) |
| N(1)–H(1N)···O(1) | 3.0584(18) |

[a] Symmetry transformations used to generate equivalent atoms: (i) $-x + 1, -y, -z + 1$; (ii) $x, y - 1, z + 1$; (iii) $-x + 2, -y + 1, -z + 1$; (iv) $x, y - 1, z + 1$.

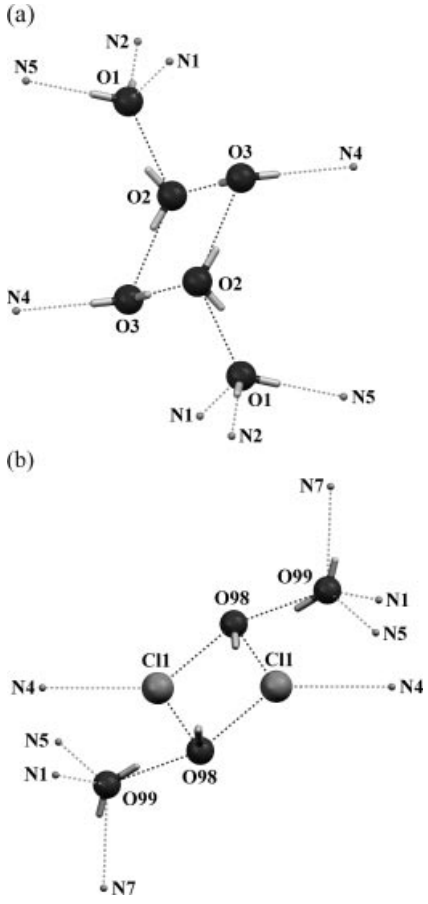


Figure 2. Perspective representations along the *a* crystallographic axis of discrete hexameric water (a) and water–chloride (b) clusters found in the crystal cells of **1′** (a) and **2′** (b). H-bonds are shown as dotted lines; water oxygen atoms and chloride atoms forming clusters are represented as spheres. Hydrogen-bond geometry parameters are those of Tables 1 and 2. Selected angles [°] within water-containing clusters: **1′**: O(1)···O(2)···O(3) 124.24 and 82.76, O(2)···O(3)···O(2) 76.89, O(3)···O(2)···O(3) 103.11; **2′**: O(99)···O(98)··· Cl(1) 137.73 and 85.80, O(98)···Cl(1)···O(98) 70.20, Cl(1)···O(98)··· Cl(1) 109.80.

structure stabilization and formation of an extended 3D hydrogen-bonded supramolecular assembly (Figure 3a). The separations between neighboring horizontal and vertical $(H_2O)_6$ clusters depicted in Figure 3a are within 8.7894(3) and 12.1448(6) Å, respectively, being equivalent to the *b* and *c* unit-cell dimensions.

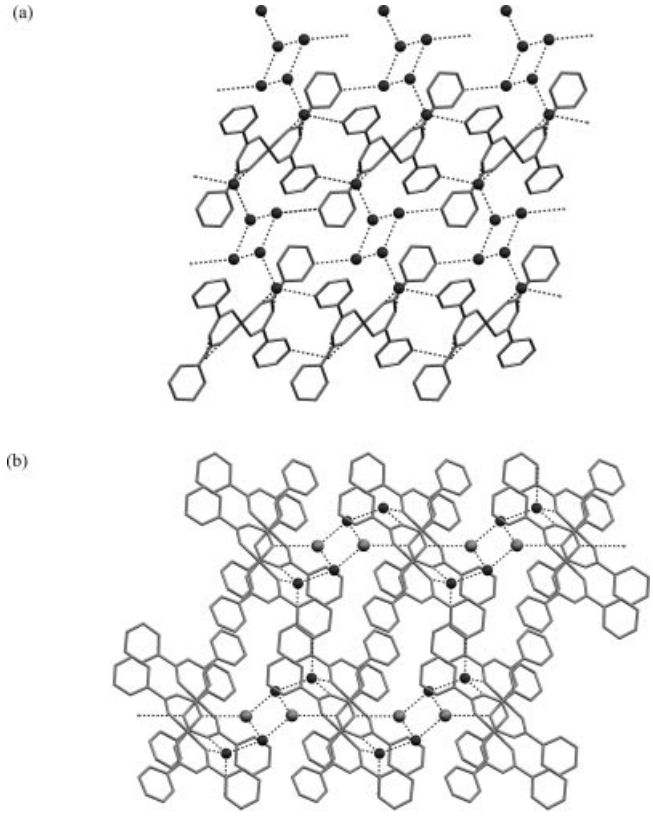


Figure 3. Fragments of the crystal packing diagrams along the *a* crystallographic axis of **1′** (a) and **2′** (b) with extensive hydrogen-bonded networks showing the interactions within the $(H_2O)_6$ and $[(H_2O)_4(Cl)_2]^{2-}$ clusters and between these clusters and the metal–organic matrixes; hydrogen atoms are omitted for clarity. Water oxygen atoms and chloride atoms forming clusters are shown as spheres.

### X-ray Crystal Structure of $[Ni\{HN{=}C(3\text{-py})N(H)_{0.5}C(3\text{-py}){=}NH\}_2]Cl{\cdot}2H_2O$ (2′)

The molecular structure of **2′** is composed of the cationic bis(imidoylamidine) $[Ni\{HN{=}C(3\text{-py})NC(3\text{-py}){=}NH\}\{HN{=}C(3\text{-py})N(H)C(3\text{-py}){=}NH\}]^+$ unit (Figure 1b), represented by $[Ni\{HN{=}C(3\text{-py})N(H)_{0.5}C(3\text{-py}){=}NH\}_2]^+$, with two water molecules of crystallization and one chloride counterion equalizing the positive charge. The latter is caused by protonation of the middle nitrogen atom in one of the two imidoylamidine ligands which, nevertheless, possess almost identical geometry and bonding parameters, both being also similar to those found in **1′** (Figure 1a). Thus, the basic structure of **2′** is not discussed in detail.

As in the case of **1′**, the analysis of hydrogen-bonding interactions in **2′** (Table 2) reveals the formation of hexameric water-containing clusters. Besides, they possess a geometry that is similar to that of **1′** and consists of a cyclic planar tetranuclear core and two dangling water molecules (Figure 2). The main difference arises from the substitution

 © 2007 Wiley-VCH Verlag GmbH & Co. KGaA, Weinheim 

of two water molecules in the $(H_2O)_4$ core of **1′** for two chloride atoms, thus leading to the formation of the $[(H_2O)_2(Cl)_2]^{2-}$ core and resulting in a hexanuclear hybrid $[(H_2O)_4(Cl)_2]^{2-}$ cluster in **2′** (Figure 2b). Hence, two symmetry-equivalent water molecules of crystallization O(98) and chloride ions Cl(1) from neighboring units are doubly hydrogen-bonded [O(98)–H(98B)···Cl(1)$^{i}$ 3.172(7) Å] generating the tetranuclear core, which is further connected through the O(99)–H(99A)···O(98) [2.706(9) Å] interactions to give the hexanuclear associate. Within this cluster the O···O and O···Cl separations as well as the corresponding angles (Figure 2b) lie in the range found in other previously identified water–chloride assemblies, which include, for example, discrete cyclic $[(H_2O)_4(Cl)]^-$[5g] and $[(H_2O)_6(Cl)_2]^{2-}$[5a] clusters, as well as various 1D or 2D hydrogen-bonded networks with $\{[(H_2O)_4(Cl_2)]^{2-}\}_n$,[5h] $\{[(H_2O)_6(Cl)_2]^{2-}\}_n$,[5h] $[(H_2O)_7(HCl)_2]_n$,[5f] $\{[(H_2O)_{11}(Cl)_7]^{7-}\}_n$,[5b] $\{[(H_2O)_{14}(Cl)_2]^{2-}\}_n$,[5d] $\{[(H_2O)_{14}(Cl)_4]^{4-}\}_n$,[5e] and $\{[(H_2O)_{14}(Cl)_5]^{5-}\}_n$[5c] compositions.

Table 2. Hydrogen bonds [Å] in **2′**.[a]

| D–H···A | *d*(D···A) |
|---|---|
| Within hexameric water–chloride cluster | |
| O(99)–H(99A)···O(98) | 2.706(9) |
| O(98)–H(98B)···Cl(1)$^{i}$ | 3.172(7) |
| Between water–chloride cluster and metal–organic matrix | |
| O(99)–H(99B)···N(7)$^{ii}$ | 2.808(8) |
| N(5)–H(05)···O(99) | 2.765(8) |
| N(1)–H(01)···O(99)$^{i}$ | 3.115(8) |
| N(4)–H(04)···Cl(1) | 3.277(7) |

[a] Symmetry transformations used to generate equivalent atoms: (i) $-x + 1, -y, -z$; (ii) $x, y - 1, z - 1$.

The $[(H_2O)_4(Cl)_2]^{2-}$ clusters are held in cavities between the monomeric metal–organic units in the crystal cell of **2′** (Figure 3b) by means of extensive H-bonding contacts. Three types have been identified and include the O–H···N, N–H···O, and N–H···Cl interactions ranging from 2.808(8) to 3.277(7) Å (Table 2). As in the case of the $(H_2O)_6$ cluster in **1′**, the pendent water molecules O(99) in **2′** act as both hydrogen-bond donors or acceptors, bridging concurrently between three imidoylamidine nitrogen atoms (Figure 2b), thus leading, along with the N(4)–H(04)···Cl(1) interactions, to the multidimensional linkage of eight different Ni(imam)$_2$ units and resulting in the 3D hydrogen-bonded supramolecular pattern (Figure 3b). The separations between neighboring horizontal and vertical $[(H_2O)_4(Cl)_2]^{2-}$ clusters shown in Figure 3b are also equivalent to the *b* and *c* unit-cell dimensions, respectively (Table 3).

## Conclusion

In the present work we have shown that the previously reported (ketoxime)nickel(II)-mediated transformations of various organonitriles[8] can be applied to 3-cyanopyridine, resulting in the direct synthesis of Ni(imam)$_2$ complexes **1** and **2** with symmetrical 3-pyridyl substituents. We have also demonstrated that the modification of a starting nickel salt [i.e. $Ni(MeCO_2)_2{\cdot}4H_2O$ vs. $NiCl_2{\cdot}2H_2O$] leads to either neutral (**1**) or cationic (**2**) (imidoylamidine)nickel(II) compounds. In spite of being insoluble in water, upon recrystallization **1** and **2** exhibit a high affinity for water, absorbing its traces from organic solvents and/or air, and giving the derivatives **1′** and **2′** with a higher content of water of crystallization.

The single-crystal X-ray diffraction analysis of **1′** and **2′** reveals the formation of hexameric water or hybrid water–chloride clusters, respectively, which are geometrically related, but distinctly different, in composition. They are shown to play the principal role in the formation of 3D supramolecular networks in the solid state through multiple hydrogen-bonding interactions. Hence, the current work provides well-identified examples of such cases and expands the constantly growing family of water[1–3] and, to a lesser extent, water–chloride[5] clusters trapped by various crystalline materials, as well as showing that imidoylamidine compounds can act as suitable matrixes to host different types of water-containing assemblies.

Further developments of this study towards widening of the family of imidoylamidine complexes and the search for their potential applications in various areas (e.g. as coloring materials and/or analogues of phthalocyanines), as well as the identification of new types of hybrid water clusters in diverse crystalline environments, are currently in progress.

## Experimental Section

**General Materials and Procedures:** All synthetic work was performed in air. The reagents and solvents were obtained from commercial sources and used as received, i.e. without further purification or drying. $NiCl_2{\cdot}2H_2O$ was prepared according to an earlier described procedure.[8c] C, H, and N elemental analyses were carried out by the Microanalytical Service of the Instituto Superior Técnico. Melting points were determined with a Leica Gallen III instrument. Positive-ion FAB mass spectra were obtained with a Trio 2000 instrument by bombarding 3-nitrobenzyl alcohol (*m*NBA) matrices of the samples with 8 keV (ca. 1.18 $10^{15}$ J) Xe atoms. Mass calibration for data system acquisition was achieved using CsI. Infrared spectra (4000–400 $cm^{-1}$) were recorded on KBr pellets with a BIO-RAD FTS 3000MX or Jasco FT/IR-430 instrument. $^1H$ and $^{13}C\{^1H\}$ NMR spectra were measured with a Varian UNITY 300 or Bruker 300 UltraShield™ spectrometer at ambient temperature.

**[Ni{HN=C(3-py)NC(3-py)=NH}$_2$]·H$_2$O·MeOH (1):** $Ni(MeCO_2)_2{\cdot}4H_2O$ (248 mg, 1.00 mmol; Aldrich) was stirred in 2-butanone oxime (5 mL; Aldrich) at 70 °C for 30 min, giving a homogeneous light green solution (solution **a**). 3-Cyanopyridine (416 mg, 4.00 mmol; Aldrich) was stirred separately in 2-butanone oxime (5 mL; Aldrich) at 70 °C for 30 min and then added to the above-mentioned solution **a**. The resulting reaction mixture was heated at 70 °C for 12 h, which resulted in the transformation of the clear green solution to a brownish-orange suspension. This was left to cool to room temperature yielding a dark orange product that was separated by filtration, washed with ethanol (15 mL), diethyl ether (10 mL), and then dried in air at room temperature. Recrystallization of the product from hot methanol with addition of

 © 2007 Wiley-VCH Verlag GmbH & Co. KGaA, Weinheim 

Table 3. Crystal data and structure refinement details for complexes **1′** and **2′**.

| | **1′** | **2′** |
|---|---|---|
| Empirical formula | $C_{24}H_{32}N_{10}NiO_6$ | $C_{24}H_{25}ClN_{10}NiO_2$ |
| Formula mass | 615.31 | 579.70 |
| Temperature [K] | 120(2) | 100(2) |
| $\lambda$ [Å] | 0.71073 | 0.71073 |
| Crystal system | triclinic | triclinic |
| Space group | $P\bar{1}$ | $P\bar{1}$ |
| $a$ [Å] | 7.2503(4) | 9.4184(14) |
| $b$ [Å] | 8.7894(3) | 10.972(3) |
| $c$ [Å] | 12.1448(6) | 13.017(3) |
| $\alpha$ [°] | 92.115(3) | 110.330(10) |
| $\beta$ [°] | 105.803(2) | 97.629(13) |
| $\gamma$ [°] | 112.183(3) | 102.445(13) |
| $V$ [Å$^3$] | 681.03(6) | 1199.7(4) |
| Z | 1 | 2 |
| $\rho_{calcd.}$ [Mg m$^{-3}$] | 1.500 | 1.605 |
| $\mu$(Mo-$K_a$) [mm$^{-1}$] | 0.772 | 0.967 |
| No. of collected reflections | 8289 | 10611 |
| No. of unique reflections | 3115 | 4178 |
| $R_{int.}$ | 0.0448 | 0.1071 |
| Final $R_1$,[a] $wR_2$[b] ($I \geq 2\sigma$) | 0.0344, 0.0739 | 0.0769, 0.1601 |
| $R_1$, $wR_2$ (all data) | 0.0447, 0.0781 | 0.1609, 0.1987 |
| GOF on $F^2$ | 1.106 | 1.064 |
| Largest difference in peak/hole [e Å$^{-3}$] | 0.282/–0.464 | 0.564/–0.443 |

[a] $R_1 = \Sigma||F_o| - |F_c||/\Sigma|F_o|$. [b] $wR_2 = \{\Sigma[w(F_o^2 - F_c^2)^2]/\Sigma[w(F_o^2)^2]\}^{1/2}$.

1.00 mmol of ethylenediamine gave a bright yellow crystalline precipitate of [Ni{HN=C(3-py)NC(3-py)=NH}$_2$]·H$_2$O·MeOH (**1**). Yield: 58%, based on nickel acetate. The compound does not have a characteristic melting point and upon heating decomposes at >300 °C. $C_{25}H_{26}N_{10}NiO_2$ (557.2): calcd. C 53.89, H 4.70, N 25.14; found C 53.67, H 5.06, N 24.55. FAB-MS(+) (*m*NBA): *m*/*z* = 507 [M + H]$^+$ (M = molecular ion of the complex part of the compound). IR (KBr): $\tilde{\nu}$ = 3397 [(s br.) $\nu$(H$_2$O+OH)], 3292 (s br.) [$\nu$(NH)], 1655 [(m-w) $\nu$(C=N)], 1548 [(s) $\delta$(NH)] cm$^{-1}$. $^1$H NMR (300 MHz, [D$_6$]acetone, Me$_4$Si): $\delta$ = 9.22 [s, 4 H, 2-C*H*(3-py)], 8.67 [d, *J* = 6.3 Hz, 4 H, 4-C*H*(3-py)], 8.37 [d, *J* = 7.8 Hz, 4 H, 6-C*H*-(3-py)], 7.46 [dd, *J* = 7.8 and 7.5 Hz, 4 H, 5-C*H*(3-py)], 6.93 (br. s, 4 H, N*H*), 4.11 (s, 1 H, MeO*H*), 3.49 (s, 3 H, C*H*$_3$OH), 3.31 (s, 2 H, *H*$_2$O) ppm. No reliable $^{13}$C{$^1$H} NMR spectrum could be accumulated due to the poor solubility of **1** in common deuterated solvents. The X-ray quality crystals of {Ni[HN=C(3-py)NC-(3-py)=NH]$_2$}·6H$_2$O (**1′**) were grown by slow concentration in air at ca. 25 °C of an acetone/toluene (1:10, v/v) solution of **1**.

**[Ni{HN=C(3-py)N(H)C(3-py)=NH}$_2$]Cl$_2$ (2):** NiCl$_2$·2H$_2$O (166 mg, 1.00 mmol) was stirred in 2-butanone oxime (5 mL; Aldrich) for 5 min, whereupon 3-cyanopyridine (416 mg, 4.00 mmol; Aldrich) was added and the reaction mixture heated at 70 °C for 1 d. Upon addition of 3-cyanopyridine, the homogenization of the reaction mixture was observed for 10 min, giving a greenish-brown solution. The color of the reaction mixture changed with time (ca. 1 h) from greenish-brown to dark brown, and a yellow powder began to form after ca. 3 h, which after 24 h was separated by filtration, washed with three 15-mL portions of acetone and dried in vacuo at room temperature to give **2**. Yield: 55% based on nickel chloride. Compound **2** does not have a characteristic melting point and upon heating decomposes at >300 °C. $C_{24}H_{22}Cl_2N_{10}Ni$ (580.1): calcd. C 49.69, H 3.82, N 24.15; found C 49.30, H 4.02, N 24.19. FAB-MS (+) (*m*NBA): *m*/*z* = 507 [M – H]$^+$. IR (KBr): $\tilde{\nu}$ = 3169 [(s br.) $\nu$(NH)], 1642 [(s) $\nu$(C=N)], 1547 [(s) $\delta$(NH)] cm$^{-1}$. $^1$H NMR [300 MHz, CDCl$_3$ (90%) + CD$_3$OD (10%), Me$_4$Si]: $\delta$ = 8.98 [s, 4 H, 2-C*H*(3-py)], 8.53 [d, *J* = 4.4 Hz, 4 H, 4-C*H*(3-py)], 8.26 [d, *J* = 7.9 Hz, 4 H, 6-C*H*(3-py)], 7.34 [dd, *J* = 7.9 and 7.8 Hz, 4 H, 5-C*H*(3-py)] ppm; NH signals were not observed due to proton exchange with the solvent. $^{13}$C{$^1$H} NMR (75.4 MHz, CDCl$_3$ (90%) + CD$_3$OD (10%), Me$_4$Si): $\delta$ = 123.5 [5-*C*H(3-py)], 134.4 [*1*-*C*H-(3-py)], 135.6 [*6*-*C*H(3-py)], 147.7 [*2*-*C*H(3-py)], 149.9 [*4*-*C*H(3-py)], 162.7 [*C*=N(–N)] ppm. Slow concentration in air at ca. 25 °C of a methanol/chloroform (1:1, v/v) solution of **2** resulted in its dehydrochlorination, giving X-ray quality crystals of [Ni{HN=C(3-py)-N(H)$_{0.5}$C(3-py)=NH}$_2$]Cl·2H$_2$O (**2′**).

**X-ray Crystal Structure Determinations:** X-ray quality single crystals of **1′** and **2′** were mounted in inert oil within the cold gas stream of the diffractometer. The X-ray diffraction data were collected with a Nonius Kappa CCD diffractometer at 120 (**1′**) or 100 (**2′**) K. Since the crystals of **2′** were poorly diffracting leading to a lower data quality, the data were collected at lower temperature in order to obtain a satisfactory structure. The Denzo-Scalepack[11] program package was used for cell refinements and data reduction. Structures were solved by direct methods using the SIR-2004 (**1′**) or SHELXS-97 (**2′**) programs.[12,13] A multiscan absorption correction based on equivalent reflections (XPREP in SHELXTL)[14] was applied to all data. The structures were refined with SHELXL-97[15] and the WinGX graphical user interface.[16] Only NH (in **1′** and **2′**) and H$_2$O (in **1′**) hydrogen atoms were located from the difference Fourier map, but not refined. Other hydrogen atoms were placed in idealized positions and constrained to ride on their parent atoms. The hydrogen-bond geometry parameters as well as the crystallographic data for **1′** and **2′** are summarized in Tables 1–3. The molecular structures of **1′** and **2′** are depicted in Figure 1, the perspective representations of hexameric water-containing clusters found in these compounds are drawn in Figure 2, while the crystal packing diagrams exhibiting the formation of extended hydrogen-bonded polymeric patterns are shown in Figure 3. All symmetry codes in the discussion are those of Tables 1 and 2. CCDC-644970 (**1′**) and -644971 (**2′**) contain the supplementary crystallographic data for this paper. These data can be obtained free of charge from The Cambridge Crystallographic Data Centre via www.ccdc.cam.ac.uk/data_request/cif.

 © 2007 Wiley-VCH Verlag GmbH & Co. KGaA, Weinheim 

## Acknowledgments

This work has been partially supported by the Foundation for Science and Technology (FCT), Portugal, and its POCI 2010 programme (FEDER funded), a HRTM Marie Curie Research Training Network (AQUACHEM project, CMTN-CT-2003-503864), the Russian Fund for Basic Research (grant 06-03-90901), and a Grant of St. Petersburg (2006).

[1] a) L. Infantes, S. Motherwell, *CrystEngComm* **2002**, *4*, 454; b) L. Infantes, J. Chisholm, S. Motherwell, *CrystEngComm* **2003**, *5*, 480; c) M. Mascal, L. Infantes, J. Chisholm, *Angew. Chem. Int. Ed.* **2006**, *45*, 32; d) R. Ludwig, *Angew. Chem. Int. Ed.* **2001**, *40*, 1808; e) S. Supriya, S. K. Das, *J. Cluster Sci.* **2003**, *14*, 337.

[2] a) W. H. Zhu, Z. M. Wang, S. Gao, *Dalton Trans.* **2006**, 765; b) J. Wang, L. L. Zheng, C. J. Li, Y. Z. Zheng, M. L. Tong, *Cryst. Growth Des.* **2006**, *6*, 357; c) J. Yang, J.-F. Ma, Y.-Y. Liu, J.-C. Ma, H.-Q. Jia, N.-H. Hu, *Eur. J. Inorg. Chem.* **2006**, 1208; d) S. K. Ghosh, P. K. Bharadwaj, *Inorg. Chem.* **2003**, *42*, 8250.

[3] a) Y. Y. Karabach, A. M. Kirillov, M. F. C. G. da Silva, M. N. Kopylovich, A. J. L. Pombeiro, *Cryst. Growth Des.* **2006**, *6*, 2200; b) M. V. Kirillova, A. M. Kirillov, M. F. C. G. da Silva, M. N. Kopylovich, J. J. R. Fraústo da Silva, A. J. L. Pombeiro, *Inorg. Chim. Acta*, DOI:10.1016/j.ica.2006.12.016.

[4] a) M. C. Das, P. K. Bharadwaj, *Eur. J. Inorg. Chem.* **2007**, 1229; b) I. Ravikumar, P. S. Lakshminarayanan, E. Suresh, P. Ghosh, *Cryst. Growth Des.* **2006**, *6*, 2630; c) P. Ren, B. Ding, W. Shi, Y. Wang, T. B. Lu, P. Cheng, *Inorg. Chim. Acta* **2006**, *359*, 3824; d) Z. G. Li, J. W. Xu, H. Q. Via, N. H. Hu, *Inorg. Chem. Commun.* **2006**, *9*, 969; e) P. S. Lakshminarayanan, D. K. Kumar, P. Ghosh, *Inorg. Chem.* **2005**, *44*, 7540; f) K. Raghuraman, K. K. Katti, L. J. Barbour, N. Pillarsetty, C. L. Barnes, K. V. Katti, *J. Am. Chem. Soc.* **2003**, *125*, 6955.

[5] a) J. R. Butchard, O. J. Curnow, D. J. Garrett, R. G. A. R. Maclagan, *Angew. Chem. Int. Ed.* **2006**, *45*, 7550; b) P. S. Lakshminarayanan, E. Suresh, P. Ghosh, *Angew. Chem. Int. Ed.* **2006**, *45*, 3807; c) M. S. Deshpande, A. S. Kumbhar, V. G. Puranik, K. Selvaraj, *Cryst. Growth Des.* **2006**, *6*, 743; d) A. K. Ghosh, D. Ghoshal, J. Ribas, G. Mostafa, N. R. Chaudhuri, *Cryst. Growth Des.* **2006**, *6*, 36; e) D. L. Reger, R. F. Semeniuc, C. Pettinari, F. Luna-Giles, M. D. Smith, *Cryst. Growth Des.* **2006**, *6*, 1068; f) M. Prabhakar, P. S. Zacharias, S. K. Das, *Inorg. Chem. Commun.* **2006**, *9*, 899; g) R. Custelcean, M. G. Gorbunova, *J. Am. Chem. Soc.* **2005**, *127*, 16362; h) M. K. Saha, I. Bernal, *Inorg. Chem. Commun.* **2005**, *8*, 871.

[6] a) P. Jungwirth, D. J. Tobias, *J. Phys. Chem. B* **2002**, *106*, 6361; b) D. J. Tobias, P. Jungwirth, M. Parrinello, *J. Chem. Phys.* **2001**, *114*, 7036; c) J. H. Choi, K. T. Kuwata, Y. B. Cao, M. Okumura, *J. Phys. Chem. A* **1998**, *102*, 503; d) S. S. Xantheas, *J. Phys. Chem.* **1996**, *100*, 9703; e) G. Markovich, S. Pollack, R. Giniger, O. Cheshnovsky, *J. Chem. Phys.* **1994**, *101*, 9344; f) J. E. Combariza, N. R. Kestner, J. Jortner, *J. Chem. Phys.* **1994**, *100*, 2851; g) L. Perera, M. L. Berkowitz, *J. Chem. Phys.* **1991**, *95*, 1954; h) L. X. Dang, J. E. Rice, J. Caldwell, P. A. Kollman, *J. Am. Chem. Soc.* **1991**, *113*, 2481.

[7] a) M. V. Kirillova, M. F. C. G. da Silva, A. M. Kirillov, J. J. R. Fraústo da Silva, A. J. L. Pombeiro, *Inorg. Chim. Acta* **2007**, *360*, 506; b) C. Di Nicola, Y. Y. Karabach, A. M. Kirillov, M. Monari, L. Pandolfo, C. Pettinari, A. J. L. Pombeiro, *Inorg. Chem.* **2007**, *46*, 221; c) D. S. Nesterov, V. N. Kokozay, V. V. Dyakonenko, O. V. Shishkin, J. Jezierska, A. Ozarowski, A. M. Kirillov, M. N. Kopylovich, A. J. L. Pombeiro, *Chem. Commun.* **2006**, 4605; d) A. M. Kirillov, M. N. Kopylovich, M. V. Kirillova, E. Y. Karabach, M. Haukka, M. F. C. G. da Silva, A. J. L. Pombeiro, *Adv. Synth. Catal.* **2006**, *348*, 159; e) A. M. Kirillov, M. N. Kopylovich, M. V. Kirillova, M. Haukka, M. F. C. G. da Silva, A. J. L. Pombeiro, *Angew. Chem. Int. Ed.* **2005**, *44*, 4345.

[8] a) M. N. Kopylovich, V. Y. Kukushkin, M. Haukka, K. V. Luzyanin, A. J. L. Pombeiro, *J. Am. Chem. Soc.* **2004**, *126*, 15040; b) M. N. Kopylovich, M. Haukka, A. M. Kirillov, V. Y. Kukushkin, A. J. L. Pombeiro, *Chem. Eur. J.* **2007**, *13*, 786; c) M. N. Kopylovich, A. J. L. Pombeiro, A. Fischer, L. Kloo, V. Y. Kukushkin, *Inorg. Chem.* **2003**, *42*, 7239.

[9] a) T. Kajiwara, A. Kamiyama, T. Ito, *Chem. Commun.* **2002**, 1256; b) J. Guo, W.-K. Wong, W.-Y. Wong, *Eur. J. Inorg. Chem.* **2004**, 267; c) J.-P. Zhang, Y.-Y. Lin, X.-C. Huang, X.-M. Chen, *J. Am. Chem. Soc.* **2005**, *127*, 5495; d) I. A. Guzei, K. R. Crozier, K. J. Nelson, J. C. Pinkert, N. J. Schoenfeldt, K. E. Shepardson, R. W. McGaff, *Inorg. Chim. Acta* **2006**, *359*, 1169.

[10] S. V. Kryatov, A. Y. Nazarenko, M. B. Smith, E. V. Rybak-Akimova, *Chem. Commun.* **2001**, 1174.

[11] Z. Otwinowski, W. Minor, "Processing of X-ray Diffraction Data Collected in Oscillation Mode" in *Methods in Enzymology, Macromolecular Crystallography*, Part A (Eds.: C. W. Carter Jr, R. M. Sweet), Academic Press, New York, **1997**, vol. 276, pp. 307–326.

[12] M. C. Burla, R. Caliandro, M. Camalli, B. Carrozzini, G. L. Cascarano, L. De Caro, C. Giacovazzo, G. Polidori, R. Spagna, *J. Appl. Crystallogr.* **2005**, *38*, 381.

[13] G. M. Sheldrick, *SHELXS-97*, University of Göttingen, Germany, **1997**.

[14] G. M. Sheldrick, *SHELXTL*, version 6.14-1, Bruker AXS, Inc., Madison, WI, **2005**.

[15] G. M. Sheldrick, *SHELXL-97*, University of Göttingen, Germany, **1997**.

[16] L. J. Farrugia, *J. Appl. Crystallogr.* **1999**, *32*, 837.

Received: June 26, 2007
Published Online: August 15, 2007

 © 2007 Wiley-VCH Verlag GmbH & Co. KGaA, Weinheim 

DOI: 10.1002/ejic.200700466

# Preparation of Thiocarboxylate, Thiocarbamate and Xanthate Complexes of Pentacoordinate Nickel(II): Insertion of Heterocumulenes Into Nickel(II) Hydroxido Complexes

**M. Dolores Santana,*[a] Magalí Sáez-Ayala,[a] Luís García,[b] José Pérez,[b] and Gabriel García[a]**

**Keywords:** Nickel / Macrocyclic ligands / S ligands / Insertion / NMR spectroscopy / X-ray diffraction

The hydroxido complexes $[Ni(N_3\text{-mc})(\mu\text{-OH})]_2[PF_6]_2$ [$N_3$-mc = 2,4,4-trimethyl-1,5,9-triazacyclododec-1-ene ($N_3$-mc1) or 2,4,4,9-tetramethyl-1,5,9-triazacyclododec-1-ene ($N_3$-mc2)] react in the presence of alcohols with $CS_2$ or PhNCS to yield xanthate $[(N_3\text{-mc})Ni\{S_2C(OR')\}][PF_6]$ or *O*-alkyl *N*-phenylthiocarbamate $[(N_3\text{-mc})Ni\{PhNC(OR')S\}][PF_6]$ complexes; these compounds represent the first examples of N,S-chelating thiocarbamates bound to nickel(II). The reactions of $[Ni(N_3\text{-mc})(\mu\text{-OH})]_2[PF_6]_2$ with thiocarboxylic acids yield the corresponding thiocarboxylate derivatives $[(N_3\text{-mc})Ni\{SC(O)R'\}][PF_6]$. These paramagnetic nickel(II) complexes were characterized by both one- and two-dimensional (COSY) $^1H$ NMR spectroscopic techniques. The crystal structures of $[(N_3\text{-mc2})Ni(S_2COCH_3)][PF_6]$ (**2**), $[(N_3\text{mc2})Ni\{PhNC(OCH_2CH_3)S\}][PF_6]$ (**8**), $[(N_3\text{-mc2})Ni\{SC(O)CH_3\}][PF_6]$ (**10**) and $[(N_3\text{-mc1})Ni\{SC(O)Ph\}][PF_6]$ (**11**) were determined.
(© Wiley-VCH Verlag GmbH & Co. KGaA, 69451 Weinheim, Germany, 2007)

## Introduction

Dimeric hydroxido complexes $[Ni(N_3\text{-mc})(\mu\text{-OH})]_2[PF_6]_2$ [$N_3$-mc = 2,4,4-trimethyl-1,5,9-triazacyclododec-1-ene ($N_3$-mc1) or 2,4,4,9-tetramethyl-1,5,9-triazacyclododec-1-ene ($N_3$-mc2)] have been shown to be good precursors in the synthesis of new coordination compounds. The acid–base reaction of these hydroxido complexes with protic acids leads to the formation of mono-[1–3] or dinuclear[4–6] complexes depending on the nature of the deprotonated ligand.

Dithioacid ligands have rich coordination and organometallic chemistry.[7] These ligands and their metal complexes deserve continuous attention due to their interesting structural and chemical properties, as well as their wide range of applications, for example, industrially as pesticides, vulcanization accelerators, lubricants but also as potent biological pesticides.[8] Those metal complexes were generally prepared by metathesis reactions of transition halides with the alkali metal salt of the corresponding thioacid.[8]

In the past decade, growing interest has been directed towards nickel as a biological and spectroscopically relevant metal. The nickel-containing enzyme urease degrades urea to ammonia and carbamate (and finally $CO_2$). The widely accepted mechanism for urease activity suggests that urea is activated by coordination to one nickel(II) ion in conjunction with extensive hydrogen bonding within the active-site pocket of the protein, and it is subsequently attacked by nucleophilic hydroxide ion bound to the opposite nickel(II) centre; the resulting carbamate species then decomposes further to yield carbonic acid and another molecule of ammonia.[9] Bioinorganic synthetic complexes are particularly relevant to the study of the active site of metalloenzymes, because they provide spectroscopic information against which theoretical results can be compared, and they can also be used to carry out hydrolytic transformations at dinuclear nickel(II) cores that mimic the urease active site.[10]

In previous studies we described the preparation of binuclear carbonate complexes $[\{Ni(N_3\text{-mc})\}_2(\mu\text{-}CO_3)][PF_6]_2$ when $CO_2$ was bubbled (or taken up directly from the atmosphere) through a solution of $[Ni(N_3\text{-mc})(\mu\text{-OH})]_2[PF_6]_2$ in acetone [or if $(NH_4)HCO_3$ was added].[11] Following our systematic study of the reactivity of hydroxido complexes of nickel, we next investigated the reactivity of nonorganometallic hydroxido nickel complexes such as $[Ni(N_3\text{-mc})(\mu\text{-OH})]_2[PF_6]_2$ with related heterocumulenes; carbon disulfide, $CS_2$, or phenylisothiocyanate, PhCNS, in the presence of alcohols R′OH, to form *O*-alkyl dithiocarbonate (xanthate) or *O*-alkyl *N*-phenylthiocarbamate pentacoordinate nickel(II) complexes, respectively. We report herein the first crystal structure of a N,S-chelating *N*-phenylthiocarbamate nickel complex (3D Search using the Cambridge Structural Database, CSD version 5.27, Aug. 2006 release). Thiocarboxylate complexes were also prepared by the acid–base re-

[a] Departamento de Química Inorgánica, Universidad de Murcia, 30071 Murcia, Spain
Fax: +34-968-364-148
E-mail: dsl@um.es
[b] Departamento de Ingeniería Minera, Geológica y Cartográfica – Área de Química Inorgánica, Universidad Politécnica de Cartagena, 30203 Cartagena, Spain

 © 2007 Wiley-VCH Verlag GmbH & Co. KGaA, Weinheim 

action of the hydroxido complexes and the corresponding thioacid. These paramagnetic nickel(II) complexes were characterized by both one- and two-dimensional (COSY) $^1$H NMR spectroscopic techniques; these techniques can provide a wealth of unique information on the electronic, magnetic and molecular properties of the metal-binding sites; however, relatively few two-dimensional $^1$H NMR spectroscopic studies involving $Ni^{II}$ ions in either model complexes or biological systems have been reported.[12]

## Results and Discussion

### Xanthate and Thiocarbamate Complexes

The hydroxido complexes $[Ni(N_3\text{-mc})(\mu\text{-OH})]_2[PF_6]_2$ ($N_3$-mc = $N_3$-mc1, $N_3$-mc2) react with $CS_2$ in R′OH solution to yield the nickel xanthate complexes $[(N_3\text{-mc})Ni\{S_2C(OR')\}][PF_6]$ (**1**–**4**) shown in Scheme 1. The reaction of the nickel hydroxido complexes with PhNCS and alcohols proceeds likewise to yield the *O*-alkyl *N*-phenylthiocarbamate complexes $[(N_3\text{-mc})Ni\{PhNC(OR')S\}][PF_6]$ (**5**–**8**; Scheme 1). The complexes are air-stable, both in solid state and in solution. The new complexes were characterized by partial elemental analyses, $FAB^+$ mass spectrometry and spectroscopic methods (IR, UV/Vis and $^1$H NMR). In acetone solution, these complexes behave as 1:1 electrolytes.[13] The nucleophilicity of the Ni–OH unit in $[Ni(N_3\text{-mc})(\mu\text{-OH})]_2[PF_6]_2$ was used here for the attack on cumulated double bond systems. In these reactions, supposedly, the first step consists of the addition of OH across one double bond, and the second step is an esterification of the coordinated acid $[Ni(N_3\text{-mc})(S\text{–}CS\text{–}OH)]^+$ by the alcohol solvent leading to complexes **1**–**8**.

As observed before for related systems,[14] $CS_2$ was inserted in the presence of one equivalent of methanol to yield xanthogenate complexes. The insertion of *p*-nitrophenyl isothiocyanate in ethanol-stabilized chloroform produced iminothiocarbonate complexes.[15]

Moreover, the reactions of $[NBu_4]_2[\{(C_6F_5)_2Ni(\mu\text{-OH})\}_2]$ with alcohols or amines in the presence of carbon disulfide to afford the corresponding xanthate or dithiocarbamate complexes were previously reported.[16]

Xanthate complexes **1**–**4** exhibit three IR bands in the 1240–1030 cm$^{-1}$ region that are related to the vibrations of the $S_2COR'$ group.[17–20] The 1240 cm$^{-1}$ band has a substantial contribution from C–O–C stretching, the band around 1170 cm$^{-1}$ is mainly a contribution of the ν(C–O) mode and the absorption around 1040 cm$^{-1}$ is entirely ν(C=S).[21]

The presence of the thiocarbamate ligand in **5**–**8** is supported by the IR spectra, which show a band at 1537 or 1524 cm$^{-1}$ assignable to ν(C=N). These values are comparable to those reported for thiocarbamate palladium complexes where the thiocarbamate is coordinated to the metal in a N,S-chelating mode.[22] The IR spectra of complexes **1**–**8** also show the characteristic absorptions of the macrocyclic ligands $N_3$-mc1 and $N_3$-mc2 at 3290–3230 cm$^{-1}$ ν(N–H) and ca. 1660 cm$^{-1}$ ν(C=N) and two strong bands as a result of the presence of the $PF_6^-$ ion at 840 and 560 cm$^{-1}$.[4]

The electronic spectra of **1**–**8** are quite similar and show two d–d transitions in acetone solution with $\lambda_{max}$ between 602 and 639 nm (100–70 M$^{-1}$cm$^{-1}$) and between 360 and 380 nm (ca. 300 M$^{-1}$cm$^{-1}$), which could be assigned to the $^3B_1(F) \rightarrow {}^3E(F)$ and $^3B_1(F) \rightarrow {}^3A_2, {}^3E(P)$ transitions, respectively. Both $\lambda_{max}$ values and molar absorptivities are consistent with a pentacoordinate environment around nickel(II).[23]

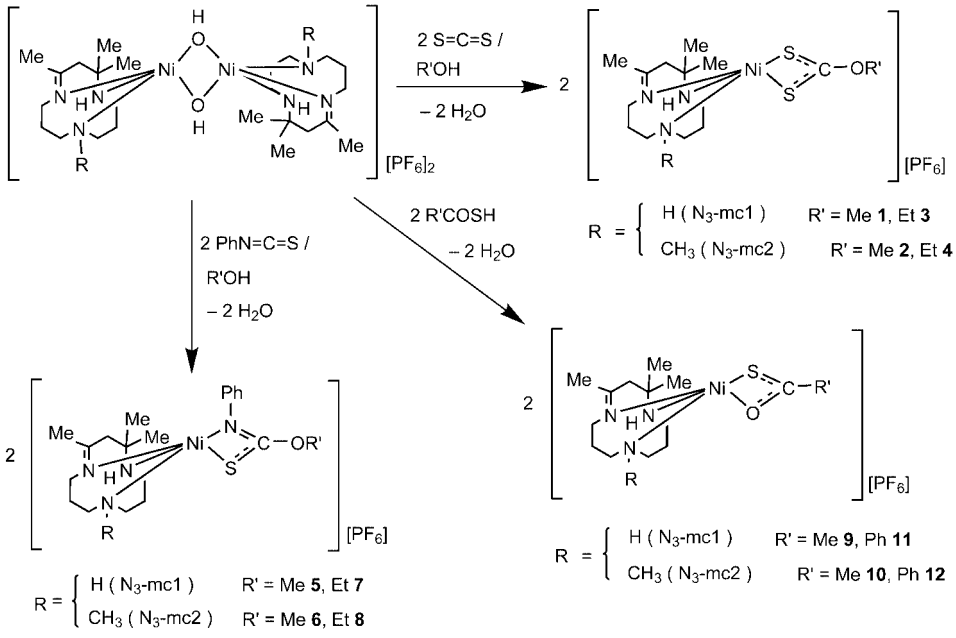


Scheme 1.

 © 2007 Wiley-VCH Verlag GmbH & Co. KGaA, Weinheim 

X-ray diffraction studies were carried out on [($N_3$-mc2)-Ni($S_2COCH_3$)][$PF_6$]·1/2 $(CH_3)_2CO$ (**2**). A thermal ellipsoid drawing of the cation of **2** with a partial labelling scheme is shown in Figure 1. Selected geometric data are given in Table 1. The $Ni^{II}$ ion in **2** adopts a distorted square-pyramidal geometry, and the parameter $\tau$[24] shows a value of 0.16. The three nitrogen atoms of the macrocyclic ligand constitute a trigonal face of the pyramid. The two sulfur atoms from the xanthate and the two nitrogen atoms of the macrocycle form the basal plane (rmsd 0.0591). The nickel ion lies above this plane and is displaced 0.3976 Å toward the N3 nitrogen, which constitutes the axial donor. The plane of the chelate moiety defined by S1, S2, C14 and O1 (rms 0.0015) is inclined by 17.19(6)° to the basal plane. The Ni–N distances lie within the range reported in complexes containing the {Ni($N_3$-mc)} moiety.[11] The Ni–S bond lengths are slightly different [2.3930(9) and 2.5119(9) Å]; thus the xanthate ligand is bonded in an asymmetric chelating mode. These bond lengths are longer than those reported for other crystallographically characterized nickel–xanthate complexes with iminophosphanes in a distorted square-planar geometry.[25] Octahedral nickel–xanthate complexes containing phenanthroline[26] or pyrazine,[27] as well as pentacoordinate nickel–xanthate complexes containing triphosphanes,[28]have shorter Ni–S bond lengths. The bite angle of the chelating xanthate anion shows values of 73.46(3)°. The distortion from square-pyramidal geometry is also reflected in the bond angles between the *trans* ligands. The N1–Ni–S2 and N2–Ni–S1 bond angles are 162.05(9) and 152.61(8)°, respectively. The deviation of these angles from the idealized square-pyramidal geometry is also due to the four-membered chelating ring of the xanthate ligand.

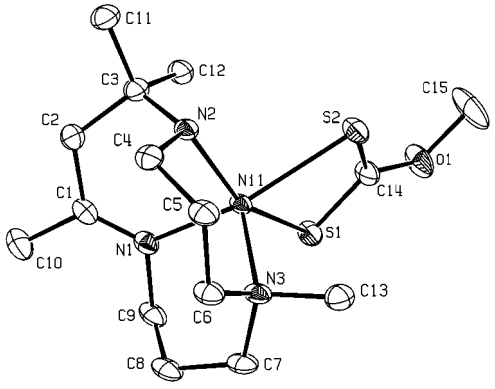


Figure 1. ORTEP drawing of the cation of complex **2** (ellipsoids at 50% probability level) with atom-labelling scheme. For clarity hydrogen atoms are omitted.

Structural studies were also carried out for the complex [($N_3$-mc2)Ni{PhNC($OCH_2CH_3$)S}][$PF_6$] (**8**). As shown in Figure 2 (selected bond lengths and angles in Table 2) the Ni atom has a distorted square-pyramidal geometry with a value of 0.14 for $\tau$. Distortions from the idealized square pyramidal geometry are almost localized in the equatorial plane where the bidentate ligand subtends an angle of 68.17(6)° to the metal. The Ni atom lies above of the basal plane (rmsd 0.0330) by 0.3642 Å. The plane of the chelate moiety defined by the S1, N4, C14 and O1 (rmsd 0.0066) atoms is inclined by 9.49(9)° to the basal plane, and the attached phenyl ring is somewhat rotated [65.33(7)°] about the N4–C17 axis. The C14–O1–C15 angle of 119.26(19)° suggests that the oxygen atom can be considered to be in the $sp^2$-hybridized state, and the C–O bond lengths agree with the values expected for a C($sp^2$)–O–C($sp^3$) system.[29] The C14–S1 bond length of 1.722(2) Å is indicative of a C($sp^2$)–S single bond,[30] whereas double bond character is well-defined in the N4–C14 bond of 1.301(3) Å. Thus, the negative charge within the bidentate ligand seems to be mainly localized on the sulfur atom.[31]

Table 1. Selected bond lengths and angles for complex **2**.[a]

| Bond lengths [Å] | | | |
|---|---|---|---|
| Ni1–N2 | 2.038(3) | Ni1–S1 | 2.3930(9) |
| Ni1–N1 | 2.039(3) | Ni1–S2 | 2.5119(9) |
| Ni1–N3 | 2.062(3) | | |
| **Bond angles [°]** | | | |
| N2–Ni1–N1 | 90.46(11) | N3–Ni1–S1 | 102.64(8) |
| N2–Ni1–N3 | 102.71(11) | N2–Ni1–S2 | 90.26(8) |
| N1–Ni1–N3 | 92.87(11) | N1–Ni1–S2 | 162.05(9) |
| N2–Ni1–S1 | 152.61(8) | N3–Ni1–S2 | 104.45(8) |
| N1–Ni1–S1 | 98.48(8) | S1–Ni1–S2 | 73.46(3) |

[a] Symmetry transformations used to generate equivalent atoms: #1: $-x + 1$, $y$, $-z + 5/2$.

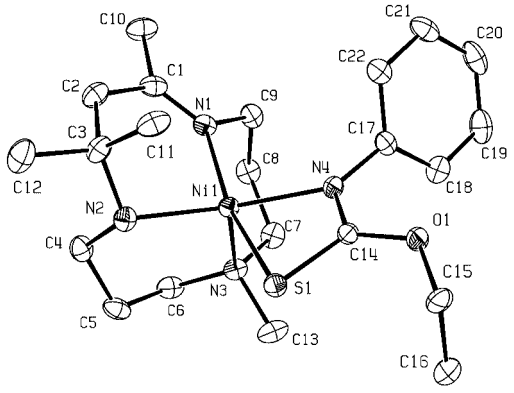


Figure 2. ORTEP drawing of the cation of complex **8** (ellipsoids at 50% probability level) with atom-labelling scheme. For clarity hydrogen atoms are omitted.

Table 2. Selected bond lengths and angles for complex **8**.

| Bond lengths [Å] | | | |
|---|---|---|---|
| Ni1–N1 | 2.034(2) | Ni1–N3 | 2.089(2) |
| Ni1–N2 | 2.048(2) | Ni1–S1 | 2.4927(6) |
| Ni1–N4 | 2.067(2) | | |
| **Bond angles [°]** | | | |
| N1–Ni1–N2 | 90.42(9) | N4–Ni1–N3 | 101.95(8) |
| N1–Ni1–N4 | 100.95(8) | N1–Ni1–S1 | 161.37(6) |
| N2–Ni1–N4 | 152.82(8) | N2–Ni1–S1 | 93.68(6) |
| N1–Ni1–N3 | 93.39(8) | N4–Ni1–S1 | 68.17(6) |
| N2–Ni1–N3 | 101.91(8) | N3–Ni1–S1 | 103.50(6) |

 © 2007 Wiley-VCH Verlag GmbH & Co. KGaA, Weinheim 

The $^1$H NMR spectra of complexes **1**–**8** exhibit sharp isotropically shifted signals from 375 to –40 ppm, in acetone solution. The spectra show the resonance line pattern observed for the $N_3$-mc ligands that was assigned on the basis of previous studies of nickel macrocyclic complexes.[1–6] A representative $^1$H NMR spectrum for complex **1** is shown in Figure 3. The eight resonance signals due to the α-CH protons were shifted downfield, whereas the six resonance signals for the β-CH protons were shifted upfield relative to the diamagnetic position because of a dominant spin polarization mechanism.[32] Moreover, the equatorial protons were expected to experience larger contact shifts than the axial protons because of the angular dependence of the hyperfine coupling constant,[33] and therefore, the most downfield resonances are due to the α-$CH_{eq}$ protons and the most upfield ones to the β-$CH_{eq}$ protons. The isotropically shifted $^1$H NMR signals observed for the methyl groups [2-Me, 4-Me(a, b) and 9-Me-N] and the alkyl groups of the xanthates and thiocarbamates can be initially assigned by inspection of their peak areas. Therefore, on the basis of X-ray structures of **2** and **8**, the larger distortions in the square-pyramid for **8** as a result of the small bite of the N,S-chelating thiocarbamate moiety (68.17°) results in a larger magnetic anisotropy that in turn induces a larger dipolar shift[34] for the *O*-alkyl substituents. The complete assignment of these isotropically shifted signals required the use of two-dimensional $^1$H NMR spectroscopic techniques. A magnitude COSY spectrum of **6** (Figure 4), recorded at 25 °C, clearly shows cross signals between the resonances at $\delta$ = 27.2 and 17.8 ppm and also between resonances at 17.8, –0.9 and –4.8 ppm. These signals can be assigned to the $CH_3O$- and *N*-phenyl *m*-H (17.8), *o*-H (–0.9) and *p*-H (–4.8) protons, respectively, of the *O*-alkyl *N*-phenylthiocarbamate ligand. The shift direction alternation of the *N*-phenyl protons is characteristic if the π-contact shift is dominant. The net spin density in the $d_\pi$ orbitals could be polarized by the unpaired electrons in the $d_{x^2-y^2}$ and $d_{z^2}$ orbitals through spin-orbit coupling. A similar behaviour was observed elsewhere.[35]

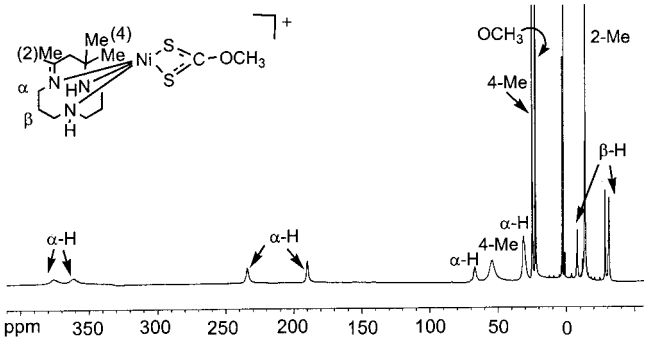


Figure 3. $^1$H NMR spectra [in $(CD_3)_2CO$ solution at room temperature] of complex **1**.

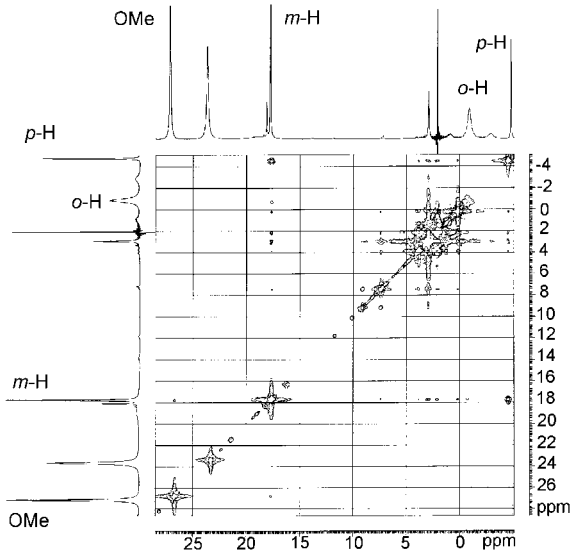


Figure 4. Portion of the $^1$H COSY spectrum of complex **6** [in $(CD_3)_2CO$ solution at 25 °C]. Only the relevant region to assign the *O*-alkyl *N*-phenylthiocarbamate resonances is shown in the top trace.

## Thiocarboxylate Complexes

When $[Ni(N_3\text{-mc})(\mu\text{-OH})]_2[PF_6]_2$ was treated with thioacids $HSC(O)CH_3$ or HSC(O)Ph in acetone, complexes **9**–**12** were obtained in moderate-to-high yields (Scheme 1). The acid–base reaction occurred at room temperature in acetone with the concomitant liberation of water for complexes **9**–**12**. The thiocarboxylates anions, $RC(O)S^-$, constitute an interesting class of ligand having a soft sulfur donor site and a hard oxygen donor site.[36] Furthermore, the chemistry of these ligands was relatively unexplored relative to thiolate or thiocarbamate ligands.[37,38] The IR spectra of complexes **9**–**12** show characteristic absorptions for the $N_3$-mc ligands at 3294–3264 $cm^{-1}$ ν(N–H) and ca. 1660 $cm^{-1}$ ν(C=N), and two strong bands due to the presence of the $PF_6^-$ ion at 840 and 560 $cm^{-1}$ are also observed. The thiocarboxylate ligand in compounds **9**–**12** exhibits a $\kappa^2$-coordination mode to the nickel atom, which is suggested by the IR spectra. The spectra show strong absorption bands at ca. 1500 and ca. 980 $cm^{-1}$, which can be assigned to ν(CO) and ν(CS), respectively, and they are consistent with a symmetrical bidentate coordination.[39] This coordination mode was authenticated by X-ray crystal structure determination on **10** and **11** (vide infra). The crystal structures of cations $[(N_3\text{-mc2})Ni\{SC(O)CH_3\}][PF_6]$ (**10**) and $[(N_3\text{-mc1})Ni\{SC(O)Ph\}][PF_6]$ (**11**) are shown in Figures 5 and 6. Selected distances and angles for these complexes are given in Tables 3 and 4. In each crystallized cation, the nickel atom is five-coordinate, with a square-pyramid arrangement of the chelating atoms. The structure of complex **10** shows the presence of two independent molecules. In each one, the Ni atom shows $\tau$ values of 0.26 and 0.27 for **10** and 0.35 for **11**. The three nitrogen atoms of the $N_3$-macrocycle hold the apical position and two adjacent basal ones, whereas the other two basal positions correspond to the *S*,*O*-thiocarboxylate group. The basal plane is

 © 2007 Wiley-VCH Verlag GmbH & Co. KGaA, Weinheim 

formed by N1, N2, O1 and S1, with a rms deviation of fitted atoms of 0.1076, by N4, N5, O2 and S2, rmsd 0.1132, for **10** and by N1, N2, O1 and S1, rmsd 0.1448, for complex **11**. The Ni atoms are 0.3850(17) and 0.3888(18) Å above of the corresponding basal plane towards the apical N3 or N6 atom in complex **10** and 0.3346(8) Å in **11**. The Ni–O bond lengths in **10** are 2.119(3) and 2.121(3) Å; in complex **11** the Ni–O bond length is 2.1000(15) Å. These bond lengths are comparable to those reported for other crystallographically characterized homoleptic nickel–thiobenzoate complexes with distorted octahedral[38] geometries. The bite angle of the carboxylate anion shows values of 68.73(10) and 68.42(10)° for complex **10** and 69.05(4)° for **11**. The plane of the chelate moiety defined by S1, O1, C14 and C15 (rmsd 0.0066) is inclined 13.93(15)° with respect to the basal plane N1, N2, O1 and S1; and the plane S2, O2, C29 and C30 (rmsd 0.0020) is inclined by 18.96(16)° to the basal N4, N5, O2 and S2 in complex **10**. In complex **11**, the plane of the chelate moiety defined by S1, O1, C13 and C14 (rmsd 0.0041) is inclined by 18.51(8)° to the basal plane N1, N2, O1 and S1, and the angle between the phenyl ring and the nickel-bounded thiocarboxylate group is 16.29(10)°.

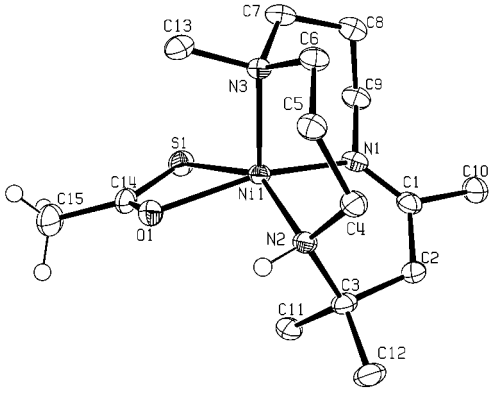


Figure 5. ORTEP drawing of the cation of complex **10** (ellipsoids at 50% probability level) with atom-labelling scheme. For clarity hydrogen atoms are omitted.

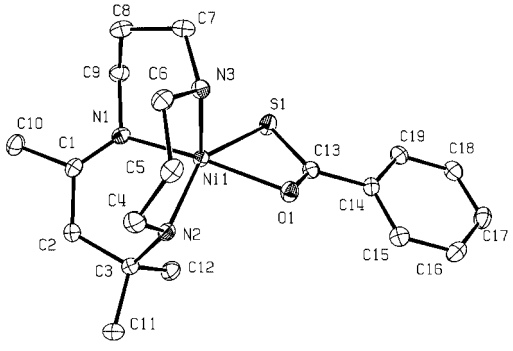


Figure 6. ORTEP drawing of the cation of complex **11** (ellipsoids at 50% probability level) with atom-labelling scheme. For clarity hydrogen atoms are omitted.

Complexes **9**–**12** exhibit relatively sharp hyperfine-shifted $^1$H NMR signals in acetone solution spanning from 390 to –35 ppm. The spectra were assigned on the basis of our previous studies of paramagnetic nickel(II) macrocyclic complexes. The spectra show the expected resonance line pattern because of a dominant spin-polarization mechanism.[32] The spectra of thiocarboxylate derivatives **9**–**12** are similar to those of corresponding complexes **1**–**8** in signals and magnitudes of contact shifts. The mean difference is the large isotropic shift for the $-CH_3$ and –Ph protons, which are consistent with the close proximity of theses groups to the paramagnetic nickel(II) centre. The spectrum of complex **12** is shown in Figure 7, and from its inspection it can be seen that all the resonances of the phenyl rings

Table 3. Selected bond lengths and angles for complex **10**.

| Bond lengths [Å] | | | |
|---|---|---|---|
| Ni1–N1 | 2.013(4) | Ni2–N4 | 2.014(4) |
| Ni1–N2 | 2.030(4) | Ni2–N5 | 2.017(4) |
| Ni1–N3 | 2.047(4) | Ni2–N6 | 2.054(4) |
| Ni1–O1 | 2.119(3) | Ni2–O2 | 2.121(3) |
| Ni1–S1 | 2.4045(13) | Ni2–S2 | 2.4047(13) |
| **Bond angles [°]** | | | |
| N1–Ni1–N2 | 92.25(15) | N4–Ni2–N5 | 91.93(16) |
| N1–Ni1–N3 | 94.47(15) | N4–Ni2–N6 | 94.45(16) |
| N2–Ni1–N3 | 102.78(15) | N5–Ni2–N6 | 102.31(15) |
| N1–Ni1–O1 | 163.40(14) | N4–Ni2–O2 | 163.65(14) |
| N2–Ni1–O1 | 89.70(14) | N5–Ni2–O2 | 89.50(14) |
| N3–Ni1–O1 | 101.17(14) | N6–Ni2–O2 | 101.16(15) |
| N1–Ni1–S1 | 102.17(11) | N4–Ni2–S2 | 102.87(12) |
| N2–Ni1–S1 | 148.10(11) | N5–Ni2–S2 | 147.34(11) |
| N3–Ni1–S1 | 104.24(11) | N6–Ni2–S2 | 105.31(11) |
| O1–Ni1–S1 | 68.73(10) | O2–Ni2–S2 | 68.42(10) |

Table 4. Selected bond lengths and angles for complex **11**.

| Bond lengths [Å] | | | |
|---|---|---|---|
| Ni1–N1 | 2.0016(18) | Ni1–O1 | 2.1000(15) |
| Ni1–N3 | 2.0202(18) | Ni1–S1 | 2.4028(6) |
| Ni1–N2 | 2.0274(17) | | |
| **Bond angles [°]** | | | |
| N1–Ni1–N3 | 93.21(7) | N2–Ni1–O1 | 88.41(6) |
| N1–Ni1–N2 | 93.04(7) | N1–Ni1–S1 | 104.65(5) |
| N3–Ni1–N2 | 101.79(7) | N3–Ni1–S1 | 104.33(5) |
| N1–Ni1–O1 | 168.51(7) | N2–Ni1–S1 | 147.34(5) |
| N3–Ni1–O1 | 97.66(7) | O1–Ni1–S1 | 69.05(4) |

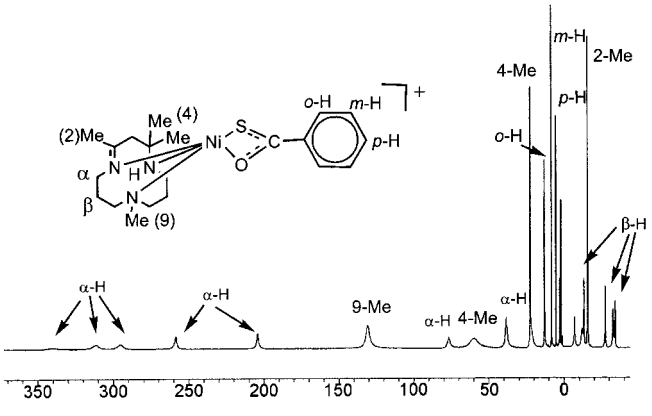


Figure 7. $^1$H NMR spectra [in $(CD_3)_2CO$ solution at room temperature] of complex **12**.

 © 2007 Wiley-VCH Verlag GmbH & Co. KGaA, Weinheim 

are shifted downfield relative to TMS in accordance with a dominant σ-delocalization pattern of spin density that is consistent with the ground state of nickel(II) although the unpaired electrons could polarize the net spin density in the $d_\pi$ orbitals.[6]

## Conclusions

Because many questions still remain about the mechanism of action of the urease metalloenzyme, such as the nature of the hydrolytic attack[40] and the feasibility of carbamate as the first intermediate formed in the reaction,[41] this study investigated the possibility of attack on cumulated double bond systems. In these reactions the proposed first step is the addition of OH across one double bond followed by esterification; however, the external attack by $R'O^-$ of the coordinated heterocumulene cannot be ruled out. Moreover, the proton resonances of the synthetic mononuclear pentacoordinate nickel(II) complexes of relevance to urease were completely assigned by using 1D and 2D $^1H$ NMR spectroscopic methods.

## Experimental Section

**Materials:** Chemicals were purchased from Aldrich and were used without further purification. Solvents were dried and distilled by general methods before use. The complexes $[Ni(N_3\text{-mc})(\mu\text{-OH})]_2[PF_6]_2$ [$N_3$-mc = 2,4,4-trimethyl-1,5,9-triazacyclododec-1-ene ($N_3$-mc1) or 2,4,4,9-tetramethyl-1,5,9-triazacyclododec-1-ene ($N_3$-mc2)] were prepared by previously described procedures.[42,43]

**Physical Measurements:** C, H, N and S analyses were carried out with a microanalyzer Carlo Erba model EA 1108. Fast atom bombardment (FAB) mass spectra were obtained with a Fisons VG Autospec spectrometer operating in the positive mode. Infrared spectra were recorded with a Perkin–Elmer 16F PC FTIR spectrophotometer by using Nujol mulls between polyethylene sheets. UV/Vis spectra (in acetone) were recorded with a UNICAM 520 spectrophotometer equipped with matched quartz cells in the 300–800 nm range. $^1H$ NMR spectra were recorded with a Bruker model AV 200E or AV 300 spectrometer. Chemical shifts (in ppm) are reported with respect to the residual solvent signal. The $^1H$ COSY spectrum was obtained at 25 °C for **6** with 512 data points in the $F^1$ dimension and 4096 data points in the $F^2$ dimension with a delay time of 150 ms. An unshifted sine-bell-squared weighting function was applied prior to Fourier transformation followed by baseline correction in both dimensions and symmetrization. Molar conductivities were measured in acetone solutions (ca. $10^{-3}$ mol L$^{-1}$) with a Crison 525 conductimeter.

**$[(N_3\text{-mc})Ni(S_2COCH_3)][PF_6]$:** To a suspension of $[Ni(N_3\text{-mc})(\mu\text{-OH})]_2[PF_6]_2$ (0.15 mmol) in methanol (60 mL) was added $CS_2$ (0.30 mmol). The mixture was stirred at room temperature for 24 h, and the solvent was partially evaporated under reduced pressure to ca. 15 mL. The mixture was filtered and the addition of diethyl ether caused the precipitation of a green solid, which was collected by filtration, washed with diethyl ether and air-dried.

**$[(N_3\text{-mc1})Ni(S_2COCH_3)][PF_6]$ 1:** Yield: 46 mg (36%). $\Lambda_M$ = 142 Ω$^{-1}$ cm$^2$ mol$^{-1}$. $^1H$ NMR [300 MHz, $(CD_3)_2CO$, TMS]: δ = 375.8 (α-H), 361.7 (α-H), 234.1 (α-H), 189.9 (α-H), 67.0 (α-H), 54.5 (4-Me, 3 H), 31.3 (2 α-H), 24.8 (4-Me, 3 H), 24.0 (α-H), 22.5 ($CH_3O$-, 3 H), –7.9 (β-H), –13.3 (2 β-H), –13.9 (2-Me, 3 H), –28.5 (β-H), –31.0 (β-H), –31.4 (β-H) ppm. IR (nujol): ṽ = 3271, 3237 (N–H), 1658 (C=N), 1238 (COC), 1178 (CO), 1046 (CS) cm$^{-1}$. UV/Vis (acetone): λ (ε, M$^{-1}$cm$^{-1}$) = 611 (100), 384 (446) nm. MS (FAB+): *m/z* (%) = 376 (100) $[M]^+$. $C_{14}H_{28}F_6N_3NiOPS_2$ (522.18): calcd. C 32.20, H 5.40, N 8.05, S 12.28; found C 32.33, H 5.26, N 7.97, S 11.84.

**$[(N_3\text{-mc2})Ni(S_2COCH_3)][PF_6]$ (2):** Yield: 62 mg (51%). $\Lambda_M$ = 139 Ω$^{-1}$ cm$^2$ mol$^{-1}$. $^1H$ NMR [300 MHz, $(CD_3)_2CO$, TMS]: δ = 286.2 (α-H), 243.3 (α-H), 173.3 (α-H), 113.8 (9-Me, 3 H), 59.2 (α-H), 49.4 (4-Me, 3 H), 34.1 (α-H), 30.6 (α-H), 24.3 (4-Me, 3 H), 22.6 (α-H), 20.7 ($CH_3O$-, 3 H), 18.9 (α-H), –6.4 (β-H), –11.2 (β-H), –14.4 (2-Me, 3 H), –17.6 (β-H), –26.9 (β-H), –29.4 (β-H), –33.3 (β-H) ppm. IR (nujol): ṽ = 3271 (N–H), 1651 (C=N), 1228 (COC), 1170 (CO), 1044 (CS) cm$^{-1}$. UV/Vis (acetone): λ (ε, M$^{-1}$cm$^{-1}$) = 639 (100), 392 (395) nm. MS (FAB+): *m/z* (%) = 390 (100) $[M]^+$. Green crystals suitable for X-ray diffraction studies were obtained by diffusion of diethyl ether into an acetone solution of the compound. $C_{15}H_{30}F_6N_3NiOPS_2$ (536.21): calcd. C 33.60, H 5.64, N 7.84, S 11.96; found C 33.15, H 5.57, N 8.00, S 11.53.

**$[(N_3\text{-mc})Ni(S_2COCH_2CH_3)][PF_6]$:** To a suspension of $[Ni(N_3\text{-mc})(\mu\text{-OH})]_2[PF_6]_2$ (0.15 mmol) in ethanol (50 mL) $CS_2$ (0.30 mmol) was added and the resulting mixture was refluxed for 3 h. The solvent was partially evaporated under reduced pressure until ca. 10 mL and then the suspension was filtered. On addition of $Et_2O$ the blue-green complexes precipitated. The solids were filtered off and air-dried.

**$[(N_3\text{-mc1})Ni(S_2COCH_2CH_3)][PF_6]$ (3):** Yield: 50 mg (40%). $\Lambda_M$ = 133 Ω$^{-1}$ cm$^2$ mol$^{-1}$. $^1H$ NMR [300 MHz, $(CD_3)_2CO$, TMS]: δ = 371.0 (α-H), 357.1 (α-H), 231.4 (α-H), 186.2 (α-H), 66.5 (α-H), 53.3 (4-Me, 3 H), 31.4 (2 α-H), 24.5 (4-Me, 3 H), 21.7 (α-H), 9.4 (-$CH_2O$-, 2 H), 8.8 ($CH_3$-, 3 H), –7.8 (β-H), –13.2 (2 β-H), –13.6 (2-Me, 3 H), –28.1 (β-H), –30.4 (β-H), –30.9 (β-H) ppm. IR (nujol): ṽ = 3274, 3247 (N–H), 1652 (C=N), 1237 (COC), 1159 (CO), 1031 (CS) cm$^{-1}$. UV/Vis (acetone): λ (ε, M$^{-1}$cm$^{-1}$) = 616 (96), 385 (418) nm. MS (FAB+): *m/z* (%) = 390 (100) $[M]^+$. $C_{15}H_{30}F_6N_3NiOPS_2$ (536.21): calcd. C 33.60, H 5.64, N 7.84, S 11.96; found C 33.56, H 5.46, N 7.55, S 11.56.

**$[(N_3\text{-mc2})Ni(S_2COCH_2CH_3)][PF_6]$ (4):** Yield: 46 mg (37%). $\Lambda_M$ = 154 Ω$^{-1}$ cm$^2$ mol$^{-1}$. $^1H$ NMR [300 MHz, $(CD_3)_2CO$, TMS]: δ = 289.2 (α-H), 246.5 (α-H), 173.8 (α-H), 113.9 (9-Me, 3 H), 59.7 (α-H), 49.8 (4-Me, 3 H), 34.2 (α-H), 30.7 (α-H), 24.6 (4-Me, 3 H), 22.3 (α-H), 18.8 (α-H), 8.3 (-$CH_2O$-, 2 H), 7.4 ($CH_3$-, 3 H), –6.5 (β-H), –11.4 (β-H), –14.5 (2-Me, 3 H), –17.0 (β-H), –27.3 (β-H), –29.7 (β-H), –33.6 (β-H) ppm. IR (nujol): ṽ = 3271 (N–H), 1651 (C=N), 1217 (COC), 1158 (CO), 1046 (CS) cm$^{-1}$. UV/Vis (acetone): λ (ε, M$^{-1}$cm$^{-1}$) = 633 (115), 391 (454) nm. MS (FAB+): *m/z* (%) = 404 (100) $[M]^+$. $C_{16}H_{32}F_6N_3NiOPS_2$ (550.23): calcd. C 34.93, H 5.86, N 7.64, S 11.66; found C 35.03, H 5.76, N 7.38, S 11.39.

**$[(N_3\text{-mc})Ni\{PhNC(OCH_3)S\}][PF_6]$:** To a suspension of $[Ni(N_3\text{-mc})(\mu\text{-OH})]_2[PF_6]_2$ (0.15 mmol) in methanol (60 mL) was added PhNCS (0.30 mmol). The mixture was stirred at room temperature for 24 h. The solvent was removed under reduced pressure until a blue solid began to precipitate, and then diethyl ether was added to complete precipitation. The solid was filtered off, washed with diethyl ether and air-dried.

**$[(N_3\text{-mc1})Ni\{PhNC(OCH_3)S\}][PF_6]$ (5):** Yield: 94 mg (70%). $\Lambda_M$ = 133 Ω$^{-1}$ cm$^2$ mol$^{-1}$. $^1H$ NMR [300 MHz, $(CD_3)_2CO$, TMS]: δ =

 © 2007 Wiley-VCH Verlag GmbH & Co. KGaA, Weinheim 

367.2 (α-H), 347.8 (α-H), 230.4 (2 α-H), 182.9 (α-H), 75.7 (α-H), 51.0 (4-Me, 3 H), 33.7 (α-H), 30.3 (α-H), 27.9 ($CH_3O$-, 3 H), 23.1 (4-Me, 3 H), 17.5 (2 *m*-H), –2.5 (2 *o*-H), –6.1 (*p*-H), –8.8 (2 β-H), –9.6 (β-H), –13.2 (2-Me, 3 H), –28.6 (β-H), –29.4 (2 β-H) ppm. IR (nujol): $\tilde{\nu}$ = 3290, 3253 (N–H), 1657 (C=N), 1537 (CN) $cm^{-1}$. UV/Vis (acetone): $\lambda$ ($\varepsilon$, $M^{-1}cm^{-1}$) = 602 (70), 366 (272) nm. MS (FAB+): *m/z* (%) = 435 (100) $[M]^+$. $C_{20}H_{33}F_6N_4NiOPS$ (581.23): calcd. C 41.33, H 5.72, N 9.64, S 5.52; found C 40.71, H 5.52, N 9.73, S 5.41.

**[($N_3$-mc2)Ni{PhNC($OCH_3$)S}][$PF_6$] (6):** Yield: 105 mg (79%). $\Lambda_M$ = 136 $\Omega^{-1}cm^2mol^{-1}$. $^1H$ NMR [300 MHz, $(CD_3)_2CO$, TMS]: $\delta$ = 290.4 (α-H), 281.7 (α-H), 251.7 (α-H), 163.5 (α-H), 151.0 (α-H), 112.4 (9-Me, 3 H), 66.2 (α-H), 47.3 (4-Me, 3 H), 38.7 (α-H), 34.1 (α-H), 27.2 ($CH_3O$-, 3 H), 23.7 (4-Me, 3 H), 17.8 (2 *m*-H), –0.9 (2 *o*-H), –4.8 (*p*-H), –7.5 (β-H), –10.6 (β-H), –11.8 (β-H), –13.9 (2-Me, 3 H), –25.8 (β-H), –27.5 (β-H), –31.7 (β-H) ppm. IR (nujol): $\tilde{\nu}$ = 3270 (N–H), 1659 (C=N), 1524 (CN) $cm^{-1}$. UV/Vis (acetone): $\lambda$ ($\varepsilon$, $M^{-1}cm^{-1}$) = 629 (79) 384 (285) nm. MS (FAB+): *m/z* (%) = 449 (100) $[M]^+$. $C_{21}H_{35}F_6N_4NiOPS$ (595.25): calcd. C 42.37, H 5.93, N 9.41, S 5.39; found C 42.62, H 5.73, N 9.27, S 5.17.

**[($N_3$-mc)Ni{PhNC($OCH_2CH_3$)S}][$PF_6$]:** To a suspension of [Ni($N_3$-mc)(μ-OH)]$_2$[$PF_6$]$_2$ (0.15 mmol) in ethanol (40 mL) was added PhNCS (0.30 mmol), and the resulting mixture was heated at reflux for 1 h. The solvent was partially evaporated under reduced pressure until a solid began to precipitate. Upon the addition of diethyl ether, the blue-green complexes precipitated completely. The solid was filtered off and air-dried.

**[($N_3$-mc1)Ni{PhNC($OCH_2CH_3$)S}][$PF_6$] (7):** Yield: 54 mg (40%). $\Lambda_M$ = 137 $\Omega^{-1}cm^2mol^{-1}$. $^1H$ NMR [300 MHz, $(CD_3)_2CO$, TMS]: $\delta$ = 363.9 (α-H), 344.5 (α-H), 228.7 (2 α-H), 180.3 (α-H), 74.9 (α-H), 49.9 (4-Me, 3 H), 33.4 (α-H), 30.0 (α-H), 22.9 (4-Me, 3 H), 17.5 (2 *m*-H), 13.7 (-$CH_2O$-, 2 H), 13.0 ($CH_3$-, 3 H), –2.3 (2 *o*-H), –6.0 (*p*-H), –8.7 (2 β-H), –9.5 (β-H), –13.0 (2-Me, 3 H), –28.3 (β-H), –29.1 (2 β-H) ppm. IR (nujol): $\tilde{\nu}$ = 3292, 3252 (N–H), 1659 (C=N), 1537 (CN) $cm^{-1}$. UV/Vis (acetone): $\lambda$ ($\varepsilon$, $M^{-1}cm^{-1}$) = 607 (75), 364 (293) nm. MS (FAB+): *m/z* (%) = 449 (100) $[M]^+$. $C_{21}H_{35}F_6N_4NiOPS$ (595.25): calcd. C 42.37, H 5.93, N 9.41, S 5.39; found C 42.49, H 5.84, N 9.30, S 5.47.

**[($N_3$-mc2)Ni{PhNC($OCH_2CH_3$)S}][$PF_6$] (8):** Yield: 58 mg (42%). $\Lambda_M$ = 134 $\Omega^{-1}cm^2mol^{-1}$. $^1H$ NMR [300 MHz, $(CD_3)_2CO$, TMS]: $\delta$ = 288.2 (α-H), 280.1 (α-H), 251.1 (α-H), 160.6 (α-H), 149.5 (α-H), 117.1 (9-Me, 3 H), 65.1 (α-H), 46.5 (4-Me, 3 H), 38.3 (α-H), 34.0 (α-H), 23.6 (4-Me, 3 H), 17.8 (2 *m*-H), 14.0 (-$CH_2O$-, 2 H), 12.2 ($CH_3$-, 3 H), –0.6 (2 *o*-H), –4.6 (*p*-H), –7.5 (β-H), –10.4 (β-H), –11.8 (β-H), –13.8 (2-Me, 3 H), –27.3 (β-H), –28.3 (β-H), –31.6 (β-H) ppm. IR (nujol): $\tilde{\nu}$ = 3279 (N–H), 1659 (C=N), 1537 (CN) $cm^{-1}$. UV/Vis (acetone): $\lambda$ ($\varepsilon$, $M^{-1}cm^{-1}$) = 623 (78), 384 (281) nm. MS (FAB+): *m/z* (%) = 463 (100) $[M]^+$. Green crystals suitable for X-ray diffraction studies were obtained by slow evaporation of the reaction mixture. $C_{22}H_{37}F_6N_4NiOPS$ (609.28): calcd. C 43.37, H 6.12, N 9.20, S 5.26; found C 43.29, H 5.96, N 9.02, S 5.47.

**[($N_3$-mc)Ni(A)][$PF_6$] [$N_3$-mc = $N_3$-mc1, A = SC(O)$CH_3$ (9), SC(O)Ph (11); $N_3$-mc = $N_3$-mc2, A = SC(O)$CH_3$ (10), SC(O)Ph (12)]:** These complexes were prepared by reaction of [Ni($N_3$-mc)(μ-OH)]$_2$-[$PF_6$]$_2$ (0.12 mmol) with the corresponding thiocarboxylic acid [HSC(O)$CH_3$ or HSC(O)Ph, 0.24 mmol] in acetone (25 mL). After stirring for 1 h, the solution was filtered and concentrated under reduced pressure to ca. 8 mL. The addition of diethyl ether caused the precipitation of green solids, which were collected by filtration, washed with diethyl ether and air-dried.

**[($N_3$-mc1)Ni{SC(O)$CH_3$}][$PF_6$] (9):** Yield: 90 mg (79%). $\Lambda_M$ = 140 $\Omega^{-1}cm^2mol^{-1}$. $^1H$ NMR [300 MHz, $(CD_3)_2CO$, TMS]: $\delta$ = 370.1 (α-H), 357.9 (α-H), 235.5 (α-H), 213.6 (α-H), 87.0 (α-H), 81.9 ($CH_3$-, 3 H), 72.7 (α-H), 54.9 (4-Me, 3 H), 36.7 (α-H), 31.2 (α-H), 21.8 (4-Me, 3 H), –8.5 (2 β-H), –12.9 (β-H), –13.7 (2-Me, 3 H), –27.2 (β-H), –29.0 (β-H), –30.5 (β-H) ppm. IR (nujol): $\tilde{\nu}$ = 3294, 3269 (N–H), 1659 (C=N), 1503 (C=O), 978 (CS) $cm^{-1}$. UV/Vis (acetone): $\lambda$ ($\varepsilon$, $M^{-1}cm^{-1}$) = 627 (84), 385 (181) nm. MS (FAB+): *m/z* (%) = 344 (100) $[M]^+$. $C_{14}H_{28}F_6N_3NiOPS$ (490.11): calcd. C 34.31, H 5.76, N 8.57, S 6.54; found C 34.55, H 5.80, N 8.63, S 6.44.

**[($N_3$-mc1)Ni{SC(O)Ph}][$PF_6$] (11):** Yield: 120 mg (94%). $\Lambda_M$ = 144 $\Omega^{-1}cm^2mol^{-1}$. $^1H$ NMR [200 MHz, $(CD_3)_2CO$, TMS]: $\delta$ = 384.7 (α-H), 364.5 (α-H), 239.6 (α-H), 240.7 (α-H), 220.3 (α-H), 89.8 (α-H), 56.7 (4-Me, 3 H), 37.5 (α-H), 32.2 (α-H), 22.2 (4-Me, 3 H), 12.2 (2 *o*-H), 8.6 (2 *m*-H), 5.0 (*p*-H), –8.7 (2 β-H), –13.1 (β-H), –13.8 (2-Me, 3 H), –27.6 (β-H), –29.3 (β-H), –30.8 (β-H) ppm. IR (nujol): $\tilde{\nu}$ = 3285, 3268 (N–H), 1656 (C=N), 1594 (C=C), 966 (CS) $cm^{-1}$. UV/Vis (acetone): $\lambda$ ($\varepsilon$, $M^{-1}cm^{-1}$) = 631 (86), 387 (183) nm. MS (FAB+): *m/z* (%) = 406 (100) $[M]^+$. $C_{19}H_{30}F_6N_3NiOPS$ (552.18): calcd. C 41.33, H 5.48, N 7.61, S 5.81; found C 41.45, H 5.39, N 7.53, S 5.70.

**[($N_3$-mc2)Ni{SC(O)$CH_3$}][$PF_6$] (10):** Yield: 87 mg (77%). $\Lambda_M$ = 136 $\Omega^{-1}cm^2mol^{-1}$. $^1H$ NMR [300 MHz, $(CD_3)_2CO$, TMS]: $\delta$ = 340.0 (α-H), 304.0 (α-H), 290.5 (α-H), 252.6 (α-H), 198.6 (α-H), 128.6 (9-Me, 3 H), 79.6 ($CH_3$-, 3 H), 74.7 (α-H), 58.3 (4-Me, 3 H), 37.6 (2 α-H), 22.1 (4-Me, 3 H), –6.8 (β-H), –11.9 (β-H), –12.9 (β-H), –15.6 (2-Me, 3 H), –26.8 (β-H), –32.1 (β-H), –33.4 (β-H) ppm. IR (nujol): $\tilde{\nu}$ = 3264 (N–H), 1656 (C=N), 1519 (C=O), 980 (CS) $cm^{-1}$. UV/Vis (acetone): $\lambda$ ($\varepsilon$, $M^{-1}cm^{-1}$) = 628 (88), 384 (164). MS (FAB+): *m/z* (%) = 358 (100) $[M]^+$. $C_{15}H_{30}F_6N_3NiOPS$ (504.14): calcd. C 35.74, H 6.00, N 8.33, S 6.36; found C 35.70, H 6.00, N 8.29, S 6.32.

**[($N_3$-mc2)Ni{SC(O)Ph}][$PF_6$] (12):** Yield: 112 mg (88%). $\Lambda_M$ = 138 $\Omega^{-1}cm^2mol^{-1}$. $^1H$ NMR [200 MHz, $(CD_3)_2CO$, TMS]: $\delta$ = 340.4 (α-H), 311.6 (α-H), 295.6 (α-H), 258.8 (α-H), 204.4 (α-H), 130.8 (9-Me, 3 H), 76.2 (α-H), 60.2 (4-Me, 3 H), 38.6 (2 α-H), 22.6 (4-Me, 3 H), 13.1 (2 *o*-H), 8.5 (2 *m*-H), 5.5 (*p*-H), –6.8 (β-H), –11.8 (β-H), –12.9 (β-H), –15.5 (2-Me, 3 H), –27.1 (β-H), –32.4 (β-H), –33.7 (β-H) ppm. IR (nujol): $\tilde{\nu}$ = 3267 (N–H), 1658 (C=N), 1495 (C=O), 967 (CS) $cm^{-1}$. UV/Vis (acetone): $\lambda$ ($\varepsilon$, $M^{-1}cm^{-1}$) = 630 (87), 394 (186). MS (FAB+): *m/z* (%) = 420 (100) $[M]^+$. $C_{20}H_{32}F_6N_3NiOPS$ (566.21): calcd. C 42.42, H 5.70, N 7.42, S 5.66; found C 42.49, H 5.65, N 7.39, S 5.56.

**Structure Determination and Refinement:** Single crystals of complexes **2** (blue block), **8** (blue block), **10** (green block) and **11** (blue block) suitable for X-ray diffraction studies were obtained by slow diffusion of diethyl ether onto an acetone solution (**10**, **11** and **2**) or by slowly evaporation of the reaction solution (**8**) of the complex. Crystals were selected and mounted on a glass fibre for data collection. Diffraction data were measured with a Bruker SMART APEX by using Mo-$K_\alpha$ radiation ($\lambda$ = 0.71073 Å). Crystallographic data are summarized in Table 5. The diffraction frames were integrated by using the SAINT package[44] and corrected for absorption with SADABS.[45] The raw intensity data were converted (including corrections for Lorentz and polarization effects) to structure amplitudes and their esd by using the SAINT program. The structures were solved by direct methods[46] and refined[46] by full-matrix least-squares techniques by using anisotropic thermal parameters for non-hydrogen atoms. Hydrogen atoms were set at calculated positions. CCDC-645172 (for **2**), -645173 (for **8**), -645174 (for **10**) and -645175 (for **11**) contain the supplementary crystallographic data for this paper. These data can be obtained free of

 © 2007 Wiley-VCH Verlag GmbH & Co. KGaA, Weinheim 

Table 5. Crystallographic data for complexes **2**, **8**, **10** and **11**.

| Complex | **2** | **8** | **10** | **11** |
|---|---|---|---|---|
| Formula | $C_{15}H_{30}F_6N_3NiOPS_2 \cdot 1/2Me_2CO$ | $C_{22}H_{37}F_6N_4NiOPS$ | $C_{15}H_{30}F_6N_3NiO_1PS \cdot 1/2 Me_2CO$ | $C_{19}H_{30}F_6N_3NiOPS$ |
| $M$ | 565.26 | 609.30 | 533.20 | 552.20 |
| $T$ [K] | 100(2) | 100(2) | 100(2) | 293(2) K |
| Wavelength [Å] | 0.71073 | 0.71073 | 0.71073 | 0.71073 |
| Crystal system | monoclinic | triclinic | triclinic | monoclinic |
| Space group | *C*2/*c* | P1 | $P\bar{1}$ | $P2_1/c$ |
| $a$ [Å] | 22.773(2) | 8.1229(4) | 13.5659(11) | 8.2180(4) |
| $b$ [Å] | 15.2834(15) | 9.0655(5) | 13.8759(11) | 14.3034(6) |
| $c$ [Å] | 14.2077(14) | 10.5412(6) | 14.1725(11) | 19.6944(9) |
| α [°] | 90 | 74.3280(10) | 77.0060(10) | 90 |
| β [°] | 105.6810(10) | 74.4370(10) | 77.2380(10) | 98.4990(10) |
| $\gamma$ [°] | 90 | 67.7310(10) | 62.8690(10) | 90 |
| $V$ [Å$^3$] | 4760.9(8) | 679.54(6) | 2291.8(3) | 2289.56(18) |
| $Z$ | 8 | 1 | 4 | 4 |
| $D_{calcd.}$ [Mg m$^{-3}$] | 1.577 | 1.489 | 1.545 | 1.602 |
| μ [mm$^{-1}$] | 1.121 | 0.914 | 1.071 | 1.074 |
| $F$(000) | 2352 | 318 | 1112 | 1144 |
| Reflections collected | 26434 | 7946 | 26502 | 26189 |
| Independent reflections | 5487 (*R*int = 0.0374) | 5786 (*R*int = 0.0159) | 10217 (*R*int = 0.0284) | 5329 (*R*int = 0.0222) |
| Goodness-of-fit on $F^2$ | 1.260 | 0.807 | 1.203 | 1.090 |
| Final $R$ indices | $R_1$ = 0.0563 | $R_1$ = 0.0304 | $R_1$ = 0.0716 | $R_1$ = 0.0388 |
| $[I > 2\sigma(I)]$[a,b] | $wR_2$ = 0.1424 | $wR_2$ = 0.0730 | $wR_2$ = 0.1709 | $wR_2$ = 0.0938 |
| $R$ indices (all data) | $R_1$ = 0.0572 | $R_1$ = 0.0319 | $R_1$ = 0.0765 | $R_1$ = 0.0395 |
| | $wR_2$ = 0.1430 | $wR_2$ = 0.0739 | $wR_2$ = 0.1737 | $wR_2$ = 0.0943 |
| Max/min $\Delta\rho$[e Å$^{-3}$] | 1.021/–0.572 | 0.515/–0.258 | 1.340/–0.654 | 0.767/–0.666 |

[a] $R_1 = \Sigma \, ||F_o|-|F_c|| / \Sigma |F_o|$ for reflections with $I > 2\sigma I$. [b] $wR_2 = \{\Sigma[w(F_o^2 - F_c^2)^2] / \Sigma[w(F_o^2)^2]\}^{1/2}$ for all reflections; $w^{-1} = \sigma^2(F^2) + (aP)^2 + bP$, in which $P = (2F_c^2 + F_o^2)/3$ and $a$ and $b$ are constants set by the program.

charge from The Cambridge Crystallographic Data Centre via www.ccdc.cam.ac.uk/data_request/cif.

## Acknowledgments

Financial support from the Comunidad Autónoma de la Región de Murcia (Projects 00484/PI/04 and 03010/PI/05), Spain, is gratefully acknowledged.

[1] M. D. Santana, G. García, J. Pérez, E. Molins, G. López, *Inorg. Chem.* **2001**, *40*, 5701–5703.
[2] J. Pérez, L. García, A. G. Orpen, M. D. Santana, P. Saez, G. García, *New J. Chem.* **2002**, *26*, 726–731.
[3] J. Ruiz, M. D. Santana, A. Lozano, C. Vicente, G. García, G. López, J. Pérez, L. García, *Eur. J. Inorg. Chem.* **2005**, 3049–3056.
[4] M. D. Santana, G. García, A. A. Lozano, G. López, J. Tudela, J. Pérez, L. García, L. Lezama, T. Rojo, *Chem. Eur. J.* **2004**, *10*, 1738–1746.
[5] M. D. Santana, G. García, M. Julve, F. Lloret, J. Pérez, M. Liu, F. Sanz, J. Cano, G. López, *Inorg. Chem.* **2004**, *43*, 2132–2140.
[6] M. D. Santana, A. A. Lozano, G. García, G. López, J. Pérez, *Dalton Trans.* **2005**, 104–109.
[7] M. El-khatteb, K. J. Asali, A. Lataifeh, *Polyhedron* **2006**, *25*, 1695–1699.
[8] A. Decken, C. R. Eisnor, R. A. Gossage, S. M. Jackson, *Inorg. Chim. Acta* **2006**, *359*, 1743–1753.
[9] F. Meyer, E. Kaifer, P. Kircher, K. Heinze, H. Pritzkow, *Chem. Eur. J.* **1999**, *5*, 1617–1630.
[10] G. Estiu, K. M. Merz Jr, *J. Am. Chem. Soc.* **2004**, *126*, 11832–11842.
[11] A. A. Lozano, M. Sáez, J. Pérez, L. García, L. Lezama, T. Rojo, G. López, G. García, M. D. Santana, *Dalton Trans.* **2006**, 3906–3911.
[12] Examples of $^1$H NMR spectra of nickel(II) complexes: a) R. C. Holz, E. A. Evodokimov, F. T. Gobena, *Inorg. Chem.* **1996**, *35*, 3808–3814; b) C. Belle, C. Bougault, M.-T. Averbuch, A. Durif, J.-L. Pierre, J.-M. Latour, L. Le Pape, *J. Am. Chem. Soc.* **2001**, *123*, 8053–8066; c) E. Szajna, P. Dobrowolski, A. L. Fuller, A. M. Arif, L. Berreau, *Inorg. Chem.* **2004**, *43*, 3988–3997; d) A. Sánchez-Méndez, J. M. Benito, E. de Jesús, F. J. de la Mata, J. C. Flores, R. Gómez, P. Gómez-Sal, *Dalton Trans.* **2006**, 5379–5389.
[13] W. J. Geary, *Coord. Chem. Rev.* **1971**, *7*, 81–122.
[14] M. Ruf, H. Vahrenkamp, *Inorg. Chem.* **1996**, *35*, 6571–6578.
[15] M. Rombach, H. Brombacher, H. Vahrenkamp, *Eur. J. Inorg. Chem.* **2002**, 153–159.
[16] G. López, G. Sánchez, G. García, J. García, A. Sanmartín, M. D. Santana, *Polyhedron* **1991**, *10*, 2821–2825.
[17] M. C. Cornock, R. O. Gould, C. L. Jones, J. D. Owen, D. F. Steele, T. A. Stephenson, *J. Chem. Soc. Dalton Trans.* **1977**, 496–501.
[18] A. A. M. Aly, M. S. El-Meligy, A. S. A. Zidau, *Transition Met. Chem.* **1989**, *14*, 366–368.
[19] M. Moran, I. Cuadrado, C. Muñoz-Reja, J. R. Masaguer, J. Losada, *J. Chem. Soc. Dalton Trans.* **1988**, 149–154.
[20] D. Coucouvanis, J. P. Fackler, *Inorg. Chem.* **1967**, *6*, 2047–2053.
[21] U. Agarwala, P. B. Rao, *Inorg. Chim. Acta* **1968**, *2*, 337–339.
[22] J. Ruiz, V. Rodriguez, C. de Haro, J. Pérez, G. López, *Inorg. Chim. Acta* **2004**, *357*, 2331–2338.
[23] A. B. P. Lever, *Inorganic Electronic Spectroscopy*, Elsevier, Amsterdam, **1984**, pp. 513–520.
[24] A. W. Addison, T. N. Rao, J. Reedijk, J. V. Rijn, G. C. Verschoor, *J. Chem. Soc. Dalton Trans.* **1984**, 1349–1356.
[25] J. L. Serrano, L. García, J. Pérez, E. Pérez, G. Sánchez, J. García, G. López, G. García, E. Molins, *Inorg. Chim. Acta* **2003**, *355*, 33–40.
[26] R.-G. Xiong, C.-M. Liu, J.-L. Zuo, H.-Z. Li, X.-Z. You, H.-K. Fun, K. Sivakumar, *Polyhedron* **1997**, *16*, 2315–2319.
[27] Z. Trávícek, R. Pastorek, Z. Šindelár, J. Kamenícek, *Polyhedron* **1996**, *15*, 2975–2981.

 © 2007 Wiley-VCH Verlag GmbH & Co. KGaA, Weinheim 

[28] L. Ballester, A. Gutierrez, M. F. Perpiñan, C. Ruiz-Valero, *Polyhedron* **1996**, *15*, 1103–1112.
[29] L. E. Sutton, *Tables of Interatomic Distances and Configuration in Molecules and Ions: Special Publication No. 18 (Supplement)*, The Chemical Society, London, **1956**–**1959**.
[30] R. D. G. Jones, L. F. Pawer, *Acta Crystallogr., Sect. B* **1976**, *32*, 1801–1806.
[31] R. Rossi, A. Marchi, S. Aggio, L. Magon, A. Duatti, U. Casellato, R. Graziani, *J. Chem. Soc. Dalton Trans.* **1990**, 477–481.
[32] R. H. Holm, C. J. Hawkins, *NMR of Paramagnetic Molecules: Principles and Applications* (Eds.: G. N. La Mar, W. Horrocks Jr, R. H. Holm), Academic Press, New York, **1973**, pp. 243–332.
[33] A. Dei, M. Wicholas, *Inorg. Chim. Acta* **1989**, *166*, 151–154.
[34] I. Bertini, C. Luchinat, *NMR of Paramagnetic Molecules in Biological Systems*, Benjamin & Cummings, Menlo Park, CA, **1986**.
[35] M. D. Santana, A. Rufete, G. García, G. López, J. Casabó, A. Cabrero, E. Molins, C. Miravitlles, *Polyhedron* **1997**, *16*, 3713–3721.
[36] R. Devy, J. J. Vittal, P. A. W. Dean, *Inorg. Chem.* **1998**, *37*, 6939–6941.
[37] T. C. Deivaraj, J. J. Vittal, *Acta Crystallogr., Sect. C* **2000**, *56*, 775–776.
[38] J. J. Vittal, M. Tack NG, *Acc. Chem. Res.* **2006**, *39*, 869–877.
[39] V. V. Savant, J. Gopalakrishnan, C. C. Patel, *Inorg. Chem.* **1970**, *9*, 748–751.
[40] M. Zimmer, *J. Biomol. Struct. Dyn.* **2000**, *17*, 787–797.
[41] A. M. Barrios, S. J. Lippard, *Inorg. Chem.* **2001**, *40*, 1250–1255.
[42] J. W. L. Martin, J. H. Johnston, N. F. Curtis, *J. Chem. Soc. Dalton Trans.* **1978**, 68–75.
[43] A. Escuer, R. Vicente, J. Ribas, *Polyhedron* **1992**, *11*, 453–456.
[44] *SAINT version 6.02*, Bruker Analytical X-ray Systems, Madison, WI, **1996**.
[45] G. M. Sheldrick, *SADABS: Empirical Absorption Program*, University of Göttingen, Göttingen, Germany, **1996**.
[46] G. M. Sheldrick, *SHELXS-97 and SHELXL-97*, *Programs for Crystals Structure Solution and Refinement*, University of Göttingen, Göttingen, Germany, **1997**.

Received: April 27, 2007
Published Online: August 17, 2007

 © 2007 Wiley-VCH Verlag GmbH & Co. KGaA, Weinheim 

DOI: 10.1002/ejic.200700469

# Methylation of a Terdentate Schiff Base Ligand *NNO*-Coordinated to Palladium with Nitromethane

**Ana M. Arnaiz,[a] Arancha Carbayo,[a] José V. Cuevas,*[a] Virginia Diez,[a] Gabriel García-Herbosa,[a] Roberto González,[a] Abigail Martínez,[a] and Asunción Muñoz[a]**

**Keywords:** Palladium / Henry reaction / Nucleophilic attack / Nitroaldol / Schiff bases

The reaction of the complex [Pd(κ$^3$-NN′O)CH$_3$] [NN′O = 2-Py-CH=N-(*o*-C$_6$H$_4$)O$^-$] (**1a**) with nitromethane affords a mixture of **2a** and **2b**. In this reaction methylation of the ligand takes place. These complexes display exchange equilibrium in solution. The methylation reaction is proposed to occur through nucleophilic attack of the nitronate anion on the iminic carbon atom. DFT calculations are presented in order to support a part of the mechanism and these calculations show that the participation of water in the migration of a proton is important. The crystal structure of the derivative product after spontaneous release of methane (**3**) is presented as well. Attempts to extend the reaction to other nitroalkanes resulted in a mixture of complexes that was not easy to characterize.

(© Wiley-VCH Verlag GmbH & Co. KGaA, 69451 Weinheim, Germany, 2007)

## Introduction

There has been increasing interest in the inorganic and organometallic chemistry of nitroalkanes. Nitroaldol (Henry) condensation is a highly versatile carbon–carbon bond formation reaction, which allows the synthesis of a huge number of interesting molecular frameworks.[1,2] In recent years considerable efforts have been devoted to developing asymmetric versions of the Henry reaction.[3] The work of Palomo et al.[3] highlights the advances in stereocontrol in these reactions that have been achieved by the use of catalysts such as cinchona alkaloids, guanidine bases, quaternary ammonium salts, or complexes of copper, zinc, or lithium/lanthanum. Recent advances on complexes of copper,[4–11] lanthanum,[12] cobalt,[13] or zinc,[11] which can act as catalysts for the asymmetric nitroaldol reaction, have been reported.

It is proposed that the metal-catalyzed nitroaldol reaction occurs through a mechanism involving *O* coordination of monodentate nitronate to the metal center.[14,15] To the best of our knowledge there are only two complexes that have a nitronate ligand coordinated to a metallic center in this way.[16] Additionally, Evans et al. reported that weakly Lewis acidic metal complexes bearing moderately basic, charged ligands may facilitate the deprotonation of nitroalkanes.[4]

In previous works of our group we have studied the dynamic behavior and the catalytic activity of palladium complexes with bi- and tridentate nitrogen donor ligands.[17,18] Those complexes have pyridine–imine donor ligands. Pelagatti et al.[19] have reported the synthesis of a palladium complex very similar to the complexes that we have studied, incorporating an additional coordination position with basic character, which could be a good candidate to catalyze the Henry reaction. In this work we report the behavior of the nitronate as a nucleophilic reagent towards this palladium complex.

## Results and Discussion

The deep purple solution of complex **1a** in nitromethane at room temperature afforded a yellow precipitate that was characterized as **2** where the *N*,*N*′,*O* tridentate ligand became only *N*,*N*′ bidentate and was methylated at the iminic carbon (see Scheme 1). For complex **2** it is possible to propose two isomers, labeled in Scheme 1 as **2a** and **2b**.

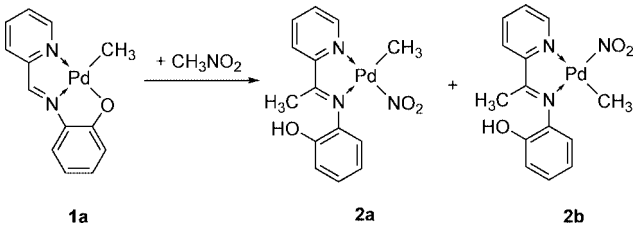


**1a** **2a** **2b**

Scheme 1.

The $^1$H NMR characterization of the reaction products was carried out in [D$_6$]DMSO because of their low solubility in other less coordinating solvents. This NMR spectrum shows two signals belonging to methyl groups bonded to

[a] Departamento de Química, Universidad de Burgos, Plaza Misael Bañuelos S/N, 09001 Burgos, Spain
E-mail: jvcv@ubu.es

Supporting information for this article is available on the WWW under http://www.eurjic.org or from the author.

 © 2007 Wiley-VCH Verlag GmbH & Co. KGaA, Weinheim 

palladium at $\delta$ = 0.60 and 0.14 ppm, which is consistent with the presence of both isomers in solution. In the analysis of the values of the integrals, the isomer where the methyl group appears at $\delta$ = 0.14 ppm is ten times more abundant than the other isomer. The comparison of these chemical shifts with the values reported for similar palladium–methyl complexes with pyridine–imine ligands[20] indicates that the signal of the palladium–methyl group located in *cis* position to the pyridine ring appears downfield when compared with the same signal in the complex with the methyl group in *trans* position to the pyridine ring. Therefore, in this case, the values of the integrals indicate that the dominant isomer is **2b**. Furthermore, isomers **2a** and **2b** undergo a dynamic equilibrium in solution. A NOESY experiment (see Figure 1) shows that the signal appearing at $\delta$ = 0.14 ppm has peaks out of the diagonal; the signals belong to the $H^6$ of the pyridine ring and the *ortho*-hydrogen of the phenyl ring, which is consistent with such equilibrium. The EXSY phase of the same experiment (see Figure 2) shows peaks out of the diagonal for the signals appearing at $\delta$ = 0.14 and 0.60 ppm, also indicating the presence of the equilibrium between **2a** and **2b**.

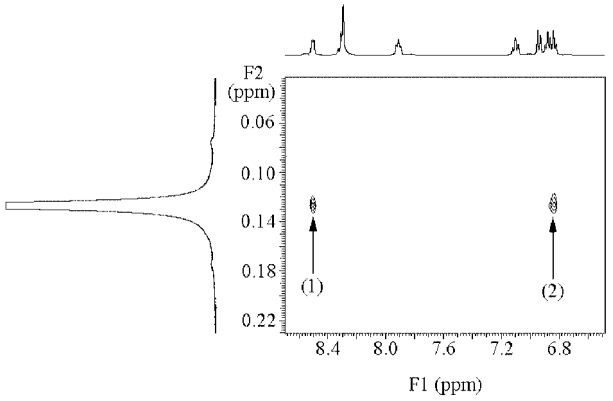


Figure 1. Expansion of the NOESY spectrum for mixture of complexes **2a** and **2b**. (1) Peak out of diagonal of the peak Pd–Me in **2b** with the $H^6$ signal of the pyridine ring. (2) Peak out of diagonal of the peak Pd–Me in **2b** with the *ortho*-hydrogen of the phenyl.

At first glance, the product of the reaction is similar to a Henry reaction product,[1,2] but there are some important differences. In our case, the bond between the nitrogen atom and the methyl carbon is broken, and the resulting nitro group is coordinated to the palladium atom. The other important difference is that the bond between the carbonylic carbon and the nitrogen atom remains as a double bond and is not transformed into a single bond as occurs in Henry reactions. For the process that we have found, the acid/base equilibrium of nitromethane can be taken into account.[21,22] This equilibrium generates a nitronate carbanionic nucleophile and a proton. We suggest that in the first step the proton attacks the phenoxide to generate the phenolic group, as shown in Scheme 2. The next step, which can be simultaneous to the previous step, is the attack of the nucleophile on the carbonylic carbon of the coordinated imine. Nucleophilic attacks on coordinated imines are

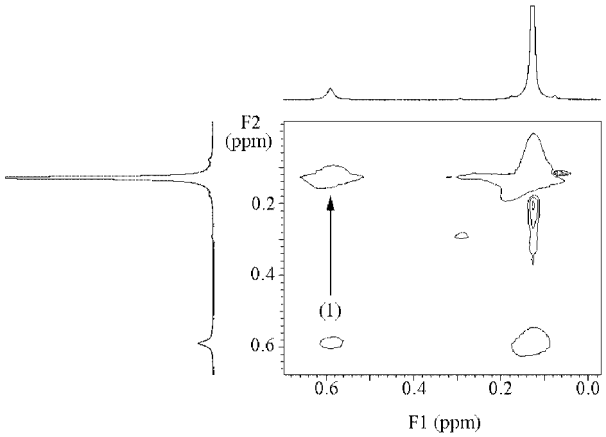


Figure 2. Expansion of the NOESY spectrum for mixture of complexes **2a** and **2b**. (1) EXSY signal out of the diagonal showing the exchange between Pd–Me groups in isomers **2a** and **2b**.

known,[23–27] and the nucleophilic behavior of nitronates has been reported as well;[14,28,29] even the nitronate attack on an imine coordinated to cobalt has been reported.[30] In our proposed mechanism, this nucleophilic attack is followed by the breaking up of the C–N bond of the nitronate fragment in an analogous way to that described for a cobalt[23] or a nickel complex[31] (see Scheme 3).

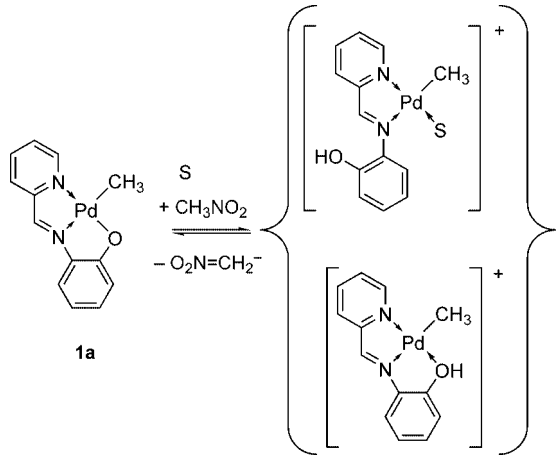


Scheme 2.

In this process, the nucleophilic attack of the carbanion on the iminic carbon atom generates the compound with structure II. This compound can release nitrous acid to afford the compound of structure III. Next, the hydrogen atom bonded to the aminic nitrogen atom "jumps" to the methylenic carbon to generate the complex with structure IV in a process of imine–enamine tautomerism. This migration of the proton has to be aided by a molecule of water, as we have found in theoretical calculations (see below). The process without water displays high activation barriers, as we will discuss later. Finally, the protonation of structure IV with the nitrous acid released earlier affords the observed products **2a** and **2b**.

In order to support this proposed mechanism, we carried out $^1$H NMR measurements of **1a** dissolved in $CD_3NO_2$

 © 2007 Wiley-VCH Verlag GmbH & Co. KGaA, Weinheim 

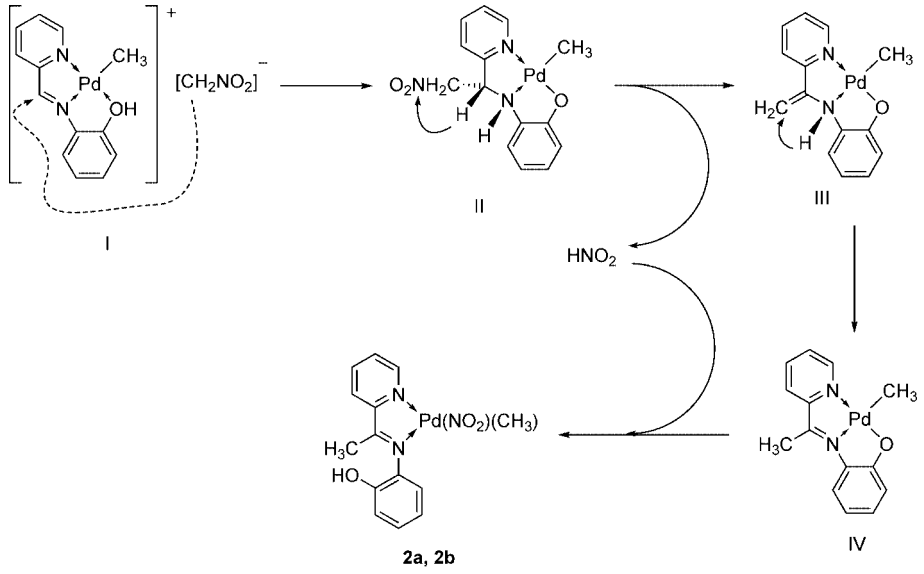


Scheme 3.

and in $CD_3NO_2/D_2O$, and $^1H$ NMR measurements of the products of these reactions dissolved in [$D_6$]DMSO, but they did not shed light on the proposal.

The slow evaporation of the mother liquors of the reaction for the preparation of complexes **2** afforded a crystal suitable for structural X-ray analysis, but not enough crystals for spectroscopic characterization. The structure of the crystal is not the structure proposed for complexes **2a** or **2b** but a complex **3** in which one molecule of methane has been lost by deprotonation of the phenolic proton, (see Scheme 4). The acidity of the phenolic proton seems to be sufficient to cause such slow methane elimination.[19,32]

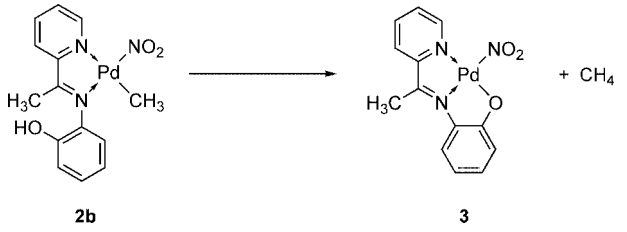


Scheme 4.

## Structure of Complex 3

The molecular structure of complex **3** is shown in Figure 3, and selected bond lengths, bond angles, and torsion angles are given in Table 1. The chelating ligand binds to the metal through a pyridyl donor N(1), secondary imine donor N(2), and aryloxide oxygen O(1). The N(1)–Pd(1)–N(2) bond angle is 81.25(13)° and the N(2)–Pd(1)–O(1) bond angle is 84.95(12)°. The pyridyl donor makes a slightly larger bond to the metal than the imine does. The torsion angles N(1)–C(5)–C(6)–N(2) and N(2)–C(8)–C(13)–O(1) are close to planarity, with values of 5.0(5)° and 0.9(5)° respectively. The nitro group is out of the coordination plane of the palladium as the torsion angle O(1)–Pd(1)–N(3)–O(3) is –136.5(3)°.

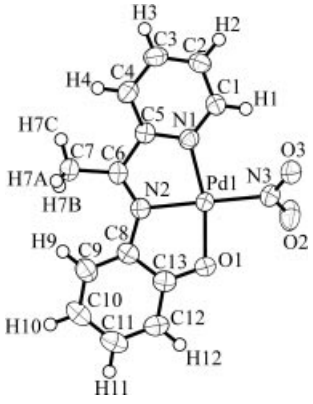


Figure 3. Molecular geometry for complex **3**.

Table 1. Selected bond lengths [Å] and angles [°] for compound **3**.

| Distances [Å] | | Angles [°] | |
|---|---|---|---|
| Pd(1)–N(2) | 1.979(3) | N(2)–Pd(1)–O(1) | 84.95(12) |
| Pd(1)–O(1) | 1.997(3) | N(2)–Pd(1)–N(3) | 178.06(11) |
| Pd(1)–N(3) | 2.011(3) | O(1)–Pd(1)–N(3) | 94.41(13) |
| Pd(1)–N(1) | 2.013(3) | N(2)–Pd(1)–N(1) | 81.25(13) |
| N(1)–C(5) | 1.355(5) | O(1)–Pd(1)–N(1) | 166.17(12) |
| N(2)–C(6) | 1.293(5) | N(3)–Pd(1)–N(1) | 99.40(13) |
| N(3)–O(2) | 1.229(4) | O(2)–N(3)–O(3) | 119.3(3) |
| N(3)–O(3) | 1.247(4) | | |
| O(1)–C(13) | 1.321(5) | N(1)–C(5)–C(6)–N(2) | 5.0(5) |
| C(5)–C(6) | 1.489(5) | N(2)–C(8)–C(13)–O(1) | 0.9(5) |
| | | O(1)–Pd(1)–N(3)–O(3) | –136.5(3) |
| | | N(1)–Pd(1)–N(3)–O(3) | 43.1(3) |

The packing of the crystal is built up through hydrogen bonds and π–π interactions. There are two weak intermolecular hydrogen bonds between the oxygen atoms of the nitro group and several hydrogen atoms of the ligand of neighbor complexes. The oxygen atom labeled as O(2) es-

 © 2007 Wiley-VCH Verlag GmbH & Co. KGaA, Weinheim 

tablishes bifurcated hydrogen bonds to the methyl group and arylic hydrogen atoms. The oxygen atom labeled as O(3) establishes trifurcated hydrogen bonds to the methyl group and arylic hydrogen atoms. The values of these hydrogen bonds are displayed in Table 2 and they are in good agreement with the values reported in the literature.[33–35] Additionally, there is a π–π interaction between the π systems of couples of molecules, with a separation between parallel planes (defined by the aromatics systems of the ligand) of 3.385 Å.[36] The combination of all these interactions packs the molecules in columns, as shown in Figure 4.

Table 2. Distances and angles of weak interactions in complex **3**.

| Hydrogen bonds | | | |
|---|---|---|---|
| O(2), bifurcated | | O(3), trifurcated | |
| O(2)–H(2) | 2.603 Å | O(3)–H(1) | 2.678 Å |
| O(2)–C(2) | 3.402 Å | O(3)–C(1) | 3.290 Å |
| O(2)–H(2)–C(2) | 144.37° | O(3)–H(1)–C(1) | 123.95° |
| O(2)–H(7)B | 2.448 Å | O(3)–H(7)A | 2.487 Å |
| O(2)–C(7) | 3.384 Å | O(3)–C(7) | 3.442 Å |
| O(2)–H(7)B–C(7) | 165.01° | O(3)–H(7)A–C(7) | 173.12° |
| | | O(3)–H(3) | 2.472 Å |
| | | O(3)–C(3) | 3.265 Å |
| | | O(3)–H(3)–C(3) | 143.29° |
| Interaction π–π | | | |
| Cj [N(1)–C(5)–C(6)–N(2)–Pd(1)] | | Ci [C(8)–C(9)–C(10)–C(11)–C(12)–C(13)] | |
| Ci–Cj | 3.515 Å | H(12)–Cj–Ci | 35.74° |

Figure 4. Packing of the molecules of complex **3** forming columns. The weak interactions are displayed.

## Deprotonation of 2

The presence of the O–H group in complexes **2** encouraged us to explore its deprotonation. Thus, as shown in Scheme 5, the reaction of the mixture of compounds **2a** and **2b** with KO*t*Bu afforded the expected O–H deprotonation to yield a new compound, **1b**, which is garnet in color. This compound has been characterized by spectroscopic techniques. The $^1$H NMR spectrum shows the presence of the two different methyl groups, a singlet at $\delta$ = 0.51 ppm (belonging to the palladium-bonded methyl) and another singlet at $\delta$ = 2.54 ppm (belonging to the carbonylic methyl).

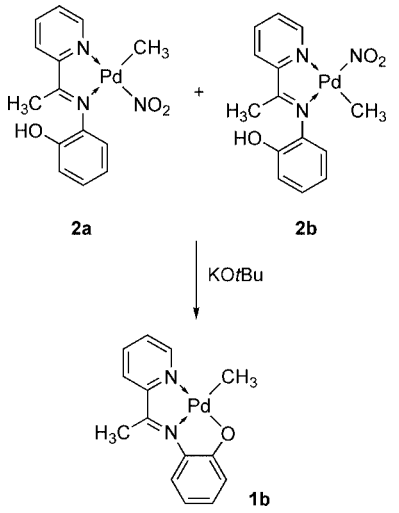


Scheme 5.

The synthesis of complex **1b** was also attempted following an alternate pathway, like that reported for **1a**.[19] However, we were unable to synthesize the *N*,*N*′,*O* tridentate ligand through the conventional condensation of 2-acetylpyridine with 2-aminophenol using Dean–Stark equipment in the presence of a catalytic amount of *p*-toluenesulfonic acid.

## DFT Calculations

In order to rationalize the observed results, DFT quantum chemical calculations were carried out on a model of complex **1a**. The positions of nucleophilic attack should display positive charge. The process starts with the protonation of complex **1a**. It is reasonable to think that the protonation occurs on the oxygen atom, as the NBO analysis[37,38] displays a negative charge on that atom (–0.67). Although the oxygen atom is not the most negatively charged atom (we have found that the methyl carbon atom bonded to the metal has a charge of –0.90), the participation of the $p_z$ atomic orbital of the oxygen in the HOMO and the nonparticipation of any atomic orbital of the carbon atom reinforces this proposal. In addition to the protonation of the oxygen atom, there is a nucleophilic attack of the nitronate anion on the iminic carbon atom. An NBO analysis displays a positive charge on the iminic carbon (0.016). Although this value is not the most positive value (palladium atom has a value of 0.690), there is strong participation of the orbitals of the π system in the LUMO of the complex and the iminic carbon atom is a place for nucleophilic attack analogous to that observed for the Henry reaction,[1,2] accounting for the observed reaction of the nitromethane.

We have modeled the migration of the hydrogen atom from the nitrogen atom to the carbon atom, as depicted in steps III–IV in Scheme 3. This process was proposed by other authors[23,31] on similar systems. The compound with structure III comes from the compound with structure II through the loss of nitrous acid. We have found that glob-

 © 2007 Wiley-VCH Verlag GmbH & Co. KGaA, Weinheim 

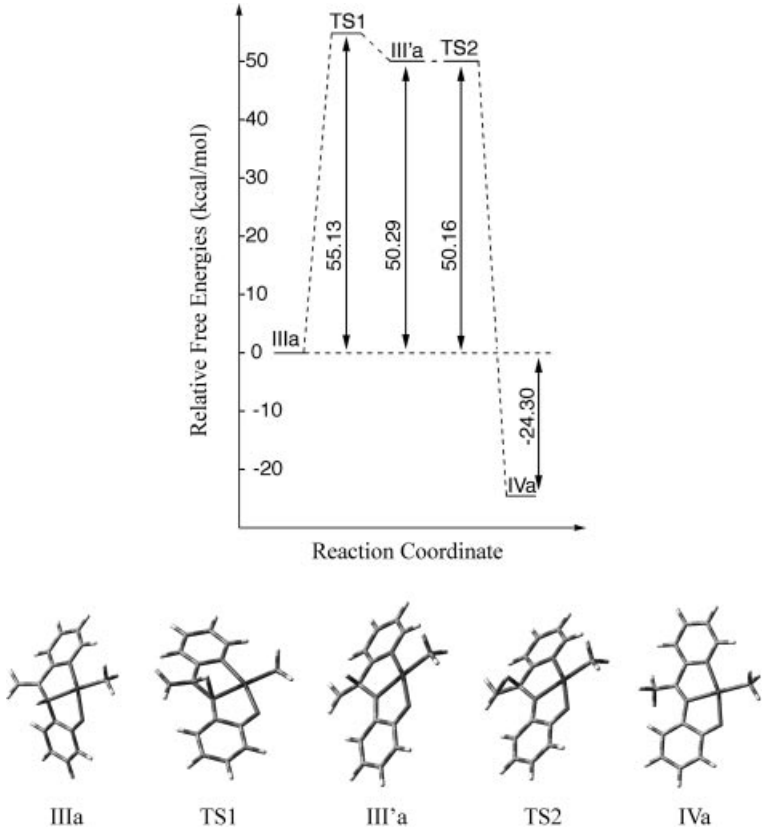


Figure 5. Calculated reaction pathway in the migration of the hydrogen atom without any molecule of water.

ally this process is an imine–enamine tautomerism through two steps. The first step is the migration of the aminic hydrogen atom from the nitrogen to the adjacent carbon atom (structure III′ in Scheme 6). This first step is highly endothermic (50.3 kcal/mol), with a high activation energy (55.1 kcal/mol). The second step of the tautomerism is a new migration of the hydrogen atom to generate the methyl and the double bond C=N (structure IV in Scheme 3; see Figure 5). This step has an activation energy very close to 0 kcal/mol, and the complete process is exothermic (–24.3 kcal/mol), taking as reference the energy of structure III.

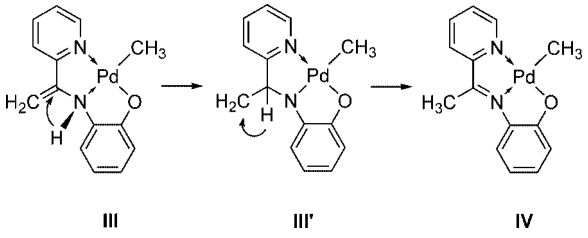


Scheme 6.

The high value of the activation energy makes this mechanism unreliable. We thought that perhaps a molecule of water could help the migration of the proton. The addition of a molecule of water to structure III (see Scheme 3) established a hydrogen bond with the oxygen atom of the aryloxide fragment, stabilizing the structure. A second molecule of water established a hydrogen bond with the amine hydrogen atom, and this molecule is the carrier of the hydrogen atom to the carbon atom (see Figure 6). In

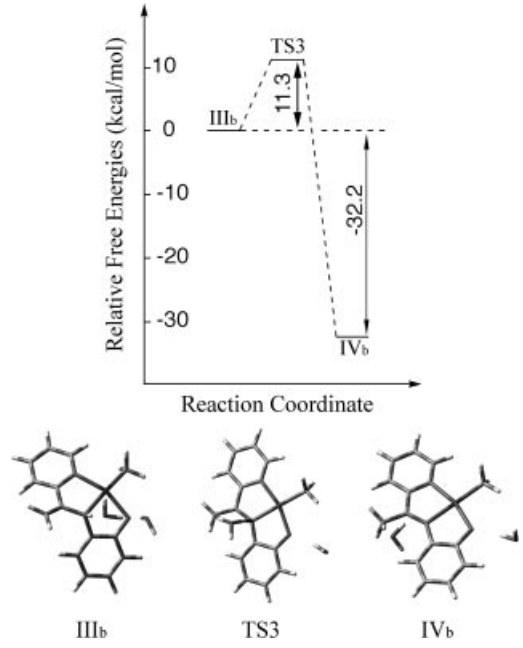


Figure 6. Calculated reaction pathway in the migration of the hydrogen atom assisted by molecules of water.

 © 2007 Wiley-VCH Verlag GmbH & Co. KGaA, Weinheim 

this mechanism the molecule of water takes the proton bonded to the amine nitrogen and gives another proton to the carbon. Intrinsic reaction coordinate (IRC) calculations[39] verified this process. This process is exothermic, with a free energy of –32.2 kcal/mol and activation energy of 11.3 kcal/mol.

## Experimental Section

**General:** Elemental analyses (C,H,N) were performed with a LECO CHNS-932 apparatus. Infrared spectra were recorded with a Nicolet Impact 410 FTIR spectrophotometer in the 4000–400 $cm^{-1}$ range, as KBr disks. $^1H$ NMR spectra were obtained on a Varian Unity Inova 400-MHz spectrometer with $SiMe_4$ as internal standard at 25 °C. Complex **1a** was synthesized as reported in the literature.[19] Nitromethane and potassium *tert*-butoxide were commercial grade and were used without further purification.

**[$C_{14}H_{15}N_3O_3Pd$] (2):** Complex **1a** (50 mg, 0.157 mmol) was dissolved in nitromethane (3.5 mL). The mixture was stirred for 20 h. During this time the initial purple color disappeared and a yellow precipitate was formed. The solid was filtered off, washed with diethyl ether, and then dried under vacuum. Yield: 45.4 mg (76%). $^1H$ NMR (signals of complex **2b**) (400 MHz, [$D_6$]DMSO, 20 °C): $\delta$ = 9.73 (s, 1 H, O-H), 8.52 (d, $^3J_{H,H}$ = 4.6 Hz, 1 H, 6-H py), 8.31 (m, 2 H, 4-H, 3-H py), 7.92 (m, 1 H, 5-H py), 7.13 (dd, $^3J_{H,H}$ = 7.4, $^3J_{H,H}$ = 7.4 Hz, 1 H, 4-H Ar), 6.95 (d, $^3J_{H,H}$ = 8.2 Hz, 1 H, 3-H Ar), 6.88 (m, 2 H, 5-H, 6-H Ar), 2.28 [s, 3 H, C**H$_3$**-C(py)=N], 0.14 (s, 3 H, C**H$_3$**-Pd) ppm. IR: $\tilde{\nu}$ = 1660 [m (C=N)] $cm^{-1}$. $C_{14}H_{15}N_3O_3Pd$ (379.69): calcd. C 44.28, H 3.98, N 11.07; found C 43.96, H 3.92, N 11.13.

**[$C_{14}H_{14}N_2OPd$] (1b):** Complex **2** (30 mg, 0.079 mmol) was dissolved in dichloromethane (10 mL), and potassium *tert*-butoxide (8.9 mg, 0.079 mmol) was added. The mixture was stirred for 45 min. The solvent of this red solution was removed under vacuum and the residue was dissolved in dichloromethane, filtered through Celite, and concentrated under vacuum. The addition of hexanes affords a purple solid that was filtered off, washed with cold diethyl ether, and then dried under vacuum. Yield: 19.2 mg (73%). $^1H$ NMR (400 MHz, $CDCl_3$, 20 °C): $\delta$ = 8.14 (d, $^3J_{H,H}$ = 5.3 Hz, 1 H, 6-H py), 7.80 (m, 1 H, 4-H py), 7.50 (d, $^3J_{H,H}$ = 8.1 Hz, 1 H, 3-H py), 7.22 (m, 1 H, 5-H py), 7.10 (m, 1 H, 6-H Ar), 6.96 (m, 1 H, 4-H Ar), 6.72 (d, $^3J_{H,H}$ = 8.5 Hz, 1 H, 3-H Ar), 6.36 (m, 1 H, 5-H Ar), 2.54 [s, 3 H, C**H$_3$**-C(py)=N], 0.51 (s, 3 H, C**H$_3$**-Pd) ppm. IR: $\tilde{\nu}$ = 1627 [m (C=N)] $cm^{-1}$. $C_{14}H_{14}N_2OPd$: calcd. C 50.54, H 4.24, N 8.42; found C 49.80, H 4.47, N 8.82.

**X-ray Structure Determination:** Crystallographic data for compound **3** were collected on a Bruker SMART CCD area-detector diffractometer with Mo-$K_\alpha$ radiation ($\lambda$ = 0.71073 Å).[40] Intensities were integrated[41] from several series of exposures, each exposure covering 0.3° in $\omega$, and the total dataset being a sphere. Absorption corrections were applied, based on multiple and symmetry-equivalent measurements.[42] The structure was solved by direct methods and refined by least-squares on weighted $F^2$ values for all reflections (see Table 3).[43] All non-hydrogen atoms were assigned anisotropic displacement parameters and refined without positional constraints. All hydrogen atoms were constrained to ideal geometries and refined with fixed isotropic displacement parameters. Refinement proceeded smoothly to give the residuals shown in Table 3. Complex neutral-atom scattering factors were used.[44]

CCDC-645201 contains the supplementary crystallographic data for **3**. These data can be obtained free of charge from The Cam-

Table 3. Crystal data for complex **3**.

| | |
|---|---|
| Empirical formula | $C_{13}H_{11}N_3O_3Pd$ |
| Temperature [K] | 273(2) |
| Crystal system | triclinic |
| Space group | $P\bar{1}$ |
| $a$ [Å] | 7.4316(17) |
| $b$ [Å] | 8.596(3) |
| $c$ [Å] | 10.274(4) |
| $\alpha$ [°] | 76.215(17) |
| $\beta$ [°] | 76.56(3) |
| $\gamma$ [°] | 85.287(16) |
| $V$ [Å$^3$] | 619.7(4) |
| $Z$ | 2 |
| $D_{calcd}$ [Mg/m$^3$] | 1.949 |
| Absorption coefficient [mm$^{-1}$] | 1.508 |
| $F$(000) | 360 |
| Crystal size [mm] | 0.60 × 0.30 × 0.20 |
| $\theta$ range for data collection [°] | 2.09–25.00 |
| Index ranges | $-8 \le h \le 8$, $-10 \le k \le 9$, $-12 \le l \le 12$ |
| Reflections collected | 3285 |
| Independent reflections | 2114 [$R_{int}$ = 0.0185] |
| Completeness to $\theta$ = 25.00° [%] | 97.2 |
| Absorption correction | Semi-empirical from equivalents |
| Max. and min. transmission | 0.740 and 0.514 |
| Refinement method | Full-matrix least-squares on $F^2$ |
| Data/restraints/parameters | 2114/0/182 |
| Goodness-of-fit on $F^2$ | $S$ = 1.185 |
| $R$ indices [for 2008 reflections with $I > 2\sigma(I)$] | $R_1$ = 0.0281, $wR_2$ = 0.0843 |
| $R$ indices (for all 2114 data points) | $R_1$ = 0.0295, $wR_2$ = 0.0853 |
| Weighting scheme | $w^{-1} = \sigma^2(F_o2) + (aP)^2 + (bP)$ |
| | $P = [\max(F_o^2, 0) + 2F_c^2]/3$ |
| | $a$ = 0.0508, $b$ = 0.0000 |
| Largest diff. peak and hole [e/Å$^3$] | 0.516 and –0.682 |

 © 2007 Wiley-VCH Verlag GmbH & Co. KGaA, Weinheim 

bridge Crystallographic Data Centre via www.ccdc.cam.ac.uk/data_request/cif.

**Computational Study:** DFT calculations were performed with the hybrid method known as B3LYP, in which the Becke three-parameter exchange functional[45] and the Lee–Yang–Parr correlation functional were used,[46] implemented in the Gaussian 03 (Revision B.04) program suite.[47] The effective core potentials (ECPs) of Hay and Wadt with a double-ζ valence basis set (Lanl2DZ)[48] adding polarization functions ($\zeta_f$ = 1.472)[49] were used in describing Pd. The basis set for the main group elements was split-valence and included polarization functions in all atoms [C, N, O, and H, abbreviated as 6-31G(d,p)].[50] The structures were optimized at the level B3LYP/Lanl2DZ and transition states were confirmed by a vibrational analysis (one imaginary frequency) and IRC calculations.[39] Energies of the structures were calculated with the specific basis sets.

**Supporting Information** (see also the footnote on the first page of this article): Tables of atomic coordinates of optimized structures (Tables S1–S8).

## Acknowledgments

The authors gratefully acknowledge the European Commission (LIFE05 ENV/E/000333), the Spanish Ministerio de Educación y Ciencia (BQ2002-01039 and CTQ2005-03141), and the Junta de Castilla y León (BU14/03) for financial support. We also acknowledge the Servicios Centrales de Apoyo a la Investiación (SCAI) of the Universidad de Burgos for technical support.

[1] G. Rosini in Comprehensive Organic Synthesis (Eds.: B. M. Trost, I. Fleming), Pergamon, New York, **1991**, vol. 2, pp. 321–340.
[2] N. Ono, *The Nitro Group in Organic Synthesis*, Wiley-VCH, New York, **2001**, p. 392.
[3] C. Palomo, M. Oiarbide, A. Mielgo, *Angew. Chem. Int. Ed.* **2004**, *43*, 5442–5444.
[4] D. A. Evans, D. Seidel, M. Rueping, H. W. Lam, J. T. Shaw, C. W. Downey, *J. Am. Chem. Soc.* **2003**, *125*, 12692–12693.
[5] C. S. Gan, G. Y. Lai, Z. H. Zhang, Z. Y. Wang, M. M. Zhou, *Tetrahedron: Asymmetry* **2006**, *17*, 725–728.
[6] H. Maheswaran, K. L. Prasanth, G. G. Krishna, K. Ravikumar, B. Sridhar, M. L. Kantam, *Chem. Commun.* **2006**, 4066–4068.
[7] M. Sedlak, P. Drabina, R. Keder, J. Hanusek, I. Cisarova, A. Ruzicka, *J. Organomet. Chem.* **2006**, *691*, 2623–2630.
[8] M. Bandini, F. Piccinelli, S. Tommasi, A. Umani-Ronchi, C. Ventrici, *Chem. Commun.* **2007**, 616–618.
[9] Y. Xiong, F. Wang, X. Huang, Y. H. Wen, X. M. Feng, *Chem. Eur. J.* **2007**, *13*, 829–833.
[10] G. Blay, E. Climent, I. Fernandez, V. Hernandez-Olmos, J. R. Pedro, *Tetrahedron: Asymmetry* **2006**, *17*, 2046–2049.
[11] D. M. Du, S. F. Lu, T. Fang, J. X. Xu, *J. Org. Chem.* **2005**, *70*, 3712–3715.
[12] J. M. Saá, F. Tur, J. González, M. Vega, *Tetrahedron: Asymmetry* **2006**, *17*, 99–106.
[13] Y. Kogami, T. Nakajima, T. Ashizawa, S. Kezuka, T. Ikeno, T. Yamada, *Chem. Lett.* **2004**, *33*, 614–615.
[14] C. Christensen, K. Juhl, R. G. Hazell, K. A. Jorgensen, *J. Org. Chem.* **2002**, *67*, 4875–4881.
[15] S. Kiyooka, T. Tsutsui, H. Maeda, Y. Kaneko, K. Isobe, *Tetrahedron Lett.* **1995**, *36*, 6531–6534.
[16] X. W. Zhang, T. J. Emge, R. Ghosh, K. Krogh-Jespersen, A. S. Goldman, *Organometallics* **2006**, *25*, 1303–1309.
[17] A. Arnaiz, J. V. Cuevas, G. Garcia-Herbosa, A. Carbayo, J. A. Casares, E. Gutierrez-Puebla, *J. Chem. Soc. Dalton Trans.* **2002**, 2581–2586.
[18] A. Arnaiz, G. Garcia-Herbosa, J. V. Cuevas, O. Lavastre, C. Hillairet, L. Toupet, *Collect. Czech. Chem. Commun.* **2002**, *67*, 1200–1214.
[19] A. Bacchi, M. Carcelli, C. Pelizzi, G. Pelizzi, P. Pelagatti, S. Ugolotti, *Eur. J. Inorg. Chem.* **2002**, 2179–2187.
[20] S. P. Meneghetti, P. J. Lutz, J. Kress, *Organometallics* **1999**, *18*, 2734.
[21] D. Turnbull, S. H. Maron, *J. Am. Chem. Soc.* **1943**, *65*, 212–218.
[22] G. W. Wheland, J. Farr, *J. Am. Chem. Soc.* **1943**, *65*, 1433.
[23] J. M. Harrowfield, A. M. Sargeson, *J. Am. Chem. Soc.* **1979**, *101*, 1514–1520.
[24] G. A. Stark, J. A. Gladysz, *Inorg. Chim. Acta* **1998**, *269*, 167–180.
[25] G. A. Stark, A. M. Arif, J. A. Gladysz, *Organometallics* **1994**, *13*, 4523–4530.
[26] G. C. Martin, J. M. Boncella, E. J. Wucherer, *Organometallics* **1991**, *10*, 2804–2811.
[27] G. C. Martin, J. M. Boncella, *Organometallics* **1989**, *8*, 2968–2970.
[28] E. Foresti, G. Palmieri, M. Petrini, R. Profeta, *Org. Biomol. Chem.* **2003**, *1*, 4275–4281.
[29] T. Risgaard, K. V. Gothelf, K. A. Jorgensen, *Org. Biomol. Chem.* **2003**, *1*, 153–156.
[30] P. A. Butler, C. G. Crane, B. T. Golding, A. Hammershoi, D. C. Hockless, T. B. Petersen, A. M. Sargeson, D. C. Ware, *Inorg. Chim. Acta* **2002**, *331*, 318–321.
[31] B. Korybutdaszkiewicz, *J. Coord. Chem.* **1992**, *27*, 219–221.
[32] P. Pelagatti, M. Carcelli, F. Franchi, C. Pelizzi, A. Bacchi, A. Fochi, H. W. Fruhauf, K. Goubitz, K. Vrieze, *Eur. J. Inorg. Chem.* **2000**, 463–475.
[33] T. Steiner, *Angew. Chem. Int. Ed.* **2002**, *41*, 48–76.
[34] T. Steiner, G. R. Desiraju, *Chem. Commun.* **1998**, 891–892.
[35] G. A. Jeffrey, *Introduction to Hydrogen Bonding*, Oxford University Press, Oxford, **1997**.
[36] C. Janiak, *J. Chem. Soc. Dalton Trans.* **2000**, 3885–3896.
[37] A. E. Reed, L. A. Curtiss, F. Weinhold, *Chem. Rev.* **1988**, *88*, 899–926.
[38] E. D. Glendening, A. E. Reed, J. E. Carpenter, F. Weinhold in *NBO Version 3.1*.
[39] C. Gonzalez, H. B. Schlegel, *J. Chem. Phys.* **1989**, *90*, 2154–2161.
[40] *SMART diffractometer control software*, Bruker Analytical X-ray Instrumets Inc., Madison, WI, **2000**.
[41] *SAINT integration software*, Siemens Analytical X-ray Instruments Inc., Madison, WI, **2000**.
[42] G. M. Sheldrick, *SADABS: A program for absorption correction with the Siemens SMART system*, University of Göttingen, Germany, **2001**.
[43] *SHELXTL program system version 6.1*, Bruker Analytical X-ray Instruments Inc., Madison, WI, **2000**.
[44] *International Tables for Crystallogarphy* Kluwer, Dordrecht, **1992**, vol. C.
[45] A. D. Becke, *J. Chem. Phys.* **1993**, *98*, 5648–5652.
[46] C. T. Lee, W. T. Yang, R. G. Parr, *Phys. Rev. B: Condens. Matter* **1988**, *37*, 785–789.
[47] M. J. Frisch, G. W. Trucks, H. B. Schlegel, G. E. Scuseria, M. A. Robb, J. R. Cheeseman, J. J. A. Montgomery, T. Vreven, K. N. Kudin, J. C. Burant, J. M. Millam, S. S. Iyengar, J. Tomasi, V. Barone, B. Mennucci, M. Cossi, G. Scalmani, N. Rega, G. A. Petersson, H. Nakatsuji, M. Hada, M. Ehara, K. Toyota, R. Fukuda, J. Hasegawa, M. Ishida, T. Nakajima, Y. Honda, O. Kitao, H. Nakai, M. Klene, X. Li, J. E. Knox, H. P. Hratchian, J. B. Cross, C. Adamo, J. Jaramillo, R. Gomperts, R. E. Stratmann, O. Yazyev, A. J. Austin, R. Cammi, C. Pomelli, J. W. Ochterski, P. Y. Ayala, K. Morokuma, G. A. Voth, P. Salvador, J. J. Dannenberg, V. G. Zakrzewski, S. Dapprich, A. D. Daniels, M. C. Strain, O. Farkas, D. K. Malick, A. D. Rabuck, K. Raghavachari, J. B. Foresman, J. V. Ortiz, Q. Cui, A. G. Baboul, S. Clifford, J. Cioslowski, B. B. Stefanov, G. Liu, A. Lia-

 © 2007 Wiley-VCH Verlag GmbH & Co. KGaA, Weinheim 

shenko, P. Piskorz, I. Komaromi, R. L. Martin, D. J. Fox, T. Keith, M. A. Al-Laham, C. Y. Peng, A. Nanayakkara, M. Challacombe, P. M. W. Gill, B. Johnson, W. Chen, M. W. Wong, C. Gonzalez, J. A. Pople, *Gaussian 03, revision B.04*, Gaussian, Inc., Pittsburgh, PA, **2003**.
[48] P. J. Hay, W. R. Wadt, *J. Chem. Phys.* **1985**, *82*, 299–310.
[49] A. W. Ehlers, M. Bohme, S. Dapprich, A. Gobbi, A. Hollwarth, V. Jonas, K. F. Kohler, R. Stegmann, A. Veldkamp, G. Frenking, *Chem. Phys. Lett.* **1993**, *208*, 111–114.
[50] P. C. Harihara, J. A. Pople, *Theor. Chim. Acta* **1973**, *28*, 213–222.
Received: April 30, 2007
Published Online: August 22, 2007

 © 2007 Wiley-VCH Verlag GmbH & Co. KGaA, Weinheim 

DOI: 10.1002/ejic.200700532

# On the Mechanism of Palladium-Catalyzed Cross-Coupling of Diazonium Salts with Aryltrifluoroborates: A Combined ESI-MS/NMR Study

**Nicola Taccardi,[a] Rossella Paolillo,[a] Vito Gallo,[a] Piero Mastrorilli,*[a] Cosimo F. Nobile,[a] Minna Räisänen,[b] and Timo Repo[b]**

**Keywords:** Homogeneous catalysis / Metallacycles / Mass spectrometry / Cross-coupling / Diazo compounds

A combined ESI-MS/NMR mechanistic study on the palladium-catalysed cross-coupling reaction between aryldiazonium salts and aryltrifluoroborates with bis(μ-acetato)bis(4,4′-difluoroazobenzene-$C^2$,$N$)dipalladium(II) (**4**) as the precatalyst is reported. The reaction follows a $Pd^0/Pd^{II}$ cycle after reduction of **4** to a molecular $Pd^0$ species (**I**), which according to the combined ESI-MS and $^{19}F$ NMR studies, bears an arylated azobenzene ligand. Oxidative addition by the diazonium salt generates the arylpalladium(II) intermediate (**II**), which was also detected in solution. The catalytic cycle is completed with a transmetallation between **II** and the organoborate, which is followed by fast reductive elimination of the cross-coupling product to restore the molecular $Pd^0$ species **I**. A concurrent activation path was also observed which consists of the formation of (4,4′-difluoroazobenzene-$C^2$,$N$)dipalladium(II) tetrafluoroborate (**7**) by the reaction of **4** with the diazonium salt and subsequent reduction by the aryltrifluoroborate to give **I**.
(© Wiley-VCH Verlag GmbH & Co. KGaA, 69451 Weinheim, Germany, 2007)

## Introduction

An innovative route to biaryls by palladium-catalysed cross-coupling between diazonium salts and aryltrifluoroborates has been proposed recently.[1] This protocol, which is an improved modification of the more popular Suzuki cross-coupling reaction,[2] does not require either temperatures higher than ambient or the addition of a base.

We have recently published a paper on the title reaction carried out in IL/methanol (IL = ionic liquid) mixtures where several (zero- and divalent) palladium complexes were used as precatalysts.[3] In this framework it was found that palladacycles of general formula $[(C^{\frown}N)Pd(\mu\text{-}OAc)]_2$ (see Scheme 1) were outstanding in terms of activity and selectivity of the reaction.

Our preliminary mechanistic investigations of this reaction demonstrated that the catalysis is molecular and is influenced by the ligand on palladium. Moreover, we found that an excess of diazonium salt (but not of aryltrifluoroborate) allowed the catalytic solutions to be recycled.[3]

In this paper we report a combined ESI-MS and $^{19}F$ NMR mechanistic study on the title reaction using $KPhBF_3$ and $p\text{-}XC_6H_4N_2BF_4$ (X = $CH_3$ or F) as substrates, [bis(μ-acetato)bis(4,4′-difluoroazobenzene-$C^2$,$N$)dipalladium(II)] (**4**) as a precatalyst and methanol as solvent (Scheme 2).

The rationale for the use of the fluorinated substrate and precatalyst resides in the possibility of monitoring the reaction progress by $^{19}F$ NMR spectroscopy, while methanol was used instead of IL/MeOH mixtures in order to simplify the experimental procedures.[4] ESI-MS, which is used here as a complementary analytical method, is a rapidly emerging technique for mechanistic investigations due to the possibility of easily revealing all species present in an actual catalyst solution.[5] The classical Suzuki cross-coupling[6] and other palladium-catalyzed reactions,[7] for example, have recently been studied by means of ESI-MS.[8]

In order to ascertain the effect of fluorine substitution of the azobenzene moiety in complex **3** on the catalysis, we preliminarily checked the catalytic activity of **4** in methanol using *p*-tolyldiazonium tetrafluoroborate ($p\text{-}CH_3C_6H_4N_2BF_4$) and $KPhBF_3$. Precatalyst **4** (1% mol) gave an 81% yield after 80 min while the non-fluorinated analogue **3** gave a 55% yield after 15 min[3] (the reactions were stopped when quantitative conversions were reached). The effect of the fluorine substitution on the ligand further confirms the molecular nature of the catalysis.

## Results and Discussion

The commonly accepted catalytic cycle for a $Pd^{II}$-initiated Suzuki cross-coupling is depicted in Scheme 3.[2] It consists of a preliminary reduction of $Pd^{II}$ to $Pd^0$ followed by the oxidative addition of the electrophile ArX (where X is typically a halide or triflate), subsequent transmetallation

[a] Dipartimento di Ingegneria delle Acque e di Chimica del Politecnico di Bari,
via Orabona 4, 70125 Bari, Italy
Fax: +39-080-596-3611
E-mail: p.mastrorilli@poliba.it
[b] Laboratory of Inorganic Chemistry, Department of Chemistry, University of Helsinki,
P.O. Box 55, 00014 Helsinki, Finland
Supporting information for this article is available on the WWW under http://www.eurjic.org or from the author.

 © 2007 Wiley-VCH Verlag GmbH & Co. KGaA, Weinheim 

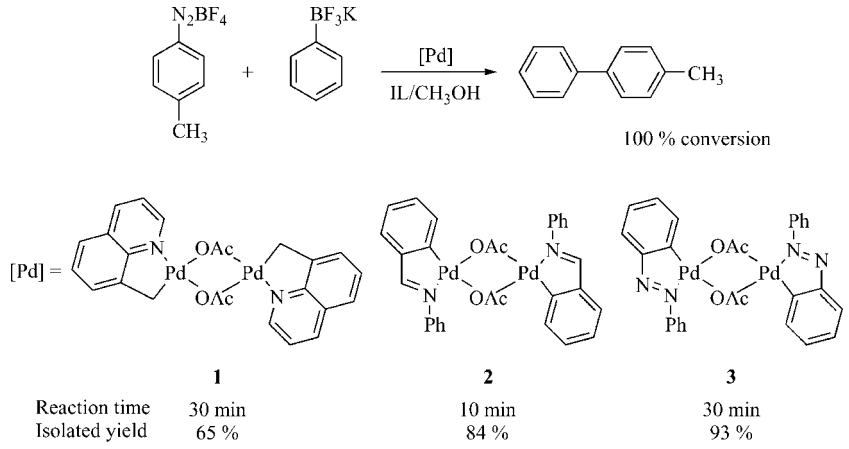


Scheme 1. Examples of highly active palladacycles for the cross-coupling reaction.[3] IL = 1-*n*-butyl-3-methylimidazolium tetrafluoroborate.

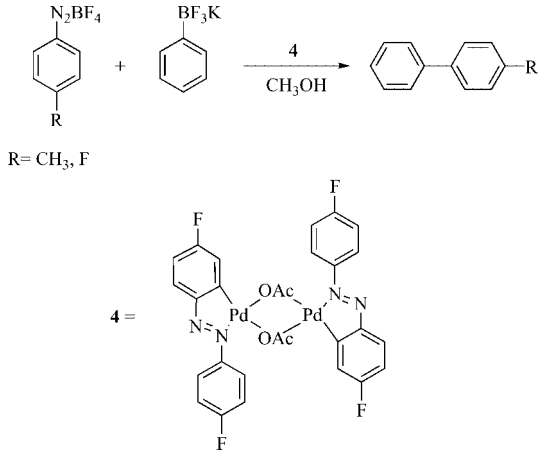


Scheme 2. Cross-coupling reaction with a fluorinated substrate and precatalyst **4**.

of the organoborate and reductive elimination leading to the cross-coupling product and regeneration of the $Pd^0$ species, which restarts the catalytic cycle.

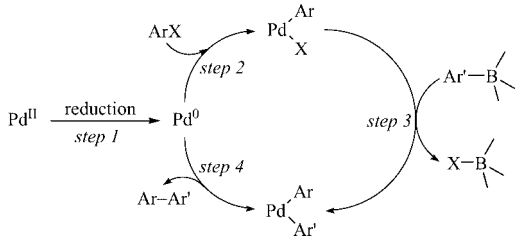


Scheme 3. General catalytic cycle for the Suzuki cross-coupling leading to biaryls.

In order to verify whether such a cycle also holds when ArX is replaced by an aryldiazonium salt and the organoboron compound is changed to $KPhBF_3$, every single step shown in Scheme 3 was examined.

### Reaction of the Precatalyst with $KPhBF_3$

The reaction mixture comprised of **4** and $KPhBF_3$ in methanol was monitored by $^{19}F$ NMR spectroscopy at room temperature (Figure 1). The lack of signals attributable to **4** is due to its poor solubility in methanol.

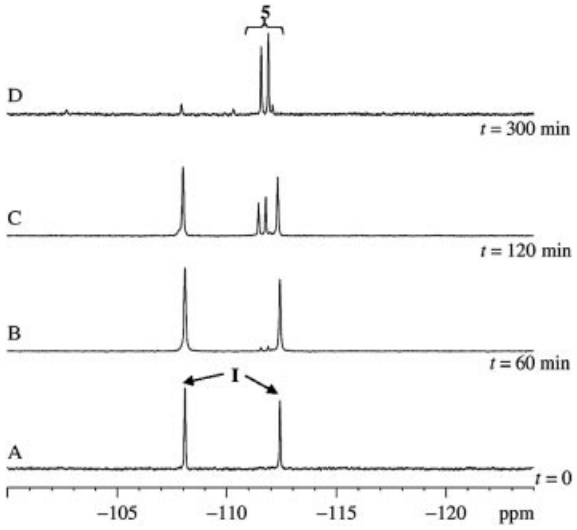


Figure 1. $^{19}F$ NMR spectroscopic monitoring of reaction mixtures of **4** and $KPhBF_3$ in methanol as a function of time (Pd:$KPhBF_3$ = 1:15 mol/mol).

It is apparent that a new species **I** with $^{19}F$ NMR resonances at $\delta$ = –108.1 and –112.4 ppm forms immediately upon mixing $KPhBF_3$ with azapalladacycle **4**. The signals assigned to **I** progressively decrease in intensity over 5 h, with concomitant appearance of two new signals at $\delta$ = –111.7 and –111.9 ppm and formation of palladium black. These latter signals belong to 4,4′-difluoro-2-phenylazobenzene (**5**), which was isolated and fully characterized. The formation of Pd black and **5** indicates two possible struc-

 © 2007 Wiley-VCH Verlag GmbH & Co. KGaA, Weinheim 

tures for **I**, one of which is a $Pd^{II}$ complex in which the bridging acetate of **4** has been replaced by a σ-bonded phenyl group and the other of which consists of already formed ligand **5** bonded to $Pd^0$ (Scheme 4; in this and in the following structures the solvent molecules possibly bound to palladium are omitted).

High resolution ESI-MS (HRMS) analysis of the solution showed an intense peak at *m/z* 419 (negative ion mode). This peak represents the fluoride adduct of **I** (exact mass = 400.00 daltons), as confirmed by the simulation of its isotopic pattern (Figure 2). The presence of other anions at *m/z* 399 $[M - HF]^-$ and 293 $[M - Pd - HF]^-$ in the MS/MS spectrum provided the basis to discriminate between the two structures depicted in Scheme 4. The latter ion, which corresponds to the deprotonated form of **5**, clearly indicates that species **I** seen in the $^{19}F$ NMR spectrum is a $Pd^0$ complex of **5**.

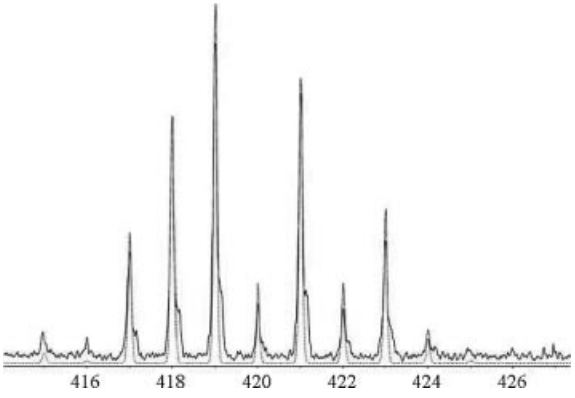


Figure 2. Experimental (solid line) and simulated (dotted line) HRMS(–) spectrum of **I** as its fluoride adduct. The error between simulated and observed isotopic patterns is –1.72 ppm.

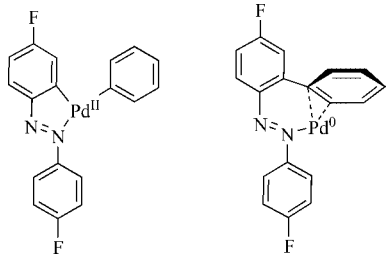

Scheme 4. Two possible structures for species **I**.

Although different structures with the same molecular formula (e.g. coordination of the other N atom, $\eta^2$ coordination of the N=N moiety or different coordination modes for the dangling phenyl) cannot be definitively ruled out,[9] the $^{19}F$ NMR resonances of **I** are in agreement with the structure depicted in Scheme 5. As suggested by a comparison of the $^{19}F$ NMR signals of **I** with those of **4**[10] and **5**, the signal at $\delta$ = –108.1 ppm in **I** can be attributed to $F^1$ while that at $\delta$ = –112.4 ppm, which is compatible with a fluorine on a 2-phenylated aryl ring in **5**, can be attributed to $F^2$.

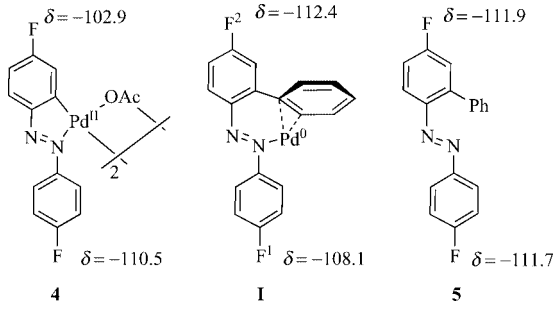


Scheme 5. $^{19}F$ NMR features of **4**, **I** and **5**. All the chemical shifts are given for the species in methanol.

The formation of **I** and its subsequent decomposition, as shown in Figure 1, are depicted in Scheme 6. Such a process is not unexpected for a $Pd^0$ species such as **I** and has already been suggested for analogous palladacycles.[11]

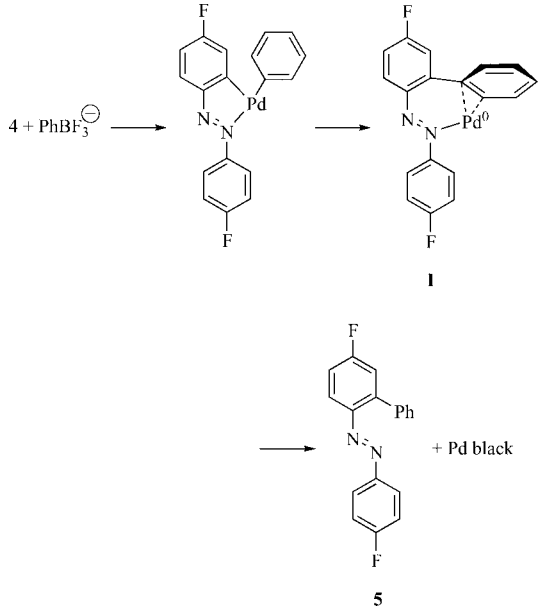


Scheme 6. Reaction of **4** with phenyltrifluoroborate generates $Pd^0$ complex **I**, which slowly decomposes to **5**.

## Reaction of I with Diazonium Salts

The addition of a slight excess of diazonium salt to the catalyst solution caused the disappearance of **I** and concomitant formation of coupling products (GLC analysis) and **5** ($\delta$ = –111.7 and –111.9 ppm). Depending on the applied diazonium salts (in this case *p*-$FC_6H_4N_2BF_4$ and *p*-$CH_3C_6H_4N_2BF_4$), two new species were also formed (see parts B in Figures 3 and 4).

 © 2007 Wiley-VCH Verlag GmbH & Co. KGaA, Weinheim 

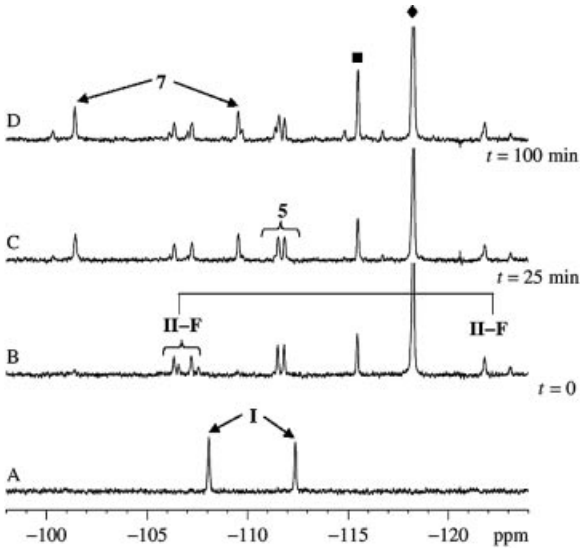


Figure 3. $^{19}F$ NMR monitoring of the reaction mixture of **4**/$KPhBF_3$ and *p*-$FC_6H_4N_2BF_4$ in methanol. A: **4**/$KPhBF_3$; B: immediately after addition of *p*-$FC_6H_4N_2BF_4$; C and D: after 25 and 100 min, respectively. ■ = 4,4′-difluorobiphenyl; ♦ = 4-fluorobiphenyl. Pd/diazonium/$KPhBF_3$ molar ratio of 1:18:15.

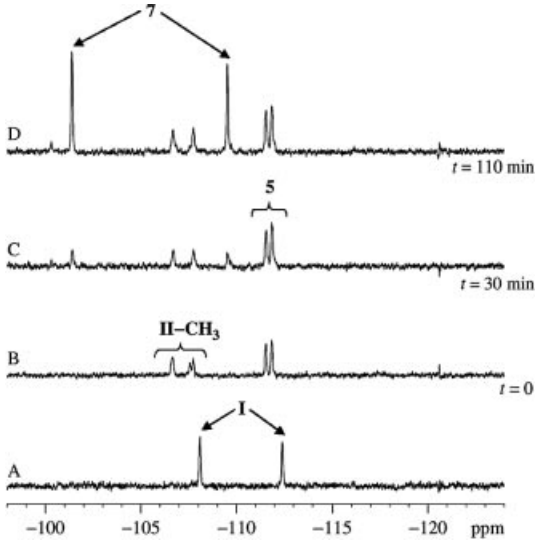


Figure 4. $^{19}F$ NMR monitoring of the reaction mixture of **4**/$KPhBF_3$ and *p*-$CH_3C_6H_4N_2BF_4$ in methanol. A: **4**/$KPhBF_3$; B: immediately after addition of *p*-$CH_3C_6H_4N_2BF_4$; C and D: after 30 and 110 min, respectively. Pd/diazonium/$KPhBF_3$ molar ratio of 1:18:15.

The new species formed in the case of *p*-fluorobenzenediazonium (**II-F**) shows three broad signals at $\delta$ = –106.4, –107.2 and –121.8 ppm that integrate in a 1:1:1 ratio (Figure 3), while that formed with *p*-tolyldiazonium (**II-CH$_3$**) shows only two broad signals at $\delta$ = –106.7 and –107.8 ppm that integrate in a 1:1 ratio (Figure 4).

HRMS(+) analysis of a solution containing **II-F** (that of Figure 3, B) revealed the presence of species with *m*/*z* values of 399, 417, 495 and 789. Analysis of the isotopic pattern of these peaks indicated the structures depicted in Scheme 7.

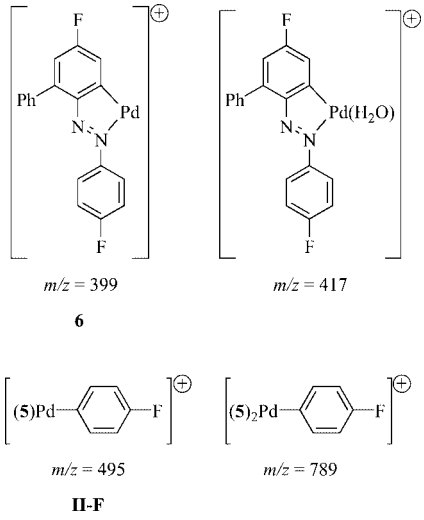


Scheme 7. $Pd^{II}$ species detected by HRMS(+) in the reaction mixture of **4**/$KPhBF_3$ after the addition of *p*-$FC_6H_4N_2BF_4$.

As already mentioned, the $^{19}F$ NMR signals of intermediate **II-F** at $\delta$ = –106.4, –107.2 and –121.8 ppm integrate in a 1:1:1 ratio and can therefore be assigned to the three fluorine atoms of the structure with *m*/*z* 495 (see Supporting Information),[12] with the downfield ones being due to the fluorine atoms of coordinated **5** and the upfield one being due to the fluorine of the σ-bonded *p*-fluorophenyl group.[13]

A structure similar to **II-F**, but with a *p*-tolyl ligand in the place of *p*-fluorophenyl, can be attributed to **II-CH$_3$**. Complexes **II-F** and **II-CH$_3$** are the products of oxidative addition of *p*-fluorophenyldiazonium and *p*-tolyldiazonium salts, respectively, to **I**.

When the reaction between **I** and *p*-$FC_6H_4N_2BF_4$ was carried out in the presence of an excess of $KPhBF_3$ (Pd/$KPhBF_3$/diazonium molar ratio of 1:18:15) the same intermediates as in Figure 3 were detected (Figure 5). However, addition of the diazonium salt did not result in the immediate disappearance of **I**, as shown in part B of Figure 5, and

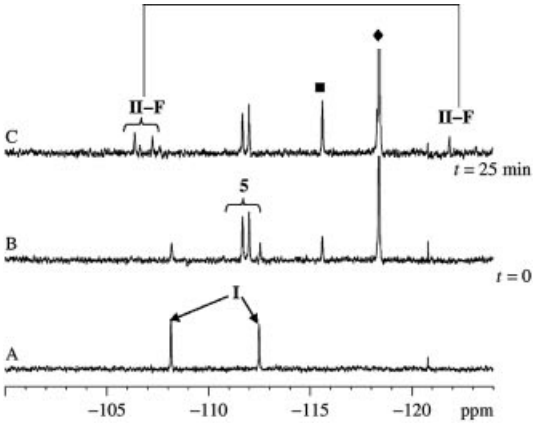


Figure 5. Reaction of **4** with excess $KPhBF_3$ and *p*-$FC_6H_4N_2BF_4$. A: **4**/$KPhBF_3$; B: immediately after addition of *p*-$FC_6H_4N_2BF_4$; C after 25 min. ■ = 4,4′-difluorobiphenyl; ♦ = 4-fluorobiphenyl. Pd/diazonium/$KPhBF_3$ molar ratio of 1:15:18.

 © 2007 Wiley-VCH Verlag GmbH & Co. KGaA, Weinheim 

the signals of **II-F** appeared only after consumption of **I** (Figure 5, C). Accordingly, HRMS analysis of the solution resulting from the addition of *p*-$FC_6H_4N_2BF_4$ (Figure 5, B) did not show the cations with *m*/*z* 399, 417, 495 and 789 whereas anions with *m*/*z* 419 ([**I** + F]$^-$), 399 ([**I** – H]$^-$), 487 ([**I** + $BF_4$]$^-$) and 499 ([**I** + $BF_3OMe$]$^-$) were detected in negative ion mode.

### Concurrent Activation of the Precatalyst

$^{19}F$ NMR analysis of the reaction solutions prepared from **4**, $KPhBF_3$ and diazonium salt in excess showed the formation of a new Pd complex (**7**; $\delta$ = –101.3 and –109.5 ppm) which after 1.5 h is the main Pd species in solution (see parts D in Figures 3 and 4).

Complex **7** was characterized as (4,4′-difluoroazobenzene-$C^2$,*N*)palladium(II) tetrafluoroborate, which arises from the reaction of *p*-fluorobenzenediazonium tetrafluoroborate with residual **4** (Scheme 8). Pure **7** was isolated in 80% yield from the reaction between **4** and *p*-$FC_6H_4N_2BF_4$ (1:1 Pd:diazonium salt molar ratio) in methanol at room temperature. The formation of **7** results from the abstraction of the bridging acetate of **4** by the diazonium salt[14] rather than simple metathesis of the acetate ligands with tetrafluoroborate, as demonstrated by the lack of reaction between **4** and $NaBF_4$ or [bmim]$BF_4$ (bmim = 1-*n*-butyl-3-methylimidazolium). Related (azobenzene-$C^2$,*N*)palladium(II) tetrafluoroborates have been previously synthesized by Heck starting from bis(μ-chloro)bis(azobenzene-$C^2$,*N*)-dipalladium(II) and $AgBF_4$.[15]

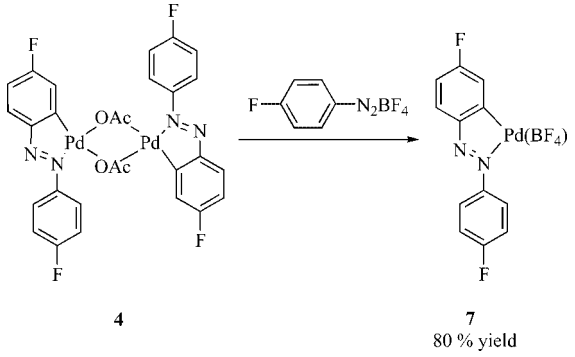


Scheme 8. Formation of complex **7**.

Complex **7** was found to be catalytically active. Thus, when **7** was used as precatalyst in the cross-coupling reaction between *p*-$CH_3C_6H_4N_2BF_4$ and $KPhBF_3$ in methanol an 88% yield of 4-methylbiphenyl was obtained in 15 min. A similar yield was obtained with the parental complex **4** only after 80 min. The higher activity of **7** compared with that of **4** can be explained by two considerations: i) complex **4** is poorly soluble in the reaction medium, while **7** is completely soluble, and ii) complex **7** is a coordinatively unsaturated species and therefore highly reactive towards prereduction reaction with $KPhBF_3$. In fact, the quantitative conversion of **7** into **I** and the subsequent slow decomposition of the latter into **5** and palladium black could be observed when following the reaction between **7** and $KPhBF_3$ by $^{19}F$ NMR spectroscopy. Thus, complex **7** can contribute to the formation of **I** and accumulates only when the aryltrifluoroborate has been consumed.

The fact that **7** survived the work-up procedures suggests that it could be responsible for the aforementioned recyclability of the catalytic solutions for reactions carried out in IL/MeOH mixtures in the presence of excess diazonium salt.[3]

### Catalytic Cycle

On the basis of the experimental data described above, the catalytic cycle shown in Scheme 9 can be proposed for palladium-catalyzed cross-coupling of diazonium salts with aryltrifluoroborates.

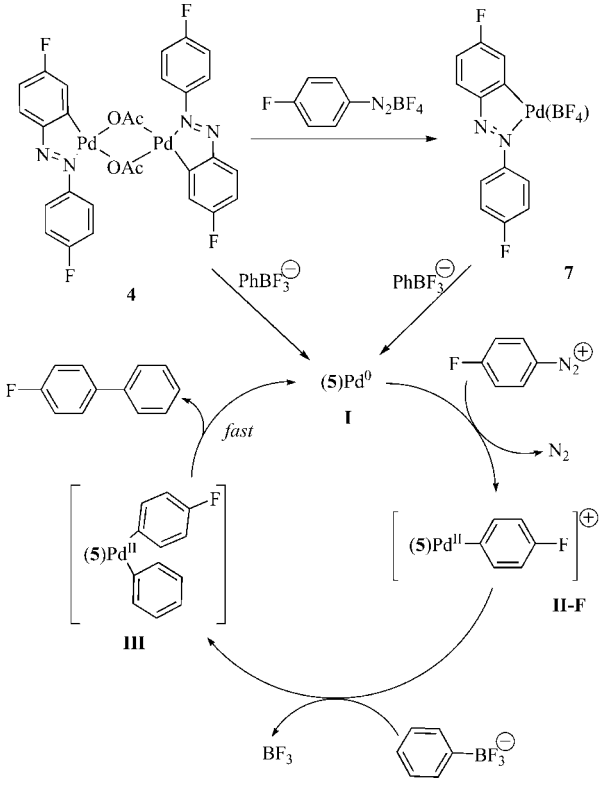


Scheme 9. Proposed catalytic cycle for the palladium-catalyzed cross-coupling of diazonium salts with aryltrifluoroborates.

The catalyst precursor **4** reacts with the trifluorophenylborate to give the $Pd^0$ species **I**, which is responsible for the observed catalytic activity. This species undergoes oxidative addition of the aryldiazonium salt to give the cationic arylpalladium(II) complex **II-F**, which bears the azobenzene **5** as a ligand. The catalytic cycle is completed by a transmetallation reaction between **II-F** and the organoborate to give the neutral compound **III**, which is followed by reductive elimination of the cross-coupling product. Compound **I** can also be formed from the reaction between **7** (formed from **4** and the aryldiazonium salt) and $PhBF_3^-$.

No transmetallation intermediates were detected, which indicates that the reductive elimination step from **III** is very

 © 2007 Wiley-VCH Verlag GmbH & Co. KGaA, Weinheim 

fast.[16] The $^{19}F$ NMR spectroscopic data (Figure 4) allowed us to extend this mechanism to the reaction with a *p*-tolyldiazonium salt, where an intermediate analogous to **II-F** was detected.

## Conclusions

We have demonstrated that the cross-coupling between aryltrifluoroborates and diazonium salts facilitated by the acetato(azobenzene-$C^2$,*N*)palladium(II) complex **4** follows a catalytic cycle involving $Pd^0$ and $Pd^{II}$ species. The active species is a $Pd^0$ complex (**I**) bearing an arylated azobenzene as a ligand that can form by two different pathways, namely direct reaction of **4** with the arylborate or by arylation of (azobenzene-$C^2$,*N*)Pd($BF_4$) (**7**), which is generated by action of the diazonium salt on **4**. The $Pd^0$ complex **I** undergoes addition of the diazonium salt to give the cationic arylpalladium(II) complex **II** which, upon transmetallation with organoborate and fast reductive elimination, restores the active species **I**.

A combination of $^{19}F$ NMR and ESI-MS data has therefore allowed us to detect both intermediates **I** and **II** from the actual catalyst solutions.

## Experimental Section

**General:** Unless otherwise specified, all manipulations were carried out in air. Potassium phenyltrifluoroborate,[1] *p*-tolyldiazonium tetrafluoroborate[17] and *p*-fluorobenzenediazonium tetrafluoroborate[17] were synthesized according to literature methods. All the other reagents were commercial and used as received. All the solvents were HPLC grade and were purified by standard techniques. Flash chromatography was performed on $SiO_2$ Kieselgel (230–400 mesh). The NMR spectra were recorded with a Bruker AX400 spectrometer (400 MHz for $^1H$) at 295.0 K; chemical shifts are reported in ppm relative to $SiMe_4$ for $^1H$ and $^{13}C$, and $CFCl_3$ for $^{19}F$; $^1H$ and $^{13}C$ signals were attributed by means of $^{13}C\{^1H\}$APT, $^{13}C\{^1H\}$DEPT, $^1H$ COSY, $^1H$-$^{13}C$ HMQC and $^1H$-$^{13}C$ HMBC experiments. Deuterated solvents were purchased from Aldrich or Acros and used as received. Mass spectrometric analyses were performed using an ion-trap mass spectrometer equipped with an electrospray ion source (Bruker Esquire3000$^{plus}$). All analyses were carried out in both positive- and negative-ion modes. The sample solutions were introduced by continuous infusion with the aid of a syringe pump at a flow-rate of 180 μL min$^{-1}$. The instrument was operated in the positive-ion mode ($ESI^+$) with an end-plate offset of –500 V and a capillary offset of –4000 V. The nebuliser pressure was 0.8 bar ($N_2$) and the drying gas ($N_2$) flow 7 L h$^{-1}$. The capillary exit and skimmer 1 voltages were 90 and 30 V, respectively. The drying gas temperature was set at 200 °C. The mass spectrometric parameters in the negative ion mode ($ESI^-$) were as follows: end-plate offset: –500 V; capillary: –4000 V; capillary exit: –120 V; skimmer 1: –50 V; nebulizer pressure: 0.4 bar; drying gas flow: 5 L h$^{-1}$; drying gas temperature: 200 °C. All the samples for mechanistic studies were prepared and handled in air using HPLC-grade methanol. The software used for the simulations was Bruker Daltonics DataAnalysis (version 3.3).

C, H, N elemental analyses were carried out with a Carlo Erba EA1108 CHNS-O elemental analyzer. Pd analyses were performed with a Perkin–Elmer SIMAA6000 atomic absorption spectrometer. The IR spectra were recorded with a Bruker Vector 22 FT-IR spectrometer. GLC analyses were performed on an HP5890 instrument equipped with a Supelco SPB-1 capillary column (30 m × 320 μm × 0.25 μm). GC-MS analyses were performed on an HP6890-HP5973MSD instrument equipped with an HP-5MS capillary column (30 m × 250 μm × 0.25 μm).

**Synthesis of 4,4′-Difluoroazobenzene**[18]

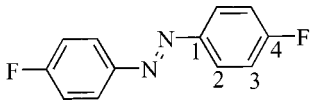


Sodium perborate (10.86 g, 0.109 mol) was added to a solution of 4-fluoroaniline (12.51 g, 0.113 mol) in 150 mL of glacial acetic acid. The system was heated at 50 °C under vigorous stirring and the reaction monitored by TLC. When the aniline has been completely consumed the system was cooled and the reaction mixture poured into a beaker containing 500 mL of cold water. The resulting suspension was neutralized with sodium carbonate and extracted with diethyl ether (3 × 150 mL). The organic phases were collected and washed with saturated sodium hydrogen carbonate (2 × 150 mL), water (2 × 250 mL) and brine (2 × 250 mL) then dried with anhydrous sodium sulfate, filtered and the solvents evaporated. The crude material was purified by column chromatography with petroleum ether (boiling range 40–70 °C) as eluent. Yield 2.46 g (20%) ppm. MS (70 eV, EI): *m*/*z* 218 (53) [$M^+$], 123 (28), 95 (100), 75 (34). $C_{12}H_8F_2N_2$ (218.20): calcd. C 66.05, H 3.70, N 12.84; found C 65.98, H 3.78, N 12.60. IR (KBr): $\tilde{\nu}$ = 430, 462, 540, 643, 668, 721, 755, 840, 951, 1008, 1093, 1141, 1201, 1232, 1288, 1302, 1415, 1499, 1593, 1653, 1896, 3061 cm$^{-1}$. $^1H$ NMR (400 MHz, $CDCl_3$): $\delta$ = 7.2 (m, 4 H, $H^3$), 7.9 (m, 4 H, $H^2$) ppm. $^{13}C$ NMR (101 MHz, $CDCl_3$): $\delta$ = 116.1 (d, $^2J_{C,F}$ = 23 Hz, $C^3$), 124.9 (d, $^3J_{C,F}$ = 9 Hz, $C^2$), 149.0 (d, $^4J_{C,F}$ = 2 Hz, $C^1$), 164.4 (d, $^1J_{C,F}$ = 252 Hz, $C^4$) ppm. $^{19}F$ NMR (376 MHz, $CD_3OD$): $\delta$ = –111.6 ppm (m).

**Synthesis of Bis(μ-acetato)bis(4,4′-difluoroazobenzene-$C^2$,*N*)dipalladium(II) (4)**

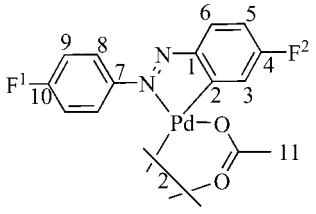


Palladium acetate (0.450 g, 0.0020 mol) and 4,4′-difluoroazobenzene (0.436 g, 0.0020 mol) were dissolved in glacial acetic acid (50 mL) and the mixture was stirred at 50 °C. Once the 4,4′-difluoroazobenzene had been completely consumed (TLC monitoring) the system was cooled down to room temperature and methanol (200 mL) added to precipitate **4** as a black microcrystalline solid. This solid was filtered off, washed with diethyl ether (10 mL) and pentane (3 × 10 mL) and air-dried. Yield 0.629 g (82%). ESI-MS ($CH_2Cl_2$/$CH_3CN$): exact mass calcd. for $C_{28}H_{20}F_4N_4O_4Pd_2$: 763.95; found 364.0 [M/2 – OAc + $CH_3CN$]$^+$. $C_{28}H_{20}F_4N_4O_4Pd_2$ (765.32): calcd. C 43.94, H 2.63, N 7.32, Pd 27.81; found C 43.69, H 2.58, N 7.20, Pd 27.95. IR (KBr): $\tilde{\nu}$ = 436, 470, 534, 685, 779, 810, 844, 877, 1101, 1153, 1184, 1234, 1246, 1320, 1348, 1416, 1501, 1560, 1597, 3077 cm$^{-1}$. $^1H$ NMR (400 MHz, $CDCl_3$): $\delta$ = 2.1 (s, 6 H, $H^{11}$), 6.1 (m, 2 H, $H^3$), 6.8 (m, 2 H, $H^5$), 7.0 (m, 4 H, $H^9$), 7.4 (m, 4 H, $H^8$), 7.7 (m, 2 H, $H^6$) ppm. $^{13}C$ NMR (101 MHz, $CDCl_3$):

 © 2007 Wiley-VCH Verlag GmbH & Co. KGaA, Weinheim 

$\delta$ = 24.5 (s, $C^{11}$), 113.2 (d, $^2J_{C,F}$ = 25 Hz, $C^5$), 115.1 (d, $^2J_{C,F}$ = 23 Hz, $C^9$), 119.5 (d, $^2J_{C,F}$ = 21 Hz, $C^3$), 125.4 (d, $^3J_{C,F}$ = 9 Hz, $C^8$), 130.5 (d, $^3J_{C,F}$ = 10 Hz, $C^6$), 146.9 (d, $^4J_{C,F}$ = 3 Hz, $C^7$), 158.2 (d, $^3J_{C,F}$ = 7 Hz, $C^2$), 159.9 (d, $^4J_{C,F}$ = 3 Hz, $C^1$), 162.2 (d, $^1J_{C,F}$ = 264 Hz, $C^4$), 164.1 (d, $^1J_{C,F}$ = 253 Hz, $C^{10}$), 181.4 (s, COO) ppm. $^{19}$F NMR (376 MHz, $CD_3OD$): $\delta$ = –110.5 (m, $F^1$), –102.9 (m, $F^2$) ppm.

**Synthesis of 4,4′-Difluoro-2-phenylazobenzene (5)**

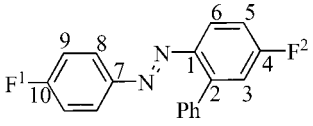


Complex **4** (0.380 g, 0.50 mmol), potassium phenyltrifluoroborate (0.250 g, 1.4 mmol) and potassium carbonate (0.225 g, 1.6 mmol) were suspended in methanol (10 mL). The system was refluxed for 1 h, then cooled and the methanol evaporated. The residue was extracted with diethyl ether (4 × 25 mL), then the organic fractions were collected and washed with water (2 × 50 mL) and brine (2 × 50 mL), dried with anhydrous sodium sulfate, filtered and the solvents evaporated. The crude product was purified by column chromatography with petroleum ether (boiling range 40–70 °C) as eluent. Yield 0.073 g (25%). MS (70 eV, EI): *m*/*z* 293 (99) [$M^+$ – 1], 184 (14), 170 (100), 151 (12), 123 (12), 95 (66), 75 (18). $C_{18}H_{12}F_2N_2$ (294.30): calcd. C 73.46, H 4.11, N 9.52; found C 73.69, H 4.28, N 9.30. IR (KBr): $\tilde{\nu}$ = 461, 542, 698, 737, 762, 781, 843, 880, 893, 1109, 1136, 1186, 1271, 1444, 1477, 1570, 1594 cm$^{-1}$. $^1$H NMR (400 MHz, $CDCl_3$): $\delta$ = 6.9–7.0 (m, $H^9$, $H^5$), 7.1 (m, $H^3$), 7.2 (m, Ph), 7.5–7.6 (m, $H^8$, $H^6$) ppm. $^{13}$C NMR (101 MHz, $CDCl_3$): $\delta$ = 115.2 (d, $^2J_{C,F}$ = 23 Hz, $C^5$), 116.0 (d, $^2J_{C,F}$ = 22 Hz, $C^9$), 117.2 (d, $^2J_{C,F}$ = 22 Hz, $C^3$), 118.0 (d, $^3J_{C,F}$ = 9 Hz, $C^6$), 125.1 (d, $^3J_{C,F}$ = 9 Hz, $C^8$), 127.7 (s, CH), 127.8 (s, CH), 130.7 (s, CH), 137.7 (d, $^4J_{C,F}$ = 2 Hz; 1 C), 143.6 (d, $^3J_{C,F}$ = 9 Hz, $C^2$), 145.8 (d, $^4J_{C,F}$ = 3 Hz, $C^1$), 149.2 (d, $^4J_{C,F}$ = 3 Hz, $C^7$), 164.0 (d, $^1J_{C,F}$ = 252 Hz, $C^4$), 164.2 (d, $^1J_{C,F}$ = 252 Hz, $C^{10}$) ppm. $^{19}$F NMR (376 MHz, $CD_3OD$): $\delta$ = –112.0 (m, $F^2$), –111.7 (m, $F^1$) ppm.

**Synthesis of (4,4′-Difluoro-6-phenylazobenzene-*C*$^2$,*N*)palladium(II) Tetrafluoroborate (6)**

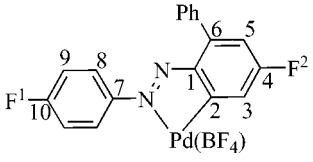


$PdCl_2$ (36 mg, 0.2 mmol) and **5** (60 mg, 0.2 mmol) were placed in a centrifuge tube and dmso (1 mL) was added. The system was heated to 140 °C for 10 min, then cooled to room temperature. Methanol (3 mL) was added to the resulting deep red solution to precipitate an orange solid, which was centrifuged, washed with methanol (3 × 3 mL) and diethyl ether (3 × 3 mL) and vacuum dried. A 25-mg portion of this solid was placed in an NMR tube and a solution of $AgBF_4$ (12 mg, 0.06 mmol) in $CD_3OD$ (0.5 mL) was added. The NMR tube was sonicated briefly and the resulting suspension allowed to settle before analysis. $^1$H NMR (400 MHz, $CD_3OD$): $\delta$ = 6.8 (m, 1 H), 7.2 (m, 1 H), 7.3 (m, 2 H, $H^9$), 7.5 (m, 3 H, Ph), 7.6 (m, 2 H, Ph), 7.7 (m, 2 H, $H^8$) ppm. $^{13}$C NMR (101 MHz, $CD_3OD$): $\delta$ = 116.0 (d, $^2J_{C,F}$ = 24 Hz, CH), 117.1 (d, $^2J_{C,F}$ = 24 Hz, $C^9$), 119.3 (d, $^2J_{C,F}$ = 23 Hz, CH), 126.5 (d, $^3J_{C,F}$ = 9 Hz, $C^8$), 129.3 (s, CH), 130.0 (s, CH), 131.2 (s, CH), 138.8 (C), 148.0 (d, $^3J_{C,F}$ = 10 Hz, 1 C), 148.9 (C), 157.9 (d, $^3J_{C,F}$ = 7 Hz, 1 C), 158.9 (C), 163.8 (d, $^1J_{C,F}$ = 265 Hz, 1 C), 165.7 (d, $^1J_{C,F}$ = 252 Hz, 1 C) ppm. $^{19}$F NMR (376 MHz, $CD_3OD$): $\delta$ = –109.9 (m, $F^1$), –100.4 (m, $F^2$) ppm.

**Synthesis of (4,4′-Difluoroazobenzene-*C*$^2$,*N*)palladium(II) Tetrafluoroborate (7)**

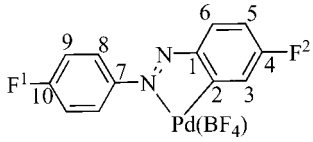


Complex **4** (0.380 g, 0.50 mmol) and *p*-fluorobenzenediazonium tetrafluoroborate (0.210 g, 1.0 mmol) were suspended in dry methanol (10 mL) at room temperature under nitrogen. The suspension was vigorously stirred and the gas (dinitrogen) evolved monitored by means of a gas burette. Once the diazonium salt had completely reacted (approx. 24 mL of gas) the methanol was evaporated. The residue was treated with dry dichloromethane (3 × 10 mL) and the resulting suspension was filtered under $N_2$ through a Celite® pad. The filtrate was concentrated to about one third and dry *n*-hexane (50 mL) added to precipitate **7** as an orange powder. The product was decanted, washed with small portions of *n*-hexane and dried under vacuum. Yield 0.330 g (80%). ESI-MS ($CH_3CN$): exact mass calcd. for $C_{12}H_7BF_6N_2Pd$: 322.96; found 323.0 [M]$^+$. $C_{12}H_7BF_6N_2Pd$: 409.96; found 323.0 [M – $BF_4$]$^+$. $C_{12}H_7BF_6N_2Pd$ (410.42): calcd. C 35.12, H 1.72, N 6.83, Pd 26.93; found C 35.02, H 1.69, N 6.49, Pd 26.81. IR (nujol): $\tilde{\nu}$ = 470, 593, 779, 845, 1064, 1154, 1193, 1257, 1499, 1568, 1583, 2050 cm$^{-1}$. $^1$H NMR (400 MHz, [$D_6$]dmso): $\delta$ = 7.1 (m, 1 H, $H^3$), 7.3 (m, 1 H, $H^5$), 7.5 (m, 2 H, $H^9$), 7.9 (m, 2 H, $H^8$), 8.1 (m, 1 H, $H^6$) ppm. $^{13}$C NMR (101 MHz, [$D_6$]dmso): $\delta$ = 114.3 (d, $^2J_{C,F}$ = 24 Hz, $C^5$), 116.1 (d, $^2J_{C,F}$ = 23 Hz, $C^9$), 119.2 (d, $^2J_{C,F}$ = 23 Hz, $C^3$), 126.0 (d, $^3J_{C,F}$ = 9 Hz, $C^8$), 132.3 (d, $^3J_{C,F}$ = 10 Hz, $C^6$), 147.1 (d, $^4J_{C,F}$ = 3 Hz, $C^7$), 156.3 (d, $^3J_{C,F}$ = 7 Hz, $C^2$), 160.5 (d, $^4J_{C,F}$ = 3 Hz, $C^1$), 161.8 (d, $^1J_{C,F}$ = 263 Hz, $C^4$), 163.6 (d, $^1J_{C,F}$ = 250 Hz, $C^{10}$) ppm. $^{19}$F NMR (376 MHz, $CD_3OD$): $\delta$ = –154.6 (br. s, $BF_4$), –109.6 (br. s, $F^1$), –101.6 (br. s, $F^2$) ppm.

**Catalysis with Precatalyst 4:** $KPhBF_3$ (221 mg, 1.2 mmol) and *p*-$CH_3C_6H_4N_2BF_4$ (206 mg, 1.0 mmol) were added, with vigorous stirring, to a suspension of **4** (7.65 mg, 0.010 mmol) in methanol (4 mL) in a 10-mL Schlenk tube. At the end of the reaction (80 min) the mixture was diluted with water (100 mL) and the products were extracted with diethyl ether (3 × 25 mL); the organic phases were collected and dried with $Na_2SO_4$. The products were purified by flash chromatography and characterized by GC-MS. The yield was determined by GLC using naphthalene as an internal standard.

**Reaction of 4 with Potassium Phenyltrifluoroborate:** HPLC-grade methanol (0.5 mL) was added to a vial containing complex **4** (7 mg, 9 μmol) and potassium phenyltrifluoroborate (25 mg, 137 μmol) and the mixture shaken for half a minute. The resulting suspension was transferred into an NMR tube containing an internal insert of $CDCl_3$ for the deuterium lock. A 0.05-mL aliquot of the same suspension was diluted to 5 mL with HPLC-grade methanol and used in ESI-MS experiments.

**Reaction of Complex 4 with Potassium Phenyltrifluoroborate and Diazonium Salts:** HPLC-grade methanol (0.5 mL) was added to a vial containing complex **4** (7 mg, 9 μmol) and potassium phenyltrifluoroborate (25 mg, 137 μmol) and the mixture shaken for half a minute. A solution of diazonium salt (165 μmol) in HPLC-grade methanol (0.5 mL) was added to the resulting suspension and the

 © 2007 Wiley-VCH Verlag GmbH & Co. KGaA, Weinheim 

vial again shaken for half a minute. About 0.5 mL of the suspension was transferred into an NMR tube containing an internal insert of $CDCl_3$ for the deuterium lock. A 0.1-mL aliquot was diluted to 5 mL with HPLC-grade methanol and used in ESI-MS experiments. The reaction mixtures were analyzed by GLC and GC-MS to identify the coupling products.

**Supporting Information** (see also the footnote on the first page of this article): $^{19}F$, $^{1}H$ and $^{13}C$ NMR spectra of **4**–**7**. HR mass spectra of a methanol solution of complex **4**, *p*-$FC_6H_4N_2BF_4$ and $KPhBF_3$; experimental and simulated HRMS(+) spectrum of **II-F**.

## Acknowledgments

Financial support from the European Cooperation in the field of Scientific and Technical Research (COST, D30 action, fellowship to N. T.) is gratefully acknowledged. We thank Ms. E. Andriani for experimental assistance.

[1] S. Darses, G. Michaud, J. Genêt, *Eur. J. Org. Chem.* **1999**, 1875–1883.
[2] a) N. Miyaura, A. Suzuki, *Chem. Rev.* **1995**, *95*, 2457–2483; b) A. Suzuki, *J. Organomet. Chem.* **1999**, *576*, 147–168.
[3] V. Gallo, P. Mastrorilli, C. F. Nobile, R. Paolillo, N. Taccardi, *Eur. J. Inorg. Chem.* **2005**, 582–588.
[4] The role of the ionic liquid in generating the active species has already been ruled out in our system (see ref.[3]).
[5] L. S. Santos, L. Knaack, J. O. Metzger, *Int. J. Mass. Spectrom.* **2005**, *246*, 84–104 and references cited therein.
[6] A. O. Aliprantis, J. W. Canary, *J. Am. Chem. Soc.* **1994**, *116*, 6985–6986.
[7] a) P. Endquist, P. Nilson, P. Sjöberg, M. Larhed, *J. Org. Chem.* **2006**, *71*, 8779–8786; b) I. Pantcheva, K. Osakada, *Organometallics* **2006**, *25*, 1735–1741; c) H. Guo, R. Qian, Y. Liao, S. Ma, Y. Guo, *J. Am. Chem. Soc.* **2005**, *127*, 13060–13064 and references cited therein; d) A. A. Sabino, A. H. L. Machado, C. R. D. Correia, M. N. Eberlin, *Angew. Chem. Int. Ed.* **2004**, *43*, 2514–2518; e) M. A. Aramendia, F. Lafont, M. Moreno-Mañas, R. Pleixats, A. Roglans, *J. Org. Chem.* **1999**, *64*, 3592–3594.
[8] A paper on the mechanism of $Pd^0$-catalysed cross-coupling reactions between arenediazonium salts and potassium organotrifluoroborates appeared after submission of this manuscript: J. Masllorens, I. González, A. Roglans, *Eur. J. Org. Chem.* **2007**, 158–166.
[9] The $^{1}H$ NMR spectra of the reaction solution were poorly informative due to the overlap of phenyl signals coming from the ligand and the borate species.
[10] These signals were observed after 1024 scans when a $^{19}F$ NMR spectrum of a methanol suspension of **4** was recorded at 50 °C.
[11] a) R. B. Bedford, S. L. Welch, *Chem. Commun.* **2001**, 129–130; b) R. Huang, K. H. Shaughnessy, *Organometallics* **2006**, *25*, 4105–4112.
[12] See electronic supporting information (Figure S25).
[13] a) T. I. Wallow, F. E. Goodson, B. M. Novak, *Organometallics* **1996**, *15*, 3708–3716; b) Y. P. Espinet, J. M. Martínez-Ilarduya, C. Pérez-Briso, A. L. Casado, M. A. Alonso, *J. Organomet. Chem.* **1998**, *551*, 9–20; c) G. W. Parshall, *J. Am. Chem. Soc.* **1974**, *96*, 2360–2366.
[14] Diazonium salts are known to undergo radical reactions with acetate ions that lead to decomposition products: H. Zollinger, *Azo and Diazo Chemistry, Aliphatic and Aromatic Compounds*, Interscience Publishers, London, **1961**, p. 153.
[15] a) G. Wu, A. L. Rheingold, R. F. Heck, *Organometallics* **1986**, *5*, 1922–1924; b) G. Wu, A. L. Rheingold, R. F. Heck, *Organometallics* **1987**, *6*, 2386–2391.
[16] G. B. Smith, G. C. Dezeny, D. L. Hughes, A. O. King, T. R. Verhoeven, *J. Org. Chem.* **1994**, *59*, 8151–8156.
[17] A. Roe, *Org. React.* **1949**, *5*, 193–228.
[18] E. Leyva, E. Monreal, C. Medina, S. Leyva, *Tetrahedron Lett.* **1997**, *38*, 7847–7848.

Received: May 21, 2007
Published Online: August 9, 2007

 © 2007 Wiley-VCH Verlag GmbH & Co. KGaA, Weinheim 

DOI: 10.1002/ejic.200700550

# Fine-Tuning Ligands for Catalysis Using Supramolecular Strategies

Vincent F. Slagt,[a][‡] Patrick Kaiser,[b] Albrecht Berkessel,[b] Mark Kuil,[a] Alexander M. Kluwer,[a] Piet W. N. M. van Leeuwen,[a] and Joost N. H. Reek*[a]

**Keywords:** Supramolecular catalysts / Self-assembly / Ligand effects / Phosphorus ligands / Porphyrinoids

Coordinative bonds have been used to prepare *supramolecular ligands* leading to well-defined catalysts formed by assembly. The construction of these ligands is based on selective metal–ligand interactions between nitrogen donor atoms of phosphorus-nitrogen building blocks and various zinc(II) porphyrins. The major advantage of this supramolecular approach of catalyst preparation is the simplification of ligand variation enabling straightforward modification of steric, electronic and chiral properties of the supramolecular ligand. A large number of new ligands becomes accessible by this modular variation of the building blocks. The ligand assembly based on pyridyl phosphites and zinc(II) porphyrin with electron-withdrawing substituents led to a twelve-fold increase in activity and an increase in enantioselectivity from 17 to 50 % in the rhodium-catalyzed hydrogenation of dimethyl itaconate. The first examples of assemblies based on non-chiral ligands and chiral zinc(II) porphyrin template molecules show, as proof of principle, an enantiomeric excess up to 18 % in the asymmetric palladium-catalyzed allylic alkylation.
(© Wiley-VCH Verlag GmbH & Co. KGaA, 69451 Weinheim, Germany, 2007)

## Introduction

In the past three decades, the exploration of ligand effects in transition-metal catalysis has proven to be a very powerful tool in homogeneous catalysis. Variation of steric[1] and electronic properties,[2] as well as the "natural bite angle"[3] for bidentate ligands, has been used to optimize many catalytic reactions. These ligand parameters have proven to control key features of catalysts, like activity, selectivity and stability, and systematic variation has resulted in better understanding of ligand effects in catalysis.[1–14] For example, electron-withdrawing substituents on the aryl ring of the phosphorus donor atom of mono- and bidentate phosphane ligands increases the activity and selectivity of the catalyst in the rhodium-catalyzed hydroformylation of 1-octene.[15] In the palladium-catalyzed arylation of alkenes, bulky phosphorus amidite ligands yielded very fast catalysts.[16] Both electronic and steric parameters of these ligands were found to be extremely important. The ligand has to be sufficiently bulky to impose formation of monoligated palladium complexes as active catalysts, but ligands that are too large retard the reaction rate.

[a] Van't Hoff Institute for Molecular Sciences, University of Amsterdam,
Nieuwe Achtergracht 166, 1018 WV Amsterdam, The Netherlands
Fax: +31-20-525-6422
E-mail: reek@science.uva.nl
[b] Institut für Organische Chemie der Universität zu Köln,
Greinstrasse 4, 50939 Köln, Germany
[‡] Current address: Syncom BV,
Kadijk 3, 9747 AT Groningen, The Netherlands

Recently, we[17,18] and others[19] have introduced a new class of bidentate ligands that are formed by a self-assembly process of two monodentate ligands. We demonstrated that the SUPRAphos[18b,18e,18f] concept – bringing two monodentate ligands together via zinc(II)–porphyrin–pyridyl interactions to form bidentate ligands – provides easy access to large bidentate ligand libraries, and that these ligands can successfully be applied to various reactions including the rhodium-catalyzed asymmetric hydrogenation. High-throughput screening of a part of the library revealed a catalyst that hydrogenates a trisubstituted cyclic enamide, a notoriously difficult substrate, with the highest enantioselectivity known to date.[18f] This unambiguously shows that the supramolecular approach to create bidentate ligands is a very powerful tool that brings about new catalysts with properties that surpass those already known. In addition, from the library of 64 SUPRAphos ligands that was investigated, only one provided a catalyst that induced high *ee* values, stressing the point that for challenging asymmetric conversion such as the hydrogenation of the trisubstituted cyclic enamide, large ligand libraries are required. One of the advantages typical of supramolecular ligands is the easy access to these large libraries. After the successful exploration of our SUPRAphos[18b,18e,18f] library based on porphyrin-appended ligands we have extended our approach to urea-based homo-bidentate ligands[20] and chiral analogues thereof for the use in asymmetric conversions.[21] This class of supramolecular bidentate ligands are easily accessible, in large variety and at an industrially interesting scale.

 © 2007 Wiley-VCH Verlag GmbH & Co. KGaA, Weinheim InterScience 

Although the preparation of monodentate ligands[22] is much easier than bidentate ligands,[23] a novel supramolecular strategy could also facilitate the preparation of large libraries of monodentate ligands. Here we report such a supramolecular strategy to change the electronic and steric properties of ligands that are equipped with pyridine and amine functional groups for the assembly of phosphorus ligands on zinc(II) porphyrin template molecules (Figure 1). The typical binding motif was previously used in the SUPRAphos concept and for the encapsulation of transition metal catalysts[24] by assembly of zinc(II) porphyrin building blocks.[25] By using the same binding motif we now show that we can vary the steric and electronic properties of phosphorus ligands by the association of the zinc(II) porphyrin templates. In this way, a series of new supramolecular ligands is prepared by just mixing the components. NMR, IR, and UV/Vis spectroscopy have been used to study the selective metal–ligand interactions and to quantify the steric and electronic properties of these supramolecular ligands. The supramolecular ligands control the activity and (enantio)selectivity of the transition metal catalysts as observed in rhodium-catalyzed hydroformylation, asymmetric hydrogenation, and asymmetric palladium-catalyzed allylic alkylation. The approach is extended to the assembly of a chiral environment around a non-chiral catalyst.

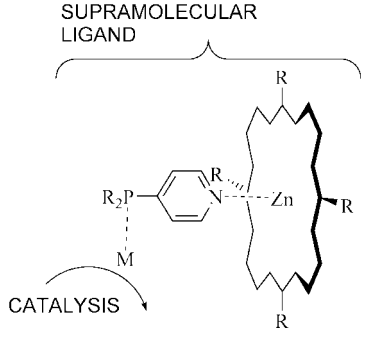


Figure 1. Schematic representation of the assembly of a phosphorus ligand on a zinc(II) porphyrin template molecule.

## Results and Discussion

### The Assembly of Phosphorus Ligands and Zinc(II) Porphyrin Building Blocks

For the preparation of supramolecular ligands with different steric and electronic properties, we synthesized several phosphorus ligands functionalized with a nitrogen donor atom and zinc(II) porphyrins (Figure 2). The phosphite ligands **2**–**4** were obtained in high yields by a reaction of the phosphor chloridite[26] with 3-hydroxypyridine. Zinc(II) *meso*,*meso*,*meso*,*meso*-tetraphenylporphyrin (**1a**) was prepared according to standard procedures.[27,28] All new compounds were fully characterized with $^{1}$H NMR, $^{31}$P-NMR and $^{13}$C-NMR spectroscopy, elemental analysis and mass spectrometry.

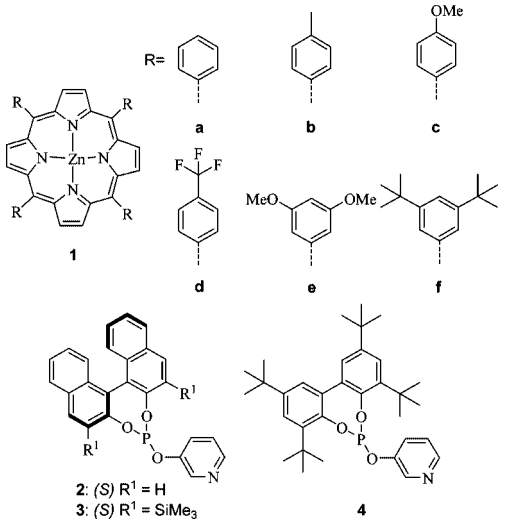


Figure 2. Various building blocks used to construct supramolecular ligands.

The coordination behavior of the pyridine phosphorus ligands **2** to **1a** has been studied using NMR and UV/Vis spectroscopy.[29,30] The addition of **1a** to a solution of **2** resulted in large upfield shifts of the protons on the pyridyl ring in $^{1}$H NMR spectroscopy ($\Delta\delta^{H1}$ = 5.7 ppm, $\Delta\delta^{H2}$ = 5.8 ppm), which is typical of axial binding of pyridine ligands to zinc(II) porphyrins (Scheme 1).[24,25] Also in $^{31}$P

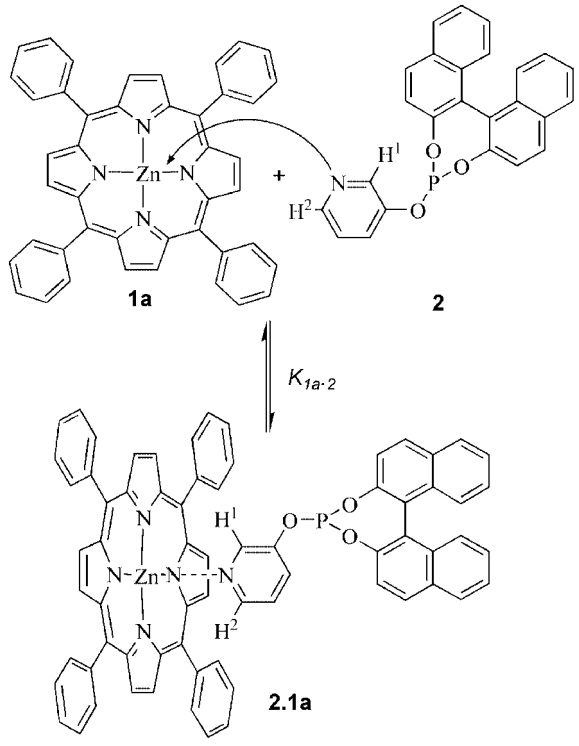


Scheme 1. Assembly of (*S*)-(1,1′-binaphthyl-2,2′-diyl) (3-pyridyl) phosphite (**2**) on zinc(II) *meso*,*meso*,*meso*,*meso*-tetraphenylporphyrin (**1a**).

 © 2007 Wiley-VCH Verlag GmbH & Co. KGaA, Weinheim 

NMR spectroscopy, a large shift to higher field ($\Delta\delta^P$ = 4.6 ppm) was observed on binding of **2** to the complex **1a**. In the UV/Vis spectrum of **1a** the typical red-shift of the Q-bands of the porphyrin on the addition of **2** was observed, indicating axial coordination of the pyridine to the zinc, and the associated binding constant determined by UV titrations was found to be high ($K_{1a.2} = 1.3 \times 10^3$ M$^{-1}$).

The binding of zinc(II) porphyrin building blocks through the nitrogen donor atom is very selective and therefore the phosphorus atom is available for coordination to transition metals that potentially can act as catalysts. Mixing two equivalents **1a** (with respect to the complex and one equivalent with respect to the ligand) with in situ formed [Rh(acac)(**2**)$_2$] yielded an assembly in which the transition metal is embedded between the two porphyrin building blocks [Rh(acac)(**2**·**1a**)$_2$], as was evident from the shifts in NMR spectroscopy. In the $^{31}$P NMR spectra the addition of the porphyrin **1a** resulted in an interestingly large upfield shift of the phosphite signals, from $\delta$ = 151.3 ppm (doublet, $J_{P-Rh}$ = 303 Hz) to $\delta$ = 144.5 ppm (doublet, $J_{P-Rh}$ = 304 Hz) (Figure 3). The large shift of $\Delta\delta^P$ = 6.8 ppm is attributed to a combination of effects: changes in the electronic and steric properties of the phosphite and the ring-current effect of the nearby complexed zinc(II) porphyrin **1a**.

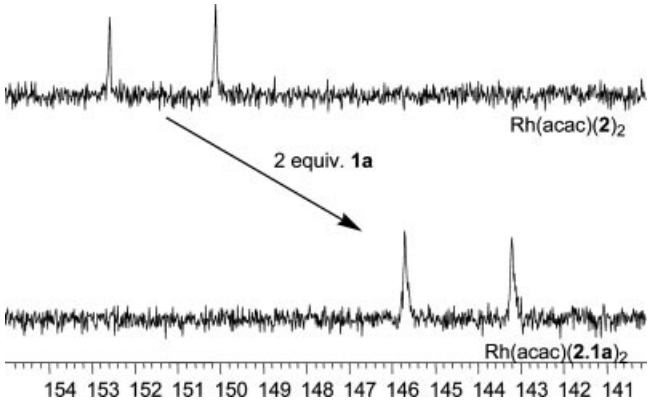


Figure 3. $^{31}$P NMR spectra before (above) and after (below) addition of two equivalents of zinc(II) *meso*,*meso*,*meso*,*meso*-tetraphenylporphyrin (**1a**) to the complex [Rh(acac)(**2**)$_2$].

## Assemblies of Zinc(II) Porphyrin and Phosphorus Ligands in Transition-Metal Catalysis

The supramolecular complexes based on the zinc(II) porphyrin **1a** and pyridyl phosphite ligands **2** and **4** were studied in the rhodium-catalyzed hydroformylation of 1-octene (Scheme 2).[9,31] The experiments were carried out in toluene under 20 bar of syngas ($H_2$/CO = 1:1) and the results are summarized in Table 1. The catalyst formed by ligand **2** yielded a moderate activity and reasonable selectivity in the hydroformylation of 1-octene at 120 °C, and the isomerization side reaction resulted in 25% internal alkenes. The assembly based on the zinc(II) porphyrin **1a** and **2** did not influence the catalytic behavior and similar activity, selectivity and isomerization were observed.[32] The more bulky ligand **4** yielded a catalyst with different properties; an increase in activity and decrease in selectivity (linear-branched ratio, l/b = 2.1) was observed for this system compared to ligand **2**. These differences are explained by the formation of monoligated rhodium phosphite complexes, as previously observed for other bulky phosphite ligands.[33] Upon using assembly **4**·**1a** an increase in activity and isomerization was observed, showing that the assembly of zinc(II) porphyrin templates to ligands with nitrogen donor atoms influences the performance of the transition metal catalyst based on these ligands, which stimulated further studies on these assembled ligand systems.

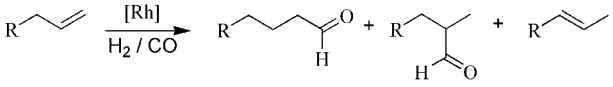


Scheme 2. The rhodium-catalyzed hydroformylation leading to the linear and branched aldehyde.

Table 1. Rhodium-catalyzed hydroformylation of 1-octene using assemblies of pyridyl phosphite and zinc(II) porphyrins template as ligands.[a]

| Ligand[b] | Temp. [°C] | T.O.F.[c] | l/b[d] | % 2-Octene[e] |
|---|---|---|---|---|
| **2** | 120 | $1.2 \times 10^3$ | 6.0 | 24.6 |
| **2**·**1a** | 120 | $1.3 \times 10^3$ | 7.0 | 19.8 |
| **4** | 80 | $2.3 \times 10^3$ | 2.1 | 21.6 |
| **4**·**1a** | 80 | $3.0 \times 10^3$ | 2.0 | 26.0 |

[a] [Rh(acac)(CO)$_2$] = 0.084 mmol/L in toluene, pressure: 20 bar (CO/$H_2$ = 1:1), 1-octene/rhodium = 5160. [b] [Phosphorus ligand **2** or **4**] = 2.1 mmol/L, [porphyrin] = 2.1 mmol/L. [c] T.O.F. = average turn over frequency: (mol aldehyde)(mol Rh)$^{-1}$ h$^{-1}$, the reaction was stopped after 1 h. [d] l/b = linear/branched. [e] Percent isomerization to 2-octene (and some 3- and 4-octene).

## Changing the Electronic Properties of Phosphorus Ligands

To study these new self-assembled ligands based on selective nitrogen–zinc interactions in more detail, several zinc(II) porphyrins **1a**–**d** were synthesized with different electron-withdrawing and -donating substituents.[27,28] The binding constants of zinc(II) porphyrins **1a**–**d** to diphenyl(4-pyridyl)-phosphane (**7**) (Figure 4) in toluene were determined using UV/Vis spectroscopy. It was found that the porphyrin with the most electron-withdrawing substituents yielded the highest binding constant (Table 2) and a linear relation between binding constants and the Hammett values[34] was observed, with a corresponding electronic dependence value of $\rho$ = 0.285 (Figure 5).

 © 2007 Wiley-VCH Verlag GmbH & Co. KGaA, Weinheim 

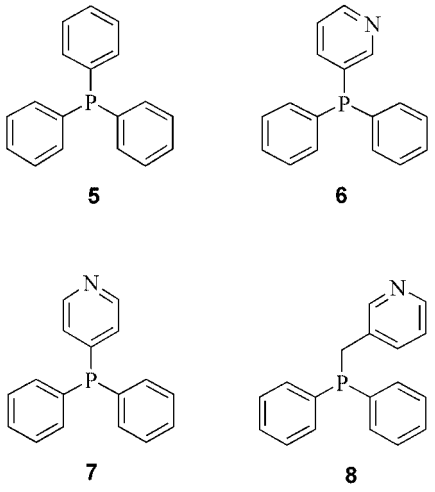


Figure 4. Various ligand building blocks used to construct supramolecular ligands.

Table 2. Binding constants observed for diphenyl(4-pyridyl)phosphane (**7**) to various zinc(II) porphyrin templates measured by UV/Vis titrations and the IR-carbonyl frequencies of the corresponding metal complexes [Rh(**7**)$_2$(CO)Cl] with the attached zinc(II) porphyrin.

| Porphyrin | $K$ [M$^{-1}$] | log $K$ | 4σ | $\tilde{\nu}$[a] [cm$^{-1}$] |
|---|---|---|---|---|
| **1c** ($OCH_3$-porphyrin) | $2.9\times10^3$ | 3.469 | –1.08 | 1983 |
| **1b** ($CH_3$-porphyrin) | $3.7\times10^3$ | 3.564 | –0.68 | 1984 |
| **1a** (H-porphyrin) | $6.1\times10^3$ | 3.785 | 0 | 1985 |
| **1d** ($CF_3$-porphyrin) | $24.4\times10^3$ | 4.387 | 2.16 | 1986/87 |

[a] Measured in dichloromethane, carbonyl region.

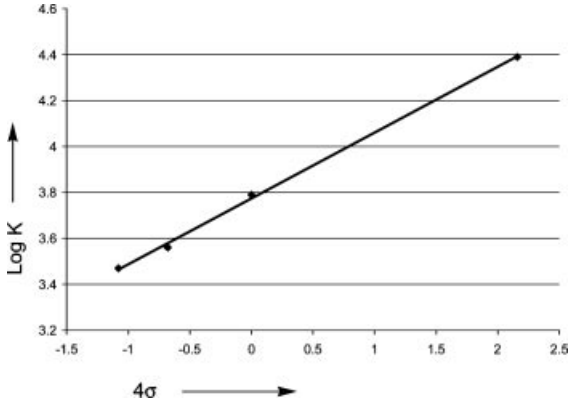


Figure 5. Plot log $K$ vs. 4σ (sigma *para*) for the assembly of zinc(II) porphyrin complexes **1a**–**d** and diphenyl(4-pyridyl)phosphane (**7**).

The substituents on the zinc(II) porphyrin template **1a**–**d** change the π back bonding of the zinc(II) metal ion to the porphyrin macrocycle, hence influencing the electron density of the pyridine moiety ring fragment.[35] Therefore, also an effect in electron density on the phosphorus donor atom is expected. Zinc(II) porphyrins containing more electron-withdrawing substituents will increase the electron-withdrawing capacity of the pyridine ring, which will result in a lower basicity of the phosphorus donor atom. (Diphenyl)(4-pyridyl)phosphane (**7**) and [Rh(CO)$_2$(Cl)]$_2$ were mixed in a 4:1 ratio to form in situ [Rh(**7**)$_2$(CO)Cl] and subsequently a stoichiometric amount of zinc(II) porphyrin **1a**–**d** was added.[36] The IR spectra of these assembled rhodium complexes show that addition of zinc(II) porphyrin changes the shift of the carbonyl ($\tilde{\nu}_{CO}$ = 1982 cm$^{-1}$) of [Rh(**7**)$_2$(CO)Cl] to higher wave numbers (up to $\tilde{\nu}_{CO}$ = 1986 cm$^{-1}$). The $\tilde{\nu}_{CO}$ band shows a gradual shift with decreasing phosphane basicity (Table 2). The lower electron density on the rhodium leads to a decrease in back bonding from the rhodium to the carbonyl ligand and hence higher CO stretching frequencies are observed. For comparison, when the strongly electron-withdrawing tris(4-α,α,α-trifluorotoluyl)phosphane is used, the $\tilde{\nu}_{CO}$ band is at 1990 cm$^{-1}$, which is a shift of 12 cm$^{-1}$ compared to triphenylphosphane, ($\tilde{\nu}_{CO}$ = 1978 cm$^{-1}$).[36,37] These results show that the effects induced by the zinc(II) porphyrin templates **1a**–**d** are significant. For phosphane **7**, the pyridine is directly attached to the phosphorus, and therefore changes on the nitrogen donor atom were expected to change the basicity of the phosphorus. Upon using a different spacer between the phosphorus and the nitrogen one can envisage that electronic effects on the phosphorus caused by the assembly of zinc(II) porphyrin templates **1a**–**d** will be different. Indeed, the use of diphenyl(3-pyridylmethyl)phosphane (**8**), a similar building block as **7** but with a spacer that has changed from 4-pyridine to 3-methylpyridine, shows that the carbonyl peak in the infrared spectrum of complex [Rh(**8**)$_2$(CO)Cl] hardly changes upon assembling the zinc(II) porphyrin templates **1a**–**d** ($\tilde{\nu}_{CO}$ = 1979–1980 cm$^{-1}$). Thus, these experiments show that electron-withdrawing substituents on the zinc(II) porphyrin that is used as a template can modify the electronic properties of the phosphane ligands, depending on the spacer between the nitrogen and phosphorus donor atom of the ligand building block.

The electronic effect of zinc(II) porphyrin templates **1a**–**d** on diphenyl(4-pyridyl)phosphane (**7**) and diphenyl(3-pyridylmethyl)phosphane (**8**) were studied in the rhodium-catalyzed hydroformylation of 1-octene (Table 3). The assemblies of zinc(II) porphyrin **1a**–**d** and **7** show a small but distinct trend in activity (**7**·**1c**<**7**·**1b**<**7**·**1a**<**7**·**1d**). The assemblies based on more electron-withdrawing zinc(II) porphyrin templates and **7** show a small increase in conversion in the rhodium-catalyzed hydroformylation of 1-octene. From the infrared spectra we know that this effect is caused by the lower basicity of the phosphane donor atoms. In the literature a similar trend has been reported for systems in which the electronic properties of the ligands were varied in a covalent manner.[15] For the various ligand assemblies based on phosphane **8** and zinc(II) porphyrin **1a**–**d** the differences in activity are negligible. This is in line with the almost identical infrared CO stretching frequencies observed for the rhodium complexes. The catalytic results obtained for the assemblies based on zinc(II) porphyrin **1a**–**d** and ligands **7** and **8** show that the spacer between the nitrogen and phosphorus donor atoms is of great importance for the small but distinct electronic influences on the phosphorus induced by the assembly process.

 © 2007 Wiley-VCH Verlag GmbH & Co. KGaA, Weinheim 

Table 3. Rhodium-catalyzed hydroformylation of 1-octene using assemblies of pyridylphosphane and zinc(II)porphyrin templates as ligands.[a]

| Ligand[b] | % Conversion[c] | T.O.F.[d] | l/b[e] | % 2-Octene[f] |
|---|---|---|---|---|
| **7·1c** | 56.0 | $2.7\times10^3$ | 2.9 | 1.9 |
| **7·1b** | 59.1 | $2.8\times10^3$ | 2.9 | 2.8 |
| **7·1a** | 59.6 | $2.8\times10^3$ | 2.9 | 2.9 |
| **7·1d** | 62.6 | $3.0\times10^3$ | 2.9 | 3.4 |
| **8·1c** | 74.7 | $3.5\times10^3$ | 2.4 | 1.1 |
| **8·1b** | 75.2 | $3.5\times10^3$ | 2.3 | 1.2 |
| **8·1a** | 75.1 | $3.6\times10^3$ | 2.3 | 0.7 |
| **8·1d** | 75.8 | $3.6\times10^3$ | 2.4 | 1.0 |

[a] [Rh] = 0.084 mmol/L in toluene, pressure: 20 bar ($CO/H_2$ = 1:1), $T$ = 80 °C, 1-octene/rhodium = 5160. [b] [phosphorus ligand (**7** or **8**)] = 0.84 mmol/L, [porphyrin] = 0.84 mmol/L. [c] Percent total conversion of 1-octene to aldehydes and isomers. [d] T.O.F. = average turn over frequency: (mol aldehyde)(mol Rh)$^{-1}$ h$^{-1}$, the reaction was stopped after 1 h. [e] l/b = linear/branched. [f] Percent isomerization to 2-octene (and some 3- and 4-octene).

## Application of Supramolecular Ligands in Asymmetric Hydrogenation

The supramolecular ligands were used in the asymmetric rhodium-catalyzed hydrogenation[49] of dimethyl itaconate to dimethyl methylsuccinate (Scheme 3). The ligands were based on the assembly of (*S*)-[3,3′-bis(trimethylsilyl)-1,1′-binaphthyl-2,2′-diyl] (3-pyridyl) phosphite (**3**) and zinc(II) porphyrins **1a**–**f**. Ligand **3** shows low conversion and enantioselectivity in the hydrogenation of dimethyl itaconate (Table 4). In contrast, the assemblies based on zinc(II) porphyrin template **1a**–**d** and ligand **3** give higher conversion and enantioselectivity. Electron-withdrawing substituents on the zinc(II) porphyrin **1a**–**d** have a positive effect on the activity, a twelve-fold increase for the most electron-withdrawing zinc(II) porphyrin **1d** was observed. Interestingly, the ligand based on the assembly of **1d** and **3** increases the enantioselectivity from 16% to 50% (*R*).

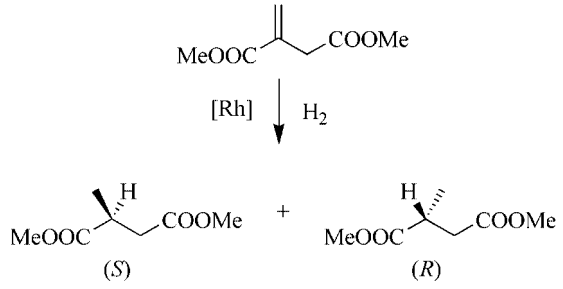


Scheme 3. The rhodium-catalyzed hydrogenation of dimethyl itaconate.

After having observed a clear electronic effect, we decided to look at the effect of the size of various ligand assemblies in catalysis by changing the substituents on the zinc(II) porphyrin **1a**–**d**. The ligand assemblies **3·1a**–**3·1d** and the more bulky ligand assemblies **3·1e** and **3·1f** were tested in the rhodium-catalyzed hydrogenation of dimethyl itaconate. The different substituents on the aryl groups of the zinc(II) porphyrins **1e** and **1f** not only change the size of the ligand, but also lead to different electronic properties of the assembled ligand system. The assembled **3·1e** yielded

Table 4. Hydrogenation of dimethyl itaconate using different rhodium catalyst assemblies: variation of the zinc(II)porphyrin template.[a]

| Ligand[b] | % Conversion[c] | % *ee*[d] |
|---|---|---|
| **3** | 1.6 | 16 (*R*) |
| **3·1a** | 8.1 | 33 (*R*) |
| **3·1b** | 6.2 | 21 (*R*) |
| **3·1c** | 4.3 | 31 (*R*) |
| **3·1d** | 18.8 | 50 (*R*) |
| **3·1e** | 2.5 | 2 (*R*) |
| **3·1f** | 3.1 | 40 (*R*) |

[a] [$Rh(nbd)_2(BPh_4)$] = 1.0 mmol/L, [dimethyl itaconate] = 100 mmol/L, pressure: 5 bar hydrogen, $T$ = 40 °C. [b] [phosphite] = 3.0 mmol/L, [porphyrin] = 3.0 mmol/L. [c] The reaction was stopped after 17 h. [d] *ee* = enantiomeric excess.

no enantioselectivity, and a low conversion was detected in the hydrogenation. The low conversion is explained by the strong electron-donating capacity of the methoxy groups of **1e**. The more bulky ligand **3·1f** resulted in a catalyst that gave an enantiomeric excess of 40% (*R*), but at low activity.

The use of selective metal–ligand interactions to change ligand properties can be extended easily to bidentate ligands (Figure 6). The chiral (2*S*,4*S*)-(–)-4-(diphenylphosphanyl)-2-(diphenylphosphanylmethyl)pyrrolidine (**9**)[38] binds to zinc(II) porphyrins by axial coordination of the nitrogen donor atom in the pyrrolidine ring to the zinc(II) ion. $^1$H NMR spectroscopy in [D]chloroform showed a large shift for the pyrrolidine protons of **9** on addition of one equivalent of zinc(II) porphyrin **1a**, as is typical of this type of binding. Also in the $^{31}$P NMR spectra a change in chemical shifts was observed, $\Delta\delta$P(2*S*) = 4.3 ppm (Figure 7).

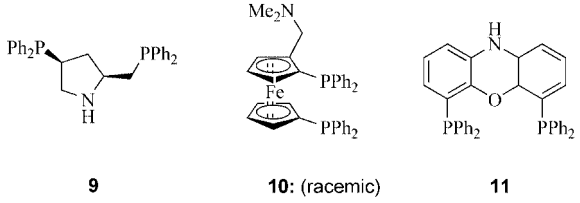


Figure 6. Various diphosphane ligand building blocks that were used to construct supramolecular ligands via nitrogen coordination to zinc(II) porphyrins.

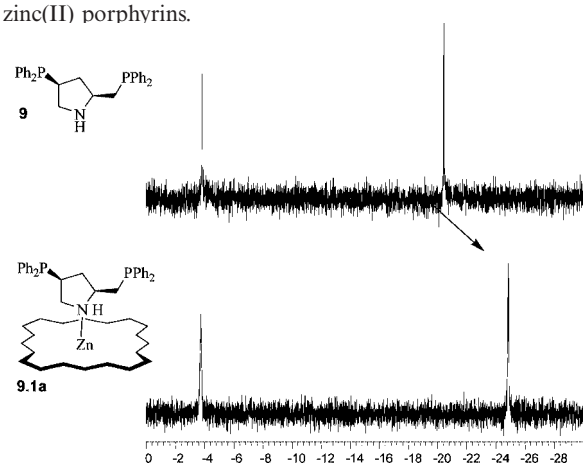


Figure 7. $^{31}$P NMR spectra of (2*S*,4*S*)-(–)-4-(diphenylphosphanyl)-2-(diphenylphosphanylmethyl)pyrrolidine (**9**) in absence (above) and presence (below) of zinc(II) porphyrin **1a**.

 © 2007 Wiley-VCH Verlag GmbH & Co. KGaA, Weinheim 

### Application of Supramolecular Ligands in Asymmetric Hydroformylation

The zinc(II) porphyrins **1a**, **1e** and **1f** were used to form new ligand assemblies with the diphosphane **9**, which were applied in the asymmetric rhodium-catalyzed hydroformylation[9,50] of styrene (40 °C, toluene, 20 bar $CO/H_2$). As is shown in Table 5, the catalyst based on the bidentate ligand **9** resulted in moderate enantioselectivity [19% *ee*, (*S*)-product] and activity in the hydroformylation of styrene. The ligand assembly based on zinc(II) porphyrin **9·1a** resulted in small increase in enantioselectivity and a decrease in activity. Electronic changes on phosphorus caused by the assembly of the zinc(II) porphyrin template are considered to be very small, because the use of the zinc(II) *meso*-*p*-$CF_3$-phenylporphyrin **1d** yielded similar results as **1a**. Increasing the bulk of the porphyrin building block by using **1f**, the enantioselectivity further improved to 29% (*S*), at the cost of a lower activity and lower branched to linear ratio. These results indicate that variation of steric bulk around the catalyst introduced by supramolecular interactions using different porphyrin building blocks modifies the ligand properties and the catalytic performance of their metal complexes, both for mono- and bidentate ligands.

Table 5. Hydroformylation of styrene using assemblies based on the chiral diphosphane **9**: variation of the zinc(II) porphyrin template.[a]

| Ligand[b] | % Conversion[c] | T.O.F.[d] | b/l[e] | % *ee*[f] |
|---|---|---|---|---|
| **9** | 54 | 14.2 | 5.2 | 19 (*S*) |
| **9·1a** | 25 | 6.7 | 5.6 | 23 (*S*) |
| **9·1e** | 15 | 4.0 | 3.9 | 26 (*S*) |
| **9·1f** | 9 | 2.3 | 2.4 | 29 (*S*) |

[a] [Rh] = 0.33 mmol/L in toluene, pressure: 20 bar ($CO/H_2$ = 1:1), $T$ = 40 °C, styrene/rhodium = 1750, in none of the reactions hydrogenation was observed. [b] [phosphane] = 1.67 mmol/L, [porphyrin] = 1.67 mmol/L. [c] Percent conversion, the reaction was stopped after 66.5 h. [d] T.O.F. = average turn over frequency: (mol aldehyde)(mol Rh)$^{-1}$h$^{-1}$. [e] b/l = branched/linear. [f] *ee* = enantiomeric excess.

### Introducing a Chiral Environment around a Non-Chiral Catalyst

In the previous section we described the fine-tuning of catalyst properties by the introduction of steric bulk around a chiral catalyst by supramolecular interactions. An even greater challenge would be the introduction of a chiral environment around a non-chiral catalyst via a selective assembly process, resulting in a chiral catalyst assembly for asymmetric catalysis. Towards this goal, chiral zinc(II) porphyrin building blocks based on octahydro-1,4:5,8-dimethanoanthracene **12a**–**12d** were synthesized (Figure 8).[39] This type of porphyrin is known to be very selective in the ruthenium- or manganese-catalyzed epoxidation[39,40] and cyclopropanation[41] of alkenes. The crystal structure[39] of the zinc(II) porphyrin **12a** shows that the chiral moieties are highly symmetrically positioned around the core of the porphyrin and molecular modeling[42] suggests that there is enough space for axial ligand coordination to the zinc metal (Figure 9).

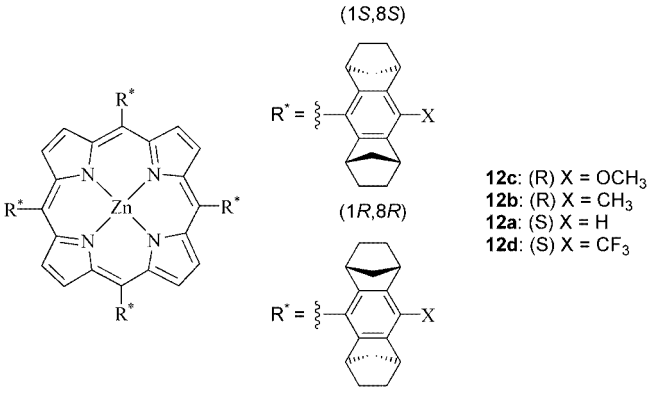


Figure 8. Various chiral porphyrin building blocks used to construct supramolecular ligands.

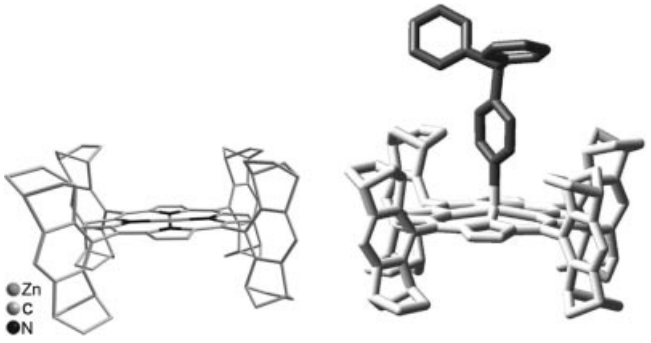


Figure 9. Crystal structure of the zinc(II) complex of *meso*,*meso*,-*meso*,*meso*-tetrakis(octahydro-1,4:5,8-dimethanoanthryl)porphyrin (**12a**) (left) and modeled structure of the assembly of **12a** (white) and diphenyl(4-pyridyl)phosphane (**7**) (dark gray, right).

Upon mixing the ligands **6**–**8** in a 1:1 ratio with the zinc(II) porphyrin **12a** supramolecular complexes were formed by complexation of the nitrogen donor atom to the axial position of zinc(II). Binding constants were determined with UV/Vis spectroscopy titrations in toluene (Table 6). Phosphane **7** has the strongest affinity for **12a** ($K$ = $3.5 \times 10^3$ M$^{-1}$) and the binding constant of phosphane **6** is approximately three times smaller ($K = 8.7 \times 10^2$ M$^{-1}$).

Table 6. Binding constants of various pyridylphosphane ligands to zinc(II) porphyrin template **12a** (and **1a** for comparison) measured by UV/Vis titrations in toluene.

| Ligand | $K$ [M$^{-1}$] | Ligand | $K$ [M$^{-1}$] |
|---|---|---|---|
| **6·12a** | $0.87 \times 10^3$ | **6·1a** | $2.3 \times 10^3$ |
| **7·12a** | $3.5 \times 10^3$ | **7·1a** | $6.1 \times 10^3$ |
| **8·12a** | $1.6 \times 10^3$ | **8·1a** | $4.0 \times 10^3$ |

A similar trend for these ligands was already observed with the complexation to the zinc(II) porphyrin **1a**, and the small differences observed for **6**–**8** are likely due to electronic effects. Titrations monitored with UV/Vis spectroscopy to determine binding constants between chiral zinc(II) porphyrins **12a**–**12d** and **7** in toluene showed that electron-withdrawing substituent X on the porphyrin resulted in higher binding constant ($OMe < Me < H < CF_3$) (Table 7), which corroborates the results obtained for **7** and

 © 2007 Wiley-VCH Verlag GmbH & Co. KGaA, Weinheim 

zinc(II) porphyrin **1a**–**1d**. A similar linear relation between binding constants and the Hammett values is observed, with a corresponding electronic dependence value of $\rho$ = 0.201 (Figure 10), which is comparable with results reported in literature.[43]

Table 7. Binding constants $K$ of diphenyl(4-pyridyl)phosphane (**7**) to various zinc(II) porphyrin templates **12a**–**12d** measured by UV/Vis titrations.

| Porphyrin | $K$ [M$^{-1}$] | log $K$ | 4σ |
|---|---|---|---|
| (*R*)-$OCH_3$-porphyrin-Zn, **12c** | $2.2 \times 10^3$ | 3.346 | –1.08 |
| (*R*)-$CH_3$-porphyrin-Zn, **12b** | $2.8 \times 10^3$ | 3.444 | –0.68 |
| (*S*)-H-porphyrin-Zn, **12a** | $3.5 \times 10^3$ | 3.545 | 0 |
| (*S*)-$CF_3$-porphyrin-Zn, **12d** | $10.0 \times 10^3$ | 4.000 | 2.16 |

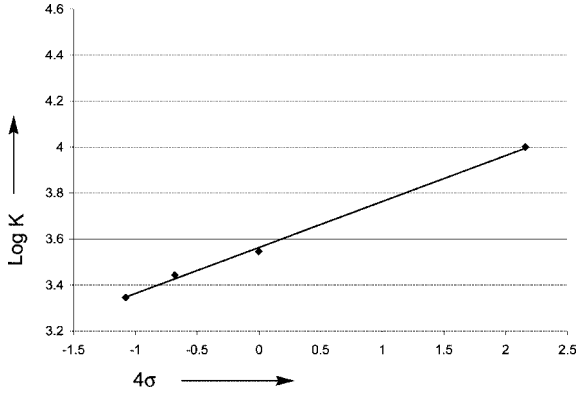


Figure 10. Plot log $K$ vs. 4σ for the reaction of zinc(II) porphyrins **12a**–**d** and diphenyl(4-pyridyl)phosphane (**7**).

To study the effect of the "associated" chiral environment, assemblies based on zinc(II) porphyrin **12a** and **4**–**8** were tested as ligands in the asymmetric palladium-catalyzed allylic alkylation[51] using 1,3-diphenylallyl acetate as the substrate and dimethyl malonate as the nucleophile (Scheme 4). Table 8 shows that the chiral zinc(II) porphyrin **12a** was not active in the palladium-catalyzed allylic alkylation and that the palladium complexes based on triphenylphosphane (**5**) in the presence of enantiopure **12a** did not induce enantioselectivity. The assembly of the pyridine phosphite ligand **4** and chiral zinc(II) porphyrin **12a** resulted in an enantioselectivity of 8% (*S*) and a concomitant low activity. The activity was much higher upon using pyridylphosphane **6**–**8** as ligands for the assembly with **12a** and complete conversion was observed for all phosphane-based catalysts. The enantiomeric excesses for the assemblies of zinc(II) porphyrin **12a** and phosphane ligands **6**–**8** are found to be comparable with the result obtained for the assembly **4·12a**. The electronic properties of the ligand assembly were varied with the use of zinc(II) porphyrin building blocks **12a**–**12d** and phosphane **7**, but this did not affect the enantioselectivity in the palladium-catalyzed allylic alkylation. The use of the assemblies based on the other enantiomer (*R*) as zinc(II) porphyrin template (**7·12b** and **7·12c**) yields indeed the other enantiomeric product in excess. Although the chiral inductions in palladium-catalyzed allylic alkylation found for the assemblies based on monodentate phosphorus ligands **4**–**8** on the chiral zinc(II) porphyrins **12a**–**12d** do not exceed 10% yet, these first results do show that it is *possible* to create a chiral catalyst by nearby complexation of a chiral co-factor.

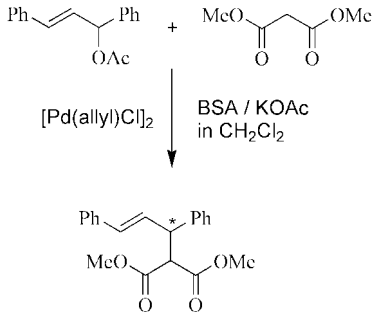


Scheme 4. Palladium-catalyzed allylic alkylation.

Table 8. Palladium-catalyzed allylic alkylation of 1,3-diphenylallyl acetate, using various ligand assemblies based on chiral zinc(II) porphyrin templates.[a]

| Ligand[b] | % Conversion[c] | % *ee*[d] |
|---|---|---|
| **12a** (*S*) | 0 | 0 |
| **4·12a** (*S*) | 30 | 9 (*S*) |
| **5** + **12a** (*S*) | >99 | 0 |
| **6·12a** (*S*) | >99 | 9 (*S*) |
| **7·12c** (*R*) | >99 | 8 (*R*) |
| **7·12b** (*R*) | >99 | 10 (*R*) |
| **7·12a** (*S*) | >99 | 9 (*S*) |
| **7·12d** (*S*) | >99 | 8 (*S*) |
| **8·12** (*S*) | >99 | 5 (*S*) |
| **10·12d** (*S*) | >99 | 18 (*S*) |
| **11·12d** (*S*) | >99 | 12 (*S*) |

[a] [[Pd(allyl)Cl]$_2$] = 0.100 mmol/L, $T$ = 25 °C. [b] [phosphite] = 0.6 mmol/L, [porphyrin] = 0.6 mmol/L. [c] The reaction was stopped after 24 h. [d] *ee* = enantiomeric excess.

This approach has also been used for bidentate phosphorus ligands with nitrogen donor atoms, i.e. ligands **10** and **11** (Figure 6).[44,45] These bidentate phosphorus ligands have been assembled on zinc(II) porphyrin template **12d** with associated binding constants of ($K_{10\cdot12d}$ = 515 M$^{-1}$) and ($K_{11\cdot12d}$ = 150 M$^{-1}$), as determined by UV/Vis spectroscopy titrations in toluene. Although the binding constants are not sufficiently high to prevent the formation of non-templated ligand under the reaction conditions, these ligand assemblies were tested in the palladium-catalyzed asymmetric allylic alkylation. It was found that the supramolecular ligands **10·12d** and **11·12d** resulted in moderate enantioselectivities, up to 18%. Attempts to increase the *ee* by shifting the equilibrium from free **11** to fully assembled **11·12d**, by adding excess of **12d**, failed due to the limited solubility of this porphyrin.

## Conclusions

A new class of supramolecular monodentate ligands is reported, which is based on selective metal–ligand interactions. The supramolecular ligands are obtained by just mixing simple building blocks, typically zinc(II) porphyrin tem-

 © 2007 Wiley-VCH Verlag GmbH & Co. KGaA, Weinheim 

plate molecules and phosphorus ligands containing nitrogen donor atoms. These unique supramolecular ligand systems provide a new tool to modify key catalyst properties, such as activity and selectivity, in a very simple manner. The major advantage of this supramolecular approach is the ease of ligand variation and accessibility of a large number of new ligand systems by variation of template molecules and phosphorus nitrogen building blocks. In the rhodium-catalyzed hydroformylation of 1-octene small but distinct changes have been observed, upon using different electron-donating and withdrawing zinc(II) porphyrin building blocks for the catalyst assemblies. Interesting changes have also been observed in the enantioselective rhodium-catalyzed hydrogenation of dimethyl itaconate. The ligand assemblies based on zinc(II) porphyrin with electron-withdrawing substituents led to a twelve fold increase of activity and an increase of enantioselectivity from 17 to 50%. We also have used, for the first time, assemblies based on non-chiral ligands and chiral zinc(II) porphyrin template molecules and used these as ligands in the asymmetric palladium-catalyzed allylic alkylation. Although the enantioselectivities observed so far are rather low (up to 18%), it demonstrates that with a chiral template a chiral environment around the metal center can be obtained. In general, the use of coordinative binding in order to construct supramolecular ligands simplifies the preparation of new (chiral) ligand systems, which enables novel (chiral) catalyst systems. We are currently expanding the scope of ligands and template molecules of which the results will be reported in due time.

## Experimental Section

**General Procedures:** Unless stated otherwise, reactions were carried out under argon using standard Schlenk techniques. THF, hexane and diethyl ether were distilled from sodium benzophenone ketyl; $CH_2Cl_2$, 2-propanol and methanol were distilled from $CaH_2$ and toluene was distilled from sodium under nitrogen. NMR spectra ($^1H$, $^{31}P$ and $^{13}C$) were measured with a Bruker DRX 300 MHz and Varian Mercury 300 MHz. $CDCl_3$ was used as a solvent, if not further specified. Mass spectra were recorded with a JEOL JMS SX/SX102A four sector mass spectrometer; for FAB-MS 3-nitrobenzyl alcohol was used as matrix. Elemental analyses were obtained with an Elementar Vario EL apparatus. Gas chromatographic analyses were run with an Interscience HR GC Mega 2 apparatus (split/splitless injector, J&W Scientific, DB-1 J&W 30 m column, film thickness 3.0 μm, carrier gas 70 kPa He, FID Detector) equipped with a Hewlett–Packard Data system (Chrom-Card). Chiral GC separations were conducted with a Chirasil-L-Val capillary column (0.25 mm × 25 m). Chiral HPLC analyses were carried out using a Daicel Chiralcel-OD column (0.46 × 25 cm).

**Materials:** With exception of the compounds given below, all reagents were purchased from commercial suppliers and used without further purification. Diisopropylethylamine and triethylamine were distilled from $CaH_2$ under argon. 1-Octene was filtered through a plug of alumina. The following compound were synthesized according to published procedures: zinc(II) porphyrins **1a**–**f**,[27,28] binaphthyl or biphenyl phosphorochloridites,[26] chiral zinc(II) porphyrin **a**–**d**,[39] pyridylphosphanes **6**–**8**[46,47] and diphosphanes **9**–**11**.[38,44–45]

**Synthesis of (*S*)-(1,1′-Binaphthyl-2,2′-diyl) (3-Pyridyl) Phosphite (2):** 3-Hydroxypyridine (1.44 g, 15.1 mmol), azeotropically dried with toluene (3 × 5 mL), and triethylamine (2.3 mL, 16.6 mmol) were dissolved in THF (40 mL) and the solution was cooled to –40 °C. Freshly prepared (*S*)-2,2′-binaphthyl phosphorochloridite (5.3 g, 15.1 mmol) was dissolved in THF (20 mL) and added dropwise. The cooling bath was removed and the solution was warmed to room temperature, stirring was continued for 1 h. The reaction mixture was filtered and the solvent evaporated. A mixture of toluene/hexane, 1:3 (40 mL) was added to extract the product. After filtration the solvent was removed in vacuo, giving **2** (5.4 g, 13.2 mmol, 87%) as a white solid. $^1H$ NMR (300 MHz): $\delta$ = 8.54 (d, $J$ = 2.4 Hz, 1 H), 8.40 (d, $J$ = 4.2 Hz, 1 H), 8.02 (d, $J$ = 8.7 Hz, 1 H), 7.95 (d, $J$ = 8.7 Hz, 1 H), 7.92 (d, $J$ = 8.7 Hz, 2 H), 7.56–7.16 (m, 10 H) ppm. $^{31}P$ NMR (121.5 MHz): $\delta$ = 143.05 ppm. $^{13}C$ NMR (75.465 MHz): $\delta$ = 148.88 (d, $J_{cp}$ = 6.1 Hz), 147.52 (d, $J_{cp}$ = 4.8 Hz), 146.84 (d, $J_{cp}$ = 1.4 Hz), 145.80 (s), 142.71 (d, $J_{cp}$ = 7.3 Hz), 133.02 (s), 132.75 (s), 132.01 (s), 131.55 (s), 130.97 (s), 130.36 (s), 129.29 (s), 128.67 (d, $J_{cp}$ = 4.8 Hz), 128.48 (s), 127.945 (s), 127.83 (s), 127.28 (s), 127.19 (s), 126.80 (s), 126.67 (s), 125.68 (s), 125.49 (s), 124.49 (s) 121.77 (s), 121.59 (s) ppm. HRMS (FAB+): *m*/*z* calcd. for $C_{25}H_{17}NO_3P$ [$MH^+$]: 410.0946; obsd. 410.0952. $C_{25}H_{16}NO_3P$ (409.09): calcd. C 73.35, H 3.94, N 3.42; found C 73.20, H 4.16, N 3.25.

**Synthesis of (*S*)-(3,3′-Bis(trimethylsilyl)-1,1′-binaphthyl-2,2′-diyl) (3-Pyridyl) Phosphite (3):** This compound was prepared as described for **2**, using freshly prepared (*S*)-3,3′-bis(trimethylsilyl)-2,2′-binaphthyl phosphorochloridite. Yield (66%) as a white solid. $^1H$ NMR (300 MHz): $\delta$ = 8.30 (d, $J$ = 2.7 Hz, 1 H), 8.27 (d, $J$ = 5.1 Hz, 1 H), 8.08 (d, $J$ = 2.7 Hz, 2 H), 7.92 (dd, $J$ = 2.7, 8.1 Hz, 2 H), 7.45–7.40 (m, 2 H), 7.39–7.31 (m, 1 H), 7.26–7.09 (m, 5 H), 0.43 (s, 9 H), 0.38 (s, 9 H) ppm. $^{31}P$ NMR (121.5 MHz): $\delta$ = 138.99 ppm. HRMS (FAB+): *m*/*z* calcd. for $C_{31}H_{33}NO_3PSi_2$ ([$MH^+$]): 554.1737; obsd. 554.1725. $C_{31}H_{32}NO_3PSi_2$ (553.2): calcd. C 67.24, H 5.82, N 2.53; found C 67.18, H 5.89, N 2.42.

**Synthesis of (3,3′-5,5′-Tetra-*tert*-butyl-1,1′-biphenyl-2,2′-diyl) (3-Pyridyl) Phosphite (4):** 3-Hydroxypyridine (0.95 g, 10 mmol), azeotropically dried with toluene (3 × 2 mL), and triethylamine (1.4 mL, 10 mmol) were dissolved in THF (20 mL) and the solution was cooled to 0 °C. Freshly prepared 3,3′,5,5′-tetra-*tert*-butyl-1,1′-biphenyl phosphorochloridite (4.75 g, 10 mmol) was dissolved in THF (20 mL) and added dropwise, stirring was continued for 10 min. The cooling bath was removed and the solution was warmed to room temperature, stirring was continued for 1 h. The reaction mixture was filtered and the solvent evaporated. A mixture of toluene/hexane, 1:3 (40 mL) was added to extract the product. After filtration the solvent was removed in vacuo, giving **4** (3.4 g, 6.4 mmol, 64%) as a white solid. $^1H$ NMR (300 MHz): $\delta$ = 8.39 (d, $J$ = 2.4 Hz, 1 H), 8.31 (dd, $J$ = 2.4, 4.2 Hz, 1 H), 7.45 (d, $J$ = 2.7 Hz, 2 H), 7.22–7.19 (m, 1 H), 7.18 (d, $J$ = 2.7 Hz, 2 H), 7.16–7.12 (m, 1 H), 1.47 (s, 18 H), 1.35 (s, 18 H) ppm. $^{31}P$ NMR (121.5 MHz): $\delta$ = 137.49 ppm. $^{13}C$ NMR (75.465 MHz): $\delta$ = 147.34 (C), 145.72 (CH), 142.92 (CH), 140.37 (C), 132.86 (C), 127.95 (CH), 127.90 (C), 126.94 (CH), 125.29 (CH), 124.74 (C), 124.16 (CH), 35.66 (C), 34.93 (C), 31.75 (CH), 31.39 (CH) ppm. HRMS (FAB+): *m*/*z* calcd. for $C_{33}H_{45}NO_3P$ ([$MH^+$]): 534.3137; obsd. 534.3147; $C_{33}H_{44}NO_3P$ (533.3): calcd. C 74.27, H 8.31, N 2.62; found C 74.35, H 8.27, N 2.75.

**Catalysis:** The hydroformylation experiments were performed as follows. A stainless steel 25 mL autoclave, equipped with a Teflon stirring bar, was charged with 0.42 μmol of [Rh(acac)$(CO)_2$], 10.4 μmol of phosphane (and 1 equiv. of porphyrin template) and

 © 2007 Wiley-VCH Verlag GmbH & Co. KGaA, Weinheim 

0.017 mL of diisopropylethylamine, as a base, in 4.0 mL of toluene. The solution was stirred for 1 h under 20 bar $CO/H_2$ (1:1) at 80 °C. The pressure was reduced to 1 bar and a mixture of 0.34 mL 1-octene (styrene) and 0.17 mL of decane in 0.67 mL of toluene was added. Subsequently the $CO/H_2$ pressure was adjusted to 20 bar. The mixture was stirred for 1 h (80 °C or 120 °C) and 18 h (40 °C). Then the autoclave was cooled to 0 °C in ice and the pressure was reduced to 1.0 bar. The products were analyzed by GC. A sample was taken and the conversion was checked by GC measurement of the crude product after filtration through a plug of silica to remove the catalyst. In none of the reactions hydrogenated side-products were observed. The crude product mixture of styrene was subjected to reduction with $NaBH_4$ by stirring in 5.0 mL methanol for 30 min. Quenching with water, extraction with a mixture of ethyl acetate/hexane = 1:1, drying of the organic layer, filtrations and removal of solvent gave the corresponding alcohols, for which the enantiomeric purities were determined by chiral GC (Cyclosil-B, isothermal; $T$ = 90 °C, $t_R$ (*R*) = 63.5 min. and $t_S$ (*S*) = 64.8 min.).

The allylic alkylation experiments were performed as follows. Under Schlenk conditions 0.50 μmol of $[Pd(allyl)Cl]_2$, 3.0 μmol phosphite and 3.0 μmol phosphane were dissolved in 5.0 mL of $CH_2Cl_2$ and stirred for 30 min. Then 50 μmol of 1,3-diphenylallyl acetate, 150 μmol of dimethyl malonate, 150 μmol of BSA and 50 μmol of decane and a catalytic amount of KOAc were added. The mixture was stirred for 24 h at 25 °C and the reaction was subsequently stopped by adding saturated aq. ammonium chloride. Subsequently, 5.0 mL of petroleum ether was added and the solution was washed once more with a saturated $NH_4Cl$ solution. The organic phase was dried with $Na_2SO_4$, filtered and the conversion was checked by GC measurement. The solution was chromatographed ($SiO_2$; petroleum ether/$CH_2Cl_2$ = 1:1) to give analytically pure products.[48] Enantiomeric purities were determined by chiral HPLC (OD column, eluent 0.5% 2-propanol in hexane $t_R$ (*R*) = 33.2 min. and $t_S$ (*S*) = 34.9 min.).

Asymmetric hydrogenation reactions were performed as follows. A 150-mL stainless-steel autoclave, equipped with 15 vessels and teflon stirring bars, was charged with 0.5 μmol of $[Rh(nbd)_2(BPh_4)]$, 1.5 μmol of phosphane, 1.5 μmol of porphyrin, 1.0 μL of dipea, 50 μmol dimethyl itaconate and 50 μmol of decane in 0.5 mL of toluene. The $H_2$ pressure was adjusted to 5 bar and the mixture was stirred, for 17 h at 40 °C. Then the autoclave was cooled to 0 °C and the pressure was reduced to 1.0 bar. The conversion was checked by GC measurement of the crude product after filtration through a plug of magnesium sulfate and subsequently silica. Enantiomeric purities were determined by chiral GC (Chirasil-L-Val, isothermal; $T$ = 70 °C, $t_R$ (*R*) = 34.4 min. and $t_S$ (*S*) = 35.2 min.).

## Acknowledgments

This work was financially supported by National Research School Combination Catalysis and by the Fonds der Chemischen Industrie.

[1] C. A. Tolman, *J. Am. Chem. Soc.* **1970**, *92*, 2953.
[2] C. A. Tolman, *Chem. Rev.* **1977**, *77*, 313.
[3] a) C. P. Casey, G. T. Whiteker, *Isr. J. Chem.* **1990**, *30*, 299; b) P. Dierkes, P. W. N. M. van Leeuwen, *J. Chem. Soc. Dalton Trans.* **1999**, 1519; c) Z. Freixa, P. W. N. M. van Leeuwen, *Dalton Trans.* **2003**, 1890; d) P. W. N. M. van Leeuwen, P. C. J. Kamer, J. N. H. Reek, P. Dierkes, *Chem. Rev.* **2000**, *100*, 2741; e) M. Kranenburg, P. C. J. Kamer, P. W. N. M. van Leeuwen, D. Vogt, W. Keim, *J. Chem. Soc. Chem. Commun.* **1995**, 2177; f) W. Goertz, W. Keim, D. Vogt, U. Englert, M. D. K. Boele, L. A. van der Veen, P. C. J. Kamer, P. W. N. M. van Leeuwen, *J. Chem. Soc. Dalton Trans.* **1998**, 2981.
[4] a) R. L. Pruett, J. A. Smith, *J. Org. Chem.* **1969**, *34*, 327; b) L. H. Slaugh, R. D. Mullineaux, *J. Organomet. Chem.* **1968**, *13*, 469; c) E. S. Brown, *Aspects of Homogeneous Catalysis* (Ed.: R. Ugo), vol. 2, p. 57, Reidel, Dordrecht, **1974**; d) R. D. Cramer, E. L. Jenner, U. G. Stolberg, *J. Am. Chem. Soc.* **1963**, *85*, 1691.
[5] a) O. R. Hughes, D. A. Young, *J. Am. Chem. Soc.* **1981**, *103*, 6636; b) T. V. RajanBabu, A. L. Casalnuovo, *Pure Appl. Chem.* **1994**, *66*, 1535; c) T. Benincori, S. Rizzo, F. Sannicolo, *J. Heterocycl. Chem.* **2002**, *39*, 471; d) G. Helmchen, A. Pfaltz, *Acc. Chem. Res.* **2000**, *33*, 336; e) A. M. Trzreciak, J. J. Ziólkowski, *Coord. Chem. Rev.* **1999**, *190–192*, 883.
[6] a) T. Bartik, T. Himler, H. G. Schulte, K. Seevogel, *J. Organomet. Chem.* **1984**, *272*, 29; b) S. O. Frim, A. W. Yankowsky, *J. Org. Chem.* **1977**, *42*, 716.
[7] a) R. Burch, *Acc. Chem. Res.* **1982**, *15*, 24; b) J. Dupont, M. Pfeffer, J. Spencer, *Eur. J. Inorg. Chem.* **2001**, *8*, 1917; c) A. Schnyder, L. Hintermann, A. Togni, *Angew. Chem.* **1995**, *107*, 996; *Angew. Chem. Int. Ed. Engl.* **1995**, *34*, 931; d) C. P. Casey, E. L. Paulsen, E. W. Beuttenmueller, B. R. Proft, B. A. Matter, D. R. Powell, *J. Am. Chem. Soc.* **1999**, *121*, 63.
[8] a) M. R. Wilson, H. Liu, A. Prock, W. P. Gierling, *Organometallics* **1993**, *12*, 2044; b) S. Joerg, R. S. Drago, S. Sales, *Organometallics* **1998**, *17*, 589.
[9] a) P. W. N. M. van Leeuwen, C. Claver, *Rhodium-Catalyzed Hydroformylation*, Kluwer, Dordrecht, **2000**.
[10] Y. Koide, S. G. Bott, A. R. Barron, *Organometallics* **1996**, *15*, 2213.
[11] a) T. L. Brown, K. J. Lee, *Coord. Chem. Rev.* **1993**, *128*, 89; b) T. L. Brown, *Inorg. Chem.* **1992**, *31*, 1286; c) D. White, B. C. Taverner, P. G. L. Leach, N. J. Coville, *J. Organomet. Chem.* **1994**, *478*, 205; d) D. White, B. C. Taverner, N. J. Coville, P. W. Wade, *J. Organomet. Chem.* **1995**, *495*, 41.
[12] K. Angermund, W. Baumann, E. Dinjus, R. Fornika, H. Görls, M. Kessler, C. Krüger, W. Leitner, F. Lutz, *Chem. Eur. J.* **1997**, *3*, 755.
[13] a) A. K. Rappe, W. M. Skiff, C. J. Casewit, *Chem. Rev.* **2000**, *100*, 1435; b) T. R. Cundari, J. Deng, W. Fu, T. R. Klinckman, A. Yoshikawa, *J. Chem. Inf. Comput. Sci.* **1998**, *38*, 941.
[14] a) L. Gonsalvi, H. Adams, G. J. Sunley, E. Ditzel, A. Haynes, *J. Am. Chem. Soc.* **2002**, *124*, 13597; b) J. J. Carbó, F. Maseras, C. Bo, P. W. N. M. van Leeuwen, *J. Am. Chem. Soc.* **2001**, *123*, 7630; c) R. J. Haaren, van H. Oevering, B. B. Coussens, G. P. F. van Strijdonck, J. N. H. Reek, P. C. J. Kamer, P. W. N. M. van Leeuwen, *Eur. J. Inorg. Chem.* **1999**, 1237.
[15] a) W. R. Moser, C. J. Papile, D. A. Brannon, R. A. Duwell, S. J. Weininger, *J. Mol. Catal.* **1987**, *41*, 271; b) J. D. Unruh, J. R. Christenson, *J. Mol. Catal.* **1982**, *14*, 19; c) L. A. van der Veen, M. D. K. Boele, F. R. Bregman, P. C. J. Kamer, P. W. N. M. van Leeuwen, K. Goubitz, J. Fraanje, H. Schenk, C. Bo, *J. Am. Chem. Soc.* **1998**, *120*, 11616.
[16] G. P. F. van Strijdonck, M. D. K. Boele, P. C. J. Kamer, J. G. de Vries, P. W. N. M. van Leeuwen, *Eur. J. Inorg. Chem.* **1999**, 1073.
[17] For reviews see: a) M. J. Wilkinson, P. W. N. M. van Leeuwen, J. N. H. Reek, *Org. Biomol. Chem.* **2005**, *3*, 2371; b) B. Breit, *Angew. Chem., Int. Ed.* **2005**, *44*, 6816; c) A. J. Sandee, J. N. H. Reek, *Dalton Trans.* **2006**, 3385.
[18] a) V. F. Slagt, P. W. N. M. van Leeuwen, J. N. H. Reek, *Chem. Commun.* **2003**, *19*, 2474–2475; b) V. F. Slagt, M. Röder, P. C. J. Kamer, P. W. N. M. van Leeuwen, J. N. H. Reek, *J. Am. Chem. Soc.* **2004**, *126*, 4056–4057; c) V. F. Slagt, P. W. N. M. van Leeuwen, J. N. H. Reek, *Angew. Chem.* **2003**, *115*, 5771–5781; *Angew. Chem. Int. Ed.* **2003**, *42*, 5619–5623; d) V. F. Slagt, P. W. N. M. van Leeuwen, J. N. H. Reek, *Dalton Trans.* **2007**, 2302; e) J. N. H. Reek, M. Röder, P. E. Goudriaan, P. C. J. Kamer, P. W. N. M. van Leeuwen, V. F. Slagt, *J. Organomet. Chem.* **2005**, *605*, 4505–4516; f) X.-B. Jiang, L. Lefort, P. E. Goudriaan, A. H. M. de Vries, P. W. N. M.

 © 2007 Wiley-VCH Verlag GmbH & Co. KGaA, Weinheim 

van Leeuwen, J. G. de Vries, J. N. H. Reek, *Angew. Chem., Int. Ed.* **2006**, *45*, 1223; g) M. Kuil, P. E. Goudriaan, P. W. N. M. van Leeuwen, J. N. H. Reek, *Chem. Commun.* **2006**, 4679; h) M. Kuil, P. E. Goudriaan, A. W. Kleij, D. M. Tooke, A. L. Spek, P. W. N. M. van Leeuwen, J. N. H. Reek, *Dalton Trans.* **2007**, 2311.

[19] a) B. Breit, W. Seiche, *J. Am. Chem. Soc.* **2003**, *125*, 6608; b) B. Breit, W. Seiche, *Angew. Chem. Int. Ed.* **2005**, *44*, 1640; c) P. A. Duckmanton, A. J. Blake, J. B. Love, *Inorg. Chem.* **2005**, *44*, 7708; d) W. Seiche, A. Schuschkowski, B. Breit, *Adv. Synth. Catal.* **2005**, *347*, 1488; e) B. Breit, W. Seiche, *Pure Appl. Chem.* **2006**, *78*, 249; f) M. Weis, C. Waloch, W. Seiche, B. Breit, *J. Am. Chem. Soc.* **2006**, *128*, 4188; g) F. Chevallier, B. Breit, *Angew. Chem., Int. Ed.* **2006**, *45*, 1599; h) J. M. Takacs, D. S. Reddy, S. A. Moteki, D. Wiu, H. Palencia, *J. Am. Chem. Soc.* **2004**, *126*, 4494; i) J. M. Takacs, P. M. Hrvatin, J. M. Atkins, D. S. Reddy, J. L. Clark, *New J. Chem.* **2005**, *29*, 263; j) K. Chaiseeda, S. A. Moteki, D. S. Reddy, D. Wu, K. Chandra, J. M. Takacs, *Fudan Xuebao, Ziran Kexueban* **2005**, *44*, 631; k) J. M. Takacs, K. Chaiseeda, S. A. Moteki, D. S. Reddy, D. Wu, K. Chandra, *Pure Appl. Chem.* **2006**, *78*, 501; l) J. M. Atkins, S. A. Moteki, S. G. DiMagn, J. M. Takacs, *Org. Lett.* **2006**, *8*, 2759.

[20] L. K. Knight, Z. Freixa, P. W. N. M. van Leeuwen, J. N. H. Reek, *Organometallics* **2006**, *25*, 954.

[21] A. J. Sandee, A. M. van der Burg, J. N. H. Reek, *Chem. Commun.* **2007**, 864.

[22] a) T. Hayashi, *Acc. Chem. Res.* **2000**, *33*, 354; b) B. L. Feringa, *Acc. Chem. Res.* **2000**, *33*, 346; c) I. V. Komarov, A. Börner, *Angew. Chem.* **2001**, *113*, 1237; *Angew. Chem. Int. Ed.* **2001**, *40*, 1197.

[23] a) H. Brunner, W. Zettlmeier, *Handbook of Enantioselective Catalysis*; VCH, Weinheim, Germany, **1993**; b) K. M. Pietrusiewicz, M. Zablocka, *Chem. Rev.* **1994**, *94*, 1375; c) B. Wolfe, T. Livinghouse, *J. Am. Chem. Soc.* **1998**, *120*, 5116.

[24] a) V. F. Slagt, J. N. H. Reek, P. C. J. Kamer, P. W. N. M. van Leeuwen, *Angew. Chem.* **2001**, *113*, 4401; *Angew. Chem. Int. Ed.* **2001**, *40*, 4271; b) V. F. Slagt, P. C. J. Kamer, P. W. N. M. van Leeuwen, J. N. H. Reek, *J. Am. Chem. Soc.* **2004**, *126*, 1526; c) A. W. Kleij, M. Lutz, A. L. Spek, P. W. N. M. van Leeuwen, J. N. H. Reek, *Chem. Commun.* **2005**, 3661; d) A. W. Kleij, M. Kuil, D. M. Tooke, A. L. Spek, J. N. H. Reek, *Inorg. Chem.* **2005**, *44*, 7696; e) M. Kuil, T. Soltner, P. W. N. M. van Leeuwen, J. N. H. Reek, *J. Am. Chem. Soc.* **2006**, *128*, 11344.

[25] For reviews on porphyrins in assembly processes see: a) T. Imamura, K. Fukushima, *Coord. Chem. Rev.* **2000**, *198*, 133; b) J. Wojaczynski, L. Latos-Grazynski, *Coord. Chem. Rev.* **2000**, *198*, 113.

[26] G. J. H. Buisman, L. A. van der Veen, A. Klootwijk, W. G. J. de Lange, P. C. J. Kamer, P. W. N. M. van Leeuwen, D. Vogt, *Organometallics* **1997**, *16*, 2929.

[27] J. B. Cooper, C. T. Brewer, G. Brewer, *Inorg. Chim. Acta* **1987**, *129*, 25.

[28] Synthesized using the method by a) A. D. Adler, F. R. Longo, J. D. Finarelli, J. Goldmacher, J. Assour, L. Korsakoff, *J. Org. Chem.* **1967**, *32*, 476; b) A. D. Adler, F. R. Longo, F. Kampas, J. Kim, *J. Inorg. Nucl. Chem.* **1970**, *32*, 2443.

[29] a) U. Michelsen, C. A. Hunter, *Angew. Chem.* **2000**, *112*, 780; *Angew. Chem. Int. Ed.* **2000**, *39*, 764; b) G. Szintay, A. Horvath, *Inorg. Chim. Acta* **2000**, *310*, 175.

[30] P. N. Taylor, H. L. Anderson, *J. Am. Chem. Soc.* **1999**, *121*, 11538.

[31] a) D. Evans, J. A. Osborn, G. Wilkinson, *J. Chem. Soc. A* **1968**, 3133; b) M. Beller, B. Cornils, C. D. Frohning, C. W. Kohlpaintner, *J. Mol. Catal. A* **1995**, *104*, 17.

[32] Similar hydroformylation experiments at 80 °C yielded comparable results only in this case lower activity was observed.

[33] A. van Rooy, P. C. J. Kamer, P. W. N. M. van Leeuwen, *Organometallics* **1996**, *15*, 835.

[34] C. Hansch, A. Leo, R. W. Taft, *Chem. Rev.* **1991**, *91*, 165.

[35] J. B. Cooper, C. T. Brewer, G. Brewer, *Inorg. Chim. Acta* **1987**, *129*, 25.

[36] L. M. Wu, M. J. Desmond, R. S. Drago, *Inorg. Chem.* **1979**, *18*, 679.

[37] a) S. Serron, S. P. Nolan, K. G. Moloy, *Organometallics* **1996**, *15*, 4301; b) S. C. van der Slot, P. C. J. Kamer, P. W. N. M. van Leeuwen, J. Fraanje, K. Goubitz, M. Lutz, A. L. Spek, *Organometallics* **2000**, *19*, 2504; c) P. Suomalainen, H. Riihimaki, S. Jaaskelainen, M. Haukka, J. T. Pursiainen, T. A. Pakkanen, *Catal. Lett.* **2001**, *77*, 125; d) P. Serp, M. Hernandez, B. Richard, P. Kalck, *Eur. J. Inorg. Chem.* **2001**, *9*, 2327.

[38] a) I. Ojima, T. Kogure, N. Yoda, *J. Org. Chem.* **1980**, *45*, 4728; b) K. Achiwa, P. A. Chaloner, D. Parker, *J. Organomet. Chem.* **1981**, *218*, 249; c) C. Yang, Y. T. Wong, Z. Li, J. J. Krepinsky, G. Jia, *Organometallics* **2001**, *20*, 5220; d) Y. Xie, R. Lou, Z. Li, A. Mi, Y. Jiang, *Tetrahedron: Asymmetry* **2000**, *11*, 1487.

[39] a) R. L. Halterman, S.-T. Jan, *J. Org. Chem.* **1991**, *56*, 5253; b) A. Berkessel, P. Kaiser, J. Lex, *Chem. Eur. J.* **2003**, *9*, 4746.

[40] a) A. Berkessel, M. Frauenkron, *J. Chem. Soc. Perkin Trans. 1* **1997**, 2265; b) R. Zhang, W.-Y. Yu, K.-Y. Wong, C.-M. Che, *J. Org. Chem.* **2001**, *66*, 8145.

[41] a) M. Frauenkron, A. Berkessel, *Tetrahedron Lett.* **1997**, *38*, 7175; b) W.-C. Lo, K.-F. Che, K.-F. Cheng, T. C. W. Mak, *Chem. Commun.* **1997**, 1205.

[42] Molecular modeling was performed using semi-empirical (PM3) calculations on a Unix workstation using the Spartan software.

[43] $\rho$ = 0.188 for pyridine with zinc(II) *meso*-phenylporphyrin; G. C. Vogel, B. A. Beckman, *Inorg. Chem.* **1976**, *15*, 483 or $\rho$ = 0.208 for a copper-imidazole complex with zinc(II) *meso*-phenylporphyrin see ref.[27].

[44] B. R. Manzano, F. A. Jalon, F. Gomez-de la Torre, A. M. Lopez-Agenjo, A. M. Rodriguez, K. Mereiter, W. Weissensteiner, T. Sturm, *Organometallics* **2002**, *21*, 789.

[45] L. A. van der Veen, P. H. Keeven, G. C. Schoemaker, J. N. H. Reek, P. C. J. Kamer, P. W. N. M. van Leeuwen, M. Lutz, A. L. Spek, *Organometallics* **2000**, *19*, 872.

[46] a) R. J. Bowen, A. C. Garner, S. J. Berners-Price, I. D. Jenkins, R. E. Sue, *J. Organomet. Chem.* **1998**, *554*, 181; b) A. Buhling, P. C. J. Kamer, P. W. N. M. van Leeuwen, *J. Mol. Catal. A* **1995**, *98*, 69; c) G. R. Newkome, *Chem. Rev.* **1993**, *93*, 2067.

[47] Diphenyl(3-pyridylmethyl)phosphane (**8**) was kindly donated by Shell Research & Technology Center, Amsterdam, The Netherlands.

[48] Product characterization data were found in agreement with the reported literature, see for example: a) P. von Matt, O. Loiseleur, G. Koch, A. Pfaltz, C. Lefeber, T. Feucht, G. Helmchen, *Tetrahedron: Asymmetry* **1994**, *5*, 573; b) J. F. Bower, R. Jumnah, A. C. Williams, J. M. J. Williams, *J. Chem. Soc. Perkin Trans. 1* **1997**, 1411.

[49] For reviews see: a) I. V. Komarov, A. Monsees, R. Kadyrov, C. Fischer, U. Schmidt, A. Borner, *Tetrahedron: Asymmetry* **2002**, *13*, 1615; b) W. Tang, X. Zhang, *Chem. Rev.* **2003**, *103*, 3029.

[50] For reviews see: a) F. Agbossou, J.-F. Carpentier, A. Mortreux, *Chem. Rev.* **1995**, *95*, 2485; b) S. Gladiali, J. C. Bayón, C. Claver, *Tetrahedron: Asymmetry* **1995**, *6*, 1453.

[51] For reviews see: a) B. M. Trost, D. L. Van Vranken, *Chem. Rev.* **1996**, *96*, 395; b) C. Grazia Arena, D. Drommi, F. Faraone, *Tetrahedron: Asymmetry* **2000**, *11*, 2765; c) B. M. Trost, D. L. Van Vranken, *Chem. Rev.* **2003**, *103*, 2921; d) G. Helmchen, A. Pfaltz, *Acc. Chem. Res.* **2000**, *33*, 336.

Received: May 25, 2007
Published Online: September 4, 2007

 © 2007 Wiley-VCH Verlag GmbH & Co. KGaA, Weinheim 

DOI: 10.1002/ejic.200700602

# Synthesis and Characterization of Bis(dithiolene) Tungsten(VI), -(V), and -(IV) Complexes and Their Reactivities in Coupled Electron–Proton Transfer: A New Series of Active Site Models of Tungstoenzymes

**Hideki Sugimoto,*[a] Makoto Tarumizu,[a] Hiroyuki Miyake,[a] and Hiroshi Tsukube[a]**

**Keywords:** Bioinorganic chemistry / Enzyme models / Molybdenum / S ligands / Tungsten

New tungsten(VI), -(V), and -(IV) complexes containing 3,6-dichloro-1,2-benzenedithiolate ($bdtCl_2$), $(Et_4N)_2[W^{VI}O_2(bdtCl_2)_2]$ {$(Et_4N)_2$[**1**]}, $(Et_4N)[W^{V}O(bdtCl_2)_2]$ {$(Et_4N)$[**2**]}, and $(Et_4N)_2[W^{IV}O(bdtCl_2)_2]$ {$(Et_4N)_2$[**3**]} were synthesized and characterized as active site models of tungstoenzymes. $(Et_4N)_2$[**1**] was prepared in high yield by the reaction of $WO_2Cl_2$ with $2bdtCl_2$ at low temperature, and its crystal structure was determined. Isomerization between octahedral structures (Δ and Λ forms) of the tungsten center of $(Bu_4N)_2$[**1**] was characterized by variable-temperature $^1H$ NMR (VT $^1H$ NMR) spectral analysis, which offers the first example of six-coordinate bis(dithiolene) tungsten(VI) complexes. The isomerization of the molybdenum center of $(Bu_4N)_2[Mo^{VI}O_2(bdtCl_2)_2]$ {$(Bu_4N)_2$[**4**]} was similarly characterized. A comparison of their activation energies indicated that the tungsten center underwent slower isomerization than that of the molybdenum one. $(Et_4N)_2$[**1**] underwent an irreversible reduction at –2.1 V vs. SCE in $CH_3CN$ by a coupled electron–proton transfer (CEPT) process to yield $(Et_4N)_2$[**3**], while $(Et_4N)_2$[**3**] underwent an irreversible oxidation by a CEPT process at –0.27 V in the presence of 2 equiv. of $Et_4NOH$ in $CH_3CN$ to yield $(Et_4N)_2$[**1**]. $(Et_4N)$[**2**] disproportionated into 0.5 equiv. of $(Et_4N)_2$[**1**] and 0.5 equiv. of $(Et_4N)_2$[**3**] when treated with 1 equiv. of $Et_4NOH$ in $CH_3CN$.

(© Wiley-VCH Verlag GmbH & Co. KGaA, 69451 Weinheim, Germany, 2007)

## Introduction

Since the characterization of tungstoenzymes by crystallographic and EXAFS studies,[1] many coordination chemists have paid much attention to intriguing coordination structures of their catalytic centers.[2] Mononuclear tungsten complexes containing two pyranopterin dithiolenes occur as the catalytic centers of the aldehyde ferredoxin oxidoreductase (AOR) family and the formate dehydrogenase (FDH) family, varying the oxidation number between +6, +5, and +4 and the coordination structure between that of a trigonal prism and a square pyramid (Scheme 1).[1,3] Therefore, synthetic tungsten(VI), -(V), and -(IV) complexes with identical dithiolenes are of special interest as active site models of these families.[2] However, such a series of tungsten complexes is still limited.[2] A number of six-coordinate bis(dithiolene) tungsten(VI) complexes have been prepared and structurally characterized.[2] The tungsten(VI) centers of the previously reported six-coordinate complexes were best described as octahedrons, rather than trigonal prisms, in the solid state, while their solution structures have rarely been reported. In contrast, a large number of $[WX(dithiolene)_2]^{2-/-}$ (X = monodentate ligand) complexes containing a square-pyramidal tungsten(IV) center have been reported.[2]

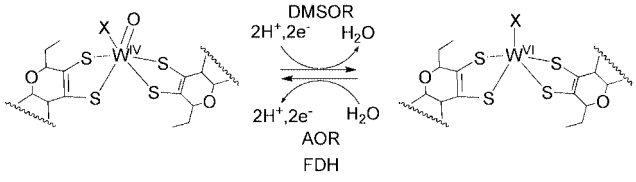


Scheme 1. Active site structures of DMSOR, AOR, and FDH families and their CEPT processes (X = O, OR, SR, SeR, etc.).

From the viewpoint of the functions of the AOR and the FDH families, a coupled electron–proton transfer (CEPT) process is essentially involved in the catalytic reactions, where the five-coordinate tungsten(IV) center changes to the six-coordinate tungsten(VI) center and a water molecule is utilized as the source of an oxygen atom, protons, and electrons.[1,3] A similar structural change of a tungsten center by the CEPT process is involved in tungsten-substituted DMSO reductase, where the six-coordinate tungsten(VI) center changes to the five-coordinate tungsten(IV) center, converting a net oxygen atom of DMSO to water.[3] The CEPT process is further involved in the catalytic reaction mediated by molybdenum containing arsenite oxidase.[1] Until now, no involvement of the bis(dithiolene) tungsten

[a] Department of Chemistry, Graduate School of Science, Osaka City University,
Sumiyoshi-ku 3-3-138, Osaka 558-8585, Japan
Fax: +81-6-6605-2522
E-Mail: sugimoto@sci.osaka-cu.ac.jp

 © 2007 Wiley-VCH Verlag GmbH & Co. KGaA, Weinheim 

complex in a CEPT process has been reported. We recently demonstrated that the CEPT process enabled the conversion from $(Et_4N)_2[MoO_2(bdtCl_2)_2]$ {$(Et_4N)_2$[**4**]} to $(Et_4N)_2$-$[MoO(bdtCl_2)_2]$ {$(Et_4N)_2$[**5**]} and its back reaction from $(Et_4N)_2$[**5**] to $(Et_4N)_2$[**4**].[5,6] Our crystallographic study on a series of $(X)_2[M(bdtCl_2)_3]$ (X = $Et_3NH$, $Et_4N$, $Ph_4P$; M = Mo, W) complexes revealed that the metal centers can adopt both trigonal-prismatic and octahedral structures depending on the size of the counter cations.[7] A similar conversion between a trigonal prism and an octahedron was not observed in other $(X)_2[M(dithiolene)_3]$ (M = Mo and W) complexes.

We herein report the synthesis and characterization of the novel $(Et_4N)_2[WO_2(bdtCl_2)_2]$ {$(Et_4N)_2$[**1**]}, $(Et_4N)[WO(bdtCl_2)_2]$ {$(Et_4N)$[**2**]}, and $(Et_4N)_2[WO(bdtCl_2)_2]$ {$(Et_4N)_2$-[**3**]} complexes. The structural isomerization of the tungsten center of $(Bu_4N)_2$[**1**] in [$D_8$]THF is characterized using the variable-temperature $^1H$ NMR (VT $^1H$ NMR) spectroscopic technique. Conversions between $(Et_4N)_2$[**1**] and $(Et_4N)_2$[**3**] by a CEPT process are described. The UV/Vis, IR, and EPR spectroscopic studies of the reaction of $(Et_4N)$[**2**] with $Et_4NOH$ indicate that $(Et_4N)$[**2**] disproportionated into 0.5 eqiv. $(Et_4N)_2$[**1**] and 0.5 equiv. $(Et_4N)_2$[**3**] and that the disproportionation is involved in the conversion of $(Et_4N)_2$[**3**] to $(Et_4N)_2$[**1**]. Since $(Et_4N)_2$[**1**] and $(Et_4N)_2$[**3**] are isostructural complexes of $(Et_4N)_2$[**4**] and $(Et_4N)_2$[**5**], the present study is useful for understanding roles of the tungsten centers of the AOR and the FDH families (Figure 1).

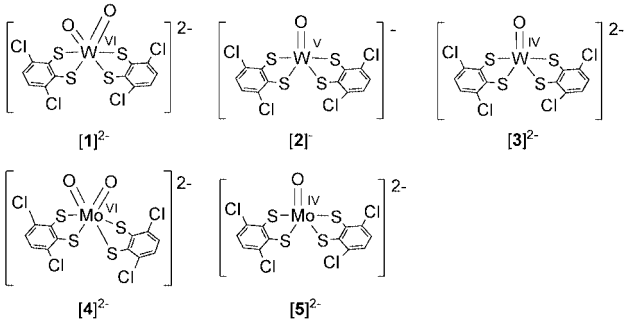


Figure 1. Structures of tungsten and molybdenum complexes.

## Results and Discussion

### Preparation of $W^{VI}O_2$ and $W^{IV}O/W^{V}O$ Complexes of $bdtCl_2$

Three synthetic methods have been established for bis(dithiolene) $W^{VI}O_2$ complexes. In the synthesis of $(Bu_4N)_2$-$[WO_2(mnt)_2]$, $Na_2WO_4$, starting compound, was treated with $Na_2$mnt and $NaHSO_3$ at pH 5.5 (yield 59%).[2a] Several bis(dithiolene) $W^{VI}O_2$ complexes of bdt and its derivatives were obtained in modest yields (1–15%) by several steps {$WCl_6 \rightarrow [WOCl_3(THF)_2] \rightarrow [WO(SC_6H_5)_4]^- \rightarrow [WO(SC_6H_5)_4]^{2-} \rightarrow [WO(benzendithiolates)_2]^{2-} \rightarrow [WO_2$-$(benzendithiolates)_2]^{2-}$}.[8,9] The yields of bis(dithiolene) $W^{VI}O_2$ complexes of aliphatic dithiolenes were also modest (20–30%) because the following reactions were required {$[Ni(dithiolene)_2] \rightarrow [W(CO)_2(dithiolene)_2] \rightarrow [WO(dithiolene)_2]^{2-} \rightarrow [WO_2(dithiolene)_2]^{2-}$}.[10] Here, we directly synthesized the bis(dithiolene) $W^{VI}O_2$ complex of $bdtCl_2$ from commercially available reagents. When $WO_2Cl_2$ was treated with 2 equiv. of $H_2bdtCl_2$ and 2 equiv. of $Et_4NI$ or $Bu_4NBr$ in the presence of 4 equiv. of $Et_3N$ at –40 °C, a red microcrystalline powder of $(Et_4N)_2$[**1**] or $(Bu_4N)_2$[**1**] precipitated in 65% yield. $(Et_4N)$[**2**] and $(Et_4N)_2$[**3**] were prepared according to literature procedures by Nakamura et al. and Holm et al.[8,11]

### Crystal Structure of $(Et_4N)_2[WO_2(bdtCl_2)_2]$

Figure 2 shows the crystal structure of the anionic part of $(Et_4N)_2$[**1**]. Selected bond lengths and angles are shown

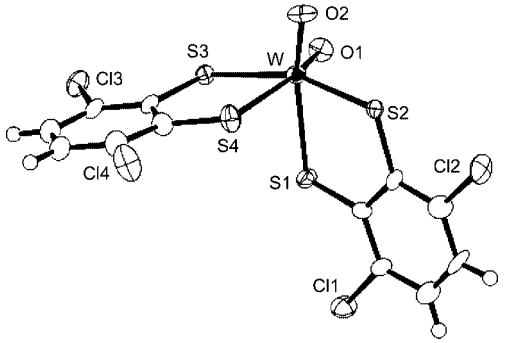


Figure 2. Crystal structure of $[1]^{2-}$ shown with 50% ellipsoids.

Table 1. Selected bond lengths [Å] and angles [°] for $(Et_4N)_2$-$[WO_2(bdtCl_2)_2]$ {$(Et_4N)_2$[**1**]} and $(Et_4N)_2[MoO_2(bdtCl_2)_2]$ {$(Et_4N)_2$-[**4**]}.

| | $(Et_4N)_2$[**1**] | $(Et_4N)_2$[**4**][a] |
|---|---|---|
| M–O1 | 1.741(6) | 1.726(3) |
| M–O2 | 1.749(7) | 1.739(3) |
| M–S1 | 2.563(2) | 2.596(1) |
| M–S2 | 2.443(2) | 2.4462(9) |
| M–S3 | 2.426(2) | 2.4486(9) |
| M–S4 | 2.592(2) | 2.561(1) |
| C1–S1 | 1.72(1) | 1.741(3) |
| C2–S2 | 1.762(9) | 1.755(4) |
| C7–S3 | 1.766(8) | 1.750(4) |
| C8–S4 | 1.707(9) | 1.728(4) |
| O1–M–O2 | 102.6(3) | 103.2(1) |
| M–S1–C1 | 108.5(3) | 108.2(1) |
| S1–M–S2 | 79.71(7) | 78.90(4) |
| S1–M–S3 | 85.72(7) | 86.07(4) |
| S1–M–S4 | 85.55(7) | 85.85(5) |
| S1–M–O1 | 88.6(2) | 87.9(1) |
| S1–M–O2 | 160.3(2) | 160.5(1) |
| S2–M–S3 | 159.21(7) | 158.97(5) |
| S2–M–S4 | 84.64(7) | 85.01(4) |
| S2–M–O1 | 111.0(3) | 111.1(1) |
| S2–M–O2 | 81.2(2) | 82.0(1) |
| S3–M–S4 | 79.49(7) | 79.30(4) |
| S3–M–O1 | 83.2(3) | 81.5(1) |
| S3–M–O2 | 111.4(2) | 112.5(1) |
| S4–M–O1 | 162.0(3) | 160.2(1) |
| S4–M–O2 | 88.2(2) | 89.0(1) |
| M–S2–C2 | 111.1(3) | 111.6(6) |
| M–S3–C7 | 111.3(3) | 110.8(1) |
| M–S4–C8 | 108.0(3) | 108.4(2) |

[a] Ref.[5]

 © 2007 Wiley-VCH Verlag GmbH & Co. KGaA, Weinheim 

in Table 1. The tungsten center was coordinated by two oxo groups in a *cis* position and four sulfur atoms from the two $bdtCl_2$ ligands in a similar fashion to that observed for $(Et_4N)_2$[**4**].[5] The geometry around the metal centers of $(Et_4N)_2$[**1**] and $(Et_4N)_2$[**4**] is described as a distorted-octahedral structure on the basis of the torsion angles[4a] made by the four sulfur atoms {S2–S1–S3–S4, 101.1° for $(Et_4N)_2$[**1**] and 100.4° for $(Et_4N)_2$[**4**]}. The W=O bond lengths [1.749(7) Å and 1.741(6) Å] of $(Et_4N)_2$[**1**] are not significantly different from those of $(Et_4N)_2$[**4**]. The W–S2 and W–S3 distances [2.563(2) Å and 2.592(2) Å, respectively] of $(Et_4N)_2$[**1**] are longer than the W–S1 and W–S4 distances [2.443(2) Å and 2.426(2) Å, respectively] due to the *trans* influence of the two W=O bonds. The long W–S (2 and 3) bond lengths and the short W–S (1 and 4) bond lengths affect the S–C bond lengths of $(Et_4N)_2$[**1**]. The S1–C1 and S4–C8 bonds [1.762(9) Å and 1.766(8) Å, respectively] are longer than the S2–C2 and S3–C7 bonds [1.72(1) Å and 1.707(9) Å, respectively].

### VT $^1$H NMR Spectroscopic Study of $[MO_2(bdtCl_2)_2]^{2-}$ (M = W and Mo)

As described in the crystal structural study, the tungsten center of $[WO_2(bdtCl_2)_2]^{2-}$ ([**1**]$^{2-}$) offers two distinguishable S atoms in one $bdtCl_2$ ligand, consequently, two protons on one $bdtCl_2$ ligand, Ha and Hb, are not equivalent in the crystal structure. Unexpectedly, the $^1$H NMR spectra of $(Bu_4N)_2$[**1**] at 25 °C in [$D_6$]acetone, [$D_3$]acetonitrile, and [$D_8$]THF show one singlet at $\delta$ = 6.61 ppm in the aromatic region, revealing that the Ha and Hb protons are apparently equivalent in solution.[12] This singlet broadens as the [$D_8$]THF solution temperature decreases from +40 °C to –60 °C. Two separate peaks are observed at –70 °C and each peak is further divided into two peaks at –90 °C (Figure 3). The singlet from $bdtCl_2$ of $(Bu_4N)_2$[**4**] similarly broadens at low temperature and is divided into two peaks at –110 °C (Figure 3). When the temperature of the [$D_8$]THF solutions of $(Bu_4N)_2$[**1**] and $(Bu_4N)_2$[**4**] was again increased to +40 °C their original $^1$H NMR spectra at +40 °C were regenerated. Since these VT $^1$H NMR spectral changes are independent of the complex concentrations, $(Bu_4N)_2$[**1**] and $(Bu_4N)_2$[**4**] exhibit structural isomerisation between the octahedral structures (50% Δ and 50% Λ forms, Scheme 2) without dissociation of the M–S bonds in solution. The trigonal-prismatic structures probably occur in the transition states where the structural isomerization of the metal center of $(Bu_4N)_2$[**1**] and $(Bu_4N)_2$[**4**] is faster than the NMR timescale at high temperatures.

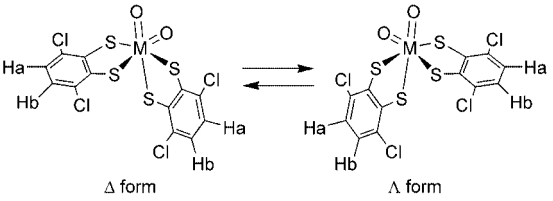


Scheme 2. Structural isomerization of anions of $(Bu_4N)_2$[**1**] and $(Bu_4N)_2$[**4**].

Δ*G* values for the isomerizations of $(Bu_4N)_2$[**1**] and $(Bu_4N)_2$[**4**] were calculated to be 43.2 and 36.4 kJ mol$^{-1}$, respectively, which are similar to the energy difference (37.2 kJ mol$^{-1}$) between the octahedron and the trigonal prism of $[Mo^{VI}(OCH_3)(OSMe_2)(S_2C_2Me_2)_2]^-$.[4a] The fact that the value of Δ*G* calculated for $(Bu_4N)_2$[**1**] is larger than that for $(Bu_4N)_2$[**4**] means that the tungsten center is kinetically more stable than the molybdenum one. This is consistent with the fact that the AOR family of tungsten enzymes belongs to the hyperthermophilic archaea.

### Redox Properties of $[W^{VI}O_2(bdtCl_2)_2]^{2-}$ and $[WO(bdtCl_2)_2]^{-/2-}$

Figure 4 shows a cyclic voltammogram of $(Et_4N)_2$[**1**] in $CH_3CN$. $(Et_4N)_2$[**1**] undergoes one irreversible reduction at $E_{pc}$ = –2.1 V vs. SCE, indicating that the octahedral structure of the tungsten center is unstable below –2.1 V. The coulometric measurement during the electrolysis at –2.2 V indicated that 2.3 electrons were consumed for the completion of the electrolysis. The electrolysis at –2.2 V caused the color to change from orange to pale yellow. Since the resulting pale yellow species exhibited an identical absorption spectrum and CV to those of $(Et_4N)_2$[**3**], $(Et_4N)_2$-[**1**] was suggested to change to $(Et_4N)_2$[**3**] by a two-electron-reduction coupled process accompanied by $H_2O$ production, with contaminant protons arising from the $CH_3CN$ solution (Scheme 3).

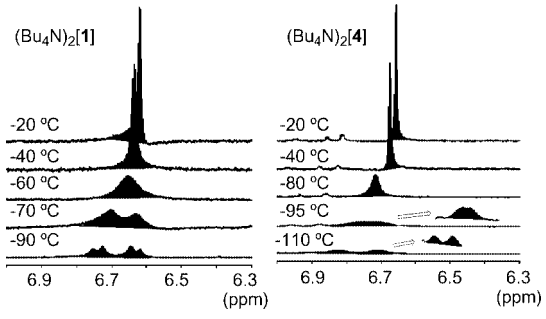


Figure 3. VT $^1$H NMR spectra of $(Bu_4N)_2$[**1**] (4.1 mM, left) and $(Bu_4N)_2$[**4**] (4.1 mM, right) in [$D_8$]THF.

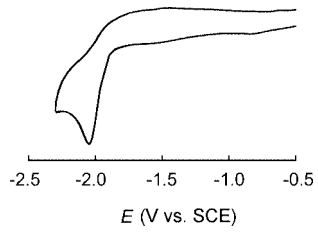


Figure 4. Cyclic voltammogram of $(Et_4N)_2$[**1**] (0.1 mM, 100 mV s$^{-1}$) in 0.1 M $TBAPF_6$ containing $CH_3CN$.

 © 2007 Wiley-VCH Verlag GmbH & Co. KGaA, Weinheim 

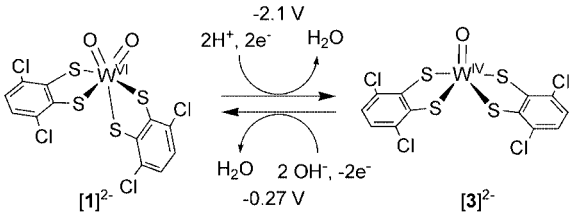


Scheme 3. Reversible structural change between $(Et_4N)_2$[**1**] and $(Et_4N)_2$[**3**] via CEPT processes.

$(Et_4N)_2$[**3**] shows one reversible oxidation wave at –0.27 V [Figure 5 (solid line)] in $CH_3CN$, which is assigned to the $[WO(bdtCl_2)_2]^{2-/-}$ process. The redox potential is more positive than those of $[WO(bdt)_2]^{2-/-}$ (–0.63 V) and $[WO(naphthalenedithiolate)_2]^{2-/-}$ (–0.52 V),[8,9] suggesting that the Cl atoms attached to the benzene ring decrease the S → W electron donations. Because the isostructural $Mo^{IV}O$ complex, $(Et_4N)_2$[**5**], changes to the $Mo^{VI}O_2$ complex, $(Et_4N)_2$[**4**], in the presence of 2 equiv. of $OH^-$ under oxidative conditions,[6] the CV change of $(Et_4N)_2$[**3**] was investigated. The reversible $W^{V/IV}$ couple at –0.27 V became an irreversible wave upon addition of $Et_4NOH$ to the $CH_3CN$ solution of $(Et_4N)_2$[**3**], increasing the current intensity of the $E_{pa}$ while decreasing that of the $E_{pc}$. The CV change depended on the added amount of $Et_4NOH$, and was completed when 2 equiv. of $Et_4NOH$ and 1 equiv. of $[WO(bdtCl_2)_2]^{2-}$ was added to the solution (dashed line in Figure 5). The absorption spectrum of the orange solution obtained after electrolysis of $(Et_4N)_2$[**3**] at –0.1 V in the presence of 2 equiv. of $Et_4NOH$ was identical to that of $(Et_4N)_2$[**1**]. The coulometric measurement taken during the electrolysis indicated that 1.9 electrons were consumed for the completion of the electrolysis. Thus, $(Et_4N)_2$[**3**] was revealed to be converted to $(Et_4N)_2$[**1**] by the CEPT process as in the case of the isostructural molybdenum complex, $(Et_4N)_2$[**5**]. Since $(Et_4N)_2$[**3**] was also changed to $(Et_4N)_2$[**1**] by the CEPT process, the tungsten center coordinated with two $bdtCl_2$ ligands was demonstrated to be convertible between the six-coordinate $W^{VI}O_2$ structure, $(Et_4N)_2$[**1**], and the five-coordinate $W^{IV}O$ structure, $(Et_4N)_2$[**3**], by CEPT processes (Scheme 3).

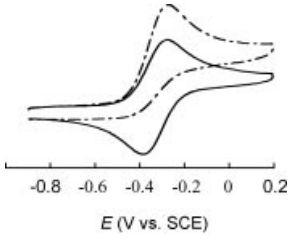


Figure 5. Cyclic voltammograms of $(Et_4N)_2$[**3**] (0.1 mM, 100 mV $s^{-1}$): complex only (solid line) and complex + 2 equiv. of $Et_4NOH$ (dashed line) in 0.1 M $TBAPF_6$ containing $CH_3CN$.

The absorption spectrum of $(Et_4N)_2$[**3**] in $CH_3CN$ remained the same when 2 equiv. of $Et_4NOH$ was added, indicating that the tungsten(IV) center does not bind $OH^-$. Whereas $(Et_4N)$[**2**] reacted with $Et_4NOH$. When $Et_4NOH$ was added to the $CH_3CN$ solution of $(Et_4N)$[**2**] the absorption band at 600 nm decreased while the bands at 470 nm and 421 nm increased (Figure 6). The plots of absorbance at 600 nm and 421 nm against the equivalence of the added $Et_4NOH$ per $(Et_4N)$[**2**] indicated that $(Et_4N)$[**2**] reacted with 1 equiv. of $OH^-$ (Figure 6, inset). The anisotropic EPR signal at $g_{av}$ = 1.96 for $(Et_4N)$[**2**] completely disappeared when 1 equiv. of $Et_4NOH$ was added. In the IR spectrum of $(Et_4N)$[**2**] the $\nu(W^{5+}{=}O)$ stretching band at 953 $cm^{-1}$ also disappears with the appearance of three new bands at 911, 892, and 848 $cm^{-1}$ when 1 equiv. of $Et_4NOH$ is added. The band at 911 $cm^{-1}$ is identical to the $\nu(W^{4+}{=}O)$ stretching band of $(Et_4N)_2$[**3**] and the other two bands are identical to the $\nu(W^{6+}{=}O)_{sym}$ and $\nu(W^{6+}{=}O)_{asym}$ stretching bands of $(Et_4N)_2$[**1**] (Figure 7). Thus, it is concluded that the disproportionation of $(Et_4N)$[**2**], when treated with 1 equiv. of $Et_4NOH$ in $CH_3CN$, yields 0.5 equiv. of $(Et_4N)_2$[**1**] and 0.5 equiv. of $(Et_4N)_2$[**3**] [Equation (1)], where $(Et_4N)_2[W^{V}O(OH)(bdtCl_2)_2]$ was proposed as an intermediate involved in the conversion process from $(Et_4N)_2$[**3**] to $(Et_4N)_2$[**1**].

$$2[W^{V}O(bdtCl_2)_2]^- + 2OH^- \rightarrow [W^{VI}O_2(bdtCl_2)_2]^{2-} + [W^{IV}O(bdtCl_2)_2]^{2-} + H_2O \quad (1)$$

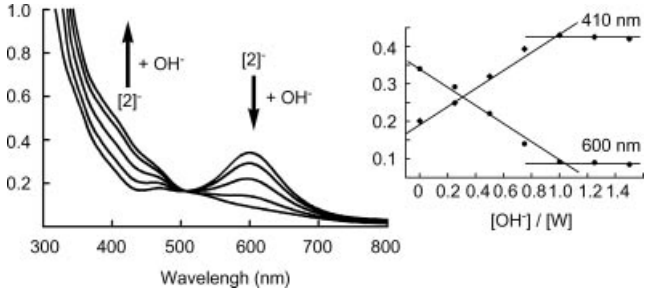


Figure 6. Absorption spectral changes of $(Et_4N)$[**2**] ($1.7 \times 10^{-4}$ M) upon addition of *n* equiv. of $Et_4NOH$ in $CH_3CN$ (left). Titration plots of the absorbance at 410 and 600 nm (right) against the *n* values.

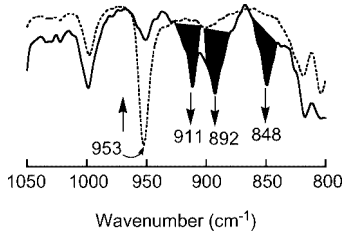


Figure 7. IR spectra of $(Et_4N)$[**2**] (dashed line) and an equimolar mixture (solid line) of $(Et_4N)$[**2**] and $Et_4NOH$.

## Conclusion

Tungsten(VI), -(V), and -(IV) complexes with two $bdtCl_2$ ligands were synthesized and characterized as a new series of active site models of tungstoenzymes as well as tungsten-

 © 2007 Wiley-VCH Verlag GmbH & Co. KGaA, Weinheim 

substituted DMSO reductase. The tungsten center of $(Et_4N)_2$[**1**] adopted an octahedral structure and underwent isomerization between the Δ and Λ forms. This is the first observation involving six-coordinate bis(dithiolene) tungsten(VI) complexes. Its isomerization rate was slower than that of the isostructural molybdenum(VI) complex, [**4**]$^{2-}$. $(Et_4N)_2$[**1**] changed to $(Et_4N)_2$[**3**] by the CEPT process below –2.1 V vs. SCE, whereas $(Et_4N)_2$[**3**] was similarly converted to $(Et_4N)_2$[**1**] above –0.27 V in the presence of 2 equiv. of $Et_4NOH$. $(Et_4N)_2[W^VO(OH)(bdtCl_2)_2]$ was suggested to be an intermediate in the CEPT process from $(Et_4N)_2$[**3**] to $(Et_4N)_2$[**1**].

## Experimental Section

**General:** All reagents and solvents were used as received unless otherwise noted. $CH_3CN$ was dried with $CaH_2$ and then $P_2O_5$, and distilled under nitrogen prior to use. All manipulations were carried out under argon in Schlenk tubes. $(Bu_4N)_2[MoO_2(bdtCl_2)_2]$ {$(Bu_4N)_2$[**4**]} was synthesized by a procedure that was reported in the literature.[5,6]

**$(Et_4N)_2[WO_2(bdtCl_2)_2]$ {$(Et_4N)_2$[1]}:** $WO_2Cl_2$ (87 mg, 0.3 mmol) was added to an ethanol solution (15 mL) containing $H_2bdtCl_2$ (126 mg, 0.60 mmol), $Et_3N$ (169 μL, 1.2 μmol), and $Et_4NI$ (231 mg, 0.9 mmol) at –40 °C. After stirring for 10 h at 0 °C, the orange solution that was obtained was concentrated to 3 mL. An orange microcrystalline powder precipitated, which was collected and dried in vacuo. Yield: 174 mg (65%). $C_{28}H_{44}Cl_4N_2O_2S_4W$ (894.59): calcd. C 37.59, H 4.96, N 3.13; found C 37.64, H 4.85, N 3.07. ESI-mass: *m*/*z* = 764 [(M + $Et_4N)^-$], 634 [$(M)^-$]. UV/Vis spectrum ($CH_3CN$): λ (ε, $dm^3\,mol^{-1}\,cm^{-1}$) = 470 (sh, 1320), 421 (2820), 344 (sh, 13300) nm. IR (KBr): $\tilde{\nu}_{max}$ = 892 [$\nu(W{=}O)_{sym}$] and 848 [$\nu(W{=}O)_{asym}$] $cm^{-1}$. Raman (solid): $\tilde{\nu}_{max}$ = 893 [$\nu(W{=}O)_{sym}$] and 848 [$\nu(W{=}O)_{asym}$] $cm^{-1}$.

**$(Bu_4N)_2[WO_2(bdtCl_2)_2]$ {$(Bu_4N)_2$[1]}:** The synthesis was carried out in the same manner as that of $(Et_4N)_2$[**1**] using $Bu_4NBr$ instead of $Et_4NI$. The UV/Vis and IR spectral profiles based on the anion were consistent with those of $(Et_4N)_2$[**1**].

**$(Et_4N)[WO(bdtCl_2)_2]$ {$(Et_4N)$[2]}:** The synthesis was carried out by a similar procedure to that of $(Et_4N)[WO(bdt)_2]$ reported by Holm et al.[11] A $CH_3CN$ solution (5 mL) of 3,6-dichloro-1,2-benzenedithiol (55 mg, 0.26 mmol) and $Et_3N$ (73 μL, 0.52 mmol) was slowly added to a $CH_3CN$ solution (5 mL) of $(Et_4N)[WO(benzenethiol)_4]$ (100 mg, 0.13 mmol) at –40 °C. The temperature of the solution was increased to 25 °C and the resultant solution was stirred for 1 h. The deep blue solution that was obtained was reduced to a volume of 1 mL. Diffusion of ether into the solution gave a black powder, which was collected by filtration and dried in vacuo. Yield: 66 mg (68%). $C_{20}H_{24}Cl_4NOS_4W$ (748.34): calcd. C 32.10, H 3.23, N 1.87; found C 32.21, H 3.38, N 2.04. ESI-mass: *m*/*z* = 618 [$(M)^-$]. UV/Vis spectrum ($CH_3CN$): λ (ε, $dm^3\,mol^{-1}\,cm^{-1}$) = 600 (2050), 468 (1070) nm. IR (KBr): $\tilde{\nu}_{max}$ = 953 [$\nu(W{=}O)$] $cm^{-1}$.

**$(Et_4N)_2[WO(bdtCl_2)_2]$ {$(Et_4N)$[3]}:** A $CH_3CN$ solution (2 mL) of $Et_4NBH_4$ (4 mg, 0.027 mmol) was added to a THF solution (10 mL) of $(Et_4N)_2$[**2**] (20 mg, 0.027 mmol). After the solution was stirred for 30 min a white yellow powder precipitated out of the solution, which was collected by filtration and dried in vacuo. Yield: 19 mg (82%). $C_{28}H_{44}Cl_4N_2OS_4W$ (878.60): calcd. C 38.28, H 5.05, N 3.19; found C 38.50, H 4.95, N 3.20. ESI-mass: *m*/*z* = 748 [M + $Et_4N^+]^-$, 618 $[M]^-$. UV/Vis spectrum ($CH_3CN$): λ (ε, $dm^3\,mol^{-1}\,cm^{-1}$) = 415 (1200), 330 (11100) nm. IR (KBr): $\tilde{\nu}_{max}$ = 911 [$\nu(W{=}O)$] $cm^{-1}$.

**Other Measurements:** $^1H$ NMR spectra were measured with a JEOL-Lambda 300. IR and Electronic spectra were recorded with a Perkin–Elmer Spectrum One and a Shimazu-U2550 spectrometer at room temperature. CV measurements and bulk electrolyses were performed with a Hokuto HZ-3000, and the working and counter electrodes were a glassy-carbon disk and a platinum wire, respectively. The complex solutions of 1.0 mM (complexes = 0.01 mmol) were deoxygenated with a stream of nitrogen gas. The reference electrode that was used was SCE. The coulometric measurements performed during the electrolyses were recorded with a Hokuto HF-201 coulomb/ampere meter.

**Calculation of Activation Free Energies ($\Delta G^{\ddagger}$ Values):** The values were calculated according to the equation $\Delta G/RT_c = 22.96 + \ln(T_c/\delta\nu)$, where $T_c$ and $\delta\nu$ are the coalescence point and the frequency difference between sites in the exchange system, respectively.[13] $T_c$ = –65 and $\delta\nu$ = 32.5 for $(Bu_4N)$[**1**], and $T_c$ = –95 and $\delta\nu$ = 34.4 for $(Bu_4N)$[**4**] were employed.

**X-ray Crystallographic Study:** A single crystal of $(Et_4N)$[**1**] was recrystallized from acetonitrile/ether and mounted on top of a glass fiber. X-ray data of the crystal were collected with graphite-monochromated Mo-$K_\alpha$ radiation with a Rigaku/MSC Mercury CCD diffractometer at –130 °C. The structure was solved by direct methods (SIR-97)[14] and expanded using the program DIRDIF 99.[15] The structure was refined anisotropically by full-matrix least-squares on $F^2$. The non-hydrogen atoms in the structure were attached at the idealized positions on carbon atoms and not refined. The structure converted in the final stages of the refinement showed no movement in the atom positions. All calculations were performed using Single-Crystal Structure Analysis Software, Ver. 3.6.0.[16] Further crystal data and agreement factors are listed in Table 2.

Table 2. Crystallographic data for $(Et_4N)_2[WO_2(bdtCl_2)_2]$ {$(Et_4N)_2$-[**1**]}.

| | $(Et_4N)_2$[**1**] |
|---|---|
| Formula | $C_{28}H_{44}Cl_4N_2O_2S_4W$ |
| Molecular weight ($g\,mol^{-1}$) | 894.57 |
| Temperature (°C) | –130 |
| Crystal system | orthorhombic |
| Space group | *Fdd*2 |
| *a* (Å) | 28.113(6) |
| *b* (Å) | 21.888(4) |
| *c* (Å) | 22.688(4) |
| *V* (Å$^3$) | 13961(5) |
| *Z* | 16 |
| $D_{calcd.}$ ($g\,cm^{-3}$) | 1.702 |
| Unique data | 18901 |
| Observed data | 7323 |
| *R* | 0.0460 |
| *wR* | 0.1200 |
| GOF | 1.001 |

CCDC-616400 contains the supplementary crystallographic data for this paper. These data can be obtained free of charge from The Cambridge Crystallographic Data Centre via www.ccdc.cam.ac.uk/data_request/cif.

## Acknowledgments

This work was partly supported by the Japan Society for Promotion of Science, Grant No. 18750052 to H. S.

 © 2007 Wiley-VCH Verlag GmbH & Co. KGaA, Weinheim 

[1] a) R. Hille, *Chem. Rev.* **1996**, *96*, 2757–2816; b) M. K. Johnson, D. C. Rees, M. W. W. Adams, *Chem. Rev.* **1996**, *96*, 2817–2839; c) S. J. N. Burgmayer, *Prog. Inorg. Chem.* **2004**, *52*, 491–532.
[2] a) S. K. Das, D. Biswas, R. Maiti, S. Sarkar, *J. Am. Chem. Soc.* **1996**, *118*, 1387–1397; b) E. S. Davis, G. M. Aston, R. L. Beddoes, D. Collison, A. Dinsmore, A. Docrat, J. A. Joule, C. R. Wilson, C. D. Garner, *J. Chem. Soc. Dalton Trans.* **1998**, 3647–3656; c) J. Jiang, R. H. Holm, *Inorg. Chem.* **2004**, *43*, 1302–1310; d) J. H. Enemark, J. J. A. Cooney, J.-J. Wang, R. H. Holm, *Chem. Rev.* **2004**, *104*, 1175–1200; e) J. McMaster, J. M. Tunney, C. D. Garner, *Prog. Inorg. Chem.* **2004**, *52*, 539–583. Authors' examples: f) H. Sugimoto, M. Harihara, M. Shiro, K. Sugimoto, K. Tanaka, H. Miyake, H. Tsukube, *Inorg. Chem.* **2005**, *44*, 6386–6392; g) H. Sugimoto, T. Sakurai, H. Miyake, K. Tanaka, H. Tsukube, *Inorg. Chem.* **2005**, *44*, 6927–6929; h) H. Sugimoto, R. Tajima, T. Sakurai, H. Ohi, H. Miyake, S. Itoh, H. Tsukube, *Angew. Chem. Int. Ed.* **2006**, *45*, 3520–3522.
[3] a) M. K. Chan, S. Mukund, A. Kletzin, M. W. W. Adams, D. C. Rees, *Science* **1995**, *267*, 1463–1469; b) H. Schindelin, C. Kisker, J. Hilton, K. V. Rajagopalan, D. C. Rees, *Science* **1996**, *272*, 1615–1621; c) Y. Hu, S. Faham, R. Roy, M. W. W. Adams, D. C. Rees, *J. Mol. Biol.* **1999**, *286*, 899–914; d) J. M. Dias, M. E. Than, A. Humm, R. Huber, G. P. Bourenkov, H. D. Bartunik, S. Bursakov, J. Calvete, J. Caldeira, C. Carneiro, J. J. G. Moura, I. Moura, M. J. Romao, *Structure* **1999**, *7*, 65–79; e) H.-K. Li, C. Temple, K. V. Rajagopalan, H. Schindelin, *J. Am. Chem. Soc.* **2000**, *122*, 7673–7680; f) L. J. Stewart, S. Bailey, B. Bennett, J. M. Charnock, C. D. Garner, A. S. McAlpine, *J. Mol. Biol.* **2000**, *299*, 593–600.
[4] a) C. E. Edwin, M. B. Hall, *J. Am. Chem. Soc.* **2001**, *123*, 5820–5821; b) A. Thapper, R. J. Deeth, E. Nordlander, *Inorg. Chem.* **2002**, *41*, 6695–6702; c) M. Kaupp, *Angew. Chem. Int. Ed.* **2004**, *43*, 546–549; d) J. P. McNamara, J. A. Joule, I. H. Hiller, C. D. Garner, *Chem. Commun.* **2005**, 177–179.
[5] H. Sugimoto, M. Tarumizu, K. Tanaka, M. Miyake, H. Tsukube, *Dalton Trans.* **2005**, 3558–3564.
[6] H. Sugimoto, M. Tarumizu, H. Miyake, H. Tsukube, *Eur. J. Inorg. Chem.* **2006**, 4494–4497.
[7] H. Sugimoto, Y. Furukawa, M. Tarumizu, H. Miyake, K. Tanaka, H. Tsukube, *Eur. J. Inorg. Chem.* **2005**, 3088–3091.
[8] N. Ueyama, H. Oku, A. Nakamura, *J. Am. Chem. Soc.* **1992**, *114*, 7310–7311.
[9] H. Oku, N. Ueyama, A. Nakamura, *Bull. Chem. Soc. Jpn.* **1996**, *69*, 3139–3150.
[10] K.-M. Sung, R. H. Holm, *Inorg. Chem.* **2001**, *40*, 4518–4525.
[11] C. Lorber, J. P. Donahue, C. A. Goddard, E. Nordlander, R. H. Holm, *J. Am. Chem. Soc.* **1998**, *120*, 8102–8112.
[12] Because $(Et_4N)_2$[**1**] and $(Et_4N)_2$[**4**] did not dissolve in THF, $(Bu_4N)_2$[**1**] and $(Bu_4N)_2$[**4**] were employed.
[13] R. J. Abraham, J. Fisher, P. Loftus, *Introduction to NMR Spectroscopy*, John Wiley & Sons Ltd., England, **1988**.
[14] A. Altomare, M. Burla, M. Camalli, G. Cascarano, C. Giacovazzo, A. Guagliardi, A. Moliterni, G. Polidori, R. Spagna, *J. Appl. Crystallogr.* **1999**, *32*, 115–119.
[15] P. T. Beurskens, G. Admiraal, G. Beurskens, W. P. Bosman, R. de Gelder, R. Israel, J. M. M. Smits, **1999**. The DIRDIF-99 program system, Technical Report of the Crystallography Laboratory, University of Nijmegen, The Netherlands.
[16] *Crystal Structure Analysis Package*, Rigaku and Rigaku/MSC, **2000**–**2004**, 9009 New Trails Dr., The Woodlands, TX 77381, US.

Received: June 11, 2007
Published Online: August 28, 2007

 © 2007 Wiley-VCH Verlag GmbH & Co. KGaA, Weinheim 

DOI: 10.1002/ejic.200700658

# Evidence for Ligand-Centered Reactivity of a 17e Radical Cationic 2*H*-Azaphosphirene Complex

**Holger Helten,[a] Christoph Neumann,[b] Arturo Espinosa,[c] Peter G. Jones,[b] Martin Nieger,[d] and Rainer Streubel*[a]**

**Keywords:** Ligand-centered reactivity / Phosphorus heterocycles / Electron transfer

Reactions of 2*H*-azaphosphirene complex **1** with electron-rich nitrile derivatives **2a–e** in the presence of substoichiometric amounts of ferrocenium hexafluorophosphate yielded regioselectively 2*H*-1,4,2-diazaphosphole complexes **3a–e** under mild conditions. The dependence of the reaction on the amount of ferrocenium hexafluorophosphate is discussed. In the reactions of **1** with electron-poor nitrile derivatives HCN (**2f**), EtOC(O)CN (**2g**), and $C_6F_5CN$ (**2h**), byproducts possessing a P–F bond are formed, which indicates that the hexafluorophosphate anion is involved in the reaction course. Apart from NMR spectroscopic (**3a–f**) and X-ray data (**3b**, **3d–e**), a detailed DFT study is included that provides first insight into the reaction pathway.

(© Wiley-VCH Verlag GmbH & Co. KGaA, 69451 Weinheim, Germany, 2007)

## Introduction

The generation of radical cationic intermediates has emerged as a useful synthetic tool in organic[1–4] and organometallic chemistry.[5] Oxidation of closed-shell organic molecules by single-electron transfer (SET) results in strongly destabilized odd-electron species that very often tend to fragment. Thus, upon pulse radiolysis or $^{60}Co$ γ radiolysis, phenylaziridines either form transient radical cations with retention of the closed ring structure or undergo ring opening with formation of radical cationic azomethine ylides depending on their substitution patterns.[6] Although the spin density of most organometallic radicals is localized mainly at the metal center, organometallic radicals can show both metal-centered and/or ligand-centered reactivity, whereas 17e cationic complexes often show the latter behavior.[7] For the generation of radical cations in solution four major routes are currently in use: (1) anodic oxidation, (2) photoinduced electron transfer (PET), (3) oxidation by radicals generated by pulse or γ radiolysis, and (4) chemical oxidation.[1,2] In this work, ferrocenium salts are used as mild single-electron oxidants, which have the further advantage that they are more easily recycled than most other heavy metal oxidants. Ferrocenium salts have been successfully applied in organic[8] and organometallic syntheses.[5] Recently, they were employed in the oxidation of N-heterocyclic carbenes.[9]

In the course of our studies concerning the applicability of 2*H*-azaphosphirene metal complexes **I**[10] (Scheme 1) in heterocyclic ligand syntheses,[11] we discovered that **I** undergoes P–N bond-selective ring-expansion reactions in the presence of substoichiometric amounts of typical single-electron oxidants such as tetracyanoethylene[12] and/or ferrocenium hexafluorophosphate.[13]

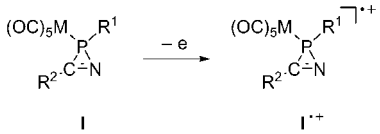


I  I•+

Scheme 1. 2*H*-Azaphosphirene complexes **I** and radical cationic 2*H*-azaphosphirene complexes $\mathbf{I}^{\bullet+}$ (M = Cr, Mo, W; $R^1$, $R^2$ = ubiquitous organic substituents).

Preliminary studies showed that these reactions require polar solvents such as dichloromethane or carbonitriles, reactants with a π system having a lone pair of electrons at one terminus, and substituents that are not (too) bulky. In all ferrocenium hexafluorophosphate induced ring expansions, the formation of small amounts of ferrocene is observed,[13b,13c] which indicates the transient formation of radical cationic species such as $\mathbf{I}^{\bullet+}$ (Scheme 1). Further evidence for the intermediate formation of $\mathbf{I}^{\bullet+}$ was obtained by the finding that reaction rates are reduced if *ortho*-phenyl-

[a] Institut für Anorganische Chemie, Rheinische Friedrich-Wilhelms-Universität Bonn,
Gerhard-Domagk-Strasse 1, 53121 Bonn, Germany
Fax: +49-228-73-9616
E-mail: r.streubel@uni-bonn.de
[b] Institut für Anorganische und Analytische Chemie der Technischen Universität Braunschweig,
Postfach 3329, 38023 Braunschweig, Germany
[c] Departamento de Química Orgánica, Facultad de Química, Universidad de Murcia,
Campus de Espinardo, 30100 Murcia, Spain
[d] Laboratory of Inorganic Chemistry, Department of Chemistry, University of Helsinki,
P. O. Box 55 (A.I. Virtasen aukio 1), 00014 Helsinki, Finland
Supporting information for this article is available on the WWW under http://www.eurjic.org or from the author.

 © 2007 Wiley-VCH Verlag GmbH & Co. KGaA, Weinheim 

substituted 2*H*-azaphosphirene complexes with electron-donating substituents were employed.[13b] Despite all these indications, fundamental questions remained open regarding reaction pathways, for example, at which stage does the three-membered ring open and/or do transition-metal coordination spheres increase during the reactions.

Here, reactions of 2*H*-azaphosphirene complex **1** with nitriles of varying donor abilities under SET conditions are reported. A detailed DFT study on the reaction pathway is included.

## Results and Discussion

Reactions of 2*H*-azaphosphirene complex **1**[10] with dimethylcyanamide (**2a**) and electron-rich five-membered heterocyclic nitrile derivatives RCN (**2b**–**e**; Scheme 2) in the presence of substoichiometric amounts (0.05 equiv.) of ferrocenium hexafluorophosphate ([FcH]$PF_6$) at ambient temperature regioselectively yielded 2*H*-1,4,2-diazaphosphole complexes **3a**–**e** (Scheme 2). The molecular structures of **3a**–**e** were unambiguously established by multinuclear NMR spectroscopic experiments and mass spectrometry.

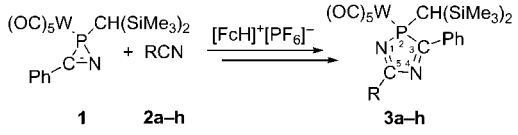


Scheme 2. Synthesis of 2*H*-1,4,2-diazaphosphole complexes **3a**–**h** (**a**: R = $NMe_2$; **b**: R = 1,5-dimethyl-2-pyrryl; **c**: R = 2-furyl; **d**: R = 2-thienyl; **e**: R = 3-thienyl; **f**: R = H; **g**: R = $CO_2Et$; **h**: R = $C_6F_5$).[14]

We monitored the ring expansion reaction of **1** + **2d** → **3d** (Scheme 2) at different concentrations of [FcH]$PF_6$ by using $^{31}P\{^1H\}$ NMR spectroscopy (Figure 1). These series revealed that the reaction progression depends strongly on the amount of [FcH]$PF_6$, but it can be reduced to 0.03 equiv. (0.01 mol $L^{-1}$) without a significant decrease in the conversion. If only 0.02 equiv. of [FcH]$PF_6$ was used, the conversion leveled off at around 80%; in the presence of 0.01 equiv. of [FcH]$PF_6$ even after 3 d the ratio of **3d** did not exceed 18%, and in the absence of [FcH]$PF_6$ no conversion of **1** was detected within 10 d (not shown). For ratios ≥0.02 equiv. of [FcH]$PF_6$, the curves show a steep ascending slope after a comparably flat trend at the start, and again a flattening at the end. As no resonances other than those of **1** and **3d** were detected by $^{31}P\{^1H\}$ NMR spectroscopic monitoring during the reaction course, the time dependent decrease of **1** follows the same trend as the increase of **3d**. Because we were interested in understanding the start of the reaction, we decided to monitor the reaction of **1** with **2d** with 0.025 equiv. of [FcH]$PF_6$ at more frequent time intervals (Figure 2).

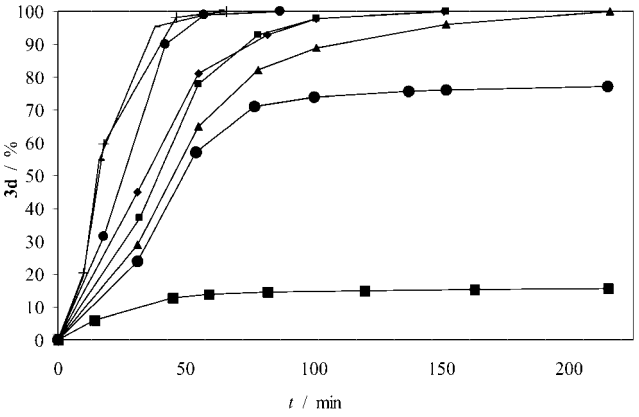


Figure 1. Ratio of **3d** over reaction time for the reaction of **1** with **2d** in the presence of varying amounts of [FcH]$PF_6$: ■ 0.01, ● 0.02, ▲ 0.03, ■ 0.04, ♦ 0.05, · 0.10, + 0.15, - 0.20 equiv.

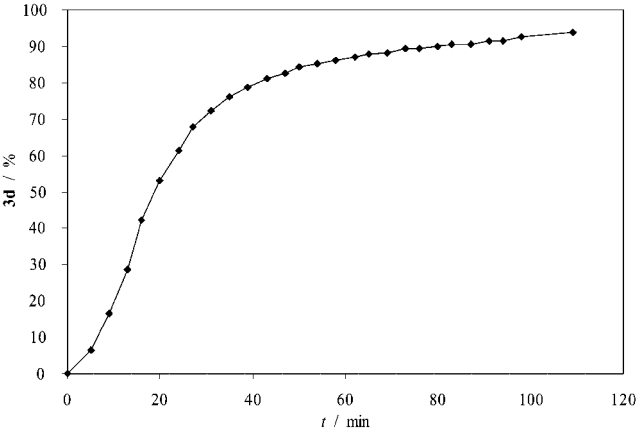


Figure 2. Ratio of **3d** over reaction time for the reaction of **1** with **2d** in the presence of 0.025 equiv. of [FcH]$PF_6$. The reaction is complete after 1 d.

The flat trend at the start is quite obvious. The fastest increase in the amount of **3d** is recorded between 29 and 42% conversion. It should be noted that a flat trend at the start of the reaction is characteristic for autocatalytic reactions, and in reactions with a very low starting concentration of the autocatalytic species the peak of the reaction rate is recorded at around 50% conversion.[15]

On the basis of these results and the finding that ferrocene is formed during the reaction, we suppose a radical cation chain reaction mechanism initiated by oxidation of **1** by the ferrocenium cation with formation of radical cation $\mathbf{1}^{\cdot+}$ and ferrocene (Scheme 3).[16]

The observed acceleration in the reaction rate at the start (Figures 1 and 2) can be explained by assuming slow oxidation of **1** followed by a fast ring-expansion reaction of highly reactive radical cation $\mathbf{1}^{\cdot+}$ with nitrile **2a**–**e**. The cycle is closed by reduction of radical cationic 2*H*-1,4,2-diazaphosphole complexes $\mathbf{3}^{\cdot+}$**a**–**e** by **1** to yield **3a**–**e** and $\mathbf{1}^{\cdot+}$, which then can restart the chain reaction. In consequence, the generation of $\mathbf{1}^{\cdot+}$ causes its multiplication, and it may be regarded as the autocatalytic species of this cycle. If

 © 2007 Wiley-VCH Verlag GmbH & Co. KGaA, Weinheim 

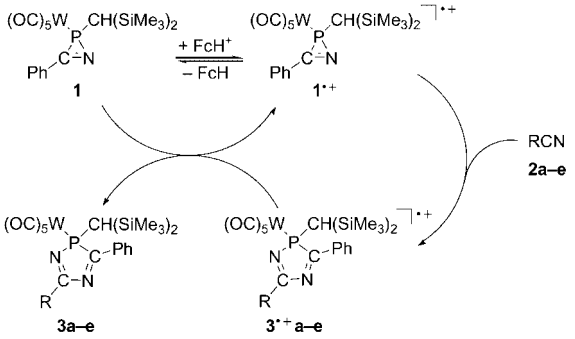


Scheme 3. Proposed chain reaction of 2*H*-azaphosphirene complex **1** with nitrile derivatives **2a**–**e** initiated by the ferrocenium cation $[FcH]^+$.

0.02 equiv. of $[FcH]PF_6$ was employed (Figure 1), the chain reaction was terminated at some point. Obviously, 0.01 equiv. of $[FcH]PF_6$ is not sufficient for the successful initiation of the chain reaction (Figure 1).

In contrast to **2a**–**e**, the reaction of **1** with HCN (**2f**) proceeded much more slowly and was unselective. Reaction monitoring showed that even after a short time (1.5 h) a variety of $^{31}P$ NMR spectroscopic resonances was detected, including a resonance at $\delta$ = 105.5 ppm (Table 1) with a tungsten–phosphorus coupling constant of 225.1 Hz and a phosphorus–hydrogen coupling constant of 34.3 Hz, which revealed the formation of **3f** (ca. 16%). Even though an excess of **2f** (2.6 equiv.) was employed, after 4 d the reaction solution still contained 16% (ratio estimation by $^{31}P\{^1H\}$ NMR spectroscopic resonance integration) of unreacted **1** and only 20% of **3f**, besides numerous unidentified byproducts. Some of the latter showed large phosphorus–fluorine coupling constants (see Experimental Section), thus revealing that the hexafluorophosphate anion, which is usually regarded as weakly coordinating, had taken part in the reaction course. As reported recently, highly electrophilic cationic species are able to abstract fluoride from the hexafluorophosphate anion.[17] Byproducts bearing a P–F bond were also found in the reaction of **1** with electron-poor nitrile derivative **2g** (see below and Experimental Section). After 6 d, 41% of **1** remained unreacted, and a product with a $^{31}P$ NMR spectroscopic resonance at $\delta$ = 110.7 ppm (21%) was observed that featured a tungsten–phosphorus coupling constant of 227.6 Hz. These data are too close to those of **3b**–**e** and, therefore, an assignment to **3g** is not supported; even more vexing is the finding that in the reaction of **1** with **2f** a byproduct having analogous $^{31}P\{^1H\}$ NMR spectroscopic data was detected. Reaction of **1** with **2h** showed a similar behavior to that of **1** with **2g**, and again, a product with a $^{31}P$ NMR spectroscopic resonance at $\delta$ = 110.7 ppm with a tungsten–phosphorus coupling constant of 228.9 Hz was observed (12% after 6 d) as well as numerous byproducts, some of which showed large phosphorus–fluorine coupling constants (see Experimental Section). Even after 6 d, 48% of **1** − and the entire amount of **2h** [by $^{19}F\{^1H\}$ NMR spectroscopy] − remained unreacted, thus indicating that **2h** had not reacted at all even though an excess of 6.4 equiv. was employed. The $^{19}F\{^1H\}$ NMR spectroscopic resonance of the hexafluorophosphate anion decreased in the course of the reaction, and after 6 d its $^{31}P\{^1H\}$ NMR spectroscopic resonance was no longer detected.

Table 1. $^{31}P\{^1H\}$ NMR spectroscopic data of **3a**–**f**.

| | **3a**[a] | **3b**[a] | **3c**[a] | **3d**[a] | **3e**[a] | **3f**[b] |
|---|---|---|---|---|---|---|
| $\delta$ / ppm | 102.1 | 108.4 | 110.6 | 110.5 | 109.1 | 105.5 |
| $^1J_{W,P}$ / Hz | 240.3 | 233.9 | 230.6 | 229.5 | 229.8 | 225.1 |

[a] In $CDCl_3$. [b] In $CH_2Cl_2$.

The $^{31}P\{^1H\}$ NMR spectroscopic data of **3b**–**e**, displayed in Table 1, are similar, and each complex has a resonance at about 110 ppm. Concerning the magnitudes of the tungsten–phosphorus coupling constant, a definite trend can be seen: $^1J_{W,P}$ constants increase with increasing donor ability[18] of the substituent at C-5 in the order: 3-thienyl ≈ 2-thienyl < 2-furyl < 1,5-dimethyl-2-pyrryl. The tungsten–phosphorus coupling constant of complex **3a**, which has a very strong electron-donating substituent ($NMe_2$) attached to C-5, is about 6 Hz larger than that of complex **3b**, whereas the $^{31}P$ NMR spectroscopic resonance is shifted by around 6 ppm to higher field. Consequently, the smallest tungsten–phosphorus coupling constant ($^1J_{W,P}$ = 225.1 Hz) was exhibited by complex **3f**, which has no substituent in the C-5 position, which lends further support to the assignment made beforehand. A further consequence can be expected from this trend: for **3g** and **3h** even lower values are expected.

To examine the aforementioned formation of products with a P–F bond, we investigated the role of the counteranion. In the reaction of **1** with **2d** we exchanged hexafluorophosphate for the weaker nucleophilic counteranion tetraphenylborate, which could not serve as a fluoride source. The outcome was a clean reaction yielding complex **4d** (by $^{31}P$ NMR spectroscopy), which also indicated that the counteranion did not play a crucial role for the ring expansions of **1** as induced by ferrocenium salts. So, the products bearing a P–F bond in the reaction of **1** with **2f** and **2g** do not constitute intermediates of the ring-expansion reaction pathway. Instead, these should be regarded as byproducts emerging from the reaction of transiently formed highly electrophilic species with hexafluorophosphate through fluoride transfer. To elucidate further the effect that $[FcH]BPh_4$ might have on reactions of **1**, we looked again at the reactions with electron-poor nitrile derivatives **2f**–**h** by using this SET reagent. Under these conditions, **1** was treated with **2f** to afford the product (again) having a $^{31}P\{^1H\}$ NMR spectroscopic resonance at $\delta$ = 110.6 ppm ($^1J_{W,P}$ = 227.6 Hz; ca. 15%) and at $\delta$ = 105.5 ppm ($^1J_{W,P}$ = 225.1 Hz: ca. 5%) that we assign to **3f** and traces of unidentified byproducts; ca. 66% of **1** remained unreacted, which did not change significantly within 4 d. Reactions of **1** with **2g** and **2h** in the presence of $[FcH]BPh_4$ showed almost no conversion of **1** within 1 d. Nevertheless, the $^{31}P\{^1H\}$ NMR spectroscopic resonance at $\delta$ = 110.6 ppm ($^1J_{W,P}$ = 227.6 Hz) slowly increased after sev-

 © 2007 Wiley-VCH Verlag GmbH & Co. KGaA, Weinheim 

eral days in both reactions, and again, complex **1** did not react with **2h**.

The molecular structures of **3b** and **3d**–**e** were determined by single-crystal X-ray diffraction analysis[19] (Figures 3, 4, and 5).

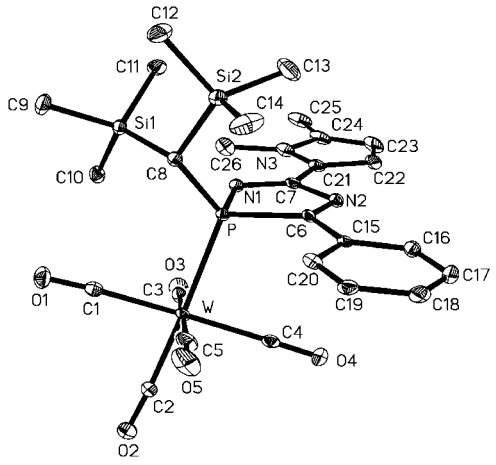


Figure 3. Molecular structure of complex **3b** in the crystal (30% probability level, hydrogen atoms are omitted for clarity). Selected bond lengths [Å] and angles [°]: W–P 2.5324(13), P–C8 1.8345(47), P–N1 1.7006(39), P–C6 1.8701(45), C6–N2 1.2947(57), N2–C7 1.4344(57), C7–N1 1.2946(59), C7–C21 1.4228(62), C6–C15 1.4876(60), N1–P–C6 89.86(19), P–C6–N2 110.00(32), C6–N2–C7 109.92(37), N2–C7–N1 119.98(40), C7–N1–P 109.80(31), P–C6–C15 127.42(33), N1–C7–C21 124.78(44).

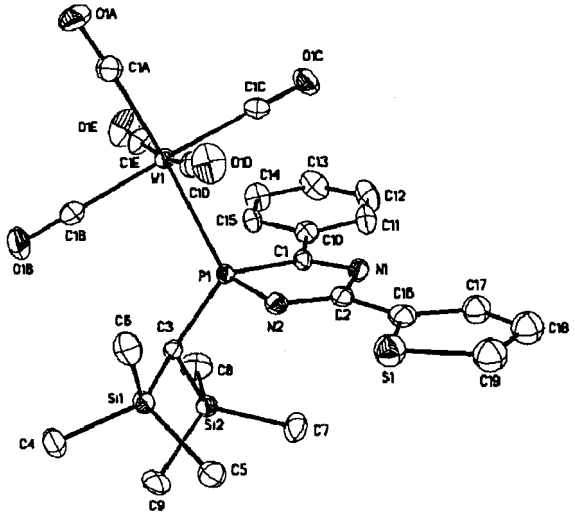


Figure 4. Molecular structure of complex **3d** in the crystal (50% probability level, hydrogen atoms and minor disordered part of the thiophene substituent are omitted for clarity). Selected bond lengths [Å] and angles [°]: W1–P1 2.531(10), P1–C3 1.835(3), P1–N2 1.707(3), P1–C1 1.877(4), C1–N1 1.304(5), N1–C2 1.424(5), C2–N2 1.293(5), C2–C16 1.441(5), C1–C10 1.457(6), N2–P1–C1 90.1(2), P1–C1–N1 109.2(3), C1–N1–C2 110.1(3), N1–C2–N2 121.0(3), C2–N2–P1 109.1(3), P1–C1–C10 129.3(3), N2–C2–C16 121.5(4).

Complexes **3b** and **3d**,**e** are isotypic. They feature almost planar phosphorus heterocycles and, to a large extent, a coplanar arrangement of the three ring systems. The torsion angles between the planes of the phosphorus heterocycle

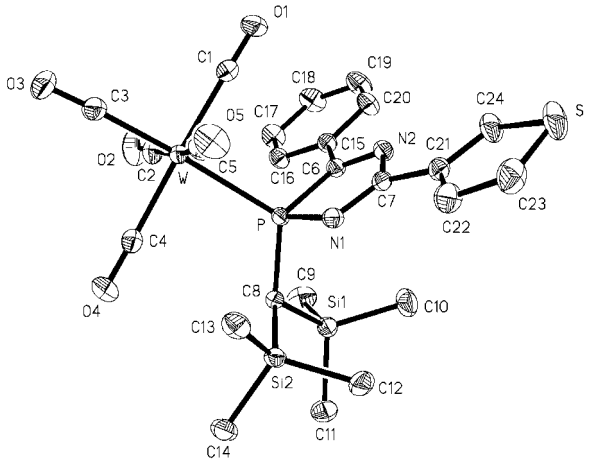


Figure 5. Molecular structure of complex **3e** in the crystal (50% probability level, hydrogen atoms are omitted for clarity). Selected bond lengths [Å] and angles [°]: W–P 2.5321(5), P–C8 1.8335(16), P–N1 1.7042(14), P–C6 1.8767(16), C6–N2 1.2990(21), N2–C7 1.4213(22), C7–N1 1.2903(21), C7–C21 1.4592(22), C6–C15 1.4675(23), N1–P–C6 90.02(7), P–C6–N2 109.14(12), C6–N2–C7 110.33(14), N2–C7–N1 120.74(14), C7–N1–P 109.31(12), P–C6–C15 128.99(12), N1–C7–C21 122.28(16).

and the particular cyclic substituent and the torsion angles between the planes of the cyclic substituents are given in Table 2. The smallest deviation from planarity is found in complex **3b**. Bond lengths and angles in the diazaphosphole ring systems of **3b** and **3d**–**e** are almost identical.

Table 2. Torsion angles of ring planes[a] for **3b** and **3d**–**e**.

| | Diazaphosphole / 5-Ph | Diazaphosphole / 3-hetaryl | 3-Hetaryl / 5-Ph |
|---|---|---|---|
| **3b** | 6.68(17) | 1.88(22) | 5.25(20) |
| **3d** | 4.29 | 3.47 / 9.96[b] | 3.52 / 7.63[b] |
| **3e** | 4.24(8) | 2.79(8) | 2.26(9) |

[a] Torsion angles with respect to least square planes; all atoms of particular ring system involved. [b] Molecule is disordered in the crystal. Values are given for both conformations.

## Theoretical Approach

The stationary points of a plausible ring-expansion pathway were calculated by DFT methods [B3LYP/TZVP//ECP-60-MWB (W)] on a model system for complex **1**, i.e. **4**. For the nitrile component, three model compounds were used, which might be classified according to their nucleophilicity: (1) medium (**2f**: R = H), (2) strong (**2i**: R = $NH_2$), and (3) weak (**2j**: R = CN). The influence of the solvent was taken into account by employing the COSMO approach with $\varepsilon$ = 8.93 to mimic dichloromethane. It was shown that this approach is appropriate.[21] In consequence, computed relative free energies (Tables 3 and 4) for reactions in solution are discussed hereafter; computed stationary points are shown in Schemes 4 and 5. All relative energies, enthalpies, and free energies are available in the Supporting Information.

 © 2007 Wiley-VCH Verlag GmbH & Co. KGaA, Weinheim 

Table 3. Calculated thermochemical data for reactions shown in Scheme 4 (all values in kJ mol$^{-1}$).

| Reaction | | $\Delta G_{298}^{\neq}$ | $\Delta_R G_{298}$ |
|---|---|---|---|
| i | **4** + FcH$^+$ → **4**$^{\cdot+}$ + FcH | [a] | +139.2 |
| ii | **4**$^{\cdot+}$ + HCN (**2f**) → **5**$^{\cdot+}$**f** | +59.8 | +24.0 |
| | **4**$^{\cdot+}$ + $H_2NCN$ (**2i**) → **5**$^{\cdot+}$**i** | [b] | –13.4 |
| iii | **4**$^{\cdot+}$ + NCCN (**2j**) → **6**$^{\cdot+}$**j** + HCN (**2f**) | +74.7 | –39.5 |
| iv | **5**$^{\cdot+}$**i** → **7**$^{\cdot+}$**i** | +22.3 | –102.6 |
| v | **5**$^{\cdot+}$**f** → **6**$^{\cdot+}$**f** + HCN (**2f**) | –1.7 | –96.2 |
| | **5**$^{\cdot+}$**i** → **6**$^{\cdot+}$**i** + HCN (**2f**) | +5.0 | –87.5 |

[a] The activation barrier was not calculated. We assume an outer sphere mechanism. [b] Transition state could not be located.

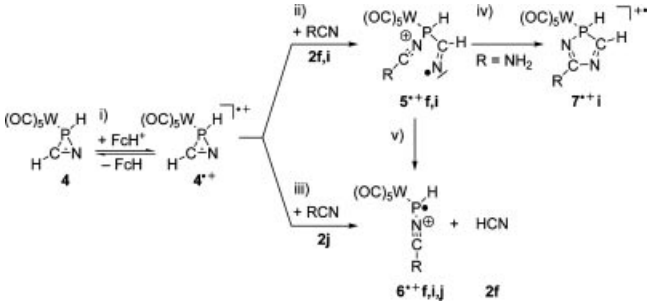


Scheme 4. Computed pathways for the reactions of 2*H*-azaphosphirene complex **4**$^{\cdot+}$ with nitrile derivatives **2f** (R = H), **2i** (R = $NH_2$), and **2j** (R = CN).

Table 4. Calculated thermochemical data for reactions shown in Scheme 5 (all values in kJ mol$^{-1}$).

| Reaction | | $\Delta G_{298}^{\neq}$ | $\Delta_R G_{298}$ |
|---|---|---|---|
| vi | **6**$^{\cdot+}$**f** + HCN (**2f**) → **7**$^{\cdot+}$**f** | +99.1 | –20.5 |
| | **6**$^{\cdot+}$**i** + HCN (**2f**) → **7**$^{\cdot+}$**i** | +100.6 | –15.0 |
| | **6**$^{\cdot+}$**j** + HCN (**2f**) → **7**$^{\cdot+}$**j** | +94.9 | –52.6 |
| vii | **6**$^{\cdot+}$**f** + HCN (**2f**) → **8**$^{\cdot+}$**f** | +116.9 | –41.4 |
| | **6**$^{\cdot+}$**i** + HCN (**2f**) → **8**$^{\cdot+}$**i** | +114.3 | –42.6 |
| | **6**$^{\cdot+}$**j** + HCN (**2f**) → **8**$^{\cdot+}$**j** | +92.9 | –78.9 |
| viii | **6**$^{\cdot+}$**f** + HCN (**2f**) → **9**$^{\cdot+}$**f** | +90.3 | +75.1 |
| | **6**$^{\cdot+}$**i** + HCN (**2f**) → **9**$^{\cdot+}$**i** | [a] | +108.7 |
| | **6**$^{\cdot+}$**j** + HCN (**2f**) → **9**$^{\cdot+}$**j** | +77.2 | +50.3 |
| ix | **9**$^{\cdot+}$**f** → **7**$^{\cdot+}$**f** | +28.8 | –95.6 |
| | **9**$^{\cdot+}$**i** → **7**$^{\cdot+}$**i** | [a] | –123.7 |
| | **9**$^{\cdot+}$**j** → **7**$^{\cdot+}$**j** | +32.3 | –102.9 |
| | **7**$^{\cdot+}$**f** + **4** → **7f** + **4**$^{\cdot+}$ | [b] | –12.7 |
| | **7**$^{\cdot+}$**i** + **4** → **7i** + **4**$^{\cdot+}$ | [b] | –8.3 |
| | **7**$^{\cdot+}$**j** + **4** → **7j** + **4**$^{\cdot+}$ | [b] | –22.2 |

[a] Transition state could not be located. [b] The activation barrier was not calculated. We assume an outer sphere mechanism.

The overall free energy balance for net ring-expansion reactions is exergonic (cf. Schemes 4 and 5; **4** + **2f** → **7f**: $\Delta_R G_{298}$ = –104 kJ mol$^{-1}$, **4** + **2i** → **7i**: $\Delta_R G_{298}$ = –124 kJ mol$^{-1}$, and **4** + **2j** → **7j**: $\Delta_R G_{298}$ = –114 kJ mol$^{-1}$). Upon oxidation of **4**, 17e cationic complex **4**$^{\cdot+}$ is predicted to retain a closed-ring structure (Scheme 4); an isomer with a broken P–N bond could not be localized as an energy minimum. The oxidation by the ferrocenium cation (Scheme 4, reaction i) is predicted to be highly endergonic ($\Delta_R G_{298}$ = +139 kJ mol$^{-1}$), which may be due to simplification resulting from the replacement of $CH(SiMe_3)_2$ and

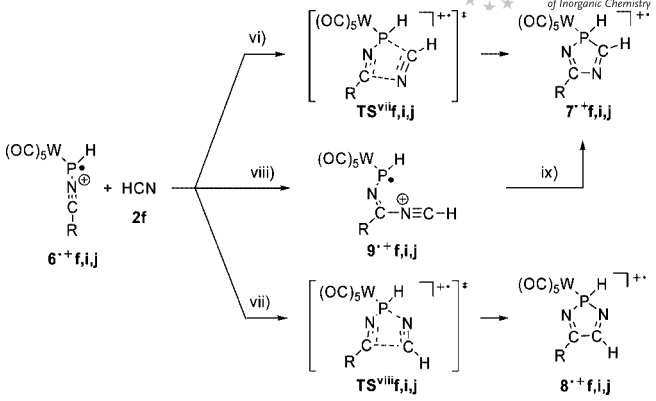


Scheme 5. Calculated pathways for the reactions of radical cationic nitrilium phosphane ylide complexes **6**$^{\cdot+}$**f,i,j** with HCN (**2f**) (**f**: R = H, **i**: R = $NH_2$, **j**: R = CN).

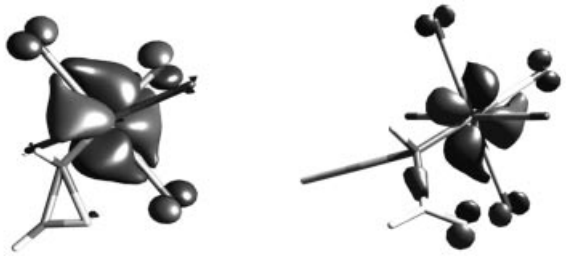

Figure 6. Highest singly occupied molecular orbitals (α-SOMO) of **4**$^{\cdot+}$ (left) and **5**$^{\cdot+}$**f** (right).

phenyl in **1** by a hydrogen atom, and thus radical cation **4**$^{\cdot+}$ is destabilized with respect to **4**. We also expect the free energy for the real system (compound **1**) to be somewhat lower but still endergonic, so the equilibrium between **1** and **1**$^{\cdot+}$ may support a low concentration of radical cation **1**$^{\cdot+}$. Most synthetically applicable radical cation chain reactions require an endergonic SET preequilibrium to initiate selective follow up reactions of highly electrophilic radical cations.[1] To save computing time we investigated the hypersurface of radical cationic model system **4**$^{\cdot+}$ by assuming that all stationary points of the reaction are affected in approximately the same way.

The highest singly occupied molecular orbital (α-SOMO) of 17e complex **4**$^{\cdot+}$, depicted in Figure 6, is mainly localized at the metal center. Only a minor participation of the nitrogen atom is apparent. An intermediate heptacoordinated tungsten complex, however, bearing one of the nitriles **2f,i,j** as ligand could not be located as an energy minimum. This ruled out a metal-centered reactivity of **4**$^{\cdot+}$ towards nitriles. Instead, a plausible pathway is the ring opening of **4**$^{\cdot+}$ by nucleophilic attack of nitriles **2f,i** with formation of intermediates **5**$^{\cdot+}$**f,i** (Scheme 4, reaction ii). The highest singly occupied molecular orbital of **5**$^{\cdot+}$**f** (Figure 6, right) also has a large contribution of the metal center, whereas a certain contribution of the nitrogen atom is apparent. This can be rationalized by the resonance structure given in Scheme 4. The barrier **TS**$^{\mathbf{ii}}$**f** for the formation of **5**$^{\cdot+}$**f** (R = H) is $\Delta G_{298}^{\neq}$ = +60 kJ mol$^{-1}$. For R = $NH_2$ no transition state

 © 2007 Wiley-VCH Verlag GmbH & Co. KGaA, Weinheim 

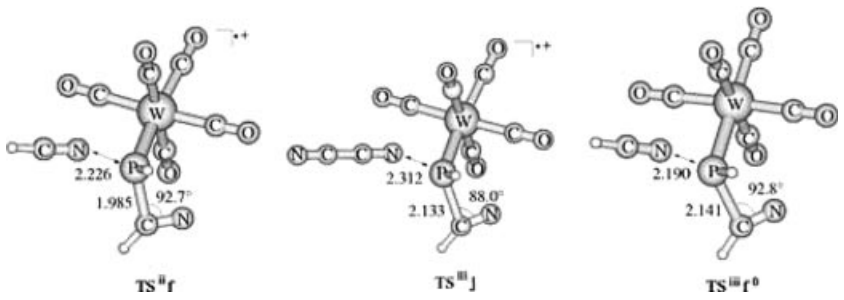


Figure 7. Transition states of the nucleophilic attack of **2f** on $\mathbf{4}^{\bullet+}$ ($\mathbf{TS}^{\mathbf{ii}}\mathbf{f}$, left), on **4** ($\mathbf{TS}^{\mathbf{iii}}\mathbf{f}^{\mathbf{0}}$, right) and of **2j** on $\mathbf{4}^{\bullet+}$ ($\mathbf{TS}^{\mathbf{iii}}\mathbf{j}$, middle).

could be located even in a constrained search, which indicates a very flat barrier. The formation of $\mathbf{5}^{\bullet+}\mathbf{f}$ is slightly endergonic ($\Delta_R G_{298}$ = +24 kJ mol$^{-1}$), whereas the formation of $\mathbf{5}^{\bullet+}\mathbf{i}$ is slightly exergonic ($\Delta_R G_{298}$ = –13 kJ mol$^{-1}$). With **2j** (R = CN), no intermediate $\mathbf{5}^{\bullet+}\mathbf{j}$ could be located. The binding of NCCN (through N) to the phosphorus center of $\mathbf{4}^{\bullet+}$ is associated with dissociation of the HCN moiety of $\mathbf{4}^{\bullet+}$ and exergonic formation of radical cationic nitrilium phosphane ylide complex $\mathbf{6}^{\bullet+}\mathbf{j}$ (Scheme 4, reaction iii; $\Delta_R G_{298}$ = –40 kJ mol$^{-1}$). The dissociation of HCN is indicated in transition state $\mathbf{TS}^{\mathbf{iii}}\mathbf{j}$ (Figure 7, middle) by the imaginary frequency, a 0.15 Å longer P–C distance and a 4.7° smaller P–C–N angle relative to ring-opening transition state $\mathbf{TS}^{\mathbf{ii}}\mathbf{f}$ (Figure 7, left). For the one-step substitution of HCN from $\mathbf{4}^{\bullet+}$ by nucleophilic attack of **2j**, the free activation energy $\mathbf{TS}^{\mathbf{iii}}\mathbf{j}$ was determined as $\Delta G_{298}^{\neq}$ = +75 kJ mol$^{-1}$. A further interesting question was to clarify the outcome of the nucleophilic attack of nitriles at the phosphorus atom of neutral 2*H*-azaphosphirene complex **4**. As indicated in the transition state, denoted as $\mathbf{TS}^{\mathbf{iii}}\mathbf{f}^{\mathbf{0}}$ (Figure 7, right), dissociation of HCN occurs also from neutral **4** upon attack of **2f**, and this reaction is also exergonic ($\Delta_R G_{298}$ = –15 kJ mol$^{-1}$) but the barrier is significantly higher ($\Delta G_{298}^{\neq}$ = +92 kJ mol$^{-1}$) than for corresponding radical cation $\mathbf{4}^{\bullet+}$. This, together with steric factors for real system **1**, might be the reason why 2*H*-azaphosphirene complex **1** does not react with nitriles in the absence of single-electron oxidants at ambient temperature.

Compound $\mathbf{5}^{\bullet+}\mathbf{i}$ (R = $NH_2$) can undergo cyclization to $\mathbf{7}^{\bullet+}\mathbf{i}$, a process that is predicted to be exergonic (Scheme 4, reaction iv; $\Delta_R G_{298}$ = –103 kJ mol$^{-1}$) and proceeding over a barrier with $\mathbf{TS}^{\mathbf{iv}}\mathbf{i}$ ($\Delta G_{298}^{\neq}$ = +22 kJ mol$^{-1}$). For $\mathbf{5}^{\bullet+}\mathbf{f}$ (R = H), transition state $\mathbf{TS}^{\mathbf{iv}}\mathbf{f}$ for the cyclization could not be located. A constrained decrease in the CN distance is associated with the breaking of the P–C bond. The dissociation of HCN from $\mathbf{5}^{\bullet+}\mathbf{f}$ proceeds over a very flat barrier $\mathbf{TS}^{\mathbf{v}}\mathbf{f}$ ($\Delta G_{298}^{\neq}$ = –2 kJ mol$^{-1}$, $\Delta E_{298}^{\neq}$ = +13 kJ mol$^{-1}$) yielding HCN and radical cationic nitrilium phosphane ylide complex $\mathbf{6}^{\bullet+}\mathbf{f}$ (Scheme 4, reaction v; $\Delta_R G_{298}$ = –96 kJ mol$^{-1}$). For $\mathbf{6}^{\bullet+}\mathbf{i}$ (R = $NH_2$), the HCN dissociation constitutes a competing pathway to the cyclization (Scheme 4, reaction iv). Calculated free activation energy for $\mathbf{TS}^{\mathbf{v}}\mathbf{i}$ is $\Delta G_{298}^{\neq}$ = +5 kJ mol$^{-1}$, and the free reaction energy is $\Delta_R G_{298}$ = –88 kJ mol$^{-1}$. In summary, the association of NCCN to $\mathbf{4}^{\bullet+}$ is simultaneously associated with a substitution of HCN, and on the other hand, upon the attack of HCN or $H_2NCN$ on $\mathbf{4}^{\bullet+}$ the HCN substitution can proceed in two steps, that is, under intermediate formation of $\mathbf{5}^{\bullet+}\mathbf{f,i}$. Alternatively, for $\mathbf{5}^{\bullet+}\mathbf{i}$ (R = $NH_2$), cyclization to $\mathbf{7}^{\bullet+}\mathbf{i}$ is feasible.

In the highest singly occupied molecular orbital (α-SOMO) of $\mathbf{6}^{\bullet+}\mathbf{f}$ (Figure 8, left) a significant contribution of the phosphorus atom is clear (as represented by the resonance structure in Scheme 4), which is in accord with the interpretation that $\mathbf{6}^{\bullet+}\mathbf{f}$ lacks one electron of the lone pair that is assigned to phosphorus in neutral nitrilium phosphane ylide complexes.[22] In 17e cationic 2*H*-1,4,2-diazaphosphole complex $\mathbf{7}^{\bullet+}\mathbf{f}$, the α-SOMO is almost exclusively located at the metal center (Figure 8, right).

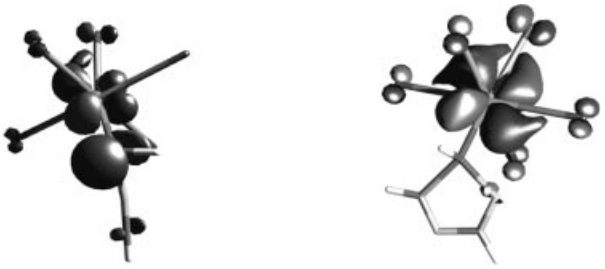

Figure 8. Highest singly occupied molecular orbitals (α-SOMO) of $\mathbf{6}^{\bullet+}\mathbf{f}$ (left) and $\mathbf{7}^{\bullet+}\mathbf{f}$ (right).

In all reactions of $\mathbf{4}^{\bullet+}$ with the three model nitrile derivatives there are plausible pathways leading to the formation of $\mathbf{6}^{\bullet+}\mathbf{f,i,j}$ with release of HCN, which in turn can (in principle) react with $\mathbf{6}^{\bullet+}\mathbf{f,i,j}$ in two regiochemically different [3+2] cycloaddition reactions, that is, with formation of radical cationic 2*H*-1,4,2-diazaphosphole complexes $\mathbf{7}^{\bullet+}\mathbf{f,i,j}$ (Scheme 5, reaction vi) or radical cationic 2*H*-1,3,2-diazaphosphole complexes $\mathbf{8}^{\bullet+}\mathbf{f,i,j}$ (Scheme 5, reaction vii). All reactions are exergonic (Table 4) and 2*H*-1,3,2-diazaphosphole complexes $\mathbf{8}^{\bullet+}\mathbf{f,i,j}$ are ca. 20–30 kJ mol$^{-1}$ more stable than corresponding 2*H*-1,4,2-diazaphosphole complexes $\mathbf{7}^{\bullet+}\mathbf{f,i,j}$. For the reactions of $\mathbf{6}^{\bullet+}\mathbf{f,i}$ (R = H and R = $NH_2$) with HCN the barriers $\mathbf{TS}^{\mathbf{vi}}\mathbf{f,i}$ for the formation of $\mathbf{7}^{\bullet+}\mathbf{f,i}$ are 18 and 14 kJ mol$^{-1}$ lower than those for the formation of $\mathbf{8}^{\bullet+}\mathbf{f,i}$ ($\mathbf{TS}^{\mathbf{vii}}\mathbf{f,i}$). For the reactions of $\mathbf{6}^{\bullet+}\mathbf{j}$ (R = CN) with HCN the barriers $\mathbf{TS}^{\mathbf{vi}}\mathbf{j}$ and $\mathbf{TS}^{\mathbf{vii}}\mathbf{j}$ are approximately equal.

For the reaction of $\mathbf{6}^{\bullet+}\mathbf{f,i,j}$ with HCN a further alternative pathway is plausible, namely a stepwise mechanism starting with the addition of HCN to $\mathbf{6}^{\bullet+}\mathbf{f,i,j}$, which leads to the

 © 2007 Wiley-VCH Verlag GmbH & Co. KGaA, Weinheim 

formation of a C–N bond to yield intermediates **9**$^{\cdot+}$**f**,**i**,**j** (Scheme 5, reaction viii), with subsequent cyclization to **7**$^{\cdot+}$**f**,**i**,**j** (Scheme 5, reaction ix). The barriers for C–N bond formation **TS**$^{\mathbf{viii}}$**f**,**j** ($\Delta G_{298}^{\neq}$ = +90 kJ mol$^{-1}$ for the reaction of HCN with **6**$^{\cdot+}$**f** and $\Delta G_{298}^{\neq}$ = +77 kJ mol$^{-1}$ for the reaction with **6**$^{\cdot+}$**j**) are slightly lower than those for the corresponding direct [3+2] cycloaddition **TS**$^{\mathbf{vi}}$**f**,**j**, whereas the barriers for the second step **TS**$^{\mathbf{ix}}$**f**,**j** are almost negligible ($\Delta G_{298}^{\neq}$ = +29 kJ mol$^{-1}$ for **9**$^{\cdot+}$**f** and $\Delta G_{298}^{\neq}$ = +32 kJ mol$^{-1}$ for **9**$^{\cdot+}$**j**). The formation of **9**$^{\cdot+}$**f**,**i**,**j** (Scheme 5, reaction viii) is predicted to be endergonic for our three model reactions, that is, for the reaction of HCN with **6**$^{\cdot+}$**f** $\Delta_R G_{298}$ = +75 kJ mol$^{-1}$, for the reaction with **6**$^{\cdot+}$**j** $\Delta_R G_{298}$ = +50 kJ mol$^{-1}$, and especially for the reaction with **6**$^{\cdot+}$**i** $\Delta_R G_{298}$ = +109 kJ mol$^{-1}$.

Once **7**$^{\cdot+}$**f**,**i**,**j** are formed, the cycle is closed by the oxidation of 2*H*-azaphosphirene complex **4** by **7**$^{\cdot+}$**f**,**i**,**j** (for **7**$^{\cdot+}$**f**: $\Delta_R G_{298}$ = –13 kJ mol$^{-1}$, for **7**$^{\cdot+}$**i**: $\Delta_R G_{298}$ = –8 kJ mol$^{-1}$, for **7**$^{\cdot+}$**j**: $\Delta_R G_{298}$ = –22 kJ mol$^{-1}$) to yield 2*H*-1,4,2-diazaphosphole complexes **7f**,**i**,**j** and **4**$^{\cdot+}$, which then can restart the chain reaction (Scheme 3).

## Conclusions

A combined experimental and theoretical investigation on the ring expansion of 2*H*-azaphosphirene complex **1** with a wide variety of electronically different nitriles revealed that electron-rich nitrile derivatives **2a**–**e** furnish regioselectively 2*H*-1,4,2-diazaphosphole complexes **3a**–**e** in the presence of substoichiometric amounts of ferrocenium hexafluorophosphate. The reaction course shows characteristics of an autocatalytic reaction and is interpretable in terms of a ligand-centered reactivity of an organometallic radical cation (**1**$^{\cdot+}$). In contrast, reactions of complex **1** with **2f**–**h** proceeded differently. With HCN (**2f**) complex **3f** was formed slowly and not selectively; byproducts having a P–F bond were also formed. This provides the first strong evidence that transiently formed highly electrophilic phosphorus-containing species had reacted with hexafluorophosphate through fluoride transfer. In reactions of complex **1** with weak nucleophilic nitrile derivatives **2g**,**h**, byproducts bearing a P–F bond were also formed, but the formation of 2*H*-1,4,2-diazaphosphole complexes **3g**,**h** could not be detected.

The computational results can be summarized as follows: The barrier of the nucleophilic attack of the nitrile at radical cationic complex **4**$^{\cdot+}$ depends strongly on its nucleophilicity. As a result of steric factors in the real system of **1**, this step may be crucial. The further course of the ring expansion with strong nucleophilic nitrile derivatives[23] can proceed by direct cyclization of the intermediately formed complex **5**$^{\cdot+}$ or with moderately nucleophilic nitrile derivatives by formation of complex **6**$^{\cdot+}$ accompanied by the release of nitrile and subsequent [3+2] cycloaddition. Because the reactions are performed at ambient temperature, the kinetically controlled pathway proceeding via the more favorable transition state may be preferred, which yields regioselectively 2*H*-1,4,2-diazaphosphole complexes **7**$^{\cdot+}$. As experimentally shown, complex **1** reacts with weak nucleophilic nitrile derivatives **2g**,**h** in the presence of ferrocenium salts neither to 2*H*-1,4,2-diazaphosphole complexes **3g**,**h** nor to 2*H*-1,3,2-diazaphosphole complexes **8g**,**h**. If hexafluorophosphate is present, products bearing a P–F bond are formed. So, in the presence of weak nucleophilic nitrile derivatives a completely different reaction course is taken, which proceeds with the participation of the hexafluorophosphate anion.

## Experimental Section

**General Procedures:** All reactions and manipulations were carried out under an atmosphere of deoxygenated, dried nitrogen or argon by using standard Schlenk techniques with conventional glassware. Solvents were dried according to standard procedures. 2*H*-Azaphosphirene complex **1** was synthesized according to the method described in the literature.[10d] NMR spectra were recorded with a Bruker AC-200 spectrometer or a Bruker Avance 300 spectrometer with [D$_6$]benzene or [D]chloroform as solvent and internal standard; shifts are given relative to external tetramethylsilane ($^1$H, $^{13}$C), neat $CFCl_3$ ($^{19}$F), and 85% $H_3PO_4$ ($^{31}$P). Mass spectra were recorded with a Finnigan MAT 8430 (70 eV) or a Kratos Concept 1H spectrometer (FAB+, *m*NBA); apart from *m*/*z* values of the molecule ions, only *m*/*z* values having intensities more than 10% are given. Infrared spectra were recorded with a Biorad FTIR 165 (selected data given) or a Bruker FTIR IFS113V spectrometer. UV/Vis spectra were recorded with a Shimadzu UV-1650 PC spectrometer. Melting points were obtained with a Büchi 535 capillary apparatus or a Büchi apparatus Type S. The values are not corrected. Elemental analyses were performed using a Carlo Erba analytical gas chromatograph or an Elementar VarioEL instrument.

**General Procedure for the Synthesis of 3a–e:** To a solution of 2*H*-azaphosphirene complex **1** (617 mg, 1.00 mmol) in $CH_2Cl_2$ (3 mL) was added the appropriate nitrile (**2a**: 122 μL, 1.50 mmol; **2b**: 120 mg, 1.00 mmol; **2c**: 180 μL, 2.06 mmol; **2d**: 94 μL, 1.01 mmol; **2e**: 94 μL, 1.03 mmol) and ferrocenium hexafluorophosphate (17 mg, 0.05 mmol). The reaction mixture was stirred for 6 h at ambient temperature [reaction monitoring by $^{31}$P{$^1$H} NMR spectroscopy]. After the solvent was removed in vacuo, the product was separated and purified by column chromatography ($SiO_2$, –10 °C, petroleum ether ether/$Et_2O$, 97.5:2.5).

**Complex 3a:** Yield: 406 mg (0.59 mmol, 59%). Yellow solid, recrystallized from *n*-pentane. M.p. 122 °C. $^1$H NMR (300.13 MHz, $C_6D_6$, 30 °C): $\delta$ = –0.22 (s, 9 H, $SiMe_3$), 0.50 (s, 9 H, $SiMe_3$), 1.01 [d, $^2J_{P,H}$ = 5.8 Hz, 1 H, C*H*($SiMe_3$)$_2$], 2.78 (s, 3 H, NMe), 2.92 (s, 3 H, NMe), 7.11 (m$_c$, 3 H, *meta*, *para* Ph), 8.17 (m$_c$, 2 H, *ortho* Ph) ppm. $^{13}$C{$^1$H} NMR (75.5 MHz, $C_6D_6$, 30 °C): $\delta$ = 3.1 [d, $^3J_{P,C}$ = 1.6 Hz, Si($CH_3$)$_3$], 4.1 [d, $^3J_{P,C}$ = 2.6 Hz, Si($CH_3$)$_3$], 22.0 [d, $^1J_{P,C}$ = 5.8 Hz, *C*H($SiMe_3$)$_2$], 37.6 (s, $NCH_3$), 37.6 (s, $NCH_3$), 128.8 (s, *para* Ph), 131.6 (d, $^3J_{P,C}$ = 1.9 Hz, *ortho* Ph), 132.8 (d, $^2J_{P,C}$ = 20.7 Hz, *ipso* Ph), 133.3 (s, *meta* Ph), 165.0 (s, PNC), 198.6 (d$_{sat}$, $^2J_{P,C}$ = 6.5 Hz, $^1J_{W,C}$ = 126.7 Hz, *cis* CO), 199.6 (d, $^2J_{P,C}$ = 22.3 Hz, *trans* CO), 200.3 (d, $^{[1+4]}J_{P,C}$ = 25.5 Hz, PCN) ppm. $^{31}$P{$^1$H} NMR (121.5 MHz, $C_6D_6$, 30 °C): $\delta$ = 101.8 (s$_{sat}$, $^1J_{W,P}$ = 241.6 Hz) ppm. IR (KBr): $\tilde{\nu}$ = 2068 (CO), 1980 (CO), 1922 (CO) cm$^{-1}$. MS (FAB+, *m*NBA): *m*/*z* (%) = 688.1 (12) [M + H]$^+$, 659.1 (49) [M – CO]$^+$, 631.1 (38) [M – 2 CO]$^+$, 603.1 (10) [M – 3 CO]$^+$, 364.2 (100) [M – W(CO)$_5$ + H]$^+$. $C_{22}H_{30}N_3O_5PSi_2W$ (687.48): calcd. C 38.44, H 4.40, N 6.11; found C 38.49, H 4.54, N 5.86.

 © 2007 Wiley-VCH Verlag GmbH & Co. KGaA, Weinheim 

**Complex 3b:** Yield: 398 mg (0.54 mmol, 54%). Orange solid, recrystallized from *n*-pentane. M.p. 123 °C. $^1$H NMR (200 MHz, $CDCl_3$, 25 °C): $\delta$ = –0.10 (s, 9 H, $SiMe_3$), 0.52 (s, 9 H, $SiMe_3$), 1.19 (d, $^2J_{P,H}$ = 3.9 Hz, 1 H, C*H*$SiMe_3$), 2.37 (s, 3 H, CMe), 4.08 (s, 3 H, NMe), 6.11 (d, $^3J_{H,H}$ = 3.9 Hz, 1 H, 3-pyrryl), 7.52 ($m_c$, 5 H, *meta*, *para* Ph, 4-pyrryl), 8.23 (dd, $^4J_{H,H}$ = 2.2 Hz, $^3J_{H,H}$ = 7.6 Hz, 2 H, *ortho* Ph) ppm. $^{13}$C{$^1$H} NMR (50.3 MHz, $CDCl_3$, 25 °C): $\delta$ = 2.9 [d, $^3J_{P,C}$ = 2.0 Hz, $Si(CH_3)_3$], 3.7 [d, $^3J_{P,C}$ = 2.7 Hz, $Si(CH_3)_3$], 13.0 (s, CMe), 19.8 [d, $^1J_{P,C}$ = 5.4 Hz, *C*H$(SiMe_3)_2$], 109.0 (s, 4-pyrryl), 122.4 (s, 3-pyrryl), 127.6 (d, $^2J_{P,C}$ = 12.1 Hz, 2-pyrryl), 128.7 (s, *meta* Ph), 131.2 (d, $^3J_{P,C}$ = 2.0 Hz, *ortho* Ph), 132.4 (d, $^2J_{P,C}$ = 23.5 Hz, *ipso* Ph), 132.9 (s, *para* Ph), 139.7 (s, 5-pyrryl), 162.3 (d, $^{[2+3]}J_{P,C}$ = 5.8 Hz, PNC), 197.5 (d, $^2J_{P,C}$ = 6.4 Hz, *cis* CO), 197.0 (d, $^{[1+4]}J_{P,C}$ = 22.7 Hz, PCN), 198.8 (d, $^2J_{P,C}$ = 13.5 Hz, *trans* CO) ppm. $^{31}$P{$^1$H} NMR (81.0 MHz, $CDCl_3$, 25 °C): $\delta$ = 108.4 ($s_{sat}$, $^1J_{W,P}$ = 233.9 Hz) ppm. IR (KBr): $\tilde{\nu}$ = 2071 (CO), 1994 (CO), 1926 (CO), 1873 (CO) cm$^{-1}$. MS (EI, 70 eV, $^{184}$W): *m/z* (%) = 726 (8) $[M]^+$, 698 (16) $[M – CO]^+$, 670 (32) $[M – 2\ CO]^+$, 533 (52) [M – 3 CO – $C_7H_9N_2]^+$, 73 (100) $[SiMe_3]^+$. $C_{26}H_{32}N_3O_5PSi_2W$ (737.53): calcd. C 42.22, H 4.51, N 5.48; found C 42.29, H 4.50, N 5.51.

**Complex 3c:** Yield: 404 mg (0.57 mmol, 57%). Orange solid, recrystallized from *n*-pentane. M.p. 119 °C. $^1$H NMR (200 MHz, $CDCl_3$, 25 °C): $\delta$ = –0.10 (s, 9 H, $SiMe_3$), 0.54 (s, 9 H, $SiMe_3$), 1.16 (d, 1 H, $^2J_{P,H}$ = 4.1 Hz, 1 H, C*H*$SiMe_3$), 6.64 (dd, $^3J_{H,H}$ = 3.5 Hz, $^3J_{H,H}$ = 1.8 Hz, 2 H, 4-furanyl), 7.56 ($m_c$, 4 H, *meta*, *para* Ph, 4-furanyl), 7.72 ($m_c$, $^3J_{H,H}$ = 1.8 Hz, 1 H, 5-furanyl), 8.21 (dd, 2 H, $^4J_{H,H}$ = 2.7 Hz, $^3J_{H,H}$ = 5.9 Hz, 2 H, *ortho* Ph) ppm. $^{13}$C{$^1$H} NMR (50.3 MHz, $CDCl_3$, 25 °C): $\delta$ = 2.9 [d, $^3J_{P,C}$ = 2.0 Hz, $Si(CH_3)_3$], 3.7 [d, $^3J_{P,C}$ = 2.8 Hz, $Si(CH_3)_3$], 18.8 [d, $^1J_{P,C}$ = 5.2 Hz, *C*H-$(SiMe_3)_2$], 112.5 (s, 4-furanyl), 119.6 (s, 3-furanyl), 128.9 (s, *meta* Ph), 131.3 (d, $^3J_{P,C}$ = 2.1 Hz, *ortho* Ph), 132.2 (d, $^2J_{P,C}$ = 22.7 Hz, *ipso* Ph), 133.6 (s, *para* Ph), 147.4 (s, 5-furanyl), 149.3 (d, $^3J_{P,C}$ = 14.5 Hz, 2-furanyl), 160.2 (d, $^{[2+3]}J_{P,C}$ = 3.8 Hz, PNC), 197.1 (d, $^2J_{P,C}$ = 6.1 Hz, *cis* CO), 198.2 (d, $^{[1+4]}J_{P,C}$ = 22.4 Hz, PCN), 202.1 (d, $^2J_{P,C}$ = 22.7 Hz, *trans* CO) ppm. $^{31}$P{$^1$H} NMR (81.0 MHz, $CDCl_3$, 25 °C): $\delta$ = 110.6 ($s_{sat}$, $^1J_{W,P}$ = 230.6 Hz). MS (EI, 70 eV, $^{184}$W): *m/z* (%) = 710 (11) $[M]^+$, 682 (11) $[M – CO]^+$, 654 (85) $[M – 3\ CO]^+$, 533 (52) [M – 3 CO – $C_5H_3NO]^+$, 477 (52) [M – 5 CO – $C_5H_3NO]^+$, 73 (100) $[SiMe_3]^+$. $C_{24}H_{27}N_2O_6PSi_2W$ (710.47): calcd. C 40.57, H 3.83, N 3.94; found C 40.72, H 3.83, N 3.94.

**Complex 3d:** Yield: 371 mg (0.51 mmol, 51%). Orange solid, recrystallized from *n*-pentane. M.p. 112 °C. $^1$H NMR (200 MHz, $CDCl_3$, 25 °C): $\delta$ = –0.09 (s, 9 H, $SiMe_3$), 0.53 (s, 9 H, $SiMe_3$), 1.19 [d, $^2J_{P,H}$ = 4.0 Hz, 1 H, $CH(SiMe_3)_2$], 7.24 ($m_c$, 1 H, 3-thienyl), 7.57 ($m_c$, 4 H, *meta*, *para* Ph, 4-thienyl), 8.22 ($m_c$, 1 H, 2-thienyl), 8.24 (dd, $^4J_{H,H}$ = 1.7 Hz, $^3J_{H,H}$ = 7.5 Hz, 2 H, *ortho* Ph) ppm. $^{13}$C{$^1$H} NMR (50.3 MHz, $C_6D_6$, 25 °C): $\delta$ = 2.9 [d, $^3J_{P,C}$ = 2.1 Hz, $Si(CH_3)_3$], 3.7 [d, $^3J_{P,C}$ = 2.6 Hz, $Si(CH_3)_3$], 18.9 [d, $^1J_{P,C}$ = 5.0 Hz, *C*H$(SiMe_3)_2$], 128.5 (s, 4-thienyl), 128.9 (s, *meta* Ph), 131.4 (d, $^3J_{P,C}$ = 2.1 Hz, *ortho* Ph), 132.3 (d, $^2J_{P,C}$ = 22.5 Hz, *ipso* Ph), 133.1 (s, 5-thienyl), 133.6 (s, *para* Ph), 134.0 (s, 3-thienyl), 138.5 (d, $^3J_{P,C}$ = 14.4 Hz, *2*-thienyl), 164.4 (d, $^{[2+3]}J_{P,C}$ = 4.0 Hz, PNC), 197.1 (d, $^2J_{P,C}$ = 6.3 Hz, *cis* CO), 198.2 (d, $^2J_{P,C}$ = 22.4 Hz, *trans* CO), 201.3 (d, $^{[1+4]}J_{P,C}$ = 23.2 Hz, PCN) ppm. $^{31}$P{$^1$H} NMR (81.0 MHz, $C_6D_6$, 25 °C): $\delta$ = 110.5 ($s_{sat}$, $^1J_{W,P}$ = 229.5 Hz) ppm. IR (KBr): $\tilde{\nu}$ = 2952 (CH), 2899 (CH), 2073 (CO), 2001 (CO), 1909 (CO), 1413 (thienyl), 1253 (thienyl) cm$^{-1}$. MS (EI, 70 eV, $^{184}$W): *m/z* (%) = 726 (8) $[M]^+$, 698 (16) $[M – CO]^+$, 670 (32) $[M – 2\ CO]^+$, 73 (100) $[SiMe_3]^+$. $C_{24}H_{27}N_2O_5PSSi_2W$ (726.53): calcd. C 39.68, H 3.75, N 3.86, S 4.41; found C 39.82, H 3.70, N 4.64, S 3.79.

**Complex 3e:** Yield: 378 mg (0.52 mmol, 52%). Orange solid, recrystallized from *n*-pentane. M.p. 112 °C. $^1$H NMR (200 MHz, $CDCl_3$, 25 °C): $\delta$ = 0.00 (s, 9 H, $SiMe_3$), 0.64 (s, 9 H, $SiMe_3$), 1.30 (d, $^2J_{P,H}$ = 4.1 Hz, 1 H, C*H*$SiMe_3$), 6.87 ($m_c$, 1 H, 4-thienyl), 7.65 ($m_c$, 3 H, *meta*, *para* Ph), 7.99 (d, $^3J_{H,H}$ = 4.9 Hz, 1 H, 5-thienyl), 8.34 (d, $^3J_{H,H}$ = 6.8 Hz, 2 H, *ortho* Ph) ppm. $^{13}$C{$^1$H} NMR (50.3 MHz, 25 °C, $CDCl_3$): $\delta$ = 2.9 [d, $^3J_{P,C}$ = 1.9 Hz, $Si(CH_3)_3$], 3.7 [d, $^3J_{P,C}$ = 2.6 Hz, $Si(CH_3)_3$], 18.6 [d, $^1J_{P,C}$ = 4.8 Hz, *C*H$(SiMe_3)_2$], 126.6 (s, 2-thienyl), 128.1 (s, 5-thienyl), 128.6 (s, *meta* Ph), 131.2 (d, $^3J_{P,C}$ = 2.1 Hz, *ortho* Ph), 132.6 (d, $^2J_{P,C}$ = 23.8 Hz, *ipso* Ph), 133.4 (s, *para* Ph), 133.6 (s, 4-thienyl), 137.2 (d, $^3J_{P,C}$ = 13.6 Hz, 3-thienyl), 165.0 (d, $^{[2+3]}J_{P,C}$ = 4.9 Hz, PNC), 197.1 (d, $^2J_{P,C}$ = 5.9 Hz, *cis* CO), 198.2 (d, $^{[1+4]}J_{P,C}$ = 22.4 Hz, PCN), 201.8 (d, $^2J_{P,C}$ = 22.8 Hz, *trans* CO) ppm. $^{31}$P{$^1$H} NMR (81.0 MHz, $CDCl_3$, 25 °C): $\delta$ = 109.1 ($s_{sat}$, $^1J_{W,P}$ = 229.8 Hz). IR (KBr): $\tilde{\nu}$ = 2073 (s, CO), 2000 (s, CO), 1921 (s, sh, CO), 1253 (m, thienyl), 834 (w, thienyl) cm$^{-1}$. MS (EI, 70 eV, $^{184}$W): *m/z* (%) = 726 (12) $[M]^+$, 698 (26) $[M – CO]^+$, 670 (100) $[M – 2\ CO]^+$, 533 (26) [M – 3 CO – $C_5H_3NS]^+$, 477 (38) [M – 5 CO – $C_5H_3NS]^+$, 73 (74) $[SiMe_3]^+$. $C_{24}H_{27}N_2O_5PSSi_2W$ (726.53): calcd. C 39.69, H 3.75, N 3.86, S 4.41; found C 39.34, H 3.98, N 3.46, S 4.36.

**Investigation of the Dependence of the Reaction Progression of 1 with 2d on the Amount of Ferrocenium Hexafluorophosphate:** To a solution of 2*H*-azaphosphirene complex **1** (123 mg, 0.20 mmol) in $CH_2Cl_2$ (0.6 mL) was added 2-thiophene carbonitrile **2d** (19 μL, 0.20 mmol) and the appropriate amount of ferrocenium hexafluorophosphate (0.7 mg, 0.002 mmol; 1.3 mg, 0.004 mmol; 2.0 mg, 0.006 mmol; 2.6 mg, 0.008 mmol; 3.3 mg, 0.010 mmol; 6.6 mg, 0.020 mmol; 9.9 mg, 0.030 mmol; 13.2 mg, 0.040 mmol). Product ratios were estimated by $^{31}$P{$^1$H} NMR spectroscopic resonance integration (30 °C, 100 scans each, measurement duration 159 s, recorded reaction time corresponds to the end of the respective measurement). For the investigations corresponding to Figure 2, a solution of $[FcH]PF_6$ (1.6 mg, 0.005 mmol) and 2-thiophene carbonitrile **2d** (19 μL, 0.20 mmol) in $CH_2Cl_2$ was added to 2*H*-azaphosphirene complex **1** (123 mg, 0.20 mmol) to ensure that the entire amount of $[FcH]PF_6$ was diluted at the start of the reaction. Product ratios were estimated by $^{31}$P{$^1$H} NMR spectroscopic resonance integration (30 °C, 32 scans each, measurement duration 56 s).

**Attempted Synthesis of Complex 3f with the Use of Ferrocenium Hexafluorophosphate:** To a solution of 2*H*-azaphosphirene complex **1** (123 mg, 0.20 mmol) in $CH_2Cl_2$ (0.6 mL) was added hydrogen cyanide **2f** (20 μL, 0.51 mmol) and ferrocenium hexafluorophosphate (12 mg, 0.04 mmol). The reaction mixture was stirred at ambient temperature [reaction monitored by $^{31}$P{$^1$H} NMR spectroscopy]. After 4 d the reaction mixture containing unidentified products **A**–**F** and **3f** was analyzed by $^{31}$P{$^1$H} NMR and $^{19}$F{$^1$H} NMR spectroscopy at 30 °C [ratio estimation by $^{31}$P{$^1$H} NMR resonance integration]. $^{31}$P{$^1$H} NMR (121.5 MHz, $CH_2Cl_2$): $\delta$ = 206.9 [d, $^1J_{P,F}$ = 855.8 Hz, **A** (1%)], 206.2 [d, $^1J_{P,F}$ = 841.8 Hz, **B** (3%)], 197.3 [d, $^1J_{P,F}$ = 824.0 Hz, **C** (9%)], 191.2 [d, $^1J_{P,F}$ = 989.3 Hz, **D** (4%)], 161.2 [$s_{sat}$, $^1J_{W,P}$ = 289.9 Hz, **E** (6%)], 110.7 [$s_{sat}$, $^1J_{W,P}$ = 227.6 Hz, **F** (5%)], 105.5 [$s_{sat}$, $^1J_{W,P}$ = 225.1 Hz, **3f** (20%)], –109.9 [$s_{sat}$, $^1J_{W,P}$ = 293.7 Hz, **1** (16%)], –143.5 [sept, $^1J_{P,F}$ = 714.0 Hz, $PF_6^-$ (3%)] ppm. $^{19}$F{$^1$H} NMR (282.4 MHz, $CH_2Cl_2$): $\delta$ = –31.0 [d, $^1J_{P,F}$ = 991.8 Hz, **D** (4%)], –72.5 [d, $^1J_{P,F}$ = 713.6 Hz, $PF_6^-$ (3%)], –109.1 [d, $^1J_{P,F}$ = 841.5 Hz, **B** (3%)], –111.4 [d, $^1J_{P,F}$ = 854.9 Hz, **A** (1%)], –117.2 [d, $^1J_{P,F}$ = 823.5 Hz, **C** (9%)] ppm.

**Attempted Synthesis of Complex 3g with the Use of Ferrocenium Hexafluorophosphate:** To a solution of 2*H*-azaphosphirene complex **1** (123 mg, 0.20 mmol) in $CH_2Cl_2$ (0.6 mL) was added ethyl cyanoformate **2g** (30 μL, 0.30 mmol) and ferrocenium hexafluorophos-

 © 2007 Wiley-VCH Verlag GmbH & Co. KGaA, Weinheim 

phate (12 mg, 0.04 mmol). The reaction mixture was stirred at ambient temperature [reaction monitored by $^{31}P\{^1H\}$ NMR spectroscopy]. After 6 d, the reaction mixture was analyzed by $^{31}P\{^1H\}$ NMR and $^{19}F\{^1H\}$ NMR spectroscopy at 30 °C [ratio estimation by $^{31}P\{^1H\}$ NMR resonance integration]. $^{31}P\{^1H\}$ NMR (121.5 MHz, $CH_2Cl_2$): $\delta$ = 197.3 [d, $^1J_{P,F}$ = 822.7 Hz, **A** (12%)], 177.2 [d, $^1J_{P,F}$ = 967.7 Hz, **B** (2%)], 160.8 [$s_{sat}$, $^1J_{W,P}$ = 284.8 Hz, **C** (6%)], 110.7 [$s_{sat}$, $^1J_{W,P}$ = 227.6 Hz, **D** (21%)], 18.5 [d, $^1J_{P,F}$ = 1044.0 Hz, **E** (3%)], –110.1 [$s_{sat}$, $^1J_{W,P}$ = 293.7 Hz, **1** (41%)], –143.8 [sept, $^1J_{P,F}$ = 714.0 Hz, $PF_6^-$ (6%)] ppm. $^{19}F\{^1H\}$ NMR (282.4 MHz, $CH_2Cl_2$): $\delta$ = –66.7 [d, $^1J_{P,F}$ = 1046.8 Hz, **E** (3%)], –73.8 [d, $^1J_{P,F}$ = 712.5 Hz, $PF_6^-$ (6%)], –74.4 [d, $^1J_{P,F}$ = 968.3 Hz, **B** (2%)], –117.2 [d, $^1J_{P,F}$ = 823.5 Hz, **A** (12%)] ppm.

**Attempted Synthesis of Complex 3h with the Use of Ferrocenium Hexafluorophosphate:** To a solution of 2*H*-azaphosphirene complex **1** (123 mg, 0.20 mmol) in $CH_2Cl_2$ (0.6 mL) was added 2,3,4,5,6-pentafluorobenzonitrile **2h** (160 μL, 1.27 mmol) and ferrocenium hexafluorophosphate (12 mg, 0.04 mmol). The reaction mixture was stirred at ambient temperature [reaction monitored by $^{31}P\{^1H\}$ NMR spectroscopy]. After 6 d the reaction mixture containing unidentified products **A**–**F**, **1**, and **2h** was analyzed by $^{31}P\{^1H\}$ NMR and $^{19}F\{^1H\}$ NMR spectroscopy at 30 °C [ratio estimation by $^{31}P\{^1H\}$ NMR resonance integration]. $^{31}P\{^1H\}$ NMR (121.5 MHz, $CH_2Cl_2$): $\delta$ = 197.4 [d, $^1J_{P,F}$ = 824.0 Hz, $^1J_{W,P}$ = 286.1 Hz, **A** (11%)], 183.1 [s, **B** (5%)], 176.3 [s, **C** (5%)], 160.9 [$s_{sat}$, $^1J_{W,P}$ = 282.3 Hz, **D** (5%)], 110.7 [$s_{sat}$, $^1J_{W,P}$ = 228.9 Hz, **E** (12%)], 18.4 [d, $^1J_{P,F}$ = 1041.4 Hz, **F** (3%)], –110.4 [$s_{sat}$, $^1J_{W,P}$ = 293.7 Hz, **1** (48%)] ppm. $^{19}F\{^1H\}$ NMR (282.4 MHz, $CH_2Cl_2$): $\delta$ = –67.6 [d, $^1J_{P,F}$ = 1041.2 Hz, **F** (3%)], –75.5 (d, $^1J_{P,F}$ = 713.6 Hz, $PF_6^-$), –117.6 [d, $^1J_{P,F}$ = 823.5 Hz, **A** (11%)], –134.0 ($m_c$, **2h**), –144.7 ($m_c$, **2h**), –160.6 ($m_c$, **2h**) ppm.

**Synthesis of 3d with the Use of Ferrocenium Tetraphenylborate:** To a solution of 2*H*-azaphosphirene complex **1** (62 mg, 0.10 mmol) in $CH_2Cl_2$ (0.3 mL) was added 2-thiophene carbonitrile **2d** (10 μL, 0.11 mmol) and ferrocenium tetraphenylborate (9 mg, 0.02 mmol). The reaction mixture was stirred for 8 h at ambient temperature, and the complete formation of **3d** was evidenced by analysis of the reaction mixture by $^{31}P\{^1H\}$ NMR spectroscopy.

**Attempted Synthesis of Complex 3f with the Use of Ferrocenium Tetraphenylborate:** To a solution of 2*H*-azaphosphirene complex **1** (123 mg, 0.20 mmol) in $CH_2Cl_2$ (0.6 mL) was added hydrogen cyanide **2f** (20 μL, 0.51 mmol) and ferrocenium tetraphenylborate (18 mg, 0.04 mmol). The reaction mixture was stirred at ambient temperature [reaction monitored by $^{31}P\{^1H\}$ NMR spectroscopy]. After 4 d the reaction mixture containing unidentified products **A**–**D** and **1** was analyzed by $^{31}P\{^1H\}$ NMR spectroscopy at 30 °C [ratio estimation by $^{31}P\{^1H\}$ NMR resonance integration]. $^{31}P\{^1H\}$ NMR (121.5 MHz, $CH_2Cl_2$): $\delta$ = 110.6 [$s_{sat}$, $^1J_{W,P}$ = 227.6 Hz, **A** (13%)], 105.5 [$s_{sat}$, $^1J_{W,P}$ = 223.8 Hz, **3f** (3%)], 20.7 [$s_{sat}$, $^1J_{W,P}$ = 236.5 Hz, **B** (3%)], 13.2 [$s_{sat}$, $^1J_{W,P}$ = 236.5 Hz, **C** (8%)], –68.9 [$s_{sat}$, $^1J_{W,P}$ = 242.9 Hz, **D** (17%)], –109.9 [$s_{sat}$, $^1J_{W,P}$ = 293.7 Hz, **1** (37%)] ppm.

**Attempted Synthesis of Complex 3g with the Use of Ferrocenium Tetraphenylborate:** To a solution of 2*H*-azaphosphirene complex **1** (123 mg, 0.20 mmol) in $CH_2Cl_2$ (0.6 mL) was added ethyl cyanoformate **2g** (30 μL, 0.30 mmol) and ferrocenium tetraphenylborate (18 mg, 0.04 mmol). The reaction mixture was stirred at ambient temperature [reaction monitored by $^{31}P\{^1H\}$ NMR spectroscopy]. After 6 d the reaction mixture containing unidentified products **A**–**G** and **1** was analyzed by $^{31}P\{^1H\}$ NMR spectroscopy at 30 °C [ratio estimation by $^{31}P\{^1H\}$ NMR resonance integration]. $^{31}P\{^1H\}$ NMR (121.5 MHz, $CH_2Cl_2$): $\delta$ = 204.9 [**A** (1%)], 184.5 [**B** (1%)], 163.3 [**C** (1%)], 110.7 [**D** (1%)], 97.4 [**E** (1%)], 54.5 [**F** (1%)], 34.1 [**G** (10%)], –110.1 [$s_{sat}$, $^1J_{W,P}$ = 293.7 Hz, **1** (81%)] ppm.

**Attempted Synthesis of Complex 3h with the Use of Ferrocenium Tetraphenylborate:** To a solution of 2*H*-azaphosphirene complex **1** (123 mg, 0.20 mmol) in $CH_2Cl_2$ (0.6 mL) was added 2,3,4,5,6-pentafluorobenzonitrile **2h** (160 μL, 1.27 mmol) and ferrocenium hexafluorophosphate (18 mg, 0.04 mmol). The reaction mixture was stirred at ambient temperature [reaction monitored by $^{31}P\{^1H\}$ NMR spectroscopy]. After 6 d the reaction mixture containing unidentified products **A**–**H** and **2h** was analyzed by $^{31}P\{^1H\}$ NMR and $^{19}F\{^1H\}$ NMR spectroscopy at 30 °C [ratio estimation by $^{31}P\{^1H\}$ NMR resonance integration]. $^{31}P\{^1H\}$ NMR (121.5 MHz, $CH_2Cl_2$): $\delta$ = 183.0 [$s_{sat}$, $^1J_{W,P}$ = 254.3 Hz, **A** (9%)], 176.2 [$s_{sat}$, $^1J_{W,P}$ = 277.2 Hz, **B** (3%)], 172.5 [$s_{sat}$, $^1J_{W,P}$ = 309.0 Hz, **C** (6%)], 126.1 [**D** (1%)], 110.7 [**E** (1%)], 95.5 [$s_{sat}$, $^1J_{W,P}$ = 277.2 Hz, **F** (3%)], 54.4 [$s_{sat}$, $^1J_{W,P}$ = 270.8 Hz, **G** (1%)], 40.0 [**H** (1%)], –110.4 [$s_{sat}$, $^1J_{W,P}$ = 295.0 Hz, **1** (69%)] ppm. $^{19}F\{^1H\}$ NMR: $\delta$ = –134.0 ($m_c$, **2h**), –144.7 ($m_c$, **2h**), –160.6 ($m_c$, **2h**) ppm.

**Theoretical Methods:** DFT calculations were carried out with the TURBOMOLE V5.8 program package.[24] For optimizations the gradient corrected exchange functional by Becke[25] (B88) in combination with the gradient corrected correlation functional by Lee, Yang, and Parr[26] (LYP) with the RI approximation[27] and the valence-double-ζ basis set SV(P)[28] was used. For tungsten the effective core potential ECP-60-MWB[29] derived from the Stuttgart-Dresden group was used. The influence of the polar solvent was taken into account by employing the COSMO approach[30] with $\varepsilon$ = 8.93. For cavity construction the atomic radii of Bondi[31] were used, which are obtained from crystallographic data. For tungsten the atomic radius was set to 2.2230 Å. The stationary points were characterized by numerical vibrational frequencies calculations by using the SNF 3.3.0 program package.[32] Single point calculations were carried out by using the Three Parameter Hybrid Functional Becke3[33] (B3) in combination with the LYP correlation functional[26] and the valence-triple-ζ basis set TZVP[34] and ECP-60-MWB for tungsten.

**Supporting Information** (see footnote on the first page of this article): Relative energies, enthalpies, and free energies for the reactions depicted in Schemes 4 and 5.

## Acknowledgments

We are grateful to the Deutsche Forschungsgemeinschaft, the Fonds der Chemischen Industrie (Kekulé Stipendium for H. H.), the SFB 624 "Template", the John von Neumann Institute for Computing (HBN12), and Prof. Dr. B. Engels for computing time. A. E. wishes to acknowledge the grants from MEC-Spain (CTQ 2004–02201) and Fundación Séneca (CARM-Spain) (02970/PI/05). We thank G. von Frantzius for fruitful discussions.

[1] M. Schmittel, A. Burghart, *Angew. Chem.* **1997**, *109*, 2658–2699; *Angew. Chem. Int. Ed. Engl.* **1997**, *36*, 2550–2589.
[2] E. Baciocchi, M. Bietti, O. Lanzalunga, *Acc. Chem. Res.* **2000**, *33*, 243–251.
[3] M. Mella, M. Fagnoni, M. Freccero, A. Albini, *Chem. Soc. Rev.* **1998**, *27*, 81–89.
[4] A. A. Fokin, P. R. Schreiner, *Chem. Rev.* **2002**, *102*, 1551–1593.
[5] N. G. Connelly, W. E. Geiger, *Chem. Rev.* **1996**, *96*, 877–910.
[6] C. Gaebert, J. Mattay, M. Toubartz, S. Steenken, B. Müller, T. Bally, *Chem. Eur. J.* **2005**, *11*, 1294–1304.
[7] K. E. Torraca, L. McElwee-White, *Coord. Chem. Rev.* **2000**, *206–207*, 469–491.

 © 2007 Wiley-VCH Verlag GmbH & Co. KGaA, Weinheim 

[8] For example, see: U. Jahn, P. Hartmann, *Chem. Commun.* **1998**, 209–210, and references cited therein.
[9] T. Ramnial, I. McKenzie, B. Gorodetsky, E. M. W. Tsang, J. A. C. Clyburne, *Chem. Commun.* **2004**, 1054–1055.
[10] a) R. Streubel, A. Kusenberg, J. Jeske, P. G. Jones, *Angew. Chem.* **1994**, *106*, 2564–2566; *Angew. Chem. Int. Ed. Engl.* **1994**, *33*, 2427–2429; b) R. Streubel, J. Jeske, P. G. Jones, R. Herbst-Irmer, *Angew. Chem.* **1994**, *106*, 115–117; *Angew. Chem. Int. Ed. Engl.* **1994**, *33*, 80–82; c) R. Streubel, A. Kusenberg, *Phosphorus Sulfur Relat. Elem.* **1994**, *93–94*, 281–284; d) R. Streubel, A. Ostrowski, S. Priemer, U. Rohde, J. Jeske, P. G. Jones, *Eur. J. Inorg. Chem.* **1998**, 257–261.
[11] a) F. G. N. Cloke, P. B. Hitchcock, J. F. Nixon, U. Schiemann, R. Streubel, D. J. Wilson, *Chem. Commun.* **2000**, 1659–1660; b) H. Wilkens, A. Ostrowski, J. Jeske, F. Ruthe, P. G. Jones, R. Streubel, *Organometallics* **1999**, *18*, 5627–5642; c) R. Streubel, H. Wilkens, P. G. Jones, *Chem. Commun.* **1999**, 2127–2128; d) H. Wilkens, F. Ruthe, P. G. Jones, R. Streubel, *Chem. Eur. J.* **1998**, *4*, 1542–1553; e) R. Streubel, H. Wilkens, A. Ostrowski, C. Neumann, F. Ruthe, P. G. Jones, *Angew. Chem.* **1997**, *109*, 1549–1550; *Angew. Chem. Int. Ed. Engl.* **1997**, *36*, 1492–1493.
[12] R. Streubel, H. Wilkens, P. G. Jones, *Chem. Eur. J.* **2000**, *6*, 3997–4000.
[13] a) R. Streubel, C. Neumann, P. G. Jones, *J. Chem. Soc. Dalton Trans.* **2000**, 2495–2496; b) C. Neumann, E. Ionescu, U. Schiemann, M. Schlenker, M. Bode, F. Ruthe, P. G. Jones, R. Streubel, *J. Organomet. Chem.* **2002**, *643–644*, 253–264; c) C. Neumann, A. Prehn Junquera, C. Wismach, P. G. Jones, R. Streubel, *Tetrahedron* **2003**, *59*, 6213–6220.
[14] The numbering of atoms in heterocyclic complexes **3a**–**h** according to the Hantzsch-Widmann-Patterson nomenclature is used in this paper.
[15] P. W. Atkins, *Physical Chemistry*, 5th ed., Oxford University Press, Oxford, **1994**.
[16] Cyclovoltammetric measurements did not reveal conclusive results.
[17] M. A. Alvarez, G. García, M. E. García, V. Riera, M. A. Ruiz, *Organometallics* **1999**, *18*, 4509–4517.
[18] The ease of electrophilic aromatic substitution increases in the order: thiophene < furane < pyrrol. For example, see: D. T. Davies, *Aromatic Heterocyclic Chemistry*, Oxford University Press, Oxford, **1992**.
[19] X-ray crystallographic analysis of **3d**: Suitable yellow single crystals of **3d** were obtained from a concentrated *n*-pentane solution upon decreasing the temperature from ambient temperature to +4 °C. Data were collected with a Nonius KappaCCD diffractometer equipped with a low-temperature device (Cryostream, Oxford Cryosystems) at 123 K by using graphite monochromated Mo-$K_\alpha$ radiation ($\lambda$ = 0.71073 Å). The structure was solved by Patterson methods (SHELXS-97)[20a] and refined by full-matrix least-squares on $F^2$ (SHELXL-97).[20b] All non-hydrogen atoms were refined anisotropically. The hydrogen atoms were included isotropically by using the riding model on the bound atoms. The thiophene substituent is disordered [occupancy: 0.81(1): 0.19(1)]. Semiempirical absorption correction was carried out from equivalents (min./max. transmissions = 0.27295/0.61685). $C_{24}H_{27}N_2O_5PSSi_2W$; crystal size 0.45 × 0.30 × 0.12 mm, triclinic, $P\bar{1}$ (No.2), $a$ = 10.9114(2) Å, $b$ = 12.1675(2) Å, $c$ = 13.1114(2) Å, $\alpha$ = 96.695(1)°, $\beta$ = 110.108(1)°, $\gamma$ = 109.554(1)°, $V$ = 1486.63(4) Å$^3$, $Z$ = 2, $\rho_{calcd.}$ = 1.623 Mg m$^{-3}$, $2\theta_{max}$ = 55°, collected (independent) reflections = 14224 (6590), $R_{int}$ = 0. 0716, $\mu$ = 4.124 mm$^{-1}$, 318 refined parameters, 51 restraints, $R_1$ [for $I > 2\sigma(I)$] = 0. 0361, $wR_2$ (for all data) = 0.0935, max./min. residual electron density = 2.745/–3.017 e Å$^{-3}$. X-ray crystallographic analysis of **3b**, **3e**: Crystals were obtained from a concentrated *n*-pentane solution. Data were collected with a Bruker SMART 1000 CCD diffractometer equipped with a low-temperature device. Structure solution and refinement as above. **3b**: $C_{26}H_{32}N_3O_5PSi_2W$; crystal size 0.19 × 0.14 × 0.06 mm, triclinic, $P\bar{1}$ (No.2), $a$ = 10.823(2) Å, $b$ = 12.207(2) Å, $c$ = 13.395(3) Å, $\alpha$ = 96.101(6)°, $\beta$ = 110.126(6)°, $\gamma$ = 107.666(6)°, $V$ = 1538.7(5) Å$^3$, $Z$ = 2, $\rho_{calcd.}$ = 1.592 Mg m$^{-3}$, $2\theta_{max}$ = 60°, collected (independent) reflections = 30876 (8933), $R_{int}$ = 0.0501, $\mu$ = 3.92 mm$^{-1}$, 351 refined parameters, 63 restraints, $R_1$ [for $I > 2\sigma(I)$] = 0. 0451, $wR_2$ (for all data) = 0.1125, max./min. residual electron density = 3.80/–5.13 e Å$^{-3}$. **3e**: $C_{24}H_{27}N_2O_5PSSi_2W$; crystal size 0.35 × 0.23 × 0.16 mm, triclinic, $P\bar{1}$ (No. 2), $a$ = 10.8501(12) Å, $b$ = 12.2138(12) Å, $c$ = 13.1138(14) Å, $\alpha$ = 96.171(3)°, $\beta$ = 110.016(3)°, $\gamma$ = 110.191(3)°, $V$ = 1481.5(3) Å$^3$, $Z$ = 2, $\rho_{calcd.}$ = 1.629 Mg m$^{-3}$, $2\theta_{max}$ = 61°, collected (independent) reflections = 24334 (8967), $R_{int}$ = 0. 0250, $\mu$ = 4.14 mm$^{-1}$, 331 refined parameters, 31 restraints, $R_1$ [for $I > 2\sigma(I)$] = 0. 0179, $wR_2$ (for all data) = 0.0455, max./min. residual electron density = 1.417/–1.308 e Å$^{-3}$. CCDC-646819 (for **3b**), -639472 (for **3d**), and -646820 (for **3e**) contain the supplementary crystallographic data for this paper. These data can be obtained free of charge from The Cambridge Crystallographic Data Centre via www.ccdc.cam.ac.uk/data_request/cif.
[20] a) SHELXS-97: G. M. Sheldrick, *Acta Crystallogr., Sect. A* **1990**, *46*, 467–473; b) G. M. Sheldrick, SHELXL-97, University of Göttingen, **1997**.
[21] H. Helten, T. Schirmeister, B. Engels, *J. Phys. Chem. A* **2004**, *108*, 7691–7701.
[22] R. Streubel, *Top. Curr. Chem.* **2002**, *223*, 91–101.
[23] The model reaction using **4** and $H_2NCN$ may be representative for the reaction of **1** with $Me_2NCN$ (**2a**), but also for the reactions with the electron-rich five-membered heterocyclic nitrile derivatives **2b**–**e**.
[24] TURBOMOLE V5.8: see http://www.cosmologic.de/Quantum-Chemistry/ main_turbomole.html.
[25] A. D. Becke, *Phys. Rev. A* **1988**, *38*, 3098–3100.
[26] C. Lee, W. Yang, R. G. Parr, *Phys. Rev. B* **1988**, *37*, 785–789.
[27] a) K. Eichkorn, O. Treutler, H. Öhm, M. Häser, R. Ahlrichs, *Chem. Phys. Lett.* **1995**, *240*, 283–290; b) K. Eichkorn, O. Treutler, H. Öhm, M. Häser, R. Ahlrichs, *Chem. Phys. Lett.* **1995**, *242*, 652–660; c) K. Eichkorn, F. Weigend, O. Treutler, R. Ahlrichs, *Theor. Chem. Acc.* **1997**, *97*, 119–124.
[28] A. Schäfer, H. Horn, R. Ahlrichs, *J. Chem. Phys.* **1992**, *97*, 2571–2577.
[29] D. Andrae, U. Häußermann, M. Dolg, H. Stoll, H. Preuß, *Theor. Chim. Acta* **1990**, *77*, 123–141.
[30] A. Klamt, G. Schürmann, *J. Chem. Soc. Perkin Trans. 2* **1993**, 799–805.
[31] A. Bondi, *J. Phys. Chem.* **1964**, *68*, 441–451.
[32] J. Neugebauer, M. Reiher, C. Kind, B. A. Hess, *J. Comput. Chem.* **2002**, *23*, 895–910.
[33] A. D. Becke, *J. Chem. Phys.* **1993**, *98*, 5648–5652.
[34] A. Schäfer, C. Huber, R. Ahlrichs, *J. Chem. Phys.* **1994**, *100*, 5829–5835.

Received: June 27, 2007
Published Online: August 22, 2007

 © 2007 Wiley-VCH Verlag GmbH & Co. KGaA, Weinheim 

DOI: 10.1002/ejic.200700402

# Organometallic and Classical Coordination Sites in Highly Preorganized Pyrazolate-Based Hybrid Systems: The Mn/Ni Case

**Huaxin Zhang,[a] Sebastian Dechert,[a] Michael Linseis,[b] Rainer F. Winter,[b] and Franc Meyer*[a]**

**Keywords:** Bridging ligands / Cyclopentadienyl ligands / Manganese / Nickel / Heterometallic complexes

A series of unsymmetric heterodinuclear Mn/Ni complexes is reported in which an organometallic $CpMn(CO)_2$ fragment and a classical Werner-type nickel(II) subunit are arranged in close proximity by means of a bridging pyrazolate. The two metalloligand scaffolds (**1** and **2**) employed differ in the chelate size of the tripodal tetradentate $\{N_4\}$ binding site for nickel. Molecular structures have been determined for ($\mathbf{1}_{-H}$)-Ni($NO_3$) (**3**), ($\mathbf{2}_{-H}$)Ni($NO_3$) (**4**), and ($\mathbf{2}_{-H}$)Ni(OAc) (**5**). Comparison with the molecular structures of the related Mn/Mn, Mn/Co, and Mn/Zn systems confirms that structural flexibility is greater for the complexes based on ligand **2** due to the longer chelate arms. According to IR and UV/Vis spectroelectrochemistry, oxidation of the heterobimetallic systems is highly localized at the organometallic manganese site. Structural and spectroscopic features as well as trends for the redox potentials of the $Mn^I/Mn^{II}$ couple suggest that ligand variations at the nickel(II) Werner-type subunit exert only a small influence on the properties of the organometallic part. In contrast, reduction occurs at the nickel site and is strongly dependent on the anion present. The effects at the organometallic $CpMn(CO)_2$ subunit upon reduction of the proximate nickel ion are most pronounced for **5**.
(© Wiley-VCH Verlag GmbH & Co. KGaA, 69451 Weinheim, Germany, 2007)

## Introduction

The pyrazolate heterocycle is a well established and useful bridging unit in bimetallic complexes.[1] Further preorganization of the two metal ions as well as modulation of their structural and electronic properties can be achieved by attaching chelating side arms to the 3- and 5-positions of the heterocycle.[2,3] The majority of such pyrazolate-derived dinucleating ligand scaffolds are symmetric, which means that these scaffolds provide two identical coordination pockets and favor the formation of homobimetallic complexes. Unsymmetrical pyrazolate ligands that allow the targeted assembly of heterobimetallic complexes, despite the intriguing metal ion cooperativity that can be expected for those systems,[4] are relatively scarce due to their more laborious synthesis.[5] An interesting situation with respect to the mutual effects of the proximate metal ions arises when the distinction between the two binding sites becomes very pronounced, such as in hybrid systems that contain an organometallic subunit next to a classical Werner-type subunit.

We have recently reported a series of unsymmetrical homo- and heterobimetallic complexes of type **A** that formally combine an organometallic $CpMn(CO)_2$ fragment **B** and a classical subunit of type **C** (Scheme 1).[6–8] The latter is reminiscent of the tripodal tetradentate tris(pyridylmethyl)amine systems that are well established in mononuclear coordination chemistry.[9] Manganese(II), cobalt(II), or zinc(II) ions with different co-ligands X can be accommodated in the Werner-type compartment of complexes **A**, with only subtle changes of the spectroscopic and redox properties of the organometallic site.[6–8] It appears that the two metal ions in these complexes are electronically quite independent. In contrast, strong electronic coupling was observed in the symmetric dimanganese complex **D**, which was shown to undergo two sequential metal-centered one-electron oxidations with fast intramolecular thermal electron transfer ($k_{ET} \approx 2.6 \times 10^{10}\ s^{-1}$ at 298 K) in the mixed-valent $Mn^IMn^{II}$ species, which has a formal low-spin $d^5d^6$ electronic configuration.[10] The coincidence of the π plane of the heterocycle with the mirror plane of the $Mn(CO)_2$ moiety in **D** is an ideal arrangement for Mn-pyrazolate π-interactions and hence for electronic communication between the two Mn centers.[10–12]

In the present work we have now investigated a series of new heterobimetallic complexes of type **A** with nickel(II) in the tripodal tetradentate $\{N_4\}$ coordination site and different counteranions Y. A large separation of the metal-centered redox potentials was anticipated for this particular combination since oxidation of the manganese ion might

[a] Institut für Anorganische Chemie, Georg-August-Universität Göttingen
Tammanstraße 4, 37077 Göttingen, Germany
Fax: +49-551-393063
E-mail: franc.meyer@chemie.uni-goettingen.de
[b] Institut für Anorganische Chemie, Universität Regensburg
Universitätsstraße 31, 93040 Regensburg, Germany
Supporting information for this article is available on the WWW under http://www.eurjic.org or from the author.

 © 2007 Wiley-VCH Verlag GmbH & Co. KGaA, Weinheim 

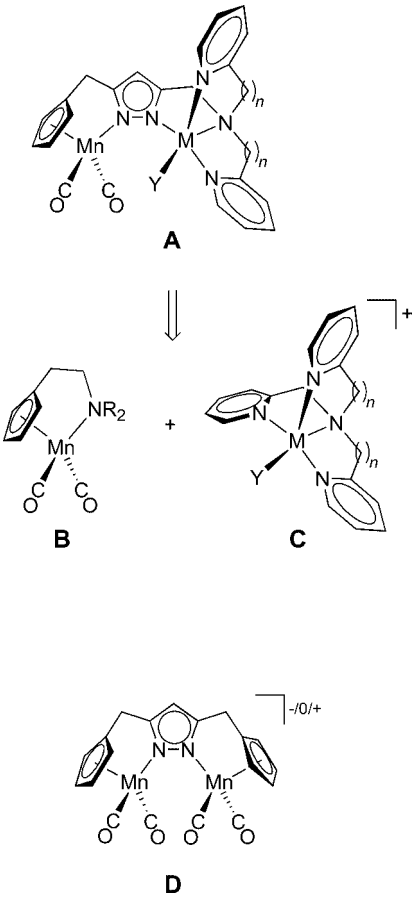


Scheme 1.

occur easily while nickel(I) or nickel(III) should be much harder to access. It therefore appeared interesting to probe whether one-electron redox processes would be strictly confined to one site and to what extent a mutual influence of the adjacent metal ions might be discernible for the Mn/Ni case.

## Results and Discussion

### Synthesis and Structural Characterization of the Complexes

Cymantrene derivatives **1** and **2** are the basic scaffolds for this particular class of heterobimetallic complexes (Scheme 2). They were prepared in several steps from simple pyrazole derivatives as reported previously,[6] with different lengths of the pyridylalkyl side-arms appended to the pyrazole heterocycle. The latter variation allows us to probe the effect of small changes of the Werner-type $\{N_4\}$ binding pockets on the properties of the bimetallic array. Photolysis of **1** or **2** with a high pressure mercury lamp in a quartz tube at –40 °C leads to CO release and intramolecular coordination of the pyrazole nitrogen atom to manganese, and subsequent deprotonation with one equivalent of KO*t*Bu followed by addition of the appropriate nickel salt [$Ni(NO_3)_2 \cdot 6H_2O$ or $Ni(OAc)_2 \cdot 4H_2O$] fills the $\{N_4\}$ donor compartment. This synthetic sequence is best carried out as a one-pot reaction.

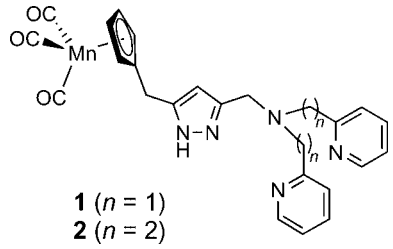


Scheme 2.

Single crystals of **3**·dmf, **4**, and **5** were obtained by slow diffusion of $Et_2O$ into dmf solutions of the products (Scheme 3), and details of the constitution of all three complexes were elucidated by X-ray crystallography. The molecular structures are depicted in Figures 1, 2, and 3, together with selected interatomic distances and bond angles.

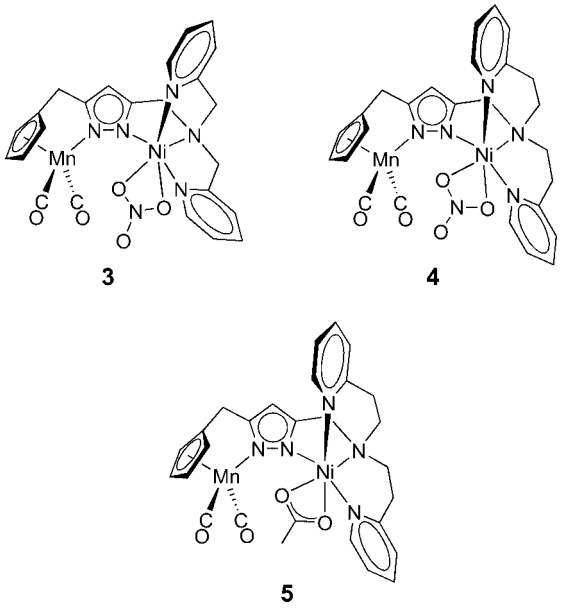


Scheme 3. Heterobimetallic Mn/Ni complexes.

The pyrazolate bridges the two metal ions in all three complexes **3**–**5** and the nickel(II) is hosted in the classical $\{N_4\}$ coordination site, as anticipated. Only complex **3** features crystallographically imposed mirror symmetry. Sixfold coordination of the nickel ion is completed by (slightly asymmetric) bidentate coordination of either a nitrate (**3**, **4**) or acetate anion (**5**), which results in a strongly distorted octahedral environment of the metal center. The metal–metal separation depends strongly on the length of the ligand side-arms. Thus, a larger Mn···Ni distance of around 4.50 Å is induced by the longer chelate arms in **4** and **5** whereas a distinctly shorter distance of 4.25 Å is observed for **3**. This variation is accompanied by different chelate arrangements of the Werner-type site: in the case of the shorter side-arms (**3**) the pyridyl nitrogens are located *trans* to each other and a nitrate oxygen is *trans* to the pyrazolate

 © 2007 Wiley-VCH Verlag GmbH & Co. KGaA, Weinheim 

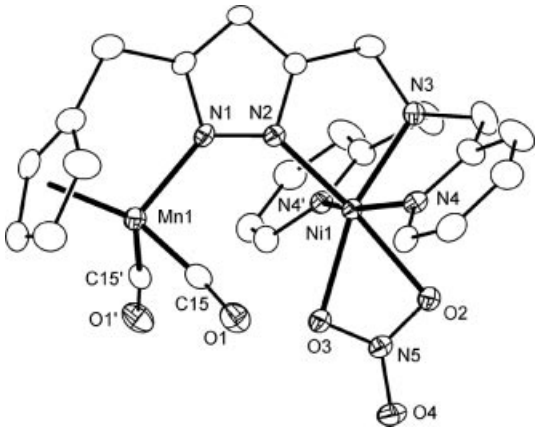


Figure 1. ORTEP plot (30% probability thermal ellipsoids) of the molecular structure of **3**. All hydrogen atoms have been omitted for the sake of clarity. Selected bond distances [Å] and angles [°] (Cg1 defines the centroid of the Cp ring atoms): Mn1–Cg1 1.771(3), Mn1–N1 2.017(4), Mn1–C15 1.764(4), Mn1···Ni1 4.247(1), Ni1–O2 2.192(4), Ni1–O3 2.093(4), Ni1–N2 2.008(4), Ni1–N3 2.090(4), Ni1–N4 2.064(3), O1–C15 1.165(5); Cg1–Mn1–N1 111.9(2), Cg1–Mn1–C15 124.0(2), C15–Mn(1)–C15′ 91.8(3), C15–Mn1–N1 100.1(2), O1–C15–Mn1 174.1(3), N2–Ni1–N3 84.5(2), N2–Ni1–N4 94.5(1), N2–Ni1–O2 174.1(2), N2–Ni1–O3 113.3(2), N3–Ni1–N4 82.1(1), N3–Ni1–O2 101.5(2), N3–Ni1–O3 162.2(2), N4–Ni1–N4′ 160.9(2), N4–Ni1–O2 86.4(1), N4–Ni1–O3 95.9(1), O2–Ni1–O3 60.8(1). Symmetry transformation used to generate equivalent atoms: (′) *x*, 3/2 – *y*, *z*.

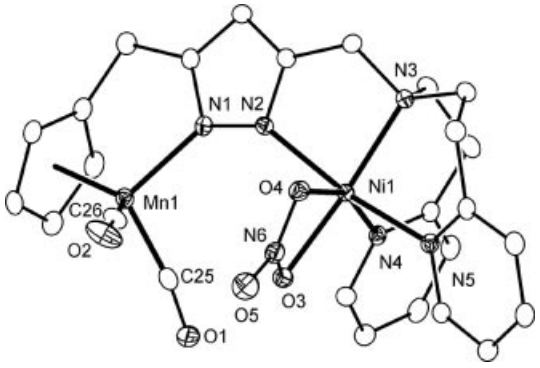


Figure 2. ORTEP plot (30% probability thermal ellipsoids) of the molecular structure of **4**. All hydrogen atoms have been omitted for the sake of clarity. Selected bond distances [Å] and angles [°] (Cg1 defines the centroid of the Cp ring atoms): Mn1–Cg1 1.773(1), Mn1–N1 2.050(2), Mn1–C25 1.760(3), Mn1–C26 1.766(3), Mn1···Ni1 4.5091(5), Ni1–O3 2.109(2), Ni1–O4 2.208(2), Ni1–N2 2.100(2), Ni1–N3 2.110(2), Ni1–N4 2.058(2), Ni1–N5 2.122(2), O1–C25 1.171(3), O2–C26 1.167(3); Cg1–Mn1–N1 112.8(1), Cg1–Mn1–C25 124.0(1), Cg1–Mn1–C26 123.7(1), C25–Mn(1)–C26 90.3(1), C25–Mn1–N1 104.9(1), C26–Mn1–N1 95.9(1), O1–C25–Mn1 170.9(2), O2–C26–Mn1 174.9(2), N2–Ni1–N3 81.9(1), N2–Ni1–N4 100.9(1), N2–Ni1–N5 166.9(1), N2–Ni1–O3 98.1(1), N2–Ni1–O4 88.6(1), N3–Ni1–N4 96.6(1), N3–Ni1–N5 90.8(1), N3–Ni1–O3 165.3(1), N3–Ni1–O4 105.3(1), N4–Ni1–N5 90.7(1), N4–Ni1–O3 97.9(1), N4–Ni1–O4 157.3(1), N5–Ni1–O3 86.1(1), N5–Ni1–O4 82.7(1), O3–Ni1–O4 60.1(1).

nitrogen, while for the longer side-arms (**4**, **5**) the pyrazolate is found *trans* to a pyridine nitrogen. Similar features and differences of the Mn···M separation of approximately 0.3 Å have been found for related Mn/Zn and Mn/Co com-

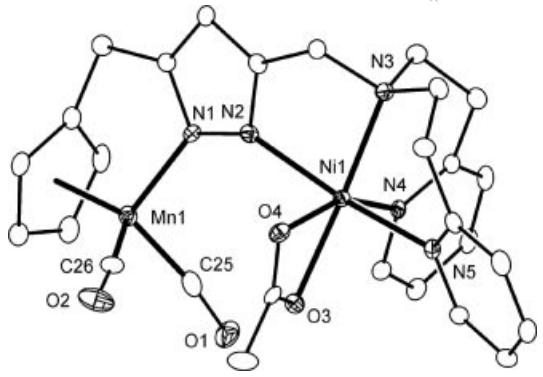


Figure 3. ORTEP plot (30% probability thermal ellipsoids) of the molecular structure of **5**. All hydrogen atoms have been omitted for the sake of clarity. Selected bond distances [Å] and angles [°] [Cg(1) defines the centroid of the Cp ring atoms]: Mn1–Cg1 1.773(2), Mn1–N1 2.045(3), Mn1–C25 1.751(5), Mn1–C26 1.759(5), Mn1···Ni1 4.507(1), Ni1–O3 2.072(3), Ni1–O4 2.193(3), Ni1–N2 2.118(3), Ni1–N3 2.114(4), Ni1–N4 2.075(3), Ni1–N5 2.143(3), O1–C25 1.184(5), O2–C26 1.174(5); Cg1–Mn1–N1 112.7(1), Cg1–Mn1–C25 123.8(2), Cg1–Mn1–C26 123.9(2), C25–Mn(1)–C26 90.3(2), C25–Mn1–N1 104.5(2), C26–Mn1–N1 96.5(2), O1–C25–Mn1 171.2(4), O2–C26–Mn1 174.3(5), N2–Ni1–N3 81.5(1), N2–Ni1–N4 101.0(1), N2–Ni1–N5 166.0(1), N2–Ni1–O3 100.2(1), N2–Ni1–O4 89.0(1), N3–Ni1–N4 95.9(1), N3–Ni1–N5 89.9(1), N3–Ni1–O3 166.6(1), N3–Ni1–O4 105.0(1), N4–Ni1–N5 90.8(1), N4–Ni1–O3 96.8(1), N4–Ni1–O4 158.0(1), N5–Ni1–O3 85.7(1), N5–Ni1–O4 82.5(1), O3–Ni1–O4 61.9(1).

plexes with the same pyrazole-based ligands.[6,8] The binding mode of the acetate or nitrate co-ligand (chelating, semi-chelating, or monodentate) depends on the radii and the particular stereoelectronic preferences of the metal ion in the $\{N_4\}$ binding pocket.

The Ni–O/N bond lengths of **3**–**5** lie within the range usually reported for octahedral nickel(II) complexes with a comparable $N_4O_2$ coordination sphere.[13] In particular, embedding of the nickel ion in the $\{N_4\}$ pocket is reminiscent of the situation found for a mononuclear nickel(II) acetate complex of type **C** with the tripodal tetradentate tris(pyridylmethyl)amine (TPA) ligand **E**.[14] This is in line with the description of complexes **3**–**5** as hybrids of an organometallic type **B** and a classical type **C** subunit. In the case of **E**, however, the acetate co-ligand is only monodentate and the remaining coordination site is occupied by a water molecule.

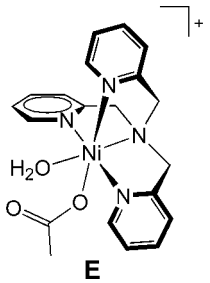


**E**

A comparison of the Mn–Cg (Cg defines the centroid of the ring atoms of the cyclopentadienido-anion), Mn–CO, Mn–N, and C≡O bond lengths of **3**–**5** and related Mn/Zn,

 © 2007 Wiley-VCH Verlag GmbH & Co. KGaA, Weinheim 

Table 1. Comparison of selected bond lengths [Å] and angles [°].

| | Mn only[6] | Mn···Mn[7] | Mn···Co[8] | Mn···Zn[6] | Mn···Ni |
|---|---|---|---|---|---|
| Mn–Cg | 1.77 | 1.76–1.77 | 1.76–1.77 | 1.77 | 1.77 |
| Mn–N | 2.01–2.02 | 2.01–2.03 | 2.01–2.05 | 1.99–2.03 | 2.02–2.05 |
| Mn–CO | 1.77–1.78 | 1.76–1.78 | 1.75–1.77 | 1.76–1.77 | 1.75–1.77 |
| C≡O | 1.16–1.17 | 1.16–1.17 | 1.17–1.20 | 1.16–1.19 | 1.17–1.18 |
| Cg–Mn–N | 111.2 | 111.6–112.7 | 112.1–112.5 | 110.8–112.5 | 111.9–112.8 |
| Cg–Mn–CO | 123.9–127.2 | 121.2–126.0 | 121.7–125.0 | 122.4–128.3 | 123.7–124.0 |
| CO–Mn–CO | 89.4–91.4 | 91.4–92.8 | 93.4–93.8 | 90.3–93.2 | 90.3–91.8 |
| CO–Mn–N | 96.0–102.2 | 94.8–102.7 | 99.5–104.1 | 94.6–101.4 | 95.9–104.9 |

Mn/Co, and Mn/Mn complexes, as well as complexes where the $\{N_4\}$ site is unoccupied, reveals that the choice of metal in the classical Werner-type site seems to have only a small influence on the bonding parameters of the organometallic $CpMn(CO)_2$ site (Table 1). Only the CO–Mn–N angles appear to be somewhat flexible and span a range from 94.8° to 104.1° (Table 1).

In order to visualize the extent of preorganization and the flexibility of the dimetallic arrangement based on **1** and **2**, a superposition of the pyrazolate-bridged cores of all Mn/Mn, Mn/Co, Mn/Ni, and Mn/Zn dinuclear complexes with either short or long chelate arms is shown in Figure 4. Structural variations should reflect the conformational freedom of the pyrazolate-centered dimetallic array, with the metal ions swinging above and below the heterocyclic plane. It seems that the range of displacements out of the plane of the pyrazolate heterocycle that is accessible to the two metal ions is greater in the case of the longer (and more flexible) side-arms at the $\{N_4\}$ compartment. The maximum angle between the pyrazolate plane and the N1–Mn bond is 11.1° for systems derived from **1** and 22.5° for systems derived from **2**; the maximum angle between the pyrazolate plane and the N2–M bond is 14.5° for systems derived from **1** and 17.9° for systems derived from **2**.

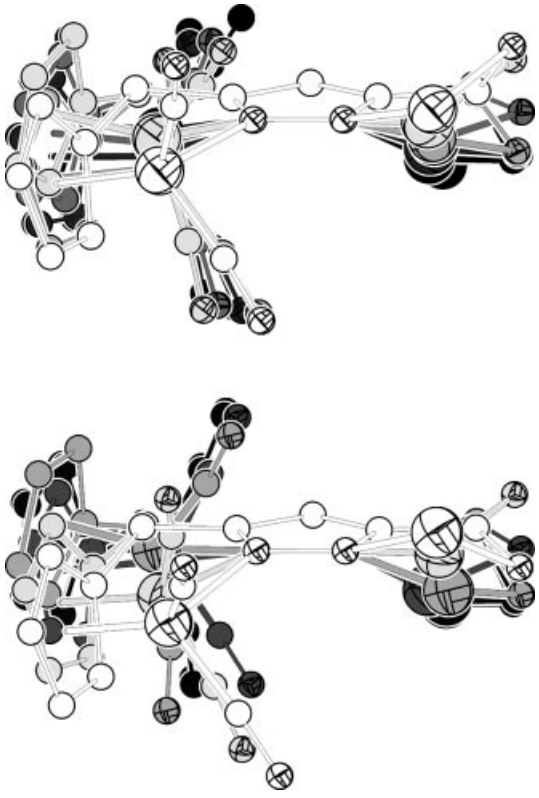

Figure 4. Overlay of the pyrazolate-bridged heterobimetallic arrangements for the series of Mn/Mn, Mn/Co, Mn/Ni, and Mn/Zn complexes based on **1** (short chelate arms; top) or **2** (long chelate arms; bottom). The appended chelate arms and the co-ligands at the Werner-type site have been omitted for clarity.

### Spectroscopic and Electrochemical Trends

All Mn/Ni complexes show two strong IR bands of similar relative intensities for the $\nu_{as}(CO)$ and $\nu_s(CO)$ vibrations of the $\{Mn(CO)_2\}$ fragment at around 1900 and 1825 $cm^{-1}$, respectively (Table 2). Neither the chelate ring size of the $\{N_4\}$ ligand compartment (**3** vs. **4**) nor the co-ligand at nickel (nitrate in **4** vs. acetate in **5**) seem to have any considerable effect on the energies of the CO stretches. Complex **5** features strong bands at 1550 and 1447 $cm^{-1}$ that are absent in the spectrum of **4** and are thus assigned to the acetate ligand. The small difference between $\nu_{as}(COO)$ and $\nu_s(COO)$ is in accordance with bidentate acetate coordination.[15]

Table 2. IR absorptions [$cm^{-1}$] in the CO stretching range.

| | dce solution[a] | KBr pellets |
|---|---|---|
| **3** | 1902, 1825 | 1902, 1822 |
| **3**$^+$ | 2029, 1949 | |
| **4** | 1906, 1829 | 1906, 1822 |
| **4**$^+$ | 2029, 1950 | |
| **5** | 1904, 1827 | 1890, 1823 |
| **5**$^+$ | 2029, 1950 | |

[a] dce = 1,2-dichloroethane.

Cyclic voltammograms in MeCN (**3**) or dmf (**4**, **5**) solution feature a reversible redox wave in the range $E_{1/2}$ = –0.50 to –0.66 V and an irreversible reduction at much lower potential (Table 3).[16] The cyclic voltammograms of **4** and **5** depicted in Figures 5 and 6, respectively, show that variations in the co-ligand at nickel (nitrate in **4** vs. acetate in **5**) barely influence the first redox process at around –0.6 V but have a pronounced effect on the reduction at lower potential. The former is thus assigned to the $Mn^I/Mn^{II}$ couple while the latter process likely corresponds to the $Ni^{II} \rightarrow Ni^I$ reduction. Potentials for the $Mn^I/Mn^{II}$ interconversions of $[CpMn(CO)_2L]$ complexes are known to

 © 2007 Wiley-VCH Verlag GmbH & Co. KGaA, Weinheim 

vary over a potential range of more than 2 V, depending of the nature of the ligand L.[11,12,17] The rather low oxidation potentials of **3**–**5** indicate significant stabilization of the $Mn^{II}$ state by the anionic pyrazolate ligand and reflect the high nucleophilicity of the nitrogen heterocycle in these heterobimetallic species.[17] Small influences of the ligand chelate ring size (**3** vs. **4**) or of the co-ligand at nickel (**4** vs. **5**) on the $Mn^{I}/Mn^{II}$ redox potential suggest a certain degree of electronic communication between the proximate metal ions. For example, the oxidation wave of the nitrate complex with shorter chelate arms at nickel (**3**) is shifted anodically by 60 mV with respect to the congener with longer chelate arms (**4**), and the more electron-donating acetate at nickel facilitates oxidation of the manganese site by 100 mV (**5** vs. **4**). These trends are in good agreement with findings for the related Mn/Mn, Mn/Co, and Mn/Zn systems.[6–8]

Table 3. Formal potentials for the $Mn^{I}/Mn^{II}$ couple in MeCN/0.1 M $n$Bu$_4$NClO$_4$ (**3**) or dmf/0.1 M $n$Bu$_4$NPF$_6$ (**4**, **5**).[16]

| Complex | $E_{1/2}(Mn^{I}Ni^{II}/Mn^{II}Ni^{II})$ | $E^{p}_{red}(Mn^{I}Ni^{II}/Mn^{I}Ni^{I})$ |
|---|---|---|
| **3** | –0.50 | –1.70[a] |
| **4** | –0.56 | –1.83[a] |
| **5** | –0.66 | –2.72[a] |

[a] Peak potentials for irreversible reduction process at 100 mV s$^{-1}$.

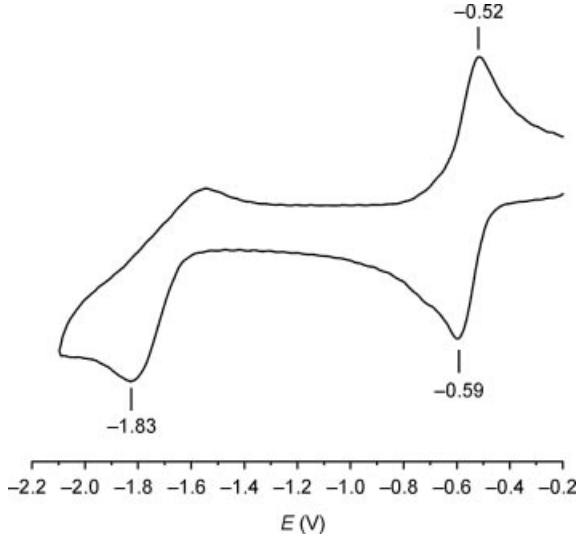


Figure 5. Cyclic voltammogram of **4** recorded with a platinum electrode in dmf containing approximately 0.1 M $n$Bu$_4$NPF$_6$; scan speed: 100 mV s$^{-1}$; potentials are given in volts vs. the Fc/Fc$^+$ couple.

IR and UV/Vis spectroelectrochemistry have proven valuable for establishing the site of redox processes in such heterobimetallic complexes and to characterize the resulting species. Oxidation of the Mn/Ni systems **3**–**5** in 1,2-dichloroethane (dce) was thus followed by IR and UV/Vis spectroscopy in an OTTLE cell (Figures 7 and 8, and Figures S1–S4 in the Supporting Information). The intensity of the pair of CO stretching vibrations at around 1905 and 1825 cm$^{-1}$ decreases at the expense of two new bands at around 2030 and 1950 cm$^{-1}$ upon gradual electrolysis, thus confirming the structural integrity of the $CpMn(CO)_2$ frag-

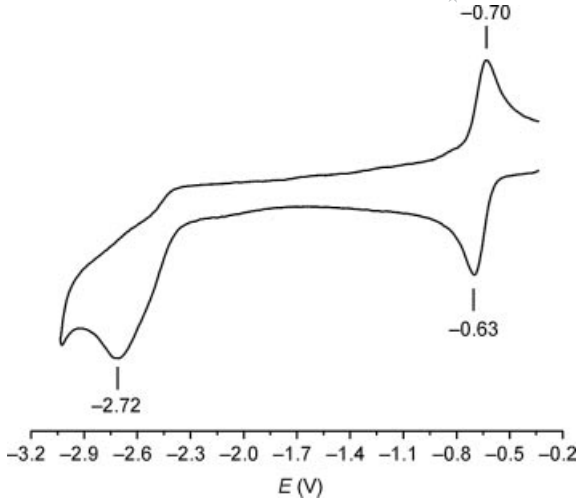


Figure 6. Cyclic voltammogram of **5** recorded with a platinum electrode in dmf containing approximately 0.1 M $n$Bu$_4$NPF$_6$; scan speed: 100 mV s$^{-1}$; potentials are given in volts vs. the Fc/Fc$^+$ couple.

ment upon generation of the oxidized species **3**$^+$–**5**$^+$. The slightly lower intensity of the new bands is in agreement with our expectations since spectral intensities in M–CO moieties usually decrease with increasing oxidation state.[18] The shift of about 125 cm$^{-1}$ to higher frequencies is very similar to the shift observed in the corresponding Mn/Zn, Mn/Co and Mn/Mn complexes.[6–8] It is typical for a one-unit increase in the oxidation state of the metal ion and reflects the diminished backbonding ability in the oxidized $CpMn^{II}(CO)_2$ subunit. This confirms that the anodic process in the present Mn/Ni systems is fully localized at the organometallic site, which means that nickel remains in the +II oxidation state. The presence of several isosbestic points confirms clean conversion between the $Mn^{I}Ni^{II}$ and $Mn^{II}$-$Ni^{II}$ species. However, the original spectra of the starting materials **3**–**5** are not fully restored upon re-reduction. Furthermore, the intensities of the CO stretching vibrations

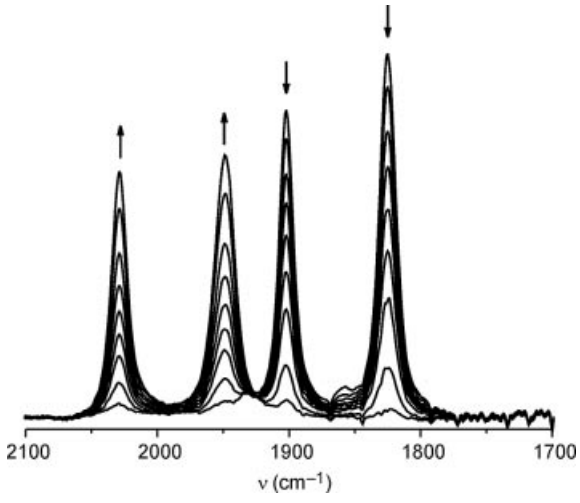


Figure 7. IR spectroscopic changes during the gradual oxidation of **3** in dce/$n$Bu$_4$PF$_6$ solution in an OTTLE cell.

 © 2007 Wiley-VCH Verlag GmbH & Co. KGaA, Weinheim 

are somewhat lower than their original values, which suggests that the oxidized complexes have only limited stabilities in solution. Accordingly, attempts to crystallize the $Mn^{II}Ni^{II}$ complexes after chemical oxidation have so far proved unsuccessful.

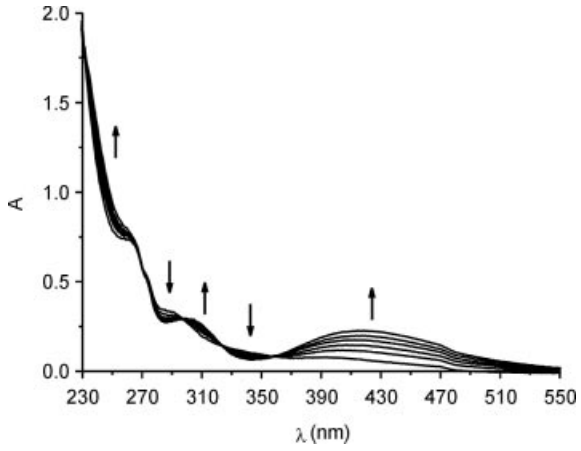


Figure 8. UV/Vis spectroscopic changes during the gradual oxidation of **3** in dce/$n$Bu$_4$PF$_6$ solution in an OTTLE cell.

The oxidation of **3**–**5** is accompanied in UV/Vis spectroelectrochemistry by the appearance of a new band peaking in the range 395–421 nm (**3**: 415 nm; **4**: 396 nm; **5**: 421 nm, Figure 8 and S3, S4). The rise of a similar band at about 400 nm has also been observed upon oxidation of the corresponding Mn/Zn, Mn/Co and Mn/Mn systems[6–8] and can thus be safely assigned to the π(pyrazolate)→CpMn$^{II}$-(CO)$_2$ LMCT transition, which is obviously relatively insensitive to the identity of the metal ion within the adjacent Werner-type {N$_4$} compartment.

According to IR spectroelectrochemistry, reduction of **4** is also an almost reversible process. Shifts to lower energy in the CO stretching range are only minor (Figures 9 and 10; 1906/1829→1902/1827 cm$^{-1}$ for **4**; 1906/1829→1896/1819 cm$^{-1}$ for **5**), in accordance with the idea that reduction occurs within the nickel subunit. It is interesting to note, however, that the CO stretches are clearly more affected in **5**, where a noticeable shift of 10 cm$^{-1}$ is observed compared to an almost negligible shift of about 3 cm$^{-1}$ for **4**. Since **4** and **5** are derived from the same pyrazolate-based ligand scaffold, this distinction must stem solely from the different anion at nickel (nitrate vs. acetate). Re-oxidation of **5**$^-$ does not reproduce the original spectrum but gives rise to a new species with two IR bands that are shifted by 18 cm$^{-1}$ to lower energy with respect to the CO absorptions of **5**. While the typical pattern of two CO stretches suggests that the integrity of the CpMn(CO)$_2$ subunit is retained, the chemical reaction that apparently follows upon electrochemical reduction may involve a ligand exchange at nickel or ligand fragmentation at the Werner-type site. The rather different behavior of **4** and **5** upon reduction is in accordance with the strongly different reduction potentials determined electrochemically for these two complexes (compare Figures 5 and 6).

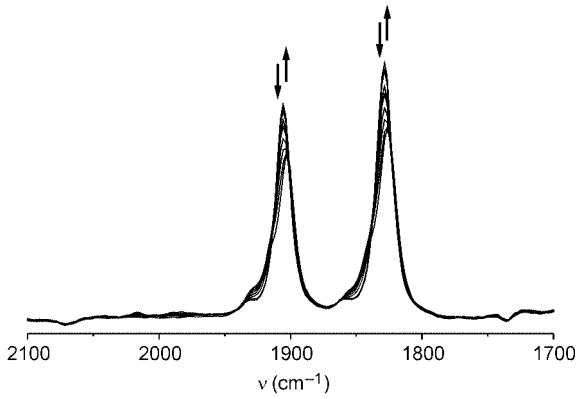


Figure 9. IR spectroscopic changes during the gradual reduction of **4** in dce/$n$Bu$_4$PF$_6$ solution in an OTTLE cell.

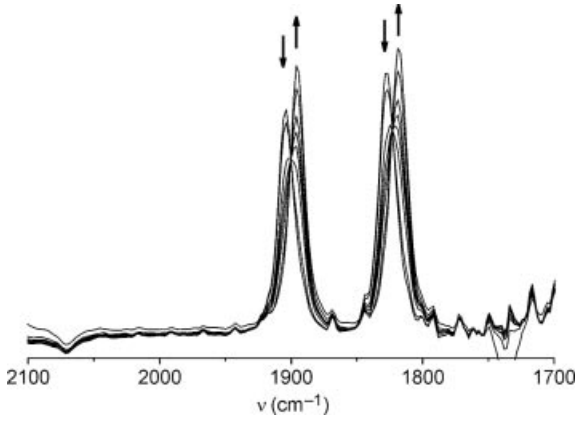


Figure 10. IR spectroscopic changes during the gradual reduction of **5** in dce/$n$Bu$_4$PF$_6$ solution in an OTTLE cell.

## Conclusions

The present set of Mn/Ni complexes complements a series of unique heterobimetallic systems in which an organometallic CpMn(CO)$_2$ fragment is bridged via a pyrazolate to a nearby metal ion ($Mn^{2+}$, $Co^{2+}$, $Ni^{2+}$, $Zn^{2+}$) that is nested in a classical Werner-type compartment with an {N$_4$} donor set. The pronounced asymmetry of the bimetallic array results in strong localization of redox events in those systems: oxidation occurs at relatively low potential and is strictly confined to the organometallic site, while reduction (in the case of $Mn^{2+}$, $Co^{2+}$, or $Ni^{2+}$ as the second metal ion) appears to occur solely within the Werner-type subunit, with very little mutual interaction. Ligand variations at the {N$_4$} compartment (such as different lengths of the chelate arms or different co-ligands) exert only minor influences on the CpMn(CO)$_2$ fragment, but have a clear effect on the properties of the second metal ion, as expected. Further modifications of the Werner-type subunit, including donor sets other than the tripodal tetradentate {N$_4$} motif of the present complexes, should allow us to shift the redox potential of the second metal ion closer to that of the organometallic Mn site. It will be interesting to monitor the changes of intermetallic communication that might accompany such modifications and to probe the co-

 © 2007 Wiley-VCH Verlag GmbH & Co. KGaA, Weinheim 

operative redox transformation of substrates that bind to the second metal but exploit the strong reduction potential of the nearby organometallic site.

## Experimental Section

**General Procedures and Methods:** Manipulations were carried out under an atmosphere of dry nitrogen by employing standard Schlenk techniques. Complexes **1** and **2** were prepared as reported previously.[6] Solvents were dried according to established procedures. All other chemicals were obtained from commercial sources and used as received. IR spectra were recorded for KBr pellets with a Digilab Excalibur. ESI mass spectra were measured with a Finnigan MAT LCQ spectrometer. Elemental analyses were performed by the analytical laboratory of the Institut für Anorganische Chemie der Universität Göttingen using a Heraeus CHN-O-RAPID instrument. Cyclic voltammetry was carried out with a Perkin–Elmer Model 263A potentiostat/galvanostat with glassy carbon working electrode and platinum reference and counter electrodes, in 0.1 M $n$Bu$_4$NClO$_4$/CH$_3$CN or 0.1 M $n$Bu$_4$NPF$_6$/dmf; ferrocene (the potential in dmf being 0.45 V against SCE)[19] was used as internal standard. Spectroelectrochemistry (IR and UV/Vis) was performed with a self-constructed OTTLE cell comprising a Pt-mesh working and counter electrode and a silver wire as pseudeo-reference electrode sandwiched in between the $CaF_2$ windows of a conventional liquid IR cell. The working electrode is positioned in the center of the spectrometer beam with all other parts of the cell made non-transparent to the incident beam by means of an absorbing tape.[20]

**Synthesis of Complex 3:** A solution of **1** (0.256 g, 0.52 mmol) in thf (200 mL) was irradiated with a high-pressure mercury lamp in a quartz tube at –40 °C. Within one hour the color of the solution had changed from light yellow to yellow. The solution was then warmed to room temperature and KO$t$Bu (0.058 g, 0.52 mmol) and Ni(NO$_3$)$_2$·6H$_2$O (0.151 g, 0.52 mmol) were added. The reaction mixture was stirred overnight to produce a yellow precipitate, which was separated by filtration, washed with light petroleum ether, and dried under vacuum. Single crystals were obtained after several days by slow diffusion of diethyl ether into a concentrated dmf solution of the crude product. The crystals were separated by filtration, washed with diethyl ether, and dried under vacuum. Yield: 31 mg (9%). IR (KBr): $\tilde{\nu}$ = 2929 (w), 2869 (w), 1902 (vs), 1822 (vs), 1672 (m), 1605 (m), 1479 (m), 1384 (m), 1287 (m), 1157 (w), 1097 (w), 1056 (w), 1024 (w), 958 (w), 884 (w), 818 (w), 771 (m), 653 (w), 611 (w), 588 (w), 512 (w), 474 (w), 427 (w) cm$^{-1}$. $C_{27}H_{28}MnN_7NiO_6$ (660.2): calcd. C 49.12, H 4.27, N 14.85; found C 49.27, H 4.44, N 13.98.

**Synthesis of Complex 4:** A solution of **2** (0.230 g, 0.44 mmol) in thf (200 mL) was irradiated with a high pressure mercury lamp in a quartz tube at –40 °C. Within about one hour the color of the solution had changed from light yellow to yellow. The solution was then warmed to room temperature and KO$t$Bu (0.049 g, 0.44 mmol) and Ni(NO$_3$)$_2$·6H$_2$O (0.128 g, 0.44 mmol) were added. The reaction mixture was stirred overnight to produce a yellow precipitate, which was separated by filtration, washed with light petroleum, and dried under vacuum. Single crystals were obtained after several days by slow diffusion of diethyl ether into a concentrated dmf solution of the crude product. The crystals were separated by filtration, washed with diethyl ether, and dried under vacuum. Yield: 40 mg (15%). IR (KBr): $\tilde{\nu}$ = 2963 (w), 2916 (w), 2864 (w), 1906 (vs), 1822 (vs), 1662 (w), 1607 (m), 1578 (w), 1487 (m), 1451 (m), 1387 (m), 1340 (w), 1276 (m), 1155 (w), 1105 (m), 1052 (w), 1022 (m), 950 (w), 807 (w), 765 (m), 656 (w), 591 (w), 528 (w), 474 (w), 432 (w) cm$^{-1}$. HR-MS (ESI+, MeCN): $m/z$ calcd. for $C_{26}H_{25}MnN_6NiO_5$ [M]$^+$: 614.06149; found 614.06132. $C_{26}H_{25}MnN_6NiO_5$ (615.2): calcd. C 50.77, H 4.10, N 13.66; found C 49.50, H 4.27, N 13.62.

**Synthesis of Complex 5:** A solution of **2** (0.200 g, 0.38 mmol) in thf (200 mL) was irradiated with a high pressure mercury lamp in a quartz tube at –40 °C. Within about one hour the color of the solution had changed from light yellow to yellow. The solution was

Table 4. Crystal data and refinement details for **3**, **4**, and **5**.

| | **3**·dmf | **4** | **5** |
|---|---|---|---|
| Formula | $C_{24}H_{21}MnN_6NiO_5$, $C_3H_7NO$ | $C_{26}H_{25}MnN_6NiO_5$ | $C_{28}H_{28}MnN_5NiO_4$ |
| $M_r$ | 660.21 | 615.17 | 612.20 |
| Crystal size [mm] | 0.38 × 0.25 × 0.15 | 0.49 × 0.31 × 0.20 | 0.20 × 0.13 × 0.08 |
| Crystal system | monoclinic | monoclinic | monoclinic |
| Space group | $P2_1/m$ (no. 11) | $P2_1/n$ (no. 14) | $P2_1/n$ (no. 14) |
| $a$ [Å] | 8.2387(6) | 9.8289(6) | 9.8625(8) |
| $b$ [Å] | 16.1559(8) | 21.7710(15) | 22.0007(18) |
| $c$ [Å] | 11.2310(7) | 11.8129(7) | 12.1508(11) |
| $\beta$ [°] | 107.879(5) | 99.659(5) | 101.311(7) |
| $V$ [Å$^3$] | 1422.69(15) | 2491.9(3) | 2585.3(4) |
| $Z$ | 2 | 4 | 4 |
| $\rho_{calcd.}$ [g cm$^{-3}$] | 1.541 | 1.640 | 1.573 |
| $F$(000) | 680 | 1264 | 1264 |
| $\mu$ [mm$^{-1}$] | 1.160 | 1.314 | 1.262 |
| $T_{max}/T_{min}$ | 0.8422/0.6728 | 0.7909/0.6217 | 0.8754/0.6491 |
| $hkl$ range | ±9, ±18, ±13 | ±11, –25 to 24, ±13 | –11 to 10, ±25, ±14 |
| $\theta$ range [°] | 1.91–24.69 | 1.87–24.83 | 1.85–24.81 |
| Measured reflections | 23598 | 15798 | 13272 |
| Unique reflections [$R_{int}$] | 2516 [0.0641] | 4270 [0.0405] | 4434 [0.0993] |
| Observed reflections $I > 2\sigma(I)$ | 2159 | 3460 | 2844 |
| Data/restraints/parameters | 2516/2/210 | 4270/0/352 | 4434/0/353 |
| Goodness-of-fit | 1.066 | 1.002 | 1.005 |
| $R1$ [$I > 2\sigma(I)$] | 0.0498 | 0.0293 | 0.0492 |
| $wR2$ (all data) | 0.1480 | 0.0706 | 0.0669 |
| Residual electron density [e Å$^{-3}$] | 1.505/–0.538 | 0.313, –0.320 | 0.451/–0.401 |

 © 2007 Wiley-VCH Verlag GmbH & Co. KGaA, Weinheim 

then warmed to room temperature and KO*t*Bu (0.043 g, 0.38 mmol) and $Ni(CH_3COO)_2 \cdot 4H_2O$ (0.095 g, 0.38 mmol) were added. The reaction mixture was stirred overnight to produce a yellow precipitate, which was separated by filtration, washed with light petroleum, and dried under vacuum. Single crystals were obtained after several days by slow diffusion of diethyl ether into a concentrated dmf solution of the crude product. The crystals were separated by filtration, washed with diethyl ether, and dried under vacuum. Yield: 36 mg (16%). IR (KBr): $\tilde{\nu}$ = 2964 (w), 2917 (m), 2861 (w), 1890 (vs), 1823 (vs), 1666 (m), 1607 (m), 1550 (m), 1478 (m), 1447 (m), 1335 (m), 1259 (m), 1208 (w), 1148 (w), 1107 (m), 1052 (m), 1021 (m), 950 (w), 896 (w), 812 (m), 771 (m), 668 (w), 608 (w), 528 (w), 467 (w), 433 (w), 410 (w) $cm^{-1}$. HR-MS (ESI+, MeCN): *m*/*z* calcd. for $C_{28}H_{28}MnN_5NiO_4$ $[M]^+$: 611.08698; found 611.08634. $C_{28}H_{28}MnN_5NiO_4$ (612.2): calcd. C 54.93, H 4.61, N 11.44; found C 53.91, H 4.70, N 11.36.

**X-ray Crystallography of Complexes 3–5:** X-ray data were collected with a STOE IPDS II diffractometer (graphite-monochromated Mo-$K_\alpha$ radiation, $\lambda$ = 0.71073 Å) using the ω-scans technique at –140 °C (Table 4). The structures were solved by direct methods and refined on $F^2$ using all reflections with SHELX-97.[21] The non-hydrogen atoms were refined anisotropically. Hydrogen atoms were placed in calculated positions and assigned an isotropic displacement parameter of 0.08 $Å^2$. Face-indexed absorption corrections were performed numerically with the program X-RED.[22] The geometrical aspects of the structures were analyzed with the PLATON program.[23] The dmf solvent molecule in **3**·dmf was found to be disordered about a center of inversion and was refined at half occupancy.

CCDC-638867 (for **3**·dmf), -638868 (for **4**), and -638869 (for **5**) contain the supplementary crystallographic data for this paper. These data can be obtained free of charge from The Cambridge Crystallographic Data Centre via www.ccdc.cam.ac.uk/data_request/cif.

**Supporting Information** (see also the footnote on the first page of this article): IR spectroscopic changes during gradual oxidation **4**→**4**$^+$ and **5**→**5**$^+$ in dce/$n$Bu$_4$PF$_6$ solution in an OTTLE cell (Figures S1 and S2); UV/Vis spectroscopic changes during gradual oxidation **4**→**4**$^+$ and **5**→**5**$^+$ in dce/$n$Bu$_4$PF$_6$ solution in an OTTLE cell (Figures S3 and S4).

## Acknowledgments

Support by the Alexander von Humboldt foundation (research fellowship to H. Z.) is gratefully acknowledged. We thank J. Teichgräber for performing the CV measurements.

[1] a) S. Trofimenko, *Progr. Inorg. Chem.* **1986**, *34*, 115–210; b) G. La Monica, G. A. Ardizzoia, *Progr. Inorg. Chem.* **1997**, *46*, 151–238; c) R. Mukherjee, *Coord. Chem. Rev.* **2000**, *203*, 151–218.
[2] C. Incarvito, A. L. Rheingold, A. L. Gavrilova, C. J. Qin, B. Bosnich, *Inorg. Chem.* **2001**, *40*, 1386–1390.
[3] J. Klingele, S. Dechert, F. Meyer, *Coord. Chem. Rev.*, manuscript in preparation.
[4] a) D. E. Fenton, H. Okawa, *Chem. Ber./Recueil* **1997**, *130*, 433–442; b) D. E. Fenton, *Inorg. Chem. Commun.* **2002**, *5*, 537–547; c) R. Bosnich, *Inorg. Chem.* **1999**, *38*, 2554–2562; d) C. J. Qin, A. Gavrilova, B. Bosnich, *Pure Appl. Chem.* **2001**, *73*, 221–226; e) C. Belle, J.-L. Pierre, *Eur. J. Inorg. Chem.* **2003**, 4137–4146.
[5] a) M. Konrad, F. Meyer, K. Heinze, L. Zsolnai, *J. Chem. Soc. Dalton Trans.* **1998**, 199–205; b) M. Konrad, S. Wuthe, F. Meyer, E. Kaifer, *Eur. J. Inorg. Chem.* **2001**, 2233–2240.
[6] a) J. C. Röder, F. Meyer, E. Kaifer, *J. Organomet. Chem.* **2002**, *641*, 113–120; b) T. Sheng, S. Dechert, A. C. Stückl, F. Meyer, *Eur. J. Inorg. Chem.* **2005**, 1293–1302.
[7] T. Sheng, S. Dechert, I. Hyla-Kryspin, R. F. Winter, F. Meyer, *Inorg. Chem.* **2005**, *44*, 3863–3874.
[8] H. Zhang, S. Dechert, J. Maurer, M. Linseis, R. F. Winter, F. Meyer, *J. Organomet. Chem.* **2007**, *692*, 2956–2964.
[9] A. G. Blackman, *Polyhedron* **2005**, *24*, 1–39.
[10] a) J. C. Röder, F. Meyer, E. Kaifer, *Angew. Chem.* **2002**, *114*, 2414–2417; *Angew. Chem. Int. Ed.* **2002**, *41*, 2304–2306; b) J. C. Röder, F. Meyer, I. Hyla-Kryspin, R. F. Winter, E. Kaifer, *Chem. Eur. J.* **2003**, *9*, 2636–2648.
[11] K. G. Caulton, *Coord. Chem. Rev.* **1981**, *38*, 1–43.
[12] W. Kaim, R. Gross, *Comments Inorg. Chem.* **1988**, *7*, 269–285.
[13] F. Meyer, H. Kozlowski, in *Comprehensive Coordination Chemistry II* (Eds.: J. A. McCleverty, T. J. Meyer), Elsevier, Oxford, UK, **2004**, vol. 6, pp. 247–554.
[14] T. Nagataki, Y. Tachi, S. Itoh, *Chem. Commun.* **2006**, 4016–4018.
[15] a) G. B. Deacon, R. J. Phillips, *Coord. Chem. Rev.* **1980**, *33*, 227–250; b) V. Robert, G. Lemercier, *J. Am. Chem. Soc.* **2006**, *128*, 1183–1187.
[16] Values vs. the ferrocene/ferrocenium couple. $\Delta E_p = E_p^{ox} - E_p^{red}$ = 64 (for **3**), 88 (for **4**), or 65 mV (for **5**) with $\Delta E_p(Cp_2Fe/Cp_2Fe^+)$ = 60 (for **3**), 69 (for **4**), or 80 mV (for **5**) under the same experimental conditions.
[17] R. Gross, W. Kaim, *Angew. Chem.* **1985**, *97*, 869–870; *Angew. Chem. Int. Ed. Engl.* **1985**, *24*, 856–858; P. M. Zizelman, C. Amatore, K. Kochi, *J. Am. Chem. Soc.* **1984**, *106*, 3771–3784.
[18] a) J. P. Bullock, K. R. Mann, *Inorg. Chem.* **1989**, *28*, 4006–4011; b) D. T. Pierce, W. E. Geiger, *Inorg. Chem.* **1994**, *33*, 373–381.
[19] N. G. Connelly, W. E. Geiger, *Chem. Rev.* **1996**, *96*, 877–910.
[20] M. Kreijcik, M. Daniek, F. Hartl, *J. Electroanal. Chem.* **1991**, *317*, 179–187.
[21] G. M. Sheldrick, *SHELXL-97, Program for Crystal Structure Refinement*, University of Göttingen, Germany, **1997**; G. M. Sheldrick, *SHELXS-97, Program for Crystal Structure Solution*, University of Göttingen, Germany, **1997**.
[22] *X-RED*, STOE & CIE GmbH, Darmstadt, **2002**.
[23] A. L. Spek, *PLATON, A Multipurpose Crystallographic Tool*, Utrecht University, **2003**.

Received: April 12, 2007
Published Online: August 22, 2007

 © 2007 Wiley-VCH Verlag GmbH & Co. KGaA, Weinheim 

DOI: 10.1002/ejic.200700493

# Environmentally Friendly Growth of Layered $K_4Nb_6O_{17}$ Crystals from a KCl Flux

**Katsuya Teshima,*[a] Yuki Niina,[a] Kunio Yubuta,[b] Takaomi Suzuki,[a] Nobuo Ishizawa,[c] Toetsu Shishido,[b] and Shuji Oishi[a]**

**Keywords:** Flux growth / Environmental chemistry / Layered compounds / Photocatalyst

Environmentally friendly, high-quality layered $K_4Nb_6O_{17}$ crystals were easily grown by two different flux methods involving supersaturation, that is, flux evaporation and cooling of the solution. To fabricate them, potassium chloride (KCl) was chosen as the flux. Transparent and colorless plate-like layered crystals of $K_4Nb_6O_{17}$ were prepared with well-developed {010} faces of the orthorhombic system. The crystal sizes obviously depended on the evaporation loss (evaporation method), the holding temperature, and the cooling rate (cooling method). Transmission electron microscopy (TEM) images showed that the grown plate-like crystals were of a very good crystallinity. The major constituents were homogeneously distributed throughout them. The crystals exhibited good photocatalytic activity under ultraviolet light irradiation. Potassium chloride was found to be a very suitable flux for the environmentally friendly growth of photocatalytic $K_4Nb_6O_{17}$ crystals.

(© Wiley-VCH Verlag GmbH & Co. KGaA, 69451 Weinheim, Germany, 2007)

## Introduction

A variety of metal oxide compounds were studied for use as semiconductor photocatalysts, such as degradation of toxic substances, decomposition of pure water, and photoactive electrodes for dye-sensitized solar cells.[1–5] Photoinduced decomposition of pure water on $TiO_2$ electrodes was first reported in 1972.[4a] After this discovery, $TiO_2$ was widely studied, and has now became one of the most well-known semiconductor photocatalysts. Titanium(IV) oxide has several advantages, for example, it is harmlessness to the environment, it has a low cost, and it is highly stable. It, however, does not work efficiently as a photocatalyst under visible light irradiation, because it has a relatively wide bandgap of 3.0–3.2 eV.[4] Numerous attempts have, therefore, been made to improve its performance under visible light irradiation. In a few decades, several kinds of metal oxides, such as titanates, niobates, tantalates, and multioxides have also been found to exhibit photocatalytic performance.

The crystal of potassium hexaniobate ($K_4Nb_6O_{17}$), which is one kind of metal niobate, is orthorhombic with the space group $P2_1nb$.[6a] $K_4Nb_6O_{17}$ was reported to have lattice parameters of $a$ = 0.783 nm, $b$ = 3.321 nm, and $c$ = 0.646 nm, and a density of 3.898 g cm$^{-3}$.[3,6a] The congruent melting point of this compound is 1163 °C.[7] From a crystal structure viewpoint, $K_4Nb_6O_{17}$ is unique in that it is layered (Figure 1),[6b] and it consists of negatively charged sheets of linked $NbO_6$ octahedral units with potassium ions between the sheets. A variety of characteristics of the layered $K_4Nb_6O_{17}$ crystals, such as their ability to undergo ion exchange and photocatalysis, as well as their intercalation properties, are attributed to their unique crystal structure (layered structure).

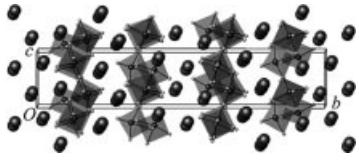


Figure 1. Schematic representation of the layered structure of $K_4Nb_6O_{17}$.

There have been many studies on $K_4Nb_6O_{17}$ crystallite syntheses and single crystal growth including flux growth, the Czochralski method, and solid-state reactions.[1,5a,8,9] Among these techniques, flux growth is an environmentally friendly process[10] and can produce $K_4Nb_6O_{17}$ crystals at temperatures below the melting point of the solute. In previous research, the following fluxes were used successfully: $K_2CO_3$, $K_2MoO_4$, and $K_2WO_4$.[5a,8] For the $K_2CO_3$ flux, however, detailed results such as the optimal growth conditions, crystal structure, size, and photocatalytic activity have not been described.[8] In our previous study,[5a] $K_4Nb_6O_{17}$

[a] Department of Environmental Science and Technology, Faculty of Engineering, Shinshu University, Nagano 380–8553, Japan
Fax: +81-26-269-5550
E-mail: teshima@gipwc.shinshu-u.ac.jp
[b] Institute for Materials Research, Tohoku Univeristy, Sendai 980–8577, Japan
[c] Ceramics Research Laboratory, Nagoya Institute of Technology, Gifu 507–0071, Japan

 © 2007 Wiley-VCH Verlag GmbH & Co. KGaA, Weinheim 

crystals were grown from $K_2MoO_4$ and $K_2WO_4$ fluxes, and their photocatalytic and adsorption properties were examined in detail. Here we report the growth of high-quality $K_4Nb_6O_{17}$ plate-like crystals from a KCl flux at a growth temperature much less than the melting point of $K_4Nb_6O_{17}$. Furthermore, their photocatalytic properties were also evaluated. Potassium chloride has some advantages for the growth of $K_4Nb_6O_{17}$ crystals; its melting point (776 °C) is much lower than those of $K_2CO_3$ (891 °C), $K_2MoO_4$ (about 930 °C), and $K_2WO_4$ (921 °C) fluxes.[11–13] In addition, it has a common cation ($K^+$) with the solute. It is abundant in nature and is also harmless to human beings and the environment, much like NaCl. Furthermore, KCl is easily soluble in warm water. Until now, no report on the growth of $K_4Nb_6O_{17}$ crystals from a KCl flux has been published.

## Results and Discussion

Photocatalytic, layered, transparent, and colorless plate-like crystals of $K_4Nb_6O_{17}$ were grown from the KCl flux (Table 1, all growth runs). In addition, byproduct crystals of $KNbO_3$ (bulk) and $K_2Nb_8O_{21}$ (whisker) were also grown in runs 1 and 10, and in run 4, respectively. The typical $K_4Nb_6O_{17}$ crystals (Table 1, run 1, solute concentration = 1 mol-%, holding temperature = 1100 °C) grown by the evaporation of the KCl flux isothermally are shown in Figure 2. Well-developed layered crystals of $K_4Nb_6O_{17}$ were clearly observed, and printed characters beneath the crystals were obviously readable. Moreover, numerous small plate-like crystals were relatively regularly layered on the well-developed surface, and the growth process was implied on the grown $K_4Nb_6O_{17}$ surface (Figure 2b). The SEM photographs of typical layered $K_4Nb_6O_{17}$ crystals are shown in Figure 3. The holding temperatures are, respectively, (a) 900 (Table 1, run 6), (b) 1000 (Table 1, run 5), and (c) 1100 °C (Table 1, run 3). The grown crystals gradually adopted rounded corners with decreasing holding temperatures as clearly shown in Figure 3. The evaporation loss of the KCl flux increased with the holding temperatures. The crystal sizes were obviously dependent on the flux evaporation ratio (and the holding temperature). In general, flux evaporation had a considerable influence on crystal growth. In the case where the holding temperature was 900 °C, the flux evaporation loss and the median diameter (D50) were, respectively, only approximately 34 wt.-% and 11.2 μm. However, they drastically increased with holding temperature, reaching about 86 wt.-% and 30.3 μm at 1000 °C, and 96 wt.-% and 27.6 μm at 1100 °C. The crystals grown at the holding temperature of 1000 °C might be slightly larger than those grown at 1100 °C, because the evaporation rate of the KCl flux at 1000 °C was smaller than that at 1100 °C. In general, crystals could grow large when the evaporation rate was suitable. When the holding temperature was 900 °C or below, the driving force for crystal growth could not distinguish between flux evaporation and solution cooling (rapid cooling) after a power supply cut of the furnace, as the evaporation loss was sufficiently low.

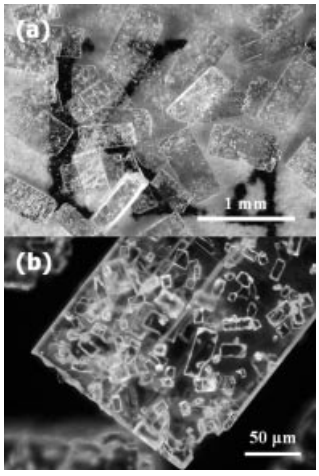


Figure 2. Optical micrographs showing plate-like $K_4Nb_6O_{17}$ crystals grown by the evaporation of a KCl flux: (a) low magnification and (b) high magnification.

Figure 4 shows the typical $K_4Nb_6O_{17}$ crystals grown by the cooling of the KCl flux (Figure 4a and b, Table 1, run 11; Figure 4c and d, Table 1, run 12). Like the $K_4Nb_6O_{17}$ crystals grown by the evaporation method (Figures 2 and 3), their basic form was a well-developed thin plate. There were a great number of the small plate-like crystals in the

Table 1. Typical growth conditions of the $K_4Nb_6O_{17}$ crystals.

| Run No. | Solute concentration / mol-% | Solute $K_2CO_3$ / g | Solute $Nb_2O_5$ / g | Flux KCl / g | Holding temperature / °C | Holding time / h | Cooling rate / °C h$^{-1}$ |
|---|---|---|---|---|---|---|---|
| 1 | 1 | 0.826 | 2.383 | 22.054 | 1100 | 60 | – |
| 2 | 10 | 4.171 | 12.033 | 10.124 | 1100 | 60 | – |
| 3 | 20 | 5.382 | 15.526 | 5.806 | 1100 | 60 | – |
| 4 | 40 | 6.297 | 18.166 | 2.546 | 1100 | 60 | – |
| 5 | 20 | 5.382 | 15.526 | 5.806 | 1000 | 60 | – |
| 6 | 20 | 5.382 | 15.526 | 5.806 | 900 | 60 | – |
| 7 | 20 | 5.382 | 15.526 | 5.806 | 1000 | 5 | 60 |
| 8 | 20 | 5.382 | 15.526 | 5.806 | 900 | 5 | 60 |
| 9 | 20 | 5.382 | 15.526 | 5.806 | 800 | 5 | 60 |
| 10 | 20 | 5.382 | 15.526 | 5.806 | 700 | 5 | 60 |
| 11 | 20 | 5.382 | 15.526 | 5.806 | 800 | 5 | 300 |
| 12 | 20 | 5.382 | 15.526 | 5.806 | 800 | 5 | >10000 |

 © 2007 Wiley-VCH Verlag GmbH & Co. KGaA, Weinheim 

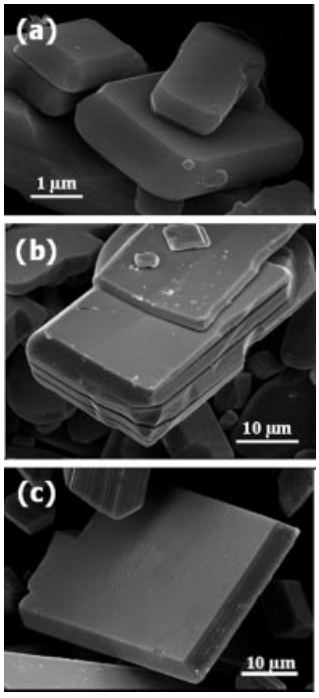


Figure 3. SEM images showing typical layered plate-like $K_4Nb_6O_{17}$ crystals grown by the evaporation of a KCl flux [holding temperature: (a) 900, (b) 1000, and (c) 1100 °C].

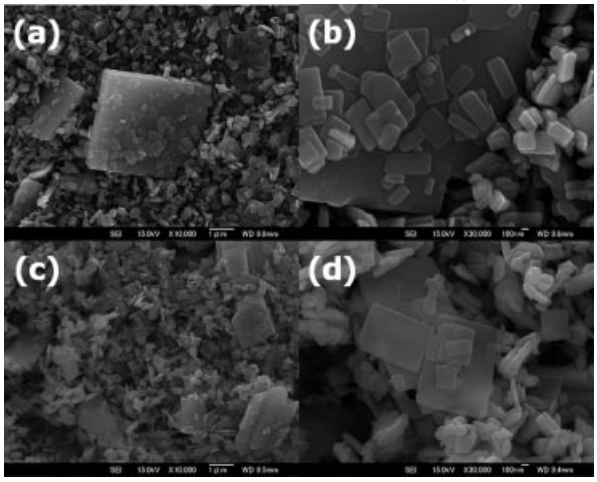


Figure 4. SEM images showing typical layered plate-like $K_4Nb_6O_{17}$ crystals grown by the rapid cooling of a KCl flux: (a) low magnification and (b) high magnification (Table 1, run 11, holding temperature 800 °C and cooling rate 300 °C $h^{-1}$), (c) low magnification and (d) high magnification (Table 1, run 12, 800 °C and quenching).

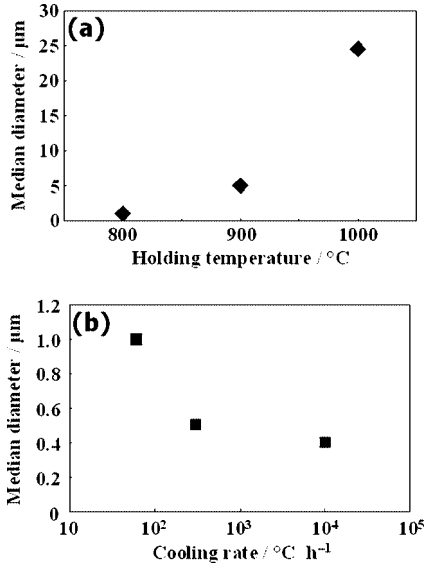


Figure 5. Variation in the median diameter of the $K_4Nb_6O_{17}$ crystals with (a) holding temperatures (solute content 20 mol-%, cooling rate 60 °C $h^{-1}$) and (b) cooling rates (solute content 20 mol-%, holding temperature 800 °C).

SEM image, although only a few of the relatively large crystals (>1 μm) were observed. However, relative to the evaporation method, the median diameters decreased drastically. Figure 5 shows the variation in the median diameter of the $K_4Nb_6O_{17}$ crystals grown by the cooling of the KCl flux with (a) the holding temperature and (b) the cooling rate. The cooling rate and the holding temperature were fixed at 60 °C $h^{-1}$ and 800 °C in Figure 5a and b, respectively. Small crystals with D50 = 1.0 μm were grown at a holding temperature of 800 °C (Figure 5a). The D50 values gradually increased with increasing holding temperatures, and they reached about 5.0 μm (900 °C) and 24.5 μm (1000 °C). In contrast, the median diameter gradually decreased with an increase in the cooling rate, and it reached 0.5 μm at 300 °C $h^{-1}$ and 0.4 μm at quenching (Figure 5b). In the previous studies, $K_4Nb_6O_{17}$ crystals were grown from a $K_2CO_3$ flux and by the Czochralski method at temperatures in excess of their melting points, or from $K_2MoO_4$ and $K_2WO_4$ fluxes at temperatures in excess of 1100 °C (in our laboratory). In this study, however, high-quality $K_4Nb_6O_{17}$ crystals were successfully grown from a KCl flux at temperatures from 800 to 1100 °C. To make environmentally functional materials, it is very important to reduce the environmental load. A low-temperature/rapid-cooling process is more environmentally friendly than other high-temperature flux ones[8] and our previous slow cooling one.[5a]

Figure 6 shows the XRD profiles of data for the well-developed layered crystals grown by the evaporation method (Figure 6a), pulverized crystallites grown by the evaporation method (Figure 6b) and by the cooling method (Figure 6c), and $K_4Nb_6O_{17}$ ICDD PDF[6] (Figure 6d). Both the grown crystals had approximately the same XRD pattern as ICDD PDF,[6] and they were identified as $K_4Nb_6O_{17}$. Byproduct crystals of $KNbO_3$ and $K_2Nb_8O_{21}$ were also identified by powder XRD patterns.[14,15] In our previous study,[5a] layered $K_4Nb_6O_{17}$ crystals were bound by two basal and eight sided faces. The indices of well-developed basal faces were {010}. In this study, the XRD patterns of oriented plate-like crystals showed that the diffraction intensity of the (040) plane was predominant, and the indices were the same as our previous study. Figure 7a and b show a bright field TEM image and the corresponding selected area diffraction (SAD) pattern of a typical crys-

 © 2007 Wiley-VCH Verlag GmbH & Co. KGaA, Weinheim 

tal grown by the flux evaporation method (Table 1, run 2). In Figure 7a, the existence of some facets, which are related to the *a* and *c* planes, is evidently observed at the upper, lower, and right regions. The SAD pattern indicated that the crystal has orthorhombic symmetry with lattice parameters $a$ = 0.769 nm and $c$ = 0.639 nm, which are in good agreement with those found in the previous study.[6] Because the incident electron beam is parallel to the [010] direction, the lattice parameter *b* cannot be measured by only this incident beam. The crystal planes in the SAD pattern were confirmed to be in accordance with a $K_4Nb_6O_{17}$ layered structure. The lattice image obtained from a $K_4Nb_6O_{17}$ crystal is shown in Figure 7c, which was taken with the incident beam along the [010] direction. The crystal was of very good crystallinity because no defects were observed in this image. From these TEM observations, the development of the *a*–*c* plane was clearly observed. With the consideration of the lattice parameters (extremely long *b* axis), it seems reasonable to develop the plane, and moreover, this is in good agreement with previous research[5a] and the XRD results as mentioned above. Additionally, the EDS data showed that potassium and niobium atoms were homogeneously distributed in the crystals. Chlorine atoms from the flux were not detected in the crystals.

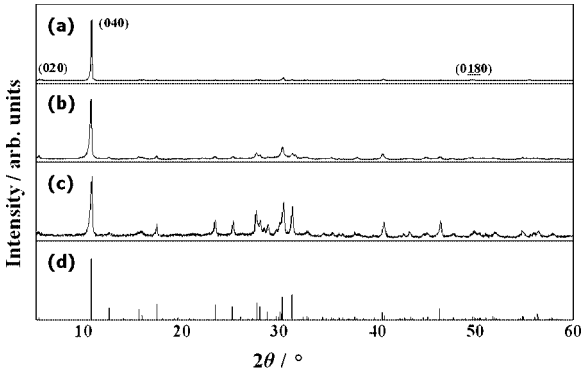


Figure 6. X-ray diffraction patterns (Cu-$K_\alpha$) of $K_4Nb_6O_{17}$ crystals: (a) plate-like crystals of which well-developed faces were laid in parallel with the holder plate (Table 1, run 4), (b) pulverized crystallites (evaporation method; Table 1, run 3), (c) pulverized crystallites (cooling method; Table 1, run 9), and (d) $K_4Nb_6O_{17}$ ICDD PDF.[6a]

The UV/Vis diffuse reflectance spectrum of the $K_4Nb_6O_{17}$ crystals was investigated. The spectrum (Figure 8) shows the onset wavelength of absorption at around 365 nm and a maximum at around 250 nm. Typical absorption spectra of $TiO_2$ (anatase) powders and $Na_2Ti_6O_{13}$ whiskers shift, respectively, to longer wavelength by about 35 and 15 nm at the onset. This result is in fair accord with that of our previous studies.[5a,5b] Furthermore, the $K_4Nb_6O_{17}$ layered crystals acted efficiently as a photocatalyst under UV light irradiation, and the characteristic colors of organic dyes (e.g., methylene blue and methyl orange) faded by the photocatalytic effect. For example, the pulverized $K_4Nb_6O_{17}$ crystals (0.5 g) and methylene blue

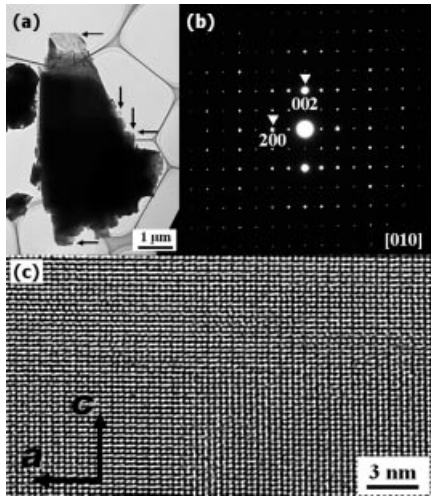


Figure 7. (a) TEM micrograph, (b) diffraction pattern, and (c) lattice image of a typical plate-like $K_4Nb_6O_{17}$ crystals.

(0.25 mg) were placed in distilled water (100 $cm^3$). The suspension was irradiated with UV light for 0–9 h. In this case, the color of the suspension decolorized gradually with an increase in irradiation time and finally changed from blue to colorless. The color of the suspension irradiated with UV light for 9 h was unchanged by the addition of any acid or base. When no $K_4Nb_6O_{17}$ crystal was added, the color of the methylene blue solution with UV light for 9 h remained unchanged.

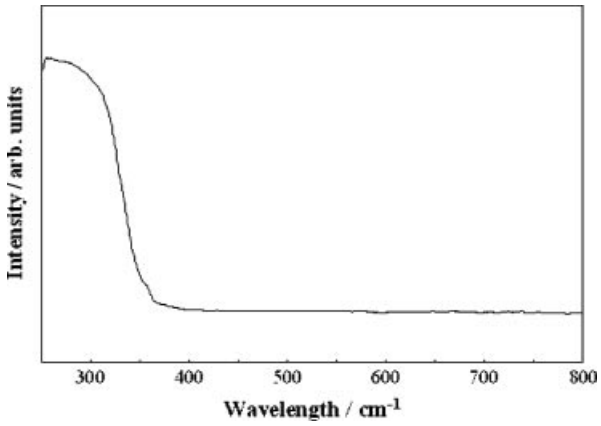


Figure 8. UV/Vis diffuse reflection spectrum of $K_4Nb_6O_{17}$ crystals.

## Conclusions

Highly crystalline photocatalytic crystals of $K_4Nb_6O_{17}$ were successfully grown by the evaporation or the rapid cooling of KCl used as the flux. Furthermore, this low holding temperature (ca. 800 °C)/rapid cooling (≥300 °C $h^{-1}$) technique is more environmentally friendly than other high-temperature flux techniques[8] and our previous slow cooling method.[5a] The layered $K_4Nb_6O_{17}$ crystals were trans-

 © 2007 Wiley-VCH Verlag GmbH & Co. KGaA, Weinheim 

parent and colorless, and they were plate-like in form with well-developed {010} faces (XRD analysis and TEM observation). The crystal sizes were dependent on the holding temperature and the cooling rate. In the case of the flux evaporation, the crystal sizes decreased gradually with a decrease in evaporation rate, and they reached 11.2 μm at 34 wt.-%. In contrast, for flux cooling, the crystal size drastically decreased with a decrease in holding temperature and gradually decreased with an increase in cooling rate, and the size was reduced to 0.4 μm (holding temperature of 800 °C and quenching). The obtained crystals had no defects (TEM observation) and major components were homogeneously distributed in the crystals (EDS analysis). Furthermore, plate-like layered $K_4Nb_6O_{17}$ crystals exhibited photocatalytic properties for organic dye decolorization. In our growth technique of functional oxide crystals, environmental damages (e.g., by exhausting greenhouse gases) and product costs are thought to be reduced greatly. In the future, it will become more and more important to develop various functional materials (including crystals) with the use of environmentally friendly processes.

## Experimental Section

Potassium hexaniobate layered crystals were grown by a cooling method and an evaporation method of the KCl flux. Reagent grade $K_2CO_3$ (Wako Pure Chemical Industries, Ltd.), $Nb_2O_5$ (99.9%, Wako Pure Chemical Industries, Ltd.), and KCl (Wako Pure Chemical Industries, Ltd.) were used for the growth of the $K_4Nb_6O_{17}$ crystals. A stoichiometric mixture of $K_2CO_3$ and $Nb_2O_5$ powders and KCl were, respectively, used as a solute and flux. The typical growth conditions are given in Table 1.

**Flux Evaporation Method:** The solute concentration was varied from 1 to 40 mol-% of the KCl flux. These masses of the reagents were kept at approximately 25 g for all growth runs (Table 1, runs 1–6). Each of the mixtures was put into platinum crucibles of 30-$cm^3$ capacity. After the lids were loosely closed, the crucibles were placed in an electric furnace. The crucibles were heated to 900, 1000, or 1100 °C at a rate of 45 °C $h^{-1}$ and then held at each temperature for 60 h. Subsequently, the electric power was turned off, and the crucible was cooled quickly to room temperature in the furnace.

**Cooling Method:** The crucibles containing each mixture (Table 1, runs 7–12) were heated to 700, 800, 900, or 1000 °C at a rate of 45 °C $h^{-1}$ and held at each temperature for 5 h. The crucibles were then cooled to 500 °C at a rate of 60, 300, or >10000 (quenching) °C $h^{-1}$. The cooling rates of 60 and 300 °C $h^{-1}$ were controlled by the cooling program, and the crucibles were cooled to room temperature in the furnace. The cooling rate of >10000 °C $h^{-1}$ was not able to be attained by the cooling program in the furnace. For >10000 °C $h^{-1}$, the crucibles were held at 800 °C for 5 h, and then removed from the furnace and cooled rapidly to room temperature (quenching in air). In both cases (flux evaporation and cooling), the crystal products were separated from the remaining flux in warm water.

The obtained crystals were observed by an optical microscope and field emission scanning electron microscope (FE-SEM, JEOL, JSM-7000F). Phases and elongated directions of the crystals were studied by X-ray diffraction (XRD, SHIMADZU, XRD-6000). An energy-dispersive X-ray spectrometer (EDS, HORIBA, EMAX-5770Q) was used to study any variation in the concentration of the major constituents in the grown crystals. The presence of impurities from the KCl flux and platinum crucible was also observed. The high-resolution transmission electron microscopy (HRTEM) and electron diffraction observations were carried out with JEM-2010 (JEOL) and JEM-2000EXII (JEOL) instruments operated at 200 kV to analyze the crystallinity and elongated direction of the grown crystals. The average sizes were measured with a laser diffraction particle size analyzer (SHIMADZU, SALD-300V). The ultraviolet/visible (UV/Vis) light diffuse reflectance spectrum of the grown crystals was obtained with a spectrophotometer (SHIMADZU, UV3150). Photocatalytic properties of the grown crystals were examined by the photodecolorization of aqueous organic dyes under an atmosphere.[5a,5b] The UV light source employed in this study was a commercial black light (15 W × 2). The center wavelength of the UV light was 352 nm.

## Acknowledgments

This research was partially supported by the TEPCO Research Foundation and The Salt Science Research Foundation, No.0609 and No.0706. A part of this work was performed under the inter-university cooperative research program of Advanced Research Center Metallic Glasses, Institute for Materials Research, Tohoku University.

[1] a) K. Domen, A. Kudo, A. Shinozaki, A. Tanaka, K. Maruya, T. Onishi, *J. Chem. Soc. Chem. Commun.* **1986**, 356–357; b) T. Nakato, K. Kuroda, C. Kato, *J. Chem. Soc. Chem. Commun.* **1989**, 1144–1145.
[2] a) Y. Inoue, T. Kubokawa, K. Sato, *J. Chem. Soc. Chem. Commun.* **1990**, 1298–1299; b) J. Ramirez-Salgado, E. Djurada, P. Fabry, *J. Eur. Ceram. Soc.* **2004**, *24*, 2477–2483.
[3] a) H. Kato, A. Kudo, *Chem. Phys. Lett.* **1998**, *295*, 487–492; b) M. Machida, J. Yabunaka, T. Kijima, *Chem. Commun.* **1999**, 1939–1940; c) K. Shimizu, Y. Tsuji, T. Hatamachi, K. Toda, T. Kodama, M. Sato, Y. Kitayama, *Phys. Chem. Chem. Phys.* **2004**, *6*, 1064–1069.
[4] a) A. Fujishima, K. Honda, *Nature* **1972**, *238*, 37–38; b) M. R. Hoffmann, S. T. Martin, W. Choi, D. W. Bahnemann, *Chem. Rev.* **1995**, *95*, 69–96.
[5] a) K. Teshima, K. Horita, T. Suzuki, N. Ishizawa, S. Oishi, *Chem. Mater.* **2006**, *18*, 3693–3697; b) K. Teshima, K. Yubuta, S. Sugiura, T. Suzuki, T. Shishido, S. Oishi, *Bull. Chem. Soc. Jpn.* **2006**, *79*, 1725–1728; c) K. Teshima, D. Tomomatsu, T. Suzuki, N. Ishizawa, S. Oishi, *Cryst. Growth Des.* **2006**, *6*, 18–19.
[6] a) ICDD-PDF 76–977; b) M. Gasperin, M. T. Le Bihan, *J. Solid State Chem.* **1982**, *43*, 346–353.
[7] E. M. Levin, C. R. Robbins, H. F. McMurdie in *Phase Diagrams for Ceramists*, The American Ceramic Society, Westerville, OH, **1964**, fig. 171, p. 88.
[8] M. Kestigian, F. D. Leipziger, J. R. Carter, F. G. Garabedian, *J. Am. Ceram. Soc.* **1966**, *49*, 517.
[9] K. Nassau, J. W. Shiever, J. L. Bernstein, *J. Electrochem. Soc.* **1969**, *116*, 348–353.
[10] a) S. Oishi, K. Teshima, H. Kondo, *J. Am. Chem. Soc.* **2004**, *126*, 4768–4769; b) K. Teshima, A. Takano, T. Suzuki, S. Oishi, *Chem. Lett.* **2005**, *34*, 1620–1621; c) K. Teshima, K. Yubuta, S. Sugiura, Y. Fujita, T. Suzuki, M. Endo, T. Shishido, S. Oishi, *Cryst. Growth Des.* **2006**, *6*, 1598–1601; d) K. Teshima, Y. Kikuchi, T. Suzuki, S. Oishi, *Cryst. Growth Des.* **2006**, *6*, 1766–

 © 2007 Wiley-VCH Verlag GmbH & Co. KGaA, Weinheim 

1768; e) K. Teshima, K. Yubuta, S. Ooi, T. Suzuki, T. Shishido, S. Oishi, *Cryst. Growth Des.* **2006**, *6*, 2538–2542.
[11] E. M. Levin, H. F. McMurdie in *Phase Diagrams for Ceramists 1975 Supplement*, The American Ceramic Society, Westerville, OH, **1975**, fig. 4889, p. 392.
[12] E. M. Levin, C. R. Robbins, H. F. McMurdie in *Phase Diagrams for Ceramists*, The American Ceramic Society, Westerville, OH, **1964**, fig. 176, p. 89.
[13] E. M. Levin, C. R. Robbins, H. F. McMurdie in *Phase Diagrams for Ceramists*, The American Ceramic Society, Westerville, OH, **1964**, fig. 177, p. 90.
[14] ICDD-PDF 32–822.
[15] ICDD-PDF 31–1060.

Received: May 8, 2007
Published Online: August 13, 2007

 © 2007 Wiley-VCH Verlag GmbH & Co. KGaA, Weinheim 

DOI: 10.1002/ejic.200700857

# The Bromination of Bulky Trialkylphosphane Selenides $R_2R'PSe$ (R, R′ = *i*Pr or *t*Bu) Studied by Physical and Computational Methods

**Cristian G. Hrib,[a] Frank Ruthe,[a] Emma Seppälä,[a] Michael Bätcher,[a] Christian Druckenbrodt,[a] Cathleen Wismach,[a] Peter G. Jones,[a] Wolf-W. du Mont,*[a] Vito Lippolis,[b] Francesco A. Devillanova,[b] and Michael Bühl[c]**

**Keywords:** Phosphane selenide dibromides / Heteronuclear NMR / Raman spectroscopy / X-ray structures / Bromine exchange / Ab initio calculations

*Table 2 on page 90 of the original article*[1] *contains errors; the correct version is given below.*

*The Authors*

Table 2. $^{31}P$ NMR shifts [ppm] and coupling constants $^1J$ ($^{77}Se,^{31}P$) [Hz] of phosphane selenides $R_2R'PSe$ (R, R′ = *i*Pr or *t*Bu) **1a**–**d** and of phosphane selenide dibromides **2a**–**d**.

| | | $R_2R'P$ | $R_2R'PSe$ (**1**) | | $R_2R'PSeBr_2$ (**2**) | |
|---|---|---|---|---|---|---|
| | | $\delta^{31}P$ | $\delta^{31}P$ | $\lvert^1J(^{77}Se,^{31}P)\rvert$ | $\delta^{31}P$ | $\lvert^1J(^{77}Se,^{31}P)\rvert$ |
| $tBu_3P$ | **a** | 62.0[a] | 93.8[a]<br>93.3[b] | 709[a]<br>693[b] | 83.0[c] | 514[c] |
| $tBu_2(iPr)P$ | **c** | 46.9[a] | 84.6[a]<br>84.4[b] | 706[a]<br>688[b] | 82.9[b] | 520[b] |
| $tBu(iPr)_2P$ | **d** | 33.3[a] | 79.9[a]<br>79.5[b] | 713[a]<br>696[b] | 77.4[b] | 526[b] |
| $iPr_3P$ | **b** | 19.3[a] | 71.1[a]<br>70.6[b] | 709[a]<br>692[b] | 69.8[c] | 521[c] |

[a] $C_6D_6$. [b] $CD_2Cl_2$. [c] $CH_2Cl_2/C_6D_6$.

[1] C. G. Hrib, F. Ruthe, E. Seppälä, M. Bätcher, C. Druckenbrodt, C. Wismach, P. G. Jones, W.-W. du Mont, V. Lippolis, F. A. Devillanova, M. Bühl, *Eur. J. Inorg. Chem.* **2006**, 88–100.

Received: August 16, 2007
Published Online: September 7, 2007

[a] Institut für Anorganische und Analytische Chemie der Technischen Universität Braunschweig,
Postfach 3329, 38023 Braunschweig, Germany
Fax: +49-531-3915387
E-mail: w.du-mont@tu-bs.de
[b] Dipartimento di Chimica Inorganica ed Analitica, Complesso Universitario di Monserrato, Università degli Studi di Cagliari, S. S. 554 Bivio per Sestu, 09042 Monserrato (CA), Italy
Fax: +39-0706754456
E-mail: devilla@unica.it
[c] Max-Planck-Institut für Kohlenforschung,
Kaiser-Wilhelm-Platz 1, 45470 Mülheim/Ruhr, Germany
Fax: +49-306-2996
E-mail: buehl@mpi-muelheim.mpg.de

 © 2007 Wiley-VCH Verlag GmbH & Co. KGaA, Weinheim

**The EUChemSoc Societies have taken the significant step into the future by merging their traditional journals, to form two leading chemistry journals, the *European Journal of Inorganic Chemistry* and the *European Journal of Organic Chemistry.* Three further EUChemSoc Societies (Austria, Czech Republic and Sweden) are Associates of the two journals.**

## COVER PICTURE

**The cover picture shows** an example of combined organometallic and enzymatic catalysis in aqueous solution. The rhodium complex $[(C_5Me_5)Rh(phenanthroline)Cl]^+$ continuously regenerates NADH from $NAD^+$ by using formate as hydrogen source, and the enzyme alcohol dehydrogenase from *Rhodococcus erythropolis* enantioselectively reduces the ketone to the corresponding alcohol by means of the NADH formed. This work illustrates the increasing interest in enantioselective catalysis with the environmentally friendly water as solvent. Details are discussed in the article by G. Süss-Fink et al. on p. 4736ff.

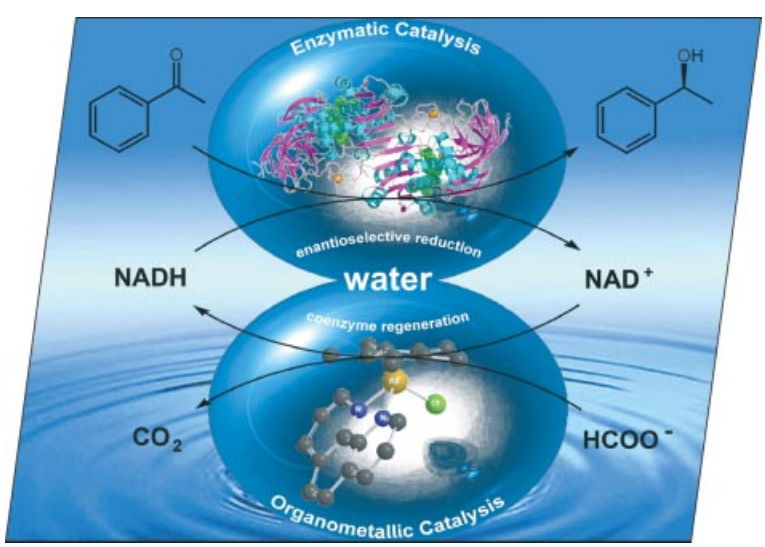


 © 2007 Wiley-VCH Verlag GmbH & Co. KGaA, Weinheim 

# CONTENTS

## MICROREVIEW


### Pt Intermolecular Hydroamination

**J.-J. Brunet,* N.-C. Chu, M. Rodriguez-Zubiri* ..... 4711–4722**

Platinum-Catalyzed Intermolecular Hydroamination of Alkenes: Halide-Anion-Promoted Catalysis

**Keywords:** Alkenes / Homogeneous catalysis / Intermolecular hydroamination / Ionic liquids / Platinum

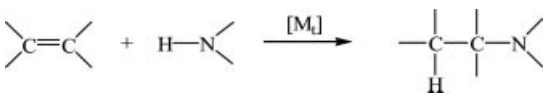


Tetraalkylphosphonium halides play the role of "promoters" for the $Pt^{II}$-catalyzed hydroamination of alkenes. The promoting effect of these "cocatalysts" depends only upon their anionic moiety. The $Pt^{II}$/$n$Bu$_4$PBr system exhibits an unprecedented catalytic activity (aerobic conditions) for the hydroamination of ethylene and 1-hexene (regioselectivity > 95%, Markovnikov).


## SHORT COMMUNICATION


### A Bis(trifluoromethyl)carbene Complex

**J. Yuan, R. P. Hughes,* A. L. Rheingold ..... 4723–4725**

The First Example of a Bis(trifluoromethyl)carbene Transition-Metal Complex and Its Reduction to a Perfluoroallene Complex

**Keywords:** Carbene / Iridium / Fluorine / Ligands / Structure

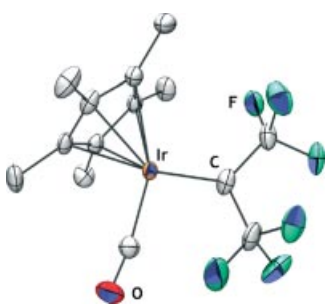


Na/Pb alloy reduction of the (perfluoroisopropyl)iridium complex Cp*(CO)IrI[CF(CF$_3$)$_2$] afforded the first example of a bis(trifluoromethyl)carbene complex, Cp*(CO)Ir=C(CF$_3$)$_2$, which has been crystallographically characterized. Further reduction of this carbene complex with KC$_8$ yielded the (perfluoroallene)iridium complex Cp*Ir(CO)($\eta^2$-CF$_2$CCF$_2$).


## FULL PAPERS


### Supramolecular Conductors

**T. Imakubo,* T. Shirahata, M. Kibune, H. Yoshino ..... 4727–4735**

Hybrid Organic/Inorganic Supramolecular Conductors $D_2[Au(CN)_4]$ [D = Diiodo(ethylenedichalcogeno)tetrachalcogenofulvalene], Including a New Ambient Pressure Superconductor

**Keywords:** Supramolecular chemistry / Conducting materials / Iodine / Superconductors / Selenium heterocycles

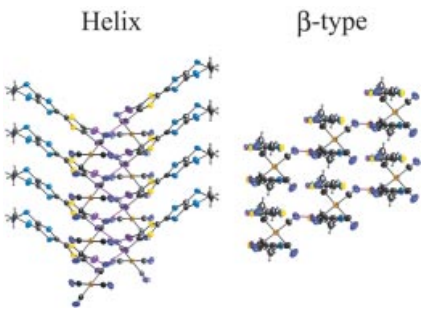


Depending on the number and positions of the selenium atoms on the iodinated donor molecule, a helical or β-type structure has been tailored by the characteristic I···N iodine bonds in the crystals of $D_2[Au(CN)_4]$, and one of the β-type salts shows superconducting transition at around 2 K (onset, ambient pressure).


 © 2007 Wiley-VCH Verlag GmbH & Co. KGaA, Weinheim 

## Organometallic–Enzymatic Catalysis

Water-soluble (chlorido)(cyclopentadienyl)rhodium and -iridium complex cations, accessible from dinuclear precursors and phenanthroline derivatives, catalyse the transfer hydrogenation of $NAD^+$ to NADH in aqueous solution by using HCOONa as hydrogen source. The combination of an alcohol dehydrogenase with this NADH-regenerating system for the chemoenzymatic reduction of prochiral ketones results in *ee* values up to 98 % under biological conditions.

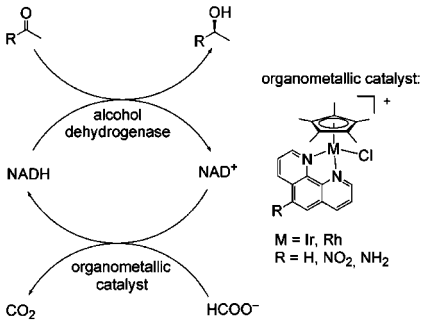


**J. Canivet, G. Süss-Fink,***
**P. Štěpnička ..... 4736–4742**

Water-Soluble Phenanthroline Complexes of Rhodium, Iridium and Ruthenium for the Regeneration of NADH in the Enzymatic Reduction of Ketones

**Keywords:** Cationic complexes / Cofactor regeneration / Chemoenzymatic catalysis / Enantioselective catalysis / Transfer hydrogenation

## Energetic Materials

Copper bis(1-methyl-5-nitrimino-tetrazole) (**1**) was synthesized by a facile route and investigated as a new primary explosive. It shows the unusual combination of high impact and moderate friction sensitivity, which are five times higher and ten times lower than that of lead azide, respectively. In addition, **1** is stable up to 250°C and shows long term stability up to 200°C.

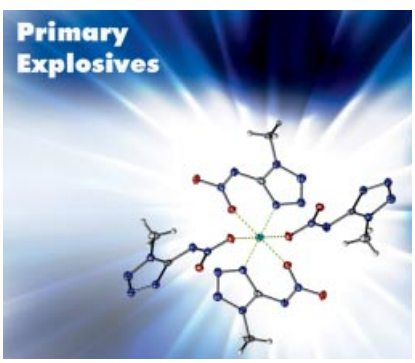


**G. Geisberger, T. M. Klapötke,***
**J. Stierstorfer ..... 4743–4750**

Copper Bis(1-methyl-5-nitriminotetrazolate): A Promising New Primary Explosive

**Keywords:** Primary explosives / Copper / Nitrogen heterocycles / Pyrotechnics / X-ray

## Radical Anion Salts

The title heterocycles are prepared and electrochemically and chemically reduced to their long-lived radical anions, which can be isolated in the form of the thermally stable salts of the $[K(18\text{-crown-6})]^+$ cation. These salts reveal low-temperature antiferromagnetic ordering of the spin system ($J = -1.65\ cm^{-1}$). Color code: gray = C, blue = N, yellow = S, magenta = Se.

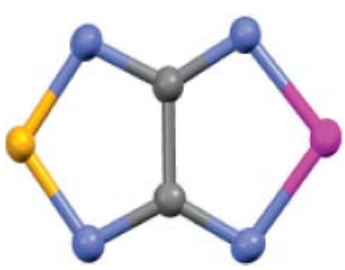

**I. Yu. Bagryanskaya, Yu. V. Gatilov, N. P. Gritsan,* V. N. Ikorskii, I. G. Irtegova, A. V. Lonchakov, E. Lork, R. Mews,* V. I. Ovcharenko,* N. A. Semenov, N.V. Vasilieva, A.V. Zibarev* ... 4751–4761**

[1,2,5]Selenadiazolo[3,4-*c*][1,2,5]thiadiazole and [1,2,5]Selenadiazolo[3,4-*c*][1,2,5]thiadiazolidyl – A Synthetic, Structural, and Theoretical Study

**Keywords:** Density functional calculations / Magnetic properties / Nitrogen heterocycles / Radical anions / Sulfur / Selenium

## Exogenous Bridging Coligands

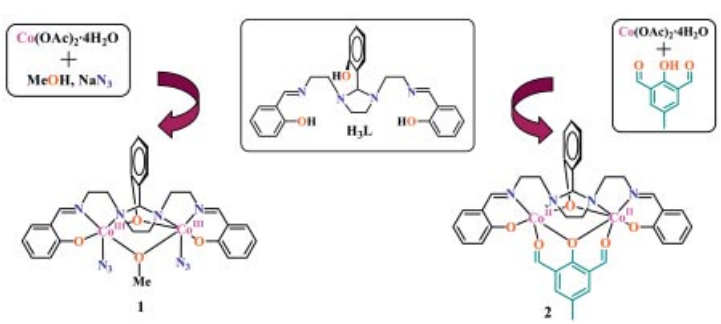


**A. R. Paital, M. Sarkar, M. Mikuriya, D. Ray* ..... 4762–4769**

[(Tmp)$Co_2$L] Complexes through Preassembly on 2,6-Diformyl- and 2,6-Bis(benzylimino)-4-methylphenolate Templates

**Keywords:** Cobalt complexes / Bridging ligands / Template synthesis / Imidazolidine / Magnetic properties

Using what are normally dinucleating ligands themselves (Hdfp and Hbip), the desired [$Co_2$L] species were crystallized by phenolate templation; $dfp^-$ and $bip^-$ acted as exogenous bridging coligands.

 © 2007 Wiley-VCH Verlag GmbH & Co. KGaA, Weinheim 

# CONTENTS

## Metallosupramolecular Chemistry

**N. K. Al-Rasbi, H. Adams, L. P. Harding, M. D. Ward* ..... 4770–4780**

Coordination Behaviour of Bis-Terdentate N-Donor Ligands: Double- and Single-Stranded Helicates, Mesocates, and Cyclic Oligomers

**Keywords:** Chelating ligands / Coordination chemistry / Helical structures / Self-assembly

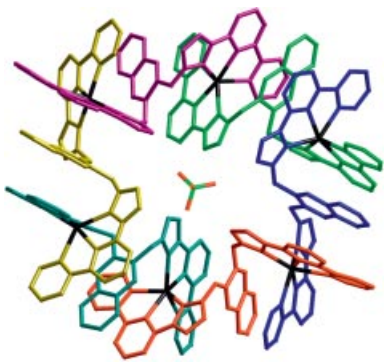

A series of potentially hexadentate ligands comprising two terdentate pyrazolyl-bipyridine units connected to a central aromatic spacer forms a range of structures including single- and double-stranded and cyclic polynuclear helicates; the Figure shows a cyclic hexanuclear helicate encapsulating a perchlorate anion.

## Bis-Intercalating Metal Complexes

**C. R. Brodie, J. R. Aldrich-Wright* ..... 4781–4793**

Synthesis of Flexible Bis-Intercalating Ruthenium(II) Complexes

**Keywords:** Ruthenium(II) / Synthesis / Chiral resolution / TRISPHAT / Dinuclear complexes / Bis-intercalators

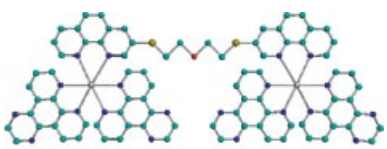

$[\{Ru(dpq)_2\}_2(\mu\text{-phen-5-SOS-5-phen})]^{4+}$

Three dinuclear ruthenium(II) complexes with the flexible linker bis(2-mercaptoethyl) ether have been syntheisied in their enantiomerically pure forms and characterised by $^1$H NMR, ESI-MS, CD and UV/Vis spectrometery.

## Manganese(II) Selenolate Complexes

**A. Eichhöfer,* P. T. Wood, R. Viswanath, R. A. Mole ..... 4794–4799**

Synthesis, Structure and Magnetic Behaviour of Manganese(II) Selenolate Complexes $^1_\infty[Mn(SePh)_2]$, $[Mn(SePh)_2(bipy)_2]$ and $[Mn(SePh)_2(phen)_2]$ (bipy = bipyridyl, phen = phenanthroline)

**Keywords:** Transition-metal complexes / Manganese / X-ray structure analysis / Magnetism

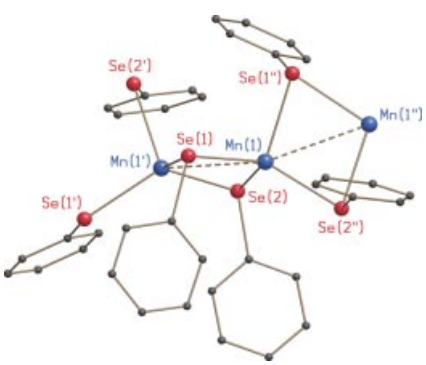


The manganese selenolate complexes $^1_\infty[Mn(SePh)_2]$ and $[Mn(SePh)_2(L)_2]$ (L = 2,2′-bipy, 1,10-phen) have been prepared and their structures characterised by X-ray analysis. The magnetic and optical properties have been investigated.

## Heteroleptic Tris(phthalocyaninates)

**A. G. Martynov, O. V. Zubareva, Yu. G. Gorbunova,* S. G. Sakharov, S. E. Nefedov, F. M. Dolgushin, A. Yu. Tsivadze ..... 4800–4807**

Diphthalocyaninatolanthanum as a New Phthalocyaninato-Dianion Donor for the Synthesis of Heteroleptic Triple-Decker Rare Earth Element Crown-Phthalocyaninato Complexes

**Keywords:** Rare earths / Macrocyclic ligands / Phthalocyanines / Sandwich complexes / Heteroleptic complexes

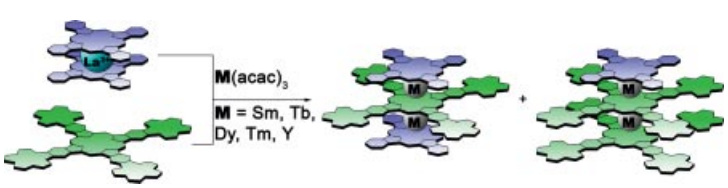


A new source of phthalocyaninato-dianion – diphthalocyaninatolanthanum – has been discovered. Its reaction with tetra-15-crown-5-phthalocyanine and rare-earth element (REE) acetylacetonato complexes leads to heteroleptic triple-decker phthalocyaninato complexes (Pc)M[(15C5)$_4$-Pc]M(Pc) and [(15C5)$_4$Pc]M[(15C5)$_4$Pc]-M(Pc) both of which are potential components of new supramolecular materials.

 © 2007 Wiley-VCH Verlag GmbH & Co. KGaA, Weinheim 

## Electrophosphorescent Ir Complexes

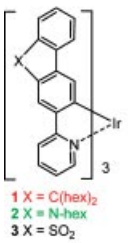


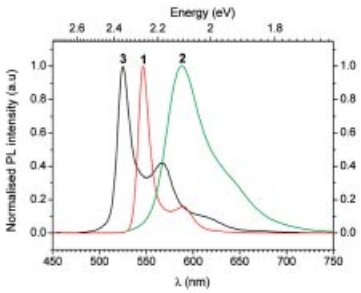


The substituent *para* to the Ir atom, i.e. $CR_2$ in **1**, NR in **2** and $SO_2$ in **3**, has a major influence on the redox and emission properties in this series of tris-cyclometalated complexes.

**M. Tavasli, S. Bettington, I. F. Perepichka, A. S. Batsanov, M. R. Bryce,* C. Rothe, A. P. Monkman** ..... **4808–4814**

A Tris-Cyclometalated Iridium(III) Complex of 2-(5,5-Dioxido-dibenzothiophen-3-yl)pyridine: Synthesis, Structural, Redox and Photophysical Properties

**Keywords:** Dibenzothiophene *S*,*S*-dioxide / Iridium / Cyclometalation / Luminescence / Electrochemistry

## Self-Assembly of Metallacryptates

An appropriate choice of ligand substitution and metal ions enables the syntheses of {2}-metallacryptates or linear/meandering coordination polymers in the solid state. Exemplarily, a detailed analysis of the stereogenic centres in racemic $\Delta/\Lambda$-$(\mathbf{2})_n$ revealed the formation of homochiral layers in the crystal [see picture; $\Lambda$-$(\mathbf{2})_n$: Mg gold, Cs silver, O red, C white].

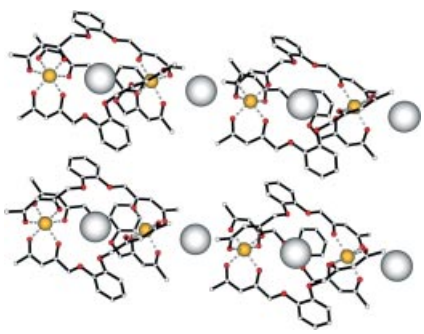

**R. W. Saalfrank,* N. Mooren, A. Scheurer, H. Maid, F. W. Heinemann, F. Hampel, W. Bauer** ..... **4815–4822**

Synthesis and Structure of Self-Complementary {2}-Metallacryptates and Their Linear or Meandering Infinite Arrangements in the Solid State

**Keywords:** Metallacryptate / Coordination polymers / O ligands / X-ray diffraction / Chirality

## Ag Nanoparticles

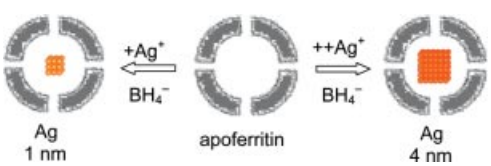


Size-controlled Ag nanoparticles were prepared by using an $Ag^+$-loaded apoferritin as a nanoconfined environment for their construction. The protein shell of the particles prevents bulk aggregation of the metal particles, which renders them water soluble and extremely stable.

**J. M. Domínguez-Vera,* N. Gálvez, P. Sánchez, A. J. Mota, S. Trasobares, J. C. Hernández, J. J. Calvino*** ..... **4823–4826**

Size-Controlled Water-Soluble Ag Nanoparticles

**Keywords:** Silver / Nanoparticles / Apoferritin / Water-soluble particles

## Copper(II) Sandwich Complex

A new hexanuclear copper(II) sandwich complex based on two 12-membered macrocyclic methylsiloxanolate ligands, $[Cu_6\{(MeSiO_2)_6\}_2]\cdot 6DMF$, was synthesized and characterized by single-crystal X-ray diffraction analysis and magnetic measurements.

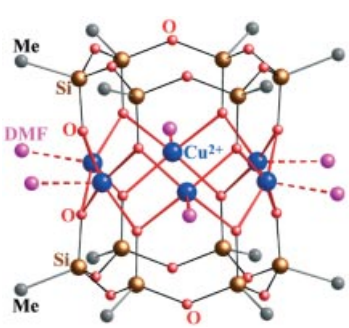


**L. Zherlitsyna, N. Auner*, M. Bolte, Yu. Pozdniakova, O. Shchegolikhina, K. Lyssenko, V. Pashchenko*, B. Wolf, M. Lang, F. Schütz, M. Kollar, F. Sauli, P. Kopietz** ..... **4827–4838**

Synthesis, Structure and Magnetic Properties of a Novel Hexanuclear Copper Methylsiloxane Complex

**Keywords:** Copper / Cluster compounds / Sandwich complexes / Magnetic properties

 © 2007 Wiley-VCH Verlag GmbH & Co. KGaA, Weinheim 

# CONTENTS

## Carbene Complexes

**D. Zhang* ..... 4839–4845**

Dinuclear Titanium(IV) Complexes Bearing Phenoxide-Tethered N-Heterocyclic Carbene Ligands with *cisoid* Conformation through Control of Hydrolysis

**Keywords:** Titanium / Carbene ligands / Phenoxides

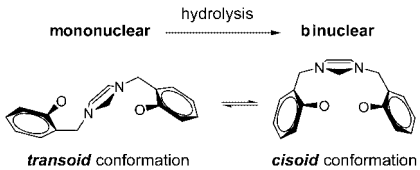


Two oxygen-bridged titanium dimers, {[(L)TiBr]$_2$(μ-O)} (**4**) and {[(L)Ti(μ-O)]$_2$} (**5**) – [H$_3$(L)]Br = 1,3-bis(4,6-di-*tert*-butyl-2-hydroxybenzyl)imidazolium bromide) – were obtained by control of hydrolysis of [(L)TiBr$_2$(thf)] (**1**) and [(L)Ti(CH$_2$Ph)$_2$] (**3**) in tetrahydrofuran and diethyl ether. The phenoxide-functionalized NHC ligand adopts *transoid* conformation in mononuclear complex **2** but rare *cisoid* conformation in dinuclear complexes **4** and **5**.

**If not otherwise indicated in the article, papers in issue 29 were published online on September 25, 2007**

 © 2007 Wiley-VCH Verlag GmbH & Co. KGaA, Weinheim

**The EUChemSoc Societies have taken the significant step into the future by merging their traditional journals, to form two leading chemistry journals, the *European Journal of Inorganic Chemistry* and the *European Journal of Organic Chemistry.* Three further EUChemSoc Societies (Austria, Czech Republic and Sweden) are Associates of the two journals.**

## COVER PICTURE

**The cover picture shows** an example of combined organometallic and enzymatic catalysis in aqueous solution. The rhodium complex $[(C_5Me_5)Rh(phenanthroline)Cl]^+$ continuously regenerates NADH from $NAD^+$ by using formate as hydrogen source, and the enzyme alcohol dehydrogenase from *Rhodococcus erythropolis* enantioselectively reduces the ketone to the corresponding alcohol by means of the NADH formed. This work illustrates the increasing interest in enantioselective catalysis with the environmentally friendly water as solvent. Details are discussed in the article by G. Süss-Fink et al. on p. 4736ff.

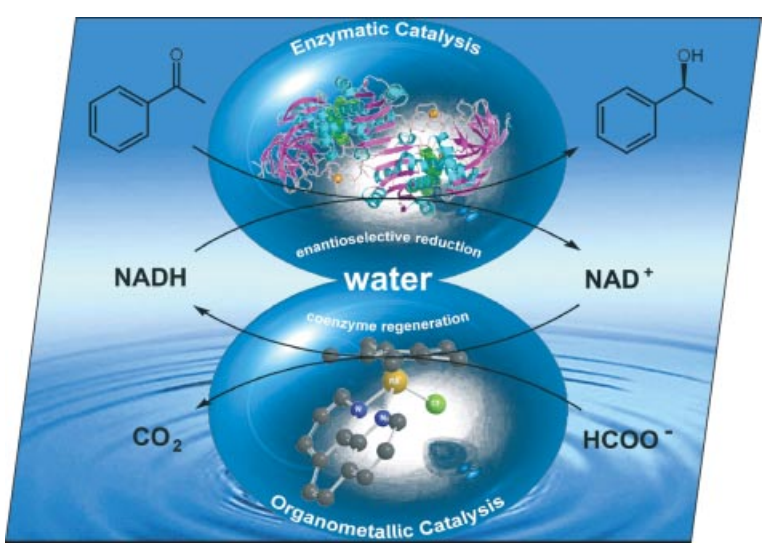


 © 2007 Wiley-VCH Verlag GmbH & Co. KGaA, Weinheim 

# SPOTLIGHTS …

## *Phase-Transfer Catalysis*

S. Shirakawa, M. Ueda, Y. Tanaka, T. Hashimoto, K. Maruoka*

**Design of Binaphthyl-Modified Symmetrical Chiral Phase-Transfer Catalysts: Substituent Effect of 4,4′,6,6′-Positions of Binaphthyl Rings in the Asymmetric Alkylation of a Glycine Derivative**

*Chem. Asian J.*
DOI: **10.1002/asia.200700117**

**Designer rings**: Chiral phase-transfer catalysts with 4,4′,6,6′-tetrasubstituted binaphthyl units give excellent enantioselectivity in the asymmetric alkylation of *tert*-butylglycinate–benzophenone Schiff base with various alkyl halides. A highly fluorinated version can also be used as a recyclable chiral phase-transfer catalyst by simple extraction with fluorous solvents.

## *Aminoglycosides*

J. Kondo, M. Hainrichson, I. Nudelman, D. Shallom-Shezifi, C. M. Barbieri, D. S. Pilch,* E. Westhof,* T. Baasov*

**Differential Selectivity of Natural and Synthetic Aminoglycosides towards the Eukaryotic and Prokaryotic Decoding A Sites**

*ChemBioChem*
DOI: **10.1002/cbic.200700271**

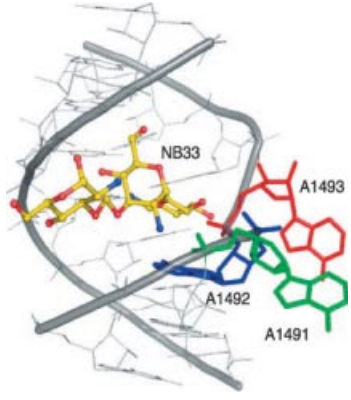


**Tuning the selectivity**. The lack of absolute prokaryotic selectivity of natural antibiotics is widespread and a significant problem clinically. By using a combined biochemical and structural analysis of the synthetic aminoglycoside NB33 bound to the *H. sapiens* cytoplasmic A site RNA fragment we demonstrate the general molecular principles that determine the selectivity interplay of 2-deoxystreptamine-based aminoglycosides between the prokaryotic and eukaryotic decoding sites.

## *Ion-Pair Surfactants*

R. Bordes, M. Vedrenne, Y. Coppel, S. Franceschi, E. Perez,* I. Rico-Lattes

**Micelle–Vesicle Transition of Fatty Acid Based Ion-Pair Surfactants: Interfacial Evidence and Influence of the Ammonium Counterion Structure**

*ChemPhysChem*
DOI: **10.1002/cphc.200700289**

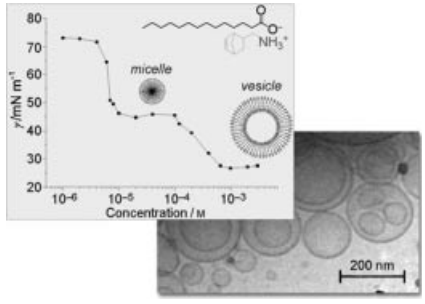


**Micelles or Vesicles?** Single-tailed surfactants have been associated with various organic counterions. Depending on the structure of the ion-paired surfactant, a micelle-to-vesicle transition is observed (see picture), thus demonstrating the key role played by the positioning of the counterion in supramolecular self-assembly.

## *Antibacterial Agents*

T. S. Mansour,* C. E. Caufield, B. Rasmussen, R. Chopra, G. Krishnamurthy, K. M. Morris, K. Svenson, J. Bard, C. Smeltzer, S. Naughton, S. Antane, Y. Yang, A. Severin, D. Quagliato, P. J. Petersen, G. Singh

**Naphthyl Tetronic Acids as Multi-Target Inhibitors of Bacterial Peptidoglycan Biosynthesis**

*ChemMedChem*
DOI: **10.1002/cmdc.200700094**

**A pathway screen** targeting multiple muramyl peptide synthesis inhibitors identified the naphthyl tetronic acids series. Optimization of this series based on $IC_{50}$, $K_d$ and MIC values led to potent inhibitors. Compound **5h** was co-crystallized in the active site of *E. coli* MurB.

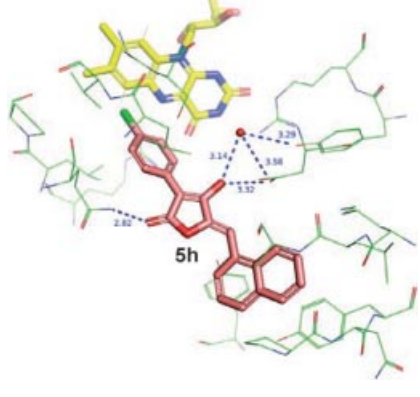


 © 2007 Wiley-VCH Verlag GmbH & Co. KGaA, Weinheim 

# … ON OUR SISTER JOURNALS

EurJIC European Journal of Inorganic Chemistry

## *Iron Complexes*

**Broken-symmetry** density functional theoretical calculations (B3LYP) have been performed on 13 five-coordinate complexes of iron that contain zero, one, or two π-radical monoanions derived from redox noninnocent dianionic dithiolates, phenylene diamides (shown here), or *o*-aminodithiolates.

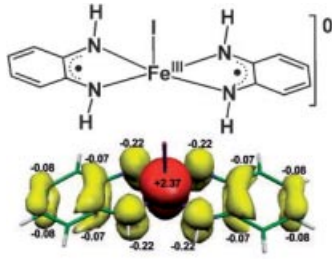


K. Chłopek, N. Muresan, F. Neese,* K. Wieghardt*

**Electronic Structures of Five-Coordinate Complexes of Iron Containing Zero, One, or Two π-Radical Ligands: A Broken-Symmetry Density Functional Theoretical Study**

*Chem. Eur. J.*
DOI: **10.1002/chem.200700897**

## *Organocatalysis*

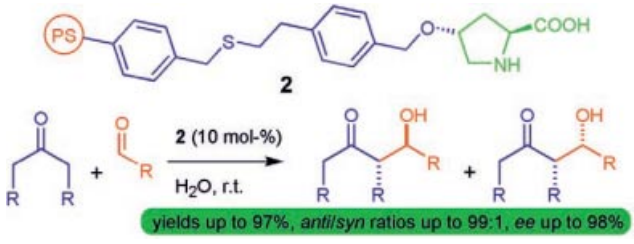


A polystyrene-supported L-proline material has been prepared and used as a catalyst in direct asymmetric aldol reactions, with high yields and stereoselectivities. The catalyst works only in the presence of water, and this material can be reused, without loss in levels of conversion and stereoselectivity, for at least five cycles.

M. Gruttadauria,* F. Giacalone, A. Mossuto Marculescu, P. Lo Meo, S. Riela, R. Noto

**Hydrophobically Directed Aldol Reactions: Polystyrene-Supported L-Proline as a Recyclable Catalyst for Direct Asymmetric Aldol Reactions in the Presence of Water**

*Eur. J. Org. Chem.*
DOI: **10.1002/ejoc.200700586**

## *Analytical Methods*

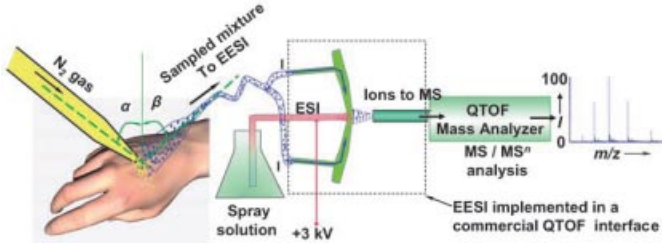


**MS comes to life**: A novel method to sample surfaces of biological objects uses a neutral gas beam for in vivo EESI mass spectrometric analysis without sample pretreatment (see picture; QTOF = quadropole time-of-flight). The sampling process results in rapid in vivo analyses with reduced ion suppression and without chemical contamination. This strategy can be used in food quality monitoring, homeland security, metabolomics, and clinical diagnosis.

H. Chen,* S. Yang, A. Wortmann, R. Zenobi*

**Neutral Desorption Sampling of Living Objects for Rapid Analysis by Extractive Electrospray Ionization Mass Spectrometry**

*Angew. Chem. Int. Ed.*
DOI: **10.1002/anie.200702200**

On these pages, we feature a selection of the excellent work that has recently been published in our sister journals. If you are reading these pages on a computer, click on any of the items to read the full article. Otherwise please see the DOIs for easy online access through Wiley InterScience.

 © 2007 Wiley-VCH Verlag GmbH & Co. KGaA, Weinheim 

DOI: 10.1002/ejic.200700737

# Platinum-Catalyzed Intermolecular Hydroamination of Alkenes: Halide-Anion-Promoted Catalysis

**Jean-Jacques Brunet,*[a] Ngoc-Chau Chu,[a] and Mireia Rodriguez-Zubiri*[a]**

**Keywords:** Alkenes / Homogeneous catalysis / Intermolecular hydroamination / Ionic liquids / Platinum

Tetraalkylphosphonium halides play the role of "promoters" for the previously unknown $Pt^{II}$-catalyzed hydroamination of alkenes. The promoting effect of these "cocatalysts" depends only upon their anionic moiety. The $Pt^{II}/nBu_4PBr$ system exhibits an unprecedented catalytic activity (aerobic conditions) for the hydroamination of ethylene and 1-hexene (regioselectivity > 95 %, Markovnikov).

(© Wiley-VCH Verlag GmbH & Co. KGaA, 69451 Weinheim, Germany, 2007)

## 1. Introduction

Amines are important chemicals for both industry and everyday life.[1–4] Since the discovery of ammonia,[5] chemists have developed synthetic methods for the production of amines, and many methods are available.[6] However, most of them are unsuitable for industrial purposes, mainly because they involve very expensive starting materials, reagents, or purification steps. The condensation of ammonia [Equation (1)] or amines [Equation (2)] with alcohols in the presence of various catalysts, first pointed out by Sabatier et al. in 1909,[7,8] is nowadays the main method for the industrial production of light amines. This reaction is also used in some cases for the production of fatty amines or diamines.[2]

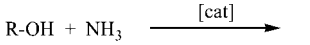


(1)

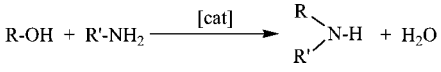


(2)

With the exception of methanol and ethanol, most primary alcohols are industrially produced from alkenes (hydroformylation–hydrogenation sequence).[9,10] It is thus obvious that the direct transformation alkene → amine would be a more economic process since it would suppress at least one step (Scheme 1) and would avoid the coproduction of water [Equations (1) and (2)].

[a] Laboratoire de Chimie de Coordination du CNRS, Unité No. 8241, liée par conventions à l'Université Paul Sabatier et à l'Institut National Polytechnique,
205 route de Narbonne, 31077 Toulouse Cedex 04, France
Fax: +33-5-61553003
E-mail: brunet@lcc-toulouse.fr
mireia.rodriguez@lcc-toulouse.fr

*Jean-Jacques Brunet was born in Clermont-Ferrand, France, in 1945. He attended the Faculté des Sciences and the Ecole Nationale Supérieure de Chimie de Clermont-Ferrand, where he received his Chemical Engineering degree in 1968. He obtained his PhD (Thèse d'Etat) in 1972 at the University of Nancy under the supervision of Pr P. Caubère. In 1985, he joined the Laboratoire de Chimie de Coordination of the CNRS (Toulouse), where he is one of the group leaders. Starting from organic synthesis and the study of reaction mechanisms, his current research interest lies now in organometallic chemistry and homogeneous catalysis directed towards organic synthesis, with some emphasis on carbonylation reactions and on the functionalization of alkenes by hydroamination.*

*Ngoc-Chau Chu was a PhD student at the Laboratoire de Chimie de Coordination du CNRS (Toulouse) from 2000 to 2005 and returned to Vietnam in 2006.*

*Mireia Rodríguez i Zubiri, born in Spain (1975), studied Chemistry at the University of Valencia in Spain (1993–1998) and completed her MSc in the group of Prof. J. Reedijk at the University of Leiden (1999). After her PhD studies with Prof. J. D. Woollins and Prof. D.J. Cole-Hamilton at the University of St. Andrews (1999–2002), she moved to France where she had a postdoctoral position in the group of Dr. P. Braunstein (2003–2004). In 2004, she joined the group of Prof. Y. Fort as assistant professor. In 2005, she became a CNRS Researcher in the team of J-J. Brunet at the Laboratoire de Chimie de Coordination in Toulouse. Her research interests include the development of new catalytic systems based on transition-metal precursors for the intermolecular hydroamination of nonactivated olefins, the mechanistic and kinetic aspects of this reaction, and the use of ionic liquids, aqueous media or supercritical fluids in this reaction.*

 © 2007 Wiley-VCH Verlag GmbH & Co. KGaA, Weinheim 

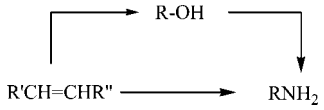


Scheme 1. From alkenes to amines.

The necessity to develop atom-economic reactions is often highlighted. The direct addition of the N–H bond of ammonia or amines on carbon–carbon multiple bonds (hydroamination) belongs to this desired class of reactions,[11] especially in the case of alkenes [Equation (3)], the subject of this review.

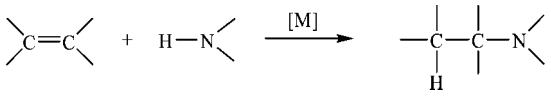


(3)

Consequently, intense efforts have long been devoted to the hydroamination of different kinds of multiple carbon–carbon bonds, alkenes, alkynes, vinylarenes, and dienes by intramolecular and intermolecular additions. Several reviews have been published since 1983.[12–23] The main conclusion that can be given (in 2006) is that significant progress has been made for the hydroamination of vinylarenes[24] and dienes,[25] which includes the inter- and intramolecular versions of this reaction. The hydroamination of vinylarenes must be highlighted since catalysts that allow fully regioselective additions (Markovnikov or anti-Markovnikov) and enantioselective Markovnikov additions have been designed.[26] In the case of nonactivated alkenes, several efficient catalytic systems have been reported for *intramolecular* hydroamination, which include highly enantioselective reactions.[22,23,27] In contrast, the *intermolecular* hydroamination of alkenes with *amines* is much less developed. Exceptions include the industrial production (BASF) of $t$BuNH$_2$ by addition of ammonia to isobutene (zeolite catalyst),[21] the organolanthanide-catalyzed (neodymium, 20% catalyst) hydroamination of 1-pentene with $n$PrNH$_2$ (fully regioselective Markovnikov addition),[27n] and the Li-catalyzed hydroamination of ethylene.[27p] This review is devoted to results developed in our group since 2002 for the platinum-catalyzed *intermolecular* hydroamination of nonactivated alkenes (some previous results with Rh catalysts are also included).

First, it is important to recall that the addition of ammonia or amines to ethylene is thermodynamically feasible (Table 1).[28] It is also noteworthy that the entropy term is highly negative, which means that very high temperatures would favor the reverse reaction and thus make the desired reaction impossible. However, this thermodynamic data gives no information on the activation barrier. It is conceivable that the approach of the nitrogen atom lone pair to the electron density of the carbon–carbon double bond of the alkene induces an electrostatic repulsion that corresponds to a high-energy barrier. The objective is thus to lower this energy barrier. Two possibilities can be considered:[14] (1) activation of the alkene (to make it more "electrophilic") and (2) activation of the amine (to make it more "nucleophilic"). The mechanisms corresponding to these two possibilities are represented in Scheme 2.[16]

Table 1. Thermodynamic data for the hydroamination of ethylene ($T$ = 298 K, $P$ = 101325 Pa).

| Reaction | $\Delta G°$ [kJ mol$^{-1}$] | $\Delta H°$ [kJ mol$^{-1}$] | $\Delta S°$ [J mol$^{-1}$ K$^{-1}$] |
|---|---|---|---|
| $C_2H_4 + NH_3 \rightarrow EtNH_2$ | –14.4 | –52.4 | –127.4 |
| $C_2H_4 + EtNH_2 \rightarrow Et_2NH$ | –33.3 | –78.6 | –152.1 |
| $C_2H_4 + Et_2NH \rightarrow Et_3N$ | –29.9 | –79.5 | –166.2 |

The most significant results on the *homogeneously* catalyzed *intermolecular* hydroamination of nonactivated alkenes have already been reviewed.[21] However, in view of the subject of this article, it is interesting to note that intense efforts have been devoted to the addition of amines to alkenes coordinated to transition metals, especially Pt$^{II}$ and Pd$^{II}$. In the case of Pt$^{II}$ alkene complexes,[29–34] attack by sufficiently basic amines (p$K_a$ of conjugated acid > 5) has been shown to afford zwitterionic complexes [Equation (4)], one of which could be characterized by X-ray dif-

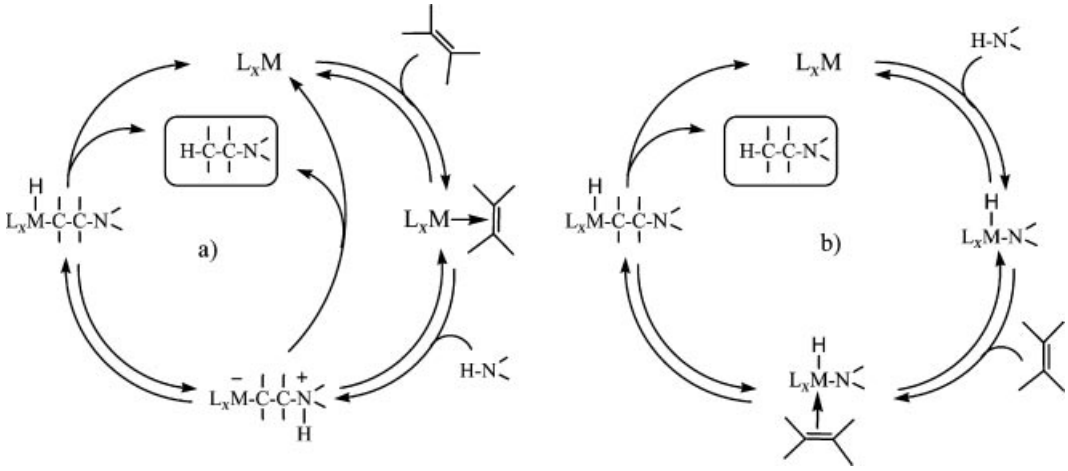


Scheme 2. a) Hydroamination by alkene activation; b) hydroamination by N–H activation.[16]

 © 2007 Wiley-VCH Verlag GmbH & Co. KGaA, Weinheim 

fraction study.[30d] However, liberation of the alkylated amine by cleavage of the carbon–platinum bond needs a further step (reaction with HCl or $NaBH_4$) [Equation (5)],[30–33] so that the hydroamination reaction is only *stoichiometric*.[34]

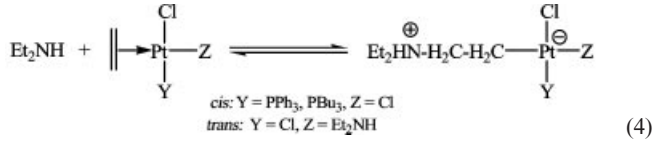


(4)

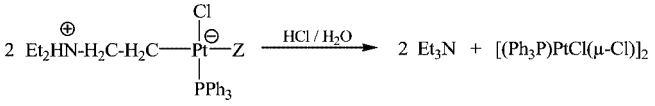


(5)

Soon after the publication of our paper on the Pt-catalyzed *hydroamination* of ethylene with aniline in ionic liquids (see below),[35] Widenhoefer et al. reported that the dinuclear $Pt^{II}$ complex $[PtCl_2(C_2H_4)]_2$, associated with $PPh_3$, is an active catalyst for the intermolecular *hydroamidation* of ethylene with *carboxamides*.[36] Extension to the hydroamidation of alkenes with poorly basic *sulfonamides* catalyzed by $[PtCl_2(C_2H_4)]_2/[AgBF_4]$ has also been reported recently.[37]

## 2. New Catalytic Systems for the Intermolecular Hydroamination of Alkenes

After our contribution on anionic $Rh^I$ anilido species as possible hydroamination catalysts,[38–41] we were tempted to take advantage of our simultaneous involvement[42] in the use of molten salts or ionic liquids as possible candidates to replace classical organic solvents – an important aspect in the development of "greener" chemical processes.[43–46]

Examination of the patent by Coulson[47] on the $Rh^{III}$-catalyzed hydroamination of ethylene with secondary amines showed that highly polar solvents, such as hexamethylphosphoramide (HMPA), have a positive effect on the reaction. We showed that some ionic solvents apparently exhibit properties similar to those of the well-known but more hazardous (carcinogenic) dipolar aprotic solvents such as DMF or HMPA.[42]

### 2.1. Hydroamination of Norbornene by Aniline in Ionic Liquids

The above results led us to examine the $Rh^{III}$-catalyzed hydroamination of alkenes in ionic solvents. The hydroamination of norbornene with aniline was selected [Equation (6)], (see Table 2).

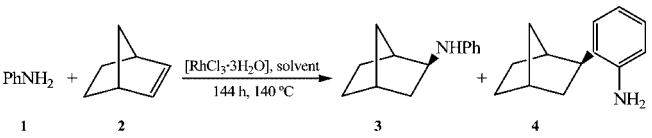


(6)

Table 2. $[RhCl_3{\cdot}3H_2O]$-catalyzed hydroamination of norbornene with aniline in ionic solvents.[a]

| Run | Solvent | Reaction products: TON | | |
|---|---|---|---|---|
| | | **3** | **4** | Total (**3** + **4**) |
| 1 | thf (7.5 mL) | 0 | 0 | 0 |
| 2 | [EMIM][Cl] (3.0 g) | ≈0 | ≈0 | ≈0 |
| 3 | [BMIM][Cl] (3.6 g) | ≈0 | ≈0 | ≈0 |
| 4 | [BMIM][Cl] (7.2 g) | ≈0 | ≈0 | ≈0 |
| 5 | [BMIM][$PF_6$] (6 g) | 5.1 | 2.6 | 7.7 |
| 6 | [BMIM][Br] (5.7 g) | 8.3 | 1.5 | 9.8 |
| 7 | [HMIM][Br] (7.1 g) | 10.1 | 1.9 | 12 |
| 8 | $n$Bu$_4$PBr (7.1 g) | 7.7 | 2.5 | 10.2 |

[a] 144 h at 140 °C, $[RhCl_3{\cdot}3H_2O]$: 0.13 mmol, norbornene: 13 mmol, aniline: 45 mmol.

As expected,[47,48] no reaction was observed when thf was used as solvent (run 1, Table 2). The use of different imidazolium chlorides resulted in only traces of reaction products (runs 2 and 3). In contrast, the replacement of the chloride ion by [$PF_6^-$] led to the formation higher-than-stoichiometric amounts of both **3** and **4** (run 5). A higher catalytic activity was obtained when imidazolium bromides were used (runs 6 and 7). Finally, the positive effect of the bromide ions was confirmed when $n$Bu$_4$PBr (mp = 100–103 °C) was used as solvent (run 8).

Thus, the reaction of norbornene with aniline, catalyzed by $[RhCl_3{\cdot}3H_2O]$, does not occur in thf, but it can occur in the presence of imidazolium or phosphonium *bromides* as solvents. It is also worthy to note that the above ionic solvents allow the $Rh^{III}$-catalyzed hydroamination by a weakly basic amine ($pK_a$ = 4.63).

In the early 2000s, Togni et al. published a very interesting theoretical study of the hydroamination through alkene activation and subsequent nucleophilic attack by the amine.[49] They considered $d^8$ transition-metal complexes of the type $[MCl(PH_3)_2]^{z+}$ {M = Co, Rh, Ir [$z$ = 0] and M = Ni, Pd, Pt [$z$ = 1]} for the hydroamination of ethylene with ammonia. For group 9 metals, nucleophilic attack was identified as the rate-determining step, while cleavage of the M–C bond was the rate-determining step for group 10 metals. Overall, metals from group 10 are more efficient than those from group 9 (lower activation barriers), and $Ni^{II}$ precursors appeared to be the best candidates. These results led us to examine the catalytic activity of group 10 transition-metal precursors in combination with $n$Bu$_4$PBr as solvent. For comparison, the reaction of aniline with norbornene under the same experimental conditions as those used for the $Rh^{III}$ catalysts was considered.

The results reported in Table 3[50] show that group 10 transition-metal precursors exhibit some activity for the test reaction. However, contrary to that expected from the cal-

 © 2007 Wiley-VCH Verlag GmbH & Co. KGaA, Weinheim 

culations by Togni and coworkers, the best results were clearly obtained with the $Pt^{II}$ catalysts. The latter gave catalytic activities and chemoselectivities similar to those observed with [$RhCl_3 \cdot 3H_2O$] (Table 2).

Table 3. Hydroamination of norbornene with aniline in $n$Bu$_4$PBr: catalysis by group 10 transition metals.[a]

| Run | Catalytic precursor [mmol] | Reaction products: TON **3** | **4** | Total (**3** + **4**) |
|---|---|---|---|---|
| 9 | [$NiBr_2$] (0.40) | 1.0 | 0 | 1.0 |
| 10 | [$PdBr_2$] (0.17) | 2.5 | 1.6 | 4.1 |
| 11 | [$PtBr_2$] (0.13) | 8.6 | 1.0 | 9.6 |
| 12 | [$PtCl_2$] (0.13) | 8.2 | 2.0 | 10.2 |
| 13 | [$PtI_2$] (0.13) | 9.8 | 1.2 | 11.0 |

[a] 144 h at 140 °C, norbornene: 13 mmol, aniline: 45 mmol, $n$Bu$_4$PBr: 7 g.

The nature of the halide ion associated with the platinum precursor plays a minor role (runs 11–13, Table 3). This is not surprising since the [$PtX_2$]/$n$Bu$_4$PBr ratio is 1:150, and this implies that the bromide ions are by far the main halogen ligands. Under these conditions, the platinum salts are soluble in the ionic solvent and can be considered as $[PtBr_4]^{2-}$ species [Equation (7)].[51]

$$[PtBr_2] + 2\,n\mathrm{Bu_4PBr} \rightleftharpoons [PtBr_4]^{2-} + 2\,[n\mathrm{Bu_4P}]^{+} \quad (7)$$

The above results were particularly exciting because, as previously noted, no platinum-catalyzed alkene hydroamination had been reported until then. Since extensive information is available on the reactivity of $Pt^{II}$–ethylene complexes with amines,[29–34] we were prompted to examine the possible catalytic hydroamination of ethylene with aniline in the presence of the newly developed [$PtBr_2$]/$n$Bu$_4$PBr system.

### 2.2. Hydroamination of Ethylene by Aniline in Ionic Liquids

Our first experiments were aimed at comparing the influence of the nature of the solvent on the reaction of aniline with ethylene (25 bar at room temperature) in the presence of catalytic amounts (0.3%) of [$PtBr_2$]. In all cases, the reaction leads to the hydroamination product, *N*-ethylaniline (**6**) (with traces of *N*,*N*-diethylaniline, **7**), together with minor amounts of 2-methylquinoline (**8**) [Equation (8)].

The results in Table 4 show that, contrary to literature data, the hydroamination reaction is catalyzed by [$PtBr_2$] in aniline or thf with significant TONs (runs 14 and15). It should be noted that no zwitterionic complex has ever been evidenced from the reaction of aniline with any $Pt^{II}$–ethylene complex.[29–33] This fact was explained by the insufficient basicity of aniline ($pK_a$ = 4.63), relative to that of, for example, diethylamine ($pK_a > 10$) for which the zwitterionic addition complex had been fully characterized.[30d] We tentatively suggest that the addition of aniline to a $Pt^{II}$–ethylene complex occurs to a very small extent and that the equilibrium is displaced toward the right because the zwitterionic complex evolves at high temperatures (150 °C) to liberate *N*-ethylaniline.

Table 4. Hydroamination of ethylene with aniline: influence of the nature of the solvent.[a]

| Run | Solvent | Reaction products: TON PhNHEt | $PhNEt_2$ | "2-Me-quinoline" |
|---|---|---|---|---|
| 14 | aniline (10 mL) | 23 | 1 | 3 |
| 15 | thf (7.5 mL) | 34 | 1 | 4 |
| 16 | $n$Bu$_4$PBr (7 g) | 80 | 1 | 11 |

[a] [$PtBr_2$]: 0.13 mmol, ethylene: 25 bar at room temperature, aniline: 45 mmol, 10 h at 150 °C.

The beneficial effect of $n$Bu$_4$PBr is again highlighted: under nonoptimized conditions, the highest catalytic activity ever reported for the hydroamination of ethylene (TON = 80) was obtained.

On the basis of the above observations, we briefly examined the influence of some classical reaction parameters.

The reaction temperature is an important parameter: at 150 °C, the TON was nearly twice that obtained at 120 °C (from 80 to 43 catalytic cycles after 10 h of reaction). Higher temperatures (180 °C) did not significantly improve the catalytic activity. Thus, further experiments were conducted at 150 °C.

The influence of the ethylene pressure was considered in the range 10–50 bar. By increasing the ethylene pressure from 10 to 50 bar, the formation of *N*-ethylaniline (TON from 73 to 90 after 10 h of reaction) was slightly increased. In contrast, the formation of the quinoline derivative was significantly favored by a high ethylene pressure (TON from 8 to 20).[52]

The next parameter that we examined was the amount of aniline used, whilst keeping all other parameters as stated in Table 4 (run 16An increase in the TON for the two main reaction products (TON for *N*-ethylaniline: from 30 to 99; TON for 2-methylquinoline: from 4 to 15) was observed by increasing the amount of aniline.

The evolution of the reaction with time was also considered. Runs were performed with different reaction times (1–10 h). The turnover frequency (TOF) for the formation of *N*-ethylaniline reached 37 $h^{-1}$ for the first hour, which is apparently the highest TOF reported for ethylene hydroamination. The reaction rate then decreased, and the average

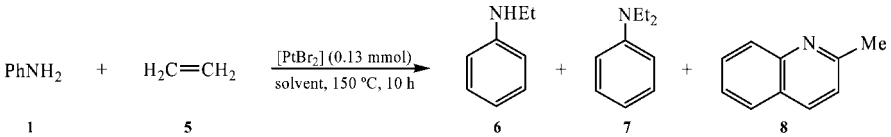


1 5 6 7 8 (8)

 © 2007 Wiley-VCH Verlag GmbH & Co. KGaA, Weinheim 

TOF for 10 h was 8 $h^{-1}$. In order to verify the possible poisoning by either of the two main reaction products, new runs were performed under the same conditions but in the presence of added 2-methylquinoline (1.5 mmol) or *N*-ethylaniline (15 mmol). After 10 h at 150 °C and in the presence of 2-methylquinoline, there was no significant difference in the reaction, whereas for the reaction conducted in the presence of added *N*-ethylaniline, a TON of less than 40 cycles was reached. Even more convincing is the following observation. A [$PtBr_2$]/aniline/*N*-ethylaniline (1:350:100 mmol) mixture was preheated (in the absence of ethylene) for 10 h at 150 °C. Ethylene was then added (25 bar at room temperature). This procedure resulted in a relatively inactive system for the production of **6**, but still active for the formation of **8** (9 cycles after 10 h). These results confirm that during the hydroamination reaction [Equation (8)], the increase in the concentration of *N*-ethylaniline induces a gradual poisoning of the catalyst.

Therefore, it was decided to perform the reaction in a biphasic medium consisting of *n*$Bu_4PBr$ and a high-boiling-point nonmiscible hydrocarbon. By performing the hydroamination of aniline with ethylene under the same conditions but in the presence of decane (4.5 mL for 7.2 g of *n*$Bu_4PBr$), higher TONs (**6**: 115 cycles, **7**: 2 cycles and **8**: 17 cycles) were effectively reached.[53]

Finally, the possible influence of a proton source was examined. When the hydroamination of ethylene [Equation (8)] was performed in the presence of anilinium sulfate (3 equiv. per mol of [$PtBr_2$]), the TON increased from 80 to 130. Under biphasic conditions (*n*$Bu_4PBr$/decane), the presence of anilinium sulfate led to an increase in the TON for *N*-ethylaniline from 115 to 145, the highest TON observed in the present work for the hydroamination of ethylene with aniline. Similar results were obtained when using $CF_3SO_3H$ (3 equiv. per mol of [$PtBr_2$]) instead of anilinium sulfate.

As already mentioned, the reaction of amines with coordinated ethylene in [$Pt(C_2H_4)Cl_2L$] complexes is only stoichiometric and, furthermore, is limited to amines of sufficient basicity ($pK_a > 5$). We have pointed out that aniline ($pK_a = 4.63$) reacts catalytically with ethylene in the presence of the [$PtBr_2$]/*n*$Bu_4PBr$ system. Consequently, it seemed interesting to explore the scope of the reaction with regard to the basicity of the arylamine. Thus, anilines bearing different substituents were treated with ethylene under the conditions of [Equation (8)]. The results are reported in Table 5.

The results from Table 5 indicate that the lower the basicity of the arylamine, the higher the TON for the formation of the ArNHEt derivative. This observation is in contrast with that been reported for the stoichiometric reaction of amines with ethylene coordinated to $Pt^{II}$ centers (see above). It must be noted, however, that the observed dependence of the TON on the basicity of the arylamine may be the result of several effects, such as an increase in reactivity of the expected zwitterionic intermediate (see below), and a reduction in the poisoning ability of the ArNHEt derivative (the lower the basicity of $ArNH_2$, the lower the poisoning effect of ArNHEt). Interestingly, hydroamination of ethylene with 2-chloroaniline was fully chemoselective (run 22).

Table 5. Hydroamination of ethylene:[a,b] influence of the basicity of arylamines.[c]

| Run | Ar ($ArNH_2$) | $pK_a$ | Reaction products: TON | | |
|---|---|---|---|---|---|
| | | | PhNHEt | $PhNEt_2$ | "2-Me-quinoline" |
| 17 | 4-$MeOC_6H_4$ | 5.34 | 22 | ≈1 | 11 |
| 18 | 4-$MeC_6H_4$ | 5.08 | 55 | ≈1 | 17 |
| 19 | $C_6H_5$ | 4.63 | 80 | ≈1 | 11 |
| 20 | 2-$MeC_6H_4$ | 4.44 | 85 | ≈1 | 11 |
| 21 | 4-$ClC_6H_4$ | 4.15 | 93 | ≈1 | 11 |
| 22 | 2-$ClC_6H_4$ | 2.65 | 110 | – | – |

[a] [$PtBr_2$]: 0.13 mmol, *n*$Bu_4PBr$: 7.2 g. [b] 25 bar at room temperature, 10 h at 150 °C. [c] 45 mmol.

Finally, hydroamination of ethylene with 2-chloroaniline was performed by using the [$PtBr_2$]/*n*$Bu_4PBr$ system in the presence of $CF_3SO_3H$ (3 equiv. per mol of the Pt species). The reaction selectively afforded *N*-ethyl-2-chloroaniline with a TON of 250 after 10 h, corresponding to a 70% yield based on 2-chloroaniline. A nearly quantitative conversion of 2-chloroaniline was observed when using 1% of the catalyst system ([$PtBr_2$]/$3H^+$) in *n*$Bu_4PBr$ for 72 h at 150 °C [Equation (9)].

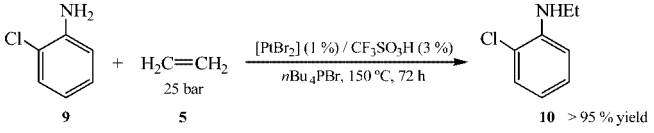


**9** **5** **10** > 95 % yield (9)

These results show, for the first time, that the platinum-catalyzed hydroamination of ethylene with arylamines is possible. The best results have been obtained for the hydroamination of ethylene with 2-chloroaniline by using a [$PtBr_2$]/*n*$Bu_4PBr$/3 $CF_3SO_3H$ system as catalyst. Such unprecedented catalytic performances for the hydroamination of ethylene led us to examine the catalytic activity of [$PtBr_2$]/*n*$Bu_4PBr$ systems for the hydroamination of higher alkenes.

### 2.3. Hydroamination of Higher Alkenes

The literature indicates that, in most cases, systems that exhibit activity for the hydroamination of ethylene fail when applied to higher olefins.[48,54,55] Thus, it was interesting to consider the [$PtBr_2$]/*n*$Bu_4PBr$ system for the hydroamination of a higher alkene such as 1-hexene. Furthermore, it was important to determine the regioselectivity of this reaction, in view of possible enantioselective intermolecular hydroamination reactions of simple alkenes.[22,23]

The first experiment was performed by reacting aniline with 1-hexene in the presence of [$PtBr_2$] in *n*$Bu_4PBr$ (150 equiv. per mol of the Pt species) for 10 h at 150 °C [Equation (10)]. The major product formed was the Markovnikov-type addition product *N*-(2-hexyl)aniline (**12**). The other regioisomer (anti-Markovnikov-type), *N*-(*n*-

 © 2007 Wiley-VCH Verlag GmbH & Co. KGaA, Weinheim 

hexyl)aniline (**13**), formed in much lower amounts (**12/13** ≈ 95:5).[56] Other side-products were identified as 2-propylquinoline (**14**, trace amounts)[57] and *N*-(2-hexenyl)aniline (**15**).

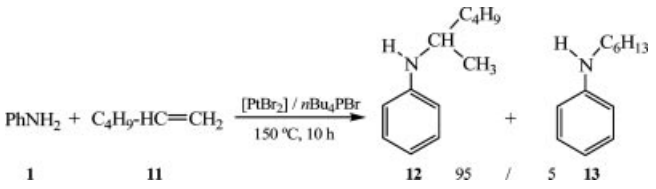


(10)

As expected, the reaction conducted in $n$Bu$_4$PBr was more efficient (10 cycles) than that conducted in thf (<1 cycle, control experiments). As for the hydroamination of ethylene (see above), the influence of the 1-hexene/Pt ratio was considered.

When the amount of 1-hexene was increased, the TON for (**12** + **13**) increased up to a maximum of 42 for a 1-hexene/Pt ratio of about 700. Higher ratios tended to decrease the TON. The regioselectivity of **12/13** is 95:5 (±1%), irrespective of the amount of 1-hexene used.

The very high regioselectivity (Markovnikov/anti-Markovnikov) was rather unexpected. Indeed, although no literature data is available on the stoichiometric addition of *aniline* to alkenes coordinated to $Pt^{II}$ complexes, it has been reported that the *Markovnikov* addition of other amines is favored only when steric factors do not interfere. This conclusion was drawn from the study of *stoichiometric* reactions of $Et_2NH$ with *cis*-[Pt(olefin)($PBu_3$)$Cl_2$] complexes [Equation (11)].[30b]

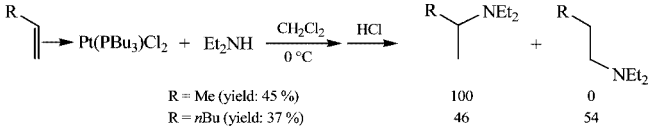


(11)

These literature data reveal a great difference in regioselectivity between the (stoichiometric) hydroaminations of propene (100% Markovnikov) and 1-hexene (46% Markovnikov, 54% anti-Markovnikov).[30b] The catalytic hydroamination of 1-hexene with our $Pt^{II}$ system thus appears remarkable, both from the point of view of catalytic efficiency and regioselectivity.

Considering now the ratio of the reagents for the best results in terms of TON, we were interested in better understanding the role of $n$Bu$_4$PBr. For the experiment, 7 g of $n$Bu$_4$PBr for 4.1 mL of aniline and 11.5 mL of 1-hexene was used. Under these conditions, $n$Bu$_4$PBr cannot truly be considered as a solvent. We therefore studied the influence of the amount of $n$Bu$_4$PBr for reactions conducted with a 1-hexene/aniline/[$PtBr_2$] ratio of 700:350:1. When the amount of $n$Bu$_4$PBr was increased from 0 to 65 equiv. per mol of [$PtBr_2$], an increase in the hydroamination TON for (**12** + **13**) from ca. 1 to 57 was observed. The TON slightly decreased to 42 when using higher $n$Bu$_4$PBr/[$PtBr_2$] ratios. The regioselectivity **12**:**13** is unchanged, irrespective of the $n$Bu$_4$PBr/[$PtBr_2$] ratio used.

These experiments confirm that $n$Bu$_4$PBr has a promoting role on the catalytic activity of the [$PtBr_2$] precursor. Furthermore, they show that the phosphonium bromide has also a limiting effect when used in larger amounts. This observation may suggest the participation of the bromide ions of $n$Bu$_4$PBr in an equilibrium implicating the active platinum species (vide infra).

On the basis of these promising results, we examined the evolution of the reaction with time under the best conditions determined so far. This study was intended to detect possible catalyst poisoning. The results indicate some activity decrease with time, but this is much less pronounced than that for the corresponding hydroamination of ethylene. This observation may be due to several facts. Firstly, the main reaction product, *N*-(2-hexyl)aniline is much more sterically demanding than *N*-ethylaniline, which results in the retarded formation of the inactive bis(*N*-alkylaniline)platinum(II) species. Secondly, this decrease in activity could simply be due to the decrease in the 1-hexene concentration, which was shown to be an important parameter (see above). Finally, this observation could also be due to the isomerization of 1-hexene. Hence, the composition of the alkene fraction was examined at the end of several runs ($^1$H NMR spectroscopic analysis). The results indicate that the [$PtBr_2$]/$n$Bu$_4$PBr system is a poor isomerization catalyst (irrespective of the reaction pathway).[58]

The promoting effect of $n$Bu$_4$PBr for the [$PtBr_2$]-catalyzed hydroamination of alkenes was thus confirmed, but remained to be explained. The study of the hydroamination of norbornene with aniline (vide supra) indicates that for a given cationic moiety, ionic solvents associated with a bromide ion give a higher catalytic efficiency than those associated with a chloride ion. This observation was confirmed for the hydroamination of 1-hexene with aniline. Indeed, replacement of $n$Bu$_4$PBr by $n$Bu$_4$PCl resulted in the formation of (**12** + **13**) with a TON of 5 (instead of 57). It is thus clear that the anionic part of the phosphonium salt plays an important role: in contrast to chloride ions, bromide ions strongly enhance the catalytic activity. Such halide ion effects have already been observed, but are generally poorly understood,[59–61] except in some cases.[62]

A possible explanation for the promoting role of $n$Bu$_4$PBr is outlined below (Scheme 3). For simplicity, the alkene considered is ethylene and the [$n$Bu$_4$P]$^+$ cation has been omitted.

Equilibria (a) and (b) represent the solubilization of [$PtBr_2$] in phosphonium bromide and the coordination of ethylene. These steps are analogous to the formation of the Zeise's salt from $K_2$[$PtCl_4$] and ethylene in water.[29] Note that the platinum–olefin bond in [$PtBr_3(C_2H_4)$]$^-$ is known to be stronger than that in the chlorido equivalent.[63] In such complexes, the ethylene ligand is displaced by halide ions at high concentrations,[29] which could be the reason for the decrease in activity when very large amounts of $n$Bu$_4$PBr are present (vide supra).

 © 2007 Wiley-VCH Verlag GmbH & Co. KGaA, Weinheim 

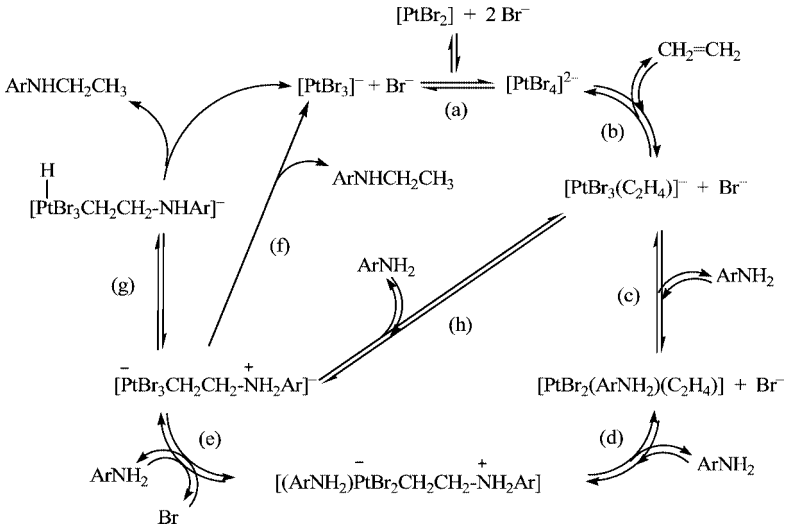


Scheme 3. $Pt^{II}$-catalyzed hydroamination of ethylene promoted by bromide ions.

Equilibrium (c) represents the displacement of a halide ligand by aniline, similar to that involved in the formation of e.g. *trans*-$[PtCl_2(C_2H_4)(amine)]$ by reaction of $K[PtCl_3(C_2H_4)]$ with an amine.[64] This equilibrium may be shifted to the left in the presence of a very large excess of bromide ions.

Equilibrium (d) corresponds to the *external*[30c] nucleophilic attack of aniline on the neutral $[PtBr_2(C_2H_4)(C_6H_5NH_2)]$ complex to generate the corresponding zwitterionic complex. However, as indicated above, zwitterionic complexes derived from the attack of aniline have never been observed in detectable quantities (NMR spectroscopy), a failure attributed to the insufficient basicity of aniline. Nevertheless, from our work, the hydroamination of 1-hexene by aniline conducted at *150 °C* with $[PtBr_2]$ in the *absence* of $nBu_4PBr$ afforded (**12** + **13**) in nearly stoichiometric amounts. This confirms that the attack of aniline on an alkene coordinated to $[PtBr_2]$ is possible, provided that the reaction is conducted at high temperature. This result may be due to a temperature-promoted evolution of the zwitterionic complex by a further proton-transfer step (vide infra).

DFT calculations by Togni et al. strongly suggest that the platinum–carbon bond cleavage by protonolysis should be the determining step for the *catalytic* hydroamination of ethylene with ammonia.[49] In our opinion, this proton transfer should be facilitated by two parameters: the acidity of the N–H proton (ammonium part) and the basicity of the platinum center. The acidity of the proton is inversely related to the basicity of the aniline: the less basic the starting arylamine, the easier the proton transfer to the negative center. This hypothesis seems to be confirmed by our observation that the less basic aniline gave the highest TONs for the hydroamination of ethylene. For the basicity of the platinum center in the zwitterionic complex, the intervention of equilibrium (e) may possibly explain the promoting role of the bromide ions (generation of a platinum center bearing *formally* two negative charges). Note that the direct addition of aniline to $[PtBr_3(C_2H_4)]^-$ should lead to the same highly reactive zwitterionic complex [equilibrium (h)]. The liberation of the alkylated aniline proceeds either by direct protonolysis of the platinum–carbon bond [path (f)] or via a platinum hydride, followed by reductive elimination [path (g)].

Another point has to be considered. During the *catalytic* hydroamination of ethylene with aniline, a gradual poisoning effect was observed, which could be attributed to the reaction product *N*-ethylaniline. Apparently, the possible poisoning by aniline itself is not significant, and the poisoning effect of *N*-ethylaniline does not prohibit catalysis, at least to some extent (TON = 80). It is tentatively proposed that the poisoning effect by the alkylated aniline is attenuated by the presence of an excess of bromide ions. The latter may prevent the competitive formation of catalytically inactive species by keeping the platinum species in the forms involved in equilibria (a)–(c). A more complete study of the effect of the halide ions on hydroamination reactions has recently been carried out and is presented further on in this review.

Finally, the role of an added catalytic source of protons was examined. Reactions performed under standard conditions, except for the additional presence of anilinium sulfate (3 equiv. per mol of the Pt species), allowed the formation of (**12** + **13**) with 70 cycles for a reaction time of 10 h, 180 cycles after 48 h, and finally 243 cycles after 96 h [Equation (12)] (70% yield based on aniline). Interestingly,

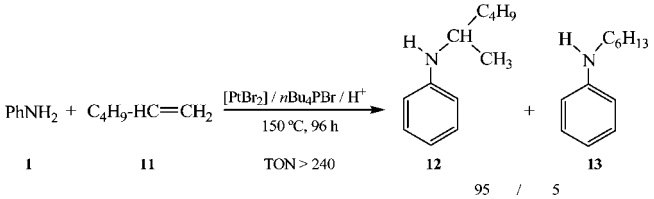


(12)

 © 2007 Wiley-VCH Verlag GmbH & Co. KGaA, Weinheim 

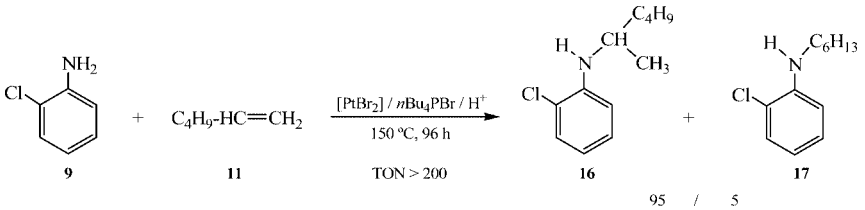


(13)

under the above conditions, the formation of the side-products **14** and **15** is limited to only traces (TON < 1).

Control experiments showed that, in the *absence* of $n$Bu$_4$PBr, the [PtBr$_2$]/H$^+$ system allowed the formation of (**12** + **13**) with a TON of about 10, thus evidencing that the major activation is induced by $n$Bu$_4$PBr. Furthermore, in the absence of [PtBr$_2$], the $n$Bu$_4$PBr/H$^+$ system yielded (**12** + **13**) with a TON of 2 (vs. H$^+$ catalyst), which indicates that simple Brønsted catalysis is not significant.

Lastly, the hydroamination of 1-hexene with 2-chloroaniline, catalyzed by the [PtBr$_2$]/$n$Bu$_4$PBr/CF$_3$SO$_3$H system, afforded the expected alkylated chloroanilines (**16** + **17**) with TON = 200 and a 95% Markovnikov selectivity [Equation (13)].

From a practical point of view, it is very important to note that the above *Pt$^{II}$-catalyzed hydroamination reactions can be conducted under aerobic conditions without loss in yield*. To the best of our knowledge, the ligandless, cheap and nontoxic [PtBr$_2$]/$n$Bu$_4$PBr/H$^+$ system is the most efficient ever reported (up to the end of 2006) for the catalytic *intermolecular* hydroamination of an α-olefin such as 1-hexene.

### 2.4. Platinum-Catalyzed Transformation of Anilines into 2-Alkylquinolines

During the above studies, some unexpected observations involving the formation of quinoline derivatives were noticed. These have been examined in more detail, which allows the very interesting properties of Pt$^{II}$-based catalysts for different C–H activation processes to be highlighted.[65] Although these studies are beyond the scope of this paper, we have evidenced, for the first time, that 2-alkylquinolines are formed by a multistep, platinum(II)-catalyzed, in situ transformation of *N*-alkylanilines (Scheme 4).[66] In other words, quinoline derivatives originate from the primary hydroamination products. This new, platinum(II)-catalyzed transformation is strongly favored by the presence of an alkene (hydrogen acceptor) and compares favorably with the recently reported ruthenium-catalyzed formation of 2-alkylquinoline from aniline and trialkylamines.[67]

### 2.5. The Promoting Effect of Halide Ions for the Pt$^{II}$-Catalyzed Hydroamination of Alkenes

In the early stages of this work, ionic liquids and molten salts were first considered as solvents. The beneficial effect of some of them, especially $n$Bu$_4$PBr, was identified for the hydroamination of norbornene and ethylene. However, for the hydroamination of 1-hexene, it was pointed out that the catalytic efficiency depended upon both the $n$Bu$_4$PX/[PtBr$_2$] ratio and the nature of the anion (Br$^-$ >> Cl$^-$). This is obviously the heart of the matter since, under classical conditions, the reaction of amines with Pt$^{II}$–alkene complexes leads to stable zwitterionic species.[30d]

In order to deepen our understanding, we investigated the influence of the $n$Bu$_4$PX/[PtBr$_2$] ratio as well as that of the nature of the associated halide anion X$^-$ on the hydroamination of ethylene with aniline. For this study, experiments were conducted without the H$^+$ cocatalyst in order to better observe, if possible, the influence of the phosphonium halides.

At first, it was verified that in the absence of [PtBr$_2$] no reaction occurred between aniline (45 mmol) and ethylene (25 bar, ca. 100 mmol) over 96 h at 150 °C. For these control experiments, the presence of $n$Bu$_4$PBr (ca. 7 g) had no effect. In contrast, [PtBr$_2$]-based systems exhibited catalytic activity for the formation of hydroamination products. Two parameters have been considered: the nature of the halide anion X$^-$ associated with the phosphonium salt $n$Bu$_4$PX and the $n$Bu$_4$PX/[PtBr$_2$] ratio. The most general reaction is represented by [Equation (14)].

Compounds **6** and **7** are direct hydroamination products. Since the formation of **8** was shown to occur in situ from 2 equiv. of **6** (vide supra), the activity of the catalytic system is best represented by the total TON calculated for the amount of **6** initially formed (Table 6, see footnote [b]).[68]

As shown in Table 6, the three phosphonium halides enhance the catalytic activity. For $n$Bu$_4$PCl, the maximum activity was obtained using 65 equiv. of phosphonium halide, whereas for both $n$Bu$_4$PBr and $n$Bu$_4$PI, the maximum catalytic activity was reached with a $n$Bu$_4$PX/[PtBr$_2$] ratio of approximately 10. It is quite clear that these phosphonium halides, first intended to play the role of ionic solvents,[50,53]

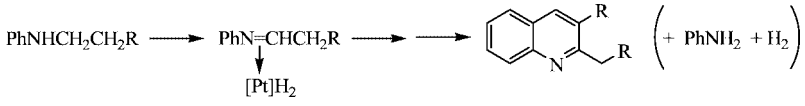


Scheme 4. Formation of 2-alkylquinolines from *N*-alkylanilines.

 © 2007 Wiley-VCH Verlag GmbH & Co. KGaA, Weinheim 

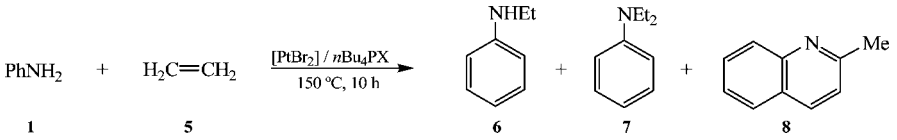


1 5 6 7 8 (14)

Table 6. Hydroamination of ethylene with aniline catalyzed by $[PtBr_2]/nBu_4PX$ systems.[a]

| Run | $nBu_4PX$ (equiv. per mol Pt) | $[PtBr_2]$ [mmol] | Total TON[b] | Reaction products: % 6 | 7 | 8 |
|---|---|---|---|---|---|---|
| 23 | – | – | – | – | – | – |
| 24 | – | 0.13 | 20 | 100 | – | – |
| 25 | $nBu_4PCl$ (10) | 0.13 | 50 | 91 | – | 9 |
| 26 | $nBu_4PCl$ (65) | 0.13 | 105 | 92 | 2 | 6 |
| 27 | $nBu_4PCl$ (150) | 0.13 | 80 | 95 | 1 | 3 |
| 28 | $nBu_4PBr$ (5) | 0.13 | 140 | 88 | 4 | 7 |
| 29 | $nBu_4PBr$ (10) | 0.13 | 150 | 89 | 3 | 8 |
| 30 | $nBu_4PBr$ (65) | 0.13 | 130 | 87 | 2 | 11 |
| 31 | $nBu_4PBr$ (150) | 0.13 | 88 | 86 | 1 | 11 |
| 32 | $nBu_4PI$ (5) | 0.13 | 110 | 93 | 2 | 4 |
| 33 | $nBu_4PI$ (10) | 0.13 | 135 | 90 | 2 | 7 |
| 34 | $nBu_4PI$ (65) | 0.13 | 100 | 80 | 1 | 17 |
| 35 | $nBu_4PI$ (150) | 0.13 | 5 | 100 | – | – |

[a] Aniline: 45 mmol, ethylene: 25 bar at room temperature (ca. 100 mmol), 150 °C, 10 h. [b] Turnover number, TON calculated as $TON_6 + TON_7 + 2\ TON_8$.

must rather be considered as promoters or cocatalysts. However, very large quantities of these "promoters" decrease their positive effect, so that their role is difficult to rationalize. The "promoting" order of the $nBu_4PX$ salts for the hydroamination of ethylene seems to be $Br^- > I^- > Cl^-$.

The $[PtBr_2]/nBu_4Br$ system is the only efficient catalyst reported so far for the hydroamination of 1-hexene with aniline. Since this reaction occurs with a particularly promising regioselectivity (95% Markovnikov), it was interesting to compare the activating ability of several $nBu_4PX$ salts associated with $[PtBr_2]$ with their possible influence on the regioselectivity [Equation (15)]. The most significant results are summarized in Table 7.[68]

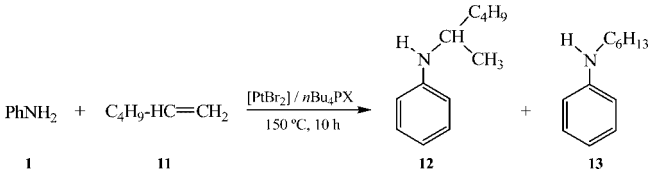


1 11 12 13 (15)

As may be seen from Table 7,[68] $[PtBr_2]$ alone did not catalyze the hydroamination of 1-hexene with aniline (run 36). In the same way, association of $[PtBr_2]$ with either $nBu_4PPF_6$ or $nBu_4PCl$ (runs 37 and 38) resulted in very low TONs. In contrast, as already found, association with $nBu_4PBr$ promoted a significant catalytic activity (TON = 57, run 39). An even higher activity was obtained with the $[PtBr_2]/nBu_4PI$ system, for which a TON of 83 was reached (run 40). For Equation (15), the "promoting" effect of the

Table 7. Hydroamination of 1-hexene with aniline catalyzed by $[PtBr_2]/nBu_4PX$ systems.[a]

| Run | Catalytic system | Total TON (**12** + **13**) | Regioselectivity (**12**/**13**) |
|---|---|---|---|
| 36 | $[PtBr_2]$ | 1 | n.d. |
| 37 | $[PtBr_2]/nBu_4PPF_6$ | 3 | n.d. |
| 38 | $[PtBr_2]/nBu_4PCl$ | 5 | n.d. |
| 39 | $[PtBr_2]/nBu_4PBr$ | 57 | 95:5 |
| 40 | $[PtBr_2]/nBu_4PI$ | 83 | 95:5 |
| 41 | $[PtBr_2]/nBu_4PBr/I_2$[b] | 115 | 95:5 |

[a] Aniline: 45 mmol, 1-hexene: 90 mmol, $[PtBr_2]$: 0.13 mmol, $nBu_4PX$: 8.45 mmol, 150 °C, 10 h. [b] $I_2$: 0.13 mmol.

phosphonium halides varies as $I^- > Br^- >> Cl^-$. The nature of the halide anion has no effect on the regioselectivity.

Iodide effects in transition-metal-catalyzed reactions are well known, and in some cases their role has been rationalized.[62] The beneficial effect of molecular iodine (generally used in large amounts) has also been observed in some transition-metal-catalyzed reactions.[69] This proved to be the case also for the $Pt^{II}$-catalyzed hydroamination of 1-hexene. With the new $[PtBr_2]/nBu_4PBr/I_2$ system (1:65:1 ratio), an even higher activity (TON = 115, run 41) than that obtained with the $[PtBr_2]/nBu_4PBr$ system (TON = 57, run 39) was reached. The use of higher amounts of iodine (vs. $[PtBr_2]$) had no beneficial effect on the TON.

These results agree with the general mechanism proposed (see Scheme 3), but suggest that the halide anions also play a role in other step(s) of the catalytic cycle, such as the coordination of the alkene and the attack of aniline on the coordinated alkene, or even by postponing poisoning effects.

Drent et al. recently reported a detailed study of the halide-anion-promoted palladium-catalyzed hydroformylation of internal alkenes to linear alcohols.[70] In the case of the [(bcope)Pd(OTf)$_2$] complex [bcope = bis(cyclooctyl)phosphinoethane], they found that the use of substoichiometric amounts (vs. Pd) of added halide anions strongly promoted the reaction rate. Most of their observations were rationalized in a qualitative way. However, it is clear that the halide-anion-promoting effect pointed out in the present work is different (no phosphorus ligand), and further detailed studies are required to gain a complete insight into these phenomena.

We have nevertheless shown that $nBu_4PX$ salts (X = $Cl^-$, $Br^-$, $I^-$) have a strong promoting effect on the $Pt^{II}$-catalyzed hydroamination of ethylene and 1-hexene with aniline. In the case of ethylene, $nBu_4PBr$ is the most efficient activator, whereas $nBu_4PI$ is more efficient than $nBu_4PBr$ in the case of 1-hexene. A special effect of molecular iodine has also been pointed out.[68]

 © 2007 Wiley-VCH Verlag GmbH & Co. KGaA, Weinheim 

### 2.6. $Pt^{IV}$ Salts Also Allow the Hydroamination Reaction!

In the course of the above studies, we examined the properties of $Pt^{IV}$ salts as catalytic precursors for the hydroamination of ethylene with aniline [see Equation (14)]. To the best of our knowledge, no hydroamination reaction, neither stoichiometric nor catalytic, has ever been reported by using $Pt^{IV}$ precursors.[21,29] The first results of this study are summarized in Table 8. Both $Pt^{IV}$ salts and $Pt^{IV}/n$Bu$_4$X systems (1:65 ratio) have been considered.

Table 8. Hydroamination of ethylene with aniline catalyzed by $Pt^{IV}$-based systems.[a]

| Run | $Pt^{IV}$ system | $n$Bu$_4$PX/[PtBr$_2$] ratio | Total TON[b] | Reaction products:% 6 | 7 | 8 |
|---|---|---|---|---|---|---|
| 42 | [PtBr$_4$] | – | 50 | 89 | 4 | 7 |
| 43 | [PtBr$_4$]/$n$Bu$_4$PCl | 65 | 75 | 84 | 14 | 2 |
| 44 | [PtBr$_4$]/$n$Bu$_4$PBr | 65 | 135 | 85 | 6 | 7 |
| 45 | [PtBr$_4$]/$n$Bu$_4$PI | 65 | 110 | 84 | 2 | 13 |
| 46 | [PtCl$_4$] | – | 15 | 100 | – | – |
| 47 | [PtCl$_4$]/$n$Bu$_4$PCl | 65 | 45 | 98 | 2 | – |
| 48 | [PtCl$_4$]/$n$Bu$_4$PBr | 65 | 120 | 90 | 3 | 7 |
| 49 | [PtCl$_4$]/$n$Bu$_4$PI | 65 | 110 | 86 | 2 | 11 |

[a] Aniline: 45.5 mmol, ethylene: 25 bar at room temperature (ca. 100 mmol), [PtX$_4$]: 0.13 mmol, 150 °C, 10 h. [b] Turnover number, TON calculated as $TON_6 + TON_7 + 2\,TON_8$.

The first and most important feature that emerges from Table 8 is that $Pt^{IV}$ bromide and chloride are shown for the first time to exhibit a catalytic activity for the hydroamination reaction: [PtBr$_4$] (run 42) is even more active than [PtBr$_2$] (run 24, Table 6).[71] Secondly, association of $n$Bu$_4$PX with these catalytic precursors promotes a significant increase in the catalytic activity. Although the role of the $n$Bu$_4$PX/$Pt^{IV}$ ratio has not yet been studied, the most efficient "promoter" seems to be $n$Bu$_4$PBr, as was the case for the $Pt^{II}$ systems (see above). For both $Pt^{II}$ and $Pt^{IV}$ catalytic precursors, the promoting ability exhibited by the phosphonium halide seems to follow the order $Br^- > I^- >> Cl^-$. It is again tentatively suggested that this unusual order is indicative that these halide anions play a role in different steps of the catalytic cycle.

## Conclusions

In the previous sections, we have described our progress in the study of the catalytic hydroamination of *nonactivated* alkenes with arylamines. Starting from the idea that molten salts or ionic liquids may be used as solvents for such reactions, we managed to show that tetraalkylphosphonium halides, in fact, play the role of "promoters", especially $n$Bu$_4$PBr and $n$Bu$_4$PI. It has been clearly evidenced that the promoting effect of these "cocatalysts" depends only upon their anionic moiety. The role of these anions is difficult to rationalize at the present time. Nevertheless, we succeeded in designing catalytic $Pt^{II}$- and $Pt^{IV}/n$Bu$_4$PX systems that are the most active catalysts reported to date for the hydroamination of ethylene with amines, especially weakly basic amines such as anilines. The $Pt^{II}/n$Bu$_4$PBr combination exhibits an unprecedented catalytic activity for the hydroamination of a higher alkene such as 1-hexene. In addition, the hydroamination of α-olefins has been found to occur with a very high regioselectivity (> 95%, Markovnikov), which opens the possibility to study an enantioselective version of this reaction. The interest in these promising catalytic systems for possible applications is heightened by the fact that the reactions can be conducted under aerobic conditions without loss of yield.

## Acknowledgments

The Centre National de la Recherche Scientifique (France) is acknowledged for financial support. The authors gratefully acknowledge Dr. F. Malbosc (Solvionic) for helpful discussions.

[1] M. Turcotte, K. S. Hayes in *Kirk-Othmer Encyclopedia of Chemistry and Technology*, Wiley & Sons, New York, **2001**, vol. 2, pp. 537–553.
[2] K. Visek in *Kirk-Othmer Encyclopedia of Chemistry and Technology*, Wiley & Sons, New York, **2003**, vol. 2, pp. 518–537.
[3] P. J. Chenier in *Survey of Industrial Chemistry*, 2nd ed., VCH, Weinheim, **1992**.
[4] K. Weissermel, H.-J. Harpe in *Industrial Organic Chemistry*, 2nd ed., VCH, Weinheim, **1993**.
[5] V. Grignard in *Traité de Chimie Organique*, Masson & Cie, Paris, **1935**, vol. 12.
[6] J. March in *Advanced Organic Chemistry*, 4th ed., Wiley & Sons, New York, **1992**.
[7] P. Sabatier, A. Mailhe, *Compt. Rend. Sc. Heb. Acad. Sci.* **1909**, *148*, 898.
[8] A. Baiker, J. Kijenski, *Catal. Rev. Sci. Eng.* **1985**, *27*, 653–697.
[9] S. A. Lawrence in *Amines*, Cambridge University Press, Cambridge, **2004**.
[10] J. Falbe in *New Syntheses with Carbon Monoxide*, Springer Verlag, Berlin, **1980**.
[11] F. Alonso, I. P. Beletskaya, M. Yus, *Chem. Rev.* **2004**, *104*, 3079–3159.
[12] *Tetrahedron* Report 144, M. B. Gasc, A. Lattes, J. J. Perié, *Tetrahedron* **1983**, *39*, 703–731.
[13] D. Steinborn, R. Taube, *Z. Chem.* **1986**, 349–359.
[14] J. J. Brunet, D. Neibecker, F. Niedercorn, *J. Mol. Catal.* **1989**, *49*, 235–259.
[15] D. M. Roundhill, *Chem. Rev.* **1992**, *92*, 1–27.
[16] R. Taube in *Applied Homogeneous Catalysis with Organometallic Complexes* (Eds.: B. Cornils, W. Herrmann), VCH, Weinheim, **1996**, vol. 2, pp. 507–521.
[17] D. M. Roundhill, *Catal. Today* **1997**, *37*, 155–165.
[18] J. J. Brunet, *Gazz. Chim. Ital.* **1997**, *127*, 111–118.
[19] a) T. E. Müller, M. Beller, *Chem. Rev.* **1998**, *98*, 675–703; b) T. E. Müller, M. Beller in *Transition Metals for Organic Synthesis* (Eds.: M. Beller, C. Bolm), Wiley-VCH, Weinheim, **1998**, vol. 2, pp. 316–330; c) M. Beller, J. Seyad, A. Tillack, H. Jiao, *Angew. Chem. Int. Ed.* **2004**, *43*, 3368–3398.
[20] H. F. Koch, L. A. Girard, D. M. Roundhill, *Polyhedron* **1999**, *18*, 2275–2279.
[21] a) J-J. Brunet, D. Neibecker in *Catalytic Heterofunctionalization* (Eds.: A. Togni, H. Grützmacher), VCH, Weinheim, **2001**, pp. 91–141; b) M. Beller, C. Breindl, M. Eichberger, C. Hartung, J. Seayad, O. R. Thiel, A. Tillack, H. Trauthwein, *Synlett* **2002**, *10*, 1579–1594.
[22] P. W. Roesky, T. E. Müller, *Angew. Chem. Int. Ed.* **2003**, *42*, 2708–2710.
[23] K. C. Hultzsch, *Adv. Synth. Catal.* **2005**, *347*, 367–391.
[24] *Transition metal catalysts*: a) U. Nettekoven, J. F. Hartwig, *J. Am. Chem. Soc.* **2002**, *124*, 1166–1167; b) M. Utsunomiya, R.

 © 2007 Wiley-VCH Verlag GmbH & Co. KGaA, Weinheim 

Kuwano, M. Kawatsura, J. F. Hartwig, *J. Am. Chem. Soc.* **2003**, *125*, 5608–5609; c) M. Utsunomiya, J. F. Hartwig, *J. Am. Chem. Soc.* **2003**, *125*, 14286–14287; d) M. Utsunomiya, J. F. Hartwig, *J. Am. Chem. Soc.* **2004**, *126*, 2702–2703; e) J. F. Hartwig, *Pure Appl. Chem.* **2004**, *76*, 507–516; f) H. Qian, R. A. Widenhoefer, *Org. Lett.* **2005**, *7*, 2635–2638; g) L. T. Kaspar, B. Fingerhut, L. Ackermann, *Angew. Chem. Int. Ed.* **2005**, *44*, 5972–5974; h) O. Jimenez, T. E. Müller, C. Sievers, A. Spirkl, J. A. Lercher, *Chem. Commun.* **2006**, 2974–2976. *Base catalysts*: i) M. Beller, C. Breindl, *Tetrahedron* **1998**, *54*, 6359–6368; j) M. Beller, C. Breindl, T. H. Riermeier, M. Eichberger, H. Trauthwein, *Angew. Chem. Int. Ed.* **1998**, *37*, 3389–3391; k) J. Herwig, M. Beller, C. Breindl, WO 9936412, **1999**; l) D. Tzalis, C. Koradin, P. Knochel, *Tetrahedron Lett.* **1999**, *40*, 6193–6195.

[25] a) J. Pawlas, Y. Nakao, M. Kawatsura, J. F. Hartwig, *J. Am. Chem. Soc.* **2002**, *124*, 3669–3679; b) C. Brouwer, C. He, *Angew. Chem. Int. Ed.* **2006**, *45*, 1744–1747; c) A. M. Johns, M. Utsunomiya, C. D. Incarvito, J. F. Hartwig, *J. Am. Chem. Soc.* **2006**, *128*, 1828–1839; d) H. Qin, N. Yamagiwa, S. Matsunaga, M. Shibasaki, *J. Am. Chem. Soc.* **2006**, *128*, 1611–1614.

[26] For an external analysis of the work developed by Hartwig et al. on the hydroamination of vinylarenes, see: J. J. Brunet, R. Poli, *Chemtracts: Inorg. Chem.* **2004**, *17*, 381–387.

[27] a) Y. K. Kim, T. Livinghouse, Y. Horino, *J. Am. Chem. Soc.* **2003**, *125*, 9560–9561; b) J. Collin, J.-C. Daran, E. Schulz, A. Trifonov, *Chem. Commun.* **2003**, 3048–3049; c) K. C. Hultzsch, F. Hampel, T. Wagner, *Organometallics* **2004**, *23*, 2601–2612; d) S. Hong, T. J. Marks, *Acc. Chem. Res.* **2004**, *37*, 673–686; e) J. Y. Kim, T. Livinghouse, *Org. Lett.* **2005**, *7*, 4391–4393; f) K. Komeyama, T. Morimoto, K. Takaki, *Angew. Chem. Int. Ed.* **2006**, *45*, 2938–2941; g) X. Y. Liu, C. H. Li, C. M. Che, *Org. Lett.* **2006**, *8*, 2707–2710; h) S. Bambirra, H. Tsurugi, D. van Leusen, B. Hessen, *Dalton Trans.* **2006**, 1157–1161; i) M. Rastätter, A. Zulys, P. W. Roesky, *Chem. Commun.* **2006**, 874–876; j) D. Riegert, J. Collin, A. Medour, E. Schultz, A. Trifonov, *J. Org. Chem.* **2006**, *71*, 2514–2517; k) A. Takemiya, J. F. Hartwig, *J. Am. Chem. Soc.* **2006**, *128*, 6042–6043; l) C. Müller, C. Loos, N. Schulenberg, S. Doye, *Eur. J. Org. Chem.* **2006**, 2499–2503; m) D. A. Watson, M. Chiu, R. G. Bergman, *Organometallics* **2006**, *25*, 4731–4733; n) J. Zhao, T. J. Marks, *Organometallics* **2006**, *25*, 4763–4772; o) D. V. Gribkov, K. C. Hultzsch, F. Hampel, *J. Am. Chem. Soc.* **2006**, *128*, 3748–3759; p) K. Khedkar, A. Tillack, C. Benisch, J. P. Melder, M. Beller, *J. Mol. Catal. A* **2005**, *241*, 175–183.

[28] a) T. E. Daubert, R. P. Danner in *Physical Thermodynamic Properties of Pure Chemicals: Data Compilation*, Taylor & Francis, Washington, DC, **1993**; b) J. B. Pedley, R. D. Naylor, S. P. Kirby in *Thermochemical Data of Organic Compounds*, 2nd ed., Chapman and Hall, London, **1986**, Appendix Table 1.2.

[29] F. R. Hartley in *Comprehensive Organometallic Chemistry*, (Eds: G. Wilkinson, F. G. A Stone, E. W. Abel), Pergamon Press, **1982**, vol 6, pp. 471–762.

[30] a) A. Panunzi, R. Palumbo, A. De Renzi, G. Paiaro, *Chim. Ind. (Milan)* **1968**, *50*, 924–925; b) A. Panunzi, A. De Renzi, R. Palumbo, G. Paiaro, *J. Am. Chem. Soc.* **1969**, *91*, 3879–3883; c) A. Panunzi, A. De Renzi, G. Paiaro, *J. Am. Chem. Soc.* **1970**, *92*, 3488–3489; d) E. Benedetti, A. De Renzi, G. Paiaro, A. Panunzi, C. Pedone, *Gazz. Chim. Ital.* **1972**, *102*, 744–754; e) V. Romano, G. Paiaro, *Chim. Ind. (Milan)* **1972**, *54*, 658–659; f) P. D. Kaplan, P. Schmidt, M. Orchin, *J. Am. Chem. Soc.* **1968**, *90*, 4175–4176.

[31] D. Hollings, M. Green, D. V. Claridge, *J. Organomet. Chem.* **1973**, *54*, 399–402.

[32] a) J. Ambühl, P. S. Pregosin, L. M. Venanzi, G. Ughetto, L. Zambonelli, *Angew. Chem. Int. Ed. Engl.* **1975**, *14*, 369; b) J. Ambuehl, P. S. Pregosin, L. M. Venanzi, G. Ughetto, *J. Organomet. Chem.* **1978**, *160*, 329–335; c) J. Ambuehl, P. S. Pregosin, L. M. Venanzi, G. Consiglio, F. Bachechi, L. Zambonelli, *J. Organomet. Chem.* **1979**, *181*, 255–269.

[33] a) I. M. Al-Najjar, M. Green, S. J. Kerrison, P. J. Sadler, *J. Chem. Soc. Chem. Commun.* **1979**, 311–312; b) I. M. Al-Najjar, M. Green, *J. Chem. Soc. Dalton Trans.* **1979**, 1651–1656; c) M. Green, J. K. K. Sarhan, I. M. Al-Najjar, *J. Chem. Soc. Dalton Trans.* **1981**, 1565–1571; d) J. K. K. Sarhan, M. Green, I. M. Al-Najjar, *J. Chem. Soc. Dalton Trans.* **1984**, 771–777.

[34] Venanzi et al.[32] reported a platinum-promoted cyclization of aminoalkenes (e.g. 1-pentenylamine) that may appear catalytic in character. However, as noted by the authors, the reaction rates are so low that "its synthetic exploitation would not represent a significant improvement over existing stoichiometric processes".

[35] J. J. Brunet, M. Cadena, N. C. Chu, O. Diallo, K. Jacob, E. Mothes, *Organometallics* **2004**, *23*, 1264–1268.

[36] a) X. Wang, R. A. Widenhoefer, *Organometallics* **2004**, *23*, 1649–1651; b) C. F. Bender, R. A. Widenhoefer, *J. Am. Chem. Soc.* **2005**, *127*, 1070–1071.

[37] D. Karshtedt, A. T. Bell, T. D. Tilley, *J. Am. Chem. Soc.* **2005**, *127*, 12640–12646.

[38] J. J. Brunet, D. Neibecker, K. Philippot, *J. Chem. Soc. Chem. Commun.* **1992**, 1215–1216.

[39] J. J. Brunet, G. Commenges, D. Neibecker, K. Philippot, *J. Organomet. Chem.* **1994**, *469*, 221–228.

[40] J. J. Brunet, G. Commenges, D. Neibecker, K. Philippot, L. Rosenberg, *Inorg. Chem.* **1994**, *33*, 6373–6379.

[41] J. J. Brunet, G. Commenges, D. Neibecker, L. Rosenberg, *J. Organomet. Chem.* **1996**, *522*, 117–122.

[42] M. Badri, J. J. Brunet, R. Perron, *Tetrahedron Lett.* **1992**, *33*, 4435–4438.

[43] a) T. Welton, *Chem. Rev.* **1999**, *99*, 2071–2083; b) P. Wasserscheid, W. Keim, *Angew. Chem. Int. Ed.* **2000**, *39*, 3772–3789; c) R. Sheldon, *Chem. Commun.* **2001**, 2399–2407.

[44] H. Olivier-Bourbigou, L. Magna, *J. Mol. Catal. A* **2002**, *182–183*, 419–437.

[45] J. Dupont, R. F. De Souza, P. A. Z. Suarez, *Chem. Rev.* **2002**, *102*, 3667–3692.

[46] P. Wasserscheid, T. Welton (Eds.), *Ionic Liquids in Synthesis*, Wiley-VCH, Verlag GmbH & Co, Weinheim, **2002**.

[47] D. R. Coulson (E. I. du Pont de Nemours and Co.), US 3,758,586, **1973**.

[48] D. R. Coulson, *Tetrahedron Lett.* **1971**, *12*, 429–430.

[49] H. M. Senn, P. E. Blöchl, A. Togni, *J. Am. Chem. Soc.* **2000**, *122*, 4098–4107.

[50] J. J. Brunet, N. C. Chu, O. Diallo, E. Mothes, *J. Mol. Catal. A* **2003**, *198*, 107–110.

[51] E. R. Perez, R. M. Carvalho, R. H. A. Santos, M. T. P. Gambardella, B. S. Lima-Neto, *Polyhedron* **2003**, *22*, 3289–3292.

[52] a) S. E. Diamond, A. Szalkiewicz, F. Mares, *J. Am. Chem. Soc.* **1979**, *101*, 490–491; b) S. E. Diamond, F. Mares (Allied Chemical Corp.), US 4,215,218, **1980**.

[53] J. J. Brunet, M. Cadena, N. C. Chu, O. Diallo, K. Jacob, E. Mothes, *Organometallics* **2004**, *23*, 1264–1268.

[54] a) G. Pez, J. E. Galles, *Pure Appl. Chem.* **1985**, *57*, 1917–1926; b) G. Pez (Allied Chemical Corp.), US 4,302,603, **1981**.

[55] S. E. Diamond, A. Szalkiewicz, F. Mares, *Fund. Res. Homogeneous Catal.* **1979**, *3*, 345–358.

[56] F. Y. Kwong, A. Klapars, S. L. Buchwald, *Org. Lett.* **2002**, *4*, 581–584.

[57] M. Novotny, R. Kump, F. Merli, L. J. Todd, *Anal. Chem.* **1980**, *52*, 401–406.

[58] J. J. Brunet, N. C. Chu, O. Diallo, *Organometallics* **2005**, *24*, 3104–3110.

[59] S. T. Handy, M. Okello, *Tetrahedron Lett.* **2003**, *44*, 8395–8397, and references herein.

[60] T. Jeffery, *Tetrahedron* **1996**, *52*, 10113–10130.

[61] C. Amatore, A. Jutand, *J. Organomet. Chem.* **1999**, *576*, 254–278.

[62] P. M. Maitlis, A. Haynes, B. R. James, M. Catellani, G. P. Chiusoli, *Dalton Trans.* **2004**, 3409–3419.

 © 2007 Wiley-VCH Verlag GmbH & Co. KGaA, Weinheim 

[63] R. G. Denning, L. M. Venanzi, *J. Chem. Soc. A* **1967**, 328–337.
[64] a) A. C. Cope, C. R. Ganellin, H. W. Johnson, T. V. Van Auken, H. J. S. Winkler, *J. Am. Chem. Soc.* **1963**, *85*, 3276–3279; b) S. Hupp, G. Dahlgreen, *Inorg. Chem.* **1976**, *15*, 2349–2353.
[65] S. Anguille, J. J. Brunet, N. C. Chu, O. Diallo, C. Pages, S. Vincendeau, *Organometallic* **2006**, *25*, 2943–2948.
[66] a) S. I. Murahashi, N. Yoshimura, T. Tsumiyama, T. Kojima, *J. Am. Chem. Soc.* **1983**, *105*, 5002–5011; b) S. I. Murahashi, *Angew. Chem. Int. Ed. Engl.* **1995**, *34*, 2443–2465.
[67] a) C. S. Cho, B. H. Oh, T. J. Kim, S. C. Shim, *Chem. Commun.* **2000**, 1885–1888; b) C. S. Cho, J. S. Kim, T. J. Oh, S. C. Shim, N. S. Yoon, *Tetrahedron* **2000**, *56*, 7747–7750; c) C. S. Cho, T. K. Kim, B. T. Kim, T. J. Kim, S. C. Shim, *J. Organomet. Chem.* **2002**, *650*, 65–68.
[68] M. Rodriguez-Zubiri, J. J. Brunet, S. Anguille, *J. Mol. Catal. A* **2007**, *271*, 146–151.
[69] See, for example: a) X. Wang, S. M. Lu, P. Y. Yang, X. W. Han, Y. G. Zhou, *J. Am. Chem. Soc.* **2003**, *125*, 10536–10537; b) D. Xiao, X. Zhang, *Angew. Chem. Int. Ed.* **2001**, *40*, 3425–3428.
[70] D. Konya, K. Q. Almeida Leñero, E. Drent, *Organometallics* **2006**, *25*, 3166–3174.
[71] [$PtCl_2$] and [$PtCl_4$] have recently been reported to exhibit similar catalytic activities for the cycloisomerization of polyunsaturated precursors: J. Marco-Contelles, N. Arroyo, S. Anjum, E. Mainetti, N. Marion, K. Cariou, G. Lemière, V. Mouriès, L. Fensterbank, M. Malacria, *Eur. J. Org. Chem.* **2006**, 4618–4633.

Received: April 27, 2007
Published Online: September 18, 2007

 © 2007 Wiley-VCH Verlag GmbH & Co. KGaA, Weinheim 

DOI: 10.1002/ejic.200700814

# The First Example of a Bis(trifluoromethyl)carbene Transition-Metal Complex and Its Reduction to a Perfluoroallene Complex

**Jian Yuan,[a] Russell P. Hughes,*[a] and Arnold L. Rheingold[b]**

*Dedicated to Dr. Robert M. Ross on the occasion of his 90th birthday*

**Keywords:** Carbene / Iridium / Fluorine / Ligands / Structure

Na/Pb alloy reduction of the (perfluoroisopropyl)iridium complex Cp*(CO)IrI[CF(CF$_3$)$_2$] afforded the first example of a bis(trifluoromethyl)carbene complex, Cp*(CO)Ir=C(CF$_3$)$_2$, which has been crystallographically characterized. Further reduction of this carbene complex with $KC_8$ yielded the perfluoroallene iridium complex Cp*Ir(CO)($\eta^2$-CF$_2$CCF$_2$).
(© Wiley-VCH Verlag GmbH & Co. KGaA, 69451 Weinheim, Germany, 2007)

## Introduction

Transition-metal complexes with carbene ligands have been known for more than four decades,[1,2] and they have been extensively utilized in organic synthesis and catalysis.[3,4] Other than compounds of the parent methylene ligand,[5] all such complexes isolated to date contain at least one carbene substituent (alkyl, aryl, heteroatom) that is electron-donating in a σ- or π-sense. Recently we reported a simple reductive conversion of primary (perfluoroalkyl)-iridium complexes to difluorocarbene complexes **1** and **2**. The (difluorocarbene)iridium complexes are stable, crystalline solids, unlike the $CH_2$ analogue of **1**, which can only be observed spectroscopically at low temperatures,[6] even though other terminal methylene complexes of iridium are stable enough for isolation.[7,8] Similarly, fluoro(perfluoroalkyl)carbene complexes **3**–**6** can be isolated by using sodium naphthalenide (NaNp), potassium graphite ($KC_8$), or magnesium graphite [$C_{16}Mg(KCl)_2$] as electron sources.[9,10] While compounds **3**–**6** contain one perfluoroalkyl substituent, which is an exclusively electron-withdrawing group,[11–14] the other fluorine substituent at the carbene carbon is still capable of π-donation. Here we report the first example of a complex with a carbene ligand bearing two electron-withdrawing trifluoromethyl substituents, which can be isolated as a stable, sublimable solid.

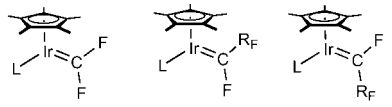

**1** L = PMe$_3$
**2** L = CO

**3a–6a** **3b–6b**

**3a,b** L = PMe$_3$, R$_F$ = CF$_3$
**4a,b** L = CO, R$_F$ = CF$_3$
**5a,b** L = PMe$_3$, R$_F$ = CF$_2$CF$_3$
**6a,b** L = CO, R$_F$ = CF$_2$CF$_3$

## Results and Discussion

Careful two-electron reduction of perfluoroisopropyl complex **7**[15] in thf by using Na/Pb alloy (Na ca.10%) afforded bis(trifluoromethyl)carbene complex **8** in 87% yield as a yellow, crystalline, sublimable, air-stable compound, unambiguously characterized by a single-crystal X-ray diffraction study. An ORTEP is shown in Figure 1 (Figure 1). The Ir–C double bond length of 1.928(7) Å is significantly shorter than the Ir–C single bond in **7** [2.11(3) Å][15] and slightly longer than the double bond in its difluorocarbene analogue **2** [1.855(13) Å].[10] Not unexpectedly, the CF$_3$–Ir–CF$_3$ angle in **8** [110.0(6)°] is substantially larger than the F–C–F angle in **2** [103.5(10)°].[10]

Complex **8** represents the first unambiguously characterized compound of a carbene ligand bearing two perfluoroalkyl groups; an early attempt by others to prepare such a compound by reaction of *trans*-(Ph$_2$MeP)$_2$Ir(CO)Cl with the diazo precursor (CF$_3$)CN$_2$ gave a poorly characterized product in which it was not possible to distinguish between structure **9a** or **9b** (L = PMePh$_2$).[16] Notably, a terminal methylene analogue of **9b** can be isolated in a similar reaction by using diazomethane.[7]

While the mono(perfluoroalkyl)carbene analogues **3**–**6** are inert to further reduction, the new bis(trifluoromethyl)-

[a] Department of Chemistry, Dartmouth College, 6128 Burke Laboratories
Hanover, NH 03755, USA
Fax: +1-603-646-3946
E-mail: rph@dartmouth.edu
[b] Department of Chemistry, University of California, San Diego
San Diego, CA 92093, USA

 © 2007 Wiley-VCH Verlag GmbH & Co. KGaA, Weinheim 

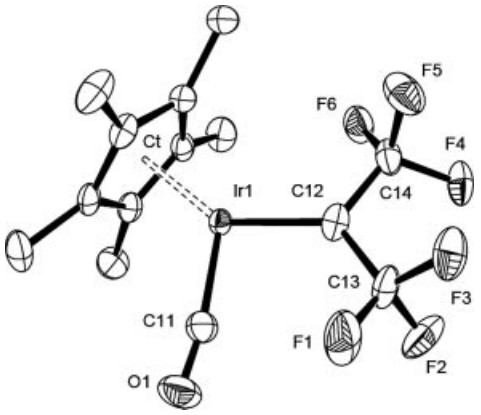


Figure 1. ORTEP diagram of the non-hydrogen atoms of **8**, showing the partial atom-labeling scheme. Thermal ellipsoids are shown at the 30% level. Selected bond lengths [Å] and angles [°]: Ir1–C11 1.860(7), Ir1–C12 1.928(7), Ir1–Ct 1.889(6), C12–C14 1.481(11), C12–C13 1.489(10), O1–C11 1.129(8); Ct–Ir1–C12 140.5(3), Ct–Ir1–C11 124.9(3), C11–Ir1–C12 94.7(3), C14–C12–C13 110.0(6), C14–C12–Ir1 123.6(5), C13–C12–Ir1 126.4(6).

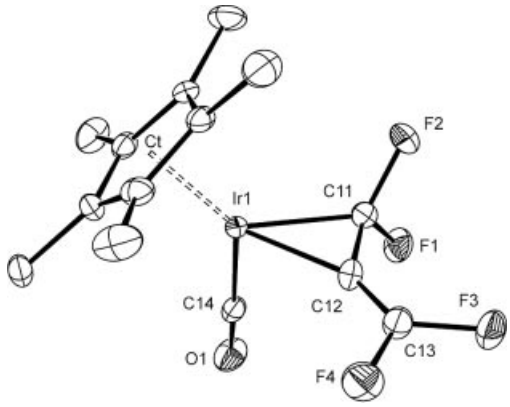


Figure 2. ORTEP diagram of the non-hydrogen atoms of **10** showing the partial atom-labeling scheme. Thermal ellipsoids are shown at the 30% level. Selected bond lengths [Å] and angles [°]: Ir1–C11 2.035(7), C11–F1 1.381(8), C11–F2 1.362(8), Ir1–C12 2.030(7), C11–C12 1.426(10), C12–C13 1.281(10), C13–F3 1.337(8), C13–F4 1.340(9), Ir1–C14 1.862(6), C14–O1 1.133(7); Ir1–C11–C12 69.3(4), Ir1–C12–C11 69.6(4), C12–Ir1–C11 41.1(3), C11–C12–C13 138.8(7), C13–C12–Ir1 151.3(6).

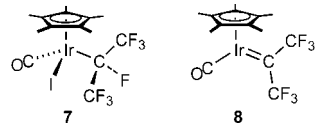


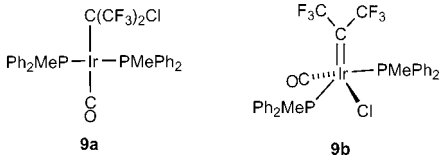


carbene complex **8** is more reactive, undergoing reduction by $KC_8$ to eliminate two more fluorides and afford (perfluoroallene)iridium complex **10** in 60% yield as a white crystalline compound. It was also possible to synthesize **10** from the direct reduction of **7** with excess $KC_8$. The structure is also unambiguously defined by means of a single-crystal X-ray diffraction study; an ORTEP representation of the structure is shown in Figure 2. As expected, the allene ligand is bent with a C–C–C angle of 138.8(7)°, and the coordinated alkene [1.426(10) Å] is longer than the uncoordinated one [1.281(10) Å]. This is only the third example of a structurally characterized perfluoroallene complex and differs from its first-row metal analogues **11**[17] and **12**[18] in that the two Ir–C distances [2.035(7) Å and 2.030(7) Å] are equal within experimental error. In compounds **11** and **12**, the distance of the metal to the internal allene carbon is significantly shorter than that to the terminal carbon. Observation of four well-resolved doublet of doublet of doublet signals in the solution $^{19}F$ NMR spectrum indicate that there is a high barrier to propeller rotation of the allene ligand in **10**; propeller rotation on the NMR timescale would interconvert the resonances of F1 and F2. All four resonances were unambiguously assigned by means of a $^{19}F\{^1H\}$ HOESY experiment.

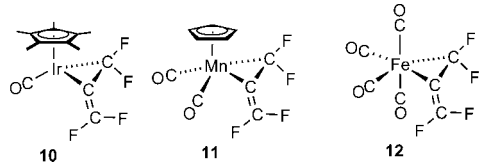


## Conclusions

This methodology illustrates that the presence of donor substituents other than H is not a requirement for stability in transition-metal carbene complexes. In addition, it demonstrates that reductive inner-sphere construction of unsaturated fluorocarbon ligands like tetrafluoroallene and the previously reported example of tetrafluorobutatriene[19] represent useful alternative methods for their synthesis as opposed to the direct ligand substitution required when starting with the free fluorocarbon,[18,20,21] which itself can be difficult to prepare and handle. Further experimental and computational studies of the structures and reactivity of this new class of carbene complexes will be reported in due course.

## Experimental Section

**Complex 8:** To a Schlenk flask containing Na/Pb alloy (353 mg, 10 equiv.) and thf (6 mL) was added $Cp^*Ir(CO)(I)[CF(CF_3)_2]$ (100 mg, 0.154 mmol) as a solid, and the mixture was stirred at room temperature for 3 h. The solvent was removed, and the product was extracted into hexanes. Removal of solvent gave a yellow solid (68 mg, 87%). Crystals were obtained by sublimation (5 Torr, 70 °C). $C_{14}H_{15}F_6IrO$ (505.46): calcd. C 33.27, H 3.00; found C 33.19, H 3.45. IR (hexanes): ν(CO) = 2017 $cm^{-1}$. $^1H$ NMR (500 MHz, $C_6D_6$, 21 °C): $\delta$ = 1.51 (s, $C_5Me_5$) ppm. $^{19}F$ NMR (470.31 MHz, $C_6D_6$, 21 °C): $\delta$ = –54.5 (q, $^5J_{FF}$ = 8 Hz, 3 F, $CF_3$), –57.1 (q, $^5J_{FF}$ = 8 Hz, 3 F, $CF_3$) ppm. $^{13}C\{^1H\}$ NMR (125.7 Hz, $C_6D_6$, 21 °C): $\delta$ = 9.5 (q, $^5J_{CF}$ = 1.2 Hz, $C_5Me_5$), 100.7 (s, $C_5Me_5$),

 © 2007 Wiley-VCH Verlag GmbH & Co. KGaA, Weinheim 

134.6 (qq, $^1J_{CF}$ = 275, $^3J_{CF}$ = 5 Hz, $CF_3$), 137.0 (qq, $^1J_{CF}$ = 275, $^3J_{CF}$ = 6 Hz, $CF_3$), 177.9 (qq, $^4J_{CF}$ = 5, $^3J_{CF}$ = 1 Hz, CO), 182.1 (qq, $^2J_{CF}$ = $^2J_{CF}$ = 32 Hz, IrC) ppm. Crystal data for **8**: $C_{14}H_{15}F_6IrO$, $M_r$ = 505.46, triclinic, space group $P\bar{1}$, $V$ = 783.8(4) Å$^3$, $a$ = 8.457(2) Å, $b$ = 8.686(3) Å, $c$ = 11.577(3) Å, $\alpha$ = 85.951(5)°, $\beta$ = 76.850(6)°, $\gamma$ = 71.198(5)°, $Z$ = 2, $T$ = 208(2) K, Mo-$K_\alpha$ = 0.71073 Å. GOF = 1.079. The final $R1(F^2)$ was 0.0343 for 3450 reflections $I > 2\sigma(I)$.

**Complex 10:** *Method A:* To a Schlenk flask containing $KC_8$ (183 mg, 1.35 mmol, 10 equiv.) and thf (6 mL) was added a solution of **8** (68 mg, 0.135 mmol) in thf (2 mL). The suspension was stirred at room temperature for 2 h. The solvent was removed, and the product was extracted into hexanes. Removal of solvent gave an off-white solid, (38 mg, 60%). *Method B:* To a Schlenk flask containing $KC_8$ (311.5 mg, 2.30 mmol, 10 equiv.) and thf (6 mL) was added. Cp*Ir(CO)(I)[$CF(CF_3)_2$] (150 mg, 0.230 mmol) as a solid. The suspension was stirred at room temperature for 2 h. The solvent was removed, and the product was extracted into hexanes. Removal of solvent gave an off-white solid (65 mg, 61%). Crystals were obtained from diffusion of neopentane into an ethyl isopropyl ether solution. $C_{14}H_{15}F_4IrO$ (467.49): calcd. C 35.97, H 3.23; found C 36.07, H 3.15. IR(hexane): ν(CO) = 2017 cm$^{-1}$, ν(C=$CF_2$) = 1787 cm$^{-1}$. $^1$H NMR (500 MHz, $C_6D_6$, 21 °C): $\delta$ = 1.56 (s, $C_5Me_5$) ppm. $^{19}$F NMR (470.31 MHz, $C_6D_6$, 21 °C): $\delta$ = –55.3 (ddd, $^2J_{FF}$ = 61, $^4J_{FF}$ = 9, $^4J_{FF}$ = 8 Hz 1 F, $CF_2$), F3; –84.7 (ddd, $^2J_{FF}$ = 133, $^4J_{FF}$ = 9, $^4J_{FF}$ = 9 Hz, 1 F, Ir$CF_2$), F1; –93.8 (ddd, $^2J_{FF}$ = 61, $^4J_{FF}$ = 9, $^4J_{FF}$ = 9 Hz, 1 F, $CF_2$), F4; –101.1 (ddd, $^2J_{FF}$ = 133, $^4J_{FF}$ = 9, $^4J_{FF}$ = 8 Hz, 1 F, Ir$CF_2$), F2 ppm. $^{13}$C{$^1$H} NMR (125.7 Hz, $C_6D_6$, 21 °C): $\delta$ = 9.1 (s, $C_5Me_5$), 45.0 (dddd, $^2J_{CF}$ = 51, $^2J_{CF}$ = 12, $^2J_{CF}$ = 7, $^2J_{CF}$ = 5 Hz, IrC), 99.1 (s, $C_5Me_5$), 97.4 (tdd, $^1J_{CF}$ = 316, $^3J_{CF}$ = 21, $^3J_{CF}$ = 2 Hz, C=$CF_2$), 148.5 (ddt, $^1J_{CF}$ = 294, $^1J_{CF}$ = 274, $^3J_{CF}$ = 2 Hz, Ir$CF_2$), 169.7 (dd, $^3J_{CF}$ = 11, $^3J_{CF}$ = 2 Hz, CO) ppm. Crystal data for **10**: $C_{14}H_{15}F_4IrO$, $M_r$ = 467.46, orthorhombic, space group *Pbca*, $V$ = 2949.4(5) Å$^3$, $a$ = 14.3156(13) Å, $b$ = 13.9844(13) Å, $c$ = 14.7327(13) Å, $\alpha = \beta = \gamma$ = 90°, dummy 90°, 90 °C, 90 °C, (2)°, (2)° dummy $Z$ = 8, $T$ = 208(2) K, Mo-$K_\alpha$ = 0.71073 Å. GOF = 1.040. The final $R1(F^2)$ was 0.0482 for 3554 reflections $I > 2\sigma(I)$.

CCDC-655232 (**8**) and CCDC-655233 (**10**) contain the supplementary crystallographic data for this paper. These data can be obtained free of charge from the Cambridge Crystallographic data Centre via http://www.ccdc.uk/data_request/cif.

## Acknowledgments

This work was supported by the U. S. National Science Foundation and the Petroleum Research Fund administered by the American Chemical Society.

[1] E. O. Fischer, A. Maasböl, *Angew. Chem.* **1964**, *76*, 645; *Angew. Chem. Int. Ed. Engl.* **1964**, *3*, 580–581.
[2] R. R. Schrock, *J. Am. Chem. Soc.* **1974**, *96*, 6796–6797.
[3] R. R. Schrock, *Angew. Chem. Int. Ed.* **2006**, *45*, 3748–3759.
[4] R. H. Grubbs, *Angew. Chem. Int. Ed.* **2006**, *45*, 3760–3765.
[5] R. R. Schrock, *J. Am. Chem. Soc.* **1975**, *97*, 6577–6578.
[6] D. P. Klein, R. G. Bergman, *J. Am. Chem. Soc.* **1989**, *111*, 3079–3080.
[7] G. R. Clark, W. R. Roper, A. H. Wright, *J. Organomet. Chem.* **1984**, *273*, C17–C19.
[8] M. D. Fryzuk, X. Gao, K. Joshi, P. A. MacNeil, R. L. Massey, *J. Am. Chem. Soc.* **1993**, *115*, 10581–10590.
[9] R. P. Hughes, R. B. Laritchev, J. Yuan, J. A. Golen, A. N. Rucker, A. L. Rheingold, *J. Am. Chem. Soc.* **2005**, *127*, 15020–15021.
[10] C. J. Bourgeois, R. P. Hughes, J. Yuan, A. G. DiPasquale, A. L. Rheingold, *Organometallics* **2006**, *25*, 2908–2910.
[11] B. E. Smart in *Chemistry of Functional Groups*, supplement D, vol. 1, chapter 14 (Eds.: S. Patai, Z. Rappoport), Wiley, New York, **1983**, pp. 603–655.
[12] B. E. Smart, *Mol. Struct. Eng.* **1986**, *3*, 141–191.
[13] R. E. Banks, B. E. Smart, J. C. Tatlow (Eds.), *Organofluorine Chemistry: Principles and Commercial Applications*, Plenum Press, New York, **1994**, pp. 644.
[14] B. E. Smart, *J. Fluorine Chem.* **2001**, *109*, 3–11.
[15] R. P. Hughes, J. M. Smith, L. M. Liable-Sands, T. E. Concolino, K.-C. Lam, C. Incarvito, A. L. Rheingold, *J. Chem. Soc. Dalton Trans.* **2000**, 873–879.
[16] J. Cooke, W. R. Cullen, M. Green, F. G. A. Stone, *Chem. Commun. (London)* **1968**, 170–171.
[17] D. Lentz, S. Willemsen, *Organometallics* **1999**, *18*, 3962–3964.
[18] D. Lentz, N. Nickelt, S. Willemsen, *Chem. Eur. J.* **2002**, *8*, 1205–1217.
[19] R. P. Hughes, R. B. Laritchev, L. N. Zakharov, A. L. Rheingold, *J. Am. Chem. Soc.* **2004**, *126*, 2308–2309.
[20] F. A. Akkerman, D. Lentz, *Angew. Chem. Int. Ed.* **2007**, *46*, 4902–4904.
[21] D. Lentz, *J. Fluorine Chem.* **2004**, *125*, 853–861.

Received: August 2, 2007
Published Online: September 12, 2007

 © 2007 Wiley-VCH Verlag GmbH & Co. KGaA, Weinheim 

DOI: 10.1002/ejic.200700530

# Hybrid Organic/Inorganic Supramolecular Conductors $D_2[Au(CN)_4]$ [D = Diiodo(ethylenedichalcogeno)tetrachalcogenofulvalene], Including a New Ambient Pressure Superconductor

**Tatsuro Imakubo,*[a] Takashi Shirahata,[a] Megumi Kibune,[a] and Hiroko Yoshino[a]**

**Keywords:** Supramolecular chemistry / Conducting materials / Iodine / Superconductors / Selenium heterocycles

Five diiodo(ethylenedichalcogeno)tetrachalcogenofulvalenes, DIEDSS {2-(5,6-dihydro[1,3]diselenolo[4,5-*b*][1,4]diselenin-2-ylidene)-4,5-diiodo-1,3-dithiole}, DIET-STF {2-(4,5-diiodo-1,3-diselenol-2-ylidene)-5,6-dihydro[1,3]dithiolo[4,5-*b*][1,4]dithiine}, DIEDS-STF {2-(4,5-diiodo-1,3-diselenol-2-ylidene)-5,6-dihydro[1,4]diselenino[2,3-*d*][1,3]dithiole}, DIETSe {2-(4,5-diiodo-1,3-diselenol-2-ylidene)-5,6-dihydro[1,3]diselenolo[4,5-*b*][1,4]dithiine}, and DIEDSSe {2-(4,5-diiodo-1,3-diselenol-2-ylidene)-5,6-dihydro[1,3]diselenolo[4,5-*b*][1,4]diselenine}, have been synthesized without the use of the highly toxic reagent $CSe_2$, and their $Au(CN)_4$ salts have been prepared by electrochemical oxidation. Characteristic I···N iodine bonds are constructed in all crystals, and their packing motifs are classified into two groups by the difference in the space group symmetry. The salt of DIEDSS crystallizes in the monoclinic *C*2/*c* space group and a novel helical supramolecular architecture is constructed by the strong and directional I···N iodine bond. On the other hand, the rest of the four salts crystallize in the triclinic $P\bar{1}$ space group and their donor packing motifs belong to the so-called β-type. Conducting properties of the β-type salts strongly depend on the number and positions of the selenium atoms on the donor molecule. The salts based on the diselenadithiafulvalene (DSDTF) derivatives, DIET-STF and DIEDS-STF, show metal–semiconductor transition and the salt of fully selenated π-donor DIEDSSe shows stable metallic behavior down to 1.6 K. On the other hand, $(DIETSe)_2[Au(CN)_4]$ is semimetallic down to low temperature and the superconducting transition occurs at around 2 K (onset).

(© Wiley-VCH Verlag GmbH & Co. KGaA, 69451 Weinheim, Germany, 2007)

## Introduction

The development of novel organic conductors based on tetrathiafulvalene (TTF) derivatives, which show interesting physical properties, depends not only on the design and synthesis of an independent donor molecule but also on the design of crystal structure, which is strongly related to the bulk physical properties. For designing crystal structures of organic conductors from the viewpoint of crystal engineering,[1] we have proposed the introduction of the iodine bond,[2–6] which is a special case of the halogen bond.[7] A large number of supramolecular conductors based on the iodinated TTFs have been synthesized,[8,9] and one of them, θ-$(DIETS)_2[Au(CN)_4]$ {DIETS = 2-(4,5-diiodo-1,3-dithiol-2-ylidene)-5,6-dihydro[1,3]diselenolo[4,5-*b*][1,4]dithiine}, shows superconductivity under uniaxial strain applied along the I···N iodine bond.[3c] It is well known that replacement of the sulfur atom in the TTF skeleton by the selenium atom is an effective method of increasing electrical conductivity and the development of organic superconductors.[10] Recently, we have reported a new $CSe_2$-free synthesis of 1,3-diselenole-2-thione, which may be a good alternative to 1,3-diselenole-2-selone, together with its applications to the synthesis of 4,5-diiodo-1,3-diselenole-2-one[5] and 4,5-alkylenedichalcogeno-1,3-diselenole-2-ones.[6] Cross-coupling reactions using these 1,3-diselenole-2-ones provide a number of selenium analogues of DIETS, i.e., DIEDSS {2-(5,6-dihydro[1,3]diselenolo[4,5-*b*][1,4]diselenin-2-ylidene)-4,5-diiodo-1,3-dithiole}, DIET-STF {2-(4,5-diiodo-1,3-diselenol-2-ylidene)-5,6-dihydro-[1,3]dithiolo[4,5-*b*][1,4]dithiine}, DIEDS-STF {2-(4,5-diiodo-1,3-diselenol-2-ylidene)-5,6-dihydro[1,4]diselenino-[2,3-*d*][1,3]dithiole}, DIETSe {2-(4,5-diiodo-1,3-diselenol-2-

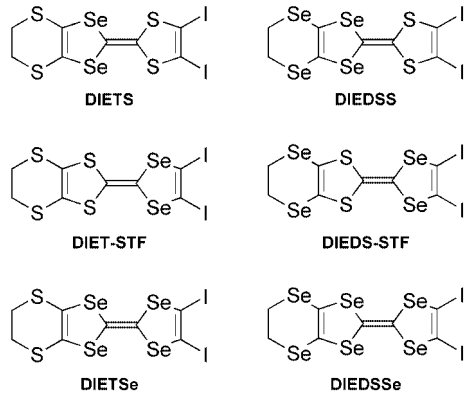


Figure 1. Molecular structure of iodinated TTFs.

[a] Imakubo Initiative Research Unit, RIKEN,
2-1 Hirosawa, Wako, Saitama 351-0198, Japan
E-mail: imakubo@riken.jp

 © 2007 Wiley-VCH Verlag GmbH & Co. KGaA, Weinheim 

ylidene)-5,6-dihydro[1,3]diselenolo[4,5-*b*][1,4]dithiine}, and DIEDSSe {2-(4,5-diiodo-1,3-diselenol-2-ylidene)-5,6-dihydro[1,3]diselenolo[4,5-*b*][1,4]diselenine}, and these organic π-donors are suitable candidates for the exploration of novel supramolecular organic conductors and superconductors. In this article, we report on the synthesis, crystal structure, and physical properties of novel supramolecular organic conductors $D_2[Au(CN)_4]$ (D = organic π-donors mentioned above, see Figure 1) together with the details of the synthesis of the neutral π-donors.

## Results and Discussion

### Donor Synthesis

The first synthesis of 4,5-ethylenediseleno-1,3-diselenole-2-selone (**1a**) was accomplished by the electrochemical reduction of $CSe_2$.[11] However, the reduction process of $CSe_2$ is dangerous and not ideal from the viewpoint of a safe laboratory environment. A modified synthesis of **1a** using bis(selenocyanato)ethane as the electrophile was reported by Otsubo et al.,[12] however $CSe_2$ is still indispensable for the synthesis of the starting material 1,3-diselenole-2-selone.[13] Recently, we have reported a $CSe_2$-free synthesis of 1,3-diselenole-2-thione, which seems to be a good starting material for the synthesis of the thione **1b**. At first, we applied the same reaction conditions for the synthesis of **1a** from 1,3-diselenole-2-selone to the synthesis of **1b** from 1,3-diselenole-2-thione. However, the main product of the reaction was the 1,3-thiaselenole-2-selone **2** (20%) and the desired thione **1b** was obtained in only 3% yield. To avoid the unfavorable transformation of 1,3-diselenole-2-thione to 1,3-thiaselenole-2-selone, we changed the reaction sequence as well as the iodination of 1,3-diselenole-2-thione,[5] that is, LDA was added last to a solution of 1,3-diselenole-2-thione and 1,2-bis(selenocyanato)ethane. This inverted sequence afforded **1b** without a selenium–sulfur exchange side reaction in a yield of under 5%. The low yield of **1b** was improved under the diluted conditions, which avoided the polymerization of the intermediate anions. In the optimized reaction conditions, the yield of **1b** exceeded 20%, and about 40% of the starting material 1,3-diselenole-2-thione, which can be recycled for the same reaction, was recovered. The thione **1b** was easily converted into the corresponding ketone **1c** (89%) by the conventional $Hg(OAc)_2/CHCl_3$ method. Phosphite-mediated cross-coupling reactions between the 1,3-dichalcogenole units in Scheme 1 gave diiodo(ethylenedichalcogeno)tetrachalcogenofulvalenes, DIEDSS, DIET-STF, DIEDS-STF, DIETSe,[4] and DIEDSSe. The results of the cross-coupling reactions and the redox potentials of a series of DIETS analogues are summarized in Table 1. These π-donors show two reversible waves and their donor abilities mainly depend on the inner fulvalene skeleton. The diselenadithiafulvalene (DSDTF) derivatives, DIETS, DIEDSS, DIET-STF, and DIEDS-STF, show lower $E_1^{1/2}$ than tetraselenafulvalene (TSeF) derivatives, DIETSe and DIEDSSe. On the other hand, the smaller $\Delta E$ values of TSeFs suggest the smaller on-site Coulombic repulsion thanks to the introduction of larger selenium atoms, which extend the highest occupied molecular orbital (HOMO).

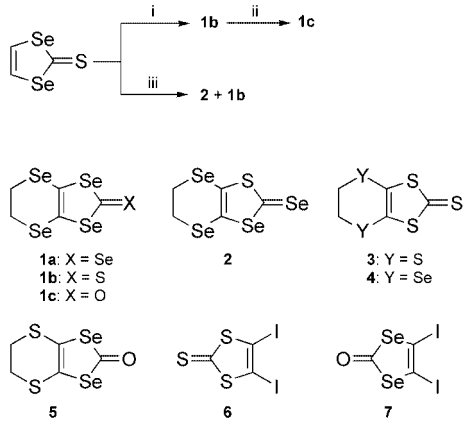


Scheme 1. Reagents and conditions: (i) 1,2-bis(selenocyanato)ethane (1.2 equiv.), then LDA (2.5 equiv.), –78 °C; (ii) $Hg(OAc)_2$, $AcOH/CHCl_3$; (iii) LDA (2.2 equiv.) then 1,2-bis(selenocyanato)ethane (1.6 equiv.), –78 °C.

### Preparation of the $Au(CN)_4$ Salts

Single crystals of the $Au(CN)_4$ salts were prepared by the galvanostatic oxidation of a $CH_2Cl_2$ solution containing DIEDSS, DIET-STF, DIEDS-STF, DIETSe, or DIEDSSe and tetrabutylammonium tetracyanoaurate as the supporting electrolyte. The five cation radical salts, $(DIEDSS)_2[Au(CN)_4]$ (**8**), $(DIET\text{-}STF)_2[Au(CN)_4]$ (**9**), $(DIEDS\text{-}STF)_2[Au(CN)_4]$ (**10**), $(DIETSe)_2[Au(CN)_4]$ (**11**), and $(DIEDSSe)_2[Au(CN)_4]$ (**12**), are classified into two groups according to the difference in their space group symmetry. The salt **8**

Table 1. Results of the cross-coupling reactions and cyclic voltammetry data[a] for diiodo(ethylenedichalcogeno)tetrachalcogenofulvalenes.

| Donor | Materials | Solvent | % Yield[b] | Color | $E_1^{1/2}$ [V] | $E_2^{1/2}$ [V] | $\Delta E$ (=$E_2^{1/2} - E_1^{1/2}$) |
|---|---|---|---|---|---|---|---|
| TTF | | | | | –0.10 | 0.32 | 0.42 |
| DIETS[c] | **5** + **6** | toluene | 74 | orange-red | 0.22 | 0.49 | 0.27 |
| DIEDSS | **1c** + **6** | toluene | 48 | orange-brown | 0.24 | 0.51 | 0.27 |
| DIET-STF | **3** + **7** | benzene | 76 | purplish-brown | 0.21 | 0.49 | 0.28 |
| DIEDS-STF | **4** + **7** | benzene | 71 | orange-brown | 0.19 | 0.47 | 0.28 |
| DIETSe[d] | **5** + **7** | toluene | 28 | dark green | 0.31 | 0.55 | 0.24 |
| DIEDSSe | **1b** + **7** | toluene | 21 | orange | 0.29 | 0.52 | 0.23 |

[a] vs. $Cp_2Fe$–$Cp_2Fe^+$ couple, in PhCN with 0.1 M $nBu_4NBF_4$, glassy carbon working electrode, 100 mV $s^{-1}$, room temp. [b] Isolated yields. [c] From ref.[3]. [d] From ref.[4].

 © 2007 Wiley-VCH Verlag GmbH & Co. KGaA, Weinheim 

Table 2. Crystal data for $D_2[Au(CN)_4]$.[a]

| | **8** | **9** | **10** | **11** | **12** |
|---|---|---|---|---|---|
| Donor | DIEDSS | DIET-STF | DIEDS-STF | DIETSe | DIEDSSe |
| Empirical formula | $C_{20}H_8AuI_4N_4S_4Se_8$ | $C_{20}H_8AuI_4N_4S_8Se_4$ | $C_{20}H_8AuI_4N_4S_4Se_8$ | $C_{20}H_8AuI_4N_4S_4Se_8$ | $C_{20}H_8AuI_4N_4Se_{12}$ |
| Formula mass | 1768.79 | 1581.19 | 1768.79 | 1768.79 | 1956.39 |
| Crystal system | monoclinic | triclinic | triclinic | triclinic | triclinic |
| Space group | *C*2/*c* (#15) | $P\bar{1}$ (#2) | $P\bar{1}$ (#2) | $P\bar{1}$ (#2) | $P\bar{1}$ (#2) |
| *a* [Å] | 35.567(11) | 7.4187(15) | 7.4317(17) | 7.3866(17) | 7.4097(18) |
| *b* [Å] | 4.8049(15) | 8.0234(16) | 8.1410(19) | 8.0530(19) | 8.153(2) |
| *c* [Å] | 23.150(7) | 16.212(3) | 16.304(4) | 16.413(4) | 16.498(4) |
| *α* [°] | 90 | 79.077(4) | 78.999(5) | 79.272(5) | 79.021(5) |
| *β* [°] | 112.379(6) | 78.369(4) | 78.441(4) | 78.358(5) | 78.479(4) |
| *γ* [°] | 90 | 68.194(4) | 69.144(4) | 68.177(4) | 68.911(5) |
| *V* [Å$^3$] | 3658(2) | 870.5(3) | 895.4(4) | 881.0(4) | 903.5(4) |
| *Z* | 4 | 1 | 1 | 1 | 1 |
| $D_{calcd}$ [g cm$^{-3}$] | 3.212 | 3.016 | 3.280 | 3.334 | 3.596 |
| $\mu$(Mo-$K_\alpha$) [mm$^{-1}$] | 15.608 | 12.456 | 15.942 | 16.202 | 19.597 |
| Collected reflections | 12382 | 6485 | 6686 | 6601 | 6737 |
| Independent reflections | 4649 | 4225 | 4344 | 4299 | 4418 |
| $R_{int}$ | 0.1253 | 0.0525 | 0.0662 | 0.0647 | 0.0728 |
| $R_1$, $wR_2$ [$I > 2\sigma(I)$] | 0.0582, 0.1136 | 0.0338, 0.0882 | 0.0369, 0.0956 | 0.0477, 0.1244 | 0.0422, 0.1042 |
| $R_1$, $wR_2$ (all data) | 0.1574, 0.1363 | 0.0384, 0.0988 | 0.0436, 0.0976 | 0.0574, 0.1344 | 0.0525, 0.1164 |
| Gof | 0.869 | 1.034 | 0.979 | 0.987 | 0.963 |
| $d_{I\cdots N}$ [Å][b] | 2.99(2), 3.28(1) | 2.856(9) | 2.86(1) | 2.83(1) | 2.86(1) |

[a] Measured at 293 K. [b] Sum of the van der Waals radii: I···N = 3.53 Å.[14]

based on DIEDSS, which contains a 4,5-diiodo-1,3-dithiole unit, crystallizes in the monoclinic *C*2/*c* space group, whereas the salts **9**–**12** based on the π-donors containing the 4,5-diiodo-1,3-diselenole unit crystallize in the triclinic $P\bar{1}$ space group (Table 2).

## Crystal Structure

The salt **8** crystallizes in the monoclinic *C*2/*c* space group (Table 2) and its crystal structure is shown in Figure 2. The donor/anion ratio is 2:1 and one crystallographically independent donor molecule stacks uniformly in a head-to-head manner along the crystallographic *b* axis. The gold atom of the $Au(CN)_4$ anion is located on the twofold axis and the almost planar $Au(CN)_4$ anion also stacks along the crystallographic *b* axis. The molecular packing motif of **8** basically resembles that of θ-$(DIETS)_2[Au(CN)_4]$,[3c] which is also based on the π-donor containing the 4,5-diiodo-1,3-dithiole unit. However, the donor columns A and B (A′ and B′) solid-cross along the side-by-side direction (Figure 3a). On the other hand, the donor columns A and A′ (B and B′) are parallel and they correspond to a part of the so-called β"-type structure, as shown in Figure 3b. Differences in the crystal structure between θ-$(DIETS)_2[Au(CN)_4]$ and **8** originate from the external form of the donor molecule. The steric hindrance between the donor molecules along the side-by-side direction in the crystal of **8** is larger than that in θ-$(DIETS)_2[Au(CN)_4]$ because DIEDSS contains a larger ethylenediseleno group than DIETS, which contains a smaller ethylenedithio group. A solid-crossing molecular arrangement of the DIEDSS molecule seems favorable for

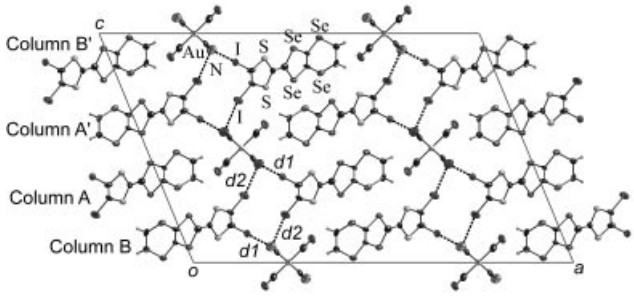


Figure 2. Crystal structure of **8** viewed along the crystallographic *b* axis. The dotted lines indicate I···N iodine bonds [*d*1 = 2.99(2), *d*2 = 3.28(1) Å].

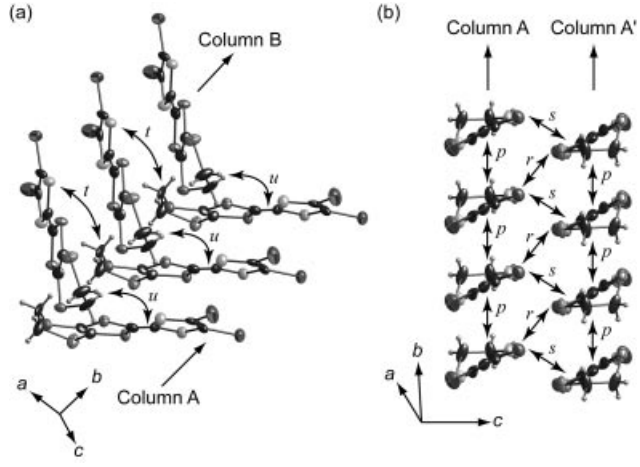


Figure 3. Molecular arrangement of the donor molecule of **8**: (a) solid-crossing arrangement for Column A and B viewed along the side-by-side direction of the donor molecule of Column A; (b) β"-type arrangement for Column A and A′ viewed along the long molecular axis of DIEDSS. The calculated overlap integrals ($\times 10^{-3}$) are *p* = –1.49, *r* = 1.41, *s* = –11.34, *t* = 0.17, *u* = 2.55.

 © 2007 Wiley-VCH Verlag GmbH & Co. KGaA, Weinheim 

avoiding steric repulsion between the larger ethylenediseleno groups.

As well as the other organic conductors based on iodinated TTFs, strong I···N iodine bonds are observed in **8**. The I···N distances are $d1$ = 2.99(2) Å and $d2$ = 3.28(1) Å and they are 7–15% shorter than the sum of the van der Waals radii (3.53 Å).[14] Along the crystallographic $b$ axis, there is a helix of ···I–C=C–I···N···I–C=C–I···N··· and the helices are connected along the $c$ axis through the $Au(CN)_4$ anions, as shown in Figure 4.

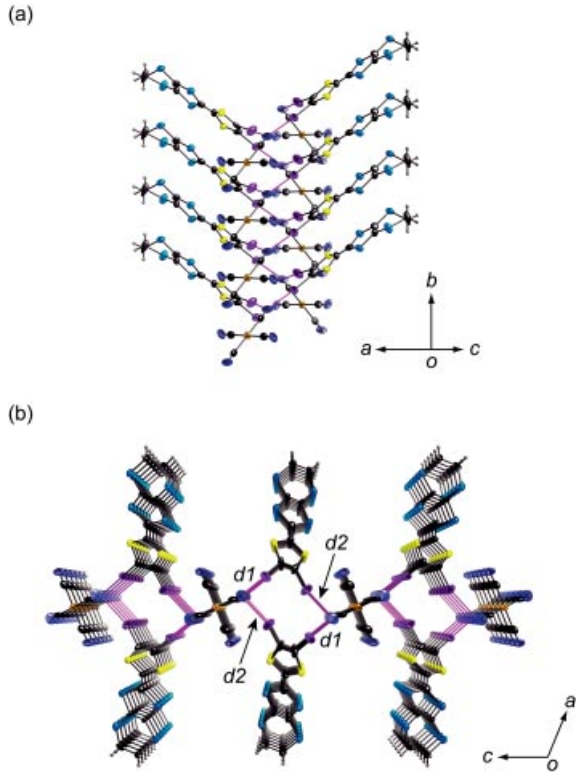


Figure 4. Helical supramolecular architecture in **8** constructed by the iodine bond (a) viewed along the $a + c$ axis; (b) projection onto the $ac$ plane. The pink lines indicate I···N iodine bonds [$d1$ = 2.99(2), $d2$ = 3.28(1) Å].

On the other hand, the $Au(CN)_4$ salts **9**–**12** based on the π-donors containing the 4,5-diiodo-1,3-diselenole unit, DIET-STF, DIEDS-STF, DIETSe, and DIEDSSe, are isostructural and crystallize in the triclinic $P\bar{1}$ space group (Table 2). The crystal structure of **11** is shown in Figure 5 as a representative of the isomorphic salts **9**–**12**. The unit cell contains two donor molecules and one $Au(CN)_4$ anion, and the donor/anion ratio is 2:1. The donor molecules stack in a head-to-tail manner along the crystallographic $b$ axis and the so-called β-type structure is constructed within the $ab$ plane. Short I···N iodine bonds ($d3$ = 2.83–2.86 Å, see the last row of Table 2), which are 19–20% shorter than the sum of the van der Waals radii, are observed.

Three types of iodine bonds, $d1$ and $d2$ for **8**, and $d3$ for **11** as the representative of the β-type salts **9**–**12**, are depicted in Figure 6 together with the lowest unoccupied molecular orbitals (LUMOs) of DIEDSS and DIETSe. In the

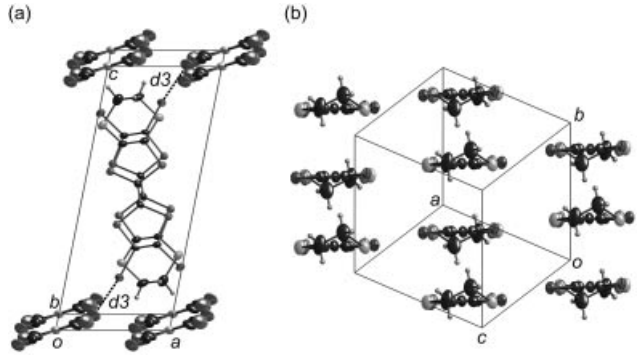


Figure 5. Crystal structure of **11**. (a) A projection onto the $ac$ plane. The dotted lines indicate I···N iodine bonds [$d3$ = 2.83(1) Å] shorter than the sum of the van der Waals radii. (b) Molecular arrangement of the donor molecule viewed along the long molecular axis of DIETSe.

case of $d1$, the donor molecule and the $Au(CN)_4$ anion are almost parallel, which is similar to the situation in θ-$(DIETS)_2[Au(CN)]_4$,[3c] and nearly orthogonal arrangements of the donor molecule and the $Au(CN)_4$ anion are observed in the cases of $d2$ and $d3$. From the viewpoint of the relationship between the molecular structure and the geometrical conformation of the iodine bond, the chalcogen element of the dichalcogenole ring on the iodine-bonded side of the molecule seems essential. A "parallel" arrangement like $d1$ is observed only in the salts based on the donor molecules containing the 4,5-diiodo-1,3-dithiole unit, that is, **8** and θ-$(DIETS)_2[Au(CN)]_4$. On the other hand, an "orthogonal" arrangement is preferred in the salts **9**–**12**, which are based on the donor molecules containing the 4,5-diiodo-1,3-diselenole unit. According to the calculated coefficients of the LUMOs on the 4,5-diiodo-1,3-dichalcogenole

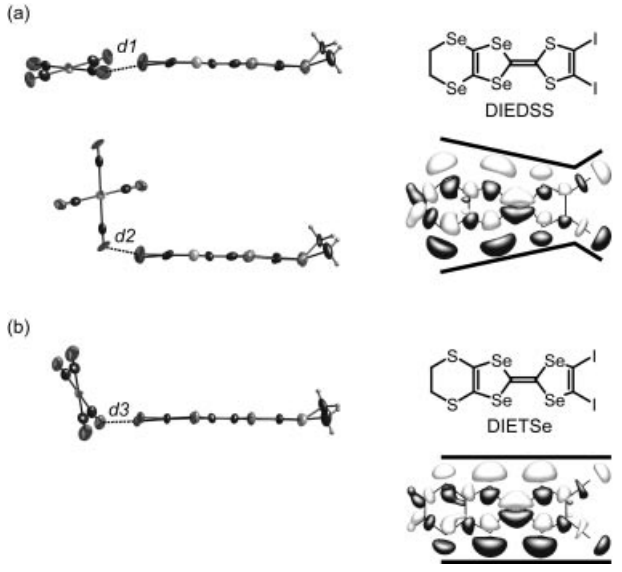


Figure 6. Three types of iodine bond, $d1$, $d2$, and $d3$, and LUMO of DIEDSS and DIETSe calculated by the MNDO–PM3 method;[15] (a) $d1$ and $d2$ for the salt **8** and LUMO of DIEDSS; (b) $d3$ for the salt **11** and LUMO of DIETSe. The solid lines are a guide for the eyes.

 © 2007 Wiley-VCH Verlag GmbH & Co. KGaA, Weinheim 

unit, the coefficients of the LUMO on the sulfur atoms of the 4,5-diiodo-1,3-dithiole unit are clearly smaller than those of the selenium atoms on the 4,5-diiodo-1,3-diselenole unit. Therefore, the differences in the geometrical conformation of the iodine bonds seem to be related not only to the external form of the donor molecules but also to the spatial extent of the frontier molecular orbitals around the 4,5-diiodo-1,3-dichalcogenole unit. In the salt **8**, there are two types of iodine bond, that is, "parallel" *d*1 and "orthogonal" *d*2, and the coexistence of these two types of iodine bond is essential to the helical supramolecular architecture.

## Band Calculation

Intermolecular overlap integrals for the salt **8** calculated by the extended Hückel method[16] are shown in Figure 3. The overlap integral *s* is considerably larger than the other overlap integrals *p*, *r*, *t*, and *u*, and the donor molecules are strongly dimerized along the side-by-side direction. The calculated band dispersion and the Fermi surfaces for **8** based on the tight-binding approximation using these overlap integrals are shown in Figure 7. There are four bands built from the HOMOs of the four donor molecules within the primitive cell [$a_p = (a + b)/2$, $b_p = b$, $c_p = c$] and they are separated by a gap in the upper and lower bands because of the strong dimerization mentioned above. Although the calculated Fermi surfaces are warped and quasi-one-dimensional, the calculated bandwidth of the upper band (ca. 0.08 eV) is much smaller than those of the usual organic conductors based on TTFs, and the strong electron correlation must be disadvantageous to achieving the metallic conductivity.

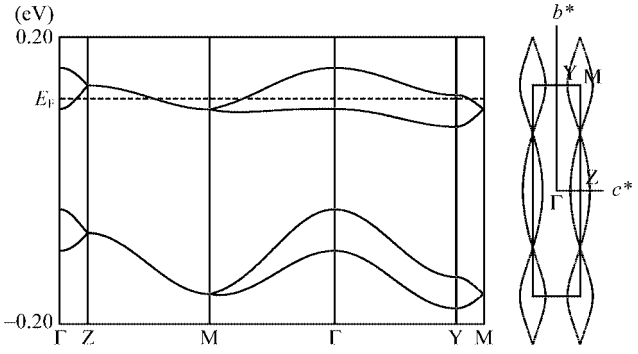


Figure 7. Calculated electronic band dispersion (left) and Fermi surfaces (right) for **8**.

Figure 8 shows a schematic view of the molecular arrangement within the donor layer for the β-type salts **9**–**12**, and the calculated overlap integrals are listed in Table 3. Differences in the intrastack overlap integrals between *p* and *q* are small enough to be regarded as a regular column structure. The interstack overlap integrals *r*, *s*, and *t* are about 1/7–1/19 of the intrastack overlap integrals *p* and *q*, and the quasi-one-dimensional character of the electronic band structure is suggested. The enhancement of the overlap integrals for **9** and **10** compared with those of **11** and **12** is accomplished by the replacement of sulfur atoms on the DSDTF skeleton with selenium atoms. On the other hand, the calculated overlap integrals of the side-by-side direction *s* and *t* for **9** based on the ethylenedithio derivative are slightly larger than those of **10** based on the ethylenediseleno derivative. There is a similar relationship between **11** and **12**, indicating that the overlap integrals *s* and *t* for the salts **10** and **12** are reduced by the steric repulsion of the larger ethylenediseleno group. The calculated band dispersion and the Fermi surfaces for **11** are shown in Figure 9 as a representative of the β-type salts **9**–**12**. There are two

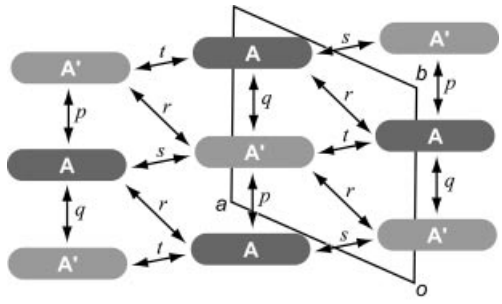


Figure 8. Schematic view of the donor layer for **9**–**12**.

Table 3. Calculated overlap integrals for **9**–**12** ($\times 10^{-3}$).[a]

| | 9 | 10 | 11 | 12 |
|---|---|---|---|---|
| *p* | –12.63 | –13.42 | –18.36 | –16.61 |
| *q* | –14.82 | –14.48 | –18.55 | –17.17 |
| *r* | –0.77 | –0.82 | –1.03 | –1.07 |
| *s* | 1.71 | 1.52 | 2.20 | 1.78 |
| *t* | 1.67 | 1.15 | 2.01 | 1.51 |

[a] See Figure 8 for the symbols of the overlap integrals.

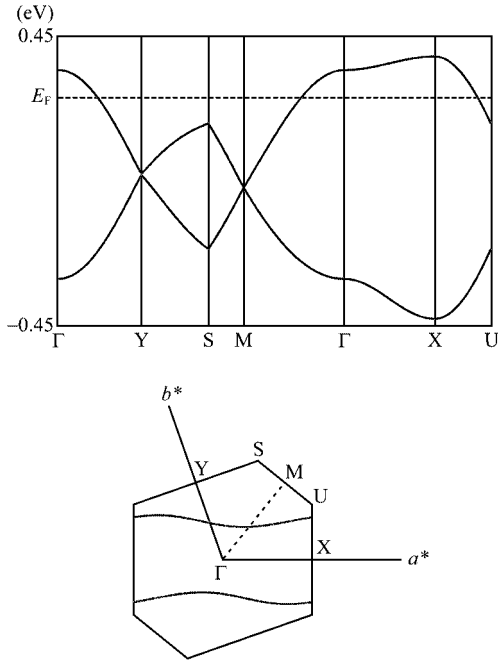


Figure 9. Calculated electronic band dispersion (top) and Fermi surfaces (bottom) for **11**.

 © 2007 Wiley-VCH Verlag GmbH & Co. KGaA, Weinheim 

bands built from the HOMOs of the two donor molecules within the unit cell, and there is no gap between the upper and lower bands. This is consistent with the regular column structure of the donor molecule. The calculated Fermi surfaces are quasi-one-dimensional along the *b* axis, which is the stacking direction of the donor molecule. The Fermi surfaces and electronic band dispersions for the salts **9**–**12** are almost the same except for the calculated bandwidth, and thanks to the TSeF skeleton, the bandwidths of **11** and **12** (about 0.7–0.8 eV) are larger than those of **9** and **10** (about 0.6 eV), and **11** and **12** are expected to have a stable metallic nature.

### Conducting Property

The single crystal of the salt **8** is a semiconductor with a small activation energy ($E_a$ = 98 meV) and the room temperature resistivity is 2.3 Ω cm. There are a few examples of helical architecture in organic crystals based on TTFs, however they are insulators.[17] To the best of our knowledge, the salt **8** is the first example of a highly conductive crystal that has helical architecture based on TTFs.

The room-temperature resistivities of the single crystals of the β-type salts **9**–**12** are $1.8 \times 10^{-2}$, $1.7 \times 10^{-2}$, $1.4 \times 10^{-2}$, and $1.6 \times 10^{-2}$ Ω cm, respectively. Figure 10 shows the temperature dependence of the resistivities for **9**–**12**. The conducting behavior of **9**–**12** strongly depends on the number and the positions of the selenium atoms on the donor molecule. The salts **9** and **10** based on the DSDTF derivatives show metal–semiconductor transition at 85 K for **9** and at 155 K for **10**. The metallic state of **9** based on the ethylenedithio derivative DIET-STF is more stable than that of **10** based on the ethylenediseleno derivative DIEDS-STF. It is consistent with the band calculation mentioned above, that is, the ethylenediseleno group reduces the overlap integrals of the side-by-side direction because of the steric repulsion and lowers the dimensionality of the electronic band structure.

The salt **12** based on the fully selenated π-donor DIEDSSe shows metallic behavior down to 1.6 K and the stable metallic nature is derived from the full replacement of the sulfur atoms in the diiodo(ethylenedichalcogeno)tetrachalcogenofulvalene with selenium atoms. On the other hand, the salt **11** shows semimetallic behavior down to 2 K and then a distinct resistivity drop, which is characteristic of the onset of superconductivity, was observed for several crystals (Figure 10b). Complete superconductivity with zero resistivity has not been confirmed because of its low transition temperature and the limit of the measurement apparatus. In spite of the identical crystal morphology among samples 1–4, there is a sample dependency of the onset temperature of the superconducting transition ($T_c$): 1.8 K for samples 1–3 and 2.1 K for sample 4. The crystals of **11** are fragile and the sample dependence of the $T_c$ may be affected by cracks in the crystals. Resistivity jumps were observed in all samples at higher temperatures, that is, at around 80 K for sample 1, 60 K for sample 2, 90 K for sample 3, and 100 K for sample 4. Samples 1 and 2 were harvested from the same crystallization cell (Batch A), and samples 3 and 4 were obtained from a different experiment (Batches B and C, respectively). The conditions of electrochemical oxidation for Batches A and B are almost the same and no clear relationship was observed between the conditions of crystal preparation and the $T_c$ of superconductivity.

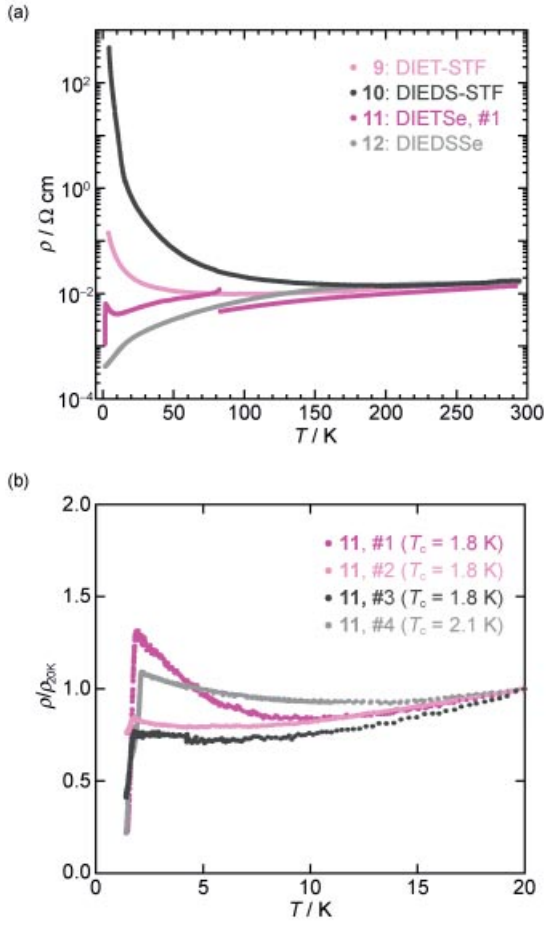


Figure 10. (a) Temperature dependence of the resistivities for **9** (light magenta), **10** (dark grey), **11** (sample 1, dark magenta), and **12** (light grey). (b) Normalized resistivities for **11** in the low-temperature region (samples 1: dark magenta, 2: light magenta, 3: dark grey, 4: light grey).

Figure 11 shows the temperature dependence of the DC magnetizations for the crystals of **11** obtained from Batches A, B, and C, which include samples 1 and 2, 3, and 4, respectively. The onset of the diamagnetic transition occurred at 1.8 K for Batches A and B, and at 1.9 K for Batch C. The higher transition temperature of Batch C is consistent with the resistivity measurement for sample 4. Owing to the very low applied field of 10 Oe and the low $T_c$, absolute values of magnetic susceptibility ($\chi$) and the volume fraction of superconductivity cannot be calculated, however the appearance of the diamagnetic transition is clear evidence for the superconducting transition of the salt **11**. The inset of Figure 11 shows the temperature dependence of the magnetic susceptibility for **11** under an applied field of 50 kOe. Magnetic susceptibility $\chi$ is almost independent of

 © 2007 Wiley-VCH Verlag GmbH & Co. KGaA, Weinheim 

temperature above $T_c$ and shows Pauli paramagnetism. It is also confirmed that the jumps of resistivity at 60–100 K are not intrinsic but result from the fragility of the crystals.

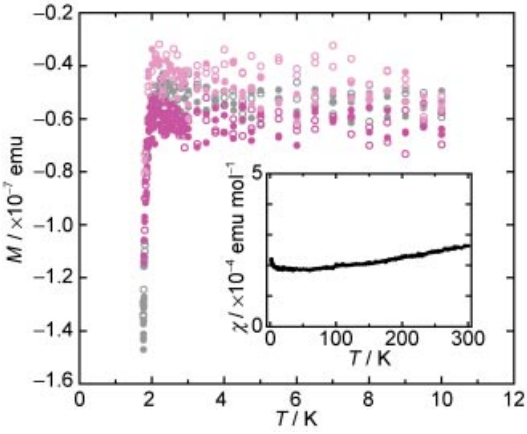


Figure 11. Temperature dependence of ZFC (filled circles) and FC (open circles) DC magnetizations for **11** (raw data). The dark magenta circles are data on Batch A including samples 1 and 2 in Figure 10b, the light magenta circles are data on Batch B including sample 3 in Figure 10b, and the light grey circles are data on Batch C including sample 4 in Figure 10b under an applied field of 10 Oe. The inset shows the temperature dependence of the magnetic susceptibility for **11** under an applied field of 50 kOe.

## Conclusions

We have synthesized five selenium-rich π-donors, DIEDSS, DIET-STF, DIEDS-STF, DIETSe, and DIEDSSe, without the use of $CSe_2$, and the crystal structure and electronic properties of their $Au(CN)_4$ salts were systematically investigated. The chalcogen element of the 4,5-diiodo-1,3-dichalcogenole unit of the donor molecule is essential to the packing motif of the crystals. The $Au(CN)_4$ salt of DIEDSS, which contains the 4,5-diiodo-1,3-dithiole unit, includes a novel helical architecture tailored by two types of the characteristic iodine bond. This salt is also the first example of a highly conductive crystal that has helical architecture based on TTFs. On the other hand, the crystal structure of the $Au(CN)_4$ salts based on donor molecules containing the 4,5-diiodo-1,3-diselenole unit, DIET-STF, DIEDS-STF, DIETSe, and DIEDSSe, is of the so-called β-type. Their conducting behavior strongly depends on the number and positions of the selenium atoms on the donor molecule and varies from semiconductor to superconductor. Among the four β-type crystals, the salt of DIETSe shows superconducting transition at around 2 K (onset), and this is the first ambient pressure organic superconductor based on halogenated TTFs. These results indicate that a combination of supramolecular architecture based on the iodine bond and enhancement of electrical conductivity by sulfur–selenium replacement is a promising method for the stepwise development of new organic superconductors.

## Experimental Section

**General:** All chemicals and solvents were of reagent grade. All reactions were conducted under argon except for the oxidation reactions using $Hg(OAc)_2$. Dehydrated THF and 4,5-ethylenedithio-1,3-dithiole-2-thione (**3**) were purchased from Kanto Chemical Co., Inc. and Tokyo Chemical Industry Co., Ltd., respectively, and used without further purification. A THF solution of LDA was prepared from diisopropylamine with an *n*-hexane solution of *n*BuLi prior to use. Column chromatography was carried out with silica gel (Kanto Chemical Co., Inc., 100–210 μm). Preparative gel permeation chromatography (GPC) was performed on a Japan Analytical Industry Co., Ltd. LC-908W equipped with a JAI-GEL 1H, 2H column assembly. $^1$H NMR spectra were recorded with a JEOL JNM-Excalibur 270 spectrometer. The chemical shifts are given in $\delta$ ppm, downfield from internal $Me_4Si$. Mass spectra were taken in the EI mode with ionization energy of 70 eV, using a Shimadzu QP-5050A quadrupole mass spectrometer. The melting points were determined from the TG-DTA analyses using a SII EXSTAR6000 analyzer. IR spectra were recorded with a Shimadzu FTIR-8100M spectrometer with a PIKE MIRacle diamond ATR. Elemental analyses were performed at the Advanced Development & Supporting Center, RIKEN. Cyclic voltammetry measurements were performed under argon using a BAS ALS-model610A analyzer.

**4,5-Ethylenediseleno-1,3-diselenole-2-thione (1b):** A THF solution of LDA (0.40 M, 2.8 mL, 1.1 mmol) was slowly added to a mixture of 1,3-diselenole-2-thione[5] (102 mg, 0.45 mmol) and 1,2-bis(selenocyanato)ethane[13] (129 mg, 0.54 mmol) in dehydrated THF (100 mL) at –78 °C for a period of 5 min. The reaction mixture was stirred for 1 h at –78 °C, then quenched by addition of $H_2O$/THF (1 mL, v:v = 1:1) and warmed to room temperature. After stirring overnight at room temperature, the resulting reddish brown solution was poured into dichloromethane (100 mL), washed with water (100 mL, three times), dried with $MgSO_4$, and then concentrated under reduced pressure. The residue was subjected to silica-gel column chromatography. The first yellow fraction eluted with $CS_2$/*n*-hexane (4:1) was **1b** (39 mg, 21%) as an ocher powder upon concentration, and the second yellow band gave the recovered 1,3-diselenole-2-thione (44 mg, 43%) as a yellow-brown solid upon concentration. Analytically pure **1b** was obtained by further purification by preparative GPC. M.p. 130 °C. MS (EI, 70 eV): *m*/*z* = 414 [$M^+$ for $C_5H_4S^{78}Se^{80}Se_3$], 370 [$M^+$ – C=S]. $^1$H NMR (270 MHz, $CDCl_3$): $\delta$ = 3.47 (s, 4 H) ppm. IR (neat): $\tilde{\nu}$ = 1001 (s), 1024 (s), 1096 (w), 1130 (w), 1217 (w), 1262 (m), 1395 (m), 1416 (w), 1458 (w), 1509 (w), 1522 (w) cm$^{-1}$. $C_5H_4SSe_4$ (411.99): calcd. C 14.58, H 0.98; found C 14.34, H 0.82.

**4,5-Ethylenediseleno-1,3-diselenol-2-one (1c):** Acetic acid (5 mL) was added to a suspension of **1b** (209 mg, 0.51 mmol) and $Hg(OAc)_2$ (339 mg, 1.06 mmol) in chloroform (25 mL), and the resulting suspension was then stirred for 5 h at room temperature. The resulting yellow-white suspension was filtered through Celite and washed with dichloromethane. The combined filtrate was washed with aqueous $NaHCO_3$ (100 mL, three times) and water (100 mL, twice), dried with $MgSO_4$, and then concentrated under reduced pressure. The residue was subjected to silica-gel column chromatography eluted with dichloromethane and pure **1c** was obtained as a cream powder (179 mg, 89%). The analytical data are identical to the reported data.[12]

**4,5-Ethylenediseleno-1,3-thiaselenol-2-selone (2):** A THF solution of LDA (0.75 M, 1.2 mL, 0.92 mmol) was added to a solution of 1,3-diselenole-2-thione[5] (96 mg, 0.42 mmol) in THF (100 mL) at –78 °C, and the resulting solution was stirred for 1 h at the same temperature. 1,2-Bis(selenocyanato)ethane[13] (157 mg, 0.66 mmol)

 © 2007 Wiley-VCH Verlag GmbH & Co. KGaA, Weinheim 

was added to this reaction mixture in one portion. After 15 min, the mixture was warmed to room temperature, then the resulting dark red solution was poured into dichloromethane (200 mL), washed with water (100 mL, four times), dried with $MgSO_4$, and then concentrated under reduced pressure. The residue was subjected to silica-gel column chromatography. The first yellow fraction eluted with $CS_2$ was **1b** (6 mg, 3%) as an ocher powder upon concentration, and the second orange band eluted with $CS_2$ gave **2** (35 mg, 20%) as a purplish-brown crystal upon concentration. M.p. 170 °C (dec.). MS (EI, 70 eV): $m/z$ = 414 [$M^+$ for $C_5H_4S^{78}Se^{80}Se_3$]. $^1H$ NMR (270 MHz, $CDCl_3$): $\delta$ = 3.44 (m, 2 H), 3.45 (m, 2 H) ppm. IR (neat): $\tilde{\nu}$ = 922 (s), 939 (m), 1021 (w), 1086 (w), 1136 (w), 1223 (w), 1258 (m), 1402 (m), 1453 (m) $cm^{-1}$. $C_5H_4SSe_4$ (411.99): calcd. C 14.58, H 0.98; found C 14.59, H 0.91.

**2-(5,6-Dihydro[1,3]diselenolo[4,5-*b*][1,4]diselenin-2-ylidene)-4,5-diiodo-1,3-dithiole (DIEDSS):** $P(OEt)_3$ (2.8 mL) was added dropwise over a period of 10 min to a refluxing solution of **6**[3b,8a] (154 mg, 0.40 mmol) and **1c** (128 mg, 0.26 mmol) in toluene (20 mL), followed by stirring under reflux for 30 min. After cooling to room temperature, the solution was evaporated under reduced pressure to eliminate the solvent and excess phosphite. The residue was subjected to silica-gel column chromatography. The second violet fraction eluted with $CS_2$ was collected, and DIEDSS was obtained as orange-brown crystals (114 mg, 48%). M.p. 157 °C (dec.). MS (EI, 70 eV): $m/z$ = 736 [$M^+$ for $C_8H_4I_2S_2{}^{78}Se^{80}Se_3$]. $^1H$ NMR (270 MHz, $CDCl_3$): $\delta$ = 3.37 (s, 4 H) ppm. IR (neat): $\tilde{\nu}$ = 1092 (s), 1136 (m), 1219 (w), 1262 (s), 1399 (m), 1416 (m), 1480 (w), 1507 (w) $cm^{-1}$. $C_8H_4I_2S_2Se_4$ (733.90): calcd. C 13.09, H 0.55; found C 13.14, H 0.53.

**2-(4,5-Diiodo-1,3-diselenol-2-ylidene)-5,6-dihydro[1,3]dithiolo[4,5-*b*]-[1,4]dithiine (DIET-STF):** $P(OEt)_3$ (3.7 mL) was added dropwise over a period of 5 min to a refluxing solution of **7**[5] (100 mg, 0.22 mmol) and **3** (58 mg, 0.26 mmol) in benzene (20 mL), followed by stirring under reflux for 1.5 h. The same procedure as for DIEDSS was adopted for the separation of the products. Evaporation of the second red-orange fraction afforded purplish-brown crystals of DIET-STF (104 mg, 76%). M.p. 175 °C (dec.). MS (EI, 70 eV): $m/z$ = 642 [$M^+$ for $C_8H_4I_2S_4{}^{80}Se_2$]. $^1H$ NMR (270 MHz, $CDCl_3$): $\delta$ = 3.30 (s, 4 H) ppm. IR (neat): $\tilde{\nu}$ = 1125 (s), 1173 (m), 1258 (m), 1283 (s), 1404 (m), 1499 (m), 1509 (m) $cm^{-1}$. $C_8H_4I_2S_4Se_2$ (640.11): calcd. C 15.01, H 0.63; found C 14.96, H 0.53.

**2-(4,5-Diiodo-1,3-diselenol-2-ylidene)-5,6-dihydro[1,4]diselenino[2,3-*d*]-[1,3]dithiole (DIEDS-STF):** $P(OEt)_3$ (3.7 mL) was added dropwise over a period of 3 min to a refluxing solution of **7**[5] (100 mg, 0.22 mmol) and **4**[18] (82 mg, 0.26 mmol) in benzene (20 mL), followed by stirring under reflux for 3 h. The same procedure as for DIEDSS was adopted for the separation of the products. Evaporation of the second red-orange fraction afforded orange-brown crystals of DIEDS-STF (112 mg, 71%). M.p. 154 °C (dec.). MS (EI, 70 eV): $m/z$ = 736 [$M^+$ for $C_8H_4I_2S_2{}^{78}Se^{80}Se_3$]. $^1H$ NMR (270 MHz, $CDCl_3$): $\delta$ = 3.35 (s, 4 H) ppm. IR (neat): $\tilde{\nu}$ = 1088 (m), 1132 (m), 1217 (m), 1223 (m), 1260 (s), 1399 (s), 1416 (m), 1480 (w), 1507 (w) $cm^{-1}$. $C_8H_4I_2S_2Se_4$ (733.90): calcd. C 13.09, H 0.55; found C 13.16, H 0.50.

**2-(4,5-Diiodo-1,3-diselenol-2-ylidene)-5,6-dihydro[1,3]diselenolo[4,5-*b*]-[1,4]diselenine (DIEDSSe):** $P(OEt)_3$ (3.0 mL) was added dropwise over a period of 3 min to a refluxing solution of **7**[5] (58 mg, 0.12 mmol) and **1b** (63 mg, 0.15 mmol) in toluene (10 mL), followed by stirring under reflux for 80 min. The same procedure as for DIEDSS was adopted for the separation of the products except for the eluent of the silica-gel column chromatography [$CS_2$/*n*-hexane (9:1)]. Evaporation of the second orange fraction afforded orange-red crystals of DIEDSSe (22 mg, 21%). M.p. 167 °C (dec.). MS (EI, 70 eV): $m/z$ = 830 [$M^+$ for $C_8H_4I_2{}^{78}Se_2{}^{80}Se_4$]. $^1H$ NMR (270 MHz, $CDCl_3$): $\delta$ = 3.38 (s, 4 H) ppm. IR (neat): $\tilde{\nu}$ = 1092 (m), 1132 (m), 1223 (m), 1260 (s), 1399 (s), 1416 (m), 1507 (w) $cm^{-1}$. $C_8H_4I_2Se_6$ (827.69): calcd. C 11.61, H 0.49; found C 11.71, H 0.44.

**Crystal Preparation:** Single crystals of the salts **8**–**12** were prepared by the electrochemical oxidation (4–6 d) of a $CH_2Cl_2$ (20 mL) solution containing the corresponding donor molecule (3–6 mg) and $nBu_4NAu(CN)_4$ as a supporting electrolyte (15–39 mg). Platinum electrodes (1.0 mm diameter wire or $1.0 \times 2.0$ $mm^2$ rectangular pillar-shaped) and standard H-shaped cells were employed, and a constant current of 0.5 μA was applied at 20 °C for **8**, **10**–**12** and at 5 °C for **9**. Details of the conditions of Batch A for **11** are as follows: DIETSe (6 mg, 6.8 μmol) and $nBu_4NAu(CN)_4$ (39 mg, 72 μmol) in a standard H-shaped cell were dissolved by $CH_2Cl_2$ (50 mL) and a small amount of remaining crystals of DIETSe were placed at the side of the anode. Black elongated plate-like crystals (typical size: $0.40 \times 0.06 \times 0.01$ $mm^3$) grew on the platinum rectangular pillar-shaped electrode under an applied current of 0.5 μA at 20 °C after 5 d.

**Crystal Structure Analysis:** The diffraction data were collected with a Bruker AXS SMART-APEX CCD system with graphite-monochromated Mo-$K_\alpha$ radiation ($\lambda$ = 0.71073 Å) (Table 2). Raw frame data were integrated using SAINT[19] and face-indexed absorption corrections[20] were applied. The structures were solved by the direct method (SHELXS-97[21]) and refined by full-matrix least-squares on $F^2$ with the program package SHELXTL.[22]

CCDC-642673 (for **8**), -642674 (for **9**), -642670 (for **10**), -642671 (for **11**), and -642672 (for **12**) contain the supplementary crystallographic data for this paper. These data can be obtained free of charge from The Cambridge Crystallographic Data Centre via www.ccdc.cam.ac.uk/data_request/cif.

**Electronic Band Calculations:** Intermolecular overlap integrals were calculated using HOMOs of the donor molecules obtained by the extended Hückel MO calculations using semiempirical parameters for the s and p Slater-type atomic orbitals listed in Table 4. The electronic band dispersions and Fermi surfaces were calculated using the intermolecular overlap integrals under the tight-binding approximation.[16]

Table 4. Semiempirical parameters for Slater-type orbitals.

| Orbitals | $\zeta$ | $I_P$/Ryd |
|---|---|---|
| I 5s | 2.681 | –1.713 |
| I 5p | 2.322 | –0.809 |
| Se 4s | 2.44 | –1.40 |
| Se 4p | 2.07 | –0.74 |
| S 3s | 2.122 | –1.47 |
| S 3p | 1.827 | –0.79 |
| C 2s | 1.625 | –1.573 |
| C 2p | 1.625 | –0.838 |
| H 1s | 1.30 | –1.0 |

**Electrical Resistivity:** The electrical resistivities were measured using the standard four-probe method in the temperature range of 1.6–300 K. Gold wires (10 or 18 μm) were attached to a single crystal using carbon paste, and silver paste was used for wiring the sample to the measurement substrate.

**Magnetic Susceptibility:** The magnetic properties for **11** were measured with a Quantum Design SQUID magnetometer (MPMS-XL5) for randomly oriented samples operating in the temperature range of 1.8–300 K with a DC magnetic field of 10 Oe or 50 kOe.

 © 2007 Wiley-VCH Verlag GmbH & Co. KGaA, Weinheim 

The absolute value of molar magnetic susceptibility $\chi$ cannot be calculated because of the low applied field of 10 Oe and the discussions of the diamagnetic transition are based on raw data of the magnetization without subtraction of the diamagnetism of the sample holder, DIETSe, and $Au(CN)_4$ anion. The absolute value of $\chi$ is obtained by the measurement under the field of 50 kOe. The diamagnetism of the sample holder and DIETSe were obtained from blank experiments under the same conditions as those for the sample measurements. The diamagnetic core susceptibility of the $Au(CN)_4$ anion was evaluated with Pascal's table.

## Acknowledgments

This work was partially supported by a Grant-in-Aid for scientific research from the Japan Society for the Promotion of Science (JSPS) and the Ministry of Education, Culture, Sports, Science and Technology (MEXT) (nos. 14740390 and 14204033).

[1] G. R. Desiraju, *Angew. Chem. Int. Ed. Engl.* **1995**, *34*, 2311–2327.

[2] a) T. Imakubo, H. Sawa, R. Kato, *Synth. Met.* **1995**, *73*, 117–122; b) T. Imakubo, H. Sawa, R. Kato, *J. Chem. Soc. Chem. Commun.* **1995**, 1097–1098; c) T. Imakubo, T. Maruyama, H. Sawa, K. Kobayashi, *Chem. Commun.* **1998**, 2021–2022; d) R. Suizu, T. Imakubo, *Org. Biomol. Chem.* **2003**, *1*, 3629–3631; e) K. Hervé, O. Cador, S. Golhen, K. Costuas, J.-F. Halet, T. Shirahata, T. Muto, T. Imakubo, A. Miyazaki, L. Ouahab, *Chem. Mater.* **2006**, *18*, 790–797; f) T. Imakubo, M. Kibune, H. Yoshino, T. Shirahata, K. Yoza, *J. Mater. Chem.* **2006**, *16*, 4110–4116.

[3] a) T. Imakubo, H. Sawa, R. Kato, *J. Chem. Soc. Chem. Commun.* **1995**, 1667–1668; b) T. Imakubo, H. Sawa, R. Kato, *Synth. Met.* **1997**, *86*, 1883–1884; c) T. Imakubo, N. Tajima, M. Tamura, R. Kato, Y. Nishio, K. Kajita, *J. Mater. Chem.* **2002**, *12*, 159–161.

[4] a) T. Imakubo, T. Shirahata, K. Hervé, L. Ouahab, *J. Mater. Chem.* **2006**, *16*, 162–173; b) T. Shirahata, M. Kibune, M. Maesato, T. Kawashima, G. Saito, T. Imakubo, *J. Mater. Chem.* **2006**, *16*, 3381–3390.

[5] T. Imakubo, T. Shirahata, *Chem. Commun.* **2003**, 1940–1941.

[6] T. Shirahata, T. Imakubo, *Org. Biomol. Chem.* **2004**, *2*, 1685–1687.

[7] a) P. Metrangolo, G. Resnati, *Chem. Eur. J.* **2001**, *7*, 2511–2519; b) P. Metrangolo, H. Neukirch, T. Pilati, G. Resnati, *Acc. Chem. Res.* **2005**, *38*, 386–395 and references cited therein.

[8] For other examples of organic conductors based on iodinated TTFs, see: a) R. Gompper, J. Hock, K. Polborn, E. Dormann, H. Winter, *Adv. Mater.* **1995**, *7*, 41–43; b) A. S. Batsanov, A. J. Moore, N. Robertson, A. Green, M. R. Bryce, J. A. K. Howard, A. E. Underhill, *J. Mater. Chem.* **1997**, *7*, 387–389; c) A. S. Batsanov, M. R. Bryce, A. Chesney, J. A. K. Howard, D. E. John, A. J. Moore, C. L. Wood, H. Gershtenman, J. Y. Becker, V. Y. Khodorkovsky, A. Ellern, J. Bernstein, I. F. Perepichka, V. Rotello, M. Grey, A. O. Cuello, *J. Mater. Chem.* **2001**, *11*, 2181–2191; d) B. Domercq, T. Devic, M. Fourmigué, P. Auban-Senzier, E. Canadell, *J. Mater. Chem.* **2001**, *11*, 1570–1575; e) T. Devic, B. Domercq, P. Auban-Senzier, P. Molinié, M. Fourmigué, *Eur. J. Inorg. Chem.* **2002**, 2844–2849; f) J. Nishijo, E. Ogura, J. Yamaura, A. Miyazaki, T. Enoki, T. Takano, Y. Kuwatani, M. Iyoda, *Synth. Met.* **2003**, *133*, 539–541; g) A. Ranganathan, A. El-Ghayoury, C. Mézière, E. Harté, R. Clérac, P. Batail, *Chem. Commun.* **2006**, 2878–2880.

[9] For reviews of organic conductors based on halogenated TTFs, see: a) M. Fourmigué, P. Batail, *Chem. Rev.* **2004**, *104*, 5379–5418; b) T. Imakubo in *TTF Chemistry – Fundamentals and Applications of Tetrathiafulvalene: Halogenated TTFs* (Eds.: J. Yamada, T. Sugimoto), Kodansha & Springer, Tokyo, **2004**, chapter 3 and references cited therein.

[10] For reviews of organic conductors based on selenium analogues of TTFs, see: a) K. Takimiya, T. Otsubo, *Phosphorus Sulfur Silicon Relat. Elem.* **2005**, *180*, 873–881; b) T. Otsubo, K. Takimiya in *TTF Chemistry – Fundamentals and Applications of Tetrathiafulvalene: Selenium Analogues of TTFs* (Eds: J. Yamada, T. Sugimoto), Kodansha & Springer, Tokyo, **2004**, chapter 5 and references cited therein.

[11] V. Y. Lee, E. M. Engler, R. R. Schumaker, S. S. P. Parkin, *J. Chem. Soc. Chem. Commun.* **1983**, 235–236.

[12] A. Morikami, K. Takimiya, Y. Aso, T. Otsubo, *Org. Lett.* **1999**, *1*, 23–25.

[13] For examples of $CSe_2$-free synthesis of TSeFs see: a) Y. A. Jackson, C. L. White, M. V. Lakshmikantham, M. P. Cava, *Tetrahedron Lett.* **1987**, *28*, 5635–5636; b) G. C. Papavassiliou, S. Y. Yiannopoulos, J. S. Zambounis, K. Kobayashi, K. Umemoto, *Chem. Lett.* **1987**, 1279–1282; c) R. Kato, H. Kobayashi, A. Kobayashi, *Synth. Met.* **1991**, *42*, 2093–2096; d) T. Imakubo, T. Shirahata, M. Kibune, *Chem. Commun.* **2004**, 1590–1591; e) K. Takimiya, H. J. Jeon, T. Otsubo, *Synthesis* **2005**, 2810–2813.

[14] A. Bondi, *J. Phys. Chem.* **1964**, *68*, 411–451.

[15] The LUMOs of the donor molecules, DIEDSS and DIETSe, were calculated by the MNDO-PM3 method using WinMOPAC ver. 3.5 (Fujitsu Ltd.).

[16] T. Mori, A. Kobayashi, Y. Sasaki, H. Kobayashi, G. Saito, H. Inokuchi, *Bull. Chem. Soc. Jpn.* **1984**, *57*, 627–633.

[17] a) M. Munakata, T. Kuroda-Sowa, M. Maekawa, A. Hirota, S. Kitagawa, *Inorg. Chem.* **1995**, *34*, 2705–2710; b) N. Kobayashi, T. Naito, T. Inabe, *Adv. Mater.* **2004**, *16*, 1803–1806.

[18] a) P. J. Nigrey, B. Morosin, E. Duesler, *Synth. Met.* **1988**, *27*, B481–B486; b) N. Svenstrup, J. Becher, *Synthesis* **1995**, 215–235.

[19] *SAINT*, Version 6.45, Bruker AXS, **2003**.

[20] *XPREP*, Bruker AXS, **2003**.

[21] G. M. Sheldrick, *SHELXS97, a program for the solution of crystal structures from X-ray Data*, University Göttingen, Germany, **1997**.

[22] *SHELXTL Reference Manual*, Version 5.03, Siemens Energy & Automation, Inc., Analytical Instrumentation, Madison, WI, USA, **1996**.

Received: May 21, 2007
Published Online: August 29, 2007

 © 2007 Wiley-VCH Verlag GmbH & Co. KGaA, Weinheim 

DOI: 10.1002/ejic.200700505

# Water-Soluble Phenanthroline Complexes of Rhodium, Iridium and Ruthenium for the Regeneration of NADH in the Enzymatic Reduction of Ketones

Jérôme Canivet,[a] Georg Süss-Fink,*[a] and Petr Štěpnička[b]

**Keywords:** Cationic complexes / Cofactor regeneration / Chemoenzymatic catalysis / Enantioselective catalysis / Transfer hydrogenation

The nicotinamide coenzyme NADH, consumed in enantioselective reduction of ketones catalysed by alcohol dehydrogenases, needs to be regenerated in order to maintain enzymatic activity. We therefore studied the catalytic potential of the cationic complexes $[(\eta^5\text{-}C_5Me_5)Rh(N\cap N)Cl]^+$ (**1**: N∩N = 1,10-phenanthroline; **2**: N∩N = 5-nitro-1,10-phenanthroline; **3**: N∩N = 5-amino-1,10-phenanthroline), $[(\eta^5\text{-}C_5Me_5)Ir(N\cap N)Cl]^+$ (**4**: N∩N = 5-nitro-1,10-phenanthroline) and $[(\eta^6\text{-}C_6Me_6)Ru(N\cap N)Cl]^+$ (**5**: N∩N = 5-nitro-1,10-phenanthroline), isolated as the water-soluble chloride salts, for transfer hydrogenation of $NAD^+$ to give NADH in aqueous solution. The best results were obtained with rhodium complex **1**, which gave catalytic turnover frequencies up to 2000 $h^{-1}$ in aqueous solution at pH 7 and 60 °C with sodium formate as the hydrogen source. When this NADH-regenerating catalytic system is combined with NADH-dependent enzymes, it is possible to chemoenzymatically reduce prochiral ketones such as acetophenone or 4-phenylbutan-2-one with high enantioselectivity. Combination of horse liver alcohol dehydrogenase (HLADH) or alcohol dehydrogenase from *Rhodococcus sp.* (S-ADH) with **1**/formate as the NADH-regenerating system resulted in *ee* values up to 98%, depending on the nature of the substrate and the enzyme. In order to explain the different catalytic activities, the electrochemical behaviour of complexes **1**–**5** has been studied.

(© Wiley-VCH Verlag GmbH & Co. KGaA, 69451 Weinheim, Germany, 2007)

## Introduction

There is an increasing demand for enantiopure biologically active compounds and their precursors.[1] The transition-metal-based enantioselective hydrogenation or transfer hydrogenation of ketones in organic solvents[2–10] as well as in aqueous solutions[11–21] is one of the most commonly used synthetic approaches. Biotransformations of organic substrates by various enzymes have also found widespread applications, particularly because of their capability to efficiently perform enantioselective transformations. The use of redox enzymes for synthetic purposes, however, has been limited by the need of cofactor regeneration.[22] Therefore, practical methods for the regeneration of coenzyme 1,4-NADH, the reduced form of nicotinamide adenine dinucleotide ($NAD^+$), are still of significant importance in the field of biocatalysis.

Conversion of $NAD^+$ to NADH by enzymatic,[23–26] photo- or electrochemical[27–29] methods has been extensively studied in order to increase the rate of cofactor regeneration while maintaining the necessary 1,4-dihydro regioselectivity. More than ten years ago Steckhan et al. introduced the dicationic (aqua)(bipyridine)rhodium complex $[(\eta^5\text{-}C_5Me_5)Rh(bipy)(OH_2)]^{2+}$ as a catalyst for the regeneration of NADH by using the formate anion as the hydrogen source in aqueous solution.[30,31] In a pioneering paper, Fishpp et al. extensively studied kinetic and mechanistic details of regioselective catalytic reduction by using a variety of 3-pyridinium $NAD^+$ models in the presence of $[(\eta^5\text{-}C_5Me_5)Rh(bipy)(OH_2)]^{2+}$.[32–35] This NADH-regenerating catalytic system was applied to the coupled chemoenzymatic enantioselective transfer hydrogenation of ketones in aqueous solution by combining NADH regeneration by an organorhodium complex and enantioselective ketone reduction performed by an alcohol dehydrogenase (ADH). Steckhan et al. described the transfer hydrogenation of 4-phenylbutan-2-one to the corresponding alcohol using ADH from horse liver with enantiomeric excesses up to 96%.[22] More recently, Schmid et al. reported a system based on ADH from *Thermus sp.* coupled with $[(\eta^5\text{-}C_5Me_5)Rh(bipy)(OH_2)]^{2+}$-promoted regeneration of NADH, which allowed the reduction of 3-methylcyclohexanone with an enantiomeric excess up to 97%.[1]

In this paper we report a series of water-soluble rhodium, iridium and ruthenium complexes containing 1,10-phenanthroline or its 5-substituted analogues as chelating *N*,*N*-donor ligands and the catalytic potential of these complexes for the regeneration of NADH in the chemoenzymatic re-

[a] Institut de Chimie, Université de Neuchâtel,
Case postale 158, 2009 Neuchâtel, Switzerland
E-mail: georg.suess-fink@unine.ch
[b] Department of Inorganic Chemistry, Faculty of Natural Science, Charles University in Prague
Hlavova 2030, 12840 Prague, Czech Republic

 © 2007 Wiley-VCH Verlag GmbH & Co. KGaA, Weinheim 

duction of ketones. The electrochemical behaviour of the complexes is also discussed.

## Results and Discussion

### Synthesis of Phenanthroline Complexes

Complexes $[(\eta^5\text{-}C_5Me_5)MCl_2]_2$ (M = Rh, Ir) react at room temperature in dichloromethane solution with 1,10-phenanthroline (phen) or with its 5-nitro or 5-amino derivatives to afford quantitatively the cationic complexes $[(\eta^5\text{-}C_5Me_5)M(N\cap N)Cl]^+$ (**1**: M = Rh, N∩N = phen; **2**: M = Rh, N∩N = 5-$NO_2$-phen; **3**: M = Rh, N∩N = 5-$NH_2$-phen; and **4**: M = Ir, N∩N = 5-$NO_2$-phen) [Equation (1)]. These cations are easily isolated as their chloride salts.

$$\tfrac{1}{2}[(\eta^5\text{-}C_5Me_5)MCl_2]_2 + N\cap N \rightarrow [(\eta^5\text{-}C_5Me_5)Rh(N\cap N)Cl]^+ + Cl^- \quad (1)$$

The chloride salts of **1**–**4** are yellow-orange solids that have a high solubility in water, a property that is used to remove unreacted starting material after the synthesis. As there is a risk of slow hydrolysis in water, the aqueous solutions are immediately filtered, and the filtrates are concentrated to dryness to give the analytically pure salts [**1**–**4**]Cl. All compounds have been characterised by $^1H$ and $^{13}C$ NMR spectroscopy, mass spectroscopy and elemental analysis.

In all cases, the phenanthroline ligand is coordinated in the *N*,*N*-chelating fashion to the metal centre. In contrast to the known, symmetrical 1,10-phenanthroline complex **1**,[36] the new 5-nitro- and 5-amino-1,10-phenanthroline cations **2**, **3** and **4** are chiral, and compounds [**2**]Cl, [**3**]Cl and [**4**]Cl are produced as racemic mixtures.

### Catalytic Reduction of $NAD^+$ to NADH in Aqueous Solution

Inspired by the pioneering studies of Steckhan[30] and Fish[33] on the use of ($\eta^5$-cyclopentadienyl)rhodium bipyridine complexes as catalysts for the regioselective reduction of $NAD^+$ models with the formate anion as the hydrogen source in aqueous solution, we studied this reaction catalysed by cations **1**–**4** as well as by the previously described complex $[(\eta^6\text{-}C_6Me_6)Ru(5\text{-}NO_2\text{-phen})Cl]^+$ (**5**),[37] which is known to be active for the reduction of ketones in water (Scheme 1).

Cations **1**–**5** were found to promote the reduction of $NAD^+$ to NADH in aqueous solution with sodium formate as the hydrogen donor (Table 1). The best results were obtained with rhodium complexes **1**–**3**, which led to TOFs ranging from 1500 to 2000 $h^{-1}$ at 60 °C and pH = 7. In comparison with the analogous bipy complex $[(\eta^5\text{-}C_5Me_5)Rh(bipy)Cl]^+$ (TOF = 875 $h^{-1}$), commonly used as a catalyst for this reaction, phen analogue **1** is more than twice as active (TOF = 2000 $h^{-1}$) under the same conditions.

Ruthenium complex **5** shows a catalytic activity fifteen times lower than that observed with the related rhodium complex **2** (entries 6 and 21). The low activity of the ruthenium complex observed in this study is similar to the results recently published by Sadler et al. describing the use of (arene)(ethylenediamine)ruthenium complexes for the reduction of $NAD^+$ to NADH in aqueous solution at 37 °C

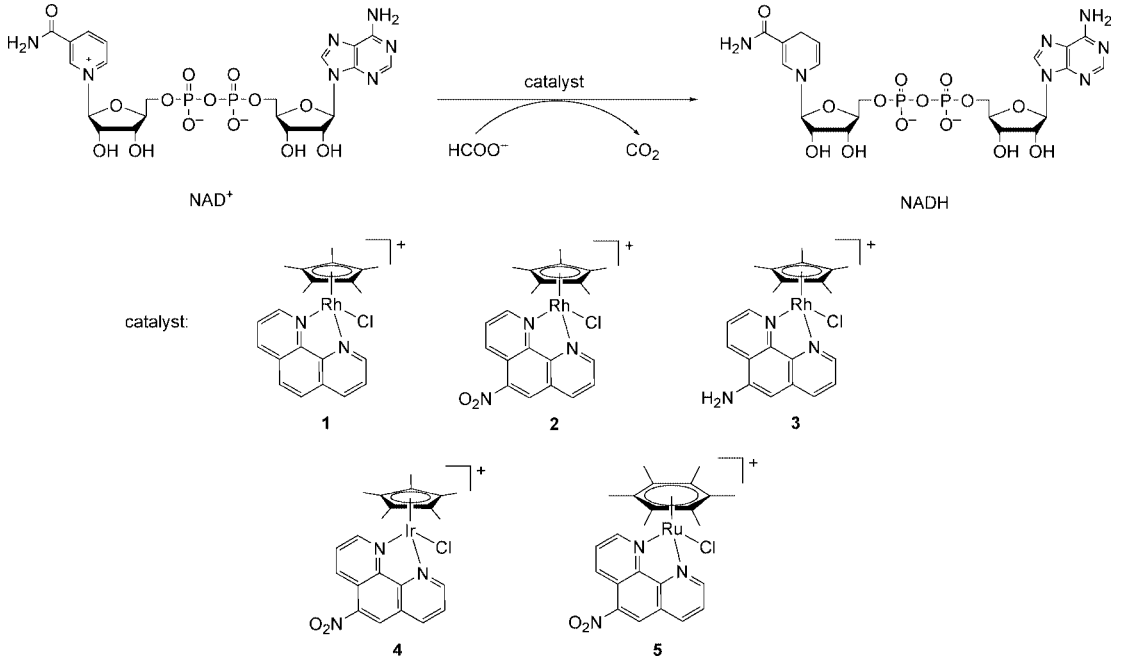


Scheme 1. Transfer hydrogenation of $NAD^+$ to NADH in aqueous solution catalysed by cationic chlorido complexes **1** to **5** by using the formate anion as the hydrogen source.

 © 2007 Wiley-VCH Verlag GmbH & Co. KGaA, Weinheim 

Table 1. Transfer hydrogenation of $NAD^+$ to NADH in aqueous solution by using the formate anion as the hydrogen source.[a]

| Entry | Catalyst | $n_s/n_c$[b] | $T$[°C] | pH | Conversion [%] (Time [h])[c] | TOF [$h^{-1}$][c,d] |
|---|---|---|---|---|---|---|
| 1 | **1** | 1000 | 38 | 7 | 100 (2.5) | 560 |
| 2 | | 1000 | 60 | 7 | 100 (0.5) | 2000 |
| 3 | **2** | 15 | 25 | 7 | 100 (3) | 19.5 |
| 4 | | 15 | 38 | 7 | 100 (0.25) | 30 |
| 5 | | 50 | 38 | 7 | 100 (0.5) | 100 |
| 6 | | 100 | 38 | 7 | 100 (2.5) | 150 |
| 7 | | 500 | 38 | 7 | 100 (3.5) | 380 |
| 8 | | 1000 | 38 | 7 | 100 (4) | 400 |
| 9 | | 1000 | 60 | 7 | 100 (0.75) | 1740 |
| 10 | | 15 | 38 | 4[e] | 100 (0.5) | 29 |
| 11 | **3** | 1000 | 38 | 7 | 100 (4) | 400 |
| 12 | | 1000 | 60 | 7 | 100 (1) | 1500 |
| 13 | **4** | 15 | 25 | 7 | 100 (5) | 14.4 |
| 14 | | 15 | 38 | 7 | 100 (2.5) | 23 |
| 15 | | 50 | 38 | 7 | 100 (4.5) | 47 |
| 16 | | 100 | 38 | 7 | 100 (7) | 58 |
| 17 | | 15 | 38 | 4[e] | 100 (3) | 22.5 |
| 18 | **5** | 15 | 25 | 7 | 35 (24) | 1.5 |
| 19 | | 15 | 38 | 7 | 70 (24) | 6 |
| 20 | | 50 | 38 | 7 | 50 (24) | 8 |
| 21 | | 100 | 38 | 7 | 20 (24) | 10 |
| 22 | | 15 | 38 | 4[e] | 55 (24) | 5.4 |
| 23 | $[(\eta^5\text{-}C_5Me_5)Rh(bipy)Cl]^+$ | 1000 | 60 | 7 | 100 (2) | 875 |

[a] Conditions: [$NAD^+$] = 8 mM, [$NaHCO_2$] = 350 mM; reactions carried out in 1 mL of phosphate buffer (pH 7). [b] Mol of substrate per mol of catalyst. [c] Determined by UV-absorption at 340 nm. [d] Turnover frequencies determined after 30 minutes and expressed in mol of product/(mol of metal·h). [e] Reactions carried out in phthalate buffer.

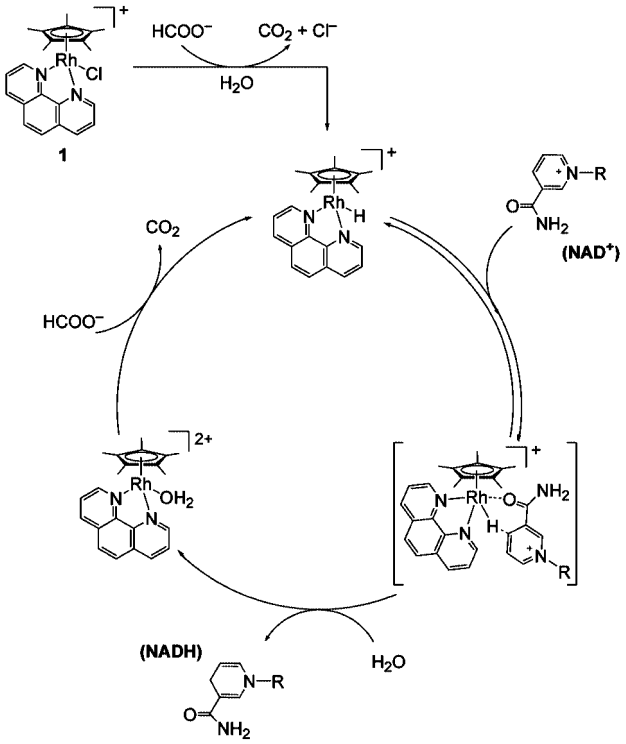


Scheme 2. Postulated catalytic cycle, based on the work of Fish, for the reduction of $NAD^+$ to NADH in aqueous solution with **1** as the catalyst.

and pH = 7.2.[38] Iridium complex **4** is also two times less active than the rhodium analogue **2** under the same conditions (entries 6 and 16). The results with varied pH demonstrate that the catalytic activity does not show any significant pH dependence.

According to the mechanistic scheme proposed by Fish et al. for the analogous bipy complexes,[33] cationic complex **1** is supposed to react with the formate anion to afford the corresponding hydrido complex, which can reduce $NAD^+$ to NADH (Scheme 2). The postulated catalytic cycle involves a transition state for hydride transfer from the rhodium centre to the pyridinium group, in which the $NAD^+$ and the metal hydride form a kinetically stable six-membered ring.

## Electrochemical Behaviour of the Phenanthroline Complexes

The electrochemical behaviour of complexes **1**–**4** has been studied by cyclic voltammetry at a stationary platinum disc and by voltammetry at a rotating platinum disc electrode (RDE) by using acetonitrile solutions (analyte concentration: ca. $5 \times 10^{-4}$ M) containing $Bu_4N[PF_6]$ (0.1 M) as the supporting electrolyte. Relevant data together with the parameters for the related Ru complexes[39] are summarised in Table 2.[40]

The redox response of phenanthroline complex **1** is shown in Figure 1. The first reduction occurs as a two-electron irreversible process (up to 500 $mV\,s^{-1}$), which is, however, fast and diffusion controlled ($i_{pa} \propto v^{1/2}$, $i_{lim} \propto \omega^{1/2}$). The associated oxidative peak (B) retains the diffusion control ($i_p \propto v^{1/2}$) but shows a peak current lower than that of the corresponding reduction wave (A). Such behaviour parallels that of the related cations $[L_nMCl(bipy)]^+$ [$L_nM$ = $(\eta^5\text{-}C_5Me_5)Rh$, $(\eta^5\text{-}C_5Me_5)Ir$ and $(\eta^6\text{-arene})Ru$; bipy =

 © 2007 Wiley-VCH Verlag GmbH & Co. KGaA, Weinheim 

Table 2. Summary of the electrochemical data.[a]

| Compound | $E_p$[V] | Reference |
|---|---|---|
| $[(\eta^5\text{-}C_5Me_5)RhCl(phen)]^+$ (**1**) | –1.32 (A), –1.10 (B), ≈ +0.64 (C) | this work |
| $[(\eta^5\text{-}C_5Me_5)RhCl(5\text{-}NO_2\text{-}phen)]^+$ (**2**) | –1.01/–0.93 ($NO_2$),[b] –1.43 (A), ≈ +0.64 (C) | this work |
| $[(\eta^5\text{-}C_5Me_5)RhCl(5\text{-}NH_2\text{-}phen)]^+$ (**3**) | –1.28 (A), –1.16 (B) | this work |
| $[(\eta^5\text{-}C_5Me_5)IrCl(phen)]^+$ (**4**) | –0.99 (A), –0.90 (B), ≈ +0.64 (C) | this work |
| $[(\eta^6\text{-}C_6Me_6)RuCl(phen)]^+$ (**5**) | –1.59 (A) | [39] |
| $[(\eta^6\text{-}C_6Me_6)RuCl(5\text{-}NO_2\text{-}phen)]^+$ | –0.99 ($E^{\circ\prime}$ for $NO_2$) | [39] |
| $[(\eta^6\text{-}C_6Me_6)RuCl(5\text{-}NH_2\text{-}phen)]^+$ | –1.58 (A) | [39] |

[a] The potentials are given relative to the ferrocene/ferrocenium reference (see the Experimental Section for details). Peak potentials for irreversible processes were obtained at a scan rate of 100 mV s$^{-1}$. Definitions: $E^{\circ\prime} = \frac{1}{2}(E_{pa} + E_{pc})$, $\Delta E_p = E_{pa} - E_{pc}$. [b] $E_{pc}/E_{pa}$ for the reversible reduction of the nitro group.

2,2′-bipyridine] and $[(\eta^5\text{-}C_5Me_5)MCl(bpym)]^+$ (M = Rh and Ir; bipym = 2,2′-bipyrimidine)[41–43] and can be explained by reductive removal of the chlorido ligand as shown in Equation (2).

$$[(\eta^5\text{-}C_5Me_5)M(phen)Cl]^+ + 2e^- \rightarrow [(\eta^5\text{-}C_5Me_5)M(phen)] + Cl^- \quad (2)$$

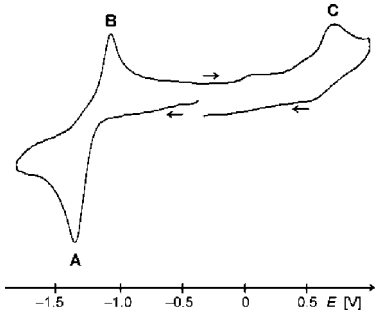


Figure 1. Cyclic voltammogram of **1** as recorded at a platinum disc electrode in acetonitrile solution at 100 mV s$^{-1}$ scan rate. The potentials are given relative to the ferrocene/ferrocenium reference.

The neutral electrogenerated species $[(\eta^5\text{-}C_5Me_5)M(phen)]$ is probably rather unstable and becomes oxidised in a single step, giving rise to wave B. A broad wave (C), observed in the anodic region, can be attributed to oxidation of some decomposition product(s). However, the exact nature of this redox process remains unclear.

The presence of an amino group at the phenanthroline ligand in **3** has only a minor influence on the electrochemical behaviour, manifested mainly by a slight shift of the A and B waves to higher potentials and also by a diminished A–B separation. On the contrary, substitution with a nitro group markedly changes the redox response, as the nitro group is reduced first in a reversible, one-electron process ($–NO_2 + e^- \rightleftarrows –NO_2^{-\cdot}$), the potential of which is independent of the metal (Rh vs. Ir). Such an "inserted" redox step naturally influences the following one(s).

In the case of **2**, the metal-centred reduction occurs at –1.44 V (wave A), while for **5** only a broad wave at around –1.6 V could be detected. The associated counterwave (if any) is difficult to detect. This could explain the higher activity of rhodium catalyst **2** as compared with that found for ruthenium catalyst **5** in the reduction of $NAD^+$ to NADH described above, the more difficult-to-reduce species being less catalytically active.

## Chemoenzymatic Enantioselective Reduction of Ketones

In light of the findings by Steckhan[22] and Schmid[1] on organometallic NADH regeneration for enzymatic ketone reductions, we studied the chemoenzymatic enantioselective transfer hydrogenation of 4-phenylbutan-2-one and acetophenone in aqueous solution. We used the NADH-dependent enzymes horse liver alcohol dehydrogenase (HLADH) or alcohol dehydrogenase from *Rhodococcus sp.* (S-ADH) and **1** as the NADH-regenerating catalyst with the formate anion as the hydrogen source (Scheme 3).

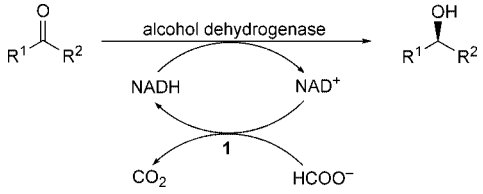


Scheme 3. Organometallic NADH regeneration for the stereoselective reduction of ketones with alcohol dehydrogenase.

The NADH-regenerating catalytic system with **1** as the catalyst was found to be active in combination with the two enzymes used (HLADH and S-ADH) for the enantioselective reduction of the test substrates (Table 3). The reaction proceeds with good to excellent enantioselectivity, producing predominantly the *S* enantiomer.

The results show the enantioselectivities to be similar to those found without the organometallic NADH regeneration catalyst with *ee* values up to 92 and 98%. However, the enzymatic activity with NADH regeneration is somewhat lower relative to enzymatic ketone reduction with excess NADH. This could be explained by a deactivation of the organometallic catalyst during the reaction, probably due to coordination of functional enzyme groups to the rhodium centre.

The mechanistic aspects of the combined organometallic–enzymatic catalysis are summarised in Scheme 4, which is a combination of Scheme 2 and Scheme 3. The organometallic intermediates $[(\eta^5\text{-}C_5Me_5)Rh(phenanthroline)H]^+$ and $[(\eta^5\text{-}C_5Me_5)Rh(phenanthroline)(OH_2)]^{2+}$ work hand-in-hand with the coenzyme intermediates $NAD^+$ and NADH to perform the enantioselective reduction of a ketone to give the corresponding alcohol, with aqueous sodium formate as hydrogen source and a dehydrogenase enzyme as chiral inducer.

 © 2007 Wiley-VCH Verlag GmbH & Co. KGaA, Weinheim 

Table 3. Chemoenzymatic enantioselective transfer hydrogenation of ketones with alcohol dehydrogenase and **1** as NADH-regenerating catalysts in aqueous solution.[a]

| Entry | Ketone | Enzyme | Conc. of Rh [mM] | *t* [h] | Conversion [%][b] | *ee* [%][b] |
|---|---|---|---|---|---|---|
| 1[c] | 4-phenylbutan-2-one | HLADH | 0 | 24 | 80 | 96 |
| 2[d] | 4-phenylbutan-2-one | none | 0.5 | 24 | 4 | n.d. |
| 3 | 4-phenylbutan-2-one | HLADH | 0.5 | 24 | 62 | 92 |
| 4 | 4-phenylbutan-2-one | HLADH | 0.1 | 24 | 47 | 88 |
| 5 | 4-phenylbutan-2-one | HLADH | 0.01 | 24 | 1.2 | n.d. |
| 6 | 4-phenylbutan-2-one | HLADH | 0.002 | 24 | 0.5 | n.d. |
| 7 | acetophenone | HLADH | 0.5 | 24 | 2 | n.d. |
| 8[c] | acetophenone | S-ADH | 0 | 24 | 78 | 98 |
| 9[d] | acetophenone | none | 0.5 | 24 | 8 | n.d. |
| 10 | acetophenone | S-ADH | 0.5 | 24 | 58 | 74 |
| 11 | acetophenone | S-ADH | 0.1 | 24 | 20 | 98 |

[a] Conditions: [$NAD^+$] = 1 mM, [$NaHCO_2$] = 100 mM, [ketone] = 33 mM, reactions carried out with 1 unit of alcohol dehydrogenase in 1 mL of phosphate buffer (pH 7) at 37 °C. [b] Determined by chiral HPLC analysis. [c] Conditions: [NADH] = 40 mM, [$NaHCO_2$] = 100 mM, [ketone] = 33 mM, reactions carried out with 1 unit of alcohol dehydrogenase in 1 mL of phosphate buffer (pH 7) at 37 °C. [d] Reaction carried out without HLADH or S-ADH and $NAD^+$.

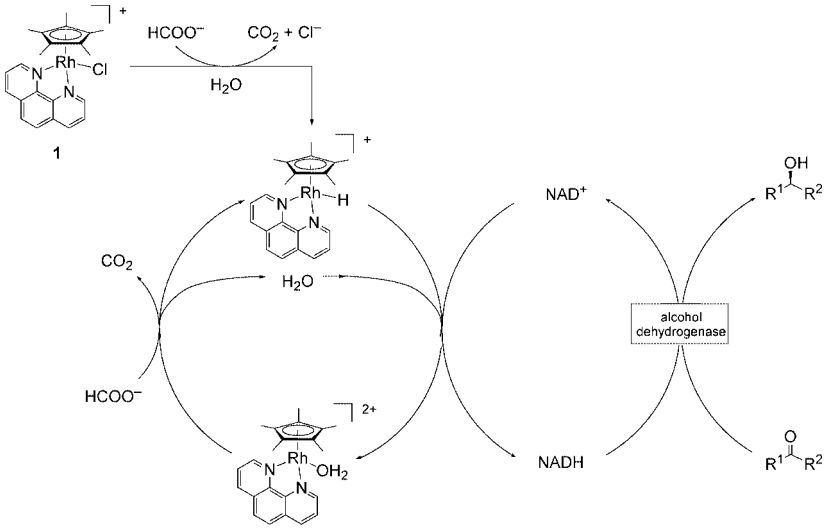


Scheme 4. Catalytic cycle for the chemoenzymatic enantioselective transfer hydrogenation of ketones with **1** as NADH regenerating catalyst in aqueous solution.

## Conclusions

In conclusion, we report here a series of five water-soluble rhodium, iridium and ruthenium complexes containing 1,10-phenanthroline and derivatives thereof as chelating ligands. All these complexes were found to catalyse the 1,4-regioselective reduction of $NAD^+$ to NADH in aqueous solution. TOF values up to 2000 $h^{-1}$ have been obtained by using [($\eta^5$-$C_5Me_5$)Rh(phen)Cl]$^+$ (**1**) as a catalyst at 60 °C and pH = 7. Furthermore, rhodium catalyst **1** has been found to be active as an NADH-regenerating catalyst for the chemoenzymatic enantioselective transfer hydrogenation of ketones in aqueous solution. Under biological conditions (37 °C, pH = 7), this system, which combines organometallic NADH regeneration and enzymatic reduction in aqueous solution, converts ketones into the corresponding chiral alcohols with good activities and enantioselectivities.

## Experimental Section

**General:** All manipulations were carried out with freshly distilled solvents. The 5-amino-1,10-phenanthroline[44] and [($\eta^6$-$C_6Me_6$)-Ru(5-$NO_2$-phen)Cl]$^+$ (**5**)[37] were prepared according to the published methods. All other reagents were commercially available and were used without further purification. NMR spectra were recorded with a Bruker 400 MHz spectrometer by using sodium 2,2-dimethyl-2-silapentane-5-sulfonate in $D_2O$ as an internal standard. Electrospray mass spectra were obtained in the positive-ion mode with an LCQ Finnigan mass spectrometer. Microanalyses were carried out by the Laboratoire de Chimie Pharmaceutique, Université de Genève (Switzerland).

Electrochemical measurements were carried out with a multipurpose polarograph PA3 interfaced to a Model 4103 XY recorder (Laboratorní přístroje, Prague) at room temperature by using a standard three-electrode cell with a rotating platinum disc electrode (RDE; 1 mm diameter) as the working electrode, platinum wire as

 © 2007 Wiley-VCH Verlag GmbH & Co. KGaA, Weinheim 

the auxiliary electrode and a saturated calomel electrode (SCE) as the reference electrode. The reference electrode was separated from the analysed solution by a salt bridge (0.1 M $Bu_4N[PF_6]$ in acetonitrile). The samples were dissolved in acetonitrile (Riedel-de Haën, purissimum p.a.), to give an analyte concentration of $5 \times 10^{-4}$ M, and in 0.1 M $Bu_4N[PF_6]$ (Fluka, purissimum for electrochemistry). The solutions were purged with argon prior to the measurement and then kept under an argon blanket. Cyclic voltammograms were recorded at a stationary platinum disc electrode (scan rates 50–500 mV/s), while the voltammograms were obtained at a RDE (1000–2500 rpm, scan rate 20 mV/s). The redox potentials are given relative to the ferrocene/ferrocenium reference.

**Preparation of Chlorido Complexes $[(\eta^5\text{-}C_5Me_5)M(N\cap N)Cl]^+$ (M = Rh, Ir and N∩N = phen, 5-$NO_2$-phen, 5-$NH_2$-phen):** Two equivalents (0.30 mmol) of the appropriate phenanthroline donor were added to a suspension of $[(\eta^5\text{-}C_5Me_5)MCl_2]_2$ (M = Rh, Ir; 0.15 mmol) in dichloromethane (30 mL). The mixture was stirred for 3 h at room temperature, while the colour changed from dark orange to yellow-orange. After concentration to dryness, the residue was dissolved in water. This solution was filtered, and the filtrate was concentrated to dryness, which gave the product as a yellow powder in good yield.

**$[(\eta^5\text{-}C_5Me_5)Rh(phen)Cl]Cl$ ([1]Cl):** Yield: 74%, 80.8 mg. $^1$H NMR (400 MHz, $D_2O$, 21 °C): $\delta$ = 1.70 (s, $CH_3$), 7.99 (s, CH), 8.05–8.12 (dd, $^3J_{H,H}$ = 5.1 Hz, $^3J_{H,H}$ = 8.1 Hz, CH), 8.67–8.71 (d, $^3J_{H,H}$ = 8.1 Hz, CH), 9.28–9.31 (d, $^3J_{H,H}$ = 5.1 Hz, CH) ppm. $^{13}$C NMR (200 MHz, $D_2O$, 21 °C): $\delta$ = 8.32 [$C_5(CH_3)_5$], 97.9 [$C_5(CH_3)_5$], 126.63 (CH), 127.62 (CH), 130.98 (CH), 139.47 (CH), 146.08 (C), 155.62 (C) ppm. MS (ESI): *m*/*z* = 453 $[M]^+$. $C_{22}H_{23}Cl_2N_2Rh$ (489.24): calcd. C 54.01, H 4.74, N 5.73; found C 53.91, H 4.82, N 5.68.

**$[(\eta^5\text{-}C_5Me_5)Rh(NO_2\text{-}phen)Cl]Cl$ ([2]Cl):** Yield: 85%, 85.4 mg. $^1$H NMR (400 MHz, $D_2O$, 21 °C): $\delta$ = 1.68 (s, $CH_3$), 7.99 (s, CH), 8.16–8.21 (quint, $^3J_{H,H}$ = 4.5 Hz, CH), 8.83–8.85 (d, $^3J_{H,H}$ = 8.2 Hz, CH), 8.96 (s, CH), 9.19–9.22 (d, $^3J_{H,H}$ = 8.7 Hz, CH), 9.36 (d, $^3J_{H,H}$ = 4.7 Hz, CH), 9.41 (d, $^3J_{H,H}$ = 4.8 Hz, CH) ppm. $^{13}$C NMR (200 MHz, $D_2O$, 21 °C): $\delta$ = 8.52 [$C_5(CH_3)_5$], 98.8 [$C_5(CH_3)_5$], 123.62 (C), 127.63 (CH), 127.81 (C), 128.38 (CH), 128.41 (CH), 136.51 (CH), 141.71 (CH), 144.31 (C), 145.72 (C), 146.98 (C), 153.44 (CH), 155.14 (CH) ppm. MS (ESI): *m*/*z* = 498 $[M^+]$. $C_{22}H_{22}Cl_2N_3O_2Rh$ (534.24): calcd. C 49.46, H 4.15, N 7.87; found C 49.32, H 4.18, N 7.63.

**$[(\eta^5\text{-}C_5Me_5)Rh(NH_2\text{-}phen)Cl]Cl$ ([3]Cl):** Yield: 80%, 78.7 mg. $^1$H NMR (400 MHz, $D_2O$, 21 °C): $\delta$ = 1.64 (s, $CH_3$), 6.60 (s, CH), 7.72–7.79 (dd, $^3J_{H,H}$ = 5.4 Hz, $^3J_{H,H}$ = 8.7 Hz, CH), 7.96–8.07 (m, $^3J_{H,H}$ = 8.8 Hz, CH), 8.54–8.58 (d, $^3J_{H,H}$ = 8.4 Hz, CH), 8.88–8.90 (d, $^3J_{H,H}$ = 4.4 Hz, CH), 9.22–9.24 (d, $^3J_{H,H}$ = 4.1 Hz, CH) ppm. $^{13}$C NMR (200 MHz, $D_2O$, 21 °C): $\delta$ = 8.47 [$C_5(CH_3)_5$], 97.9 [$C_5(CH_3)_5$], 107.56 (CH), 126.52 (C), 126.80 (CH), 128.02 (CH), 128.91 (CH), 134.49 (CH), 136.00 (C), 138.41 (C), 145.54 (C), 148.94 (C), 151.81 (CH), 155.71 (CH) ppm. MS (ESI): *m*/*z* = 468 $[M]^+$. $C_{22}H_{24}Cl_2N_3Rh$ (504.26): calcd. C 52.40, H 4.80, N 8.33; found C 52.18, H 4.92, N 8.16.

**$[(\eta^5\text{-}C_5Me_5)Ir(NO_2\text{-}phen)Cl]Cl$ ([4]Cl):** Yield: 84%, 81.2 mg. $^1$H NMR (400 MHz, $D_2O$, 21 °C): $\delta$ = 1.53 (s, $CH_3$), 8.05–8.09 (dd, $^3J_{H,H}$ = 5.3 Hz, $^3J_{H,H}$ = 8.8 Hz, CH), 8.94 (s, CH), 9.08–9.11 (d, $^3J_{H,H}$ = 8.7 Hz, CH), 9.22 (d, $^3J_{H,H}$ = 5.2 Hz, CH), 9.27 (d, $^3J_{H,H}$ = 5.4 Hz, CH) ppm. $^{13}$C NMR (200 MHz, $D_2O$, 21 °C): $\delta$ = 8.14 [$C_5(CH_3)_5$], 90.72 [$C_5(CH_3)_5$], 124.02 (C), 127.75 (CH), 128.02 (C), 128.76 (CH), 128.83 (CH), 136.59 (CH), 141.64 (CH), 144.53 (C), 147.14 (C), 148.28 (C), 153.17 (CH), 154.76 (CH) ppm. MS (ESI): *m*/*z* = 588 $[M]^+$. $C_{22}H_{22}Cl_2IrN_3O_2$ (623.55): calcd. C 42.38, H 3.56, N 6.74; found C 42.24, H 3.67, N 6.54.

**Catalytic NADH Regeneration:** The reduction of $NAD^+$ (8 mM) catalysed by complexes [**1**–**5**]Cl with sodium formate (350 mM) as the hydrogen source was carried out in phosphate buffer (1 mL, pH 7) or in phthalate buffer (1 mL, pH 4). The conversion was determined by UV absorption at 340 nm. The pH was monitored with a pH meter (Mettler Toledo InLab® 413). Turnover frequencies were calculated for all the catalytic reactions from the conversions observed after 30 min for the hydrogenation reaction of $NAD^+$ to NADH. The results are summarised in Table 1.

**Chemoenzymatic Hydrogenation of Ketones:** The enzymatic transfer hydrogenation reactions of acetophenone or 4-phenylbutan-2-one (33 mM) were carried out in phosphate buffer (1 mL, pH 7) at 37 °C with 1 unit of alcohol dehydrogenase S-ADH or HLADH respectively, in the presence of $NAD^+$ (1 mM) and [**1**]Cl as NADH-regenerating catalyst and $NaHCO_2$ (100 mM) as the hydrogen source. The reactions without rhodium catalyst were performed with NADH instead of $NAD^+$ (40 mM), and the reactions without enzymatic reduction were performed without enzyme and $NAD^+$. The products were extracted with diethyl ether, filtered through silica and identified (and conversion and enantiomeric excess were determined) by HPLC on a Chiracel OD-H capillary column (hexane/2-propanol 9:10, 0.7 mL min$^{-1}$, 215 nm). The pH was monitored with a pH meter (Mettler Toledo InLab® 413).

## Acknowledgments

This work was financially supported by the Swiss National Science Foundation and is a part of the long-term research projects supported by the Ministry of Education, Youth and Sports of the Czech Republic (project nos. MSM0021620857 and LC06070). The generous loan of ruthenium(III) chloride hydrate from the Johnson Matthey Research Centre is gratefully acknowledged.

[1] F. Holmann, A. Kleeb, K. Otto, A. Schmid, *Tetrahedron: Asymmetry* **2005**, *16*, 3512–3519.
[2] K. Everaere, A. Mortreux, M. Bulliard, J. Brussee, A. van der Gen, G. Nowogrocki, J. F. Carpentier, *Eur. J. Org. Chem.* **2001**, 275–291.
[3] J. Diez, M. P. Gamasa, E. Lastra, A. Garcia-Fernandez, M. P. Tarazona, *Eur. J. Inorg. Chem.* **2006**, 2855–2864.
[4] S. Hashiguchi, A. Fujii, J. Takehara, T. Ikariya, R. Noyori, *J. Am. Chem. Soc.* **1995**, *117*, 7562–7563.
[5] N. Dahlin, A. Bogevig, H. Adolfsson, *Adv. Synth. Catal.* **2004**, *346*, 1101–1105.
[6] W. He, P. Liu, B. L. Zhang, X. L. Sun, S. Y. Zhang, *Appl. Organomet. Chem.* **2006**, *20*, 328–334.
[7] P. F. Yan, C. H. Nie, G. M. Li, G. F. Hou, W. B. Sun, J. S. Gao, *Appl. Organomet. Chem.* **2006**, *20*, 338–343.
[8] W. He, B. L. Zhang, R. Jiang, P. Liu, X. L. Sun, S. Y. Zhang, *Tetrahedron Lett.* **2006**, *47*, 5367–5370.
[9] B. Z. Li, J. S. Chen, Z. R. Dong, Y. Y. Li, Q. B. Li, J. X. Gao, *J. Mol. Catal. A: Chem.* **2006**, *258*, 113–117.
[10] K. Matsumura, S. Hashiguchi, T. Ikariya, R. Noyori, *J. Am. Chem. Soc.* **1997**, *119*, 8738–8739.
[11] T. Abura, S. Ogo, Y. Watanabe, S. Fukuzumi, *J. Am. Chem. Soc.* **2003**, *125*, 4149–4154.
[12] X. H. Li, J. Blacker, I. Houson, X. F. Wu, J. L. Xiao, *Synlett* **2006**, 1155–1160.
[13] X. G. Li, X. F. Wu, W. P. Chen, F. E. Hancock, F. King, J. L. Xiao, *Org. Lett.* **2004**, *6*, 3321–3324.
[14] X. F. Wu, X. G. Li, F. King, J. L. Xiao, *Angew. Chem. Int. Ed.* **2005**, *44*, 3407–3411.

 © 2007 Wiley-VCH Verlag GmbH & Co. KGaA, Weinheim 

[15] J. Canivet, G. Labat, H. Stoeckli-Evans, G. Süss-Fink, *Eur. J. Inorg. Chem.* **2005**, 4493–4500.
[16] Y. Arakawa, N. Haraguchi, S. Itsuno, *Tetrahedron Lett.* **2006**, *47*, 3239–3243.
[17] L. Jiang, T. F. Wu, Y. C. Chen, J. Zhu, J. G. Deng, *Org. Biomol. Chem.* **2006**, *4*, 3319–3324.
[18] H. Y. Rhyoo, H. J. Park, W. H. Suh, Y. K. Chung, *Tetrahedron Lett.* **2002**, *43*, 269–272.
[19] Y. P. Ma, H. Liu, L. Chen, X. Cui, J. Zhu, J. E. Deng, *Org. Lett.* **2003**, *5*, 2103–2106.
[20] F. Wang, H. Liu, L. F. Cun, J. Zhu, J. G. Deng, Y. Z. Jiang, *J. Org. Chem.* **2005**, *70*, 9424–9429.
[21] D. S. Matharu, D. J. Morris, G. J. Clarkson, M. Wills, *Chem. Commun.* **2006**, 3232–3234.
[22] D. Westerhausen, S. Herrmann, W. Hummel, E. Steckhan, *Angew. Chem. Int. Ed. Engl.* **1992**, *31*, 1529–1531.
[23] A. Liese in *Technology Transfer in Biotechnology: from Lab to Industry to Production*, **2005**, *92*, 197–224.
[24] H. M. Zhao, W. A. van der Donk, *Curr. Opin. Biotechnol.* **2003**, *14*, 583–589.
[25] W. A. van der Donk, H. M. Zhao, *Curr. Opin. Biotechnol.* **2003**, *14*, 421–426.
[26] H. Groger, W. Hummel, S. Buchholz, K. Drauz, T. Van Nguyen, C. Rollmann, H. Husken, K. Abokitse, *Org. Lett.* **2003**, *5*, 173–176.
[27] F. Hollmann, A. Schmid, *Biocatal. Biotransform.* **2004**, *22*, 63–88.
[28] K. Vuorilehto, S. Lutz, C. Wandrey, *Bioelectrochemistry* **2004**, *65*, 1–7.
[29] R. Ruppert, S. Herrmann, E. Steckhan, *Tetrahedron Lett.* **1987**, *28*, 6583–6586.
[30] E. Steckhan, S. Herrmann, R. Ruppert, J. Thommes, C. Wandrey, *Angew. Chem. Int. Ed. Engl.* **1990**, *29*, 388–390.
[31] R. Ruppert, S. Herrmann, E. Steckhan, *J. Chem. Soc. Chem. Commun.* **1988**, 1150–1151.
[32] J. Lutz, F. Hollmann, T. V. Ho, A. Schnyder, R. H. Fish, A. Schmid, *J. Organomet. Chem.* **2004**, *689*, 4783–4790.
[33] H. C. Lo, C. Leiva, O. Buriez, J. B. Kerr, M. M. Olmstead, R. H. Fish, *Inorg. Chem.* **2001**, *40*, 6705–6716.
[34] S. Ogo, O. Buriez, J. B. Kerr, R. H. Fish, *J. Organomet. Chem.* **1999**, *589*, 66–74.
[35] H. C. Lo, O. Buriez, J. B. Kerr, R. H. Fish, *Angew. Chem. Int. Ed.* **1999**, *38*, 1429–1432.
[36] U. Kolle, M. Grutzel, *Angew. Chem. Int. Ed. Engl.* **1987**, *26*, 567–570.
[37] J. Canivet, L. Karmazin-Brelot, G. Süss-Fink, *J. Organomet. Chem.* **2005**, *690*, 3202–3211.
[38] Y. K. Yan, M. Melchart, A. Habtemariam, A. F. A. Peacock, P. J. Sadler, *J. Biol. Inorg. Chem.* **2006**, *11*, 483–488.
[39] P. Stepnicka, J. Ludvik, J. Canivet, G. Süss-Fink, *Inorg. Chim. Acta* **2006**, *359*, 2369–2374.
[40] $E_{pa}$ and $E_{pc}$ are anodic and cathodic peak potentials, respectively. Similarly, $i_{pa}$ and $i_{pc}$ denote the anodic and cathodic peak currents in cyclic voltammetry; $i_{lim}$ is the limiting current in voltammetry at Pt-RDE, $\nu$ is the scan rate, and $\omega$ is the rotation frequency of the disc electrode.
[41] M. Ladwig, W. Kaim, *J. Organomet. Chem.* **1991**, *419*, 233–243.
[42] M. Ladwig, W. Kaim, *J. Organomet. Chem.* **1992**, *439*, 79–90.
[43] W. Kaim, R. Reinhardt, M. Sieger, *Inorg. Chem.* **1994**, *33*, 4453–4459.
[44] D. Garcia-Fresnadillo, G. Orellana, *Helv. Chim. Acta* **2001**, *84*, 2708–2730.

Received: May 9, 2007
Published Online: August 13, 2007

 © 2007 Wiley-VCH Verlag GmbH & Co. KGaA, Weinheim 

DOI: 10.1002/ejic.200700395

# Copper Bis(1-methyl-5-nitriminotetrazolate): A Promising New Primary Explosive

**Georg Geisberger,[a] Thomas M. Klapötke,*[a] and Jörg Stierstorfer[a]**

**Keywords:** Primary explosives / Copper / Nitrogen heterocycles / Pyrotechnics / X-ray

Copper bis(1-methyl-5-nitriminotetrazolate) (**1**) was synthesized and investigated as a new primary explosive. Compound **1** was obtained by dehydration of diaquabis(1-methylnitriminotetrazolato)copper(II) dihydrate (**2**) or diaquabis(1-methylnitriminotetrazolato)copper(II) (**3**) at 120 °C. Complexes **2** and **3** are easily formed by the reaction of 1-methyl-5-nitrimino-1,2,3,4-tetrazole (**4**) with copper(II) nitrate in aqueous solution in high yields. Single crystals of **1** were obtained by recrystallization from dry methanol, whereas wet methanol favors the yield of diaquabis(1-methyl-nitriminotetrazolato)copper(II) dimethanolate (**5**). Compound **1** was characterized by using single-crystal X-ray diffraction, IR spectroscopy, elemental analysis, and differential scanning calorimetry (DSC). The sensitivities were investigated by using the BAM drophammer and friction tests, and the heat of formation was calculated on the basis of electronic energies at the B3LYP/SDD level of theory. Compound **1** shows an impact sensitivity that is five times higher and a friction sensitivity that is ten times lower than that of lead azide, which is appropriate. In addition, the long-term stability of **1** at higher temperatures was tested by using isothermal safety calorimetry (TSC). Compounds **2** and **3** were characterized by single-crystal X-ray diffraction, IR spectroscopy, elemental analysis, DSC, bomb calorimetry, and BAM sensitivity tests. In addition, compound **5** was characterized by single-crystal X-ray diffraction and elemental analysis. The dehydration of **2** was determined by using thermal gravimetry (TG) to occur by the loss of crystal water in one discrete step.
(© WILEY-VCH Verlag GmbH & Co. KGaA, 69451 Weinheim, Germany, 2007)

## Introduction

Commonly used primary explosives[1,2] still include poisonous and polluting compounds (illustrated in Figure 1) like lead azide $[Pb(N_3)_2]$,[3–5] and lead styphnate (2,4,6-trinitroresorcinate),[6] which replaced mercury fulminate $[Hg(CNO)_2]$[7] early in the last century. Primary explosives are highly sensitive and are characterized by detonation velocities of 3500–5500 $ms^{-1}$. The discovery of suitable new substitutes for lead-containing primary explosives is an important aspect of current energetic materials research. Primary explosives consisting only of C, N, and H such as tetrazene,[8] which is used as a sensitizer, exist but are often difficult to synthesize.

A recently employed idea is the formation of nontoxic metal complexes containing zinc or copper instead of toxic heavy metals.[9] Because several tetrazoles[10,11] and tetrazolates[12,13] are known to be promising energetic compounds[14] with appropriate properties such as high densities, a positive heat of formation, and a high nitrogen content, one possible alternative for the development of new primary explosives is the use of copper tetrazole complexes.[15–17]

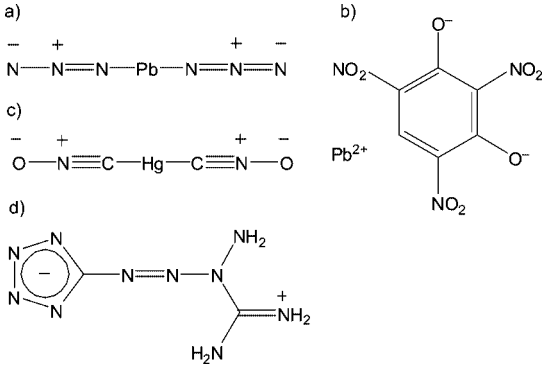


Figure 1. Common primary explosives: (a) lead azide, (b) lead styphnate, (c) mercury fulminate, and (d) tetrazene.

Copper tetrazole complexes are also suitable materials for modern pyrotechnical compositions. Common pyrotechnic compositions are nonexplosive combustible mixtures consisting of fuels and oxidizers, which generate bright-colored light, heat, or acoustic effects.[18] High-nitrogen materials have been investigated for use in pyrotechnic compositions in order to reduce smoke production.[19] A low-smoke pyrotechnic composition should include a nitrogen-rich energetic material (e.g. tetrazoles) with a low carbon content, an oxidizer, and a colorant. Copper(II) 1-

[a] Chair of Inorganic Chemistry, Energetic Materials Research, Ludwig-Maximilian University of Munich,
Butenandtstr. 5-13, 81377 Munich, Germany
Fax: +49-89-2180-77492
E-mail: tmk@cup.uni-muenchen.de

 © 2007 Wiley-VCH Verlag GmbH & Co. KGaA, Weinheim 

methyl-5-nitriminotetrazolates **2** and **3** are suitable new compounds for use as green-coloring pyrotechnic materials acting as substitutes for toxic barium salts.

## Results and Discussion

### Synthesis

The copper complexes $[Cu(C_2H_3N_6O_2)_2(H_2O)_2]\cdot 2H_2O$ (**2**) and $[Cu(C_2H_3N_6O_2)_2(H_2O)_2]$ (**3**) were synthesized according to Scheme 1 by the addition of an aqueous solution of copper nitrate trihydrate to an aqueous solution containing two equivalents of 1-methyl-5-nitriminotetrazole (**4**)[20] at 80 °C. Compound **2** was observed as the main product (85% yield), whereas **3** was obtained when the mother liquor was allowed to stand for a few days. Compound **4** was synthesized by the nitration of 1-methyl-5-aminotetrazole[21,22] by using fuming $HNO_3$.

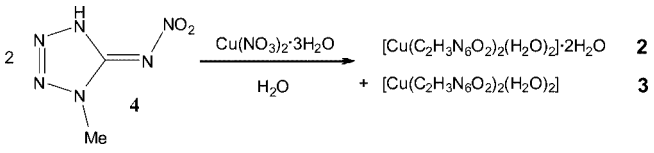


Scheme 1. Synthesis of compounds **2** and **3**.

The highly explosive $[Cu(C_2H_3N_6O_2)_2]$ (**1**), which does not contain crystal water, was obtained by dehydration of **2** by using high vacuum ($1 \times 10^{-2}$ bar) at 120 °C for two hours (Scheme 2). To remove the four water molecules, heating to 120 °C is sufficient but it requires twice the time. Single crystals of **1** were obtained by recrystallization of **1** from dry methanol, whereas recrystallization from wet methanol led to the formation of crystals of compound **5**, which contains two coordinated water molecules and two free methanol molecules.

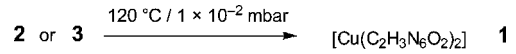


Scheme 2. Synthesis of **1** by dehydration of **2** or **3**.

### Molecular Structures

The single-crystal X-ray diffraction data were collected with an Oxford Xcalibur3 diffractometer with a Spellman generator (voltage 50 kV, current 40 mA) and a KappaCCD detector. Data collection was undertaken by using the CrysAlis CCD software,[23] and the data reductions were performed with the CrysAlis RED software.[24] The structures were solved by using SIR-92[25] and refined with SHELXL-97[26] and finally checked with PLATON.[27] In the structures, the hydrogen atoms were located and refined. The absorptions of **1**, **2**, **3**, and **5** were corrected by using the SCALE3 ABSPACK multiscan method.[28] Selected data from the X-ray data collections and refinements are given in Table 3. Further information regarding crystal structure determination was deposited with the Cambridge Crystallographic Data Centre.[29]

Primary explosive **1** crystallizes in the monoclinic space group $P2_1/c$ with 2 molecules in the unit cell and a density of 2.067 g cm$^{-3}$. The copper cations lay on the center of inversion and are coordinated in a distorted octahedral arrangement by two nitrogen atoms [$d$(Cu–N4) = 1.923(2) Å], which is also found in copper nitrogen complexes such as $[Cu(NH_3)_4(NO_3)_2]$,[30] and four oxygen atoms [$d$(Cu–O1) = 1.974(2) Å, $d$(Cu–O4$^i$) = 2.589(2) Å (i: 2 –$x$, –0.5 + $y$, 1.5 – $z$)]. The shorter coordination distances Cu–N4 and Cu–O1 are between one chelating 1-methyl-5-nitriminotetrazolato ligand, whereby a longer coordination to the other oxygen atom of the nitro group is also observed, which is longer than in typical Jahn–Teller distorted d$^9$ copper complexes (see structures of **2**, **3**, and **5**). Accordingly, every nitro group participates in coordination with two copper centers, which results in an endless 3-dimensional network. The extended molecular structure of **1**, which illustrates the coordination of the nitro groups in the crystalline state, is shown in Figure 2.

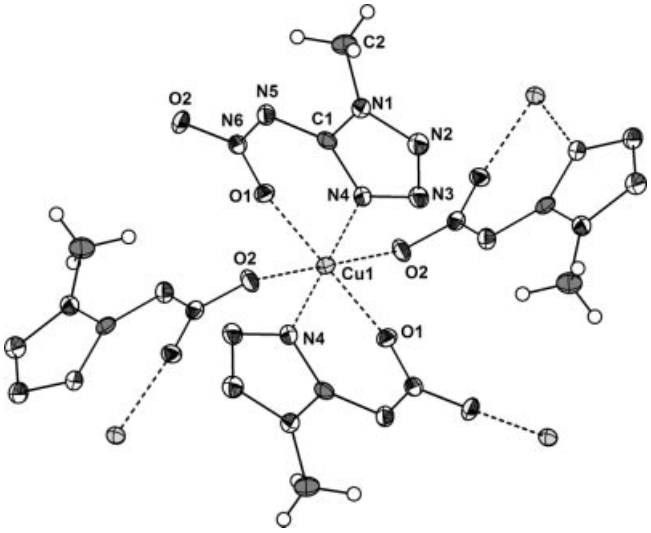


Figure 2. Crystal structure of **1** showing an extended molecular unit and atom-labeling scheme. Ellipsoids represent 50% probability.

The reaction of ligand **4** with copper(II) nitrate yields two different compounds {$[Cu(C_2H_3N_6O_2)_2(H_2O)_2]\cdot 2H_2O$ (**2**) and $[Cu(C_2H_3N_6O_2)_2(H_2O)_2]$ (**3**)}, which can be easily distinguishable by their color. Blue-colored main product **2** is characterized by the inclusion of two water molecules that do not participate in the coordination sphere. In these two structures, the effects of the inclusion of water can clearly be seen for example in the variation of the density (**2** 1.870 g cm$^{-3}$, **3** 2.035 g cm$^{-3}$). Both compounds crystallize with two molecules in the unit cell in the monoclinic crystal system: **2** in the space group $P2_1/c$ and **3** in the alternative

 © 2007 Wiley-VCH Verlag GmbH & Co. KGaA, Weinheim 

setting $P2_1/n$. The coordination geometry of the copper cations is characterized by an elongated octahedral arrangement due to the Jahn–Teller effect. This coordination geometry is typical for transition-state metals with $d^9$ valence electron configurations distorted by the Jahn–Teller[31] effect and is similar to those found for other complexes of both 2-substituted and 1-substituted tetrazoles.[32] The Cu–N bond lengths show considerable variation. Whereas a typical Cu–N4 distance of 1.997(1) Å is found in **2**, which is comparable to complexes with ligand systems such as 1,10-phenanthroline,[33] in compound **3** the distance Cu–N4 of 1.919(2) Å is importantly shorter. The differences in the Cu–O bond lengths are, however, less significant [**2**: *d*(Cu–O3) = 1.971(1) Å, *d*(Cu–O1) = 2.393(1) Å, **3**: *d*(Cu1–O1) = 2.048(2) Å, *d*(Cu1–O3) = 2.337(2) Å]. The geometries of the 1-methyl-5-nitriminotetrazolate moieties in **2** and **3** are essentially unaffected by the inclusion of water in **3**. In Figures 3 and 4 the molecular moieties of complexes **2** and **3** are shown.

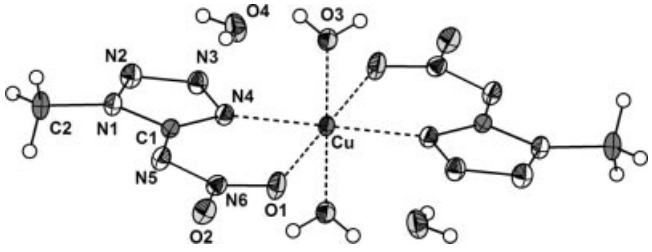


Figure 3. Crystal structure of **2** showing the molecular unit and atom-labeling scheme. Ellipsoids represent 50% probability.

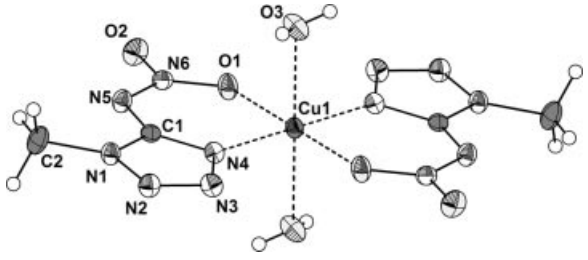


Figure 4. Crystal structure of **3** showing the molecular unit and atom-labeling scheme. Ellipsoids represent 50% probability.

Compound **5** crystallizes in the monoclinic space group $P2_1/c$ with two molecules in the unit cell and the lowest density of 1.74 g cm$^{-3}$ observed in this work. The structure is analogues to that of **2**; however, instead of two water molecules in **2**, two methanol molecules complete the packing of compound **5**. The methanol is not coordinated to any copper centers; therefore, it is not further discussed. The molecular structure of **5** in the crystalline state is shown in Figure 5.

The bond lengths and bond lengths of the discussed crystal structures **1**, **2**, **3**, and **5** are given in Table 1.

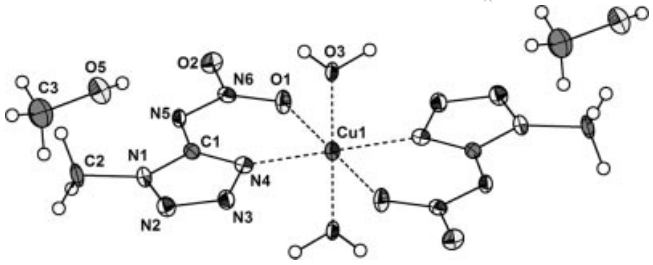


Figure 5. Crystal structure of **5** showing the molecular unit and atom-labeling scheme. Ellipsoids represent 50% probability.

Table 1. Bond lengths and angles.

| Atoms A–B | **1** *d* [Å] | **2** *d* [Å] | **3** *d* [Å] | **5** *d* [Å] |
|---|---|---|---|---|
| Cu–O3 | – | 1.971(1) | 2.337(2) | 1.998(2) |
| Cu–N4 | 1.923(2) | 1.997(1) | 1.919(2) | 1.960(2) |
| Cu–O1 | 1.974(2) | 2.393(1) | 2.048(2) | 2.326(2) |
| O2–N6 | 1.248(3) | 1.261(2) | 1.241(3) | 1.252(2) |
| O1–N6 | 1.291(3) | 1.246(2) | 1.284(3) | 1.255(2) |
| N1–C1 | 1.340(3) | 1.347(2) | 1.344(3) | 1.339(3) |
| N1–N2 | 1.352(3) | 1.349(2) | 1.352(3) | 1.353(3) |
| N1–C2 | 1.467(4) | 1.462(2) | 1.467(3) | 1.466(3) |
| N5–N6 | 1.306(3) | 1.324(2) | 1.311(3) | 1.328(3) |
| N5–C1 | 1.362(3) | 1.365(2) | 1.366(3) | 1.361(3) |
| N2–N3 | 1.287(3) | 1.294(2) | 1.293(3) | 1.288(3) |
| N3–N4 | 1.365(3) | 1.365(2) | 1.365(3) | 1.365(3) |
| N4–C1 | 1.334(3) | 1.343(2) | 1.337(3) | 1.343(3) |
| Atoms A–B–C | Angle [°] | Angle [°] | Angle [°] | Angle [°] |
| O3–Cu–N4 | – | 89.84(6) | 87.08(9) | 89.27(8) |
| O3–Cu–O1 | – | 88.97(5) | 91.39(8) | 88.35(7) |
| N4–Cu–O1 | 86.23(8) | 76.57(5) | 85.57(8) | 78.18(7) |
| C1–N1–N2 | 108.8(2) | 109.5(1) | 109.4(2) | 109.8(2) |
| C1–N1–C2 | 129.5(2) | 128.8(1) | 129.2(2) | 128.4(2) |
| N2–N1–C2 | 121.7(2) | 121.7(1) | 121.1(2) | 121.8(2) |
| N6–N5–C1 | 117.5(2) | 117.8(2) | 118.3(2) | 118.5(2) |
| N3–N2–N1 | 107.4(2) | 106.6(1) | 107.0(2) | 107.1(2) |
| O1–N6–O2 | 117.8(2) | 120.8(1) | 117.6(2) | 121.0(2) |
| O1–N6–N5 | 125.2(2) | 124.9(1) | 125.1(2) | 124.0(2) |
| O2–N6–N5 | 116.9(2) | 114.3(1) | 117.4(2) | 115.0(2) |
| N2–N3–N4 | 109.6(2) | 110.6(1) | 109.7(2) | 109.5(2) |
| C1–N4–N3 | 107.1(2) | 106.5(1) | 107.4(2) | 107.7(2) |

## Thermogravimetry

Thermogravimetry was used to investigate the dehydration step and was performed with a Setaram TG-DTA 92-16[34] under a helium atmosphere with a heating rate of 1° min$^{-1}$ to a maximum temperature of 350 °C. For the measurement, 5.351 mg of a pulverized sample in an aluminum oxide pan was used. The TG curve as well the DTA curve are shown in Figure 6, and they show that the loss of water occurs over a wide range that starts before 50 °C and ends at about 85 °C. The loss of water depends on the heating rate and occurs at higher temperatures when higher heating rates are used (see DSC measurements). The loss of 0.878 mg weight corresponds to the loss of all four water molecules in compound **2**, and therefore, it was not possible to stop the dehydration at compound **3**. In the second step

 © 2007 Wiley-VCH Verlag GmbH & Co. KGaA, Weinheim 

at about 245 °C, a mass of 3.932 mg was lost, which is more than the expected mass for the remaining copper(II) oxide as solid residues. Through the explosion that releases a huge amount of nitrogen, some of the $Cu^{II}O$ must be removed from the open setup.

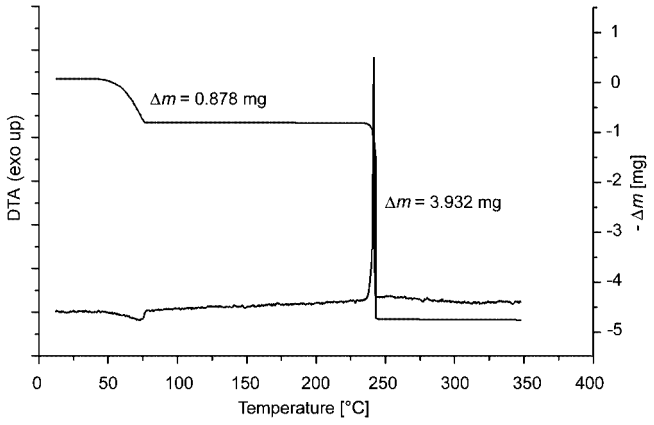


Figure 6. Thermogravimetry plot of compound **2** showing the loss of mass (right axis) and the DTA curve (left axis).

## Energetic Properties

### Differential Scanning Calorimetry (DSC)

DSC measurements used to determine the thermal behavior of the copper(II) 1-methyl-5-nitriminotetrazolate complexes were performed in covered Al containers with a nitrogen flow of 20 mL min$^{-1}$ with a Perkin–Elmer Pyris 6 DSC,[35] which was calibrated by standard pure indium and zinc at a heating rate of 5 °C min$^{-1}$. Compound **1** decomposes at a temperature of 252 °C at a heating rate of 5° min$^{-1}$ and at 248 °C at a heating rate of 2° min$^{-1}$. The DSC plots in Figure 7 show the thermal behavior of ca. 1.5 mg of **1**–**3** in the temperature range from 50 to 300 °C. Interestingly, the deprotonation in combination with the coordination to the copper(II) centers results in a substantial increase in the decomposition points in relative to neutral ligand **4**, which decomposes at temperatures above 125 °C.

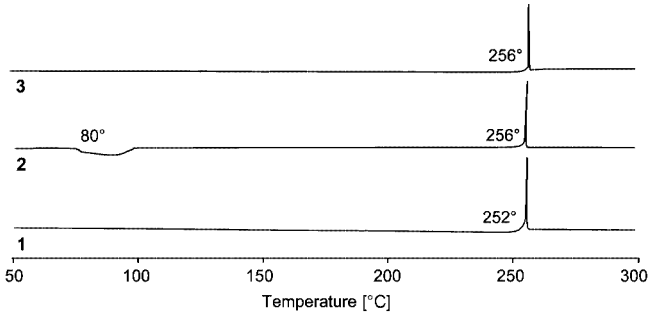


Figure 7. DSC plots of compounds **1**, **2**, and **3** (heating rate 5° min$^{-1}$).

To determine the heats of decomposition, a Linseis DSC PT10[36] instrument was used. Three samples (ca. 1 mg) were heated with a heating rate of 2° min$^{-1}$ and a fixed nitrogen flow of 5 L h$^{-1}$ over the decomposition peaks. The surface was integrated by using Linseis software, and the average of three measurements was used to calculate the heats of decomposition: for **1** $\Delta_{dec.}H_m°$ = 2739 J g$^{-1}$ (958 kJ mol$^{-1}$) and for **2** $\Delta_{dec.}H_m°$ = 2218 J g$^{-1}$ (936 kJ mol$^{-1}$).

### Bomb Calorimetry

As a result of its explosive character, it was not possible to combust compound **1** completely in the bomb calorimeter; therefore, only complex **2** was investigated by using bomb calorimetry (Scheme 3). For the calorimetric measurements of **2**, a Parr 1356 bomb calorimeter (static jacket) equipped with a Parr 1108CL oxygen bomb for the combustion of highly energetic materials was used.[37] The reported value of the energy of combustion $\Delta U_c$ = –1610 cal g$^{-1}$ (–2841 kJ mol$^{-1}$) is the average of three single measurements. The calorimeter was calibrated by combustion of certified benzoic acid (SRM, 39i, NIST) under an oxygen atmosphere at a pressure of 3.05 MPa. The standard molar enthalpy of combustion ($\Delta_c H°$) was derived from $\Delta_c H° = \Delta U_c + \Delta nRT$ [$\Delta n = \Delta n_i$ (products, g) – $\Delta n_i$ (reactants, g); where $\Delta n_i$ is the total molar amount of gases in the products or reactants]. The enthalpy of formation, $\Delta_f H°$, of –904 kJ mol$^{-1}$ for **2** was calculated at 298.15 K by using the Hess thermochemical cycle and the combustion reaction outlined in Scheme 3. After combustion, only a brown compound was left in the bomb, which was identified as copper(II) oxide.

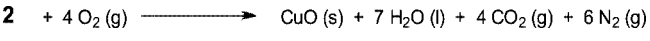


Scheme 3. Combustion equation of **2**.

To estimate the heat of formation of solid $[Cu(C_2H_3N_6O_2)_2]$ (**1**), we calculated[38] the electronic energies of all species involved in the gas-phase reaction (Scheme 4) at the B3LYP/SDD level of theory to be $\Delta E^{el}$(**1**) = –1859 kJ mol$^{-1}$.

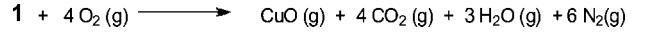


Scheme 4. Gas-phase combustion equation of **1**.

This gas-phase electronic energy was converted after correction for the work term and the vibrational, translational, and rotational corrections into the gas-phase enthalpy of $\Delta H$(**1**) = –1883.4 kJ mol$^{-1}$.

With the known enthalpy of sublimation for CuO of $\Delta H_{sub.}$(CuO) = 462.7 kJ mol$^{-1}$[39] and the estimated heat of sublimation for **1** of $\Delta H_{sub.}$(**1**) = 175.9 kJ mol$^{-1}$ [this value was taken to be equal to the enthalpy of sublimation of the Cu(salen) complex,[40] the enthalpy of combustion of **1** according to the equation in Scheme 5 could be calculated to be $\Delta H_{comb.}$(**1**,s) = –2169.3 kJ mol$^{-1}$.

 © 2007 Wiley-VCH Verlag GmbH & Co. KGaA, Weinheim 

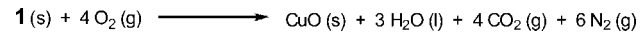


Scheme 5. Combustion equation of solid **1**.

The enthalpy of formation was then calculated by using the known literature[41] values for the enthalpies of formation of water [$\Delta H°_f(H_2O,g) = -242\ kJ\,mol^{-1}$] and carbon dioxide [$\Delta H°_f(CO_2,g) = -393\ kJ\,mol^{-1}$] to be $\Delta H°_f$ (**1**,s) = $-83.7\ kJ\,mol^{-1}$.

### Sensitivities

For initial safety testing, the impact and friction sensitivities were tested according to BAM methods[42,43] with the "BAM Fallhammer" and "BAM friction tester". Compound **1** is very sensitive towards impact (0.7 J) and friction (40 N), and because the value is comparable with lead azide, it should be considered to be a primary explosive; it should therefore only be handled with appropriate precautions. Compounds **2** and **5** are not sensitive towards impact (<100 J) and friction (<360 N). Compound **3** shows only a very low impact sensitivity (>55 J) and is not sensitive towards friction.

### Comparison with Lead Azide

Because lead azide is still used in modern priming charges and the U. S. army alone consumes more than 1000 lbs of it,[9] a comparison of its properties with those of compound **1** is shown in Table 2.

Table 2. Energetic properties of **1** and lead azide.

| | **1** | Lead azide |
|---|---|---|
| Impact sensitivity | >0.7 J | 2.5–4.0 J (pure)<br>3.0–6.5 J (techn.) |
| Friction sensitivity | >40 N | 0.1–1 N |
| Decomposition temperature | 252 °C | >315 °C |

### Long-Term Stability Tests

The long-term stability test of **1** was performed with a Systag FlexyTSC[44] (thermal safety calorimetry) in combination with a RADEX V5 oven and the SysGraph software. The test was undertaken as long-term isoperibolic evaluations in glass test vessels at atmospheric pressure with 500 mg of the compound. It was shown that tempering the substance for 48 h at 40 °C below the decomposition point results in storage periods that are over 50 years at room temperature. Initially, for **1** a temperature of 210 °C was chosen and possible occurrences of exo- or endothermic behavior were investigated over period of 48 h (Figure 8). Compound **1** was not stable for 48 h at a temperature of 210 °C. After 25 h there was an explicit increase in the temperature that was passed again after a few hours. After 48 h the compound in the test vessel was mainly brown-colored $Cu^{II}O$. The second test was performed at a temperature of 190 °C, and the compound was completely stable during this period. It can therefore be reasoned that the compound shows long-term stability even at higher temperatures, which is a basic requirement for possible applications.

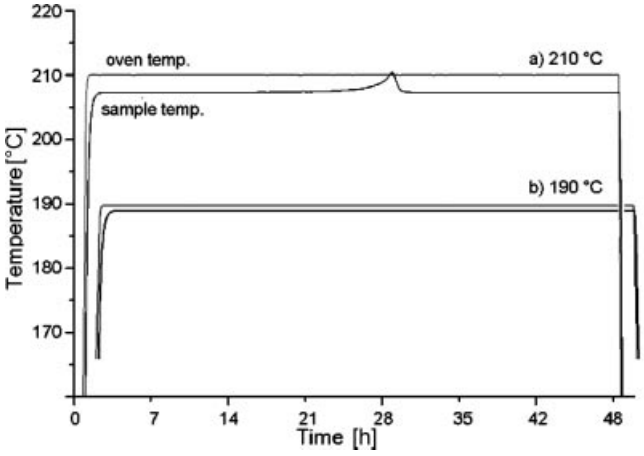


Figure 8. TSC plots of compound **1** over a period of 48 h at (a) 210 °C and (b) 190 °C (the upper curve represents the oven temperature, the curve below the sample temperature).

## Conclusions

From this experimental study the following conclusions can be drawn: (1) 1-Methyl-5-nitriminotetrazole can be used as a bidentate ligand in novel copper complexes forming compounds with different amounts of crystal water depending on the reaction conditions. The crystal water can be completely removed at higher temperatures to form highly explosive bis(1-methyl-5-nitriminotetrazolate) copper(II) (**1**). The dehydration proceeds in discrete steps and is determined by differential thermo gravimetry. (2) Bis(1-methyl-5-nitriminotetrazolato) copper(II) is a primary explosive due to its high sensitivity towards impact (0.7 J), but it shows a lower sensitivity towards friction (40 N) relative to common primary explosives. It is stable up to 250 °C and even shows long-term stability when tested at a temperature of 190 °C. In comparison with the commonly used lead azide, it shows suitable properties, in particular, its friction and impact sensitivities and its lower toxicity. The thermal decomposition provides a heat of decomposition of $2730\ J\,g^{-1}$, which was measured by using differential scanning calorimetry. (3) The crystal structures presented show common copper coordinations that are characterized by a Jahn–Teller distorted elongated octahedral coordination sphere.

## Experimental Section

All reagents and solvents were used as received (Sigma–Aldrich, Fluka, Acros Organics) if not stated otherwise. Melting points were measured with a Perkin–Elmer Pyris6 DSC apparatus by using a heating rate of $5°\,min^{-1}$. Otherwise, melting points were determined with a Büchi melting point B-450 apparatus and are not corrected.

 © 2007 Wiley-VCH Verlag GmbH & Co. KGaA, Weinheim 

Infrared (IR) spectra were recorded with a Perkin–Elmer Spectrum One FTIR instrument. Elemental analyses were performed with a Netsch STA 429 simultaneous thermal analyzer. Bomb calorimetry was done with a Parr 1356 bomb calorimeter with a Parr 1108CL oxygen bomb. The sensitivity data were performed with a BAM drophammer and a BAM friction tester.

***CAUTION!***

*Compounds **1** and **4** are highly energetic materials that show increased sensitivities towards various stimuli. Proper protective measures (safety glasses, face shield, leather coat, earthened equipment and shoes, Kevlar gloves and ear plugs) should be used when handling these compounds, especially when compound **1** is prepared on a larger scale.*

**$[Cu(C_2H_3N_6O_2)_2]$ (1):** The highly explosive copper complex **1** was obtained by dehydration of powdered **2** at 120 °C and reduced pressure ($1 \times 10^{-2}$ mbar) for 2h. Single crystals suitable for X-ray diffraction were grown from dry methanol. M.p. 252 °C (dec.). IR (KBr): $\tilde{\nu}$ = 3498 (m), 3456 (m), 3223 (m), 2861 (m), 2926 (m), 2346 (w), 1618 (m), 1528 (m), 1494 (m), 1477 (m), 1438 (m), 1384 (m), 1339 (s), 1303 (s), 1245 (m), 1229 (m), 1120 (m), 1037 (w), 1001 (m), 873 (m), 776 (w), 733 (w), 698 (w), 588 (w), 512 (w) $cm^{-1}$. $C_4H_6CuN_{12}O_4$ (349.71): calcd. C 13.74, H 1.73, N 48.06; found C 13.77, H 1.83, N 48.29.

**$[Cu(C_2H_3N_6O_2)_2(H_2O)_2]\cdot(H_2O)_2$ (2):** Copper(II) nitrate trihydrate (240 mg, 1.0 mmol) was dissolved in hot water (2 mL) and combined with a hot solution of 1-methyl-5-nitriminotetrazole (288 mg, 2 mmol) in water (15 mL) and heated at reflux for 5 min. After cooling to room temperature and standing for 24 h, blue crystals of **2** started to precipitate (299 mg, 71%). After filtration, the mother liquid was left, whereby green crystals of **3** were obtained (39 mg, 10%). M.p. 256 °C (dec.). IR (KBr): $\tilde{\nu}$ = 3504 (m), 3461 (m), 3220 (m), 2963 (m), 2148 (w), 1801 (w), 1662 (w), 1526 (m), 1476 (s), 1398 (m), 1384 (m), 1339 (s), 1305 (s), 1256 (m), 1120 (m), 1037 (m), 1010 (w), 929 (w), 887 (w), 859 (w), 776 (w), 737 (w), 654 (w), 585 (w) $cm^{-1}$. $C_4H_{14}CuN_{12}O_8$ (421.78): calcd. C 11.39, H 3.35, Cu 15.07, N 39.85, O 30.35; found C 11.32, H 3.38, N 39.69.

**$[Cu(C_2H_3N_6O_2)_2(H_2O)_2]$ (3):** M.p. 251 °C (dec.). IR (KBr): $\tilde{\nu}$ = 3481 (m), 2963 (w), 1798 (w), 1628 (m), 1539 (m), 1487 (m), 1417 (s), 1404 (s), 1385 (s), 1339 (m), 1298 (s), 1247 (m), 1125 (m), 1030 (m), 877 (w), 772 (w), 757 (w), 734 (m), 701 (m), 537 (w) $cm^{-1}$. $C_4H_{10}CuN_{12}O_6$ (385.75): calcd. C 12.45, H 2.61, Cu 16.47, N 43.57; found C 12.28, H 2.71, N 43.11.

**4:** 1-Methyl-5-nitriminoterazole was obtained by the nitration of 1-methyl-5-aminotetrazole by using fuming $HNO_3$. The nitration reaction was quenched with ice water, and the solvent was removed by using high vacuum until the product started to precipitate.

**$[Cu(C_2H_3N_6O_2)_2(H_2O)_2]\cdot(MeOH)_2$:** The light-blue colored methanol containing complex **5** was obtained by recrystallization of **1** from a wet methanol solution. $C_6H_{18}CuN_{12}O_8$ (449.83): calcd. C 16.02, H 4.03, N 37.37; found C 15.8, H 3.92, N 37.65.

Table 3 contains the parameters and data obtained from the single-crystal X-ray determinations.

Table 3. Crystallographic data.

| | **1** | **2** | **3** | **5** |
|---|---|---|---|---|
| Formula | $CuC_4H_6N_{12}O$ | $CuC_4H_{14}N_{12}O_8$ | $CuC_4H_{10}N_{12}O_6$ | $C_6H_{18}CuN_{12}O_8$ |
| Formula weight | 349.75 | 421.81 | 385.78 | 449.87 |
| Crystal system | monoclinic | monoclinic | monoclinic | monoclinic |
| Space group | $P2_1/c$ (14) | $P2_1/c$ (14) | $P2_1/n$ (14) | $P2_1/n$ (14) |
| Color / habit | green / rods | blue / rods | green / plates | light blue / needles |
| Size [mm] | $0.03 \times 0.04 \times 0.10$ | $0.08 \times 0.17 \times 0.18$ | $0.08 \times 0.12 \times 0.16$ | $0.03 \times 0.05 \times 0.12$ |
| $a$ [Å] | 9.1982(5) | 5.9934(4) | 5.7451(6) | 6.9382(3) |
| $b$ [Å] | 6.7004(3) | 14.3068(8) | 9.482(1) | 12.1607(7) |
| $c$ [Å] | 9.3453(4) | 8.9967(6) | 11.574(1) | 10.1950(5) |
| $\alpha$ [°] | 90.0 | 90.0 | 90.0 | 90.0 |
| $\beta$ [°] | 102.653(5) | 103.753(6) | 92.935(9) | 93.188(5) |
| $\gamma$ [°] | 90.0 | 90.0 | 90.0 | 90.0 |
| $V$ [Å$^3$] | 561.98(5) | 749.32(8) | 629.7(1) | 858.86(7) |
| $Z$ | 2 | 2 | 2 | 2 |
| $\rho_{calcd.}$ [g cm$^{-3}$] | 2.067 | 1.870 | 2.035 | 1.740 |
| $\mu$ [mm$^{-1}$] | 1.991 | 1.529 | 1.799 | 1.340 |
| $F$(000) | 350 | 430 | 390 | 462 |
| $\lambda$Mo-$K_\alpha$ [Å] | 0.71073 | 0.71073 | 0.71073 | 0.71073 |
| $T$ [K] | 100(2) | 120(2) | 200(2) | 100(2) |
| $\theta$ min, max [°] | 3.8, 26.0 | 4.5, 26.5 | 4.1, 26.5 | 3.7, 26.0 |
| Data set | –11/11; –8/8; –11/11 | –7/7; –17/17; –11/11 | –7/7; –11/11; –14/14 | –8/8; –13/15; –12/12 |
| Reflections collected | 5473 | 7776 | 6422 | 4363 |
| Indep. reflections | 1102 | 1551 | 1295 | 1689 |
| $R_{int}$ | 0.044 | 0.025 | 0.038 | 0.041 |
| Observed reflections | 837 | 1473 | 1170 | 1060 |
| No. parameters | 109 | 143 | 126 | 160 |
| $R_1$ (obs) | 0.0267 | 0.0254 | 0.0352 | 0.0291 |
| $wR_2$ (all data) | 0.0669 | 0.0616 | 0.0782 | 0.0612 |
| GooF | 0.96 | 1.12 | 1.16 | 0.88 |
| Min./Max. Resd. [e Å$^{-3}$] | –0.32, 0.42 | –0.24, 0.34 | –0.31, 0.39 | –0.33, 0.41 |
| Device type | Oxford Xcalibur3 CCD | Oxford Xcalibur3 CCD | Oxford Xcalibur3 CCD | Oxford Xcalibur3 CCD |
| Solution | SIR-92 | SIR-92 | SIR-92 | SIR-92 |
| Refinement | SHELXL-97 | SHELXL-97 | SHELXL-97 | SHELXL-97 |
| Absorption correction | multiscan | multiscan | multiscan | multiscan |
| CCDC No. | 642162 | 641972 | 641973 | 642161 |

 © 2007 Wiley-VCH Verlag GmbH & Co. KGaA, Weinheim 

## Acknowledgments

Financial support of this work by the University of Munich (LMU), the Fonds der Chemischen Industrie, the European Research Office (ERO) of the U. S. Army Research Laboratory (ARL) under contract no. N 62558-05-C-0027 and the Bundeswehr Research Institute for Materials, Explosives, Fuels and Lubricants (WIWEB) under contract no. E/E210/4D004/X5143 is gratefully acknowledged. The authors are indebted to and thank Prof. Dr. Wolfgang Schnick and Dipl.-Chem. Andreas Sattler for thermal gravimetry measurements. The authors also thank Dr. habil. M.-J. Crawford for correcting the manuscript and Ms. Susanne Scheuzow for the thermal safety calorimetric measurements.

[1] J. Köhler, R. Meyer, *Explosivstoffe*, 9th ed., Wiley-VCH, Weinheim, **1998**, p. 174.
[2] K. Karaghiosoff, T. M. Klapötke, A. N. Michailovski, H. Nöth, M. Suter, G. Holl, *Propellants Explos. Pyrotech.* **2003**, *28*, 1.
[3] a) G. Pfefferkorn, *Z. Naturforsch., Teil A* **1948**, *3*, 364; b) B. Reitzner, R. P. Manno, *Nature* **1963**, *198*, 4884; c) C. M. Ho, S. T. Lee, P. C. Chen, G. H. Wei, J. S. Shiau, P. H. Chen, H. C. Fan, J. Y. Huan, *Huoyao Jishu* **1992**, *8*, 31; d) G. L. Glen, *J. Am. Chem. Soc.* **1963**, *85*, 3892.
[4] a) M. Stammler, J. E. Abel, R. C. Ling, *Nature* **1961**, *192*, 626; b) M. Stammler, J. E. Abel, J. V. R. Kaufman, *Nature (London, U.K.)* **1960**, *185*, 4560; c) J. Roth, *J. Chem. Phys.* **1964**, *41*, 1929; d) G. Todd, E. Parry, *Nature* **1962**, *196*, 250.
[5] J. Köhler, R. Meyer, *Explosivstoffe*, 9th ed., Wiley-VCH, Weinheim, **1998**, p. 54.
[6] a) A. Stettbacher, *Nitrocellulose* **1937**, *8*, 3–6; A. Stettbacher, *Nitrocellulose* **1937**, *8*, 21–27; b) J. R. Payne, *Thermochim. Acta* **1994**, *242*, 13; c) H. C. J. Saint, J. Hewson, *Analyst* **1959**, *84*, 183; d) F. C. Tompkins, D. A. Young, *J. Chem. Soc.* **1956**, 3331; e) W. C. McCrone, O. W. Adams, *Anal. Chem.* **1955**, *27*, 2014; f) J. F. Hobbs, W. Melville, *Ger. Offen.* **1974**.
[7] a) S. Singh, *J. Phys. Soc. Jpn.* **1959**, *14*, 540; b) L. Wohler, A. Berthmann, *Angew. Chem.* **1930**, *43*, 59; c) A. Langhans, *J. Soc. Chem. Ind. (London)* **1918**, *38*, 389A; d) M. E. Brown, G. M. Swallowe, *Thermochim. Acta* **1981**, *49*, 333.
[8] a) S. H. Patinkin, J. P. Horwitz, E. Lieber, *J. Am. Chem. Soc.* **1955**, *77*, 562; b) J. R. C. Duke, *J. Chem. Soc. Sect. D* **1971**, *1*, 2; c) G. C. Mei, J. W. Pickett, *Propellants Explos. Pyrotech.* **1998**, *23*, 172.
[9] M. H. V. Huynh, M. A. Hiskey, T. J. Meyer, M. Wetzler, *Proc. Natl. Acad. Sci. USA* **2006**, *103*, 5409.
[10] R. P. Singh, R. D. Verma, D. T. Meshri, J. M. Shreeve, *Angew. Chem. Int. Ed.* **2006**, *45*, 3584.
[11] T. M. Klapötke, P. Mayer, A. Schulz, J. J. Weigand, *Propellants Explos. Pyrotech.* **2004**, *29*, 325.
[12] A. Hammerl, M. A. Hiskey, G. Holl, T. M. Klapötke, K. Polborn, J. Stierstorfer, J. J. Weigand, *Chem. Mater.* **2005**, *17*, 3784.
[13] C. Ye, J.-C. Xiao, B. Twamley, J. M. Shreeve, *Chem. Commun.* **2005**, *21*, 2750.
[14] T. M. Klapötke in *Moderne Anorganische Chemie* (Ed.: E. Riedel), 2nd ed., Walter de Gruyter, Berlin, New York, **2003**, pp. 95–100.
[15] a) T. M. Klapötke, P. Mayer, K. Polborn, J. Stierstorfer, J. J. Weigand, *New Trends in Research of Energetic Materials, Proceedings of the Seminar*, 9th ed., Pardubice, Czech Republic, **2006**, vol. 2, p. 641; b) T. M. Klapötke, P. Mayer, K. Polborn, J. Stierstorfer, J. J. Weigand, *37th International Annual Conference of ICT*, Karlsruhe, Federal Republic of Germany, **2006**.
[16] a) P. N. Gaponik, M. M. Degtyarik, A. S. Lyakhov, V. E. Matulis, O. A. Ivashkevich, M. Quesada, J. Reedijk, *Inorg. Chim. Acta* **2005**, *358*, 3949; b) A. S. Lyakhov, P. N. Gaponik, M. M. Degtyarik, L. S. Ivashkevich, *Acta Crystallogr., Sect. C* **2003**, *59*, 204; c) A. F. Stassen, H. Kooijman, A. L. Spek, L. Jos de Jongh, J. G. Haasnoot, J. Reedijk, *Inorg. Chem.* **2002**, *41*, 6468; d) T. Wu, B.-H. Yi, D. Li, *Inorg. Chem.* **2005**, *44*, 4130.
[17] M. Friedrich, J. C. Gálvez-Ruiz, T. M. Klapötke, P. Mayer, B. Weber, J. J. Weigand, *Inorg. Chem.* **2005**, *44*, 8044.
[18] J. Köhler, R. Meyer, *Explosivstoffe*, 9th ed., Wiley-VCH, Weinheim, **1998**, p. 138.
[19] a) D. E. Chavez, M. A. Hiskey, M. H. Huynh, D. L. Naud, S. F. Son, B. C. Tappan, *J. Pyrotech.* **2006**, *23*, 70; b) D. E. Chavez, M. A. Hiskey, D. L. Naud, *J. Pyrotech.* **1999**, *10*, 17; c) M. A. Hiskey, D. E. Chavez, D. L. Naud, *U. S. patent* **2001**, US 6214139.
[20] T. M. Klapötke, J. Stierstorfer, *New Trends in Research of Energetic Materials*, Proceedings, Pardubice, **2007**, 674–690.
[21] R. A. Henry, W. G. Finnegan, *J. Am. Chem. Soc.* **1954**, *76*, 923.
[22] R. M. Herbst, C. W. Roberts, E. J. Harvill, *J. Org. Chem.* **1951**, *16*, 139.
[23] *CrysAlis CCD*, Oxford Diffraction Ltd., Version 1.171.27p5 beta (release 01–04–2005 CrysAlis171.NET) (compiled Apr 1 **2005**,17:53:34).
[24] *CrysAlis RED*, Oxford Diffraction Ltd., Version 1.171.27p5 beta (release 01–04–2005 CrysAlis171.NET) (compiled Apr 1 **2005**,17:53:34).
[25] SIR-92, *A Program for Crystal Structure Solution*: A. Altomare, G. Cascarano, C. Giacovazzo, A. Guagliardi, *J. Appl. Crystallogr.* **1993**, *26*, 343.
[26] G. M. Sheldrick, *SHELXL97: Program for the Refinement of Crystal Structures*, University of Göttingen, Germany, **1994**.
[27] A. L. Spek, *PLATON: A Multipurpose Crystallographic Tool*, Utrecht University, Utrecht, The Netherlands, **1999**.
[28] *SCALE3 ABSPACK: An Oxford Diffraction Program* (1.0.4, gui:1.0.3) (C), Oxford Diffraction Ltd., **2005**.
[29] CCDC-642162 (for **1**), -641972 (for **2**), -641973 (for **3**), and -642161 (for **5**) contains the supplementary crystallographic data for this paper. These data can be obtained free of charge from The Cambridge Crystallographic Data Centre via www.ccdc.cam.ac.uk/data_request/cif.
[30] B. Morosin, *Acta Crystallogr., Sect. B* **1976**, *32*, 1237.
[31] E. Riedel, *Anorganische Chemie*, 4th ed., de Gryter, Berlin, **1999**, p. 677 and 722.
[32] a) R. Prins, M. Biagini-Cingi, R. A. G. De Graff, J. Haasnoot, A.-M. Manotti-Lanfredi, P. Rabu, P. Reedijk, E. Ugozzli, *Inorg. Chim. Acta* **1996**, *248*, 35; b) R. Bronisz, *Inorg. Chim. Acta* **2004**, *357*, 396; c) P. Børsting, J. J. Steel, *Eur. J. Inorg. Chem.* **2004**, 376; d) P. E. M. Wijnands, J. S. Wood, J. Reedijk, W. J. A. Maaskant, *Inorg. Chem.* **1996**, *35*, 1214.
[33] a) H. Nakai, Y. Deguchi, *Bull. Chem. Soc. Jpn.* **1975**, *48*, 2557; b) H. E. Heldal, J. Sletten, *Acta Chem. Scand.* **1997**, *51*, 122.
[34] http://www.setaram.com.
[35] http://www.perkinelmer.com.
[36] http://www.linseis.com.
[37] http://www.parrinst.de
[38] M. J. Frisch, G. W. Trucks, H. B. Schlegel, G. E. Scuseria, M. A. Robb, J. R. Cheeseman, J. A. Montgomery Jr, T. Vreven, K. N. Kudin, J. C. Burant, J. M. Millam, S. S. Iyengar, J. Tomasi, V. Barone, B. Mennucci, M. Cossi, G. Scalmani, N. Rega, G. A. Petersson, H. Nakatsuji, M. Hada, M. Ehara, K. Toyota, R. Fukuda, J. Hasegawa, M. Ishida, T. Nakajima, Y. Honda, O. Kitao, H. Nakai, M. Klene, X. Li, J. E. Knox, H. P. Hratchian, J. B. Cross, C. Adamo, J. Jaramillo, R. Gomperts, R. E. Stratmann, O. Yazyev, A. J. Austin, R. Cammi, C. Pomelli, J. W. Ochterski, P. Y. Ayala, K. Morokuma, G. A. Voth, P. Salvador, J. J. Dannenberg, V. G. Zakrzewski, S. Dapprich, A. D. Daniels, M. C. Strain, O. Farkas, D. K. Malick, A. D. Rabuck, K. Raghavachari, J. B. Foresman, J. V. Ortiz, Q. Cui, A. G. Baboul, S. Clifford, J. Cioslowski, B. B. Stefanov, G. Liu, A. Liashenko, P. Piskorz, I. Komaromi, R. L. Martin, D. J. Fox, T. Keith, M. A. Al-Laham, C. Y. Peng, A. Nanayakkara, M. Challacombe, P. M. W. Gill, B. Johnson, W. Chen, M. W.

 © 2007 Wiley-VCH Verlag GmbH & Co. KGaA, Weinheim 

Wong, C. Gonzalez, J. A. Pople, *Gaussian 03*, Revision A.1, Gaussian Inc., Pittsburgh, PA, **2003**.
[39] CuO: $C_{\infty v}$, $E$ = –272.499622 a.u., *zpe* = 0.9 kcal mol$^{-1}$; $O_2$: $D_{\infty h}$, $E$ = –150.315318 a.u., *zpe* = 2.1 kcal mol$^{-1}$; $CO_2$: $D_{\infty h}$, $E$ = –188.541219 a.u., *zpe* = 6.8 kcal mol$^{-1}$; $H_2O$: $C_{2v}$, $E$ = –76.414392 a.u., *zpe* = 13.0 kcal mol$^{-1}$; $N_2$: $D_{\infty h}$, $E$ = –109.481395 a.u., *zpe* = 3.2 kcal mol$^{-1}$; **A**: $C_i$, $E$ = –1310.826700 a.u., *zpe* = 102.7 kcal mol$^{-1}$.
[40] M. D. M. C. Ribeiro da Silva, J. M. Goncalves, A. L. R. Silva, P. C. F. C. Oliveira, B. Schröder, M. A. V. Ribeiro da Silva, *J. Mol. Catal. A Chem.* **2004**, *224*, 207.
[41] NIST Chemistry WebBook, *NIST Standard Reference Database Number 69*, Release: June **2005**. http://webbook.nist.gov/chemistry/.
[42] a) M. Suceska, *Test Methods for Explosives*, Springer, New York, **1995**, p. 21 (impact), p. 27 (friction); b) http://www.bam.de
[43] Impact: insensitive > 40 J, less sensitive ≥ 35 J, sensitive ≥ 4 J, very sensitive ≤ 3 J; Friction: insensitive > 360 N, less sensitive = 360 N, sensitive < 360 N, very sensitive ≤ 80 N, extremely sensitive ≤ 10 N (according to the UN Recommendations on the Transport of Dangerous Goods).
[44] http://www.systag.ch

Received: April 10, 2007
Published Online: August 31, 2007

 © 2007 Wiley-VCH Verlag GmbH & Co. KGaA, Weinheim 

DOI: 10.1002/ejic.200700501

# [1,2,5]Selenadiazolo[3,4-*c*][1,2,5]thiadiazole and [1,2,5]Selenadiazolo-[3,4-*c*][1,2,5]thiadiazolidyl – A Synthetic, Structural, and Theoretical Study

**Irina Yu. Bagryanskaya,[a] Yuri V. Gatilov,[a] Nina P. Gritsan,*[b,c] Vladimir N. Ikorskii,[d] Irina G. Irtegova,[a] Anton V. Lonchakov,[c] Enno Lork,[e] Ruediger Mews,*[e] Victor I. Ovcharenko,*[d] Nikolay A. Semenov,[f] Nadezhda V. Vasilieva,[a] and Andrey V. Zibarev*[a,c]**

*Dedicated to Professor Neil Bartlett on the occasion of his 75th birthday*

**Keywords:** Density functional calculations / Magnetic properties / Nitrogen heterocycles / Radical anions / Sulfur / Selenium

A new heterocyclic system, namely [1,2,5]selenadiazolo[3,4-*c*][1,2,5]thiadiazole (**1**), has been prepared in 60 % yield by the 1:1 condensation of 3,4-diamino-1,2,5-thiadiazole (**4**) with $SeCl_4$ in the presence of pyridine. The structures of **1** and its 1:1 complex with pyridinium chloride (**5**) have been elucidated by X-ray diffraction (XRD). The reversible electrochemical reduction of **1**, as well as its chemical reduction with $PhS^-$ anion, provide the long-lived [1,2,5]selenadiazolo[3,4-*c*][1,2,5]thiadiazolidyl radical anion (**2**), which has been isolated in the form of the thermally stable salt [K(18-crown-6)][**2**] (**3**) in 75 % yield. The experimental structural and spectral characteristics of **1** and **2** agree fairly well with those obtained from density functional (DFT) calculations. The salt **3** has been characterized by ESR spectroscopy (in the solid state and in solution) and XRD. The radical anion **2** acts as a bridging ligand in crystalline **3**. Magnetic measurements on salt **3** reveal weak antiferromagnetic interactions ($J = -1.65$ cm$^{-1}$). The magnetic structures of **3** and its disulfur congener **11** have been analyzed in terms of dimeric exchange integrals calculated by spin-unrestricted broken-symmetry DFT and post-HF methods.

(© Wiley-VCH Verlag GmbH & Co. KGaA, 69451 Weinheim, Germany, 2007)

## Introduction

Chalcogen-nitrogen chemistry[1] has begun to play an increasingly important role in the design and synthesis of molecular materials, especially conducting, superconducting and magnetic materials, during the past two decades.[2–7] In particular, numerous spin-carrying chalcogen-nitrogen compounds, mostly neutral and positively charged heterocyclic thiazyl radicals (radical cations), have been carefully explored as molecular magnets and/or conductors. Related negatively charged systems (radical anions) have been less studied as they are much rarer.[1–6]

We have recently described the preparation and X-ray diffraction (XRD) and ESR characterization of thermally stable salts of the [1,2,5]thiadiazolo[3,4-*c*][1,2,5]thiadiazolidyl radical anion.[8] This π-delocalized radical anion might be of interest in materials science as a building block for molecular ion-based magnets and/or conductors.[8–10] Indeed, the results of magnetic susceptibility ($\chi$) measurements on its salts in the temperature range 2–300 K have revealed low-temperature antiferromagnetic ordering of their spin systems. Investigation of the electrical properties of the salts is in progress. One of the directions of further development in this field relates to the Se analogue of [1,2,5]-thiadiazolo[3,4-*c*][1,2,5]thiadiazolidyl, namely [1,2,5]selenadiazolo[3,4-*c*][1,2,5]thiadiazolidyl.

[a] Institute of Organic Chemistry, Russian Academy of Sciences, 630090 Novosibirsk, Russia
Fax: +7-383-330-9752
E-mail: zibarev@nioch.nsc.ru
[b] Institute of Chemical Kinetics and Combustion, Russian Academy of Sciences, 630090 Novosibirsk, Russia
Fax: +7-383-330-7350
E-mail: gritsan@kinetics.nsc.ru
[c] Department of Physics, Novosibirsk State University, 630090 Novosibirsk, Russia
[d] International Tomography Center, Russian Academy of Sciences, 630090 Novosibirsk, Russia
Fax: +7-383-333-1399
E-mail: Victor.Ovcharenko@tomo.nsc.ru
[e] Institute for Inorganic and Physical Chemistry, University of Bremen, 28334 Bremen, Germany
Fax: +49-421-218-4267
E-mail: mews@chemie.uni-bremen.de
[f] Department of Natural Sciences, Novosibirsk State University, 630090 Novosibirsk, Russia

 © 2007 Wiley-VCH Verlag GmbH & Co. KGaA, Weinheim 

Herein we report on the synthesis of [1,2,5]selenadiazolo[3,4-*c*][1,2,5]thiadiazole (**1**) and its electrochemical and chemical reduction to [1,2,5]selenadiazolo[3,4-*c*][1,2,5]thiadiazolidyl (**2**), which is isolated in the form of the thermally stable salt [K(18-crown-6)][**2**] (**3**; Scheme 1). The crystal and molecular structures of **1** and **3** are elucidated by XRD and the radical anion **2** is characterized by ESR spectroscopy in solution. The salt **3** is also characterized by ESR spectroscopy as well as by magnetic susceptibility measurements in the temperature range 2–300 K. The experimental structural and spectral characteristics of **1** and **2** and the magnetic properties of **3** are compared with those calculated by density functional (DFT) and post-Hartree–Fock (HF) techniques.

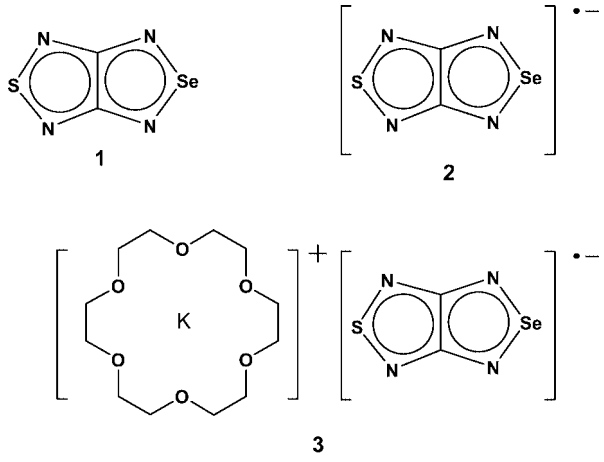

Scheme 1.

It should be noted that beyond the field of chalcogen-nitrogen chemistry, π-delocalized radical anions suitable as spin-carrying units for molecular materials are also very rare and are represented mainly by those derived from nitrogen heterocycles, such as tetrazines,[11] cyanocarbons, such as tetracyanoethylene and 7,7,8,8-tetracyanoquinodimethane,[12] and semiquinones.[13]

## Results and Discussion

### Preparation and Characterization of [1,2,5]Selenadiazolo[3,4-*c*][1,2,5]thiadiazole (1)

An initial attempt to prepare compound **1** by treating 3,4-diamino-1,2,5-thiadiazole (**4**) with $SeOCl_2$ in the presence of pyridine was unsuccessful. The reaction product was described as an unstable solid with no reported characteristics (even melting point) other than a low-resolution mass spectrum.[14]

In this work, compound **1** is synthesized in 60% yield by the 1:1 condensation of diamine **4** with $SeCl_4$ in the presence of pyridine (Scheme 2). This approach is an extension of the chalcogen tetrahalide based methodology, previously suggested for the synthesis of 2,1,3-benzochalcogenadiazoles, to non-benzoid systems (chalcogen tetrahalides are $SF_4$, $SeCl_4$, and $TeCl_4$).[15] Unexpectedly, compound **1** was isolated from the reaction mixture in the form of a 1:1 complex with pyridinium chloride (**5**; Scheme 2). Pure **1**, which was obtained by decomposition of complex **5** with water, was found to be thermally stable and stable to air in both the solid state and in solution.

The structures of **1** and **5** were confirmed by XRD (Figures 1 and 2, respectively). The pyridinium cation in the crystal of **5** is disordered over two positions in each of which the N atom is also disordered over two positions (Figure 2). In the crystal of **1**, the molecules lie in the crystallographic *m* plane. Only half a molecule is crystallographically independent since the crystallographic $C_2$ axis passes through the center of the C–C bond, which means that either S or Se atoms can be placed in the same position. The best refinement was achieved with occupation factors (SOF) of 0.25 for both S and Se (Figure 1). As a result, the experimental accuracy of the molecular geometry of **1** is higher in the case of its co-crystal with pyridinium chloride **5** than in the case of its homo-crystal (see Figures 1 and 2). The experimental geometry of **1** in complex **5** agrees well with its geometry calculated at the DFT/B3LYP/6-31G(d) level of theory (Figure 2).

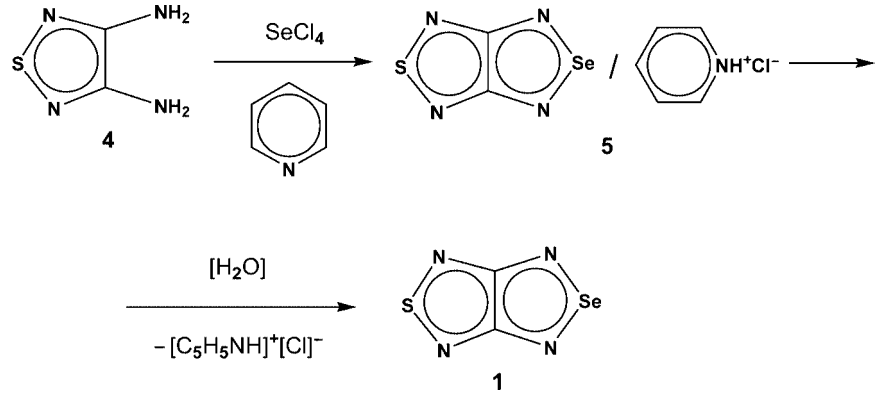

Scheme 2.

 © 2007 Wiley-VCH Verlag GmbH & Co. KGaA, Weinheim 

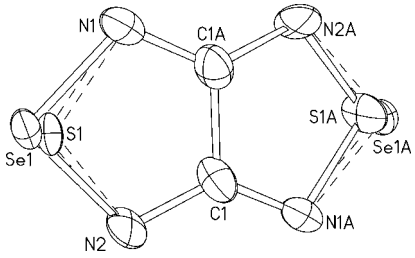


Figure 1. Structure of compound **1**. Bond lengths [pm] and angles [°]: Se1–N1 177.6(9), Se1–N2 182.1(9), S1–N2 158(2), S1–N1 165(2), N2–C1 134.1(8), N1–C1A 130.9(8), C1–C1A 148.9(13); N1–Se1–N2 93.0(4), N2–S1–N1 107.8(9), C1–N2–S1 101.4(8), C1–N2–Se1 107.4(5), C1A–N1–S1 100.7(8), C1A–N1–Se1 109.6(5), N1A–C1–N2 129.7(6), N1A–C1–C1A 115.4(8), N2–C1–C1A 114.6(8) [symmetry transformation used: $-x$, $y$, $-z + 2$].

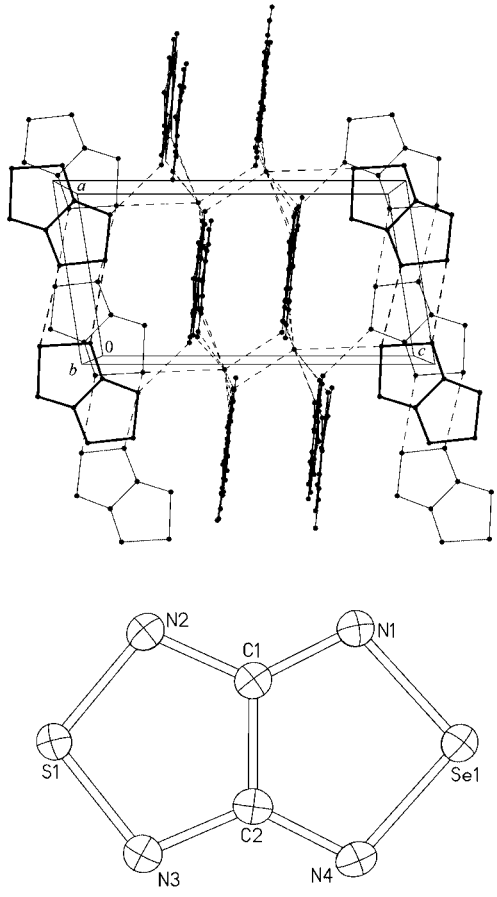





Figure 2. Top: structure of compound **5** (dotted lines show shortened intermolecular contacts). Bottom: compound **1** (XRD numbering is used) moiety in **5**; bond lengths [pm] and angles [°]: Se1–N1 179.0(4), Se1–N4 179.7(4), N1–C1 133.2(6), N4–C2 133.0(6), C1–C2 144.7(6), S1–N2 163.0(5), S1–N3 162.6(4), N2–C1 135.3(6), N3–C2 136.0(6); N1–Se1–N4 95.74(18), Se1–N1–C1 105.0(3), N1–C1–C2 117.3(4), C2–C1–N2 114.2(4), C1–N2–S1 104.9(3), N2–S1–N3 102.5(2), S1–N3–C2 105.2(3), N3–C2–C1 113.3(4), C1–C2–N4 117.0(4), C2–N4–Se1 105.0(3). Bond lengths [pm] and angles [°] of the same moiety obtained from DFT/B3LYP/6-31G(d) calculations: Se1–N1 (Se1–N4) 179.5, N1–C1 (N4–C2) 133.0, C1–C2 147.0, S1–N2 (S1–N3) 163.0, N2–C1 (N3–C2) 135.0; N1–Se1–N4 97.4, Se1–N1–C1 104.1, N1–C1–C2 117.3, C2–C1–N2 113.6, C1–N2–S1 (S1–N3–C2) 104.7, N2–S1–N3 102.9, N3–C2–C1 113.5, C1–C2–N4 116.8, C2–N4–Se1 104.6.

The formation of [1,2,5]selenadiazolo[3,4-*c*][1,2,5]selenadiazole (**6**) as a minor by-product in the preparation of **1** was observed by mass spectrometry and confirmed by XRD characterization in the form of a statistically disordered co-crystal of **1** with **6** ("compound" **7**; Scheme 3, Figure 3). The best refinement was achieved with occupation factors (SOF) in the S2/Se2 position of 0.56 for S and 0.44 for Se (Figure 3). As a result, the experimental accuracy was relatively low, which makes a correct comparison of the changes in molecular geometry on going from the archetypal [1,2,5]thiadiazolo[3,4-*c*][1,2,5]thiadiazole (**8**)[8b] to **1** and **6** impossible.

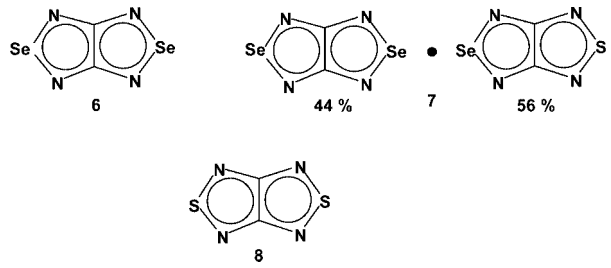


Scheme 3.

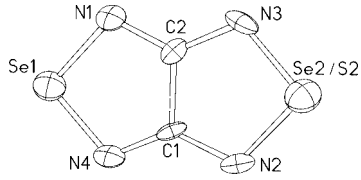


Figure 3. Structure of complex **7** between **1** and **6** (56:44). Bond lengths [pm] and angles [°]: Se1–N1 178(1), Se1–N4 175(1), Se2/S2–N2 169(1), Se2/S2–N23 166(1), N1–C2 132(2), N2–C1 132(2), N3–C2 132(2), N4–C1 131(2), C1–C2 146(2); N1–Se1–N4 94.5(5), N2–Se2/S2–N3 98.0(5), Se1–N1–C2 107.0(9), Se2/S2–N2–C1 107.6(9); Se2/S2–N3–C2 107.0(8), Se1–N4–C1 107.8(8), N4–C1–C2 115.9(12), N1–C2–C1 114.8(11), N2–C1–C2 112.2(11), N3–C2–C1 115.2(12).

A comparison of the spectroscopic properties of **1** and **8** showed the expected similarities. Thus, the maximum absorption wavelength ($\lambda_{max}$) of the long-wave band in the electronic absorption spectra (EAS) of **1** and **8** (DME solutions) is found at 353 and 319 nm, respectively. The theoretical EAS of **1** and **8**, calculated at the TD-DFT/B3LYP/6-31+G(d) level of theory, reveal two $\pi \rightarrow \pi^*$ transitions at 359 ($f$ = 0.0430) and 310 nm ($f$ = 0.3203) in the case of **1** and at 331 ($f$ = 0.0522) and 285 nm ($f$ = 0.3361) in the case of **8** ($f$ is the oscillator strength). These theoretical transitions appear as one unresolved band in the experimental EAS of both compounds (Figure 4). In the NMR spectra, the $^{13}C$ chemical shift of **1** is only 3 ppm downfield from that of **8**.[8b]

 © 2007 Wiley-VCH Verlag GmbH & Co. KGaA, Weinheim 

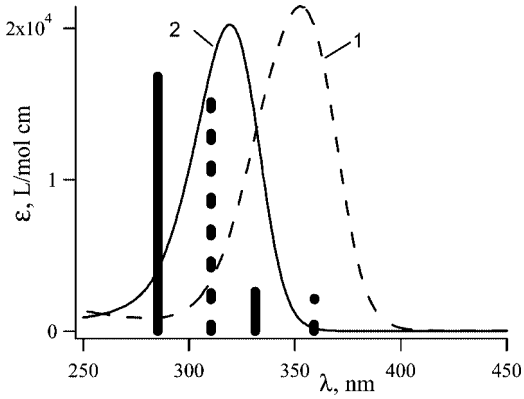


Figure 4. Experimental (curves) EAS of **1** (1) and **8** (2) and theoretical (bars) spectra of **1** (dotted bars) and **8** (solid bars) calculated at the TD-B3LYP/6-31+G(d) level of theory.

### Preparation and Characterization of the [1,2,5]Selenadiazolo[3,4-*c*][1,2,5]thiadiazolidyl Radical Anion (2) and the Salt [K(18-crown-6)][2] (3)

Cyclic voltammetry (CV) of a solution of **1** in MeCN in the potential range from 0 to –2.5 V revealed two diffusion-controlled one-electron reduction peaks (1C and 2C, Figure 5) corresponding to consecutive transformations of **1** into the radical anion **2** (peak 1C) and the dianion **9** (peak 2C; Scheme 4). The oxidation peak 1A, which is observed

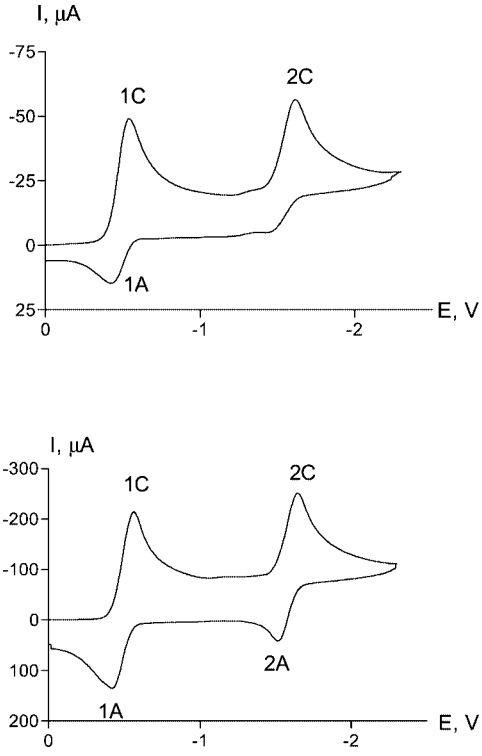


Figure 5. CV of **1** at scan rates of 100 mV s$^{-1}$ (top) and 2 V s$^{-1}$ (bottom).

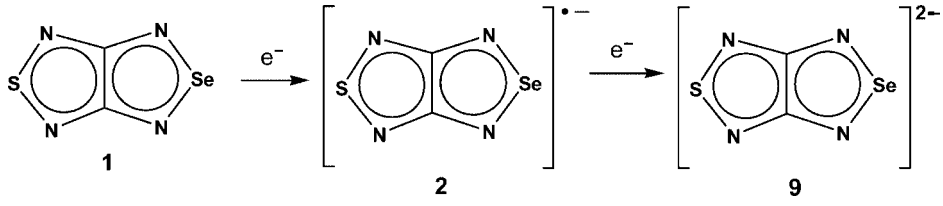


Scheme 4.

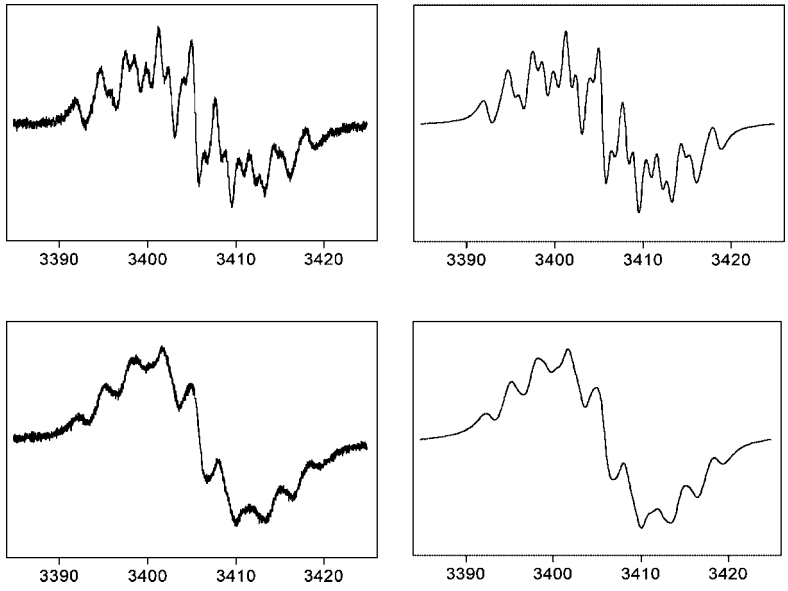


Figure 6. Experimental (in MeCN, left) and simulated (right) ESR spectra of **2** at 223 K (top) and 243 K (bottom). $|H| = 10^{-4}$ T.

 © 2007 Wiley-VCH Verlag GmbH & Co. KGaA, Weinheim 

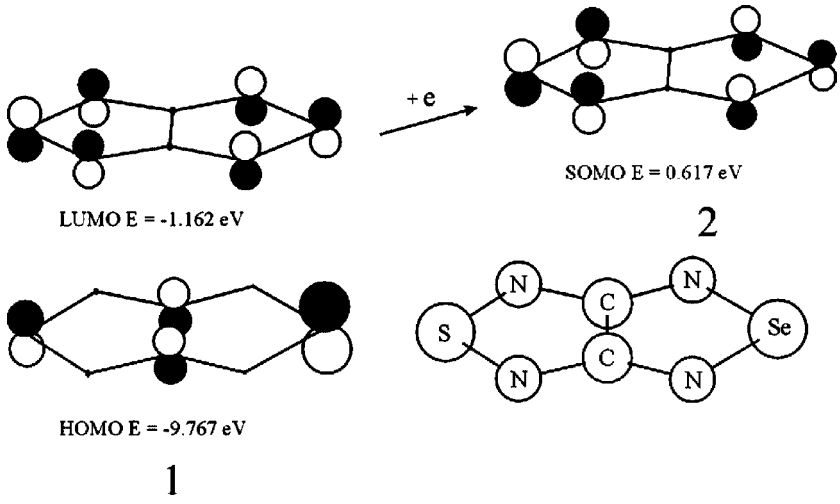


Figure 7. The frontier MOs of **1** and the SOMO of **2** obtained from the HF/6-31G(d) and ROHF/6-31G(d) calculations, respectively, for the molecular geometries optimized at the (U)B3LYP/6-31G(d) level.

even at low scan rates (approx. 10 mV s$^{-1}$), proves that **2** is a rather long-lived species. The peak potential of reduction 1C in **1** ($E_p^{red}$ = –0.53 V) is only 0.03 V less than the corresponding peak potential of its analog **8**.[8b] Reversibility of the 2C peak of **1** is observed only at scan rates >1 V s$^{-1}$ (Figure 5), which implies that dianion **9** is less stable under the CV conditions than the dianion of **8**.[8b]

The formation of **2** was confirmed by variable-temperature ESR spectroscopy (Figure 6). For **2**, two hfc constants $a(^{14}N \times 2)$ are 0.379 and 0.269 mT, whereas for [1,2,5]thiadiazolo[3,4-*c*][1,2,5] thiadiazolidyl (**10**) $a(^{14}N \times 4)$ is 0.314 mT.[8b] The theoretical hfc constants of **2** calculated at the DFT/UB3LYP/6-31G(d) level of theory [$a(^{14}N_1, ^{14}N_4)$ = 0.360 and $a(^{14}N_2, ^{14}N_3)$ = 0.309 mT] are close to the experimental values.

The ESR spectrum of **2** is temperature-dependent (Figure 6). In the range of 223–295 K it reveals lines broadening with increasing temperature (decreasing solvent viscosity), and at 295 K the spectrum is an unresolved singlet. This behavior is rather uncommon as the inverse situation is normally observed due to better averaging of the anisotropy of both the hfc and the *g*-tensor at higher temperatures. It is not, however, unprecedented, as a similar behavior has been reported for 1,2,3-benzodithiazolyls,[16a] which are neutral thiazyl radicals related to **2**, and explained by spin-rota-

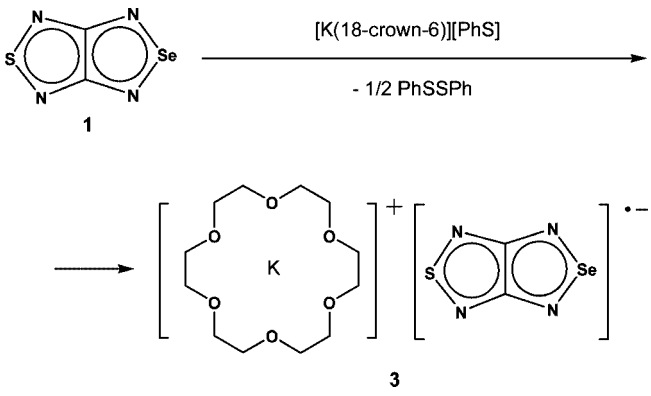


Scheme 5.

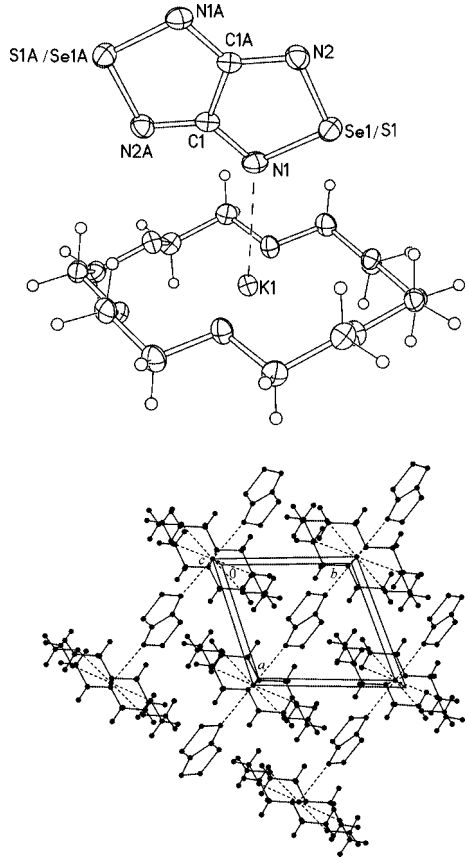


Figure 8. The structure (top) and crystal packing (bottom) of salt **3**. Bond lengths [pm] and bond angles [°] of radical anion **2**: Se1/S1–N1 175.6(4), Se1/S1–N2 174.1(4), N1–C1 133.4(6), N2–C1A 133.8(6), C1–C1A 147.2(8); N1–Se1–N2 97.72(18), Se1–N1–C1 105.3(3), N1–C1–N2A 128.4(4), N1–C1–C1A 115.7(5), N2–C1–C1A115.9(5), C1A–N2–Se1 105.4(3) [symmetry transformation used: –*x* + 1, –*y* + 1, –*z*].

 © 2007 Wiley-VCH Verlag GmbH & Co. KGaA, Weinheim 

tional relaxation,[16a] which gives an inversely proportional dependence of linewidth on viscosity.[17]

On the basis of the ESR data, the half-life of the electrochemically generated radical anion **2** can be estimated as $\tau_{1/2}$ = 930 s at 243 K and $\tau_{1/2}$ = 750 s at 295 K.

Figure 7 depicts the frontier MOs of **1** and the SOMO of **2** obtained from the HF/6-31G(d) and ROHF/6-31G(d) calculations, respectively, with geometries optimized at the DFT/(U)B3LYP/6-31G(d) level of theory. As usual, the SOMO of **2** is very similar to the LUMO of its neutral precursor **1**.

The thermally stable salt [K(18-crown-6)][**2**] (**3**) was obtained in 75% yield by chemical reduction of **1** with [K(18-crown-6)][PhS] (Scheme 5; see also ref.[8a]).

The structure of salt **3** was confirmed by XRD (Figure 8). As in the case of **1**, either S or Se atoms can be placed in the same position. The best refinement was achieved with occupation factors (SOF) of 0.50 for both S and Se (Figure 8). The crystal packing of **3** is very similar to that of [K(18-crown-6)][**10**][8b] (**11**) and reveals chains along the (01$\bar{1}$) crystallographic direction formed by uniform N···K contacts of 286.7 pm (288.5 pm in salt **11**).[8b] Thus, reduction of the molecular symmetry (disappearance of the inversion center) and the resulting appearance of a dipole moment on going from **10** to **2** essentially does not affect the crystal packing of salts **3** and **11**.

The solid-state ESR spectrum of salt **3**, with an unresolved hyperfine structure and $g_\perp$ = 2.0163 and $g_\parallel$ = 1.9971, is shown in Figure 9. The solution ESR spectrum of **3** in dmf is rather different to the spectrum of the electrochemically generated **2** in MeCN as the spectrum in dmf reveals two hfc constants [$a(^{14}N)$ = 0.380 and $a(^{14}N \times 3)$ = 0.292 mT; Figure 9] with $g$ = 2.001. This difference can be tentatively explained by the reduced molecular symmetry of **2** in the dmf solution of salt **3** (cf., for example, the data for the 2,2′-bipyrimidinyl radical anion in high- and low-symmetry complexes[16b]). The reduced symmetry can be proposed, for example, for a non-dissociated complex [K(18-crown-6)(dmf)][**2**] featuring $K^+$···**2** coordination similar to that observed in the solid state (Figure 8) and additional coordination of dmf to $K^+$ (instead of a second molecule of **2** as in the solid state).

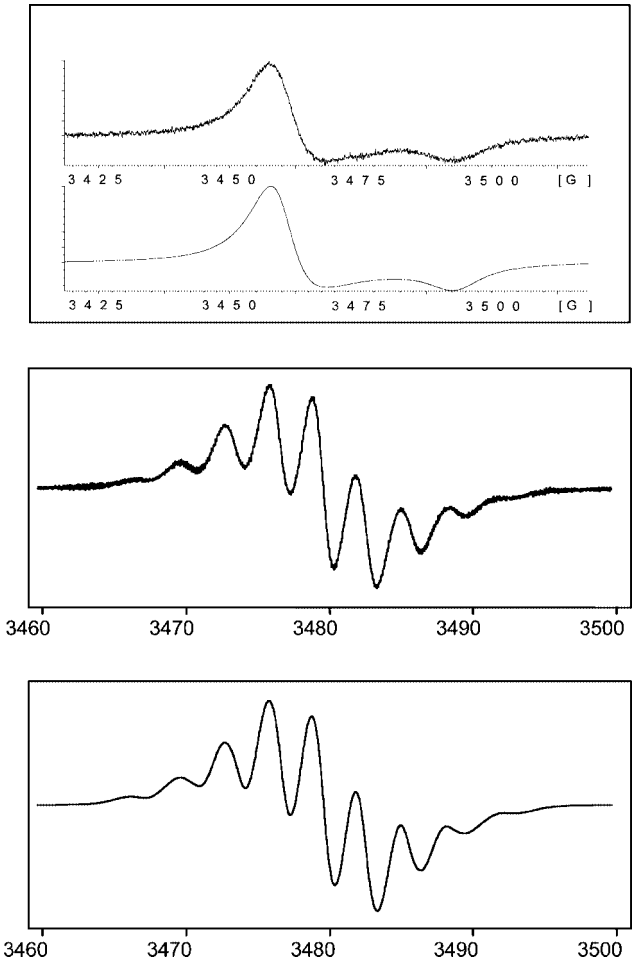


Figure 9. ESR spectra of **3** in the solid state (top: experimental and simulated) and dmf solution (center: experimental; bottom: simulated) at 295 K. $|H|$ $10^{-4}$ T.

## Magnetic Properties of [K(18-crown-6)][2] (3) in Comparison with Those of [K(18-crown-6)][10] (11)

The crystal lattices of salts **3** (this work) and **11**[8a] are very similar; therefore some similarity in their magnetic properties is to be expected. Indeed, the magnetic susceptibility, $\chi$, increases steadily for both salts with a decrease in temperature in the range 300–2 K (Figure 10). The experimental data are best fitted by the Bonner–Fisher uniform chain model[18] with exchange parameters, $J$, of $-1.65 \pm 0.03$ cm$^{-1}$ ($R_2$ = 0.997) for **3** and $-1.22 \pm 0.10$ cm$^{-1}$ ($R_2$ = 0.9997) for **11**.[8a] Thus, within this model, replacement of sulfur by selenium strengthens the antiferromagnetic exchange interactions in the discussed radical anion salts by 35%.

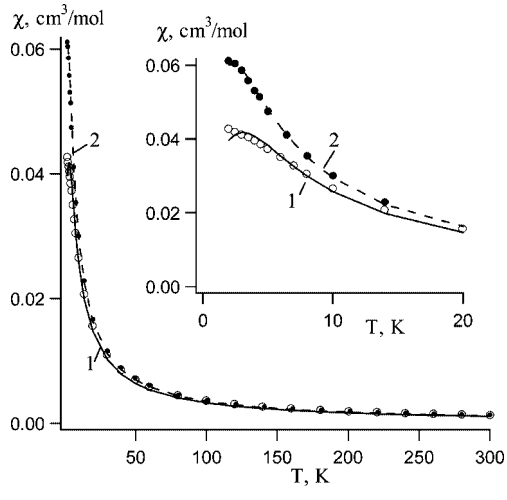


Figure 10. Temperature dependence of $\chi$ in the temperature ranges 2–300 K and 2–20 K (inset) for salts **3** (open circles) and **11** (black circles). Theoretical curves: Bonner–Fisher uniform chain model with $J$ = –1.65 cm$^{-1}$ for **3** (1) and $J$ = –1.22 cm$^{-1}$ for **11** (2).

 © 2007 Wiley-VCH Verlag GmbH & Co. KGaA, Weinheim 

Disordered salt **3** is less suitable for a theoretical analysis of the magnetic properties than salt **11**. Additionally, the symmetry of the radical anion **2** is lower than that of the radical anion **10**, therefore a detailed analysis of the pair exchange interactions ($J_{AB}$) based on the spin-unrestricted broken-symmetry DFT/UB3LYP/6-31+G(d) calculations was first performed for salt **11**. All radical anions **10** in the crystal of **11** are structurally equivalent. It is therefore possible to select a radical anion and calculate the $J_{AB}$ values with all first-nearest neighbors and then with the closest second-nearest neighbors.

Figure 11 demonstrates that every radical anion **10** has ten first-nearest neighbors, two of which are separated from it by $[K(18\text{-crown-6})]^+$ cations. These ten first-nearest neighbors give only five unique pairs (r1–r5, Figure 11) with the calculated $J_{AB}$ values presented in Table 1. This table also displays the shortest S···S (N···N for r4) distances in the pairs. Only for three of these five pairs are the calculated $J_{AB}$ values higher than the given accuracy of the calculations (0.04 $cm^{-1}$). All $J_{AB}$ values with closest second-nearest neighbors were found to be less than 0.04 $cm^{-1}$.

The influence of $[K(18\text{-crown-6})]^+$ cations separating radical anions **10**, as well as that of their 18-crown-6 fragments, on the values of the calculated $J_{AB}$ was estimated in the context of superexchange interactions. $J_{AB}$ was found to be zero for the "bare" r4 pair as well as for r4 pair divided by the $[K(18\text{-crown-6})]^+$ cation (Figure 11). Calculations for the clusters containing pairs r1–r3 and fragments of 18-crown-6 showed a noticeable change of the $J_{AB}$ values

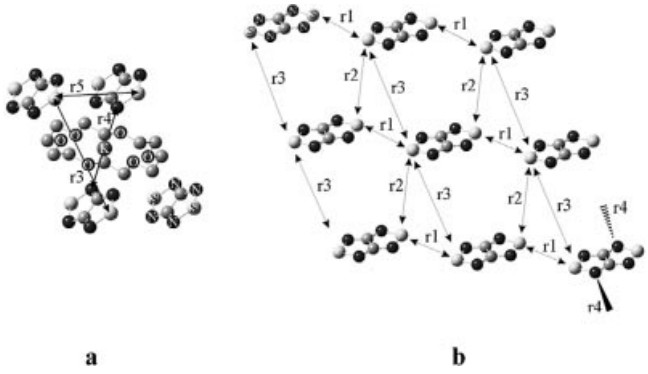


Figure 11. Crystal packing of salt **11** analyzed in terms of shortest intermolecular distances between radical anions **10**: (a) along the $(01\bar{1})$ crystallographic direction (hydrogen atoms of 18-crown-6 are omitted); (b) in the plane perpendicular to this direction.

(Table 1). Figure 12 displays the cluster containing the r3 pair together with two fragments of 18-crown-6 as an example.

Figure 12. Structure of the cluster containing the r3 pair and two fragments of 18-crown-6.

On the whole, the calculations demonstrate that the full magnetic structure of salt **11** is three-dimensional, although $J_{AB}$ for the r1 pair is much larger than all the others (Table 1, Figure 11). The magnetic motif for this salt can therefore be described approximately as a linear spin chain. This is why the $\chi(T)$ dependence is very well fitted by the Bonner–Fisher uniform chain model.[8a] At the same time, the experimentally estimated value of $J$ ($-1.22 \pm 0.01$ $cm^{-1}$) is about twice as small as $J_{AB}$ calculated for the r1 pair using the spin-unrestricted broken-symmetry approach at the DFT/UB3LYP/6-31+G(d) level of theory.

The HF and post-HF calculations of $J_{AB}$ for the r1 pair, with the same basis set as above, revealed (Table 1) that the UHF and UMP2 calculations considerably underestimate $J_{AB}$. Note that similar results were recently obtained for model systems such as H···H and H···He···H, where the $J_{AB}$ values were overestimated more than twice with the spin-polarized DFT approach and underestimated by the UHF method; only the UMP4 results agreed well with the data of high-level calculations such as full-CI ones.[19]

As mentioned above, the case of salt **3** is rather complicated since there are three different mutual orientations of the radical anions **2** in the selected pairs (Figure 13). The influence of these orientations on $J_{AB}$ was tested (Table 2). A comparison of Tables 1 and 2 clearly demonstrates that the $J_{AB}$ values for **3** are considerably larger than those for **11**. This observation agrees qualitatively with the difference in the exchange parameter ($J$) values obtained from the fitting of the $\chi(T)$ dependencies for salts **3** and **11**. At the same time, Table 2 shows that the obtained theoretical mag-

Table 1. Spin-unrestricted broken-symmetry results obtained by the UB3LYP, UHF and UMP2 techniques with the 6-31+G(d) basis set for the dimeric exchange interaction ($J_{AB}$) of the radical anion **10** with first-nearest neighbors in the crystal of salt **11**.

| Pair | Shortest distance in pair [Å] | $J_{AB}$ [$cm^{-1}$] | | | |
|---|---|---|---|---|---|
| | | UB3LYP | | UHF | UMP2 |
| | | "bare" | with 18-crown-6 | "bare" | |
| r1 | S···S, 5.34 | 2.13 | 2.79 | 0.44 | 0.75 |
| r2 | S···S, 6.22 | 0.09 | 0.09 | – | – |
| r3 | S···S, 8.25 | 0.26 | 0.07 | – | – |
| r4 | N···N, 5.77 | <\|0.04\| | <\|0.04\| | – | – |
| r5 | S···S, 8.55 | <\|0.04\| | <\|0.04\| | – | – |

 © 2007 Wiley-VCH Verlag GmbH & Co. KGaA, Weinheim 

netic motif for salt **3** cannot be correctly described as a uniform spin-chain since three different $J_{AB}$ values alternate along the chain. Indeed, although the experimental $\chi(T)$ dependence for **3** can be fairly well fitted by the Bonner–Fisher uniform chain model, the agreement is not as good as for **11** (see above).

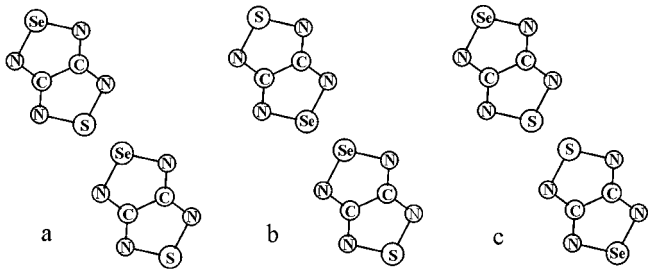


Figure 13. Different mutual orientations of the radical anions **2** reveal the highest $J_{AB}$ values in crystals of salt **3**.

Table 2. Spin-unrestricted broken-symmetry results obtained at the UB3LYP/6-31+G(d) level for the dimeric exchange interaction ($J_{AB}$) of the radical anion **2** with first-nearest neighbors in the crystal of salt **3** at different mutual orientations (Figure 13).

| Pair | $J_{AB}$ [cm$^{-1}$] | | |
|---|---|---|---|
| | *a* | *b* | *c* |
| r1 | 4.02 | 8.08 | 1.69 |
| r3 | 0.37 | 0.37 | 0.26 |

## Conclusions

A new heterocyclic system, namely [1,2,5]selenadiazolo[3,4-*c*][1,2,5]thiadiazole (**1**), has been prepared and characterized by XRD. The reversible electrochemical reduction of **1**, as well as its chemical reduction with the PhS$^-$ anion, provide the long-lived [1,2,5]selenadiazolo[3,4-*c*]-[1,2,5]thiadiazolidyl radical anion (**2**), which has been characterized by ESR spectroscopy and isolated in the form of the thermally stable salt [K(18-crown-6)][**2**] (**3**). According to the XRD data, the radical anion **2** acts as a bridging ligand in salt **3**. Magnetic measurements on salt **3** have revealed weak antiferromagnetic interactions ($J$ = –1.65 cm$^{-1}$). A comparison of **3** with its disulfur congener **11** assuming the Bonner–Fisher uniform chain model has shown that replacement of sulfur by selenium in these radical anion salts enhances the antiferromagnetic exchange interactions by 35%. Theoretical calculations of the exchange interactions in crystals of **3** and **11** have confirmed this trend. At the same time, these calculations demonstrate that the genuine magnetic structures of salts **3** and **11** are three-dimensional. In the case of salt **11**, the exchange interaction ($J_{AB}$) calculated for one particular type of radical anion pair in the solid state is much larger than for all the others, therefore the theoretical magnetic motif for this salt can be approximately described as a uniform spin chain. The obtained theoretical magnetic motif for salt **3** cannot be correctly described as a uniform spin chain since three different $J_{AB}$ values alternate along the chain.

## Experimental Section

**General:** 3,4-Dichloro-1,2,5-thiadiazole, $SeCl_4$, 18-crown-6, and Ph–S–$SiMe_3$ were used as received from Aldrich, whereas K*t*BuO was sublimed in vacuo before use. 3,4-Diamino-1,2,5-thiadiazole (**4**) was synthesized from the 3,4-dichloro derivative by a known procedure[14] and purified by vacuum sublimation. The complex [K(18-crown-6)][*t*BuO] was prepared as described previously.[20] The syntheses described below were performed under argon in absolutely dry solvents. The $^1$H and $^{13}$C NMR spectra were measured with a Bruker DRX-500 spectrometer at frequencies of 500.13 and 125.76 MHz, respectively, for solutions in $CDCl_3$, with TMS as standard. High-resolution mass spectra (EI, 70 eV) were recorded with a Finnigan MAT MS 8200 mass spectrometer. API-ES mass spectra were recorded with an Agilent 1100 Series LC/MSD instrument. The GC-MS measurements were performed with a Hewlett–Packard G1800A GCD device for solutions in $CH_2Cl_2$. EAS spectra were recorded with a Hewlett–Packard 8453 instrument for solutions in 1,2-dimethoxyethane (DME). The CV measurements on **1** were performed at 298 K under argon for a $2 \times 10^{-3}$ M solution of depolarizer in absolute MeCN at a stationary platinum electrode with 0.1 M $Et_4NClO_4$ as supporting electrolyte, with potential scan rates of 0.01–100 V s$^{-1}$. Both the 1C and 2C peaks were diffusion-controlled ($I_p^c v^{-1/2}$ = const, where $I_p$ is a current value in the peak and $v$ is a scan rate). Peak potentials are quoted relative to a saturated calomel electrode. The solid-state and solution ESR spectra were recorded with a Bruker ESP-300 spectrometer (MW frequency: 9.7641 GHz; MW power: 265 mW; modulation frequency: 100 kHz; modulation amplitude: 0.005 mT) equipped with a rectangular double resonator and a BST-100/700 temperature control unit. Electrochemical generation of the radical anion **2** from the neutral precursor **1** was performed with a $5 \times 10^{-3}$ M solution in MeCN (supporting electrolyte: 0.1 M $Et_4NClO_4$) with a standard cell for variable-temperature ESR measurements under anaerobic conditions. Simulations of the experimental solution ESR spectra were carried out with the Winsim 32 program using the Simplex algorithm of many-parameter optimization for hfc and linewidths. The accuracy in calculating $a$ values is ±0.0001 mT. The solid-state ESR spectrum of salt **3** was simulated with the Simfonia program in the $x$, $y$ and $z$ directions. Anisotropic hyperfine effects due to the $^{14}$N nuclei affect the general linewidth and do not appear directly in the spectrum (Figure 9). The half-life ($\tau_{1/2}$) of the electrochemically generated radical anion **2** in MeCN solution was calculated from the time dependency of the integral intensities of the ESR signals in the absence of an applied potential using the first-order kinetic equation for radical anion decay ($I = Ae^{(-kt)} + B$, $\tau_{1/2} = 0.69\ k^{-1}$). Because of the low solubility of salt **3** in MeCN, its ESR spectrum was recorded in dmf. The $g$ factors of salt **3** in the solid state and dmf solution were measured using a double resonator and MnO standard (six-line spectrum) with an accuracy of ±0.0002. The magnetic measurements were carried out with an MPMS-XL Quantum Design SQUID magnetometer in the temperature range 2–300 K in a magnetic field of 5000 Oe. The molar magnetic susceptibility, $\chi$, of salt **3** was calculated using the standard diamagnetism correction.

**Calculations:** The quantum chemical calculations were performed with the GAUSSIAN98 program suite.[21] The geometries of the closed-shell compounds and their radical anions were fully opti-

 © 2007 Wiley-VCH Verlag GmbH & Co. KGaA, Weinheim 

mized at the DFT/(U)B3LYP/6-31G(d) level of theory.[22] The hfc constants were calculated by the same method. The HOMO and LUMO of the closed-shell species and the SOMO of the radical anions were characterized at the HF and ROHF levels of theory, respectively. The EAS were calculated by the TD-DFT/B3LYP/6-31+G(d) technique.[23] For the theoretical analysis of the magnetic structures of **3** and **11**, the exchange integrals ($J_{AB}$) between selected pairs of radical anions (**2** or **10**, respectively) were calculated using the spin-unrestricted broken-symmetry approach.[24] The $J_{AB}$ values were obtained from the following equation:

$$J_{AB} = E^{S}_{BS} - E^{T}$$

where $E^T$ is the energy of the triplet state of the pair of radical anions and $E^S_{BS}$ is the energy of the open-shell singlet state within the broken-symmetry approach.[24] In all cases the $<S^2>$ value for the broken-symmetry singlet state was about 1.02. The $E^T$ and $E^S_{BS}$ values were calculated using the DFT (UB3LYP), HF (UHF), and post-HF (UMP2) methods with the 6-31+G(d) basis set. The accuracy of the energy calculations was chosen to be $10^{-7}$ H, which provided values for $J_{AB}$ with an accuracy of 0.04 $cm^{-1}$.

**Crystallographic Analysis:** The XRD data (Table 3) for **1**, **3**, **5**, and **7** were collected with a Siemens P4 diffractometer using graphite-monochromated Mo-$K_\alpha$ ($\lambda$ = 71.073 pm) radiation. The structures were solved by direct methods using the SHELXS-97 program[25] and refined by the least-squares method in the full-matrix anisotropic (isotropic for H atoms) approximation using the SHELXL-97 program.[25] The structures obtained were analyzed for shortened contacts between non-bonded atoms with the PLATON program.[26] CCDC-645192 (for **1**), -644966 (for **3**), -644965 (for **5**), and -645193 (for **7**) contain the supplementary crystallographic data for this paper. These data can be obtained free of charge from The Cambridge Crystallographic Data Centre via www.ccdc.cam.ac.uk/data_request/cif.

**Synthesis of Compound 1:** A solution of $SeCl_4$ (1.11 g, 0.005 mol) in 15 mL of DME was added dropwise during 10 min to a refluxed and stirred solution of **4** (0.58 g, 0.005 mol) and pyridine (1.58 g, 0.02 mol) in 15 mL of the same solvent. The reaction mixture was refluxed and stirred for an additional 30 min, then filtered hot and cooled to 20 °C. The complex **1**·[$C_5H_5NH$][Cl] (**5**) was obtained as transparent light-yellow needles (yield: 1.04 g, 68%). M.p. (sealed capillary): 155–157 °C (dec.). $C_7H_6ClN_5SSe$ (306.64): calcd. C 27.42, H 1.97, Cl 11.56, N 22.84; found C 27.27, H 1.82, Cl 11.43, N 22.79. Complex **5** was subsequently treated with $H_2O$, EtOH, and $Et_2O$, and the residue was dried under vacuum at 20 °C followed by sublimation at 90 °C/0.1 Torr. According to the API-ES and GC-MS data, the sublimed product was compound **1** ($m/z$ = 191.9 [$C_2N_4S^{80}Se$]) containing approx. 5% of [1,2,5]selenadiazolo[3,4-*c*][1,2,5]selenadiazole (**6**; $m/z$ = 239.8 [$C_2N_4{}^{80}Se_2$]). The

Table 3. Crystal data and structure refinement for compounds **1**, **3**, **5**, and **7**.

| Compound | **1** | **3** | **5** | **7** |
|---|---|---|---|---|
| Empirical formula | $C_2N_4SSe$ | $C_{14}H_{24}KN_4O_6SSe$ | $C_7H_6ClN_5SSe$ | $C_2N_4S_{0.56}Se_{1.44}$ |
| Formula mass | 191.08 | 494.49 | 306.64 | 211.91 |
| Temperature [K] | 293(2)[a] | 173(2) | 173(2) | 293(2) |
| Wavelength [pm] | 71.073 | 71.073 | 71.073 | 71.073 |
| Crystal system | monoclinic | triclinic | monoclinic | monoclinic |
| Space group | *C*2/*m* | $P\bar{1}$ | $P2_1/m$ | $P2_1/c$ |
| *a* [pm] | 640.4(1) | 829.6(2) | 639.8(1) | 385.0(1) |
| *b* [pm] | 672.2(2) | 852.8(3) | 694.2(2) | 2208.1(6) |
| *c* [pm] | 639.4(1) | 913.0(2) | 1210.6(2) | 628.0(2) |
| *α* [°] | 90 | 71.08(2) | 90 | 90 |
| *β* [°] | 105.61(1) | 63.38(2) | 98.93(1) | 105.77(3) |
| *γ* [°] | 90 | 64.92(2) | 90 | 90 |
| Volume [$nm^3$] | 0.2651(1) | 0.5158(2) | 0.53117(19) | 0.5137(3) |
| *Z* | 2 | 1 | 2 | 4 |
| Density (calcd.) [$Mg\,m^{-3}$] | 2.394 | 1.592 | 1.917 | 2.737 |
| Absorption coefficient [$mm^{-1}$] | 7.351 | 2.160 | 3.954 | 10.552 |
| *F*(000) | 180 | 253 | 300 | 392 |
| Crystal size [mm] | 0.31 × 0.30 × 0.03 | 0.50 × 0.30 × 0.10 | 0.60 × 0.40 × 0.25 | 0.20 × 0.20 × 0.07 |
| *θ* range for data collection [°] | 3.31–27.49 | 2.53–27.49 | 3.22–27.49 | 3.50–25.01 |
| Index range | $0 \le h \le 8$<br>$-8 \le k \le 0$<br>$-8 \le l \le 8$ | $-1 \le h \le 10$<br>$-10 \le k \le 10$<br>$-11 \le l \le 11$ | $-8 \le h \le 8$<br>$-9 \le k \le 8$<br>$-15 \le l \le 15$ | $0 \le h \le 4$<br>$0 \le k \le 26$<br>$-7 \le l \le 6$ |
| Reflections collected | 364 | 2856 | 4898 | 910 |
| Independent reflections | 335 [*R*(int) = 0.0313] | 2330 [*R*(int) = 0.0302] | 1315 [*R*(int) = 0.0334] | 774 [*R*(int) = 0.0981] |
| Completeness to *θ* [%] | 100.0 | 98.3 | 99.9 | 84.9 |
| Absorption correction | empirical | empirical | empirical | empirical |
| Max./min. transmission | 0.661/0.204 | 0.813/0.411 | 0.382/0.159 | 0.651/0.179 |
| Refinement method | full-matrix least squares on $F^2$ | full-matrix least squares on $F^2$ | full-matrix least squares on $F^2$ | full-matrix least squares on $F^2$ |
| Data/restraints/parameters | 335/1/32 | 2330/0/125 | 1315/12/96 | 774/0/74 |
| Goodness-of-fit on $F^2$ | 1.132 | 1.033 | 1.092 | 1.110 |
| Final *R* indices [$I > 2\sigma(I)$] | $R_1$ = 0.0461,<br>$wR_2$ = 0.1270 | $R_1$ = 0.0624,<br>$wR_2$ = 0.1483 | $R_1$ = 0.0366,<br>$wR_2$ = 0.0896 | $R_1$ = 0.0743,<br>$wR_2$ = 0.1851 |
| *R* indices (all data) | $R_1$ = 0.0509,<br>$wR_2$ = 0.1270 | $R_1$ = 0.0932,<br>$wR_2$ = 0.1649 | $R_1$ = 0.0439,<br>$wR_2$ = 0.0946 | $R_1$ = 0.1044,<br>$wR_2$ = 0.2090 |
| Largest difference peak/hole [e Å$^3$] | 0.557/–0.825 | 0.656/–0.834 | 0.662/–1.076 | 0.860/–0.863 |

[a] The XRD data collected for **1** at 173 K could not be finally refined due to accretion/twinning of the crystal.

 © 2007 Wiley-VCH Verlag GmbH & Co. KGaA, Weinheim 

product was recrystallized from toluene to give compound **1** as small yellow crystals (yield: 0.57 g, 60%). M.p. (sealed capillary): 231–233 °C. MS: calcd. for $C_2N_4S^{80}Se$ 191.9009; found 191.9028. $^{13}C$ NMR ($CDCl_3$): $\delta$ = 173.6 ppm. EAS (DME): $\lambda_{max}$ (log $\varepsilon$) = 353 nm (4.33). $C_2N_4SSe$ (191.08): calcd. C 12.57, N 29.32; found C 12.49, N 29.28. The use of $Et_3N$ instead of pyridine led to a mixture of unidentified products. The single crystal of **1** suitable for XRD was obtained by slowly concentrating a DME solution at ambient temperature. The single crystal of **7** (molecular complex between **1** and **6**) was found in the same sample.

**Synthesis of Salt 3:** A solution of Ph–S–$SiMe_3$ (0.182 g, 0.001 mol) in 2 mL of thf was added to a solution of [K(18-crown-6)][*t*BuO] (0.376 g, 0.001 mol) in 5 mL of the same solvent at –30 °C. The solution was warmed to 20 °C, stirred for 1 h, and the solvent distilled off under vacuum to give a white crystalline residue. Compound **1** (0.191 g; 0.001 mol) and 10 mL of MeCN were then added at –30 °C, and the wine-red solution obtained was warmed to 20 °C, stirred for 1 h, filtered, and the solvents were evaporated under vacuum. The residue was washed with 10 mL of thf, then dissolved in 5 mL of boiling MeCN under normal pressure of argon and the solution cooled to 20 °C. The solvent was removed with a syringe and the crystals that had formed were washed with 10 mL of thf and dried under vacuum. Salt **3** forms transparent ruby plates, Yield: 0.371 g (75%). M.p. (sealed capillary): 138 °C (dec.). $C_{14}H_{24}KN_4O_6SSe$ (494.50): calcd. C 34.00, H 4.89, N 11.33; found C 34.09, H 4.71, N 11.36. Concentration of the initially obtained thf solution gave PhSSPh (98%), as identified by GC-MS techniques by comparison with an authentic sample.

## Acknowledgments

The authors are grateful to Prof. Yuri N. Molin and Dr. Leonid A. Shundrin for valuable discussions, to Dr. Alexander Yu. Makarov and Mr. Peter Brackmann for their assistance in the preparative and XRD experiments, respectively, and to the Deutsche Forschungsgemeinschaft (grant 436 RUS 113/486/0-3 R), the Russian Foundation for Basic Research (grants 06-03-32229, 06-03-32742, and 07-03-00467), and the Siberian Division of the Russian Academy of Sciences (interdisciplinary project No. 25) for financial support of this work. N. G. gratefully acknowledges the Ohio Supercomputing Center, USA, for providing computational facilities.

[1] T. Chivers, *A Guide to Chalcogen-Nitrogen Chemistry*, World Scientific, New Jersey, **2005**.

[2] a) K. Awaga, T. Tanaka, T. Shirai, Y. Umezono, W. Fujita, *C. R. Chim.* **2007**, *10*, 52–59; b) K. Awaga, T. Tanaka, T. Shirai, M. Fujimori, Y. Suzuki, H. Yoshikava, W. Fujita, *Bull. Chem. Soc. Jpn.* **2006**, *79*, 25–34; K. Okamoto, T. Tanaka, W. Fujita, K. Awaga, T. Inabe, *Angew. Chem. Int. Ed.* **2006**, *45*, 4516–4518.

[3] a) M. Deumal, S. LeRoux, J. M. Rawson, M. A. Robb, J. J. Novoa, *Polyhedron* **2007**, *26*, 1949–1958; b) J. M. Rawson, A. Alberola, A. Whalley, *J. Mater. Chem.* **2006**, *16*, 2560–2575; c) J. M. Rawson, J. Luzon, F. Palacio, *Coord. Chem. Rev.* **2005**, *249*, 2631–2641; d) J. M. Rawson, F. Palacio, *Struct. Bonding (Berlin)* **2001**, *100*, 93–128; e) J. M. Rawson, G. D. MacManus, *Coord. Chem. Rev.* **1999**, *189*, 135–168; f) J. M. Rawson, A. J. Banister, I. Lavender, *Adv. Heterocycl. Chem.* **1995**, *62*, 137–247.

[4] a) J. L. Brusso, K. Cvrkalj, A. A. Leitch, R. T. Oakley, R. W. Reed, C. M. Robertson, *J. Am. Chem. Soc.* **2006**, *128*, 15080–15081; b) J. L. Brusso, S. Derakhshan, M. E. Itkis, H. Kleinke, R. C. Haddon, R. T. Oakley, R. W. Reed, J. F. Richardson, C. M. Robertson, L. K. Thompson, *Inorg. Chem.* **2006**, *45*, 10958–10966; c) L. Beer, J. L. Brusso, R. C. Haddon, M. E. Itkis, R. T. Oakley, R. W. Reed, J. F. Richardson, R. A. Secco, X. Yu, *Chem. Commun.* **2005**, 5745–5747; d) W. Cordes, R. C. Haddon, R. T. Oakley, *Adv. Mater.* **1994**, *6*, 798–802; e) R. T. Oakley, *Prog. Inorg. Chem.* **1988**, *36*, 299–391.

[5] a) T. S. Cameron, A. Decken, R. M. Kowalczyk, E. J. L. McInnes, J. Passmore, J. M. Rawson, K. V. Shuvaev, L. K. Thompson, *Chem. Commun.* **2006**, 2277–2279; b) A. Decken, S. M. Mattar, J. Passmore, K. V. Shuvaev, L. K. Thompson, *Inorg. Chem.* **2006**, *45*, 3878–3886; c) T. S. Cameron, M. T. Lemaire, J. Passmore, J. M. Rawson, K. V. Shuvaev, L. K. Thompson, *Inorg. Chem.* **2005**, *44*, 2576–2578; d) G. Antorrena, S. Brownridge, T. S. Cameron, F. Palacio, S. Parsons, J. Passmore, L. K. Thompson, F. Zarlaida, *Can. J. Chem.* **2002**, *80*, 1568–1583; e) S. Parsons, J. Passmore, *Acc. Chem. Res.* **1994**, *27*, 101–108.

[6] R. T. Boere, T. L. Roemmele, *Coord. Chem. Rev.* **2000**, *210*, 369–445.

[7] J. Banister, I. B. Gorrell, *Adv. Mater.* **1998**, *10*, 1415–1429.

[8] a) V. N. Ikorskii, I. G. Irtegova, E. Lork, A. Yu. Makarov, R. Mews, V. I. Ovcharenko, A. V. Zibarev, *Eur. J. Inorg. Chem.* **2006**, 3061–3067; b) Yu. Makarov, I. G. Irtegova, N. V. Vasilieva, I. Yu. Bagryanskaya, T. Borrmann, Yu. V. Gatilov, E. Lork, R. Mews, W.-D. Stohrer, A. V. Zibarev, *Inorg. Chem.* **2005**, *44*, 7194–7199.

[9] a) D. Kovisto, R. G. Hicks, *Coord. Chem. Rev.* **2005**, *249*, 2612–2630; b) R. G. Hicks, *Austr. J. Chem.* **2001**, *54*, 597–600.

[10] a) D. Luneau, P. Rey, *Coord. Chem. Rev.* **2005**, *249*, 2591–2611; b) V. I. Ovcharenko, R. Z. Sagdeev, *Russ. Chem. Rev.* **1999**, *68*, 345–365.

[11] a) M. Gloekle, K. Hueber, H.-J. Kuemmerer, G. Denninger, W. Kaim, *Inorg. Chem.* **2001**, *40*, 2263–2269; b) M. Schwach, H.-D. Hausen, W. Kaim, *Inorg. Chem.* **1999**, *38*, 2242–2243.

[12] a) G. Saito, Y. Yoshida, *Bull. Chem. Soc. Jpn.* **2007**, *80*, 1–137; b) K. I. Pokhodnya, M. Bonner, J.-H. Her, P. W. Stephens, J. S. Miller, *J. Am. Chem. Soc.* **2006**, *128*, 15592–15593; c) H. Zhao, R. A. Heintz, X. Ouyang, K. R. Dunbar, C. F. Campana, R. D. Rogers, *Chem. Mater.* **1999**, *11*, 736–746; d) P. J. Kunkeler, P. J. van Koningsbruggen, J. P. Cornelissen, A. N. van der Horst, A. M. van der Kraan, A. L. Spek, J. G. Haasnoot, J. Reedijk, *J. Am. Chem. Soc.* **1996**, *118*, 2190–2197; e) A. Böhm, C. Vazquez, R. S. McLean, J. C. Calabrese, S. E. Kalm, J. L. Manson, A. J. Epstein, J. S. Miller, *Inorg. Chem.* **1996**, *35*, 3083–3088.

[13] a) A. Bencini, C. A. Daul, A. Dei, F. Mariotti, H. Lee, D. A. Shultz, L. Sorace, *Inorg. Chem.* **2001**, *40*, 1582–1590; b) A. Shultz, S. H. Bodnar, K. E. Vostrikova, J. W. Kampf, *Inorg. Chem.* **2000**, *39*, 6091–6093; c) G. Pierpont, C. W. Lange, *Prog. Inorg. Chem.* **1994**, *41*, 331–442; d) M. Adams, A. Dei, A. L. Rheingold, D. N. Hendrickson, *Angew. Chem. Int. Ed. Engl.* **1993**, *32*, 880–882; e) A. Dei, D. Gatteschi, *Inorg. Chim. Acta* **1992**, *198–200*, 813–822.

[14] A. P. Komin, M. Carmack, *J. Heterocycl. Chem.* **1976**, *13*, 13–22.

[15] a) A. V. Zibarev, O. M. Fugaeva, A. O. Miller, S. N. Konchenko, I. K. Korobeinicheva, G. G. Furin, *Khim. Geterotsikl. Soedin.* **1990**, 1124–1133 (in Russian; *Chem. Abstr.* **1991**, *114*, 100927); b) V. Zibarev, A. O. Miller, *J. Fluorine Chem.* **1990**, *50*, 359–563; c) V. N. Kovtonyuk, A. Yu. Makarov, M. M. Shakirov, A. V. Zibarev, *Chem. Commun.* **1996**, 1991–1992; d) F. Cozzolino, J. F. Britten, I. Vargas-Baca, *Cryst. Growth Des.* **2006**, *6*, 181–186.

[16] a) V. Vlasyuk, V. A. Bagryansky, N. P. Gritsan, Yu. N. Molin, A. Yu. Makarov, Yu. V. Gatilov, V. V. Shcherbukhin, A. V. Zibarev, *Phys. Chem. Chem. Phys.* **2001**, *3*, 409–415; b) W. Kaim, *Inorg. Chem.* **1984**, *23*, 3365–3368.

[17] P. W. Atkins, D. Kivelson, *J. Chem. Phys.* **1966**, *44*, 169–174.

[18] W. E. Hatfield, *J. Appl. Phys.* **1981**, *52*, 1985–1990.

[19] T. Soda, Y. Kitagawa, T. Onishi, Y. Takano, Y. Shigeta, H. Nagao, Y. Yoshioka, K. Yamaguchi, *Chem. Phys. Lett.* **2000**, *319*, 223–230.

 © 2007 Wiley-VCH Verlag GmbH & Co. KGaA, Weinheim 

[20] T. Borrmann, E. Lork, R. Mews, M. M. Shakirov, A. V. Zibarev, *Eur. J. Inorg. Chem.* **2004**, 2452–2458.
[21] M. J. Frisch, G. W. Trucks, H. B. Schlegel, G. E. Scuseria, M. A. Robb, J. R. Cheeseman, V. G. Zakrzewski, J. A. Montgomery Jr, R. E. Stratmann, J. C. Burant, S. Dapprich, J. M. Millam, A. D. Daniels, K. N. Kudin, M. C. Strain, O. Farkas, J. Tomasi, V. Barone, M. Cossi, R. Cammi, B. Mennucci, C. Pomelli, C. Adamo, S. Clifford, J. Ochterski, G. A. Petersson, P. Y. Ayala, Q. Cui, K. Morokuma, D. K. Malick, A. D. Rabuck, K. Raghavachari, J. B. Foresman, J. Cioslowski, J. V. Ortiz, B. B. Stefanov, G. Liu, A. Liashenko, P. Piskorz, I. Komaromi, R. Gomperts, R. L. Martin, D. J. Fox, T. Keith, M. A. Al-Laham, C. Y. Peng, A. Nanayakkara, C. Gonzalez, M. Challacombe, P. M. W. Gill, B. Johnson, W. Chen, M. W. Wong, J. L. Andres, C. Gonzalez, M. Head-Gordon, E. S. Replogle, J. A. Pople, *Gaussian 98 (Revision A.9)*, Gaussian Inc., Pittsburgh, PA, **1998**.
[22] a) P. Geerlings, F. De Proft, W. Langenaeker, *Chem. Rev.* **2003**, *103*, 1793–1873; b) D. Becke, *J. Chem. Phys.* **1993**, *98*, 5648–5652; c) C. Lee, W. Yang, R. G. Parr, *Phys. Rev. B* **1988**, *37*, 785–789.
[23] a) A. Dreuw, M. Head-Gordon, *Chem. Rev.* **2005**, *105*, 4009–4037; b) M. E. Casida, C. Jamorski, K. C. Casida, D. R. Salahub, *J. Chem. Phys.* **1998**, *108*, 4439–4449; c) K. B. Wiberg, R. E. Stratmann, M. J. Frisch, *Chem. Phys. Lett.* **1998**, *297*, 60–64.
[24] a) L. Nudlemann, *J. Chem. Phys.* **1981**, *74*, 5737–5743; b) L. Nudlemann, E. R. Davidson, *Chem. Phys.* **1986**, *109*, 131–143; c) L. Nudlemann, D. A. Case, J. M. Mouesca, *Coord. Chem. Rev.* **1995**, *144*, 199–244; d) H. Nagao, M. Nishino, Y. Shigeta, T. Soda, Y. Kitagawa, T. Onishi, Y. Yoshioka, K. Yamaguchi, *Coord. Chem. Rev.* **2000**, *198*, 265–295; e) M. Deumal, M. J. Bearpark, J. Novoa, M. A. Robb, *J. Phys. Chem. A* **2002**, *106*, 1299–1315.
[25] G. M. Sheldrick, *SHELX-97 – Programs for Crystal Structure Analysis (Release 97-2)*, Institute for Inorganic Chemistry, University of Göttingen, Germany, **1997**.
[26] a) A. L. Spek, *PLATON, A Multipurpose Crystallographic Tool (Version 10 M)*, Utrecht University, The Netherlands, **2003**; b) L. Spek, *J. Appl. Crystallogr.* **2003**, *36*, 7–13.

Received: May 9, 2007
Published Online: September 14, 2007

 © 2007 Wiley-VCH Verlag GmbH & Co. KGaA, Weinheim 

DOI: 10.1002/ejic.200700551

# [(Tmp)$Co_2$L] Complexes through Preassembly on 2,6-Diformyl- and 2,6-Bis(benzylimino)-4-methylphenolate Templates

**Alok Ranjan Paital,[a] Mrinal Sarkar,[a] Masahiro Mikuriya,[b] and Debashis Ray*[a]**

**Keywords:** Cobalt complexes / Bridging ligands / Template synthesis / Imidazolidine / Magnetic properties

The reaction of the dinucleating ligand $H_3L$ {2-(2′-hydroxyphenyl)-1,3-bis[4-(2-hydroxyphenyl)-3-azabut-3-enyl]-1,3-imidazolidine} with $Co(OAc)_2{\cdot}4H_2O$ and $NaN_3$ in MeOH produces the methoxide-bridged dicobalt complex [$Co^{III}_2$(μ-OMe)L$(N_3)_2$] (**1**) under aerobic conditions. If the reaction occurs in the presence of either 2,6-diformyl-4-methylphenolate ($dfp^-$) or 2,6-bis(benzyliminomethyl)-4-methylphenolate ($bip^-$), a preassembly of the [$Co^{II}_2(OPh)]^{3+}$ units takes place on these templates before coordination with $L^{3-}$ in [$Co^{II}_2$(μ-dfp)L]·$3H_2O$ (**2**·$3H_2O$) and [$Co^{II}_2$(μ-bip)L]·$3H_2O$ (**3**·$3H_2O$), respectively. Incorporation of these coligands into the structure leads to stabilization of 3+ and 2+ oxidation states of the cobalt. In complex **2**, the $Co^{II}$ ions are engaged in a weak antiferromagnetic interaction.
(© Wiley-VCH Verlag GmbH & Co. KGaA, 69451 Weinheim, Germany, 2007)

## Introduction

Dinuclear high-spin cobalt(II) complexes have been the subject of recent investigations in molecular magnetism and magnetic analysis.[1] These high-spin cobalt(II) complexes show interesting magnetic properties, where the ground term possesses an orbital angular moment.[2] Cobalt can also give rise to mixed-valent complexes because of its ready access to 2+ and 3+ oxidation states. These complexes have attracted attention because of their fascinating magnetic properties as well as their biological relevance. They can serve as synthetic models of dimetallic biosites, such as in methionine aminopeptidase,[3] and can show DNA cleavage activity.[4] This type of metallohydrolase is known to require two or more metal ions for hydrolysis of phosphate ester and peptide bonds.[5] Recently, Love and co-workers have used a binucleating macrocycle to prepare low-spin square-planar $Co^{II}Co^{II}$ diporphyrin complexes having a pacman-like cleft showing interesting dioxygen reduction chemistry.[6] Because of these various interesting features of cobalt ions, we studied their reactivity toward imidazolidinyl ligands.[7] We and others have been exploring the dinucleating properties of the ligand $H_3L$ (Scheme 1) {2-(2′-hydroxyphenyl)-1,3-bis[4-(2-hydroxyphenyl)-3-azabut-3-enyl]-1,3-imidazolidine}[8] and its close derivative $H_3L'$ {2-(2′-hydroxyphenyl)-1,3-bis[4-(2-hydroxyphenyl)-4-methyl-3-azabut-3-enyl]-2-methyl-1,3-imidazolidine}[9] for various reasons, including their importance in coordination chemistry, molecular magnetism, and catalysis.[9–16]

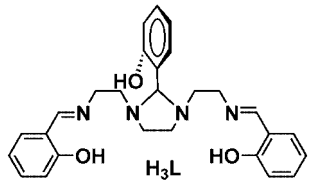


Scheme 1.

During the course of these investigations, we have observed that in certain conditions, complexation reactions with $Mn^{III}$, $Fe^{III}$, $Co^{III}$, or $Cu^{II}$ led to the hydrolysis of the imidazolidine ring[17,18] and even the destruction of one of the imine linkages of the hexadentate proligand.[19] We have also investigated the hydrolysis of $H_3L$ as triggered by $Co^{III}$ and isolated the mononuclear complex resulting from the hydrolyzed ligand.[7] Previously Fondo et al. showed that this type of ligand leads to either $Co^{III}_2$ or mixed-valent $Co^{III}Co^{II}$ complexes[20] by spontaneous oxidation of $Co^{II}$ salts in air. The main objectives of the present investigation are (i) to scrutinize the role of the different ligand templates in inhibition of the coordination-induced hydrolysis of the imidazolidine ring of the trisphenolate ligands, (ii) to synthesize a new $Co_2$ complex of this ligand incorporating template ligands, and (iii) to stabilize the 2+ oxidation states of cobalt in phenolate environments. We have successfully achieved our goal by using 2,6-diformyl-4-methylphenol (Hdfp) and 2,6-bis(benzyliminomethyl)-4-methylphenol (Hbip) as coligands (Scheme 2).

[a] Department of Chemistry, Indian Institute of Technology, Kharagpur 721 302, India
Fax: +91-3222-255303
+91-3222-82252
E-mail: dray@chem.iitkgp.ernet.in
[b] School of Science and Technology, Kwansei Gakuin University, 2-1 Gakuen, Sanda 669-1337, Japan
Supporting information for this article is available on the WWW under http://www.eurjic.org or from the author.


InterScience
© 2007 Wiley-VCH Verlag GmbH & Co. KGaA, Weinheim

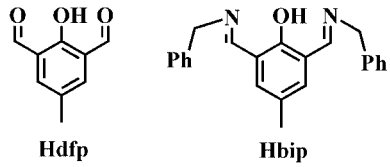


Scheme 2.

These coligands not only inhibit hydrolysis of $L^{3-}$ but also serve as templates to stabilize the metal ions in 2+ oxidation states in two new [$Co_2$] complexes. Hydroxy carboxaldehydes of this type have been used extensively as precursors in the preparation of more complicated ligands,[21] however their use as exogenous bridging ligands is very uncommon.[22] While exploring the metal ion coordination processes toward $L^{3-}$, we found that the reactions of a particular metal salt control the production of the desired complex in the presence and absence of externally added or solvent-derived template bridges. Herein complexes [$Co^{III}_2$(μ-OMe)L($N_3$)$_2$] (**1**), [$Co^{II}_2$(μ-dfp)L]·3$H_2O$ (**2**·3$H_2O$), and [$Co^{II}_2$(μ-bip)L]·3$H_2O$ (**3**·3$H_2O$) derived from ligand $H_3L$ following two different (solvent-derived or external) template routes are reported. Complexes **1** and **2**·3$H_2O$ were crystallographically characterized and the magnetic properties of **2**·3$H_2O$ were also studied.

## Results and Discussion

### Syntheses, Reactivity, and Spectroscopic Characterizations

The ligand $H_3L$ {2-(2′-hydroxyphenyl)-1,3-bis[4-(2-hydroxyphenyl)-3-azabut-3-enyl]-1,3-imidazolidine} (Scheme 1) was prepared according to a literature procedure[8] and its reaction with cobalt(II) salts has been investigated, as shown in Scheme 3.

In MeOH, the reaction of $Co(OAc)_2$·4$H_2O$ and $NaN_3$ followed by addition of a methanolic solution of $H_3L$ in a 2:2:1 molar ratio yields brown [$Co^{III}_2$(μ-OMe)L($N_3$)$_2$] (**1**) in 75% yield while stirring in air at room temperature (300 K). Complex **1** could be isolated in high purity and shows aerial oxidation of metal centers. It has also been observed that use of excess $NaN_3$ up to a molar ratio of 1:6 could not substitute the bridging $MeO^-$ group by $N_3^-$ and afforded **1** exclusively. In a previous report, we noticed that in solution $H_3L$ is unstable during reactions with cobalt(II) salts and produced crystals of the mononuclear complex cations [CoL′]$^+$ in low yield ($H_2L'$ is the hexadentate proligand formed from the imidazolidine ring hydrolysis of $H_3L$).[7] As an *o*-formylphenolate moiety is generated from the hydrolysis of $L^{3-}$, which indicates that the ligand decomposition is possibly inhibited by this. Therefore the solution stability of $L^{3-}$ as part of new [$Co_2$] complexes could be enhanced with the introduction of diformyl- and bis(benzylimino)phenolates as template ligands. 2,6-Diformyl-4-meth-

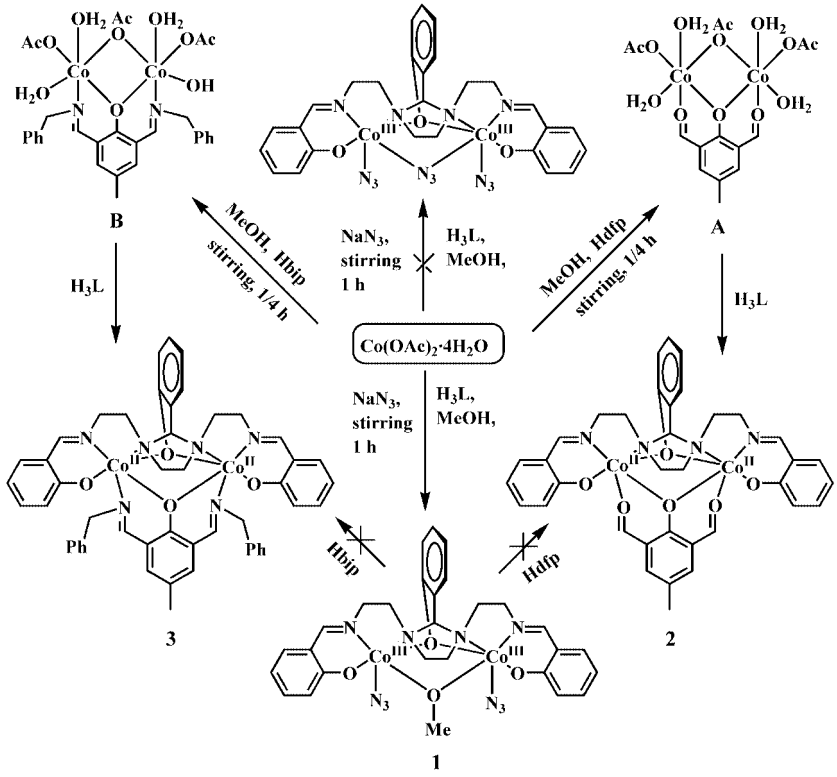


Scheme 3.

 © 2007 Wiley-VCH Verlag GmbH & Co. KGaA, Weinheim 

ylphenol (Hdfp)[21] and 2,6-bis(benzyliminomethyl)-4-methylphenol (Hbip)[23] have been synthesized following the methods previously described and satisfactorily characterized by elemental analysis, IR, and $^1$H NMR spectroscopy. Binucleating ligands based on this dialdehyde as introduced by Robson[24] and Okawa[25] have been extensively studied for the preparation of different dimetal complexes. The process of ligand hydrolysis, however, was inhibited completely if Hdfp or Hbip had previously been mixed with the solution of $Co(OAc)_2{\cdot}4H_2O$. Presumably this led to the formation of intermediate **A** or **B** (Scheme 3), to result in the formation of complexes **2** and **3**, after addition of $H_3L$ where the deprotonated dicarbonyl phenolate ($dfp^-$) and bis(benzylimino)phenolate ($bip^-$) behave as bisdidentate bridging ligands stabilizing the $Co^{II}_2$ complexes. The formulation of all the complexes is consistent with the elemental and metal analysis, and solution electrical conductivity data in $CH_3CN$. The red complex **2** forms in 80% yield whilst stirring in MeOH at 300 K. Similarly, compound **3** was isolated in 75% yield as a red powder. All the compounds are insoluble in water and separate directly from the reaction mixture following the completion of the reactions in air at room temperature. Stabilization of the metal oxidation states within these $Co_2$ complexes is template-ligand-dependent. Template interconversions within this family of the complexes are not possible in the presence of external oxidizing and reducing agents. This clearly identifies that the templates are present as an integral part within these assemblies.

### Infrared Spectroscopy

The sharp peak in the FTIR spectra of complexes **1**, **2**·3$H_2O$, and **3**·3$H_2O$, at 1629, 1625, and 1624 $cm^{-1}$ respectively, are characteristic of the C=N functionality of the ligand $L^{3-}$. The C=N stretching frequency of the free Hbip ligand is shifted from 1636 $cm^{-1}$ to 1601 $cm^{-1}$ in **3**·3$H_2O$. Broad medium bands at 3396 and 3422 $cm^{-1}$ are observed corresponding to $\nu$(OH) vibrations from lattice water molecules in complexes **2**·3$H_2O$ and **3**·3$H_2O$, respectively. In addition, complex **1** shows a very strong sharp band at 2025 $cm^{-1}$ for the $\nu_{as}(N_3^-)$ stretching[26] and the $\nu_s(N_3^-)$ appears at 1322 $cm^{-1}$. The position of this band is consistent with terminal azide coordinations, as observed in other cobalt(III) complexes.[27] Complex **2** also shows a sharp band at 1597 $cm^{-1}$ due to the coordinated $\nu$(C=O) functionality of the $dfp^-$ ligand.

### Electronic Spectroscopy

In MeCN solution, the brown compound **1** shows a band at 639 nm ($\varepsilon$ = 470 $L\,mol^{-1}\,cm^{-1}$) and is characteristic of the octahedral cobalt(III) environment ($^1A_{1g} \rightarrow {}^1T_{1g}$) in the d–d spectra. The charge transfer transitions ($L \rightarrow Co^{III}$ and intraligand) occur at 349 nm ($\varepsilon$ = 4600 $L\,mol^{-1}\,cm^{-1}$) and 271 nm (7600 $L\,mol^{-1}\,cm^{-1}$) with an overlapping contribution of $^1A_{1g} \rightarrow {}^1T_{2g}$ in the former. Complex **2** shows d–d transition at 562 nm ($\varepsilon$ = 310 $L\,mol^{-1}\,cm^{-1}$) and charge transfer transitions at 375 and 271 nm with molar extinction coefficients of 2400 and 12500 $L\,mol^{-1}\,cm^{-1}$. Similarly, complex **3** shows d–d transition at 591 nm ($\varepsilon$ = 361 $L\,mol^{-1}\,cm^{-1}$) and charge transfer transitions at 401 (2100 $L\,mol^{-1}\,cm^{-1}$) and 274 nm (8700 $L\,mol^{-1}\,cm^{-1}$). In a reported octahedral $Co^{II}$ compound, observation of the three bands around 450, 550, and 850 nm are assigned to spin-allowed excitations from the $^4T_{1g}$(F) ground state.[28] So for compounds **2** and **3** the bands at 562 and 591 nm may be assigned to the spin-allowed transitions from $^4T_{1g}$(F) to $^4A_{2g}$.

### The Role of Template Anions in the Stabilization of the Ligand Imidazolidine Ring

Earlier we showed that expulsion of 1 mol of 2-hydroxybenzaldehyde molecules takes place when cobalt ions react with the ligand $H_3L$ in aqueous MeOH solution in air, which is different from the selective imidazolidine ring-opening reaction for a different ligand system with no loss of aldehyde molecule.[29] In the presence of solvent-generated $MeO^-$ template and terminal $N_3^-$ coordination, a similar situation did not arise leading to imidazolidine ring hydrolysis. Thus the presence of both $MeO^-$ and $N_3^-$ stabilizes the imidazolidine ring and cobalt ions in 3+ oxidation states. Also terminal double $N_3^-$ coordination did not provide any tetranucleation through *cis*-1,3-$N_3^-$ bridges. In exactly the same fashion 2,6-diformyl- and 2,6-bis(benzylimino)-4-methylphenolate templates (Tmp) stabilize the $L^{3-}$ against imidazolidine ring hydrolysis and 2+ oxidation states of cobalt ions in a new family of $Co_2$ complexes. The nature of the final reaction product is greatly influenced by the ligands used in different steps, the solvent system, and the sequence of addition of reactants.

### X-ray Crystallographic Procedures for 1 and 2·3$H_2O$

The intensity data of complexes **1** and **2** were collected on a Nonius CAD4 X-ray diffractometer using single-crystal graphite-monochromated Mo-$K_\alpha$ radiation ($\lambda$ = 0.71073 Å) by the $\omega$-scan method. Data were collected at 293 K. Information concerning X-ray data collection and structure refinement of the compound is summarized in Table 1. For complex **1**, a total of 4926 reflections were recorded with Miller indices $h_{min}$ = –11, $h_{max}$ = 0, $k_{min}$ = 0, $k_{max}$ = 24, $l_{min}$ = –16, and $l_{max}$ = 16. For complex **2**, a total of 6861 reflections were recorded with Miller indices $h_{min}$ = 0, $h_{max}$ = 23, $k_{min}$ = 0, $k_{max}$ = 23, $l_{min}$ = 0, and $l_{max}$ = 21. In the final cycles of full-matrix least-squares on $F^2$ all non-hydrogen atoms were assigned anisotropic thermal parameters. The positions of the H atoms bonded to C atoms were added (C–H distance 0.97 Å) in the riding model. The structure was solved using the SHELX-97[30] program system.

 © 2007 Wiley-VCH Verlag GmbH & Co. KGaA, Weinheim 

Table 1. Crystallographic data for **1** and **2**·3$H_2O$.

| | **1** | **2**·3$H_2O$ |
|---|---|---|
| Empirical formula | $C_{28}H_{30}Co_2N_{10}O_4$ | $C_{36}H_{39}Co_2N_4O_9$ |
| Formula mass | 688.477 | 896.63 |
| Crystal system | monoclinic | tetragonal |
| Space group | $P2_1/c$ | $P42_1c$ |
| $a$ [Å] | 9.749 (2) | 19.8524(10) |
| $b$ [Å] | 21.000(10) | 19.8524(10) |
| $c$ [Å] | 14.155(3) | 18.499(2) |
| $\beta$ [°] | 96.96(2) | |
| $D_{calcd}$ [g cm$^{-3}$] | 1.590 | 1.429 |
| $Z$ | 2 | 8 |
| $F$(000) | 1416 | 3231 |
| Crystal size [mm] | 0.26 × 0.18 × 0.16 | 0.34 × 0.28 × 0.24 |
| $\mu$ [mm$^{-1}$] | 1.208 | 0.968 |
| $\theta$ range [°] | 1.74–24.99 | 1.45–24.98 |
| $R_1$[a], $wR_2$ [$I > 2\sigma(I)$] | 0.1030, 0.2289 | 0.0588, 0.1410 |
| Gof on $F^2$ | 0.933 | 1.048 |
| Final difference map | | |
| Max., min. [e Å$^{-3}$] | 0.849, –1.528 | 0.633, –0.375 |

[a] $R_1 = \Sigma(||F_o| - |F_c||)/\Sigma|F_o|$. $wR_2 = [\Sigma w(|F_o| - |F_c|)^2/\Sigma w(F_o)^2]^{1/2}$. $w = 0.75/[\sigma^2(F_o) + 0.0010F_o^2]$.

## Description of Structures

Single crystals suitable for X-ray structure determinations were obtained by slow evaporation of a MeOH/$CH_3CN$ (1:1) solution of **1** and a MeOH solution of **2**·3$H_2O$ after a week. The atom labeling scheme and molecular views (ORTEP) of the complexes are shown in Figures 1, 2, 3, and 4. Selected interatomic distances and angles are collected in Tables 2 and 3.

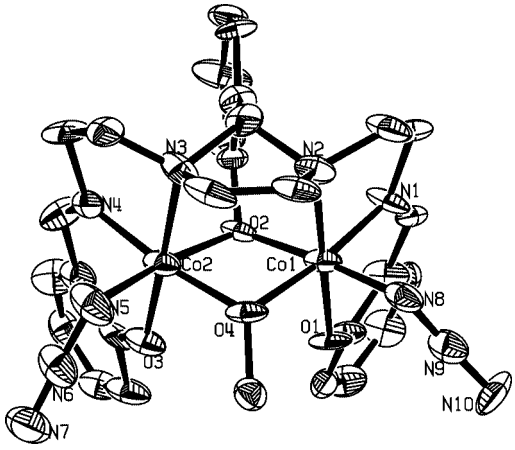


Figure 1. ORTEP representation of [$Co^{III}_2$(μ-OMe)L($N_3$)$_2$] (**1**) at the 40% probability level. Hydrogen atoms are omitted for clarity. Only independent non-carbon atoms are labeled.

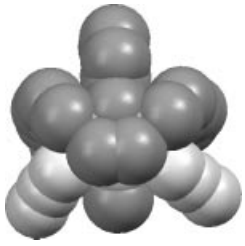

Figure 2. The ψ-like shape of the ligand covers the Co(μ-OMe)Co unit of **1** in a space-filling model when viewed along one intermediate axis (deep grey: ligand carbon; light grey: nitrogen).

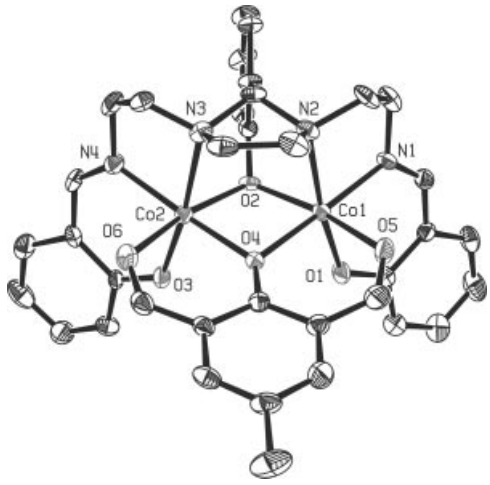


Figure 3. ORTEP representation of [$Co_2$(μ-dfp)L] (**2**) at the 30% probability level. Hydrogen atoms are omitted for clarity. Only independent non-carbon atoms are labeled.

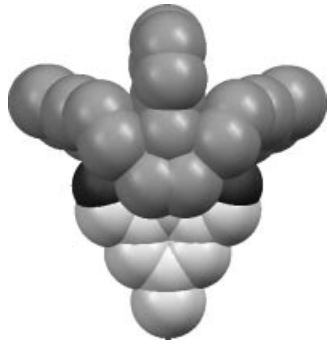

Figure 4. The template ligand in an "ice-cream cone" shape holds the Co(μ-OPh)Co unit in a space-filling model when viewed along one intermediate axis (light grey: template carbon; dark grey: ligand carbon; black: oxygen).

### *[$Co^{III}_2$(μ-OMe)L($N_3$)$_2$] (1)*

Complex **1** (Figure 1) is a neutral aggregate of two $Co^{III}$ ions linked by the template action of solvent-derived $MeO^-$ and capping coordination of the heptadentate ligand $L^{3-}$.

The unit cell of **1** consists of [$Co^{III}_2$(L)(μ-OMe)($N_3$)$_2$] neutral molecules, without any solvent of crystallization. Each tetradentate $N_2O_2$ pocket binds $Co^{III}$ ions in *cis* fashion; *facial* coordination involves bridging phenolate O, imidazolidine, and imine N atoms. The bridging function is accomplished by the central imidazolidine group (NCN group) and phenolate moiety (one μ-O) of $L^{3-}$, while the imine N-atom and the phenoxide O-donor at each side of the ligand saturate two additional coordination sites of each $Co^{III}$ center. The $MeO^-$ group, in preference to the $N_3^-$ group, contributes to the bridging within the complex and functions as a template in the absence of any externally added chelating exogenous template ligand. Hexacoordina-

 © 2007 Wiley-VCH Verlag GmbH & Co. KGaA, Weinheim 

Table 2. Selected interatomic distances [Å] and angles [°] for complex **1**.

| | | | |
|---|---|---|---|
| Co1–O1 | 1.867(8) | N5–Co2–O2 | 172.3(6) |
| Co1–N1 | 1.871(11) | O3–Co2–N3 | 178.2(6) |
| Co1–N8 | 1.883(15) | O4–Co2–N3 | 89.5(5) |
| Co1–O4 | 1.894(9) | N4–Co2–N3 | 84.8(6) |
| Co1–O2 | 1.899(10) | N5–Co2–N3 | 88.3(5) |
| Co1–N2 | 2.031(11) | O2–Co2–N3 | 91.8(4) |
| Co2–O3 | 1.851(9) | O1–Co1–N1 | 95.5(4) |
| Co2–O4 | 1.875(11) | O1–Co1–N8 | 92.3(5) |
| Co2–N4 | 1.879(15) | N1–Co1–N8 | 90.9(5) |
| Co2–N5 | 1.930(13) | O1–Co1–O4 | 90.7(4) |
| Co2–O2 | 1.955(9) | N1–Co1–O4 | 172.5(5) |
| Co2–N3 | 2.032(11) | N8–Co1–O4 | 93.1(5) |
| Co2···Co1 | 2.869(3) | O1–Co1–O2 | 87.6(4) |
| | | N1–Co1–O2 | 94.6(5) |
| O3–Co2–O4 | 92.2(4) | N8–Co1–O2 | 174.4(5) |
| O3–Co2–N4 | 93.4(5) | O4–Co1–O2 | 81.4(4) |
| O4–Co2–N4 | 172.3(5) | O1–Co1–N2 | 179.0(5) |
| O3–Co2–N5 | 92.3(5) | N1–Co1–N2 | 85.1(5) |
| O4–Co2–N5 | 91.9(6) | N8–Co1–N2 | 86.9(5) |
| N4–Co2–N5 | 93.0(6) | O4–Co1–N2 | 88.8(4) |
| O3–Co2–O2 | 87.9(4) | O2–Co1–N2 | 93.2(4) |
| O4–Co2–O2 | 80.4(4) | Co1–O2–Co2 | 96.2(4) |
| N4–Co2–O2 | 94.6(5) | Co2–O4–Co1 | |

Table 3. Selected interatomic distances [Å] and angles [°] for complex **2**.

| | | | |
|---|---|---|---|
| Co1–O1 | 1.960(9) | O4–Co2–O6 | 84.7(4) |
| Co1–N1 | 2.019(10) | O3–Co2–N3 | 173.0(4) |
| Co1–O2 | 2.050(9) | N4–Co2–N3 | 81.6(5) |
| Co1–O4 | 2.085(8) | O2–Co2–N3 | 87.1(3) |
| Co1–O5 | 2.103(9) | O4–Co2–N3 | 90.0(4) |
| Co1–N2 | 2.254(11) | O6–Co2–N3 | 90.8(4) |
| Co2–O3 | 1.998(9) | O1–Co1–N1 | 90.0(4) |
| Co2–N4 | 2.026(12) | O1–Co1–O2 | 94.5(3) |
| Co2–O2 | 2.051(7) | N1–Co1–O2 | 102.7(4) |
| Co2–O4 | 2.057(8) | O1–Co1–O4 | 97.4(3) |
| Co2–O6 | 2.144(9) | N1–Co1–O4 | 170.9(4) |
| Co2–N3 | 2.261(10) | O2–Co1–O4 | 82.0(3) |
| | | O1–Co1–O5 | 89.8(4) |
| O3–Co2–N4 | 91.4(4) | N1–Co1–O5 | 89.6(4) |
| O3–Co2–O2 | 93.7(3) | O2–Co1–O5 | 167.0(3) |
| N4–Co2–O2 | 102.1(4) | O4–Co1–O5 | 85.2(3) |
| O3–Co2–O4 | 96.9(4) | O1–Co1–N2 | 172.2(4) |
| N4–Co2–O4 | 170.1(4) | N1–Co1–N2 | 82.2(4) |
| O2–Co2–O4 | 82.7(3) | O2–Co1–N2 | 87.0(3) |
| O3–Co2–O6 | 89.9(4) | O4–Co1–N2 | 90.4(4) |
| N4–Co2–O6 | 90.1(4) | O5–Co1–N2 | 90.5(4) |
| O2–Co2–O6 | 167.2(4) | Co2–O4–Co1 | 95.8(4) |
| | | Co1–O2–Co2 | 97.0(3) |

tion around each Co ion is achieved through terminal binding of two $N_3^-$ ions. Each Co atom is thus coordinated in a distorted octahedral $N_3O_3$ environment in which the two octahedra sharing the edge are defined by the bridging phenolate and methoxide O atoms (Scheme 4 with N5 and N8). The planes intersecting at this edge form an angle of 162.95°, as a result of the folding imposed by the imidazolidine ring [N2···N3 distance of 2.342(4) Å]. The geometric restrictions resulting from $L^{3-}$ also cause the Co–O–Co angles to be different [96.2(4)° and 99.1(4)°] for endogenous phenolate and exogenous methoxide oxygen atoms, respectively. The sums of the angles around the oxygen atoms of the central phenolate and methoxide bridges are 330.37° and 342.03° and demonstrate that the pyramidal distortion is more pronounced in the case of phenolate O atom because of a folding of the ligand $L^{3-}$ around the imidazolidine backbone. The intramolecular Co···Co distance is 2.869(3) Å. The O–Co–O angles [81.4(4)° and 80.4(4)°] within the metallacyclic $Co_2(\mu\text{-}O)_2$ diamond core indicate distortions at the metal ion octahedra. The degree of distortion from an ideal octahedral (90°) geometry is reflected in the *cisoid* [95.4(4)–80.4(4)°] and the *transoid* [179.0(5)–172.3(5)°] angles. The bridging Co–O(phenolate) distances [1.955(9) Å] are longer than the terminal distances (av. 1.859 Å).

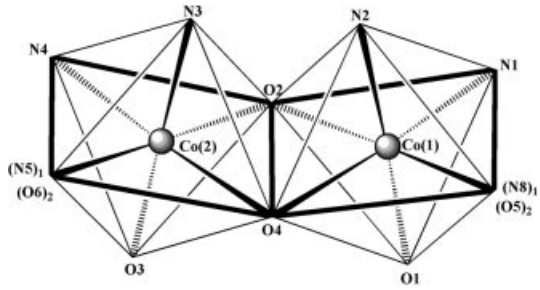


Scheme 4.

The Co–N(imidazolidine) [2.031(11) and 2.032(11) Å] and Co–N(imine) [1.871(11) and 1.879(15) Å] distances are clearly different. The terminal Co–N(azide) distances [1.883(15) and 1.930(13) Å] are intermediate between the above two distances.[31] The azide terminals are almost linear, with N–N–N angles 172.6(19)–172.8(17)°. The nonlinear monodentate coordination of $N_3^-$ is reflected in the Co–N–N angles of 121.0(11) and 118.0(10)°. Perfect covering of the Co(μ-OMe)Co unit by a ψ-like appearance of the ligand in a space-filling model is shown in Figure 2.

In crystal packing no H-bonding network is present because of the absence of solvate molecules within the crystal lattice. The crystal-packing diagram is shown in Figure S1 (see Supporting Information).

### *[$Co^{II}_2$(μ-dfp)L]·3$H_2O$ (2·3$H_2O$)*

The unit cell of **2**·3$H_2O$ consists of a dinuclear complex [$Co_2$(μ-dfp)L] (**2**) (Figure 3) along with three water molecules. Complex **2** is a neutral aggregate of $Co^{II}$ ions bridged and chelated by the ligand $L^{3-}$ in the same manner as in complex **1**. The bridging and hexacoordination of both metals is completed by a symmetric 2,6-diformylphenolate ($dfp^-$) ligand that terminally binds both metals through each of its carbonyl groups, while linking them through the central phenolate μ-O. This type of exogenous bridging coordination mode of the 2,6-diformyl-4-methylphenolate anion is quite unusual. The bridging bisdidentate ligand $dfp^-$ naturally binds the edges offered by the $[Co_2L]^+$ moiety (Scheme 4), therefore the exchange of two $N_3^-$ and $MeO^-$ ions for $dfp^-$ in going from **1** to **2** does not introduce significant changes to the overall metric parameters of the complex. Each Co atom is thus coordinated in a distorted octahedral $N_2O_4$ environment in which the two octahedra

 © 2007 Wiley-VCH Verlag GmbH & Co. KGaA, Weinheim 

sharing the edge are defined by the bridging phenolate oxygen atoms of different origin (Scheme 4 with O5 and O6). The planes intersecting at this edge form an angle of 160.94° as a result of the folding imposed by the imidazolidine ring (N2···N3 distance of 2.303 Å). The geometric restrictions resulting from $L^{3-}$ also cause the Co–O–Co angles to be different [97.0(3)° and 95.8(4)°] for endogenous and exogenous phenolate O atoms, respectively. The sums of the angles around the oxygen atoms of the central endogenous and exogenous phenolates are 333.28° and 359.16°, indicating the pyramidal and planar nature of phenolate oxygen atoms of different origin. The Co···Co separation at 3.073 Å is longer than 2.869(3) Å in **1** and is due to the different oxidation levels of cobalt ions in octahedral geometries. The O–Co–O angles [82.0(3) and 82.7(3)] within the metallacyclic $Co_2(\mu\text{-}O)_2$ diamond core indicate distortions at the metal ion octahedra.

The degrees of distortion from an ideal octahedral (90°) geometry are reflected in the *cisoid* [102.7(4)–82.0(3)°] and the *transoid* [173.0(4)–167.0(3)°] angles. Compared to $Cu_2$ binding[9,19] in *meridional* mode with apical $AcO^-$ or $N_3^-$ bridging, the $dfp^-$ template in the present case forces a *facial* binding [chelate bite angles are 102.7(4), 87.0(3), and 82.2(4)° around Co1 and 102.1(4), 87.1(3), and 81.6(5)° around Co2] of the O(central phenolate)N(imidazolidine)-N(imine) part of $L^{3-}$.

Earlier we showed that in $Cu_2$ complexes each tetradentate $N_2O_2$ pocket endorses either square-pyramidal or distorted trigonal-bipyramidal geometry. Now we report its potential to accommodate $Co^{II}$ ions in octahedral geometries that have *facial* coordination involving the bridging phenolate O, and imidazolidine and imine nitrogen atoms. The bridging Co–O(phenolate) distances [av. 2.050 Å] are longer than terminal distances (av. 1.979 Å). The Co–N-(imidazolidine) [2.254(11) to 2.261(10) Å] and Co–N(imine) [2.019(10) to 2.026(12) Å] distances are clearly different. The terminal Co–O(carbonyl) distances [2.103(9) and 2.144(9)] are intermediate between the above two distances and the angle between the chelate rings of $dfp^-$ is 160.94°. The template ligand in an "ice-cream cone" shape holds the Co(μ-OPh)Co unit in a space-filling model of the complex (Figure 4). Intramolecular hydrogen bonding was found between lattice water molecules and terminal phenolate oxygen atoms of ligand $L^{3-}$ (Figure S2). A crystal-packing diagram along the *c* axis is shown in Figure S3.

### Magnetochemistry of $[Co^{II}_2(\mu\text{-dfp})L]\cdot 3H_2O$ ($2\cdot 3H_2O$)

The magnetic property of complex $2\cdot 3H_2O$ was investigated by means of bulk magnetization methods. Measurements were collected under a constant magnetic field of 0.5 T in the 4.5–300 K temperature range. The effective magnetic moment at 300 K of **2** is measured to be $6.24\mu_B$ against $5.38\mu_B$ at 4.5 K per molecule of the complex. The temperature dependence of the magnetic moment was analyzed by the expression $\chi_M = f(T)$[32] derived from the Van Vleck equation, where

$$\chi_M = \frac{2Ng^2\beta^2}{kT}\left[\frac{14 + 5\exp(-6J/kT) + \exp(-10J/kT)}{7 + 5\exp(-6J/kT) + 3\exp(-10J/kT) + \exp(-12J/kT)}\right]$$

The results for the complex are represented in Figure 5 in the form of $\chi_M$ and $\mu_{eff}$ versus *T* plots ($\chi_M$ is the molar paramagnetic susceptibility and $\mu_{eff}$ is the effective magnetic moment). The parameters emerging from this fit are $J = -0.38\ cm^{-1}$ and $g = 2.27$, and *Na* was set to $0\ cm^3\ mol^{-1}$. The experimental behavior clearly shows that the intramolecular coupling is antiferromagnetic, leading to a ground state $S = 3/2{:}3/2$ dimer model applicable because the distortion from octahedral symmetry is so large.[2a] So the small antiferromagnetic intramolecular coupling might be ascribed to the $Co^{II}$–O–$Co^{II}$ angles formed by the phenolate bridges (between 95.79° and 97°), which are within the range predicted to lead to antiferromagnetic interactions in $Co^{II}_2$ systems.[33]

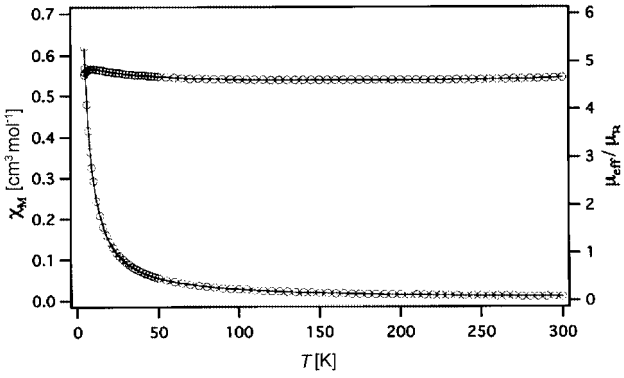


Figure 5. Plot of the temperature dependence of $\chi_M$ and $\mu_{eff}$ for complex $2\cdot 3H_2O$.

## Conclusions

We have shown that both solvent-derived and externally added templates control the synthesis of a new family of $Co^{III}Co^{III}$ and $Co^{II}Co^{II}$ complexes using a binucleating imidazolidinyl ligand $H_3L$. As part of the interesting chemistry of the ligand $L^{3-}$ with $Co^{II}$ and $Co^{III}$, we have shown that in situ generation of methoxide in the presence of $N_3^-$ and external addition of diformylphenolate and bis(benzylimino)phenolate to the system inhibit the imidazolidine ring hydrolysis of the $L^{3-}$ and lead to the high-yield formation of the assemblies $[Co^{III}_2(\mu\text{-OMe})L(N_3)_2]$ (**1**), $[Co^{II}_2(\mu\text{-dfp})L]\cdot 3H_2O$ ($2\cdot 3H_2O$), and $[Co^{II}_2(\mu\text{-bip})L]\cdot 3H_2O$ ($3\cdot 3H_2O$). The crystal structure of **1** shows that aerial oxidation in the presence of anions yields the $Co_2$ complex in 3+ oxidation state, whereas this oxidation is prevented when bisdidentate bridging template ligands are used. Interconversion of the templates within this family of the complexes is not permissible, which in turn identifies the templates as an integral part of these assemblies. Magnetic measurements indicate that complex **2** exhibits weak antiferromagnetic coupling between the $Co^{II}$ centers bridged by two phenolate groups of different origin. We are currently working to exploit the

 © 2007 Wiley-VCH Verlag GmbH & Co. KGaA, Weinheim 

asymmetry induced by external bridges in this reaction system in order to induce the formation of heterometallic and high nuclearity complexes.

## Experimental Section

**Materials and Physical Measurements:** The chemicals used were obtained from the following sources: Triethylenetetramine, sodium azide, and cobalt acetate tetrahydrate from S.D. Fine Chem. (India) and 2-hydroxybenzaldehyde from SRL (India). 2,6-Diformyl-4-methylphenol (Hdfp) and 2,6-bis(benzyliminomethyl)-4-methylphenolate (Hbip) were prepared by the literature procedures.[21,23] All other chemicals and solvents were reagent-grade materials and were used as received without further purification. The elemental analyses (C,H,N) were performed with a Perkin–Elmer model 240C elemental analyzer. FTIR spectra were recorded with a Perkin–Elmer RX1 spectrometer. The solution electrical conductivity and electronic spectra were obtained using a Unitech type U131C digital conductivity meter with a solute concentration of about $10^{-3}$ M and a Shimadzu UV 3100 UV/Vis/NIR spectrophotometer respectively. The room-temperature magnetic susceptibilities in the solid state were measured using a home-built Gouy balance fitted with a Polytronic d.c. power supply. The experimental magnetic susceptibilities were corrected for the diamagnetic response using Pascal's constants. Magnetic measurements were carried out on polycrystalline samples (about 30 mg) using a Quantum Design MPMS-5S SQUID magnetometer operating at a constant magnetic field of 5000 G between 4.5 and 300 K. The experimental magnetic moment was corrected for the diamagnetic contribution from the sample holder and the diamagnetic response from the sample, which was evaluated from Pascal's constants.

**General:** All experimental procedures were carried out under air at room temperature. The ligand $H_3L$ {2-(2′-hydroxyphenyl)-1,3-bis[4-(2-hydroxyphenyl)-3-azabut-3-enyl]-1,3-imidazolidine} was prepared according to a literature procedure.[8]

**Synthesis of Complexes:** One single high-yield method was followed for the synthesis and isolation of complexes **1**–**3**. For complex **1**, a nontemplate procedure was followed in which the methoxide template was generated in solution, while for **2** and **3** prior addition of template ligands was necessary. In the absence of these templates and in the presence of azides, only **1** is isolated exclusively. Details are given below for the representative cases.

**$[Co^{III}_2(\mu\text{-}OMe)L(N_3)_2]$ (1):** $NaN_3$ (0.13 g, 2.00 mmol) in MeOH was added dropwise to the methanolic solution (20 mL) of $Co(OAc)_2{\cdot}4H_2O$ (0.5 g, 2.00 mmol) and stirred for 15 min. Methanolic solution (15 mL) of ligand $H_3L$ (0.458 g, 1.00 mmol) was then added dropwise to the above solution, and stirring was continued in air for 1 h leading to the oxidation of both the metal ions to $Co^{III}$. After evaporation of the reaction mixture a brown solid was obtained (about 75% yield). The reaction in the presence of up to 6 mmol of $NaN_3$ yields complex **1** exclusively, with no sign of azido bridging. The solid was isolated, washed with cold methanol, and dried under vacuum over $P_4O_{10}$. $C_{28}H_{30}Co_2N_{10}O_4$ (688.48): calcd. C 48.84, H 4.39, N 20.34; found C 48.76, H 4.28, N 20.08. Selected FTIR bands (KBr): $\tilde{\nu}$ = 2025 (vs), 1629 (vs), 1531 (m), 1451 (s), 1322 (m), 1264 (m), 1146 (m), 1093 (m), 949 (m), 755 (m) $cm^{-1}$. Molar conductance, $\Lambda_M$ ($CH_3CN$ solution): 6 $ohm^{-1}cm^2mol^{-1}$. UV/Vis spectra ($CH_3CN$ solution): $\lambda_{max}$ ($\varepsilon$, $L\,mol^{-1}cm^{-1}$) = 639 (470), 349 (4600), 275 (7600) nm.

***Caution!*** Metal azide complexes are potential explosives. Only a small amount of material should be prepared and handled with caution.

**$[Co^{II}_2(\mu\text{-}dfp)L]{\cdot}3H_2O$ (2·3H$_2$O):** 2,6-Diformyl-4-methylphenol (Hdfp) (0.164 g, 1.00 mmol) in MeOH was added dropwise to a methanolic solution (50 mL) of $Co(OAc)_2{\cdot}4H_2O$ (0.5 g, 2.00 mmol) for 15 min whilst stirring. Ligand $H_3L$ (0.458 g, 1.00 mmol) in hot methanol (20 mL) was added to the resulting solution and the mixture was stirred for another 1 h. The resulting solution was filtered and left undisturbed to slowly evaporate. After 4 d, a red crystalline product was obtained (about 80% yield). The solid was isolated, washed with cold methanol, and dried under vacuum over $P_4O_{10}$. $C_{36}H_{39}Co_2N_4O_9$ (789.59): calcd. C 54.76, H 4.97, N 7.09; found C 54.66, H 4.88, N 6.92. Selected FTIR bands (KBr): $\tilde{\nu}$ = 3396 (b), 1625 (s), 1597 (s), 1528 (s), 1443 (s), 1397 (m), 1341 (m), 1230 (m), 1185 (m), 1146 (m), 1034 (m), 988 (m), 756 (m) $cm^{-1}$. Molar conductance, $\Lambda_M$ ($CH_3CN$ solution): 6 $ohm^{-1}cm^2mol^{-1}$. UV/Vis spectra ($CH_3CN$ solution): $\lambda_{max}$ ($\varepsilon$, $L\,mol^{-1}cm^{-1}$) = 562 (310), 375 (2400), 271 (12500) nm.

**$[Co^{II}_2(L)(\mu\text{-}bip)]{\cdot}3H_2O$ (3·3H$_2$O):** 2,6-Bis(benzyliminomethyl)-4-methylphenolate (Hbip) (0.342 g, 1.00 mmol) was added dropwise to a methanolic solution (50 mL) of $Co(OAc)_2{\cdot}4H_2O$ (0.5 g, 2.00 mmol) for 15 min whilst stirring. Ligand $H_3L$ (0.458 g, 1.00 mmol) in hot methanol (20 mL) was added to the resulting solution and the mixture was stirred for another 1 h. The resulting solution was filtered and left undisturbed to slowly evaporate. After 7 d, a red crystalline product was obtained (about 75% yield). The solid was isolated, washed with cold methanol, and dried under vacuum over $P_4O_{10}$. $C_{50}H_{54}Co_2N_6O_7$ (968.88): calcd. C 61.98, H 5.61, N 8.67; found C 61.88, H 5.54, N 8.48. Selected FTIR bands (KBr): $\tilde{\nu}$ = 3422 (b), 1624 (vs), 1601 (s), 1560 (s), 1451 (vs), 1400 (m), 1320 (m), 1233 (m), 1028 (m), 754 (m) $cm^{-1}$. Molar conductance, $\Lambda_M$ ($CH_3CN$ solution): 8 $ohm^{-1}cm^2mol^{-1}$. UV/Vis spectra ($CH_3CN$ solution): $\lambda_{max}$ ($\varepsilon$, $L\,mol^{-1}cm^{-1}$) = 591 (361), 401 (2100), 274 (8700) nm.

CCDC-644647 (for **1**) and -644648 (for **2**) contain the supplementary crystallographic data for this paper. These data can be obtained free of charge from The Cambridge Crystallographic Data Centre via www.ccdc.cam.ac.uk/data_request/cif.

**Supporting Information** (see also the footnote on the first page of this article): Figures S1, S2, and S3.

## Acknowledgments

We are thankful to the Council of Scientific and Industrial Research, New Delhi, for financial support. M. M. acknowledges financial support from the "Open Research Center" Project for Private Universities: matching fund subsidy and Grants-in-Aid for Scientific Research No. 19550074 from the Ministry of Education, Culture, Sports, Science and Technology, Government of Japan.

[1] a) J.-L. Tian, L. Feng, W. Gu, G.-J. Xu, S.-P. Yan, D.-Z. Liao, Z.-H. Jiang, P. Cheng, *J. Inorg. Biochem.* **2007**, *101*, 196–202; b) G. Vučković, S. B. Tanasković, U. Rychlewska, D. D. Radanović, J. Mroziński, M. Korabik, *J. Mol. Struct.* **2007**, *827*, 80–87; c) L. Vaiana, C. Platas-Iglesias, D. Esteban-Gómez, F. Avecilla, J. M. Clemente-Juan, J. A. Real, A. Blas, T. Rodríguez-Blas, *Dalton Trans.* **2005**, 2031–2037; d) L.-Y. Wang, B. Zhao, C.-X. Zhang, D.-Z. Liao, Z.-H. Jiang, S.-P. Yan, *Inorg. Chem.* **2003**, *42*, 5804–5806; e) M. J. Hossain, M. Yamasaki, M. Mikuriya, A. Kuribayashi, H. Sakiyama, *Inorg. Chem.* **2002**, *41*, 4058–4062.

[2] a) S. M. Ostrovsky, K. Falk, J. Pelikan, D. A. Brown, Z. Tomkowicz, W. Haase, *Inorg. Chem.* **2006**, *45*, 688–694; b) R. Hernandez-Molina, A. Mederos, P. Gili, S. Dominguez, F. Lloret, J. Cano, M. Julve, C. Ruiz-Perez, X. Solans, *J. Chem. Soc.*

 © 2007 Wiley-VCH Verlag GmbH & Co. KGaA, Weinheim 

*Dalton Trans.* **1997**, 4327–4334; c) H. Sakiyama, R. Ito, H. Kumagai, K. Inoue, M. Sakamoto, Y. Nishida, M. Yamasaki, *Eur. J. Inorg. Chem.* **2001**, 2027–2032.
[3] S. L. Roderick, B. W. Matthews, *Biochemistry* **1993**, *32*, 3907–3912.
[4] Y. Nishida, S. Nishino, L. L. Guo, M. Kunita, H. Matsushima, T. Tokii, *Inorg. Chem. Commun.* **1999**, *2*, 609–611.
[5] a) L. M. Rossi, A. Neves, A. J. Bortoluzzi, R. Hörner, B. Szpoganicz, H. Terenzi, A. S. Mangrich, E. Pereira-Maia, E. E. Castellano, W. Haase, *Inorg. Chim. Acta* **2005**, *358*, 1807–1822; b) D. A. Brown, W. Errington, W. K. Glass, W. Haase, T. J. Kemp, H. Nimir, S. M. Ostrovsky, R. Werner, *Inorg. Chem.* **2001**, *40*, 5962–5971.
[6] G. Givaja, M. Volpe, M. A. Edwards, A. J. Blake, C. Wilson, M. Schröder, J. B. Love, *Angew. Chem. Int. Ed.* **2007**, *46*, 584–586.
[7] P. K. Nanda, D. Mandal, D. Ray, *Polyhedron* **2006**, *25*, 702–710.
[8] E. Wong, S. Liu, T. Lugger, F. E. Hahn, C. Orvig, *Inorg. Chem.* **1995**, *34*, 93–101.
[9] M. Bera, W. T. Wong, G. Aromí, D. Ray, *Eur. J. Inorg. Chem.* **2005**, 2526–2535.
[10] A. R. Paital, C. S. Hong, H. C. Kim, D. Ray, *Eur. J. Inorg. Chem.* **2007**, 1644–1653.
[11] P. K. Nanda, G. Aromí, D. Ray, *Chem. Commun.* **2006**, 3181–3183.
[12] P. K. Nanda, G. Aromi, D. Ray, *Inorg. Chem.* **2006**, *45*, 3143–3145.
[13] M. Fondo, A. M. García-Deibe, M. Corbella, E. Ruiz, J. Tercero, J. Sanmartín, M. R. Bermejo, *Inorg. Chem.* **2005**, *44*, 5011–5020.
[14] M. Fondo, N. Ocampo, A. M. García-Deibe, M. Corbella, M. R. Bermejo, J. Sanmartín, *Dalton Trans.* **2005**, 3785–3794.
[15] M. Fondo, A. M. Garcia-Deibe, J. Sanmartin, M. R. Bermejo, L. Lezama, T. Rojo, *Eur. J. Inorg. Chem.* **2003**, 3703–3706.
[16] M. Fondo, N. Ocampo, A. M. Garcia-Deibe, R. Vicente, M. Corbella, M. R. Bermejo, J. Sanmartin, *Inorg. Chem.* **2006**, *45*, 255–262.
[17] M. Bera, U. Mukhopadhyay, D. Ray, *Inorg. Chim. Acta* **2005**, *358*, 437–443.
[18] M. Bera, K. Biradha, D. Ray, *Inorg. Chim. Acta* **2004**, *357*, 3556–3562.
[19] P. K. Nanda, M. Bera, G. Aromí, D. Ray, *Polyhedron* **2006**, *25*, 2791–2799.
[20] a) M. Fondo, N. Ocampo, A. M. Garcia-Deibe, M. Corbella, M. S. El Fallah, J. Cano, J. Sanmartin, M. R. Bermejo, *Dalton Trans.* **2006**, 4905–4913; b) M. Fondo, A. M. García-Deibe, N. Ocampo, M. R. Bermejo, J. Sanmartín, *Z. Anorg. Allg. Chem.* **2005**, *631*, 2041–2045.
[21] R. R. Gagne, C. L. Spiro, T. J. Smith, C. A. Hamann, W. R. Thies, A. K. Shiemke, *J. Am. Chem. Soc.* **1981**, *103*, 4073–4081.
[22] S. Cromie, F. Launay, V. McKee, *Chem. Commun.* **2001**, 1918–1919.
[23] J. J. Grzybowski, F. L. Urbach, *Inorg. Chem.* **1980**, *19*, 2604–2608.
[24] a) I. E. Dickson, R. Robson, *Inorg. Chem.* **1974**, *13*, 1301–1306; b) W. D. McFayden, R. Robson, *J. Coord. Chem.* **1976**, *5*, 49–53; c) B. F. Hoskins, R. Robson, G. A. Williams, *Inorg. Chim. Acta* **1976**, *16*, 121–133 and references cited therein.
[25] a) H. Okawa, *Bull. Chem. Soc. Jpn.* **1970**, *43*, 3019; b) H. Okawa, I. Ando, S. Kida, *Bull. Chem. Soc. Jpn.* **1974**, *47*, 3041–3044; c) T. Ichinose, Y. Nishida, H. Okawa, S. Kida, *Bull. Chem. Soc. Jpn.* **1974**, *47*, 3045–3048 and references cited therein.
[26] M. A. S. Goher, A. A. Youssef, F. A. Mautner, *Polyhedron* **2006**, *25*, 1531–1536.
[27] A. B. P. Lever, *Inorganic Electronic Spectroscopy*, 2nd ed., Elsevier, New York, **1984**, p. 477.
[28] R. P. John, A. Steekanth, R. Maliyekal, P. Kurup, S. M. Mobin, *Polyhedron* **2002**, *21*, 2515–2521.
[29] M. Boca, P. Baran, R. Boca, H. Fuess, G. Kickelbick, W. Linert, F. Renz, I. Svoboda, *Inorg. Chem.* **2000**, *39*, 3205–3212.
[30] G. M. Sheldrick, *SHELXS-97*, *Program for the Refinement of Crystal Structures*, University of Göttingen, Germany, **1997**.
[31] S. H. Rahaman, H. Chowdhury, H. L. Milton, A. M. Z. Slawin, J. D. Woollins, B. K. Ghosh, *Inorg. Chem. Commun.* **2005**, *8*, 1031–1035.
[32] M. Fondo, A. M. Garcia-Deibe, N. Ocampo, J. Sanmartin, M. R. Bermejo, A. L. Llamas-Saiz, *Dalton Trans.* **2006**, 4260.
[33] L. Rodríguez, E. Labisbal, A. Sousa-Pedrares, J. A. García-Vázquez, J. Romero, M. L. Durán, J. A. Real, A. Sousa, *Inorg. Chem.* **2006**, *45*, 7903–7914.

Received: May 25, 2007
Published Online: August 31, 2007

 © 2007 Wiley-VCH Verlag GmbH & Co. KGaA, Weinheim 

DOI: 10.1002/ejic.200700715

# Coordination Behaviour of Bis-Terdentate N-Donor Ligands: Double- and Single-Stranded Helicates, Mesocates, and Cyclic Oligomers

**Nawal K. Al-Rasbi,[a] Harry Adams,[a] Lindsay P. Harding,[b] and Michael D. Ward*[a]**

**Keywords:** Chelating ligands / Coordination chemistry / Helical structures / Self-assembly

Three new ligands have been prepared in which two terdentate chelating pyrazolyl-bipyridine units are connected by a central aromatic spacer via methylene "hinges": the spacers are *o*-phenylene ($L^{Ph}$), 2,6-pyridine-diyl ($L^{Py}$) and 2,3-naphthalenediyl ($L^{naph}$). The ligands act as potentially hexadentate bridging ligands, with the central pyridyl N atom of $L^{Py}$ not involved in coordination. The following complexes were prepared and structurally characterised: $[M_2(L^{Ph})_2][ClO_4]_4$ (M = Ni, Cu), which are dinuclear double helicates; $[Ag_2(L^{Ph})(MeCN)_2][BF_4]_2$, a dinuclear complex with an Ag···Ag bond in which the ligand adopts a helical twist around the pair of metal ions; $[Ni_2(L^{Py})_2][BF_4]_4$, an achiral "mesocate" with a box-like structure and a face-to-face arrangement of ligands; $[Ag_3(L^{naph})_2](BF_4)_3$, which contains a linear trinuclear array of $Ag^I$ ions with the two ligands arranged in a shallow helical twist, each ligand spanning one terminal and the central metal ion; and $[Cd_6(L^{naph})_6](ClO_4)_{12}$, a cyclic hexanuclear helicate with a perchlorate anion in the central cavity. Both $[Cu_2(L^{Ph})_2][ClO_4]_4$ and $[Cd_6(L^{naph})_6](ClO_4)_{12}$, which have architecturally similar bridging ligands, show evidence by electrospray mass spectrometry for formation of a range of cyclic oligomers in solution up to 11-mers for the $Cd^{II}/L^{naph}$ system.

(© Wiley-VCH Verlag GmbH & Co. KGaA, 69451 Weinheim, Germany, 2007)

## Introduction

Complexes with double or triple helical structures ("helicates") have been of interest in the field of coordination chemistry for many years. These assemblies have elegantly demonstrated how the formation of architecturally complex systems is directed by the interplay between simple parameters such as the stereoelectronic preference of the metals ion and the disposition of the binding sites in the ligand.[1]

Despite that the fact that very many helical complexes are known, the field remains as popular as ever because of the development of new research areas which involve them. These are remarkably diverse as some very recent examples will illustrate. Hannon and co-workers have shown how relatively simple dinuclear helicates bind to DNA and stabilise a triple junction.[2] Rice and co-workers have prepared ligands in which the degree of twist between the two binding domains can be controlled by allosteric means, allowing the assembly of helicate complexes to be controlled by an external perturbation.[3] A double helical ligand array has been used as a scaffold for a dinuclear $Cu^I/Cu^{II}$ complex which shows unusual electronic delocalisation behaviour.[4] Piguet has used polynuclear helicate complexes to understand and illustrate the phenomenon of cooperativity in self-assembly processes,[5] and has used heterodinuclear d/f helicates for studies on photoinduced energy-transfer between d-block and f-block luminophores.[6] Nitschke has used structurally relatively simple dinuclear $Cu^I$ helicates with different combinations of ligands to probe the concept of "valence frustration" which plays an important role in controlling self-assembly processes.[7] Triple helicates with a pendant hydrogen-bonding group attached to each ligand have been found to bind anions in the resultant pocket, and such anion binding can control the orientation of the three ligands in the helical scaffold.[8] Williams and co-workers showed how dinuclear helicates can display unusual stepwise spin-crossover properties, associated with mechanical coupling between the two metal centres.[9] Certain anions can template formation of cyclic helicates in which the anion occupies the central cavity, and the size of the anion dictates the size of the metal/ligand circular helical array around it.[10]

We report here the preparation and coordination chemistry of a set of three new bis-tridentate ligands $L^{Ph}$, $L^{py}$, and $L^{naph}$ (Scheme 1), in which two terdentate arms, each based on a pyrazolyl–pyridyl–pyridyl sequence of donors, are connected to various different aromatic spacers (*o*-phenylene, pyridine-2,6-diyl, and 2,3-naphthalenediyl, respectively). Flexibility in the ligand backbone is provided by the methylene "hinges" which connect the terdentate arms to the central spacer. These belong to a general class of bridging

[a] Department of Chemistry, University of Sheffield, Sheffield S3 7HF, UK
Fax: +44-114-2229346
E-mail: m.d.ward@sheffield.ac.uk
[b] Department of Chemical and Biological Sciences, University of Huddersfield, Huddersfield HD1 3DH, UK

 © 2007 Wiley-VCH Verlag GmbH & Co. KGaA, Weinheim 

ligand that we have studied extensively in the last few years and which have proven to be particularly effective at providing polynuclear complexes with elaborate and often unexpected structures.[10b,11]

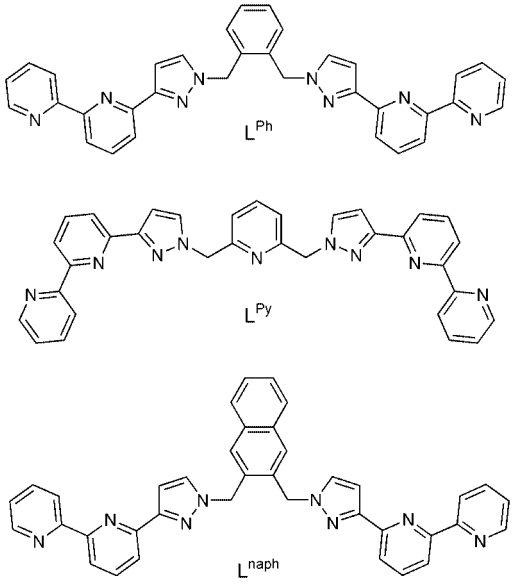


Scheme 1.

## Results and Discussion

### Ligand Syntheses

The new ligands (Scheme 1) were prepared by the reaction of two equivalents of 6-(pyrazol-3-yl)-2,2′-bipyridine[12] with the appropriate bis(bromomethyl)-substituted organic spacer, in the presence of hydroxide ion under phase-transfer conditions, according to the method we have used for related ligands in this series.[13] All of the spectroscopic and analytical data were consistent with the formulation of the ligands. Needles of $L^{Ph}$ suitable for X-ray analysis were obtained by slow evaporation of a dilute dichloromethane solution of the ligand. The crystal structure is presented in Figure 1. Individual bond lengths and angles within the ligand are unremarkable. The crystal packing shows an extensive combination of weak CH···N hydrogen bonds and π–π stacking interactions between adjacent molecules.

### Complexes with $L^{Ph}$

Reaction of $L^{Ph}$ with perchlorate salts of $Ni^{II}$ or $Cu^{II}$ in MeCN afforded crystalline products of empirical formula $M(L^{ph})(ClO_4)_2$ by elemental analysis, that is 1:1 $M^{2+}/L^{Ph}$ stoichiometry. X-ray quality crystals could be grown for M = Cu and Ni by diffusion of diethyl ether vapour into MeCN solutions of the complexes.

Both complexes $[M_2(L^{Ph})_2][ClO_4]_4$ (M = Ni, Cu) proved to be dinuclear double helicates with two ligands wrapped around two metal ions; each ligand donates one terdentate site to each metal ion, and each metal ion is six-coordinate from coordination by two terdentate fragments, one from each ligand. Their gross structures are very similar (Figure 2), with minor differences arising from the distorted coordination environment around $Cu^{II}$ due to the Jahn–Teller effect. Thus the $Ni^{II}$ complex has fairly regular coordination around the $Ni^{II}$ ions, with the Ni–N(pyridine) bond lengths in the range 2.00–2.10 Å and the Ni–N(pyrazole) distances being slightly longer at 2.12–2.18 Å. The angles between the two Ni(NNN) planes at Ni(1) and Ni(2) are 92.5° and 94.2°, respectively (Table 1). Areas of overlap between aromatic rings on adjacent ligands are clear, resulting in some degree of stabilisation of the structure by π-stack-

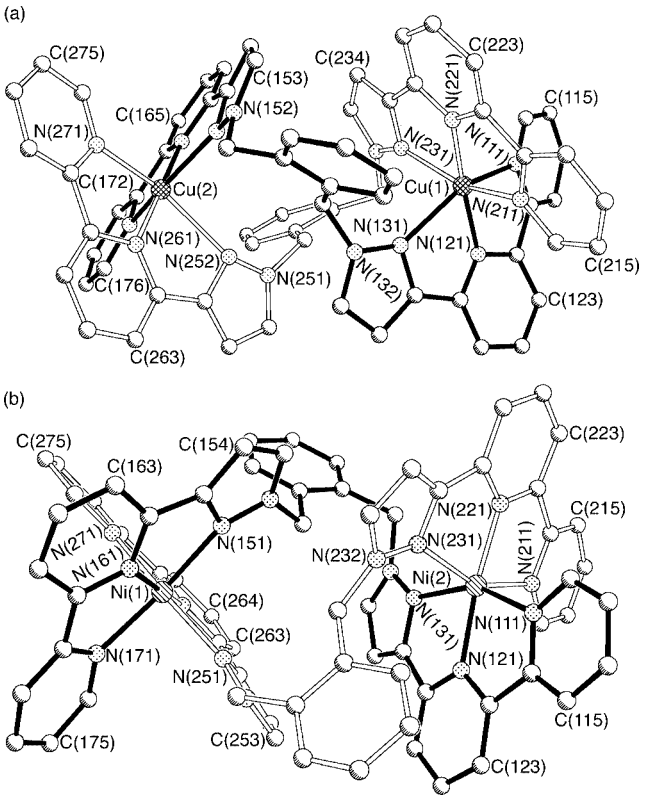


Figure 2. Structures of the double helical complex cations of (a) $[Cu_2(L^{Ph})_2][ClO_4]_4 \cdot 2MeCN \cdot 0.5H_2O$ and (b) $[Ni_2(L^{Ph})_2][ClO_4]_4 \cdot MeCN$, with the ligands shaded differently for clarity.

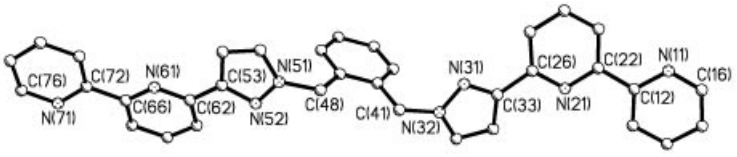


Figure 1. Structure of $L^{Ph}$.

 © 2007 Wiley-VCH Verlag GmbH & Co. KGaA, Weinheim 

Table 1. Selected bond lengths [Å] and angles [°] for $[Ni_2(L^{Ph})_2][ClO_4]_4 \cdot MeCN$.

| | | | |
|---|---|---|---|
| Ni(1)–N(161) | 2.001(4) | Ni(2)–N(221) | 2.005(4) |
| Ni(1)–N(261) | 2.008(4) | Ni(2)–N(121) | 2.019(4) |
| Ni(1)–N(171) | 2.102(4) | Ni(2)–N(211) | 2.106(4) |
| Ni(1)–N(271) | 2.110(4) | Ni(2)–N(111) | 2.110(4) |
| Ni(1)–N(251) | 2.118(4) | Ni(2)–N(131) | 2.153(4) |
| Ni(1)–N(151) | 2.164(4) | Ni(2)–N(231) | 2.180(4) |
| N(161)–Ni(1)–N(261) | 170.80(17) | N(221)–Ni(2)–N(121) | 173.31(16) |
| N(161)–Ni(1)–N(171) | 78.35(17) | N(221)–Ni(2)–N(211) | 78.24(17) |
| N(261)–Ni(1)–N(171) | 101.28(16) | N(121)–Ni(2)–N(211) | 99.81(17) |
| N(161)–Ni(1)–N(271) | 92.77(17) | N(221)–Ni(2)–N(111) | 96.41(15) |
| N(261)–Ni(1)–N(271) | 78.12(16) | N(121)–Ni(2)–N(111) | 77.59(16) |
| N(171)–Ni(1)–N(271) | 96.67(16) | N(211)–Ni(2)–N(111) | 100.81(16) |
| N(161)–Ni(1)–N(251) | 111.74(17) | N(221)–Ni(2)–N(131) | 109.15(16) |
| N(261)–Ni(1)–N(251) | 77.37(16) | N(121)–Ni(2)–N(131) | 76.93(16) |
| N(171)–Ni(1)–N(251) | 88.42(15) | N(211)–Ni(2)–N(131) | 85.73(15) |
| N(271)–Ni(1)–N(251) | 155.49(16) | N(111)–Ni(2)–N(131) | 154.42(16) |
| N(161)–Ni(1)–N(151) | 76.44(16) | N(221)–Ni(2)–N(231) | 76.18(15) |
| N(261)–Ni(1)–N(151) | 104.76(16) | N(121)–Ni(2)–N(231) | 106.46(16) |
| N(171)–Ni(1)–N(151) | 153.78(16) | N(211)–Ni(2)–N(231) | 153.30(16) |
| N(271)–Ni(1)–N(151) | 91.64(16) | N(111)–Ni(2)–N(231) | 89.57(15) |
| N(251)–Ni(1)–N(151) | 94.25(15) | N(131)–Ni(2)–N(231) | 95.47(14) |

Table 2. Selected bond lengths [Å] and angles [°] for $[Cu_2(L^{Ph})_2][ClO_4]_4 \cdot 2MeCN \cdot 0.5H_2O$.

| | | | |
|---|---|---|---|
| Cu(1)–N(221) | 1.973(4) | Cu(2)–N(161) | 1.980(5) |
| Cu(1)–N(121) | 2.007(5) | Cu(2)–N(261) | 1.995(5) |
| Cu(1)–N(211) | 2.115(6) | Cu(2)–N(171) | 2.114(6) |
| Cu(1)–N(231) | 2.170(5) | Cu(2)–N(271) | 2.184(6) |
| Cu(1)–N(111) | 2.233(5) | Cu(2)–N(151) | 2.274(5) |
| Cu(1)–N(131) | 2.355(7) | Cu(2)–N(252) | 2.438(7) |
| N(221)–Cu(1)–N(121) | 171.61(11) | N(161)–Cu(2)–N(261) | 176.12(11) |
| N(221)–Cu(1)–N(211) | 79.1(2) | N(161)–Cu(2)–N(171) | 78.8(2) |
| N(121)–Cu(1)–N(211) | 92.79(19) | N(261)–Cu(2)–N(171) | 97.29(19) |
| N(221)–Cu(1)–N(231) | 78.3(2) | N(161)–Cu(2)–N(271) | 102.77(15) |
| N(121)–Cu(1)–N(231) | 109.7(2) | N(261)–Cu(2)–N(271) | 78.32(15) |
| N(211)–Cu(1)–N(231) | 157.29(10) | N(171)–Cu(2)–N(271) | 108.87(13) |
| N(221)–Cu(1)–N(111) | 105.69(19) | N(161)–Cu(2)–N(151) | 77.1(2) |
| N(121)–Cu(1)–N(111) | 77.7(2) | N(261)–Cu(2)–N(151) | 106.8(2) |
| N(211)–Cu(1)–N(111) | 99.95(16) | N(171)–Cu(2)–N(151) | 154.84(11) |
| N(231)–Cu(1)–N(111) | 88.54(17) | N(271)–Cu(2)–N(151) | 83.52(14) |
| N(221)–Cu(1)–N(131) | 102.05(14) | N(161)–Cu(2)–N(252) | 104.70(11) |
| N(121)–Cu(1)–N(131) | 75.79(15) | N(261)–Cu(2)–N(252) | 75.08(11) |
| N(211)–Cu(1)–N(131) | 91.84(11) | N(171)–Cu(2)–N(252) | 88.11(11) |
| N(231)–Cu(1)–N(131) | 90.43(11) | N(271)–Cu(2)–N(252) | 150.04(14) |
| N(111)–Cu(1)–N(131) | 151.41(12) | N(151)–Cu(2)–N(252) | 91.14(10) |

ing. In the $Cu^{II}$ complex in contrast the coordination geometry about the $Cu^{II}$ ions is more distorted (Table 2). Cu(1) has a *trans*-related pair of Cu–N bonds from the same ligand (using a terminal pyridyl ring and the pyrazolyl ring) and that are significantly longer than the other four; for Cu(2) in contrast the distortion is expressed as an elongation of both Cu–N(pyrazolyl) bonds, which are *cis* to one another.

Electrospray mass spectra of both complexes revealed several peaks at the *m*/*z* values expected for the dinuclear complexes (see Experimental section). However in both cases there are very weak peaks identifiable whose *m*/*z* values are consistent with formation of higher oligomers. For redissolved crystals of $[Cu_2(L^{Ph})_2][ClO_4]_4$ for example, the ES mass spectrum has a weak peak at *m*/*z* 979.1, assigned as $\{Cu_4(L^{Ph})_4(ClO_4)_5\}^{3+}$; and redissolved crystals of $[Ni_2(L^{Ph})_2][ClO_4]_4$ show numerous weak peaks at high *m*/*z* values of which those at 972.4 and 1508.1 can be assigned as belonging to $\{Ni_4(L^{Ph})_4(ClO_4)_5\}^{3+}$ and $\{Ni_4(L^{Ph})_4(ClO_4)_6\}^{2+}$ respectively. Thus, both complexes which were isolated as dinuclear species in the solid state show evidence for traces of a tetrameric (presumably, cyclic helical) species existing in solution.[10]

Reaction of $L^{Ph}$ with $AgBF_4$ in MeCN, followed by diffusion of diisopropyl ether vapour into the solution, afforded crystals of $[Ag_2(L^{Ph})(MeCN)_2][BF_4]_2$ (Figure 3) which, in contrast to the two structures above, is a dinuclear *single* stranded helicate. The hexadentate ligand $L^{Ph}$ is arranged in a shallow spiral which is wound around a central axis of two $Ag^{I}$ ions; the two metals end up close enough together to be considered as having an argentophilic bond between them [Ag(1)···Ag(2), 3.07 Å]. Somewhat surprisingly, the two $Ag^{I}$ ions are in markedly different coordination environments. It might be expected [cf. the structures

 © 2007 Wiley-VCH Verlag GmbH & Co. KGaA, Weinheim 

with $Cu^{II}$ and $Ni^{II}$, above] that $L^{Ph}$ would donate a terdentate pyrazolyl-bipyridine arm to each $Ag^{I}$ ion. Instead the partitioning of the ligand into two binding sites occurs within one of the terdentate units, such that one terdentate arm of the ligand donates only a bipyridyl unit to Ag(1), with the adjacent pyrazolyl donor [N(51)] closer to Ag(2) (2.43 Å) than to Ag(1) (2.78 Å). Such ambiguous bridging interactions of a single N-donor ligand to a pair of $Ag^{I}$ ions is known in other cases.[14] The remaining terdentate arm of the ligand is bound in its entirety to Ag(2). Thus, $L^{Ph}$ acts as a "2+4"-dentate donor [or, possibly, a "2.5+3.5" donor if N(51) is considered as genuinely bridging] to the two $Ag^{I}$ centres, each of which also has one MeCN ligand. The differences in coordination number of Ag(1) and Ag(2) are reflected in significantly longer average Ag–N bond lengths around Ag(2) (see Table 3).

A consequence of the single-stranded helical structure is that the bipyridyl groups at each end of the ligand are overlapping and π-stacked with each other. This is emphasised in Figure 3(b). These two bipyridyl groups are near-parallel, and the separation between them is ca. 3.3 Å. It is convenient that the separation between the two $Ag^{I}$ ions is almost exactly that required for aromatic ligands coordinated to them to have an optimal π-stacking separation.

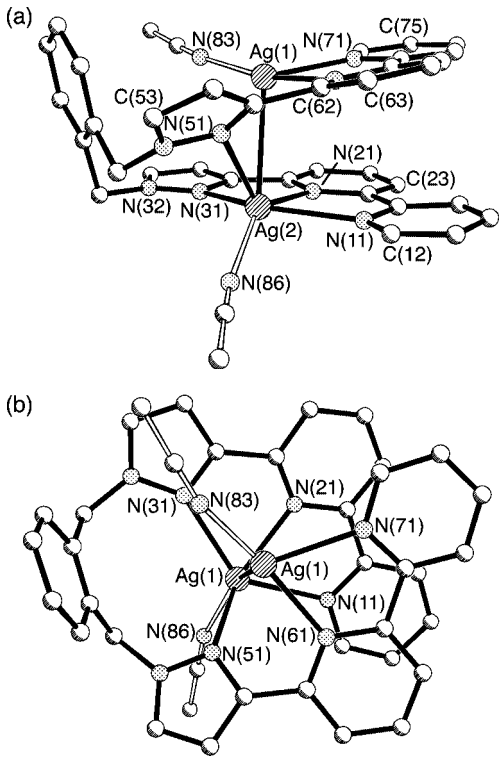


Figure 3. Structure of the complex cation of $[Ag_2(L^{Ph})(MeCN)_2][BF_4]_2$ (MeCN ligands are shown shaded differently for clarity).

Table 3. Selected bond lengths [Å] and angles [°] for $[Ag_2(L^{Ph})(MeCN)_2][BF_4]_2$.

| | |
|---|---|
| Ag(1)–N(71) | 2.386(8) |
| Ag(1)–Ag(2) | 3.0697(12) |
| Ag(2)–N(21) | 2.344(7) |
| Ag(2)–N(86) | 2.366(9) |
| Ag(2)–N(51) | 2.428(7) |
| Ag(2)–N(11) | 2.451(8) |
| Ag(2)–N(31) | 2.514(8) |
| N(83)–Ag(1)–N(61) | 167.3(3) |
| N(83)–Ag(1)–N(71) | 112.1(3) |
| N(61)–Ag(1)–N(71) | 70.6(3) |
| N(21)–Ag(2)–N(86) | 143.5(3) |
| N(21)–Ag(2)–N(51) | 129.5(2) |
| N(86)–Ag(2)–N(51) | 84.2(3) |
| N(21)–Ag(2)–N(11) | 68.9(3) |
| N(86)–Ag(2)–N(11) | 91.1(3) |
| N(51)–Ag(2)–N(11) | 104.9(3) |
| N(21)–Ag(2)–N(31) | 68.9(3) |
| N(86)–Ag(2)–N(31) | 120.4(3) |
| N(51)–Ag(2)–N(31) | 105.9(2) |
| N(11)–Ag(2)–N(31) | 137.5(2) |

## $Ni^{II}$ Complex with $L^{Py}$

Reaction of $L^{Py}$ with $Ni(BF_4)_2$ in a 1:1 ratio in nitromethane afforded, after crystallisation, $[Ni_2(L^{Py})_2][BF_4]_4$ which has the structure of a box-like achiral complex, sometimes called a "*meso*-helicate" or "mesocate",[15] in which the two ligands are side-by-side rather than twisted around one another (Figure 4, Table 4). This suits the coordination preference of $Ni^{II}$ for octahedral geometry as it allows the

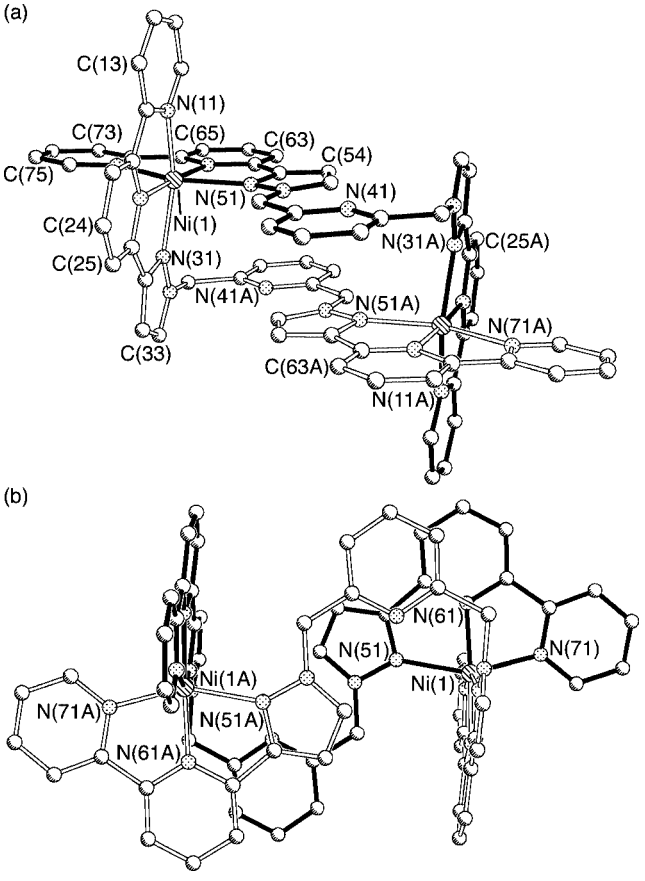


Figure 4. Two views of the complex cations of the mesocate $[Ni_2(L^{Py})_2][BF_4]_4 \cdot 2MeNO_2$, with the ligands shaded differently for clarity.

 © 2007 Wiley-VCH Verlag GmbH & Co. KGaA, Weinheim 

Table 4. Selected bond lengths [Å] and angles [°] for $[Ni_2(L^{Py})_2][BF_4]_4 \cdot 2MeNO_2$.

| | | | |
|---|---|---|---|
| Ni(1)–N(21) | 2.009(4) | Ni(1)–N(11) | 2.094(4) |
| Ni(1)–N(61) | 2.013(4) | Ni(1)–N(51) | 2.154(4) |
| Ni(1)–N(71) | 2.083(4) | Ni(1)–N(31) | 2.172(4) |
| N(21)–Ni(1)–N(61) | 177.12(16) | N(71)–Ni(1)–N(51) | 154.70(15) |
| N(21)–Ni(1)–N(71) | 104.50(15) | N(11)–Ni(1)–N(51) | 90.63(15) |
| N(61)–Ni(1)–N(71) | 78.20(16) | N(21)–Ni(1)–N(31) | 76.77(15) |
| N(21)–Ni(1)–N(11) | 78.17(16) | N(61)–Ni(1)–N(31) | 102.26(14) |
| N(61)–Ni(1)–N(11) | 102.85(16) | N(71)–Ni(1)–N(31) | 92.46(15) |
| N(71)–Ni(1)–N(11) | 92.20(15) | N(11)–Ni(1)–N(31) | 154.89(15) |
| N(21)–Ni(1)–N(51) | 100.68(14) | N(51)–Ni(1)–N(31) | 95.56(14) |
| N(61)–Ni(1)–N(51) | 76.66(15) | | |

two Ni(NNN) planes to be essentially perpendicular to one another (89° between them), and also allows a region of overlap between parallel and overlapping ligand fragments in the space between the two metal ions, involving the pyrazolyl ring of one ligand [N(51)–C(55)] and the non-coordinated central pyridyl ring of the other [N(41A)–C(46A)], whose mean planes are separated by ca. 3.3 Å. The Ni–N bonds to the two pyrazolyl donors (average 2.16 Å) are slightly longer than to the four pyridyl donors (average 2.05 Å). Notably, the central pyridyl ring of each ligand [containing N(41)] does not participate in coordination but acts like a *meta*-phenylene spacer such that the ligand coordinated only via its terdentate pyrazolyl-bipyridine arms.

### Complexes with $L^{naph}$

This ligand is architecturally similar to $L^{Ph}$ in that it has the same geometry spacer (an *ortho*-disubstituted six-membered aromatic ring) separating the two fragments. However, replacement of the 1,2-phenylene spacer by 2,3-naphthalenediyl spacer results in formation of some quite different structural types.

Reaction of $L^{naph}$ with $AgBF_4$ in MeCN afforded a clear solution, from which X-ray quality crystals were obtained following slow diffusion of diethyl ether vapour into the solution. The peak at the highest *m*/*z* value in the ES mass spectrum was at 1691.2, consistent with the 3:2 Ag/L fragment $\{[Ag_3(L^{naph})_2][BF_4]_2\}^+$, implying that the neutral complex should be $[Ag_3(L^{naph})_2](BF_4)_3$. This was confirmed by X-ray crystallography; the structure is in Figure 5, and shows some interesting similarities to that of the simpler complex $[Ag_2(L^{Ph})(MeCN)_2][BF_4]_2$. The trinuclear complex cation has $C_2$ symmetry, and consists of a linear sequence of three $Ag^I$ ions with two ligands each spanning two of them. Thus one ligand presents four of its six donor atoms (one entire tridentate arm, and the pyrazolyl donor of the next arm) to the terminal $Ag^I$ ion, and the remaining two (a bipyridyl unit) to the next $Ag^I$ at the centre of the array. We are seeing again how each ligand is partitioned into a "4 + 2-dentate" coordination mode rather than the more natural "3 + 3" mode which might be expected. The central $Ag^I$ ion [Ag(1)] is therefore in a four-coordinate environment, connected to a terminal bipyridyl fragment from each of the two ligands; the terminal $Ag^I$ ions are also four coordinate with all four donors coming from the same ligand (see Table 5). As with $[Ag_2(L^{Ph})(MeCN)_2][BF_4]_2$, each ligand adopts a shallow monohelical twist such that the bipyridyl units at each end of a given ligand overlap with one another. The $C_2$ symmetry of the complex cation means that both ligands have the same helical arrangement as one another, so the complex superstructure contains a pair of mono-helical ligands with the same configuration.

The Ag···Ag separations are considerably higher than in dinuclear $[Ag_2(L^{Ph})(MeCN)_2][BF_4]_2$, where it was 3.07 Å. Actually Ag(2) at the end of the sequence (and its symmetry equivalent at the other end) is disordered over two closely

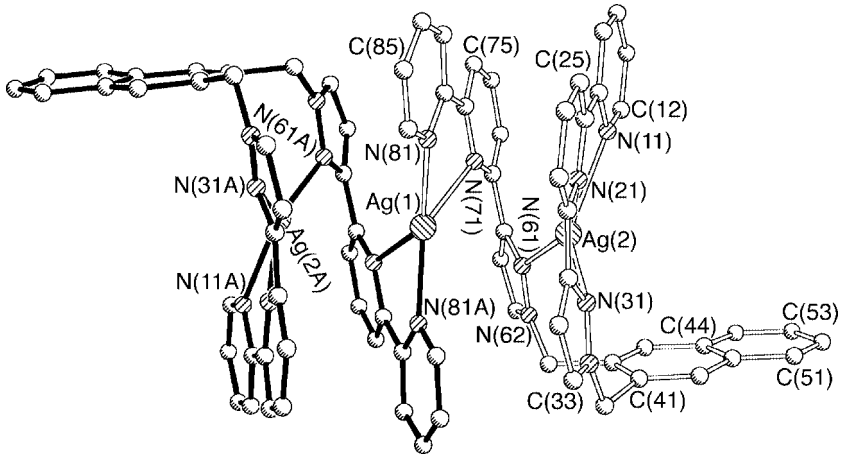


Figure 5. Structure of the complex cation of $[Ag_3(L^{naph})_2](BF_4)_3 \cdot 2MeCN$, with the two ligands shaded differently for clarity.

 © 2007 Wiley-VCH Verlag GmbH & Co. KGaA, Weinheim 

Table 5. Selected bond lengths [Å] and angles [°] for $[Ag_3(L^{naph})_2](BF_4)_3 \cdot 2MeCN$.

| | | | |
|---|---|---|---|
| Ag(1)–N(81) | 2.216(3) | Ag(2)–N(31)[b] | 2.358(4) |
| Ag(1)–N(81)#1[a] | 2.216(3) | Ag(2)–N(11)[b] | 2.571(4) |
| Ag(1)–N(71)#1 | 2.442(3) | Ag(3)–N(11)[c] | 2.330(5) |
| Ag(1)–N(71) | 2.442(3) | Ag(3)–N(61)[c] | 2.360(4) |
| Ag(2)–N(61)[b] | 2.234(3) | Ag(3)–N(21)[c] | 2.454(4) |
| Ag(2)–N(21)[b] | 2.249(4) | Ag(3)–N(31)[c] | 2.590(4) |
| N(81)–Ag(1)–N(81)#1 | 149.64(16) | N(61)–Ag(2)–N(11) | 111.63(13) |
| N(81)–Ag(1)–N(71)#1 | 133.99(10) | N(21)–Ag(2)–N(11) | 67.05(14) |
| N(81)#1–Ag(1)–N(71)#1 | 71.15(10) | N(31)–Ag(2)–N(11) | 130.67(13) |
| N(81)–Ag(1)–N(71) | 71.15(10) | N(11)–Ag(3)–N(61) | 116.11(14) |
| N(81)#1–Ag(1)–N(71) | 133.99(10) | N(11)–Ag(3)–N(21) | 67.96(15) |
| N(71)#1–Ag(1)–N(71) | 89.64(14) | N(61)–Ag(3)–N(21) | 130.54(19) |
| N(61)–Ag(2)–N(21) | 154.59(11) | N(11)–Ag(3)–N(31) | 131.13(15) |
| N(61)–Ag(2)–N(31) | 117.07(12) | N(61)–Ag(3)–N(31) | 104.52(15) |
| N(21)–Ag(2)–N(31) | 72.34(13) | N(21)–Ag(3)–N(31) | 65.20(13) |

[a] Symmetry transformations used to generate equivalent atoms: #1 $-x + 2$, $y$, $-z + 1/2$. [b] Ag(2) has a site occupancy of 58%. [c] Ag(3) has a site occupancy of 42%.

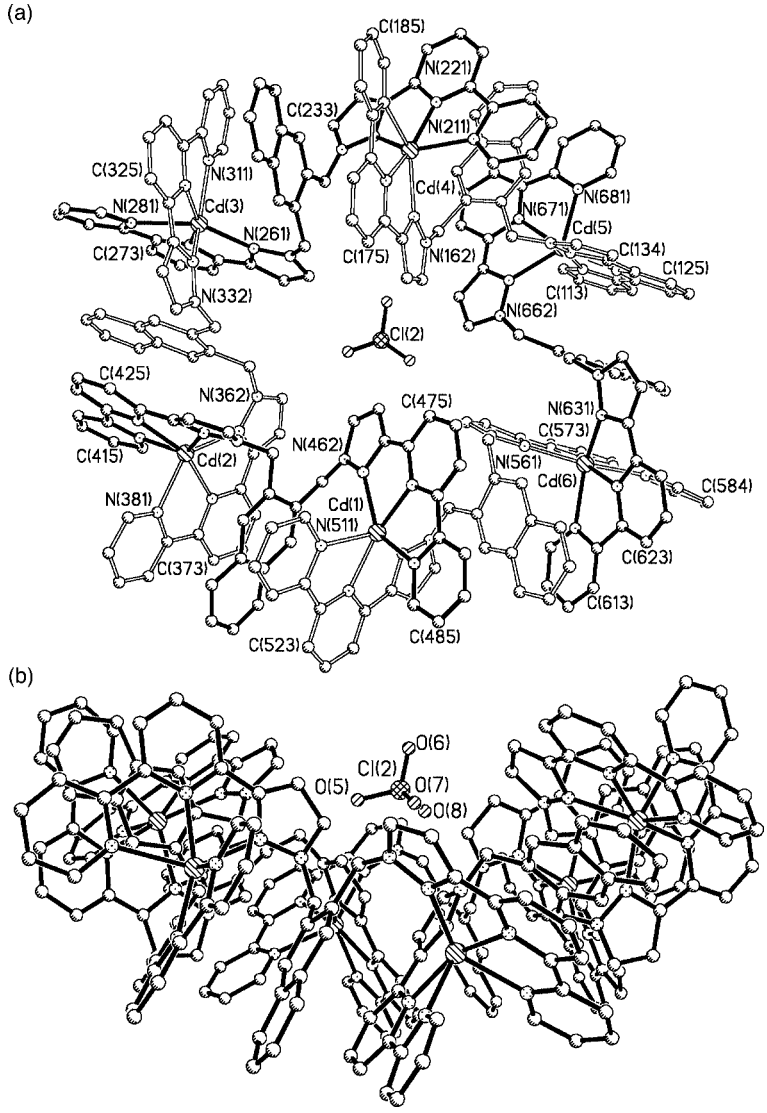


Figure 6. Two views of the structure of the complex cation of $[Cd_6(L^{naph})_6](ClO_4)_{12}$: (a) a face-on view, with the ligands shaded alternately dark and light for clarity, emphasising the cyclic helical structure and the encapsulated anion in the centre; (b) an edge-on view showing the shallow bowl shape of the cation.

 © 2007 Wiley-VCH Verlag GmbH & Co. KGaA, Weinheim 

spaced sites, with the Ag(1)···Ag(2) separation being 3.35 Å and Ag(1)···Ag(2′) being 3.88 Å, such that argentophilic interactions are clearly much less significant than for $[Ag_2(L^{Ph})(MeCN)_2][BF_4]_2$. The structure of this complex may be compared with those of other linear polynuclear complexes of $Ag^I$ with polypyridine-type ligands.[16]

Reaction of $L^{naph}$ with $Cd(ClO_4)_2$ in MeCN (1:1 ratio), followed by diffusion of diethyl ether vapour into the resultant solution, afforded X-ray quality colourless needles. On the basis of the common preference of $Cd^{II}$ for six-coordinate geometry, we were expecting a dinuclear double helicate to form similar to what we observed for $[M_2(L^{Ph})_2][ClO_4]_4$ (M = Ni, Cu). Instead however the structure is that of a circular hexanuclear helicate $[Cd_6(L^{naph})_6](ClO_4)_{12}$ (Figure 6), in which the 1:1 ratio of metal ions to ligands ensures that each $Cd^{II}$ centre is in a six-coordinate geometry (Cd–N separations lie in the range 2.21–2.41 Å, see Table 6). There are two significant non-covalent interactions involved, beyond the metal-ligand bonding, which appear to play a significant role in the structure. Firstly, each of the six naphthyl units is sandwiched between two pyridylpyrazole chelating units (from different ligands) to form a three-layer π-stack with separations of ca. 3.5 Å between the approximately parallel layers. Secondly, there is a perchlorate ion inside the ring which is involved in numerous short O···HC contacts with H atoms from the ligands. The anion is not actually centrally located in the cavity because the ring is not planar but slightly bowl-shaped; a view of the structure emphasising this is in Figure 6 (b).

Table 6. Selected bond lengths [Å] for $[Cd_6(L^{naph})_6](ClO_4)_{12}$.

| | | | |
|---|---|---|---|
| Cd(1)–N(471) | 2.301(7) | Cd(4)–N(221) | 2.271(6) |
| Cd(1)–N(521) | 2.305(6) | Cd(4)–N(171) | 2.301(7) |
| Cd(1)–N(531) | 2.325(7) | Cd(4)–N(231) | 2.302(8) |
| Cd(1)–N(461) | 2.331(6) | Cd(4)–N(161) | 2.346(7) |
| Cd(1)–N(511) | 2.334(6) | Cd(4)–N(211) | 2.358(8) |
| Cd(1)–N(481) | 2.371(7) | Cd(4)–N(181) | 2.406(7) |
| Cd(2)–N(421) | 2.294(6) | Cd(5)–N(131) | 2.213(9) |
| Cd(2)–N(371) | 2.312(6) | Cd(5)–N(121) | 2.216(9) |
| Cd(2)–N(411) | 2.325(7) | Cd(5)–N(661) | 2.312(10) |
| Cd(2)–N(431) | 2.343(8) | Cd(5)–N(671) | 2.317(10) |
| Cd(2)–N(361) | 2.349(7) | Cd(5)–N(681) | 2.352(11) |
| Cd(2)–N(381) | 2.357(6) | Cd(5)–N(111) | 2.380(10) |
| Cd(3)–N(271) | 2.229(8) | Cd(6)–N(571) | 2.208(10) |
| Cd(3)–N(321) | 2.288(7) | Cd(6)–N(631) | 2.323(9) |
| Cd(3)–N(261) | 2.295(7) | Cd(6)–N(611) | 2.326(8) |
| Cd(3)–N(331) | 2.309(7) | Cd(6)–N(561) | 2.338(9) |
| Cd(3)–N(311) | 2.363(6) | Cd(6)–N(621) | 2.342(9) |
| Cd(3)–N(281) | 2.474(9) | Cd(6)–N(581) | 2.451(9) |

Circular helicates have been reported by several groups[10,17] and, in addition to their appealing structures, can have two features of interest. Firstly, there is often an anion located in the centre of the cavity which has acted as a template to induce assembly of the metal/ligand array around it. Thus, use of a differently-sized templating anion can lead to a larger circular helicate containing more metal ions and more ligands in the peripheral assembly to accommodate a larger anion in the central cavity. Secondly, there can be a dynamic equilibrium in solution between differently-sized assemblies ($M_3L_3$, $M_4L_4$, $M_5L_5$ etc.), even if a single component crystallises preferentially such that solid-state studies indicate that only a single product has formed. Accordingly we examined the $^1H$ NMR spectrum and electrospray mass spectra of redissolved crystals of $[Cd_6(L^{naph})_6](ClO_4)_{12}$. The $^1H$ NMR spectrum in $CD_3CN$ showed no evidence for a mixture of species being present, with a clean spectrum being observed indicative of a structure with all ligands in a chiral twofold symmetric environment, viz. half of the ligand being unique, and the two $CH_2$ protons being inequivalent (diastereotopic) and coupled to one another (AB doublets) as a consequence of the chirality of the helicate.

The ES mass spectrum however reveals more complicated behaviour in solution that is not apparent from the $^1H$ NMR spectrum (Figure 7). The most intense peak at *m*/*z* 809.1 is ascribable to the mononuclear fragment $\{Cd(L^{naph})(ClO_4)\}^+$, implying either that dissociation of the complex occurs in solution, or that fragmentation occurs under mass spectroscopic conditions. The latter explanation is likely to be correct as the $^1H$ NMR spectrum shows that the main species in solution is chiral, i.e. at least a $[Cd_2(L^{naph})_2]^{4+}$ dinuclear double helicate. More interestingly, at higher *m*/*z* values are numerous much weaker peaks (< 2% of intensity of the main peak at *m*/*z* 809.1) whose *m*/*z* values match exactly to a range of oligomers ranging from a dimer [the peak at *m*/*z* 1717.2 corresponds to $\{Cd_2(L^{naph})_2(ClO_4)_3\}^{4+}$, presumably a double helicate] up to an 11-mer [the peak at *m*/*z* 3229.2 corresponds to $\{Cd_{11}(L^{naph})_{11}(ClO_4)_9\}^{2+}$, presumably a large cyclic helical assembly of the same nature as the crystal structure]. Altogether, peaks corresponding to $\{Cd(L^{naph})\}_n$ oligomers with $n$ = 2, 4, 5, 7, 8, 10, 11 can be identified unambiguously; and a peak at *m*/*z* 2624.2 could correspond to either the $n$ = 3 species $\{Cd_3(L^{naph})_3(ClO_4)_5\}^+$ or the $n$ = 6 species $\{Cd_6(L^{naph})_6(ClO_4)_{10}\}^{2+}$ (or both, superimposed). It is clear that in solution an equilibrium mixture of cyclic helicates species exists.[10b] The fact that this is not apparent in the NMR spectrum implies either that they all have essentially

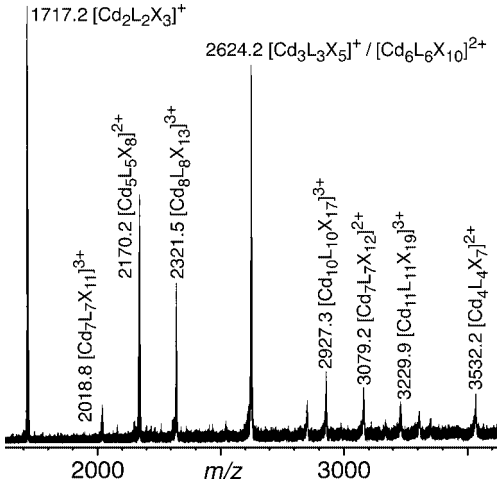


Figure 7. Part of the electrospray mass spectrum of redissolved crystals of $[Cd_6(L^{naph})_6](ClO_4)_{12}$, showing the presence of a range of cyclic oligomers in solution.

 © 2007 Wiley-VCH Verlag GmbH & Co. KGaA, Weinheim 

identical NMR spectra, or that one species is present in abundance and dominates the NMR spectrum, with the minor components being invisible. Either possibility is perfectly plausible.

A final interesting point about these complexes of $L^{naph}$ is their luminescence spectra. The free ligand has a characteristic intense naphthalene-based fluorescence band at 347 nm. For the $Ag^{I}$ complex $[Ag_3(L^{naph})_2](BF_4)_3$ in MeCN solution, the fluorescence is reduced in intensity by about 90% but remains at exactly the same wavelength. In $[Cd_6(L^{naph})_6](ClO_4)_{12}$ in MeCN solution however the fluorescence is significantly red-shifted, to 363 nm (Figure 8). We ascribe this to the extensive aromatic stacking of the emissive naphthyl units between pyridyl/pyrazolyl units of adjacent ligands in the cyclic helical array (see Figure 6), which results in stabilisation of the naphthyl-based π-π* excited state and hence a red-shift of the emission.[18] Even if other cyclic oligomers are present in solution, as the ES mass spectrum suggests, similar structures are plausible in which this type of stacking is retained. Thus the red-shifted luminescence of the ligand is indicative of the nature of the self-assembled structure formed in solution.

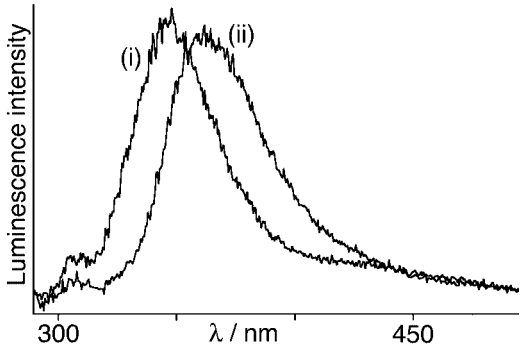


Figure 8. Luminescence spectra of solutions of (i) $[Ag_3(L^{naph})_2](BF_4)_3$ and (ii) $[Cd_6(L^{naph})_6](ClO_4)_{12}$ in MeCN, concentration ca. $10^{-6}$ M; the solutions had the same optical density at the excitation wavelength.

## Conclusions

This series of relatively simple bridging ligands has generated a range of structures in which the ligands all span two metal ions – an essential prerequisite for formation of polynuclear assemblies – resulting in double helicates, a mesocate, some single-stranded helicates based on $Ag^{I}$, and a cyclic hexanuclear helicate based on $Cd^{II}$. In some cases there are obvious factors controlling the structures, such as the presence of Ag···Ag interactions in the $Ag^{I}$ complexes. In other cases apparently very similar metal/ligand combinations generate quite different structures, cf. the difference between the dinuclear double helicates $[M_2(L^{Ph})_2][ClO_4]_4$ (M = Ni, Cu) and the cyclic hexanuclear helicate $[Cd_6(L^{naph})_6](ClO_4)_{12}$; both of these structural types have arisen from combination of bis-terdentate ligands (with similar spacers separating the binding sites) with six-coordinate metal ions. Significant factors favouring the formation of $[Cd_6(L^{naph})_6](ClO_4)_{12}$ could include the aromatic π-stacking between the naphthyl units, and the ability of $Cd^{II}$ to tolerate a more highly distorted coordination environment than $Cu^{II}$ or $Ni^{II}$ on stereoelectronic grounds.

However, although it is tempting to try and rationalise such structural variations in a facile manner, it is not appropriate to over-do this for two reasons. Firstly, the number of variables involved is large: some of the more obvious factors include the charge and radius of the metal cation; stereoelectronic preferences arising from partially filled d-shells [for $Cu^{II}$ and $Ni^{II}$]; the presence of attractive Ag···Ag interactions in the $Ag^{I}$ complexes; the nature of the anion, which may exert a templating effect in the hexanuclear $Cd^{II}$ circular helicate; and the presence of other supramolecular interactions such as aromatic π-stacking between ligands. Secondly, the solid-state structures are not necessarily thermodynamic minima but may represent kinetically stable assemblies which happened to crystallise well; for example the ES mass spectroscopic data for $[Cd_6(L^{naph})_6](ClO_4)_{12}$ clearly shows that there is a mixture of oligomers in solution. Rationalising the appearance of one kinetic product in the solid state therefore does not tell the whole story.

## Experimental Section

**General Details:** 6-Acetyl-2,2′-bipyridine,[19] 6-(pyrazol-3-yl)-2,2′-bipyridine,[12] 2,6-bis(bromomethyl)pyridine,[20] and 2,3-bis(bromomethyl)naphthalene[21] were prepared as described previously. Other organic reagents and metal salts were obtained from Aldrich and Avocado and used as received. Instrumentation used for spectroscopic analysis were as follows: $^1$H NMR spectra, a Bruker AC 250 spectrometer. EI mass spectra, a VG AutoSpec magnetic sector instrument; ES mass spectra, a Bruker MicroTOF instrument in positive ion mode, with capillary exit and first skimmer voltages of 30 V and 60 V respectively. UV/Vis absorption spectra, a Cary 50 spectrophotometer, using MeCN solutions of the complexes.

### Syntheses of Ligands

**$L^{Ph}$:** A mixture of 1,2-bis(bromomethyl)benzene (0.539 g, 2.04 mmol), 6-(pyrazol-3-yl)-2,2′-bipyridine (0.852 g, 3.84 mmol), 10 M aqueous NaOH (3 $cm^3$), $NBu_4OH$ (3 drops of 40% aqueous solution) and toluene (15 $cm^3$) was heated with vigorous stirring to 85 °C for 24 h. After cooling, the organic layer was washed with water and then dried with $MgSO_4$. The solvent was removed to afford a pale yellow solid which was purified by column chromatography (5:95 EtOAc/$CH_2Cl_2$ on alumina) to give 0.861 g (65%) of $L^{Ph}$ as a white powder. EI MS: *m*/*z* (%) = 546 (3) [$M^+$] and 324 (35) [$M^+$ – pzbpy]. $^1$H NMR (250 MHz, $CDCl_3$): $\delta$ = 8.67 (d, 2 H, bpy $H^{6'}$), 8.57 (d, 2 H, bpy $H^{3'}$), 8.33 (dd, 2 H, bpy $H^3$), 8.01 (dd, 2 H, bpy $H^5$), 7.76–7.85, (m, 4 H, bpy $H^{5'}$ and $H^{4'}$), 7.37 (d, 2 H, pz $H^5$), 7.24–7.33 (m, 4 H, bpy $H^4$ and phenyl $H^3$ and $H^4$), 7.17 (m, 2 H, phenyl $H^2$ and $H^5$), 7.07 (d, 2 H, pz $H^4$) and 5.49 (s, 4 H, $CH_2$) ppm. $C_{34}H_{26}N_8$ (546.63): calcd. C 74.7, H 4.8, N 20.5; found C 74.9, H 4.7, N 20.3.

**$L^{py}$:** A mixture of 2,6-bis(bromomethyl)pyridine (0.602 g, 2.27 mmol) and 6-(pyrazol-3-yl)-2,2′-bipyridine (1.00 g, 4.50 mmol) were reacted in exactly the same manner as described above for the synthesis of $L^{Ph}$. The crude product was purified by column chromatography (1% MeOH in $CH_2Cl_2$, on alumina) to give 0.593 g (47%) of $L^{py}$ as yellow foam. EI MS: *m*/*z* (%) = 547

 © 2007 Wiley-VCH Verlag GmbH & Co. KGaA, Weinheim 

(5) [M$^+$] and 325 (100) [M$^+$ – pzbpy]. $^1$H NMR (250 MHz, $CDCl_3$): $\delta$ = 8.66 (d, 2 H, bipy H$^{6\prime}$), 8.58 (d, 2 H, bpy H$^{3\prime}$), 8.32 (dd, 2 H, bpy H$^3$), 8.02 (dd, 2 H, bpy H$^5$), 7.83 (t, 4 H, bpy H$^{4\prime}$ and H$^{5\prime}$), 7.61–7.52 (m, 3 H, py H$^3$, H$^4$ and H$^5$), 7.33 (t, 2 H, bpy H$^4$), 7.11 (d, 2 H, pz H$^5$), 6.93 (d, 2 H, pz H$^4$) ppm. $C_{33}H_{25}N_9 \cdot H_2O$ (565.63): calcd. C 70.1, H 4.8, N 22.3; found C 70.5, H 4.6, N 22.4.

**L$^{naph}$:** A mixture of 2,3-bis(bromomethyl)naphthalene[9] (0.314 g, 1.00 mmol) and 6-(pyrazol-3-yl)-2,2′-bipyridine were reacted in the same manner as described above for the synthesis of L$^{Ph}$. The crude solid was purified by column chromatography (0.5% MeOH in $CH_2Cl_2$, on alumina) to give 0.390 g (69%) of yellow powder. EI-MS: *m*/*z* (%) = 596 (5) [M$^+$], 374 (100) M$^+$ – pzBipy]. $^1$H NMR (250 MHz, $CDCl_3$): $\delta$ = 8.65 (d, 2 H, bipy H$^{6\prime}$), 8.56 (d, 2 H, bipy H$^{3\prime}$), 8.33 (dd, 2 H, bipy H$^3$), 8.04 (dd, 2 H, bipy H$^5$), 7.71–7.85, (m, 6 H, bipy H$^{5\prime}$, H$^{4\prime}$and naphthyl H$^5$/H$^8$), 7.59 (s, 2 H, naphthyl H$^1$/H$^4$) 7.43–7.47 (m, 2 H, naphthyl H$^6$/H$^7$), 7.43 (d, 2 H, pz H$^5$), 7.24 (t, 2 H, bipy H$^4$), 7.10 (d, 2 H, pz H$^4$) and 5.56 (s, 4 H, $CH_2$) ppm. $C_{38}H_{28}N_8$ (596.69): calcd. C 76.5, H 4.7, N 18.8; found C 76.1, H 4.7, N 18.4.

### Syntheses of Complexes

Complexes were prepared by the reaction of the ligand (0.05 g) with the appropriate metal salt [in a 2:1 metal/ligand ratio for Ag$^I$ complexes and in a 1:1 ratio for the Ni$^{II}$, Co$^{II}$, Cu$^{II}$, and Cd$^{II}$ complexes] in nitromethane or acetonitrile. Diffusion of diisopropyl ether vapour into the resulting solutions afforded single crystals suitable for X-ray crystallography and other analyses. Characterisation data for the complexes are as follows.

**[Ni$_2$L$^{Ph}_2$](ClO$_4$)$_4$:** Yield: 0.050 g (68%). UV/Vis (MeCN): $\lambda_{max}$/nm ($\varepsilon$, dm$^3$mol$^{-1}$cm$^{-1}$) = 245 (32400), 260 (32600), 327 (18800), 340 (16700), 548 (29), 848 (71). ESMS: *m*/*z* = 704.1 {[Ni$_2$L$^{Ph}_2$](ClO$_4$)$_2$}$^{2+}$, 436.4 {[Ni$_2$L$^{Ph}_2$](ClO$_4$)}$^{3+}$, 302.6 {[Ni$_2$L$^{Ph}_2$]}$^{4+}$. $Ni_2C_{68}H_{52}N_{16}Cl_4O_{16} \cdot 2H_2O$ (1644.48): calcd. C 49.7, H 3.4, N 13.6; found C 49.3, H 3.5, N 13.6.

**[Cu$_2$L$^{Ph}_2$](ClO$_4$)$_4$:** Yield 0.046 g (62%). UV/Vis (MeCN): $\lambda_{max}$/nm ($\varepsilon$, dm$^3$mol$^{-1}$cm$^{-1}$) = 210 (67600), 245 (23000), 686 (69). ES MS: *m*/*z* = 1518.1 {[Cu$_2$L$^{Ph}_2$](ClO$_4$)$_3$}$^+$, 979.1 {[Cu$_4$L$^{Ph}_4$](ClO$_4$)$_5$}$^{3+}$, 709.1 {[Cu$_2$L$^{Ph}_2$](ClO$_4$)$_2$}$^{2+}$, 439.7 {[Cu$_2$L$^{Ph}_2$](ClO$_4$)}$^{3+}$, 305.1 {[Cu$_2$L$^{Ph}_2$]}$^{4+}$. $Cu_2C_{68}H_{52}N_{16}Cl_4O_{16} \cdot 2H_2O$ (1654.19): calcd. C 49.4, H 3.4, N 13.5; found C 48.3, H 3.3, N 13.3.

**[Ag$_2$L$^{Ph}$(MeCN)$_2$](BF$_4$)$_2$:** Yield 0.051 g (55%). $^1$H NMR (250 MHz, $CD_3CN$): $\delta$ = 8.06 (d, 2 H, bpy H$^{6\prime}$), 7.90–7.97 (m, 4 H, bpy H$^{3\prime}$, H$^3$), 7.75 (d, 2 H, bpy H$^5$), 7.68 (d, 2 H, bpy H$^{5\prime}$), 7.56 (d, 4 H, phenyl H$^2$, H$^3$), 7.53 (d, 2 H, pz H$^5$), 7.44 (m, 2 H, py H$^{4\prime}$), 7.12 (dt, 2 H, py H$^4$), 6.95 (d, 2 H, pz H$^4$), 5.32 (s, 4 H, $CH_2$) ppm. UV/Vis (MeCN): $\lambda_{max}$/nm ($\varepsilon$, dm$^3$mol$^{-1}$cm$^{-1}$) = 238 (40000), 265 (sh), 310 (19400). ES MS: *m*/*z* = 849.0 {[Ag$_2$L$^{Ph}$][BF$_4$]}$^+$, 380.0 {[Ag$_2$L$^{Ph}$]}$^{2+}$. $C_{38}H_{32}Ag_2B_2F_8N_{10}$ (1018.07): calcd. C 44.8, H 3.2, N 13.8; found C 44.5, H 2.9, N 13.4.

**[Ni$_2$L$^{py}_2$](BF$_4$)$_4$:** Yield 0.035 g (49%). UV/Vis (MeCN): $\lambda_{max}$/nm ($\varepsilon$, dm$^3$mol$^{-1}$cm$^{-1}$) = 247 (54800), 326 (19600), 845 (83). ES MS: *m*/*z* = 692.2 {[Ni$_2$L$^{py}_2$](BF$_4$)$_2$}$^{2+}$, 433.1 {[Ni$_2$L$^{py}_2$](BF$_4$)}$^{3+}$, 302.6 {[Ni$_2$L$^{py}_2$]}$^{4+}$. This sample was hygroscopic and gave variable elemental analyses consistent with the presence of several molecules of water per complex.

**[Ag$_3$(L$^{naph}$)$_2$](BF$_4$)$_3$:** Yield 0.034 g (46%). UV/Vis (MeCN): $\lambda_{max}$/nm ($\varepsilon$, dm$^3$mol$^{-1}$cm$^{-1}$) = 227 (160000), 260 (89500), 310 (37100). ES MS: *m*/*z* = 1691.2 {[Ag$_3$(L$^{naph}$)$_2$][BF$_4$]$_2$}$^+$, 899.1 {[Ag$_2$(L$^{naph}$)][BF$_4$]}$^+$. $C_{76}H_{56}Ag_3B_3F_{12}N_{16} \cdot 2H_2O$ (1813.42): calcd. C 50.3, H 3.3, N, 12.4; found C 50.3, H 3.0, N 12.3.

**[Cd$_6$(L$^{naph}$)$_6$](ClO$_4$)$_{12}$:** Yield 0.032 g (42%). $^1$H NMR (250 MHz, $CD_3CN$): $\delta$ = 8.44 (d, 2 H, bipy H$^{6\prime}$), 8.43 (br, 2 H, bipy H$^3$), 8.29 (m, 2 H, bipy H$^{3\prime}$), 8.28 (m, 2 H, bipy H$^5$), 8.13 (s, 2 H, naphthyl H$^1$/H$^4$), 7.99 (t, 2 H, bipy H$^{5\prime}$), 7.95 (d, 2 H, naphthyl H$^5$/H$^8$), 7.90 (d, 2 H, pz H$^5$), 7.65–7.68 (2 H, naphthyl H$^6$/H$^7$), 7.52 (dt, 2 H, bipy H$^{4\prime}$), 7.31 (dt, 2 H, bipy H$^{4\prime}$), 7.27 (dt, 2 H, pz H$^4$), 5.38 (d, 2 H, $CH_2$), 5.76 (d, 2 H, $CH_2$) ppm. UV/Vis (MeCN): $\lambda_{max}$/nm ($\varepsilon$, dm$^3$mol$^{-1}$cm$^{-1}$) = 320 (22800), 268 (30200), 226 (55700). ES MS: *m*/*z* = 809.1 {[Cd(L$^{naph}$)](ClO$_4$)}$^+$, 1717.2 {[Cd$_2$(L$^{naph}$)$_2$](ClO$_4$)$_3$}$^+$, 2624.2 {[Cd$_3$(L$^{naph}$)$_3$](ClO$_4$)$_5$}$^+$, 3532.2 {[Cd$_4$(L$^{naph}$)$_4$](ClO$_4$)$_7$}$^+$, 1717.2 {[Cd$_4$(L$^{naph}$)$_4$](ClO$_4$)$_6$}$^{2+}$, 2170.2 {[Cd$_5$(L$^{naph}$)$_5$](ClO$_4$)$_8$}$^{2+}$, 2624.2 {[Cd$_6$(L$^{naph}$)$_6$](ClO$_4$)$_{10}$}$^{2+}$, 3079.2 {[Cd$_7$(L$^{naph}$)$_7$](ClO$_4$)$_{12}$}$^{2+}$,

Table 7. Crystallographic data.

| Complex | L$^{Ph}$ | [Ni$_2$(L$^{Ph}$)$_2$][ClO$_4$]$_4$·MeCN | [Cu$_2$(L$^{Ph}$)$_2$][ClO$_4$]$_4$·2MeCN·0.5H$_2$O | [Ag$_2$(L$^{Ph}$)(MeCN)$_2$][BF$_4$]$_2$ |
|---|---|---|---|---|
| Empirical formula | $C_{34}H_{26}N_8$ | $C_{70}H_{55}Cl_4N_{17}Ni_2O_{16}$ | $C_{72}H_{59}Cl_4Cu_2N_{18}O_{16.5}$ | $C_{38}H_{32}Ag_2B_2F_8N_{10}$ |
| Formula mass | 546.6 | 1649.53 | 1709.25 | 1018.1(0) |
| *T* [K] | 100(2) | 150(2) | 100(2) | 150(2) |
| Crystal system, space group | monoclinic, $P2_1/n$ | triclinic, $P\bar{1}$ | triclinic, $P\bar{1}$ | triclinic, $P\bar{1}$ |
| *a* [Å] | 10.181(5) | 13.6741(18) | 13.73(4) | 12.6315(16) |
| *b* [Å] | 23.562(12) | 14.3285(19) | 14.37(4) | 13.1407(18) |
| *c* [Å] | 11.711(6) | 21.426(3) | 21.66(6) | 13.6001(16) |
| $\alpha$ [°] | 90 | 102.679(3) | 102.22(5) | 72.745(7) |
| $\beta$ [°] | 95.079(16) | 93.931(3) | 94.69(3) | 83.475(7) |
| $\gamma$ [°] | 90 | 113.108(2) | 112.83(4) | 62.214(6) |
| *V* [Å$^3$] | 2798(2) | 3710.5(9) | 3786(17) | 1906.4(4) |
| Z | 4 | 2 | 2 | 2 |
| $D_{calcd.}$ [Mg/m$^3$] | 1.298 | 1.476 | 1.499 | 1.774 |
| $\mu$ [mm$^{-1}$] | 0.081 | 0.730 | 0.783 | 1.112 |
| Crystal size [mm] | 0.14 × 0.06 × 0.04 | 0.32 × 0.14 × 0.09 | 0.27 × 0.20 × 0.07 | 0.35 × 0.16 × 0.08 |
| Reflections collected | 25235 | 32968 | 83182 | 43039 |
| Independent reflections | 4804 ($R_{int}$ = 0.126) | 13042 ($R_{int}$ = 0.108) | 14172 ($R_{int}$ = 0.059) | 6605 ($R_{int}$ = 0.0333) |
| Data/restraints/parameters | 4804/0/380 | 13042/5/982 | 14172/8/1020 | 6605/0/543 |
| Final *R* indices[a] | 0.0576, 0.1518 | 0.0644, 0.1675 | 0.0456, 0.1199 | 0.0784, 0.1934 |
| Largest diff. peak/hole [e Å$^{-3}$] | +0.22/–0.30 | +0.77/–0.73 | +0.92/–0.63 | +2.42/–2.19 |

[a] The first value is *R*1, based on "observed data" with $I > 2\sigma(I)$; the second value is *wR*2, based on all data.

 © 2007 Wiley-VCH Verlag GmbH & Co. KGaA, Weinheim 

Table 8. Crystallographic data.

| Complex | $[Ni_2(L^{Py})_2][BF_4]_4\cdot 2MeNO_2$ | $[Ag_3(L^{naph})_2](BF_4)_3\cdot 2MeCN$ | $[Cd_6(L^{naph})_6](ClO_4)_{12}$ |
|---|---|---|---|
| Empirical formula | $C_{68}H_{56}B_4F_{16}N_{20}Ni_2O_4$ | $C_{80}H_{62}Ag_3B_3F_{12}N_{18}$ | $C_{228}H_{168}Cd_6Cl_{12}N_{48}O_{48}$ |
| Formula mass | 1681.98 | 1859.52 | 5447.90 |
| $T$ [K] | 100(2) | 100(2) | 100(2) |
| Crystal system, space group | monoclinic, $P2_1/n$ | monoclinic, $C2/c$ | monoclinic, $P2_1/n$ |
| $a$ [Å] | 12.3638(7) | 15.1250(9) | 25.350(2) |
| $b$ [Å] | 12.3036(7) | 23.7334(15) | 26.015(2) |
| $c$ [Å] | 23.4297(13) | 20.9965(17) | 41.398(3) |
| $\alpha$ [°] | 90 | 90 | 90 |
| $\beta$ [°] | 97.427(4) | 103.930(3) | 95.762(5) |
| $\gamma$ [°] | 90 | 90 | 90 |
| $V$ [Å$^3$] | 3534.2(3) | 7315.4(9) | 27163(4) |
| Z | 2 | 4 | 4 |
| $D_{calcd.}$ [Mg/m$^3$] | 1.581 | 1.688 | 1.332 |
| $\mu$ [mm$^{-1}$] | 0.641 | 0.887 | 0.654 |
| Crystal size [mm] | $0.18\times0.16\times0.14$ | $0.06\times0.04\times0.03$ | $0.24\times0.16\times0.06$ |
| Reflections collected | 49325 | 55542 | 304166 |
| Independent reflections | 7161 ($R_{int}$ = 0.0836) | 8612 ($R_{int}$ = 0.0546) | 47783 ($R_{int}$ = 0.1166) |
| Data/restraints/parameters | 7161/4/514 | 8612/83/581 | 47783/1419/2197 |
| Final $R$ indices[a] | 0.0680, 0.1934 | 0.0457, 0.1267 | 0.1195, 0.3615 |
| Largest diff. peak/hole [e Å$^{-3}$] | +0.94/–0.72 | +1.66/–1.01 | +2.33/–1.38 |

[a] The first value is $R1$, based on "observed data" with $I > 2\sigma(I)$; the second value is $wR2$, based on all data.

2018.8 $\{[Cd_7(L^{naph})_7](ClO_4)_{11}\}^{3+}$, 3532.2 $\{[Cd_8(L^{naph})_8](ClO_4)_{14}\}^{2+}$, 2321.5 $\{[Cd_8(L^{naph})_8](ClO_4)_{13}\}^{3+}$, 2927.2 $\{[Cd_{10}(L^{naph})_{10}](ClO_4)_{17}\}^{3+}$, 3229.2 $\{[Cd_{11}(L^{naph})_{11}](ClO_4)_{19}\}^{3+}$. $C_{228}H_{168}Cd_6Cl_{12}N_{48}O_{48}\cdot 10H_2O$ (5628.19): calcd. C 48.7, H 3.4, N 11.9; found C 48.0, H 3.0, N 11.4.

**Crystallography**

X-ray crystallographic data are summarised in Tables 7 and 8. In each case a suitable crystal was coated with hydrocarbon oil and attached to the tip of a glass fibre and transferred to a Bruker APEX-2 CCD diffractometer (graphite-monochromated Mo-$K_\alpha$ radiation, $\lambda$ = 0.71073 Å) under a stream of cold $N_2$. After collection and integration the data were corrected for Lorentz and polarisation effects and for absorption by semi-empirical methods (SADABS) based on symmetry-equivalent and repeated reflections.[22] The structures were solved by direct methods or heavy atom Patterson methods and refined by full-matrix least-squares methods on $F^2$. Hydrogen atoms were placed geometrically and refined with a riding model and with $U_{iso}$ constrained to be 1.2 (1.5 for methyl groups) times $U_{eq}$ of the carrier atom. Structures were solved and refined using the SHELX suite of programs.[23] Significant bond lengths and angles for the structures of the metal complexes are in Tables 1–6. Particular problems associated with the refinements are as follows.

The complex cation of $[Ni_2(L^{Py})_2][BF_4]_4\cdot 2MeNO_2$ lies on an inversion centre with only one metal ion in the asymmetric unit. Crystals of $[Cd_6(L^{naph})_6](ClO_4)_{12}$ scattered relatively weakly and only data with $2\theta \leq 50°$ were used in the final refinement. Several of the perchlorate anions showed disorder of the oxygen atoms which were in many cases disordered over two sites. Extensive use of geometric restraints was required to keep the Cl–O distances and the geometries of the perchlorate anions reasonable. Areas of electron density which presumably corresponded to disordered solvent molecules, but which could not be modelled as anything reasonable, were removed using the SQUEEZE command in PLATON. In $[Ag_3(L^{naph})_2](BF_4)_3\cdot 2MeCN$ the complex cation lies on a twofold rotation axis which passes through Ag(1) and B(2). The "terminal" ion is disordered over two closely spaced sites [Ag(2), 58% site occupancy; Ag(3), 42% site occupancy]; only Ag(2) is shown in Figure 5. Some of the F atoms of the tetrafluoroborate ions are disordered over two positions with the same fractional occupancies (0.58/0.42). None of the other structural determinations presented any significant problems.

CCDC-653275 to -653281 contain the supplementary crystallographic information for this paper. These data can be obtained free of charge from the Cambridge Crystallographic Data Centre via www.ccdc.cam.ac.uk/data_request/cif.

## Acknowledgments

We thank theGovernment of the Sultanate of Oman for a PhD studentship to N. K. A.

[1] a) C. Piguet, G. Bernardinelli, G. Hopfgartner, *Chem. Rev.* **1997**, *97*, 2005; b) E. C. Constable, *Polynuclear Transition Metal Helicates,* in *Comprehensive Supramolecular Chemistry*, vol. 9 (Ed.: J.-P. Sauvage), Elsevier, Oxford, **1996**, p. 213; c) M. Albrecht, *Chem. Rev.* **2001**, *101*, 3457; d) M. J. Hannon, L. J. Childs, *Supramol. Chem.* **2004**, *16*, 7; e) A. F. Williams, *Chimia* **2000**, *54*, 585.

[2] A. Oleksi, A. G. Blanco, R. Boer, I. Uson, J. Aymami, A. Rodger, M. J. Hannon, M. Coll, *Angew. Chem. Int. Ed.* **2006**, *45*, 1227.

[3] T. Riis-Johannessen, L. P. Harding, J. C. Jeffery, R. Moon, C. R. Rice, *Dalton Trans.* **2007**, 1577.

[4] J. C. Jeffery, T. Riis-Johannessen, C. J. Anderson, C. J. Adams, A. Robinson, S. P. Argent, M. D. Ward, C. R. Rice, *Inorg. Chem.* **2007**, *46*, 2417.

[5] C. Piguet, M. Borkovec, J. Hamacek, K. Zeckert, *Coord. Chem. Rev.* **2005**, *249*, 705.

[6] M. Cantuel, F. Gumy, J.-C. G. Bünzli, C. Piguet, *Dalton Trans.* **2006**, 2647.

[7] J. R. Nitschke, *Acc. Chem. Res.* **2007**, *40*, 103.

[8] a) L. P. Harding, J. C. Jeffery, T. Riis-Johannessen, C. R. Rice, Z. T. Zeng, *Chem. Commun.* **2004**, 654; b) L. P. Harding, J. C. Jeffery, T. Riis-Johannessen, C. R. Rice, Z. Zeng, *Dalton Trans.* **2004**, 2396.

[9] S. G. Telfer, B. Bocquet, A. F. Williams, *Inorg. Chem.* **2001**, *40*, 4818.

[10] a) C. S. Campos-Fernandez, B. L. Schottel, H. T. Chifotides, J. K. Bera, J. Basca, J. M. Koomen, D. H. Russell, K. R. Dun-

 © 2007 Wiley-VCH Verlag GmbH & Co. KGaA, Weinheim 

bar, *J. Am. Chem. Soc.* **2005**, *127*, 12909; b) S. P. Argent, H. Adams, T. Riis-Johannessen, J. C. Jeffery, L. P. Harding, O. Mamula, M. D. Ward, *Inorg. Chem.* **2006**, *45*, 3905; c) P. L. Jones, K. J. Byrom, J. C. Jeffery, J. A. McCleverty, M. D. Ward, *Chem. Commun.* **1997**, 1361; d) B. Hasenknopf, J.-M. Lehn, B. O. Kneisel, G. Baum, D. Fenske, *Angew. Chem. Int. Ed. Engl.* **1996**, *35*, 1838; e) B. Hasenknopf, J.-M. Lehn, N. Boumediene, A. Dupont-Gervais, A. van Dorsselaer, B. Kneisel, D. Fenske, *J. Am. Chem. Soc.* **1997**, *119*, 10956.

[11] a) T. K. Ronson, H. Adams, L. P. Harding, S. J. A. Pope, D. Sykes, S. Faulkner, M. D. Ward, *Dalton Trans.* **2007**, 1006; b) S. P. Argent, H. Adams, T. Riis-Johannessen, J. C. Jeffery, L. P. Harding, W. Clegg, R. W. Harrington, M. D. Ward, *Dalton Trans.* **2006**, 4996; c) S. P. Argent, H. Adams, T. Riis-Johannessen, J. C. Jeffery, L. P. Harding, M. D. Ward, *J. Am. Chem. Soc.* **2006**, *128*, 72; d) S. P. Argent, H. Adams, L. P. Harding, M. D. Ward, *Dalton Trans.* **2006**, 542.

[12] J. S. Fleming, E. Psillakis, S. M. Couchman, J. C. Jeffery, J. A. McCleverty, M. D. Ward, *J. Chem. Soc. Dalton Trans.* **1998**, 537.

[13] Z. R. Bell, J. A. McCleverty, M. D. Ward, *Aust. J. Chem.* **2003**, *56*, 665.

[14] E. R. Humphrey, Z. R. Reeves, J. C. Jeffery, J. A. McCleverty, M. D. Ward, *Polyhedron* **1999**, *18*, 1335.

[15] T. K. Ronson, H. Adams, M. D. Ward, *New J. Chem.* **2006**, *30*, 26.

[16] a) G. Baum, E. C. Constable, D. Fenske, C. E. Housecroft, T. Kulke, *Chem. Commun.* **1998**, 2659; b) G. Baum, E. C. Constable, D. Fenske, C. E. Housecroft, T. Kulke, M. Neuburger, M. Zehnder, *J. Chem. Soc. Dalton Trans.* **2000**, 945; c) S. Binsilong, J. D. Kildea, W. C. Patalinghug, B. W. Skelton, A. H. White, *Aust. J. Chem.* **1994**, *47*, 1545; d) L. Hou, D. Li, *Inorg. Chem. Commun.* **2005**, *8*, 128; e) M. J. Hannon, C. L. Painting, E. A. Plummer, L. J. Childs, N. W. Alcock, *Chem. Eur. J.* **2002**, *8*, 2225; f) C. Provent, S. Hewage, G. Brand, G. Bernardinelli, L. J. Charbonnière, A. F. Williams, *Angew. Chem. Int. Ed. Engl.* **1997**, *36*, 1287.

[17] a) G. Baum, E. C. Constable, D. Fenske, C. E. Housecroft, T. Kulke, *Chem. Commun.* **1999**, 195; b) F. Tuna, J. Hamblin, A. Jackson, G. Clarkson, N. W. Alcock, M. J. Hannon, *Dalton Trans.* **2003**, 2141; c) O. Mamula, A. von Zelewsky, P. Brodard, C. W. Schlapfer, G. Bernardinelli, H. Stoeckli-Evans, *Chem. Eur. J.* **2005**, *11*, 3049.

[18] N. K. Al-Rasbi, C. Sabatini, F. Barigelletti, M. D. Ward, *Dalton Trans.* **2006**, 4769.

[19] E. C. Constable, F. Heirtzler, M. Neuburger, M. Zehnder, *J. Am. Chem. Soc.* **1997**, *119*, 5606.

[20] H. Scheytza, O. Rademacher, H.-U. Reißig, *Eur. J. Org. Chem.* **1999**, 2373.

[21] C. Wang, H. I. Mosberg, *Tetrahedron Lett.* **1995**, *36*, 3623.

[22] G. M. Sheldrick: *SADABS*, A program for absorption correction with the Siemens SMART area-detector system, University of Göttingen, **1996**.

[23] G. M. Sheldrick: *SHELXS-97* and *SHELXL-97*, programs for crystal structure solution and refinement, University of Göttingen, **1997**.

Received: July 9, 2007
Published Online: August 29, 2007

 © 2007 Wiley-VCH Verlag GmbH & Co. KGaA, Weinheim 

DOI: 10.1002/ejic.200700079

# Synthesis of Flexible Bis-Intercalating Ruthenium(II) Complexes

**Craig R. Brodie[a] and Janice R. Aldrich-Wright*[a]**

**Keywords:** Ruthenium(II) / Synthesis / Chiral resolution / TRISPHAT / Dinuclear complexes / Bis-intercalators

We report the synthesis, resolution and characterisation of a number of novel ruthenium(II) complexes. Four mononuclear complexes, $[Ru(dpq)_2(3\text{-Br-phen})]^{2+}$, $[Ru(dpq)_2(4\text{-Cl-phen})]^{2+}$, $[Ru(dpq)_2(5\text{-Cl-phen})]^{2+}$ and $[Ru(dpq)_2(phen)]^{2+}$ were synthesised (dpq = dipyrido[3,2-*d*:2′,3′-*f*]quinoxaline, phen = 1,10-phenanthroline, 3-Br-phen = 3-bromo-1,10-phenanthroline, 4-Cl-phen = 4-chloro-1,10-phenanthroline, 5-Cl-phen = 5-chloro-1,10-phenanthroline). These complexes were resolved using the chiral TRISPHAT anion, [tris(tetrachlorocatecholato)phosphate(V)]$^-$. Racemic mononuclear complexes were used in the synthesis of the racemic dinuclear complexes, $[\{Ru(dpq)_2\}_2\mu\text{-(phen-}n\text{-SOS-}n\text{-phen)}]^{4+}$ (SOS = 2-mercaptoethyl ether, $n$ = 3, 4 or 5). Resolved mononuclear complexes were used to synthesise stereoselectively the ΔΔ- and ΛΛ-enantiomers of their respective dinuclear complexes. All metal complexes were characterised by $^1$H NMR, ESI-MS, UV/Vis and luminescence spectroscopy. Resolved metal complexes were further characterised using CD spectroscopy and chiral $^1$H NMR titrations.

(© Wiley-VCH Verlag GmbH & Co. KGaA, 69451 Weinheim, Germany, 2007)

## Introduction

The widespread interest in ruthenium(II) complexes as DNA probes was initially sparked by the study of these complexes as potential anticancer agents.[1] Since then, ruthenium(II) complexes have displayed potential as medical diagnostic tools through their ability to act as "molecular light switches"; complexes which exhibit fluorescence only in the presence of DNA,[2–4] while others have been shown to induce the breakage of DNA strands by photocleavage.[5–9] By incorporating certain ligands, such as dipyrido[3,2-*d*:2′,3′-*f*]quinoxaline (dpq), it is possible to produce ruthenium(II) complexes that display some measure of DNA sequence selectivity,[8,10] enantioselectivity[11–14] and/or preference for DNA base mismatches.[15]

Mononuclear ruthenium(II) complexes are relatively small, can only span 2–4 DNA base pairs, and bind to the double helix over a range of $K_b \approx 10^4$–$10^6$ M$^{-1}$, depending on the intercalating ligand such as dpq $K_b = 5.9 \times 10^4$,[16] dpqc $K_b = 8.5 \times 10^4$[17] and dppz $K_b > 10^6$.[8,18] Researchers have theorised that it may be possible to increase the DNA binding affinity, and therefore biological efficacy of ruthenium complexes, by producing complexes of higher nuclearity. There have been relatively few examples, however, of the application of dinuclear complexes as DNA probes.

Flexibly linked dinuclear ruthenium(II) complexes incorporating 1,10-phenanthroline (phen) and 2,2′-bipyridine (bpy) ligands bind to DNA with a ca. 50-fold increase in $K_b$ compared to the mononuclear analogues of these complexes.[19,20] The length of the linking chain was found to be a critical factor in determining binding strength,[21] with $n$ = 7 being the optimal chain length. Nordén et al.[22–27] have focused on metal complexes derived from $[Ru(phen)_2(dppz)]^{2+}$ (dppz = dipyrido[3,2-*a*:2′,3′-*c*]phenazine). The two-component metal-based units are linked through an intercalating dppz ligand and their DNA binding was found to be extremely strong (ca. $10^{11}$–$10^{13}$ M$^{-1}$).[26,28] Other dinuclear ruthenium complexes, where the metal centre is linked by a rigid bridge,[29] such as 2,2′-bipyrimidine,[30–33] display modest affinity for DNA bulge sites,[33] with significant enantioselectivity being observed between the three stereoisomeric forms ΔΔ, ΛΛ and *meso* (ΔΛ = ΛΔ).[30–33]

We have synthesised flexibly linked dinuclear complexes incorporating the intercalating ligand, dpq, in the hope of achieving high DNA binding strength and some measure of sequence selectivity (Figure 1). The dpq ligand is known to possess some purine-purine base specificity,[10] and adding flexibility to dinuclear intercalators may enhance the DNA binding ability of the complexes as they will be better able to fit within the DNA grooves. While only one intercalating ligand (dpq) per complex may be needed to increase the DNA affinity, two dpq ligands may allow for a more effective intercalation geometry given the specific orientation of each metal complex to DNA is not known. It is anticipated that these resolved dinuclear intercalating complexes, linked by a flexible linker and with a 4+ charge, will bind with a higher binding affinity than a mononuclear

[a] School of Biomedical and Health Sciences, University of Western Sydney,
Locked Bag 1797, Penrith South DC NSW 1797, Australia
Fax: +61-2-4620-3025
E-mail: j.aldrich-wright@uws.edu.au

Supporting information for this article is available on the WWW under http://www.eurjic.org or from the author.

 © 2007 Wiley-VCH Verlag GmbH & Co. KGaA, Weinheim 

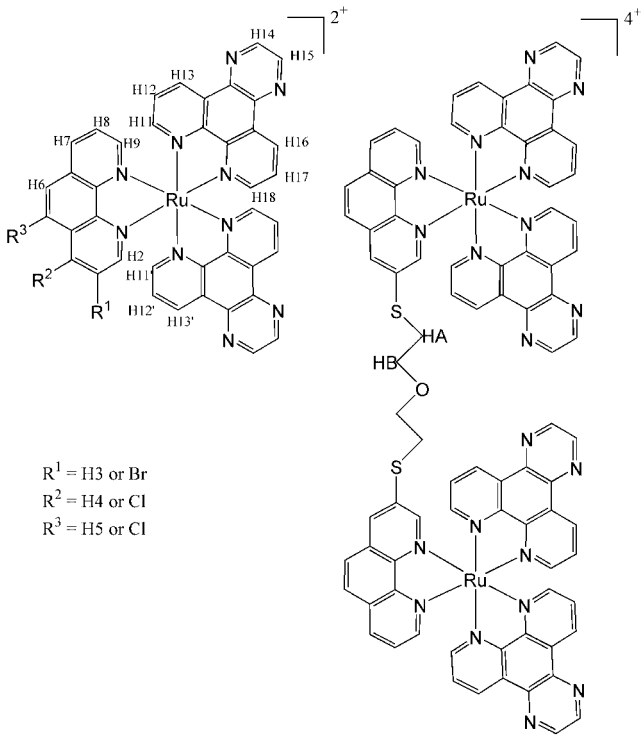


Figure 1. $[Ru(dpq)_2(R\text{-phen})]^{2+}$ and $[\{Ru(dpq)_2\}_2\mu\text{-(phen-3-SOS-3-phen)}]^{4+}$ showing the proton numbering scheme used in $^1H$ NMR assignments. Anions have been omitted for clarity.

complex.[34] It is also possible that the presence of additional intercalating ligands could cause unfavourable steric hindrance when the metal complex is bound to DNA. Varying the position of linker attachment (3-, 4- or 5-position on the phenanthroline ligand) causes subtle variations in the distance between the metal centres and complex geometry, which may affect the nature of the DNA adduct formed and the overall binding affinity.

Herein we expand an earlier communication[34] on the DNA binding of *rac*-$[\{Ru(dpq)_2\}_2\mu\text{-(phen-}n\text{-SOS-}n\text{-phen)}]^{4+}$ ($n$ = 3, 4 or 5, SOS = bis(2-mercaptoethyl) ether). We now report the synthesis of the mononuclear precursors to these complexes, the synthsis of *rac*/*meso* dinuclear complexes, the resolution of the mononuclear precursors and the stereo-retentive synthesis of the dinuclear complexes as their ΔΔ- and ΛΛ-enantiomers (see Figures 1, 2 and 3).

## Results and Discussion

### Synthesis of Mononuclear Complexes

**Synthesis and Characterisation of $[Ru(dpq)_2(pp')](PF_6)_2$.** $[Ru(dpq)_2(pp')]^{2+}$ (pp′ = phen, 3-Br-phen, 4-Cl-phen or 5-Cl-phen) were synthesised by refluxing $[Ru(dpq)_2Cl_2]$ with pp′ in water. Purification was achieved using silica gel and alumina chromatography. Assignment of the $^1H$ NMR

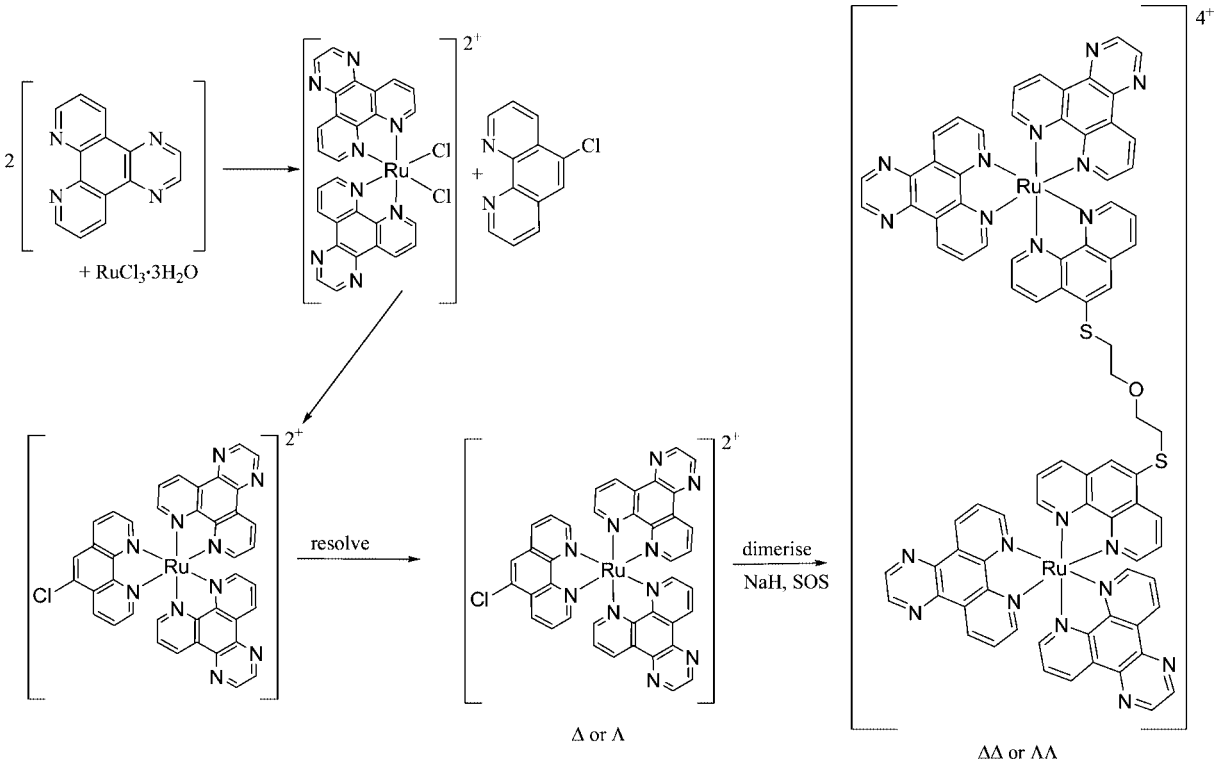


Figure 2. Synthetic route for the synthesis of dinuclear complexes of $[\{Ru(dpq)_2\}_2(\mu\text{-phen-5-SOS-5-phen})]^{4+}$. The same Scheme was also applied to synthesise $[\{Ru(dpq)_2\}_2(\mu\text{-phen-3-SOS-3-phen})]^{4+}$ and $[\{Ru(dpq)_2\}_2(\mu\text{-phen-4-SOS-4-phen})]^{4+}$. The resolution is described further in Figure 3.

 © 2007 Wiley-VCH Verlag GmbH & Co. KGaA, Weinheim 

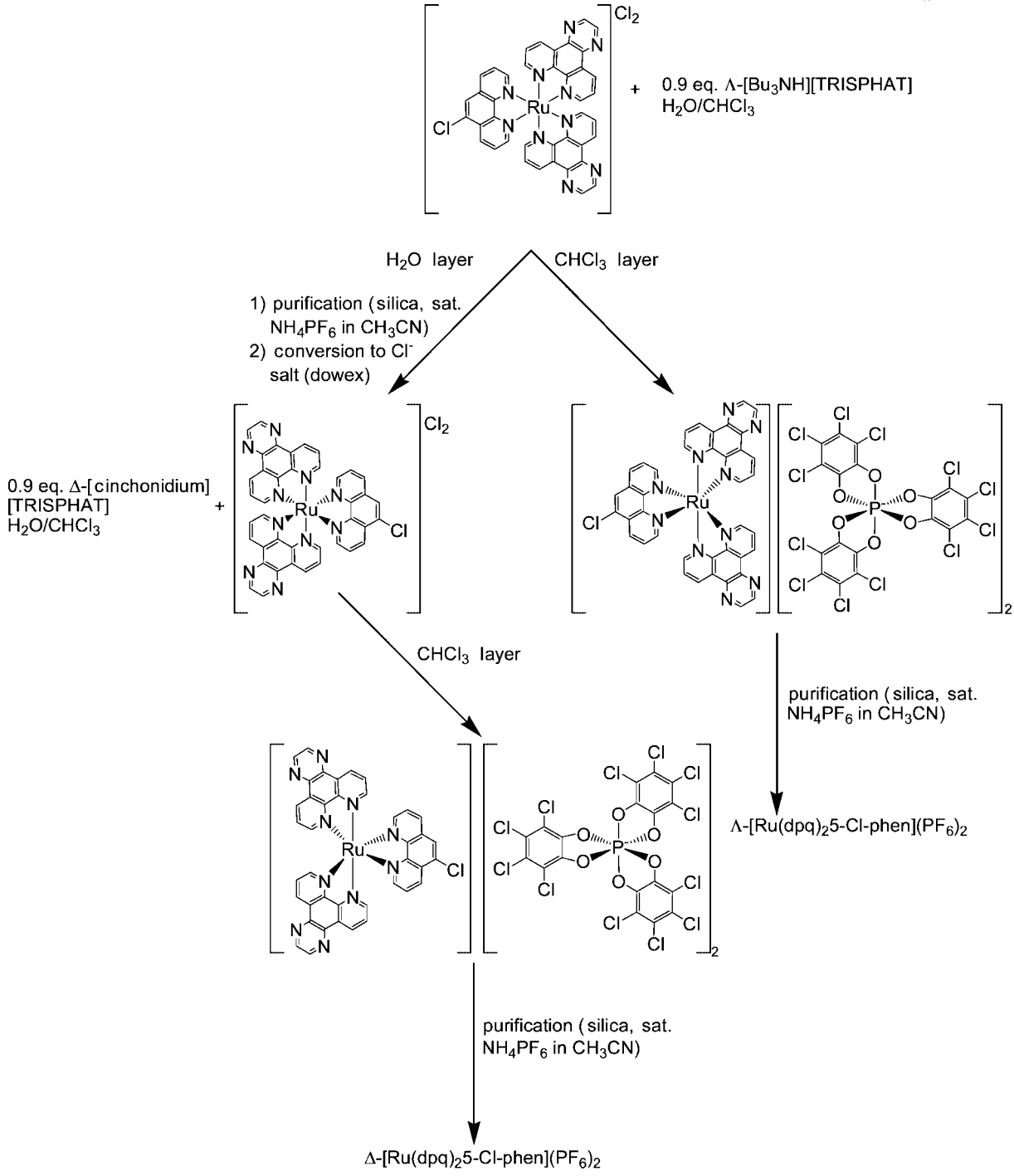


Figure 3. Resolution of $[Ru(dpq)_2(5\text{-Cl-phen})](PF_6)_2$ using the TRISPHAT anion.

spectra of the mononuclear complexes was made using NOESY and g-DQCOSY experiments. Each of the metal complexes exhibit similar resonances with comparative chemical shifts and splitting patterns observed for protons at the same relative positions. $[Ru(dpq)_2(phen)]^{2+}$ is an octahedral complex with two different types of bidentate ligands, and as such it belongs to point group $C_2$. This complex exhibits the simplest $^1H$ NMR spectrum of all the mononuclear complexes due to the presence of the $C_2$ axis. Since the halide substituent occupies the 3-, 4- and 5-position in the 3-Br-phen, 4-Cl-phen and 5-Cl-phen ligands, the complexes of these ligands feature $C_1$ symmetry (i.e. are dissymmetric) and the spectra for $[Ru(dpq)_2(pp')]^{2+}$ are slightly more complicated (see Supporting Information).

**Resolution of Mononuclear Complexes.** Attempts to resolve the $[Ru(dpq)_2(pp')]^{2+}$ complexes using solvent recycled chromatography employing SP-Sephadex® as the stationary phase and the chiral anions *O*,*O*′-dibenzoyl-L-tar-

 © 2007 Wiley-VCH Verlag GmbH & Co. KGaA, Weinheim 

taric acid and *O*,*O*′-ditoluoyl-L-tartaric acid by the methods of Rutherford et al.[35] were unsuccessful. Likewise, fractional recrystallisation employing (+)- and (–)-antimonyl tartrate was also unsuccessful.

The method of [(tris(tetrachlorocatecholato)phosphate(V))]$^-$ (TRISPHAT) extraction was developed from the technique of Lacour et al.[36] for analogous ruthenium(II) complexes. $[Ru(dpq)_2(pp')]Cl_2$ in water was added to a solution of $[Bu_3NH][\Lambda$-TRISPHAT] (0.9 equiv.) in chloroform. The solutions were stirred to allow complete equilibration to occur and the layers separated, with the organic layer containing $[Ru(dpq)_2(pp')][(\Lambda$-TRISPHAT$)_2]$. The reaction was subsequently repeated on the remaining aqueous layer using [cinchonidium][Δ-TRISPHAT] to give $[Ru(dpq)_2(pp')][(\Delta$-TRISPHAT$)_2]$.

The CD spectrum of each sample was obtained and the Δε values calculated as a means of characterising the optical properties of the metal complexes. The assignment of the absolute configurations of the resolved complexes in this study is based on CD and comparison with similar complexes whose absolute configuration has been determined by X-ray crystallography, such as the complex $[Ru(phen)_2(dpq)](PF_6)_2$.[35] In this work, relative enantiomeric purity of the chloride salt was determined by CD to be 99.0–93.3% for the monomers (Tables 1 and 2). The CD spectra for Δ- and Λ-$[Ru(dpq)_2(5\text{-Cl-phen})](PF_6)_2$ are shown in Figure 4 and those of Δ,Λ-$[Ru(dpq)_2(phen)]^{2+}$, Δ,Λ-$[Ru(dpq)_2(3\text{-Br-phen})]^{2+}$ and Δ,Λ-$[Ru(dpq)_2(4\text{-Cl-phen})]^{2+}$ are shown in the Supporting Information. As expected for a pair of enantiomers, there is a mirror–image relationship between the CD curves of the Δ- and Λ-enantiomers as well as the presence of isosbetic points, where the spectra of the Δ- and Λ-enantiomers intercept on the *x*-axis.

The enantiopurity of the samples was also confirmed by the use of a $^1$H NMR TRISPHAT titration.$^1$H NMR experiments using chiral shifting agents have been applied previously[37] and were necessary in order to confirm that complete resolution had been achieved. The TRISPHAT anion has previously been shown to be a successful chiral shift reagent, specifically with complexes such as $[Ru(phen)_3]$.[38,39] The TRISPHAT titration was performed initially on *rac*/*meso* mixtures of the metal complexes to demonstrate that selective resonance shifts would be induced in the $^1$H NMR spectrum of each metal complex. As can be

Table 1. CD data obtained for the metal complexes. All measurements conducted in $CH_3CN$ at 25 °C.

| Metal complex | CD, $\lambda$ / nm (Δε, mdeg M$^{-1}$ cm$^{-1}$) |
|---|---|
| Δ-$[Ru(dpq)_2(phen)](PF_6)_2$ | 462.5 (–24.9), 415.5 (+21.2), 298.0 (–139.7), 265.0 (–189.9), 248.5, (+109.4), 216.0, (+73.7) |
| Λ-$[Ru(dpq)_2(phen)](PF_6)_2$ | 462.5, (+21.8), 415.0 (–20.4), 298.0 (+123.3), 265.5 (+188.5), 249.0, (–109.6), 216.0, (–66.6) |
| Δ-$[Ru(dpq)_2(3\text{-Br-phen})](PF_6)_2$ | 463.0 (–23.2), 414.5 (+22.7), 300.0 (–148.1), 275.0 (–109.8), 247.0 (+45.5), 219.0, (+51.8) |
| Λ-$[Ru(dpq)_2(3\text{-Br-phen})](PF_6)_2$ | 463.0 (+24.8), 414.5 (–23.4), 300.0 (+155.3), 275.0 (+112.8), 247.0 (–47.6), 216.5, (–55.9) |
| Δ-$[Ru(dpq)_2(4\text{-Cl-phen})](PF_6)_2$ | 465.0 (–26.7), 415.5 (+22.8), 299.0 (–139.5), 267.5 (–175.5), 249.5 (+95.6), 218.5, (+60.9) |
| Λ-$[Ru(dpq)_2(4\text{-Cl-phen})](PF_6)_2$ | 465.5 (+24.8), 417.0 (–21.1), 299.0 (+129.8), 267.5 (+163.9), 249.5 (–90.0), 216.5, (–57.1) |
| Δ-$[Ru(dpq)_2(5\text{-Cl-phen})](PF_6)_2$ | 463.5 (–26.2), 414.5 (+23.1), 299.0 (–140.0), 270.5 (–171.4), 250.5 (+88.0), 216.0, (+69.5) |
| Λ-$[Ru(dpq)_2(5\text{-Cl-phen})](PF_6)_2$ | 463.5 (+26.7), 414.5 (–22.9), 298.5 (+141.4), 271.0 (+176.5), 251.0 (–90.3), 217.0, (–68.6) |
| ΔΔ-$[\{Ru(dpq)_2\}_2\mu\text{-(phen-3-SOS-3-phen)}](PF_6)_4$ | 464.0 (–48.3), 415.0 (+46.1), 299.0 (–269.6), 260.0 (–188.3), 242.0 (+188.9), 213.0, (+111.8) |
| ΛΛ-$[\{Ru(dpq)_2\}_2\mu\text{-(phen-3-SOS-3-phen)}](PF_6)_4$ | 463.0 (+54.9), 415.5 (–55.1), 299.0 (+317.1), 260.0 (+222.8), 242.0 (–220.4), 212.0, (–133.1) |
| ΔΔ-$[\{Ru(dpq)_2\}_2\mu\text{-(phen-4-SOS-4-phen)}](PF_6)_4$ | 470.0 (–44.9), 419.0 (+35.1), 298.5 (–218.6), 263.5 (–293.0), 247.0 (+163.6), 213.5, (+152.4) |
| ΛΛ-$[\{Ru(dpq)_2\}_2\mu\text{-(phen-4-SOS-4-phen)}](PF_6)_4$ | 468.5 (+45.5), 418.5 (–36.2), 298.5 (+213.3), 263.5 (+280.5), 247.5 (–169.3), 213.5, (–149.6) |
| ΔΔ-$[\{Ru(dpq)_2\}_2\mu\text{-(phen-5-SOS-5-phen)}](PF_6)_4$ | 464.0 (–59.2), 415.0 (+43.7), 299.0 (–309.1), 260.5 (–101.1), 241.0 (+25.1), 216.5, (+163.0) |
| ΛΛ-$[\{Ru(dpq)_2\}_2\mu\text{-(phen-5-SOS-5-phen)}](PF_6)_4$ | 464.0 (+53.5), 416.0 (–49.4), 299.0 (+307.6), 260.5 (+101.6), 240.0 (–35.1), 216.5, (–173.2) |

Table 2. Relative enantiomeric purity, quantum yield, emission and absorption data of the metal complexes. All measurements conducted in $CH_3CN$ at 25 °C.

| Metal complex | Relative enantiomeric purity %[a] | Quantum yield $\Phi$ | Emission $\lambda_{max}$ / nm | Absorption $\lambda_{max}$ / nm ($\varepsilon \times 10^4$ mol$^{-1}$ dm$^3$ cm$^{-1}$) |
|---|---|---|---|---|
| Δ-$[Ru(dpq)_2(phen)](PF_6)_2$ | 93.9 ± 5.3 | | | 447 (1.7), 290 (4.6) sh[b], 258 (10.6), 206 (6.7) |
| Λ-$[Ru(dpq)_2(phen)](PF_6)_2$ | | 0.061 | 604–608 | |
| Δ-$[Ru(dpq)_2(3\text{-Br-phen})](PF_6)_2$ | 95.3 ± 1.9 | | | 447 (1.9), 257 (10.0), 207 (7.8) |
| Λ-$[Ru(dpq)_2(3\text{-Br-phen})](PF_6)_2$ | | 0.042 | 590–600 | |
| Δ-$[Ru(dpq)_2(4\text{-Cl-phen})](PF_6)_2$ | 93.3 ± 0.6 | | | 449 (2.1), 291 (5.4) sh, 257 (12.0), 207 (8.1) |
| Λ-$[Ru(dpq)_2(4\text{-Cl-phen})](PF_6)_2$ | | 0.050 | 590–600 | |
| Δ-$[Ru(dpq)_2(5\text{-Cl-phen})](PF_6)_2$ | 99.0 ± 1.8 | | | 448 (2.0), 291 (5.1) sh, 257 (11.6), 207 (7.7) |
| Λ-$[Ru(dpq)_2(5\text{-Cl-phen})](PF_6)_2$ | | 0.059 | 598–598 | |
| ΔΔ-$[\{Ru(dpq)_2\}_2\mu\text{-(phen-3-SOS-3-phen)}](PF_6)_4$ | 85.1 ± 1.6 | | | 448 (3.7), 255 (20.8), 215 (13.6) |
| ΛΛ-$[\{Ru(dpq)_2\}_2\mu\text{-(phen-3-SOS-3-phen)}](PF_6)_4$ | | 0.062 | 603–608 | |
| ΔΔ-$[\{Ru(dpq)_2\}_2\mu\text{-(phen-4-SOS-4-phen)}](PF_6)_4$ | 99.9 ± 3.2 | | | 452 (4.8), 257 (20.5), 215 (15.1) |
| ΛΛ-$[\{Ru(dpq)_2\}_2\mu\text{-(phen-4-SOS-4-phen)}](PF_6)_4$ | | 0.053 | 607–610 | |
| ΔΔ-$[\{Ru(dpq)_2\}_2\mu\text{-(phen-5-SOS-5-phen)}](PF_6)_4$ | 94.1 ± 13.3 | | | 450 (4.8), 256 (20.2), 217 (14.1) |
| ΛΛ-$[\{Ru(dpq)_2\}_2\mu\text{-(phen-5-SOS-5-phen)}](PF_6)_4$ | | 0.048 | 602–603 | |

[a] The relative enantiomeric purity has been determined by dividing the intensity of each of the peaks of one enantiomer by the corresponding peaks of the other. The averages for all the peaks in the spectrum are given as percentage purity along with the standard deviation. [b] sh = shoulder band.

 © 2007 Wiley-VCH Verlag GmbH & Co. KGaA, Weinheim 

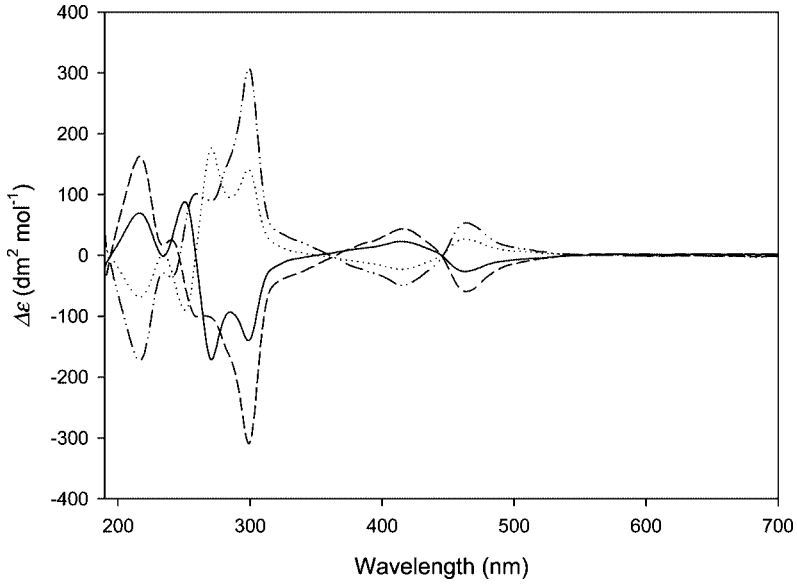


Figure 4. CD spectra ($CH_3CN$) of Δ-[Ru(dpq)$_2$(5-Cl-phen)](PF$_6$)$_2$ (solid line), Λ-[Ru(dpq)$_2$(5-Cl-phen)](PF$_6$)$_2$ (dotted line), ΔΔ-[{Ru(dpq)$_2$}$_2$-μ-(phen-5-SOS-5-phen)](PF$_6$)$_4$ (dashed line) and ΛΛ-[{Ru(dpq)$_2$}$_2$μ-(phen-5-SOS-5-phen)](PF$_6$)$_4$ (dashed and dotted line).

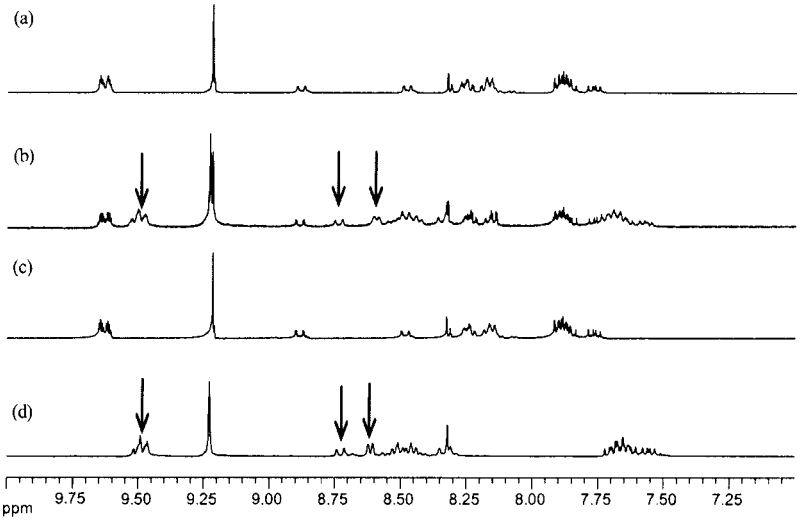


Figure 5. $^1$H NMR ($CD_3CN$, 25 °C) titration of [Ru(dpq)$_2$(5-Cl-phen)](PF$_6$)$_2$ with [Bu$_3$NH][Λ-TRISPHAT]. Arrows indicate the splitting and shifting of the Δ-[Ru(dpq)$_2$(5-Cl-phen)](PF$_6$)$_2$ proton resonances from the Λ-[Ru(dpq)$_2$(5-Cl-phen)](PF$_6$)$_2$ proton resonances; (a) *rac*-[Ru(dpq)$_2$(5-Cl-phen)](PF$_6$)$_2$, (b) *rac*-[Ru(dpq)$_2$(5-Cl-phen)](PF$_6$)$_2$ + 1 mol-equiv. of [Bu$_3$NH][Λ-TRISPHAT], (c) Δ-[Ru(dpq)$_2$(5-Cl-phen)](PF$_6$)$_2$ + 1 mol-equiv. of [Bu$_3$NH][Λ-TRISPHAT] and (d) Λ-[Ru(dpq)$_2$(5-Cl-phen)](PF$_6$)$_2$ + 1 mol-equiv. of [Bu$_3$NH][Λ-TRISPHAT].

seen in Figure 5, the addition of 1 mol-equiv. of [Bu$_3$NH][Λ-TRISPHAT] to *rac*-[Ru(dpq)$_2$(5-Cl-phen)](PF$_6$)$_2$ causes the resonances for the metal complex to broaden and split into two groups – one complete set of resonances for each enantiomer.

The three most downfield resonances, corresponding to the H13/16, H14/15 and H4 protons are the signals most easily used for the assessment of optical purity, because each of them is isolated from other overlapping resonances. The resonance for H13/16 splits into two multiplets, one resonance (due to Δ-[Ru(dpq)$_2$(5-Cl-phen)](PF$_6$)$_2$) remains at $\delta$ = 9.63 ppm while the resonance for Λ-[Ru(dpq)$_2$(5-Cl-phen)](PF$_6$)$_2$ shifts upfield to 9.50 ppm. Similarly, the H14/15 and H4 resonances also split, with separations of 0.01 ppm and 0.15 ppm, respectively, observed between the Δ- and Λ-resonances. The addition of 1 mol-equiv. of [Bu$_3$NH][Λ-TRISPHAT] does not induce any change in the $^1$H NMR spectrum of Δ-[Ru(dpq)$_2$(5-Cl-phen)](PF$_6$)$_2$, while the addition of [Bu$_3$NH][Λ-TRISPHAT] to Λ-[Ru(dpq)$_2$(5-Cl-phen)](PF$_6$)$_2$ induces chemical shift changes in all resonances of the metal complex.

The results from the chiral $^1$H NMR titration experiment shown in Figure 5 agree with those published previously for [Ru(4,7-Me$_2$phen)$_3$]$^{2+}$ and [Ru(Me$_2$bpy)$_3$]$^{2+}$, where it was shown that Λ-TRISPHAT will interact more strongly with the Λ-enantiomer of a metal complex than with the Δ-en-

 © 2007 Wiley-VCH Verlag GmbH & Co. KGaA, Weinheim 

Table 3. Summary of the MS data obtained for the metal complexes. All measurements conducted in $CH_3CN$ at 25 °C.

| Metal complex | ESI-MS (calcd., found) (*m*/*z*) |
|---|---|
| Δ-[Ru(dpq)$_2$(phen)](PF$_6$)$_2$ | [M(PF$_6$) + H]$^+$ (891.7, 891.2), [M]$^{2+}$ (372.9, 372.4) |
| Λ-[Ru(dpq)$_2$(phen)](PF$_6$)$_2$ | [M(PF$_6$) + H]$^+$ (891.7, 891.4), [M]$^{2+}$ (372.9, 371.0) |
| Δ-[Ru(dpq)$_2$(3-Br-phen)](PF$_6$)$_2$ | [M(PF$_6$) + H]$^+$ (970.7, 970.5), [M]$^{2+}$ (412.3, 412.7) |
| Λ-[Ru(dpq)$_2$(3-Br-phen)](PF$_6$)$_2$ | [M(PF$_6$) + H]$^+$ (970.7, 970.5), [M]$^{2+}$ (412.3, 412.7) |
| Δ-[Ru(dpq)$_2$(4-Cl-phen)](PF$_6$)$_2$ | [M(PF$_6$)]$^+$, (925.2, 924.6). [M]$^{2+}$ (390.1, 390.0) |
| Λ-[Ru(dpq)$_2$(4-Cl-phen)](PF$_6$)$_2$ | [M(PF$_6$)]$^+$ (925.2, 924.6), [M]$^{2+}$ (390.1, 390.0) |
| Δ-[Ru(dpq)$_2$(5-Cl-phen)](PF$_6$)$_2$ | [M(PF$_6$)]$^+$ (925.2, 924.7), [M]$^{2+}$ (390.1, 390.0) |
| Λ-[Ru(dpq)$_2$(5-Cl-phen)](PF$_6$)$_2$ | [M(PF$_6$)]$^+$ (925.2, 924.7), [M]$^{2+}$ (390.1, 390.0) |
| ΔΔ-[{Ru(dpq)$_2$}$_2$μ-(phen-3-SOS-3-phen)](PF$_6$)$_4$ | [M(PF$_6$)$_2$]$^{2+}$ (957.8, 958.0), [M(PF$_6$)]$^{3+}$ (590.2, 590.7), [M]$^{4+}$ (406.4, 407.0) |
| ΛΛ-[{Ru(dpq)$_2$}$_2$μ-(phen-3-SOS-3-phen)](PF$_6$)$_4$ | [M(PF$_6$)$_2$]$^{2+}$ (957.8, 958.1), [M(PF$_6$)]$^{3+}$ (590.2, 590.4), [M]$^{4+}$ (406.4, 406.6) |
| ΔΔ-[{Ru(dpq)$_2$}$_2$μ-(phen-4-SOS-4-phen)](PF$_6$)$_4$ | [M(PF$_6$)$_2$]$^{2+}$ (957.8, 958.3), [M(PF$_6$)]$^{3+}$ (590.2, 590.7), [M]$^{4+}$ (406.4, 407.0) |
| ΛΛ-[{Ru(dpq)$_2$}$_2$μ-(phen-4-SOS-4-phen)](PF$_6$)$_4$ | [M(PF$_6$)$_2$]$^{2+}$ (957.8, 958.3), [M(PF$_6$)]$^{3+}$ (590.2, 590.7), [M]$^{4+}$ (406.4, 406.9) |
| ΔΔ-[{Ru(dpq)$_2$}$_2$μ-(phen-5-SOS-5-phen)](PF$_6$)$_4$ | [M(PF$_6$)$_4$ + H]$^+$ (2206.6, 2206.4), [M(PF$_6$)$_3$]$^+$ (2060.6, 2061.3), [M(PF$_6$)$_2$]$^{2+}$ (957.8, 958.4), [M(PF$_6$)]$^{3+}$ (590.2, 590.7), [M]$^{4+}$ (406.4, 406.9) |
| ΛΛ-[{Ru(dpq)$_2$}$_2$μ-(phen-5-SOS-5-phen)](PF$_6$)$_4$ | [M(PF$_6$)$_2$]$^{2+}$ (957.8, 957.3), [M(PF$_6$)]$^{3+}$ (590.2, 589.7), [M]$^{4+}$ (406.4, 406.3) |

antiomer of the same metal complex.[35] The TRISPHAT titrations were repeated for all the resolved metal complexes and similar results were observed for each.

The mononuclear metal complexes were also analysed using electrospray ionisation mass spectrometry (ESI-MS) as an additional method of characterisation (Table 3). Although the parent ions, [M(PF$_6$)$_2$ + H]$^+$ were not observed, peaks were generally observed for the [M(PF$_6$)]$^+$ and [M]$^{2+}$ ions of each complex (e.g. Δ-[Ru(dpq)$_2$(5-Cl-phen)](PF$_6$)$_2$ ([M(PF$_6$)]$^+$ *m*/*z* calcd. 925.2, found 924.7); ([M]$^{2+}$ *m*/*z* calcd. 390.1, found 390.0)), confirming the molecular weights of the metal complexes. The isotopic splitting patterns observed agree closely with those calculated. The peak due to the [M(PF$_6$)]$^+$ ion was approximately twice the intensity of that due to the [M]$^{2+}$ ion, and this ratio was observed for all the mononuclear complexes studied.

## Dinuclear Complexes

**Synthetic Method Development:** Synthesising [{Ru(dpq)$_2$}$_2$μ-(phen-*n*-SOS-*n*-phen)](PF$_6$)$_4$ (*n* = 3, 4 or 5) by reacting the bridging SOS linker with the mononuclear complexes (DMF, $N_{2(g)}$, NaH, 25 °C) resulted in a number of side-products, in addition to the required complex. The impurities were characterised by TLC and $^1$H NMR spectroscopy. The simplest component in the mixture was the unreacted mononuclear complex [Ru(dpq)$_2$(5-Cl-phen)]$^{2+}$. A mononuclear ruthenium complex with a non-bridging dithiol linker attached, that had not dimerised with a second monomer of [Ru(dpq)$_2$(phen-*n*-SOS-H)]$^{2+}$ was also identified. A third species was also found in which the linker had reacted with itself forming a dinuclear ruthenium(II) complex, bridged by a disulfide-bonded linker, forming a 14 unit chain instead of the desired seven. The desired dinuclear ruthenium(II) complexes were isolated from solution by precipitation with diethyl ether followed by silica gel chromatography.

In the initial method development the synthesis of the dinuclear metal complexes using racemic (unresolved) mononuclear precursors was tried and it was expected that this would afford a mixture consisting of 25% of each of the two homochiral enantiomers, ΔΔ and ΛΛ, and 50% of the *meso* (ΔΛ/ΛΔ) diastereoisomer. The $^1$H NMR spectra of the ΔΔ- and ΛΛ-enantiomers of the metal complexes are

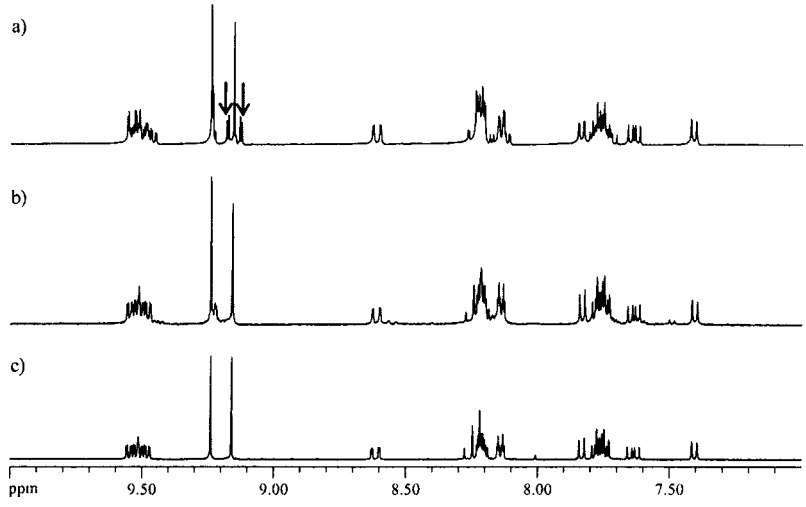


Figure 6. $^1$H NMR spectra ($CD_3CN$, 25 °C) of the stereoisomers of [{Ru(dpq)$_2$}$_2$μ-(phen-4-SOS-4-phen)](PF$_6$)$_4$; (a) *rac*/*meso* (ΔΔ/ΛΛ/ΔΛ/ΛΔ-), (b) ΔΔ- and (c) ΛΛ- showing the presence of the *meso* (ΔΛ/ΛΔ-) complex (indicated by arrows).

 © 2007 Wiley-VCH Verlag GmbH & Co. KGaA, Weinheim 

slightly different from those of the *meso* (ΔΛ/ΛΔ)-diastereoisomer, giving rise to overlapping resonances due to the chemically identical ΔΔ- and ΛΛ- enantiomers with the *meso* (ΔΛ/ΛΔ) form. Due to resonance overlap, it was not possible to determine the ratio of the enantiomers formed in these experiments.

When the dinuclear metal complexes were synthesised using enantiopure starting materials, resonances due to the *meso* diastereoisomer were absent from the $^1$H NMR spectra of the ΔΔ- and ΛΛ complexes (Figure 6).

**UV/Vis:** The extinction coefficients for ΔΔ- and ΛΛ-[{Ru(dpq)$_2$}$_2$μ-(phen-3-SOS-3-phen)]$^{4+}$ exhibited an increase in intensity of 220% compared to *rac*-[Ru(dpq)$_2$(3-Br-phen)]$^{2+}$. The extinction coefficients for the ΔΔ- and ΛΛ-[{Ru(dpq)$_2$}$_2$μ-(phen-4-SOS-4-phen)]$^{4+}$ and ΔΔ- and ΛΛ-[{Ru(dpq)$_2$}$_2$μ-(phen-5-SOS-5-phen)]$^{4+}$ complexes also increased by 180 and 200%, respectively, compared to their mononuclear analogues ([Ru(dpq)$_2$(4-Cl-phen)]$^{2+}$ and [Ru(dpq)$_2$(5-Cl-phen)]$^{2+}$). Three main peaks were observed in the UV/Vis spectra of the metal complexes, in the ranges of 206–217 nm, 256–258 nm and 447–452 nm. For the mononuclear metal complexes, the transitions observed in the region of 447–452 nm are attributed to metal-to-ligand charge transfer (MLCT). For both the mono- and dinuclear metal complexes, the bands in the region of 206–256 are attributed predominantly to overlapping π→π* transitions. In the spectrum of each of the dinuclear complexes, the MLCT bands were observed at slightly higher wavelength (lower energy) than the MLCT bands of the analogous mononuclear complexes.

**Luminescence Quantum Yields:** The luminescence quantum yields of the complexes were determined and are shown in Table 2. Excitation at 450 nm of the metal complexes in $CH_3CN$ at 25 °C results in an emission maximum at 600 ± 10 nm (depending on the position of substitution shown in Table 2) and is due to both the phen and dpq ligands. The luminescence quantum yields of the mononuclear metal complexes are in the range of $\Phi = 4.2 \times 10^{-2}$ to $5.9 \times 10^{-2}$ and for the dinuclear complexes are in the range of $\Phi = 4.8 \times 10^{-2}$ to $6.2 \times 10^{-2}$. It is not expected that the excitation and emission maxima and $\Phi$ would vary significantly between the mono- and dinuclear complexes (as was the case with $\varepsilon_{max}$). The metal centres in the dinuclear complexes are separated by a relatively long aliphatic linker and therefore the electronic configuration of the ruthenium(II) centres is not significantly changed upon dimerisation.

**Circular Dichroism:** The CD spectrum of each of the resolved dinuclear metal complexes was obtained and the Δε values calculated as a means of characterising the optical properties of the complexes (see Tables 1 and 2, Figure 4 and Supporting Information). The relative enantiomeric purity of the chloride salt of each of the complexes was determined by CD spectroscopy to be 99.9–85.1% for the dimers. Each pair of enantiomers shows a mirror–image relationship between the CD curves of the ΔΔ and ΛΛ enantiomers and the presence of isosbetic points, but when compared with the spectra of the corresponding mononuclear complex subtle differences are observed.

The main CD features for the mononuclear complexes Δ-[Ru(dpq)$_2$(phen)]$^{2+}$, Δ-[Ru(dpq)$_2$(4-Cl-phen)]$^{2+}$ and Δ-[Ru(dpq)$_2$(5-Cl-phen)]$^{2+}$ are two sets of bisignate curves due to the excition coupling of the π–π* transitions of the diimine chromophores that are centred around 250 nm. The two bands between 200–250 nm are positive, the two bands between 250–350 nm are negative and the intensities between the monomeric complexes are comparable. The CD spectra of Δ-[Ru(dpq)$_2$(4-Cl-phen)]$^{2+}$ and Δ-[Ru(dpq)$_2$(5-Cl-phen)]$^{2+}$ show very slight differences, about 10% in intensity in peaks at ca. 265, 247 and 216 nm. Δ-[Ru(dpq)$_2$(3-Br-phen)]$^{2+}$ has a similar CD spectrum, however, the intensities are significantly reduced for the peaks (% reduction) at 275 (58%), 247 (42%) and 219 (70%) nm when compared with Δ-[Ru(dpq)$_2$(phen)]$^{2+}$.

Telfer et al.[29] have shown that the energy ordering of the positive and negative Cotton effects is related directly to the absolute configuration of the metal centre. The contribution of intranuclear excition coupling to the CD spectra is dependent strongly upon the length of the bridging ligand and is not simply double the intensity of the appropriate mononuclear complex, as one might expect, even though a flexible linker connects the two metal complexes in this case. The CD spectra that are produced are uniquely different for each of the dimers indicating that although the linker does not rigidly orientate the molecules there must be some coupling between the chromophores and that the resulting CD spectra are not simply additive.

The CD spectrum of Δ-[Ru(dpq)$_2$(phen)]$^{2+}$ contains four intraligand π–π* transitions, between 190–300 nm (216, 248, 265 and 298 nm at Δε = 73, 109, –190, and –140 respectively), while the weak band at 462.5 nm is most likely to be an MLCT transition. The intense CD bands at ca. 298 and 265 nm (long-axis polarization transition) for Δ-[Ru(dpq)$_2$(phen)]$^{2+}$ is strongly negative and the CD bands at higher energy (ca. 247 and 216 nm) positive, confirming the assignment as the Δ-enantiomer.[35] As expected, the CD spectrum of Λ-[Ru(dpq)$_2$(phen)]$^{2+}$ exhibits peaks of opposite intensity.

The CD spectra of Δ- and Λ-[Ru(dpq)$_2$(5-Cl-phen)](PF$_6$)$_2$, and ΔΔ- and ΛΛ-[{Ru(dpq)$_2$}$_2$μ-(phen-5-SOS-5-phen)](PF$_6$)$_4$ are shown in Figure 4. The spectra of both the mono- and dinuclear metal complexes are characterised by the peak wavelengths and their intensity in the 190 to 500 nm region. The two peaks at higher wavelength (465 to 415 nm), due to the MLCT, are similar in shape for both the mono- and dinuclear metal complexes and the peaks are approximately double (2.26 and 1.89 times intensity respectively) the intensity for the dinuclear metal complexes compared to the mononuclear complexes. The peaks at 299 and 216 nm also are approximately double (2.21 and 2.35 times intensity respectively) however, the peaks at 261 and 241 nm are considerably less (0.59 and 0.29 times intensity, respectively) than the mononuclear complex.

The CD spectra of Δ- and Λ-[Ru(dpq)$_2$-(4-Cl-phen]$^{2+}$, ΔΔ- and ΛΛ-[{Ru(dpq)$_2$}$_2$μ-(phen-4-SOS-4-phen)]$^{4+}$ are provided in the Supporting Information. For ΔΔ-[{Ru(dpq)$_2$}$_2$μ-(phen-4-SOS-4-phen)]$^{4+}$ the two peaks at higher

 © 2007 Wiley-VCH Verlag GmbH & Co. KGaA, Weinheim 

wavelength (468 to 418 nm), due to the MLCT, are similar in shape for both the mono- and dinuclear metal complexes and the peaks are 1.68 and 1.54 the intensity, respectively, for the dinuclear metal complexes compared to the mononuclear complexes. The peaks at 289, 263 and 247 nm have all similarly increased in intensity (1.57, 1.67 and 1.71 times, respectively) whereas the peak at 213 nm is the only peak which is approximately double (2.50 times) in intensity when compared to Δ-$[Ru(dpq)_2$-(4-Cl-phen)$]^{2+}$.

The CD spectra of Δ- and Λ-$[Ru(dpq)_2$-(3-Br-phen)$]^{2+}$, ΔΔ- and ΛΛ-$[\{Ru(dpq)_2\}_2\mu$-(phen-3-SOS-3-phen)$]^{4+}$ are provided in the Supporting Information. For ΔΔ-$[\{Ru(dpq)_2\}_2\mu$-(phen-3-SOS-3-phen)$]^{4+}$ the two peaks at higher wavelength (463 to 415 nm), due to the MLCT, are similar in shape for both the mono- and dinuclear metal complexes and the peaks are more than double (2.21 and 2.35) the intensity, respectively, for the dinuclear metal complexes compared to the mononuclear complexes. The peaks at 299, 260 and 212 nm are also about double the intensity (2.04, 1.98 and 2.38 times intensity, respectively) whereas the peak at 242 nm is 4.63 times the intensity when compared to Δ-$[Ru(dpq)_2$-(3-Br-phen)$]^{2+}$.

These differences in the CD spectra indicate that the location of the flexible linker attachment in the 3-, 4- or 5-positions on the phenanthroline ligand contribute differently to internuclear excitation coupling. The transitions at ca. 216 and 299 nm and the intensity of the MLCT band for all of the complexes are about double that of the mononuclear complex indicating that the linker position has a limited effect on these transitions. The transitions at ca. 241 and 261 nm are particularly sensitive to the orientation of the coordinated ligands when the linker attachment is in the 3- (0.29 and 0.29 times the mononuclear respectively), 4- (1.71 and 1.67 times the mononuclear respectively) or 5- (4.65 and 1.98 times the mononuclear respectively) positions.

For ΔΔ- and ΛΛ-$[\{Ru(dpq)_2\}_2\mu$-(phen-3-SOS-3-phen)$]^{4+}$ the distance between the complexes and the orientation with respect to one another is sufficient for all of the transitions to be additive and in the case of the transition at 242 nm four times. For ΔΔ- and ΛΛ-$[\{Ru(dpq)_2\}_2\mu$-(phen-4-SOS-4-phen)$]^{4+}$ the internuclear excitation coupling is 1.5–2 for all transitions indicating that in this case each of the observed transitions for the complexes is almost independent. In the case of ΔΔ- and ΛΛ-$[\{Ru(dpq)_2\}_2\mu$-(phen-5-SOS-5-phen)$]^{4+}$ the distance between the complexes appears to be adequate to produce a reduction in the band intensity which is accompanied by a wavelength shift of –10 nm for the dinuclear complex at 240 nm (the mononuclear complex peak occurs at 250 nm).

**ESI-MS:** As with the mononuclear complexes, the racemic and resolved dinuclear complexes were also characterised by ESI-MS (Table 3). The parent ions, $[M(PF_6)_4 + H]^+$ were not observed for any of the complexes. In the case of ΔΔ-$[\{Ru(dpq)_2\}_2\mu$-(phen-5-SOS-5-phen)$](PF_6)_4$, the mass spectrum displayed $[M(PF_6)_2]^{2+}$ (*m*/*z* calcd. 957.8, found 958.4), $[M(PF_6)]^{3+}$ (*m*/*z* calcd. for 590.2, found 590.7) and $[M]^{4+}$ (*m*/*z* calcd. 406.4, found 406.9). The intensity of the peaks increased as the charge on the metal complexes increased, such that the order of intensity was $[M]^{4+} > [M(PF_6)]^{3+} > [M(PF_6)_2]^{2+}$ (100%, 50% and 18%, respectively). The other dinuclear metal complexes also exhibited isotopic patterns for the $[M(PF_6)_2]^{2+}$, $[M(PF_6)]^{3+}$ and $[M]^{4+}$ ions, in similar ratios to those observed for ΔΔ-$[\{Ru(dpq)_2\}_2\mu$-(phen-5-SOS-5-phen)$](PF_6)_4$. The *m*/*z* values and isotopic ratios for the peaks observed in the ESI-MS of all the metal complexes are in close agreement with the calculated values.

## Conclusions

Here we have demonstrated that the mononuclear complexes Δ,Λ-$[Ru(dpq)_2$(3-Br-phen)$]^{2+}$, Δ,Λ-$[Ru(dpq)_2$(4-Cl-phen)$]^{2+}$, Δ,Λ-$[Ru(dpq)_2$(5-Cl-phen)$]^{2+}$ and Δ,Λ-$[Ru(dpq)_2$-(phen)$]^{2+}$ can be used to produce enantiomerically pure dinuclear complexes ΔΔ- and ΛΛ-$[\{Ru(dpq)_2\}_2\mu$-(phen-3-SOS-3-phen)$]^{4+}$, ΔΔ- and ΛΛ-$[\{Ru(dpq)_2\}_2\mu$-(phen-4-SOS-4-phen)$]^{4+}$ and ΔΔ- and ΛΛ-$[\{Ru(dpq)_2\}_2\mu$-(phen-5-SOS-5-phen)$]^{4+}$. The resolution of the mononuclear complexes could only be achieved using the chiral TRISPHAT anion, as column chromatography and classical resolution techniques were not effective in this case. Resolution of the mononuclear metal complexes was confirmed by CD and chiral $^1$H NMR titrations using the TRISPHAT anion. The production of the enantiomerically pure dinuclear complexes was assessed by CD. When compared to the monomeric form, the intensity of the peaks in the CD spectra the dinuclear complexes were not simply double that of their mononuclear analogues. This suggests that the position of attachment of the flexible linker affects the internuclear excitation coupling between the chromophores located on each of the metal centres differently. Binding studies using the dinuclear metal complexes are under way for these potential DNA probes.

## Experimental Section

**Materials** Dowex® 1X8–200 ($Cl^-$ form), 1,10-phenanthroline, lithium chloride, 5-chloro-1,10-phenanthroline, aluminium oxide (activated, neutral, Brockman I), potassium hexafluorophosphate, ammonium hexafluorophosphate, anhydrous *N*,*N*′-dimethylformamide (99.9%), NaH, $KNO_3$ and silica gel (TLC grade) were all obtained from the Aldrich chemical company. Ruthenium trichloride $(RuCl_3)\cdot xH_2O$ was purchased from Precious Metals Online. Silica gel 60 (0.040–0.063 mm) for column chromatography was obtained from Merck. Bis(2-mercaptoethyl) ether was purchased from Lancaster. Deuterated solvents, [$D_2O$ (99.9% D), $CD_2Cl_2$ (99.8% D) and $CD_3CN$ (99.8% D)] were purchased from Cambridge Isotope Laboratories. 3-Br-phen was made by the method of Tzalis et al.,[40] 4-Cl-phen was made by the method of Snyder and Freier,[41] dpq was made by the method of Collins et al.[17] Tetrachlorocatechol was made by the method of Renner and Hopfer,[42] TRISPHAT was synthesised and resolved by the methods of Favarager et al.[43] and $[Ru(dpq)_2Cl_2]$ was synthesised by the method of Anderson et al.[44] as for the analogous bpy complex. All general reagents and solvents were used as received (unless specifically stated) and were of analytical reagent grade or higher.

 © 2007 Wiley-VCH Verlag GmbH & Co. KGaA, Weinheim 

**NMR Spectroscopy:** Routine NMR was carried out on a 300-MHz Varian Mercury spectrometer equipped with a variable temperature accessory. For one-dimensional $^1$H spectra, a spectral width of 4500 Hz was used with 18000 data points and relaxation delay of 1 s, with the temperature kept constant at 25 °C. The spectra were referenced internally to the solvent resonances. Two dimensional NOESY spectra were accumulated using a 4200 Hz spectral width with 256 increments in the $t_1$ dimension, 2048 points in the $t_2$ dimension and mixing times of 300–800 ms. Two dimensional g-DQCOSY experiments were recorded over a spectral width of 4200 Hz using 256 increments in the $t_1$ dimension, 2048 points in the $t_2$ dimension and a pulse repetition delay of 1.5–2.0 s.

**ESI-MS:** Electrospray ionisation mass spectrometry was carried out by the mass spectroscopic service provided by the Research School of Chemistry, Australian National University.

**Circular Dichroism:** Circular dichroism spectra were recorded using a Jasco J-810 CD spectropolarimeter at room temperature. Samples of metal complexes (approx. 0.22 mg) were weighed directly into a 1-cm cell. The samples were dissolved by the addition of $CH_3CN$ (3.000 mL) then diluted so that the absorbance maximum was in the range $2.2 \pm 0.2$ absorbance units. The spectrum of each sample was then reacquired (in the range of 190–700 nm), the data pitch was set at 0.5 nm, the scan speed at 500 nm/min and the response time at 1 s. Spectra are shown as an average of 20 accumulations. The value of the molar absorptivity ($\Delta\varepsilon$) was calculated according to Equation (1).[45]

$$\Delta\varepsilon = \frac{\theta}{32.982 \times c \times l} \quad (1)$$

**TRISPHAT Titrations:** Samples of metal complexes $[Ru(dpq)_2(pp')]^{2+}$ (pp′ = phen, 3-Br-phen, 4-Cl-phen or 5-Cl-phen) (approx. $4.4 \times 10^{-4}$ mmol) were weighed out and dissolved in $CD_2Cl_2$ (650 μL) in NMR tubes. A solution of [$Bu_3NH$][Λ-TRISPHAT] was also prepared in $CD_2Cl_2$ at such a concentration that 25 μL of this solution would be 1 equiv. of the metal complex. $^1$H NMR spectra were acquired for each sample before and after the addition of [$Bu_3NH$][Λ-TRISPHAT].

**UV/Vis:** Absorption spectra were measured at 25 °C in the range 200–800 nm using a Varian Cary 300 Bio UV/Vis double-beam spectrophotometer referenced to $H_2O$. Extinction coefficients were determined by repeated measurements of the absorbance of aqueous metal complex solutions of known concentration. The solutions were serially diluted so that for all peaks, three measurements within the range 0.3–0.8 were obtained. The gradient of the lines of best fit of a plot of concentration vs. absorbance at each $\lambda_{max}$ gave the extinction coefficients, $\varepsilon_{max}$.

**Radiative Quantum Yield:** Radiative quantum yield ($\Phi$) measurements were performed using an adaptation of the method of Damrauer et al.[46] UV spectra were recorded on a Varian Cary 300-Bio spectrophotometer equipped with temperature controller set at 298 K. Luminescence spectra were recorded on a Varian Cary Eclipse fluorescence spectrophotometer, also equipped with a temperature controller at 298 K. All metal complexes were used as $PF_6^-$ salts in $CH_3CN$. Values of $\Phi$ are reported relative to $[Ru(bpy)_3]^{2+}$ in $CH_3CN$ ($\Phi_r = 0.062$)[47] and were calculated using Equation (2),[48] where $\Phi_{unk}$ is the radiative quantum yield of the sample, $\Phi_{std}$ is the radiative quantum yield of the standard, $I_{unk}$ and $I_{std}$ are the integrated emission intensities of the sample and standard, respectively. $A_{unk}$ and $A_{std}$ are the absorbance of the sample and standard, respectively, at the wavelength of excitation (450 nm). $\eta_{unk}$ and $\eta_{std}$ are the indices of refraction of the sample and standard solutions, respectively. Values of $\eta$ corresponding to the pure solvent are generally used. Since all measurements were conducted in the same solvent, $\eta_{unk}/\eta_{std} = 1$.

$$\Phi_{unk} = \Phi_{std}\left(\frac{I_{unk}}{A_{unk}}\right)\left(\frac{A_{std}}{I_{std}}\right)\left(\frac{\eta_{unk}}{\eta_{std}}\right)^2 \quad (2)$$

## Metal Complex Synthesis

**Synthesis of $[Ru(dpq)_2(pp')](PF_6)_2$ (pp′ = phen, 3-Br-phen, 4-Cl-phen or 5-Cl-phen):** In a typical experiment, $[Ru(dpq)_2Cl_2]$ (1.0 g, 1.58 mmol) was suspended in $H_2O$ (800 mL) and the solution heated to reflux (30 min). The ligand pp′ (1.16 mmol) was dissolved in $CH_3CH_2OH$ (200 mL) and added dropwise over a period of 1 h. The mixture was kept at reflux for another 48 h, during which time it changed colour from black to deep red. After cooling, the solution was reduced in volume to ca. 100 mL before the addition of saturated $KPF_6$ solution (3 mL), which caused precipitation of the complex. The suspension was extracted with $CH_2Cl_2$ ($5 \times 200$ mL), into which the orange complex redissolved and the combined extracts were dried with anhydrous $Na_2SO_4$. The solution was evaporated to dryness to give the crude product as a red solid, which was purified on silica gel (eluent: 89% $CH_3CN$, 1% saturated $KNO_3$ solution, 10% $H_2O$). The fractions containing pure $[Ru(dpq)_2(pp')](PF_6)_2$ were identified by $^1$H NMR, combined and extracted with $CH_2Cl_2$. The compound was dissolved in acetone and then precipitated by the addition of $H_2O$. The complex was collected by vacuum filtration, washed with diethyl ether and air-dried. The complex was subsequently purified by column chromatography on alumina, eluting with $CH_3CN$. The single fraction was collected and the solvents evaporated to dryness to yield the product as an orange solid.

***rac*-$[Ru(dpq)_2(phen)](PF_6)_2$:** Yield 0.11 g (30%). UV ($CH_3CN$): $\lambda_{max}$ ($\varepsilon \times 10^4$, $mol^{-1}\,dm^3\,cm^{-1}$) = 447 (1.7), 290 (4.6), 258 (10.6), 206 (6.7) nm. Quantum luminescence yield ($\Phi$): 0.061. $^1$H NMR (300 MHz, $CD_3CN$): $\delta$ = 9.57 (dd, $J$ = 1.4 Hz, 4 H, H13/16), 9.26 (d, $J$ = 1.4 Hz, 4 H, H14/15), 8.66 (ddd, $J$ = 1.3, 1.3, 8.3 Hz, 4 H, H4/7), 8.30 (d, $J$ = 1.3 Hz, 2 H, H5/6), 8.26 (d, $J$ = 5.4 Hz, 4 H, H2/9), 8.16 (dddd, $J$ = 1.3, 1.3, 2.6, 5.2 Hz, 4 H, H11/18), 7.80 (m, 4 H, H12/17), 7.67 (ddd, $J$ = 1.3, 5.3, 8.3 Hz, 2 H, H3/8) ppm. ESI-MS $CH_3CN$ $m/z$ calcd. for $C_{40}H_{24}F_6N_{10}PRu$ $[M(PF_6) + H]^+$, 891.7, found 891.4, $m/z$ calcd. for $C_{40}H_{24}N_{10}Ru$ $[M]^{2+}$, 372.9, found 371.0.

***rac*-$[Ru(dpq)_2(3\text{-}Br\text{-}phen)](PF_6)_2$:** Yield 0.75 g (45%). UV ($CH_3CN$): $\lambda_{max}$ ($\varepsilon \times 10^4$, $mol^{-1}\,dm^3\,cm^{-1}$) = 447 (1.9), 257 (10.0), 207 (7.8). Quantum luminescence yield ($\Phi$): 0.042. $^1$H NMR (300 MHz, $CD_3CN$): $\delta$ = 9.55 (m, 4 H, H13/16), 9.24 (d, $J$ = 3.0 Hz, 4 H, H14/15), 8.88 (d, $J$ = 1.9 Hz, 1 H, H4), 8.65 (dd, $J$ = 1.2, 8.3 Hz, 1 H, H7), 8.33 (d, $J$ = 8.9 Hz, 1 H, H5), 8.24 (m, 4 H, H11/18), 8.14 (dd, $J$ = 1.2, 9.1 Hz, 1 H, H2), 8.14 (dd, $J$ = 1.3, 1.3 Hz, 1 H, H6), 8.10 (dd, $J$ = 1.3, 5.3 Hz, 1 H, H9), 7.80 (m, 4 H, H12/17), 7.68 (dd, $J$ = 5.3, 8.3 Hz, 1 H, H8) ppm. ESI-MS $CH_3CN$ $m/z$ calcd. for $C_{40}H_{24}BrF_6N_{10}PRu$ $[M(PF_6) + H]^+$, 970.7, found 972.2, $m/z$ calcd. for $C_{40}H_{23}BrN_{10}Ru$ $[M]^{2+}$, 412.3, found 409.9.

***rac*-$[Ru(dpq)_2(4\text{-}Cl\text{-}phen)](PF_6)_2$:** Yield 0.44 g (52%). UV ($CH_3CN$): $\lambda_{max}$ ($\varepsilon \times 10^4$, $mol^{-1}\,dm^3\,cm^{-1}$) = 449 (2.1), 291 (5.4), 257 (12.0), 207 (8.1). Quantum luminescence yield ($\Phi$): 0.050. $^1$H NMR (300 MHz, $CD_3CN$): $\delta$ = 9.55 (m, 4 H, H13/16), 9.24 (d, $J$ = 0.9 Hz, 4 H, H14/15), 8.67 (dd, $J$ = 1.3, 8.3 Hz, 1 H, H7), 8.52 (d, $J$ = 9.1 Hz, 1 H, H5), 8.40 (d, $J$ = 9.2 Hz, 1 H, H6), 8.20 (m, 4 H, H11/18), 8.12 (dd, $J$ = 1.3, 5.3 Hz, 2 H, H2/9), 8.03 (d, $J$ = 5.8 Hz, 1 H, H3),

 © 2007 Wiley-VCH Verlag GmbH & Co. KGaA, Weinheim 

7.78 (m, 4 H, H12/17), 7.68 (dd, $J$ = 5.3, 8.3 Hz, 1 H, H8) ppm. ESI-MS $CH_3CN$ $m/z$ calcd. for $C_{40}H_{23}ClF_6N_{10}PRu$ $[M(PF_6)]^+$, 925.2, found 926.1, $m/z$ calcd. for $C_{40}H_{23}BrN_{10}Ru$ $[M]^{2+}$, 390.1, found 390.3.

***rac*-[Ru(dpq)$_2$(5-Cl-phen)](PF$_6$)$_2$:** Yield 0.587 g (58%). UV ($CH_3CN$): $\lambda_{max}$ ($\varepsilon \times 10^4$, $mol^{-1}\,dm^3\,cm^{-1}$) = 448 (2.0), 291 (5.1), 257 (11.6), 207 (7.7). Quantum luminescence yield ($\Phi$): 0.059. $^1H$ NMR (300 MHz, $CD_3CN$): $\delta$ = 9.57 (ddd, $J$ = 1.5, 2.9, 8.3 Hz, 4 H, H13/16), 9.26 (d, $J$ = 0.7 Hz, 4 H, H14/15), 8.89 (dd, $J$ = 1.2, 8.5 Hz, 1 H, H4), 8.58 (dd, $J$ = 1.2, 8.3 Hz, 1 H, H7), 8.48 (s, 1 H, H6), 8.24 (m, 3 H, H2/11), 8.15 (m, 3 H, H9/18), 7.80 (m, 4 H, H12/17), 7.75 (d, $J$ = 5.3 Hz, 1 H, H3), 7.68 (dd, $J$ = 5.3, 8.3 Hz, 1 H, H8) ppm. ESI-MS $CH_3CN$ $m/z$ calcd. for $C_{40}H_{23}ClF_6N_{10}PRu$ $[M(PF_6)]^+$, 925.2, found 925.6, $m/z$ calcd. for $C_{40}H_{23}ClN_{10}Ru$ $[M]^{2+}$, 390.1, found 390.2.

**Resolution of Mononuclear Complexes:** TRISPHAT extraction was carried out using modifications of the methods of Lacour et al.[36] In a typical experiment, [Ru(dpq)$_2$(pp′)](PF$_6$)$_2$ pp′ = phen, 3-Br-phen, 4-Cl-phen or 5-Cl-phen) (approx. 0.83 mmol, 1 equiv.) was suspended in $H_2O$ (1.8 L) and the solution stirred with Dowex® 1X8–200 (2.0 g) for 4 h to convert the metal complex to a chloride salt. The solution was filtered to remove the resin and [$Bu_3NH$][Λ-TRISPHAT] (approx. 0.75 mmol, 0.9 equiv.) in chloroform (600 mL) was added. The solution was stirred in darkness for 4 h, and then filtered to remove any precipitate. The organic layer was removed, dried with anhydrous $MgSO_4$ and the solvents evaporated to dryness to give an orange solid (first isolate, Λ-[Ru(dpq)$_2$(pp′)](Λ-TRISPHAT)$_2$).

To the remaining aqueous layer was added saturated $KPF_6$ (5 mL), causing the formation of an orange precipitate which was subsequently extracted with $CH_2Cl_2$ (3 × 250 mL). The extracts were dried with anhydrous $MgSO_4$ and the solvents evaporated to dryness to give an orange solid (Δ-[Ru(dpq)$_2$(pp′)](PF$_6$)$_2$) (pp′ = phen, 3-Br-phen, 4-Cl-phen or 5-Cl-phen). This complex was dissolved in $CH_3CN$ and purified on silica gel using saturated $NH_4PF_6$ in $CH_3CN$ as eluent. A single orange band was collected and the solvents evaporated to dryness (intermediate isolate).

The intermediate isolate was suspended in $H_2O$ (900 mL) and converted into the chloride salt by stirring with Dowex® 1X8–200 (1.0 g) for 4 h. The solution was filtered to remove the resin and a suspension of [cinchonidium][Δ-TRISPHAT] (approx. 0.75 mmol, 0.9 equiv.) in chloroform (600 mL) was added. The solution was stirred in darkness for 4 h, and then filtered to remove any precipitate. The organic layer was separated, dried with anhydrous $MgSO_4$ and the solvents evaporated to dryness to give an orange solid (second isolate, Δ-[Ru(dpq)$_2$(pp′)](Δ-TRISPHAT)$_2$).

The removal of TRISPHAT counterions and conversion of the metal complexes back to $PF_6^-$ salts was achieved using flash chromatography. The two isolates were separately pre-absorbed onto silica gel (5 g) using $CH_2Cl_2$ (50 mL). The $CH_2Cl_2$ was removed under reduced pressure prior to dry loading each of the fractions onto separate pre-prepared columns of silica gel equilibrated with $CH_3CN$. The complexes were eluted from the columns as a single orange band in each case using saturated $NH_4PF_6$ in $CH_3CN$. $H_2O$ (50 mL) was added to each fraction and the $CH_3CN$ was removed under reduced pressure to precipitate the complex as a finely divided orange solid. The solid was collected under vacuum, washed with diethyl ether (50 mL) and air dried. The first isolate was found to contain Λ-[Ru(dpq)$_2$(pp′)](PF$_6$)$_2$ while the second isolate contained Δ-[Ru(dpq)$_2$(pp′)](PF$_6$)$_2$. The information gained from the characterisation of Δ- and Λ-[Ru(dpq)$_2$(pp′)](PF$_6$)$_2$ (where pp′ = phen, 3-Br-phen, 4-Cl-phen or 5-Cl-phen) is detailed below.

**Δ-[Ru(dpq)$_2$(phen)](PF$_6$)$_2$:** Yield 36 mg, (13%). $^1H$ NMR (300 MHz, $CD_3CN$): $\delta$ = 9.57 (dddd, $J$ = 1.5, 3.0, 5.3, 9.0 Hz, 3 H, H13/16), 9.26 (s, 2 H, H14/15), 9.25 (s, 2 H, H14/15), 8.89 (d, $J$ = 1.9 Hz, 1 H, H2), 8.65 (dd, $J$ = 1.3, 8.3 Hz, 1 H, H7), 8.33 (d, $J$ = 8.9 Hz, 1 H, H6), 8.24 (m, 4 H, H11/18), 8.24 (s, 1 H, H4), 8.22 (d, $J$ = 2.6 Hz, 1 H, H5), 8.13 (ddd, $J$ = 1.3, 3.9, 5.2 Hz, 1 H, H9), 8.09 (dd, $J$ = 1.3, 5.4 Hz, 1 H, H13′), 7.80 (m, 3 H, H12/17), 7.81 (d, $J$ = 8.5 Hz, 1 H, H12′) 7.68 (dd, $J$ = 5.3, 8.3 Hz, 1 H, H8) ppm. ESI-MS $CH_3CN$ $m/z$ calcd. for $C_{40}H_{24}F_6N_{10}PRu$ $[M(PF_6) + H]^+$, 891.7, found 891.2, $m/z$ calcd. for $C_{40}H_{24}N_{10}Ru$ $[M]^{2+}$, 372.9, found 372.4. CD ($CH_3CN$, $1.60 \times 10^{-5}$ M, r.t.): $\lambda$ ($\Delta\varepsilon$, $mdeg\,M^{-1}\,cm^{-1}$) = 462.5 (–24.9), 415.5 (+21.2), 298.0 (–139.7), 282.5 (–77.0), 265.0 (–189.9), 248.5, (+109.4), 232.5 (+9.4), 216.0, (+73.7) nm.

**Λ-[Ru(dpq)$_2$(phen)](PF$_6$)$_2$:** Yield 90 mg, (34%). ESI-MS $CH_3CN$ $m/z$ calcd. for $C_{40}H_{24}F_6N_{10}PRu$ $[M(PF_6) + H]^+$, 891.7, found 891.4, $m/z$ calcd. for $C_{40}H_{24}N_{10}Ru$ $[M]^{2+}$, 372.9, found 371.0. CD ($CH_3CN$, $1.77 \times 10^{-5}$ M, r.t.): $\lambda$ ($\Delta\varepsilon$; $mdeg\,M^{-1}\,cm^{-1}$) = 462.5, (+21.8), 415.0 (–20.4), 298.0 (+123.3), 283.0, (+69.6), 265.5 (+188.5), 249.0, (–109.6), 232.0, (–9.3), 216.0, (–66.6) nm.

**Δ-[Ru(dpq)$_2$(3-Br-phen)](PF$_6$)$_2$** Yield 297 mg, (64%). $^1H$ NMR (300 MHz, $CD_3CN$): $\delta$ = 9.57 (dddd, $J$ = 1.5, 3.0, 5.3, 9.0 Hz, 3 H, H13/16), 9.26 (s, 2 H, H14/15), 9.25 (s, 2 H, H14/15), 8.89 (d, $J$ = 1.9 Hz, 1 H, H2), 8.65 (dd, $J$ = 1.3, 8.3 Hz, 1 H, H7), 8.33 (d, $J$ = 8.9 Hz, 1 H, H6), 8.24 (m, 4 H, H11/18), 8.24 (s, 1 H, H4), 8.22 (d, $J$ = 2.6 Hz, 1 H, H5), 8.13 (ddd, $J$ = 1.3, 3.9, 5.2 Hz, 1 H, H9), 8.09 (dd, $J$ = 1.3, 5.4 Hz, 1 H, H13′), 7.80 (m, 3 H, H12/17), 7.81 (d, $J$ = 8.5 Hz, 1 H, H12′) 7.68 (dd, $J$ = 5.3, 8.3 Hz, 1 H, H8) ppm. ESI-MS $CH_3CN$ $m/z$ calcd. for $C_{40}H_{24}BrF_6N_{10}PRu$ $[M(PF_6) + H]^+$, 970.7, found 970.5, $m/z$ calcd. for $C_{40}H_{23}BrN_{10}Ru$ $[M]^{2+}$, 412.3, found 412.7. CD ($CH_3CN$, $1.24 \times 10^{-5}$ M, r.t.): $\lambda$ ($\Delta\varepsilon$; $mdeg\,M^{-1}\,cm^{-1}$) = 463.0 (–23.2), 414.5 (+22.7), 300.0 (–148.1), 275.0 (–109.8), 247.0 (+45.5), 219.0, (+51.8) nm.

**Λ-[Ru(dpq)$_2$(3-Br-phen)](PF$_6$)$_2$:** Yield 288 mg, (62%). ESI-MS $CH_3CN$ $m/z$ calcd. for $C_{40}H_{24}BrF_6N_{10}PRu$ $[M(PF_6) + H]^+$, 970.7, found 970.5, $m/z$ calcd. for $C_{40}H_{23}BrN_{10}Ru$ $[M]^{2+}$, 412.3, found 412.7. CD ($CH_3CN$, $1.18 \times 10^{-5}$ M, r.t.): $\lambda$ ($\Delta\varepsilon$; $mdeg\,M^{-1}\,cm^{-1}$) = 463.0 (+24.8), 414.5 (–23.4), 300.0 (+155.3), 275.0 (+112.8), 247.0 (–47.6), 216.5, (–55.9) nm.

**Δ-[Ru(dpq)$_2$(4-Cl-phen)](PF$_6$)$_2$** Yield 137 mg, (81%). $^1H$ NMR (300 MHz, $CD_3CN$): $\delta$ = 9.54 (m, 4 H, H13/16), 9.23 (d, $J$ = 0.9 Hz, 4 H, H14/15), 8.66 (dd, $J$ = 1.3, 8.3 Hz, 1 H, H7), 8.51 (d, $J$ = 9.1 Hz, 1 H, H5), 8.39 (d, $J$ = 9.1 Hz, 1 H, H6), 8.19 (m, 4 H, H11/18), 8.11 (dd, $J$ = 1.3, 5.4 Hz, 2 H, H2/9), 8.02 (d, $J$ = 5.8 Hz, 1 H, H3), 7.77 (dddd, $J$ = 2.0, 3.9, 5.7, 7.1 Hz, 1 H, H12/17), 7.67 (dd, $J$ = 5.3, 8.3 Hz, 1 H, H8) ppm. ESI-MS $CH_3CN$ $m/z$ calcd. for $C_{40}H_{23}ClF_6N_{10}PRu$ $[M(PF_6)]^+$, 925.2, found 924.6, $m/z$ calcd. for $C_{40}H_{23}BrN_{10}Ru$ $[M]^{2+}$, 390.1, found 390.0. CD ($CH_3CN$, $1.04 \times 10^{-5}$ M, r.t.): $\lambda$ ($\Delta\varepsilon$ $mdeg\ M^{-1}\,cm^{-1}$) = 465.0 (–26.7), 415.5 (+22.8), 299.0 (–139.5), 267.5 (–175.5), 249.5 (+95.6), 218.5, (+60.9) nm.

**Λ-[Ru(dpq)$_2$(4-Cl-phen)](PF$_6$)$_2$:** Yield 139 mg, (82%). ESI-MS $CH_3CN$ $m/z$ calcd. for $C_{40}H_{23}ClF_6N_{10}PRu$ $[M(PF_6)]^+$, 925.2, found 924.6, $m/z$ calcd. for $C_{40}H_{23}ClN_{10}Ru$ $[M]^{2+}$, 390.1, found 390.0. CD ($CH_3CN$, $1.14 \times 10^{-5}$ M, r.t.): $\lambda$ ($\Delta\varepsilon$; $mdeg\,M^{-1}\,cm^{-1}$) = 465.5 (+24.8), 417.0 (–21.1), 299.0 (+129.8), 267.5 (+163.9), 249.5 (–90.0), 216.5, (–57.1) nm.

**Δ-[Ru(dpq)$_2$(5-Cl-phen)](PF$_6$)$_2$** Yield 262 mg, (73%). $^1H$ NMR (300 MHz, $CD_3CN$): $\delta$ = 9.54 (dddd, $J$ = 1.7, 1.7, 3.8, 6.6 Hz, 4 H, H13/16), 9.23 (d, $J$ = 0.7 Hz, 4 H, H14/15), 8.85 (dd, $J$ = 1.2,

 © 2007 Wiley-VCH Verlag GmbH & Co. KGaA, Weinheim 

8.5 Hz, 1 H, H4), 8.54 (dd, $J$ = 1.3, 8.3 Hz, 1 H, H7), 8.44 (s, 1 H, H6), 8.20 (m, 3 H, H2/11), 8.12 (m, 3 H, H9/18), 7.77 (m, 4 H, H12/17), 7.72 (d, $J$ = 5.3 Hz, 1 H, H3), 7.64 (dd, $J$ = 5.3, 8.3 Hz, 1 H, H8) ppm. ESI-MS $CH_3CN$ $m/z$ calcd. for $C_{40}H_{23}ClF_6N_{10}PRu$ $[M(PF_6)]^+$, 925.2, found 924.7, $m/z$ calcd. for $C_{40}H_{23}ClN_{10}Ru$ $[M]^{2+}$, 390.1, found 390.0. CD ($CH_3CN$, $1.08 \times 10^{-5}$ M, r.t.): $\lambda$ ($\Delta\varepsilon$; mdeg $M^{-1}$ $cm^{-1}$) = 463.5 (–26.2), 414.5 (+23.1), 299.0 (–140.0), 270.5 (–171.4), 250.5 (+88.0), 216.0, (+69.5) nm.

**Λ-[Ru(dpq)$_2$(5-Cl-phen)](PF$_6$)$_2$:** Yield 231 mg, (65%). ESI-MS $CH_3CN$ $m/z$ calcd. for $C_{40}H_{23}ClF_6N_{10}PRu$ $[M(PF_6)]^+$, 925.2, found 924.7, $m/z$ calcd. for $C_{40}H_{23}ClN_{10}Ru$ $[M]^{2+}$, 390.1, found 390.0. CD ($CH_3CN$, $1.19 \times 10^{-5}$ M, r.t.): $\lambda$ ($\Delta\varepsilon$, mdeg $M^{-1}$ $cm^{-1}$) = 463.5 (+26.7), 414.5 (–22.9), 298.5 (+141.4), 271.0 (+176.5), 251.0 (–90.3), 217.0, (–68.6) nm.

**Synthesis of Racemic Dinuclear Complexes:** In a typical experiment, anhydrous $(CH_3)_2NCOH$ was de-aerated prior to use by bubbling with $N_{2(g)}$ for 10 min in a round-bottomed flask fitted with a rubber septum. *rac*-[Ru(dpq)$_2$(pp′)](PF$_6$)$_2$ (pp′ = 3-Br-phen, 4-Cl-phen or 5-Cl-phen, 0.10 mmol) was dissolved in de-aerated anhydrous $(CH_3)_2NCOH$ (2 mL). In a separate vessel NaH (70% dispersion in mineral oil, 0.0024 g, 0.10 mmol) was suspended $(CH_3)_2NCOH$ (2 mL) and the solution was purged by bubbling with $N_{2(g)}$ for 5 min. Under a strong stream of $N_{2(g)}$, bis(2-mercaptoethyl) ether (SOS) (5.6 μL, 0.05 mmol) in $(CH_3)_2NCOH$ (100 μL) was added to the solution by micropipette. The solution of SOS/NaH was allowed to stir under $N_{2(g)}$ to complete dissolution of the NaH, at which point the solution went clear (c.a. 2 min). The separate solutions containing the monomer and linker were mixed using cannulation at which time the solution underwent a rapid colour change from deep red to black. The solution was allowed to stir under $N_{2(g)}$ for a further 5 min before $(CH_3CH_2)_2O$ (50 mL) was added causing a black precipitate to form. The solution was stored at 0 °C for 2 h before the product was collected under vacuum and washed with copious amounts of $(CH_3CH_2)_2O$.

The crude mixture was purified using flash chromatography on silica gel (20 × 2.5 cm, eluent: 89% $CH_3CN$, 10% $H_2O$, 1% saturated aqueous $KNO_3$). The fractions containing pure [{Ru(dpq)$_2$}$_2$μ-(phen-*n*-SOS-*n*-phen)]$^{4+}$ ($n$ = 3, 4 or 5, SOS = –S–$CH_2$–$CH_2$–O–$CH_2$–$CH_2$–S–) were identified by TLC (silica gel, $CH_3CN$/$H_2O$/saturated $KNO_3$, 45:5:2) and were combined. Saturated $KPF_6$ (1 mL) was added before extraction with $CH_2Cl_2$ (3 × 50 mL) to remove the $KNO_3$. The extracts were dried with anhydrous $MgSO_4$, filtered and the solvent removed under reduced pressure. The complex was purified a second time on silica gel, (20 × 2.5 cm, eluent:saturated $NH_4PF_6$ in $CH_3CN$), and the single orange band was collected and the solvents evaporated to dryness under reduced pressure. The resultant orange solid was dissolved in a minimum volume of $CH_3CN$ and precipitated by the addition of $H_2O$. The complex was collected by vacuum filtration, washed with $(CH_3CH_2)_2O$ and air dried. The yields and characterisation data of the dinuclear complexes synthesised are given below.

***raclmeso*-[{Ru(dpq)$_2$}$_2$μ-(phen-3-SOS-3-phen)](PF$_6$)$_4$:** Yield 111 mg (56%). UV ($CH_3CN$): $\lambda_{max}$ ($\varepsilon$ × $10^4$ $mol^{-1}$ $dm^3$ $cm^{-1}$) = 215 (13.6), 255 (20.8), 289 (11.9), 342 (4.0), 448 (3.7) nm. Quantum luminescence Yield ($\Phi$): 0.062. $^1$H NMR (300 MHz, $CD_3CN$): $\delta$ = 9.55 (d, $J$ = 8.0 Hz, 4 H), 9.48 (dd, $J$ = 8.5, 16.8 Hz, 2 H), 9.37 (d, $J$ = 8.2 Hz, 2 H), 9.23 (s, 4 H), 9.08 (d, $J$ = 2.4 Hz, 2 H), 9.00 (d, $J$ = 2.5 Hz, 1 H), 8.63 (d, $J$ = 8.3 Hz, 2 H), 8.40 (d, $J$ = 7.5 Hz, 2 H), 8.25 (m, 8 H), 8.14 (m, 8 H), 7.95 (dd, $J$ = 1.7, 3.4 Hz, 2 H), 7.79 (m, 4 H), 7.69 (m, 5 H), 3.52 (m, 4 H), 2.96 (dd, $J$ = 5.7, 12.1 Hz, 4 H) ppm. ESI-MS $m/z$ calcd. for $C_{84}H_{54}F_{12}N_{20}OP_2Ru_2S_2$ $[M(PF_6)_2]^{2+}$, 957.8, found 958.2, $m/z$ calcd. for $C_{84}H_{54}F_6N_{20}OPRu_2S_2$ $[M(PF_6)]^{3+}$, 590.2, found 590.5, $m/z$ calcd. for $C_{84}H_{54}N_{20}ORu_2S_2$ $[M]^{4+}$, 406.4, found 406.5.

***raclmeso*-[{Ru(dpq)$_2$}$_2$μ-(phen-4-SOS-4-phen)](PF$_6$)$_4$:** Yield 62 mg (31%). UV ($CH_3CN$): $\lambda_{max}$ ($\varepsilon$ × $10^4$, $mol^{-1}$ $dm^3$ $cm^{-1}$) = 215 (15.1), 257 (20.5), 452 (4.8) nm. Quantum luminescence Yield ($\Phi$): 0.053. $^1$H NMR (300 MHz, $CD_3CN$): $\delta$ = 9.55 (m, 4 H), 9.50 (m, 2 H), 9.47 (d, $J$ = 1.3 Hz, 1 H), 9.26 (s, 4 H), 9.17 (s, 2 H), 9.17 (dd, $J$ = 2.2, 12.7 Hz, 2 H), 8.63 (d, $J$ = 8.5 Hz, 2 H), 8.29 (d, $J$ = 1.4 Hz, 1 H), 8.24 (m, 8 H), 8.20 (d, $J$ = 3.5 Hz, 1 H), 8.16 (d, 4 H), 8.13 (d, $J$ = 1.4 Hz, 1 H), 7.86 (d, $J$ = 6.4 Hz, 2 H), 7.78 (m, 8 H), 7.66 (dd, $J$ = 3.3, 5.1 Hz, 2 H), 7.43 (d, $J$ = 6.1 Hz, 2 H), 3.74 (dd, $J$ = 5.5, 11.6 Hz, 4 H), 2.74 (dd, $J$ = 4.8, 5.8 Hz, 4 H) ppm. ESI-MS $m/z$ calcd. for $C_{84}H_{54}F_{12}N_{20}OP_2Ru_2S_2$ $[M(PF_6)_2]^{2+}$, 957.8, found 958.3, $m/z$ calcd. for $C_{84}H_{54}F_6N_{20}OPRu_2S_2$ $[M(PF_6)]^{3+}$, 590.2, found 590.7, $m/z$ calcd. for $C_{84}H_{54}N_{20}ORu_2S_2$ $[M]^{4+}$, 406.4, found 406.9;

***raclmeso*-[{Ru(dpq)$_2$}$_2$μ-(phen-5-SOS-5-phen)](PF$_6$)$_4$:** Yield 95 mg (48%). UV ($CH_3CN$): $\lambda_{max}$ ($\varepsilon$ × $10^4$, $mol^{-1}$ $dm^3$ $cm^{-1}$) = 217 (14.1), 256 (20.2), 450 (4.8) nm. Quantum luminescence Yield ($\Phi$): 0.048. $^1$H NMR (300 MHz, $CD_3CN$): $\delta$ = 9.55 (dd, $J$ = 7.3, 14.7 Hz, 7 H), 9.50 (s, 1 H), 9.26 (d, $J$ = 1.0 Hz, 4 H), 9.24 (dd, $J$ = 2.7, 8.5 Hz, 4 H), 8.84 (dd, $J$ = 2.7, 8.5 Hz, 2 H), 8.50 (d, $J$ = 7.9 Hz, 2 H), 8.24 (dd, $J$ = 4.7, 9.9 Hz, 4 H), 8.18 (m, 8 H), 8.06 (d, $J$ = 5.0 Hz, 2 H), 7.80 (m, 8 H), 7.63 (m, 4 H), 3.93 (dd, $J$ = 6.1, 12.3 Hz, 4 H), 3.48 (m, 4 H) ppm. $C_{84}H_{54}F_{12}N_{20}OP_2Ru_2S_2$ $[M(PF_6)_2]^{2+}$, 957.8, found 958.2, $m/z$ calcd. for $C_{84}H_{54}F_6N_{20}OPRu_2S_2$ $[M(PF_6)]^{3+}$, 590.2, found 590.5, $m/z$ calcd. for $C_{84}H_{54}N_{20}ORu_2S_2$ $[M]^{4+}$, 406.4, found 406.5.

**Synthesis of Homochiral Dinuclear Complexes:** The homochiral dinuclear complexes were synthesised in a manner analogous to that used for the diastereoisomeric mixtures synthesised above using resolved mononuclear metal complexes. Their yields and characterisation data are provided below.

**ΔΔ-[{Ru(dpq)$_2$}$_2$μ-(phen-3-SOS-3-phen)](PF$_6$)$_4$:** Yield 22 mg (31%). $^1$H NMR (300 MHz, $CD_3CN$): $\delta$ = 9.54 (dd, $J$ = 1.3, 8.3 Hz, 4 H, H13/16) 9.40 (dd, $J$ = 1.3, 8.3 Hz, 4 H, H13/16) 9.24 (s, 4 H, H14/15) 9.11 (s, 4 H, H14/15) 8.59 (dd, $J$ = 1.2, 8.3 Hz, 2 H, H7) 8.37 (d, $J$ = 1.8 Hz, 2 H, H2/H4) 8.20 (m, 4 H, H11/18) 8.19 (d, $J$ = 1.35 Hz, 4 H, H11/18) 8.15 (dd, $J$ = 1.3, 5.3 Hz, 2 H, H5/H6) 8.10 (d, $J$ = 1.3 Hz, 2 H, H5/6) 8.07 (m, 2 H, H9) 7.89 (d, $J$ = 1.9 Hz, 2 H, H2/H4) 7.78 (dd, $J$ = 1.6, 5.3, 8.3 Hz, 4 H, H12/17) 7.69 (m, $J$ = 5.3, 8.3, 13.1 Hz, 4 H, H12/17) 7.61 (dd, $J$ = 5.3, 8.6 Hz, 2 H, H8) 3.35 (m, $J$ = 1.9, 6.2 Hz, 4 H, HB) 2.94 (m, $J$ = 3.6, 6.1 Hz, 4 H, HA) ppm. ESI-MS $m/z$ calcd. for $C_{84}H_{54}F_{12}N_{20}OP_2Ru_2S_2$ $[M(PF_6)_2]^{2+}$, 957.8, found 958.0, $m/z$ calcd. for $C_{84}H_{54}F_6N_{20}OPRu_2S_2$ $[M(PF_6)]^{3+}$, 590.2, found 590.7, $m/z$ calcd. for $C_{84}H_{54}N_{20}ORu_2S_2$ $[M]^{4+}$, 406.4, found 407.0. CD ($CH_3CN$, $4.12 \times 10^{-6}$ M, r.t.): $\lambda$ ($\Delta\varepsilon$, mdeg $M^{-1}$ $cm^{-1}$) = 464.0 (– 48.3), 415.0 (+46.1), 299.0 (–269.6), 260.0 (–188.3), 242.0 (+188.9), 213.0, (+111.8) nm.

**ΛΛ-[{Ru(dpq)$_2$}$_2$μ-(phen-3-SOS-3-phen)](PF$_6$)$_4$:** Yield 24 mg (24%). ESI-MS $m/z$ calcd. for $C_{84}H_{54}F_{12}N_{20}OP_2Ru_2S_2$ $[M(PF_6)_2]^{2+}$, 957.8, found 958.1, $m/z$ calcd. for $C_{84}H_{54}F_6N_{20}OPRu_2S_2$ $[M(PF_6)]^{3+}$, 590.2, found 590.4, $m/z$ calcd. for $C_{84}H_{54}N_{20}ORu_2S_2$ $[M]^{4+}$, 406.4, found 406.6. CD ($CH_3CN$, $4.15 \times 10^{-6}$ M, r.t.): $\lambda$ ($\Delta\varepsilon$, mdeg $M^{-1}$ $cm^{-1}$) = 463.0 (+54.9), 415.5 (–55.1), 299.0 (+317.1), 260.0 (+222.8), 242.0 (–220.4), 212.0, (–133.1) nm.

**ΔΔ-[{Ru(dpq)$_2$}$_2$μ-(phen-4-SOS-4-phen)](PF$_6$)$_4$:** Yield 17 mg (17%). $^1$H NMR (300 MHz, $CD_3CN$): $\delta$ = 9.54 (m, $J$ = 1.3, 5.1, 8.3, 12.4 Hz, 8 H, H13/16), 9.26 (s, 4 H, H14/15), 9.18 (s, 1 H, H14/15), 8.64 (dd, $J$ = 1.2, 8.3 Hz, 2 H, H7), 8.24 (m, $J$ = 3.4, 4.9,

 © 2007 Wiley-VCH Verlag GmbH & Co. KGaA, Weinheim 

6.4 Hz, 8 H, H11/18), 8.16 (m, $J$ = 1.2, 1.2, 5.4 Hz, 4 H, H5/6), 7.86 (d, $J$ = 5.9 Hz, 2 H, H2/9), 7.78 (m, 10 H, H2/9/12/17), 7.66 (dd, $J$ = 5.2, 8.3 Hz, 2 H, H8), 7.43 (d, $J$ = 6.0 Hz, 2 H, H3), 3.75 (dd, $J$ = 5.8, 5.8 Hz, 4 H, HB), 3.28 (dd, $J$ = 5.7, 10.6 Hz, 4 H, HA) ppm. ESI-MS *m/z* calcd. for $C_{84}H_{54}F_{12}N_{20}OP_2Ru_2S_2$ $[M(PF_6)_2]^{2+}$, 957.8, found 958.3, *m/z* calcd. for $C_{84}H_{54}F_6N_{20}OPRu_2S_2$ $[M(PF_6)]^{3+}$, 590.2, found 590.7, *m/z* calcd. for $C_{84}H_{54}N_{20}ORu_2S_2$ $[M]^{4+}$, 406.4, found 407.0. CD ($CH_3CN$, $6.25\times10^{-6}$ M, r.t.): $\lambda$ ($\Delta\varepsilon$, mdeg M$^{-1}$ cm$^{-1}$) = 470.0 (–44.9), 419.0 (+35.1), 298.5 (–218.6), 263.5 (–293.0), 247.0 (+163.6), 213.5, (+152.4) nm.

**ΛΛ-[{Ru(dpq)$_2$}$_2$μ-(phen-4-SOS-4-phen)](PF$_6$)$_4$:** Yield 51 mg (50%). ESI-MS *m/z* calcd. for $C_{84}H_{54}F_{12}N_{20}OP_2Ru_2S_2$ $[M(PF_6)_2]^{2+}$, 957.8, found 958.3, *m/z* calcd. for $C_{84}H_{54}F_6N_{20}OPRu_2S_2$ $[M(PF_6)]^{3+}$, 590.2, found 590.7, *m/z* calcd. for $C_{84}H_{54}N_{20}ORu_2S_2$ $[M]^{4+}$, 406.4, found 406.9. CD ($CH_3CN$, $6.88\times10^{-6}$ M, r.t.): $\lambda$ ($\Delta\varepsilon$, mdeg M$^{-1}$ cm$^{-1}$) = 468.5 (+45.5), 418.5 (–36.2), 298.5 (+213.3), 263.5 (+280.5), 247.5 (–169.3), 213.5, (–149.6) nm.

**ΔΔ-[{Ru(dpq)$_2$}$_2$μ-(phen-5-SOS-5-phen)](PF$_6$)$_4$:** Yield 32 mg (31%). $^1$H NMR (300 MHz, $CD_3CN$): $\delta$ = 9.56 (m, 8 H, H13/16), 9.26 (m, 8 H, H14/15), 8.83 (dd, $J$ = 1.2, 8.5 Hz, 2 H, H4), 8.50 (dd, $J$ = 1.2, 8.3 Hz, 2 H, H7), 8.24 (m, $J$ = 1.3, 4.2, 5.5 Hz, 4 H, H11/18), 8.20 (s, 2 H, H6), 8.16 (m, 6 H, H11/18/2/9), 8.06 (dd, $J$ = 1.2, 5.3 Hz, 2 H, H2/9), 7.80 (m, 8 H, H12/17), 7.62 (m, $J$ = 5.3, 8.4, 11.4 Hz, 4 H, H3/8), 3.93 (dd, $J$ = 6.0, 6.0 Hz, 4 H, HB), 3.49 (m, $J$ = 3.1, 6.0, 6.3 Hz, 4 H, HA) ppm. ESI-MS *m/z* calcd. for $C_{84}H_{55}F_{24}N_{20}OP_4Ru_2S_2$ $[M(PF_6)_4 + H]^+$, 2206.6, found 2206.4, *m/z* calcd. for $C_{84}H_{54}F_{18}N_{20}OP_3Ru_2S_2$ $[M(PF_6)_3]^+$, 2060.6, found 2061.3, *m/z* calcd. for $C_{84}H_{54}F_{12}N_{20}OP_2Ru_2S_2$ $[M(PF_6)_2]^{2+}$, 957.8, found 958.4, *m/z* calcd. for $C_{84}H_{54}F_6N_{20}OPRu_2S_2$ $[M(PF_6)]^{3+}$, 590.2, found 590.7, *m/z* calcd. for $C_{84}H_{54}N_{20}ORu_2S_2$ $[M]^{4+}$, 406.4, found 406.9. CD ($CH_3CN$, $5.02\times10^{-6}$ M, r.t.): $\lambda$ ($\Delta\varepsilon$, mdeg M$^{-1}$ cm$^{-1}$) = 464.0 (–59.2), 415.0 (+43.7), 299.0 (–309.1), 260.5 (–101.1), 241.0 (+25.1), 216.5, (+163.0) nm.

**ΛΛ-[{Ru(dpq)$_2$}$_2$μ-(phen-5-SOS-5-phen)](PF$_6$)$_4$:** Yield 52 mg (51%). ESI-MS *m/z* calcd. for $C_{84}H_{54}F_{12}N_{20}OP_2Ru_2S_2$ $[M(PF_6)_2]^{2+}$, 957.8, found 957.3, *m/z* calcd. for $C_{84}H_{54}F_6N_{20}OPRu_2S_2$ $[M(PF_6)]^{3+}$, 590.2, found 589.7, *m/z* calcd. for $C_{84}H_{54}N_{20}ORu_2S_2$ $[M]^{4+}$, 406.4, found 406.3. CD ($CH_3CN$, $5.24\times10^{-6}$ M, r.t.): $\lambda$ ($\Delta\varepsilon$, mdeg M$^{-1}$ cm$^{-1}$) = 464.0 (+53.5), 416.0 (–49.4), 299.0 (+307.6), 260.5 (+101.6), 240.0 (–35.1), 216.5, (–173.2) nm.

**Supporting Information** (see also the footnote on the first page of this article): Additional CD spectra of the metal complexes and a comparison of the NMR spectra of all the mononuclear complexes.

## Acknowledgments

C. R. B. was supported by a University of Western Sydney PhD and writing scholarship. We gratefully acknowledge the support of the Australian Research Council (Grant no. DP0343480), UWS Research Grant Scheme (No. 82802), Prof. Jérôme Lacour (University of Geneva) for helpful advice and Dr. Nial Wheate (University of Western Sydney) for assistance in the preparation of this manuscript.

[1] N. J. Wheate, C. R. Brodie, J. G. Collins, S. Kemp, J. R. Aldrich-Wright, *Mini Rev. Med. Chem.* **2006**, *7*, 627–648.
[2] J. K. Barton, A. E. Friedman, J. C. Chambron, J. P. Sauvage, N. J. Turro, *J. Am. Chem. Soc.* **1990**, *112*, 4960–4962.
[3] E. J. C. Olson, D. Hu, A. Hoermann, A. M. Jonkman, M. R. Arkin, E. D. A. Stemp, J. K. Barton, P. F. Barbara, *J. Am. Chem. Soc.* **1997**, *119*, 11458–11467.
[4] Y. Jenkins, J. K. Barton, *J. Am. Chem. Soc.* **1992**, *114*, 8736–8738.
[5] L. A. Basile, J. K. Barton, *J. Am. Chem. Soc.* **1987**, *109*, 7548–7550.
[6] C. S. Chow, J. K. Barton, *J. Am. Chem. Soc.* **1990**, *112*, 2839–2841.
[7] J.-P. Lecomte, A. Kirsch-De Mesmaeker, M. M. Feeney, J. M. Kelly, *Inorg. Chem.* **1995**, *34*, 6481–6491.
[8] T. P. Shields, J. K. Barton, *Biochemistry* **1995**, *34*, 15037–15048.
[9] A. B. Tossi, J. M. Kelly, *Photochem. Photobio.* **1989**, *49*, 545–556.
[10] J. G. Collins, J. R. Aldrich-Wright, I. D. Greguric, P. A. Pellegrini, *Inorg. Chem.* **1999**, *38*, 5502–5509.
[11] C. M. Dupureur, J. K. Barton, *Inorg. Chem.* **1997**, *36*, 33–43.
[12] C. Hiort, B. Nordén, *Nucleosides. Nucleotides.* **1988**, *7*, 661–665.
[13] C. Hiort, B. Nordén, A. Rodger, *J. Am. Chem. Soc.* **1990**, *112*, 1971–1982.
[14] L. N. Ji, X. H. Zou, J. G. Liu, *Coord. Chem. Rev.* **2001**, *216–217*, 513–536.
[15] E. Rueba, J. R. Hart, J. K. Barton, *Inorg. Chem.* **2004**, *43*, 4570–4578.
[16] S. Delaney, M. Pascaly, P. K. Bhattacharya, K. Han, J. K. Barton, *Inorg. Chem.* **2002**, *41*, 1966–1974.
[17] J. G. Collins, A. D. Sleeman, J. R. Aldrich-Wright, I. Greguric, T. W. Hambley, *Inorg. Chem.* **1998**, *37*, 3133–3141.
[18] R. M. Hartshorn, J. K. Barton, *J. Am. Chem. Soc.* **1992**, *114*, 5919–5925.
[19] F. O'Reilly, J. Kelly, A. Kirsch-De Mesmaeker, *Chem. Commun.* **1996**, 1013–1014.
[20] F. M. O'Reilly, J. M. Kelly, *New J. Chem.* **1998**, *22*, 215–217.
[21] F. M. O'Reilly, J. M. Kelly, *J. Phys. Chem. B* **2000**, *104*, 7206–7213.
[22] L. M. Wilhelmsson, F. Westerlund, P. Lincoln, B. Nordén, *J. Am. Chem. Soc.* **2002**, *124*, 12092–12093.
[23] L. M. Wilhelmsson, E. K. Esbjoerner, F. Westerlund, B. Nordén, P. Lincoln, *J. Phys. Chem. B* **2003**, *107*, 11784–11793.
[24] F. Westerlund, L. M. Wilhelmsson, B. Nordén, P. Lincoln, *J. Am. Chem. Soc.* **2003**, *125*, 3773–3779.
[25] P. Lincoln, B. Nordén, *J. Chem. Society, Chem. Commun.* **1996**, 2145–2146.
[26] B. Önfelt, P. Lincoln, B. Nordén, *J. Am. Chem. Soc.* **1999**, *121*, 10846–10847.
[27] F. Westerlund, F. Pierard, M. P. Eng, B. Nordén, P. Lincoln, *J. Phys. Chem. B* **2005**, *109*, 17327–17332.
[28] B. Önfelt, L. Gostring, P. Lincoln, B. Nordén, A. Onfelt, *Mutagenesis* **2002**, *17*, 317–320.
[29] G. Telfer Shane, N. Tajima, R. Kuroda, *J. Am. Chem. Soc.* **2004**, *126*, 1408–1418.
[30] J. A. Smith, J. G. Collins, B. T. Patterson, F. R. Keene, *Dalton Trans.* **2004**, 1277–1283.
[31] F. M. Foley, F. R. Keene, J. G. Collins, *J. Chem. Soc. Dalton Trans.* **2002**, 2968–2974.
[32] A. Brodkorb, A. K.-D. Mesmaeker, T. J. Rutherford, F. R. Keene, *Eur. J. Inorg. Chem.* **2001**, 2151–2160.
[33] B. T. Patterson, J. G. Collins, F. M. Foley, F. R. Keene, *J. Chem. Soc. Dalton Trans.* **2002**, 4343–4350.
[34] J. R. Aldrich-Wright, C. Brodie, E. C. Glazer, N. W. Luedtke, L. Elson-Schwab, Y. Tor, *Chem. Commun.* **2004**, 1018–1019.
[35] T. J. Rutherford, P. A. Pellegrini, J. R. Aldrich-Wright, P. C. Junk, F. R. Keene, *Eur. J. Inorg. Chem.* **1998**, *11*, 1677–1688.
[36] J. Lacour, C. Goujon-Ginglinger, S. Troche-Haldimann, J. J. Jordry, *Angew. Chem. Int. Ed.* **2000**, *39*, 3695–3697.
[37] T. J. Wenzel, J. D. Wilcox, *Chirality* **2003**, *15*, 256–270.
[38] J. Lacour, C. Ginglinger, C. Grivet, G. Bernardinelli, *Angew. Chem. Int. Ed. Engl.* **1997**, *36*, 608–610.
[39] G. Bruylants, C. Bresson, A. Boisdenghien, F. Pierard, A. Kirsch-De Mesmaeker, J. Lacour, K. Bartik, *New J. Chem.* **2003**, *27*, 748–751.
[40] D. Tzalis, Y. Tor, *Tetrahedron Lett.* **1995**, *36*, 6017–6020.

 © 2007 Wiley-VCH Verlag GmbH & Co. KGaA, Weinheim 

[41] R. Snyder, H. E. Freier, *J. Am. Chem. Soc.* **1946**, *68*, 1320–1322.
[42] G. Renner, C. Hopfer, *Chemosphere* **1982**, *11*, 363–366.
[43] F. Favarger, C. Goujon-Ginglinger, D. Monchaud, J. Lacour, *J. Org. Chem.* **2004**, *69*, 8521–8524.
[44] P. A. Anderson, R. F. Anderson, M. Furue, P. C. Junk, F. R. Keene, B. T. Patterson, B. D. Yeomans, *Inorg. Chem.* **2000**, *39*, 2721–2728.
[45] A. Rodger, B. Nordén, *Circular and Linear Dichroism*, Oxford University Press, Oxford, **1997**.
[46] N. H. Damrauer, T. R. Boussie, M. Devenney, J. K. McCusker, *J. Am. Chem. Soc.* **1997**, *119*, 8253–8268.
[47] J. V. Casper, T. J. Meyer, *J. Am. Chem. Soc.* **1983**, *105*, 5583–5590.
[48] J. N. Demas, G. A. Crosby, *J. Phys. Chem.* **1971**, *78*, 991–1024.
Received: January 23, 2007
Published Online: September 4, 2007

 © 2007 Wiley-VCH Verlag GmbH & Co. KGaA, Weinheim 

DOI: 10.1002/ejic.200700129

# Synthesis, Structure and Magnetic Behaviour of Manganese(II) Selenolate Complexes $^1_\infty$[Mn(SePh)$_2$], [Mn(SePh)$_2$(bipy)$_2$] and [Mn(SePh)$_2$(phen)$_2$] (bipy = bipyridyl, phen = phenanthroline)

**Andreas Eichhöfer,*[a] Paul T. Wood,[b] Raghavan Viswanath,[a] and Richard A. Mole[c]**

**Keywords:** Transition-metal complexes / Manganese / X-ray structure analysis / Magnetism

The manganese selenolate complex $^1_\infty$[Mn(SePh)$_2$] has been prepared by reaction of Mn(OOCCH$_3$)$_2$ with 2 equiv. PhSeSiMe$_3$ in thf. In the crystal structure, the compound forms one-dimensional chains, and the bridging selenolate ligands result in relatively short metal–metal contacts of about 3 Å. Reaction with two equivalents of the Lewis bases 2,2′-bipyridine and 1,10-phenanthroline yielded the monomeric octahedral complexes [Mn(SePh)$_2$(2,2′-bipy)$_2$] and [Mn(SePh)$_2$(1,10-phen)$_2$], respectively. The magnetic and optical properties of these complexes have been investigated.
(© Wiley-VCH Verlag GmbH & Co. KGaA, 69451 Weinheim, Germany, 2007)

## Introduction

Metal chalcogenolato complexes have attracted interest because of their rich structural chemistry,[1–3] their potential use as precursors for M/Se materials[4,5] and their relevance as models for active sites of chalcogen-containing metalloproteins.[6,7] Manganese, for example, plays a role as a dopant for 12–16 semiconductor films and nanocrystals, referred to as dilute magnetic semiconductors (DMS),[8,9] as well as in some manganese–oxido cluster complexes such as [Mn$_{12}$O$_{12}$(O$_2$CCH$_3$)$_{16}$][10] and [Mn$_{84}$O$_{72}$(O$_2$CMe)$_{78}$(OMe)$_{24}$(MeOH)$_{12}$(H$_2$O)$_{42}$(OH)$_6$],[11] which are known as single-molecule magnets (SMMs). With respect to manganese chalcogenolato complexes, two synthetic approaches have been widely used. The reaction of a manganese(II) halide with NaEPh (E = S, Se, Te) in the presence of quarternary ammonium or phosphonium salts yields anionic monomeric and oligomeric complexes {for example, [Mn(EPh)$_4$]$^{2-}$ (E = S, Se, Te),[12,13] [Mn$_2$(SPh)$_6$]$^{2-}$[14] and [Mn$_4$(SPh)$_{10}$]$^{2-}$[12]}. In contrast, a few neutral complexes containing bulky organic groups, such as [Mn{N(SiMe$_3$)$_2$}-(μ-SeC$_6$H$_2$-2,4,6-*i*Pr$_3$)(THF)],[15] [Mn(SeMes*)$_2$C$_4$H$_8$O] (Mes* = C$_6$H$_2$-2,4,6-*t*Bu$_3$), [Mn(SeC$_6$H$_3$-2,6-Mes$_2$)$_2$] (Mes = C$_6$H$_2$-2,4,6-Me$_3$)[16] and $^1_\infty$[Mn(SeC$_6$H$_2$-2,4,6-CH$_3$)$_2$],[17] have been synthesised by reaction of [Mn{N(SiMe$_3$)$_2$}$_2$] with the corresponding selenol RSeH (R = organic group).

Reported here is the organometallic synthesis of three manganese selenolate complexes by reaction of manganese acetate with PhSeSiMe$_3$. Structural characterization and investigation of the magnetic and optical properties of these complexes is also presented.

[a] Institut für Nanotechnologie, Forschungszentrum Karlsruhe, Postfach 3640, 76021 Karlsruhe, Germany
Fax: +7247-82-6368
E-mail: eichhoefer@int.fzk.de
[b] University Chemical Laboratory, Lensfield Rd., Cambridge CB2 1EW, UK
[c] ZWE FRM-II, Lichtenbergstrasse 1, 85747 Garching, Germany

## Results and Discussion

### Synthesis and Structure

The manganese selenolate complex $^1_\infty$[Mn(SePh)$_2$] (**1**) was prepared by reaction of anhydrous Mn(OOCCH$_3$)$_2$ with 2 equiv. PhSeSiMe$_3$ in thf, as shown in Scheme 1. Reaction of **1** with 2 equiv. of the Lewis bases 2,2′-bipyridine and 1,10-phenanthroline yielded dark red crystals of the monomeric octahedral complexes [Mn(SePh)$_2$(2,2′-bipy)$_2$] (**2**) and [Mn(SePh)$_2$(1,10-phen)$_2$] (**3**), respectively.

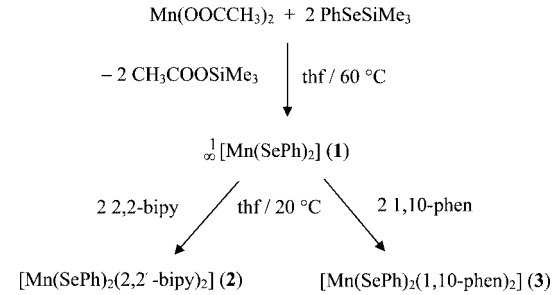


Scheme 1.

Compound **1** crystallises in the tetragonal space group $I4_1/a$. In the crystal structure of **1**, the manganese atoms are μ$_2$-bridged in one dimension by the phenylselenolato ligands to form infinite chains (Figure 1). The Mn–Se distances of 254.7(1) and 257.3(1) pm are comparable to those found in similar compounds such as [Mn(SePh)$_4$]$^{2-}$ (average 256.7 pm)[13] and $^1_\infty$[Mn(SeC$_6$H$_2$-2,4,6-CH$_3$)$_2$] (259.0 pm);[17]

 © 2007 Wiley-VCH Verlag GmbH & Co. KGaA, Weinheim 

the latter compound also forms a one-dimensional chain structure in the crystal lattice. However, different orientations of the phenyl rings in the structures of **1** and $^{1}_{\infty}$[Mn(SeC$_6$H$_2$-2,4,6-CH$_3$)$_2$] results in different coordination geometries around the manganese atoms. In **1**, four selenium atoms [Se(1), Se(2), Se(1′) and Se(2′)] of the phenylselenolato ligands form a distorted tetrahedral coordination environment around the manganese atom with five similar Se–Mn–Se bond angles [104.63(3)° for Se(1)–Mn(1)–Se(1′), 106.0° for Se(2′)–Mn(1)–Se(1′), 105.88(3)° for Se(1)–Mn(1)–Se(2), 107.97° for Se(2′)–Mn(1)–Se(2) and 105.42° for Se(1′)–Mn(1)–Se(2)] and only one distinctly larger angle of 125.4(1)° for Se(1)–Mn(1)–Se(2′). The $Mn_2Se_2$ four-membered rings in **1** have a much more rhombic–like shape [angles of 73.0(1)° for Mn(1)–Se(1)–Mn(1′) and 72.9(1)° for Mn(1)–Se(2)–Mn(1′)] than in [Mn(SeC$_6$H$_2$-2,4,6-CH$_3$)$_2$], where the manganese and selenium atoms form nearly planar quadratic rings (Mn–Se–Mn 88.0°, Se–Mn–Se 92.0°). In addition, the ring in **1** is twisted by 18.24° from ideal planarity to form a butterfly-type shape. This reduces the distance between the manganese atoms in the one dimensional chains distinctly from 359.3 pm in $^{1}_{\infty}$[Mn(SeC$_6$H$_2$-2,4,6-CH$_3$)$_2$] to 304.6 pm in **1**, which is closer to the distance between the metal atoms in [Mn(CO)$_5$]$_2$ (290.4 pm).[18]

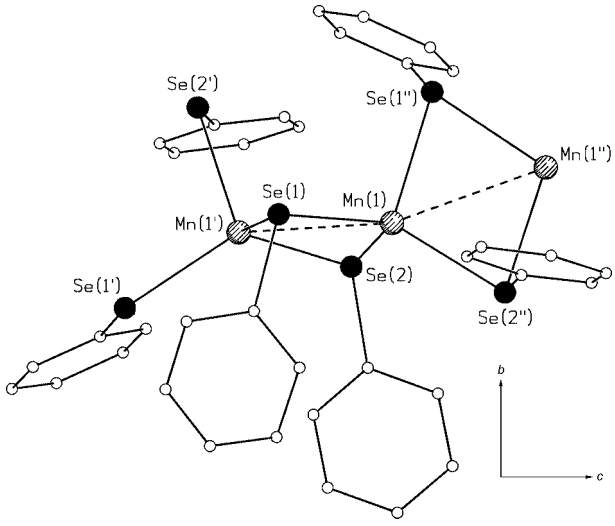


Figure 1. Section of the one-dimensional chain structure of $^{1}_{\infty}$[Mn(SePh)$_2$] (**1**) viewed down *a*. Symmetry transformation for generation of equivalent atoms: ′: *y* – 3/4, –*x* + 5/4, *z* + 1/4 ": –*y* + 5/4, *x* + 3/4, *z* – 1/4. Selected bond lengths [pm] and angles [°]: Se(1)–Mn(1) 254.7(1), Se(1)–Mn(1′) 257.3(1), Se(2)–Mn(1′) 254.8(1), Se(2)–Mn(1) 257.8(1), Mn(1)–Mn(1") 304.6(1). Mn(1)–Se(1)–Mn(1′) 73.01(3), Mn(1′)–Se(2)–Mn(1) 72.93(3), Se(1)–Mn(1)–Se(2) 105.88(3), Se(1)–Mn(1)–Se(2") 125.39(4), Se(1)–Mn(1)–Se(1") 104.63(3), Se(2′′)–Mn(1)–Se(1") 106.00(3), Se(2")–Mn(1)–Se(2) 107.97(3), Se(1")–Mn(1)–Se(2) 105.42(4), Mn(1")–Mn(1)–Mn(1′) 151.86(3).

The monomeric compound **2** crystallises in the monoclinic space group $P2_1/c$ (Figure 2) and exhibits a distorted octahedral coordination sphere around the manganese atom. The coordination sphere involves four nitrogen atoms [N(1), N(2), N(3), N(4)] from the two bidentate bipyridine ligands and two selenium atoms [Se(1), Se(2)] from the phenylselenolato ligands, which coordinate in a *cis* geometry. The Mn–Se distances are 265.3 pm and 265.5 pm, which are slightly longer than in **1**. The Mn–N distances [224.6–231.9(4) pm] as well as the N–Mn–N bite angle [N(1)–Mn(1)–N(2): 71.9(2)°, N(3)–Mn(1)–N(4): 71.5(2)°] are comparable to those in related transition-metal complexes.

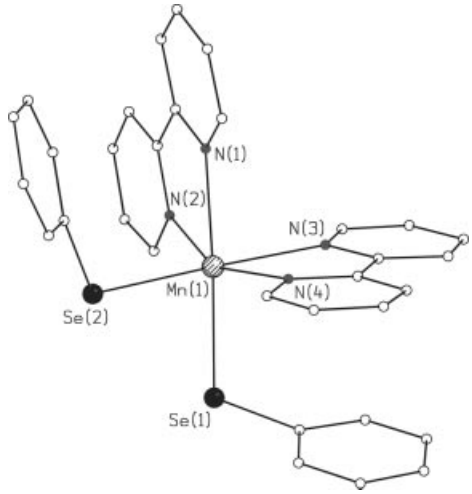


Figure 2. Molecular structure of [Mn(SePh)$_2$(2,2′-bipy)$_2$] (**2**). Selected bond lengths [pm] and angles [°]: Se(1)–Mn(1) 265.3(1), Se(2)–Mn(1) 265.5(1), Mn(1)–N(4) 224.6(4), Mn(1)–N(2) 228.3(4), Mn(1)–N(1) 228.9(4), Mn(1)–N(3) 231.9(5). N(4)–Mn(1)–N(1) 91.06(15), N(2)–Mn(1)–N(1) 71.91(16), N(4)–Mn(1)–N(3) 71.54(16), N(2)–Mn(1)–N(3) 88.81(16), N(1)–Mn(1)–N(3) 86.22(16), N(4)–Mn(1)–Se(1) 98.69(11), N(2)–Mn(1)–Se(1) 97.49(12), N(3)–Mn(1)–Se(1) 92.81(11), N(4)–Mn(1)–Se(2) 100.32(12), N(2)–Mn(1)–Se(2) 98.92(13), N(1)–Mn(1)–Se(2) 93.71(12), Se(1)–Mn(1)–Se(2) 88.74(4).

Complex **3** crystallises in the acentric space group *Cc* and is isostructural to **2**, with only slight differences in the bond lengths and bond angles.

## Magnetic Properties

The magnetic behaviour of chain compounds such as **1** is well understood.[19] For materials with an antiferromagnetic exchange interaction there should be a broad maximum in the temperature dependence of the susceptibility that is typical of short-range order found in low dimensional materials. The temperature at which the maximum occurs is dependent on the size of the *intra*chain exchange coupling, *J*. For small spins, the susceptibility is normally well modelled by the approach of Bonner and Fisher,[20] which was subsequently modified by Weng.[21] For $Mn^{II}$ chains, the larger $S = 5/2$ spin is usually better modelled[22] by the classical approach of Fisher.[23] In the case of compound **1**, the magnitude of the susceptibility is much lower than expected (the susceptibility of an array of non-interacting $S = 5/2$ ions at 300 K should be approximately 0.015 cm$^3$ mol$^{-1}$, almost an order of magnitude larger than the observed value) and it decreases smoothly down to 25 K (Figure 3). This is indica-

 © 2007 Wiley-VCH Verlag GmbH & Co. KGaA, Weinheim 

tive of very strong superexchange as the broad maximum must occur at a temperature far higher than 300 K. Strong exchange is expected for bridging ligands that have heavy donor atoms, although this does not seem to always be the case.[19] However, sulfur-mediated superexchange has recently been shown to give strong exchange and relatively high magnetic ordering temperatures.[24]

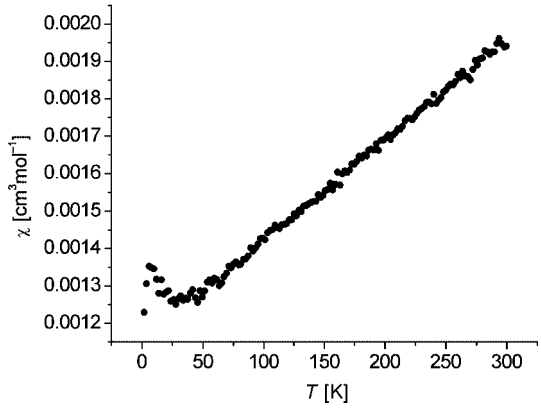


Figure 3. Susceptibility versus temperature for $^{1}_{\infty}$[Mn(SePh)$_2$] (**1**).

At the suggestion of a referee we prepared the previously reported compound $^{1}_{\infty}$[Mn(SeC$_6$H$_2$-2,4,6-CH$_3$)$_2$][17] and measured its magnetic susceptibility (Figure 4). The presence of the broad maximum centred close to 100 K shows that the exchange is strong, but not as strong as that in **1**. Fits to the Weng (Equation 1) and Fisher (Equation 2) equations give satisfactory agreement for the position of the maximum, but fail to model the low-temperature data. Fits obtained by using the Weng equation are superior to those obtained from the Fisher equation, which is surprising given the way these functions were derived (see above). These fits give values for $J$ of –13.50(5) K and –11.2(3) K, respectively. Below 25 K there is a discontinuity in the susceptibility for both **1** and $^{1}_{\infty}$[Mn(SeC$_6$H$_2$-2,4,6-CH$_3$)$_2$], which we ascribe to the onset of long-range order.

MnSe has an analogous structure to sodium chloride and orders antiferromagnetically at 249 K,[25] which indicates that coupling is strong in this compound. In compound **1**, the Mn–Se–Mn bridging angle is approximately 73° in comparison with 90° in MnSe and 88° in $^{1}_{\infty}$[Mn(SeC$_6$H$_2$-2,4,6-CH$_3$)$_2$]. As the strength of the superexchange is dependent on the bridging angle, it is reasonable that the ordering temperatures for these three compounds should be different. Whilst there has been much study of the variation in exchange coupling with bridging angle for angles of 90° and greater, the lack of compounds with more acute bridges has meant that there has been no equivalent study for angles less than 90°. Selenolate bridges appear to favour more acute bridging angles than either alkoxide or thiolate ligands, hence further study of how the selenolate-mediated exchange interaction varies with angle would be useful. For compound **1** it is also important to remember that the Mn–Mn distance is very small, and we cannot rule out some contribution from direct exchange.

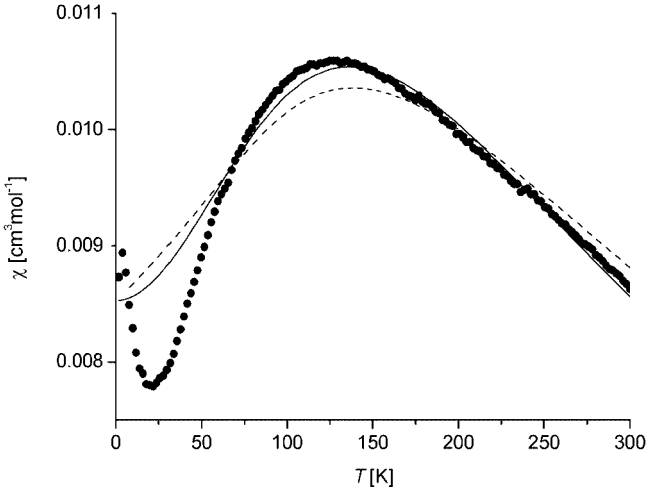


Figure 4. Susceptibility versus temperature for $^{1}_{\infty}$[Mn(SeC$_6$H$_2$-2,4,6-CH$_3$)$_2$] (dotted line). The fits according to either the Weng (straight) or Fisher (dashed) equation (see text).

For the spin Hamiltonian $\hat{H} = -2J\sum_i S_i \cdot S_{i+1}$, these equations, Equation (1) and Equation (2), have the form:

$$\chi = \frac{Ng^2\beta^2}{kT}\left(\frac{2.9167 + 208.04(J/kT)^2}{1 + 15.543(J/kT) + 2707.2(J/kT)^3}\right) \quad (1)$$

$$\chi = \frac{Ng^2\beta^2 S(S+1)}{3kT}\left(\frac{1+u}{1-u}\right)$$
$$u = \coth[2JS(S=1)/kT] - kT/[2JS(S+1)] \quad (2)$$

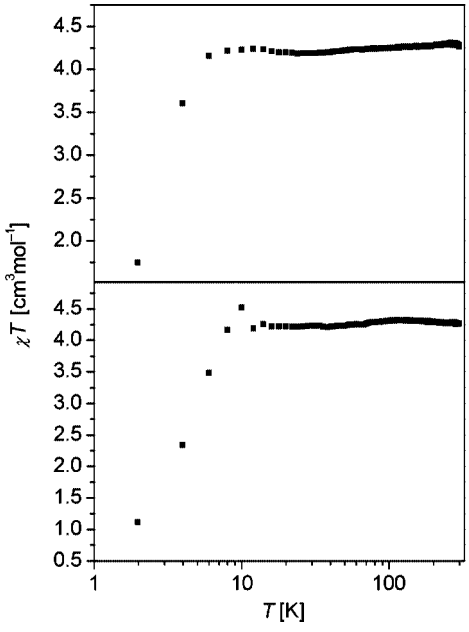


Figure 5. Graph of $\chi T$ vs. $T$ for [Mn(SePh)$_2$(2,2′-bipy)$_2$] (**2**) (bottom) and for [Mn(SePh)$_2$(1,10-phen)$_2$] (**3**) (top).

 © 2007 Wiley-VCH Verlag GmbH & Co. KGaA, Weinheim 

Compounds **2** and **3** are both well-isolated octahedral molecules with somewhat distorted coordination environments. They both obey the Curie law at temperatures above 10 K to give Curie constants of 4.27(8) and 4.31(1) $cm^3 mol^{-1} K$, respectively, in comparison to the expected value of 4.375 $cm^3 mol^{-1} K$ for $g = 2$ (Figure 5). Below 10 K, both compounds exhibit a local maximum in $\chi$, followed by a sharp decrease. The single ion anisotropy of a high spin $d^5$ ion may be modelled according to ref.[19], however, this approach alone does not successfully model the low temperature data for either compound. We therefore suggest that the low temperature behaviour is a combination of very weak single ion anisotropy and dipolar coupling.

## Optical Properties

Crystals of **1** appear red-brown in compact form but turn light rose-red when ground to a powder. The UV/Vis spectrum of **1** dissolved in thf is displayed in the lower part of Figure 6. The spectrum shows three distinct regions of absorption features, which differ significantly in their absorption intensity. The broad and intense band centred around 260 nm ($\varepsilon = 2.4 \times 10^4$ $M^{-1} cm^{-1}$), which comprises a weakly resolved shoulder, can be assigned to π–π* transitions of the phenylselenolato ligands. In the region between 340 and 400 nm, two additional weakly resolved shoulders with extinction coefficients between 200 and 400 $M^{-1} cm^{-1}$ can be thought to originate from ligand-to-metal charge transfer transitions, although they are relatively low in intensity, as well as from d–d transitions in $Mn^{2+}$ ions. Between 400 and 700 nm one observes one sharp band at 431 nm ($\varepsilon = 12$ $M^{-1} cm^{-1}$) followed by two shoulders at 476 and 552 nm, which can be assigned because of their low intensity as d–d transitions in $Mn^{2+}$ [$^4T_1(G) \leftarrow {}^6A_1$ 552 nm (18116 $cm^{-1}$), $^4T_2(G) \leftarrow {}^6A_1$ 476 nm (21008 $cm^{-1}$), $^4E(G) \leftarrow {}^6A_1$ 431 nm (23202 $cm^{-1}$)].[26] The solid-state spectrum as a nujol mull (Figure 6, upper part) displays, in principle, similar absorption features as observed in solutions of **1**, although the bands differ slightly in intensity, position and shape. The strong band of the π–π* transitions of the $SePh^-$ ligands is shifted to 243 nm, and the intensity of the shoulder is reduced. Bands for the transitions at 378 and 357 nm observed in the solution spectrum are obscured by a broad band centred around 324 nm in the solid-state spectrum. A shoulder is visible at 400 nm in the solid-state spectrum, which has no equivalent in the solution spectrum. In the region of the d–d transitions, the solid-state spectrum shows a weakly resolved maximum at 436 nm, a shoulder at 464 nm and a comparatively strong band at 481 nm. The shoulder in the solution spectrum at 552 nm is only visible in the solid-state spectrum as a tail of the absorption at 481 nm. The differences observed between the solution and solid-state spectra, which are due in part to the non-validity of the Lambert–Beer law for the solid-state spectra, might also indicate different coordination geometries of the $Mn^{2+}$ ions in thf and in the solid state. In the crystal structure of **1**, the $Mn^{2+}$ ions are coordinated by four selenium atoms of the phenylselenolato ligands in a tetrahedrally distorted arrangement. In solution, the one-dimensional polymeric structure might be destroyed with additional coordination of thf solvent molecules, which can either result in a tetrahedral or octahedral geometry or a mixture of both.

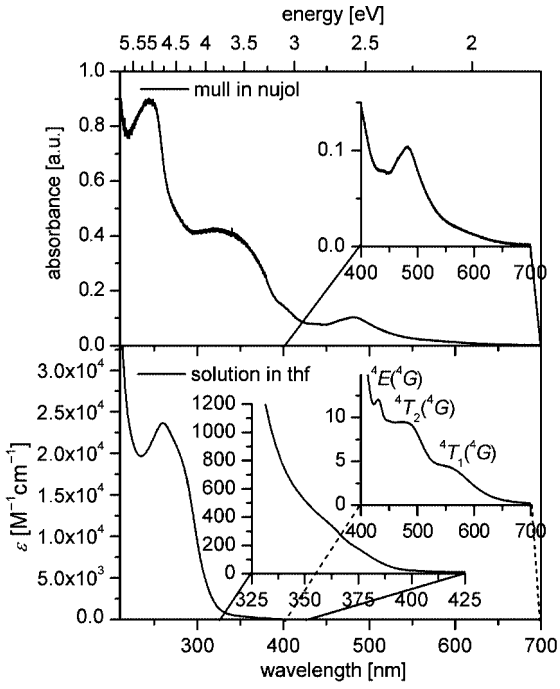


Figure 6. UV/Vis spectra of $^1_\infty$[Mn(SePh)$_2$] (**1**) in thf.

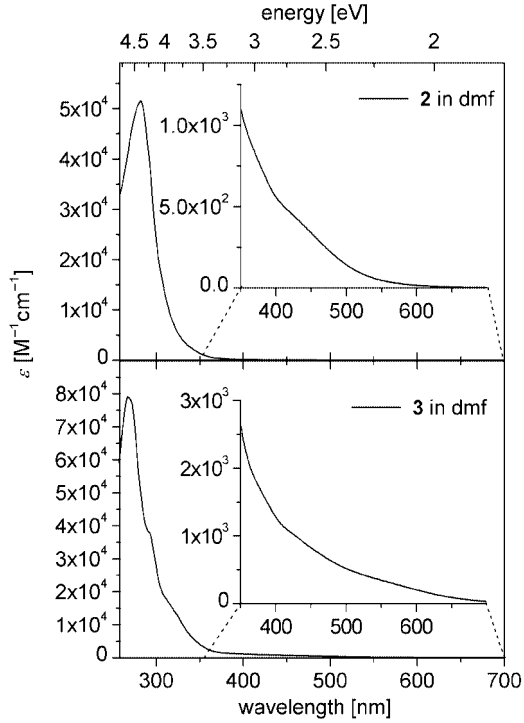


Figure 7. UV/Vis spectra of [Mn(SePh)$_2$(2,2′-bipy)$_2$] (**2**) (top) and [Mn(SePh)$_2$(1,10-phen)$_2$] (**3**) (bottom) in dmf.

 © 2007 Wiley-VCH Verlag GmbH & Co. KGaA, Weinheim 

The dark red crystals of **2** and **3** mostly keep their colour when ground to a powder. In dmf solutions, **2** and **3** display strong absorption features at 284 nm and 267 nm, respectively, which can be assigned to π–π* transitions of either the bidentate amine ligands or the $PhSe^-$ ligands, or a mixture of both (Figure 7). The UV/Vis spectrum of **3** displays several shoulders at 292, 313 and 322 nm. Apart from the strong absorption, weakly resolved shoulders between 350 and 600 nm (**2**), and 350 and 700 nm (**3**) could originate from metal-to-ligand charge transfer transitions into low-lying, empty π* orbitals of the bipyridyl and phenanthroline ligands, respectively. An assignment as d–d transitions seems to be unlikely because of extinction coefficients in the region between 500 and 2000 $M^{-1}cm^{-1}$. These transitions are most probably obscured by the charge-transfer bands.

## Experimental Section

**Synthesis:** Standard Schlenk techniques were employed throughout the syntheses by using a double manifold vacuum line with high-purity dry nitrogen. The solvents thf and diethyl ether were dried with sodium benzophenone and distilled under nitrogen. Anhydrous dimethylformamide (dmf) ($H_2O < 0.005\%$) obtained from Aldrich was degassed, freshly distilled and stored over molecular sieves under nitrogen. $Mn(OOCCH_3)_2$, 2,2′-bipyridine and 1,10-phenanthroline were purchased from Aldrich. $PhSeSiMe_3$ was prepared according to a literature procedure.[27]

**$^1_\infty$[Mn(SePh)$_2$] (1):** An ultrasonic bath was used to suspend $Mn(OOCCH_3)_2$ (0.42 g, 2.45 mmol) in thf (45 mL) for 45 min. $PhSeSiMe_3$ (0.98 mL, 5.1 mmol) was then added, and the mixture was stirred overnight to give an orange solution. Careful addition of diethyl ether (50 mL) resulted in the crystallisation of dark red needles of $^1_\infty$[Mn(SePh)$_2$] (**1**). Filtration of the crude product, and further addition of diethyl ether to the filtrate resulted in a total yield of 90% (0.81 g) of **1**. $C_{12}H_{10}MnSe_2$ (367.1): calcd. C 39.3, H 2.8; found C 39.8, H 3.1.

**[Mn(SePh)$_2$(2,2′-bipy)$_2$] (2):** $^1_\infty$[Mn(SePh)$_2$] (0.15 g, 0.41 mmol) was dissolved in thf (25 mL ) to give an orange-brown solution. A solution of 2,2′-bipyridine (0.13 g, 0.83 mmol) in thf (6 mL) was then added, and the mixture immediately turned dark red. Overnight, a dark red crystalline precipitate of [Mn(SePh)$_2$(2,2′-bipy)$_2$] (**2**) was formed from this solution with a total yield of 79% (0.22 g). Compound **2** was insoluble in thf and could be recrystallised for purification from dmf/thf. $C_{32}H_{26}MnN_4Se_2$ (679.4): calcd. C 56.6, H 3.7, N 8.3; found C 56.4, H 4.1, N 8.1. Crystals suitable for single-crystal X-ray analysis were grown by layering dmf solutions of **2** with diethyl ether.

**[Mn(SePh)$_2$(1,10-phen)$_2$] (3):** $^1_\infty$[Mn(SePh)$_2$] (0.081 g, 0.22 mmol) was dissolved in thf (20 mL) to give an orange-brown solution. A solution of 1,10-phenanthroline (0.083 g, 0.46 mmol) in thf (5 mL) was then added, which led to the immediate formation of [Mn(SePh)$_2$(1,10-phen)$_2$] (**3**) as a cherry red crystalline precipitate with a total yield of 84% (0.15 g). $C_{36}H_{26}MnN_4Se_2{\cdot}C_3H_7NO$ (800.6): calcd. C 58.6, H 4.2, N 8.8; found C 58.7, H 4.2, N 8.7. Crystals suitable for single-crystal X-ray analysis were grown by layering dmf solutions of **3** with diethyl ether.

**Crystallography:** Crystals suitable for single-crystal X-ray diffraction were taken directly from the reaction solution of the compound and then selected under perfluoroalkylether oil. Single-crystal X-ray diffraction data of compounds **1**–**3** were collected by using graphite-monochromatised Mo-$K_\alpha$ radiation ($\lambda$ = 0.71073 Å) on a STOE IPDS II (Imaging Plate Diffraction System) equipped with a Schneider rotating anode. Raw intensity data were collected and treated with the STOE X-Area software Version 1.27. Data for all compounds were corrected for Lorentz and polarisation effects. The structures were solved with the direct methods program SHELXS[28] of the SHELXTL PC suite programs and were refined with the use of the full-matrix least-squares program SHELXL.[28] Molecular diagrams were prepared with SCHAKAL 97.[29]

All Mn, Se, N and C atoms, with the exception of the C atoms of thf in **1**, were refined with anisotropic displacement parameters, whilst H atoms were calculated in fixed positions (Table 1).

Table 1. Crystallographic data for $^1_\infty$[Mn(SePh)$_2$] (**1**), [Mn(SePh)$_2$(2,2′-bipy)$_2$] (**2**) and [Mn(SePh)$_2$(1,10-phen)$_2$] (**3**).

| | **1**·0.4thf | **2** | **3**·dmf |
|---|---|---|---|
| $F_w$ [g mol$^{-1}$] | 395.9 | 679.4 | 800.6 |
| Crystal system | tetragonal | monoclinic | monoclinic |
| Space group | $I4_1/a$ | $P2_1/c$ | $Cc$ |
| $a$ [Å] | 22.051(3) | 10.238(2) | 15.406(3) |
| $b$ [Å] | | 17.444(4) | 16.747(3) |
| $c$ [Å] | 11.443(2) | 16.651(3) | 13.578(3) |
| $\beta$ [°] | | 102.99(3) | 101.74(3) |
| $V$ [Å$^3$] | 5563.8(16) | 2897.7(10) | 3430.1(12) |
| $Z$ | 16 | 4 | 4 |
| $T$ [K] | 190 | 180 | 190 |
| $d_c$ [g cm$^{-3}$] | 1.891 | 1.557 | 1.550 |
| $\mu$(Mo-$K_\alpha$) [mm$^{-1}$] | 6.159 | 2.996 | 2.547 |
| $F$[000] | 3056 | 1356 | 1612 |
| $2\theta_{max}$ [°] | 52 | 49 | 49 |
| Measured reflections | 4236 | 16985 | 10401 |
| Unique reflections | 2372 | 4616 | 5163 |
| $R_{int}$ | 0.0446 | 0.0666 | 0.1128 |
| Reflections with $I > 2\sigma(I)$ | 1746 | 3306 | 4441 |
| Parameters | 139 | 352 | 429 |
| $R_1[I > 2\sigma(I)]$[a] | 0.0459 | 0.0498 | 0.0667 |
| $wR_2$(all data)[b] | 0.1295 | 0.1292 | 0.1892 |
| Abs. struct. param. | | | 0.27(2) |

[a] $R_1 = \Sigma||F_o| - |F_c||/\Sigma|F_o|$. [b] $wR_2 = \{\Sigma[w(F_o^2 - F_c^2)^2] / \Sigma[w(F_o^2)^2]\}^{1/2}$.

CCDC-603930(**1**), -603931(**2**) and -603932(**3**) contain the supplementary crystallographic data for this paper. These data can be obtained free of charge from The Cambridge Crystallographic Data Centre via www.ccdc.cam.ac.uk/data_request/cif.

**Physical Measurements:** Field-cooled SQUID measurements were performed at 1 T with an extraction magnetometer (Quantum Design PPMS) in DC extraction mode, and the response to the vertical movement of the sample (10 $ms^{-1}$) through the detection coils was recorded, under a dry helium environment. The samples were contained in high-precision quartz glass sample holders owing to the high degree of moisture sensitivity of the compounds. The data were corrected for the sample holder and for diamagnetism using Pascal's constants.[19] UV/Vis absorption spectra of cluster molecules in solution were measured on a Varian Cary 500 spectrophotometer in quartz cuvettes. Solid-state reflection spectra were measured as micron-sized crystalline powders between quartz plates with a Labsphere integrating sphere.

## Acknowledgments

This work was supported by the Deutsch-Israelisches Programm (DIP) and the Deutsche Forschungsgemeinschaft (center for func-

 © 2007 Wiley-VCH Verlag GmbH & Co. KGaA, Weinheim 

tional nanostructures CFN). The authors are grateful to Prof. Dr. D. Fenske for helpful discussions and generous support and to E. Tröster for her assistance in the practical work.

[1] I. Dance, K. Fisher, *Prog. Inorg. Chem.* **1994**, *41*, 637–803.
[2] S. Dehnen, A. Eichhöfer, D. Fenske, *Eur. J. Inorg. Chem.* **2002**, 279–317.
[3] M. W. DeGroot, J. F. Corrigan, *Comprehensive Coordination Chemistry II* (Eds.: M. Fujita, A. Powell, C. Creutz), Pergamon, Oxford, **2004**, Vol. 7, pp. 57–123.
[4] J. Arnold, *Prog. Inorg. Chem.* **1995**, *43*, 353.
[5] M. Bochmann, *Chem. Vap. Deposition* **1996**, *2*, 85–96.
[6] B. Krebs, G. Henkel, *Angew. Chem.* **1991**, *103*, 785–804; *Angew. Chem. Int. Ed. Engl.* **1991**, *30*, 769–788.
[7] B. Krebs, G. Henkel, *Chem. Rev.* **2004**, *104*, 801–824.
[8] J. K. Furdyna, *J. Appl. Phys.* **1988**, *64*, R29–R64.
[9] D. J. Norris, N. Yao, F. T. Charnock, T. A. Kennedy, *Nanoletters* **2001**, *1*, 3–7.
[10] R. Sessoli, H.-K. Tsai, A. R. Schake, S. Wang, J. B. Vincent, K. Folting, D. Gatteschi, G. Cristou, D. N. Hendrickson, *J. Am. Chem. Soc.* **1993**, *115*, 1804–1816.
[11] A. J. Tasiopoulous, A. Vinslava, W. Wernsdorfer, K. A. Abboud, G. Christou, *Angew. Chem. Int. Ed.* **2004**, *43*, 2117–2121.
[12] T. Costa, J. Dorfman, K. S. Hagen, R. H. Holm, *Inorg. Chem.* **1983**, *22*, 4091–4099.
[13] W. Tremel, B. Krebs, K. Greiwe, W. Simon, H. Stephan, G. Henkel, *Z. Naturforsch., Teil B* **1992**, *47*, 1580–1592.
[14] H. Stephan, K. Griesar, W. Haase, G. Henkel, *Z. Naturforsch.* **1994**, *49b*, 1620–1632.
[15] M. Bochmann, A. K. Powell, X. Song, *Inorg. Chem.* **1994**, *33*, 400–401.
[16] J. J. Ellison, K. Ruhlandt-Senge, H. H. Hope, P. P. Power, *Inorg. Chem.* **1995**, *34*, 49–54.
[17] M. Bochmann, A. K. Powell, X. Song, *J. Chem. Soc. Dalton Trans.* **1995**, 1645–1648.
[18] R. Bianchi, G. Gervasio, D. Marabello, *Inorg. Chem.* **2000**, *39*, 2360–2366.
[19] O. Kahn, *Molecular Magnetism*, Wiley-VCH, Weinheim, **1993**.
[20] J. C. Bonner, M. E. Fisher, *Phys. Rev. A* **1964**, *135*, A640.
[21] C. Y. Weng, Ph. D. Thesis, Carnegie Mellon University, Pittsburgh PA, USA, **1969**.
[22] S. O. H. Gutschke, D. J. Price, A. K. Powell, P. T. Wood, *Inorg. Chem.* **2000**, *39*, 3705.
[23] M. E. Fisher, *Am. J. Phys.* **1964**, *32*, 343.
[24] S. M. Humphrey, A. Alberola, C. J. Gomez Garcia, P. T. Wood, *Chem. Commun.* **2006**, 1607.
[25] T. Ito, K. Ito, M. Oka, *Jpn. J. Appl. Phys.* **1978**, *17*, 371.
[26] A. B. P. Lever, *Inorganic Electronic Spectroscopy*, 2nd ed., Elsevier, Amsterdam, **1984**, p. 448.
[27] N. Miyoshi, H. Ishii, K. Kondo, S. Mui, N. Sonoda, *Synthesis* **1979**, 301–304.
[28] G. M. Sheldrick, *SHELXTL PC version 5.1 An Integrated System for Solving, Refining, and Displaying Crystal Structures from Diffraction Data*, Bruker Analytical X-ray Systems, Karlsruhe, **2000**.
[29] E. Keller, *SCHAKAL 97*, *A Computer Program for the Graphic Representation of Molecular and Crystallographic Models*, University of Freiburg, **1997**.

Received: January 30, 2007
Published Online: September 4, 2007

 © 2007 Wiley-VCH Verlag GmbH & Co. KGaA, Weinheim 

DOI: 10.1002/ejic.200700489

# Diphthalocyaninatolanthanum as a New Phthalocyaninato-Dianion Donor for the Synthesis of Heteroleptic Triple-Decker Rare Earth Element Crown-Phthalocyaninato Complexes

**Alexander G. Martynov,[a,b] Olga V. Zubareva,[a] Yulia G. Gorbunova,*[a,b] Sergey G. Sakharov,[b] Sergey E. Nefedov,[b] Fedor M. Dolgushin,[c] and Aslan Yu. Tsivadze[a,b]**

**Keywords:** Rare earths / Macrocyclic ligands / Phthalocyanines / Sandwich complexes / Heteroleptic complexes

A novel synthetic approach towards heteroleptic triple-decker crown-phthalocyaninato complexes $[(15C5)_4Pc]$-M$[(15C5)_4Pc]$M(Pc) and (Pc)M$[(15C5)_4Pc]$M(Pc) [where $(15C5)_4Pc^{2-}$ = 2,3,9,10,16,17,24,25-tetrakis(15-crown-5)-phthalocyaninato dianion; $Pc^{2-}$ = phthalocyaninato dianion; M = Sm, Tb, Dy, Tm and Y] has been developed. It utilises the application of diphthalocyaninatolanthanum, $La(Pc)_2$, as a new source of the phthalocyaninato dianion instead of well known $Li_2(Pc)$. In contrast to the highly hygroscopic $Li_2(Pc)$, $La(Pc)_2$ is quite air-stable and its use allowed a significant decrease in reaction times. All the synthesised complexes were characterised by UV/Vis and $^1H$ NMR spectroscopy as well as MALDI TOF mass spectrometry. The X-ray structure of heteroleptic triple-decker crown-phthalocyaninato (Pc)-Sm$[(15C5)_4Pc]$Sm(Pc) was determined. These new heteroleptic phthalocyaninato complexes are interesting because of their potential as components in new supramolecular materials.

(© Wiley-VCH Verlag GmbH & Co. KGaA, 69451 Weinheim, Germany, 2007)

## Introduction

The development of novel supramolecular devices requires both an understanding of the supramolecular interactions between individual molecules and also the possibility of tuning the structure of the supramolecular aggregates which determine the device performance.[1]

Tetrapyrrolic macrocycles (porphyrins, phthalocyanines, etc.) exhibit highly delocalised π electron systems and are thus prominent components of novel supramolecular materials with unique optical, electrochemical and magnetic properties. When tetrapyrrolic ligands are held in close proximity by metal ions in sandwich-type double- and triple-decker complexes, there exist strong intramolecular π-π interactions between macrocycles which results in the characteristic features of this class of compound. These interactions depend both on the nature of the ligand and the metal ion and can be tuned by the synthesis of heteroleptic and heteronuclear complexes.[2]

The intermolecular stacking π-π interactions are the main driving force of the formation of supramolecular assemblies by tetrapyrrolic compounds.[3a] The introduction of functional groups into the periphery of the macrocycles provides an opportunity for obtaining supramolecules of various architectures based on ionic interactions,[3b] hydrogen bonds[3c] etc. The introduction of crown-ether substituents enables the formation of supramolecular assemblies by the addition of alkali metal ions. In the case of the double-decker lutetium crown-phthalocyaninato $Lu[(15C5)_4Pc]_2^0$, the formation of a 1D oligomeric supramolecular aggregate $\{Lu[(15C5)_4Pc]_2 \cdot 4K^+\}_n$, $M_w = 8.1 \times 10^5$ g mol$^{-1}$, was identified by UV/Vis studies,[4a] light scattering measurements[4b] and atom force microscopy.[4c]

The heteroleptic double-decker 15-crown-5-phthalocyaninato complexes $[(15C5)_4Pc]$M(Pc) were synthesised previously for studying the intermolecular interactions between double-decker complexes.[5] The raise-by-one-story method was applied in the cases of the Sm, Dy and Tm complexes, whereas for the La complex a new synthetic approach was developed. This was based on the synthesis of the intermediate heteroleptic triple-decker complex $[(15C5)_4Pc]$La(Pc)-La(Pc) by means of the interaction between $H_2[(15C5)_4Pc]$, $La(Pc)_2$ and $La(acac)_3 \cdot nH_2O$. It was shown that $[(15C5)_4Pc]$-La(Pc)La(Pc) undergoes decomposition with the formation of the heteroleptic double-decker complex $[(15C5)_4Pc]$-La(Pc) due to the low stability of triple-decker lanthanum complexes.[6]

[a] A. N. Frumkin Institute of Physical Chemistry and Electrochemistry RAS
Leninsky Prosp. 31, Moscow 119991, Russia
E-mail: yulia@igic.ras.ru
[b] N. S. Kurnakov Institute of General and Inorganic Chemistry RAS
Leninsky Prosp. 31, Moscow 119991, Russia
[c] A. N. Nesmeyanov Institute of Organoelement Compounds RAS
Moscow, Vavilova str. 28, Moscow 119991, Russia

 © 2007 Wiley-VCH Verlag GmbH & Co. KGaA, Weinheim 

The formation of the intermediate heteroleptic heteronuclear triple-decker complexes $[(15C5)_4Pc]M(Pc)La(Pc)$ was assumed to occur as a result of the reaction between $H_2[(15C5)_4Pc]$, $La(Pc)_2$ and acetylacetonato complexes of the other lanthanides. Unexpectedly, there were isolated two types of heteroleptic homonuclear triple-decker phthalocyaninato species. Thus, we herein report the novel synthetic approach towards heteroleptic triple-decker phthalocyaninato compounds which enabled us to obtain, at first, (Pc)M[(15C5)$_4$Pc]M(Pc) and [(15C5)$_4$Pc]M[(15C5)$_4$Pc]M(Pc).

It was previously demonstrated that amphiphilic heteroleptic triple-decker complexes [(15C5)$_4$Pc]M[(15C5)$_4$Pc]M[$(C_8H_{17}O)_8$Pc] [M = Eu, Ho, Lu] form Langmuir–Blogett films which can been fabricated into field-effect transistor devices with almost the highest carrier mobilities achieved thus far for all LB film-based organic field-effect transistors.[7a] The mixed ligand triple-decker complex [(15C5)$_4$Pc]Eu[(15C5)$_4$Pc]Eu(TPP) forms well-ordered monolayers on an Au(111) surface. The molecular orientation of the complex is reversed during the electrochemical redox reaction.[7b] Thus, we suppose, that the heteroleptic tris(phthalocyaninato) complexes reported herein could be important components of new supramolecular materials.

## Results and Discussion

### Synthesis of (Pc)M[(15C5)$_4$Pc]M(Pc) and [(15C5)$_4$Pc]M-[(15C5)$_4$Pc]M(Pc)

We performed the reactions between $H_2[(15C5)_4Pc]$, $La(Pc)_2$ and $M(acac)_3{\cdot}H_2O$ [M = Sm, Tb, Dy, Tm and Y] in 1-chloronaphthalene at reflux. It was expected that the intermediate heteroleptic heteronuclear complex [(15C5)$_4$Pc]M(Pc)La(Pc) would eliminate the $La(Pc)^+$ fragment with the formation of the target heteroleptic double-decker complexes. Indeed, chromatographic separation of the reaction mixture afforded the corresponding [(15C5)$_4$Pc]M(Pc) complex although the yield was low (<5%). Unexpectedly, the major products were heteroleptic homonuclear triple-decker complexes, viz. (Pc)M[(15C5)$_4$Pc]M(Pc) and [(15C5)$_4$Pc]-M[(15C5)$_4$Pc]M(Pc) which contained no lanthanum ions (Scheme 1). The progress of the reaction was monitored by UV/Vis spectroscopy. The bands of the initial material $La(Pc)_2$ disappeared immediately after the reaction mixture started to reach reflux and the band of intermediate monophthalocyaninato species was observed. We suppose that the decomposition of $La(Pc)_2$ with the formation of the $Pc^{2-}$ species may occur under the synthetic conditions used. $Pc^{2-}$ reacts with metal acetylacetonato complexes and $H_2[(15C5)_4Pc]$ with the formation of heteroleptic triple-decker complexes. Free lanthanum ions remain in solution and do not participate in subsequent reactions as was demonstrated by MALDI TOF mass spectrometry. The reaction time decreased from 1 h in the case of M = Tm and Y to 30 min for Tb and Dy and to 10 min for Sm. The complexes (Pc)M[(15C5)$_4$Pc]M(Pc) form with lower yield for M = Y and Tm (10–12%) in comparison with M = Sm, Tb and Dy (19–25%). The yields of the [(15C5)$_4$Pc]M[(15C5)$_4$-Pc]M(Pc) complexes do not significantly change with a decrease in the ionic radii (39–46%) (Table 1). Previously, the related heteroleptic triple-decker complexes (Pc)M-[$(C_8H_{17}O)_8$Pc]M(Pc) and [$(C_8H_{17}O)_8$Pc]M[$(C_8H_{17}O)_8$Pc]M-(Pc) were prepared using a wide range of metals.[8] Phthalocyaninatodilithium $Li_2(Pc)$ was used as a soluble donor of $Pc^{2-}$ and the reactions were carried out over more than 12 h. The authors carried out the reaction between $M[(C_8H_{17}O)_8Pc]_2$ and (Pc)M(acac) which was generated in situ from $Li_2Pc$ and $M(acac)_3{\cdot}nH_2O$.

The partial decomposition of sandwich complexes under the synthetic conditions and the formation of scrambling products are common in the preparation of heteroleptic compounds. Previously[8] it was demonstrated that in the synthesis of [$(C_8H_{17}O)_8$Pc]M[$(C_8H_{17}O)_8$Pc]M(Pc), the formation of the scrambling product (Pc)M[$(C_8H_{17}O)_8$Pc]-M(Pc) occurs due to decomposition of the starting double-decker complex $M[(C_8H_{17}O)_8Pc]_2$. The contraction of the rare-earth element (REE) ion along the investigated series of elements leads to an increase of the target compound yield and a decrease in the formation of side products.

Lanthanum has the biggest covalent radius in the series of REEs and so its complexes are less stable than those of middle and late REEs. Unsubstituted diphthalocyaninato-

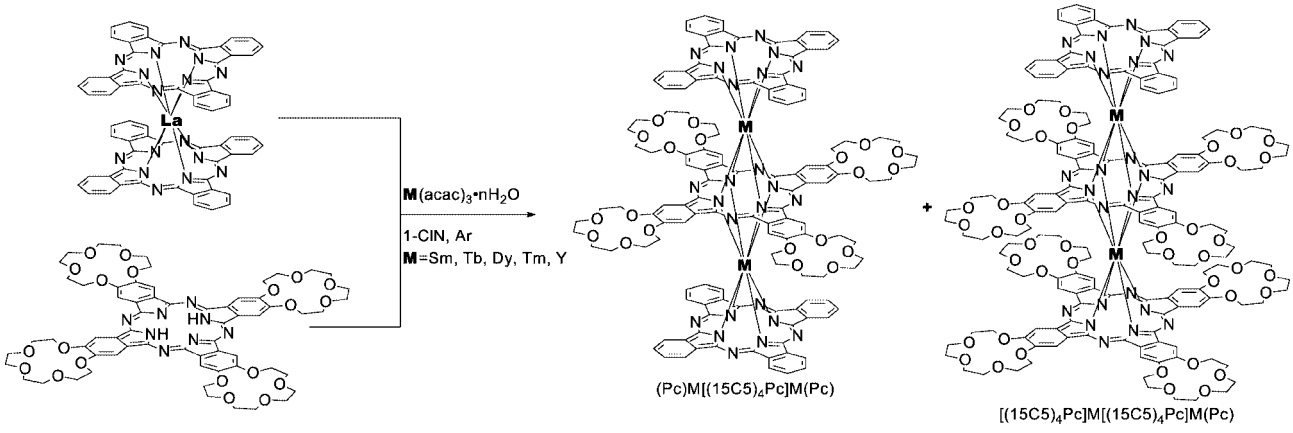


Scheme 1. The synthesis of complexes (Pc)M[(15C5)$_4$Pc]M(Pc) and [(15C5)$_4$Pc]M[(15C5)$_4$Pc]M(Pc) [M = Sm, Tb, Dy, Tm and Y].

 © 2007 Wiley-VCH Verlag GmbH & Co. KGaA, Weinheim 

Table 1. Yields and MALDI TOF mass spectrometric data for heteroleptic triple-decker crown-substituted phthalocyaninato complexes.

| | % Yield | MALDI TOF MS, *m/z* [a] | |
|---|---|---|---|
| | | Observed | Calculated |
| (Pc)M[(15C5)$_4$Pc]M(Pc)[b] | | | |
| M | | | |
| Sm | 23 | 2599.14 | 2599.11 |
| Tb | 19 | 2614.48 | 2614.64 |
| Dy | 25 | 2323.10 | 2623.38 |
| Tm | 10 | 2635.94 | 2636.26 |
| Y | 12 | 2474.57 | 2476.20 |
| [(15C5)$_4$Pc]M[(15C5)$_4$Pc]M(Pc)[c] | | | |
| M | | | |
| Sm | 39 | 3360.35 | 3359.90 |
| Tb | 38 | 3375.79 | 3374.97 |
| Dy | 45 | 3384.52 | 3384.17 |
| Tm | 46 | 3396.65 | 3397.04 |
| Y | 39 | 3236.51 | 3236.99 |

[a] Average *m/z* are given. [b] $[M]^+$ calculated for $C_{128}H_{104}M_2N_{24}O_{20}$. [c] $[M]^+$ calculated for $C_{160}H_{160}N_{24}O_{40}M_2$.

lanthanum should be even less stable towards the decomposition process than M[$(C_8H_{17}O)_8$Pc]$_2$ [M = Pr–Tm] and liberate $Pc^{2-}$ under the synthetic conditions utilised. Comparative studies of the chemical behaviour of other M(Pc)$_2$ complexes in this reaction will be reported elsewhere.

The low stability of some early lanthanide sandwich phthalocyaninato complexes, which has been mentioned previously,[9] makes them prospective donors of phthalocyaninato-dianions for the synthesis of more stable complexes. However, this feature has never been utilised for the synthesis of sandwich complexes with other metals by means of the metal exchange reaction. This reaction is comparatively rarely applied in the chemistry of tetrapyrrolic compounds in contrast to reactions of direct metallation and template synthesis. The above mentioned phthalocyaninatolithium was also used for the synthesis of REE monophthalocyaninato complexes.[10] Magnesium complexes can be transmetallated in acidic media[11] and cadmium ions in porphyrin complexes can be exchanged by cobalt or zinc ions in polar solvents.[12] However, REE exchange was never reported previously. Thus, the reaction described herein is also interesting in relation to the development of the coordination chemistry of tetrapyrrolic compounds.

Thus, we have proposed the alternative $Pc^{2-}$ donor – diphthalocyaninatolanthanum La(Pc)$_2$ – for the synthesis of heteroleptic triple-decker complexes. In contrast to highly hygroscopic Li$_2$(Pc), La(Pc)$_2$ is quite air-stable and its application allowed us to significantly decrease the reaction times in comparison with the synthesis of the related heteroleptic trisphthalocyaninato complexes (Pc)M[$(C_8H_{17}O)_8$Pc]M(Pc) and [$(C_8H_{17}O)_8$Pc]M[$(C_8H_{17}O)_8$Pc]M(Pc).[8]

## Spectroscopic Characterisation

All the synthesised heteroleptic complexes were isolated by column chromatography on neutral alumina using gradient elution with CHCl$_3$/MeOH mixtures and were subsequently characterised by various physical and chemical methods.

No elemental analyses were performed because the complexes undergo sublimation under the experimental conditions without complete decomposition and combustion.

Table 2. UV/Vis spectroscopic data for heteroleptic triple-decker crown-substituted phthalocyaninato complexes.

| (Pc)M[(15C5)$_4$Pc]M(Pc) | | | | |
|---|---|---|---|---|
| M | UV/Vis, CHCl$_3$, $\lambda_{max}$ / nm | | | |
| Sm | 682 (sh.) | 643 | 334 | 293 |
| Tb | 695 | 641 | 333 | 292 |
| Dy | 700 | 640 | 333 | 293 |
| Tm | 709 | 635 | 333 | 292 |
| Y | 702 | 639 | 333 | 294 |
| [(15C5)$_4$Pc]M[(15C5)$_4$Pc]M(Pc) | | | | |
| Sm | 690 (sh.) | 644 | 353 | 292 |
| Tb | 696 | 642 | 355 | 292 |
| Dy | 702 | 640 | 354 | 291 |
| Tm | 713 | 636 | 355 | 292 |
| Y | 705 | 639 | 355 | 291 |

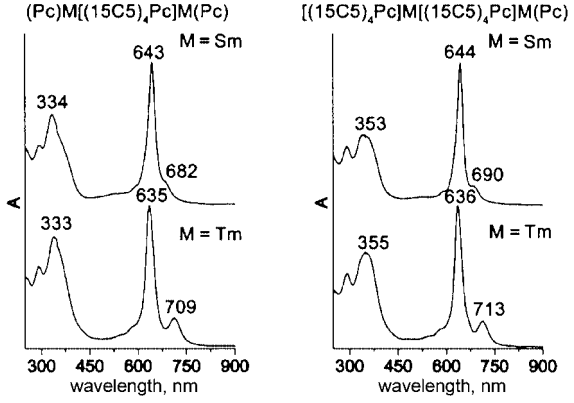


Figure 1. UV/Vis spectra of the heteroleptic triple-decker complexes (Pc)M[(15C5)$_4$Pc]M(Pc) and [(15C5)$_4$Pc]M[(15C5)$_4$Pc]M(Pc) [M = Sm, Tm] in CHCl$_3$.

 © 2007 Wiley-VCH Verlag GmbH & Co. KGaA, Weinheim 

Moreover, crown-ethers can contain solvent molecules which can affect the results of elemental analyses. However, these new complexes gave satisfactory MALDI-TOF mass spectra (Table 1) and the observed average *m*/*z* values and isotopic distribution patterns are in good agreement with simulated spectra. It should be pointed out that in the MALDI TOF mass spectra there were no peaks observed which could correspond to the lanthanum complexes.

The position and the shape of the Q-band in the UV/Vis spectra are mainly determined by the metal ion. It hypsochromically shifts and splits into two components upon a decrease in the metal ion's radius. It is noteworthy that the shape of the Soret band is lanthanide independent and is determined by the number and position of the crown-ether substituents (Table 2, Figure 1). The increase of the number of electron-donating crown-ether substituents leads to a bathochromic shift of the Soret band and to an increase in the relative intensity of the N-band at 292 nm.

$^1$H NMR spectra for all the heteroleptic triple-decker complexes were recorded in $CDCl_3$ and the data are collected in Table 3. Hydrazine-hydrate was added to the solutions to suppress their possible partial air oxidation so that well-resolved NMR spectra could be obtained

The positions the of signals are strongly affected by the lanthanide induced shift (LIS) effect[13] in the case of paramagnetic lanthanides. LIS depends both on the lanthanide

Table 3. $^1$H NMR spectroscopic data for heteroleptic triple-decker crown-substituted phthalocyaninates.

| (Pc)M[(15C5)$_4$Pc]M(Pc) M | $H_{Ar}$ $\delta$ values (ppm) | –$OCH_2$– $\delta$ values (ppm) |
|---|---|---|
| Sm | 8.02 (dd, $^3J$ = 5.4 Hz, $^4J$ = 2.8 Hz, 16 H, α-$H_{Ar}^o$) 7.56 (dd, $^3J$ = 5.4 Hz, $^4J$ = 2.8 Hz, 16 H, β-$H_{Ar}^o$) 6.59 (s, 8 H, $H_{Ar}^{*i}$) | 4.42 (m, 16 H, 1-$CH_2^i$), 4.29 (m, 16 H, 2-$CH_2^i$), 4.06 (m, 32 H, 3,4-$CH_2^i$) |
| Tb | –154.76 (s, 8 H, $H_{Ar}^{*i}$) –67.60 (s, 16 H, α-$H_{Ar}^o$) –30.07 (s, 16 H, β-$H_{Ar}^o$) | –67.60 (s, 16 H, 1-$CH_2^i$), –35.27 (s, 16 H, 2-$CH_2^i$), –21.68 (s, 16 H, 3-$CH_2^i$), –19.23 (s, 16 H, 4-$CH_2^i$) |
| Dy | –74.00 (s, 8 H, $H_{Ar}^{*i}$) –21.51 (s, 16 H, α-$H_{Ar}^o$) –11.57 (s, 16 H, β-$H_{Ar}^o$) | –31.59 (s, 16 H, 1-$CH_2^i$), –15.37 (s, 16 H, 2-$CH_2^i$), –8.70 (s, 16 H, 3-$CH_2^i$), –7.46 (s, 16 H, 4-$CH_2^i$) |
| Tm | 53.58 (s, 8 H, $H_{Ar}^{*i}$) 25.10 (s, 16 H, α-$H_{Ar}^o$) 17.76 (s, 16 H, β-$H_{Ar}^o$) | 23.40 (s, 16 H, 1-$CH_2^i$), 15.99 (s, 16 H, 2-$CH_2^i$), 11.64 (s, 16 H, 3-$CH_2^i$), 10.89 (s, 16 H, 4-$CH_2^i$) |
| Y | 8.58 (dd, $^3J$ = 5.4 Hz, $^4J$ = 2.4 Hz, 16 H, α-$H_{Ar}^o$) 8.25 (s, 8 H, $H_{Ar}^{*i}$) 7.92 (dd, $^3J$ = 5.4 Hz, $^4J$ = 2.4 Hz, 16 H, β-$H_{Ar}^o$) | 5.13 (m, 16 H, 1-$CH_2^i$), 4.67 (m, 16 H, 2-$CH_2^i$), 4.31 (m, 16 H, 3-$CH_2^i$), 4.26 (m, 16 H, 4-$CH_2^i$) |
| [(15C5)$_4$Pc]M[(15C5)$_4$Pc]MPc | | |
| Sm | 8.03 (dd, $^3J$ = 5.5 Hz, $^4J$ = 3.0 Hz, 8 H, α-$H_{Ar}^o$) 7.67 (dd, $^3J$ = 5.5 Hz, $^4J$ = 3.0 Hz, 8 H, β-$H_{Ar}^o$) 7.37 (s, 8 H, $H_{Ar}^{*o}$) 6.66 (s, 8 H, $H_{Ar}^{*i}$) | 4.47–3.74 (overlapping multiplet, 128 H) |
| Tb | –157.94 (s, 8 H, $H_{Ar}^{*i}$) –56.34 (s, 16 H, $H_{Ar}^{*o}$ and α-$H_{Ar}^o$) –34.72 (s, 8 H, β-$H_{Ar}^o$) | –69.43 and –66.77 (2 s, 2 × 8 H, 1,1′-$CH_2^i$),[a] –36.99 and –36.25 (2 s, 2 × 8 H, 2,2′-$CH_2^i$), –33.84 (s, 8 H, 1-$CH_2^o$), –22.27 and –22.10 (2 s, 2 × 8 H, 3,3′-$CH_2^i$), –18.88 and –18.58 (2 s, 2 × 8 H, 4,4′-$CH_2^i$), –17.78 (s, 8 H, 1′-$CH_2^o$), –14.48 (s, 8 H, 2-$CH_2^o$), –10.84 (s, 16 H, 2′,3-$CH_2^o$), –10.30 (s, 8 H, 3′-$CH_2^o$), –7.37 (s, 8 H, 4-$CH_2^o$), –4.28 (s, 8 H, 4′-$CH_2^o$) |
| Dy | –74.15 (s, 8 H, $H_{Ar}^{*i}$) –24.32 (s, 16 H, $H_{Ar}^{*o}$ and α-$H_{Ar}^o$) –15.01 (s, 8 H, β-$H_{Ar}^o$) | –32.66 and –31.23 (2 s, 2 × 8 H, 1,1′-$CH_2^i$), –16.34 and –15.94 (2 s, 2 × 8 H, 2,2′-$CH_2^i$), –13.41 (s, 8 H, 1-$CH_2^o$), –9.20 and –9.07 (2 s, 2 × 8 H, 3,3′-$CH_2^i$), –7.39 and –7.26 (2 s, 2 × 8 H, 4,4′-$CH_2^i$), –6.68 (s, 8 H, 1′-$CH_2^o$), –5.08 (s, 8 H, 2-$CH_2^o$), –2.95 (s, 16 H, 2′,3-$CH_2^o$), –1.47 (s, 8 H, 3′-$CH_2^o$), –1.05 (s, 8 H, 4-$CH_2^o$), 0.35 (s, 8 H, 4′-$CH_2^o$) |
| Tm | 55.07 (s, 8 H, $H_{Ar}^{*i}$) 27.12 (s, 8 H, $H_{Ar}^{*o}$) 25.46 (s, 8 H, α-$H_{Ar}^o$) 19.16 (s, 8 H, β-$H_{Ar}^o$) | 26.29 and 25.46 (2 s, 2 × 8 H, 1,1′-$CH_2^i$), 16.50 and 16.32 (2 s, 2 × 8 H, 2,2′-$CH_2^i$), 16.14 (s, 8 H, 1-$CH_2^o$), 11.80 (s, 16 H, 1′-$CH_2^o$ and 2-$CH_2^o$), 10.73 and 10.62 (2 s, 2 × 8 H, 3,3′-$CH_2^i$), 10.38 (s, 8 H, 2′-$CH_2^o$), 9.89 (s, 8 H, 3-$CH_2^o$), 7.91 (2 s, 2 × 8 H, 4,4′-$CH_2^i$), 6.84 (s, 8 H, 3′-$CH_2^o$), 6.53 (s, 8 H, 4-$CH_2^o$), 5.65 (s, 8 H, 4′-$CH_2^o$) |
| Y | 8.58 (dd, $^3J$ = 5.2 Hz, $^4J$ = 2.8 Hz, 8 H, α-$H_{Ar}^o$) 8.27 (s, 8 H, $H_{Ar}^{*i}$) 8.02 (dd, $^3J$ = 5.2 Hz, $^4J$ = 2.8 Hz, 8 H, β-$H_{Ar}^o$) 7.95 (s, 8 H, $H_{Ar}^{*o}$) | 5.17 (m, 16 H, 1,1′-$CH_2^i$), 4.76 and 4.61 (2 s, 2 × 8 H, 2,2′-$CH_2^o$), 4.63 (m, 16 H, 2,2′-$CH_2^i$), 4.25–3.84 (m, 64 H, 3,4-$CH_2^i$, 2,2′,3,3′,4,4′-$CH_2^o$)[a] |

[a] Primes ′ indicate *exo*-protons.

 © 2007 Wiley-VCH Verlag GmbH & Co. KGaA, Weinheim 

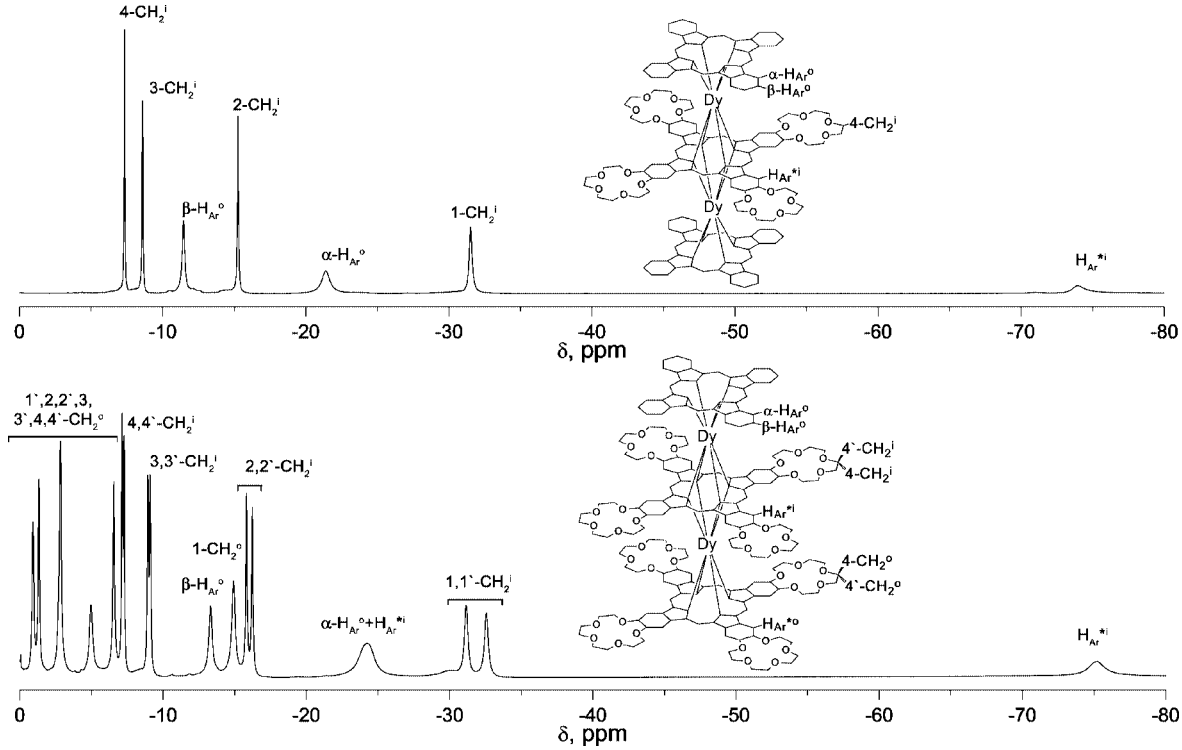


Figure 2. $^1$H NMR spectra of (Pc)Dy[(15C5)$_4$Pc]Dy(Pc) and [(15C5)$_4$Pc]Dy[(15C5)$_4$Pc]Dy(Pc) in $CDCl_3$.

ion and on the orientation of the proton relative to the paramagnetic nuclei. For Dy and Tb complexes, a strong upfield shift can be observed resulting in negative values for the chemical shifts of all resonance signals. Sm causes a slight upfield shift whereas Tm leads to a strong downfield shift of the resonance signals. Because of the paramagnetic broadening, the spin-spin coupling constants cannot be observed in the case of the Tb, Dy and Tm complexes. In the spectra of the Sm and Y complexes the multiplets, which correspond to the resonance signals of the unsubstituted ligands, are well resolved. The attribution of signals can be made using the previously reported assignment of signals in the $^1$H NMR spectra of (Pc)M[($C_8H_{17}O)_8$Pc]M(Pc) and [($C_8H_{17}O)_8$Pc]M[($C_8H_{17}O)_8$Pc]M(Pc).[13a]

In the NMR spectra of (Pc)M[(15C5)$_4$Pc]M(Pc), the resonance signals from the α- and β-aromatic protons of the outer unsubstituted rings (α- and β-$H_{Ar}$º), the aromatic protons of the inner crown-substituted ligands ($H_{Ar}$*$^i$) and the methylene protons of crown-ether macrocycles can be observed. Two protons at each $CH_2$ group are equivalent resulting in four resonance signals (Figure 2).

Along with the resonance signals of α- and β-$H_{Ar}$º and $H_{Ar}$*$^i$ there can also be observed a signal for the aromatic protons of the outer crown-substituted ligand $H_{Ar}$*$^o$ in the NMR spectra of [(15C5)$_4$Pc]M[(15C5)$_4$Pc]M(Pc). Due to lower the symmetry of the molecules, two protons at each methylene-group of the crown-ethers are nonequivalent with respect to the neighbouring ligands (*exo* and *endo*). This significantly complicates the aliphatic region of $^1$H NMR spectra of [(15C5)$_4$Pc]M[(15C5)$_4$Pc]M(Pc) in comparison with (Pc)M[(15C5)$_4$Pc]M(Pc) (Figure 2).

## Structural Studies

The molecular structure of (Pc)Sm[(15C5)$_4$Pc]Sm(Pc) was determined by single-crystal X-ray analysis. Although the structures of some heteroleptic trisphthalocyaninato complexes have been determined previously,[14] no structural data on heteroleptic triple-decker crown-phthalocyaninato complexes have been reported so far. Moreover, to date,[15a] no binuclear samarium phthalocyaninato complexes have been structurally characterised with the exception of ($\eta^2$-dpm)$_4$Sm$_2$(μ-Pc) (dpm = 2,2,6,6-tetramethylheptane-3,5-dionato ion).[15b]

According to the X-ray analysis of (Pc)Sm[(15C5)$_4$Pc]-Sm(Pc), each Sm atom is sandwiched between an outer Pc ring and the inner [(15C5)$_4$Pc] ring giving a symmetrical structure (see Figures 3 and 4). Two Sm atoms are located at a nonbonding Sm···Sm distance of 3.5111(4) Å. They are linked with four nitrogen atoms from the central bridging crown-substituted macrocycle [Sm–N(9) 2.613(3) Å, Sm–N(11) 2.599(3) Å] and each of them is linked with four isoindole nitrogen atoms of the outer Pc ligands [(Sm–N(1) 2.372(3) Å, Sm–N(3) 2.385(3) Å, Sm–N(5) 2.397(3) Å, Sm–N(7) 2.395(3) Å)]. Each metal adopts a distorted square antiprismatic geometry with an average twist angle of 43°. The inequality of the Sm–N distances and the significant decrease in the Sm–$N_{outer}$ distance compared with the Sm–$N_{inner}$ distance is in agreement with the previously reported data for the homoleptic lutetium phthalocyaninato $Lu_2$[Pc(15C5)$_4$]$_3$[16] and the heteroleptic triple-decker complexes (Pc)M[($OC_8H_{17})_8$Pc]M′(Pc)[14a] and [(α-$OC_5H_{11})_4$-Pc]M(Pc)M(Pc)[14b] (Table 4).

 © 2007 Wiley-VCH Verlag GmbH & Co. KGaA, Weinheim 

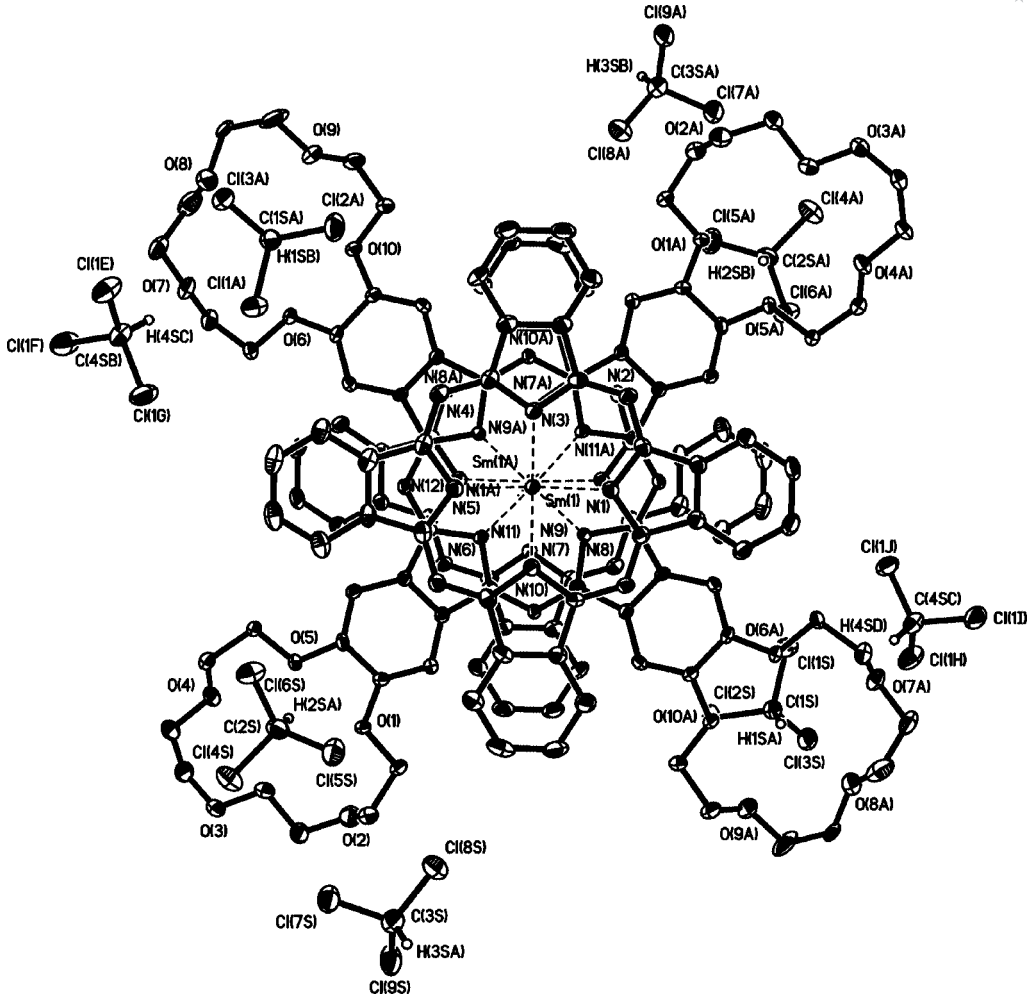


Figure 3. Molecular structure of the complex (Pc)Sm[(15C5)$_4$Pc]Sm(Pc)·8CHCl$_3$ with thermal ellipsoids drawn at the 50% probability level, top view.

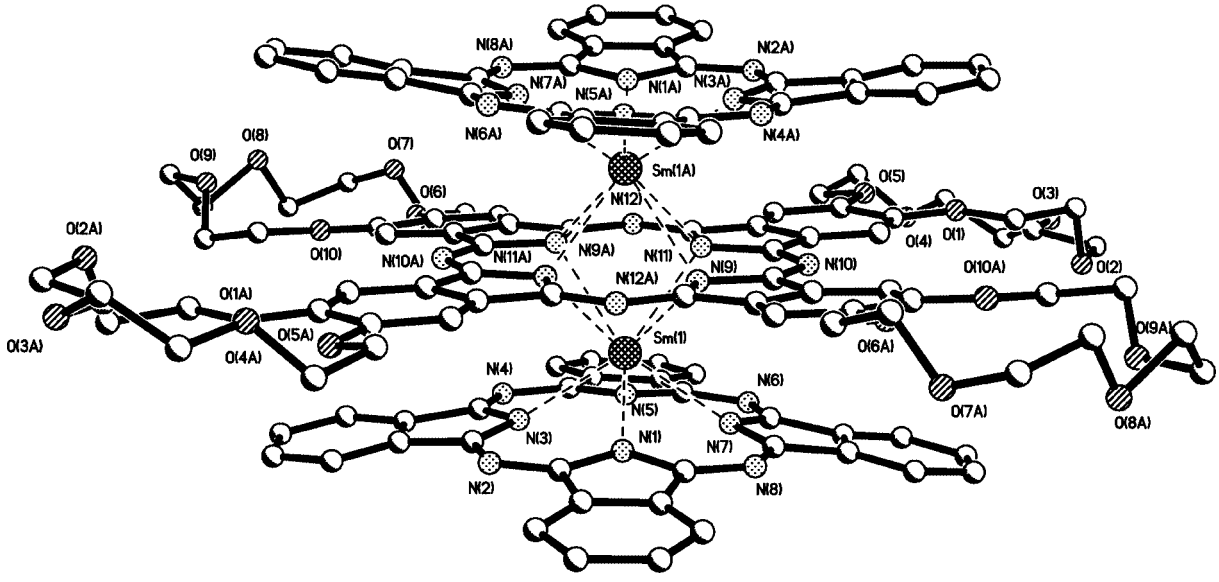


Figure 4. Molecular structure of the complex (Pc)Sm[(15C5)$_4$Pc]Sm(Pc), side view.

 © 2007 Wiley-VCH Verlag GmbH & Co. KGaA, Weinheim 

Table 4. Comparison of M–$N_{iso}$ for different lanthanide trisphthalocyaninates.

| Complex | M–$N_{outer}$ / Å | M–$N_{inner}$ / Å | Ref. |
|---|---|---|---|
| (Pc)Sm[(15C5)$_4$Pc]Sm(Pc) | 2.372(3)–2.397(3) | 2.599(3)–2.613(3) | present work |
| $Lu_2$[(15C5)$_4$Pc]$_3$ | 2.297(7)–2.323(7) | 2.538(8)–2.587(7) | [16] |
| (Pc)Er[(OC$_8$H$_{17}$)$_8$Pc]Er(Pc) | 2.332 | 2.573 | [14a] |
| (Pc)Lu[(OC$_8$H$_{17}$)$_8$Pc]Lu(Pc) | 2.283 | 2.507 | [14a] |
| (Pc)Er[(OC$_8$H$_{17}$)$_8$Pc]Lu(Pc) | 2.30 | 2.55 | [14a] |
| [(α-OC$_5$H$_{11}$)$_4$Pc]Gd(Pc)Gd(Pc) | 2.364, 2.386 | 2.634, 2.654 | [14b] |
| [(α-OC$_5$H$_{11}$)$_4$Pc]Lu(Pc)Lu(Pc) | 2.297, 2.307 | 2.588 | [14b] |

The Sm···Sm distance of 3.5111(4) Å in (Pc)Sm[(15C5)$_4$Pc]Sm(Pc) is different from the metal–metal separation in the binuclear complex [($\eta^2$-dpm)$_4$Sm$_2$(μ-Pc)] [Sm···Sm 3.627(3) Å].[15] This can be explained both by the nature of the axial ligands and the phthalocyanine bridge. The Sm–$N_{outer}$ distance (2.37–2.39 Å) is close to the Sm–N distance in the double-decker ionic phthalocyaninato complexes [Sm(Pc$^{2-}$)$_2$]$^-$(NBu$_4$)$^+$ (Sm–N 2.452–2.471 Å)[17a] and [Sm(Pc$^{\cdot-}$)$_2$]$^+$Br$^-$ (Sm–N 2.457 Å).[17b] It is also significantly shorter than in [Sm(Pc$^{\cdot-}$)$_2$]$^+$(ClO$_4$)$^-$ (Sm–N 2.607 Å).[17b] It is noteworthy that eight solvated $CHCl_3$ molecules are present in the crystallographic cell. The hydrogen atoms of 6 molecules form very weak contacts with the oxygen atoms of the crown-ether substituents, notwithstanding affecting their conformation [H(1SA)···O(8),O(9) 2.66 Å, H(2SA)···O(1) 2.59 Å, H(2SA)···O(5) 2.22 Å, H(4SA)··· O(7) 2.14 Å]. The molecules adopt a brick wall type packing arrangement.

## Conclusions

A simple methodology for preparing a series of heteroleptic crown-substituted REE(III) triple-decker phthalocyaninato complexes (Pc)M[(15C5)$_4$Pc]M(Pc) and [(15C5)$_4$Pc]M[(15C5)$_4$Pc]M(Pc) [M = Sm, Tb, Dy, Tm and Y] has been developed. This method involves the application of the diphthalocyaninatolanthanum La(Pc)$_2$ as a new Pc$^{2-}$ donor species. The advantages of this method are that it results in the complexes being formed in high yield under mild conditions and a significant decrease in the reaction times. All the complexes were fully characterised by MALDI TOF mass spectrometry as well as UV/Vis and $^1$H NMR spectroscopy. The molecular structure of (Pc)Sm[(15C5)$_4$Pc]Sm(Pc) was also determined and it represents the first structure reported for a heteroleptic triple-decker crown-phthalocyaninato complex.

## Experimental Section

The compounds H$_2$[(15C5)$_4$Pc],[18a] La(Pc)$_2$[5] and M(acac)$_3$·H$_2$O[18b] were prepared according to published procedures. 1-Chloronaphthalene was used as received (1-ClN, Acros Organics). Chloroform was dried with anhydrous $CaCl_2$ followed by distillation over $CaH_2$. Methanol was dried with 4 Å molecular sieves. Column chromatography was carried out on neutral alumina (Merck, 0.063–0.200 mm, activity II–III according to Brockmann).

The electronic (UV/Vis) spectra were recorded on a Cary-100 spectrophotometer (Varian) in $CHCl_3$ in quartz cells (1–10 mm). MALDI-TOF mass spectra were recorded on an Ultraflex mass spectrometer (Bruker Daltonics) with nicotinic acid as a matrix. Sonication was performed in an ElmasonicS70H ultrasonic bath (Elma) at 37 kHz. $^1$H NMR spectra were recorded on Bruker Avance-400 spectrometer (400 MHz) in $CDCl_3$ solution in the presence of 10 μL of a 1% solution of $N_2H_4$·$H_2O$ in [D$_6$]DMSO. Chemical shifts, $\delta$ values, are reported in ppm relative to the internal standard (residual $CHCl_3$, $\delta$ = 7.25 ppm) at $T$ = 298 K.

**Preparation of Heteroleptic Triple-Decker Complexes:** A mixture of La(Pc)$_2^0$ (15.0 mg, 12 μmol), H$_2$[(15C5)$_4$Pc] (16.4 mg, 12 μmol) and M(acac)$_3$·$H_2O$ (36 μmol) (M = Sm, Tb, Dy, Tm, Y) was dissolved in 1-ClN (4 mL) with sonication and heated to reflux until no further changes in the UV/Vis spectrum of the reaction mixture were observed. The resultant blue solution was subsequently cooled. The reaction mixture treated with hexane to bring about precipitation and was then filtered. The precipitate was dissolved in $CHCl_3$ and chromatographed on neutral alumina. $CHCl_3$ was used to remove M(Pc)$_2^{0\cdot}$ and M$_2$(Pc)$_3$. The complexes (Pc)M[(15C5)$_4$Pc]M(Pc) were eluted with a mixture of $CHCl_3$ and 0.75 vol.-% MeOH. The complexes [(15C5)$_4$Pc)M[(15C5)$_4$Pc]M(Pc) were eluted with a mixture of $CHCl_3$ and 1.25 vol.-% MeOH. The physical and chemical data and yields for all the complexes are summarised in Tables 1, 2 and 3.

**X-Ray Crystallographic Analysis of (Pc)M[(15C5)$_4$Pc]M(Pc):** Single crystals of (Pc)M[(15C5)$_4$Pc]M(Pc)·8$CHCl_3$ were grown by slow diffusion of heptane into a chloroform solution of the complex. The crystals ($C_{136}H_{112}Cl_{24}N_{24}O_{20}Sm_2$, $M$ = 3554.00, crystal size 0.07 × 0.08 × 0.40 mm) are triclinic, space group $P\bar{1}$, $a$ = 13.2279(9), $b$ = 15.5561(11), $c$ = 19.0738(14) Å, $\alpha$ = 69.145(1), $\beta$ = 74.402(1), $\gamma$ = 89.489(2)°, $V$ = 3516.2(4) Å$^3$, $Z$ = 1, $\rho_{calcd.}$ = 1.678 g cm$^{-3}$, $\mu$(Mo-$K_\alpha$) = 13.60 cm$^{-1}$. The intensities of 39384 reflections (16902 independent reflections, $R_{int}$ = 0.0616) were measured on a Bruker SMART APEX II diffractometer (graphite monochromated Mo-$K_\alpha$ radiation, $\lambda$ = 0.71073 Å, $\omega$-scan technique, $2\theta_{max}$ = 56°, $T$ = 100 K). The APEX II software[19] was used for collecting frames of data, indexing reflections, determination of lattice constants, integration of intensities of reflections, scaling and absorption correction ($T_{min}/T_{max}$ = 0.707/0.911) and SHELXTL[20] was used for space group and structure determination, refinements, graphics and structure reporting. The structure was solved by direct methods and refined by the full-matrix least-squares technique against $F^2$ with the anisotropic temperature factors for all non-hydrogen atoms. All hydrogen atoms were placed geometrically and included in the structure factor calculations in the riding motion approximation. The refinement converged to $wR_2$ = 0.1085 and a $GOF$ = 0.994 for all independent reflections [$R_1$ = 0.0463 was calculated against $F$ for 12032 observed reflections with $I > 2\sigma(I)$], 936 refined parameters.

CCDC-641195 contains the supplementary crystallographic data for this paper. These data can be obtained free of charge from The Cambridge Crystallographic Data Centre via www.ccdc.cam.ac.uk/data_request/cif.

 © 2007 Wiley-VCH Verlag GmbH & Co. KGaA, Weinheim 

## Acknowledgments

This work was supported by the Russian Foundation for Basic Research (Grant No. 05-03-32984), Russian Academy of Science Programs and European Research Association "Suprachem".

[1] F. J. M. Hoeben, P. Jonkheijm, E. W. Meijer, A. P. H. J. Schenning, *Chem. Rev.* **2005**, *105*, 1491–1546.
[2] D. K. P. Ng, J. Jiang, *Chem. Soc. Rev.* **1997**, *26*, 433–442.
[3] a) A. W. Snow in *The Porphyrin Handbook*, vol. 17 (Eds.: K. M. Kadish, K. M. Smith, R. Guilard), Academic Press, San Diego, **2000**, pp. 129–179; b) T.-H. Tran-Thi, *Coord. Chem. Rev.* **1997**, *160*, 53–91; c) A. Lutzen, S. D. Starnes, D. M. Rudkevich, J. J. Rebek, *Tetrahedron Lett.* **2000**, *41*, 3777–3780.
[4] a) T. Toupance, V. Ahsen, J. Simon, *J. Am. Chem. Soc.* **1994**, *116*, 5352–5361; b) T. Toupance, H. Benoit, D. Sarazin, J. Simon, *J. Am. Chem. Soc.* **1997**, *119*, 9191–9197; c) T. Thami, C. Chassenieux, C. Fretigny, J.-P. Roger, F. Steybe, *J. Porphyrins Phthalocyanines* **2002**, *6*, 563–570.
[5] A. G. Martynov, Yu. G. Gorbunova, *Inorg. Chim. Acta* **2007**, *360*, 122–130.
[6] A. G. Martynov, I. V. Nefedova, Y. G. Gorbunova, A. Yu. Tsivadze, *Mendeleev Commun.* **2007**, *17*, 66–67.
[7] a) Y. Chen, W. Su, M. Bai, J. Jiang, X. Li, Y. Liu, L. Wang, S. Wang, *J. Am. Chem. Soc.* **2005**, *127*, 15700–15701; b) S. Yoshimoto, T. Sawaguchi, W. Su, J. Jiang, N. Kobayashi, *Angew. Chem. Int. Ed.* **2007**, *46*, 1071–1074.
[8] W. Lui, J. Jiang, N. Pan, D. P. Arnold, *Inorg. Chim. Acta* **2000**, *310*, 140–146.
[9] a) M. M'Sadak, J. Roncali, F. Garnier, *J. Chim. Phys. Phys.-Chim. Biol.* **1986**, *83*, 211–216; b) D. K. P. Arnold, J. Jiang, *J. Phys. Chem.* **2001**, *105*, 7525–7533.
[10] N. B. Subbotin, L. G. Tomilova, N. A. Kostromina, E. A. Luk'yanets, *J. Gen. Chem. USSR (Engl. Transl.)* **1986**, *56*, 345–348.
[11] A. A. Stuzhin, E. M. Bauer, C. Ercolani, *Inorg. Chem.* **1998**, *37*, 1533–1539.
[12] S. V. Zvezdina, M. B. Berezin, B. D. Berezin, *Russ. J. Inorg. Chem.* **2006**, *51*, 112–117.
[13] a) D. P. Arnold, J. Jiang, *J. Phys. Chem. A* **2001**, *105*, 7525–7533; b) N. Ishikawa, T. Iino, Y. Kaizu, *J. Phys. Chem. A* **2003**, *107*, 7879–7884.
[14] a) P. Zhu, N. Pan, R. Li, J. Dou, Y. Zhang, D. Y. Y. Cheng, D. Wang, D. K. K. Ng, J. Jiang, *Chem. Eur. J.* **2005**, *11*, 1425–1432; b) Y. Bian, L. Li, D. Wang, C.-F. Choi, D. Y. Y. Cheng, P. Zhu, R. Li, J. Dou, R. Wang, N. Pan, D. K. P. Ng, N. Kobayashi, J. Jiang, *Eur. J. Inorg. Chem.* **2005**, 2612–2618.
[15] a) CSD version 5.28, Nov. **2006**, update 1 (Jan. **2007**) ; b) H. Sugimoto, T. Higashi, A. Maeda, M. Mori, H. Masuda, T. Taga, *J. Chem. Soc. Chem. Commun.* **1983**, 1234–1235.
[16] S. I. Troyanov, L. A. Lapkina, V. E. Larchenko, A. Yu. Tsivadze, *Dokl. Chem. (Engl. Transl.)* **1999**, *367*, 192–197.
[17] a) H. Hückstädt, A. Tutaß, M. Göldner, U. Cornelissen, H. Homborg, *Z. Anorg. Allg. Chem.* **2001**, *627*, 485–497; b) G. Ostendorp, H. W. Rotter, H. Homborg, *Z. Anorg. Allg. Chem.* **1996**, *622*, 235–244.
[18] a) V. Ahsen, E. Yilmazer, M. Ertas, Ö. Bekâroğlu, *J. Chem. Soc. Dalton Trans.* **1988**, 401–406; b) J. G. Stites, C. N. McCarty, L. L. Quill, *J. Am. Chem. Soc.* **1948**, *70*, 3142–3143.
[19] *APEX II software package*, Bruker AXS Inc., 5465, East Cheryl Parkway, Madison, WI 5317, 2005.
[20] *SHELXTL v. 5.10*, Structure Determination Software Suite, Bruker AXS, Madison, Wisconsin, USA, **1998**.

Received: May 7, 2007
Published Online: August 28, 2007

 © 2007 Wiley-VCH Verlag GmbH & Co. KGaA, Weinheim 

DOI: 10.1002/ejic.200700578

# A Tris-Cyclometalated Iridium(III) Complex of 2-(5,5-Dioxido-dibenzothiophen-3-yl)pyridine: Synthesis, Structural, Redox and Photophysical Properties

**Mustafa Tavasli,[a] Sylvia Bettington,[a] Igor F. Perepichka,[a,b] Andrei S. Batsanov,[a] Martin R. Bryce,*[a] Carsten Rothe,[c] and Andrew P. Monkman[c]**

**Keywords:** Dibenzothiophene *S*,*S*-dioxide / Iridium / Cyclometalation / Luminescence / Electrochemistry

The first cyclometalated dibenzothiophene *S*,*S*-dioxide derivative, namely [*fac*-2-(5,5-dioxidodibenzothiophen-3-yl)-pyridine]iridium(III) (**3**) has been synthesised in high yield and characterised by X-ray crystallography, solution electrochemistry, absorption and emission spectroscopy. The Ir atom has a *fac*-octahedral coordination with three chelating ligands (*A, B* and *C*); each Ir–N bond is in *trans* position to an Ir–C bond. In cyclic voltammetry experiments in dichloromethane, complex **3** undergoes a reversible metal-centred $Ir^{III}/Ir^{IV}$ oxidation at $E_{1/2}^{ox}$ = +1.04 V vs. $Ag/Ag^+$ reference electrode. Complex **3** exhibits bright green photoluminescence ($\lambda_{max}$ = 525 nm in toluene) from mixed $^3MLCT/^3\pi\rightarrow\pi^*$ states with quantum yield ($\Phi_{PL}$) of 0.26 in toluene solution. The phosphorescence emission decay follows first order kinetics, with a lifetime of 4.9 μs. A comparison of complex **3** with analogues **1** and **2**, where the dibenzothiophene *S*,*S*-dioxide unit is replaced by 9,9-dihexylfluorene and *N*-hexylcarbazole respectively, establish that the substituent *para* to the Ir metal atom, i.e. $CR_2$ in **1**, NR in **2** and $SO_2$ in **3**, has a major influence on the redox and emission properties in this series. Organic light-emitting diodes (OLEDs) were fabricated by spin-coating techniques using a polyspirobifluorene copolymer (PSBF) as a host and complex **3** as dopant. In a single-layer blend configuration ITO/PEDOT:PSS/PSBF:**3**(8 wt.-%)/Ba/Al OLEDs showed pale blue/white light emission (CIE coordinates: x = 0.29, y = 0.31) arising from a combination of fluorescence from the host copolymer ($\lambda_{max}$ = 450 nm) and phosphorescence from **3** ($\lambda_{max}$ = 530 nm).
(© Wiley-VCH Verlag GmbH & Co. KGaA, 69451 Weinheim, Germany, 2007)

## Introduction

Since Baldo et al.[1] first reported an organic light-emitting diode (OLED) with *fac*-tris(2-phenylpyridine)iridium [$Ir(ppy)_3$] as an emitting guest in a blend with a host material, a variety of transition metal–ligand complexes have been studied from the viewpoint of their fundamental photophysical properties and for their optoelectronic applications. Mixing of the electrogenerated singlet and triplet excited states by intersystem crossing removes the spin-forbidden nature of the radiative relaxation of the triplet excited state so singlet and triplet excited states both contribute to light emission. Additionally, the triplet-state lifetime is shortened, thereby suppressing triplet–triplet annihilation. Particular emphasis has been placed on tris-cyclometalated *CN* iridium(III) complexes with their emission colours spanning the blue, green and red regions.[2–5] Colour tuning in these complexes is achieved either by the peripheral functionalisation[2,3] of the parent 2-phenylpyridine with electron-withdrawing/donating substituents, or through variation of the cyclometalating ligands.[2,4] With regard to the latter, 2-(9,9-dialkylfluoren-2-yl)pyridine-based iridium(III) complexes **1** (alkyl = *n*-hexyl[6,7] or methyl[8]) and 2-(*N*-alkylcarbazol-2-yl)pyridine-based iridium(III) complexes **2** (alkyl = hexyl[9] or ethyl[10]) have been explored by us and others.

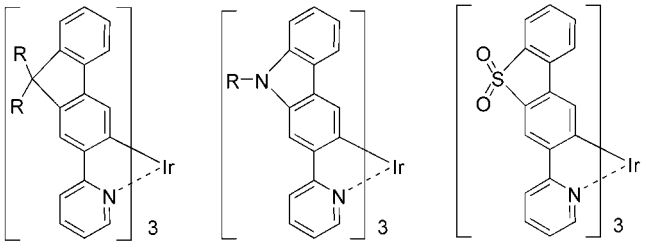


**1** **2** **3**

We were interested in incorporating a new unit, namely dibenzothiophene *S*,*S*-dioxide (DBThD), into the ligands of cyclometalated complexes. This moiety is of current interest in the field as linearly-conjugated co-oligomers and

[a] Department of Chemistry, Durham University, Durham DH1 3LE, United Kingdom
Fax: +44-191-384-4737
E-Mail: m.r.bryce@durham.ac.uk
[b] National Academy of Sciences of Ukraine, L. M. Litvinenko Institute of Physical Organic and Coal Chemistry, Donetsk 83114, Ukraine
[c] Department of Physics, Durham University, Durham DH1 3LE, United Kingdom
Supporting information for this article is available on the WWW under http://www.eurjic.org or from the author.

 © 2007 Wiley-VCH Verlag GmbH & Co. KGaA, Weinheim 

copolymers incorporating DBThD and 9,9-dialkylfluorene units are bright blue emitters in OLEDs, with the DBThD units imparting high stability, high fluorescence quantum yields and increased electron-transporting properties.[11,12] Other small-molecule DBThD derivatives have been used as an efficient electron-transporting layer (not the emitter) in OLEDs.[13]

We now report the synthesis of the first cyclometalated DBThD derivative, namely the *fac*-2-(5,5-dioxidodibenzothiophen-3-yl)pyridine iridium(III) complex (**3**), along with its structural, electrochemical and photophysical properties. Complex **3** is an analogue of complexes **1** and **2**, from which it differs in terms of the bridging group being $SO_2$, instead of $CR_2$ in **1** or NR in **2** . These complexes constitute an interesting series for comparative redox and photophysical studies.

## Results and Discussion

### Synthesis

Ligand **6** was readily prepared by Stille[14] reaction of 3-bromodibenzothiophene *S*,*S*-dioxide **4**[15] with commercially available 2-tris(*n*-butyl)stannylpyridine (**5**)[16] in moderate yield (58%). An excess of ligand **6** was then treated with $Ir(acac)_3$ in glycerol at 220 °C[17] to give the *fac*-tris-cyclometalated iridium(III) complex **3** in 82% yield. The TGA analysis showed that complex **3** exhibits good thermal stability with a very high $T_d$ value of 490 °C (estimated at 5% weight loss temperature), which is ca. 75–100 °C higher than for complexes **1** and **2** and for $Ir(ppy)_3$.[8] The synthesis and X-ray molecular structure of the related 2-(5,5-dioxidodibenzothiophen-2-yl)pyridine *N*-oxide (**7**) is given in the Supporting Information (see footnote on the first page of this article). This compound was prepared during unsuccessful attempts to obtain an isomer of complex **3** (Scheme 1).

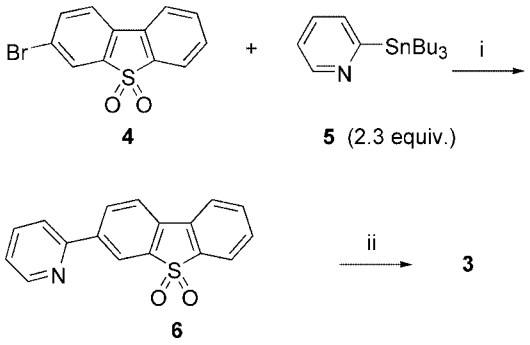


Scheme 1. Reagents and conditions: i) $Pd(PPh_3)_2Cl_2$ (13% equiv.), toluene, 110 °C, 48 h (58% yield); ii) $Ir(acac)_3$, glycerol, 220 °C, 48 h (82% yield).

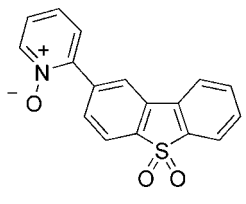


### X-ray Crystal Structures of Iridium Complex 3 and Its Precursor Ligand 6

Crystallisation of **3** from $CH_2Cl_2$/MeOH yielded three pseudo-polymorphs, containing different (non-stoichiometric) amounts of disordered solvents, of which the triclinic form **3a** gave the most precise structure (Figure 1). The asymmetric unit comprises one molecule of **3** and an intermolecular void of ca. 80 Å$^3$ shared by a DCM molecule and a methanol molecule (modeled with occupancies 0.2 and 0.8, respectively), the latter hydrogen-bonded to a sulfone group. The Ir atom has a *fac*-octahedral coordination with three chelating ligands (*A, B* and *C*); each Ir–N bond is in a *trans* position to an Ir–C bond. Lengths of these bonds (Table 1) agree with X-ray studies of *fac*-$Ir(ppy)_3$[1b] and its derivatives.[6,18,19] The X-ray crystal structure of the free ligand **6** (Figure 2) revealed a practically planar molecule (except for the two oxygen atoms) with *cis* disposition of the N atom and the sulfone group. Upon coordination in complex **3**, the pyridine substituent adopts the opposite (*trans*) orientation, although the ligands are not entirely planar, as indicated by the dihedral angles between the pyridine ring and the two benzene rings (Table 1). Interestingly,

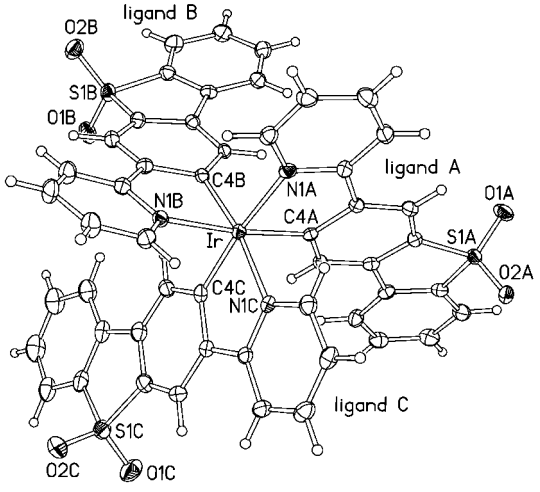


Figure 1. Molecule of **3** in the crystal of **3a** (50% thermal ellipsoids). For the atom and ring notation in the ligands see Figure 2.

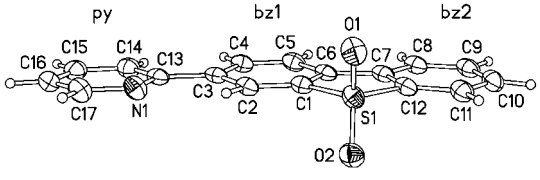


Figure 2. X-ray molecular structure of the free ligand **6** (50% thermal ellipsoids).

 © 2007 Wiley-VCH Verlag GmbH & Co. KGaA, Weinheim 

Table 1. Bond lengths [Å], bond and interplanar angles [°] in **3** and **6**.

| Ligand | **6** | **3a** *A* | **3a** *B* | **3a** *C* | **3b** *A* |
|---|---|---|---|---|---|
| Ir–N | | 2.111(2) | 2.130(2) | 2.132(2) | 2.101(9) |
| Ir–C(4) | | 2.005(3) | 1.994(3) | 2.017(3) | 2.004(11) |
| N–C(13) | 1.344(3) | 1.369(3) | 1.357(4) | 1.375(3) | 1.368(14) |
| N–C(17) | 1.338(3) | 1.347(3) | 1.338(4) | 1.343(4) | 1.354(14) |
| C(3)–C(4) | 1.404(3) | 1.423(4) | 1.427(4) | 1.425(4) | 1.451(16) |
| C(3)–C(13) | 1.481(3) | 1.474(4) | 1.475(4) | 1.464(4) | 1.448(18) |
| C(4)–C(5) | 1.387(3) | 1.418(4) | 1.411(4) | 1.421(4) | 1.361(15) |
| N–Ir–C(4) | | 79.7(1) | 79.8(1) | 79.9(1) | 80.2(4) |
| py/bz1 | 1.9 | 5.3 | 15.2 | 6.3 | 3.2 |
| py/bz2 | 2.0 | 6.3 | 28.6 | 7.4 | 3.1 |
| bz1/bz2 | 0.7 | 4.5 | 13.4 | 2.5 | 1.0 |

| Ligand | **3b** *B* | **3b** *C* | **3c** *A* | **3c** *B* | **3c** *C* |
|---|---|---|---|---|---|
| Ir–N | 2.148(8) | 2.092(9) | 2.116(4) | 2.134(3) | 2.124(4) |
| Ir–C(4) | 2.050(11) | 2.010(10) | 2.008(4) | 2.010(4) | 2.005(4) |
| N–C(13) | 1.368(13) | 1.353(15) | 1.353(7) | 1.361(5) | 1.357(5) |
| N–C(17) | 1.309(15) | 1.378(15) | 1.337(6) | 1.352(5) | 1.351(5) |
| C(3)–C(4) | 1.453(14) | 1.441(15) | 1.428(6) | 1.431(5) | 1.428(5) |
| C(3)–C(13) | 1.474(15) | 1.457(17) | 1.475(7) | 1.464(6) | 1.471(5) |
| C(4)–C(5) | 1.362(15) | 1.364(15) | 1.406(6) | 1.414(6) | 1.408(5) |
| N–Ir–C(4) | 81.1(4) | 79.5(4) | 79.71(17) | 80.05(14) | 79.98(14) |
| py/bz1 | 0.7 | 8.1 | 2.6 | 2.3 | 12.8 |
| py/bz2 | 4.7 | 9.6 | 5.9 | 6.9 | 15.8 |
| bz1/bz2 | 4.4 | 3.3 | 3.4 | 5.3 | 7.3 |

the looser is the molecular packing in a pseudo-polymorph of **3** (see the Experimental Section) the more planar are the ligands.

## Solution Electrochemical Properties

The cyclic voltammogram (CV) of complex **3** in dichloromethane displayed a reversible one-electron oxidation wave at $E_{1/2}^{ox}$ = +1.04 V vs. $Ag/Ag^+$ reference (internal $Fc/Fc^+$ reference gave +0.28 V vs. $Ag/Ag^+$ in these conditions). DFT calculations predict that dibenzothiophene *S*,*S*-dioxide has a LUMO energy level of 1.04 eV lower than that of 9,9-dialkylfluorene[11] and the substantial increase in oxidation potential of **3**, compared to complexes **1** and **2** ($E_{1/2}^{ox}$ = +0.40 V[7] and + 0.14 V,[9] respectively), indicates that the bridging $SO_2$ group has dramatically reduced the electron density on the iridium centre. On the contrary, the carbazole nitrogen of **2** donates electron density to the Ir centre and hence the ease of oxidation in the series is **2** > **1** > **3**. Generally, oxidation processes which involve an Ir–aryl moiety are considered as a metal-centered couple,[20] i.e. $Ir^{III}/Ir^{IV+}$ in the present series. Similar to complexes **1** and **2**, complex **3** shows good chemical and electrochemical reversibility in CV experiments. The half-wave oxidation potentials ($E_{1/2}^{ox}$) of the complexes **1**, **2** and **3** and ferrocene are summarised in Table 2; CV traces are shown in Figure 3.

Table 2. Summary of the half-wave oxidation potentials ($E_{1/2}^{ox}$/V) obtained by cyclic voltammetry for complexes **1**, **2** and **3** and ferrocene (Fc) vs. $Ag/Ag^+$ reference electrode.[a]

| Compound | $E_{1/2}^{ox}$ (V) [$\Delta E$ (mV)] |
|---|---|
| **1** | +0.40 [83] |
| **2** | +0.14 [64] |
| **3** | +1.04 [71] |
| Fc | +0.28 [70] |

[a] Dichloromethane, 0.1 M $nBu_4NPF_6$, scan rate = 100 mV $s^{-1}$; $\Delta E = E_{pa} - E_{pc}$.

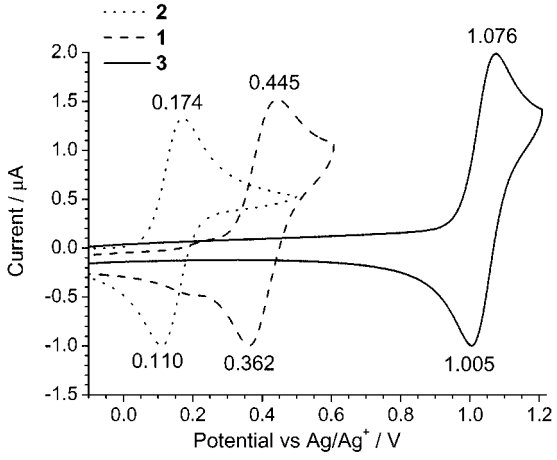


Figure 3. Cyclic voltammograms of complexes **1**, **2** and **3** in dichloromethane, electrolyte 0.1 M $nBu_4NPF_6$, scan rate 100 mV $s^{-1}$.

## Solution-State Photophysical Properties

### *Absorption*

The absorption spectrum of complex **3** in toluene solution is shown in Figure 4. Ligand **6** showed no absorption at all in the region of $\lambda$ = 360 to 600 nm; for complex **3** the

 © 2007 Wiley-VCH Verlag GmbH & Co. KGaA, Weinheim 

Table 3. Absorption and emission spectra data for complexes **1**, **2**, and **3**, and ligand **6** in toluene.

| Compound | Absorption, $\lambda_{max}$ (nm) [$\varepsilon$ (L mol$^{-1}$ cm$^{-1}$)] | Emission, $\lambda_{max}$ (nm) |
|---|---|---|
| **1** | 335 [55000], 350 [51000], 368 [48500], 445 [13500] | 546, 583 |
| **2** | 313 sh [85000], 324 [111000], 340 [91000], 402 [26000], 448 [10500], 475 sh [6700] | 587, 640 sh |
| **3** | 300.5 [97500], 316 [98000], 331 sh [60000], 385 [19500], 434 [7500], 455 sh [4500] | 525, 567, 610 sh |
| **6** | 313 [43500], 330 sh [20000] | |

strong peaks below 360 nm are therefore assigned to spin-allowed ligand-centered $^1\pi$–$\pi^*$ transitions, whereas the less intense absorption features seen above 360 nm are attributed to the metal-to-ligand charge-transfer (MLCT) transitions. As evident from their relative extinction coefficients, the absorption bands seen at around 385 nm and 450 nm are assigned to spin-allowed $^1$MLCT ($\lambda$ = 385 nm, $\varepsilon$ = 19500 M$^{-1}$ cm$^{-1}$) and spin-orbit coupling enhanced mixed $^3$MLCT-$^3$LC ($\lambda$ = 455 sh nm, $\varepsilon \approx$ 4500 M$^{-1}$ cm$^{-1}$) transitions, respectively (Table 3). The whole spectrum of **3** is blue shifted compared to analogous fluorene and carbazole complexes **1**[7] and **2**,[9] indicating that the bridging $SO_2$ group lowers the highest occupied molecular orbital (HOMO) energy level by withdrawing electrons from the system. These assignments were made on the basis of the literature data reported for other iridium complexes.[21]

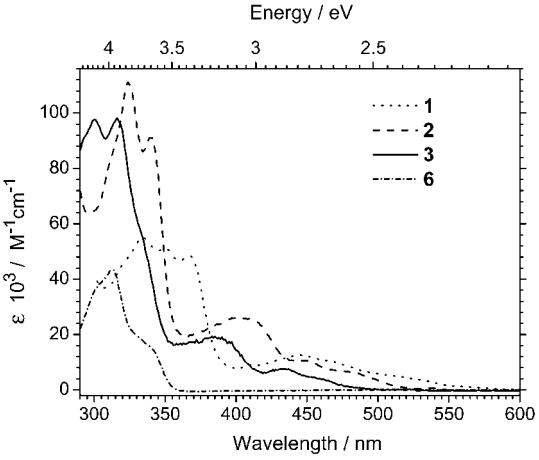


Figure 4. The absorption spectra of ligand **6** and its complex **3** in toluene at room temperature. Spectra of analogous complexes **1** and **2** have also been shown for comparison.

### *Emission*

The photoluminescence (PL) spectrum of complex **3** obtained from degassed solutions in toluene (excitation at 400 nm) is shown in Figure 5, along with comparative spectra for **1** and **2**. The PL of complex **3** is characterised by a structured spectrum with two emission peaks around $\lambda$ = 525 and 567 nm (vibronic progression of 1410 cm$^{-1}$) with a shoulder around $\lambda$ = 610 nm (Table 3). The highest energy emission peak is blue-shifted by ca. 21 nm and 62 nm from those of the complexes **1** ($\lambda_{em}$ = 546 nm)[7] and **2** ($\lambda_{em}$ = 587 nm),[9] respectively. The blue-shift in **3** is again attributed to the presence of $SO_2$ group, which increases the HOMO–LUMO energy gap by withdrawing electrons from the iridium centre. The emission intensities, upon degassing, increased without any change in the spectral profiles. Its sensitivity towards oxygen and long lifetime observed in the microsecond (4.9 μs) region both suggest that the emitting state has a triplet character.[22] The well-resolved vibronic structure, a large Stokes' shift (difference between the $^3$MLCT absorption and emission bands) and longer lifetime indicates that complex **3** emits from mixed $^3$MLCT/$^3\pi\rightarrow\pi^*$ states, with a substantial $^3\pi\rightarrow\pi^*$ contribution to the emitting states.[23]

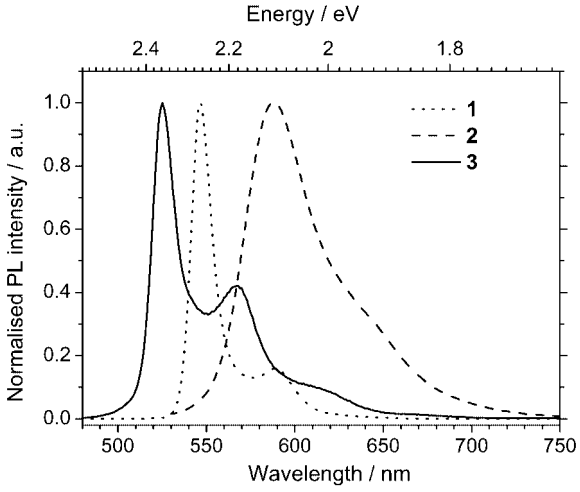


Figure 5. Photoluminesence (PL) spectra for complex **3** (PL of analogous complexes **1** and **2** are also shown) in degassed toluene at room temperature, $\lambda_{ex}$ = 400 nm.

### Phosphorescence Lifetimes and Photoluminescence Quantum Yields

Time-resolved luminescence decay measurements for the complex **3** (OD < 0.1 at $\lambda_{ex}$ = 355 nm) were performed at 298 K in degassed toluene. The emission was collected at $\lambda_{max}$ and the phosphorescence decay was found to follow first order kinetics, with a lifetime ($\tau_p$) of 4.9 μs. This lifetime is comparable with the values for **1** (2.8 μs)[7] and **2** (3.2 μs).[9] The phosphorescent quantum yield ($\Phi_{PL}$) of **3** is 0.26, measured at 298 K in thoroughly degassed toluene solution using Ir(ppy)$_3$ ($\lambda_{ex}$ = 450 nm, $\Phi_{PL}$ = 0.40 in toluene)[8,19] as the standard. This value is comparable with those for **1** ($\Phi_{PL}$ = 0.24)[7] and **2** ($\Phi_{PL}$ = 0.28).[9]

### Organic Light Emitting Devices

Preliminary studies of OLEDs have been performed for single-layer devices with spin-coated PSBF:**3** layer, in the

 © 2007 Wiley-VCH Verlag GmbH & Co. KGaA, Weinheim 

following configuration: ITO/PEDOT:PSS/PSBF:**3**(8 wt.-%)/Ba/Al (PSBF is the host polyspirobifluorene copolymer; full details are given in the Supporting Information). Turn-on voltages were ca. 3 V. At driving voltages of 5–10 V, the diodes emit a pale blue/white light (CIE coordinates: $x$ = 0.29, $y$ = 0.31); the electroluminescence (EL) spectrum (Figure 6) demonstrates emission both from the host PSBF polymer around $\lambda_{max}$ = 450 nm and the characteristic emission of guest emitter (complex **3**) peaking at $\lambda_{max}$ = 530 nm. The latter phosphorescence is very similar in spectral shape to the emission spectrum of **3** in dilute solution (Figure 5) but is red shifted by ca. 5 nm in the devices. At ca. $0.9 \times 10^6$ V cm$^{-1}$ the light output of the device reached a maximum of 300 cd/m$^2$, which however, is accompanied by large currents, reducing the luminance efficiency to $< 1$ cd/A. Thus, both the luminance and the luminance efficiency are lower than complexes **1** (25000 cd/m$^2$ and 7.0 cd/A)[7] and **2** (4500 cd/m$^2$ and 1.7 cd/A).[9] The reason for this reduced performance of **3** is likely to be a combination of unbalanced charge injection and the inefficient excitation confinement at the guest emitter. Considering the latter, the triplet energies of both guest and host are of order of 2.3 eV.[24] Also, complex **3** has a high oxidation potential (HOMO level) compared to the other, better performing, complexes. Considering this, the holes may be less confined at the guest sites, implying that charge carrier recombination takes place at the host rather than the guest. This also explains the significant contribution of the host to the emission of the diode even at very low driving voltages. After exceeding ca. 0.9 V/cm the diode emission irreversibly changes from pale blue to orange with most of the host fluorescence now being quenched (Figure 6). At the same time, the guest emission becomes significantly broader and shifts to slightly lower energies. These simultaneous spectral changes indicate the formation of a new radiative site between guest emitter and host polymer.

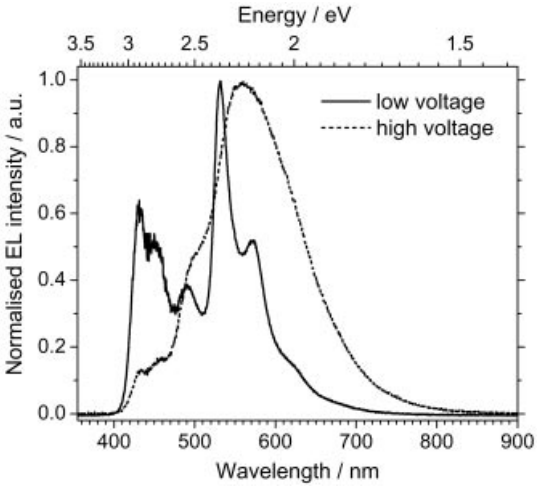


Figure 6. Electroluminescence (EL) spectrum of complex **3**, blended into polyspirobifluorene copolymer host. Device structure: ITO/PEDOT:PSS/PSBF:**3**(8 wt.-%)/Ba/Al. The spectra were taken at low (5 V) and high (15 V) applied voltage.

## Conclusions

The first cyclometalated dibenzothiophene *S*,*S*-dioxide derivative, namely *fac*-2-(5,5-dioxidodibenzothiophen-3-yl)-pyridine iridium(III) **3** has been synthesised in high yield. The structure of the homoleptic $C\widehat{N}$ $Ir^{III}$ complex **3** has been confirmed by X-ray crystallography. The complex exhibits good thermal stability with a very high $T_d$ value of 490 °C. The electron-withdrawing DBThD unit, with its $SO_2$ unit *para* to the Ir centre, significantly raises the oxidation potential of complex **3** ($Ir^{III}/Ir^{IV}$ transition; $E_{1/2}^{ox}$ = +1.04 V vs. $Ag/Ag^+$ reference) compared to the fluorene (**1**) and carbazole (**2**) analogs (+0.40 V and +0.14 V, respectively). Complex **3** displays green photoluminescence ($\lambda_{max}$ = 525 nm) attributed to mixed $^3$MLCT/$^3\pi\rightarrow\pi^*$ states, which is blue shifted compared to fluorene and carbazole complexes **1** and **2**. The phosphorescent quantum yield of **3** is $\Phi_{PL}$ = 0.26 in toluene solution; the decay followed first order kinetics, with a lifetime of 4.9 μs. Single-layer organic light-emitting diodes (OLEDs) were fabricated from a blend of complex **3** as a guest and polyspirobifluorene copolymer as a host demonstrated pale blue/white light emission (CIE coordinates: $x$ = 0.29, $y$ = 0.31) arising from a combination of fluorescence from the host copolymer ($\lambda_{max}$ = 450 nm) and phosphorescence from **3** ($\lambda_{max}$ = 530 nm). Future work will involve variations on the chemical structure of the 2-(5,5-dioxidodibenzothiophen-3-yl)pyridine ligand to form new homoleptic and heteroleptic complexes, with the aim of tuning their photophysical properties, probing deeper into the fundamental properties of this fascinating class of materials and exploiting them as emitters in electrophosphorescent devices.

## Experimental Section

**2-(5,5-Dioxidodibenzothiophen-3-yl)pyridine (6):** A mixture of 3-bromodibenzothiophene *S*,*S*-dioxide (**4**, 0.70 g, 2.73 mmol), LiCl (1.0 g, 22.5 mmol), 2-tris(-*n*-butyl)stannylpyridine (**5**, 2.6 g, 6.36 mmol) and anhydrous toluene (50 mL) was placed in a flame-dried flask and purged with argon for 30 min at room temperature. Subsequently, $[Pd(PPh_3)_2Cl_2]$ (0.22 g, 13 mol.%) was added and the mixture was heated at 110 °C for 48 h. The warm reaction mixture was passed through a sinter and the remaining black residue was washed repeatedly ($5 \times 30$ mL) with hot toluene. The combined filtrates were evaporated to dryness to give a pale orange solid. The crude product was column chromatographed [silica gel; eluent DCM to remove fast running impurities and then eluted with a mixture of DCM/EtOAc (95:5 v/v)] to give **6** which was finally washed with *n*-hexane to obtain a white solid (0.70 g, 58%), $R_f$ = 0.74 (EtOAc), m.p. 245–246 °C. $^1$H NMR (500 MHz, $CDCl_3$): $\delta$ = 8.71 (d, $J$ = 5.0 Hz, 1 H), 8.44 (d, $J$ = 1.5 Hz, 1 H), 8.36 (dd, $J$ = 6.0 Hz, 1 H), 7.87 (d, $J$ = 8.0 Hz, 1 H), 7.84–7.76 (m, 4 H), 7.64 (td, $J$ = 8.0 Hz, 1 H), 7.53 (td, $J$ = 7.5 Hz, 2 H), 7.30 (m, 1 H) ppm. $^{13}$C NMR (125 MHz, $CDCl_3$): $\delta$ = 155.0, 150.3, 142.0, 138.8, 138.5, 137.6, 134.3, 132.7, 132.2, 131.7, 130.8, 123.6, 122.6, 122.3, 122.2, 120.8, 117.3 ppm. MS (ES+): $m/z$ = 294.2 $[M + H]^+$. $C_{17}H_{11}NO_2S{\cdot}0.2H_2O$: calcd. C 68.76, H 3.87, N 4.72; found C 68.50, H 3.76, N 4.60. Crystals for X-ray analysis were grown from chloroform.

 © 2007 Wiley-VCH Verlag GmbH & Co. KGaA, Weinheim 

Table 4. Crystal data.

| Compound | **3a** | **3b** | **3c** | **6** | **7** |
|---|---|---|---|---|---|
| CCDC number | 645914 | 645915 | 645916 | 645913 | 645917 |
| Formula | $C_{51}H_{30}IrN_3S_3O_6{\cdot}xCH_2Cl_2{\cdot}y$MeOH | | | $C_{17}H_{11}NO_2S$ | $C_{17}H_{11}NO_3S$ |
| Solvent content[a] | $x$ = 0.2, $y$ = 0.8 | $x$ = 2, $y$ = 2 | $x$ = 1, $y$ = 3 | – | – |
| Formula weight | 1111.78 | 1303.10 | 1252.23 | 293.33 | 309.33 |
| $T$ [K] | 120 | 120 | 120 | 120 | 120 |
| Symmetry | triclinic | orthorhombic | orthorhombic | monoclinic | monoclinic |
| Space group | $P\bar{1}$ (# 2) | *Pbca* (# 61) | *Pbca* (# 61) | $P2_1/c$ (# 14) | $P2_1/c$ (# 14) |
| $a$ [Å] | 10.529(1) | 19.189(2) | 18.3159(14) | 7.2777(8) | 9.7017(9) |
| $b$ [Å] | 11.374(1) | 11.558(1) | 11.8180(8) | 10.9635(10) | 11.5570(11) |
| $c$ [Å] | 18.317(2) | 45.717(5) | 45.561(3) | 16.5451(14) | 12.4184(12) |
| $\alpha$ [°] | 93.15(1) | 90 | 90 | 90 | 90 |
| $\beta$ [°] | 92.41(1) | 90 | 90 | 93.14(1) | 103.945(10) |
| $\gamma$ [°] | 91.81(1) | 90 | 90 | 90 | 90 |
| $V$ [Å$^3$] | 2187.1(4) | 10140(2) | 9862(1) | 1318.1(2) | 1351.3(2) |
| $Z$ | 2 | 8 | 8 | 4 | 4 |
| $\mu$ [mm$^{-1}$] | 3.28 | 3.03 | 3.01 | 0.25 | 0.25 |
| Crystal size [mm] | 0.15 × 0.14 × 0.06 | 0.32 × 0.24 × 0.08 | 0.51 × 0.26 × 0.11 | 0.49 × 0.07 × 0.05 | 0.25 × 0.20 × 0.10 |
| Transmission | 0.647–0.828 | 0.493–0.793 | 0.393–0.744 | 0.932–0.988 | – |
| Reflections collected | 27393 | 55652 | 107923 | 10612 | 14217 |
| Unique reflections | 12646, 10513[b] | 8894, 6309[b] | 14365, 11304[b] | 2319, 1730[b] | 3590, 2928[b] |
| $R_{int}$, % | 5.0 (7.2[c]) | 7.5 (14.5[c]) | 7.7 (11.0[c]) | 7.1 | 4.7 |
| $R(F)$[b], w$R(F^2)$, % | 3.1, 6.3 | 8.3, 18.4 | 4.9, 9.8 | 3.7, 10.2 | 4.2, 10.3 |

[a] Tentative estimate, especially for **3b** and **3c**. [b] Reflections with $I > 2\sigma(I)$. [c] Before absorption correction.

***fac*-2-(5,5-Dioxidodibenzothiophen-3-yl)pyridine Iridium(III) Complex (3):** A mixture of **6** (0.35 g, 1.19 mmol), Ir(acac)$_3$ (97%, 0.12 g, 0.23 mmol) and glycerol (10 mL) were heated to 220 °C under argon for 48 h. The mixture was cooled to room temperature and water (20 mL) was added. The suspension was extracted with DCM (4 × 30 mL) and the solvents evaporated to dryness giving an orange-brown solid. The crude material was column chromatographed [$SiO_2$; eluent EtOAc, then toluene/EtOAc (8:2 v/v)] to give **3** as a bright orange solid (0.20 g, 82%), $R_f$ = 0.42 (EtOAc). M.p. ca. 230 °C (broad). $^1$H NMR (500 MHz, $CDCl_3$): $\delta$ = 8.13 (s, 3 H), 8.04 (d, $J$ = 8.0 Hz, 1 H), 7.83 (t, $J$ = 5.0 Hz, 1 H), 7.77 (d, $J$ = 8.0 Hz, 1 H), 7.50–7.47 (m, 2 H), 7.43–7.40 (m, 2 H), 7.32 (s, 1 H), 7.10 (t, $J$ = 6.5 Hz, 1 H) ppm. $^{13}$C NMR (125 MHz, $CDCl_3$): $\delta$ = 169.7, 164.1, 147.6, 146.3, 138.9, 138.2, 133.9, 132.6, 133.3, 131.2, 130.4, 129.3, 124.2, 122.8, 122.0, 120.4, 117.6 ppm. MALDI-ToF $m/z$ = 1069.2 (M)$^+$. $C_{51}H_{30}IrN_3O_6S_3H_2O$: calcd. C 56.34, H 2.97, N 3.86; found C 56.49, H 2.68, N 3.79. Single crystals for X-ray analysis were grown from a mixture of methanol and dichloromethane.

**X-ray Crystallography:** Single-crystal X-ray diffraction data were collected with Bruker 3-circle diffractometers with 1 K (for **3b**) or 6 K CCD area detectors, using graphite-monochromated Mo-$K_\alpha$ radiation ($\lambda$ = 0.71073 Å) and Cryostream (Oxford Cryosystems) open-flow $N_2$ cryostats, and corrected for absorption by numerical integration based on crystal face-indexing. The structures were solved by direct methods and refined by full-matrix least-squares against $F^2$ of all data, using SHELXTL software.[25] Crystal data and other experimental details are listed in Table 4. CCDC-645913 to -645917 contain the supplementary crystallographic data for this paper, which can be obtained free of charge from The Cambridge Crystallographic Data Centre via www.ccdc.cam.ac.uk/data_request/cif.

Crystallisations of **3** from DCM/MeOH produced three pseudo-polymorphs, always containing one molecule of the complex per asymmetric unit, but differing by the (non-stoichiometric) amounts of disordered solvents. In the triclinic form **3a** a closed intermolecular void of ca. 80 Å$^3$ is shared by DCM and methanol molecules (with estimated occupancies of 0.2 and 0.8, respectively), so that the methyl carbon of the latter coincides with a chlorine atom of the former. The guest methanol is hydrogen-bonded to a sulfone group of **3**.

Two orthorhombic (space group *Pbca*) pseudo-polymorphs, **3b** and **3c**, crystallize in broadly similar unit cells with similar positions of the host molecules, which are packed in layers along the $z$ = 0 and $z$ = 1/2 planes, and leave in each unit cell four large voids, of ca. 630 Å$^3$ (**3b**) or 565 Å$^3$ (**3c**) each, filled with chaotically disordered solvents, for which no meaningful model could be found. The total volume of these voids amounts to ca. 25% and 23% of the crystal volume, respectively (cf. 7% in **3a**). From these volumes and the amount of residual electron density (much higher in **3b** than in **3c**) the compositions can be tentatively estimated as **3**·2$CH_2Cl_2$·2MeOH (**3b**) and **3**·$CH_2Cl_2$·3MeOH (**3c**). The crystallization of **3b** and **3c** in fact precedes that of **3a**, in agreement with Ostwald's rule of stages. The structures of **3b** and **3c** were refined using the back-Fourier transformation of the continuous density found in a masked region of the difference map,[26] to account for the missing solvent.

**Supporting Information** (see also the footnote on the first page of this article): General details of procedures and equipment used in this work. Chemical structure of the host PSBF copolymer used in the OLEDs. Detailed procedures for the synthesis of 2-(dibenzothiophen-2-yl)pyridine and 2-(5,5-dioxidodibenzothiophen-2-yl)-pyridine *N*-oxide. X-ray crystal structure of 2-(5,5-dioxidodibenzothiophen-2-yl)pyridine *N*-oxide.

## Acknowledgments

We thank Durham County Council (Project SP/082), Cenamps (Newcastle upon Tyne, U.K.) and the University of Durham Photonic Materials Institute for funding this work.

[1] a) M. A. Baldo, S. Lamansky, P. E. Burrows, M. E. Thompson, S. R. Forrest, *Appl. Phys. Lett.* **1999**, *75*, 4–6; b) For a structure

 © 2007 Wiley-VCH Verlag GmbH & Co. KGaA, Weinheim 

determination of *fac*-Ir(ppy)$_3$ see: J. Breu, P. Stössel, S. Schrader, A. Starukhin, W. J. Finkenzeller, H. Yersin, *Chem. Mater.* **2005**, *17*, 1745–1752.
[2] A. B. Tamayo, B. D. Alleyne, P. I. Djurovich, S. Lamansky, I. Tsyba, N. N. Ho, R. Bau, M. E. Thompson, *J. Am. Chem. Soc.* **2003**, *125*, 7377–7387.
[3] a) R. Ragni, E. A. Plummer, K. Brunner, J. W. Hofstraat, F. Babudri, G. M. Farinola, F. Naso, L. De Cola, *J. Mater. Chem.* **2006**, *16*, 1161–1170; b) V. V. Grushin, N. Herron, D. D. LeCloux, W. J. Marshall, V. A. Petrov, Y. Wang, *Chem. Commun.* **2001**, 1494–1495; c) T. Tsuzuki, N. Shirasawa, T. Suzuki, S. Tokito, *Adv. Mater.* **2003**, *15*, 1455–1458; d) K. Ono, M. Joho, K. Saito, M. Tomura, Y. Matsushita, S. Naka, H. Okada, H. Onnagawa, *Eur. J. Inorg. Chem.* **2006**, 3676–3683; e) A. S. Ionkin, W. J. Marshall, D. C. Roe, Y. Wang, *Dalton Trans.* **2006**, 2468–2478; f) J. Nishida, H. Echizen, T. Iwata, Y. Yamashita, *Chem. Lett.* **2005**, *34*, 1378–1379.
[4] a) T. Sajoto, P. I. Djurovich, A. Tamayo, M. Yousufuddin, R. Bau, M. E. Thompson, *Inorg. Chem.* **2005**, *44*, 7992–8003; b) X. Zhang, C. Yang, L. Chen, K. Zhang, J. Qin, *Chem. Lett.* **2005**, *35*, 72–73; c) X. Zhang, J. Gao, C. Yang, L. Zhu, Z. Li, K. Zhang, J. Qin, H. You, D. Ma, *J. Organomet. Chem.* **2006**, *691*, 4312–4319.
[5] Reviews: a) E. Holder, B. M. W. Langeveld, U. S. Schubert, *Adv. Mater.* **2005**, *17*, 1109–1121; b) P.-T. Chou, Y. Chi, *Chem. Eur. J.* **2007**, *13*, 380–395.
[6] J. C. Ostrowski, M. R. Robinson, A. J. Heeger, G. C. Bazan, *Chem. Commun.* **2002**, 784–785.
[7] M. Tavasli, S. Bettington, M. R. Bryce, H. A. Al Attar, F. B. Dias, S. King, A. P. Monkman, *J. Mater. Chem.* **2005**, *15*, 4963–4970.
[8] A. Tsuboyama, H. Iwawaki, M. Furugori, T. Mukaide, J. Kamatani, S. Igawa, T. Moriyama, S. Miura, T. Takiguchi, S. Okada, M. Hoshino, K. Ueno, *J. Am. Chem. Soc.* **2003**, *125*, 12971–12979.
[9] S. Bettington, M. Tavasli, M. R. Bryce, A. Beeby, H. Al-Attar, A. P. Monkman, *Chem. Eur. J.* **2007**, *13*, 1423–1431.
[10] X. Zhang, C. Yang, L. Chen, K. Zhang, J. Qin, *Chem. Lett.* **2006**, *35*, 72–73.
[11] I. I. Perepichka, I. F. Perepichka, M. R. Bryce, L.-O. Pålsson, *Chem. Commun.* **2005**, 3397–3399.
[12] F. B. Dias, S. Pollock, G. Hedley, L.-O. Pålsson, A. Monkman, I. I. Perepichka, I. F. Perepichka, M. Tavasli, M. R. Bryce, *J. Phys. Chem. B* **2006**, *110*, 19329–19339.
[13] T.-H. Huang, W.-T. Whang, J. Y. Shen, Y.-S. Wen, J. T. Lin, T.-H. Ke, L.-Y. Chen, C.-C. Wu, *Adv. Funct. Mater.* **2006**, *16*, 1449–1456.
[14] Y. D. M. Champouret, R. K. Chaggar, I. Dadhiwala, J. Fawcett, G. A. Solan, *Tetrahedron* **2006**, *62*, 79–89.
[15] I. I. Perepichka, I. F. Perepichka, M. R. Bryce, manuscript in preparation.
[16] V. Fargeas, F. Favresse, D. Mathieu, I. Beaudet, P. Charrue, B. Lebret, M. Piteau, J.-P. Quintard, *Eur. J. Org. Chem.* **2003**, 1711–1721.
[17] K. Dedeian, P. I. Djurovich, F. O. Garces, C. Carlson, R. J. Watts, *Inorg. Chem.* **1991**, *30*, 1685–1687.
[18] F. O. Garces, K. Dedeian, N. L. Keder, R. J. Watt, *Acta Crystallogr., Sect. C* **1993**, *49*, 1117–1120.
[19] S. Jung, Y. Kang, H.-S. Kim, Y.-H. Kim, C.-L. Lee, J.-J. Kim, S.-K. Lee, S.-K. Kwon, *Eur. J. Inorg. Chem.* **2004**, 3415–3423.
[20] J. Brooks, Y. Babayan, S. Lamansky, P. I. Djurovich, I. Tsyba, R. Bau, M. E. Thompson, *Inorg. Chem.* **2002**, *41*, 3055–3066.
[21] a) M. G. Colombo, T. C. Brunold, T. Riedener, H. U. Güdel, M. Fürtsch, H.-B. Bürgi, *Inorg. Chem.* **1994**, *33*, 545–550; b) S. Lamansky, P. Djurovich, D. Murphy, F. Abdel-Razzaq, R. Kwong, I. Tsyba, M. Bortz, B. Mui, R. Bau, M. E. Thompson, *Inorg. Chem.* **2001**, *40*, 1704–1711.
[22] P. Coppo, E. A. Plummer, D. De Cola, *Chem. Commun.* **2004**, 1774–1775.
[23] a) S. Lamansky, P. Djurovich, D. Murphy, F. Abdel-Razzaq, H.-E. Lee, C. Adachi, P. E. Burrows, S. R. Forrest, M. E. Thompson, *J. Am. Chem. Soc.* **2001**, *123*, 4304–4312; b) Y.-Y. Lyu, Y. Byun, O. Kwon, E. Han, W. S. Jeon, R. R. Das, K. Char, *J. Phys. Chem. B* **2006**, *110*, 10303–10314.
[24] C. Rothe, S. King, A. P. Monkman, *Phys. Rev. B* **2006**, *73*, 245208-1/9.
[25] *SHELXTL*, version 6.14; Bruker AXS, Madison, Wisconsin, U. S. A., **2003**.
[26] P. van der Sluis, A. L. Spek, *Acta Crystallogr., Sect. A* **1990**, *46*, 194–201.

Received: June 4, 2007
Published Online: September 4, 2007

 © 2007 Wiley-VCH Verlag GmbH & Co. KGaA, Weinheim 

DOI: 10.1002/ejic.200700579

# Synthesis and Structure of Self-Complementary {2}-Metallacryptates and Their Linear or Meandering Infinite Arrangements in the Solid State[‡]

**Rolf W. Saalfrank,*[a] Nicolai Mooren,[a] Andreas Scheurer,[a] Harald Maid,[a] Frank W. Heinemann,[a] Frank Hampel,[b] and Walter Bauer[b]**

*Dedicated to Professor Herbert Mayr on the occasion of his 60th birthday*

**Keywords:** Metallacryptate / Coordination polymers / O ligands / X-ray diffraction / Chirality

Reaction of bis(1,3-diketone) $H_2L^1$ in the presence of cesium acetate with magnesium acetate yielded crystalline one-dimensional coordination polymer *rac*-(**2**)$_n$. The {2}-metallacryptand core $[Mg_2(L^1)_3]^{2-}$ is composed of two magnesium centres linked through three bis(1,3-diketo) dianions $(L^1)^{2-}$. These {2}-metallacryptands are homochiral with either (Δ,Δ)-*fac* or (Λ,Λ)-*fac* stereochemistry at the magnesium centres, and they are capable to host a cesium ion in the cavity. Charge compensation of the thus formed {2}-metallacryptates $\{Cs\subset[Mg_2(L^1)_3]\}^-$ is achieved through extra external cesium ions to give the neutral self-complementary building blocks [{Cs⊂[(Δ,Δ)/(Λ,Λ)-$Mg_2(L^1)_3$]}Cs], which aggregate end-on across the external cesium ions to give the *homochiral* one-dimensional strings [{Cs⊂[(Δ,Δ)-$Mg_2(L^1)_3$]}Cs]$_n$ [Δ-(**2**)$_n$] and [{Cs⊂[(Λ,Λ)-$Mg_2(L^1)_3$]}Cs]$_n$ [Λ-(**2**)$_n$], which are packed in the crystal in alternating homochiral layers. However, reaction of bulkier phenyl-substituted bis(1,3-diketone) $H_2L^2$ instead of methyl-substituted $H_2L^1$ with cesium or rubidium acetate and magnesium, cobalt or zinc acetate yielded the meandering polymer *meso*-{[({$M^1\subset[(\Delta,\Delta)$-$M^2{}_2(L^2)_3$]}$M^1{}_{end}$)({$M^1\subset[(\Lambda,\Lambda)$-$M^2{}_2(L^2)_3$]}$M^1{}_{side}$)][({$M^1\subset[(\Lambda,\Lambda)$-$M^2{}_2(L^2)_3$]}$M^1{}_{end}$)({$M^1\subset[(\Delta,\Delta)$-$M^2{}_2(L^2)_3$]}$M^1{}_{side}$)]}$_n$ [*meso*-(**3**)$_n$] ($M^1$ = $Cs^+$, $Rb^+$; $M^2$ = $Mg^{2+}$, $Co^{2+}$, $Zn^{2+}$). In this case, the {2}-metallacryptates $\{M^1\subset[(\Delta,\Delta/\Lambda,\Lambda)\text{-}M^2{}_2(L^2)_3]\}^-$ are linked by only one cesium ion end-on to give the fragments *meso*-[({$M^1\subset[(\Delta,\Delta)$-$M^2{}_2(L^2)_3$]}$M^1{}_{end}$)({$M^1\subset[(\Lambda,\Lambda)$-$M^2{}_2(L^2)_3$]}$M^1{}_{side}$)], which are connected by the second cesium ions side-on. The one-dimensional meander strands of isostructural *meso*-(**3**)$_n$ are packed in the crystal in parallel. Reaction of 4 equiv. of zinc acetate and 1 equiv. of cesium or rubidium acetate with 2 equiv. of $H_2L^2$ afforded the {$M^1\subset[Zn_2(L^2)_2OAc]$} cryptates **4a**,**b** ($M^1$ = $Cs^+$, $Rb^+$).
(© Wiley-VCH Verlag GmbH & Co. KGaA, 69451 Weinheim, Germany, 2007)

## Introduction

In earlier work, we demonstrated that hexacoordinate nickel(II) in the presence of cesium ions reacts with bis(1,3-diketo) dianion $(L^1)^{2-}$ to yield the neutral {2}-metallacryptate [{Cs⊂[$Ni_2(L^1)_3$]}Cs] with either (Δ,Δ)-*fac* or (Λ,Λ)-*fac* stereochemistry at the nickel centres. These building blocks are self-complementary and aggregate across the external cesium ions alternately *end-on* to yield in the solid state the one-dimensional coordination polymer *meso*-[({Cs⊂[(Δ,Δ)-$Ni_2(L^1)_3$]}Cs)({Cs⊂[(Λ,Λ)-$Ni_2(L^1)_3$]}Cs)]$_n$ [*meso*-(**1**)$_n$] (Figure 1).[2]

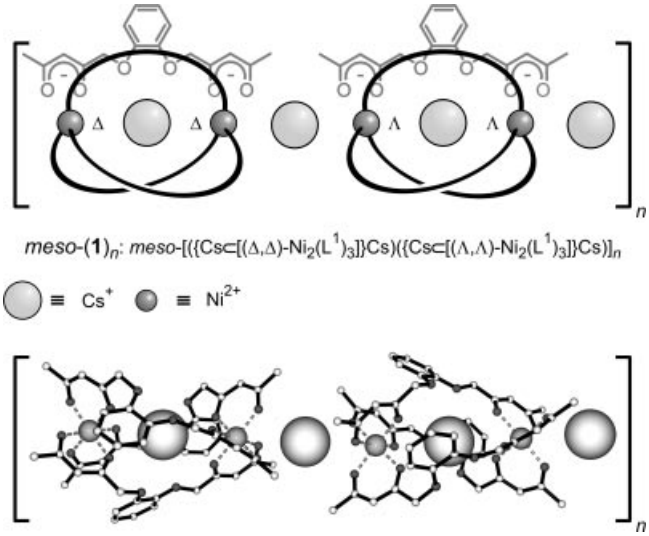


Figure 1. Schematic presentation of the repeating unit of crystalline 1D coordination polymer *meso*-(**1**)$_n$ (top) and the POVRAY presentation of the repeating unit of the molecular structure of *meso*-(**1**)$_n$ (bottom).

[‡] Chelate Complexes, Part 37. Part 36: Ref.[1]
[a] Institut für Anorganische Chemie, Universität Erlangen-Nürnberg
Egerlandstraße 1, 91058 Erlangen, Germany
Fax: +49-9131-85-27396
E-mail: saalfrank@chemie.uni-erlangen.de
[b] Institut für Organische Chemie, Universität Erlangen-Nürnberg
91054 Erlangen, Germany

 © 2007 Wiley-VCH Verlag GmbH & Co. KGaA, Weinheim 

## Results and Discussion

In the course of our ongoing studies on supramolecular coordination chemistry with nickel(II)[2] and copper(II),[2–4] we focused on the development of new oligonuclear complexes by self-assembly[5] with the bis(1,3-diketo) dianion $(L^1)^{2-}$. To this end, we treated $H_2L^1$ with magnesium acetate in the presence of cesium acetate in methanol. As in the nickel case, the cesium ions function as templates for the formation of crystalline one-dimensional coordination polymer *rac*-(**2**)$_n$ (Scheme 1). Cuboids obtained by vapour diffusion of diethyl ether into a solution of the reaction product in acetonitrile were subjected to X-ray crystal analysis, which revealed that Δ/Λ-(**2**)$_n$ crystallizes in the triclinic space group $P\bar{1}$ (Table 1).[6] In Δ/Λ-(**2**)$_n$, the {2}-metallacryptand $[Mg_2(L^1)_3]^{2-}$ core is composed of two magnesium centres linked through three hexadentate catecholate-spacered bis(1,3-diketo) dianions $(L^1)^{2-}$. Therefore, each magnesium ion is coordinated octahedrally by six diketo oxygen donors. The resulting {2}-metallacryptands are homochiral with either (Δ,Δ)-*fac* or (Λ,Λ)-*fac* stereochemistry at the magnesium centres and capable to host a cesium ion in the cavity, which is coordinated by six carbonyl and six catecholate oxygen donors each. Charge compensation of the thus formed enantiomers $\{Cs\subset[(\Delta,\Delta)/(\Lambda,\Lambda)\text{-}Mg_2(L^1)_3]\}^-$ is achieved through extra external cesium ions to give the neutral self-complementary building blocks $[\{Cs\subset[(\Delta,\Delta)/(\Lambda,\Lambda)\text{-}Mg_2(L^1)_3]\}Cs]$. However, contrary to *meso*-(**1**)$_n$, these building blocks aggregate in the solid state end-on across the external cesium ions to give the *homochiral* strings $[\{Cs\subset[(\Delta,\Delta)\text{-}Mg_2(L^1)_3]\}Cs]_n$ [Δ-(**2**)$_n$] and $[\{Cs\subset[(\Lambda,\Lambda)\text{-}Mg_2(L^1)_3]\}Cs]_n$ [Λ-(**2**)$_n$],[6] which are packed in the crystal in alternating homochiral layers (Figure 2). In Δ/Λ-(**2**)$_n$, the coupling external cesium ions are coordinated by two sets of three peripheral carbonyl oxygen donors and two acetonitrile molecules. An additional noncoordinating acetonitrile molecule per monomer unit, trapped in the crystal, leads to the final overall stoichiometry Δ/Λ-(**2**·3MeCN)$_n$. Therefore, the stereogenic metal centres are controlled, simply by varying hexacoordinate $Ni^{II}$ in *meso*-(**1**)$_n$ to $Mg^{II}$ in Δ/Λ-(**2**)$_n$.

To suppress the formation of self-complementary monomers and their aggregation in the solid state by making the external pockets of the cryptates too small to host the external cesium ions, we used $H_2L^2$ with bulkier phenyl groups instead of $H_2L^1$ with methyl substituents at the end. For that purpose, the reaction of stoichiometric amounts of $H_2L^2$, cesium or rubidium acetate and magnesium, cobalt or zinc acetate in acetonitrile was performed, and we isolated microcrystalline materials after vapour diffusion of diethyl ether into a solution of the reaction products (Scheme 2).

Single crystals obtained for *meso*-(**3b**,**e**)$_n$ were subjected to X-ray crystal analyses (Table 1).[6] According to these analyses, *meso*-(**3b**,**e**)$_n$ are isostructural and crystallize in the monoclinic space group $P2_1/n$. Therefore, only the structure of *meso*-(**3e**)$_n$ is discussed in detail. Contrary to our expectation, a strand *meso*-(**3e**)$_n$ was obtained in the solid state.

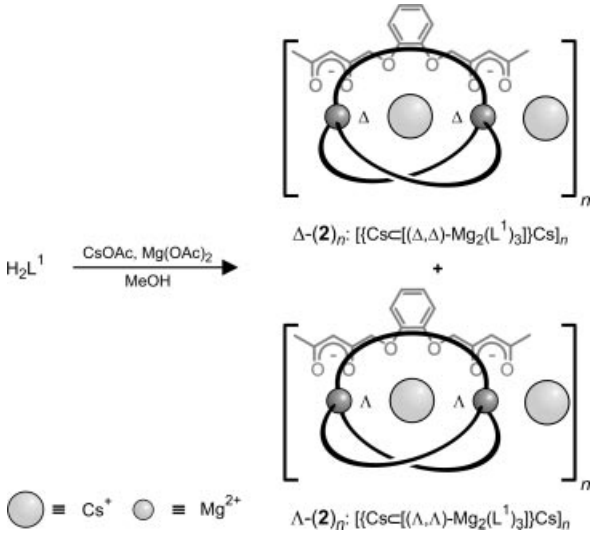


Scheme 1. Synthesis and schematic presentation of the repeating units of the homochiral strings Δ-(**2**)$_n$ and Λ-(**2**)$_n$ [= *rac*-(**2**)$_n$].

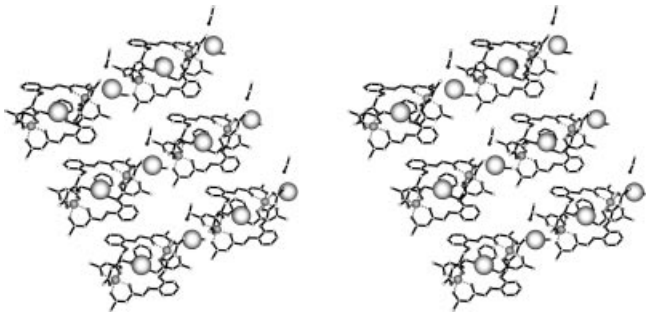

Figure 2. Stereo presentation (POVRAY) of a layer of Λ-(**2**)$_n$ in the crystal together with the coordinating acetonitrile solvent molecules. Mg grey, Cs light grey.

In *meso*-(**3e**)$_n$, two enantiomers $\{Cs\subset[(\Delta,\Delta/\Lambda,\Lambda)\text{-}Co_2(L^2)_3]\}^-$ are linked by only one cesium ion *end-on* and a second one is coordinated *side-on* to connect these units to finally give *meso*-$\{[(\{Cs\subset[(\Delta,\Delta)\text{-}Co_2(L^2)_3]\}Cs_{end})(\{Cs\subset[(\Lambda,\Lambda)\text{-}Co_2(L^2)_3]\}Cs_{side})][(\{Cs\subset[(\Lambda,\Lambda)\text{-}Co_2(L^2)_3]\}Cs_{end})(\{Cs\subset[(\Delta,\Delta)\text{-}Co_2(L^2)_3]\}Cs_{side})]\}_n$ [*meso*-(**3e**)$_n$]. Therefore, the $Cs_{end}$ links two enantiomers $\{Cs\subset[(\Delta,\Delta/\Lambda,\Lambda)\text{-}Co_2(L^2)_3]\}^-$, whereas the $Cs_{side}$ links the *meso*-$[(\{Cs\subset[(\Delta,\Delta)\text{-}Co_2(L^2)_3]\}Cs_{end})(\{Cs\subset[(\Lambda,\Lambda)\text{-}Co_2(L^2)_3]\}Cs_{side})]$ fragments across their homochiral {2}-metallacryptate halves. The explanation for the formation of this structure is the fact that when an external cesium splits the {2}-metallacryptate building block at one end, the pocket at the other end is compressed and incapable to host another $Cs_{end}$. The $Cs_{side}$ ion is coordinated to eight oxygen donors of four ligands $(L^2)^{2-}$ (one carbonyl oxygen donor of one ligand and one carbonyl oxygen donor together with two catecholate oxygen donors of another ligand of one cryptate each) and to two acetonitrile molecules. The meander strands of isostructural *meso*-(**3b**,**e**)$_n$ are packed in the crystal in parallel. The repetitive unit of the structure in the crystal is therefore

 © 2007 Wiley-VCH Verlag GmbH & Co. KGaA, Weinheim 

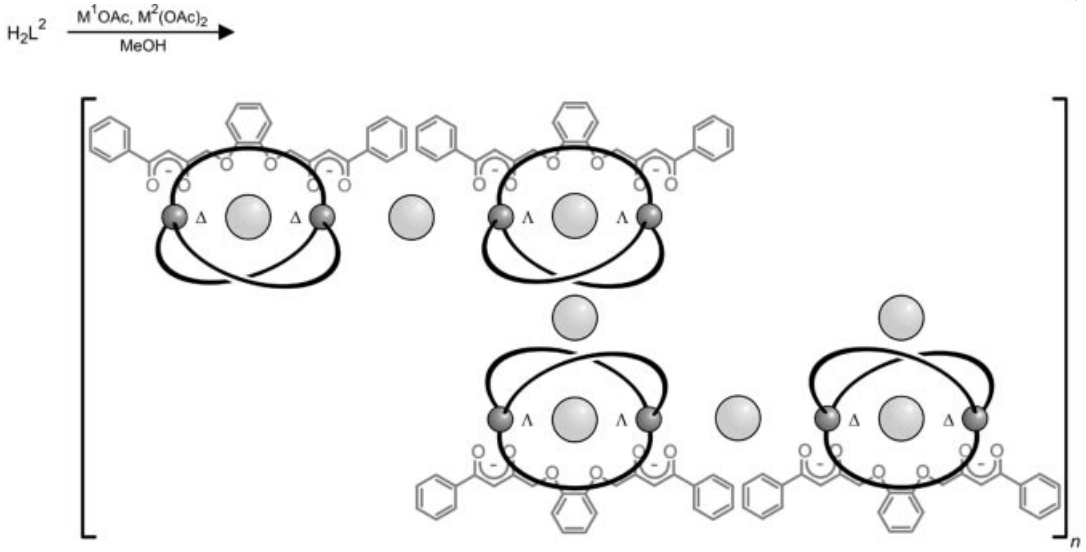


*meso*-(**3**)$_n$: *meso*-{[({M$^1$⊂[(Δ,Δ)-M$^2_2$(L$^2$)$_3$]}M$^1_{end}$)({M$^1$⊂[(Λ,Λ)-M$^2_2$(L$^2$)$_3$]}M$^1_{side}$)][({M$^1$⊂[(Λ,Λ)-M$^2_2$(L$^2$)$_3$]}M$^1_{end}$)({M$^1$⊂[(Δ,Δ)-M$^2_2$(L$^2$)$_3$]}M$^1_{side}$)]}$_n$

| *meso*-(**3**)$_n$ | **a** | **b** | **c** | **d** | **e** |
|---|---|---|---|---|---|
| ≡ (M$^1$)$^+$ | $Cs^+$ | $Rb^+$ | $Cs^+$ | $Rb^+$ | $Cs^+$ |
| ≡ (M$^2$)$^{2+}$ | $Mg^{2+}$ | $Mg^{2+}$ | $Zn^{2+}$ | $Zn^{2+}$ | $Co^{2+}$ |

Scheme 2. Synthesis and schematic presentation of the complex repeating unit of infinite one dimensional meander *meso*-(**3**)$_n$.

rather complex. Figure 3 exemplarily exhibits the stereo presentation of the repeating unit of *meso*-(**3e**)$_n$. The stereo view of Figure 4 presents only the metal centres of two strands of *meso*-(**3e**)$_n$.

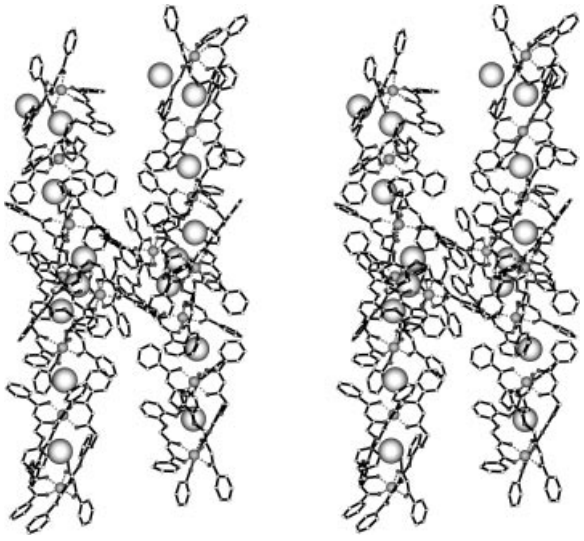

Figure 3. Stereo presentation (POVRAY) of the repeating unit of *meso*-(**3e**)$_n$ in the crystal without solvent molecules. Co grey, Cs light grey.

Figure 4. Simplified stereo presentation (POVRAY) of meander *meso*-(**3e**)$_n$. The Cs⊂, $Cs_{end}$ and Co centres are connected by lines and are arranged in angles, linked by the $Cs_{side}$ ions. Co grey, Cs light grey.

 © 2007 Wiley-VCH Verlag GmbH & Co. KGaA, Weinheim 

Surprisingly, when stoichiometric amounts of $H_2L^2$, zinc acetate and cesium acetate were combined, a mixture of two compounds was generated. However, both components can be synthesized separately by using the appropriate stoichiometry (Scheme 3). The reaction of 1 equiv. of zinc acetate and 2 equiv. of cesium acetate with 3 equiv. of $H_2L^2$ in a mixture of acetonitrile and methanol (3:1) yielded one-dimensional meander polymer *meso*-(**3c**)$_n$. In contrast, the reaction of 4 equiv. of zinc acetate and 1 equiv. of cesium acetate with 2 equiv. of $H_2L^2$ afforded {Cs⊂[Zn$_2$($L^2$)$_2$OAc]} cryptate **4a**, which readily crystallized from a mixture of acetonitrile and methanol (3:1) (Scheme 3, Figure 5). Analogously, supramolecular *meso*-(**3d**)$_n$ as well as metallacryptate **4b** are accessible with rubidium (Schemes 2 and 3). Metallacryptate **4a** crystallizes in space group $P2_1/c$ and has idealized $C_{2v}$ molecule symmetry (Table 1).[6] Two hexadentate bis(1,3-diketo) dianions $(L^2)^{2-}$ together with an encapsulated cesium ion formally create a {2}-metallacoronate that is folded by an acetate bridge. In the heteroleptic cryptate, one acetate oxygen atom functions as a $\mu_1$-donor to one zinc ion and the other as a $\mu_2$-donor to the other zinc ion, but also to the cesium ion. In **4a**, the cesium ion at one side is coordinatively unsaturated and, therefore, two molecules of **4a** form a dimer due to cation–π interaction of neighboring phenyl groups (Figure 5 bottom).[7]

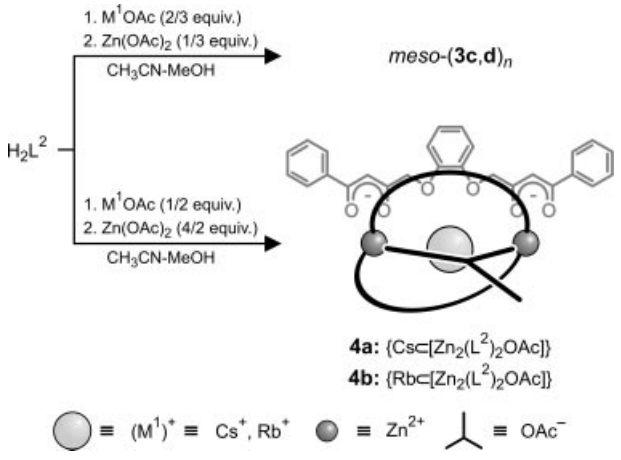


Scheme 3. Synthesis of one-dimensional meandering polymers *meso*-(**3c**,**d**)$_n$ and heteroleptic {2}-cryptates **4** (schematic presentation).

To prove the existence of the supramolecular cryptate monomers of crystalline *rac*-(**2**)$_n$ and *meso*-(**3**)$_n$ also in solution, we carried out $^1$H and $^{13}$C NMR spectroscopic studies of diamagnetic *rac*-(**2**)$_n$ and *meso*-(**3a**–**d**)$_n$. It turned out that the spectra of all five compounds were not very significant [5 $^1$H and 8 $^{13}$C NMR signals for *rac*-(**2**)$_n$ and 7 $^1$H and 11 $^{13}$C NMR signals for *meso*-(**3a**–**d**)$_n$]. We were unable to detect an AB pattern for the diastereotopic $OCH_2$ protons, even by using variable temperature techniques.[8] The compounds *meso*-(**3a**)$_n$ and *meso*-(**3c**)$_n$ are identical except for the metal ions magnesium or zinc. Exemplarily, their spectra are discussed here in detail. They differ only slightly in their chemical shifts. To evaluate the intermolecular exchange processes, we also recorded a $^{13}$C NMR spectrum

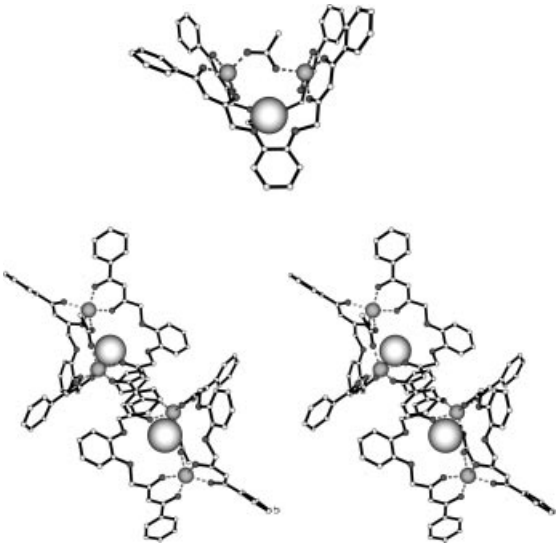

Figure 5. Structure of heteroleptic cryptate **4a** (top) and stereo presentation (POVRAY) of the dimer of **4a** (bottom). Zn grey, Cs light grey.

of a 1:1 mixture of *meso*-(**3a**)$_n$ and *meso*-(**3c**)$_n$ in [$D_6$]acetone. A total of 22 signals was detected, which is twice the number of signals for each individual compound. We thus concluded that any Mg/Zn exchange process must be extremely slow on the NMR timescale. Unequivocally, we observed intact cryptate monomers also in solution. For convenience, we present only the carbonyl $^{13}$C NMR signals for cryptates *meso*-(**3a**)$_n$ and *meso*-(**3c**)$_n$ and their 1:1 mixture in [$D_6$]acetone (Figure 6).

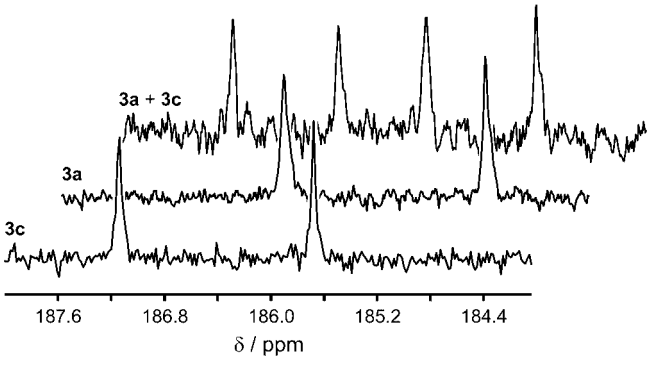


Figure 6. $^{13}$C NMR signals for the carbonyl atoms of *meso*-(**3a**)$_n$ and *meso*-(**3c**)$_n$ and their 1:1 mixture in [$D_6$]acetone at ca. 25 °C.

The number of $^{13}$C NMR signals found for *meso*-(**3a**)$_n$ and *meso*-(**3c**)$_n$ observed in solution (11 each) suggests that a homochiral (Δ,Δ/Λ,Λ) monomeric species exists as proposed from the X-ray data. However, the $^{13}$C NMR spectroscopic data would also match a heterochiral (Δ,Λ) monomeric species. The monomeric homochiral species represents the racemate, the heterochiral species is a monomeric *meso* compound. Therefore, provided that there are only minute chemical shift differences between the racemate and *meso* compounds, there might be a mixture of both diastereomers present. Normal $^{13}$C NMR spectroscopic pro-

 © 2007 Wiley-VCH Verlag GmbH & Co. KGaA, Weinheim 

cessing yields only a single set of signals. However, we are currently exploring whether these signals can be resolved further. This requires $^{13}C$ NMR spectroscopic data with very high signal-to-noise ratios and resolution enhancement techniques. We will report in forthcoming papers on these results.

## Conclusions

We presented the synthesis of the homochiral linear one-dimensional polymers $[\{Cs\subset[(\Delta,\Delta)\text{-}Mg_2(L^1)_3]\}Cs]_n$ [$\Delta$-(**2**)$_n$] and $[\{Cs\subset[(\Lambda,\Lambda)\text{-}Mg_2(L^1)_3]\}Cs]_n$ [$\Lambda$-(**2**)$_n$] and the one dimensional meander polymers *meso*-$\{[(\{M^1\subset[(\Delta,\Delta)\text{-}M^2{}_2(L^2)_3]\}M^1{}_{end})(\{M^1\subset[(\Lambda,\Lambda)\text{-}M^2{}_2(L^2)_3]\}M^1{}_{side})][(\{M^1\subset[(\Lambda,\Lambda)\text{-}M^2{}_2(L^2)_3]\}M^1{}_{end})(\{M^1\subset[(\Delta,\Delta)\text{-}M^2{}_2(L^2)_3]\}M^1{}_{side})]\}_n$ [*meso*-(**3**)$_n$] ($M^1$ = $Cs^+$, $Rb^+$; $M^2$ = $Mg^{2+}$, $Co^{2+}$, $Zn^{2+}$). The structures of complexes **1**–**4** were solved by the combination of mass spectroscopy, single-crystal X-ray analyses and $^1H$ and $^{13}C$ NMR spectroscopy. Most importantly, the $^{13}C$ NMR spectrum of a mixture of *meso*-(**3a**,**c**) unequivocally proved the existence of the intact cryptates $\{Cs\subset[Mg_2(L^2)_3]\}^-$ of *meso*-(**3a**)$_n$ and $\{Cs\subset[Zn_2(L^2)_3]\}^-$ of *meso*-(**3c**)$_n$ in solution.

## Experimental Section

**General Techniques:** All solvents used were purified according to standard procedures. All reagents employed were commercially available, high-grade purity materials and used as supplied (Fluka, Aldrich and Acros). Melting points were determined with a WAGNER-MUNZ apparatus and are uncorrected. IR spectra were recorded as powder films with a ASI React IR-1000 spectrometer. NMR spectra were obtained from dilute solutions in $CDCl_3$, unless stated otherwise, and recorded with a JEOL EX400 or a BRUKER Avance 300 spectrometer. The residual solvent signals were used as internal standards: $CDCl_3$ ($^1H$ 7.27 ppm, $^{13}C$ 77.0 ppm); [D$_6$]acetone ($^1H$ 2.05 ppm; $^{13}C$ 29.85 ppm).[9] The resonance multiplicity is indicated as s (singlet), d (doublet) and m (multiplet). MS (FAB) spectra were recorded with a Micromass ZAB-Spec ($Cs^+$) spectrometer with *m*-NBA as matrix. Elemental analyses were performed with a Carlo Erba EA1110 CHN instrument and with a HERAEUS CHN-Mikroautomat.

**General Procedure for $H_2L^{1,2}$:**[2,10] To a suspension of sodium amide (7.8 g, 200 mmol) in THF (200 mL) was added a solution of the corresponding methyl ketone (100 mmol) in THF (20 mL) by a dropping funnel. After 15 min, a solution of ester 1,2-bis(methylacetoxy)benzene[11] (12.71 g, 50 mmol) in THF (20 mL) was added. After heating at reflux for 4 h, cooling to room temp. and the addition of water (5 mL), the mixture was concentrated under reduced pressure. The residue was taken up in water (100 mL) and acidified with concentrated HCl (30 mL). Extraction of the aqueous phase with chloroform (3 × 100 mL), drying (over sodium sulfate) and evaporation of the combined organic phases yielded the crude reaction product, which was further purified by recrystallization. In solution, the ligands $H_2L^{1,2}$ are present as a tautomeric mixture of the diketo, monoenol and bisenol species. Below, only signals of the dominating bisenol form are listed.

**$H_2L^1$:** Acetone (7.34 mL). Yield: 5.5 g (36%), bright-beige crystals (methanol). M.p. 92 °C. $^1H$ NMR (300.1 MHz): $\delta$ = 15.26 (br. s, 2 H, O*H*), 6.98–6.95 (m, 2 H, Ar-*H*), 6.89–6.86 (m, 2 H, Ar-*H*), 5.98 (s, 2 H, C*H*), 4.65 (s, 4 H, C$H_2$), 2.10 (s, 6 H, C$H_3$) ppm. $^{13}C$ NMR (75.5 MHz): $\delta$ = 191.88 (2 *C*-OH), 190.50 (2 *C*=O), 148.04 (2 Ar-*C*-O), 122.57 (2 Ar-*C*-H, *m*-$C_6H_4$), 114.69 (2 Ar-*C*-H, *o*-$C_6H_4$), 97.44 (2 *C*H), 70.24 (2 *C*$H_2$), 24.47 (2 *C*$H_3$) ppm. IR: $\tilde{\nu}$ = 2922, 1609, 1589, 1509, 1225, 1124 cm$^{-1}$. MS: *m*/*z* (%) = 307 (100) [M + H]$^+$, 222 (9) [M – $COCH_2COMe$]$^+$. $C_{16}H_{18}O_6$ (306.32): calcd. C 62.74, H 5.92; found C 62.85, H 6.04.

**$H_2L^2$:** Acetophenone (11.67 mL). Yield: 10.3 g (48%), colorless cotton-like crystals (methanol). M.p. 117 °C. $^1H$ NMR (300.1 MHz): $\delta$ = 15.87 (br. s, 2 H, O*H*), 7.78–7.76 (m, 4 H, Ar-*H*, *o*-$C_6H_5$), 7.41–7.36 (m, 2 H, Ar-*H*, *p*-$C_6H_5$), 7.30–7.25 (m, 4 H, Ar-*H*, *m*-$C_6H_5$), 6.93–6.86 (m, 4 H, Ar-*H*, $C_6H_4$), 6.66 (s, 2 H, C*H*), 4.72 (s, 4 H, C$H_2$) ppm. $^{13}C$ NMR (75.5 MHz): $\delta$ = 193.70 (2 *C*-OH), 182.75 (2 *C*=O), 147.95 (2 Ar-*C*-O), 133.90 (2 Ar-*C*-C=O), 132.67 (2 Ar-*C*-H, *p*-$C_6H_5$), 128.62 (4 Ar-*C*-H, $C_6H_5$), 127.11 (4 Ar-*C*-H, $C_6H_5$), 122.54 (2 Ar-*C*-H, *m*-$C_6H_4$), 114.68 (2 Ar-*C*-H, *o*-$C_6H_4$), 93.44 (2 *C*H), 70.73 (2 *C*$H_2$) ppm. IR: $\tilde{\nu}$ = 3050, 2890, 2830, 1610, 1575, 1509, 1262, 1227, 1127 cm$^{-1}$. MS: *m*/*z* (%) = 431 (100) [M]$^+$. $C_{26}H_{22}O_6$ (430.46): calcd. C 72.55, H 5.15; found C 72.19, H 5.13.

**$\Delta/\Lambda$-(2)$_n$:** A solution of cesium acetate (25 mg, 131 μmol) in MeOH (1 mL) was added to a solution of ligand $H_2L^1$ (40 mg, 131 μmol) in MeOH (3 mL). The mixture was heated to boiling. Then a solution of $Mg(OAc)_2{\cdot}4H_2O$ (19 mg, 87 μmol) in MeOH (1 mL) was prepared at boiling heat and added dropwise. After cooling and filtration of the resulting mixture, the crude product was obtained in the form of microcrystals by vapour diffusion of diethyl ether into the filtrate. Recrystallisation from acetonitrile by vapour diffusion of diethyl ether gave colourless crystals of $\Delta/\Lambda$-(**2**·3$CH_3CN$)$_n$, suitable for X-ray structure determination. Yield: 25 mg (47%) of $\Delta/\Lambda$-(**2**)$_n$ after drying for 8 h under reduced pressure ($10^{-3}$ mbar). M.p. >260 °C (decomp). $^1H$ NMR (300.1 MHz, XXXX): $\delta$ = 6.76 (br. s, 6 H, Ar-*H*), 6.46 (br. s, 6 H, Ar-*H*), 4.75 (br. s, 6 H, C*H*), 4.03 (br. s, 12 H, C$H_2$), 1.78 (br. s, 18 H, C$H_3$) ppm. $^{13}C$ NMR (100.5 MHz, XXXX): $\delta$ = 191.66 (6 *C*=O), 183.23 (6 *C*=O), 146.42 (6 Ar-*C*-O), 120.67 (6 Ar-*C*-H), 111.67 (6 Ar-*C*-H), 95.11 (6 *C*H), 68.24 (6 *C*$H_2$), 28.21 (6 *C*$H_3$) ppm. IR: $\tilde{\nu}$ = 3065, 2910, 1613, 1521, 1235, 1127, 1054 cm$^{-1}$. MS: *m*/*z* (%) = 1359 (15) [Cs⊂$Mg_2L_3$ + 2Cs]$^+$, 1227 (22) [Cs⊂$Mg_2L_3$ + Cs]$^+$, 789 (100) [$Mg_2L_2$ + Cs]$^+$, 691 (16) [$Mg_2L_2$ + Cs – $CH_2COCHCOCH_3$]$^+$. $C_{48}H_{48}Cs_2Mg_2O_{18}$ (1227.40): calcd. C 46.97, H 3.95; found C 46.47, H 4.13.

**General Procedure for *meso*-(3a,b,e)$_n$:** A solution of cesium or rubidium acetate (77 μmol) in MeOH (1 mL) was added to a solution of ligand $H_2L^2$ (50 mg, 116 μmol) in acetonitrile (3 mL). The mixture was heated to boiling. Then a solution of $M^2(OAc)_2{\cdot}xH_2O$ (77 μmol) in MeOH (1 mL) was prepared at boiling heat and added dropwise. After cooling and filtration of the resulting mixture, the product was obtained in the form of crystals by vapour diffusion of diethyl ether into the filtrate.

***meso*-(3a)$_n$:** CsOAc (15 mg) and $Mg(OAc)_2{\cdot}4H_2O$ (17 mg). Yield: 38 mg (62%), colorless crystals after drying for 8 h under reduced pressure ($10^{-3}$ mbar). M.p. >220 °C (decomp). $^1H$ NMR (300.1 MHz, [D$_6$]acetone): $\delta$ = 7.88–7.85 (m, 12 H, Ar-*H*, *o*-$C_6H_5$), 7.41–7.31 (m, 18 H, Ar-*H*, *m*- and *p*-$C_6H_5$), 6.61–6.58 (m, 6 H, Ar-*H*, $C_6H_4$), 6.33–6.30 (m, 6 H, Ar-*H*, $C_6H_4$), 5.63 (br. s, 6 H, C*H*), 4.33 (br. s, 12 H, C$H_2$) ppm. $^{13}C$ NMR (75.5 MHz, [D$_6$]acetone): $\delta$ = 186.32 (6 *C*=O), 184.80 (6 *C*=O), 147.65 (6 Ar-*C*-O), 142.54 (6 Ar-*C*-C=O), 130.71 (6 Ar-*C*-H, *p*-$C_6H_5$), 128.64 (12 Ar-*C*-H, $C_6H_5$), 128.16 (12 Ar-*C*-H, $C_6H_5$), 121.41 (6 Ar-*C*-H, *m*-$C_6H_4$), 112.57 (6 Ar-*C*-H, *o*-$C_6H_4$), 92.30 (6 *C*H), 69.60 (6 *C*$H_2$) ppm. IR:

 © 2007 Wiley-VCH Verlag GmbH & Co. KGaA, Weinheim 

$\tilde{\nu}$ = 3065, 2918, 1610, 1575, 1502, 1247, 1127, 1042 $cm^{-1}$. MS: *m*/*z* (%) = 1732 (83) $[Cs\subset Mg_2L_3 + 2Cs]^+$, 1601 (23) $[Cs\subset Mg_2L_3 + Cs]^+$, 1038 (100) $[Mg_2L_2 + Cs]^+$, 877 (32) $[Mg_2L_2 + Cs - CH_2COCHCOC_6H_5]^+$, 718 (21) $[Mg_2L_2 + Cs - 2CH_2COCHCOC_6H_5]^+$. $C_{78}H_{60}O_{18}Cs_2Mg_2$ (1599.82): calcd. C 58.56, H 3.79; found C 57.71, H 3.93.

***meso*-(3b)$_n$:** RbOAc (11 mg) and $Mg(OAc)_2{\cdot}4H_2O$ (17 mg), colorless crystals of *meso*-(**3b**·$2CH_3CN$)$_n$ suitable for X-ray structure determination. Yield: 21 mg (36%) of *meso*-(**3b**)$_n$ after drying for 8 h under reduced pressure ($10^{-3}$ mbar). M.p. >190 °C (decomp). $^1$H NMR (300.1 MHz, [D$_6$]acetone): $\delta$ = 7.88–7.85 (br. s, 12 H, Ar-*H*, *o*-$C_6H_5$), 7.40–7.30 (m, 18 H, Ar-*H*, *m*- and *p*-$C_6H_5$), 6.57 (br. s, 6 H, Ar-*H*, $C_6H_4$), 6.26 (br. s, 6 H, Ar-*H*, $C_6H_4$), 5.60 (br. s, 6 H, C*H*), 4.28 (br. s, 12 H, C$H_2$) ppm. $^{13}$C NMR (75.5 MHz, [D$_6$]acetone): $\delta$ = 185.79 (6 *C*=O), 184.40 (6 *C*=O), 147.34 (6 Ar-*C*-O), 141.86 (6 Ar-*C*-C=O), 130.15 (6 Ar-*C*-H, *p*-$C_6H_5$), 128.03 (12 Ar-*C*-H, $C_6H_5$), 127.63 (12 Ar-*C*-H, $C_6H_5$), 120.85 (6 Ar-*C*-H, *m*-$C_6H_4$), 112.07 (6 Ar-*C*-H, *o*-$C_6H_4$), 92.12 (6 *C*H), 69.24 (6 *C*$H_2$) ppm. IR: $\tilde{\nu}$ = 3065, 2922, 1606, 1575, 1502, 1247, 1127, 1038 $cm^{-1}$. MS: *m*/*z* (%) = 1590 (27) $[Rb\subset Mg_2L_3 + 2\,Rb]^+$, 1505 (28) $[Rb\subset Mg_2L_3 + Rb]^+$, 991 (100) $[Mg_2L_2 + Rb]^+$, 831 (25) $[Mg_2L_2 + Rb - CH_2COCHCOC_6H_5]^+$. $C_{78}H_{60}Mg_2O_{18}Rb_2$ (1504.94): calcd. C 62.26, H 4.02; found C 63.00, H 3.89.

***meso*-(3e)$_n$:** CsOAc (15 mg) and $Co(OAc)_2{\cdot}4H_2O$ (19 mg), red crystals of *meso*-(**3e**·$10CH_3CN{\cdot}18CH_3OH$)$_n$ suitable for X-ray structure determination. Yield: 45 mg (70%) of *meso*-(**3e**)$_n$ after drying for 8 h under reduced pressure ($10^{-3}$ mbar). M.p. >220 °C (decomp). IR: $\tilde{\nu}$ = 3061, 2918, 1598, 1571, 1502, 1243, 1127, 1038 $cm^{-1}$. MS: *m*/*z* (%) = 1799 (42) $[Cs\subset Co_2L_3 + 2Cs]^+$, 1669 (74) $[Cs\subset Co_2L_3 + Cs]^+$, 1536 (31) $[Cs\subset Co_2L_3]^+$, 1107 (100) $[Co_2L_2 + Cs]^+$, 947 (27) $[Co_2L_2 + Cs - CH_2COCHCOC_6H_5]^+$. $C_{78}H_{60}O_{18}Co_2Cs_2$ (1669.06): calcd. C 56.13, H 3.63; found C 56.68, H 3.81.

**General Procedure for *meso*-(3c,d)$_n$:** A solution of cesium or rubidium acetate (116 μmol) in MeOH (1 mL) was added to a solution of ligand $H_2L^2$ (75 mg, 174 μmol) in acetonitrile (5 mL). The mixture was heated to boiling. Then a solution of $Zn(OAc)_2{\cdot}2H_2O$ (13 mg, 58 μmol) in MeOH (1 mL) was prepared at boiling heat and added dropwise. After cooling and filtration of the resulting mixture, the product precipitated from the filtrate during 12 h in the form of crystals.

***meso*-(3c)$_n$:** CsOAc (22 mg). Yield: 32 mg (66%), colorless crystals of *meso*-(**3c**)$_n$ after drying for 8 h under reduced pressure ($10^{-3}$ mbar). M.p. >190 °C (decomp). $^1$H NMR (300.1 MHz, [D$_6$]-acetone): $\delta$ = 7.85–7.83 (m, 12 H, Ar-*H*, *o*-$C_6H_5$), 7.31–7.41 (m, 18 H, Ar-*H*, *m*- and *p*-$C_6H_5$), 6.57 (br. s, 6 H, Ar-*H*, $C_6H_4$), 6.35 (br. s, 6 H, Ar-*H*, $C_6H_4$), 5.56 (br. s, 6 H, C*H*), 4.27 (br. s, 12 H, C$H_2$) ppm. $^{13}$C NMR (100.5 MHz, [D$_6$]acetone): $\delta$ = 187.14 (6 *C*=O), 185.68 (6 *C*=O), 147.65 (6 Ar-*C*-O), 142.61 (6 Ar-*C*-C=O), 130.74 (6 Ar-*C*-H, *p*-$C_6H_5$), 128.68 (12 Ar-*C*-H, $C_6H_5$), 128.10 (12 Ar-*C*-H, $C_6H_5$), 121.43 (6 Ar-*C*-H, *m*-$C_6H_4$), 112.57 (6 Ar-*C*-H, *o*-$C_6H_4$), 92.11 (6 *C*H), 69.58 (6 *C*$H_2$) ppm. IR: $\tilde{\nu}$ = 3065, 2918, 1598, 1571, 1502, 1243, 1127, 1038 $cm^{-1}$. MS: *m*/*z* (%) = 1813 (33) $[Cs\subset Zn_2L_3 + 2Cs]^+$, 1683 (11) $[Cs\subset Zn_2L_3 + Cs]^+$, 1121 (100) $[Zn_2L_2 + Cs]^+$, 961 (16) $[Zn_2L_2 + Cs - CH_2COCHCOC_6H_5]^+$. $C_{78}H_{60}O_{18}Cs_2Zn_2$ (1681.98): calcd. C 55.70, H 3.60; found C 55.56, H 3.69.

***meso*-(3d)$_n$:** RbOAc (17 mg). Yield: 14 mg (45%), colorless crystals of *meso*-(**3d**)$_n$ after drying for 8 h under reduced pressure ($10^{-3}$ mbar). M.p. >180 °C (decomp). $^1$H NMR (300.1 MHz, [D$_6$]-acetone): $\delta$ = 7.81 (br. s, 12 H, Ar-*H*, *o*-$C_6H_5$), 7.38–7.32 (m, 18 H, Ar-*H*, *m*- and *p*-$C_6H_5$), 6.56 (br. s, 6 H, Ar-*H*, $C_6H_4$), 6.30 (br. s, 6 H, Ar-*H*, $C_6H_4$), 5.52 (br. s, 6 H, C*H*), 4.24 (br. s, 12 H, C$H_2$) ppm. $^{13}$C NMR (75.5 MHz, [D$_6$]acetone): $\delta$ = 186.70 (6 *C*=O), 185.30 (6 *C*=O), 147.33 (6 Ar-*C*-O), 141.95 (6 Ar-*C*-C=O), 130.21 (6 Ar-*C*-H, *p*-$C_6H_5$), 128.11 (12 Ar-*C*-H, $C_6H_5$), 127.60 (12 Ar-*C*-H, $C_6H_5$), 120.87 (6 Ar-*C*-H, *m*-$C_6H_4$), 112.15 (6 Ar-*C*-H, *o*-$C_6H_4$), 92.02 (6 *C*H), 69.22 (6 *C*$H_2$) ppm. IR: $\tilde{\nu}$ = 3065, 2918, 1598, 1571, 1513, 1247, 1127, 1038 $cm^{-1}$. MS: *m*/*z* (%) = 1671 (32) $[Rb\subset Zn_2L_3 + 2Rb]^+$, 1587 (17) $[Rb\subset Zn_2L_3 + Rb]^+$, 1073 (100) $[Zn_2L_2 + Rb]^+$, 913 (27) $[Zn_2L_2 + Rb - CH_2COCHCOC_6H_5]^+$. $C_{78}H_{60}O_{18}Rb_2Zn_2$ (1587.10): calcd. C 59.02, H 3.82; found C 58.76, H 3.97.

**General Procedure for 4a,b:** A solution of cesium or rubidium acetate (29 μmol) in MeOH (1 mL) was added to a solution of ligand $H_2L^2$ (25 mg, 58 μmol) in acetonitrile (3 mL). The mixture was heated to boiling. Then a solution of $Zn(OAc)_2{\cdot}2H_2O$ (25 mg, 116 μmol) in MeOH (1 mL) was prepared at boiling heat and added dropwise. After cooling and filtration of the resulting mixture, the product precipitated from the filtrate during 12 h in the form of crystals.

**4a:** CsOAc (6 mg). Colorless crystals of **4a**·$3CH_3CN$ suitable for X-ray structure determination by vapour diffusion of diethyl ether into a mother liquor of **4a** in acetonitrile. Yield: 59 mg (86%) of **4a** after drying for 8 h under reduced pressure ($10^{-3}$ mbar). M.p. >210 °C (decomp). $^1$H NMR (300.1 MHz): $\delta$ = 7.93–7.91 (m, 8 H, Ar-*H*, *o*-$C_6H_5$), 7.42–7.31 (m, 12 H, Ar-*H*, *m*- and *p*-$C_6H_5$), 6.95 (*ps*-s, 8 H, Ar-*H*, $C_6H_4$), 5.97 (s, 4 H, C*H*), 4.71 (d, $^2J$ = 12.0 Hz, 4 H, C$H_2$), 4.36 (d, $^2J$ = 12.0 Hz, 4 H, C$H_2$), 2.20 (s, 3 H, $CH_3$) ppm. $^{13}$C NMR (75.5 MHz): $\delta$ = 188.30 (4 *C*=O), 186.51 (4 *C*=O), 180.38 ($H_3C$-*C*$O_2$), 148.46 (4 Ar-*C*-O), 139.72 (4 Ar-*C*-C=O), 131.05 (2 Ar-*C*-H, *p*-$C_6H_5$), 128.03 (4 Ar-*C*-H, $C_6H_5$), 127.57 (8 Ar-*C*-H, $C_6H_5$), 122.82 (4 Ar-*C*-H, *m*-$C_6H_4$), 115.95 (4 Ar-*C*-H, *o*-$C_6H_4$), 93.79 (4 *C*H), 73.90 (4 *C*$H_2$), 24.56 (*C*$H_3$-$CO_2$) ppm. IR: $\tilde{\nu}$ = 3065, 2903, 2849, 1598, 1567, 1521, 1254, 1119, 1034 $cm^{-1}$. MS: *m*/*z* (%) = 1121 (84) $[Cs\subset Zn_2L_2]^+$, 959 (11) $[Cs\subset Zn_2L_2 - CH_2COCHCOC_6H_5]^+$, 625 (17) $[ZnL + Cs]^+$. $C_{54}H_{43}O_{14}CsZn_2$ (1179.66): calcd. C 54.98, H 3.68; found C 54.81, H 3.69.

**4b:** RbOAc (4 mg). Colorless crystals of **4b**·$2CH_3CN{\cdot}CH_3OH$ suitable for X-ray structure determination by vapour diffusion of diethyl ether into a mother liquor of **4b** in acetonitrile. Yield: 47 mg (72%) of **4b** after drying for 8 h under reduced pressure ($10^{-3}$ mbar). M.p. >210 °C (decomp). $^1$H NMR (300.1 MHz): $\delta$ = 7.94–7.91 (m, 8 H, Ar-*H*, *o*-$C_6H_5$), 7.43–7.32 (m, 12 H, Ar-*H*, *m*- and *p*-$C_6H_5$), 6.99 (*ps*-s, 8 H, Ar-*H*, $C_6H_4$), 5.94 (s, 4 H, C*H*), 4.71 (d, $^2J$ = 12.6 Hz, 4 H, C$H_2$), 4.37 (d, $^2J$ = 12.6 Hz, 4 H, C$H_2$), 2.25 (s, 3 H, C$H_3$) ppm. $^{13}$C NMR (75.5 MHz): $\delta$ = 188.10 (4 *C*=O), 186.79 (4 *C*=O), 180.67 ($H_3C$-*C*$O_2$), 148.76 (4 Ar-*C*-O), 139.69 (4 Ar-*C*-C=O), 131.05 (2 Ar-*C*-H, *p*-$C_6H_5$), 128.04 (4 Ar-*C*-H, $C_6H_5$), 127.53 (8 Ar-*C*-H, $C_6H_5$), 123.07 (4 Ar-*C*-H, *m*-$C_6H_4$), 116.71 (4 Ar-*C*-H, *o*-$C_6H_4$), 93.31 (4 *C*H), 73.78 (4 *C*$H_2$), 24.74 (*C*$H_3$-$CO_2$) ppm. IR: $\tilde{\nu}$ = 3065, 2903, 2845, 1594, 1563, 1521, 1254, 1119, 1034 $cm^{-1}$. MS: *m*/*z* (%) = 1073 (100) $[Rb\subset Zn_2L_2]^+$, 913 (23) $[Rb\subset Zn_2L_2 - CH_2COCHCOC_6H_5]^+$, 579 (39) $[ZnL + Rb]^+$. $C_{54}H_{43}O_{14}RbZn_2$ (1132.22): calcd. C 57.28, H 3.84; found C 56.82, H 3.91.

**Single Crystal X-ray Structure Analyses:** Details of crystal data, data collection and refinement are given in Table 1. X-ray data for Δ/Λ-(**2**)$_n$, *meso*-(**3e**)$_n$, **4a** and **4b** were collected with a Nonius Kappa CCD area detector by using Mo-$K_\alpha$ radiation ($\lambda$ = 0.71073 Å). The structures were solved by direct methods with SHELXS-97[12] and refined with full-matrix least-squares against $F^2$ using the SHELXL-97 program system.[13] All non-hydrogen atoms were refined anisotropically. The positions of the hydrogen atoms were fixed in ideal positions (riding model) and were included without refinement and with fixed isotropic *U*. Data for *meso*-(**3b**)$_n$ were collected with a Bruker-Nonius KappaCCD dif-

 © 2007 Wiley-VCH Verlag GmbH & Co. KGaA, Weinheim 

Table 1. Crystal and structure refinement data for complexes Δ/Λ-(**2**)$_n$, *meso*-(**3b**)$_n$, *meso*-(**3e**)$_n$, **4a** and **4b**.

| | Δ/Λ-(**2**)$_n$ | *meso*-(**3b**)$_n$ | *meso*-(**3e**)$_n$ |
|---|---|---|---|
| Empirical formula | $C_{48}H_{48}Cs_2Mg_2O_{18}\cdot 3CH_3CN$ | $C_{156}H_{120}Mg_4O_{36}Rb_4\cdot 2CH_3CN$ | $C_{312}H_{240}Co_8Cs_8O_{72}\cdot 10CH_3CN\cdot 18CH_3OH$ |
| $Mr$ [g mol$^{-1}$] | 1350.47 | 3091.84 | 7663.06 |
| Crystal size [mm] | 0.35 × 0.20 × 0.15 | 0.18 × 0.16 × 0.13 | 0.25 × 0.20 × 0.20 |
| Crystal system | triclinic | monoclinic | monoclinic |
| Space group | $P\bar{1}$ | $P2_1/n$ | $P2_1/n$ |
| $a$ [Å] | 11.9122(3) | 25.643(2) | 25.9749(3) |
| $b$ [Å] | 16.1944(2) | 21.655(2) | 21.6357(2) |
| $c$ [Å] | 17.7467(3) | 29.756(2) | 30.2700(3) |
| $\alpha$ [°] | 114.852(1) | | |
| $\beta$ [°] | 96.960(1) | 90.502(6) | 90.077(3) |
| $\gamma$ [°] | 95.055(1) | | |
| $V$ [Å$^3$] | 3046.65(10) | 16523(2) | 17011.3(3) |
| $Z$ | 2 | 4 | 2 |
| $\rho_{calcd.}$ [Mg m$^{-3}$] | 1.472 | 1.243 | 1.496 |
| $T$ [K] | 173(2) | 100(2) | 173(2) |
| Absorption coeff. [mm$^{-1}$] | 1.286 | 1.263 | 1.308 |
| $F$(000) | 1360 | 6336 | 7776 |
| $\theta$ range [°] | 1.74 to 27.50 | 3.38 to 27.00 | 1.03 to 26.01 |
| Index ranges | $-15 \le h \le 15$ | $-32 \le h \le 32$ | $-31 \le h \le 32$ |
| | $-21 \le k \le 21$ | $-27 \le k \le 27$ | $-24 \le k \le 26$ |
| | $-23 \le l \le 23$ | $-37 \le l \le 37$ | $-37 \le l \le 37$ |
| Reflections collected | 26391 | 166961 | 88290 |
| Independent reflections | 13968 | 35804 | 31901 |
| Refl. observed [$I \ge 2\sigma(I)$] | 10176 | 22949 | 19074 |
| Absorption correction | Scalepack | SADABS | Scalepack |
| Refinement method | full-matrix least-squares on $F^2$ | full-matrix least-squares on $F^2$ | full-matrix least-squares on $F^2$ |
| Max./Min. transm. | 0.8305/0.6617 | 0.850/0.783 | 0.7799/0.7357 |
| [$R_{int}$] | 0.0226 | 0.0699 | 0.0705 |
| Data/parameters | 13968/732 | 35804/1922 | 31901/2093 |
| Goodness-of-fit on $F^2$ | 0.983 | 1.067 | 0.929 |
| Final $R_1$ [$I \ge 2\sigma(I)$] | 0.0430 | 0.0537 | 0.0484 |
| $wR_2$ (all data) | 0.1470 | 0.1425 | 0.1520 |
| Largest residuals [e Å$^{-3}$] | 2.019/–1.330 | 2.913/–1.162 | 1.263/–1.252 |

| | **4a** | **4b** |
|---|---|---|
| Empirical formula | $C_{54}H_{43}CsO_{14}Zn_2\cdot 3CH_3CN$ | $C_{54}H_{43}O_{14}RbZn_2\cdot 2CH_3CN\cdot CH_3OH$ |
| $Mr$ [g mol$^{-1}$] | 1302.70 | 1246.24 |
| Crystal size [mm] | 0.30 × 0.30 × 0.30 | 0.20 × 0.20 × 0.20 |
| Crystal system | monoclinic | monoclinic |
| Space group | $P2_1/c$ | $P2_1/c$ |
| $a$ [Å] | 19.0036(3) | 18.7116(4) |
| $b$ [Å] | 14.4150(2) | 14.6150(3) |
| $c$ [Å] | 20.5309(3) | 20.3408(4) |
| $\alpha$ [°] | | |
| $\beta$ [°] | 103.511(1) | 103.419(1) |
| $\gamma$ [°] | | |
| $V$ [Å$^3$] | 5468.52(14) | 5410.73(19) |
| $Z$ | 4 | 4 |
| $\rho_{calcd.}$ [Mg m$^{-3}$] | 1.582 | 1.530 |
| $T$ [K] | 173(2) | 173(2) |
| Absorption coeff. [mm$^{-1}$] | 1.605 | 1.852 |
| $F$(000) | 2640 | 2552 |
| $\theta$ range [°] | 1.10 to 27.49 | 2.06 to 27.48 |
| Index ranges | $-24 \le h \le 24$ | $-24 \le h \le 24$ |
| | $-18 \le k \le 17$ | $-18 \le k \le 17$ |
| | $-26 \le l \le 26$ | $-26 \le l \le 26$ |
| Reflections collected | 23739 | 22634 |
| Independent reflections | 12546 | 12355 |
| Refl. observed [$I \ge 2\sigma(I)$] | 9906 | 7781 |
| Absorption correction | Scalepack | Scalepack |
| Refinement method | full-matrix least-squares on $F^2$ | full-matrix least-squares on $F^2$ |
| Max./Min. transm. | 0.6446/0.6446 | 0.7083/0.7083 |
| [$R_{int}$] | 0.0247 | 0.0417 |
| Data/parameters | 12546/721 | 12355/712 |
| Goodness-of-fit on $F^2$ | 1.022 | 1.000 |
| Final $R_1$ [$I \ge 2\sigma(I)$] | 0.0328 | 0.0479 |
| $wR_2$ (all data) | 0.1049 | 0.1321 |
| Largest residuals [e Å$^{-3}$] | 0.745/–0.841 | 1.149/–0.583 |

 © 2007 Wiley-VCH Verlag GmbH & Co. KGaA, Weinheim 

fractometer by using Mo-$K_\alpha$ radiation ($\lambda$ = 0.71073 Å), and a graphite monochromator. The structure was solved by direct methods; full-matrix least-squares refinements were carried out on $F^2$ using SHELXTL NT 6.12.[14] A semiempirical absorption correction based on multiple scans (SADABS)[15] was performed. All non-hydrogen atoms were refined anisotropically. The H atoms were geometrically positioned with isotropic displacement parameters being either 1.2 U(eq) or 1.5 U(eq) of the proceeding C atom. Disorder: Two of the aromatic rings (C99–C104 and C125–C130) are disordered with 42.6(5) and 57.4(5)% and 47.8(4) and 52.2(4)%, respectively. In the crystal structure two huge cavities are present that are occupied by different disordered solvent molecules. Attempts to solve this disorder did not lead to reasonable results and therefore the SQUEEZE algorithm was employed to treat the rest electron density in this part of the structure.[16]

## Acknowledgments

This work was supported by the Deutsche Forschungsgemeinschaft Sa 276/27-1-2, SFB 583, GK 312, SPP 1137 "Molecular Magnetism" (Sa 276/26-1-3), the Bayerisches Langzeitprogrammm Neue Werkstoffe, and the Fonds der Chemischen Industrie. N. M. thanks the Freistaat Bayern for a scholarship. The generous allocation of premises by Prof. Dr. K. Meyer at the Institut für Anorganische Chemie (University of Erlangen-Nürnberg) is gratefully acknowledged.

[1] R. W. Saalfrank, A. Scheurer, R. Prakash, F. W. Heinemann, T. Nakajima, F. Hampel, R. Leppin, B. Pilawa, H. Rupp, P. Müller, *Inorg. Chem.* **2007**, *46*, 1586–1592.

[2] R. W. Saalfrank, H. Maid, N. Mooren, F. Hampel, *Angew. Chem.* **2002**, *114*, 323–326; *Angew. Chem. Int. Ed.* **2002**, *41*, 304–307.

[3] R. W. Saalfrank, A. Scheurer, R. Puchta, F. Hampel, H. Maid, F. W. Heinemann, *Angew. Chem.* **2007**, *119*, 269–272; *Angew. Chem. Int. Ed.* **2007**, *46*, 265–268.

[4] R. W. Saalfrank, C. Schmidt, H. Maid, F. Hampel, W. Bauer, A. Scheurer, *Angew. Chem.* **2006**, *118*, 322–325; *Angew. Chem. Int. Ed.* **2006**, *45*, 315–318.

[5] a) R. W. Saalfrank, B. Demleitner in *Perspectives in Supramolecular Chemistry* (Ed.: J. P. Sauvage), Wiley-VCH, Weinheim, **1999**, vol. 5, pp. 1–51; b) E. Uller, B. Demleitner, I. Bernt, R. W. Saalfrank in *Structure and Bonding* (Ed.: M. Fujita), Springer, Berlin, **2000**, vol. 96, pp. 149–175; c) D. L. Caulder, K. N. Raymond, *Acc. Chem. Res.* **1999**, *32*, 975–982; d) M. Fujita, *Chem. Soc. Rev.* **1998**, *27*, 417–425; e) C. J. Jones, *Chem. Soc. Rev.* **1998**, *27*, 289–299; f) F. Hof, S. L. Craig, C. Nuckolls, J. Rebek Jr, *Angew. Chem.* **2002**, *114*, 1556–1578; *Angew. Chem. Int. Ed.* **2002**, *41*, 1488–1508; g) B. J. Holliday, C. A. Mirkin, *Angew. Chem.* **2001**, *113*, 2076–2098; *Angew. Chem. Int. Ed.* **2001**, *40*, 2022–2043; h) S. R. Seidel, P. J. Stang, *Acc. Chem. Res.* **2002**, *35*, 972–983; i) L. R. MacGillivray, J. L. Atwood, *Angew. Chem.* **1999**, *111*, 1080–1096; *Angew. Chem. Int. Ed.* **1999**, *38*, 1018–1033; j) E. Barea, J. A. R. Navarro, J. M. Salas, M. Quirós, M. Willermann, B. Lippert, *Chem. Eur. J.* **2003**, *9*, 4414–4421; k) R. E. P. Winpenny in *Perspectives in Supramolecular Chemistry* (Ed.: J. P. Sauvage), Wiley-VCH, Weinheim, **1999**, vol. 5, pp. 193–223; l) A. D. Cutland, R. G. Malkani, J. W. Kampf, V. L. Pecoraro, *Angew. Chem.* **2000**, *112*, 2801–2803; *Angew. Chem. Int. Ed.* **2000**, *39*, 2689–2691; m) H. Oshio, N. Hoshino, T. Ito, M. Nakano, F. Renz, P. Gütlich, *Angew. Chem.* **2003**, *115*, 233–235; *Angew. Chem. Int. Ed.* **2003**, *42*, 223–225; n) M. Albrecht, *Chem. Rev.* **2001**, *101*, 3457–3497; o) S. P. Watton, P. Fuhrmann, L. E. Pence, S. J. Lippard, A. Caneschi, A. Cornia, G. L. Abbati, *Angew. Chem.* **1997**, *109*, 2917–2919; *Angew. Chem. Int. Ed. Engl.* **1997**, *36*, 2774–2776.

[6] CCDC-637293 [for *meso*-(**3b**)$_n$], -641321 (for **4b**), -641322 [for *meso*-(**3e**)$_n$], -641323 [for Δ/Λ-(**2**)$_n$] and -641652 (for **4a**) contain the supplementary crystallographic data for this paper. These data can be obtained free of charge from the Cambridge Crystallographic data centre via www.ccdc.cam.ac.uk/data_request/cif. For further details of crystal data, data collection and refinement, see Table 1 and the Experimental Section.

[7] a) A. Åhman, M. Nissinen, *Chem. Commun.* **2006**, 1209–1211; b) A. B. Rozhenko, W. W. Schoeller, M. C. Letzel, B. Decker, C. Agena, J. Mattay, *J. Mol. Struct. (Theochem.)* **2005**, *732*, 7–20; c) M. T. Gamer, P. W. Roesky, *Inorg. Chem.* **2005**, *44*, 5963–5965.

[8] Geminal diastereotopic nuclei are inherently nonisochronous. However, chemical shift differences and/or coupling constants may be vanishingly small.

[9] H. E. Gottlieb, V. Kotlyar, A. Nudelman, *J. Org. Chem.* **1997**, *62*, 7512–7515.

[10] D. E. Fenton, J. R. Tate, U. Casellato, S. Tamburini, P. A. Vigato, M. Vidali, *Inorg. Chim. Acta* **1984**, *83*, 23–31.

[11] D. T. Gryko, P. Piątek, J. Jurczak, *Tetrahedron* **1997**, *53*, 7957–7966.

[12] G. M. Sheldrick, C. Krüger, P. Goddard, *Crystallographic Computing 3*, Oxford University Press, Oxford, **1985**, p. 175.

[13] G. M. Sheldrick, *SHELXL-97, Program for Crystal Structure Refinement*, University Göttingen, **1997**.

[14] *SHELXTL NT 6.12*, Bruker AXS Inc., Madison, WI, USA, **2002**.

[15] *SADABS 2.06*, Bruker AXS Inc., Madison, WI, USA, **2002**.

[16] P. v. d. Sluis, A. L. Spek, *Acta Crystallogr., Sect. A* **1990**, *46*, 194–201.

Received: June 4, 2007
Published Online: August 28, 2007

 © 2007 Wiley-VCH Verlag GmbH & Co. KGaA, Weinheim 

DOI: 10.1002/ejic.200700606

# Size-Controlled Water-Soluble Ag Nanoparticles

José M. Domínguez-Vera,*[a] Natividad Gálvez,[a] Purificación Sánchez,[a] Antonio J. Mota,[a] Susana Trasobares,[b] Juan C. Hernández,[b] and Jose J. Calvino*[b]

**Keywords:** Silver / Nanoparticles / Apoferritin / Water-soluble particles

Ag nanoparticles of two different sizes (1 and 4 nm) were prepared within an apoferritin cavity by using an $Ag^+$-loaded apoferritin as a nanoconfined environment for their construction. The initial amount of $Ag^+$ ions injected in the apoferritin cavity dictates the size of the final Ag particles. The protein shell prevents bulk aggregation of the metal particles, which renders them water soluble and extremely stable.

(© Wiley-VCH Verlag GmbH & Co. KGaA, 69451 Weinheim, Germany, 2007)

## Introduction

Metallic nanoparticles are attracting considerable attention for their intriguing properties and potential applications. Because of their small size, the nanoparticles exhibit magnetic, electrical, optical, and chemical properties that cannot be achieved by bulk materials. Advances in the study of the properties of nanoparticles and in their technological applications depend on the development of new methods that are able to control the size and chemical stability of the nanoparticles. In this sense, it must be considered that traditional methods often restrict the flexibility in the preparation of small-size particles (<10 nm).[1] On the other hand, the chemical stability of the nanoparticles is crucial to avoid degradation processes such as partial oxidation or agglomeration. This is one of the reasons why noble metals have been the more usual candidates to be prepared and studied at the nanometer regimen. Among noble metals, Au and Ag exhibit a strong UV/Vis absorption band that is not present in the spectrum of the bulk metals. This absorption band results when the incident photon frequency is resonant with the collective excitation of the conduction electrons and is known as the surface plasmon resonance (SPR).[2] The SPR can be tuned by changing particle size, shape, as well as the surrounding dielectric medium. This tunability confers to Au and Ag nanoparticles potential applications for surface-enhanced spectroscopy,[3] optical filters,[4] and plasmonic devices[5] and sensors.[6] This potentiality is exploited more in the case of Au nanoparticles than it is for Ag nanoparticles despite the known fact that Ag nanoparticles exhibit higher efficiency of plasmon excitation.[2] However, the propensity of pure Ag nanoparticles to undergo oxidative corrosion[7] and aggregation in electrolytic solutions[8] limit their usage, especially for biological applications. The oxidative corrosion and aggregation of Ag nanoparticles can be attenuated or eliminated with a protective layer, such as organic cap ligands or inorganic coatings, which allow stable nanoparticle solutions to exist even at high NaCl concentrations and over a wide range of pH values. An alternative route for avoiding the agglomeration of the particles is the use of a preorganized molecular matrix as a chemical and spatial nanocage for building the Ag nanoparticle. An example of this underexploited route is the use of genetically engineered apoferritin expressing a silver-binding peptide.[9] Native apoferritin consists of a spherical protein shell surrounding an aqueous cavity of about 8 nm.[10] It was reported that apoferritin binds or concentrates metal ions in its cavity[11] and that, interestingly, the loaded metal ions can be chemically reduced to form the corresponding zero-valent cluster, which remains encapsulated.[12] Moreover other inorganic nanoparticles (especially oxides and hydroxides) can be prepared within the apoferritin cavity by using different strategies.[13] The final particle size should be directly determined by the number of metal ions previously encapsulated. However, size tuning by metal ion loading control was only reported for native ferritin, which was prepared with a different iron content.[14] We herein report the preparation of apoferritin-encapsulated silver nanoparticles, and we demonstrate that the initial amount of $Ag^+$ ions injected in the apoferritin capsule dictates the size of the resulting Ag particles.

[a] Departamento de Química Inorgánica, Facultad de Ciencias, Universidad de Granada,
Fuentenueva s/n 18071 Granada, Spain
Fax: +34-958-248526
E-mail: josema@ugr.es
[b] Departamento Ciencia de Materiales e Ingeniería Metalúrgica y Química Inorgánica, Universidad de Cádiz,
Campus Río San Pedro, 11510 Cádiz, Spain
E-mail: jose.calvino@uca.es

## Results and Discussion

Sodium chloride free horse spleen apoferritin was incubated with $AgNO_3$ at two different stoichiometries (500 and

 © 2007 Wiley-VCH Verlag GmbH & Co. KGaA, Weinheim InterScience 

5000 $Ag^+$ per apoferritin) to afford homogeneous solutions that were chromatographed (Sephadex G-25). Every collected fraction was added to a $NaBH_4$ solution and the apoferritin and Ag concentrations were then measured (see Experimental Section). The elution profile does not change with the $Ag^+$/apoferritin stoichiometry. As an example, the elution profile of the solution corresponding to the experiment of higher $Ag^+$/apoferritin is shown in Figure 1. The Ag-associated apoferritin peak (fractions 4–7) was separated from free Ag (fractions 10–12), which trailed well behind (Figure 1). The coelution was an indication that Ag was attached to apoferritin. In fact, fraction 4–7 contained water-soluble particles of sizes smaller than the apoferritin cavity (see below) whereas fractions 10–12 consisted of insoluble and heterogeneous larger Ag particles (20–80 nm).

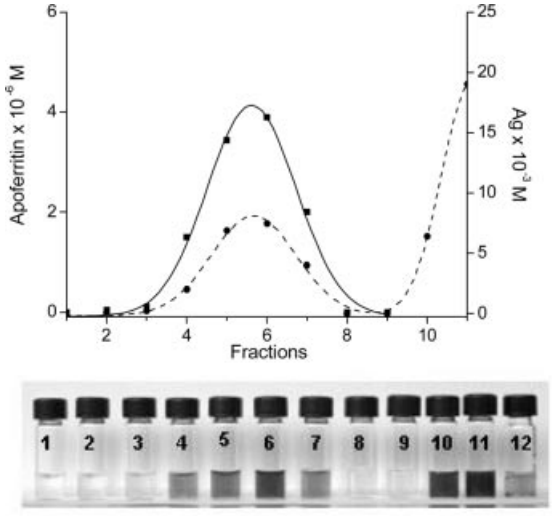


Figure 1. Elution profile of Ag-containing apoferritin. Protein (solid line) was measured by UV/Vis spectroscopy and Ag (dashed line) by atomic absorption spectroscopy.

The solutions corresponding to fractions 5–7 were dialyzed against water at 4 °C and then examined by transmission electron microscopy (TEM). A typical image obtained from the material corresponding to the experiments made in a 5000:1 $Ag^+$/apoferritin stoichiometry shows discrete electron-dense cores, which are spherical in shape (Figure 2). The mean diameter was statistically measured to be $(4 \pm 0.5)$ nm. X-ray energy dispersive spectroscopy (EDS) confirmed that the particles contained Ag (Figure 2d), which was not detected outside the particles. TEM images of samples negatively stained with uranyl acetate (to visualize the protein shell) confirmed that the particles were actually produced within the apoferritin interior (Figure 2b). The presence of the apoferritin coat prevents irreversible aggregation of the Ag particles and their precipitation. For this reason, apoferritin-free Ag particles (fractions 10 and 11) resulted in bulk precipitation.

The use of the apoferritin cavity as a nanoreactor to build the Ag particle allows initial control over the size, because the particles cannot be larger than the cavity (approximately 8 nm). In fact, particles from fractions 5–7 are smaller than 8 nm, whereas those of the apoferritin-free ones (fractions 10–12) are significantly larger (20–80 nm). However, more exhaustive control over the particle size is possible: the initial amount of $Ag^+$ injected in the apoferritin cavity plays a key role in dictating the size of the particles and then the size may be tuned by changing the molar ratio of $Ag^+$/apoferritin. Thus, with a lower $Ag^+$/apoferritin ratio (500:1) and the use of the same experimental procedure (incubation time, chromatography, and dialysis), particles of smaller size were obtained. The detection and structural characterization of these smaller particles requires the use of alternative electron microscopy techniques. Given the large difference in atomic number between Ag ($Z$ = 47) and C ($Z$ = 6), high angle annular dark field imaging (HAADF) was used, which extends the detection limit below the nanometer range. Figure 3a shows a representative HAADF image of the $Ag^+$/apoferritin (500:1) sample. Bright spot contrasts correspond to the high atomic number component, namely, the silver particles. As shown in Figure 3a, a large number of nanosized Ag particles can be detected in the HAADF images.

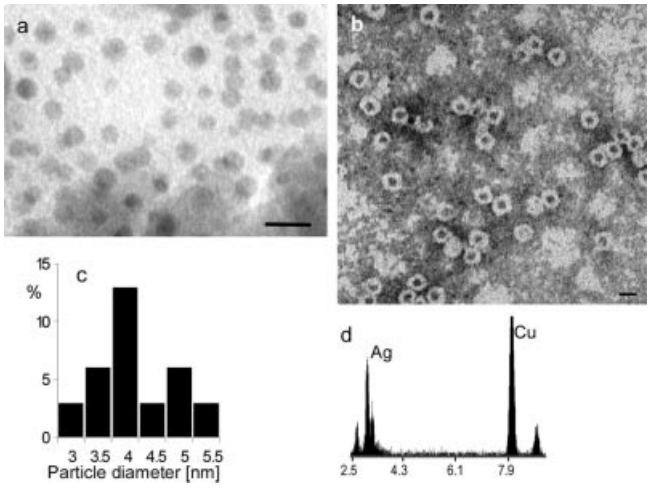


Figure 2. (a) TEM image of Ag nanoparticles prepared in a Ag/apoferritin stoichiometry of 5000:1; (b) negatively stained TEM image showing the metallic core surrounded by the apoferritin shell (scale bars are 10 nm); (c) size-distribution in nm; and (d) representative EDS recorded inside the particles. Cu peaks are due to the sample grid.

EDS obtained from locations inside these particles by using a finely focused 0.5-nm electron probe (Figure 3b) confirm the presence of Ag in these bright areas. From the particle size histogram established from HAADF images (Figure 3c) an average Ag particle size of $(1 \pm 0.1)$ nm can be estimated in this sample.

The structure of the small particles containing Ag was further investigated by means of high-resolution electron microscopy (HREM). Figure 4 shows some representative HREM images. Measurements of lattice spacings and interplanar angles on the diffractograms of these images (included as insets) confirm that the particles are fcc Ag. Some

 © 2007 Wiley-VCH Verlag GmbH & Co. KGaA, Weinheim 

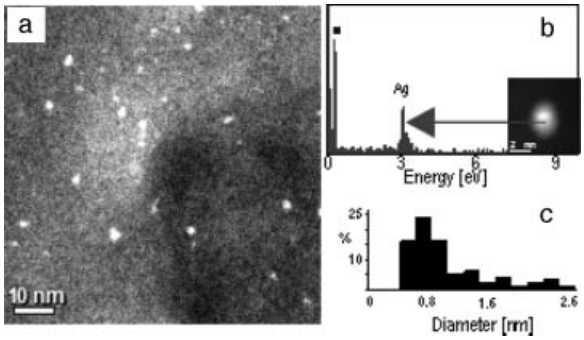


Figure 3. (a) STEM-HAADF image of the 500:1 $Ag^+$/apoferritin sample; (b) X-EDS spectrum obtained from inside one of the particles (shown as inset); (c) particle diameter histogram of this sample established from a collection of HAADF images.

of them are monocrystalline domains (Figure 4a,b), whereas in some other cases they are made of several singly or multiply twinned smaller fcc domains (Figure 4c,d). In the diffractograms of the former, {002} reflections at 0.204 nm, {022} at 0.14 nm, and {111} at 0.235 nm can be clearly identified. Twinning on the {111} planes complicates the appearance of the diffractograms in the case of the latter, but these same reflections can still be clearly identified. Note that the size of the domains in these twinned particles is smaller than 1 nm.

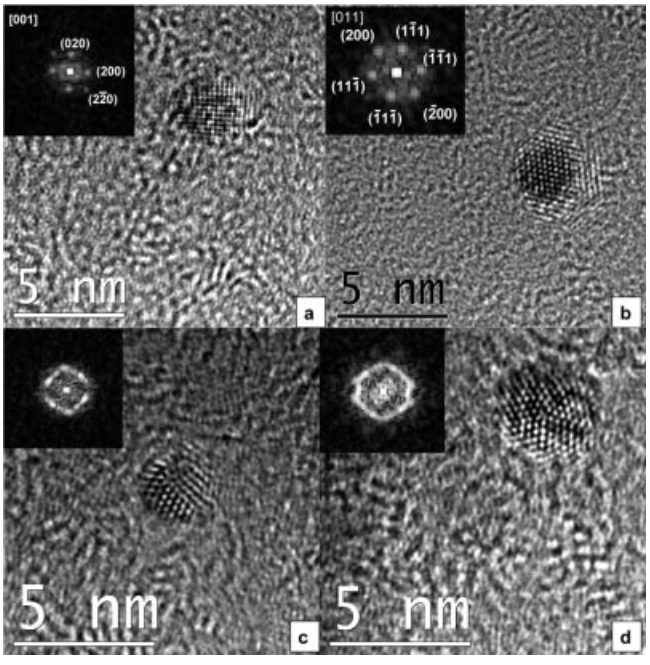


Figure 4. HREM images recorded of the 500:1 $Ag^+$/apoferritin sample: (a) shows a fcc Ag particle down the [001] zone axis; (b) Ag particle down the [110] zone axis; (c) and (d) correspond to multiply twinned Ag particles. Diffractograms are included as insets. Multiply-twinned particles illustrate the structure of larger particles.

These results demonstrate that $Ag^+$-apoferritin acts as a reactor because the trapped $Ag^+$ ions are able to react with a chemical reagent that is small enough to traverse the apoferritin channels to build a new material. Thus, $Ag^+$ ions are reduced with $NaBH_4$ to yield zero-valent silver. As a result of the reduction, the UV/Vis spectrum of the solution dramatically changed and showed the typical absorption band attributable to the SPR of the Ag particles. The position of the SPR can be tuned by changing the particle size and shape, as well as the surrounding dielectric medium. In Figure 5, the UV/Vis spectra of the solution corresponding to the particles of 1 and 4 nm show the presence, in both cases, of the SPR at 392 and 434 nm, respectively. This significant shift must be a direct consequence of the different particle sizes[15] and/or their different dielectric surrounding media: the lower the Ag particle size, the less contact with the apoferritin takes place. In fact, particles of 1 nm exhibit a SPR (392 nm) that is typical for uncoated Ag nanoparticles, whereas that (434 nm) of the 4-nm sized particle is more characteristic of Ag particles surrounded with a high refractive index shell.[16]

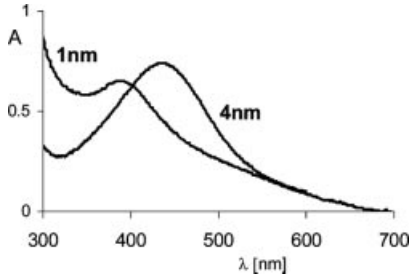


Figure 5. UV/Vis spectra of the Ag particles. The SPR showed a redshift with a reduced particle size.

Stability is a key point for silver nanoparticles. Previous studies showed that silver nanoparticles were often unstable in solution and easily aggregated at high concentration of the particles or NaCl. The apoferritin-encapsulated Ag nanoparticles we have prepared exhibited excellent stability in solution and no significant UV/Vis spectral changes were observed over one month at room temperature. Likewise, the addition of NaCl to reach a 0.1 M concentration did not produce either precipitation or UV/Vis spectral change. Moreover, the solution can be lyophilized and the particles kept in the solid state under ambient conditions for months without showing significant changes on the basis of X-ray powder diffraction analysis.

## Conclusions

Ag nanoparticles were prepared by using the apoferritin cavity as a nanoreactor to reduce the $Ag^+$ ions. The size of the nanoparticles can be tuned by changing the $Ag^+$ loading. The presence of the apoferritin coat is responsible for the water solubility and stability of these particles.

 © 2007 Wiley-VCH Verlag GmbH & Co. KGaA, Weinheim 

## Experimental Section

Horse spleen apoferritin (53 mg mL$^{-1}$) was exhaustively dialyzed for 3 d with several changes of the milli-Q water at 4 °C to remove NaCl. After this treatment, apoferritin (5.3 mg mL$^{-1}$) was incubated with $AgNO_3$ at two different concentrations (6 and 60 mM) at room temperature, which corresponds to 500 and 5000 $Ag^+$/apoferritin stoichiometries. No precipitation of AgCl occurred. After 1 d, the resulting solutions were dialyzed against water for 15 min and then passed through a 1.5 cm × 5.5 cm column of Sephadex G-25 equilibrated with water. Fractions were collected every minute, and then, the concentrations of apoferritin and Ag were obtained by the absorbance values at 280 nm ($\varepsilon^{280} \approx 468000$ M$^{-1}$) and atomic absorption spectroscopy, respectively. In a parallel experiment, the chromatographed fractions were directly added to a water solution containing $NaBH_4$ (4.5 mg mL$^{-1}$). The samples used for electron microscopy (TEM) studies were prepared by diluting the dialyzed solutions of particles with milli-Q water and then placing a drop onto a carbon-coated Cu grid and drying it in a glove box. To record images in high-resolution electron microscopy (HREM) and high angle annular dark field (HAADF) modes, the samples were deposited onto holey carbon Cu grids. The average particle sizes and the standard deviations were estimated from measurements of diameters performed either with TEM or HAADF images of a statistically adequate number of particles (about a hundred). Electron micrographs were recorded with two different microscopes: a Philips CM-20 HR analytical electron microscope operating at 200 keV (TEM) and a JEOL 2010F (HREM, HAADF) working also at 200 kV. Structural resolution of the last instrument was 0.19 nm, which allowed structural analysis of noble metals as it is the case of silver. Moreover operating this instrument in scanning transmission electron microscopy mode (STEM) allows forming electron probes with diameters as small as 0.2 nm, which opens the possibility, in combination with X-EDS detectors, to perform chemical analysis with a spatial resolution better than 1 nm.

## Acknowledgments

Financial support from the Spanish Ministerio de Educación y Ciencia (project CTQ2006-02840) and Junta de Andalucía (Proyecto Excelencia FQM-00425 and FQM-334) are gratefully acknowledged. N. G. and S. T. thank the Spanish Ministerio de Ciencia y Tecnología for a research contract (programa Ramón y Cajal).

[1] D. D. Evanoff Jr, G. Chumanov, *ChemPhysChem* **2005**, *6*, 1221–1231; I. Sondi, D. V. Goia, E. Matijevic, *J. Colloid Interface Sci.* **2003**, *260*, 75–81; M. P. Pileni, *J. Phys. Chem.* **1993**, *97*, 6961; N. Shirtcliffe, U. Nickel, S. Schneider, *J. Colloid Interface Sci.* **1999**, *211*, 122–129; K. P. Velikov, G. E. Zegeres, A. V. Blaaderen, *Langmuir* **2003**, *19*, 1384–1389; Y. Tan, X. Dai, Y. Li, D. Zhu, *J. Mater. Chem.* **2003**, *13*, 1069–1075; K. K. Caswell, C. M. Bender, C. J. Murphy, *Nano Lett.* **2003**, *3*, 667–669; D. L. Van Hyning, C. F. Zukoski, *Langmuir* **1998**, *14*, 7034–7046.

[2] U. Kreibig, M. Vollmer in *Springer Series in Materials Science Vol. 25: Optical Properties of Metal Clusters*, New York, Springer, **1995**.

[3] G. C. Schatz, R. P. Van Duyne in *Electromagnetic Mechanism of Surface-Enhanced Spectroscopy*, **2002**, Wiley, New York, vol. 1; C. L. Haynes, R. P. Van Duyne, *J. Phys. Chem. B* **2003**, *107*, 7426–7433; Z.-G. Shang, D. N. Ting, Y. T. Wong, Y. C. Tan, B. Ying, Y.-J. Mo, *J. Mol. Struct.* **2007**, *826*, 64–67.

[4] Y. Dirix, C. Bastiaansen, W. Caseri, P. Smith, *Adv. Mater.* **1999**, *11*, 223–227; C. L. Haynes, R. P. Van Duyne, *Nano Lett.* **2003**, *3*, 939–943.

[5] S. A. Maier, M. L. Brongersma, P. G. Kik, S. Meltzer, A. A. G. Requicha, H. A. Atwater, *Adv. Mater.* **2001**, *13*, 1501–1505; R. A. Shelby, D. R. Smith, S. Schultz, *Science* **2001**, *292*, 77–78.

[6] A. J. Haes, R. P. Van Duyne, *J. Am. Chem. Soc.* **2002**, *124*, 10596–10604; R. C. Mucic, J. J. Storhoff, C. A. Mirkin, R. L. Letsinger, *J. Am. Chem. Soc.* **1998**, *120*, 12674–12675.

[7] A. Henglein, *Chem. Mater.* **1998**, *10*, 444.

[8] T. Huang, R. W. Murray, *J. Phys. Chem. B* **2003**, *107*, 7434.

[9] R. M. Kramer, C. Li, D. C. Carter, M. O. Stone, R. R. Naik, *J. Am. Chem. Soc.* **2004**, *126*, 13282–13286.

[10] P. M. Harrison, P. Arosio, *Biochim. Biophys. Acta* **1996**, *1275*, 161; P. M. Proulx-Curry, N. D. Chasteen, *Coord. Chem. Rev.* **1995**, *144*, 347.

[11] S. Pead, E. Durrant, B. Webb, C. Larsen, D. Heaton, J. Johnson, G. D. Watt, *J. Inorg. Biochem.* **1995**, *59*, 15.

[12] N. Gálvez, P. Sánchez, J. M. Domínguez-Vera, *Dalton Trans.* **2005**, 2492; N. Gálvez, P. Sánchez, J. M. Domínguez-Vera, A. Soriano-Portillo, M. Clemente-León, E. Coronado, *J. Mater. Chem.* **2006**, *16*, 2757; M. Clemente-Leon, E. Coronado, A. Soriano-Portillo, N. Galvez, J. M. Dominguez-Vera, *J. Mater. Chem.* **2007**, *17*, 49–51.

[13] K. Yoshizawa, K. Iwahori, K. Sugimoto, I. Yamashita, *Chem. Lett.* **2006**, *35*, 1192; K. Iwahori, T. Morioka, I. Yamashita, *Phys. Status Solid A* **2006**, *203*, 2658; K. Iwahori, K. Yoshizawa, M. Muraoka, I. Yamashita, *Inorg. Chem.* **2005**, *44*, 6393; M. Uchida, M. T. Klem, M. Allen, P. S. uci, M. Flenniken, E. Gillitzer, Z. Varpness, L. O. Liepold, M. Young, T. Douglas, *Adv. Mater.* **2007**, *19*, 1025 and references cited therein.

[14] S. Gider, D. D. Awschalon, T. Douglas, S. Mann, M. Chaparala, *Science* **1995**, *268*, 77.

[15] A. S. Kumbhar, M. K. Kinnan, G. Chumanov, *J. Am. Chem. Soc.* **2005**, *127*, 12444–12445; S. Hussain, R. K. Roy, A. K. Pal, *Mater. Chem. Phys.* **2006**, *99*, 375.

[16] I. Pastoriza-Santos, D. S. Koktysh, A. A. Mamedov, M. Giersig, N. A. Kotov, L. M. Liz-Marzán, *Langmuir* **2000**, *16*, 2731–2735.

Received: June 11, 2007
Published Online: August 28, 2007

 © 2007 Wiley-VCH Verlag GmbH & Co. KGaA, Weinheim 

DOI: 10.1002/ejic.200601194

# Synthesis, Structure and Magnetic Properties of a Novel Hexanuclear Copper Methylsiloxane Complex

Larissa Zherlitsyna,[a] Norbert Auner,*[a] Michael Bolte,[a] Yulia Pozdniakova,[b] Olga Shchegolikhina,[b] Konstantin Lyssenko,[b] Vladimir Pashchenko,*[c] Bernd Wolf,[c] Michael Lang,[c] Florian Schütz,[d,e] Marcus Kollar,[f] Francesca Sauli,[d] and Peter Kopietz[d]

**Keywords:** Copper / Cluster compounds / Sandwich complexes / Magnetic properties

A new hexanuclear copper(II) sandwich complex based on two 12-membered macrocyclic methylsiloxanolate ligands, $[Cu_6\{(MeSiO_2)_6\}_2]\cdot 6DMF$, was synthesized and characterized by single-crystal X-ray diffraction analysis and magnetic measurements. The cluster compound crystallizes in the monoclinic system, space group $P2_1/n$ (No. 14), with $a$ = 13.3728(5) Å, $b$ = 15.4281(7) Å, $c$ = 17.4335(7) Å, $\beta$ = 98.932(3)° and $Z$ = 2. The unit cell contains two identical molecular clusters, each consisting of six interacting $Cu^{2+}$ ($S$ = ½) ions. Within the cluster the six oxygen-bridged $Cu^{2+}$ ions are arranged in an almost regular hexagon. An analysis of the high-temperature part of the magnetic susceptibility reveals that the complex has a strong average ferromagnetic Cu–Cu exchange interaction of $|J_{av}/k_B|$ = (50.4 ± 1) K with a high-spin $S$ = 3 ground state. A satisfactory fit for the magnetic susceptibility and the magnetization in the whole accessible temperature range is obtained from a Heisenberg model with nonuniform exchange couplings within a ring, corresponding to a system of two weakly coupled trimers with a ferromagnetic intratrimer exchange coupling of $|J/k_B|$ = 72.5 K and a ferromagnetic intertrimer exchange coupling of $|J'/k_B|$ = 7 K.
(© Wiley-VCH Verlag GmbH & Co. KGaA, 69451 Weinheim, Germany, 2007)

## Introduction

Because of their unusual physical properties, large metal clusters have attracted much attention during the past two decades.[1,2] In particular, the ability of transition-metal clusters to form single-molecule magnets has stimulated the research community to synthesize new compounds with various exchange interactions between the magnetic ions within a cluster.[1–3] In addition, different spin configurations within a cluster, together with possible magnetic exchange between neighbouring clusters, are of interest in molecular and low-dimensional magnetism because these systems may play an important role in future applications.

From a widespread series of molecular polymetallaorganosiloxane complexes, we have concentrated our interest on the family $[M_N\{(RSiO_2)_N\}_2]\cdot N$(Ligand) (where M = Ni, Mn, Co, Cu,…; $N$ = 6, 8, 10,…; R = Et, Ph, Me,…; Ligand = EtOH, DMF,…), having a sandwich-like molecular structure. In the past decades, some representatives of this family have been obtained and their molecular structures have been established by single-crystal X-ray analysis.[4–8] These clusters are composed of two 2$N$-membered ($N$ Si + $N$ O) cycloorganosiloxanolate fragments linked together through $N$ metal atoms. These polymetallaorganosiloxane complexes offer the potential to study the magnetic properties of molecular quantum rings experimentally. It should be noted that in a subfamily of copper-containing organosiloxanes with $N$ = 6, only three representatives of hexanuclear copper(II) siloxanes with phenyl substituents at silicon atoms, $[Cu_6\{(PhSiO_2)_6\}_2]\cdot 6EtOH$, $\{[Cu_6\{(PhSiO_2)_6\}_2]\cdot 6DMF\}\cdot 4DMF$ and $\{[Cu_6\{(PhSiO_2)_6\}_2]\cdot 5BuOH\}\cdot 3^nBuOH$, have been described in the literature.[4,6,8] For the previously reported ring-shaped molecular complex $[Cu_6\{(PhSiO_2)_6\}_2]\cdot 6EtOH$,[9] it was demonstrated that the six copper ions within the ring are ferromagnetically coupled ($J/k_B$ = –60 K) with a total spin $S_{tot}$ = 3 ground state. The complex $\{[Cu_6\{(PhSiO_2)_6\}_2]\cdot 5BuOH\}\cdot 3^nBuOH$ also has a high-spin $S_{tot}$ = 3 ground state, but its magnetic data indicate a strong nonequivalence of exchange pathways

[a] Institut für Anorganische Chemie, J. W. Goethe-Universität Frankfurt, FOR 412,
60439 Frankfurt (M), Germany
Fax: +49-69-798-29188
E-mail: auner@chemie.uni-frankfurt.de
[b] A. N. Nesmeyanov Institute of Organoelement Compounds of RAS (INEOS),
28 Vavilov Str., 117813 Moscow, Russia
[c] Physikalisches Institut, J. W. Goethe-Universität Frankfurt, FOR 412,
60438 Frankfurt (M), Germany
Fax: +49-69-798-47250
E-mail: pashchenko@physik.uni-frankfurt.de
[d] Institut für Theoretische Physik, J. W. Goethe-Universität Frankfurt, FOR 412,
60438 Frankfurt (M), Germany
[e] Department of Physics, Brown University,
Providence, RI 02912, USA
[f] Theoretische Physik III, Universität Augsburg,
86135 Augsburg, Germany
Supporting information for this article is available on the WWW under http://www.eurjic.org or from the author.

 © 2007 Wiley-VCH Verlag GmbH & Co. KGaA, Weinheim 

within the ring ($J_1/k_B$ = –89.2 K, $J_2/k_B$ = –15.3 K).[8] For more detailed investigations on the mechanisms leading to the formation of a high-spin ground state and the influence of various substituents and/or ligands of the molecule on the magnetic behaviour of the quantum ring, we have attempted to expand the existing class of copper-containing molecular magnets by the synthesis of new isostructural molecular complexes.

Here we report on the synthesis, structure and magnetic properties of a novel sandwich-like hexacopper hexamethylcyclohexasiloxane complex, $[Cu_6\{(MeSiO_2)_6\}_2]\cdot 6DMF$. In contrast to the phenyl analogues previously reported,[4,6,8] the present complex has methyl groups as substituents at the silicon atoms. Preliminary results of this work have been published in ref.[10], in which the high-temperature susceptibility of this complex has been analyzed and an initial comparative investigation of the structural and magnetic properties has been carried out.

## Results and Discussion

The synthesis of sandwich-like polyhedral metallaorganosiloxanes containing transition metals is commonly based on an exchange reaction of alkali-metal organosiloxanolates[11] with transition-metal chlorides in alcohol-containing media.[4–6,12,13]

Similarly, the novel copper methylsiloxane $[Cu_6\{(MeSiO_2)_6\}_2]\cdot 6DMF$ (**E**) has been obtained in a two-step reaction (Scheme 1). The first step involves an alkaline hydrolysis of methyltriethoxysilane $MeSi(OEt)_3$ (Si/KOH ratio of 1:1) in a toluene/methanol mixture generating in situ a potassium methylsiloxanolate intermediate **A**. A spontaneous association of potassium methylsiloxanolate intermediates **A** leads to the formation of aggregates **B**, in which an ionic network containing alcohol and water molecules is surrounded by organosilicon species with functional groups. In a second step, the addition of a methanolic solution of $CuCl_2$ (Cu/K ratio of 1:2) initiates an irreversible exchange reaction that substitutes the potassium ions with copper ions. Consequently, potassium chloride precipitates from the reaction. Thus, aggregates **B**, originally containing only alkali metals, are reorganized into new aggregates **C**, now possessing only copper atoms. Finally, condensation of EtO– and OH– functional groups at silicon results in the formation of the cyclic siloxane fragments.

After filtration of precipitated KCl, complete evaporation of the solvent from aggregates **C** gives a greenish-blue product **D** with a yield up to 82.5%. A powder X-ray diffraction analysis (XRD) of the obtained product **D** proved that the product was in the crystalline state. However, the crystals were too small for single-crystal X-ray analysis.

To identify product **D**, we used a well-known approach applied in organosilicon chemistry, preparing the trimethylsilyl-substituted derivative of the functional system. This general route was optimized for the treatment of metallaorganosiloxanes.[13] According to Scheme 2, the cyclic siloxane fragments of the starting metallaorganosiloxanes were isolated as a trimethylsiloxy derivative with retention of the

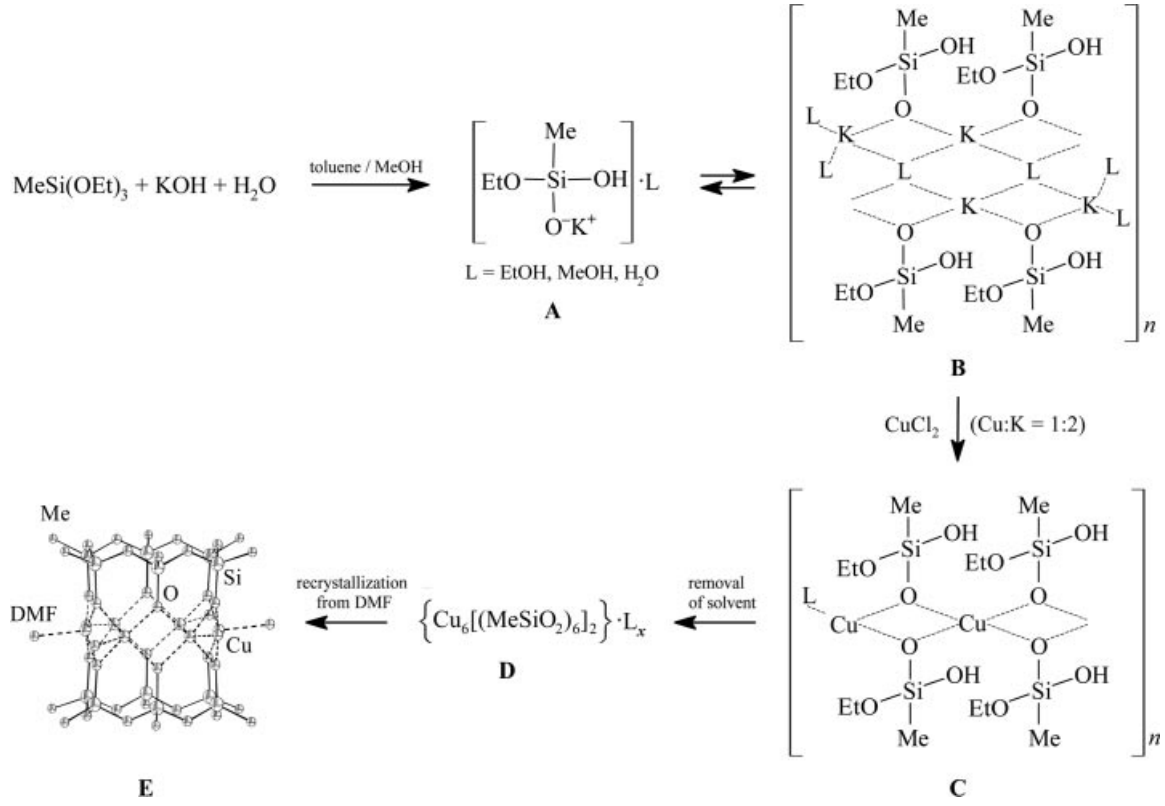


Scheme 1.

 © 2007 Wiley-VCH Verlag GmbH & Co. KGaA, Weinheim 

size and configuration of the rings. Consequently, the correspondence of crystalline **D** to the formula $[Cu_6\{(MeSiO_2)_6\}_2]\cdot L_x$ was confirmed by its trapping reaction with $Me_3SiCl$ and subsequent NMR spectroscopy investigations on the resulting product.

$$\left\{Cu_6[(MeSiO_2)_6]_2\right\}\cdot L_x + Me_3SiCl \xrightarrow[-\,CuCl_2]{\text{py, hexane}} \left[MeSi(O)(OSiMe_3)\right]_6$$

Scheme 2.

The $^1H$ NMR spectrum of $[MeSi(O)(OSiMe_3)]_6$ exhibits two nonequivalent signals for the methyl groups: one singlet at 0.11 ([–$SiMe_3$]) and one singlet at $\delta$ = 0.03 ppm ([MeSi–]), with an integrated intensity ratio of 3:1.

The $^{29}Si$ NMR spectrum of $[MeSi(O)(OSiMe_3)]_6$ shows two signals: one singlet at $\delta$ = 8.50 ppm corresponds to the [–$OSiMe_3$] groups and the second one at –68.18 ppm ([Me-$SiO_3$–]) to the Si atoms in the hexamethylcyclohexasiloxanolate ring $[MeSi(O)O^-]_6$.

As the dried product **D** is insoluble in methanol, toluene or ethanol, DMF was used as a solvent for recrystallization, giving greenish-blue crystals **E** after a few months. X-ray analysis on suitable single crystals proved the product to be $[Cu_6\{(MeSiO_2)_6\}_2]\cdot 6DMF$. It should be noted that the crystals are very unstable in air because the desolvating occurs within a short time period, thereby reducing the properties of the crystal transparency.

### Crystal Structure of $[Cu_6\{(MeSiO_2)_6\}_2]\cdot 6DMF$

In accordance with the single-crystal X-ray analysis, the complex $[Cu_6\{(MeSiO_2)_6\}_2]\cdot 6DMF$ crystallizes in the monoclinic system, space group $P2_1/n$ (no. 14) with $a$ = 13.3683(14) Å, $b$ = 15.388(2) Å, $c$ = 17.4383(14) Å, $\beta$ = 98.88(7)° and $Z$ = 2.

The complex $[Cu_6\{(MeSiO_2)_6\}_2]\cdot 6DMF$ exhibits a ring-shaped sandwich-like structure (Figure 1). The molecule consists of two hexamethylcyclohexasiloxanolate ligands, $[(MeSiO_2)_6]^{6-}$, sandwiched by six $Cu^{2+}$ ions. Within the ring, the adjacent $Cu^{2+}$ ions are linked by pairs of siloxanolate oxygen atoms, which provide the main magnetic exchange path for the copper $S$ = 1/2 spins. The overall molecular building topology is analogous to that of the hexacopper(II) cyclohexaphenylsiloxanolates $[Cu_6\{(PhSiO_2)_6\}_2]\cdot 6EtOH$,[4] $\{[Cu_6\{(PhSiO_2)_6\}_2]\cdot 6DMF\}\cdot 4DMF$[6] and $\{[Cu_6\{(PhSiO_2)_6\}_2]\cdot 5BuOH\}\cdot 3^nBuOH$[8] described earlier.

It is important to note that the molecular structure of $[Cu_6\{(MeSiO_2)_6\}_2]\cdot 6DMF$ is centrosymmetric, with a crystallographic inversion centre at the midpoint of the molecule. The molecules of the complexes $\{[Cu_6\{(PhSiO_2)_6\}_2]\cdot 6DMF\}\cdot 4DMF$ and $\{[Cu_6\{(PhSiO_2)_6\}_2]\cdot 5BuOH\}\cdot 3^nBuOH$ also contain a crystallographic centre of inversion, while the complex $[Cu_6\{(PhSiO_2)_6\}_2]\cdot 6EtOH$ shows a higher local symmetry of the molecules (trigonal symmetry $C_3$), giving only two symmetry-independent positions for copper atoms.

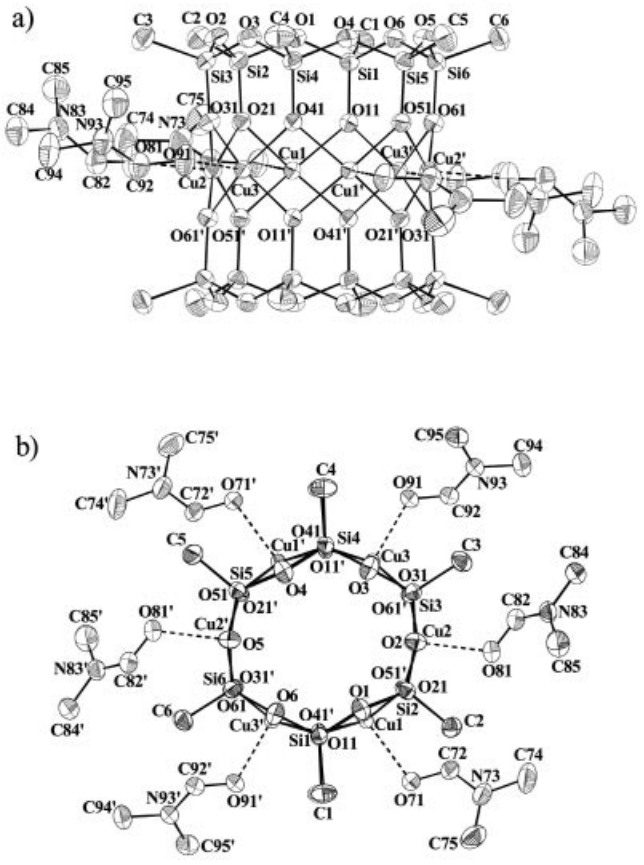


Figure 1. Side view (a) and top view (b) of the molecular structure of the complex $[Cu_6\{(MeSiO_2)_6\}_2]\cdot 6DMF$ with the atomic labelling. The hydrogen atoms have been omitted for clarity. The dashed bonds indicate the apical coordination of the copper atoms. Displacement ellipsoids are drawn at the 50% probability level.

The hexamethylcyclohexasiloxanolate ligands have an *all-cis* configuration; the olate groups are directed towards the plane of the Cu atoms. The two 12-membered siloxanolate $(Si–O)_6$ rings are coaxial and parallel to each other. The Si–O(Si) bond lengths vary in the range of 1.624–1.636 Å and the Si–O–Si angles in the range of 133.98–136.64°, which are usual for this class of compounds.[4,5,7] The standard deviations of the Si and O atoms from the mean planes do not exceed 0.0004 Å and 0.0012 Å, respectively. The Si–O(Cu) bond lengths are significantly shorter (1.609–1.613, av. 1.611 Å) than the corresponding Si–O(Si) bond lengths in the hexasiloxane macrocycle. The Si–O–Si sections of the siloxanolate ring are nearly perpendicular to the mean plane of the Si atoms (dihedral angles 74.3–89.3°). The methyl group, attached to each of the $2\times 6$ Si atoms, points away from the molecule.

A metal group of the six $Cu^{II}$ atoms is arranged as an almost flat (standard deviation from the mean plane is 0.0002 Å) hexagon. In contrast to the complex $[Cu_6\{(PhSiO_2)_6\}_2]\cdot 6EtOH$,[4] which has a high (trigonal) crystal symmetry, the hexagon in the complex $[Cu_6\{(MeSiO_2)_6\}_2]\cdot 6DMF$ is slightly distorted. However, this distortion of the hexahedron is significantly smaller compared with the observed one in the complex

 © 2007 Wiley-VCH Verlag GmbH & Co. KGaA, Weinheim 

{[$Cu_6${$(PhSiO_2)_6$}$_2$]·6DMF}·4DMF.[6] In all cases the Cu, Si, O skeleton approaches 6/*mmm* symmetry. In the complex [$Cu_6${$(MeSiO_2)_6$}$_2$]·6DMF the nonbounded Cu–Cu distances are 2.816, 2.841 and 2.861 Å (av. 2.839 Å) and the distance between opposite copper atoms varies between 5.495(7) and 5.820(6) Å (av. 5.677 Å).

The coordination surrounding of the copper atoms in the complex [$Cu_6${$(MeSiO_2)_6$}$_2$]·6DMF is a slightly distorted oxygen square-pyramidal (SP) configuration. It should be noted that, similarly to the known sandwich-like complexes,[4,6,8] the copper–oxygen moiety is organized in the cyclic form by the oxygen atoms of the siloxanolate ligands and the SP configuration arises from the apical oxygen bonding with the solvent molecules. In the further discussion, the oxygen atoms of the siloxanolate ligands bound to the copper atoms will be indicated as equatorial, whereas the others, belonging to the DMF solvent, will be mentioned as apical or axial.

The equatorial Cu–O bonds in the complex vary in the range of 1.946–1.974 Å (av. 1.957 Å), which is close to the expected values for copper atoms with a square-pyramidal coordination environment. In the recently reported copper-containing siloxanolate complexes,[4,6,8] it was demonstrated that the average Cu–O bond lengths in the basal plane for SP (av. 1.96 Å) and in the case of square-planar configuration (av. 1.90 Å) are significantly different. The Cu–O–Cu angles at the bridging equatorial oxygen atoms, which mainly determine the magnetochemical behaviour of polynuclear clusters, vary in the range 91.26–94.59°, which is typical for other copper-containing sandwich-like organosiloxanes.[4,6,8] The average value of the Cu–O–Cu angle is about 93.02°.

All copper atoms are shifted from the mean planes of the slightly distorted basal squares of the equatorial oxygen atoms by 0.324 (for Cu1), 0.290 (Cu2) and 0.323 Å (Cu3) towards the external axially coordinated oxygen of DMF molecules. In the close analogues [$Cu_6${$(PhSiO_2)_6$}$_2$]·6EtOH and {[$Cu_6${$(PhSiO_2)_6$}$_2$]·6DMF}·4DMF, the shifts are 0.285(Cu1)–0.290(Cu2) and 0.345(Cu1)–0.288(Cu2)–0.349(Cu3) Å, respectively.

The six apical positions of all copper polyhedra in the complex $Cu_6[(MeSiO_2)_6]_2$·6DMF are occupied by the DMF oxygen atoms and the corresponding Cu–O bonds are always significantly longer than the equatorial ones. The apical Cu–O bonds vary in the range of 2.229(3)–2.322(6) Å (av. 2.273 Å).

Selected bond lengths and bond angles are summarized in Table 1.

Interestingly, in contrast to the complex {[$Cu_6${$(PhSiO_2)_6$}$_2$]·6DMF}·4DMF described earlier,[6] which was also recrystallized from DMF, the crystal structure of [$Cu_6${$(MeSiO_2)_6$}$_2$]·6DMF does not contain any additional solvate molecules within the intermolecular space.

It should be noted that the central cavity of the molecule contains a relatively large empty inner channel, suitable for small molecules or ions to enter the interior of the complex. The estimated diameter of the free cross-section is about 2.5 Å. Despite the similarity in the overall molecular building topology, the presence of an additional small anion, occupying the central cavity, was observed only for non-copper-containing metallasiloxanes (with Ni, Co, Mn).[5,7]

Table 1. Selected bond lengths [Å] and angles [°] for [$Cu_6${$(MeSiO_2)_6$}$_2$]·6DMF.

| Bond lengths [Å] | | | |
|---|---|---|---|
| Cu1–O11 | 1.9457(10) | Si1–O1 | 1.6235(12) |
| Cu1–O41′[a] | 1.9460(10) | Si1–O11 | 1.6095(11) |
| Cu1–O21 | 1.9606(10) | Si1–O6 | 1.6244(11) |
| Cu1–O51′ | 1.9611(10) | Si1–C1 | 1.8424(18) |
| Cu1–O71 | 2.3256(12) | Si2–O1 | 1.6315(12) |
| Cu2–O31 | 1.9485(11) | Si2–O21 | 1.6091(11) |
| Cu2–O21 | 1.9531(10) | Si2–O2 | 1.6282(13) |
| Cu2–O51′ | 1.9543(11) | Si2–C2 | 1.8523(16) |
| Cu2–O61′ | 1.9654(10) | Si3–O2 | 1.6328(12) |
| Cu2–O81 | 2.2625(13) | Si3–O31 | 1.6092(11) |
| Cu3–O11′ | 1.9481(10) | Si3–O3 | 1.6285(12) |
| Cu3–O31 | 1.9613(10) | Si3–C3 | 1.8411(18) |
| Cu3–O41 | 1.9664(10) | Si4–O3 | 1.6219(12) |
| Cu3–O61′ | 1.9739(10) | Si4–O41 | 1.6123(11) |
| Cu3–O91 | 2.2311(13) | Si4–O4 | 1.6258(13) |
| Cu1–Cu2 | 2.8412(3) | Si4–C4 | 1.8458(19) |
| Cu2–Cu3 | 2.8159(3) | Si5–O4 | 1.6285(12) |
| Cu1–Cu3′ | 2.8614(3) | Si5–O51 | 1.6110(12) |
| **Bond angles [°]** | | | |
| Cu1–O11–Cu3′ | 94.589(44) | Cu2–O61′–Cu3 | 91.258(45) |
| Cu1–O41′–Cu3′ | 93.998(45) | Cu2–O21–Cu1 | 93.098(47) |
| Cu2–O31–Cu3 | 92.141(45) | Cu2–O51′–Cu1 | 93.047(46) |

[a] Symmetry transformations used to generate equivalent atoms: (′) $-x + 1, -y + 1, -z + 1$.

The crystal packing of the complex is shown in Figure 2. The structure consists of two nonequivalent layers of [$Cu_6${$(MeSiO_2)_6$}$_2$]·6DMF molecules, which are parallel to the crystallographic (*ac*) plane. The local axis of the molecules for the neighbouring layers are turned from the normal to the (*ac*) plane and make up an angle of 25.76° with the crystallographic *b* axis.

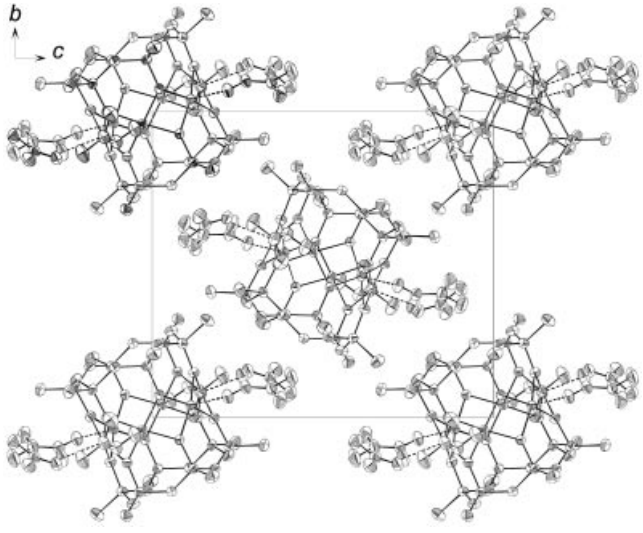


Figure 2. Crystal packing of the complex [$Cu_6${$(MeSiO_2)_6$}$_2$]·6DMF, viewed along the [100] direction. The hydrogen atoms have been omitted for clarity.

 © 2007 Wiley-VCH Verlag GmbH & Co. KGaA, Weinheim 

### Magnetic Properties of $[Cu_6\{(MeSiO_2)_6\}_2]$·6DMF

Magnetic susceptibility and magnetization measurements were performed on polycrystalline samples of $[Cu_6\{(MeSiO_2)_6\}_2]$·6DMF. The data were corrected for the contribution of the sample holder and for the diamagnetic core contribution. Notably, the temperature-independent contribution of $\chi_0 = -3.29 \times 10^{-3}$ cm$^3$/mol, determined by analyzing the high-temperature magnetic behaviour, is in reasonable agreement with the sum of the sample holder contribution of $\chi_{sholder} \approx -1.9 \times 10^{-3}$ cm$^3$/mol and the core contribution of $\chi_{core} = -1.37 \times 10^{-3}$ cm$^3$/mol calculated by using tabulated values for Pascal's constants.[14]

Figure 3 shows the molar magnetic susceptibility $\chi(T) = M(T)/B$ of complex $[Cu_6\{(MeSiO_2)_6\}_2]$·6DMF, where $M$ denotes the magnetic moment of the sample per mole. The data were found to be reversible upon cooling and heating, with no indications for hysteretic behaviour. Moreover, no sign of long-range magnetic ordering was observed in the temperature range under investigation. From isothermal magnetization measurements in dc fields from 0 to 5 T at varying temperatures (see Figure 6), we have also extracted the data for the differential magnetic susceptibility $[dM(T)/dB]_{B\to 0}$, which are indicated as the solid star symbols in Figure 3. The collapse of the susceptibility data onto a single curve shows that no significant field dependence occurs over the whole temperature (2–350 K) and field (0.01–0.2 T) range under investigation.

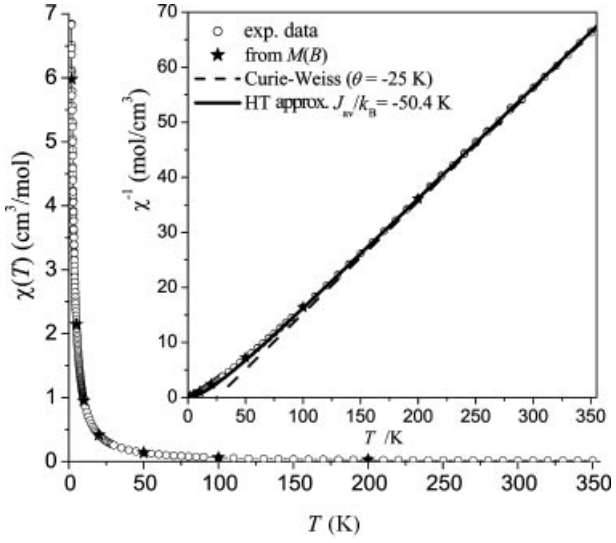


Figure 3. Temperature dependence of the magnetic susceptibility of complex $[Cu_6\{(MeSiO_2)_6\}_2]$·6DMF for temperatures 2–350 K. The data have been taken at magnetic fields of 0.01–0.2 T. Star symbols denote the susceptibility data extracted from isothermal magnetization measurements. The inset shows the inverse magnetic susceptibility. The solid line corresponds to the best fit using the high-temperature approximation Equation (2) with the parameter $J_{av}/k_B = (-50.4 \pm 1)$ K in the range 100–350 K. The dashed line corresponds to the calculated curve by using a simple Curie–Weiss law $\chi(T) = C/(T + \theta)$ for the six-site ring ($S = 1/2$; $g = 2.10$) with $\theta = -25$ K.

The analysis of the magnetic properties of the complex $[Cu_6\{(MeSiO_2)_6\}_2]$·6DMF was performed in the following three steps. First, in the high-temperature range, we used a Curie–Weiss law to obtain preliminary information on the sign and average magnitude of the exchange interactions between the six $Cu^{2+}$ ($S = 1/2$) ions inside the molecule. Next, in analogy to what has been done for other ring-shaped complexes,[8,9] we attempted to analyze the obtained experimental data within the framework of a model with uniform exchange couplings between nearest-neighbour spins within the ring. We found that this uniform exchange coupling model, even with the possible extensions such as significant intermolecular interactions, weakly anisotropic intramolecular exchange interactions or next-nearest neighbour exchange couplings, is not capable of satisfactorily reproducing the low-temperature part of the magnetic behaviour of this compound. In a third step, taking into account the structural symmetry properties of the molecule, we thus considered the most general Heisenberg model for the six-site ring with three a priori nonequivalent exchange couplings. This nonuniform nearest-neighbour exchange model, which has a parameter set corresponding to a pair of weakly coupled trimers with a strong ferromagnetic intratrimer coupling and a weak ferromagnetic intertrimer coupling, yields a satisfactory agreement with the observed experimental data.

### Magnetic Susceptibility at High Temperatures

In a first attempt at setting up a simple model capable of describing the main features of the magnetic susceptibility of the complex $[Cu_6\{(MeSiO_2)_6\}_2]$·6DMF at high temperatures, the magnetic behaviour can be assigned to a Curie–Weiss-like temperature dependence $\chi(T) = C/(T + \theta)$ with a Curie constant $C$ and a Weiss temperature $\theta$. In the temperature range 100–350 K, the best fit yields $C = 5.041$ cm$^3$ K/mol and $\theta = -17.7$ K. The obtained Curie constant is consistent with the presence of six $Cu^{2+}$ ions per molecule (two molecules per unit cell) yielding a spin-only value of $C_{theory} = 4.914$ cm$^3$ K/mol. The latter number is based on an average spectroscopic $g$-value of $2.10 \pm 0.02$, as determined by our high-temperature ESR measurements operated at X- and Q-band frequencies. It should be noted that all known ring-shaped copper complexes[4,6,8] have a similar square-pyramidal oxygen configuration of the nearest environment of the copper ions, therefore a quite close value of the average spectroscopic $g$-factor for the local magnetic centre is expected. For the recently reported phenyl analogues,[8,9] it was found that the average $g$-values of the $Cu^{2+}$ ions are in the range 2.11–2.12. The negative Weiss constant $\theta$ indicates a dominant ferromagnetic spin–spin interaction. It should be noted that a simple Curie–Weiss law implies a temperature-independent effective moment of the magnetic centres, which results in a strictly linear behaviour of the inverse magnetic susceptibility. As can be seen in the inset of Figure 3, the inverse magnetic susceptibility of the complex exhibits a weak nonlinearity over the entire high-temperature region and an appropriate microscopic magnetic model would be desirable.

 © 2007 Wiley-VCH Verlag GmbH & Co. KGaA, Weinheim 

In search of a minimal microscopic model, we first assume isotropic Heisenberg exchange between nearest-neighbour spins in the ring, ignoring possible complications such as next-nearest neighbour couplings or anisotropic exchange interactions. Because of the inversion centre of the molecule (see Figure 1, b), bonds on opposite sites of the ring that are mapped onto each other by the symmetry transformation are equal and the most general Heisenberg model is given by Equation (1)

$$H = J_1(\mathbf{S}_1 \cdot \mathbf{S}_2 + \mathbf{S}_4 \cdot \mathbf{S}_5) + J_2(\mathbf{S}_2 \cdot \mathbf{S}_3 + \mathbf{S}_5 \cdot \mathbf{S}_6) + J_3(\mathbf{S}_3 \cdot \mathbf{S}_4 + \mathbf{S}_6 \cdot \mathbf{S}_1) - g\mu_B B \sum_{i=1}^{6} S_i^z \quad (1)$$

with three a priori nonequivalent exchange couplings, $J_1$, $J_2$ and $J_3$, which, from the molecular structure, might be expected to be close in magnitude. However, this expectation turns out not to be justified, as we will discuss in the next section. In Equation (1), $\mathbf{S}_i$ are spin-1/2 operators located at the Cu sites of the ring, $\mu_B$ is the Bohr magneton and $g$ is an average spectroscopic $g$-value of $Cu^{2+}$ ions.

A first estimate of the strength of the exchange couplings can be obtained from a high-temperature expansion of the magnetic susceptibility. The first terms are given by Equation (2)

$$\chi|_{h=0} = \frac{N\mu_B^2 g^2}{k_B} \frac{3}{2T}\left\{1 - \frac{J_{av}}{2k_B T} + O\left(\frac{Ji^2}{T^2}\right)\right\} \quad (2)$$

where $J_{av} = (J_1 + J_2 + J_3)/3$ is the average exchange interaction within the ring.[10,15] In Equations (2)–(4), $N$ is the number of spins and $k_B$ is the Boltzmann constant. For uniform exchange couplings $J_1 = J_2 = J_3$, we have compared this high-temperature approximation with results of a complete numerical diagonalization for spin $S = 1/2$ rings with $N = 6$ and concluded that this is in satisfactory agreement with the exact solution for temperatures above $3/2 \cdot J_{av}$.

In the inset of Figure 3 the solid line shows the best fit of the high-temperature expansion Equation (2) to the experimental data with the parameter $J_{av}/k_B = (-50.4 \pm 1)$ K. It should be noted that at high temperatures, the leading terms in the high-temperature expansion agree with the Curie–Weiss law, where, by expanding the latter in powers of $1/T$, one obtains $J_{av}/k_B = 2\theta$.

### Magnetic Behaviour at Low Temperatures

Before starting the discussion of the low-temperature part, a few interesting peculiarities of the low-temperature magnetic behaviour of the present complex observed in the experiment should be underlined. At $T = 2$ K, the product $\chi(T) \cdot T$ reaches a value of approximately 12 $cm^3/mol\,K$, which is close to what would be expected for two effective spins $S = 3$ per unit cell, but with an effective spectroscopic $g$-value $g = 2.00$, yielding $\chi \cdot T = 12.004\ cm^3/mol\,K$. Of course, this can be due to the fact that at the given temperature ($T = 2\ K \approx \frac{1}{25}|J_{av}/k_B|$) the system has not yet frozen into the state with full ferromagnetic alignment and a tendency toward the higher value of $2 \times (S = 3;\ g = 2.10) \rightarrow 13.234\ cm^3/mol\,K$ is observable (see the inset of Figure 4). Note that Figure 4 shows the normalized square of the effective moment $\chi \cdot T/(N\mu_B^2 g^2/k_B)$ of the complex $[Cu_6\{(MeSiO_2)_6\}_2] \cdot 6DMF$ (where we set $g = 2.10$) as a function of normalized temperature $T/J_{av}$. Additionally, the experimentally observed magnetization $M(B)$ of the complex at $T = 2$ K can be nicely reproduced by a Brillouin function for an effective spin $S = 3$, again with $g = 2.00$ (see the dashed line in Figure 6). The reason for this "high symmetry" isotropic behaviour of the effective $g$-tensor of the magnetic molecular cluster is not clear.

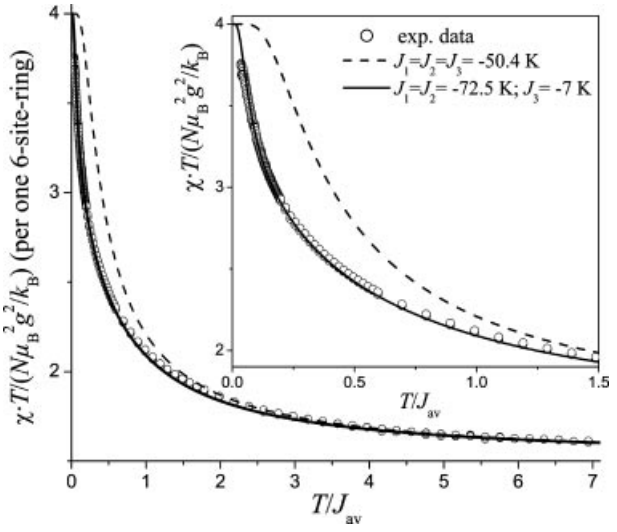


Figure 4. The product $\chi \cdot T/(N\mu_B^2 g^2/k_B)$ as a function of normalized temperature $T/J_{av}$. The inset shows the low-temperature behaviour on expanded scales. The dashed line indicates the theoretical result of a complete numerical diagonalization for uniform ferromagnetic exchange couplings within the ring. The solid line corresponds to the best fit for a nonuniform exchange coupling model.

In the case of uniform ferromagnetic couplings $J_1 = J_2 = J_3$ within the ring (as well as in the presence of weak anisotropy of these interactions), the parameter $J_{av}/k_B = -50.4$ K strictly determines the initial structure of the energy spectrum and, therefore, the quantitative characteristics of the crossover (the temperature evolution of the effective magnetic moment of the molecular cluster) from a low-temperature plateau of width $\sim\Delta/2 = \frac{1}{4}|J_{av}/k_B| = 12.6$ K to the $1/T$ behaviour at high temperatures discussed in the previous section. Here, $\Delta = |J| \cdot [1 - \cos(2\pi/N)] = |J|/2$ is the finite-size gap of spin-wave excitations above the high-spin ferromagnetic ground state corresponding to the splitting between the lowest two levels. The lowest levels of the resulting energy-level scheme for a model with uniform exchange couplings with $J_{av}/k_B = -50.4$ K are sketched in Figure 5 (left part). In Figure 4, the numerical result for the product $\chi \cdot T/(N\mu_B^2 g^2/k_B)$ for the uniform-exchange model with $J_{av}/k_B = -50.4$ K is shown as a black dashed line. A

 © 2007 Wiley-VCH Verlag GmbH & Co. KGaA, Weinheim 

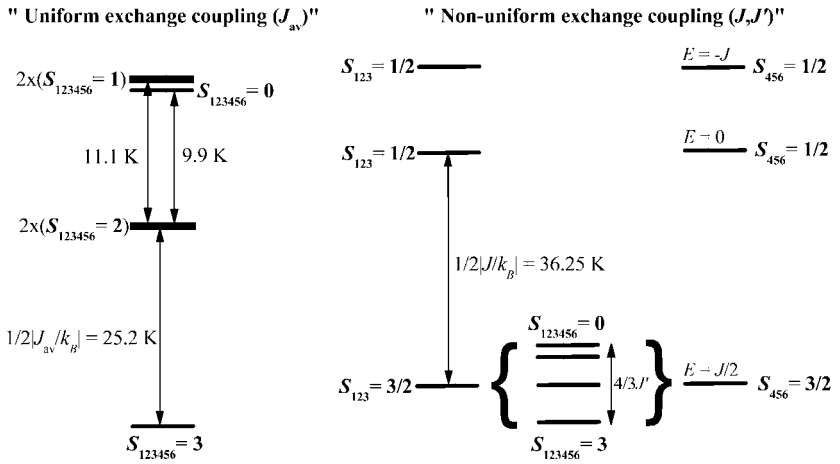


Figure 5. Energy-level schemes for a uniform ferromagnetically coupled ring (left part) with $J_{av}$ and for two weakly coupled trimers (right part) with a strong ferromagnetic intratrimer coupling $J$ and a weak ferromagnetic intertrimer coupling $J'$. Only the splitting of the high-spin ground state of the complex due to the coupling $J'$ is considered, as the splitting of excited states is not relevant for the thermodynamic quantities in the temperature and field range considered here.

closer look at the experimental data in Figure 4 reveals that $\chi \cdot T/(N\mu_B{}^2g^2/k_B)$ does not show a low-temperature plateau in the accessible temperature range. This indicates that the ground state of the magnetic cluster might be composite, and the presence of other energy levels at a distance of a few Kelvin from the ground $S_{123456} = 3$ multiplet is possible. Furthermore, Figure 4 reveals that significant deviations of the experimental data from the results for the uniform-exchange model with $J_{av}/k_B = -50.4$ K become visible at temperatures below approximately 100 K. A comparison to the total width of the spectrum of $|E_{FM} - E_{AFM}| = 8.6 \times 50.4/2 \approx 217$ K for this case already hints at the fact that to account for these deviations a significant adaptation of the model is required.

In order to fix further the parameters of the microscopic model, we analyzed the low-temperature behaviour of the magnetic susceptibility more carefully. To this end, the Hamiltonian in Equation (1) can easily be diagonalized numerically, as the dimension of the largest subspace to be considered is only 20 using the conservation of the $z$ component of the total spin. For uniform exchange couplings $J_1 = J_2 = J_3$, even analytic results can be obtained exploiting translational invariance.[16] For convenience, we will only use numerical results here, as well as a perturbative treatment for $J_1 = J_2 \equiv J$ and $J_3 \equiv J'$, $|J'| << |J|$. In Figure 4 the presentation of the product $\chi \cdot T/(N\mu_B{}^2g^2/k_B)$ as a function of normalized temperature $T/J_{av}$ has been chosen in order to simplify the comparison of the data with various theoretical predictions. Note also that the set of exchange coupling parameters $\{J_1, J_2, J_3\}$, extracted for a particular model, always have to be in agreement with the average value $J_{av}/k_B = -50.4$ K obtained from the high-temperature fit in the previous section.

The absence of a sizeable finite-size gap above the high-spin ferromagnetic ground state might be attributed to intermolecular interactions, either of dipolar or exchange type. However, rather large intermolecular distances and the absence of an apparent exchange path between neighbouring molecules lead us to search for intramolecular mechanisms to explain the low-temperature behaviour. As candidates, we have envisioned anisotropic intramolecular exchange and next-nearest neighbour exchange, as well as a nonuniform exchange.

Our low-temperature ESR measurements show a zero-field splitting in the order of 1 K, so that it seems natural to analyze the influence of anisotropies on the low-temperature behaviour of the susceptibility. Microscopically, such anisotropies can arise from anisotropic exchange interactions as well as intramolecular dipolar interactions. In the high-spin low-energy subspace they lead to an effective single-ion anisotropy term of the form $H = D(S^z_{tot})^2$, where $\mathbf{S}_{tot} = \mathbf{S}_1 + \ldots + \mathbf{S}_6$ and $D$ can in principle be obtained as an average over the microscopic anisotropic exchange parameters. Yet, a quantitative analysis of such anisotropy terms reveals that the angular average of the susceptibility is only changed below a temperature scale in the order of $D$. Furthermore, $\chi \cdot T$ is reduced for $T \rightarrow 0$ and shows a maximum at a temperature $\sim D$. This behaviour is clearly not observed in the experiment and we conclude that the anisotropies seen in ESR measurements are too small to be relevant to thermodynamic quantities in the temperature range under consideration.

From a numerical treatment of next-nearest-neighbour exchange we find a slightly better fit to the experimental data than with just the nearest-neighbour exchange. Yet, the agreement is not satisfactory, as the functional form with a very steep decrease of $\chi \cdot T$ at low temperatures does not correspond to the experimentally observed curve.

To analyze nonuniform exchange, we consider $J_1 = J_2 = J$ and $J_3 = J'$, which might correspond, for example, to the following exchange links between the Cu1–Cu2, Cu2–Cu3 and Cu3–Cu1′ atoms, respectively. It turns out that for $|J'| << |J|$ a good fit of the experimental data can indeed be achieved. The model then reduces to two weakly coupled

 © 2007 Wiley-VCH Verlag GmbH & Co. KGaA, Weinheim 

trimers with a strong ferromagnetic intratrimer coupling $J$ and a weak ferromagnetic intertrimer coupling $J'$. The solid line in Figure 4 shows the best fit of the effective magnetic moment with nonuniform exchange couplings, yielding $J/k_B$ = –72.5 K and $J'/k_B$ = –7 K. For these parameters, a perturbative treatment of the intertrimer coupling is possible. The resulting level scheme is sketched in Figure 5 (right part). The energy spectrum of an isolated ferromagnetic trimer consists of a quartet ground state separated from two excited doublets by an energy gap $|J/2|$ and $|3J/2|$, respectively. The ground-state splitting $4/3|J'|$ of two ferromagnetic trimers within the molecule is due to ferromagnetic intertrimer coupling. For the magnetization and the magnetic susceptibility, only the splitting of the high-spin ground state due to the intertrimer coupling $J'$ is relevant and we can obtain analytic formulas, for example, the magnetic susceptibility is given by Equation (3)

$$\chi(T) = \frac{N\mu_B^2 g^2}{k_B}\,\frac{1}{2T}\,\frac{x^{-6}\left(1+x^2+2x^3\right)\left(1+x^2+10x^3\right)+\left(14y^9+5y^{-3}+y^{-11}-20\right)}{x^{-6}\left(1+x^2+2x^3\right)^2+\frac{1}{4}\left(7y^9+5y^{-3}+3y^{-11}+y^{-15}-16\right)} \tag{3}$$

where $x = \exp[-(J/2k_BT)]$ and $y = \exp[-(J'/18k_BT)]$. Equation (3) can be checked by comparison with numerical diagonalization for the full model. At least up to $|J'/J| \leq 0.1$, we obtain excellent agreement with the exact result. Note that for $J' \to 0$ Equation (3) results as expected in twice the susceptibility of an isolated ferromagnetic trimer. In contrast to the antiferromagnetically coupled trimer model described earlier,[3] the influence of $J'$ on the magnetic susceptibility is rather strong and the deviations from the pure ferromagnetic trimer model become visible even at relatively high temperatures. This can be understood by noting that the saturation value of the product $\chi T|_{J' \to 0,\ T \to 0} = 5/2$ for two isolated trimers within a molecule is significantly reduced compared to $\chi T|_{J' \neq 0,\ T \to 0} = 4$ for the high-spin $S = 3$ ground state.

### Magnetization Curves

The magnetization of the complex $[Cu_6\{(MeSiO_2)_6\}_2]\cdot 6DMF$ at various temperatures is shown in Figure 6 as a function of the applied magnetic field. In order to check the main result obtained from the analysis of the magnetic susceptibility, we have also calculated the isothermal magnetization curves for the above-discussed models of a uniform ferromagnetically coupled ring with $J_{av}/k_B$ = –50.4 K and nonuniform exchange couplings with $J/k_B$ = –72.5 K and $J'/k_B$ = –7 K. The uniform-exchange model progressively departs from the experimental data below 100 K (calculated curves are not shown). On the other hand, a very good description, except for the data taken at the lowest temperature of 2 K, can be achieved by the model with nonuniform exchange couplings.

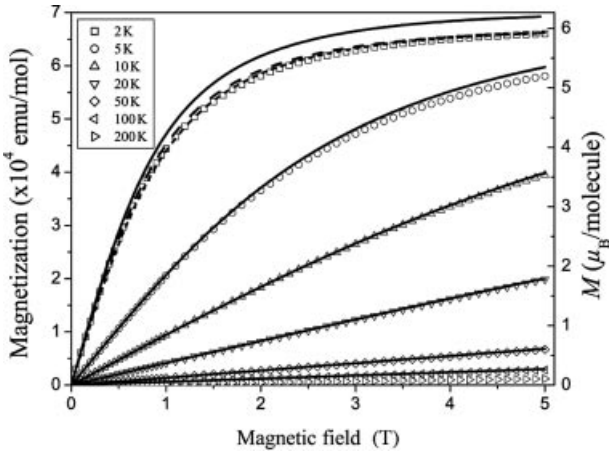


Figure 6. Isothermal magnetization measurements in dc fields from 0 to 5 T at varying temperatures as indicated in the figure. The right scale of the main panel is given in units of $\mu_B$ per molecule. The solid lines indicate the theoretical results for a nonuniform exchange coupling model with $J/k_B$ = –72.5 K and $J'/k_B$ = –7 K ($g$ = 2.10). The dashed and short dashed lines correspond to the calculated magnetization curve (Brillouin function) at $T$ = 2 K for isolated magnetic quasiparticles with $S$ = 3 and $g$ = 2.00 and for the above-mentioned nonuniform coupling model with $g$ = 2.00, respectively.

For the model with nonuniform exchange couplings, we can obtain a perturbative analytic expression for the magnetization in Equation (4)

$$M(T,h) = N\mu_B g \cdot \frac{2x^{-6}\left(Z'_{½}+Z'_{½}x^2+Z'_{½}x^3\right)\left(Z_{½}+Z_{½}x^2+Z_{½}x^3\right)+\left(Z'_3y^9+Z'_2y^{-3}+Z'_1y^{-11}-2Z'_{½}Z_{½}\right)}{x^{-6}\left(Z_{½}+Z_{½}x^2+Z_{½}x^3\right)^2+\left(Z_3y^9+Z_2y^{-3}+Z_1y^{-11}+y^{-15}-Z_{½}^2\right)} \tag{4}$$

where $h = \frac{g\mu_B}{k_B}B$, $Z_s(t) = \frac{\sinh(t[s+1/2])}{\sinh(t/2)}$ is the partition function of a single half-integer spin $s$ as a function of the dimensionless magnetic field $t = \frac{h}{T}$, and its derivative is given by

$$Z'_s(t) = (s+1/2)\frac{\cosh(t[s+1/2])}{\sinh(t/2)} - \frac{\sinh(t[s+1/2])\cosh(t/2)}{2\sinh^2(t/2)}.$$

$x$ and $y$ are defined below Equation (3). The approximate result in Equation (4) can again be checked against the complete numerical solution yielding very good agreement for at least $|J'/J| \leq 0.1$ for all relevant temperatures.

The calculated magnetization curves for a model with nonuniform exchange couplings with $J/k_B$ = –72.5 K and $J'/k_B$ = –7 K ($g$ = 2.10) are shown in Figure 6 as solid lines. As shown in Figure 6, we have obtained a very satisfactory agreement with the experimental data for the complex $[Cu_6\{(MeSiO_2)_6\}_2]\cdot 6DMF$ over the whole temperature range under investigation, except for data taken at $T$ = 2 K. The deviations between theory and experiment become visible below 5 K. However, we should note once more that the magnetization curve at $T$ = 2 K can be nicely simulated

 © 2007 Wiley-VCH Verlag GmbH & Co. KGaA, Weinheim 

by using a Brillouin function for isolated particles with $S$ = 3 and $g$ = 2.00 (dashed line) or by using our nonuniform exchange model with an effective $g$-value of 2.00 (short dashed line). We would like to point out however that the same conceptual problem arises in ref.[8]: The low-temperature magnetization of the complex $\{[Cu_6\{(PhSiO_2)_6\}_2]\cdot 5BuOH\}\cdot 3^nBuOH$ also shows a saturation value expected for $S$ = 3 with $g$ = 2.00.

## ESR Measurements

In two papers reported only recently,[8,9] high-frequency ESR (HF-ESR) techniques were used to investigate polycrystalline powder samples of $[Cu_6\{(PhSiO_2)_6\}_2]\cdot 6EtOH$ and $\{[Cu_6\{(PhSiO_2)_6\}_2]\cdot 5BuOH\}\cdot 3^nBuOH$ to study the nature of the ground spin state of ferromagnetic rings and to obtain the effective magnetic anisotropy parameters of paramagnetic clusters. It was demonstrated that two sets of the equally spaced resonances at high exciting frequency might be attributed to the parallel and perpendicular transitions of an anisotropic paramagnet with an effective $S$ = 3 spin and unresolved rhombicity ($E$ = 0). The sign of the zero-field splitting parameter $D > 0$ corresponds to a hard-axis type anisotropy. The molecular $g$-tensor shows an axial symmetry with an unusual feature of "reversed" $g$-values ($g_\parallel < g_\perp$), which is not in accordance with the expected correlation ($g_\parallel > g_\perp$) for the local $g$-tensor with a square-pyramidal environment of the copper centres. Notably, there are still two small questions in the interpretation of magnetic data based on a uniform/nonuniform microscopical model, which the HF-ESR measurements on polycrystalline powder samples did not answer. (i) The reported magnetic anisotropy parameters $D$ (0.3 and 0.308 $cm^{-1}$) are quite similar, showing that the initial splitting of the $S$ = 3 manifold remains almost insensitive to the anisotropy of exchange interactions within the ring (uniform and nonuniform exchange cases). (ii) The absence of additional transitions to the variable-temperature HF-ESR polycrystalline spectra in the temperature range up to 100 K may indicate that the ground $S$ = 3 state of a molecular cluster is well thermally isolated from the other excited multiplets.

Performing the resonance measurements on single crystals of $[Cu_6\{(MeSiO_2)_6\}_2]\cdot 6DMF$, a more complicated situation than that described in the literature was found. Single-crystal ESR spectra were recorded using the cavity technique in the frequency range 26–56 GHz with an opportunity of a sample rotation in three mutually perpendicular planes. The ESR spectra at 38.816 GHz ($T$ = 1.5 K) for two different directions of the magnetic field are shown in parts a and b of Figure 7. Each spectrum consists of up to 20 well-resolved absorption lines (ESR active) with an average line width in the order of 28 mT. The angular dependence of the resonance line positions shows the strong magnetic anisotropy. The appearance of the spectrum with multicomponent structure may be interpreted as follows: (1) The energy spectrum of individual clusters is strongly anisotropic; consequently the presence of two nonequivalent molecules in the unit cell with an angle of 51.5° between the local axial axis might double the ESR spectrum (in the literature[8,9] this effect is not observed or discussed for polycrystalline powder samples). (2) According to a nonuniform model, the excited states ($S$ = 2, 1, 0) of the molecular cluster of $[Cu_6\{(MeSiO_2)_6\}_2]\cdot 6DMF$ are close to each other and to the ground multiplet $S$ = 3 (in the distance of a few Kelvins); all of the states are split, consequently the extra transitions between different sublevels inside and/or between different multiplets are possible.

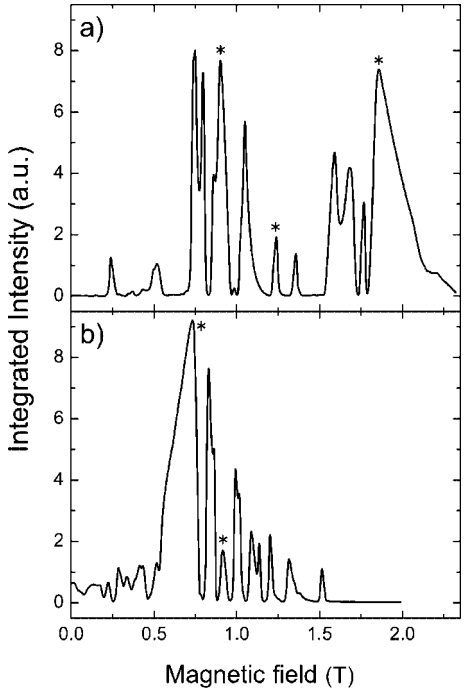


Figure 7. ESR spectra recorded on a single-crystal sample of $[Cu_6\{(MeSiO_2)_6\}_2]\cdot 6DMF$ at 38.816 GHz ($T$ = 1.5 K). (a) Parallel and (b) perpendicular to the axial axis of a molecule.

In the case of a few close multiplets, the ESR spectra for a $S$ = 3, 2 or 1 system can be interpreted separately for each manifold by the effective spin Hamiltonian

$$H = D[S_x^2 - 1/3S(S+1)] + E(S_x^2 - S_y^2) + \mu_B \mathbf{S}\cdot\mathbf{g}\mathbf{B},$$

in which each set of anisotropic parameters $D$, $E$, $\mathbf{g}$ will correspond to the given effective spin $S$ = 3, 2 or 1. It should be stressed that $D$, $E$, $g_\parallel$, $g_\perp$ are effective parameters for an effective spin $S$, and they cannot be used directly in the microscopic model (1). A single ion anisotropy is not possible for a spin $S$ = 1/2 ($Cu^{2+}$ ions) and only an effective anisotropy term $D$ of the complete molecule can arise from an anisotropy of the exchange interactions within the ring. The molecular $g$-tensor for a given geometry is related in a complicated way to the local $g$-tensors of individual Cu sites.

Analysis of the resonance data reveals that some lines of the spectrum (marked by * symbols in Figure 7) might be attributed to transitions for the split $S$ = 3 multiplet with unresolved rhombicity, as reported for polycrystalline pow-

 © 2007 Wiley-VCH Verlag GmbH & Co. KGaA, Weinheim 

der measurements.[8,9] The magnetic anisotropic parameters obtained for the split $S = 3$ multiplet are: $g_{\parallel} = 2.05$, $g_{\perp} = 2.22$, $D = 14.5$ GHz (0.48 $cm^{-1}$) and $E = 0$. The value of the zero-field splitting parameter $D$ is in good agreement with the estimation obtained from the single-crystal X-band spectra of $[Cu_6\{(MeSiO_2)_6\}_2]$·6DMF. Single-crystal ESR measurements have confirmed an unchangeable character of the molecular $g$-tensor with good accuracy for polymetallaorganosiloxane complexes. It should be noted that the larger magnitude of the effective anisotropy parameter $D$ of the $S = 3$ manifold for the given complex indicates the larger anisotropy of exchange interactions within the ring compared to the previously reported analogues.[8,9]

A weak ferromagnetic intertrimer coupling $|J'/k_B| = 7$ K produces the total energy splitting of $4/3|J'/k_B| = 9.33$ K between idealized (non-split) $S = 3$ and $S = 0$ states (see energy-level scheme for the coupling of two "effective $S = 3/2$ spins" in Figure 5). Note, the energy interval to the nearest excited state $S = 2$ takes half of this value and is 4.67 K. For the obtained effective parameter $D = 14.5$ GHz the expected total splitting of the $S = 3$ state is 6.26 K. Thus, if we assume that all close states $S = 3, 2, 1$ are split by anisotropy of exchange interactions within the ring then the energy overlap or superposition of the different sublevels associated with the different manifolds is expected. According to this complication, a classification of all detected resonances in the frame of all possible transitions for excited and ground states was avoided. We consider that the other ESR-active lines, which are not marked in Figure 7, might be associated to the sublevel transitions for the split $S = 2$ and $S = 1$ states and their satellites arising from a second independent molecule. The slightly different values of the effective anisotropy parameter $D$ for the $S = 2$ and $S = 1$ states compared with the corresponding value for the $S = 3$ state are expected.

## Conclusions

This paper reports on the synthesis, X-ray crystal structure and magnetic properties of a new oxygen-bridged hexanuclear copper(II) hexamethylcyclohexasiloxane complex, $[Cu_6\{(MeSiO_2)_6\}_2]$·6DMF. In contrast to the known phenyl analogues, the present complex has methyl groups as substituents at the silicon atoms. This compound has a sandwich-like molecular structure. The molecule contains a planar ring of six oxygen-bridged $Cu^{II}$ atoms arranged in an almost regular hexagon and sandwiched by two hexamethylcyclohexasiloxanolate ligands.

Investigations of the magnetic properties in the high-temperature region have shown that the molecular complex has a strong average ferromagnetic Cu–Cu exchange interaction of $|J_{av}/k_B| = (50.4 \pm 1)$ K, which produces a high-spin $S = 3$ molecular ground state. Yet, at temperatures below about 100 K, significant deviations between the experimental susceptibility data and the theory for a model with uniform nearest-neighbour exchange couplings become visible. Because of rather large intermolecular distances and the absence of an apparent exchange path, intermolecular interactions of either dipolar or exchange type do not seem likely. Attempts to modify the uniform-exchange model by including weakly anisotropic intramolecular exchange terms (because of slight distortions of copper–oxygen exchange bridges) or next-nearest neighbour exchange do not lead to a satisfactory agreement with the experimentally observed curve either. However, good fits for the magnetic susceptibility and the magnetization in the whole accessible temperature and field range can be obtained from an isotropic Heisenberg model that has nonuniform nearest-neighbour exchange couplings corresponding to weakly coupled trimers with a strong ferromagnetic intratrimer exchange coupling of $|J/k_B| = 72.5$ K and a weak ferromagnetic intertrimer exchange coupling of $|J'/k_B| = 7$ K.

Such dramatic variations in the magnitude of the exchange couplings within the ring might seem surprising in light of the almost regular hexagonal arrangement of the $Cu^{2+}$ ions. However, it is well known that small variations in the bonding angles of oxygen exchange bridges can significantly influence the exchange couplings. For the family of the ring-shaped polynuclear $Cu^{II}$ cyclomethylsiloxanolate complexes, the critical bonding angle of the oxygen bridge Cu–O–Cu for a transition between ferromagnetic and antiferromagnetic exchange is approximately 96°.[10] Yet, it seems plausible that the highest bonding angles of about 94° (see Table 1) might be close enough to the critical angle that the corresponding exchange coupling is significantly reduced compared to the other two. Our results thus seem to suggest that the magnetic properties of quantum rings are very susceptible to small structural infringements of symmetry, which at once effectively split the ring as a whole into a system with simpler blocks: poorly cooperating trimers or dimers.

## Experimental Section

**General Remarks:** All chemicals used were of high quality and purchased from Aldrich. The solvents were dried and distilled prior before use. Calculations on KOH were made based on the content of KOH (85%, Aldrich).

**Synthesis of $[Cu_6\{(MeSiO_2)_6\}_2]$·6DMF:** $MeSi(OEt)_3$ (10 mL, 0.05 mol), KOH (3.3 g, 0.05 mol), water (0.9 mL, 0.05 mol) and MeOH (80 mL) were added to toluene (80 mL) under vigorous stirring. The reaction mixture was stirred for 45 min at room temperature and then heated up to the boiling point. A solution of $CuCl_2$ (3.4 g, 0.025 mol) in MeOH (80 mL) was added dropwise. The reaction mass was refluxed for 10 min and filtered. The solution was evaporated and dried in vacuo (1 Torr, at 80 °C). A greenish-blue crystalline product **D** (see Scheme 1) was obtained. Yield: 4.43 g (82.5%). This product was dissolved in DMF (50 mL) under heating and left to crystallize. The recrystallization process took a few months and transparent greenish-blue crystals, suitable for the X-ray structure analysis, were obtained. $C_{30}H_{78}Cu_6N_6O_{30}Si_{12}$ (1721.30): C 20.93, H 4.57, N 4.88; found C 20.19, H 4.53, N 4.58.

**Trimethylsilylation of Product D:** A mixture of product **D** (1.5 g, 1.2 mmol) and pyridine (3.5 mL, 43.2 mmol) was slowly stirred for 15 min. $Me_3SiCl$ (7.28 mL, 7.6 mmol) was added while slowly stirring. The reaction mixture was stirred for another 10 min at room

 © 2007 Wiley-VCH Verlag GmbH & Co. KGaA, Weinheim 

temperature and then hexane (30 mL) was added. The solution was heated and refluxed for 55 min. The mixture was cooled to room temperature, washed with water to remove $Cl^-$, dried with $Na_2SO_4$ and the solvent was evaporated. A viscous colourless product was obtained after drying in vacuo (1 Torr, at 50 °C, 1 h). Yield: 0.56 g (53.57%). $^1$H NMR: $\delta$ = 0.11 (s, 9 H, –OSiMe$_3$), 0.03 (s, 3 H, MeSiO$_3$–) ppm. $^{29}$Si NMR: $\delta$ = 8.50 (s, –OSiMe$_3$), –68.18 (s, MeSiO$_3$–) ppm.

**Single-Crystal X-ray Crystallography:** A single crystal (greenish-blue block with dimensions $0.52 \times 0.49 \times 0.37$ mm) was measured on a Stoe-IPDS-II diffractometer in $\omega$-scan mode. An empirical absorption correction was performed using the MULABS option[17] in PLATON.[18] Structure solution was performed by direct methods using SHELXS-97[19] and structure refinement by full-matrix least-squares on $F^2$ with SHELXL-97.[20] Hydrogen atoms were placed at ideal positions and refined with fixed isotropic displacement parameters using a riding model.

Detailed crystal data and experimental parameters are given in Table 2.

Table 2. Crystal data and structure refinement for [Cu$_6${(MeSiO$_2$)$_6$}$_2$]·6DMF.

| | |
|---|---|
| Empirical formula | $C_{30}H_{78}Cu_6N_6O_{30}Si_{12}$ |
| Crystal dimensions [mm] | $0.52 \times 0.49 \times 0.37$ |
| $F_w$ [g/mol] | 1721.30 |
| $T$ [K] | 173(2) |
| $\lambda$ [Å] | 0.71073 |
| Crystal system, space group | monoclinic, $P2_1/n$ |
| $a$ [Å] | 13.3728(5) |
| $b$ [Å] | 15.4281(7) |
| $c$ [Å] | 17.4335(7) |
| $\beta$ [°] | 98.932(3) |
| $V$ [Å$^3$] | 3553.2(3) |
| $Z$ | 2 |
| Absorption coefficient [mm$^{-1}$] | 2.048 |
| $F$(000) | 1764 |
| $\rho_{calcd}$ [g/cm$^3$] | 1.609 |
| $\theta$ range for data collection [°] | 2.64–30.55 |
| Reflections collected/unique | 64952/10746 [$R_{int}$ = 0.0494] |
| Completeness to $\theta$ = 30.55 [%] | 98.7 |
| Absorption correction | semiempirical |
| Max. and min. transmission | 0.5187 and 0.4164 |
| Data/restraints/parameters | 10746/0/385 |
| Goodness-of-fit | 0.938 |
| $R_1$, $wR_2$ [$I > 2\sigma(I)$] | 0.0257, 0.0659 |
| $R_1$, $wR_2$ [all data] | 0.0334, 0.0678 |
| Max./min. peak [e/Å$^3$] | 0.381, –0.960 |

CCDC-630857 contains the supplementary crystallographic data for this paper. These data can be obtained free of charge from The Cambridge Crystallographic Data Centre via www.ccdc.cam.ac.uk/data_request/cif.

**Magnetic Susceptibility and Magnetization Measurements:** Variable-temperature magnetic susceptibility measurements in the temperature range 2–350 K and magnetic fields 0.01–0.2 T were carried out on a polycrystalline sample ($m$ = 97.85 mg) using a Quantum Design SQUID magnetometer MPMS-XL. These measurements were complemented by isothermal magnetization runs at temperatures between 2 and 200 K for fields up to 5 T.

**NMR Measurements:** $^1$H and $^{29}$Si NMR spectra were recorded with a Bruker Avance 400 spectrometer ($^1$H, 400.13 MHz; $^{29}$Si, 79.495 MHz) at 30 °C in $CDCl_3$. Chemical shifts ($\delta$, ppm) were measured relative to TMS ($\delta$ = 0.00 ppm).

**ESR Measurements:** Powder and single-crystal ESR spectra of the compound [Cu$_6${(MeSiO$_2$)$_6$}$_2$]·6DMF were recorded employing various spectrometers operating on different fixed frequencies in the range 9.5–134 GHz equipped with a variable-temperature Oxford cryostat with an accessible temperature range of 1.4–300 K.

**Supporting Information** (see also footnote on the first page of this article): View of the crystals (Figure S1), comparison of the magnetic susceptibility data with calculations for alternative models (Figures S2, S3 and S4) and the calculated magnetization curves for uniform and nonuniform models (Figure S5).

## Acknowledgments

The work was supported by the Deutsche Forschungsgemeinschaft (DFG) (Forschergruppenprogramm "Spin- und Ladungskorrelationen in niedrigdimensionalen metallorganischen Festkörpern", FOR412). We thank J. Bats (Institut für Anorganische Chemie, J. W. Goethe-Universität Frankfurt) for the collection of the X-ray data.

[1] D. Gatteschi, A. Caneschi, L. Pardi, R. Sessoli, *Science* **1994**, *265*, 1054–1058.
[2] S. P. Watton, P. Fuhrmann, L. E. Pence, A. Caneschi, A. Cornia, G. L. Abbati, S. J. Lippard, *Angew. Chem. Int. Ed. Engl.* **1997**, *36*, 2774–2776.
[3] V. Pashchenko, B. Brendal, B. Wolf, M. Lang, K. Lyssenko, O. Shchegolikhina, Yu. Molodtsova, L. Zherlitsyna, N. Auner, F. Schütz, M. Kollar, P. Kopietz, N. Harrison, *Eur. J. Inorg. Chem.* **2005**, *22*, 4617–4625.
[4] V. A. Igonin, O. I. Shchegolikhina, S. V. Lindeman, M. M. Levitsky, Yu. T. Struchkov, A. A. Zhadnov, *J. Organomet. Chem.* **1992**, *423*, 351–360.
[5] C. Zucchi, O. I. Shchegolikhina, M. Borsari, A. Cornia, G. Gavioli, A. C. Fabretti, E. Rentschler, D. Gatteschi, R. Ugo, R. Psaro, Yu. A. Pozdniakova, S. V. Lindeman, A. A. Zhdanov, G. Pályi, *J. Mol. Catal. A* **1996**, *107*, 313–321, and references therein.
[6] S. V. Lindeman, O. I. Shchegolikhina, Yu. A. Molodtsova, A. A. Zhdanov, *Acta Crystallogr., Sect. C: Cryst. Struct. Commun.* **1997**, *53*, 305–309.
[7] Yu. T. Struchkov, S. V. Lindeman, *J. Organomet. Chem.* **1995**, *488*, 9–14.
[8] G. L. Abbati, A.-L. Barra, A. Caneschi, A. Cornia, A. F. Costantino, D. Gatteschi, Yu. A. Pozdniakova, O. I. Shchegolikhina, *C. R. Chim.* **2003**, *6*, 645–656.
[9] E. Rentschler, D. Gatteschi, A. Cornia, A. C. Fabretti, A.-L. Barra, O. Shchegolikhina, A. A. Zhdanov, *Inorg. Chem.* **1996**, *35*, 4427–4431.
[10] V. Pashchenko, M. Lang, B. Wolf, L. Zherlitsyna, N. Auner, O. Shchegolikhina, Yu. Pozdnyakova, F. Schütz, P. Kopietz, M. Kollar, *C. R. Chim.* **2007**, *10*, 89–95.
[11] Yu. A. Pozdniakova, M. Antipin, O. I. Shchegolikhina, D. Katsoulis, N. Auner, B. Herrschaft, *Organometallics* **2000**, *19*, 1077–1082.
[12] O. I. Shchegolikhina, I. V. Blagodatskikh, A. A. Zhdanov in *Tailor-Made Silicon-Oxygen Compounds. From Molecules to Materials* (Eds.: R. Corriu, P. Jutzi), Vieweg, Wiesbaden, Germany, **1996**, p. 177.
[13] Yu. A. Molodtsova, Yu. A. Pozdniakova, K. A. Lyssenko, I. V. Blagodatskikh, D. E. Katsoulis, O. I. Shchegolikhina, *J. Organomet. Chem.* **1998**, *571*, 31–36.
[14] a) E. König, *Magnetic Properties of Coordination and Organo-Metallic Transition Metal Compounds*, in Landolt-Börnstein, Neue Serie, Springer, Berlin, **1966**, vol. II/2, pp. 1–16; b) R. Boča, *Theoretical Foundations of Molecular Magnetism*, vol. 1, *Current Methods in Inorganic Chemistry*, Elsevier, Amsterdam, **1999**, appendix 4.

 © 2007 Wiley-VCH Verlag GmbH & Co. KGaA, Weinheim 

[15] D. C. Johnston, R. K. Kremer, M. Troyer, X. Wang, A. Klümper, S. L. Bud'ko, A. F. Panchula, P. C. Canfield, *Phys. Rev. B: Condens. Matter* **2000**, *61*, 9558–9606 and references cited therein.
[16] D. Kouzoudis, *J. Magn. Magn. Mater.* **1998**, *189*, 366–376; D. Kouzoudis, *J. Magn. Magn. Mater.* **1997**, *173*, 259–265.
[17] R. H. Blessing, *Acta Crystallogr., Sect. A: Found. Crystallogr.* **1995**, *51*, 33–38.
[18] A. L. Spek, *J. Appl. Crystallogr.* **2003**, *36*, 7–13.
[19] G. M. Sheldrick, *Acta Crystallogr., Sect. A: Found. Crystallogr.* **1990**, *46*, 467–473.
[20] G. M. Sheldrick, *SHELXL-97, A Program for the Refinement of Crystal Structures*, University of Göttingen, Germany, **1997**.
Received: December 15, 2006
Published Online: August 28, 2007

 © 2007 Wiley-VCH Verlag GmbH & Co. KGaA, Weinheim 

DOI: 10.1002/ejic.200700464

# Dinuclear Titanium(IV) Complexes Bearing Phenoxide-Tethered N-Heterocyclic Carbene Ligands with *cisoid* Conformation through Control of Hydrolysis

**Dao Zhang*[a]**

**Keywords:** Titanium / Carbene ligands / Phenoxides

In situ generated N-heterocyclic carbene salt derivative $Na_2(L)$ of 1,3-bis(4,6-di-*tert*-butyl-2-hydroxybenzyl)imidazolium bromide, $[H_3(L)]Br$, reacted with 1 equiv. of $TiBr_4$ at –78 °C to give a titanium complex of the composition $[(L)TiBr_2(thf)]$ (**1**), while the reaction in a 2:1 ratio under the same conditions afforded bisligand titanium complex $[(L)_2Ti]$ (**2**). Two oxygen-bridged titanium dimers, $\{[(L)TiBr]_2(\mu\text{-}O)\}$ (**4**) and $\{[(L)Ti(\mu\text{-}O)]_2\}$ (**5**), were obtained by control of hydrolysis of **1** and $[(L)Ti(CH_2Ph)_2]$ (**3**) in tetrahydrofuran and diethyl ether. The molecular structures of **2**, **4**, and **5** have been confirmed by X-ray single-crystal analysis. The phenoxide-functionalized NHC ligand adopts *transoid* conformation in mononuclear complex **2** but rare *cisoid* conformation in dinuclear complexes **4** and **5**.
(© Wiley-VCH Verlag GmbH & Co. KGaA, 69451 Weinheim, Germany, 2007)

## Introduction

N-Heterocyclic carbene (NHC) ligands are heterocycles that bind as soft, two-electron donors through the NCN carbon atom, and are now used widely as strongly basic phosphane analogs, to support transition-metal complexes.[1] The overwhelming majority of NHCs are functionalized (with respect to the N and N′ substituents) by incorporating neutral donor or anionic groups such as pyridyl, phosphane, NHC, amide, alkoxide, and cyclopentadienyl.[1–14] In contrast, the diversity of NHC ligands found in high-oxidation-state transition-metal chemistry and homogeneous catalysis is conspicuously absent in early transition-metal NHC systems because of the ease of dissociation of the NHC ligand from the electron-deficient metal center, which makes it difficult to study the chemistry of NHCs in early transition metals and f-elements.[2–8]

In recent years, we have been investigating the use of aryl oxides linked to the NHC donor by a $C_1$ alkyl chain to generate asymmetric, heterobidentate and symmetric, heterotridentate ligands (Scheme 1) through which we can explore the NHC binding to *s*-block and early transition metal cations.[8] Earlier we reported the application of the bisphenoxy-substituted NHC ligand $(L)^{2-}$ – $[H_3(L)]Br$ = 1,3-bis(4,6-di-*tert*-butyl-2-hydroxybenzyl)imidazolium bromide) – and its corresponding aryloxy–NHC IVB metal complexes $[(L)MX_2]$ (M = Ti, Zr; X = Cl, $CH_2Ph$).[8a,8c] Among these complexes, the dichloride titanium complex has been proven to be a highly active procatalyst (up to $10^5$ g PE $mol^{-1}$ Ti $h^{-1}$) for polymerization of ethylene under methylaluminoxane (MAO) activation.[8c] The X-ray crystallography analysis of these Ti and Zr compounds revealed that only *transoid* conformation ligands were observed (Scheme 2). Herein, we wish to describe the synthesis and structural characterization of the first dinuclear titanium complexes supported by phenoxide-tethered N-heterocyclic carbene ligands, the tridentate chelate bianionic $(L)^{2-}$ with *cisoid* conformation (Scheme 3).

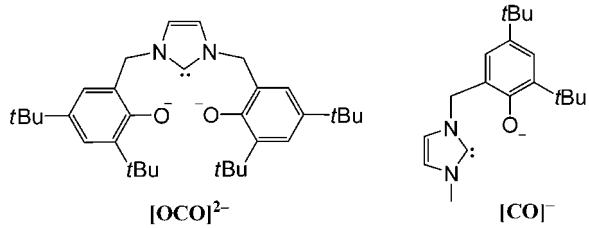


Scheme 1.

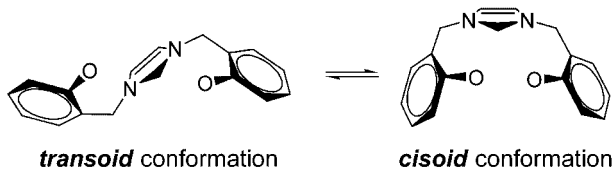


Scheme 2.

[a] Department of Chemistry, Fudan University, Shanghai 200433, P. R. China
Fax: +86-21-65641740
E-mail: daozhang@fudan.edu.cn

 © 2007 Wiley-VCH Verlag GmbH & Co. KGaA, Weinheim 

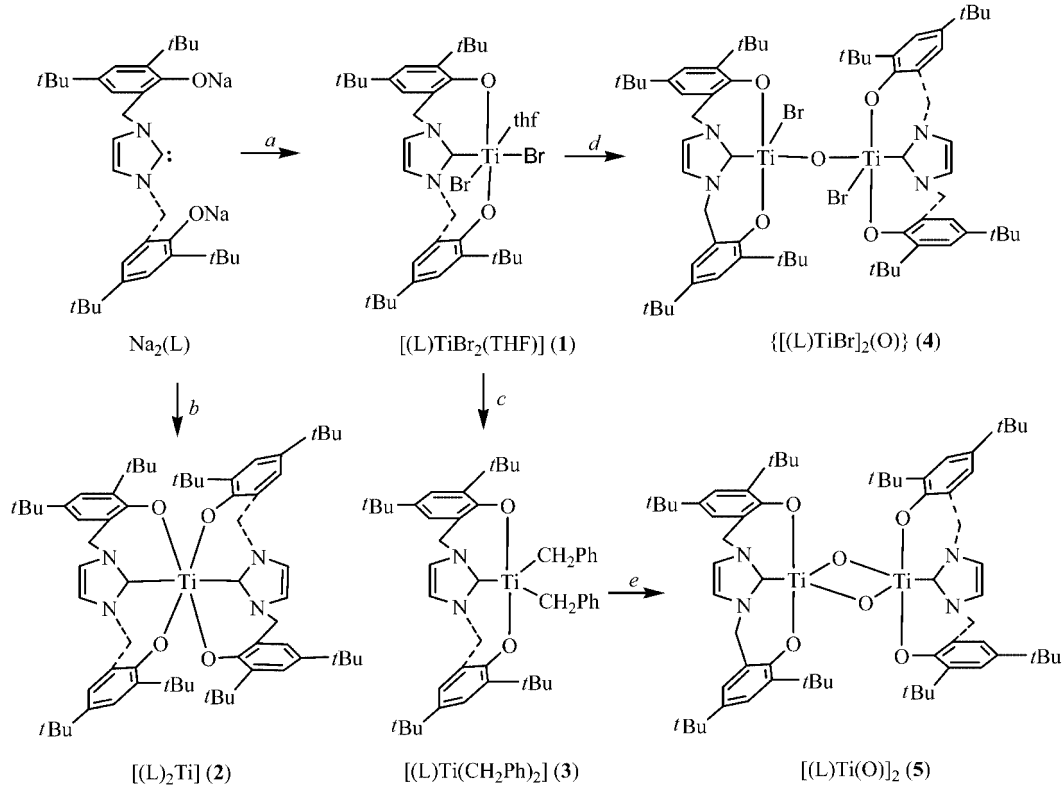


Scheme 3. Synthesis of titanium complexes **1**–**5**. Reaction conditions: *a*: $TiBr_4$/THF, –78 °C to room temp. *b*: 0.5 $TiBr_4$/THF, –78 °C to room temp. *c*: 2 $PhCH_2MgCl/Et_2O$, –78 °C to room temp. (d) $H_2O$/THF, room temp. (e) $H_2O/Et_2O$, room temp.

## Results and Discussion

The bromide titanium complex [(L)$TiBr_2$(THF)] (**1**) is easily prepared in 76% yield by the in situ reaction at low temperature of 3 equiv. of $NaN(SiMe_3)_2$ with [$H_3$(L)]Br, followed by addition to $TiBr_4$ in 1:1 ratio in THF. The temperature-dependent NMR spectroscopic features of **1** are similar to those of the reported [(L)$TiCl_2$(THF)].[8c] $TiBr_4$, a more expensive reagent than $TiCl_4$, was also chosen to study the influence of different halide ions on the solid-state structures of titanium complexes. Unfortunately the poor quality of the orange-red crystals of **1** prevented us from carrying out X-ray analysis to determine its molecular structure.

Attempts to prepare the titanium complex [$(L)_2$Ti] (**2**), a NHC phenoxide titanium derivative analogous to [$(L)_2$Zr],[8a] were successful by the reaction of $TiCl_4(THF)_2$ or $TiBr_4$ with 2.0 equiv. of in situ generated $Na_2$(L) in THF. The structure of **2** was determined crystallographically (Figure 1). The selected bond lengths and angles of **2** are listed in Table 1, which includes the data of zirconium complex [$(L)_2$Zr][8a] for comparison. The titanium center shows a slightly distorted octahedral geometry and features two meridionally coordinated tridentate $(L)^{2-}$ ligands, each with mutually *trans* NHC donors [C8–Ti–C25, 179.9(2)°; O1–Ti–O2, 177.3(1)°; O3–Ti–O4, 176.6(1)°]. The molecule has approximate $C_2$ symmetry and the ligands adopt a *transoid* conformation. The Ti–C(carbene) [2.2053(4) and 2.196(4) Å] and Ti–O(phenoxide) distances [average 1.909 Å] are comparable to the corresponding distances found in [(L)$TiCl_2$(THF)].[8c]

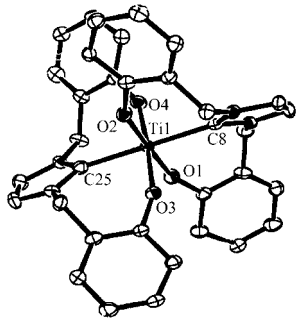


Figure 1. The molecular structure of **2**. All *t*Bu groups, solvent molecules, and hydrogen atoms are omitted for clarity.

The NMR spectroscopic data of **2** in [$D_1$]chloroform are consistent with the solid-state structure, and signals for only a single $D_2$ symmetric bis(phenoxide)–NHC ligand environment are seen, although the slight broadening of signals assigned to the N–$CH_2$ protons at $\delta$ = 3.88 and 6.42 ppm indicates some fluxional process at room temperature. The *tert*-butyl groups appear as two singlets at $\delta$ = 1.11 and 1.42 ppm, and the NHC ring protons are observed as a singlet at $\delta$ = 6.18 ppm. In the $^{13}C\{^1H\}$ NMR spectrum, the NHC carbon is observed at $\delta$ = 182.4 ppm.

 © 2007 Wiley-VCH Verlag GmbH & Co. KGaA, Weinheim 

Table 1. Selected bond lengths [Å] and bong angles [°] of **2** and $[(L)_2Zr]$.[8a]

| Bond lengths | $[(L)_2Zr]$ | **2** | Bond angles | $[(L)_2Zr]$ | **2** |
|---|---|---|---|---|---|
| M–C8(carbene) | 2.385(30) | 2.205(4) | C8–M–C25 | 160.23(10) | 179.9(2) |
| M–C25(carbene) | 2.381(3) | 2.196(4) | O1–M–O2 | 161.85(8) | 177.3(1) |
| M–O1 | 2.028(1) | 1.910(3) | O3–M–O4 | 161.00(8) | 176.6(1) |
| M–O2 | 2.041(2) | 1.914(3) | C8–M–O1 | 84.57(9) | 89.2(1) |
| M–O3 | 2.018(2) | 1.912(3) | C8–M–O2 | 80.05(9) | 88.3(1) |
| M–O4 | 2.035(2) | 1.898(3) | C25–M–O3 | 83.79(9) | 88.3(1) |
| | | | C25–M–O4 | 79.82(9) | 88.5(2) |

Complex $[(L)Ti(Ch_2Ph)_2]$ (**3**) has been prepared from $[(L)TiCl_2(thf)]$ by salt metathesis in toluene at room temperature and characterized by X-ray analysis, but a lower yield (30%) was obtained with this method.[8a] We modified this method by changing the reaction solvent and temperature. Reaction of **1** with 2 equiv. of $PhCH_2MgCl$ in $Et_2O$ at –78 °C (Scheme 1) affords an orange microcrystalline solid of alkyl derivatives **3** in high yield (>88%) after washing with hexamethyldisiloxane (HMDSO), in which they are insoluble. As we previously reported, these derivatives are air- and moisture-sensitive and soluble in common organic solvents, including benzene, toluene, and dimethyl ether.

Hydrolysis of **1** with 0.5 equiv. of water in THF affords a dinuclear titanium complex $\{[(L)TiBr]_2(\mu\text{-}O)\}$ (**4**) with the release of 1 equiv. of hydrogen bromide (Scheme 1). The proton resonances of N–$CH_2$–Ar appeared at $\delta$ = 4.27 and 6.00 ppm as two broad signals and $^{13}C\{^1H\}$ NMR spectra revealed the coordinated carbene carbon signal at $\delta$ = 185.0 ppm.

The X-ray single-crystal analysis of needle crystals of **4** showed that the titanium center binds to the carbene–phenoxide ligand, a bromide, and a bridged oxygen atom to form a pseudo-trigonal-bipyramidal geometry in the solid state (see Figures 2 and 4a). The aryloxy–NHC ligands are bound in a meridional fashion; the phenoxide donors occupy axial positions and two tops are occupied by bromide and carbene carbon. The most notable feature of this structure is that each carbene–phenoxide ligand coordinated to titanium favors *cisoid* conformation, but not *transoid* conformation. Bond lengths Ti–Br [2.5759(7) Å] and Ti–O(phenoxide) [1.822(3)–1.810(5) Å] (Table 2) are longer than those in monomeric aryl oxide complexes $[Ti(OC_6H_3Ph_2)_2Br_2]$ [2.3719(4) Å; 1.746(2) Å][15] and $[Ti(ebmp)Br_2]$ [ebmp = (3-*t*Bu-5-Me-2-O-$C_6H_2CH_2$)$_2$] [2.372(2), 2.363(2) Å; 1.754(4), 1.747(4) Å].[16]

Alkyl titanium complex **3** reacts with 1.0 equiv. of $H_2O$ in $Et_2O$ to afford $\{[(L)Ti]_2(\mu\text{-}O)_2\}$ (**5**) as a light yellow solid in almost quantitative yield. Its $^1H$ NMR spectrum exhibits

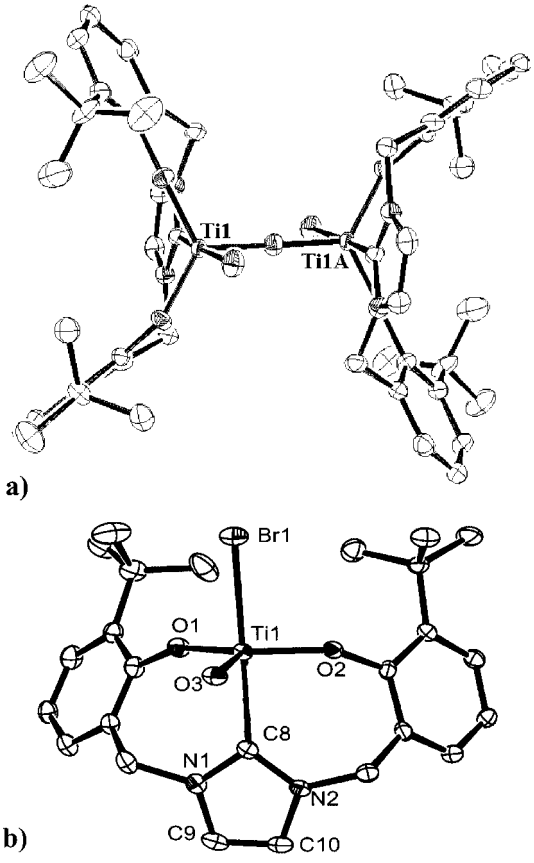


Figure 2. The molecular structure of **4**. All *t*Bu groups, solvent molecules, and hydrogen atoms are omitted for clarity. (a) The side view of the whole molecule; (b) one of the two symmetrically related Ti units.

resonances at 3.98 and 6.06 ppm attributable to the N–$CH_2$–Ar protons of the carbene–phenoxide ligand.

Light yellow single crystals of **5** suitable for X-ray diffraction were obtained by recrystallization from hexane/THF at –20 °C. X-ray analysis of **5** revealed the dinuclear

Table 2. Selected bond lengths [Å] and angles [°] of **4** and **5**.

| Bond lengths | **4** | **5** | Bond angles | **4** | **5** |
|---|---|---|---|---|---|
| Ti1–C8 | 2.208(5) | 2.250(5) | C8–Ti1–O3A | | 177.0(2) |
| Ti1–O1 | 1.822(4) | 1.862(3) | C8–Ti1–Br | 176.4(1) | |
| Ti1–O2 | 1.841(3) | 1.868(4) | C8–Ti1–O1 | 87.0(2) | 86.7(1) |
| Ti1–O3 | 1.8074(8) | 1.760(3) | C8–Ti1–O2 | 87.0(2) | 87.4(2) |
| Ti1–O3(2) | | 1.970(2) | O1–Ti1–O2 | 125.4(2) | 131.7(1) |
| Ti1–Br | 2.5700(9) | | O1–Ti1–O3 | 115.9(1) | 113.4(2) |
| Ti1···Ti1A | | 2.7804(8) | O2–Ti1–O3 | 117.5(1) | 114.8(1) |

 © 2007 Wiley-VCH Verlag GmbH & Co. KGaA, Weinheim 

titanium structure to be linked by two μ-oxygen atoms; the geometry around the titanium atom is distorted trigonal-bipyramidal (Figures 3 and 4b). Each aryloxy–NHC ligand coordinated to titanium favors *cisoid* conformation, as titanium complex **4** does. The coordinated dianionic [Ti(μ-O)$_2$-Ti] core strongly compresses the carbene–phenoxide ligand to *cisoid* conformation. The titanium–carbene distance [2.249(5) Å] is obviously longer than those in other titanium complexes bearing a *transoid* conformation ligand because of the presence of two bridged $O^{2-}$ groups that strongly bind to the titanium centers. A similarly short Ti···Ti distance of 2.704(8) Å has been observed in other titanium compounds where the dianionic groups such as oxo, imido, or alkylidene bridge the $d^0$ metals. Examples include [{$C_5H_2(SiMe_3)_3$}ClTi(μ-O)$_2$TiCl {$C_5H_2(SiMe_3)_3$}] 2.7071(4) Å,[17] [(2,6-$Me_2C_6H_3$)$_2$Ti(μ-N*t*Bu)$_2$Ti(O$C_6H_3Me_2$-2,6)$_2$] 2.7909(7) Å,[18] [(cb)$_2$ClTi(μ-CHSi$Me_3$)$_2$Ti(cb)$_2$] (Hcb = carbazole) 2.9504(8) Å,[19] and [($Cy_2N$)$_2$ClTi(μ-$CH_2$)$_2$-Ti($NCy_2$)$_2$] 2.934(2) Å.[20]

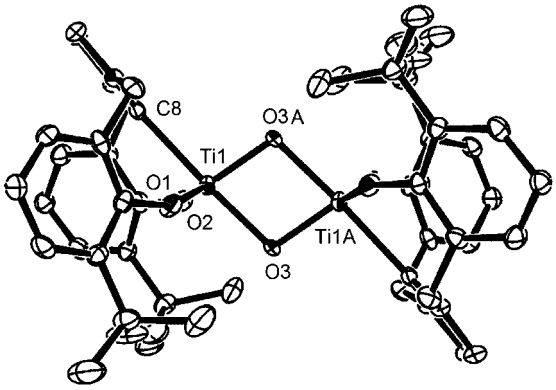


Figure 3. The molecular structure of **5**. All *t*Bu groups, solvent molecules, and hydrogen atoms are omitted for clarity.

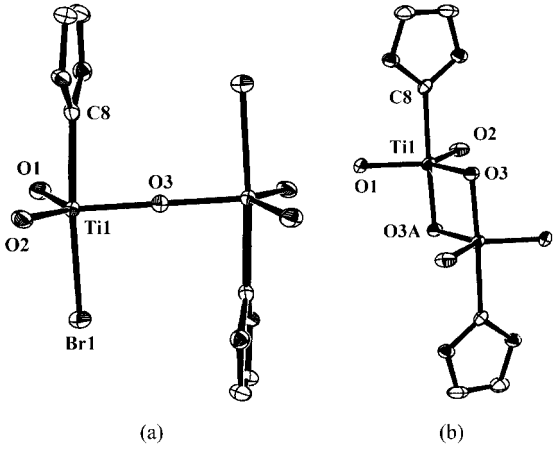


Figure 4. The coordinate sphere of dinuclear titanium complexes **4** (a) and **5** (b) with trigonal-bipyramidal geometry around the metal centers.

Compounds **1**, **4**, and **5** were found to catalyze the polymerization of ethylene at ambient temperature to give polyethylene with MAO as cocatalyst (Table 3). Compared with **1** and previously reported [(L)TiCl$_2$(thf)],[8a] which reveal high activity up to $10^5$ g PE mol$^{-1}$ Ti h$^{-1}$, the dinuclear complexes **4** and **5** show very low activities for polymerization of ethylene. The catalytic activity in the polymerization of ethylene decreases in the order of **1** > **4** > **5**. We are not convinced there is any relationship between conformation (*cisoid* or *transoid*) of the auxiliary carbene ligand and activity in polymerization reactions, because the ground-state conformation of the procatalysts is largely irrelevant to what happens following the addition of a MAO cocatalyst. We tried but failed to obtain information from theory calculation to support this idea. A possible reason for this is that the oxo compounds **4** and **5** are less reactive than **1** following MAO activation.

Table 3. Results of polymerization of ethylene.[a]

| Complex | *T* [°C] | Polymer [g] | Activity[b] |
|---|---|---|---|
| [(L)TiCl$_2$(thf)][c] | 30 | – | 290 |
| **1** | 25–35 | 2.3 | 164 |
| **4** | 25–35 | 0.5 | 39 |
| **5** | 25–35 | 0.3 | 21 |

[a] Polymerization conditions: 2 μmol of titanium, activated by MAO (Al/Ti = 1000), 1 h, 250 mL of toluene, 7 bar. [b] kg PE mol$^{-1}$ Ni h$^{-1}$ bar$^{-1}$. [c] See ref.[8a], 1 L of toluene, 0.5 h, 9 bar.

## Conclusions

In summary, the present work demonstrated that two unique dinuclear titanium phenoxide-tethered N-heterocyclic carbene compounds, **4** and **5**, could be synthesized by control of the hydrolysis of **1** and **2** with the right amount of water. The phenoxide-functionalized NHC ligand adopts *transoid* conformation in mononuclear complexes but rare *cisoid* conformation in dinuclear complexes. This synthetic strategy may be applied to the preparation of other early transition-metal complexes. We are currently working on the synthesis of multinuclear macrocyclic metal compounds with a similar phenoxide-functionalized carbene ligand.

## Experimental Section

**General Considerations:** All manipulations were carried out under dry oxygen-free argon using standard Schlenk techniques. Solvents were dried by refluxing with appropriate drying agents (sodium/benzophenone for toluene, diethyl ether, THF, and hexane; $CaH_2$ for dichloromethane) and distilled under argon prior to use. $CDCl_3$ and $C_6D_6$ were distilled from $CaH_2$ or K and degassed by three freeze–pump–thaw cycles prior to use. The chemicals $TiBr_4$, NaN($SiMe_3$)$_2$ (1.1 M in THF), and $C_6H_5CH_2MgCl$ (1.0 M in diethyl ether) were obtained commercially and used as received. Ligand [$H_3$(L)]Br and complexes [(L)TiCl$_2$(thf)] and [(L)Ti($CH_2Ph$)$_2$] were prepared according to the literature.[8] $^1$H and $^{13}$C{$^1$H} NMR spectra were recorded with a JEOL Lambda-500 spectrometer. Chemical shifts are reported in parts per million. Elemental analyses were measured using Yanaco MT-6 and MSU-32 microanalyzers.

**Synthesis of [(L)TiBr$_2$(THF)] (1):** Complex **1** was prepared using $TiBr_4$ instead of $TiCl_4(THF)_2$ according to a similar way of preparing [(L)TiCl$_2$(THF)].[8a] A 200-mL round-bottomed flask was

 © 2007 Wiley-VCH Verlag GmbH & Co. KGaA, Weinheim 

charged with $[H_3L]Br$ (1.930 g, 3.3 mmol). THF (50 mL) was added and the mixture was cooled to –78 °C. A solution of 3.0 equiv. $NaN(SiMe_3)_2$ (9.9 mmol) in THF (1.0 M, 9.9 mL) was added drop by drop using a syringe. The reaction mixture was kept at –78 °C and stirred for another 30 min to afford the suspended solution of sodium salt of the ligand $Na_2[L]$. The obtained sodium salt was slowly transferred to a suspension of $TiBr_4$ (1.237 g, 3.3 mmol) in THF (50 mL) at –78 °C by cannula. The dark red solution was slowly warmed to room temperature and stirred for another 12 h. The metathesis reaction was evident by the formation of NaBr; all volatile compounds were removed under vacuum, and the crude product was extracted with toluene (50 mL) and filtered through a layer of Celite to remove NaBr. The extracts were concentrated to 10 mL and hexane (30 mL) was added. Filtration followed by drying in vacuo gave an orange-red solid, **1** (0.958 g). The mother liquid was cooled to –30 °C overnight to yield a second crop of **1** (1.023 g). Yield 75.8%. $^1$H NMR (500 MHz, $CDCl_3$): $\delta$ = 1.27 (s, 18 H, $CH_3$ of *t*Bu), 1.52 (s, 18 H, $CH_3$ of *t*Bu), 1.85 (m, 2 H, $CH_2$ of THF), 3.76 (m, 2 H, $CH_2$ of THF), 4.5–6.0 (br. m, 4 H, Ar–$CH_2$–N), 6.93 (br. s, 2 H, Ar-H), 7.10 (br. s, 2 H, N–CH=), 7.27 (br. s, 2 H, Ar-H) ppm. $^{13}$C{$^1$H} NMR (127 MHz, $CDCl_3$): $\delta$ = 24.8 ($CH_2$ of THF), 31.0 ($CH_3$ of *t*Bu), 34.2, 35.10 ($CMe_3$), 52.2 (N–$CH_2$–Ar), 67.5 (O–$CH_2$ of THF), 119.4 (CH of imidazol), 123.7, 124.3, 124.9, 128.6, 137.8, 145.3, 164.8 (NCN) ppm. $C_{37}H_{54}Br_2N_2O_3Ti$ (782.51): calcd. C 56.79, H 6.96, N 3.58; found C 56.84, H 7.04, N 3.61.

**Synthesis of [(L)$_2$Ti] (2):** $TiBr_4$ (0.187 g, 0.50 mmol) in THF (20 mL) was slowly added by channel transfer to a suspended solution of sodium salt $Na_2(L)$ obtained from the reaction of $[H_3(L)]$-Br (0.587 g, 1.0 mmol) with $NaN(SiMe_3)_2$ (3.3 mL, 1.1 M in THF) at –78 °C. The mixture was warmed to room temperature and stirred for another 12 h. The residue was evaporated to dryness and extracted with hexane/toluene (30 mL/20 mL), and the salt was removed by centrifugation. The light yellow solution was concentrated to dryness, washed with HMDSO and dried in vacuo to give a yellow solid of **2** in 73% yield. $^1$H NMR (500 MHz, $CDCl_3$): $\delta$ = 1.11 (s, 36 H, $CH_3$ of *t*Bu), 1.42 (s, 36 H, $CH_3$ of *t*Bu), 3.88 (d, 4 H, $CH_2$), 6.18 (s, 4 H, CH), 6.41 (d, 4 H, $CH_2$), 6.96 (s, 4 H, ArH), 7.46 (s, 4 H, Ar-H) ppm. $^{13}$C{$^1$H} NMR (127 MHz, $CDCl_3$): $\delta$ = 30.4, 31.8 ($CH_3$ of *t*Bu), 34.1, 34.9 ($CMe_3$), 53.7 ($CH_2$), 119.5 (CH of imidazol), 123.1, 123.7, 124.4, 136.2, 138.0, 161.8, 182.4 (NCN) ppm. $C_{66}H_{94}N_4O_4Ti$ (1055.34): calcd. C 75.11, H 8.98, N 5.31; found C 75.05, H 8.92, N 5.47.

**Synthesis of [(L)Ti(CH$_2$Ph)$_2$] (3):** Complex **3** was prepared from [(L)$TiBr_2$(thf)] (**1**) instead of [(L)$TiCl_2$(thf)] using a modified method. Benzylmagnesium chloride (1.4 mL, 1.0 M in diethyl ether, 1.4 mmol) was added dropwise to a precooled suspension of **1** (0.536 g, 0.69 mmol) in $Et_2O$ (30 mL) at –78 °C. The mixture was slowly warmed to 0 °C and stirred for another 4 h at 0 °C. The solvent was removed under vacuum, and $CH_2Cl_2$ (20 mL) was added to the solid residue. The suspension was centrifuged to remove the formed salt and the upper clear solution was evacuated to dryness. The orange-red crude product was washed with HMDSO (5 mL) and dried in vacuo, yielding an orange solid, **3** (0.439 g). Yield 88%. $C_{47}H_{60}N_2O_2Ti$ (732.86): calcd. C 77.03, H 8.25, N 3.82; found C 76.87, H 8.33, N 3.91.

**Synthesis of {[(L)TiBr]$_2$(μ-O)} (4):** Water (1.0 M in $Et_2O$) (193 μL, 0.193 mmol) was added dropwise to a THF solution (20 mL) of **1** (0.300 g, 0.386 mmol) with an ice–water bath. The mixture was stirred overnight at room temperature and was evaporated to dryness. The crude mixture was recrystallized from THF/hexane to give red plate microcrystals (0.206 g). Yield 84%. $^1$H NMR (500 MHz, $C_6D_6$): $\delta$ = 0.88 (t, $CH_3$ of hexane), 1.24 (m, $CH_2$ of hexane), 1.28 (s, 18 H, $CH_3$ of *t*Bu), 1.41 (m, $OCH_2CH_2$ of THF), 1.75 (s, 18 H, $CH_3$ of *t*Bu), 3.57 (m, $OCH_2CH_2$ of THF), 4.27 (br. s, 2 H, N–$CH_2$–Ar), 6.00 (br. s, 1 H, N–$CH_2$–Ar), 6.93 (br. s, 2 H, N–CH=), 7.17 (s, overlapped by 7.15 of $C_6D_6$), 7.49 (d, $J$ = 6.4 Hz, 2 H, H-Ar) ppm. $^{13}$C{$^1$H} NMR (127 MHz, $C_6D_6$): $\delta$ = 14.3 ($CH_3$ of hexane), 23.0 ($CH_2$ of hexane), 25.8 ($OCH_2CH_2$ of THF), 31.4, 32.7 ($CH_3$ of *t*Bu), 31.9 ($CH_2$ of hexane), 34.5, 35.8 ($CMe_3$), 53.2 (N–$CH_2$–Ar), 67.8 ($OCH_2CH_2$ of THF), 119.2 (CH of imidazol), 124.8, 124.9, 125.6, 127.9, 128.1, 128.3, 138.4, 143.5 (arom.), 164.0 (Ti–O–C), 185.0 (NCN) ppm. $C_{66}H_{94}Br_2N_4O_5Ti_2$ (1279.02): calcd. C 61.98, H 7.41, N 4.38; found C 61.41, H 7.12, N 3.89.

**Synthesis of {[(L)Ti(μ-O)]$_2$} (5):** $H_2O$ (1 M $Et_2O$) (0.35 mL, 0.35 mmol) was added dropwise to a THF solution (20 mL) of **3** (0.350 mmol) with an ice–water bath. The mixture was stirred over-

Table 4. Summary of data collection and structure refinement details for **2**, **4**, and **5**.

| | **2**·5$C_6H_6$ | **4**·$C_4H_8O$·$C_6H_{12}$ | **5**·$C_4H_8O$ |
|---|---|---|---|
| Empirical formula | $C_{99}H_{125}N_4O_4Ti$ | $C_{40}H_{61}BrN_2O_4Ti$ | $C_{37}H_{54}N_2O_4Ti$ |
| $F_w$ | 1483.00 | 761.74 | 638.74 |
| $T$ [K] | 123 | 123 | 123 |
| Crystal system | triclinic | triclinic | triclinic |
| Space group | $P\bar{1}$ | $P\bar{1}$ | $P\bar{1}$ |
| $a$ [Å] | 12.608(6) | 10.387(6) | 9.523(4) |
| $b$ [Å] | 14.217(6) | 13.419(7) | 13.419(6) |
| $c$ [Å] | 24.70(1) | 15.916(8) | 15.086(7) |
| α [°] | 90.831(7) | 69.00(3) | 76.60(2) |
| $\beta$ [°] | 97.75(1) | 74.25(3) | 77.53(2) |
| $\gamma$ [°] | 94.51(1) | 76.89(3) | 75.40(2) |
| $V$ [Å$^3$] | 4371(3) | 1972.5(18) | 1789.1(13) |
| $Z$ | 2 | 2 | 2 |
| $D_{calcd.}$ [g cm$^{-3}$] | 1.127 | 1.282 | 1.186 |
| $\mu$(Mo-$K_\alpha$) [mm$^{-1}$] | 1.503 | 12.733 | 2.78 |
| Measured reflections | 70112 | 31334 | 28788 |
| Unique reflections | 19241 | 8684 | 7857 |
| $R_1/wR_2$[a] | 0.098/0.286 | 0.075/0.217 | 0.092/0.182 |
| Gof | 1.000 | 1.001 | 1.217 |
| Min./max. electron density [e Å$^{-3}$] | –2.38/0.82 | –1.15/3.59 | –1.10/2.25 |

[a] Definitions: $R_1 = \Sigma||F_o| - |F_c||/\Sigma|F_o|$, $wR_2 = \{\Sigma[w(F_o^2 - F_c^2)^2]/\Sigma w(F_o^2)^2\}^{1/2}$.

 © 2007 Wiley-VCH Verlag GmbH & Co. KGaA, Weinheim 

night at room temperature and was evaporated to dryness. The crude mixture was recrystallized from THF/hexane to give 0.167 g of **5** as light yellow plate crystals. Yield 84%. $^1$H NMR (500 MHz, $C_6D_6$): $\delta$ = 1.43 (s, 36 H, $CH_3$ of *t*Bu), 1.63 (s, 36 H, $CH_3$ of *t*Bu), 3.96, 3.99 (br. s, 4 H, N–$CH_2$–Ar), 5.74 (s, 4 H, N–CH=), 6.04, 6.07 (br. s, 4 H, N–$CH_2$–Ar), 7.07 (d, $J$ = 2.5 Hz, 4 H, H-Ar), 7.51 (d, $J$ = 2.5 Hz, 4 H, H-Ar) ppm. $^{13}$C{$^1$H} NMR (127 MHz, $CDCl_3$): $\delta$ = 30.8, 32.0 ($CH_3$ of *t*Bu), 34.4, 35.4 ($CMe_3$), 53.1 (N–$CH_2$–Ar), 119.2 (CH of imidazol), 124.4, 124.6, 124.7, 128.3 138.2, 140.6 (arom.), 162.5 (Ti–O–C), 188.4 (NCN) ppm. $C_{66}H_{94}N_4O_6Ti_2$ (1135.21): calcd. C 69.83, H 8.35, N 4.94; found C 69.74, H 8.43, N 4.97.

**Ethylene Polymerization:** A 500-mL autoclave was charged with 240 mL of toluene under argon and a mixture of titanium complex/MAO (the molar ratio of Al:Ti was 1000) in 10 mL toluene was added. After three ethylene gas exchanges, the ethylene pressure was raised to 7 bar and maintained for 1 h. The polymerization was terminated by the addition of methanol and diluted HCl (10%). The solid polyethylene was filtered, washed with methanol, and dried at 40 °C in vacuo.

**X-ray Crystal Structure Determination:** A suitable crystal was immersed in mineral oil and mounted on a nylon loop in a random orientation under a cold stream of dry nitrogen (Rigaku GNNP low-temperature device). Diffraction experiments were performed with Mo-$K_\alpha$ radiation ($\alpha$ = 0.71070 Å) on a Rigaku CCD diffractometer. The data were collected in a hemisphere of data in 720 frames with 20–40-s exposure times. The data sets were collected ($4.0 < 2\theta < 45$–$55°$). The data were processed using CrystalClear (Rigaku) Processing packages.[21] The structures were determined by routine heavy-atom and Fourier methods by using SHELXS-97[22] and refined by full-matrix least-squares. The non-hydrogen atoms were refined with anisotropic parameters and the hydrogen atoms with fixed isotropic thermal parameters of 0.07 Å by means of the SHELXL-97[23] program. The hydrogen atoms were partially located from difference electron-density maps and the rest were fixed at predetermined positions. Scattering factors were from common sources. Some details of data collection and refinement are given in Table 4.

CCDC-639449, -639453, and -639454 contain the supplementary crystallographic data for this paper. These data can be obtained free of charge from The Cambridge Crystallographic Data Centre via www.ccdc.cam.ac.uk/data_request/cif.

## Acknowledgments

This work was financially supported by the National Natural Science Foundation of China, Grant No. 20671021.

[1] For recent reviews see: a) F. E. Hahn, *Angew. Chem. Int. Ed.* **2006**, *45*, 1348–1352; b) N. M. Scott, S. P. Nolan, *Eur. J. Inorg. Chem.* **2005**, 1815–1828; c) K. J. Cavell, D. S. McGuinness, *Coord. Chem. Rev.* **2004**, *248*, 671–681; d) V. César, S. Bellemin-Lapnnaz, L. H. Gade, *Chem. Soc. Rev.* **2004**, *33*, 619–636; e) C. M. Crudden, D. P. Allen, *Coord. Chem. Rev.* **2004**, *248*, 2247–2273; f) W. Kirmse, *Angew. Chem. Int. Ed.* **2004**, *43*, 1767–1769; g) W. A. Herrmann, *Angew. Chem. Int. Ed.* **2002**, *41*, 1290–1309; h) P. L. Arnold, *Heteroat. Chem.* **2002**, *13*, 534–542; i) D. Bourissou, O. Guerret, F. P. Gabbai, G. Bertrand, *Chem. Rev.* **2000**, *100*, 39–92; j) For abnormal carbenes bound to the metal center, see S. Gründemann, A. Kovacevic, M. Albrecht, J. W. Faller, R. H. Crabtree, *Chem. Commun.* **2001**, 2274–2275.

[2] a) N. A. Jones, S. T. Liddle, C. Wilson, P. L. Arnold, *Organometallics* **2007**, *26*, 755–757; b) P. L. Arnold, S. T. Liddle, *Chem. Commun.* **2006**, 3959–3971; c) D. Patel, S. T. Liddle, S. A. Mungur, M. Rodden, A. J. Blake, P. L. Arnold, *Chem. Commun.* **2006**, 1124–1126; d) S. A. Mungur, A. J. Blake, C. Wilson, J. McMaster, P. L. Arnold, *Organometallics* **2006**, *25*, 1861–1867; e) S. T. Liddle, P. L. Arnold, *Organometallics* **2005**, *24*, 2597–2605; f) P. L. Arnold, A. C. Scarisbrick, *Organometallics* **2004**, *23*, 2519–2521; g) P. L. Arnold, S. A. Mungur, A. J. Blake, C. Wilson, *Angew. Chem. Int. Ed.* **2003**, *42*, 5981–5984.

[3] a) S. P. Downing, A. A. Danopoulos, *Organometallics* **2006**, *25*, 1337–1340; b) D. Pugh, J. A. Wright, S. Freeman, A. A. Danopoulos, *Dalton Trans.* **2006**, 775–782.

[4] a) L. P. Spencer, M. D. Fryzuk, *J. Organomet. Chem.* **2005**, *690*, 5788–5803; b) L. P. Spencer, S. Winston, M. D. Fryzuk, *Organometallics* **2004**, *23*, 3372–3374.

[5] a) M. Tamm, S. Randoll, E. Herdtweck, N. Kleigrewe, G. Kehr, G. Erker, B. Rieger, *Dalton Trans.* **2006**, 459–467; b) M. Tamm, S. Randoll, T. Bannenberg, E. Herdtweck, *Chem. Commun.* **2004**, 876–877; c) M. Niehues, G. Erker, G. Kehr, P. Schwab, R. Froehlich, O. Blacque, H. Berke, *Organometallics* **2002**, *21*, 2905–2911; d) M. Tamm, F. E. Hahn, *Coord. Chem. Rev.* **1999**, *182*, 175–209.

[6] a) W. A. Herrmann, C. Köcher, *Angew. Chem. Int. Ed. Engl.* **1997**, *36*, 2162–2187; b) W. A. Herrmann, F. C. Munck, G. R. J. Artus, O. Runte, R. Anwander, *Organometallics* **1997**, *16*, 682–688; c) W. A. Herrmann, G. M. Lobmaier, M. Elison, *J. Organomet. Chem.* **1996**, *520*, 231–234; d) W. A. Herrmann, K. Oefele, M. Elison, F. E. Kuehn, P. W. Roesky, *J. Organomet. Chem.* **1994**, *480*, C7–C9.

[7] P. Shukla, J. A. Johnson, D. Vidovic, A. H. Cowley, C. D. Abernethy, *Chem. Commun.* **2004**, 360–361.

[8] a) D. Zhang, H. Aihara, T. Watanabe, T. Matsuo, H. Kawaguchi, *J. Organomet. Chem.* **2007**, *692*, 234–242; b) D. Zhang, H. Kawaguchi, *Organometallics* **2006**, *25*, 5506–5509; c) H. Aihara, T. Matsuo, H. Kawaguchi, *Chem. Commun.* **2003**, 2204–2205.

[9] a) D. Zhang, G. Jin, N. Hu, *Chem. Commun.* **2002**, 574–575; b) D. Zhang, G. Jin, *Eur. J. Inorg. Chem.* **2003**, 1570–1576; c) D. Zhang, G. Jin, *Organometallics* **2003**, *22*, 2851–2854; d) D. Zhang, G. Jin, L. Weng, F. S. Wang, *Organometallics* **2004**, *23*, 3270–3275; e) D. Zhang, G. Jin, *J. Polym. Sci., Part A: Polym. Chem.* **2004**, *42*, 1018–1024; f) D. Zhang, G. Jin, *Appl. Catal., A* **2004**, *262*, 85–91; g) D. Zhang, G. Jin, *Appl. Catal., A* **2004**, *262*, 13–18; h) D. Zhang, G. Jin, *Inorg. Chem. Commun.* **2006**, *9*, 1322–1325; i) D. Zhang, *Eur. J. Inorg. Chem.* **2007**, 3077–3082.

[10] a) A. A. Danopoulos, N. Tsoureas, J. A. Wright, M. E. Light, *Organometallics* **2004**, *23*, 166–168; b) A. A. Danopoulos, J. A. Wright, W. B. Motherwell, S. Ellwood, *Organometallics* **2004**, *23*, 4807–4810; c) N. Tsoureas, A. A. Danopoulos, A. A. D. Tulloch, M. E. Light, *Organometallics* **2003**, *22*, 4750–4758; d) A. A. Danopoulos, S. Winston, W. B. Motherwell, *Chem. Commun.* **2002**, 1376–1377; e) A. A. Danopoulos, S. Winston, T. Gelbrich, M. B. Hursthouse, R. P. Tooze, *Chem. Commun.* **2002**, 482–483; f) A. A. D. Tulloch, A. A. Danopoulos, S. Kleinhenz, M. E. Light, M. B. Hursthouse, G. Eastham, *Organometallics* **2001**, *20*, 2027–2031; g) A. A. D. Tulloch, A. A. Danopoulos, G. J. Tizzard, S. J. Coles, M. B. Hursthouse, R. S. Hay-Motherwell, W. B. Motherwell, *Chem. Commun.* **2001**, 1270–1271; h) A. A. D. Tulloch, A. A. Danopoulos, R. P. Tooze, S. M. Cafferkey, S. Kleinhenz, M. B. Hursthouse, *Chem. Commun.* **2000**, 1247–1248.

[11] a) A. W. Waltman, T. Ritter, R. H. Grubbs, *Organometallics* **2006**, *25*, 4238–4239; b) A. W. Waltman, R. H. Grubbs, *Organometallics* **2004**, *23*, 3105–3107.

[12] a) Z. Wang, H. Sun, H. Yao, Q. Shen, Y. Zhang, *Organometallics* **2006**, *25*, 4436–4438; b) W. Li, H. Sun, M. Chen, Z. Wang, D. Hu, Q. Shen, Y. Zhang, *Organometallics* **2005**, *24*, 5925–5928.

 © 2007 Wiley-VCH Verlag GmbH & Co. KGaA, Weinheim 

[13] a) D. S. McGuinness, V. C. Gibson, J. W. Steed, *Organometallics* **2004**, *23*, 6288–6292; b) D. S. McGuinness, V. C. Gibson, D. F. Wass, J. W. Steed, *J. Am. Chem. Soc.* **2003**, *125*, 12716–12717.
[14] M. Muehlhofer, T. Strassner, W. A. Herrmann, *Angew. Chem. Int. Ed.* **2002**, *41*, 1745–1747.
[15] G. F. Eade, P. E. Fanwick, I. P. Rothwell, *Dalton Trans.* **2003**, 1061–1064.
[16] S. Fokken, T. O. Spaniol, J. Okuda, *Organometallics* **1997**, *16*, 4240–4242.
[17] J. Okuda, E. Herdtweck, *Inorg. Chem.* **1991**, *30*, 1516–1520.
[18] P. Collier, A. J. Blake, P. Mountford, *J. Chem. Soc. Dalton Trans.* **1997**, 2911–2916.
[19] P. N. Riley, P. E. Fanwick, I. P. Rothwell, *Chem. Commun.* **1997**, 1109–1110.
[20] L. Scoles, R. Minhas, R. Duchateau, J. Jubb, S. Gambarotta, *Organometallics* **1994**, *13*, 4978–4983.
[21] a) CrystalClear Software Package, Rigaku and Molecular Structure Corp., **1999**; b) J. W. Pflugrath, *Acta Crystallogr., Sect. D: Biol. Crystallogr.* **1999**, *55*, 1718–1725.
[22] *Crystal Structure Analysis Package*, Rigaku and Molecular Structure Corp., **2001**.
[23] G. M. Sheldrick, *SHELX-97 Programs for Crystal Structure Analysis*, University of Göttingen, Germany, **1997**.

Received: April 27, 2007
Published Online: September 4, 2007

 © 2007 Wiley-VCH Verlag GmbH & Co. KGaA, Weinheim

**The EUChemSoc Societies have taken the significant step into the future by merging their traditional journals, to form two leading chemistry journals, the *European Journal of Inorganic Chemistry* and the *European Journal of Organic Chemistry*. Three further EUChemSoc Societies (Austria, Czech Republic and Sweden) are Associates of the two journals.**

## COVER PICTURE

**The cover picture shows** one of donor-stabilized phosphenium compounds which have been obtained by direct addition of chlorophosphanes to the 1,3-dimethylimidazolium-2-carboxylate without any further purification step. Their stronger π-acceptor character similar to phosphites and their ionic nature render these ligands very promising in the development of new continuous-flow catalytic processes. Details of phosphorylation mechanisms of imidazolium-2-carboxylate as well as the electronic and steric properties of these adducts are discussed in the article by J. Andrieu et al. on p. 4877 ff.

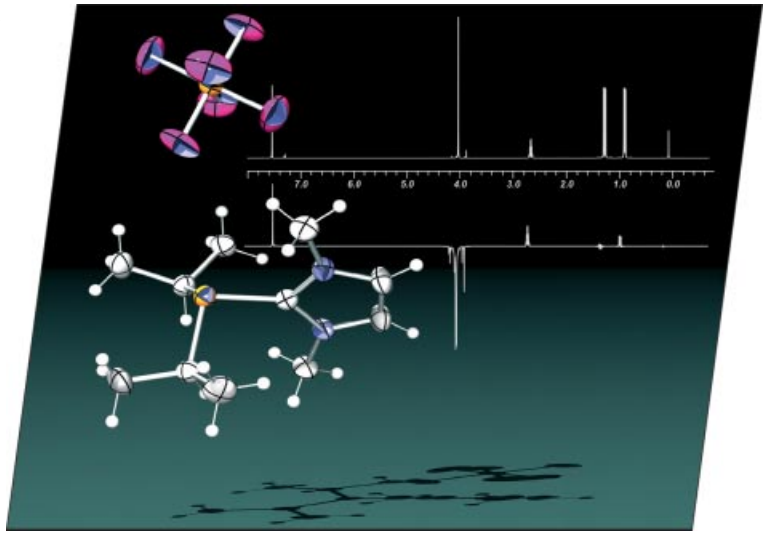

 © 2007 Wiley-VCH Verlag GmbH & Co. KGaA, Weinheim 

# CONTENTS

## SHORT COMMUNICATION


### Heterogeneous Asymmetric Catalysts

**S.-H. Cho, T. Gadzikwa, M. Afshari, S. T. Nguyen,* J. T. Hupp* .... 4863–4867**

[Bis(catechol)salen]$Mn^{III}$ Coordination Polymers as Support-Free Heterogeneous Asymmetric Catalysts for Epoxidation

**Keywords:** Asymmetric catalysis / Heterogeneous catalysis / Manganese / Salen ligands / Coordination polymers

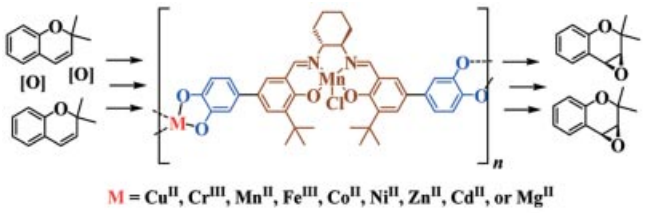


Amorphous coordination polymers, formed by the linkage of [bis(catechol)salen]$Mn^{III}$ units, function as recyclable heterogeneous asymmetric epoxidation catalysts.

### Phosphorus Cations

**J. J. Weigand,* N. Burford,* A. Decken, A. Schulz ..... 4868–4872**

Preparation and Characterization of a Ligand-Stabilized Trimethylphosphane Dication

**Keywords:** Phosphane dication / Donor–acceptor complexes

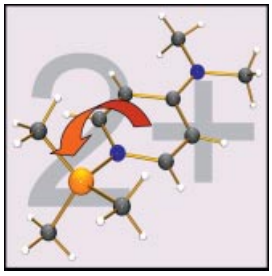

Chlorotrimethylphosphonium triflate reacts with 4-(dimethylamino)pyridine (DMAP) in the presence of trimethylsilyltriflate to give the DMAP-stabilized trimethylphosphane dication as a ditriflate salt. The new salt is also formed from DMAP-dimethylphosphenium triflate by reaction with methyltriflate. Ligand exchange of DMAP for $PMe_3$ yields the hexamethyldiphosphonium dication.

### Turbostratic Boron Nitride

**S. K. Klitgaard, K. Egeblad, M. Brorson, K. Herbst, C. H. Christensen* ..... 4873–4876**

Turbostratic Boron Nitride Coated on High-Surface Area Metal Oxide Templates

**Keywords:** Boron nitride / Turbostratic / Metal oxide templates / Catalyst support material / Nanostructure

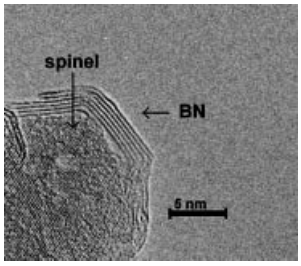


Boron nitride coatings on high-surface area $MgAl_2O_4$ and $Al_2O_3$ have been synthesized and characterized by TEM and by X-ray powder diffraction. The metal oxide templates were coated with BN using a simple nitridation in a flow of ammonia starting from ammonium borate adsorbed onto $MgAl_2O_4$ or $\gamma$-$Al_2O_3$. This procedure resulted in the formation of a turbostratic boron nitride film with a thickness of a few individual BN layers.


## FULL PAPERS


### Donor–Acceptor Systems

**M. Azouri, J. Andrieu* M. Picquet, P. Richard, B. Hanquet, I. Tkatchenko ..... 4877–4883**

Straightforward Synthesis of Donor-Stabilised Phosphenium Adducts from Imidazolium-2-carboxylate and Their Electronic Properties

**Keywords:** Carboxylates / Phosphanes / Electronic properties / Synthesis / Coordination modes

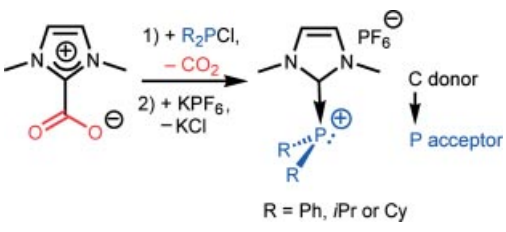


A very convenient method for the generation of donor-stabilised phosphenium compounds from imidazolium-2-carboxylate and chlorophosphanes is presented; the ligands show phosphite-like π-acceptor character.


 © 2007 Wiley-VCH Verlag GmbH & Co. KGaA, Weinheim 

## Vanadium Coordination Chemistry

Simple bis(imidazol-2-yl) derivatives form mono- and bis-chelate complexes under acidic and neutral conditions with the $V^{IV}O$ ion. The bis-chelates show *cis-trans* isomerism. With bis(imidazol-2-yl) amino acid derivatives the complexation process takes place also in the basic pH range with the deprotonation and coordination of the amide nitrogen to give $VOLH_{-1}$ and $VOLH_{-2}$.

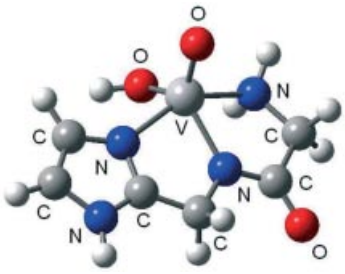


**K. Várnagy, T. Csorba, D. Kiss, E. Garribba,* G. Micera,* D. Sanna ..... 4884–4896**

$V^{IV}O$ Complexes of Bis(imidazol-2-yl) Derivatives: A Potentiometric, Spectroscopic and DFT Study

**Keywords:** Vanadium / Bioinorganic chemistry / pH potentiometry / EPR spectroscopy / Density functional calculations

## Germanium Chemistry

Detailed structural and spectroscopic studies have been carried out on a series of $GeF_4$ complexes of N-donor ligands, and their properties compared with analogues containing $GeX_4$ (X = Cl or Br).

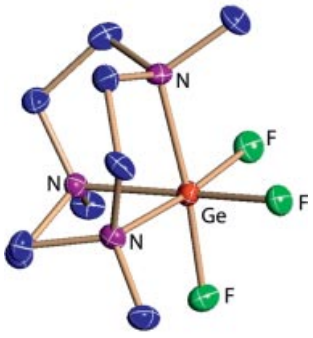


**F. Cheng, M. F. Davis, A. L. Hector, W. Levason,* G. Reid, M. Webster, W. Zhang ..... 4897–4905**

Synthesis, Spectroscopic and Structural Systematics of Complexes of Germanium(IV) Halides ($GeX_4$, X = F, Cl, Br or I) with Mono-, Bi- and Tri-Dentate and Macrocyclic Nitrogen Donor Ligands

**Keywords:** Germanium / Nitrogen ligands / Fluorido complexes

## Nanotechnology

Integrative synthesis of nanoparticles, -tubes, -rods, and -wires in the same reverse micelle system is successfully achieved. The growth process is studied in detail. The stepwise assembly-growth mechanism is significant in guiding the synthesis of one-dimensional nanomaterials in micelle systems.

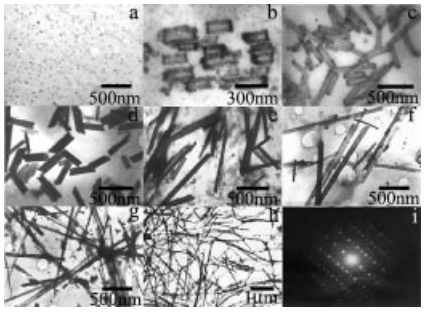


**Y. Chen, Q.-S. Wu,* Y.-P. Ding ..... 4906–4910**

Stepwise Assembly of Nanoparticles, -tubes, -rods, and -wires in Reverse Micelle Systems

**Keywords:** Stepwise-assembly synthesis / Nanomaterials / $CaSO_4{\cdot}2H_2O$ / Reverse micelles

## "Disobedient Skeleton" of $[B_{11}H_{11}]^{2-}$

The molecular graph of the $[B_{11}H_{11}]^{2-}$ dianion obtained as a result of AIM analysis of the electron-density distribution demonstrates the absence of some edge-localized B–B bond paths, leading to the formation of two effectively six-membered "open faces" in the cluster.

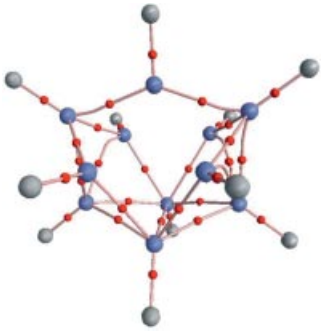

**E. G. Kononova, L. A. Leites,* S. S. Bukalov, I. V. Pisareva, I. T. Chizhevsky, J. D. Kennedy, J. Bould ..... 4911–4918**

Vibrational Spectrum and Electronic Structure of the $[B_{11}H_{11}]^{2-}$ Dianion

**Keywords:** Boron / Cage compounds / Vibrational spectra / Electronic structure / Fluxionality

 © 2007 Wiley-VCH Verlag GmbH & Co. KGaA, Weinheim 

# CONTENTS


## Ligand-Supported Al Compounds

**Z. Yang, X. Ma, H. W. Roesky,* Y. Yang, V. M. Jiménez-Pérez, J. Magull, A. Ringe, P. G. Jones ..... 4919–4922**

Syntheses, Characterizations, and X-ray Single-Crystal Structures of 1,8-Bis(trimethylsilylamino)naphthalene Aluminum Hydride and the Methyl Derivative

**Keywords:** Aluminum / Arene ligands / Structure elucidation

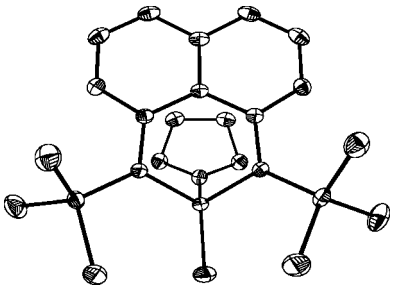

The reaction of 1,8-bis(trimethylsilylamino)naphthalene with $H_3Al{\cdot}NMe_3$ results in the formation of $[1,8\text{-}(Me_3SiN)_2C_{10}H_6]AlH(NMe_3)$ (**3**). The compound $[1,8\text{-}(Me_3SiN)_2C_{10}H_6](Li)_2(thf)_3$ reacts with $MeAlCl_2$ to yield $[1,8\text{-}(Me_3SiN)_2C_{10}H_6]$-Al(Me)thf (**4**). Compounds **3** and **4** are the first mononuclear aluminum compounds to contain the 1,8-diaminonaphthalene ligand.

## [(η⁶-arene)Cr(CO)₃]-Based Ligands

**E. Alberico,* W. Braun, B. Calmuschi-Cula, U. Englert, A. Salzer,* D. Totev ..... 4923–4945**

Expanding the Range of "Daniphos"-Type P∩P- and P∩N-Ligands: Synthesis and Structural Characterisation of New [(η⁶-arene)Cr(CO)₃] Complexes

**Keywords:** N,P ligands / Phosphane ligands / Asymmetric catalysis / Arene complexes / Chromium

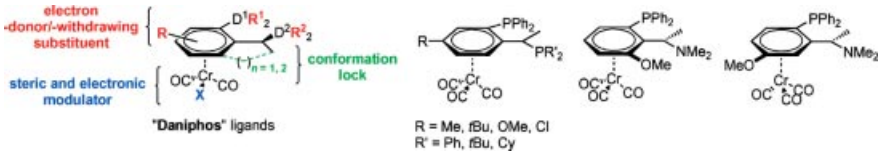


New P∩P- and P∩N-ligands have been synthesised whose core structure is an [(η⁶-arene)Cr(CO)₃] unit. These new ligands, which expand the range of "Daniphos" ligands, are endowed with central and planar chirality and have been prepared by a stereoselective synthetic strategy from optically pure benzylamines bearing a second substituent on the arene other than the benzyldimethylamino group.

## Gold Photochemistry

**J. B. Foley,* S. E. Gay, M. J. Vela, B. M. Foxman, A. E. Bruce, M. R. M. Bruce* ..... 4946–4951**

Structure and Photochemical Isomerization of the Dinuclear Gold(I) Halide Bis(diphenylphosphanyl)ethylene Complexes: Correlation Between Quantum Yield and Aurophilicity

**Keywords:** Aurophilicity / Metal–metal interactions / Gold / Photochemistry / Olefin isomerization / Quantum yield

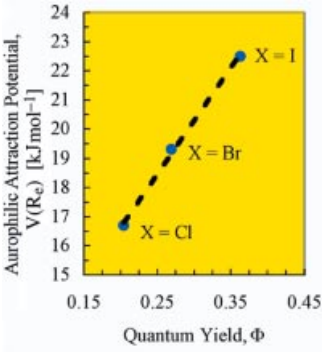


The quantum yields for the photochemical isomerization of *cis*-$(Ph_2PCH{=}CHPPh_2)(AuX)_2$, $\Phi_{(cis\rightarrow trans)}$, were measured (for X = Cl, Br, and I, respectively) and found to correlate with the aurophilic attraction potential $V(R_e)$. The crystal structures for *cis*-$(Ph_2PCH{=}CHPPh_2)(AuI)_2$ and *trans*-$(Ph_2PCH{=}CHPPh_2)(AuI)_2$ are also reported.

## Conformations of Cyclohexagermanes

**M. Hölbling, M. Flock, J. Baumgartner, K. Hassler* ..... 4952–4957**

$Ge_6Me_{12}$ and $Ge_6H_{12}$ Cyclohexagermanes: Conformer Equilibria Studied by Raman Spectroscopy and Quantum Chemical Calculations

**Keywords:** Cyclohexagermanes / Conformational analysis / Raman spectroscopy / X-ray structure / Ab initio calculations

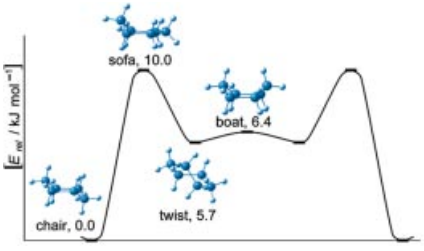


The conformational equilibria of cyclohexagermanes have been investigated with ab initio calculations. Two stable conformers were located on the potential energy surface for $Ge_6H_{12}$, whereas three were located for $Ge_6Me_{12}$. With the aid of Raman spectroscopy, two conformers were detected for $Ge_6Me_{12}$, a chair and an averaged twist/boat conformer, with an enthalpy difference of 2.4 kJ mol$^{-1}$ between them.


 © 2007 Wiley-VCH Verlag GmbH & Co. KGaA, Weinheim 

## Platinum Sulfide Aggregates

Dibromo-organic compounds with an extended skeleton can function as an overhead bridge across the sulfide centers in $[Pt_2(\mu\text{-}S)_2(PPh_3)_4]$. If it is stereochemically too restrictive to serve as an intramolecular bridge within the $Pt_2$ core, it could be switched to the intermolecular mode and interlink two $Pt_2$ cores, giving an open $Pt_4$ aggregate of $Pt_2\cdots(spacer)\cdots Pt_2$, $[(PPh_3)_4Pt_2(\mu\text{-}S)(\mu\text{-}SRS)(\mu\text{-}S)Pt_2(PPh_3)_4](PF_6)_2$.

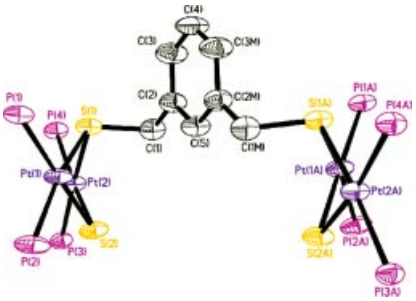

**S. H. Chong, W. Henderson, T. S. A. Hor* ..... 4958–4964**

Open Platinum Aggregate Frameworks with Overhead Dithiolate Bridges

**Keywords:** Platinum / Sulfide / Aggregate / Alkylation / Dithiolate

## Energetic Ionic Liquids

Comparison is made of heats of formation and densities of dicyanamide and dinitramide salts.

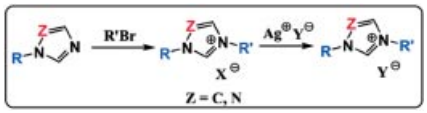


**Y. Gao, H. Gao, C. Piekarski, J. M. Shreeve* ..... 4965–4972**

Azolium Salts Functionalized with Cyanomethyl, Vinyl, or Propargyl Substituents and Dicyanamide, Dinitramide, Perchlorate and Nitrate Anions

**Keywords:** Energetic salts / Density / Heat of formation / Thermal stability

## Rhodium Phosphane Complexes

The influence of phosphane "arm-on, arm-off" association/dissociation in rhodium catalysed alkene hydrogenation using $[Rh(COD)(\kappa^3\text{-triphos})]PF_6$ has been investigated, including comparison of catalytic activity of this complex to the related diphosphane complex, $[Rh(COD)(\kappa^2\text{-dppp})]PF_6$, with added triphenylphosphane.

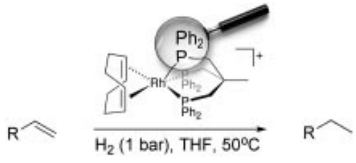


**A. B. Chaplin, P. J. Dyson* ... 4973–4979**

On the Influence of "Arm-on, Arm-off" Processes on Alkene Hydrogenation Catalysed by a Rhodium Triphos Complex

**Keywords:** Rhodium / Homogeneous catalysis / Hydrogenation / Tripodal ligands / Phosphane ligands

## Benzotriazole Surface Coordination

The surface coordination chemistry of benzotriazole on a Cu electrode was investigated by electrochemical synthesis combined with in situ electrochemical surface-enhanced Raman spectroscopy in non-aqueous solution. Two different surface complexes were prepared in the solution with or without triphenylphosphane. The surface coordination mechanism was proposed.

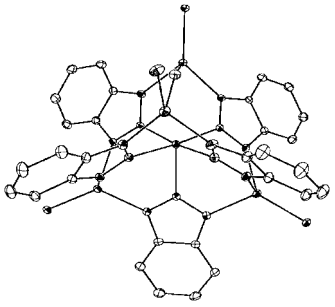

**Y.-X. Yuan, P.-J. Wei, W. Qin, Y. Zhang, J.-L. Yao,* R.-A. Gu ..... 4980–4987**

Combined Studies on the Surface Coordination Chemistry of Benzotriazole at the Copper Electrode by Direct Electrochemical Synthesis and Surface-Enhanced Raman Spectroscopy

**Keywords:** Benzotriazoles / Copper / Surface coordination / Electrochemistry / Raman spectroscopy

 © 2007 Wiley-VCH Verlag GmbH & Co. KGaA, Weinheim 

# CONTENTS

## Heterometallic Complexes

**P. Chandrasekaran, J. T. Mague, R. Venkateswaran, M. S. Balakrishna* ..... 4988–4997**

Cyclodiphosphazane *cis*-{(*o*-$MeOC_6H_4O$)-P(μ-N*t*Bu)}$_2$ as a Bridging Bidentate Ligand: Synthesis, Structures of Heterometallic Complexes, and Halogen Exchange Between Rh–Cl and Cu–X (X = Br, I)

**Keywords:** Heterometallic complexes / Cyclodiphosphazanes / P,N ligands / Halogen exchange / Rhodium

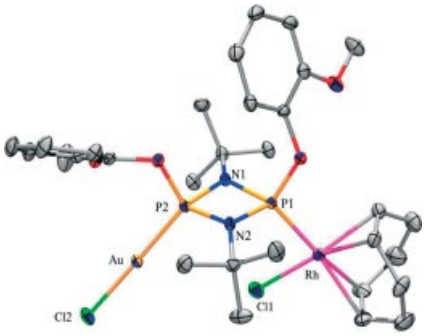


The heterometallic complexes of cyclodiphosphazanes *cis*-{(*o*-$MeOC_6H_4O$)P(μ-N*t*Bu)}$_2$ containing $Rh^I/Au^I$, $Rh^I/2Au^I$, $2Rh^I/2Cu^I$, and $Rh^I/Pd^{II}$ metal centers have been synthesized. The selective mono- and bidentate coordination modes of cyclodiphosphazane with respect to diverse metal precursors gives a facile synthetic approach for the preparation of heterometallic complexes. Halogen exchange reactions were observed between Rh–Cl and CuX (X = Br, I) during the preparation of $Rh^I/Cu^I$ heteronuclear complexes.

**If not otherwise indicated in the article, papers in issue 30 were published online on October 9, 2007**

 © 2007 Wiley-VCH Verlag GmbH & Co. KGaA, Weinheim

**The EUChemSoc Societies have taken the significant step into the future by merging their traditional journals, to form two leading chemistry journals, the *European Journal of Inorganic Chemistry* and the *European Journal of Organic Chemistry*. Three further EUChemSoc Societies (Austria, Czech Republic and Sweden) are Associates of the two journals.**

## COVER PICTURE

**The cover picture shows** one of donor-stabilized phosphenium compounds which have been obtained by direct addition of chlorophosphanes to the 1,3-dimethylimidazolium-2-carboxylate without any further purification step. Their stronger π-acceptor character similar to phosphites and their ionic nature render these ligands very promising in the development of new continuous-flow catalytic processes. Details of phosphorylation mechanisms of imidazolium-2-carboxylate as well as the electronic and steric properties of these adducts are discussed in the article by J. Andrieu et al. on p. 4877 ff.

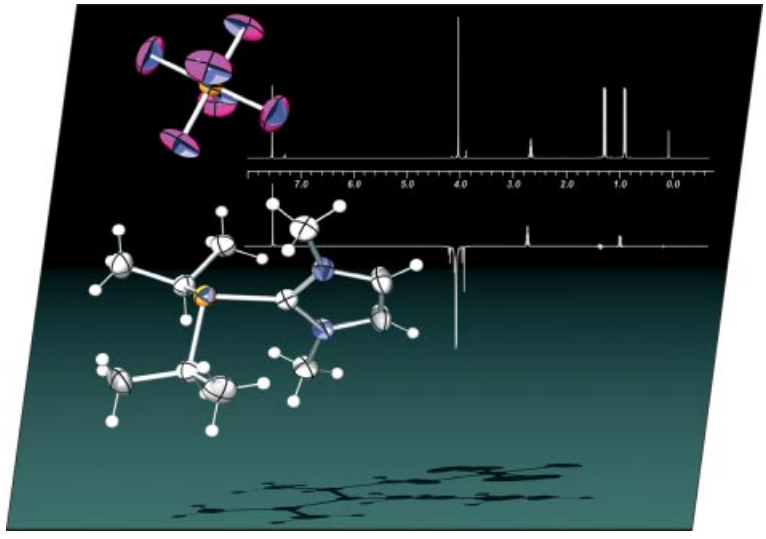

 © 2007 Wiley-VCH Verlag GmbH & Co. KGaA, Weinheim 

# SPOTLIGHTS …

## *Helical Structures*

K. Nagai, K. Maeda, Y. Takeyama, T. Sato, E. Yashima*

**Temperature-Induced Chiroptical Changes in a Helical Poly(phenylacetylene) Bearing *N*,*N*-Diisopropylaminomethyl Groups with Chiral Acids in Water**

*Chem. Asian J.*
DOI: **10.1002/asia.200700185**

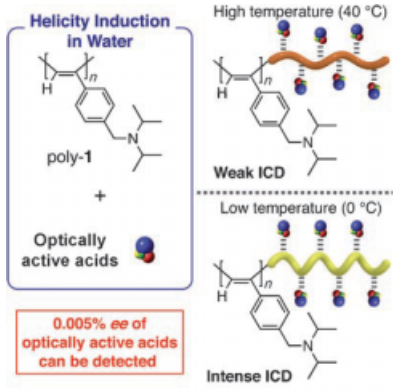


**Blowing hot and cold**: The title compound (poly-**1**) is highly sensitive to the chirality of chiral acids and can detect small enantiomeric imbalances in these acids in water. Its one-handed helical structure produces induced circular dichroism (ICD), whose signal intensity and pattern depend on the temperature and concentration of poly-**1**.

## *Protein Translation*

N. Muranaka, M. Miura, H. Taira, T. Hohsaka*

**Incorporation of Unnatural Non-α-Amino Acids into the N Terminus of Proteins in a Cell-Free Translation System**

*ChemBioChem*
DOI: **10.1002/cbic.200700249**

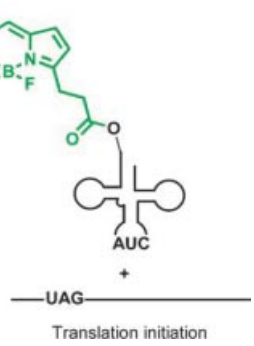


**Expanding translation initiation**. Incorporation of unnatural carboxylic acids without α-amino groups was achieved by using chemically acylated initiator tRNA (see figure). The results suggest that various unnatural compounds with a carboxyl group can be incorporated into the N terminus of proteins.

## *Xenon Biosensor*

V. Roy, T. Brotin, J.-P. Dutasta, M.-H. Charles, T. Delair, F. Mallet, G. Huber, H. Desvaux, Y. Boulard, P. Berthault*

**A Cryptophane Biosensor for the Detection of Specific Nucleotide Targets through Xenon NMR Spectroscopy**

*ChemPhysChem*
DOI: **10.1002/cphc.200700384**

**DNA sensor**: A xenon host composed of a cryptophane structure with a DNA strand (see picture) serves to detect its complementary strand in the micromolar range through laser-polarized $^{129}Xe$ NMR spectroscopy.

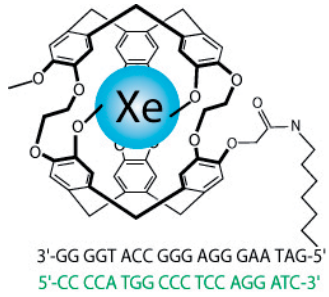


## *Drug Stability*

R. K. Haynes,* H.-W. Chan, C.-M. Lung, N.-C. Ng, H.-N. Wong, L. Y. Shek, I. D. Williams, A. Cartwright, M. F. Gomes

**Artesunate and Dihydroartemisinin (DHA): Unusual Decomposition Products Formed under Mild Conditions and Comments on the Fitness of DHA as an Antimalarial Drug**

*ChemMedChem*
DOI: **10.1002/cmdc.200700064**

**The front-line** antimalarial drugs artesunate and DHA undergo thermal decomposition under mild conditions to give unusual dimeric peroxides, a glycal and a rearranged peroxide, in addition to benign decomposition products. The implications of the decomposition in relation to shelf-life determination according to the International Conference of Harmonization guidelines and use of DHA as an antimalarial drug are discussed.

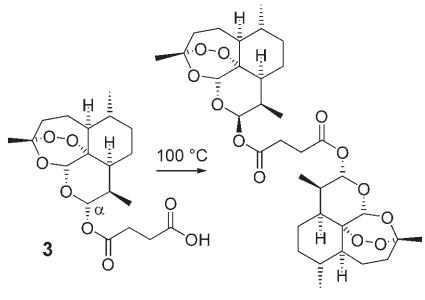


 © 2007 Wiley-VCH Verlag GmbH & Co. KGaA, Weinheim 

# … ON OUR SISTER JOURNALS

EurJIC European Journal of Inorganic Chemistry

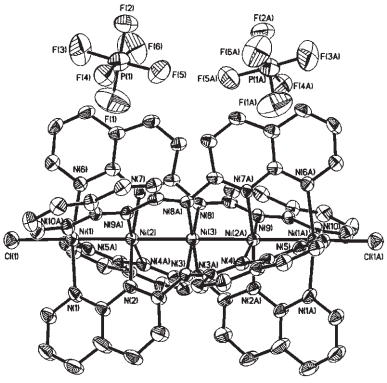

**Metal string!** The first linear nickel framework in which the usual sequence of $Ni^{II}$ atoms has been reduced by two electrons is presented. The electronic structure of the metal framework appears intermediate between a localized picture corresponding to $Ni^{II}$-$Ni^{I}$-$Ni^{II}$-$Ni^{I}$-$Ni^{II}$ and a fully delocalized model represented as $(Ni_2)^{3+}$-$Ni^{II}$-$(Ni_2)^{3+}$.

## *Mixed-Valent Compounds*

I. P.-C. Liu, M. Bénard,* H. Hasanov, I.-W. P. Chen, W.-H. Tseng, M.-D. Fu, M.-M. Rohmer, C.-h. Chen, G.-H. Lee, S.-M. Peng*

**A New Generation of Metal String Complexes: Structure, Magnetism, Spectroscopy, Theoretical Analysis, and Single Molecular Conductance of an Unusual Mixed-Valence Linear $[Ni_5]^{8+}$ Complex**

*Chem. Eur. J.*
DOI: **10.1002/chem.200700750**

The reactions between glycidol and either the nonglycosylated protein BSA or the glycoprotein avidin (AV), followed by mild oxidation of the intermediate glycol moieties, afforded reactive aldehyde functionalities. As an application, the functionalized proteins were derivatized with the fluorescent dye Lucifer Yellow CH, affording highly fluorescent bioprobes.

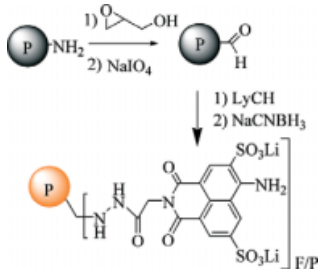


## *Bioconjugation Using Glycidol*

J.-M. Heldt, N. Fischer-Durand, M. Salmain, A. Vessières,* G. Jaouen

**The Use of Glycidol to Introduce Aldehyde Functions Into Proteins – Application to the Fluorescent Labelling of Bovine Serum Albumin and Avidin**

*Eur. J. Org. Chem.*
DOI: **10.1002/ejoc.200700429**

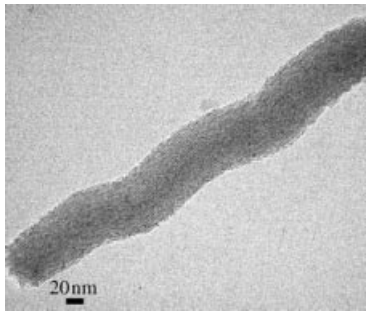


**Keep this handy**! Periodic mesoporous organosilica-based compounds with chiral channels are prepared by using an achiral fluorinated surfactant (FC-4911) and cetyltrimethylammonium bromide as structure-directing agents. Spiral samples synthesized from 1,4-bis(triethoxysilyl)benzene exhibit structural periodicity and a crystal-like mesoporous wall (see TEM image).

## *Mesoporous Materials*

X. Meng, T. Yokoi, D. Lu, T. Tatsumi*

**Synthesis and Characterization of Chiral Periodic Mesoporous Organosilicas**

*Angew. Chem. Int. Ed.*
DOI: **10.1002/anie.200702666**

On these pages, we feature a selection of the excellent work that has recently been published in our sister journals. If you are reading these pages on a computer, click on any of the items to read the full article. Otherwise please see the DOIs for easy online access through Wiley InterScience.

 © 2007 Wiley-VCH Verlag GmbH & Co. KGaA, Weinheim 

DOI: 10.1002/ejic.200700302

# [Bis(catechol)salen]Mn$^{III}$ Coordination Polymers as Support-Free Heterogeneous Asymmetric Catalysts for Epoxidation

So-Hye Cho,[a] Tendai Gadzikwa,[a] Mitra Afshari,[a] SonBinh T. Nguyen,*[a] and Joseph T. Hupp*[a]

**Keywords:** Asymmetric catalysis / Heterogeneous catalysis / Manganese / Salen ligands / Coordination polymers

The formation of coordination polymers by the reaction of [bis(catechol)salen]Mn$^{III}$ with several di- and trivalent metal ions is reported. These polymers are insoluble in a wide range of organic solvents and water but can be dissolved upon addition of excess pyrocatechol. They function as enantioselective heterogeneous epoxidation catalysts and exhibit catalytic activity comparable to that of the homogeneous [bis(catechol)salen]Mn$^{III}$ building block alone when used for the enantioselective epoxidation of 2,2-dimethyl-2*H*-chromene. After catalysis, catalyst isolation from the reaction mixture can be readily achieved by centrifugation and decantation. Under practical oxidant concentrations, the catalyst can be recycled up to ten times with little loss of activity and no loss of enantioselectivity.
(© Wiley-VCH Verlag GmbH & Co. KGaA, 69451 Weinheim, Germany, 2007)

## Introduction

Porous coordination polymers – especially crystalline ones – have recently received much attention for their potential applications in the areas of heterogeneous catalysis, separations, and gas storage.[1,2] Although the coordination polymerization of chiral homogeneous catalysts has been suggested as a strategy to obtain practically useful heterogeneous asymmetric catalysts,[3] to date there are only a few demonstrations of this approach.[4] Among these are heterogenized catalysts for the addition of $ZnEt_2$ to aromatic aldehydes[4a] and for enantioselective Michael addition.[4b] In addition, coordination polymers have been used in asymmetric Lewis acid catalysis.[4c,4d] Examples of coordination polymers in chiral oxidative catalysis are scarcer. Suslick and co-workers have reported that a porphyrin-based material catalyzes organic oxidations;[4e] however, this system is not chiral. To the best of our knowledge, our recent report of the enantioselective epoxidation of 2,2-dimethyl-2*H*-chromene by a microporous, crystalline metal–organic framework (MOF) material constitutes the first example of chiral oxidation catalyzed by a coordination polymer.[5] While this work successfully illustrates the translation of a homogeneous chiral (salen)Mn$^{III}$ catalyst into the heterogeneous realm, the (salen)Mn-based MOF material has limited recyclability. Specifically, fragmentation of MOF particles and loss of the catalyst (4 to 7% per cycle) can occur during each batch reaction, reflecting the inherent weakness of the Zn$^{II}$–N(pyridine) bond. The required usage of zinc or similar divalent ions as framework nodes in these particular MOFs also limits the diversity of functional materials that can potentially be obtained by this approach.

If the requirement of crystallinity were relaxed, however, stronger chelate-type metal–ligand linkages (such as metal–catecholate or –semiquinone links) could be used, and the resulting amorphous coordination polymers may still exhibit heterogeneous catalytic competency.[6] Previously, we reported the immobilization of mono-catechol-functionalized (salen)Mn$^{III}$ complexes on alumina membranes.[7] The modified membranes functioned well as heterogeneous asymmetric epoxidation catalysts, achieving high one-pass conversion and excellent turnover numbers, albeit with moderate recyclability due to catalyst leaching. We hypothesized that a more permanent approach to heterogenization would be coordination polymerization of [bis(catechol)-salen]Mn (**1**). By combining **1** with various soluble metal ions, linear and/or branched coordination polymers should form, ideally as isolable solids that can be used as catalysts. While there is no precedent for the use of catechol-based coordination polymers in heterogeneous catalysis, catechol has long been known as an effective bidentate ligand for many metal ions.[8] The redundantly chelating (salen)Mn moieties in the polymer networks might well display reduced leaching and higher stability/recyclability compared to the alumina-supported species. Herein, we report that a series of exceptionally stable enantioselective heterogeneous epoxidation catalysts can be made by the coordination po-

[a] Department of Chemistry and the Institute for Energy in Catalytic Processes, Northwestern University
2145 Sheridan Road, Evanston, IL 60208-3113, USA
Fax: +1-847-491-7713
E-mail: stn@northwestern.edu
j-hupp@northwestern.edu
Supporting information for this article is available on the WWW under http://www.eurjic.org or from the author.

 © 2007 Wiley-VCH Verlag GmbH & Co. KGaA, Weinheim 

lymerization of **1** and several metal ions. These catalysts can be recycled numerous times with minimal leaching and no loss of enantioselectivity.

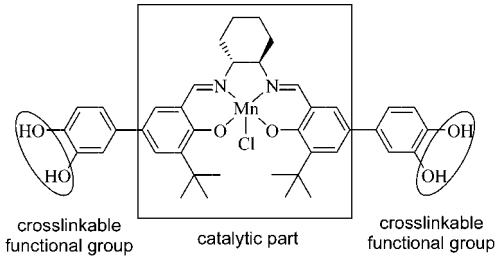


**1**

## Results and Discussion

The bis(catechol)-functionalized salen ligand of **1** can be prepared easily from (1*R*,2*R*)-diaminocyclohexane (see Supporting Information). Metalation with $MnCl_2$ under an $N_2$ atmosphere, followed by oxidation in air, afforded complex **1** in good yield. Coordination polymerization of **1** with $Cu^{II}$ was accomplished under an $N_2$ atmosphere by adding $CuCl_2$ to a 1:4 mixture of compound **1** and triethylamine (TEA) dissolved in deoxygenated dimethylformamide (DMF). Vigorous stirring of the resulting reaction mixture led to a spontaneous formation of precipitates, which were then filtered and thoroughly washed with DMF to afford the Cu-linked (salen)Mn polymer **poly(Cu-1)** as a brown solid (Figure 1).[9]

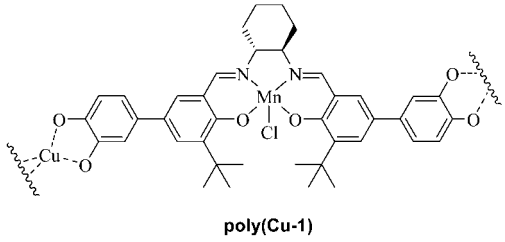


**poly(Cu-1)**

Figure 1. A schematic drawing of the coordination polymer formed between $Cu^{II}$ and [bis(catechol)salen]$Mn^{III}Cl$ [**poly(Cu-1)**].

**Poly(Cu-1)** is insoluble in a wide range of organic solvents (toluene, methanol, DMF, and dimethyl sulfoxide) and water. Inductively coupled plasma (ICP) mass spectrometric measurements performed on **poly(Cu-1)** yielded a Mn/Cu ratio of approximately 1:1.1, suggesting that **poly(Cu-1)** exhibits a quasi-one-dimensional structure, in which **1** is connected by bis(catecholate)copper linkages. The formation of **poly(Cu-1)** can be reversed: addition of excess pyrocatechol to a DMF slurry of **poly(Cu-1)** dissolves the particles within a few hours. Electrospray ionization mass spectrometry conducted on the resulting solution clearly showed mass peaks associated with the (salen)Mn building block ($[M - Cl]^+$ = 703.92 and $[M - Cl + DMF]^+$ = 776.56, see Supporting Information).

Thermal gravimetric analysis (TGA) performed on the as-synthesized **poly(Cu-1)** revealed a weight loss of ca. 18% between 25–200 °C, followed by several additional losses up to 700 °C (see Supporting Information). We attribute the initial weight loss to the liberation of DMF and water and the latter ones to the decomposition of the polymer. As further evidence for the initial solvent loss, TGA of a sample polymer that had been evacuated (30 mTorr) for 18 h at 80 °C showed only ca. 2% weight loss in the temperature range of 25–200 °C. The TGA trace of an evacuated polymer sample that was then resolvated showed a lower loss of solvent than the as-synthesized product (8% vs. 18%), suggesting that **poly(Cu-1)** may have undergone further aggregation upon evacuation and become less porous than freshly prepared samples. However, it still has moderate porosity (total BET surface area = 72 $m^2 g^{-1}$) and an amorphous structure as evidenced by scanning electron microscopy (SEM; Figure 2) and by the absence of peaks in powder X-ray diffraction measurements.

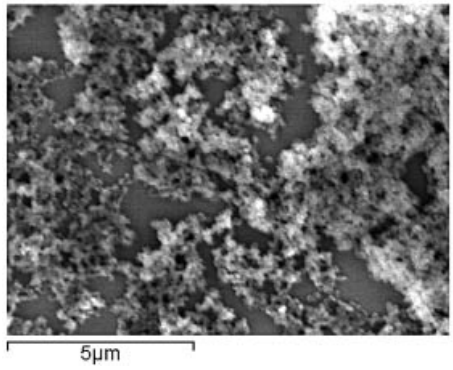


Figure 2. SEM image of **poly(Cu-1)**.

Catalytic epoxidations of 2,2-dimethyl-2*H*-chromene were carried out in dichloromethane[10] solution under ambient conditions with **poly(Cu-1)** by using 2-(*tert*-butylsulfonyl)iodosylbenzene as the oxidant [Equation (1)]. For comparison, [bis(dimethoxyphenyl)salen]$Mn^{III}Cl$ (**2**), the protected soluble analogue of **poly(Cu-1)**, was also tested for epoxidation activity.[11] Although a slightly lower enantioselectivity was observed for **poly(Cu-1)** relative to **2** [76% *ee* for **poly(Cu-1)** vs. 86% *ee* for **2**], their epoxidation activities were comparable (Table 1, entries 1 and 2). As reduced enantioselectivity is often seen with homogeneous catalysts immobilized in constrained environments such as cross-linked polymers and zeolites,[12] this slight decrease in enantioselectivity may be attributed to structural constraints resulting from the immobilization. Indeed, when **poly(Cu-1)** is dissolved in the presence of pyrocatechol (vide supra) and used as a catalyst for reaction (1), its enantioselectivity (82%) becomes quite close to that of free **1**.

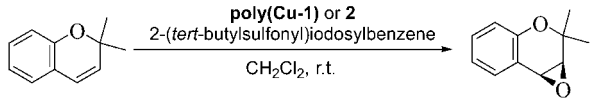


(1)

 © 2007 Wiley-VCH Verlag GmbH & Co. KGaA, Weinheim 

Table 1. Recyclability of **poly(Cu-1)** in the asymmetric epoxidation of 2,2-dimethyl-2*H*-chromene with 2-(*tert*-butylsulfonyl)iodosylbenzene.[a]

| Entry | Catalyst | Reuse cycle | Yield [%][b] | *ee* [%][c] | Leaching [%][d] of Cu/Mn |
|---|---|---|---|---|---|
| 1 | **2** | 1st | 87 | 86 | not applicable |
| 2 | **poly(Cu-1)** | 1st | 79 | 76 | 2.9:1.5 |
| 3 | **poly(Cu-1)** | 2nd | 74 | 76 | 1.8:1.6 |
| 4 | **poly(Cu-1)** | 3rd | 78 | 75 | 0.5:0.9 |
| 5 | **poly(Cu-1)** | 4th | 80 | 76 | 0.1:0.3 |
| 6 | **poly(Cu-1)** | 5th | 80 | 75 | 0.1:0.1 |
| 7 | **poly(Cu-1)** | 6th | 73 | 76 | 0.1:0.1 |
| 8 | **poly(Cu-1)** | 7th | 79 | 76 | $< 0.1$: $< 0.1$ |
| 9 | **poly(Cu-1)** | 8th | 72 | 75 | $< 0.1$: $< 0.1$ |
| 10 | **poly(Cu-1)** | 9th | 69 | 75 | not detectable |
| 11 | **poly(Cu-1)** | 10th | 70 | 76 | not detectable |

[a] Molar ratio olefin/oxidant/catalyst = 100:150:1. [b] GC yield after 2 h with undecane as an internal standard. [c] Determined by using a Supelco β-DEX 120 chiral GC column. [d] Measured by ICP mass spectrometry.

Encouraged by the persistence of catalytic activity for **poly(Cu-1)**, we examined its recyclability. Samples of **poly(Cu-1)** were easily recovered by centrifugation after catalysis and rinsed with dichloromethane and acetone before being used again for epoxidation. Remarkably, **poly(Cu-1)** can be recycled up to ten times with little loss in activity (79% → 70% yield) and no loss in enantioselectivity (75–76% *ee*) (Table 1, entries 2–11). Evaluation of the product solutions by ICP mass spectrometry, after removing the catalyst particles, showed that 3.1% of the manganese and 4.7% of the copper initially leached out during the first two cycles (Table 1, entries 2 and 3). However, this metal loss quickly decreased during the next four cycles (Table 1, entries 4–7), and no leaching was detected in the last stages of recycling (Table 1, entries 10 and 11). Together with the retention of activity and selectivity mentioned above, it is conceivable that the initial leaching could have arisen from Cu$^{II}$ ions and **1** that were weakly bound or entrapped in **poly(Cu-1)**. As **poly(Cu-1)** undergoes successive recycling, these weakly bound or entrapped ions and compounds are removed, leading to a substantial decrease in leaching after the second cycle.

Figure 3 compares the epoxidation activity of **poly(Cu-1)** to that of compound **2** in dichloromethane solution over a 3-h period under high-oxidant conditions (ca. 13 times the concentration used for the experiments in Table 1). As is often observed for homogeneous epoxidation catalysts, **2** is initially highly effective; however, it loses much of its activity after the first few minutes, followed by complete deactivation in less than 0.5 h. In contrast, the insoluble catalyst **poly(Cu-1)** exhibits a lifetime that is significantly greater ($> 3$ h) than that of **2**.[13] In addition, the enantioselectivity of **poly(Cu-1)** stays consistent throughout the reaction, indicating that it is inherent to the nature of the system and that the Cu-coordinated **1** is probably more stable than **1** itself during the epoxidation. Although the rate of catalysis by **poly(Cu-1)** is slower than that by **2**, presumably because of the biphasic nature of its reaction, a total turnover number (TON) greater than 2000 can be obtained within 3 h. Employing a filtered homogeneous reaction mixture as catalyst in the epoxidation of chromene provides no significant TON, suggesting that the catalysis occurs heterogeneously. Interestingly, use of the recovered **poly(Cu-1)** under the same high-oxidant conditions only affords about 600 turnovers in the 3-h period and with a slightly lower *ee* (ca. 60%). These data suggest that although **poly(Cu-1)** is highly stable under practical synthetic laboratory scale (0.17 M), it is not immortal and can eventually be degraded under highly oxidative environments.

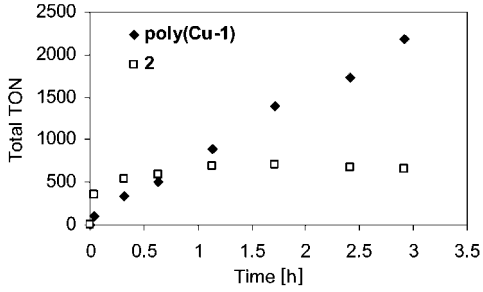


Figure 3. Plots of total turnover number (TON) vs. time for the epoxidation of 2,2-dimethyl-2*H*-chromene catalyzed by **poly(Cu-1)** (diamonds) and **2** (empty squares).

The catechol-based coordination-polymer-formation strategy is general for a wide range of metal ions, including Cr$^{III}$, Mn$^{II}$, Fe$^{III}$, Co$^{II}$, Ni$^{II}$, Zn$^{II}$, Cd$^{II}$, and Mg$^{II}$. Similar to the procedure for the formation of **poly(Cu-1)**, separately prepared solution mixtures of compound **1** and TEA were exposed to deoxygenated DMF solutions of $CrCl_3$, $MnCl_2$, $FeCl_3$, $CoCl_2$, $NiCl_2$, $ZnCl_2$, $Cd(NO_3)_2{\cdot}4H_2O$, or $MgCl_2$. All mixtures yielded spontaneous precipitation of the desired **poly(M-1)** products as dark brown solids except for the polymer derived from Fe$^{III}$ [**poly(Fe-1)**], which was red brown.

The catalytic activities of **poly(M-1)** were also examined through the asymmetric epoxidation of 2,2-dimethyl-2*H*-chromene with 2-(*tert*-butylsulfonyl)iodosylbenzene as the oxidant. As shown in Table 2, all **poly(M-1)** compounds catalyzed this epoxidation but to varying extents. Polymers assembled with Cr$^{III}$, Mn$^{II}$, Cd$^{II}$, and Mg$^{II}$ nodes gave the highest yields ($> 70$%; Table 2, entries 1–4) followed by those with Co$^{II}$ and Zn$^{II}$ (Table 2, entries 5 and 6). While enantioselectivities for **poly(Cr-1)**, **poly(Cd-1)**, **poly(Mg-1)**, and **poly(Zn-1)** were the same as that of **poly(Cu-1)** (76% *ee*), **poly(Mn-1)** and **poly(Co-1)** gave slightly lower *ee* values (60 and 52%, respectively). ICP mass spectrometric analysis for Mn was also performed for each epoxidation to estimate the extent of catalyst leaching. Similar to **poly(Cu-1)**, polymers assembled with Cr$^{III}$, Mn$^{II}$, Cd$^{II}$, Mg$^{II}$, Co$^{II}$, and Zn$^{II}$ exhibited ca. 1–3% catalyst leaching during catalysis.

Polymers assembled from Fe$^{III}$ and Ni$^{II}$ afforded poor epoxide yields (Table 2, entries 7 and 8). These low activities are accompanied by low enantioselectivities (48% and 20% *ee*), which suggests either potential competing oxidation from the added linker ions or that the Mn-based catalytic sites of **poly(Fe-1)** and **poly(Ni-1)** are damaged or inaccessible. Notably, a large amount of manganese (19%) was

 © 2007 Wiley-VCH Verlag GmbH & Co. KGaA, Weinheim 

Table 2. Catalytic performance of **poly(M-1)** in the asymmetric epoxidation of 2,2-dimethyl-2*H*-chromene with 2-(*tert*-butylsulfonyl)iodosylbenzene.[a][14]

| Entry | Catalyst | Yield [%][b] | *ee* [%][c] | Manganese leaching [%][d] |
|---|---|---|---|---|
| 1 | **poly(Cr-1)** | 78 | 76 | 2.6 |
| 2 | **poly(Mn-1)** | 89 | 60 | 1.8[e] |
| 3 | **poly(Cd-1)** | 71 | 76 | 1.8 |
| 4 | **poly(Mg-1)** | 70 | 76 | 2.2 |
| 5 | **poly(Co-1)** | 49 | 52 | 2.6 |
| 6 | **poly(Zn-1)** | 66 | 76 | 2.2 |
| 7 | **poly(Fe-1)** | 22 | 48 | 19 |
| 8 | **poly(Ni-1)** | 31 | 20 | 0.5 |

[a] Molar ratio olefin/oxidant/catalyst = 100:150:1. [b] GC yield after 2 h with undecane as an internal standard. [c] Determined by using a Supelco β-DEX 120 chiral GC column. [d] Measured by ICP mass spectrometry. [e] Combined amount of Mn leached from complex **1** and the catechol complex.

found to leach from **poly(Fe-1)**, conceivably as a result of the displacement of $Mn^{III}$ by $Fe^{III}$. A color change from dark brown to red brown [the color of (salen)$Fe^{III}$ complexes, which are known to give lower *ee* than (salen)$Mn^{III}$ in epoxidation][15] during polymerization also supports this argument. Interestingly, **poly(Ni-1)** exhibited substantially less Mn leaching than the other polymers, suggesting that its Mn-based catalytic sites are not as readily accessible, which in turn may explain its low activity and selectivity.

## Conclusion

We have demonstrated that heterogeneous asymmetric catalysts can be formed by the coordination polymerization of chiral [bis(catechol)salen]$Mn^{III}$ catalysts and any of several di- or trivalent metal ions. These catalysts show catalytic activity comparable to their homogeneous counterpart, complex **1**, when used for epoxidation and exhibit great potential as recyclable catalysts. This polymerization approach provides a facile and efficient strategy for support-free heterogenization of molecular catalysts.

## Experimental Section

**Materials and Methods:** Please see Supporting Information.

**Preparation of poly(M-1):** In a 20-mL vial equipped with a magnetic stir bar were combined **1** (30 mg, $4.1 \times 10^{-2}$ mmol), TEA (19.0 mg, 0.16 mmol), and degassed DMF (10 mL) under a nitrogen atmosphere. In another vial was prepared a DMF solution of corresponding metal salts (0.10 M). To the DMF solution of **1** was added the salt solution in appropriate amount ([**1**]/[salts] = 1:1 for dicationic salts or [**1**]/[salts] = 3:2 for tricationic salts) over 10 min with vigorous stirring. Precipitates formed instantaneously, and the resulting slurry was left to stir for an additional 2 h under a nitrogen atmosphere. The solids were collected by filtration in air, washed with DMF ($3 \times 10$ mL), and dried under vacuum overnight. The samples were stored under $N_2$ prior to being used.

**General Procedure for the Asymmetric Epoxidation of 2,2-Dimethyl-2*H*-chromene:** To a 2-mL conical vial were added 2,2-dimethyl-2*H*-chromene (17.6 mg, $1.1 \times 10^{-4}$ mol), undecane (9.8 mg), and dichloromethane (1 mL). Catalyst ($1.1 \times 10^{-6}$ mol) was next placed in the vial along with a micro magnetic stir bar. The oxidant, 2-(*tert*-butylsulfonyl)iodosylbenzene (18.7 mg, $5.5 \times 10^{-5}$ mol), was then added as a solid to the mixture to start the reaction. The same quantity of oxidant was added twice more at 20-min intervals (total amount added = $1.7 \times 10^{-4}$ mol). Aliquots (40 μL) of the reaction mixture were taken, filtered through a silica gel plug (120 mg), and washed with $CH_2Cl_2$ (5 mL). The combined filtrate was analyzed by GC and chiral GC for yield and enantioselectivity, respectively.

**General Procedure for Recycling of poly(Cu-1):** After being used for the catalytic reaction, the mixture was centrifuged on a Hermle Z230MA centrifuge at 12,000 rpm for 1 min. The supernatant solution was decanted for analysis by GC. The remaining solid was washed with acetone ($3 \times 1$ mL) followed by dichloromethane ($3 \times 1$ mL) before being dried in air for 0.5 h prior to being reused.

**General Procedure for the Asymmetric Epoxidation of 2,2-Dimethyl-2*H*-chromene under High-Oxidant Conditions:** To a 3.7-mL screw-threaded vial (15 mm × 45 mm) were added a dichloromethane solution of 2,2-dimethyl-2*H*-chromene (2.25 mM, 2 mL, $5.5 \times 10^{-3}$ mol) and undecane (100 mg) as an internal standard. The catalyst ($1.1 \times 10^{-6}$ mol) was next placed in the vial along with a micro magnetic stir bar. The oxidant, 2-(*tert*-butylsulfonyl)iodosylbenzene (136 mg, $4.0 \times 10^{-4}$ mol), was then added as a solid to the reaction mixture to start it. The same quantity of oxidant was added 10 more times at 10 min intervals (total amount added = $4.4 \times 10^{-3}$ mol). Aliquots (20 μL) of the reaction mixture were taken periodically over 3 h, filtered through a silica gel plug (60 mg), and washed with $CH_2Cl_2$ (5 mL). The combined filtrate was analyzed by GC and chiral GC for yield and enantioselectivity, respectively.

**Supporting Information** (see footnote on the first page of this article): Synthetic procedures and characterization data for **1** and **2**; ESI-MS, FTIR, TGA, and BET isotherm data for **poly(Cu-1)**; ICP mass spectroscopic analysis of **poly(M-1)**; and procedure for catalyst dissolution.

## Acknowledgments

We gratefully acknowledge the U. S. National Science Foundation, the American Association of University Women (fellowship for S.-H. C.), and the Institute for Energy in Catalytic Processes at Northwestern University (DOE grant # DE-FG02-01ER15244) for financial support. We also thank Dr. Michael Schwartz and Ms. Karen Mulfort for BET measurements and Dr. Jun-Hyun Kim for SEM measurements.

[1] For general reviews in coordination polymers, see: a) S. Kitagawa, R. Kitaura, S. Noro, *Angew. Chem. Int. Ed.* **2004**, *43*, 2334–2375; b) A. K. Cheetham, C. N. R. Rao, R. K. Feller, *Chem. Commun.* **2006**, 4780–4795; c) C. Janiak, *Dalton Trans.* **2003**, 2781–2804.

[2] For recent reviews in the applications of coordination polymers: a) U. Mueller, M. Schubert, F. Teich, H. Puetter, K. Schierle-Arndt, J. Pastre, *J. Mater. Chem.* **2006**, *16*, 626–636; b) A. Y. Robin, K. M. Fromm, *Coord. Chem. Rev.* **2006**, *250*, 2127–2157; c) Y. Y. Liu, J. F. Ma, J. Yang, Z. M. Su, *Inorg. Chem.* **2007**, *46*, 3027–3037.

[3] B. Kesanli, W. B. Lin, *Coord. Chem. Rev.* **2003**, *246*, 305–326.

[4] a) C. D. Wu, A. Hu, L. Zhang, W. Lin, *J. Am. Chem. Soc.* **2005**, *127*, 8940–8941; b) S. Takizawa, H. Somei, D. Jayaprakash, H. Sasai, *Angew. Chem. Int. Ed.* **2003**, *42*, 5711–5714; c) J. S. Seo, D. Whang, H. Lee, S. I. Jun, J. Oh, Y. J. Jeon, K. Kim, *Nature* **2000**, *404*, 982–986; d) O. R. Evans, H. L. Ngo, W. Lin, *J. Am.*

 © 2007 Wiley-VCH Verlag GmbH & Co. KGaA, Weinheim 

*Chem. Soc.* **2001**, *123*, 10395–10396; e) K. S. Suslick, P. Bhyrappa, J. H. Chou, M. E. Kosal, S. Nakagaki, D. W. Smithenry, S. R. Wilson, *Acc. Chem. Res.* **2005**, *38*, 283–291.
[5] S.-H. Cho, B. Ma, S. T. Nguyen, J. T. Hupp, T. E. Albrecht-Schmitt, *Chem. Commun.* **2006**, 2563–2565.
[6] See also the work of Lin and co-workers on noncrystalline zirconium phosphonate polymers: a) A. Hu, H. L. Ngo, W. B. Lin, *Angew. Chem. Int. Ed.* **2003**, *42*, 6000–6003; b) H. L. Ngo, A. G. Hu, W. B. Lin, *J. Mol. Catal. A* **2004**, *215*, 177–186.
[7] S.-H. Cho, N. D. Walther, S. T. Nguyen, J. T. Hupp, *Chem. Commun.* **2005**, 5331–5333.
[8] a) F. Rohrsche, A. L. Balch, R. H. Holm, *Inorg. Chem.* **1966**, *5*, 1542–1551; b) C. G. Pierpont, C. W. Lange, *Prog. Inorg. Chem.* **1994**, *41*, 331–442.
[9] Subsequent exposure to oxidant or air almost certainly converts the catecholates to semiquinones, see ref.[8]
[10] In our hands, reactions proceed slowly in toluene, both homogeneously and heterogeneously. Since it was not our primary intention to engineer a practical system, we did not explore other "greener" solvents.
[11] While the comparison between **1** and **poly(Cu-1)** would be more exact, **1** decomposes quickly in the presence of the oxidant because of its unprotected catechol functionality.
[12] a) F. Bedioui, *Coord. Chem. Rev.* **1995**, *144*, 39–68; b) L. Canali, D. C. Sherrington, *Chem. Soc. Rev.* **1999**, *28*, 85–93.
[13] Lifetime enhancement of a catalyst upon immobilization has precedents in porphyrin- and salen-based catalysis, see: a) D. A. Annis, E. N. Jacobsen, *J. Am. Chem. Soc.* **1999**, *121*, 4147–4154; b) M. Bonnet, L. Schmid, A. Baiker, F. Diederich, *Adv. Funct. Mater.* **2002**, *12*, 39–42; c) G. J. Kim, S. H. Kim, *Catal. Lett.* **1999**, *57*, 139–143; d) M. A. Martinez-Lorente, P. Battioni, W. Kleemiss, J. F. Bartoli, D. Mansuy, *J. Mol. Catal. A* **1996**, *113*, 343–353.
[14] As a consequence of catalyst exposure to oxidant, it is likely that the $Mn^{II}$, $Co^{II}$, and $Ni^{II}$ linking ions are oxidized as well.
[15] S. K. Edulji, Ph. D. Thesis in Chemistry, Northwestern University, Evanston, **2004**.

Received: March 19, 2007
Final Revision Received: August 24, 2007
Published Online: September 26, 2007

 © 2007 Wiley-VCH Verlag GmbH & Co. KGaA, Weinheim 

DOI: 10.1002/ejic.200700826

# Preparation and Characterization of a Ligand-Stabilized Trimethylphosphane Dication

**Jan J. Weigand,*[a] Neil Burford,*[a] Andreas Decken,[b] and Axel Schulz[c]**

*In memoriam of Prof. Dr. Nils Wiberg*

**Keywords:** Phosphane dication / Donor–acceptor complexes

The ditriflate salt of the DMAP-stabilized trimethylphosphane dication is formed from the reaction of chlorotrimethylphosphonium triflate with DMAP (4-dimethylaminopyridine) in the presence of trimethylsilyltriflate and also from the reaction of DMAP-dimethylphosphenium triflate with methyltriflate. The coordinative nature of the DMAP–phosphorus bond is demonstrated by a ligand exchange of DMAP for $PMe_3$ to give the hexamethyldiphosphonium dication.
(© Wiley-VCH Verlag GmbH & Co. KGaA, 69451 Weinheim, Germany, 2007)

## Introduction

Phosphorus exhibits a broad range of bonding environments and coordination numbers, and the chemistry of phosphorus is further diversified by the ability of compounds to accommodate negative or positive charges. Nevertheless, new electronic and structural arrangements for phosphorus are regularly reported. The Lewis acceptor properties of phosphorus have recently provided new synthetic approaches to new bonding environments.[1] Cations of phosphorus are the most versatile acceptors as classified in Figure 1 according to the coordination number and the charge.

Also summarized in Figure 1 are generic examples of donor–acceptor complexes that have been structurally characterized for monocations of type **A**,[2–8] **B**,[9–13] **C**,[1,14–18] **D**,[19–21] **E**[22,23] and **F**.[24] Complexes of a phosphorus dication of type **G** have been proposed on the basis of spectroscopic and chemical analysis data,[25–28] but solid-state structures have been confirmed for only two examples.[6,14,18] There are no structural reports of complexes involving cations of the type **H**, **I**, **J**, **K**, **L** or **M**.

We now report the preparation and isolation of complex **1** representing a 4-(dimethylamino)pyridine (DMAP) ligand on the dication of trimethylphosphane, the first example of a ligand-stabilized bonding environment **H**. Two preparative reactions demonstrate synthetic versatility and the solid-state structure provides fundamental comparisons with the DMAP complex of the isoelectronic group 13 Lewis acid $AlMe_3$.

Reaction of $[Me_3PCl][OTf]$ (OTf = trifluoromethanesulfonate; **2**[OTf], $\delta^{31}P$ = 94.0 ppm, $[D_3]$MeCN, room temp.) with DMAP in the presence of $Me_3SiOTf$ (Scheme 1, a) results in quantitative formation (isolated 93%) of the new salt **1**$[OTf]_2$ ($\delta^{31}P$ = 89.0 ppm, $[D_3]$MeCN, room temp.). The reaction represents a chloride ion displacement or ligand (neutral DMAP for chloride ion) exchange from monocation **2** (OTf = trifluoromethanesulfonate). Compound **1**$[OTf]_2$ is also formed quantitatively (isolated 95%) from the DMAP-phosphenium complex cation in **3**[OTf] ($\delta^{31}P$ = 91.3 ppm, $[D_3]$MeCN, room temp.) by reaction with MeOTf in the absence of solvent (Scheme 1, b). As illustrated in part c of Scheme 1, DMAP·$AlMe_3$ (**4**) was prepared quantitatively by reaction of $AlMe_3$ with DMAP in hexane.

The solid-state structure of **2**[OTf] (Figure 2) exhibits weak inter-ion contacts that give strands of alternating cations and anions along the *c* axis. The P–Cl distance [1.990(1) Å] is slightly shorter than that in $[Ph_3P–Cl\cdots Cl\cdots Cl–PPh_3]Cl·2CH_2Cl_2$ [2.015(9)].[29] The position of O1 [O1–P–Cl 178.33(5)°, P–O cation–anion contact 3.355(2) Å; cf. sum of the van der Waals radii $r_w(P) + r_w(O)$ = 3.32 Å][30] is envisaged as the associative site for DMAP in an $S_N2$ displacement of chloride. The cation in the solid-state structure of **3**(OTf) is shown in Figure 3, and is comparable to that of the previously reported $(DMAP·PPh_2)(OTf)$.[15]

[a] Dalhousie University, Department of Chemistry, Halifax, NS, B3H 4J3, Canada
Fax: +902-494-1310
E-mail: Neil.Burford@dal.ca
Jan.Weigand@dal.ca
[b] Department of Chemistry, University of New Brunswick Fredericton, NB, E3A 6E2, Canada
[c] Universität Rostock, Institut für Chemie, Abteilung Anorganische Chemie, Albert-Einstein-Straße 3a, 18059 Rostock, Germany
Supporting information for this article is available on the WWW under http://www.eurjic.org or from the author.

 © 2007 Wiley-VCH Verlag GmbH & Co. KGaA, Weinheim 

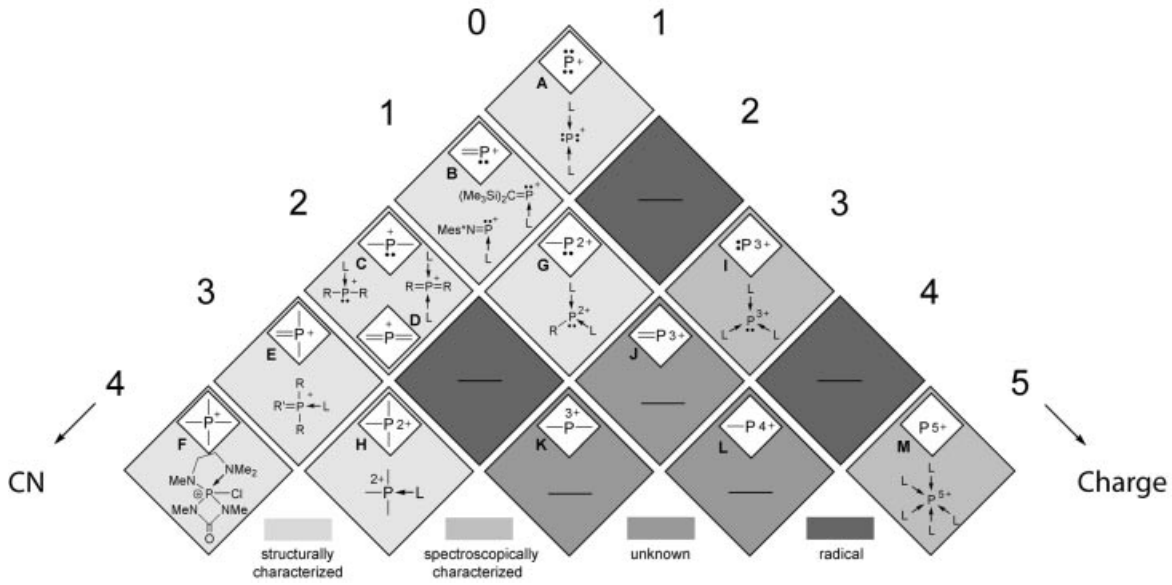


Figure 1. Bonding environments of cationic phosphorus centers and generic representations of isolated complexes.

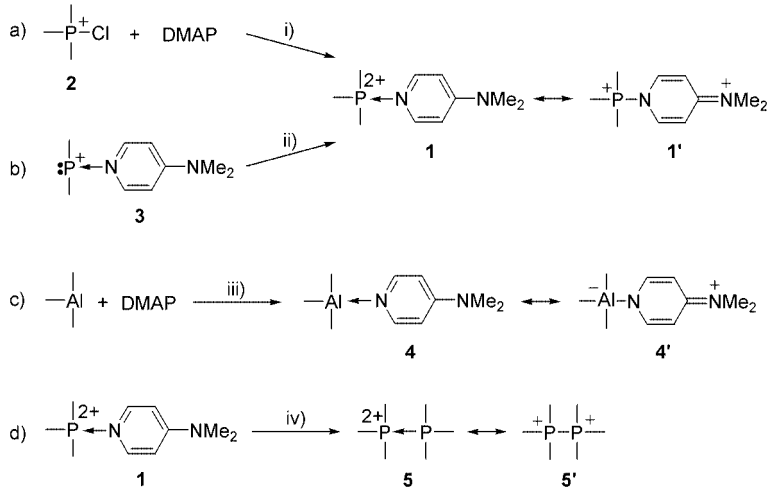


Scheme 1. Preparative routes to **1**[OTf]$_2$, **4**, and **5**[OTf]$_2$ [i) $Me_3SiOTf$, MeCN, – $Me_3SiCl$; ii) MeOTf; iii) hexane; iv) excess. $PMe_3$, – DMAP, MeCN].

Figure 4 shows the $^{31}P$ and $^{1}H$ NMR spectra for **1**[OTf]$_2$ as well as the bandshape analysis.[31] The phosphorus-coupled $^{1}H$ NMR spectrum exhibits a doublet centered at $\delta$ = 2.60 ppm assigned to the methyl groups attached to the phosphorus atom and the complex patterns at $\delta$ = 8.19 ppm and 7.13 ppm have been fitted as an AA′BB′$M_9X$ spin system. The $^{1}H$ and $^{13}C$ NMR signals for the *ortho* positions are upfield shifted, while those for the *meta* position are downfield shifted with respect to free DMAP (cf. $\delta^{1}_{H}$ = 8.21 and 6.46 ppm, [$D_3$]MeCN, room temp.).[32]

The solid-state structure of the dication in **1**[OTf]$_2$ is compared in Figure 3 with the structures of the monocation in **3**[OTf] and the neutral compound **4**. Selected bond lengths for DMAP,[33] **1**[OTf]$_2$, **2**[OTf], **3**[OTf] and **4** are listed in Table 1. The distinctly pyramidal geometry at phosphorus in monocation **3** is comparable with that in the diphenyl derivative, as is the P–N distance [**3**(OTf), 1.801(2) Å; ($Ph_2$P·DMAP)$^+$, 1.789(1) Å[15]]. The tetrahedral geometry of the phosphorus center in **1**[OTf]$_2$ is less distorted than that for the Al center in **4** (Figure 3). The DMAP ligand in all three complexes exhibits minimal structural adjustments with respect to free DMAP.[33] The Al–N distance [2.005(2) Å] in **4** is in the typical range for four-coordinate nitrogen-atoms involved in a donor–acceptor bond to an aluminium center (1.93–2.13 Å).[34] The P–N distance in **1**[OTf]$_2$ [1.720(3) Å] is significantly shorter than those in other DMAP complexes of phosphorus acceptors,[13,15,35] including **3**[OTf] [1.801(2) Å]. In addition, the P–C bonds in **1**[OTf]$_2$ [1.777(3), 1.772(3), 1.774(3) Å] are significantly shorter than those in **3**[OTf] [1.824(3), 1.826(3) Å] and in **4** [1.975(2), 1.971(2), 1.978(2) Å] (Table 1), all consistent with the greater positive molecular charge in **1**.

 © 2007 Wiley-VCH Verlag GmbH & Co. KGaA, Weinheim 

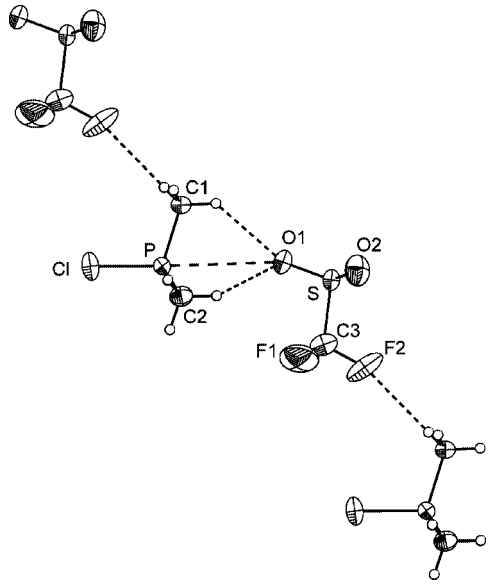


Figure 2. ORTEP view of a portion of the solid-state structure for **2**[OTf] along the *c* axis. Atoms Cl, P, C1, C3, S and F2 lie on a mirror plane, and atoms C2′, F1′ and O2′ are not shown. Amplitude displacement ellipsoids are depicted at 50% probability and hydrogen atoms with arbitrary radii.

The quinoidal character of the pyridine framework (Scheme 1, **1**′ and **4**′) is demonstrated in Table 1, by the C2–C3, C5–C6 and C4–N7 bonds being shorter in all complexes than in the free ligand. The trend in length for these bonds is **1** < **3** < **4** < DMAP, which we correlate with the relative strength of the N–E (E = P or Al) interaction in the complexes. Moreover, the N–E bond is shortest in the dicationic **1** and longest in **4**.

NBO analyses[36] and MO analyses of **4**, **3**, **1**, $AlMe_3$, $PMe_2^+$ and $PMe_3^{2+}$ at the B3LYP/6-31+G(d,p)[37] level provide charge-transfer and charge-distribution values that are summarized in Table 2. The donor–acceptor NP bond in **1** is purely σ in character and is strongly polarized (N: 75%, P: 25%) with a partial charge of 1.806 *e* at phosphorus, representing a substantial increase with respect to neutral $PMe_3$ (0.734 *e*). The calculated charge at phosphorus in the free $PMe_3^{2+}$ dication is 1.906 *e* (cf. 1.539 *e* at Al in $AlMe_3$) so that formation of **1** effects only a slight decrease in charge at phosphorus in the complex, although polarization of the P–C bonds in the $PMe_3$ fragment (P: 42%, C: 58%) contributes to the positive charge on phosphorus. The total charge transfer $Q_{CT}$ (from DMAP to acceptor, Table 2) in dication **1** (0.540 *e*) is significantly greater than that in **4** (0.158 *e*) and only slightly greater than that in **3** (0.411 *e*) consistent with the relative positive charge in each acceptor.

Reaction of **1** in MeCN with an excess of $PMe_3$ results in the displacement of DMAP and formation of **5**$[OTf]_2$ ($\delta^{31}P$ = 28.4 ppm, [D$_3$]MeCN, room temp.; isolated by $Et_2O$ diffusion into the reaction mixture)[38] (Scheme 1, d), which is understood in terms of a ligand exchange of DMAP in **1** by $Me_3P$.

## Summary

Compound **1**$[OTf]_2$ has been prepared by two methods and represents a ligand-stabilized $PMe_3^{2+}$, which is compared with the isoelectronic group 13 analog $AlMe_3$. The synthetic versatility of the first phosphane dication bodes well for the discovery and development of a series of ligand-stabilized multiply-charge phosphorus cations.

CCDC-650300 (for **1**$[OTf]_2$), -650302 (for **2**[OTf]), -650299 (for **3**[OTf]) and -650301 (for **4**) contain the supplementary crystallographic data for this paper. These data can be obtained free of charge from The Cambridge Crystallographic Data Centre via www.ccdc.cam.ac.uk/data_request/cif.

**Supporting Information** (see also the footnote on the first page of this article): Experimental and crystallographic details, NBO and MO data.

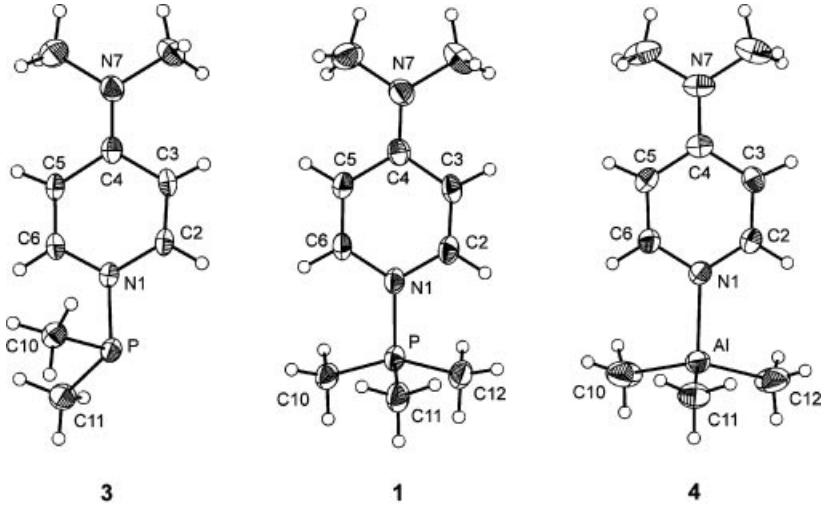


Figure 3. ORTEP views of the cations in **3**[OTf] and **1**$[OTf]_2$, and the neutral **4**. Amplitude displacement ellipsoids are depicted at 50% probability and hydrogen atoms with arbitrary radii.

 © 2007 Wiley-VCH Verlag GmbH & Co. KGaA, Weinheim 

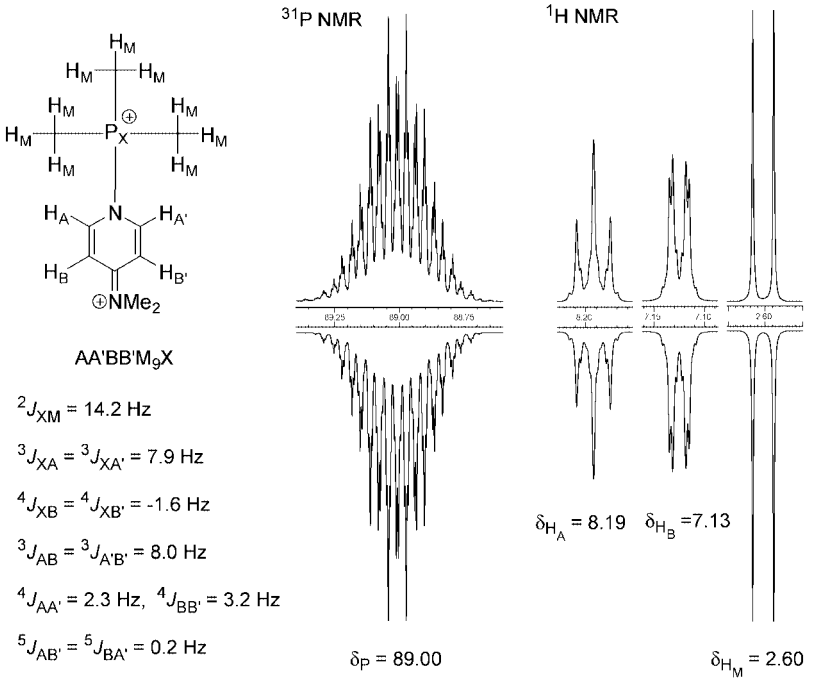


Figure 4. Experimental (upper) and simulated (lower) $^{31}P$ and $^{1}H$ NMR spectra of **1**[OTf]$_2$ (in [D$_3$]MeCN, room temp. [ppm]), cf. free DMAP, 8.21, 6.46 (in [D$_3$]MeCN).

Table 1. Selected interatomic distances [Å] for DMAP, **4**, **3**[OTf], **1**[OTf]$_2$, and **2**[OTf].

| | DMAP | **4** (E = Al, X = N1) | **3**[OTf] (E = P, X = N1) | **1**[OTf]$_2$ (E = P, X = N1) | **2**[OTf] (E = P, X = Cl) |
|---|---|---|---|---|---|
| E–C10(C1)[a] | – | 1.975(2) | 1.824(3) | 1.777(3) | 1.772(2) |
| E–C11(C2)[a] | – | 1.971(2) | 1.826(3) | 1.772(3) | 1.773(3) |
| E–C12(C2$^i$)[a] | – | 1.978(2) | – | 1.774(3) | 1.773(3) |
| E–X | – | 2.005(2) | 1.801(2) | 1.720(3) | 1.990(1) |
| C2–C3 | 1.381(3) | 1.369(2) | 1.354(3) | 1.340(4) | – |
| C3–C4 | 1.403(2) | 1.418(2) | 1.437(3) | 1.431(4) | – |
| C4–C5 | 1.404(3) | 1.409(2) | 1.416(3) | 1.432(4) | – |
| C5–C6 | 1.375(3) | 1.368(2) | 1.349(3) | 1.342(4) | – |
| C2–N1 | 1.337(3) | 1.348(2) | 1.367(3) | 1.380(3) | – |
| C6–N1 | 1.335(3) | 1.350(2) | 1.374(3) | 1.386(4) | – |
| C4–N7 | 1.367(2) | 1.350(2) | 1.339(3) | 1.319(4) | – |

[a] Atom labeling for **2**[OTf] in brackets [symmetry code: i) $x$, 0.5 – $y$, $z$].

Table 2. Charge-transfer ($Q_{CT}$) values and selected NPA charges in the DMAP complexes **4**, **3**, and **1** in *e*.

| | **4** | **3** | **1** | $PMe_3$ |
|---|---|---|---|---|
| $Q_{CT}$[a,b] | –0.158 | –0.411 | –0.540 | 1.387 |
| $Q_{CT}$(E)[c,d] | –0.056 | –0.316 | –0.100 | 1.073 |
| $Q_{CT}$(N1$_{ring}$)[e] | –0.094 | –0.098 | –0.178 | – |
| $Q_{CT}$(N7$_{amino}$)[e] | 0.019 | 0.064 | 0.125 | – |
| E[f] | 1.538[g] | 1.003[h] | 1.806[i] | 0.734 |
| N1[j] | –0.599 | –0.617 | –0.697 | – |
| N7[j] | –0.431 | –0.382 | –0.321 | – |

[a] For **1** and **4**: $Q_{CT}$ = –Σ $q$(E, DMAP, adduct), (ii) = Σ $q$(E, AlMe$_3$, adduct), (ii) = [Σ $q$(E, PMe$_3$, adduct)] – 2 = Σ [$q$(E, PMe$_3$, adduct) – $q$(E, PMe$_3^{2+}$)] (charge transfer based on PMe$_3^{2+}$) and for **3**: $Q_{CT}$ = –Σ $q$(E, DMAP, adduct). [b] In **1**: $Q_{CT}$ = Σ [$q$(E, PMe$_3$, adduct) – $q$(E, PMe$_3$)] charge transfer based on neutral PMe$_3$. [c] In **1**: $Q_{CT}$(P) = $q$(P, adduct) – $q$(P, PMe$_3^{2+}$), in **3**: $Q_{CT}$(P) = $q$(P, adduct) – $q$(P, PMe$_2^{+}$) and in **4**: $Q_{CT}$(Al) = $q$(Al, adduct) – $q$(Al, AlMe$_3$). [d] $Q_{CT}$(P) = $q$(P, adduct) – $q$(P, PMe$_3$), $q$(P, PMe$_3$) – $q$(P, PMe$_3^{2+}$) = 1.173 *e*. [e] $Q_{CT}$(N) = $q$(N, adduct) – $q$(N, DMAP). [f] E = P in **3** and **1**, Al in **4**. [g] 1.593 *e* In AlMe$_3$. [h] 1.319 *e* In PMe$_2^{+}$. [i] 1.906 *e* In PMe$_3^{2+}$. [j] –0.520 (N1) and –0.441 (N7) *e* in neutral DMAP.

## Acknowledgments

We thank the Natural Sciences and Engineering Research Council of Canada, the Killam Foundation, the Canada Research Chairs Program and the Alexander von Humboldt-Stiftung (Feodor Lynen program, fellowship for J. J. W.) for funding.

[1] N. Burford, P. J. Ragogna, *J. Chem. Soc. Dalton Trans.* **2002**, 4307–4315.
[2] A. Schmidpeter, S. Lochschmidt, W. S. Sheldrick, *Angew. Chem. Int. Ed. Engl.* **1982**, *21*, 63–64.
[3] A. Schmidpeter, S. Lochschmidt, W. S. Sheldrick, *Angew. Chem. Int. Ed. Engl.* **1985**, *24*, 226–227.
[4] B. Ellis, M. Carlesimo, C. Macdonald, *Chem. Commun.* **2003**, 1946–1947.
[5] P. Kilian, A. M. Z. Slawin, J. D. Woollins, *Dalton Trans.* **2006**, 2175–2183.
[6] A. Schmidpeter, S. Lochschmidt, K. Karaghiosoff, W. S. Sheldrick, *J. Chem. Soc. Chem. Commun.* **1985**, 1447–1448.
[7] A. Schmidpeter, S. Lochschmidt, *Inorg. Synth.* **1990**, *27*, 253–258.

 © 2007 Wiley-VCH Verlag GmbH & Co. KGaA, Weinheim 

[8] B. D. Ellis, C. L. B. Macdonald, *Inorg. Chem.* **2006**, *45*, 6864–6874.
[9] G. David, E. Niecke, M. Nieger, J. Radseck, W. W. Schoeller, *J. Am. Chem. Soc.* **1994**, *116*, 2191–2192.
[10] E. Niecke, M. Nieger, F. Reichert, *Angew. Chem. Int. Ed. Engl.* **1988**, *27*, 1715–1716.
[11] N. Burford, J. A. C. Clyburne, P. K. Bakshi, T. S. Cameron, *Organometallics* **1995**, *14*, 1578–1585.
[12] N. Burford, T. S. Cameron, J. A. C. Clyburne, K. Eichele, K. N. Robertson, S. Sereda, R. E. Wasylishen, W. A. Whitla, *Inorg. Chem.* **1996**, *35*, 5460–5467.
[13] N. Burford, H. A. Spinney, M. J. Ferguson, R. McDonald, *Chem. Commun.* **2004**, 2696–2697.
[14] G. Bouhadir, R. W. Reed, R. Réau, G. Bertrand, *Heteroat. Chem.* **1995**, *6*, 371–375.
[15] N. Burford, P. Losier, A. D. Phillips, P. J. Ragogna, T. S. Cameron, *Inorg. Chem.* **2003**, *42*, 1087–1091.
[16] N. Burford, P. J. Ragogna, R. McDonald, M. Ferguson, *J. Am. Chem. Soc.* **2003**, *125*, 14404–14410.
[17] N. Burford, C. A. Dyker, A. Decken, *Angew. Chem. Int. Ed.* **2005**, *44*, 2364–2367.
[18] R. Reed, R. Réau, F. Dahan, G. Bertrand, *Angew. Chem. Int. Ed. Engl.* **1993**, *32*, 399–401.
[19] P. Rovnaník, L. Kapièka, J. Taraba, M. Cerník, *Inorg. Chem.* **2004**, *43*, 2435–2442.
[20] M. Meisel, P. Lönnecke, A. R. Grimmer, D. Wulff-Molder, *Angew. Chem. Int. Ed. Engl.* **1997**, *36*, 1869–1870.
[21] M. Blättner, M. Nieger, A. Ruban, W. W. Schoeller, E. Niecke, *Angew. Chem. Int. Ed.* **2000**, *39*, 2768–2771.
[22] K. Huynh, A. J. Lough, I. Manners, *J. Am. Chem. Soc.* **2006**, *128*, 14002–14003.
[23] E. Rivard, K. Huynh, A. J. Lough, I. Manners, *J. Am. Chem. Soc.* **2004**, *126*, 2286–2287.
[24] T. Kaukorat, L. Ernst, R. Schmutzler, *Polyhedron* **1990**, *9*, 1463–1467.
[25] R. Weiss, S. Engel, *Synthesis* **1991**, 1077–1079.
[26] R. Weiss, S. Engel, *Angew. Chem. Int. Ed. Engl.* **1992**, *31*, 216–217.
[27] K. B. Dillon, R. J. Olivey, *Heteroat. Chem.* **2004**, *15*, 150–154.
[28] J. D. Burton, R. M. K. Deng, K. B. Dillon, P. K. Monks, R. J. Olivey, *Heteroat. Chem.* **2005**, *16*, 447–452.
[29] S. M. Godfrey, C. A. McAuliffe, R. G. Pritchard, J. M. Sheffield, *Chem. Commun.* **1996**, 2521–2522.
[30] F. Neumann, H. Teramae, J. H. Dowing, J. Michl, *J. Am. Chem. Soc.* **1998**, *120*, 582.
[31] Budzelaar, P. H. M. gNMR for Windows. [4.0]. **1997**. The Magdalen Centre, Oxford Science Park, Oxford OX4 4GA, UK, Cherwell Scientific Publishing Limited. Ref Type: Computer Program.
[32] T. J. Batterham, NMR Spectra of Simple *Heterocycles*, Wiley, New York, **1973**.
[33] U. Ohms, H. Guth, *Z. Kristallogr.* **1984**, *166*, 213–217.
[34] F. Thomas, T. Bauer, S. Schultz, M. Nieger, *Z. Anorg. Allg. Chem.* **2003**, *629*, 2018–2027.
[35] N. Burford, A. D. Phillips, H. A. Spinney, M. D. Lumsden, U. Werner-Zwanziger, M. J. Ferguson, R. McDonald, *J. Am. Chem. Soc.* **2005**, *127*, 3921–3927.
[36] a) E. D. Glendening, A. E. Reed, J. E. Carpenter, F. Weinhold, *NBO Version 3.1*; b) J. E. Carpenter, F. Weinhold, *J. Mol. Struc. (Theochem)* **1988**, *169*, 41–62; c) F. Weinhold, J. E. Carpenter, *The Structure of Small Molecules and Ions*, Plenum Press, **1988**, 227; d) F. Weinhold, C. Landis, *Valency and Bonding*. *A Natural Bond Orbital Donor-Acceptor Perspective*, Cambridge University Press, **2005** and references cited therein.
[37] Single point calculations were computed with a tight conversion criterion using the program package Gaussian 98. For computational details see Supporting Information; M. J. Frisch, G. W. Trucks, H. B. Schlegel, G. E. Scuseria, M. A. Robb, J. R. Cheeseman, V. G. Zakrzewski, J. A. Montgomery Jr., R. E. Stratmann, J. C. Burant, S. Dapprich, J. M. Millam, A. D. Daniels, K. N. Kudin, M. C. Strain, O. Farkas, J. Tomasi, V. Barone, M. Cossi, R. Cammi, Mennucci, B. C. Pomelli, C. Adamo, S. Clifford, J. Ochterski, G. A. Petersson, P. Y. Ayala, Q. Cui, Morokuma, K. D. K. Malick, A. D. Rabuck, K. Raghavachari, J. B. Foresman, J. Cioslowski, J. V. Ortiz, B. B. Stefanov, G. Liu, A. Liashenko, P. Piskorz, I. Komaromi, R. Gomperts, R. L. Martin, D. J. Fox, T. Keith, M. A. Al-Laham, C. Y. Peng, A. Nanayakkara, C. Gonzalez, M. Challacombe, P. M. W. Gill, B. Johnson, W. Chen, M. W. Wong, J. L. Andres, M. Head-Gordon, E. S. Replogle, J. A. Pople, *Gaussian 98*, Revision A7 and A11, Gaussian Inc., Pittsburgh PA, **1998**.
[38] J. J. Weigand, S. D. Riegel, N. Burford, A. Decken, *J. Am. Chem. Soc.* **2007**, *129*, 7969–7976.

Received: June 16, 2007
Published Online: September 21, 2007

 © 2007 Wiley-VCH Verlag GmbH & Co. KGaA, Weinheim 

DOI: 10.1002/ejic.200700839

# Turbostratic Boron Nitride Coated on High-Surface Area Metal Oxide Templates

Søren K. Klitgaard,[a] Kresten Egeblad,[a] Michael Brorson,[b] Konrad Herbst,[b] and Claus H. Christensen*[a]

**Keywords:** Boron nitride / Turbostratic / Metal oxide templates / Catalyst support material / Nanostructure

Boron nitride coatings on high-surface area $MgAl_2O_4$ and $Al_2O_3$ have been synthesized and characterized by transmission electron microscopy and by X-ray powder diffraction. The metal oxide templates were coated with boron nitride using a simple nitridation in a flow of ammonia starting from ammonium borate adsorbed on $MgAl_2O_4$ or $\gamma$-$Al_2O_3$. This procedure resulted in the formation of a turbostratic boron nitride film with a thickness of a few individual BN layers.

(© Wiley-VCH Verlag GmbH & Co. KGaA, 69451 Weinheim, Germany, 2007)

## Introduction

The importance of boron nitride (BN) as a ceramic material, a lubricant, and for other industrial purposes is increasing. Whereas boron nitride in many respects is similar to carbon because of the isoelectronic relation, some important differences between the properties of the two materials remain. On one hand, boron nitride, like carbon, exists in several allotropic forms, including a diamond-like cubic structure and a graphite-like hexagonal layer structure. Even boron nitride nanotubes[1] and an intriguing boron nitride nanomesh[2] were recently reported. On the other hand, white hexagonal BN (occasionally referred to as "white graphite") is a good insulator with a bandgap around ca. 5.3 eV,[3] whereas black graphite is a semimetallic conductor. Both materials are resistant towards most reagents, but boron nitride is slightly less so due to its more polarized bonds. However, boron nitride is superior to carbon when it comes to thermal stability, in air and also in hydrogen. This has led to numerous studies on the use of boron nitride as a non-oxide ceramic material.[4–6] Due to the excellent stability of boron nitride at high temperatures and under harsh chemical conditions it has found application as a support material for heterogeneous catalysts.[7–12] The growing interest in using boron nitride as a catalyst support material, in particular for reactions where carbon is not stable, has increased the need for simple ways of synthesizing high-surface area boron nitride – an undertaking that normally involves considerable technical difficulties.[3,13] Very recently, the use of organic-inorganic block copolymers have been used to produce BN and BCN nanostructured ceramics with very high-surface areas.[14]

## Results and Discussion

Here we present a simple, versatile procedure for the formation of high-surface area turbostratic boron nitride by high-temperature nitridation of ammonium borate adsorbed on high-surface area $MgAl_2O_4$ or $\gamma$-$Al_2O_3$ with ammonia.

Previously, reports of BN thin films on different substrates have appeared in the literature.[3,7,15,16–19] Paine et al. showed that large $Al_2O_3$, $TiO_2$ and MgO single crystals could be covered by BN thin films using pyrolysis of a solid polymer formed by cross-linking chloroborazenes with hexamethyldisilazane.[4,16] Also, the preparation of BN films on metallic surfaces obtained by thermal decomposition of borazine or related compounds have been reported.[17,18]

In the present work, BN was synthesized by impregnating high-surface area $MgAl_2O_4$ and $Al_2O_3$ with aqueous precursor solutions of ammonium borate, using readily available boric acid as the source of boron, followed by high temperature nitridation in a flow of ammonia.[15,20] One advantage of the present procedure is its simplicity and the fact that it can be easily modified to control the extent of BN coverage on the metal oxide. $Al_2O_3$ and $MgAl_2O_4$ was chosen as the templates because they are considered completely inactive in redox processes and both known as inert support materials from the literature.[21,22] Given the stability, a removal of the metal oxides has not been attempted here even though new interesting structures could be envis-

[a] The Center for Sustainable and Green Chemistry, Department of Chemistry, Building 206, Technical University of Denmark, 2800 Lyngby, Denmark
E-mail: chc@kemi.dtu.dk
[b] Haldor Topsøe A/S,
Nymøllevej 55, 2800 Lyngby, Denmark

Supporting information for this article is available on the WWW under http://www.eurjic.org or from the author.

 © 2007 Wiley-VCH Verlag GmbH & Co. KGaA, Weinheim 

aged. Other templating approaches to produce high-surface area BN have been reported recently. For instance, a soft-template approach involving surfactant assembly[23] and also a hard-template method involving the use of carbon as mesopore hard-template for making boron nitride and boron carbon nitride, BCN, using $B_2O_3$ as precursor was reported.[19] These materials were prepared by reaction with $N_2$ which require very high reaction temperatures (1500–1750 °C) due to the thermodynamic stability of $N_2$. By conducting the nitridation with ammonia the reaction temperature can be lowered.

The boron content of all the samples was determined by elemental analysis using Inductively Coupled Plasma (ICP) analysis. Prior to ICP analysis, the boron nitride coated samples were pretreated with aqua regia in a microwave oven leading to decomposition of boron nitride and its dissolution as boric acid. As shown in Table 1, the measured boron contents are in good agreement with those calculated. Table 1 also lists the surface areas measured at liquid-nitrogen temperature with a Micromeritics ASAP 2020, and calculated using the BET (Brunauer–Emmett–Teller) method.[24] As seen in Table 1, the BET surface areas of all the samples are moderate to high, though not as high as the parent metal oxide templates. The surface area of the boron nitride is very much dependent on the choice of metal oxide. By choosing a high-surface area metal oxide it will give a high-surface area boron nitride. Not surprisingly, a further decrease in the surface area is observed with successive BN coatings of the $MgAl_2O_4$ sample. This can be interpreted as encapsulation of the individual metal oxide crystals into larger agglomerates giving an overall smaller surface area.

Figure 1 shows a representative high-resolution transmission electron microscopy (TEM) image of the prepared BN-coated $MgAl_2O_4$, impregnated once with the precursor solution. The images were obtained by means of a JEM 2000FX microscope operated at an accelerating voltage of 300 kV. For sample preparation, ground powders were dispersed in ethanol and deposited on a 300 mesh copper grid coated with a holey carbon film. Figure 1 shows $MgAl_2O_4$ particles coated with a thin film of BN. The BN films, which coat and apparently fully encapsulate the metal oxide particles, have thicknesses between 0.5 and 3 nm. These films consist of 2 to 6 individual BN sheets. Judged from Figure 1, the thickness of a stack of 6 sheets is estimated to be ca. 1.8 nm resulting in an interlayer distance between the sheets of ca. 0.3 nm. This distance compares well with the 0.333 nm interlayer distance of bulk hexagonal BN.[3] The composition of the BN film was qualitatively confirmed by elemental analysis using energy-dispersive X-ray (EDX) analysis. TEM analyses of the samples with higher BN content, i.e. samples impregnated two or three times with precursor solution, showed BN coating of agglomerates of metal oxide particles already coated with BN (see electronic supporting information, Figure S1).

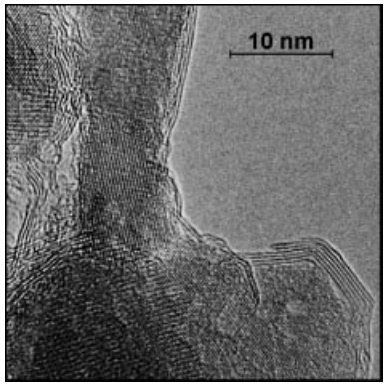


Figure 1. TEM image of BN on $MgAl_2O_4$ impregnated once. A thin film of BN encapsulates the $MgAl_2O_4$ particles. The film consists of 2–6 layers of BN.

Figure 2 shows a TEM image of BN-coated $Al_2O_3$ obtained by impregnating once with the precursor solution. $Al_2O_3$ is encapsulated by BN in a manner very similar to that of $MgAl_2O_4$, as 2–6 BN layers are formed. Multiple impregnations of $Al_2O_3$ are expected to show a similar behaviour as those of $MgAl_2O_4$.

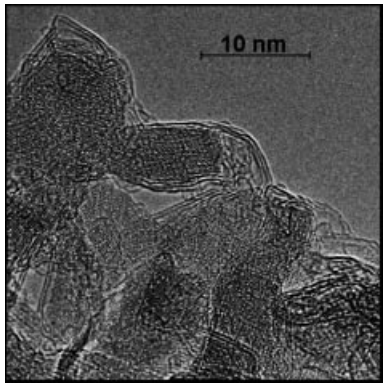


Figure 2. TEM image of BN on $Al_2O_3$. The $Al_2O_3$ particles are coated with a thin BN film.

Table 1. Boron contents and BET surface areas.

| Support material | Number of impregnations | Boron content measured [wt.-%] | Boron content calculated [wt.-%] | BET Surface area [$m^2/g$] |
|---|---|---|---|---|
| $MgAl_2O_4$ | 0 | 0 | 0 | 72 |
| $MgAl_2O_4$ | 1 | 4.67 | 4.49 | 39 |
| $MgAl_2O_4$ | 2 | 7.77 | 8.13 | 27 |
| $MgAl_2O_4$ | 3 | 10.70 | 11.16 | 14 |
| $Al_2O_3$ | 0 | 0 | 0 | 228 |
| $Al_2O_3$ | 1 | 4.30 | 4.49 | 175 |

 © 2007 Wiley-VCH Verlag GmbH & Co. KGaA, Weinheim 

X-ray powder diffraction (XRPD) patterns of all samples were recorded after nitridation. Figure 3 shows the XRPD patterns of the $MgAl_2O_4$ sample coated (a) twice and (b) three times with BN; the remaining XRPD patterns are available as supplementary information (Figures S2–S3). In the XRPD patterns of BN-coated $MgAl_2O_4$ and $Al_2O_3$ samples that were impregnated once with precursor solution, only the parent metal oxide templates are observed, whereas the BN films are X-ray amorphous. This is because the BN film is too thin to give rise to any diffraction showing that all BN in the samples is present as film and that no bulk BN is present. However, when increasing the BN content by impregnating a second or third time, the BN phase appears as broad diffraction peaks at $2\theta$ ca. 26° and 43° in the diffraction pattern of BN-coated $MgAl_2O_4$. These diffraction maxima can be assigned to a boron nitride phase which has previously been described in the literature as turbostratic BN.[25] Turbostratic materials are characterized by having a structure of roughly parallel layers, these layers, however, showing random rotation and translation about the layer normal.[26] In an X-ray diffraction pattern, turbostratic BN can be indexed on the basis of the diffraction maxima of well-defined hexagonal BN, although some reflections of hexagonal BN alter their shape and other reflections are missing. The most characteristic changes caused by the layer disorder in turbostratic relative to hexagonal BN are seen in a broadening of the (002) reflection at $2\theta$ = 26.4°, the appearance of a two-dimensional (10) reflection at $2\theta$ = 42.4° merged from the (100) and (101) reflections and the disappearance of higher indexed reflections (102), (004) and (103) above $2\theta$ = 45°.[25] These features, although partially covered by the diffraction maxima of the spinel phase, are most clearly visible in the diffraction pattern shown in Figure 3, (b).

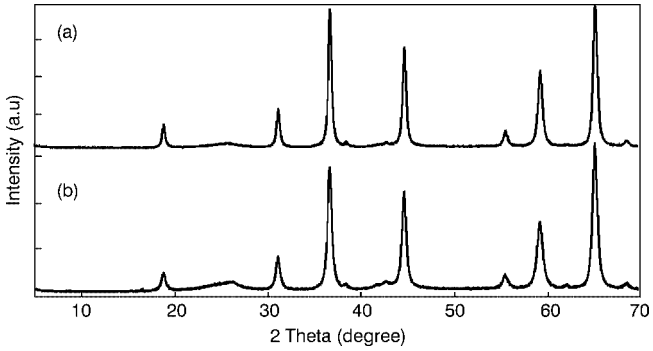


Figure 3. XRPD patterns of the BN samples coated (a) twice and (b) three times on $MgAl_2O_4$. The turbostratic BN phase appears at $2\theta$ ca: 26° and 43°.

Both diffraction maxima of turbostratic boron nitride can be used for the calculation of the particle size, although different information is obtained from the three-dimensional (002) reflection and the two-dimensional (10) reflection. The (002) reflection renders information about the crystallite size along the *c* axis, i.e. the thickness $L_c$ of the crystallite. From the (002) reflections in Figure 3, (a) and (b), $L_c$ parameters of 2.5 and 2.2 nm, respectively, can be determined. The interlayer spacings $d_{(002)}$, obtained from the exact position of the (002) peak maxima, are 0.344 nm in Figure 3, (a) and 0.339 nm in Figure 3, (b). This means that the BN film is, on average, 7 individual layers of BN thick confirming the impression from the TEM image shown in Figure S1. The slightly higher value for the *d* spacing in samples containing turbostratic BN compared to well-ordered hexagonal BN is consistent with the layer disorder in these samples, and several subpolytypes of turbostratic BN have been discussed in the literature.[27] On the other hand, the two-dimensional (10) reflection can be used to calculate the width of the crystallite layer. However, in the diffraction patterns of the BN-coated $MgAl_2O_4$ samples, the (10) reflection at $2\theta$ ca. 43° is partially covered by the (400) reflection of spinel, preventing an unambiguous determination of the line width of the (10) reflection.

The presence of a turbostratic boron nitride phase implies the presence of boron oxynitride ($BN_xO_y$) and amorphous boric oxide zones interconnecting the peripheries of the hexagonal planar boron nitride networks.[27–29] On the other hand, no indication for the presence of crystalline boric oxide with diffraction peaks at $2\theta$ = 13.58° and 27.98° is seen in the diffraction patterns shown in Figure 3. A removal of the oxygen impurities, coinciding with the growth and ordering of the BN layers to form crystalline BN, requires temperatures above 1350 °C.[29,30]

The diffraction pattern of BN coated on alumina (Figure S3) shows a mixture of two alumina phases, γ-alumina and θ-alumina, the latter being obtained by thermal degradation of γ-alumina at temperatures above 800 °C. Remarkably, no indication was found in the diffraction pattern for the formation of the thermodynamically stable α-alumina during the nitridation process, despite the thermal treatment of the coated material at 1100 °C for 24 h.

## Conclusions

In summary, composite materials of turbostratic boron nitride coated in various concentrations on high-surface area metal oxides, $MgAl_2O_4$ and $Al_2O_3$, were prepared by nitridation of ammonium borate with ammonia. This provides a simple way for the synthesis of high-surface area BN which could be an ideal support material for many heterogeneous catalytic applications.

## Experimental Section

In a typical synthesis of BN, a precursor solution was prepared by suspending $H_3BO_3$ (5.72 g, containing 1 g of boron) in $H_2O$ (7 mL) whilst stirring, followed by addition of aqueous $NH_3$ (3 mL, 24 wt.-%) resulting in a clear solution. Aqueous $NH_3$ was used to raise the solubility of $H_3BO_3$. The BN precursor solution (0.5 mL) was impregnated once onto high-surface area powders of $MgAl_2O_4$ or γ-$Al_2O_3$ (1 g) to incipient wetness, giving boron loads of ca. 4.5 wt.-% in each of the final the samples after the formation of boron nitride. Prior to nitridation, all samples were dried for at least 30 min at 100 °C. Nitridation was performed by passing a gentle flow of ammonia over the samples at 1100 °C for 24 h. Attempts

 © 2007 Wiley-VCH Verlag GmbH & Co. KGaA, Weinheim 

to lower the reaction temperature for nitridation resulted in incomplete BN coverage of the metal oxide particles. In order to increase the amount of boron nitride, samples obtained by first impregnation were dried for 30 min at 100 °C and then impregnated a second and third time.

**Supporting Information** (see also the footnote on the first page of this article): Figure S1 shows a TEM image of BN on $MgAl_2O_4$ impregnated three times (boron content ca. 11 wt.-%). Figure S2 and S3 show XRPD patterns of BN coated on $MgAl_2O_4$ and $Al_2O_3$ impregnated once.

## Acknowledgments

Center for Sustainable and Green Chemistry is sponsored by the Danish National Research Foundation.

[1] N. G. Chopra, R. J. Luyken, K. Cherrey, V. H. Crespi, M. L. Cohen, S. G. Louie, A. Zettl, *Science* **1995**, *269*, 966–967.
[2] M. Corso, W. Auwärter, M. Muntwiler, A. Tamai, T. Greber, J. Osterwalder, *Science* **2004**, *303*, 217–220.
[3] R. T. Paine, C. K. Narula, *Chem. Rev.* **1990**, *90*, 73–91.
[4] C. K. Narula, R. Schaeffer, R. T. Paine, *J. Am. Chem. Soc.* **1987**, *109*, 5556–5557.
[5] R. W. Rice, C. V. Matt, W. J. McDonough, K. McKinney, C. C. Wu, *Ceram. Eng. Sci. Proc.* **1982**, *3*, 698.
[6] S. D. Peteves, *Ceram. Int.* **1996**, *22*, 527–533.
[7] T. W. Hansen, J. B. Wagner, P. L. Hansen, S. Dahl, H. Topsøe, C. J. H. Jacobsen, *Science* **2001**, *294*, 1508–1510.
[8] J. C. S. Wu, W.-C. Chen, *Appl. Catal. A* **2005**, *289*, 179–185.
[9] G. Postole, M. Caldararu, N. I. Ionescu, B. Bonnetot, A. Auroux, C. Guimon, *Thermochim. Acta* **2005**, *434*, 150–157.
[10] C. J. H. Jacobsen, *J. Catal.* **2001**, *200*, 1–3.
[11] G. Postole, A. Gervasini, C. Guimon, A. Auroux, B. Bonnetot, *J. Phys Chem. B* **2006**, *110*, 12572–12580.
[12] G. Postole, B. Bonnetot, A. Gervasini, C. Guimon, A. Auroux, N. I. Ionescu, M. Caldararu, *Appl. Catal.* **2007**, *316*, 250–258.
[13] J. A. Perdigon-Melon, A. Auroux, D. Cornu, P. Miele, B. Toury, B. Bonnetot, *J. Organomet. Chem.* **2002**, *657*, 98–106.
[14] P. R. L. Malenfant, J. Wan, S. T. Taylor, M. Manoharan, *Nature* **2007**, *2*, 43–46.
[15] S. E. Nielsen, C. J. H. Jacobsen, H. Udesen, T. Shim and N. K. Sørensen, *U. S. Patent*, 7 025 944.
[16] R. T. Paine, C. K. Narula, R. Schaeffer, A. K. Datye, *Chem. Mater.* **1989**, *1*, 486–489.
[17] M. Corso, T. Greber, J. Osterwalder, *Surf. Sci.* **2005**, *577*, L78–L84.
[18] F. Müller, K. Stöwe, H. Sachdev, *Chem. Mater.* **2005**, *17*, 3464–3467.
[19] A. Vinu, M. Terrones, D. Golberg, S. Hishita, K. Ariga, T. Mori, *Chem. Mater.* **2005**, *17*, 5887–5890.
[20] A. Meller, *Gmelin Handbuch der Anorganischen Chemie*, *Borverbindungen*; Springer-Verlag: Berlin, **1974**, vol. 1, p, 1.
[21] M. Trueba, S. P. Trasatti, *Eur. J. Inorg. Chem.* **2005**, 3393–3403.
[22] C. H. Christensen, B. Jørgensen, J. Rass-Hansen, K. Egeblad, R. Madsen, S. K. Klitgaard, S. M. Hansen, M. R. Hansen, H. C. Andersen, A. Riisager, *Angew. Chem. Int. Ed.* **2006**, *45*, 4648–4651.
[23] P. Dibandjo, L. Bois, F. Chassagneux, P. Miele, *J. Eur. Ceram. Soc.* **2007**, *27*, 313–317.
[24] S. Brunauer, P. H. Emmett, E. Teller, *J. Am. Chem. Soc.* **1938**, *60*, 309–319.
[25] J. Thomas Jr, N. E. Weston, T. E. O'Connor, *J. Am. Chem. Soc.* **1963**, *84*, 4619–4622.
[26] J. Biscoe, B. E. Warren, *J. Appl. Phys.* **1942**, *13*, 364–371.
[27] M. Hubáček, T. Sato, T. Ishii, *J. Solid State Chem.* **1994**, *109*, 384–390.
[28] T. Masui, H. Hirai, R. Hamada, N. Imanaka, G. Adachi, T. Sakata, H. Mori, *J. Mater. Chem.* **2003**, *13*, 622–627.
[29] M. Hubáček, M. Ueki, T. Sato, V. Brožek, *Thermochim. Acta* **1996**, *282/283*, 359–367.
[30] Brožek, M. Hubáček, *J. Solid State Chem.* **1992**, *100*, 120–129.
Received: August 10, 2007
Published Online: September 28, 2007

 © 2007 Wiley-VCH Verlag GmbH & Co. KGaA, Weinheim 

DOI: 10.1002/ejic.200700590

# Straightforward Synthesis of Donor-Stabilised Phosphenium Adducts from Imidazolium-2-carboxylate and Their Electronic Properties

Michèle Azouri,[a] Jacques Andrieu,*[a] Michel Picquet,[a] Philippe Richard,[a] Bernard Hanquet,[a] and Igor Tkatchenko[a]

**Keywords:** Carboxylates / Phosphanes / Electronic properties / Synthesis / Coordination modes

Cationic imidazolium-2-phosphanes were obtained by the addition of a chlorophosphane ($R_2PCl$, R = Ph, *i*Pr or Cy) to 1,3-dimethylimidazolium-2-carboxylate without the need for a purification step. An additional anion exchange reaction with $KPF_6$ led to the corresponding halide-free ligands in excellent yields. The molecular structure of one of them was examined both in the solid state and in solution. The lone pair of electrons on the phosphorus atom is not delocalised to the imidazolium fragment and thus remains available for further metal coordination. As such compounds can be described as phosphenium cations stabilised by a N-heterocarbene donor base, the electronic properties of the Lewis acceptor phosphorus centre was evaluated upon nickel tricarbonyl coordination, and the properties are surprisingly similar to those found for phosphites. The stronger π-acceptor character of these imidazolium-2-phosphanes relative to that of neutral tertiary phosphanes can thus explain the higher catalytic activities observed with the corresponding rhodium complexes in styrene hydroformylation reactions. Additionally, a preliminary study of platinum coordination chemistry indicated that the steric demand of 1,3-dimethylimidazolium-2-phosphanes is comparable to mixed arylalkylphosphanes.
(© Wiley-VCH Verlag GmbH & Co. KGaA, 69451 Weinheim, Germany, 2007)

## Introduction

Imidazolium-functionalised phosphanes, when compared to neutral phosphane ligands, represent an interesting opportunity to decrease strongly the metal leaching in homogeneous polyphasic catalysis, especially with the use of an ionic liquid phase.[1–3] However, if the C-2 position of the imidazolium ring is unprotected, this type of cationic ligand can sometimes decrease the activity of the catalyst and/or the enantioselectivity of the reaction because of the production of zerovalent metals[4,5] induced by the formation of the corresponding chelating N-heterocarbene phosphane.[6] To overcome such a limitation, we thus focused our investigations on imidazolium-2-phosphanes. Moreover, these particular structures represent rare examples of "base donor, P acceptor complexes" involving an electron rich $P^{III}$ centre as the Lewis acceptor.[7] It is also noteworthy that a simple change in the substituent on the nitrogen atom can easily tune their electronic and steric properties.

There are few examples of imidazolium-2-phosphanes in the literature.[8] They are obtained either by selective N alkylation of the corresponding free[9] or metal-coordinated[10] neutral imidazolyl-2-phosphane or by the addition of chlorodiphenylphosphane to isolated[11] or in situ generated imidazol-2-ylidenes from the related imidazolium salts in the presence of a strong base.[1] However, all these preparations require several steps, most of which are quite difficult due to the air-sensitive phosphorus intermediates or the use of strong alkyllithium bases. Thus, we developed a short and easy synthetic method allowing the obtention of the expected products on a large scale. Our synthetic approach is thus based on the use of 1,3-dimethylimidazolium-2-carboxylate (**1**) as a N heterocarbene source,[12] as it was reported in the preparation of N heterocarbene metal complexes[13,14] or ionic liquids,[15,16] as well as in the study of its reactivity towards several chlorophosphanes.

## Results and Discussion

### Synthesis and Characterisation of Imidazolium-2-phosphanes

The chlorophosphanes $Ph_2PCl$ and $iPr_2PCl$ react smoothly with **1** to afford pure imidazolium-2-phosphanes **2a** and **2b**, respectively (see Experimental Section) after 4 h (Scheme 1). When the more sterically hindered chloroalkylphosphane $Cy_2PCl$ was used, complete conversion leading to cationic ligand **2c** was achieved after a longer period (ca. 8 h), which also favoured the formation of small amounts of 1,3-dimethylimidazolium chloride [MMIM]Cl as a result of the competitive hydrolysis of the chlorophosphane by trace amounts of water in the solution and the subsequent protonation–decarboxylation of **1** with HCl.[15,16] This side reaction is, however, inhibited by the addition of molecular

[a] Institut de Chimie Moléculaire de l'Université de Bourgogne (ICMUB) – UMR 5260 CNRS,
9, av. Alain Savary 21078 Dijon
E-mail: Jacques.Andrieu@u-bourgogne.fr

 © 2007 Wiley-VCH Verlag GmbH & Co. KGaA, Weinheim 

sieves. It is noteworthy that the bulky chlorodialkylphosphane $t$Bu$_2$PCl does not react with imidazolium-2-carboxylate at room temperature even after 24 h.

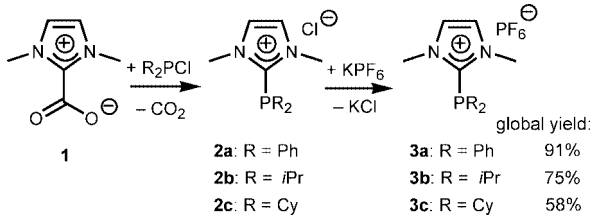


Scheme 1.

An anion exchange reaction of **2a**–**c** with $KPF_6$ in $CH_2Cl_2$, which can be done in a one-pot synthesis, led to the corresponding halide free ligands **3a**–**c** in excellent yields. Compounds **3a** and **3c** could be crystallised from dichloromethane/pentane as white plates in poor quality and as a white crystalline powder, respectively, which were therefore unsuitable for crystallographic studies. However, suitable crystals for X-ray structure determination were obtained for compound **3b** (Figure 1) from the same mixture of solvents.

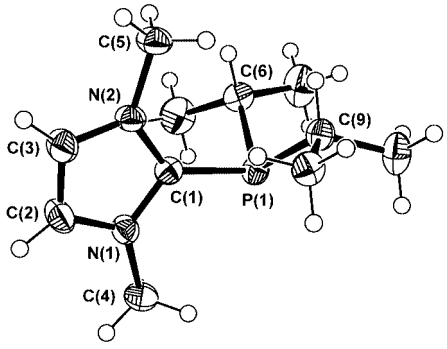


Figure 1. Molecular structure of **3b** with thermal ellipsoids presented at the 50% probability level. The $PF_6^-$ anion is omitted for clarity.

The ORTEP view shows that the P(1)–C(1) bond length of 1.840(3) Å (Table 1) is similar to that found in the 1,3-diisopropyl-4,5-dimethylimidazolium-2-phosphane analogue (1.813 Å)[11] obtained from the reaction of $Ph_2PCl$ and the corresponding imidazol-2-ylidene.

Table 1. Selected bond lengths [Å] and bond angles [°] for **3b**.

| | | | |
|---|---|---|---|
| P(1)–C(1) | 1.840(3) | P(1)–C(6) | 1.859(3) |
| P(1)–C(9) | 1.855(3) | C(1)–N(1) | 1.344(4) |
| C(1)–N(2) | 1.354(4) | C(4)–N(1) | 1.476(4) |
| C(5)–N(2) | 1.474(4) | C(2)–C(3) | 1.341(5) |
| N(1)–C(1)–N(2) | 105.6(3) | N(1)–C(1)–P(1) | 121.3(2) |
| N(2)–C(1)–P(1) | 133.0(2) | C(1)–P(1)–C(9) | 102.47(15) |
| C(1)–P(1)–C(6) | 98.96(15) | C(9)–P(1)–C(6) | 105.58(16) |
| C(9)–P(1)–C(1)–N(2) | 51.8(4) | C(6)–P(1)–C(1)–N(2) | –56.5(4) |

The imidazolium heterocycle is in the bisector plan of the C(9)–P(1)–C(6) angle [dihedral angles C(6,9)–P(1)–C(1)–N(2), Table 1], analogously to the structure of the above-mentioned cationic compound, possibly because of the strong steric hindrance of the methyl groups in the solid state. In $CDCl_3$ solution, we observed two different signals for the C(6,9)–$CH_3$ methyl groups. To obtain more information, an additional 1D-NMR NOE experiment was recorded at 298 K. Figure 2 shows a strong Overhauser effect of 2.5% between the irradiated N–Me groups and the C(6,9)H protons. This effect decreases from 1 to <0.2% for the C(6,9)Me$_{endo}$ and C(6,9)Me$_{exo}$ methyl groups, respectively. Such a difference in the Overhauser effect observed for the latter fragments proves that the spatial organisation of the isopropyl groups observed in the solid state is maintained in solution. However, the unique signals obtained at

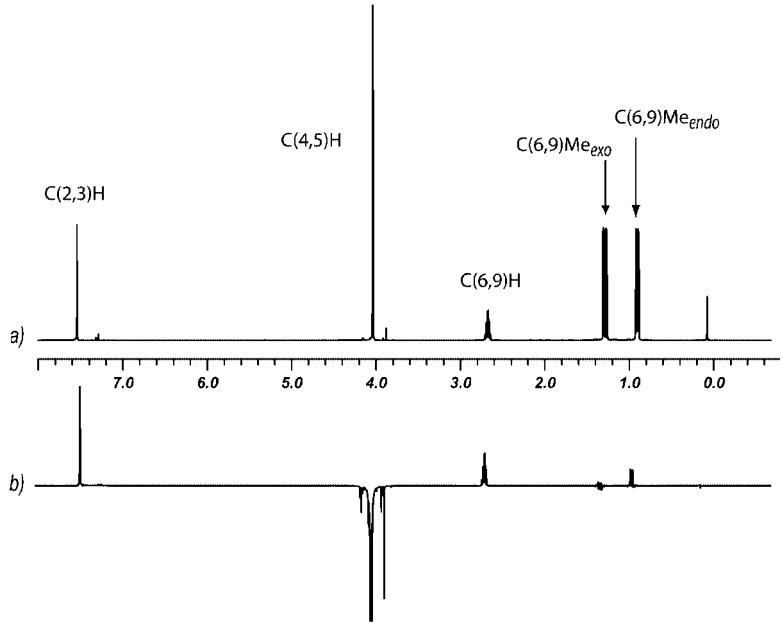


Figure 2. (a) $^1$H NMR spectrum and (b) NOE difference spectrum of **3b** in $CDCl_3$ at room temperature.

 © 2007 Wiley-VCH Verlag GmbH & Co. KGaA, Weinheim 

298 K for the N–Me group and for the olefinic CH moiety of compound **2** in the $^1$H and $^{13}$C NMR spectra (for example Figure 2, spectrum a) seemed to indicate free rotation of the imidazolium ring. Indeed, VT-NMR spectroscopic experiments in $CD_2Cl_2$ solutions were investigated at lower temperature and differentiation between the two N–Me signals and between the two olefinic CH was found at 193 K in the $^1$H and $^{13}$C NMR for **2a**, whereas the same phenomena was observed at 273 K for **2b**. These observations show unambiguously that the cationic fragment rotates around the P(1)–C(1) bond at room temperature, whereas the isopropyl groups do not rotate around the P–C(6,9) bonds. In addition, and in line with previous calculations,[7] this easy rotation of the imidazolium ring confirms that the lone pair of electrons on the P centre remains selectively localised on the phosphorus atom, which thus makes it available for further metal coordination.

## Mechanistic Aspects in the Formation of Imidazolium-2-phosphane

As our phosphorylation reaction contrasts other preparations of imidazolium-2-phosphanes because it does not involve the use of additional alkyllithium for the formation of the N heterocyclic carbene intermediate, different mechanistic pathways can reasonably be proposed to explain the formation of **2** (Scheme 2).

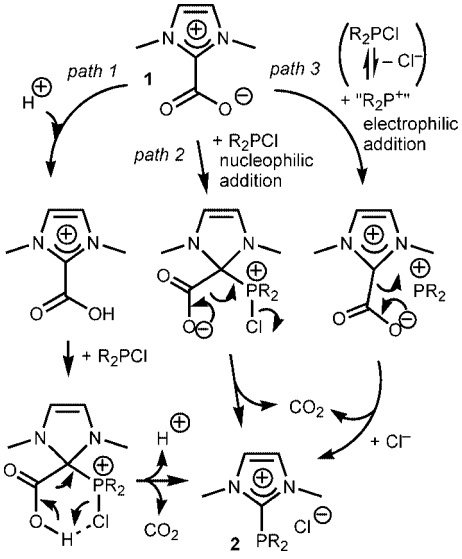


Scheme 2. Possible phosphorylation mechanisms of the imidazolium-2-carboxylate.

A first kinetic experiment in $CH_2Cl_2$ solution with $Ph_2PCl$ showed that the addition of a stoichiometric amount of $K_2CO_3$ did not prevent the formation of **2a**, although an increased reaction time from 4 to 14 h was needed to reach complete conversion. This observation is more consistent with the strong stabilizing interaction observed in our laboratory between **1** and alkali metals[17] rather than with an acid-catalysed mechanism. A second experiment based on the direct addition of $Ph_2PCl$ to the pure carboxylic acid form [MMIM-2-$CO_2H$]($BF_4$)[15,17] of **1** in a $CH_2Cl_2/C_6D_6$ mixture did not proceed even after 18 h at room temperature. Both observations exclude the possibility of an acid-catalysed phosphorylation reaction.

Notably, a mechanism involving the formation of a P–O bond followed by P migration to the N–C–N carbon atom can also be excluded, as no adduct was observed after the addition of $t$Bu$_2$PCl to the imidazolium-2-carboxylate. Therefore, two alternative mechanisms both involving the direct addition of $R_2PCl$ were examined (Scheme 2, paths 2 and 3); these mechanisms differ in their nucleophilic and electrophilic nature. To distinguish between them, we envisioned the use of a chlorophosphane reagent in which the nucleophilic character would be masked by metal coordination. The reactivity of imidazolium-2-carboxylate towards *cis*-$PtCl_2(PPh_2Cl)_2$ was then investigated in $CD_2Cl_2$ solution. $^{31}$P NMR spectroscopic analysis of the crude product performed after 2 d showed the absence of a signal at $\delta$ = 71.4 ppm, which is due to the platinum starting material, and the presence of two new peaks at $\delta$ = –26.9 and 2.2 ppm; the latter peak showed a $^1J_{Pt,P}$ value of 3420 Hz. This spectrum indicates that the *cis*-$PtCl_2(PPh_2Cl)_2$ complex had totally disappeared while free ligand **2a** and a new monophosphane platinum complex were formed. The latter complex was assigned to the [$PtCl_3$(**2a**)] complex **4**, which was independently prepared by treating [$PtCl_2(NCPh)_2$] with one equivalent of compound **2a** (Scheme 3), and by using reaction conditions similar to those described for a platinum analogue complex.[18] Because the imidazolium-2-phosphane was formed in the above experiment in spite of the platinum coordination, which masks the lone pair of electrons on the phosphorus atom in chlorodiphenylphosphane, we can suggest that $PR_2Cl$ likely reacts as an electrophilic reagent[19] toward imidazolium-2-carboxylate (Scheme 2, path 3). This assumption is supported by the lack of reactivity when the less electron rich carboxylic acid [MMIM-2-$CO_2H$]($BF_4$) is used under the conditions described for imidazolium-2-carboxylate (Scheme 2, path 1). Nevertheless, the presence of free ligand **2a** could also be the result of the direct addition of imidazolium-2-carboxylate to free $PPh_2Cl$, which thus illustrates the electrophilic character of compound **1**. However, the release of $Ph_2PCl$

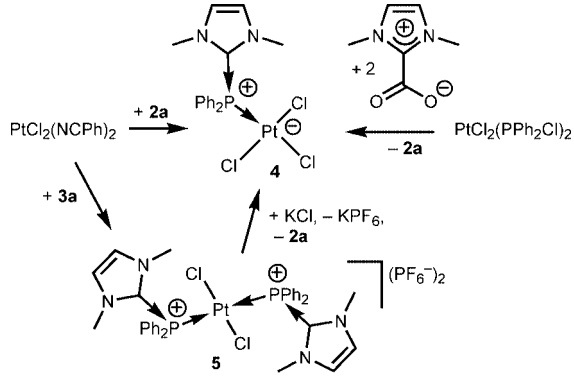


Scheme 3.

 © 2007 Wiley-VCH Verlag GmbH & Co. KGaA, Weinheim 

from *cis*-$PtCl_2(PPh_2Cl)_2$ is unlikely at room temperature, as the reaction would then induce *cis*/*trans*-$PtCl_2(PPh_2Cl)_2$ isomerisation, which was shown to require higher temperatures.[20] Therefore, in our case the presence of free ligand **2a** in solution seems to be the consequence of imidazolium-2-phosphane displacement by a chloride anion, which leads to more stable complex **4**.

### Electronic Properties of the Ligands and Catalytic Properties

As mentioned in the introduction, there is only one report of the use of imidazolium-2-phosphanes in homogeneous catalysis.[1] In that paper, the authors observed that the presence of a *para*-phenylene spacer between the phosphorus atom and the imidazolium fragment decreased the TOF from 552 to 51 $h^{-1}$ for rhodium catalysts in hydroformylation reactions of 1-octene and also decreased the *n:i* aldehyde ratio.[1] Besides, terminal alkenes are hydroformylated at higher rates when bulky phosphites[21] or arylphosphanes containing electron-withdrawing substituents[22] are used instead of triphenylphosphane. All results agree with the fact that the nature of the phosphorus ligand plays an important role in the stabilisation of the active species in hydroformylation reactions and the associated kinetic behaviour (alkene coordination vs. hydrogenolysis step), which drastically modify the conversion rate and selectivity in the catalytic reaction.[23] However, recent calculations performed on imidazolium-2-phosphanes describe these compounds as nonmetal complexes with a coordination bond between the electron rich N–C–N carbon and the P acceptor centre instead of a P–C covalent bond.[7] Therefore, we thought that the different hydroformylation experiments performed with an imidazolium-2-phosphane could be correlated with its specific σ-donor/π-acceptor character, which should certainly be different to those of the unmodified $PPh_3$, although the lone pair of electrons on the phosphorus atom is not delocalised (see above). The electronic/donor properties of the P atom was then evaluated by measurement of the $A_1$ symmetric stretching frequency of nickel complexes prepared in situ by replacement of a CO group in $[Ni(CO)]_4$ by phosphane **2a**. Although less-toxic compounds than $Ni(CO)_4$ {prepared in situ from $[Ni(cod)_2]$} are now more commonly used to characterise the electronic properties of phosphanes {for example, the $[Rh(CO)_2Cl]_2$ dimer}, we opted to prepare a nickel–carbonyl complex to compare easily the imidazolium-2-phosphane complex parameters directly with the large database tabulated by Tolman for adducts of the $Ni(CO)_3$ moiety.[24] We thus reacted **2a** with an equimolar amount of $Ni(CO)_4$ to afford [$Ni(CO)_3$(**2a**)] (Scheme 4).

The new nickel complex was not isolated but was recognised by its characteristic $\nu_{CO}(A_1)$ carbonyl stretching mode in the infrared spectrum of the crude mixture, which was found at 2082 $cm^{-1}$ in a toluene/$CH_2Cl_2$ solution. This value classifies **2a** as less electron-donating than the common arylphosphanes [$\nu_{CO}(A_1)$ = 2069 $cm^{-1}$ with $PPh_3$]. The

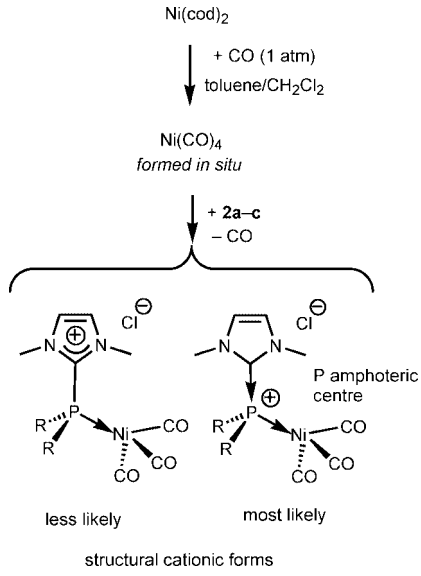


Scheme 4.

replacement of the aryl groups by isopropyl or cyclohexyl substituents in imidazolium-2-phophanes **2b** and **2c** led to new stretching frequencies at 2075 and 2078 $cm^{-1}$, respectively, in the infrared spectra for the corresponding phosphane–nickel tricarbonyl complexes. The latter values are slightly shifted to lower frequencies owing to the presence of better electron-donating alkyl groups. Nevertheless, the electronic parameters of compounds **2a**–**c** are wedged in the range of strong π-acceptor ligands such as phosphites, from $P(OiPr)_3$ [with $\nu_{CO}(A_1)$ = 2076 $cm^{-1}$] and $P(OPh)_3$ ligands [with $\nu_{CO}(A_1)$ = 2085 $cm^{-1}$][24] and clearly illustrate the strong acceptor properties of a donor-stabilised phosphenium cation reinforced by the presence of its positive charge (Scheme 4).

In addition to the above electronic properties studied, a preliminary determination of the steric demands of imidazolium-2-phosphanes was investigated in platinum dichloride complexes with the smallest ligand. So, the addition of one (or two) equivalent(s) of ligand **2a** to $PtCl_2(NCPh)_2$ in $CH_2Cl_2$ solution at room temperature led selectively to the formation of [$PtCl_3$(**2a**)] complex **4**. When the same reaction was performed under similar conditions with two equivalents of related halide-free ligand **3a**, the selective formation of new [$PtCl_2$(**3a**)$_2$] complex **5** was observed with a typical $^1J_{Pt,P}$ value of 2785 Hz for a P *trans* geometry around the metal centre (Scheme 3). Additionally, the $^{31}P\{^1H\}$ NMR spectrum of **5** recorded in $CH_2Cl_2/C_6D_6$ after introduction of KCl in a 1:1 ratio showed the presence of complex **4** and free ligand **2a**. This observation confirms the higher stability of the latter platinum trichloride complex **4**, and noteworthy is the phosphane decoordination from the platinum centre by halide addition (Scheme 3).

It is interesting to note that the nature of the counter anion perfectly controls the metal/ligand ratio in the metal–imidazoliumphosphane complexes. Nevertheless, the latter reaction contrasts those with other tertiary phosphanes $Ph_2PR$ (R = Ph, Cl, OMe or $NEt_2$[20]), which selectively

 © 2007 Wiley-VCH Verlag GmbH & Co. KGaA, Weinheim 

lead, under similar mild conditions, to the corresponding *cis*-[$PtCl_2(Ph_2PR)_2$] isomers. The results seem to indicate that compound **2a** behaves as a bulky phosphane like the mixed arylalkylphosphanes. Other investigations on the electronic and steric properties of the cationic imidazolium-2-phosphanes, as well as their catalytic properties, are currently in progress.

## Conclusions

In this paper, we report that imidazolium-2-carboxylate is an interesting starting material in the simple and straightforward synthesis of imidazolium-2-phosphanes, and the reaction could easily be extended to large-scale preparation. The synthesis of other base-stabilised phosphenium cation complexes, in addition to their optically pure forms, are currently in progress in our laboratory. Moreover, the measurements of the $A_1$ symmetric stretching frequency of related $Ni(CO)_3$(imidazolium-2-phosphane) complexes have shown that such compounds behave as stronger π-acceptor ligands like phosphites. The result seems to be the consequence of the C→P bond present in imidazolium-2-phosphanes, which displaces the positive charge from the imidazolium ring to the phosphorus centre. This electronic property combined with the ionic nature of the compounds renders these ligands very promising in the development of new continuous-flow catalytic processes that are currently being investigated.

## Experimental Section

**General Procedures:** All reactions were performed in Schlenk-type flasks under an argon atmosphere. Solvents were purified and dried by conventional methods and distilled under an argon atmosphere. With the exception of compound **1** and the *trans*-$PtCl_2$(**3a**)$_2$ complex, all $^1H$, $^{31}P\{^1H\}$ and $^{13}C\{^1H\}$ NMR spectra were recorded with a Bruker Avance 300 instrument at 298 K. Complete assignment was achieved by COSY, DEPT and HMQC experiments. All chemical shifts are reported relative to $SiMe_4$ ($^1H$ and $^{13}C$ NMR) and 85% $H_3PO_4$ ($^{31}P$ NMR) and are given in ppm. Electrospray spectra were performed with a Bruker micrOTOF-Q instrument. The IR instrument was calibrated with solutions of $Ni(CO)_3(PPh_3)$, for which the $A_1$ $\nu_{CO}$ stretching band was reported to be 2068.9 $cm^{-1}$.[24] Elemental analyses were performed with a Fisons EA 1108 apparatus at the ICMUB in Dijon. The chlorophosphanes $Ph_2PCl$, *i*$Pr_2PCl$ and $Cy_2PCl$ were commercial products from Aldrich and Ni(1,5-cod)$_2$ was a commercial product from Strem, and all were used as received. 1,3-Dimethylimidazolium-2-carboxylate (**1**) and the $PtCl_2(NCPh)_2$ complex were prepared according to the literature.[15,17,25] Nickel tetracarbonyl $Ni(CO)_4$ was prepared from Ni(1,5-cod)$_2$ and CO according to the literature;[26] however, owing to its highly toxic nature, this preparation was handled with extreme care in a dedicated facility (CECUB, Université de Bourgogne).

**Compound 2a:** To a mixture of **1** (0.164 g, 1.17 mmol) and $Ph_2PCl$ (0.258 g, 1.17 mmol) was added $CH_2Cl_2$ (5 mL). The mixture was stirred for 4 h at room temp. The solvent was then removed under vacuum to afford a white powder (359 mg, 97%) that was dried for 3 h under vacuum. M.p. 200 °C. $^1H$ NMR (300 MHz, $CDCl_3$): $\delta$ = 8.46 (s, 2 H, CH=), 7.42–7.23 (m, 10 H, aromatics), 3.78 (d, $J_{P,H}$ = 7.2 Hz, 6 H, $NCH_3$) ppm. $^{13}C\{^1H\}$ NMR (75 MHz, $CDCl_3$): $\delta$ = 142.24 (d, $J_{P,C}$ = 52.1 Hz, 1 C, NCN), 132.74–130.95 (m, 12 C, aromatics), 128.52 (s, 2 C, CH=), 37.71 (d, $^3J_{P,C}$ = 9.1 Hz, 2 C, $NCH_3$) ppm. $^{31}P\{^1H\}$ NMR (121 MHz, $CDCl_3$): $\delta$ = –27.31 (s) ppm. $C_{17}H_{18}N_2PCl$ (316.76): calcd. C 64.46, H 5.73, N 8.84; found C 64.23, H 5.78, N 8.84.

**Compound 2b:** Prepared in an analogous manner to **2a** and obtained as white powder (250 mg, 86%). M.p. 133 °C. $^1H$ NMR (300 MHz, $CDCl_3$): $\delta$ = 8.50 (s, 2 H, CH=), 4.18 (s, 6 H, $NCH_3$), 2.62 (hept., $^3J_{H,H}$ = 6.6 Hz, 2 H, PCH), 1.23 (dd, $^3J_{H,H}$ = 6.6 Hz, $^3J_{P,H}$ = 12.6 Hz, 6 H, $CCH_3$ *exo*), 0.83 (dd, $^3J_{H,H}$ = 6.9 Hz, $^3J_{P,H}$ = 7.2 Hz, 6 H, $CCH_3$ *endo*) ppm. $^{13}C\{^1H\}$ NMR (75 MHz, $CDCl_3$): $\delta$ = 145.07 (d, $J_{P,C}$ = 60.4 Hz, 1 C, NCN), 127.17 (s, 2 C, CH=), 37.86 (d, $^3J_{P,C}$ = 9.1 Hz, 2 C, $NCH_3$), 24.07 (d, $^3J_{P,C}$ = 10.6 Hz, 2 C, PCH), 21.33 (d, $^3J_{P,C}$ = 27.2 Hz, 4 C, $CH_3$ *exo*), 20.75 (d, $^3J_{P,C}$ = 9.1 Hz, 4 C, $CH_3$ *endo*) ppm. $^{31}P\{^1H\}$ NMR (121 MHz, $CDCl_3$): $\delta$ = –9.44 (s) ppm. $C_{11}H_{22}N_2PCl$ (248.73): calcd. C 53.12, H 8.91, N 11.26; found C 53.05, H 8.71, N 11.70.

**Compound 2c:** Prepared in an analogous manner to **2a** over molecular sieves and obtained as a white powder (277 mg, 72%). $^1H$ NMR (300 MHz, $CDCl_3$): $\delta$ = 8.61 (s, 2 H, CH=), 4.14 (s, 6 H, $NCH_3$), 2.33 (m, 1 H, PCH), 1.77 (m, 8 H, $CH_2$), 1.24 (m, 10 H, $CH_2$) ppm. $^{13}C\{^1H\}$ NMR (75 MHz, $CDCl_3$): $\delta$ = 144.5 (d, $J_{P,C}$ = 60.4 Hz, 1 C, NCN), 127.4 (s, 2 C, CH=), 37.79 (s, 2 C, $NCH_3$), 33.99 (d, $J_{P,C}$ = 11.3 Hz, 2 C, PCH), 31.85 (d, $^2J_{P,C}$ = 24.2 Hz, 2 C, $CH_2$), 30.39 (d, $^2J_{P,C}$ = 6.0 Hz, 2 C, $CH_2$), 26.33 (d, $^3J_{P,C}$ = 8.3 Hz, 2 C, $CH_2$), 26.08 (d, $^3J_{P,C}$ = 15.1 Hz, 2 C, $CH_2$), 25.51 (s, 2 C, $CH_2$) ppm. $^{31}P\{^1H\}$ NMR (121 MHz, $CDCl_3$): $\delta$ = –19.77 (s) ppm. $C_{17}H_{30}N_2PCl$ (328.86): No satisfactory elemental analysis was obtained for **2a** owing to its strong hygroscopic character.

**Compound 3a:** To a solution of **2a** (0.380 g, 1.20 mmol) in acetone (5 mL) was added $KPF_6$ (0.277 g, 1.50 mmol), and the resulting suspension was stirred for 2 d at room temp. The solvent was removed under vacuum at 50 °C for 2 h. The residue was dissolved in $CH_2Cl_2$ (5 mL), and the resulting solution was filtered. Evaporation of solvent under vacuum afforded compound **3a**, which was crystallised from $CH_2Cl_2$/pentane as white plates (481 mg, 94%). M.p. 176 °C. $^1H$ NMR (300 MHz, $CDCl_3$): $\delta$ = 7.49 (s, 2 H, CH=), 7.45–7.24 (m, 10 H, aromatics), 3.57 (s, 6 H, $NCH_3$) ppm. $^{13}C\{^1H\}$ NMR (75 MHz, $CDCl_3$): $\delta$ = 143.08 (d, $J_{P,C}$ = 54.3 Hz, 1 C, NCN), 133.06–130.07 (m, 12 C, aromatics), 127.00 (s, 2 C, CH=), 37.65 (d, $^3J_{P,C}$ = 7.6 Hz, 2 C, $NCH_3$) ppm. $^{31}P\{^1H\}$ NMR (121 MHz, $CDCl_3$): $\delta$ = –25.89 (s, $P_{phosphane}$), –144.14 (hept., $J_{P,F}$ = 712 Hz, $PF_6^-$) ppm. $C_{17}H_{18}N_2P_2F_6$ (426.27): calcd. C 47.90, H 4.25, N 6.57; found C 47.80, H 4.08, N 6.49.

**Compound 3b:** Prepared in an analogous manner to **3a** and obtained as white solid (374 mg, 87%). M.p. 154 °C. $^1H$ NMR (300 MHz, $CDCl_3$): $\delta$ = 7.46 (s, 2 H, CH=), 3.96 (s, 6 H, $NCH_3$), 2.60 (hept., $^3J_{H,H}$ = 6.9 Hz, 2 H, PCH), 1.20 (dd, $^3J_{H,H}$ = 6.9 Hz, $^3J_{P,H}$ = 12.3 Hz, 6 H, $CCH_3$ *exo*), 0.82 (dd, $^3J_{H,H}$ = 6.9 Hz, $^3J_{P,H}$ = 7.20 Hz, 6 H, $CCH_3$ *endo*) ppm. $^{13}C\{^1H\}$ NMR (75 MHz, $CDCl_3$): $\delta$ = 145.89 (d, $J_{P,C}$ = 62.4 Hz, 1 C, NCN), 126.14 (s, 2 C, CH=), 37.35 (d, $^3J_{P,C}$ = 9.8 Hz, 2C, $NCH_3$), 23.88 (d, $J_{C,P}$ = 10.5 Hz, 2 C, PCH), 21.16 (d, $^3J_{P,C}$ = 27.2 Hz, 4 C, $CH_3$ *exo*), 20.46 (d, $^3J_{P,C}$ = 9.8 Hz, 4 C, $CH_3$ *endo*) ppm. $^{31}P\{^1H\}$ NMR (121 MHz, $CDCl_3$): $\delta$ = –8.57 (s, $P_{phosphane}$), –144.40 (hept., $J_{P,F}$ = 712 Hz, $PF_6^-$) ppm. $C_{11}H_{22}N_2P_2F_6$ (358.24): calcd. C 36.88, H 6.19, N 7.82; found C 36.39, H 6.08, N 7.54.

 © 2007 Wiley-VCH Verlag GmbH & Co. KGaA, Weinheim 

**Compound 3c:** Prepared in an analogous manner to **3a** and obtained as white solid (421 mg; 80%). M.p. 193 °C. $^1$H NMR (300 MHz, $CDCl_3$): $\delta$ = 7.51 (s, 2 H, CH=), 3.95 (s, 6 H, $NCH_3$), 2.37 (m, 2 H, PCH), 1.75 (m, 8 H, $CH_2$), 1.23 (m, 10 H, $CH_2$) ppm. $^{13}$C{$^1$H} NMR (75 MHz, $CDCl_3$): $\delta$ = 144.53 (d, $J_{P,C}$ = 62.6 Hz, 1 C, NCN), 125.6 (s, 2 C, CH=), 36.57 (s, 2 C, $NCH_3$), 32.86 (d, $J_{P,C}$ = 11.3 Hz, 2 C, PCH), 30.87 (d, $^2J_{P,C}$ = 24.2 Hz, 2 C, $CH_2$), 29.33 (d, $^2J_{P,C}$ = 6.8 Hz, 2 C, $CH_2$), 25.22 (d, $^3J_{P,C}$ = 8.3 Hz, 2 C, $CH_2$), 25.02 (d, $^3J_{P,C}$ = 15.1 Hz, 2 C, $CH_2$), 24.56 (s, 2 C, $CH_2$) ppm. $^{31}$P{$^1$H} NMR (121 MHz, $CDCl_3$): $\delta$ = –18.89 (s, $P_{phosphane}$), –144.33 (hept., $J_{P,F}$ = 712 Hz, $PF_6^-$) ppm. $C_{17}H_{30}N_2P_2F_6$ (438.37): calcd. C 46.58, H 6.90, N 6.39; found C 44.99, H 7.54, N 6.05.

**Formation of [Ni(CO)$_3$(2a–c)]:** $Ni(CO)_4$ was prepared by treating a solution of [Ni(1,5-cod)$_2$] (50.1 mg, 0.182 mmol) in toluene (1 mL) with CO at 0 °C for 5 min, followed by the addition of **2a** (0.0545 mg, 0.172 mmol) in $CH_2Cl_2$ (1 mL). The mixture was stirred for 15 min. A light-green solution was obtained, which was analysed by infrared spectroscopy. IR (toluene/$CH_2Cl_2$): $\nu_{CO}$ = 2082 ($A_1$), 2013 cm$^{-1}$ (E). The formation of the analogous [Ni(CO)$_3$(**2b**)] and [Ni(CO)$_3$(**2c**)] complexes was performed under similar conditions. IR (toluene/$CH_2Cl_2$): $\nu_{CO}$ = 2075 ($A_1$), 2051 cm$^{-1}$(E) for [Ni(CO)$_3$(**2b**)] and $\nu_{CO}$ = 2078 ($A_1$), 2005 cm$^{-1}$ (E) for [Ni(CO)$_3$(**2c**)].

**Platinum Complex 4:** To a mixture of **2a** (60.1 mg, 0.19 mmol) was added $PtCl_2(PhCN)_2$ (86.6 mg, 0.19 mmol) in $CH_2Cl_2$ (2 mL), and the mixture was stirred for 7 h. A yellow suspension was obtained. The suspension was filtered off, and the yellow solid was washed with diethyl ether and dried under vacuum to afford $PtCl_3$(**2a**) (94 mg, 85%). M.p. >200 °C (dec.). $^1$H NMR (300 MHz, [D$_6$]acetone): $\delta$ = 7.56–7.78 (m, 12 H, aromatics and CH=), 2.03 (s, 6 H, $NCH_3$) ppm. $^{31}$P{$^1$H} NMR (121 MHz, [D$_6$]acetone): $\delta$ = 2.24 (s, $J_{Pt,P}$ = 3425 Hz, $P_{phosphane}$) ppm. MS: *m*/*z* = 510.060 [M – Cl – HCl]$^+$. $C_{17}H_{18}Cl_3N_2PPt$ (582.76): calcd. C 35.04, H 3.11, N 4.81; found C 35.51, H 2.78, N 4.26.

**Platinum Complex 5:** To a mixture of **3a** (0.0396 mg, 0.093 mmol) was added $PtCl_2(PhCN)_2$ (0.0224 mg, 0.049 mmol) in $CH_2Cl_2$ (1.5 mL), and the mixture was stirred for 12 h. A yellow suspension was obtained. The suspension was filtered off, and the yellow solid was dried under vacuum to afford *trans*-$PtCl_2$(**3a**)$_2$ (100 mg, 95%). M.p. 216 °C. $^1$H NMR (300 MHz, [D$_6$]acetone): $\delta$ = 8.43–7.80 (m, 20 H, aromatics), 7.97 (s, 4 H, CH=), 3.75 (s, 12 H, $NCH_3$) ppm. $^{13}$C{$^1$H} NMR (75 MHz, [D$_6$]acetone): $\delta$ = 141.64 (d, $J_{P,C}$ = 7.5 Hz, 2 C, NCN), 139.51–127.09 (m, 24 C, aromatics), 126.68 (s, 4 C, CH=), 44.04 (s, 4 C, $NCH_3$) ppm. $^{31}$P{$^1$H} NMR (121 MHz, [D$_6$]acetone): $\delta$ = 17.83 (s, $J_{Pt,P}$ = 2785 Hz, $P_{phosphane}$), –139.08 (hept, $J_{P,F}$ = 712 Hz, $PF_6^-$) ppm. $C_{34}H_{48}Cl_2F_{12}N_4P_4Pt$ (1130.64): calcd. C 36.12, H 4.28, N 4.96; found C 36.30, H 3.86, N 4.66.

**Crystal Structure Determination for 3b:** Crystal data and refinement figures are reported in Table 2. The data set was collected with an Enraf–Nonius Kappa CCD diffractometer at 110 K with Mo-$K_\alpha$ radiation. The structure was solved by direct methods and refined with full-matrix least-squares methods[27] based on $|F^2|$ with the aid of the WINGX program.[28] All non-hydrogen atoms were refined with anisotropic thermal parameters. The positions of the hydrogen atoms were either calculated or located on final Fourier difference maps and refined, after idealization, with a riding model. CCDC-649689 contains the supplementary crystallographic data for this paper. These data can be obtained free of charge from The Cambridge Crystallographic Data Centre via www.ccdc.cam.ac.uk/data_request/cif.

Table 2. Crystallographic and refinement data for complex **3b**.

| | |
|---|---|
| Formula | $C_{11}H_{22}F_6N_2P_2$ |
| *M* | 358.25 |
| *T* [K] | 110(2) |
| Crystal system | monoclinic |
| Space group | $P2_1/c$ |
| *a* [Å] | 12.5537(4) |
| *b* [Å] | 11.1571(4) |
| *c* [Å] | 13.0473(6) |
| $\alpha = \gamma$ [°] | 90 |
| $\beta$ [°] | 112.897(1) |
| *V* [Å$^3$] | 1683.45(11) |
| Z | 4 |
| *F*(000) | 744 |
| $D_{calcd.}$ [g cm$^{-3}$] | 1.413 |
| Diffractometer | Enraf–Nonius KappaCCD |
| Scan type | mixture: $\phi$ rotations and $\omega$ scans |
| $\lambda$ [Å] | 0.71073 |
| $\mu$ [mm$^{-1}$] | 0.311 |
| Crystal size [mm] | $0.25 \times 0.07 \times 0.01$ |
| $\sin(\theta)/\lambda$ max [Å$^{-1}$] | 0.65 |
| Index ranges | *h* –16; 16<br>*k* –14; 9<br>*l* –16; 16 |
| RC = refl. collected | 5899 |
| IRC = independent RC | 3831 [*R*(int) = 0.0414] |
| IRCGT = IRC and [$I > 2\sigma(I)$] | 2580 |
| Refinement method | full-matrix L.S. on $F^2$ |
| Data/restraints/parameters | 3831/0/192 |
| R for IRCGT | $R_1$[a] = 0.064, $wR_2$[b] = 0.137 |
| R for IRC | $R_1$[a] = 0.105, $wR_2$[b] = 0.159 |
| Goodness-of-fit[c] | 1.024 |
| Largest diff. peak and hole [e Å$^{-3}$] | 0.758 and –0.446 |

[a] $R_1 = \Sigma(||F_o| - |F_c||)/\Sigma|F_o|$. [b] $wR_2 = \{\Sigma w(F_o^2 - F_c^2)^2/\Sigma[w(F_o^2)^2]\}^{1/2}$ where $w = 1/[\sigma^2(F_o^2)+(0.049P)^2+3.10P]$ where $P = [\max(F_o^2,0) + 2\cdot F_c^2]/3$. [c] Goodness of fit = $[\Sigma w(F_o^2 - F_c^2)^2/(N_o - N_v)]^{1/2}$.

## Acknowledgments

We wish to acknowledge the Ministère de la Recherche for support and for a PhD fellowship to M. A. We also thank the Université de Bourgogne, the Centre National de la Recherche Scientifique and the Conseil Régional de Bourgogne for financial support of this work.

[1] D. J. Brauer, K. W. Kottsieper, C. Liek, O. Stelzer, H. Waffenschmidt, P. Wasserscheid, *J. Organomet. Chem.* **2001**, *630*, 177–184.
[2] S.-G. Lee, Y. J. Zhang, J. Y. Piao, C. E. Song, J. H. Choi, J. Hong, *Chem. Commun.* **2003**, 2624–2625.
[3] R. P. J. Bronger, S. M. Silva, P. C. J. Kamer, P. W. N. M. van Leeuwen, *Dalton Trans.* **2004**, 1590–1596.
[4] C. M. Crudden, D. P. Allen, *Coord. Chem. Rev.* **2004**, *248*, 2247–2273.
[5] L. Magna, Y. Chauvin, P. G. Niccolai, J.-M. Basset, *Organometallics* **2003**, *22*, 4418–4425.
[6] L. D. Field, B. A. Messerle, K. Q. Vuong, P. Turner, *Organometallics* **2005**, *24*, 4241–4250.
[7] B. D. Ellis, P. J. Ragogna, C. L. B. Macdonald, *Inorg. Chem.* **2004**, *43*, 7857–7867.
[8] N. Burford, P. J. Ragogna, *J. Chem. Soc. Dalton Trans.* **2002**, 4307–4315.
[9] A. A. Tolmachev, A. A. Yurchenko, A. S. Merculov, M. G. Semenova, E. V. Zarudnitskii, V. V. Ivanov, A. M. Pinchuk, *Heteroat. Chem.* **1999**, *10*, 585–597.

 © 2007 Wiley-VCH Verlag GmbH & Co. KGaA, Weinheim 

[10] I. V. Komarov, M. Y. Kornilov, *Tetrahedron* **1995**, *51*, 11271–11280.
[11] N. Kuhn, J. Fahl, D. Bläser, R. Boese, *Z. Anorg. Allg. Chem.* **1999**, *625*, 729–734.
[12] J. D. Holbrey, W. M. Reichert, I. Tkatchenko, E. Bouajila, O. Walter, I. Tommasi, R. D. Rogers, *Chem. Commun.* **2003**, 28–29.
[13] A. M. Voutchkova, L. N. Appelhans, A. R. Chianese, R. H. Crabtree, *J. Am. Chem. Soc.* **2005**, *127*, 17624–17625.
[14] A. Tudose, A. Demonceau, L. Delaude, *J. Organomet. Chem.* **2006**, *691*, 5356–5365.
[15] M. Picquet, D. Poinsot, S. Stutzmann, I. Tkatchenko, I. Tommasi, P. Wasserscheid, J. Zimmermann, *Top. Catal.* **2004**, *29*, 139–143.
[16] M. Smiglak, J. D. Holbrey, S. T. Griffin, W. M. Reichert, R. P. Swatloski, A. R. Katritzky, H. Yang, D. Zhang, K. Kirichenko, R. D. Rogers, *Green Chem.* **2007**, *9*, 90–98.
[17] E. Bouajila, *Thèse de doctorat*, Université de Bourgogne, France, **2004**.
[18] N. Kuhn, M. Goëhner, G. Henkel, *Z. Anorg. Allg. Chem.* **1999**, *625*, 1415–1416.
[19] J. Andrieu, P. Braunstein, A. Tiripicchio, F. Ugozzoli, *Inorg. Chem.* **1996**, *35*, 5975–5985.
[20] P. W. Dyer, J. Fawcett, M. J. Hanton, R. D. W. Kemmitt, R. Padda, N. Singh, *Dalton Trans.* **2003**, 104–113.
[21] A. van Rooy, J. N. H. de Bruijn, F. K. Roobeek, C. J. Kamer, P. W. N. M. van Leeuwen, *J. Organomet. Chem.* **1996**, *507*, 69–73.
[22] D. R. Palo, C. Erkey, *Organometallics* **2000**, *19*, 81–86.
[23] *Rhodium Catalyzed Hydroformylation* (Eds.: P. W. N. M. van Leeuwen, C. Claver), Kluwer, Dordrecht, **2000**, vol. 22.
[24] C. A. Tolman, *Chem. Rev.* **1977**, *77*, 313–348.
[25] P. Braunstein, R. Bender, J.-M. Jud, *Inorg. Synth.* **1989**, *26*, 341–350.
[26] P. W. Jolly, G. Wilke, *The Organic Chemistry of Nickel*, Academic Press, New York, London, **1974**, vol. 1.
[27] G. M. Sheldrick, *SHELX97: Programs for Crystal Structure Analysis (Includes SHELXS97 and SHELXL97)*, Release 97–2, University of Göttingen, Göttingen, Germany, **1998**.
[28] L. J. Farrugia, *J. Appl. Crystallogr.* **1999**, *32*, 837–838.

Received: June 7, 2007
Published Online: August 23, 2007

 © 2007 Wiley-VCH Verlag GmbH & Co. KGaA, Weinheim 

DOI: 10.1002/ejic.200700502

# $V^{IV}O$ Complexes of Bis(imidazol-2-yl) Derivatives: A Potentiometric, Spectroscopic and DFT Study

Katalin Várnagy,[a] Timea Csorba,[a] Dóra Kiss,[a] Eugenio Garribba,*[b] Giovanni Micera,*[b] and Daniele Sanna[c]

**Keywords:** Vanadium / Bioinorganic chemistry / pH potentiometry / EPR spectroscopy / Density functional calculations

The complexation of the $V^{IV}O$ ion with four amino acid derivatives of bis(imidazol-2-yl)methylamine [*N*-glycyl-bis(imidazol-2-yl)methylamine = Gly-BIMA, *N*-α-aspartyl-bis(imidazol-2-yl)methylamine = α-Asp-BIMA, *N*-α-glutamyl-bis(imidazol-2-yl)methylamine = α-Glu-BIMA and *N*-histidyl-bis(imidazol-2-yl)methylamine = His-BIMA] was studied in aqueous solution through the combined application of potentiometric and spectroscopic (UV/Vis and EPR) techniques. For comparison, the complexing capability of three simple bis(imidazol-2-yl) derivatives [bis(imidazol-2-yl)methane = BIM, bis(imidazol-2-yl)methylamine = BIMA and bis(imidazol-2-yl)-nitromethane = BINM] and two benzyloxycarbonyl (Z) derivatives (Z-Gly-BIMA and Z-Ala-BIMA) was reported. Mono- and bis-chelated species with the ($N_{im}$, $N_{im}$) donor set were formed in both acid and neutral pH conditions, with the bis-chelated complexes being characterised by a *cis-trans* isomerism. In the basic pH range the complexation process continues with the formation of a mono-hydroxo *cis*-$VOL_2H_{-1}$ complex in systems with BIM, BIMA and BINM, and with the deprotonation and coordination of the amide nitrogen to give $VOLH_{-1}$ and $VOLH_{-2}$ in those with Gly-BIMA, α-Asp-BIMA, α-Glu-BIMA and His-BIMA. The results demonstrate that the bis(imidazol-2-yl)methyl residue is an anchoring group of intermediate strength, capable of avoiding extensive hydrolysis of the $V^{IV}O$ ion in the presence of a slight excess of ligand (L/M from 3:1 to 5:1). DFT calculations with progressively more complex basis sets were performed in order to obtain information on the structure of the $VOLH_{-1}$ and $VOLH_{-2}$ complexes. Finally, a discussion on the $^{51}V$ anisotropic parallel hyperfine coupling constant ($A_{\parallel}$) of $VOLH_{-1}$ and $VOLH_{-2}$ and on the EPR properties connected to the V–$N^-$(amide) bond in $V^{IV}O$ complexes is presented.
(© Wiley-VCH Verlag GmbH & Co. KGaA, 69451 Weinheim, Germany, 2007)

## Introduction

Vanadium plays a number of roles in biological systems.[1] It is accumulated by tunicates (ascidians or sea squirts)[2] and the fan worm *Pseudopotamilla occelata*,[3] and by some species of the mushroom genus *Amanita*.[4] Vanadium is also present in two enzymes, vanadium-dependent haloperoxidases,[5] and nitrogenase.[6] In the human organism it elicits a number of physiological responses, for example, the inhibition of phosphate-metabolising enzymes,[7] such as phosphatases, ribonuclease and ATPases, and its compounds show insulin-mimetic activity.[8]

The presence of vanadium in all these systems suggests it interacts with biomolecules. Among the biomolecules present in intra- and extra-cellular fluids, proteins and peptides have a special importance because of their high amount in the cellular environment and their possible interaction with the metal ions through a number of donor groups. For instance, glutathione is believed to play an important role in the processes of reduction of $V^V$ to $V^{IV}O$ and in the subsequent complexation reactions.[9]

The interaction of vanadium, mainly in the oxidation states +IV and +V, with different proteins and enzymes has been reported in the literature.[10] Of special importance is interaction with human transferrin (hTF) and human serum albumin (HSA), since they could be involved in the transport of vanadium and insulin-mimetic compounds towards physiological target sites.[11–16]

Oligopeptides are the most closely related models for proteins; they may mimic specific metal ion binding sites, for example, GlyGlyHis for serum albumin.[17] Detailed studies on synthetic models of the vanadium–protein interaction can greatly contribute to the knowledge of its biological activity. Oligopeptides can interact with a metal ion through the terminal amino and carboxylate groups, intermediate peptide bond and side-chain donors, but all these groups are not strong enough to keep metal ions in solution at the physiological pH. However, they can play the role of "anchoring group" and promote the deprotonation of the

[a] Department of Inorganic and Analytical Chemistry, University of Debrecen,
4010 Debrecen, Hungary
[b] Department of Chemistry, University of Sassari,
Via Vienna 2, 07100 Sassari, Italy
Fax: +39-079-212069
E-mail: garribba@uniss.it
[c] Istituto C.N.R. di Chimica Biomolecolare,
Trav. La Crucca 3, 07040 Li Punti, Sassari, Italy
Supporting information for this article is available on the WWW under http://www.eurjic.org or from the author.

 © 2007 Wiley-VCH Verlag GmbH & Co. KGaA, Weinheim 

amide bond and its coordination in the $–N^-$ form, as proved with $Pt^{II}$, $Pd^{II}$, $Cu^{II}$, $Ni^{II}$, $Zn^{II}$ and $Co^{II}$.[18]

Recently, the role of the anchoring groups was studied with $V^{IV}O$ and it was found that their effectiveness in promoting peptide amide deprotonation and coordination follows the order: phenolate-$O^-$ > alcoholate-$O^-$ > thiolate-$S^-$ > carboxylate-$COO^-$ > amino-$NH_2$.[19] Subsequent results demonstrated that a histidyl residue in the *N*-terminal position can act as a valid anchor because the coordination of the amino group is assisted by the imidazole nitrogen of the side-chain.[20] Many examples of $V^{IV}O$ complexes containing a V–$N^-$(amide) bond, both in solution and in the solid state, have been characterised in the last few years.[19–21]

A particularly interesting case of anchoring group is represented by the bis(imidazol-2-yl)methyl moiety, in which two imidazole rings are linked via a methylene group, since it can potentially mimic the binding sites and catalytic activities of the metal-enzymes with the binding of imidazole nitrogen donors belonging to histidine residues (for example, copper and zinc enzymes).[22] It has been proved that amino acid derivatives containing the bis(imidazol-2-yl)-methyl residue form very stable complexes with $Cu^{II}$, $Zn^{II}$, $Ni^{II}$ and $Co^{II}$ ions, promoting the deprotonation and coordination of the amide nitrogens.[23]

In this work, we report the complexation of the $V^{IV}O$ ion with four amino acid derivatives of bis(imidazol-2-yl)-methylamine: *N*-glycyl-bis(imidazol-2-yl)methylamine (Gly-BIMA), *N*-α-aspartyl-bis(imidazol-2-yl)methylamine (α-Asp-BIMA), *N*-α-glutamyl-bis(imidazol-2-yl)methylamine (α-Glu-BIMA) and *N*-histidyl-bis(imidazol-2-yl)methylamine (His-BIMA). In addition, two protected benzyloxycarbonyl (Z) derivatives were considered, where the terminal amino group of glycine and alanine was transformed into a Ph–$CH_2$–O–C(O)–NH– function: Z-Gly-BIMA and Z-Ala-BIMA. This allows us to evaluate how the transformation of an amino into a carbamate function, which can be considered as an analogue of the peptide group, modifies the complexation process. Bis(imidazol-2-yl)methane (BIM), bis(imidazol-2-yl)methylamine (BIMA) and bis(imidazol-2-yl)nitromethane (BINM) were studied for comparison. The structure of all the examined ligands is reported in Scheme 1. The study was performed through the combined application of potentiometric and spectroscopic (UV/Vis and EPR) techniques. DFT calculations were used to obtain information on the structure of $V^{IV}O$ complexes containing a V–$N^-$(amide) bond.

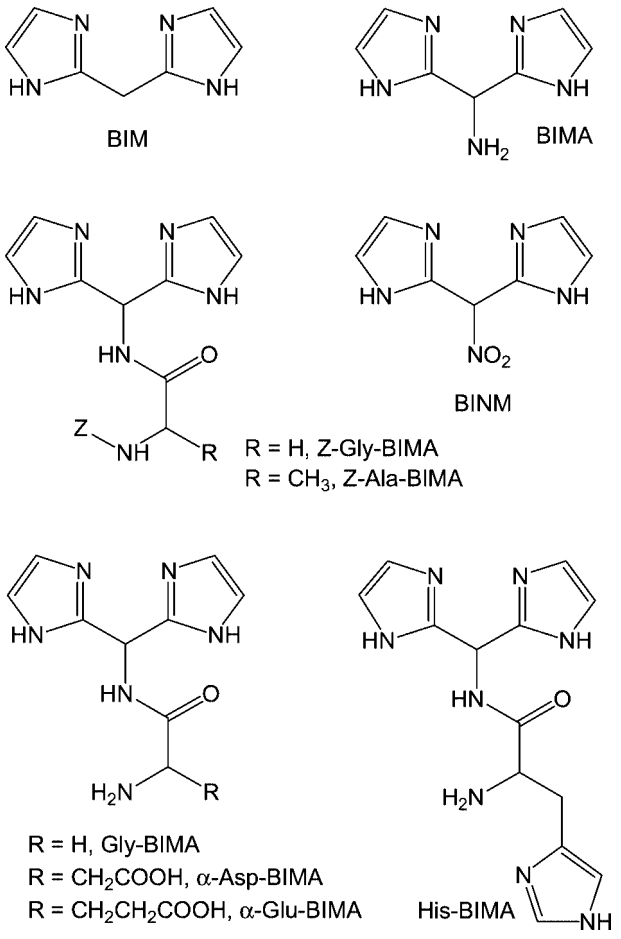


Scheme 1. Structure of the ligands (Z = benzyloxycarbonyl).

## Results and Discussion

### BIM, BIMA, BINM, Z-Gly-BIMA and Z-Ala-BIMA

All these ligands have two titrable protons in water and can be indicated in the fully protonated form as $H_2L$. The two protons belong to the two imidazole rings except for BIMA, for which the higher p$K_a$ refers to the deprotonation of the ammonium group $–NH_3^+$. Protonation constants of the ligands are reported in Table 1. The measured p$K_a$ values are comparable with those already reported for BIM and BIMA.[23a] As previously observed, the interaction between the two aromatic rings decreases the first p$K_a$ value in the bis(imidazol-2-yl)methyl moiety with respect to imidazole.[23a] Substitution at the methylene group has a marked effect on the p$K_a$ values of the ligands; the positive charge on the ammonium group results in a further decrease in the basicity of the aromatic nitrogens and the first p$K_a$ of BIMA cannot be determined. In the case of BINM an increase of acidity of one imidazole group can be observed [p$K_{a1}$ = log$\beta$($H_2L$) – log$\beta$(HL) is 4.00 for BINM and 4.72 for BIM]; the formation of the hydrogen bond between the two aromatic nitrogens, however, results in a decrease of acidity of the second imidazole group.

If the amino group of BIMA is transformed into an amide nitrogen the decrease of p$K_a$ values is smaller than for BIMA itself, but the imidazole nitrogens are still less basic than those of BIM. This is well reflected by the p$K_a$ of the two imidazole nitrogens of the bis(imidazol-2-yl)methyl moiety of Z-Gly-BIMA and Z-Ala-BIMA (Table 1). Their values, however, are in good agreement with those of peptide derivatives of the bis(imidazol-2-yl)methyl group with a protected terminal amino group (e.g. Ac-ProLeuGly-BIMA).[23a]

All the five ligands show analogous complexing behaviour, different from that of the derivatives of amino acids (see below). Stability constants of the $V^{IV}O$ complexes are

 © 2007 Wiley-VCH Verlag GmbH & Co. KGaA, Weinheim 

Table 1. Stability constants (log$\beta$) of proton and $V^{IV}O$ complexes for BIM, BIMA, BINM, Z-Gly-BIMA, Z-Ala-BIMA at 25.0 ± 0.1 °C and $I$ = 0.2 M (KCl).[a]

| Species | BIM | BIMA | BINM | Z-Gly-BIMA | Z-Ala-BIMA |
|---|---|---|---|---|---|
| $H_2L$ | 11.65(1) | 10.52(1) | 12.08(1) | 9.19(2) | 8.86(1) |
| HL | 6.93(1) | 6.46(1) | 8.08(1) | 5.82(1) | 5.65(1) |
| p$K_a$($Im_1$) | 4.72 | <1 | 4.00 | 3.37 | 3.21 |
| p$K_a$($Im_2$) | 6.93 | 4.06 | 8.08 | 5.82 | 5.65 |
| p$K_a$($NH_2$) | | 6.46 | | | |
| VOLH | | 10.01(1) | | | |
| VOL | 7.26(1) | 6.75(1) | 9.21(2) | 6.22(1) | 6.15(1) |
| $VOL_2H_2$ | | 19.56(5) | | | |
| $VOL_2$ | 12.94(2) | 12.07(1) | 16.62(3) | 11.28(2) | 10.95(2) |
| $(VO)_2L_2H_{-2}$ | 6.95(5) | 6.08(4) | 11.30(7) | 5.27(6) | 4.98(6) |
| $VOL_2H_{-1}$ | 5.80(5) | 5.10(3) | 8.86(6) | | |
| p$K$($VOL_2$)[b] | 7.14 | 6.97 | 7.76 | | |

[a] The uncertainties (σ values) of the protonation and stability constants are given in parentheses. [b] p$K$($VOL_2$) = log$\beta$($VOL_2$) – log$\beta$($VOL_2H_{-1}$).

reported in Table 1. From these data, the distribution curves of the species as a function of pH can be obtained; as an example, the distribution diagram for the system with BIM with a ligand-to-metal molar ratio of 5:1 is represented in Figure 1.

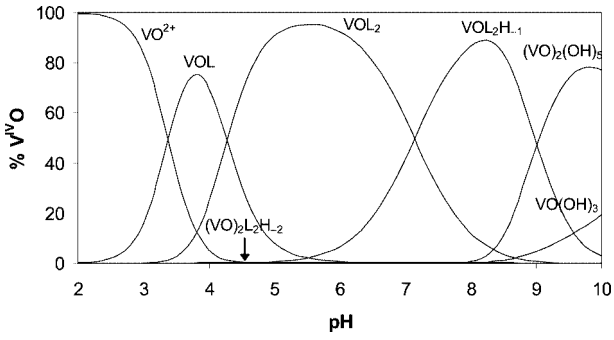


Figure 1. Species distribution for the $V^{IV}O$/BIM system as a function of pH with a ligand-to-metal molar ratio of 5:1 and a $V^{IV}O$ concentration of 1 mM.

In all the systems a mono-chelated VOL complex in acid solution, a bis-chelated $VOL_2$ in the pH range 4–7, and a mono-hydroxo $VOL_2H_{-1}$ species above pH 7 are formed. With BIMA, besides VOL and $VOL_2$, VOLH and $VOL_2H_2$ exist, because of the presence of one and two additional protons on the amino group (Table 1). $(VO)_2L_2H_{-2}$ is probably an EPR-silent dimeric di-μ-hydroxo complex with antiferromagnetic coupling between the two $V^{IV}O$ ions.[24]

The complexation reactions can be followed by EPR spectroscopy, since the anisotropic hyperfine coupling constant along the $z$ axis ($A_\parallel$) between the unpaired electron and the nucleus of $^{51}V$ in tetragonal complexes of the $V^{IV}O$ ion is particularly sensitive to the donors coordinated in the equatorial plane. $A_\parallel$ can be calculated from the sum of the contribution of each equatorial donor function, according to the "additivity rule" proposed by Wüthrich,[25] and subsequently developed by Chasteen, see Equation (1).[26]

$$A_\parallel = \sum_{i=1}^{4} A_\parallel(\text{donor i}) = A_\parallel(\text{donor 1}) + A_\parallel(\text{donor 2}) + A_\parallel(\text{donor 3}) + A_\parallel(\text{donor 4}) \quad (1)$$

This is an empirical rule that allows one to correlate $A_\parallel$ to the number and type of ligands present in the equatorial plane of the $V^{IV}O$ ion and has been proved and accepted in a large number of subsequent works.[27] The contribution to $A_\parallel$ is approximately inverse to the electron donor capacity of the ligand, with the most donating ligands contributing the least to the hyperfine coupling constant $A_\parallel$. Usually, the experimental $A_\parallel$ falls in the range of ca. $3 \times 10^{-4}$ $cm^{-1}$ with respect to the calculated value.[26,27]

EPR parameters for the complexes formed by BIM, BIMA, BINM and Z-Gly-BIMA are listed in Table 2. Anisotropic EPR spectra, recorded on frozen samples as a function of pH, for the system with BIM are displayed in Figure 2.

According to the potentiometric data (Figure 1), with a total $V^{IV}O$ concentration of 4 mM and a total BIM concentration of 20 mM, the first species is recognised between pH 3 and 4 as the mono-chelated complex VOL. Spectral parameters support a [($N_{im}$, $N_{im}$); $H_2O$; $H_2O$] equatorial donor set (Scheme 2).[26]

At pH values higher than 4, the appearance of two new sets of resonances attributable to a complex with $VOL_2$ stoichiometry is detected (Figure 2). Since in the pH range 4.5–7.5 we observe the same EPR spectra with the presence of two species with an almost identical relative amount, it is obvious to suppose that these are the two isomeric *cis* and *trans* forms of the species $VOL_2$.

In bis-chelated $V^{IV}O$ complexes, *cis* species are hexacoordinate with one solvent molecule coordinated in the fourth equatorial position; *trans* species can be penta- or hexacoordinate according to the absence or presence of a solvent molecule weakly bound in the axial position, which can be revealed through the combined application of IR and UV/Vis spectroscopy.[28] As usual, because of the higher contri-

 © 2007 Wiley-VCH Verlag GmbH & Co. KGaA, Weinheim 

Table 2. EPR parameters of $V^{IV}O$ complexes.[a]

| Ligand | VOL[b] | | *cis*-$VOL_2$[c] | | *trans*-$VOL_2$[d] | | *cis*-$VOL_2H_{-1}$[e] | | $VOLH_{-1}$[f] | | | $VOLH_{-2}$[g] | | |
|---|---|---|---|---|---|---|---|---|---|---|---|---|---|---|
| | $g_\parallel$ | $A_\parallel$ | $g_\parallel$ | $A_\parallel$ | $g_\parallel$ | $A_\parallel$ | $g_\parallel$ | $A_\parallel$ | $g_\parallel$ | $A_\parallel$ exp. | $A_\parallel$ calcd. | $g_\parallel$ | $A_\parallel$ exp. | $A_\parallel$ calcd. |
| BIM | 1.948 | 169.5 | 1.950 | 164.3 | 1.959 | 159.7 | 1.956 | 161.0 | | | | | | |
| BIMA | 1.946 | 169.2 | 1.951 | 164.2 | 1.958 | 158.7 | 1.951 | 160.8 | | | | | | |
| BINM | 1.950 | 167.6 | 1.951 | 163.0 | | | 1.952 | 159.1 | | | | | | |
| Z-Gly-BIMA | 1.947 | 169.5 | 1.952 | 164.1 | 1.958 | 158.9 | | | | | | | | |
| Gly-BIMA | 1.947 | 169.5 | 1.953 | 165.2 | 1.961 | 158.3 | | | ≈1.952–1.954[h] | ≈163–165[h] | 163.6 | 1.954 | 160.0 | 158.9 |
| α-Asp-BIMA | 1.947 | 168.7 | 1.950 | 164.8 | 1.958 | 158.2 | | | ≈1.952–1.954[h] | ≈163–165[h] | 163.6 | 1.953 | 158.5 | 158.9 |
| α-Glu-BIMA | 1.953 | 170.3 | 1.954 | 163.7 | [i] | [i] | | | ≈1.952–1.954[h] | ≈163–165[h] | 163.6 | 1.956 | 159.7 | 158.9 |
| His-BIMA | 1.949 | 169.8 | 1.951 | 164.9 | 1.958 | 158.4 | | | ≈1.952–1.954[h] | ≈163–165[h] | 163.6 | 1.952 | 160.0 | 158.9 |

[a] $A_\parallel$ measured in $10^{-4}$ $cm^{-1}$. [b] Species characterised by the [($N_{im}$, $N_{im}$); $H_2O$; $H_2O$] donor set; in the systems with BIMA, Gly-BIMA, α-Asp-BIMA, α-Glu-BIMA and His-BIMA, VOL can have various degrees of protonation (see Table 1 and Table 3). [c] Species characterised by the [($N_{im}$, $N_{im}$); ($N_{im}$, $N_{im}^{ax}$); $H_2O$] donor set; in the systems with BIMA, Gly-BIMA, α-Asp-BIMA, α-Glu-BIMA and His-BIMA, *cis*-$VOL_2$ can have various degrees of protonation (see Table 1 and Table 3). [d] Species characterised by the [($N_{im}$, $N_{im}$); ($N_{im}$, $N_{im}$)] donor set; in the systems with BIMA, Gly-BIMA, α-Asp-BIMA, α-Glu-BIMA and His-BIMA, *trans*-$VOL_2$ can have various degrees of protonation (see Table 1 and Table 3). [e] Species characterised by the [($N_{im}$, $N_{im}$); ($N_{im}$, $N_{im}^{ax}$); $OH^-$] donor set. [f] Species characterised by the [($N_{im}$, $N^-$, $NH_2$); $H_2O$] donor set. [g] Species characterised by the [($N_{im}$, $N^-$, $NH_2$); $OH^-$] donor set. [h] Parameters not exactly measurable for the low concentration of the species and/or the contemporaneous presence of $VOL_2$ and $VOLH_{-2}$. [i] Parameters not exactly measurable for the contemporaneous presence of $VOLH_{-1}$ and $VOLH_{-2}$.

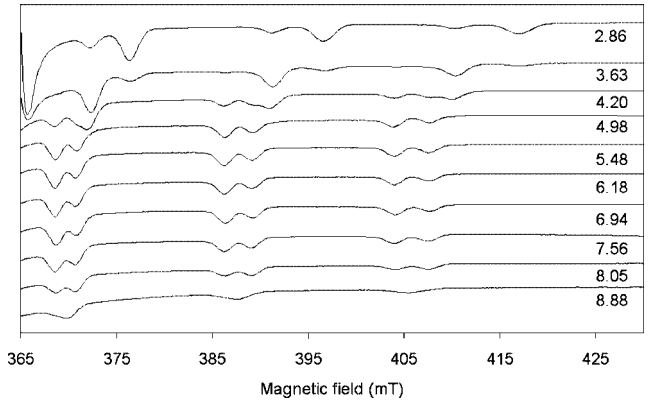


Figure 2. High field region of the X-Band anisotropic EPR spectra recorded at 140 K as a function of pH for an aqueous solution of the $V^{IV}O$/BIM system with a ligand-to-metal molar ratio of 5:1 and a $V^{IV}O$ concentration of 4 mM.

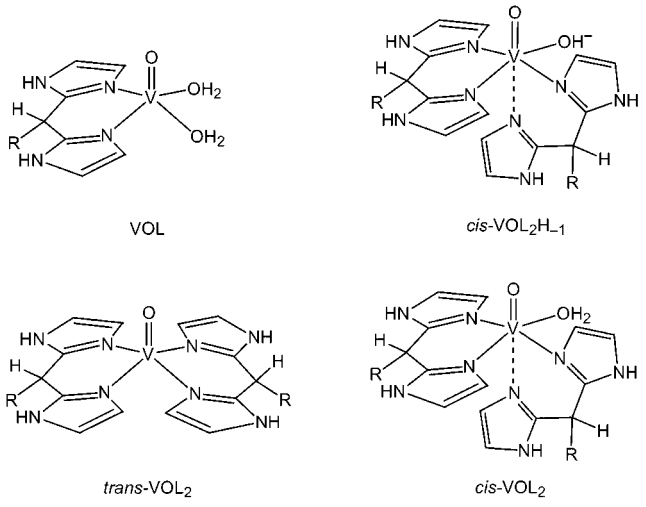


Scheme 2. Structure of the $V^{IV}O$ complexes formed by BIM (R = H), BIMA (R = $NH_2$), BINM (R = $NO_2$), Z-Gly-BIMA (R = Z-Gly) and Z-Ala-BIMA (R = Z-Ala). *Trans*-$VOL_2$ complex does not form with BINM, and *cis*-$VOL_2H_{-1}$ with Z-Gly-BIMA and Z-Ala-BIMA.

bution of water to $A_\parallel$ than the other donor functions, the *cis* complex corresponds to the species with the higher $A_\parallel$ value and the *trans* to that with the lower $A_\parallel$ (Table 2). Their structure is proposed in Scheme 2. The donor set is [($N_{im}$, $N_{im}$); ($N_{im}$, $N_{im}^{ax}$); $H_2O$] for the *cis*, and [($N_{im}$, $N_{im}$); ($N_{im}$, $N_{im}$)] for the *trans* isomer. Only the system with BINM constitutes an exception, since only the *cis* isomer for $VOL_2$ is observed.

*cis*-*trans* isomerism is not unusual for $V^{IV}O$ complexes and, of course, is due to the comparable stability of the two species. To date, many examples of such an isomerism have been reported in the literature.[28,29] The relative stability of the two isomers is influenced by a number of factors, including the ligand bite, the size of the chelate ring, the basicity and the steric requirements of the ligands, the hydrophobicity of the complexes; usually, large ligand bites, six-membered chelate rings, strong ligands and hydrophobicity of the complexes favour the *trans* isomer.[29,30] To the best of our knowledge, this is the first example of *cis*-*trans* isomerism with bidentate ligands forming six-membered chelate rings provided with only nitrogen donors.

In the systems with BIM, BIMA and BINM, potentiometry suggests a further deprotonation process above pH 7 and the species formed has been identified as $VOL_2H_{-1}$. p$K$ values for the deprotonation of $VOL_2$ to give $VOL_2H_{-1}$ fall in the range 6.97–7.76 (Table 1). As previously observed, a water molecule bound in the equatorial position of a *cis* complex with $VOL_2$ stoichiometry is more

 © 2007 Wiley-VCH Verlag GmbH & Co. KGaA, Weinheim 

acid than the bulk water,[28,30,31] and can be easily deprotonated to form the corresponding mono-hydroxo complex, *cis*-$VOL_2H_{-1}$ or *cis*-$VOL_2(OH)$. This transformation can be followed by EPR spectroscopy, since the replacement of a water molecule with a hydroxo ion implies a marked decrease of $A_{\parallel}$. In fact, with BIM, BIMA and BINM, above pH 7.5 EPR spectra change considerably, suggesting the transformation of *cis*-$VOL_2$ into *cis*-$VOL_2H_{-1}$ species (Figure 2); the decrease of the $A_{\parallel}$ value from 163.0–164.3 × $10^{-4}$ $cm^{-1}$ of *cis*-$VOL_2$ to 159.1–161.0 × $10^{-4}$ $cm^{-1}$ of *cis*-$VOL_2H_{-1}$ (Table 2) is that expected on the basis of the "additivity rule",[26] and is similar to what has been previously observed in the literature.[30,31]

It is worth noting that Z-Gly-BIMA and Z-Ala-BIMA, even if they have a carbamide group in their structure, behave like the simple BIM, BIMA or BINM derivatives, with the only difference being that they do not form the hydroxo complex $VOL_2H_{-1}$ (Table 1). The binding of the two bis(imidazol-2-yl)methyl moieties does not promote the deprotonation and the subsequent coordination of the (carb)amide nitrogen, unlike Gly-BIMA, α-Asp-BIMA, α-Glu-BIMA or His-BIMA (see below); this seems to be due to the lack of a third strong donor in the ligand chain, able to close a second chelate ring after the coordination of the amide nitrogen-$N^-$.

### Gly-BIMA, α-Asp-BIMA, α-Glu-BIMA, His-BIMA

Gly-BIMA, α-Asp-BIMA, α-Glu-BIMA, and His-BIMA can be considered as amino acid derivatives of BIMA, in which the carboxylic group of the amino acid forms an amide bond with the amino group of BIMA (Scheme 1).

Gly-BIMA in the fully protonated form has three titrable protons, α-Glu-BIMA and His-BIMA four (i.e. the formula is $H_3L$ for Gly-BIMA, and $H_4L$ for α-Glu-BIMA and His-BIMA), as reported in Table 3. The p$K_a$ values of imidazole nitrogens are similar to those of other amino acid and peptide derivatives of the bis(imidazol-2-yl)methyl group; the highest value corresponds to the deprotonation of the ammonium group of the amino acid residue. The additional deprotonation process measured for α-Glu-BIMA and His-BIMA is due to the carboxylic group and to the imidazole nitrogen of the amino acid side-chain, respectively. The p$K_a$ values recalculated in this work are in good agreement with those previously reported by some of the present authors.[23b,23d,23g]

For this group of ligands, the complexation scheme derived from the potentiometric and spectroscopic studies is similar to that of BIM, BIMA, BINM, Z-Gly-BIMA and Z-Ala-BIMA in the acid and neutral solution, but includes two different species at pH >7, $VOLH_{-1}$ and $VOLH_{-2}$, in which the amino and deprotonated amide group take part in the coordination. The stability constants of the complexes are presented in Table 3. The distribution curves for the $V^{IV}O$/Gly-BIMA system with a ligand-to-metal molar ratio of 5:1 are shown in Figure 3 as an example.

The EPR analysis allows us to confirm the results of the potentiometric titrations. Anisotropic EPR spectra recorded as a function of pH for the system with Gly-BIMA are displayed in Figure 4, and EPR parameters are listed in Table 2.

Table 3. Stability constants (log$\beta$) of proton and $V^{IV}O$ complexes for Gly-BIM, α-Glu-BIMA, His-BIMA at 25.0 ± 0.1 °C and $I$ = 0.2 M (KCl).[a]

| Species | Gly-BIMA | α-Glu-BIMA | His-BIMA |
|---|---|---|---|
| $H_4L$ | | 19.59(7) | 20.16(3) |
| $H_3L$ | 16.23(1) | 16.94(5) | 17.58(1) |
| $H_2L$ | 13.19(1) | 13.22(3) | 13.06(1) |
| HL | 7.79(1) | 7.59(1) | 7.28(1) |
| p$K_a$($Im_1$) | 3.04 | 2.65 | 2.58 |
| p$K_a$($Im_2$) | 5.40 | 5.63 | 5.78 |
| p$K_a$($NH_2$) | 7.79 | 7.59 | 7.28 |
| p$K_a$(COOH) | | 3.72 | |
| p$K_a$($Im_{His}$) | | | 4.52 |
| $VOLH_2$ | | 17.09(2) | 17.99(2) |
| VOLH | 13.56(1) | 13.51(2) | 13.31(8) |
| VOL | 8.60(3) | 9.18(1) | 8.76(3) |
| $VOL_2H_4$ | | 33.18(11) | 34.36(14) |
| $VOL_2H_3$ | | 30.00(5) | |
| $VOL_2H_2$ | 25.49(3) | 25.49(6) | 24.88(13) |
| $VOL_2H$ | 19.17(10) | | |
| $VOLH_{-1}$ | 2.12(5) | 2.51(4) | 2.96(4) |
| $VOLH_{-2}$ | –4.93(4) | –4.72(3) | –5.00(8) |
| p$K$(VOL)[b] | 6.48 | 6.67 | 5.80 |
| p$K$($VOLH_{-1}$)[c] | 7.05 | 7.23 | 7.96 |

[a] The uncertainties (σ values) of the protonation and stability constants are given in parentheses. [b] p$K$(VOL) = log$\beta$(VOL) – log$\beta$($VOLH_{-1}$). [c] p$K$($VOLH_{-1}$) = log$\beta$($VOLH_{-1}$) – log$\beta$($VOLH_{-2}$).

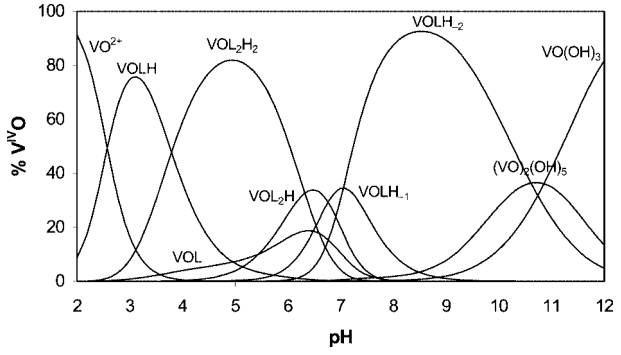


Figure 3. Species distribution for the $V^{IV}O$/Gly-BIMA system as a function of pH with a ligand-to-metal molar ratio of 5:1 and a $V^{IV}O$ concentration of 1 mM.

In all the systems we can identify two mono-chelated species with the compositions VOLH and VOL, with similar EPR parameters, $A_{\parallel}$ = 168.7–170.3 × $10^{-4}$ $cm^{-1}$, and equatorial donor set [($N_{im}$, $N_{im}$); $H_2O$; $H_2O$]; the only difference is the protonation of the terminal amino group, $–NH_3^+$ in VOLH and $–NH_2$ in VOL. For α-Glu-BIMA and His-BIMA, the additional species $VOLH_2$ has the carboxylate or the imidazole nitrogen of the amino acid residue protonated.

At excess of ligand, a number of $VOL_2H_x$ (with $x$ = 1–4) complexes predominate if pH >4 (Table 3). They are characterised by the same donor set and a *cis*-*trans* isomer-

 © 2007 Wiley-VCH Verlag GmbH & Co. KGaA, Weinheim 

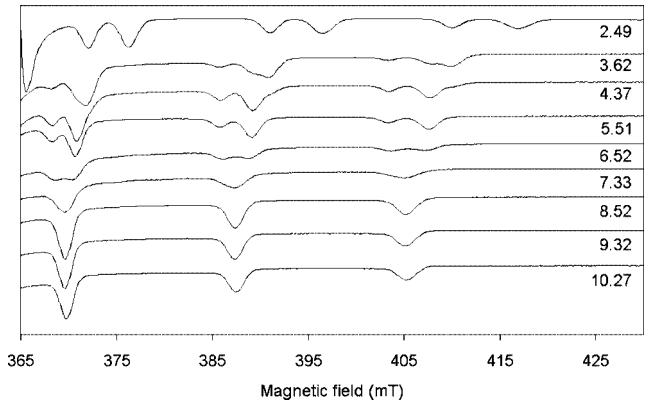


Figure 4. High field region of the X-Band anisotropic EPR spectra recorded at 140 K as a function of pH for an aqueous solution of the $V^{IV}O$/Gly-BIMA system with a ligand-to-metal molar ratio of 5:1 and a $V^{IV}O$ concentration of 4 mM.

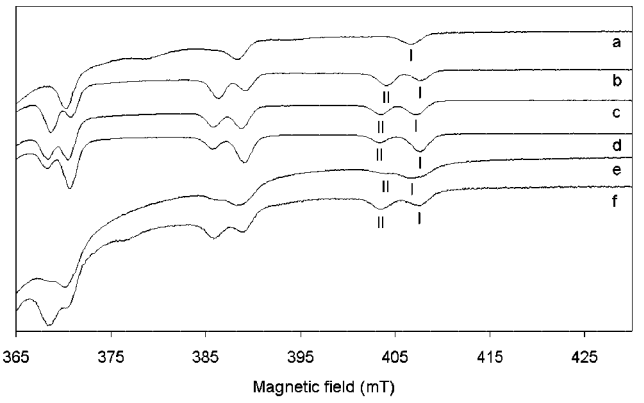


Figure 5. High field region of the X-Band anisotropic EPR spectra of the bis-chelated complexes formed by BINM, BIM, BIMA, GlyBIMA, α-Glu-BIMA and HisBIMA recorded in aqueous solutions at 140 K with a $V^{IV}O$ concentration of 4 mM: a) BINM: L/M = 1, pH = 7.20; b) BIM: L/M = 5, pH = 6.95; c) BIMA: L/M = 5, pH = 6.60; d) Gly-BIMA: L/M = 5, pH = 5.50; e) α-Glu-BIMA: L/M = 3, pH = 5.65; f) HisBIMA: L/M = 3, pH = 6.60. I and II denote *cis* and *trans* species, respectively.

ism similar to that discussed for BIM, BIMA, BINM and Z-Gly-BIMA (Table 2). The difference is the protonation degree of the ligands (for example, $VOL_2H_2$ and $VOL_2H$ species formed by Gly-BIMA have two and one non-coordinating amino group protonated, respectively). Analogously to the previous systems, the *cis* complexes are characterised by a higher $A_{\parallel}$ value ($A_{\parallel}$ = 163.7–165.2 × $10^{-4}$ $cm^{-1}$) and a [($N_{im}$, $N_{im}$); ($N_{im}$, $N_{im}^{ax}$); $H_2O$] donor set, whereas the *trans* species shows lower $A_{\parallel}$ values ($A_{\parallel}$ = 158.2–158.4 × $10^{-4}$ $cm^{-1}$), as expected on the basis of the "additivity rule",[26] and a [($N_{im}$, $N_{im}$); ($N_{im}$, $N_{im}$)] donor set. The relative amount of the two isomers does not change in the pH range 4–7 for a given ligand, but it can vary depending on the ligand; in particular, the relative amount of the *cis* isomer with respect to the *trans* increases in the order: His-BIMA < Gly-BIMA < α-Glu-BIMA ≈ α-Asp-BIMA.

In Figure 5 a comparison between the EPR spectra for a number of bis-chelated complexes formed by bis(imidazol-2-yl)methyl ligands is shown. As mentioned above, some of the present authors recently demonstrated that for ligands with the same bite, basicity and size of the chelate ring, the hydrophilicity of the complexes is the critical factor in determining the relative amount of the *cis* and *trans* species in water; particularly, hydrophilic complexes prefer the *cis* arrangement.[29] This could also explain the results displayed in Figure 5: the hydrophilic bis-chelated complexes formed by BIMA, Gly-BIMA, α-Glu-BIMA and His-BIMA prefer *cis* arrangement, whereas the most hydrophobic complex formed by BIM prefer the *trans* one. With this rule in mind, the reason for which BINM forms only a *cis* bis-chelated complex can be rationalised: BINM is the most hydrophilic ligand, because of the presence of a formal positive charge on the nitrogen and a formal negative charge on one of the oxygen atoms for each of the two $–NO_2$ groups.

Differently from the BIM, BIMA, BINM, Z-Gly-BIMA and Z-Ala-BIMA systems, above pH 7 the formation of two new species, with the composition $VOLH_{-1}$ and $VOLH_{-2}$, is observed. These species cannot be confused at all with the hydroxo complexes $VOL_2H_{-1}$ present in the previously examined systems because they exist in a wider pH range and are characterised by a higher intensity of the EPR signals, indicating a different coordination mode. Moreover, the formation of these complexes is accompanied by a new absorption maximum in the UV/Vis spectra around 390 nm, as demonstrated by an examination of Figure 6, where the distribution curves of $V^{IV}O$/His-BIMA species and the variation of molar absorptivity of the system at 386 nm are depicted as a function of pH. The appearance of this new band suggests the coordination of a "strong" donor atom, as a consequence of the deprotonation and coordination of the amide nitrogen. Similar changes in the electronic spectra were observed in the case of the $V^{IV}O$/SalGly system (SalGly = salicylglycine), where simultaneously to the deprotonation and coordination of the amide-$N^-$ a new absorption band is observed around 400 nm.[21f]

For Gly-BIMA, α-Asp-BIMA, α-Glu-BIMA and His-BIMA, in contrast with Z-Gly-BIMA and Z-Ala-BIMA, the presence of a terminal amino group allows the deprotonation and coordination of the amide nitrogen, with the closure of two five-membered chelate rings; this possibility results in the formation of $VOLH_{-1}$ and $VOLH_{-2}$ with [($N_{im}$, $N^-$, $NH_2$); $H_2O$] and [($N_{im}$, $N^-$, $NH_2$); $OH^-$] donor sets. Their structure is represented in Scheme 3. As noted above, with Z-Gly-BIMA and Z-Ala-BIMA, the second chelate ring does not form because the amino group is involved in a "carbamate-like" bond with the benzyloxycarbonyl group. For α-Asp-BIMA and α-Glu-BIMA, the formation of the final species $VOLH_{-2}$ takes place at higher pH values with respect to Gly-BIMA and His-BIMA, probably because of the presence of a negative charge on the carboxylate group which prevents the deprotonation of the amide nitrogen.

 © 2007 Wiley-VCH Verlag GmbH & Co. KGaA, Weinheim 

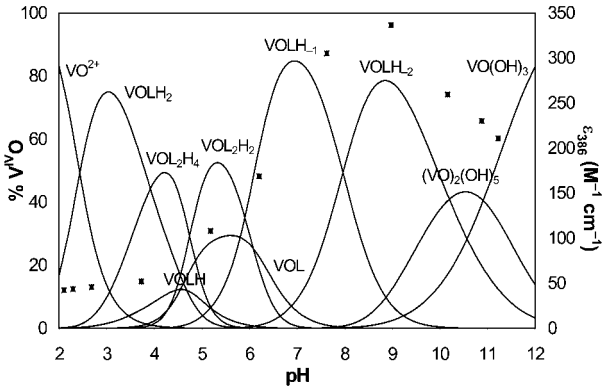


Figure 6. Species distribution for the $V^{IV}O$/His-BIMA system as a function of pH with a ligand-to-metal molar ratio of 4:1 and a $V^{IV}O$ concentration of 1 mM. The superimposed squares show the variation of molar absorptivity $\varepsilon$ at 386 nm.

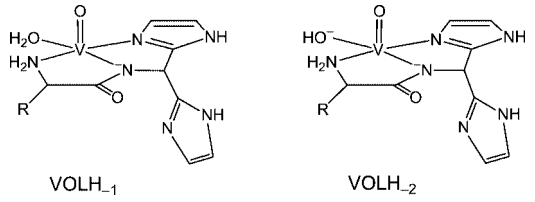


Scheme 3. Structure of the $VOLH_{-1}$ and $VOLH_{-2}$ complexes formed by Gly-BIMA (R = H), α-Asp-BIMA (R = $CH_2COO^-$), α-Glu-BIMA (R = $CH_2CH_2COO^-$) and His-BIMA (R = 4-$CH_2$-imidazole).

Since Gly-BIMA, α-Asp-BIMA, α-Glu-BIMA and His-BIMA display a comparable complexing scheme, this allows us to rule out the participation of the side-chain of α-Asp, α-Glu or His amino acids to the coordination.

As a final comment, we propose some observations on the differences between the behaviour at basic pH values of BIM, BIMA, BINM, Z-Gly-BIMA and Z-Ala-BIMA which form *cis*-$VOL_2H_{-1}$ on the one hand, and Gly-BIMA, α-Asp-BIMA, α-Glu-BIMA, His-BIMA which form $VOLH_{-2}$ on the other hand: (i) *cis*-$VOL_2H_{-1}$ undergoes hydrolytic reactions to give $[(VO)_2(OH)_5]^-$ and $[VO(OH)_3]^-$ above pH 9, whereas $VOLH_{-2}$ exists in a rather wide pH range (7.0–11.0), suggesting the coordination of stronger donors like the deprotonated amide nitrogen; (ii) UV/Vis electronic absorption spectra recorded at pH >7 on equimolar solutions of $V^{IV}O$ ions and His-BIMA are characteristic of a limpid solution: this allows us to rule out the presence of a 1:2 complex, which should result in the precipitation of the remaining part of the $V^{IV}O$ ion as $VO(OH)_2$, and supports the formation of 1:1 species like $VOLH_{-1}$ and $VOLH_{-2}$; (iii) the linewidth of the EPR signal due to $VOLH_{-2}$ is notably narrower than *trans*-$VOL_2$, indicating a lower number of nitrogen atoms coordinated (three instead of four): indeed, the nitrogen atoms on the equatorial plane increase the linewidth of the EPR signal because of the superhyperfine coupling between the unpaired electron on the $V^{IV}O$ ion and the $^{14}N$ nucleus ($I$ = 1).

## Density Functional Calculations of the $VOLH_{-1}$ and $VOLH_{-2}$ Structures

An optimised geometry of the $VOLH_{-1}$ and $VOLH_{-2}$ complexes formed by Gly-BIMA, α-Asp-BIMA, α-Glu-BIMA and His-BIMA was calculated by performing Density Functional Theory (DFT) calculations with the Gaussian 03 program.[32] In the last few years, there has been growing use of DFT methods because they give rather good results in the optimisation of the geometries of transition-metal complexes.[33] The functional B3LYP,[34,35] which has been demonstrated to yield good agreement with the experimental structures for many vanadium compounds,[33d,36] and the mixed basis set 6-311g for vanadium and 6-31g(d) for the other elements were used. With this latter set, differences of 0.023 Å in V–C and 0.010 Å in C–O bond lengths are obtained for $[V(CO)_6]^-$ and of 0.001 Å in Cr–C and 0.009 Å in C–O distances for $[Cr(CO)_6]$.[36a]

Attempts to simulate the structure of $VOLH_{-1}$ and $VOLH_{-2}$ complexes with the second imidazole ring coordinated in the axial position, in *trans* to the oxo group of the V=O unit, were unsuccessful. Therefore, in order to speed up the calculation time, we simulated the structure of $VOLH_{-1}$ and $VOLH_{-2}$ by replacing one imidazole ring with a hydrogen atom and abbreviating with Gly-IMA the obtained ligand *N*-glycyl-(imidazol-2-yl)methylamine. The results are listed in Table 4. The structure of the $VOLH_{-2}$ complex with Gly-IMA, simulated with the mixed 6-311g/6-31g(d) basis set, is displayed in Figure 7.

From an examination of Table 4 it can be noticed that beginning from the 6-31g basis set comparable results are obtained, suggesting that also simple sets can provide a satisfactory agreement with a real structure, whereas more complete basis sets supply only a marginal improvement in the geometric parameters. The distance of V=O(oxo) bond ranges were between 1.588 and 1.622 Å, that of V–N(amino) between 2.150 and 2.163 Å, that of V–$N^-$(amide) between 2.009 and 2.021 Å, that of V–N(imidazole) between 2.112 and 2.140 Å and that of V–O(hydroxo) between 1.860 and 1.882 Å.[37] An important structural parameter, which will be used for estimating the $A_\parallel$ value for $VOLH_{-1}$ and $VOLH_{-2}$ species, is the dihedral angle $\theta$, defined by the vanadyl oxo, the vanadium atom, the coordinated imidazole N and the carbon atom that bridges the two imidazole nitrogen atoms.[27,38] From an examination of Table 4, it can be noticed that it falls in the range 111.1–112.8°, suggesting an almost perpendicular arrangement of the imidazole ring with respect to the V=O bond.[27,38] The structural data of our simulations are comparable with those of the [VO(Gly-L-Val)(phen)]·$H_2O$ complex (see Table 4), characterised by a similar equatorial donor set: [($NH_2$, $N^-$, $COO^-$); ($N_{pyr}$, $N_{pyr}^{ax}$)].[21] A shorter V–O(hydroxo) distance (1.785 Å) has been measured for the complex *cis*-[VO(OH)(4,4′-dtbipy)$_2$]-$BF_4$·1.2$H_2O$ (Table 4).[36c] We have no explanation for this.

For the complex $VOLH_{-1}$, simulated with Gly-IMA with a water molecule replacing the $OH^-$ ion, bond lengths of 1.567, 2.155, 1.948, 2.091 and 2.130 Å are obtained for V=O(oxo), V–N(amino), V–$N^-$(amide), V–N(imidazole)

 © 2007 Wiley-VCH Verlag GmbH & Co. KGaA, Weinheim 

Table 4. Details and structural parameters of the DFT calculations on [VO(Gly-IMAH$_{-1}$)(OH)] and [VO(Gly-IMAH$_{-1}$)($H_2O$)]$^+$ and comparison with similar species reported in the literature.[a]

| Complex | Basis set | Basis functions | V=O | V–N(amino) | V–N$^-$(amide) | V–N(aromatic) | V–O[b] | Dihedral angle $\theta$[c] |
|---|---|---|---|---|---|---|---|---|
| [VO(Gly-IMAH$_{-1}$)(OH)] | 3-21g | 166 | 1.609 | 2.140 | 1.985 | 2.077 | 1.839 | 109.94 |
| [VO(Gly-IMAH$_{-1}$)(OH)] | 6-31g | 166 | 1.617 | 2.150 | 2.009 | 2.118 | 1.868 | 111.59 |
| [VO(Gly-IMAH$_{-1}$)(OH)] | 6-31g(d) | 171 | 1.589 | 2.163 | 2.017 | 2.139 | 1.862 | 111.87 |
| [VO(Gly-IMAH$_{-1}$)(OH)] | 6-31g+ | 231 | 1.622 | 2.156 | 2.010 | 2.112 | 1.882 | 111.11 |
| [VO(Gly-IMAH$_{-1}$)(OH)] | 6-311g | 238 | 1.609 | 2.158 | 2.017 | 2.115 | 1.864 | 112.14 |
| [VO(Gly-IMAH$_{-1}$)(OH)] | 6-311g for V/ 6-31g(d) for C,H,N,O | 241 | 1.588 | 2.163 | 2.021 | 2.140 | 1.860 | 112.76 |
| [VO(Gly-IMAH$_{-1}$)($H_2O$)]$^+$ | 6-311g for V/ 6-31g(d) for C,H,N,O | 243 | 1.567 | 2.155 | 1.948 | 2.091 | 2.130 | 105.85 |
| [VO(Gly-L-Val)(phen)] [d] | | | 1.587 | 2.158 | 1.978 | 2.155 | | |
| *cis*-[VO(OH)(4,4′-dtbipy)$_2$]$^+$ [e] | | | 1.659 | | | 2.134 [f] | 1.785 | |

[a] Gly-IMA is *N*-glycyl-(imidazol-2-yl)methylamine. [b] O belonging to an $OH^-$ ion or to a $H_2O$ molecule. [c] Defined by the vanadyl oxo, the vanadium atom, the coordinated imidazole nitrogen and the carbon atom that bridges the two imidazole nitrogens.[27,38] [d] [VO(Gly-L-Val)(phen)]·$H_2O$, where Gly-L-Val is glycyl-L-valinato and phen is 1,10-phenanthroline.[21l] [e] *cis*-[VO(OH)(4,4′-dtbipy)$_2$]-$BF_4$·1.2$H_2O$, where 4,4′-dtbipy is 4,4′-di-*tert*-butyl-2,2′-bipyridine.[36c] [f] Mean values.

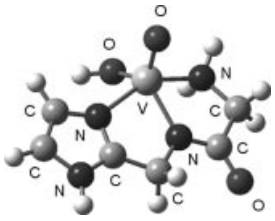


Figure 7. Simulated structure of the complex [VO(Gly-IMA)(OH)] calculated by the DFT method using the 6-311g basis set for vanadium and 6-31g(d) for the other elements (see Table 4). Gly-IMA is *N*-glycyl-(imidazol-2-yl)methylamine.

and V–O(water), respectively.[39] The dihedral angle $\theta$ is 105.9° (Table 4).[39] As expected, V–N$^-$(amide) becomes shorter as the length of the bond in the *trans* position increases; thus, V–N$^-$(amide) in VOLH$_{-1}$ is shorter than in VOLH$_{-2}$ (1.948 vs. 2.021 Å)[39] because $H_2O$ replaces the $OH^-$ ion.

### Effect of the V–N$^-$(amide) Bond on the $A_\parallel$ Value

By continuing the discussion of a previous work,[20] we would now analyse the bond between a deprotonated amide-N$^-$ and a vanadyl ion and its effect on the $^{51}V$ anisotropic parallel hyperfine constant of $V^{IV}O$ complexes. The latter is indicated with $A_\parallel$ or $A_z$, depending on the symmetry of the complexes, axial or rhombic (here we consider only axial species with two $g$, $g_\parallel$ and $g_\perp$, and two $A$, $A_\parallel$ and $A_\perp$, values). For the $^{51}V$ nucleus, $A_\parallel$ can be expressed as shown in Equation (2).[40]

$$A_{\parallel} = P_d\left[\beta^2\left(-\kappa-\frac{4}{7}\right)+(g_{\parallel}-2.0023)+\frac{3}{7}(g_{\perp}-2.0023)\right] \quad (2)$$

In this equation $P_d = g_N\beta_N g\beta\langle r^{-3}\rangle$ is the dipolar interaction between the unpaired electron and the $^{51}V$ nucleus and is determined by the spatial distribution of the *d* electron,[40] $\kappa$ is the Fermi contact term and measures the unpaired *s*-electron spin density at the nucleus, and $\beta^2$ is, to a good approximation, the population of the ground state *d* orbital containing the unpaired spin (for $V^{IV}O$ species with $C_{2v}$ symmetry or higher, it measures the population of the $d_{xy}$ orbital). Pecoraro assumed the terms $\kappa$ and $P_d$ as constants and reported a value of 0.85 for $\kappa$ and of $128\times10^{-4}$ cm$^{-1}$ for $P_d$.[38] A similar value for $P_d$ ($125\times10^{-4}$ cm$^{-1}$) has been used by Deligiannakis and Kabanos.[21h] Mabbs and Collison report a significantly higher value ($173.5\times10^{-4}$ cm$^{-1}$).[41]

In the "additivity rule",[26] Chasteen estimated $A_\parallel$ or $A_z$ of a $V^{IV}O$ species from the contribution of each of the four equatorial donor groups, see Equation (1).[26] The contribution of the various groups to $A_\parallel$ is listed in Table 5.

The rule provides a valid criterion for the identification of the equatorial donor atoms. Additions or corrections concerning the contribution of N(imino),[20] $Cl^-$ and $SCN^-$,[21j] CO(carbonyl)[42] and $COO^-$,[21m] appeared subsequently in the literature. Pecoraro and co-workers proposed that for imidazole the overlap of the π orbitals of the aromatic ring with the $d_{xy}$ vanadium atomic orbital bearing the unpaired electron would increase the covalence of the metal–ligand bond and produce a decrease of the $\beta^2$ value and of the contribution of an imidazole nitrogen to $A_\parallel$, see Equation (2).[27,38] They determined an empiric equation to calculate the value of $A_\parallel$(imidazole) as a function of the dihedral $\theta$ angle, see Equation (3) where $x = 42.72\times10^{-4}$ cm$^{-1}$ and $y = 2.96\times10^{-4}$ cm$^{-1}$.[27,38]

$$A_\parallel(\text{imidazole}) = x + y\sin(2\theta - 90) \quad (3)$$

With the data reported in Table 5, an expected value of $A_\parallel$ for the complexes VOLH$_{-1}$ and VOLH$_{-2}$ formed by Gly-BIMA, α-Asp-BIMA, α-Glu-BIMA and His-BIMA can be calculated. The values of $32.7\times10^{-4}$ cm$^{-1}$ and $35.3\times10^{-4}$ for $A_\parallel$(amide) in VOLH$_{-1}$ (total equatorial charge of –1, Table 5) and VOLH$_{-2}$ (total equatorial charge of –2, Table 5), and of $45.2\times10^{-4}$ and $44.8\times10^{-4}$ cm$^{-1}$ for $A_\parallel$(imidazole) in VOLH$_{-1}$ and VOLH$_{-2}$ calculated with the dihe-

 © 2007 Wiley-VCH Verlag GmbH & Co. KGaA, Weinheim 

dral $\theta$ angles obtained from DFT simulations (Table 4) were used.[39] $A_{\parallel}$ of $163.6 \times 10^{-4}$ cm$^{-1}$ for $VOLH_{-1}$ and $158.9 \times 10^{-4}$ cm$^{-1}$ for $VOLH_{-2}$ are derived, comparable to the experimental ones (Table 2).

Table 5. Contribution of the various groups to $^{51}$V hyperfine coupling constants $A_{\parallel}$.[a]

| Donor group[b] | Contribution to $A_{\parallel}$[c] | Ref. |
|---|---|---|
| $H_2O$ | 45.6 | [26] |
| $COO^-$ | 42.1 | [21m] |
| CO | 43.5 | [42] |
| $OH^-$ | 38.7 | [26] |
| $O_{aromatic}^-$ ($O_{ar}^-$) | 38.9 | [26] |
| $RO^-$ | 35.3 | [26] |
| $S_{aromatic}^-$ ($S_{ar}^-$) | 35.3 | [26] |
| $RS^-$ | 31.9 | [26] |
| $NH_2$ | 40.1 | [26] |
| $N_{imino}$ | 41.6 | [20] |
| $N_{imidazole}$ ($N_{im}$) | $42.72 + 2.96 \cdot \sin(2\theta - 90)$[d] | [27,38] |
| $N_{pyridine}$ ($N_{pyr}$) | 40.7 | [26] |
| $N_{amide}$ ($N^-$) | 32.7 (–1), 35.3 (–2), 38.6 (–3), 40.9 (–4)[e] | [20] |
| $Cl^-$ | 44.2 | [21j] |
| $SCN^-$ | 43.2 | [21j] |

[a] Contribution measured in $10^{-4}$ cm$^{-1}$. [b] Between round brackets are given the symbols used in Table S1 of the electronic supporting information and in other parts of the text. [c] In many parts of the text the contribution of each donor group to $A_{\parallel}$ is also indicated with $A_{\parallel}$(donor). [d] $\theta$ is the dihedral angle defined by the vanadyl oxo, the vanadium atom, the coordinated imidazole nitrogen and the carbon atom that bridges the two imidazole nitrogen atoms.[27,38] [e] Between round brackets, the total charge present in the equatorial plane of the $V^{IV}O$ ion (including that of the amide nitrogen).

Concerning the amide contribution to $A_{\parallel}$, $A_{\parallel}$(amide), it was found to be sensitive to the total charge of the donor atoms in the equatorial plane; in particular, its value decreases with a decrease in the total equatorial charge.[20,21b,21h] By taking into account the $A_{\parallel}$(amide) values for 37 $V^{IV}O$ compounds with a V–N$^-$(amide) bond, we recently calculated 35.5, 38.3 and $40.9 \times 10^{-4}$ cm$^{-1}$ for the contribution to $A_{\parallel}$ when the total equatorial charge is –4, –3 or –2 (including that of the amide nitrogen) and by extrapolation $32.7 \times 10^{-4}$ cm$^{-1}$ for the –1 equatorial charge (Table 5),[20] in good agreement with the results of Tasiopoulos et al.[21h]

On the basis of the methods reported in the literature for rationalising some cases of anomalous EPR behaviour displayed by $V^{IV}O$ complexes, three different hypotheses could be advanced to explain the unusual reduction of $A_{\parallel}$(amide) with the total equatorial charge:

(i) Two limit resonance structures for a deprotonated amide group coordinated through nitrogen, one "amide-like" with the nitrogen atom negatively charged and a double bond between the carbon and oxygen atoms of the carbonyl group, and another "imine-like" with the carbonyl oxygen negatively charged and a double bond between the carbon and nitrogen atoms, can be assumed.[21b] With a decrease in the total equatorial charge around vanadium the importance of the "amide-like" arrangement should increase, to which a lower $A_{\parallel}$(amide) contribution corresponds.[21b] This explanation would result in a change in C–N, C=O and V–N distances as a function of $A_{\parallel}$(amide), but is not supported by the data of the structures resolved through a single-crystal X-ray diffraction analysis for which EPR parameters are reported.[20]

(ii) A reduction of the $P_d$ parameter, which should decrease the electron density on the metal ion and hence the V=O bond length, could be proposed. A similar explanation was put forward by Kabanos and co-workers to explain the reduction of $A_{\parallel}$ by about 10%, relative to the value predicted with the "additivity rule", for the complexes [VOX(capca)], where Hcapca is *N*-{2-[(2-pyridylmethylene)amino]phenyl}pyridine-2-carboxamide and $X^-$ is an anion ($Cl^-$, $SCN^-$, $CH_3COO^-$ or $PhCOO^-$) occupying the axial position.[21j] This mechanism can be ruled out for $V^{IV}O$ complexes involving a V–N$^-$(amide) bond, because no correlation between the $A_{\parallel}$(amide) values and V=O length is observable.[20] According to the theoretic treatment of Mabbs and Collison,[41] to Pecoraro and co-workers[27,38] and to a previous paper of Deligiannakis and Kabanos,[21h] we believe that the value of $P_d$ can be assumed to be constant.

(iii) An overlap between the π orbitals of the ligand and $d_{xy}$ atomic orbital of vanadium, which increases the covalence of the V–N$^-$(amide) bond and decreases $\beta^2$ and $A_{\parallel}$ values [see Equation (2)] could be suggested, i.e. a mechanism similar to that proposed by Pecoraro and co-workers to justify the reduction of $A_{\parallel}$(imidazole) when the aromatic ring is perpendicular to the V=O group.[27,38] However, this possibility is not applicable to the V–N$^-$(amide) bond if the amide group remains perpendicular to the V=O group, because the delocalised π system is not in a favourable position to overlap with the $d_{xy}$ orbital.

The question arising is: why only the V–N$^-$(amide) bond (and not the other V-donor bonds) should compensate a lower electronic density in the equatorial plane of a $V^{IV}O$ complex through an increase of the covalence? In order to evaluate the effect of the total equatorial charge on $A_{\parallel}$, we re-analysed the EPR parameters of the structures containing a V–N$^-$(amide) bond (see Table S1 in the electronic supporting information). We compared several couples of $V^{IV}O$ structures, in which the only variable is the equatorial charge; in particular, we examined four couples which only differ in one donor and in one unit of the total equatorial charge (two couples with –4/–3 and two with –3/–2 equatorial charge), two couples which differ in one donor but two units of equatorial charge (–4/–2) and, for comparison, six couples which differ in one donor but not in equatorial charge (two couples with –4/–4, two with –3/–3 and two with –2/–2). To avoid taking into account the influence of the donor which changes going from higher to lower equatorial charge, for each couple we considered the experimental $A_{\parallel}$ value ($A_{\parallel}$ exp.) for the complex with higher equatorial charge and, from it, calculated $A_{\parallel}$ ($A_{\parallel}$ calcd.) for the complex with lower charge by subtracting the contribution of the donor which is replaced and adding that of the donor which replaces it (indicated in bold in Table S1 of Supporting Information), with the contribution of several donors taken from Table 5.[43] If $A_{\parallel}$ was only dependent on the do-

 © 2007 Wiley-VCH Verlag GmbH & Co. KGaA, Weinheim 

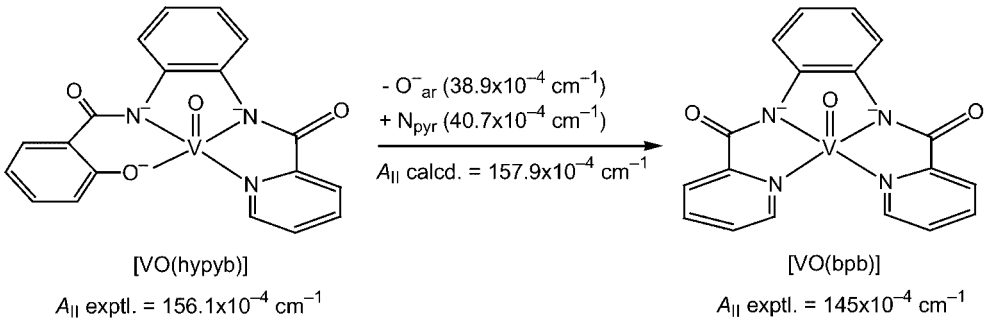


Scheme 4. Methods for calculating $A_{\parallel}$ ($A_{\parallel}$ calcd.) for a $V^{IV}O$ complex containing a V–$N^{-}$(amide) bond from the experimental $A_{\parallel}$ value ($A_{\parallel}$ exp.) of the species with higher total equatorial charge. $H_3$hypyb = 1-(2-hydroxybenzamido)-2-(2-pyridinecarboxamido)benzene,[21e] and $H_2$bpb = 1,2-bis(2-pyridinecarboxamido)benzene.[21i]

nor functions bound to the $V^{IV}O$ ion and not on the equatorial charge, we should expect an almost exact coincidence between $A_{\parallel}$ calcd. and $A_{\parallel}$ exp. for the species with lower charge; every difference between the two values can be attributable only to the decrease of the equatorial charge. This is illustrated in Scheme 4.

The conclusion is that the decrease of the equatorial charge always results in a decrease of the $A_{\parallel}$ value for a $V^{IV}O$ complex, whereas if the equatorial charge remains the same no significant changes in the $A_{\parallel}$ value can be observed. In particular, in the two couples with –4/–3 equatorial charge, in the two with –3/–2 and in the two with –4/–2 a reduction in the range 3.0–3.8, 3.2–8.9 and 7.6–10.2% is observed, respectively; on the other hand, in the six couples with the same equatorial charge the maximum difference (negative or positive) is 1.2%. It is worth noting that the most marked reduction is observed when changing the equatorial charge from –4 to –2. The comparison between the $VOLH_{-2}$ complex studied in this work (total equatorial charge of –2) and two $V^{IV}O$ species with a charge of –3 and –2 follows the same trend.

It is obvious that, if the contribution to $A_{\parallel}$ of all the donor functions is considered constant, the decrease in $A_{\parallel}$ for $V^{IV}O$ complexes containing a V–$N^{-}$(amide) bond must be entirely attributed to the decrease of $A_{\parallel}$(amide). However, analysing the 14 couples of $V^{IV}O$ complexes in Table S1 of the electronic supporting information, the hypothesis that all the donors participate in the reduction of $A_{\parallel}$ could be advanced, i.e. all the contributions of the four equatorial donors could decrease with a decrease in the total equatorial charge. Of course, this reduction can be almost negligible; for example, in the couple **I** in Table S1 of the supporting information it is enough if the contribution of every donor to $A_{\parallel}$ decreases by 3.0% to obtain an agreement with the calculated value, i.e. the contribution of phenolate ($O_{ar}^{-}$) will be of $37.7 \times 10^{-4}$ cm$^{-1}$ instead of $38.9 \times 10^{-4}$ cm$^{-1}$. This effect is not evident when bis-chelated complexes of bidentate ligands (often with the same donor function),[44] like those analysed by Chasteen in formulating the "additivity rule", are considered.[26] However, this difference falls within the uncertainty of ca. $3 \times 10^{-4}$ cm$^{-1}$ for the $A_{\parallel}$ value estimated by Chasteen and Pecoraro.[26,27] Therefore, we would stress that the "additivity rule" is respected; what should be taken into account in its application is that the contribution of the various donor functions could vary in a narrow range, probably centred around the value reported in Table 5, depending on the type of $V^{IV}O$ complex under examination.

Since the $\kappa$ and probably $P_d$ terms can be considered constant for vanadyl complexes,[21h,38,41] a reduction of $A_{\parallel}$ could be only connected to a reduction of coefficient $\beta^2$ in Equation (2). By following the discussion of Ballhausen and Gray, in a square pyramidal $V^{IV}O$ complex the $d_{xy}$ atomic orbital with $b_{2g}$ symmetry which bears the unpaired electron can covalently interact with the ligand orbitals only through a π bond, see Equation (4).[45]

$$\psi(b_{2g}) = \beta d_{xy} + (\gamma_1\pi_{x1} + \gamma_2\pi_{y2} - \gamma_3\pi_{x3} - \gamma_4\pi_{y4}) \quad (4)$$

where $\beta$ is the coefficient of the $d_{xy}$ vanadium atomic orbital, see Equation (2), and $\gamma_i$ are the coefficients of the ligand orbitals $\pi_i$ with suitable symmetry to overlap with $d_{xy}$.[46] A value of 1 for $\beta^2$ indicates that the unpaired electron is localised exclusively on the vanadium $d_{xy}$ orbital and that there is no delocalisation onto the ligands; on the other hand, a value of $\beta^2$ lower than 1 indicates that a $(1–\beta^2)$ fraction of the spin density is delocalised onto the ligands, causing a decrease of $A_{\parallel}$ value through Equation (2).

By analysing the data reported in Table S1 of the electronic supporting information, we think that it can not be excluded that the reduction of $A_{\parallel}$ is due to an increase of the covalence of all or part of the four equatorial V-donor bonds through a π interaction between the $d_{xy}$ orbital of vanadium and the π wavefunction of the ligands with $b_{2g}$ symmetry in the $C_{4v}$ group (for example, p atomic orbitals of oxygen in $O_{aromatic}^{-}$, $RO^{-}$, $OH^{-}$, $COO^{-}$, and of sulfur in $S_{aromatic}^{-}$, $RS^{-}$, or π aromatic orbitals of phenols, thiols, imidazole and pyridine rings, imino groups with suitable orientation to overlap with the $d_{xy}$ orbital). Probably, such a π interaction is necessary when the total equatorial charge around vanadium diminishes and the four σ bonds are not sufficient to neutralise the +2 charge of the vanadyl ion. We do not believe that the decreased contribution of the deprotonated $N^{-}$(amide) function to $A_{\parallel}$ is the only reason for the decrease in $A_{\parallel}$. Further studies are, however, necessary to clarify this topic.

 © 2007 Wiley-VCH Verlag GmbH & Co. KGaA, Weinheim 

## Conclusions

Simple amino acid derivatives of bis(imidazol-2-yl)-methylamine coordinate the $V^{IV}O$ ion at acid pH values and keep it in solution until the deprotonation and the coordination of the amide group occurs. A ligand-to-metal molar ratio between 3:1 and 5:1 is enough to avoid the hydrolysis of $V^{IV}O$ solutions; on the other hand, for ligands with weaker anchoring groups higher ratios are required: for example 10:1 for HisGlyGly provided with the ($NH_2$, CO, $N_{im}^{ax}$) donor set,[21o] and 15:1 for GlyGlyHis and GlyGlyCys with the ($COO^-$, CO) set.[21o] This suggests that the bis(imidazol-2-yl)methyl residue is an anchoring group of intermediate strength, weaker than phenolate-$O^-$ or thiolate-$S^-$ but stronger than amino-$NH_2$ or carboxylate-$COO^-$.

The presence of a free terminal amino group seems to be a necessary condition to promote the deprotonation of the amide bond through the closure of a second chelate ring besides that formed by imidazole and deprotonated amide nitrogens; its absence, like with Z-Gly-BIMA and Z-Ala-BIMA, stops the complexation to the $VOL_2$ complex.

The identical complexing behaviour of Gly-BIMA, α-Asp-BIMA, α-Glu-BIMA and His-BIMA indicates that the side-chain of the α-Asp, α-Glu or His residues does not take part in the coordination. This is not too surprising because the carboxylate group of α-Asp-BIMA and α-Glu-BIMA should close seven- and eight-membered chelate rings, and the imidazole nitrogen of His-BIMA a seven-membered ring. Moreover, the lower affinity of the $V^{IV}O$ ion for nitrogen atoms with respect to $Cu^{II}$ hinders the formation of the dinuclear structures observed for α-Asp-BIMA,[23g] α-Glu-BIMA[23g] and His-BIMA.[23b]

Also with Gly-BIMA, α-Asp-BIMA, α-Glu-BIMA and His-BIMA the "additivity rule" for calculating the $^{51}V$ anisotropic parallel hyperfine coupling constant ($A_\parallel$) is followed,[20,21j,21m,26,27,38,42] but only attributing a reduced contribution to $A_\parallel$(amide) when the total equatorial charge around the vanadyl ion decreases.[20,21b,21h] This simplification allows us to obtain a good agreement between the calculated and experimental $A_\parallel$ values,[20,21o] but is justified only if the contribution of all the other donors is considered constant so that the reduction of $A_\parallel$ can be entirely attributed to a reduction of $A_\parallel$(amide). In this work we present the new idea that all four equatorial donors could contribute to reducing the positive charge of the vanadyl ion when a decrease in the total equatorial charge is considered; the mechanism could be based on an increase of the covalence of V-donor bonds through π interactions involving the overlap of the ligand orbitals with $d_{xy}$ bearing the unpaired electron, which in turn results in a decrease of the $A_\parallel$ value, according to Equation (2). However, further experimental data must be collected to confirm this hypothesis.

## Experimental Section

**Syntheses:** The synthetic procedures for preparation of simple amino acid derivatives containing the bis(imidazoly-2-yl)methyl moiety have already been reported.[23b,47] The purities of products were checked by $^1H$ NMR and concentrations were determined by potentiometric titration. $V^{IV}O$ solutions were prepared following literature methods.[48]

**Potentiometric Measurements:** The stability constants of proton and $V^{IV}O$ complexes were determined by pH-potentiometric titrations on 3–10 mL of samples. The ligand-to-metal molar ratio was between 1:1 and 5:1 and $V^{IV}O$ concentration was 0.001–0.004 M. Titrations were performed from pH 2.0 until precipitation or very extensive hydrolysis by adding carbonate-free KOH of known concentration (ca. 0.2 M KOH).[49] The pH was measured with a Metrohm 6.0234.100 combined electrode, calibrated for hydrogen concentration by the method of Irving et al.[50] Measurements were carried out at 25.0 ± 0.1 °C and at a constant ionic strength of 0.2 M KCl with a Radiometer ABU91 automatic titration system or MOLSPIN pH-meter equipped with a digitally operated syringe (1.00 mL) controlled by a computer. Purified argon was bubbled through the samples to ensure the absence of oxygen. The number of experimental points was 50–100 for each titration curve and the reproducibility of the points included in the evaluation was within 0.005 pH units in the whole pH range examined. The stability of the complexes, reported as the logarithm of the overall formation constant $\beta_{pqr} = [VO_pL_qH_r]/[VO]^p[L]^q[H]^r$, where VO stands for the $V^{IV}O$ ion, L is the deprotonated form of the ligand and H is the proton, was calculated with the aid of the SUPERQUAD[51] and PSEQUAD programs.[52] Standard deviations were calculated by assuming random errors. Conventional notation was used: negative indices for protons indicate either the dissociation of groups which do not deprotonate in the absence of $V^{IV}O$ coordination, or hydroxo ligands. Hydroxo complexes of $V^{IV}O$ were taken into account and the following species were assumed: $[VO(OH)]^+$ ($\log\beta_{10-1} = -5.94$), $[(VO)_2(OH)_2]^{2+}$ ($\log\beta_{20-2} = -6.95$), with stability constants calculated from the data of Henry et al.[53] and corrected for the different ionic strengths by use of the Davies equation,[54] $[VO(OH)_3]^-$ ($\log\beta_{10-3} = -18.0$) and $[(VO)_2(OH)_5]^-$ ($\log\beta_{20-5} = -22.0$).[55]

**Spectroscopic Measurements:** Anisotropic EPR spectra were recorded for aqueous solutions with an X-band (9.35 GHz) Bruker EMX spectrometer in the temperature range 120–140 K. As usual for low temperature measurements, a few drops of DMSO were added to the samples to ensure good glass formation. The spectra were simulated with the computer program Bruker WinEPR SimFonia.[56] Although the temperature is different during the potentiometric and EPR measurements, according to the data in the literature the same stoichiometry and coordination mode of the main species can be supposed.[19] Electronic spectra were recorded with Perkin–Elmer Lambda 25 or 35 spectrophotometers in the same concentration range as used for potentiometry. All operations were performed under a purified argon atmosphere in order to avoid oxidation of the $V^{IV}O$ ion.

**Computational Details:** All calculations presented in this paper were performed using the Gaussian 03 program (revision C.02)[32] and DFT methods.[57] The hybrid exchange-correlation functional B3LYP was employed.[34,35] Several basis functions were used for the calculations: 3-21g, 6-31g, 6-31g(d), 6-31+g, 6-31g(d,p) and 6-311g; finally, the mixed set with 6-311g for vanadium and 6-31g(d) for the other elements was chosen. Full geometry optimisations were carried out on the $VOLH_{-1}(H_2O)$ and $VOLH_{-1}(OH)$ complexes (i.e. $VOLH_{-1}$ and $VOLH_{-2}$), using the ligand L in which one imidazole ring of the bis(imidazol-2-yl) residue was replaced by a hydrogen atom [L = *N*-glycyl-(imidazol-2-yl)methylamine, Gly-IMA]. Minima were verified through frequency calculations.

 © 2007 Wiley-VCH Verlag GmbH & Co. KGaA, Weinheim 

Minimisations of the structures formed by Gly-BIMA with the second imidazole ring coordinated in the axial position of the $V^{IV}O$ ion were unsuccessful.

**Supporting Information** (see also the footnote on the first page of this article): Details of DFT calculations. Comparison between the experimental and calculated $A_{\parallel}$ values for $V^{IV}O$ complexes containing a V–$N^{-}$(amide) bond, characterised by different and same total equatorial charge (Table S1).

## Acknowledgments

This work was supported by the Hungarian Scientific Research Fund (OTKA T042722). The authors thank Helga Süli-Vargha, Ágnes Seprényi and Péter Buglyó for the synthesis of ligands.

[1] a) D. Rehder in *Metal Ions in Biological Systems* (Eds.: A. Sigel, H. Sigel), Marcel Dekker, New York, **1995**, vol. 31, p. 1–43; b) D. C. Crans, J. J. Smee, E. Gaidamauskas, L. Yang, *Chem. Rev.* **2004**, *104*, 849–902.

[2] a) M. J. Smith, D. E. Ryan, K. Nakanishi, P. Frank, K. O. Hodgson in *Metal Ions in Biological Systems* (Eds.: A. Sigel, H. Sigel), Marcel Dekker, New York, **1995**, vol. 31, p. 423–490; b) H. Michibata, T. Uyama, K. Kanamori in *Vanadium Compounds: Chemistry, Biochemistry and Therapeutic Applications* (Eds.: A. S. Tracey, D. C. Crans), ACS Symposium Series 711, Washington, DC, **1998**, p. 248–258.

[3] T. Ishii, I. Nakai, K. Okoshi in *Metal Ions in Biological Systems* (Eds.: A. Sigel, H. Sigel), Marcel Dekker, New York, **1995**, vol. 31, p. 491–509.

[4] E. Bayer in *Metal Ions in Biological Systems* (Eds.: A. Sigel, H. Sigel), Marcel Dekker, New York, **1995**, vol. 31, p. 407–421.

[5] a) H. Vilter in *Metal Ions in Biological Systems* (Eds.: A. Sigel, H. Sigel), Marcel Dekker, New York, **1995**, vol. 31, p. 325–362; b) V. L. Pecoraro, C. A. Slebodnick, B. J. Hamstra in *Vanadium Compounds: Chemistry, Biochemistry and Therapeutic Applications* (Eds.: A. S. Tracey, D. C. Crans), ACS Symposium Series 711, Washington, DC, **1998**, p. 157–167.

[6] a) R. L. Robson, R. R. Eady, T. J. Richardson, R. W. Miller, M. Hawkins, J. R. Postgate, *Nature* **1986**, *322*, 388–390; b) R. R. Eady in *Metal Ions in Biological Systems* (Eds.: A. Sigel, H. Sigel), Marcel Dekker, New York, **1995**, vol. 31, p. 363–405.

[7] P. J. Stankiewicz, A. S. Tracey, D. C. Crans in *Metal Ions in Biological Systems* (Eds.: A. Sigel, H. Sigel), Marcel Dekker, New York, **1995**, vol. 31, p. 287–324.

[8] a) Y. Shechter, S. J. D. Karlish, *Nature* **1980**, *284*, 556–558; b) K. H. Thompson, J. H. McNeill, C. Orvig, *Chem. Rev.* **1999**, *99*, 2561–2571 and references cited therein; c) K. H. Thompson, C. Orvig, *Coord. Chem. Rev.* **2001**, *219–221*, 1033–1053 and references cited therein; d) Y. Shechter, I. Goldwaser, M. Mironchik, M. Fridkin, D. Gefel, *Coord. Chem. Rev.* **2003**, *237*, 3–11; e) K. Kawabe, Y. Yoshikawa, Y. Adachi, H. Sakurai, *Life Sci.* **2006**, *78*, 2860–2866.

[9] a) M. Garner, J. Reglinski, W. E. Smith, J. McMurray, I. Abdullah, R. Wilson, *J. Biol. Inorg. Chem.* **1997**, *2*, 235–241; b) D. C. Crans, M. Mahroof-Tahir, A. D. Keramidas, *Mol. Cell. Biochem.* **1995**, *153*, 17–24.

[10] N. D. Chasteen in *Metal Ions in Biological Systems* (Eds.: A. Sigel, H. Sigel), Marcel Dekker, New York, **1995**, vol. 31, p. 231–247.

[11] N. D. Chasteen, E. M. Lord, H. J. Thompson in *Frontiers in Bioinorganic Chemistry* (Ed.: A. V. Xavier), VCH, Weinheim, **1986**, p. 133–141.

[12] N. D. Chasteen, J. K. Grady, C. E. Holloway, *Inorg. Chem.* **1986**, *25*, 2754–2760.

[13] T. Kiss, E. Kiss, E. Garribba, H. Sakurai, *J. Inorg. Biochem.* **2000**, *80*, 65–73.

[14] G. R. Willsky, A. B. Goldfine, P. J. Kostyniak, J. H. McNeill, L. Q. Yang, H. R. Khan, D. C. Crans, *J. Inorg. Biochem.* **2001**, *85*, 33–42.

[15] B. D. Liboiron, K. H. Thompson, G. R. Hanson, E. Lam, N. Aebischer, C. Orvig, *J. Am. Chem. Soc.* **2005**, *127*, 5104–5115 and references cited therein.

[16] T. Kiss, T. Jakusch, S. Bouhsina, H. Sakurai, E. A. Enyedy, *Eur. J. Inorg. Chem.* **2006**, 3607–3614.

[17] C. Harford, B. Sarkar, *Acc. Chem. Res.* **1997**, *30*, 123–130.

[18] I. Sóvágó in *Biocoordination Chemistry* (Ed.: K. Burger), Ellis Horwood, New York, **1990**, p. 135–184.

[19] T. Kiss, T. Jakusch, J. Costa Pessoa, I. Tomaz, *Coord. Chem. Rev.* **2003**, *237*, 123–133.

[20] E. Garribba, E. Lodyga-Chruscinska, G. Micera, A. Panzanelli, D. Sanna, *Eur. J. Inorg. Chem.* **2005**, 1369–1382.

[21] a) G. R. Hanson, T. A. Kabanos, A. D. Keramidas, D. Mentzafos, A. Terzis, *Inorg. Chem.* **1992**, *31*, 2587–2594; b) C. R. Cornman, E. P. Zovinka, Y. D. Boyajina, K. M. Geisre-Bush, P. D. Boyle, P. Singh, *Inorg. Chem.* **1995**, *34*, 4213–4219; c) I. Cavaco, J. Costa Pessoa, S. M. Luz, M. T. Duarte, P. M. Matias, R. T. Henriques, R. D. Gillard, *Polyhedron* **1995**, *14*, 429–439; d) A. J. Tasopoulos, A. T. Vlahos, A. D. Keramidas, T. A. Kabanos, Y. G. Deligiannakis, C. P. Raptopoulou, A. Terzis, *Angew. Chem. Int. Ed. Engl.* **1996**, *35*, 2531–2533; e) A. D. Keramidas, A. P. Papaioannou, A. Vlahos, T. A. Kabanos, G. Bonas, A. Makriyannis, C. P. Raptopoulou, A. Terzis, *Inorg. Chem.* **1996**, *35*, 357–367; f) T. Kiss, K. Petrohán, P. Buglyó, D. Sanna, G. Micera, J. Costa Pessoa, C. Madeira, *Inorg. Chem.* **1998**, *37*, 6389–6391; g) J. Costa Pessoa, T. Gajda, R. D. Gillard, T. Kiss, S. M. Luz, J. J. G. Moura, I. Tomaz, J. P. Telo, I. Török, *J. Chem. Soc. Dalton Trans.* **1998**, 3587–3600; h) A. J. Tasiopoulos, A. N. Troganis, A. Evangelou, C. P. Raptopoulou, A. Terzis, Y. Deligiannakis, T. A. Kabanos, *Chem. Eur. J.* **1999**, *5*, 910–921; i) A. T. Vlahos, E. I. Tolis, C. P. Raptopoulou, A. Tsohos, M. P. Sigalas, A. Terzis, T. A. Kabanos, *Inorg. Chem.* **2000**, *39*, 2977–2985; j) E. J. Tolis, V. I. Teberekidis, C. P. Raptopoulou, A. Terzis, M. Sigalas, Y. Deligiannakis, T. A. Kabanos, *Chem. Eur. J.* **2001**, *7*, 2698–2710; k) J. Costa Pessoa, I. Correia, T. Kiss, T. Jakusch, M. M. C. A. Castro, C. F. G. C. Geraldes, *J. Chem. Soc. Dalton Trans.* **2002**, 4440–4450; l) A. J. Tasiopoulos, E. J. Tolis, J. M. Tsangaris, A. Evangelou, J. D. Woollins, A. M. Z. Slawin, J. Costa Pessoa, I. Correia, T. A. Kabanos, *J. Biol. Inorg. Chem.* **2002**, *7*, 363–374; m) T. Jakusch, P. Buglyó, A. I. Tomaz, J. Costa Pessoa, T. Kiss, *Inorg. Chim. Acta* **2002**, *339*, 119–128; n) T. Jakusch, A. Dörnyei, I. Correia, L. M. Rodriguez, G. K. Tóth, T. Kiss, J. Costa Pessoa, S. Marcão, *Eur. J. Inorg. Chem.* **2003**, 2113–2122; o) E. Garribba, G. Micera, E. Lodyga-Chruscinska, D. Sanna, G. Sanna, *Eur. J. Inorg. Chem.* **2005**, 4953–4963.

[22] a) G. J. Anthony, A. Koolhaas, P. M. van Berkel, S. C. van der Slot, G. Mendoza-Diaz, W. L. Driessen, J. Reedijk, *Inorg. Chem.* **1996**, *35*, 3525–3532 and references cited therein; b) L. Zhou, D. Powell, K. M. Nicholas, *Inorg. Chem.* **2007**, *46*, 2316–2321 and references cited therein.

[23] a) K. Várnagy, I. Sóvágó, K. Ágoston, Z. Likó, H. Süli-Vargha, D. Sanna, G. Micera, *J. Chem. Soc. Dalton Trans.* **1994**, 2939–2945; b) K. Várnagy, I. Sóvágó, W. Goll, H. Süli-Vargha, G. Micera, D. Sanna, *Inorg. Chim. Acta* **1998**, *283*, 233–242; c) K. Várnagy, I. Sóvágó, H. Süli-Vargha, D. Sanna, G. Micera, *J. Inorg. Biochem.* **2000**, *81*, 35–41; d) K. Ősz, K. Várnagy, H. Süli-Vargha, D. Sanna, G. Micera, I. Sóvágó, *Inorg. Chim. Acta* **2002**, *339*, 373–382; e) K. Ősz, K. Várnagy, H. Süli-Vargha, D. Sanna, G. Micera, I. Sóvágó, *Dalton Trans.* **2003**, 2009–2016; f) K. Ősz, K. Várnagy, H. Süli-Vargha, A. Csámpay, D. Sanna, G. Micera, I. Sóvágó, *J. Inorg. Biochem.* **2004**, *98*, 24–32; g) C. Kállay, M. Cattari, D. Sanna, K. Várnagy, H. Süli-Vargha, A. Csámpai, I. Sóvágó, G. Micera, *New J. Chem.* **2004**, *28*, 727–734; h) O. Szilágyi, K. Ősz, K. Várnagy, D. Sanna, H. Süli-Vargha, I. Sóvágó, G. Micera, *Polyhedron* **2006**, *25*, 3173–3182.

 © 2007 Wiley-VCH Verlag GmbH & Co. KGaA, Weinheim 

[24] J. Felcman, J. J. R. Fraústo da Silva, *Talanta* **1983**, *30*, 565–570.
[25] K. Wüthrich, *Helv. Chim. Acta* **1965**, *48*, 1012–1017.
[26] N. D. Chasteen in *Biological Magnetic Resonance* (Eds.: L. J. Berliner, J. Reuben), Plenum Press, New York, **1981**, vol. 3, p. 53–119.
[27] T. S. Smith II, R. LoBrutto, V. L. Pecoraro, *Coord. Chem. Rev.* **2002**, *228*, 1–18.
[28] E. Garribba, G. Micera, D. Sanna, *Inorg. Chim. Acta* **2006**, *359*, 4470–4476.
[29] E. Garribba, G. Micera, E. Lodyga-Chruscinska, D. Sanna, *Eur. J. Inorg. Chem.* **2006**, 2690–2700 and references cited therein.
[30] P. Buglyó, E. Kiss, I. Fábián, T. Kiss, D. Sanna, E. Garribba, G. Micera, *Inorg. Chim. Acta* **2000**, *306*, 174–183.
[31] E. Kiss, D. Petrohán, D. Sanna, E. Garribba, G. Micera, T. Kiss, *Polyhedron* **2000**, *19*, 55–61.
[32] M. J. Frisch, G. W. Trucks, H. B. Schlegel, G. E. Scuseria, M. A. Robb, J. R. Cheeseman, J. A. Montgomery Jr, T. Vreven, K. N. Kudin, J. C. Burant, J. M. Millam, S. S. Iyengar, J. Tomasi, V. Barone, B. Mennucci, M. Cossi, G. Scalmani, N. Rega, G. A. Petersson, H. Nakatsuji, M. Hada, M. Ehara, K. Toyota, R. Fukuda, J. Hasegawa, M. Ishida, T. Nakajima, Y. Honda, O. Kitao, H. Nakai, M. Klene, X. Li, J. E. Knox, H. P. Hratchian, J. B. Cross, C. Adamo, J. Jaramillo, R. Gomperts, R. E. Stratmann, O. Yazyev, A. J. Austin, R. Cammi, C. Pomelli, J. W. Ochterski, P. Y. Ayala, K. Morokuma, G. A. Voth, P. Salvador, J. J. Dannenberg, V. G. Zakrzewski, S. Dapprich, A. D. Daniels, M. C. Strain, O. Farkas, D. K. Malick, A. D. Rabuck, K. Raghavachari, J. B. Foresman, J. V. Ortiz, Q. Cui, A. G. Baboul, S. Clifford, J. Cioslowski, B. B. Stefanov, G. Liu, A. Liashenko, P. Piskorz, I. Komaromi, R. L. Martin, D. J. Fox, T. Keith, M. A. Al-Laham, C. Y. Peng, A. Nanayakkara, M. Challacombe, P. M. W. Gill, B. Johnson, W. Chen, M. W. Wong, C. Gonzalez, J. A. Pople, *Gaussian 03*, Revision C.02, Gaussian, Inc., Wallingford CT, **2004**.
[33] a) T. Ziegler, *Chem. Rev.* **1991**, *91*, 651–667; b) S. Niu, M. B. Hall, *Chem. Rev.* **2000**, *100*, 353–405; c) T. Ziegler, J. Autschbach, *Chem. Rev.* **2005**, *105*, 2695–2722; d) M. Bühl, H. Kabrede, *J. Chem. Theory Comput.* **2006**, *2*, 1282–1290.
[34] A. D. Becke, *J. Chem. Phys.* **1993**, *98*, 5648–5652.
[35] C. Lee, W. Yang, R. G. Parr, *Phys. Rev. B* **1988**, *37*, 785–789.
[36] a) K. G. Spears, *J. Phys. Chem. A* **1997**, *101*, 6273–6279; b) A. C. Saladino, S. C. Larsen, *J. Phys. Chem. A* **2002**, *106*, 10444–10451; c) G. D. Triantafillou, E. I. Tolis, A. Terzis, Y. Deligiannakis, C. P. Raptopoulou, M. P. Sigalas, T. A. Kabanos, *Inorg. Chem.* **2004**, *43*, 79–91; d) C. P. Aznar, Y. Deligiannakis, E. J. Tolis, T. Kabanos, M. Brynda, R. D. Britt, *J. Phys. Chem. A* **2004**, *108*, 4310–4321; e) I. Correia, J. Costa Pessoa, M. T. Duarte, R. T. Henriques, M. F. M. Piedade, L. F. Veiros, T. Jakusch, T. Kiss, Á. Dörnyei, M. M. C. A. Castro, C. F. G. C. Geraldes, F. Avecilla, *Chem. Eur. J.* **2004**, *10*, 2301–2317.
[37] The reported values do not include the calculation with the 3-21g basis set.
[38] T. S. Smith II, C. A. Roof, J. W. Kampf, P. G. Rasmussen, V. L. Pecoraro, *J. Am. Chem. Soc.* **2000**, *122*, 767–775.
[39] Results of the DFT calculations obtained using the 6-311g basis set for vanadium and 6-31g(d) for the other elements.
[40] B. R. McGarvey, *J. Phys. Chem.* **1967**, *71*, 51–67.
[41] F. E. Mabbs, D. Collison, *Electron Paramagnetic Resonance of d-Transition Metal Compounds*, Elsevier, Amsterdam, **1992**.
[42] B. J. Hamstra, A. P. L. Houseman, G. J. Colpas, J. W. Kampf, R. LoBrutto, W. D. Frasch, V. L. Pecoraro, *Inorg. Chem.* **1997**, *36*, 4866–4874.
[43] For example, in the couple **III** of Table S1 $A_{\parallel}$ calcd. for [VO(bpb)] [equatorial donor set ($N_{pyr}$, $N^-$, $N^-$, $N_{pyr}$) and total equatorial charge –2] has been obtained from $A_{\parallel}$ exptl. of [VO(hypyb)] [$156.1 \times 10^{-4}$ cm$^{-1}$ [21e]], equatorial donor set ($N_{pyr}$, $N^-$, $N^-$, $O_{ar}^-$) and total equatorial charge –3] with this formula: $A_{\parallel}$ calcd.([VO(bpb)]) = {$A_{\parallel}$ exptl.([VO(hypyb)]) – $A_{\parallel}(O^-_{ar})$ + $A_{\parallel}(N_{pyr})$} = {$156.1 \times 10^{-4}$ cm$^{-1}$ – $38.9 \times 10^{-4}$ cm$^{-1}$ + $40.7 \times 10^{-4}$ cm$^{-1}$} = $157.9 \times 10^{-4}$ cm$^{-1}$. Subsequently, $A_{\parallel}$ calcd. ($157.9 \times 10^{-4}$ cm$^{-1}$) has been compared with $A_{\parallel}$ exptl. ($145 \times 10^{-4}$ cm$^{-1}$).[21b,21i] The reduction is 8.9%.
[44] For example, Chasteen calculated the contribution to $A_{\parallel}$ for $NH_2$ and $O_{ar}^-$ from the experimental $A_{\parallel}$ value of $[VO(en)_2]^{2+}$ and $[VO(cat)_2]^{2-}$ complexes, where en = ethylenediamine and cat = catecholate, and for $H_2O$ from experimental $A_{\parallel}$ of aqua ion $[VO(H_2O)_5]^{2+}$[26].
[45] C. J. Ballhausen, H. B. Gray, *Inorg. Chem.* **1962**, *1*, 111–122.
[46] D. Kivelson, S. K. Lee, *J. Chem. Phys.* **1964**, *41*, 1896–1903.
[47] a) M. Joseph, T. Leigh, M. L. Swain, *Synthesis* **1977**, 459–461; b) Z. Likó, H. Süli-Vargha, *Tetrahedron Lett.* **1993**, *34*, 1673–1676.
[48] I. Nagypál, I. Fábián, *Inorg. Chim. Acta* **1982**, *61*, 109–113.
[49] G. Gran, *Acta Chem. Scand.* **1950**, *4*, 559–577.
[50] H. Irving, M. G. Miles, L. D. Pettit, *Anal. Chim. Acta* **1967**, *38*, 475–488.
[51] P. Gans, A. Vacca, A. Sabatini, *J. Chem. Soc. Dalton Trans.* **1985**, 1195–1200.
[52] L. Zékány, I. Nagypál in *Computation Methods for the Determination of Formation Constants* (Ed.: D. J. Leggett), Plenum Press, New York, **1985**, p. 291–353.
[53] R. P. Henry, P. C. H. Mitchell, J. E. Prue, *J. Chem. Soc. Dalton Trans.* **1973**, 1156–1159.
[54] C. W. Davies, *J. Chem. Soc.* **1938**, 2093–2098.
[55] a) A. Komura, M. Hayashi, H. Imanaga, *Bull. Chem. Soc. Jpn.* **1977**, *50*, 2927–2931; b) L. F. Vilas Boas, J. Costa Pessoa in *Comprehensive Coordination Chemistry* (Eds.: G. Wilkinson, R. D. Gillard, J. A. McCleverty), Pergamon Press, Oxford, **1987**, vol. 3, p. 453–583.
[56] *WINEPR SimFonia*, version 1.25, Bruker Analytische Messtechnik GmbH, Karlsruhe, **1996**.
[57] R. G. Parr, W. Yang, *Density-Functional Theory of Atoms and Molecules*, Oxford University Press, Oxford, **1989**.

Received: May 9, 2007
Published Online: September 12, 2007

 © 2007 Wiley-VCH Verlag GmbH & Co. KGaA, Weinheim 

DOI: 10.1002/ejic.200700727

# Synthesis, Spectroscopic and Structural Systematics of Complexes of Germanium(IV) Halides ($GeX_4$, X = F, Cl, Br or I) with Mono-, Bi- and Tri-Dentate and Macrocyclic Nitrogen Donor Ligands

**Fei Cheng,[a] Martin F. Davis,[a] Andrew L. Hector,[a] William Levason,*[a] Gillian Reid,[a] Michael Webster,[a] and Wenjian Zhang[a]**

**Keywords:** Germanium / Nitrogen ligands / Fluorido complexes

The six-coordinate adducts *cis*-[$GeX_4$(L–L)] (L–L = 2,2′-bipyridyl, 1,10-phenanthroline, or $Me_2NCH_2CH_2NMe_2$, X = F, Cl or Br) have been synthesised and characterised by IR and VT $^1H$ and $^{19}F\{^1H\}$ NMR spectroscopy. X-ray crystal structures reveal distorted octahedral geometries and the trends in *d*(Ge–N) with halide are interpreted in terms of varying Lewis acidity within the series. The *trans*-[$GeX_4(py)_2$] were similarly characterised. In contrast, $GeI_4$ does not form similar adducts, although it appears to co-crystallise with some of the ligands, and the structure of $GeI_4 \cdot (1,10\text{-phenH})_3 \cdot I_3$ which contains phenanthrolinium cations, iodide anions and tetrahedral $GeI_4$ molecules is reported. Multidentate nitrogen donor ligands including cyclam (1,4,8,11-tetraazacyclotetradecane) and $Me_4$-cyclam (1,4,8,11-tetramethyl-1,4,8,11-tetraazacyclotetradecane) react with [$GeF_4(MeCN)_2$] to form insoluble compounds [{$GeF_4$}$_2$(macrocycle)] ($F_4N_2$ donor sets). In contrast, $Me_3$[9]ane$N_3$ (1,4,7-trimethyl-1,4,7-triazacyclononane) forms the cation [$GeF_3${$Me_3$[9]ane$N_3$}]$^+$ with a facial geometry ($N_3F_3$ donor set) which is the first example of displacement of fluoride from $GeF_4$ by a neutral ligand.
(© Wiley-VCH Verlag GmbH & Co. KGaA, 69451 Weinheim, Germany, 2007)

## Introduction

The coordination chemistry of tin(IV), especially complexes derived from the three tetrahalides, $SnX_4$ (X = Cl, Br or I), is among the most extensive of the *p*-block elements.[1–5] Tin(IV) fluoride has been much less studied (see ref.[4,5] and citations therein), but is a very strong Lewis acid. In marked contrast, the coordination chemistry of the lighter analogue germanium(IV) is little known. Surveys in the 1950–1960s established that germanium(IV) halides exhibited modest Lewis acidity, markedly less than that of the tin(IV) analogues, but provided little detail.[6] A few more examples have been reported in the intervening years,[7–13] but data on series of complexes, solution speciation studies or even establishment of the boundaries of complex formation are elusive. We have begun a detailed examination of the coordination chemistry of germanium(IV), and have recently reported a series of phosphane oxide adducts of the tetrahalides,[14] including *trans*-[$GeF_4(R_3PO)_2$] (R = Me, Et or Ph), *trans*-[$GeCl_4(Et_3PO)_2$], *fac*-[$GeCl_3(Me_3PO)_3$]$_2$-[$GeCl_6$], and *cis*-[$GeX_2(Me_3PO)_4$]$X_2$ (X = Cl or Br). The ability of $R_3PO$ to displace Cl or Br from the $GeX_4$ to form the cationic complexes was unexpected and is unknown in the corresponding tin(IV) systems. Similarly, whilst $GeF_4$ forms *trans*-[$GeF_4(Ph_3AsO)_2$] on reaction with the arsane oxide, reaction of $Ph_3AsO$ or $Me_3AsO$ with $GeCl_4$ leads to the corresponding $R_3AsCl_2$, again contrasting with the tin(IV) systems.[14]

This present study focuses on nitrogen donor ligands of a variety of architectures and denticities, especially the complexes with $GeF_4$. A more limited range of examples with $GeCl_4$ and $GeBr_4$ were examined for comparison purposes.

## Results and Discussion

### Mono- and Bi-Dentate Nitrogen Donor Ligands

The germanium(IV) halides and their complexes are moisture sensitive to varying degrees and all syntheses were carried out using rigorously anhydrous conditions. $GeF_4$ is a gas (sub. 236 K) and inconvenient to handle in this form, and the nitrile adduct, [$GeF_4(MeCN)_2$][14] is a more convenient precursor. The reaction of [$GeF_4(MeCN)_2$] with the bidentate N-donors 2,2′-bipyridyl, 1,10-phenanthroline and $Me_2N(CH_2)_2NMe_2$ (L–L) in anhydrous MeCN solution afforded white solid [$GeF_4$(L–L)] complexes which were unaffected by exposure to moist air and stable in solution in dry MeCN or $CH_2Cl_2$. The $^{19}F\{^1H\}$ NMR spectra in $CH_2Cl_2$ or MeCN each show two triplets consistent with the presence of *cis* isomers ($^2J_{FF}$ = 55–65 Hz), and the IR spectra show several strong bands in the region 590–660 cm$^{-1}$ assigned as ν(Ge–F) (theory: 4 IR-active stretches $2a_1 + b_1 + b_2$). The $^1H$ NMR spectra are also simple showing resonances only due to the coordinated ligands. In contrast the

[a] School of Chemistry, University of Southampton, Southampton SO17 1BJ, UK
E-mail: wxl@soton.ac.uk

 © 2007 Wiley-VCH Verlag GmbH & Co. KGaA, Weinheim 

monodentates, pyridine and $Et_3N$ (L) give $[GeF_4(L)_2]$ which exhibit singlet $^{19}F\{^1H\}$ NMR resonances in $CDCl_3$ solution consistent with *trans* isomers. The $^1H$ NMR spectra of solutions of $[GeF_4(NEt_3)_2]$ in $CH_2Cl_2$ at 298 K shows broad $\delta$(Me) and $\delta(CH_2)$ resonances with no couplings, but on cooling four resonances appear, two quartets and two triplets ($^3J_{HH} \approx 7$ Hz) with approximately equal intensities in each case, assigned from their chemical shifts to $[GeF_4(NEt_3)_2]$ and free $NEt_3$, showing significant ligand dissociation in solution. The presence of only the *trans* isomer contrasts with the behaviour found for $[GeF_4(R_3PO)_2]$ where varying amounts of *cis* and *trans* isomers were found in solution in chlorocarbons.[14]

The structure of $[GeF_4(2,2'\text{-bipy})]$[9] is the only literature structure of a $GeF_4$ adduct with a bidentate N-donor ligand. We have determined the structures of $[GeF_4$-(1,10-phenanthroline)] and $[GeF_4(Me_2NCH_2CH_2NMe_2)]$ (Table 1, Figures 1 and 2) which show close to octahedral coordination at the Ge with F–Ge–F angles slightly greater than 90° and F–Ge–N slightly smaller than 90°, and with N–Ge–N 80.0(2)° and 85.2(3)° respectively. The Ge–$F_{trans F}$ are typically longer than Ge–$F_{trans N}$, with the *trans* F–Ge–F unit bent towards the neutral ligand, as is usually found in compounds of this type.[5,9] The structure of $[GeF_4(py)_2]$ in contrast, is of a *trans* isomer, a centrosymmetric molecule, with unexceptional bond lengths (Table 2, Figure 3).

Table 1. Selected bond lengths [Å] and angles (°) for $[GeF_4$(1,10-phenanthroline)]·0.5MeCN and $[GeF_4(Me_2NCH_2CH_2NMe_2)]$.

| (a) $[GeF_4$(1,10-phenanthroline)]·0.5MeCN[a] | | | |
|---|---|---|---|
| Ge1–F1 | 1.781(2) | Ge1–F2 | 1.753(2) |
| Ge1–N1 | 2.046(3) | | |
| F1–Ge1–F2 | 93.11(13) | F1–Ge1–F2a | 92.70(12) |
| F1–Ge1–F1a | 171.11(14) | F2–Ge1–F2a | 98.40(18) |
| F1–Ge1–N1 | 86.58(11) | F1–Ge1–N1a | 86.61(12) |
| F2–Ge1–N1 | 90.81(12) | N1–Ge1–N1a | 79.98(16) |
| (b) $[GeF_4(Me_2NCH_2CH_2NMe_2)]$ | | | |
| Ge1–F1 | 1.773(3) | Ge1–F2 | 1.763(2) |
| Ge1–F3 | 1.756(4) | Ge1–F4 | 1.774(4) |
| Ge1–N1 | 2.087(3) | Ge1–N2 | 2.068(5) |
| F1–Ge1–F2 | 91.6(2) | F1–Ge1–F3 | 92.0(2) |
| F1–Ge1–F4 | 174.6(2) | F2–Ge1–F3 | 94.7(2) |
| F2–Ge1–F4 | 91.6(2) | F3–Ge1–F4 | 91.9(1) |
| F1–Ge1–N1 | 88.4(2) | F3–Ge1–N1 | 89.5(2) |
| F4–Ge1–N1 | 88.0(2) | F1–Ge1–N2 | 90.0(1) |
| F2–Ge1–N2 | 90.4(2) | F4–Ge1–N2 | 85.7(2) |
| N2–Ge1–N1 | 85.3(2) | N1–C3–C4–N2 | –54.5(6) |

[a] Symmetry operation: $a = 1 - x, 1/2 - y, z$.

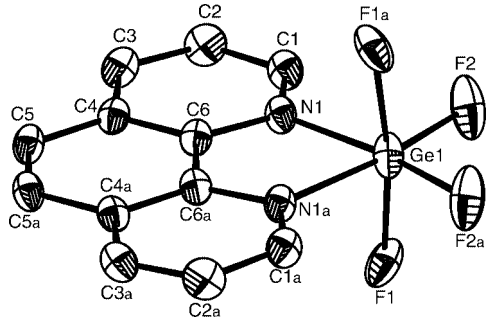


Figure 1. Structure of $[GeF_4$(1,10-phenanthroline)]·0.5MeCN showing the atom labelling scheme. The solvate and the H atoms have been omitted for clarity and the atom displacement ellipsoids are drawn at the 50% probability level. Symmetry operation: $a = 1 - x, 1/2 - y, z$.

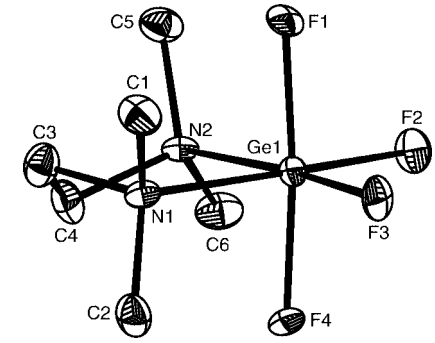


Figure 2. Structure of $[GeF_4(Me_2NCH_2CH_2NMe_2)]$ showing the atom labelling scheme. The H atoms have been omitted for clarity and the atom displacement ellipsoids are drawn at the 50% probability level.

Table 2. Selected bond lengths [Å] and angles (°) for $[GeF_4(py)_2]$.

| | | | |
|---|---|---|---|
| Ge1–F1 | 1.780(2) | Ge1–F2 | 1.782(3) |
| Ge1–N1 | 2.011(4) | N1–C | 1.348(5), 1.354(5) |
| F1–Ge1–F2 | 89.86(12) | F1–Ge1–N1 | 90.21(13) |
| F2–Ge1–N1 | 90.25(13) | | |

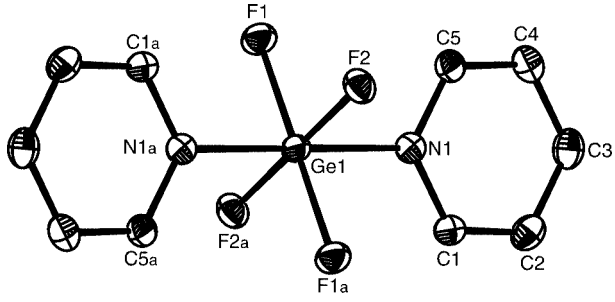


Figure 3. Structure of $[GeF_4(py)_2]$ showing the atom labelling scheme. The H atoms have been omitted for clarity and the atom displacement ellipsoids are drawn at the 50% probability level. The Ge is positioned on a centre of symmetry. Symmetry operation: $a = -x, -y, -z$.

In contrast to the fluorides, the complexes of $GeCl_4$ and $GeBr_4$ are hydrolytically very sensitive and must be handled in a glove box and in dry solvents. The complexes $[GeX_4$-(L–L)] (X = Cl or Br; L–L = 2,2′-bipy, 1,10-phen, $Me_2NCH_2CH_2NMe_2$) were obtained as white powders by combining the constituents in dry $CH_2Cl_2$ solution, and in several cases, as colourless crystals on recrystallisation from dry MeCN in a freezer. The structures of $[GeCl_4(2,2'$-bipy)][12] and $[GeCl_4(Me_2NCH_2CH_2NMe_2)]$[8] have been reported previously, and we report here the structures of $[GeX_4$(1,10-phenanthroline)], $[GeBr_4(2,2'$-bipy)] and $[GeBr_4$-

 © 2007 Wiley-VCH Verlag GmbH & Co. KGaA, Weinheim 

($Me_2NCH_2CH_2NMe_2$)] (Tables 3, 4, and 5, Figures 4, 5, 6, and 7). The structural features generally mimic those discussed above for the fluorides, with X–Ge–X angles rather greater than 90° and X–Ge–N angles rather less. The N–Ge–N angles are 79.5(1)° [$GeCl_4$(1,10-phenanthroline)], 78.8(3)° [$GeBr_4$(1,10-phenanthroline)], 79.0(2)° [$GeBr_4$-(2,2′-bipy)] and 82.3(2)° [$GeBr_4(Me_2NCH_2CH_2NMe_2)$], reflecting the slightly different ligand bites. The availability of the present data combined with that in the literature permits a detailed comparison of structural features within the [$GeX_4$(L–L)] series as a function of X and hence an examination of the Lewis acidity of the $GeX_4$. The trends reflect two major contributions, the strength of the Ge–N bond

Table 3. Selected bond lengths [Å] and angles (°) for [$GeX_4$(1,10-phenanthroline)] (X = Cl and Br).

| (a) [$GeCl_4$(1,10-phenanthroline)]·0.5MeCN[a] | | | |
|---|---|---|---|
| Ge1–Cl1 | 2.2619(6) | Ge1–Cl2 | 2.2232(6) |
| Ge1–Cl3 | 2.2244(6) | Ge1–Cl4 | 2.2799(6) |
| Ge1–N1 | 2.0716(17) | Ge1–N2 | 2.0759(17) |
| Cl1–Ge1–Cl2 | 93.61(2) | Cl1–Ge1–Cl3 | 92.15(2) |
| Cl1–Ge1–Cl4 | 171.81(2) | Cl2–Ge1–Cl3 | 96.81(2) |
| Cl2–Ge1–Cl4 | 91.65(2) | Cl3–Ge1–Cl4 | 93.46(2) |
| N1–Ge1–Cl1 | 86.40(5) | N1–Ge1–Cl2 | 92.07(5) |
| N1–Ge1–Cl4 | 87.13(5) | N2–Ge1–Cl1 | 87.21(5) |
| N2–Ge1–Cl3 | 91.66(5) | N2–Ge1–Cl4 | 86.66(5) |
| N1–Ge1–N2 | 79.49(7) | | |
| (b) [$GeBr_4$(1,10-phenanthroline)]·0.4$CH_2Cl_2$ | | | |
| Ge1–Br1 | 2.3902(14) | Ge1–Br2 | 2.4289(16) |
| Ge1–Br3 | 2.3792(15) | Ge1–Br4 | 2.4719(17) |
| Ge1–N1 | 2.069(7) | Ge1–N2 | 2.078(7) |
| Br1–Ge1–Br2 | 93.52(5) | Br1–Ge1–Br3 | 95.40(5) |
| Br1–Ge1–Br4 | 91.95(5) | Br2–Ge1–Br3 | 94.99(5) |
| Br2–Ge1–Br4 | 171.16(6) | Br3–Ge1–Br4 | 91.40(5) |
| N1–Ge1–Br2 | 86.0(2) | N1–Ge1–Br3 | 93.4(2) |
| N1–Ge1–Br4 | 87.5(2) | N2–Ge1–Br1 | 92.4(2) |
| N2–Ge1–Br2 | 87.6(2) | N2–Ge1–Br4 | 85.3(2) |
| N1–Ge1–N2 | 78.8(3) | | |

[a] There are two molecules in the asymmetric unit and the second molecule is very similar.

Table 4. Selected bond lengths [Å] and angles (°) for [$GeBr_4$(2,2′-bipy)].

| | | | |
|---|---|---|---|
| Ge1–Br1 | 2.4438(7) | Ge1–Br2 | 2.4202(6) |
| Ge1–Br3 | 2.4280(7) | Ge1–Br4 | 2.4157(6) |
| Ge1–N1 | 2.070(3) | Ge1–N2 | 2.073(4) |
| Br1–Ge1–Br2 | 92.64(2) | Br1–Ge1–Br3 | 173.13(2) |
| Br1–Ge1–Br4 | 92.12(2) | Br2–Ge1–Br3 | 91.70(2) |
| Br2–Ge1–Br4 | 92.99(2) | Br3–Ge1–Br4 | 92.96(2) |
| N1–Ge1–Br1 | 86.84(10) | N1–Ge1–Br2 | 94.09(10) |
| N1–Ge1–Br3 | 87.54(10) | N2–Ge1–Br1 | 87.48(10) |
| N2–Ge1–Br3 | 87.57(10) | N2–Ge1–Br4 | 93.97(10) |
| N1–Ge1–N2 | 78.95(14) | N1–C5–C6–N2 | 0.7(6) |

Table 5. Selected bond lengths [Å] and angles (°) for [$GeBr_4(Me_2NCH_2CH_2NMe_2)$].

| | | | |
|---|---|---|---|
| Ge1–Br1 | 2.4388(10) | Ge1–Br2 | 2.4587(10) |
| Ge1–Br3 | 2.4372(10) | Ge1–Br4 | 2.4506(11) |
| Ge1–N1 | 2.188(5) | Ge1–N2 | 2.193(5) |
| Br1–Ge1–Br2 | 89.72(3) | Br1–Ge1–Br3 | 95.35(4) |
| Br1–Ge1–Br4 | 88.53(4) | Br2–Ge1–Br3 | 88.89(4) |
| Br2–Ge1–Br4 | 177.28(4) | Br3–Ge1–Br4 | 89.21(4) |
| N1–Ge1–Br1 | 90.45(14) | N1–Ge1–Br2 | 90.19(15) |
| N1–Ge1–Br4 | 91.89(15) | N2–Ge1–Br2 | 92.81(13) |
| N2–Ge1–Br3 | 91.99(15) | N2–Ge1–Br4 | 89.20(13) |
| N1–Ge1–N2 | 82.3(2) | N1–C3–C4–N2 | –61.7(8) |

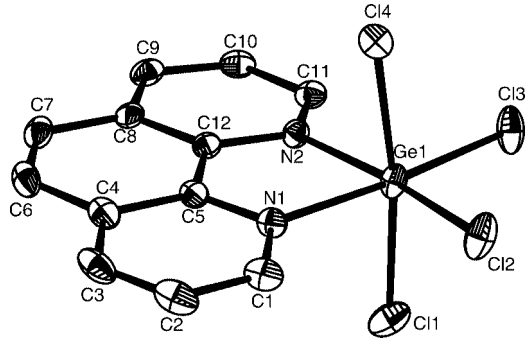


Figure 4. Structure of [$GeCl_4$(1,10-phenanthroline)]·0.5MeCN showing the atom labelling scheme. There are two molecules in the asymmetric unit and the second molecule is very similar. The solvate and the H atoms have been omitted for clarity and the atom displacement ellipsoids are drawn at the 50% probability level.

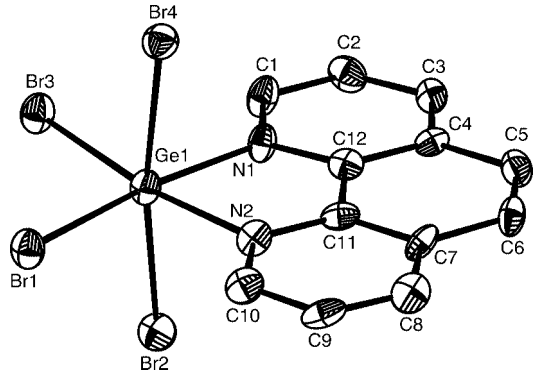


Figure 5. Structure of [$GeBr_4$(1,10-phenanthroline)]·0.4$CH_2Cl_2$ showing the atom labelling scheme. The solvate and the H atoms have been omitted for clarity and the atom displacement ellipsoids are drawn at the 50% probability level.

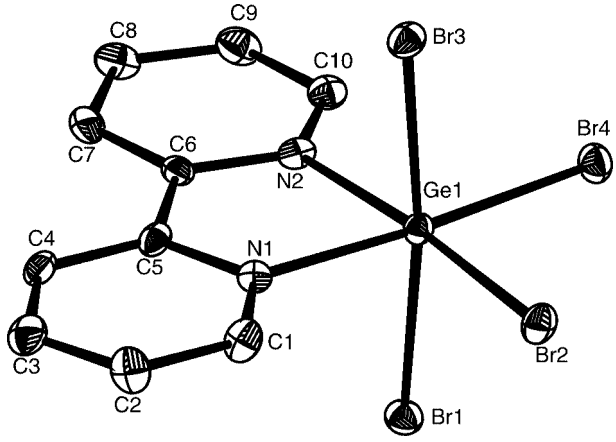


Figure 6. Structure of [$GeBr_4$(2,2′-bipy)] showing the atom labelling scheme. The H atoms have been omitted for clarity and the atom displacement ellipsoids are drawn at the 50% probability level.

 © 2007 Wiley-VCH Verlag GmbH & Co. KGaA, Weinheim 

Table 6. Comparison of Ge–N and Ge–X bond lengths (Å).

| Complex | Ge–N | Ge–$X_{trans X}$ | Ge–$X_{trans N}$ | N···N | Ref. |
|---|---|---|---|---|---|
| [$GeF_4$(1,10-phenanthroline)] | 2.046(3) | 1.781(2) | 1.753(2) | 2.629(6) | this work |
| [$GeCl_4$(1,10-phenanthroline)] | 2.076(2), 2.072(2) | 2.262(1), 2.280(1) | 2.223(1), 2.224(1) | 2.652(2) | this work |
| [a] | 2.074(2), 2.093(2) | 2.237(1), 2.245(1) | 2.227(1), 2.249(1) | 2.656(2) | |
| [$GeBr_4$(1,10-phenanthroline)] | 2.069(7), 2.078(7) | 2.492(2), 2.472(2) | 2.390(2), 2.379(2) | 2.632(10) | this work |
| [$GeF_4$(2,2′-bipy)] | 2.023(4), 2.029(4) | 1.777(2) | 1.757(3), 1.761(3) | 2.585(5) | [9] |
| [$GeCl_4$(2,2′-bipy)] | 2.062(4), 2.068(4) | 2.272(1), 2.262(1) | 2.241(1), 2.246(1) | 2.629(–) | [12] |
| [$GeBr_4$(2,2′-bipy)] | 2.070(3), 2.073(4) | 2.428(1), 2.444(1) | 2.416(1), 2.420(1) | 2.634(5) | this work |
| [$GeF_4(Me_2NCH_2CH_2NMe_2)$] | 2.073(6), 2.090(4) | 1.766(4), 1.782(4) | 1.766(2), 1.750(4) | 2.815(7) | this work |
| [$GeCl_4(Me_2NCH_2CH_2NMe_2)$] | 2.148(12), 2.156(10) | 2.253(5), 2.248(4) | 2.247(3), 2.236(4) | 2.908(–) | [8] |
| [$GeBr_4(Me_2NCH_2CH_2NMe_2)$] | 2.188(5), 2.193(5) | 2.451(1), 2.459(1) | 2.437(1), 2.439(1) | 2.881(8) | this work |

[a] There are two molecules in the asymmetric unit. The first line refers to the Ge1 centred molecule.

and the reorganisation energy necessary to convert the tetrahedral $GeX_4$ to the four-coordinate fragment of the octahedron produced on bonding the Lewis base. For comparison the key bond lengths are summarised in Table 6.

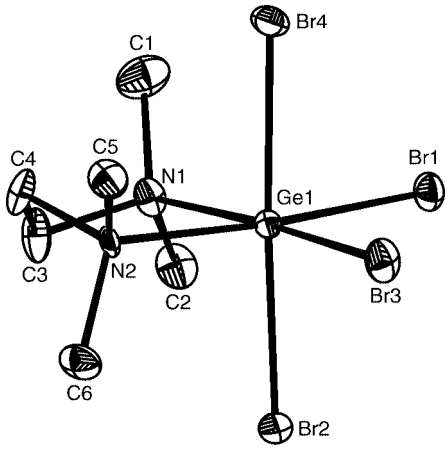


Figure 7. Structure of [$GeBr_4(Me_2NCH_2CH_2NMe_2)$] showing the atom labelling scheme. The H atoms have been omitted for clarity and the atom displacement ellipsoids are drawn at the 40% probability level.

The Ge–X bonds are all longer than in the parent (tetrahedral) $GeX_4$ {X = F, 1.661(1) Å at 133 K; X = Cl, 2.082(7) Å; X = Br, 2.262(2), 2.269(1) Å}[15–17] reflecting the increased coordination number. Looking at the [$GeX_4(Me_2NCH_2CH_2NMe_2)$] series there is a very clear lengthening of Ge–N as the halide changes F → Cl → Br, showing reduced Lewis acidity in this order. There is a corresponding small decrease in the N–Ge–N angle along the series. For the diimine series the Ge–N are markedly shorter in the fluorido complexes, but the differences are small between the chlorides and bromides (although marginally longer in the latter), possibly reflecting the effects of the rigid ligand skeleton in 1,10-phenanthroline and to a lesser extent 2,2′-bipyridyl (the two rings are essentially co-planar in the bipy complexes and the angles N–Ge–N change by ≤ 1° between the three complexes in each series). The two independent molecules in the unit cell of [$GeCl_4$(1,10-phenanthroline)] show small but significant differences and this is presumably attributable to packing,[18] and effects of a similar magnitude in other cases could mask trends in Ge–N distances with changing halogen co-ligands. The decreasingly strong binding of the nitrogen ligands as the halide becomes heavier is also reflected in the solution properties. Thus, whilst the fluorides show simple spectra due to coordinated ligand with high frequency shifts for the resonances in the $^1$H NMR spectra at 295 K in $CDCl_3$ or $CD_3CN$, the diimine bromide complexes show evidence for both coordinated and "free" ligand, indicative of partial dissociation in solution at ambient temperatures. The $^1$H NMR spectrum of [$GeBr_4(Me_2NCH_2CH_2NMe_2)$] at 295 K shows broad features consistent with fast exchange, whilst at low temperatures separate resonances are seen for coordinated and "free" diamine as exchange slows. The chlorides are intermediate in properties with the [$GeCl_4$(1,10-phenanthroline)] showing sharp resonances for the coordinated ligand only, but [$GeCl_4$(2,2′-bipy)] shows both "free" and coordinated ligand resonances.

The older literature contains a few reports of brown or red complexes derived from $GeI_4$ and nitrogen donor ligands[19] mostly characterised only by (partial) microanalytical data. We have obtained similar products in a number of cases. The IR spectra show the presence of the nitrogen ligand (protonated in some examples) and a strong band at 250 ± 5 $cm^{-1}$ which corresponds to the $t_2$ vibration of tetrahedral $GeI_4$, but are otherwise uninformative, and since extensive dissociation is expected in solution, NMR spectroscopic data are of little help. For the 1,10-phenanthroline/$GeI_4$ system in $CH_2Cl_2$, a few good quality crystals were obtained, the structure revealed the composition to be $GeI_4$·(1,10-phenH)$_3$·$I_3$, presumably formed by trace hydrolysis (Table 7). This contained tetrahedral $GeI_4$, 1,10-phenanthrolinium cations, and iodide ions. Two of the three protonated 1,10-phenanthrolines were involved in N–H···I H-bonding and one $I^-$ (I5) showed a weak interaction to an iodine atom of $GeI_4$ (3.483 Å), rather shorter than that found in $Et_4NI$·2$GeI_4$ (3.660–3.792 Å).[20] The unit cell is

Table 7. Selected bond lengths [Å] and angles (°) for $GeI_4$·3[$C_{12}H_9N_2$]·3I.

| | | | |
|---|---|---|---|
| Ge1–I1 | 2.5388(6) | Ge1–I3 | 2.5281(6) |
| Ge1–I2 | 2.5332(6) | Ge1–I4 | 2.5339(6) |
| I4···I5 | 3.4832(5) | | |
| I1–Ge1–I2 | 111.54(2) | I2–Ge1–I3 | 107.17(2) |
| I1–Ge1–I3 | 112.35(2) | I2–Ge1–I4 | 108.00(2) |
| I1–Ge1–I4 | 107.46(2) | I3–Ge1–I4 | 110.27(2) |

 © 2007 Wiley-VCH Verlag GmbH & Co. KGaA, Weinheim 

shown in Figure 8. In our work on the $GeI_4/R_3PO$ systems[14] we also obtained crystals of $GeI_4$ and $R_3POH^+ I_3^-$, but no adducts from reactions of $GeI_4$ with the ligands, and there appear to be no structurally authenticated examples of $GeI_4$ complexes with neutral ligands.

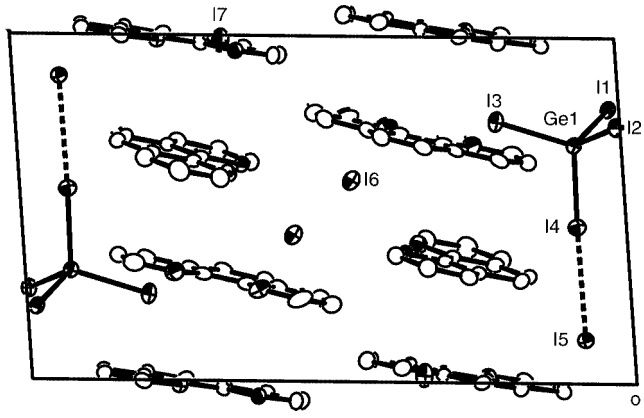


Figure 8. Unit cell packing diagram of $GeI_4 \cdot 3[C_{12}H_9N_2] \cdot 3I$ viewed along the *a* direction. The H atoms have been omitted for clarity, only Ge and I are labelled with C drawn as boundary ellipsoids, and the atom displacement ellipsoids are drawn at the 50% probability level. The weak I···I interaction is shown as a dotted bond. I6 and I7 are involved in N–H···I H-bonds (not shown). The origin is in the lower right corner with *c* along the horizontal direction and *b* near vertical. The packing consists of nearly parallel 1,10-phenanthrolinium cations ($C_{12}H_9N_2$) lying in the *ac* plane. The cations stack to form a sheet in the *ab* plane $\{[(C_{12}H_9N_2)_3I_2]^+\}$ interleaved with a sheet of composition $[(GeI_4) \cdot I]^-$.

## Polydentate and Macrocyclic N-Ligands

Polydentate N-donor macrocycles displace halide from the appropriate $GeX_4$ (X = Cl or Br) in forming $[GeCl_3\{Me_3[9]aneN_3\}]^+$ and $[GeBr_3(1,3,5\text{-trimethyl-}1,3,5\text{-triazacyclohexane})]^+$,[7] and it was therefore of interest to establish if it was possible to displace fluoride from $GeF_4$ by similar ligands. The reaction of $Me_3[9]aneN_3$ with $[GeF_4(MeCN)_2]$ in $CH_2Cl_2$ produced a white solid identified as $[GeF_3\{Me_3[9]aneN_3\}]_2[GeF_6]$ by microanalysis, which was insoluble in MeCN or chlorocarbons. The IR spectrum showed two strong broad features at 629 and 602 $cm^{-1}$ attributable to the ν(Ge–F) stretching modes of the cation and anion respectively, and a strong feature at 340 $cm^{-1}$ which is δ(Ge–F) of the anion. Unfortunately crystals of this salt could not obtained due to insolubility in common solvents, but a few crystals were isolated by slow evaporation of an MeCN extract of the white solid from the preparation and were found to be (Figure 9, Table 8) $[GeF_3\{Me_3[9]aneN_3\}]Cl$. The adventitious chloride anion is believed to arise from the displaced fluoride ion reacting with the chlorocarbon solvent.[21] The structure shows the expected facial geometry for the cation with Ge–N 2.043(3) Å which may be compared with 2.106(2)–2.125(2) Å in the chloride analogue $[GeCl_3\{Me_3[9]aneN_3\}]^+$.[7] The N–Ge–N angle in the former is 85.53(13)° compared to 82.59(8)–83.17(8)° in the latter. The Ge–F distance in the cation is 1.767(2) Å not significantly different from that in the $[GeF_4(diimine)]$ complexes despite the cation charge. This complex is the first example in which fluoride has been displaced from $GeF_4$ by a neutral ligand.

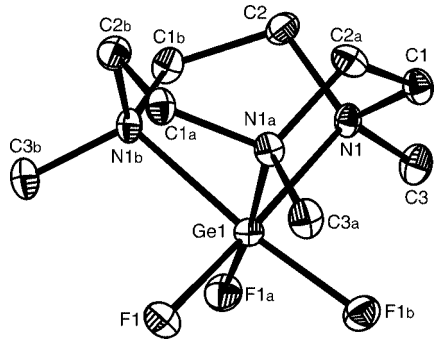


Figure 9. Structure of the cation of $[GeF_3(Me_3[9]aneN_3)]Cl$ showing the atom labelling scheme. The H atoms have been omitted for clarity and the atom displacement ellipsoids are drawn at the 50% probability level. The cation has threefold crystallographic symmetry. Symmetry operations: $a = 1 - y, x - y, z$; $b = 1 - x + y, 1 - x, z$.

Table 8. Selected bond lengths [Å] and angles (°) for $[GeF_3(Me_3[9]aneN_3)]Cl$.[a]

| | | | |
|---|---|---|---|
| Ge1–F1 | 1.767(2) | Ge1–N1 | 2.043(3) |
| F1–Ge1–F1a | 92.86(10) | N1–Ge1–N1a | 85.53(13) |
| F1–Ge1–N1a | 88.77(12) | F1–Ge1–N1b | 92.68(11) |

[a] Symmetry operations: $a = 1 - y, x - y, z$; $b = 1 - x + y, 1 - x, z$.

The reactions of cyclam (1,4,8,11-tetra-azacyclotetradecane) and $Me_4$-cyclam (1,4,8,11-tetramethyl-1,4,8,11-tetra-azacyclotetradecane) with $[GeF_4(MeCN)_2]$ in $CH_2Cl_2$ in either a 1:1 or 1:2 molar ratio, precipitated white powders which were identified by microanalysis as $[(GeF_4)_2(\text{azamacrocycle})]$. The solids are air-stable and the IR spectra reveal the presence of the macrocycle and terminal Ge–F modes. The isolated solids are insoluble in chlorocarbons and MeCN, precluding NMR studies, but the $^{19}F\{^1H\}$ NMR spectra of the reaction mixtures (in situ) show a number of resonances in the regions expected for $\delta F_{trans F}$ and $\delta F_{trans N}$ and on cooling the solutions these show t or d,t patterns consistent with *cis* octahedral-$GeF_4$ units with $\kappa^2$ coordination to the macrocycles (depending upon the rate of pyramidal inversion at N or reversible dissociation, resonances due to the presence of *meso* and DL forms of the $\kappa^2$ coordinated macrocycle may be expected). Notably absent were any features attributable to $[GeF_6]^{2-}$ $\{\delta(^{19}F) = -139\}$ or significant amounts of $F^-$, which would be present if fluoride had been displaced from the germanium centre. Confirmation of the $\kappa^2$-bonding mode came from the crystal structure of $[GeF_4(Me_4\text{-cyclam})]$, a few crystals of which were obtained from the filtrate of the 1:1 reaction mixture after removal of the precipitated 2:1 complex. The crystals were very small and the data quality modest, but the structure (Figure 10, Table 9) shows $[GeF_4(\kappa^2\text{-}Me_4\text{-cyclam})]$ with the *meso* conformation at the coordinated nitrogens, and the other two N-donors bent away from and not interacting with the germanium. The failure of the cyclam type ligands

 © 2007 Wiley-VCH Verlag GmbH & Co. KGaA, Weinheim 

to form cationic complexes is rationalised in that they are not well suited to $\kappa^3$ coordination (in contrast to $Me_3$[9]-ane$N_3$), and the displacement of two fluorides to form $[GeF_2(\kappa^4\text{-cyclam})]^{2+}$ is probably energetically unfavourable. Reaction of 2,2′,6′,2′′-terpyridyl with $[GeF_4(MeCN)_2]$ in $CH_2Cl_2$ gave a white solid of composition $[(GeF_4)_3(2,2',6',2''\text{-terpy})_2]$ which was insoluble in MeCN or chlorocarbons. The IR spectrum showed terpy and terminal Ge–F stretches at similar frequencies to the $[GeF_4(diimine)]$ complexes. The insolubility prevented further study, but it seems likely that the terpy is $\kappa^2$ coordinated to one $GeF_4$ residue and $\kappa^1$ to a second $GeF_4$, producing oligomers with six-coordinate germanium centres ($F_4N_2$ coordinated).

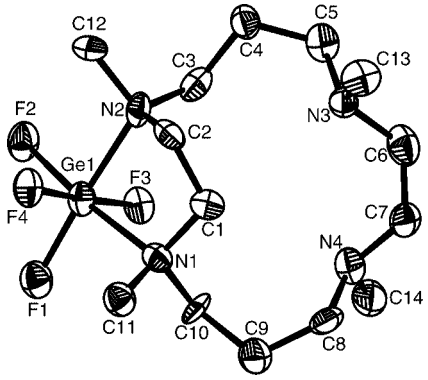


Figure 10. Structure of $[GeF_4(\kappa^2\text{-}Me_4\text{-cyclam})]$ showing the atom labelling scheme. The H atoms have been omitted for clarity and the atom displacement ellipsoids are drawn at the 50% probability level.

Table 9. Selected bond lengths [Å] and angles (°) for $[GeF_4(\kappa^2\text{-}Me_4\text{-cyclam})]$.

| | | | |
|---|---|---|---|
| Ge1–F1 | 1.771(7) | Ge1–F2 | 1.775(6) |
| Ge1–F3 | 1.779(5) | Ge1–F4 | 1.775(5) |
| Ge1–N1 | 2.121(8) | Ge1–N2 | 2.086(9) |
| F1–Ge1–F2 | 95.7(3) | F2–Ge1–F3 | 89.8(3) |
| F1–Ge1–F3 | 92.5(3) | F2–Ge1–F4 | 90.5(3) |
| F1–Ge1–F4 | 91.2(3) | F3–Ge1–F4 | 176.2(3) |
| F1–Ge1–N1 | 90.3(3) | F1–Ge1–N2 | 173.2(3) |
| F2–Ge1–N1 | 174.0(3) | F2–Ge1–N2 | 90.1(3) |
| F3–Ge1–N1 | 90.0(3) | F3–Ge1–N2 | 90.8(3) |
| F4–Ge1–N1 | 89.4(3) | F4–Ge1–N2 | 85.4(3) |
| N1–Ge1–N2 | 83.9(3) | | |

## Conclusions

This study has shown that $GeF_4$ forms robust complexes with a variety of neutral nitrogen donor ligands, all but one example containing six-coordinate germanium with $F_4N_2$ donor sets. The exception, $[GeF_3\{Me_3[9]aneN_3\}]^+$ reflects the strong pre-organisation in the macrocycle for $\kappa^3$ coordination which in this case achieves the displacement of one fluorido ligand. The complexes are generally only slightly moisture sensitive, whereas the corresponding complexes with $GeX_4$ (X = Cl or Br) are very sensitive to moisture, and often partially dissociated in solution. Structural studies confirm that Lewis acidity decreases along the series $GeF_4 >> GeCl_4 > GeBr_4$. There is no evidence that simple N-donor complexes form with $GeI_4$. The much stronger acceptor ability of $GeF_4$ may well mean that an extensive coordination chemistry is accessible, including complexes with other neutral donor types, e.g. tertiary phosphanes, thio- or seleno-ethers (none of which form simple adducts with $GeCl_4$)[10,22] and work is underway in our laboratory to explore this possibility.

## Experimental Section

The germanium(IV) halides $GeF_4$, $GeBr_4$ and $GeI_4$ were obtained from Aldrich and used as received. $GeCl_4$ (Aldrich) was distilled from a mixture of $CaCl_2/Na_2CO_3$, which removes traces of water and HCl. MeCN and $CH_2Cl_2$ were dried by distillation from $CaH_2$. All reactions were conducted using Schlenk, vacuum line and glove-box techniques and under a dry dinitrogen atmosphere. $Me_3$[9]ane$N_3$ was made as described.[23] 2,2′-Bipyridyl, 1,10-phenanthroline, 2,2′,6′2′′-terpyridyl and cyclam and $Me_4$-cyclam were dried by heating in vacuo. Pyridine was dried by distillation from potassium, and $Me_2N(CH_2)_2NMe_2$ and $NEt_3$ by distillation from BaO. $[GeF_4(MeCN)_2]$ was made as described.[14]

Infrared spectra were recorded as Nujol mulls on a Perkin–Elmer PE 983G spectrometer, $^1$H NMR spectra in $CDCl_3$, $CD_2Cl_2$ or $CD_3NO_2$ solutions on a Bruker AV300, $^{19}F\{^1H\}$ NMR spectra on a Bruker DPX400 and referenced to $CFCl_3$. Microanalytical measurements on new complexes were performed by the microanalytical service at Strathclyde University. Representative syntheses of the complexes are given below.

Yields of the complexes were at least 80% based upon germanium.

**$[GeF_4(2,2'\text{-bipy})]$:** 2,2′-Bipyridyl (0.04 g, 0.25 mmol) was added to a solution of $[GeF_4(MeCN)_2]$ (0.057 g, 0.25 mmol) in MeCN (10 mL) at room temperature with stirring, which led to the slow formation of a white precipitate. After stirring for 20 min, the solvent was removed in vacuo to leave a white solid. Air-stable colourless crystals were obtained by vapour diffusion of diethyl ether into solution of the compound in MeCN. $C_{10}H_8F_4GeN_2$ (304.8): calcd. C 39.4, H 2.7, N 9.2; found C 39.6, H 2.6, N 9.2. $^1$H NMR ($CD_3CN$, 295 K): $\delta$ = 9.03 (d, 2 H), 8.52 (m, 2 H), 8.37 (m, 2 H), 7.89 (m, 2 H) ppm. $^{19}F\{^1H\}$ NMR ($CDCl_3$, 295 K): $\delta$ = –116.2 (t, $^2J_{F,F}$ = 58 Hz, 2 F), –151.2 (t, 2 F) ppm. IR (Nujol): $\tilde{\nu}$ = 635 (sh), 618 (s), 605 (sh) ν(Ge–F) cm$^{-1}$.

**$[GeF_4(1,10\text{-phenanthroline})]$:** Was made analogously to the 2,2′-bipyridyl complex. $C_{12}H_8F_4GeN_2{\cdot}0.5MeCN$ (350.8): calcd. C 44.5, H 3.2, N 10.0; found C 44.5, H 2.7, N 10.0. $^1$H NMR ($CD_3CN$, 295 K): $\delta$ = 9.26 (d 2 H), 8.89 (d,d 2 H), 8.24 (s, 2 H), 8.15 (m 2 H) ppm. $^{19}F\{^1H\}$ NMR ($CDCl_3$, 295 K): $\delta$ = –115.7 (t, $^2J_{F,F}$ = 62 Hz, 2 F), –150.1 (t, 2 F) ppm. IR (Nujol): $\tilde{\nu}$ = 664 (s), 618 (s), 597 (s) ν(Ge–F) cm$^{-1}$.

**$[GeF_4(Me_2NCH_2CH_2NMe_2)]$:** Was made similarly to the 2,2′-bipyridyl complex and the white solid obtained was washed with diethyl ether and dried in vacuo. $C_6H_{16}F_4GeN_2$ (264.8): calcd. C 27.2, H 6.1, N 10.6; found C 27.3, H 5.9, N 10.1. $^1$H NMR ($CDCl_3$, 295 K): $\delta$ = 2.97 (m, 1 H) 2.83 (t, 3 H) ppm. $^{19}F\{^1H\}$ NMR ($CDCl_3$, 295 K): $\delta$ = –132.7 (t, $^2J_{F,F}$ = 60 Hz, 2 F), –150.9 (t, 2 F) ppm. IR (Nujol): $\tilde{\nu}$ = 619 (vs), 605 (s), 590 (sh) ν(Ge–F) cm$^{-1}$.

**$[GeF_4(py)_2]$:** Was made similarly to the 2,2′-bipyridyl complex using a 2:1 molar ratio of pyridine to $[GeF_4(MeCN)_2]$ in $CH_3CN$ solution. $C_{10}H_{10}F_4GeN_2$ (306.8): calcd. C 39.2, H 3.3, N 9.1; found C 39.0, H 2.7, N 9.1. $^1$H NMR ($CD_3CN$, 295 K): $\delta$ = 8.89 (m, 2 H),

 © 2007 Wiley-VCH Verlag GmbH & Co. KGaA, Weinheim 

8.29 (m, 1 H), 7.81 (s, 2 H) ppm. $^{19}F\{^1H\}$ NMR ($CDCl_3$, 295 K): $\delta$ = –125.7 (s) ppm. IR (Nujol): $\tilde{\nu}$ = 617 (vs) ν(Ge–F) $cm^{-1}$.

**[$GeF_4(NEt_3)_2$]:** Triethylamine (0.020 g, 0.20 mmol) was added to a solution of [$GeF_4(MeCN)_2$] (0.023 g, 0.10 mmol) in $CH_2Cl_2$ (15 mL) at room temperature with stirring. After stirring for 10 min, the volatiles were evaporated slowly from the static solution which gave colourless crystalline solid. $^1H$ NMR ($CD_2Cl_2$, 295 K): $\delta$ = 1.2 (s, 3 H) 3.0 (s, 2 H) ppm; (253 K): $\delta$ = 1.10 (t, $^3J_{HH}$ = 6 Hz, 3 H), 1.27 (t, $^3J_{HH}$ = 6 Hz, 3 H), 2.98 (q, 2 H), 3.11 (q, 2 H). $^{19}F\{^1H\}$ NMR ($CD_2Cl_2$, 295 K): $\delta$ = –129 (br); 253 K $\delta$ = –118.5 (s) ppm. IR (Nujol): $\tilde{\nu}$ = 602 ν(Ge–F) $cm^{-1}$.

**[$GeCl_4$(2,2′-bipy)]:** $GeCl_4$ (0.22 g, 1.0 mmol) and 2,2′-bipyridyl (0.15 g, 1.0 mmol) were combined in dry dichloromethane (20 mL) producing an immediate white precipitate. The solvent was removed in vacuo and the white solid recrystallised from MeCN (20 mL). Colourless crystals were obtained by keeping the filtrate in a freezer for 3 d. $C_{10}H_8Cl_4GeN_2$ (370.6): calcd. C 32.4, H 2.2, N 7.6; found C 31.7, H 2.1, N 7.2. $^1H$ NMR ($CDCl_3$, 295 K): $\delta$ = 8.85 (br., H), 8.80 (br., H), 8.38 (m, H), 8.15 (m, H); (273 K): $\delta$ = 9.01 (d, $J$ = 8 Hz, 1 H), 8.92 (m, 1 H), 8.40 (m, 1 H), 8.20 (m, 1 H) ppm. IR (Nujol): $\tilde{\nu}$ = 335, 317, 295 ν(Ge–Cl) $cm^{-1}$.

**[$GeCl_4$(1,10-phenanthroline)]:** The complex was prepared analogously to the 2,2′-bipyridyl analogue. Colourless crystals were obtained from the MeCN filtrate after several days in a freezer. $C_{12}H_8Cl_4GeN_2$ (394.6): calcd. C 36.5, H 2.0, N 7.1; found C 36.6, H 1.9, N 7.2. $^1H$ NMR ($CD_3CN$, 295 K): $\delta$ = 10.17 (d, 2 H), 9.08 (d, 2 H), 8.42 (br., 2 H), 8.36 (m, 2 H) ppm. IR (Nujol): $\tilde{\nu}$ = 357, 332, 320 (sh), 275 ν(Ge–Cl) $cm^{-1}$.

**[$GeCl_4(Me_2NCH_2CH_2NMe_2)$]:** The complex was made similarly to the 2,2′-bipyridyl analogue. $C_6H_{16}Cl_4GeN_2$ (330.6): calcd. C 21.8, H 4.9, N 8.5; found C 22.4, H 5.2, N 8.2. $^1H$ NMR ($CDCl_3$, 295 K): $\delta$ = 2.90 (s, 3 H), 3.05 (s, 1 H) (little change at 220 K) ppm. IR (Nujol): $\tilde{\nu}$ = 324, 303, 282 ν(Ge–Cl) $cm^{-1}$.

**[$GeCl_4(py)_2$]:** Pyridine (0.16 g, 1.0 mmol) was added to a solution of $GeCl_4$ (0.11 g, 0.5 mmol) in $CH_2Cl_2$ (20 mL) resulting in an immediate white precipitate, which was isolated by filtration and dried in vacuo. $C_{10}H_{10}Cl_4GeN_2$ (372.6): calcd. C 32.2, H 2.7, N 7.5; found C 31.9, H 2.5, N 7.2. $^1H$ NMR ($CDCl_3$, 295 K): $\delta$ = 8.71 (d, 2 H), 8.54 (m, 1 H), 8.01 (m, 2 H) ppm. IR (Nujol): $\tilde{\nu}$ = 323 (vbr) ν(Ge–Cl) $cm^{-1}$.

**[$GeBr_4$(2,2′-bipy)]:** Was made similarly to the chloride as pale yellow crystals. $C_{10}H_8Br_4GeN_2$ (548.4): calcd. C 21.9, H 1.5, N 5.1; found C 22.1, H 1.7, N 5.2. $^1H$ NMR ($CDCl_3$, 295 K): $\delta$ = 8.92 (m, 2 H), 8.20 (m, H), 7.69 (m, H); (253 K): $\delta$ = 9.01 (d. H), 8.90 (d, $J$ = 8 Hz, 1 H), 8.32 (m, 1 H), 7.70 (m, 1 H) ppm. IR (Nujol): $\tilde{\nu}$ = 284 (s), 237 (s), 218 (s) ν(Ge–Br) $cm^{-1}$.

**[$GeBr_4$(1,10-phenanthroline)]:** Was made similarly to the 2,2-bipy complex. $C_{12}H_8Br_4GeN_2$ (572.4): calcd. C 25.2, H 1.4, N 4.9; found C 25.5, H 1.9, N 5.3. $^1H$ NMR ($CD_3CN$, 298 K): $\delta$ = 10.33 (d, 2 H), 9.10 (d, 2 H), 8.45 (s, 2 H), 8.40 (m, 2 H) ppm. IR (Nujol): $\tilde{\nu}$ = 247 (s), 232 (s), 203 (sh), ν(Ge–Br) $cm^{-1}$.

**[$GeBr_4(Me_2NCH_2CH_2NMe_2)$]:** The diamine (0.06 g, 0.50 mmol) was added to a solution of $GeBr_4$ (0.19 g, 0.50 mmol) in $CH_2Cl_2$ (10 mL) at room temperature with stirring, which lead to an immediate colour change to pale yellow and slow precipitation of a yellow solid. After stirring for 10 min the solution was filtered and the pale yellow solid was dried in vacuo. Pale yellow crystals were obtained from a concentrated solution in MeCN in the freezer. $C_6H_{16}Br_4GeN_2$ (508.4): calcd. C 14.2, H 3.2, N 5.5; found C 14.5, H 3.8, N 5.7. $^1H$ NMR ($CDCl_3$, 298 K): $\delta$ = 2.46 (s, 3 H), 2.75 (s, H); (235 K): $\delta$ = 2.45 (s, 1 H), 2.63 (s, 1 H), 3.00 (s, 3 H), 3.12 (s, 1 H) ppm. IR (Nujol): $\tilde{\nu}$ = 238 (sh), 216 (s), ν(Ge–Br) $cm^{-1}$.

**[$GeBr_4$(py)$_2$]:** Was made similarly to the chloride analogue above, as a pale yellow powder. $C_{10}H_{10}Br_4GeN_2$ (540.4): calcd. C 21.8, H 1.8, N 5.1; found C 22.0, H 2.6, N 5.2. $^1H$ NMR ($CDCl_3$, 295 K): $\delta$ = 8.71 (d, 2 H), 8.33 (m, 1 H), 7.83 (m, 2 H) ppm. IR (Nujol): $\tilde{\nu}$ = 237 (vbr) ν(Ge–Br) $cm^{-1}$.

**[$(GeF_4)_3$(2,2′,6′,2′′-terpy)$_2$]:** Was made analogously to the 2,2′-bipyridyl complex, using $MeCN/CH_2Cl_2$ solvent mixture. $C_{30}H_{22}F_{12}Ge_3N_6{\cdot}0.5CH_2Cl_2$ (954.7): calcd. C 38.4, H 2.4, N 8.8; found C 38.2, H 2.3, N 9.1. IR (Nujol): $\tilde{\nu}$ = 645 (br., s), 580 (s) ν(Ge–F) $cm^{-1}$.

**[$(GeF_4)_2$($Me_4$-cyclam)]:** $Me_4$-cyclam (0.025 g, 0.10 mmol) was added to a solution of [$GeF_4(MeCN)_2$] (0.046 g, 0.20 mmol) in $CH_2Cl_2$ (20 mL) at room temperature with stirring, which led to slow precipitation of a white solid. After stirring for 15 min the white precipitate was separated by filtration and dried in vacuo. $C_{14}H_{32}F_8Ge_2N_4{\cdot}0.5CH_2Cl_2$ (596.1): calcd. C 29.2, H 5.5, N 9.4; found C 28.4, H 5.3, N 9.2. IR (Nujol): $\tilde{\nu}$ = 615 (vbr, s), 590 (sh) ν(Ge–F) $cm^{-1}$. A small number of colourless crystals of [$GeF_4$($Me_4$-cyclam)] were obtained by slow evaporation of the solvent from the filtrate.

**[$(GeF_4)_2$(cyclam)]:** Cyclam (0.020 g, 0.10 mmol) was added to a solution of [$GeF_4(MeCN)_2$] (0.046 g, 0.20 mmol) in $CH_2Cl_2$ (20 mL) at room temperature with stirring which lead to immediate precipitation of a white solid. After stirring for 15 min the white precipitate was separated by filtration and dried in vacuo. $C_{10}H_{24}F_8Ge_2N_4$ (497.5): calcd. C 24.1, H 4.8, N 11.3; found C 25.5, H 4.7, N 11.7. IR (Nujol): $\tilde{\nu}$ = 3100 (br) ν(N–H), 1650 (br) δ(N–H), 624 (br., s), 572 (br., s) ν(Ge–F) $cm^{-1}$.

**[$GeF_3${$Me_3$[9]aneN$_3$}]$_2$[$GeF_6$]:** $Me_3$[9]aneN$_3$ (0.018 g, 0.10 mmol) was added to a solution of [$GeF_4(CH_3CN)_2$] (0.035 g, 0.15 mmol) in $CH_2Cl_2$ (20 mL) at room temperature with stirring which lead to the precipitation of a white solid. After stirring for 30 min the white precipitate was separated by filtration and washed with diethyl ether. A few crystals of [$GeF_3$($Me_3$[9]aneN$_3$)]Cl were obtained by extracting the crude solid in $CH_3CN$ with heating followed by filtration and slow evaporation of the filtrate at room temperature. $C_{18}H_{42}F_{12}Ge_3N_6{\cdot}CH_2Cl_2$ (873.3): calcd. C 26.1, H 5.1, N 9.6; found C 26.6, H 5.1, N 10.1. IR (Nujol): $\tilde{\nu}$ = 629 (s), 602 (s) ν(Ge–F), 340 δ(Ge–F) $cm^{-1}$.

**X-ray Crystallography:** Details of the crystallographic data collection and refinement parameters are given in Table 10. Crystals were mostly obtained directly from the preparations as described. Data collections used a Bruker-Nonius Kappa CCD diffractometer fitted with Mo-$K_\alpha$ radiation ($\lambda$ = 0.71073 Å) and with the crystals held at 120 K in a nitrogen gas stream. Structure solution and refinement were straightforward[24–27] with H atoms introduced into the models in calculated positions using the default C–H distance.

CCDC-652869 [for F/N(phen)], -652870 [for F/N(diamine)], -652871 [for F/N(py)], -652872 (for Cl/N), -652873 [for Br/N(phen)], -652874 [for Br/N(bipy)], -652875 [for Br/N(diamine)], -652876 [for F/N(cyclam)], -652877 (*I*), and -652878 ($F_3N_3$) contain the supplementary crystallographic data for this paper (the atoms in parentheses indicate the species bonded to Ge in the compound). These data can be obtained free of charge from The Cambridge Crystallographic Data Centre via www.ccdc.cam.ac.uk/data_request/cif.

 © 2007 Wiley-VCH Verlag GmbH & Co. KGaA, Weinheim 

Table 10. Crystal data and structure refinement details.[a]

| Compound | $[GeF_4(1,10\text{-phen})]\cdot 0.5MeCN$ | $[GeF_4\{Me_2N(CH_2)_2NMe_2\}]$ | $[GeF_4(py)_2]$ | $[GeCl_4(1,10\text{-phen})]\cdot 0.5MeCN$ | $[GeBr_4(1,10\text{-phen})]\cdot 0.4CH_2Cl_2$ |
|---|---|---|---|---|---|
| Formula | $C_{13}H_{9.5}F_4GeN_{2.5}$ | $C_6H_{16}F_4GeN_2$ | $C_{10}H_{10}F_4GeN_2$ | $C_{13}H_{9.5}Cl_4GeN_{2.5}$ | $C_{12.4}H_{8.8}Br_4Cl_{0.8}GeN_2$ |
| $M$ | 349.32 | 264.80 | 306.79 | 415.12 | 606.40 |
| Crystal system | tetragonal | monoclinic | triclinic | triclinic | orthorhombic |
| Space group | $I4_1/a$ (no. 88) | $P2_1$ (no. 4) | $P\bar{1}$ (no. 2) | $P\bar{1}$ (no. 2) | $Pbca$ (no. 61) |
| $a$ (Å) | 9.2446(15) | 6.359(2) | 6.386(3) | 7.5868(10) | 14.211(4) |
| $b$ (Å) | 9.2446(15) | 10.731(4) | 7.073(3) | 12.4792(15) | 12.454(3) |
| $c$ (Å) | 29.725(4) | 7.693(3) | 7.154(3) | 16.622(3) | 18.278(6) |
| $\alpha$ (°) | 90 | 90 | 116.13(3) | 89.688(6) | 90 |
| $\beta$ (°) | 90 | 112.99(2) | 93.67(3) | 88.027(10) | 90 |
| $\gamma$ (°) | 90 | 90 | 109.73(3) | 78.982(10) | 90 |
| $V$ (Å$^3$) | 2540.4(7) | 483.3(3) | 264.3(2) | 1543.8(4) | 3234.9(16) |
| $Z$ | 8 | 2 | 1 | 4 | 8 |
| $\mu$(Mo-$K_\alpha$) [mm$^{-1}$] | 2.453 | 3.188 | 2.931 | 2.668 | 11.898 |
| $F$(000) | 1384 | 268 | 152 | 820 | 2262 |
| Total no. of observations | 9921 | 3942 | 4537 | 21764 | 28439 |
| $R_{int}$ | 0.065 | 0.040 | 0.056 | 0.032 | 0.173 |
| Unique observations | 1445 | 2060 | 1195 | 7032 | 3181 |
| Parameters, restraints | 93, 0 | 123, 1 | 79, 0 | 371, 0 | 188, 3 |
| $R_1$, $wR_2$ [$I>2\sigma(I)$][b] | 0.045, 0.097 | 0.036, 0.070 | 0.045, 0.103 | 0.028, 0.061 | 0.054, 0.104 |
| $R_1$, w$R_2$ [all data] | 0.060, 0.107 | 0.045, 0.073 | 0.049, 0.105 | 0.033, 0.064 | 0.110, 0.124 |

| Compound | $[GeBr_4(2,2'\text{-bipy})]$ | $[GeBr_4\{Me_2N(CH_2)_2NMe_2\}]$ | $[GeF_4(Me_4\text{-cyclam})]$ | $GeI_4\cdot 3[C_{12}H_9N_2]\cdot 3I$ | $[GeF_3(Me_3[9]aneN_3)]Cl$ |
|---|---|---|---|---|---|
| Formula | $C_{10}H_8Br_4GeN_2$ | $C_6H_{16}Br_4GeN_2$ | $C_{14}H_{32}F_4GeN_4$ | $C_{36}H_{27}GeI_7N_6$ | $C_9H_{21}ClF_3GeN_3$ |
| $M$ | 548.41 | 508.44 | 405.03 | 1504.53 | 336.33 |
| Crystal system | monoclinic | orthorhombic | orthorhombic | triclinic | trigonal |
| Space group | $Pn$ (no. 7) | $Pna2_1$ (no. 33) | $P2_12_12_1$ (no. 19) | $P\bar{1}$ (no. 2) | $R3c$ (no. 161) |
| $a$ (Å) | 8.2473(10) | 14.877(4) | 9.650(3) | 10.6183(15) | 8.8068(12) |
| $b$ (Å) | 6.9155(10) | 7.4172(15) | 12.621(4) | 10.6674(10) | 8.8068(12) |
| $c$ (Å) | 12.566(2) | 11.947(4) | 15.120(4) | 18.606(2) | 29.556(6) |
| $\alpha$ (°) | 90 | 90 | 90 | 85.261(10) | 90 |
| $\beta$ (°) | 102.346(10) | 90 | 90 | 85.491(5) | 90 |
| $\gamma$ (°) | 90 | 90 | 90 | 86.619(10) | 120 |
| $V$ (Å$^3$) | 700.11(17) | 1318.3(6) | 1841.6(9) | 2090.9(4) | 1985.2(6) |
| $Z$ | 2 | 4 | 4 | 2 | 6 |
| $\mu$(Mo-$K_\alpha$) [mm$^{-1}$] | 13.58 | 14.41 | 1.704 | 5.934 | 2.535 |
| $F$(000) | 508 | 952 | 848 | 1376 | 1032 |
| Total no. of observations | 9565 | 9995 | 19108 | 42764 | 3306 |
| $R_{int}$ | 0.054 | 0.070 | 0.162 | 0.045 | 0.032 |
| Unique observations | 3124 | 3002 | 3228 | 9567 | 914 |
| Parameters, restraints | 154, 2 | 123, 1 | 208, 0 | 451, 0 | 52, 1 |
| $R_1$, $wR_2$ [$I>2\sigma(I)$][b] | 0.026, 0.053 | 0.040, 0.056 | 0.080, 0.141 | 0.032, 0.067 | 0.026, 0.057 |
| $R_1$, w$R_2$ [all data] | 0.027, 0.054 | 0.071, 0.062 | 0.133, 0.165 | 0.044, 0.072 | 0.031, 0.062 |

[a] Common items: temperature = 120 K; wavelength (Mo-$K_\alpha$) = 0.71073 Å; $\theta$(max) = 27.5°. [b] $R_1 = \Sigma||F_o| - |F_c||/\Sigma|F_o|$; $wR_2 = [\Sigma w(F_o^2 - F_c^2)^2/\Sigma\ wF_o^4]^{1/2}$.

## Acknowledgments

We thank Research Councils U.K. (EP/C006763/1) and the Engineering and Physical Sciences Research Council (GR/T09613/01) for support. A. L. H. thanks the Royal Society for a University Research Fellowship.

[1] P. G. Harrison (Ed.), *The Chemistry of Tin*, Blackie, London, **1984**.
[2] P. G. Harrison in *Comprehensive Coordination Chemistry* (Eds.: G. Wilkinson, R. D. Gillard, J. A. McCleverty), Pergamon Press, Oxford, **1987**, vol. 3, chapter 26.
[3] a) A. R. J. Genge, W. Levason, G. Reid, *Inorg. Chim. Acta* **1999**, *288*, 142–149; b) N. Bricklebank, S. M. Godfrey, C. A. McAuliffe, R. G. Pritchard, *J. Chem. Soc. Chem. Commun.* **1994**, 695–696; c) S. H. Hunter, V. M. Langford, G. A. Rodley, C. J. Wilkins, *J. Chem. Soc. A* **1968**, 305–308; d) J. E. Fergusson, W. R. Roper, C. J. Wilkins, *J. Chem. Soc.* **1965**, 3716–3720.
[4] M. F. Davis, W. Levason, G. Reid, M. Webster, *Polyhedron* **2006**, *25*, 930–936.
[5] M. F. Davis, M. Clarke, W. Levason, G. Reid, M. Webster, *Eur. J. Inorg. Chem.* **2006**, 2773–2782.
[6] F. Glockling, *The Chemistry of Germanium*, Academic Press, NY, **1969**.
[7] G. R. Willey, T. J. Woodman, U. Somasundaram, D. R. Aris, W. Errington, *J. Chem. Soc. Dalton Trans.* **1998**, 2573–2576.
[8] J. Ejfler, S. Szafert, H. Jiao, P. Sobota, *New J. Chem.* **2002**, *26*, 803–805.
[9] A. D. Adley, P. H. Bird, A. R. Fraser, M. Onyszchuk, *Inorg. Chem.* **1972**, *11*, 1402–1409.
[10] S. M. Godfrey, I. Mushtaq, R. G. Pritchard, *J. Chem. Soc. Dalton Trans.* **1999**, 1319–1323.
[11] N. W. Mitzel, U. Losehand, K. Vojinovic, *Inorg. Chem.* **2001**, *40*, 5302–5303.
[12] G. R. Willey, U. Somasundaram, D. R. Aris, W. Errington, *Inorg. Chim. Acta* **2001**, *315*, 191–195.
[13] A. V. Yatsenko, S. V. Medvedev, L. A. Aslanov, *Koord. Khim.* **1991**, *17*, 1338–1341.
[14] F. Cheng, A. L. Hector, W. Levason, G. Reid, M. Webster, W. Zhang, *Eur. J. Inorg. Chem.* **2007**, 2488–2495.
[15] J. Köhler, A. Simon, R. Hoppe, *J. Less-Common Met.* **1988**, *137*, 333–341.
[16] a) I. R. Beattie, P. J. Jones, G. Reid, M. Webster, *Inorg. Chem.* **1998**, *37*, 6032–6034; b) K. Mertz, M. Driess, *Acta Crystallogr., Sect. C* **2002**, *58*, 101–102.
[17] a) J. Köhler, H. Okudera, D. Reuter, A. Simon, *Z. Kristallogr.* **2005**, *220*, 523; b) J. Köhler, H. Okudera, A. Simon, *Z. Kristallogr.* **2005**, *220*, 524.

 © 2007 Wiley-VCH Verlag GmbH & Co. KGaA, Weinheim 

[18] A. G. Orpen, A. Martin, *J. Am. Chem. Soc.* **1996**, *118*, 1464–1470.
[19] a) N. Klouras, A. Galinos, *Monatsh. Chem.* **1982**, *113*, 49–52; b) J. E. Ferguson, W. R. Roper, C. J. Wilkins, *J. Chem. Soc.* **1965**, 3716–3720.
[20] U. Müller, V. Krug, *Acta Crystallogr., Sect. C* **1990**, *46*, 523–525.
[21] K. O. Christe, W. W. Wilson, *J. Fluorine Chem.* **1990**, *47*, 117–120.
[22] A. R. J. Genge, W. Levason, G. Reid, *J. Chem. Soc. Dalton Trans.* **1997**, 4549–4553.
[23] K. Wieghardt, P. Chaudhuri, B. Nuber, J. Weiss, *Inorg. Chem.* **1982**, *21*, 3086–3090.
[24] G. M. Sheldrick, SHELXS-97, *Program for crystal structure solution*, University of Göttingen, Germany, **1997**.
[25] G. M. Sheldrick, SHELXL-97, *Program for crystal structure refinement*, University of Göttingen, Germany, **1997**.
[26] G. M. Sheldrick, SADABS, *Bruker-Nonius area detector scaling and absorption correction* (V2.10), University of Göttingen, Germany, **2003**.
[27] H. D. Flack, *Acta Crystallogr., Sect. A* **1983**, *39*, 876–881.

Received: July 10, 2007
Published Online: September 10, 2007

 © 2007 Wiley-VCH Verlag GmbH & Co. KGaA, Weinheim 

DOI: 10.1002/ejic.200700196

# Stepwise Assembly of Nanoparticles, -tubes, -rods, and -wires in Reverse Micelle Systems

Yun Chen,[a] Qingsheng Wu,*[a] and Yaping Ding[b]

**Keywords:** Stepwise-assembly synthesis / Nanomaterials / $CaSO_4 \cdot 2H_2O$ / Reverse micelles

A traditional facile method was used for the stepwise-assembly synthesis of $CaSO_4 \cdot 2H_2O$ nanoparticles, -tubes, -rods, and -wires. Sizes of these nanostructures vary from tens of nanometers to tens of microns. The key point of the stepwise-assembly process is the reaction time. The growth process was studied as a function of the reaction time and this was used to guide the synthesis of other one-dimensional nanomaterials in reverse micelle systems. The results showed that this growth process is somewhat universal in synthesizing inorganic salts with zero/one-dimensional and solid/hollow structures in reverse micelle systems. The growing mechanism was also explored and it was believed to be an assembly-based growth in association and concurrent with the surfactant-templating mechanism.
(© Wiley-VCH Verlag GmbH & Co. KGaA, 69451 Weinheim, Germany, 2007)

## Introduction

The reverse micelle or microemulsion system is a traditional synthesis method that has been widely used to prepare nanomaterials because of its facility, speediness, and efficiency. Being a soft template system with affluent diversification, reverse micelles were used to fabricate nanomaterials with different novel morphologies.[1–14] However, it is the variety that makes it difficult to effectively control the morphology. Thus, how to regulate the shapes and structures effectively in reverse micelle systems has become the target that most scientists seek. Although considerable efforts have been made to control the synthesis at will in reverse micelle systems,[15–19] to date no one has achieved the successful synthesis of a series of different nanostructures in one reverse micelle system. Somewhat controllable methods are involved such as changing surfactant concentration, reactant concentration, $\omega_0$, and using different surfactants.[20–22] In these methods it is found that the structures of the micelle templates are changed fundamentally to tune nanostructures. However, the structures and behavior of micelle templates are still not clear so much uncertainty is involved in these methods. Consequently there is an urgent need to explore the entire picture of the growth process in such a system.

The development of nanoscience and -technology over the last two decades shows that some interesting new nanostructures can be fabricated based on the mechanism called "oriented attachment".[23–24] In this mechanism, inorganic nanocrystals are the fundamental building blocks for the creation of highly ordered extended nanostructures. Although there are now feasible ways for the formation of low-dimensional complex nanostructures using nanoparticles as building blocks,[25] the challenge for the organization of nanoparticles into higher dimensional structures still remains. Nanotubes are higher structures constructed by initial nano building blocks and are thought to be a sort of the most promising nanomaterials.[26–27] However, most of the obtained nanotubes are oxides or have graphite-like structures:[28–32] noncarbon, nonoxide, and nonlaminated nanotubes are difficult to fabricate through ordinary methods.[33–34] The simple and easy way to make nanotubes at room temperature described in this paper can offer more opportunities for the research of noncarbon, nonoxide, and nonlaminated nanotubes.

Reaction time was investigated as an impact factor in the microemulsion system and its main role is believed to be to control the crystal growth and crystallinity.[5,35] However, after many trials other important functions of aging time were discovered. It can control the dimension, morphology, and structure of the products under certain circumstances. In this work, by controlling reaction time step by step, according to the characteristics of different inorganic salts, stepwise-assembly synthesis of non-oxide ionic-crystal nanomaterials from nanoparticles to nanotubes, nanorods, and nanowires is successfully realized for the first time in reverse micelle soft-template systems. Thus this study provides a new route in selectively synthesizing low-dimensional nanomaterials in identical reverse micelle systems. It can also bring new vitality to this traditional facile synthesis method.

[a] Department of Chemistry, Tongji University, Shanghai, P. R. China, 200092
E-mail: qswu@mail.tongji.edu.cn
[b] Department of Chemistry, Shanghai University, Shanghai, P. R. China, 200444
Supporting information for this article is available on the WWW under http://www.eurjic.org or from the author.

 © 2007 Wiley-VCH Verlag GmbH & Co. KGaA, Weinheim 

## Results and Discussion

### Results

The phase composition and phase structure of the samples were examined by X-ray powder diffraction (XRD). Because samples with different shapes all have the same composition, only the XRD pattern of the nanotubular products was given. The products were deposited on a glass base when characterized by XRD. As shown in Figure 1, all of the peaks can be perfectly indexed to a pure monoclinic phase (space group $C2/c$[15]) of $CaSO_4 \cdot 2H_2O$ with lattice constants (a) 6.286 Å, (b) 15.213 Å, and (c) 5.678 Å (JCPDS card No. 33–0311). No other impurities have been detected in the synthesized products. The broad peak between 10 and 30° ($2\theta$) is caused by the amorphous-phase glass base on which the product deposited.

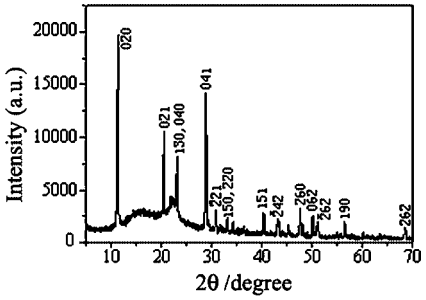


Figure 1. XRD curve of $CaSO_4 \cdot 2H_2O$ obtained in the reverse micelle system.

The morphologies of the synthesized products were examined by transmission electron microscopy (TEM). Figure 2 shows the typical TEM images of the sample prepared in $C_{12}E_9$ reverse micelles with different reaction times. $\omega_0$ of the reverse micelle was 8 when the concentration of $CaCl_2$ and $Na_2SO_4$ was 0.1 M. Tunable shapes of $CaSO_4$ nanocrystals can be readily produced at different reaction times.

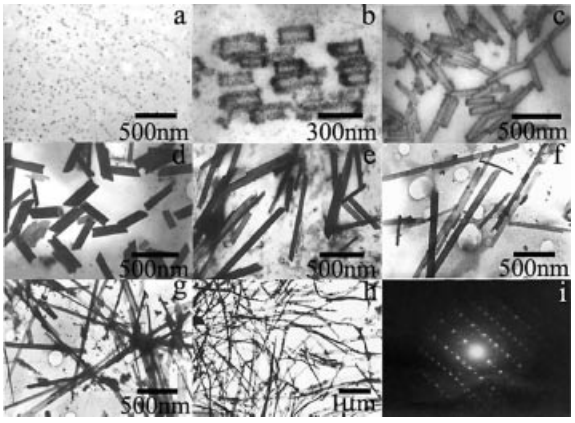


Figure 2. TEM and SAED images of $CaSO_4 \cdot 2H_2O$ at different aging times: (a) 1 min, (b) 3 min, (c) 5 min, (d) 40 min, (e) 3 h, (f) 12 h, (g) 36 h, (h) 108 h, (i) SAED image.

As shown in Figure 2 (a), the products are primarily nanoparticles with a diameter of about 15 nm when the reaction time is 1 min; there are some signals showing nanoparticles tending to form a one-dimensional morphology. This trend is realized when the reaction time extends to 3 min. Nanotubes with a diameter of about 50 nm and a length of nearly 200 nm are formed as shown in part b of Figure 2. From further observations it can be seen that the walls of the nanotubes are composed of nanoparticles, and that the walls become solid when the reaction time is 5 min. But there are few changes in the size of the nanotubes (see Figure 2, c). This process can be described as the assembly from nanoparticles to nanotubes and the increase in the firmness of the nanotubes. The simple method reported in this paper can produce inorganic salt nanotubes at room temperature, which provides a contribution to the research on nanotubes.

Interestingly, when the reaction time is prolonged to 40 min well-dispersed short rods are observed (Figure 2, d), and the growth of the rods keeps for tens of hours as revealed in parts d and g of Figure 2. With the extension of the reaction time both the length and the diameter increased and the increment in length was much larger than that in diameter. When the reaction time is long enough rods grow into wires and the lengths reach nearly 100 μm as shown in part h of Figure 2. The Selected Area Electron Diffraction (SAED) image (Figure 2, i) taken from a single nanotube shown in Figure 2 (c) exhibits single-crystalline diffraction dots that can be indexed to the monoclinic structure of $CaSO_4 \cdot 2H_2O$, which is in good agreement with the XRD result presented above.

The experimental results above demonstrate the possibility of synthesizing nanoparticles, nanotubes, nanorods, and nanowires under certain circumstances in reverse micelle systems. Furthermore, it is found that the reaction time has a significant effect on the morphologies and dimensions of the final products. The effect of the reaction time on the shape and size of the nanomaterials is shown in Figure 3. The size becomes larger with an increase in the reaction time, and the curve reveals that the increase in length is much bigger than that in diameter. Thus the aspect ratio is enhanced when the reaction time becomes longer. The size can vary from tens of nanometers to tens of microns.

By tracking the observed results, the growth process shows that nanoparticles assemble to nanotubes, nanorods, and then to nanowires in a step-by-step fashion as the reaction time increases. The aspect ratio increases along with the reaction time. In order to justify this deduction another two inorganic salts have been synthesized by the same method. The results are shown in Figure 4 and Figure 5. Firstly, Pb(OH)Cl was prepared in the same reverse micelle system ($C_{12}E_9$, *n*-pentanol, cyclohexane and $Pb^{2+}$, $Cl^-$ water solution) as $CaSO_4$. TEM pictures taken at different reaction times are shown in Figure 4. The results demonstrate that the deduced growth process is reasonable. Another experiment was carried out in a different reverse micelle system to justify the growth process. In this system, $C_{12}E_9$ was replaced by Triton X-100 and CdS nanoparticles, -tubes,

 © 2007 Wiley-VCH Verlag GmbH & Co. KGaA, Weinheim 

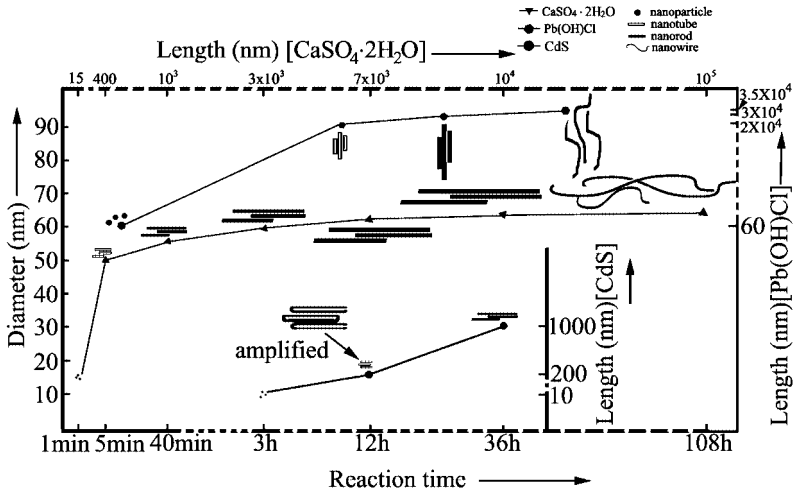


Figure 3. The effect of reaction time on the shape and size of nanomaterials obtained in the reverse micelle systems.

and -rods were prepared stepwise with reaction times becoming longer (as shown in Figure 5). It indicates that the deduction could be used to guide the stepwise-assembly formation in different reverse micelle systems.

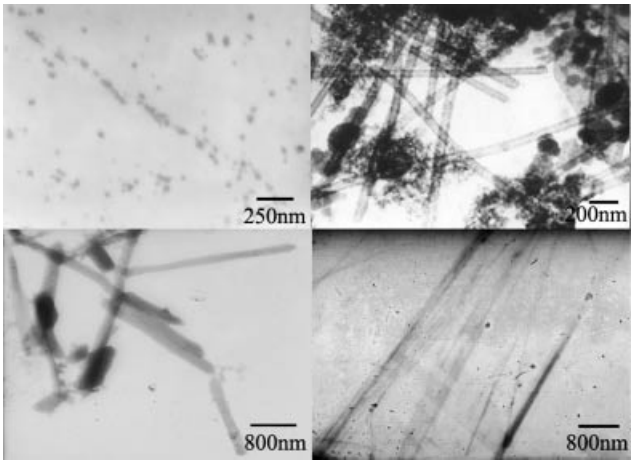


Figure 4. TEM images of as-obtained Pb(OH)Cl nanomaterials in the reverse micelles ($C_{12}E_9$ as surfactant) at different reaction times.

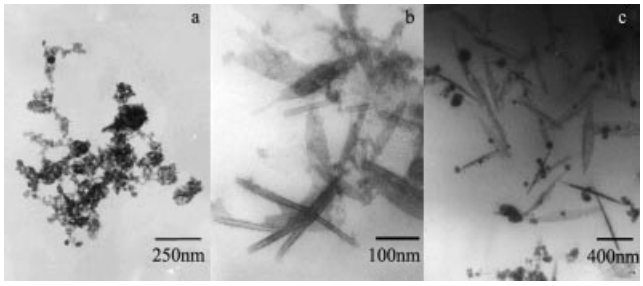


Figure 5. TEM images of CdS obtained in the reverse micelle systems (Triton X-100 as surfactant) at different reaction times: (a) 3 h, (b) 12 h, (c) 36 h.

Similar to the synthesis of CdS, ZnS, and $Ag_2S$ nanoparticles, nanotubes, and nanorods are also synthesized using sulfocarbamide as the sulfur source in the reverse micelle system (see Supporting Information). All results obtained above show that the stepwise-assembly synthesis has universality in preparing inorganic salts in reverse micelle systems. What is important is that ZnS and $Ag_2S$ nanotubes and nanorods synthesized by this method have never been reported before.

## Discussion

The mechanism of stepwise-assembly synthesis is discussed according to the results. The surfactant used in this system is AEO ($C_{12}E_9$), which is a long-chain molecule. It contains two indented hydrophobic and hydrophilic chains, which can easily form a one-dimensional template.[36] The products obtained in such reverse micelles are commonly one-dimensional materials. The mechanism diagram of the growth procedure is shown in Figure 6.

When two reverse micelle solutions are mixed only micelles containing two different reactants have effective collisions. These effectively collided reverse micelles then fuse and inorganic ions filter to form nucleation. These nuclei grow up to form nanoparticles with micelles attached to the surface. The nanotubes are then assembled in association and concurrent with the self-organization of stacked micellar aggregates (see Figure 7, Figure 2, a and b). It is clearly seen that incompact particles are assembling into wandering tubes, which indicates that nanoparticles are firstly formed and then assembled into tubes. Because these nanotubes are surfactant coated, micelles containing different ions can be absorbed onto the faces by the interaction between the hydrophobic tails of AEO.[37] When the micelles attach to the surface the surface tension is broken and the ions enter the nanotubes through the interstices of nanoparticles in the wall of the nanotube. Thus different ions react to form $CaSO_4$ nuclei inside nanotubes. These nuclei then grow bigger and the hollow tubes are filled. Lateral growth can still take place since the surfactant-$CaSO_4$ particles are not depleted.[38] The fact that the size of the nanotubes becomes larger in both length and width is evidence

 © 2007 Wiley-VCH Verlag GmbH & Co. KGaA, Weinheim 

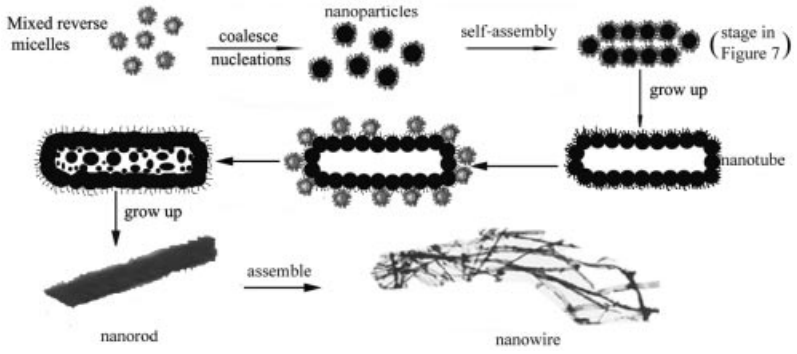


Figure 6. Formation mechanism diagram of stepwise-assembly synthesis.

for this process (Figure 2, b and c). After enough growth nanorods are obtained (Figure 2, d). These short rods coated with surfactant can also assemble into long nanowires with an extension of the aging time (Figure 2, e and f). Thus stepwise-assembly synthesis of nanoparticles, nanotubes, nanorods, and nanowires is successfully realized.

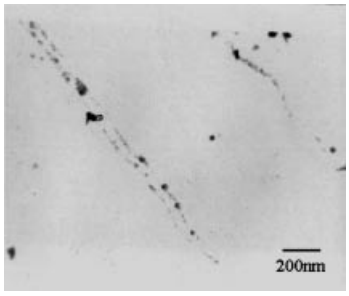


Figure 7. TEM image of Pb(OH)Cl, reaction time is 1 h at 37 °C.

## Conclusions

In conclusion, a facile reverse micelle method for the stepwise preparation of $CaSO_4$ nanoparticles, -tubes, -rods, and -wires in one reverse micelle system is described. By controlling the reaction time in a certain reverse micelle system, $CaSO_4$ nanocrystals with tunable shapes and sizes are presented. The growth process in this system is deduced to be a stepwise-assembly-growth process. This deduction is demonstrated by several experimental results. This deduction can perceptibly make a contribution not only to the research on inorganic salt nanotubes, nanorods, and nanowires, but also to the application of reverse micelles or micoremulsions in fabricating one-dimensional nanomaterials. The products obtained in this work also have potential applications in many fields, such as nanoreactors and drug carriers.

## Experimental Section

**Reagents:** Anhydrous calcium chloride, sodium sulfate, *n*-pentanol, and cyclohexane used in this work were A.R. reagents purchased from Shanghai Chemical Reagent Factory, China. They were used without any pretreatment. $C_{12}E_9$ (AEO) [polyoxyethylene (9) dodecyl ether] was used as received from Henkel.

**Stepwise Synthesis of $CaSO_4$ Nanoparticles, Nanotubes, Nanorods, and Nanowires:** In a typical procedure a calculated amount of 0.1 M $CaCl_2$ solution was first placed in a conical flask, and then certain amounts of $C_{12}E_9$, *n*-pentanol, and cyclohexane were added in turn to form a reverse micelle when stirred vigorously. Another reverse micelle system was prepared through the same method except that the $CaCl_2$ solution was replaced by a 0.1 M $Na_2SO_4$ solution. The corresponding volume ratio of $Ca^{2+}/SO_4^{2-}$/AEO is 1:1:0.3. Thereafter, the above two reverse micelle solutions were mixed quickly. The mixture was stirred for a few minutes, and then a slightly viscous and optically transparent single-phase liquid was formed. This liquid was then aged for 1 min, 3 min, 5 min, 40 min, 3 h, 12 h, 36 h, and 108 h statically at 30 °C. The solid products were separated by centrifugation and repeatedly washed with anhydrous ethanol. These products were then kept in anhydrous ethanol for further characterization.

**Characterization of $CaSO_4$ Nanomaterials with Different Morphologies:** X-ray powder diffraction (XRD) analyses of the products were carried out with a Rigaku D/mx2550 X-ray diffractometer with Cu-$K_\alpha$ radiation ($\lambda$ = 1.5418 Å). Transmission electron microscopic (TEM) images were recorded using a Hitachi-800 transmission electron microscope. And the TEM images were obtained on thin films deposited on Cu gauze from a dilute ethanol solution of as-prepared products.

**Supporting Information** (see also the footnote on the first page of this article): Stepwise synthesis of ZnS and $Ag_2S$ nanoparticles, nanotubes and nanorods. Two figures with transmission electron microscopy images (ZnS at different reaction times and $Ag_2S$ after different aging times).

## Acknowledgments

The authors are grateful for the financial support from the National Natural Science Foundation of China (grant numbers 20471042, 20571051), the State Key Project of Fundamental Research (973 Project) for Nanoscience and Nanotechnology (grant number 2006CB932300) and the Nano-Foundation of Shanghai in China (grants 0652nm007, 0552nm048).

[1] S. Mann, G. Ozin, *Nature* **1996**, *382*, 313–318.
[2] X. J. Zhao, R. P. Bagwe, W. H. Tan, *Adv. Mater.* **2004**, *16*, 173–176.
[3] S. P. Moulik, G. C. De, A. K. Panda, B. B. Bhowmik, A. R. Das, *Langmuir* **1999**, *15*, 8361–8367.

 © 2007 Wiley-VCH Verlag GmbH & Co. KGaA, Weinheim 

[4] D. Ma, M. Li, A. J. Patil, S. Mann, *Adv. Mater.* **2004**, *16*, 1838–1841.
[5] Z. L. Yin, Y. Sakamoto, J. H. Yu, S. X. Sun, O. Terasaki, R. R. Xu, *J. Am. Chem. Soc.* **2004**, *126*, 8882–8883.
[6] B. Yoon, C. M. Wai, *J. Am. Chem. Soc.* **2005**, *127*, 17174–17175.
[7] J. Zhang, X. Ju, Z. Y. Wu, T. D. Hu, Y. N. Xie, Z. J. Zhang, *Chem. Mater.* **2001**, *13*, 4192–4197.
[8] H. Ohde, F. Hunt, C. M. Wai, *Chem. Mater.* **2001**, *13*, 4130–4135.
[9] J. H. Xiang, S. H. Yu, X. Geng, B. H. Liu, Y. Xu, *Cryst. Growth Des.* **2005**, *5*, 1157–1161.
[10] J. C. Liu, P. Raveendran, Z. Shervani, Y. Ikushima, Y. Hakuta, *Chem. Eur. J.* **2005**, *11*, 1854–1860.
[11] F. Teng, J. G. Xu, Z. J. Tian, J. W. Wang, Y. P. Xu, Z. S. Xu, G. X. Xiong, *Chem. Commun.* **2004**, 1858–1859.
[12] T. Tago, T. Hatsuta, K. Miyajima, M. Kishida, S. Tashiro, K. Wakabayashi, *J. Am. Ceram. Soc.* **2002**, *85*, 2188–2194.
[13] A. J. Zarur, J. Y. Ying, *Nature* **2000**, *403*, 65–67.
[14] J. P. Ge, S. Xu, L. P. Liu, Y. D. Li, *Chem. Eur. J.* **2006**, *12*, 3672–3677.
[15] M. M. Wu, J. B. Long, A. H. Huang, Y. J. Luo, S. H. Feng, R. R. Xu, *Langmuir* **1999**, *15*, 8822–8825.
[16] P. Zhang, L. Gao, *Langmuir* **2003**, *19*, 208–210.
[17] M. Roth, R. Hempelmann, *Chem. Mater.* **1998**, *10*, 78–82.
[18] G. B. Sun, M. H. Cao, Y. H. Wang, C. W. Hu, L. Ren, K. L. Huang, *Chem. Commun.* **2005**, 1740–1742.
[19] M. Haeger, K. Holmberg, *Chem. Eur. J.* **2004**, *10*, 5460–5466.
[20] M. H. Cao, X. L. Wu, X. Y. He, C. W. Hu, *Langmuir* **2005**, *21*, 6093–6096.
[21] A. J. Zarur, H. H. Hwu, J. Y. Ying, *Langmuir* **2000**, *16*, 3042–3049.
[22] G. D. Rees, R. Evans-Gowing, S. J. Hammond, B. H. Robinson, *Langmuir* **1999**, *15*, 1993–2002.
[23] A. P. Alivisatos, *Science* **2000**, *289*, 736–737.
[24] R. L. Penn, J. F. Banfield, *Geochim. Cosmochim. Acta* **1999**, *63*, 1549–1557.
[25] S. A. Davis, M. Breulmann, K. H. Rhodes, B. Zhang, S. Mann, *Chem. Mater.* **2001**, *13*, 3218–3226.
[26] M. Terrones, W. K. Hsu, H. W. Kroto, D. R. M. Walton, *Top. Curr. Chem.* **1999**, *199*, 189–234.
[27] M. Remskar, *Adv. Mater.* **2004**, *16*, 1497–1504.
[28] X. L. Li, Y. D. Li, *Chem. Eur. J.* **2003**, *9*, 2726–2731.
[29] R. Tenne, *Adv. Mater.* **1995**, *7*, 965–972.
[30] L. M. Dai, A. Patil, X. Y. Gong, Z. X. Guo, L. Q. Liu, Y. Liu, D. B. Zhu, *ChemPhysChem* **2003**, *4*, 1150–1169.
[31] C. S. Rout, S. Hari Krishna, S. R. C. Vivekchand, A. Govindaraj, C. N. R. Rao, *Chem. Phys. Lett.* **2006**, *418*, 586–590.
[32] G. R. Patzke, F. Krumeich, R. Nesper, *Angew. Chem. Int. Ed.* **2002**, *41*, 2446–2461.
[33] V. V. Pokropivny, *Powder Metall. Met. Ceram.* **2001**, *40*, 485–496.
[34] H. J. Niu, M. Y. Gao, *Angew. Chem. Int. Ed.* **2006**, *45*, 6462–6466.
[35] W. Liu, W. Zhong, X. L. Wu, N. J. Tang, Y. W. Du, *J. Cryst. Growth* **2005**, *284*, 446–452.
[36] X. H. Yang, Q. S. Wu, L. Li, Y. P. Ding, G. X. Zhang, *Colloids. Surf. A* **2005**, *264*, 172–178.
[37] M. Li, H. Schnablegger, S. Mann, *Nature* **1999**, *402*, 393–395.
[38] M. Li, S. Mann, *Langmuir* **2000**, *16*, 7088–7094.

Received: February 11, 2007
Published Online: September 12, 2007

 © 2007 Wiley-VCH Verlag GmbH & Co. KGaA, Weinheim 

DOI: 10.1002/ejic.200700461

# Vibrational Spectrum and Electronic Structure of the $[B_{11}H_{11}]^{2-}$ Dianion

**Elena G. Kononova,[a] Larissa A. Leites,*[a] Sergey S. Bukalov,[a] Irina V. Pisareva,[a] Igor T. Chizhevsky,[a] John D. Kennedy,[b] and Jonathan Bould[b]**

**Keywords:** Boron / Cage compounds / Vibrational spectra / Electronic structure / Fluxionality

The vibrational spectrum, geometrical structure and electron-density distribution (EDD) of the formally *closo* (2*n*+2)-electron cluster species $[B_{11}H_{11}]^{2-}$ have been studied. The presence of two low-frequency vibrational modes is evidence of cluster nonrigidity. A rationale for this lies in the results of EDD calculations which show that the polyhedron lacks two-centre edge-localized B–B bonds of the 6**k**–5**k** type and that its surface exhibits two six-membered rings with low electron density. Thus, the polyhedron does not consist of deltahedral faces only and therefore does not have a genuine *closo* structure. The data obtained also allow further elucidation of the "diamond-square-diamond" mechanism as commonly applied to the fluxionality of $[B_{11}H_{11}]^{2-}$ in solution.

(© Wiley-VCH Verlag GmbH & Co. KGaA, 69451 Weinheim, Germany, 2007)

## Introduction

The eleven-vertex *closo* boranes and *closo* carbaboranes differ from their twelve-vertex and ten-vertex *closo* congeners in that (i) their cages contain a boron atom with the highest cluster connectivity of six, designated 6**k** in Williams' notation,[1] and in that (ii) they exhibit unusual NMR spectroscopic and chemical properties.[2–7]

Recently we studied the vibrational spectra of two representatives of the eleven-vertex *closo*-carbaborane family, namely the neutral molecule 2,3-$C_2B_9H_{11}$ (**1**) and the [2-$CB_{10}H_{11}]^-$ anion (**2**) (see Figure 1 for atom numbering), and showed that both species exhibited two low-frequency large-amplitude vibrational modes, at ca. 200 and ca. 300 $cm^{-1}$.[8,9] In this regard they contrast to all of the previously studied[10–12] unsubstituted twelve-, ten-, and six-vertex *closo*-boranes and *closo*-carbaboranes, which exhibit **no** normal modes with frequencies lower than 450 $cm^{-1}$. This lack of low-frequency modes is a consequence of the rigidity of the latter polyhedral cages. The cage rigidity, when present, permits the treatment of a *closo*-carbaboranyl moiety as a *pseudo*-atom, "Cb", and this model approach has worked well for the interpretation of the vibrational spectra of Cb–Cb and Cb–X molecules.[10,13,14]

By contrast, the presence of the low-frequency "soft modes" in the vibrational spectra of both **1** and **2** suggested cage nonrigidity, which, we surmised, was associated with the 6**k** feature. Based on the analysis of the published experimental and computed data on interboron distances in the structures of **1** and **2**, together with the results of the topological analysis of the electron-density distribution in both species, we thence concluded[8,9] that each of the polyhedra **1** and **2** does not actually have the deltahedral *closo* structure traditionally associated with them by the formal [2*n*+2] electron-count.[1,15]

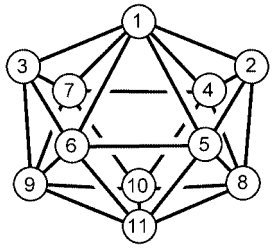


Figure 1. A traditional representation of the $\{B_{11}\}$ *closo* polyhedron depicting the atom numbering.

It was of interest similarly to investigate the other principal representative of the eleven-vertex *closo* polyhedral class, the $[B_{11}H_{11}]^{2-}$ boron cluster dianion (**3**), of which a well-known and interesting characteristic is its very simple, averaged $^{11}B$ NMR spectrum in solution, which was first reported by Tolpin and Lipscomb in 1973,[2] and which arises from a fluxionality due to a rapid polyhedral rearrangement.[2,6]

In this paper we present the Raman and IR spectra of **3** as its di-$K^+$ and di-$Cs^+$ salts and the Raman data on an aqueous solution of the di-$Cs^+$ salt. These vibrational spectra of **3** are previously unreported. Quantum-chemical DFT B3LYP calculations of the geometry of the undistorted dianion **3** and its vibrational mode frequencies and eigenvec-

[a] A. N. Nesmeyanov Institute of Organoelement Compounds, 28 ul. Vavilova, Moscow 119991, Russia
Fax: +7-495-135-5085
E-mail: buklei@ineos.ac.ru
[b] The School of Chemistry of the University of Leeds, Leeds, UK LS2 9JT, England

 © 2007 Wiley-VCH Verlag GmbH & Co. KGaA, Weinheim 

tors are also reported, and the electron density distribution (EDD) in **3** has been reconstructed using Bader's theory of "atoms in molecules" (AIM),[16] based on the optimized structure arising from DFT calculations. The results are related to the mechanism of the fluxionality of the anion.

## Results and Discussion

### Synthesis

A sample of $K_2[B_{11}H_{11}]$ (**3a**) was synthesized essentially according to a literature method.[6] The cation exchange reaction, substituting $Cs^+$ for $K^+$, between **3a** and a solution in methanol of CsCl, did not lead to $Cs_2[B_{11}H_{11}]$ (**3b**) but to a mixed salt of which the elemental analysis was consistent with the formulation $Cs_2[B_{11}H_{11}]$·CsCl (**3c**). Here it may be noted that an analogous double salt has been obtained for the $[B_{12}H_{12}]^{2-}$ dianion.[17] Subsequent attempts to prepare the simple di-$Cs^+$ salt of **3** using CsCl were made by variation of the concentrations of the reagents and by changing the order of reagent addition, but, in both cases, only the mixed salt **3c** with a 1:1 $Cs_2[B_{11}H_{11}]$: CsCl ratio was obtained. Use of CsF, however, did yield $Cs_2[B_{11}H_{11}]$ (**3b**). The Raman spectra of both $Cs^+$ salts **3b** and **3c** were almost identical, as were the IR spectra; the presence of $Cl^-$ anions in **3c** resulted only in small shifts of several bands in the spectrum of solid **3c** (Table 1).

Table 1. Vibrational spectrum of the $[B_{11}H_{11}]^{2-}$ anion.[a]

| Calculated frequency [$cm^{-1}$] | IR intensity (arbitrary units) | Experimental frequencies [$cm^{-1}$] | | | | | Symmetry species | Assignment |
|---|---|---|---|---|---|---|---|---|
| | | IR spectrum of the solid salt $Cs_2B_{11}H_{11}$·CsCl | Raman spectrum of the salt $Cs_2B_{11}H_{11}$·CsCl solid sample | Raman spectrum of the salt $Cs_2B_{11}H_{11}$·CsCl aqueous solution | Raman spectra of the solid salts $Cs_2B_{11}H_{11}$ | Raman spectra of the solid salts $K_2B_{11}H_{11}$ | | |
| 2526 | 0 | | 2517 vs | 2511 s p | 2514 vs | 2516 vs br | $A_1$ | |
| 2497, 2492 | 10.0 | 2498 vvs | | | | | | |
| 2482, 2475 | 9.0 | 2480 vs | 2484 s br | 2475 w | | | | νBH |
| 2465 | | 2463 vvs | 2461 s br | 2460 m dp | 2474 s sh | 2467 vs br | $A_1$, $B_2$ | |
| 2450 | 0.3 | | | | | 2429 sh | | |
| | | 1208 vw | | | | | | |
| | | 1168 sh | | | | | | |
| 1066 | 0.3 | 1154 m | | | | | | |
| 1049 | 0.2 | 1076 m | | | | | $B_1$ | |
| 1037 | 0.2 | 1059 s | 1061 m | 1064 mw p | 1062 m | 1070 mw | $A_1$ $B_2$ | |
| | | | 1040 vw | | | 1035 vw | | δBH |
| | | 1024 sh | | | | | | |
| 942 | 0.1 | 960 m br | 963 m | 950 mw p | 952 m | 948 m | $A_1$ | |
| 941 | 0.1 | 942 sh | | | | | $B_2$ | |
| 921 | 0 | | | | | 914 vw | | |
| 893 | 0 | 891 vw | 905 mw | 879 m p | 871 sh | 873 m | $A_1$ | |
| 860 | 0.1 | 863 sh | | | | | $B_2$ | δBH |
| 862 | 0.0 | 851 mw | 856 vs | 843 s p | 845 s | 841 s | $A_1$,$B_1$ | +νBB |
| 832 | 0.1 | 812 mw | 814 vw | | | | $A_1$,$B_2$ | |
| 822 | 0 | | | | | | $A_2$ | |
| 802 | 0 | 806 sh | | | | | $B_1$ | |
| 786 | 0.1 | | | | | | $B_1$ | |
| 781 | 0 | 769 w | | | | | $B_2$ | |
| 751 | 0.04 | | 748 vs | 749 s p | 746 vs | 751 vs | $A_1$ | cage stretch |
| 740 | 0.04 | 730 sh | | | | | | |
| 717, 726 | 0.04 | 725 sh | 726 s | 725 s p | 732 s sh | 724 s | $A_1$ | cage stretch |
| 695 | 0.02 | 680 w | 683 vw | | | 689 vw | $B_2$ | νBB+δBBB |
| 675 | 0.01 | 664 vw | 661 vw | | 662 w | 664 vw | $A_1$ | |
| 640 | 2.0 | | | | | 638 sh | $B_2$ | |
| 617 | 1.0 | 631 vw | 627 m | 626 m p | 626 m | 623 m | $A_1$,$B_1$ | |
| | | | 608 w | | 612 w sh | | | |
| 598 | 0 | | 594 m | 594 w dp | 592 m | 594 m | $B_2$ | |
| 579 | 0 | | | | | | $B_1$ | δBBB |
| 546 | 2.0 | | 575 m | 577 w p | 575 m | 578 m | $A_1$ | cage |
| 539 | 0 | | 541 m | 543 w dp | 541 m | 541 m | $A_2$ | deformations |
| 495 | 2.0 | 510 w | 519 m | 518 w p | 514 m | 525 m | $A_1$ | |
| 473 | 7.0 | 460 vw | 464 mw | 466 m dp | 465 m | 459 mw | $B_2$ | |
| 282 | 0.02 | 310 vvw ? | 300 w br | | 312 mw br | 310 mw | $B_2$ | wB1 |
| 173 | 0 | | 210 m | | 212 m br | 220 m | $A_2$ | δB(4,5,6,7) |

[a] s: strong, m: medium, w: weak, sh: shoulder, br: broad, p: polarized, dp: depolarized.

 © 2007 Wiley-VCH Verlag GmbH & Co. KGaA, Weinheim 

### Vibrational Spectra and Electronic Structure

The undistorted dianion $[B_{11}H_{11}]^{2-}$ belongs to the $C_{2v}$ symmetry point group; its 60 normal modes are distributed among the symmetry species as follows:

$\Gamma = 19\ A_1 + 11\ A_2 + 16\ B_1 + 14\ B_2$

The vibrations of the $A_1$, $B_1$ and $B_2$ species are both IR-active and Raman-active, whereas the $A_2$ ones are only Raman-active. The spectra obtained are given in Figure 2 and Table 1. The latter also presents the calculated, unscaled harmonic frequencies and IR intensities of some normal modes, along with band assignment. The assignment was based on the Raman and IR activities, depolarization ratios of the Raman lines and on the results of normal-coordinate analysis. Previously, the low-resolution IR spectrum of the Nujol mull of the di-$Cs^+$ salt has been presented as a picture in ref.[18], where its Raman spectrum was also mentioned, but no particularly specific data were reported.

As is seen from Figure 2 and Table 1, the number of spectral features is much less than the theoretical value of 60. This observation can be rationalized in terms of the results of the normal-coordinate analysis, which shows that the frequencies of some normal modes, having close displacement eigenvectors but belonging to different symmetry species, nearly coincide (Table 1). An analogous situation was also observed for the spectra of both **1** and **2**.[8,9] It is of interest that the calculation for **3** reproduces the frequencies of ν(BH) stretching vibrations quite well without any scaling, unlike in the cases of the carbaboranes **1** and **2**, for which the computed ν(BH) frequencies were highly overvalued.

The vibrational spectrum of **3** is as specific as those of **1** and **2** in that it also exhibits two low-frequency modes at about 200 and 300 $cm^{-1}$. The exact frequency values of these modes depend slightly on the nature of the cation. The normal-coordinate analysis for the free anion **3** reproduces these low-frequency modes, but with somewhat lowered frequencies compared to the experimental values, as if they are now free from cation influences. Notably, by contrast, in the spectra of the two rigid-cage species $[B_{12}H_{12}]^{2-}$ and $[B_{10}H_{10}]^{2-}$ there are no frequencies lower than 588 $cm^{-1}$ [19] and 515 $cm^{-1}$,[20] respectively. However, all the rest of the salient spectral features, for example the ν(BH) frequencies or the cage breathing modes, are very much alike for all three borane dianions $[B_nH_n]^{2-}$, where $n$ is 12, 11 and 10.[10] There are two totally symmetric cage vibrations in the spectra of all of the salts of **3**, to which very intense Raman lines at ca. 725 $cm^{-1}$ and ca. 750 $cm^{-1}$ correspond.

The incidence of low frequencies in the spectrum of **3**, as for those of **1** and **2**, is explained by the nonrigidity of the cage that is caused by the peculiarities of geometrical and electronic structure of the eleven-vertex polyhedron. To the best of our knowledge, three molecular structures, as determined by X-ray crystallography, are available for salts containing $\{B_{11}\}$ cluster anions. These are for $A_2[B_{11}H_{11}]$, where A is $[Li(thp)_3]$ (**4**) or $[NBzlEt_3]$ (**5**),[6b] and for $[NEt_4][4\text{-}(SMe_2)B_{11}H_{10}]$ (**6**).[21] Short interionic contacts in the crystal structure of **4** strongly distort the symmetry of the anion from regular $C_{2v}$. However, the less interactive ammonium cations in **5** and **6** leave the geometry of the anion closer to the idealized one. Dimensions derived by X-

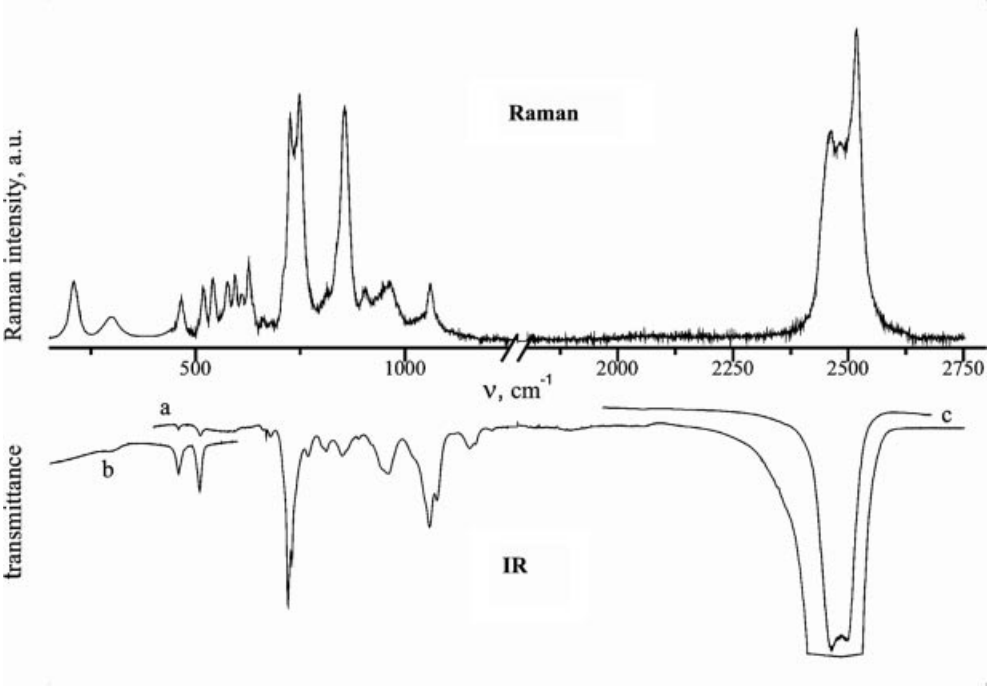


Figure 2. The Raman and IR spectra of solid $Cs_2[B_{11}H_{11}]$·CsCl. The IR spectra: (a) KBr pellet, (b) polyethylene pellet, (c) Nujol mull.

 © 2007 Wiley-VCH Verlag GmbH & Co. KGaA, Weinheim 

Table 2. Interatomic distances and bond electron density $\rho_b(\mathbf{r})$ inside the $\{B_{11}\}$ polyhedron of the $[B_{11}H_{11}]^{2-}$ dianion (**3**).

| Pairs of cage atoms | Interatomic distances [Å] | | | | | | Presence of the (3,–1) bond critical points in **3** | $\rho_b(\mathbf{r})$ a.u. |
|---|---|---|---|---|---|---|---|---|
| | X-ray data for **5**[a][6b] | for **6**[a][21] | X-ray data [23] | [22] | calculated for isolated **3** [6] | this work | | |
| B(1)B(2) = B(1)B(3) | 1.747, 1.744 | 1.768, 1.722 | 1.746 | 1.726 | 1.745 | 1.745 | + | 0.117 |
| B(2)B(8) = B(3)B(9) | 1.743, 1.746 | 1.786, 1.757 | 1.753 | 1.746 | 1.760 | 1.759 | + | 0.120 |
| B(2)B(4) = B(2)B(5) = B(3)B(6) = B(3)B(7) | 1.658, 1.660, 1.665, 1.664 | 1.650, 1.662, 1.632, 1.677 | 1.670 | 1.634 | 1.672 | 1.670 | + | 0.142 |
| B(1)B(4) = B(1)B(5) = B(1)B(6) = B(1)B(7) | 2.024, 1.999, 2.026, 1.988 | 2.001, 2.025, 2.048, 1.971 | 2.004 | 1.990 | 2.026 | 2.028 | – | |
| B(8)B(10) = B(8)B(11) = B(9)B(10) = B(9)B(11) | 1.767, 1.781, 1.772, 1.775 | 1.804, 1.757, 1.731, 1.772 | 1.785 | 1.760 | 1.790 | 1.789 | + | 0.116 |
| B(4)B(7) = B(5)B(6) | 1.861, 1.846 | 1.806, 1.901 | 1.856 | 1.847 | 1.871 | 1.873 | – | |
| B(4)B(10) = B(5)B(11) = B(6)B(11) = B(7)B(10) | 1.779, 1.775, 1.770, 1.784 | 1.759, 1.812, 1.775, 1.795 | 1.780 | 1.775 | 1.786 | 1.785 | + | 0.116 |
| B(4)B(8) = B(5)B(8) = B(6)B(9) = B(7)B(9) | 1.761, 1.783, 1.785, 1.795 | 1.791, 1.797, 1.757, 1.782 | 1.791 | 1.783 | 1.796 | 1.794 | + | 0.117 |
| B(10)B(11) | 1.809 | 1.781 | 1.814 | 1.821 | 1.830 | 1.830 | + | 0.108 |

[a] The corresponding B–B interatomic distances in **5** and **6** are crystallographically non-equivalent as well as being subject to differing cation and substituent influences.

ray crystallography for **5** and **6**,[6b,21] as well as the results of geometry optimization for the undistorted **3**, both as reported previously[6a,22,23] and as obtained in this study, are given in Table 2. Both the experimental data and the computed data show that the interatomic distances between the B(1) and the B(4), B(5), B(6) and B(7) boron atoms, that average at 2.02 Å, are anomalously long for B–B bonds in *closo*-boranes, which typically vary from 1.58 to 1.99 Å.[22] Analogously long 6**k**–5**k** distances are similarly observed for **1** and **2**.[8,9] It is pertinent to mention here that Wade estimated the 6**k**–5**k** type of B–B interatomic distance to be 1.95 Å on the basis of fractional bond order.[15b] Long interboron connectivities have been recognized in some "disobedient" *closo* clusters to be typical for "fragile" structures.[24]

Explanation for these peculiar properties of the eleven-vertex *closo* polyhedra can be attempted by means of a topological analysis of the electron-density function according to Bader's "atoms in molecules" (AIM) approach.[16] This method has proven to be a useful and successful tool in understanding several other electron-deficient borane and carbaborane structures.[25,26] The results of such calculations for the $[B_{11}H_{11}]^{2-}$ anion **3** are given in Table 2. The corresponding molecular graph is presented in Figure 3, where the bond critical points are indicated and denoted by small circles.

The electron density values $\rho_b(\mathbf{r})$ for the (3,–1) critical points [i.e. bond critical points (BCPs)] of the BH and BB two-centre bonds lie in the intervals 0.166–0.162 and 0.142–0.108 a.u., respectively. These values are close to those obtained for the $[B_{12}H_{12}]^{2-}$ dianion.[25a] The electron-density values $\rho_r(\mathbf{r})$ for the (3,+1) critical points [i.e. ring critical points (RCPs)] that characterize the three-membered rings are as follows: for the eqivalent B(3,9,6) = B(3,9,7) = B(2,5,8) = B(2,4,8) faces: 0.116 a.u., for the equivalent B(6,9,11) = B(5,8,11) = B(4,8,10) = B(7,9,10) faces: 0.109 a.u., for the equivalent B(9,10,11) = B(8,10,11) faces: 0.105 a.u.

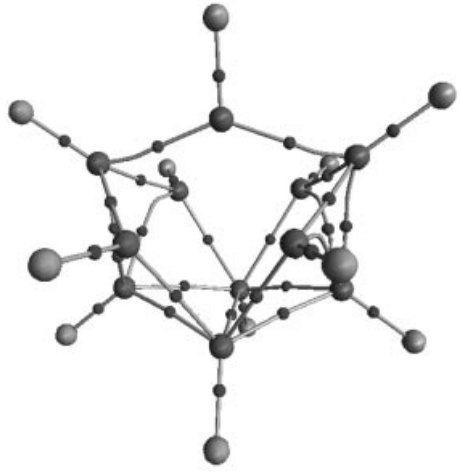

Figure 3. Molecular graph of the $[B_{11}H_{11}]^{2-}$ dianion **3** obtained as a result of the AIM topological analysis of electron-density distribution.

It is evident from these data that the $\rho_r(\mathbf{r})$ values for the above-mentioned three-membered rings in the structure of **3** are of comparable magnitude to those of $\rho_b(\mathbf{r})$ for the pairwise B–B interactions (Table 2). This is typical for boron polyhedra[25,26] and shows that the three-centre bonding plays almost the same role as the two-centre bonding; in other words, stabilization of the cage is attained both by the accumulation of electron density along the edge-localized bond paths and by its delocalization over the triangular polyhedral faces. There is a (3,+3) critical point in

 © 2007 Wiley-VCH Verlag GmbH & Co. KGaA, Weinheim 

the cage interior: this is consistent with the essentially closed volume of **3**. The electron density value $\rho_c(\mathbf{r})$ in the centre of the cage **3** is low, at 0.0196 a.u., close to those[8,9] of the other eleven-vertex cages, for **1** at 0.0211 a. u. and for **2** at 0.0195 a.u.

However, the results also show that there are no (3,–1) BCPs between members of each of the following pairs of boron atoms: B(1)–B(4), B(1)–B(5), B(1)–B(6) and B(1)–B(7); that is, there are no edge-localized two-centre 6**k**–5**k** bonds in the bonding network of **3**. This obviously leads to the longer interatomic distances from the B(1) atom to B(4), B(5), B(6) and B(7). Also, however, no BCPs were found between the B(5) and B(6) atoms, or between the B(4) and B(7) atoms, for which the interboron distances, which average at 1.86 Å, are significantly shorter than the 1.99 Å upper limit mentioned above, although elongated compared to the typical expected value of 1.79 Å[15b] for a 5**k**–5**k** cluster interboron linkage. The reason for this is not clear yet; the atoms in each of the B(4)–B(7) and B(5)–B(6) pairs would seem to be drawn together by the whole delocalized bonding system of the cage **3**. An analogous situation occurs for the *closo*-1,5-$C_2B_3H_5$ molecule, for which the AIM treatment, both theoretical[25a] and experimental,[26b] reveals no B–B bond paths, although the corresponding experimental B–B interatomic distances are also of closely similar magnitude, at 1.853 Å.

Thus, according to the analysis of the topology of electron density with AIM, six of the 27 edges of the octadecahedron of **3**, specifically B(1)–B(4), B(1)–B(5), B(1)–B(6) and B(1)–B(7), together with B(5)–B(6) and B(4)–B(7), do not correspond to two-centre bond paths. The absence of these leads to the presence in the structure of **3** of two equivalent six-membered rings encompassing the B(1,2,5,11,6,3) and B(1,2,4,10,7,3) atoms. These rings are characterized by two (3,+1) RCPs with low values for the electron density $\rho_r(\mathbf{r})$ of 0.070 a.u. The $\rho_r(\mathbf{r})$ values for the RCPs of the three-membered rings are much higher (see above), all being greater than 0.105 a.u. Thus in the structure of **3**, multicentre bonding in the six-membered rings is significantly weakened. These rings can therefore be regarded to some extent as "open faces", although it is pertinent to mention here that, according to our computations, the $\rho_r(\mathbf{r})$ value for a conventionally recognized five-membered open face, as in the *nido*-dicarbaborane anion [7,8-$C_2B_9H_{12}]^-$, is much lower, at 0.020 a.u.

The weaker bonding interaction between the B(1) and the B(4), B(5), B(6) and B(7) atoms (compared to those between other pairs of boron atoms) inevitably gives a freer mobility to these atoms, and thus accounts for the low frequencies and large amplitudes of the corresponding vibrational "soft modes" that involve this set of boron atoms. The normal-coordinate analysis shows that the mode at ca. 200 $cm^{-1}$ is of the $A_2$ type and involves mainly displacements of equivalent B(4), B(5), B(6) and B(7) atoms. During this vibration, atoms B(4) and B(6) are approaching B(1) whereas atoms B(5) and B(7) are moving away from it. The mode at ca. 300 $cm^{-1}$ of the $B_2$ type is a wagging of the 6**k** B(1) atom in the B(2)B(1)B(3) "handle" back and forth in the symmetry plane defined by the B(1), B(10) and B(11) atoms.

Hence, all the data presented here and in the previous papers on 2,3-$C_2B_9H_{11}$ (**1**) and $[2\text{-}CB_{10}H_{11}]^-$ (**2**)[8,9] suggest that the formally closed eleven-vertex polyhedra **1**, **2** and **3** are **not formed by triangular faces only**, and therefore do not have genuine *closo* structures, in spite of having (2*n*+2) skeletal bonding electrons. It is obvious that they can be regarded as belonging to a category of "disobedient skeletons".[24]

It is of interest to attempt to reconcile the molecular graph that emerges from Bader's AIM approach with a more familiar Lipscomb-type "semi-localised" bonding diagram, which is based on two-electron two-centre and two-electron three-centre bonds. A schematic as in **I** (Scheme 1) below may be sketched as a representation of the bond paths and bond critical points of the molecular graph presented in Figure 3. In this diagram the hatched lines from B(1) to the B(4), B(7), B(5) and B(6) atoms, as well as from the B(4) to B(7) and from the B(5) to B(6) atoms, correspond to the "missing" two-centre bond paths and point to the thinning of the bonding "electronic glue" layer in these regions of the cage surface.

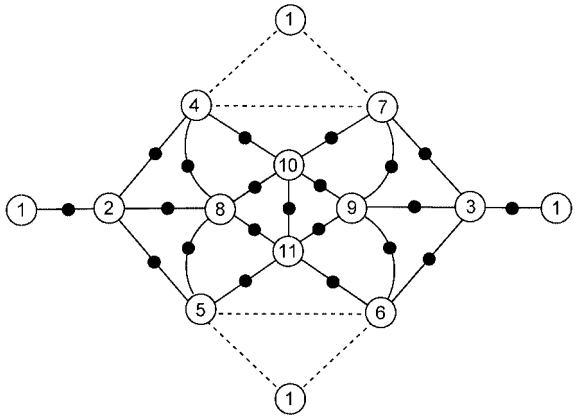


Scheme 1.

This schematic **I** can be supplemented by a schematic **II** (Scheme 2) to approximately reflect the rings and ring critical points of the molecular graph.

A corresponding classical Lipscomb-type semi-localized diagram, which seems to be a reasonable approximation of the electron density in terms of a factorization into localised two-electron bonding units, may be sketched as in schematic **III** (Scheme 3): this accommodates the 2*n*+2 cluster electrons required for a formal *closo* cluster-electron count if the dotted lines among the B(1), B(4), B(7), B(5) and B(6) atoms are taken to account for an overall total two-electron bonding interaction between B(1) and the B(4)B(7)B(5) B(6)B(10)B(11) region of the molecule.

The bonding representations involving the hatched lines, between B(2), B(4) and B(8), and also at the other three equivalent sites, B(2)B(5)B(8), B(3)B(6)B(9), and B(3)B(7) B(9), represent Lipscomb's semi-localised "partial-three-

 © 2007 Wiley-VCH Verlag GmbH & Co. KGaA, Weinheim 

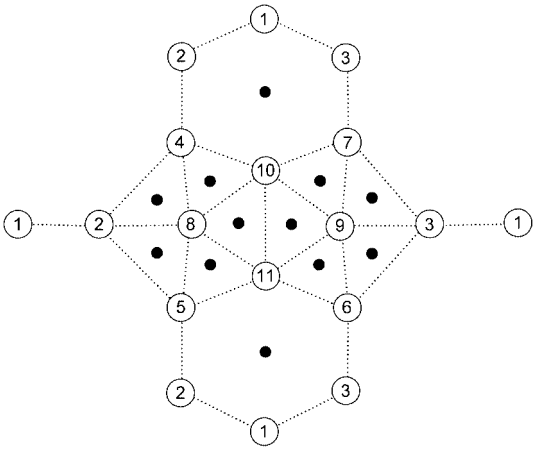


Scheme 2.

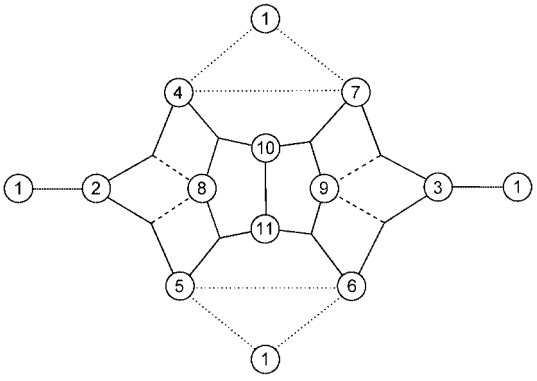


Scheme 3.

centre bonds". Which of these two approaches to a description of the bonding is adopted is a matter of taste and habit.

The data obtained also shed new light on the long-recognized phenomenon of the very facile fluxionality of anion **3**, which mutually "scrambles" all the cluster vertices. A Lipscomb diamond-square-diamond (*dsd*) mechanism is reasonably established for the dynamic framework rearrangements in the 11-vertex *closo* polyhedra.[3a,6] Repeated *dsd* processes, involving the B(1)B(2)B(5)B(6) quadrangle or one of the three other equivalent units, lead to the time-average equivalence of all the boron atoms in **3** in the $^{11}$B NMR spectrum in solution.[2,3,6] On the presumption that each of the quadrangles consists of two deltahedral faces, the *dsd* mechanism requires that, in its initiating diamond-to-square stage, a 6**k**–5**k** linkage [e.g. B(1)–B(5)] be broken, thus generating a square face, and then the nearest boron atoms undergo a slight rotation, and in the final square-to-diamond stage a new interboron linkage is formed, between B(2) and B(6). The B(6) atom thereby becomes a 6**k** vertex [instead of B(1)], and by repetition of this process, the 6**k** and all the 5**k** and 4**k** positions move over the whole polyhedron. However, the present results suggest that 6**k**–5**k** two-centre edge-localized bonds from B(1) to the B(4), B(5), B(6) and B(7) atoms are in fact absent, and, further, that multicentre bonding between B(1) and the B(4)B(5)B(6)B(7) quartet is weak. This bonding perception, together with the vibrational analysis, indicates that the process for the permutation of the 6**k** position can be regarded as being initiated simply via large-amplitude vibrations entailing the B(1) and the B(4), B(5), B(6), and B(7) atoms. Hence there is no need for a "*deus ex machina*" initially to "break" a (non-existent) 6**k**–5**k** linkage in the process of this cluster rearrangement.

These factors imply a very low activation energy for this process. Indeed, Paetzold and co-workers have calculated this value as 9.1 kJ mol$^{-1}$.[6] Incidental to this present work we have also obtained a similarly low calculated activation energy. This low value is clearly in accord with the experimental finding that fluxionality cannot be slowed sufficiently for individual resonances to be observed in the solution-state $^{11}$B NMR spectrum down to 200 K,[2] which implies an experimental activation energy upper limit of ca. 30 kJ·mol$^{-1}$. The low activation energy adds further to the perception that distortions away from the $C_{2v}$ ideal should be frequently observable in solid-state structures, since asymmetric crystal packing forces of even a few kJ mol$^{-1}$ will easily force distortions along the *dsd* rearrangement coordinate. This last phenomenon is manifested, for example, in the crystallographically determined square-open-faced structure of the interesting fluxional eleven-vertex formally *closo* $[B_{11}H_9(Se_3)]^{2-}$ anion.[27]

## Conclusions

Two low-frequency large-amplitude modes (at ca. 200 cm$^{-1}$ and ca. 300 cm$^{-1}$) in the vibrational spectra of the salts of the $[B_{11}H_{11}]^{2-}$ anion **3** have been found, and these are shown by normal coordinate analysis to involve the 6**k** B(1) and the neighbouring 5**k** B(4), B(5), B(6) and B(7) atoms. A critical review of the published experimental and computed data on the geometry of $[B_{11}H_{11}]^{2-}$ species reveals that the interboron distances between the 6**k** and the 5**k** atoms are greater than the generally accepted interboron bonding limit of 2.0 Å. Calculations of the electron-density distribution in **3**, performed according to Bader's approach and grounded on DFT results, show that there are no two-centre bond paths between the 6**k** B(1) and 5**k** B(4), B(5), B(6), and B(7) atoms; nor are there any between the members of each of the B(4)–B(7) and B(5)–B(6) pairs. Hence the cage of the $[B_{11}H_{11}]^{2-}$ anion **3** contains two six-membered rings with low electron density. These consistent data lead to the conclusion that the eleven-vertex polyhedron of $[B_{11}H_{11}]^{2-}$, although possessing $2n+2$ skeletal bonding electrons, is not in fact a pure deltahedron and not a straightforward *closo* cluster. A similar conclusion was made previously for the two corresponding eleven-vertex carbaboranes: the neutral 2,3-$C_2B_9H_{11}$ molecule **1** and the [2-$CB_{10}H_{11}]^-$ monoanion **2**.[8,9] The terminology "*quasi-closo*-polyhedron" has been suggested as a nomenclature to be associated with this interesting phenomenon.[9] Molecules **1**, **2** and **3** can therefore be placed in a category of "disobe-

 © 2007 Wiley-VCH Verlag GmbH & Co. KGaA, Weinheim 

dient skeletons".[24] The data obtained also allow a refinement of the interpretation of the "diamond-square-diamond" mechanism as commonly applied to the fluxionality of anion **3** in solution.

Overall the results well illustrate the important general point that an allegedly triangulated deltahedron does not necessarily merit such a description when the actual bonding is considered in appropriate detail. More generally, it is important to recognise that the bonding within any cluster may often be much less uniform than a simple consideration of the polyhedral shape of the cluster may be taken to imply.

## Experimental Section

**Preparation of $Cs_2[B_{11}H_{11}]\cdot CsCl$ (3c). Procedure A:** A filtered solution of $K_2[B_{11}H_{11}]$ (0.083 g, 0.4 mmol; prepared essentially as in ref.[6]) in absolute MeOH (2 mL) was added in drops to a stirred solution of CsCl (0.2 g, 1.2 mmol) in the same solvent (5 mL). After 10 min of vigorous stirring, the mother liquid was removed with a pipette from the white precipitate formed. The residue was washed with MeOH (2 × 3 mL) and thoroughly dried in vacuo, affording the mixed salt $Cs_2[B_{11}H_{11}]\cdot CsCl$ (**3c**) (0.15 g, 68%). $B_{11}H_{11}ClCs_3$ (564.20): calcd. B 21.06, H 1.95, Cl 6.29, Cs 70.69; found: B 21.02, H 2.08, Cl 5.76, Cs 70.27.

**Procedure B:** Analogous to procedure A, but with an inverse order of reagent addition, the same mixed salt $Cs_2[B_{11}H_{11}]\cdot CsCl$ (**3c**) was obtained in 56% yield. $B_{11}H_{11}ClCs_3$ (564.20) calcd. B 21.06, H 1.95, Cl 6.29, Cs 70.69; found: B 21.55, H 2.04, Cl 5.65, Cs 69.21.

**Preparation of $Cs_2[B_{11}H_{11}]$ (3b):** The salt $Cs_2[B_{11}H_{11}]$ was obtained in the same manner, but using CsF in EtOH instead of CsCl in MeOH.

**Vibrational Spectra:** Raman spectra for the solid salts sealed in capillaries, and also for a saturated aqueous solution of the salt **3c**, were recorded in the region 30–3500 $cm^{-1}$ using LabRAM and U-1000 Jobin–Yvon laser Raman spectrometers. The spectra were excited by the 632.8 nm line of a He-Ne laser and the 514.5 nm line of an $Ar^+$ laser (Spectra Physics 2020). Depolarization ratios of the Raman lines in the spectrum of the aqueous solution of **3c** were estimated qualitatively. IR spectra in the region 150–3500 $cm^{-1}$ for the salts **3b** and **3c** pressed with polyethylene, and for their Nujol mulls and KBr pellets, were obtained using a M-82 Carl Zeiss spectrophotometer and a Nicolet Magna-750 FTIR spectrometer.

**Computational Details:** Geometry optimization and calculations of the vibrational-mode frequencies and eigenvectors for the isolated anion **3** were carried out at the DFT B3LYP/6-31++G(d,p) level, using the G94W program suite.[28] Topological analysis of the theoretical electron-density distribution (based on the results of the DFT calculation) was accomplished using the AIMpac program package.[29] Calculations for the rearrangement process were carried out at the B3LYP/6-31G* level using the Gaussian 98 and Gaussian 03 packages,[30,31] and gave a value of 9.3 kJ $mol^{-1}$, comparable to the result of 9.1 kJ $mol^{-1}$ reported from a higher-level B3LYP/6-31++G(d,p) calculation.[6]

## Acknowledgments

The Russian authors acknowledge partial financial support from the Russian Academy of Sciences in the framework of the program "Theoretical and experimental study of chemical bonding" (grant number 591-07), as well as from the Russian Foundation for Basic Research (project number 03-03-32651). The English authors thank the University of Leeds for facilities.

[1] a) R. E. Williams, *Inorg. Chem.* **1971**, *1*, 210–214; b) R. E. Williams, *Adv. Inorg. Chem. Radiochem.* **1976**, *18*, 67–142; c) R. E. Williams, *Chem. Rev.* **1992**, *92*, 177–208; d) R. E. Williams, J. W. Bausch, in: Yu. N. Bubnov (Ed.), *Boron Chemistry at the Beginning of the 21st Century,* Editorial URSS, Moscow, **2003**, pp. 3–16.
[2] E. I. Tolpin, W. N. Lipscomb, *J. Am. Chem. Soc.* **1973**, *95*, 2384–2386.
[3] a) R. J. Wiersema, M. F. Hawthorne, *Inorg. Chem.* **1973**, *12*, 785–788; b) E. L. Muetterties, E. L. Hoel, C. G. Salentine, M. F. Hawthorne, *Inorg. Chem.* **1975**, *14*, 950–951.
[4] F. W. E. Carrol, M. Green, F. G. A. Stone, A. J. Welch, *J. Chem. Soc. Dalton Trans.* **1975**, 2263–2270.
[5] a) M. P. Garcia, M. Green, F. G. A. Stone, R. G. Somerville, A. J. Welch, C. E. Briant, *J. Chem. Soc. Chem. Commun.* **1981**, 871–872; b) M. P. Garcia, M. Green, F. G. A. Stone, R. G. Somerville, A. J. Welch, C. E. Briant, D. N. Cox, D. M. P. Mingos, *J. Chem. Soc. Dalton Trans.* **1985**, 2343–2348.
[6] a) O. Volkov, K. Radacki, P. Paetzold, X. Zheng, *Z. Anorg. Allg. Chem.* **1999**, *625*, 1185–1191; b) O. Volkov, W. Dirk, U. Englert, P. Paetzold, *Z. Anorg. Allg. Chem.* **1999**, *625*, 1193–1201; c) O. Volkov, P. Paetzold, *J. Organomet. Chem.* **2003**, *680*, 301–311.
[7] a) V. E. Konoplev, *Reactions of carborane "polyhedral contraction" initiated by 16-electron complexes of Ru and Os,* Ph. D. Thesis, Institute of Organoelement Compounds of the Russian Academy of Sciences, Moscow **2004**; b) V. E. Konoplev, I. V. Pisareva, I. T. Chizhevsky *to be published*.
[8] E. G. Kononova, L. A. Leites, S. S. Bukalov, A. V. Zabula, I. V. Pisareva, V. E. Konoplev, I. T. Chizhevsky, *Chem. Phys. Lett.* **2004**, *390*, 279–284.
[9] E. G. Kononova, L. A. Leites, S. S. Bukalov, I. V. Pisareva, I. T. Chizhevsky, *J. Mol. Struct.* **2006**, *794*, 148–153.
[10] L. A. Leites, *Chem. Rev.* **1992**, *92*, 279–322.
[11] E. G. Kononova, S. S. Bukalov, L. A. Leites, K. A. Lyssenko, V. A. Ol'shevskaya, *Russ. Chem. Bull.* **2003**, *52*, 85–92.
[12] A. Salam, M. S. Deleuze, J.-P. Francois, *Chem. Phys.* **2003**, *286*, 45–61; A. Salam, M. S. Deleuze, J.-P. Francois, *Chem. Phys.* **2001**, *271*, 17–30.
[13] L. E. Vinogradova, L. A. Leites, S. S. Bukalov, A. I. Kovredov, L. I. Zakharkin, *Izv. Akad. Nauk SSSR, Ser. Khim. (Proc. USSR Acad. Sci.)* **1977**, 2337–2339 (in Russian).
[14] Z. Mingyu, Z. Jianwei, Yu. Weizhou, *J. Mol. Struct. (Theochem)* **1999**, *458*, 263–267.
[15] a) K. Wade, *Adv. Inorg. Chem. Radiochem.* **1976**, *18*, 1–66; b) M. A. Fox, K. Wade, in: Yu. N. Bubnov (Ed.), *Boron Chemistry at the Beginning of the 21st Century*, Editorial URSS, Moscow, **2003**, pp. 17–26.
[16] R. F. W. Bader, *Atoms in Molecules: a Quantum Theory*, Clarendon Press, Oxford, UK, **1990**, 438 pp.
[17] E. L. Muetterties, J. H. Balthis, Y. T. Chia, W. H. Knoth, H. C. Miller, *Inorg. Chem.* **1964**, *3*, 444–451.
[18] P. Brint, B. Sangchakr, P. W. Fowler, W. J. Weldon, *J. Chem. Soc. Dalton Trans.* **1989**, 2253–2260.
[19] L. A. Leites, S. S. Bukalov, A. P. Kurbakova, M. M. Kaganski, Yu. L. Gaft, N. T. Kuznetsov, I. A. Zakharova, *Spectrochim. Acta* **1982**, *38 A*, 1047–1056.
[20] L. A. Leites, A. P. Kurbakova, M. M. Kaganski, Yu. L. Gaft, I. A. Zakharova, N. T. Kuznetsov, *Izv. Akad. Nauk SSSR, Ser. Khim. (Proc. USSR Acad. Sci.)* **1983**, 2284–2292.
[21] E. H. Wong, L. Prasad, E. J. Gabe, M. G. Gatter, *Inorg. Chem.* **1983**, *22*, 1143–1146.
[22] J. Joseph, B. M. Gimarc, M. Zhao, *Polyhedron* **1993**, *12*, 2841–2848.

 © 2007 Wiley-VCH Verlag GmbH & Co. KGaA, Weinheim 

[23] P. v. R. Schleyer, K. Najafian, *Inorg. Chem.* **1998**, *37*, 3454–3470.
[24] J. D. Kennedy, in J. Casanova (Ed.), *The Borane-Carborane-Carbocation Continuum*, Wiley, New York, **1998**, pp. 85–116, and references therein.
[25] a) R. F. W. Bader, D. A. Legare, *Can. J. Chem.* **1992**, *70*, 657–676; b) T. A. Keith, R. F. W. Bader, Y. Aray, *Int. J. Quantum Chem.* **1996**, *57*, 183–198.
[26] a) M. Yu. Antipin, A. V. Polyakov, V. G. Tsirel'son, M. Kappkhan, V. V. Grushin, Yu. T. Struchkov, *Organomet. Chem. USSR* **1990**, *3*, 421–426; b) M. Antipin, R. Boese, D. Blaser, A. Maulitz, *J. Am. Chem. Soc.* **1997**, *119*, 326–333; c) K. A. Lyssenko, M. Yu. Antipin, V. N. Lebedev, *Inorg. Chem.* **1998**, *37*, 5834–5843.
[27] G. D. Friesen, J. L. Little, J. C. Huffman, L. J. Todd, *Inorg. Chem.* **1979**, *18*, 755.
[28] M. J. Frisch, G. W. Trucks, H. B. Schlegel, P. M. W. Gill, B. G. Johnson, M. A. Robb, J. R. Cheeseman, T. Keith, G. A. Petersson, J. A. Montgometry, K. Raghavachari, M. A. Al-Laham, V. G. Zakrzewski, J. V. Ortiz, J. B. Foresman, J. Cioslowski, B. B. Stefanov, A. Nanayakkara, M. Challacombe, C. Y. Peng, P. Y. Ayala, W. Chen, M. W. Wong, J. L. Andres, E. S. Replogle, R. Gomperts, R. L. Martin, D. J. Fox, J. S. Binkley, D. J. Defrees, J. Baker, J. P. Stewart, M. Head-Gordon, C. Gonzalez, J. A. Pople, *Gaussian 94W*, revision E.2, Gaussian, Inc., Pittsburgh, PA, **1995**.
[29] J. Cheeseman, T. A. Keith, R. W. F. Bader, *AIMpac Program Package*, McMaster University, Hamilton, Ontario, **1992**.
[30] M. J. Frisch, G. W. Trucks, H. B. Schlegel, G. E. Scuseria, M. A. Robb, J. R. Cheeseman, V. G. Zakrzewski, J. A. Montgomery, Jr., R. E. Stratmann, J. C. Burant, S. Dapprich, J. M. Millam, A. D. Daniels, K. N. Kudin, M. C. Strain, O. Farkas, J. Tomasi, V. Barone, M. Cossi, R. Cammi, B. Mennucci, C. Pomelli, C. Adamo, S. Clifford, J. Ochterski, G. A. Petersson, P. Y. Ayala, Q. Cui, K. Morokuma, D. K. Malick, A. D. Rabuck, K. Raghavachari, J. B. Foresman, J. Cioslowski, J. V. Ortiz, A. G. Baboul, B. B. Stefanov, G. Liu, A. Liashenko, P. Piskorz, I. Komaromi, R. Gomperts, R. L. Martin, D. J. Fox, T. Keith, M. A. Al-Laham, C. Y. Peng, A. Nanayakkara, C. Gonzalez, M. Challacombe, P. M. W. Gill, B. Johnson, W. Chen, M. W. Wong, J. L. Andres, C. Gonzalez, M. Head-Gordon, E. S. Replogle, J. A. Pople, *Gaussian 98*, revision A.7, Gaussian, Inc., Pittsburgh, PA, **1998**.
[31] M. J. Frisch, G. W. Trucks, H. B. Schlegel, G. E. Scuseria, M. A. Robb, J. R. Cheeseman, J. A. Montgomery, Jr., T. Vreven, H. N. Kudin, J. C. Burant, J. M. Millam, S. S. Iyengar, J. Tomasi, V. Barone, B. Mennucci, M. Cossi, G. Scalmani, N. Rega, G. A. Petersson, H. Nakatsuji, M. Hada, M. Ehara, K. Toyota, R. Fukuda, J. Hasegawa, M. Ishida, T. Nakajima, Y. Honda, O. Kitao, H. Nakai, M. Klene, X. Li, J. E. Knox, H. P. Hratchian, J. B. Cross, C. Adamo, J. Jaramillo, R. Gomperts, R. E. Stratmann, O. Yazyev, A. J. Austin, R. Cammi, C. Pomelli, J. W. Ochterski, P. Y. Ayala, K. Morokuma, G. A. Voth, P. Salvador, J. J. Dannenberg, V. G. Zakrzewski, S. Dapprich, A. D. Daniels, M. C. Strain, O. Farkas, D. K. Malick, A. D. Rabuck, K. Raghavachari, J. B. Foresman, J. V. Ortiz, Q. Cui, A. G. Baboul, S. Clifford, J. Cioslowski, B. B. Stefanov, G. Liu, A. Liashenko, P. Piskorz, I. Komaromi, R. L. Martin, D. J. Fox, T. Keith, M. A. Al-Laham, C. Y. Peng, A. Nanayakkara, M. Challacombe, P. M. W. Gill, B. Johnson, W. Chen, M. W. Wong, C. Gonzalez, J. A. Pople, *Gaussian 03*, revision B.05, Gaussian, Inc., Pittsburgh, PA, **2003**.

Received: April 26, 2007
Published Online: September 10, 2007

 © 2007 Wiley-VCH Verlag GmbH & Co. KGaA, Weinheim 

DOI: 10.1002/ejic.200700477

# Syntheses, Characterizations, and X-ray Single-Crystal Structures of 1,8-Bis(trimethylsilylamino)naphthalene Aluminum Hydride and the Methyl Derivative

**Zhi Yang,[a] Xiaoli Ma,[a] Herbert W. Roesky,*[a] Ying Yang,[b] Víctor Manuel Jiménez-Pérez,[a] Jörg Magull,[a] Arne Ringe,[a] and Peter G. Jones[c]**

*Dedicated to Professor K. Mach*

**Keywords:** Aluminum / Arene ligands / Structure elucidation

The reaction of 1,8-bis(trimethylsilylamino)naphthalene ($LH_2$) (**1**) with *n*BuLi yields the dilithium compound [1,8-$(Me_3SiN)_2C_{10}H_6$]$(Li)_2(thf)_3$ (**2**). Compound **1** reacts with $H_3Al{\cdot}NMe_3$ with elimination of hydrogen gas to produce [1,8-$(Me_3SiN)_2C_{10}H_6$]$AlH(NMe_3)$ (**3**), and the reaction of **2** with $MeAlCl_2$ leads to [1,8-$(Me_3SiN)_2C_{10}H_6$]Al(Me)thf (**4**). Compounds **3** and **4** are the first two aluminum mononuclear compounds to contain the 1,8-diaminonaphthalene ligand. These compounds were characterized by elemental analysis, NMR and IR spectroscopy, MS, and single-crystal X-ray structural analysis.

(© Wiley-VCH Verlag GmbH & Co. KGaA, 69451 Weinheim, Germany, 2007)

## Introduction

Aluminum hydrides and their alkyl derivatives are involved in many aluminum-containing reactions, and thus are extraordinarily important in aluminum chemistry. Aluminum hydrides are good reducing agents and are used in a wide range of inorganic and organic transformations.[1] In addition, they are excellent precursors in the synthesis of alumoxanes by controlled hydrolysis,[2] and they can be used in the preparation of carbaalane clusters in conjunction with acetylenes or substituted acetylenes[3,4] and for the generation of amidoalane clusters from organic nitriles.[5] Recent research in our group showed that they can be used as very efficient starting materials in the preparation of aluminum chalcogenides[6–10] and also in the preparation of aluminum-containing heterocycles[11] by the elimination of $H_2$ gas. Alkylaluminum compounds are important cocatalysts used in polymerization reactions for the production of polypropylene, medium-to-low pressure polyethylene, and polybutadiene. They can also be converted into aluminum halides or oxides. A series of aluminum oxides and hydroxides was synthesized by the hydrolysis of alkylaluminum compounds,[12] and a very important product is methylaluminum oxide (MAO). MAO is a highly active cocatalyst for group 4 metallocenes and catalyzes ethylene and propylene polymerization.[13,14]

A bulky organic ligand is usually employed to stabilize the aluminum center both electronically and sterically. The introduction of a bulky organic ligand at the Al center can efficiently reduce the condensation of the resulting products. In recent years, a number of aluminum compounds with monovalent bulky chelating ligands have been reported, although there are not many aluminum compounds known that are supported by bivalent bulky ligands. In 1998, a series of new bivalent bulky 1,8-diaminonaphthalene ligands was synthesized.[15–19] The interest in these ligands is currently growing as a result of their specific steric and electronic properties, and these properties can efficiently control the geometry at the metal center. The known complexes containing these ligands, or naphthalene-based substrates, include main group (Al, Ge, In, Li, Na, Mg, Si, Sn, Tl) and transition-metal (Ni, Ti, Zr, Zn) derivatives.[16,20–27] Previously, aluminum mononuclear complexes were unknown, but herein we report the synthesis and characterization of bulky 1,8-bis(trimethylsilylamino)naphthalene (L) aluminum monohydride and its aluminum monomethyl derivative.

## Results and Discussion

The reaction of 1,8-bis(trimethylsilylamino)naphthalene ($LH_2$) (**1**) with *n*BuLi leads to the starting material [1,8-

[a] Institut für Anorganische Chemie, Universität Göttingen, Tammannstrasse 4, 37077 Göttingen, Germany
Fax: +49-551-39-3373
E-mail: hroesky@gwdg.de
[b] College of Chemistry and Chemical Engineering, Central South University,
410083 Changsha, P. R. China
[c] Institut für Anorganische und Analytische Chemie der Technischen Universität Braunschweig,
Postfach 3329, 38023 Braunschweig, Germany

 © 2007 Wiley-VCH Verlag GmbH & Co. KGaA, Weinheim 

$(Me_3SiN)_2C_{10}H_6](Li)_2(thf)_3$ (**2**). Synthesis of [1,8-$(Me_3SiN)_2$-$C_{10}H_6$]AlH($NMe_3$) (**3**) was accomplished by the reaction of $LH_2$ (**1**) with $H_3Al{\cdot}NMe_3$ at 0 °C in high yield. The compound [1,8-$(Me_3SiN)_2C_{10}H_6$]Al(Me)thf (**4**) was prepared from the reaction of **2** in situ with $MeAlCl_2$ at –30 °C. Compounds **3** and **4** (Scheme 1) are both mononuclear aluminum compounds containing the 1,8-diaminonaphthalene ligand (L). Only one aluminum compound of the form $L(AlMe_2)_2$ is known to contain the 1,8-diaminonaphthalene ligand,[25] and it is a binuclear compound synthesized by the reaction of $LH_2$ (**1**) with $AlMe_3$. We found, whether in a ratio of 1:1 or 1:2, the reaction of compound **1** with $AlMe_3$ always leads to $L(AlMe_2)_2$. Mononuclear LAlMe compounds are unknown. This is explained by the fact that after the formation of the $LH(AlMe_2)$ intermediate, the second Me group at the same Al center is not reactive enough to interact with the other proton of the ligand to eliminate another molecule of methane. In the reaction of **1** with $H_3Al{\cdot}NMe_3$, only mononuclear LAlH($NMe_3$) (**3**) was obtained independently whether the reaction was conducted in the ratio of 1:1 or 1:2. This is due to the reactivity of the second hydride at the same Al center, which is high enough to interact with the other proton of the ligand to result in the elimination of $H_2$ gas. Consequently, the question as to whether it is possible to prepare the mononuclear methylaluminum compound of the general form LAlMe is raised. To prepare LAlMe, we used $LLi_2(thf)_3$ (**2**) and $MeAlCl_2$ as the starting materials. This reaction involved the elimination of two molecules of LiCl, and we successfully prepared the mononuclear methylaluminum compound LAl(Me)thf (**4**). The lithium salt **2** was prepared in situ at –30 °C, and the reaction with $MeAlCl_2$ was conducted also at –30 °C. Compounds **3** and **4** are soluble in common solvents such as toluene, dichloromethane, and tetrahydrofuran, and they can be kept in the glove box for several months without decomposition.

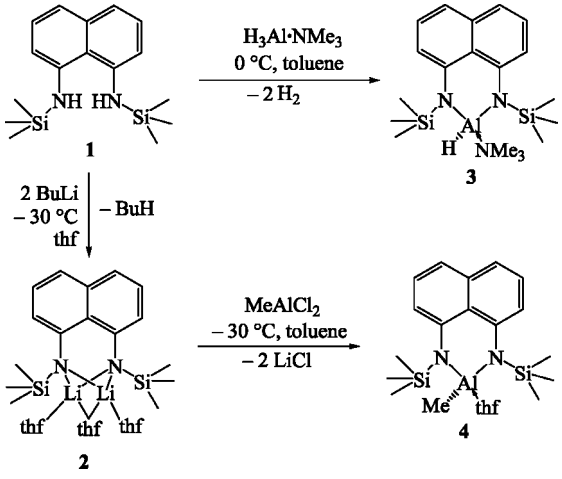


Scheme 1. Preparation of compounds **3** and **4**.

Compounds **3** and **4** were characterized by multinuclear NMR and IR (for **3**) spectroscopy, MS (EI), and elemental analysis. The presence of an Al–H bond in **3** is evident from the analysis of the IR spectrum. The broad IR band around 1869 $cm^{-1}$ was assigned to the Al–H stretching frequency, which compares well with the known value of 1860 $cm^{-1}$.[28] In the $^1H$ NMR spectra of compounds **3** and **4**, resonances in the ranges from $\delta$ = 6.6 to 7.2 ppm and $\delta$ = 0.3 to 0.1 ppm in the ratio of 6:18 are present, which were assigned to the $C_{10}H_6$ and $SiMe_3$ groups, respectively. They confirm the existence of the backbone of the 1,8-bis(trimethylsilylamino)naphthalene ligand. In the $^1H$ NMR spectrum of **3**, the resonance at $\delta$ = 2.66 ppm suggests the existence of the $NMe_3$ group. In the $^1H$ NMR spectrum of **4**, the resonances at $\delta$ = 3.79 and 1.57 ppm in a ratio of 1:1 were assigned to the thf molecule coordinated to the aluminum center, and the resonance at $\delta$ = –0.55 ppm indicates the existence of the Al–Me bond in the molecule. The $^{13}C$ NMR spectra of **3** and **4** for the arene part exhibit almost the same resonances for both compounds.

Compounds **3** (Figure 1) and **4** (Figure 2) crystallize in the orthorhombic system *Ama*2 and in the monoclinic system $P2_1/n$, respectively. In both structures, the aluminum centers have a tetrahedral environment. The tetrahedral aluminum center in **3** indicates the existence of an H atom. Compounds **3** and **4** have almost the same Al–N bond lengths (av. 1.828 Å for **3** and 1.830 Å for **4**), whereas the Al–N bonds in the binuclear compound $L(AlMe)_2$ are much longer (av. 2.00 Å). The Al centers in $L(AlMe_2)_2$ are much more crowded than those in mononuclear **3** and **4**.[25] Thus, the two Al centers in $L(AlMe_2)_2$ are in close proximity, which results in the longer bond lengths of the Al–N bonds in $L(AlMe_2)_2$ in comparison to those in **3** and **4**. In the binuclear structure of $L(AlMe_2)_2$, it is obvious that the two Me groups at the same aluminum atom have different chemical environments. One Me group is near the naphthalene ligand and the other Me group is positioned away from the arene ring ($\delta$ = –0.11 and –1.14 ppm).[25] There is only one Me group at the aluminum atom in mononuclear **4**, which results in only one chemical shift. The Al→N2 bond

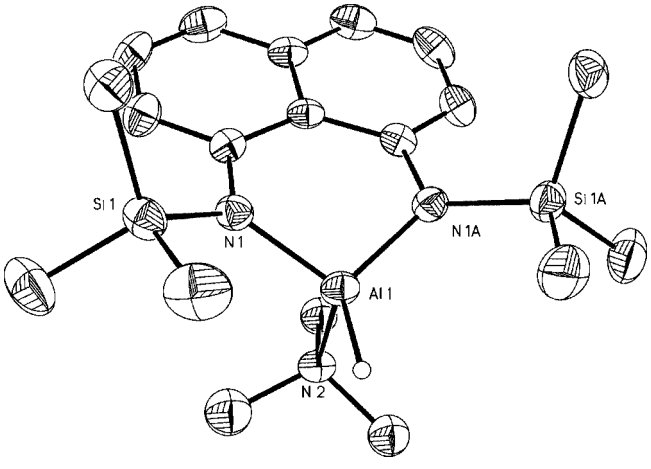


Figure 1. Molecular structure of **3**. Thermal ellipsoids are drawn at the 50% probability level and the hydrogen atoms are omitted for clarity, while the hydrogen atom on the aluminum atom was set. Selected bond lengths [Å] and angles [°]: Al1–N1 1.828(2), Al1–N1A 1.828(2), Al1–N2 2.021(3), N1–Si1 1.744(2); N1–Al1–N1A 102.95(13), N1–Al1–N2 106.85(8), N1A–Al1–N2 106.86(8).

 © 2007 Wiley-VCH Verlag GmbH & Co. KGaA, Weinheim 

length (2.021 Å) in **3** and the Al→O bond length (1.920 Å) in **4** are longer than the normal σ bonds of compounds containing Al–N and Al–O moieties.

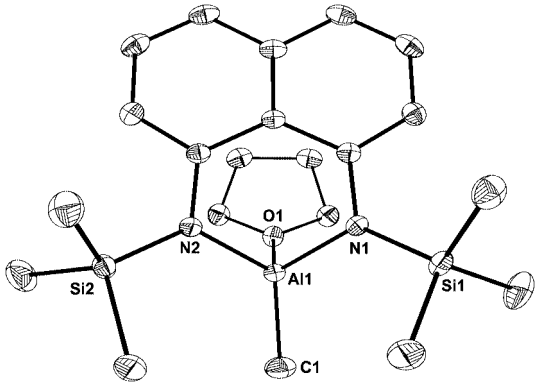


Figure 2. Molecular structure of **4**. Thermal ellipsoids are drawn at the 50% probability level and the hydrogen atoms are omitted for clarity. Selected bond lengths [Å] and angles [°]: Al1–N1 1.8298(13), Al1–N2 1.8311(12), Al1–O1 1.9202(11), Al1–C1 1.9482(16); N1–Al1–N2 100.82(6), N1–Al1–O1 101.88(5), N2–Al1–O1 100.33(5), N1–Al1–C1 121.37(7), N2–Al1–C1 125.87(7), O1–Al1–C1 102.09(7).

## Conclusions

Herein, we described the syntheses, characterizations, and X-ray structures of aluminum hydride and methyl compounds supported by the 1,8-bis(trimethylsilylamino)naphthalene ligand. The resulting compounds are interesting precursors for the preparation of new aluminum compounds.

## Experimental Section

**[1,8-(Me$_3$SiN)$_2$C$_{10}$H$_6$]AlH(NMe$_3$) (3):** To a solution of [1,8-(Me$_3$SiNH)$_2$C$_{10}$H$_6$] (3.02 g, 10 mmol) in toluene (40 mL) at 0 °C was added dropwise H$_3$Al·NMe$_3$ (1 M in toluene, 10 mL, 10 mmol). The resulting solution was stirred and warmed to room temperature. After additional stirring for 2 h, the solution was evaporated to dryness in vacuo, and the residue was washed with cold *n*-hexane (2 × 5 mL) to yield crystalline **3** (3.29 g, 85%). M.p. 213 °C. $^1$H NMR (500.13 MHz, CDCl$_3$, 298 K): $\delta$ = 0.30 (s, 18 H, Si-*Me*), 2.66 (s, 9 H, N*Me*$_3$), 6.70 (m, 2 H, C$_{10}$*H*$_6$), 7.25–7.45 (m, 4 H, C$_{10}$*H*$_6$) ppm. $^{13}$C NMR (125.77 MHz, CDCl$_3$, 298 K): $\delta$ = 2.91 (Si-*Me*), 47.60 (N*Me*$_3$), 116.19 (*C*H, *C*$_{10}$H$_6$), 118.54 (*C*H, *C*$_{10}$H$_6$), 125.32 (*C*, *C*$_{10}$H$_6$), 137.98 (*C*H, *C*$_{10}$H$_6$), 144.75 (*C*, *C*$_{10}$H$_6$), 150.64 (*C*N, C$_{10}$H$_6$) ppm. $^{29}$Si NMR (99.36 MHz, CDCl$_3$, 298 K): $\delta$ = –0.55 ppm. IR (KBr, plate): $\tilde{\nu}$ = 1869 (m, AlH) cm$^{-1}$. MS (EI): *m*/*z* (%) = 387 (16) [M]$^+$, 328 (100) [M – NMe$_3$]$^+$. C$_{19}$H$_{34}$AlN$_3$Si$_2$ (387.64): calcd. C 58.87, H 8.84, N 10.84; found C 57.76, H 8.62, N 10.44.

**[1,8-(Me$_3$SiN)$_2$C$_{10}$H$_6$]Al(Me)thf (4):** To a solution of [1,8-(Me$_3$SiNH)$_2$C$_{10}$H$_6$] (3.02 g, 10 mmol) in thf (40 mL) at –30 °C was added dropwise *n*BuLi (2.5 M, 8 mL, 20 mmol). The mixture was stirred and warmed to room temperature. After additional stirring for 1 h, all volatiles were removed in vacuo and toluene (40 mL) was added to the solid residue. The solution was cooled to –30 °C and MeAlCl$_2$ (1 M, 10 mL, 10 mmol) was added. The resulting solution was warmed to room temperature and stirred for 2 h. After workup, the insoluble LiCl was removed by filtration, and the residue was dried in vacuo and washed with cold *n*-hexane (2 × 5 mL) to yield solid **4** (2.94 g, 71%). M.p. 154–155 °C. $^1$H NMR (500.13 MHz, CDCl$_3$, 298 K): $\delta$ = –0.55 (s, 3 H, Al-*Me*), 0.23 (s, 18 H, Si-*Me*), 1.57 [m, 4 H, O(CH$_2$C*H*$_2$)$_2$], 3.79 [m, 4 H, O(C*H*$_2$CH$_2$)$_2$], 6.63 (m, 2 H, C$_{10}$*H*$_6$), 7.01–7.05 (m, 4 H, C$_{10}$*H*$_6$) ppm. $^{13}$C NMR (125.77 MHz, CDCl$_3$, 298 K): $\delta$= 2.70 (Si-*Me*), 24.93 [O(CH$_2$*C*H$_2$)$_2$], 69.78 [O(*C*H$_2$CH$_2$)$_2$], 116.68 (*C*H, *C*$_{10}$H$_6$), 118.21 (*C*H, *C*$_{10}$H$_6$), 125.17 (*C*, *C*$_{10}$H$_6$), 137.66 (*C*H, *C*$_{10}$H$_6$), 144.15 (*C*, *C*$_{10}$H$_6$), 151.01 (*C*N, C$_{10}$H$_6$) ppm. $^{29}$Si NMR (99.36 MHz, CDCl$_3$, 298 K): $\delta$ = –1.12 ppm. MS (EI): *m*/*z* (%) = 342 (100) [M – thf]$^+$. C$_{21}$H$_{35}$AlN$_2$OSi$_2$ (414.67): calcd. C 60.83, H 8.51, N 6.76; found C 58.94, H 7.99, N 6.93. The slight difference in the found and calculated analytical data is due to the extreme moisture sensitivity of the product.

**X-ray Structure Determination of 3 and 4:** Suitable crystals of **3** and **4** were mounted on a glass fiber and coated with paraffin oil. Data for **3** was obtained with a STOE-IPDS II image-plate diffractometer with graphite-monochromated Mo-$K_\alpha$ radiation ($\lambda$ = 0.71073 Å). Data for **4** was collected with a Bruker SMART 1000 CCD diffractometer. The structures were solved by direct methods by using SHELXS-97[29] and refined against $F^2$ on all data by using full-matrix least-squares with SHELXL-97.[30] All non-hydrogen atoms were refined anisotropically. Hydrogen atoms connected to carbon atoms were included at geometrically calculated positions and refined by using a riding model (Table 1).

CCDC-645712 (**3**) and -644929 (**4**) contain the supplementary crystallographic data for this paper. These data can be obtained free

Table 1. X-ray crystallographic data for **3** and **4**.

| | **3** | **4** |
|---|---|---|
| Empirical formula | C$_{19}$H$_{33}$AlN$_3$Si$_2$ | C$_{21}$H$_{35}$AlN$_2$OSi$_2$ |
| Formula weight | 386.64 | 414.67 |
| Temperature [K] | 133(2) | 133(2) |
| Wavelength [Å] | 0.71073 | 0.71073 |
| Crystal system | orthorhombic | monoclinic |
| Space group | *Ama*2 | *P*2$_1$/*n* |
| *a* [Å] | 18.5497(19) | 7.2999(8) |
| *b* [Å] | 12.2030(7) | 16.7801(18) |
| *c* [Å] | 10.1856(7) | 19.187(2) |
| $\alpha$ [°] | 90 | 90 |
| $\beta$ [°] | 90 | 94.074(4) |
| $\gamma$ [°] | 90 | 90 |
| *V* [Å$^3$] | 2305.6(3) | 2344.3(4) |
| *Z* | 4 | 4 |
| $D_{calcd.}$ [Mg m$^{-3}$] | 1.114 | 1.175 |
| Absorption coefficient [mm$^{-1}$] | 0.199 | 0.202 |
| *F*(000) | 836 | 896 |
| $\theta$ range for data collection [°] | 2.20 to 24.80 | 1.61 to 30.50 |
| Index ranges | $-21 \le h \le 21$ | $-10 \le h \le 10$ |
| | $-14 \le k \le 14$ | $-23 \le k \le 23$ |
| | $-12 \le l \le 12$ | $-27 \le l \le 27$ |
| Reflections collected | 16394 | 49652 |
| $R_{int}$ | 0.0837 | 0.0424 |
| Data/restraints/parameters | 2050/1/127 | 7143/0/251 |
| Goodness-of-fit on $F^2$ | 0.890 | 1.037 |
| Final $R_{int}$ [$I > 2\sigma(I)$] | $R_1$ = 0.0327 | $R_1$ = 0.0392 |
| | $wR_2$ = 0.0623 | $wR_2$ = 0.0939 |
| $R_{int}$ (all data) | $R_1$ = 0.0471 | $R_1$ = 0.0646 |
| | $wR_2$ = 0.0654 | $wR_2$ = 0.1087 |
| Largest difference peak and hole [e Å$^{-3}$] | 0.182 and –0.204 | 0.456 and –0.299 |

 © 2007 Wiley-VCH Verlag GmbH & Co. KGaA, Weinheim 

of charge from The Cambridge Crystallographic Data Centre via www.ccdc.cam.ac.uk/data_request/cif.

## Acknowledgments

This work was supported by the Deutsche Forschungsgemeinschaft, the Fonds der Chemischen Industrie, and the Göttinger Akademie der Wissenschaften. V. M. J.-P. thanks the German Academic Exchange Service for a postdoctoral DAAD fellowship.

[1] K. B. Starowieyski in *Chemistry of Aluminum, Gallium, Indium and Thallium* (Ed.: A. J. Downs), Chapman & Hall, London, UK, **1993**.
[2] Y. Peng, G. Bai, H. Fan, D. Vidovic, H. W. Roesky, J. Magull, *Inorg. Chem.* **2004**, *43*, 1217–1219.
[3] A. Stasch, M. Ferbinteanu, J. Prust, W. Zheng, F. Cimpoesu, H. W. Roesky, J. Magull, H.-G. Schmidt, M. Noltemeyer, *J. Am. Chem. Soc.* **2002**, *124*, 5441–5448.
[4] S. S. Kumar, J. Rong, S. Singh, H. W. Roesky, D. Vidovic, J. Magull, D. Neculai, *Organometallics* **2004**, *23*, 3496–3500.
[5] N. D. Reddy, S. S. Kumar, H. W. Roesky, D. Vidovic, J. Magull, M. Noltemeyer, H.-G. Schmidt, *Eur. J. Inorg. Chem.* **2003**, 442–448.
[6] Z. Yang, X. Ma, R. B. Oswald, H. W. Roesky, C. M. Cui, H.-G. Schmidt, M. Noltemeyer, *Angew. Chem.* **2006**, *118*, 2335–2338; *Angew. Chem. Int. Ed.* **2006**, *45*, 2277–2280.
[7] C. Cui, H. W. Roesky, H. Hao, H.-G. Schmidt, M. Noltemeyer, *Angew. Chem.* **2000**, *112*, 1885–1887; *Angew. Chem. Int. Ed.* **2000**, *39*, 1815–1817.
[8] V. Jancik, Y. Peng, H. W. Roesky, J. Li, D. Neculai, A. M. Neculai, R. Herbst-Irmer, *J. Am. Chem. Soc.* **2003**, *125*, 1452–1453.
[9] Z. Yang, X. Ma, V. Jancik, Z. Zhang, H. W. Roesky, J. Magull, M. Noltemeyer, H.-G. Schmidt, R. Cea-Olivares, R. A. Toscano, *Inorg. Chem.* **2006**, *45*, 3312–3315.
[10] Z. Yang, X. Ma, H. W. Roesky, Y. Yang, J. Magull, A. Ringe, *Inorg. Chem.* **2007**, *46*, 7903–7906.
[11] Z. Yang, X. Ma, R. B. Oswald, H. W. Roesky, M. Noltemeyer, *J. Am. Chem. Soc.* **2006**, *128*, 12406–12407.
[12] For example, see: a) A. Storr, K. Jones, A. W. Laubengayer, *J. Am. Chem. Soc.* **1968**, *90*, 3173–3177; b) M. Bolesławski, S. Pasynkiewicz, A. Minorska, W. Hryniów, *J. Organomet. Chem.* **1974**, *65*, 165–167.
[13] H. Sinn, W. Kaminsky, H. J. Vollmer, R. Woldt, *Angew. Chem.* **1980**, *92*, 396–402; *Angew. Chem. Int. Ed. Engl.* **1980**, *19*, 390–392.
[14] H. Sinn, W. Kaminsky, *Adv. Organomet. Chem.* **1980**, *18*, 99–149.
[15] S. Danièle, C. Drost, B. Gehrhus, S. M. Hawkins, P. B. Hitchcock, M. F. Lappert, P. G. Merle, S. G. Bott, *J. Chem. Soc. Dalton Trans.* **2001**, 3179–3188.
[16] a) C. H. Galka, D. J. M. Trösch, I. Rüdenauer, L. H. Gade, I. Scowen, M. McPartlin, *Inorg. Chem.* **2000**, *39*, 4615–4620; b) D. R. Armstrong, D. Barr, W. Clegg, S. R. Drake, R. J. Singer, R. Snaith, D. Stalke, D. S. Wright, *Angew. Chem.* **1991**, *103*, 1702–1704; *Angew. Chem. Int. Ed. Engl.* **1991**, *30*, 1707–1709.
[17] K. W. Hellmann, C. Galka, L. H. Gade, A. Steiner, D. S. Wright, T. Kottke, D. Stalke, *Chem. Commun.* **1998**, 549–551.
[18] J. L. Smith, J. L. Beck, W. J. A. VandenHeuvel, *Org. Mass. Spectrom.* **1971**, *5*, 473–480.
[19] L. H. Gade, C. H. Galka, K. W. Hellmann, R. M. Williams, L. D. Cola, I. J. Scowen, M. McPartlin, *Eur. J. Org. Chem.* **2002**, *8*, 3732–3746.
[20] A. G. Avent, C. Drost, B. Gehrhus, P. B. Hitchcock, M. F. Lappert, *Z. Anorg. Allg. Chem.* **2004**, *630*, 2090–2096.
[21] K. W. Hellmann, C. H. Galka, I. Rüdenauer, L. H. Gade, I. J. Scowen, M. McPartlin, *Angew. Chem.* **1998**, *110*, 2053–2057; *Angew. Chem. Int. Ed.* **1998**, *37*, 1948–1952.
[22] P. Bazinet, G. P. A. Yap, G. A. DiLabio, D. S. Richeson, *Inorg. Chem.* **2005**, *44*, 4616–4621.
[23] C. Drost, P. B. Hitchcock, M. F. Lappert, *Angew. Chem.* **1999**, *111*, 1185–1187; *Angew. Chem. Int. Ed.* **1999**, *38*, 1113–1116.
[24] P. Bazinet, G. P. A. Yap, D. S. Richeson, *J. Am. Chem. Soc.* **2001**, *123*, 11162–11167.
[25] C. H. Lee, Y.-H. La, S. J. Park, J. W. Park, *Organometallics* **1998**, *17*, 3648–3655.
[26] K. Nomura, N. Naga, K. Takaoki, *Macromolecules* **1998**, *31*, 8009–8015.
[27] a) K. Nomura, N. Naga, K. Takaoki, A. Imai, *J. Mol. Catal. A* **1998**, *130*, 209–213; b) W. Clegg, S. H. Dale, E. Hevia, L. M. Hogg, G. W. Honeyman, R. E. Mulvey, C. T. O'Hara, *Angew. Chem.* **2006**, *118*, 6698–6700; *Angew. Chem. Int. Ed.* **2006**, *45*, 6548–6550.
[28] J. L. Atwood, S. M. Lawrence, C. L. Raston, *J. Chem. Soc. Chem. Commun.* **1994**, 73–74.
[29] *SHELXS-90: Program for Structure Solution:* G. M. Sheldrick, *Acta Crystallogr., Sect. A* **1990**, *46*, 467–473.
[30] G. M. Sheldrick, *SHELXL-97: Program for Crystal Structure Refinement*, University of Göttingen, Germany, **1997**.

Received: May 2, 2007
Published Online: September 10, 2007

 © 2007 Wiley-VCH Verlag GmbH & Co. KGaA, Weinheim 

DOI: 10.1002/ejic.200700568

# Expanding the Range of "Daniphos"-Type P∩P- and P∩N-Ligands: Synthesis and Structural Characterisation of New [(η⁶-arene)Cr(CO)₃] Complexes

**Elisabetta Alberico,*[a] Wolfgang Braun,[b] Beatrice Calmuschi-Cula,[b] Ulli Englert,[b] Albrecht Salzer,*[b] and Daniel Totev[b]**

**Keywords:** N,P ligands / Phosphane ligands / Asymmetric catalysis / Arene complexes / Chromium

New P∩P- and P∩N-ligands have been synthesised whose core structure is an [(η⁶-arene)Cr(CO)₃] unit. These new ligands, which extend the range of "Daniphos" ligands, are endowed with central and planar chirality and have been prepared through a stereoselective synthetic strategy from optically pure benzylamines bearing a second substituent on the arene other than the benzyldimethylamino group. Because the two faces of unsymmetrically 1,2- and 1,3-disubstituted benzylamine are diastereotopic, which means that diastereomeric complexes arise upon coordination of the Cr(CO)₃ fragment to either of these two faces, the synthetic plan has been adjusted by exploiting the trimethylsilyl group as a temporary steric modulator in order to access both complexes with high diastereoselectivity.
(© Wiley-VCH Verlag GmbH & Co. KGaA, 69451 Weinheim, Germany, 2007)

## Introduction

"Daniphos" ligands are a class of ligands suitable for application in catalysis whose core structure is an [(η⁶-arene)Cr(CO)₃] unit. A stereoselective synthetic strategy developed recently in our laboratories has provided these ligands with a modular and tunable character (Scheme 1).[1] Daniphos ligands are usually prepared from commercially available optically pure benzylamines and are characterised by the presence of a stereogenic plane and a stereocentre. Planar chirality is introduced by means of a diastereoselective directed orthometallation (DOM) assisted by the benzylic amino group and subsequent electrophilic substitution on the arene ring. Central chirality is preserved by the stereoselective replacement of the dimethylamino group for a chloride by treatment with chloroethyl chloroformate (ACE-Cl) and subsequent stereoselective nucleophilic substitution of the chloro substituent for a different nucleophile. A library of ligands, which comprises mono- and bidentate P∩N and P∩P ligands, has been prepared following this approach.[1–3] The steric and/or electronic properties of these ligands can be easily tuned by varying the $R^1$/$R^2$ substituents on the donor atoms D or by reducing their conformational flexibility by tethering the donor atoms to an annelated framework[3e] (Scheme 2). These ligands have been tested in a number of enantioselective homogeneous catalytic processes such as hydrogenation,[3] hydroamination,[3a] allylic sulfonation,[3a] hydrovinylation,[1b] transfer hydrogenation[4] and, more recently, nucleophilic asymmetric ring opening (ARO) of oxabenzonorbornadienes.[5]

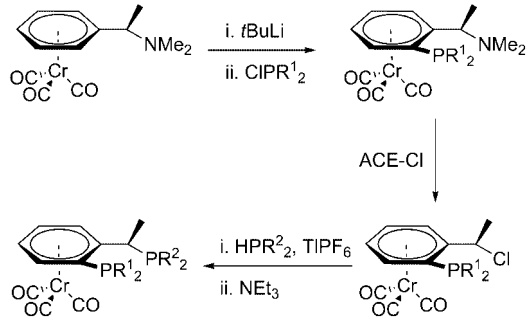


Scheme 1. General synthetic strategy for the preparation of "Daniphos"-like diphosphanes. ACE-Cl = 1-chloroethyl chloroformate.

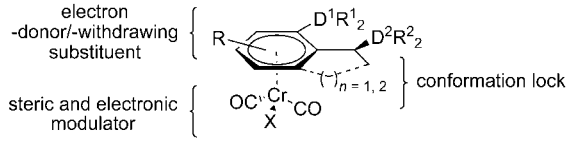


Scheme 2. Accessibility of a modular ligand architecture based on [(η⁶-arene)Cr(CO)₃] complexes.

As shown in Scheme 2, a further possibility for altering the basic structure of Daniphos ligands is to introduce a substituent R onto the arene ring. Such substituents might be important in modulating the electronic properties of the donor atoms D and, depending on their location on the arene, also their steric properties. Such substituents can be introduced at the stage of complexation of the arene to the

[a] Istituto di Chimica Biomolecolare,
CNR, trav. La Crucca 3, Li Punti, 07040 Sassari, Italy,
Fax: +39-079-3961036
E-mail: elisabetta.alberico@icb.cnr.it
[b] Institut für Anorganische Chemie der RWTH,
Landoltweg 1, 52074 Aachen, Germany,
Fax: +49-241-8092288
E-mail: albrecht.salzer@ac.rwth-aachen.de

 © 2007 Wiley-VCH Verlag GmbH & Co. KGaA, Weinheim 

$Cr(CO)_3$ moiety as a range of chiral amines related to 1-phenylethylamine that already bear the R substituent are commercially available. In this paper we detail the synthesis of these complexes and explore the influence of the R group on the outcome of some steps of our established synthetic strategy. The X-ray structures of some intermediates and some of the target ligands are also provided, which, in cases of uncertainty, serve to define the stereochemical outcome of a reaction.

## Results and Discussion

The amines used to prepare the "Daniphos" ligands reported in this paper are shown in Figure 1. The corresponding primary benzylamines were reductively methylated with formaldehyde and formic acid following the Eschweiler–Clarke procedure.[6] Protection of the amino group prior to complexation to the $Cr(CO)_3$ moiety is necessary in order to reduce its coordinating ability towards chromium as this might lead to incomplete complex formation. The diphosphanes P∩P were prepared from the *para*-substituted benzylamines (*S*)-**1**, (*S*)-**2**, (*R*)-**3** and (*R*)-**6** while the bidentate P∩N ligands were prepared from *ortho*- and *meta*-methoxy-substituted benzylamines (*S*)-**4** and (*S*)-**5**.

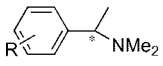


| | |
|---|---|
| R = 4-Me | (*S*)-**1** |
| R = 4-*t*Bu | (*S*)-**2** |
| R = 4-Cl | (*R*)-**3** |
| R = 2-OMe | (*S*)-**4** |
| R = 3-OMe | (*S*)-**5** |
| R = 4-OMe | (*R*)-**6** |

Figure 1. Phenylethylamines which have been complexed to the $Cr(CO)_3$ moiety to synthesise the "Daniphos" ligands reported in this paper.

### Preparation of Daniphos Diphosphanes P∩P

The coordination of amines (*S*)-**1**, (*S*)-**2**, (*R*)-**3** and (*R*)-**6** was accomplished by thermolysis with $Cr(CO)_6$ (Scheme 3). The reactions weren carried out under the conditions reported by Mahaffy and Pauson.[7] The protected benzylamine and $Cr(CO)_6$ were heated (temperature of the oil bath: 140 °C) in an 8:1 mixture of di-*n*-butyl ether and tetrahydrofuran until the evolution of CO ceased or onset of decomposition was observed. The best yield was obtained with the *para*-*tert*-butyl-substituted benzylamine (*S*)-**2**. It is known that π-electron-withdrawing groups (e.g. CHO or COOH) slow down complexation and are best protected before complexation, while electron-donating arene substituents accelerate complexation.[8a,8b] Complexation of (*R*)-**3** to the $Cr(CO)_3$ moiety gave a modest 43% yield of the expected complex. In this case, decomposition during the reaction, as indicated by formation of a grey-green precipitate, was difficult to avoid. This appears to be progressive and the reaction had to be stopped. The poor yield might also be due to reductive dehalogenation.[9]

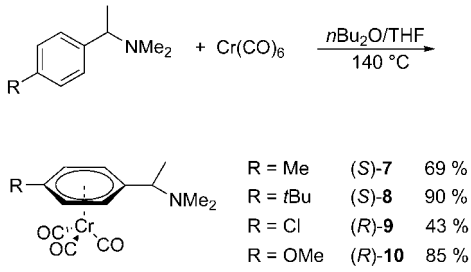


| | | |
|---|---|---|
| R = Me | (*S*)-**7** | 69 % |
| R = *t*Bu | (*S*)-**8** | 90 % |
| R = Cl | (*R*)-**9** | 43 % |
| R = OMe | (*R*)-**10** | 85 % |

Scheme 3. Yields obtained in the complexation of protected *para*-substituted benzylamines with $Cr(CO)_6$.

DOM of complexes (*S*)-**7**, (*S*)-**8**, (*R*)-**9** and (*R*)-**10** was carried out according to a general procedure consisting of treatment with *t*BuLi in diethyl ether at –78 °C for 1.5 h, subsequent quenching with $ClPPh_2$, and warming to room temperature overnight. The relative amounts of products formed were calculated based on integration of the corresponding $^{31}P$ NMR signals in the spectra of crude reaction mixtures in all cases. The diastereomeric excesses reported in the schemes were calculated in a similar manner. Products of very high purity were obtained by flash chromatography.

Coordination of the $Cr(CO)_3$ group to the arene enhances the kinetic acidity of the ring C–H bonds due to the strong electron-withdrawing character of the $Cr(CO)_3$ moiety,[8c] therefore direct lithiation of the arene ring occurs more easily than that of the parent chromium-free arene. Because of the presence of a heteroatom-containing functionality, lithiation can be extremely selective towards the *ortho* position due to specific coordination of the base through its lithium counterion.[10]

The two hydrogen atoms *ortho* to the ethylamino group in complexes (*S*)-**7**, (*S*)-**8**, (*R*)-**9** and (*R*)-**10** are diastereotopic because of the α-stereogenic centre, which means that preferential replacement of either of them gives rise to unequal amounts of two molecules endowed with the same central chirality but opposite planar chirality.[11] When the related complex [{(*R*)-*N*,*N*-dimethyl-1-phenylethylamine}$Cr(CO)_3$] is treated with *tert*-butyllithium in diethyl ether at –78 °C, the ortholithiated species derived from preferential abstraction of the $H_S$ proton is formed with 96% diastereoselectivity (Figure 2).[12] The origin of this high diastereoselectivity stems from a preferential average solution-state conformation in which both the α-methyl and α-dimethylamino groups lie above the plane of the arene ring, opposite the bulky $Cr(CO)_3$ unit (Figure 2, a). This "sensible" spatial arrangement has been inferred by deuterium-labelling and difference NOE $^1H$ NMR experiments. According to these data, it can be expected that the *ortho*-directing dimethylamino group preferentially directs a precoordinated lithium base towards the closest $H_S$ proton (Figure 2, b). Removal of the $H_R$ proton would force the benzylic methyl group below the plane of the arene, thereby causing an unfavourable steric interaction with the tricarbonylchromium unit. The absolute configuration of the α-stereogenic centre dictates the relative planar chirality, thus

 © 2007 Wiley-VCH Verlag GmbH & Co. KGaA, Weinheim 

indicating that the sense of asymmetric induction is determined in the deprotonation step. The greater discrimination between the two diastereotopic hydrogens achieved with a sterically more demanding base such as *t*BuLi is consistent with this assumption. In fact, although high *ortho* diastereoselectivity has been demonstrated with both *n*BuLi and *t*BuLi, only the latter allows for complete transfer of side-chain chirality on to the arene ring.

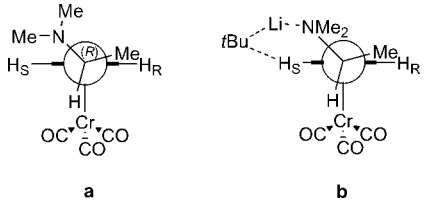


Figure 2. (a) Average solution-state conformation of the benzylic side chain of [{(*R*)-*N*,*N*-dimethyl-1-phenylethylamine}$Cr(CO)_3$] as inferred from NOEDS. (b) Newman projection of the possible directed orthometallation intermediate along the $C_\alpha$–$C_{ipso}$ bond.

Uemura and Hayashi prepared the first ever reported P,N ligand of the "Daniphos" type by diastereoselective lithiation of [{(*R*)-*N*,*N*-dimethyl-1-phenylethylamine}$Cr(CO)_3$] and subsequent reaction with chlorodiphenylphosphane.[13]

DOM of (*S*)-**7** and (*S*)-**8** proceeds with high diastereoselectivity to give the expected products (*S*,*R*p)-**11** and (*S*,*R*p)-**12**, respectively (Scheme 4). No competitive α-proton abstraction was observed in the *ortho* functionalisation of (*S*)-**7** either from the dimethylaminoethyl group or from

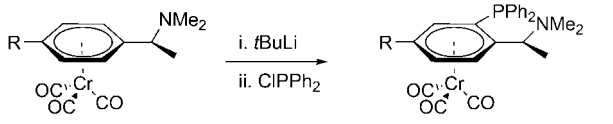


R = Me (*S*)-**7** (*S*,*R*p)-**11** *de* = 92% (90%)

R = *t*Bu (*S*)-**8** (*S*,*R*p)-**12** *de* > 99% (78%)

Scheme 4. Products obtained in the *ortho*-functionalisation of (*S*)-**7** and (*S*)-**8**.

the *para*-substituted methyl group − α-proton abstraction from [($\eta^6$-arene)$Cr(CO)_3$] complexes is in fact the thermodynamically favoured process and the high yield of ring-substituted products clearly demonstrates that proton abstraction by *tert*-butyllithium is kinetically controlled.[14]

*ortho*-Functionalisation of [{$\eta^6$-(*R*)-1-(4-methoxyphenyl)-*N*,*N*-dimethylethylamine}$Cr(CO)_3$] [(*R*)-**10**] according to the procedure described above affords a mixture of products due to the presence of two coordinating substituents (Scheme 5).

A very useful study has demonstrated that the substituent effects on regioselectivity in the deprotonation of free arenes are distinctly different from those found for [$Cr(CO)_3$]-complexed arenes.[15] A series of *para*-disubstituted arenes were complexed and deprotonated, and the ratio of the two possible products in each case allowed a reactivity series to be generated. The following ratio of *ortho*-directing abilities of functional groups was deduced:

$F > CONHR > NHCOR > CH_2NR_2 \approx OMe >> CH_2OMe$

According to this study, when lithiation is performed at –78 °C with *s*BuLi for 1.5 h and is followed by electrophilic quenching with $Me_3SiCl$, the relative kinetic acidity of a ring proton takes precedence over simple base coordination by a heteroatom in the substituent group as the principal factor in determining the site of metallation in disubstituted arene complexes. The chromium complex of *p*-methoxy-*N*,*N*-dimethylbenzylamine provides a comparison of the directing effect of the OMe and $CH_2NMe_2$ groups. In this case, the two effects, namely OMe-induced labilisation of the *ortho* proton by electron withdrawal and $CH_2NMe_2$ coordination of the incoming base, are almost exactly balanced. In line with this result, D*O*M of (*R*)-**10** produces similar amounts of products in which lithiation has occurred *ortho* to the benzylic amino group and *ortho* to the methoxy group.

The products reported in Scheme 5 were separated by means of flash chromatography, although (*R*)-**14M** (the more abundant isomer) and (*R*)-**14m** (the less abundant iso-

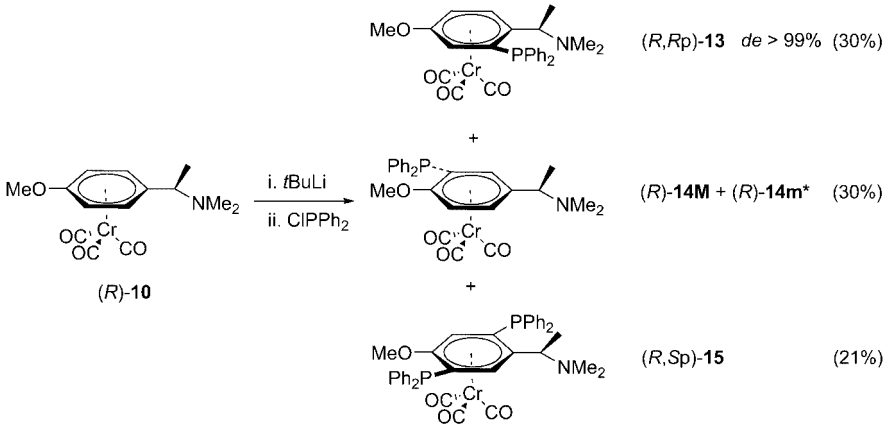


Scheme 5. Products obtained in the *ortho*-functionalisation of (*R*)-**10**. Yields of isolated products are reported in parentheses. * This notation indicates the two regioisomeric products bearing a diphenylphosphanyl group *ortho* to the OMe substituent; the absolute configurations, however, could not be assigned.

 © 2007 Wiley-VCH Verlag GmbH & Co. KGaA, Weinheim 

Table 1. Products obtained in the *ortho*-functionalisation of (*R*)-**10** along with diagnostic chemical shifts.

| Complex | Relative amounts[a] [%] | Yield[b] [%] | $\delta_{^1H}$ [ppm] (mult) C*H*(Me)NMe$_2$ | $\delta_{^{31}P}$ [ppm] PPh$_2$ *ortho* to CH(Me)NMe$_2$ | OMe |
|---|---|---|---|---|---|
| (*R*)-**10** | – | – | 2.96 (q) | – | – |
| (*R*,*R*p)-**13** | 32 | 30 | 4.41 (m) | –14.22 | – |
| (*R*)-**14M** | 26 | 30[c] | 2.69 (q) | – | –18.57 |
| (*R*)-**14m** | 10 | | 2.86 (q) | – | –17.92 |
| (*R*,*S*p)-**15** | 32 | 30 | 4.22 (m) | –14.23 | –17.69 |

[a] Ratio of products based on peak integration in the $^{31}P$ NMR spectrum of the crude reaction mixture. [b] Yield of product isolated after flash chromatography. [c] The two regioisomeric products could not be separated by flash chromatography and were isolated as a single fraction.

mer), which are the two regioisomeric products bearing a diphenylphosphanyl group *ortho* to the -OMe substituent, could not be separated and were collected as a single fraction.

The identity of the products was assigned based on the mass, $^1H$ and $^{31}P$ NMR, and 2D NMR spectra (Table 1). The location of the diphenylphosphanyl group *ortho* to the dimethylethylamino group was easily inferred from the $^1H$ NMR spectrum due to the phosphorus-hydrogen coupling, which further splits the signal of the α-hydrogen compared to the corresponding signal in complex (*R*)-**10**. Furthermore, this resonance is shifted nearly 2 ppm to lower field due to the proximity of the phenyl groups and their "ring current" effect. This is observed both in the spectrum of the desired (*R*,*R*p)-**13** [its diastereomeric product (*R*,*S*p)-**13** could not be detected in the $^1H$ NMR spectrum of the crude reaction mixture] and in the spectrum of disubstituted (*R*,*S*p)-**15**. The chemical shift of the α-hydrogen signal is nearly unchanged and no H-P coupling is detected in the spectrum of (*R*)-**14M** or (*R*)-**14m**, which were identified as the species in which lithiation has occurred *ortho* to the OMe group. The two regioisomers are formed in a 72:28 ratio, thereby suggesting a possible influence of the remote stereogenic centre; the absolute planar chirality was not assigned.

Formation of complex (*R*,*S*p)-**15** might proceed via a dianion stabilized by the strongly electron-withdrawing Cr(CO)$_3$ moiety, which could mean that the mono-lithiated arene ring is sufficiently acidic to allow a second deprotonation or the second deprotonation is faster than the first one.[16] Unfortunately, to the best of our knowledge, there is no reliable structural and spectroscopic information on lithiated [(η$^6$-arene)Cr(CO)$_3$] complexes which would make it possible to determine whether the electronic effect of Li as a substituent does or does not deactivate the aromatic ring towards further H-abstraction. The existence of an intermediate polycarbanion has been postulated recently in a detailed investigation of multiple substitution of [(η$^6$-arene)Cr(CO)$_3$] complexes.[17] The treatment of representative complexes such as [{η$^6$-1-(*tert*-butyl-sulfonyl)-benzene}Cr(CO)$_3$], [(η$^6$-anisole)Cr(CO)$_3$] and [(η$^6$-*N*,*N*-dimethylbenzylamine)Cr(CO)$_3$] with three equivalents of 2,2,6,6-tetramethylpiperidyllithium (LiTMP), followed by electrophilic quenching with Me$_3$SiCl, provided a series of di- and trisilylated complexes. Deuteration studies using lithium diisopropylamide (LDA) as the base and deuteroacetic acid as the electrophile led to the observation of a trideuterated species presumably derived from a trianionic species formed during the reaction. Alternatively, complex (*R*,*S*p)-**15** might arise from successive deprotonation/trapping/deprotonation processes enabled by the unreacted *t*BuLi. This would imply that electrophilic trapping of the base itself is rather slower than deprotonation of the arene complex, although the isolation of *t*BuPPh$_2$ as a by-product in some cases suggests that this might not be the case.

The stereochemistry of complex (*R*,*S*p)-**15** was tentatively assigned based on the most stable charge arrangement of the intermediate dianion considering that both the dimethylethylamino group and the methoxy group favour the formation of the corresponding *ortho* anion and that the dimethylethylamino group stereoselectively promotes abstraction of the pro-$S_P$ *ortho* H atom.

Lithiation of [{η$^6$-(*R*)-1-(4-chlorophenyl)-*N*,*N*-dimethylethylamine}Cr(CO)$_3$] [(*R*)-**9**] with *t*BuLi followed by treatment of the lithiated species with ClPPh$_2$ afforded the expected *ortho*-functionalised diastereomeric complexes (*R*,*S*p)-**16** and (*R*,*R*p)-**16** and the product of metal/halogen exchange [(*R*)-**17**; Scheme 6]. According to the $^{31}P$ NMR spectrum of the crude reaction mixture, the relative ratio of (*R*,*S*p)-**16** and (*R*,*R*p)-**16** is 94:6, which corresponds to an 88% diastereoselectivity of the ortholithiation reaction (Table 2). Pure (*R*,*S*p)-**16** was obtained by flash chromatography. A second fraction contained (*R*,*R*p)-**16** as the main product. Attempts to further purify this complex failed, however, and its structure was assigned based on its $^1H$ NMR spectrum, where the diagnostic H-P coupling and shift of the -C*H*(Me)NMe$_2$ signal to lower field are observed. Although directed orthometallation is predominant, competitive chloride/lithium exchange leads to the formation of complex (*R*)-**17**. Interestingly, no lithiation *ortho* to the chloro substituent was detected.

Because lithium amides enable metallation to be achieved in preference to metal/halogen exchange,[18a] lithiation of (*R*)-**9** was repeated with LDA under otherwise identical conditions. However, only the two diastereoisomers corresponding to lithiation *ortho* to the chloro substituent were detected in a nearly 1:1 ratio (Scheme 6). The steric bulk of the base most likely prevents coordination by the ethyldimethylamino group and the electron-withdrawing effect of the chloro substituent prevails in dictating the regiochemis-

 © 2007 Wiley-VCH Verlag GmbH & Co. KGaA, Weinheim 

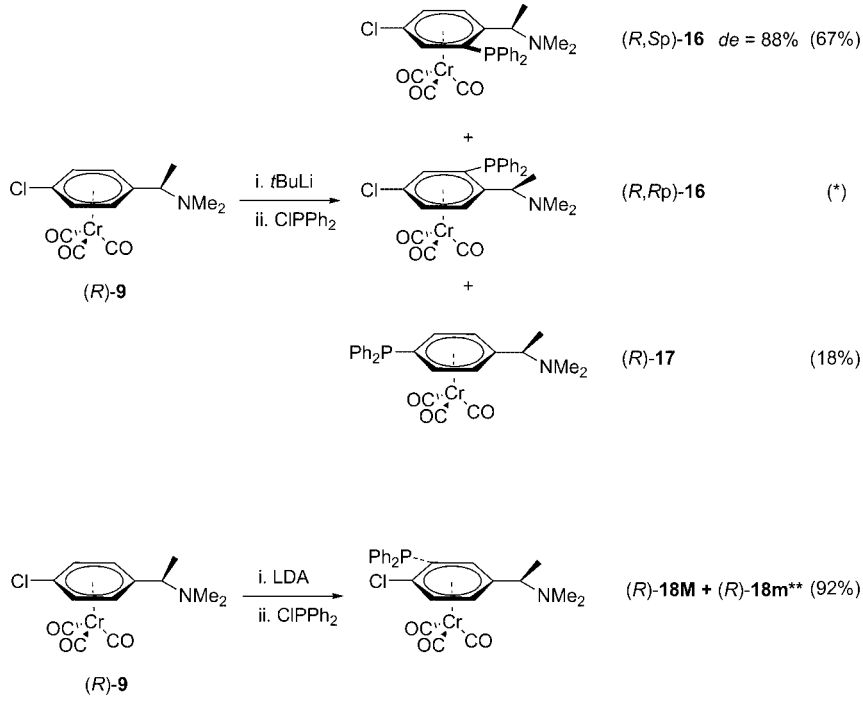


Scheme 6. Products obtained in the *ortho*-functionalisation of (*R*)-**9**. Yields of isolated products are reported in parentheses. * See Table 2. ** This notation indicates the two regioisomeric products bearing a diphenylphosphanyl group *ortho* to the Cl substituent whose absolute configuration could not be assigned.

Table 2. Products obtained in the *ortho*-functionalisation of (*R*)-**9** along with diagnostic chemical shifts.

| Complex | Rel. amounts[a] [%] | Yield[b] [%] | $\delta_{1H}$ [ppm] (mult.) C*H*(Me)NMe$_2$ | $\delta_{31P}$ [ppm] |
|---|---|---|---|---|
| (*R*)-**9** | – | – | 2.88 (q) | |
| (*R*,*S*p)-**16** | 77 | 67 | 4.39 (m) | –14.41 |
| (*R*,*R*p)-**16** | 5 | [c] | 3.57 (m) | –17.53 |
| (*R*)-**17** | 18 | 18 | 3.25 (q) | –7.83 |
| (*R*)-**18M** | 54 | 92[d] | 2.64 (q) | –12.06 |
| (*R*)-**18m** | 46 | | 2.75 (q) | –11.83 |

[a] Relative amounts of products based on peak integration in the $^{31}$P NMR spectrum of the crude reaction mixture. [b] Yield of product isolated after flash chromatography. [c] The collected fraction was not clean and contained some (*R*,*S*p)-**16** and (*R*)-**17**. [d] The two diastereomeric products (*R*)-**18M** and (*R*)-**18m** could not be separated by flash chromatography and were isolated as a single fraction (see text).

try of deprotonation.[18b] These complexes could not be separated by flash chromatography and the regiochemistry of lithiation was assigned based on the $^1$H NMR spectrum of the mixture of the two diastereoisomers. The two compounds, the absolute planar chirality of which could not be defined, are labelled as the major [(*R*)-**18M**] and minor [(*R*)-**18m**] diastereoisomers in Table 2.

After the first phosphorus donor has been introduced into the *ortho* position, a second one has to be appropriately placed in the benzylic position for subsequent metal chelation. This was achieved in two steps, both of which are highly stereoconservative (Scheme 7). The first step involves transformation of the phosphanylamino complex into a chlorobenzyl derivative by treatment of the former with an excess of 1-chloroethyl chloroformate (ACE-Cl). This procedure, which has been developed in our laboratory,[1a] relies on the ability of chloroformates to promote the mild debenzylation of tertiary amines.[19] Replacement of the dimethylamino group by chloride takes place with retention of configuration and no evidence of epimerisation was observed. All the desired α-chloro derivatives were obtained in good yields after purification by flash chromatography except the *para*-chloro one [(*R*,*S*p)-**22**], which readily decomposes while adsorbed on silica gel. The reported yield of (*R*,*S*p)-**22** therefore refers to the crude product after the removal of excess ACE-Cl and carbamate by-product.

The new $C_1$-symmetric diphosphane ligands were finally prepared by treatment of the corresponding benzyl chloride complexes with a slight excess of a secondary phosphane (HPR′$_2$) in acetone at room temperature in the presence of $TlPF_6$, which acts as a chloride scavenger by precipitation of highly insoluble TlCl. The $^{31}$P NMR spectra of all ligands display two doublets − one for each non-equivalent phosphorus atom − whose splitting is due to coupling to the other phosphorus atom in the molecule (Table 3). Large low-field shifts are observed upon changing the substituent on the α-phosphorus atom from phenyl to cyclohexyl and, to a larger extent, to *tert*-butyl. This downfield shift with increasing steric bulk at phosphorus can be explained by a concomitant change in the hybridisation at phosphorus.[20] However, within the same set of diphosphanes having the

 © 2007 Wiley-VCH Verlag GmbH & Co. KGaA, Weinheim 

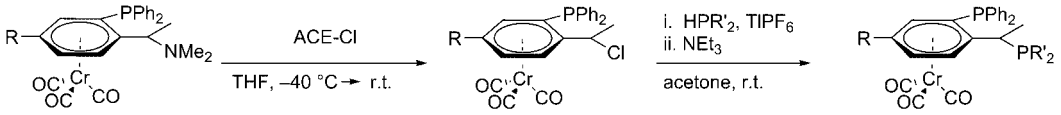


| | | | | | | | | |
|---|---|---|---|---|---|---|---|---|
| R = Me | (*S*,*R*p)-**11** | R = Me | (*S*,*R*p)-**19** | 86% | R = Me | R' = Ph | (*S*,*R*p)-**23a** | 64% |
| | | | | | | R' = Cy | (*S*,*R*p)-**23b** | 63% |
| | | | | | | R' = *t*Bu | (*S*,*R*p)-**23c** | 62% |
| R = *t*Bu | (*S*,*R*p)-**12** | R = *t*Bu | (*S*,*R*p)-**20** | 80% | R = *t*Bu | R' = Cy | (*S*,*R*p)-**24** | 61% |
| R = OMe | (*R*,*R*p)-**13** | R = OMe | (*R*,*R*p)-**21** | 85% | R = OMe | R' = Ph | (*R*,*R*p)-**25a** | 88% |
| | | | | | | R' = Cy | (*R*,*R*p)-**25b** | 77% |
| | | | | | | R' = *t*Bu | (*R*,*R*p)-**25c** | 78% |
| R = Cl | (*R*,*S*p)-**16** | R = Cl | (*R*,*S*p)-**22** | 90%* | R = Cl | R' = Ph | (*R*,*S*p)-**26a** | 28% |
| | | | | | | R' = Cy | (*R*,*S*p)-**26b** | 36% |
| | | | | | | R' = *t*Bu | (*R*,*S*p)-**26c** | 31% |

Scheme 7. Yields of isolated products (* yield of crude product) obtained from the nucleophilic replacement of the dimethylamino group by chloride and of diphosphanes prepared by replacement of benzyl chloride with a secondary phosphane $HPR'_2$. Both reactions take place with retention of configuration.

same substituents on the phosphorus donors, replacing a hydrogen on the arene directly complexed to chromium with either a methoxy, methyl, *tert*-butyl or chloro substituent does not bring about any meaningful change in the properties of the phosphorus donors, as measured by the corresponding chemical shifts. This means that the influence of the $Cr(CO)_3$ moiety on the electron richness of the arene, either as an aryl substituent on the phosphorus directly attached to the arene or a benzyl substituent on the α-phosphorus, is too strong and levels out any electronic contribution due to substituents on the arene.

Table 3. $^{31}P$ NMR spectroscopic data for the diphosphanes reported in this paper.

| Ligand | R | R′ | $\delta_{^{31}P}$ [ppm][a] *o*-$PPh_2$ | $\delta_{^{31}P}$ [ppm] α-PR′ | $J_{P,P}$ [Hz] |
|---|---|---|---|---|---|
| (*R*,*S*p)-**27a**[b] | H | Ph | –18.74 | 10.12 | 26.5 |
| (*S*,*R*p)-**23a** | Me | | –17.56 | 8.47 | 18.3 |
| (*R*,*R*p)-**25a** | OMe | | –17.99 | 5.02 | 11.0 |
| (*R*,*S*p)-**26a** | Cl | | –18.93 | 7.33 | 18.3 |
| (*R*,*S*p)-**27b**[b] | H | Cy | –19.95 | 16.66 | 46.7 |
| (*S*,*R*p)-**23b** | Me | | –18.71 | 15.85 | 38.3 |
| (*S*,*R*p)-**24** | *t*Bu | | –20.83 | 15.73 | 46.7 |
| (*R*,*R*p)-**25b** | OMe | | –17.48 | 15.49 | 26.0 |
| (*R*,*S*p)-**26b** | Cl | | –20.17 | 15.20 | 39.3 |
| (*R*,*S*p)-**27c**[b] | H | *t*Bu | –20.19 | 50.49 | 68.0 |
| (*S*,*R*p)-**23c** | Me | | –19.79 | 49.33 | 61.7 |
| (*R*,*R*p)-**25c** | OMe | | –18.58 | 48.07 | 54.3 |
| (*R*,*S*p)-**26c** | Cl | | –21.06 | 48.78 | 63.2 |

[a] NMR spectra recorded in $C_6D_6$. [b] These data, which are provided for comparison, have been taken from ref.[3a].

The diphosphanes are characterised by large four-bond phosphorus-phosphorus coupling constants whose values increase from 11–26 Hz in $PPh_2/PPh_2$ diphosphanes to 54–68 Hz in $PPh_2/PtBu_2$ ones. A similar trend has been reported for the analogous ferrocene-based ligands.[21] The two phosphorus donors are bound to an allylic fragment (P–$C_o$=$C_{ipso}$–$C_\alpha$–P) and π-systems usually lead to unexpectedly large long-range couplings.[22] The large value of the $^4J_{P,P}$ coupling might stem from "through-space" nuclear spin-spin coupling made possible by partial overlap of the two phosphorus lone pairs.[23a] The steric crowding provided by the substituents on phosphorus locks the molecule in a preferred time-average conformation in solution which, by keeping the substituents on the *ortho*- and α-donors far apart, brings the lone pairs into close proximity. The X-ray structure of ligand (*S*,*R*p)-**23b** supports this hypothesis (Figure 3).[24a] The larger values observed for the derivatives bearing bulky cyclohexyl and *tert*-butyl groups compared to those which only possess phenyl substituents might reflect the further restricted conformational freedom caused by the former substituents, although formal hybridisation of the coupled nuclei and the electronegativity of their substituents also play a role.[22,23b]

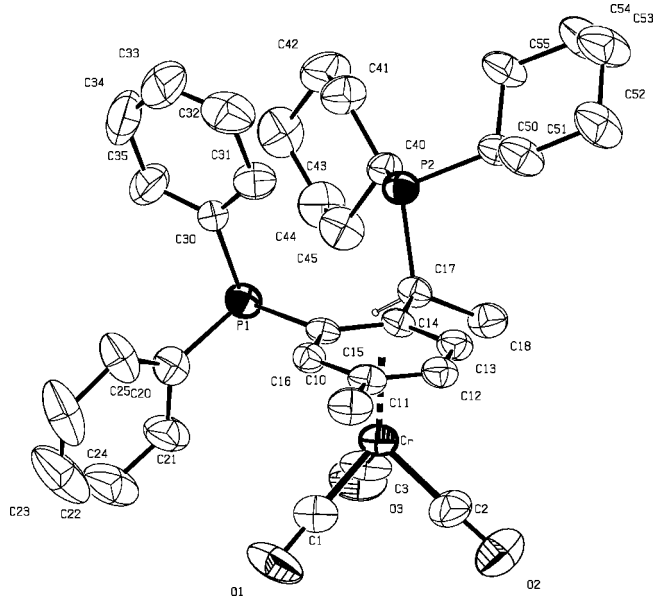


Figure 3. Displacement ellipsoids plot (PLATON) of (*S*,*R*p)-**23b**. Ellipsoids are shown at the 30% probability level. The H-atom attached to the stereogenic centre is shown with arbitrary radius; other H-atoms have been omitted for clarity.

 © 2007 Wiley-VCH Verlag GmbH & Co. KGaA, Weinheim 

The diphosphanes were tested in a variety of hydrogenations in comparison with the complexes without R substituents. Some of the results of these studies have already been published elsewhere.[3c] In most reactions there was a general trend in that the more electron-rich *para*-substituted ligands gave better *ee* values in enantioselective hydrogenations.

## Synthesis of Daniphos N∩P Ligands

The two faces of unsymmetrically 1,2- and 1,3-disubstituted benzylamine (*S*)-**4** and (*S*)-**5**, respectively, are diastereotopic, which means that diastereomeric complexes arise upon coordination of the $Cr(CO)_3$ fragment to either of these two faces.[25]

When complexation of (*S*)-**4** is carried out under harsh conditions [$Cr(CO)_6$, $nBu_2O$/thf, 150 °C] the isomer (*S*,*R*p)-**28** is preferentially formed with a diastereoselectivity of 50% (Scheme 8). An excellent diastereoselectivity in favour of the other diastereoisomer (*S*,*S*p)-**28** is achieved when complexation is carried out using Kündig's reagent [(naphthalene)$Cr(CO)_3$]. The latter is a good starting material for the mild synthesis of other [(arene)$Cr(CO)_3$] compounds by $Cr(CO)_3$ fragment transfer.[26] The absolute configuration of complex (*S*,*S*p)-**28** was confirmed by X-ray crystallographic analysis (Figure 4).

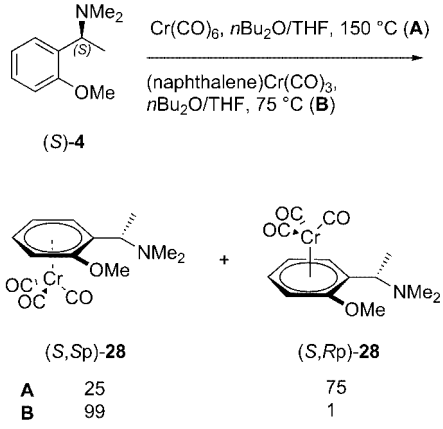


Scheme 8. Relative amounts of diastereomeric complexes obtained in the complexation of (*S*)-**4** under thermodynamic (A) and kinetic (B) conditions.

These results can be explained on the basis of the preferred average conformation adopted by (*S*)-**4** in solution at room temperature (Figure 5a), which was inferred by difference NOE/$^1$H NMR experiments. Thus, a much greater NOE enhancement of the α-$CH_3$ signal is observed compared to the α-H signal upon irradiation of the *ortho*-hydrogen, thus suggesting that, in order to minimize non-bonding interactions between the α-substituents and the *ortho* OMe group, the dimethylamino group is preferentially located below the pro-*R*p face of the arene. Under thermodynamic conditions, the $Cr(CO)_3$ fragment coordinates to the less crowded pro-$S_P$ face of the arene; under milder conditions, it is delivered to the pro-*R*p face due to temporary coordination by the amino group.

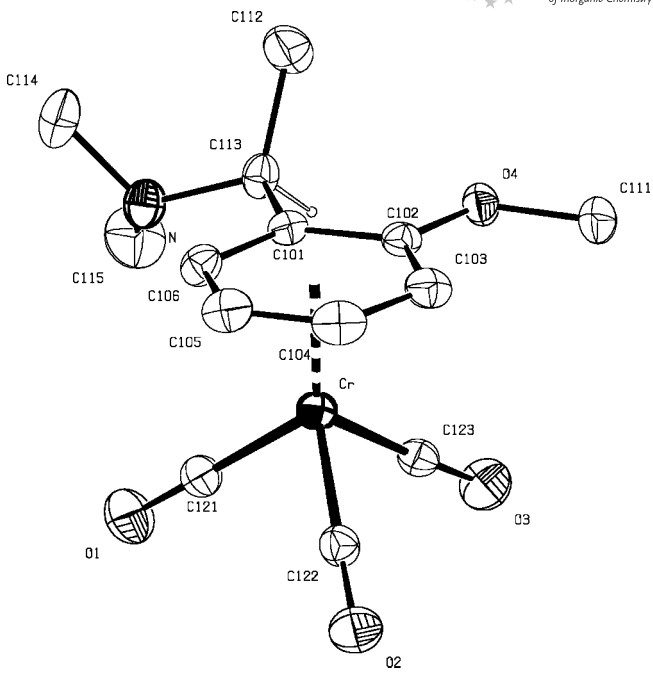


Figure 4. Displacement ellipsoids plot (PLATON) of (*S*,*S*p)-**28**. Ellipsoids are shown at the 30% probability level. The H-atom attached to the stereogenic centre is shown with arbitrary radius; other H-atoms have been omitted for clarity.

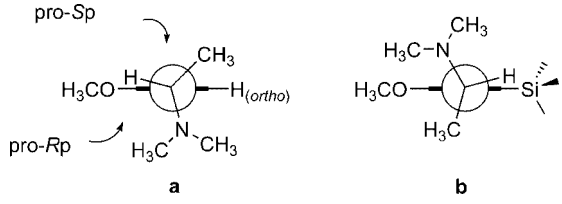


Figure 5. (a) Preferred average conformation adopted by (*S*)-**4** in solution at room temperature as inferred by difference NOE/$^1$H NMR experiments. (b) Preferred conformation in the presence of a bulky $–SiMe_3$ group in the *ortho* position.

Because flash chromatography and fractional crystallisation failed to provide the (*S*,*R*p)-**28** isomer in acceptable yield and purity, an alternative synthetic strategy was devised in order to obtain it as a single diastereoisomer. This strategy is based on the direct complexation of a benzylamine derivative in which a sterically bulky and easily removable trimethylsilyl group has been temporarily introduced at the *ortho* position of the 1-*N*,*N*-dimethylaminoethyl group in (*S*)-**4**.[27] The presence of this group should restrict rotation of the benzylic group at high temperature and favour a conformation which, while limiting interaction of the α-Me with the $SiMe_3$ group, preferentially confines the dimethylamino group to the "upper" face, thus enhancing the diastereoselectivity of the complexation (Figure 5b). However, treatment of (*S*)-**4** with *t*BuLi at –50 °C followed by quenching with $ClSiMe_3$ afforded benzylamine (*S*)-**29** in which lithiation has taken place at the most acidic site of the molecule *ortho* to the methoxy group, instead.[10b,28]

 © 2007 Wiley-VCH Verlag GmbH & Co. KGaA, Weinheim 

As shown in Scheme 9, the presence of an $SiMe_3$ group improves the diastereoselectivity of the complexation which, however, is still not satisfactory in the (*S*,*R*p)-**30** isomer, the absolute configuration of which was unambiguously assigned based on an X-ray crystallographic analysis (Figure 6).

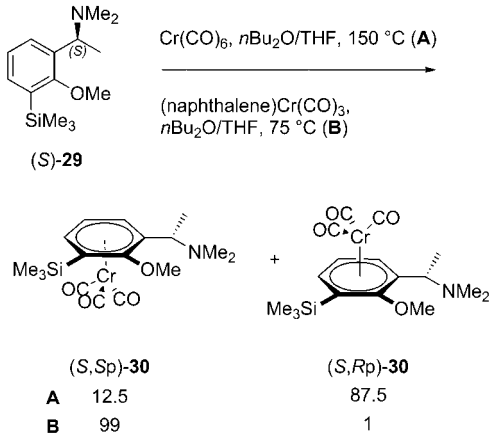


Scheme 9. Relative amounts of diastereomeric complexes obtained in the complexation of (*S*)-**29** under thermodynamic (A) and kinetic (B) conditions.

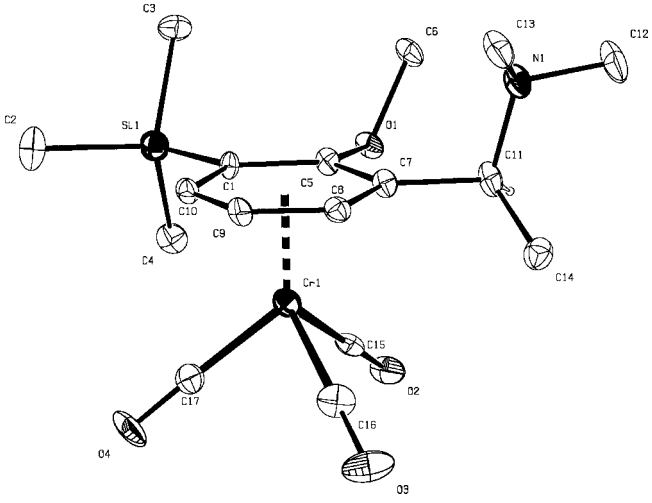


Figure 6. Displacement ellipsoids plot (PLATON) of one independent molecule of (*S*,*R*p)-**30**. Ellipsoids are shown at the 30% probability level. The H-atom attached to the stereogenic centre is shown with arbitrary radius; other H-atoms have been omitted for clarity.

Complexation of (*S*)-**31**, in which a second $SiMe_3$ group has been introduced *ortho* to the benzylamino group by lithiation and subsequent electrophilic quenching of (*S*)-**29** with $ClSiMe_3$, turned out to be highly selective for the desired isomer (*S*,*R*p)-**32** (Scheme 10).[24b] Notably, the (*S*,*R*p) isomer is formed preferentially even under the rigorous conditions of the thermal complexation due to hampered rotation of the amino group around the benzylic bond. The $SiMe_3$ groups are easily removed by treatment with $Bu_4NF$, thereby opening a stereoselective route to (*S*,*R*p)-**28**.

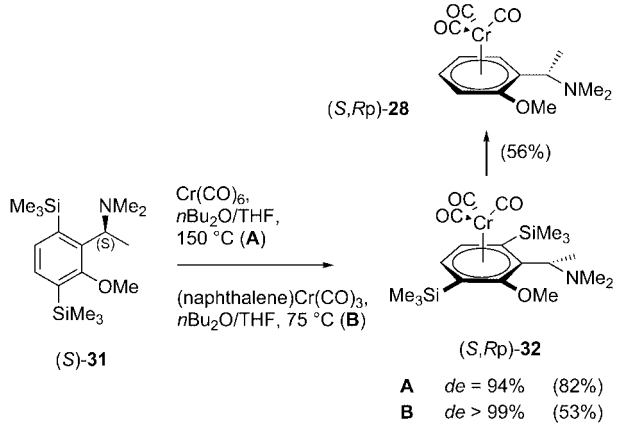


Scheme 10. Stereoselective route to (*S*,*R*p)-**28**.

Complexation of the *meta*-substituted benzylamine (*S*)-**5** to the $Cr(CO)_3$ moiety gives rise to equal amounts of the two possible diastereomers whatever the method of complexation. The same approach used for (*S*)-**4** was therefore applied to (*S*)-**5** by introduction of an $SiMe_3$ group as steric modulator. According to a previous report, metallation of the related compound *m*-methoxy-*N*,*N*-dimethylbenzylamine occurs exclusively at the position mutually *ortho* to both the methoxy and the amine side chain.[27] This was explained by assuming that the combined *ortho*-directing effects of both coordinating substituents and inductive electron withdrawal by the methoxy group serve to stabilize metallation at the position mutually *ortho* to these two substituents. In the case of (*S*)-**5**, optimisation of the metallation conditions was carried out using $ClPPh_2$ as electrophile since this compound allows an easy monitoring of the reaction course by $^{31}P$ NMR spectroscopy (Scheme 11). Table 4 summarises the relative amounts of products formed when lithiation was carried out using different RLi reagents under different reaction conditions.

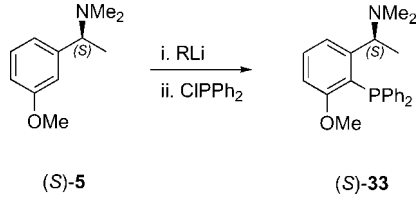


Scheme 11. Lithiation and subsequent electrophilic quenching of (*S*)-**5**.

Treatment of (*S*)-**5** with *t*BuLi at –78 °C for 4 h in $Et_2O$ and subsequent quenching of the Li salt formed with $ClPPh_2$ did not provide the expected product (*S*)-**33** (Table 4, entry 5) – $tBuPPh_2$ and unreacted (*S*)-**5** were isolated instead. The bulkiness of the $tBu^-$ anion might hamper its access to the *ortho* position between the two coordinating groups in (*S*)-**5**. However, the use of *n*BuLi both at –78 °C and –50 °C (Table 4, entries 1 and 2, respectively) was also unsuccessful. Formation of (*S*)-**33** was observed when either *s*BuLi or *t*BuLi were used at –50 °C (Table 4, entries 3 and 6, respectively). A further temperature increase up to room temperature favoured formation of a side

 © 2007 Wiley-VCH Verlag GmbH & Co. KGaA, Weinheim 

Table 4. Relative amounts of products formed in the lithiation of (*S*)-**5** and subsequent quenching with $ClPPh_2$.

| Entry | RLi | *T* [°C] | Deprotonation time [h] | Products[a] (relative amounts) | | |
|---|---|---|---|---|---|---|
| | | | | $RPPh_2$ | (*S*)-**33** | other product |
| 1 | *n*BuLi | –78 | 4 | 1 | n.d.[b] | n.d. |
| 2 | | –50 | 4 | 10 | n.d. | 1 |
| 3 | *s*BuLi | –50 | 4 | 5 | 1 | 0.5 |
| 4 | | room temp. | 4 | n.d. | 1 | 3.5 |
| 5 | ***t*BuLi** | –78 | 4 | 1 | n.d. | n.d. |
| 6 | | –50 | 4 | 3 | 3 | 1 |
| 7[c] | | **–50** | **24** | n.d. | 1 | n.d. |
| 8 | | room temp. | 4 | n.d. | 1 | 1 |

[a] The ratio of the three products was calculated based on integration of the areas of the corresponding $^{31}P$ NMR signals of the crude reaction mixture: (*S*)-**33**: $\delta_{31P}$ = –24 ppm; *n*BuPPh$_2$: $\delta_{31P}$ = –17.8 ppm; *s*BuPPh$_2$: $\delta_{31P}$ = –0.8 ppm; *t*BuPPh$_2$: $\delta_{31P}$ = 16.8 ppm; other unidentified product: $\delta_{31P}$ = 115 ppm. [b] n.d. = non detected. [c] The best reaction conditions are printed in bold.

product ($\delta_{31P}$ = 115 ppm) which, unfortunately, could not be identified (Table 4, entries 4 and 8, respectively). The best selectivity and yield for the desired *ortho*-substituted product (*S*)-**33** were achieved by carrying out the metallation with *t*BuLi at –50 °C for 24 h (Table 4, entry 7). The identity of this product was unambiguously assigned by X-ray crystallographic analysis (Figure 7).

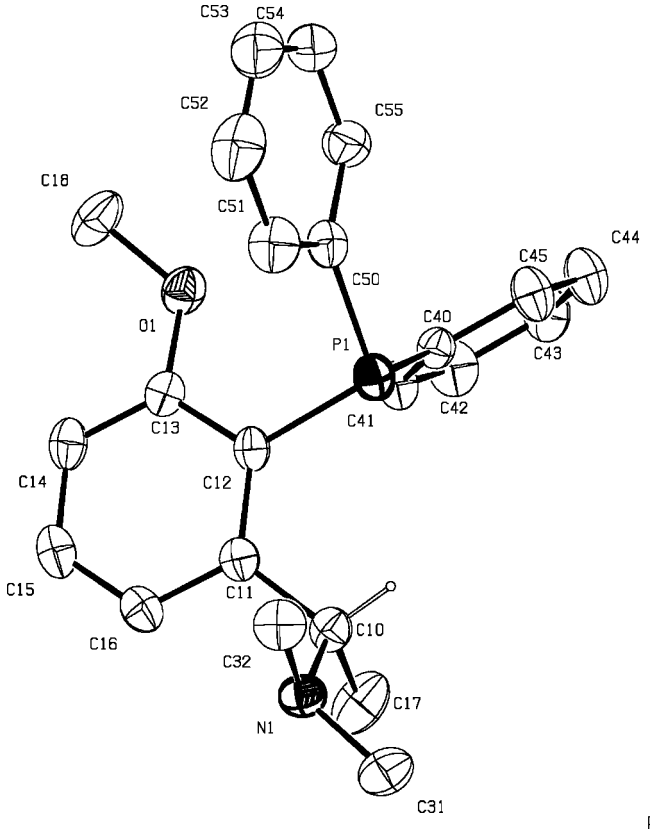


Figure 7. Displacement ellipsoids plot (PLATON) of one independent molecule of (*S*)-**33**. Ellipsoids are shown at the 30% probability level. The H-atom attached to the stereogenic centre is shown with arbitrary radius; other H-atoms have been omitted for clarity.

The optimised conditions were applied to the preparation of (*S*)-**34** (Scheme 12), although a large excess of $ClSiMe_3$ had to be used and the electrophilic trapping following metallation required ten days at room temperature.

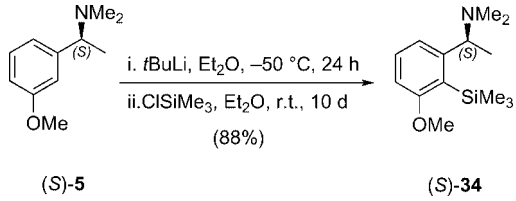


Scheme 12. Synthesis of (*S*)-**34**.

Complexation of (*S*)-**34** to $Cr(CO)_3$ was carried out using Kündig's reagent under mild conditions (Scheme 13). The diastereoselectivity was 86% in favour of the (*S*,*R*p)-**35** isomer, as established from the NMR spectra of the crude reaction mixture. This complex could be obtained as a single diastereoisomer after flash chromatography [the other diastereoisomer (*S*,*S*p)-**35** was not isolated]. Desilylation of (*S*,*R*p)-**35** afforded complex (*S*,*S*p)-**36**, the absolute configuration of which was confirmed by X-ray crystallographic analysis (Figure 8).

(*S*,*S*p)-**37** was obtained by treatment of complex (*S*,*S*p)-**28** with *t*BuLi at –78 °C for four hours and then with $ClPPh_2$ (Scheme 14). The site of ortholithiation was confirmed by an X-ray crystallographic analysis (Figure 9). The NMR spectrum of the crude reaction mixture did not show the formation of other regioisomers. This result is surprising because the OMe group and the $CH_2NMe_2$ group have a similar *ortho*-directing ability in [($\eta^6$-arene)$Cr(CO)_3$] complexes.[15c] Lithiation of the diastereomeric complex (*S*,*R*p)-**28** with opposite planar chirality under analogous conditions failed and was also unsuccessful at higher temperatures or when using the less bulky base *n*BuLi. Directed orthometallation adjacent to the OMe group might be expected in (*S*,*R*p)-**28**, as is the case for (*S*,*S*p)-**28**, whereas lithiation adjacent to the $CH(Me)NMe_2$ group is hampered due to steric reasons. Removal of the *ortho* proton by a lithium base pre-coordinated by the amino group would

 © 2007 Wiley-VCH Verlag GmbH & Co. KGaA, Weinheim 

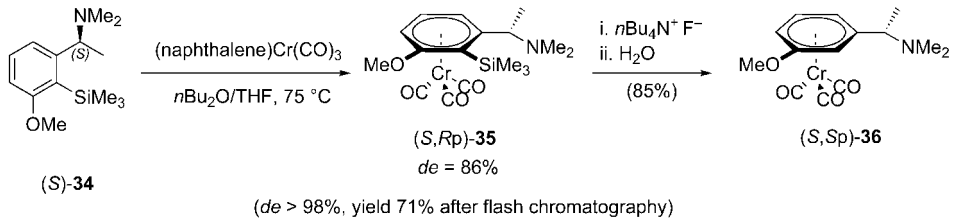


Scheme 13. Stereoselective route to (*S*,*S*p)-**36**.

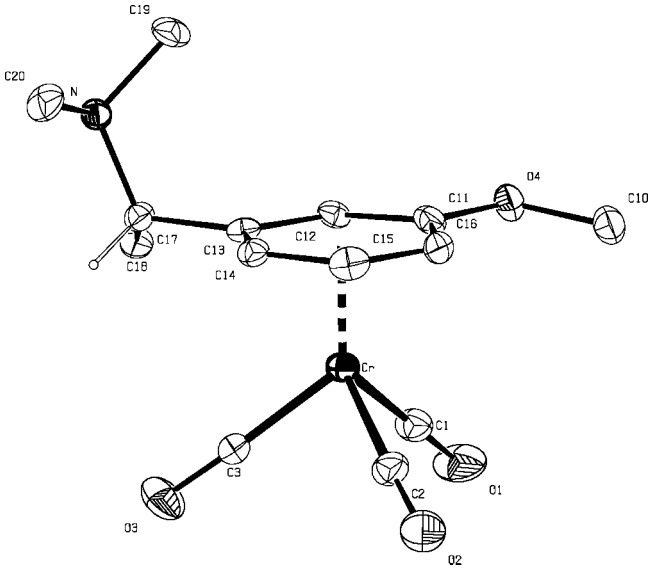


Figure 8. Displacement ellipsoids plot (PLATON) of (*S*,*S*p)-**36**. Ellipsoids are shown at the 30% probability level. The H-atom attached to the stereogenic centre is shown with arbitrary radius; other H-atoms have been omitted for clarity.

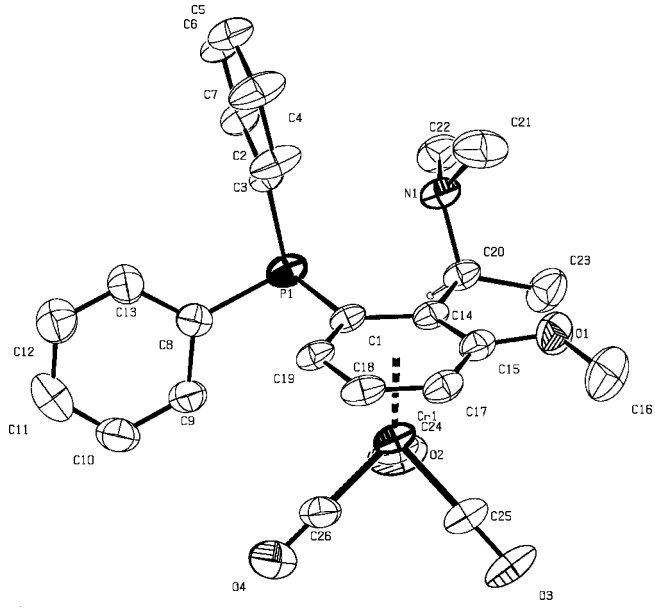


Figure 9. Displacement ellipsoids plot (PLATON) of (*S*,*S*p)-**37**. Ellipsoids are shown at the 30% probability level. The H-atom attached to the stereogenic centre is shown with arbitrary radius; other H-atoms have been omitted for clarity.

force the benzylic methyl group below the plane of the arene, thereby causing unfavourable steric interaction with the $Cr(CO)_3$ unit (Figure 10).

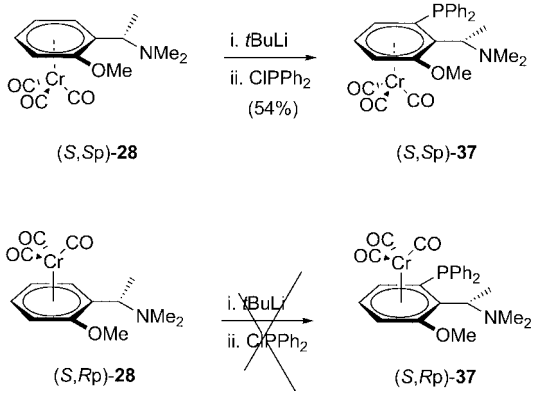


Scheme 14. Lithiation of diastereomeric complexes (*S*,*S*p)-**28** and (*S*,*R*p)-**28** and subsequent electrophilic quenching with $ClPPh_2$. The latter complex fails to react (see text for experimental conditions).

The inertness of (*S*,*R*p)-**28** towards *ortho*-functionalisation was advantageously exploited to separate the diastereomeric mixture of (*S*,*S*p)-**28** and (*S*,*R*p)-**28** obtained in

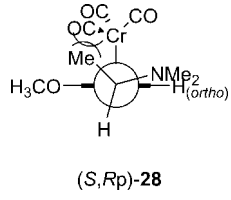


(*S*,*R*p)-**28**

Figure 10. Conformation of (*S*,*R*p)-**28** required for ortholithiation assisted by the benzylic dimethylamino group.

the thermal complexation of (*S*)-**4** with $Cr(CO)_6$. Thus, after treatment of this mixture with *t*BuLi and $ClPPh_2$, (*S*,*S*p)-**37** and unreacted (*S*,*R*p)-**28** were easily separated and purified by flash chromatography.

When complex (*S*,*S*p)-**36** was treated with *t*BuLi and then with $ClPPh_2$, the $^{31}P$ NMR spectrum of the crude reaction mixture indicated the formation of two products in a 10:1 ratio, as established from the areas of the corresponding NMR signals [81 MHz, $CDCl_3$; (*S*,*S*p)-**38**: $\delta$ = –16.74 ppm; **39**: $\delta$ = –12.67 ppm; Scheme 15]. An X-ray crystallographic analysis of the major product (*S*,*S*p)-**38**

 © 2007 Wiley-VCH Verlag GmbH & Co. KGaA, Weinheim 

indicated that lithiation had occurred *ortho* to the benzylic amino group and *para* to the methoxy group (Figure 11). The minor product **39** could not be isolated in a pure form.

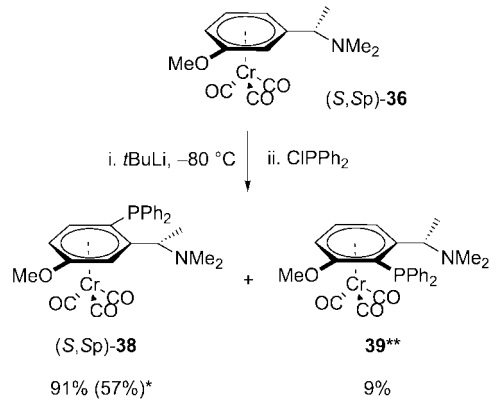


Scheme 15. Lithiation of (*S*,*S*p)-**36** and subsequent electrophilic quenching with $ClPPh_2$. * Yield of isolated products. ** The structure of complex **39** is only a proposal.

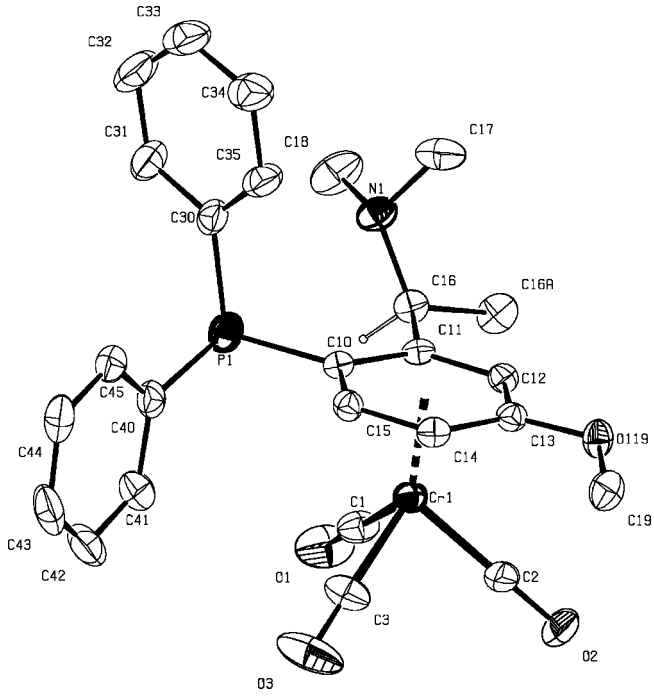


Figure 11. Displacement ellipsoids plot (PLATON) of one independent molecule of (*S*,*S*p)-**38**. Ellipsoids are shown at the 30% probability level. The H-atom attached to the stereogenic centre is shown with arbitrary radius; other H-atoms have been omitted for clarity.

Because (*S*,*R*p)-**36** was not available in a pure form, the 1:1 diastereomeric mixture of (*S*,*S*p)-**36** and (*S*,*R*p)-**36** was lithiated instead (Scheme 16). A third product [(*S*,*S*p)-**40**] was detected along with (*S*,*S*p)-**38** and **39** in the $^{31}P$ NMR spectrum of the crude product [(*S*,*S*p)-**40**: $\delta = -10.70$ ppm]. This complex was isolated and its structure confirmed by an X-ray crystallographic analysis (Figure 12). (*S*,*S*p)-**40** is formed from (*S*,*R*p)-**36** by selective abstraction of the proton *ortho* to both substituents on the arene. The relative amounts of (*S*,*S*p)-**38**, **39** and (*S*,*S*p)-**40** depend on the temperature at which lithiation is carried out. Thus, at 0 °C and at room temperature (*S*,*S*p)-**38** is not detected and **39** and (*S*,*S*p)-**40** are formed in equal amounts. This might suggest that **39** is the product derived from (*S*,*S*p)-**36** when the dimethylamino group can overcome restricted rotation

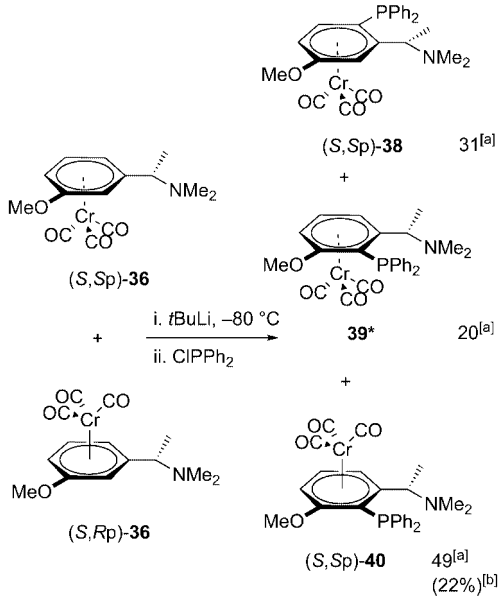


Scheme 16. Products arising from *ortho*-functionalisation of a 1:1 diastereomeric mixture of (*S*,*S*p)-**36** and (*S*,*R*p)-**36**. * The structure of complex **39** is only a proposal. [a] Relative amounts of products as inferred from the $^{31}P$ NMR spectrum of the crude reaction mixture. [b] Yield after flash chromatography; only this product was isolated.

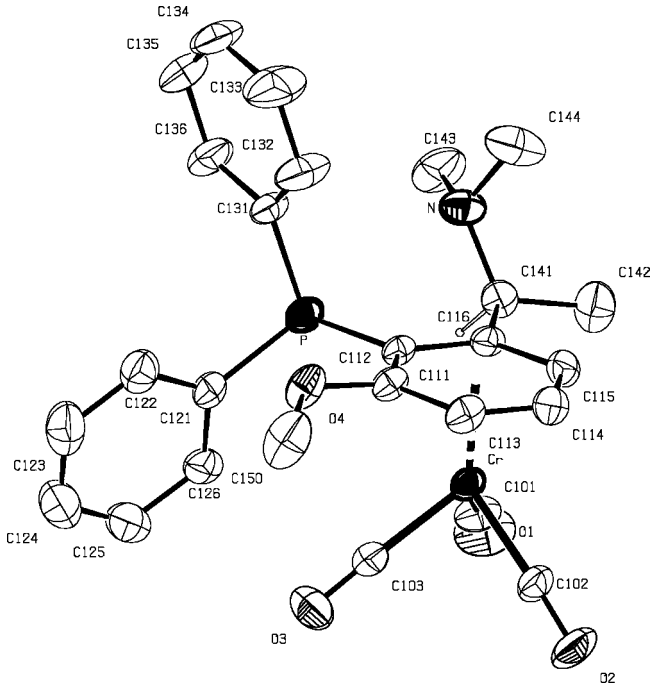


Figure 12. Displacement ellipsoids plot (PLATON) of (*S*,*S*p)-**40**. Ellipsoids are shown at the 30% probability level. The H-atom attached to the stereogenic centre is shown with arbitrary radius; other H-atoms have been omitted for clarity.

 © 2007 Wiley-VCH Verlag GmbH & Co. KGaA, Weinheim 

around the benzylic bond at higher temperature and the base is delivered to the other *ortho* proton through chelation by both substituents on the arene.

Some of the complexes containing P∩N ligands coordinated to the $Cr(CO)_3$ moiety have been successfully tested by us in asymmetric transfer hydrogenation. The results of these studies have been reported elsewhere.[4]

## Conclusions

The range of "Daniphos" ligands has been expanded to include N∩P and P∩P ligands bearing a substituent R on the arene of the [($\eta^6$-arene)$Cr(CO)_3$] unit, which might serve to modulate the steric and electronic properties of the donor atoms. The stereoselective synthetic strategy originally devised for the preparation of this class of ligands has been successfully applied to their preparation. In the case of N∩P ligands derived from 1,2- and 1,3-disubstituted benzylamines, because the two faces of such amines are diastereotopic and diastereomeric complexes arise from the coordination of the $Cr(CO)_3$ fragment to either of the two faces, the synthetic plan has been adjusted by exploiting the trimethylsilyl group as a temporary steric modulator in order to access both complexes with high diastereoselectivity.

## Experimental Section

**Materials and Methods:** All reactions involving air- and moisture-sensitive compounds, and their subsequent workup, were carried out under nitrogen using Schlenk and syringe techniques. Reactions were monitored by analytical TLC using either Merck silica gel 60 F 254 or Merck aluminium oxide F 254 aluminium cards. The chromatograms were visualized with UV light. Solutions of crude reaction mixtures were filtered through a short bed of the filter aid Fluka Celite 535. The solvent was then evaporated. Flash chromatography of the crude products was performed either on silica gel 60 [Merck; particle size: 0.063–0.200; pH 7.0 (0.5)] or aluminium oxide 90 II–III [Merck; particle size: 0.063–0.200; pH 9.0 (0.5)]. Solvents were dried and deoxygenated by standard procedures. NMR spectra were recorded with a Varian Mercury 200 spectrometer operating at 200 (for $^1H$), 50 (for $^{13}C$) or 81 MHz (for $^{31}P$), a Varian Unity 300 spectrometer operating at 300 (for $^1H$), 75.5 (for $^{13}C$) or 121.5 MHz (for $^{31}P$), a Varian Mercury Plus spectrometer operating at 400 (for $^1H$), 100.5 (for $^{13}C$) or 162 MHz (for $^{31}P$), or a Varian Unity 500 spectrometer operating at 500 (for $^1H$), 125 (for $^{13}C$) or 202 MHz (for $^{31}P$) at ambient temperature. Chemical shifts ($\delta$) are given in ppm relative to TMS ($^1H$, $^{13}C$) or 85% $H_3PO_4$ as external standards ($^{31}P$). IR spectra were recorded with a Perkin–Elmer FT-IR Model 1720-X spectrometer. Optical rotations were measured in 1-dm cells with a Perkin–Elmer Model 341 polarimeter at ambient temperature. Mass spectra were obtained by electron impact (EI) or chemical ionisation (CI) with isobutane with a Finnigan MAT 95 spectrometer. Elemental analyses were performed with a Carlo Erba Strumentazione Element Analyzer (Model 1106). Generous loans of chiral amines were kindly provided by BASF GmbH. [($\eta^6$-naphthalene)$Cr(CO)_3$]. was prepared according to published procedure.[9,26] All other chemicals were purchased and used without further purification.

**General Methods**

**A. Methylation of Amines:** Benzylamines were methylated according to the Eschweiler–Clarke procedure with formic acid and formaldehyde.[6] Formaldehyde (37% aqueous solution, $d$ = 1.090, 3 equiv.) and formic acid (98% aqueous solution, $d$ = 1.220, 5 equiv.) were added dropwise to the amine (1 equiv.) at 0 °C. The solution was heated at 80 °C for the reported time, then cooled and acidified with 10 N HCl. The solution was extracted with diethyl ether and then basified with 50% aqueous NaOH. The basic aqueous phase was extracted three times with diethyl ether and the combined ether extracts were washed with water and dried with $MgSO_4$. Diethyl ether was evaporated and the crude product finally distilled under reduced pressure.

**B. Synthesis of [($\eta^6$-Arene)$Cr(CO)_3$] Complexes by Thermolysis with $Cr(CO)_6$:** [($\eta^6$-arene)$Cr(CO)_3$] complexes were prepared according to the Pauson–Mahaffy procedure.[7] $Cr(CO)_6$ (1.2 equiv.) and the protected benzylamine (1 equiv.) were refluxed (bath temperature: 140 °C) in an 8:1 di-*n*-butyl ether/thf mixture ([Cr] = 0.36 M) for the reported time. The solution was cooled and filtered through a short pad of Celite on a sintered glass filter, which was then washed with some additional solvent. The solvents were distilled off on a rotary evaporator from a water bath held at 60 °C (an oil pump was required to remove the solvents completely). The crude product was purified by column chromatography and crystallised from suitable solvents.

**C. Directed Orthometallation and Functionalisation of [($\eta^6$-arene)-$Cr(CO)_3$] Complexes:** The appropriate [($\eta^6$-arene)$Cr(CO)_3$] complex (1 equiv.) was dissolved in dry diethyl ether ([Cr] = 0.05 M). The solution was cooled to –78 °C and *tert*-butyllithium (1.7 M in pentane, 1.14 equiv.) was added dropwise with a syringe. After 1.5 h, chlorodiphenylphosphane (1.14 equiv.) was added dropwise. The reaction mixture was warmed slowly to room temperature overnight and then filtered through a short pad of Celite on a sintered glass filter. The solvent was distilled off on a rotary evaporator and the crude product purified by column chromatography.

**D. Replacement of $NMe_2$ with Cl:** The appropriate [($\eta^6$-arene)-$Cr(CO)_3$] complex (1 equiv.) was dissolved in dry thf ([Cr] = 0.05 M). The solution was cooled to –40 °C and 1-chloroethyl chloroformate ($d$ = 1.312, 4 equiv.) was added dropwise. The reaction mixture was warmed up to room temperature overnight. The course of the reaction was monitored by $^{31}P$ NMR spectroscopy on a small sample of the crude reaction mixture dissolved in $C_6D_6$. The solvent and unreacted 1-chloroethyl chloroformate were distilled off. The residue was redissolved in diethyl ether and the solution filtered through a short pad of Celite on a sintered glass filter to eliminate the insoluble by-product [$(CH_3)_2NC(O)CHClCH_3$]. The crude product was purified by column chromatography after removal of the solvent.

**E. Replacement of Cl with $PR_2$:** The appropriate [($\eta^6$-arene)Cr-$(CO)_3$] complex (1 equiv.) was dissolved in dry acetone and $HPR_2$ (1.1 equiv.) was added. A suspension of $TlPF_6$ (1.1 equiv.) in dry acetone (final concentration of Cr in acetone = 0.05 M) was added dropwise to this solution very slowly. A fine white precipitate consisting of TlCl formed immediately. The solution was stirred at room temperature overnight. $NEt_3$ (1.5 mL per millimol of Cr) was added, the solution stirred for a further 15 min and then filtered through a short pad of Celite on a sintered glass filter to remove TlCl. The solvent and excess $NEt_3$ were distilled off and the crude product purified by column chromatography.

**(*S*)-*N*,*N*-Dimethyl-1-(*p*-tolyl)ethylamine [(*S*)-1]:** This compound was prepared according to general procedure A from formaldehyde

 © 2007 Wiley-VCH Verlag GmbH & Co. KGaA, Weinheim 

(66.1 mL, 0.89 mol), formic acid (55.8 mL, 1.45 mol) and (*S*)-**1**-(*p*-tolyl)ethylamine (40.0 g, 0.30 mol). The reaction mixture was heated at 80 °C for 18 h. Distillation of the crude product under reduced pressure gave the protected amine as a colourless oil. Yield 37.1 g (77%). $^1$H NMR (500 MHz, $C_6D_6$): $\delta$ = 1.27 (d, $J$ = 6.7 Hz, 3 H, α-Me), 2.12 (s, 6 H, N*Me*$_2$), 2.15 (s, 3 H, *p*-Me), 3.10 (q, $J$ = 6.7 Hz, 1 H, α-C*H*), 7.04 (d, $J$ = 7.6 Hz, 2 H, $H_{Ar}$), 7.25 (d, $J$ = 7.9 Hz, 2 H, $H_{Ar}$) ppm. $^{13}$C NMR (125 MHz, $C_6D_6$): $\delta$ = 20.77 (α-Me), 21.06 (*p*-Me), 43.34 (N*Me*$_2$), 65.92 (α-*C*H), 127.64 ($C_{Ar}$), 129.15 ($C_{Ar}$), 136.17 ($C_{Ar,ipso}$), 142.50 ($C_{Ar,ipso}$) ppm. MS (EI): *m*/*z* (%) 163 (13) [M$^+$], 148 (100) [M – Me], 132 (54) [M – NMe$_2$]. B.p. (30 Torr): 115 °C. $[\alpha]_D^{r.t.}$ = –61.4 (neat). $C_{11}H_{17}N$ (163.26): calcd. C 80.93, H 10.49, N 8.58; found C 80.40, H 10.27, N 9.03.

**(*S*)-*N*,*N*-Dimethyl-1-(*p*-*tert*-butylphenyl)ethylamine [(*S*)-2]:** This compound was prepared according to general procedure A by methylation of (*S*)-1-(4-*tert*-butylphenyl)ethylamine (10.00 g, 56.5 mmol) with formaldehyde (12.8 mL, 169.5 mmol) and formic acid (10.6 mL, 282.5 mmol). The crude product was purified by column chromatography (aluminium oxide; diethyl ether/hexane = 1:2) and the protected amine was isolated as a colourless oil. Yield 9.70 g (84%). $^1$H NMR (200 MHz, $CDCl_3$): $\delta$ = 1.30 (s, 9 H, *p*-*t*Bu), 1.35 (d, $J$ = 6.8 Hz, 3 H, α-Me), 2.17 (s, 6 H, N*Me*$_2$), 3.22 (q, $J$ = 6.8 Hz, 1 H, α-C*H*), 7.19 (d, $J$ = 8.3 Hz, 2 H, $H_{Ar}$), 7.31 (d, $J$ = 8.3 Hz, 2 H, $H_{Ar}$) ppm. $^{13}$C NMR (125 MHz, $CDCl_3$): $\delta$ = 25.05 (α-Me), 31.38 (*p*-C*Me*$_3$), 34.46 (*p*-*C*Me$_3$), 43.40 (N*Me*$_2$), 50.98 (α-*C*H), 125.43 ($C_{Ar}$), 125.48 ($C_{Ar}$), 143.78 ($C_{Ar,ipso}$), 149.90 ($C_{Ar,ipso}$) ppm.

**(*R*)-*N*,*N*-Dimethyl-1-(*p*-chlorophenyl)ethylamine [(*R*)-3]:** This compound was prepared according to general procedure A from formaldehyde (44.0 mL, 0.59 mol), formic acid (37.0 mL, 0.96 mol) and (*R*)-1-(*p*-chlorophenyl)ethylamine (30.5 g, 0.20 mol). The reaction mixture was heated at 80 °C for 38 h. Distillation of the crude product under reduced pressure gave the protected amine as a colourless oil. Yield 28.8 g (80%) $^1$H NMR (500 MHz, $C_6D_6$): $\delta$ = 1.09 (d, $J$ = 6.7 Hz, 3 H, α-Me), 2.00 (s, 6 H, N*Me*$_2$), 2.92 (q, $J$ = 6.7 Hz, 1 H, α-C*H*), 7.02 (m, $J$ = 8.5 Hz, 2 H, $H_{Ar}$), 7.13 (m, $J$ = 7.9 Hz, 2 H, $H_{Ar}$) ppm. $^{13}$C NMR (125 MHz, $C_6D_6$): $\delta$ = 20.34 (α-Me), 43.09 (N*Me*$_2$), 65.28 (α-*C*H), 128.58 ($C_{Ar}$), 128.97 ($C_{Ar}$), 132.56 ($C_{Ar,ipso}$), 143.98 ($C_{Ar,ipso}$) ppm. MS (EI): *m*/*z* (%) 183 (12) [M$^+$], 168 (100) [M – Me], 132 (54) [M – NMe$_2$]. B.p. (0.1 Torr): 54 °C. $[\alpha]_D^{r.t.}$ = +60.1 (neat).

**(*S*)-*N*,*N*-Dimethyl-1-(*o*-anisyl)ethylamine [(*S*)-4]:** This compound was prepared according to general procedure A by methylation of (*S*)-1-(2-methoxyphenyl)ethylamine (50.00 g, 0.33 mol) with formaldehyde (75 mL, 0.99 mol) and formic acid (62.5 mL, 1.66 mol). The crude product was purified by column chromatography (aluminium oxide; diethyl ether/hexane = 1:2) and the protected amine was isolated as a light yellow oil. Yield 51.60 g (87%) $^1$H NMR (500 MHz, $CDCl_3$): $\delta$ = 1.31 (d, $J$ = 6.7 Hz, 3 H, α-Me), 2.21 (s, 6 H, N*Me*$_2$), 3.80 (s, 3 H, O*Me*), 3.84 (q, $J$ = 6.7 Hz, 1 H, α-C*H*), 6.86 (d, $J$ = 7.6 Hz, 1 H, $H_{Ar}$), 6.94 (t, $J$ = 7.6 Hz, 1 H, $H_{Ar}$), 7.19 (t, $J$ = 7.6 Hz, 1 H, $H_{Ar}$), 7.39 (d, $J$ = 7.6 Hz, 1 H, $H_{Ar}$) ppm. $^{13}$C NMR (50 MHz, $C_6D_6$): $\delta$ = 21.16 (α-Me), 43.81 (N*Me*$_2$), 54.94 (O*Me*), 57.89 (α-*C*H), 110.63 ($C_{Ar}$), 121.01 ($C_{Ar}$) 127.49 ($C_{Ar}$), 128.00 ($C_{Ar}$), 133.84 ($C_{Ar,ipso}$), 157.09 ($C_{Ar,ipso}$) ppm.

**(*S*)-*N*,*N*-Dimethyl-1-(*m*-anisyl)ethylamine [(*S*)-5]:** This compound was prepared according to general procedure A by methylation of (*S*)-1-(3-methoxyphenyl)ethylamine (10.00 g, 66.20 mmol) with formaldehyde (15 mL, 0.20 mol) and formic acid (12.5 mL, 0.33 mol). The crude product was purified by column chromatography ($Al_2O_3$; diethyl ether/hexane = 1:2) and the protected amine was isolated as a light yellow oil. Yield 9.36 g (79%). $^1$H NMR (200 MHz, $CDCl_3$): $\delta$ = 1.30 (d, $J$ = 6.6 Hz, 3 H, α-Me), 2.16 (s, 6 H, N*Me*$_2$), 3.11 (q, $J$ = 6.6 Hz, 1 H, α-C*H*), 3.78 (s, 3 H, O*Me*), 6.75–6.88 (m, 3 H, $H_{Ar}$), 7.20 (t, $J$ = 8.1 Hz, 1 H, $H_{Ar}$) ppm. $^{13}$C NMR (50 MHz, $CDCl_3$): $\delta$ = 20.35 (α-Me), 43.17 (N*Me*$_2$), 54.84 (O*Me*), 65.91 (α-*C*H), 111.97 ($C_{Ar}$), 112.63 ($C_{Ar}$) 119.60 ($C_{Ar}$), 128.84 ($C_{Ar}$), 145.76 ($C_{Ar,ipso}$), 159.30 ($C_{Ar,ipso}$) ppm.

**(*R*)-*N*,*N*-Dimethyl-1-(*p*-anisyl)ethylamine [(*R*)-6]:** This compound was prepared according to general procedure A from formaldehyde (54.0 mL, 0.72 mol), formic acid (45.0 mL, 1.17 mol) and (*R*)-1-(*p*-methoxyphenyl)ethylamine (36.0 g, 0.24 mol). The reaction mixture was heated at 80 °C for 13 h. Distillation of the crude product under reduced pressure gave the protected amine as a colourless oil. Yield 20.7 g (48%). $^1$H NMR (500 MHz, $C_6D_6$): $\delta$ = 1.27 (d, $J$ = 6.7 Hz, 3 H, α-Me), 2.12 (s, 6 H, N*Me*$_2$), 3.10 (q, $J$ = 6.7 Hz, 1 H, α-C*H*), 3.34 (s, 3 H, O*Me*), 6.82 (d, $J$ = 8.9 Hz, 2 H, $H_{Ar}$), 7.25 (d, $J$ = 8.2 Hz, 2 H, $H_{Ar}$) ppm. $^{13}$C NMR (125 MHz, $C_6D_6$): $\delta$ = 20.65 (α-Me), 43.26 (N*Me*$_2$), 54.73 (α-*C*H), 65.45 (O*Me*), 113.90 ($C_{Ar}$), 128.63 ($C_{Ar}$), 137.34 ($C_{Ar,ipso}$), 159.05 ($C_{Ar,ipso}$) ppm. MS (EI): *m*/*z* (%) 179 (13) [M$^+$], 164 (100) [M – Me], 135 (35) [M – NMe$_2$], 105 (21) [M – NMe$_2$ – OMe]. B.p. (0.5 Torr): 68 °C. $[\alpha]_D^{r.t.}$ = +55.8 (neat). $C_{11}H_{17}NO$ (179.26): calcd. C 73.70, H 9.56, N 7.81; found C 73.65, H 9.00, N 8.40.

**[{η$^6$-(*S*)-*N*,*N*-Dimethyl-1-(*p*-tolyl)ethylamine}Cr(CO)$_3$] [(*S*)-7]:** This complex was prepared from $Cr(CO)_6$ (24.3 g, 110.0 mmol) and (*S*)-**1** (15.0 g, 92.0 mmol) in an 8:1 di-*n*-butyl ether/thf mixture (327 mL) according to general procedure B. The reaction mixture was refluxed for 60 h. The crude product was purified by column chromatography over aluminium oxide using diethyl ether as the sole eluent ($R_f$ = 0.74). The yellow solid was crystallised from dichloromethane/hexane at –30 °C. Yield 19.1 g (69%). $^1$H NMR (500 MHz, $C_6D_6$): $\delta$ = 1.08 (d, $J$ = 6.7 Hz, 3 H, α-Me), 1.59 (s, 3 H, *p*-Me), 1.88 (s, 6 H, N*Me*$_2$), 3.07 (q, $J$ = 6.7 Hz, 1 H, α-C*H*), 4.33 (d, $J$ = 6.6 Hz, 1 H, $H_{Ar}$), 4.39 (d, $J$ = 6.4 Hz, 1 H, $H_{Ar}$), 4.87 (d, $J$ = 6.4 Hz, 1 H, $H_{Ar}$), 5.02 (d, $J$ = 6.6 Hz, 1 H, $H_{Ar}$) ppm. $^{13}$C NMR (125 MHz, $C_6D_6$): $\delta$ = 13.26 (α-Me), 19.91 (*p*-Me), 40.72 (N*Me*$_2$), 61.33 (α-*C*H), 91.28 ($C_{Ar}$), 92.09 ($C_{Ar}$), 93.08 ($C_{Ar}$), 97.27 ($C_{Ar}$), 109.29 ($C_{Ar,ipso}$), 109.63 ($C_{Ar,ipso}$), 233.92 (*C*O) ppm. MS (EI): *m*/*z* (%) 299 (16) [M$^+$], 255 (100) [M – NMe$_2$], 243 (31) [M – 2 CO], 215 (5) [M – 3 CO]. $[\alpha]_D^{r.t.}$ = –18.7 (*c* = 2.01, $CHCl_3$). IR ($CHCl_3$): $\nu_{CO}$ = 1959, 1876 cm$^{-1}$. $C_{14}H_{17}CrNO_3$ (299.29): calcd. C 56.18, H 5.72, N 4.68; found C 56.02, H 5.68, N 4.73.

**[{η$^6$-(*S*)-*N*,*N*-Dimethyl-1-(*p*-*tert*-butylphenyl)ethylamine}Cr(CO)$_3$] [(*S*)-8]:** This complex was prepared from $Cr(CO)_6$ (12.50 g, 56.78 mmol) and (*S*)-**2** (9.70 g, 47.32 mmol) in an 8:1 mixture of di-*n*-butyl ether and thf (169 mL) according to general procedure B. The reaction mixture was refluxed for 55 h. The crude product was purified by column chromatography over aluminium oxide using diethyl ether as eluent. A yellow microcrystalline product was obtained after recrystallisation from diethyl ether/hexane at –30 °C. Yield 14.31 g (89%). $^1$H NMR (500 MHz, $CDCl_3$): $\delta$ = 1.27 (br. s, 12 H, *p*-*t*Bu, α-Me), 2.21 (s, 6 H, N*Me*$_2$), 3.49 (q, $J$ = 6.7 Hz, 1 H, α-C*H*), 5.14–5.70 (br. m, 4 H, $H_{Ar}$) ppm. $^{13}$C NMR (125 MHz, $CDCl_3$): $\delta$ = 11.68 (α-Me), 31.42 (*p*-C*Me*$_3$), 34.22 (*p*-*C*Me$_3$), 41.12 (N*Me*$_2$), 61.39 (α-*C*H), 90.21 ($C_{Ar}$), 91.65 ($C_{Ar}$), 92.31 ($C_{Ar}$), 94.33 ($C_{Ar}$), 112.84 ($C_{Ar,ipso}$), 123.12 ($C_{Ar,ipso}$), 233.74 (*C*O) ppm. IR (hexane): $\nu_{CO}$ = 1969, 1899 cm$^{-1}$.

**[{η$^6$-(*R*)-*N*,*N*-Dimethyl-1-(*p*-chlorophenyl)ethylamine}Cr(CO)$_3$] [(*R*)-9]:** This complex was prepared from $Cr(CO)_6$ (21.6 g, 98.0 mmol) and (*R*)-**3** (15.0 g, 82.0 mmol) in an 8:1 di-*n*-butyl ether/thf mixture (281 mL) according to general procedure B. The reaction mixture was refluxed for 62 h. The product was purified by flash chromatography (aluminium oxide; diethyl ether, $R_f$ = 0.73)

 © 2007 Wiley-VCH Verlag GmbH & Co. KGaA, Weinheim 

and recrystallisation from a layered mixture of di-*n*-butyl ether and hexane at –30 °C. Yield yellow crystals (43%). $^1$H NMR (500 MHz, $C_6D_6$): $\delta$ = 0.85 (d, $J$ = 6.8 Hz, 3 H, α-Me), 1.78 (s, 6 H, N$Me_2$), 2.88 (q, $J$ = 6.8 Hz, 1 H, α-C$H$), 4.61 (br. d, $J$ = 6.7 Hz, 1 H, $H_{Ar}$), 4.64 (br. d, $J$ = 6.4 Hz, 1 H, $H_{Ar}$), 4.68 (br. d, $J$ = 6.4 Hz, 1 H, $H_{Ar}$), 4.81 (br. d, $J$ = 6.1 Hz, 1 H, $H_{Ar}$) ppm. $^{13}$C NMR (125 MHz, $C_6D_6$): $\delta$ = 13.32 (α-Me), 40.62 (N$Me_2$), 60.92 (α-$C$H), 89.80 ($C_{Ar}$), 90.34 ($C_{Ar}$), 91.93 ($C_{Ar}$), 95.92 ($C_{Ar}$), 108.34 ($C_{Ar,ipso}$), 112.89 ($C_{Ar,ipso}$), 232.28 ($C$O) ppm. MS (CI, isobutane): $m/z$ (%) 320 (1) [M + H], 275 (100) [M – $NMe_2$], 263 (18) [M – 2 CO]. $[a]_D^{r.t.}$ = +9.7 ($c$ = 1.18, $CHCl_3$). IR ($CHCl_3$): $\nu_{CO}$ = 1981, 1888 cm$^{-1}$. $C_{13}H_{14}ClCrNO_3$ (319.71): calcd. C 48.84, H 4.41, N 4.38; found C 50.06, H 4.58, N 4.30.

**[{η$^6$-(*R*)-*N*,*N*-Dimethyl-1-(*p*-anisyl)ethylamine}Cr(CO)$_3$] [(*R*)-10]:** This complex was prepared from $Cr(CO)_6$ (22.1 g, 0.10 mol) and (*R*)-**6** (15.0 g, 0.84 mol) in an 8:1 di-*n*-butyl ether/thf mixture (281 mL) according to general procedure B. The crude product was purified by column chromatography (aluminium oxide; diethyl ether). $R_f$ = 0.73 Crystallisation from dichloromethane/hexane at –30 °C afforded the product as yellow crystals. Yield 22.3 g (85%). $^1$H NMR (500 MHz, $C_6D_6$): $\delta$ = 1.04 (d, $J$ = 6.7 Hz, 3 H, α-Me), 1.90 (s, 6 H, N$Me_2$), 2.96 (q, $J$ = 6.7 Hz, 1 H, α-C$H$), 2.99 (s, 3 H, O$Me$), 4.42 (d, $J$ = 6.4 Hz, 1 H, $H_{Ar}$), 4.45 (d, $J$ = 6.4 Hz, 1H $H_{Ar}$), 5.03 (d, $J$ = 6.4 Hz, 1 H, $H_{Ar}$), 5.12 (d, $J$ = 6.4 Hz, 1 H, $H_{Ar}$) ppm. $^{13}$C NMR (125 MHz, $C_6D_6$): $\delta$ = 14.43 (α-Me), 40.87 (N$Me_2$), 55.09 (O$Me$), 61.22 (α-$C$H), 76.25 ($C_{Ar}$), 77.71 ($C_{Ar}$), 93.60 ($C_{Ar}$), 97.70 ($C_{Ar}$), 105. 70 ($C_{Ar,ipso}$), 143.34 ($C_{Ar,ipso}$), 233.86 ($C$O) ppm. MS: $m/z$ (%) 315 (12) [M$^+$], 271 (100) [M – $NMe_2$], 259 (22) [M – 3 CO]. $[a]_D^{r.t.}$ = –9.5 ($c$ = 1.00, $CHCl_3$). IR ($CHCl_3$): $\nu_{CO}$ = 1970, 1873 cm$^{-1}$. $C_{14}H_{17}CrNO_4$ (315.29): calcd. C 53.33, H 5.43, N 4.44; found C 53.21, H 5.41, N 4.47.

**[{η$^6$-(*S*,*R*p)-*N*,*N*-Dimethyl-1-[2-(diphenylphosphanyl)-4-tolyl]ethylamine}Cr(CO)$_3$] [(*S*,*R*p)-11]:** This complex was prepared according to general procedure C by lithiation of (*S*)-**7** (6.0 g, 20.0 mmol) with *tert*-butyllithium (1.7 M in pentane; 13 mL, 22.8 mmol) and treatment of the lithiated species with chlorodiphenylphosphane (5.0 g, 22.8 mmol) in dry diethyl ether (400 mL). The crude product was purified by column chromatography (silica gel; diethyl ether/hexane, 1:4, $R_f$ = 0.44). Yield yellow crystals 8.7 g (90%). $^1$H NMR (500 MHz, $C_6D_6$): $\delta$ = 0.79 (d, $J$ = 6.7 Hz, 3 H, α-Me), 1.46 (s, 3 H, *p*-Me), 1.55 (s, 6 H, N$Me_2$), 4.52 (m, $J$ = 6.4 Hz, 1 H, α-C$H$), 4.66 (dd, $J$ = 6.1, $J$ = 3.2 Hz, 1 H, $H_{Ar}$), 4.74 (d, $J$ = 6.1 Hz, 1 H, $H_{Ar}$), 4.91 (s, 1 H, $H_{Ar}$), 7.03–7.13 (m, 6 H, *m*/*p*-$H_{PAr}$), 7.27 (m, $J$ = 7.94 Hz, 2 H, *o*-$H_{PAr}$), 7.61 (m, $J$ = 7.02 Hz, 2 H, *o*-$H_{PAr}$) ppm. $^{13}$C NMR (125 MHz, $C_6D_6$): $\delta$ = 6.02 (α-Me), 19.75 (*p*-Me), 37.81 (N$Me_2$), 58.56 (d, $^3J_{C,P}$ = 14.3 Hz, α-$C$H), 88.75 (d, $J_{C,P}$ = 3.8 Hz, α-$C$H), 94.13 ($C_{Ar}$), 101.72 (d, $J_{C,P}$ = 3.9 Hz, $C_{Ar}$), 105 80 (d, $J_{C,P}$ = 1.7 Hz, $C_{Ar,ipso}$), 107.00 (d, $J_{C,P}$ = 25.7 Hz, $C_{Ar,ipso}$), 118.23 (d, $J_{C,P}$ = 19.2 Hz, $C_{Ar,ipso}$), 128.07 (d, $J_{C,P}$ = 1.6 Hz, $C_{PAr}$), 128.67 (d, $J_{C,P}$ = 6.0 Hz, $C_{PAr}$), 129.26 ($C_{PAr}$), 132.43 (d, $J_{C,P}$ = 20.3 Hz, $C_{PAr}$), 135.05 (d, $J_{C,P}$ = 19.7 Hz, $C_{PAr}$), 137.29 (d, $J_{C,P}$ = 15.9 Hz, $C_{PAr}$), 138.58 (d, $J_{C,P}$ = 6.0 Hz, $C_{PAr}$), 233.28 ($C$O) ppm. $^{31}$P NMR (81 MHz, $C_6D_6$): $\delta$ = –14.32 ppm. MS (CI, isobutane): $m/z$ (%) 484 (15) [M + 1], 439 (100) [M – $NMe_2$], 399 (34) [M – 3 CO], 348 (18) [M – 3 CO – Cr]. $[a]_D^{r.t.}$ = +452.3 ($c$ = 1.09, $CHCl_3$). IR ($CHCl_3$): $\nu_{CO}$ = 1965, 1894 cm$^{-1}$. $C_{26}H_{26}CrNO_3P$ (483.47): calcd. C 64.59, H 5.42, N 2.90; found C 64.58, H 5.31, N 2.77.

**[{η$^6$-(*S*,*R*p)-*N*,*N*-Dimethyl-1-[4-*tert*-butyl-2-(diphenylphosphanyl)-phenyl]ethylamine}Cr(CO)$_3$] [(*S*,*R*p)-12]:** This complex was prepared according to general procedure C by lithiation of (*S*)-**8** (10.00 g, 29.33 mmol) with *tert*-butyllithium (1.7 M in pentane; 19.70 mL, 33.43 mmol) and treatment of the lithiated species with chlorodiphenylphosphane (7.38 g, 33.43 mmol) in dry diethyl ether (400 mL). The crude product was purified by column chromatography (aluminium oxide; diethyl ether). Yield yellow crystals 4.59 g (78%). $^1$H NMR (200 MHz, $CDCl_3$): $\delta$ = 1.26 (br. s, 12 H, *p*-*t*Bu, α-Me), 1.89 (s, 6 H, N$Me_2$), 4.61 (m, $J$ = 6.1 Hz, 1 H, α-C$H$), 5.21 (dd, $J$ = 6.6, $J$ = 3.4 Hz, 1 H, $H_{Ar}$), 5.34 (s, 1 H, $H_{Ar}$), 5.78 (dd, $J$ = 6.6, $J$ = 1.2 Hz, 1 H, $H_{Ar}$), 7.39–7.52 (m, 10 H, $H_{PAr}$) ppm. $^{13}$C NMR (125 MHz, $CDCl_3$): $\delta$ = 5.78 (α-Me), 31.06 (*p*-C$Me_3$), 33.81 (*p*-$C$Me$_3$), 37.96 (N$Me_2$), 58.29 (d, $J$ = 13.7 Hz, α-$C$H),88.60 ($C_{Ar}$), 92.76 ($C_{Ar}$), 99.45 ($C_{Ar}$), 104.11 (d, $J$ = 24.5 Hz, $C_{Ar,ipso}$), 119.89 ($C_{Ar,ipso}$), 120.14 ($C_{Ar,ipso}$), 127.79–138.20 ($C_{PAr}$), 233.07 ($C$O) ppm. $^{31}$P NMR (121.5 MHz, $CDCl_3$): $\delta$ = –16.79 ppm. IR ($CH_2Cl_2$): $\nu_{CO}$ = 1970, 1904 cm$^{-1}$.

**Lithiation of [{η$^6$-(*R*)-*N*,*N*-Dimethyl-1-(*p*-anisyl)ethylamine}Cr(CO)$_3$]:** Following general procedure C, lithiation of (*R*)-**10** (4.26 g, 13.5 mmol) with *tert*-butyllithium (1.7 M in pentane; 9.5 mL, 16.2 mmol), followed by addition of chlorodiphenylphosphane (3.58 g, 16.2 mmol), produced a mixture of products. Column chromatography (aluminium oxide; hexane/diethyl ether 4:1→1:4) gave (*R*,*S*p)-**15**, (*R*,*R*p)-**13** and (*R*)-**14M**/(*S*)-**14m** in that order.

**[{η$^6$-(*R*,*S*p)-*N*,*N*-Dimethyl-1-[2,5-bis(diphenylphosphanyl)-4-methoxyphenyl]ethylamine}Cr(CO)$_3$] [(*R*,*S*p)-15]:** Yield orange crystals (1.92 g, 21%). $R_f$ = 0.73 (aluminium oxide; diethyl ether/hexane, 1:1). $^1$H NMR (500 MHz, $C_6D_6$): $\delta$ = 0.66 (d, $J$ = 6.7 Hz, 3 H, α-Me), 1.55 (s, 6 H, N$Me_2$), 2.80 (s, 3 H, O$Me$), 4.22 (m, $J$ = 6.7 Hz, 1 H, α-C$H$), 4.91 (d, $J$ = 2.44 Hz, 1 H, $H_{Ar}$), 5.16 (t, $J$ = 2.44 Hz, 1 H, $H_{Ar}$), 7.01–7.16 (m, 12 H, *m*/*p*-$H_{P1Ar}$, *m*/*p*-$H_{P2Ar}$), 7.36 (m, $J$ = 7.33 Hz, 2 H, *o*-$H_{PAr}$), 7.49 (m, $J$ = 7.33 Hz, 2 H, *o*-$H_{PAr}$), 7.69 (m, $J$ = 7.33 Hz, 2 H, *o*-$H_{PAr}$), 7.74 (m, $J$ = 7.33 Hz, 2 H, *o*-$H_{PAr}$) ppm. $^{13}$C NMR (125 MHz, $C_6D_6$): $\delta$ = 6.93 (α-Me), 37.98 (N$Me_2$), 55.44 (O$Me$), 58.61 (d, $J_{C,P}$ = 13.7 Hz, α-$C$H), 80.27 (d, $J_{C,P}$ = 3.3 Hz, $C_{Ar}$), 93.87 (d, $J_{C,P}$ = 25.7 Hz, $C_{Ar,ipso}$), 95.19 (d, $J_{C,P}$ = 3.3 Hz, $C_{Ar}$), 108.73 (d, $J_{C,P}$ = 27.9 Hz, $C_{Ar,ipso}$), 112.43 (d, $J_{C,P}$ = 18.1 Hz, $C_{Ar,ipso}$), 128.28 ($C_{PAr}$), 128.72 (d, $J_{C,P}$ = 6.0 Hz, $C_{PAr}$), 128.84 (d, $J_{C,P}$ = 6.6 Hz, $C_{PAr}$), 128.98 (d, $J_{C,P}$ = 7.1 Hz, $C_{PAr}$), 129.65 ($C_{PAr}$), 129.90 ($C_{PAr}$), 132.45 (d, $J_{C,P}$ = 20.2 Hz, $C_{PAr}$), 133.26 (d, $J_{C,P}$ = 20.8 Hz, $C_{PAr}$), 134.81 (d, $J_{C,P}$ = 15.4 Hz, $C_{PAr}$), 135.55 (d, $J_{C,P}$ = 21.9 Hz, $C_{PAr}$), 135.72 (d, $J_{C,P}$ = 20.9 Hz, $C_{PAr}$), 136.42 (d, $J_{C,P}$ = 16.5 Hz, $C_{PAr}$), 137.52 (d, $J_{C,P}$ = 14.3 Hz, $C_{PAr}$), 139.00 (d, $J_{C,P}$ = 6 Hz, $C_{Ar,ipso}$), 143.39 (d, $J_{C,P}$ = 9.9 Hz, $C_{PAr}$), 233.18 ($C$O) ppm. $^{31}$P NMR (81 MHz, $C_6D_6$): $\delta$ = –14.23 ($P_{o\text{-}CHMeNMe_2}$), –17.69 ($P_{o\text{-}OMe}$) ppm. MS (CI, isobutane): $m/z$ (%) 684 (4) [M + 1], 599 (6) [M – 3 CO], 548 (38) [M – 3 CO – Cr], 455 (29) [M + H – $NMe_2$ – $PPh_2$], 364 (100) [M + H – 3 CO – Cr – $PPh_2$], 319 (41) [M + H – 3 CO – Cr – $PPh_2$ – H $NMe_2$]. $[a]_D^{r.t.}$ = –358.3 ($c$ = 0.24, $CHCl_3$). IR ($CHCl_3$): $\nu_{CO}$ = 1962, 1893 cm$^{-1}$. $C_{38}H_{35}CrNO_4P_2$ (683.64): calcd. C 66.76, H 5.16, N 2.05; found C 66.63, H 5.24, N 2.53.

**[{η$^6$-(*R*,*R*p)-*N*,*N*-Dimethyl-1-[2-(diphenylphosphanyl)-4-methoxyphenyl]ethylamine}Cr(CO)$_3$] [(*R*,*R*p)-13]:** Yield yellow crystals (2.02 g, 30%). $R_f$ = 0.64 (aluminium oxide; diethyl ether/hexane, 1:1). $^1$H NMR (500 MHz, $C_6D_6$): $\delta$ = 0.82 (d, $J$ = 6.7 Hz, 3 H, α-Me), 1.54 (s, 6 H, N$Me_2$), 2.87 (s, 3 H, O$Me$), 4.41 (m, $J$ = 6.4 Hz, 1 H, α-C$H$), 4.58 (dd, $J$ = 6.7, $J$ = 2.4 Hz, 1 H, $H_{Ar}$) 4.80 (dd, $J$ = 7.0, $J$ = 3.0 Hz, 1H $H_{Ar}$), 5.10 (d, $J$ = 2.1 Hz, 1 H, $H_{Ar}$), 6.68–7.11 (m, 6 H, *m*/*p*-$H_{PAr}$), 7.29 (m, $J$ = 7.9 Hz, 2 H, *o*-$H_{PAr}$), 7.66 (m, $J$ = 7.0 Hz, 2 H, *o*-$H_{PAr}$) ppm. $^{13}$C NMR (125 MHz, $C_6D_6$): $\delta$ = 6.93 (α-Me), 37.89 (N$Me_2$), 55.27 (O$Me$), 58.40 (d, $J_{C,P}$ = 14.3 Hz, α-$C$H), 76.78 ($C_{Ar}$), 88.97 (d, $J_{C,P}$ = 3.3 Hz, $C_{Ar}$), 89.51 (d, $J_{C,P}$ = 3.8 Hz, $C_{Ar}$), 108.3 (d, $J_{C,P}$ = 27.4 Hz, $C_{Ar,ipso}$), 114.39 (d, $J_{C,P}$ = 18.6 Hz, C $C_{Ar,ipso}$), 127.91 ($C_{PAr}$), 128.07 (d, $J_{C,P}$ = 7.7 Hz, $C_{PAr}$), 128.71 (d, $J_{C,P}$ = 6.0 Hz, $C_{PAr}$), 129.47 ($C_{PAr}$), 132.53

 © 2007 Wiley-VCH Verlag GmbH & Co. KGaA, Weinheim 

(d, $J_{C,P}$ = 20.9 Hz, $C_{PAr}$), 135.17 (d, $J_{C,P}$ = 19.7 Hz, $C_{PAr}$), 136.67 (d, $J_{C,P}$ = 15.9 Hz, $C_{PAr}$), 138.45 (d, $J_{C,P}$ = 6.0 Hz, $C_{PAr}$), 140.25 (d, $J_{C,P}$ = 2.7 Hz, $C_{Ar,ipso}$), 233.45 (d, $J_{C,P}$ = 1.7 Hz, *C*O) ppm. $^{31}$P NMR (81 MHz, $C_6D_6$): $\delta$ = –14.22 ppm. MS (CI, isobutane): *m*/*z* (%) 500 (4) [M + 1], 455 (100) [M – $NMe_2$], 415 (43) [M – 3 CO], 364 (45) [M – 3 CO – Cr], 319 (45) [M – 3 CO – Cr – $HNMe_2$]. $[\alpha]_D^{r.t.}$ = –480.9 (*c* = 0.22, $CHCl_3$). IR ($CHCl_3$): $\nu_{CO}$ = 1965, 1882 cm$^{-1}$. $C_{26}H_{26}CrNO_4P$ (499.46): calcd. C 62.52, H 5.25, N 2.80; found C 62.08, H 5.01, N 2.97.

**[{η$^6$-(*R*,*R*p)-*N*,*N*-Dimethyl-1-(3-(diphenylphosphanyl)-4-methoxyphenyl)ethylamine}Cr(CO)$_3$] [(*R*)-14M] and [{η$^6$-(*R*,*S*p)-*N*,*N*-Dimethyl-1-(3-(diphenylphosphanyl)-4-methoxyphenyl)ethylamine}Cr(CO)$_3$] [(*S*)-14m]:** Yield yellow crystals (1.98 g, 30%). $R_f$ = 0.15 (aluminium oxide; diethyl ether/hexane, 1:1) The two compounds eluted as a single fraction. Further attempts to separate the two diastereoisomers by column chromatography failed.
**(*R*)-14M:** $^1$H NMR (500 MHz, $C_6D_6$): $\delta$ = 0.97 (d, *J* = 6.71 Hz, 3 H, α-Me), 1.88 (s, 6 H, N*Me*$_2$), 2.69 (q, *J* = 6.71 Hz, 1 H, α-C*H*), 2.91 (s, 3 H, O*Me*), 4.15 (dd, *J* = 6.71, *J* = 3.35 Hz, 1 H, $H_{Ar}$), 5.02 (t, *J* = 1.67 Hz, 1 H, $H_{Ar}$), 5.13 (dd, *J* = 6.71, *J* = 1.67 Hz, 1 H, $H_{Ar}$), 7.01–7.10 (m, 6 H, *m*/*p*-$H_{PAr}$), 7.43 (m, *J* = 7.33 Hz, 2 H, *o*-$H_{PAr}$), 7.59 (m, *J* = 7.33 Hz, 2 H, *o*- $H_{PAr}$) ppm. $^{13}$C NMR (125 MHz, $C_6D_6$): $\delta$ = 15.60 (α-Me), 41.04 (N*Me*$_2$), 55.63 (O*Me*), 61.33 (α-*C*H), 71.61 ($C_{Ar}$), 92.66 (d, $J_{C,P}$ = 24.6 Hz, $C_{Ar,ipso}$), 92.84 ($C_{Ar}$), 101.73 ($C_{Ar}$), 104.753 ($C_{Ar,ipso}$), 128.29 ($C_{PAr}$), 128.79 ($C_{PAr}$), 128.98 ($C_{PAr}$), 133.22 (d, $J_{C,P}$ = 20.3 Hz, $C_{PAr}$), 134.92 (d, $J_{C,P}$ = 14.8 Hz,, $C_{PAr}$), 135.26 (d, $J_{C,P}$ = 20.9 Hz, $C_{PAr}$), 137.44 (d, $J_{C,P}$ = 14.8 Hz, $C_{PAr}$), 146.14 (d, $J_{C,P}$ = 13.7 Hz, $C_{Ar,ipso}$), 233.11 (*C*O) ppm. $^{31}$P NMR (81 MHz, $C_6D_6$): $\delta$ = –18.57 ppm.

**(*R*)-14m:** $^1$H NMR (500 MHz, $C_6D_6$): $\delta$ = 0.87 (d, *J* = 6.8 Hz, 3 H, α-Me), 1.92 (s, 6 H, N*Me*$_2$), 2.86 (q, *J* = 6.7 Hz, 1 H, α-C*H*), 2.91 (s, 3 H, O*Me*), 4.12 (dd, *J* = 6.7, *J* = 3.4 Hz, 1 H, $H_{Ar}$), 5.10 (t, *J* = 1.7 Hz, 1 H, $H_{Ar}$), 5.25 (dd, *J* = 6.7, *J* = 1.7 Hz, 1 H, $H_{Ar}$), 7.01–7.10 (m, 6 H, *m*/*p*-$H_{PAr}$), 7.43 (m, 2 H, *o*-$H_{PAr}$), 7.59 (m, *J* = 7.3 Hz, 2 H, *o*-$H_{PAr}$) ppm. $^{13}$C NMR (125 MHz, $C_6D_6$): $\delta$ = 14.50 (α-Me), 40.87 (N*Me*$_2$), 55.58 (O*Me*), 61.23 (α-*C*H), 71.84 ($C_{Ar}$), 91.83 (d, $J_{C,P}$ = 24.1 Hz, $C_{Ar,ipso}$), 96.72 ($C_{Ar}$), 97. 34 ($C_{Ar}$), 128.77 (d, $J_{C,P}$ = 6.6 Hz, $C_{PAr}$), 128.98 (d, $J_{C,P}$ = 9.9 Hz, $C_{PAr}$), 129.81 ($C_{PAr}$), 133.09 (d, $J_{C,P}$ = 20.3 Hz, $C_{PAr}$), 135.06 (d, $J_{C,P}$ = 14.8 Hz, $C_{PAr}$), 135.33 (d, $J_{C,P}$ = 21.4 Hz, $C_{PAr}$), 137.54 (d, $J_{C,P}$ = 14.8 Hz, $C_{PAr}$), 146.26 (d, $J_{C,P}$ = 15.3 Hz, $C_{Ar}$), 233.26 (*C*O) ppm. $^{31}$P NMR (81 MHz, $C_6D_6$): $\delta$ = –17.92 ppm. The absolute configuration of the two diastereomers has not been assigned.

**Lithiation of [{η$^6$-(*R*)-*N*,*N*-Dimethyl-1-(*p*-chlorophenyl)ethylamine}-Cr(CO)$_3$] [(*R*)-9]:** Following general procedure C, lithiation of (*R*)-**9** (4.77 g, 14.9 mmol) with *tert*-butyllithium (1.7 M in pentane; 8.8 mL, 14.9 mmol), followed by addition of chlorodiphenylphosphane (3.29 g, 14.9 mmol), produced a mixture of three products. Column chromatography (aluminium oxide; hexane→hexane/diethyl ether, 3:2) gave (*R*,*S*p)-**16**, (*R*,*R*p)-**16** and (*R*)-**17** in that order.

**[{η$^6$-(*R*,*S*p)-*N*,*N*-Dimethyl-1-[4-chloro-2-(diphenylphosphanyl)phenyl]ethylamine}Cr(CO)$_3$] [(*R*,*S*p)-16]:** Yield yellow crystals 5.0 g (67%). $R_f$ = 0.54 (aluminium oxide; hexane/diethyl ether, 2:1). $^1$H NMR (500 MHz, $C_6D_6$): $\delta$ = 0.66 (d, *J* = 6.7 Hz, 3 H, α-Me), 1.47 (s, 3 H, N*Me*$_2$), 4.39 (m, *J* = 6.7 Hz, 1 H, α-C*H*), 4.45 (dd, *J* = 6.4, *J* = 2.8 Hz, 1 H, $H_{Ar}$), 5.04 (d, *J* = 5.8 Hz, 1 H, $H_{Ar}$), 5.26 (br. s, 1 H, $H_{Ar}$), 6.69 (m, 4 H, *m*/*p*-$H_{PAr}$), 7.09 (m, *J* = 7.3 Hz, 2 H, *m*/*p*-$H_{PAr}$), 7.20 (m, 2 H, *o*-$H_{PAr}$), 7.56 (m, *J* = 7.0 Hz, 2 H, *o*-$H_{PAr}$) ppm. $^{13}$C NMR (125 MHz, $C_6D_6$): $\delta$ = 6.02 (α-Me), 37.78 (N*Me*$_2$), 58.40 (d, $J_{C,P}$ = 14.2 Hz, α-*C*H), 87.76 (d, $J_{C,P}$ = 3.3 Hz, $C_{Ar}$), 93.01 ($C_{Ar}$), 99.69 (d, $J_{C,P}$ = 3.8 Hz, $C_{Ar}$), 106.58 (d, $J_{C,P}$ = 29.7 Hz, $C_{Ar,ipso}$), 108.3 (d, $J_{C,P}$ = 4.4 Hz, $C_{Ar,ipso}$), 117.40 (d, $J_{C,P}$ = 19.2 Hz, $C_{Ar,ipso}$), 127.91 ($C_{PAr}$), 128.19 ($C_{PAr}$), 128.30 ($C_{PAr}$), 128.90 (d, $J_{C,P}$ = 6.1 Hz, $C_{PAr}$), 129.73 ($C_{PAr}$), 132.30 (d, $J_{C,P}$ = 20.8 Hz, $C_{PAr}$), 135.01 (d, $J_{C,P}$ = 20.3 Hz, $C_{PAr}$), 136.50 (d, $J_{C,P}$ = 14.8 Hz, $C_{PAr}$), 137.95 (d, $J_{C,P}$ = 6.0 Hz, $C_{PAr}$), 231.61 (*C*O) ppm. $^{31}$P NMR (81 MHz, $C_6D_6$): $\delta$ = –14.41 ppm. MS (CI, isobutane): *m*/*z* (%) 504 (21) [M + H], 459 (100) [M – $NMe_2$], 419 (46) [M – 3 CO], 368 (15) [M – 3 CO – Cr]. $[\alpha]_D^{r.t.}$ = –401.9 (*c* = 0.21, $CHCl_3$). IR ($CHCl_3$): $\nu_{CO}$ = 1976, 1912 cm$^{-1}$. $C_{25}H_{23}ClCrNO_3P$ (503.87): calcd. C 59.59, H 4.60, N 2.78; found C 60.56, H 4.81, N 2.74.

**[{η$^6$-(*R*,*R*p)-*N*,*N*-Dimethyl-1-[4-chloro-2-(diphenylphosphanyl)phenyl]ethylamine}Cr(CO)$_3$] [(*R*,*R*p)-16]:** Yield yellow crystals (0.53 g). The yield is only indicative as this fraction also contained the other diastereoisomer and traces of the product derived from metal–halogen exchange. Attempts to further purify the product by means of crystallisation failed. Only the $^1$H and $^{31}$P NMR spectra are reported. $R_f$ = 0.42 (aluminium oxide; hexane/diethyl ether, 2:1). $^1$H NMR (500 MHz, $C_6D_6$): $\delta$ = 0.87 (d, *J* = 6.8 Hz, 3 H, α-Me), 2.00 (s, 3 H, N*Me*$_2$), 3.57 (m, 1 H, α-C*H*), 4.86 (dd, *J* = 4.9, *J* = 1.2 Hz, 1 H, $H_{Ar}$), 5.06 (dd, *J* = 1.7, *J* = 1.0 Hz, 1 H, $H_{Ar}$), 5.21 (dd, *J* = 6.8, *J* = 2.4 Hz, 1 H, $H_{Ar}$), 6.69 (m, 4 H, $H_{PAr}$), 7.02–7.05 (m, 6 H, $H_{PAr}$), 7.20–7.35 (m, 2 H, $H_{PAr}$), 7.51–7.65 (m, 2 H, $H_{PAr}$) ppm. $^{31}$P NMR (81 MHz, $C_6D_6$): $\delta$ = –17.53 ppm.

**[{η$^6$-(*R*)-*N*,*N*-Dimethyl-1-[4-(diphenylphosphanyl)phenyl]ethylamine}Cr(CO)$_3$] [(*R*)-17]:** Yield yellow crystals (1.30 g, 18%). $R_f$ = 0.30 (aluminium oxide; hexane/diethyl ether, 3:2). $^1$H NMR (500 MHz, $C_6D_6$): $\delta$ = 0.92 (d, *J* = 7.0 Hz, 3 H, α-Me), 1.89 (s, 6 H, N*Me*$_2$), 3.25 (q, *J* = 7.0 Hz, 1 H, α-C*H*), 4.40 (dd, *J* = 6.4, *J* = 1.5 Hz, 1 H, $H_{Ar}$), 4.75 (m, *J* = 6.8 Hz, 1 H, $H_{Ar}$), 4.84 (ddd, *J* = 6.4, *J* = 4.2, *J* = 1.2 Hz, 1 H, $H_{Ar}$), 5.00 (ddd, *J* = 6.6, *J* = 5.4, *J* = 1.5 Hz, 1 H, $H_{Ar}$), 7.04–7.13 (m, 6 H, *m*/*p*-$H_{PAr}$), 7.39 (m, *J* = 7.3, *J* = 1.5 Hz, 2 H, *o*-$H_{PAr}$), 7.45 (m, *J* = 7.3 Hz, 2 H, *o*-$H_{PAr}$) ppm. $^{13}$C NMR (125 MHz, $C_6D_6$): $\delta$ = 10.89 (α-Me), 40.55 (N*Me*$_2$), 61.04 (α-*C*H), 89.55 (d, $J_{C,P}$ = 3.3 Hz, $C_{Ar}$), 93.91 (d, $J_{C,P}$ = 6.0 Hz, $C_{Ar}$), 97.24 (d, $J_{C,P}$ = 11.5 Hz, $C_{Ar}$), 98.42 (d, $J_{C,P}$ = 19.2 Hz, $C_{Ar}$), 102.36 (d, $J_{C,P}$ = 19.2 Hz, $C_{Ar,ipso}$), 113.71 ($C_{Ar,ipso}$), 128.94 (d, $J_{C,P}$ = 1.1 Hz, $C_{PAr}$), 129.00 (d, $J_{C,P}$ = 1.1 Hz, $C_{PAr}$), 129.58 (d, $J_{C,P}$ = 12.1 Hz, $C_{PAr}$), 134.13 (d, $J_{C,P}$ = 10.9 Hz, $C_{PAr}$), 134.29 (d, $J_{C,P}$ = 11.0 Hz, $C_{PAr}$), 135.76 (d, $J_{C,P}$ = 12.6 Hz, $C_{PAr}$), 136.11 (d, $J_{C,P}$ = 12.6 Hz, $C_{PAr}$), 232.93 (*C*O) ppm. $^{31}$P NMR (81 MHz, $C_6D_6$): $\delta$ = –7.83 ppm. MS (EI): *m*/*z* (%) 469 (8) [M$^+$], 385 (100) [M – 3 CO]. $[\alpha]_D^{r.t.}$ = –27.4 (*c* = 1.08, $CHCl_3$). IR ($CHCl_3$): $\nu_{CO}$ = 1970, 1893 cm$^{-1}$. $C_{25}H_{24}CrNO_3P$ (469.44): calcd. C 63.96, H 5.15, N 3.00; found C 63.56, H 4.82, N 3.10.

**[{η$^6$-(*R*,*S*p)-1-[4-Chloro-3-(diphenylphosphanyl)phenyl]ethylamine}Cr(CO)$_3$] [(*R*)-18M] and [{η$^6$-(*R*,*R*p)-1-[4-chloro-3-(diphenylphosphanyl)phenyl]ethylamine}Cr(CO)$_3$] [(*S*)-18m]:** Following general procedure C, lithiation of (*R*)-**9** (056 g, 1.75 mmol) with LDA (2 M in pentane, 1.0 mL, 2.0 mmol), followed by addition of chlorodiphenylphosphane (0.44 g, 2.0 mmol), produced a nearly 1:1 ratio of two compounds. The two were collected as a single fraction after column chromatography ($R_f$ = 0.47; aluminium oxide, diethyl ether). Further attempts to separate them failed. Analytical data refer to the clean fraction collected after flash chromatography. Yield yellow crystals 0.81 g (92%). M = major diastereoisomer; m = minor diastereoisomer. $^1$H NMR (500 MHz, $C_6D_6$): $\delta$ = 0.74 (d, *J* = 6.8 Hz, 3 H, α-$Me_m$), 0.80 (d, *J* = 6.8 Hz, 3 H, α-$Me_M$), 1.78 (s, 6 H, N*Me*$_{2M}$), 1.83 (s, 6 H, N*Me*$_{2m}$), 2.64 (q, *J* = 6.8 Hz, 1 H, α-C*H*$_M$), 2.75 (q, *J* = 7.1 Hz, 1 H, α-C*H*$_m$), 4.66–4.94 (overlapping peaks, 3 $H_{ArM}$ + 3 $H_{Arm}$), 7.04–7.10 (m, overlapping peaks, 6 H, $H_{PArM}$ + 6 H, $H_{PArm}$), 7.27–7.40 (m, overlapping peaks, 2 H, $H_{PArM}$ + 2 H, $H_{PArm}$), 7.50–7.60 (m, overlapping peaks, 2 H, $H_{PArM}$ + 2 H, $H_{PArm}$) ppm. $^{31}$P NMR (81 MHz, $C_6D_6$): $\delta$ = –12.06 ($P_M$), –11.83 ($P_m$) ppm.

 © 2007 Wiley-VCH Verlag GmbH & Co. KGaA, Weinheim 

**[{η⁶-(*S*,*R*p)-1-[2-(Diphenylphosphanyl)-4-tolyl]chloroethyl}Cr(CO)₃] [(*S*,*R*p)-19]:** This complex was prepared from (*S*,*R*p)-**11** (6.45 g, 13.0 mmol) and 1-chloroethyl chloroformate (5.8 mL, 53.4 mmol) in thf (260 mL) according to general procedure D. The crude product was purified by column chromatography ($R_f$ = 0.54; silica gel, ethyl acetate/hexane, 1:1). Yield yellow crystals (5.5 g, 86%). $^1$H NMR (500 MHz, $C_6D_6$): $\delta$ = 1.39 (s, 3 H, *p*-Me), 1.47 (d, $J$ = 6.7 Hz, 3 H, α-Me), 4.52 (d, $J$ = 6.1 Hz, 1 H, $H_{Ar}$), 4.65 (s, 1 H, $H_{Ar}$), 4.87 (dd, $J$ = 6.1, $J$ = 2.5 Hz, 1 H, $H_{Ar}$), 5.89 (m, $J$ = 8.8, $J$ = 6.7 Hz, 1 H, α-C*H*), 7.01–7.12 (m, 6 H, *m*/*p*-$H_{PAr}$), 7.39 (m, $J$ = 7.3 Hz, 2 H, *o*-$H_{PAr}$), 7.56 (t, $J$ = 7.3 Hz, 2 H, *o*-$H_{PAr}$) ppm. $^{13}$C NMR (125 MHz, $C_6D_6$): $\delta$ = 19.71 (*p*-Me), 23.84 (α-Me), 54.18 (d, $J_{C,P}$ = 29.6 Hz, α-*C*H), 89.63 (d, $J_{C,P}$ = 2.8 Hz, $C_{Ar}$), 93.50 ($C_{Ar}$), 98.30 (d, $J_{C,P}$ = 2.8 Hz, $C_{Ar}$), 104.88 (d, $J_{C,P}$ = 24.7 Hz, $C_{Ar,ipso}$), 107.60 ($C_{Ar,ipso}$), 115.28 (d, $J_{C,P}$ = 20.8 Hz, $C_{Ar,ipso}$), 128.71 (d, $J_{C,P}$ = 7.2 Hz, $C_{PAr}$), 129.98 (d, $J_{C,P}$ = 6.6 Hz, $C_{PAr}$), 129.42 ($C_{PAr}$), 130.02 ($C_{PAr}$), 134.12 (d, $J_{C,P}$ = 20.3 Hz, $C_{PAr}$), 134.54 (d, $J_{C,P}$ = 13.1 Hz, $C_{PAr}$), 134.94 (d, $J_{C,P}$ = 19.8 Hz, $C_{PAr}$), 135.76 (d, $J_{C,P}$ = 8.8 Hz, $C_{PAr}$), 232.49 (d, $J_{C,P}$ = 2.2 Hz, *C*O) ppm. $^{31}$P NMR (81 MHz, $C_6D_6$): $\delta$ = –17.74 ppm. MS (CI, isobutane): *m*/*z* (%) 475 (66) [M + 1], 439 (33) [M – Cl], 390 (61) [M – 3 CO], 354 (22) [M – 3 CO – HCl], 305 (100). $[\alpha]_D^{r.t.}$ = +291.0 (*c* = 1.10, $CHCl_3$). IR ($CHCl_3$): $\nu_{CO}$ = 1971, 1888 cm$^{-1}$. $C_{24}H_{20}ClCrO_3P$ (474.84): calcd. C 60.71, H 4.24; found C 60.87, H 4.38.

**[{η⁶-(*S*,*R*p)-1-[4-*tert*-Butyl-2-(diphenylphosphanyl)phenyl]chloroethyl}Cr(CO)₃] [(*S*,*R*p)-20]:** This complex was prepared according to general procedure D from (*S*,*R*p)-**12** (6.00 g, 11.43 mmol) and 1-chloroethyl chloroformate (6.54 g, 45.70 mmol) in dry thf (250 mL). The crude product was purified by column chromatography (aluminium oxide; ethyl acetate/hexane, 4:1). Yield yellow crystals 4.59 g (78%). $^1$H NMR (300 MHz, $CDCl_3$): $\delta$ = 1.12 (s, 9 H, *p*-*t*Bu), 1.56 (d, $J$ = 6.7 Hz, 3 H, α-Me), 5.12 (s, 1 H, $H_{Ar}$), 5.32 (br. s, 1 H, $H_{Ar}$), 5.65 (d, $J$ = 5.5 Hz, 1 H, $H_{Ar}$), 5.93 (m, 1 H, α-C*H*), 7.35–7.39 (m, 10 H, $H_{PAr}$) ppm. $^{13}$C NMR (75 MHz, $CDCl_3$): $\delta$ = 22.85 (α-Me), 30.93 (*pC*$Me_3$), 33.96 (*pC*$Me_3$), 54.15 (d, $J$ = 28.2 Hz, α-*C*H), 86.12 ($C_{Ar}$), 92.87 ($C_{Ar}$), 97.10 ($C_{Ar}$), 101.55 (d, $J$ = 24.5 Hz, $C_{Ar,ipso}$), 116.82 (d, $J$ = 22.1 Hz, $C_{Ar,ipso}$), 121.48 ($C_{Ar,ipso}$), 128.34–135.95 ($C_{PAr}$), 232.19 (*C*O) ppm. $^{31}$P NMR (121.5 MHz, $CDCl_3$): $\delta$ = –16.79 ppm. IR ($CHCl_3$): $\nu_{CO}$ = 1974, 1912 cm$^{-1}$.

**[{η⁶-(*R*,*R*p)-1-[2-(Diphenylphosphanyl)-4-methoxyphenyl]chloroethyl}Cr(CO)₃] [(*R*,*R*p)-21]:** This complex was prepared from (*R*,*R*p)-**13** and 1-chloroethyl chloroformate (2.07 mL, 19.0 mmol) according to general procedure D. The crude product was purified by column chromatography ($R_f$ = 0.40 (silica gel; ethyl acetate/hexane, 3:7). Yield yellow crystals 2.02 g (85%). $^1$H NMR (500 MHz, $C_6D_6$): $\delta$ = 1.52 (d, $J$ = 6.7 Hz, 3 H, α-Me), 2.78 (s, 3 H, O*Me*), 4.29 (dd, $J$ = 6.7, $J$ = 2.1 Hz, 1 H, $H_{Ar}$), 4.77 (dd, $J$ = 2.1, $J$ = 1.2 Hz, 1 H, $H_{Ar}$), 5.08 (dd, $J$ = 6.7, $J$ = 2.7 Hz, 1 H, $H_{Ar}$), 5.72 (dq, $J$ = 9.2, $J$ = 6.7 Hz, 1 H, α-C*H*), 6.95–7.10 (m, 6 H, *m*/*p*-$H_{PAr}$), 7.41 (m, $J$ = 7.6 Hz, 2 H, *o*-$H_{PAr}$), 7.58 (tm, $J$ = 7.6 Hz, 2 H, *o*-$H_{PAr}$) ppm. $^{13}$C NMR (125 MHz, $C_6D_6$): $\delta$ = 25.12 (α-Me), 53.89 (d, $J_{C,P}$ = 27.4 Hz, α-*C*H), 55.09 (O*Me*), 75.95 ($C_{Ar}$), 84.85 (d, $J_{C,P}$ = 1.7 Hz, $C_{Ar}$), 91.22 (d, $J_{C,P}$ = 3.3 Hz, $C_{Ar}$), 102.00 ($C_{PAr}$), 106.62 (d, $J_{C,P}$ = 24.6 Hz, $C_{Ar,ipso}$), 110.10 ($C_{PAr}$), 111.16 (d, $J_{C,P}$ = 19.7 Hz, $C_{Ar,ipso}$), 133.79 (d, $J_{C,P}$ = 13.7 Hz, $C_{PAr}$), 134.32 (d, $J_{C,P}$ = 20.8 Hz, $C_{PAr}$), 135.03 (d, $J_{C,P}$ = 29.8 Hz, $C_{PAr}$), 135.37 (d, $J_{C,P}$ = 8.8 Hz, $C_{PAr}$), 141.67 (d, $J_{C,P}$ = 1.6 Hz, $C_{Ar,ipso}$), 232.52 (d, $J_{C,P}$ = 2.7 Hz, *C*O) ppm. $^{31}$P NMR (81 MHz, $C_6D_6$): $\delta$ = –16.69 ppm. MS (CI, isobutane): *m*/*z* (%) 491 (35) [M + 1], 455 (100) [M – Cl], 427 (33) [M – Cl – CO], 319 (91) [M – Cl – 3 CO – Cr]. $[\alpha]_D^{r.t.}$ = –311.9 (*c* = 0.21, $CHCl_3$). IR ($CHCl_3$): $\nu_{CO}$ = 1970, 1894 cm$^{-1}$. $C_{24}H_{20}ClCrO_4P$ (490.84): calcd. C 58.73, H 4.11; found C 58.99, H 4.01.

**[{η⁶-(*R*,*S*p)-1-[4-chloro-2-(diphenylphosphanyl)phenyl]chloroethyl}-Cr(CO)₃] [(*R*,*S*p)-22]:** This complex was prepared as follows. (*R*,*S*p)-**16** (1.80 g, 3.6 mmol) was dissolved in dry diethyl ether (70 mL), the solution was cooled to –40 °C and 1-chloroethyl chloroformate (1.56 mL, 14.3 mmol) added dropwise. This solution was warmed slowly overnight. As a $^{31}$P NMR check revealed only 50% conversion, the solution was again cooled to –40 °C and two more equivalents of 1-chloroethyl chloroformate (0.78 mL, 7.1 mmol) were added. The mixture was stirred at room temperature until complete conversion. Solvent and volatiles were distilled off, dry diethyl ether was added and the mixture filtered through a short pad of Celite on a sintered glass filter. The solvent was evaporated and the crude product was used for the next step. Yield (of crude product): yellow crystals (1.42 g, 90%). $^1$H NMR (200 MHz, $C_6D_6$): $\delta$ = 1.32 (d, $J$ = 6.8 Hz, 3 H, α-Me), 4.66 (dd, $J$ = 6.6, $J$ = 2.9 Hz, 1 H, $H_{Ar}$), 4.82 (dd, $J$ = 6.6, $J$ = 1.7 Hz, 1 H, $H_{Ar}$), 4.99 (dd, $J$ = 1.7, $J$ = 0.7 Hz, 1 H, $H_{Ar}$), 5.72 (dq, $J$ = 9.3, $J$ = 6.8 Hz, 1 H, α-C*H*), 7.10–6.99 (m, 6 H, *m*/*p*-$H_{PAr}$), 7.33 (m, 2 H, *o*-$H_{PAr}$), 7.49 (m, 2 H, *o*-$H_{PAr}$) ppm. $^{31}$P NMR (81 MHz, $C_6D_6$): $\delta$ = –17.53 ppm.

**[{η⁶-(*S*,*R*p)-1-[2-(Diphenylphosphanyl)-4-tolyl]ethyldiphenylphosphane}Cr(CO)₃] [(*S*,*R*p)-23a]:** This complex was prepared from (*S*,*R*p)-**19** (1.07 g, 2.5 mmol), diphenylphosphane (0.51 g, 2.7 mmol) and $TlPF_6$ (0.95 g, 2.7 mmol) in dry acetone (50 mL) according to general procedure E. The crude product was purified by column chromatography ($R_f$ = 0.42; aluminium oxide; dichloromethane/hexane, 1:4). Yield yellow crystals (1.0 g, 64%). $^1$H NMR (500 MHz, $C_6D_6$): $\delta$ = 1.34 (dd, $J$ = 7.0, $J$ = 5.0 Hz, 3 H, α-Me), 1.44 (s, 3 H, *p*Me), 4.39 (ddd, $J$ = 6.7, $J$ = 3.4, $J$ = 1.5 Hz, 1 H, $H_{Ar}$), 4.47 (dd, $J$ = 6.7, $J$ = 1.0 Hz, 1 H, $H_{Ar}$), 4.91 (dq, $J$ = 9.5, $J$ = 7.0 Hz, 1 H, α-C*H*), 5.00 (t, $J$ = 1.5 Hz, $H_{Ar}$), 6.95–7.16 (m, 12 H, $H_{PAr}$), 7.21 (m, 2 H, $H_{PAr}$), 7.25 (m, $J$ = 7.0 Hz, 2 H, $H_{PAr}$), 7.52 (m, $J$ = 7.0 Hz, 2 H, $H_{PAr}$), 7.74 (m, $J$ = 7.6 Hz, 2 H, $H_{PAr}$) ppm. $^{13}$C NMR (125 MHz, $C_6D_6$): $\delta$ = 16.25 (α-Me), 19.71 (*p*Me), 33.14 (dd, $J$ = 24.4 Hz, α-*C*H), 90.10 (dd, $J_{C,P}$ = 4.8 Hz, $C_{Ar}$), 94.00 ($C_{Ar}$), 100.04 (d, $J_{C,P}$ = 2.2 Hz, $C_{Ar}$), 104.86 (d, $J_{C,P}$ = 18.7 Hz, $C_{Ar,ipso}$), 106.23 ($C_{Ar,ipso}$), 121.44 (dd, $J_{C,P}$ = 22.5 Hz, $C_{Ar,ipso}$), 128.57 (d, $J_{C,P}$ = 7.6 Hz, $C_{PAr}$), 128.62 (d, $J_{C,P}$ = 4.4 Hz, $C_{PAr}$), 128.93 (d, $J_{C,P}$ = 6.6 Hz, $C_{PAr}$), 129.24 ($C_{PAr}$), 129.83 (d, $J_{C,P}$ = 3.9 Hz, $C_{PAr}$), 131.60 (d, $J_{C,P}$ = 15.3 Hz, $C_{PAr}$), 134.15 (d, $J_{C,P}$ = 23.6 Hz, $C_{PAr}$), 134.54 (dd, $J_{C,P}$ = 20.3, $J_{C,P}$ = 2.2 Hz, $C_{PAr}$), 135.05 (d, $J_{C,P}$ = 19.7 Hz, $C_{PAr}$), 135.77 (d, $J_{C,P}$ = 13.7 Hz, $C_{PAr}$), 136.28 (d, $J_{C,P}$ = 9.8 Hz, $C_{PAr}$) 136.44 (d, $J_{C,P}$ = 22.5 Hz, $C_{PAr}$), 137.04 (d, $J_{C,P}$ = 19.2 Hz, $C_{PAr}$), 233.34 (*C*O) ppm. $^{31}$P NMR (202 MHz, $C_6D_6$): $\delta$ = –17.56 (d, $J_{P,P}$ = 18.3 Hz, *o*$PPh_2$), 8.47 (d, $J_{P,P}$ = 18.3 Hz, α-$PPh_2$) ppm. MS (CI, isobutane): *m*/*z* (%) 625 (20) [M + 1], 540 (22) [M – 3 CO], 489 (54) [M – 3 CO – Cr], 439 (100) [M – $PPh_2$]. $[\alpha]_D^{r.t.}$ = +293.6 (*c* = 1.00, $CHCl_3$). IR ($CHCl_3$): $\nu_{CO}$ = 1965, 1894 cm$^{-1}$. $C_{36}H_{30}CrO_3P_2$ (624.57): calcd. C 69.23, H 4.84; found C 69.14, H 5.26.

**[{η⁶-(*S*,*R*p)-1-[2-(Diphenylphosphanyl)-4-tolyl]ethyldicyclohexylphosphane}Cr(CO)₃] [(*S*,*R*p)-23b]:** This complex was prepared from (*S*,*R*p)-**19** (1.45 g, 3.0 mmol), dicyclohexylphosphane (0.59 g, 3.0 mmol) and $TlPF_6$ (1.04 g, 3.0 mmol) in dry acetone (60 mL) according to general procedure E. The crude product was purified by column chromatography ($R_f$ = 0.54; aluminium oxide; diethyl ether/hexane, 1:4). Yield yellow crystals (1.2 g, 63%). Crystals suitable for X-ray structure determination were grown from a layered mixture of dichloromethane and hexane at –30 °C. $^1$H NMR (500 MHz, $C_6D_6$): $\delta$ = 1.00–1.23 (m, 10 H, $H_{PCy_2}$), 1.34 (m, 1 H,

 © 2007 Wiley-VCH Verlag GmbH & Co. KGaA, Weinheim 

$H_{PCy_2}$), 1.39 (dd, $J$ = 7.0, $J$ = 3.4 Hz, 3 H, α-Me), 1.45 (s, 3 H, *p*Me), 1.48–1.80 (m, 11 H, $H_{PCy_2}$), 4.24 (dq, $J$ = 7.0 Hz, 1 H, α-C*H*), 4.78 (br. d, $J$ = 6.4 Hz, 1 H, $H_{Ar}$), 4.84 (m, $J$ = 6.4, $J$ = 3.35, $J$ = 0.6 Hz, 1 H, $H_{Ar}$), 5.10 (t, $J$ = 1.2 Hz, 1 H, $H_{Ar}$), 7.14 (m, $J$ = 7.3 Hz, 4 H, $H_{PPh_2}$), 7.47 (m, $J$ = 7.6 Hz, 2 H, $H_{PPh_2}$), 7.65 (m, $J$ = 7.6 Hz, 2 H, $H_{PPh_2}$), 7.70 (m, $J$ = 7.6 Hz, 2 H, $H_{PPh_2}$) ppm. $^{13}$C NMR (125 MHz, $C_6D_6$): $\delta$ = 15.32 αMe), 19.63 (*p*Me), 26.64 (d, $J_{C,P}$ = 3.9 Hz, $C_{PCy_2}$), 27.03 (d, $J_{C,P}$ = 12.1 Hz, $C_{PCy_2}$), 27.45 (d, $J_{C,P}$ = 8.2 Hz, $C_{PCy_2}$), 27.82 (d, $J_{C,P}$ = 5.4 Hz, $C_{PCy_2}$), 28.05 (d, $J_{C,P}$ = 13.7 Hz, $C_{PCy_2}$), 30.02 (d, $J_{C,P}$ = 9.3 Hz, $C_{PCy_2}$), 30.38 (d, $J_{C,P}$ = 5.5 Hz, $C_{PCy_2}$), 31.58 (dd, $J_{C,P}$ = 21.4 Hz, α-*C*H), 31.70 (d, $J_{C,P}$ = 12.6 Hz, $C_{PCy_2}$), 33.48 (d, $J_{C,P}$ = 21.4 Hz, $C_{PCy_2}$), 33.89 (d, $J_{C,P}$ = 23.5 Hz, $C_{PCy_2}$), 88.93 (dd, $J_{C,P}$ = 4.1, $J_{C,P}$ = 3.8 Hz, $C_{Ar}$), 94.92 ($C_{Ar}$), 101.98 (d, $J_{C,P}$ = 2.8 Hz, $C_{Ar}$), 104.70 (dd, $J_{C,P}$ = 24.1, $J_{C,P}$ = 3.3 Hz, $C_{Ar,ipso}$), 105 41 ($C_{Ar,ipso}$), 124.78 (dd, $J_{C,P}$ = 22.5, $J_{C,P}$ = 19.2 Hz, $C_{Ar,ipso}$), 128.47 ($C_{PPh_2}$), 128.78 (d, $J_{C,P}$ = 7.1 Hz, $C_{PPh_2}$), 133.90 (dd, $J_{C,P}$ = 18.6, $J_{C,P}$ = 2.7 Hz, $C_{PPh_2}$), 135.39 (d, $J_{C,P}$ = 20.9 Hz, $C_{PPh_2}$), 137.35 (dd, $J_{C,P}$ = 14.3, $J_{C,P}$ = 3.9 Hz, $C_{PPh_2}$),138.42 (dd, $J_{C,P}$ = 7.1, $J_{C,P}$ = 2.7 Hz, $C_{PPh_2}$), 233.41 (*C*O) ppm. $^{31}$P NMR (202 MHz, $C_6D_6$): $\delta$ = –18.71 (d, $J_{P,P}$ = 38.3 Hz, $PPh_2$), 15.85 (d, $J_{P,P}$ = 38.3 Hz, $PCy_2$) ppm. MS (CI, isobutane): *m*/*z* (%) 637 (82) [M + 1], 580 (16) [M – 2 CO], 552 (100) [M – 3 CO], 501 (16) [M – 3 CO – Cr]. $[\alpha]_D^{r.t.}$ = +549.7 (*c* = 0.62, $CHCl_3$). IR ($CHCl_3$): $\nu_{CO}$ = 1963, 1887 cm$^{-1}$. $C_{36}H_{42}CrO_3P_2$ (636.67): calcd. C 67.91, H 6.65; found C 69.12, H 7.75.

**[{η$^6$-(*S*,*R*p)-1-[2-(Diphenylphosphanyl)-4-tolyl]ethyldi-*tert*-butylphosphane}Cr(CO)$_3$] [(*S*,*R*p)-23c]:** This complex was prepared from (*S*,*R*p)-**19** (1.02 g, 2.4 mmol), di-*tert*-butylphosphane (0.34 g, 2.6 mmol) and $TlPF_6$ (0.91 g, 2.6 mmol) in dry acetone (48 mL) according to general procedure E. The crude product was purified by column chromatography (aluminium oxide; dichloromethane/hexane, 1:4). $R_f$ = 0.71. Yield yellow crystals (0.88 g, 62%). $^1$H NMR (500 MHz, $C_6D_6$): $\delta$ = 0.92 [d, $J$ = 9.0 Hz, 9 H, P(C*Me*$_3$)$_2$], 1.21, [d, $J$ = 10.7 Hz, 9 H, P(C*Me*$_3$)$_2$], 1.48 (s, 3 H, *p*Me), 1.55 (dd, $J$ = 7.0, $J$ = 2.7 Hz, 3 H, α-Me), 4.44 (m, $J$ = 7.0 Hz, 1 H, α-C*H*), 4.75 (dd, $J$ = 6.7, $J$ = 3.4 Hz, 1 H, $H_{Ar}$), 4.80 (br. d, $J$ = 6.7 Hz, 1 H, $H_{Ar}$), 5.23 (br. s, 1 H, $H_{Ar}$), 7.06 (m, $J$ = 7.3 Hz, 2 H, $H_{PPh_2}$), 7.10–7.16 (m, 4 H, $H_{PPh_2}$), 7.45 (m, $J$ = 7.0 Hz, 2 H, $H_{PPh_2}$), 7.71 (m, $J$ = 7.0 Hz, 2 H, $H_{PPh_2}$) ppm. $^{13}$C NMR (125 MHz, $C_6D_6$): $\delta$ = 15.54 (α-Me), 19.58 (*p*Me), 31.59 [dd, $J_{C,P}$ = 13.2, $J_{C,P}$ = 3.3 Hz, P(C*Me*$_3$)$_2$], 32.20 [dd, $J_{C,P}$ = 13.2, $J_{C,P}$ = 3.3 Hz, P(C*Me*$_3$)$_2$], 34.67 (d, $J_{C,P}$ = 31.8 Hz, α-*C*H), 34.85 [d, $J_{C,P}$ = 22 Hz, P(*C*Me$_3$)$_2$], 35.15 [d, $J_{C,P}$ = 23 Hz, P(*C*Me$_3$)$_2$], 89.44 (d, $J_{C,P}$ = 3.8 Hz, $C_{Ar}$), 95.05 ($C_{Ar}$), 103.26 (d, $J_{C,P}$ = 2.8 Hz, $C_{Ar}$), 104.15 (d, $J_{C,P}$ = 28.5 Hz, $C_{Ar,ipso}$), 105.09 ($C_{Ar,ipso}$), 125.28 (dd, $J_{C,P}$ = 20.9 Hz, $C_{Ar,ipso}$), 128.08 (d, $J_{C,P}$ = 4.9 Hz, $C_{PPh_2}$), 128.9 ($C_{PPh_2}$), 128.72 (d, $J_{C,P}$ = 6.6 Hz, $C_{PPh_2}$), 129.55 ($C_{PPh_2}$), 133.66 (dd, $J_{C,P}$ = 18.7, $J_{C,P}$ = 2.8 Hz, $C_{PPh_2}$), 135.56 (d, $J_{C,P}$ = 20.9 Hz, $C_{PPh_2}$), 138.11 (dd, $J_{C,P}$ = 15.4, $J_{C,P}$ = 7.7 Hz, $C_{PPh_2}$), 139 67 (dd, $J_{C,P}$ = 5 Hz, $C_{PPh_2}$), 233.42 (*C*O) ppm. $^{31}$P NMR (202 MHz, $C_6D_6$): $\delta$ = –19.79 (d, $J_{P,P}$ = 61.7 Hz, $PPh_2$), 49.33 [d, $J_{P,P}$ = 61.7 Hz, P(CMe$_3$)$_2$] ppm. MS (CI, isobutane): *m*/*z* (%) 585 (87) [M + 1], 527 (100) [M – CMe$_3$], 500 (22) [M – 3 CO], 439 (74) [M – P(CMe$_3$]$_2$. $[\alpha]_D^{r.t.}$ = +435.2 (*c* = 1.01, $CHCl_3$). IR ($CHCl_3$): $\nu_{CO}$ = 1962, 1891 cm$^{-1}$. $C_{32}H_{38}CrO_3P_2$ (584.59): calcd. C 65.75, H 6.55; found C 65.56, H 6.39.

**[{η$^6$-(*S*,*R*p)-1-[4-*tert*-Butyl-2-(diphenylphosphanyl)phenyl]dicyclohexylphosphanylethane}Cr(CO)$_3$] [(*S*,*R*p)-24]:** This complex was prepared according to general procedure E from (*S*,*R*p)-**20** (4.59 g, 8.88 mmol), dicyclohexylphosphane (2.00 g, 10.13 mmol) and $TlPF_6$ (3.10 g, 8.88 mmol) in dry acetone (170 mL). The crude product was purified by column chromatography (aluminium oxide; diethyl ether). Yield yellow microcrystalline powder (3.70 g, 61%). $^1$H NMR (500 MHz, $C_6D_6$): $\delta$ = 0.95 (s, 9 H, C*Me*$_3$), 1.00–1.23 (m, 11 H, $H_{PCy_2}$), 1.44 (dd, $J$ = 7.0, $J$ = 3.7 Hz, 3 H, α-Me), 1.47–1.91 (m, 11 H, $H_{PCy_2}$), 4.35 (dq, $J$ = 7.0 Hz, 1 H, α-C*H*), 4.69 (dd, $J$ = 6.7, $J$ = 4 Hz, 1 H, $H_{Ar}$), 5.40 (dd, $J$ = 6.7, $J$ = 1.5 Hz, 1 H, $H_{Ar}$), 5.62 (t, $J$ = 1.5 Hz, 1 H, $H_{Ar}$), 7.02–7.48 (m, 10 H, $H_{PPh_2}$) ppm. $^{13}$C NMR (125 MHz, $C_6D_6$): $\delta$ = 14.48 (α-Me), 26.64–30.35 (10 C, $C_{PCy_2}$), 30.93 (C*Me*$_3$), 31.14 (*C*Me$_3$), 31.82 (dd, $J_{C,P}$ = 21.3 Hz, α-*C*H), 33.63 (d, $J_{C,P}$ = 22.1 Hz, $C_{PCy_2}$), 33.83 (d, $J_{C,P}$ = 16.3 Hz, $C_{PCy_2}$), 86.54 (t, $J_{C,P}$ = 3.8 Hz, $C_{Ar}$), 88.17 ($C_{Ar}$), 99.77 (d, $J_{C,P}$ = 3.8 Hz, $C_{Ar}$), 101.48 (d, $J_{C,P}$ = 24.0 Hz, $C_{Ar,ipso}$), 119.58 ($C_{Ar,ipso}$), 126.47 ($C_{Ar,ipso}$), 126.66–139.11 (m, 12 C, $C_{PPh_2}$), 233.50 (*C*O) ppm. $^{31}$P NMR (81 MHz, $C_6D_6$): $\delta$ = –20.83 (d, $J_{P,P}$ = 46.7 Hz, $PPh_2$), 15.73 (d, $J_{P,P}$ = 46.7 Hz, $PCy_2$) ppm. $[\alpha]_D^{r.t.}$ = +306.27 (*c* = 0.07, $CHCl_3$). IR ($CHCl_3$): $\nu_{CO}$ = 1968, 1903 cm$^{-1}$. $C_{39}H_{48}CrO_3P_2$ (678.75): calcd. C 69.01, H 7.13; found C 69.01, H 7.13.

**[{η$^6$-(*R*,*R*p)-1-[2-(Diphenylphosphanyl)-4-methoxyphenyl]ethyldiphenylphosphane}Cr(CO)$_3$] [(*R*,*R*p)-25a]:** This complex was prepared from (*R*,*R*p)-**21** (0.78 g, 1.59 mmol), diphenylphosphane (0.32 g, 1.70 mmol) and $TlPF_6$ (0.60 g, 1.70 mmol) in acetone (32 mL) according to general procedure E. The crude product was purified by column chromatography ($R_f$ = 0.42; aluminium oxide; hexane/dichloromethane, 4:1). Yield yellow crystals (0.90 g, 88% yield). $^1$H NMR (500 MHz, $C_6D_6$): $\delta$ = 1.41 (dd, $J$ = 6.9, $J$ = 5.6 Hz, 3 H, α-Me), 2.81 (s, 3 H, O*Me*), 4.20 (dd, $J$ = 7.0, $J$ = 2.4 Hz, 1 H, $H_{Ar}$), 4.65 (dq, $J$ = 9.1, $J$ = 7.0 Hz, 1 H, α-C*H*), 4.68 (ddd, $J$ = 7.0, $J$ = 3.0, $J$ = 1.8 Hz, 1 H, $H_{Ar}$), 5.09 (dd, $J$ = 2.4, $J$ = 1.2 Hz, 1 H, $H_{Ar}$), 6.94–7.15 (m, 14 H, $H_{PPh_2}$), 7.29 (m, $J$ = 7.0 Hz, 2 H, $H_{PPh_2}$), 7.51 (m, $J$ = 7.9 Hz, 2 H, $H_{PPh_2}$), 7.74 (m, $J$ = 7.0 Hz, 2 H, $H_{PPh_2}$) ppm. $^{13}$C NMR (125 MHz, $C_6D_6$): $\delta$ = 18.12 (α-Me), 32.48 (t, $J_{C,P}$ = 23.1 Hz, α-*C*H), 56.18 (O*Me*), 76.05 ($C_{Ar}$), 86.82 ($C_{Ar}$), 91.24 (dd, $J_{C,P}$ = 7.0, $J_{C,P}$ = 3.0 Hz, $C_{Ar}$), 106.48 (d, $J_{C,P}$ = 22.5 Hz, $C_{Ar,ipso}$), 117.20 (t, $J_{C,P}$ = 21.2 Hz, $C_{Ar,ipso}$), 128.71 (d, $J_{C,P}$ = 7.7 Hz, $C_{PPh_2}$), 128.97 (d, $J_{C,P}$ = 6.5 Hz, $C_{PPh_2}$), 129.53 ($C_{PPh_2}$), 131.73 (d, $J_{C,P}$ = 15.9 Hz, $C_{PPh_2}$), 134.57 (d, $J_{C,P}$ = 22.5 Hz, $C_{PPh_2}$), 134.85 (d, $J_{C,P}$ = 20.9 Hz, $C_{PPh_2}$), 135.06 (d, $J_{C,P}$ = 20.3 Hz, $C_{PPh_2}$), 135.59 (d, $J_{C,P}$ = 7.7 Hz, $C_{PPh_2}$), 136.28 (d, $J_{C,P}$ = 22.5 Hz, $C_{PPh_2}$), 137.25 (d, $J_{C,P}$ = 18.6 Hz, $C_{PPh_2}$), 140.80 ($C_{Ar,ipso}$), 233.51 (*C*O) ppm. $^{31}$P NMR (202 MHz, $C_6D_6$): $\delta$ = 5.02 (d, $J_{P,P}$ = 11.0 Hz, α-$PPh_2$), –17.99 (d, $J_{P,P}$ = 11.0 Hz, *o*$PPh_2$) ppm. MS (CI, isobutane): *m*/*z* (%) 505 (22) [M + H – 3 CO – Cr], 319 (100) [M – 3 CO – Cr –HP$Ph_2$]. $[\alpha]_D^{r.t.}$ = –286.4 (*c* = 0.22, $CHCl_3$). IR ($CHCl_3$): $\nu_{CO}$ = 1964, 1892 cm$^{-1}$. $C_{36}H_{30}CrO_4P_2$ (640.57): calcd. C 67.50, H 4.72; found C 67.57, H 5.27.

**[{η$^6$-(*R*,*R*p)-1-[2-(Diphenylphosphanyl)-4-methoxyphenyl]ethyldicyclohexylphosphane}Cr(CO)$_3$] [(*R*,*R*p)-25b]:** This complex was prepared from (*R*,*R*p)-**21**, dicyclohexylphosphane (0.47 g, 2.36 mmol) and $TlPF_6$ (0.82 g, 2.36 mmol) in acetone (47 mL) according to general procedure E. The crude product was purified by column chromatography ($R_f$ = 0.51; aluminium oxide; hexane/diethyl ether, 2:1). Yield yellow crystals (1.18 g, 77% yield). $^1$H NMR (500 MHz, $C_6D_6$): $\delta$ = 1.08–1.36 (m, 8 H, $H_{PCy_2}$), 1.45–1.70 (m, 14 H, $H_{PCy_2}$), 1.47 (dd, $J$ = 7.0, $J$ = 4.5 Hz, 3 H, α-Me), 2.84 (s, 3 H, O*Me*), 4.00 (m, $J$ = 7.0 Hz, 1 H, α-C*H*), 4.47 (dd, $J$ = 7.0, $J$ = 2.4 Hz, 1 H, $H_{Ar}$), 5.13 (ddd, $J$ = 7.0, $J$ = 3.0, $J$ = 1.5 Hz, 1 H, $H_{Ar}$), 5.19 (dd, $J$ = 2.4, $J$ = 0.9 Hz, 1 H, $H_{Ar}$), 7.00–7.11 (m, 6 H, $H_{PPh_2}$), 7.47 (m, $J$ = 7.0 Hz, 2 H, $H_{PPh_2}$), 7.70 (m, $J$ = 7.3 Hz, 2 H, $H_{PPh_2}$) ppm. $^{13}$C NMR (125 MHz, $C_6D_6$): $\delta$ = 17.60 (α-Me), 26.65 (d, $J_{C,P}$ = 10.4 Hz, $C_{PCy_2}$), 27.12 (d, $J_{C,P}$ = 11.5 Hz, $C_{PCy_2}$), 27.41 (d, $J_{C,P}$ = 8.2 Hz, $C_{PCy_2}$), 27.89 (d, $J_{C,P}$ = 6.0 Hz, $C_{PCy_2}$), 28.01 (d, $J_{C,P}$ = 13.2 Hz, $C_{PCy_2}$), 30.13 (d, $J_{C,P}$ = 10.4 Hz, $C_{PCy_2}$), 30.44 (d, $J_{C,P}$ = 6.6 Hz, $C_{PCy_2}$), 30.68 (dd, $J_{C,P}$ = 26.3, $J_{C,P}$ = 19.7 Hz, α-*C*H), 31.43 (d, $J_{C,P}$ = 17.0 Hz, $C_{PCy_2}$), 31.79 ($C_{PCy_2}$), 31.95 (d, $J_{C,P}$

 © 2007 Wiley-VCH Verlag GmbH & Co. KGaA, Weinheim 

= 7.7 Hz, $C_{PCy_2}$), 33.43 (d, $J_{C,P}$ = 20.9 Hz, $C_{PCy_2}$), 33.65 (d, $J_{C,P}$ = 21.9 Hz, $C_{PCy_2}$), 55.25 (O*Me*), 77.13 ($C_{Ar}$), 88.36 (d, $J_{C,P}$ = 2.2 Hz, $C_{Ar}$), 90.58 (dd, $J_{C,P}$ = 7.1, $J_{C,P}$ = 3.3 Hz, $C_{Ar}$), 105.37 (dd, $J_{C,P}$ = 24.7, $J_{C,P}$ = 3.3 Hz, $C_{Ar,ipso}$), 120.89 (dd, $J_{C,P}$ = 21.4, $J_{C,P}$ = 19.8 Hz, $C_{Ar,ipso}$), 128.41 (d, $J_{C,P}$ = 7.1 Hz, $C_{PPh_2}$), 128.84 (d, $J_{C,P}$ = 7.1 Hz, $C_{PPh_2}$), 129.89 ($C_{PPh_2}$), 134.22 (dd, $J_{C,P}$ = 19.2, $J_{C,P}$ = 2.2 Hz, $C_{PPh_2}$), 135.46 (d, $J_{C,P}$ = 20.3 Hz, $C_{PPh_2}$), 136.09 (dd, $J_{C,P}$ = 14.8, $J_{C,P}$ = 2.7 Hz, $C_{PPh_2}$), 137.74 (d, $J_{C,P}$ = 7.7 Hz, $C_{PPh_2}$), 140.00 (d, $J_{C,P}$ = 1.7 Hz, $C_{Ar,ipso}$), 233.68 (d, $J_{C,P}$ = 1.7 Hz, *C*O) ppm. $^{31}$P NMR (202 MHz, $C_6D_6$): $\delta$ = 15.49 (d, $J_{P,P}$ = 26.0 Hz, $PCy_2$), –17.48 (d, $J_{P,P}$ = 26.0 Hz, $PPh_2$) ppm. MS (CI, isobutane): *m*/*z* (%) 653 (72) [M + H], 568 (100) [M – 3 CO], 517 (85) [M – 3 CO – Cr], 433 (44) [M – 3 CO – Cr – $C_6H_{12}$]. $[\alpha]_D^{r.t.}$ = –309.5 (*c* = 0.21, $CHCl_3$). IR ($CHCl_3$): $\nu_{CO}$ = 1963, 1886 cm$^{-1}$. $C_{36}H_{42}CrO_4P_2$ (652.67): calcd. C 66.25, H 6.49; found C 66.00, H 6.74.

**[{η$^6$-(*R*,*R*p)-1-[2-(Diphenylphosphanyl)-4-methoxyphenyl]ethyldi-*tert*-butylphosphane}Cr(CO)$_3$] [(*R*,*R*p)-25c]:** This complex was prepared from (*R*,*R*p)-**21** (0.91 g, 1.82 mmol), di-*tert*-butylphosphane (0.29 g, 2.00 mmol) and $TlPF_6$ (0.70 g, 2.00 mmol) in acetone (36 mL) according to general procedure E. The crude product was purified by column chromatography ($R_f$ = 0.34; aluminium oxide; hexane/dichloromethane, 4:1→neat dichloromethane). Yield yellow crystals (0.84 g, 78%). $^1$H NMR (500 MHz, $C_6D_6$): $\delta$ = 0.94 [d, *J* = 11.0 Hz, 9 H, P(C*Me*$_3$)$_2$], 1.18 [d, *J* = 10.7 Hz, 9 H, P(C*Me*$_3$)$_2$], 1.58 (dd, *J* = 7.4, *J* = 2.5 Hz, 3 H, α-Me), 2.86 (s, 3 H, O*Me*), 4.32 (m, *J* = 7.0 Hz, 1 H, α-C*H*), 4.86 (dd, *J* = 6.7, *J* = 3.0 Hz, 1 H, $H_{Ar}$), 4.55 (dd, *J* = 6.7, *J* = 1.6 Hz, 1 H, $H_{Ar}$), 5.40 (d, *J* = 1.5 Hz, 1 H, $H_{Ar}$), 7.00–7.10 (m, 6 H, $H_{PPh_2}$), 7.44 (dd, *J* = 7.4 Hz, 2 H, $H_{PPh_2}$), 7.70 (dd, *J* = 7.0 Hz, 2 H, $H_{PPh_2}$) ppm. $^{13}$C NMR (125 MHz, $C_6D_6$): $\delta$ = 16.32 (α-Me), 31.51 [dd, $J_{C,P}$ = 13.2, $J_{C,P}$ = 3.3 Hz, P(C*Me*$_3$)$_2$], 32.22 [d, $J_{C,P}$ = 14.3 Hz, P(C*Me*$_3$)$_2$], 34.29 [d, $J_{C,P}$ = 15.4 Hz, P(*C*Me$_3$)$_2$], 34.51 (dd, $J_{C,P}$ = 22.5, $J_{C,P}$ = 15.3 Hz, α-*C*H), 34.98 [d, $J_{C,P}$ = 35.6 Hz, P(*C*Me$_3$)$_2$], 55.38 (O*Me*), 77.96 ($C_{Ar}$), 89.69 (d, $J_{C,P}$ = 3.9 Hz, $C_{Ar}$), 90.76 ($C_{Ar}$), 104.83 (d, $J_{C,P}$ = 30.2 Hz, $C_{Ar,ipso}$), 121.53 (m, $J_{C,P}$ = 20.8 Hz, $C_{Ar}$), 128.72 (d, $J_{C,P}$ = 6.5 Hz, $C_{PPh_2}$), 129.68 ($C_{PPh_2}$), 133.81 (dd, $J_{C,P}$ = 19.2, $J_{C,P}$ = 2.9 Hz, $C_{PPh_2}$), 135.63 (d, $J_{C,P}$ = 20.3 Hz, $C_{PPh_2}$), 137.20 ($C_{PPh_2}$), 139.10 ($C_{Ar,ipso}$), 139.34 (d, $J_{C,P}$ = 5.0 Hz, $C_{PPh_2}$), 233.63 (*C*O) ppm. $^{31}$P NMR (202 MHz, $C_6D_6$): $\delta$ = –18.58 (d, $J_{P,P}$ = 54.3 Hz, $PPh_2$), 48.07 [d, $J_{P,P}$ = 54.3 Hz, P(CMe$_3$)$_2$] ppm. MS (CI, isobutane): *m*/*z* (%) 601 (39) [M + H], 543 (32) [M – CMe$_3$], 516 (54) [M – 3 CO], 465 (100) [M – 3 CO – Cr], 407 (83) [M – 3 CO – Cr – HCMe$_3$]. $[\alpha]_D^{r.t.}$ = –436.4 (*c* = 0.22, $CHCl_3$). IR ($CHCl_3$): $\nu_{CO}$ = 1963, 1889 cm$^{-1}$. $C_{32}H_{38}CrO_4P_2$ (600.599): calcd. C 63.99, H 6.38; found C 63.83, H 6.32.

**[{η$^6$-(*R*,*S*p)-1-[4-Chloro-2-(diphenylphosphanyl)phenyl]ethyldiphenylphosphane}Cr(CO)$_3$] [(*R*,*S*p)-26a]:** This complex was prepared from (*R*,*S*p)-**22** (0.54 g, 1.1 mmol), diphenylphosphane (0.23 g, 1.2 mmol) and $TlPF_6$ (0.44 g, 1.2 mmol) in dry acetone (22 mL) according to general procedure E. The crude product was purified by column chromatography ($R_f$ = 0.53; aluminium oxide; diethyl ether/hexane, 1:4). Yield yellow crystals (0.20 g, 28%). $^1$H NMR (500 MHz, $C_6D_6$): $\delta$ = 1.22 (dd, *J* = 6.9, *J* = 4.9 Hz, 3 H, α-Me), 4.24 (d, *J* = 6.6 Hz, 1 H, $H_{Ar}$), 4.76 (d, *J* = 6.8 Hz, 1 H, $H_{Ar}$), 4.80 (dd, *J* = 9.1, *J* = 6.9 Hz, 1 H, α-C*H*), 5.36 (d, *J* = 1.4 Hz, 1 H, $H_{Ar}$), 6.93–7.12 (m, 16 H, $H_{PPh_2}$), 7.45 (m, *J* = 7.7 Hz, 2 H, $H_{PPh_2}$), 7.66 (m, *J* = 7.7 Hz, 2 H, $H_{PPh_2}$) ppm. $^{13}$C NMR (125 MHz, $C_6D_6$): $\delta$ = 16.07 (α-Me), 33.01 (m, $J_{C,P}$ = 24.2 Hz, α-*C*H), 89.06 ($C_{Ar}$), 92.97 ($C_{Ar}$), 98.10 ($C_{Ar}$), 104.43 (d, $J_{C,P}$ = 25.7 Hz, $C_{Ar,ipso}$), 108.84 ($C_{Ar,ipso}$), 120.68 (m, $J_{C,P}$ = 21.4 Hz, $C_{Ar,ipso}$), 128.54 ($C_{PPh_2}$), 128.66 ($C_{PPh_2}$), 128.72 ($C_{PPh_2}$), 129.14 (d, $J_{C,P}$ = 7.1 Hz, $C_{PPh_2}$), 129.40 ($C_{PPh_2}$), 129.95 ($C_{PPh_2}$), 130.25 ($C_{PPh_2}$), 131.55 (d, $J_{C,P}$ = 15.9 Hz, $C_{PPh_2}$), 133.76 (d, $J_{C,P}$ = 23.1 Hz, $C_{PPh_2}$), 134.43 (d, $J_{C,P}$ = 20.8 Hz, $C_{PPh_2}$), 134.98 (d, $J_{C,P}$ = 20.9 Hz, $C_{PPh_2}$), 135.53 (d, $J_{C,P}$ = 7.1 Hz, $C_{PPh_2}$), 126.20 (d, $J_{C,P}$ = 22.5 Hz, $C_{PPh_2}$), 136.68 (d, $J_{C,P}$ = 19.2 Hz, $C_{PPh_2}$), 231.71 (*C*O) ppm. $^{31}$P NMR (202 MHz, $C_6D_6$): $\delta$ = 7.33 (d, $J_{P,P}$ = 18.3 Hz, *a*$PPh_2$), –18.93 (d, $J_{P,P}$ = 18.3 Hz, *o*$PPh_2$) ppm. MS (CI, isobutane): *m*/*z* (%) 645 (22) [M + H], 560 (14) [M – 3 CO], 509 (48) [M + H – 3 CO – Cr], 459 (100) [M – $PPh_2$], 432 (28) [M – 3 CO – Cr – Ph], 323 (42) [M – 3 CO – Cr – $PPh_2$]. $[\alpha]_D^{r.t.}$ = –248.1 (*c* = 0.10, $CHCl_3$). IR ($CHCl_3$): $\nu_{CO}$ = 1976, 1912 cm$^{-1}$. $C_{35}H_{27}ClCrO_3P_2$ (644.99): calcd. C 65.18, H 4.22; found C 65.84, H 4.74.

**[{η$^6$-(*R*,*S*p)-1-[4-Chloro-2-(diphenylphosphanyl)phenyl]ethyldicyclohexylphosphane}Cr(CO)$_3$] [(*R*,*S*p)-26b]:** This complex was prepared from (*R*,*S*p)-**22** (0.62 g, 1.25 mmol), dicyclohexylphosphane (0.25 g, 1.25 mmol) and $TlPF_6$ (0.44 g, 1.25 mmol) in dry acetone (25 mL) according to general procedure E. The crude product was purified by column chromatography ($R_f$ = 0.69, aluminium oxide; diethyl ether/hexane, 1:4). Yield yellow crystals (0.30 g, 36%). $^1$H NMR (500 MHz, $C_6D_6$): $\delta$ = 1.00–1.19 (m, 7 H, $H_{PCy_2}$), 1.27 (dd, *J* = 7.3, *J* = 3.7 Hz, 3 H, α-Me), 1.30–1.46 (m, 4 H, $H_{PCy_2}$), 1.48–1.76 (m, 11 H, $H_{PCy_2}$), 4.13 (m, *J* = 7.3 Hz, 1 H, α-C*H*), 4.66 (ddd, *J* = 6.7, *J* = 3.4, *J* = 0.9 Hz, 1 H, $H_{Ar}$), 5.08 (dd, *J* = 6.7, *J* = 1.8 Hz, 1 H, $H_{Ar}$), 5.49 (m, *J* = 1.8 Hz, 1 H, $H_{Ar}$), 7.01–7.10 (m, 6 H, $H_{PPh_2}$), 7.40 (m, *J* = 7.6 Hz, 2 H, $H_{PPh_2}$), 7.74 (m, *J* = 7.6 Hz, 2 H, $H_{PPh_2}$) ppm. $^{13}$C NMR (125 MHz, $C_6D_6$): $\delta$ = 15.17 (α-Me), 26.59 (d, $J_{C,P}$ = 4.9 Hz, $C_{PCy_2}$), 27.01 (d, $J_{C,P}$ = 11.5 Hz, $C_{PCy_2}$), 27.44 (d, $J_{C,P}$ = 7.7 Hz, $C_{PCy_2}$), 27.80 (d, $J_{C,P}$ = 15.9 Hz, $C_{PCy_2}$), 27.88 (d, $J_{C,P}$ = 23.5 Hz, $C_{PCy_2}$), 30.40 (d, $J_{C,P}$ = 9.3 Hz, $C_{PCy_2}$), 30.18 ($C_{PCy_2}$), 30.33 (d, $J_{C,P}$ = 6.6 Hz, $C_{PCy_2}$), 31.57 (dd, $J_{C,P}$ = 26.8, $J_{C,P}$ = 20.3 Hz, α-*C*H), 31.59 (d, $J_{C,P}$ = 12.0 Hz, $C_{PCy_2}$), 31.74 (d, $J_{C,P}$ = 20.8 Hz, $C_{PCy_2}$), 33.55 (d, $J_{C,P}$ = 14.8 Hz, $C_{PCy_2}$), 33.72 (d, $J_{C,P}$ = 15.9 Hz, $C_{PCy_2}$), 87.89 (dd, $J_{C,P}$ = 3.8 Hz, $C_{Ar}$), 93.89 ($C_{Ar}$), 100.10 (d, $J_{C,P}$ = 2.8 Hz, $C_{Ar}$), 103.57 (dd, $J_{C,P}$ = 27.9, $J_{C,P}$ = 2.7 Hz, $C_{Ar,ipso}$), 107.52 (d, $J_{C,P}$ = 3.8 Hz, $C_{Ar,ipso}$), 124.13 (dd, $J_{C,P}$ = 21.9, $J_{C,P}$ = 19.2 Hz, $C_{Ar,ipso}$), 128.29 ($C_{PPh_2}$), 128.35 ($C_{PPh_2}$), 128.59 ($C_{PPh_2}$), 129. 01 (d, $J_{C,P}$ = 7.7 Hz, $C_{PPh_2}$), 130.42 ($C_{PPh_2}$), 133.76 (dd, $J_{C,P}$ = 18.6, $J_{C,P}$ = 2.7 Hz, $C_{PPh_2}$), 135.33 (d, $J_{C,P}$ = 21.4 Hz, $C_{PPh_2}$), 136.80 (dd, $J_{C,P}$ = 14.3, $J_{C,P}$ = 4.4 Hz, $C_{PPh_2}$), 137.83 (dd, $J_{C,P}$ = 7.1, $J_{C,P}$ = 2.7 Hz, $C_{PPh_2}$), 231.75 (*C*O) ppm. $^{31}$P NMR (81 MHz, $C_6D_6$): $\delta$ = 15.20 (d, $J_{P,P}$ = 39.3 Hz, $PCy_2$), –20.17 (d, $J_{P,P}$ = 39.3 Hz, $PPh_2$) ppm. MS (CI, isobutane): *m*/*z* (%) 657 (68) [M + H], 572 (44) [M – 3 CO], 521 (100) [M – 3 CO – Cr], 433 (32) [M – 3 CO – Cr – $C_6H_{12}$]. $[\alpha]_D^{r.t.}$ = –346.0 (*c* = 0.20, $CHCl_3$). IR ($CHCl_3$): $\nu_{CO}$ = 1973, 1906 cm$^{-1}$.

**[{η$^6$-(*R*,*S*p)-1-[4-Chloro-2-(diphenylphosphanyl)phenyl]ethyldi-*tert*-butylphosphane}Cr(CO)$_3$] [(*R*,*S*p)-26c]:** This complex was prepared from (*R*,*S*p)-**22** (0.48 g, 0.97 mmol), di-*tert*-butylphosphane (0.16 g, 1.07 mmol) and $TlPF_6$ (0.37 g, 1.07 mmol) in dry acetone (20 mL) according to general procedure E. The crude product was purified by column chromatography ($R_f$ = 0.54; aluminium oxide; dichloromethane/hexane, 4:1). Yield yellow crystals (0.18 g, 31%). $^1$H NMR (500 MHz, $C_6D_6$): $\delta$ = 0.86 [d, *J* = 10.7 Hz, 9 H, P(C*Me*$_3$)$_2$], 1.17 [d, *J* = 10.5 Hz, 9 H, P(C*Me*$_3$)$_2$], 1.41 (dd, *J* = 7.3, *J* = 2.7 Hz, 3 H, α-Me), 4.32 (m, *J* = 4.6 Hz, 1 H, α-C*H*), 4.56 (dd, *J* = 6.8, *J* = 3.7 Hz, 1 H, $H_{Ar}$), 5.12 (dd, *J* = 6.8, *J* = 1.7 Hz, 1 H, $H_{Ar}$), 5.61 (d, *J* = 1.7 Hz, 1 H, $H_{Ar}$), 7.02–7.11 (m, 6 H, $H_{PPh_2}$), 7.36 (m, *J* = 7.6 Hz, 2 H, $H_{PPh_2}$), 7.62 (m, *J* = 7.6, *J* = 1.9 Hz, $H_{PPh_2}$) ppm. $^{13}$C NMR (125 MHz, $C_6D_6$): $\delta$ = 15.35 (α-Me), 31.55 [dd, $J_{C,P}$ = 13.2, $J_{C,P}$ = 3.8 Hz, P(C*Me*$_3$)$_2$], 32.15 [d, $J_{C,P}$ = 13.7 Hz, P(C*Me*$_3$)$_2$], 34.54 [d, $J_{C,P}$ = 32.0 Hz, P(*C*Me$_3$)$_2$], 34.74 (d, $J_{C,P}$ = 37.0 Hz, α-*C*H), 35.08 [d, $J_{C,P}$ = 32.0 Hz, P(C*Me*$_3$)$_2$], 88.37 ($C_{Ar}$), 94.09 ($C_{Ar}$), 101.36 ($C_{Ar}$), 103.62 (d, $J_{C,P}$ = 29.6 Hz, $C_{Ar,ipso}$), 107.02 (d, $J_{C,P}$ = 3.9 Hz, $C_{Ar,ipso}$), 124.65 (dd, $J_{C,P}$ = 21.1 Hz, $C_{Ar,ipso}$), 127.91

 © 2007 Wiley-VCH Verlag GmbH & Co. KGaA, Weinheim 

($C_{PPh_2}$), 128.13 ($C_{PPh_2}$), 128.29 ($C_{PPh_2}$), 128.94 (d, $J_{C,P}$ = 6.6 Hz, $C_{PPh_2}$), 129.94 ($C_{PPh_2}$), 133.45 (dd, $J_{C,P}$ = 18.6, $J_{C,P}$ = 3.3 Hz, $C_{PPh_2}$), 135.49 (d, $J_{C,P}$ = 21.4 Hz, $C_{PPh_2}$), 137.56 (dd, $J_{C,P}$ = 15.3, $J_{C,P}$ = 7.7 Hz, $C_{PPh_2}$), 139.03 (m, $J_{C,P}$ = 4.4 Hz, $C_{PPh_2}$), 231.75 (*C*O) ppm. $^{31}$P NMR (81 MHz, $C_6D_6$): $\delta$ = –21.06 (d, $J_{P,P}$ = 63.2 Hz, $PPh_2$), 48.78 [d, $J_{P,P}$ = 63.2 Hz, $P(CMe_3)_2$] ppm. MS (CI, isobutane): *m*/*z* (%) 605 (88) [M + H], 547 (45) [M – $CMe_3$], 520 (15) [M – 3 CO], 459 (14) [M – $P(CMe_3)_2$, 391 (100) [M – 3 CO – Cr – Ph], 407 (83) [M – 3 CO – Cr – $HCMe_3$]. $[\alpha]_D^{r.t.}$ = –445.4 (*c* = 0.22, $CHCl_3$). IR ($CHCl_3$): $\nu_{CO}$ = 1974, 1910 cm$^{-1}$.

**Preparation of [{η$^6$-(*S*)-*N*,*N*-Dimethyl-1-(2-methoxyphenyl)ethylamine}Cr(CO)$_3$] [(*S*,*S*p)-28] and [(*S*,*R*p)-28]. Thermolysis with Cr(CO)$_6$:** Reaction of (*S*)-**4** (4.00 g, 22.00 mmol) and $Cr(CO)_6$ (6.00 g, 27.00 mmol) in a 8:1 mixture of di-*n*-butyl ether and thf (81 mL) for 50 h according to general procedure B afforded (*S*,*S*p)-**28** and (*S*,*R*p)-**28** in a 25:75 ratio (Scheme 8). The two diastereomers were collected as a single fraction after flash chromatography (aluminium oxide; diethyl ether). Yield 4.65 g (66%).

**Arene Exchange with [(η$^6$-Naphthalene)Cr(CO)$_3$]:** (*S*,*S*p)-**28** was prepared in a high-pressure Schlenk tube from (*S*)-**4** (0.86 g, 4.78 mmol) and [(η$^6$-naphthalene)$Cr(CO)_3$] (1.50 g, 5.68 mmol) in di-*n*-butyl ether (25 mL). After all reagents and the solvent had been mixed, a catalytic amount of thf (0.53 g, 7.35 mmol) was added, the reaction mixture was degassed by means of ultrasound and three freeze-pump-thaw cycles and then heated in the dark at 75 °C for 95 h. The reaction mixture was then filtered through a short pad of Celite, the solvent was distilled off on a rotary evaporator and the residue was taken up in diethyl ether and purified by flash chromatography (aluminium oxide; diethyl ether/hexane = 1:10→1:2). A yellow crystalline product was isolated after evaporation of the solvents. Crystals suitable for X-ray analysis were grown by slow diffusion of hexane into a solution of the compound in diethyl ether at –30 °C. Yield 0.91 g (60%).

**[{η$^6$-(*S*,*S*p)-*N*,*N*-Dimethyl-1-(2-methoxyphenyl)ethylamine}Cr(CO)$_3$] [(*S*,*S*p)-28]:** $^1$H NMR (500 MHz, $CDCl_3$): $\delta$ = 1.38 (d, *J* = 6.8 Hz, 3 H, α-Me), 2.37 (s, 6 H, N*Me*$_2$), 3.35 (q, *J* = 6.8 Hz, 1 H, α-C*H*), 3.74 (s, 3 H, O*Me*), 4.89 (t, *J* = 6.3 Hz, 1 H, $H_{Ar}$), 5.00 (d, *J* = 6.6 Hz, 1 H, $H_{Ar}$), 5.50 (t, *J* = 6.6 Hz, 1 H, $H_{Ar}$), 5.84 (d, *J* = 6.6 Hz, 1 H, $H_{Ar}$) ppm. $^{13}$C NMR (125 MHz, $CDCl_3$): $\delta$ = 19.84 (α-Me), 43.46 (N*Me*$_2$), 55.61 (O*Me*), 60.60 (α-*C*H), 73.88 ($C_{Ar}$), 84.83 ($C_{Ar}$), 94.17 ($C_{Ar}$), 96.56 ($C_{Ar}$), 105.39 ($C_{Ar,ipso}$), 141.39 ($C_{Ar,ipso}$), 233.41 (*C*O) ppm. IR (hexane): $\nu_{CO}$ = 1972, 1903. $^1$H NMR (200 MHz, $C_6D_6$): $\delta$ = 1.12 (d, *J* = 6.6 Hz, 3 H, α-Me), 2.23 (s, 6 H, N*Me*$_2$), 2.93 (s, 3 H, O*Me*), 3.37 (q, *J* = 6.8 Hz, 1 H, α-C*H*), 4.01 (d, *J* = 6.3 Hz, 1 H, $H_{Ar}$), 4.15 (t, *J* = 6.1 Hz, 1 H, $H_{Ar}$), 4.64 (t, *J* = 6.3 Hz, 1 H, $H_{Ar}$), 5.62 (d, *J* = 6.3 Hz, 1 H, $H_{Ar}$) ppm.

**[{η$^6$-(*S*,*R*p)-*N*,*N*-Dimethyl-1-(2-methoxyphenyl)ethylamine}Cr(CO)$_3$] [(*S*,*R*p)-28]:** $^1$H NMR (500 MHz, $CDCl_3$): $\delta$ = 1.32 (d, *J* = 7.1 Hz, 3 H, α-Me), 2.24 (s, 6 H, N*Me*$_2$), 3.74 (s, 3 H, O*Me*), 4.00 (q, *J* = 7.1 Hz, 1 H, α-C*H*), 4.90 (t, *J* = 6.1 Hz, $H_{Ar}$), 5.66 (d, *J* = 6.1 Hz, 1 H, $H_{Ar}$), 5.52 (t, *J* = 6.3 Hz, 1 H, $H_{Ar}$), 4.98 (d, *J* = 6.6 Hz, 1 H, $H_{Ar}$) ppm. $^{13}$C NMR (125 MHz, $CDCl_3$): $\delta$ = 14.10 (α-Me), 41.16 (N*Me*$_2$), 54.35 (O*Me*), 55.93 (α-*C*H), 73.12 ($C_{Ar}$), 84.36 ($C_{Ar}$), 94.46 ($C_{Ar}$), 94.61 ($C_{Ar}$), 102.65 ($C_{Ar,ipso}$), 142.29 ($C_{Ar,ipso}$), 233.12 (*C*O) ppm. IR (hexane): $\nu_{CO}$ = 1973, 1903 cm$^{-1}$. $^1$H NMR (200 MHz, $C_6D_6$): $\delta$ = 1.22 (d, *J* = 6.8 Hz, 3 H, α-Me), 1.95 (s, 6 H, N*Me*$_2$), 2.93 (s, 3 H, O*Me*), 3.86 (q, *J* = 7.1 Hz, 1 H, α-C*H*), 3.99 (d, *J* = 6.6 Hz, 1 H, $H_{Ar}$), 4.08 (t, *J* = 6.3 Hz, $H_{Ar}$), 4.68 (t, *J* = 6.1 Hz, 1 H, $H_{Ar}$), 5.19 (d, *J* = 6.1 Hz, 1 H, $H_{Ar}$) ppm.

**(*S*)-*N*,*N*-Dimethyl-1-[2-methoxy-3-(trimethylsilyl)phenyl]ethylamine [(*S*)-29]:** (*S*)-**4** (5 g, 27.93 mmol, 1 equiv.) was dissolved in diethyl ether (200 mL) and the solution cooled to –50 °C. *t*BuLi (1.7 M in pentane; 19.00 mL, 32.30 mmol, 1.15 equiv.) was added dropwise and the reaction mixture stirred at –50 °C for 24 h. After addition of chlorotrimethylsilane (15.17 g, 139.65 mmol, 5 equiv.), the resulting mixture was warmed to room temperature, stirred at that temperature for 80 h and then filtered through a short pad of Celite in order to remove LiCl. The solvent and excess $ClSiMe_3$ were distilled off on a rotary evaporator and the crude product was purified by column chromatography (aluminium oxide; diethyl ether/hexane, 1:1) to afford (*S*)-**29** as a light yellow oil. Yield 6.89 g (98%). $^1$H NMR (500 MHz, $CDCl_3$): $\delta$ = 0.41 (s, 9 H, Si*Me*$_3$), 1.47 (d, *J* = 6.7 Hz, 3 H, α-Me), 2.30 (s, 6 H, N*Me*$_2$), 3.75 (q, *J* = 6.7 Hz, 1 H, α-C*H*), 3.85 (s, 3 H, O*Me*), 6.23 (t, *J* = 7.3 Hz, 1 H, $H_{Ar}$), 7.42 (d, *J* = 7.3 Hz, 1 H, $H_{Ar}$), 7.59 (d, *J* = 7.6 Hz, 1 H, $H_{Ar}$) ppm. $^{13}$C NMR (125 MHz, $CDCl_3$): $\delta$ = –0.03 (Si*Me*$_3$), 20.91 (α-Me), 43.43 (N*Me*$_2$), 57.95 (O*Me*), 62.79 (α-*C*H), 124.16 ($C_{Ar}$), 129.58 ($C_{Ar}$), 132.52 ($C_{Ar,ipso}$), 133.84 ($C_{Ar}$), 136.90 ($C_{Ar,ipso}$), 163.14 ($C_{Ar,ipso}$) ppm.

**Preparation of [{η$^6$-(*S*)-*N*,*N*-Dimethyl-1-[2-methoxy-3-(trimethylsilyl)phenyl]ethylamine}Cr(CO)$_3$] [(*S*,*S*p)-30 and (*S*,*R*p)-30]. Thermolysis with Cr(CO)$_6$:** Reaction of (*S*)-**29** (2.80 g, 11.00 mmol) and $Cr(CO)_6$ (3.00 g, 14.00 mmol) in an 8:1 mixture of di-*n*-butyl ether and thf (40.5 mL) for 48 h according to general procedure B afforded (*S*,*R*p)-**30** and (*S*,*S*p)-**30** in an 87.5:12.5 ratio (Scheme 9). The two diastereomers were collected as a single fraction after flash chromatography (aluminium oxide; diethyl ether). Yield 3.03 g (79%). Crystals of (*S*,*R*p)-**30** suitable for X-ray analysis were grown by slow diffusion of hexane into a solution of this fraction in diethyl ether.

**Arene Exchange with [(η$^6$-Naphthalene)Cr(CO)$_3$]:** (*S*,*S*p)-**30** was prepared in a high-pressure Schlenk tube from (*S*)-**29** (1.20 g, 4.78 mmol) and [(η$^6$-naphthalene)$Cr(CO)_3$] (1.50 g, 5.68 mmol) in di-*n*-butyl ether (25 mL). After all reagents and the solvent had been mixed, a catalytic amount of thf (0.53 g, 7.35 mmol) was added, the reaction mixture was degassed by means of ultrasound and three freeze-pump-thaw cycles and then heated in the dark at 75 °C for 78 h. The reaction mixture was filtered through a short pad of Celite, the solvent was distilled off on a rotary evaporator and the residue was taken up in diethyl ether and purified by flash chromatography (aluminium oxide; diethyl ether/hexane, 3:1). After evaporation of the solvents, the product was obtained as a yellow-orange powder in a mixture with unreacted [(η$^6$-naphthalene)-$Cr(CO)_3$]. The desired product was isolated in high purity after a second chromatographic purification (silica gel; diethyl ether/hexane, 1:7). Yield yellow crystals (1.30 g, 70%).

**[{η$^6$-(*S*,*S*p)-*N*,*N*-Dimethyl-1-[2-methoxy-3-(trimethylsilyl)phenyl]-ethylamine}Cr(CO)$_3$] [(*S*,*S*p)-30]:** $^1$H NMR (200 MHz, $CDCl_3$): $\delta$ = 0.35 (s, 9 H, Si*Me*$_3$), 1.43 (d, *J* = 6.3 Hz, 3 H, α-Me), 2.34 (s, 6 H, N*Me*$_2$), 3.06 (q, *J* = 6.3 Hz, 1 H, α-C*H*), 3.89 (s, 3 H, O*Me*), 4.83 (t, *J* = 7.1 Hz, 1 H, $H_{Ar}$), 5.44 (d, *J* = 5.9 Hz, 1 H, $H_{Ar}$), 5.79 (d, *J* = 6.6 Hz, 1 H, $H_{Ar}$) ppm. $^{13}$C NMR (50 MHz, $CDCl_3$): $\delta$ = 0.31 (Si*Me*$_3$), 21.31 (α-Me), 44.06 (N*Me*$_2$), 62.07 (O*Me*), 64.11 (α-*C*H), 86.39 ($C_{Ar}$), 94.13 ($C_{Ar,ipso}$), 97.96 ($C_{Ar}$), 100.57 ($C_{Ar}$), 109.75 ($C_{Ar,ipso}$), 146.36 ($C_{Ar,ipso}$), 233.42 (*C*O) ppm. IR (hexane): $\nu_{CO}$ = 1975, 1906 cm$^{-1}$.

**[{η$^6$-(*S*,*R*p)-*N*,*N*-Dimethyl-1-[2-methoxy-3-(trimethylsilyl)phenyl]-ethylamine}Cr(CO)$_3$] [(*S*,*R*p)-30]:** $^1$H NMR (400 MHz, $CDCl_3$): $\delta$ = 0.48 (s, 9 H, Si*Me*$_3$), 1.40 (d, *J* = 6.0 Hz, 3 H, α-Me), 2.36 (s, 6 H, N*Me*$_2$), 3.93 (q, *J* = 6.8 Hz, 1 H, α-C*H*), 4.00 (s, 3 H, O*Me*), 4.97 (t, *J* = 6.0 Hz, 1 H, $H_{Ar}$), 5.58 (d, *J* = 5.8 Hz, 1 H, $H_{Ar}$), 5.88 (d, *J* = 6.0 Hz, 1 H, $H_{Ar}$) ppm. The X-ray structure is shown in Figure 6.

 © 2007 Wiley-VCH Verlag GmbH & Co. KGaA, Weinheim 

**(*S*)-*N*,*N*-Dimethyl-1-[2-methoxy-3,6-bis(trimethylsilyl)phenyl]ethylamine [(*S*)-31]:** This complex was prepared by deprotonation of (*S*)-**29** (4.00 g, 15.94 mmol, 1 equiv.) with *t*BuLi (1.7 M in pentane; 10.70 mL, 18.17 mmol, 1.14 equiv.) for 24 h at –50 °C in diethyl ether (150 mL) and then treatment of the lithiated species with chlorotrimethylsilane (8.65 g, 79.70 mmol, 5 equiv.). The reaction mixture was warmed up to room temperature overnight and then filtered through short pad of Celite in order to remove LiCl. The solvent and the excess of $ClSiMe_3$ were distilled off on a rotary evaporator and the crude product was purified by column chromatography (aluminium oxide; diethyl ether/hexane, 1:1). Yield light yellow oil (4.62 g, 90%). $^1$H NMR (500 MHz, $CDCl_3$): $\delta$ = 0.34 (s, 9 H, Si$Me_3$), 0.35 (s, 9 H, Si$Me_3$), 1.47 (d, $J$ = 7.0 Hz, 3 H, α-Me), 2.20 (s, 6 H, N$Me_2$), 3.61 (q, $J$ = 7.0 Hz, 1 H, α-C$H$), 3.80 (s, 3 H, O$Me$), 7.35 (d, $J$ = 7.3 Hz, 1 H, $H_{Ar}$), 7.42 (d, $J$ = 7.3 Hz, 1 H, $H_{Ar}$) ppm. $^{13}$C NMR (125 MHz, $CDCl_3$): $\delta$ = 0.24 (Si$Me_3$), 2.72 (Si$Me_3$), 21.23 (α-Me), 45.03 (N$Me_2$), 62.81 (O$Me$), 62.97 (α-$C$H), 131.83 ($C_{Ar}$), 133.60 ($C_{Ar}$), 134.37 ($C_{Ar,ipso}$), 141.44 ($C_{Ar,ipso}$), 144.72 ($C_{Ar,ipso}$), 163.60 ($C_{Ar,ipso}$) ppm.

**Preparation of [{η$^6$-(*S*,*R*p)-*N*,*N*-Dimethyl-1-[2-methoxy-3,6-bis(trimethylsilyl)phenyl]ethylamine}Cr(CO)$_3$] [(*S*,*R*p)-32]. Thermolysis with Cr(CO)$_6$:** Treatment of (*S*)-**31** (2.50 g, 7.74 mmol) with $Cr(CO)_6$ (2.21 g, 10.00 mmol) in an 8:1 mixture of di-*n*-butyl ether and thf (40.5 mL) for 45 h according to general procedure B afforded (*S*,*R*p)-**32** in 94% diastereomeric purity (NMR; Scheme 10). The crude product was purified by column chromatography (aluminium oxide; diethyl ether/hexane, 1:1). Yield 2.90 g (82%).

**Arene Exchange with [(η$^6$-Naphthalene)Cr(CO)$_3$]:** (*S*,*R*p)-**32** was prepared in a high-pressure Schlenk tube from (*S*)-**31** (1.51 g, 4.68 mmol) and [(η$^6$-naphthalene)$Cr(CO)_3$] (1.50 g, 5.68 mmol) in di-*n*-butyl ether (25 mL). After all reagents and the solvent had been mixed, a catalytic amount of thf (0.53 g, 7.35 mmol) was added, the reaction mixture was degassed by means of ultrasound and three freeze-pump-thaw cycles and then heated in the dark at 75 °C for 140 h. The reaction mixture was filtered through a short pad of Celite and the solvent distilled off on a rotary evaporator to afford (*S*,*R*p)-**31** in >99% *de* (NMR). The crude product was purified by flash chromatography (aluminium oxide; diethyl ether/hexane, 1:7) to yield 1.14 g of yellow crystals (53%). $^1$H NMR (500 MHz, $CDCl_3$): $\delta$ = 0.37 (s, 9 H, Si$Me_3$), 0.42 (s, 9 H, Si$Me_3$), 1.44 (d, $J$ = 7.0 Hz, 3 H, α-Me), 2.16 (s, 6 H, N$Me_2$), 3.13 (q, $J$ = 7.0 Hz, 1 H, α-C$H$), 3.74 (s, 3 H, O$Me$), 4.84 (d, $J$ = 6.4 Hz, 1 H, $H_{Ar}$), 5.51 (d, $J$ = 6.1 Hz, 1 H, $H_{Ar}$) ppm. $^{13}$C NMR (125 MHz, $CDCl_3$): $\delta$ = 0.40 (Si$Me_3$), 2.38 (Si$Me_3$), 25.07 (α-Me), 45.35 (N$Me_2$), 59.66 (O$Me$), 62.67 (α-$C$H), 91.28 ($C_{Ar,ipso}$), 93.32 ($C_{Ar}$), 103.03 ($C_{Ar}$), 105.12 ($C_{Ar,ipso}$), 118.63 ($C_{Ar,ipso}$), 146.41 ($C_{Ar,ipso}$), 233.60 ($C_{Ar,ipso}$) ppm. IR (hexane): $\nu_{CO}$ = 1970, 1900 cm$^{-1}$.

**Preparation of [{η$^6$-(*S*,*R*p)-*N*,*N*-Dimethyl-1-(2-methoxyphenyl)ethylamine}Cr(CO)$_3$] [(*S*,*R*p)-28]:** (*S*,*R*p)-**31** (1.61 g, 3.51 mmol) was dissolved in thf (30 mL) and the solution cooled to 0 °C. Tetra-*n*-butylammonium fluoride (1 M in thf; 9.00 mL, 9.00 mmol) was added dropwise and the solution stirred at 0 °C for 4 h (Scheme 10). After addition of distilled water the reaction mixture was extracted several times with diethyl ether. The combined organic phases were concentrated on a rotary evaporator and the residue was purified by column chromatography (aluminium oxide; diethyl ether) to afford (*S*,*R*p)-**28** in diastereomerically pure form as yellow crystals. Yield 0.62 g (56%).

**(*S*)-*N*,*N*-Dimethyl-1-[2-(diphenylphosphanyl)-3-methoxyphenyl]-ethylamine [(*S*)-33]:** This complex was prepared by deprotonating (*S*)-**5** (1.00 g, 5.58 mmol, 1 equiv.) with *t*BuLi (1.7 M in pentane; 3.75 mL, 6.37 mmol, 1.14 equiv.) for 24 h at –50 °C in diethyl ether (100 mL) and then treating the lithiated species with chlorodiphenylphosphane (1.4 g, 6.37 mmol, 1.14 equiv.). The reaction mixture was warmed to room temperature overnight and then filtered through a short pad of Celite in order to remove LiCl. The solvent was distilled off on a rotary evaporator and the crude product purified by column chromatography (silica gel; diethyl ether/hexane, 1:1). Yield white crystals (1.25 g, 89%). Crystals suitable for X-ray analysis were grown by slow diffusion of hexane into a solution of the compound in diethyl ether at –30 °C (diethyl ether/hexane, 1:3). $^1$H NMR (500 MHz, $CDCl_3$): $\delta$ = 1.25 (d, $J$ = 6.4 Hz, 3 H, α-Me), 2.10 (s, 6 H, N$Me_2$), 3.11 (s, 3 H, O$Me$), 4.62 (m, $J$ = 6.4, $J$ = 2.4 Hz, 1 H, α-C$H$), 6.59 (dd, $J$ = 8.2, $J$ = 1.2 Hz, 1 H, $H_{Ar}$), 7.10–7.34 (m, 12 H, $10H_{PPh_2}$ + $2H_{Ar}$) ppm. $^{13}$C NMR (125 MHz, $CDCl_3$): $\delta$ = 19.72 (α-Me), 42.98 (N$Me_2$), 54.64 (O$Me$), 62.48 (d, $J_{C,P}$ = 31.8 Hz, α-$C$H), 110.25 ($C_{Ar}$), 119.35 (d, $J_{C,P}$ = 7.1 Hz, $C_{Ar}$), 122.54 (d, $J_{C,P}$ = 20.3 Hz, $C_{Ar,ipso}$), 127.01 ($C_{PPh_2}$), 127.15 ($C_{PPh_2}$), 127.54 ($C_{PPh_2}$), 127.60 ($C_{PPh_2}$), 127.62 ($C_{PPh_2}$), 127.65 ($C_{PPh_2}$), 131.62 ($C_{Ar}$), 131.64 ($C_{PPh_2}$), 131.90 ($C_{PPh_2}$), 132.06 ($C_{PPh_2}$), 132.22 ($C_{PPh_2}$), 137.44 (d, $J_{C,P}$ = 9.3 Hz, $C_{PPh_2}$), 138.35 (d, $J_{C,P}$ = 11.0 Hz, $C_{PPh_2}$), 154.45 (d, $J_{C,P}$ = 24.7 Hz, $C_{Ar,ipso}$), 161.80 (d, $J_{C,P}$ = 3.3 Hz, $C_{Ar,ipso}$) ppm. $^{31}$P NMR (81 MHz, $CDCl_3$): $\delta$ = –23.98 ppm.

**(*S*)-*N*,*N*-Dimethyl-1-[3-methoxy-2-(trimethylsilyl)phenyl]ethylamine [(*S*)-34]:** This complex was prepared by deprotonation of (*S*)-**5** (5.00 g, 27.93 mmol, 1 equiv.) with *t*BuLi (1.7 M in pentane; 19.00 mL, 32.30 mmol, 1.14 equiv.) for 24 h at –50 °C in diethyl ether (200 mL) and then treatment of the lithiated species with chlorotrimethylsilane (15.17 g, 139.65 mmol, 5 equiv.). The reaction mixture was warmed to room temperature, stirred at that temperature for 10 d and then filtered through a short pad of Celite in order to remove LiCl. The solvent and excess $ClSiMe_3$ were distilled off on a rotary evaporator and the crude product was purified by column chromatography (aluminium oxide; diethyl ether/hexane, 1:1). Yield light yellow oil (6.16 g, 88%). $^1$H NMR (200 MHz, $CDCl_3$): $\delta$ = 0.35 (s, 9 H, Si$Me_3$), 1.29 (d, $J$ = 6.4 Hz, 3 H, α-Me), 2.19 (s, 6 H, N$Me_2$), 3.49 (q, $J$ = 6.4 Hz, 1 H, α-C$H$), 3.75 (s, 3 H, O$Me$), 6.69 (d, $J$ = 7.3 Hz, 1 H, $H_{Ar}$), 7.17–7.35 (m, 2 H, $H_{Ar}$) ppm. $^{13}$C NMR (125 MHz, $CDCl_3$): $\delta$ = 3.12 (Si$Me_3$), 22.91 (α-Me), 44.16 (N$Me_2$), 54.87 (O$Me$), 63.85 (α-$C$H), 107.95 ($C_{Ar}$), 119.24 ($C_{Ar}$), 125.56 ($C_{Ar,ipso}$), 130.50 ($C_{Ar}$), 153.91 ($C_{Ar,ipso}$), 164.46 ($C_{Ar,ipso}$) ppm. $[\alpha]_D^{r.t.}$ = –80.36 ($c$ = 0.21, $CHCl_3$).

**[{η$^6$-(*S*,*R*p)-*N*,*N*-Dimethyl-1-[3-methoxy-2-(trimethylsilyl)phenyl]-ethylamine}Cr(CO)$_3$] [(*S*,*R*p)-35]:** This complex was prepared in a high-pressure Schlenk tube from (*S*)-**34** (2.03 g, 8.10 mmol) and [(η$^6$-naphthalene)$Cr(CO)_3$] (2.56 g, 9.70 mmol) in di-*n*-butyl ether (40 mL). After all reagents and the solvent had been mixed, a catalytic amount of thf (0.9 g, 10.88 mmol) was added, the reaction mixture was degassed by means of ultrasound and three freeze-pump-thaw cycles and then heated in the dark at 75 °C for 72 h. The reaction mixture was then filtered through a short pad of Celite and the solvent was distilled off on a rotary evaporator to give the desired product in 86% *de* (NMR). The crude product was taken up in diethyl ether and purified by flash chromatography (aluminium oxide; diethyl ether/hexane, 3:1). A yellow-orange powder contaminated with unreacted [(η$^6$-naphthalene)$Cr(CO)_3$] was obtained after evaporation of the solvents. The product was isolated in high purity (*de* > 98%) after a second chromatographic purification (silica gel; diethyl ether/hexane, 1:7). Yield 2.24 g (71%). $^1$H NMR (200 MHz, $CDCl_3$): $\delta$ = 0.45 (s, 9 H, Si$Me_3$), 11.01 (d, $J$ = 6.8 Hz, 3 H, α-Me), 2.22 (s, 6 H, N$Me_2$), 3.00 (s, 3 H, O$Me$), 3.53 (q, $J$ = 7.2 Hz, 1 H, α-C$H$), 4.15 (d, $J$ = 6.8 Hz, 1 H, $H_{Ar}$), 5.07 (t, $J$ = 6.8 Hz, 1 H, $H_{Ar}$), 5.33 (d, $J$ = 6.4 Hz, 1 H, $H_{Ar}$) ppm. $^{13}$C NMR (125 MHz, $CDCl_3$): $\delta$ = 2.98 (Si$Me_3$), 23.21

 © 2007 Wiley-VCH Verlag GmbH & Co. KGaA, Weinheim 

(α-Me), 44.02 (N*Me*$_2$), 54.93 (O*Me*), 60.54 (α-*C*H), 75.05 ($C_{Ar}$), 85.51 ($C_{Ar}$), 93.94 ($C_{Ar}$), 100.00 ($C_{Ar,ipso}$), 115.40 ($C_{Ar,ipso}$), 147.25 ($C_{Ar,ipso}$), 234.74 (*C*O) ppm. IR (hexane): $\nu_{CO}$ = 1965, 1895 cm$^{-1}$.

**[{η$^6$-(*S*,*S*p)-*N*,*N*-Dimethyl-1-(3-methoxyphenyl)ethylamine}Cr(CO)$_3$] [(*S*,*S*p)-36]:** (*S*,*R*p)-**35** (2.03 g, 5.23 mmol) was dissolved in thf (18 mL) and the solution cooled to 0 °C. Tetra-*n*-butylammonium fluoride (1 M in thf, 6.38 mL, 6.38 mmol) was added dropwise and the solution was stirred at 0 °C for 4 h. After addition of distilled water the reaction mixture was extracted several times with diethyl ether. The combined organic phases were concentrated on a rotary evaporator and the residue was purified by column chromatography (silica gel; diethyl ether/acetone) to afford (*S*,*S*p)-**36** as yellow crystals. Yield 1.41 g (85%). $^1$H NMR (200 MHz, $CDCl_3$): $\delta$ = 0.99 (d, *J* = 6.8 Hz, 3 H, α-Me), 1.89 (s, 6 H, N*Me*$_2$), 3.02 (s, 3 H, O*Me*), 3.39 (q, *J* = 6.8 Hz, 1 H, α-C*H*), 4.25 (d, *J* = 6.6 Hz, $H_{Ar}$), 4.52 (d, *J* = 6.3 Hz, 1 H, $H_{Ar}$), 4.80 (t, *J* = 6.6 Hz, 1 H, $H_{Ar}$), 4.95 (s, 1 H, $H_{Ar}$) ppm. $^{13}$C NMR (50 MHz, $CDCl_3$): $\delta$ = 10.49 (α-Me), 40.58 (N*Me*$_2$), 55.65 (O*Me*), 61.20 (α-*C*H), 75.78 ($C_{Ar}$), 79.26 ($C_{Ar}$), 88.48 ($C_{Ar}$), 93.98 ($C_{Ar}$), 114.42 ($C_{Ar,ipso}$), 142.53 ($C_{Ar,ipso}$), 233.06 (*C*O) ppm. IR (hexane): $\nu_{CO}$ = 1970, 1900 cm$^{-1}$.

**[{η$^6$-(*S*,*S*p)-*N*,*N*-Dimethyl-1-[2-(diphenylphosphanyl)-6-methoxyphenyl]ethylamine}Cr(CO)$_3$] [(*S*,*S*p)-37]:** This complex was prepared according to general procedure C by lithiation of (*S*,*S*p)-**28** (0.45 g, 1.43 mmol) with *tert*-butyllithium (1.7 M in pentane; 0.96 mL, 1.63 mmol) and treatment of the lithiated species with chlorodiphenylphosphane (0.36 g, 1.63 mmol) in dry diethyl ether (25 mL). The crude product was purified by column chromatography (aluminium oxide; diethyl ether/hexane, 2:1). Yield yellow crystals (0.38 g, 54%). Crystals suitable for X-ray analysis were grown by means of slow diffusion of hexane into a solution of the compound in diethyl ether at –30 °C. $^1$H NMR (500 MHz, $CDCl_3$): $\delta$ = 1.29 (d, *J* = 6.7 Hz, 3 H, α-Me), 1.76 (s, 6 H, N*Me*$_2$), 3.72 (s, 3 H, O*Me*), 4.47 (d, *J* = 5.2 Hz, 1 H, $H_{Ar}$), 4.55 (dq, *J* = 6.7, *J* = 2.4 Hz, 1 H, α-C*H*), 5.25–5.29 (m, 2 H, $H_{Ar}$), 7.20–7.33 (m, 10 H, $H_{PPh_2}$) ppm. $^{13}$C NMR (125 MHz, $CDCl_3$): $\delta$ = 10.74 (α-Me), 38.90 (N*Me*$_2$), 56.01 (O*Me*), 60.17 (d, $J_{C,P}$ = 19.2 Hz, α-*C*H), 77.54 ($C_{Ar}$), 90.74 ($C_{Ar}$), 94.18 (d, $J_{C,P}$ = 1.9 Hz, $C_{Ar}$), 107.83 (d, $J_{C,P}$ = 18.2 Hz, $C_{Ar,ipso}$), 110.54 (d, $J_{C,P}$ = 24.0 Hz, $C_{Ar,ipso}$), 127.74–134.83 (10 C, $C_{PPh_2}$), 136.56 (d, $J_{C,P}$ = 17.3 Hz, $C_{PPh_2}$), 137.58 (d, $J_{C,P}$ = 5.6 Hz, $C_{PPh_2}$), 140.52 (d, $J_{C,P}$ = 3.8 Hz $C_{Ar,ipso}$), 233.36 (*C*O) ppm. $^{31}$P NMR (81 MHz, $CDCl_3$): $\delta$ = –11.22 ppm. IR (hexane): $\nu_{CO}$ = 1970, 1896 cm$^{-1}$. $C_{26}H_{26}CrNO_4P$: calcd. C 62.52, H 5.21, N 2.80; found 62.61, H 6.05, N 2.39.

**[{η$^6$-(*S*,*S*p)-*N*,*N*-Dimethyl-1-[2-(diphenylphosphanyl)-5-methoxyphenyl]ethylamine}Cr(CO)$_3$] [(*S*,*S*p)-38]:** This complex was prepared according to general procedure C by lithiation of (*S*,*S*p)-**36** (1.36 g, 4.30 mmol) with *tert*-butyllithium (1.7 M in pentane; 2.90 mL, 4.90 mmol) and treatment of the lithiated species with chlorodiphenylphosphane (1.80 g, 4.90 mmol) in dry diethyl ether (250 mL; see Scheme 15). The crude product was purified by column chromatography (silica gel; diethyl ether/hexane, 1:6). Yield 1.22 g (57%); yellow crystals. $^1$H NMR (500 MHz, $CDCl_3$): $\delta$ = 0.82 (d, *J* = 6.7 Hz, 3 H, α-Me), 1.45 (s, 6 H, N*Me*$_2$), 3.01 (s, 3 H, O*Me*), 3.97 (d, *J* = 6.4 Hz, 1 H, $H_{Ar}$), 4.65 (m, 1 H, α-C*H*), 4.92 (d, *J* = 6.7 Hz, 1 H, $H_{Ar}$), 5.05 (s, 1 H, $H_{Ar}$), 7.06–7.56 (m, 10 H, $H_{PPh_2}$) ppm. $^{13}$C NMR (125 MHz, $CDCl_3$): $\delta$ = 5.48 (α-Me), 37.85

Table 5. Crystallographic data, data collection and structure refinement parameters for (*S*,*R*p)-**23b**, (*S*,*S*p)-**28**, (*S*,*R*p)-**30** and (*S*)-**33**.

| | 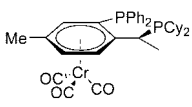 (*S*,*R*p)-**23b** | 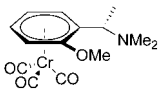 (*S*,*S*p)-**28** | 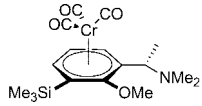 (*S*,*R*p)-**30** | 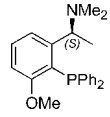 (*S*)-**33** |
|---|---|---|---|---|
| Empirical formula | $C_{36}H_{42}Cr_1O_3P_2$ | $C_{14}H_{17}CrNO_4$ | $C_{17}H_{25}CrNO_4Si$ | $C_{23}H_{26}NOP$ |
| Formula mass | 636.68 | 315.29 | 387.47 | 363.44 |
| Crystal habit, colour | hexagonal prism, yellow | rod, yellow | rod, yellow | rod, colourless |
| Crystal dimensions [mm] | 0.74 × 0.39 × 0.37 | 0.90 × 0.16 × 0.14 | 0.22 × 0.05 × 0.05 | 0.53 × 0.26 × 0.16 |
| Crystal system | orthorhombic | orthorhombic | monoclinic | monoclinic |
| Space group | $P2_12_12_1$ | $P2_12_12_1$ | $C_2$ | $P2_1$ |
| *a* [Å] | 12.7113(14) | 6.612(6) | 41.416(7) | 9.099(12) |
| *b* [Å] | 34.4771(17) | 9.932(10) | 6.7122(12) | 12.294(16) |
| *c* [Å] | 7.8497(4) | 22.04(2) | 22.578(4) | 18.36(2) |
| *β* [°] | | | 112.069(4) | 92.79(3) |
| *V* [Å$^3$] | 3440.1(5) | 1447(2) | 5816.6(18) | 2051(4) |
| *Z* | 4 | 4 | 12 | 4 |
| *D* [g cm$^{-3}$] | 1.229 | 1.447 | 1.327 | 1.177 |
| *F*(000) | 1344 | 656 | 2448 | 776 |
| $\mu$(Mo-$K_\alpha$) [cm$^{-1}$] | 0.458 | 0.802 | 0.671 | 0.145 |
| Diffractometer | Enraf Nonius CAD4 | Bruker Smart CCD | Bruker Smart CCD | Bruker Smart CCD |
| *T* [K] | 293(2) | 153(2) | 110(2) | 293(2) |
| $\theta$ range [°] | 3.1–26.0 | 1.9–28.3 | 1.7–25.2 | 2.0–28.3 |
| Reflections collected | 9867 | 19784 | 24383 | 50905 |
| Unique refl. | 6725 | 3582 | 9823 | 8929 |
| $R_{int}$ | 0.083 | 0.0283 | 0.0941 | 0.0365 |
| Reflections observed | 3278 | 3464 | 6761 | 7561 |
| Parameters refined | 381 | 185 | 655 | 477 |
| $R_1$ | 0.0740 | 0.0412 | 0.0611 | 0.0407 |
| $wR_2$ | 0.1507 | 0.1001 | 0.1337 | 0.1093 |
| Flack parameter | –0.01(4) | 0.03(3) | 0.00(3) | –0.06(6) |
| GooF | 0.999 | 1.313 | 1.002 | 1.026 |
| Diff. peak/hole [e Å$^{-3}$] | 0.34/–0.24 | 0.55/–0.29 | 0.40/–0.51 | 0.30/–0.141 |

 © 2007 Wiley-VCH Verlag GmbH & Co. KGaA, Weinheim 

(N*Me*$_2$), 55.08 (O*Me*), 58.98 (d, $J_{C,P}$ = 14.4 Hz, α-*C*H), 73.95 ($C_{Ar}$), 79.62 ($C_{Ar}$), 99.61 ($C_{Ar}$), 100.33 (d, $J_{C,P}$ = 24.0 Hz, $C_{Ar,ipso}$), 120.88 (d, $J_{C,P}$ = 21.1 Hz, $C_{Ar,ipso}$), 128.75 (d, $J_{C,P}$ = 5.8 Hz $C_{PPh_2}$), 129.18 ($C_{PPh_2}$), 132.31 (d, $J_{C,P}$ = 20.1 Hz, $C_{PPh_2}$), 135.24 (d, $J_{C,P}$ = 21.1 Hz, $C_{PPh_2}$), 137.62 (d, $J_{C,P}$ = 14.4 Hz, $C_{PPh_2}$), 139.00 (d, $J_{C,P}$ = 6.7 Hz, $C_{PPh_2}$), 142.94 ($C_{Ar,ipso}$), 233.01 (*C*O) ppm. $^{31}$P NMR (81 MHz, $CDCl_3$): $\delta$ = –16.74 ppm. IR (hexane): $\nu_{CO}$ = 1972, 1908 cm$^{-1}$. $C_{26}H_{26}NO_4PCr$ (499.46): calcd. C 62.52, H 5.21, N 2.80; found C 62.78, H 5.54, N 2.89.

**[{η$^6$-(*S*,*Sp*)-*N*,*N*-Dimethyl-1-[2-(diphenylphosphanyl)-3-methoxyphenyl]ethylamine}Cr(CO)$_3$] [(*S*,*Sp*)-40]:** A 1:1 mixture of (*S*,*Sp*)-**36** and (*S*,*Rp*)-**36** (4.20 g, 13.33 mmol, 1 equiv.) was dissolved in diethyl ether (250 mL). The solution was cooled to –80 °C and *tert*-butyllithium (1.7 M in pentane; 8.94 mL, 15.20 mmol, 1.14 equiv.) was added dropwise (Scheme 16). After stirring for 4 h at –80 °C, chlorodiphenylphosphane (3.35 g, 15.20 mmol, 1.14 equiv.) was added dropwise. The reaction mixture was warmed to room temperature overnight, filtered through a short pad of celite to remove LiCl and the solvent removed in vacuo. Three compounds were detected in the NMR spectrum of the crude product: (*S*,*Sp*)-**38**, **39** and (*S*,*Sp*)-**40** in a 31:20:49 ratio. The crude product was purified by column chromatography (aluminium oxide; diethyl ether/hexane, 1:7). Only (*S*,*Sp*)-**40** was isolated and further purified by column chromatography on silica gel. Yield yellow crystals (0.64 g, 22%). Crystals suitable for X-ray analysis were grown by slow diffusion of hexane into a solution of the complex in diethyl ether at –30 °C. $^1$H NMR (200 MHz, $C_6D_6$): $\delta$ = 0.85 (d, $J$ = 6.3 Hz, 3 H, α-Me), 1.69 (s, 6 H, N*Me*$_2$), 2.59 (s, 3 H, O*Me*), 3.87 (d, $J$ = 7.3 Hz, 1 H, $H_{Ar}$), 4.20 (d, $J$ = 7.3 Hz, 1 H, $H_{Ar}$), 4.83 (m, 1 H, α-C*H*), 4.97 (t, $J$ = 7.3 Hz, 1 H, $H_{Ar}$), 7.07–7.31 (m, 8 H, $H_{PPh_2}$), 7.79 (t, $J$ = 8.3 Hz, 2 H, $H_{PPh_2}$) ppm. $^{13}$C NMR (125 MHz, $CDCl_3$): $\delta$ = 5.80 (α-Me), 38.03 (N*Me*$_2$), 54.51 (O*Me*), 58.88 (d, $J_{C,P}$ = 22.1 Hz, α-*C*H), 71.48 ($C_{Ar}$), 82.47 ($C_{Ar}$), 94.03 ($C_{Ar}$), 121.98 (d, $J_{C,P}$ = 8.6 Hz, $C_{Ar,ipso}$), 123.60 (d, $J_{C,P}$ = 25.9 Hz, $C_{Ar,ipso}$), 127.41–135.83 (10 C, $C_{PPh_2}$), 137.60 (d, $J_{C,P}$ = 14.2 Hz, 1 C, $C_{PPh_2}$), 139.90 (d, $J_{C,P}$ = 6.5 Hz, 1 C, $C_{PPh_2}$), 146.80 ($C_{Ar,ipso}$), 233.24 (*C*O) ppm. $^{31}$P NMR (81 MHz, $C_6D_6$): $\delta$ = –10.70 ppm. IR (hexane): $\nu_{CO}$ = 1971, 1903 cm$^{-1}$.

**X-ray Structure Determination:** Crystal data and details of the structure determinations are listed in Tables 5 and 6. Data collection was performed with a Bruker Smart CCD (Mo-$K_\alpha$ radiation, $\lambda$ = 0.71073 Å, graphite monochromator) fitted with an area detector for (*S*,*Sp*)-**28**, (*S*,*Rp*)-**30**, (*S*)-**33**, and (*S*,*Sp*)-**40** and an Enraf Nonius CAD4 diffractometer (Mo-$K_\alpha$ radiation, $\lambda$ = 0.71073 Å, graphite monochromator) for (*S*,*Rp*)-**23b**, (*S*,*Sp*)-**36**, (*S*,*Sp*)-**37** and (*S*,*Sp*)-**38**. The unit-cell parameters were obtained by least-squares refinement of up to 8096 reflections for the area detector and 25 reflections for the CAD4 point detector. The structures were solved by direct methods (SHELXS-97)[29] and refined by full-matrix least-squares procedures based on $F^2$ with all measured reflections (SHELXL-97).[29] The SADABS[30] program was used for absorption correction of the structures. All non-hydrogen atoms were refined anisotropically. All H-atoms were introduced at their idealised positions and were refined using a riding model. The absolute configuration was confirmed by evaluation of the Flack[31] parameter. Displacement ellipsoid plots were obtained with PLATON.[32]

Table 6. Crystallographic data, data collection and structure refinement parameters for (*S*,*Sp*)-**36**, (*S*,*Sp*)-**37**, (*S*,*Sp*)-**38** and (*S*,*Sp*)-**40**.

| | 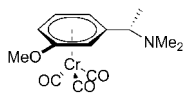 (*S*,*Sp*)-**36** | 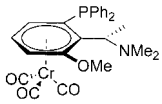 (*S*,*Sp*)-**37**[a] | 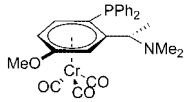 (*S*,*Sp*)-**38** | 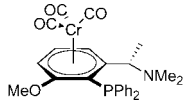 (*S*,*Sp*)-**40** |
|---|---|---|---|---|
| Empirical formula | $C_{14}H_{17}CrNO_4$ | $C_{26}H_{26}CrNO_4P$ | $C_{26}H_{26}CrNO_4P$ | $C_{26}H_{26}CrNO_4P$ |
| Formula mass | 315.29 | 499.45 | 499.45 | 499.45 |
| Crystal habit, colour | plate, pale yellow | rod, yellow | irregular, yellow | platelet, yellow |
| Crystal dimensions [mm] | 0.52 × 0.35 × 0.12 | 0.83 × 0.20 × 0.15 | 0.70 × 0.60 × 0.20 | 0.85 × 0.28 × 0.06 |
| Crystal system | orthorhombic | orthorhombic | orthorhombic | orthorhombic |
| Space group | $P2_12_12_1$ | $P2_12_12_1$ | $P2_12_12_1$ | $P2_12_12_1$ |
| $a$ [Å] | 7.012(3) | 12.0203(10) | 7.8948(5) | 8.2725(10) |
| $b$ [Å] | 8.509(4) | 13.3439(10) | 14.8611(17) | 10.8788(13) |
| $c$ [Å] | 24.36(1) | 15.6855(10) | 42.615(5) | 29.045(3) |
| $V$ [Å$^3$] | 1453.4(11) | 2515.9(3) | 4999.8(9) | 2613.9(5) |
| $Z$ | 4 | 4 | 8 | 4 |
| $D$ [g cm$^{-3}$] | 1.44 | 1.319 | 1.327 | 1.269 |
| $F$(000) | 656 | 1040 | 2080 | 1040 |
| $\mu$(Mo-$K_\alpha$) [cm$^{-1}$] | 0.798 | 0.549 | 0.053 | 0.0529 |
| Diffractometer | Enraf Nonius CAD4 | Enraf Nonius CAD4 | Enraf Nonius CAD4 | Bruker Smart CCD |
| $T$ [K] | 223(2) | 293(2) | 223(2) | 200(2) |
| $\theta$ range [°] | 2.4–26.0 | 2.0–25.0 | 2.4–26.0 | 2.0–28.3 |
| Reflections collected | 12629 | 6688 | 14852 | 36050 |
| Unique refl. | 2851 | 3419 | 9801 | 6499 |
| $R_{int}$ | 0.145 | 0.0426 | 0.0536 | 0.0614 |
| Reflections observed | 1940 | 2492 | 7770 | 5482 |
| Parameters refined | 185 | 302 | 655 | 477 |
| $R_1$ | 0.0656 | 0.0416 | 0.0436 | 0.0547 |
| $wR_2$ | 0.1459 | 0.0895 | 0.0915 | 0.1325 |
| Flack parameter | 0.02(5) | –0.02(3) | –0.008(17) | 0.01(3) |
| GooF | 0.954 | 1.034 | 1.065 | 1.066 |
| Diff. peak/hole [e Å$^{-3}$] | 0.73/–1.46 | 0.19/–0.24 | 0.35/–0.28 | 0.60/–0.36 |

[a] Due to a technical problem with the diffractometer the intensity data collection for the crystal of (*S*,*Sp*)-**37** had to be stopped at about 73% completion; the data are, however, sufficient to ensure a reliable assignment of the absolute configuration.

 © 2007 Wiley-VCH Verlag GmbH & Co. KGaA, Weinheim 

Due to a technical problem with the diffractometer the intensity data collection for the sample of (*S*,*S*p)-**37** had to be stopped at about 73% completion; the data are, however, sufficient to ensure a reliable assignment of the absolute configuration.

CCDC-648702 to -648709 contain the supplementary crystallographic data for this paper. These data can be obtained free of charge from The Cambridge Crystallographic Data Centre via www.ccdc.cam.ac.uk/data_request/cif.

## Acknowledgments

The authors are grateful for financial support from the Deutsche Forschungsgemeinschaft DFG within the Collaborative Research Center (SFB, 380) "Asymmetric Synthesis with Chemical and Biological Means" and the Graduiertenkolleg 440 "Methods in Asymmetric Synthesis" for three scholarships for E. A., B. C.-C. and D. T. We also thank Dr. K. Ditrich from BASF Corporation for a generous gift of various chiral phenylethylamines.

[1] a) U. Englert, A. Salzer, D. Vasen, *Tetrahedron: Asymmetry* **1998**, *9*, 1867–1870; b) U. Englert, R. Härter, D. Vasen, A. Salzer, E. Eggeling, D. Vogt, *Organometallics* **1999**, *18*, 4390–4398.

[2] a) A. Salzer, *Coord. Chem. Rev.* **2003**, *242*, 59–72; b) K. Muñiz, *Planar Chiral Arene Chromium(0) Complexes as Ligands for Asymmetric Catalysis*, in *Topics in Organometallic Chemistry*, vol. 7 (Ed.: E. P. Kündig), Springer Verlag, Heidelberg, **2004**, pp. 205–233; A. Salzer, W. Braun, *The "Daniphos" Ligands: Synthesis and Catalytic Applications*, in *Asymmetric Synthesis with Chemical and Biological Methods* (Eds.: D. Enders, K.-E. Jaeger), Wiley-VCH Verlag, Weinheim, **2007**, pp. 115–130.

[3] a) D. Vasen, A. Salzer, F. Gerhards, J. Gais, R. Stürmer, N. H. Bieler, A. Togni, *Organometallics* **2000**, *19*, 539–546; b) W. Braun, A. Salzer, H.-J. Drexler, A. Spannenberg, D. Heller, *Dalton Trans.* **2003**, 1606–1612; c) W. Braun, A. Salzer, F. Spindler, E. Alberico, *Appl. Catal., A* **2004**, *274*, 191–203; d) W. Braun, B. Calmuschi, J. Haberland, W. Hummel, A. Liese, T. Nickel, O. Stelzer, A. Salzer, *Eur. J. Inorg. Chem.* **2004**, 2235–2243; e) U. Englert, C. Hu, A. Salzer, E. Alberico, *Organometallics* **2004**, *23*, 5419–5431; f) W. Braun, W. Müller, B. Calmuschi-Cula, A. Salzer, V. Groehn, *J. Organomet. Chem.* **2006**, *691*, 2263–2269.

[4] D. Totev, A. Salzer, D. Carmona, L. A. Oro, F. J. Lahoz, I. T. Dobrinovitch, *Inorg. Chim. Acta* **2004**, *357*, 2889–2898.

[5] W. Braun, W. Müller, B. Calmuschi, A. Salzer, *J. Organomet. Chem.* **2005**, *690*, 1166–1171.

[6] S. H. Pine, B. L. Sanchez, *J. Org. Chem.* **1971**, *36*, 829–832.

[7] C. A. Mahaffy, P. L. Pauson, *Inorg. Synth.* **1990**, *28*, 136–140.

[8] a) H. G. Schmalz, F. Dehmel, in *Transition Metals for Organic Synthesis: Building Blocks and Fine Chemicals*, 2nd ed. (Eds.: M. Beller, C. Bolm), Wiley-VCH Verlag, Weinheim, **2004**, p. 601, and references cited therein; b) E. P. Kündig, *Synthesis of Transition Metal $\eta^6$-Complexes*, in *Topics in Organometallic Chemistry*, vol. 7 (Ed.: E. P. Kündig), Springer Verlag, Heidelberg, **2004**, pp. 3–20; c) M. F. Semmelhack, A. Chlenov, *[$\eta^6$-(arene)Cr(CO)$_3$] Complexes: Arene Lithiation/Reaction with Electrophiles*, in *Topics in Organometallic Chemistry*, vol. 7 (Ed.: E. P. Kündig), Springer Verlag, Heidelberg, **2004**, pp. 21–42.

[9] M. Hudecek, S. Toma, *J. Organomet. Chem.* **1990**, *393*, 115–118.

[10] a) V. Snieckus, *Chem. Rev.* **1990**, *90*, 879–933; b) M. C. Whisler, S. MacNeil, V. Snieckus, P. Beak, *Angew. Chem. Int. Ed.* **2004**, *43*, 2206–2225.

[11] K. Schlögl, *Top. Stereochem.* **1967**, *1*, 39. According to Schlögl's rules, to assign the stereochemical descriptor for an element of planar chirality, the arene is monitored from the side which is not coordinated to the chromium moiety. The priority of the substituents is then determined by employing the Cahn–Ingold–Prelog (CIP) rules. If the shortest path from the substituent displaying highest priority to the following one is clockwise, the absolute configuration is denoted as *R*p, while the opposite case is referred to as *S*p.

[12] J. A. Heppert, J. Aubé, E. M. Thomas-Miller, M. L. Milligan, F. Takusagawa, *Organometallics* **1990**, *9*, 727–739.

[13] M. Uemura, R. Miyake, H. Nishimura, Y. Matsumoto, T. Hayashi, *Tetrahedron: Asymmetry* **1992**, *3*, 213–216.

[14] R. J. Card, W. S. Trahanovsky, *J. Org. Chem.* **1980**, *45*, 2560–2566.

[15] a) J. P. Gilday, D. A. Widdowson, *J. Chem. Soc. Chem. Commun.* **1986**, 1235–1237; b) J. P. Gilday, J. T. Negri, D. A. Widdowson, *Tetrahedron* **1989**, *45*, 4605–4618; c) I. K. Sebhat, Y.-L. Tan, D. A. Widdowson, R. Wilhelm, A. J. P. White, D. J. William, *Tetrahedron* **2000**, *56*, 6121–6134.

[16] A. Berger, J.-P. Djukic, C. Michon, *Coord. Chem. Rev.* **2002**, *225*, 215–238.

[17] S. E. Gibson (née Thomas), J. W. Steed, S. Sur, *J. Chem. Soc. Perkin Trans. 1* **2001**, 636–641.

[18] a) B. J. Wakefield, in *Comprehensive Organic Chemistry* (Eds.: D. Barton, W. D. Ollis), Pergamon Press, **1979**, vol. 3, p. 943; b) R. Maggi, M. Schlosser, *J. Org. Chem.* **1996**, *61*, 5430–5434.

[19] V. Y. Bingwei, D. O'Rourke, L. Jancheng, *Synlett* **1993**, 195–196.

[20] C. A. Tolman, *Chem. Rev.* **1977**, *77*, 313–348.

[21] A. Togni, A. Breutel, M. C. Soares, N. Zanetti, T. Gerfin, V. Gramlich, F. Spindler, G. Rihs, *Inorg. Chim. Acta* **1994**, *222*, 213–224.

[22] *$^{31}$P NMR Spectroscopy in Stereochemical Analysis, Methods in Stereochemical Analysis* (Eds.: J. G. Verkade and L. D. Quin), VCH, Deerfield Beach, FL, **1987**, vol. 8, 215–227.

[23] a) J.-C. Hierso, A. Fihri, V. V. Ivanov, B. Hanquet, N. Pirio, B. Donnadieu, B. Rebière, R. Amardeil, P. Meunier, *J. Am. Chem. Soc.* **2004**, *126*, 11077–11087. b) In the series of Daniphos diphosphanes supported on the more rigid scaffold provided by the indane framework the $^4J$ phosphorus-phosphorus coupling constants are even larger at 58 Hz for the $PPh_2/PPh_2$ diphosphane, 64.1 Hz for the $PPh_2/PCy_2$ one and 89.7 Hz for the $PPh_2/PtBu_2$ one (see ref.[3e]).

[24] a) Crystal structures of other Daniphos ligands and of their metal complexes have been reported in refs.[3b,3d,4] and in W. Braun, B. Calmuschi, H. J. Drexler, U. Englert, D. Heller, A. Salzer, *Acta Crystallogr., Sect. C* **2004**, *60*, m532; b) The absolute configuration of complex (*S*,*R*p)-**32** has been confirmed by an X-ray crystallographic analysis: W. Braun, B. Calmuschi, D. Totev, A. Salzer, *Acta Crystallogr., Sect. E* **2005**, *61*, m647.

[25] R. S. Paley, *Chem. Rev.* **2002**, *102*, 1493–1523.

[26] E. P. Kündig, C. Perret, S. Spichinger, G. Bernardinelli, *J. Organomet. Chem.* **1985**, *286*, 183–200.

[27] M. Uemura, T. Kobayashi, K. Isobe, T. Minami, Y. Hayashi, *J. Org. Chem.* **1986**, *51*, 2859–2863.

[28] D. W. Slocum, C. A. Jennings, *J. Org. Chem.* **1976**, *41*, 3653–3664.

[29] G. M. Sheldrick, *SHELXS-97*, *Program for solution of crystal structures*, University of Göttingen, Germany, **1997**.

[30] G. M. Sheldrick, *SADABS*, University of Göttingen, Germany, **1996**.

[31] H. D. Flack, *Acta Crystallogr., Sect. A* **1983**, *39*, 876–881.

[32] A. L. Spek, *J. Appl. Cryst.* **2003**, *36*, 7–13.

Received: June 1, 2007
Published Online: September 12, 2007

 © 2007 Wiley-VCH Verlag GmbH & Co. KGaA, Weinheim 

DOI: 10.1002/ejic.200700575

# Structure and Photochemical Isomerization of the Dinuclear Gold(I) Halide Bis(diphenylphosphanyl)ethylene Complexes: Correlation Between Quantum Yield and Aurophilicity

**Janet B. Foley,*[a] Stanley E. Gay,[b] Michael J. Vela,[c] Bruce M. Foxman,[c] Alice E. Bruce,[b] and Mitchell R. M. Bruce*[b]**

**Keywords:** Aurophilicity / Metal–metal interactions / Gold / Photochemistry / Olefin isomerization / Quantum yield

The crystal structures for *cis*-$(Ph_2PCH{=}CHPPh_2)(AuI)_2$ and *trans*-$(Ph_2PCH{=}CHPPh_2)(AuI)_2$ are reported. The structure of *cis*-$(Ph_2PCH{=}CHPPh_2)(AuI)_2$ reveals a short intramolecular Au–Au distance of 2.9526(5) Å, while the structure of *trans*-$(Ph_2PCH{=}CHPPh_2)(AuI)_2$ shows intermolecular Au–Au distances of 3.2292(7) Å. Structural data for the iodide complexes are compared to previously reported crystal structural data for *cis*- and *trans*-$(Ph_2PCH{=}CHPPh_2)(AuCl)_2$ and dppbz$(AuCl)_2$. The quantum yields for the photochemical isomerization of *cis*-$(Ph_2PCH{=}CHPPh_2)(AuX)_2$ with 334-nm light, $\Phi(_{cis\rightarrow trans})$, are 0.204, 0.269, and 0.363 for X = Cl, Br, and I, respectively. Prior results from ab initio calculations on the model *cis*- and *trans*-$Au_2X_2C_2H_2(PH_2)_2$ complexes aid in the interpretation of the correlation between the quantum yield for isomerization and the calculated aurophilic attraction potential $V(R_e)$.
(© Wiley-VCH Verlag GmbH & Co. KGaA, 69451 Weinheim, Germany, 2007)

## Introduction

In the 1980s, the X-ray structures of the *cis*- and *trans* isomers of dppee$(AuCl)_2$ (dppee: $Ph_2PCH{=}CHPPh_2$) were reported by Jones,[1] and Eggleston, McArdle, and Zuber,[2] respectively. The crystal structure of *cis*-dppee$(AuCl)_2$ ($\mathbf{1}_{cis}$) reveals short intramolecular Au–Au interactions of 3.05(1) Å, whereas *trans*-dppee$(AuCl)_2$ ($\mathbf{1}_{trans}$) shows only intermolecular Au–Au interactions of 3.043(1) Å. In the structure for $\mathbf{1}_{cis}$ reported in 1980, Jones comments that "radiation damage, the exact nature of which is uncertain, causes the cell constants to increase." Subsequently, it was shown by Foley et. al that the series of *cis* complexes involving X = Cl, Br, I, and thiolate [Equation (1)] are photochemically reactive in solution, which results in a clean isomerization to the *trans* isomers.[3] In addition, the *cis* complexes show changes in crystal morphology upon exposure to room light, which suggests the interesting possibility of solid-state photochemical reactivity,[4] consistent with Jones' observations noted above.

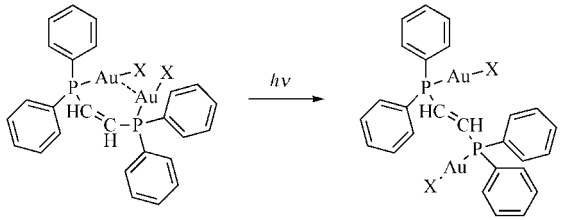


$\mathbf{1}_{cis}$ (X = Cl)
$\mathbf{2}_{cis}$ (X = Br)
$\mathbf{3}_{cis}$ (X = I)

$\mathbf{1}_{trans}$ (X = Cl)
$\mathbf{2}_{trans}$ (X = Br)
$\mathbf{3}_{trans}$ (X = I) (1)

The photochemical conversions depicted in Equation (1) are rapid and efficient. For example, photolysis of a 2.1 mM solution of *cis*-(dppee)$(AuI)_2$ in $CDCl_3$ with a 300 W Hg arc lamp ($\lambda \geq 320$ nm) results in complete conversion of the *cis* isomer to the *trans* isomer within 3 min [as monitored by $^{31}P(^1H)$ NMR spectroscopy].[3] The quantum yields for isomerization of $\mathbf{1}_{cis}$–$\mathbf{3}_{cis}$ to the respective *trans* complexes were estimated to be greater than 0.1, and control reactions establish that the isomerization process is not thermally activated.

In contrast, the free *cis*- and *trans*-dppee ligands do not undergo photochemical isomerization under similar conditions or when light of higher energy ($\lambda \geq 220$ nm) is used.[3] In addition, the *trans*-dppee gold complexes $\mathbf{1}_{trans}$–$\mathbf{3}_{trans}$ do not photochemically convert into the *cis*-dppee gold complexes. The photochemical reactivity of $\mathbf{3}_{trans}$ appears to be limited to a decomposition pathway that is consistent with release of $I_2$.[4]

[a] Bennington College, Division of Natural Sciences and Mathematics, Bennington College,
Bennington, Vermont 05201, USA
E-mail: jfoley@bennington.edu
[b] University of Maine, Department of Chemistry, University of Maine,
Orono, Maine 04469, USA
E-mail: mbruce@maine.edu
[c] Brandeis University, Department of Chemistry, Brandeis University,
Waltham, Massachusetts 02454, USA

 © 2007 Wiley-VCH Verlag GmbH & Co. KGaA, Weinheim 

The *cis*- and *trans*-dppee ligands have been used extensively to prepare metal complexes, and examples are reported for nearly every transition metal.[5] In addition, there are a few reports of thermal isomerization processes involving dppee. For example, *cis*-dppee isomerizes to *trans*-dppee in the presence of $GaBr_3$, $GaCl_3$, and $AlBr_3$ at elevated temperatures in a catalytic process that is correlated with Lewis acidity.[6] The *cis*-dppee disulfide and *cis*-dppee dioxide also thermally isomerize to the *trans* isomers in refluxing thf in the presence of $PCl_3$.[7] However, photochemical reactivity for dppee is rare, and to date, as far we are aware the photoisomerization of dppee has been reported only for the gold(I) complexes $\mathbf{1}_{cis}$–$\mathbf{3}_{cis}$. These observations suggest a pivotal role for gold atoms in photoisomerization. In this report, we present the crystal structures for $\mathbf{3}_{cis}$ and $\mathbf{3}_{trans}$, details of the quantum yield measurements for the photoisomerization reactions of $\mathbf{1}_{cis}$–$\mathbf{3}_{cis}$ to $\mathbf{1}_{trans}$–$\mathbf{3}_{trans}$, and the correlation between quantum yield and aurophilicity.[8]

## Results and Discussion

### Structural Characterization of $3_{cis}$ and $3_{trans}$ Complexes

Selected bond lengths and angles for $\mathbf{3}_{cis}$ and $\mathbf{3}_{trans}$ are presented in Tables 1, 2, and 3, and ORTEP diagrams are shown in Figure 1. In both $\mathbf{3}_{cis}$ and $\mathbf{3}_{trans}$, the dppee ligands bridge two gold atoms and the Au–P (average = 2.25 Å) and Au–I (average = 2.55 Å) bond lengths are typical for gold(I).[9–13] The P–Au–I angles are approximately linear.

Table 1. Selected bond lengths [Å] and angles [°] for compound $\mathbf{3}_{cis}$.

| Bond lengths [Å] | | | |
|---|---|---|---|
| Au1–Au2 | 2.9526(5) | Au1–I1 | 2.5629(9) |
| Au1–P1 | 2.256(3) | Au2–I2 | 2.5385(9) |
| Au2–P2 | 2.253(2) | P1–C1 | 1.81(1) |
| P1–C11 | 1.81(1) | P1–C31 | 1.82(1) |
| P2–C2 | 1.831(11) | P2–C21 | 1.82(1) |
| P2–C41 | 1.832(9) | C1–C2 | 1.332(14) |
| **Bond Angles [°]** | | | |
| Au2–Au1–I1 | 90.24(2) | Au1–P1–C31 | 112.8(4) |
| Au2–Au1–P1 | 94.21(6) | C1–P1–C31 | 98.9(5) |
| I1–Au1–P1 | 174.80(7) | C11–P1–C31 | 107.6(4) |
| Au1–Au2–I2 | 105.40(3) | Au2–P2–C2 | 115.1(3) |
| Au1–Au2–P2 | 82.30(6) | Au2–P2–C21 | 116.3(3) |
| I2–Au2–P2 | 170.36(7) | C2–P2–C21 | 105.0(5) |
| Au1–P1–C1 | 119.1(3) | Au2–P2–C41 | 110.2(3) |
| Au1–P1–C11 | 113.3(3) | C2–P2–C41 | 102.0(4) |
| C1–P1–C11 | 103.7(5) | C21–P2–C41 | 106.9(4) |

In $\mathbf{3}_{cis}$, the *cis* orientation of the rigid phosphane ligand promotes formation of an intramolecular Au–Au bond of 2.9526(5) Å. The Au–Au distance in $\mathbf{3}_{cis}$ is 0.1 Å shorter than that found in the related complex $\mathbf{1}_{cis}$ and 0.05 Å shorter than the intramolecular Au–Au distance in the *cis*-dppbz$(AuCl)_2$[14] (Table 3). These distances all fall within the accepted values for aurophilic interactions, which range from 2.8 Å (strong interaction) to 3.5 Å (weak interaction).[15] The two P–Au–I arms in $\mathbf{3}_{cis}$ "cross" at the Au centers with an I–Au···Au–I torsion angle of 63.61°. The structure of $\mathbf{3}_{trans}$ is very similar to that reported for the related complex $\mathbf{1}_{trans}$.[2] Both crystallize in the centrosymmetric space group *C*2/*c* with an inversion center at the midpoint of the ethylene backbone. Only one half of each *trans* molecule is crystallographically unique. In $\mathbf{3}_{trans}$, a partially disordered dichloromethane molecule is also present. The intermolecular Au–Au interactions in $\mathbf{3}_{trans}$ [3.2292(7) Å] are 0.19 Å longer than in $\mathbf{1}_{trans}$.

Table 2. Selected bond lengths [Å] and angles [°] for compound $\mathbf{3}_{trans}$.

| Bond lengths [Å] | | | |
|---|---|---|---|
| Au1–Au1 | 3.2292(7) | Au1–I1 | 2.5435(8) |
| Au1–P1 | 2.250(2) | P1–C1 | 1.811(9) |
| P1–C2 | 1.812(9) | P1–C8 | 1.796(9) |
| C1–C1 | 1.309(17) | | |
| **Bond Angles [°]** | | | |
| Au1–Au1–I1 | 83.51(2) | C1–P1–C2 | 104.1(4) |
| Au1–Au1–P1 | 101.42(6) | Au1–P1–C8 | 115.9(3) |
| I1–Au1–P1 | 174.81(6) | C1–P1–C8 | 103.7(4) |
| Au1–P1–C1 | 113.3(3) | C2–P1–C8 | 104.4(4) |
| Au1–P1–C2 | 114.1(3) | P1–C1–C1 | 123.5(9) |

### Electronic Spectra of dppee Gold Complexes and Quantum Yield Measurements

The *cis*- and *trans*-dppee$(AuX)_2$ complexes (X = Cl, Br, I) exhibit featureless, broad absorptions above 300 nm. The bands for each *cis* complex are slightly redshifted relative to that of its *trans* isomer. Quantum yield measurements were carried out at 334 nm where the molar absorptivities of the *cis* complexes range from $0.9–3.0 \times 10^3\ M^{-1}\,cm^{-1}$ and those of the *trans* complexes are near zero.[3] The quantum yields for disappearance, $\Phi_{disappearance}$, of the *cis*-dppee$(AuX)_2$ complexes measured at 334 nm are: $\Phi(\mathbf{1}_{cis,disappearance}) = 0.204 \pm 0.062$; $\Phi(\mathbf{2}_{cis,disappearance}) = 0.269 \pm 0.092$; $\Phi(\mathbf{3}_{cis,disappearance}) = 0.363 \pm 0.055$. Because

Table 3. Selected bond lengths and angles for $\mathbf{3}_{cis}$ and $\mathbf{3}_{trans}$ and related phosphane gold(I) complexes.

| Complex | Au–P [Å] | Au–X [Å] | P–Au–X [°] | X–Au···Au–X Torsion [°] | Intramolecular Au···Au [Å] (≤ 3.5 Å) | Intermolecular Au···Au [Å] (≤ 3.5 Å) | Ref. |
|---|---|---|---|---|---|---|---|
| *cis*-dppee$(AuI)_2$ ($\mathbf{3}_{cis}$) | 2.256(3), 2.253(2) | 2.5629(9), 2.5385(9) | 174.80(7), 170.36(7) | 63.61 | 2.9526(5) | *none* | this work |
| *cis*-dppee$(AuCl)_2$ ($\mathbf{1}_{cis}$) | 2.226(4), 2.239(5) | 2.299(5), 2.289(5) | 172.5(2), 173.3(2) | 52.49 | 3.05(1) | *none* | [1] |
| *cis*-dppbz$(AuCl)_2$ | 2.2408(15), 2.2360(16) | 2.2921(16), 2.2925(16) | 173.07(6), 173.21(6) | –63.92 | 2.996(1) | *none* | [12] |
| *trans*-dppee$(AuI)_2$ ($\mathbf{3}_{trans}$) | 2.250(2) | 2.5435(9) | 174.81(6) | 180.00 | *none* | 3.2292(7) | this work |
| *trans*-dppee$(AuCl)_2$ ($\mathbf{1}_{trans}$) | 2.235(2) | 2.291(2) | 173.5(1) | 180.00 | *none* | 3.043(1) | [2] |

 © 2007 Wiley-VCH Verlag GmbH & Co. KGaA, Weinheim 

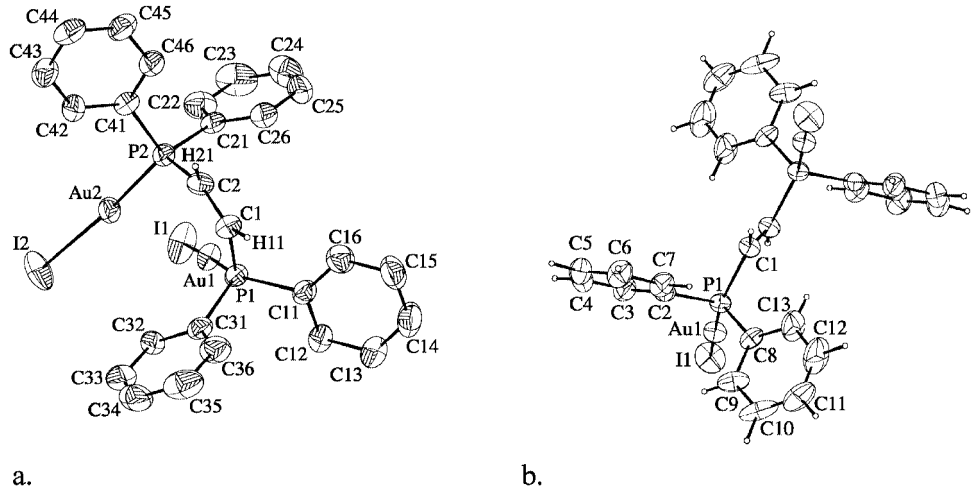


Figure 1. ORTEP drawings of a) $\mathbf{3}_{cis}$ and b) $\mathbf{3}_{trans}$ at the 50% probability level.

the photochemical isomerization processes are clean and appear to be irreversible, the quantum yields are reasonable estimates of the relative photoefficiencies of the *cis* to *trans* isomerizations, e.g. $\Phi(\mathbf{1}_{cis,\text{disappearance}}) = \Phi(\mathbf{1}_{cis} \rightarrow \mathbf{1}_{trans})$.

It is interesting to note that the increase in quantum yield in this series is correlated with an increase in the aurophilic attraction potential[16] (Figure 2). The quantum yield is also correlated with a decrease in electronegativity of the halide ligand X[16] (not shown). Both correlations give linear correlation coefficients above 0.99. The aurophilic attraction potential is a measure of the energy of interaction between a dimer and a pair of monomers and has been calculated[16] as well as estimated experimentally. Experimental values for the aurophilic attraction potential, $V(R_e)$, have been reported in the range 29–42 kJ mol$^{-1}$.[15,17–22] The ligand dependence on aurophilic attraction has been studied on the interacting, perpendicular X–Au–$PH_3$ monomer by using 19-valence electron quasirelativistic pseudopotentials for gold.[16] The study estimates that in interacting X–Au–$PH_3$ monomers, the aurophilic potentials, $V(R_e)$, are 16.7, 19.3, and 22.5 kJmol$^{-1}$ for X = Cl, Br, and I, respectively. Thus, the aurophilic potential increases as the electronegativity of X decreases.

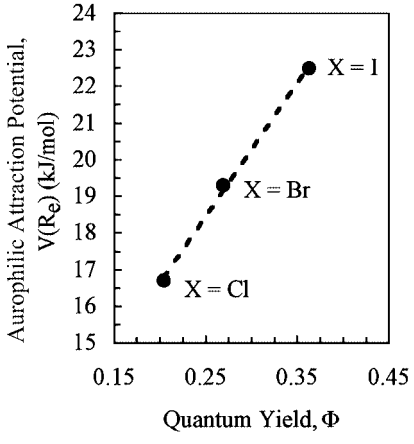


Figure 2. Correlation between aurophilic attraction potential[14] and quantum yield for isomerization of $\mathbf{1}$–$\mathbf{3}_{cis}$ to $\mathbf{1}$–$\mathbf{3}_{trans}$.

## Photochemical Isomerization of Alkenes – Direct and Photosensitized

The direct and triplet sensitized photochemical isomerization of alkenes and polyenes has been extensively studied and reviewed. The ground state of the *cis* olefin is usually slightly higher in energy than that of the *trans* isomer, and photochemical processes have been shown to proceed through either discrete singlet or triplet pathways. For many organic dienes, e.g. stilbenes or 1,2-diphenylpropenes, photoisomerization originating from either the *cis* or *trans* isomer produces a photostationary state as a result of direct photolysis or photolysis with the addition of a triplet sensitizer.[23]

While the molar absorptivity of the two isomers at a particular wavelength affects the direct population of the *cis** and *trans** excited states, it is the shape of the excited state potential surface that is often critical for understanding the mechanism and photoefficiency of isomerization.[24–29] The research of Hammond and coworkers in the 1960s laid the groundwork for an explosion of interest in this field by illustrating how suitable photosensitizers could be used to understand reactivity that ensues after photoexcitation.[28]

To explain the basic photochemical phenomena, we have included Figure 3, which shows *cis* and *trans* olefin ground states, and an excited state potential surface reached by photoexcitation. This is a generic diagram similar to many diagrams used to discuss olefin photoisomerization,[26–28] and precise details of energy changes of the ground state as a function of olefin twist angle have been omitted. Excitation, according to the Franck–Condon principle, produces vertical transitions and initial excited states possess identical geometries as in the ground state. Three critical points are important to keep in mind: (a) excitation of

 © 2007 Wiley-VCH Verlag GmbH & Co. KGaA, Weinheim 

either isomer populates a common potential surface, (b) the energy of the excited state is a function of the degree of olefin twist, and (c) deactivation pathways (e.g. thermal relaxation, luminescence) as well as the lifetime of the excited state dictate how far the excited state travels along the excited state potential surface. The excited state perpendicular geometry, *p**, with a twist angle of 90° may be thought of ideally as the state from which it is equally possible to convert to either isomer (see Figure 3). In the diagram in Figure 3, the excited states *trans** or *p** occur at local minima while *cis** is found at a transient position. However, the actual shape of the process under consideration varies and has a significant effect on the ensuing chemistry.

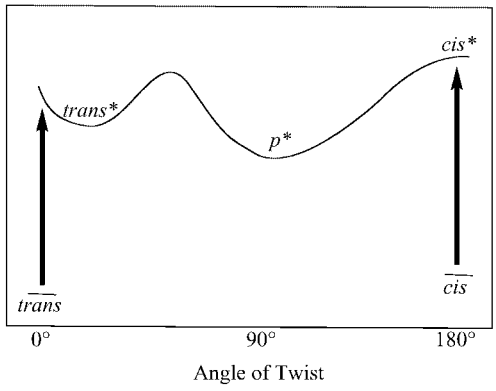


Figure 3. Relative energy of ground and excited states as a function of the angle of twist around the C–C olefin bond.

We may also consider photolysis of a system that contains a photosensitizer. In this case, photolysis produces an excited state sensitizer that must either become covalently attached or is pre-complexed to the olefin in order for photoisomerization to occur. Examples of sensitizers in both categories exist. In order for the sensitizer to influence the olefin, energy transfer must occur. If the excited state lifetimes are short compared to processes involving rotation about the carbon–carbon double bond or if rotation is hindered, the excited state will undoubtedly relax with little or no photoisomerization. However, if the lifetime is sufficiently long for either a system involving a sensitizer or for direct photolysis of an olefin, then the shape of the excited state potential surface and the energy available to the excited state complexes will dictate the process that occurs.

### The Photochemical Process and Quantum Efficiency

To consider why the quantum yield for photoisomerization of $\mathbf{1}_{cis}$–$\mathbf{3}_{cis}$ is correlated with the aurophilic potential, it is useful to consider the overall photoisomerization as occurring in distinct steps involving absorption of a photon by a ground state molecule, the creation of an excited state complex, rotation about the C=C bond, and relaxation to various isomers. The gold complexes may be thought of as an assembly involving a chromophore (X–Au) that is covalently attached to the olefin through phosphorus atoms in the dppee ligand [see Equation (1)]. Thus, the ground state, excited state, and mixing of X, Au, and C=C orbitals all play important roles in the observed photoisomerization reaction.

Ab initio MP2 calculations on the model complexes *cis*- and *trans*-$Au_2X_2C_2H_2(PH_2)_2$ were previously reported and the excited states were investigated by the CIS (configuration interaction with single excitations only) and CAS-LMP2 procedures.[30] The results show that in the *cis* compounds the degree of aurophilic interaction increases with an increase in the softness of the ligand. Thus, $\mathbf{3}_{cis}$ would be expected to have a greater aurophilic interaction than $\mathbf{1}_{cis}$. The aurophilic interactions stabilize the ground state of the *cis* complexes relative to that of the *trans* complexes. In addition, the aurophilic interactions stabilize the first excited state, which leads to a red shift and an increased transition moment for the *cis* complexes, in contrast to that observed for the *trans* complexes. While the overall effect lowers the energy needed for promotion into the first excited state of the $\mathbf{1}_{cis}$–$\mathbf{3}_{cis}$ complexes (i.e. the red shift), it does not explain the increase in photoefficiency, since quantum yield measures the ratio of the number of *cis* molecules that isomerize relative to those that absorb light, regardless of what the energy gap is at 334 nm.

The stabilization of the first excited state was found to be critically dependent on the intramolecular Au–Au distance. The CIS calculations produce results that suggest that the HOMO–LUMO transitions (as well as the first few singlet excitations) are primarily halide to gold [Au(5d6s6p)] charge transfer transitions. However, there were significant admixtures from a variety of other orbitals. For both the *cis* and *trans* complexes, phosphorus p orbital character is found in the LUMO orbitals. In addition, for the *cis* complexes, the HOMO has some gold character, and in the LUMO, there is significant ethylene π* character. Population of an orbital with ethylene π* character in the *cis* complexes would be predicted to weaken the carbon–carbon double bond. The shorter Au–Au bond length in $\mathbf{3}_{cis}$ than in $\mathbf{1}_{cis}$ may indicate a higher degree of aurophilic interaction. Although the ab initio calculations do not easily permit quantification of orbital mixing, it seems reasonable to suggest that the aurophilic interaction in the *cis* complexes facilitates mixing of ethylene π* character in the excited states. Thus, it may be inferred that $\mathbf{3}_{cis}$ would have a greater degree of ethylene π* character in the excited state than $\mathbf{1}_{cis}$.

The relatively high quantum yield for photoisomerization of $\mathbf{1}_{cis}$–$\mathbf{3}_{cis}$ suggests that the HOMO–LUMO transition directly populates an orbital with sufficient ethylene π* character to weaken the C=C bond and permit rotation. Our results can be compared to the $ReX(CO)_3L_2$ complexes {see [Equation (2)]; X = Cl, Br; L = *trans*-4-styrylpyridine} whose IL transitions involve a spin-allowed π–π* transition, which directly weakens the C=C bond, permitting rotation and high quantum yields ($\Phi$ = 0.49–0.64). In this case, the quantum yields are very similar to that of the free ligand.[31] In contrast, the quantum yield for photoisomerzation of *cis*-styrylferrocene [Equation (3)] is ca. 0.001. The inef-

 © 2007 Wiley-VCH Verlag GmbH & Co. KGaA, Weinheim 

ficiency of this isomerization is attributed to rapid deactivation of the triplet *cis* excited state by the heavy atom effect.[26,32]

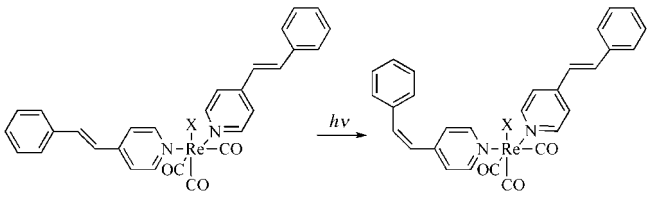


(2)

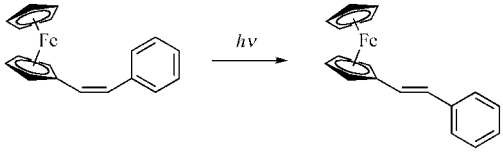


(3)

We are continuing to explore the correlation between quantum yield and aurophilic potential as a function of the ligands attached to gold. Preliminary results indicate that substitution of thiolate ligands for halides increases the photoefficiency, while substitution of arsenic for phosphorus in dppee decreases the photoefficiency.

## Summary

The crystal structure of the *cis*-$(AuI)_2$dppee shows a shorter gold–gold distance than the analogous chloride and bromide complexes. This is consistent with the assertion, made by Pyykkö and others, that soft ligands should increase the gold–gold interaction. We have demonstrated that the quantum yield for the photoisomerization of *cis*-$(AuX)_2$dppee to the *trans*-$(AuX)_2$dppee [X = Cl($\Phi$ = 0.204); Br($\Phi$ = 0.269); I($\Phi$ = 0.363)] increases as the aurophilic attraction potential increases. We suggest that the increase in quantum yield is indicative of increased ethylene π* character in the first excited state of the iodide complex ($\mathbf{3}_{cis}$) relative to that in the chloride complex ($\mathbf{1}_{cis}$). This experimental approach allows a quantitative comparison of the effect of different ligands on the strength of gold–gold interactions.

## Experimental Section

**General Procedures:** Methylene chloride (spectral grade) was obtained from Aldrich and used as received. Complexes $\mathbf{1}_{cis}$–$\mathbf{3}_{cis}$ and $\mathbf{3}_{trans}$ were synthesized and purified as previously reported.[3,4] The following abbreviations are used: dppee = 1,2-bis(diphenylphosphanyl)ethylene; dppbz = 1,2-bis(diphenylphosphanyl)benzene.

**Quantum Yield Measurements:** A 200-W Oriel mercury arc lamp was used for quantum yield measurements. The wavelengths for the experiments were isolated by using a model 77250 Oriel monochrometer with 6-mm gratings. Ferrioxalate actinometry was used for determining lamp flux for quantum yield calculations.[33] The flux for the 200-W lamp had an average value of $6.12 \times 10^{15}$ photons/Ls. Gold(I) complexes were dissolved in dichloromethane, and the solutions were protected from light while transferring them to a dark room for quantum yield experiments. No attempts were made to exclude oxygen from the solutions. Previous studies confirmed that the presence of oxygen does not affect the photochemical isomerization reaction.[4] Solutions were irradiated at room temperature in 1-cm quartz cells and were stirred during irradiation. Absolute quantum yield measurements for the *cis* to *trans* isomerization were made by monitoring the decrease in absorbance for the *cis* complexes at 334 nm (X = I, Br, Cl). Absorbances were measured by using a Beckman DU spectrophotometer. Quantum yield measurements were replicated 4–6 times for each complex.

**Crystal Structure Determination:** Details of the X-ray experiments and crystal data for $\mathbf{3}_{cis}$ and $\mathbf{3}_{trans}$ are summarized in Table 4. Crystals of $\mathbf{3}_{cis}$ and $\mathbf{3}_{trans}$ were grown from $CH_2Cl_2$/$Et_2O$. Crystals of $\mathbf{3}_{trans}$ turned opaque when exposed to the atmosphere owing to loss of solvent, and no longer diffract X-rays. In order to prevent loss of solvent, crystals of $\mathbf{3}_{trans}$ were coated with a thin film of epoxy. Crystals of $\mathbf{3}_{cis}$ did not require any special treatment.

Table 4. Crystallographic data for compounds $\mathbf{3}_{cis}$ and $\mathbf{3}_{trans}$·$2CH_2Cl_2$.

| | $\mathbf{3}_{cis}$ | $\mathbf{3}_{trans}$·$2CH_2Cl_2$ |
|---|---|---|
| Chemical formula | $C_{26}H_{22}Au_2I_2P_2$ | $C_{28}H_{26}Au_2Cl_4I_2P_2$ |
| Formula mass | 1044.15 | 1214.02 |
| Space group | P1 21/*n* 1 | C 1 2/*c* 1 |
| *a* [Å] | 12.6165(15) | 11.7391(14) |
| *b* [Å] | 14.505(1) | 20.3363(16) |
| *c* [Å] | 15.2955(9) | 15.634(3) |
| $\beta$ [°] | 103.457(7) | 108.255(17) |
| *V* [Å$^3$] | 2722.3(4) | 3544.6(9) |
| *Z* | 4 | 4 |
| *T* [°C] | 21 | 21 |
| $\lambda$ [Å] | 0.71073 | 0.71073 |
| $\rho_{calcd.}$ [g cm$^{-1}$] | 2.547 | 2.267 |
| $\mu$ [cm$^{-1}$] | 13.164 | 10.419 |
| *R*[a] | 0.0476 | 0.0380 |
| $R_w$[b] | 0.0548 | 0.0379 |

[a] $R = \Sigma||F_o| - |F_c||/\Sigma|F_o|$. [b] $R_w = [\Sigma w(|F_o| - |F_c|)^2/\Sigma w|F_o|^2]^{1/2}$.

Data on $\mathbf{3}_{cis}$ and $\mathbf{3}_{trans}$ were collected with an Enraf–Nonius CAD4-Turbo diffractometer at Brandeis University by using the Enraf–Nonius EXPRESS program with Mo-$K_\alpha$ radiation ($\lambda$ = 0.71073 Å). The structures were solved by direct methods by using SHELXS-86 and refined with the Oxford CRYSTALS package. Drawings were made (50% probability ellipsoids) with the Oxford CAMERON program. All non-hydrogen atoms were located from successive difference-Fourier syntheses for both structures. Final refinement of positional and anisotropic displacement parameters for all non-hydrogen atoms in compound $\mathbf{3}_{cis}$ led to $R$ = 0.0476 and $R_w$ = 0.0548 by using 4602 data for which $I > 1.96\sigma(I)$. For compound $\mathbf{3}_{trans}$, final refinement of positional and isotropic displacement parameters for all non-hydrogen atoms [anisotropic displacement parameters for Au, P, I, C(1), C(2), and C(8), a total of 77 parameters] led to $R$ = 0.0380 and $R_w$ = 0.0379 by using 2272 data for which $I > 1.96\sigma(I)$. Attempts to refine all non-hydrogen atoms by using anisotropic displacement parameters led to unsatisfactory values. Hence the non-*ipso* carbon atoms in each of the phenyl rings were refined by using isotropic displacement parameters. The hydrogen atoms were placed in calculated positions ($d_{C-H}$ = 0.95 Å) in both structures.

For the solvent molecule present in $\mathbf{3}_{trans}$, only atom Cl(1) was refined by using an anisotropic displacement parameter, while the other atoms in the solvent molecule were refined by using isotropic

 © 2007 Wiley-VCH Verlag GmbH & Co. KGaA, Weinheim 

displacement parameters. The $CH_2Cl_2$ solvent was found to be partially disordered over two sites with the major component occupancy equal to 0.67(2). The Cl–C distances and the Cl–C–Cl angles were restrained to be at 1.75(5) Å and 111.0(5)°. Occupancy constraints were also applied to the disordered atoms in the solvent molecule.

**Supplementary Crystallographic Data:** CCDC-646580 and -646581 contain the supplementary crystallographic data for this paper. These data can be obtained free of charge from The Cambridge Crystallographic Data Centre via www.ccdc.ac.uk/data_request/cif.

## Acknowledgments

We thank Whitney King for use of photochemical and photoactinometry equipment.

[1] P. Jones, *Acta Crystallogr., Sect. B: Struct. Sci.* **1980**, *36*, 2775–2776.
[2] D. S. Eggleston, J. V. McArdle, G. E. Zuber, *J. Chem. Soc. Dalton Trans.* **1987**, 677–679.
[3] J. B. Foley, A. E. Bruce, M. R. M. Bruce, *J. Am. Chem. Soc.* **1995**, *117*, 9596–9597.
[4] J. B. Foley Ph. D. Thesis, University of Maine, Orono, ME **1996**.
[5] See ref.[3].
[6] M. Sigl, A. Schier, H. Schmidbaur, *Z. Naturforsch., B: Chem. Sci.* **1998**, *53*, 1301–1306.
[7] A. M. Aguiar, D. Daigle, *J. Am. Chem. Soc.* **1964**, *86*, 5354–5355.
[8] Preliminary communication of bond length and quantum yields was presented at the 4th International Conference on Gold and Silver in Medicine and was published as part of the conference proceedings in Metal Based Drugs. However, no crystal structure experimental details, CIF files, or details of the quantum yield measurements were published at that time. See J. B. Foley, S. E. Gay, C. Turmel, G. Wei, T. Jiang, R. Narayanaswamy, B. M. Foxman, M. J. Vela, A. E. Bruce, M. R. M. Bruce, "Proceedings of the 4th International Conference on Gold and Silver in Medicine", *Metal-Based Drugs* **1999**, *6*, 255–260.
[9] P. F. Barron, L. M. Engelhardt, P. C. Healy, J. Oddy, A. H. White, *Aust. J. Chem.* **1987**, *40*, 1545–1555.
[10] S. Ahrland, K. Dreisch, B. Noren, A. Oskarsson, *Acta Chem. Scand., Ser. A* **1987**, *A41*, 173–177.
[11] R. C. Bott, G. A. Bowmaker, R. W. Buckley, P. C. Healy, M. C. S. Perera, *Aust. J. Chem.* **1999**, *52*, 271–277.
[12] R. C. Bott, P. C. Healy, G. Smith, *Aust. J. Chem.* **2004**, *57*, 213–218.
[13] D. Schneider, A. Schier, H. Schmidbaur, *Dalton Trans.* **2004**, 1995–2005.
[14] A. A. Mohamed, J. A. Krause Bauer, A. E. Bruce, M. R. M. Bruce, *Acta Crystallogr,. Sect. C: Cryst. Struct. Commun.* **2003**, *C59*, m84–m86.
[15] P. Pyykkö, *Angew. Chem. Int. Ed.* **2004**, *43*, 4412–4456.
[16] P. Pyykkö, J. Li, N. Runeberg, *Chem. Phys. Lett.* **1994**, *218*, 133–138.
[17] P. Pyykkö, *Chem. Rev. (Washington, DC, United States)* **1997**, *97*, 597–636.
[18] H. Schmidbaur, W. Graf, G. Mueller, *Angew. Chem. Int. Ed.* **1988**, *27*, 417–419.
[19] H. Schmidbaur, K. Dziwok, A. Grohmann, G. Mueller, *Chem. Ber.* **1989**, *122*, 893–895.
[20] K. Dziwok, J. Lachmann, G. Mueller, H. Schmidbaur, D. L. Wilkinson, *Chem. Ber.* **1990**, *123*, 423–431.
[21] R. Narayanaswamy, M. A. Young, E. Parkhurst, M. Ouellette, M. E. Kerr, D. M. Ho, R. C. Elder, A. E. Bruce, M. R. M. Bruce, *Inorg. Chem.* **1993**, *32*, 2506–2517.
[22] D. E. Harwell, M. D. Mortimer, C. B. Knobler, F. A. L. Anet, M. F. Hawthorne, *J. Am. Chem. Soc.* **1996**, *118*, 2679–2685.
[23] F. A. Carey and R. J. Sundberg, *Advanced Organic Photochemistry, Part A, Structure and Mechanisms*, Plenum/Rosetta, **1980**, p.
[24] R. S. H. Liu, G. S. Hammond, *Photochem. Photobiol. Sci.* **2003**, *2*, 835–844.
[25] R. S. H. Liu, G. S. Hammond, *Acc. Chem. Res.* **2005**, *38*, 396–403.
[26] T. Arai, K. Tokumaru, *Chem. Rev.* **1993**, *93*, 23–39.
[27] D. G. Whitten, *Acc. Chem. Res.* **1993**, *26*, 502–509.
[28] G. S. Hammond, J. Saltiel, A. A. Lamola, N. J. Turro, J. S. Bradshaw, D. Cowan, R. C. Covnsell, V. Vogt, A. C. Dalton, *J. Am. Chem. Soc.* **1964**, *86*, 3198–3217.
[29] B. Liaw, S. W. Orchard, C. Kutal, *Inorg. Chem.* **1988**, *27*, 1311–1316.
[30] P. Schwerdtfeger, A. E. Bruce, M. R. M. Bruce, *J. Am. Chem. Soc.* **1998**, *120*, 6587–6597.
[31] M. S. Wrighton, D. L. Morse, L. Pdungsap, *J. Am. Chem. Soc.* **1975**, *97*, 2073–2079.
[32] T. Arai, Y. Ogawa, H. Sakuragi, K. Tokumaru, *Chem. Phys. Lett.* **1992**, *196*, 145–149.
[33] J. Calvert, J. Pitts, *Photochemistry*, John Wiley & Sons: New York, **1967**.

Received: June 1, 2007
Published Online: September 14, 2007

 © 2007 Wiley-VCH Verlag GmbH & Co. KGaA, Weinheim 

DOI: 10.1002/ejic.200700577

# $Ge_6Me_{12}$ and $Ge_6H_{12}$ Cyclohexagermanes: Conformer Equilibria Studied by Raman Spectroscopy and Quantum Chemical Calculations

**Margit Hölbling,[a] Michaela Flock,[a] Judith Baumgartner,[a] and Karl Hassler*[a]**

**Keywords:** Cyclohexagermanes / Conformational analysis / Raman spectroscopy / X-ray structure / Ab initio calculations

In the first experimental study of rotational isomerism of a compound possessing a fourth row element backbone, the totally symmetric Ge–Ge stretching mode of dodecamethylcyclohexagermane ($Ge_6Me_{12}$), which is the most intense Raman band in the range 200–300 $cm^{-1}$, was analyzed with temperature-dependent vibrational Raman spectroscopy in both the crystalline and solution states. Below 50 °C, the Raman spectrum of the solid shows a single band at 232 $cm^{-1}$ originating from the chair conformer. Between 50 and 60 °C, a shoulder at 227 $cm^{-1}$ appears, which is associated with a twisted conformer. In solution, the band attributed to the chair conformer displays a shoulder arising from an averaged twist/boat conformer, even at –80 °C. The intensity of the shoulder increases with temperature. By using the van't Hoff relationship, an enthalpy difference of 2.4 kJ $mol^{-1}$ between chair and twist/boat conformers was obtained. An improved X-ray crystal structure of $Ge_6Me_{12}$ was also obtained, and an average Ge–Ge bond length of 242 pm was found, about 5 pm longer than previously reported. With the help of quantum chemical DFT and MP2 calculations, the geometries and energies of the conformers of $Ge_6Me_{12}$ and of the parent $Ge_6H_{12}$ compound were investigated thoroughly by employing 6-31+G*, D95V and aug-cc-pVTZ basis sets, as well as SDD and aug-cc-pVTZ-PP pseudopotentials on the Ge atoms. B3LYP/aug-cc-pVTZ calculations predict two conformers for $Ge_6H_{12}$, chair and twist, with zero-point vibrational energy (ZPVE) corrected relative energies of 0.0 and 5.7 kJ $mol^{-1}$, respectively. They predict three conformers, chair (0.0), twist (5.2) and boat (9.2), for $Ge_6Me_{12}$. They also give reasonable geometry parameters, relative energies and barriers for the conformer interconversion.

(© Wiley-VCH Verlag GmbH & Co. KGaA, 69451 Weinheim, Germany, 2007)

## Introduction

In the early days of stereochemistry, which at the time was essentially carbon chemistry, it was assumed that rotation about single bonds was free. Yet by the middle of the third decade of the twentieth century, the idea that rotation around the C–C bond in ethane and related carbon compounds was not free had been widely accepted. In 1936, Kemp and Pitzer[1] calculated the barrier for the internal rotation in ethane to be 13.2 kJ $mol^{-1}$ from entropy data, a value which is very similar (±10%) to the most recent results (12.1–12.3 kJ $mol^{-1}$).[2] About forty years later, the barrier for disilane, $Si_2H_6$, was determined to be 5.1 kJ $mol^{-1}$.[3] The barrier for $Ge_2H_6$ was estimated with the aid of vibrational spectroscopy to be about 6 kJ $mol^{-1}$.[4] However, no experimental data for $Sn_2H_6$ and $Pb_2H_6$ are available as they have not even been prepared.

With the availability of quantum chemical calculations, the origin of these barriers could be investigated. Schleyer et al. analyzed the barriers for $X_2H_6$ (X = C, Si, Ge, Sn and Pb) in detail.[5] In the natural bond orbital (NBO) picture, the stabilizing vicinal σ(XH)→σ*(XH) delocalization is responsible for the more stable staggered rather than eclipsed conformation, and decreased overlap due to longer X–X bonds is responsible for the smaller rotational barriers of the heavier species.[5] These results contradict the long and widely held belief that the steric repulsion of X–H bonds is responsible for hindered rotation. The debate is ongoing; for instance a more recent ab initio valence bond (VB) study by Mo et al. [HF/6-31G(d) and HF/6-311G(d,p)] reinstated that the barrier for ethane and its congeners is overwhelmingly dominated by steric repulsion.[2a–2d]

In disubstituted ethane-like molecules such as $FH_2XXH_2F$, the conformer stabilities are influenced by the relative magnitudes of σ(XH) and σ(XF) delocalization into the antibonding σ*(XH) and σ*(XF) orbitals. For instance, in $FH_2CCH_2F$, the gauche form is preferred even in the gas phase, despite the repulsive dipole–dipole interactions.

Of course, steric effects due to the increasing size of the pendant groups will increasingly dominate the conformational potential. While conformer stabilities and equilibria due to hindered rotation about C–C bonds have been determined for a huge number of compounds and various pendant groups, experimental data for Si–Si bonds remain

[a] Institute of Inorganic Chemistry, University of Technology, Stremayrgasse 16, 8010 Graz, Austria
Fax: +43-316-873-8701
E-mail: margit.hoelbling@TUGraz.at
michaela.flock@TUGraz.at
baumgartner@TUGraz.at
karl.hassler@TUGraz.at

Supporting information for this article is available on the WWW under http://www.eurjic.org or from the author.

 © 2007 Wiley-VCH Verlag GmbH & Co. KGaA, Weinheim 

scarce.[6] Generally, not only barrier heights but also energy differences between conformers decrease from carbon- to silicon-containing molecules, and this is accompanied by a considerable decrease in the conformer mean lifetimes. The increased rate constants for conformer interconversion make NMR spectroscopy − so successful in organic chemistry − an inadequate method for the monitoring of many silicon compounds. The NMR time scale of $10^{-1}$ to $10^{-9}$ seconds demands temperatures as low as –160 °C or lower to slow down reaction rates sufficiently for conformer observation. For instance, the splitting of the $^{13}C$ resonances of the methyl groups of $Si_6Me_{12}$ as a result of them being in axial and equatorial positions was observed at –165 °C, and a ring inversion barrier of ca. 20 kJ mol$^{-1}$ was deduced. However, the signals were barely detectable due to low solubility.[7]

So far, no experimental studies of hindered rotation about Ge–Ge, Sn–Sn or Pb–Pb bonds have been reported in the literature. Surely NMR spectroscopy is not a suitable method for exploring these systems, and the question arises whether vibrational spectroscopy, possessing a time scale which on average is six orders of magnitudes smaller (about $10^{-13}$ seconds) than that of NMR spectroscopy, might be able to resolve these fast processes. If vibrational transitions originating from two different conformers are separated by 10 cm$^{-1}$ or by a frequency difference $\Delta\nu$ of $3 \times 10^{11}$ Hz, the lifetime of the conformers has to be longer than $\Delta\nu^{-1}$ to give resolved vibrational spectra. By using the theory of the activated complex, a barrier height of about 4 kJ mol$^{-1}$ or larger is estimated for this to occur at 300 K.[8,9] Alternatively, it can be argued that the barrier must be noticeably larger than the Boltzmann energy *RT*, which is 2.5 kJ mol$^{-1}$ at 300 K.

Recent ab initio calculations for digermane predict a barrier of 3.1 to 3.6 kJ mol$^{-1}$; this result is dependent on the methods and basis sets that were used.[2b,10] These results support the expectation that the conformer equilibria of digermanes and oligogermanes will be borderline cases as far as the use of vibrational spectroscopy is concerned. We have therefore set out to investigate some germanes that are expected to possess at least two conformational minima on the potential energy surface (PES) by employing Raman spectroscopy combined with quantum chemical ab initio calculations. Here we report on cyclohexagermane studied by quantum chemical calculations and on dodecamethylcyclohexagermane studied by both theory and Raman spectroscopy. Results for 1,2-dichlorotetramethyldigermane, tetramethyldigermane, and hexamethyldigermane will be published elsewhere.[11]

We were led to choose $Ge_6Me_{12}$ because, by analogy with $C_6Me_{12}$ and $Si_6Me_{12}$, we expected the barriers for the chair-to-chair and chair-to-twist interconversions to be larger than the barrier in digermane itself. Dynamic NMR spectroscopic studies for $C_6Me_{12}$ and $Si_6Me_{12}$ gave barriers for the chair-to-chair interconversion of 70 kJ mol$^{-1}$ and 20 kJ mol$^{-1}$, respectively.[7,12] In two Raman spectroscopic studies of $Si_6Me_{12}$ and $Si_6Me_{11}X$ (X = H, F, Cl, Br and I), we were able to identify chair and twist conformers and to determine their enthalpy differences.[13,14] It turned out that boat conformations also represent minima for these cyclohexasilanes, and that the boat-to-twist interconversion is fast even on the timescale of Raman spectroscopy. Therefore, a three-conformer equilibrium between chair (**A**), twist (**B**) and boat (**C**) must also be expected for $Ge_6Me_{12}$.

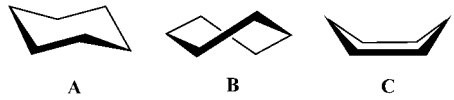


Generally, reports of experimental studies of conformer equilibria for molecules composed of fourth or higher row elements (group 14: Ge, Sn, Pb; group 15: As, Sb, Bi; group 16: Se. Te) are virtually absent from the literature. To the best of our knowledge, group 14 and group 16 elements have not been studied at all. Of the group 15 elements, tetramethyldistibane has been examined by photoelectron spectroscopy, and the existence of *gauche* and *anti* conformers in the gas phase was observed. No enthalpy data or barrier heights were given.[15] A gas-phase electron diffraction study of tetrakis(trifluoromethyl)diarsane showed quite a different behaviour: only the trans conformer was present.[16]

## Results and Discussion

### Cyclohexagermane, $Ge_6H_{12}$

$Ge_6Me_{12}$ was prepared by known methods.[17] It is now well established by extensive calculations on $Ge_2H_6$ (and also $SiH_3GeH_3$) that experimental geometrical parameters are reproduced well at correlated levels by employing triple-zeta basis sets augmented with f polarization functions on the heavy atoms.[10b,18] The calculated Ge–Ge distance was 0.013 Å longer than the experimental value at the CISD/TZP(f) level. MP2 and DFT calculations, which may be used for larger molecules, performed satisfactorily in computing geometries and vibrational spectra. The Ge–Ge distances were longer than the experimental value by about 0.030–0.035 Å, and consequently, the barriers were generally about 10% too small.

DFT calculations for $Ge_6H_{12}$ employing the B3LYP functional and all-electron basis set 6-31+G* predict three conformers, chair, twist and boat, with relative energies of 0.0, 10.2 and 12.1 kJ mol$^{-1}$, respectively. DFT and MP2 calculations with SDD predict only two conformers, chair and twist, with relative energies of 4.4 and 4.2 kJ mol$^{-1}$, respectively. Finally, B3LYP/aug-cc-pVTZ calculations also led to two conformers, again chair and twist, with respective energies of 0.0 and 5.7 kJ mol$^{-1}$. The boat turned out to be a transition structure for the twist-to-twist interconversion with a relative energy of 6.4 kJ mol$^{-1}$.

We know from calculations of the ring inversion barriers of cyclohexasilanes $Si_6H_{12}$ and $Si_6Me_{12}$ that sofa and half-chair transition structures have almost the same energy.[13]

 © 2007 Wiley-VCH Verlag GmbH & Co. KGaA, Weinheim 

To obtain a representative value for the barrier of $Ge_6H_{12}$, we calculated the energy of the sofa transition structure to be 10.0 kJ mol$^{-1}$, and we anticipated that it would not differ significantly from that of the half-chair. The energy profile for ring inversion at the B3LYP/aug-cc-pVTZ level is depicted in Figure 1. It is of some note that B3LYP/6-31+G* calculations gave an energy of 40 kJ mol$^{-1}$ for the half-chair transition structure, thus predicting a ring inversion barrier that is considerably larger than that found for $Si_6H_{12}$ (15 kJ mol$^{-1}$) and $Si_6Me_{12}$ (16 kJ mol$^{-1}$). This large value can be explained with the shorter Ge–Ge bonds and the much larger Ge–Ge–Ge–Ge dihedral angles (up to 70°) obtained by using nonrelativistic basis sets on the Ge atoms. Even when the small SDD quasi-relativistic basis set for Ge is used, this barrier is more appropriately estimated [7.4/7.6 kJ mol$^{-1}$ (DFT/MP2)]. However, the large-core effective core pseudopotential (ECP) in the SDD basis sets is known to result in bond lengths that are too long. The aug-cc-pVTZ basis set with the small-core ECP gives more accurate bond lengths. Nevertheless, it is obvious that relativistic effects in the Ge atom have to be taken into consideration, and to this purpose the ECP approximation seems to be satisfactory.

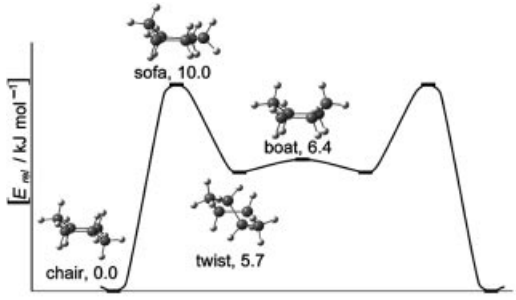


Figure 1. Calculated minima and transition structures of $Ge_6H_{12}$ at the B3LYP/aug-cc-pVTZ level of theory. All relative energies are ZPVE-corrected.

### Dodecamethylcyclohexagermane, $Ge_6Me_{12}$

#### *X-ray Structure Determination*

A first crystal structure of dodecamethylcyclohexagermane obtained at 298 K with $R$ = 0.131 was published in 1975; an average Ge–Ge bond length of 2.37 Å was reported.[19] In the present work, an improved structure ($R$ = 0.101) determined at 100(2) K is presented and is depicted in Figure 2.[20] The average Ge–Ge bond length is found to be 2.42 Å, which is 5 pm longer than that previously reported, whereas the Ge–Ge–Ge angles are the same. Other structural parameters do not differ significantly from the parameters determined for $Si_6Me_{12}$.[21] The average Ge–Ge–Ge–Ge dihedral angle is ±52.97°, the same as that in the silicon ring (53.4°). Further, the average Ge–Ge–Ge angle of 112.0° is only 0.1° smaller than the average Si–Si–Si angle of 111.9°.

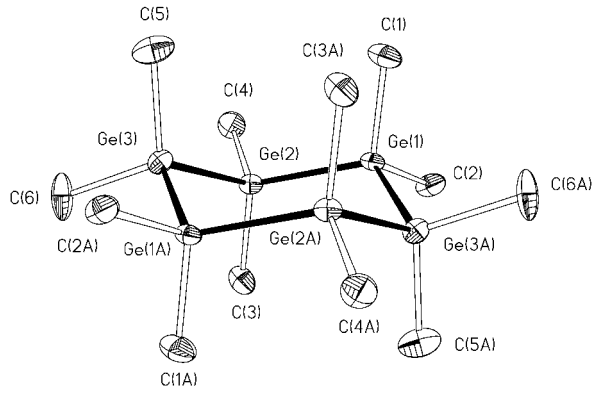


Figure 2. ORTEP plot (30% probability) of the molecular structure of $Ge_6Me_{12}$, including numbering of the atoms. Hydrogen atoms have been omitted for clarity. Selected bond lengths [Å] and bond angles [°] (with standard deviations): Ge(1)–Ge(2) 2.4094(19), Ge(1)–Ge(3A) 2.4242(17), Ge(2)–Ge(3) 2.4300(16), Ge(1)–C(1) 1.971(11), Ge(1)–C(2) 1.979(11), Ge(2)–C(3) 1.994(11), Ge(2)–C(4) 1.969(11), Ge(3)–C(5) 1.987(11), Ge(3)–C(6) 1.982(13), Ge(1)–Ge(2)–Ge(3) 111.13(6), Ge(2)–Ge(3)–Ge(1A) 111.56(6), Ge(2)–Ge(1)–Ge(3A) 113.32(6), C(1)–Ge(1)–Ge(2) 109.0(4), C(1)–Ge(1)–Ge(3A) 106.7(4), C(1)–Ge(1)–C(2) 108.4(5), C(1)–Ge(1)–Ge(2)–Ge(3) –65.2(4), C(2)–Ge(1)–Ge(2)–Ge(3) 177.0(3), Ge(3A)–Ge(1)–Ge(2)–Ge(3) 53.45(8), Ge(1)–Ge(2)–Ge(3)–Ge(1A) –52.49(8).

For comparison, the Ge–Ge bond length in $Ge_6Ph_{12}$ was determined to be 2.466 Å, and the dihedral angles to be 49.16° and –48.92° ($R$ = 7.1%, r.t.).[22] In $Ge_2Ph_6$, this bond length is 2.437 Å ($R$ = 3.3%, r.t.).[23] A shorter Ge–Ge bond of 2.419 Å was found in $Ph_3GeGeMe_3$ ($R$ = 3.6%, r.t.).[24] The longest Ge–Ge bond of 2.713 Å was detected in $Ge_2(t\text{Bu})_6$ ($R$ = 2.8%, r.t.).[25]

#### *Ab Initio Calculations*

As observed for $Ge_6H_{12}$, the optimized geometry parameters for $Ge_6Me_{12}$ also strongly depend on the basis sets employed. We will therefore present results for B3LYP/aug-cc-pVTZ calculations only. Additional results are summarized in the Supporting Information (Figure S1, Tables S1–S4). Three minima closely related to those of $Si_6Me_{12}$,[13] chair, twist and boat, with ZPVE-corrected relative energies of 0.0, 5.2 and 9.2 kJ mol$^{-1}$, respectively, were found. Table 1 summarizes the most important geometry parameters for the conformers of both $Ge_6Me_{12}$ and $Ge_6H_{12}$, including the wavenumbers and Raman intensities of the symmetric ring-breathing modes. As can be seen from Table 1, the calculations overestimate Ge–Ge bond lengths by about 5 pm relative to those obtained from the X-ray results, but agree reasonably well with experimental bond angles and dihedral angles.

In order to assign the vibrational spectra, calculations of the Raman and infrared intensities were also performed. In the range expected for Ge–Ge stretching vibrations between 200 and 300 cm$^{-1}$, where rotational isomerism is expected to show up most clearly, the symmetric Ge–Ge stretch possessing the smallest wavenumber (henceforth denoted as the ring-breathing mode) has by far the largest Raman intensity for all the conformers. Although the absolute wavenumbers

 © 2007 Wiley-VCH Verlag GmbH & Co. KGaA, Weinheim 

Table 1. Calculated relative energies, wavenumbers and Raman intensities of the ring-breathing modes, and selected geometry parameters for the conformers of $Ge_6H_{12}$ and $Ge_6Me_{12}$ obtained at the B3LYP/aug-cc-pVTZ level.

| | $Ge_6H_{12}$ | | $Ge_6Me_{12}$ | | |
|---|---|---|---|---|---|
| | Chair | Twist | Chair | Twist | Boat |
| $E_{rel}$ [kJ mol$^{-1}$] | 0.0 | 5.7 | 0.0 | 5.2 | 9.2 |
| $\nu_s$(Ge–Ge) [cm$^{-1}$] | 198.4 | 197.8 | 214.7 | 209.4 | 211.5 |
| Raman intensity [Å$^4$ amu$^{-1}$] | 51 | 52 | 18 | 16 | 14 |
| av. $r$(Ge–Ge) [Å] | 2.450 | 2.453 | 2.473 | 2.475 | 2.477 |
| av. ∠(Ge–Ge–Ge) [°] | 111.2 | 111.6 | 112.3 | 113.1 | 113.9 |
| av. ∠(Ge–Ge–Ge–Ge) [°] | ±55.5 | ±63.3/±30.5 | ±52.2 | ±57.5/±27.8 | ±0.1/±46.7 |

of the modes shift depend on the basis set and method used, the wavenumber differences between the various conformers remain almost constant. Table 1 includes the most important predictions, and further details of the calculations can be retrieved from the Supporting Information. As we will show shortly, the chair conformer can be distinguished experimentally from the twist and boat conformers by a close examination of the ring-breathing mode. It is noteworthy that the calculations also show that the $CH_3$-group vibrations $\nu_s$, $\nu_{as}$, $\delta_s$, $\delta_{as}$, $\rho(CH_3)$ and $\nu_s$, $\nu_{as}$, $\delta$, $\gamma$, $\tau$, $\rho(GeC_2)$ cannot be used for this purpose.

To estimate the ring inversion barrier of $Ge_6Me_{12}$, the energy of the half-chair structure was calculated at the B3LYP/SDD level to be 10.1 kJ mol$^{-1}$. For cyclohexasilanes it is known that the calculated barriers are almost the same for both $Si_6H_{12}$ (ca. 15 kJ mol$^{-1}$) and $Si_6Me_{12}$ (ca. 16 kJ mol$^{-1}$).[13,14,26] Therefore, a calculation at the aug-cc-pVTZ level was not performed for $Ge_6Me_{12}$ in the interest of conserving time (the barrier is 10.0 kJ mol$^{-1}$ for $Ge_6H_{12}$ at the B3LYP/aug-cc-pVTZ level). The predicted barrier for the twist-to-chair interconversion of about 10 kJ mol$^{-1}$ for $Ge_6Me_{12}$ is realistic when compared with $C_6Me_{12}$ (70 kJ mol$^{-1}$) and $Si_6Me_{12}$. This value is considerably larger than $RT$ (2.5 kJ mol$^{-1}$ at 300 K) and supports the expectation that the chair and twist conformers will give separate Raman spectra.

### *Solid-State Raman Spectra*

For $Si_6Me_{12}$, a phase transition in the solid state from a crystalline phase containing only the chair conformer into a plastic phase with chair and twist conformers has been reported. The transition occurs between 70 and 80 °C.[7] A similar transition was also detected for $Ge_6Me_{12}$ between 50 and 60 °C. Figure 3 shows the ring-breathing mode of crystalline $Ge_6Me_{12}$ for different temperatures. At 60 °C, a shoulder suddenly appears at lower wavenumbers, certainly originating from a second conformer, which can be either twist or boat in nature. However, a detailed investigation of its nature was not performed in this work.

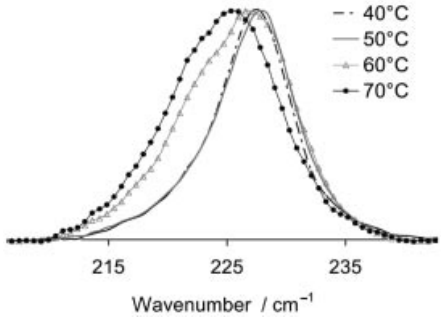


Figure 3. Shape of the ring-breathing mode of crystalline $Ge_6Me_{12}$ for different temperatures.

### *Solution Raman Spectra*

With a band shape closely resembling that in the solid state, a second band on the low-wavenumber side of the ring-breathing mode of the chair conformer is observed in thf solution. On the basis of quantum chemical calculations, it is identified as the signal for the twist or the averaged twist/boat conformer. At –80 °C, the band is barely observed as a small shoulder separated by about 5 cm$^{-1}$, and it gains intensity with increasing temperature. At room temperature, it is more intense than the band of the chair conformer. The band shapes for two temperatures as well as the relevant deconvolutions are shown in Figure 4.

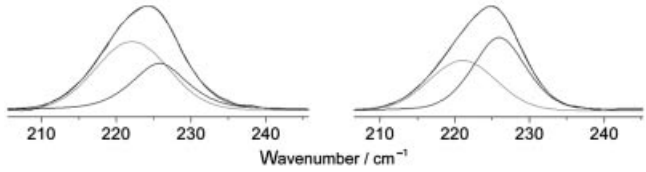


Figure 4. Appearance and deconvolution of the ring-breathing mode of $Ge_6Me_{12}$ in the Raman spectrum of a thf solution for 0 °C (left) and –40 °C (right).

According to Boltzmann statistics, the population of two conformational states varies with temperature. To analyze temperature-dependent Raman spectra of a compound possessing two conformational minima, I and II, the van't Hoff relation is used. The simple formula, $\ln(A_I/A_{II}) = -\Delta H/RT$ + constant, can be derived by assuming that $\Delta H$ and the ratio of Raman scattering coefficients, $a_I$ and $a_{II}$, are temperature independent ($a_I$, $a_{II}$ and $\Delta S$ are incorporated into the constant term). $A_I$ and $A_{II}$ are the intensities of the lines originating from conformers I and II (either band areas or band heights resulting from deconvolution may be used). The enthalpy difference, $\Delta H$, can then be obtained from the slope of a plot of $\ln(A_I/A_{II})$ against $T^{-1}$.

The calculated wavenumber difference between the chair and the averaged twist conformations is only ca. 5 cm$^{-1}$. To get the line intensities $A$, a band deconvolution was per-

 © 2007 Wiley-VCH Verlag GmbH & Co. KGaA, Weinheim 

formed. First, peak positions were obtained by calculating the second derivative, which clearly indicates the presence of two overlapping peaks. Deconvolution was then achieved by free peak fitting using Lorentzian band shapes, and an enthalpy difference of 2.4 kJ mol$^{-1}$ was obtained between the chair and the averaged twist/boat conformer. A graphical reproduction of the resulting van't Hoff plot is shown in Figure 5. The statistical errors of the experimental results are not given here because the standard deviation obtained from van't Hoff analysis certainly underestimates the actual error of the method, which originates, amongst other things, from the assumptions made in the van't Hoff analysis[27] and from ambiguities in the band deconvolution. The overall accuracy of the experimental method is estimated to be no better than ± 20%.

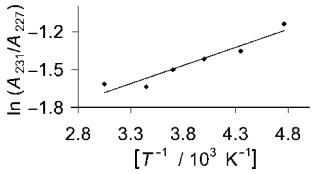


Figure 5. van't Hoff plot for the 231/227 cm$^{-1}$ band pair of $Ge_6Me_{12}$ in thf solution.

As the quantum chemical calculations refer to the isolated molecule in the gas phase, the calculated enthalpy values of 4–5 kJ mol$^{-1}$, which depend on the method and basis set used, compare fairly well with the experimental $\Delta H$ value of 2.4 kJ mol$^{-1}$.

## Conclusions

Third and higher row $E_6H_{12}$ and $E_6Me_{12}$ ring systems behave somewhat differently from cyclohexanes because the ring inversion barriers and the energy differences between stable conformers are considerably larger in the cyclohexanes. By using quantum chemical calculations, two minima, belonging to chair and twist conformations, were located on the PES for $Ge_6H_{12}$, and three minima, belonging to chair, twist, and boat conformations, were found for $Ge_6Me_{12}$. Relativistic effects have to be taken into account for the Ge atoms.

As in the case for $Si_6Me_{12}$, an averaged twist/boat conformer was observed in the Raman spectrum of $Ge_6Me_{12}$ in solution in addition to the most stable chair conformer, even at low temperatures. In the spectrum of the solid, a phase transition was observed between 50 and 60 °C. It should be noted though that $Ge_6Me_{12}$ represents a borderline case for the successful application of temperature-dependent Raman spectroscopy in terms of conformational analyses. Substituted digermanes with fairly small substituents, such as H, Me or Cl, which possess smaller rotational barriers between stable conformers, cannot be detected separately in a Raman spectrum. As we will report elsewhere, they must be investigated with the faster gas-phase electron diffraction technique.

## Experimental Section

**Synthesis:** $Ge_6Me_{12}$ was synthesized as described by Carberry et al.[17] by a coupling reaction of dimethyldichlorogermane with excess Li granulate in thf and was purified by recrystallization from acetone. The purity of the compound was checked with $^1$H NMR spectroscopy, GC-MS and Raman spectroscopy. Data were compared with literature data.[17]

**Quantum Chemical Calculations:** Geometry optimizations were initiated by using the previously published structures of $Si_6H_{12}$ and $Si_6Me_{12}$ as a starting point.[13] All geometry optimizations and minimum energy calculations, as well as the calculations of vibrational frequencies and intensities, were performed with the Gaussian03 program package at the DFT and MP2 levels of theory.[28] MP2 and B3LYP[29] density functional with the 6-31+G*[30] basis sets were employed to scan the potential energy surface, as well as the combination of D95V[31] basis sets for the C and H atoms and the quasi-relativistic Stuttgart Dresden large-core pseudopotentials (ECP28MWB[32]) for the Ge atoms. This combination is incorporated in Gaussian03 and is denoted as SDD. Geometry optimizations for located stationary points of $Ge_6H_{12}$ and $Ge_6Me_{12}$ were performed by using B3LYP with the aug-cc-pVTZ[33,34] basis set for the H atoms and aug-cc-pVTZ-PP,[35] a small-core relativistic pseudopotential correlation consistent basis set, for the Ge atoms. However, in the interest of reduced computational costs, the 6-31+G* basis set was used for the C and H atoms in $Ge_6Me_{12}$. In order to simplify the discussion, both of these methods are referred to as B3LYP/aug-cc-pVTZ.. The minima possess all real frequencies, while the transition structures have one single imaginary frequency. No symmetry restraints were employed to ensure a full investigation of the PES.

**X-ray Structure Determination:** For X-ray structure analyses, the crystals were mounted onto the tip of glass fibers, and data collection was performed with a BRUKER-AXS SMART APEX CCD diffractometer using graphite-monochromated Mo-$K_\alpha$ radiation (0.71073 Å). The data were reduced to $F^2_o$ and corrected for absorption effects with SAINT[36] and SADABS,[37] respectively. The structures were solved by direct methods and refined by the full-matrix least-squares method (SHELXL97).[38] All non-hydrogen atoms were refined with anisotropic displacement parameters. All hydrogen atoms were located in calculated positions to correspond to standard bond lengths and angles. CCDC-642005 contains the supplementary crystallographic data for this paper. These data can be obtained free of charge from The Cambridge Crystallographic Data Centre via www.ccdc.cam.ac.uk/data_request/cif.

**Raman Spectroscopy:** Raman spectra were recorded with a Jobin Yvon T64000 spectrometer equipped with a triple monochromator and a CCD camera. The samples were transferred into 1-mm glass capillary tubes and irradiated with the green 532-nm line of a frequency-doubled Nd-YAG laser (Coherent DPSS model 532–20, 20 mW). Spectra were recorded for both solid samples and solutions in thf. For high-temperature measurements, a metal block of copper with filament heating, on which the capillary was mounted, and a thermocouple for temperature monitoring were used. A continuous-flow cryostat (Oxford Instruments OptistatCF™ using liquid nitrogen for cooling) was employed for the low-temperature measurements.

**Supporting Information** (see footnote on the first page of this article): Due to space limitations, a compilation of geometric parameters for the chair, twist and boat conformers of $Ge_6H_{12}$ and $Ge_6Me_{12}$ obtained with various basis sets at the MP2 and B3LYP levels is presented.

 © 2007 Wiley-VCH Verlag GmbH & Co. KGaA, Weinheim 

## Acknowledgments

We gratefully acknowledge the financial support of the "Fonds zur Förderung der wissenschaftlichen Forschung", Vienna (project number P-17435).

[1] J. D. Kemp, K. S. Pitzer, *J. Chem. Phys.* **1936**, *4*, 749.
[2] See for instance: a) Y. Mo, J. Gao, *Acc. Chem. Res.* **2007**, *40*, 113–119; b) L. Song, Y. Lin, W. Wu, Q. Zhang, Y. Mo, *J. Phys. Chem. A* **2005**, *109*, 2310–2316; c) F. Weinhold, *Angew. Chem.* **2003**, *115*, 4320–4326; d) F. M. Bickelhaupt, E. J. Bearends, *Angew. Chem.* **2003**, *115*, 4315–4320; e) E. L. Eliel, S. H. Wilen, *Stereochemistry of Organic Compounds*, Wiley, New York, **1994**.
[3] B. Beagley, A. R. Conrad, J. M. Freeman, J. J. Monaghan, B. G. Norton, G. C. Halywell, *J. Mol. Struct.* **1972**, *11*, 371–380.
[4] J. E. Griffiths, G. E. Walrafen, *J. Chem. Phys.* **1964**, *40*, 321–328.
[5] P. v. R. Schleyer, M. Kaupp, F. Hampel, M. Bremer, K. Mislow, *J. Am. Chem. Soc.* **1992**, *114*, 6791–6797.
[6] See for instance: a) A. Jähn, K. Schenzel, R. Zink, K. Hassler, *Spectrochim. Acta Part A* **1999**, *55*, 2677–2686; b) D. Hnyk, R. S. Fender, H. E. Robertsson, D. W. H. Rankin, M. Brühl, K. Hassler, K. Schenzel, *J. Mol. Struct.* **1995**, *346*, 215–229; c) S. L. Hinchley, H. Robertson, A. Parkin, D. W. H. Rankin, G. Tekautz, K. Hassler, *Dalton Trans.* **2004**, *5*, 759–766.
[7] D. Casarini, L. Lunazzi, A. Mazzanti, *J. Org. Chem.* **1998**, *63*, 9125–9127.
[8] See for instance: D. A. McQuarrie, J. D. Simon, *Physical Chemistry, A Molecular Approach*, University Science Books, Sausalito, USA, **1997**.
[9] The rate constant $k$ is given by $k = \chi k_b T h^{-1} \exp(-\Delta G^*/RT)$ ($k_b$ = Boltzmann constant, $T$ = temperature, $h$ = Planck constant, $\Delta G^*$ = barrier height, $\chi$ = transmission coefficient). We have assumed $\chi = 0.5$.
[10] a) L. Goodman, V. Pophristic, W. Wang, *Int. J. Quantum Chem.* **2002**, *90*, 657–662; b) J. Urban, P. R. Schreiner, G. Vacek, P. v. R. Schleyer, J. Q. Huang, J. Leszczynski, *Chem. Phys. Lett.* **1997**, *264*, 441–448.
[11] M. Hölbling, S. L. Masters (née Hinchley), M. Flock, J. Baumgartner, K. Hassler, H. E. Robertson, D. A. Wann, D. W. H. Rankin, *ChemPhysChem*, submitted.
[12] L. Fitjer, H.-J. Scheuermann, D. Wehle, *Tetrahedron Lett.* **1984**, *25*, 2329–2332.
[13] G. Tekautz, A. Binter, K. Hassler, M. Flock, *ChemPhysChem* **2006**, *7*, 421–429.
[14] M. Hölbling, M. Flock, K. Hassler, *ChemPhysChem* **2007**, *8*, 735–744.
[15] B. Sztaray, A. Nagy, L. Szepes, H. J. Breunig, *J. Organomet. Chem.* **1996**, *515*, 249–252.
[16] G. Becker, W. Golla, J. Grobe, K. W. Klinkhammer, D. L. Van, A. H. Maulitz, O. Mundt, H. Oberhammer, M. Sachs, *Inorg. Chem.* **1999**, *38*, 1099–1107.
[17] E. Carberry, D. Dombek, S. C. Cohen, *J. Organomet. Chem.* **1972**, *36*, 61–70.
[18] J. Leszczynski, J. Q. Huang, P. R. Schreiner, G. Vacek, J. Kapp, P. v. R. Schleyer, H. F. Schaefer, *Chem. Phys. Lett.* **1995**, *244*, 252–257 and citations herein.
[19] W. Jensen, R. Jacobson, J. Benson, *Cryst. Struct. Comm.* **1975**, *4*, 299–301.
[20] Crystal data: Monoclinic, space group *C*2/*c*, $a$ = 18.057(4) Å, $b$ = 10.274(2) Å, $c$ = 13.941(3) Å, $\alpha$ = 90°, $\beta$ = 108.89(3)°, $\gamma$ = 90°, $V$ = 2447.1(9) Å$^3$, $Z$ = 4, $\rho_{calc.}$ = 1.672 Mg m$^{-3}$, $\mu$ (Mo-$K_\alpha$) = 7.264 mm$^{-1}$, $F$(000) = 1200, collected reflections 8018, unique reflections 2156, $R$(int) = 0.21114, $\theta$-range 2.31 to 24.99°, data/restraints/parameters: 2156/0/88, final $R$ indices [$I > 2\sigma(I)$]: $R_1$ = 0.0733, $wR_2$ = 0.1651, $R$ indices (all data): $R_1$ = 0.1001, $wR_2$ = 0.1775, largest diff. peak and hole: 1.400 and –1.308 e Å$^{-3}$.
[21] H. L. Carrell, J. Donohue, *Acta Crystallogr., Sect. B* **1972**, *28*, 1566–1571.
[22] M. Draeger, L. Ross, *Z. Anorg. Allg. Chem.* **1981**, *476*, 95–104.
[23] M. Draeger, L. Ross, *Z. Anorg. Allg. Chem.* **1980**, *460*, 207–216.
[24] L. Parkanyi, A. Kalman, S. Sharma, D. M. Nolen, K. H. Pannell, *Inorg. Chem.* **1994**, *33*, 180–182.
[25] M. Weidenbruch, F.-T. Grimm, M. Herrndorf, A. Schaefer, K. Peters, H. G. von Schnering, *J. Organomet. Chem.* **1988**, *341*, 335–343.
[26] M. K. Leong, V. S. Mastryukov, J. E. Boggs, *J. Phys. Chem.* **1994**, *98*, 6961–6966.
[27] P. Klaeboe, *Vib. Spectrosc.* **1995**, *9*, 3–17.
[28] M. J. Frisch, G. W. Trucks, H. B. Schlegel, G. E. Scuseria, M. A. Robb, J. R. Cheeseman, J. A. Montgomery Jr, T. Vreven, K. N. Kudin, J. C. Burant, J. M. Millam, S. S. Iyengar, J. Tomasi, V. Barone, B. Mennucci, M. Cossi, G. Scalmani, N. Rega, G. A. Petersson, H. Nakatsuji, M. Hada, M. Ehara, K. Toyota, R. Fukuda, J. Hasegawa, M. Ishida, T. Nakajima, Y. Honda, O. Kitao, H. Nakai, M. Klene, X. Li, J. E. Knox, H. P. Hratchian, J. B. Cross, C. Adamo, J. Jaramillo, R. Gomperts, R. E. Stratmann, O. Yazyev, A. J. Austin, R. Cammi, C. Pomelli, J. W. Ochterski, P. Y. Ayala, K. Morokuma, G. A. Voth, P. Salvador, J. J. Dannenberg, V. G. Zakrzewski, S. Dapprich, A. D. Daniels, M. C. Strain, O. Farkas, D. K. Malick, A. D. Rabuck, K. Raghavachari, J. B. Foresman, J. V. Ortiz, Q. Cui, A. G. Baboul, S. Clifford, J. Cioslowski, B. B. Stefanov, G. Liu, A. Liashenko, P. Piskorz, I. Komaromi, R. L. Martin, D. J. Fox, T. Keith, M. A. Al-Laham, C. Y. Peng, A. Nanayakkara, M. Challacombe, P. M. W. Gill, B. Johnson, W. Chen, M. W. Wong, C. Gonzalez, and J. A. Pople, *Gaussian 03, Revision B.03*, Gaussian, Inc., Pittsburgh PA, **2003**.
[29] As implemented in Gaussian03: a) A. D. Becke, *J. Chem. Phys.* **1993**, *98*, 5648–5652; C. Lee, W. Yang, R. G. Parr, *Phys. Rev. B* **1988**, *37*, 785–789; b) B. Miehlich, A. Savin, H. Stoll, H. Preuss, *Chem. Phys. Lett.* **1989**, *157*, 200–206; c) S. H. Vosko, L. Wilk, M. Nusair, *Can. J. Phys.* **1980**, *58*, 1200–1211.
[30] The 6-31+G* basis sets for the H, C and Ge atoms are used as implemented in Gaussian03.
[31] T. H. Dunning Jr, P. J. Hay, in *Modern Theoretical Chemistry* (Ed.: H. F. Schaefer III), Plenum, New York, **1976**, vol. 3, pp. 1–28.
[32] A. Bergner, M. Dolg, W. Kuechle, H. Stoll, H. Preuss, *Mol. Phys.* **1993**, *80*, 1431–1441.
[33] a) T. H. Dunning Jr, *J. Chem. Phys.* **1989**, *90*, 1007–1023; b) R. A. Kendall, T. H. Dunning Jr, R. J. Harrison, *J. Chem. Phys.* **1992**, *96*, 6796–6806.
[34] These augmented-correlation-consistent triple zeta basis sets can easily be obtained from the EMSL Basis Set Library, http://www.emsl.pnl.gov/cgi-bin/ecce/basis_old.pl.
[35] a) K. A. Peterson, *J. Chem. Phys.* **2003**, *119*, 11099–11112; b) B. Metz, H. Stoll, M. Dolg, *J. Chem. Phys.* **2000**, *113*, 2563–2569.
[36] *SAINTPLUS: Software Reference Manual, Version 6.45*, Bruker-AXS, Madison, WI, **1997**–**2003**.
[37] R. H. Blessing, Acta Crystallogr., *Sect. A* **1995**, *51*, 33–38: SADABS: Version 2.1 Bruker AXS **1998**.
[38] G. M. Sheldrick, *SHELX97 Programs for Crystal Structure Analysis (Release 97–2)*, University of Göttingen, Göttingen (Germany) **1998**.

Received: June 4, 2007
Published Online: September 12, 2007

 © 2007 Wiley-VCH Verlag GmbH & Co. KGaA, Weinheim 

DOI: 10.1002/ejic.200700620

# Open Platinum Aggregate Frameworks with Overhead Dithiolate Bridges

Siew Huay Chong,[a] William Henderson,[b] and T. S. Andy Hor*[a]

**Keywords:** Platinum / Sulfide / Aggregate / Alkylation / Dithiolate

A convenient method has been developed to bring together two discrete moieties of $[Pt_2(\mu\text{-}S)_2(PPh_3)_4]$ to give an open $Pt_4$ aggregate of $Pt_2\cdots(spacer)\cdots Pt_2$, as exemplified in the isolation of $[(PPh_3)_4Pt_2(\mu\text{-}S)(\mu\text{-}SRS)(\mu\text{-}S)Pt_2(PPh_3)_4](PF_6)_2$ [R = *m*-$CH_2C_6H_4CH_2$, *p*-$CH_2C_6H_4CH_2$, $CH_2C_{10}H_6CH_2$, and $CH_2(C_6H_4)_2CH_2$]. The spacer is a dithiolate with an extended skeletal backbone formed from the alkylation of sulfide with a suitable dibromo-organic compound. This synthetic methodology can tolerate a range of conformationally contrasting thiolate substituents with different chemical functionalities. Shorter or stereochemically more restrictive spacers could opt to be an intramolecular bridge over the $Pt_2$ core, as given in $[Pt_2(\mu\text{-}S\text{-}o\text{-}CH_2C_6H_4\text{-}C_6H_4CH_2S)(PPh_3)_4](PF_6)_2$. A few representative complexes have been characterized by single-crystal X-ray diffraction analysis.

(© Wiley-VCH Verlag GmbH & Co. KGaA, 69451 Weinheim, Germany, 2007)

## Introduction

Owing to the rich nucleophilicity of the $\{Pt_2(\mu\text{-}S)_2\}$ core, the $[Pt_2(\mu\text{-}S)_2(P\text{-}P)_2]$ (P-P = diphosphane or $2\times PR_3$) (**1**) complexes have evolved to be a versatile metalloligand[1] and an efficacious thio-template for organic reactions.[2] The well-developed metallation chemistry of **1** has resulted in a large number of homo-, hetero-, and intermetallic polynuclear structures, which are best described as metal aggregates, not clusters, as they generally do not have active and direct M–M bonds. One of the objectives for this type of supramolecular assembly is to construct a mega-aggregate framework using sub-aggregates as building blocks. Parallel to this development is the use of organic moieties, instead of metal species, to connect the aggregate and build up the nuclearity. Conceptually, this can be viewed as an application of the growing alkylation chemistry of $[Pt_2(\mu\text{-}S)_2(P\text{-}P)_2]$.[1c,3–4] The nuclearity growth is controlled by the electronic and geometric features of the spacer. Adjusting the nucleophilicity of both sulfide centers could help to control the mono- or dialkylation selectivity, as evidenced from our recent study of the alkylation and arylation chemistry of $[Pt_2(\mu\text{-}S)_2(PPh_3)_4]$ (**1a**) using Electrospray Ionization Mass Spectrometry (ESI-MS).[3a] While simple monohalides predominantly give monoalkylated products of the type, $[Pt_2(\mu\text{-}SR)(\mu\text{-}S)(PPh_3)_4]^+$ (**2**), reactive halides, dimethyl sulfate, and α,ω-dialkylating agents result in dialkylated products, such as $[Pt_2(\mu\text{-}SR)_2(PPh_3)_4]^{2+}$ (**3**) and $[Pt_2(\mu\text{-}S_2R)(PPh_3)_4]^{2+}$ (**4**). Of particular interest here is the use of α,ω-dialkylating agents, with more rigid spacers; the spacer length between the alkylating groups [typically halides (X), e.g. XRX] determines the extent of functionalization in **1a**. For example, with a spacer containing up to four carbons, the end product of the reaction is the bridged complex (**4**), but with a longer separation, monoalkylation tends to dominate, resulting in complexes of the type $[Pt_2(\mu\text{-}SRX)(\mu\text{-}S)(PPh_3)_4]^+$ (**5**). In the case where the dihalides have a hydrocarbon chain which is too long to fit into the overhead S···S bridge, they can opt to intermolecularly bridge two sulfides, thus resulting in $Pt_4$ dications.[3a]

We herein present a synthetic application of our earlier ESI-MS study by preparing, isolating, and characterizing the tetranuclear platinum ($Pt_4$) sulfide aggregates $[(PPh_3)_4Pt_2(\mu\text{-}S)(\mu\text{-}SRS)(\mu\text{-}S)Pt_2(PPh_3)_4]^{2+}$ (**6**), which up to now have only been observed spectroscopically.[3a] This type of high-nuclearity platinum complex, in which the metal centers interact through ligand bridges, has attracted attention for their structural diversity,[5] luminescent[6] and redox[7] properties, electronics,[8] catalysis,[7] and as molecular precursors for inorganic materials under mild conditions,[9] as possible models in redox-active metalloproteins,[10] and as anti-cancer agents.[11]

## Results and Discussion

### Constructing Linkages to Build Platinum Sulfide Aggregates

The use of dihalides (XRX) of an appropriate spacer length to cross both sulfur atoms in $[Pt_2(\mu\text{-}S)_2(P\text{-}P)_2]$ (**1**) has provided the first solution to stable dialkylated derivatives of **1**.[2,3b] Early alkylation studies of $[Pt_2(\mu\text{-}S)_2(PPh_3)_4]$ (**1a**) demonstrate that while monoalkylation is facile, dialky-

[a] Department of Chemistry, National University of Singapore, 3, Science Drive 3, Singapore 117543, Singapore
Fax: +65-6516-1324
E-mail: andyhor@nus.edu.sg
[b] Department of Chemistry, University of Waikato, Private Bag 3105, Hamilton, New Zealand

 © 2007 Wiley-VCH Verlag GmbH & Co. KGaA, Weinheim 

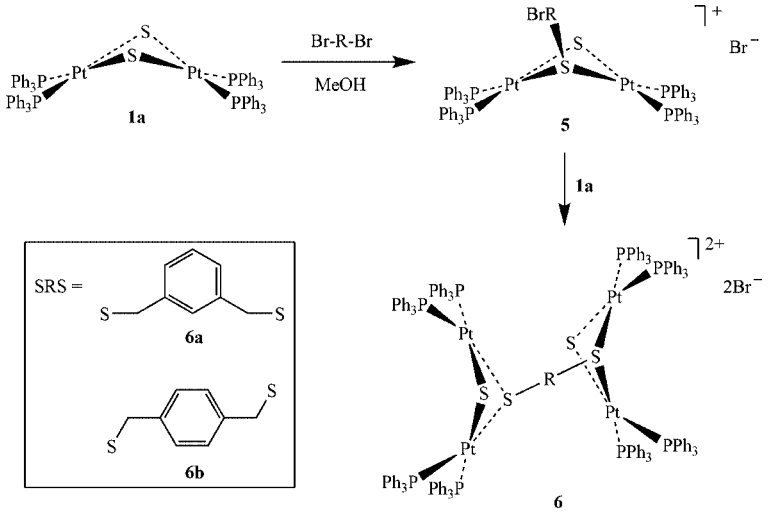


Scheme 1. Formation of a $Pt_4$ aggregate (**6**) through the linkage of two moieties of **1a**.

lation is elusive since the second sulfide is deactivated upon alkylation of the first in the initially formed monocation, $[Pt_2(\mu\text{-}SR)(\mu\text{-}S)(PPh_3)_4]^+$ (**2**)[3a–3b] or disintegration of the $\{Pt_2(\mu\text{-}S)_2\}$ core that follows dialkylation with $CH_2Cl_2$[4a–4c] and protic acids.[12] This method of sulfide functionalization in **1** leads to the isolation of stable overhead-bridged dialkylated products, such as $[Pt_2(\mu\text{-}SC_nH_{2n}S)(PPh_3)_4](PF_6)_2$ ($n$ = 2 and 4)[3b] and $[Pt_2(\mu\text{-}S\text{-}o\text{-}CH_2C_6H_4CH_2S)(P\text{-}P)_2](PF_6)_2$ [P-P = 2 × $PPh_3$ and $Ph_2PC_3H_6PPh_2$ (dppp)].[2a] The latter complex has been shown to be a useful precursor in the catalytic-like preparation of dithiacyclophanes.

As mentioned previously, dihalides with a hydrocarbon chain which is too long or insufficiently flexible to fit into the overhead S···S bridge will lead to monoalkylation, giving $[Pt_2(\mu\text{-}SRX)(\mu\text{-}S)(PPh_3)_4]^+$ (**5**).[3a–3b] By taking advantage of the dehalogenation capability of $\{Pt_2(\mu\text{-}S)_2\}$[3d] to displace the halide in **5**, $Pt_4$ dications of the type, $[(PPh_3)_4Pt_2(\mu\text{-}S)(\mu\text{-}SRS)(\mu\text{-}S)Pt_2(PPh_3)_4]^{2+}$ (**6**) can be readily obtained (Scheme 1). Initial alkylation of **1a** with one equivalent of α,α′-dibromo-*m*-xylene gives the stable monoalkylated $[Pt_2(\mu\text{-}S\text{-}m\text{-}CH_2C_6H_4CH_2Br)(\mu\text{-}S)(PPh_3)_4]^+$ (**5a**) (*m*/*z* 1687, 100%), followed by the formation of $[(PPh_3)_4Pt_2(\mu\text{-}S)(\mu\text{-}S\text{-}m\text{-}CH_2C_6H_4CH_2S)(\mu\text{-}S)Pt_2(PPh_3)_4](PF_6)_2$ (**6a**) upon addition of another equivalent of **1a**, and metathesis with $NH_4PF_6$. Single-crystal X-ray diffraction analysis of **6a** (Figure 1) reveals two $\{Pt_2(\mu\text{-}S)_2\}$ butterflies joined together by -$CH_2C_6H_4CH_2$- at each of their sulfides, resulting in a "coat hanger-like" structure. Similarly, in the case of the *para* isomer (α,α′-dibromo-*p*-xylene), the two $\{Pt_2(\mu\text{-}S)_2\}$ butterflies are connected at both ends of the xylyl bridge (Figure 2) to give the intermolecularly bridged complex, $[(PPh_3)_4Pt_2(\mu\text{-}S)(\mu\text{-}S\text{-}p\text{-}CH_2C_6H_4CH_2S)(\mu\text{-}S)Pt_2(PPh_3)_4](PF_6)_2$ (**6b**). It is expected that the dihedral angles in each of the $\{Pt_2(\mu\text{-}S)_2\}$ moieties would be the same within the same molecule, and that is observed in the case of complex

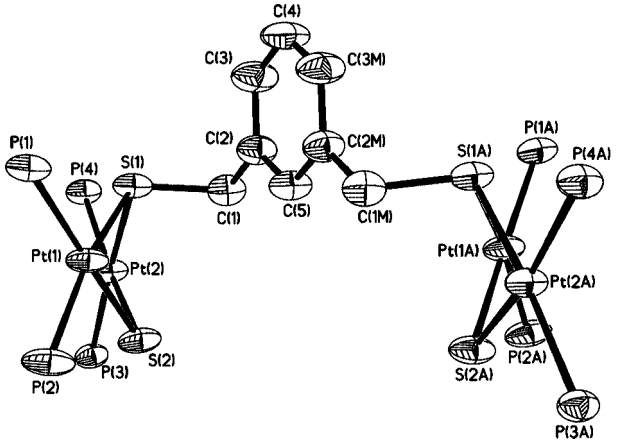


Figure 1. A 50% thermal ellipsoid representation of the cation of $[(PPh_3)_4Pt_2(\mu\text{-}S)(\mu\text{-}S\text{-}m\text{-}CH_2C_6H_4CH_2S)(\mu\text{-}S)Pt_2(PPh_3)_4](PF_6)_2$ (**6a**). The phenyl rings of $PPh_3$ and hydrogen atoms are omitted for clarity.

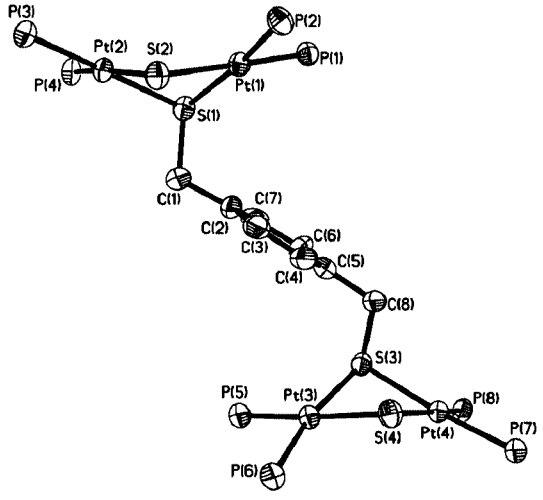


Figure 2. A 50% thermal ellipsoid representation of the cation of $[(PPh_3)_4Pt_2(\mu\text{-}S)(\mu\text{-}S\text{-}p\text{-}CH_2C_6H_4CH_2S)(\mu\text{-}S)Pt_2(PPh_3)_4](PF_6)_2$ (**6b**). The phenyl rings of $PPh_3$ and hydrogen atoms are omitted for clarity.

 © 2007 Wiley-VCH Verlag GmbH & Co. KGaA, Weinheim 

**6a** where both $\{Pt_2(\mu\text{-}S)_2\}$ rings are hinged with the dihedral angle of 132°. Interestingly, each of the $\{Pt_2(\mu\text{-}S)_2\}$ rings in complex **6b** are hinged to a slightly different extent – the moiety with the Pt(1)–S(1)–S(2)–Pt(2) core has a dihedral angle of 133° while the one with the Pt(3)–S(3)–S(4)–Pt(4) core has a dihedral angle of 138°. The slight difference in the dihedral angles is a result of having two noncrystallographically related $\{Pt_2(\mu\text{-}S)_2\}$ rings in **6b**. In contrast, the asymmetric unit for complex **6a** is half a molecule, so the two $\{Pt_2(\mu\text{-}S)_2\}$groups are symmetry-related and must therefore have exactly the same dihedral angle.

The $^{31}P\{^1H\}$ NMR characteristics of the two complexes are similar. The two sets of phosphanes have very similar chemical shifts and are differentiated by the different Pt-P couplings; a multiplet due to the overlap of the two phosphane signals at $\delta_P$ 23.2–23.8 ppm ($^1J_{Pt,P(1)}$ = 3292, $^1J_{Pt,P(2)}$ = 2627 Hz) and $\delta_P$ 23.3–23.6 ppm ($^1J_{Pt,P(1)}$ = 3293, $^1J_{Pt,P(2)}$ = 2591 Hz) for **6a** and **6b**, respectively. The thiolate ligand, $SCH_2C_6H_4CH_2S$ has a lower *trans* influence than a sulfido ligand, so the Pt–P bond *trans* to thiolate is shorter and has a larger $J_{Pt,P}$ coupling.

Isolation of complexes **6a** and **6b** suggested that we could conveniently control the directionality of the aggregate alignment by adjusting the geometry effect of the spacer. This synthetic methodology opens up the opportunity for the preparation of platinum sulfide aggregates that can be linked by a variety of organic alkyl or aryl chains. Application of this technique to two other dihalides: 2,6-bis(bromomethyl)naphthalene and 4,4′-bis(chloromethyl)-1,1′-biphenyl results in similar $Pt_4$ aggregates; $[(PPh_3)_4Pt_2(\mu\text{-}S)(\mu\text{-}SCH_2C_{10}H_6CH_2S)(\mu\text{-}S)Pt_2(PPh_3)_4](PF_6)_2$ (**6c**) and $[(PPh_3)_4Pt_2(\mu\text{-}S)(\mu\text{-}SCH_2(C_6H_4)_2CH_2S)(\mu\text{-}S)Pt_2(PPh_3)_4](PF_6)_2$ (**6d**). $^{31}P\{^1H\}$ NMR confirms successful syntheses and displays a multiplet from the overlap of the two phosphane signals at $\delta_P$ 23.5–24.2 ppm ($^1J_{Pt,P(1)}$ = 3289, $^1J_{Pt,P(2)}$ = 2630 Hz) and $\delta_P$ 23.7–24.4 ppm ($^1J_{Pt,P(1)}$ = 3282, $^1J_{Pt,P(2)}$ = 2628 Hz) for **6c** and **6d**, respectively.

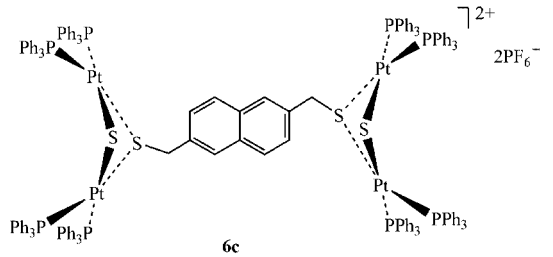


**6c**

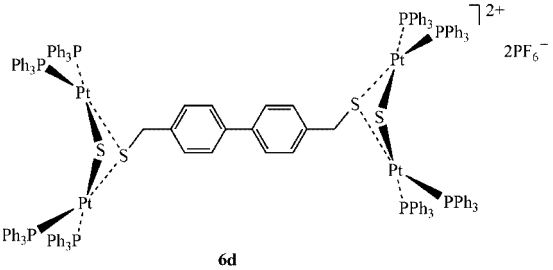


**6d**

## From Linker to a Bridge

An unexpected overhead-bridged dialkylated complex, $[Pt_2(\mu\text{-}S\text{-}o\text{-}CH_2C_6H_4\text{-}C_6H_4CH_2S)(PPh_3)_4](PF_6)_2$ (**7**) with a long ($C_6$) spacer between the alkylating groups has been successfully isolated using 2,2′-bis(bromomethyl)-1,1′-biphenyl as the difunctional alkylating agent. Prior to this, dihalides with a spacer more than four C–C bonds long impeded dialkylation significantly and resulted predominantly in monoalkylation (**6**).[2] Despite the long $C_6$ distance that would normally result in monoalkylation of **1a**, dialkylation occurs rapidly and is completed within 2 h. Any signal corresponding to monoalkylation is absent in the ESI mass spectrum of the reaction monitored in MeOH. The bridging nature of the dithiolate ($\mu$-S-*o*-$CH_2C_6H_4\text{-}C_6H_4CH_2S$) ligand as opposed to the expected monothiolate ($\mu$-$SCH_2C_6H_4\text{-}C_6H_4CH_2Br$) ligand is confirmed by the single-crystal X-ray diffraction analyses of

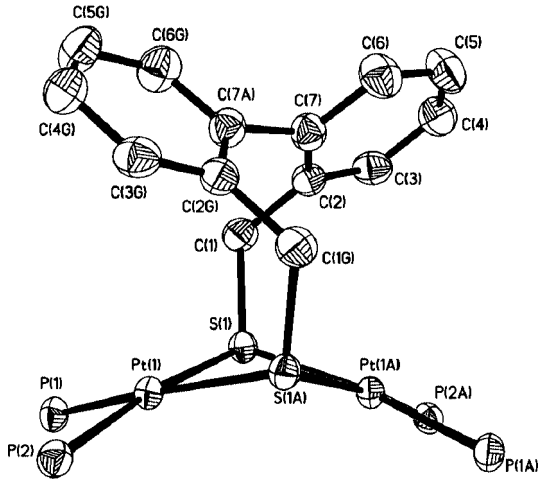


Figure 3. A 50% thermal ellipsoid representation of the cation of $[Pt_2(\mu\text{-}S\text{-}o\text{-}CH_2C_6H_4\text{-}C_6H_4CH_2S)(PPh_3)_4](PF_6)_2$ (**7**). The phenyl rings of $PPh_3$ and hydrogen atoms are omitted for clarity.

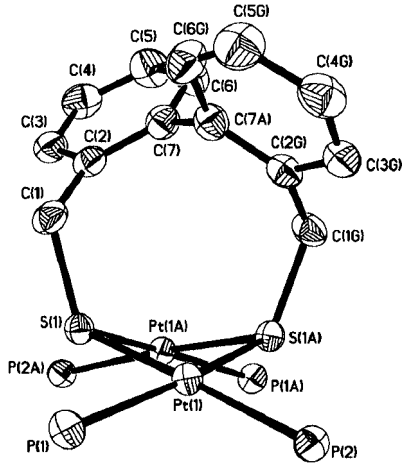


Figure 4. View along the Pt(1)–Pt(1A) axis. A 50% thermal ellipsoid representation of the cation of $[Pt_2(\mu\text{-}S\text{-}o\text{-}CH_2C_6H_4\text{-}C_6H_4CH_2S)(PPh_3)_4](PF_6)_2$ (**7**). The phenyl rings of $PPh_3$ and hydrogen atoms are omitted for clarity.

 © 2007 Wiley-VCH Verlag GmbH & Co. KGaA, Weinheim 

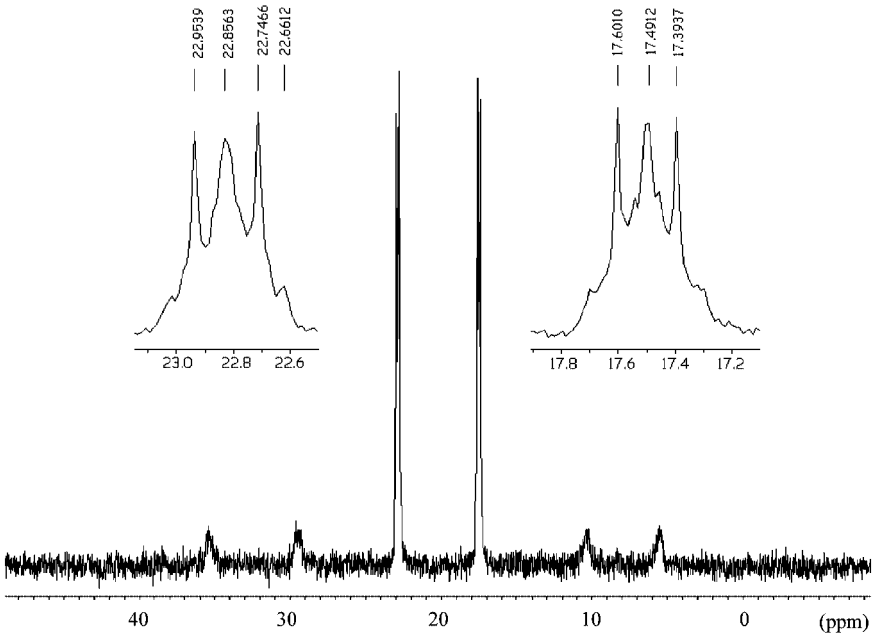


Figure 5. $^{31}P\{^{1}H\}$ NMR spectrum of $[Pt_2(\mu\text{-}S\text{-}o\text{-}CH_2C_6H_4\text{-}C_6H_4CH_2S)(PPh_3)_4](PF_6)_2$ (**7**) in $[D_6]$DMSO.

complex **7** in Figures 3 and 4. When viewed along the S(1A)–S(1) axis (Figure 3), the two phenyl groups which are joined at the C(7A)–C(7) bond are pointing away from one another as they are bent about the $\{S_2C_2\}$ plane. The conformationally flexible C(7A)–C(7) bond appears almost perpendicular to the S(1)–C(1) and S(1A)–C(1G) bonds, which are in a *syn-exo* conformation, pointing away from the sterically bulky triphenylphosphanes. These conformational features allow the flexible $C_6$ chain to fit into the S···S bridge. When viewed along the Pt(1)–Pt(1A) axis (Figure 4), complex **7** shows a unique and unusual bicyclic nine-membered metallosulfur-carbon ring. Its structure has a bent $\{Pt_2(\mu\text{-}S)_2\}$ ring and a dihedral angle of 147°. The dissymmetry created by the bridge generated two sets of inequivalent phosphanes that give two discrete resonances at $\delta_P$ = 17.5 (m, $^1J_{Pt,P}$ = 2923, $^2J_{P,P}$ = 13 Hz) and 22.9 ppm (m, $^1J_{Pt,P}$ = 3043, $^2J_{P,P}$ = 13 Hz) in its $^{31}P\{^{1}H\}$ NMR spectrum (Figure 5). Such NMR characteristics have been observed in the xylyl dithiolato-bridged complex, $[Pt_2(\mu\text{-}S\text{-}o\text{-}CH_2C_6H_4CH_2S)(PPh_3)_4](PF_6)_2$.[2a]

## Conclusions

The isolation of tetranuclear platinum sulfide aggregates that can be linked by a variety of organic chains marks an extension to the scope of alkylation chemistry in the $\{Pt_2(\mu\text{-}S)_2\}$ systems. The choice of appropriate alkylating agents coupled with the excellent dehalogenation capability of the sulfide centers in $[Pt_2(\mu\text{-}S)_2(PPh_3)_4]$ (**1a**) makes the preparation possible. In principle, all dibromo-organic compounds with an extended skeleton can function as an overhead bridge across the sulfide centers. If it is stereochemically too restrictive to serve as an intramolecular bridge within the $Pt_2$ core, it could be switched to the intermolecular mode and interlink two $Pt_2$ cores, giving $[(PPh_3)_4Pt_2(\mu\text{-}S)(\mu\text{-}SRS)(\mu\text{-}S)Pt_2(PPh_3)_4](PF_6)_2$ (**6**). Our next synthetic target is to activate the unsubstituted sulfide atoms of the aggregate. The strategies used could be adapted from the method we recently developed for the alkylation of the $[Pt_2(S)(SR)]^+$ core to $[Pt_2(SR)_2]^{2+}$.[13] The success of such a synthesis would pave the way to stepwise alignment of Pt aggregates ···$Pt_2$···$Pt_2$···$Pt_2$··· with sole dithiolate spacers.

## Experimental Section

### Materials and Methods

All manipulations were carried out at room temperature under an atmosphere of dinitrogen. Solvents used were generally of analytical grade (Tedia) and were dried and deoxygenated before being used. The complex $[Pt_2(\mu\text{-}S)_2(PPh_3)_4]$ (**1a**) was synthesized by metathesis of *cis*-$[PtCl_2(PPh_3)_2]$ with $Na_2S{\cdot}9H_2O$ (Riedel-de Haën) in benzene. Complex **1a** was obtained in 86% yield {ESI-MS (80% MeOH/20% $H_2O$): *m*/*z* 1504 (100%) $[M + H]^+$}. The following chemicals were used as supplied from Aldrich: α,α′-dibromo-*m*/*p*-xylenes, 2,2′-bis(bromomethyl)-1,1′-biphenyl, 2,6-bis(bromomethyl)naphthalene, 4,4′-bis(chloromethyl)-1,1′-biphenyl, and ammonium hexafluorophosphate ($NH_4PF_6$).

Electrospray mass spectra were obtained in the positive-ion mode with a Finnigan/MAT LCQ mass spectrometer coupled with a TSP4000 HPLC system and the crystal 310 CE system. The mobile phase was 80% methanol/20% $H_2O$ (flow rate: 0.4 mL min$^{-1}$). The capillary temperature was 150 °C. Peaks were assigned from the *m*/*z* values and from the isotope-distribution patterns. The charge(s) on the species could be confirmed by comparing the experimental and calculated isotope-distribution patterns. Elemental analyses were performed with a Perkin–Elmer PE 2400 CHNS elemental analyzer. $^1H$ NMR spectra were recorded at 25 °C with a Bruker ACF 300 spectrometer (at 300 and 75.47 MHz, respectively) with $Me_4Si$

 © 2007 Wiley-VCH Verlag GmbH & Co. KGaA, Weinheim 

as internal standard. The $^{31}P$ NMR spectra were recorded at 25 °C and 121.50 MHz with 85% $H_3PO_4$ as external reference. The $^{31}P$ NMR spectra of **6a**–**d** and **7** obtained are generally higher-order spectra which were treated with first-order approximations. Detailed analysis of similar six-spin systems ($4\times{}^{31}P + 2\times{}^{195}Pt$) has been reported.[4d]

**Syntheses**

**$[(PPh_3)_4Pt_2(\mu\text{-}S)(\mu\text{-}S\text{-}m\text{-}CH_2C_6H_4CH_2S)(\mu\text{-}S)Pt_2(PPh_3)_4](PF_6)_2$ (6a):** Compound **1a** (29.6 mg, 0.020 mmol) and a stoichiometric amount of α,α′-dibromo-*m*-xylene (5.0 mg, 0.019 mmol) in methanol (15 mL) was stirred for 2 h, followed by the addition of a slight excess of **1a** (36.2 mg, 0.024 mmol, 1.2 equiv.). The yellow suspension was stirred for a further 2.5 h and filtered to remove any unreacted **1a**. Excess $NH_4PF_6$ (20.0 mg, 0.123 mmol) was added to give a yellow suspension. Deionized water (40 mL) was then used to complete the precipitation. A yellow powder of **6a** (56.2 mg, 76%) was obtained by washing with deionized water (100 mL) and diethyl ether (100 mL) using vacuum suction filtration. $^{31}P\{^1H\}$ NMR ($CD_2Cl_2$): $\delta_P$ = 23.6 ppm (m, $^1J_{Pt,P(1)}$ = 3292, $^1J_{Pt,P(2)}$ = 2627 Hz). $^1H$ NMR ($CD_2Cl_2$): $\delta_H$ = 3.84 (br. s, 4 H, 2 $SCH_2$), 5.82–5.85 (d, $J$ = 8.0 Hz, 2 H, $CH_2C_6H_4CH_2$), 6.49 (b t, $J$ = 7.7 Hz, 1 H, $CH_2C_6H_4CH_2$), 6.76 (s, 1 H, $CH_2C_6H_4CH_2$), 7.03–7.43 ppm (m, 120 H, 24 $C_6H_5$). ESI-MS (MeOH/$H_2O$): *m*/*z* (%) = 1555 (100) $[M]^{2+}$. $C_{152}H_{128}F_{12}P_{10}Pt_4S_4$ (3400.94): calcd. C 53.68, H 3.79, S 3.77; found C 53.65, H 3.76, S 3.98. Yellow crystals of $[(PPh_3)_4Pt_2(\mu\text{-}S)(\mu\text{-}S\text{-}m\text{-}CH_2C_6H_4CH_2S)(\mu\text{-}S)Pt_2(PPh_3)_4](PF_6)_2$ suitable for X-ray crystallographic analysis were obtained from dichloromethane/benzene (1:1).

**$[(PPh_3)_4Pt_2(\mu\text{-}S)(\mu\text{-}S\text{-}p\text{-}CH_2C_6H_4CH_2S)(\mu\text{-}S)Pt_2(PPh_3)_4](PF_6)_2$ (6b):** A procedure similar to that used above was employed. A stoichiometric amount of α,α′-dibromo-*p*-xylene (6.8 mg, 0.026 mmol) was introduced into an orange suspension of compound **1a** (40.0 mg, 0.027 mmol) in methanol (20 mL). The mixture changed from an orange suspension to a yellow solution in 2 h. Another 40.5 mg (0.027 mmol) of **1a** was added, resulting in a yellow suspension. The mixture was stirred for a further 2 h, and the resultant suspension was filtered, followed by the addition of excess $NH_4PF_6$ (20.0 mg, 0.123 mmol). Deionized water (50 mL) was used to complete the precipitation. A yellow powder of **6b** (64.2 mg, 71%) was obtained by washing with deionized water (100 mL) and diethyl ether (100 mL) using vacuum suction filtration. $^{31}P\{^1H\}$ NMR ($CD_2Cl_2$): $\delta_P$ = 23.5 ppm (br. s, $^1J_{Pt,P(1)}$ = 3293, $^1J_{Pt,P(2)}$ = 2591, $^2J_{P(1)-P(2)}$ = 18 Hz). $^1H$ NMR ($CD_2Cl_2$): $\delta_H$ = 3.39 (br. s, 4 H, 2 $SCH_2$), 6.12 (s, 4 H, $CH_2C_6H_4CH_2$), 6.99–7.43 ppm (m, 120 H, 24 $C_6H_5$). ESI-MS (MeOH/$H_2O$): *m*/*z* (%) = 1555 (100) $[M]^{2+}$. $C_{152}H_{128}F_{12}P_{10}Pt_4S_4$ (3400.94): calcd. C 53.68, H 3.79, S 3.77; found C 53.43, H 3.75, S 3.47. Yellow crystals of $[(PPh_3)_4Pt_2(\mu\text{-}S)(\mu\text{-}S\text{-}p\text{-}CH_2C_6H_4CH_2S)(\mu\text{-}S)Pt_2(PPh_3)_4](PF_6)_2$ suitable for X-ray crystallographic analysis were obtained from dichloromethane/ethanol (1:1).

**$[(PPh_3)_4Pt_2(\mu\text{-}S)(\mu\text{-}SCH_2C_{10}H_6CH_2S)(\mu\text{-}S)Pt_2(PPh_3)_4](PF_6)_2$ (6c):** Stoichiometric amount of 2,6-bis(bromomethyl)naphthalene (8.0 mg, 0.026 mmol) was introduced into an orange suspension of compound **1a** (39.1 mg, 0.026 mmol) in methanol (22 mL). The mixture changed from an orange suspension to a yellow solution in 2 h. Another 40.4 mg (0.027 mmol) of **1a** was added, resulting in a yellow solution in 2 h, and the mixture was left to stir overnight. The resultant yellow solution which was slightly cloudy was filtered, followed by the addition of excess $NH_4PF_6$ (20.0 mg, 0.123 mmol). Deionized water (50 mL) was used to complete the precipitation. A yellow powder of **6c** (48.5 mg, 53%) was obtained by washing with deionized water (100 mL) and diethyl ether (100 mL) using vacuum suction filtration. $^{31}P\{^1H\}$ NMR ($CD_2Cl_2$): $\delta_P$ = 23.5–24.2 ppm (m, $^1J_{Pt,P(1)}$ = 3289, $^1J_{Pt,P(2)}$ = 2630 Hz). $^1H$ NMR ($CD_2Cl_2$): $\delta_H$ = 3.82 (br. s, 4 H, 2 $SCH_2$), 6.83–7.45 (m, 6 H, $C_{10}H_6$), 6.83–7.45 ppm (m, 120 H, 24 $C_6H_5$). ESI-MS (MeOH/$H_2O$): *m*/*z* (%) = 1580 (100) $[M]^{2+}$. $C_{156}H_{130}F_{12}P_{10}Pt_4S_4$ (3451.0): calcd. C 54.29, H 3.80, S 3.72; found C 54.44, H 3.72, S 3.54.

**$[(PPh_3)_4Pt_2(\mu\text{-}S)(\mu\text{-}SCH_2(C_6H_4)_2CH_2S)(\mu\text{-}S)Pt_2(PPh_3)_4](PF_6)_2$ (6d):** A stoichiometric amount of 4,4′-bis(chloromethyl)-1,1′-biphenyl (4.8 mg, 0.019 mmol) was introduced into an orange sus-

Table 1. Selected bond lengths [Å] and angles [°] for complexes **6a**, **6b**, and **7**.

| $[(PPh_3)_4Pt_2(\mu\text{-}S)(\mu\text{-}S\text{-}m\text{-}CH_2C_6H_4CH_2S)(\mu\text{-}S)Pt_2(PPh_3)_4](PF_6)_2$ (**6a**) | | | |
|---|---|---|---|
| Pt(1)–P(1) | 2.289(15) | Pt(2)–S(2) | 2.322(13) |
| Pt(1)–P(2) | 2.293(15) | Pt(2A)–S(1A) | 2.373(13) |
| Pt(2A)–P(4A) | 2.308(14) | Pt(2A)–S(2A) | 2.322(13) |
| Pt(2A)–P(3A) | 2.273(14) | Pt(1A)–S(1A) | 2.345(14) |
| Pt(1)–S(1) | 2.345(14) | Pt(1A)–S(2A) | 2.334(15) |
| Pt(1)–S(2) | 2.334(15) | S(1)–C(1) | 1.842(6) |
| Pt(2)–S(1) | 2.373(13) | | |
| | | | |
| Pt(1)–S(1)–Pt(2) | 87.30(5) | P(2)–Pt(1)–S(1) | 166.66(6) |
| Pt(1)–S(2)–Pt(2) | 88.77(5) | P(2)–Pt(1)–S(2) | 174.19(5) |
| Pt(2A)–S(1A)–Pt(1A) | 87.30(5) | P(4A)–Pt(2A)–S(1A) | 87.49(5) |
| Pt(2A)–S(2A)–Pt(1A) | 88.77(5) | P(4A)–Pt(2A)–S(2A) | 168.06(5) |
| S(1)–Pt(1)–S(2) | 81.06(5) | P(3A)–Pt(2A)–S(1A) | 172.31(5) |
| S(1A)–Pt(2A)–S(2A) | 80.70(5) | P(3A)–Pt(2A)–S(2A) | 91.65(5) |
| P(1)–Pt(1)–P(2) | 99.04(6) | C(1)–S(1)–Pt(1) | 105.54(18) |
| P(4A)–Pt(2A)–P(3A) | 100.13(5) | C(1)–S(1)–Pt(2) | 102.50(18) |
| P(1)–Pt(1)–S(1) | 94.16(5) | $\theta$[a] | 132 |
| P(1)–Pt(1)–S(2) | 174.19(5) | | |

| $[(PPh_3)_4Pt_2(\mu\text{-}S)(\mu\text{-}S\text{-}p\text{-}CH_2C_6H_4CH_2S)(\mu\text{-}S)Pt_2(PPh_3)_4](PF_6)_2$ (**6b**) | | | |
|---|---|---|---|
| Pt(1)–P(1) | 2.296(3) | Pt(2)–S(2) | 2.327(2) |
| Pt(1)–P(2) | 2.287(3) | Pt(3)–S(3) | 2.355(2) |
| Pt(3)–P(5) | 2.296(3) | Pt(3)–S(4) | 2.337(2) |
| Pt(3)–P(6) | 2.291(3) | Pt(4)–S(3) | 2.370(2) |
| Pt(1)–S(1) | 2.341(2) | Pt(4)–S(4) | 2.329(2) |
| Pt(1)–S(2) | 2.340(2) | S(1)–C(1) | 1.850(10) |
| Pt(2)–S(1) | 2.377(2) | S(3)–C(8) | 1.845(9) |
| | | | |
| Pt(1)–S(1)–Pt(2) | 90.04(8) | P(2)–Pt(1)–S(2) | 84.57(9) |
| Pt(1)–S(2)–Pt(2) | 91.32(8) | P(5)–Pt(3)–S(3) | 94.17(9) |
| Pt(3)–S(3)–Pt(4) | 87.93(8) | P(5)–Pt(3)–S(4) | 175.12(9) |
| Pt(3)–S(4)–Pt(4) | 89.35(8) | P(6)–Pt(3)–S(3) | 166.68(9) |
| S(1)–Pt(1)–S(2) | 81.19(8) | P(6)–Pt(3)–S(4) | 85.89(9) |
| S(3)–Pt(3)–S(4) | 80.95(9) | C(1)–S(1)–Pt(1) | 104.8(4) |
| P(1)–Pt(1)–P(2) | 100.05(9) | C(1)–S(1)–Pt(2) | 99.8(3) |
| P(5)–Pt(3)–P(6) | 98.99(9) | C(8)–S(3)–Pt(3) | 106.3(3) |
| P(1)–Pt(1)–S(1) | 94.25(9) | C(8)–S(3)–Pt(4) | 98.1(3) |
| P(1)–Pt(1)–S(2) | 174.63(9) | $\theta$ [Pt(1)–S(1)–S(2)–Pt(2)] | 133 |
| P(2)–Pt(1)–S(1) | 165.66(9) | $\theta$ [Pt(3)–S(3)–S(4)–Pt(4)] | 138 |

| $[Pt_2(\mu\text{-}S\text{-}o\text{-}CH_2C_6H_4\text{-}C_6H_4CH_2S)(PPh_3)_4](PF_6)_2$ (**7**) | | | |
|---|---|---|---|
| Pt(1)–P(1) | 2.304(8) | Pt(1)–S(1A) | 2.357(7) |
| Pt(1)–P(2) | 2.306(8) | Pt(1A)–S(1) | 2.357(7) |
| Pt(1)–S(1) | 2.377(7) | S(1)–C(1) | 1.856(3) |
| | | | |
| Pt(1)–S(1)–Pt(1A) | 92.67(3) | P(2)–Pt(1)–S(1) | 173.22(3) |
| S(1)–Pt(1)–S(1A) | 81.92(3) | P(2)–Pt(1)–S(1A) | 93.71(3) |
| P(1)–Pt(1)–P(2) | 97.86(3) | C(1)–S(1)–Pt(1) | 113.90(12) |
| P(1)–Pt(1)–S(1) | 85.97(3) | C(1)–S(1)–Pt(1A) | 113.44(11) |
| P(1)–Pt(1)–S(1A) | 166.77(3) | $\theta$[a] | 147 |

[a] $\theta$ = Dihedral angle between the two $PtS_2$ planes.

 © 2007 Wiley-VCH Verlag GmbH & Co. KGaA, Weinheim 

pension of compound **1a** (30.5 mg, 0.020 mmol) in methanol (15 mL). The mixture was stirred for 3.5 h followed by the addition of another 30.6 mg (0.020 mmol) of **1a**. The resultant yellow suspension was left to stir overnight. The suspension was then filtered, followed by the addition of excess $NH_4PF_6$ (20.0 mg, 0.123 mmol). Deionized water (30 mL) was used to complete the precipitation. A yellow powder of **6d** (45.8 mg, 66%) was obtained by washing with deionized water (100 mL) and diethyl ether (100 mL) using vacuum suction filtration. $^{31}P\{^1H\}$ NMR ($CD_2Cl_2$): $\delta_P$ = 23.7–24.4 ppm (m, $^1J_{Pt,P(1)}$ = 3282, $^1J_{Pt,P(2)}$ = 2628 Hz). $^1H$ NMR ($CD_2Cl_2$): $\delta_H$ = 3.73 (br. s, 4 H, 2 $SCH_2$), 6.65–7.45 (m, 8 H, 2 $C_6H_4$), 6.65–7.45 ppm (m, 120 H, 24 $C_6H_5$). ESI-MS (MeOH/$H_2O$): *m*/*z* (%) = 1592 (100) $[M]^{2+}$. $C_{158}H_{132}F_{12}P_{10}Pt_4S_4$ (3477.03): calcd. C 54.58, H 3.83, S 3.69; found C 54.57, H 3.36, S 3.40.

**[$Pt_2$(μ-S-*o*-$CH_2C_6H_4$-$C_6H_4CH_2$S)($PPh_3$)$_4$]($PF_6$)$_2$ (7):** 2,2′-Bis(bromomethyl)-1,1′-biphenyl (32.3 mg, 0.095 mmol, 3 equiv.) and compound **1a** (48.7 mg, 0.032 mmol) in methanol (20 mL) gave a pale yellow solution in 15 min and was left to stir for 2 h. Excess $NH_4PF_6$ (20.0 mg, 0.123 mmol) was then added, resulting in an off-white suspension. Deionized water (40 mL) was used to complete the precipitation. A cream-colored powder of **7** (58.7 mg, 92%) was obtained by washing with deionized water (100 mL) and diethyl ether (100 mL) using vacuum suction filtration. $^{31}P\{^1H\}$ NMR ([D$_6$]DMSO): $\delta_P$ = 17.5 (m, $^1J_{Pt,P}$ = 2923, $^2J_{P,P}$ = 13 Hz), 22.9 ppm (m, $^1J_{Pt,P}$ = 3043, $^2J_{P,P}$ = 13 Hz). $^1H$ NMR ([D$_6$]DMSO): $\delta_H$ = 3.32 (s, 4 H, 2 $SCH_2$), 6.85–6.88 (d, *J* = 7.6 Hz, 2 H, $C_6H_4$-$C_6H_4$), 6.76–6.78 (d, *J* = 7.4 Hz, 2 H, $C_6H_4$-$C_6H_4$), 7.86 (t, *J* = 7.4 Hz, 2 H, $C_6H_4$-$C_6H_4$), 7.56 (t, *J* = 6.8 Hz, 2 H, $C_6H_4$-$C_6H_4$), 6.99 (br. s, 12 H, 12 $C_6H_5$), 7.15 (br. s, 24 H, 12 $C_6H_5$), 7.43 ppm (br. s, 24 H, 12 $C_6H_5$). ESI-MS (MeOH/$H_2O$): *m*/*z* (%) = 842 (100) $[M]^{2+}$, 1827 (10) $[[M]^{2+}[PF_6]^-]$. $C_{86}H_{74}F_{12}OP_6Pt_2S_2$ (1991.62): calcd. C 51.86, H 3.74, S 3.22; found C 51.85, H 3.49, S 3.59. Pale yellow crystals of [$Pt_2$(μ-S-*o*-$CH_2C_6H_4$-$C_6H_4CH_2$S)($PPh_3$)$_4$]($PF_6$)$_2$ suitable for X-ray crystallographic analysis were obtained from dichloromethane/ethanol (1:1).

**X-ray Crystal Structure Determination and Refinement**

Selected bond lengths and angles for complexes **6a**, **6b**, and **7** are given in Table 1. All measurements were made with a Bruker AXS SMART APEX diffractometer equipped with a CCD area detector by using Mo-$K_\alpha$ radiation ($\lambda$ = 0.71073 Å). The software SMART[14] was used for the collection of data frames, for indexing reflections, and to determine lattice parameters; SAINT[14] was used for the integration of the intensity of the reflections and for scaling; SADABS[15] was used for empirical absorption correction; and SHELXTL[16] was used for space group and structure determination, refinements, graphics, and structure reporting. The structure was refined by full-matrix least-squares on $F^2$ with anisotropic thermal parameters for non-hydrogen atoms. A summary of crystallographic parameters for the data collections and refinements is given in Table 2.

For **6a**, the asymmetrical unit contains half a titled cation, two halves of the $PF_6^-$ counteranion, one benzene, and one and a half dichloromethane molecules. The whole of the molecule can be generated by a twofold symmetry. One of the half $PF_6^-$ counteranions is at a special position and the other is disordered. The disordered $PF_6^-$ counteranion is refined only with isotropic thermal parameters. The half dichloromethane molecule is also disordered. For **6b**, the asymmetric unit contains one titled cation, two counter $PF_6^-$ counteranions, seven dichloromethane solvent molecules, and one disordered water molecule. One of the dichloromethane molecules is slightly disordered. The phenyl rings are refined as fixed hexagon rings with anisotropic thermal parameters. For **7**, the asymmetrical unit contains one half of the titled cation, two halves of $PF_6^-$, and two disordered dichloromethane molecules.

CCDC-646073 (for **6a**), -646074 (for **6b**), and -646075 (for **7**) contain the supplementary crystallographic data for this paper. These data can be obtained free of charge from The Cambridge Crystallographic Data Centre via www.ccdc.cam.ac.uk/data_request/cif.

Table 2. Crystallographic data for complexes **6a**, **6b**, and **7**.

| Complex | **6a**·3$CH_2Cl_2$·2$C_6H_6$ | **6b**·7$CH_2Cl_2$·$H_2O$ | **7**·4$CH_2Cl_2$ |
|---|---|---|---|
| Formula | $C_{167}H_{146}Cl_6F_{12}P_{10}Pt_4S_4$ | $C_{159}H_{144}Cl_{14}F_{12}O\ P_{10}Pt_4S_4$ | $C_{90}H_{80}Cl_8F_{12}\ P_6Pt_2S_2$ |
| *M* | 3811.84 | 4011.33 | 2313.26 |
| Crystal system | monoclinic | triclinic | monoclinic |
| Space group | *P*2/*n* | $P\bar{1}$ | *C*2/*c* |
| *a* [Å] | 18.932(6) | 19.279(5) | 14.525(7) |
| *b* [Å] | 18.241(6) | 19.532(5) | 24.413(12) |
| *c* [Å] | 23.469(7) | 22.936(6) | 26.261(13) |
| *α* [°] | 90 | 98.30(6) | 90 |
| *β* [°] | 105.210(10) | 93.838(7) | 94.972(10) |
| *γ* [°] | 90 | 103.42(6) | 90 |
| *V* [Å$^3$] | 7820.7(4) | 8267(4) | 9277(8) |
| *Z* | 2 | 2 | 4 |
| $\rho_{calcd.}$ [g cm$^{-3}$] | 1.619 | 1.611 | 1.656 |
| $\mu$ [mm$^{-1}$] | 3.890 | 3.810 | 3.460 |
| Temperature [K] | 223(2) | 223(2) | 223(2) |
| Reflections measured | 54806 | 90694 | 32398 |
| Independent reflections | 17962 | 29107 | 10646 |
| $R_{int}$ | 0.0583 | 0.0988 | 0.0356 |
| Parameters | 927 | 1416 | 567 |
| $R$ ($F$, $F^2 > 2\sigma$) | 0.0466 | 0.0576 | 0.0290 |
| $R_w$ ($F^2$, all data) | 0.1149 | 0.1479 | 0.0725 |
| Goodness of fit $F^2$ | 0.993 | 1.009 | 1.033 |
| Max., min. electron density [e Å$^{-3}$] | 1.817, –1.345 | 1.518, –1.047 | 1.237, –1.028 |

 © 2007 Wiley-VCH Verlag GmbH & Co. KGaA, Weinheim 

## Acknowledgments

We acknowledge the National University of Singapore (NUS) for financial support and S. H. C. thanks NUS for a Kiang Ai Kim Graduate Research Scholarship. We are grateful to L. L. Koh and G. K. Tan for assistance in the X-ray single-crystal crystallographic data collection and analyses.

[1] a) S. W. A. Fong, T. S. A. Hor, *J. Chem. Soc. Dalton Trans.* **1999**, 639; b) Z. Li, S.-W. A. Fong, J. S. L. Yeo, W. Henderson, K. F. Mok, T. S. A. Hor in *Modern Coordination Chemistry: The Legacy of Joseph Chatt* (Eds.: G. J. Leigh, N. Winterton), Royal Society of Chemistry, Cambridge, **2002**, pp. 355; c) P. González-Duarte, A. Lledos, R. Mas-Balleste, *Eur. J. Inorg. Chem.* **2004**, 3585.

[2] a) S. H. Chong, D. J. Young, T. S. A. Hor, *J. Organomet. Chem.* **2006**, *691*, 349; b) J. S. L. Yeo, J. J. Vittal, T. S. A. Hor, *Eur. J. Inorg. Chem.* **2003**, 277.

[3] a) W. Henderson, S. H. Chong, T. S. A. Hor, *Inorg. Chim. Acta* **2006**, *359*, 3440; b) S. H. Chong, A. Tjindrawan, T. S. A. Hor, *J. Mol. Catal. A* **2003**, *204–205*, 267; c) S. H. Chong, L. L. Koh, W. Henderson, T. S. A. Hor, *Chem. Asian J.* **2006**, *1*, 264; d) A. Nova, P. González-Duarte, A. Lledós, R. Mas-Ballesté, G. Ujaque, *Inorg. Chim. Acta* **2006**, *359*, 3736.

[4] a) M. Zhou, C. F. Lam, K. F. Mok, P.-H. Leung, T. S. A. Hor, *J. Organomet. Chem.* **1994**, *476*, C32; b) R. Mas-Ballesté, M. Capdevila, P. A. Champkin, W. Clegg, R. A. Coxall, A. Lledós, C. Mégret, P. González-Duarte, *Inorg. Chem.* **2002**, *41*, 3218; c) R. R. Gukathasan, R. H. Morris, A. Walker, *Can. J. Chem.* **1983**, *61*, 2490; d) C. E. Briant, C. J. Gardner, T. S. A. Hor, N. D. Howells, D. M. P. Mingos, *J. Chem. Soc. Dalton Trans.* **1984**, 2645.

[5] a) J. Forniés, C. Fortuno, R. Gil, A. Martin, *Inorg. Chem.* **2005**, *44*, 9534; b) M. Ohashi, A. Yagyu, Q. Xu, K. Mashima, *Chem. Lett.* **2006**, *35*, 954; c) D. E. Janzen, K. N. Patel, D. G. VanDerveer, G. J. Grant, *Chem. Commun.* **2006**, *33*, 3540.

[6] a) C.-H. Tao, K. M.-C. Wong, N. Zhu, V. W.-W. Yam, *New J. Chem.* **2003**, *27*, 150; b) C.-H. Tao, N. Zhu, V. W.-W. Yam, *Chem. Eur. J.* **2005**, *11*, 1647.

[7] B. F. Ali, A. Nassar, M. Al-Refai, M. H. Zaghal, K. H. Al-Obaidi, *J. Coord. Chem.* **2006**, *59*, 873.

[8] a) R. Uson, J. Fornies, M. A. Uson, M. Tomas, M. A. Ibaiiez, *J. Chem. Soc. Dalton Trans.* **1994**, 401; b) A. Singhal, V. K. Jain, A. Klein, M. Niemeyer, W. Kaim, *Inorg. Chim. Acta* **2004**, *357*, 2134.

[9] a) S. P. Huangand, M. G. Kanatzidis, *J. Am. Chem. Soc.* **1992**, *114*, 5477; b) Z. Nomikov, B. Schubert, R. Hoffmann, M. L. Steigerwald, *Inorg. Chem.* **1992**, *31*, 2201; c) J. G. Brennan, T. Siegrists, S. M. Struczynski, M. L. Steigerwald, *J. Am. Chem. Soc.* **1990**, *112*, 9233; d) S. Dey, V. K. Jain, J. Singh, V. Trehan, K. K. Bhasin, B. Varghese, *Eur. J. Inorg. Chem.* **2003**, 744; e) S. Dey, V. K. Jain, S. Chaudhury, A. Knoedler, F. Lissner, W. Kaim, *J. Chem. Soc. Dalton Trans.* **2001**, 723.

[10] a) D. Gibson, S. J. Lippard, *Inorg. Chem.* **1986**, *25*, 219; b) P. P. Power, S. C. Shoner, *Angew. Chem. Int. Ed. Engl.* **1991**, *30*, 330; c) B. Oskui, M. Mintert, W. S. Sheldrick, *Inorg. Chim. Acta* **1999**, *287*, 72; d) N. J. Wheate, C. Cullinane, L. K. Webster, J. G. Collins, *Anti-Cancer Drug Des.* **2001**, *16*, 91.

[11] a) N. Farrell, *Comments Inorg. Chem.* **1995**, *16*, 373; b) C. Manzotti, G. Pratesi, E. Menta, R. Di Domenico, E. Cavalletti, H. H. Fiebig, L. R. Kelland, N. Farrell, D. Polizzi, R. Supino, G. Pezzoni, F. Zunino, *Clin. Cancer Res.* **2000**, *6*, 2626; c) N. J. Wheate, J. G. Collins, *Coord. Chem. Rev.* **2003**, *241*, 133; d) S. L. Woodhouse, L. M. Rendina, *Dalton Trans.* **2004**, *21*, 3669; e) N. J. Wheate, A. I. Day, R. J. Blanch, A. P. Arnold, *Chem. Commun.* **2004**, *12*, 1424; f) N. J. Wheate, D. P. Buck, A. I. Day, J. G. Grant, *Dalton Trans.* **2006**, *3*, 451.

[12] R. Mas-Ballesté, G. Aullón, P. A. Champkin, W. Clegg, C. Mégret, P. González-Duarte, A. Lledós, *Chem. Eur. J.* **2003**, *9*, 5023.

[13] S. H. Chong, W. Henderson, T. S. A. Hor, manuscript submitted.

[14] *SMART & SAINT Software Reference Manuals*, version 4.0, Siemens Energy & Automation, Inc., Analytical Instrumentation, Madison, WI, USA, **1996**.

[15] G. M. Sheldrick, *SADABS*, a software for empirical adsorption correction, University of Göttingen, Göttingen, Germany, **1993**.

[16] G. M. Sheldrick, *SHELXTL*, VERSION 5.03, Siemens Energy & Automation, Inc., Analytical Instrumentation, Madison, WI, USA, **1996**.

Received: June 14, 2007
Published Online: September 7, 2007

 © 2007 Wiley-VCH Verlag GmbH & Co. KGaA, Weinheim 

DOI: 10.1002/ejic.200700666

# Azolium Salts Functionalized with Cyanomethyl, Vinyl, or Propargyl Substituents and Dicyanamide, Dinitramide, Perchlorate and Nitrate Anions

Ye Gao,[a] Haixiang Gao,[b] Crystal Piekarski,[a] and Jean'ne M. Shreeve*[a]

**Keywords:** Energetic salts / Density / Heat of formation / Thermal stability

A series of functionalized imidazolium and 1,2,4-triazolium salts with cyanomethyl, vinyl and propargyl substituents coupled with energetic anions, viz., perchlorate, nitrate, dicyanamide and dinitramide were prepared and characterized by NMR and IR spectroscopy, and elemental analyses. Since some melt < 100 °C, they can be classed as ionic liquids. Their densities range between 1.25–1.76 g cm$^{-3}$. The standard enthalpies of formation of the salts were calculated by using the computationally feasible DFT(B3LYP) and MP2 methods in conjunction with an empirical approach based on calculated densities of the salts. These values range from $\Delta H°_f$ = –56 (**12a**) to 851 (**21c**) kJ mol$^{-1}$. Of the salts synthesized, the dicyanamides exhibit the highest positive heats of formation, but also the lowest densities.
(© Wiley-VCH Verlag GmbH & Co. KGaA, 69451 Weinheim, Germany, 2007)

## Introduction

Ionic liquids have been extensively studied, e.g., as novel solvents,[1] in separation processes,[2] in electrochemistry,[3] and as lubricants.[4] The introduction of functional groups into the azolium cation modifies the properties of the salt which enables the enhancement of certain characteristics which may be tailored to particular applications.[1g–1i]

Syntheses of energetic materials continue to attract considerable interest. Salt-based energetic materials often possess some advantage over molecular compounds since they tend to have lower vapor pressures and higher densities.[5–7] Many new members of heterocyclic-based energetic, low-melting salt families have been reported. Theoretical calculations of enthalpies of formation of salts, based on the heats of formation of cation, anion, and lattice energy, show that when $\Delta H_f$ for analogous species with various functional groups are determined, the values decrease CN > $NO_2$ > $NH_2$ > H.[8a–8d] Initially, this appears to suggest that introduction of the nitrile moiety would give rise to the most energetic species, i.e., a compound with the highest detonation pressure and velocity. However, nearly invariably and not surprisingly, the density of the nitrile is less than that of the nitro or amino-substituted salt and thus detonation properties are diminished given that the detonation pressure is dependent on the square of the density and detonation velocity is proportional to the density. Calculations show that $\Delta H°_f$ for the vinyl group is also slightly higher than that of hydrogen; $\Delta H°_f$ for ethylene is 52.4 kJ mol$^{-1}$; and $\Delta H°_f$ for acetylene is 226.7 kJ mol$^{-1}$.[8d] Therefore, $\Delta H°_f$ for propargyl is expected to be higher than vinyl.

This paper describes the synthesis and characterization of a series of azolium salts with cyanomethyl-, vinyl- and propargyl-substituted imidazolium and 1,2,4-triazolium cations coupled with energetic inorganic anions – nitrate, perchlorate, dicyanamide and dinitramide. Their thermal properties were determined and the standard enthalpies of formation calculated.

## Results and Discussion

1-Substituted 1,2,4-triazoles, **1**, **2**, and **19**, were obtained by reacting sodium triazolate with methyl iodide, chloroacetonitrile and propargyl bromide. The remaining starting materials, 4-amino triazole, 1-vinyl imidazole, 1-methyl imidazole, 1-methyl triazole are commercially available. Compounds **3**, **4**, **7**, **9**, **10**, **11**, **15**, **16**, and **20** were obtained via quaternization reactions between the azole and the corresponding halide. These were then metathesized with silver nitrate, silver perchlorate, silver dicyanamide[9] or silver dinitramide[10] to give salts **5**, **6**, **8**, **12**, **13**, **14**, **17**, **18**, or **21** (Scheme 1).

Phase-transition temperatures (midpoints of melting points, $T_m$, or glass transition temperature, $T_g$) for all the salts were determined using differential scanning calorimetry (DSC) (Table 1). Most of the phase-transition temperatures are lower than 100 °C, and some of the salts are room temperature ionic liquids. With a common cation, phase-transition temperatures recorded for perchlorates > nitrates (with the exception of **8** and **12**) > dicyanamides > dinitra-

[a] Department of Chemistry, University of Idaho
Moscow, Idaho 83844-2343, USA
Fax: +1-208-885-9146
E-mail: jshreeve@uidaho.edu
[b] Department of Applied Chemistry, China Agricultural University
Beijing 100094, China

 © 2007 Wiley-VCH Verlag GmbH & Co. KGaA, Weinheim 

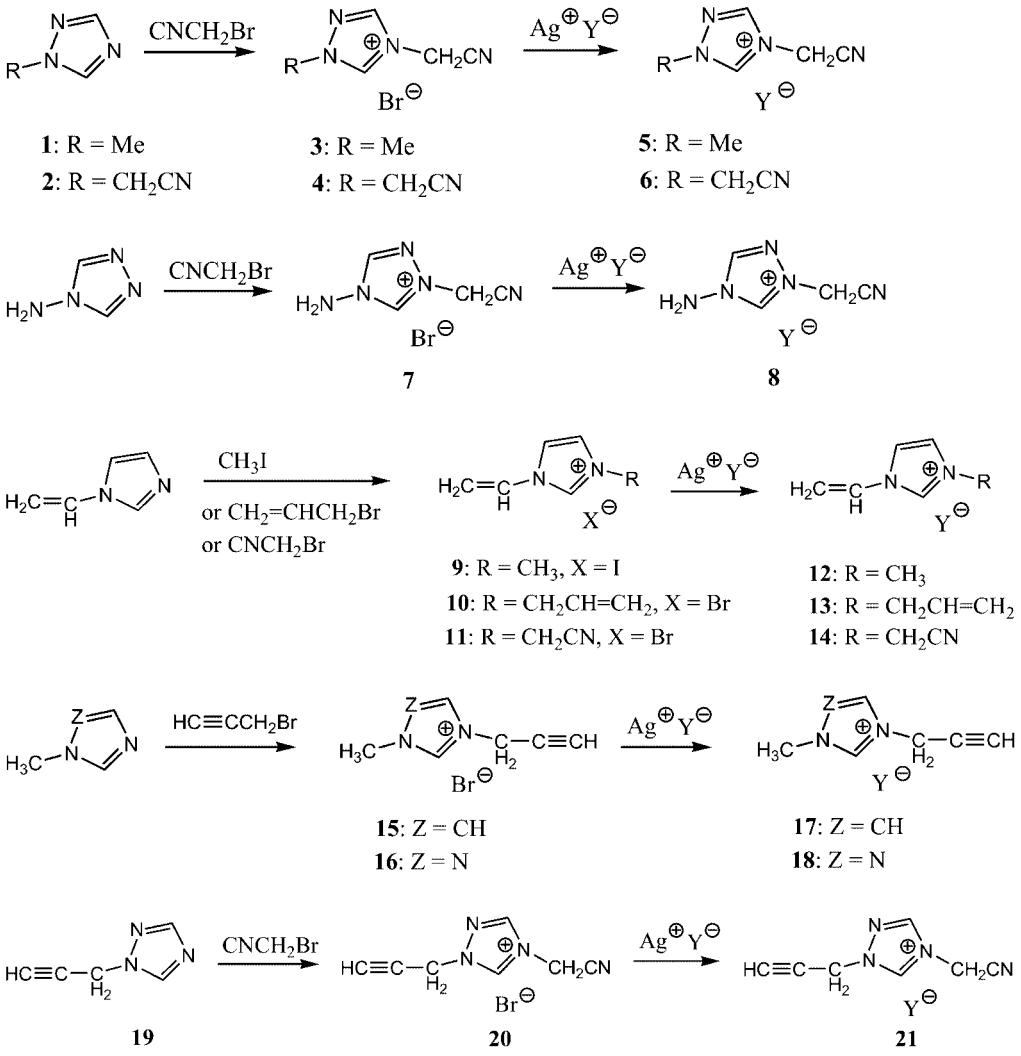


Scheme 1.

mides (with the exception of **8** and **17**). Invariably the perchlorate salts are the most thermally stable, sometimes by > 100 °C and with thermal decomposition temperatures ≥ 200 °C. Comparing compounds **5**, **6**, and **8** that have common anions, the melting points or phase transition points ($T_m$/$T_g$) of the triazolium salts substituted with two cyanomethyl ($CNCH_2$-) groups were highest (**6a**–**d**). When the substituents were one $CNCH_2$– group and 1-methyl (**5a**–**d**) or 4-amino (**8a**–**d**), the $T_m$/$T_g$ decreased, and the latter two sets were similar (except **8b**). For vinyl imidazolium salts, **14a**–**d** with a $CNCH_2$– substituent exhibit the highest $T_m$/$T_g$ followed by the salts with a methyl group (**12a**, **d**), and finally the allyl-substituted salts (except **12b**). Similar relationships were observed for propargyl-substituted salts **18** and **21**.

When comparing densities, it is seen that the 1-methylcyano-4-aminotriazolium salts (**8a**–**d**) exhibit the highest values, from perchlorate (1.76 g cm$^{-3}$) to dicyanamide (1.43 g cm$^{-3}$).[11–13] Not surprisingly, the presence of the amino-substituted cation with its enhanced proclivity to form hydrogen bonds gives rise to higher density followed by $CNCH_2^- > CH_3$. Similar ordering is observed in moving from **14a**–**d** > **12a**,**b**,**d** > **13a**–**d** as the cation substituent changes from $CNCH_2^-$ to $CH_3$ to allyl. Densities of **21a**–**c** exceed those of **18a**–**d** due to the presence of the dicyanomethyl vis-à-vis methyl. The densities of **18a**–**d** > **17a**–**d** because, in general, the densities of triazolium salts are higher than imidazolium. Regardless of the cation, with few exceptions, the density order is $ClO_4^- > N(NO_2)_2^- > NO_3^- > N(CN)_2^-$.

One of the purposes of this work is to compare the energetic properties of salts that contain the dicyanamide anion with their dinitramide analogues. As predicted,[8] the calculated heats of formation for the dicyanamide salts are invariably more positive than those of the analogous dinitramide salts, and, in fact, the dicyanamides have values higher than any of their counterparts in this study followed by dinitramides > perchlorates > nitrates in each of the cation

 © 2007 Wiley-VCH Verlag GmbH & Co. KGaA, Weinheim 

Table 1. Properties of azolium salts.

| Cation | Anion | | $T_m$ /°C | $T_d$[a] /°C | $D$[b] /g·cm$^{-3}$ | ? $H_f$[298][c] /kJ·mol$^{-1}$ |
|---|---|---|---|---|---|---|
| 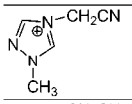 | $NO_3^-$ | **5a** | 115 | 152 | 1.51 | 167 |
| | $ClO_4^-$ | **5b** | 140 | 250 | 1.65 | 209 |
| | $N(CN)_2^-$ | **5c** | 66 | 115 | 1.35 | 605 |
| | $N(NO_2)_2^-$ | **5d** | –45[d] | 143 | 1.55 | 336 |
| 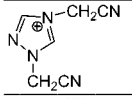 | $NO_3^-$ | **6a** | 133 | 135 | 1.53 | 359 |
| | $ClO_4^-$ | **6b** | 147 | 220 | 1.66 | 400 |
| | $N(CN)_2^-$ | **6c** | 114 | 114 | 1.39 | 796 |
| | $N(NO_2)_2^-$ | **6d** | –22[d] | 141 | 1.57 | 526 |
| 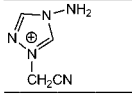 | $NO_3^-$ | **8a** | 93 | 158 | 1.61 | 267 |
| | $ClO_4^-$ | **8b** | –23[d] | 193 | 1.76 | 310 |
| | $N(CN)_2^-$ | **8c** | 66 | 105 | 1.43 | 707 |
| | $N(NO_2)_2^-$ | **8d** | –41[d] | 180 | 1.64 | 438 |
| 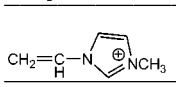 | $NO_3^-$ | **12a** | 70 | 155 | 1.41 | –56 |
| | $ClO_4^-$ | **12b** | –63[d] | 207 | 1.57 | –14 |
| | $N(NO_2)_2^-$ | **12d** | 50 | 145 | 1.47 | 113 |
| 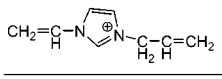 | $NO_3^-$ | **13a** | 17 | 85 | 1.39 | 26 |
| | $ClO_4^-$ | **13b** | 70 | 225 | 1.53 | 66 |
| | $N(CN)_2^-$ | **13c** | 2[d] | 168 | 1.27 | 462 |
| | $N(NO_2)_2^-$ | **13d** | – | 127 | 1.45 | 191 |
| 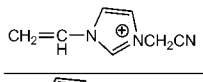 | $NO_3^-$ | **14a** | 83 | 161 | 1.44 | 156 |
| | $ClO_4^-$ | **14b** | 130 | 225 | 1.58 | 197 |
| | $N(CN)_2^-$ | **14c** | 73 | 155 | 1.31 | 593 |
| | $N(NO_2)_2^-$ | **14d** | 70 | 153 | 1.50 | 323 |
| 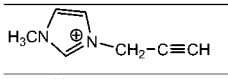 | $NO_3^-$ | **17a** | 63 | 180 | 1.38 | 104 |
| | $ClO_4^-$ | **17b** | 74 | 221 | 1.52 | 144 |
| | $N(CN)_2^-$ | **17c** | 17 | 131 | 1.25 | 540 |
| 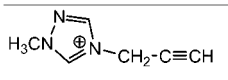 | $NO_3$ | **18a** | 74 | 176 | 1.42 | 205 |
| | $ClO_4^-$ | **18b** | 98 | 236 | 1.57 | 246 |
| | $N(CN)_2^-$ | **18c** | –54[d] | 119 | 1.28 | 642 |
| | $N(NO_3)_2$ | **18d** | –59[d] | 121 | 1.48 | 372 |
| 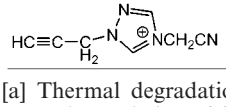 | $NO_3^-$ | **21a** | 112 | 134 | 1.45 | 415 |
| | $ClO_4^-$ | **21b** | 125 | 139 | 1.59 | 455 |
| | $N(CN)_2$ | **21c** | –23[d] | 101 | 1.32 | 851 |
| | $N(NO_2)_2^-$ | **21d** | –31[d] | 136 | 1.50 | 581 |

[a] Thermal degradation. [b] Calculated density, references.[11–13] [c] Molar enthalpy of formation, calcd. [d] $T_g$.

families. As is usually the case, the nitrate salts have the lowest heats of formation.

However, the performance of energetic materials is measured by detonation pressure and detonation velocity where the former is dependent on the square of the density and the latter is proportional to the density.[14] Some of these values (based on the traditional Chapman–Jouget thermodynamic detonation theory) were obtained by using CHEETAH 4.0 (Table 2).[15]

As is shown in Table 1, the dicyanamide salts exhibit the lowest densities of the anion salts studied. The importance of density in performance is easily seen since in every case, while the dinitramide is more dense and exhibits a lower heat of formation than its dicyanamide counterpart, it displays an appreciably higher detonation pressure and velocity. It should be noted that **5d**, **6d**, **8d**, **18d**, and **21d** have performance characteristics resembling those of TNT. None of the dicyanamides approaches this value.

Comparing the heats of formation of **5**, **6**, and **8**, it can be seen that the $CNCH_2$– group contributes most, greater than $NH_2$ with the $CH_3$ substituent contributing least. From **12**–**14**, the order of the heats of formation is **14** > **13** > **12**, once again indicating that the $CNCH_2$-substituent contributes most, greater than allyl with $CH_3$– last. Based on **17**, **18**, and **21**, the results further indicate that the 1,2,4-triazolium cation contributes more positively to the heat of formation of a salt than imidazolium does, and again the $CNCH_2$– group is a stronger contributor than methyl.

Table 2. Comparison of detonation pressures and velocities for dicyanamide and dinitramide salts with common cations.[a]

| Compd. | Anion | Detonation pressure[b] | Detonation velocity[c] |
|---|---|---|---|
| **5c** | $N(CN)_2^-$ | 11.60 | 6.21 |
| **5d** | $N(NO)_2^-$ | 21.53 | 7.51 |
| **6c** | $N(CN)_2^-$ | 11.64 | 6.21 |
| **6d** | $N(NO)_2^-$ | 21.38 | 7.44 |
| **8c** | $N(CN)_2^-$ | 14.83 | 6.88 |
| **8d** | $N(NO)_2^-$ | 24.82 | 7.85 |
| **14c** | $N(CN)_2^-$ | 9.27 | 5.65 |
| **14d** | $N(NO)_2^-$ | 17.28 | 6.97 |
| **18c** | $N(CN)_2^-$ | 10.05 | 5.89 |
| **18d** | $N(NO)_2^-$ | 18.72 | 7.16 |
| **21c** | $N(CN)_2^-$ | 10.16 | 5.90 |
| **21d** | $N(NO)_2^-$ | 18.87 | 7.13 |

[a] TNT: 19.53 GPa, 6.88 m/s. [b] Detonation pressure, GPa. [c] Detonation velocity, m/s.

## Thermochemistry

Computations were performed with the Gaussian 03 (Revision D.01) suite of programs.[16] The geometric optimization of the structures based on single-crystal structures, where available, and frequency analyses are carried out by using B3LYP functional with 6-31+G** basis set,[17] and single energy points were calculated at the MP2(full)/6-311++G** level.[18,19] All of the optimized structures were characterized to be true local energy minima on the potential energy surface without imaginary frequencies. Based on Born–Haber energy cycles, the heats of formation of an ionic salt can be simplified by the formula:

$$\Delta H_f^\circ \text{ (ionic salt, 298 K)} = \Delta H_f^\circ \text{ (cation, 298 K)} + \Delta H_f^\circ \text{ (anion, 298 K)} - \Delta H_L$$

where $\Delta H_L$ is the lattice energy of the ionic salt which can be predicted by the formula suggested by Jenkins[20] as:

$$\Delta H_L = U_{POT} + [p(n_M/2 - 2) + q(n_X/2 - 2)]RT$$

where $n_M$ and $n_X$ depend on the nature of the ions $M_p^+$ and $Xq^-$, respectively, and are equal to 3 for monatomic ions, 5 for linear polyatomic ions, and 6 for nonlinear polyatomic ions. The equation for lattice potential energy $U_{POT}$ has the form

$$U_{POT}/\text{kJ mol}^{-1} = \gamma\,(\rho_m/M_m)^{1/3} + \delta$$

where $\rho_m$ [g/cm$^3$] density, $M_m$ [g] is the chemical formula mass of the ionic material, and the coefficients $\gamma$ [kJ/mol cm] and $\delta$ [kJ/mol] take the values from the literature.[20]

For $NO_3^-$, $ClO_4^-$, and $N(NO_2)_2^-$, the proton affinities (PA) were taken from literature results calculated by using the G2 or G3 method.[21] For $N(CN)_2^-$, the PA was calculated by using G2. The heats of formation of $NO_3^-$, $ClO_4^-$, $N(NO_2)_2^-$, and $N(CN)_2^-$ were calculated to be –308, –278, –162, and 113 kJ mol$^{-1}$, respectively. Thus with a common

 © 2007 Wiley-VCH Verlag GmbH & Co. KGaA, Weinheim 

cation, the heats of formation of these salts (positive to negative) is $N(CN)_2^- > N(NO_2)_2^- > ClO_4^- > NO_3^-$.

## Conclusions

A series of imidazolium and 1,2,4-triazolium salts functionalized with vinyl, propargyl and cyanomethyl substituents and paired with nitrate, perchlorate, dicyanoamide, and dinitroamide anions have been prepared and characterized. Some of them melt at less than 100 °C and can be classified as ionic liquids. The densities of these salts range between 1.25–1.76 g cm$^{-3}$ with those of the dicyanamides being the lowest. The heats of formation for these salts which were calculated with the Gaussian 03 (Revision D.01) suite of programs indicate that the dicyanamides have the highest values. However, they unfortunately show the least promise for useful applications since they have the lowest energetic performance characteristics which are primarily a function of density.

## Experimental Section

***Caution:*** While we have experienced no difficulties with shock and friction sensitivity of these compounds that have high nitrogen content and rather high heats of formation, they must be synthesized in mmol amounts and handled with extreme care.

**General Methods:** $^1$H and $^{13}$C NMR spectra were recorded on a 300 MHz (Bruker AMX 300) spectrometer operating at 300.1 and 75.5 MHz, respectively. Chemical shifts are reported in parts per million relative to the appropriate standard ($Me_4Si$ for $^1$H and $^{13}$C NMR spectra). Phase-transition temperatures and decomposition temperatures were determined by using a differential scanning calorimeter (DSC, TA Instruments TA10) at a scan rate of 10 °C min$^{-1}$. IR spectra (BioRad FTS 3000 Excalibur series infrared spectrometer) were measured by using KBr pellets. Elemental analyses were carried out by using a CE-440 elemental analyzer (EAI Exeter Analytical). In some cases the experimental values for nitrogen are lower than the required values. This is sometimes observed for compounds with large amounts of nitrogen.

1-Substituted 1,2,4-triazoles, **1**, **2** and **19**, were obtained by reacting sodium triazolate with methyl iodide, chloroacetonitrile and propargyl bromide. The remaining starting materials, 4-aminotriazole, 1-vinylimidazole, 1-methylimidazole, 1-methyltriazole are commercially available. Compounds **3**, **4**, **7**, **9**, **10**, **11**, **15**, **16**, and **20** were obtained via quaternization reactions between the azole and the corresponding halide. These were then metathesized with silver nitrate, silver perchlorate, silver dicyanamide[9] or silver dinitramide[10] to give salts **5**, **6**, **8**, **12**, **13**, **14**, **17**, **18**, or **21**.

Sodium hydride (25 mmol, 1.00 g, 60% yield) in dry THF (40 mL) was added to a two-necked round-bottomed flask (100 mL) maintained under $N_2$ and containing a magnetic stir bar. 1,2,4-Triazole (25 mmol, 1.70 g) in THF (5 mL) was then added slowly to the stirring solution and the mixture was refluxed for 12 h and then cooled to room temp. Chloroacetonitrile (40 mmol, 3.12 g) was added and the mixture was refluxed for 12 h. Then the mixture was cooled to room temp. filtered. The filtrate was concentrated under vacuum then isolated by chromatography (silica gel column), eluted by hexane/ethyl acetate (80:20). The light brown solid **2** was obtained (1.9 g, 70% yield), $T_m$ = 60 °C.

Sodium 1,2,4-triazolate (25 mmol) was prepared as above. Propargyl bromide (40 mmol, 4.72 g) was added and the mixture was refluxed for 12 h. Workup was similar to above. A light brown liquid **19** (1.6 g, 60% yield), $^1$H NMR ($CHCl_3$): $\delta$ = 2.60 (t, $J$ = 2.6 Hz, 1 H), 5.40 (d, $J$ = 2.6 Hz, 2 H), 7.97 (s, 1 H), 8.30 (s, 1 H) ppm. $^{13}$C NMR ($CHCl_3$): $\delta$ = 153.2, 143.6, 76.7, 75.8, 40.3 ppm.

A typical preparation of an iodide salt was to dissolve **1** (10 mmol, 0.83 g) and methyl iodide (20 mmol, 2.8 g) in ethyl acetate (5 mL) in a Pyrex glass tube (20 mL) that was subsequently evacuated, sealed, and stirred at 60 °C for 24 h. The precipitate was washed with ethyl acetate (3 × 5 mL) and dried under vacuum for 24 h to give the colorless solid 3-cyanomethyl-1-methyl-1,2,4-triazolium iodide (**3**) (1.8 g, 80% yield), $T_m$ = 168 °C. IR (KBr): $\tilde{\nu}$ = 3062, 2953, 2906, 1580, 1402, 1227, 1163, 1070 cm$^{-1}$. $^1$H NMR ($D_2O/H_2O$): $\delta$ = 4.22 (s, 3 H), 5.67 (s, 2 H), 9.10 (s, 1 H), 10.10 (s, 1 H) ppm. $^{13}$C NMR ($D_2O/H_2O$): $\delta$ = 145.7, 144.4, 114.2, 40.5, 37.1 ppm. $C_5H_7BrN_4$ (203.04): calcd. C 29.58, H 3.47, N 27.59; found C 29.53, H 3.33, N 26.80.

**1,4-Bis(cyanomethyl)-1,2,4-triazolium Bromide (4):** 1.6 g, 70% yield, grey solid; $T_m$ = 184 °C. IR (KBr): $\tilde{\nu}$ = 3113, 2965, 2918, 1788, 1570, 1537, 1421, 1382, 1342, 1231, 1155, 1035, 1003 cm$^{-1}$. $^1$H NMR ($H_2O/D_2O$): $\delta$ = 5.78 (s, 2 H), 5.89 (s, 2 H), 9.33 (s, 1 H), 10.50 (s, 1 H) ppm. $^{13}$C NMR ($H_2O/D_2O$): $\delta$ = 146.2, 145.6, 113.4, 113.1, 41.4, 37.1 ppm. $C_6H_6BrN_5$ (228.05): calcd. C 31.60, H 2.65, N 30.71; found C 31.54, H 2.54, N 30.84.

**1-Cyanomethyl-1,2,4-triazolium Bromide (7):** 1.8 g, 90% yield, colorless solid; $T_m$ = 102 °C. IR (KBr): $\tilde{\nu}$ = 3107, 2932, 2071, 1638, 1560, 1520, 1406, 1287, 1162, 1034, 998 cm$^{-1}$. $^1$H NMR ([D$_6$]-DMSO): $\delta$ = 5.92 (s, 2 H), 7.22 (s, 2 H), 9.35 (s, 1 H), 10.37 (s, 1 H) ppm. $^{13}$C NMR (DMSO): $\delta$ = 147.2, 145.3, 115.1, 41.7 ppm. $C_4H_6BrN_5$ (204.03): calcd. C 23.55, H 2.96, N 34.33; found C 23.45, H 2.86, N 34.43.

**3-Methyl-1-vinylimidazolium Iodide (9):**[22] 2.3 g, 96% yield, light yellow liquid, $T_m$ = 75 °C.

**3-Allyl-1-vinyl-imidazolium Bromide (10):** 1.8 g, 85% yield, orange solid, $T_m$ = 253 °C. IR (KBr): $\tilde{\nu}$ = 3124, 3065, 2994, 1651, 1549, 1423, 1370, 1308, 1172 cm$^{-1}$. $^1$H NMR ([D$_3$]acetonitrile): $\delta$ = 4.97 (d, $J$ = 6.2 Hz, 2 H), 5.33–5.49 (m, 3 H), 6.01 (dd, $J$ = 2.7, $J$ = 15.6 Hz, 1 H), 6.10 (tdd, $J$ = 6.2, $J$ = 10.3, $J$ = 17.0 Hz, 1 H), 7.39 (dd, $J$ = 8.7, $J$ = 15.6 Hz, 1 H), 7.67 (t, $J$ = 1.8 Hz, 1 H), 8.02 (t, $J$ = 1.8 Hz, 1 H), 10.06 (s, 1 H) ppm. $^{13}$C NMR ([D$_3$]acetonitrile): $\delta$ = 136.3, 131.5, 129.5, 123.7, 122.0, 120.6, 109.9, 52.4 ppm. $C_8H_{11}BrN_2$ (215.09): calcd. C 44.67, H 5.15, N 13.02; found C 44.40, H 5.03, N 12.34.

**3-Cyanomethyl-1-vinylimidazolium Bromide (11):** 1.5 g, 70% yield, colorless solid, $T_m$ = 148 °C. IR (KBr): $\tilde{\nu}$ = 3103, 3063, 3034, 2983, 1647, 1555, 1406, 1177 cm$^{-1}$. $^1$H NMR ($D_2O/H_2O$): $\delta$ = 5.53 (dd, $J$ = 3.0, $J$ = 8.7 Hz, 1 H), 5.55 (s, 2 H), 5.89 (dd, $J$ = 3.0, $J$ = 15.5 Hz, 1 H), 7.20 (dd, $J$ = 8.7, $J$ = 15.5 Hz, 1 H), 7.79 (t, $J$ = 1.8 Hz, 1 H), 7.91 (t, $J$ = 1.8 Hz, 1 H), 9.31 (s, 1 H) ppm. $^{13}$C NMR ($D_2O/H_2O$): $\delta$ = 136.6, 128.9, 124.1, 121.4, 114.5, 111.9, 38.3 ppm. $C_7H_8BrN_3$ (214.06): calcd. C 39.28, H 3.77, N 19.63; found C 39.19, H 3.68, N 19.31.

**1-Methyl-3-propargylimidazolium Bromide (15):** 1.8 g, 90% yield, colorless solid, $T_m$ = 68 °C. IR (KBr): $\tilde{\nu}$ = 3196, 3086, 2126, 1627, 1570, 1437, 1342, 1164 cm$^{-1}$. $^1$H NMR ([D$_3$]acetonitrile): $\delta$ = 3.23 (t, $J$ = 2.6 Hz, 1 H), 3.95 (s, 3 H), 5.33 (d, $J$ = 2.6 Hz, 2 H), 7.63 (s, $J$ = 1.8 Hz, 1 H), 7.72 (s, $J$ = 1.8 Hz, 1 H), 9.54 (s, 1 H) ppm. $^{13}$C NMR ([D$_3$]acetonitrile): $\delta$ = 137.6, 124.9, 122.9, 78.4, 75.9, 40.0, 37.1 ppm. $C_7H_9BrN_2$ (201.06): calcd. C 41.82, H 4.51, N 13.93; found C 41.31, H 4.50, N 13.42.

 © 2007 Wiley-VCH Verlag GmbH & Co. KGaA, Weinheim 

**1-Methyl-4-propargyl-1,2,4-triazolium Bromide (16):** 1.4 g, 70% yield, colorless solid, $T_m$ = 201 °C. IR (KBr): $\tilde{\nu}$ = 3223, 3011, 2939, 1566, 1425, 1356, 1230, 1199, 1153 cm$^{-1}$. $^1$H NMR ($D_2O/H_2O$): $\delta$ = 3.20 (t, $J$ = 2.6 Hz, 1 H), 4.18 (s, 3 H), 5.25 (d, $J$ = 2.6 Hz, 2 H), 8.99 (s, 1 H), 9.95 (s, 1 H) ppm. $^{13}$C NMR ($D_2O/H_2O$): $\delta$ = 145.0, 143.4, 79.4, 74.5, 39.9, 39.1 ppm. $C_6H_8BrN_3$ (202.05): calcd. C 35.67, H 3.99, N 20.80; found C 35.83, H 3.86, N 20.19.

**4-Cyanomethyl-1-propargyl-1,2,4-triazolium Bromide (20):** 1.4 g, 62% yield, light brown solid, $T_m$ = 179 °C. IR (KBr): $\tilde{\nu}$ = 3123, 2965, 2117, 1570, 1412, 1379, 1341, 1231, 1152, 1069 cm$^{-1}$. $^1$H NMR ($D_2O/H_2O$): $\delta$ = 3.23 (t, $J$ = 2.6 Hz, 1 H), 5.40 (d, $J$ = 2.6 Hz, 2 H), 5.69 (s, 2 H), 9.18 (s, 1 H), 10.36 (s, 1 H) ppm. $^{13}$C NMR ($D_2O/H_2O$): $\delta$ = 146.0, 144.3, 113.8, 80.0, 73.7, 43.9, 36.9 ppm. $C_7H_7BrN_4$ (227.06): calcd. C 37.03, H 3.11, N 24.67; found C 37.38, H 3.04, N 24.44.

All metathesis reactions were carried out by using halide salts (1 mmol) reacted with silver nitrate or silver perchlorate or silver dicyanoamide or silver dinitroamide (1 mmol) in water (10 mL) in a test tube (100 mL). The mixture was filtered, the water pumped off, and the remaining residue dried under vacuum at 40 °C for 24 h. The yields were essentially quantitative.

**4-Cyanomethyl-1-methyl-1,2,4-triazolium Nitrate (5a):** Colorless solid, $T_m$ = 115 °C. IR (KBr): $\tilde{\nu}$ = 3059, 2952, 2395, 1761, 1580, 1380, 1163 cm$^{-1}$. $^1$H NMR ($D_2O/H_2O$): $\delta$ = 4.21 (s, 3 H), 5.66 (s, 2 H), 9.09 (s, 1 H), 10.08 (s, 1 H) ppm. $^{13}$C NMR ($D_2O/H_2O$): $\delta$ = 145.7, 144.4, 114.2, 40.4, 36.9 ppm. $C_5H_7N_5O_3$ (185.14): calcd. C 32.44, H 3.81, N 37.83; found C 32.46, H 3.67, N 38.01.

**4-Cyanomethyl-1-methyl-1,2,4-triazolium Perchlorate (5b):** Colorless solid, $T_m$ = 140 °C. IR (KBr): $\tilde{\nu}$ = 3059, 2951, 2904, 1578, 1466, 1363, 1072 cm$^{-1}$. $^1$H NMR ([D$_6$]acetone): $\delta$ = 4.12 (s, 3 H), 5.40 (s, 2 H), 8.81 (s, 1 H), 9.59 (s, 1 H) ppm. $^{13}$C NMR ([D$_6$]-acetone): $\delta$ = 145.2, 144.0, 113.7, 40.5, 37.0 ppm. $C_5H_7ClN_4O_4$ (222.59): calcd. C 26.98, H 3.17, N 25.17; found C 27.09, H 3.14, N 24.49.

**4-Cyanomethyl-1-methyl-1,2,4-triazolium Dicyanamide (5c):** Colorless solid, $T_m$ = 66 °C. IR (KBr): $\tilde{\nu}$ = 3082, 3019, 2239, 2198, 2136, 1582, 1418, 1318, 1161, 1071 cm$^{-1}$. $^1$H NMR ([D$_6$]acetonitrile): $\delta$ = 4.12 (s, 3 H), 5.47 (s, 2 H), 8.89 (s, 1 H), 9.82 (s, 1 H) ppm. $^{13}$C NMR ([D$_6$]acetonitrile): $\delta$ = 145.3, 144.1, 120.7, 113.8, 40.4, 37.0 ppm. $C_7H_7N_7$ (189.18): calcd. C 44.44, H 3.73, N 51.83; found C 43.88, H 3.65, N 49.59.

**4-Cyanomethyl-1-methyl-1,2,4-triazolium Dinitramide (5d):** Colorless liquid, $T_g$ = –45 °C. IR (KBr): $\tilde{\nu}$ = 3091, 2997, 1584, 1518, 1434, 1182, 1013 cm$^{-1}$. $^1$H NMR ([D$_6$]acetonitrile): $\delta$ = 4.11 (s, 3 H), 5.44 (s, 2 H), 8.87 (s, 1 H), 9.75 (s, 1 H) ppm. $^{13}$C NMR ([D$_6$]-acetonitrile): $\delta$ = 145.2, 144.1, 113.7, 40.3, 36.8 ppm. $C_5H_7N_7O_4$ (229.15): calcd. C 26.21, H 3.08, N 42.79; found C 25.45, H 2.85, N 42.92.

**1,4-Bis(cyanomethyl)-1,2,4-triazolium Nitrate (6a):** Colorless solid, $T_m$ = 133 °C. IR (KBr): $\tilde{\nu}$ = 3101, 3003, 2957, 2378, 2264, 1755, 1574, 1355, 1073, 934 cm$^{-1}$. $^1$H NMR ($H_2O/D_2O$): $\delta$ = 5.70 (s, 2 H), 5.82 (s, 2 H), 9.25 (s, 1 H), 10.44 (s, 1 H) ppm. $^{13}$C NMR ($H_2O$/$D_2O$): $\delta$ = 146.1, 145.5, 113.3, 113.0, 41.1, 36.8 ppm. $C_6H_6N_6O_3$ (210.15): calcd. C 34.29, H 2.88, N 39.99; found C 34.46, H 2.70, N 39.83.

**1,4-Bis(cyanomethyl)-1,2,4-triazolium Perchlorate (6b):** Colorless solid, $T_m$ = 147 °C. IR (KBr): $\tilde{\nu}$ = 3116, 2925, 2364, 1572, 1419, 1386, 1068 cm$^{-1}$. $^1$H NMR ([D$_3$]acetone): $\delta$ = 5.93 (s, 2 H), 6.04 (s, 2 H), 9.51 (s, 1 H), 10.53 (s, 1 H) ppm. $^{13}$C NMR ([D$_3$]acetone): $\delta$ = 146.4, 146.3, 113.4, 112.9, 41.3, 37.2 ppm. $C_6H_6ClN_5O_4$ (247.61): calcd. C 29.11, H 2.44, N 28.29; found C 29.12, H 2.15, N 27.72.

**1,4-Bis(cyanomethyl)-1,2,4-triazolium Dicyanamide (6c):** Colorless solid, $T_m$ = 114 °C. IR (KBr): $\tilde{\nu}$ = 3121, 2991, 2245, 2201, 2139, 1576, 1318, 1161, 1069 cm$^{-1}$. $^1$H NMR ([D$_3$]acetonitrile): $\delta$ = 5.53 (s, 2 H), 5.64 (s, 2 H), 9.05 (s, 1 H), 10.09 (s, 1 H) ppm. $^{13}$C NMR ([D$_3$]acetonitrile): $\delta$ = 146.1, 145.5, 120.6, 113.4, 113.0, 41.5, 37.3 ppm. $C_8H_6N_8$ (214.19): calcd. C 44.86, H 2.82, N 52.32; found C 44.43, H 3.01, N 51.98.

**1,4-Bis(cyanomethyl)-1,2,4-triazolium Dinitramide (6d):** Colorless liquid, $T_g$ = –22 °C. IR (KBr): $\tilde{\nu}$ = 3135, 3080, 2997, 1578, 1518, 1433, 1337, 1179, 1015 cm$^{-1}$. $^1$H NMR ([D$_3$]acetonitrile): $\delta$ = 5.56 (s, 2 H), 5.66 (s, 2 H), 9.06 (s, 1 H), 10.11 (s, 1 H) ppm. $^{13}$C NMR ([D$_3$]acetonitrile): $\delta$ = 146.1, 145.7, 113.3, 112.9, 41.5, 37.2 ppm. $C_6H_6N_8O_4$ (254.16): calcd. C 28.35, H 2.38, N 44.09; found C 27.87, H 2.21, N 44.09.

**4-Amino-1-cyanomethyl-1,2,4-triazolium Nitrate (8a):** Colorless solid, $T_m$ = 93 °C. IR (KBr): $\tilde{\nu}$ = 3201, 3103, 2988, 1701, 1626, 1562, 1366, 1166, 1071 cm$^{-1}$. $^1$H NMR ([D$_3$]acetonitrile): $\delta$ = 5.61 (s, 2 H), 6.60 (s, 2 H), 8.81 (s, 1 H), 10.16 (s, 1 H) ppm. $^{13}$C NMR ([D$_3$]-acetonitrile): $\delta$ = 146.8, 145.6, 113.4, 41.3 ppm. $C_4H_6N_6O_3$ (186.13): calcd. C 25.81, H 3.25, N 45.15; found C 25.62, H 3.12, N 45.00.

**4-Amino-1-cyanomethyl-1,2,4-triazolium Perchlorate (8b):** Colorless liquid, $T_g$ = –23 °C. IR (KBr): $\tilde{\nu}$ = 3345, 3140, 2962, 2023, 1634, 1567, 1418, 1360, 1171, 1095 cm$^{-1}$. $^1$H NMR ([D$_3$]acetonitrile): $\delta$ = 5.49 (s, 2 H), 6.10 (s, 2 H), 8.76 (s, 1 H), 9.59 (s, 1 H) ppm. $^{13}$C NMR ([D$_3$]acetonitrile): $\delta$ = 147.2, 145.4, 113.4, 41.7 ppm. $C_4H_6ClN_5O_4$ (223.57): calcd. C 21.49, H 2.70, N 31.32; found C 21.47, H 2.66, N 31.49.

**4-Amino-1-cyanomethyl-1,2,4-triazolium Dicyanamide (8c):** Light yellow solid, $T_m$ = 66 °C. IR (KBr): $\tilde{\nu}$ = 3278, 2985, 2237, 2196, 2136, 1638, 1527, 1330, 1180, 1021 cm$^{-1}$. $^1$H NMR ([D$_3$]acetonitrile): $\delta$ = 5.55 (s, 2 H), 6.44 (s, 2 H), 8.80 (s, 1 H), 9.79 (s, 1 H) ppm. $^{13}$C NMR ([D$_3$]acetonitrile): $\delta$ = 146.9, 145.0, 121.1, 113.4, 41.6 ppm. $C_6H_6N_8$ (190.17): calcd. C 37.90, H 3.18, N 58.92; found C 37.76, H 3.09, N 58.49.

**4-Amino-1-cyanomethyl-1,2,4-triazolium Dinitramide (8d):** Colorless liquid, $T_g$ = –41 °C. IR (KBr): $\tilde{\nu}$ = 3322, 3134, 2998, 1632, 1518, 1433, 1336, 1181, 1017 cm$^{-1}$. $^1$H NMR ([D$_3$]acetonitrile): $\delta$ = 5.55 (s, 2 H), 6.32 (s, 2 H), 8.81 (s, 1 H), 9.79 (s, 1 H) ppm. $^{13}$C NMR ([D$_3$]acetonitrile): $\delta$ = 146.9, 145.2, 113.1, 41.3 ppm. $C_4H_6N_8O_4$ (230.14): calcd. C 20.88, H 2.63, N 48.69; found C 20.39, H 2.50, N 48.02.

**3-Methyl-1-vinylimidazolium Nitrate (12a):** Colorless solid, $T_m$ = 70 °C. IR (KBr): $\tilde{\nu}$ = 3144, 3097, 1655, 1581, 1553, 1346, 1176 cm$^{-1}$. $^1$H NMR ([D$_3$]acetonitrile): $\delta$ = 3.91 (s, 3 H), 5.29 (dd, $J$ = 2.6, $J$ = 8.7 Hz, 1 H), 5.82 (dd, $J$ = 2.6, $J$ = 15.6 Hz, 1 H), 7.19 (dd, $J$ = 8.7, $J$ = 15.6 Hz, 1 H), 7.64 (t, $J$ = 1.8 Hz, 1 H), 7.93 (t, $J$ = 1.8 Hz, 1 H), 9.41 (s, 1 H) ppm. $^{13}$C NMR ([D$_3$]acetonitrile): $\delta$ = 137.0, 129.5, 125.3, 120.1, 109.4, 36.8 ppm. $C_6H_9N_3O_3$ (171.15): calcd. C 42.11, H 5.30, N 24.55; found C 41.68, H 5.29, N 23.63.

**3-Methyl-1-vinylimidazolium Perchlorate (12b):** Light yellow liquid, $T_g$ = –63 °C. IR (KBr): $\tilde{\nu}$ = 3117, 3157, 1657, 1583, 1555, 1369, 1177, 1092 cm$^{-1}$. $^1$H NMR ([D$_3$]acetone): $\delta$ = 4.03 (s, 3 H), 5.46 (dd, $J$ = 2.7, $J$ = 8.7 Hz, 1 H), 5.97 (dd, $J$ = 2.7, $J$ = 15.6 Hz, 1 H), 7.32 (dd, $J$ = 8.7, $J$ = 15.6 Hz, 1 H), 7.75 (t, $J$ = 1.8 Hz, 1 H), 8.02 (t, $J$ = 1.8 Hz, 1 H), 9.22 (s, 1 H) ppm. $^{13}$C NMR ([D$_3$]acetone): $\delta$ = 136.7, 129.6, 125.5, 120.2, 109.8, 37.0 ppm. $C_6H_9ClN_2O_4$ (208.60): calcd. C 34.55, H 4.35, N 13.43; found C 3.92, H 4.34, N 13.36.

**3-Methyl-1-vinylimidazolium Dinitramide (12d):** Colorless solid, $T_m$ = 50 °C. IR (KBr): $\tilde{\nu}$ = 3154, 3097, 1659, 1518, 1434, 1227, 1190,

 © 2007 Wiley-VCH Verlag GmbH & Co. KGaA, Weinheim 

1011 cm$^{-1}$. $^1$H NMR ($D_2O/H_2O$): $\delta$ = 4.00 (s, 3 H), 5.47 (dd, $J$ = 2.7, $J$ = 8.7 Hz, 1 H), 5.84 (dd, $J$ = 2.7, $J$ = 15.7 Hz, 1 H), 7.20 (dd, $J$ = 8.7, $J$ = 15.7 Hz, 1 H), 7.58 (t, $J$ = 1.8 Hz, 1 H), 7.80 (t, $J$ = 1.8 Hz, 1 H), 9.02 (s, 1 H) ppm. $^{13}$C NMR ($D_2O/H_2O$): $\delta$ = 136.2, 129.3, 125.3, 120.4, 110.3, 37.2 ppm. $C_6H_9N_5O_4$ (215.17): calcd. C 33.49, H 4.22, N 32.55; found C 32.83, H 4.05, N 32.42.

**3-Allyl-1-vinylimidazolium Nitrate (13a):** Light yellow liquid, $T_g$ = –64 °C; $T_m$ = 17 °C. IR (KBr): $\tilde{\nu}$ = 3134, 3091, 1651, 1552, 1377, 1171 cm$^{-1}$. $^1$H NMR ([D$_3$]acetonitrile): $\delta$ = 4.88 (d, $J$ = 6.2 Hz, 2 H), 5.45–5.44 (m, 3 H), 5.90 (dd, $J$ = 2.6, $J$ = 15.6 Hz, 1 H), 6.05 (tdd, $J$ = 6.2, $J$ = 10.3, $J$ = 17.1 Hz, 1 H), 7.25 (dd, $J$ = 8.7, $J$ = 15.6 Hz, 1 H), 7.63 (t, $J$ = 1.8 Hz, 1 H), 7.94 (t, $J$ = 1.8 Hz, 1 H), 9.61 (s, 1 H) ppm. $^{13}$C NMR ([D$_3$]acetonitrile): $\delta$ = 136.7, 131.6, 129.6, 123.9, 121.8, 120.6, 109.7, 52.5 ppm. $C_8H_{11}N_3O_3$ (197.19): calcd. C 48.73, H 5.62, N 21.31; found C 48.32, H 5.53, N 21.18.

**3-Allyl-1-vinylimidazolium Perchlorate (13b):** Colorless solid, $T_m$ = 70 °C. IR (KBr): $\tilde{\nu}$ = 3142, 3099, 1652, 1578, 1549, 1425, 1368, 1169, 1096 cm$^{-1}$. $^1$H NMR ([D$_3$]acetone): $\delta$ = 5.02 (d, $J$ = 6.2 Hz, 2 H), 5.42–5.57 (m, 3 H), 6.01 (dd, $J$ = 2.5, $J$ = 15.6 Hz, 1 H), 6.17 (tdd, $J$ = 6.4, $J$ = 10.3, $J$ = 16.9 Hz, 1 H), 7.36 (dd, $J$ = 8.7, $J$ = 15.6 Hz, 1 H), 7.80 (t, $J$ = 1.8 Hz, 1 H), 8.10 (t, $J$ = 1.8 Hz, 1 H), 9.35 (s, 1 H) ppm. $^{13}$C NMR ([D$_3$]acetone): $\delta$ = 136.2, 131.6, 129.7, 124.2, 122.3, 120.6, 109.9, 52.8 ppm. $C_8H_{11}ClN_2O_4$ (234.64): calcd. C 40.95, H 4.73, N 11.92; found C 40.73, H 4.68, N 11.76.

**3-Allyl-1-vinylimidazolium Dicyanamide (13c):** Brown liquid, $T_g$, 2 °C. IR (KBr): $\tilde{\nu}$ = 3096, 3019, 2235, 2195, 2134, 1652, 1552, 1311, 1171 cm$^{-1}$. $^1$H NMR ([D$_3$]acetonitrile): $\delta$ = 4.84 (d, $J$ = 6.3 Hz, 2 H), 5.39–5.48 (m, 3 H), 5.86 (dd, $J$ = 2.6, $J$ = 15.6 Hz, 1 H), 6.06 (tdd, $J$ = 6.2, $J$ = 10.1, $J$ = 17.3 Hz, 1 H), 7.18 (dd, $J$ = 8.7, $J$ = 15.6 Hz, 1 H), 7.55 (t, $J$ = 1.8 Hz, 1 H), 7.82 (t, $J$ = 1.8 Hz, 1 H), 9.08 (s, 1 H) ppm. $^{13}$C NMR ([D$_3$]acetonitrile): $\delta$ = 135.8, 131.2, 129.4, 124.0, 122.4, 120.6, 118.4, 110.2, 52.7 ppm. $C_{10}H_{11}N_5$ (201.23): calcd. C 59.69, H 5.51, N 34.80; found C 59.24, H 5.45, N 34.73.

**3-Allyl-1-vinylimidazolium Dinitramide (13d):** No $T_g$. IR (KBr): $\tilde{\nu}$ = 3141, 3100, 1653, 1514, 1429, 1184, 1007 cm$^{-1}$. $^1$H NMR ([D$_3$]-acetonitrile): $\delta$ = 4.83 (d, $J$ = 6.2 Hz, 2 H), 5.40–5.45 (m, 3 H), 5.91 (dd, $J$ = 2.7, $J$ = 15.6 Hz, 1 H), 6.04 (tdd, $J$ = 6.3, $J$ = 10.1, $J$ = 17.3 Hz, 1 H), 7.17 (dd, $J$ = 8.7, $J$ = 15.6 Hz, 1 H), 7.52 (t, $J$ = 1.8 Hz, 1 H), 7.78 (t, $J$ = 1.8 Hz, 1 H), 8.98 (s, 1 H) ppm. $^{13}$C NMR ([D$_3$]acetonitrile): $\delta$ = 135.9, 131.3, 129.5, 124.1, 122.5, 120.7, 110.4, 52.9 ppm. $C_8H_{11}N_5O_4$ (241.20): calcd. C 39.84, H 4.60, N 29.03; found C 39.83, H 4.64, N 28.61.

**3-Cyanomethyl-1-vinylimidazolium Nitrate (14a):** Colorless solid, $T_m$ = 83 °C. IR (KBr): $\tilde{\nu}$ = 3109, 3032, 1647, 1561, 1371, 1177 cm$^{-1}$. $^1$H NMR ($D_2O/H_2O$): $\delta$ = 5.55 (dd, $J$ = 3.0, $J$ = 8.7 Hz, 1 H), 5.57 (s, 2 H), 5.90 (dd, $J$ = 3.0, $J$ = 15.6 Hz, 1 H), 7.22 (dd, $J$ = 8.7, $J$ = 15.6 Hz, 1 H), 7.81 (t, $J$ = 1.8 Hz, 1 H), 7.92 (t, $J$ = 1.8 Hz, 1 H), 9.32 (s, 1 H) ppm. $^{13}$C NMR ($D_2O/H_2O$): $\delta$ = 136.7, 128.9, 124.1, 121.4, 114.5, 111.8, 38.2 ppm. $C_7H_8N_4O_3$ (196.16): calcd. C 42.87, H 4.11, N 28.56; found C 43.05, H 3.94, N 28.37.

**3-Cyanomethyl-1-vinylimidazolium Perchlorate (14b):** Colorless solid, $T_m$ = 130 °C. IR (KBr): $\tilde{\nu}$ = 3154, 3098, 3063, 2983, 1652, 1555, 1406, 1368, 1177, 1104 cm$^{-1}$. $^1$H NMR ([D$_3$]acetone): $\delta$ = 5.57 (dd, $J$ = 3.1, $J$ = 8.7 Hz, 1 H), 5.77 (s, 2 H), 6.10 (dd, $J$ = 3.1, $J$ = 15.5 Hz, 1 H), 7.46 (dd, $J$ = 8.7, $J$ = 15.5 Hz, 1 H), 8.09 (t, $J$ = 1.8 Hz, 1 H), 8.24 (t, $J$ = 1.8 Hz, 1 H), 9.66 (s, 1 H) ppm. $^{13}$C NMR ([D$_3$]acetone): $\delta$ = 137.6, 129.6, 124.5, 121.3, 114.2, 111.0, 38.2 ppm. $C_7H_8ClN_3O_4$ (233.61): calcd. C 35.99, H 3.45, N 17.99; found C 35.89, H 3.32, N 17.60.

**3-Cyanomethyl-1-vinylimidazolium Dicyanamide (14c):** Colorless solid, $T_m$ = 73 °C. IR (KBr): $\tilde{\nu}$ = 3105, 2239, 2197, 2135, 1653, 1557, 1425, 1313, 1175 cm$^{-1}$. $^1$H NMR ($D_2O/H_2O$): $\delta$ = 5.59 (dd, $J$ = 3.0, $J$ = 8.7 Hz, 1 H), 5.60 (s, 2 H), 5.95 (dd, $J$ = 3.0, $J$ = 15.5 Hz, 1 H), 7.26 (dd, $J$ = 8.7, $J$ = 15.5 Hz, 1 H), 7.85 (t, $J$ = 1.8 Hz, 1 H), 7.98 (t, $J$ = 1.8 Hz, 1 H), 9.36 (s, 1 H) ppm. $^{13}$C NMR ($D_2O/H_2O$): $\delta$ = 136.7, 129.0, 124.2, 121.5, 120.9, 114.5, 112.0, 38.3 ppm. $C_9H_8N_6$ (200.20): calcd. C 53.99, H 4.03, N 41.98; found C 53.70, H 4.01, N 41.82.

**3-Cyanomethyl-1-vinylimidazolium Dinitramide (14d):** Colorless solid, $T_m$ = 70 °C. IR (KBr): $\tilde{\nu}$ = 3144, 3075, 2996, 1652, 1557, 1515, 1434, 1336, 1182, 1011 cm$^{-1}$. $^1$H NMR ([D$_3$]acetonitrile): $\delta$ = 5.45 (s, 2 H), 5.48 (dd, $J$ = 2.8, $J$ = 8.8 Hz, 1 H), 5.88 (dd, $J$ = 2.8, $J$ = 15.6 Hz, 1 H), 7.20 (dd, $J$ = 8.8, $J$ = 15.6 Hz, 1 H), 7.74 (t, $J$ = 1.8 Hz, 1 H), 7.85 (t, $J$ = 1.8 Hz, 1 H), 9.21 (s, 1 H) ppm. $^{13}$C NMR ([D$_3$]acetonitrile): $\delta$ = 137.0, 129.2, 124.2, 121.2, 114.1, 111.5, 38.3 ppm. $C_7H_8N_6O_4$ (240.19): calcd. C 35.01, H 3.36, N 34.99; found C 34.37, H 3.15, N 34.74.

**1-Methyl-3-propargylimidazolium Nitrate (17a):** Colorless solid, $T_m$ = 63 °C. IR (KBr): $\tilde{\nu}$ = 3222, 3151, 3104, 1570, 1378, 1164 cm$^{-1}$. $^1$H NMR ($D_2O/H_2O$): $\delta$ = 3.17 (t, $J$ = 2.6 Hz, 1 H), 3.97 (s, 3 H), 5.14 (d, $J$ = 2.6 Hz, 2 H), 7.54 (t, $J$ = 1.8 Hz, 1 H), 7.64 (t, $J$ = 1.8 Hz, 1 H), 8.93 (s, 1 H) ppm. $^{13}$C NMR ($D_2O/H_2O$): $\delta$ = 137.1, 124.9, 123.0, 78.5, 75.7, 40.0, 36.9 ppm. $C_7H_9N_3O_3$ (183.16): calcd. C 45.90, H 4.95, N 22.94; found C 45.04, H 4.93, N 22.53.

**1-Methyl-3-propargylimidazolium Perchlorate (17b):** Colorless solid, $T_m$ = 74 °C. IR (KBr): $\tilde{\nu}$ = 3268, 3150, 2984, 1607, 1566, 1442, 1387, 1355, 1165, 1093 cm$^{-1}$. $^1$H NMR ([D$_6$]acetone): $\delta$ = 3.35 (t, $J$ = 2.6 Hz, 1 H), 4.10 (s, 3 H), 5.30 (d, $J$ = 2.6 Hz, 2 H), 7.76 (t, $J$ = 1.8 Hz, 1 H), 7.81 (t, $J$ = 1.8 Hz, 1 H), 9.13 (s, 1 H) ppm. $^{13}$C NMR ([D$_6$]acetone): $\delta$ = 137.7, 125.2, 123.2, 78.6, 75.8, 39.8, 36.9 ppm. $C_7H_9ClN_2O_4$ (220.61): calcd. C 38.11, H 4.11, N 12.70; found C 37.85, H 4.02, N 12.62.

**1-Methyl-3-propargylimidazolium Dicyanamide (17c):** Colorless liquid, $T_m$ = 17 °C. IR (KBr): $\tilde{\nu}$ = 3233, 3106, 2236, 2195, 2135, 1570, 1440, 1312, 1164 cm$^{-1}$. $^1$H NMR ([D$_3$]acetonitrile): $\delta$ = 3.16 (t, $J$ = 2.6 Hz, 1 H), 3.88 (s, 3 H), 5.07 (d, $J$ = 2.6 Hz, 2 H), 7.47 (t, $J$ = 1.8 Hz, 1 H), 7.55 (t, $J$ = 1.8 Hz, 1 H), 8.84 (s, 1 H) ppm. $^{13}$C NMR ([D$_3$]acetonitrile): $\delta$ = 137.2, 125.0, 123.0, 120.4, 78.6, 75.5, 40.0, 37.0 ppm. $C_9H_9N_5$ (187.20): calcd. C 57.74, H 4.85, N 37.41; found C 58.28, H 4.89, N 38.27.

**1-Methyl-3-propargylimidazolium Dinitramide (17d):** $T_m$ = 62 °C. IR (KBr): $\tilde{\nu}$ = 3258, 3153, 2978, 1515, 1434, 1339, 1183, 1008 cm$^{-1}$. $^1$H NMR ([D$_3$]acetonitrile): $\delta$ = 3.10 (t, $J$ = 2.6 Hz, 1 H), 3.87 (s, 3 H), 5.05 (d, $J$ = 2.6 Hz, 2 H), 7.44 (t, $J$ = 1.8 Hz, 1 H), 7.52 (t, $J$ = 1.8 Hz, 1 H), 8.76 (s, 1 H) ppm. $^{13}$C NMR ([D$_3$]acetonitrile): $\delta$ = 137.4, 125.1, 123.1, 78.5, 75.6, 40.0, 37.1 ppm. IR (KBr): $\tilde{\nu}$ = 3258, 3153, 2978, 1515, 1434, 1339, 1183, 1008 cm$^{-1}$. $C_7H_9N_5O_4$ (227.18): calcd. C 37.01, H 3.99, N 30.83; found C 36.43, H 3.97, N 30.78.

**1-Methyl-4-propargyl-1,2,4-triazolium Nitrate (18a):** Colorless solid, $T_m$ = 74 °C. IR (KBr): $\tilde{\nu}$ = 3267, 3085, 2994, 2395, 2130, 1757, 1577, 1375, 1155, 1070 cm$^{-1}$. $^1$H NMR ($D_2O/H_2O$): $\delta$ = 3.16 (t, $J$ = 2.6 Hz, 1 H), 4.14 (s, 3 H), 5.21 (d, $J$ = 2.6 Hz, 2 H), 8.95 (s, 1 H), 9.91 (s, 1 H) ppm. $^{13}$C NMR ($D_2O/H_2O$): $\delta$ = 145.0, 143.4, 79.2, 74.4, 39.7, 38.9 ppm. $C_6H_8N_4O_3$ (184.15): calcd. C 39.13, H 4.38, N 30.42; found C 39.15, H 4.34, N 29.58.

**1-Methyl-4-propargyl-1,2,4-triazolium Perchlorate (18b):** Colorless solid, $T_m$ = 98 °C. IR (KBr): $\tilde{\nu}$ = 3289, 3102, 2988, 1573, 1439, 1373, 1153, 1096 cm$^{-1}$. $^1$H NMR ([D$_6$]acetone): $\delta$ = 3.39 (t, $J$ = 2.6 Hz, 1 H), 4.26 (s, 3 H), 5.37 (d, $J$ = 2.6 Hz, 2 H), 9.09 (s, 1 H), 9.94 (s, 1 H) ppm. $^{13}$C NMR ([D$_6$]acetone): $\delta$ = 144.9, 143.8, 79.6,

 © 2007 Wiley-VCH Verlag GmbH & Co. KGaA, Weinheim 

74.7, 39.9, 38.8 ppm. $C_6H_8ClN_3O_4$ (221.60): calcd. C 32.52, H 3.64, N 18.96; found C 32.52, H 3.45, N 18.89.

**1-Methyl-4-propargyl-1,2,4-triazolium Dicyanamide (18c):** Colorless liquid, $T_g$ = –54 °C. IR (KBr): $\tilde{\nu}$ = 3252, 3067, 2237, 2196, 2135, 1580, 1440, 1314, 1158, 1069 cm$^{-1}$. $^1$H NMR ([D$_3$]acetonitrile): $\delta$ = 3.21 (t, $J$ = 2.6 Hz, 1 H), 4.10 (s, 3 H), 5.17 (d, $J$ = 2.6 Hz, 2 H), 8.83 (s, 1 H), 9.77 (s, 1 H) ppm. $^{13}$C NMR ([D$_3$]acetonitrile): $\delta$ = 144.7, 143.3, 120.4, 79.3, 74.5, 39.9, 39.0 ppm. $C_8H_8N_6$ (188.19): calcd. C 51.06, H 4.28, N 44.66; found C 51.35, H 4.33, N 43.88.

**1-Methyl-4-propargyl-1,2,4-triazolium Dinitramide (18d):** Colorless liquid, $T_g$ = –59 °C. IR (KBr): $\tilde{\nu}$ = 3265, 3091, 1582, 1518, 1437, 1184, 1012 cm$^{-1}$. $^1$H NMR ([D$_3$]acetonitrile): $\delta$ = 3.13 (t, $J$ = 2.6 Hz, 1 H), 4.11 (s, 3 H), 5.18 (d, $J$ = 2.6 Hz, 2 H), 8.80 (s, 1 H), 9.68 (s, 1 H) ppm. $^{13}$C NMR ([D$_3$]acetonitrile): $\delta$ = 144.8, 143.5, 79.3, 74.6, 40.1, 39.1 ppm. $C_6H_8N_6O_4$ (228.17): calcd. C 31.58, H 3.53, N 36.83; found C 30.97, H 3.42, N 37.22.

**4-Cyanomethyl-1-propargyl-1,2,4-triazolium Nitrate (21a):** Colorless solid, $T_m$ = 112 °C. IR (KBr): $\tilde{\nu}$ = 3135, 2951, 1683, 1569, 1347, 1151, 1070 cm$^{-1}$. $^1$H NMR (D$_2$O/H$_2$O): $\delta$ = 3.18 (t, $J$ = 2.6 Hz, 1 H), 5.36 (d, $J$ = 2.6 Hz, 2 H), 5.64 (s, 2 H), 9.13 (s, 1 H), 10.31 (s, 1 H) ppm. $^{13}$C NMR (D$_2$O/H$_2$O): $\delta$ = 146.1, 144.5, 113.9, 80.0, 73.9, 44.0, 36.9 ppm. $C_7H_7N_5O_3$ (209.16): calcd. C 40.20, H 3.37, N 33.48; found C 40.10, H 3.45, N 33.68.

**4-Cyanomethyl-1-propargyl-1,2,4-triazolium Perchlorate (21b):** Colorless solid, $T_m$ = 125 °C. IR (KBr): $\tilde{\nu}$ = 3271, 3135, 2988, 1574, 1423, 1348, 1100 cm$^{-1}$. $^1$H NMR ([D$_6$]acetone): $\delta$ = 3.45 (t, $J$ = 2.6 Hz, 1 H), 5.57 (d, $J$ = 2.6 Hz, 2 H), 5.87 (s, 2 H), 9.40 (s, 1 H), 10.45 (s, 1 H) ppm. $^{13}$C NMR ([D$_6$]acetone): $\delta$ = 146.0, 144.7, 113.6, 79.5, 74.2, 43.5, 36.9 ppm. $C_7H_7ClN_4O_4$ (246.61): calcd. (246.61) C, 34.09; H, 2.86; N, 22.72. Found: C, 34.14; H, 2.49; N, 21.99.

**4-Cyanomethyl-1-propargyl-1,2,4-triazolium Dicyanamide (21c):** Colorless liquid, $T_g$ = –23 °C. IR (KBr): $\tilde{\nu}$ = 3126, 2985, 2239, 2131, 1673, 1574, 1428, 1317, 1154 cm$^{-1}$. $^1$H NMR ([D$_3$]acetonitrile): $\delta$ = 3.18 (t, $J$ = 2.6 Hz, 1 H), 5.31 (d, $J$ = 2.6 Hz, 2 H), 5.48 (s, 2 H), 8.97 (s, 1 H), 10.03 (s, 1 H) ppm. $^{13}$C NMR ([D$_3$]acetonitrile): $\delta$ = 145.9, 144.3, 121.5, 113.7, 79.7, 74.0, 43.9, 37.2 ppm. $C_9H_7N_7$ (213.20): calcd. C 50.70, H 3.31, N 45.99; found C 50.16, H 3.04, N 44.10.

**4-Cyanomethyl-1-propargyl-1,2,4-triazolium Dinotramide (21d):** Colorless solid, $T_m$ = 100 °C. IR (KBr): $\tilde{\nu}$ = 3140, 2955, 1697, 1570, 1349, 1152, 1071 cm$^{-1}$. $^1$H NMR (D$_2$O/H$_2$O): $\delta$ = 3.12 (t, $J$ = 2.6 Hz, 1 H), 5.30 (d, $J$ = 2.6 Hz, 2 H), 5.59 (s, 2 H), 9.08 (s, 1 H), 10.26 (s, 1 H) ppm. $^{13}$C NMR (D$_2$O/H$_2$O): $\delta$ = 145.9, 144.2, 113.6, 79.7, 73.6, 43.7, 36.7 ppm. $C_7H_7N_7O_4$ (253.17): calcd. C 33.21, H 2.79, N 38.73; found C 33.07, H 2.73, N 37.52.

## Acknowledgments

The authors gratefully acknowledge the support of the Air Force Office of Scientific Research (AFOSR) (F49 620-03-1-0209), the National Science Foundation (NSF) (Grant CHE0315 275), and the Office of Naval Research (ONR) (Grant N00014-06-1-1032). We are grateful to Dr. Alex Blumenfeld for NMR analyses.

[1] For reviews see: a) T. Welton, *Chem. Rev.* **1999**, *99*, 2071; b) P. Wasserscheid, W. Keim, *Angew. Chem. Int. Ed.* **2000**, *39*, 3772; c) K. R. Seddon, *J. Chem. Technol. Biotechnol.* **1997**, *68*, 351; d) *Ionic Liquids in Synthesis* (Eds.: P. Wasserscheid, T. Welton), Wiley-VCH Weinheim, Germany, **2003**; e) *Ionic Liquids IIIB: Fundamentals, Progress, Challenges, and Opportunities: Transformations and Processes* (Eds.: R. D. Rogers, K. R. Seddon), ACS Symposium Series 901, American Chemical Society, Washington, DC, **2005**; f) *Ionic Liquids*: *Industrial Applications for Green Chemistry* (Eds.: R. D. Rogers, K. R. Seddon), ACS Symposium Series 818, American Chemical Society, Washington, DC, **2002**; g) Z. Fei, T. J. Geldbach, D. Zhao, P. J. Dyson, *Chem. Eur. J.* **2006**, *12*, 2122–2130; h) J. Dupont, P. A. Suarez, *Phys. Chem. Chem. Phys.* **2006**, *8*, 2441–2452; i) J. H. Davis Jr, *Chem. Lett.* **2004**, *33*, 1072–1077.

[2] A. E. Visser, R. P. Swatloski, W. M. Reichert, R. Mayton, S. Sheff, A. Wierzbicki, J. H. Davis Jr, R. D. Rogers, *Chem. Commun.* **2001**, 135.

[3] a) D. Demberelnyamba, B. K. Shin, H. Lee, *Chem. Commun.* **2002**, 1538; b) *Electrochemical Aspects of Ionic Liquids* (Ed.: H. Ohno), John Wiley & Sons, New Jersey, **2005**, chapters 14–17; c) M. C. Buzzeo, R. G. Evans, R. G. Copton, *ChemPhysChem* **2004**, *5*, 1106–1120.

[4] a) C.-M. Jin, C. Ye, B. S. Phillips, J. S. Zabinski, X. Liu, W. Liu, J. M. Shreeve, *J. Mater. Chem.* **2006**, *16*, 1529–1535; b) C. Ye, W. Liu, Y. Chen, L. Yu, *Chem. Commun.* **2001**, 2244.

[5] a) K. O. Christe, W. W. Wilson, M. A. Petrie, H. H. Michels, J. C. Bottaro, R. Gilardi, *Inorg. Chem.* **1996**, *35*, 5068–5071; b) M. A. Petrie, J. A. Sheehy, J. A. Boatz, G. Rasul, G. K. Surya Prakash, G. A. Olah, K. O. Christe, *J. Am. Chem. Soc.* **1997**, *119*, 8802–8808; c) J. C. Bottaro, P. E. Penwell, R. J. Schmitt, *J. Am. Chem. Soc.* **1997**, *119*, 9405–9410; d) R. Gilardi, J. Flippen-Anderson, C. George, R. J. Butcher, *J. Am. Chem. Soc.* **1997**, *119*, 9411–9416; e) T. M. Klapötke, P. Mayer, A. Schulz, J. J. Weigand, *J. Am. Chem. Soc.* **2005**, *127*, 2032–2033; f) D. E. G. Jones, Q. S. M. Kwok, M. Vachon, C. Badeen, W. Ridley, *Propellants Explos. Pyrotech.* **2005**, *30*, 140–147; g) T. M. Klapotke, K. Karaghiosoff, P. Mayer, A. Penger, J. M. Welch, *Propellants Explos. Pyrotech.* **2006**, *31*, 188–195.

[6] a) G. Drake, T. Hawkins, A. Brand, L. Hall, M. Mckay, A. Vij, I. Ismail, *Propellants Explos. Pyrotech.* **2003**, *28*, 174–180; b) G. Drake, US Patent 6,509,473, Jan. 21, **2003**; G. Drake, T. Hawkins, AFOSR Ionic Liquids Workshop, Dulles, VA. October **2002**; c) G. Drake, AFOSR Ionic Liquids Workshop, Aberdeen, MD. September **2003**; d) G. Kaplan, G. Drake, K. Tollison, L. Hall, T. Hawkins, *J. Heterocycl. Chem.* **2005**, *42*, 19–27; e) G. W. Drake, T. M. Hawkins, J. Boatz, L. Hall, A. Vij, *Propellants Explos. Pyrotech.* **2005**, *30*, 156–163; f) G. Drake, T. Hawkins, K. Tollison, L. Hall, A. Vij, S. Sobaski, (1*R*)-4-Amino-1,2,4-triazolium salts: New Families of Ionic Liquids. In *Ionic Liquids IIIB: Fundamentals, Progress, Challenges, and Opportunities: Transformations and Processes* (Eds.: R. D. Rogers, K. R. Seddon), ACS Symposium Series 902, American Chemical Society, Washington, DC, **2005**, pp. 259–302.

[7] a) H. Xue, Y. Gao, B. Twamley, J. M. Shreeve, *Chem. Mater.* **2005**, *17*, 191–198; b) H. Xue, S. W. Arritt, B. Twamley, J. M. Shreeve, *Inorg. Chem.* **2004**, *43*, 7972–7977; c) Y. Gao, S. W. Arritt, B. Twamley, J. M. Shreeve, *Inorg. Chem.* **2005**, *44*, 1704–1712; d) C. Ye, J. M. Shreeve, *Chem. Commun.* **2005**, 2570–2572; e) H. Xue, Y. Gao, B. Twamley, J. M. Shreeve, *Inorg. Chem.* **2005**, *44*, 5068–5072; f) H. Xue, B. Twamley, J. M. Shreeve, *J. Mater. Chem.* **2005**, *15*, 3459–3465; g) H. Xue, B. Twamley, J. M. Shreeve, *Inorg. Chem.* **2005**, *44*, 7009–7013; h) C.-M. Jin, C. Ye, C. Piekarski, B. Twamley, J. M. Shreeve, *Eur. J. Inorg. Chem.* **2005**, *18*, 3760–3767; i) H. Xue, H. Gao, B. Twamley, J. M. Shreeve, *Eur. J. Inorg. Chem.* **2006**, *15*, 2959–2965; j) H. Gao, C. Ye, R. W. Winter, G. L. Gard, M. E. Sitzmann, J. M. Shreeve, *Eur. J. Inorg. Chem.* **2006**, *15*, 3221–3226; k) Y. Gao, C. Ye, B. Twamley, J. M. Shreeve, *Chem. Eur. J.* **2006**, *12*, 9010–9018; l) H. Gao, R. Wang, B. Twamley, M. A. Hiskey, J. M. Shreeve, *Chem. Commun.* **2006**, 4007–4009; m) H. Xue, H. Gao, B. Twamley, J. M. Shreeve, *Chem. Mater.* **2007**, *19*, 1731–1739; n) H. Gao, C. Ye, O. D. Gupta, J.-C. Xiao, M. A. Hiskey, B. Twamley, J. M. Shreeve, *Chem. Eur. J.* **2007**, *13*, 3853–3860; o) Y. Huang, H. Gao, B. Twamley, J. M. Shreeve, *Eur. J. Inorg. Chem.* **2007**, 2025–2030; p) R. Wang, H.

 © 2007 Wiley-VCH Verlag GmbH & Co. KGaA, Weinheim 

Gao, C. Ye, J. M. Shreeve, *Chem. Mater.* **2007**, *19*, 144–152; q) C. Ye, H. Gao, J. A. Boatz, G. W. Drake, B. Twamley, J. M. Shreeve, *Angew. Chem. Int. Ed.* **2006**, *45*, 7262–7265; r) R. P. Singh, R. D. Verma, D. T. Meshri, J. M. Shreeve, *Angew. Chem. Int. Ed.* **2006**, *45*, 3584–3601, and references therein.

[8] a) M. W. Schmidt, M. S. Gordon, J. A. Boatz, *J. Phys. Chem. A* **2005**, *109*, 7285–7295; b) K. E. Gutowski, R. D. Rogers, D. A. Dixon, *J. Phys. Chem. B* **2007**, *111*, 4788 –4800; c) K. E. Gutowski, J. D. Holbrey, R. D. Rogers, D. A. Dixon, *J. Phys. Chem. B* **2005**, *109*, 23196 –23208; d) NIST Chemistry Web Book.

[9] D. Gerhard, S. C. Alpaslan, H. J. Gores, M. Uerdingen, P. Wasserscheid, *Chem. Commun.* **2005**, 5080–5082.

[10] H. G. Ang, W. Fraenk, K. Karaghiosoff, T. M. Klapotke, P. Mayer, H. Nöth, J. Sprott, M. Warchhold, *Z. Anorg. Allg. Chem.* **2002**, *628*, 2894–2900.

[11] J. P. Ritchie, S. M. Bachrach, *J. de Physique C4, Suppl. 9* **1987**, *48*, 377–391.

[12] H. L. Ammon, S. Mitchell, *Propellants Explos. Pyrotech.* **1998**, *23*, 260–265.

[13] C. Ye, J. M. Shreeve, *J. Phys. Chem. A* **2007**, *111*, 1456–1461.

[14] a) P. Politzer, J. S. Murray, M. E. Grice, P. Sjoberg, in *Chemistry of Energetic Materials* (Eds.: G. A. Olah, D. R. Squire), Academic Press, San Diego, CA, **1991**, p. 77; b) J. Köhler, R. Mayer, *Explosivstoffe*, 9th ed., Wiley-VCH, Weinheim, **1998**.

[15] a) L. E. Fried, K. R. Glaesemann, W. M. Howard, P. C. Souers, *CHEETAH 4.0 User's Manual*, Lawrence Livermore National Laboratory, **2004**; b) J. P. Lu, *Evaluation of the Thermochemical Code, CHEETAH 2.0 for Modelling Explosives Performance*, DSTO-TR-1199, DSTO, Edinburgh, **2001**.

[16] M. J. Frisch, G. W. Trucks, H. B. Schlegel, G. E. Scuseria, M. A. Robb, J. R. Cheeseman, J. A. Montgomery Jr, T. Vreven, K. N. Kudin, J. C. Burant, J. M. Millam, S. S. Iyengar, J. Tomasi, V. Barone, B. Mennucci, M. Cossi, G. Scalmani, N. Rega, G. A. Petersson, H. Nakatsuji, M. Hada, M. Ehara, K. Toyota, R. Fukuda, J. Hasegawa, M. Ishida, T. Nakajima, Y. Honda, O. Kitao, H. Nakai, M. Klene, X. Li, J. E. Knox, H. P. Hratchian, J. B. Cross, V. Bakken, C. Adamo, J. Jaramillo, R. Gomperts, R. E. Stratmann, O. Yazyev, A. J. Austin, R. Cammi, C. Pomelli, J. W. Ochterski, P. Y. Ayala, K. Morokuma, G. A. Voth, P. Salvador, J. J. Dannenberg, V. G. Zakrzewski, S. Dapprich, A. D. Daniels, M. C. Strain, O. Farkas, D. K. Malick, A. D. Rabuck, K. Daghavachari, J. B. Foresman, J. V. Ortiz, Q. Cui, A. G. Baboul, S. Clifford, J. Cioslowski, B. B. Stefanov, G. Liu, A. Liashenko, P. Piskorz, I. Komaromi, R. L. Martin, D. J. Fox, T. Keith, M. A. Al-Laham, C. Y. Peng, A. Nanayakkara, M. Challacombe, P. M. W. Gill, B. Johnson, W. Chen, M. W. Wong, C. Gonzalez, J. A. Pople, *Gaussian 03*, revision D.01, Gaussian, Inc., Wallingford CT, **2004**.

[17] R. G. Parr, W. Yang, *Density Functional Theory of Atoms and Molecules*, Oxford University Press, New York, **1989**.

[18] C. M. Møller, M. S. Plesset, *Phys. Rev.* **1934**, *46*, 618.

[19] J. A. Pople, J. S. Binkely, R. Seeger, *Int. J. Quantum Chem.* **1976**, *10*, 1–19.

[20] H. D. B. Jenkins, D. Tudeal, L. Glasser, *Inorg. Chem.* **2002**, *41*, 2364–2367.

[21] J. C. Gálvez-Ruiz, G. Holl, K. Karaghiosoff, T. M. Klapötke, K. Löhnwitz, P. Mayer, H. Nöth, K. Polborn, C. J. Rohbogner, M. Suter, J. J. Weigand, *Inorg. Chem.* **2005**, *44*, 4237–4253.

[22] B. K. M. Chan, N.-H. Chang, M. R. Grimmett, *Aust. J. Chem.* **1977**, *30*, 2005–2013.

Received: June 28, 2007
Published Online: September 7, 2007

 © 2007 Wiley-VCH Verlag GmbH & Co. KGaA, Weinheim 

DOI: 10.1002/ejic.200700496

# On the Influence of "Arm-on, Arm-off" Processes on Alkene Hydrogenation Catalysed by a Rhodium Triphos Complex

**Adrian B. Chaplin[a] and Paul J. Dyson*[a]**

**Keywords:** Rhodium / Homogeneous catalysis / Hydrogenation / Tripodal ligands / Phosphane ligands

The influence of phosphane "arm-on, arm-off" association/dissociation in rhodium catalysed alkene hydrogenation using [Rh(COD)($\kappa^3$-triphos)]$PF_6$ {**1**, COD = cyclooctadiene, triphos = 1,1,1-tris(diphenylphosphanylmethyl)ethane} has been investigated by comparison of the activity of **1** to mixtures of the related diphosphane complex, [Rh(COD)($\kappa^2$-dppp)]$PF_6$ {**2**, dppp = 1,3-bis(diphenylphosphanyl)propane} and triphenylphosphane (THF, 50 °C, 1 bar $H_2$). These investigations are supplemented by a demonstration of the $\kappa^2$–$\kappa^3$ fluxionally of the triphos coordination in **1** by reversible reaction with $[RuCl_2(p\text{-cymene})]_2$ at room temperature in $CH_2Cl_2$. The product of this reaction, the bimetallic complex [(*p*-cymene)$Cl_2$Ru{($PPh_2CH_2$)CMe($CH_2PPh_2$)$_2$}Rh(COD)]$PF_6$, was isolated and fully characterized, including determination of the solid-state structure by X-ray diffraction analysis. Despite this evidence for facile arm-off dissociation of the triphos ligand in **1**, complex **2**, with or without triphenylphosphane, was found to be more efficient for the hydrogenation of styrene and cyclohexene. Notably, use of triphenylphosphane together with **2** was found to have beneficial effects – increasing the rate of styrene hydrogenation (in some cases) and helping to stabilise the metal center during cyclohexene hydrogenation. These observations are supported by mercury poisoning experiments and reactivity experiments with **2** in medium pressure sapphire NMR tubes.

(© Wiley-VCH Verlag GmbH & Co. KGaA, 69451 Weinheim, Germany, 2007)

## Introduction

Tripodal triphosphane ligands have found widespread application in inorganic and organometallic chemistry.[1] Among these ligands, the $C_3$ symmetric 1,1,1-tris(diphenylphosphanylmethyl)ethane (triphos) and it's derivatives are among the most extensively investigated, forming a large variety of transition metal complexes, many of which have found applications in catalysis.[1,2] Bianchini and co-workers, in particular, have pioneered the use of this ligand in transition metal catalysis, using platinum group metals for a number of processes, including hydrogenation and hydroformylation of alkenes,[3] oxidation of catechols,[4] coupling reactions of alkynes,[5] and the hydrogenation, hydrogenolyis and hydrodesulfurisation of thiophenes.[6] Functionalisation of the triphos ligand by derivation of the bridgehead atom with appropriate moieties has allowed the formation of metallo-dendrimers[7] or immobilisation of metal complexes on silica[8] or into biphases;[9] facilitating catalyst reuse or modifying reactivity. Such immobilization is complemented by the tridentate nature of the ligand, stabilising the metal center during catalysis and reducing leaching.

Although commonly found in a tridentate ($\kappa^3$) coordination mode,[1] $\kappa^2$-coorindination of triphos is also observed in a number of transition metal complexes.[10] The interconversion between these $\kappa^2$ and $\kappa^3$ coordination modes by "arm-on, arm-off" association/dissociation of one of the phosphane arms has been implicated in the reactivity and catalytic activity of triphos complexes, particularly those of rhodium.[10c,11] Notably, Kiss and Hováth demonstrated a reversible arm-off dissociation in [Rh(CO)H($\kappa^3$-triphos)], an active hydroformylation catalyst,[3a] and addition of CO under hydroformylation conditions at room temperature by high pressure IR and $^{31}$P NMR spectroscopy (Scheme 1).[12] Caulton and co-workers have further affirmed the importance of this arm-off mechanism in hydroformylation catalysis by reactions of related hydride, alkyl and acetyl rhodium triphos complexes.[13] During their investigation of rhodium triphos, and related tripodal phosphane complexes, Huttner and co-workers suggested that the $\kappa^3$-coordination of the phosphane hinders hydrogenation,[14] and

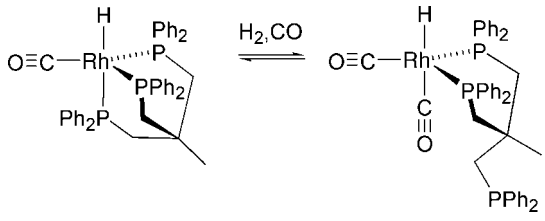


Scheme 1.

[a] Institut des Sciences et Ingénierie Chimiques, Ecole Polytechnique Fédérale de Lausanne (EPFL),
1015 Lausanne, Switzerland
E-mail: paul.dyson@epfl.ch

Supporting information for this article is available on the WWW under http://www.eurjic.org or from the author.

 © 2007 Wiley-VCH Verlag GmbH & Co. KGaA, Weinheim 

they demonstrated that related diphosphane complexes are significantly more active for the hydrogenation of (*Z*)-α-*N*-acetamidocinnamic acid.[15] Burk and co-workers have also reported similar behaviour for other rhodium tripodal phosphane systems.[16]

To further investigate the importance of phosphane arm-on, arm-off processes in the hydrogenation activity of rhodium triphos complexes, we report here a comparison of the activity of [Rh(COD)(κ$^3$-triphos)]$PF_6$ (**1**) with mixtures of the related diphosphane complex, [Rh(COD)(κ$^2$-dppp)]-$PF_6$ (**2**), and triphenylphosphane (Scheme 2).[14a,15] To complement these investigations, relevant in situ reactivity studies are also presented together with the demonstration of the κ$^2$–κ$^3$ interconversion in complex **1** using a ruthenium complex.

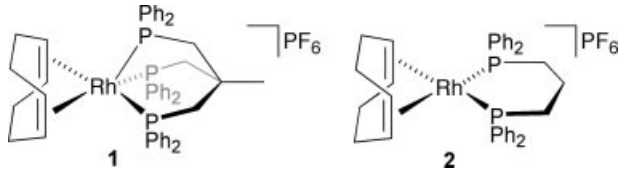


Scheme 2.

## Results and Discussion

### 1. Reaction of 1 with [$RuCl_2$(*p*-cymene)]$_2$

To probe the presence of an arm-on, arm-off process, **1** was reacted at room temperature with the dinuclear ruthenium complex [$RuCl_2$(*p*-cymene)]$_2$, well known to react rapidly with phosphane ligands,[17] in an attempt to trap the κ$^2$-coordination mode of the triphos ligand. After 30 minutes, analysis of the reaction solution by $^{31}$P NMR spectroscopy revealed the formation of the bimetallic complex, [(*p*-cymene)$Cl_2$Ru{($PPh_2CH_2$)CMe($CH_2PPh_2$)$_2$}-Rh(COD)]-$PF_6$ **3**, identified by the presence of characteristic singlet and doublet ($^1J_{RhP}$ = 141 Hz) resonances at $\delta$ = 16.6 and 13.1 ppm, respectively, in a 1:2 ratio together with a small quantity of **1** (Scheme 3). Subsequently, **3** was isolated, albeit in moderate yield (54%), following recrystallisation and the structure was further verified by $^1$H and $^{13}$C NMR spec-

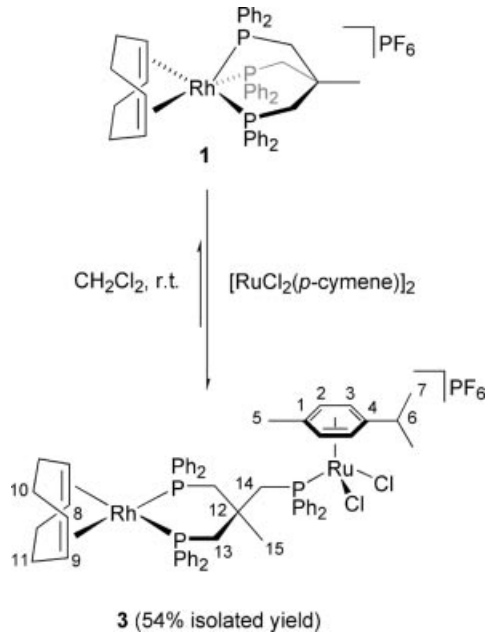


Scheme 3. Formation and equilibrium of complex **3** (with NMR numbering scheme).

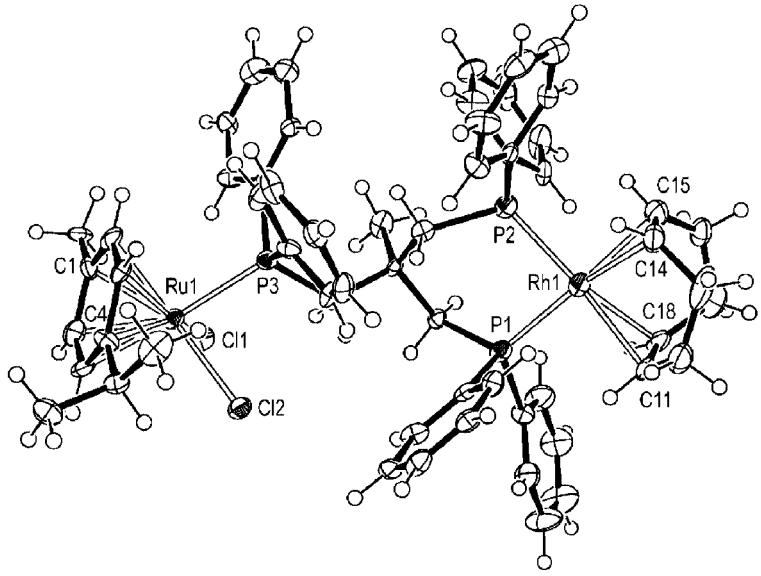


Figure 1.ORTEP representation of **3**; thermal ellipsoids drawn at 50%. Solvent molecules and counter anion omitted for clarity. Key bond lengths [Å] and angles [°]: Ru1–Cl1 2.420(3), Ru1–Cl2 2.421(2), Ru1–P3 2.356(3); Cl1–Ru1–Cl2 88.23(8), Cl1–Ru1–P3 88.37(9), Cl2–Ru1–P1 83.78(8); Ru1–C1 2.200(9), Ru1–C4 2.227(9), Ru1–$C_{avg}$ 2.21(2), Rh1–P1 2.287(3), Rh1–P2 2.286(3); P2–Rh1–P3 88.06(10); Rh1–C11 2.274(8), Rh1–C18 2.263(9), Rh1–C14 2.217(10), Rh1–C15 2.226(10).

 © 2007 Wiley-VCH Verlag GmbH & Co. KGaA, Weinheim 

troscopy and electrospray ionization mass spectrometry (ESI-MS). Furthermore, the solid-state structure of **3** has been established by X-ray diffraction analysis – depicted in Figure 1. The bonding parameters about the Ru center are similar to related [$RuCl_2$($\kappa^1$-phosphane)(*p*-cymene)] (Ru–P ≈ 2.4 Å)[18] complexes, while those about the Rh center are similar to [Rh(COD)($\kappa^2$-dppp)]$BF_4$ {**1**·$BF_4$, Rh–P 2.311(2), 2.319(2) Å; P–Rh–P 90.81(4)°},[19] although the Rh–P bond length and P–Rh–P angle are slightly contracted in **3** in comparison to **1**·$BF_4$ {Rh1–P1, 2.287(3) Å; Rh1–P2, 2.286(3) Å; P1–Rh–P2, 88.06(10)°}. In $CD_2Cl_2$ solution at room temperature, **3** undergoes a slow equilibration reaction ($t_{1/2}$ = 22 ± 3 h) in which dissociation of the phosphane from the ruthenium-arene moiety results in an mixture of **1**, **3**, and [$RuCl_2$(*p*-cymene)]$_2$ with a equilibrium constant, *K*, of approximately 2, demonstrating the reversible nature of the triphos coordination.

## 2. Catalytic Activity

The catalytic activity of **1** and solutions of **2** containing various quantities of triphenylphosphane were first investigated for the hydrogenation of styrene. The hydrogenation experiments were carried out in THF, a weakly coordinating solvent,[20] at 50 °C under 1 bar of $H_2$ with a substrate to catalyst (S/C) ratio of 200:1; **2** was investigated with 0, 0.5, 1, 2, and 5 equiv. of triphenylphosphane. Conversion was monitored by GC during the reaction and results are listed in Table 1 with selected data depicted in Figure 2. Both complexes were found to exhibit incubation periods, consistent with previously reported kinetic studies on diphosphane rhodium complexes containing the COD ligand (attributed to hydrogenation of the diene).[21] From the hydrogenation curves (Figure 2) it is apparent that **1** is significantly less active than **2** under these conditions. Catalytic runs carried out with **2** in the presence of added triphenylphosphane showed enhanced rates of hydrogenation at 50% conversion in comparison to **2** alone – most pronounced with 1 equiv. of the phosphane. However, in the presence of excess triphenylphosphane significant reductions in the rate of hydrogenation with **2** are observed close to complete conversion (> 90%), resulting in longer reactions times than in the absence of triphenylphosphane (see insert in Figure 2). Addition of mercury, a selective poison for heterogeneous catalysis, did not inhibit catalytic activity for **2** + *n*$PPh_3$ (*n* = 0 or 1) significantly.[22]

Table 1. Hydrogenation of styrene using **1** and **2** + *n*$PPh_3$.[a]

| | *n* | 50% Conversion Time/h | TOF[b]/$h^{-1}$ | > 99% Conversion Time/h |
|---|---|---|---|---|
| **1** | | 2.83 | 32 | 10 |
| **2** | 0 | 1.72 | 68 | 3.5 |
| **2**[c] | 0 | 1.81 | 62 | 4.5 |
| **2** | 0.5 | 1.63 | 74 | 3.5 |
| **2** | 1 | 1.50 | 80 | 3.0 |
| **2**[c] | 1 | 1.49 | 80 | 3.5 |
| **2** | 2 | 1.65 | 72 | 4.0 |
| **2** | 5 | 1.65 | 70 | 4.5 |

[a] Conditions: $2.6 \times 10^{-5}$ mol pre-catalyst, S/C = 200:1, 20 mL of THF, 0.1 mL of octane (internal standard), 1 bar $H_2$. Conversion determined by GC analysis of reaction aliquots. [b] Calculated at 50% conversion from hydrogenation progress. [c] 0.1 mL of Hg added.

In comparison to styrene, the initial rate of cyclohexene hydrogenation using **2** is significantly reduced by the addition of 1 equiv. of triphenylphosphane (Figure 3). However, mercury poisoning experiments suggest a significant degree of heterogeneous character to the active species for **2** alone, whereas, with 1 equiv. of triphenylphosphane there is no significant change in activity in the presence of mercury (Figure 3 and Table 2). This difference is also apparent to some degree by significant darkening of the reaction solution after ca. 90 min in the absence of triphenylphosphane, whereas with 1 equiv. of triphenylphosphane the solution remains yellow throughout the reaction. For **1**, the initial rate of hydrogenation is comparable to **2** with 1 equiv. of triphenylphosphane, although activity is gradually reduced and is accompanied by the reaction solution becoming green/brown – consistent with decomposition into inactive molecular species.

Together, these results are consistent with the ability of the triphos ligand to undergo reversible phosphane arm-off coordination during catalysis. While the catalytic activity of

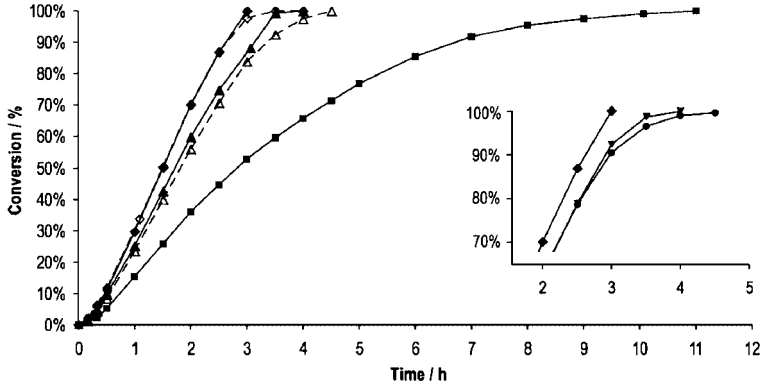


Figure 2. Hydrogenation of styrene using **1** (–■–) and **2** + *n*$PPh_3$ (*n* = 0, –▲–; 1, –♦–; 2, –▼– insert only; 5, –●– insert only). Mercury poisoning experiments for **2** + *n*$PPh_3$ (*n* = 0, --Δ--; 1, --◇--) are shown with dashed lines.

 © 2007 Wiley-VCH Verlag GmbH & Co. KGaA, Weinheim 

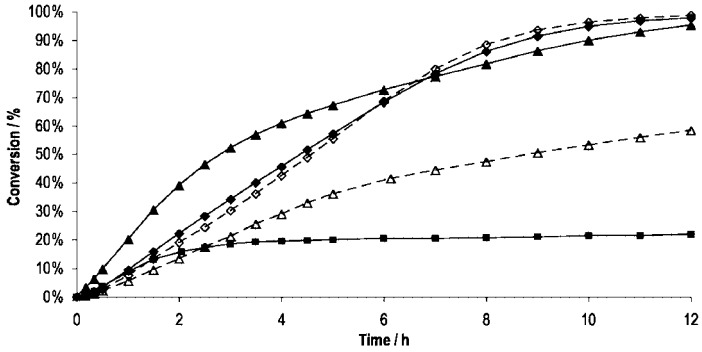


Figure 3. Hydrogenation of styrene using **1** (–■–) and **2** + *n*$PPh_3$ (*n* = 0, –▲–; 1, –♦–). Mercury poisoning experiments for **2** + *n*$PPh_3$ (*n* = 0, --Δ--; 1, --◇--) are shown with dashed lines.

Table 2. Hydrogenation of cyclohexene using **1** and **2** + *n*$PPh_3$.[a]

| | *n* | 50% Conversion Time/h | TOF[b]/$h^{-1}$ |
|---|---|---|---|
| **1** | | _[c] | _[c] |
| **2** | 0 | 2.81 | 24 |
| **2**[d] | 0 | 8.78 | 6 |
| **2** | 1 | 4.36 | 22 |
| **2**[d] | 1 | 4.59 | 26 |

[a] Conditions: $2.6 \times 10^{-5}$ mol pre-catalyst, S/C = 200:1, 20 mL of THF, 0.1 mL of octane (internal standard), 1 bar $H_2$. Conversion determined by GC analysis of reaction aliquots. [b] Calculated at 50% conversion from hydrogenation progress. [c] Conversion < 50%. [d] 0.1 mL of Hg added.

**1** is attributed to the ability of the triphos ligand to undergo an arm-off dissociation process, leading to active species containing the $\kappa^2$-coordinated ligand and a vacant coordination site (i.e. becoming directly analogous to **2**), the adoption of the $\kappa^3$-mode during catalysts is suggested to complete with substrate significantly during catalysis resulting in significantly lower activity than **2**. This suggestion is supported by similar reductions in activity observed for the hydrogenation of styrene with **2** and excess triphenylphosphane, but only near reaction completion, when substrate concentration is low. The reduced effect of triphenylphosphane coordination in comparison to the arm-on, arm-off process in **1** is presumably due to the absence of the chelate effect and the bulky nature of triphenylphosphane. (*Note:* no reaction with **2** and triphenylphosphane can be detected in THF cf. $\kappa^3$-coordination of the triphos ligand in **1**.) The failure of **1** to hydrogenate cyclohexene to completion may also be rationalised by the tendency of the triphos ligand in **1** to adopt a $\kappa^3$-coordination mode. This feature together with the more hindered nature of cyclohexene could be responsible for the decomposition observed with this substrate in comparison with styrene.

While the arm-on coordination appears to be detrimental the catalytic activity of **1**, the addition of triphenylphosphane, in an attempt to mimic this behaviour,[23] during catalysis with **2** had a number of beneficial outcomes. For example, in the hydrogenation of cyclohexene with **2**, addition of triphenylphosphane appeared to stabilise the metal center, i.e. by reversible coordination, preventing decomposition with only a minor decrease in activity. For styrene, addition of, for example, one equivalent of triphenylphosphane noticeably increased the rate of hydrogenation. As Osborn-type rhodium and iridium complexes are known to react with arenes under hydrogenation conditions to form inactive species of the type, $[M(\eta^6\text{-arene})L_2]^+$,[20] reversible coordination of triphenylphosphane may help prevent the formation of species of this nature and thus enhance the rate of hydrogenation. This possibility was thus investigated further (see below).

### 3. Effect of Triphenylphosphane on the Formation of $[Rh(\eta^6\text{-toluene})(\kappa^2\text{-dppp})]^+$

To further investigate the enhancement of catalytic activity of **2** with triphenylphosphane for styrene hydrogenation, reactions of **2** with hydrogen (ca. 12 bar) in the presence of toluene (ca. 80 equiv.) and triphenylphosphane were carried out in medium pressure sapphire NMR tubes.[24,25] In the absence of triphenylphosphane, following COD hydrogenation, $[Rh(\eta^6\text{-toluene})(\kappa^2\text{-dppp})]^+$ **4** is formed quantitatively.[26] However, in the presence of 5 equiv. of triphenylphosphane **4** cannot be detected and instead a species assigned to *cis*-$[RhH_2(PPh_3)_2(\kappa^2\text{-dppp})]^+$ **5** is observed in ca. 94% yield.[27] The identity and geometry of this species is deduced primarily from the $^{31}P\{^1H\}$ NMR spectrum, which exhibits four distinct phosphorus resonances with characteristic multiplicity and coupling constants (Figure 4). Notably, those centred at $\delta$ = 31.3 and 18.3 ppm exhibit large $^2J_{PP}$ coupling constants of 318 Hz, suggesting a *trans* arrangement of two of the phosphane moieties,[28] and $^1J_{RhP}$ coupling constants of ca. 100 Hz. The other phosphorus resonances, centred at 21.6 and –3.6 ppm, have smaller $^1J_{RhP}$ coupling constants (82 and 85 Hz) consistent with phosphane moieties *trans* to hydride ligands.[29] The remaining $^2J_{PP}$ coupling constants, ca. 20 Hz, are typical for *cis*-coordinated phosphane ligands.[28] Furthermore, the $^1H$ NMR spectrum exhibits two broad doublets at –10.55 and –11.33 ppm with $^2J_{PH}$ coupling constants of 132 and 136 Hz, respectively. A similar species, containing instead a tetradentate phosphane, has been reported by Bianchini and co-workers.[30]

 © 2007 Wiley-VCH Verlag GmbH & Co. KGaA, Weinheim 

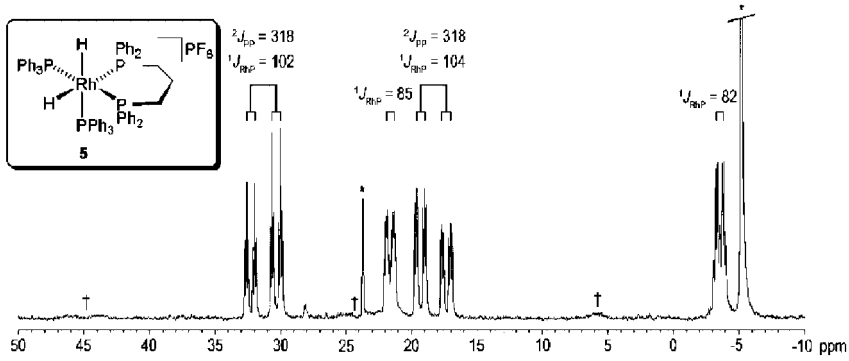


Figure 4. $^{31}P\{^1H\}$ NMR spectrum of **5**. * $PPh_3$ ($\delta \approx 5$ ppm) and $OPPh_3$ ($\delta \approx 24$ ppm), † denotes complex **6**.

In the presence of 1 equiv. of triphenylphosphane **4** is formed, although only in modest yield (ca. 24%), together with a new species, exhibiting two broad doublets of doublets at 45.0 ($^2J_{PP}$ = 340 Hz, $^1J_{RhP}$ = 112 Hz) and 24.0 ppm ($^2J_{PP}$ = 340 Hz, $^1J_{RhP}$ = 112 Hz) and a broad resonance at 5.8 ppm (ca. 54%), and a small amount of **5** (ca. 12%). This new species is tentatively assigned as *cis*-$[RhH_2(THF)(PPh_3)(\kappa^2\text{-dppp})]^+$ (**6**, Scheme 4) on the basis of these data and their good agreement with that of the known complex *cis*-$[RhH_2Cl(PPh_3)(\kappa^2\text{-}\{PPh_2CH_2\}_2CHOH)]$ **7** (Scheme 4).[27,31] A small quantity of this complex is also observed during the reaction with 5 equiv. (ca. 4%).

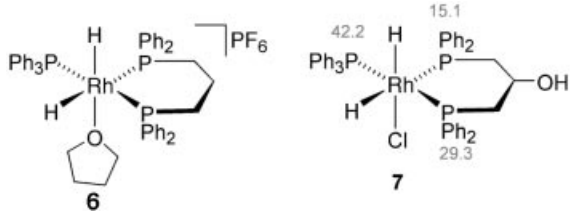


Scheme 4. Proposed structure of **6** and the known compound **7** {annotated with $^{31}P$ NMR spectroscopic data ([$D_8$]toluene / ppm)}.[31]

Combined these data are consistent with the ability of triphenylphosphane to hinder the coordination of arene substrates or products under catalytic conditions, supporting the observation of enhanced activity on addition of triphenylphosphane during hydrogenation of styrene with complex **2**.

## Concluding Remarks

The influence of the phosphane arm-on, arm-off process in rhodium triphos complexes for hydrogenation catalysis has been further established by comparison to related dppp systems with added triphenylphosphane. Despite further evidence for facile dissociation of one of the triphos arms in these systems, by the reaction of **1** with $[RuCl_2(p\text{-cymene})]_2$, the tendency of this ligand to adopt a $\kappa^3$-coordination appears to significantly encumber catalytic activity by competing with the substrate for vacant coordination sites on the metal. In comparison, in an attempt to mimic the $\kappa^3$-coordination motif in the triphos complex, added triphenylphosphane results in the enhancement of the rate of catalytic activity during the hydrogenation of styrene with **2**, although with excess triphenylphosphane, reduction in the hydrogenation rate close to completion is observed – upholding the proposed reduction of activity by $\kappa^3$-coordination of the triphos ligand in **1**. The enhanced rate of styrene hydrogenation is attributed to the ability of triphenylphosphane to prevent the coordination of the substrate or product (by weak and reversible coordination) during catalysis, and this hypothesis is supported by medium pressure in situ reactions of **2** with $H_2$, toluene and different quantities of triphenylphosphane. The use of triphenylphosphane with **2** also has the beneficial effect of stabilizing the metal center towards decomposition during catalysis as demonstrated in the hydrogenation of cyclohexene.

## Experimental Section

**General:** All organometallic manipulations were carried out under a nitrogen atmosphere using standard Schlenk techniques. Solvents ($CH_2Cl_2$, THF, toluene) were dried catalytically under dinitrogen using a solvent purification system, manufactured by Innovative Technology Inc. All other solvents were p.a. quality and saturated with nitrogen prior to use. Styrene and cyclohexene were saturated with nitrogen and stored over activated molecular sieves. $[Rh(COD)(\kappa^3\text{-triphos})]PF_6$ (**1**),[15] $[Rh(COD)(\kappa^2\text{-dppp})]PF_6$ (**2**),[14a] and $[RuCl_2(p\text{-cymene})]_2$[32] were prepared as described elsewhere. All other chemicals are commercial products and were used as received. NMR spectra were recorded with a Bruker Avance 400 spectrometer at room temperature, unless otherwise stated. Chemical shifts are given in ppm and coupling constants (*J*) in Hz. The NMR labelling for complex **3** is given in Scheme 3. ESI-MS were recorded on a Thermo Finnigan LCQ DecaXP Plus quadrupole ion trap instrument according to a literature protocol;[33] $CH_2Cl_2$ was used as the solvent for all experiments with a capillary temperature of 80 °C and spray voltage of 5.0 kV.

**Preparation of $[(p\text{-Cymene})Cl_2Ru\{(PPh_2CH_2)CMe(CH_2PPh_2)_2\}Rh(COD)]PF_6$ (3):** A solution of $[Rh(COD)(\kappa^3\text{-triphos})]PF_6$ (0.070 g, 0.071 mmol) and $[RuCl_2(p\text{-cymene})]_2$ (0.022 g, 0.036 mmol) in $CH_2Cl_2$ (10 mL) was stirred at room temp. for 30 min. The solution was then concentrated to ca. 5 mL and hexane (ca. 10 mL) added precipitating out a small amount of a un-

 © 2007 Wiley-VCH Verlag GmbH & Co. KGaA, Weinheim 

identified brown impurity, which was removed by filtration. The product was obtained as a microcrystalline orange solid from the filtrate upon standing at –20 °C. Yield 0.049 g (54%). Crystals suitable for X-ray diffraction were obtained from a $CH_2Cl_2$/hexane solution of the complex at –20 °C. $^1$H NMR ($CD_2Cl_2$): $\delta$ = 7.26–7.92 (m, 30 H), 5.12 (d, $^3J_{HH}$ = 6.1, 2 H, H$^3$), 5.07 (d, $^3J_{HH}$ = 5.7, 2 H, H$^2$), 4.74–4.84 (m, 2 H, H$^8$), 4.01–4.11 (m, 2 H H$^9$), 3.00–3.10 (m, 2 H, H$^{13}$), 2.70–2.78 (m, 2 H, H$^{14}$), 2.59 (sept, $^3J_{HH}$ = 6.9, 1 H, H$^6$), 2.41–2.50 (m, 2 H, H$^{10}$), 2.30–2.41 (m, 2 H, H$^{10'}$), 2.06–2.21 (m, 4 H, H$^{11}$), 1.83–1.96 (m, 2 H, H$^{13'}$), 1.78 (s, 3 H, H$^5$), 1.05 (d, $^3J_{HH}$ = 7.0, 6 H, H$^7$), –0.09 (s, 3 H, H$^{15}$) ppm. $^{13}$C{$^1$H} NMR ($CD_2Cl_2$): $\delta$ = 127–135 (m), 109.6 (s, C$^4$), 104.4–104.9 (m, C$^9$), 98.8–99.3 (m, C$^8$), 95.3 (s, C$^1$), 89.9 (d, $^2J_{PC}$ = 3, C$^2$), 86.3 (d, $^2J_{PC}$ = 6, C$^3$), 45.0–45.7 (m, C$^{14}$), 39.7 (d, $^2J_{PC}$ = 6, C$^{12}$), 36.2–36.9 (m, C$^{13}$), 31.4 (s, C$^{15}$), 30.3 (s, C$^6$), 30.0 (s, C$^{10}$), 29.9 (s, C$^{11}$), 21.4 (s, C$^7$), 17.1 (s, C$^5$) ppm. $^{31}$P{$^1$H} NMR ($CD_2Cl_2$): $\delta$ = 16.6 (s, 1 P, Ru*P*Ph$_2$), 13.1 (d, $^1J_{RhP}$ = 141, 2 P, Rh*P*Ph$_2$), –144.4 (sept, $^1J_{PF}$ = 711, 1 P, *P*F$_6$) ppm. ESI-MS ($CH_2Cl_2$, 80 °C, 5 kV) positive ion: *m*/*z*, 834 (30%) [M –RuCymeneCl$_2$]$^+$, 1141 [M]$^+$. ESI-MS$^2$ (+1141): *m*/*z*, 834 [M – RuCymeneCl$_2$]$^+$. $C_{59}H_{65}Cl_2F_6P_4RhRu$ (1286.94 g mol$^{-1}$): calcd. C 55.07, H 5.09; found C 55.14, H 5.11.

**Medium Pressure NMR Experiments:** Reactions of **2** (9 mg) with $H_2$ (12 bar) and toluene (0.1 mL, ca. 80 equiv.) were carried out in 10 mm sapphire NMR tubes in THF (2.5 mL) with the appropriate quantity of triphenylphosphane. All samples were prepared under nitrogen. Reaction progress was followed by $^{31}$P NMR spectroscopy until complete consumption of **2** was observed, typically < 5 h (no further change in product distributions were observed). Selected $^1$H and $^{31}$P{$^1$H} NMR spectroscopic data for **5** and **6** follow; referenced externally to TMS and 85% $H_3PO_4$, respectively. $^1$H NMR (**5**, THF, hydride region): $\delta$ = –10.55 (br. d, $^2J_{PH}$ = 132, 1 H), –11.33 (br. d, $^2J_{PH}$ = 136, 1 H) ppm. $^{31}$P{$^1$H} NMR (**5**, THF): $\delta$ = 31.3 (ddt, $^2J_{PP}$ = 318, $^1J_{RhP}$ = 102, $^2J_{PP}$ = 21, 1 P), 21.6 (dq, $^1J_{RhP}$ = 85, $^2J_{PP}$ = 20, 1 P), 18.3 (dddd, $^2J_{PP}$ = 318, $^1J_{RhP}$ = 104, $^2J_{PP}$ = 26, $^2J_{PP}$ = 16, 1 P), 3.6 (dq, $^1J_{RhP}$ = 82, $^2J_{PP}$ = 23, 1 P) ppm. $^{31}$P{$^1$H} NMR (**6**, THF): $\delta$ = 45.0 (br. d, $^2J_{PP}$ = 340, $^1J_{RhP}$ = 112, 1 P), 24.0 (br. d, $^2J_{PP}$ = 340, $^1J_{RhP}$ = 112, 1 P) 5.8 (br., 1 P) ppm. The hydride region of the $^1$H NMR spectrum of **6** was broad and uninformative.

**Catalytic Evaluations:** Catalytic experiments were conducted in a 50 mL three-necked round-bottomed flask equipped with a 2.0 L latex balloon (Dräger/2165694) connected via a 6 cm reflux condenser and gas tap, a septum cap and gas adaptor. Following pressurisation of the balloon with hydrogen (1 bar), via successive vacuum hydrogen cycles, the flask was charged with pre-catalyst ($2.6\times10^{-5}$ mol) and magnetic stirring bar and placed under an inert atmosphere. THF (20 mL), octane (0.1 mL), substrate ($5.2\times10^{-3}$ mol) and, for the poisoning experiments, mercury (0.1 mL) were then added via syringe through the septum cap. The system was then placed under $H_2$ by three vacuum/$H_2$ cycles and then heated at 50 °C. The hydrogenation was followed by sampling the reaction solution at *t* = 10, 20, 30, 60, 90, 120, 180, 210, 240, 270, 300 min and every successive hour up to *t* = 12 h by GC (Varian chrompack CP-3380 gas chromatograph) or until reaction completion. Full hydrogenation data is given in the supplementary material.

**Crystallography:** Relevant details for the structure refinement are given in Table 3 and selected geometrical parameters for **3** are found in caption of Figure 1. Data collection for the X-ray structure determination was performed on a KUMA CCD diffractometer system using graphite monochromated Mo-$K_\alpha$ radiation (0.71073 Å) and a low-temperature device [140(2) K]. Data reduction was performed using CrysAlis RED.[34] The structure was solved using SIR97,[35] and refined (full-matrix least-squares on $F^2$) using SHELXTL.[36] An absorption correction was applied to the data set (empirical, DELABS).[37] All non-hydrogen atoms were refined anisotropically, with hydrogen atoms placed in calculated positions using the riding model. The occupancy of one of the $CH_2Cl_2$ molcules was refined to 66% and it was necessary to retrain the displacement parameters of some atoms. The graphical representation of **3** was made with ORTEP3.[38]

Table 3. Crystal data and details of the structure determinations of **3**.

| Formula | $C_{59}H_{65}Cl_2F_6P_4RhRu\cdot4.66\,CH_2Cl_2$ |
|---|---|
| *M* | 1682.81 |
| Crystal system | triclinic |
| Space group | $P\bar{1}$ |
| *a* /Å | 11.8544(10) |
| *b* /Å | 16.506(2) |
| *c* /Å | 19.485(2) |
| *α* /° | 105.563(10) |
| *β* /° | 90.054(8) |
| *δ* /° | 100.954(9) |
| *V* /Å$^3$ | 3600.5(7) |
| *Z* | 2 |
| Density /g cm$^{-3}$ | 1.552 |
| *μ* /mm$^{-1}$ | 1.002 |
| *θ* range /° | $3.09 < \theta < 25.25$ |
| Measured reflections | 21093 |
| Unique reflections | 11146 [$R_{int}$ = 0.0832] |
| Number of data/restraints/parameters | 11146/126/798 |
| *R*1, *wR*2 [$I > 2\sigma(I)$][a] | *R*1 = 0.0622, *wR*2 = 0.1122 |
| Largest diff. peak and hole /e Å$^{-3}$ | 1.377 and –0.975 [rms = 0.112] |
| GoF[b] | 0.819 |

[a] $R1 = \Sigma||F_o| - |F_c||/\Sigma|F_o|$, $wR2 = \{\Sigma[w(F_o^2 - F_c^2)^2]/\Sigma[w(F_o^2)^2]\}^{1/2}$. [b] $GoF = \{\Sigma[w(F_o^2 - F_c^2)^2]/(n-p)\}^{1/2}$ where *n* is the number of data and *p* is the number of parameters refined.

CCDC-645738 contains the supplementary crystallographic data for this paper. These data can be obtained free of charge from The Cambridge Crystallographic Data Centre via www.ccdc.cam.ac.uk/data_request/cif.

**Supporting Information** (see also the footnote on the first page of this article): Full hydrogenation profiles for catalysis with **1** and **2**.

## Acknowledgments

This work was supported by the Ecole Polytechnique Fédérale de Lausanne (EPFL) and the Swiss National Science Foundation. We are grateful to Dr. R. Scopelliti and Dr. E. Solari for assistance with crystallography. We also thank the New Zealand Foundation for Research, Science and Technology for a Top Achiever Doctoral Fellowship (to A. B. C.).

[1] a) J.-C. Hierso, R. Amardeil, E. Bentabet, R. Boussier, B. Gautheron, P. Meunier, P. Kalck, *Coord. Chem. Rev.* **2004**, *236*, 143; b) H. A. Mayer, W. C. Kaska, *Chem. Rev.* **1994**, *94*, 1239; c) F. A. Cotton, B. Hong, *Prog. Inorg. Chem.* **1992**, *40*, 179.

[2] For example see: a) M. Rosales, R. Vallejo, J. J. Soto, G. Chacón, Á. González, B. González, *Catal. Lett.* **2006**, *106*, 101; b) J.-X. Chen, J. F. Daeuble, D. M. Brestensky, J. M. Stryker, *Tetrahedron* **2000**, *56*, 2153; c) V. Sernau, G. Huttner, M. Friz, L. Zsolnai, O. Walter, *J. Organomet. Chem.* **1993**, *453*, C23; d) C. Bianchini, A. Meli, M. Peruzzini, F. Vizza, F. Zanobni, *Coord. Chem. Rev.* **1992**, *120*, 193; e) J. Ott, G. M. R. Tombo, B. Schmid, L. M. Venanzi, G. Wang, T. R. Ward, *Tetrahedron Lett.* **1989**, *30*, 6151.

 © 2007 Wiley-VCH Verlag GmbH & Co. KGaA, Weinheim 

[3] a) C. Bianchini, A. Meli, M. Peruzzini, F. Vizza, P. Frediani, P. Frediani, J. A. Ramirez, *Organometallics* **1990**, *9*, 226; b) C. Bianchini, A. Meli, M. Peruzzini, F. Vizza, Y. Fujiwara, T. Jintoku, H. Taniguchi, *J. Chem. Soc. Chem. Commun.* **1988**, 299; c) C. Bianchini, A. Meli, F. Laschi, J. A. Ramirez, P. Zanello, *Inorg. Chem.* **1988**, *27*, 4429.
[4] a) P. Barbaro, C. Bianchini, P. Frediani, A. Meli, F. Vizza, *Inorg. Chem.* **1992**, *31*, 1523; b) P. Barbaro, C. Bianchini, C. Mealli, A. Meli, *J. Am. Chem. Soc.* **1991**, *113*, 3181; c) C. Bianchini, P. Frediani, F. Laschi, A. Meli, F. Vizza, P. Zanello, *Inorg. Chem.* **1990**, *29*, 3402.
[5] C. Bianchini, A. Meli, M. Peruzzini, A. Vacca, F. Vizza, *Organometallics* **1991**, *10*, 645.
[6] a) C. Bianchini, A. Meli, F. Vizza, *J. Organomet. Chem.* **2004**, *689*, 4277; b) C. Bianchini, A. Meli, *J. Chem. Soc. Dalton Trans.* **1996**, 801; c) C. Bianchini, A. Meli, *Acc. Chem. Res.* **1998**, *31*, 109.
[7] R. A. Findeis, L. H. Gade, *Eur. J. Inorg. Chem.* **2003**, 99.
[8] Metal impregnated silica: a) P. Barbaro, C. Bianchini, V. D. Santo, A. Meli, S. Moneti, R. Psaro, A. Scaffidi, L. Sordelli, F. Vizza, *J. Am. Chem. Soc.* **2006**, *128*, 7065; b) C. Bianchini, V. D. Santo, A. Meli, S. Moneti, M. Moreno, W. Oberhauser, R. Psaro, L. Sordelli, F. Vizza, *Angew. Chem. Int. Ed.* **2003**, *42*, 2536; Silica Alone: c) C. Bianchini, V. D. Santo, A. Meli, S. Moneti, M. Moreno, W. Oberhauser, R. Psaro, L. Sordelli, F. Vizza, *J. Catal.* **2003**, *213*, 47; d) C. Bianchini, V. D. Santo, A. Meli, W. Oberhauser, R. Psaro, F. Vizza, *Organometallics* **2000**, *19*, 2433; e) C. Bianchini, D. G. Burnaby, J. Evans, P. Frediani, A. Meli, W. Oberhauser, R. Psaro, L. Sordelli, F. Vizza, *J. Am. Chem. Soc.* **1999**, *121*, 5961.
[9] a) I. Rojas, F. L. Linares, N. Valencia, C. Bianchini, *J. Mol. Catal. A* **1999**, *144*, 1; b) C. Bianchini, P. Frediani, V. Sernau, *Organometallics* **1995**, *14*, 5458.
[10] a) M. Kandiah, G. S. McGrady, A. Decken, P. Sirsch, *Inorg. Chem.* **2005**, *44*, 8650; b) P. K. Baker, M. Al-Jahdali, M. M. Meehan, *J. Organomet. Chem.* **2002**, *648*, 99; c) C. Boxwell, P. J. Dyson, D. J. Ellis, T. Welton, *J. Am. Chem. Soc.* **2002**, *124*, 9334; d) D. H. Gibson, H. He, M. S. Mashuta, *Organometallics* **2001**, *20*, 1456; e) M. A. Rida, C. Copéret, A. K. Smith, *J. Organomet. Chem.* **2001**, *628*, 1; f) A. M. Bond, R. Colton, A. v. d. Bergen, J. N. Walter, *Inorg. Chem.* **2000**, *39*, 4696 (and references cited therein); g) G. Reinhard, R. Soltek, G. Huttner, A. Barth, O. Walter, L. Zsolnai, *Chem. Ber.* **1996**, *129*, 97; h) S. G. Davis, S. J. Simpson, H. Felkin, F. Tadj, O. Watts, *J. Chem. Soc. Dalton Trans.* **1983**, 981; i) S. G. Davis, H. Felkin, T. Fillebeen-Khan, F. Tadj, O. Watts, *J. Chem. Soc. Chem. Commun.* **1981**, 341.
[11] a) C. Landgrafe, W. S. Sheldrick, M. Südfed, *Eur. J. Inorg. Chem.* **1998**, 407; b) D. J. Rauscher, E. G. Thaler, J. C. Huffman, K. G. Caulton, *Organometallics* **1991**, *10*, 2209; c) J. Ott, L. M. Venanzi, C. A. Ghilardi, S. Midollini, A. Orlandini, *J. Organomet. Chem.* **1985**, *291*, 89; d) A. R. Sanger, *J. Chem. Soc. Dalton Trans.* **1977**, 121; e) W. O. Siegl, S. Lapporte, J. P. Collman, *Inorg. Chem.* **1973**, *12*, 674; f) W. O. Siegl, S. Lapporte, J. P. Collman, *Inorg. Chem.* **1971**, *10*, 2158.
[12] G. Kiss, I. Hováth, *Organometallics* **1991**, *10*, 3798.
[13] E. G. Thaler, K. Folting, K. G. Caulton, *J. Am. Chem. Soc.* **1990**, *112*, 2664.
[14] a) J. Scherer, G. Huttner, O. Walter, B. C. Janssen, L. Zsolnai, *Chem. Ber.* **1996**, *129*, 1603; b) J. Scherer, G. Huttner, M. Büchner, J. Bakos, *J. Organomet. Chem.* **1996**, *520*, 45.
[15] A. Jacobi, G. Huttner, U. Winterhalter, *J. Organomet. Chem.* **1998**, *571*, 231.
[16] M. J. Burk, J. E. Feaster, R. L. Harlow, *Tetrahedron: Asymmetry* **1991**, *2*, 569.
[17] J. Gimeno, V. Cardierno and P. Crochet, *Comprehensive Organometallic Chemistry III* (Eds.: D. M. P. Mingos, R. H. Crabtree, M. Bruce), Elsevier, Oxford, **2007**, Vol. 6, 465.
[18] a) M. R. J. Elsegood, M. B. Smith, N. M. Sanchez-Ballester, *Acta Crystallogr., Sect. E* **2006**, *62*, 2838; b) A. B. Chaplin, R. Scopelliti, P. J. Dyson, *Eur. J. Inorg. Chem.* **2005**, 4762.
[19] R. Kempe, A. Spannenberg, D. Heller, *Z. Kristallogr. - New Cryst. Struct.* **2001**, *216*, 153.
[20] P. A. Chaloner, M. A. Esteruelas, F. Joó and L. A. Oro, *Homogenous Hydrogenation*, Kluwer Academic, Dordrecht, **1994**.
[21] H.-J. Drexler, W. Baumann, A. Spannenberg, C. Fischer, D. Heller, *J. Organomet. Chem.* **2001**, *621*, 89.
[22] D. R. Anton, R. H. Crabtree, *Organometallics* **1983**, *2*, 855.
[23] This approach is inherently limited owing to the different possible coordination geometries that could be obtained and the chelate effect. For example, the triphos ligand adopts a *fac*-coordination geometry, while in the dppp-$PPh_3$ system the *mer*-geometry is more likely (see section 3). However, despite these limitations similar impacts on catalytic activity could be expected with high concentrations of $PPh_3$.
[24] No reactions of **2** with $PPh_3$ where observed before pressurisation with $H_2$.
[25] A. Cusanelli, U. Frey, D. T. Richens, A. E. Merbach, *J. Am. Chem. Soc.* **1996**, *118*, 5265.
[26] E. T. Singewald, C. S. Slone, C. L. Stern, C. A. Mirkin, G. P. A. Yap, L. M. Liable-Sands, A. L. Rheingold, *J. Am. Chem. Soc.* **1997**, *119*, 3048.
[27] Complexes **5** and **6** are only stable under hydrogen pressure, precluding full characterisation.
[28] J. Manson, *Multinuclear NMR*, Plenum Press, New York, **1987**, pg. 369.
[29] For example see ref.[31] and P. Meakin, J. P. Jesson, C. A. Tolman, *J. Am. Chem. Soc.* **1972**, *94*, 3240.
[30] C. Bianchini, D. Masi, A. Mali, M. Peruzzini, F. Zanobini, *J. Am. Chem. Soc.* **1988**, *110*, 6411.
[31] C. Merckle, S. Haubrich, J. Blümel, *J. Organomet. Chem.* **2001**, *627*, 44.
[32] M. A. Bennett, A. K. Smith, *J. Chem. Soc. Dalton Trans.* **1974**, 233.
[33] P. J. Dyson, J. S. McIndoe, *Inorg. Chim. Acta* **2003**, *354*, 69–74.
[34] Oxford Diffraction Ltd., Abingdon, Oxfordshire, U. K., **2003**.
[35] A. Altomare, M. C. Burla, M. Camalli, G. L. Cascarano, C. Giacovazzo, A. Guagliardi, A. G. Moliterni, G. G. Polidori, R. Spagna, *J. Appl. Crystallogr.* **1999**, *32*, 115.
[36] a) Bruker AXS, Inc., Madison, WI, **1997**; b) G. M. Sheldrick, *SHELXTL*, University of Göttingen, Germany, **1997**.
[37] N. Walker, D. Stuart, *Acta Crystallogr., Sect. A* **1983**, *39*, 158.
[38] L. J. Farrugia, *J. Appl. Crystallogr.* **1997**, *30*, 565.

Received: May 8, 2007
Published Online: September 11, 2007

 © 2007 Wiley-VCH Verlag GmbH & Co. KGaA, Weinheim 

DOI: 10.1002/ejic.200700436

# Combined Studies on the Surface Coordination Chemistry of Benzotriazole at the Copper Electrode by Direct Electrochemical Synthesis and Surface-Enhanced Raman Spectroscopy

**Ya-Xian Yuan,[a] Ping-Jie Wei,[a] Wei Qin,[a] Yong Zhang,[a] Jian-Lin Yao,*[a] and Ren-Ao Gu[a]**

**Keywords:** Benzotriazoles / Copper / Surface coordination / Electrochemistry / Raman spectroscopy

The surface coordination chemistry of benzotriazole (BTAH) on a Cu electrode was investigated by electrochemical synthesis of surface complexes and in situ electrochemical surface-enhanced Raman spectroscopy (SERS) in nonaqueous solution. Two different surface complexes were prepared in solution with or without triphenylphosphane ($PPh_3$). A new mixed-valence Cu–N cluster compound containing BTAH was synthesized by direct electrochemical oxidation of Cu in nonaqueous solutions with $PPh_3$. The final product, $Cu_5Cl(BTA)_5(PPh_3)_4$ was crystallized and characterized by microanalysis and Raman spectroscopy together with X-ray crystallographic determinations. The complex crystallized in a monoclinic space group ($P2_1/n$) with lattice parameters $a$ = 16.739(2) Å, $b$ = 18.919(2) Å, $c$ = 31.042(4) Å, $\beta$ = 103.194(3)°, $V$ = 9571.0(19) Å$^3$, $R_1$ = 0.0704, $wR_2$ = 0.1643. The results showed that the complex was a pentanuclear compound. The central $Cu^{II}$ atom is coordinated to four equatorial and one axial $BTA^-$ ligands to form a distorted tetragonal pyramidal coordination polyhedron, whereas each surrounding $Cu^I$ ion is in a distorted tetrahedral environment. The in situ SERS studies revealed that the $BTA^-$ ion was coordinated to a Cu surface through its two N atoms of the triazole ring to form a surface polymer complex of $[Cu(BTA)]_n$, which suppressed the dissolution and oxidation of Cu effectively. The introduction of $PPh_3$ blocked the surface coordination of BTAH with the electrode, and a complex of $BTA^-$ and $PPh_3$ with Cu was formed in the bulk solution.

(© Wiley-VCH Verlag GmbH & Co. KGaA, 69451 Weinheim, Germany, 2007)

## Introduction

The coordination chemistry of metal surfaces exposed to a corrosion medium has attracted considerable attention from the coordination chemists and surface scientists because of its economic importance.[1–5] For example, some organic molecules adsorbed on particular metal surfaces form a compact complex layer that can inhibit the corrosion of the surface effectively.[6–12] Despite the importance of special organic inhibitors, little attention has been paid to the investigation of how they bind or coordinate to the metal surfaces or as to why seemingly minor modifications in the structures of the active organic compounds can have a profound effect on their efficiency. Therefore, investigation into the interaction or the coordination chemistry of organic ligands with metal surfaces could be beneficial to obtain deeper insight into the adsorption behavior of ligands and their relevant surface coordination processes.

Generally, the deduction of the surface reaction mechanisms that include strong chemisorption or the formation of films (surface complexes) should be based on the known habits of the components and the structures of the surface complexes. One reliable and direct way to obtain such components is by the preparation of the corresponding surface complexes under conditions similar to those of the electrode surface. So far, many methods have been used to synthesize the relevant surface complexes. For example, the soluble metal salt and the ligands can simply be mixed in aqueous/nonaqueous solutions to produce the corresponding complexes, or the metal salt and the ligand solid powders can be mixed to form the complexes, a so-called solid-phase synthesis.[13] However, the direct electrochemical synthesis performed for the first time by Tuck and coworkers has exhibited several advantages for providing the comparable conditions of the surface.[14–21] This method consists in oxidizing a sacrificial metal anode in the nonaqueous solution with one or more appropriate kinds of ligands. Therefore, the synthetic conditions, including the bulk metal electrode, applied potential/current, solution (aqueous or nonaqueous), and electrolyte resemble the real electrode reaction system. As a consequence, on the basis of the interactions and chemical bonding between the ligand and the metal, it is reasonable to deduce the surface adsorption processes with the participation of some ligands on the electrode in the complex prepared by the electrochemical synthetic

[a] Department of Chemistry, Suzhou University (Dushu Lake campus),
Suzhou 215123, China
Fax: +86-512-65880089
E-mail: jlyao@suda.edu.cn

 WILEY InterScience DISCOVER SOMETHING GREAT © 2007 Wiley-VCH Verlag GmbH & Co. KGaA, Weinheim 

method. Moreover, no oxidant or reductant is introduced into the system of the electrochemical synthesis, and this avoids the possible complicated processes resulting from redox reactions. Alternatively, the oxidation of the metal electrode and the reduction of the ligands were carried out by the "clean" electron, which was removed or added on the anode and cathode by the applied potential/current. This dramatically decreased the contamination due to extraneous chemicals not only in the reaction processes but also in the separation of the final products. Most importantly, the adjustable applied potential/current made the reaction become highly selective, and thus enabled us to obtain the expected final products. However, the introduction of supporting electrolytes might be found in the final product in the form of anions or cations. In low concentrations, the appropriate amount of supporting electrolyte can, to some extent, minimize its negative effect on the complexes. Therefore, the direct electrochemical synthetic technique provided an effective way to simulate the electrochemical adsorption and reaction on the electrode surface, which allowed the structure and composition of the surface species to be obtained.

However, information on the dynamic and mechanistic aspects of the surface processes was not obtained by the above-mentioned techniques. Information about the processes that occur on the electrode surface can be gained by several modern surface techniques, such as scanning tunneling microscopy (STM), X-ray photoelectron spectroscopy (XPS), electron energy loss spectroscopy (EELS), sum frequency generation (SFG), and infrared and Raman spectroscopy.[10,11,22–25] Among them, Raman spectroscopy is a powerful tool for the investigation of the surface chemistry of adsorbed molecules involving adsorption and coordination at the liquid–solid interface, provided that the surface Raman signals are sufficiently enhanced.[26,27] In particular, surface-enhanced Raman scattering (SERS) has been shown to be a good method for determining the structure of molecules adsorbed on electrode surfaces.[28–34] Furthermore, unlike EELS and XPS, SERS can yield detailed surface information free from the interference of the bulk phase even at metal–liquid interfaces, and it has been widely used to investigate the dynamic and mechanisms of surface processes in situ.

To date, most coatings for metals have contained corrosion inhibitors as key constituents, and their activity was dependent on the surface coordination chemistry of the inhibitor. Benzotriazole (BTAH) is one of the most effective inhibitors for Cu and its alloys. Since the pioneering work of Cotton and coworkers,[35] the adsorption/coordination behavior and bonding structure between BTAH and a Cu substrate have been extensively studied by many authors by using various techniques, including electrochemical, surface analytical, and spectroscopic techniques.[36–40] Most of the previous work revealed that BTAH inhibited the corrosion of Cu in a wide pH range and potential region. For example, in different potential regions, BTAH can form a chemisorbed layer or a multilayer polymerized structural film with a larger thickness that increases the inhibition of corrosion significantly. The details of the mechanism by which the film forms and protects the metal are the subject of much investigation and debate.

Therefore, a powerful in situ technique with high surface sensitivity that is able to provide specific molecular information on metal surfaces has long been desired. Many researchers reported studies on the inhibition effect of BTAH by electrochemical SERS in aqueous solutions. To the best of our knowledge, there is no report on the studies of the adsorption/coordination chemistry and film formation of inhibitors in nonaqueous solutions. However, nonaqueous solvents are extremely important in both pure and applied electrochemistry, particularly as a component of the electrolyte that is in contact with the electrodes. Moreover, the involved organic molecules or inorganic ions can exhibit different inhibition efficiencies.[40,41] For example, the introduction of $I^-$ ions into solutions containing BTAH makes the inhibition efficiency for both the anodic and cathodic processes become even more remarkable,[42,43] which thus indicates the existence of a synergetic effect between the $I^-$ ions and benzotriazole on the inhibition. However, some organic ligands might play a negative role in the inhibition when it coexists with BTAH. For example, the introduction of ligands such as β-diketonate, acetylacetone, and triphenylphosphane ($PPh_3$) can result in remarkable differences in the structures of metal complexes with BTAH, specifically, the transformation of single metal nuclear to multinuclear complexes.[1,44–49] Therefore, it is worth investigating the inhibition of BTAH in nonaqueous solutions containing some organic molecules that might play an important role in the formation of surface complex films. In contrast, it is highly desirable to extend SERS studies directly to wider applications in surface science, not only for the various processes of corrosion and inhibition, but also for the surface coordination chemistry of BTAH together with other ligands. Triphenylphosphane is one of the most commonly used ligands in organometallic and coordination chemistry, and it is one of the most common ligands found in homogeneous transition-metal catalysts for the binding and transformation of organic substrates.[50–53] Phosphanes in general have been mainly used as protecting groups in organic synthesis as well as in catalytic processes, in which they were responsible for the decisive reaction step.[54] For this reason, $PPh_3$ was chosen as the second metal-binding domain in studying the surface coordination chemistry of BTAH on a Cu electrode.

In the present work, the adsorption behavior and film formation of BTAH were investigated by in situ electrochemical SERS on the surface of a Cu electrode in nonaqueous solution and by the coordination chemistry between the Cu surface and BTAH with and without $PPh_3$. Meanwhile, for the determination of the compositions and structures of the surface complexes, two kinds of complexes of BTAH and Cu with and without $PPh_3$ were synthesized by direct electrochemical synthesis and characterized by microanalysis, X-ray crystallographic measurements, and Raman spectroscopy. The modes of inhibitor on the Cu surface in nonaqueous solution were proposed.

 © 2007 Wiley-VCH Verlag GmbH & Co. KGaA, Weinheim 

## Results and Discussion

### Electrochemical Synthesis of the Complex

The electrochemical oxidation of Cu provided a convenient route to its coordination compound with the title ligands in a "one pot" procedure. One of the advantages of these techniques is that the metal in the product is frequently in a low oxidation state as the starting point is the element itself. It should be noted that the deposited layer on the anode resulted in its low conductivity. Thus, a mild voltage was applied to the system to maintain electrolysis. However, the electrochemical reaction potential was less than the applied voltage and the current density was maintained with a small value of about 5–8 $mA\,cm^{-2}$ during the electrolytic procedures. Therefore, the conditions used in the direct electrochemical synthesis were comparable to those at the Cu electrode surface, which was studied by in situ SERS. Complexes 1 and 2, which were synthesized by the electrochemical method, were expected to have the same composition as the Cu electrode surface in the electrochemical system for the in situ SERS investigation.

The stoichiometry of the electrochemical reaction is indicated by the electrochemical efficiency outlined in Equations (1) and (2), where $m$ is the weight lost at the Cu anode, $M$ is the molar mass of Cu, $z$ is the valence of the Cu ion, $i$ is the applied current, $t$ is the electrolysis time, and $F$ is Faraday constant; the value $\int_t^0 idt$ is determined by the silver coulomb meter, which is linked into the circuit, and is defined as the number of moles of metal dissolved from the anode per Faraday of charge. In the present study, the value of $E_f$ of $0.99\,mol\,F^{-1}$ and $0.98\,mol\,F^{-1}$ implied that the monovalent $Cu^I$ complex was formed on the electrode surface at the initial stage in solutions without/with $PPh_3$, respectively. The electrochemical systems can be represented as Pt(–)|$CH_3CN$, BTAH, electrolyte|Cu(+) and Pt(–)|$CH_3CN$, $PPh_3$, BTAH, electrolyte|Cu(+), respectively. The electrode reactions are outlined in Equations (3) and (4).

$$E_f = (m/M)F/\int_0 \mathrm{idt}(\mathrm{mol}/F) \quad (1)$$

$$z = 1/E_f = M\int_0^t \mathrm{idt}/mF \quad (2)$$

$$\text{cathode: } BTAH + e \rightarrow BTA^- + 1/2H_2 \quad (3)$$

$$\text{anode: } Cu \rightarrow Cu^+ + e \quad (4)$$

For the solution without $PPh_3$, the $BTA^-$ anion coordinated to the $Cu^+$ ion immediately to form a compact film that attached itself to the electrode surface. Actually, at the initial stage of the electrochemical synthesis, to be exact, as soon as the electrolytic current was applied, a yellow precipitate was produced that attached itself to the Cu electrode surface. At last, a dark yellow product was obtained after separation of the precipitate from the solution. Unfortunately, no crystal of the final product was obtained because of its poor solubility in most solvents. Elemental microanalysis of the sample gave a composition of C 61.35, H 4.18, N 11.47 (CuBTA: calcd. C 59.74, H 4.15, N 10.55) and revealed that the molar ratio of Cu to the $BTA^-$ anion was 1:1. Previous investigations of BTAH adsorbed on Cu electrodes showed that compact polymer films of $(CuBTA)_n$ were attached to the surface and inhibited the corrosion of Cu effectively in the aqueous solution;[12,29,40] this is in agreement with the synthesized sample that was prepared by mixing the $Cu^+$ compound with the BTAH solution. Therefore, it is reasonable to assume that the formula of the present sample was $(CuBTA)_n$ (complex 1). The overall reaction at the electrode surface is depicted in Equation (5). On the basis of previous experimental results, its structure was proposed as that shown in Figure 1.

$$nBTAH + nCu \xrightarrow{\text{electrolysis}} (CuBTA)_n + n/2H_2\uparrow \quad (5)$$

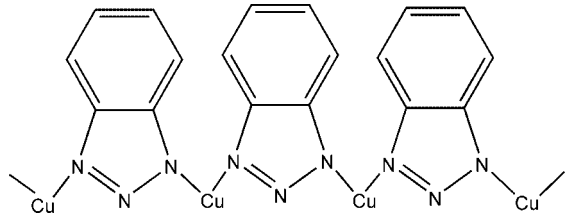


Figure 1. Proposed structure of the $(CuBTA)_n$ polymer complex.

The normal Raman spectrum of $(CuBTA)_n$ was presented with in situ SERS studies. The large blueshift of the triazole and benzene ring mode indicated the coordination of the $BTA^-$ ion with Cu. The detailed structure information will be discussed in the next section.

After the addition of $PPh_3$, no precipitation was observed on the Cu electrode surface or in the solution at the initial stage of the electrolytic reaction. With an increase in the electrolysis time, a brown-yellow precipitate was formed at the bottom of the flask. The absence of precipitation at the beginning of the electrochemical synthesis in the $CH_3CN$ solution with BTAH and $PPh_3$ indicated that no film was attached to the surface or that the prepared complex might be soluble in the $CH_3CN$ solution (normally, with a low solubility). To separate the precipitate, the nonaqueous solution was transferred into the fridge and yellow crystals were formed. Both the $BTA^-$ and $PPh_3$ signals were detected together in the normal Raman measurement of the crystal. The frequency of the triazole and benzene ring mode of $BTA^-$ was shifted to 1031 $cm^{-1}$, which is an indication of the coordination of the $BTA^-$ ion to the Cu electrode. This result revealed that both the $BTA^-$ ion and the $PPh_3$ ligand coordinate to the Cu ion. The final molecular formula and structure of this crystal should be deduced from its X-ray crystal structure.

### Crystal Structure of $Cu_5(BTA)_5(PPh_3)_4Cl$

Selected bond lengths and angles of the $Cu_5(BTA)_5(PPh_3)_4Cl$ complex are listed in Table 1. The $Cu_5(BTA)_5$-

 © 2007 Wiley-VCH Verlag GmbH & Co. KGaA, Weinheim 

$(PPh_3)_4Cl$ complex crystallizes as a pentanuclear complex, and its molecular structure is illustrated in Figure 2. Because the benzotriazolate ion has a charge of –1, the pentacopper complex is a mixed-valent material that contains four $Cu^I$ ions and one $Cu^{II}$ ion. The central $Cu^{II}$ ion is surrounded by four tetrahedrally coordinated $Cu^I$ ions held by bridging $BTA^-$ ligands. In the title complex, each tridentate $BTA^-$ ligand bridges two $Cu^I$ ions in two sides and coordinates to the central $Cu^{II}$ ion through its central nitrogen atom. The central $Cu^{II}$ ion is coordinated to four equatorial and one axial $BTA^-$ ligands at the N2, N5, N8, N11, and N14 positions, and it has a distorted tetragonal pyramidal coordination geometry with average distances of $Cu^{II}$–$N_{eq}$ 2.050(1) Å and $Cu^{II}$–$N_{ax}$ 2.294(3) Å. These values are comparable to the $Cu^{II}$–N bond lengths (2.08 and 2.29 Å, respectively) in the related $Cu_5(BTA)_6(tfpbd)_4$ complex (tfpdb = 4,4,4-trifluoro-1-phenyl-1,3-butanedione).[47] Each surrounding $Cu^I$ ion is four-coordinate with two types of coordination environments. For example, Cu3 (or Cu4) is in a distorted tetrahedral ($CuN_3P$) environment and is bound to three nitrogen atoms from different BTA ligands and a phosphorus atom in $PPh_3$. The $Cu^I$–N lengths Cu3–N9, Cu3–N3, and Cu3–N13 are about 2.061 Å and are close to those values in the complex [CuL($PPh_3$)] {L = bis(2-pyridyl)[2-(6-methoxy)pyridyl]methoxymethane} with the similar core of $CuN_3P$.[55] In addition to Cu1 (or Cu2) being coordinated to two nitrogen atoms in two different $BTA^-$ ligands and a phosphorus atom in $PPh_3$, it is also coordinated to a chloride ion that bridges two Cu centers with a Cu···Cu separation of 4.822 Å. The average value of all $Cu^I$–P bond lengths (about 2.1766 Å) is a little shorter than the value in $[Cu_4(BTA)_3(PPh_3)_4][Cu(PPh_3)_3](BF_4)_2$ [2.200(5) Å],[49] whereas the $Cu^I$–Cl bond lengths [Cu1–Cl1 2.4456(13) Å, Cu2–Cl1 2.4619(13) Å] are close to the value of about 2.455(1) Å in the $Cu_2Cl_2(PPh_3)_3$ complex together with a bridging chloride ion.[56]

Table 1. Selected bond lengths and bond angles of the $Cu_5(BTA)_5(PPh_3)_4Cl$ complex.

| Bond lengths [Å] | | | |
|---|---|---|---|
| Cu1–N1 | 2.041(3) | Cu3–N9 | 2.060(4) |
| Cu1–N4 | 2.067(3) | Cu3–N3 | 2.061(3) |
| Cu1–P1 | 2.1860(12) | Cu3–N13 | 2.062(4) |
| Cu1–Cl1 | 2.4456(13) | Cu3–P3 | 2.1813(12) |
| Cu2–N7 | 1.994(4) | Cu4–N15 | 2.031(4) |
| Cu2–N10 | 2.006(4) | Cu4–N6 | 2.081(3) |
| Cu2–P2 | 2.1435(15) | Cu4–N12 | 2.106(4) |
| Cu2–Cl1 | 2.4619(13) | Cu4–P4 | 2.1956(12) |
| Cu5–N2 | 2.033(3) | Cu5–N14 | 2.294(3) |
| Cu5–N11 | 2.050(3) | Cu5–N5 | 2.064(3) |
| Cu5–N8 | 2.052(4) | | |
| **Bond angles [°]** | | | |
| N1–Cu1–N4 | 91.89(14) | N1–Cu1–Cl1 | 97.69(10) |
| N1–Cu1–P1 | 130.91(10) | N4–Cu1–Cl1 | 93.65(10) |
| N4–Cu1–P1 | 127.92(10) | P1–Cu1–Cl1 | 105.78(5) |
| N7–Cu2–N10 | 96.33(16) | N9–Cu3–P3 | 120.67(11) |
| N7–Cu2–P2 | 128.18(11) | N3–Cu3–P3 | 122.72(10) |
| N10–Cu2–P2 | 126.78(12) | N13–Cu3–P3 | 117.46(11) |
| N7–Cu2–Cl1 | 94.95(12) | N15–Cu4–N6 | 99.40(14) |
| N10–Cu2–Cl1 | 98.03(11) | N15–Cu4–N12 | 96.11(14) |
| P2–Cu2–Cl1 | 104.44(5) | N6–Cu4 –N12 | 93.10(13) |
| N9–Cu3–N3 | 94.06(14) | N15–Cu4–P4 | 124.37(10) |
| N9–Cu3–N13 | 98.83(15) | N6–Cu4–P4 | 119.86(10) |
| N3–Cu3–N13 | 97.63(14) | N12–Cu4–P4 | 117.44(10) |
| N2–Cu5–N11 | 175.34(14) | N2–Cu5–N5 | 90.64(13) |
| N2–Cu5–N8 | 88.28(14) | N11–Cu5–N5 | 88.39(13) |
| N11–Cu5–N8 | 92.08(14) | N8–Cu5–N5 | 172.31(14) |
| N2–Cu5–N14 | 94.02(13) | N5–Cu5–N14 | 93.49(12) |
| N11–Cu5–N14 | 90.59(13) | Cu1–Cl1–Cu2 | 158.56(6) |
| N8–Cu5–N14 | 94.17(13) | | |

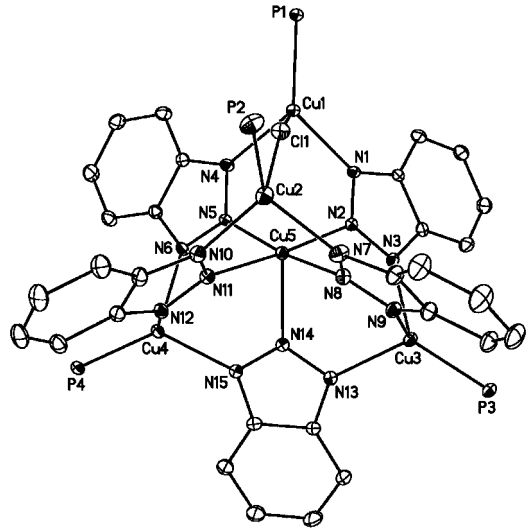


Figure 2. ORTEP drawing of the $Cu_5Cl(BTA)_5(PPh_3)_4$ complex. Hydrogen atoms are omitted for clarity.

For the $Cu^I$ ion bridged by the axial benzotriazolate anion and the chloride ion, the average distance between the surrounding $Cu^I$ ion is 5.315 Å and the distance increases to about 5.886 Å for the $Cu^I$ ion bridged by the equatorial benzotriazolate anions, whereas the average distance of about 3.500 Å between the surrounding $Cu^I$ and central $Cu^{II}$ ions is much shorter than the above-mentioned value. The structure of the complex bears resemblance to that of $Cu_5(BTA)_6(t\text{-}C_4H_9NC)_4$,[44] where the latter contains an extra $BTA^-$ group instead of the bridging chloride ion.

### In Situ Electrochemical SERS Investigation

Figure 3 presents a set of potential-dependent SERS spectra of BTAH from a roughened Cu electrode in a wide potential range in acetonitrile solution with or without $PPh_3$ together with the normal Raman spectra of two complexes prepared by an electrochemical method for comparison. The series of spectra on the right side of Figure 3 unambiguously demonstrate the change in spectral features over a narrow range. Because the surface coordination of the $BTA^-$ ion to the Cu electrode occurs in a positive potential range irreversibly, which was proven by relevant SERS studies in aqueous solution,[8,12] the potential-dependent spectra were recorded stepwise starting from a negative limit potential to more positive potentials so that all the ad-

 © 2007 Wiley-VCH Verlag GmbH & Co. KGaA, Weinheim 

sorption and surface coordination processes could be observed. It can be seen that the SERS spectra changed significantly with the applied potential not only in the intensity, but also in the frequency of the relevant bands. The spectra showed a similar spectral feature to that of the BTAH solid in the extremely negative potential region both in solution with or without $PPh_3$. For example, the surface spectra at –0.9 V without $PPh_3$ and at –1.0 V with $PPh_3$ exhibited the same frequency as the free BTAH for the triazole and benzene ring mode at 1022 $cm^{-1}$, respectively. This normally can serve as direct evidence for the determination of the coordination configuration of BTAH on the metal surface, although in this sample this band broadened significantly because of the complicated surface structure of the Cu electrode (as shown in Figure 3, right).[12] Our previous results indicated that the $BTA^-$ ion of the surface complex film showed a blueshift to ca. 1040 $cm^{-1}$ for this band. Therefore, the high similarity of the SERS spectra of BTAH on the surface to that from the bulk solution revealed the existence of an adsorption adlayer of BTAH molecules in the relative negative potential region in both solutions.

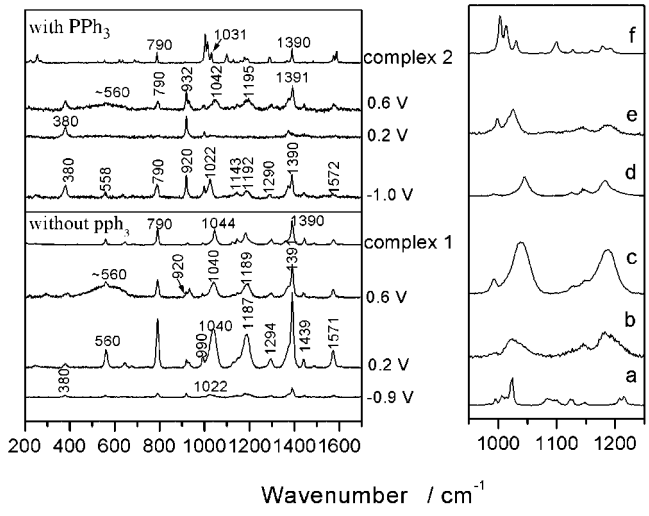


Figure 3. Potential dependent SERS spectra of BTAH adsorbed on the Cu electrode in acetonitrile solution without (bottom) and with 0.01 mol $dm^{-3}$ $PPh_3$ (upper) together with the normal Raman spectra of two surface complexes (left). The figure presented on the right is for comparison in the range from 950 to 1250 $cm^{-1}$: (a) BTAH solid; (b) without $PPh_3$ at –0.9 V; (c) 0.2 V; (d) complex 1; (e) with $PPh_3$ at –1.0 V; and (f) complex 2.

By moving the potential positively, the signal intensity also increased greatly and the frequency of the triazole and benzene ring mode shifted to 1040 $cm^{-1}$ at 0.2 V in the solution without $PPh_3$. Moreover, the surface spectrum at 0.2 V exhibited the same spectral features as that of the electrochemically synthesized $[Cu(BTA)]_n$ (complex 1; Figure 3, right). Most interestingly, the color of the electrode surface changed from brown to gray after the positive potential excursion, and the SERS measurement on the electrode in air without potential control exhibited similar spectral features to those in solution in the positive potential region. It was reported by many researchers that the $BTA^-$ ion can adsorb onto the Cu surface to form an irreversible compact polymer film of $[Cu(BTA)]_n$, which increases the inhibition efficiency dramatically in a certain potential region in aqueous solutions.[8,9,12,35–37] Therefore, it is reasonable to assume that the observed surface Raman spectrum at 0.2 V comprised contributions from this irreversible polymer film attached to the Cu surface in a wide potential range, that is, the BTAH was adsorbed on the surface by the coordination of N atoms with Cu atoms. In the extremely positive potential region, the signal of the film decreased remarkably. This occurred mainly because of the following two reasons: (1) the disappearance of or decrease in the SERS activity of the Cu surface owing to the oxidation of the Cu surface and (2) the partial breakage of the polymer film due to the formation of Cu oxide. At 0.6 V, the intensities of the bands decreased and a broad band at ca. 560 $cm^{-1}$ was detected with a sharp band at 560 $cm^{-1}$. The broad band was assigned to the stretching vibrational mode of Cu–O and the sharp band was assigned to the triazole ring torsion mode. Therefore, the observation of broad bands revealed the formation of Cu oxide in this potential region.

It is reasonable to assume that the surface complex (surface film) has the same composition as the synthesized complex. Therefore, on the basis of the fact that the potential-dependent adsorption behavior in nonaqueous solutions was similar to that in aqueous solutions, one can assume that BTAH adsorbs in the form of neutral BTAH molecules onto the Cu surface to form an adsorption layer in the negative potential region and in the form of $BTA^-$ ions to form a compact polymer film of the type $[Cu(BTA)]_n$ in the positive potential region; the polymer film partially breaks in the most positive potential region. The formation of a surface complex film results in a more compact barrier layer, which leads to a higher inhibition effect. Most interestingly, when a small amount of $PPh_3$ (the same concentration as BTAH) was introduced into the solution as above and the same experimental processes were performed, significant spectral changes were found. For example, the Raman signal of BTA/BTAH was not detected at 0.2 V, and the observed bands in this spectrum could be assigned to the vibrational modes of $CH_3CN$ and $PPh_3$. Therefore, the detected Raman signal in fact comes mainly from the bulk solvent rather than from the surface species. The great differences in the spectral features in this potential region might be caused by the differences in the compositions of the surface films on the surface, that is, the $PPh_3$ might play an important role in the formation of the surface film and it may modify the properties of the surface complex.

### The Role of $PPh_3$ in the Surface Coordination Chemistry of BTAH

It is well known that $PPh_3$ serves as a common ligand in metal coordination chemistry. On the basis of the hard–soft acid–base theory, low-valent metal ions (e.g. $Cu^+$) are a class of soft Lewis acids, whereas $PPh_3$ is a typical soft base.[57] Therefore, stabilization of the low-valent $Cu^+$ metal

 © 2007 Wiley-VCH Verlag GmbH & Co. KGaA, Weinheim 

ion was increased by the interaction of $PPh_3$ with the metal ion, which resulted in an increase in the softness by increasing the electron density on the metal ion. Generally, more than one $PPh_3$ molecule coordinated with one $Cu^+$ ion to form a $Cu(PPh_3)_n^+$ cation.[58–60] Therefore, this cation is a soft acceptor ion that can accommodate a wide range of coordination anions to form air-stable complexes.[61] In the direct electrochemical synthesis, the electrochemical efficiency $E_f$ value of ca. 1.0 mol $F^{-1}$ for both cases indicated that the Cu metal was oxidized to the $Cu^+$ ion in the electrochemical reaction. As a consequence, the central metal ion was $Cu^+$, which was quickly stabilized by the soft neutral $PPh_3$ ligand. Following that, the $BTA^-$ anion that was generated at the cathode participated to form a stable complex. In the final product, the separation of crystalline $Cu(PPh_3)_3Cl$ indicated the formation of $Cu(PPh_3)_3^+$ (Figure 4). However, the structure of the final product in the latter case of $Cu_5Cl(BTA)_5(PPh_3)_4$ indicated that the central $Cu^{II}$ was coordinated to four equatorial and one axial $BTA^-$ ligands to form a distorted tetragonal pyramidal coordination polyhedron, whereas each surrounding $Cu^I$ ion was in a distorted tetrahedral environment and coordinated with one $PPh_3$ ligand. It revealed that one $Cu^I$ ion was oxidized to $Cu^{II}$ after the electrochemical reaction, and some of the $PPh_3$ ligands that were coordinated to $Cu^I$ in the initial stage of the electrochemical procedure were exchanged by $BTA^-$ ligands in solution. The proposed surface coordination chemistry of BTAH is presented in Equation (6).

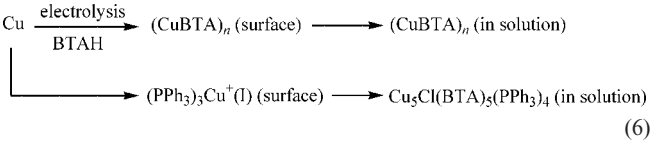


(6)

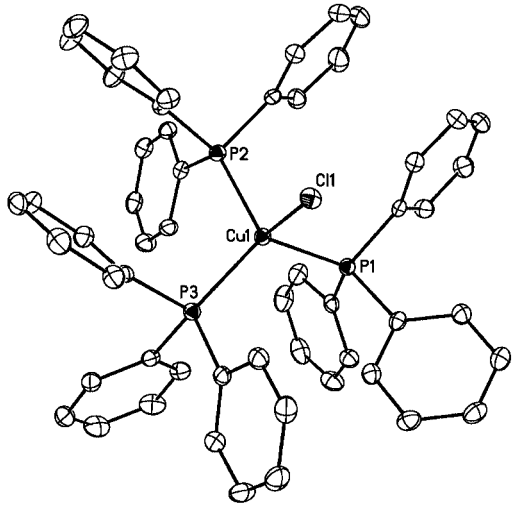


Figure 4. ORTEP drawing of the $Cu_3Cl(PPh_3)_3$ complex. Hydrogen atoms are omitted for clarity.

The in situ SERS measurements were in agreement with the processes of electrochemical synthesis, namely, the soluble $Cu(PPh_3)_3^+$ cation was firstly formed on the surface and then the complex was secondly formed in solution. Thus, the fact that no BTAH film covered the electrode surface resulted in the absence of an SERS signal at +0.2 V. There are two effects that can be attributed to the disappearance of the surface Raman signal of BTAH/$BTA^-$ at +0.2 V: (1) no compact film was formed on the electrode surface and (2) the decrease in the SERS activity because of the dissolution of Cu to form the $Cu(PPh_3)_3^+$ layer in the specific potential region. When the potential was increased again to the severe oxidization region, the surface atoms of the electrode were oxidized to $Cu^{2+}$ which were located at the borderline between being a hard acid and a soft acid. Conversely, because of the increase in the valence of Cu, an increase in the coordination numbers produces steric hindrance that hinders the participation of a large ligand such as $PPh_3$ in the coordination process. Therefore, the observation of the SERS signal from the $BTA^-$ ion and the absence of the SERS signal from the $PPh_3$ ligand in the potential region of 0.4 to 0.6 V revealed that the $Cu^{2+}$ ion could be coordinated by the $BTA^-$ anion directly to form a film on the surface again. At +0.6 V, a broad band at ca. 560 $cm^{-1}$ was detected, which was similar to that obtained in the solution without $PPh_3$. Therefore, it is reasonable to assume that the $BTA^-$ anion showed a similar adsorption or coordination behavior in the most positive potential region, specifically, the formation of surface complex film together with the Cu oxide.

The formation of longchains of the insoluble polymer $[Cu(BTA)]_n$ is suppressed because the neutral $PPh_3$ ligand participates in the formation of the complex and shows a strong stabilization effect on the complexes. As a consequence, the cation of $Cu(PPh_3)_3^+$ dissolves into $CH_3CN$ quickly and hence no strong signal of BTAH from the surface could be detected in a specific potential region. In fact, it accelerates the dissolution of the Cu electrode rather than strengthening the inhibition efficiency in that potential region; explicitly, the existence of $PPh_3$ plays a negative role in the inhibition of BTAH at the Cu surface.

## Conclusions

The surface coordination of BTAH onto the Cu surface was deduced to involve chemically adsorbed layers, a $BTA^-$ polymer film, and $PPh_3$-assisted surface dissolution. BTAH exhibits different adsorbed and filmed behaviors in different potential regions in solution. In the extremely negative potential region, the neutral BTAH molecules were adsorbed onto the Cu surface in acetonitrile solutions with or without $PPh_3$. BTAH also formed an attached polymer film on the surface in the medium without $PPh_3$, whereas a crystalline complex formed in solutions containing $PPh_3$. Our preliminary experiment showed that electrochemical synthesis combined with SERS studies could provide the surface coordination mechanism at the molecular level.

## Experimental Section

**Physical Measurements:** BTAH and $PPh_3$ (Aldrich) were used as received. Solvents were purified by standard methods. C and H

 © 2007 Wiley-VCH Verlag GmbH & Co. KGaA, Weinheim 

elemental analysis was performed with an Italy Carlo Erba MOD-1106 microanalysis instrument. Raman spectra were measured with a micro-Raman system of LabRam I with a low power He–Ne laser source.

**Electrochemical Synthesis of $(CuBTA)_n$, $Cu_5Cl(BTA)_5(PPh_3)_4$:** The electrosynthesis of the metal complex was carried out in acetonitrile by using Pt as the cathode and Cu as a sacrificial anode according to the technique described in our previous work.[21] The BTAH ligand (0.2374 g), with or without $PPh_3$ (0.5230 g), was dissolved in $CH_3CN$ (30 mL) containing a small amount of $Et_4NClO_4$ as the supporting electrolyte. The electrodes were treated with $HNO_3$, and washed and dried before use. All operations were carried out under the protection of dry Ar with rigorous exclusion of air by using standard vacuum line techniques. The voltage was regulated to obtain an initial current of 20 mA. As soon as the current flowed in the cell, bubbles of hydrogen gas were visible at the cathode. Five minutes later, pale yellow solids precipitated around the anode piece. After two hours of electrolysis, the Cu piece was rinsed, dried, and weighed to determine the electrochemical efficiency ($E_f$). A black powder was obtained in the solution without $PPh_3$ and defined as complex 1. For the system with $PPh_3$, the solid was isolated by filtration, and then dissolved in a mixture of acetonitrile/chloroform (1:1; complex 2). One week later, brown crystals of $Cu_5(BTA)_5(PPh_3)_4Cl{\cdot}2CH_3CN$ were separated out from the solution in a yield of ca. 63%. A little quantity of $Cu(PPh_3)_3Cl$ was separated from the final product and its structure was determined.

**X-ray Structure Determination:** $C_{106}H_{86}ClCu_5N_{17}P_4$ (2075.04): calcd. C 61.35, H 4.18, N 11.47; found C 59.74, H 4.15, N 10.55. A brown crystal having approximate dimensions of $0.60 \times 0.36 \times 0.35$ mm was selected and mounted on a glass fiber. All measurements were made with a Rigaku Mercury CCD diffractometer equipped with graphite-monochromated Mo-$K_\alpha$ ($\lambda$ = 0.71070 Å) radiation by using an $\omega$ scan mode in the range $3.02 < \theta < 27.48°$ at 193(2) K. A total of 99572 reflections were collected, of which 17353 with $I > 2\sigma(I)$ out of 21901 were unique ones ($R_{int}$ = 0.0512) were considered as observed. All of the calculations were performed by using the SHELXS-97package.[62] The structure was solved by direct methods and refined by full-matrix least-squares techniques on $F^2$. All non-hydrogen atoms were refined anisotropically, whereas the hydrogen atoms included in the final cycle of refinement were located on the calculated positions boned to their carrier atoms. The weighting scheme was $w = 1/[\sigma^2(F_o^2) + (0.0739P)^2 + 24.2198P]$, where $P = (F_o^2 + 2F_c^2)/3$, $S$ = 1.069. The final $R$ indices $R_1$ = 0.0704, $wR_2$ = 0.1643[$I > 2\sigma(I)$]. The crystallographic data is summarized in Table 2, and the crystal structure is presented in Figure 2. CCDC-283457 contains the supplementary crystallographic data for this paper. These data can be obtained free of charge from The Cambridge Crystallographic Data Centre via www.ccdc.cam.ac.uk/data_request/cif.

**The In Situ Electrochemical SERS Measurements:** Raman spectra were recorded with a confocal micro-Raman system (LabRam I from Dilor). The microscope attachment was based on an Olympus BX40 system and used a 50× long working length objective (≈ 8 mm) so that the objective would not be immersed into the solution. All the experiments were performed with the excitation line of 632.8 nm from an internal He–Ne laser with a power of 4 mW on the electrode surface. The electrochemical cell for the SERS measurement was made by Teflon with a quartz window for introducing the laser and collecting the Raman signal. The working electrode was a Cu disk with a geometric area of 0.1 $cm^2$ embedded in a Teflon rod. It was polished successively with 1 and 0.05 μm alumina powder and sonicated in triply distilled water. Consequently, a double potential step from –0.4 to + 0.4 V (vs. SCE) was applied to the electrode in 0.1 M KCl solution for about 2 min followed by a potential excursion at –0.4 V for 1 min, and then, it was rinsed thoroughly and dried with nitrogen to remove traces of water on the surface. A large Pt ring served as the counter electrode. The reference electrode was a solid Ag/AgCl electrode, which was prepared by electrochemical oxidation of an Ag wire with a constant anodic current of 0.4 $mA\,cm^{-2}$ in a 0.1 M HCl solution for 30 min. A detailed description of the spectroelectrochemical measurements is given elsewhere.[9,40] All experiments were performed at room temperature. All the chemicals used were analytical reagent grade. The solutions were prepared by using acetonitrile, which was pretreated to remove water.

Table 2. Crystal data for $Cu_5(BTA)_5(PPh_3)_4Cl{\cdot}2CH_3CN$.

| | |
|---|---|
| Empirical formula | $C_{106}H_{86}ClCu_5N_{17}P_4$ |
| Formula weight | 2074.95 |
| Crystal system | monoclinic |
| Space group | $P2_1/n$ |
| $a$ [Å] | 16.739(2) |
| $b$ [Å] | 18.919(2) |
| $c$ [Å] | 31.042(4) |
| $\beta$ [°] | 103.194(3) |
| $V$ [$Å^3$] | 9571.0(19) |
| $Z$ value | 4 |
| Crystal dimensions [mm] | $0.60 \times 0.36 \times 0.35$ |
| $D_{calcd.}$ [$g\,cm^{-3}$] | 1.440 |
| $F(000)$ | 4252 |
| Total reflections measured | 99572 |
| Unique | 21901 |
| Residuals: $R_1$ [$I > 2\sigma(I)$] | 0.0704 |
| Residuals: $wR_2$ [$I > 2\sigma(I)$] | 0.1643 |
| Maximum peak in final diff. map [$e\,Å^3$] | 1.764 |
| Minimum peak in final diff. map [$e\,Å^3$] | –1.382 |

## Acknowledgments

The authors gratefully acknowledge the financial support from the Nature Science Foundation of China (20503019, 20573076) and the Natural Science Foundation of Jiangsu Province (BK2005032). Y. X. Y. is partially supported by the Key Academic Discipline of Organic Chemistry of Jiangsu Province and Suzhou University for Young Teachers.

[1] J. Handley, D. Collison, C. D. Garner, M. Helliwell, R. Docherty, J. R. Lawson, P. A. Tasker, *Angew. Chem. Int. Ed. Engl.* **1993**, *32*, 1036–1038.
[2] M. Frey, S. G. Haris, J. M. Holmes, D. A. Nation, S. Parsons, P. A. Tasker, S. J. Teat, R. E. P. Winpenny, *Angew. Chem. Int. Ed.* **1998**, *37*, 2193–2197.
[3] J. M. Thorpe, R. L. Beddoes, D. Collison, C. D. Garner, M. Helliwell, J. M. Holmes, P. A. Tasker, *Angew. Chem. Int. Ed.* **1999**, *38*, 1119–1121.
[4] M. P. Soriaga, *Chem. Rev.* **1990**, *90*, 771–793.
[5] C. A. Melendres, N. Camillone, T. Tipton, *Electrochim. Acta* **1989**, *34*, 281–286.
[6] I. Dugdale, J. B. Cotton, *Corros. Sci.* **1963**, *3*, 69–74.
[7] R. Walker, R. C. Benn, *Electrochim. Acta* **1971**, *16*, 1081–1088.
[8] G. Xue, J. F. Ding, P. Lu, J. Dong, *J. Phys. Chem.* **1991**, *95*, 7380–7384.
[9] J. L. Yao, Y. X. Yuan, R. A. Gu, *J. Electroanal. Chem.* **2004**, *573*, 255–261.
[10] D. Chadwick, T. Hashemi, *Corros. Sci.* **1978**, *18*, 39–51.
[11] J. O'M. Bockris, M. A. Habib, J. L. Carbajal, *J. Electrochem. Soc.* **1984**, *131*, 3032–3033.

 © 2007 Wiley-VCH Verlag GmbH & Co. KGaA, Weinheim 

[12] J. Rubim, I. G. R. Gutz, O. Sala, W. J. Orvillethomas, *J. Mol. Struct.* **1983**, *100*, 571–583.
[13] J. P. Lang, X. Q. Xin, *J. Solid State Chem.* **1994**,*108*, 118–127.
[14] T. A. Annan, D. G. Tuck, *Organometallics* **1991**, *10*, 2159–2166.
[15] C. Oldham, M. J. Taylor, D. G. Tuck, *Inorg. Chim. Acta* **1985**, *100*, L9–L10.
[16] R. Castro, J. Romero, J. A. Garcia-Vazquez, M. L. Duran, A. Castineiras, A. Sousa, *J. Chem. Soc. Dalton Trans.* **1990**, 3255–3258.
[17] M. L. Duran, J. Romero, J. A. Garcia-Vazquez, R. Castro, A. Castineiras, A. Sousa, *Polyhedron* **1991**, *10*, 197–202.
[18] R. Castro, M. L. Duran, J. A. Garcia-Vazquez, J. Romero, A. Sousa, A. Castineiras, W. Hiller, J. Strahle, *J. Chem. Soc. Dalton Trans.* **1990**, 531–534.
[19] T. A. Annan, J. Gu, Z. Tian, D. G. Tuck, *J. Chem. Soc. Dalton Trans.* **1992**, 3061–3067.
[20] W. Y. Vivian, W. K. Lee, T. F. Lai, *Organometallics* **1993**, *12*, 2383–2387.
[21] Y. Yuan, J. Yao, J. Lu, Y. Zhang, R. Gu, *Inorg. Chem. Commun.* **2005**, *8*, 1014–1017.
[22] Y. Yamamoto, H. Nishihara, K. Aramaki, *Corrosion* **1992**, *48*, 641–648.
[23] L. J. Wan, *Acc. Chem. Res.* **2006**, *39*, 334–342.
[24] S. J. Huo, Q. X. Li, Y. G. Yan, Y. Chen, W. B. Cai, Q. J. Xu, M. Osawa, *J. Phys. Chem. B* **2005**, *109*, 15985–15991.
[25] Y. G. Yan, S. J. Huo, Q. J. Xu, W. B. Cai, *J. Phys. Chem. B* **2006**, *110*, 14911–14915.
[26] Z. Q. Tian, B. Ren, "Infrared and Raman Spectroscopy in Analysis of Surfaces" in *Encyclopedia of Analytical Chemistry* (Ed.: R. A. Meyers), John Wiley & Sons, Chichester, **2000**, pp. 9162–9201.
[27] K. Kneipp, H. Kneipp, I. Itzkan, R. R. Dasari, M. S. Feld, *Chem. Rev.* **1999**, *99*, 2957–2975.
[28] B. Pettinger in *Adsorption at Electrode Surface* (Eds.: J. Lipkowski, P. N. Ross), VCH, New York, **1992**, pp. 285–345.
[29] L. W. H. Leung, M. J. Weaver, *J. Electroanal. Chem.* **1987**, *217*, 367–384.
[30] Y. Zhang, X. Gao, M. J. Weaver, *J. Phys. Chem.* **1993**, *97*, 8656–8663.
[31] M. Fleischmann, Z. Q. Tian, L. J. Li, *J. Electroanal. Chem.* **1987**, *217*, 397–410.
[32] B. Pettinger, H. Wetzel, "Organic and Inorganic Species at Ag, Cu, and Au Electrodes" in *Surface Enhanced Raman Scattering* (Eds.: R. K. Chang, T. E. Furtak), Plenum, New York, USA, **1982**, pp. 293–314.
[33] R. K. Chang, "Raman Spectroscopic Techniques in Interfacial Electrochemistry" in *Spectroscopic and Diffraction Techniques in Interfacial Electrochemistry* (Eds.: C. Gutierrez, C. Melendres), Kluwer Academic, Drodrecht, Netherlands, **1990**, pp. 155–180.
[34] J. Lipkowski, L. Stolberg, "Molecular Adsorption at Gold and Silver Electrodes" in *Adsorption of Molecules at Metal Electrodes* (Eds.: J. Lipkowski, P. N. Ross), VCH, New York, USA, **1992**, ch. 4, pp. 171–238.
[35] J. B. Cotton, I. R. Scholes, *Br. Corros. J.* **1967**, *2*, 1–5.
[36] R. Youda, H. Nishihara, K. Aramaki, *Corros. Sci.* **1988**, *28*, 87–96.
[37] J. Kester, T. Furtak, *J. Electrochem. Soc.* **1981**, *128*, 112–112.
[38] P. G. Cao, J. L. Yao, J. W. Zheng, R. A. Gu, Z. Q. Tian, *Langmuir* **2002**, *18*, 100–104.
[39] P. G. Cao, R. A. Gu, Z. Q. Tian, *Langmuir* **2002**, *18*, 7609–7615.
[40] R. F. V. Villamil, P. Corio, J. C. Rubim, S. M. L. Agostinho, *J. Electroanal. Chem.* **1999**, *472*, 112–120.
[41] M. Fleischmann, I. R. Hill, G. Mengoli, M. M. Musiani, *Electrochim. Acta* **1983**, *28*, 1325–1333.
[42] Y. C. Wu, P. Zhang, H. W. Pickering, D. L. Allara, *J. Electrochem. Soc.* **1993**, *140*, 2791–2800.
[43] J. L. Yao, B. Ren, Z. F. Huang, P. G. Cao, R. A. Gu, Z. Q. Tian, *Electrochim. Acta* **2003**, *48*, 1263–1271.
[44] V. L. Himes, *J. Am. Chem. Soc.* **1981**, *103*, 211–212.
[45] E. G. Bakalbassis, E. Diamantopoulou, S. P. Perlepes, C. P. Raptopoulou, V. Tangoulis, A. Terzis, T. F. Zafiropoulous, *J. Chem. Soc. Chem. Commun.* **1995**, 1347–1348.
[46] E. Diamantopoulou, C. P. Raptopoulou, A. Terzis, V. Tangoulis, S. P. Perlepes, *Polyhedron* **2002**, *21*, 2117–2126.
[47] M. Murrie, D. Collison, C. Garner, M. Helliwell, P. A. Tasker, S. S. Turner, *Polyhedron* **1998**, *17*, 3031–3043.
[48] D. Collison, E. J. L. McInnes, E. K. Brechin, *Eur. J. Inorg. Chem.* **2006**, 2725–2733.
[49] D. Li, R. Li, Z. Qi, X. Feng, J. Cai, X. Shi, *Inorg. Chem. Commun.* **2001**, *4*, 483–485.
[50] G. Kickelbick, H. J. Paik, K. Matyjaszewski, *Macromolecules* **1999**, *32*, 2941–2947.
[51] I. Fenger, C. Le Drian, *Tetrahedron Lett.* **1998**, *39*, 4287–4291.
[52] K. Dehnicke, F. Weller, *Coord. Chem. Rev.* **1997**, *158*, 103–169.
[53] K. Nomiya, R. Noguchi, M. Oda, *Inorg. Chim. Acta* **2000**, *298*, 24–32.
[54] R. Pikl, F. Duschek, C. Fickert, R. Finsterer, W. Kiefer, *Vib. Spectrosc.* **1997**, *14*, 189–197.
[55] R. T. Jonas, T. D. P. Stack, *Inorg. Chem.* **1998**, *37*, 6615–6629.
[56] T. Kräuter, B. Neumüller, *Polyhedron* **1996**, *15*, 2851–2857.
[57] R. G. Pearson, *J. Am. Chem. Soc.* **1963**, *85*, 3533–3539.
[58] P. F. Barron, J. C. Dyason, P. C. Healy, L. M. Engelhardt, C. J. Pakawatchai, *J. Chem. Soc. Dalton Trans.* **1987**, 1099–1106.
[59] D. J. Fife, W. M. Moore, K. W. Morse, *Inorg. Chem.* **1984**, *23*, 1684–1691.
[60] G. Doyle, K. A. Eriksen, D. V. Engen, *Organometallics* **1985**, *4*, 830–835.
[61] R. D. Hart, P. C. Healy, G. A. Hope, D. W. Turner, A. H. White, *J. Chem. Soc. Dalton Trans.* **1994**, 773–779.
[62] G. M. Sheldrick, *SHELX-97 and SHELXL-97: Program for Crystal Structure Refinement*, University of Göttingen, Germany, **1997**.

Received: April 20, 2007
Published Online: September 10, 2007

 © 2007 Wiley-VCH Verlag GmbH & Co. KGaA, Weinheim 

DOI: 10.1002/ejic.200700554

# Cyclodiphosphazane *cis*-{(*o*-$MeOC_6H_4O$)P(μ-N*t*Bu)}$_2$ as a Bridging Bidentate Ligand: Synthesis, Structures of Heterometallic Complexes, and Halogen Exchange Between Rh–Cl and Cu–X (X = Br, I)

**P. Chandrasekaran,[a] Joel T. Mague,[b] Ramalingam Venkateswaran,[a] and Maravanji S. Balakrishna*[a]**

**Keywords:** Heterometallic complexes / Cyclodiphosphazanes / P,N ligands / Halogen exchange / Rhodium

The mononuclear rhodium complexes of cyclodiphosphazane [(cod)RhCl{L-κP}] (**1a**) (L = *cis*-{(*o*-$MeOC_6H_4O$)P(μ-N*t*Bu)}$_2$) and *trans*-[Rh(CO)Cl{L-κP}$_2$] (**1b**) react in a 1:1 molar ratio with [AuCl($SMe_2$)] to form the heteronuclear complexes [(cod)RhCl{μ-L-κP,κP}AuCl] (**2**) and *trans*-[Rh(CO)Cl{μ-L-κP,κP}$_2$(AuCl)$_2$] (**7**), respectively, in quantitative yield. The reaction between **1a** and CuCl afforded a tetranuclear complex [(cod)RhCl{μ-L-κP,κP}Cu(μ-Cl)]$_2$ (**3**). Under similar reaction conditions **1** reacts with 2 equiv. of CuX (X = Br, I) to produce the heteronuclear complexes [(cod)RhBr{μ-L-κP,κP}Cu(μ-Br)]$_2$ (**4**) and [((cod)RhI{μ-L-κP,κP})$_2$Cu(μ-X)$_2$Cu] (X ≈ 1:1 mixture of Cl and I disordered over both sites) (**5**), respectively, in which two molecules of **1a** are bridged by the rhombic, disordered, mixed halide [Cu(μ-X)$_2$Cu] (**5**: X = Br; **6**: X = Cl, I) unit. The crystal structures of **4** and **5** confirm the halogen exchange between the Rh–Cl and CuX (X = Br, I) moieties which leads to the formation of Rh–Br and Rh–I bonds. The heterodinuclear $Rh^I/Pd^{II}$ complex [(cod)RhCl{μ-L-κP,κP}PdCl($\eta^3$-$C_3H_5$)] (**6**) was synthesized by the reaction of **1a** with [PdCl($\eta^3$-$C_3H_5$)]$_2$ in a 2:1 ratio. Reaction of **1b** with CuI leads to the formation of the tetranuclear complex [Rh(CO)I{μ-L-κP,κP}$_2$Cu(μ-I)]$_2$ (**8**) containing two terminal uncoordinated phosphorus(III) centers irrespective of reactant ratio and reaction conditions. Halogen exchange reaction which leads to the formation of the Rh–I bond was also observed during the preparation of complex **8**.
(© Wiley-VCH Verlag GmbH & Co. KGaA, 69451 Weinheim, Germany, 2007)

## Introduction

The cooperativity or synergism present in heterometallic complexes gives remarkable chemical and biological properties compared to homonuclear complexes.[1] These heteromultinuclear complexes have applications in the formation of new materials with useful physicochemical properties,[2] and as polyfunctional catalysts for organic transformations.[3] The ligand design is important for the synthesis of heteronuclear complexes because the dimensionality and topology of the final structures are predominantly controlled by the location of donor sites in the ligand and their coordination preferences towards different metal centers.[4] Several phosphane ligands have been utilized for the synthesis of heterometallic complexes; however, in many cases formation of homonuclear complexes was observed along with the expected heterometallic complexes, due to the competition between different metal centers for the coordination sites and also due to the symmetric nature of bis(phosphanes). Preparation of heterometallic complexes can be made easier by choosing robust bidentate ligands which can perform as monodentate ligands under mild reaction conditions to give mononuclear complexes containing one or two free phosphorus(III) sites. These metalloligands containing uncoordinated phosphorus(III) centers can be conveniently treated with appropriate metal centers to form a variety of heterometallic complexes. In this context, cyclodiphosphazanes containing saturated four-membered $P_2N_2$ rings are interesting since they often exhibit monodentate coordination with several metal reagents under mild reaction conditions as shown in Scheme 1.[5,6] These mononuclear complexes containing uncoordinated phosphorus centers can be utilized to form heterometallic complexes. Such complexes can be of importance in homogeneous catalysis to promote

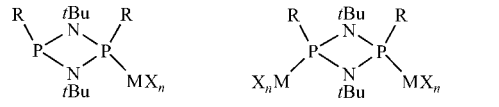


R = $OC_6H_4OMe$

| | |
|---|---|
| $MX_n$ = [$RuCl_2(\eta^6$-cymene)] | $MX_n$ = [$RhCl_2(CO)_2$] |
| [MCl(COD)] (M = Rh, Ir) | [PdCl($\eta^3$-$C_3H_5$)] |
| [$PdCl_2(PEt_3)$] | [CuX]∞ (X = Cl, Br, I) |
| [$MCl_2$(COD)L] (M = Pd, Pt) | [AgX]∞ (X = OTf, $ClO_4$) |
| [AgCN]∞ | [AuX] (X = Cl, Br, I) |

Scheme 1.

[a] Phosphorus Laboratory, Department of Chemistry, Indian Institute of Technology,
Bombay, Mumbai 400076, India
Fax: +91-22-2572-3480
E-mail: krishna@chem.iitb.ac.in
[b] Department of Chemistry, Tulane University,
New Orleans, Louisiana, LA 70118, USA

 © 2007 Wiley-VCH Verlag GmbH & Co. KGaA, Weinheim 

more than one type of catalysis and also for exploring the catalytic activity of multimetallic systems.[7] As a continuation of our work on transition metal chemistry of phosphorus-based ligands and their catalytic applications,[8] we describe in this article the synthesis and molecular structures of several heterometallic complexes of cyclodiphosphazanes.

## Results and Discussion

### Synthesis of Heterometallic Complexes

The rhodium(I) complex containing monocoordinated cyclodiphosphazane, [(cod)RhCl{L-κP}] (**1a**), chosen for the construction of heterometallic complexes was synthesized by treating *cis*-{(*o*-MeOC$_6$H$_4$O)P(μ-N*t*Bu)}$_2$ (L) with [Rh(cod)Cl]$_2$ as described previously.[6] The reaction of **1a** with 1 equiv. of [AuCl(SMe$_2$)] in dichloromethane at room temperature affords the heterodimetallic Rh$^I$/Au$^I$ complex **2** in good yield as shown in Scheme 2. The $^{31}$P NMR spectrum of **2** consists of two sets of doublets of doublets centered at δ = 104.7 and 94.1 ppm, respectively, for Au-coordinated and Rh-coordinated centers of the cyclodiphosphazane together with a low-intensity singlet at $\delta$ = 107.9 ppm attributable to the presence of a small amount of [ClAu{(*o*-MeOC$_6$H$_4$O)P(μ-N*t*Bu)}$_2$AuCl].[9] The formation of the dinuclear complex may be due to the replacement of the RhCl(cod) moiety present in **2** by [AuCl(SMe$_2$)] which was used in slight excess quantity for the complete conversion of **1a** into **2**. In order to confirm this metathesis reaction between Au and Rh centers, we carried out an NMR-tube reaction between [(cod)RhCl{L-κP}] (**1a**) and 2 equiv. of [AuCl(SMe$_2$)] in CDCl$_3$. We observed complete conversion of **1a** into dinuclear gold complex [ClAu{(*o*-MeOC$_6$H$_4$O)P(μ-N*t*Bu)}$_2$AuCl] as indicated by its $^{31}$P NMR spectrum which shows a single resonance at $\delta$ = 107.9 ppm. The gold-bound phosphorus center of **2** shows $^2J_{PP}$ and $^3J_{RhP}$ couplings of 30 and 5.5 Hz, respectively. The magnitude of $^3J_{RhP}$ is comparable with literature values,[10] while the rhodium-coordinated phosphorus atom shows a $^1J_{RhP}$ coupling of 247 Hz along with $^2J_{PP}$. However, compound **1a** did not show any $^2J_{PP}$ coupling and the $^1J_{RhP}$ coupling (229 Hz) was smaller than that of **2** (Table 1). The mass spectrum of **2** exhibits a peak at *m*/*z* = 893.21 which corresponds to the [M – Cl] ion (Figure 1).

Table 1. $^{31}$P{$^1$H} NMR spectroscopic data for complexes **1**–**7**.

| Compound | $\delta$(RhP) [ppm] | $^1J_{RhP}$ [Hz] | $\delta$(MP) [ppm] (other *J* values [Hz]) |
|---|---|---|---|
| **1a** | 102.8 (d) | 229 | 131.7 (s)[a] |
| **1b** | 112.5 (d) | 187 | 130.8 (s)[a] |
| **2** | 94.1 (dd) | 247 | 104.7 (dd, $^2J_{PP}$ = 30, $^3J_{RhP}$ = 5.58)[b] |
| **3** | 93.2 (d) | 227 | 93.8 (br. s)[c] |
| **4** | 93.0 (d) | 236 | 92.3 (br. s)[c] |
| **5** | 91.0 (d) | 259 | 90.2 (br. s)[c] |
| **6** | 94.1 (dd) | 240 | 130.6 (d, $^2J_{PP}$ = 37)[d] |
| **7** | 104.8 (d) | 219 | 106.8 (s)[b] |

[a] M = lone pair. [b] M = Au. [c] M = Cu. [d] M = Pd.

The equimolar reaction of **1a** with CuCl in CH$_3$CN/CH$_2$Cl$_2$ produces the tetranuclear, dimetallic complex **3**. The $^{31}$P NMR spectrum of **3** exhibits a doublet at $\delta$ = 93.2 ppm for the rhodium-coordinated phosphorus atom of the cyclodiphosphazane, while the signal due to the copper-coordinated phosphorus atom appears as a broad singlet at $\delta$ = 93.8 ppm. Reaction of 2 equiv. of CuX (X = Br, I) with **1a** leads to the formation of heterotetranuclear derivatives [(cod)RhBr(μ-L-κP,κP)Cu(μ-Br)]$_2$ (**4**) and [{(cod)RhI(μ-L-κP,κP)}$_2$Cu(μ-X)$_2$Cu] (**5**), respectively. The rhombic [Cu(μ-X)$_2$Cu] unit in complex **5** contains a ca. 1:1 mixture of Cl and I disordered over both sites as indicated by X-ray dif-

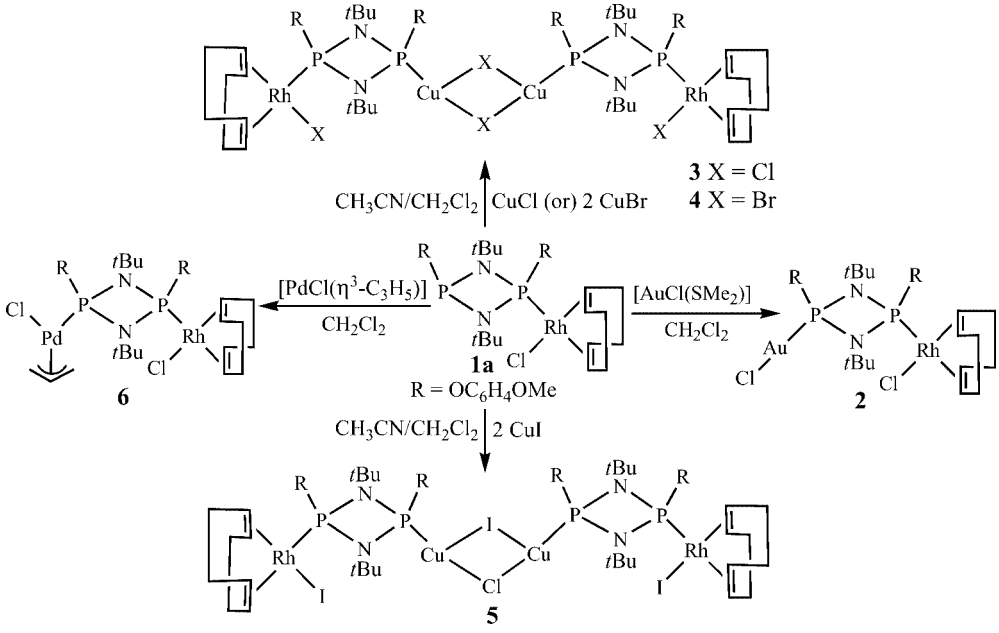


Scheme 2.

 © 2007 Wiley-VCH Verlag GmbH & Co. KGaA, Weinheim 

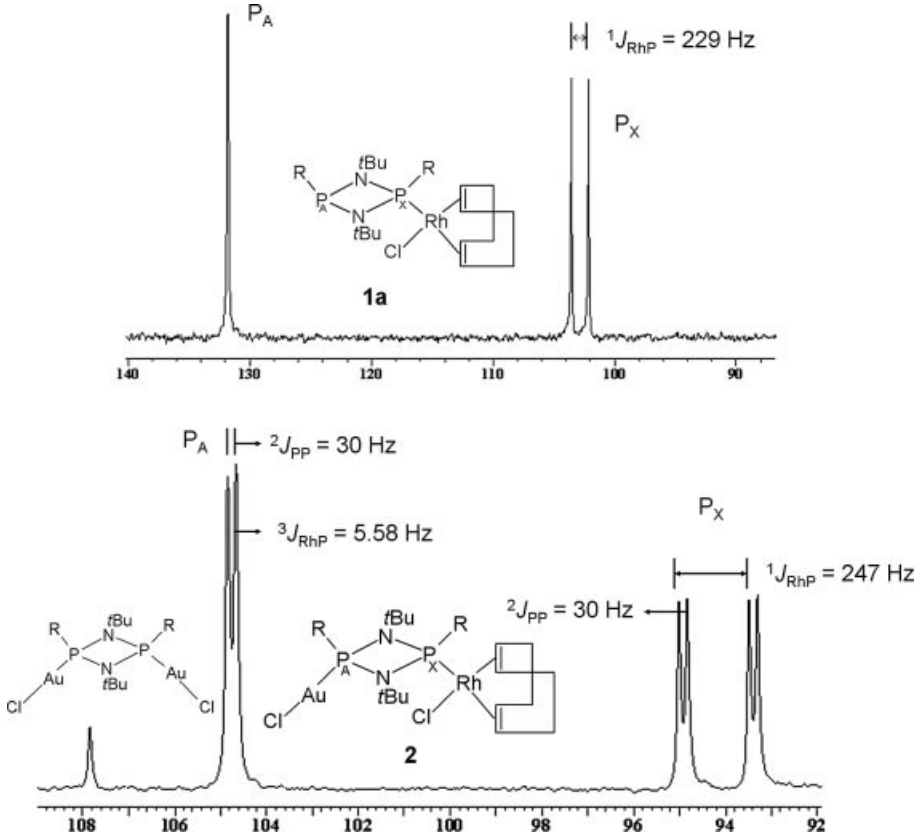


Figure 1. $^{31}P\{^{1}H\}$ NMR (161 MHz) spectrum of **1a** and **2** in $CDCl_3$.

fraction studies. Complexes **3**–**5** show a slight increase in their $^{1}J_{RhP}$ values as the halide varies from chloride to iodide (**3**: 227; **4**: 236; **5**: 259 Hz). Similar variations in $^{1}J_{RhP}$ have been seen in complexes containing the $[RhXP_3]$ unit depending on the nature of the anionic ligand X situated *cis* to the phosphorus atom in question[11] although the range is smaller than observed here. However, the remaining ligand set on Rh here is two C=C moieties which are weaker σ-donors than the two P atoms in the other examples and since the magnitude of $^{1}J_{MP}$ is sensitive to the *s*-orbital character in the M–P bond,[12] there should be more *s*-orbital character to share between Rh and X in the present case. Thus, a larger variation in the *s*-orbital character of the Rh–P bond with the nature of the halide ligand might be expected. The X-ray crystal structure of **5** reveals the presence of an Rh–I bond instead of the Rh–Cl bond present in the starting complex as well as the presence of a rhombic $[Cu(\mu\text{-}X)_2Cu]$ unit which clearly contains a mixture of chloride and iodide but because the unit sits on a crystallographic center of symmetry, the two halides are disordered over the two bridging sites. This result was unexpected since CuI was used in the reaction and suggests that the halogen exchange reaction occurs between the Rh–Cl bond present in **1a** and CuI to form the Rh–I derivative with concomitant formation of CuCl, which later coordinates to the uncoordinated phosphorus center of cyclodiphosphazane to produce a tetranuclear complex **5**. This indicates that the halogen exchange reaction occurs prior to the formation of Cu–P bonds. The formation of Rh–X (X = Br, I) through the halogen exchange between Rh–Cl and CuX (X = Br, I) as well as the preference for CuI over CuCl in coordination with phosphorus can be explained on the basis of the HSAB principle.[13]

The reaction of **1a** with $[PdCl(\eta^3\text{-}C_3H_5)]_2$ in dichloromethane in a 2:1 ratio produces the heterodinuclear complex $[(cod)RhCl(\mu\text{-}L\text{-}\kappa P,\kappa P)PdCl(\eta^3\text{-}C_3H_5)]$ (**6**) in good yield. The $^{31}P$ NMR spectrum of **6** exhibits a doublet centered at $\delta$ = 130.6 ppm with $^{2}J_{PP}$ = 37 Hz for the palladium-coordinated phosphorus atom, whereas the signal corresponding to the rhodium-coordinated phosphorus atom appears as a doublet of doublets centered at $\delta$ = 94.1 ppm ($^{1}J_{RhP}$ = 240 Hz, $^{2}J_{PP}$ = 37 Hz). Compounds **2**–**6** are stable solids and soluble in $CH_2Cl_2$, $CHCl_3$, and THF.

The complex *trans*-$[Rh(CO)Cl(L\text{-}\kappa P)_2]$ (**1b**)[6] containing two uncoordinated phosphorus centers from two *trans*-disposed cyclodiphosphazanes, when treated with 2 equiv. of $[AuCl(SMe_2)]$ in dichloromethane, afforded trinuclear complex **7** in quantitative yield (Scheme 3). The $^{31}P$ NMR spectrum of **7** consists of a singlet at $\delta$ = 106.8 ppm, which is assigned to the gold-coordinated phosphorus centers. The doublet appearing at $\delta$ = 104.8 ppm ($^{1}J_{PRh}$ = 218 Hz) is due to the rhodium-coordinated phosphorus centers. The IR spectrum of **7** shows $\nu_{CO}$ at 2019 $cm^{-1}$.

The slow addition of 2 equiv. of copper(I) iodide dissolved in acetonitrile to a dichloromethane solution of **1b** affords complex **8** containing two $Rh^{I}$ and two $Cu^{I}$ centers

 © 2007 Wiley-VCH Verlag GmbH & Co. KGaA, Weinheim 

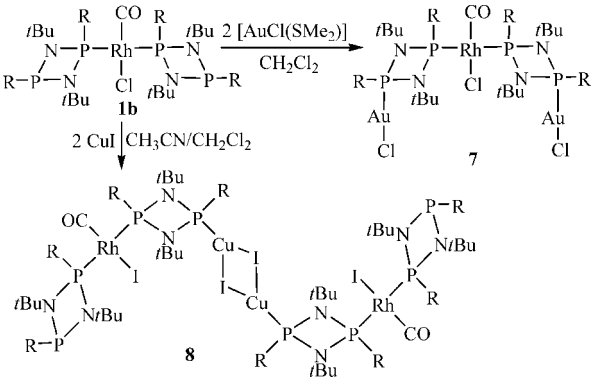


Scheme 3.

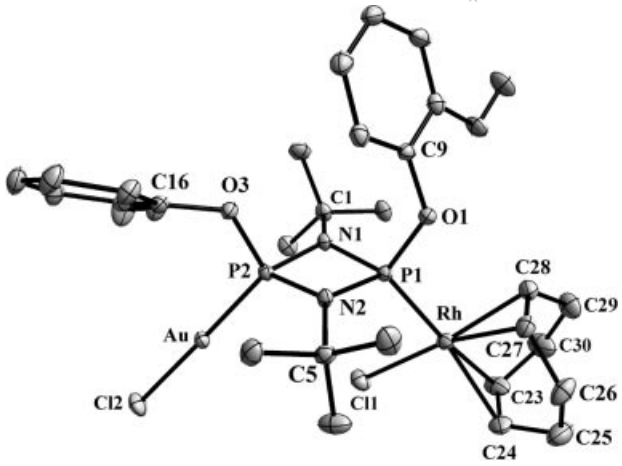


Figure 2. Molecular structure of **2**. Ellipsoids are drawn at the 50% probability level and H atoms and solvent molecules are omitted for clarity.

along with two uncoordinated P$^{III}$ ends. Complex **8** crystallizes from the mother liquor at room temperature and the X-ray quality yellow crystals obtained are insoluble in most organic solvents, thus preventing solution spectroscopic characterization. The IR spectrum of **8** shows a strong $\nu_{CO}$ band at 2021 cm$^{-1}$ which is slightly lower than that of the parent compound **1b**.[6] The analytical data for **8** indicate the formation of a 1:1 complex between **1b** and CuI, and also the presence of an Rh–I bond. The structure of **8** was confirmed by low-temperature X-ray diffraction studies. Surprisingly, only one of the two dangling phosphorus(III) centers of complex **1b** coordinates to CuI with the resulting dimetallic Rh/Cu complex dimerizing through the formation of a rhombic [Cu(μ-I)$_2$Cu] unit, leaving the other phosphorus(III) center uncoordinated. Since phosphorus prefers the softer CuI for coordination over the CuCl which is generated from the halogen exchange reaction, we carried out the reaction between **1b** and CuI in a 1:3 ratio to force coordination of CuI to the heretofore uncoordinated phosphorus atom in anticipation of the formation of a heteronuclear metallopolymer containing rhodium(I) and [Cu(μ-I)$_2$Cu] units bridged by the cyclodiphosphazane. However, we observed exclusive formation of complex **8** in this reaction as well as under various other conditions.

## Molecular Structures of 2, 4, 5, 7, and 8

Molecular structures of complexes **2**, **4**, **5**, **7**, and **8** with atom numbering schemes are shown in Figures 2, 3, 4, 5, and 6, respectively. Crystallographic information and the details of the structure determination are summarized in Table 6. The pertinent bond lengths and bond angles are listed in Tables 2, 3, and 4. A compilation of Cremer–Pople puckering parameters[14] for the cyclodiphosphazane rings in **2**, **4**, **5**, **7**, and **8** appears in Table 5.

X-ray quality crystals of **2** were grown from a 1:1 solution of $CH_2Cl_2$/$Et_2O$ at –30 °C. In complex **2**, the cyclodiphosphazane bridges the rhodium(I) and gold(I) moieties in a *cis* fashion through P-coordination. As noted in the previous section, the crystal used for the structure determination proved to contain about 3.8% of cocrystallized [ClAu{(*o*-MeOC$_6$H$_4$O)P(μ-N*t*Bu)}$_2$AuCl], but this impurity appears to have no effect on the derived structural parameters for **2**. Previously, Krishnamurthy and co-workers have reported[15] the crystal structure of a heterodimetallic Mo$^0$/W$^0$ complex containing μ-cyclodiphosphazane, *cis*-[(*p*-MeC$_6$H$_4$O)P(μ-NPh)]$_2$, which is the only structurally characterized heterometallic complex of cyclodiphosphazanes to date. The geometry around the gold center in complex **2** is linear with a P2–Au–Cl2 angle of 178.36(3)°, whereas the rhodium center is in a distorted square-planar environment. The P1–Rh bond length is 2.2269(8) Å, which is considerably shorter than that in the parent compound **1** [2.2439(9) Å]. The Rh–Cl and Rh–C bond lengths are almost equal in both the complexes [Rh–Cl 2.3605(5) Å for **1b**, 2.3612(9) Å for **2**]. The presence of a shorter Rh–P bond in **2** is also reflected in its $^{31}$P NMR spectrum, which shows a large $^1J_{RhP}$ coupling of 247 Hz, whereas that in complex **1** is 229 Hz. The Au–P2 bond length in **2** is 2.2084(8) Å, which is comparable to that found in the mononuclear gold complex [ClAu{(*o*-MeOC$_6$H$_4$O)P(μ-N*t*Bu)}$_2$] [2.210(1) Å].[9] Assessment of these bond parameters suggests a stronger metal–ligand interaction in the heterodimetallic complex **2** as compared to the homodimetallic complex. The exocyclic phenyl substituents on the phosphorus centers are arranged in an *exo*,*endo* manner. The P$_2$N$_2$ ring present in **2** is unevenly puckered (see Table 5) with the sum of the angles around N1 and N2 being 359.00(18)° and 355.46(12)°, respectively. The crystal structure of **2** contains a molecule of dichloromethane in the lattice which forms a weak C–H···Cl hydrogen bond with the chlorido ligand on the rhodium atom (C21–H31A···Cl1 153°; H31A···Cl1 2.56 Å which is significantly less than the 2.88 Å average normalized distance determined previously for this type of interaction[16]). The other hydrogen atom on this solvent molecule (H31B) makes a contact of less than the sum of the van der Waals radii with the chlorido ligand on the gold atom (Cl2), but the C–H···Cl angle is too small for this to be considered a hydrogen bond.

 © 2007 Wiley-VCH Verlag GmbH & Co. KGaA, Weinheim 

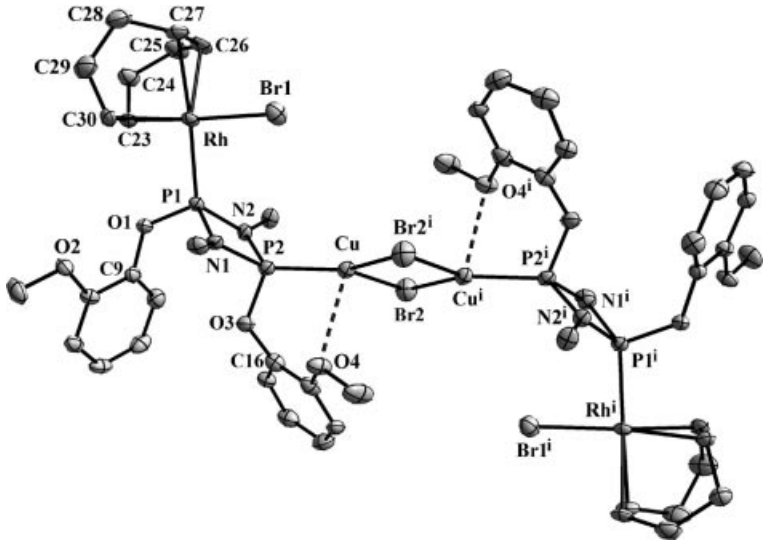


Figure 3. Molecular structure of **4**. Ellipsoids are drawn at the 50% probability level and H atoms and substituents on N (except α-C) are omitted for clarity.

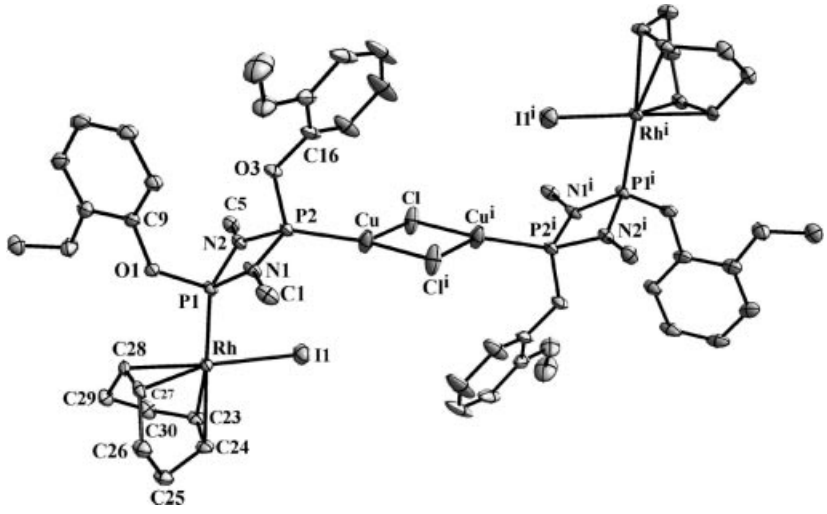


Figure 4. Molecular structure of **5**. Ellipsoids are drawn at the 50% probability level and H atoms and substituents on N (except α-C) are omitted for clarity.

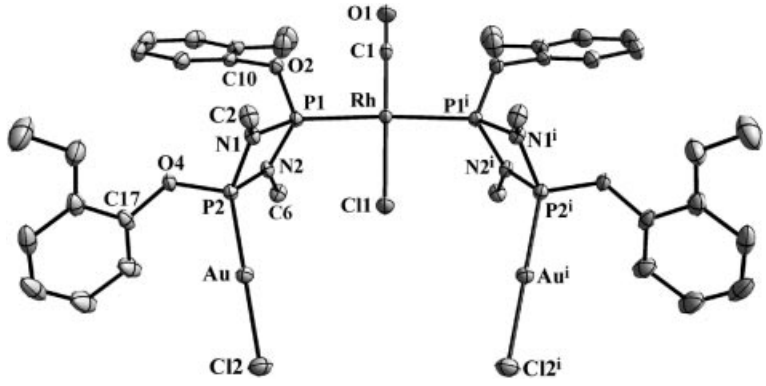


Figure 5. Molecular structure of **7**. Ellipsoids are drawn at the 50% probability level and H atoms and substituents on N (except α-C) are omitted for clarity.

 © 2007 Wiley-VCH Verlag GmbH & Co. KGaA, Weinheim 

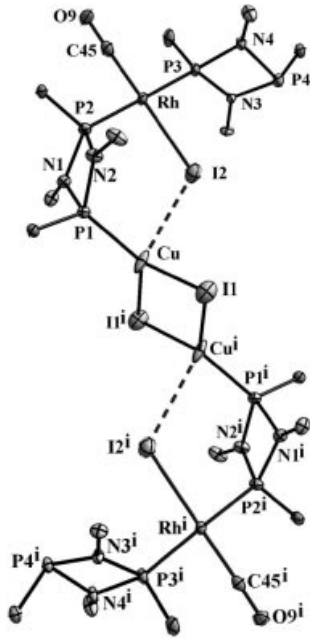


Figure 6. Molecular structure of **8**. Ellipsoids are drawn at the 50% probability level and H atoms and substituents on N (except α-C) are omitted for clarity.

Table 2. Selected bond lengths [Å] and bond angles [°] for **2**.

| Bond lengths | | Bond angles | |
|---|---|---|---|
| Rh–P1 | 2.2269(8) | P1–Rh–Cl1 | 88.91(3) |
| Au–P2 | 2.2084(8) | P2–Au–Cl2 | 178.36(3) |
| Rh–Cl1 | 2.3612(9) | P1–Rh–C23 | 164.7(1) |
| Au–Cl2 | 2.2868(8) | P1–Rh–C24 | 159.9(1) |
| Rh–C23 | 2.245(3) | P1–Rh–C27 | 91.52(9) |
| Rh–C24 | 2.254(3) | P1–Rh–C28 | 95.79(9) |
| Rh–C27 | 2.123(3) | C23–Rh–C28 | 81.6(1) |
| Rh–C28 | 2.128(3) | C23–Rh–C24 | 35.4(1) |
| P1–N1 | 1.693(2) | P1–N1–P2 | 96.2(1) |
| P1–N2 | 1.704(3) | P1–N2–P2 | 95.6(1) |
| P2–N1 | 1.667(2) | N1–P1–N2 | 82.8(1) |
| P2–N2 | 1.673(3) | N1–P2–N2 | 84.5(1) |
| P1–O1 | 1.607(2) | P1–O1–C9 | 127.7(2) |
| P2–O3 | 1.607(2) | P2–O3–C16 | 125.7(2) |
| N1–C1 | 1.494(4) | P1–N1–C1 | 131.32(20) |
| N2–C5 | 1.496(4) | P2–N1–C1 | 131.48(20) |

Crystals of **4** and **5** suitable for X-ray structure determination were obtained by slow evaporation of dichloromethane from respective 1:1 $CH_3CN/CH_2Cl_2$ solutions at room temperature. The core structures of **4** and **5** consist of a rhombic [Cu(μ-X)$_2$Cu] [X = Br (**4**) and X = apparent equimolar mixture of Cl and I (**5**)] unit bridging the two [(cod)RhX] (X = Br, I) moieties through two cyclodiphosphazanes as shown in Figures 3 and 4, respectively. Because the [Cu(μ-X)$_2$Cu] unit in **5** sits on a crystallographic center of symmetry, the bridging chlorido and iodido ligands are necessarily disordered, so it is not possible to say whether each molecule actually has a discrete [Cu(μ-Cl)(μ-I)Cu] unit at its center or if a more random distribution of Cl and I is present. The best model for refinement proved to be one in which Cl and I were given the same atomic coordinates and displacement parameters after which refinement of occupancy factors converged at ca. 0.5 for each atom type. Copper complexes containing mixed halide bridges are rare but in a copper(I) complex containing a mixed halide [$Cu_4Br_2Cl_2$] unit of distorted cubane geometry a 50:50 occupancy of all bridging halide sites was used as the model for refinement of the structure as we have done here. A similar disorder model was used in refining the structures of a series of $[Cu_2Cl_{6-x}Br_x]^{2-}$ ($x$ = 0.70–4.78) salts.[17] Copper centers adopt a distorted trigonal-planar geometry in both the molecules **4** and **5**. The bromo derivative **4** shows larger P2–Cu–Br [136.71(6)°] and short Br–Cu–Br$^i$ angles [99.50(4)°] compared with **5** [P2–Cu–X$^i$ 130.59(4)°, X–Cu–X$^i$ 103.79(2)°]. In structure **4**, the OMe groups present on exocyclic phosphorus substituents show strong interaction with the copper center [Cu···O4 2.691(4) Å], and this interaction leads to the formation of a boat-shaped six-membered ring around each copper center. However, complex **5** does not show such Cu···O interactions. The rhodium centers in **4** and **5** are located in the center of a distorted square-planar environment with the corners being occupied by iodido, phosphorus, and 1,5-cyclooctadiene ligands. The Rh–P1 bond lengths in **4** and **5** are 2.243(1) and 2.232(1) Å,

Table 3. Selected bond lengths [Å] and bond angles [°] for **4** and **5**.

| Bond lengths | | Bond angles | |
|---|---|---|---|
| Complex **4** | | | |
| Rh–P1 | 2.243(2) | Br1–Rh–P1 | 89.72(4) |
| Rh–Br1 | 2.484(2) | Br1–Rh–C26 | 91.45(18) |
| Rh–P1 | 2.243(2) | Br1–Rh–P1 | 89.72(4) |
| Rh–Br1 | 2.484(2) | Br1–Rh–C26 | 91.45(18) |
| Rh–C23 | 2.153(6) | Br1–Rh–C27 | 90.19(19) |
| Rh–C26 | 2.234(6) | P1–Rh–C23 | 93.11(16) |
| Rh–C27 | 2.261(6) | P1–Rh–C30 | 94.30(18) |
| Rh–C30 | 2.112(6) | C23–Rh–C26 | 81.0(2) |
| Cu–P2 | 2.154(2) | Br2–Cu–P2 | 136.71(6) |
| Br2–Cu | 2.370(2) | Cu–Br2–Cu$^i$ | 80.50(4) |
| P1–O1 | 1.630(4) | Br2–Cu–Br2$^i$ | 99.50(4) |
| P2–O3 | 1.625(4) | P2–Cu···O4 | 79.87(12) |
| P1–N1 | 1.685(5) | Cu–P2–O3 | 110.99(17) |
| P1–N2 | 1.690(5) | P1–O1–C9 | 128.1(4) |
| P2–N1 | 1.706(5) | P2–O3–C16 | 125.2(3) |
| P2–N2 | 1.692(5) | P1–N1–P2 | 96.5(3) |
| Cu···O4 | 2.691(4) | P1–N2–P2 | 96.8(3) |
| Cu···Cu$^i$ | 3.082 | N1–P1–N2 | 83.6(2) |
| | | N1–P2–N2 | 82.9(2) |
| Complex **5** | | | |
| Rh–P1 | 2.2318(9) | P1–Rh–I2 | 88.30(2) |
| Cu–P2 | 2.166(1) | P1–Rh–C23 | 157.5(1) |
| Rh–I2 | 2.6779(4) | P1–Rh–C24 | 167.4(1) |
| Rh–C23 | 2.256(3) | P1–Rh–C27 | 93.9(1) |
| Rh–C24 | 2.279(3) | P1–Rh–C28 | 94.8(1) |
| Rh–C27 | 2.122(3) | C23–Rh–C28 | 80.5(1) |
| Rh–C28 | 2.154(3) | C23–Rh–C24 | 35.1(1) |
| Cu– (Cl,I1) | 2.4894(7) | P2–Cu–(Cl,I1) | 130.59(4) |
| Cu– (Cl$^i$,I1$^i$) | 2.4647(7) | P2–Cu–(Cl$^i$,I1$^i$) | 123.40(3) |
| P1–N1 | 1.691(3) | (Cl,I1)–Cu–(Cl$^i$,I1$^i$) | 103.79(2) |
| P1–N2 | 1.681(3) | Cu–(Cl,I1)–Cu$^i$ | 76.21(2) |
| P2–N1 | 1.694(3) | P1–N1–P2 | 96.2(2) |
| P2–N2 | 1.686(3) | P1–N2–P2 | 96.9(2) |
| Cu···Cu$^i$ | 3.033 | N1–P1–N2 | 82.9(1) |
| | | N1–P2–N2 | 82.6(1) |

 © 2007 Wiley-VCH Verlag GmbH & Co. KGaA, Weinheim 

Table 4. Selected bond lengths [Å] and bond angles [°] for **7** and **8**.

| Bond lengths | | Bond angles | |
|---|---|---|---|
| Complex **7** | | | |
| Rh–P1 | 2.2687(7) | P1–Rh–Cl1 | 88.80(2) |
| Rh–Cl1 | 2.341(1) | P1–Rh–C1 | 91.12(2) |
| Rh–C1 | 1.841(4) | P1–Rh–P1$^{i}$ | 176.33(4) |
| Au–P2 | 2.1968(7) | Cl1–Rh–C1 | 176.6(1) |
| Au–Cl2 | 2.2720(7) | Au–P2–O4 | 113.61(8) |
| C1–O1 | 1.133(5) | P2–Au–Cl2 | 179.70(3) |
| P1–N1 | 1.699(2) | P1–N1–P2 | 95.8(1) |
| P1–N2 | 1.689(2) | P1–N2–P2 | 96.1(1) |
| P2–N1 | 1.671(2) | N1–P1–N2 | 82.9(1) |
| P2–N2 | 1.674(2) | N1–P2–N2 | 84.2(1) |
| P1–O2 | 1.608(2) | P1–O2–C10 | 126.9(2) |
| P2–O4 | 1.606(2) | P2–O4–C17 | 125.4(2) |
| Complex **8** | | | |
| P2–Rh | 2.288(2) | P2–Rh–C45 | 91.0(2) |
| P3–Rh | 2.302(2) | P3–Rh–C45 | 87.8(2) |
| P1–Cu | 2.173(2) | P2–Rh–I2 | 88.19(4) |
| Rh–I2 | 2.6799(7) | P3–Rh–I2 | 93.00(4) |
| Rh–C45 | 1.832(7) | P2–Rh–P3 | 178.25(6) |
| Cu–I1 | 2.505(1) | I2–Rh–C45 | 179.1(2) |
| Cu$^{i}$–I1 | 2.564(1) | P1–Cu–I1 | 128.95(6) |
| P1–N1 | 1.701(5) | P1–Cu–I$^{i}$ | 122.46(6) |
| P1–N2 | 1.701(5) | I1–Cu–I$^{i}$ | 105.01(3) |
| P2–N1 | 1.683(5) | Cu–I1–Cu$^{i}$ | 74.99(3) |
| P2–N2 | 1.686(5) | P1–N1–P2 | 95.9(3) |
| P3–N3 | 1.671(5) | P1–N2–P2 | 95.7(3) |
| P3–N4 | 1.685(5) | N1–P1–N2 | 82.6(3) |
| P4–N3 | 1.716(5) | N1–P2–N2 | 83.6(3) |
| P4–N4 | 1.725(6) | P3–N3–P4 | 97.7(7) |
| Cu···Cu$^{i}$ | 3.085 | P3–N4–P4 | 96.8(3) |
| Cu···I2 | 3.262 | N3–P3–N4 | 83.1(3) |
| | | N3–P4–N4 | 80.6(2) |

Table 5. Cremer–Pople puckering parameters for the cyclodiphosphazane in **2**, **5**, **7**, and **8**.

| Complex | $Q_2$ [Å] | Dihedral angle [°] P1–N1–N2 vs. N1–P2–N2 | Dihedral angle [°] P1–N1–P2 vs. P1–P2–N2 |
|---|---|---|---|
| **2** | 0.106 | 170.3 | 169.2 |
| **5** | –0.131 | 168.2 | 166.7 |
| **7** | –0.111 | 169.8 | 168.7 |
| **8** | 0.167 | 164.8 | 163.0 |
| | 0.155[a] | 166.2[b] | 164.2[c] |

[a] For the P3–N3–P4–N4 ring. [b] Dihedral angle P3–N3–N4 vs. P3–N4–P4. [c] Dihedral angle P3–N3–P4 vs. P3–P4–N4.

respectively, which is slightly shorter than that in the parent complex **1a**. The Cu···Cu$^{i}$ separation of 3.082(1) and 3.057(1) Å, respectively, in complexes **4** and **5**, indicate the absence of cuprophilicity.[18] The two rhodium moieties present in **4** and **5** are arranged in a *trans* disposition with respect to the [Cu(μ-X)$_2$Cu] plane; however, the molecules maintain the *cis* disposition of substituents on the phosphorus atom with respect to the $P_2N_2$ plane as was found in the molecular structure of **1a**.

Single crystals of **7** were grown by slow diffusion of hexane into a dichloromethane solution of the complex at room temperature. Complex **7** contains two gold centers bridged by rhodium-bound cyclodiphosphazanes to form a trinuclear complex with a conformation very similar to that of the parent complex **1b**. The geometry around the rhodium center is slightly distorted square-planar with *cis* angles varying from 88.80(2) (P1–Rh–Cl1) to 91.12(2)° (P1–Rh–C1). The gold centers are dicoordinated and have a linear geometry with a P2–Au–Cl2 angle of 179.70(3)° which is more linear than that in the monometallic complex of the same ligand [176.83(2)°] but comparable with that in $Ph_3PAuCl$ [179.63(2)°].[19] The Rh–P1 distance in **7** is 2.2687(7) Å, which is shorter than those in the parent compound [**1b**: 2.2784(6), 2.2863(6) Å] – a situation comparable to that in the Rh$^{I}$/Au$^{I}$ complex **2**. The Au–P2 bond length is 2.1968(7) Å which is slightly shorter than that in **3** but much shorter than that in the mononuclear gold complex of the same ligand, [AuCl({(*o*-MeOC$_6$H$_4$O)P(μ-N*t*Bu)}$_2$-κP)].[11] The phenyl substituents on the phosphorus centers are arranged in an *exo*,*endo* manner.

Crystals of **8** suitable for X-ray diffraction studies were obtained from a $CH_2Cl_2$/$CH_3CN$ solution at room temperature. The core structure of **8** consists of two *trans*-Rh(P$_2$N$_2$)$_2$ moieties that are bridged by a [Cu(μ-I)$_2$Cu] unit to form a heterometallic complex containing two Rh$^{I}$ and two Cu$^{I}$ centers along with an uncoordinated P$^{III}$ site at each end. These two *trans*-Rh(P$_2$N$_2$)$_2$ moieties are oriented in a *trans* manner with respect to the plane of the rhombic [Cu(μ-I)$_2$Cu] unit and gives the molecule an overall S-shape. The rhodium centers are in distorted square-planar geometries, whereas the copper centers are in trigonal-planar environments. The Rh–P2 bond [2.288(2) Å] is shorter than the Rh–P3 distance [2.302(2) Å] while the distance between the two copper atoms (Cu···Cu$^{i}$) is 3.085 Å at 100 K, which indicates the absence of metal–metal interactions in complex **8**. This stands in contrast to the low-temperature structure of (Cy$_3$P)Cu(μ-I)$_2$Cu(PCy$_3$) in which the Cu···Cu separation is 2.893(2) Å.[20] Interestingly, the molecular structure of **8** shows a weak interaction between the copper and iodine atoms to form two six-membered rings based on the observation that the Cu···I2 distance is 3.262 Å, which is distinctly shorter than the sum of the van der Waals radii for the two atoms (3.38 Å).[21] There are no unusually short intermolecular contacts apparent that would flex the molecule so as to cause I2 to approach Cu more closely than a van der Waals contact, but since the distance is much longer than normal bonding distances [2.525(4)–2.640(2) Å],[22] it is a weak attractive interaction at best. There also appears to be a distinct C–H···I hydrogen bond between the aromatic hydrogen atom H27 and I1 (H27···I1 2.993 Å; C27–H27···I1 156.05°) as the H27···I1 distance is less than the 3.15 Å mean H···I1 distance considered indicative of a C–H···I hydrogen bond.[16]

## Conclusions

Several heterodi-, -tri-, and -tetrametallic complexes [Cu$^{I}$/Rh$^{I}$ (3d/4d), Pd$^{II}$/Rh$^{I}$ (4d/4d), and Au$^{I}$/Rh$^{I}$ (5d/4d)] containing cyclodiphosphazanes are described. The selective mono- and bidentate coordination modes exhibited by cyclodiphosphazane with a range of metal precursors gives

 © 2007 Wiley-VCH Verlag GmbH & Co. KGaA, Weinheim 

a facile synthetic approach for construction of heterometallic systems. The halogen exchange reaction was observed for the first time between Rh–Cl and Cu–X (X = Br, I) during the synthesis of Cu$^{I}$/Rh$^{I}$ derivatives. Formation of rhombic [Cu(μ-X)$_2$Cu] units increases the nuclearity and can be utilized for the synthesis of a series of heterometallic coordination polymers. The work in this direction is currently underway in our laboratory.

## Experimental Section

**General:** All manipulations were performed under rigorously anaerobic conditions using high-vacuum manifolds and Schlenk techniques. All the solvents were purified by conventional procedures and freshly distilled and degassed prior to use.[23] Compounds *cis*-{(*o*-MeOC$_6$H$_4$O)P(μ-N*t*Bu)}$_2$ (L), [(cod)RhCl{L-κP}] (**1a**), *trans*-[Rh(CO)Cl{L-κP}$_2$] (**1b**),[6] [AuCl(SMe$_2$)],[24] CuX (X = Cl, Br)[25], and [PdCl(η-C$_3$H$_5$)]$_2$[26] were prepared according to published procedures. CuI was purchased from commercial sources and used as received.

**Instrumentation:** $^1$H and $^{31}$P{$^1$H} NMR (δ in ppm) spectra were recorded with a Varian Mercury Plus spectrometer operating at the appropriate frequencies using TMS and 85% $H_3PO_4$ as internal and external references, respectively. IR spectra of KBr disks were recorded with a Nicolet Impact 400 FT-IR instrument. Microanalyses were performed with a Carlo Erba Model 1112 elemental analyzer. Mass spectrometry experiments were carried out with a Waters Q-Tof micro-YA-105 instrument. Melting points were recorded in capillary tubes and are uncorrected.

**Synthesis of [(cod)RhCl{μ-L-κP,κP}AuCl] (2):** A dichloromethane solution (5 mL) of [AuCl(SMe$_2$)] (22.2 mg, 0.075 mmol) was added dropwise to a well-stirred dichloromethane solution (7 mL) of [(cod)RhCl{L-κP}] (**1a**) (52.5 mg, 0.075 mmol) at room temperature. The resulting yellow reaction mixture was stirred for 4 h. The solution was concentrated to 5 mL under reduced pressure, diluted with 5 mL of Et$_2$O and stored at –30 °C for 1 d to give the product as yellow crystals (62.4 mg, 89%). M.p. 222–224 °C (dec). $C_{30}H_{44}AuCl_2N_2O_4P_2Rh$ (929.4): calcd. C 38.76, H 4.77, N 3.01; found C 38.50, H 4.74, N 3.22. $^1$H NMR (400 MHz, CDCl$_3$, 25 °C): δ = 7.78–6.79 (m, 8 H, Ph), 5.77, 4.33 (br. s, 4 H, CH), 3.85 (s, 3 H, OMe), 3.82 (s, 3 H, OMe), 2.49–2.24 (m, 8 H, CH$_2$), 1.66 (s, 18 H, *t*Bu) ppm. $^{31}$P{$^1$H} NMR (161.9 MHz, CDCl$_3$, 25 °C): δ = 104.7 (dd, $^2J_{PP}$ = 30 Hz, $^3J_{RhP}$ = 5.58 Hz, 1 P, PAu), 94.1 (dd, $^1J_{PRh}$ = 247 Hz, 1 P, PRh) ppm. MS (EI): *m*/*z* = 893.21 [M – Cl].

**Synthesis of [(cod)RhCl{μ-L-κP,κP}Cu(μ-Cl)]$_2$ (3):** Copper(I) chloride (4.5 mg, 0.045 mmol), dissolved in acetonitrile (5 mL), was added dropwise to a well-stirred $CH_2Cl_2$ solution (10 mL) of [(cod)RhCl{L-κP}] (**1a**) (31.1 mg, 0.045 mmol) at room temperature. The resulting yellow reaction mixture was stirred for 6 h. The solution was concentrated to 5 mL under reduced pressure, diluted with Et$_2$O (5 mL) and stored at –30 °C for 1 d to afford yellow crystals of the product (33.9 mg, 61%). M.p. 228–230 °C (dec). $C_{60}H_{88}Cl_4Cu_2N_4O_8P_4Rh_2$ (1519.9): calcd. C 45.26, H 5.57, N 3.51; found C 45.53, H 5.39, N 3.44. $^1$H NMR (400 MHz, CDCl$_3$, 25 °C): δ = 7.89–6.84 (m, 16 H, Ph), 5.72, 4.32 (s, 8 H, CH), 3.93 (s, 6 H, OMe), 3.81 (s, 6 H, OMe), 2.48–2.22 (m, 16 H, CH$_2$), 1.57 (s, 36 H, *t*Bu) ppm. $^{31}$P{$^1$H} NMR (161.9 MHz, CDCl$_3$, 25 °C): δ = 93.8 (br. s, 2 P, CuP), 93.2 (d, $^1J_{PRh}$ = 227 Hz, 2 P, RhP) ppm.

**Synthesis of [(cod)RhBr{μ-L-κP,κP}Cu(μ-Br)]$_2$ (4):** The synthesis was the same as that for **3**, using copper(I) bromide (18.4 mg, 0.128 mmol) and [(cod)RhCl{L-κP}] (**1a**) (44.9 mg, 0.064 mmol). Yield: 74% (42.07 mg). M.p. 236–238 °C (dec). $C_{60}H_{88}Br_4Cu_2N_4O_8P_4Rh_2$ (1769.7): calcd. C 40.71, H 5.01, N 3.16; found C 40.94, H 5.17, N 3.24. $^1$H NMR (400 MHz, CDCl$_3$, 25 °C): δ = 7.94–6.84 (m, 16 H, Ph), 5.78, 4.44 (m, 8 H, CH), 3.93 (s, 6 H, OMe), 3.82 (s, 6 H, OMe), 2.41–2.19 (m, 16 H, CH$_2$), 1.55 (s, 36 H, *t*Bu) ppm. $^{31}$P{$^1$H} NMR (161.9 MHz, CDCl$_3$, 25 °C): δ = 93.0 (d, $^1J_{PRh}$ = 236 Hz, 2 P, RhP), 92.3 (br. s, 2 P, CuP) ppm.

**Synthesis of [((cod)RhBr{μ-L-κP,κP})$_2$Cu(μ-Cl,I)Cu] (5):** The synthesis was the same as that for **3**, using copper(I) iodide (27.5 mg, 0.144 mmol) and [(cod)RhCl{L-κP}] (**1a**) (50.3 mg, 0.072 mmol). Yield: 85% (57.10 mg). M.p. 224–226 °C (dec). $C_{60}H_{88}ClCu_2I_3N_4O_8P_4Rh_2$ (1866.3): calcd. C 38.61, H 4.75, N 3.00; found C 38.83, H 4.81, N 3.07. $^1$H NMR (400 MHz, CDCl$_3$, 25 °C): δ = 7.98–6.87 (m, 16 H, Ph), 5.87, 4.67 (br. s, 8 H, CH), 3.82 (s, 6 H, OMe), 3.81 (s, 6 H, OMe), 2.47–2.01 (m, 16 H, CH$_2$), 1.53 (s, 36 H, *t*Bu) ppm. $^{31}$P{$^1$H} NMR (161.9 MHz, CDCl$_3$, 25 °C): δ = 91.0 (d, $^1J_{PRh}$ = 259 Hz, 2 P, RhP), 90.2 (br. s, 2 P, CuP) ppm.

**Synthesis of [(cod)RhCl{μ-L-κP,κP}PdCl(η$^3$-C$_3$H$_5$)] (6):** A dichloromethane solution (5 mL) of [PdCl(η$^3$-C$_3$H$_5$)]$_2$ (16.9 mg, 0.046 mmol) was added dropwise to a well-stirred dichloromethane (10 mL) solution of [(cod)RhCl{L-κP}] (**1a**) (64.6 mg, 0.093 mmol) at room temperature. The reaction mixture was stirred for 6 h, concentrated to 5 mL under reduced pressure, diluted with diethyl ether (5 mL) and stored at –30 °C for 1 d to give a yellow crystalline solid (61.3 mg, 75%). M.p. 160–162 °C (dec). $C_{33}H_{49}Cl_2N_2O_4P_2PdRh$ (879.9): calcd. C 45.04, H 5.61, N 3.18; found C 45.31, H 5.82, N 3.37. $^1$H NMR (400 MHz, CDCl$_3$, 25 °C): δ = 7.79–6.76 (m, 8 H, Ph), 5.60 (br. s, 1 H, allyl CH), 5.73, 4.32 (s, 4 H, cod CH), 4.66, 3.65 (m, 4 H, allyl CH$_2$), 3.84 (s, 3 H, OMe), 3.82 (s, 3 H, OMe), 2.46–2.25 (m, 8 H, CH$_2$), 1.57 (s, 18 H, *t*Bu) ppm. $^{31}$P{$^1$H} NMR (161.9 MHz, CDCl$_3$, 25 °C): δ = 130.6 (d, $^2J_{PP}$ = 37 Hz, 1 P, PPd), 94.1 (dd, $^1J_{PRh}$ = 240 Hz, 1 P, PRh) ppm.

**Synthesis of *trans*-[Rh(CO)Cl{μ-L-κP,κP}$_2$(AuCl)$_2$] (7):** To a suspension of *trans*-[Rh(CO)Cl{L-κP}$_2$] (**1b**) (100 mg, 0.093 mmol) in acetonitrile (5 mL), a dichloromethane solution (10 mL) of [AuCl(SMe$_2$)] (55.1 mg, 0.187 mmol) was added dropwise at room temperature. The reaction mixture was stirred for 4 h, concentrated to 10 mL under reduced pressure, and diluted with hexane (5 mL). Storing the resulting clear yellow solution overnight afforded a crystalline product (132 mg, 93%). M.p. 236–238 °C. $C_{45}H_{64}Au_2Cl_3N_4O_9P_4Rh$ (1532.1): calcd. C 35.27, H 4.21, N 3.65; found C 35.02, H 4.10, N 3.88. IR (KBr disk): $\tilde{\nu}$ = 2019 [ν(C≡O)] cm$^{-1}$. $^1$H NMR (400 MHz, CDCl$_3$, 25 °C): δ = 7.31–6.91 (m, 16 H, Ph), 3.93 (s, 6 H, OMe), 3.91 (s, 6 H, OMe), 1.73 (s, 36 H, *t*Bu) ppm. $^{31}$P{$^1$H} NMR (161.9 MHz, CDCl$_3$, 25 °C): δ = 106.8 (s, 2 P, PAu), 104.8 (d, $^1J_{PRh}$ = 218.5 Hz, 2 P, PRh) ppm.

**Synthesis of [Rh(CO)I{μ-L-κP,κP}$_2$Cu(μ-I)]$_2$ (8):** Copper(I) iodide (0.019 g, 0.101 mmol) in $CH_3CN$ (5 mL) was added dropwise to a well-stirred dichloromethane solution (10 mL) of *trans*-[Rh(CO)Cl{L-κP}$_2$] (**1b**) (0.054 g, 0.051 mmol) at room temperature. The reaction mixture was stirred for 6 h. Upon standing at room temperature for 3 d, the yellow solution afforded compound **8** as dark yellow crystals (47.5 mg, 69%). M.p. 248–250 °C (dec). $C_{90}H_{128}Cu_2I_4N_8O_{18}P_8Rh_2$ (2698.3): calcd. 40.06, H 4.78, N 4.15; found C 40.38, H 4.42, N 4.27. IR (KBr disk): $\tilde{\nu}$ = 2021 [ν(C≡O)] cm$^{-1}$.

**X-ray Crystallography:** Crystals of **2**, **4**, **5**, **7**, and **8** were mounted in a CryoLoop with a drop of Paratone oil and placed in the cold nitrogen stream of the Kryoflex attachment of the Bruker APEX CCD diffractometer (Table 6). For each, a full sphere of data was collected using a protocol of 400 scans in ω (0.5° per scan) at φ =

 © 2007 Wiley-VCH Verlag GmbH & Co. KGaA, Weinheim 

Table 6. Crystallographic parameters and refinement details for complexes **2**, **4**, **5**, **7**, and **8**.

| | **2**·$CH_2Cl_2$ | **4** | **5** | **7** | **8** |
|---|---|---|---|---|---|
| Empirical formula | $C_{31}H_{46}AuCl_4N_2O_4P_2Rh$ | $C_{60}H_{88}Br_4Cu_2N_4O_8P_4Rh_2$ | $C_{60}H_{88}ClCu_2I_3N_4O_8P_4Rh_2$ | $C_{45}H_{64}Au_2Cl_3N_4O_9P_4Rh$ | $C_{90}H_{128}Cu_2I_4N_8O_{18}P_8Rh_2$ |
| Formula mass | 1023.61 | 1769.76 | 1866.27 | 1532.08 | 2698.29 |
| Crystal system | monoclinic | triclinic | monoclinic | orthorhombic | triclinic |
| Space group | $P2_1/c$ | $P\bar{1}$ | $P2_1/c$ | *Pnma* | $P\bar{1}$ |
| *a* [Å] | 11.161(1) | 9.863(1) | 10.7191(8) | 13.642(1) | 12.119(1) |
| *b* [Å] | 17.253(2) | 10.319(1) | 18.665(1) | 29.323(3) | 15.336(2) |
| *c* [Å] | 19.776(2) | 18.877(2) | 17.017(1) | 15.236(1) | 16.499(2) |
| *α* [°] | 90 | 91.670(1) | 90 | 90 | 106.365(1) |
| *β* [°] | 100.281(1) | 98.434(1) | 91.675(1) | 90 | 103.718(1) |
| *γ* [°] | 90 | 114.655(1) | 90 | 90 | 104.491(1) |
| *V* [Å$^3$] | 3746.9(6) | 1718.3(3) | 3403.1(4) | 6094.6(9) | 2687.8(5) |
| *Z* | 4 | 1 | 4 | 4 | 1 |
| $\rho_{calcd.}$ [g cm$^{-3}$] | 1.815 | 1.710 | 1.812 | 1.670 | 1.667 |
| $\mu$(Mo-$K_\alpha$) [mm$^{-1}$] | 4.758 | 3.554 | 2.641 | 5.355 | 2.024 |
| *F*(000) | 2015 | 888 | 1834 | 2992 | 2696 |
| Crystal size [mm] | 0.10 × 0.15 × 0.18 | 0.05 × 0.15 × 0.19 | 0.15 × 0.17 × 0.20 | 0.09 × 0.17 × 0.17 | 0.17 × 0.13 × 0.06 |
| *T* [K] | 100 | 100 | 100 | 100 | 100 |
| *θ* range [°] | 2.1–28.3 | 2.2–28.2 | 2.2–28.3 | 1.4–28.3 | 1.4–28.3 |
| Total no. reflns. | 65502 | 29820 | 59384 | 52609 | 23883 |
| No. of indep. reflns. | 9318 ($R_{int}$ = 0.041) | 8357 ($R_{int}$ = 0.051) | 8484 ($R_{int}$ = 0.035) | 7582 ($R_{int}$ = 0.037) | 12230 ($R_{int}$ = 0.025) |
| $R_1$[a] | 0.0269 | 0.0558 | 0.0381 | 0.0255 | 0.0635 |
| $wR_2$[b] | 0.0636 | 0.1602 | 0.1056 | 0.0615 | 0.1926 |
| Goodness-of-fit on $F^2$ | 1.05 | 1.03 | 0.97 | 1.04 | 1.04 |

[a] $R = \Sigma||F_o| - |F_c||/\Sigma|F_o|$. [b] $wR_2 = \{[\Sigma w(F_o^2 - F_c^2)/\Sigma w(F_o^2)^2]\}^{1/2}$.

0, 90, and 180° plus 800 scans in $\phi$ (0.45° per scan at $\omega$ = –30 and 210° for **2**, **4**, and **5**) and one of 606 scans in $\omega$ (0.3° per scan) at $\phi$ = 0, 120, and 240° for **7** and **8** using the SMART software package.[27] The raw data were reduced to $F^2$ values using the SAINT+ software[28] and global refinements of unit cell parameters employing 8555–9267 reflections chosen from the full data set were performed. Multiple measurements of equivalent reflections provided the basis for empirical absorption correction as well as a correction for any crystal deterioration during the data collection (SADABS[29]). The structures were solved by direct methods and refined by full-matrix least-squares procedures using the SHELXTL program package.[30] Hydrogen atoms were placed in calculated positions [C–H 0.95 Å (aromatic rings) or 0.98 Å (methyl groups)] and included as riding contributions with isotropic displacement parameters 1.2 (aromatic rings) or 1.5 (methyl groups) times those of the attached non-hydrogen atoms. Near the end of the refinement of the structure of **2**, two significant peaks were observed in a difference map near the rhodium atom which formed a linear unit with P1. These were treated as the second Au and Cl atoms of the [ClAu{(*o*-$MeOC_6H_4O$)P(μ-N*t*Bu)}$_2$AuCl] impurity which had been identified by NMR spectroscopy in the original sample and which presumably had cocrystallized with **2**. Addition of these to the model significantly improved the refinement and resulted in a refined occupancy of the digold complex impurity of 0.038. CCDC-642038 (**2**), -642039 (**4**), -642040 (**5**), -642041 (**7**), and -642042 (**8**) contain the supplementary crystallographic data for this paper. This can be obtained free of charge from the Cambridge Crystallographic Data Centre via www.ccdc.cam.ac.uk/data_request/cif.

## Acknowledgments

We are grateful to the Department of Science and Technology (DST), New Delhi for funding. P. C. thanks the Council of Scientific and Industrial Research (CSIR) for a Research Fellowship. J. T. M. thanks the Louisiana Board of Regents through grant LEQSF(2002-03)-ENH-TR-67 for the purchase of a Bruker APEX CCD diffractometer and the Chemistry Department of Tulane University for support of the X-ray laboratory.

[1] a) N. Wheatley, P. Kalck, *Chem. Rev.* **1999**, *99*, 3379–3419; b) C. E. Plecnik, S. Liu, S. G. Shore, *Acc. Chem. Res.* **2003**, *36*, 499–508; c) M. Sakamoto, K. Manseki, H. Okawa, *Coord. Chem. Rev.* **2001**, *219–221*, 379–414; d) H. B. Gray, B. G. Malmstrom, *Biochemistry* **1989**, *28*, 7499–7505.

[2] a) R. E. P. Winpenny, *Chem. Soc. Rev.* **1998**, *27*, 447–452; b) J. Costes, F. Dahan, J. G. Tojal, *Chem. Eur. J.* **2002**, *8*, 5430–5434; c) Y. Yang, L. McElwee-White, *Dalton Trans.* **2004**, 2352–2356; d) J. L. Dempsey, A. J. Esswein, D. R. Manke, J. Rosenthal, J. D. Soper, D. G. Nocera, *Inorg. Chem.* **2005**, *44*, 6879–6892.

[3] a) M. Shibasaki, N. Yoshikawa, *Chem. Rev.* **2002**, *102*, 2187–2209; b) P. A. Shapley, N. Zhang, J. L. Allen, D. H. Pool, H. C. Liang, *J. Am. Chem. Soc.* **2000**, *122*, 1079–1091; c) G. J. Mataare, M. E. Tess, Y. Yang, K. A. Abboud, L. McElwee-White, *Organometallics* **2002**, *21*, 711–716.

[4] a) H. Han, M. Elsmaili, S. A. Johnson, *Inorg. Chem.* **2006**, *45*, 7435–7445; b) M. Gagliardo, G. Rodriguez, H. H. Dam, M. Lutz, A. L. Spek, R. W. A. Havenith, P. Coppo, L. D. Cola, F. Hartl, G. P. M. vanKlink, G. vanKoten, *Inorg. Chem.* **2006**, *45*, 2143–2155; c) Y. Yang, K. A. Abboud, L. McElwee-White, *Dalton Trans.* **2003**, 4288–4296; d) A. H. Eisenberg, M. V. Ovchinnikov, C. A. Mirkin, *J. Am. Chem. Soc.* **2003**, *125*, 2836–2837.

[5] a) M. S. Balakrishna, V. S. Reddy, S. S. Krishnamurthy, J. F. Nixon, J. C. T. R. B. Laurent, *Coord. Chem. Rev.* **1994**, *129*, 1–90; b) M. S. Balakrishna, S. S. Krishnamurthy, *J. Organomet. Chem.* **1992**, *424*, 243–251; c) J. C. T. R. B. Laurent, P. B. Hitchcock, J. F. Nixon, *J. Organomet. Chem.* **1983**, *249*, 243–254.

[6] a) P. Chandrasekaran, J. T. Mague, M. S. Balakrishna, *Organometallics* **2005**, *24*, 3780–3783; b) P. Chandrasekaran, J. T. Mague, M. S. Balakrishna, *Inorg. Chem.* **2005**, *44*, 7925–7932; c) P. Chandrasekaran, J. T. Mague, M. S. Balakrishna, *Inorg. Chem.* **2006**, *45*, 6678–6683; d) P. Chandrasekaran, J. T. Mague, M. S. Balakrishna, *Inorg. Chem.* **2006**, *45*, 5893–5897; e) P.

 © 2007 Wiley-VCH Verlag GmbH & Co. KGaA, Weinheim 

Chandrasekaran, J. T. Mague, M. S. Balakrishna, *Dalton Trans.* **2007**, 2957–2962.
[7] a) S. Ogo, R. Kabe, K. Uehara, B. Kure, T. Nishimura, S. C. Menon, R. Harada, S. Fukuzumi, Y. Higuchi, T. Ohhara, T. Tamada, R. Kuroki, *Science* **2007**, *316*, 585–587; b) M. A. F. Hernandez-Gruel, J. J. Perez-Torrente, M. A. Ciriano, A. B. Rivas, F. J. Lahoz, I. T. Dobrinovitch, L. A. Oro, *Organometallics* **2003**, *22*, 1237–1249; c) J. Choudhury, S. Podder, S. Roy, *J. Am. Chem. Soc.* **2005**, *127*, 6162–6163; d) T. Hosokawa, M. Takano, S. Murahashi, H. Ozaki, Y. Kitagawa, K. Sakaguchi, Y. Katsube, *J. Chem. Soc. Chem. Commun.* **1994**, 1433–1434; e) D. Drommi, F. Nicolo, C. A. Arena, G. Bruno, F. Faraone, R. Gobetto, *Inorg. Chim. Acta* **1994**, *221*, 109–116; f) E. K. Van Den Beuken, B. L. Feringa, *Tetrahedron* **1998**, *54*, 12985–13011; g) P. A. Robles-Dutenhefner, E. M. Moura, G. J. Gama, H. G. L. Siebald, E. V. Gusevskaya, *J. Mol. Catal. A* **2000**, *164*, 39–47; h) H. Kato, H. Seino, Y. Mizobe, M. Hidai, *J. Chem. Soc. Dalton Trans.* **2002**, 1494–1499.
[8] a) B. Punji, J. T. Mague, M. S. Balakrishna, *Inorg. Chem.* **2006**, *45*, 9454–9464; b) B. Punji, J. T. Mague, M. S. Balakrishna, *Dalton Trans.* **2006**, 1322–1330; c) S. Priya, M. S. Balakrishna, J. T. Mague, S. M. Mobin, *Inorg. Chem.* **2003**, *42*, 1272–1281; d) S. Priya, M. S. Balakrishna, J. T. Mague, *J. Organomet. Chem.* **2003**, *679*, 116–124; e) M. S. Balakrishna, R. Panda, J. T. Mague, *Inorg. Chem.* **2001**, *40*, 5620–5625; f) R. Venkateswaran, J. T. Mague, M. S. Balakrishna, *Inorg. Chem.* **2007**, *46*, 808–817; g) R. Venkateswaran, S. M. Mobin, M. S. Balakrishna, *Eur. J. Inorg. Chem.* **2007**, 1930–1938.
[9] P. Chandrasekaran, J. T. Mague, M. S. Balakrishna, unpublished results.
[10] a) A. M. Z. Slawin, M. B. Smith, J. D. Woollins, *J. Chem. Soc. Dalton Trans.* **1996**, 1283–1293; b) A. M. Z. Slawin, M. B. Smith, J. D. Woollins, *J. Chem. Soc. Dalton Trans.* **1996**, 4575–4581.
[11] a) G. G. Christoph, P. Blum, W.-C. Liu, A. Elia, D. W. Meek, *Inorg. Chem.* **1979**, *18*, 894–897; b) T. H. Brown, P. J. Green, *J. Am. Chem. Soc.* **1970**, *92*, 2359–2362.
[12] J. G. Verkade, J. A. Mosbo in *Phosphorus-31 NMR Spectroscopy in Stereochemical Analysis* (Eds.: J. G. Verkade, L. D. Quin), VCH Publishers, Inc., Deerfield Beach, FL, USA, **1987**, p. 425–464.
[13] R. G. Pearson, *J. Am. Chem. Soc.* **1963**, *85*, 3533–3543.
[14] D. Cremer, J. Pople, *J. Am. Chem. Soc.* **1975**, *97*, 1354–1358.
[15] V. S. Reddy, S. S. Krishnamurthy, M. Nethaji, *J. Chem. Soc. Dalton Trans.* **1994**, 2661–2667.
[16] L. Brammer, E. A. Bruton, P. Sherwood, *Cryst. Growth Des.* **2001**, *1*, 277–290.
[17] a) M. Haakansson, S. Jagner, E. Clot, O. Eisenstein, *Inorg. Chem.* **1992**, *31*, 5389–5394; b) R. D. Willett, R. Butcher, C. P. Landee, B. Twamley, *Polyhedron* **2005**, *24*, 2222–2231.
[18] P. Pyykko, *Chem. Rev.* **1997**, *97*, 597–636.
[19] N. C. Baenziger, W. E. Bennett, D. M. Soboroff, *Acta Crystallogr., Sect. B* **1976**, *32*, 962–963.
[20] G. L. Soloveichik, O. Eisenstein, J. T. Poulton, W. E. Streib, J. C. Huffman, K. G. Caulton, *Inorg. Chem.* **1992**, *31*, 3306–3312.
[21] A. Bondi, *J. Phys. Chem.* **1964**, *68*, 441–451.
[22] G. A. Bowmaker, S. E. Boyd, J. V. Hanna, R. D. Hart, P. C. Healy, B. W. Skelton, A. H. White, *J. Chem. Soc. Dalton Trans.* **2002**, 2722–2730.
[23] W. L. F. Armarego, D. D. Perrin, *Purification of Laboratory Chemicals*, 4th ed., Butterworth-Heinemann, Linacre House, Jordan Hill, Oxford, U. K., **1996**.
[24] M. Brandys, M. C. Jennings, R. J. Puddephatt, *J. Chem. Soc. Dalton Trans.* **2000**, 4601–4606.
[25] B. S. Furniss, A. J. Hannaford, P. W. G. Smith, A. R. Tatchell, *Vogel's Textbook of Practical Organic Chemistry*, 5th ed., ELBS, England, **1989**.
[26] Y. Tatsuno, T. Yoshida, S. Otsuka, *Inorg. Synth.* **1990**, *28*, 342–345.
[27] *SMART*, version 5.625, Bruker-AXS, Madison, WI, **2000**.
[28] *SAINT+*, version 6.35A, Bruker-AXS, Madison, WI, **2002**.
[29] G. M. Sheldrick, *SADABS*, version 2.05, University of Göttingen, Germany, **2002**.
[30] a) *SHELXTL*, version 6.10, Bruker-AXS, Madison, WI, **2000**; b) G. M. Sheldrick, *SHELXS97* and *SHELXL97*, University of Göttingen, Germany, **1997**.

Received: May 25, 2007
Published Online: September 12, 2007

 © 2007 Wiley-VCH Verlag GmbH & Co. KGaA, Weinheim 

EurJIC
European Journal of Inorganic Chemistry

**The EUChemSoc Societies have taken the significant step into the future by merging their traditional journals, to form two leading chemistry journals, the *European Journal of Inorganic Chemistry* and the *European Journal of Organic Chemistry.* Three further EUChemSoc Societies (Austria, Czech Republic and Sweden) are Associates of the two journals.**

## COVER PICTURE

**The cover picture shows** how a novel tetranuclear $Ni^{II}$ complex $[Ni_4L_4^1(\mu\text{-tp-}\kappa_4\text{-O})(H_2O)_2(\mu\text{-tp-}\kappa_2\text{-O})]\cdot 2C_2H_5OH\cdot CH_3OH\cdot 3H_2O$ [$L^1$ = *N*-(3-aminopropyl)-5-bromosalicylaldimine] acts as an active catalyst for the partial oxidation of cyclohexene into its epoxide product when it is immobilized over a network of hexagonal mesoporous silica. Herein the catalytic sites allow the formation of epoxide over their surfaces. *tert*-Butyl hydroperoxide acts as an oxidant for the partial oxidation process. A dinuclear unit is formed, in which the $Ni^{II}$ is bridged by a phenolato group, and two such units are connected through a terephthalate moiety to form a tetranuclear nickel(II) complex. The tetranuclear units are connected to each other by another terephthalate moiety in its bis(monodentate) mode to form one-dimensional networks. Details are described in the article by P. Banerjee et al. on p. 5033 ff. The artwork was designed by Mr. Jishnunil Chakraborty and Mr. Gopal Das.

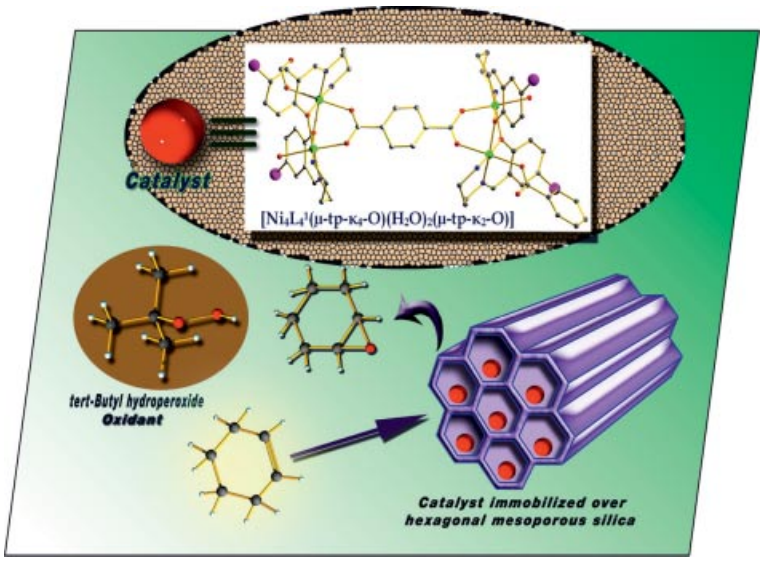


 © 2007 Wiley-VCH Verlag GmbH & Co. KGaA, Weinheim 

EurJIC
European Journal of Inorganic Chemistry

**The EUChemSoc Societies have taken the significant step into the future by merging their traditional journals, to form two leading chemistry journals, the *European Journal of Inorganic Chemistry* and the *European Journal of Organic Chemistry.* Three further EUChemSoc Societies (Austria, Czech Republic and Sweden) are Associates of the two journals.**

## COVER PICTURE

**The cover picture shows** how a novel tetranuclear $Ni^{II}$ complex $[Ni_4L_4^1(\mu\text{-tp-}\kappa_4\text{-O})(H_2O)_2(\mu\text{-tp-}\kappa_2\text{-O})]\cdot 2C_2H_5OH\cdot CH_3OH\cdot 3H_2O$ [$L^1$ = *N*-(3-aminopropyl)-5-bromosalicylaldimine] acts as an active catalyst for the partial oxidation of cyclohexene into its epoxide product when it is immobilized over a network of hexagonal mesoporous silica. Herein the catalytic sites allow the formation of epoxide over their surfaces. *tert*-Butyl hydroperoxide acts as an oxidant for the partial oxidation process. A dinuclear unit is formed, in which the $Ni^{II}$ is bridged by a phenolato group, and two such units are connected through a terephthalate moiety to form a tetranuclear nickel(II) complex. The tetranuclear units are connected to each other by another terephthalate moiety in its bis(monodentate) mode to form one-dimensional networks. Details are described in the article by P. Banerjee et al. on p. 5033 ff. The artwork was designed by Mr. Jishnunil Chakraborty and Mr. Gopal Das.

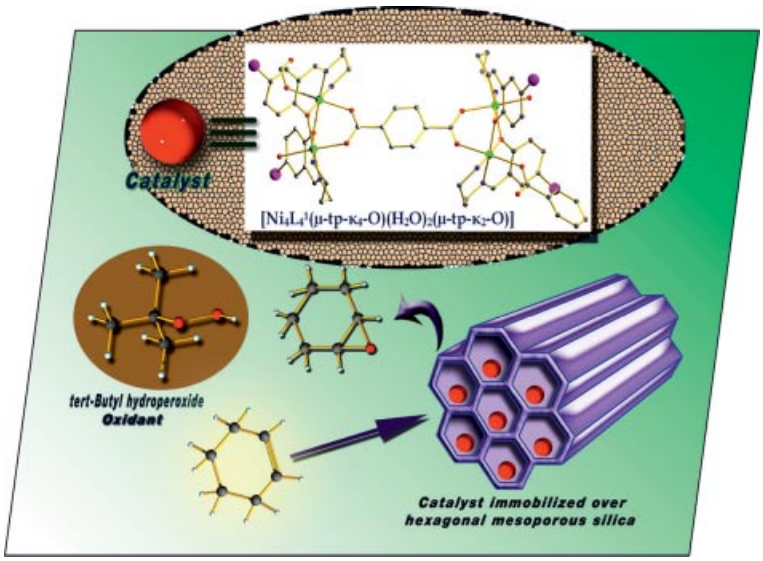


 © 2007 Wiley-VCH Verlag GmbH & Co. KGaA, Weinheim 

# CONTENTS

## MICROREVIEW


### Metallocene-Containing Dendrimers

**A. E. Kaifer*** ..... **5015–5027**

Electron Transfer and Molecular Recognition in Metallocene-Containing Dendrimers

**Keywords:** Metallocenes / Dendrimers / Electrochemistry / Molecular recognition / Supramolecular chemistry


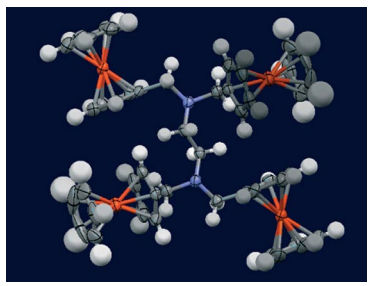


Dendrimers containing multiple metallocenes on their surface or a single metallocene in their core offer interesting properties in electron-transfer reactions and molecular recognition processes.


## SHORT COMMUNICATION


### Reductive Nitrosation

**D. Shamir, I. Zilbermann,* E. Maimon, G. Gellerman, H. Cohen, D. Meyerstein*** ..... **5029–5031**

Reductive Nitrosation of Peptides Ligated to High-Valent Metal Cations

**Keywords:** Nitrosation / Peptides / NO / High-valent transition metals


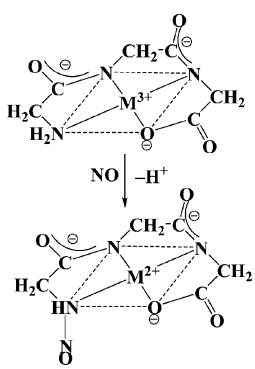



Reductive *N*-nitrosations occur according to a radical mechanism.


## FULL PAPERS


### Nickel Epoxidation Catalysts

**J. Chakraborty, M. Nandi, H. Mayer-Figge, W. S. Sheldrick, L. Sorace, A. Bhaumik, P. Banerjee*** ..... **5033–5044**

Nickel Complexes with $N_2O$ Donor Ligands: Syntheses, Structures, Catalysis and Magnetic Studies

**Keywords:** Nickel / N,O ligands / Epoxidation / Heterogeneous catalysis / Magnetic properties


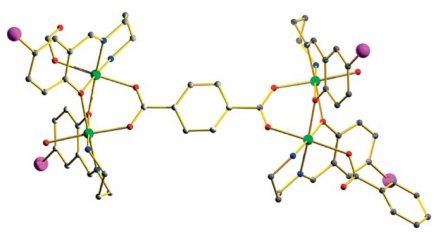


The terephthalato-bridged tetranuclear polymeric $Ni^{II}$ complexes $[Ni_4L_4^1(\mu\text{-tp-}\kappa_4\text{-O})(H_2O)_2(\mu\text{-tp-}\kappa_2\text{-O})]\cdot 2C_2H_5OH\cdot CH_3OH\cdot 3H_2O$ (**1**) and $[Ni_4L_4^2(\mu\text{-tp-}\kappa_4\text{-O})(H_2O)_2(\mu\text{-tp-}\kappa_2\text{-O})]\cdot 3H_2O$ (**2**) are synthesized along with the dicyanoargentate-bridged polymeric complexes $[Ni^{II}(L^1)(H_2O)\{Ag(CN)_2\}]_\alpha$ (**3**) and $[Ni^{II}(L^3)(MeOH)\{Ag(CN)_2\}]_\alpha$ (**4**). All four complexes are effective catalysts for the epoxidation of alkenes. Variable-temperature magnetic susceptibility measurements of complex **1** show a medium-strength antiferromagnetic coupling between the $Ni^{II}$ centers.

## Square-Planar Palladium Complexes

**L. Chahen, B. Therrien, G. Süss-Fink* 5045–5051**

Square-Planar Diacetatopalladium Complexes with *trans*-Configured Secondary Amine Ligands that Avoid Orthometalation: Ligand Synthesis, Coordination, Molecular Structure and Catalytic Potential for Suzuki Cross-Coupling Reactions

**Keywords:** Cross-coupling / Palladium / N ligands / Amines / Homogeneous catalysis

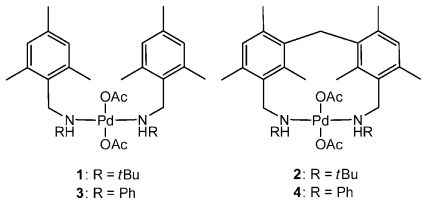


*trans*-Configured square-planar palladium complexes have been synthesized by treating palladium acetate with the amines or diamines. All complexes are found to catalyze Suzuki cross-coupling reactions of deactivated and even sterically hindered arene substrates.

## Heterodimetallic Ferrocene Complexes

**S. Clément, L. Guyard, M. Knorr,* F. Villafañe, C. Strohmann, M. M. Kubicki ..... 5052–5061**

(2,2-Dibromovinyl)ferrocene as a Building Block for the Assembly of Heterodinuclear Complexes – Preparation of an σ-Alkenylpalladium Complex and Dimetallic Dithioether Complexes

**Keywords:** Oxidative addition / Thioether ligands / Platinum / Rhenium / Palladium / Electrochemistry

The oxidative addition of (2,2-dibromovinyl)ferrocene to $[Pd(PPh_3)_4]$ yields the σ-alkenyl complex *trans*-[{Pd(Br)-$(PPh_3)_2$}–C(Br)=C(H)–Fc]. Nucleophilic attack of NaSR on $[Br_2C=C(H)–Fc]$ produces the π-conjugated dithioether compounds [(RS)CH=C(SR)–Fc], which react with $[Re(thf)(CO)_3(\mu\text{-}Br)]_2$ or $[PtCl_2(PhCN)_2]$ to afford heterodinuclear dithioether complexes.

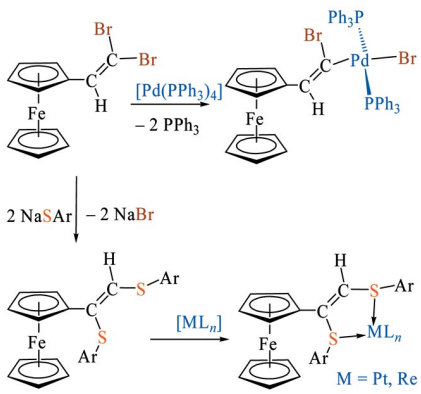


## Iron-Only Hydrogenase Models

**D. Morvan, J.-F. Capon, F. Gloaguen,* P. Schollhammer, J. Talarmin ..... 5062–5068**

Electrochemical Synthesis of Mono- and Disubstituted Diiron Dithiolate Complexes as Models for the Active Site of Iron-Only Hydrogenases

**Keywords:** Biomimetic catalysis / Iron-only hydrogenases / Diiron dithiolate / CO substitution / Electrochemistry / Proton reduction

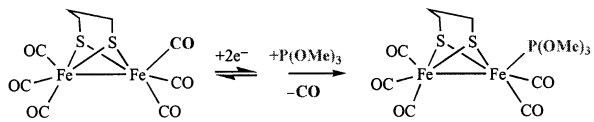


$[Fe_2(S_2C_3H_6)(CO)_5\{P(OMe)_3\}]$ (**2**) and $[Fe_2(S_2C_3H_6)(CO)_4\{P(OMe)_3\}_2]$ (**3**) were prepared by the electrochemical reduction of $[Fe_2(S_2C_3H_6)(CO)_6]$ (**1**) in the presence of trimethyl phosphite. Electrochemical data indicate a CO-displacement reaction catalyzed by electron transfer. These compouds serves as models for the active site of iron-only hydrogenases.

## NHC Thioether Ligands

**J. Wolf, A. Labande,* J.-C. Daran, R. Poli ..... 5069–5079**

Nickel(II), Palladium(II) and Rhodium(I) Complexes of New NHC-Thioether Ligands: Efficient Ketone Hydrosilylation Catalysis by a Cationic Rh Complex

**Keywords:** N-Heterocyclic carbenes / S ligands / Nickel / Palladium / Rhodium

A series of new, bifunctional imidazolium–thioether ligands have been synthesised using a general method and used as N-heterocyclic carbene (NHC) precursors for complexation studies on various transition metals ($Ni^{II}$, $Pd^{II}$ and $Rh^{I}$). $Rh^{I}$ complexes showed a good activity for the hydrosilylation of ketones.

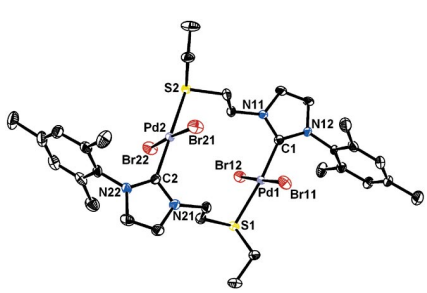


 © 2007 Wiley-VCH Verlag GmbH & Co. KGaA, Weinheim 

# CONTENTS


## Cluster Chemistry

**A. Seifert, G. Linti* ..... 5080–5086**

Synthesis and Structure of Tetrameric Gallium(I) Amides

**Keywords:** Gallium / Amides / Cluster compounds / X-ray structures / Density functional calculations

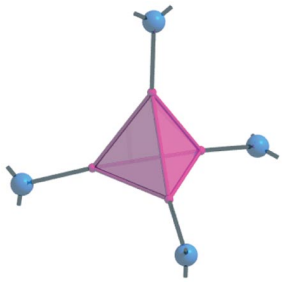

The gallium(I) amides $GaNR_2$ [$NR_2$ = tmp, $N(SiMe_3)dipp$] were prepared from "GaI". They form distorted tetrahedral tetramers in the solid state.

## Fluorescent Probes

**A. El Majzoub, C. Cadiou, I. Déchamps-Olivier, F. Chuburu,* M. Aplincourt ..... 5087–5097**

(Benzimidazolylmethyl)cyclen: A Potential Sensitive Fluorescent PET Chemosensor for Zinc

**Keywords:** Zinc / Macrocyclic ligands / X-ray diffraction / UV/Vis spectroscopy / Fluorescent probes / Fluorimetric titrations

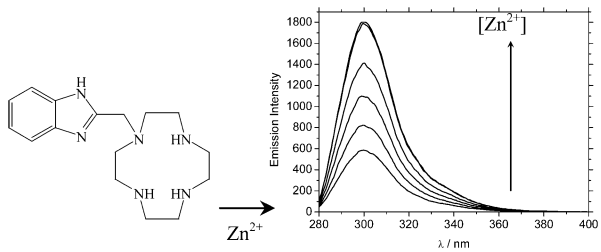


A new fluorescent probe for $Zn^{2+}$, namely (benzimidazolylmethyl)cyclen [LH], was designed and synthesised. On addition of successive amounts of $Zn^{2+}$, the fluorescence emission of LH increases linearly by a factor of 3.

## Mixed-Valence $Co^{II/III}$ Complexes

**T. C. Stamatatos, A. K. Boudalis, K. V. Pringouri, C. P. Raptopoulou, A. Terzis, J. Wolowska, E. J. L. McInnes,* S. P. Perlepes* ..... 5098–5104**

Mixed-Valence Cobalt(II/III) Carboxylate Clusters: $Co^{II}_4Co^{III}_2$ and $Co^{II}Co^{III}_2$ Complexes from the Use of 2-(Hydroxymethyl)-pyridine

**Keywords:** Mixed-valence cobalt complexes / [2-(Hydroxymethyl)pyridine]metal complexes / Linear trinuclear cobalt complexes / Hexanuclear cobalt clusters / Q-band electron paramagnetic resonance

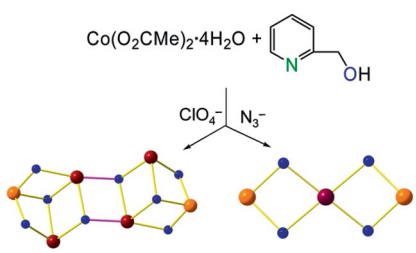


The shown reaction scheme gives a hexanuclear, mixed-valence cationic cluster containing the unprecedented $[Co^{II}_4Co^{III}_2(\mu_3\text{-}OR')_4(\mu\text{-}OR')_4]^{6+}$ core (the benzoate analogue has a similar structure) and a linear $Co^{III}Co^{II}Co^{III}$ neutral complex containing the $[Co^{II}Co^{III}_2(\mu\text{-}OR')_4]^{4+}$ core, depending on the inorganic anion present; the $Co^{II}$ ions in the hexanuclear clusters are antiferromagnetically coupled.

## Microwave-Assisted Cycloplatination

**N. Godbert, T. Pugliese, I. Aiello, A. Bellusci, A. Crispini, M. Ghedini* ..... 5105–5111**

Efficient, Ultrafast, Microwave-Assisted Syntheses of Cycloplatinated Complexes

**Keywords:** Cycloplatination / Microwave synthesis / Platinum / Antitumor agents / X-ray diffraction

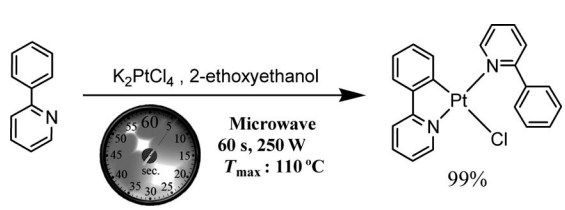


Mononuclear cycloplatinated chlorido complexes containing neutral ligands are synthesised by two different methods, namely conventional and microwave-assisted synthesis. All new complexes have been fully characterised and their crystal structures determined.


 © 2007 Wiley-VCH Verlag GmbH & Co. KGaA, Weinheim 

## N-Heterocyclic Phosphanes

A series of N-heterocyclic chlorophosphanes and 1,3,2-diazaphospholenium salts with different substitution patterns is prepared and characterised by single-crystal X-ray diffraction studies. An analysis of trends in the structural parameters supports the view that the unusual P−Cl bond lengthening is attributable to n(N)/σ*(P-Cl) hyperconjugation.

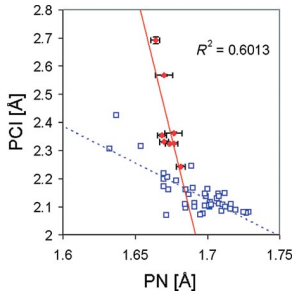


**S. Burck, D. Gudat,* K. Nättinen, M. Nieger, M. Niemeyer, D. Schmid ..... 5112−5119**

2-Chloro-1,3,2-diazaphospholenes − A Crystal Structural Study

**Keywords:** Phosphanes / Halides / X-ray diffraction / Substituent effects / Structure correlation

## Speciation of Uranyl Nitrate

Complex formation between the uranyl ion and nitrate ions is investigated in acetonitrile and the ionic liquid [$C_4$mim][$Tf_2$N] at room temperature by optical absorption, magnetic circular dichroism and EXAFS spectroscopy. The sharp peaks in the absorption spectrum are characteristic of a $[UO_2(NO_3)_3]^-$ species with $D_{3h}$ coordination symmetry. No evidence is found for the formation of uranyl nitrato complexes in aqueous solution.

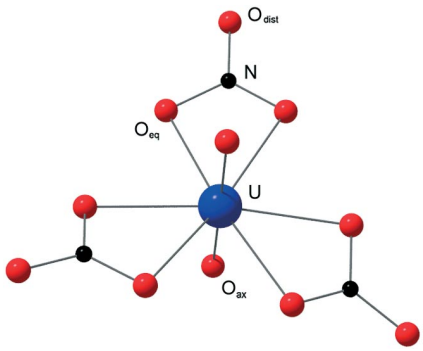


**K. Servaes, C. Hennig,* I. Billard, C. Gaillard, K. Binnemans, C. Görller-Walrand, R. Van Deun* ..... 5120−5126**

Speciation of Uranyl Nitrato Complexes in Acetonitrile and in the Ionic Liquid 1-Butyl-3-methylimidazolium Bis(trifluoromethylsulfonyl)imide

**Keywords:** EXAFS spectroscopy / Ionic liquids / Uranium / UV/Vis spectroscopy / X-ray absorption spectroscopy

## Cyclopentadienylcobalt Complexes

Chelation by the amino-functionalised side chain occurred when the Cp′-cobalt(I) dicarbonyl complexes were oxidised by iodine, resulting in the corresponding Cp′-cobalt(III) chelates via diiodocarbonyl intermediates. The stabilities of the intermediates were found to correlate with the I−Co−I angles and the repulsive force from the amino-functionalised groups in the chelates. Complex **6′** was reduced to **6** by the CO released upon chelation. Its $PPh_3$-substituted $CH_2CH_2$ solvate shows a strong N−H···I hydrogen bond.

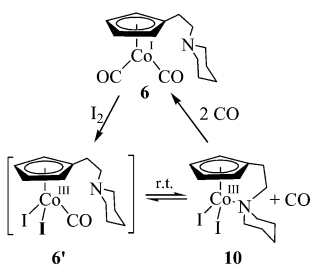


**L. Li, S. Han, Q. Li, Z. Chen, Z. Pang* ..... 5127−5137**

Synthesis and Reactivity of Cobalt Complexes with Pendant Nitrogen Functional Groups

**Keywords:** Cyclopentadienylcobalt complexes / Carbonylcobalt complexes

## Inorganic Reaction Mechanisms

The process $AuCl_3$(3R-py) + $Cl^-$ → $AuCl_4^-$ + 3R-py (3R-py = *meta*-substituted pyridines) was studied in methanol at 25 °C and the data were compared with those found for *para*-substituted pyridines (4R-py). Until now the two groups of bases have been considered to behave in the same manner in their displacement reactions but, on the contrary, the reactivity of the two classes of N donors is slightly different and follows the order: 4R-py > 3R-py. This kinetic result is explained on the basis of an energetic difference between the frontier orbitals of the $AuCl_3$(3R-py) and $AuCl_3$(4R-py) derivatives.

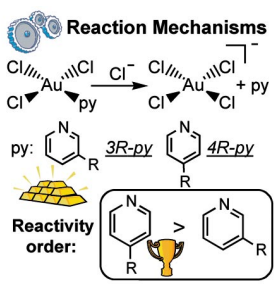


**B. Pitteri,* M. Bortoluzzi ..... 5138−5143**

Displacement of Neutral Nitrogen Donors by Chloride in $AuCl_3$(3R-py) (3R-py = *meta*-Substituted Pyridine): Comparison between *meta*- and *para*-Substituted Pyridines by Kinetics and DFT Calculations

**Keywords:** Gold / Kinetics / Nitrogen donors / Reaction Mechanism / DFT

**If not otherwise indicated in the article, papers in issue 31 were published online on October 23, 2007**

 © 2007 Wiley-VCH Verlag GmbH & Co. KGaA, Weinheim 

# SPOTLIGHTS …

## *Platinum–Thiolate Complexes*

S. H. Chong, D. J. Young, T. S. A. Hor*

**Pressure-Assisted Hetero- and Homodialkylation of Sulfide in $[Pt_2(\mu\text{-}S)_2(dppp)_2]$: One-Pot Conversion of $\{Pt_2(\mu\text{-}S)_2\}$ into $\{Pt_2(SR)_2\}$ and $\{Pt_2(SR)(SR')\}$**

*Chem. Asian J.*
DOI: **10.1002/asia.200700203**

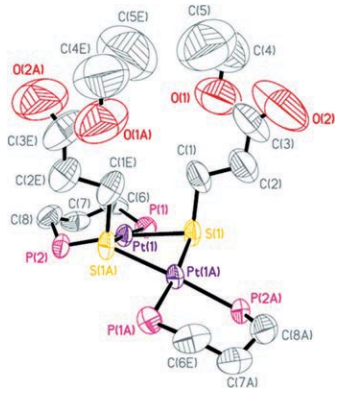


**Cool under pressure**: Elevated pressure and the use of dppp ($Ph_2P(CH_2)_3PPh_2$) to enhance the nucleophilicity of the sulfide centers in $[Pt_2(\mu\text{-}SR)(\mu\text{-}S)(dppp)_2]^+$ lead to the successful synthesis of novel diplatinum complexes that contain hetero- and homothiolate bridges. Functional alkyls and aryls are thus converted into functional thiolates.

## *Epoxides*

B. J. Albert, K. Koide*

**How Rapidly Do Epoxides Nonspecifically Form Covalent Bonds with Thiols in Water?**

*ChemBioChem*
DOI: **10.1002/cbic.200700365**

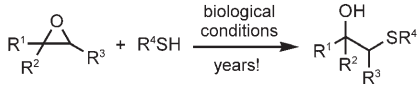


**Rating reaction rates**. Due to some concerns about the reactivity of epoxides towards the most abundant and powerful nucleophiles, thiols, in a biological setting, we report kinetic data for the consumption of five common epoxide motifs in the presence of a thiol under biologically relevant conditions.

## *Monolayers*

D. T. Pham, K. Wandelt, P. Broekmann*

**2D Ordering Phenomena Under Non-Equilibrium Conditions: An In Situ STM Approach**

*ChemPhysChem*
DOI: **10.1002/cphc.200700507**

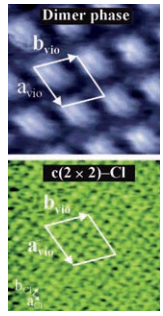


**Ordering phenomena**: The "reactive" adsorption and lateral ordering of redox-active dibenzyl viologens (DBV) on a chloride-modified Cu(100) electrode surface is studied. At electrode potentials where the first electron transfer step from the di-cationic to the radical mono-cationic viologen takes place, the preferred products at the surface are metastable viologen dimer species (see STM images).

## *Peptide Analogues*

L. Gomez-Paloma, I. Bruno, E. Cini, S. Khochbin, M. Rodriquez, M. Taddei,* S. Terracciano, K. Sadoul

**Design and Synthesis of Cyclopeptide Analogues of the Potent Histone Deacetylase Inhibitor FR235222**

*ChemMedChem*
DOI: **10.1002/cmdc.200700095**

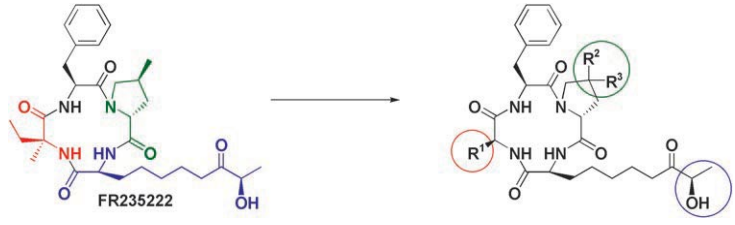


**FR235222**, one of the most potent HDAC inhibitors, is a natural tetrapeptide formed by some not easily available amino acids. We found that it is possible to build a structurally similar tetrapeptide made with simpler amino acids but maintaining Ahoda (indispensable) which has the high activity of the parent natural product and shows selective inhibition of class 1 histone deacetylase.

 © 2007 Wiley-VCH Verlag GmbH & Co. KGaA, Weinheim 

EurJIC European Journal of Inorganic Chemistry

## *Natural Poducts*

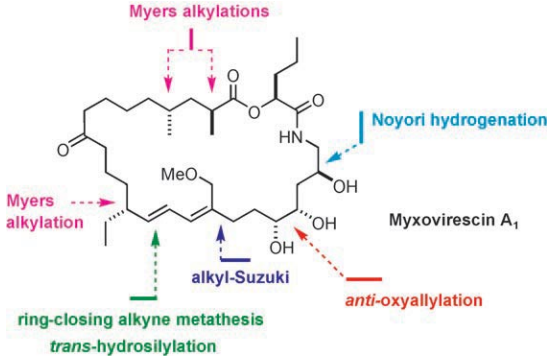


**A convergent total synthesis** of the antibiotic macrolide myxovirescin $A_1$ is described that is largely based on reagent- and catalyst-controlled transformations. This includes a highly regioselective Negishi reaction of a dibromoalkene, a palladium-catalyzed alkyl-Suzuki coupling, an exquisitely selective ring-closing alkyne metathesis, and a ruthenium-catalyzed *trans*-hydrosilylation tandem.

A. Fürstner,* M. Bonnekessel, J. T. Blank, K. Radkowski, G. Seidel, F. Lacombe, B. Gabor, R. Mynott

**Total Synthesis of Myxovirescin $A_1$**

*Chem. Eur. J.*
DOI: **10.1002/chem.200700926**

## *Enantioselective Biohydrolysis*

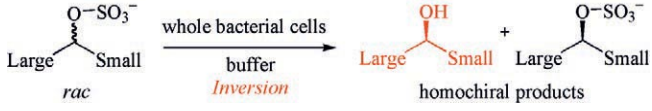


Highly enantioselective biohydrolysis of *rac-sec*-alkyl sulfate esters by *Pseudomonas* spp. proceeded with strict inversion of configuration.

P. Gadler, K. Faber*

**Highly Enantioselective Biohydrolysis of *sec*-Alkyl Sulfate Esters with Inversion of Configuration Catalysed by *Pseudomonas* spp.**

*Eur. J. Org. Chem.*
DOI: **10.1002/ejoc.200700637**

## *Macroscopic Chirality*

**Which way around?** J-aggregated zinc porphyrin dendrimer can be used to detect the macroscopic chirality of a vortex. The sign of the circular dichroism response changes quickly upon switching from clockwise (CW) to counterclockwise (CCW) stirring (see picture). The observed chiroptical activity most likely arises from a macroscopic helical alignment of nanofibers formed from the polymeric J-aggregate.

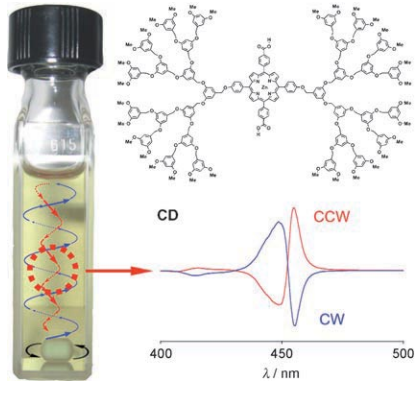


A. Tsuda,* M. A. Alam, T. Harada, T. Yamaguchi, N. Ishii, T. Aida*

**Spectroscopic Visualization of Vortex Flows Using Dye-Containing Nanofibers**

*Angew. Chem. Int. Ed.*
DOI: **10.1002/anie.200703083**

On these pages, we feature a selection of the excellent work that has recently been published in our sister journals. If you are reading these pages on a computer, click on any of the items to read the full article. Otherwise please see the DOIs for easy online access through Wiley InterScience.

 © 2007 Wiley-VCH Verlag GmbH & Co. KGaA, Weinheim 

DOI: 10.1002/ejic.200700817

# Electron Transfer and Molecular Recognition in Metallocene-Containing Dendrimers

**Angel E. Kaifer*[a]**

*Dedicated to the late Professor Moisés Morán*

**Keywords:** Metallocenes / Dendrimers / Electrochemistry / Molecular recognition / Supramolecular chemistry

This manuscript provides a summary of the relatively large body of research on the preparation and characterization of dendrimers containing (1) multiple copies of metallocene residues on their surfaces or (2) a single metallocene residue at their core. Special emphasis is placed on dendrimers functionalized with either ferrocene or cobaltocenium groups, because their reversible electrochemistry makes them particularly attractive to the author's group. Dendrimers containing multiple, peripheral metallocene residues are of interest to develop multivalent interactions with suitable receptors or receptor assemblies. With dendrimers containing a single metallocene at their cores, the key questions relate to the effects of the dendritic mass on their properties and degree of encapsulation or site isolation. We focused our work on the electrochemical properties of these dendrimers as well as on their use as guests in molecular recognition processes with freely diffusing hosts.

(© Wiley-VCH Verlag GmbH & Co. KGaA, 69451 Weinheim, Germany, 2007)

## Introduction

Dendrimers[1] are highly branched macromolecules spanning from a central core and containing a series of layers, structurally and synthetically distinct, which are usually referred to as "generations". Whereas the initial interest in dendrimers was basically related to the synthetic and structural characterization challenges that they pose, their fractal geometries, high molecular weights, and nanometer-range sizes, a little more than a decade ago many groups started to focus on their functionalization. In very simplistic terms, one can look at a functionalized dendrimer as one or more functional residues attached to a large dendritic mass that defines the shape, size, and other properties of the macromolecule. In some cases, the dendritic mass also has a pronounced influence on the chemical or physical properties of the functional residue. There are two general ways to approach dendrimer functionalization. First, one can attach many copies of a functional residue on the surface of the dendrimer (peripheral functionalization). Second, one can grow dendritic mass branching out from a functional residue (core functionalization). Both styles of functionalization (see Figure 1 for schematic drawings) have different advantages and target various purposes. Peripheral functionalization is advantageous to develop multivalent interactions with dendrimers or to achieve chemical amplification. Core functionalization is more suitable when the main interest revolves around site isolation of the residue and/or the concomitant alteration of its properties.

[a] Center for Supramolecular Science and Department of Chemistry, University of Miami
Coral Gables, FL 33124-0431, USA
Fax: +1-305-284-4571
E-mail: akaifer@miami.edu

*Angel E. Kaifer was born in Madrid, Spain, where he completed his undergraduate studies in chemistry at Universidad Autónoma. He earned his Ph.D. (with Luis Echegoyen) in 1984 at the University of Puerto Rico, Rio Piedras, and did postdoctoral work (with Allen Bard) at the University of Texas, Austin. In 1985 he joined the faculty of the University of Miami, where he is now Professor of Chemistry. His research interests focus on the electrochemistry of supramolecular systems, with current emphasis on functionalized dendrimers, molecular capsules, hydrogen-bonded systems, and the binding properties of cucurbit[n]uril hosts.*

 © 2007 Wiley-VCH Verlag GmbH & Co. KGaA, Weinheim 

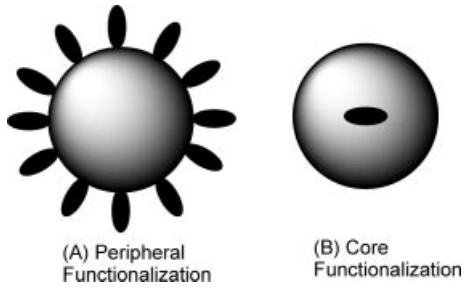


Figure 1. Main approaches to dendrimer functionalization.

In this manuscript, research work on dendrimers functionalized with metallocene residues is described, placing significant emphasis on the work done by my research group, without relegating the very important work done by other groups, from which we have gained inspiration and a healthy measure of competition. From the standpoint of my own group, reversible electrochemical properties are quite desirable, and, thus, we have mostly focused our efforts on dendrimers functionalized with either ferrocene [bis(cyclopentadienyl)iron(II)] or cobaltocenium [bis(cyclopentadienyl)-cobalt(III)] centers. Both metallocene residues are stable, 18-electron systems, which differ on the charge of their most accessible oxidation states: zero for ferrocene and +1 for cobaltocenium. Ferrocene undergoes fast one-electron oxidation to the positively charged ferrocenium form, whereas cobaltocenium exhibits fast one-electron reduction to produce the neutral cobaltocene. Both electrochemical processes take place at accessible potentials and usually maintain fast kinetics (*reversibility* in electrochemical jargon) in ferrocene- and cobaltocenium-containing compounds.

## Dendrimers Containing Multiple Peripheral Metallocene Residues

Our initial interest in this type of system was sparked by the elegant work of Cuadrado and Morán, at Universidad Autónoma de Madrid, who were among the pioneering groups reporting the preparation of dendrimers with multiple, peripheral metallocene centers.[2] Our long-standing interest on the binding interactions between water-soluble ferrocene derivatives (see compound **1** as an example) and cyclodextrins, naturally led to the investigation of the supramolecular interactions between dendrimers **2** and **3** with cyclodextrin hosts[3] (see Figure 2).

The binding interactions between **1** and β-cyclodextrin (βCD) were studied by using $^1$H NMR spectroscopy in 0.1 M NaCl/$D_2O$. An equilibrium association constant ($K$) of 1230 $M^{-1}$ was measured by using this technique.[4] The formation of inclusion complex **1**·βCD was also evident from cyclic voltammetric data. The binding interactions between dendrimers **2** and **3**, as guests, and the βCD host were harder to study, as these dendrimers are quite insoluble in aqueous media. We observed, however, that the solubility of the dendrimers in aqueous solution containing 6.0 mM βCD was substantially higher.[4] In fact, our solubility measurements suggested that a minimum number of ferrocene residues per dendrimer must be CD bound for solubilization to take place. Competition experiments with a second guest (2-naphthalenesulfonate) and voltammetric experiments revealed that all the ferrocene residues in dendrimers **2** and **3** are accessible to βCD for formation of the inclusion complexes. On the other hand, a larger dendrimer (compound **4**, structure not shown) containing 16 ferrocenyl groups on its surface, shows signs of steric peripheral congestion, as not all the ferrocene groups are accessible for βCD complexation under our experimental conditions.

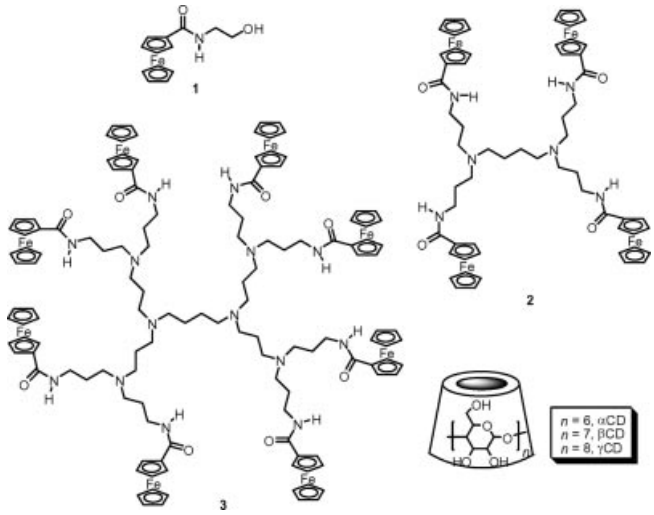


Figure 2. Structures of model compound **1**, dendrimers **2** and **3**, and the cyclodextrin hosts.

Conceptually, these dendrimers serve as three-dimensional templates for the organization of the CD receptors on their peripheries, giving rise to large supramolecular assemblies. For instance, the molecular weight of the octameric inclusion complex formed by the interaction of dendrimer **3** and excess βCD exceeds 11 kDa.[4] In addition to this, the one-electron oxidation of the ferrocene derivatives provides a reversible mechanism to release the CD receptors from these supramolecular complexes, as it is well known that the binding affinity of a ferrocene–βCD inclusion complex decreases by approximately two orders of magnitude upon oxidation of the ferrocene guest, effectively going from a $K$ value in the range $1 \times 10^3$ to $5 \times 10^3$ $M^{-1}$ to less than 50 $M^{-1}$.[5]

Our joint work with the Madrid group quickly moved to the exploration of the binding interactions between a similar series of dendrimers containing multiple cobaltocenium units on their surfaces and cyclodextrin hosts.[6] The simplest structures (dendrimers **5** and **6**) within this dendrimer series are shown in Figure 3. Unlike their ferrocene counterparts, these dendrimers have excellent aqueous solubility due to their polycationic character. Previous work from my group on the binding interactions between βCD and simple cobaltocenium revealed that the positively charged, oxidized form does not interact significantly with the CD host.[7] However, one-electron reduction leads to the formation of a stable inclusion complex between the neutral co-

 © 2007 Wiley-VCH Verlag GmbH & Co. KGaA, Weinheim 

baltocene form and βCD. These binding interactions have a strong effect on the shape of the current–potential voltammetric curves for cobaltocenium. In the absence of βCD, one-electron reduction gives rise to extensive precipitation on the electrode surface of the neutral, hydrophobic cobaltocene, which results in a distorted, very sharp peak for its reoxidation process back to cobaltocenium.[7] The sharpness of this peak is strongly related to the stripping nature of the electrochemical process, as material deposited onto the electrode surface is redissolved back into the solution as a result of the electron-transfer reaction. Not surprisingly, similar cyclic voltammograms were observed with dendrimers **5** and **6** (Figure 4), strongly suggesting that the same βCD binding mechanism operates on them as it does on simple cobaltocenium derivatives. The lack of binding interactions between βCD and the fully oxidized, cationic forms of the dendrimers was verified by $^1$H NMR spectroscopic data.[6] When comparing the behavior of ferrocene- and cobaltocenium-containing dendrimers, it is clear that dendrimers **5** and **6** interact with the cyclodextrin host only after one-electron reduction of the cobaltocenium units, whereas in the case of the ferrocene dendrimers (**2** and **3**, for instance) the binding interactions are disrupted by one-electron oxidation of the electroactive peripheral units. Whereas the behavior is similar in the sense that the neutral metallocene forms are complexed by βCD and the cationic forms are not, we must recognize that the ferrocene dendrimers are bound in their most stable and accessible oxidation state, and the cobaltocenium dendrimers are only bound after electrochemical stimulation. Therefore, electrochemical stimulation has opposite effects on these two types of dendrimers; it leads to the disassembly of the supramolecular complexes in the case of the ferrocene dendrimers and to supramolecular association for the cobaltocenium dendrimers.

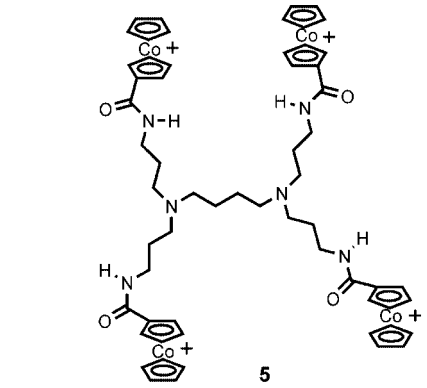


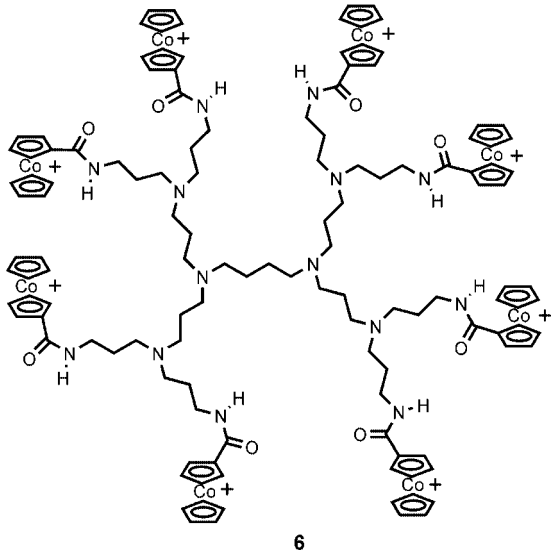


Figure 3. Representative structures of dendrimers containing multiple cobaltocenium units on their surfaces.

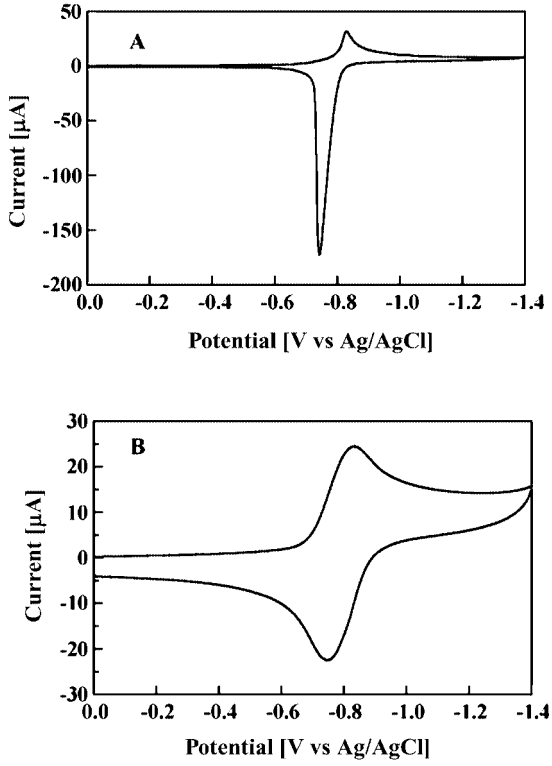


Figure 4. Cyclic voltammetric behavior on glassy carbon (0.08 cm$^2$) of a solution containing **5** (0.5 mM) and NaCl (0.1 M) (A) in the absence and (B) in the presence of βCD (7.0 mM).

We noted early that dendrimers with multiple copies of a metallocene unit on their surfaces could be interesting to express chemical amplification and or multivalency properties.[4] However, we did not explore this kind of phenomena. Reinhoudt and coworkers started to investigate the interactions between dendrimers containing multiple peripheral copies of adamantyl units with βCD and were able − by decreasing substantially the pH of the solution − to solubilize these dendrimers in aqueous media and investigate their CD binding interactions in more detail.[8] Whereas we observed limitations on the number of βCD hosts that can interact with dendrimers containing 16 peripheral ferrocene groups or more, their experimental conditions led to more open dendrimer structures that can interact easily with larger number of cyclodextrin hosts, even if considerable steric crowding is expected on the dendrimer surface. This group moved on to perform a series of elegant studies on

 © 2007 Wiley-VCH Verlag GmbH & Co. KGaA, Weinheim 

the interaction between dendrimers containing multiple surface guest units, such as adamantyl or ferrocenyl, and gold surfaces covered with self-assembled monolayers prepared with complementary host (βCD) monomers.[9] These are multivalent interactions involving several guest units from an individual dendrimer that interact simultaneously with several binding cavities in the cyclodextrin monolayer. The multivalent aspect of the interaction adds considerable thermodynamic stability to the assembly, leading to the robust immobilization of the dendrimers on the monolayer-covered surfaces. These multivalent dendrimer–monolayer interactions constitute the supramolecular basis for the development of a new class of soft nanolithographic patterning methods.

The βCD binding properties of cobaltocenium and ferrocene units were combined in a single compound (**7**), which exhibits three oxidation states that we can represent as $Fc^+$–$Cob^+$, Fc–$Cob^+$ and Fc–Cob (see Figure 5).[10] The first form ($Fc^+$–$Cob^+$) does not interact with βCD, the second forms a 1:1 inclusion complex (Fc included, $Cob^+$ not bound), and the third oxidation state interacts with two βCD hosts (both Fc and Cob units are bound). The group of Cuadrado and Morán has also prepared dendrimers containing multiple ferrocene and cobaltocenium residues,[11] but their binding interactions with βCD were not investigated.

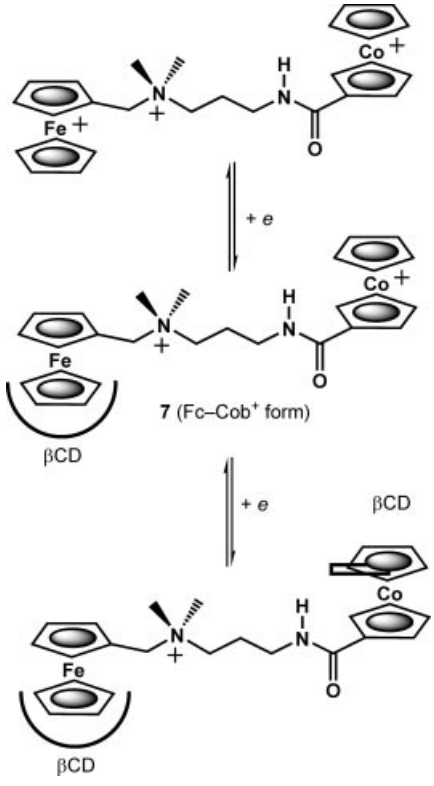


Figure 5. The three oxidation states of compound **7** and their respective binding sites for βCD.

The group of Astruc has pioneered a large amount of work with dendrimers having multiple ferrocenyl and other organometallic residues on their surfaces. Among many other goals, this group has emphasized the possible use of these systems in anion binding/sensing applications.[12] Furthermore, they have also utilized gold nanoparticles as the scaffold to assemble a multiple set of peripheral metallocene subunits for anion recognition.[13] Inspired by this work, we decided to modify the structure of our ferrocene dendrimers, such as **2** and **3**, to enhance the binding of biologically relevant anions, of which phosphate is one of the most significant examples. The preparation of **2** and **3** relies on the reaction of commercially available amine-terminated, poly(propylene imine) (PPI) dendrimers with chlorocarbonylferrocene (**8**).[2b] The final dendrimer products have multiple ferrocenyl centers covalently attached to the dendrimer through amide functional groups. Whereas amides are known to hydrogen bond to anions, ureido groups are typically more effective for this purpose. Therefore, we treated the amine-terminated PPI dendrimers with isocyanatoferrocene, which was prepared from **8** via formation of the acyl azide derivative as an intermediate.[14] We obtained a series of novel dendrimers terminated in 4, 8, 16 or 32 ferrocenyl–ureido termini (see Figure 6 for an example). These dendrimers exhibit a voltammetric behavior in DMSO solution that is quite sensitive to the presence of hydrogenphosphate anions. The addition of hydrogenphosphate (1 equiv.) shifts the observed half-wave potential for ferrocene oxidation 112 mV to less positive values, whereas hydrogensulfate and chloride cause much smaller potential shifts (40 and 16 mV, respectively). Furthermore, the selectivity of the ferrocenyl–urea dendrimers for hydrogenphosphate was excellent as judged by the potential shifts observed in the presence of anion mixtures.[14] A particularly interesting aspect of this work is that the anion binding interactions and their voltammetric sensing were performed in a relatively polar solvent (DMSO), affording a reasonable measure of optimism for the development of structur-

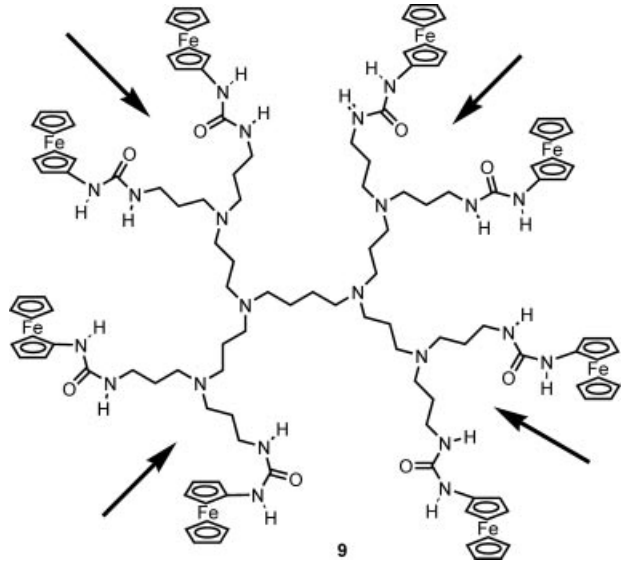


Figure 6. Representative structure of the series of anion-binding dendrimers with ferrocenyl–ureido termini. The arrows represent the four possible binding sites for hydrogenphosphate anions.

 © 2007 Wiley-VCH Verlag GmbH & Co. KGaA, Weinheim 

ally related systems that might have similar operational characteristics in aqueous environments.

When discussing the electrochemistry of dendrimers such as **2**, **3**, **5**, **6**, **9**, and related compounds having an even larger number of metallocene units on their surfaces, it is important to clearly point out that their electrochemical behavior is characterized by a single voltammetric wave (anodic in the case of ferrocene systems and cathodic for cobaltocenium dendrimers). This wave may be distorted due to precipitation effects, because these dendrimers suffer a large change in their hydrophilic/hydrophobic nature as a result of electron-transfer reactions. However, the individual oxidation of all the ferrocene centers (or reduction of all the cobaltocenium units) takes place at rather similar potentials. In other words, all metallocene units undergo electron transfer independently and no significant degree of electronic coupling among them can be discerned. This is so in spite of the spatial proximity between adjacent metallocenes forced by the crowding on the dendrimer surface. Even dendrimer systems with 64 peripheral ferrocenes, thus located very close to one another, exhibit a single, albeit relatively broad, oxidation wave.[15] In other words, the electrochemical behavior of these dendrimers clearly suggests that through space communication between adjacent metallocenes does not seem to be very effective in these systems.

A few years ago we prepared a new class of dinuclear ferrocene compounds containing a $–CH_2–N(R)–CH_2–$ bridge between the two ferrocenyl residues.[16] These compounds could be readily synthesized by thermal decomposition in polar solvents of (ferrocenylmethyl)trimethylammonium in the presence of a primary amine (Scheme 1). Interestingly, we observed that the level of electronic coupling between the two ferrocenyl residues was dependent on the state of protonation of the central nitrogen atom in the bridge. For instance, unprotonated amine **10** showed a modest level of electronic coupling between the ferrocene centers, as reflected by the measurable difference between the two half-wave potentials ($\Delta E_{1/2}$ = 82 mV), but the protonated compound exhibited a $\Delta E_{1/2}$ value of 46 mV, which was barely above that expected for fully independent redox centers. Alkylation of the bridge nitrogen atom had an effect similar to protonation on the level of communication between the two ferrocene centers.[16]

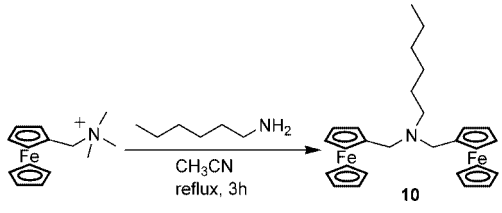


Scheme 1. The preparation of dinuclear ferrocene compound **10**.

Intrigued by these observations, we decided to express this dinuclear ferrocene motif on dendritic surfaces. By allowing the thermal decomposition of ferrocenyltrimethylammonium in the presence of amine-terminated PPI dendrimers, we successfully prepared a series of small dendrimers shown in Figure 7.[17] Unfortunately, the modest level of electronic communication existing in simple ferrocene dinuclear compounds bridged by $–CH_2–N(R)–CH_2–$ linkages is not observable on the surface of these dendrimers. However, their voltammetric behavior was interesting in a different way. For simplicity, let us discuss first the behavior of compound **13**. Our experiments were recorded in an 80:20 v/v mixture of $CH_2Cl_2/CH_3CN$, in order to minimize precipitation problems associated with the electron transfer reactions. In this solvent system the electrochemical behavior of **13** is characterized by a single reversible oxidation at a half-wave potential of 0.45 V vs. Ag/AgCl. However, the addition of HCl leads to the observation of two distinct oxidation waves at 0.45 and 0.61 V vs. Ag/AgCl. The addition of an excess amount of acid eliminates the first redox couple at 0.45 V and develops the second wave (at 0.61 V) to maximum current levels.[17] Clearly, protonation of one of the two tertiary nitrogen atoms of the compound shifts the half-wave potential of the two attached ferrocene centers to more positive values, and thus, the voltammetric behavior reveals the presence of protonated and unprotonated nitrogen centers on the periphery of the compound. This was further verified by partial methylation of one of the peripheral tertiary nitrogen atoms, leading to compound **14**, which we also prepared and characterized. The voltammetric behavior of **14** shows two oxidation processes at 0.48 and 0.67 V vs. Ag/AgCl. Protonation of **14** eliminates the redox couple at 0.48 V and leads to a single oxidation wave at the higher half-wave potential. These experiments suggest that the protonation (or methylation) of each of the peripheral nitrogen atoms leads to an anodic shift of the half-wave potential corresponding to the oxidation of the two ferrocenyl units covalently attached to it. One would expect, therefore, that the behavior of larger dendrimer **11**, containing four pairs of ferrocenyl units on its surface, would be similar. In fact, this expectation was fully realized. The voltammetric response of **11** in the absence of acid shows a single redox couple at 0.50 V vs. Ag/AgCl, which corresponds to the oxidation of eight ferrocene centers. The addition of HCl gives rise to a new redox wave at 0.61 V, which grows at the expense of the original wave as more acid is added to the solution. Eventually, upon addition of ca. 10 equiv. of HCl, the first wave disappears and the second wave at 0.61 V reaches full development.[17] This behavior reveals that it is possible to control − by the addition of suitable concentrations of acid − the relative population of the two types of ferrocene centers attached to protonated or unprotonated nitrogen atoms, which are characterized by different half-wave potentials. It is interesting to point out that compound **12** was isolated during the preparation of **11**. This defective compound (missing one ferrocenyl group in comparison to **11**) affords an interesting example on the poor diagnostic power of elemental analysis with some types of dendrimers. Both **11** and **12** gave experimental elemental compositions (C, H) that agree with the calculated compositions of both **11** and **12** within accepted error margins. This highlights the importance of mass spectrometry for the unequivocal confirmation of dendritic structures.

 © 2007 Wiley-VCH Verlag GmbH & Co. KGaA, Weinheim 

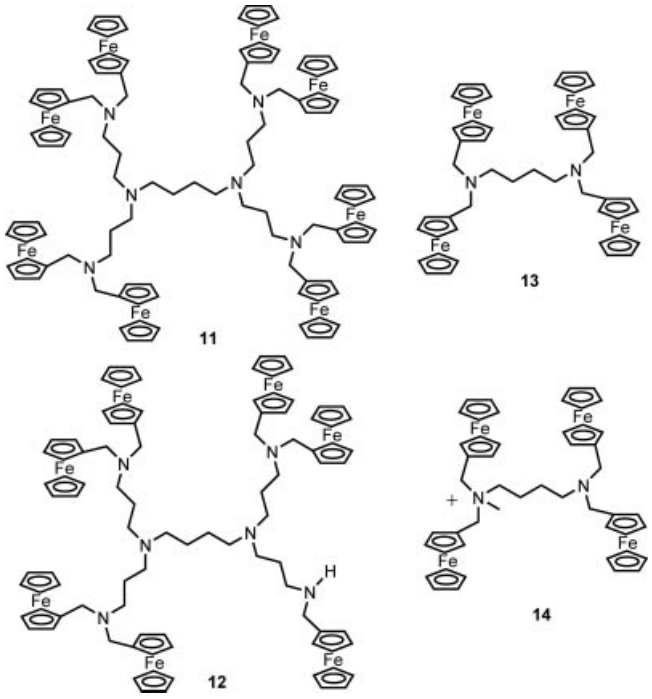


Figure 7. Small dendrimers containing Fc–$CH_2$–N(R)–$CH_2$–Fc units on their surfaces.

Dendrimers with multiple metallocene centers on their surfaces are interesting systems from the standpoint of their electrochemical properties and their possible use as guests in multivalent interactions, either in new nanolithographic surface patterning methods or in their potential applications as anion sensors.

## Dendrimers with a Single Metallocene Unit at Their Focal Positions

As discussed in the Introduction, dendrimer functionalization can take many forms. Whereas we first became interested in dendrimers with multiple metallocene units on their surfaces, our interests evolved and eventually focused on the properties of metallocene core dendrimers, that is, dendrimers containing a single metallocene residue covalently attached to one or more dendrons. Dendron growth may give rise to site isolation, that is, the partial or complete encapsulation of the metallocene unit by dendrimer mass. These dendritic systems are interesting for a number of reasons. Primarily, site isolation leads to new and intriguing properties for the dendrimer-surrounded metallocene residue, which may exhibit very different electrochemical and optical properties relative to those of the free metallocene. This has some biological overtones because in redox proteins the electrochemical reactivity of the prosthetic redox active group is often modulated by its partial encapsulation in the polypeptide framework. Therefore, we decided to start a research program to prepare and characterize dendronized metallocenes, that is, dendrimers containing a single metallocene unit attached to their focal points.

Our molecular design relies on the use of three dendrimer building blocks based on the branching architecture of a triester amine (Behera's amine, compound **15** in Figure 8) first reported by Newkome and coworkers.[18] We modified slightly the synthetic procedures published by this group and prepared Behera's amine, as well as its second and third generation analogs[19] (Figure 8). Once these amine dendrons are available, we can easily tap into the reactivity of the focal amine groups to covalently attach a variety of electroactive and fluorescent groups to the dendrons. Our group has taken advantage of this chemistry to prepare dendrimers with ferrocene,[19,20] dansyl,[21] pyrene,[22] viologen,[23] cobaltocenium,[24] and hydrogen-bonding ureidopyrimidine[25] groups attached to the focal position of the dendron. In this review, we will obviously focus our attention on the properties of dendronized ferrocene and cobaltocenium compounds, but will use some of the data obtained with other functional groups to support specific conclusions along the way.

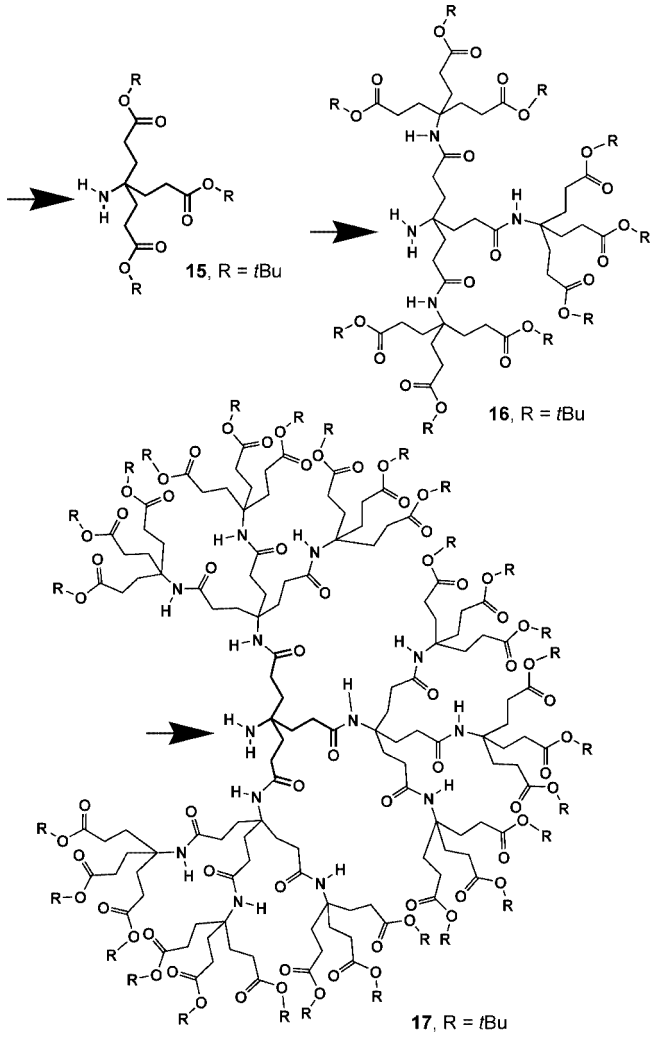


Figure 8. Structures of the Newkome dendrons used in this work. The arrows point to the focal sites used in functionalization reactions.

 © 2007 Wiley-VCH Verlag GmbH & Co. KGaA, Weinheim 

## Dendronized Ferrocenes: Electrochemistry

These compounds were readily prepared by reaction of the amine dendrimer building blocks (compounds **15**, **16**, and **17**) with chlorocarbonylferrocene.[19] The amidation reaction worked well and led to the dendronized ferrocenes in reasonable yields (31–49%). These dendrimers (Figure 9), having 3, 9 and 27 *tert*-butyl esters on their surfaces, were characterized by $^1$H and $^{13}$C NMR spectroscopy, MALDI-TOF mass spectrometry, UV/Vis and IR spectroscopy, and electrochemical data.

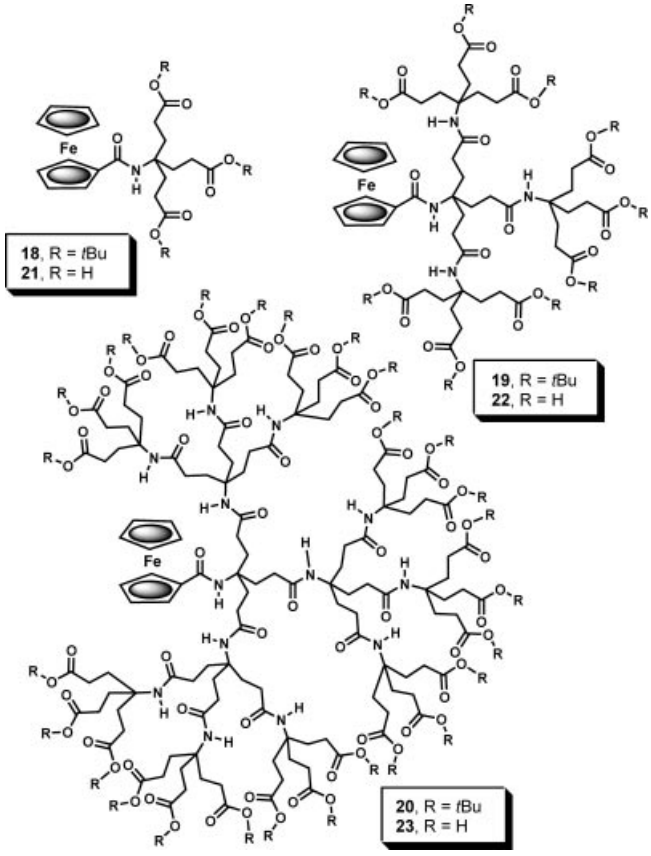


Figure 9. Hydrophobic (**18**, **19**, and **20**) and hydrophilic (**21**, **22**, and **23**) series of dendronized ferrocenes.

The anodic voltammetric behavior in dichloromethane solution is characterized by the one-electron oxidation of the ferrocenyl group. Table 1 gives the relevant electrochemical parameters obtained in voltammetric experiments. Generally, ferrocene derivatives exhibit fast (reversible) electrochemical kinetics in their one-electron oxidation processes. In agreement with this expectation, the first generation ferrocene dendrimer (compound **18**) shows reversible electrochemical behavior, characterized by a reasonably fast heterogeneous electron transfer rate constant ($k°$). However, the $k°$ values decrease quickly as the size of the attached dendron increases,[19] which is consistent with the findings of other groups who have investigated electrochemical kinetics with core dendrimers.[26] These results are understood as a straightforward effect of molecular size. As the dendrimer grows, its diffusion coefficient decreases, which leads to lower current levels due to slower mass transport of electroactive molecules to the electrode surface. However, the decrease in the $k°$ value represents an intrinsic slowdown of the electrochemical kinetics and is thought to be associated with the distance between the redox center and electrode surface when the interfacial electron transfer takes place. As electroactive molecules move towards the electrode surface, they reach a point of maximum approach, which is defined by the so-called outer Helmholtz plane (OHP). The larger the molecule, the further away from the electrode the OHP will be located. Therefore, if one considers all possible rotational orientations for the dendrimer, it is clear that the average distance between the ferrocene center and the electrode surface should increase with the molecular size. The electron transfer rate is well known to decrease exponentially with distance,[27] thus explaining the general trend observed with most core dendrimers and the $k°$ values reported in Table 1.

Table 1. Molecular weights and electrochemical parameters (0.2 M $TBA^+PF_6^-$ in $CH_2Cl_2$ at 25 °C) for the dendronized ferrocenes.

| Dendrimer | MW[a] [amu] | $E_{1/2}$ [V vs. Ag/AgCl] | $D_o$[b] [$10^6 \times cm^2 s^{-1}$] | $k°$[b] [$10^3 \times cm\,s^{-1}$] |
|---|---|---|---|---|
| **18** | 627.6 | 0.63 | $9.5 \pm 1.0$ | $80 \pm 20$ |
| **19** | 1652.0 | 0.60 | $4.0 \pm 0.5$ | $17 \pm 3$ |
| **20** | 4725.0 | 0.54 | $2.3 \pm 0.3$ | $5 \pm 1$ |

[a] Calculated and verified by MALDI-TOF mass spectrometry. [b] Determined from digital simulations of the voltammetric data obtained on glassy carbon electrodes (0.078 $cm^2$).

The data in Table 1 also shows a very interesting trend in the variation of the half-wave potentials for ferrocene oxidation, which tend to decrease with increasing size of the attached dendron. When we first reported this data, a similar trend had been reported by Diederich and coworkers for porphyrin-core dendrimers.[28] Our data clearly indicate that, in dichloromethane solution, Newkome dendrimer growth differentially stabilizes the positively charged, oxidized ferrocenium form. Although Smith and coworkers demonstrated a different trend in half-wave potentials for dendronized ferrocenes with unrelated architecture,[29] we investigated the half-wave potentials of dendrimers of the same architecture containing a single, electroactive 4,4′-bipyridinium (viologen) residue at their apical positions.[23] These dendronized viologens have more favorable solubility properties, allowing the exploration of their electrochemistry in a variety of solvents, with a large range of polarities. The results provide a very clear picture in which the variation of the half-wave potential as a function of dendron size can be rationalized by the balance of polarities between the bulk solution and the inner phase of the dendrimer. Basically, as the dendron grows, it starts to affect the microenvironment of the redox center attached to the apical position (Scheme 2). If the inner phase of the dendrimer is more polar than the bulk solution, dendrimer growth is expected to differentially stabilize the more highly charged form of the redox couple. This is why the positively charged ferrocenium form is differentially stabilized versus neutral ferrocene by the growth of the attached Newkome dendron −

 © 2007 Wiley-VCH Verlag GmbH & Co. KGaA, Weinheim 

containing polar amide groups − in a low polarity solvent, such as dichloromethane. Therefore, the half-wave potential decreases as the dendrimer size increases, as seen in Table 1.

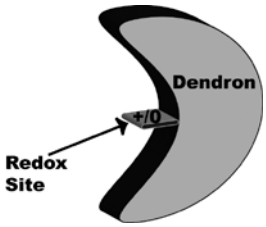


Scheme 2. Cartoon representation of the effect of dendron growth on the microenvironment of the apical redox center.

One of the advantages of our dendrimer architecture is that the set of peripheral *tert*-butyl esters can be easily hydrolyzed to yield dendrimers with multiple carboxylic acid groups on their surfaces.[19b] In fact, hydrolysis transforms a series of hydrophobic dendrimers (**18**–**20**), soluble in low polarity solvents, such as chloroform and dichloromethane, into a series of hydrophilic dendrimers (**21**–**23**, see structures in Figure 9) with moderate solubility in aqueous solution. The presence of multiple carboxylic acids on the surface immediately suggests the possibility of endowing these dendrimers with considerable negative charge (up to a maximum of 27 negative charges in the case of **23**). Charge development on these dendrimers was of interest to us because we assumed that the negative charges could favor specific dendrimer orientations at the electrode solution interface. Titration experiments with these dendrimers revealed that their p$K_a$ values are in the range 4.5–6.[20] Therefore, we started to focus our attention on a comparison of properties between solutions in the pH range 3–4, where the dendrimers are protonated and uncharged, and solutions in the pH range 7–8, in which the dendrimers are extensively deprotonated and negatively charged. Electrochemical experiments on bare gold electrodes did not show any significant differences on the electrochemical parameters measured for ferrocene oxidation in the 3–8 pH range. Faced with these initial results, we hypothesized that the surface density of positive charge on the electrode surface was probably not high enough to enforce specific dendrimer orientations at the interface. Therefore, we decided to derivatize the gold electrode surface by preparing a self-assembled monolayer (SAM) with a protonated amine in order to increase the positive charge surface density on the electrode. For simplicity, we selected cystamine as the monomer for SAM formation, as it is known that it stays protonated in the pH range 3–7, and it forms a relatively disorganized, albeit thin SAM, which is suitable for our purposes.

On gold electrodes covered with cystamine SAMs, the voltammetric behavior of the second generation dendrimer **22** was found to be extremely pH dependent.[20] At low pH (3–4) the reversible, one-electron oxidation of the ferrocene group was clearly detected, whereas at high pH (7–8) the oxidation wave basically disappeared. Similarly pronounced pH-induced changes in the voltammetric response were observed with the third generation dendrimer **23**. However, the first generation dendrimer **21** (a much smaller molecule) showed only small changes in its voltammetric response as the solution pH was changed from 3 to 8. The square wave voltammograms recorded in all these cases could be fitted to digital simulations in which the variable degree of voltammetric response could be rationalized by dramatic changes in the heterogeneous electron transfer rate constants. For instance, the $k°$ values for dendrimer **22** on cystamine-covered gold electrodes were found to decrease from $(8 \pm 1) \times 10^{-3}$ cm s$^{-1}$ at pH 4 to $(1.5 \pm 0.1) \times 10^{-5}$ cm s$^{-1}$ at pH 7.[20] This considerable decrease is completely gradual and reversible, as the measured $k°$ values oscillate between quasireversible to irreversible electrochemical behavior as the pH of the solution is titrated back and forth. What could be responsible for the pronounced change in electrochemical kinetics as the pH of the solution oscillates between these two extremes? Our interpretation of the data relies on the presence of a large negative charge on the dendrimer surface. The anionic form of the dendrimer, present at high pH, experiences strong electrostatic forces with the positively charged electrode surface, enforcing orientations in which the ferrocene group faces away from the electrode surface. Conversely, at low pH, the uncharged form of the dendrimer is free from these electrostatic forces and no specific interfacial orientations are favored, thus allowing free rotation of the dendrimer. These two extreme situations are represented in Scheme 3. When the dendrimer reaches the OHP and becomes ready for electron transfer, the average distance between the electrode surface and the ferrocene residue is larger at high pH than at low pH. Thus the electrochemical kinetics is considerably faster in the latter situation, as free rotation allows the electrode surface to sample dendrimers in which the ferrocene residue is facing it. As the pH increases, negative charge develops on the dendrimer, restricting free rotation and forcing the electrode surface to sample dendrimers in which the redox active center is facing towards the bulk solution. Therefore, dendrimers **22** and **23** are synthetic macromolecular compounds exhibiting strong pH-induced, orientational effects on their interfacial electron transfer reactions. In this sense, both dendrimers show similar electrochemical behavior to that exhibited by a number of redox proteins, providing an interesting kind of validation for our molecular design.

An aspect of these experiments that should not go unnoticed is the possible effect that surface ionization may have on the solution conformation of the dendrimers. In the polyelectrolyte field, it is well known that charge development in a polymer chain usually leads to remarkable conformational changes, as the polymer goes from a random coil arrangement to a fully extended chain, in which the charges are well solvated and separated from one another. Similarly, we could anticipate that surface ionization of the dendrimer should lead to a more expanded conformation, particularly in comparison with the more collapsed structure expected for the neutral, uncharged macromolecule. Quite recently, we looked at this issue by doing careful diffusion coefficient measurements on these dendrimers[30] with the use of pulse gradient stimulated echo (PGSE)

 © 2007 Wiley-VCH Verlag GmbH & Co. KGaA, Weinheim 

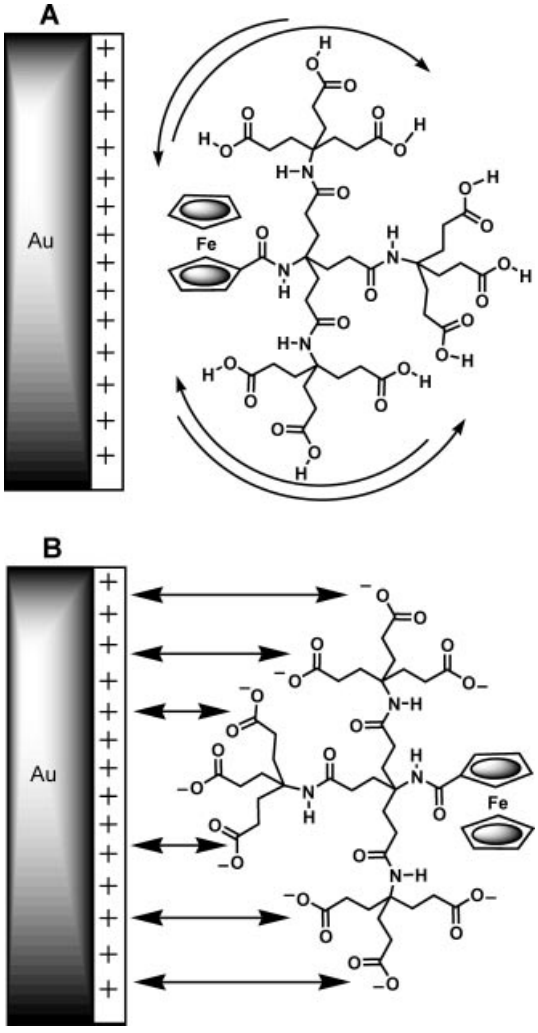


Scheme 3. Interfacial orientation of dendrimer **22** as it approaches the OHP next to a gold electrode covered by a positively charged SAM of cystamine in aqueous solution at (A) pH 3–4 and (B) pH 7–8.

NMR techniques. The data (Table 2) shows that the diffusion coefficient of any of these dendrimers is always smaller in pH 7 solution than in pH 2, which is consistent with the electrostatically expanded conformation anticipated for the ionized dendrimer. However, we must point out that these conformational changes by themselves cannot be responsible for the observed changes in electrochemical kinetics, as shown by the essentially pH independent electrochemical behavior obtained on bare gold electrodes.

Table 2. Approximate radii and diffusion coefficients at 25 °C for water-soluble dendronized ferrocenes.

| Dendrimer | Radius[a] [Å] | $D_o$ at pH 2 [$cm^2 s^{-1}$] | $D_o$ at pH 7 [$cm^2 s^{-1}$] |
|---|---|---|---|
| **21** | 3.5–8 | $4.8 \times 10^{-6}$ | $4.2 \times 10^{-6}$ |
| **22** | 3.5–12 | $3.0 \times 10^{-6}$ | $2.5 \times 10^{-6}$ |
| **23** | 3.5–18 | $1.9 \times 10^{-6}$ | $1.5 \times 10^{-6}$ |

[a] Radius range as estimated from molecular modeling.

## Dendronized Cobaltocenium Derivatives: Electrochemistry

The attachment of cobaltocenium units to the Newkome dendrons shown in Figure 8, can be readily accomplished by reaction of their apical amine groups with cobaltocenium carboxylic acid (as its chloride salt) in dry DMF by using *O*-(7-azabenzotriazol-1-yl)-*N*,*N*,*N*′,*N*′-tetramethyluronium hexafluorophosphate (*n*-HATU) to promote amide coupling.[24] As it is the case with the ferrocene derivatives, the dendrimers are initially prepared with *tert*-butyl ester peripheries (hydrophobic series, **24**–**26**) but hydrolysis with formic acid led to their water-soluble forms (hydrophilic series, **27**–**29**, see Figure 10 for structures). As expected, the cathodic electrochemical behavior of the dendrimers is dominated by the reversible one-electron reduction of cobaltocenium. The corresponding electrochemical parameters obtained in voltammetric experiments and the diffusion coefficients measured in PGSE NMR experiments are given in Table 3.

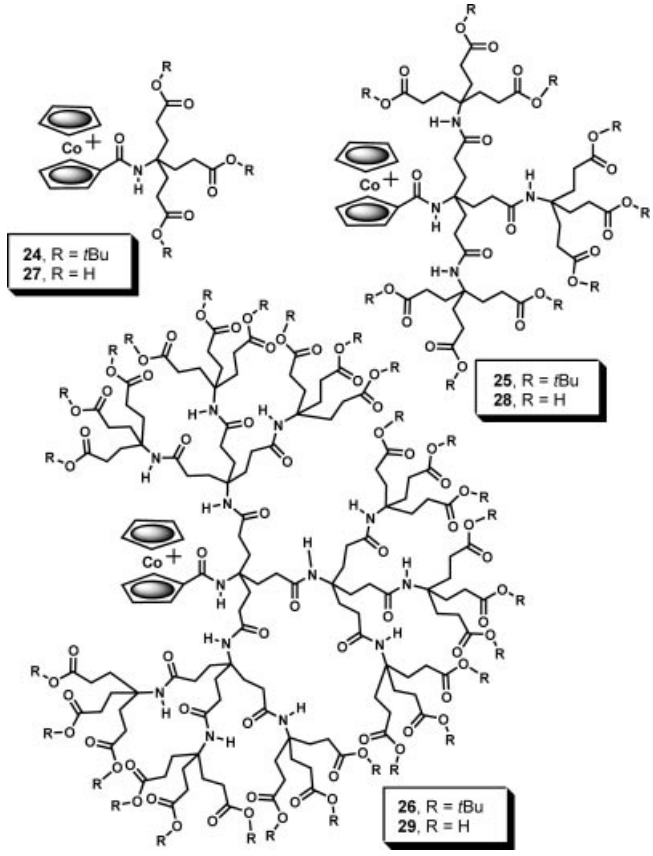


Figure 10. Hydrophobic (**24**, **25**, **26**) and hydrophilic (**27**, **28**, **29**) series of cobaltocenium-containing dendrimers.

The data in Table 3 generally follow the trends discussed before with dendronized ferrocenes. For instance, within the hydrophobic series of dendrimers (**24**–**26** surveyed in dichloromethane solution), $k°$ values and diffusion coefficients decrease with dendrimer size, as expected. The half-

 © 2007 Wiley-VCH Verlag GmbH & Co. KGaA, Weinheim 

Table 3. Electrochemical parameters and diffusion coefficients for the cobaltocenium-containing dendrimers.

| Dendrimer | $E_{1/2}$ [V vs. Ag/AgCl] | $k°$ [cm s$^{-1}$] | $10^6 \times D_o$ [cm$^2$ s$^{-1}$] |
|---|---|---|---|
| **24** | –0.66[a] | reversible[a] | 9.6[c] |
| **25** | –0.70[a] | $3.2 \times 10^{-2}$[a] | 6.8[c] |
| **26** | –0.75[a] | $3.0 \times 10^{-3}$[a] | 5.1[c] |
| **27** | –0.91[b] | $1.4 \times 10^{-2}$[b] | 4.1[d] |
| **28** | –0.92[b] | $8.0 \times 10^{-3}$[b] | 3.2[d] |
| **29** | –0.95[b] | $6.0 \times 10^{-3}$[b] | 2.1[d] |

[a] Measured in $CH_2Cl_2$ with 0.1 M $TBAPF_6$. [b] Measured in pH 7 phosphate buffer. [c] Measured in $CD_2Cl_2$ at 25 °C. [d] Measured in $D_2O$ buffered at pH 7 (phosphate) at 25 °C.

wave potential for the one-electron reduction of cobaltocenium shifts to more negative values as the dendron grows. This potential variation is consistent with the differential stabilization of the charged member of the redox couple (the positively charged cobaltocenium) by the inner phase of the dendrimer. The hydrophilic dendrimers were investigated in aqueous solution buffered at pH 7. The $k°$ values and diffusion coefficients again decrease as the size of the dendrimer grows. The half-wave potentials for cobaltocenium reduction show minor changes as the dendron size increases. However, for the third generation dendrimer (**29**) the $E_{1/2}$ value is about 30 mV more negative than in the first generation dendrimer (**27**). Because these experiments were run in a very polar, aqueous solution, we cannot attribute this small potential variation to the inner phase of the dendrimer having greater polarity than the bulk solution. We believe that this unusual potential trend may be associated to electrostatic interactions between the cobaltocenium unit and some of the carboxylate groups on the surface of the dendrimer.

## Guest Behavior of Dendronized Metallocenes

One of the most interesting aspects of these metallocene dendrimers is that their structures are "unsymmetric" in the sense that they offer two very different directions of approach for a species capable of reacting with the metallocene unit. Of course, this unsymmetric character was used to advantage in our demonstration of strong pH-induced, orientation effects on the electron transfer reactions between the dendronized ferrocene residue and a properly derivatized electrode surface.[20] Because of our long-standing interest in host–guest interactions, we decided to investigate the guest properties of dendronized metallocenes with freely diffusing hosts. These macromolecules can be used as guests because the metallocene unit is accessible to a free host that approaches the dendrimer near the apical site, where the metallocene is located. Basically, the driving force for this research work is to understand the effects of dendron size on the thermodynamic binding affinity between the partially buried, dendronized guest and the free host. We recently published a review of our research work on dendrimers as guests in molecular recognition phenomena.[31] Thus, we will limit ourselves here to provide a brief account of some of the most recent data involving dendronized metallocenes.

We started this research by investigating the binding interactions between the βCD host and dendronized ferrocenes **21**, **22**, and **23** in aqueous solution (0.1 M NaCl) buffered at pH 7 with 0.05 M tris.[19b] The complexation phenomena was monitored by using cyclic voltammetric experiments, as our group has considerable experience analyzing voltammetric data to extract information on chemical reactions, such as complexation by βCD, involving electroactive species, such as ferrocene derivatives. Fitting of the experimental current–potential curves by using digital simulation techniques is a powerful methodology to extract thermodynamic and/or kinetic parameters for the host–guest reactions coupled to the electron transfer processes. The addition of βCD to a solution containing any of the dendronized ferrocenes has two major effects on the voltammetric response: (1) the apparent half-wave potential for the one-electron oxidation of the ferrocene center shifts to more positive values and (2) the overall current levels of the voltammetric peaks decrease. The CD-induced, anodic potential shift reflects the differential stabilization of ferrocene relative to ferrocenium. This is consistent with the strong thermodynamic preference for the neutral ferrocene versus the positively charged ferrocenium of the host, which reflects the well-known selectivity of CD hosts for hydrophobic guests.[3] The CD-induced current decrease is readily explained by the lower diffusion coefficient of the ferrocene derivative due to its binding interactions with the bulky CD host. By optimizing the fitting of digitally simulated voltammograms to the experimental ones at variable βCD concentrations, we obtained 950, 250, and 50 M$^{-1}$ as the $K$ values for the βCD association with **21**, **22**, and **23**, respectively. The binding constant between the first generation dendrimer (**21**) with βCD is at the lower end of the usual range (1000–5000 M$^{-1}$) for binding of this host with small, water-soluble ferrocene derivatives. However, the binding constant comes down quite rapidly as the dendron size increases. By the third generation dendrimer, the host–guest binding interaction is almost completely quenched by the presence of the dendron.

What causes such a rapid decrease in the $K$ values as the dendron grows from first to third generation? Clearly, the larger dendron hinders the host approach towards the unsubstituted cyclopentadienyl ring of the ferrocene group, which is the main βCD binding site (Scheme 4). We also know that dendron growth leads to changes in the microenvironment around the ferrocene residue. In aqueous solution, dendrimer growth should decrease the polarity of the environment, which is expected to decrease the strength of the βCD–ferrocene binding interaction. In any instance, the effect of dendron growth on the stability of the inclusion complex formed between βCD and the dendronized ferrocenes is quite pronounced. The key question that must be asked upon examination of these data concerns the possible extrapolation of these effects to other host–guest systems.

 © 2007 Wiley-VCH Verlag GmbH & Co. KGaA, Weinheim 

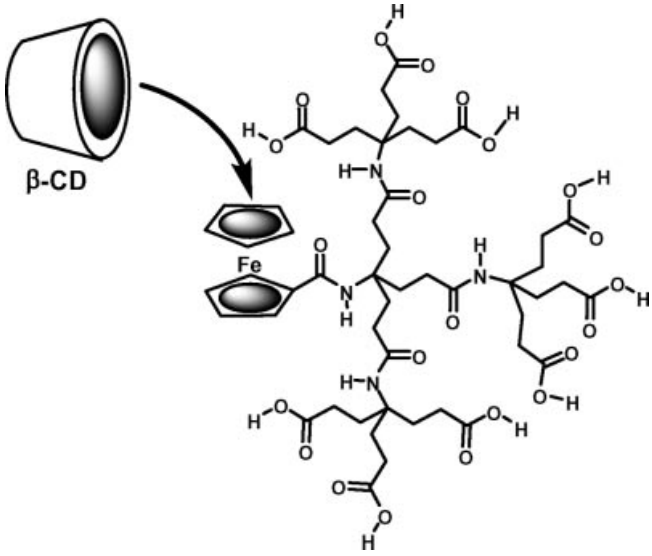


Scheme 4. Complexation of dendrimer **22** by the βCD host.

The cucurbit[*n*]urils[32] are a family of molecular receptors that can be prepared by the acid-catalyzed condensation of glycoluril with formaldehyde. Recent work on expanded cucurbiturils ($n \geq 6$) was sprung by their first isolation, reported by Kim and coworkers.[33] Whereas the cavity size of cucurbit[6]uril (CB6) is similar to αCD, cucurbit[7]-uril (CB7) resembles βCD, and the similarities between these two host families are more superficial than real.[34] CB hosts are known to be much more sensitive to guest charge, charge distribution, and shape than CD hosts. Therefore, the CBs are capable of achieving higher levels of binding selectivity. In optimal cases, CB hosts reach extremely high levels of binding affinities ($K > 10^{10}$ M$^{-1}$), which are completely unimaginable with unmodified cyclodextrins. The binding interactions between the simple ferrocene derivatives (**30**, **31**, and **32**) with βCD and CB7 provide an excellent illustration of these differences. All these ferrocene derivatives, regardless of their charge, form stable inclusion complexes with βCD, with *K* values in the range 1–$5 \times 10^3$ M$^{-1}$, as mentioned before. In contrast to this, CB7 forms a very stable complex with **30** ($K = 3 \times 10^9$ M$^{-1}$) and even more so with **31** ($K = 2 \times 10^{12}$ M$^{-1}$), but does not bind anionic **32** at all.[34] The complete lack of binding between **32** and CB7 is understood to result from the electrostatic repulsion between the carboxylate group of the guest and the negative charge density accumulated on the carbonyl oxygen-laced portals of the host (Figure 11).

As a result of our interest in cucurbit[*n*]uril chemistry, we decided to investigate the interactions between CB7 and dendrimers **21**–**23**. In this case the binding constants are readily obtained in $^1$H NMR spectroscopic experiments in which the dendronized ferrocene and a reference guest compete for a limited amount of the CB7 host.[30] The corresponding binding constants are given in Table 4. Measurements were made at two solution pH values (2 and 7) to ascertain the magnitude of the electrostatic effects between the anionic carboxylate charges on the dendrimer surface

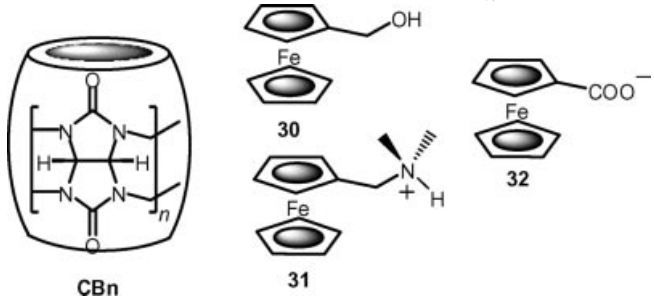


Figure 11. Structures of the cucurbituril hosts (CBn) and ferrocene derivatives **30**–**32**.

and the negatively charged portal openings on the host. These electrostatic effects are clearly evidenced by the lack of binding observed between ionized **21** (at pH 7) and CB7, in analogy with the absence of binding interactions between **32** and this host.[34] However, dendrimer growth decreases the intensity of the electrostatic repulsions opposing host–guest association, as evidenced by the measured binding constants at pH 7 with the dendronized guests **22** and **23**. In these larger macromolecules, the average distance between the peripheral carboxylates and the ferrocene site is sufficiently long for binding to take place. At pH 2, the binding constant between neutral **21** and CB7 is moderately high. Similarly the *K* value measured for neutral **22** is larger than that determined for anionic **22** (at pH 7) due to the lack of coulombic repulsion in the former case. In general terms, however, the trends observed in the *K* values with CB7 are quite different from what was observed with βCD, as dendrimer growth does not decrease the binding affinity in the quick and pronounced way that was observed with the latter host.

Table 4. Equilibrium association constants (*K*) at 25 °C measured in aqueous media between dendronized metallocenes and the CB7 host.

| Dendrimer | *K* [L mol$^{-1}$] at pH 2 | *K* [L mol$^{-1}$] at pH 7 |
|---|---|---|
| **21** | $3.9 \times 10^4$ | n.b.[a] |
| **22** | $4.2 \times 10^6$ | $3.8 \times 10^5$ |
| **23** | Insol.[b] | $7.7 \times 10^5$ |
| **27** | $3.2 \times 10^5$ | $1.0 \times 10^4$ |
| **28** | $1.1 \times 10^7$ | $3.4 \times 10^6$ |
| **29** | $4.0 \times 10^5$ | $4.0 \times 10^5$ |

[a] No binding detected. [b] Insoluble under these conditions.

We also investigated the binding interactions between CB7 and cobaltocenium-containing dendrimers[24] **27**–**29** (Table 4). The *K* values offer many similarities to those obtained with the dendronized ferrocenes. Perhaps the key difference between the two data sets is that the first generation dendrimer **27**, in its ionized form at pH 7, does form a stable complex with CB7. This is in clear contrast with unprotonated **21**. Clearly, the positive charge on the metallocene nucleus plays an important role in neutralizing the coulombic repulsions between the CB7 portal and the peripheral carboxylates on the dendrimer. In general terms, the *K* values with the cobaltocenium systems are slightly larger than the corresponding values with the dendronized

 © 2007 Wiley-VCH Verlag GmbH & Co. KGaA, Weinheim 

ferrocenes, probably a reflection of the positive charge on the cobaltocenium residue.

The differences observed in the host–guest binding interactions between our dendronized metallocenes and the hosts βCD and CB7 are part of a growing body of data,[31] which will eventually allow us to rationalize the effect of dendron size on the thermodynamic binding affinity. So far, the observed effects have proven to be very specific to the particular host–guest system under examination, and extended generalizations cannot be made at this time.

## Hybrid Dendrimers Containing Newkome and Fréchet Dendrons

Whereas all the work discussed so far on single metallocene dendrimers used Newkome-type dendrons, we recently reported a new class of dendrimers containing a single ferrocene group and two different dendrons (Newkome and Fréchet) covalently attached to a triazine nucleus.[35] Some examples are shown in Figure 12.

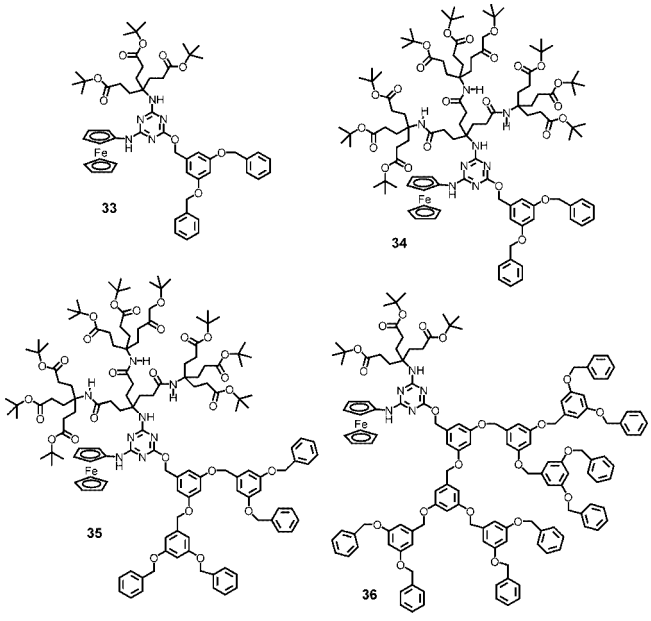


Figure 12. Hybrid dendrimers containing a ferrocene unit and Newkome and Fréchet dendrons attached to a central triazine nucleus.

This new series of dendrimers offers the possibility of comparing on the same molecule the relative effects of two different types of dendritic architectures. Because of their synthetic availability and widespread use by various research groups, we decided to use $AB_3$ Newkome-type, ester-terminated dendrons[18] and $AB_2$ Fréchet-type, aromatic ether dendrons.[36] Initially, we focused our attention on comparative dendron effects on the electrochemical parameters of the ferrocene residue and on the diffusion coefficients of the macromolecules.[35] Our preliminary data suggest that the Fréchet dendrons expand as wedges away from the core, whereas the Newkome dendrons are more effective at changing the polarity of the microenvironment around the ferrocene residue. This is probably a reflection of the more highly branched $AB_3$ architecture of the Newkome dendrons and their greater flexibility.

## Conclusions

This manuscript has addressed many aspects of the research work done by the authors' group on metallocene dendrimers. Whereas most of our work has focused on electrochemical processes and host–guest interactions in which the dendrimers act as mono- or multivalent guests, these systems also have tremendous potential as nanoscale objects for surface patterning, sensors, and other interesting applications. Furthermore, it is important to realize that the synthetic degree of sophistication of these systems is still in its infancy. Most of the synthetic work described here is based on the straightforward functionalization of existing dendritic architectures with metallocene units. More elaborate synthetic schemes, such as those leading to hybrid dendrimers **33**–**36**, may yield macromolecules with more complex structures and yet unexplored and, hopefully, exciting properties. The exploration of these novel structures and their properties is one of the major goals of our continuous research work in this field.

## Acknowledgments

The author is grateful to the U.S. National Science Foundation for continuous and generous support. This work would have been impossible without the effort and dedication of all the coworkers named in the references. A special mention should go to Claudia Cardona, who prepared the first series of dendrimers in my group. Her persistence and extraordinary ability as a chemist were crucial for the initial development of this work. Many thanks to all my friends at Universidad Autónoma de Madrid for their willingness to collaborate on these research problems and for making me feel very welcome as an Iberdrola Visiting Professor. The support of our collaborative efforts by NATO and the U.S.–Spain Fulbright Commission is also gratefully acknowledged.

[1] Some recent reviews: a) S.-C. Lo, P. L. Burn, *Chem. Rev.* **2007**, *107*, 1097–1116; b) S.-H. Hwang, C. D. Shreiner, C. N. Moorefield, G. R. Newkome, *New J. Chem.* **2007**, *31*, 1192–1217; c) D. K. Smith, *Adv. Mater.* **2006**, *18*, 2773–2778; d) U. Boas, J. B. Christensen, P. M. H. Heegaard, *J. Mater. Chem.* **2006**, *16*, 3785–3798; e) A.-M. Caminade, A. Maraval, J.-P. Majoral, *Eur. J. Inorg. Chem.* **2006**, 887–901; f) D. K. Smith, *Chem. Commun.* **2006**, 34–44.
[2] a) B. Alonso, I. Cuadrado, M. Morán, J. Losada, *J. Chem. Soc. Chem. Commun.* **1994**, 2575–2576; b) I. Cuadrado, M. Morán, C. M. Casado, B. Alonso, F. Lobete, B. Garcia, M. Ibisate, J. Losada, *Organometallics* **1996**, *15*, 5278–5280.
[3] K. A. Connors, *Chem. Rev.* **1997**, *97*, 1325–1358.
[4] R. Castro, I. Cuadrado, B. Alonso, C. M. Casado, M. Morán, A. E. Kaifer, *J. Am. Chem. Soc.* **1997**, *119*, 5760–5761.
[5] A. U. Moozyckine, J. L. Bookham, M. E. Deary, D. M. Davies, *J. Chem. Soc. Perkin Trans. 2* **2001**, 1858.
[6] B. González, C. M. Casado, B. Alonso, I. Cuadrado, M. Morán, Y. Wang, A. E. Kaifer, *Chem. Commun.* **1998**, 2569–2570.
[7] Y. Wang, S. Mendoza, A. E. Kaifer, *Inorg. Chem.* **1998**, *37*, 317–320.

 © 2007 Wiley-VCH Verlag GmbH & Co. KGaA, Weinheim 

[8] J. J. Michaels, M. W. P. L. Baars, E. W. Meijer, J. Huskens, D. N. Reinhoudt, *J. Chem. Soc. Perkin Trans. 2* **2000**, 1914–1918.

[9] a) C. A. Nijhuis, B. J. Ravoo, J. Huskens, D. N. Reinhoudt, *Coord. Chem. Rev.* **2007**, *251*, 1761–1780; b) C. A. Nijhuis, B. A. Boukamp, B. J. Ravoo, J. Huskens, D. N. Reinhoudt, *J. Phys. Chem. C* **2007**, *111*, 9799–9810; c) M. J. W. Ludden, D. N. Reinhoudt, J. Huskens, *Chem. Soc. Rev.* **2006**, *35*, 1122–1134.

[10] B. González, I. Cuadrado, B. Alonso, C. M. Casado, M. Morán, A. E. Kaifer, *Organometallics* **2002**, *21*, 3544–3551.

[11] C. M. Casado, B. González, I. Cuadrado, B. Alonso, M. Morán, J. Losada, *Angew. Chem. Int. Ed.* **2000**, *39*, 2135–2138.

[12] a) C. Ornelas, J. Ruiz Aranzaes, E. Cloutet, S. Alves, D. Astruc, *Angew. Chem. Int. Ed.* **2007**, *46*, 872–877; b) M.-C. Daniel, F. Ba, J. Ruiz Aranzaes, D. Astruc, *Inorg. Chem.* **2004**, *43*, 8649–8657; c) J. Ruiz, M. J. R. Medel, M.-C. Daniel, J.-C. Blais, D. Astruc, *Chem. Commun.* **2003**, 464–465; d) M.-C. Daniel, J. Ruiz, D. Astruc, *J. Am. Chem. Soc.* **2003**, *125*, 1150–1151.

[13] a) M.-C. Daniel, D. Astruc, *Chem. Rev.* **2004**, *104*, 293–346; b) D. Astruc, M.-C. Dabniel, J. Ruiz, *Chem. Commun.* **2004**, 2637–2649.

[14] B. Alonso, C. M. Casado, I. Cuadrado, M. Morán, A. E. Kaifer, *Chem. Commun.* **2002**, 1778–1779.

[15] K. Takada, D. J. Díaz, H. D. Abruña, I. Cuadrado, C. M. Casado, B. Alonso, M. M. Morán, J. Losada, *J. Am. Chem. Soc.* **1997**, *119*, 10763–10773.

[16] J. Alvarez, A. E. Kaifer, *Organometallics* **1999**, *18*, 5733–5734.

[17] J. Alvarez, T. Ren, A. E. Kaifer, *Organometallics* **2001**, *20*, 3543–3549.

[18] G. R. Newkome, R. K. Behera, C. N. Moorefield, G. R. Baker, *J. Org. Chem.* **1991**, *56*, 7162–7167.

[19] a) C. M. Cardona, A. E. Kaifer, *J. Am. Chem. Soc.* **1998**, *120*, 4023–4024; b) C. M. Cardona, T. D. McCarley, A. E. Kaifer, *J. Org. Chem.* **2000**, *65*, 1857–1864.

[20] Y. Wang, C. M. Cardona, A. E. Kaifer, *J. Am. Chem. Soc.* **1999**, *121*, 9756–9757.

[21] C. M. Cardona, J. Alvarez, A. E. Kaifer, T. D. McCarley, S. Pandey, G. A. Baker, N. J. Bonzagni, F. V. Bright, *J. Am. Chem. Soc.* **2000**, *122*, 6139–6144.

[22] C. M. Cardona, T. Wilkes, W. Ong, A. E. Kaifer, T. D. McCarley, S. Pandey, G. A. Baker, M. N. Kane, S. N. Baker, F. V. Bright, *J. Phys. Chem. B* **2002**, *106*, 8649–8656.

[23] a) W. Ong, A. E. Kaifer, *J. Am. Chem. Soc.* **2002**, *124*, 9358–9359; b) W. Ong, J. Grindstaff, D. Sobransingh, R. Toba, J. Quintela, C. Peinador, A. E. Kaifer, *J. Am. Chem. Soc.* **2005**, *127*, 3353–3361.

[24] D. Sobransingh, A. E. Kaifer, *Langmuir* **2006**, *22*, 10540–10544.

[25] H. Sun, A. E. Kaifer, *Org. Lett.* **2005**, *7*, 3845–3848.

[26] a) C. B. Gorman, J. C. Smith, *Acc. Chem. Res.* **2001**, *34*, 60–71; b) C. S. Cameron, C. B. Gorman, *Adv. Funct. Mater.* **2002**, *12*, 17–20.

[27] A. J. Bard, L. R. Faulkner in *Electrochemical Methods: Fundamentals and Applications*, 2nd ed., Wiley, New York, **2001**, ch. 3.

[28] P. J. Dandliker, F. Diederich, M. Gross, C. B. Knobler, A. Louati, E. M. Sadford, *Angew. Chem. Int. Ed. Engl.* **1994**, *33*, 1739–1741.

[29] D. L. Stone, D. K. Smith, P. T. McGrail, *J. Am. Chem. Soc.* **2002**, *124*, 856–864.

[30] D. Sobransingh, A. E. Kaifer, *Chem. Commun.* **2005**, 5071–5073.

[31] W. Ong, M. Gómez-Kaifer, A. E. Kaifer, *Chem. Commun.* **2004**, 1677–1683.

[32] a) J. W. Lee, S. Samal, N. Selvapalam, H.-J. Kim, K. Kim, *Acc. Chem. Res.* **2003**, *36*, 621–630; b) J. Lagona, P. Mukhopadhyay, S. Chakrabarti, L. Isaacs, *Angew. Chem. Int. Ed.* **2005**, *44*, 4844–4870.

[33] J. Kim, I.-S. Jung, S. Y. Kim, E. Lee, J. L. Kang, S. Sakamoto, K. Yamaguchi, K. Kim, *J. Am. Chem. Soc.* **2000**, *122*, 540–541.

[34] W. S. Jeon, K. Moon, S. H. Park, H. Chun, Y. H. Ko, J. Y. Lee, E. S. Lee, S. Samal, N. Selvapalam, M. V. Rekharsky, V. Sindelar, D. Sobransingh, Y. Inoue, A. E. Kaifer, K. Kim, *J. Am. Chem. Soc.* **2005**, *127*, 12984–12989.

[35] W. Wang, H. Sun, A. E. Kaifer, *Org. Lett.* **2007**, *9*, 2657–2660.

[36] C. J. Hawker, J. M. J. Fréchet, *J. Am. Chem. Soc.* **1990**, *112*, 7638–7647.

Received: August 2, 2007
Published Online: October 9, 2007

 © 2007 Wiley-VCH Verlag GmbH & Co. KGaA, Weinheim 

DOI: 10.1002/ejic.200700867

# Reductive Nitrosation of Peptides Ligated to High-Valent Metal Cations

**Dror Shamir,[a] Israel Zilbermann,*[a] Eric Maimon,[a] Gary Gellerman,[b] Haim Cohen,[b] and Dan Meyerstein*[c,d]**

**Keywords:** Nitrosation / Peptides / NO / High-valent transition metals

NO reacts with $M^{III}$–(glycylglycylglycine), M = Fe; Ni and Cu, to form the terminal *N*-nitrosated peptide complex. This reaction proceeds by a radical mechanism.

(© Wiley-VCH Verlag GmbH & Co. KGaA, 69451 Weinheim, Germany, 2007)

The role of NO in a variety of physiological processes renders its reaction mechanisms with species present in biological media of importance. Of special interest are nitrosation processes that are involved in signaling[1–2] and pathological[2] processes as well as in buffering the concentration of NO in the cell.[1,3–6] Two transition-metal-initiated reductive nitrosation mechanisms were reported:

(1) Ligation of NO to the central cation, which induces a partial positive charge on the nitrogen atom and thus enables attack of a nucleophile at the nitrogen atom[7–10] [Reaction (1)].

$$M^{n+1}L_n \xrightarrow[-L]{NO} L_{n-1}M^{n+1}\text{–}NO \xrightarrow[L]{:B} M^nL_n + BNO^- \quad (1)$$

In water: B is usually $H_2O$ or $OH^-$ and the product is $NO_2^-$.

(2) Reaction of NO with a ligand bound to the central cation with a lone electron pair on the atom ligated to the cation. This process often requires proton loss to form the lone pair. Recently,[11] it was suggested that this is a radical process as outlined in Reactions (2)–(4).

$$M^{n+1}\text{–}E(H)R_m \rightleftharpoons M^{n+1}\text{–}\ddot{E}R_m + H^+ \quad (2)$$

$$M^{n+1}\text{–}\ddot{E}R_m \rightleftharpoons M^n\text{–}\dot{E}R_m \quad (3)$$

$$M^n\text{–}\dot{E}R_m + NO \longrightarrow M^n + R_mENO \quad (4)$$

Where E = N, S and plausibly O.

Reactions of this type were previously attributed to attack of NO on the lone pair followed by electron transfer.[7–10] However, as NO does not react with strong nucleophiles, for example, $OH^-$, it is reasonable that the radical mechanism is the occurring one. As the mechanism described by Reactions (2)–(4) was observed for $E(H)R_m$ = $CH_3NH_2$, it seemed of interest to check whether it took place also for $E(H)R_m$ = peptides. The present study proves that indeed peptide *N*-nitrosations of the terminal amine occur by this mechanism.

The first peptide investigated in this study was glycylglycylglycine (glyglygly). The complexes $Ni^{III}$–(glyglygly) and $Cu^{III}$–(glyglygly) were prepared by a known procedure,[12,13] and the complex $Fe^{III}$–(glyglygly) was prepared by slow addition of 0.3 M tris buffer to a solution containing $Fe(ClO_4)_3$ and 10–20% excess of tripeptide. The solutions containing the complexes were saturated with Ar and mixed with NO saturated aqueous solutions at the same pH. By using stopped flow, the kinetic results, Figure 1, confirm that these complexes react with NO in reactions obeying pseudo-first-order rate laws. The observed rates depend linearly on the concentrations of NO and $OH^-$, Figures 2 and 3, respectively. The observed rate constants at pH 6.0 are summed up in Table 1. The pH dependence of the rate con-

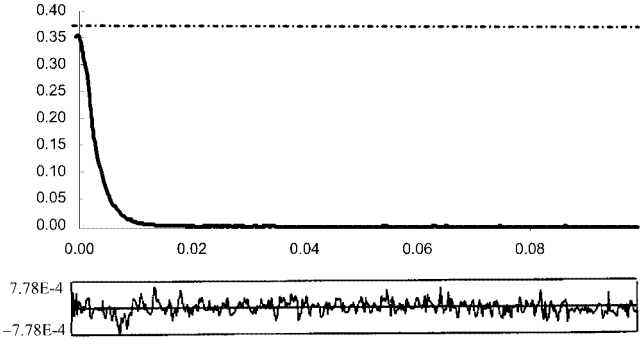


Figure 1. Kinetics of reaction of $Ni^{III}$–(glyglygly) at pH 7.0 with NO measured at 332 nm. Solution composition: (——) $Ni^{III}$ 0.0005 M, glyglygly 0.0011 M, (50% saturated NO); (-·-·-·) $Ni^{III}$ 0.0005 M, glyglygly 0.0011 M (saturated Ar).

[a] Chem. Dept., Ben-Gurion Univ. of the Negev, and Nuclear Research Centre Negev, Beer-Sheva, Israel
[b] Biol. Chem. Dept. Ariel University Center of Samaria, Ariel, Israel
[c] Chem. Dept., Ben-Gurion Univ. of the Negev, Beer-Sheva, Israel
Fax: +972-8-6461740
E-mail: danmeyer@bgu.ac.il
[d] Biol. Chem. Dept. Ariel University Center of Samaria, Ariel, Israel

Supporting information for this article is available on the WWW under http://www.eurjic.org or from the author.

 © 2007 Wiley-VCH Verlag GmbH & Co. KGaA, Weinheim 

stants, Figure 3, suggests that these reactions occur with an alkaline form of the complexes [the results suggest a p$K_a \geq 7$ for $Cu^{III}$–(glyglygly); $\geq 9$ for $Ni^{III}$–(glyglygly) and ca. 10 for $Fe^{III}$–(glyglygly)] (for the Cu and Ni complexes, measurements could not be performed at higher pH values, as they are faster than the mixing time of the stopped flow). The p$K_a$ values of the amide nitrogen atoms of these complexes are $\leq 6.0$.[14–17] Thus, the results suggest that the reactions observed require the loss of a proton from the terminal amine of the peptide.

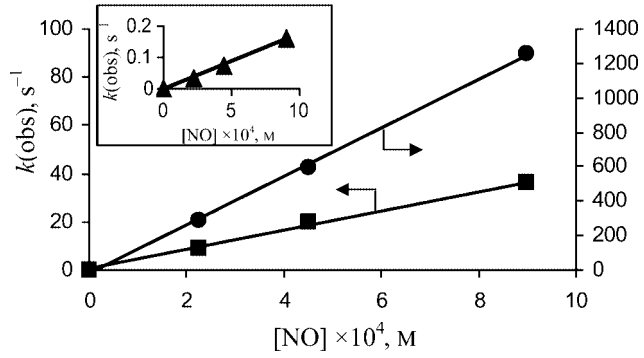


Figure 2. Dependence of the observed rate constants on [NO]. Solution composition: A: $k$(obs.) vs. [NO] pH 6.0, [bis tris buffer] = $5 \times 10^{-5}$ M, [$M^{III}$] = 0.005 M, [glyglygly] = $1.1 \times 10^{-3}$ M; (●) = $Cu^{III}$; (▲) = $Fe^{III}$; (■) = $Ni^{III}$.

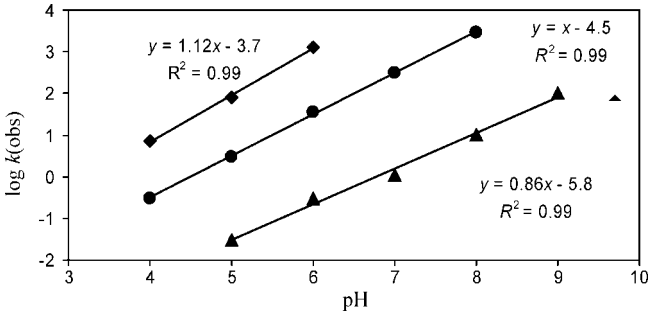


Figure 3. Dependence of the observed rate constants on pH. Solution composition: (●) $Ni^{III}$ 0.0005 M, glyglygly 0.0011 M, (■) $Cu^{III}$ 0.0005 M, glyglygly 0.0011 M, (▲) $Fe^{III}$ 0.0005 M, GGG 0.0011 M, NO 50% saturated.

Table 1. Observed rate constants at pH 6.0.

| $M^{III}$ | $K_{obs.}$, $M^{-1} s^{-1}$ (alaglygly) | $k_{obs.}$, $M^{-1} s^{-1}$ (glyglygly) |
|---|---|---|
| $Cu^{III}$ | 880 | 1260 |
| $Ni^{III}$ | 21 | 36 |
| $Fe^{III}$ | 0.090 | 0.16 |

The pH dependence of the observed rate constants of the reactions (Figure 3) suggests that the site of the nitrosation of the ligand is the terminal amine of the peptide. The observed rate constants (Table 1 and Figure 3) decrease along the series $Cu^{III} > Ni^{III} > Fe^{III}$. This result is in accord with expectations as the redox potentials vs. NHE of $M^{III/II}$–(glyglygly) complexes are 0.92,[18,19] 0.83[19,20] and –0.21 V [this study] for M = Cu, Ni and Fe, respectively. Though the rate constants decrease with the decrease in the oxidation potential of the complexes, one would expect a larger difference between the $Ni^{III}$ and $Fe^{III}$ complexes. The source of this observation is not clear although it might be due to a higher p$K_a$ of the bound terminal amine in the $Ni^{III}$ complex. Analysis of the final products was performed by the following techniques: (1) Ion chromatography, which proved that $NO_2^-$ is not a product of the reactions studied. (2) ESI MS (Supporting Information, Figure S1), which detected a product with $m/z$ = 219 in solutions that contained $M^{III}$–(glyglygly) and NO (Ar saturated and acidified to pH 3.0 after the nitrosation). This peak is absent in a blank experiment that contained Ar-saturated solutions of $M^{II}$–(glyglygly), which were then acidified. A mass of 219 fits the adduct glyglyglyH-NO, namely, the reductive nitrosation product, which as expected is obtained by adding NO to solutions containing the three $M^{III}$–(glyglygly) complexes. (3) Determination of pH − the pH dependence of the rate constants suggests that the nitrosation occurs on the terminal amine. In order to verify this assumption the $^{13}C$ NMR spectra of the peptides before and after the nitrosation reactions were measured [deaerated $D_2O$ solutions of $M^{II}$–(glyglygly) and of $M^{III}$–(glyglygly) were treated with NO then Ar saturate in order to inhibit nitrite formation, and acidified to pH 3.0 in order to release the peptide from the paramagnetic cation].

The results (Supporting Information, Figures S2, S3) show that the glyglygly peptide has $^{13}C$ NMR signals at 176.4, 170.8 and 167.7 ppm for the carboxylate and amide carbons and at 43.1, 42.3 and 40.4 ppm for the $CH_2$ carbons. For the nitrosation product, signals at 173.3, 173.2, 172.8, 50.0, 42.1 and 41.7 ppm and an additional weak signal at 41.0 ppm are observed. These results are in accordance with those obtained by approximate simulation by using the semiempirical simulation − CS ChemDraw Ultra program − for the different plausible nitrosation sites (Table 2). Comparison of the experimental results with the simulations points out that the nitrosations do not occur on the $CH_2$ groups. However, the results do not enable a decision regarding which nitrogen is nitrosated.

Table 2. Simulations of the $^{13}C$ NMR data of glyglygly, and the different plausible nitrosation products.

| Nitrosation Site | $C^1$ | $C^2$ | $C^3$ | $C^4$ | $C^5$ | $C^6$ |
|---|---|---|---|---|---|---|
| None | 43.0 | 171.1 | 42.9 | 171.1 | 42.7 | 173.2 |
| $N^1$ | 43.4 | 171.1 | 42.7 | 171.0 | 48.7 | 173.2 |
| $N^2$ | 42.8 | 171.0 | 49.1 | 171.1 | 42.7 | 173.2 |
| $N^3$ | 48.4 | 171.2 | 42.9 | 171.1 | 42.7 | 173.2 |
| $N^3$ acidic form | 50.7 | 171.1 | 42.9 | 171.1 | 42.7 | 173.2 |
| $C^1$ | 77.5 | 171.2 | 42.9 | 171.1 | 42.7 | 173.2 |

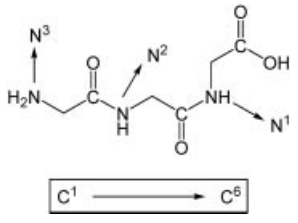


 © 2007 Wiley-VCH Verlag GmbH & Co. KGaA, Weinheim 

In order to resolve this dilemma, the experiments were repeated with the peptide alaglygly, as the $^{13}C$ NMR spectroscopic simulation (Table 3) clearly demonstrates that *N*-nitrosation at the terminal amine and the amide N adjacent to the alanine residue will have significantly different $^{13}C$ NMR spectra. The results (Supporting Information, Figures S4, S5) point out signals for the alaglygly peptide at 176.4, 171.3, 170.6, 49.0, 43.3, 42.3 and 16.2 ppm and for the nitrosation product signals at 178.9, 176.8, 170.7, 57.2, 43.1, 42.2 and 9.8 ppm and additional very weak signals 16.9 and 10.4 ppm. Comparison of the results with the simulation clearly points out that the signal of the $CH_3$ group is shifted to higher field from 16.2 to 9.8 ppm in perfect accord with the simulation results for nitrosation of the terminal amine group. In contrast, the simulation of the nitrosation product on $N^2$ predicts that the signal due to the $CH_3$ group will be shifted to a lower field. The kinetics of the reaction of the $M^{III}$–(alaglygly) with NO are very similar to those observed for the $M^{III}$–(glyglygly) complexes. The observed rate constants at pH 6.0 (Table 1) are slightly lower than those for the $M^{III}$–(glyglygly) complexes. This result is tentatively attributed to the fact that the terminal amine of alaglygly is a slightly stronger base than that of glyglygly. The corresponding p$K_a$ values are 8.16 and 7.95,[21] respectively. The stronger base is expected to stabilize better the $M^{III}$ oxidation state and probably to increase the p$K_a$ value of the terminal amine; both these effects are expected to lower the rate constant of the nitrosation reactions.

Table 3. Simulations of the $^{13}C$ NMR spectra of alaglygly and the different plausible nitrosation products.

| Nitrosation Site | $C^1$ | $C^2$ | $C^3$ | $C^4$ | $C^5$ | $C^6$ | $C^7$ |
|---|---|---|---|---|---|---|---|
| None | 173.2 | 42.7 | 171.1 | 43.2 | 172.1 | 49.3 | 20.5 |
| $N^1$ | 173.2 | 42.7 | 171.1 | 43.2 | 172.1 | 56.1 | 15.7 |
| $N^2$ | 173.2 | 42.7 | 171.1 | 49.4 | 176 | 49.1 | 21.1 |

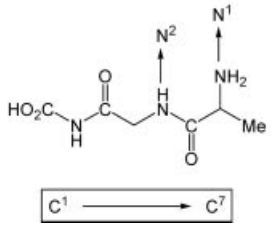


It is of interest to note that nitrosations do not occur at the amide sites although a lone electron pair is also available at these sites even at the lowest pH values used in the this study. This observation is attributed to the higher energy of the orbital of the lone pair of the terminal amine than that of the amide groups.

Finally one should consider whether the ·NO attacks the lone pair of the $M^{III}$–N̈HR group followed by an electron transfer or the NO attacks the radical isomer of this species:

$$M^{III}-\ddot{N}HR \rightleftharpoons M^{II}-\dot{N}HR$$

As the lone pair in $M^{III}$–N̈HR is a weaker base than $OH^-$ and NO does not react with the latter, it is suggested that the nitrosations proceed by a radical mechanism. This suggestion is also attractive as it suggests that the nitrosation of E(H)R and the release of NO from ON–ER[7,22,23] proceed through the same mechanism: a radical mechanism. Finally as *N*-nitroso compounds are carcinogenic[2] this mechanism of reductive *N*-nitrosation might be of biological importance.

**Supporting Information** (see footnote on the first page of this article): Mass spectra and $^{13}C$ NMR spectra of pertinent solutions studied.

## Acknowledgments

This study was supported by a grant from the Planning and Granting Committee of the Council of Higher Education and the Israel Atomic Energy Committee.

[1] S. Moncada, R. M. J. Palmer, E. A. Higges, *Pharmacol. Rev.* **1991**, *43*, 109.
[2] L. J. Ignarro, *ED Nitric Oxide: Biology and Pathobiology*, Academic press, San Diego, **2000**.
[3] D. L. H. Williams, *Chem. Commun.* **1996**, 1085.
[4] M. Feelisch, M. te Poel, R. Zamora, A. Deussen, S. Moncada, *Nature* **1994**, *368*, 92.
[5] H. H. Al-Sa′doni, I. L. Megson, S. Bisland, A. R. Butler, F. W. Flitney, *Br. J. Pharmacol.* **1997**, *121*, 1047.
[6] A. P. Dicks, H. R. Swift, D. L. H. Williams, A. R. Butler, H. H. Al-Sadonini, B. G. Cox, *J. Chem. Soc. Perkin Trans. 2* **1996**, *2*, 481.
[7] P. C. Ford, O. B. Fernandez, M. D. Lim, *Chem. Rev.* **2005**, *105*, 2439.
[8] K. Tsuge, F. Derose, D. M. Lim, P. C. Ford, *J. Am. Chem. Soc.* **2004**, *126*, 6564.
[9] S. D. Pell, J. N. Armor, *J. Am. Chem. Soc.* **1973**, *95*, 7625.
[10] M. M. deMaine, D. M. Stanbury, *Inorg. Chem.* **1991**, *31*, 2104.
[11] D. Shamir, I. Zilbermann, E. Maimon, H. Cohen, D. Meyerstein, *Inorg. Chem. Commun.* **2007**, *1*, 57.
[12] J. B. Green, T. M. Tesfai, D. W. Margerum, *Dalton Trans.* **2004**, 3508.
[13] S. T. Kirksey, T. A. Neubecker, D. W. Margerum, *J. Am. Chem. Soc.* **1979**, *101*, 1631.
[14] D. W. Margerum, *Pure Appl. Chem.* **1983**, *1*, 23.
[15] M. K. Kim, A. E. Martell, *J. Am. Chem. Soc.* **1967**, *89*, 5138.
[16] R. B. Martin, M. Chamberlin, J. T. Edsell, *J. Am. Chem. Soc.* **1960**, *82*, 495.
[17] E. J. Billo, D. W. Margerum, *J. Am. Chem. Soc.* **1970**, *92*, 6704.
[18] F. P. Bossu, K. L. Chellappa, D. W. Margerum, *J. Am. Chem. Soc.* **1977**, *99*, 2195.
[19] G. D. Owens, D. A. Phillips, J. J. Czarnecki, J. M. T. Raycheba, D. W. Margerum, *Inorg. Chem.* **1984**, *23*, 1345.
[20] F. P. Bossu, D. W. Margerum, *J. Am. Chem. Soc.* **1976**, *98*, 4003.
[21] M. N. Tursunov, U. I. Salakhutdinov, S. S. Shukurov, K. T. Poroshin, *Dokl. Akademii Nauk Tadzhikskoi SSR* **1971**, *14*, 40.
[22] P. Kapoor, T. H. Warren, The 230th ACS National Meeting and Exposition, Washington, DC, **2005**, INOR 308.
[23] M. Marie; T. H.Warren, The 230th ACS National Meeting and Exposition, Washington, DC, **2005**, INOR 98.

Received: July 31, 2007
Published Online: October 4, 2007

 © 2007 Wiley-VCH Verlag GmbH & Co. KGaA, Weinheim 

DOI: 10.1002/ejic.200700500

# Nickel Complexes with $N_2O$ Donor Ligands: Syntheses, Structures, Catalysis and Magnetic Studies

**Jishnunil Chakraborty,[a] Mahasweta Nandi,[b] Heike Mayer-Figge,[c] William S. Sheldrick,[c] Lorenzo Sorace,[d] Asim Bhaumik,[b] and Pradyot Banerjee*[a]**

**Keywords:** Nickel / N,O ligands / Epoxidation / Heterogeneous catalysis / Magnetic properties

Two new terephthalato-bridged tetranuclear polymeric $Ni^{II}$ complexes, namely $[Ni_4L_4^1(\mu\text{-tp-}\kappa_4\text{-O})(H_2O)_2(\mu\text{-tp-}\kappa_2\text{-O})]\cdot 2C_2H_5OH\cdot CH_3OH\cdot 3H_2O$ (**1**) and $[Ni_4L_4^2(\mu\text{-tp-}\kappa_4\text{-O})(H_2O)_2(\mu\text{-tp-}\kappa_2\text{-O})]\cdot 3H_2O$ (**2**) [$L^1$ = *N*-(3-aminopropyl)-5-bromosalicylaldimine and $L^2$ = *N*-(3-aminopropyl)salicylaldimine], are reported along with the syntheses and structures of the dicyanoargentate-bridged polymeric complexes $[Ni(L^1)(H_2O)\{Ag(CN)_2\}]_\alpha$ (**3**) and $[Ni(L^3)(MeOH)\{Ag(CN)_2\}]_\alpha$ (**4**) [$L^3$ = *N*-(3-amino-2,2-dimethylpropyl)-5-bromosalicylaldimine]. All four complexes are found to be effective heterogeneous catalysts for the epoxidation of alkenes such as styrene, α-methylstyrene and cyclohexene in the presence of *tert*-butyl hydroperoxide. The variable-temperature magnetic susceptibility measurements (300–2 K) of complex **1** show a fair degree of antiferromagnetic coupling between the $Ni^{II}$ centers.

(© Wiley-VCH Verlag GmbH & Co. KGaA, 69451 Weinheim, Germany, 2007)

## Introduction

Low-dimensional coordination polymers, including one-dimensional (1D) chain-like and two-dimensional (2D) layer-like structures, have received much attention in recent years owing to their intriguing structural features and unique electroconductive, nonlinear optical, and magnetic properties, which differ from those of three-dimensional (3D) coordination polymers.[1] A great variety of low-dimensional coordination polymers based on d-block transition metal ions and organic ligands have been prepared to date, many of which have potential applications in the field of functional materials.[2–6] The organic components containing N- or O- donors in the framework offer great potential for chemical and structural diversity.[7]

Organic aromatic polycarboxylates are some of the most widely employed multidentate O-donor ligands for the preparation of such coordination polymers with multidimensional networks. In this respect, terephthalate (tp) has been studied extensively as a rigid and versatile bridging ligand[8] as it contains multiple bridging moieties that lead to a variety of connection modes with transition metal centers and provide abundant structural motifs. Furthermore, it can act not only as a hydrogen-bond donor but also as an acceptor due to the existence of protonated and/or deprotonated carboxylate groups. The terephthalate ligand is therefore regarded as an excellent candidate for the construction of multidimensional coordination frameworks.

The introduction of another kind of both N- and O-donor chelating ligand, such as a tridentate Schiff base, in the {M/tp} (M = transition metal) system may induce new structural evolution as the introduction of N-donor chelating ligands into the metal sites may inhibit the expansion of the polymeric frameworks and lead to the desired low-dimensional coordination polymers. However, the synthesis of complexes containing mixed ligands is expected to be more difficult to control than that of complexes containing one ligand for several reasons, such as the different solubility of the organic ligands and competition between these ligands to coordinate the transition metal. In order to gain insight into the parameters that control these variables we have synthesized two new terephthalate-bridged tetranuclear polymeric $Ni^{II}$ complexes, namely $[Ni_4L_4^1(\mu\text{-tp-}\kappa_4\text{-O})(H_2O)_2(\mu\text{-tp-}\kappa_2\text{-O})]\cdot 2C_2H_5OH\cdot CH_3OH\cdot 3H_2O$ (**1**) and $[Ni_4L_4^2(\mu\text{-tp-}\kappa_4\text{-O})(H_2O)_2(\mu\text{-tp-}\kappa_2\text{-O})]\cdot 3H_2O$ [**2**; $L^1$ = *N*-(3-aminopropyl)-5-bromosalicylaldimine and $L^2$ = *N*-(3-aminopropyl)salicylaldimine]. $Ni^{II}$ forms a phenolate-bridged binuclear unit in these complexes and two such units are connected by a terephthalate moiety to form a tetranuclear nickel(II) complex. The crystal structure of complex **1** shows that the tetranuclear units are connected to each other by the terephthalate moiety in a bis(monodentate) mode to form a one-dimensional network. The variable-

[a] Department of Inorganic Chemistry, Indian Association for the Cultivation of Science,
Jadavpur, Kolkata-700 032, India
Fax: +91-33-2473-2805
E-mail: icpb@mahendra.iacs.res.in
[b] Department of Materials Science and Center for Advanced Materials, Indian Association for the Cultivation of Science,
Jadavpur, Kolkata-700 032, India
[c] Lehrstuhl für Analytische Chemie, Ruhr-Universität Bochum,
Universitätsstrasse 150, 44780 Bochum, Germany
[d] Laboratory for Molecular Magnetism (LAMM), Dipartimento di Chimica, Università di Firenze,
Firenze, Italy

 © 2007 Wiley-VCH Verlag GmbH & Co. KGaA, Weinheim 

temperature magnetic behavior of complex **1** is also investigated.

Like terephthalate, cyanometalate anions have been extensively used as building blocks in supramolecular coordination polymers.[9,10] Compared to the higher coordination counterparts of various transition metals, there has been considerably less investigation of two-coordinate linear cyanometalate building blocks for the construction of coordination polymers. We have chosen to examine the ability of the linear dicyanoargentate ion $[Ag(CN)_2]^-$ to form supramolecular frameworks. The syntheses and structures of two dicyanoargentate-bridged polymeric networks, namely $[Ni(L^1)(H_2O)\{Ag(CN)_2\}]_\alpha$ (**3**) and $[Ni(L^3)(MeOH)\{Ag(CN)_2\}]_\alpha$ [**4**; $L^3$ = *N*-(3-amino-2,2-dimethylpropyl)-5-bromosalicylaldimine], are therefore also included in this paper.

Intrigued by a recent study concerning the use of (salen)-$Ni^{II}$ complexes as homogeneous/heterogeneous epoxidation catalysts,[11] we extended our study to the epoxidation of alkenes such as styrene, α-methylstyrene and cyclohexene in the presence of *tert*-butyl hydroperoxide heterogeneously catalyzed by complexes **1**–**4**.

## Results and Discussion

### Synthesis

The monocondensed ligands $L^1$–$L^3$ were prepared as their nickel complexes $Ni(L^1)_2$, $Ni(L^2)_2$, and $Ni(L^3)_2$ by treating 5-bromosalicylaldehyde or salicylaldehyde with $Ni(OAC)_2{\cdot}4H_2O$ and the corresponding amine (see Experimental Section). Complex **1** was prepared by the reaction of $Ni(L^1)_2$ with equimolar amounts of $Ni(ClO_4)_2{\cdot}6H_2O$ and the disodium salt of terephthalic acid in EtOH/MeOH/$H_2O$ to produce the $\mu_2$-phenolate and terephthalate-bridged tetranuclear complex $[Ni_4L_4{}^1(\mu\text{-tp-}\kappa_4\text{-O})(H_2O)_2(\mu\text{-tp-}\kappa_2\text{-O})]{\cdot}2C_2H_5OH{\cdot}CH_3OH{\cdot}3H_2O$ (Scheme 1). Complex **2** was prepared in the same way as described for complex **1** but with salicylaldehyde for the Schiff base condensation instead of 5-bromosalicylaldehyde. Complex **3** was prepared by the reaction of $Ni(L^1)_2$ with equimolar amounts of $Ni(ClO_4)_2{\cdot}6H_2O$ and $[NaAg(CN)_2]$ in MeOH/$H_2O$ to produce the argentocyanide-bridged heterobinuclear polymeric complex $[Ni(L^1)(H_2O)\{Ag(CN)_2\}]_\alpha$ (Scheme 2). Complex **4** was syn-

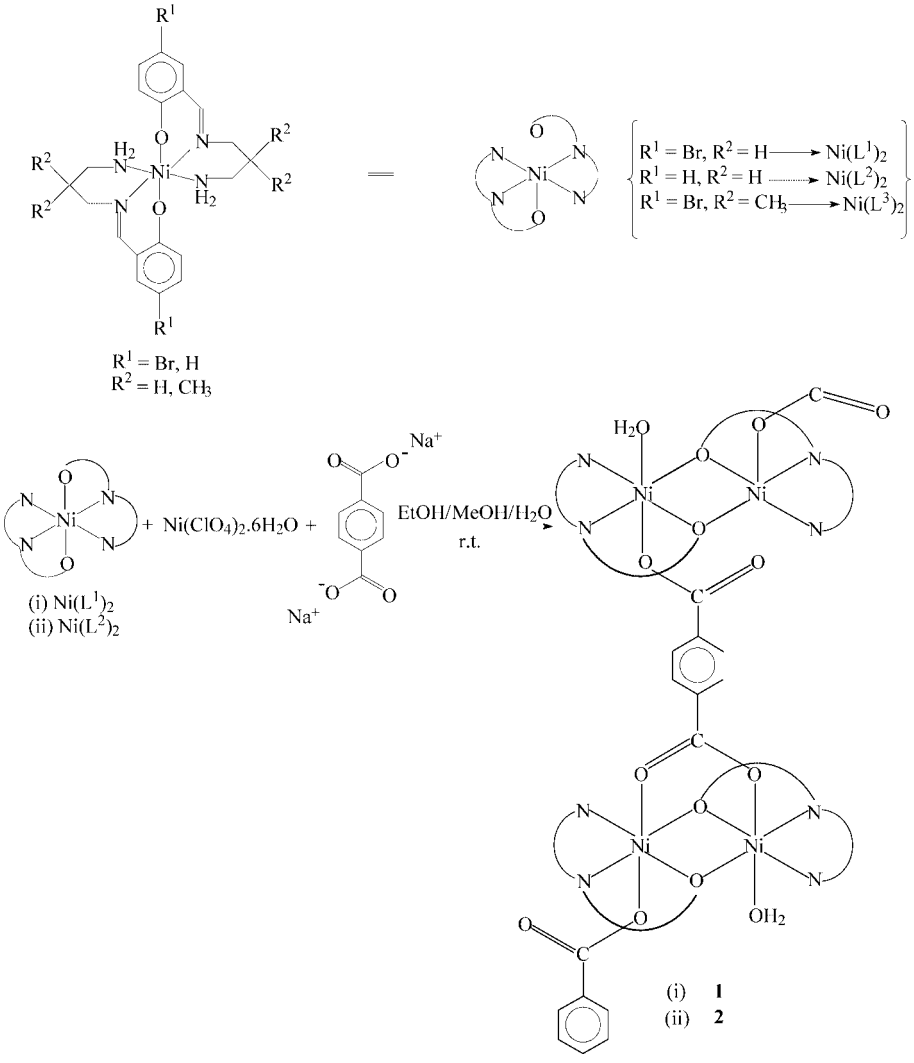


Scheme 1. Synthetic routes to complexes **1** and **2**.

 © 2007 Wiley-VCH Verlag GmbH & Co. KGaA, Weinheim 

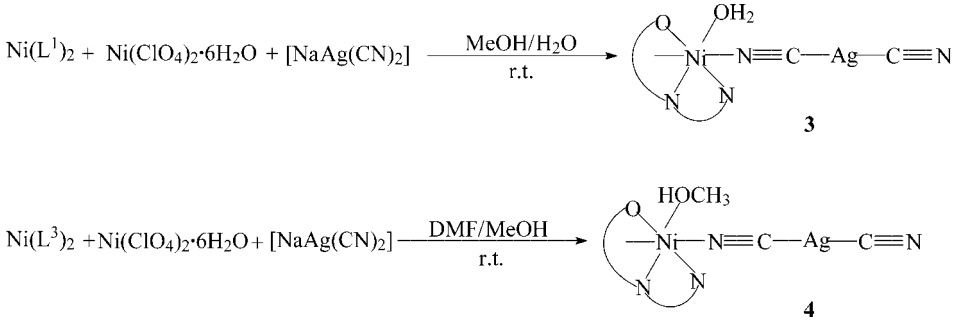


Scheme 2. Synthetic routes to complexes **3** and **4**.

thesized in dmf/MeOH by treating $Ni(L^3)_2$ with equimolar amounts of $Ni(ClO_4)_2·6H_2O$ and $[NaAg(CN)_2]$ to yield the argentocyanide-bridged polymeric species $[Ni(L^3)(MeOH)\{Ag(CN)_2\}]_\alpha$.

## IR Spectra

The IR spectra of **1** and **2** show a broad absorption band in the range 3321–3504 $cm^{-1}$ which can be assigned to the O–H stretching vibrations of the coordinated and noncoordinated water molecules and noncoordinated MeOH and EtOH molecules in the case of complex **1**. The strong band in the range 1637–1645 $cm^{-1}$ can be assigned to $\nu(CN_{iminic})$, which suggests coordination of the ligands to the metal centers through the imine nitrogen atoms. The tp unit coordinates the metal ions in both complexes in both its bis(monodentate) and bis(bidentate) coordination modes. The values of $\Delta\nu$, indicating the difference between the asymmetric stretching $\nu_a(COO^-)$ and the symmetric stretching $\nu_s(COO^-)$, for **1** are 148 and 29 $cm^{-1}$, whereas those for complex **2** are 142 and 27 $cm^{-1}$.

The strong band at 2162 $cm^{-1}$ in the IR spectrum of complex **3** is due to the $\nu(CN)$ absorption of the N-bonded argentocyanide unit and the band at 3346 $cm^{-1}$ is due to the water molecule coordinated to the $Ni^{II}$ center. Complex **4** also exhibits a strong band at 2164 $cm^{-1}$ due to the N-bonded argentocyanide unit. The broad band at 3437 $cm^{-1}$ is assigned to an O–H stretching vibration, thereby confirming the presence of the coordinated $CH_3OH$ molecule. The strong band in the range 1585–1602 $cm^{-1}$ observed for all complexes is due to the $\nu(CO)$ absorption of the phenolate-containing ligands.

## Structure of Complex 1

A view of **1** is shown in Figure 1 and key bond lengths and angles are listed in Table 1. The crystal structure of this complex shows that the asymmetric unit contains a tetranuclear molecule of the type $[Ni_4L_4^1(\mu\text{-}O_2CC_6H_4CO_2)(H_2O)_2(O_2CC_6H_4CO_2)]$ in addition to two ethanol, one methanol, and three water molecules. The tetranuclear unit is formed by two $Ni^{II}$ atoms (Ni1 and Ni2) bridged by two $\mu_2$-phenolato oxygen atoms (O1 and O2) of the Schiff-base ligands and a terephthalato ligand in its bis(bidentate) mode that connects the four $Ni^{II}$ centers. The tridentate ligand $L^1$ provides an $N_2O_2$ donor set around each metal atom. The basal $NiN_2O_2$ plane for the Ni1 center is formed by the two nitrogen atoms (N1 and N2) and the two oxygen atoms (O1 and O2) of the bridging phenolato ligands while the basal plane of the Ni2 center is formed by two different nitrogen atoms (N3 and N4) of another $L^1$ ligand and the same phenolate oxygens (O1 and O2). The O3 atom of the terminal water molecule and the O5 atom of the bridging bis(bidentate) terephthalato ligand occupy the axial positions of the Ni1 center. The coordination environment of the Ni2 center is somewhat different to that of the Ni1 center. Thus, for

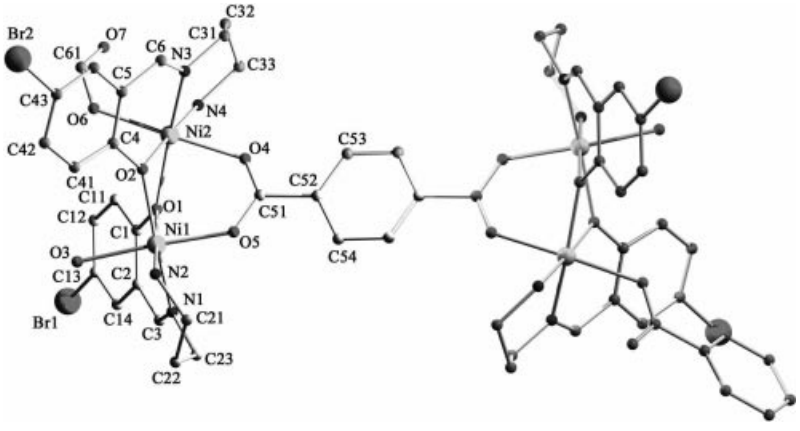


Figure 1. A view of the molecule of complex **1**.

 © 2007 Wiley-VCH Verlag GmbH & Co. KGaA, Weinheim 

the Ni2 center the axial positions are occupied by the O4 atom of the bridging terephthalato ligand and the O6 atom of another bridging terephthalato ligand in its bis(monodentate) coordination mode. Each nickel atom has a distorted octahedral environment. The phenolate-bridged nickel atoms are separated by 3.076 Å with two Ni1–O1–Ni2 and Ni1–O2–Ni2 bridging angles of 97.4(4)° and 96.5(3)°, respectively; two $Ni_2N_4O_2$ moieties are separated from each other by 10.996 Å. The basal bond lengths around Ni1 are within the range 2.020(8)–2.089(10) Å while those around Ni2 are in the range 2.044(8)–2.092(10) Å. The apical Ni1–O3, Ni1–O5, Ni2–O4, and Ni2–O6 bond lengths are 2.143(6), 2.077(8), 2.091(6), and 2.133(8) Å, respectively. The O3–Ni1–O5 bond angle is 176.8(3)° while that for O4–Ni2–O6 is 177.8(3)°. The Ni–$O_{tp}$ bond lengths are similar to those found in other terephthalate-bridged nickel complexes.[12,13]

The packing diagram of complex **1** (Figure 2) shows that the tetranuclear $Ni^{II}$ units are joined to each other by the terephthalate moiety in its bis(monodentate) mode to form an infinite one-dimensional network where symmetry-related O6 terephthalato-oxygen atoms bind two Ni2 centers in a zig-zag structure along the *a*-axis The simultaneous presence of two terephthalate ligands with different bridging modes gives rise to an unprecedented coordination chain. It is interesting to note that the adjacent layers are not parallel when viewed along the *c*-axis but are inclined to each other with an angle of 39.17° (Figure 3). The dihedral angle formed between the anion and the equatorial plane is 62.14°, and the carboxylate group O6/C61/O7 deviates from coplanarity with the phenyl ring (11.65°). This deviation is uniform throughout the chain. The Ni···Ni separation within a linear chain is 11.296 Å. This distance is

Table 1. Selected bond lengths [Å] and angles [°] in complex **1**.

| Bond lengths [Å] | | | |
|---|---|---|---|
| Ni1–O1 | 2.020(8) | Ni2–O1 | 2.075(8) |
| Ni1–O2 | 2.079(8) | Ni2–O2 | 2.044(8) |
| Ni1–O3 | 2.143(6) | Ni2–O4 | 2.091(6) |
| Ni1–O5 | 2.077(8) | Ni2–O6 | 2.133(8) |
| Ni1–N1 | 2.030(11) | Ni2–N3 | 2.047(10) |
| Ni1–N2 | 2.089(10) | Ni2–N4 | 2.092(10) |
| **Bond angles [°]** | | | |
| O1–Ni1–O2 | 79.7(3) | O1–Ni2–O2 | 79.2(3) |
| O1–Ni1–O3 | 88.0(3) | O1–Ni2–O4 | 86.8(3) |
| O1–Ni1–O5 | 94.5(3) | O1–Ni2–O6 | 95.4(3) |
| O1–Ni1–N1 | 89.0(4) | O1–Ni2–N3 | 165.5(4) |
| O1–Ni1–N2 | 174.6(4) | O1–Ni2–N4 | 97.0(3) |
| O2–Ni1–O3 | 93.9(3) | O2–Ni2–O4 | 93.0(3) |
| O2–Ni1–O5 | 88.7(3) | O2–Ni2–O6 | 86.9(3) |
| O2–Ni1–N1 | 168.6(4) | O2–Ni2–N3 | 87.6(4) |
| O2–Ni1–N2 | 94.9(4) | O2–Ni2–N4 | 176.3(3) |
| O3–Ni1–O5 | 176.8(3) | O4–Ni2–O6 | 177.8(3) |
| O3–Ni1–N1 | 86.9(4) | O4–Ni2–N3 | 87.7(4) |
| O3–Ni1–N2 | 92.8(3) | O4–Ni2–N4 | 86.3(4) |
| O5–Ni1–N1 | 91.0(4) | O6–Ni2–N3 | 90.1(3) |
| O5–Ni1–N2 | 85.0(4) | O6–Ni2–N4 | 93.9(3) |
| N1–Ni1–N2 | 96.5(4) | N3–Ni2–N4 | 96.0(4) |
| Ni1–O1–Ni2 | 97.4(4) | Ni1–O2–Ni2 | 96.5(3) |

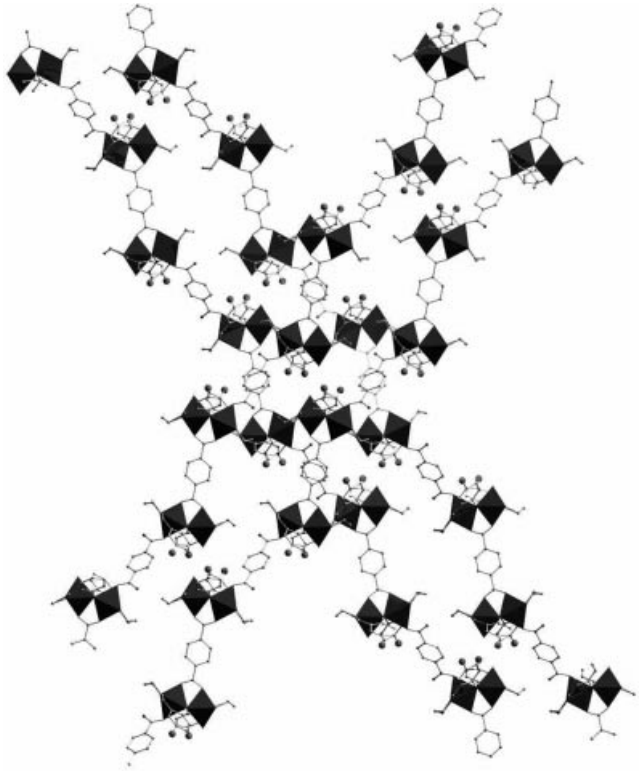

Figure 3. A view of the packing fragment showing the crossing of the 1D networks in **1**. The polyhedra represent the $Ni_2N_4O_6$ core.

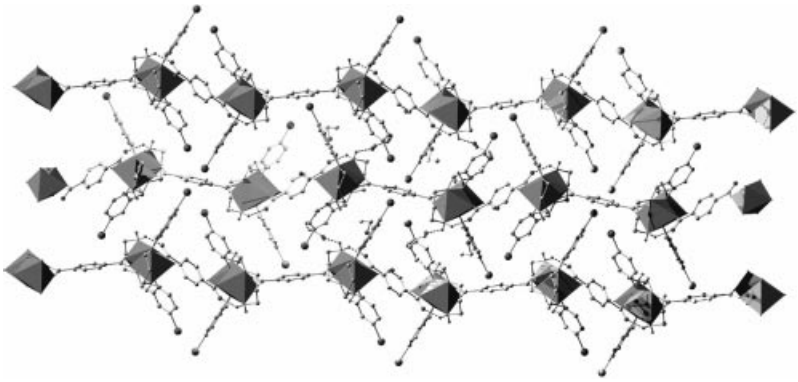

Figure 2. Packing diagram of complex **1**. The polyhedra represent the $Ni_2N_4O_6$ core.

 © 2007 Wiley-VCH Verlag GmbH & Co. KGaA, Weinheim 

shorter than in other terephthalate-bridged nickel complexes such as $[Ni(pyrazole)_4(tp)]_n$ [11.446(2) Å],[14] $[Ni(C_{12}H_{30}N_6O_2)(C_8H_4O_4)]_n{\cdot}4nH_2O$ [11.514(1) Å],[12] where $n$ is ∞, and [(μ-terephthalato){Ni(dca)(dpt)($H_2O$)}$_2$] [11.379(10) Å].[15] The one-dimensional chains are connected together by intermolecular hydrogen-bonding interactions between the oxygen atom of uncoordinated methanol and the coordinated amine of the Schiff base [N2···O300 3.33(3) Å]. In addition, one lattice ethanol molecule takes part in hydrogen bonding with another coordinated amine group of the Schiff base [N4···O200 3.12(3) Å]. There is also an intramolecular hydrogen bond connecting an amine group with a bis(monodentate) terephthalato oxygen atom [N4···O7 2.889(14) Å]. The two C–O bond lengths of the carboxylate group are practically identical even though one is coordinated to the Ni2 center [1.253(16) Å] and the other is not [1.253(19) Å]. In general, the C–O bond lengths of coordinated carboxylate groups fall in the range 1.266–1.279 Å and are longer than the free carbonyl C–O bonds (1.226–1.255 Å) when terephthalate coordinates a metal ion in a monodentate fashion.[12]

### Structure of Complex 3

The coordination environment of the $Ni^{II}$ ion in complex **3** is shown in Figure 4 along with the atom-numbering scheme. Key bond lengths and angles are listed in Table 2. The coordination environment for each nickel center is best described by a distorted octahedral geometry. Two nitrogen atoms, a phenolate oxygen atom of the tridentate Schiff-base ligand $L^1$, and an oxygen atom of the coordinated water molecule, with Ni1–N1, Ni1–N2, Ni1–O1, and Ni1–O2 distances of 2.045(4), 2.076(5), 2.015(4), and 2.152(4) Å, respectively, define the equatorial plane around the nickel atom. The axial sites are occupied by two nitrogen atoms of the bridging argentocyanide moiety with Ni1–N3 and Ni1–N4 bond lengths of 2.115(5) and 2.101 Å, respectively. The central nickel atom lies slightly above the equatorial plane (0.048 Å).

Table 2. Selected bond lengths [Å] and angles [°] in complex **3**.

| Bond lengths [Å] | | | |
|---|---|---|---|
| Ni1–O1 | 2.015(4) | N3–C8 | 1.142(9) |
| Ni1–O2 | 2.152(4) | Ag1–C8 | 2.064(7) |
| Ni1–N1 | 2.045(4) | Ag1–C9 | 2.065(7) |
| Ni1–N2 | 2.076(5) | N4–C9 | 1.139(9) |
| Ni1–N3 | 2.115(5) | | |
| **Bond angles [°]** | | | |
| O1–Ni1–O2 | 87.66(16) | O1–Ni1–N1 | 89.90(18) |
| O1–Ni1–N2 | 175.28(17) | O1–Ni1–N3 | 86.61(19) |
| O2–Ni1–N1 | 175.72(19) | O2–Ni1–N2 | 87.91(17) |
| O2–Ni1–N3 | 84.29(17) | N1–Ni1–N2 | 94.42(19) |
| N1–Ni1–N3 | 92.05(19) | N2–Ni1–N3 | 91.4(2) |
| C8–Ag1–C9 | 176.4(3) | | |
| **Hydrogen bonds [Å, °]** | | | |
| D–H–A | D···A | H···A | ∠D–H···A |
| O2–H2···O1 | 2.608(6) | 1.78(5) | 176(7) |

The crystal packing of complex **3** (Figure 5) shows that the $[Ag(CN)_2]^-$ units display an almost linear coordination [C8–Ag1–C9 176.4(3)°] with Ag1–C8 and Ag1–C9 bond lengths of 2.064(7) and 2.065(7) Å, respectively, and form endless one-dimensional chains involving the $[NiL^1(H_2O)]^+$ moiety. These chains lie parallel to each other with diagonal distances $a$ and $b$ of 8.12 and 5.95 Å, respectively, and an Ag···Ag distance of about 10.6 Å. The minimum Ag···Ag distance found between two successive layers is 4.514 Å, which is greater the van der Waals diameter of silver (3.44 Å)[16] and hence no direct Ag···Ag interactions are present. In addition to the argentocyanide bridging, there

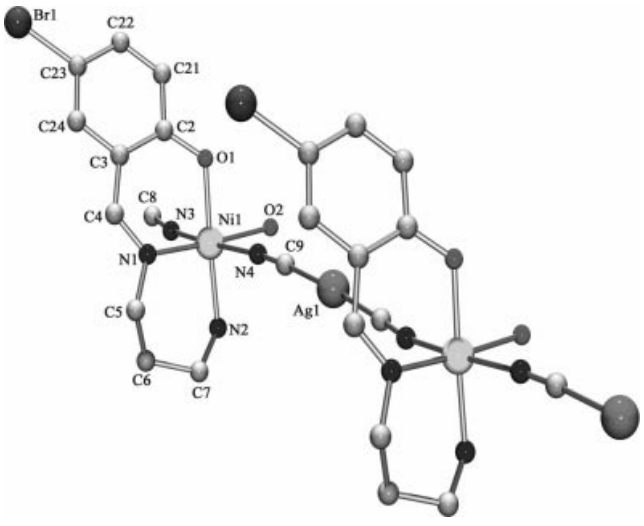


Figure 4. A view of the molecule of complex **3**.

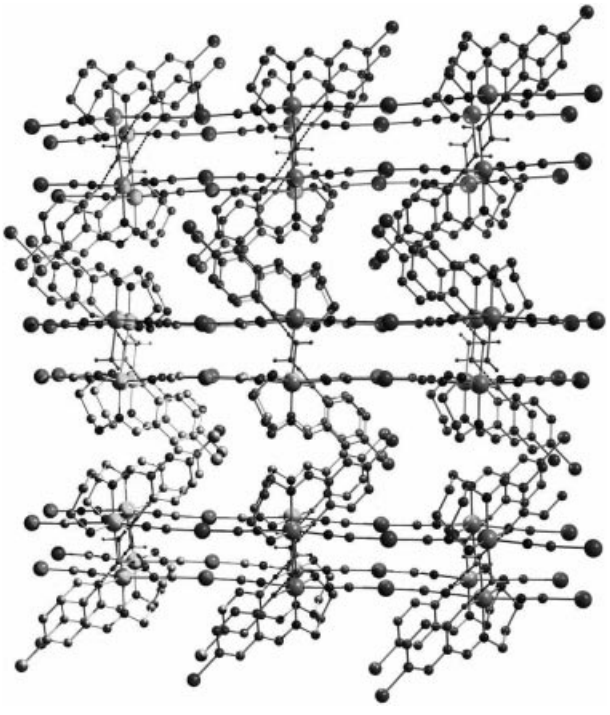

Figure 5. Packing diagram of complex **3**.

 © 2007 Wiley-VCH Verlag GmbH & Co. KGaA, Weinheim 

are intermolecular hydrogen-bonding interactions between the phenolate oxygen of the $L^1$ moiety in one layer and the coordinated water oxygen of the next layer which form stable eight-membered rings [O2···O1 2.608(6) Å; ∠O2–H20···O1 176(7)°] in an extended two-dimensional ladder-like network (Figure 6).

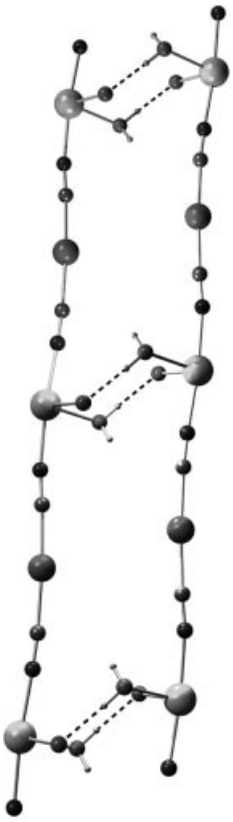

Figure 6. Packing fragment of complex **3** showing the ladder-like network.

### Structure of Complex 4

A perspective view of **4** together with the atom-labeling scheme is shown in Figure 7. Each nickel site is coordinated by two nitrogen atoms, a phenoxo oxygen atom of the tridentate $L^2$ ligand, an oxygen atom of the methanol molecule, and two bridging nitrogen atoms of the $[Ag(CN)_2]^-$ moiety. The average Ni–N bond length is 2.069 Å and the $Ni–O_{phenolato}$ and $Ni–O_{methanol}$ bond lengths are 2.0316(18) and 2.1135(19) Å, respectively. The N(O)–Ni–O(N) bond angles range from 86.77(9)° to 178.07(8)° (see Table 3), which means that the nickel centers display a distorted octahedral coordination geometry. The argentocyanide ion acts as a bridging ligand that connects the $[NiL^3(MeOH)]^+$ moieties to form endless one-dimensional chains. The Ni···Ni separation within a chain is 10.414 Å, whereas the Ni···Ni separation between two successive chains is 5.052 Å. This distance is uniform throughout two successive layers. Moreover, adjacent chains are connected together through non-covalent interactions between the two coordinated phenolato oxygen atoms (O1) in one layer and the methanol oxygen atom (O2) in the adjacent layer (O1···O2 2.586 Å) to form a 2D supramolecular network (Figure 8). It is noteworthy that this network adopts a wavelike layer (Figure 9) due to greater deviation of the bond angles [∠Ni1–N3–C8 166.4(2)° and ∠Ni1_a–N4–C9 166.6(2)°] from planarity in the bridging argentocyanide moieties along the *b*-axis. The same bond angles in complex **3** are close to planarity, which means that the formation of a wavelike network can be ruled out and a chainlike network is obtained instead.

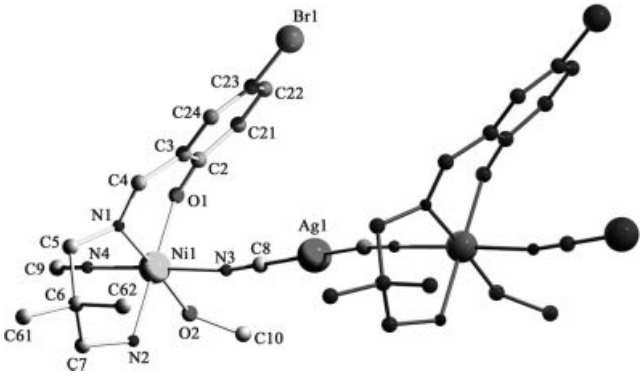


Figure 7. A view of the molecule of complex **4**.

Table 3. Selected bond lengths [Å] and angles [°] in complex **4**.

| Bond lengths [Å] | | | |
|---|---|---|---|
| Ni1–O1 | 2.0316(18) | N3–C8 | 1.147(4) |
| Ni1–O2 | 2.1135(19) | Ag1–C8 | 2.050(3) |
| Ni1–N1 | 2.045(2) | Ag1–C9 | 2.061(3) |
| Ni1–N2 | 2.088(3) | N4–C9 | 1.142(4) |
| Ni1–N3 | 2.084(2) | | |
| **Bond angles [°]** | | | |
| O1–Ni1–O2 | 95.50(9) | O1–Ni1–N1 | 86.77(9) |
| O1–Ni1–N2 | 178.07(8) | O1–Ni1–N3 | 89.69(9) |
| O2–Ni1–N1 | 177.40(9) | O2–Ni1–N2 | 85.91(9) |
| O2–Ni1–N3 | 90.66(8) | N1–Ni1–N2 | 91.86(9) |
| N1–Ni1–N3 | 90.61(9) | N2–Ni1–N3 | 88.98(9) |
| C8–Ag1–C9 | 175.27(13) | | |

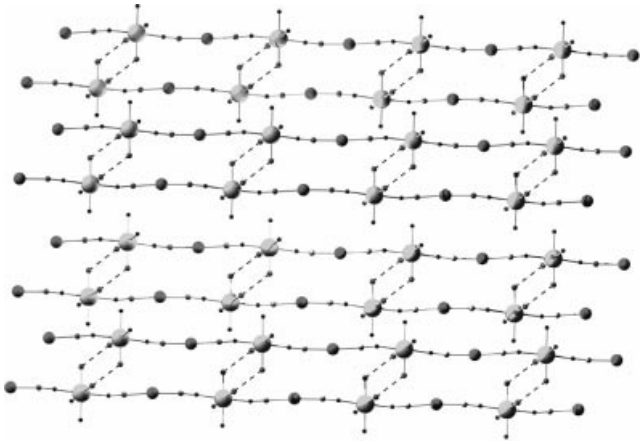

Figure 8. Packing diagram of complex **4**.

 © 2007 Wiley-VCH Verlag GmbH & Co. KGaA, Weinheim 

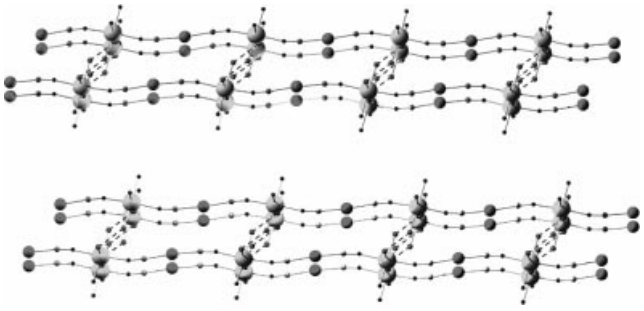

Figure 9. A view of the packing fragment of **4** showing the 2D wave-like network.

## Heterogeneous Catalysis

The use of nickel complexes with cyclam and salen ligands as active catalysts in the epoxidation of alkenes[17–22] has been reported in the literature. Some examples include the use of (salen)Ni-type complexes in faujasites for the oxidation of phenol with $H_2O_2$,[23] the epoxidation of cyclohexene and 1-hexene by NaOCl,[24,25] as well as the use of [Ni(salen)] immobilized on several solid supports as a catalyst for hydrogenation reactions.[26] More recently, Ferreira et al.[11] have carried out an extensive study of (salen)$Ni^{II}$ complexes as homogeneous catalysts and, after immobilization in zeolites (X and Y; following the "ship-in-a-bottle" procedure), as heterogeneous catalysts in the epoxidation of *trans*-β-methylstyrene by NaOCl (considered to be environmentally more friendly).

The heterogeneous oxidation reactions were carried out using 1.0 g of substrate and 0.200 g of loaded catalyst (0.050 g of solid complex in the case of complex **2**) in 10 mL of $CH_3CN$ whilst stirring in a two-necked, round-bottomed flask fitted with a water condenser in an oil bath at 333 K. *tert*-Butyl hydroperoxide (equimolar with respect to the substrate) was added immediately before the start of the reaction. The products were collected from the reaction mixture after different time intervals and analyzed by gas chromatography. They were identified by comparison with known standards.

Tables 4, 5, and 6 show the results obtained with for the various Ni complexes immobilized on silica. Acetonitrile was used as the solvent in all cases. The major products of the reactions are epoxides and the selectivities for these compounds are very high. The very high TONs obtained for the oxidation of styrene, α-methylstyrene, and cyclohexene suggest a very high catalytic efficiency for the nickel hydroperoxo species that could form in the presence of *tert*-butyl hydroperoxide. Small amounts of the corresponding diols were also obtained for all substrates.

Complex **2** is insoluble in all common solvents therefore instead of immobilizing it on mesoporous silica this pure complex was used as a solid catalyst. Our experimental results show that the TONs obtained with the immobilized catalysts are better than the pure nickel complex **2** for all the olefin substrates and that among these substrates cyclohexene shows the highest conversion and TON; the epoxide selectivities for styrene and α-methylstyrene are also very good.

Table 4. Epoxidation of styrene[a] catalyzed by complexes **1**–**4**.

| Entry | Catalyst | Conversion [%][b] | Epoxide selectivity | TON[c] |
|---|---|---|---|---|
| 1 | **1** | 39 | 81 | 121 |
| 2 | **2** | 56 | 82 | 36 |
| 3 | **3** | 41 | 91 | 127 |
| 4 | **4** | 66 | 83 | 205 |

[a] Solvent: $CH_3CN$; temperature: 333 K; complex **2** was used as a solid catalyst whereas the other catalysts were impregnated on a 2D hexagonal mesoporous silica. [b] Reaction time: 24 h; conversion and TON were measured by GC using *n*-decane as internal standard. [c] TON: mol of substrate converted per mole of $Ni^{II}$ present in catalyst used for the reaction.

Table 5. Epoxidation of α-methylstyrene[a] catalyzed by complexes **1**–**4**.

| Entry | Catalyst | Conversion [%][b] | Epoxide selectivity | TON[c] |
|---|---|---|---|---|
| 1 | **1** | 56 | 86 | 153 |
| 2 | **2** | 76 | 93 | 43 |
| 3 | **3** | 69 | 78 | 189 |
| 4 | **4** | 61 | 89 | 167 |

[a] Solvent: $CH_3CN$; temperature: 333 K; complex **2** was used as a solid catalyst whereas the other catalysts were impregnated on a 2D hexagonal mesoporous silica. [b] Reaction time: 24 h; conversion and TON were measured by GC using *n*-decane as internal standard. [c] TON: mol of substrate converted per mole of $Ni^{II}$ present in catalyst used for the reaction.

Table 6. Epoxidation of cyclohexene[a] catalyzed by complexes **1**–**4**.

| Entry | Catalyst | Conversion [%][b] | Epoxide selectivity | TON[c] |
|---|---|---|---|---|
| 1 | **1** | 82 | 82 | 323 |
| 2 | **2** | 89 | 82 | 72 |
| 3 | **3** | 81 | 87 | 319 |
| 4 | **4** | 89 | 84 | 350 |
| 5 | **4** | 87 | 79 | |
| 6 | **4** | 33 | 29 | |

[a] Solvent: $CH_3CN$; temperature: 333 K; complex **2** was used as a solid catalyst whereas the other catalysts were impregnated on a 2D hexagonal mesoporous silica. [b] Reaction time: 24 h; conversion and TON were measured by GC using *n*-decane as internal standard. [c] TON: mol of substrate converted per mole of $Ni^{II}$ present in catalyst used for the reaction.

Microporous and mesoporous titanium silicates have been widely employed in the epoxidation of aromatic and alicyclic unsaturated compounds[27] in the presence of dilute aqueous $H_2O_2$ as oxidant. The intermediate titanium hydroperoxo species formed play a crucial role in catalyzing the epoxidation reaction. The water molecules present in **1**–**3** and the methanol moiety in **4** could help the Ni complex to form such Ni hydroperoxide species in presence of $H_2O_2$, similar to the titanium silicate surface, and this could help in the catalysis of these epoxidation reactions (Scheme 3).

One control experiment was carried out for cyclohexene over immobilized catalyst **4** to check the efficiency of subsequent catalytic cycles and whether Ni leaches from these catalysts (Table 6, entry 4). After the initial experiment the catalyst was washed thoroughly with acetonitrile and then

 © 2007 Wiley-VCH Verlag GmbH & Co. KGaA, Weinheim 

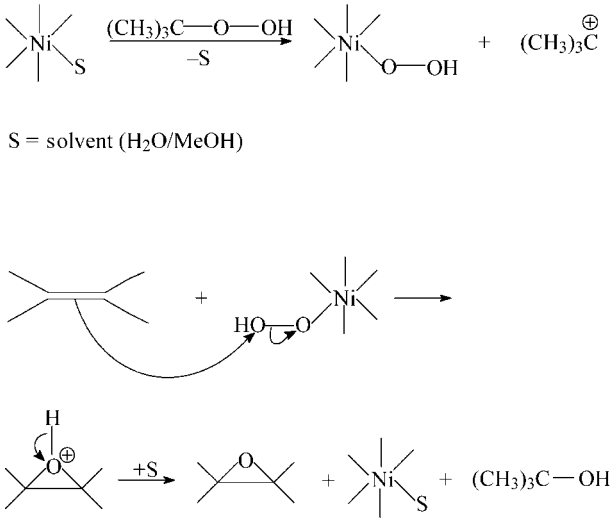


Scheme 3. Proposed mechanism for the partial oxidation of styrene, α-methylstyrene, and cyclohexene by *tert*-butyl hydroperoxide with complexes **1**–**4** as catalyst.

treated with 0.1 M HCl solution in EtOH for 8 h at 343 K and finally dried at 373 K for 2 h. It was then re-used as catalyst for a second experiment (Table 6, entry 5). The catalytic activity was found to remain practically the same, with only a marginal difference in the epoxide selectivity. This suggests that there is almost no Ni leaching into the liquid phase from these immobilized catalysts. A blank reaction of the oxidation of cyclohexene in the absence of any solid catalyst under otherwise identical reaction conditions was also carried out (Table 6, entry 6). The results show very poor conversion and epoxide selectivity in this case, thereby confirming the catalytic role of the Ni complex and the immobilized catalysts in these epoxidation reactions.

Figures 10, 11, and 12 show bar diagrams for the epoxidation of the alkenes over different immobilized catalysts at 333 K. It is clear from these figures that all the $Ni^{II}$ complexes act as efficient epoxidation catalysts in the presence of *tert*-butyl hydroperoxide as oxidant. Figure 13 shows the alkene conversion as a function of reaction time for the epoxidation of styrene catalyzed by the four $Ni^{II}$ complexes. The conversions follow a sigmoid curve and reach maximum conversion after 24 h. It is apparent from these experimental observations that immobilized Ni complex **4** is most

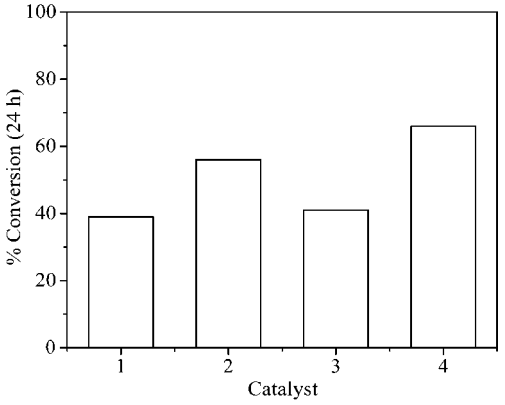


Figure 10. Bar diagram showing the catalytic activity of complexes **1**–**4** with styrene ($CH_3CN$, 333 K).

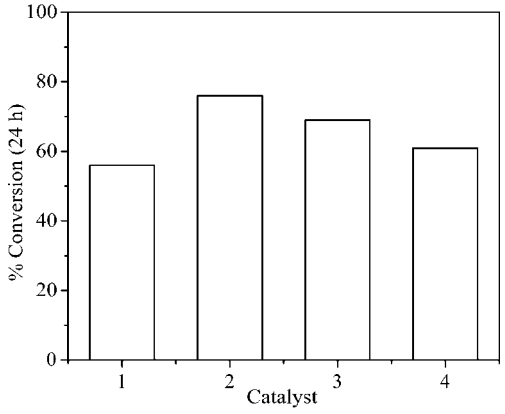


Figure 11. Bar diagram showing the catalytic activity of complexes **1**–**4** with α-methylstyrene ($CH_3CN$, 333 K).

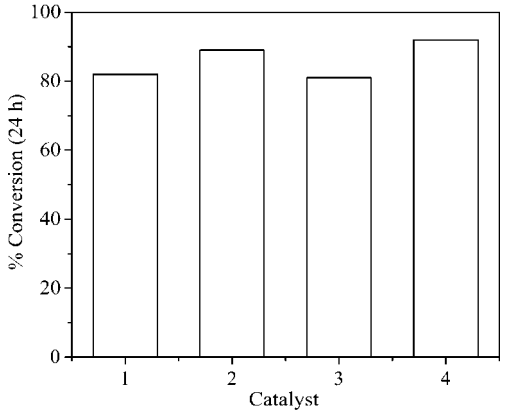


Figure 12. Bar diagram showing the catalytic activity of complexes **1**–**4** with cyclohexene ($CH_3CN$, 333 K).

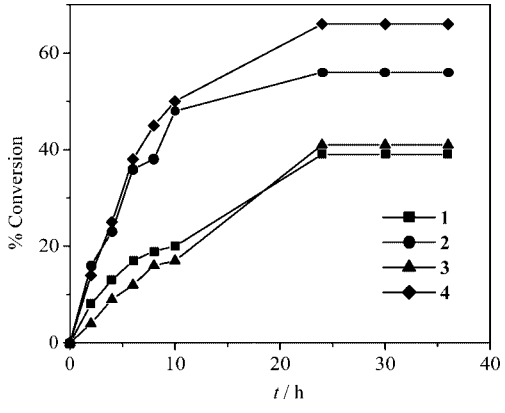


Figure 13. Conversion vs. time plot for the epoxidation of styrene with *tert*-butyl hydroperoxide catalyzed by complexes **1**–**4** ($CH_3CN$, 333 K).

 © 2007 Wiley-VCH Verlag GmbH & Co. KGaA, Weinheim 

reactive for the epoxidation of all three substrates with high TONs (205, 167, and 350 for styrene, α-methylstyrene, and cyclohexene, respectively).

### Magnetic Behavior of 1

The temperature dependencies of $\chi_M T$ and $\chi_M$ for complex **1** are plotted in Figure 14. The value of $\chi_M T$ observed at room temperature (4.54 $cm^3 mol^{-1} K$ at 300 K) is typical for four uncoupled $Ni^{II}$ ions with $g > 2.00$, as expected. On lowering the temperature the $\chi_M T$ product decreases smoothly, reaching 0.05 $cm^3 mol^{-1} K$ at 2 K. This behavior clearly points to the existence of moderate antiferromagnetic interactions between the $Ni^{II}$ centers, which result in a diamagnetic ground state. This is confirmed by the shape of the $\chi_M$ vs. $T$ curve, which passes through a maximum at around 22 K.

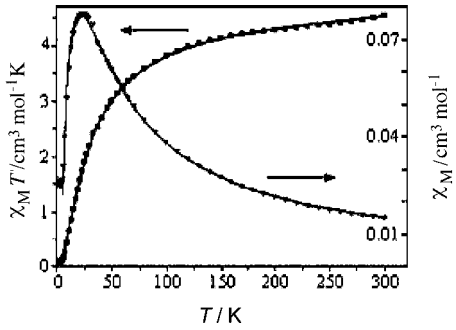


Figure 14. Temperature-dependence of $\chi_M T$ (left scale, full squares) and $\chi_M$ (right scale, full triangles) for **1** and best fit curves obtained with the parameters reported in the text. The theoretical curves calculated with the two different models cannot be discerned.

An initial quantitative analysis of the results obtained was performed using a simple isotropic Hamiltonian that considers all the possible exchange interactions in the tetramer [Equation (1)].

$$\hat{H} = J(S_1S_2 + S_3S_4) + J'(S_1S_3 + S_1S_4 + S_2S_3 + S_2S_4) + g\beta SH \quad (1)$$

where $J$ is the exchange coupling within each dinuclear moiety, in other words the exchange interactions transmitted by the two phenolato bridges and the carboxylato one, and $J'$ describes the coupling through the terephthalato bridging ligand. The fit was implemented using the CLUMAG package,[28] including a temperature-independent paramagnetism term ($N_\alpha = (8 \pm 2) \times 10^{-4}$ emu $mol^{-1}$), which yields the best fit parameters $J = 14.5 \pm 0.6$ $cm^{-1}$, $J' = 3.8 \pm 1.2$ $cm^{-1}$, and $g = 2.15 \pm 0.02$. This set of parameters results in a diamagnetic ground state, as expected, with the first triplet lying 14.5 $cm^{-1}$ higher in energy. This is in fair agreement with the $M$ vs. $H$ curve (Figure 15), which shows the beginning of a singlet–triplet field induced transition at the highest measured field.

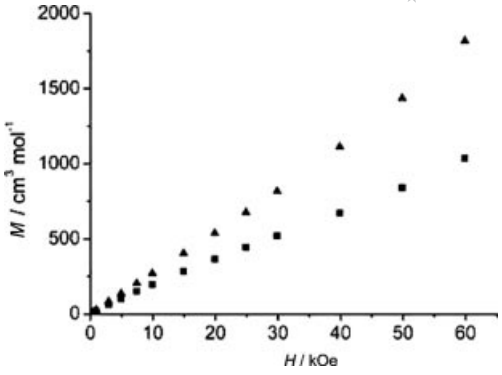


Figure 15. $M$ vs. $H$ curve for **1** measured at 2.7 (squares) and 5.1 K (triangles).

The obtained value of $J'$ appears to be relatively large and higher than would be expected on the basis of literature data.[29] This might, in principle, be due to the neglecting of the single-ion zero-field-splitting terms that affect the shape of the calculated temperature dependence of the susceptibility curve in the same way as an intermolecular coupling.[30] We therefore fitted the data by including these terms using the Ginsberg formula for dinuclear $Ni^{II}$ centers with interdimer interactions.[30,31] The best fit parameters obtained with this approach were $J = 14.5 \pm 0.2$ $cm^{-1}$, in perfect agreement with the simple isotropic approach, $2zJ' = 3.4 \pm 0.6$ $cm^{-1}$, $N_\alpha = (4.5 \pm 2) \times 10^{-4}$ emu $mol^{-1}$, $g = 2.17 \pm 0.02$, and $D = 1$–$8$ $cm^{-1}$, with the latter parameter having only a weak effect on the calculated curve. We can conclude on the basis of the two fits that the Ni–Ni interaction in each dinuclear moiety is close to 14.5 $cm^{-1}$ and that a non-negligible interaction is transmitted by the terephthalato ligand, in contrast to what is normally assumed.[32] The value of the Ni–Ni coupling constant in the dinuclear moiety is somewhat larger than would be expected on the basis of simple magnetostructural correlations derived for centrosymmetric bis(phenolate)-bridged dinuclear nickel complexes derived by Thompson's group[33] [Equation (2)].

$$J = +7.27\theta - 704.06 \quad (2)$$

where $\theta$ is the bridging Ni–O–Ni angle. Using the average value of the bridging angle (96.94°) for $\theta$ would result in a predicted value of $J = 0.8$ $cm^{-1}$ for **1**, far from what is observed experimentally. We attribute this discrepancy to the effect of the carboxylato ligand, which bridges the two nickel ions in a *syn-syn* fashion and provides an additional pathway for the antiferromagnetic coupling between the two centers.[34] Finally, we note that the importance of the interdimer exchange coupling provided by the terephthalato ligand lies in the large π-connectivity it may provide, thus providing a relatively efficient pathway whilst keeping the interacting metal centers far apart.

## Conclusions

We have prepared four polymeric nickel(II)/Schiff-base complexes with terephthalate and argentocyanide as bridg-

 © 2007 Wiley-VCH Verlag GmbH & Co. KGaA, Weinheim 

ing moieties. Complex **1** is tetranuclear and its X-ray crystal structure shows that each tetranuclear unit contains both phenolate and terephthalate bridges. These tetranuclear units are connected together by the terephthalate units in a bis(monodentate) coordination mode to form an infinite 1D network. Variable-temperature magnetic measurements show that this complex exhibits moderate antiferromagnetic coupling. Complex **2** has the same structure as complex **1**, although we were unable to obtain crystals suitable for X-ray diffraction. Both complexes **3** and **4** form 2D polymeric networks utilizing the bridging argentocyanide units and strong noncovalent interactions.

Alkene epoxidation studies have been performed with all the complexes as active heterogeneous catalysts. Styrene, α-methylstyrene, and cyclohexene are all efficiently converted into their corresponding epoxides. The experimental results show that immobilized Ni complex **4** is the most active catalyst for the epoxidation of all three substrates (TON values of 205, 167, and 350 for styrene, α-methylstyrene, and cyclohexene, respectively).

## Experimental Section

**Starting Materials:** Salicylaldehyde, 5-bromosalicylaldehyde, 1,3-diaminopropane, 1,3-diamino-2,2-dimethylpropane, terephthalic acid, and $Ni^{II}$ salts were purchased form commercial sources and used as received. Sodium terephthalate was readily prepared by the reaction of terephthalic acid with a stoichiometric amount of NaOH in water. All other chemicals (sodium hydroxide, $AgNO_3$, and NaCN) were of reagent grade. Ethanol, methanol, and dmf were of reagent grade and used without further purification. Doubly distilled water was used throughout. The acetonitrile used in the epoxidation reaction was of HPLC grade. *tert*-Butyl hydroperoxide purchased form Aldrich was used as oxidant. The substrates styrene, α-methylstyrene, and cyclohexene were also obtained from Aldrich.

**Physical Measurements:** Microanalyses (CHN) were performed with a Perkin–Elmer 240C elemental analyzer. FT-IR spectra were obtained on a Nicolet, MAGNA-IR 750 spectrometer with samples prepared as KBr pellets. A Perkin–Elmer 2380 AAS was used for wet chemical analysis. GC analysis was carried out with an Agilent Technologies 6890N network GC system equipped with a fused silica capillary column (30 m × 0.32 mm) and a FID detector. The column temperature was increased from 80 °C (4 min) to 220 °C at a rate of 5 °C $min^{-1}$. The injection temperature was 200 °C. The solid-state electronic spectra were measured with a Shimadzu UV 2401PC spectrophotometer using a $BaSO_4$ pellet as background standard. Magnetic measurements were performed with a Cryogenic SQUID S600 magnetometer operating between 2 and 300 K with applied magnetic fields of up to 65 kOe. Raw data were corrected for diamagnetic contribution of the sample holder and the intrinsic diamagnetism of the sample estimated by Pascal's constants.

**General Procedure for the Preparation of the Immobilized Catalysts:** For the synthesis of the mesoporous silica,[35] the cationic surfactant cetyl trimethylammonium bromide (2.96 g) was mixed with an aqueous solution containing sodium dodecyl sulfate (0.47 g) and vigorously stirred at room temperature for 30 min. Gel formation occurred immediately leading to a viscous suspension. Tetraethyl orthosilicate (3.5 g) was added to this suspension with continuous stirring for 30 min. After 2 h constant stirring, tetraethylammonium hydroxide was added dropwise until the color of the solution turned white. The pH value of the final mixture was about 11.0. The resultant mixture was aged overnight whilst stirring at room temperature and then transferred into a polypropylene bottle and heated at 80 °C for 72 h without stirring. The solid produced was recovered by filtration, washed several times with water, and dried at room temperature. The resulting powder was calcined at 703 K to remove the organic surfactants. The molar ratio of the various constituents was TEOS/CTAB/SDS/$H_2O$ = 50:25:5:4500. For loading of the $Ni^{II}$ complexes, 1.0 g of the calcined solid was suspended in 50 mL of dmf containing 0.2 g of complex. The mixture was stirred for 4 h at room temperature, then filtered off and washed several times with dmf and dried in vacuo at ambient temperature. The loading (immobilization) of the Ni complexes on the mesoporous host was confirmed by UV/Vis solid state spectroscopy.

**Bis(3-aminopropyl-5-bromosalicylideneiminato)nickel(II) [Ni($L^1$)$_2$]:** This complex was prepared following the method of Elder.[36] Thus, a solution of 1,3-diaminopropane (8.88 g, 120 mmol) in ethanol was heated at 60 °C and a solution of 5-bromosalicylaldehyde (4.02 g, 20 mmol) in ethanol added dropwise with stirring for 30 min. After the addition was complete, solid $Ni(CH_3COO)_2 \cdot 4H_2O$ (2.49 g, 10 mmol) was added at once. The solid dissolved rapidly to give a dark solution, which was refluxed for 20 min at 60 °C. The green precipitate that formed was filtered off, washed with a small amount of ethanol and diethyl ether, and dried in air.

**Bis(3-aminopropylsalicylideneiminato)nickel(II) [Ni($L^2$)$_2$]:** This complex was also prepared by the method described by Elder.[36]

**Bis(3-aminopropyl-5-bromo-2,2-dimethylsalicylideneiminato)nickel(II) [Ni($L^3$)$_2$]:** This complex was prepared in a similar manner to Ni($L^1$)$_2$. Thus, a solution of 1,3-diamino-2,2-dimethylpropane (6.13 g, 60 mmol) in ethanol was heated at 60 °C and a solution of 5-bromosalicylaldehyde (2.01 g, 10 mmol) in ethanol was added dropwise with stirring for 30 min. The deep yellow precipitate obtained dissolved after the addition of solid $Ni(CH_3COO)_2 \cdot 4H_2O$ (1.25 g, 5 mmol) at once. The solid dissolved rapidly to give a dark brown solution, which was refluxed for 30 min at 60 °C. The green precipitate obtained was filtered off, washed with a small amount of ethanol and diethyl ether, and dried in air.

**[$Ni_4L^1_4$(μ-tp-κ$_4$-O)($H_2O$)$_2$(μ-tp-κ$_2$-O)]·2$C_2H_5OH$·$CH_3OH$·3$H_2O$ (1):** A solution of [Ni($L^1$)$_2$] (0.057 g, 0.1 mmol) in 10 mL of hot ethanol was added to a methanolic solution (5 mL) of $Ni(ClO_4)_2 \cdot 6H_2O$ (0.036 g, 0.1 mmol) with constant stirring. The color of the solution turned deep green. An aqueous solution of $Na_2tp$ (0.021 g, 0.1 mmol) was then added to this mixture. The resulting solution was stirred for 30 min, then filtered. Slow evaporation at room temperature yielded green crystals of **1** suitable for X-ray analysis after 4 d. Yield: 0.040 g (45%). $C_{61}H_{82}Br_4N_8Ni_4O_{20}$ (1800.8): calcd. C 40.65, H 4.55, N 6.22; found C 39.40, H 4.70, N 6.40.

**[$Ni_4L^2_4$(μ-tp-κ$_4$-O)($H_2O$)$_2$(μ-tp-κ$_2$-O)]·3$H_2O$ (2):** A solution of [Ni($L^2$)$_2$] (0.083 g, 0.2 mmol) in 10 mL of hot ethanol was added to a methanolic solution (5 mL) of $Ni(ClO_4)_2 \cdot 6H_2O$ (0.073 g, 0.2 mmol) with constant stirring. The color of the solution turned deep green. An aqueous solution of $Na_2tp$ (0.042 g, 0.2 mmol) was then added to this mixture. The resulting solution was stirred for 30 min, then filtered. This solution yielded dark green crystals of **2** on standing at room temperature for 3 d. Unfortunately, it was not possible to grow single crystals of X-ray diffraction quality. Yield: 0.085 g (63%). $C_{56}H_{70}N_8Ni_4O_{17}$ (1360.8): calcd. C 49.38, H 5.14, N 8.23; found C 49.29, H 5.06, N 8.17.

 © 2007 Wiley-VCH Verlag GmbH & Co. KGaA, Weinheim 

Table 7. Crystal data and details for structure refinement for **1**, **3**, and **4**.

| | **1** | **3** | **4** |
|---|---|---|---|
| Formula | $C_{122}H_{160}Br_8N_{16}Ni_8O_{40}$ | $C_{12}H_{14}AgBrN_4NiO_2$ | $C_{15}H_{19}AgBrN_4NiO_2$ |
| Formula weight | 3599.62 | 492.76 | 533.83 |
| Crystal system | monoclinic | monoclinic | triclinic |
| Space group | $P2_1/n$ (no. 14) | $P2_1/c$ (no. 14) | $P\bar{1}$ (no. 2) |
| $a$ [Å] | 12.073(2) | 10.204(2) | 8.2964(3) |
| $b$ [Å] | 18.601(4) | 21.706(4) | 10.4145(5) |
| $c$ [Å] | 16.998(3) | 8.0562(16) | 11.3805(5) |
| $\alpha/\beta/\gamma$ [°] | 90/99.70(3)/90 | 90/110.33(3)/90 | 96.918(4)/102.963(4)/96.348(4) |
| $V$ [Å$^3$] | 3762.7(13) | 1673.2(6) | 941.60(7) |
| Z | 1 | 4 | 2 |
| $D_{calcd}$ [g cm$^{-3}$] | 1.553 | 1.956 | 1.883 |
| $\mu$ [mm$^{-1}$] | 3.180 | 4.691 | 4.175 |
| $F$(000) | 1764 | 960 | 526 |
| Temperature [K] | 294 | 294 | 108 |
| $\lambda$ [Å] | 0.71073 (Mo-$K_\alpha$) | 0.71073 (Mo-$K_\alpha$) | 0.71073 (Mo-$K_\alpha$) |
| $\theta_{min}$–$\theta_{max}$ [°] | 2.2–25.0 | 2.1–30.0 | 3.4–27.6 |
| Reflections collected | 6266 | 5787 | 9565 |
| Independent reflections | 6093 | 4857 | 4287 |
| Observed data [$I > 2\sigma(I)$] | 3140 | 2516 | 3373 |
| Data/restraints/parameters | 6093/0/429 | 4857/2/196 | 4287/0/220 |
| Goodness-of-fit on $F^2$ | 0.889 | 0.922 | 0.927 |
| Final $R$ indices [$I > 2\sigma(I)$] | $R_1$ = 0.0828 | $R_1$ = 0.0566 | $R_1$ = 0.0286 |
| | $wR_2$ = 0.1480 | $wR_2$ = 0.1145 | $wR_2$ = 0.0635 |
| $R$ indices (all data) | $R_1$ = 0.2370 | $R_1$ = 0.1145 | $R_1$ = 0.0392 |
| | $wR_2$ = 0.1872 | $wR_2$ = 0.1324 | $wR_2$ = 0.0656 |

**$[Ni(L^1)(H_2O)\{Ag(CN)_2\}]_\alpha$ (3):** A methanolic solution (5 mL) of $Ni(ClO_4)_2{\cdot}6H_2O$ (0.036 g, 0.1 mmol) was added to a methanolic solution (10 mL) of $[Ni(L^1)_2]$ (0.057 g, 0.1 mmol) and the resulting green solution stirred for 10 min. An aqueous solution (5 mL) of $Na[Ag(CN)_2]$ (0.018 g, 0.1 mmol) was then added to this mixture and the solution stirred for 20 min. The solution was filtered to remove any suspended material and kept at room temperature. Slow evaporation of solvents yielded deep green crystals suitable for X-ray analysis after 7 d. Yield: 0.018 g (73%). $C_{12}H_{14}AgBrN_4NiO_2$ (492.76): calcd. C 29.22, H 2.84, N 11.36; found C 29.16, H 2.79, N 11.23.

**$[Ni(L^3)(MeOH)\{Ag(CN)_2\}]_\alpha$ (4):** A methanolic solution (5 mL) of $Ni(ClO_4)_2{\cdot}6H_2O$ (0.036 g, 0.1 mmol) was added to a methanolic solution (10 mL) of $[Ni(L^3)_2]$ (0.057 g, 0.1 mmol) and the resulting green solution stirred for 10 min. A dmf solution (5 mL) of $Na[Ag(CN)_2]$ (0.018 g, 0.1 mmol) was then added to this mixture and the solution stirred for 20 min. It was then filtered and kept at room temperature. Slow evaporation of the solvents yielded green crystals suitable for X-ray analysis after 5 d. Yield: 0.021 g (40%). $C_{15}H_{20}AgBrN_4NiO_2$ (534.83): calcd. C 33.66, H 3.74, N 10.47; found C 33.59, H 3.70, N 10.41.

**Crystal-Structure Determination:** Single crystals of complex **1** were grown from EtOH/MeOH/$H_2O$ and those of complexes **3** and **4** were grown from MeOH/$H_2O$ and dmf/MeOH medium, respectively. The X-ray single-crystal data for complexes **1** and **3** were collected with a Siemens P4 four-circle diffractometer whereas those of complex **4** were collected on an Oxford Instruments Sapphire2-CCD diffractometer. Crystal size: $0.18 \times 0.21 \times 0.51$, $0.30 \times 0.31 \times 0.52$, and $0.08 \times 0.17 \times 0.22$ mm$^3$ for complexes **1**, **3**, and **4** respectively. Unit cell dimensions and intensity data were measured at 294 K for **1** and **3** and 108 K for **4**. The crystallographic data, conditions used for the intensity data collection and some features of the structure refinement are listed in Table 7. Graphite-monochromated Mo-$K_\alpha$ radiation ($\lambda$ = 0.71073 Å) was used to collect the data sets. Accurate unit-cell parameters for **1**, **3**, and **4** were determined from automatic centering of 14, 15, and 5214 reflections, respectively, and refined by least-square methods. 6266 Reflections were collected for **1** in the range $2.2° < \theta < 25.0°$, 5787 reflections were collected in the range $2.1° < \theta < 30.0°$ for **3**, and 7224 reflections were collected in the range $3.4° < \theta < 27.6°$ for **4**. A total of 3140, 2516, and 3373 reflections were assumed as observed [$I > 2\sigma(I)$] for complexes **1**, **3**, and **4** respectively. All calculations for data reduction, structure solution and refinement were performed using standard procedures with SHELXS-97[37] and SHELXL-97.[38] All non-hydrogen atoms were refined anisotropically by full-matrix least-squares techniques on $F^2$. The H atoms were constrained to idealized positions and refined isotropically using a riding model.

CCDC- 645841 (for **1**), -645842 (for **3**), and -645843 (for **4**) contain the supplementary crystallographic data for this paper. These data can be obtained free of charge from The Cambridge Crystallographic Data Centre via www.ccdc.cam.ac.uk/data_request/cif.

## Acknowledgments

M. N. gratefully acknowledges financial support from the Council of Scientific and Industrial Research, New Delhi for a senior research fellowship. AB wishes to thank the Department of Science and Technology, Government of India, New Delhi for a Ramanna Fellowship grant.

[1] a) P. J. Stang, B. Olenyuk, *Acc. Chem. Res.* **1997**, *30*, 502; b) S. Leininger, B. Olenyuk, P. J. Stang, *Chem. Rev.* **2000**, *100*, 853; c) G. F. Swiegers, T. J. Malefetse, *Chem. Rev.* **2000**, *100*, 3483; d) C. T. Chen, K. S. Suslick, *Coord. Chem. Rev.* **1993**, *128*, 293.

[2] a) P. J. Hagrman, D. Hagrman, J. Zubieta, *Angew. Chem. Int. Ed.* **1999**, *38*, 2638; b) D. Hagrman, R. P. Hammond, R. Haushalter, J. Zubieta, *J. Chem. Mater.* **1998**, *10*, 2091.

[3] a) X. M. Zhang, M. L. Tong, X. M. Chen, *Angew. Chem. Int. Ed.* **2002**, *41*, 1029; b) G. F. Liu, B. H. Ye, Y. H. Ling, X. M.

 © 2007 Wiley-VCH Verlag GmbH & Co. KGaA, Weinheim 

Chen, *Chem. Commun.* **2002**, 1442; c) X. H. Bu, W. Chen, S. L. Lu, R. H. Zhang, D. Z. Liao, W. M. Bu, M. Shionoya, F. Brisse, J. Ribas, *Angew. Chem. Int. Ed.* **2001**, *40*, 3201; d) X. H. Bu, W. Chen, W. F. Hou, M. Du, R. H. Zhang, F. Brisse, *Inorg. Chem.* **2002**, *41*, 3477.
[4] a) W. B. Lin, O. R. Evans, R. G. Xiong, Z. Y. Wang, *J. Am. Chem. Soc.* **1998**, *120*, 13272; b) Y. Cui, O. R. Evans, H. L. Ngo, P. S. White, W. B. Lin, *Angew. Chem. Int. Ed.* **2002**, *41*, 1159; c) Y. Cui, H. L. Ngo, W. B. Lin, *Inorg. Chem.* **2002**, *41*, 1033.
[5] a) N. Takeda, K. Umemoto, K. Yamaguchi, M. Fujita, *Nature* **1999**, *398*, 794; b) A. Caneschi, D. Gatteschi, N. Lalioti, C. Sangregorio, R. Sessoli, G. Venturi, A. Vindigni, A. Rettori, M. G. Pini, M. A. Novak, *Angew. Chem. Int. Ed.* **2001**, *40*, 1760; c) Y. Q. Tian, C. X. Cai, Y. Ji, X. Z. You, S. M. Peng, G. H. Lee, *Angew. Chem. Int. Ed.* **2002**, *41*, 1384.
[6] a) Y. H. Wang, L. Y. Feng, Y. G. Li, C. W. Hu, E. B. Wang, N. H. Hu, H. Q. Jia, *Inorg. Chem.* **2002**, *41*, 6351; b) Y. Lu, E. B. Wang, M. Yuan, G. Y. Luan, Y. G. Li, *J. Chem. Soc. Dalton Trans.* **2002**, 3029; c) Y. G. Li, E. B. Wang, H. Zhang, G. L. Luan, C. W. Hu, *J. Solid State Chem.* **2002**, *163*, 10; d) M. Yuan, Y. G. Li, E. B. Wang, Y. Lu, C. W. Hu, N. H. Hu, H. Q. Jia, *J. Chem. Soc. Dalton Trans.* **2002**, 2916; e) W. S. You, E. B. Wang, Y. Xu, Y. G. Li, L. Xu, C. W. Hu, *Inorg. Chem.* **2001**, *40*, 5468.
[7] a) M. Eddaoudi, D. B. Moler, H. Li, B. Chen, T. M. Reineke, M. O'Keeffe, O. M. Yaghi, *Acc. Chem. Res.* **2001**, *34*, 319; b) S. Kitagawa, M. Kondo, *Bull. Chem. Soc. Jpn.* **1998**, *71*, 1739; c) S. R. Batten, R. Robson, *Angew. Chem. Int. Ed.* **1998**, *37*, 1460.
[8] a) H. Li, M. Eddaoudi, O. M. Yaghi, *Nature* **1999**, *402*, 276; b) R. H. Groeneman, L. R. MacGillivray, J. L. Atwood, *Chem. Commun.* **1998**, 2735; c) Y. Zhang, J. M. Li, M. Zhu, Q. M. Wang, X. T. Wu, *Chem. Lett.* **1998**, 1051; d) C. S. Hong, Y. Do, *Inorg. Chem.* **1998**, *37*, 4470; e) L. C. Franesconi, D. R. Corbin, A. W. Clauss, D. N. Hendrickson, G. D. Stucky, *Inorg. Chem.* **1981**, *20*, 2078.
[9] a) M. Ohba, N. Usuki, N. Fukita, H. Okawa, *Angew. Chem. Int. Ed.* **1999**, *38*, 1795; b) H. Z. Kou, S. Gao, B. Q. Ma, D. Z. Liao, *Chem. Commun.* **2000**, 713; c) A. Marvilliers, S. Parsons, E. Riviere, J.-P. Audiere, T. Mallah, *Chem. Commun.* **1999**, 2217; d) J. A. Smith, J.-R. Galan-Mascaros, R. Clerac, K. R. Dunbar, *Chem. Commun.* **2000**, 1077; e) M. S. El Fallah, E. Rentschler, A. Caneschi, R. Sessoli, D. Gatteschi, *Angew. Chem. Int. Ed. Engl.* **1996**, *35*, 1947.
[10] a) L. R. Falvello, M. Tomas, *Chem. Commun.* **1999**, 273; b) F. Olbrich, J. Kopf, E. Weiss, *J. Organomet. Chem.* **1993**, *456*, 293.
[11] R. Ferreira, H. García, B. de Castro, C. Freire, *Eur. J. Inorg. Chem.* **2005**, 4272.
[12] H. J. Choi, M. P. Suh, *Inorg. Chem.* **1999**, *38*, 6309.
[13] Y. Go, X. Wang, E. V. Anokhina, A. J. Jacobson, *Inorg. Chem.* **2004**, *43*, 5360.
[14] C. S. Hong, J. H. Yoon, J. H. Lim, H. H. Ko, *Eur. J. Inorg. Chem.* **2005**, 4818.
[15] D. Ghoshal, H. Bialas, A. Escuer, M. Font-Bardía, T. K. Maji, J. Ribas, X. Solans, R. Vicente, E. Zangrando, N. Ray Chaudhuri, *Eur. J. Inorg. Chem.* **2003**, 3929.
[16] a) A. Bondi, *J. Phys. Chem.* **1964**, *68*, 441; b) M. Jansen, *Angew. Chem. Int. Ed. Engl.* **1987**, *26*, 1098.
[17] J. F. Kinneary, T. R. Wagner, C. J. Burrows, *Tetrahedron Lett.* **1988**, *29*, 877.
[18] J. F. Kinneary, J. S. Albert, C. J. Burrows, *J. Am. Chem. Soc.* **1988**, *110*, 6124.
[19] R. I. Kureshy, N. H. Khan, S. H. R. Abdi, P. Iyer, A. K. Bhatt, *J. Mol. Catal. A* **1998**, *130*, 41.
[20] R. I. Kureshy, N. H. Khan, S. H. R. Abdi, S. T. Patel, P. Iyer, E. Suresh, P. Dastidar, *J. Mol. Catal. A* **2000**, *160*, 217.
[21] H. Yoon, C. J. Burrows, *J. Am. Chem. Soc.* **1988**, *110*, 4087.
[22] H. Yoon, T. R. Wagler, K. J. O'Connor, C. J. Burrows, *J. Am. Chem. Soc.* **1990**, *112*, 4568.
[23] M. R. Maurya, S. J. J. Titinchi, S. Chand, *J. Mol. Catal. A* **2003**, *201*, 119.
[24] D. Chatterjee, A. Mitra, *J. Mol. Catal. A* **1999**, *144*, 363.
[25] D. Chatterjee, S. Mukherjee, A. Mitra, *J. Mol. Catal. A* **2000**, *154*, 5.
[26] V. Ayala, A. Corma, M. Iglesias, J. A. Rincón, F. Sanchez, *J. Catal.* **2004**, *224*, 170.
[27] A. Bhaumik, T. Tatsumi, *J. Catal.* **2000**, *189*, 31.
[28] D. Gatteschi, L. Pardi, *Gazz. Chim. Ital.* **1993**, *123*, 231.
[29] C. S. Hong, Y. S. You, *Polyhedron* **2004**, *23*, 1379.
[30] A. P. Ginsberg, R. L. Martin, R. W. Brookes, R. C. Sherwood, *Inorg. Chem.* **1972**, *11*, 2884.
[31] A. Asokan, B. Varghese, A. Caneschi, P. T. Manoharan, *Inorg. Chem.* **1998**, *37*, 228.
[32] C. Qin, X.-L. Wang, Y.-G. Li, E.-B. Wang, Z.-M. Su, L. Xu, R. Clérac, *Dalton Trans.* **2005**, 2609.
[33] K. K. Nanda, L. K. Thompson, J. N. Bridson, K. Nag, *J. Chem. Soc. Chem. Commun.* **1994**, 1337.
[34] S. K. Dey, M. S. El Fallah, J. Ribas, T. Matsushita, V. Gramlich, S. Mitra, *Inorg. Chim. Acta* **2004**, *357*, 1517.
[35] D. Chandra, A. Bhaumik, *Ind. Eng. Chem. Res.* **2006**, *45*, 4879.
[36] R. C. Elder, *Aust. J. Chem.* **1978**, *31*, 35.
[37] G. M. Sheldrick, *Acta Crystallogr., Sect. A* **1990**, *46*, 467.
[38] G. M. Sheldrick, *SHELXL-97, Program for Crystal Structure Refinement*, University of Göttingen, Germany, **1997**.

Received: May 9, 2007
Published Online: August 8, 2007

 © 2007 Wiley-VCH Verlag GmbH & Co. KGaA, Weinheim 

DOI: 10.1002/ejic.200700518

# Square-Planar Diacetatopalladium Complexes with *trans*-Configured Secondary Amine Ligands that Avoid Orthometalation: Ligand Synthesis, Coordination, Molecular Structure and Catalytic Potential for Suzuki Cross-Coupling Reactions

**Ludovic Chahen,[a] Bruno Therrien,[a] and Georg Süss-Fink*[a]**

**Keywords:** Cross-coupling / Palladium / N ligands / Amines / Homogeneous catalysis

The *trans*-configured square-planar palladium complexes $[Pd(OAc)_2(LN{t}Bu)_2]$ (**1**), $[Pd(OAc)_2(\eta^2\text{-}LN\cap N{t}Bu)]$ (**2**), $[Pd(OAc)_2(LNPh)_2]$ (**3**), and $[Pd(OAc)_2(\eta^2\text{-}LN\cap NPh)]$ (**4**), have been synthesized by treating palladium acetate with the amines $NH{t}BuCH_2\text{-}2,4,6\text{-}Me_3C_6H_2$ (LN*t*Bu) or $NHPhCH_2\text{-}2,4,6\text{-}Me_3C_6H_2$ (LNPh) or with the diamines $NH{t}BuCH_2\text{-}2,4,6\text{-}Me_3C_6H\text{-}CH_2\text{-}2,4,6\text{-}Me_3C_6H\text{-}CH_2\text{-}NH{t}Bu$ (LN∩N*t*Bu) or $NHPh\text{-}CH_2\text{-}2,4,6\text{-}Me_3C_6H\text{-}CH_2\text{-}2,4,6\text{-}Me_3C_6H\text{-}CH_2\text{-}NHPh$ (LN∩NPh). The single-crystal X-ray structure analysis of complexes **1**–**3** confirms a *trans* arrangement of the two acetato groups and of the two nitrogen atoms. Orthometalation leading to palladacycles is impossible in all cases as the *ortho* positions in the benzylic rings are blocked by methyl substituents. All complexes are found to catalyze Suzuki cross-coupling reactions of deactivated and even sterically hindered arene substrates.
(© Wiley-VCH Verlag GmbH & Co. KGaA, 69451 Weinheim, Germany, 2007)

## Introduction

The Suzuki cross-coupling reaction is one of the most important methods for the selective assembly of biaryls in the synthesis of natural products, pharmaceuticals, and advanced materials.[1] Although many palladium(II) or palladium(0) complexes catalyze this coupling reaction, significant efforts have been made to design ligands that can increase the catalytic activity of the palladium center. Some of the most widely studied Suzuki catalysts are palladium phosphane complexes that are susceptible to orthometalation or palladacycle formation.[2] However, the most efficient catalysts so far reported are palladium phosphane complexes that cannot undergo orthometalation.[3] These very active phosphane complexes require rigorous exclusion of air and water, however, due to the air sensitivity of the phosphane ligands, which is the main reason for the growing interest in Ncoordinating ligands for Suzuki catalysts. Indeed, many N-based ligands have been reported to be efficient for the Suzuki cross-coupling reactions, especially tertiary amines and imines.[4] These ligands are air-stable and are therefore easier to synthesize and handle. Boykin et al. have screened several simple and commercially available amines as ligands with palladium acetate in the Suzuki cross-coupling reaction and found that bulky primary and secondary amines appear to be better ligands than comparable tertiary amines that do not form stable complexes with palladium acetate.[5] Although these catalytic systems are efficient at low temperature and under aerobic conditions, a significantly higher amount of palladium acetate (2 mol-%) is needed compared to the molar ratio generally required with phosphane ligands (0.01 mol-%) in order to afford similar turnover numbers.

Our laboratory has recently designed new ligands that impose a *trans* geometry at the metal center, thereby preventing orthometalation.[6] As the palladium complex *trans*-$[PdCl_2(P\cap P)]$, which contains the diphosphane ligand $PPh_2CH_2\text{-}2,4,6\text{-}Me_3C_6H\text{-}CH_2\text{-}2,4,6\text{-}Me_3C_6H\text{-}CH_2\text{-}PPh_2$ (P∩P) is an active Suzuki catalyst for the cross-coupling of deactivated or hindered aryl bromides, we decided to synthesize the analogous amine ligands $NH{t}Bu\text{-}CH_2\text{-}2,4,6\text{-}Me_3C_6H_2$ (LN*t*Bu), $NHPh\text{-}CH_2\text{-}2,4,6\text{-}Me_3C_6H_2$ (LNPh), $NH{t}Bu\text{-}CH_2\text{-}2,4,6\text{-}Me_3C_6H\text{-}CH_2\text{-}2,4,6\text{-}Me_3C_6H\text{-}CH_2\text{-}NH{t}Bu$ (LN∩N*t*Bu), and $NHPh\text{-}CH_2\text{-}2,4,6\text{-}Me_3C_6H\text{-}CH_2\text{-}2,4,6\text{-}Me_3\text{-}C_6H\text{-}CH_2\text{-}NHPh$ (LN∩NPh) in order to study their coordination to palladium acetate as well as the catalytic potential of these complexes for Suzuki reactions.

## Results and Discussion

### Synthesis and Characterization of New Secondary Amine Ligands

The secondary amines $NH{t}Bu\text{-}CH_2\text{-}2,4,6\text{-}Me_3C_6H_2$ (LN*t*Bu), $NH{t}Bu\text{-}CH_2\text{-}2,4,6\text{-}Me_3C_6H\text{-}CH_2\text{-}2,4,6\text{-}Me_3C_6H\text{-}CH_2\text{-}NH{t}Bu$ (LN∩N*t*Bu), and $NHPh\text{-}CH_2\text{-}2,4,6\text{-}Me_3C_6H\text{-}CH_2\text{-}2,4,6\text{-}Me_3C_6H\text{-}CH_2\text{-}NHPh$ (LN∩NPh) are accessible in one step from the corresponding bromide and the corre-

[a] Institut de Chimie, Université de Neuchâtel,
Case Postale 158, 2009 Neuchâtel, Switzerland

 © 2007 Wiley-VCH Verlag GmbH & Co. KGaA, Weinheim 

sponding amine (Scheme 1). The synthesis of (2,4,6-trimethylbenzyl)aniline (LNPh) has been described previously.[7]

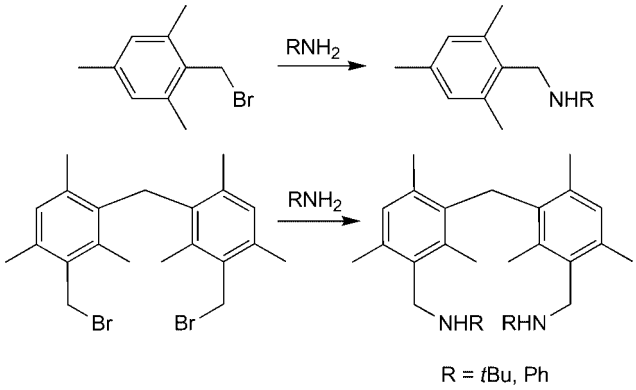


Scheme 1. Synthesis of the secondary amines LN*t*Bu, LNPh, LN∩N*t*Bu, and LN∩NPh.

All new compounds were characterized by NMR ($^1$H, $^{13}$C) spectroscopy, mass spectrometry, and elemental analysis.

## Synthesis and Molecular Structure of *trans*-Palladium Complexes

The *trans*-palladium complexes [Pd(OAc)$_2$(LN*t*Bu)$_2$] (**1**), [Pd(OAc)$_2$($\eta^2$-LN∩N*t*Bu)] (**2**), [Pd(OAc)$_2$(LNPh)$_2$] (**3**), and [Pd(OAc)$_2$($\eta^2$-LN∩NPh)] (**4**) were synthesized by treating [Pd(OAc)$_2$] with the corresponding amines or diamines in toluene at 50 °C and simple workup of the reaction mixture (Scheme 2).

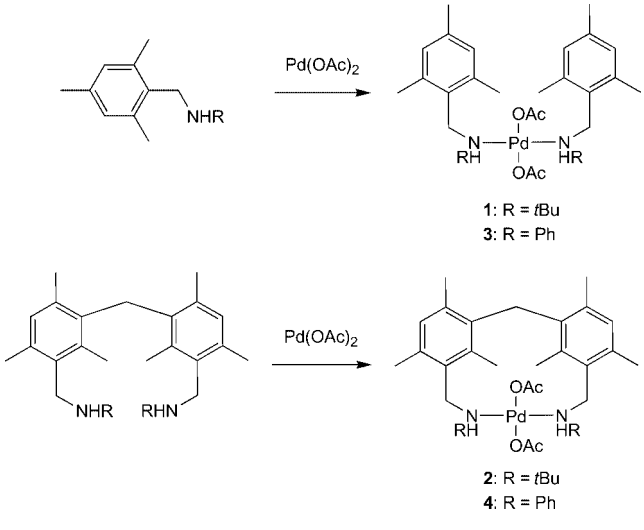


Scheme 2. Synthesis of the palladium complexes *trans*-[Pd(OAc)$_2$(LN*t*Bu)$_2$](**1**), *trans*-[Pd(OAc)$_2$($\eta^2$-LN∩N*t*Bu)](**2**), *trans*-[Pd(OAc)$_2$(LNPh)$_2$] (**3**), and *trans*-[Pd(OAc)$_2$($\eta^2$-LN∩NPh)] (**4**).

The question of stereochemistry needs to be addressed for complexes containing secondary amine ligands with three different substituents as the nitrogen atom is stereogenic (asymmetric tetrahedral geometry) due to coordination to the metal center. This problem has been solved by NMR spectroscopy and X-ray crystallography for complexes **1**–**4**.

The two asymmetric nitrogen centers in the bis-amine complexes **1** and **3** give rise, in principle, to three isomers − a pair of enantiomers (*R*,*R* and *S*,*S*) and a *meso* isomer (*R*,*S*), as shown in Scheme 3. In both cases, all three isomers are indeed formed upon coordination of LN*t*Bu or LNPh to [Pd(OAc)$_2$] as the NMR spectra show the expected signals of both diastereoisomers.

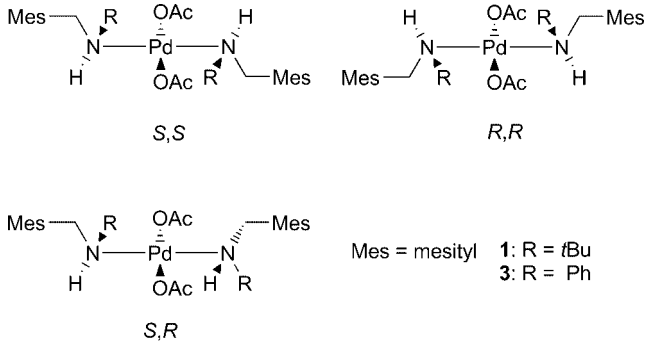


Scheme 3. Representation of the stereoisomeric configurations of complexes **1** and **3**.

While it did not prove possible to separate the three isomers of complex **3**, we succeeded in separating the diastereoisomers of **1** by extraction with diethyl ether. However, the separated diastereoisomers (*R*,*R*)/(*S*,*S*)-**1** and (*R*,*S*)-**1** were found to isomerize in solution over a period of several minutes so it was only possible to record $^1$H NMR spectra of diastereomerically pure **1a** and **1b**, but not the $^{13}$C{$^1$H} NMR spectra. Crystallization from chloroform gave only the *meso* isomer (*R*,*S*) for both complexes **1** and **3**.

The single-crystal X-ray structure analysis of **1** and **3** revealed that, in contrast to solutions of these complexes, which contain all isomers, the crystals isolated in both cases represent only the *meso* isomer. The molecular structures of **1** and **3** show the palladium atom to be in a square-planar geometry surrounded by two acetato ligands and two nitrogen atoms in a *trans* coordination geometry (Figures 1 and 2, respectively).

There are intramolecular hydrogen bonds in the crystal structures of **1** and **3** between the NH of the amino function and the C=O group of the acetato ligands [N–O 2.846(5) Å, N–H···O 141.7° in **1** and N–O 2.714(3) Å, N–H···O 150.4° in **3**; Figure 3]. The N···O distances and N–H···O angles are similar to those observed in analogous *trans* acetato(amino)-palladium complexes.[5a,8]

The rigid diamine backbone in the diamine complexes **2** and **4** generates an additional chirality upon coordination, with two enantiomers (*P* and *M*) being generated depending on the sense of helicity. Complexes **2** and **4** therefore possess three chiral elements (two chiral nitrogen atoms and a helical chirality element) and thus eight stereoisomeric species can theoretically be obtained (Scheme 4).

 © 2007 Wiley-VCH Verlag GmbH & Co. KGaA, Weinheim 

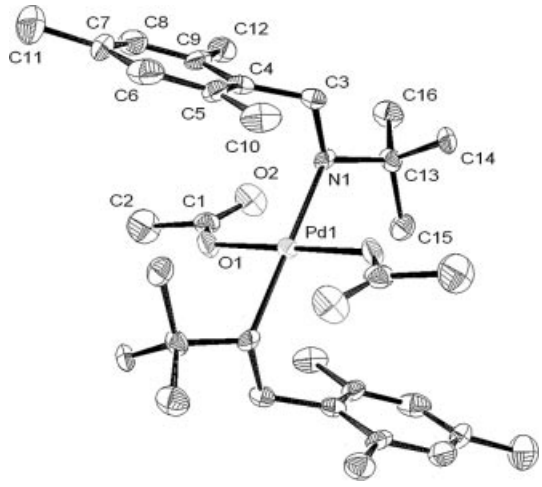


Figure 1. ORTEP drawing of **1** showing ellipsoids at the 50% probability level with hydrogen atoms omitted for clarity. Selected bond lengths [Å] and angles [°]: Pd(1)–O(1) 2.038(4), Pd(1)–N(1) 2.097(5), O(1)–C(1) 1.239(7), O(2)–C(1) 1.236(9), C(2)–C(1) 1.506(11), N(1)–C(3) 1.501(5), N(1)–C(13) 1.509(9), C(3)–C(4) 1.497(10); O(1)–Pd(1)–O(1)$^{i}$ 180.0(4), N(1)–Pd(1)–O(1) 87.3(2), N(1)–Pd(1)–N(1)$^{i}$ 180.0(1). (i = –*x*, –*y*, –*z*).

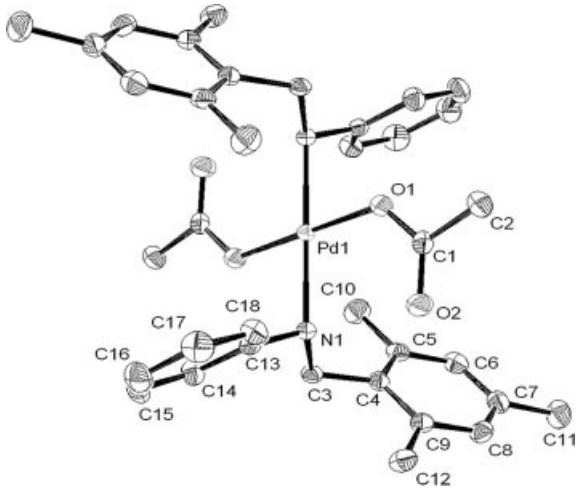


Figure 2. ORTEP drawing of **3** showing ellipsoids at the 50% probability level with hydrogen atoms omitted for clarity. Selected bond lengths [Å] and angles [°]: Pd(1)–O(1) 2.013(2), Pd(1)–N(1) 2.079(2), O(1)–C(1) 1.280(3), O(2)–C(1) 1.230(3), C(2)–C(1) 1.504(4), N(1)–C(3) 1.500(3), N(1)–C(13) 1.446(3), C(3)–C(4) 1.506(3); O(1)–Pd(1)–O(1)$^{i}$ 180.0(1), N(1)–Pd(1)–O(1) 96.14(8), N(1)–Pd(1)–N(1)$^{i}$ 180.0. (i = –*x*, –*y*, 1 – *z*).

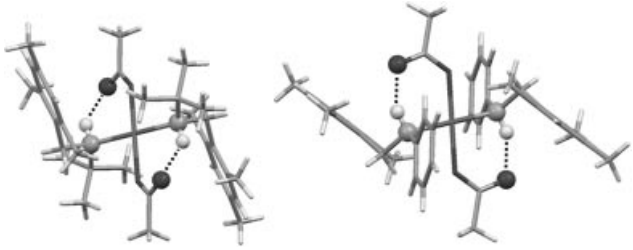

Figure 3. Intramolecular hydrogen-bonded systems in **1** (left) and **3** (right).

However, as suggested by $^{1}$H NMR spectroscopy and confirmed by the X-ray structure analysis of **2**, only one pair of enantiomers is observed for **2** and **4**.

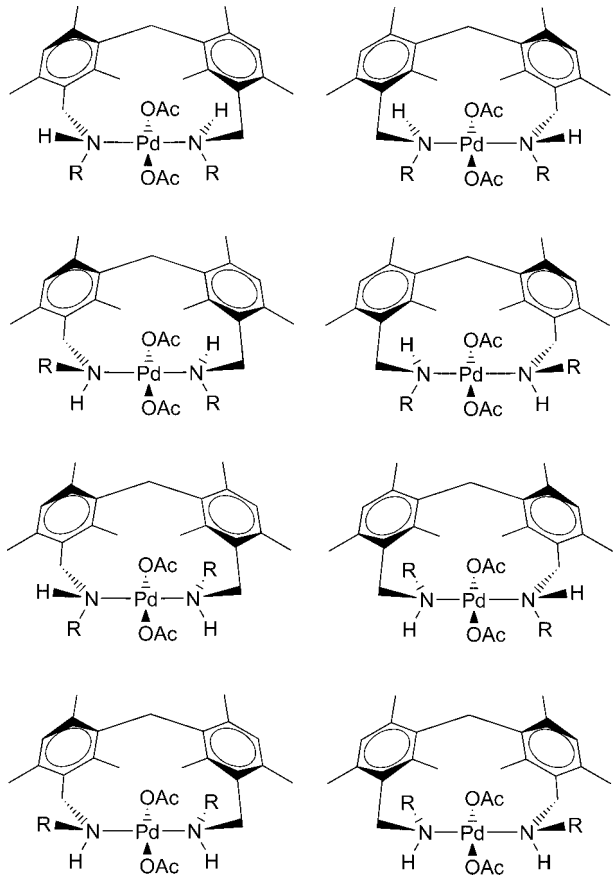


Scheme 4. Representation of the possible stereoconfigurations of complexes **2** and **4**.

Despite the high number of theoretically possible isomers, the $^{1}$H NMR spectra of complexes **2** and **4** are not complex and show only the expected signals for the ligands, thereby suggesting that only one isomer or pair of enantiomers is present in solution. As neither **2** nor **4** shows a signal in its CD spectrum, it can be assumed that both complexes exist as a pair of enantiomers. The single-crystal X-ray structure analysis of **2** confirmed this hypothesis since it reveals a racemic crystal containing two enantiomers, with the square-planar palladium center being *trans* coordinated to two acetato ligands and to the two nitrogen atoms of the diamine ligand (Figure 4).

The coordination of the chelating diamino ligand in **2** imposes a slight distortion of the planar geometry. Thus, unlike in **1** and **3**, where the O–Pd–O and N–Pd–N axes are perfectly linear by symmetry, the corresponding angles in **2** are 179.1(4)° and 178.8(4)°, respectively. A strong distortion is imposed on the diphenylmethane spacer such that the angle between the two planes of the phenyl rings is much more acute (56.4°; Figure 5) than the corresponding angle in diphenylmethane[9] (80.5°), the analogous *trans*-diphosphane complex [$PdCl_2$(P∩P)][6] (65.9°), and in the structurally constrained dinuclear chromium complex [($\mu_2$-$\eta^6$,$\eta^6$-di-

 © 2007 Wiley-VCH Verlag GmbH & Co. KGaA, Weinheim 

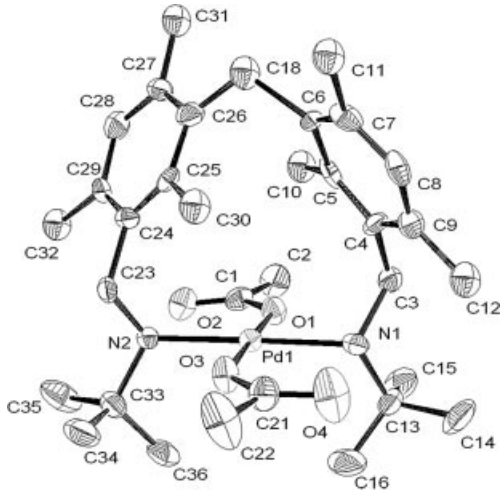


Figure 4. ORTEP drawing of **2** showing ellipsoids at the 50% probability level with hydrogen atoms omitted for clarity. Selected bond lengths [Å] and angles [°]: Pd(1)–O(1) 1.999(9), Pd(1)–O(3) 2.012(9), Pd(1)–N(1) 2.112(11), Pd(1)–N(2) 2.102(10), O(1)–C(1) 1.260(16), O(3)–C(21) 1.268(18), N(1)–C(3) 1.504(16), N(1)–C(13) 1.552(17), N(2)–C(23) 1.528(16), N(2)–C(33) 1.531(16), C(3)–C(4) 1.537(19), C(23)–C(24) 1.517(16); O(1)–Pd(1)–O(3) 179.1(4), N(1)–Pd(1)–O(1) 83.9(4), N(1)–Pd(1)–O(3) 95.5(4), N(1)–Pd(1)–N(2) 178.8(4), C(6)–C(18)–C(26) 111.4(12).

phenylmethane)-($\mu_2$-1,1,2,2-tetramethyldiphosphane-*P*,*P*′)-bis(dicarbonylchromium)] (71.9°).[10] Intramolecular hydrogen bonds are observed between the N–H amino function and the C=O oxygen of an acetato group in the crystal structure of **2**, as in **1** and **3** (Figure 5). The N···O distances are 2.801(16) and 2.765(15) Å with N–H···O angles of 149.0° and 150.3°, respectively.

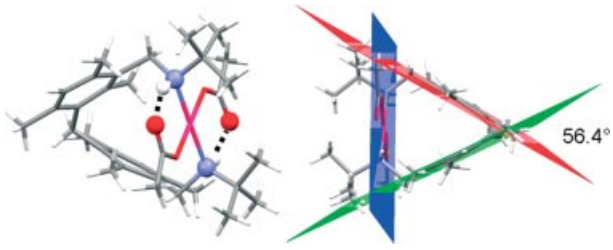


Figure 5. Intramolecular hydrogen-bonded system in **2** (left) and axial view in **2** (right).

## Catalytic Activity of Complexes 1–4 for Suzuki Cross-Coupling Reactions

The *trans*-palladium complexes **1**–**4** were studied as catalyst precursors for Suzuki cross-coupling reactions. As we wanted to study the real influence of the ligands and the geometry they impose, we decided to compare the results of these four complexes with the ligand-free compound [$Pd(OAc)_2$], which is suspected to catalyze the Suzuki cross-coupling due to nanoparticle formation, depending on the catalyst concentration.[11]

We studied two Suzuki-type reactions, namely the cross-coupling of phenylboronic acid with 4-bromotoluene, which is a deactivated bromo derivative, and the cross-coupling of phenylboronic acid with 1-bromo-2,4,6-trimethylbenzene, which is both deactivated and sterically hindered. The cross-coupling of phenylboronic acid with aliphatic bromides, which was recently reported to occur with [$Pd(OAc)_2$] in the presence of sterically hindered phosphanes,[12,13] does not work with our complexes [<5% of product formation with $CH_3(CH_2)_{11}Br$; catalyst/substrate ratio: 1:20; dioxane, *t*BuOK, 30–90 °C].

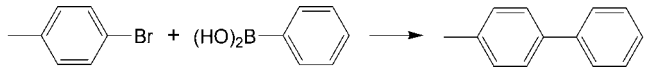


The results summarized in Table 1 show that the efficiency of the catalysts depends mainly on the temperature. Thus, at 90 °C the highest catalytic turnover number (86000) is achieved with [$Pd(OAc)_2$], which is not surprising given that recent work has shown [$Pd(OAc)_2$] to be an excellent source of highly active palladium nanoparticles during cross-coupling reactions.[14] However, at 60 °C complexes **1** and **2** are more efficient than [$Pd(OAc)_2$] and the other complexes, thereby indicating that the ligands have a strong influence on the catalytic performance − the electronic and steric effect of the *tert*-butyl groups on secondary amines is stronger than that of phenyl groups. Finally, this sequence changes again at 30 °C, since complex **2** becomes the least efficient one. This is due to the rigidity of the ligand, which means that the complex requires more energy to perform the catalytic reaction.

Table 1. Catalytic turnover numbers (TON), indicating the mol of product formed per mol of catalyst used after 18 h, for the Suzuki cross-coupling of 4-bromotoluene and phenylboronic acid catalyzed by **1**–**4** and [$Pd(OAc)_2$]. Solvent: toluene; base: $K_2CO_3$; reaction time: 18 h. Average of two runs.

| *T* [°C] | Catalyst/substrate | **1** | **2** | **3** | **4** | [$Pd(OAc)_2$] |
|---|---|---|---|---|---|---|
| 30 | 1:1000 | 410 | 250 | 130 | 230 | 240 |
| 30 | 1:10000 | 2700 | 0 | 600 | 900 | 460 |
| 60 | 1:1000 | 620 | 960 | 360 | 390 | 1000 |
| 60 | 1:10000 | 4800 | 6200 | 2300 | 2200 | 3800 |
| 60 | 1:100000 | 36000 | 38000 | 7000 | 12000 | 21000 |
| 90 | 1:1000 | 800 | 1000 | 710 | 710 | 1000 |
| 90 | 1:10000 | 6200 | 9100 | 4000 | 4900 | 9600 |
| 90 | 1:100000 | 45000 | 58000 | 28000 | 29000 | 86000 |

Nevertheless, as the TONs of the four complexes have the same order of magnitude as that of [$Pd(OAc)_2$], we compared complex **2** and [$Pd(OAc)_2$] kinetically at 60 °C with a catalyst/substrate ratio of 1:10000.

Figure 6 shows that the two precursors behave differently during the catalytic reaction. Thus, whereas [$Pd(OAc)_2$] shows a relatively constant activity, complex **2** undergoes an induction period of almost one hour, thereby indicating that it is also only a precatalyst. As we cannot exclude nanoparticle formation in the case of **2**, we performed poisoning tests with metallic mercury using a catalyst/substrate ratio of 1:1000. At 60 °C, **2** attains a TON of 300 after 1 h, while it is 960 after 18 h. When 400 equiv. of mercury is added at the beginning of the reaction, the TON falls to

 © 2007 Wiley-VCH Verlag GmbH & Co. KGaA, Weinheim 

480 after 18 h, and if mercury is added after one hour of reaction the TON is 660 after 18 h. Under the same conditions, the catalytic turnover of $[Pd(OAc)_2]$ drops to 84 or 267 if 400 equiv. of mercury is added at the beginning or after 1 h, respectively. Since the catalytic activity of metallic palladium nanoparticles should be suppressed completely by metallic mercury, we can conclude that the molecular catalysis pathway dominates for complex **2** while in the case of palladium acetate the nanoparticle pathway is dominant.

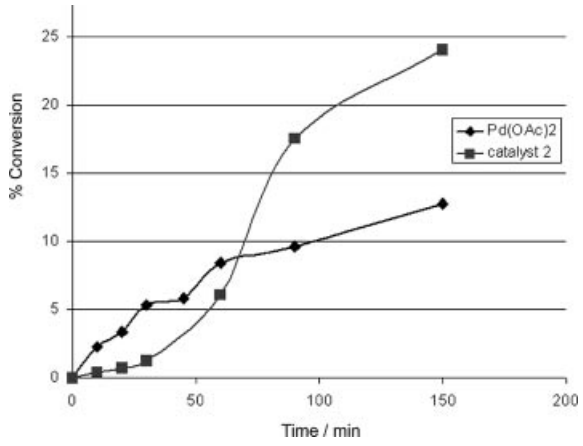


Figure 6. Kinetic comparison of complex **2** and $[Pd(OAc)_2]$ at 60 °C with a ratio of 1:10000.

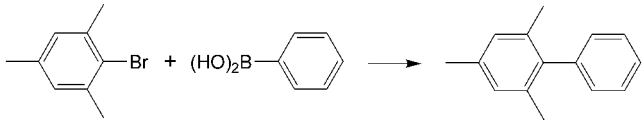


The results of the Suzuki cross-coupling of 1-bromo-2,4,6-trimethylbenzene with phenylboronic acid are summarized in Table 2. As expected with a sterically hindered and deactivated bromide, the TONs are lower than those observed for the previous reaction. Complex **2** is less active than **1** at 30 °C because of the rigidity of the ligand backbone. However, at temperatures above 60 °C complex **2** shows the best catalytic performance for sterically hindered substrates.

Table 2. Catalytic turnover numbers (TON) indicating the mol of product formed per mol of catalyst used after 18 h for the Suzuki cross-coupling of 2,4,6-trimethylphenyl bromide and phenylboronic acid catalyzed by **1**–**4** and $[Pd(OAc)_2]$. Solvent: toluene; base: $K_2CO_3$; reaction time: 18 h. Average of two runs.

| *T* [°C] | Catalyst/ substrate | **1** | **2** | **3** | **4** | $[Pd(OAc)_2]$ |
|---|---|---|---|---|---|---|
| 30 | 1:1000 | 297 | 66 | 18 | 60 | 86 |
| 60 | 1:1000 | 430 | 620 | 80 | 160 | 200 |
| 60 | 1:10000 | 2790 | 2900 | 300 | 900 | 420 |
| 90 | 1:1000 | 550 | 730 | 140 | 140 | 270 |
| 90 | 1:10000 | 3200 | 4900 | 800 | 1000 | 1300 |

## Conclusions

The *trans*-secondary amino complexes **1**–**4**, in which orthometalation is impossible because of the methyl substituents in the *ortho*-positions, catalyze the Suzuki cross-coupling of 4-bromotoluene and even of 2,4,6-trimethylphenyl bromide with phenylboronic acid. Whereas the TONs of the four complexes show the same order of magnitude as $[Pd(OAc)_2]$ in both reactions, it seems that the new ligands give rise to the formation of catalytically active molecular species rather than to metallic nanoparticles. Furthermore, we have shown that, at temperatures above 60 °C, the rigidity of the ligand backbone and the *tert*-butyl substituents increase the catalytic performance in the Suzuki cross-coupling of sterically hindered and deactivated bromides.

## Experimental Section

**General:** All reactions were carried out under argon using standard Schlenk techniques. Thf was distilled from sodium benzophenone under $N_2$ to avoid water and oxygen contamination. Toluene, *n*-hexane, and diethyl ether were purchased from Merck (puriss., pro analysi) and, along with distilled water, were saturated with argon prior to use. Dichloromethane was distilled from $CaH_2$ and saturated with $N_2$. $[Pd(OAc)_2]$ was purchased from Aldrich and used as received. Deuterated chloroform was used as received, and all NMR spectra were performed with a Bruker spectrometer [400 MHz for $^1H$ and 100 MHz for $^{13}C\{^1H\}$]. All GC analyses were performed using a GC DANI 86.10 equipped with a fused-silica capillary column OPTIMA $\delta$-3 (0.5 μm, 30 m × 0.25 mm) and an SP-4400 integrator.

**Synthesis of NH*t*Bu-$CH_2$-2,4,6-$Me_3C_6H_2$ (LN*t*Bu):** *tert*-Butylamine (2.11 mL, 20 mmol) was added to a suspension of 1-(bromomethyl)-2,4,6-trimethylbenzene (1.278 g, 6 mmol) and $K_2CO_3$ (2.76 g, 20 mmol) in toluene (20 mL). The mixture was refluxed for 15 h, then cooled to room temperature, and filtered through filter pulp. The filtrate was evaporated to dryness to give 793 mg of an oil (yield 64%). $^1H$ NMR (400 MHz, $CDCl_3$, 25 °C): $\delta$ = 6.91 (s, 2 H), 3.75 (s, 2 H), 2.44 (s, 6 H), 2.32 (s, 3 H), 1.27 (s, 9 H) ppm. $^{13}C\{^1H\}$ NMR (100 MHz, $CDCl_3$, 25 °C): $\delta$ = 136.74, 136.09, 134.25, 128.95, 50.43, 40.37, 28.89, 20.84, 19.21 ppm. EI-MS: *m*/*z* 206 $[M + H]^+$. $C_{14}H_{23}N$ (205.34): calcd. C 81.89, H 11.29, N 6.82; found C 81.95, H 11.34, N 6.75.

**Synthesis of NH*t*Bu-$CH_2$-2,4,6-$Me_3C_6H$-$CH_2$-2,4,6-$Me_3C_6H$-$CH_2$-NH*t*Bu (LN∩N*t*Bu):** *tert*-Butylamine (2.11 mL, 20 mmol) was added to a suspension of bis[3-(bromomethyl)-2,4,6-trimethylphenyl]methane (1.313 g, 3 mmol) and $K_2CO_3$ (2.76 g, 20 mmol) in toluene (20 mL) and the mixture refluxed for 15 h. The solution was then filtered through filter pulp at room temperature and the filtrate dried in vacuo (yield 80%). $^1H$ NMR (400 MHz, $CDCl_3$, 25 °C): $\delta$ = 6.78 (s, 2 H), 4.02 (s, 2 H), 3.63 (s, 4 H), 2.32 (s, 6 H), 2.08 (s, 12 H), 1.15 (s, 18 H) ppm. $^{13}C\{^1H\}$ NMR (100 MHz, $CDCl_3$, 25 °C): $\delta$ = 136.41, 135.87, 135.15, 135.13, 133.99, 130.54, 50.46, 41.07, 32.39, 28.90, 21.07, 19.37, 15.74 ppm. $C_{29}H_{46}N_2$ (422.69): calcd. C 82.40, H 10.97, N 6.63; found C 82.56, H 11.04, N 6.57.

**Synthesis of NHPh-$CH_2$-2,4,6-$Me_3C_6H$-$CH_2$-2,4,6-$Me_3C_6H$-$CH_2$-NHPh (LN∩NPh):** Phenylamine (2 mL, 20 mmol) was added to a suspension of bis[3-(bromomethyl)-2,4,6-trimethylphenyl]methane (1.313 g, 3 mmol) and $K_2CO_3$ (2.76 g, 20 mmol) in toluene (20 mL) and the mixture refluxed for 24 h. The solution was then filtered through filter pulp at room temperature and the filtrate dried in vacuo. The white residue was washed with *n*-hexane (20 mL) to remove an excess of phenylamine (yield 968 mg, 70%). $^1H$ NMR (400 MHz, $CDCl_3$, 25 °C): $\delta$ = 7.35–7.24 (m, 4 H), 6.91 (s, 2 H),

 © 2007 Wiley-VCH Verlag GmbH & Co. KGaA, Weinheim 

6.88–6.69 (m, 6 H), 4.22 (s, 4 H), 4.15 (s, 2 H), 2.38 (s, 6 H), 2.19 (s, 6 H), 2.16 (s, 6 H) ppm. $^{13}C\{^1H\}$ NMR (100 MHz, $CDCl_3$, 25 °C): $\delta$ = 148.20, 136.48, 136.22, 134.77, 133.09, 130.68, 129.25, 129.01, 128.20, 125.28, 117.42, 115.16, 112.62, 43.15, 32.36, 21.09, 19.53, 16.12 ppm. EI-MS: *m*/*z* 463 $[M + H]^+$. $C_{33}H_{38}N_2$ (462.67): calcd. C 85.67, H 8.28, N 6.05; found C 85.89, H 8.46, N 5.90.

**Synthesis of $[Pd(OAc)_2(LNtBu)_2]$ (1):** A solution of LN*t*Bu (102.5 mg, 0.5 mmol) in toluene (40 mL) was added to a suspension of $[Pd(OAc)_2]$ (56 mg, 0.25 mmol) in toluene (40 mL) and the mixture stirred at 50 °C for 3 h. The red solution became clear after 20 min, although towards the end of the reaction it became slightly cloudy again. After 3 h the cloudy solution was concentrated in vacuo to 40 mL and then filtered through filter pulp to remove the solid precipitate. The filtrate was evaporated to dryness and the residue washed with *n*-hexane (40 mL) to give analytically pure **1** as a mixture of isomers (total yield 65%). Complex **1** was separated into two diastereoisomers by extraction with diethyl ether (40 mL). After stirring at room temperature for 10 min, the diethyl ether extract was filtered through a cannula equipped with filter paper and the solvents evaporated to dryness to give isomer **1a**; diastereoisomer **1b** remained as a solid.

**1a:** $^1H$ NMR (400 MHz, $CDCl_3$, 25 °C): $\delta$ = 7.60 (br. d, $^3J_{H,H}$ = 9.6 Hz, 2 H, NH), 6.87 (s, 4 H), 3.69 (dd, $^3J_{H,H}$ = 12.8, 9.6 Hz, 2 H), 3.05 (dd, $^3J_{H,H}$ = 12.8, 2.2 Hz, 2 H), 2.40 (s, 6 H), 2.19 (s, 12 H), 1.80 (s, 6 H), 1.63 (s, 18 H) ppm. $C_{32}H_{52}N_2O_4Pd$ (635.19): calcd. C 63.72, H 8.69, N 4.64; found C 63.96, H 8.85, N 4.44.

**1b:** $^1H$ NMR (400 MHz, $CDCl_3$, 25 °C): $\delta$ = 7.11 (br. d, $^3J_{H,H}$ = 10.6 Hz, 2 H, NH), 6.90 (s, 4 H), 3.64 (t, $^3J_{H,H}$ = 10.6 Hz, 2 H), 3.00 (dd, $^3J_{H,H}$ = 12.8, 2.0 Hz, 2 H), 2.45 (s, 12 H), 2.32 (s, 6 H), 1.70 (s, 6 H), 1.41 (s, 18 H) ppm. $C_{32}H_{52}N_2O_4Pd$ (635.19): calcd. C 63.72, H 8.69, N 4.64; found C 63.88, H 8.78, N 4.50.

**Synthesis of $[Pd(OAc)_2(\eta^2\text{-}LN\cap NtBu)]$ (2):** A solution of LN∩N*t*Bu (105 mg, 0.25 mmol) in toluene (50 mL) was added to a suspension of $[Pd(OAc)_2]$ (56 mg, 0.25 mmol) in toluene (50 mL) and the mixture stirred at 50 °C for 15 h. The red solution became clear after 20 min. After 15 h the solvent was evaporated to dryness to give a yellow powder, which was washed with diethyl ether (10 mL). Yield 80%. $^1H$ NMR (400 MHz, $CDCl_3$, 25 °C): $\delta$ = 7.71 (d, $^3J_{H,H}$ = 10.6 Hz, 2 H), 6.86 (s, 2 H), 4.16 (s, 2 H), 3.61 (dd, $^3J_{H,H}$ = 12.3, 10.6 Hz, 2 H), 2.93 (d, $^3J_{H,H}$ = 12.6 Hz, 2 H), 2.51 (s, 6 H), 3.32 (s, 6 H), 1.72 (s, 6 H), 1.67 (s, 18 H), 1.66 (s, 6 H) ppm. $^{13}C\{^1H\}$ NMR (100 MHz, $CDCl_3$, 25 °C): $\delta$ = 180.16, 140.47, 138.95, 136.26, 135.70, 132.40, 129.94, 59.47, 42.90, 32.39, 28.85, 24.80, 21.48, 20.59, 18.46 ppm. $C_{33}H_{52}N_2O_4Pd$ (647.20): calcd. C 61.24, H 8.10, N 4.33; found C 61.48, H 8.28, N 4.28.

**Synthesis of $[Pd(OAc)_2(LNPh)_2]$ (3):** A solution of LNPh (225 mg, 1 mmol) in toluene (50 mL) was added to a suspension of $[Pd(OAc)_2]$ (112 mg, 0.5 mmol) in toluene (50 mL) and the mixture stirred at 50 °C for 3 h. The red solution became clear after 20 min, although towards the end of the reaction the solution became slightly cloudy again. After 3 h the cloudy solution was concentrated in vacuo to 50 mL and then filtered through filter pulp to remove the solid precipitate. The filtrate was evaporated to dryness and the residue washed with diethyl ether (20 mL) to give analytically pure **3** as a mixture of isomers (total yield 60%). $^1H$ NMR (400 MHz, $CDCl_3$, 25 °C): $\delta$ = 9.35 (m), 9.06 (m), 7.22–7.07 (m), 6.82 (s), 6.78 (s), 4.41–4.20 (m), 3.79 (dd, $^3J_{H,H}$ = 13.4, 4.6 Hz), 3.63 (dd, $^3J_{H,H}$ = 13.4, 4.7 Hz), 2.37 (s), 2.33 (s), 2.28 (s), 1.81 (s), 1.76 (s) ppm. $^{13}C\{^1H\}$ NMR (100 MHz, $CDCl_3$, 25 °C): $\delta$ = 180.78, 147.21, 138.35, 137.87, 129.52, 129.42, 129.20, 129.08, 128.90, 125.61, 122.96, 122.26, 50.78, 49.84, 29.32, 24.22, 23.15, 21.27, 20.39, 20.26 ppm. $C_{36}H_{44}N_2O_4Pd$ (675.17): calcd. C 61.20, H 6.10, N 4.46; found C 61.48, H 6.12, N 4.42.

**Synthesis of $[Pd(OAc)_2(\eta^2\text{-}LN\cap NPh)]$ (4):** A solution of LN∩NPh (230 mg, 0.5 mmol) in toluene (50 mL) was added to a suspension of $[Pd(OAc)_2]$ (112 mg, 0.5 mmol) in toluene (50 mL) and the mixture stirred at 50 °C for 15 h. The red solution became clear after 20 min, although towards the end of the reaction the solution became slightly cloudy again. After 15 h the cloudy solution was con-

Table 3. Crystallographic and selected experimental data for **1**–**3**.

| | **1** | **2** | **3** |
|---|---|---|---|
| Chemical formula | $C_{32}H_{52}N_2O_4Pd$ | $C_{33}H_{52}N_2O_4Pd$ | $C_{36}H_{44}N_2O_4Pd$ |
| Formula weight | 635.16 | 647.17 | 675.13 |
| Crystal system | triclinic | monoclinic | triclinic |
| Space group | $P\bar{1}$ | $P2_1/c$ | $P\bar{1}$ |
| Crystal color and shape | yellow block | yellow block | yellow block |
| Crystal size [mm] | $0.35\times0.22\times0.20$ | $0.18\times0.15\times0.13$ | $0.23\times0.22\times0.18$ |
| *a* [Å] | 9.095(3) | 12.5014(12) | 8.8590(9) |
| *b* [Å] | 9.113(2) | 14.5192(10) | 9.1797(10) |
| *c* [Å] | 10.093(2) | 19.354(3) | 11.2241(12) |
| *α* [°] | 107.71(3) | | 66.176(12) |
| *β* [°] | 99.14(3) | 110.856(10) | 71.855(12) |
| *γ* [°] | 91.95(3) | | 75.525(12) |
| *V* [Å$^3$] | 783.8(3) | 3282.8(6) | 785.34(14) |
| *Z* | 1 | 4 | 1 |
| *T* [K] | 173(2) | 173(2) | 173(2) |
| $D_c$ [g cm$^{-3}$] | 1.346 | 1.309 | 1.428 |
| $\mu$ [mm$^{-1}$] | 0.629 | 0.602 | 0.633 |
| Scan range [°] | $4.30 < 2\theta < 51.80$ | $4.42 < 2\theta < 51.90$ | $4.90 < 2\theta < 51.92$ |
| Unique reflections | 1552 | 6379 | 2852 |
| Reflections used $[I > 2\sigma(I)]$ | 1494 | 3759 | 2745 |
| $R_{int}$ | 0.0166 | 0.1243 | 0.0287 |
| *R* indices $[I > 2\sigma(I)]$[a] | 0.0364, $wR_2$ 0.0739 | 0.1587, $wR_2$ 0.4129 | 0.0253, $wR_2$ 0.0630 |
| *R* indices (all data) | 0.0302, $wR_2$ 0.0898 | 0.1927, $wR_2$ 0.4256 | 0.0287, $wR_2$ 0.0739 |
| Goodness-of-fit | 1.224 | 1.518 | 1.151 |
| Max, min $\Delta\rho$ [e Å$^{-3}$] | 0.535, –0.686 | 13.775, –2.481 | 0.575, –0.998 |

[a] Structures were refined on $F_o^2$: $wR_2 = \{\Sigma[w(F_o^2 - F_c^2)^2]/\Sigma w(F_o^2)^2\}^{1/2}$, where $w^{-1} = [\Sigma(F_o^2) + (aP)^2 + bP]$ and $P = [\max(F_o^2, 0) + 2F_c^2]/3$.

 © 2007 Wiley-VCH Verlag GmbH & Co. KGaA, Weinheim 

centrated in vacuo to 50 mL and then filtered through filter pulp to remove the solid precipitate. The filtrate was evaporated to dryness and the residue washed with diethyl ether (20 mL) to give **4** (yield 60%). $^1$H NMR (400 MHz, $CDCl_3$, 25 °C): $\delta$ = 10.34 (d, $^3J_{H,H}$ = 10.0 Hz, 2 H, NH), 7.35–7.31 (m, 4 H), 7.27–7.15 (m, 6 H), 6.98 (s, 2 H), 4.39 (dd, $^3J_{H,H}$ = 12.1, 10.0 Hz, 2 H), 4.23 (s, 2 H), 3.08 (d, $^3J_{H,H}$ = 12.1 Hz, 2 H), 2.56 (s, 6 H), 2.28 (s, 6 H), 1.90 (s, 6 H), 1.79 (s, 6 H) ppm. $^{13}$C{$^1$H} NMR (100 MHz, $CDCl_3$, 25 °C): $\delta$ = 181.20, 148.43, 140.28, 138.23, 136.90, 136.23, 131.37, 130.18, 129.44, 125.37, 121.29, 49.00, 32.38, 25.34, 21.62, 19.67, 18.59 ppm. $C_{37}H_{44}N_2O_4Pd$ (687.18): calcd. C 64.67, H 6.45, N 4.08; found C 64.90, H 6.59, N 3.99.

**X-ray Crystallographic Study:** Crystals of **1**–**3** were mounted on a Stoe Image Plate Diffraction system equipped with a $\phi$ circle goniometer and a Mo-$K_\alpha$ graphite-monochromated radiation source ($\lambda$ = 0.71073 Å). Data were collected in the $\phi$ range 0–200°, in increments of 1.0°, 1.2°, and 1.0°, respectively, with the 2$\theta$ range 2.0–26° and $D_{max}$–$D_{min}$ = 12.45–0.81 Å. The structures were solved by direct methods using the program SHELXS-97.[15] Refinement and all further calculations were carried out using SHELXL-97.[16] The H-atoms were included in calculated positions in all complexes and treated as riding atoms using the SHELXL default parameters. The non-H atoms were refined anisotropically using weighted full-matrix least-squares on $F^2$. Crystallographic details are summarized in Table 3. Figures 1, 2, and 4 were drawn with ORTEP[17] and Figures 3 and 5 with MERCURY.[18]

CCDC-647487 (for **1**), -647488 (for **2**), and -647489 (for **3**) contain the supplementary crystallographic data for this paper. These data can be obtained free of charge from The Cambridge Crystallographic Data Centre via www.ccdc.cam.ac.uk/data_request/cif.

**Catalytic Reactions:** The catalyst was added (in the molar ratio given in Tables 1 and 2) to a solution of $K_2CO_3$·1.5$H_2O$ (138 mg, 0.8 mmol), phenylboronic acid (91 mg, 0.75 mmol), and the aryl bromide (0.5 mmol) in toluene (5 mL) in a Schlenk tube and the mixture heated to the desired temperature (Tables 1 and 2) and stirred for 18 h. After cooling, the solution was filtered through a small silica gel column then the silica gel was eluted with diethyl ether (20 mL). The filtrate was combined with the ether washings and the solution obtained analyzed by GC.


[1] a) N. Miyaura, A. Suzuki, *Chem. Rev.* **1995**, *95*, 2457; b) S. Kotha, K. Lahiri, D. Kashinath, *Tetrahedron* **2002**, *58*, 9633; c) A. Suzuki, *J. Organomet. Chem.* **2002**, *653*, 83–90; d) F. Bellina, A. Carpita, R. Rossi, *Synthesis* **2004**, *15*, 2419.

[2] a) A. Zapf, M. Beller, *Chem. Eur. J.* **2001**, *7*, 908; b) M. Beller, H. Fischer, W. A. Herrmann, K. Öfele, C. Brossmer, *Angew. Chem. Int. Ed. Engl.* **1995**, *34*, 1848; c) R. B. Bedford, S. L. Hazelwood (née Welch), M. E. Limmert, D. A. Albisson, S. M. Draper, P. N. Scully, S. J. Coles, M. B. Hursthouse, *Chem. Eur. J.* **2003**, *9*, 3216.

[3] a) T. E. Barder, S. D. Walker, J. R. Martinelli, S. L. Buchwald, *J. Am. Chem. Soc.* **2005**, *127*, 4685; b) J. Yin, M. P. Rainka, X. Zhang, S. L. Buchwald, *J. Am. Chem. Soc.* **2002**, *124*, 1162; c) J. P. Wolfe, R. A. Singer, B. H. Yang, S. L. Buchwald, *J. Am. Chem. Soc.* **1999**, *121*, 9550; d) S. D. Walker, T. E. Barder, J. R. Martinelli, S. L. Buchwald, *Angew. Chem. Int. Ed.* **2004**, *43*, 1871.

[4] a) B. Tao, D. W. Boykin, *Tetrahedron Lett.* **2002**, *43*, 4955; b) D. A. Alonso, C. Najera, M. C. Pacheco, *Org. Lett.* **2000**, *2*, 1823; c) L. Botella, C. Najera, *Angew. Chem. Int. Ed.* **2002**, *41*, 179; d) H. Weissman, D. Milstein, *Chem. Commun.* **1999**, 1901; e) R. B. Bedford, C. S. Cazin, *Chem. Commun.* **2001**, 1540; f) G. A. Grasa, A. C. Hillier, S. P. Nolan, *Org. Lett.* **2001**, *3*, 1077.

[5] a) B. Tao, D. W. Boykin, *J. Org. Chem.* **2004**, *69*, 4330; b) B. Tao, D. W. Boykin, *Tetrahedron Lett.* **2003**, *44*, 7993.

[6] L. Chahen, B. Therrien, G. Süss-Fink, *J. Organomet. Chem.* **2006**, *691*, 4257.

[7] J. R. Miecznikowski, R. H. Crabtree, *Polyhedron* **2004**, *23*, 2857.

[8] a) S. V. Kravtsova, I. P. Romm, A. I. Stash, V. K. Belsky, *Acta Crystallogr., Sect. C* **1996**, *52*, 2201; b) S. Bouquillon, J. Rouden, J. Muzart, M.-C. Lasne, M. Hervieu, A. Leclaire, B. Tinant, *C. R. Chim.* **2006**, *9*, 1301.

[9] J. C. Barnes, J. D. Paton, J. R. Damewood, K. Mislow, *J. Org. Chem.* **1981**, *46*, 4975.

[10] W. E. Geiger, N. Van Order, D. T. Pierce, T. E. Bitterwolf, A. L. Rheingold, N. D. Chasteen, *Organometallics* **1991**, *10*, 2403.

[11] A. Alimardanov, L. Schmieder-van de Vomdervoort, A. H. M. de Vries, *Adv. Synth. Catal.* **2004**, *346*, 1812.

[12] J. H. Kirchhoff, M. R. Netherton, I. D. Hills, G. C. Fu, *J. Am. Chem. Soc.* **2002**, *124*, 13662.

[13] T. Brenstrum, D. A. Gerritsma, G. M. Adjabeng, C. S. Frampton, J. Britten, A. J. Robertson, J. McNulty, A. Capretta, *J. Org. Chem.* **2004**, *69*, 7635.

[14] A. H. M. de Vries, J. M. C. A. Mulders, J. H. M. Mommers, H. J. W. Henderickz, J. G. de Vries, *Org. Lett.* **2003**, *5*, 3285.

[15] G. M. Sheldrick, *Acta Crystallogr., Sect. A* **1990**, *46*, 467.

[16] G. M. Sheldrick, *SHELXL-97*, University of Göttingen, Germany, **1999**.

[17] L. J. Farrugia, *J. Appl. Crystallogr.* **1997**, *30*, 565.

[18] I. J. Bruno, J. C. Cole, P. R. Edgington, M. Kessler, C. F. Macrae, P. McCabe, J. Pearson, R. Taylor, *Acta Crystallogr., Sect. B* **2002**, *58*, 389.


Received: May 16, 2007
Published Online: September 12, 2007

 © 2007 Wiley-VCH Verlag GmbH & Co. KGaA, Weinheim 

DOI: 10.1002/ejic.200700470

# (2,2-Dibromovinyl)ferrocene as a Building Block for the Assembly of Heterodinuclear Complexes – Preparation of an σ-Alkenylpalladium Complex and Dimetallic Dithioether Complexes

**Sébastien Clément,[a] Laurent Guyard,[a] Michael Knorr,*[a] Fernando Villafañe,[b] Carsten Strohmann,[c] and Marek M. Kubicki[d]**

**Keywords:** Oxidative addition / Thioether ligands / Platinum / Rhenium / Palladium / Electrochemistry

The oxidative addition of (2,2-dibromovinyl)ferrocene [$Br_2C$=C(H)–Fc] (**1**) to [$Pd(PPh_3)_4$] yields the heterodinuclear σ-alkenyl complex *trans*-[{$Pd(Br)(PPh_3)_2$}–C(Br)=C(H)–Fc] (**2**). Nucleophilic attack of sodium thiolates on **1** unexpectedly affords the vinyl thioether derivatives (*Z*)-[(RS)(H)C=C(H)–Fc] (**4a**: R = Ph; **4b**: R = *t*Bu; **4c**: R = Et). Complexes **4a** and **4c** can also be prepared by addition of NaSR across the triple bond of Fc–C≡C–H (**3**). Addition of an excess of NaSR to **1** affords the dithioether derivatives (*Z*)-[(RS)(H)C=C(SR)–Fc] (**5a**: R = Ph; **5b**: R = *p*-tolyl; **5c**: R = Et). An addition/elimination sequence is suggested to account for this surprising result. The yield of **5c** is very low due to a competing formation of ethynylferrocene (**3**). Reaction of **5b** with [Re(thf)$(CO)_3$-(μ-Br)]$_2$ and [$PtCl_2(PhCN)_2$] leads to the heterodinuclear chelate complexes [Fc{C(S–*p*-tolyl)=C(H)(S–*p*-tolyl)}Re(Br)-$(CO)_3$] (**6**) and [Fc{C(S–*p*-tolyl)=C(H)(S–*p*-tolyl)}$PtCl_2$] (**7a**), respectively. Metathesis of the fluxional compound **7a** in the presence of NaI affords [Fc{C(S–*p*-tolyl)=C(H)(S–*p*-tolyl)}$PtI_2$] (**7b**). The electrochemical properties of some of these complexes have been studied by means of cyclic voltammetry, and the molecular structures of **1**, **2**, **3**, **4b**, **4c** and **6** have been determined by X-ray diffraction.
(© Wiley-VCH Verlag GmbH & Co. KGaA, 69451 Weinheim, Germany, 2007)

## Introduction

Ethynylferrocene[1] is increasingly being used as building block for the construction of di- and polymetallic organometallic systems[2–5] due to the presence of an electrochemically active ferrocenyl unit. In contrast, only a few examples of the preparation of polymetallic arrays starting from alkenylferrocenes have been reported in the literature.[6–9] In addition to a covalent connection to other metal centres, vinylferrocene has also been used as side-on bound π-ligand for the synthesis of dimetallic compounds of the type [$M(CO)_5$\{$\eta^2$-$H_2C$=C(H)Fc\}] (M = Cr, Mo, W).[10] For the past few years, we have been interested in the assembly of homo- and heterodinuclear transition metal complexes and the evaluation of their physicochemical properties (electrochemistry, luminescence).[11] Indeed, we recently published the synthesis of (dibromovinyl)[2.2]paracyclophane and investigated its reactivity towards [$M(PPh_3)_4$] (M = Pd, Pt).[11c] For comparison, we embarked on a study on the reactivity of (2,2-dibromovinyl)ferrocene (**1**), which shares some common features with (dibromovinyl)[2.2]paracyclophane such as planar chirality, redox activity and potential applications in materials science. We now wish to report the use of **1** for the synthesis of a functionalised vinylpalladium(II) complex, the reactivity of **1** towards various thiolates (NaSR) and the subsequent rearrangement reactions that lead to vinylic thioether compounds, which may also serve as ligands in coordination chemistry. This work also includes electrochemical investigations and several crystal structure determinations.

[a] Institut UTINAM UMR CNRS 6213, Université de Franche-Comté, Faculté des Sciences,
16, Route de Grey, 25030 Besançon Cedex, France
Fax: +33-3-81666438
E-mail: michael.knorr@univ-fcomte.fr
[b] IUCINQUIMA/Química Inorgánica, Facultad de Ciencias, Universidad de Valladolid,
47005 Valladolid, Spain
[c] Institut für Anorganische Chemie der Universität Würzburg, Am Hubland, 97074 Würzburg, Germany
[d] Institut de Chimie Moléculaire UMR CNRS 5260, Université de Bourgogne,
9, Avenue Alain Savary, 21078 Dijon, France
Supporting information for this article is available on the WWW under http://www.eurjic.org or from the author.

## Results and Discussion

### Oxidative Addition of (2,2-Dibromovinyl)ferrocene (1) to [$Pd(PPh_3)_4$]

The starting material **1** was prepared according to a literature procedure under Corey–Fuchs conditions by treatment of ferrocenecarbaldehyde with $CBr_4$ in the presence of zinc dust and $PPh_3$ (Scheme 1).[12,13] An X-ray diffraction study (Figure 1) revealed that, in contrast to (dibromovinyl)[2.2]paracyclophane,[11c] the alkenyl unit and the cyclopentadienido ring are almost parallel, with an interplanar angle of only 10.43°.

 © 2007 Wiley-VCH Verlag GmbH & Co. KGaA, Weinheim 

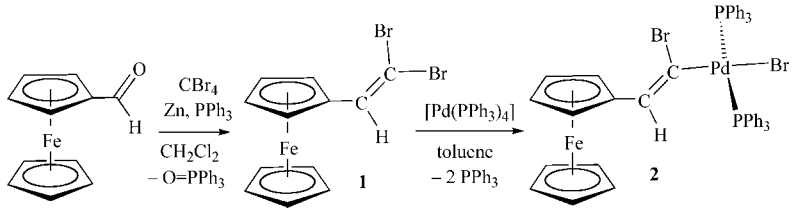


Scheme 1.

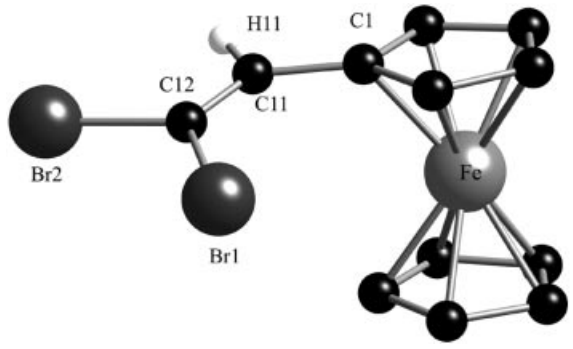


Figure 1. Ball-and-stick view of the molecular structure of **1**. Selected bond lengths [Å] and angles [°]: C(12)–Br(2) 1.892(2), C(12)–Br(1) 1.873(3), C(12)–C(11) 1.318(4), C(11)–C(1) 1.445(4); Br(1)–C(12)–Br(2) 113.56(15), Br(2)–C(12)–C(11) 120.7(2), Br(1)–C(12)–C(11) 125.7(2), C(12)–C(11)–C(1) 130.8(2).

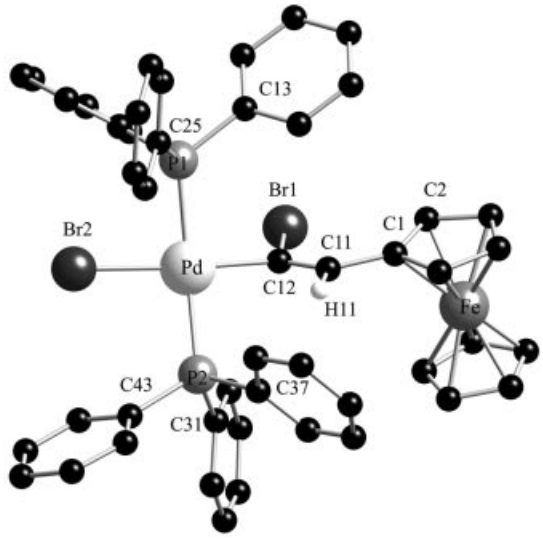


Figure 2. Ball-and-stick view of the molecular structure of **2**. For clarity, only the vinylic hydrogen atom is shown. Selected bond lengths [Å] and angles [°]: Pd–P(1) 2.3375(17), Pd–P(2) 2.3185(18), Pd–Br(2) 2.4479(8), Pd–C(12) 2.037(6), C(12)–Br(1) 1.952(6), C(12)–C(11) 1.272(9), C(11)–C(1) 1.481(8); P(1)–Pd–P(2) 166.74(5), Br(2)–Pd–C(12) 173.86(16), P(1)–Pd–C(12) 92.66(17), P(2)–Pd–C(12) 90.21(17), P(1)–Pd–Br(2) 84.76(4), P(2)–Pd–Br(2) 93.61(4), Br(1)–C(12)–Pd 108.8(3), Pd–C(12)–C(11) 120.4(5), C(12)–C(11)–C(1) 135.2(6).

Several experimental and theoretical studies have shown that the oxidative addition of vinyl halides to low-valent $Pd^0$ centres leads to $Pd^{II}$ complexes bearing a σ-alkenyl ligand.[14–18] For example, treatment of $[Pd(PPh_3)_4]$ with β-bromostyrene results in the formation of *trans*-$[PdBr(CH{=}CHPh)(PPh_3)_2]$.[18] The vinyl bromide **1** adds oxidatively to $[Pd(PPh_3)_4]$ at 60 °C in toluene solution in a similar manner to produce the heterodinuclear σ-alkenyl complex *trans*-[PdBr{C(Br)=C(H)–Fc}$(PPh_3)_2$] (**2**) in 76% yield (Scheme 1). The *trans* geometry of the $PPh_3$ ligands is evidenced by the presence of a single resonance at $\delta$ = 22.7 ppm in the $^{31}P\{^1H\}$ NMR spectrum. Unfortunately, the reaction with $[Pt(PPh_3)_4]$ under identical conditions led mainly to the formation of *cis*-$[PtBr_2(PPh_3)_2]$.

The X-ray structure of **2**, which is shown in Figure 2, reveals a slightly deformed square-planar coordination around Pd consisting of two *trans* $PPh_3$ residues, a terminal bromo ligand and a vinylferrocene moiety. The C(11)–C(12) double bond in **2** is shorter than in **1** [1.318(4) vs. 1.272(9) Å]. The latter ligands are placed almost linearly, with a Br(2)–Pd–C(12) angle of 173.86(16)°. Due to a stereoselective activation of the Br(2)–C(12) bond during the oxidative addition process, the stereochemistry about the vinylic C(11)=C(12) double bond is *anti* (*E*) with respect to the ferrocene unit and the Pd centre, with a C(1)–C(11)–C(12)–Pd dihedral angle of 164.7°.

### Reactivity of 1 Towards Various Thiolates

In the context of our work on the development of new dithioether ligands and their coordination chemistry,[19–21] we recently demonstrated that the nucleophilic attack of various thiolates on the π-conjugated 2-azabutadiene $[Cl_2C{=}C(H)N{=}CPh_2]$ in dmf affords the functionalised derivatives $[(RS)_2C{=}C(H){-}N{=}CPh_2]$ (R = Ph, *i*Pr) by replacement of the two vinylic chloro substituents by $SR^-$.[22] If the reaction with sodium thiophenolate is carried out in a 1:1 ratio, the monosubstituted product $[(PhS)(Cl)C{=}C(H){-}N{=}CPh_2]$ can be isolated. Unexpectedly, treatment of **1** with thiolates was less straightforward. Thus, when **1** is treated with just 1 equiv. of thiophenolate the reaction is incomplete and leads to the formation of a mixture of **1**, the substitution product **4a** and some ethynylferrocene (**3**). Treatment of **1** with a slight excess of NaSPh in dmf allowed us to isolate the vinylic thioether **4a** as an orange-red solid. However, the elemental analysis and NMR spectroscopic

 © 2007 Wiley-VCH Verlag GmbH & Co. KGaA, Weinheim 

data of **4a** did not match the expected values for [(PhS)(Br)-C=C(H)–Fc] but instead suggested the formulation (*Z*)-[(PhS)(H)C=C(H)–Fc] (**4a**; Scheme 2). Treatment of **1** with an excess of NaS*t*Bu in dmf also did not lead to the anticipated dithioether compound [(*t*BuS)$_2$C=C(H)–Fc]. Instead, analysis of the crude product by TLC indicated the presence of (*Z*)-[(*t*BuS)(H)C=C(H)–Fc] (**4b**) together with a large amount of ethynylferrocene (**3**). The formation of ethynylferrocene, which was isolated by column chromatography, was unambiguously confirmed by an X-ray diffraction analysis.

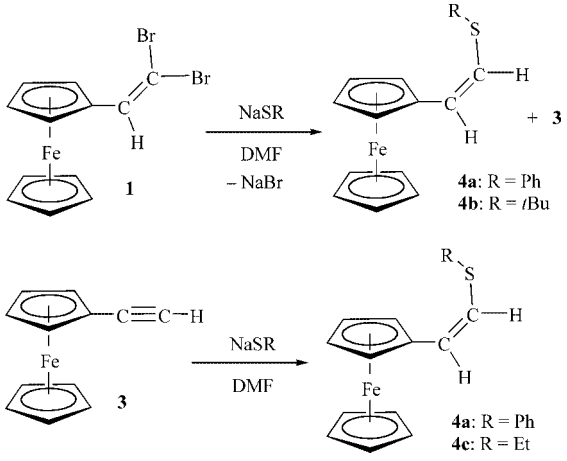


Scheme 2.

The (*Z*) stereochemistry about the vinylic double bond of **4b** and the unexpected replacement of the Br substituent by an H atom were also confirmed by X-ray diffractometry. As illustrated in Figure 3, the crystallographic data unambiguously confirm the replacement of one bromine atom in the (*Z*) position relative to the ferrocene unit by an S*t*Bu group and replacement of the second bromine atom by a hydrogen atom. The Cp ring bearing the vinyl group and the thioether function are almost coplanar, with a C(10)–C(11)–C(12)–S torsion angle of 2.8°. We were unable to synthesise the corresponding SEt derivative (*Z*)-[(EtS)(H)-C=C(H)–Fc] (**4c**) by this method as, except for some minor amounts of the dithioether compound (*Z*)-[(EtS)(H)-C=C(SEt)–Fc] (**5c**; see below), only ethynylferrocene (**3**) could be isolated from this reaction. X-ray checks carried out on several differently shaped crystals and full analysis of one sample always showed the presence of ethynylferrocene.[23,24]

A related structural motif was recently crystallographically established for the vinylferrocene derivatives **A** and **B**, which were obtained after hydrolysis or alcoholysis of 2,3-diferrocenyl-1-(methylthio)cyclopropenylium iodide (Scheme 3).[25]

The formation of large amounts of ethynylferrocene can be rationalised by a dehydrobromination reaction induced by the basic thiolate reagent. It is well established that addition of thiolates (or thiols under basic conditions) across the C≡C bond of alkynes leads to vinyl thioethers.[26–30] For example, treatment of phenylacetylene with sodium *p*-

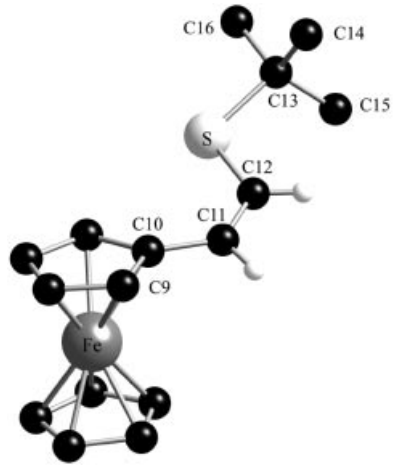


Figure 3. Ball-and-stick view of the molecular structure of **4b** showing the (*Z*) configuration around the C=C bond. For clarity, only the vinylic hydrogen atoms are shown. Selected bond lengths [Å] and angles [°]: C(10)–C(11) 1.458(7), C(11)–C(12) 1.351(8), C(12)–S 1.749(5), C(13)–S 1.845(5), C(13)–C(14) 1.545(7); C(9)–C(10)–C(11) 123.1(5), C(10)–C(11)–C(12) 128.8(5), C(11)–C(12)–S 125.0(4), C(12)–S–C(13) 103.0(3), C(14)–C(13)–S 110.1(3), C(15)–C(13)–S 110.8(4), C(16)–C(13)–S 103.5(4).

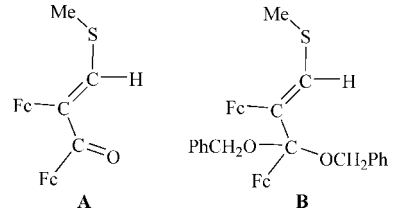


Scheme 3.

toluenethiolate in dmf produces (*Z*)-1-phenyl-2-(*p*-tolylmercapto)ethene in a stereospecific manner. According to the kinetics of the reaction, a stepwise mechanism has been suggested for this addition which is initiated by nucleophilic attack of SR$^-$ at the β-carbon atom of Ph–C≡C–H, followed by protonation of the resulting carbanionic intermediate.[27] We therefore attempted an alternative synthesis of **4c** along this route by treating Fc–C≡C–H (**3**) with NaSEt in dmf at room temperature. Indeed, **4c** was now accessible in 78% isolated yield as a red crystalline solid after workup in aqueous solution. An X-ray diffraction study confirmed the (*Z*) disposition of the Fc moiety and the SEt substituent about the C=C bond (see Figure 4). As in **4b**, the Cp ring bearing the vinyl group and the thioether function are almost coplanar, with a C(10)–C(11)–C(12)–S torsion angle of 2.7°. The Cp rings of **4c** are again placed in an eclipsed conformation.

The complex (*Z*)-[(PhS)(H)C=C(H)–Fc] (**4a**) is also accessible by this route. The (*Z*) arrangement of the two vinylic hydrogen atoms of **4a** is corroborated by the $^1$H NMR spectrum, which exhibits an AB pattern centred at $\delta$ = 6.31 ppm with a typical vicinal (*Z*) coupling constant of 10.1 Hz. Similar values ($\delta$ = 6.45 ppm, $^3J_{A,B}$ = 10.8 Hz) were recently reported for (*Z*)-[(PhS)(H)C=C(H)–C$_6$H$_4$O-Me].[31a] In contrast, a $^3J_{H,H}$ coupling constant of 15.3 Hz

 © 2007 Wiley-VCH Verlag GmbH & Co. KGaA, Weinheim 

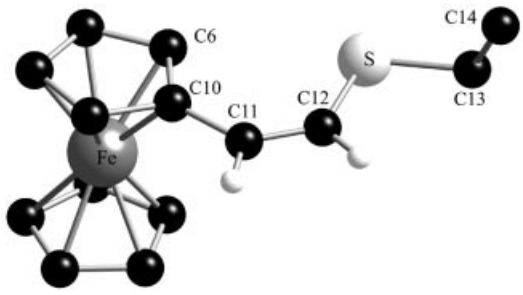


Figure 4. Ball-and-stick view of the molecular structure of **4c**. Selected bond lengths [Å] and angles [°]: C(10)–C(11) 1.463(7), C(11)–C(12) 1.314(7), C(12)–S 1.750(4), C(13)–S 1.789(6), C(13)–C(14) 1.522(5); C(10)–C(11)–C(12) 129.6(4), C(11)–C(12)–S 126.8(4), C(12)–S–C(13) 101.6(2), C(14)–C(13)–S 114.3(3).

has been reported for (*E*)-[(PhS)(H)C=C(H)–Ph], which was obtained by Rh-catalysed hydrothiolation of phenylacetylene.[31b] The NOESY spectrum (see Supporting Information) reveals a weak correlation between the unresolved Cp signal at $\delta$ = 4.62 ppm and the vinylic resonance at $\delta$ = 6.35 ppm, thereby proving the existence of a weak $^4J_{H,H}$ "W-coupling".

With the aim of synthesising ferrocene-based dithioether ligands, complex **1** was treated with an excess of aromatic thiolate (10 equiv.) at room temperature. Although the vinylic dithioether complexes (*Z*)-[(ArS)(H)C=C(SAr)–Fc] (**5a**,**b**) were formed as orange-red solids, albeit in moderate yields (46–51%) due to a competing elimination reaction that produces ethynylferrocene (**3**; Scheme 4), a closer look at the NMR spectra of **5a**,**b** and the X-ray data for the heterodinuclear compound **6** (see Figure 5 for the rhenium dithioether complex) revealed that a rearrangement reaction again occurred.[32] The overall yield of **5c** was lower still (22%) with the more basic ethyl thiolate as nucleophile, giving **3** in more than 50% yield as the main product.

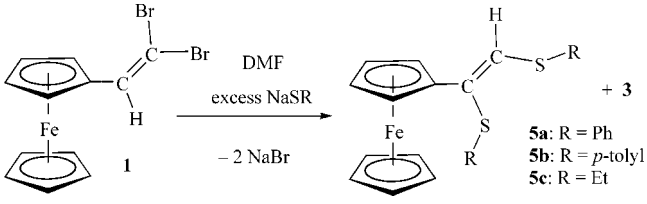


Scheme 4.

A literature survey indicates that this rearrangement has a precedent in organic chemistry. Thus, the mechanistic investigations of Truce and Boudakian on the reactivity of 1,1-dichloroethylene towards an excess of sodium *p*-toluenethiolate in EtOH demonstrate that this reaction affords exclusively (*Z*)-1,2-bis(*p*-tolylmercapto)ethene. The intermediacy of an alkyne species ArS–C≡CH was suggested to rationalize this interesting addition/elimination sequence.[33] Another research group later independently confirmed these findings with NaSPh as nucleophile and dmf as solvent.[34]

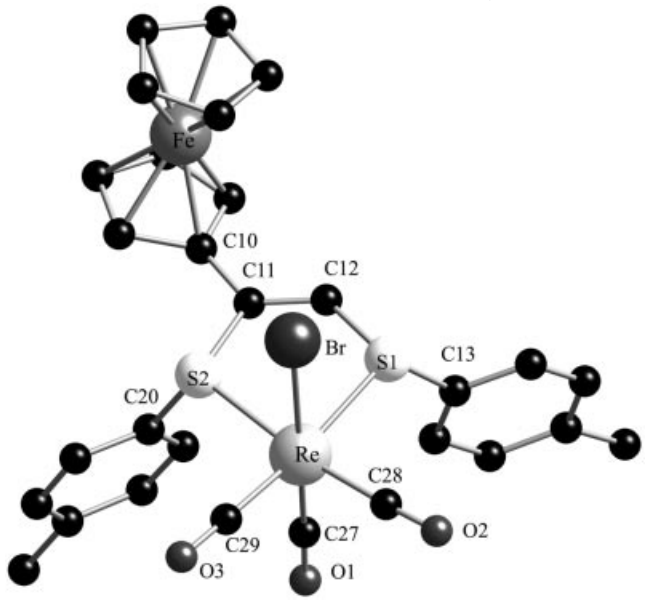


Figure 5. Ball-and-stick view of the molecular structure of **6**. Selected bond lengths [Å] and angles [°]: Re–S(1) 2.4705(18), Re–S(2) 2.4807(16), Re–Br 2.6304(8), Re–C(27) 1.908(8), Re–C(28) 1.944(9), Re–C(29) 1.947(9), C(12)–S(1) 1.755(7), C(11)–S(2) 1.807(7), C(12)–C(11) 1.331(9), C(11)–C(10) 1.466(9); Br–Re–C(27) 176.2(2), Br–Re–S(1) 79.42(5), Br–Re–S(2) 81.00(5), C(28)–Re–C(29) 90.2(3), C(28)–Re–S(1) 92.5(3), C(28)–Re–S(2) 172.5(2), C(29)–Re–S(2) 94.0(2), C(29)–Re–S(1) 172.7(2), C(10)–C(11)–C(12) 124.0(6), C(11)–C(12)–S(1) 126.9(6), C(12)–C(11)–S(2) 119.1(5), C(10)–C(11)–S(2) 116.8(5), C(12)–S(1)–C(13) 100.3(3), C(11)–S(2)–C(20) 101.3(3).

## Coordination Chemistry of the Dithioether Ligand 5b

Preliminary studies demonstrated that dithioether compounds **5** can be used as chelating ligands to assemble heterodinuclear compounds.[35] Thus, reaction monitoring by IR spectroscopy revealed that treatment of dimeric $[Re(thf)(CO)_3(\mu\text{-}Br)]_2$ with 2 equiv. of **5b** in $CH_2Cl_2$ solution led to formation of the brick-red complex [Fc{C(S–*p*-tolyl)=C(S–*p*-tolyl)(H)}–Re(Br)(CO)$_3$] (**6**; Scheme 5) almost quantitatively, within 15 min. The facial arrangement of the carbonyl groups of air-stable **6** can be deduced from the observation of three ν(CO) vibrations in KBr at 2031, 1958 and 1930 cm$^{-1}$.

The rearrangement discussed above, which results in a (*Z*) substitution of C(11) and C(12) by S–*p*-tolyl groups, was corroborated by an X-ray diffraction study. Figure 5 reveals that the octahedral coordination around the Re centre is achieved by three carbonyl groups, a chelating dithioether ligand and a bromo ligand, thus conferring an 18-electron count at the Re$^{I}$ centre. The bromo substituent and the ferrocenyl moiety of the dithioether ligand are directed in the same sense. The dithioether ligand forms a five-membered ring with mean Re–S bond lengths of 2.4807 Å, which are somewhat shorter than those found for *fac*-[{$(PhSCH_2)_2SiPh_2$}Re(Br)(CO)$_3$] (2.515 Å).[36] Like in the latter compound, the aryl rings of the thioether groups are

 © 2007 Wiley-VCH Verlag GmbH & Co. KGaA, Weinheim 

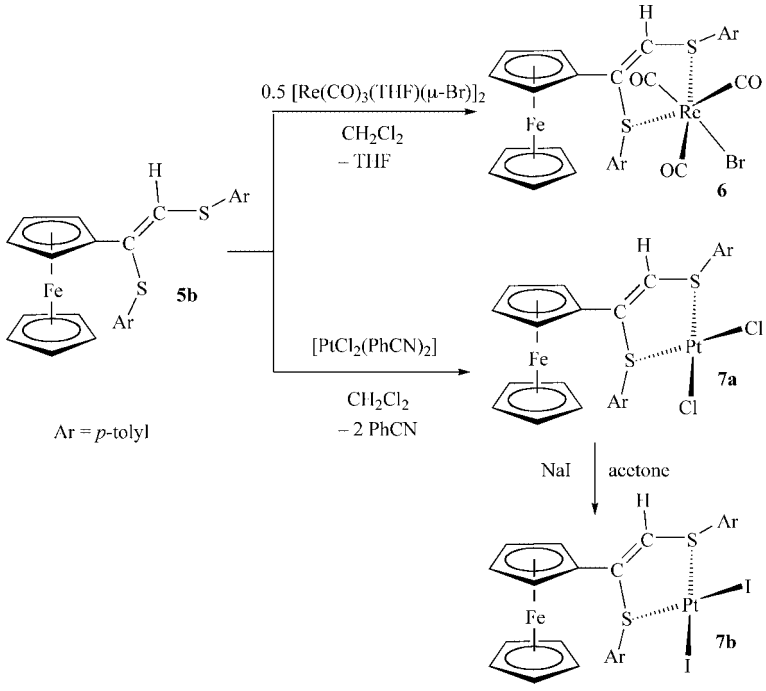


Scheme 5.

both *syn*-orientated and form a *meso* invertomer, although they point in the opposite direction to the bromo ligand.[36,37]

Similarly, treatment of $[PtCl_2(PhCN)_2]$ with a slight excess of **5b** yielded the brownish air-stable square-planar dithioether complex [Fc–{C(S–*p*-tolyl)=C(S–*p*-tolyl)-(H)}$PtCl_2$] (**7a**). The spectroscopic and elemental analysis data are in agreement with a bidentate chelating coordination mode of **5b** at the platinum atom, similar to that encountered in *cis*-$[MCl_2(MeSCH=CHSMe)]$ (M = Pd, Pt) and other related $Pd^{II}$ and $Pt^{II}$ compounds.[38] Metathesis with NaI in acetone solution converted **7a** into red-brown [Fc–{C(S–*p*-tolyl)=C(S–*p*-tolyl)(H)}$PtI_2$] (**7b**), whose $FAB^+$ mass spectrum displays the peak for the molecular ion. The $^1H$ NMR spectrum of **7a** recorded at 293 K displays a rather broad unresolved signal between $\delta$ = 4.80 and 4.10 ppm for the Cp resonances; the vinylic proton gives rise to a very broad hump centred at $\delta$ = 6.41 ppm. At 213 K, the vinylic proton appears sharper at $\delta$ = 6.54 ppm and the Cp protons give rise to several signals in the range $\delta$ = 4.58–3.92 ppm. This temperature-dependent behaviour is most probably due to a pyramidal inversion process operating for the two sulfur atoms that gives rise to *meso* and DL invertomers, as outlined in Scheme 6. Since this phenomenon has been studied by us and several other groups in the past,[20a,21a,36a,39] we did not undertake a detailed kinetic variable-temperature study. In contrast, the diiodo analogue **7b** displays well-resolved signals at room temperature, which barely sharpen upon heating to 313 K. This indicates a fast exchange such that only one "averaged planar" conformation is observed on the NMR timescale.

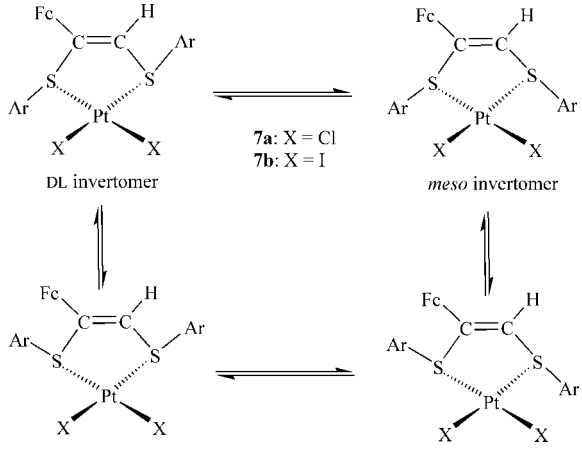


Scheme 6.

The vinylic proton signal at $\delta$ = 6.32 ppm exhibits a $^3J_{Pt,H}$ coupling of 73 Hz, and two distinct singlets are observed at $\delta$ = 2.41 and 2.34 ppm in a 1:1 ratio for the methyl groups of the *p*-tolyl rings. We and others have previously noted this finding for various $PtX_2$ complexes ligated with chelating dithioethers. The enhanced thermodynamic *trans* influence of I over Cl elongates the Pt–S bonds (as corroborated by several X-ray structures), and the concomitant weakening of the metal–sulfur bonds accounts for the lower activation barrier of the inversion process.[20a,20b,21,39]

## Electrochemistry

The anodic sweep of **1** in MeCN between –0.25 and +0.75 V vs. $Ag/Ag^+$ on a Pt electrode leads to a totally re-

 © 2007 Wiley-VCH Verlag GmbH & Co. KGaA, Weinheim 

versible peak in the cyclic voltammogram (CV), even for low scan rates (i.e. 100 mV s$^{-1}$). The separation between the anodic and cathodic peaks is about 60 mV, which indicates a fast electron transfer. The peak potential for **1** is about +0.25 V vs. Ag/Ag$^+$. In comparison with the corresponding peak values measured for the non-substituted ferrocene/ferrocenium couple ($E_p$ = 0.21 V vs. Ag/Ag$^+$) or the vinylferrocene/ferrocenium couple ($E_p$ = 0.24 V vs. Ag/Ag$^+$), the introduction of the CH=CBr$_2$ group does not significantly change the oxidation peak potential.[40a]

The CV of **2** in MeCN exhibits a reversible one-electron oxidation peak at +0.08 V vs. Ag/Ag$^+$ ($i_{pc}/i_{pa}$ = 1, $\Delta E$ = 60 mV; see Supporting Information). This oxidation is "easier" (i.e. occurs at lower positive potential) than that for precursor **1** due to the electronic communication with the electron-rich Pd(PPh$_3$)$_2$Br moiety. A contribution from a Pd(PPh$_3$)$_2$Br motif was recently observed in (vinylferrocene)Pd$^{II}$ complexes containing thiophene spacers of the type [(C$_5$H$_5$)Fe(C$_5$H$_4$CH=CH–th–Pd(PPh$_3$)$_2$(Br)] (th = 2,5-disubstituted thiophene).[41] The potentials of these complexes were reported to be lower than those without an end-capping Pd(PPh$_3$)$_2$Br unit, thereby implying the delocalisation of Pd electron density into the spacer chain through a dπ→pπ interaction. This behaviour is also observed for dithioether **5b**. The CV of **5b** between –0.25 and +0.50 V vs. Ag/Ag$^+$ on a Pt electrode at 100 mV s$^{-1}$ reveals the presence of a reversible peak also involving a fast electron transfer (see Supporting Information). Since this ferrocene derivative bears two electron-donating substituents, the oxidation is "easier" than that for **1**. The potential of the reversible peak for **5b** ($E_p$ = 0.19 V vs. Ag/Ag$^+$) is lower than that for **1**. Oxidation of **7a** between 0.00 and +0.60 V vs. Ag/Ag$^+$ on a platinum electrode at 100 mV s$^{-1}$ again leads to a reversible signal (see Supporting Information). Actually, the complexation of **5b** with a PtCl$_2$ fragment decreases the electronic density on the ferrocene moiety and the oxidation peak is therefore shifted towards higher oxidation potentials with respect to that for **1** and **5b**. The $E^0$ value ($E_p$ = 0.39 V vs. Ag/Ag$^+$) is larger than that for compound **1**. This behaviour is also observed for compound **6**. The $E^0$ value for the couple **6**/**6**$^{\cdot+}$ ($E_p$ = 0.33 V vs. Ag/Ag$^+$) is in the same range as that for the couple **7a**/**7a**$^{\cdot+}$ ($E_p$ = 0.39 V vs. Ag/Ag$^+$). A shift after complexation with metal centres has also been noted previously for other ferrocene-based thioether ligands.[35e]

The CV of **5b** between –0.40 and +2.00 V vs. Ag/Ag$^+$ on a Pt electrode at 100 mV s$^{-1}$ reveals a different shape of the voltammogram curve (Figure 6). Thus, we now observe three irreversible waves at 0.19, 1.16 and 1.29 V vs. Ag/Ag$^+$. The first irreversible wave corresponds to the oxidation of the ferrocene moiety. Surprisingly, the lifetime of the ferrocenium radical cation formed during the oxidation in this experiment is not long enough to be observed during the reversible scan. This behaviour is usually not observed for ferrocenium radical cations. This phenomenon is probably due to the low scan rate and the high value of the final potential. Partial peak reversibility is again observed when we increase the scan rate to 200 mV s$^{-1}$. The CV of **7a** between –0.40 and +2.00 V vs. Ag/Ag$^+$ at a Pt electrode at 100 mV s$^{-1}$ leads to a voltammogram similar to that of **5b** (see Supporting Information). However, the two irreversible peaks in this voltammogram obtained after oxidation of the two S-*p*-tolyl substituents are less well-defined than that for **5b**. Moreover, the ferrocenium radical cation of **7a** is more stable than the corresponding radical cation of **5b**. In fact, we observe a partial reversibility of the first oxidation peak, even at low scan rate (100 mV s$^{-1}$).

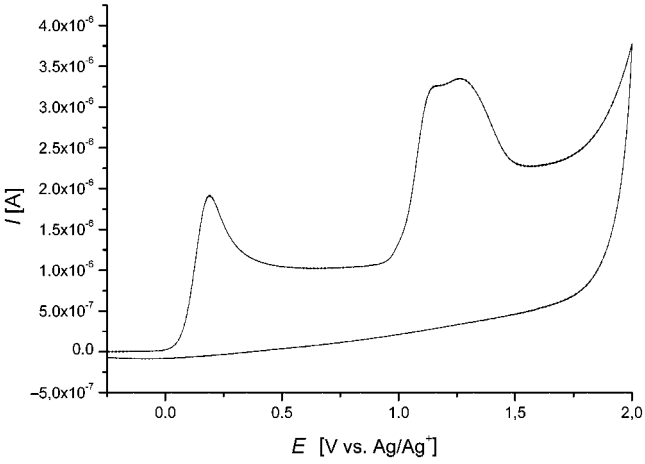


Figure 6. CV of **5b** (1 mM) in $CH_2Cl_2$ + $Bu_4NPF_6$ (0.1 M) at 100 mV s$^{-1}$ at a platinum electrode.

The same electrochemical measurements were also performed using glassy carbon electrodes. All voltammograms are very similar. The only difference observed between platinum and carbon electrodes concerns the value of $E_p$ (Table 1).

Table 1. Values of standard potentials or peak potentials for monomer/radical cation in dichloromethane (vs. Ag/Ag$^+$) deduced from CV measurements.

| Compound | $E_p$ [V] on Pt electrode | $E_p$ [V] on C electrode |
|---|---|---|
| **1** | 0.25 | 0.25 |
| **2** | | 0.08 |
| **5b** | 0.19, 1.16, 1.19 | 0.13, 1.21 |
| **6** | 0.33, 1.61 | 0.32, 1.59 |
| **7** | 0.39, 1.72 | 0.36, 1.59 |

### Solid-State Luminescence of 5b and 6

When excited at 270 nm, the solid-state emission spectra of **5b** and the heterometallic system **6** (Figure 7) at room temperature are quite similar, with a broad band at 668 and 670 nm, respectively. This band is tentatively assigned to an intraligand transition. More importantly, the incorporation of ferrocene and its derivatives in a luminescent system produced effective quenchers of excited states by energy-transfer processes.[42a] These compounds are known for their capacity to inhibit the lowest energy states of a number of molecules frequently used as photosensitizers.[42b,42c] This finding may also explain the luminescence quenching of the rhenium fragment in compound **6**.

 © 2007 Wiley-VCH Verlag GmbH & Co. KGaA, Weinheim 

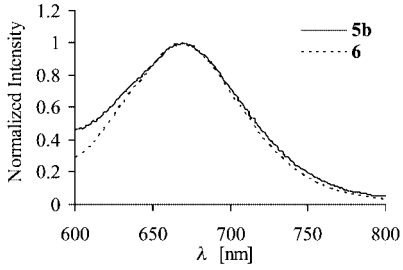


Figure 7. Corrected and normalised solid-state luminescence spectra recorded at room temperature for compounds **5b** (solid) and **6** (dotted).

## Conclusion and Perspectives

This study has demonstrated that the reactivity of **1** towards thiolates is not trivial. We are currently investigating these rearrangement reactions in more detail {isolation of intermediates, influence of temperature and solvent, utilisation of [$Cl_2C$=C(H)–Fc] instead of [$Br_2C$=C(H)–Fc] as starting material, use of other aromatic substrates such as (dibromovinyl)[2.2]paracyclophane, …} to develop a clear mechanistic understanding of these interesting transformations. Moreover, the preparation of π-conjugated thioether ligands **4** and **5** allows a promising development in organometallic coordination chemistry. We are currently working on the synthesis, reactivity and electrochemical investigation of other neutral and ionic complexes ligated by **4** and **5**. Furthermore, the substitution of the bromo substituents of **1** by $^-$OR, $^-NR_2$ or $^-PR_2$ may also lead to promising new ligand systems.

## Experimental Section

**General:** All reactions were performed using a conventional vacuum/argon line with standard Schlenk techniques. (2,2-Dibromovinyl)ferrocene (**1**), [$Pd(PPh_3)_4$], [$Re(\mu\text{-}Br)(CO)_3(thf)]_2$ and [$PtCl_2(PhCN)_2$] were prepared according to literature methods.[13,43] Thiophenol, *p*-thiocresol, 2-methyl-2-propanethiol and ethanethiol were purchased from commercial sources and used without further purification. All solvents were distilled from appropriate drying agents. IR spectra were recorded with a Nicolet Nexus 470 spectrometer. All NMR spectra were recorded in $CDCl_3$ with a Bruker AC 300 ($^1$H: 300.13 MHz; $^{13}$C: 75.48 MHz; $^{31}$P: 121.49 MHz) using the solvent as reference, except for $^{31}$P, where the chemical shifts are quoted relative to 85% $H_3PO_4$ in $D_2O$. UV/Vis spectra were recorded with a Varian Cary 50 spectrophotometer. The solid-state emission spectra were recorded at room temperature with a Jobin–Yvon Fluorolog-3 spectrometer using a cylindrical quartz capillary (diameter: 0.5 cm) with a scan speed of 1 nm s$^{-1}$. Intensity scales are presented in arbitrary units. The FAB$^+$ mass spectrum of **7b** was obtained with a VG Autospec spectrometer using NBA as matrix.

**Electrochemical Setup:** Analytical experiments were performed in a three-compartment cell fitted with an $AgClO_4$ (0.1 M in $CH_3CN$)| Ag reference electrode, a glassy carbon electrode (diameter: 3 mm) or a Pt electrode (diameter: 1 mm) and a platinum counter electrode. The electrochemical apparatus was an Autolab PGSTAT 20 Potentiostat Galvanostat (Ecochemie). The solvent was spectroscopic grade $CH_2Cl_2$ or acetonitrile with [$Bu_4N$][$PF_6$] (TBAF) as supporting electrolyte. The concentration of the monomeric substrate was $10^{-3}$ M. Under these conditions, the $E_{1/2}$ of $Cp_2Fe^{+/0}$ was found to be 0.21 V ± 0.01 V ($CH_2Cl_2$) vs. an Ag reference.

**Preparation of *trans*-[$(PPh_3)_2$PdBr{C(Br)=C(H)–Fc}] (2):** Compound **1** (185 mg, 0.5 mmol) was added to a suspension of [$Pd(PPh_3)_4$] (520 mg, 0.45 mmol) in toluene (15 mL) and the mixture was warmed to 60 °C for 1 d. The resulting clear, red solution was then concentrated to 8 mL and layered with heptane. Complex **2** crystallised as red needles after storing this solution in a refrigerator overnight. Yield: 76% (380 mg). $^1$H NMR: $\delta$ = 7.77 (m, 10 H, Ph), 7.17–7.41 (m, 20 H, Ph), 6.09 (s, 1 H, $H_{vinyl}$), 3.93 (m, 2 H, Cp), 3.81 (m, 2 H, Cp), 3.72 (s, 5 H, Cp) ppm. $^{31}$P{$^1$H} NMR: $\delta$ = 22.7 (s) ppm. UV/Vis ($CH_2Cl_2$): $\lambda_{max}$ ($\varepsilon$) = 229 nm (62800 M$^{-1}$ cm$^{-1}$), 310 (13100), 365 (13600). $C_{48}H_{40}Br_2FeP_2Pd$ (1000.9): calcd. C 57.60, H 4.03; found C 57.48, H 4.09.

**Typical Procedure for the Conversion of the Dibromo Olefin 1 into 4a–c and 5a–c:** Compound **1** (1 mmol) was stirred with an excess of thiolate (10 mmol) in dry dmf (10 mL) at room temperature for 1 d. The reaction mixture was then poured into water (10 mL). The organic layer was extracted with $Et_2O$ (2 × 25 mL), washed with brine (20 mL) and water (2 × 25 mL) and dried with $Na_2SO_4$. Evaporation of the solvents gave the crude products. Purification was carried out by chromatography on silica gel. In the case of treatment of **1** with 4 equiv. of thiolates, the ratios of thioether compounds **4a/3** and **4b/3** were both 25%/75%.

**FcCH=CH(SPh) (4a):** Eluent: $CH_2Cl_2$/petroleum ether (1:9). M.p. 50 °C. $^1$H NMR: $\delta$ = 7.25–7.52 (m, 5 H, Ph), 6.35 (d, $^3J_{H,H}$ = 10.1 Hz, 1 H, $H_{A,vinyl}$), 6.26 (d, $^3J_{H,H}$ = 10.1 Hz, 1 H, $H_{B,vinyl}$), 4.62 (br. s, 2 H), 4.27 (br. s, 2 H, Cp), 4.16 (s, 5 H, Cp) ppm. $^{13}$C{$^1$H} NMR: $\delta$ = 68.9, 69.2, 69.3, 80.8 (*Cp*HC=), 121.0 (CpH*C*=), 126.5, 126.8, 129.0, 129.3 [C-14, C-15, C-16, C-17, C-18, =*C*H(SPh)], 136.6 (C-13) ppm. $C_{18}H_{16}FeS$ (320.23): calcd. C 67.51, H 5.04, S 10.01; found C 67.42, H 5.74, S 9.80.

**FcCH=CH(S*t*Bu) (4b):** Eluent: $CH_2Cl_2$/petroleum ether (1:9). Yield: 52% (156 mg). M.p. 50–52 °C. $^1$H NMR: $\delta$ = 6.19 (d, $^3J_{H,H}$ = 10.0 Hz, 1 H, $H_{A,vinyl}$), 6.11 (d, $^3J_{H,H}$ = 10.0 Hz, 1 H, $H_{B,vinyl}$), 4.58 (br. s, 2 H, Cp), 4.23 (br. s, 2 H, Cp), 4.15 (s, 5 H, Cp), 1.43 (s, 9 H, $CH_3$) ppm. $^{13}$C{$^1$H} NMR: $\delta$ = 30.9 ($CH_3$), 43.8 [*C*-($CH_3$)$_3$], 68.5, 69.1, 69.2, 81.9 (*Cp*HC=), 119.5 (CpH*C*=), 124.1 [=*C*H(S*t*Bu)] ppm. UV/Vis ($CH_2Cl_2$): $\lambda_{max}$ ($\varepsilon$) = 229 (16200), 251 (10500), 298 (9100), 351 (7100), 452 nm (3900 M$^{-1}$ cm$^{-1}$). $C_{16}H_{20}FeS$ (300.23): calcd. C 64.00, H 6.67, S 10.67; found C 63.98, H 6.58, S 10.62.

**FcCH=CH(SEt) (4c):** Eluent: petroleum ether. M.p. 38–39 °C. $^1$H NMR: $\delta$ = 6.14 (d, $^3J_{H,H}$ = 10.4 Hz, 1 H, $H_{A,vinyl}$), 5.95 (d, $^3J_{H,H}$ = 10.4 Hz, 1 H, $H_{B,vinyl}$), 4.32 (br. s, 2 H, Cp), 4.24 (br. s, 2 H, Cp), 4.12 (s, 5 H, Cp), 2.75 (q, $^3J_{H,H}$ = 7.4 Hz, 2 H, SC$H_2$CH$_3$), 1.22 (t, $^3J_{H,H}$ = 7.4 Hz, 2 H, SCH$_2$C$H_3$) ppm. UV/Vis ($CH_2Cl_2$): $\lambda_{max}$ ($\varepsilon$) = 229 (11500), 250 (9200), 298 (10900), 351 (550), 452 nm (350 M$^{-1}$ cm$^{-1}$). $C_{14}H_{16}FeS$ (272.18): calcd. C 61.76, H 5.88, S 11.76; found C 61.68, H 5.73, S 11.67.

**Alternative Preparation of 4a and 4c:** Ethynylferrocene (210 mg, 1 mmol) was added to a stirred solution of thiolate (10 mmol) in dmf (10 mL). The solution was stirred at room temperature for 1 d and then poured into water. The organic layer was extracted with diethyl ether, washed with water (5 mL) and brine (2 × 5 mL) and dried with $Na_2SO_4$. Solvent evaporation provided the crude products. Column chromatography with petroleum ether as eluent afforded 207 mg of **4a** (yield: 76%) and 249 mg of **4c** (yield: 78%).

**FcC(SPh)=CH(SPh) (5a):** Obtained by column chromatography on silica gel with petroleum ether as eluent (197 mg, 46%). $^1$H NMR:

 © 2007 Wiley-VCH Verlag GmbH & Co. KGaA, Weinheim 

$\delta$ = 4.17 (s, 5 H, Cp), 4.23 (s, 2 H, Cp), 4.48 (br. s, 2 H, Cp), 7.13 (s, 1 H, $H_{vinyl}$), 7.23–7.52 (m, 10 H, Ph) ppm. $^{13}C\{^1H\}$ NMR: $\delta$ = 69.3, 69.8, 70.1 (C-1–C-9), 79.7 (C-10), 123.5, 125.6, 127.1, 127.3, 127.4, 129.0, 129.2, 129.9, 130.1, 130.7, 132.2, 134.7, 135.0, 135.5, 135.9, 141.2 (C-11–C-24) ppm. $C_{24}H_{20}FeS_2$ (428.39): calcd. C 67.29, H 4.67, S 14.95; found C 67.18, H 4.59, S 14.83.

**FcC(S–*p*-tolyl)=CH(S–*p*-tolyl) (5b):** Eluent: petroleum ether/$CH_2Cl_2$ (9:1). Yield: 51% (230 mg). M.p. 135–136 °C. $^1H$ NMR: $\delta$ = 7.30–7.00 (m, 9 H, $C_6H_4$ + $H_{vinyl}$), 4.40 (br. s, 2 H, Cp), 4.15 (br. s, 2 H, Cp), 4.09 (s, 5 H, Cp), 2.31 (s, 3 H, $CH_3$), 2.24 (s, 3 H, $CH_3$) ppm. $^{13}C\{^1H\}$ NMR: $\delta$ = 21.3, 21.4 ($CH_3$), 67.2, 69.2, 69.9 (Cp), 87.5 (CpH*C*=), 128.0, 128.1, 128.9, 130.1, 130.3, 130.9, 132.4, 132.8, 133.2, 135.8 ($C_6H_4$), 137.7 [=*C*($SC_6H_4CH_3$)$_2$] ppm. UV/Vis ($CH_2Cl_2$): $\lambda_{max}$ ($\varepsilon$) = 229 (64100), 257 (32200), 330 nm (9100 $M^{-1}cm^{-1}$). $C_{26}H_{24}FeS_2$ (456.44): calcd. C 68.42, H 5.30, S 14.05; found C 68.48, H 5.38, S 14.12.

**FcC(SEt)=CH(SEt) (5c):** Obtained by column chromatography on silica gel with petroleum ether as eluent (134 mg, 22%). $^1H$ NMR: $\delta$ = 6.26 (s, 1 H, $H_{vinyl}$), 4.53 (br., 2 H, Cp), 4.29 (s, 2 H, Cp), 4.11 (s, 5 H, Cp), 2.85 (m, 4 H, S*C*$H_2$CH$_3$), 2.77 (m, 4 H, SC$H_2$CH$_3$), 1.29 (m, 3 H, $SCH_2CH_3$), 1.27 (m, 3 H, $SCH_2CH_3$) ppm. $C_{16}H_{20}FeS_2$ (332.31): calcd. C 57.83, H 6.07, S 19.30; found C 57.78, H 5.93, S 19.18.

**[FcC(S–*p*-tolyl)=C(H)(S–*p*-tolyl)$_2$Re(Br)(CO)$_3$] (6):** [Re(μ-Br)(CO)$_3$-(thf)]$_2$ (127 mg, 0.15 mmol) was added in several portions to a solution of **5b** (136 mg, 0.3 mmol) in $CH_2Cl_2$ (5 mL). The reaction mixture was stirred at room temperature for 2 h and then concentrated to 3 mL under reduced pressure. Layering with heptane gave red needles after several days at 5 °C. Yield: 92% (119 mg). IR (KBr): ν(CO) = 2031 (vs), 1958 (s), 1931 (vs) $cm^{-1}$. $^1H$ NMR: $\delta$ = 7.37–7.27 (m, 8 H, $C_6H_4$), 7.07 (s, 1 H, $H_{vinyl}$), 4.83 s, (br., 2 H, Cp), 4.45 (br. s, 2 H, Cp), 4.55 (s, 5 H, Cp), 2.40 (s, 3 H, $CH_3$), 2.37 (s, 3 H, $CH_3$) ppm. UV/Vis ($CH_2Cl_2$): $\lambda_{max}$ ($\varepsilon$) = 231 (47800), 300 (16100), 382 (2200), 482 nm (1700 $M^{-1}cm^{-1}$). $C_{29}H_{24}BrFeReO_3S_2{\cdot}0.5CH_2Cl_2$ (849.09): calcd. C 41.72, H 2.95; found C 41.85, H, 3.00.

**[FcC(S–*p*-tolyl)=C(H)(S–*p*-tolyl)PtCl$_2$] (7a):** [$PtCl_2$(PhCN)$_2$] (127 mg, 0.3 mmol) was added in several portions to a solution of **5b** (136 mg, 0.3 mmol) in $CH_2Cl_2$ (8 mL). The reaction mixture was stirred at room temperature for 4 h and then concentrated to 5 mL under reduced pressure. Addition of light petroleum gave an orange powder, which was filtered off and dried under vacuum. Yield: 91% (197 mg). $^1H$ NMR (213 K): $\delta$ = 7.79–7.30 (m, 8 H, $C_6H_4$), 6.54 (br. s, 1 H, $H_{vinyl}$), 4.58–3.92 (m, 9 H, Cp), 2.40 (br. s, 3 H, $CH_3$), 2.36 (br. s, 3 H, $CH_3$) ppm. UV/Vis ($CH_2Cl_2$): $\lambda_{max}$ ($\varepsilon$) = 228 (69500), 295 (20200), 382 (2400), 487 nm (1600 $M^{-1}cm^{-1}$). $C_{26}H_{24}Cl_2FePtS_2$ (722.43): calcd. C 43.23, H 3.35, S 8.88; found C 43.02, H 3.12, S 8.54.

**[FcC(S–*p*-tolyl)=C(H)(S–*p*-tolyl)PtI$_2$] (7b):** NaI (150 mg, 10 mmol) was added to a solution of **7a** (72 mg, 0.1 mmol) in acetone (5 mL). The reaction mixture was stirred at room temperature for 1 d and then the solvent was evaporated under reduced pressure. Extraction of the crude product with $CH_2Cl_2$ (4 mL) and addition of heptane gave an orange powder, which was filtered off and dried under vacuum. Yield: 90% (76 mg). $^1H$ NMR: $\delta$ = 7.68–7.19 (m, 8 H, $C_6H_4$), 6.32 (br. s, $^3J_{Pt,H}$ = 73 Hz, 1 H, $H_{vinyl}$), 4.53–4.09 (m, 9 H, Cp), 2.41 (s, 3 H, $CH_3$), 2.34 (s, 3 H, $CH_3$) ppm. FAB$^+$ (NBA): *m*/*z* = 906.1 [M$^+$]. $C_{26}H_{24}FeI_2PtS_2$ (905.34): calcd. C 34.49, H 2.67; found C 34.12, H 2.76.

**X-ray Crystallography:** Crystal data and experimental details are given in Table 2. Data for **2** and **6** were collected with a Stoe IPDS diffractometer at 173(2) (**2**) and 193(2) K (**6**). The intensities were determined and corrected with the program INTEGRATE in IPDS (Stoe & Cie, 1999). An empirical absorption correction was employed using the FACEIT program in IPDS (Stoe & Cie, 1999). Data for **1** and **4b**,**c** were collected with a Bruker APEX-CCD (D8

Table 2. X-ray crystallographic and refinement data for **1**, **2**, **4b**, **4c** and **6**.

| | **1** | **2** | **4b** | **4c** | **6** |
|---|---|---|---|---|---|
| Empirical formula | $C_{12}H_{10}Br_2Fe$ | $C_{48}H_{40}Br_2FeP_2Pd$ | $C_{16}H_{20}FeS$ | $C_{14}H_{16}FeS$ | $C_{29}H_{24}BrFeO_3ReS_2$ |
| Formula mass [g mol$^{-1}$] | 369.87 | 1000.81 | 300.23 | 272.18 | 806.56 |
| $T$ [K] | 173(2) | 173(2) | 193(2) | 173(2) | 193(2) |
| Crystal system | orthorhombic | monoclinic | monoclinic | monoclinic | monoclinic |
| Space group | *Pbca* | $P2_1/n$ | $P2_1/n$ | $C2/c$ | $P2_1/c$ |
| $a$ [Å] | 7.5029(5) | 20.385(5) | 5.9214(12) | 31.07(3) | 10.169(2) |
| $b$ [Å] | 17.1025(11) | 7.6128(12) | 10.199(2)° | 10.509(6) | 25.404(5) |
| $c$ [Å] | 18.1892(12) | 29.280(5) | 12.232(2)° | 7.457(9) | 11.609(2) |
| $\beta$ [°] | 90 | 109.21(3) | 96.88 | 91.42(3) | 107.25(3) |
| $V$ [Å$^3$] | 2334.0(3) | 4035.4(14) | 733.4(3) | 2463(4) | 2864.2(10) |
| $Z$ | 8 | 4 | 2 | 8 | 4 |
| $\rho_{calcd.}$ [Mg m$^{-3}$] | 2.105 | 1.647 | 1.359 | 1.468 | 1.870 |
| $\mu$ [mm$^{-1}$] | 8.101 | 2.899 | 1.150 | 1.362 | 6.298 |
| $F$(000) | 1424 | 2000 | 316 | 1136 | 1560 |
| $\Theta$ range [°] | 2.24–26.43 | 2.39 –25.00 | 2.61–25.00 | 1.31–26.99 | 2.10–26.99 |
| Index ranges | $-9 \le h \le 9$ | $-10 \le h \le 10$ | $-7 \le h \le 7$ | $-39 \le h \le 39$ | $-12 \le h \le 12$ |
| | $-21 \le k \le 21$ | $-45 \le k \le 45$ | $-12 \le k \le 12$ | $-13 \le k \le 13$ | $-29 \le k \le 32$ |
| | $-22 \le l \le 22$ | $-14 \le l \le 14$ | $-14 \le l \le 14$ | $-9 \le l \le 9$ | $-14 \le l \le 8$ |
| Collected reflections | 46927 | 24804 | 6312 | 16681 | 12577 |
| Independent reflections | 2409 [$R$(int) = 0.0430] | 7081 [$R$(int) = 0.0654] | 2559 [$R$(int) = 0.0515] | 2693 [$R$(int) = 0.0287] | 6127 [$R$(int) = 0.0529] |
| Data/restraints/parameters | 2409/0/136 | 7081/0/487 | 2559/1/166 | 2693/0/146 | 6127/0/336 |
| Largest difference peak/hole [e Å$^{-3}$] | 0.663 and –0.377 | 1.027 and –1.036 | 0.8026 and 0.6562 | 0.7724 and 0.6119 | 1.704 and –1.816 |
| Final $R$ indices [$I > 2\sigma(I)$] | $R_1$ = 0.0260 | $R_1$ = 0.0517 | $R_1$ = 0.0551 | $R_1$ = 0.0335 | $R_1$ = 0.0474 |
| | $wR_2$ = 0.0622 | $wR_2$ = 0.1296 | $wR_2$ = 0.1410 | $wR_2$ = 0.0952 | $wR_2$ = 0.1140 |
| $R$ indices (all data) | $R_1$ = 0.0327 | $R_1$ = 0.0726 | $R_1$ = 0.0586 | $R_1$ = 0.0370 | $R_1$ = 0.0646 |
| | $wR_2$ = 0.0652 | $wR_2$ = 0.1412 | $wR_2$ = 0.1445 | $wR_2$ = 0.1058 | $wR_2$ = 0.1212 |
| GOF on $F^2$ | 1.067 | 1.045 | 1.023 | 1.027 | 1.036 |

 © 2007 Wiley-VCH Verlag GmbH & Co. KGaA, Weinheim 

three-circle goniometer, Bruker AXS) at 173(2) K; data collection, cell determination and refinement: Smart version 5.622 (Bruker AXS, 2001); integration: SaintPlus version 6.02 (Bruker AXS, 1999); empirical absorption correction: Sadabs version 2.01 (Bruker AXS, 1999). All structures were solved applying direct and Fourier methods, using SHELXS-90 and SHELXL-97.[44] For each structure, the non-hydrogen atoms were refined anisotropically. All of the hydrogen atoms were placed in geometrically calculated positions and each was assigned a fixed isotropic displacement parameter based on a riding model. Refinement of the structures was carried out by full-matrix least-squares methods based on $F_o^2$ using SHELXL-97. CCDC-644866 to -644869 (for **1**, **2**, **4c**, **6**), -646158 (for **3**), and -650184 (for **4b**) contain the supplementary crystallographic data for this paper. These data can be obtained free of charge from The Cambridge Crystallographic Data Centre via www.ccdc.cam.ac.uk/data_request/cif.

**Supporting Information** (see footnote on the first page of this article): Crystallographic data and view of the structure and packing of **3** (Figure S1). Cyclic voltammograms of **2**, **5b** and **7a** are depicted in Figures S2–S5. Figures S6–S10 show the thermal ellipsoid plots of **1**, **2**, **4b**, **4c** and **6**. The NOESY $^1$H NMR spectrum of **4a** is shown in Figure S11.

## Acknowledgments

We are grateful to the French Ministère de la Recherche et Technologie for a PhD grant for S. C. Financial support from the Région of Franche-Comté for the fluorescence spectrometer is also gratefully acknowledged. We thank Dr. A. Khatyr for recording the emission spectra and Dr. Harmel N. Peindy (University of Bochum, Germany) for recording the FAB$^+$ mass spectrum of **7b**.

[1] a) K. Schlögl, H. Egger, *Monatsh. Chem.* **1963**, *94*, 376–392; b) J.-G. Rodriguez, A. Oñate, R. M. Martin-Villamil, I. Fonseca, *J. Organomet. Chem.* **1996**, *513*, 71–76.

[2] a) M. Akita, M. Terada, M. Tanaka, Y. Moro-Oka, *Organometallics* **1992**, *11*, 3468–3472; b) K. Onitsuka, X.-Q. Tao, K. Sonogashira, *Bull. Chem. Soc. Jpn.* **1994**, *104*, 893–894.

[3] R. Wiedemann, R. Fleischer, D. Stalke, H. Werner, *Organometallics* **1997**, *16*, 866–870.

[4] a) E. Rüba, K. Mereiter, R. Schmid, K. Kirchner, H. Schottenberger, *J. Organomet. Chem.* **2001**, *637–639*, 70–74; b) M. V. Russo, A. Furlani, S. Licoccia, R. Paolese, A. C. Villa, C. Guastini, *J. Organomet. Chem.* **1994**, *469*, 245–452.

[5] a) P. Mathur, S. Chatterjee, A. Das, G. K. Lahiri, S. Maji, S. M. Mobin, *J. Organomet. Chem.* **2007**, *692*, 1601–1607; b) U. Siemeling, K. Bausch, H. Fink, C. Bruhn, M. Baldus, B. Angerstein, R. Plessow, A. Brockhinke, *Dalton Trans.* **2005**, 2365–2374; c) Y. Tanaka, T. Ozawa, A. Inagaki, M. Akita, *Dalton Trans.* **2007**, 928–933.

[6] A. J. Deeming, M. S. B. Felix, D. Nuel, N. I. Powell, D. A. Tocher, *J. Organomet. Chem.* **1990**, *384*, 181–191.

[7] J. Buchweitz, R. Gompper, K. Polborn, M.-T. Sailer, C. Robl, W. Weigand, *Chem. Ber.* **1994**, *127*, 23–26.

[8] J. Mata, S. Uriel, E. Peris, R. Llusar, S. Houbrechts, A. Persoons, *J. Organomet. Chem.* **1998**, *562*, 197–202.

[9] a) G. A. V. R. Toreki, R. R. Schrock, W. M. Davis, *J. Am. Chem. Soc.* **1993**, *115*, 127–137; b) I. R. Butler, S. J. Coles, M. B. Hursthouse, D. J. Roberts, N. Fujimoto, *Inorg. Chem. Commun.* **2003**, *6*, 760–762.

[10] S. Özkar, C. Kayran, N. Demir, *J. Organomet. Chem.* **2003**, *688*, 62–67.

[11] a) M. Knorr, I. Jourdain, G. Crini, K. Frank, H. Sachdev, C. Strohmann, *Eur. J. Inorg. Chem.* **2002**, 2419–2426; b) D. Evrard, S. Clément, D. Lucas, B. Hanquet, M. Knorr, C. Strohmann, A. Decken, Y. Mugnier, P. D. Harvey, *Inorg. Chem.* **2006**, *45*, 1305–1315; c) S. Clément, L. Guyard, M. Knorr, S. Dilsky, C. Strohmann, M. Arroyo, *J. Organomet. Chem.* **2007**, *692*, 839–850.

[12] B. Pedersen, G. Wagner, R. Herrmann, W. Scherer, K. Meerholz, E. Schmälzlin, C. Bräuchle, *J. Organomet. Chem.* **1999**, *590*, 129–137.

[13] N. Tsuboya, R. Hamasaki, M. Ito, M. Mitsuishi, T. Miyashita, Y. Yamamoto, *J. Mater. Chem.* **2003**, *13*, 511–513.

[14] P. Fitton, J. E. McKeon, *J. Chem. Soc. Chem. Commun.* **1968**, 4–6.

[15] M. Knorr, G. Schmitt, M. M. Kubicki, E. Vigier, *Eur. J. Inorg. Chem.* **2003**, 514–517.

[16] A. Ariafard, Z. Lin, *Organometallics* **2006**, *25*, 4030–4033.

[17] A. Jutand, S. Négri, *Organometallics* **2003**, *22*, 4229–4237.

[18] J. F. Fauvarque, A. Jutand, *J. Organomet. Chem.* **1981**, *209*, 109–114.

[19] a) C. Strohmann, S. Lüdtke, O. Ulbrich, *Organometallics* **2000**, *19*, 4223–4227; b) C. Strohmann, *Chem. Ber.* **1995**, *128*, 167–172; c) C. Strohmann, S. Lüdtke, E. Wack, *Chem. Ber.* **1996**, *129*, 799–805; d) C. Strohmann, E. Wack, *Z. Naturforsch. Teil B* **2004**, *59*, 1570–1578.

[20] a) M. Knorr, H. N. Peindy, F. Guyon, H. Sachdev, C. Strohmann, *Z. Anorg. Allg. Chem.* **2004**, *630*, 1955–1961; b) H. N. Peindy, F. Guyon, M. Knorr, A. B. Smith, J. A. Farouq, S. A. Islas, D. Rabinovich, J. A. Golen, C. Strohmann, *Inorg. Chem. Commun.* **2005**, *8*, 479–482; c) A. Hameau, F. Guyon, M. Knorr, M. Enescu, C. Strohmann, *Monatsh. Chem.* **2006**, *137*, 545–555.

[21] a) H. N. Peindy, F. Guyon, I. Jourdain, M. Knorr, D. Schildbach, C. Strohmann, *Organometallics* **2006**, *25*, 1472–1479; b) H. N. Peindy, F. Guyon, A. Khatyr, M. Knorr, C. Strohmann, *Eur. J. Inorg. Chem.* **2007**, 1823–1828.

[22] a) S. Jacquot-Rousseau, A. Khatyr, G. Schmitt, M. Knorr, M. M. Kubicki, O. Blacque, *Inorg. Chem. Commun.* **2005**, *8*, 610–613; b) S. Jacquot-Rousseau, G. Schmitt, A. Khatyr, G. Schmitt, M. Knorr, E. Vigier, M. M. Kubicki, O. Blacque, *Eur. J. Org. Chem.* **2006**, 1555–1562.

[23] The crystal structure of **3** has already been reported in two different contexts: (i) at low temperature in the search for a typical hydrogen bonding and (ii) at room temperature where **3** is considered as a promising synthon for oligonuclear synthesis: a) T. Steiner, M. Tamm, A. Grzegorzewski, N. Schulte, N. Veldman, A. M. M. Schreurs, J. A. Kanters, J. Kroon, J. van der Maas, B. Lutz, *J. Chem. Soc. Perkin Trans. 2* **1996**, 2441–2446; b) K. Wurst, O. Elsner, H. Schottenberger, *Synlett* **1995**, 833–834.

[24] Because there is no direct description of the molecular structure in ref.[23], some metric parameters along with the crystal data are given in the Supporting Information.

[25] a) T. K. Berestneva, M. Martínez García, L. Ortiz-Frade, S. Hernández-Ortega, R. A. Toscano, E. I. Klimova, *J. Organomet. Chem.* **2006**, *691*, 2872–2882; b) T. K. Berestneva, E. I. Klimova, J. M. Méndez-Stivalet, S. Hernández Ortega, M. Martínez García, *Eur. J. Org. Chem.* **2005**, 4406–4413.

[26] W. E. Truce, G. J. W. Tichenor, *J. Org. Chem.* **1972**, *37*, 2391–2396.

[27] W. E. Truce, R. F. Heine, *J. Am. Chem. Soc.* **1959**, *81*, 592–594.

[28] a) V. I. Laba, A. V. Sviridova, A. A. Kron, V. N. Dudnikova, E. N. Prilezhaeva, *Izv. Akad. Nauk SSSR, Ser. Khim.* **1974**, 2874–2877 (*Chem. Abstr.* **1975**, *82*, 86021); b) V. I. Laba, A. V. Sviridova, A. A. Kron, E. N. Prilezhaeva, *Izv. Akad. Nauk SSSR, Ser. Khim.* **1977**, 1566–1573 (*Chem. Abstr.* **1977**, *87*, 133437).

[29] a) L. K. Liu, F.-T. Luo, S.-Y. Shia, *J. Chin. Chem. Soc.* **1982**, 21–27; b) M. T. Omar, M. N. Basyouni, *Bull. Chem. Soc. Jpn.* **1974**, *47*, 2325–2326.

[30] P. Beltrame, P. L. Beltrame, M. G. Cattania, M. Simonetta, *J. Chem. Soc. Perkin Trans. 2* **1973**, 63–66.

 © 2007 Wiley-VCH Verlag GmbH & Co. KGaA, Weinheim 

[31] a) Y. Misumi, H. Seino, Y. Mizobe, *J. Organomet. Chem.* **2006**, *691*, 3157–3164; b) A. Ogawa, T. Ikeda, K. Kimura, T. Hirao, *J. Am. Chem. Soc.* **1999**, *121*, 5108–5114.

[32] The same rearrangement reaction has been encountered upon treatment of (dibromovinyl)[2.2]paracyclophane with an excess of sodium *p*-toluenethiolate, which affords the crystallographically characterised dithioether compound (*Z*)-[(*p*-tol–S)(H)C=C(S–*p*-tol)(PCP)] (PCP = [2.2]paracyclophane) (S. Clément, M. Knorr, L. Guyard, C. Strohmann, manuscript in preparation).

[33] W. E. Truce, M. M. Boudakian, *J. Am. Chem. Soc.* **1956**, *78*, 2748–2751.

[34] a) S. Tanimoto, R. Taniyasu, T. Takahashi, T. Miyake, M. Okano, *Bull. Chem. Soc. Jpn.* **1976**, *49*, 1931–1936; b) for the substitution mechanism of haloalkenes by thiolates, see also: M. Beit-Yannai, Z. Rappoport, B. A. Shainyan, Y. S. Danilevich, *J. Org. Chem.* **1997**, *62*, 8049–8057.

[35] For other examples of heterometallic complexes assembled from ferrocene-based thioether ligands, see: a) B. McCulloch, D. L. Ward, J. D. Woolins, C. H. Brubaker, *Organometallics* **1985**, *4*, 1425–1432; b) E. W. Abel, N. J. Long, K. G. Orrell, A. G. Osborne, V. Sik, *J. Organomet. Chem.* **1989**, *367*, 275–289; c) P. D. Beer, J. E. Nation, M. E. Harman, M. Hursthouse, *J. Organomet. Chem.* **1992**, *441*, 465–477; d) V. C. Gibson, N. J. Long, A. J. P. White, C. K. Williams, D. J. Williams, *Organometallics* **2000**, *19*, 4425–4428; e) K. Bushell, C. Gialou, C. H. Goh, N. J. Long, J. Martin, A. J. P. White, C. K. Williams, D. J. Williams, M. Fontani, P. Zanello, *J. Organomet. Chem.* **2001**, *637–639*, 418–425; f) V. C. Gibson, N. J. Long, C. K. Williams, M. Fontani, P. Zanello, *Dalton Trans.* **2003**, 3599–3605; g) R. C. J. Atkinson, V. C. Gibson, N. J. Long, L. J. West, A. P. White, *Dalton Trans.* **2006**, 3597–3602; h) K. Sünkel, U. Birk, A. Blum, W. Kempinger, *J. Organomet. Chem.* **1994**, *465*, 167–174.

[36] a) M. Knorr, S. Kneifel, C. Strohmann, in *Organosilicon Chemistry III: From Molecules to Materials* (Eds.: N. Auner, J. Weis), Wiley-VCH, Weinheim, **1998**, pp. 211–216; b) M. Knorr, F. Guyon, I. Jourdain, S. Kneifel, J. Frenzel, C. Strohmann, *Inorg. Chim. Acta* **2003**, *350*, 455–466.

[37] a) E. W. Abel, R. Corben, I. Moss, K. G. Orrell, N. R. Richardson, V. Sik, *J. Organomet. Chem.* **1988**, *344*, 343–350; b) S. Murray, F. R. Hartley, *Chem. Rev.* **1981**, *81*, 365–414.

[38] a) C. A. McAuliffe, S. G. Murray, *Inorg. Nucl. Chem. Lett.* **1976**, *12*, 897–898; b) T. A. K. Al-Allaf, N. H. Buttrus, P. B. Hitchcock, *Asian J. Chem.* **1997**, *9*, 187–194; c) E. W. Abel, S. K. Bhargawa, K. Kite, K. G. Orrell, V. Sik, *Polyhedron* **1982**, *1*, 289–298; d) E. W. Abel, K. Kite, B. L. Williams, *J. Chem. Soc. Dalton Trans.* **1983**, 1017–1018.

[39] a) K. G. Orrell, V. Sik, C. H. Brubaker, B. McCulloch, *J. Organomet. Chem.* **1984**, *276*, 267–279; b) F. R. Hartley, S. G. Murray, W. Levason, H. E. Soutter, C. A. McAuliffe, *Inorg. Chim. Acta* **1979**, *35*, 265–277.

[40] a) P. Zanello, G. Opromolla, G. Giorgi, G. Sasso, A. Togni, *J. Organomet. Chem.* **1996**, *506*, 61–65; b) for another electrochemical study of vinylferrocene, see: H. Scholl, K. Sochaj, *Electrochim. Acta* **1991**, *36*, 689–694.

[41] K. R. J. Thomas, J. T. Lin, K.-J. Lin, *Organometallics* **1999**, *18*, 5285–5291.

[42] a) G. L. Geoffroy, M. S. Wrighton, *Organometallic Photochemistry*, Academic Press, New York, **1979**; b) K. L. Cunningham, D. R. McMillin, *Inorg. Chem.* **1998**, *37*, 4114–4119; c) J. M. Bevilacqua, R. Eisenberg, *Inorg. Chem.* **1994**, *33*, 1886–1890.

[43] a) D. R. Coulson, *Inorg. Synth.* **1972**, *13*, 121–122; b) D. Vitali, F. Calderazzo, *Gazz. Chim. Ital.* **1972**, *102*, 587–596.

[44] a) G. M. Sheldrick, *SHELXS-90*, University of Göttingen, **1990**; b) G. M. Sheldrick, *SHELXL97*, University of Göttingen, **1997**.

Received: May 2, 2007
Published Online: September 14, 2007

 © 2007 Wiley-VCH Verlag GmbH & Co. KGaA, Weinheim 

DOI: 10.1002/ejic.200700598

# Electrochemical Synthesis of Mono- and Disubstituted Diiron Dithiolate Complexes as Models for the Active Site of Iron-Only Hydrogenases

**Didier Morvan,[a] Jean-François Capon,[a] Frederic Gloaguen,*[a] Philippe Schollhammer,[a] and Jean Talarmin[a]**

**Keywords:** Biomimetic catalysis / Iron-only hydrogenases / Diiron dithiolate / CO substitution / Electrochemistry / Proton reduction

$[Fe_2(S_2C_3H_6)(CO)_5\{P(OMe)_3\}]$ (**2**) and $[Fe_2(S_2C_3H_6)(CO)_4\{P(OMe)_3\}_2]$ (**3**) were selectively prepared by the electrochemical reduction of $[Fe_2(S_2C_3H_6)(CO)_6]$ (**1**) in the presence of trimethyl phosphite ligand. Electrochemical data indicate a CO-displacement reaction catalyzed by electron transfer. Complexes **2** and **3** were characterized by X-ray crystallography, which shows that in the solid state, the trimethyl phosphite ligands lie in the apical configuration. NMR suggests that multiple isomers exist in solution. Both **2** and **3** exhibit a primary reduction step that involves two electrons. No stable hydride derivatives could be isolated by the reaction of **2** or **3** with strong acid. However, for both **2** and **3**, proton reduction catalysis was detected at a potential less negative than that of the reduction of the diiron complex working as catalyst. The proposed mechanism involves a protonation of the diiron complex in the vicinity of the electrode, which is triggered by the more facile reduction of the protonated form (CE mechanism). The protonation and reduction steps are followed by a bimolecular reaction that regenerates the starting complex.
(© Wiley-VCH Verlag GmbH & Co. KGaA, 69451 Weinheim, Germany, 2007)

## Introduction

Hydrogenases are nickel- and iron-based enzymes that control the hydrogen production and uptake in a wide variety of microorganisms. These biomolecules have long interested biologists and chemists, as they might hold the key to a competitive hydrogen economy.[1] Recently, the active site of the iron-only hydrogenases was structurally characterized and shown to contain a dithiolate-bridged diiron moiety with carbonyl and cyanido ligands.[2] This has opened the way for the synthesis of organometallic models that could eventually work as cheap and efficient proton reduction catalysts.[3–11] The First structural models were readily accessed by the substitution of two CO ligands with two $CN^-$ ligands in $[Fe_2(S_2C_3H_6)(CO)_6]$ (**1**).[12–14] Several structural aspects of the iron-only hydrogenase active site have been modeled by diiron complexes bearing azadithiolate and related bridges,[15–18] a 2Fe3S core,[19,20] or chelating ligands.[21–26] Mimicking the catalytic activity of the hydrogenases turns out to be far more challenging. For the all-carbonyl complex **1**, the catalysis of proton reduction in acidified acetonitrile solution requires potentials more negative than –1.6 V[27,28] (all potentials in this paper are referenced to that of the reversible oxidation of ferrocene, $E_{1/2}^{ox}$ = 0.4 V vs. NHE). The substitution of one or two CO ligands by good donor ligands such as cyanido, phosphane, and/or *N*-heterocyclic carbene (NHC) yielded better functional models.[21,29–33] Good donor ligands increase the basicity of the iron–iron bond, and thus render it susceptible to protonation by relatively strong acids ($pK_a < 10$).[34,35] On protonation, the reduction potential of the complex is positively shifted by about 1 V, and catalytic hydrogen evolution can be detected at potentials around –1.4 V.[29,30] This obviously suggests that advances in designing an efficient proton reduction catalyst will follow from a greater balance between the basicity and the reduction potential of the diiron center. There are several examples of $[Fe_2(SR)_2(CO)_{6-x}L_x]$ ($x$ = 1, 2) complexes with ligands L that have a relatively modest donor ability such as phosphite or isocyanide.[36–40] However, the electrochemistry of these compounds and their reactivity toward protons have so far received little attention. In addition, they were generally prepared in rather low yields by thermal activation to give a mixture of mono-, di-, and trisubstituted derivatives. On the other hand, it was shown that electron transfer (reduction or oxidation) could also lead to substituted diiron dithiolates.[38,41,42] For example, the formation of $[Fe_2(S_2C_2H_4)(CO)_5\{P(OMe)_3\}]$ by an electron-transfer-catalyzed chain reaction was detected upon the electrochemical reduction of the all-CO parent compound in the presence of $P(OMe)_3$.[41] A similar approach allowed us to

[a] UMR CNRS 6521: Chimie, Electrochimie Moléculaires et Chimique Analytique, Université de Bretagne Occidentale, CS 93837, 29238 Brest, France
Fax: +33-298-017001
E-mail: fgloague@univ-brest.fr
Supporting information for this article is available on the WWW under http://www.eurjic.org or from the author.

 © 2007 Wiley-VCH Verlag GmbH & Co. KGaA, Weinheim 

selectively prepare $[Fe_2(S_2C_6H_4)(CO)_5\{P(OMe)_3\}]$ in good yield.[43]

We now describe the selective synthesis of $[Fe_2(S_2C_3H_6)(CO)_5\{P(OMe)_3\}]$ (**2**) and $[Fe_2(S_2C_3H_6)(CO)_4\{P(OMe)_3\}_2]$ (**3**) by bulk electrolysis of the all-CO parent compound **1** in the presence of $P(OMe)_3$. The purpose of this preliminary study was to determine whether electrochemical methods could be used as a general route for the selective preparation of mono- and disubstituted diiron dithiolates. The crystallographic and spectroscopic characterization and the electrochemical properties of complexes **2** and **3** are also reported.

## Results and Discussion

### Preparation and Characterization of Complexes 2 and 3

IR spectra recorded over a period of several hours showed that a $CH_3CN$ solution of the all-CO compound **1** was not reactive toward the addition of 1.1 molar equiv. of $P(OMe)_3$ at room temperature. However, electrolysis of this solution at a potential slightly more negative than the reduction potential of **1** readily gave the monosubstituted derivative **2**. The disubstituted complex **3** was similarly obtained by bulk electrolysis of a solution of **1** with 2.1 molar equiv. of $P(OMe)_3$ at a potential slightly more negative than the reduction potential of **2**. In each case, IR spectra indicated total consumption of **1** in 45–60 min. The charge passed in the course of electrolysis was about 0.7 F per mol of **1**, which indicates that CO-displacement reactions catalyzed by electron transfer occur (see Supporting Information).[41,43]

Compounds **2** and **3** were characterized by IR and NMR spectroscopy, elemental analysis, mass spectrometry, and X-ray crystallography. The shift in the $\nu_{CO}$ bands is considered a useful indicator of the variation in electron density in diiron models of the hydrogenase active site. The average values for the IR bands in the carbonyl stretching region are lowered by 47 and 79 $cm^{-1}$ for the monosubstituted compound **2** ($\tilde{\nu}_{CO}$: 2048, 1991, 1976, 1938 $cm^{-1}$) and the disubstituted compound **3** ($\tilde{\nu}_{CO}$ = 2004, 1966, 1937, 1917 $cm^{-1}$), respectively, relative to those in the all-CO compound **1** ($\tilde{\nu}_{CO}$: 2073, 2033, 1999 $cm^{-1}$). The redshifted values for **2** and **3** indicate that the electron-donating ability of $P(OMe)_3$ is comparable to that of $PPh_3$ and slightly better than that of $P(OEt)_3$ and *t*BuNC.[39,40] The difference in wavenumber between the highest and lowest band ($\Delta\tilde{\nu}_{CO}$ = 87 $cm^{-1}$) in **3** is smaller than that in the monosubstituted complex **2** ($\Delta\tilde{\nu}_{CO}$ = 110 $cm^{-1}$), which indicates that **3** is a symmetric diphosphite derivative.[25]

Evidence for monosubstitution in **2** was provided by $^{13}C$ NMR spectroscopy. The spectrum of **2** displays two carbonyl resonances: a doublet at $\delta$ = 211.9 ppm assigned to the two carbonyl ligands of the $Fe(CO)_2[P(OMe)_3]$ moiety and a singlet at $\delta$ = 209.6 ppm assigned to the three carbonyl ligands of the $Fe(CO)_3$ moiety. The $^{13}C$ NMR spectrum of the disubstituted complex **3** shows only one doublet at $\delta$ = 213.5 ppm for the carbonyl ligands.

The dynamic properties of complexes **2** and **3** were investigated by variable temperature $^{31}P$ NMR spectroscopy. At room temperature, the NMR spectrum of complex **2** displays one signal at $\delta$ = 177.0 ppm, which splits at 183 K into four sharp resonances (186.4, 184.4, 178.0, and 177.1 ppm, Figure 1a). This indicates that the dynamic site exchange

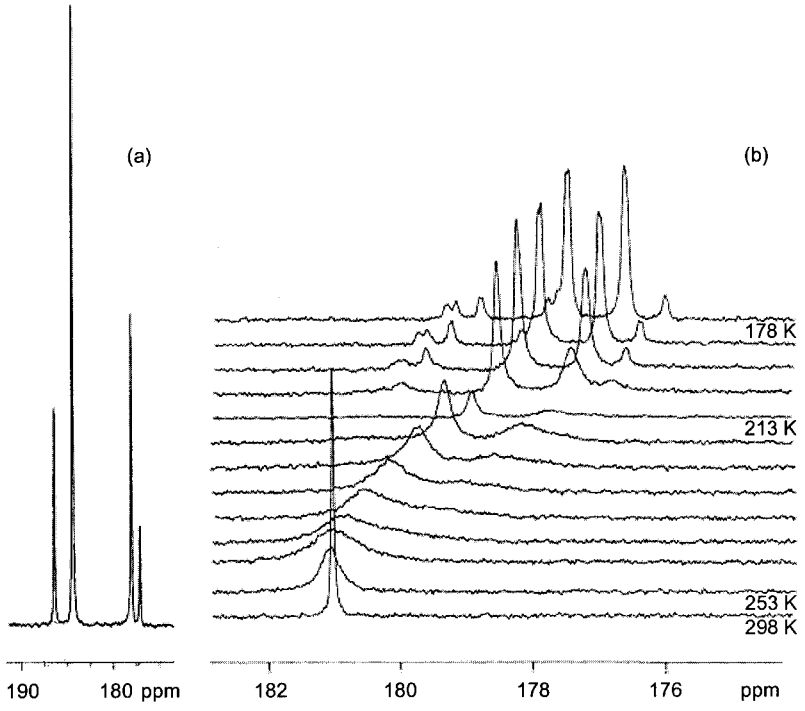


Figure 1. $^{31}P$ NMR spectra of (a) compound **2** at 183 K and (b) compound **3** at variable temperatures from 298 K to 178 K.

 © 2007 Wiley-VCH Verlag GmbH & Co. KGaA, Weinheim 

processes at low temperature are sufficiently slow on the NMR timescale to allow the detection of the four isomers expected for a monosubstituted derivative (Scheme 1). The fluxional processes that occur in solution are a basal/apical rotation of the phosphite and carbonyl ligands along with a flipping of the methylene group of the propanedithiolate ligand.[44,45]

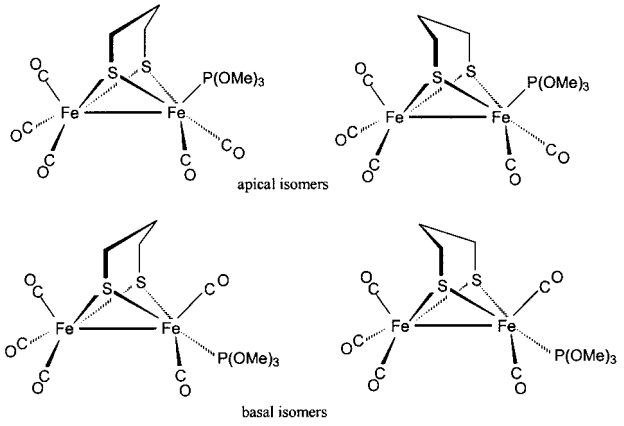


Scheme 1.

At room temperature, the $^{31}P$ NMR spectrum of **3** displays one signal at $\delta$ = 180.4 ppm (Figure 1b). The $^{31}P$ NMR pattern at 183 K suggests the presence of the four expected isomers, relative to the position of the phosphite ligands (Scheme 2). The major isomer (75%) displays four poorly resolved signals of nearly equal intensity in the range of 184.3 to 182.9 ppm. This is indicative of an apical/basal form, in which the two phosphorus atoms are nonequivalent. This observation is consistent with density functional theory calculations, which indicate that the most stable structure for $[Fe_2(S_2C_2H_4)(CO)_4(PH_3)_2]$ is the apical/basal isomer, even though the difference in energy between each isomer is weak.[46]

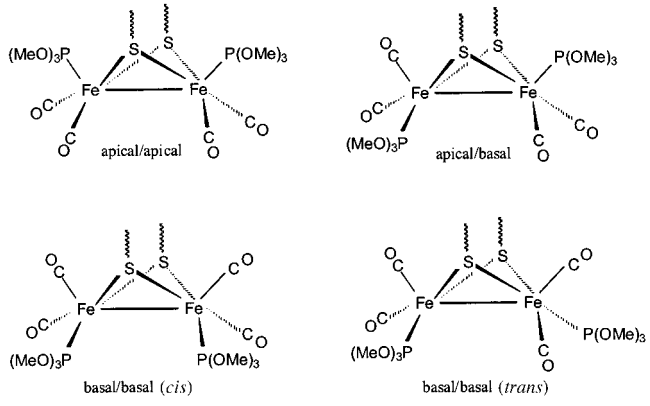


Scheme 2.

The structure of **2** in the solid state was determined by X-ray diffraction and confirms the presence of one phosphite ligand bonded to an iron atom in an apical position (Figure 2). Such an apical orientation for the incoming ligand was previously reported in $[Fe_2(S_2C_3H_6)(CO)_5L]$ when L = $PPh_3$, $PMe_2Ph$, $POEt_3$,[40] NHC,[21,32,33] and $PPh_2\{C_6H_4$-$CCSi(CH_3)_3\}$,[47] whereas the basal position was occupied when L = $P(NC_4H_8)_3$,[48] PTA (1,3,5-triaza-7-phosphaadamantane),[31] $\eta^1$-$Ph_2P$-$CH_2$-$PPh_2$,[23] and $H_2NPr$.[49] Each iron atom in **2** displays the usual pentacoordinate square-pyramidal structure, where both metal centers are displaced from the basal plane toward the apical position by 0.37 Å for Fe(1) and by 0.41 Å for Fe(2).

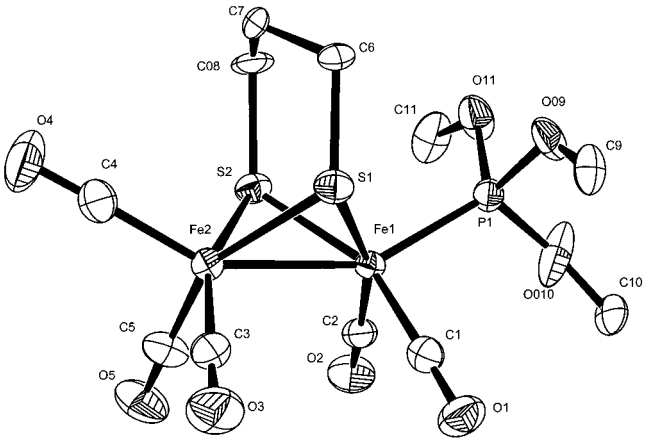


Figure 2. ORTEP diagram of compound **2** depicted with 50% thermal ellipsoids. Selected bond lengths [Å] and angles [°]: Fe(1)–Fe(2) 2.5098(12), Fe(1)–C(1) 1.777(2), Fe(1)–C(2) 1.785(2), C(1)–O(1) 1.144(3), C(2)–O(2) 1.140(3), C(3)–O(3) 1.139(3), Fe(1)–P(1) 2.1618(6), Fe(1)–S(1) 2.2595(6), C(2)–Fe(1)–P(1) 96.89(7), C(1)–Fe(1)–P(1) 97.80(7), P(1)–Fe(1)–S(1) 101.64(2), P(1)–Fe(1)–Fe(2) 150.73(4).

Crystallization of **3** afforded crystals suitable for X-ray diffraction and resulted in the formation of only one isomer in which both phosphite ligands are coordinated in an apical position (Figure 3). It is worth noting that the electrochemically synthesized complex **3** is a *symmetrically* disubstituted diiron compound, as are those prepared by the thermally-activated CO-displacement reaction. Ligand coordination in an apical/apical fashion was previously reported in complexes of type $[Fe_2(S_2C_3H_6)(CO)_4L_2]$, where L = *t*BuNC,[39] $PMe_2Ph$,[40] and $PPh_2(C_6H_4Br)$.[47] In analo-

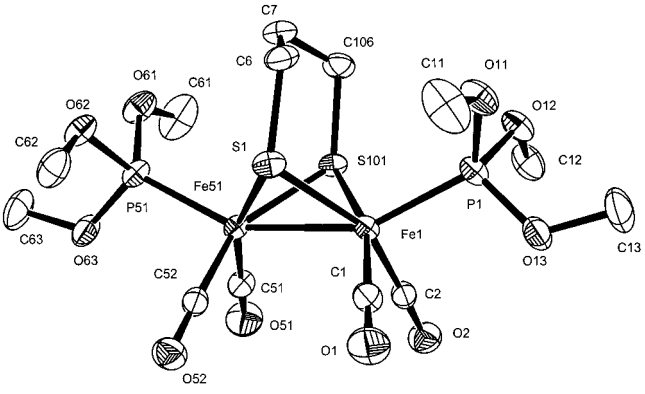


Figure 3. ORTEP diagram of compound **3** depicted with 50% thermal ellipsoids. Selected bond lengths [Å] and angles [°]: Fe(1)–Fe(51) 2.5089(4), Fe(1)–C(1) 1.7763(16), Fe(1)–C(2) 1.7633(16), C(1)–O(1) 1.1443(19), C(2)–O(2) 1.1490(19), Fe(1)–P(1) 2.1656(5), Fe(1)–S(1) 2.268(8), C(2)–Fe(1)–P(1) 97.97(5), C(1)–Fe(1)–P(1) 95.66(5), P(1)–Fe(1)–S(1) 106.8(3), P(1)–Fe(1)–Fe(51) 152.694(13).

 © 2007 Wiley-VCH Verlag GmbH & Co. KGaA, Weinheim 

gous disubstituted complexes, basal/basal *trans* isomers have also been observed in the solid state when L = $PMe_3$[50] and L = PTA,[31] while L = $CN^-$[14] and L = NHC[32] led to basal/apical isomers. These results show that the ligand size is not the determining factor that affects the structure of $[Fe_2(S_2C_3H_6)(CO)_4L_2]$ complexes in the solid state.[36]

The electrochemical properties of organometallic models are one of the interesting features that may lead to a better understanding of the structure–function relationships in the hydrogenase active site. Cyclic voltammetry of **2** and **3** was carried out in $CH_3CN/Bu_4NPF_6$ solution. The monosubstituted complex **2** exhibits two reductions at –1.98 V and –2.29 V and one oxidation at +0.37 V. The primary reduction and oxidation processes of **2** are chemically irreversible. The disubstituted complex **3** exhibits a chemically irreversible reduction at –2.30 V and a chemically reversible oxidation event at 0.12 V. In comparison to **1**, the first reduction processes of compounds **2** and **3** are negatively shifted by 0.31 V and 0.63 V, respectively, which is consistent with the increase in the electron density when one or two CO ligands are replaced by more electron-donating phosphite ligands (see IR data). Another interesting feature of these systems is that the oxidation of phosphite-disubstituted derivatives such as complex **3** and $[Fe_2(S_2C_3H_6)(CO)_4\{P(OEt)_3\}_2]$[40] is a chemically reversible process, while the oxidation of isocyanide- and phosphane-disubstituted derivatives is an irreversible process.[37,39] There is so far no clear agreement on the number of electrons involved in the reduction step of $[Fe_2(S_2C_3H_6)(CO)_{6-x}L_x]$ complexes. For example, Heinekey and co-workers[39] reported that the reduction of $[Fe_2(S_2C_3H_6)(CO)_4(t\text{BuNC})_2]$ is apparently a two-electron process, whereas Sun and co-workers[40] ascribed the first reduction peak of $[Fe_2(S_2C_3H_6)(CO)_{6-x}L_x]$ [L = $PPh_3$, $PMe_2Ph$, $P(OEt)_3$; $x$ = 1,2] to a one-electron process. To determine the number of electrons involved in the reduction and oxidation of **2** and **3**, respectively, we used $[Fe_2(S_2C_3H_6)(CO)_4(I_{Me}CH_2I_{Me})]$ ($I_{Me}$ = 1-methylimidazol-2-ylidene) as an internal standard (see Supporting Information). The chelated dicarbene derivative exhibits a diffusion-limited, reversible, one-electron oxidation process,[26] and its diffusion coefficient should be close to that of **2** and **3**. The voltammetric peak current ($I_p$) for the oxidation of **3** varies linearly with the square root of the potential scan rate ($v$) in the range of 0.02 to 2 $V s^{-1}$. Additionally, the slope of the $I_p$ vs. $v^{1/2}$ plot is more than twice that calculated for the chelated carbene-disubstituted derivative at the same concentration. This clearly demonstrates that the oxidation of **3** is a diffusion-limited, two-electron process. The same procedure allowed us to conclude that the reduction processes of **2** and **3** involve in each case two electrons.

## Protonation Study of Complexes 2 and 3

Before evaluating the electrocatalytic properties of **2** and **3** for proton reduction, it is important to check their reactivity toward protons. The all-CO compound **1** is not reactive toward strong acids such as $HBF_4{\cdot}Et_2O$. However, it is well known that in $[Fe_2(SR)_2(CO)_{6-x}L_x]$ ($x$ = 1,2), the donor ability of the ligand L has a great influence on the nucleophilicity of the $Fe^I$–$Fe^I$ bond.[34] The IR spectrum of a $CH_3CN$ solution of **2** with excess $HBF_4{\cdot}Et_2O$ remains unaltered, which indicates that the replacement of one CO ligand with one $P(OMe)_3$ ligand does not noticeably increase the basicity of the metal–metal bond. Treatment of a $CH_3CN$ solution of **3** with 10 molar equiv. $HBF_4{\cdot}Et_2O$ led to an IR spectrum that displays new $\tilde{\nu}_{CO}$ bands at 2070, 2050, and 2010 $cm^{-1}$. The positive shift of about 80 $cm^{-1}$ is characteristic of the formation of a $Fe^{II}(\mu\text{-H})Fe^{II}$ species.[34] Protonation is, however, very slow since $\nu_{CO}$ bands corresponding to the starting compound **3** were still observed one hour after excess acid was added. The $^1H$ NMR spectrum of **2** recorded at room temperature in the presence of excess $HBF_4{\cdot}Et_2O$ shows a triplet at $\delta$ = –14.8 ppm ($J_{PH}$ = 26.6 Hz) in the high field region, which confirms the formation of a bridging hydride complex.

The electrocatalytic activity of complexes **2** and **3** for proton reduction was investigated in $CH_3CN/Bu_4NPF_6$ solutions with increasing concentrations of toluenesulfonic acid (HOTs, p$K_a$ ca. 8). The addition of HOTs to a solution of **2** triggers the appearance of a new reduction process, noted as B in the cyclic voltammograms in Figure 4. This process occurs at a potential less negative than that of the

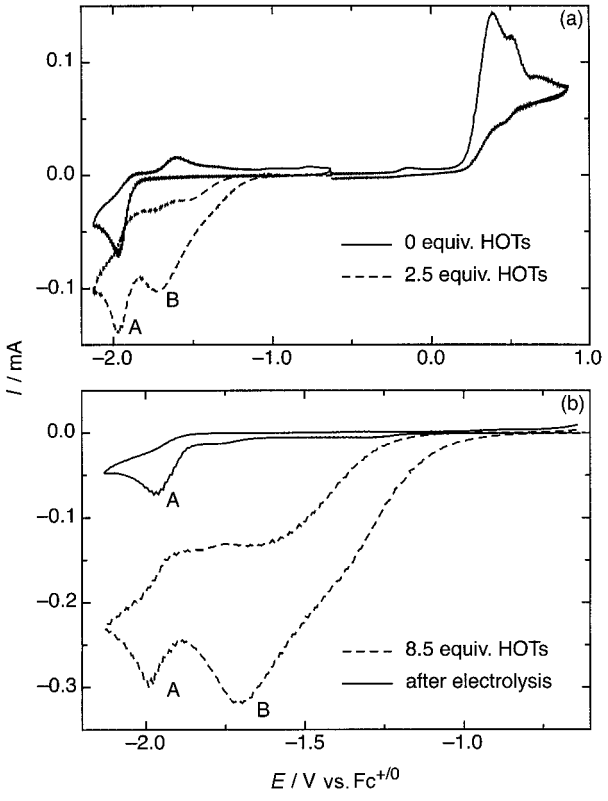


Figure 4. Cyclic voltammograms of compound **2** in $CH_3CN/Bu_4NPF_6$ (a) before and after addition of 2.5 molar equiv. HOTs and (b) after addition of 8.5 molar equiv. HOTs and after electrolysis at –1.65 V. Experimental conditions: $v$ = 0.1 $V s^{-1}$; [**2**] = 2.1 mM; glassy carbon electrode 0.071 $cm^2$ in surface area.

 © 2007 Wiley-VCH Verlag GmbH & Co. KGaA, Weinheim 

reduction of **2**, noted as A in the same Figure. The onset of wave B is at about –1.1 V, and a maximum in height is reached at about –1.7 V. The height of wave B is responsive to the acid concentration. It increases by a factor of three upon increasing the [HOTs]/[**2**] ratio from 2.5 to 8.5 (Figure 4b). Since **2** does not readily react with protons under the present conditions (see IR data above), it is most probable that wave B is due to the reduction of $\mathbf{2}H^+$ generated at the electrode according to the CE mechanism shown in Equations (1), (2), and (3).

$$\mathbf{2} + H^+ \rightleftarrows \mathbf{2}H^+ \quad (1)$$

$$\mathbf{2}H^+ + e^- \rightleftarrows \mathbf{2}H \quad (2)$$

$$2 \times \mathbf{2}H \rightarrow 2 \times \mathbf{2} + H_2 \quad (3)$$

$\mathbf{2}H^+$ does not exist in an appreciable amount in the bulk of the solution, but its reduction at the electrode displaces the protonation equilibrium to the right [Equation (1)]. The amount of acid in solution has a similar effect on this equilibrium, which explains the dependence of the height of wave B on the proton concentration. It is relevant to note that the height of peak A, which corresponds to the reduction of **2**, remains unaffected upon addition of acid. This suggests not only that all the protons available in the diffusion layer are consumed in wave B, but also that the reduction of $\mathbf{2}H^+$ regenerates the unprotonated complex **2**, likely by the release of $H_2$ [Equations (3)]. To support the proposed mechanism, we carried out an electrolysis at –1.65 V of a solution of **2** with 8.5 molar equiv. of HOTs. The charge passed after a period of 120 min was 8.2 F per mol of **2**, consistent with the stoichiometry of one electron and one proton per mol of **2** as proposed in Equations (1)–(3). Gas evolution was observed over the course of the electrolysis, which is consistent with the production of molecular hydrogen, and this has previously been reported for the electrochemical reduction of diiron complexes in the presence of acid.[17,27,29] Cyclic voltammograms recorded after the electrolysis confirms the consumption of almost all of the protons without any noticeable decomposition of **2** (Figure 4b). Despite the presence of excess acid, the hydrogen production seems to proceed through a bimolecular reaction as in Equation (3) and not through the subsequent protonation and reduction of **2**H (i.e. $\mathbf{2}H + H^+ + e^- \rightarrow \mathbf{2} + H_2$). This is most certainly because of the weakly basic character of **2**H, which is either too slowly protonated by HOTs or not protonated at all.

As in the case of compound **2**, the addition of HOTs to a solution of **3** triggers the appearance of a new reduction process, noted as D in the cyclic voltammograms in Figure 5. This process occurs at a potential less negative than that of the reduction of **3**, noted as C in the same Figure. The height of wave D is responsive to the concentration of acid, which indicates proton reduction catalysis (Figure 5b). The onset of this catalysis by **3** occurs at a potential approximately 0.4 V more negative than that for **2**, which parallels the shift in reduction potential. Although **3** seems to be a less efficient catalyst than **2** on the voltammetric timescale, bulk electrolysis at –1.90 V of a solution of **3** containing 8.3 molar equiv. HOTs consumed 8.0 F per mol of **3** over a period of about 120 min. The voltammograms in Figure 5b show that most of the protons were consumed by electrolysis, which suggests that, as in the case of **2**, the catalysis by **3** involves a bimolecular reaction [see Equation (3)].

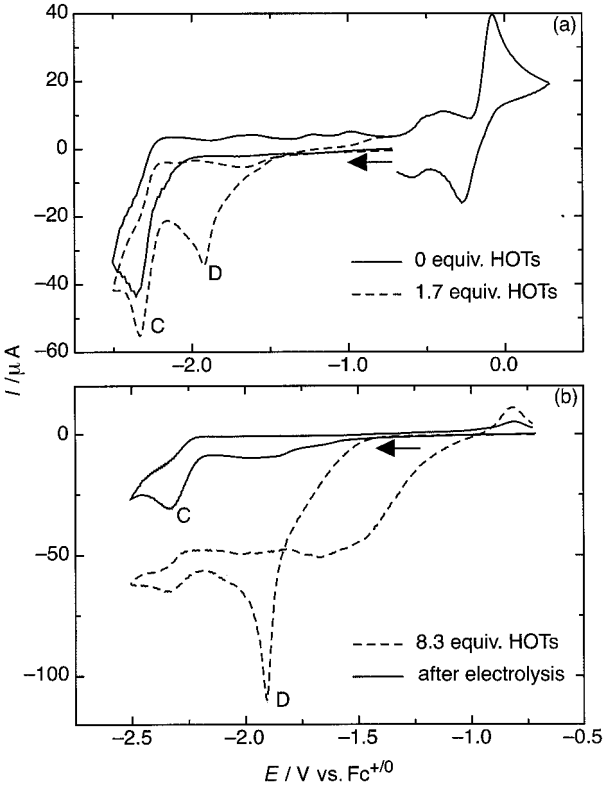


Figure 5. Cyclic voltammograms of compound **3** in $CH_3CN/Bu_4NPF_6$ (a) before and after addition of 1.7 molar equiv. HOTs and (b) after addition of 8.3 molar equiv. HOTs and after electrolysis at –1.9 V. Experimental conditions: $v$ = 0.1 V s$^{-1}$; [**3**] = 2.1 mM; glassy carbon electrode 0.071 cm$^2$ in surface area.

## Conclusions

To summarize our results, we have shown that the electrochemical route represents a convenient method for the selective synthesis of mono- and disubstituted derivatives of diiron dithiolates. We are currently extending this approach to introduce more elaborate ligands (e.g. bidentate ligands) into the coordination sphere of diiron complexes.

Substitution of one CO ligand by one $P(OMe)_3$ ligand shifts the reduction potential of the complex by about 0.3 V. This modification has little effect on the thermodynamics of proton binding. Nevertheless, the voltammogram of **2** in the presence of acid exhibits a reduction wave that does not have a counterpart in the voltammogram of **1**. This is ascribed to proton binding by **2** in the vicinity of the electrode, which is triggered by the more facile reduction of $\mathbf{2}H^+$ relative to that of **2** (CE mechanism). We are presently not able to determine whether the protonation is metal- or ligand- (e.g. sulfur) centered. Bulk electrolysis experiments

 © 2007 Wiley-VCH Verlag GmbH & Co. KGaA, Weinheim 

confirm the occurrence of a CE process and indicate that the proton reduction catalysis occurs most likely by a bimolecular reaction even in the presence of a large excess of acid. It is relevant to note that **2** appears to be a more efficient catalyst in terms of turnovers than the corresponding benzenedithiolate-bridged derivative, whereas the latter works at a significantly less negative potential.[43] This suggests that a careful tailoring of both the bridging and terminal ligands may well lead to an efficient proton reduction catalyst working at a mildly negative potential.

## Experimental Section

**General Procedures:** All reactions were performed under an atmosphere of argon or nitrogen by using conventional Schlenk techniques. Solvents were deoxygenated and dried by standard methods. Literature methods were used for the preparation of $[Fe_2(S_2C_3H_6)(CO)_6]$.[37] All other reagents were commercially available. Bulk electrolysis and cyclic voltammetry experiments were carried out as described elsewhere.[51] Chemical analyses were performed by the Service Central d'Analyse du CNRS (France). IR spectra were recorded in $CH_3CN$ solution with a Nicolet Nexus Fourier transform spectrometer. NMR spectra were recorded with Bruker AMX 3–400 and DRX 500 spectrometers. Single-crystal X-ray diffraction data were collected at 170 K on an X-CALIBUR-2 CCD diffractometer (Oxford Diffraction) with graphite-monochromated Mo-$K_\alpha$ radiation ($\lambda$ = 0.71073 Å). The structures of **2** and **3** were solved by direct methods and refined by full-matrix least-squares on $F^2$.[52] Complete crystal data and parameters for data collection and refinement are listed in Table 1. CCDC-49699 and CCDC-649700 contain the supplementary crystallographic data for this paper. These data can be obtained free of charge from The Cambridge Crystallographic Data Centre via www.ccdc.cam.ac.uk/data_request/cif.

Table 1. Crystallographic data and processing parameters for complexes **2** and **3**.

| Complex | **2** | **3** |
|---|---|---|
| Empirical formula | $C_{11}H_{15}Fe_2O_8PS_2$ | $C_{13}H_{24}Fe_2O_{10}P_2S_2$ |
| Formula weight | 482.02 | 578.08 |
| Crystal system | monoclinic | monoclinic |
| Space group | $P2_1/n$ | $C2/c$ |
| $a$ [Å] | 9.5915(3) | 19.3412(9) |
| $b$ [Å] | 8.8963(2) | 7.8440(3) |
| $c$ [Å] | 21.4503(7) | 15.1964(6) |
| $\beta$ [°] | 96.218(3) | 97.709 |
| $V$ [Å$^3$] | 1819.56(9) | 2284.65(16) |
| $Z$ | 4 | 4 |
| $\rho_{calcd.}$ [g cm$^{-3}$] | 1.756 | 1.681 |
| $\mu$ [mm$^{-1}$] | 1.945 | 1.638 |
| Crystal size [mm] | 0.50 × 0.20 × 0.05 | 0.24 × 0.17 × 0.14 |
| Range of $\theta$ [°] | 2.98–28.88 | 3.66–33.22 |
| Reflections collected | 11908 | 22481 |
| $R_{int}$ | 0.0156 | 0.0332 |
| Unique data/Parameters | 3979/245 | 4121/175 |
| $R(F)$, $wR(F^2)$ (all data) | 0.0354,0.0683 | 0.0475,0.0837 |
| Goodness-of-fit on $F^2$ | 1.063 | 1.047 |
| $\|\Delta\rho\|$ maximum [e Å$^3$] | 0.505 | 0.834 |

**Electrochemical Synthesis of $[Fe_2(S_2C_3H_6)(CO)_5\{P(OMe)_3\}]$ (2):** In a typical procedure, $[Fe_2(S_2C_3H_6)(CO)_6]$ (70 mg, 0.181 mmol) was dissolved in a $N_2$-purged $CH_3CN/Bu_4NPF_6$ solution (15 mL). $P(OMe)_3$ (24 μL, 1.1 molar equiv.) was added by using a microsyringe. Bulk electrolysis was carried out at –1.75 V under vigorous agitation. The color of the solution changed rapidly from orange to brown. After 45–60 min, the quantity of electricity passed reached a plateau value, and the IR spectrum confirmed the total consumption of the starting hexacarbonyl compound. After evaporation of $CH_3CN$ under vacuum, complex **2** was purified by column chromatography on silica gel with hexane/$CH_2Cl_2$ (8:2) as eluent. Yield: 74 mg (85%). IR ($CH_3CN$): $\tilde{\nu}_{CO}$ = 2048 (s), 1991 (vs), 1976 (s), 1938 (w) cm$^{-1}$. $^1$H NMR ($CD_2Cl_2$, 298 K): $\delta$ = 3.75 [d, $^3J_{PH}$ = 11.3 Hz, 9 H, P(O*Me*)$_3$], 2.05 {s br., 4 H, [S-(C*H*$_2$)$_3$-S]}, 1.75 {s br., 1 H, [S-(C*H*$_2$)$_3$-S]}, 1.54 {s br., 1 H, [S-(C*H*$_2$)$_3$-S]} ppm. $^{13}$C{$^1$H} NMR ($CDCl_3$, 298 K): $\delta$ = 211.90 (d, $^2J_{PC}$ = 20.5 Hz, {Fe(*C*O)$_2$[P(OMe)$_3$]}), 209.59 [Fe(*C*O)$_3$], 52.09 [P(O*Me*)$_3$], 30.26, 22.88 [S-(*C*H$_2$)$_3$-S] ppm. $^{31}$P{$^1$H} NMR ($CD_2Cl_2$, 298 K): $\delta$ = 177.04 [*P*(OMe)$_3$] ppm. $^{31}$P{$^1$H} NMR ($CD_2Cl_2$, 183 K): $\delta$ = 186.4 (17%), 184.4 (50%), 178.0 (25%), 177.1 (8%), [*P*(OMe)$_3$] ppm. LSMIS: *m*/*z* calcd. for [M]$^+$ 481.9; found 481.9. $C_{11}H_{15}Fe_2O_8PS_2$ (482.02): calcd. C 27.41, H 3.14; found C 27.90, H 3.40.

**Electrochemical Synthesis of $[Fe_2(S_2C_3H_6)(CO)_4\{P(OMe)_3\}_2]$ (3):** Complex **3** was prepared as described for complex **2** except that the amount of added $P(OMe)_3$ was 2.1 equiv. and that the electrolysis potential was set to –2.0 V. Yield (starting from 70 mg **1**): 71 mg (68%). IR ($CH_3CN$): $\tilde{\nu}_{CO}$ = 2004 (s), 1966 (vs), 1937 (s), 1917 (w) cm$^{-1}$. $^1$H NMR ($CDCl_3$, 298 K): $\delta$ = 3.77 [d, $^3J_{PH}$ = 11.7 Hz, 18 H, 2 P(O*Me*)$_3$], 1.94 {m br., 4 H, [S-(C*H*$_2$)$_3$-S]}, 1.70 {s br., 2 H, [S-(C*H*$_2$)$_3$-S]} ppm. $^{13}$C{$^1$H} NMR ($CDCl_3$, 298 K): $\delta$ = 213.50 (d, $^2J_{PC}$ = 17 Hz, {Fe(*C*O)$_2$[P(OMe)$_3$]}), 51.67 [P(O*Me*)$_3$], 29.94, 22.03 [S-(*C*H$_2$)$_3$-S] ppm. $^{31}$P{$^1$H} NMR ($CD_2Cl_2$, 298 K): $\delta$ = 180.40 [*P*(OMe)$_3$] ppm. LSMIS: *m*/*z* calcd. for [M]$^+$ 577.9; found 577.9. $C_{13}H_{24}Fe_2O_{10}P_2S_2$ (578.08): calcd. C 27.01, H 4.18, P 10.72; found C 27.04, H 4.16, P 10.32.

**Supporting Information** (see footnote on the first page of this article): Plots as a function of the potential scan rate of the oxidation current of compound **3** and $[Fe_2(S_2C_3H_6)(CO)_4(I_{Me}CH_2I_{Me})]$ ($I_{Me}$ = 1-methylimidazol-2-ylidene) used as an internal standard, cyclic voltammetry of **1** and **2** in the presence of added $P(OMe)_3$, along with the kinetic analysis of the charge-transfer-catalyzed substitution process, are presented.

## Acknowledgments

We are grateful to the Centre National de Recherche Scientifique (CNRS), the Agence National de la Recherche (ANR, project number: NT05-2_42699 – PhotoBioH2), and the University of Brest for financial support of this work.

[1] M. Frey, *ChemBioChem* **2002**, *3*, 153–160.
[2] Y. Nicolet, B. J. Lemon, J. C. Fontecilla-Camps, J. W. Peters, *Trends Biochem. Sci.* **2000**, *25*, 138–143.
[3] M. Y. Darensbourg, E. J. Lyon, J. J. Smee, *Coord. Chem. Rev.* **2000**, *206–207*, 533–561.
[4] R. B. King, T. E. Bitterwolf, *Coord. Chem. Rev.* **2000**, *206–207*, 563–579.
[5] M. Y. Darensbourg, E. J. Lyon, X. Zhao, I. P. Georgakaki, *Proc. Natl. Acad. Sci. USA* **2003**, *100*, 3683–3688.
[6] D. J. Evans, C. J. Pickett, *Chem. Soc. Rev.* **2003**, *32*, 268–275.
[7] T. B. Rauchfuss, *Inorg. Chem.* **2004**, *43*, 14–26.
[8] V. Artero, M. Fontecave, *Coord. Chem. Rev.* **2005**, *249*, 1518–1535.
[9] S. P. Best, *Coord. Chem. Rev.* **2005**, *249*, 1536–1554.
[10] J.-F. Capon, F. Gloaguen, P. Schollhammer, J. Talarmin, *Coord. Chem. Rev.* **2005**, *249*, 1664–1676.

 © 2007 Wiley-VCH Verlag GmbH & Co. KGaA, Weinheim 

[11] L. Sun, B. Akermark, S. Ott, *Coord. Chem. Rev.* **2005**, *249*, 1653–1663.
[12] A. Le Cloirec, S. P. Best, S. Borg, S. C. Davies, D. J. Evans, D. L. Hughes, C. J. Pickett, *Chem. Commun.* **1999**, 2285–2286.
[13] E. J. Lyon, I. P. Georgakaki, J. H. Reibenspies, M. Y. Darensbourg, *Angew. Chem. Int. Ed.* **1999**, *38*, 3178–3180.
[14] M. Schmidt, S. M. Contakes, T. B. Rauchfuss, *J. Am. Chem. Soc.* **1999**, *121*, 9736–9737.
[15] J. D. Lawrence, H. Li, T. B. Rauchfuss, M. Benard, M. M. Rohmer, *Angew. Chem. Int. Ed.* **2001**, *40*, 1768–1771.
[16] P. Das, J. F. Capon, F. Gloaguen, F. Y. Petillon, P. Schollhammer, J. Talarmin, K. W. Muir, *Inorg. Chem.* **2004**, *43*, 8203–8205.
[17] S. Ott, M. Kritikos, B. Akermark, L. C. Sun, R. Lomoth, *Angew. Chem. Int. Ed.* **2004**, *43*, 1006–1009.
[18] J. L. Stanley, T. B. Rauchfuss, S. R. Wilson, *Organometallics* **2007**, *26*, 1907–1911.
[19] C. Tard, X. M. Liu, S. K. Ibrahim, M. Bruschi, L. De Gioia, S. C. Davies, X. Yang, L. S. Wang, G. Sawers, C. J. Pickett, *Nature* **2005**, *433*, 610–613.
[20] G. Zampella, M. Bruschi, P. Fantucci, M. Razavet, C. J. Pickett, L. De Gioia, *Chem. Eur. J.* **2005**, *11*, 509–520.
[21] L. L. Duan, M. Wang, P. Li, Y. Na, N. Wang, L. C. Sun, *Dalton Trans.* **2007**, 1277–1283.
[22] S. Ezzaher, J. F. Capon, F. Gloaguen, F. Y. Petillon, P. Schollhammer, J. Talarmin, R. Pichon, N. Kervarec, *Inorg. Chem.* **2007**, *46*, 3426–3428.
[23] W. M. Gao, J. Ekstrom, J. H. Liu, C. N. Chen, L. Eriksson, L. H. Weng, B. Akermark, L. H. Sun, *Inorg. Chem.* **2007**, *46*, 1981–1991.
[24] G. Hogarth, I. Richards, *Inorg. Chem. Commun.* **2007**, *10*, 66–70.
[25] A. K. Justice, G. Zampella, L. DeGioia, T. B. Rauchfuss, J. I. vanderVlugt, S. R. Wilson, *Inorg. Chem.* **2007**, *46*, 1655–1664.
[26] D. Morvan, J. F. Capon, F. Gloaguen, A. LeGoff, M. Marchivie, F. Michaud, P. Schollhammer, J. Talarmin, J. J. Yaouanc, R. Pichon, N. Kervarec, *Organometallics* **2007**, *26*, 2042–2052.
[27] D. S. Chong, I. P. Georgakaki, R. Mejia-Rodriguez, J. Samabria-Chinchilla, M. P. Soriaga, M. Y. Darensbourg, *Dalton Trans.* **2003**, 4158–4163.
[28] S. J. Borg, T. Behrsing, S. P. Best, M. Razavet, X. M. Liu, C. J. Pickett, *J. Am. Chem. Soc.* **2004**, *126*, 16988–16999.
[29] F. Gloaguen, J. D. Lawrence, T. B. Rauchfuss, *J. Am. Chem. Soc.* **2001**, *123*, 9476–9477.
[30] F. Gloaguen, J. D. Lawrence, T. B. Rauchfuss, M. Benard, M. M. Rohmer, *Inorg. Chem.* **2002**, *41*, 6573–6582.
[31] R. Mejia-Rodriguez, D. S. Chong, J. H. Reibenspies, M. P. Soriaga, M. Y. Darensbourg, *J. Am. Chem. Soc.* **2004**, *126*, 12004–12014.
[32] J. F. Capon, S. ElHassnaoui, F. Gloaguen, P. Schollhammer, J. Talarmin, *Organometallics* **2005**, *24*, 2020–2022.
[33] J. W. Tye, J. Lee, H. W. Wang, R. Mejia-Rodriguez, J. H. Reibenspies, M. B. Hall, M. Y. Darensbourg, *Inorg. Chem.* **2005**, *44*, 5550–5552.
[34] K. Fauvel, R. Mathieu, R. Poilblanc, *Inorg. Chem.* **1976**, *15*, 976–978.
[35] M. Bruschi, P. Fantucci, L. De Gioia, *Inorg. Chem.* **2003**, *42*, 4773–4781.
[36] J. A. De Beer, R. J. Haines, *J. Organomet. Chem.* **1972**, *37*, 173–181.
[37] F. Gloaguen, J. D. Lawrence, M. Schmidt, S. R. Wilson, T. B. Rauchfuss, *J. Am. Chem. Soc.* **2001**, *123*, 12518–12527.
[38] J. D. Lawrence, T. B. Rauchfuss, S. R. Wilson, *Inorg. Chem.* **2002**, *41*, 6193–6195.
[39] J. L. Nehring, D. M. Heinekey, *Inorg. Chem.* **2003**, *42*, 4288–4292.
[40] P. Li, M. Wang, C. J. He, G. H. Li, X. Y. Liu, C. N. Chen, B. Akermark, L. C. Sun, *Eur. J. Inorg. Chem.* **2005**, 2506–2513.
[41] A. Darchen, H. Mousser, H. Patin, *J. Chem. Soc. Chem. Commun.* **1988**, 968–970.
[42] J. I. van der Vlugt, T. B. Rauchfuss, S. R. Wilson, *Chem. Eur. J.* **2005**, *12*, 90–98.
[43] F. Gloaguen, D. Morvan, J.-F. Capon, P. Schollhammer, J. Talarmin, *J. Electroanal. Chem.* **2007**, *603*, 15–20.
[44] E. J. Lyon, I. P. Georgakaki, J. H. Reibenspies, M. Y. Darensbourg, *J. Am. Chem. Soc.* **2001**, *123*, 3268–3278.
[45] X. Zhao, I. P. Georgakaki, M. L. Miller, R. Mejia-Rodriguez, C. Y. Chiang, M. Y. Darensbourg, *Inorg. Chem.* **2002**, *41*, 3917–3928.
[46] J. W. Tye, M. Y. Darensbourg, M. B. Hall, *Inorg. Chem.* **2006**, *45*, 1552–1559.
[47] J. Ekstrom, M. Abrahamsson, C. Olson, J. Bergquist, F. B. Kaynak, L. Eriksson, S. C. Licheng, H. C. Becker, B. Akermark, L. Hammarstrom, S. Ott, *Dalton Trans.* **2006**, 4599–4606.
[48] J. Hou, X. J. Peng, Z. Y. Zhou, S. G. Sun, X. Zhao, S. Gao, *J. Organomet. Chem.* **2006**, *691*, 4633–4640.
[49] L. Schwartz, J. Ekstrom, R. Lomoth, S. Ott, *Chem. Commun.* **2006**, 4206–4208.
[50] X. Zhao, I. P. Georgakaki, M. L. Miller, J. C. Yarbrough, M. Y. Darensbourg, *J. Am. Chem. Soc.* **2001**, *123*, 9710–9711.
[51] J.-F. Capon, F. Gloaguen, P. Schollhammer, J. Talarmin, *J. Electroanal. Chem.* **2004**, *566*, 241–247.
[52] Programs used: a) G. M. Sheldrick, *SHELX97*, University of Göttingen, Germany, **1998**; b) *WinGX – A Windows Program for Crystal Structure Analysis*: L. J. Farrugia, *J. Appl. Crystallogr.* **1999**, *32*, 837–838.

Received: June 8, 2007
Published Online: September 24, 2007

 © 2007 Wiley-VCH Verlag GmbH & Co. KGaA, Weinheim 

DOI: 10.1002/ejic.200700670

# Nickel(II), Palladium(II) and Rhodium(I) Complexes of New NHC-Thioether Ligands: Efficient Ketone Hydrosilylation Catalysis by a Cationic Rh Complex

**Joffrey Wolf,[a] Agnès Labande,*[a] Jean-Claude Daran,[a] and Rinaldo Poli[a]**

**Keywords:** N-Heterocyclic carbenes / S ligands / Nickel / Palladium / Rhodium

Five new, bifunctional imidazolium–thioether ligands of the general formula $RS(CH_2)_n(imidazolium)^+ArBr^-$ ($n$ = 2 or 3, R = Et or *t*Bu, Ar = 2,4,6-trimethylphenyl or 2,6-diisopropylphenyl) have been synthesised in good overall yields by a general method and used as N-heterocyclic carbene precursors for complexation studies on various transition metals ($Ni^{II}$, $Pd^{II}$ and $Rh^{I}$). Sulfur does not coordinate the nickel centre, whereas the two functional groups bind the palladium centre to form a dinuclear compound. Cationic rhodium(I) complexes have also been prepared and preliminary catalytic tests show that they have good activity for the hydrosilylation of ketones.
(© Wiley-VCH Verlag GmbH & Co. KGaA, 69451 Weinheim, Germany, 2007)

## Introduction

N-Heterocyclic carbenes (NHC) have been thoroughly studied over the last 15 years.[1] Whereas the high strength of metal–NHC bonds has yielded new classes of robust catalysts,[2–4] the combination of NHCs and less strongly binding heteroatom donors has been investigated in order to combine robustness and activity in the corresponding complexes. Thus NHC–phosphane[5–10] and NHC-N donor[11,12] or NHC-O donor[13] ligands have been developed. Thioethers are soft donor ligands and have been successfully used in catalysis, mostly in combination with other donors such as phosphanes.[14] In combination with NHCs, they could provide potentially useful catalytic properties. A few NHC–thioether precursors have already been described, but they have mainly been used as bioactive compounds (antibacterials, fungicides)[15] or for heavy metal extraction from water.[16] Few carbene–thioether complexes have been isolated and characterised, respectively, by Seo et al. in 2003[9] and Ros et al. recently[17,18] (Figure 1). NHC–furan and NHC–thiophene ligands have also been described, but only the NHC moiety coordinates the metal centre.[19] We have recently described an efficient synthetic pathway for phosphane–imidazolium compounds, using 1-bromoalkyl-3-arylimidazolium bromides as key intermediates.[5,6] We have now extended this methodology to the synthesis of NHC–thioether precursors and report here the characterisation of these new ligands, as well as representative products of their complexation to various metals of interest in catalysis: nickel(II), palladium(II) and rhodium(I).

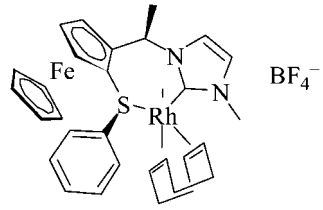


**A**

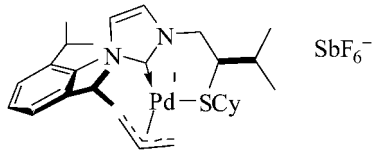


**B**

Figure 1. NHC–thioether complexes described in the literature. (A) Seo et al.[9], (B) Ros et al.[17,18]

## Results and Discussion

### Ligand Syntheses

Compounds **5**–**7** were obtained from 1-(2-bromoethyl)-3-arylimidazolium bromides **1** and **2**, and compounds **8** and **9** from 1-(3-bromopropyl)-3-arylimidazolium bromides **3** and **4**, by nucleophilic substitution with lithium alkylthiolates (Scheme 1). An optimisation study has been carried out on the reaction of compound **1** with lithium *tert*-butyl

[a] Laboratoire de Chimie de Coordination, UPR CNRS 8241 (lié par convention à l'Université Paul Sabatier et à l'Institut National Polytechnique de Toulouse),
205 route de Narbonne, 31077 Toulouse Cedex 4, France
Fax: +33-561553003
E-mail: agnes.labande@lcc-toulouse.fr
Supporting information for this article is available on the WWW under http://www.eurjic.org or from the author.

 © 2007 Wiley-VCH Verlag GmbH & Co. KGaA, Weinheim 

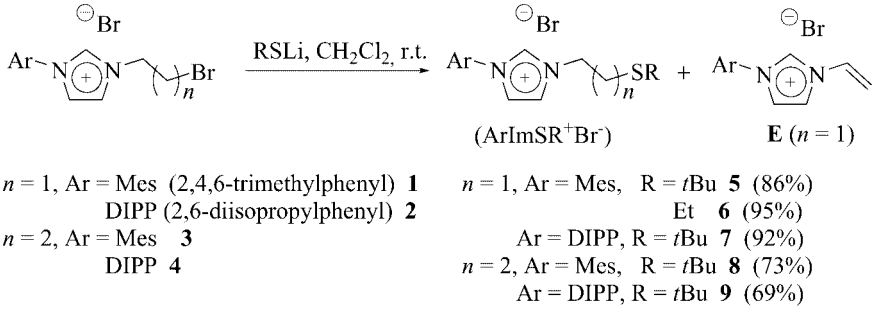


Scheme 1. Nucleophilic substitution on **1**–**4** bromides by lithium alkylthiolate reagents.

thiolate (Table 1). Alcohols and water are commonly used solvents for nucleophilic substitution reactions with thiolates,[20] whereas acetone and DMF are employed with phenolates.[21] Ethanol and DMF produced homogeneous mixtures with our substrates, contrary to acetone and dichloromethane. Our first attempt in ethanol at 60 °C, however, gave 62% of an elimination product, **E**, and only 7% of the expected compound. The temperature was lowered to 25 °C in order to improve the selectivity in favour of the substitution product: compound **5** was obtained in 14% yield, but again with 57% of elimination product (entry 1). A systematic study of the reaction conditions showed that the reaction is highly solvent-dependent, ethanol and acetone leading to substantial amounts of elimination product **E**, whereas dichloromethane and DMSO yield greater selectivity in favour of the substitution product but at slower rates. The conversion was also greatly improved when the reactions were carried out in more dilute media (entries 4 and 6). Under optimised reaction conditions (entry 6), **5** was obtained in very good yields (Scheme 1). These conditions were successfully applied to other substrates to afford thioethers **6**–**9** in good yields.

Table 1. Solvent and concentration screening for ligand **5** synthesis.[a]

| Entry | Solvent | Solvent amount (mL) | **1**/**E**/**5**[b] |
|---|---|---|---|
| 1 | EtOH | 2 | 29/57/14 |
| 2 | $Me_2CO$ | 2 | 38/50/12 |
| 3 | DMSO | 2 | 85/00/15 |
| 4 | DMSO | 3 | 60/00/40 |
| 5 | $CH_2Cl_2$ | 2 | 74/07/19 |
| 6 | $CH_2Cl_2$ | 3 | 03/03/94 |
| 7 | $CH_2Cl_2$ | 4 | 30/01/69 |

[a] **1** (0.5 mmol), *t*BuSLi (0.55 mmol), 17 h at room temperature. [b] Ratio determined by ethylene signal integration in $^1$H NMR spectra of crude products.

The $^1$H NMR signals of the acidic imidazolium protons are observed between 10.03 and 10.28 ppm for compounds **5**, **6** and **8**, and at $\delta$ = 9.87 ppm for compounds **7** and **9**, which denotes a greater shielding effect of the bulky DIPP compared to the mesityl group. Compounds **5** and **6** were analysed by single-crystal X-ray diffraction. The structures (Figure 2) show hydrogen bonds, as is typically observed for imidazolium bromides,[22] between the bromide anion and the C1 proton (Br1···H1–C1 2.637 Å for **5**, 2.624 Å for **6**).

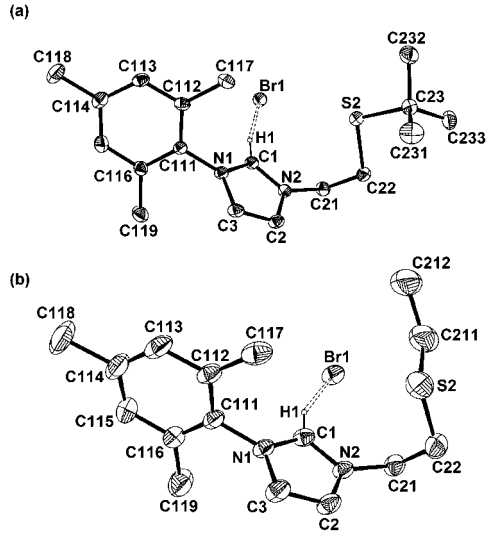


Figure 2. ORTEP views of **5** (a) and **6** (b). Ellipsoids are shown at the 30% probability level. All hydrogen atoms except H(1) and the solvent molecule ($CH_2Cl_2$) which co-crystallised with **5** are omitted for clarity.

## Nickel Complexes

Preliminary complexation studies were carried out with the catalytically relevant metals nickel, palladium and rhodium. Our previous studies of the coordination of phosphane-imidazolium salts to $Ni^{II}$ complexes of type $NiX_2L_2$ led to the isolation of zwitterionic compounds of the formula [$NiX_3(PPh_2ImAr)$], where ImAr is as defined in Scheme 1.[5,6] The analogous reaction of **5** with 1 equiv. of $NiBr_2$(DME) did not give the corresponding zwitterionic species with sulfur coordination. A $NiBr_4^{2-}$ species with two imidazolium/thioether counterions, **10**, was obtained instead (Scheme 2). Deprotonation of **10** with *t*BuOK led to the biscarbene complex **11**, with no sulfur coordination onto the nickel centre. The alternative strategy consisting of initial deprotonation of ligand **5** with a strong base, followed by reaction of the resulting free carbene with $NiBr_2$(DME), also led to the same product. The absence of sulfur coordination has two possible explanations: the bulkiness of the *tert*-butyl group prevents the coordination on the nickel, or the sulfur donor power is insufficient to compete with bromide for coordination. In order to con-

 © 2007 Wiley-VCH Verlag GmbH & Co. KGaA, Weinheim 

firm one of these hypotheses, we added 1 equiv. of **6**, which contains a less bulky ethyl substituent, to 1 equiv. of $NiBr_2(MeCN)_2$. During the treatment, unreacted nickel corresponding to half of the starting material was recovered. This result would be more in favour of the second hypothesis, although we have no further evidence to validate it.

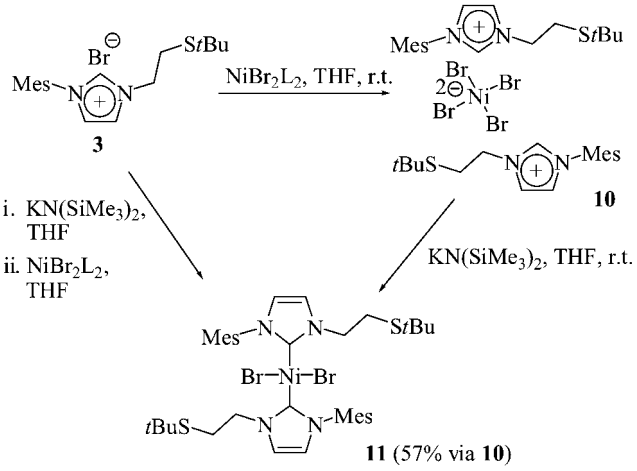


Scheme 2. Nickel(II) complex synthesis.

The crystal structure of compound **11** has been resolved by X-ray analysis (Figure 3). As the nickel atom is located on an inversion centre, the geometry around it is perfectly square-planar. The imidazol-2-ylidene ring is planar [maximum deviation of 0.005(1) Å for atom N2] and is approximately perpendicular [angle of 75.06(5)°] to the coordination plane, thus limiting steric interactions. This was already observed for other previously described $Ni^{II}$–bis(NHC) complexes.[23] The mesityl ring forms an angle of 77.63(6)° with the NHC ring, and we can notice the existence of an interaction between a hydrogen from methyl C119 and Br1 (C119···Br1$^{i}$ 2.75 Å). Selected bond lengths and angles are listed in Table 2.

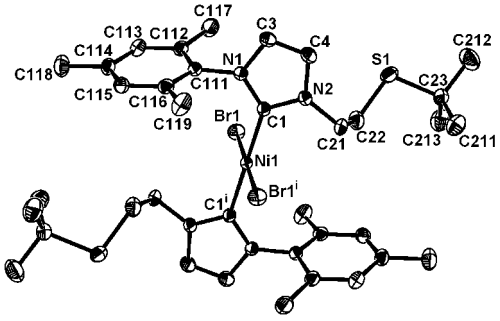


Figure 3. An ORTEP view of compound **11**. Ellipsoids are represented at the 50% probability level. Hydrogen atoms are omitted for clarity.

Although only one isomer is present in the crystal, analysis by $^1H$ and $^{13}C$ NMR revealed a mixture of two distinct isomers in solution in a ratio of 1:1.27. We believe that these

Table 2. Comparison of the main structural parameters of **11** and $NiBr_2$(1,3-dicyclohexylimidazol-2-ylidene)$_2$.

| | **11** | $NiBr_2L_2$ [a] |
|---|---|---|
| *Bond lengths* [Å] | | |
| Ni–Br | 2.3113(5) | 2.3113(4) |
| Ni–C1 | 1.9186(17) | 1.908(3) |
| C1–N1 | 1.359(2) | 1.353(4) |
| C1–N2 | 1.354(2) | 1.347(4) |
| N2–C4 | 1.385(2) | 1.394(5) |
| N1–C3 | 1.395(2) | 1.390(5) |
| C3–C4 | 1.348(3) | 1.333(5) |
| *Bond angles* [°] | | |
| C1–Ni–C1i | 180.00(9) | 180.00 |
| C1–Ni–Br1 | 89.48(5) | 89.41(10) |
| C1–Ni–Br1i | 90.52(5) | 90.59(10) |
| *Dihedral angles* [°] | | |
| N1–C1–Ni–Br1 | 74.43 | |
| N2–C1–Ni–Br1i | 75.41 | |
| N1–C1–C1i–N2i | 0.98 | |

[a] L = 1,3-dicyclohexylimidazol-2-ylidene.

are conformational isomers. In the crystalline compound, the aryl and thioether alkyl chains of the two imidazol-2-ylidene groups are mutually *anti* to afford a head-to-tail arrangement, which minimises steric interactions. Strong steric interactions between the N-substituents in a bis-NHC-$Ni^{II}$ complex have been observed for $NiCl_2$[1,3-bis(2,6-diisopropylphenyl)imidazol-2-ylidene]$_2$, resulting in a significant deviation from coplanarity for the two NHC rings.[24] For our compound, it is possible to envisage that the different N-substituents adopt a *syn* orientation in the second isomer and that there is a significant barrier for the 180° rotation that is required to interconvert them. Recent work by Gomes et al.[25] has shown that the energy barrier for a 180° rotation of a N-heterocyclic carbene along the C–Ni axis, in allyl $Ni^{II}$ complexes, is 14–15 kcal mol$^{-1}$ for NHCs bearing methyl substituents and becomes >18 kcal mol$^{-1}$ with *tert*-butyl substituents. In our case, the imidazole-2-ylidene bears a bulky mesityl group on one side and a functionalised alkyl chain on the other side. Therefore it becomes possible to independently observe two conformational isomers.

## Palladium Complexes

Contrary to the nickel system, addition of ligands **5**–**9** to $PdBr_2$(COD) led to the expected coordination of the sulfur and bromine atoms, leading to the zwitterionic complexes **12**–**16** in good yields (Scheme 3). A zwitterionic structure for these complexes, with a coordinated thioether function and a dangling imidazolium group, is suggested by the spectroscopic data. The typical signal of the acidic imidazolium proton is still present in the $^1H$ NMR spectra of all complexes and is situated between 9.00 and 9.61 ppm. Likewise, the elemental analyses of the complexes are in agreement with the calculated values. Subsequent deprotonation of **13** (Scheme 3) led to NHC complex **17**. The $^1H$ and $^{13}C$ NMR properties are consistent with the expected stoichiometry, as for the related phosphane-carbene complexes previously

 © 2007 Wiley-VCH Verlag GmbH & Co. KGaA, Weinheim 

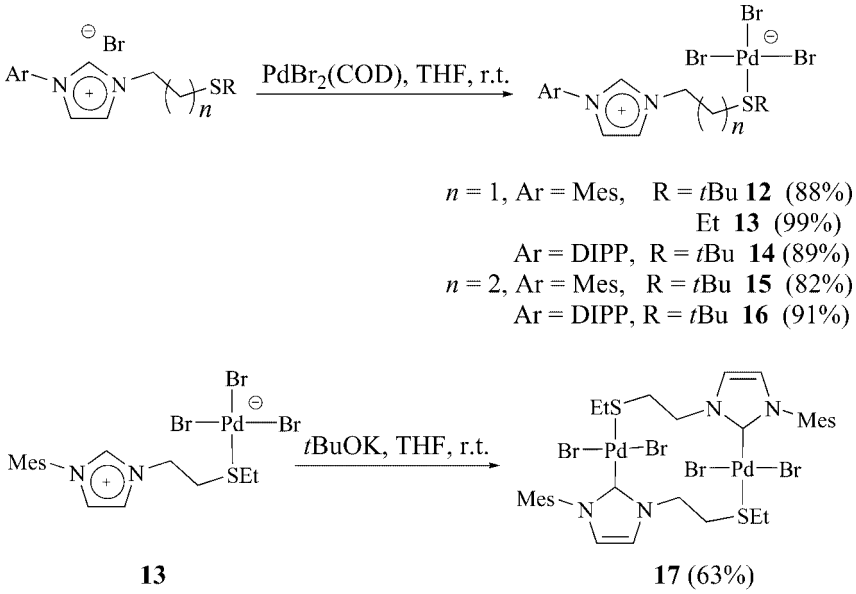


Scheme 3. Synthesis of palladium(II) complexes.

described by Danopoulos et al.[7] and Lee et al.[26] The $^{13}C$ NMR signal of the carbene C atom is observed at $\delta$ = 155.75 ppm in the case of **17**, and respectively at $\delta$ = 157.2 and 162.4 ppm for the above-mentioned phosphane-carbene complexes. Moreover, the $^{1}H$ NMR spectrum of **17** only shows two protons for the imidazole cycle, appearing as doublets, and a 2D HMBC NMR experiment confirms the existence of a long-range coupling between these protons and the carbene C atom.

However, the X-ray structure (Figure 4) reveals that **17** is a dinuclear complex where each palladium centre displays a slightly distorted square-planar coordination environment. The two square-planar moieties are located face to face and the two NHC–thioether ligands span the metal centres in a relative *trans* arrangement. Pd–C and Pd–S bond lengths are comparable to the usual NHC–$Pd^{II}$ and thioether–$Pd^{II}$ bonds.[7,26,27] A similar arrangement is adopted by related NHC–oxazoline derivatives. Only three X-ray structures of $Pd^{II}$ complexes possessing a chelating NHC–thioether ligand have been described:[17,18] in these cases, the sulfur atom is situated *cis* to the NHC moiety, with Pd–C and Pd–S distances of, respectively, 2.036–2.063 Å and 2.326–2.367 Å. Mass spectrometry analyses (FAB technique) confirm the existence of a dinuclear compound.

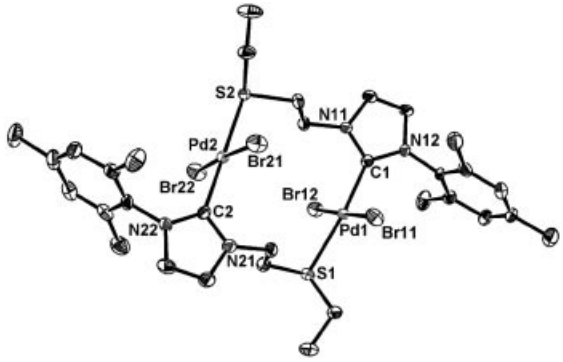


Figure 4. An ORTEP view of compound **17**. Ellipsoids are represented at the 30% probability level. Hydrogen atoms and a co-crystallised THF molecule are omitted for clarity. Selected bond lengths [Å] and angles [°]: Pd1–C1 1.990(4), Pd2–C2 1.983(4), Pd1–S1 2.3731(9), Pd2–S2 2.3622(9), Br21–Pd2–Br22 175.50(2), C1–Pd1–S1 173.10(12).

## Rhodium Complexes

Addition of compounds **5**–**7** to $[Rh(COD)Cl]_2$ in the presence of a strong base (Scheme 4) led, after halide abstraction, to the formation of NHC derivatives **18**–**20**. The

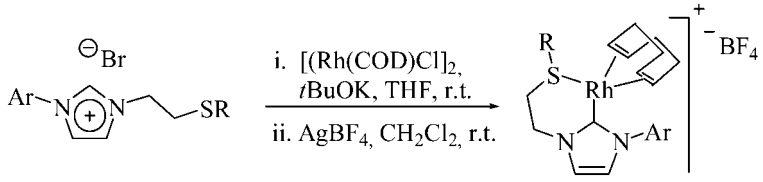


R = *t*Bu, Ar = Mes **18** (81%)
Ar = DIPP **19** (79%)
R = Et, Ar = Mes **20** (76%)

Scheme 4. Synthesis of rhodium(I) complexes.

 © 2007 Wiley-VCH Verlag GmbH & Co. KGaA, Weinheim 

nature of these products, as salts of typical square-planar $Rh^I$ complexes with *cis* chelating NHC–thioether ligands, is consistent with the spectroscopic characterisation. The $^{13}C$ NMR signals of the carbene C atoms appear around 173 ppm, which is the expected value for cationic NHC–$Rh^I$ complexes.[10,18,28] The sulfur coordination on rhodium is suggested by the downfield shift (about 7 ppm) of the quaternary carbon on sulfur for complexes **18** and **19**, and of the S–$CH_2CH_3$ carbon signal (about 6 ppm) for complex **20**.[29]

The square-planar coordination environment in complexes **18**–**20** was confirmed by X-ray diffraction studies (Figure 5). Selected bond lengths and angles are listed in Table 3. The structures reveal slightly shorter Rh1–C1 bond lengths than in Seo's NHC–thioether complex. Rh1–S1 distances are within the same range, except compound **20**, for which we observe a shorter bond of 2.351(2) Å. The Rh1–C(COD) bonds *trans* to NHC are longer than the bonds *trans* to sulfur, which indicates a stronger *trans* influence of the NHC moiety. A boat-like conformation of the six-membered metallacycle is a common feature for all these structures. In the case of compound **20**, the deviation from the ideal 90° value of the C1–Rh1–S1 angle [82.5(2)°] could be because of a close contact between the methylene of the ethyl arm on sulfur (C311) and the COD ligand [intramolecular distances: C5–C311 3.45(1) Å and H5–H31A 2.36 Å; C6–C311 3.52(1) Å and H6–H31B 2.30 Å]. This value is consistent with the previously reported data for similar complexes.[10,18,30] This distortion cannot be observed in **18** and **19**, which have a bulky *tert*-butyl substituent on sulfur.

Table 3. Comparison of the main structural parameters of **18**–**20** and of the $Rh^I$ complex described by Seo et al. (**A**).

| | **18** | **19** | **20** | **A**[7] |
|---|---|---|---|---|
| *Bond lengths* [Å] | | | | |
| Rh1–C1 | 2.032(4) | 2.020(5) | 2.042(7) | 2.051(7) |
| Rh1–S1 | 2.4076(10) | 2.3940(18) | 2.351(2) | 2.394(2) |
| Rh1–C11 | 2.145(4) | 2.127(6) | 2.149(6) | 2.137(7) |
| Rh1–C12 | 2.175(4) | 2.150(6) | 2.148(8) | 2.148(9) |
| Rh1–C15 | 2.199(4) | 2.191(6) | 2.175(6) | 2.225(9) |
| Rh1–C16 | 2.222(4) | 2.212(7) | 2.228(8) | 2.236(8) |
| C1–N1 | 1.351(5) | 1.341(7) | 1.360(9) | 1.342(9) |
| C1–N2 | 1.366(5) | 1.356(7) | 1.365(9) | 1.319(9) |
| S1–C5 | 1.827(4) | 1.791(8) | 1.806(9) | 1.785(7) |
| S1–C6[a] | 1.863(4) | 1.848(9) | 1.808(8) | 1.802(7) |
| *Bond angles* [°] | | | | |
| C1–Rh1–S1 | 88.93(11) | 89.94(16) | 82.5(2) | 89.0(2) |
| N1–C–1–N2 | 104.0(3) | 103.9(5) | 104.1(6) | 105.7(6) |

[a] This carbon is labelled C111 for **19**.

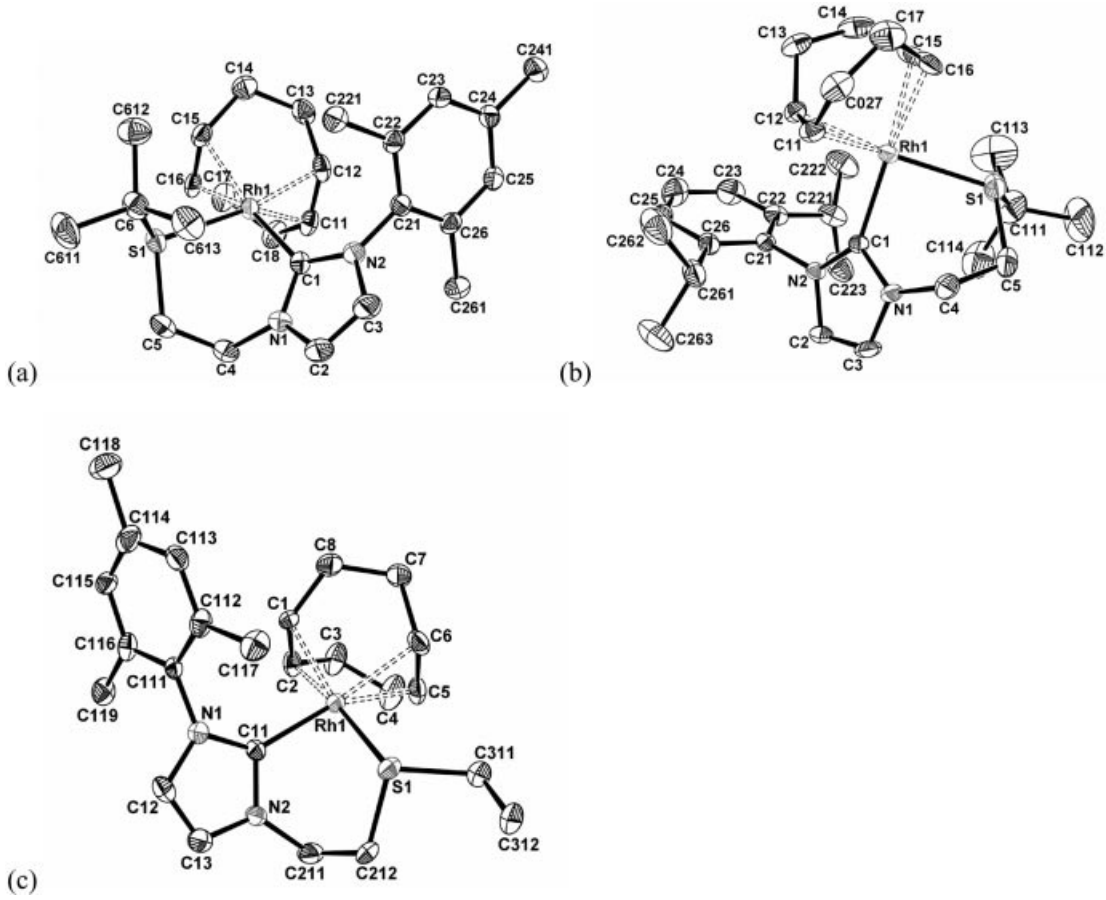


Figure 5. ORTEP views of the cations in complexes **18** (a), **19** (b) and **20** (c). Ellipsoids are represented at the 30% probability level. Hydrogen atoms, the counterion ($BF_4$) and a co-crystallised $CDCl_3$ molecule **18** are omitted for clarity.

 © 2007 Wiley-VCH Verlag GmbH & Co. KGaA, Weinheim 

**Catalytic Hydrosilylation of Methyl Aryl Ketones**

The catalysed hydrosilylation of ketones has attracted a lot of attention for many decades as it is an efficient synthetic alternative to the reduction of the carbonyl group by main group hydrides and catalytic hydrogenation.[31] Rhodium is the favoured catalytic metal for this process, even though other metals have been used. Neutral precatalysts derived from $RhCl(PPh_3)_3$,[32,33] $[RhCl(olefin)_2]_2$ [olefin = ethylene, cyclooctene; or $(olefin)_2$ = 1,5-cyclooctadiene, norbornadiene],[33–36] $RhH(PPh_3)_4$[37] or $RhCl_3L_3$[38] derivatives have most commonly been used to generate the active catalyst, but a few processes using cationic precursors have also been reported.[39,40] It has also been reported that the assistance of AgX (X = $OSO_2CF_3$, $BF_4$) is required in some cases to improve the catalytic activity,[38,41] presumably through transformation into a more active cationic species. The typical supporting ligands, including chiral versions for the enantioselective hydrosilylation of prochiral ketones, are based on P or N donors. Although several catalysts have shown outstanding activities,[36,41,42] the issue of catalyst stability and deactivation may hamper extension to large-scale production. As NHC ligands are likely to be solidly anchored to the metal centre, they may be expected to impart activity and stability to the catalytic system. Previous reports of ketone hydrosilylation using NHC ligands are limited.[12,43,44] For these reasons, we considered it of interest to test the catalytic activity of the cationic rhodium complexes **18**–**20**.

Preliminary catalytic tests have shown that these complexes are indeed active in the hydrosilylation of acetophenone and its derivatives (Tables 4 and 5, Scheme 5). The reactions were followed by TLC and the silylated intermediate was hydrolysed with MeOH before $^1H$ NMR analysis. The reactions were first carried out with 2 mol-% of **18**, in dichloromethane or THF. The yield of the expected alcohol reached 90% in dichloromethane in 17 h (Table 4, entry 1), whereas it was quantitative in THF (Table 4, entry 2). The catalyst loading was thus lowered to 1 mol-%. With a concentration of 1 M in acetophenone in THF, the yield reached 90% after 24 h. However, working in a more concentrated medium allowed us to get a total conversion of the substrate into the alcohol in only 4 h (entry 4). A similar result was obtained with complex **19** (Table 4, entries 5 and 6). Finally, complex **20** proved to be the most active, with a quantitative yield of alcohol in only 1 h at room temperature (Table 4, entry 7). The same trend was observed with 4-methoxyacetophenone (Table 5, entries 1–5): increasing the concentration allowed us to get a total conversion of the substrate into the desired alcohol in a reduced time, while **20** showed a better activity than **18** and **19**. Similar results were obtained with 4-fluoroacetophenone, bearing an electron-withdrawing substituent (Table 5, entries 6–8). The introduction of a methyl group *ortho* to the halide, however, slowed the reaction down. As an example, the reaction with **18** did not go to completion after 6 h, with only 78% conversion (Table 5, entry 9). Thus steric factors seem to have more influence than electronic factors on the issue of the reaction. Finally, no reaction occurred when other silanes ($Et_3SiH$, $MeEt_2SiH$ and $HSiCl_3$) were used with acetophenone.

Table 4. Hydrosilylation of acetophenone.[a]

| Entry | R | Catalyst (mol-%) | Solvent (concentration) | *t* (h) | Yield (%)[b] |
|---|---|---|---|---|---|
| 1 | H | **18** (2) | $CH_2Cl_2$ (1 M) | 17 | 90 |
| 2 | H | **18** (2) | THF (1 M) | 17 | 99 |
| 3 | H | **18** (1) | THF (1 M) | 24 | 90 |
| 4 | H | **18** (1) | THF (2 M) | 4 | 99 |
| 5 | H | **19** (1) | THF (1 M) | 8 | 99 |
| 6 | H | **19** (1) | THF (2 M) | 4 | 99 |
| 7 | H | **20** (1) | THF (2 M) | 1 | 99 |

[a] Ketone (1 equiv.), diphenylsilane (1.1 equiv.), room temperature, then hydrolysis with MeOH. [b] Determined by integration of signals in $^1H$ NMR spectra of crude products.

Table 5. Hydrosilylation of acetophenone derivatives.[a]

| Entry | R | Catalyst | Concentration | *t* (h) | Yield (%)[b] |
|---|---|---|---|---|---|
| 1 | 4-OMe | **18** | 1 M | 24 | 80 |
| 2 | 4-OMe | **18** | 2 M | 3 | 98 |
| 3 | 4-OMe | **19** | 1 M | 6 | 99 |
| 4 | 4-OMe | **19** | 2 M | 2.5 | 99 |
| 5 | 4-OMe | **20** | 2 M | 2 | 99 |
| 6 | 4-F | **18** | 2 M | 4 | 96 |
| 7 | 4-F | **19** | 2 M | 4.5 | 99 |
| 8 | 4-F | **20** | 2 M | 2 | 99 |
| 9 | 2-Me | **18** | 2 M | 6 | 78[c] |
| 10 | 2-Me | **19** | 2 M | 3.5 | 99 |
| 11 | 2-Me | **20** | 2 M | 3.5 | 99 |

[a] Ketone (1 equiv.), diphenylsilane (1.1 equiv.), room temperature, 1 mol-% catalyst, THF, then hydrolysis with MeOH. [b] Determined by integration of signals in $^1H$ NMR spectra of crude products. [c] The reaction was stopped before completion.

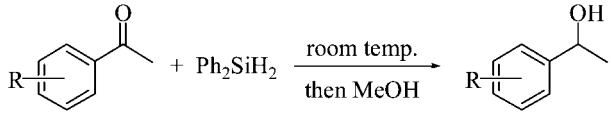


Scheme 5. Hydrosilylation of acetophenone and its derivatives with $Rh^I$ complexes.

The activity of our complexes compares well with previously reported $Rh^I$ systems bearing bifunctional NHC-oxazoline ligands. Thus, Bolm et al. obtain excellent yields of 1-phenylethanol with their system, using 2 mol-% of catalyst in THF at room temperature or at 0 °C.[44] Unfortunately there is no indication of reaction times, which does not allow a direct comparison with our results. On the other hand, César et al. report the hydrosilylation of acetophenone with diphenylsilane using 1 mol-% catalyst in dichloromethane at room temperature. In their case, the $Rh^I$ complexes tested give from 70% to 93% yield in a maximum of 5 h.[12]

The higher catalytic activity observed at higher ketone concentration is in agreement with previous reports of a saturation effect: the reaction was found to be first order in ketone at low concentrations, but eventually became [ketone] independent at high concentrations.[35,40]

 © 2007 Wiley-VCH Verlag GmbH & Co. KGaA, Weinheim 

## Conclusions

In conclusion, we have described a general and simple method for the preparation of new NHC–thioether precursors and explored their coordination chemistry. The coordination of sulfur on nickel was not observed, yielding complex **11** where the two ligands are monodentate through the NHC function and the thioether function is dangling. In the case of palladium(II), a dinuclear complex with *trans* carbene and sulfur coordination, **17**, was obtained. Rhodium(I) complexes with chelating carbene/thioether ligands were finally prepared in good yields. Preliminary catalytic studies have shown that these complexes are very active for the hydrosilylation of acetophenone and its derivatives. The asymmetric version of this reaction, as well as other catalytic reactions, is now under investigation, and the results will be published in due course.

## Experimental Section

**General Methods:** Reactions involving air- or moisture-sensitive reagents and products were carried out under dry argon using Schlenk glassware and vacuum line techniques, and dry, purified solvents. All other steps were done without particular precautions. Elemental analyses were carried out by the Service d'Analyse du Laboratoire de Chimie de Coordination in Toulouse. $^1$H and $^{13}$C{$^1$H} NMR spectroscopic data were recorded with a Bruker AV-500 spectrometer, operating at 500 MHz for $^1$H and 125.8 MHz for $^{13}$C and on a Bruker AV-200 spectrometer operating at 188 MHz for $^{19}$F. The spectra were referenced internally using the signal from the residual protiosolvent ($^1$H), the signals of the solvent ($^{13}$C) or the signal of trifluoroacetic acid, 10% in $C_6D_6$ ($^{19}$F). Mass spectra (ESI) were obtained from acetonitrile or methanol solutions on a TSQ 7000 (Thermo Electron) and (FAB) from DMSO or DMF solutions on a Nermag R10-10 instrument. Electrospray high-resolution mass spectra were performed by the Service de spectroscopie de masse CESAMO de l'université de Bordeaux I. Chromatographic work was performed on silica gel 60 Å. $PdBr_2(COD)$,[45] 1-(2-bromoethyl)-3-(2,4,6-trimethylphenyl) imidazolium bromide **1**,[6] 1-(2-bromoethyl)-3-(2,6-diisopropylphenyl)imidazolium bromide **2**[6] and 1-(3-bromopropyl)-3-(2,4,6-trimethylphenyl)imidazolium bromide **3**[6] were prepared as described in the literature. Both lithium alkylthiolates were prepared by action of methyllithium on the corresponding thiols and used rapidly after their preparation. Other reagents were obtained from commercial sources and used as received.

**1-[2-(*tert*-Butylthio)ethyl]-3-(2,4,6-trimethylphenyl)imidazolium Bromide (5):** *t*BuSLi (170 mg, 1.77 mmol) was added to a solution of **1** (610 mg, 1.63 mmol) in $CH_2Cl_2$ (10 mL). The mixture was stirred for one day at room temperature. $CH_2Cl_2$ (20 mL) was added and the mixture was washed with water (10 + 5 mL). The organic phase was dried ($MgSO_4$), filtered and concentrated under vacuum to give a white, hygroscopic solid. Yield 535 mg (86%). Suitable X-ray colourless crystals were obtained by slow diffusion of diethyl ether in a $CH_2Cl_2$ solution. M.p. 88–92 °C. $C_{18}H_{27}BrN_2S$ (383.42): HRMS (ESI) *m*/*z*: calcd. 303.189496; found 303.190467. $^1$H NMR (500 MHz, $CDCl_3$, 25 °C): $\delta$ = 10.03 (t, $^4J$ = 1.6 Hz, 1 H, NC*H*N), 8.13 (t, $^{3,4}J$ = 1.5 Hz, 1 H, MesNC*H*=), 7.19 (t, $^{3,4}J$ = 1.6 Hz, 1 H, AlkN–C*H*=), 6.97 [s, 2 H, C*H* (Mes)], 4.89 (t, $^3J$ = 6.0 Hz, 2 H, NC$H_2$), 3.17 (t, $^3J$ = 6.1 Hz, 2 H, C$H_2$S*t*Bu), 2.31 (s, 3 H, *p*-C$H_3$), 2.06 (s, 6 H, *o*-C$H_3$), 1.27 (s, 9 H, S*t*Bu) ppm. $^{13}$C NMR (125.8 MHz, $CDCl_3$, 25 °C): $\delta$ = 141.26 [*p*-*C* (Mes)], 137.77 (N–*C*H–N), 134.31 [*o*-*C* (Mes)], 130.66 [N–*C* (Mes)], 129.81 [*C*H (Mes)], 124.13 (AlkN–*C*H=), 122.74 (MesN–*C*H=), 50.33 (N–*C*$H_2$), 43.33 [S*C*$(CH_3)_3$], 31.00 [SC(*C*$H_3)_3$], 29.32 (*C*$H_2$S), 21.11 [*p*-*C*$H_3$ (Mes)], 17.66 [*o*-*C*$H_3$ (Mes)] ppm. MS (ESI, positive mode): *m*/*z* (%) = 303.35 (100) [$C_{18}H_{27}N_2S^+$]. MS (ESI, negative mode): *m*/*z* (%) = 79 (100) [$Br^-$].

**1-[2-(Ethylthio)ethyl]-3-(2,4,6-trimethylphenyl)imidazolium Bromide (6):** EtSLi (246 mg, 3.61 mmol) was added to a solution of **1** (1.125 g, 3.01 mmol) in $CH_2Cl_2$ (18 mL). The mixture was stirred for one day at room temperature. $CH_2Cl_2$ (22 mL) was added and the mixture was washed with water (2 × 15 mL). The organic phase was dried ($MgSO_4$), filtered and concentrated under vacuum to give a white hygroscopic solid. Yield 1.07 g (95%). X-ray quality crystals were obtained by slow diffusion of diethyl ether in a $CH_2Cl_2$ solution. M.p. 117 °C. $C_{16}H_{23}BrN_2S$ (355.36): calcd. C 54.08, H 6.52, N 7.88; found C 53.96, H 6.51, N 8.00. $^1$H NMR (500 MHz, $CDCl_3$, 25 °C): $\delta$ = 10.08 (s, 1 H, NC*H*N), 8.26 (s, 1 H, MesNC*H*=), 7.16 (s, 1 H, AlkNC*H*=), 6.94 [s, 2 H, C*H* (Mes)], 4.90 (t, $^3J$ = 6.0 Hz, 2 H, NC$H_2$), 3.09 (t, $^3J$ = 6.1 Hz, 2 H, C$H_2$SEt), 2.62 (q, $^3J$ = 7.4 Hz, 2 H, SC$H_2$CH$_3$), 2.29 (s, 3 H, *p*-C$H_3$), 2.02 (s, 6 H, *o*-C$H_3$), 1.16 (t, $^3J$ = 7.4 Hz, 3 H, SCH$_2$C$H_3$) ppm. $^{13}$C NMR (125.8 MHz, $CDCl_3$, 25 °C): $\delta$ = 141.11 [*p*-C (Mes)], 137.97 (N*C*HN), 134.29 [*o*-C (Mes)], 130.67 [N*C* (Mes)], 129.73 [CH (Mes)], 123.98 (AlkN*C*H=), 122.93 (MesN*C*H=), 48.88 (N*C*$H_2$), 32.14 (*C*$H_2$SEt), 25.67 (S*C*$H_2$CH$_3$), 21.07 [*p*-*C*$H_3$ (Mes)], 17.61 [*o*-*C*$H_3$ (Mes)], 14.61 (SCH$_2$*C*$H_3$) ppm. MS (ESI, positive mode): *m*/*z* (%) = 275.15 (100) [$C_{16}H_{23}N_2S^+$]. MS (ESI, negative mode): *m*/*z* (%) = 79 (100) [$Br^-$].

**1-[2-(*tert*-Butylthio)ethyl]-3-(2,6-diisopropylphenyl)imidazolium Bromide (7):** *t*BuSLi (118 mg, 1.23 mmol) was added to a solution of **2** (410 mg, 0.99 mmol) in $CH_2Cl_2$ (6 mL). The mixture was stirred for one day at room temperature. $CH_2Cl_2$ (14 mL) was added and the mixture was washed with water (2 × 4 mL). The organic phase was dried ($MgSO_4$), filtered and concentrated under vacuum to give a pale yellow hygroscopic solid. Yield 387 mg (92%). M.p. 85–90 °C. $C_{21}H_{33}BrN_2S$ (425.48). HRMS (ESI) *m*/*z*: calcd. 345.236446; found 345.236823. $^1$H NMR (500 MHz, $CDCl_3$, 25 °C): $\delta$ = 9.87 (t, $^4J$ = 1.7 Hz, 1 H, NC*H*N), 8.38 (t, $^{3,4}J$ = 1.7 Hz, 1 H, AlkNC*H*=), 7.47 [t, $^3J$ = 7.8 Hz, 1 H, *p*-C*H* (DIPP)], 7.24 [d, $^3J$ = 7.8 Hz, 2 H, *m*-C*H* (DIPP)], 7.16 [t, $^{3,4}J$ = 1.7 Hz, 1 H, (DIPP)-NC*H*=], 4.91 (t, $^3J$ = 5.9 Hz, 2 H, NC$H_2$), 3.16 (t, $^3J$ = 5.9 Hz, 2 H, C$H_2$S*t*Bu), 2.28 [h, $^3J$ = 6.8, 6.9 Hz, 2 H, C*H*$(CH_3)_2$], 1.24 (s, 9 H, S*t*Bu), 1.15 [d, $^3J$ = 6.9 Hz, 6 H, CH(C$H_3)_2$], 1.09 [d, $^3J$ = 6.8 Hz, 6 H, CH(C$H_3)_2$] ppm. $^{13}$C NMR (125.8 MHz, $CDCl_3$, 25 °C): $\delta$ = 145.42 [*o*-C (DIPP)], 137.94 (N*C*HN), 131.82 [*p*-CH (DIPP)], 130.07 [N*C* (DIPP)], 124.60 [*m*-CH (DIPP)], 124.27 (AlkN*C*H=), 123.84 [(DIPP)N*C*H=], 50.10 (N*C*$H_2$), 43.13 [S*C*$(CH_3)_3$], 30.99 [SC(*C*$H_3)_3$], 29.39 (*C*$H_2$S), 28.48 [*C*H$(CH_3)_2$], 24.40, 24.21 [CH(*C*$H_3)_2$] ppm. MS (ESI, positive mode): *m*/*z* (%) = 345.50 (100) [$C_{21}H_{33}N_2S^+$]. MS (ESI, negative mode): *m*/*z* (%) = 81 (100) [$Br^-$].

**1-[3-(*tert*-Butylthio)propyl]-3-(2,4,6-trimethylphenyl)imidazolium Bromide (8):** *t*BuSLi (130 mg, 1.35 mmol) was added to a solution of **3** (390 mg, 1.00 mmol) in $CH_2Cl_2$ (6 mL). The mixture was stirred for one day at room temperature. $CH_2Cl_2$ (14 mL) was added and the mixture was washed with water (2 × 10 mL). The organic phase was dried ($MgSO_4$), filtered and concentrated under vacuum to give a white, hygroscopic solid. Yield 290 mg (73%). M.p. 134–136 °C. $C_{19}H_{29}BrN_2S$ (397.42): HRMS (ESI) *m*/*z*: calcd. 317.205146; found 317.204589. $^1$H NMR (500 MHz, $CDCl_3$, 25 °C): $\delta$ = 10.28 (t, $^4J$ = 1.5 Hz, 1 H, NC*H*N), 7.93 (t, $^{3,4}J$ =

 © 2007 Wiley-VCH Verlag GmbH & Co. KGaA, Weinheim 

1.7 Hz, 1 H, NC*H*=), 7.24 (t, $^{3,4}J$ = 1.7 Hz, 1 H, =C*H*N), 6.98 [s, 2 H, C*H* (Mes)], 4.81 (t, $^{3}J$ = 6.9 Hz, 2 H, NC$H_2$), 2.63 (t, $^{3}J$ = 6.9 Hz, 2 H, C$H_2$S*t*Bu), 2.32 (q + s, $^{3}J$ = 6.9 Hz, 5 H, *p*-C$H_3$; NCH$_2$C$H_2$), 2.06 (s, 6 H, *o*-C$H_3$), 1.27 (s, 9 H, S*t*Bu) ppm. $^{13}$C NMR (125.8 MHz, $CDCl_3$, 25 °C): $\delta$ = 141.27 [s, *p*-C (Mes)], 137.99 (s, N*C*HN), 134.16 [s, *o*-C (Mes)], 130.67 [s, N*C* (Mes)], 129.86 [s, CH (Mes)], 123.42 (s, =*C*HN), 123.25 (s, =*C*H–N), 49.37 (s, N$CH_2$), 42.69 [s, S*C*(CH$_3$)$_3$], 30.83 [s, SC(*C*H$_3$)$_3$], 30.63 (s, NCH$_2$*C*H$_2$), 24.66 (s, *C*H$_2$S), 21.10 [s, *p*-*C*H$_3$ (Mes)], 17.71 [s, *o*-*C*H$_3$ (Mes)] ppm. MS (ESI, positive mode): *m*/*z* (%) = 317.4 (100) [$C_{19}H_{29}N_2S^+$]. MS (ESI, negative mode): *m*/*z* (%) = 81.0 (100) [$Br^-$].

**1-[3-(*tert*-Butylthio)propyl]-3-(2,6-diisopropylphenyl)imidazolium Bromide (9):** *t*BuSLi (130 mg, 1.35 mmol) was added to a solution of **4** (450 mg, 1.05 mmol) in $CH_2Cl_2$ (6 mL). The mixture was stirred for one day at room temperature. $CH_2Cl_2$ (14 mL) was added and the mixture was washed with water (2 × 15 mL). The organic phase was dried ($MgSO_4$), filtered and concentrated under vacuum to give a pale yellow hygroscopic solid. Yield 318 mg (69%). M.p. 103–104 °C. $C_{22}H_{35}BrN_2S$ (439.50): HRMS (ESI) *m*/*z*: calcd. 359.252096; found 359.253029. $^1$H NMR (500 MHz, $CDCl_3$, 25 °C): $\delta$ = 9.87 (s, 1 H, NC*H*N), 8.14 (t, $^{3,4}J$ = 1.7 Hz, 1 H, AlkNC*H*=), 7.39 [t, $^{3}J$ = 7.8 Hz, 1 H, *p*-C*H* (DIPP)], 7.25 [d, $^{3}J$ = 7.9 Hz, 2 H, *m*-C*H* (DIPP)], 7.23 [t, $^{3,4}J$ = 1.7 Hz, 1 H, (DIPP) NC*H*=], 4.84 (t, $^{3}J$ = 6.8 Hz, 2 H, NC$H_2$), 2.61 (t, $^{3}J$ = 7.1 Hz, 2 H, C$H_2$S*t*Bu), 2.30 (q, $^{3}J$ = 6.9; 7.0 Hz, 2 H, NCH$_2$C$H_2$), 2.25 [h, $^{3}J$ = 6.9 Hz, 2 H, C*H*(CH$_3$)$_2$], 1.26 (s, 9 H, S*t*Bu), 1.17 [d, $^{3}J$ = 6.8 Hz, 6 H, CH(C$H_3$)$_2$], 1.10 [d, $^{3}J$ = 6.8 Hz, 6 H, CH(C$H_3$)$_2$] ppm. $^{13}$C NMR (125.8 MHz, $CDCl_3$, 25 °C): $\delta$ = 145.29 [s, *o*-*C* (DIPP)], 138.08 (s, N*C*HN), 131.85 [s, *p*-*C*H (DIPP)], 130.13 [s, N*C* (DIPP)], 124.63 [s, *m*-*C*H (DIPP)], 124.30 (s, AlkN*C*H=), 123.75 [s, (DIPP)N*C*H=], 49.43 (s, N$CH_2$), 42.61 [s, S*C*(CH$_3$)$_3$], 30.90 [s, SC(*C*H$_3$)], 30.82 (s, NCH$_2$*C*H$_2$), 28.67 [s, *C*H(CH$_3$)$_2$], 24.59 (s, *C*H$_2$S), 24.40, 24.19 [s, CH(*C*H$_3$)$_2$] ppm. MS (ESI, positive mode): *m*/*z* (%) = 359.4 (100) [$C_{22}H_{35}N_2S^+$]. MS (ESI, negative mode): *m*/*z* (%) = 80.8 (100) [$Br^-$].

**Bis{1-[2-(*tert*-butylthio)ethyl]-3-(2,4,6-trimethylphenyl)imidazol-2-ylidene}nickel Dibromide (11):** $NiBr_2(MeCN)_2$ (140 mg, 0.47 mmol) and **3** (383 mg, 1.00 mmol) were placed in a Schlenk tube and THF (15 mL) was added. After stirring for 5 min, a homogeneous blue-green solution was obtained. A freshly prepared KN(SiMe$_3$)$_2$ solution (5 mL, 0.2 M in THF) was added over 5 min during which the mixture colour became darker and changed to deep pink-red. The mixture was stirred at room temperature for 15 min and the solvent was removed under vacuum. The residue was washed with diethyl ether (20 mL) and filtered. The filtrate was concentrated (about 5 mL), precipitated in pentane (50 mL) and filtered. The solution was concentrated to give a pink-red solid. Yield 217 mg (57%). X-ray quality crystals were obtained by slow evaporation of a pentane solution. M.p. (dec.) 195–200 °C. $C_{36}H_{52}Br_2N_4NiS_2$ (823.47): calcd. C 52.51, H 6.37, N 6.80; found C 52.45, H 6.39, N 6.56. NMR shows signals for two isomers, 1.27:1 ratio. Major isomer: $^1$H NMR (500 MHz, $CDCl_3$, 25 °C): $\delta$ = 7.09 [s, 4 H, C*H* (Mes)], 6.97 (s, 2 H, AlkNC*H*=), 6.60 (s, 2 H, MesNC*H*=), 4.92 (s, 4 H, NC$H_2$), 3.18 (s, 4 H, C$H_2$S), 2.45 [s, 6 H, *p*-C$H_3$ (Mes)], 2.23 [s, 12 H, *o*-C$H_3$ (Mes)], 1.30 (s, 18 H, S*t*Bu). $^{13}$C NMR (125.8 MHz, $CDCl_3$, 25 °C): $\delta$ = 169.74 (N*C*N), 138.41 [*p*-*C* (Mes)], 136.95 [*o*-*C* (Mes)], 136.03 [N*C* (Mes)], 129.03 [*C*H (Mes)], 122.66 (MesN*C*H=), 122.53 (AlkN*C*H=), 50.94 (N$CH_2$), 42.68 [S*C*(CH$_3$)$_3$], 31.05 [SC(*C*H$_3$)$_3$], 29.24 (*C*H$_2$S), 21.27 (*p*-*C*H$_3$), 19.99 (*o*-*C*H$_3$) ppm. Minor isomer: $^1$H NMR (500 MHz, $CDCl_3$, 25 °C): $\delta$ = 7.01 (s, 2 H, AlkNC*H*=), 6.90 [s, 4 H, C*H* (Mes)], 6.53 (s, 2 H, MesNC*H*=), 5.37 (s, 4 H, NC$H_2$), 3.62 (s, 4 H, C$H_2$S), 2.54 [s, 6 H, *p*-C$H_3$ (Mes)], 1.94 [s, 12 H, *o*-C$H_3$ (Mes)], 1.42 (s, 18 H, S*t*Bu) ppm. $^{13}$C NMR (125.8 MHz, $CDCl_3$, 25 °C): $\delta$ = 169.34 (N*C*N), 137.51 [*p*-*C* (Mes)], 136.23 [*o*-*C* (Mes)], 135.56 [N*C* (Mes)], 129.09 [*C*H (Mes)], 123.21 (MesN*C*H=), 121.90 (AlkN*C*H=), 51.26 (N$CH_2$), 42.95 [S*C*(CH$_3$)$_3$], 31.21 [SC(*C*H$_3$)$_3$], 29.43 (*C*H$_2$S), 21.38 (*p*-*C*H$_3$), 19.47(*o*-*C*H$_3$) ppm. MS (DCI[$NH_3$]): *m*/*z* (%) = 743 (100) [$C_{36}H_{52}BrN_4S_2Ni^+$].

**{1-[2-(*tert*-Butylthio)ethyl]-3-(2,4,6-trimethylphenyl)imidazolium}-palladium Tribromide (12):** $PdBr_2$(COD) (146 mg, 0.39 mmol) was added to a solution of **5** (165 mg, 0.43 mmol) in THF (15 mL). The mixture was stirred for 1 h at room temperature and filtered. The orange solid obtained was washed with THF (15 mL), dichloromethane (10 mL) and dried in vacuo. Yield 223 mg (88%). M.p. (dec.) 245 °C. $C_{18}H_{27}Br_3N_2PdS$ (649.62): calcd. C 33.28, H 4.19, N 4.31; found C 33.26, H 4.35, N 4.98. $^1$H NMR (500 MHz, [D$_6$]-DMSO, 25 °C): $\delta$ = 9.46 (s, 1 H, NC*H*N), 8.12 (s, 1 H, MesNC*H*=), 7.91 (s, 1 H, AlkNC*H*=), 7.14 [s, 2 H, C*H* (Mes)], 4.44 (s, 2 H, NC$H_2$), 3.12 (s, 2 H, C$H_2$S*t*Bu), 2.34 (s, 3 H, *p*-C$H_3$), 2.04 (s, 6 H, *o*-C$H_3$), 1.28 (s, 9 H, S*t*Bu) ppm. $^{13}$C NMR (125.8 MHz, [D$_6$]-DMSO, 25 °C): $\delta$ = 140.78 [*p*-*C* (Mes)], 138.18 (N*C*HN), 134.8 [*o*-*C* (Mes)], 131.57 [N*C* (Mes)], 129.73 [*C*H (Mes)], 124.34 (AlkN*C*H=), 123.68 (MesN*C*H=), 49.9 (N$CH_2$), 43.22 [S*C*(CH$_3$)$_3$], 31.22 [SC(*C*H$_3$)$_3$], 28.31 (S*C*H$_2$), 21.08 [*p*-*C*H$_3$ (Mes)], 17.38 [*o*-*C*H$_3$ (Mes)] ppm. MS (FAB, MNBA matrix): *m*/*z* (%) = 303 (100) [$C_{18}H_{27}N_2S^+$]; 489 (1) [$C_{18}H_{26}BrN_2SPd^+$]; 569 (1) [$C_{18}H_{27}Br_2N_2SPd^+$].

**{1-[2-(Ethylthio)ethyl]-3-(2,4,6-trimethylpenyl)imidazolium}-palladium Tribromide (13):** $PdBr_2$(COD) (170 mg, 0.44 mmol) was added to a suspension of **6** (145 mg, 0.4 mmol) in THF (2 × 10 mL). The mixture was stirred for 2 h at room temperature and filtered. The orange solid obtained was washed with THF (15 mL) and dried in vacuo. Yield 250 mg (99%). M.p. 177–179 °C. $C_{16}H_{23}Br_3N_2PdS$ (621.57): calcd. C 30.92, H 3.73, N 4.51; found C 30.58, H 3.57, N 4.56. $^1$H NMR (500 MHz, [D$_6$]Me$_2$CO, 25 °C): $\delta$ = 9.00 (t, $^{4}J$ = 1.7 Hz, 1 H, NC*H*N), 7.84 (t, $^{3,4}J$ = 1.7 Hz, 1 H, MesNC*H*=C), 7.50 (t, $^{3,4}J$ = 1.8 Hz, 1 H, AlkNC*H*=C), 7.13 [s, 2 H, C*H* (Mes)], 4.88 (t, $^{3}J$ = 4.3 Hz, 2 H, NC$H_2$), 3.49 (t, $^{3}J$ = 4.3 Hz, 2 H, C$H_2$SEt), 3.00 (q, $^{3}J$ = 7.2 Hz, 2 H, SC$H_2$CH$_3$), 2.35 (s, 3 H, *p*-C$H_3$), 2.06 (s, 6 H, *o*-C$H_3$), 1.16 (t, $^{3}J$ = 7.3 Hz, 3 H, SCH$_2$C$H_3$) ppm. $^{13}$C NMR (125.8 MHz, [D$_6$]Me$_2$CO, 25 °C): $\delta$ = 141.30 [*p*-*C* (Mes)], 137.10 (N*C*HN), 134.86 [*o*-*C* (Mes)], 130.87 [N*C* (Mes)], 129.45 [*C*H (Mes)], 124.16 (AlkN*C*H=), 123.42 (MesN*C*H=), 47.94 (N$CH_2$), 36.11 (*C*H$_2$SEt), 32.26 (S*C*H$_2$CH$_3$), 20.17 [*p*-*C*H$_3$ (Mes)], 16.90 [*o*-*C*H$_3$ (Mes)], 12.63 (SCH$_2$*C*H$_3$) ppm. MS (FAB, MNBA matrix): *m*/*z* (%) = 275 (100) [$C_{16}H_{23}N_2S^+$]; 461 (1) [$C_{16}H_{22}BrN_2PdS^+$]; 543 (0.9) [$C_{16}H_{23}Br_2N_2PdS^+$].

**{1-[2-(*tert*-Butylthio)ethyl]-3-(2,6-diisopropylphenyl)imidazolium}-palladium Tribromide (14):** $PdBr_2$(COD) (374 mg, 1.00 mmol) was added to a solution of **7** (400 mg, 0.94 mmol) in THF (15 mL). The mixture was stirred for 2 h at room temperature and filtered. The orange solid obtained was washed with THF (2 × 15 mL), $CH_2Cl_2$ (15 mL) and dried in vacuo. Yield 579 mg (89%). M.p. 210–212 °C. $C_{21}H_{33}Br_3N_2PdS$ (691.70): calcd. C 36.47, H 4.81, N 4.05; found C 36.60, H 4.49, N 3.87. $^1$H NMR (500 MHz, [D$_6$]-DMSO, 25 °C): $\delta$ = 9.59 (s, 1 H, NC*H*N), 8.16 [s, 1 H, (DIPP)-NC*H*=C], 8.10 (s, 1 H, AlkNC*H*=C), 7.64 [t, $^{3}J$ = 7.8 Hz, 1 H, *p*-C*H* (DIPP)], 7.47 [d, $^{3}J$ = 7.8 Hz, 2 H, *m*-C*H* (DIPP)], 4.47 (t, 2 H, NC$H_2$), 3.13 (t, 2 H, C$H_2$S*t*Bu), 2.51 [h, $^{3}J$ = 6.8 Hz, 2 H, C*H*(CH$_3$)$_2$], 1.28 (s, 9 H, S*t*Bu), 1.16 [d, $^{3}J$ = 6.9 Hz, 6 H, CH-(C$H_3$)$_2$], 1.14 [d, $^{3}J$ = 6.9 Hz, 6 H, CH(C$H_3$)$_2$] ppm. $^{13}$C NMR (125.8 MHz, [D$_6$]DMSO, 25 °C): $\delta$ = 145.64 [*o*-*C* (DIPP)], 138.71 (N*C*HN), 131.98 [*p*-*C*H (DIPP)], 130.98 [N*C* (DIPP)], 125.69 [(DIPP)N*C*H=], 124.91 [*m*-*C*H (DIPP)], 123.60 (AlkN*C*H=), 49.84 (N$CH_2$), 43.07 [S*C*(CH$_3$)$_3$], 31.17 [SC(*C*H$_3$)$_3$], 28.48 (*C*H$_2$S), 28.40

 © 2007 Wiley-VCH Verlag GmbH & Co. KGaA, Weinheim 

[*C*H(CH$_3$)$_2$], 24.33, 24.30 [CH(*C*H$_3$)$_2$] ppm. MS (FAB, MNBA matrix): *m*/*z* (%) = 345 (100) [$C_{21}H_{33}N_2S^+$]; 611 (1) [$C_{21}H_{33}Br_2N_2SPd^+$].

**{1-[3-(*tert*-Butylthio)propyl]-3-(2,4,6-trimethylphenyl)imidazolium}-palladium Tribromide (15):** $PdBr_2$(COD) (141 mg, 0.38 mmol) was added to a solution of **8** (180 mg, 0.45 mmol) in THF (10 mL). The mixture was stirred for 2 h at room temperature and filtered. The orange solid obtained was washed with THF (2 × 10 mL) and dried in vacuo. Yield 206 mg (82%). M.p. 200–202 °C. $C_{19}H_{29}Br_3N_2PdS$ (663.65): calcd. C 34.39, H 4.40, N 4.22; found C 35.21, H 4.34, N 3.92. $^1$H NMR (500 MHz, [D$_6$]DMSO, 25 °C): $\delta$ = 9.45 (s, 1 H, NC*H*N), 8.13 (s, 1 H, MesNC*H*=C), 7.95 (s, 1 H, AlkNC*H*=C), 7.16 [s, 2 H, C*H* (Mes)], 4.38 (s, $^3J$ = 6.7 Hz, 2 H, NC$H_2$), 2.55 (s, $^3J$ = 6.8 Hz, 2 H, C$H_2$S*t*Bu), 2.30 (s, 3 H, *p*-C$H_3$), 2.17 (t, $^3J$ = 7.0 Hz, 2 H, NCH$_2$C$H_2$), 2.04 (s, 6 H, *o*-C$H_3$), 1.27 (s, 9 H, S*t*Bu) ppm. $^{13}$C NMR (125.8 MHz, [D$_6$]DMSO, 25 °C): $\delta$ = 140.74 [s, *p*-*C* (Mes)], 137.87 (s, N*C*HN), 134.76 [s, *o*-*C* (Mes)], 131.63 [s, N*C* (Mes)], 129.73 [s, *C*H (Mes)], 124.51 (s, AlkN*C*H=), 123.73 (s, MesN*C*H=), 49.35 (s, N*C*H$_2$), 42.64 [s, S*C*(CH$_3$)$_3$], 31.08 [s, SC(*C*H$_3$)$_3$], 29.96 (s, NCH$_2$*C*H$_2$), 24.81 (s, *C*H$_2$S), 21.09 [s, *p*-*C*H$_3$ (Mes)], 17.41 [s, *o*-*C*H$_3$ (Mes)] ppm. MS (FAB, MNBA matrix): *m*/*z* (%) = 317 (100) [$C_{19}H_{29}N_2S^+$]; 503 (1) [$C_{19}H_{28}BrN_2SPd^+$]; 583 (1) [$C_{19}H_{29}Br_2N_2SPd^+$].

**{1-[3-(*tert*-Butylthio)propyl]-3-(2,6-diisopropylphenyl)imidazolium}-palladium Tribromide (16):** $PdBr_2$(COD) (374 mg, 1.00 mmol) was added to a solution of **9** (505 mg, 1.15 mmol) in THF (20 mL). The mixture was stirred for 2 h at room temperature and filtered. The orange solid obtained was washed with THF (2 × 15 mL), $CH_2Cl_2$ (15 mL) and dried in vacuo. Yield 642 mg (91%). M.p. 184–186 °C. $C_{22}H_{35}Br_3N_2PdS$ (705.73): calcd. C 37.44, H 5.00, N 3.97; found C 37.79, H 4.79, N 3.99. $^1$H NMR (500 MHz, [D$_6$]DMSO, 20 °C): $\delta$ = 9.61 (s, 1 H, NC*H*N), 8.18 (s, 1 H, AlkNC*H*=), 8.12 [s, 1 H, (DIPP)NC*H*=], 7.63 [s, 1 H, *p*-C*H* (DIPP)], 7.46 [s, 2 H, *m*-C*H* (DIPP)], 4.42 (s, 2 H, NC$H_2$), 2.53 (s, 2 H, C$H_2$S*t*Bu), 2.28 [s, 2 H, C*H*(CH$_3$)$_2$], 2.17 (s, 2 H, NCH$_2$C$H_2$), 1.27 (s, 9 H, S*t*Bu), 1.14 [s, 12 H, CH(C$H_3$)$_2$] ppm. $^{13}$C NMR (125.8 MHz, [D$_6$]DMSO, 20 °C): $\delta$ = 145.56 [s, *o*-*C* (DIPP)], 138.12 (s, N*C*HN), 130.96 [s, N*C* (DIPP)], 131.97 [s, *p*-*C*H (DIPP)], 125.73 [s, (DIPP)N*C*H=], 124.90 [s, *m*-*C*H (DIPP)], 124.00 (s, AlkN*C*H=), 49.52 (s, N*C*H$_2$), 42.58 [s, S*C*(CH$_3$)$_3$], 31.05 [s, SC(*C*H$_3$)$_3$], 29.92 (s, NCH$_2$*C*H$_2$), 28.53 [s, *C*H(CH$_3$)$_2$], 24.76 (s, *C*H$_2$S), 24.34, 24.27 [s, CH(*C*H$_3$)$_2$] ppm. MS (FAB, MNBA matrix): *m*/*z* (%) = 359 (100) [$C_{22}H_{35}N_2S^+$]; 545 (1) [$C_{22}H_{34}BrN_2SPd^+$]; 625 (1) [$C_{22}H_{35}Br_2N_2SPd^+$].

**{1-[2-(Ethylthio)ethyl]-3-(2,4,6-trimethylphenyl)imidazol-2-ylidene}-palladium Dibromide Dimer (17):** A solution of *t*BuOK (42 mg, 0.38 mmol) in THF (15 mL) was slowly added to a suspension of **13** (117 mg, 0.19 mmol) in THF (15 mL). The mixture was stirred for 2 h at room temperature and the solvent removed in vacuo. The resulting solid was dissolved in $CH_2Cl_2$ and filtered through Celite. The product was purified by column chromatography on silica gel (eluent: $CH_2Cl_2$/acetone, 9:1). The product was crystallised by layer diffusion of diethyl ether into a THF solution to give yellow orange crystals. Yield 64 mg (63%). M.p. (dec.) 240 °C. $C_{32}H_{44}Br_4N_4Pd_2S_2$ (1081.3): calcd. C 35.54, H 4.10, N 5.18; found C 36.14, H 4.04, N 5.03. $^1$H NMR (500 MHz, $CD_2Cl_2$, 25 °C): $\delta$ = 7.28 (d, $^3J$ = 1.9 Hz, 2 H, NC*H*=), 7.05 [s, 4 H, C*H* (Mes)], 6.96 (d, $^3J$ = 1.8 Hz, 2 H, MesNC*H*=), 4.60 (br. s, 4 H, C$H_2$N), 3.35 (br. s, 4 H, SC$H_2$CH$_3$), 2.75 (br. s, 4 H, C$H_2$SEt), 2.39 [s, 6 H, *p*-C$H_3$ (Mes)], 2.24 [s, 12 H, *o*-C$H_3$ (Mes)], 1.53 (t, $^3J$ = 7.3 Hz, 6 H, SCH$_2$C$H_3$) ppm. $^{13}$C NMR (125.8 MHz, $CD_2Cl_2$, 25 °C): $\delta$ = 155.75 (N*C*N), 139.28 [*p*-*C* (Mes)], 135.69 [N*C* (Mes)], 134.79 [*o*-*C* (Mes)], 129.09 [*C*H (Mes)], 125.09, 121.56 (N*C*H=), 51.67 (N*C*H$_2$), 35.81 (S*C*H$_2$CH$_3$), 32.62 (*C*H$_2$SEt), 20.88 [*p*-*C*H$_3$ (Mes)], 19.10 [*o*-*C*H$_3$ (Mes)], 14.00 (SCH$_2$*C*H$_3$) ppm. MS (FAB, MNBA matrix): *m*/*z* (%) = 245 (100) [$C_{14}H_{17}N_2S^+$]; 275 (47) [$C_{16}H_{23}N_2S^+$]; 461 (7) [$C_{16}H_{22}BrN_2SPd^+$]; 1001 (3) [$C_{32}H_{44}Br_3N_4S_2Pd_2^+$].

**{1-[2-(*tert*-Butylthio)ethyl]-3-(2,4,6-trimethylphenyl)imidazol-2-ylidene-1,4-cyclooctadienyl}rhodium(I) Tetrafluoroborate (18):** [Rh(COD)Cl]$_2$ (77.2 mg, 0.16 mmol) was stirred for 15 min at room temperature with *t*BuOK (38.6 mg, 0.34 mmol) in THF (4 mL). The dark yellow solution was slowly added to a solution of **5** (120.0 mg, 0.31 mmol) in THF (4 mL). The mixture was stirred overnight at room temperature and the solvent was removed under vacuum. $AgBF_4$ (122.0 mg, 0.63 mmol) and $CH_2Cl_2$ (10 mL) were added to the residue and the reaction was stirred at room temperature for two additional hours. The mixture was filtered through Celite, concentrated under vacuum and purified by column chromatography on silica gel (eluent: $CH_2Cl_2$/$Me_2CO$, 17:3) to give a yellow-orange hygroscopic solid (152 mg, 81%). Suitable X-ray crystals were obtained by layer diffusion of pentane into a $CDCl_3$ solution. M.p. 99–101 °C. $C_{26}H_{38}BF_4N_2RhS$ (600.38): calcd. C 52.01, H 6.38, N 4.67; found C 51.67, H 5.86, N 4.54. $^1$H NMR (500 MHz, [D$_6$]DMSO, 80 °C): $\delta$ = 7.64 (d, $^3J$ = 1.8 Hz, 1 H, AlkNC*H*=), 7.34 (d, $^3J$ = 1.7 Hz, 1 H, MesNC*H*=), 7.13 [s, 2 H, C*H* (Mes)], 4.85 [s, 2 H, C*H* (COD)], 4.62 (t, $^3J$ = 5.3 Hz, 2 H, C$H_2$N), 3.90 [br. s, 2 H, C*H* (COD)], 2.97 (t, $^3J$ = 5.3 Hz, 2 H, C$H_2$S*t*Bu), 2.36 (s, 3 H, *p*-C$H_3$), 2.11–2.26 [m + s, 8 H, *o*-C$H_3$; C$H_2$ (COD)], 1.82–2.06 [br. m, 6 H, C$H_2$ (COD)], 1.25 (s, 9 H, S*t*Bu) ppm. $^{13}$C NMR (125.8 MHz, [D$_6$]DMSO, 80 °C): $\delta$ = 173.63 (d, $^1J_{Rh-C}$ = 49.8 Hz, N*C*N), 139.41 [*p*-*C* (Mes)], 135.88 [N*C* (Mes)], 135.37 [*o*-*C* (Mes)], 129.46 [*C*H (Mes)], 125.54 (MesN*C*H=), 123.10 (AlkN*C*H=), 96.86, 81.86 [*C*H (COD)], 51.11 [S*C*(CH$_3$)$_3$], 50.06 (N*C*H$_2$), 31.90, 29.38 [*C*H$_2$ (COD)], 30.01 [SC(*C*H$_3$)$_3$], 27.54 (S*C*H$_2$), 20.88 [*p*-*C*H$_3$ (Mes)], 19.11 [*o*-*C*H$_3$ (Mes)] ppm. $^{19}$F NMR (188 MHz, $CDCl_3$, 25 °C): $\delta$ = –76.73 (s, $BF_4$) ppm. MS (ESI): *m*/*z* (%) = 513.3 (100) [$C_{26}H_{38}N_2RhS^+$].

**{1-[2-(*tert*-Butylthio)ethyl]-3-(2,6-diisopropylphenyl)imidazol-2-ylidene-1,4-cyclooctadienyl}rhodium(I) Tetrafluoroborate (19):** Compound **19** was prepared using the same procedure as for **18**, from compound **7** (95.0 mg, 0.22 mmol), [Rh(COD)Cl]$_2$ (55.0 mg, 0.11 mmol), *t*BuOK (27.6 mg, 0.25 mmol) and $AgBF_4$ (87.0 mg, 0.45 mmol). After purification, the product was recovered as a yellow-orange solid (113 mg, 79%). Suitable X-ray crystals were obtained by slow evaporation of a saturated ether solution. M.p. (slow dec.) >150 °C. $C_{29}H_{44}BF_4N_2RhS$ (642.46): calcd. C 54.22, H 6.90, N 4.36; found C 54.46, H 6.64, N 4.48. $^1$H NMR (500 MHz, [D$_6$]-DMSO, 80 °C): $\delta$ = 7.67 (s, 1 H, AlkNC*H*=), 7.57 [t, $^3J$ = 7.8 Hz, 1 H, *p*-C*H* (DIPP)], 7.43 [s, 1 H, (DIPP)NC*H*=], 7.41 [d, $^3J$ = 7.8 Hz, 2 H, *m*-C*H* (DIPP)], 4.87 [s, 2 H, C*H* (COD)], 4.68 (s, 2 H, C$H_2$N), 3.92 [br. s, 2 H, C*H* (COD)], 3.01 (s, 2 H, C$H_2$S*t*Bu), 2.5–2.6 [br. s, 2 H, C*H*(CH$_3$)$_2$], 2.14–2.24 [m, 2 H, C$H_2$ (COD)], 1.90–2.04 [m, 4 H, C$H_2$ (COD)], 1.80–1.90 [m, 2 H, C$H_2$ (COD)], 1.35 [d, $^3J$ = 4.1 Hz, 6 H, CH(C$H_3$)$_2$], 1.28 (s, 9 H, S*t*Bu), 1.08 [d, $^3J$ = 6.7 Hz, 6 H, CH(C$H_3$)$_2$] ppm. $^{13}$C NMR (125.8 MHz, [D$_6$]-DMSO, 80 °C): $\delta$ = 173.02 (d, $^1J_{Rh-C}$ = 50 Hz, N*C*N), 146.04 [*o*-*C* (DIPP)], 135.06 [N*C* (DIPP)], 130.76 [*p*-*C*H (DIPP)], 127.06 [(DIPP)N*C*H=], 124.51 [*m*-*C*H (DIPP)], 122.84 (AlkN*C*H=), 96.71, 81.21 [*C*H (COD)], 50.95 [S*C*(CH$_3$)$_3$], 50.33 (N*C*H$_2$), 31.73, 29.36 [*C*H$_2$ (COD)], 30.00 [SC(*C*H$_3$)$_3$], 28.44 [*C*H(CH$_3$)$_2$], 27.74 (S*C*H$_2$), 25.62, 23.51 [*C*H(CH$_3$)$_2$] ppm. $^{19}$F NMR (188 MHz, $CDCl_3$, 25 °C): $\delta$ = –76.83 (s, $BF_4$) ppm. MS (FAB, MNBA matrix): *m*/*z* (%) = 555 (100) [$C_{29}H_{44}N_2RhS^+$].

**{1-[β-(Ethylthio)ethyl]-3-(2,4,6-trimethylphenyl)imidazol-2-ylidene-1,4-cyclooctadienyl}rhodium(I) Tetrafluoroborate (20):** Compound

 © 2007 Wiley-VCH Verlag GmbH & Co. KGaA, Weinheim 

**20** was prepared using the same procedure as for **18**, from compound **6** (40.0 mg, 0.11 mmol), $[Rh(COD)Cl]_2$ (27.8 mg, 0.06 mmol), *t*BuOK (13.9 mg, 0.12 mmol) and $AgBF_4$ (48.0 mg, 0.25 mmol). After purification, the product was recovered as a yellow-orange solid (49 mg, 76%). M.p. (dec.) >70 °C. $C_{24}H_{34}BF_4N_2RhS$ (572.32): calcd. C 50.37, H 5.98, N 4.89; found C 48.89, H 5.59, N 4.57. HRMS (ESI) *m*/*z*: calcd. for $C_{24}H_{34}N_2RhS$ 485.1498; found 485.1512. $^1$H NMR (500 MHz, [D$_6$]DMSO, 80 °C): $\delta$ = 7.65 (d, $^3J$ = 1.8 Hz, 1 H, AlkNC*H*=), 7.34 (d, $^3J$ = 1.8 Hz, 1 H, MesNC*H*=), 7.12 [s, 2 H, C*H* (Mes)], 4.72 [s, 2 H, C*H* (COD)], 4.65 (t, $^3J$ = 5.3 Hz, 2 H, C$H_2$N), 3.97 [br. s, 2 H, C*H* (COD)], 2.93 (t, $^3J$ = 5.3 Hz, 2 H, C$H_2$SEt), 2.65 (q, $^3J$ = 7.3 Hz, 2 H, SC$H_2$CH$_3$), 2.36 (s, 3 H, *p*-C$H_3$), 2.07–2.23 [m + s, 8 H, *o*-C$H_3$; C$H_2$ (COD)], 1.86–2.05 [br. m, 6 H, C$H_2$ (COD)], 1.30 (t, $^3J$ = 7.3 Hz, 3 H, SCH$_2$C$H_3$) ppm. $^{13}$C NMR (125.8 MHz, [D$_6$]-DMSO, 80 °C): $\delta$ = 173.72 (d, $^1J_{Rh-C}$ = 50.3 Hz, N*C*N), 139.38 [*p*-*C* (Mes)], 135.85 [N*C* (Mes)], 135.28 [*o*-*C* (Mes)], 129.33 [*C*H (Mes)], 125.13 (MesN*C*H=), 122.99 (AlkN*C*H=), 94.36 [d, $^1J_{Rh-C}$ = 7.3 Hz, *C*H (COD)], 83.56 [br. s, *C*H (COD)], 51.88 (N*C*H$_2$), 32.00 (S*C*H$_2$CH$_3$), 31.91 (*C*H$_2$SEt), 31.78, 29.61 [*C*H$_2$ (COD)], 27.54 (S*C*H$_2$), 20.92 [*p*-*C*H$_3$ (Mes)], 18.45 [*o*-*C*H$_3$ (Mes)], 14.49 (SCH$_2$*C*H$_3$) ppm. $^{19}$F NMR (188 MHz, $CDCl_3$): $\delta$ = –76.08 ($BF_4$) ppm. MS (ESI): *m*/*z* (%) = 485.7 (100) [$C_{24}H_{34}N_2RhS^+$].

CCDC-631917 to -631922 and -637108 contain the supplementary crystallographic data for this paper. These data can be obtained free of charge from The Cambridge Crystallographic Data Centre via www.ccdc.cam.ac.uk/datarequest/cif.

**Supporting Information** (see footnote on the first page of this article): Synthesis and characterization of compounds **21** and **4**; crystallographic data for compounds **5**, **6**, **11**, **17**–**20**.

## Acknowledgments

We thank the Centre National de la Recherche Scientifique (C.N.R.S.) for support of this work, the Fonds Social Européen (F.S.E.) for a Ph.D. fellowship to J. W., and Yannick Coppel for NMR analysis of the rhodium complexes.

[1] D. Bourissou, O. Guerret, F. P. Gabbaï, G. Bertrand, *Chem. Rev.* **2000**, *100*, 39–91; W. A. Herrmann, *Angew. Chem. Int. Ed.* **2002**, *41*, 1290–1309; N. M. Scott, S. P. Nolan, *Eur. J. Inorg. Chem.* **2005**, 1815–1828; F. E. Hahn, *Angew. Chem. Int. Ed.* **2006**, *45*, 1348–1352.

[2] M. Scholl, T. M. Trnka, J. P. Morgan, R. H. Grubbs, *Tetrahedron Lett.* **1999**, *40*, 2247–2250; L. Jafarpour, H.-J. Schanz, E. D. Stevens, S. P. Nolan, *Organometallics* **1999**, *18*, 5416–5419; S. Díez-González, N. M. Scott, S. P. Nolan, *Organometallics* **2006**, *25*, 2355–2358.

[3] V. P. W. Böhm, T. Weskamp, C. W. K. Gstöttmayr, W. A. Herrmann, *Angew. Chem. Int. Ed.* **2000**, *39*, 1602–1604; N. Gürbüz, I. Özdemir, S. Demir, B. Çetinkaya, *J. Mol. Catal. A* **2004**, *209*, 23–28; A. C. Hillier, G. A. Grasa, M. S. Viciu, H. M. Lee, C. Yang, S. P. Nolan, *J. Organomet. Chem.* **2002**, *653*, 69–82; N. Hadei, E. A. B. Kantchev, C. J. O'Brien, M. G. Organ, *Org. Lett.* **2005**, *7*, 3805–3807.

[4] E. Mas-Marzá, E. Peris, I. Castro-Rodríguez, K. Meyer, *Organometallics* **2005**, *24*, 3158–3162; I. Özdemir, S. Demir, B. Çetinkaya, *J. Mol. Catal. A* **2004**, *215*, 45–48; C. Rivera, R. H. Crabtree, *J. Mol. Catal. A* **2004**, *222*, 59–73; F. Hanasaka, K.-i. Fujita, R. Yamaguchi, *Organometallics* **2005**, *24*, 3422–3433.

[5] J. Wolf, A. Labande, J.-C. Daran, R. Poli, *J. Organomet. Chem.* **2006**, *691*, 433–443.

[6] J. Wolf, A. Labande, M. Natella, J.-C. Daran, R. Poli, *J. Mol. Catal. A* **2006**, *259*, 205–212.

[7] N. Tsoureas, A. A. Danopoulos, A. A. D. Tulloch, M. E. Light, *Organometallics* **2003**, *22*, 4750–4758.

[8] C. L. Yang, H. M. Lee, S. P. Nolan, *Org. Lett.* **2001**, *3*, 1511–1514; T. Focken, G. Raabe, C. Bolm, *Tetrahedron: Asymmetry* **2004**, *15*, 1693–1706.

[9] H. Seo, H.-J. Park, B. Y. Kim, J. H. Lee, S. U. Son, Y. K. Chung, *Organometallics* **2003**, *22*, 618–620.

[10] L. D. Field, B. A. Messerle, K. Q. Vuong, P. Turner, *Organometallics* **2005**, *24*, 4241–4250.

[11] L. G. Bonnet, R. E. Douthwaite, R. Hodgson, J. Houghton, B. M. Kariuki, S. Simonovic, *Dalton Trans.* **2004**, 3528–3535; W. A. Herrmann, L. J. Gooßen, M. Spiegler, *Organometallics* **1998**, *17*, 2162–2168; D. S. McGuinness, K. J. Cavell, *Organometallics* **2000**, *19*, 741–748.

[12] L. H. Gade, V. César, S. Bellemin-Laponnaz, *Angew. Chem. Int. Ed.* **2004**, *43*, 1014–1017; V. César, S. Bellemin-Laponnaz, H. Wadepohl, L. H. Gade, *Chem. Eur. J.* **2005**, *11*, 2862–2873.

[13] P. L. Arnold, A. C. Scarisbrick, A. J. Blake, C. Wilson, *Chem. Commun.* **2001**, 2340–2341; P. L. Arnold, M. Rodden, C. Wilson, *Chem. Commun.* **2005**, 1743–1745; P. L. Arnold, C. Wilson, *Inorg. Chim. Acta* **2007**, *360*, 190–196; A. R. Chianese, R. H. Crabtree, *Organometallics* **2005**, *24*, 4432–4436; E. Mas-Marzá, M. Poyatos, M. Sanaú, E. Peris, *Organometallics* **2004**, *23*, 323–325; D. J. Nielsen, K. J. Cavell, B. W. Skelton, A. H. White, *Inorg. Chim. Acta* **2003**, *352*, 143–150; S. Prühs, C. W. Lehmann, A. Fürstner, *Organometallics* **2004**, *23*, 280–287; J. J. Van Veldhuizen, S. B. Garber, J. S. Kingsbury, A. H. Hoveyda, *J. Am. Chem. Soc.* **2002**, *124*, 4954–4955.

[14] J. C. Bayón, C. Claver, A. M. Masdeu-Bultó, *Coord. Chem. Rev.* **1999**, *193–195*, 73–145; L. Routaboul, S. Vincendeau, J.-C. Daran, E. Manoury, *Tetrahedron: Asymmetry* **2005**, *16*, 2685–2690; R. Malacea, E. Manoury, L. Routaboul, J.-C. Daran, R. Poli, J. P. Dunne, A. C. Whitwood, C. Godard, S. B. Duckett, *Eur. J. Inorg. Chem.* **2006**, 1803–1816; R. Malacea, J.-C. Daran, S. B. Duckett, J. P. Dunne, C. Godard, E. Manoury, R. Poli, A. C. Whitwood, *Dalton Trans.* **2006**, 3350–3359.

[15] J. Pernak, A. Skrzypczak, *Eur. Med. Chem.* **1996**, *31*, 901–903; G. Nalecz-Jawecki, E. Grabinska-Sota, P. Narkiewicz, *Ecotoxicol. Environ. Saf.* **2003**, *54*, 87–91.

[16] A. E. Visser, R. P. Swatloski, W. M. Reichert, R. Mayton, S. Sheff, A. Wierzbicki, J. H. Davis Jr, R. D. Rogers, *Chem. Commun.* **2001**, 135–136; A. E. Visser, R. P. Swatloski, W. M. Reichert, R. Mayton, S. Sheff, A. Wierzbicki, J. H. Davis Jr, R. D. Rogers, *Environ. Sci. Technol.* **2002**, *36*, 2523–2529.

[17] A. Ros, D. Monge, M. Alcarazo, E. Álvarez, J. M. Lassaletta, R. Fernández, *Organometallics* **2006**, *25*, 6039–6046.

[18] S. J. Roseblade, A. Ros, D. Monge, M. Alcarazo, E. Alvarez, J. M. Lassaletta, R. Fernandez, *Organometallics* **2007**, *26*, 2570–2578.

[19] D. J. Nielsen, K. J. Cavell, M. S. Viciu, S. P. Nolan, B. W. Skelton, A. H. White, *J. Organomet. Chem.* **2005**, *690*, 6133–6142.

[20] D. S. Tarbell, W. E. Lovett, *J. Am. Chem. Soc.* **1956**, *78*, 2259–2264; M. Zaidlewicz, J. V. B. Kanth, H. C. Brown, *J. Org. Chem.* **2000**, *65*, 6697–6702.

[21] L. A. Sayyed, V. V. Thakur, M. D. Nikalje, G. K. Dewkar, S. P. Kotkar, A. Sudalai, *Tetrahedron* **2005**, *61*, 2831; W. Kurosawa, T. Kan, T. Fukuyama, *J. Am. Chem. Soc.* **2003**, *125*, 8112–8113.

[22] T. Welton, *Chem. Rev.* **1999**, *99*, 2071–2084.

[23] W. A. Herrmann, G. Gerstberger, M. Spiegler, *Organometallics* **1997**, *16*, 2209–2212; D. S. McGuinness, W. Mueller, P. Wasserscheid, K. J. Cavell, B. W. Skelton, A. H. White, U. Englert, *Organometallics* **2002**, *21*, 175–181.

[24] A. L. MacKinnon, M. C. Baird, *J. Organomet. Chem.* **2003**, *683*, 114–119.

[25] L. C. Silva, P. T. Gomes, L. F. Veiros, S. I. Pascu, M. T. Duarte, S. Namorado, J. R. Ascenso, A. R. Dias, *Organometallics* **2006**, *25*, 4391–4403.

[26] H. M. Lee, P. L. Chiu, J. Y. Zeng, *Inorg. Chim. Acta* **2004**, *357*, 4313–4321.

 © 2007 Wiley-VCH Verlag GmbH & Co. KGaA, Weinheim 

[27] D. Enders, R. Peters, J. Runsink, J. W. Bats, *Org. Lett.* **1999**, *1*, 1863–1866; D. A. Evans, K. R. Campos, J. S. Tedrow, F. E. Michael, M. R. Gagné, *J. Am. Chem. Soc.* **2000**, *122*, 7905–7920.
[28] B. A. Messerle, M. J. Page, P. Turner, *Dalton Trans.* **2006**, 3927–3933; V. César, S. Bellemin-Laponnaz, L. H. Gade, *Eur. J. Inorg. Chem.* **2004**, 3436–3444.
[29] The influence of the deuterated solvent on $^{13}C$ NMR chemical shifts is negligible compared to the difference in $^{13}C$ NMR chemical shifts observed between compounds **5** and **18**. For **18**, the $SC(CH_3)_3$ signal is at $\delta$ = 51.11 ppm in [$D_6$]DMSO and at $\delta$ = 50.5 ppm in $CDCl_3$.
[30] G. Esquius, J. Pons, R. Yáñez, J. Ros, R. Mathieu, B. Donnadieu, N. Lugan, *Eur. J. Inorg. Chem.* **2002**, 2999–3006.
[31] I. Ojima, Z. Li, J. Zhu in *The Chemistry of Organic silicon Compounds* (Eds.: Z. Rappoport, Y. Apeloig), Wiley, New York, **1998**, vol. 2, p. 1687.
[32] I. Ojima, M. Nihonyanagi, Y. Nagai, *J. Chem. Soc. Chem. Commun.* **1972**, 938; R. J. P. Corriu, J. J. E. Moreau, *J. Organomet. Chem.* **1975**, *91*, C27–C30; I. Ojima, M. Nihonyanagi, T. Kogure, M. Kumagai, S. Horiuchi, K. Nakatsugawa, *J. Organomet. Chem.* **1975**, *94*, 449–461.
[33] I. Ojima, T. Kogure, *Organometallics* **1982**, *1*, 1390–1399.
[34] W. Dumont, J. C. Poulin, P. Dang Tuan, H. B. Kagan, *J. Am. Chem. Soc.* **1973**, *95*, 8295–8299; M. E. Wright, S. A. Svejda, *Polyhedron* **1991**, *10*, 1061–1068; H. Brunner, G. Riepl, H. Weitzer, *Angew. Chem.* **1983**, *95*, 326; H. Brunner, R. Becker, G. Riepl, *Organometallics* **1984**, *3*, 1354–1359; H. Brunner, B. Reiter, G. Riepl, *Chem. Ber.* **1984**, *117*, 1330–1354; H. Brunner, A. Kürzinger, *J. Organomet. Chem.* **1988**, *346*, 413–424; T. Kogure, I. Ojima, *J. Organomet. Chem.* **1982**, *234*, 249–256; B. Tao, G. C. Fu, *Angew. Chem. Int. Ed.* **2002**, *41*, 3892–3894; R. Corriu, J. J. E. Moreau, *J. Organomet. Chem.* **1975**, *85*, 19–33; I. Ojima, T. Kogure, M. Kumagai, S. Horiuchi, T. Sato, *J. Organomet. Chem.* **1976**, *122*, 83–97.
[35] C. Reyes, A. Prock, W. P. Giering, *Organometallics* **2002**, *21*, 546–554.
[36] T. Hayashi, C. Hayashi, Y. Uozumi, *Tetrahedron: Asymmetry* **1995**, *6*, 2503–2506.
[37] T. H. Chan, G. Z. Zheng, *Tetrahedron Lett.* **1993**, *34*, 3095–3098; G. Z. Zheng, T. H. Chan, *Organometallics* **1995**, *14*, 70–79.
[38] H. Nishiyama, H. Sakaguchi, T. Nakamura, M. Horihata, M. Kondo, K. Itoh, *Organometallics* **1989**, *8*, 846–848; H. Nishiyama, M. Kondo, T. Nakamura, K. Itoh, *Organometallics* **1991**, *10*, 500–508; H. Nishiyama, S. B. Park, K. Itoh, *Tetrahedron: Asymmetry* **1992**, *3*, 1029–1034; D. Cuervo, M. P. Gamasa, J. Gimeno, *J. Mol. Catal. A* **2006**, *249*, 60–64.
[39] T. Hayashi, K. Yamamoto, K. Kasuga, H. Omizu, M. Kumada, *J. Organomet. Chem.* **1976**, *113*, 127–137; M. Sawamura, R. Kuwano, Y. Ito, *Angew. Chem. Int. Ed. Engl.* **1994**, *33*, 111–113; T. Imamoto, T. Itoh, Y. Yamanoi, R. Narui, K. Yoshida, *Tetrahedron: Asymmetry* **2006**, *17*, 560–565.
[40] I. Kolb, J. Hetflejs, *Collect. Czech. Chem. Commun.* **1980**, *45*, 2808–2816; T. E. Waldman, G. Schaefer, D. P. Riley, *ACS Symp. Ser.* **1993**, *517*, 58–74.
[41] H. Nishiyama, S. Yamaguchi, M. Kondo, K. Itoh, *J. Org. Chem.* **1992**, *57*, 4306–4309.
[42] D. A. Evans, F. E. Michael, J. S. Tedrow, K. R. Campos, *J. Am. Chem. Soc.* **2003**, *125*, 3534–3543.
[43] M. F. Lappert, R. K. Maskell, *J. Organomet. Chem.* **1984**, *264*, 217–228; W.-L. Duan, M. Shi, G.-B. Rong, *Chem. Commun.* **2003**, 2916–2917; Q. Xu, X. Gu, S. Liu, Q. Dou, M. Shi, *J. Org. Chem.* **2007**, *72*, 2240–2242; J. W. Faller, P. P. Fontaine, *Organometallics* **2006**, *25*, 5887–5893.
[44] Y. Yuan, G. Raabe, C. Bolm, *J. Organomet. Chem.* **2005**, *690*, 5747–5752.
[45] D. Drew, J. R. Doyle, *Inorg. Synth.* **1972**, *13*, 47–55.

Received: June 28, 2007
Published Online: September 20, 2007

 © 2007 Wiley-VCH Verlag GmbH & Co. KGaA, Weinheim 

DOI: 10.1002/ejic.200700537

# Synthesis and Structure of Tetrameric Gallium(I) Amides

**Annekathrin Seifert[a] and Gerald Linti*[a]**

**Keywords:** Gallium / Amides / Cluster compounds / X-ray structures / Density functional calculations

The amino substituted gallatetrahedranes described herein, $Ga_4(tmp)_4$ [tmp = 2,2,6,6-(tetramethylpiperidino)] and $Ga_4[N(SiMe_3)dipp]_4$ (dipp = 2,6-diisopropylphenyl), are the first oligomeric gallium(I) amides to be reported. These compounds are formed in a facile manner from "GaI". A new hexagallane with an unusual structure is also described. The clusters were characterized by NMR and UV/Vis spectroscopy, single-crystal X-ray crystallography, and DFT calculations.

(© Wiley-VCH Verlag GmbH & Co. KGaA, 69451 Weinheim, Germany, 2007)

## Introduction

The cluster chemistry of gallium seems to be dominated by metal-rich compounds.[1] Prominent examples include $[Ga_8\{Si(CMe_3)_3\}_6]^{x-}$, ($x$ = 0, 2),[2] $[Ga_9\{Si(SiMe_3)_3\}_6]^-$,[3] $[Ga_{10}\{Si(SiMe_3)_3\}_6]$,[4] $Ga_{11}(C_6H_3\text{-}2,6\text{-}Mes_2)_4$,[5] $[Ga_{12}(fluorenyl)_{10}]^{2-}$,[6] $[Ga_{13}\{Si(CMe_3)_3\}_6]$,[4] $[Ga_{22}R_8]$ [R = $Si(SiMe_3)_3$],[7] $Ge(SiMe_3)_3$,[8] $Si(CMe_3)_3$,[9] $[Ga_{26}\{Si(SiMe_3)_3\}_8]^{2-}$,[10] $[Ga_{84}\{N(SiMe_3)_2\}_{20}]^{4-}$,[11] and $Ga_{23}[N(SiMe_3)_2]_{11}$.[12]

Known gallium(I) derivatives are either cluster compounds, $(GaR)_n$ where $n$ = 4–9, or monomeric species. Examples of cluster compounds are $Ga_4R_4$ [**1a** R = $C(SiMe_3)_3$,[13] **1b** $Si(SiMe_3)_3$,[14] **1c** $Si(CMe_3)_3$[15]], $Ga_6[SiMe(SiMe_3)_2]_6$,[16] and $[Ga_9(CMe_3)_9]$.[17,18] For $(GaR)_n$ clusters, $n$ skeletal electron pairs are counted, these clusters may hence be termed *hypercloso* clusters. $[Ga_6[Si(CMe_3)_3]_4(CH_2Ph)_2]^{2-}$[16] and $[Ga_8(fluorenyl)_8]^{2-}$[19] have two more electrons in their cluster core; therefore, they are *closo*-type clusters according to the Wade rules.[20–23] More bulky substituents stabilize less aggregated compounds such as the dimeric compound $[Ga(2,6\text{-}dipp_2\text{-}C_6H_3)]_2$.[24] GaCp* is monomeric in the gas phase and in solution, but it forms a weakly bound hexameric crystal structure.[25–27] [Ga{2,6-$iPr_2C_6H_2NC(CH_3)_2\}_2CH$][28] and the recently reported gallium amide $[GaN(SiMe_3)(2,6\text{-}Mes_2C_6H_3)]$ (**2**)[29] are monomers with a broad scope of applications. A very versatile starting material into this chemistry has been "GaI".[30,31]

Gallium(I) amide species are still rare. The parent compound, $GaNH_2$, has been studied in a matrix.[32] As a whole, amino groups are investigated less frequently as cluster-stabilizing substituents; with the exception of the $(Me_3Si)_2N$ group, which is used to synthesize metalloid clusters.

Here we report on reactions of "GaI" with bulky lithium amides to obtain tetrahedral clusters of gallium.

## Results and Discussion

By treating "GaI"[30] with equimolar amounts of Li[N(2,6-$iPr_2C_6H_3$)($SiMe_3$)] [Equation (1)] in a toluene/thf mixture (2:1) at –78 °C, [Ga{N(2,6-$iPr_2C_6H_3$)($SiMe_3$)}]$_4$ (**3**) is obtained. In a comparable manner, $[Ga(tmp)]_4$ (**4**) was synthesized by reaction of "GaI" and Li(tmp) [tmp = 2,2,6,6-(tetramethylpiperidino)]. Compounds **3** and **4** were isolated in moderate yields of 24% and 34%, respectively. The reactions described here allow synthetically useful amounts of material to be prepared from "GaI", whereas other reactions starting from "GaI" form a mixture of products simultaneously and mostly in very low yields, as a result of disproportionation and redox reactions that in-

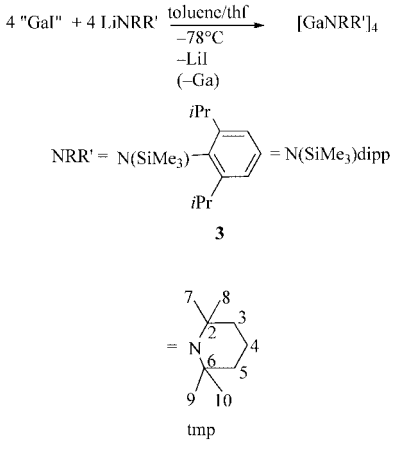


(1)

[a] University of Heidelberg, Institute of Inorganic Chemistry, Im Neuenheimer Feld 270, 69120 Heidelberg, Germany
Fax: +49-6221-546617
E-mail: Gerald.linti@aci.uni-heidelberg.de

Supporting information for this article is available on the WWW under http://www.eurjic.org or from the author.


© 2007 Wiley-VCH Verlag GmbH & Co. KGaA, Weinheim

volve the reagent LiR. This difference may be due to the lower reductive ability of amides compared to that of silanides.

Nevertheless, the formation of elemental gallium points to accompanying redox reactions. No products could be isolated, but in the case of the tmp derivative, NMR spectra of the reaction mixture indicated the formation of Ga(tmp)$_2$I[33] and Ga$_2$(tmp)$_4$,[34] which are expected byproducts. Gallium(I) amides **3** and **4** are yellow and very soluble in *n*-hexane, toluene, and tetrahydrofuran. Compound **3** is tetrameric in benzene solution, as determined by cryoscopy. Temperature-dependent NMR spectroscopic studies (20–70 °C) suggest a tetramer/monomer equilibrium in solution (see below).

In the case of LiN(SiMe$_3$)$_2$, the tetrameric species [GaN(SiMe$_3$)$_2$]$_4$ was not observed, and only the disproportionation product **5** was isolated in minor yields [Equation (2)]. This is partly in line with the results observed for the reaction of metastable GaX solutions with LiN(SiMe$_3$)$_2$, which lead to the higher metalloid Ga$_{23}$ and Ga$_{84}$ clusters. In a similar reaction, with only toluene as solvent, the only observed products were gallium and Ga[N(SiMe$_3$)$_2$]$_3$. The source of the oxygen atom that bridges two gallium atoms in **5** was not clear. Either thf was cleaved by the Lewis acidic Ga[N(SiMe$_3$)$_2$]I units or Ga[N(SiMe$_3$)$_2$]I was hydrolyzed by traces of water. Compounds **5** and **5a**, a derivative of **5** in which Li(thf) is replaced by a LiILi(thf)$_3$ unit (see Supporting Information), were formed reproducibly. This might be indicative of thf as the oxygen source.

$$\text{"GaI"} + \text{LiN(SiMe}_3\text{)}_2 \xrightarrow[-78\,^\circ\text{C}\ -\text{Ga}\ -\text{LiI}]{\text{toluene/thf}} \underset{\mathbf{5}}{\text{[Li(thf)][Ga}_6\text{IO\{N(SiMe}_3\text{)}_2\}_6\text{]}} \quad (2)$$

## Spectroscopic Characterization

Both compounds **3** and **4** were fully characterized by $^1$H-, $^{13}$C-, $^{29}$Si NMR and UV/Vis spectroscopy and elemental analyses as well as X-ray structure analysis. The signals in the proton and carbon NMR spectra were associated by HMBC correlation. For **3**, a characteristic signal for the SiMe$_3$ group was found at $\delta$ = 0.09 ppm. The proton resonance of the isopropyl moiety was detected as one set of doublets at $\delta$ = 1.26 ppm (CH$_3$) and a septet at $\delta$ = 3.4 ppm (CH). The coincidence of the diastereotopic methyl groups is indicative of a similar environment and thus of free rotation around the Ga–N bonds. The singlet observed at $\delta$ = 3.2 ppm for the SiMe$_3$ group at 293 K by $^{29}$Si NMR spectroscopy was the most characteristic for **3**. Upon heating to 333 K, a new signal at 1.4 ppm appeared, but it disappeared again upon cooling. This is indicative of the dissociation of **3** in solution. A $\Delta G$ value of 20 kJ/mol for the dissociation of **3** into monomers was derived from the NMR spectroscopic data. Quantum chemical calculations (see below) predict low tetramerization energies for GaNR$_2$ and are in line with this observation.

The $^1$H NMR spectrum for **4** shows three signal groups. The methyl groups resonate at $\delta$ = 1.65 ppm, the protons of the six-membered piperidine ring give rise to multiples at $\delta$ = 1.32 and 1.55 ppm. The carbon atoms in the ring resonate at 18.7 (C-4), 41.3 (C-3,5), and 55.6 (C-2,6) ppm in the $^{13}$C NMR spectrum, as expected. The resonance signal for the methyl groups is at $\delta$ = 36 ppm. The chemical shift for C-2,6 is typical for Ga(tmp) derivatives and is shifted to higher frequencies compared to tmpH. For comparison, the formal oxidation product of **4**, [Ga(tmp)S]$_4$, shows a signal for C-2,6 at $\delta$ = 54.9 ppm.[35] Here, too, the observation of only one set of tmp signals is indicative of free rotation around the Ga–N bond.

The mass spectra of **3** and **4** do not have the molecular peak characteristic for the tetramers. In the case of **4**, the peak at highest mass, at *m*/*z* = 419, corresponds to [Ga$_2$(tmp)$_2$]$^+$, from which one Ga is lost to give [Ga(tmp)$_2$]$^+$ at *m*/*z* = 349.

Solutions of **3** and **4** absorb in the UV range at 280 and 268 nm, respectively. The extinction coefficients suggest a weak transition. In contrast, the intensively colored silyl and organyl substituted gallatetrahedranes show absorption bands at about 500 nm.

## Crystal Structure Analyses

Tetragallane **3** crystallizes from *n*-hexane at –30 °C as yellow crystals in the monoclinic space group $P2_1c$ (Table 1), while **4** crystallizes in the monoclinic space group *Cc*. The molecular structures of molecules **3** and **4** are presented in Figure 1 and Figure 2.

The cores of **3** and **4** are distorted tetrahedra of gallium atoms. The gallium–gallium distances in **3** spread over a range of 10 pm [$d_{Ga-Ga}$ = 258.6(1)–268.5(1) pm], those for **4** cover a range of 6 pm [$d_{Ga-Ga}$ = 258.4(1)–264.2(1) pm]. This is different from the results obtained for silyl and organyl substituted gallatetrahedranes, in which nearly regular tetrahedra were observed. Silyl substituted derivatives **1b** and **1c** have shorter gallium–gallium distances [$d_{Ga-Ga}$ = 258.4 pm, **1b**;[14] 257.2 pm, **1c**[15,36,37]] than organyl substituted ones [$d_{Ga-Ga}$ = 268.8 pm, **1a**].[13] Steric as well as electronic reasons for these differences have been discussed.[1] The gallium–nitrogen bond lengths in **3** and **4** are similar. The average Ga–N distances are 186.0 and 188.5 pm for **3** and **4**, respectively. The nitrogen atoms in **3** and **4** are coordinated in a nearly planar manner by a gallium atom and two carbon atoms (or a silicon atom). In **3**, the nitrogen atoms are less than 2 pm outside the corresponding Ga–Si–C-planes. In **4**, the deviation is slightly larger, with values between 5 and 15 pm. Nevertheless, the nitrogen atoms can be regarded as coordinated in a planar fashion. The N–Si–C bond lengths and the Ga–N–Si bond angle in **3** are very similar to those observed for **2**. The gallium–nitrogen bond lengths in **3** are similar to that in a N(SiMe$_3$)dipp derivative of gallium(III).[38] The gallium–nitrogen distances of **4** are in the typical range observed for Ga(tmp) compounds like Ga$_2$(tmp)$_4$ [$d_{Ga-N}$ = 190.1(4) pm] and Ga(tmp)$_2$Ph

 © 2007 Wiley-VCH Verlag GmbH & Co. KGaA, Weinheim 

Table 1. Crystal data and data collection parameters.

| Compound | **3** | **4** | **5** |
|---|---|---|---|
| Empirical formula | $C_{60}H_{104}Ga_4N_4Si_4 \cdot 0.5C_4H_{80}$ | $C_{36}H_{72}Ga_4N_4$ | $C_{44}H_{124}Ga_6ILiN_6Si_{12}$ |
| Formula weight | 1309.8 | 839.9 | 1674.7 |
| Crystal size | $0.21 \times 0.12 \times 0.11$ | $0.13 \times 0.39 \times 0.41$ | $0.53 \times 0.33 \times 0.32$ |
| Crystal system | monoclinic | monoclinic | triclinic |
| Space group | $P2_1/c$ | $Cc$ | $P\bar{1}$ |
| $a$ [pm] | 13.112(3) | 18.843(4) | 13.492(3) |
| $b$ [pm] | 23.474(5) | 18.267(4) | 16.289(3) |
| $c$ [pm] | 25.591(5) | 12.548(3) | 21.963(4) |
| $\alpha$ [°] | | | 90.58(3) |
| $\beta$ [°] | 92.43(3) | 95.41(3) | 95.17(3) |
| $\gamma$ [°] | | | 114.15(3) |
| $V$[pm$^3$] | 7.870(3) | 4.299(2) | 4.380(2) |
| $Z$ | 4 | 4 | 2 |
| $\rho$(calcd.) [g/cm$^3$] | 1.105 | 1.297 | 1.270 |
| $\mu$ [mm$^{-1}$] | 1.449 | 2.506 | 2.367 |
| $F$(000) | 2772 | 1760 | 1728 |
| $2\theta_{max}$ [°] | 42 | 48 | 48 |
| Temp. [K] | 200 | 200 | 200 |
| Refl. collected | 33822 | 13484 | 28107 |
| Refl. unique | 8217 | 6588 | 12889 |
| Refl. observed (4σ) | 4056 | 5615 | 8788 |
| $R_{int}$ | 0.1182 | 0.0640 | 0.0478 |
| Absorption corr. | numerical | numerical | numerical |
| Min/max. transm. | 0.7361/0.8584 | 0.4286/0.7192 | 0.3558/0.5785 |
| No. variables | 724 | 414 | 739 |
| Weighting scheme[a] $x$ | 0.0499 | 0.0637 | 0.0439 |
| GOOF | 0.779 | 0.967 | 0.860 |
| Final $R$ (4σ) | 0.0480 | 0.0398 | 0.0340 |
| Final $wR_2$ | 0.1185 | 0.1000 | 0.0827 |
| Largest resid. peak [e/Å$^3$] | 0.77 | 0.92 | 0.55 |

[a] $w^{-1} = \sigma^2F_o^2 + (xP)^2$; $P = (F_o^2 + 2F_c^2)/3$.

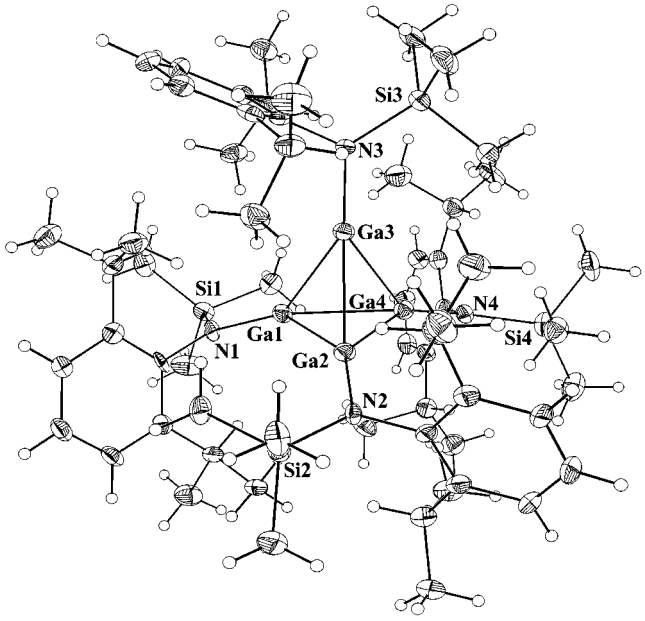


Figure 1. View of a molecule of **3**. Selected distances [pm] and angles [°]: Ga1–Ga2 260.2(1), Ga1–Ga3 267.6(1), Ga1–Ga4 258.6(1), Ga2–Ga4 261.9(1), Ga2–Ga3 268.5(1), Ga3–Ga4 262.0(1), Ga1–N1 187.2(6), Ga2–N2 187.1(7), Ga3–N3 187.5(7), Ga4–N4 182.3(6), Si–N 174.4(7)–176.6(7); N–Ga–Ga 137.9(2)–149.0(2), Ga–Ga–Ga 58.07(4)–61.87(4), C1–N1–Si1 120.0(5), C1–N1–Ga1 115.0(5), Si1–N1–Ga1 125.0(4).

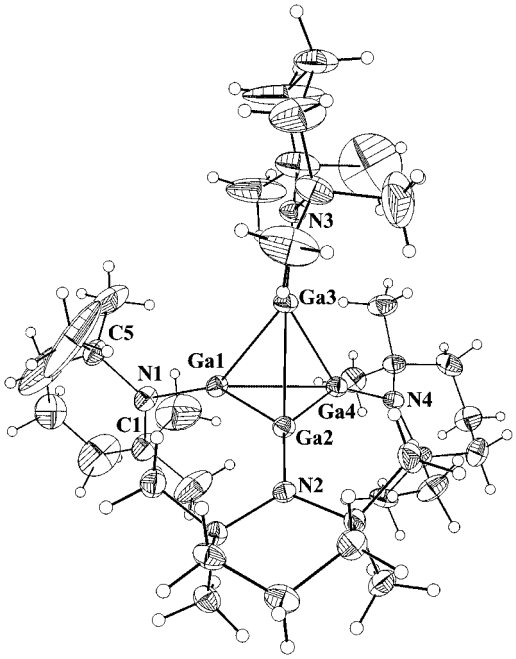


Figure 2. View of a molecule of **4**. Selected distances [pm] and angles [°]: Ga1–Ga2 258.9(1), Ga1–Ga3 264.1(1), Ga1–Ga4 261.6(1), Ga2–Ga3 258.35(9), Ga2–Ga4 264.1(1), Ga3–Ga4 261.1(1), Ga1–N1 187.6(5), Ga2–N2 188.2(4), Ga3–N3 189.6(4), Ga4–N4 188.7(5); N–Ga–Ga 142.3(1)–148.3(2), Ga–Ga–Ga 58.93(3)–61.41(3), C1–N1–C5 121.0(5), C1–N1–Ga1 119.7(4), C5–N1–Ga1 119.0(4).

 © 2007 Wiley-VCH Verlag GmbH & Co. KGaA, Weinheim 

[$d_{Ga–N}$ = 188.3(2) pm].[33] Gallium(I) amides with two- and three-coordinate gallium atoms have longer gallium–nitrogen distances, e.g. [{H(CMeCdipp$_2$N)$_2$}Ga][28] [$d_{Ga–N}$ = 205.4(2) pm], [dippNC(NCy$_2$)Ndipp]Ga[39] [$d_{Ga–N}$ = 209.1(2) pm], and Tp*t*Bu$_2$Ga [$d_{Ga–N}$ = 223.0(5) pm], where Tp*t*Bu$_2$ = tris(3,5-di-*tert*-butylpyrazolyl)hydroborato.[40] Even relative to the monomeric gallium(I) amide **2** [$d_{Ga–N}$ = 198.0(2) pm], the gallium–nitrogen bonds seem to be shortened by 10 pm. The gallium–nitrogen distances in the metalloid clusters Ga$_{23}$ and Ga$_{84}$ are in a similar range [$d_{Ga–N}$ = 186–190 pm]. A comparable shortening was observed on the tetramerization of [GaC(SiMe$_3$)$_3$].[13] The long Ga–X bonds in the monomer were explained by the influence of the lone pair. To determine whether this is valid for gallium(I) amides as well, DFT calculations were performed.

Compound **5** crystallizes in the triclinic space group $P\bar{1}$ together with a disordered molecule of tetrahydrofuran. Compound **5** (Figure 3) is a hexagallanate with six bis(trimethylsilyl)amino, one iodo, and one oxo substituents. The counterion is a lithium cation coordinated by a thf molecule. The lithium ion is bonded by a Li–O and a Li–N contact to the hexagallane core. This means that the $Ga_6X_9^-$ derivative has an intermediate formal oxidation state of 1.66, which is close to that of $Ga_4I_6$. The latter was synthesized directly from the elements[41] and could be identified[42] by means of Raman spectroscopy as a possible component of "GaI". Upon heating a suspension of "GaI" in toluene to about 100 °C for a week, crystals of $Ga_4I_6$ can be obtained.

The structure of **5** is best described as a central gallium atom coordinated by four gallium atoms in a distorted tetrahedron (angles Ga–Ga–Ga = 89.9–120.9°). Three of them are part of $GaX_2$ groups where $X_2$ is [N(SiMe$_3$)]$_2$, [N(SiMe$_3$)I], or [N(SiMe$_3$)]$_2$O$_{0.5}$. The fourth gallium atom is part of a $Ga_2$ unit and is ligated to a N(SiMe$_3$)$_2$ group and a [GaN(SiMe$_3$)$_2$O$_{0.5}$] group. Thus, a five-membered ring composed of four gallium atoms and one oxygen atom is formed in a slightly twisted conformation [torsion angles for Ga1–Ga5–Ga3–Ga2 and Ga5–Ga3–Ga2–O1 are –19.2° and 24.6°, respectively].

The iodine atom bonded to Ga4 is connected to Ga5 as well, which means that Ga5 is tetracoordinate, like the central Ga3. The gallium–iodine distances ($d_{Ga–I}$ = 289.2 and 299.0 pm) are relatively long compared to other compounds with four-membered $Ga_3I$ rings; for example, in {(Me$_3$Si)$_3$Si}$_4$Ga$_4$I$_3^-$ (**6**)[3] they are at 285 pm. The remaining gallium atoms are in a planar environment made up of their substituents. The nonplanar, four-membered $Ga_3I$ ring has an acute angle [angle (Ga–I–Ga) = 73.68(3)°] at the iodine atom. The remaining inner ring angles are between 89 and 92°. The ring is butterfly-like with a roof angle of 31.7°. Both rings are oriented orthogonally to one another. The gallium–gallium bond lengths range from 246.5 to 252.7 pm, which is typical for digallanes $R_4Ga_2$ and other oligogallanes,[1] which can be described by 2c2e gallium–gallium bonds. Also comparable is the subhalide $Ga_5Cl_7$·(OEt$_2$)$_5$,[43] in which a central gallium atom is tetrahedrally surrounded by four gallium atoms, and tetragallane **6**[3] [average $d_{Ga–Ga}$ = 253 pm].

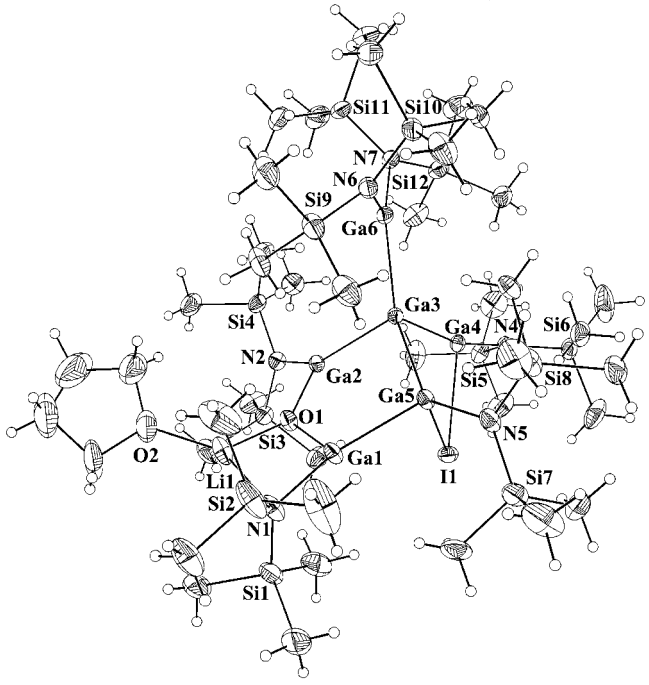


Figure 3. View of a molecule of **5**. Selected distances [pm] and angles [°]: Ga1–Ga5 250.00(9), Ga2–Ga3 250.59(8), Ga3–Ga4 246.49(8), Ga3–Ga5 248.8(1), Ga3–Ga6 252.7(1), Ga4–I1 289.2(1), Ga5–I1 299.04(9), Ga1–O1 185.1(2), Ga2–O1 185.1(2), Ga1–N1 196.8(3), Ga2–N2 190.0(3), Ga4–N4 186.4(3), Ga5–N5 190.4(3), Ga6–N6 190.0(3), Ga6–N7 191.2(3§), N–Si 174.2(3)–175.6(4); Ga2–Ga3–Ga4 96.65(3), Ga2–Ga3–Ga6 118.46(3), Ga4–Ga3–Ga6 120.88(3), Ga4–Ga3–Ga5 89.94(3), Ga6–Ga3–Ga5 128.77(3), Ga2–Ga3–Ga5 94.22(4).

The gallium–nitrogen bond lengths are between 186.4 and 196.8 pm. This is in the typical range for gallium–nitrogen bonds, e.g. Ga[N(SiMe$_3$)$_3$] [$d_{Ga–N}$ = 186.8(1) pm].[44–47] Bonds between gallium and nitrogen show considerable variations due to inductive and steric effects of gallium substituents. In general, electron-withdrawing substituents at gallium lead to shorter gallium–nitrogen bonds.[33] In **5**, the longest gallium–nitrogen bond is the Ga1–N1 bond, where N1 is coordinated to lithium. The shortest is the Ga4–N4 bond, where the gallium is also bonded to an iodine atom.

At the triply coordinated gallium centers Ga2 and Ga6, the $NSi_2$ planes are twisted by approximately 45° to the planes described by the adjacent gallium atom and its bonding partners. At the Ga1 center, the twist angle is larger (70°). This difference is due to the interaction of the nitrogen atom with the lithium ion and the resulting steric restrictions. At Ga4, the $NSi_2$ and Ga4–N4–I1–Ga3 planes are orthogonal. The N4–Ga4–Ga3 angle is very wide (165°). This might hint to an alternative description with a gallium(I) amide (Me$_3$Si)$_2$NGa as Lewis base adduct to a pentagallate residue, as depicted in Scheme 1. In line with this description are the short gallium–nitrogen bond to Ga4, the long gallium–iodine distance, and the large angle at Ga4.[44–47]

 © 2007 Wiley-VCH Verlag GmbH & Co. KGaA, Weinheim 

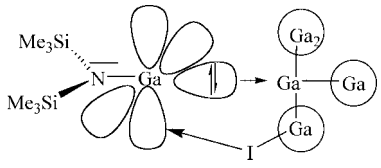


Scheme 1. Description of **5** as a gallium(I) adduct to a pentagallanate.

### Quantum Chemical Calculations

Geometry optimizations at the RI-DFT[44] level with the BP86-functional and def-SVP base sets for all atoms have been performed for monomeric gallium(I) amides **7**–**10** and the tetrameric species **11**–**14** (Table 2). The calculated structural parameters for **13** are similar to those observed for **3**, but the bonds are all a little bit elongated ($d_{Ga–Ga}$ = 263.5–272.2 pm, $d_{Ga–N}$ = 192.3 pm, $d_{N–Si}$ = 179.0 pm). Compared to the monomer **9**, the gallium–nitrogen bonds in **13** are shortened only by 2 pm. For gallium organyls, a larger shortening of the Ga–N bonds by nearly 10 pm was observed experimentally. Even the gallium–hydrogen bond lengths in GaH were calculated to be shortened by 9 pm upon tetramerization to $Ga_4H_4$. The silicon–nitrogen and nitrogen–carbon bonds were affected slightly [**9**: $d_{N–Si}$ = 179.9 pm, $d_{N–C}$ = 143.3 pm; **13**: $d_{N–Si}$ = 179.0 pm, $d_{N–C}$ = 144.0 pm]. The Si–N–C angles are 3° smaller than those in the monomer. A comparison of **9** with **2**[29] shows that the gallium–nitrogen bond is shorter in **9**. Calculations for monomeric gallium(I) amides reported previously[29,32] and in this work demonstrate quite strong gallium–nitrogen bonds, with minor participation from Ga–N π bonds. This is documented by an Ahlrichs–Heinzmann population analysis, which gives an SEN value of 1.4 to 1.6 for these amides.[45] Values of about 1.4 are typical for Ga–N single bonds.

The HOMO–1 orbitals for **7**–**10** are mainly Ga 4s orbitals, the LUMO and LUMO+1 orbitals have mainly Ga 4p character. The HOMO orbitals indicate a π bond, which is polarized to nitrogen. In the tetrameric compounds **11**–**14**, the SEN values for the gallium–nitrogen bonds are smaller, indicating the loss of π-bond participation. The HOMO of cluster **12** (Figure 4) has mainly nitrogen-pair character and gives no hint of any interaction, either stabilizing or destabilizing, between the lone pairs and the cluster core.

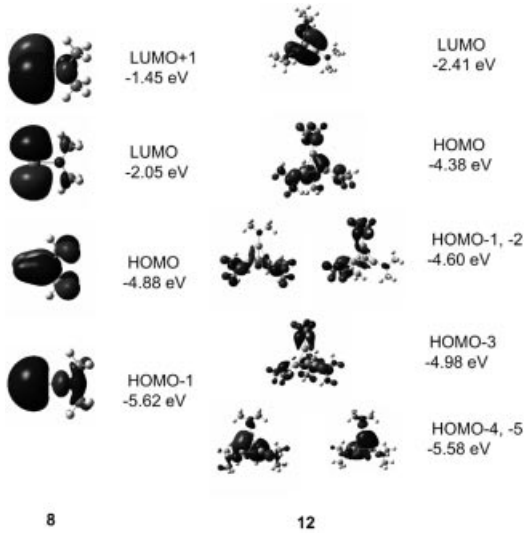


Figure 4. Kohn–Sham frontier orbitals for $GaNMe_2$ and $Ga_4(NMe_2)_4$.

The calculated HOMO–LUMO gaps of about 2.4 eV fit well with the observed absorption bands in the visible spectral region of **1** but not with those measured for **3** and **4**. Inspection of the LUMO and HOMO of **12** makes clear that population of the LUMO would weaken the cluster bonding, because the LUMO is a cluster antibonding orbital, whilst the HOMO has, as stated before, essentially lone-pair character. A more reasonable excitation of an electron from a cluster-binding orbital like HOMO–4 into the LUMO could explain the UV-absorption bands of **3** and **4** much better. The monomer would also give rise to absorptions around 300 nm. The tetramerization energy of the gallium amides ($E_{tetra}$ = 150–170 kJ/mol) is much lower than those calculated for gallium silyls ($E_{tetra}$ = 300–400 kJ/mol) and organyls ($E_{tetra}$ ≈ 200 kJ/mol). This is a consequence of the Ga–N π bond in monomeric gallium(I) amides, which has to be broken upon tetramerization. A hypothetical dimer should have a very long Ga–Ga distance [$d_{Ga–Ga}$ = 299.5 pm] and a very low dimerization energy of 16 kJ/mol. A trimer $[Ga(tmp)]_3$ is calculated to have a irregular triangular $Ga_3$ core [$d_{Ga–Ga}$ = 261.0–280.3 pm, $d_{Ga–N}$ = 193.0 pm] and has a trimerization energy of 58 kJ/mol.

Table 2. RI-DFT results (BP86 functional, def-SVP base) for **7**–**14**.

| | $H_2GaNH_2$ | $GaNH_2$ **7** | $GaNMe_2$ **8** | $GaN(SiMe_3)dipp$ **9** | Ga(tmp) **10** | $[GaNH_2]_4$ **11** | $[GaNMe_2]_4$ **12** | $[GaN(SiMe_3)dipp]_4$ **13** | $[Ga(tmp)]_4$ **14** |
|---|---|---|---|---|---|---|---|---|---|
| $d_{Ga–Ga}$ [pm] | – | – | – | – | – | 257.7–263.0 | 258.2–267.7 | 263.5–272.2 | 259.9–269.8 |
| $d_{Ga–N}$ [pm] | 182.6 | 188.8 | 190.9 | 194.3 | 193.8 | 187.1 | 187.9 | 191.7–192.9 | 191.6–193.0 |
| $E_{Tetra}$ [kJ/mol] | – | – | – | – | – | 56 | 50 | 150 | 173 |
| HOMO–LUMO [eV] | 4.55 | 3.57 | 2.84 | 3.05 | 3.31 | 2.28 | 1.96 | 2.41 | 2.31 |
| SEN Ga–N | 1.62 | 1.62 | 1.49 | 1.36 | 1.39 | 1.08 | 1.21 | 1.09 | |
| SEN Ga–Ga | – | – | – | – | – | 1.23–1.25 | 1.13–1.24 | 1.11–1.25 | |
| SEN Ga–Ga–Ga | – | – | – | – | – | 0.32 | 0.25 | 0.35 | |
| $Q_{Ga}$ [a] | 0.01 | –0.02 | 0.01 | 0.15 | 0.01 | 0.08 | 0.07 | 0.16 | |
| $Q_N$ [a] | –0.16 | –0.20 | –0.01 | –0.29 | –0.12 | –0.38 | –0.13 | –0.44 | |

[a] Charges with multicenter correction.[49]

 © 2007 Wiley-VCH Verlag GmbH & Co. KGaA, Weinheim 

The HOMO of tetramer **11** is higher in energy than that of the monomer. A similar situation is found for gallium organyls, where monomerization in gas phase and solution is easy. For gallium silyls, the HOMO energies for tetrahedral clusters are lower than those for the monomers. Compound **12** is a distorted tetrahedron, thus the HOMO is a nondegenerate molecular orbital, in contrast to the regular tetrahedral clusters with $T_d$ symmetry, where the HOMO is of the $t_2$ type.

## Conclusions

The facile synthesis of the first amino-substituted gallium(I) clusters, with functional groups attached to cluster cores, opens new reaction possibilities, which might lead to novel cluster types and give insight into cluster formation reactions.

## Experimental Section

**General Remarks:** All experiments were performed under purified argon or in vacuo with Schlenk techniques. All yields are referenced to "GaI" as starting material. Elemental analyses were performed in the microanalytical laboratory of Ruprecht-Karls-University of Heidelberg. NMR: Bruker AV400–600; The UV/Vis spectra were measured at 18 °C with a JASCO V-570 UV/Vis/NIR Spectrophotometer, using a Suprasil quartz cell (10 mm transition thickness) in n-hexane as solvent. Quantum chemical calculations: TURBOMOLE[44,47,48] and G03/GaussView.[49]

### X-ray Crystallography

Suitable crystals were mounted with a perfluorinated polyether oil on the tip of a glass fiber and cooled immediately on the goniometer head. Data collection was performed with Mo-$K_\alpha$ radiation (graphite monochromator) on a STOE IPDSI diffractometer. Structures were solved by direct methods and refined by full-matrix least-squares against $F^2$. All non-hydrogen atoms were given anisotropic displacement parameters. Hydrogen atoms were included in calculated positions. Calculations were performed by using the SHELXTL package.[46] Crystals of **3** were weakly diffracting; no reflections could be observed at $2\theta > 40°$.

CCDC-641586 (**3**), -641585 (**4**), -641587 (**5**), -650747 (**5a**) contain the supplementary crystallographic data for this paper. These data can be obtained free of charge from the Cambridge Crystallographic Data Centre via www.ccdc.cam.ac.uk/data_request/cif.

**[Ga{N(2,6-*i*Pr$_2$C$_6$H$_3$)(SiMe$_3$)}]$_4$ (3):** Into a vigorously stirred suspension of freshly prepared "GaI" (0.61 g, 3.9 mmol) in toluene (20 mL) at –78 °C was added a solution of Li[N(2,6-*i*Pr$_2$C$_6$H$_3$)-(SiMe$_3$)] (1.10 g, 4.3 mmol) in thf (8 mL). After slow warming to room temperature, the mixture was stirred for an additional hour. All volatiles were removed in vacuo. The residue was extracted with *n*-hexane (30 mL). The yellow solution was concentrated to about 10 mL. At –30 °C, yellow crystals of compound **3** were isolated. Yield 0.30 g, 0.24 mmol (24%). $^1$H NMR ($C_6D_6$): $\delta$ = 0.09 (s, 9 H, SiC$H_3$), 1.26 [d, $^3J_{HH}$ = 6.9 Hz, 12 H, CH(C$H_3$)$_2$], 3.44 [sept, 2 H, C$H$(CH$_3$)$_2$], 7.07 (m, 3 H, CH arom.) ppm. $^{13}$C NMR ($C_6D_6$): $\delta$ = 0.8 (SiCH$_3$), 23.8, [CH(*C*H$_3$)$_2$], 28.4 [*C*H(CH$_3$)$_2$], 123.3 (m-C), 124.0 (*p*-C), 139.8 (*o*-C), 144.6 (*i*-C) ppm. $^{29}$Si NMR ($C_6D_6$): $\delta$ = 3.26 ppm. UV/Vis (*n*-hexane): $\lambda_{max}$ ($\varepsilon$, L mol$^{-1}$ cm$^{-1}$) = 280 (996) nm. $C_{60}H_{104}Ga_4N_4Si_4$ (1272.7): calcd. C 56.62, H 8.24, N 4.40; found C 54.95, H 8.23, N 4.39.

**[Ga(tmp)]$_4$ (4):** Into a vigorously stirred suspension of freshly prepared "GaI"[30] (0.99 g, 51 mmol) in toluene (20 mL) at –78 °C was added a solution of Li(tmp) (0.82 g, 55 mmol) in thf (8 mL). After slow warming to room temperature, the mixture was stirred for 1 h. All volatiles were removed in vacuo. The residue was extracted with *n*-hexane (30 mL). The orange solution was concentrated to a volume of 5 mL. At –30 °C yellow crystals of compound **4** were isolated; yield 0.37 g, 0.44 mmol (34%). $^1$H NMR ($C_6D_6$): $\delta$ = 1.32 [m, 4 H, (CH$_3$)$_2$CC$H_2$], 1.55 (m, 2 H, CH$_2$C$H_2$CH$_2$) ppm. 1.65 [s, 12 H, C(C$H_3$)] ppm. $^{13}$C NMR ($C_6D_6$): $\delta$ = 18.8 (CH$_2$*C*H$_2$CH$_2$), 36.6 [C(*C*H$_3$)$_2$], 41.3 (*C*H$_2$CH$_2$*C*H$_2$), 55.6 [*C*(CH$_3$)$_2$] ppm. UV/Vis (*n*-hexane): $\lambda_{max}$ ($\varepsilon$, L mol$^{-1}$ cm$^{-1}$) = 268 (155) nm. $C_{36}H_{72}Ga_4N_4$ (839.8): calcd. C 51.48, H 8.64, N 6.64; found C 50.46, H 8.46, N 6.35.

**Ga$_6$[N(SiMe$_3$)$_2$]$_6$IOLi.thf (5):** Into a vigorously stirred suspension of freshly prepared "GaI" (0.66 g, 3.35 mmol) in toluene (20 mL) at –78 °C was added a solution of LiN(SiMe$_3$)$_2$ (0.62 g, 3.68 mmol) in thf (8 mL). After slow warming to room temperature, the mixture was stirred for an additional hour. All volatiles were removed in vacuo. The residue was extracted with *n*-hexane (30 mL). The remaining solid was not soluble in any common solvent and consisted mainly of LiI and elemental gallium. The orange solution was concentrated to a volume of 5 mL. At –30 °C, some yellow crystals of compound **5** were isolated.

**Supporting Information** (see footnote on the first page of this article): Crystal data, structure refinement, and selected bond lengths and bond angles for **5a**.

## Acknowledgments

We thank the Deutsche Forschungsgemeinschaft for financial support and Philipp Butzug for making the crystallographic measurements.

[1] G. Linti, H. Schnöckel, W. Uhl, N. Wiberg in *Molecular Clusters of the Main Group Elements* (Eds.: M. Driess, H. Nöth), Wiley-VCH, Weinheim, **2004**, pp. 126–168.
[2] N. Wiberg, T. Blank, H. Nöth, M. Suter, M. Warchold, *Eur. J. Inorg. Chem.* **2002**, 929–934.
[3] G. Linti, W. Köstler, *Angew. Chem.* **1997**, *109*, 2758–2760; *Angew. Chem. Int. Ed. Engl.* **1997**, *36*, 2644–2646.
[4] M. Kehrwald, W. Köstler, G. Linti, A. Rodig, T. Blank, N. Wiberg, *Organometallics* **2001**, *20*, 860–867.
[5] N. J. Hardman, R. J. Wright, A. D. Phillips, P. P. Power, *J. Am. Chem. Soc.* **2003**, *125*, 2667–2679.
[6] A. Schnepf, G. Stößer, R. Köppe, H. Schnöckel, *Angew. Chem. Int. Ed.* **2000**, *39*, 1637–1639.
[7] A. Schnepf, E. Weckert, G. Linti, H. Schnöckel, *Angew. Chem.* **1999**, *111*, 3578–3581; *Angew. Chem. Int. Ed.* **1999**, *38*, 3381–3383.
[8] G. Linti, A. Rodig, *Chem. Commun.* **2000**, 127–128.
[9] A. Donchev, A. Schnepf, G. Stößer, E. Baum, H. Schnöckel, T. Blank, N. Wiberg, *Chem. Eur. J.* **2001**, *7*, 3348–3353.
[10] A. Rodig, G. Linti, *Angew. Chem.* **2000**, *112*, 3076–3078; *Angew. Chem. Int. Ed.* **2000**, *39*, 2952–2954.
[11] A. Schnepf, H. Schnöckel, *Angew. Chem.* **2001**, *113*, 733–737; *Angew. Chem. Int. Ed.* **2001**, *40*, 711–715.
[12] J. Hartig, A. Stößer, P. Hauser, H. Schnöckel, *Angew. Chem.* **2007**, *119*, 1687–1691; *Angew. Chem. Int. Ed.* **2007**, *46*, 1658–1662.
[13] W. Uhl, W. Hiller, M. Layh, W. Schwarz, *Angew. Chem.* **1992**, *104*, 1378–1380; *Angew. Chem. Int. Ed. Engl.* **1992**, *31*, 1364–1366.

 © 2007 Wiley-VCH Verlag GmbH & Co. KGaA, Weinheim 

[14] G. Linti, *J. Organomet. Chem.* **1996**, *520*, 107–113.
[15] N. Wiberg, K. Amelunxen, H. W. Lerner, H. Nöth, W. Ponikwar, H. Schwenk, *J. Organomet. Chem.* **1999**, *574*, 246–251.
[16] G. Linti, S. Çoban, D. Dutta, *Z. Anorg. Allg. Chem.* **2004**, *630*, 319–323.
[17] W. Uhl, L. Cuypers, K. Harms, W. Kaim, M. Wanner, R. Winter, R. Koch, W. Saak, *Angew. Chem.* **2001**, *113*, 589–591; *Angew. Chem. Int. Ed.* **2001**, *40*, 566–568.
[18] W. Uhl, L. Cuypers, W. Kaim, B. Schwederski, R. Koch, *Angew. Chem.* **2003**, *115*, 2524–2526; *Angew. Chem. Int. Ed.* **2003**, *42*, 2422–2423.
[19] A. Schnepf, G. Stößer, H. Schnöckel, *Z. Anorg. Allg. Chem.* **2000**, *626*, 1676–1680.
[20] K. Wade, *Adv. Inorg. Chem. Radiochem.* **1976**, *18*, 1–66.
[21] R. W. Rudolph, *Acc. Chem. Res.* **1976**, *9*, 446–452.
[22] R. E. Williams, *Adv. Inorg. Chem. Radiochem.* **1976**, *18*, 67–142.
[23] D. M. P. Mingos, *Nature* **1972**, *236*, 99–102.
[24] N. J. Hardman, R. J. Wright, A. D. Phillips, P. P. Power, *Angew. Chem.* **2002**, *114*, 2966–2968; *Angew. Chem. Int. Ed.* **2002**, *41*, 2842–2844.
[25] D. Loos, H. Schnöckel, *J. Organomet. Chem.* **1993**, *463*, 37–40.
[26] P. Jutzi, B. Neumann, G. Reumann, H.-G. Stammler, *Organometallics* **1998**, *17*, 1305–1314.
[27] P. Jutzi, L. O. Schebaum, *J. Organomet. Chem.* **2002**, *654*, 176–179.
[28] N. J. Hardman, B. E. Eichler, P. P. Power, *Chem. Commun.* **2000**, 1991–1992.
[29] R. J. Wright, M. Bynda, J. C. Fettinger, A. R. Betzer, P. P. Power, *J. Am. Chem. Soc.* **2006**, *128*, 12498–12509.
[30] M. L. H. Green, P. Mountford, G. J. Smout, S. R. Speel, *Polyhedron* **1990**, *9*, 2763–2765.
[31] R. J. Baker, C. Jones, *Dalton Trans.* **2005**, 1341–1348.
[32] H.-J. Himmel, A. J. Downs, T. M. Greene, *J. Am. Chem. Soc.* **2000**, *122*, 9793–9807.
[33] G. Linti, R. Frey, K. Polborn, *Chem. Ber.* **1994**, *127*, 1387–1393.
[34] G. Linti, R. Frey, M. Schmidt, *Z. Naturforsch., Teil B* **1994**, *49*, 958–962.
[35] G. Linti, M. Bühler, H. Urban, *Z. Anorg. Allg. Chem.* **1998**, *624*, 517–520.
[36] N. Wiberg, T. Blank, W. Kaim, B. Schwerderski, G. Linti, *Eur. J. Inorg. Chem.* **2000**, 1475–1481.
[37] N. Wiberg, K. Amelunxen, T. Blank, H. Nöth, J. Knizek, *Organometallics* **1998**, *17*, 5431–5433.
[38] R. Frey, G. Linti, *Z. Anorg. Allg. Chem.* **1997**, *623*, 531–538.
[39] C. Jones, P. C. Junk, J. A. Platts, A. Stasch, *J. Am. Chem. Soc.* **2006**, *128*, 2206–2207.
[40] M. C. Kuchta, J. B. Bonanno, G. Parkin, *J. Am. Chem. Soc.* **1996**, *118*, 10914–10915.
[41] G. Gerlach, W. Höhnle, A. Simon, *Z. Anorg. Allg. Chem.* **1982**, *486*, 7–21.
[42] S. Çoban, Diplomarbeit, University of Karlsruhe, Karlsruhe, **1999**.
[43] D. Loos, H. Schnöckel, D. Fenske, *Angew. Chem.* **1993**, *105*, 1124–1125; *Angew. Chem. Int. Ed. Engl.* **1993**, *32*, 1059–1060.
[44] O. Treutler, R. Ahlrichs, *J. Chem. Phys.* **1995**, *102*, 346–354.
[45] R. Heinzmann, R. Ahlrichs, *Theor. Chim. Acta* **1976**, *42*, 33–45.
[46] G. M. Sheldrick, *SHELXTL Bruker AXS*, *Vol.* **1998**.
[47] K. Eichkorn, O. Treutler, H. Oehm, M. Haeser, R. Ahlrichs, *Chem. Phys. Lett.* **1995**, *242*, 652–660.
[48] K. Eichkorn, F. Weigend, O. Treutler, R. Ahlrichs, *Theor. Chem. Acc.* **1997**, *97*, 119–124.
[49] M. J. Frisch, G. W. Trucks, H. B. Schlegel, G. E. Scuseria, M. A. Robb, J. R. Cheeseman, J. A. M. Jr, T. Vreven, K. N. Kudin, J. C. Burant, J. M. Millam, S. S. Iyengar, J. Tomasi, V. Barone, B. Mennucci, M. Cossi, G. Scalmani, N. Rega, G. A. Petersson, H. Nakatsuji, M. Hada, M. Ehara, K. Toyota, R. Fukuda, J. Hasegawa, M. Ishida, T. Nakajima, Y. Honda, O. Kitao, H. Nakai, M. Klene, X. Li, J. E. Knox, H. P. Hratchian, J. B. Cross, C. Adamo, J. Jaramillo, R. Gomperts, R. E. Stratmann, O. Yazyev, A. J. Austin, R. Cammi, C. Pomelli, J. W. Ochterski, P. Y. Ayala, K. Morokuma, G. A. Voth, P. Salvador, J. J. Dannenberg, V. G. Zakrzewski, S. Dapprich, A. D. Daniels, M. C. Strain, O. Farkas, D. K. Malick, A. D. Rabuck, K. Raghavachari, J. B. Foresman, J. V. Ortiz, Q. Cui, A. G. Baboul, S. Clifford, J. Cioslowski, B. B. Stefanov, G. Liu, A. Liashenko, P. Piskorz, I. Komaromi, R. L. Martin, D. J. Fox, T. Keith, M. A. Al-Laham, C. Y. Peng, A. Nanayakkara, M. Challacombe, P. M. W. Gill, B. Johnson, W. Chen, M. W. Wong, C. Gonzalez, J. A. Pople, *Gaussian 03*, Gaussian, Inc., Pittsburgh PA, **2003**.

Received: May 23, 2007
Published Online: September 17, 2007

 © 2007 Wiley-VCH Verlag GmbH & Co. KGaA, Weinheim 

DOI: 10.1002/ejic.200700616

# (Benzimidazolylmethyl)cyclen: A Potential Sensitive Fluorescent PET Chemosensor for Zinc

**Abir El Majzoub,[a] Cyril Cadiou,[a] Isabelle Déchamps-Olivier,[a] Françoise Chuburu,*[a] and Michel Aplincourt[a]**

**Keywords:** Zinc / Macrocyclic ligands / X-ray diffraction / UV/Vis spectroscopy / Fluorescent probes / Fluorimetric titrations

A new fluorescent probe for $Zn^{2+}$, methylbenzimidazole-pendant cyclen [LH: 1-(benzimidazol-2-ylmethyl)-1,4,7,10-tetraazacyclododecane] was designed and synthesized. The protonation constants of (benzimidazolylmethyl)cyclen and the stability constants of the corresponding zinc complex were determined by potentiometric titrations. The single-crystal X-ray diffraction analysis showed that LH and $Zn^{2+}$ form a 1:1 complex $[ZnLH]^{2+}$. The results of potentiometric, $^1H$ NMR and UV titrations indicated that above pH 8, $[ZnLH]^{2+}$ mainly deprotonates into $[ZnL]^+$. On addition of successive amounts of $Zn^{2+}$ at pH 10.4 ($2 \times 10^{-2}$ mol L$^{-1}$ CAPS, 25 °C), the fluorescence emission of cyclen(methylbenzimidazole) increases linearly by a factor of 3.

(© Wiley-VCH Verlag GmbH & Co. KGaA, 69451 Weinheim, Germany, 2007)

## Introduction

The design and synthesis of fluorescent chemosensors is an active field of research and is of particular significance in analytical chemistry since fluorimetric analysis offers a simple method for detecting chemical species in solution.[1] Thus, the development of selective analytical reagents, which allows the quantitative analysis of trace metal ions, is very important for environmental and biological applications. Fluorescent chemosensors developed for the detection of pH and metal cations in aqueous solution generally comprise a fluorophore covalently linked to an ionophore that can bind $H^+$ or metal cations.[2–5] The principle on which the so-called fluoroionophore works is based on an enhanced or quenched fluorescence of the system when the ionophore units bind $H^+$ or metal ions. Among the metal ions, the detection of biologically important divalent cations is of great importance to elucidate their physiological roles. In particular, the detection of $Zn^{2+}$, which is the second most abundant transition metal, following iron, in biological systems, is of interest.[6,7] The most important and best-known role for zinc is as a structural cofactor in metalloproteins. Many zinc proteins possessing one or more zinc motifs have been identified.[8] In these different structures, the zinc environment is usually tetracoordinate {i.e. $[Zn(Cys)_4]$, $[Zn(Cys)_3(His)]$, $[Zn(Cys)_2(His)_2]$}. A catalytic role was also demonstrated for zinc, for instance, in carbonic anhydrase or carboxypeptidase.[9,10] The main difference in the coordination sphere of zinc when its catalytic function is involved is the existence of a vacant coordination site. Recently, the neurological roles of zinc have attracted much attention.[11] A disorder in the metabolism of zinc is closely associated with neurological diseases such as Alzheimer's disease, amyotrophic lateral sclerosis, Parkinson's disease and epilepsy. Thus, there is a great interest in developing zinc sensors, and since, unlike biological metal ions, $Zn^{2+}$ does not give any spectroscopic or magnetic signals (as a result of its $d^{10}$ configuration), fluorescence spectroscopy stands out as a method of choice. Up to now, the reported zinc sensors are chelation-enhanced fluorescent probes.[12–17] Among them, Zn-chelating macrocyclic compounds such as cyclen (1,4,7,10-tetraazacyclododecane) form stable $Zn^{II}$ complexes in aqueous solution at neutral pH. Moreover, by comparison with quinoline-based compounds such as TSQ [6-methoxy-8-(*p*-toluenesulfonamido)-quinoline] and zinquin,[12,13a] for which zinc complexation at neutral pH is not stoichiometric (mixture of ZnL and $ZnL_2$ complexes can be obtained), cyclen derivatives such as anthracene-pendant cyclen,[14] dansylamide-pendant cyclen,[15] (anthrylmethylamino)ethyl cyclen,[16] 2-[8-hydroxy-5-(dimethylaminosulfonyl)quinolinyl]methyl cyclen[17] complex with almost 100% of $Zn^{II}$ to form ZnL under physiological conditions (at pH 7.4, $10.7 < \log K_{app}$, $[ZnL] < 14.1$, where L represents the ligand and $K_{app[ZnL]} = [ZnL]/[L]_{free}[Zn]_{free}$). The $\log K_{app[ZnL]}$ value depends whether $Zn^{2+}$ is coordinated to the fluorescent unit. Furthermore, from the fluorescent point of view, comparison of the efficiency of the sensors indicates that coordination of the fluorophore to the metal improves the signal.

[a] GRECI, Université de Reims Champagne-Ardenne,
B. P. 1039, 51687 Reims Cedex 2, France
E-mail: francoise.chuburu@univ-reims.fr

Supporting information for this article is available on the WWW under http://www.eurjic.org or from the author.

 © 2007 Wiley-VCH Verlag GmbH & Co. KGaA, Weinheim 

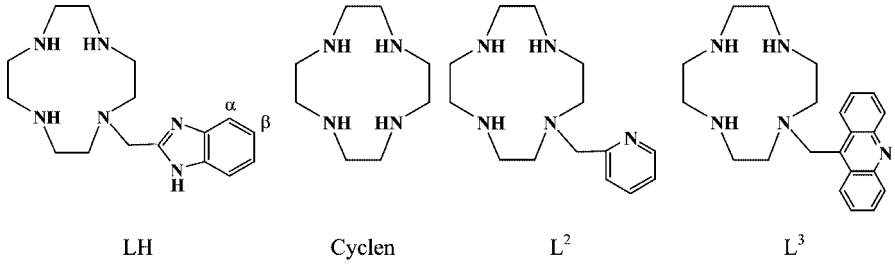


LH Cyclen $L^2$ $L^3$

Scheme 1.

Therefore, on the basis of this analysis, we present here a new fluorophore, LH (Scheme 1), in which the ionophore unit is cyclen; according to the affinity for the imidazole of histidine units in metalloenzymes of zinc, we have chosen a benzimidazole moiety as the fluorophore. This paper describes the synthesis and the coordination properties of the resulting (benzimidazolylmethyl)cyclen; protonation and coordination properties towards $Zn^{2+}$ are studied. Spectrophotometric and spectrofluorimetric investigations of the ligand in the presence of $Zn^{2+}$ are also reported in order, first, to test whether the benzimidazole moiety is a good candidate for the detection of zinc and, second, whether the system is responsive in the biological pH window.

## Results and Discussion

The ligand LH was prepared following the bisaminal methodology.[18]

### Acidity Constants of LH Determined by Potentiometric pH, UV and $^1$H NMR Titrations

Typical potentiometric pH titration curves of a mixture of (LH) $2 \times 10^{-3}$ mol L$^{-1}$ and ($HNO_3$) $10^{-2}$ mol L$^{-1}$ with $I$ = 1 ($KNO_3$) at 25 °C were analysed for acid–base equilibrium [Equation (1)]. Four protonation constants were determined for LH by using the PROTAF software (Table 1).[19] The LH macrocyclic cavity protonation assignment was made on the basis of the variation in the cyclen protonation constants upon *N*-functionalisation in relevant ligands $L^2$ and $L^3$[20,21] (Table 1). Since the presence of electron-withdrawing pendant groups results in the lowering of the cyclen protonation constants $\log K_{011}$ and $\log K_{012}$, one can conclude that the second and the third protonations of LH ($\log K_{012}$ = 10.21 and $\log K_{013}$ = 9.01) correspond to those of the macrocycle. The fourth protonation constant ($\log K_{014}$ = 4.55) cannot be associated to the cyclen moiety but to the benzimidazole ring. Effectively, this $\log K$ value has to be compared to the $\log K$ value determined for protonation of the pyrrole nitrogen atom in the benzimidazole ring [$\log K_{012}$ (benzimidazole BIH ⇆ benzimidazolium $BIH_2^+$) ≈ 5.6, see Scheme 2].[22,23] Furthermore, this value is close to that determined for the protonation of the exocyclic pyridine or acridine nitrogen atom of $L^2$ and $L^3$, respectively ($\log K_{013}$ = 3.42 and 4.44, respectively, Table 1).[21] In order to get a more precise insight into the acid–base properties of LH before pH 6, the UV absorption changes that take place upon protonation of the macrocyclic nitrogen atoms and/or the benzimidazole moiety were investigated in the 250–340 nm range (Figure 1). In this range and at pH = 6, the electronic spectrum is characteristic of the benzimidazole moiety, and two main absorptions are centred at 273 and 280 nm.[24] This absorption pattern ressembles that of a substituted benzene derivative: two absorption bands are observed in the near UV region that can be assigned to the $\pi^* \leftarrow \pi$ singlet–singlet transitions[25]($^1L_a \leftarrow S_0$ and $^1L_b \leftarrow S_0$, where $^1L_a$ and $^1L_b$ correspond to the two excited states[25c]). The extinction coefficients ($\varepsilon_{max}$ = 6700 mol$^{-1}$ L cm$^{-1}$ at 273 and 280 nm) are in agreement

Table 1. Ligand protonation constants $\log K_{0/h}$.[a]

| | | LH[b] | Cyclen[c] | $L^{2}$[d] | $L^{3}$[e] |
|---|---|---|---|---|---|
| L[f] + $H^+$ ⇌ LH | $\log K_{011}$ | 11.05(4) | 10.97 | 10.6 | 10.32 |
| LH + $H^+$ ⇌ $LH_2$ | $\log K_{012}$ | 10.21(8) | 9.87 | 9.77 | 7.78 |
| $LH_2$ + $H^+$ ⇌ $LH_3$ | $\log K_{013}$ | 9.01(5) | <2 | 3.42 | 4.44 |
| $LH_3$ + $H^+$ ⇌ $LH_4$ | $\log K_{014}$ | 4.55(9) | <2 | <2 | <2 |
| $LH_4$ + $H^+$ ⇌ $LH_5$ | $\log K_{015}$ | <2 | – | <2 | <2 |
| $LH_5$ + $H^+$ ⇌ $LH_6$ | $\log K_{016}$ | <2 | – | – | – |

[a] The numbers in parentheses refer to the estimated standard deviations for the last significant digit (95% confidence). [b] Potentiometric titrations at 25.0(1) °C, $I$ = 1 ($KNO_3$) (this work). [c] Ref.[20] [d] Ref.[21a] [e] Ref.[21b] [f] For LH, the L species corresponds to the anionic form of the ligand.

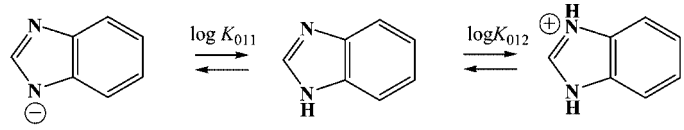


$BI^-$ BIH $BIH_2^+$

$\log K_{011}$(25°C) = 12.75 [22]; 12.78 [27] $\log K_{012}$ (25°C) = 5.58 [23]; 5.68 [23]

Scheme 2.

 © 2007 Wiley-VCH Verlag GmbH & Co. KGaA, Weinheim 

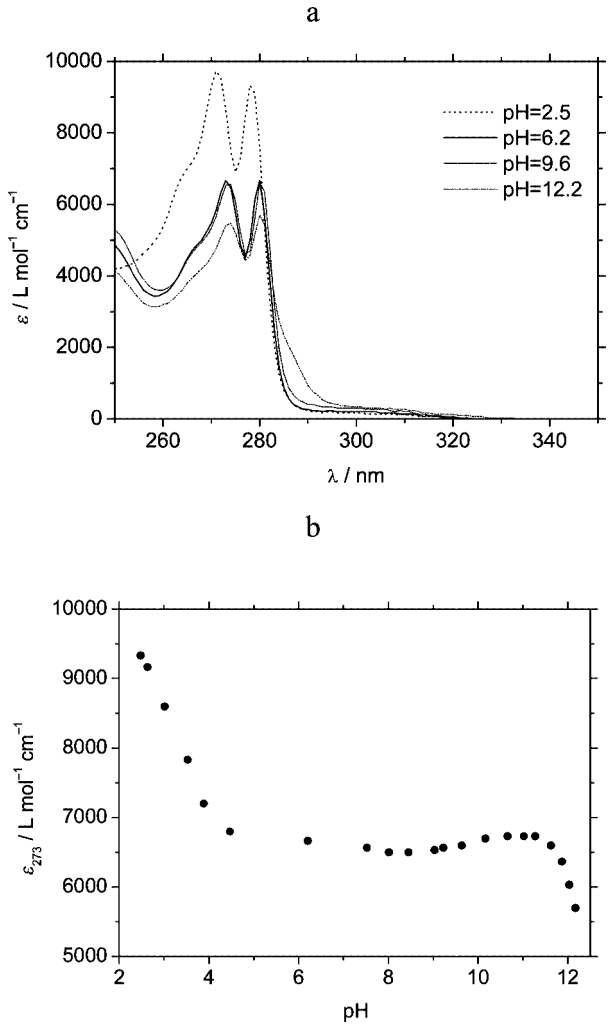


Figure 1. (a) Spectrophotometric titration of LH with KOH (0.1 mol L$^{-1}$): [LH] = $3 \times 10^{-5}$ mol L$^{-1}$ in HCl ($10^{-2}$ mol L$^{-1}$), $T$ = 25 °C, path length = 1 cm; (b) $\varepsilon_{273}$ (mol$^{-1}$ L cm$^{-1}$) as a function of pH.

with those obtained in bis(benzimidazole) macrocycles.[25,26] Acidification of the medium down to pH = 6 induces perturbations in the spectra: the previous bands undergo a slight blue shift ($\lambda$ = 2 nm) similar to that observed for the free benzimidazole under acidic conditions.[24] This slight shift is accompanied by a strong hyperchromic effect, which results in an approximately 50% increase in the parent extinction coefficient (Figure 1b). This effect can be compared to the hyperchromic effect observed under similar conditions on the $\pi^* \leftarrow \pi$ transition of cyclen- and cyclam–pyridine.[21a] This result is characteristic of the formation of a benzimidazolium cation. This analysis can be consolidated by the change in the $^1$H chemical shifts of $H_\alpha$ and $H_\beta$ of the benzimidazole moiety (for the numbering see Scheme 1) in the pH range 6.2–2.5 in $D_2O$ (Supporting Information Figure S1). The decrease in pH is accompanied with a downfield shift of the signals of the aromatic protons as expected for protonation of the aromatic ring.[21a] These convergent observations imply that the log $K$ value of 4.55 can be attributed to protonation of the benzimidazole group.

Finally, the first protonation constant (log $K_{011}$ = 11.05) determined for (benzimidazolylmethyl)cyclen LH cannot be attributed to the cyclen moiety but to the benzimidazole ring. This is supported by UV and $^1$H NMR spectroscopic experiments above pH 9. The increase in pH is accompanied by an upfield shift in the NMR spectrum of the signals for the aromatic protons (Supporting Information, Figure S1). Accordingly, in the range 250–290 nm in the absorption spectrum, a hypochromic effect is observed with a slight red shift of the bands (Figure 1), and a low-energy shoulder appears at 287 nm. These data are in agreement with the formation of a benzimidazolate species (Scheme 2).[24,27] From the sigmoidal curve observed in the plot of $\varepsilon_{273}$ versus pH (Figure 1b), one can estimate the corresponding log $K$ value to be 11, which agrees well with the

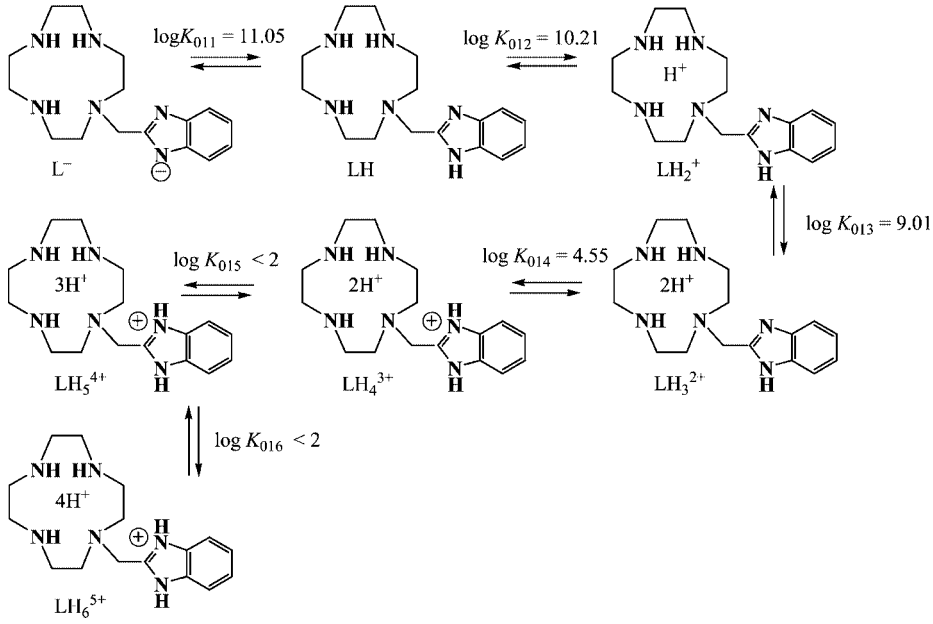


Scheme 3.

 © 2007 Wiley-VCH Verlag GmbH & Co. KGaA, Weinheim 

$\log K_{011}$ value obtained from the potentiometric pH titration. On the basis of these results, the acid–base behaviour of LH is summarised in Scheme 3.

### Zinc(II) Complex of LH

#### *Synthesis and Solid-State Structure of [ZnLH](ClO$_4$)$_2$*

[ZnLH]$X_2$, where X = $NO_3$ and $ClO_4$, were synthesised by reacting one equivalent of the ligand and one equivalent of the $ZnX_2{\cdot}nH_2O$ salt in a methanolic solution. Colorless single crystals were obtained only for [ZnLH](ClO$_4$)$_2$ by diffusion of diethyl ether in an acetonitrile solution of the complex. Selected geometrical parameters for [ZnLH](ClO$_4$)$_2$ are given in Table 2. The X-ray structure of $[ZnLH]^{2+}$ shows that the metal ion lies inside a square-based pyramid (Figure 2) and that the coordination sphere of the zinc centre consists of the four macrocyclic nitrogen atoms (N1–N4) and the imine nitrogen atom of the benzimidazole ($N_{im}$). The $Zn^{II}$ cation lies 0.781 Å above the macrocyclic nitrogen square in this distorted square-based pyramid geometry. The Zn–N(secondary) bonds (2.104–2.116 Å) are shorter than the Zn–N(tertiary) bond (2.236 Å): tertiary nitrogen atoms are not as good donors as secondary nitrogen atoms.[28–30] The $N_{im}$ atom is coordinated to the zinc cation. This type of coordination in which the imidazole is linked to the metal cation through the imine nitrogen atom and the hydrogen atom of the secondary amine nitrogen atom remains is well known for histidine and nucleoside bases such as adenine and guanine.[10] The Zn–$N_{im}$ bond of 1.982 Å is shorter than the Zn–N(cyclen) bonds, which indicates a strong interaction between the $N_{im}$ and $Zn^{II}$ atoms. This feature has already been reported for a Zn–guanidinyl cyclen complex in which the Zn–N(guanidyl) bond[31] (1.95 Å) is shorter than the average Zn–N(cyclen) bonds (2.16 Å). For $[ZnLH]^{2+}$ in the solid state, an efficient five-membered chelate ring is formed, as the $N_{im}$–Zn–N4 angle of 80.6° is noticeably smaller than the other three $N_{im}$–Zn–N angles (104.6–138.2°). This indicates that electron donation from the imine nitrogen lone pair of the benzimidazole moiety to the $Zn^{II}$ ion is strong. Furthermore, comparison of the C–N bond lengths in the imidazole ring of $[ZnLH]^{2+}$ (C2–$N_{im}$: 1.324 Å and C2–$N_{am}$: 1.347 Å) and in free benzimidazole[32] (C2–$N_{im}$: 1.297 Å and C2–$N_{am}$: 1.344 Å) shows that the C2–$N_{im}$ distance is elongated by coordination. This indicates an electronic delocalisation through the imidazole ring,[33] which results in the reinforcement of the electronic density at the $N_{im}$ nitrogen atom (Scheme 4). The driving force of this phenomenon is the $Zn^{II}$ Lewis acidity. Finally, to ensure the cohesion of the solid-state structure, hydrogen bonds between $ClO_4^-$ oxygen atoms and N1, N3 and $N_{am}$ hydrogen atoms are present.[34]

Table 2. Selected bond lengths [Å] and angles [°] for $[ZnLH]^{2+}$.

| | | | |
|---|---|---|---|
| Zn–N1 | 2.1049(15) | N1–Zn–N2 | 83.25(6) |
| Zn–N2 | 2.1147(15) | N1–Zn–N3 | 133.47(6) |
| Zn–N3 | 2.1163(16) | N1–Zn–N4 | 81.22(6) |
| Zn–N4 | 2.2369(15) | N1–Zn–$N_{im}$ | 114.79(6) |
| Zn–$N_{im}$ | 1.9829(15) | N2–Zn–N3 | 83.42(6) |
| $N_{im}$–C2 | 1.324(2) | N2–Zn–N4 | 141.03(6) |
| $N_{am}$–C2 | 1.347(7) | N2–Zn–$N_{im}$ | 138.19(6) |
| | | N3–Zn–N4 | 81.85(6) |
| | | N3–Zn–$N_{im}$ | 104.64(6) |
| | | N4–Zn–$N_{im}$ | 80.60(6) |

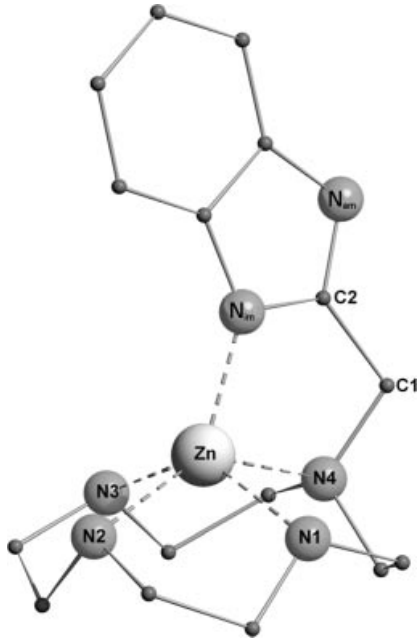


Figure 2. Schakal diagram of $[ZnLH]^{2+}$ (hydrogen atoms are omitted for clarity, with the exception of the H atom of $N_{am}$).

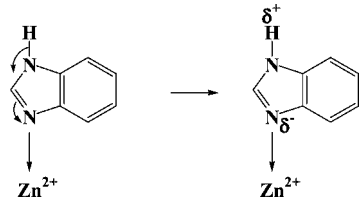


Scheme 4.

#### *Thermodynamic Stability of the Zn$^{II}$-LH Complex – Potentiometric pH, UV and $^1$H NMR Titrations*

At first, direct pH titrations of LH in the presence of one equivalent of $Zn^{2+}$ and a strong acid in excess were carried out following a published procedure for similar compounds.[35] By using this method with LH, we encountered some problems because $Zn^{2+}$complexation is very slow at low pH. This can be attributed to the protonation of the ligand nitrogen atoms (the macrocyclic nitrogen atoms and the pyrrole nitrogen atom in the benzimidazole ring). In order to counteract this drawback in acidic medium, the "batch method", which involves the preparation of LH/

 © 2007 Wiley-VCH Verlag GmbH & Co. KGaA, Weinheim 

$Zn^{2+}/HNO_3/KOH$ mixtures at each pH value, was then used.[36] This method was implemented up to pH 7, after which carbonation cannot be avoided. Direct KOH titrations of synthesised $[ZnLH]^{2+}$ were also carried out in the pH range 5–12. For comparison, similar titrations were performed with pendantless cyclen. From the analysis of the titration data, the speciation diagram of the $Zn^{2+}/LH$ system was obtained (Figure 3), and the values for the overall complexation constants of the 1:1 $Zn^{II}$ complex ($\log\beta_{mlh}$) calculated (Table 3). Firstly, the speciation diagram indicates that there is no formation of the $Zn^{II}$ complex with $LH_4^{3+}$ in acidic medium. This is confirmed by spectroscopy: the UV (Figure 4) and/or $^1H$ NMR (Figure 5 and Supporting Information Figure S2) experiments show that, under acidic conditions, the presence of the metal does not affect the signal, since the ligand is the only species detected. Secondly, the diagram indicates that at pH 3, the $[ZnLH]^{2+}$ complex starts to form: this is confirmed by $^1H$ NMR spectroscopy, since in the $^1H$ NMR spectrum, a second set of signals at $\delta$ = 7.64, 7.38 and 4.28 ppm increasingly appears, while the signals for LH collapse (from pH 3.7). Comparison of the LH and cyclen affinities for $Zn^{2+}$ before pH 4 (Supporting Information Figure S3) indicates, moreover, that the presence of the benzimidazole moiety on the cyclen framework promotes $Zn^{2+}$ complexation in acidic medium. The speciation diagram highlights that the 1:1 $Zn^{II}$ complex is quantitatively obtained between pH 5–7. In this pH range, the UV and $^1H$ NMR spectra remain unchanged. From the $\log\beta_{111}$ value and the first protonation constant, $\log K_{011}$, of the ligand, the stepwise formation constant of the species $[ZnLH]^{2+}$ was calculated to be 16.13 (Table 3). This value is higher than that of the cyclen complex $\{\log K_{[Zn(cyclen)]} = 14.20\}$. The affinity of LH for $Zn^{2+}$ is greater than that of cyclen over the whole pH range (Supporting Information Figure S3). Usually, the *N*-functionalisation of the tetraazamacrocycle induces a decrease in the stability of the complexes, which results mainly because of the poor σ-donor ability of tertiary amines relative to that of secondary amines.[16,30,38,39] Here, the enhanced stability of $[ZnLH]^{2+}$ must be due to the presence of an additional stabilising interaction, probably between the benzimidazole ring and the metal through a supplementary five-membered ring chelate. This also suggests that the solid-state structure remains in solution. Although lower, the stability of $[ZnLH]^{2+}$ compares well with that determined for the [{(anthrylmethylamino)ethyl}cyclen]$Zn^{II}$ complex ($\log K$ = 17.6).[16] This stability is even lower than that of the [{8-hydroxy-5-(dimethylaminosulfonyl)quinolin-2-

Table 3. Stability constants for the $Zn^{II}$/LH and $Zn^{II}$/cyclen systems.

| Equilibrium | LH<br>$\log\beta_{mlh}$ | Cyclen[a]<br>$\log\beta_{mlh}$ |
|---|---|---|
| Zn + L + $H^+$ ⇌ ZnLH | 27.18(8) | |
| Zn + L ⇌ ZnL | 18.53(6) | 14.20(8) (15.3[35]) |
| Zn + L ⇌ ZnL(OH) + $H^+$ | 7.5(3) | 6.3(1) (7.44[37]) |
| | $\log K$ | |
| Zn + LH ⇌ ZnLH | 16.13 | |
| ZnLH ⇌ ZnL + $H^+$ | –8.65 | |

[a] Potentiometric titrations at 25.0(1) °C, $I$ = 1 ($KNO_3$) (this work).

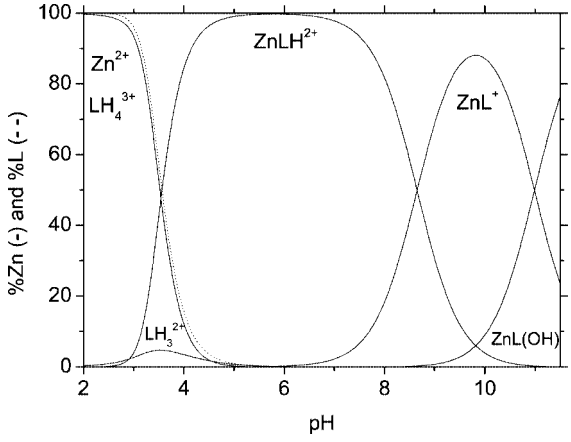


Figure 3. Speciation diagram of the $Zn^{II}$/LH system as a function of pH ($[Zn^{II}]$ = [LH] = $2\times10^{-3}$ mol $L^{-1}$). The dashed line corresponds to $Zn^{2+}$.

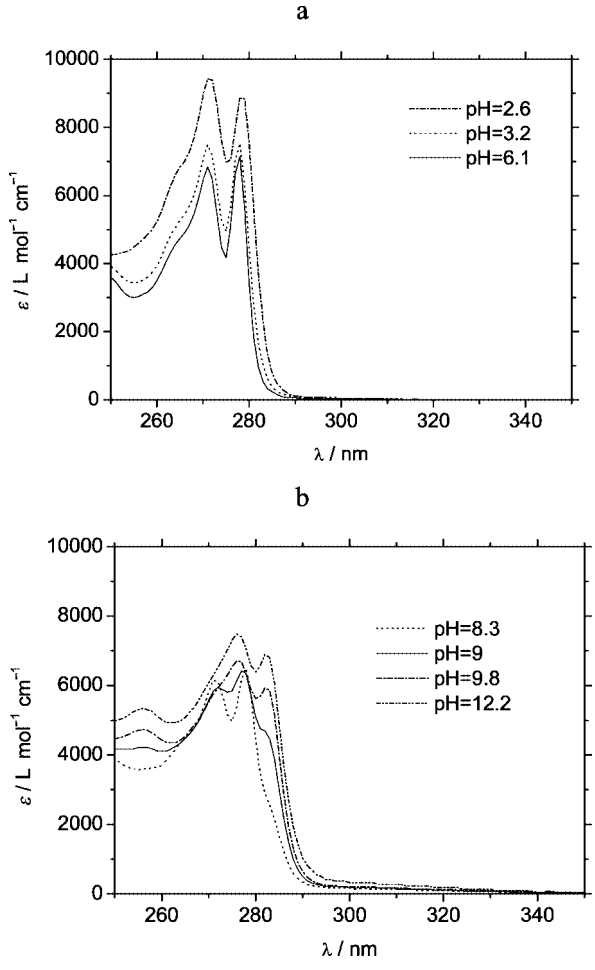


Figure 4. Spectrophotometric titration of $[ZnLH]^{2+}$ with KOH (0.1 mol $L^{-1}$): (a) $[ZnLH]^{2+}$ = $3\times10^{-5}$ mol $L^{-1}$ in HCl ($10^{-2}$ mol $L^{-1}$), pH range 2.6–6.1; (b) $[ZnLH]^{2+}$ = $3\times10^{-5}$ mol $L^{-1}$, pH range 7–12.2. $T$ = 25 °C; path length = 1 cm.

 © 2007 Wiley-VCH Verlag GmbH & Co. KGaA, Weinheim 

ylmethyl}cyclen]$Zn^{II}$ complex ($\log K$ = 22.4).[17] It can be assumed for the latter that the enhanced stability is due to the fact that the metal ion is six-coordinate rather than five-coordinate. Another way to compare the thermodynamic behaviour of different systems is to calculate the apparent complexation constant $\log K_{app}$ at a given pH. The $\log K_{app}$ value is calculated from the potentiometric pH titration results, according to $\log K_{app} = \log([ZnLH]/[Zn]_{free} \times [L]_{free})$ with $[L]_{free} = \sum_n [H_nL]_{free}$ ($n$ = 0–4 for LH) and for an equimolar mixture of $5 \times 10^{-6}$ mol $L^{-1}$ LH and $Zn^{2+}$. At pH 7.4, in the medium of the biological pH window, the $\log K_{app[ZnLH]}$ value is calculated to be 11.71. This value is between those calculated under the same conditions for [{(anthrylmethylamino)ethyl}cyclen]$Zn^{II}$ complex ($\log K_{app[ZnL]}$ = 10.7)[16] and for [{8-hydroxy-5-(dimethylaminosulfonyl)quinolin-2-ylmethyl}cyclen]$Zn^{II}$ complex ($\log K_{app[ZnL]}$ = 14.1).[17] Finally, above pH 8, the deprotonation of $[ZnLH]^{2+}$ was confirmed by $^1H$ NMR and UV spectroscopy. Thus, around pH 8.5, the $^1H$ signals for $H_\alpha$, $H_\beta$ and $N_{cyclen}CH_2$ are shifted upfield [Figure 5: $\Delta(\delta)$ = 0.15 ppm for $H_\alpha$, 0.25 ppm for $H_\beta$ and 0.3 ppm for $N_{cyclen}CH_2$]. This shielding indicates a decrease in the overall charge of the complex. Accordingly, on increasing the pH up to 12, the UV bands of the benzimidazole unit are perturbed and undergo a slight red shift of about 5 nm (Figure 4b). As indicated for the ligand, this is characteristic of deprotonation at the imidazole ring.[24] Moreover, a new band appears at 282 nm from pH 8, and up to pH 12, the extinction coefficient of this band increases by about a factor of six. From the $\log \beta_{mlh}$ values, one can calculate the deprotonation constant of $[ZnLH]^{2+}$ ($\log K$ = –8.65), which, as suggested by the UV titration, corresponds to the ionisation of the pyrrole hydrogen of the benzimidazole moiety. This value is remarkably lower than that for the analogous equilibrium in LH, which means that in the presence of $Zn^{II}$, the benzimidazole pyrrole hydrogen is $10^{2.4}$ times more acidic. This is a consequence of the Lewis acidity of the $Zn^{II}$ ion, which operates predominantly through an inductive effect and strongly alters the benzimidazole acidity.[40]

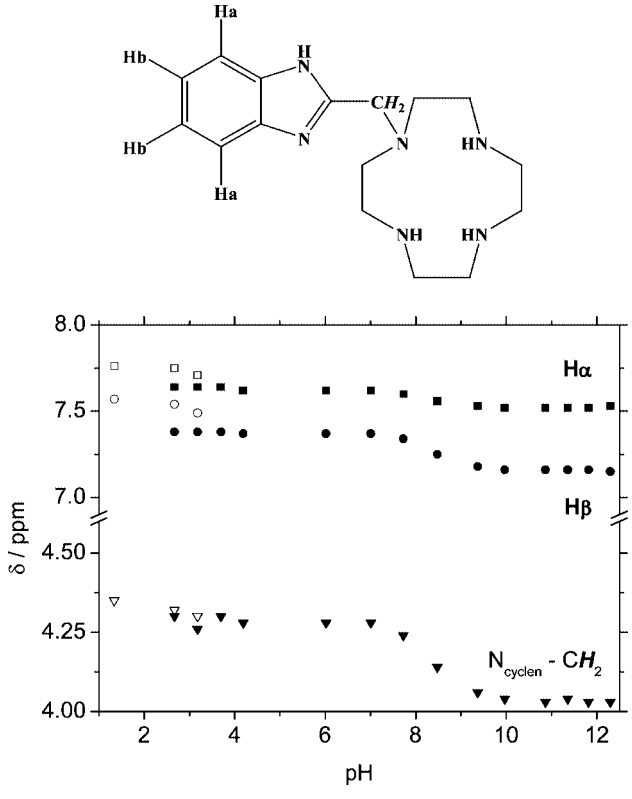


Figure 5. $^1H$ NMR chemical shifts plotted as a function of pH for a mixture of LH ($10^{-2}$ mol $L^{-1}$) and $Zn^{2+}$ ($10^{-2}$ mol $L^{-1}$) in the pH range 3.0–12.0 ($T$ = 25 °C, $D_2O$). The filled symbols correspond to the complex chemical shifts.

## Spectrofluorimetric Study of LH

The change in the fluorescent response of LH ($5 \times 10^{-7}$ mol $L^{-1}$) in the pH range 4–12 ($I$ = 0.1 $NaNO_3$) at 25 °C (excitation at 270 nm) is presented in Figure 6. Inspection of the LH deprotonation sequence indicates that the fully protonated species gives rise to the smallest emission intensity and that removal of the protons leads to an increase in the fluorescence emission intensity. Thus, as the pH is raised, emission at 301 nm increases following a sigmoidal curve with an inflexion point at pH 9. The fluorescence curve follows the formation of all the species in solution at pH > 8, i.e. $LH^{2+}$, LH and $L^-$. It is concluded that the break at pH 9 in Figure 6 denotes the $pK_{a4}$ for $LH_3^{2+} \leftrightarrows LH_2^+$. The further increase in the fluorescence emission (above pH 10.5) is due to deprotonation at the benzimidazole moiety. Consequently, the quantum yield $\Phi$ of (benzimidazolylmethyl)cyclen increases with the pH from 0.21 at pH 10.4 to 0.30 at pH 12. The enhanced effect of the fluorescence emission can be explained in terms of an intramolecular electron-transfer process from the macrocycle to the excited benzimidazole (PET process).[41] Such a mechanism involves the deactivation of the excited state of the fluorophore by addition of one electron to one of its excited-state frontier orbitals. This leaves the fluorophore in a reduced, nonemissive state. Among factors responsible for intramolecular electron transfer, the overlap S between the electron donor (macrocycle) and acceptor (benzimidazole) orbitals is, of course, crucial, and it is obvious that S is optimum when both parts of the fluoroionophore are in close proximity and in a suitable orientation. In functionalised macrocycles, it has already been shown that protonated forms of the macrocycle are stabilised by intramolecular hydrogen bonds between the cavity and the pendant arm when the latter has coordinating atoms.[21a,42] Furthermore, deprotonation at the cavity induces conformational modifications in the ligand that lead to an outward orientation of the pendant arm relative to the macrocyclic cavity. If we assume that similar conformational changes occur during deprotonation of LH, in particular between the $LH_3^{2+}$, $LH_2^+$ and LH species, then an increase in the distance between the cavity and the benzimidazole moiety results. One can then

 © 2007 Wiley-VCH Verlag GmbH & Co. KGaA, Weinheim 

explain the fluorescence enhancement observed during the deprotonation sequence by the reduced overlap of the orbitals of both parts of the fluoroionophore, which favours the emissive deactivation of benzimidazole over the PET process.

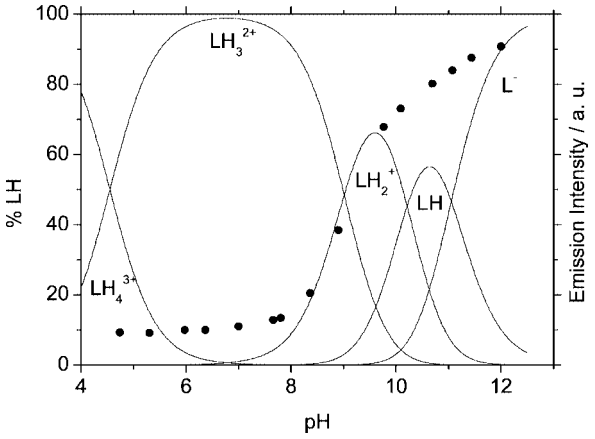


Figure 6. Speciation diagram of the LH system as a function of pH in the pH range 4.0–12.0, and the fluorescent response of LH ($5 \times 10^{-7}$ mol L$^{-1}$).

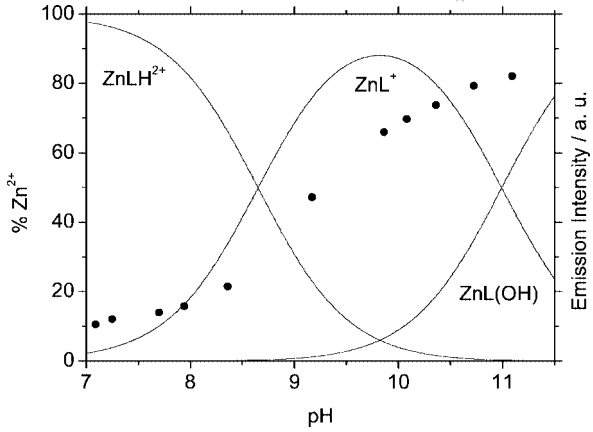


Figure 7. Speciation diagram of the LH/$Zn^{2+}$ system as a function of pH in the pH range 7.0–12.0, and fluorescent response of LH/$Zn^{2+}$.

Moreover, once formed $[ZnL]^+$ is so stable that even at such concentrations, the 1:1 complex does not dissociate and the $Zn^{2+}$-dependent fluorescence is unaffected by excess amounts of $Zn^{2+}$.

### Fluorescence of $[ZnLH]^{2+}$ and Titration of LH with $Zn^{2+}$

The change in the fluorescence emission of the zinc complex ($5 \times 10^{-7}$ mol L$^{-1}$) as a function of pH is presented in Figure 7. The fluorescence curve follows the formation of all the species in solution at pH >8, i.e. $ZnL^+$, ZnL(OH). The sensitivity of the fluorescence in the complex implicates deprotonation at the benzimidazole moiety. This behaviour should be compared with that of [(dansylamidoethyl)-cyclen]Zn.[15] Moreover, the emission of LH increased by about a factor of three with increasing $[Zn^{2+}]$ (quantum yield $\Phi$ 0.21 → 0.63). This chelation-enhanced fluorescence can be explained as follows: the metal coordination induces an energetic modification of the molecular orbitals between the free macrocycle and the corresponding $Zn^{II}$ complex that leads to the stabilisation of the HOMO. Consequently, the Zn-cyclen subunit is a less efficient donor towards the benzimidazole fluorophore than the cyclen unit in LH towards the same benzimidazole moiety. This makes PET-type fluorescence quenching less probable, and the native fluorescence of the fluorophore is thus restored.[43]

In order to test the response of LH in the presence of $Zn^{2+}$, it is then necessary to follow the fluorescence emissionat pH 10.4 where, first, a significant alteration in the signal intensity in response to the binding unit is expected, and, second, the complexation kinetics is fast. The change in fluorescence upon addition of $Zn^{2+}$ to (benzimidazolylmethyl)cyclen is presented in Figure 8. Upon excitation at 270 nm, an increase in emission is observed. The response of the system at 301 nm is linear between $5 \times 10^{-8}$ and $5 \times 10^{-7}$ mol L$^{-1}$, until a 1:1 [LH]/$[Zn^{2+}]$ ratio is reached. This implies that the increase in fluorescence is stoichiometric and is due to total formation of the $[ZnL]^+$ complex.

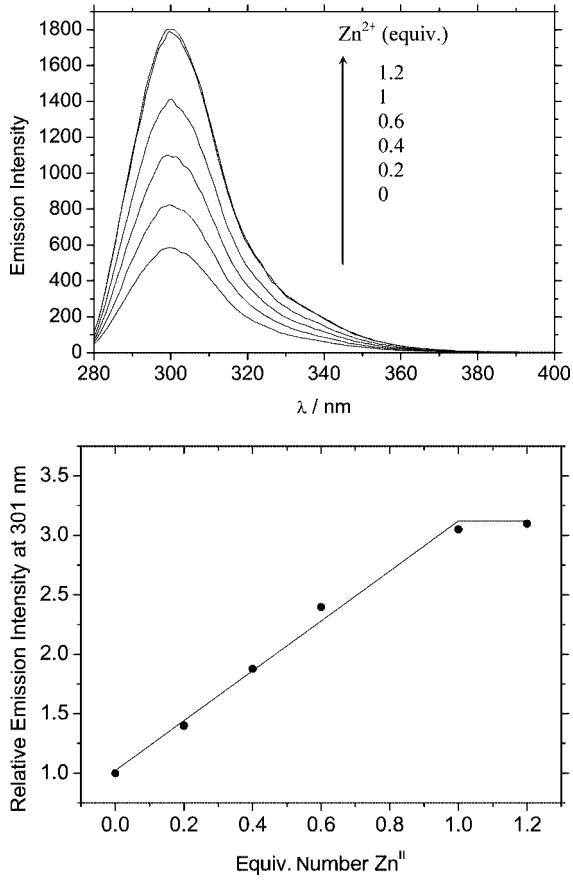


Figure 8. Change in the fluorescent response of LH ($5 \times 10^{-7}$ mol L$^{-1}$) upon addition of $Zn^{2+}$ at pH 10.4 [CAPS ($2 \times 10^{-2}$ mol L$^{-1}$), $I$ = 1 ($NaClO_4$), $T$ = 25 °C, excitation at 270 nm].

 © 2007 Wiley-VCH Verlag GmbH & Co. KGaA, Weinheim 

To determine whether LH works as a selective chemosensor for $Zn^{2+}$, the LH fluorescent spectra were recorded in the presence of various metal ions at pH 10.4 (some first-row transition metals, $Cd^{II}$ and biologically relevant alkali and alkaline earth ions, Figure 9). The fluorescent intensities slightly increase by addition of ions that are found in high concentrations in cells, such as $K^+$, $Mg^{2+}$ and $Ca^{2+}$. The selectivity of $Zn^{2+}$ over alkali or alkaline earth cations comes from the inherent binding properties of macrocyclic polyamines. Addition of transition metals such as $Mn^{2+}$ and $Fe^{3+}$ does not significantly increase the fluorescent response of (benzimidazolylmethyl)cyclen. This test also indicates that the cadmium complex is less fluorescent than the ligand (which allows $Zn^{2+}$ and $Cd^{2+}$ to be distinguished), while the copper complex does not fluoresce at all. For these two cations, the decrease in fluorescence is due to a quenching mechanism.[44]

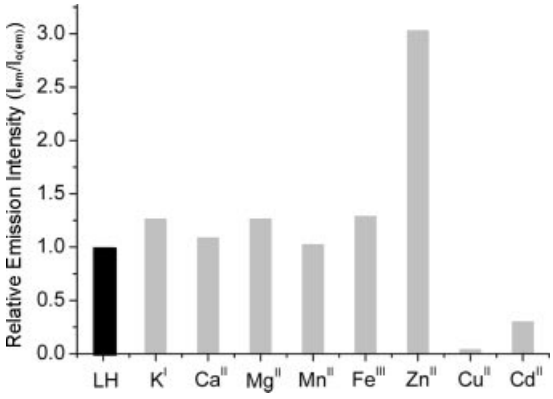


Figure 9. Relative fluorescence of LH at 301 nm responding to 1 equiv. of the metal ions at pH 10.4 [CAPS ($2\times10^{-2}$ mol L$^{-1}$), $I$ = 1 (NaCl), $T$ = 25 °C, excitation at 270 nm]. $I_{0(em)}$ is the emission intensity of LH ($5\times10^{-7}$ mol L$^{-1}$) at 301 nm in the absence of metal ions.

In comparison with the results reported for cyclen fluorophores,[15–17] the fluorimetric titration of $Zn^{2+}$ with LH shows that LH does not respond to $Zn^{2+}$ at neutral pH, which is a disadvantage. This point has to be improved in order to envisage a use under biological conditions. For that, the key mechanistic feature is the decoupling of macrocyclic electron-donor nitrogen atoms from resonance with the fluorophore. In light of the behaviour of the anthracene-pendant cyclen probe, which responds to $Zn^{2+}$ for pH values >12,[14] and the {(anthrylmethylamino)ethyl}-cyclen probe, which responds to $Zn^{2+}$ at neutral pH,[16] the introduction of an aminoethyl spacer between the macrocycle and the methylbenzimidazole moiety is to be studied. The introduction of a supplementary amine function on the spacer is expected to sufficiently change the electronic nature of the ligand and complex structures at neutral pH to be able to detect $Zn^{2+}$ under better conditions.

## Conclusions

We have designed a new ligand LH for complexation with $Zn^{2+}$ and that can be detected by fluorescence spectroscopy. The zinc(II) complex is stable and quantitatively formed at pH 5, which is comparable to zinc(II) complexes obtained from (dansylamidoethyl)cyclen[15] or {(anthrylmethylamino)ethyl}cyclen.[16] The complexation induces a PET-retarded fluorescence, which is responsible for the fluorescence enhancement in the presence of $Zn^{2+}$. Thus, in CAPS buffer and upon addition of increasing amounts of $Zn^{2+}$, the fluorescent emission of LH linearly increases. The detection limit of LH ($5\times10^{-7}$ mol L$^{-1}$) is [$Zn^{2+}$] = $5\times10^{-8}$ mol L$^{-1}$ at pH 10.4. The LH fluorescent response to $Zn^{2+}$ has to be improved in order to allow $Zn^{2+}$ detection at neutral pH. On the basis of the modification of the ligand already proposed by Aoki and al.,[16] it is envisaged that the introduction of an aminoethyl spacer between the macrocycle and the methylbenzimidazole moiety will help towards this end.

## Experimental Section

**General Information:** All solvents were HPLC grade. The metals salts were purchased from Aldrich. The other reagents (highest commercial quality) were used without further purification.

**Ligand Synthesis:** The ligand LH was synthesised according to a published procedure[18] by alkylation of the cyclen glyoxal ligand (5.1 mmol, 1.00 g) with 2-(chloromethyl)benzimidazole (5.3 mmol, 0.89 g) in thf. The solution was stirred for 6 h, after which a pale yellow precipitate forms, which corresponds to the alkylated bisaminal monosalt. This was separated from the mother solution by filtration. This salt was then deprotected with hydrazine monohydrate for 3 h at 100 °C. After cooling, a brown oil precipitates, which was collected by filtration and washed several times with ethanol. The ligand LH was finally obtained after purification in methanol in 53% yield (0.87 g). $^{13}$C NMR (62.9 MHz, $D_2O$): $\delta$ = 44.5, 45.4, 51.4, 52.8 and 73.7 ($CH_2N$), 115.2, 123.2, 118.1 and 153.9 ($C_{Ar}$) ppm. $C_{16}H_{26}N_6\cdot0.25CH_3OH\cdot0.5H_2O$ (319.44): calcd. C 61.10, H 8.84, N 26.31; found C 61.09, H 9.14, N 26.67%.

### Preparation of the Zinc Complexes

**[Zn(cyclen)$(NO_3)_2$]:** A methanolic solution of $Zn(NO_3)_2\cdot4H_2O$ (0.61 mmol, 0.16 g, 5 mL) was added dropwise to a solution of the ligand (cyclen: 0.60 mmol, 0.11 g) in methanol (10 mL). The colourless solution was heated at reflux for 4 h and concentrated by evaporation. A white powder was precipitated by addition of diethyl ether solution (0.16 g, 74%). $C_8H_{20}N_4Zn(NO_3)_2$ (361.67): calcd. C 26.57, H 5.57, N 23.24; found C 26.71, H 5.66, N, 23.39%. ESI-MS: $m/z$ calcd. for $[Zn(C_8H_{20}N_4)(NO_3)]^+$ 298.1; found 298.0.

**[ZnLH]$(NO_3)_2$:** A methanolic solution of $Zn(NO_3)_2\cdot4H_2O$ (0.68 mmol, 0.18 g, 5 mL) was added dropwise to a solution of the ligand (LH: 0.66 mmol, 0.21 g) in methanol (10 mL). The colourless solution was heated at reflux for 4 h and concentrated by evaporation. A white powder was precipitated by addition of diethyl ether solution (0.19 mg, 58%). $^{13}$C NMR (62.9 MHz, $CD_3OD$): $\delta$ = 45.1, 42.3, 47.4, 52.2 and 53.9 ($CH_2N$), 113.5, 118.5, 125.2, 125.8, 135.6, 139.3 and 153.3 ($C_{Ar}$). $C_{16}H_{26}N_6ZnN_2O_6\cdot0.25CH_3OH$ (499.83): calcd. C 39.05, H 5.44, N 22.42; found C 38.92, H 5.26, N 22.49%.

**[ZnLH]$(ClO_4)_2$:** A methanolic solution of $Zn(ClO_4)_2\cdot6H_2O$ (0.41 mmol, 0.15 g, 5 mL) was added dropwise to a solution of the ligand (LH: 0.35 mmol, 0.11 g) in methanol (5 mL). The colourless solution was heated at reflux for 4 h and concentrated by evapora-

 © 2007 Wiley-VCH Verlag GmbH & Co. KGaA, Weinheim 

tion. A white powder was precipitated by addition of diethyl ether (0.10 g, 50%). $C_{16}H_{26}N_6ZnCl_2O_8{\cdot}0.5H_2O$ (575.72): calcd. C 33.38, H 4.73, N 14.60; found C 33.62, H 4.76, N 14.42%. ESI-MS: *m*/*z* calcd. for $[Zn(C_{16}H_{26}N_6)(ClO_4)]^+$ 465.1; found 465.1. This solid was further dissolved in acetonitrile, and after slow diffusion of diethyl ether, white monocrystals of $[ZnLH](ClO_4)_2{\cdot}CH_3CN$ suitable for X-ray analysis were produced.

CAUTION: Perchlorate-containing complexes are potentially explosive and appropriate precautions should be in place for their preparation, handling and storage.

**Potentiometric Measurements:** Potentiometric titrations were carried out with an automatic titrator composed of a microprocessor burette (Metrohm dosimat 665) and a pH meter (Metrohm 713) connected to a computer. The titration procedure was fully automated.[19] All measurements were performed within a thermoregulated cell at 25.0 ± 0.1 °C under an argon stream to avoid the dissolution of carbon dioxide. The ionic strength was adjusted to 1 with potassium nitrate. The combined Type "U" glass electrode (Metrohm) used had a very low alkaline error. The complex formation constants were determined according to the "batch method". Equimolar mixtures of $Zn^{2+}$ and ligand [$2 \times 10^{-3}$ mol L$^{-1}$ in $10^{-2}$ mol L$^{-1}$ $HNO_3$ , $I$ = 1 ($KNO_3$)] were prepared in 30 stoppered flasks at different pH values by microaddition of KOH [$10^{-1}$ mol L$^{-1}$, $I$ = 1 ($KNO_3$)]. These solutions were stored under argon and placed in a thermoregulated enclosure at 40 °C for two, four or six weeks. Before pH measurements, these solutions were allowed to reach equilibrium temperature (25 °C) for 48 h. The deprotonation of the [(benzimidazolylmethyl)cyclen]zinc complex was determined by a pH titration of a complex solution [$2 \times 10^{-3}$ mol L$^{-1}$, $I$ = 1 ($KNO_3$)] prepared from the solid $[ZnLH](NO_3)_2$ monohydrate complex previously described.

The protometric data were processed by using the PROTAF program[19] to obtain the best-fit chemical model and refined overall constants, $\beta_{mlh}$.

$$mM + lL + hH^+ \rightleftharpoons M_mL_lH_h$$

$$\beta_{mlh} = \frac{[M_mL_lH_h]}{[M]^m[L]^l[H^+]^h}$$

A negative $h$ value refers to the hydroxide ion.

The stepwise protonation constants ($K_{0lh}$) related to equilibrium (1) are defined by Equation (2) and are deduced from the refined $\beta_{0lh}$ values by Equation (3).

$$LH_{h-1}^{(h-1)+} + H^+ \overset{K_{0lh}}{\rightleftharpoons} LH_h^{h+} \quad (1)$$

$$K_{0lh} \frac{[LH_h^{h+}]}{[LH_{h-1}^{(h-1)+}][H^+]} \quad (2)$$

$$\beta_{0lh} = \prod_{i=1}^{h} K_{0li} \quad (3)$$

**Spectroscopic Measurements:** $^1$H and $^{13}$C NMR spectra were recorded with a Bruker DRX 500 spectrometer. $^1$H–$^1$H and $^1$H–$^{13}$C 2D correlation experiments were performed to assign the signals. In $^1$H NMR titrations, the pD was adjusted by additions of small amounts of a 4-% diluted NaOD solution or a 3.5-% diluted DCl solution to $D_2O$ solutions containing the ligand LH ($10^{-2}$ mol L$^{-1}$). The pH was calculated from the measured pD values by using Equation (4):[26]

$$pH = pD - 0.40 \quad (4)$$

For both ligands, NMR measurements were performed after an equilibration time of one day. Mass spectra in methanol were recorded on a Micromass Q-TOF electrospray positive ionisation instrument. For both ligand and complex $[ZnLH](ClO_4)_2{\cdot}H_2O$ ($3 \times 10^{-5}$ mol L$^{-1}$), the UV spectrophotometric titrations were recorded at 25 °C in the range 200–400 nm with a thermoregulated Shimadzu UV 2401 PC spectrophotometer. For the UV pH titrations, the pH was adjusted by addition of small amounts of KOH ($10^{-1}$ to $10^{-3}$ mol L$^{-1}$) and HCl solutions ($10^{-1}$ to $10^{-2}$ mol L$^{-1}$).

**Crystal Structure Determination:** The crystal diffraction data were collected at 120 K with a Kappa CCD diffractometer (Centre de Diffractométrie X, Univ. Rennes, France) by using monochromated Mo-$K_\alpha$ radiation ($\lambda$ = 0.71073 Å). Data collection was performed with the COLLECT program.[45] Frame integration and data reduction procedures were realised with the DENZO and SCALEPACK programs of the KappaCCD software package, respectively,[46] for the [ZnLH] compound and with EVAL[47] and SADABS[48] programs, respectively. The structure was solved by using the direct methods program SIR97,[49] which revealed all non-hydrogen atoms. SHELXL97[50] was used to refine the structure. Finally, hydrogen atoms were placed geometrically and held in riding mode in the least-squares refinement procedure. Final difference maps revealed no significant maxima (Table 4). CCDC-648571 contains the supplementary crystallographic data for this paper. These data can be obtained free of charge from The Cambridge Crystallographic Data Centre via www.ccdc.cam.ac.uk/data_request/cif.

Table 4. Crystal data and details of the structure determination for $[ZnLH](ClO_4)_2{\cdot}CH_3CN$.

| | $[ZnLH](ClO_4)_2{\cdot}CH_3CN$ |
|---|---|
| Empirical formula | $C_{18}H_{29}Cl_2N_7O_8Zn$ |
| Formula weight | 607.75 |
| Temperature [K] | 100(2) |
| Crystal system | monoclinic |
| Space group | *P*21/*c* |
| colour | colourless |
| *a* [Å] | 14.7457(4) |
| *b* [Å] | 9.2669(3) |
| *c* [Å] | 18.7281(6) |
| *α* [°] | 90 |
| *β* [°] | 106.5910(10) |
| *γ* [°] | 90 |
| Volume [Å$^3$] | 2452.59(13) |
| *Z* | 4 |
| $D_{calcd.}$ [g cm$^{-3}$] | 1.646 |
| Absorption coefficient [mm$^{-1}$] | 1.278 |
| *F*[000] | 1256 |
| $\lambda$(Mo-$K_\alpha$) [Å] | 0.71073 |
| Largest diff peak/hole [e Å$^{-3}$] | 0.639/–0.514 |
| No. independent reflections | 5614 |
| No. reflections [I > 2.0σ(*I*)] | 4962 |
| $R_1$ | 0.0294 |
| $wR_2$ | 0.0768 |
| Goodness-of-fit on $F^2$ | 1.037 |

**Spectrofluorimetric Measurements:** Fluorescence emission spectra were recorded at 25 °C with a Perkin–Elmer LS50B spectrofluorimeter equipped with a Hammamastu R928 photomultiplier. The lin-

 © 2007 Wiley-VCH Verlag GmbH & Co. KGaA, Weinheim 

earity of the fluorescence emission versus the concentration was checked in the concentration range 0 to $10^{-6}$ mol L$^{-1}$. Emission spectra were normalised by the manufacturer-supplied correction curves. Quantum yields were determined by comparison of the integrated corrected emission spectrum of standard quinine sulfate[51] [the quantum yield ($\Phi$) is 0.55]. Spectrofluorimetric pH titrations of the ligand and the complex were performed as follows: the stock solutions of the ligand or the complex (ca. $3\times10^{-5}$ mol L$^{-1}$) were prepared by dissolving an appropriate amount of the ligand in a 50-mL volumetric flask and by diluting with degassed water under an argon atmosphere. The titration solution {[LH] = $5\times10^{-7}$ mol L$^{-1}$} was prepared by appropriate dilution of the stock solution. The response of LH to increased amounts of $Zn^{2+}$ was checked as follows: successive volumes of $Zn(ClO_4)_2\cdot6H_2O$ ($1.2\times10^{-3}$ mol L$^{-1}$) were added to ligand solutions ($3\times10^{-5}$ mol L$^{-1}$) for a constant pH value [CAPS buffer solution ($2\times10^{-2}$ mol L$^{-1}$)]. These solutions were further diluted in CAPS buffer in order to reach a LH concentration of $5\times10^{-7}$ mol L$^{-1}$. The emission spectra of ligand and complex solutions were recorded after excitation at a wavelength of $\lambda$ = 270 nm in the range 275–400 nm (slit width of 5 nm).

**Supporting Information** (see footnote on the first page of this article): The $^1$H NMR spectra of LH as well as the $^1$H NMR spectra of a mixture of LH and $Zn^{2+}$ as a function of pH. A comparison of the affinities of LH and cyclen for $Zn^{II}$ is also reported.

## Acknowledgments

We thank H. Ballia and D. Harakat (Université de Reims Champagne Ardenne, France) for their help with the NMR 2D measurements and with ESI-MS measurements, respectively. T. Roisnel is gratefully acknowlegded for the crystal structure determination. Prof. S. Aoki (Tokyo University of Science), Dr. C. Picard (Université Paul Sabatier, Toulouse, France) and Prof. J. Rimbault (Université de Reims Champagne Ardenne, France) are gratefully acknowledged for helpful discussions.

[1] A. W. Czarnik, *Fluorescent Chemosensors for Ion and Molecule Detection*, American Chemical Society, Washington DC, **1993**.
[2] L. Fabbrizzi, A. Poggi, *Chem. Soc. Rev.* **1995**, *24*, 197–202.
[3] A. W. Czarnik, *Acc. Chem. Res.* **1994**, *27*, 302–308.
[4] A. P. De Silva, H. Q. N. Gunaratne, T. Gunnlaugsson, A. J. Huxley, C. P. Mc Coy, J. T. Rademacher, T. E. Rice, *Chem. Rev.* **1997**, *97*, 1515–1566.
[5] B. Valeur, I. Leray, *Coord. Chem. Rev.* **2000**, *205*, 3–40.
[6] E. Kimura, T. Koike, *Chem. Soc. Rev.* **1998**, *27*, 179–184.
[7] P. Jiang, Z. Guo, *Coord. Chem. Rev.* **2004**, *248*, 205–229.
[8] E. H. Cox, G. L. Mc Lendon, *Curr. Opin. Chem. Biol.* **2000**, *4*, 162–165.
[9] J. E. Coleman, *Curr. Opin. Chem. Biol.* **1998**, *2*, 222–234.
[10] S. J. Lippard, J. M. Berg, *Principles of Bioionorganic Chemistry*, De Boeck University, Brussels, **1997**.
[11] S. Burdette, S. J. Lippard, *Coord. Chem. Rev.* **2001**, *216–217*, 333–361.
[12] a) P. D. Zalewski, I. J. Forbes, W. H. Betts, *Biochem. J.* **1993**, *296*, 403–408; b) M. S. Nasir, C. J. Fahrni, D. A. Suhy, K. J. Kolodsick, C. P. Singer, T. V. O'Halloran, *J. Biol. Inorg. Chem.* **1999**, *4*, 775–783; c) C. J. Fahrni, T. V. O'Halloran, *J. Am. Chem. Soc.* **1999**, *121*, 11448–11458.
[13] a) P. Coyle, P. D. Zalewski, J. C. Phicox, I. J. Forbes, A. D. Ward, S. F. Lincoln, I. Mahadevan, A. M. Rofe, *Biochem. J.* **1994**, *303*, 781–786; b) T. Hirano, K. Kikuchi, Y. Urano, T. Higichi, T. Nagano, *Angew. Chem. Int. Ed.* **2000**, *39*, 1052–1055.
[14] E. U. Akkaya, M. E. Huston, A. W. Czarnik, *J. Am. Chem. Soc.* **1990**, *112*, 3590–3593.
[15] T. Koike, T. Watanabe, S. Aoki, E. Kimura, M. Shiro, *J. Am. Chem. Soc.* **1996**, *118*, 12696–12703.
[16] S. Aoki, S. Kaido, H. Fujioka, E. Kimura, *Inorg. Chem.* **2003**, *42*, 1023–1030.
[17] S. Aoki, K. Sakurama, N. Matsuo, Y. Yamada, R. Takasawa, S. Tanuma, M. Shiro, K. Takeda, E. Kimura, *Chem. Eur. J.* **2006**, *12*, 9066–9080.
[18] M. Le Baccon, F. Chuburu, L. Toupet, H. Handel, M. Soibinet, I. Déchamps-Olivier, J. P. Barbier, M. Aplincourt, *New J. Chem.* **2001**, *25*, 1168–1174.
[19] a) R. Fournaise, C. Petitfaux, *Talanta* **1987**, *34*, 385–395; b) R. Fournaise, C. Petitfaux, *Analusis* **1990**, *18*, 242–249.
[20] A. Bianchi, M. Micheloni, P. Paoletti, *Coord. Chem. Rev.* **1991**, *110*, 17–113.
[21] a) S. El Ghachtouli, C. Cadiou, I. Déchamps-Olivier, F. Chuburu, M. Aplincourt, T. Roisnel, *Eur. J. Inorg. Chem.* **2006**, 3472–3481; b) M. Shionoya, T. Ikeda, E. Kimura, M. Shiro, *J. Am. Chem. Soc.* **1994**, *116*, 3848–3859.
[22] J. Catalán, R. M. Claramunt, J. Elguero, J. Laynez, M. Menéndez, F. Anvia, J. H. Quian, M. Taagepera, R. W. Taft, *J. Am. Chem. Soc.* **1988**, *110*, 4105–4111.
[23] T. J. Lane, K. P. Quinlan, *J. Am. Chem. Soc.* **1960**, *82*, 2994–2997.
[24] M. Krishnamurthy, P. Phaniraj, S. K. Dogra, *J. Chem. Soc. Perkin Trans. 2* **1986**, 1917–1925.
[25] a) M. R. Figueroa, D. E. Gomez, C. P. Iglesias, A. De Blas, T. R. Blas, *Eur. J. Inorg. Chem.* **2007**, 2198–2207; b) G. Berden, W. L. Meerts, E. Jalviste, *J. Chem. Phys.* **1995**, *103*, 9596–9606; c) J. R. Platt, *J. Chem. Phys.* **1951**, *19*, 101–118.
[26] M. Alvaro, H. García, E. Palomares, R. Achour, A. Moussaif, R. Zniber, *Chem. Phys. Lett.* **2001**, *250*, 240–246.
[27] H. Walba, R. W. Isensee, *J. Org. Chem.* **1961**, *26*, 2789–2791.
[28] A. E. Goeta, J. A. K. Howard, D. Maffeo, H. Puschmann, J. A. G. Williams, D. S. Yufit, *J. Chem. Soc. Dalton Trans.* **2000**, 1873–1880.
[29] V. J. Thöm, C. C. Fox, J. C. A. Boeyens, R. D. Hancock, *J. Am. Chem. Soc.* **1984**, *106*, 3198–3207.
[30] G. Golub, H. Cohen, P. Paoletti, A. Bencini, L. Messori, I. Bertini, D. Meyerstein, *J. Am. Chem. Soc.* **1995**, *117*, 8353–8361.
[31] S. Aoki, K. Iwaida, N. Hanamoto, M. Shiro, E. Kimura, *J. Am. Chem. Soc.* **2002**, *124*, 5256–5257.
[32] X. P. Yang, B. S. Kang, W. K. Wong, C. Y. Su, H. Q. Liu, *Inorg. Chem.* **2003**, *42*, 169–179.
[33] T. Matsubara, K. Hirao, *J. Mol. Chem. Theochem.* **2002**, *581*, 203–213.
[34] Q. X. Li, Q.-H. Luo, Y. Z. Li, C. Y. Duan, Q. Y. Tu, *Inorg. Chim. Acta* **2005**, *358*, 504–512.
[35] T. Koike, S. Kajitani, I. Nakamura, E. Kimura, M. Shiro, *J. Am. Chem. Soc.* **1995**, *117*, 1210–1219.
[36] J. Moreau, E. Guillon, J. C. Pierrard, J. Rimbault, M. Port, M. Aplincourt, *Chem. Eur. J.* **2004**, *10*, 5218–5232.
[37] T. Koike, M. Takamura, E. Kimura, *J. Am. Chem. Soc.* **1994**, *116*, 8443–8449.
[38] E. K. Barefield, H. C. Freeman, D. G. V. Derveer, *Inorg. Chem.* **1986**, *25*, 552–558.
[39] D. Meyerstein, *Coord. Chem. Rev.* **1999**, *185–186*, 141–147.
[40] M. F. Hoq, R. E. Shepherd, *Inorg. Chem.* **1984**, *23*, 1851–1858.
[41] A. P. de Silva, H. Q. N. Gunaratne, T. Gunnlaugsson, A. J. M. Huxley, C. P. Mc. Coy, J. T. Rademacher, T. E. Rice, *Chem. Rev.* **1997**, *97*, 1515–1566.
[42] S. Aoki, D. Kagata, M. Shiro, K. Takeda, E. Kimura, *J. Am. Chem. Soc.* **2004**, *126*, 13377–13390.
[43] N. C. Lim, H. C. Freake, C. Bruckner, *Chem. Eur. J.* **2005**, *11*, 38–49.
[44] J. A. Kemio, T. M. Shepherd, *Chem. Phys. Lett.* **1977**, *47*, 158–162.

 © 2007 Wiley-VCH Verlag GmbH & Co. KGaA, Weinheim 

[45] *COLLECT*, KappaCCD software, Nonius BV, Delft, The Netherlands, **1998**.
[46] Z. Otwinowski, W. Minor in *Methods in Enzymology* (Ed.: C. W. Carter Jr, R. M. Sweet), Academic Press, New York, **1997**, vol. 276, pp. 307.
[47] A. Altomare, M. C. Burla, M. Camalli, G. Cascarano, C. Giacovazzo, A. Guagliardi, A. G. G. Moliterni, G. Polidori, R. Spagna, *J. Appl. Crystallogr.* **1999**, *32*, 115.
[48] G. M. Sheldrick, *SHELX97, Program for the Refinement of Crystal Structures*, University of Göttingen, Germany, **1997**.
[49] A. J. M. Duisenberg, *Reflections on Area detectors*, PhD Thesis, Utrecht, **1998**.
[50] G. M. Sheldrick, *SADABS version 2.03*, Bruker AXS Inc., Madison, Wisconsin, USA, **2002**.
[51] P. C. Tway, L. J. Cline Love, *J. Phys. Chem.* **1982**, *86*, 5223–5226.

Received: June 13, 2007
Published Online: September 21, 2007

 © 2007 Wiley-VCH Verlag GmbH & Co. KGaA, Weinheim 

DOI: 10.1002/ejic.200700533

# Mixed-Valence Cobalt(II/III) Carboxylate Clusters: $Co^{II}_4Co^{III}_2$ and $Co^{II}Co^{III}_2$ Complexes from the Use of 2-(Hydroxymethyl)pyridine

**Theocharis C. Stamatatos,[a] Athanassios K. Boudalis,[b] Konstantina V. Pringouri,[a] Catherine P. Raptopoulou,[b] Aris Terzis,[b] Joanna Wolowska,[c] Eric J. L. McInnes,*[c] and Spyros P. Perlepes*[a]**

*Dedicated to the late F. Albert Cotton for his important contributions to Inorganic Chemistry*

**Keywords:** Mixed-valence cobalt complexes / [2-(Hydroxymethyl)pyridine]metal complexes / Linear trinuclear cobalt complexes / Hexanuclear cobalt clusters / Q-band electron paramagnetic resonance

Aerobic reactions of $Co(O_2CR)_2$ with 2-(hydroxymethyl)pyridine (hmpH), in the presence of $ClO_4^-$ counterions give the hexanuclear, mixed-valence clusters $[Co^{II}_4Co^{III}_2(O_2CR)_4(hmp)_8](ClO_4)_2$ [R = Me (**1**), Ph (**2**)] which possess the unprecedented $[Co^{II}_4Co^{III}_2(\mu_3\text{-}OR')_4(\mu\text{-}OR')_4]^{6+}$ [R′ = (2-pyridyl)-$CH_2$-] core. Replacement of $ClO_4^-$ by $N_3^-$ in the reaction mixture that gives **1** leads to the linear complex $[Co^{III,II,III}_3(O_2CMe)_2(N_3)_2(hmp)_4]$ (**3**). Q-band EPR spectra and variable-temperature magnetic susceptibility studies for **1** and **2** provide strong evidence that the $Co^{II}$ ions are antiferromagnetically coupled.

(© Wiley-VCH Verlag GmbH & Co. KGaA, 69451 Weinheim, Germany, 2007)

## Introduction

There is currently an intense interest in the synthesis and study of polynuclear 3d-metal complexes (clusters). Among the diverse reasons for this is the discovery that 3d-metal molecular clusters can show slow relaxation of magnetisation under certain circumstances. These molecular species, named "single-molecule magnets" (SMMs),[1] have attracted great interest from both a technological viewpoint – in that such single molecules represent the smallest conceivable memory devices – and from a fundamental scientific perspective, as those clusters have allowed studies of quantum mechanichal phenomena such as tunneling.[1a,1b,1d] There thus continues to be a need for new synthetic methods[2] to such molecules.

Ligands used in synthesising 3d-metal clusters are however comparatively restricted[3] and thus discovery of new combinations ("blends") of ligands remains important in the field. With this aim, we have been exploring "ligand blend" reactions involving carboxylates ($RCO_2^-$) *and* anionic bridging-chelating ligands (i.e. bridging ligands that simultaneously form chelating rings), *with* or *without* additional inorganic anions ($Cl^-$, $Br^-$, $NO_3^-$, $N_3^-$, $SCN^-$). Our results with the anionic *gem*-diol derivatives of di-2-pyridyl ketone,[4] various 2-pyridyloximates[5] and a plethora of derivatized salicylaldoximates[6] have been very encouraging, and a series of Cr, Mn, Fe, Co, Ni and Cu carboxylate clusters with nuclearities ranging from 3 to 20 and with interesting properties (including high-spin molecules[7] and SMMs[6,8]) have been prepared.

As part of our continuing search for new preparative routes to polynuclear species, we have recently turned our attention to 2-pyridyl alcohols that present a kind of structural similarity to 2-pyridyl oximes; our goals are to investigate to what extent the use of such ligands might affect the identity of the obtained products compared with 2-pyridyl oximes and to what extent this might thus prove to be a route to new cluster types. In the present work, we report interesting clusters from the use of 2-(hydroxymethyl)pyridine (hmpH) in cobalt carboxylate chemistry. Cobalt(II), which has a large single-ion anisotropy due to the orbitally degenerate ground state, may potentially be a good candidate for making SMMs, and there are few reports in the literature of $Co^{II}$-based SMMs.[9] The ligand hmpH has been used extensively in the synthesis of Fe,[10] Mn[11] and Cu[12] clusters, but has been sparingly used with other 3d-metals. The deprotonated $hmp^-$ group has been used previously in $Co^{II}$ chemistry by Christou and Hendrickson,[9a] who reported the cubane cluster $[Co^{II}_4Cl_4(hmp)_4(MeOH)_4]$;

[a] Department of Chemistry, University of Patras, 26504 Patras, Greece
E-mail: perlepes@patreas.upatras.gr
[b] Institute of Materials Science, NCSR "Demokritos", 15310 Aghia Paraskevi Attikis, Greece
[c] EPSRC Multi-frequency EPR Centre, School of Chemistry, University of Manchester, Oxford Road, Manchester M13 9PL, UK

 © 2007 Wiley-VCH Verlag GmbH & Co. KGaA, Weinheim 

this cluster proved to be the first cobalt SMM. No cobalt carboxylate clusters containing hmp$^-$ have been reported. We suspected that there might be a number of Co/$RCO_2^-$/hmp$^-$ cluster species accessible and have therefore been investigated the reactions of hmpH with $Co^{II}$ carboxylate sources under a variety of conditions.

## Results and Discussion

### Synthesis and IR Characterisation

Aerobic reactions of $Co(O_2CMe)_2{\cdot}4H_2O$ and $Co(O_2CPh)_2$ with hmpH, in the presence of $NaClO_4$ (1:1:1 molar ratio), in a solvent mixture comprising MeCN and MeOH (3:1, v/v) at room temperature led to dark red solutions, from which were subsequently isolated crystals of $[Co_6(O_2CMe)_4(hmp)_8](ClO_4)_2{\cdot}$MeOH (**1**·MeOH) and $[Co_6(O_2CPh)_4(hmp)_8](ClO_4)_2{\cdot}2$(*n*-hex) [**2**·2(*n*-hex)], respectively, upon conventional workup (*n*-hex = *n*-hexane). The formation of **1** and **2** can be represented by Equation (1).

$$6\ Co^{II}(O_2CR)_2 + 8\ hmpH + 2\ NaClO_4 + 1/2\ O_2 \xrightarrow{MeCN/MeOH} \mathbf{[Co^{II}_4Co^{III}_2(O_2CR)_4(hmp)_8](ClO_4)_2} + 6\ RCO_2H + 2\ NaO_2CR + H_2O \quad [R = Me\ (\mathbf{1}),\ Ph\ (\mathbf{2})] \tag{1}$$

The addition of the coordinating $N_3^-$ ions to the 1:1 Co$(O_2CMe)_2{\cdot}4H_2O$/hmpH (i.e. omission of $ClO_4^-$ ions) reaction mixture in MeCN/$H_2O$ (3:1, v/v), in the presence of atmospheric oxygen and layering of $Me_2CO$ onto the resulting green-brown solution gave dark red crystals of the neutral complex $[Co_3(O_2CMe)_2(N_3)_2(hmp)_4]{\cdot}H_2O$ (**3**·$H_2O$) in very good yield. The formation of **3** is summarised in Equation (2).

$$3\ Co^{II}(O_2CMe)_2{\cdot}4H_2O + 4\ hmpH + 2\ NaN_3 + 1/2\ O_2 \xrightarrow{MeCN/H_2O} \mathbf{[Co^{II}Co^{III}_2(O_2CMe)_2(N_3)_2(hmp)_4]}\ (\mathbf{3}) + 2\ MeCO_2H + 2\ NaO_2CMe + 13\ H_2O \tag{2}$$

The IR spectra of **1** and **2** exhibit bands at 1098–1092 and 628–624 $cm^{-1}$ assignable to the $\nu_3(F_2)[\nu_d(ClO)]$ and $\nu_4(F_2)[\delta_d(OClO)]$ modes, respectively, of the uncoordinated $T_d$ $ClO_4^-$ ions.[13] The spectrum of **3**·$H_2O$ exhibits an intense band centred at 2135 $cm^{-1}$ which is attributed to the asymmetric stretching mode of the coordinated azide.[13] Several bands appear in the 1610–1380 $cm^{-1}$ range in the spectra of the three complexes. Contributions from the carboxylate $\nu_{as}(CO_2)$ and $\nu_s(CO_2)$ modes are expected in this region, but overlapping with the stretching vibrations of the 2-pyridyl and benzoate (only for **2**) rings, and $\delta(CH_2)$ renders assignments tentative. The strong bands at 1574 (**1**), 1573 (**2**), 1574 (**3**·$H_2O$) and 1434 (**1**), 1438 (**2**), 1434 (**3**·$H_2O$) have $\nu_{as}(CO_2)$ and $\nu_s(CO_2)$ characters, respectively. The difference $\Delta$ [$\Delta = \nu_{as}(CO_2) - \nu_s(CO_2)$] is 140 $cm^{-1}$ for **1**, **3**·$H_2O$ and 135 $cm^{-1}$ for **2**, less than those for $NaO_2CMe$ (164 $cm^{-1}$) and $NaO_2CPh$ (184 $cm^{-1}$), as expected for the bridging mode of carboxylate ligation.[14]

### Description of Structures

The cations of **1** (Figure 1) and **2** (Figure 2) are structurally similar in many aspects and thus only the structure of complex **1**·MeOH (the quality of this structure is superior

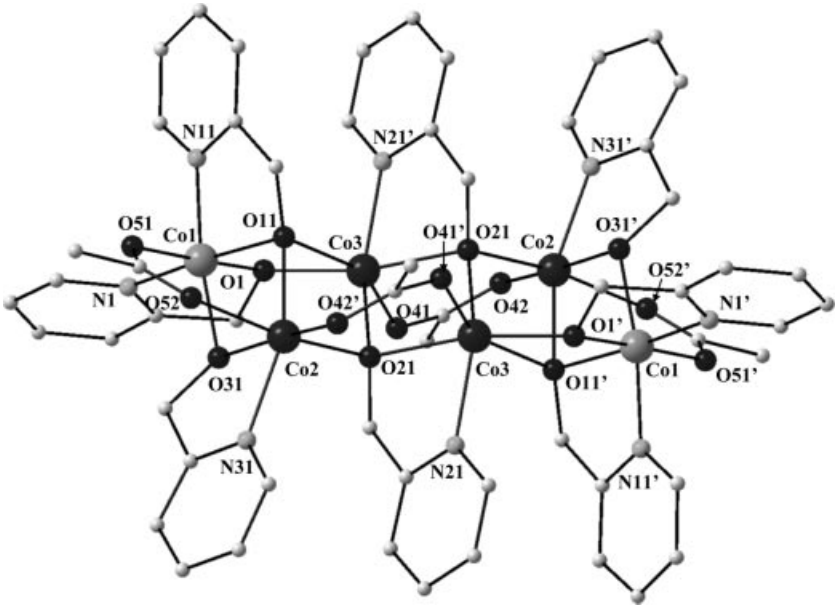


Figure 1. Partially labelled ball-and-stick presentation of the cation of **1**. H atoms are omitted for clarity. Primes are used for symmetry-related atoms.

 © 2007 Wiley-VCH Verlag GmbH & Co. KGaA, Weinheim 

to that of the benzoate cluster) will be described in detail. Selected interatomic distances and angles for the two hexanuclear complexes are listed in Tables 1 and 2. The cation of **1** lies on a crystallographic inversion centre, and consists of six distorted octahedral metal ions held together by four 3.31 (Harris notation[15]) or $\eta^1{:}\eta^3{:}\mu_3$ hmp$^-$ ligands, four 2.21 or $\eta^1{:}\eta^2{:}\mu$ hmp$^-$ ligands (Scheme 1), two *syn*,*syn* 2.11 or $\eta^1{:}\eta^1{:}\mu$ $MeCO_2^-$ groups (those containing atoms O51/O52 and their symmetry equivalents) and two *syn*,*anti* 2.11 or $\eta^1{:}\eta^1{:}\mu$ $MeCO_2^-$ (those containing atoms O41/O42 and their symmetry equivalents). Harris notation[15] describes the binding mode as $X.Y_1Y_2Y_3\cdots Y_n$, where X is the overall number of metals bound by the whole ligand, and each value of Y refers to the number of metal ions attached to the different donor atoms. The ordering of Y is listed by the Cahn–Ingold–Prelog priority rules, hence here O before N. The chromophores are $Co(1)O_4N_2$, $Co(2)O_5N$ and $Co(3)O_5N$. Charge considerations require a $4Co^{II}$, $2Co^{III}$ oxidation-state description (mixed-valent complex). Cobalt–ligand distances fall into two well-separated groups with all distances from Co(1) being less than 1.93 Å, and those from Co(2) and Co(3) being at least 2.01 Å; thus,[16] Co(1) and its symmetry-related Co(1′) are assigned as the $Co^{III}$ ions. The core of the cluster (Figure 3) appears to be $[Co^{II}_4Co^{III}_2(\mu_3\text{-}OR')_4(\mu\text{-}OR')_4]^{6+}$, where R′ is the (2-pyridyl)$CH_2$- group. It can be conveniently described as consisting of two $[Co^{II}_2Co^{III}O_4]$ partial cubanes (cubanes missing a vertex). The linking of the partial cubane subunits is achieved via the alkoxide-type oxygen atoms O(21) and O(21′) which become $\mu_3$. The four $Co^{II}$ ions define a rhombus. The $Co^{II}_3$ triangular faces are each bridged by a $\mu_3$-oxygen [O(21), O(21′)]. An alternative description of the core is as containing a $[Co_6O_8]^{6+}$ rod- or ladder-like unit which consists of four edge-sharing triangles, with Co(1) and Co(1′), respectively, below and above (0.223 Å) the plane of the central four $Co^{II}$ ions. The Co(1)–(O,N) and Co(2,3)–(O,N) bond lengths agree well with values expected for low-spin $Co^{III}$ and high-spin $Co^{II}$, respectively, in octahedral environments.[16–18]

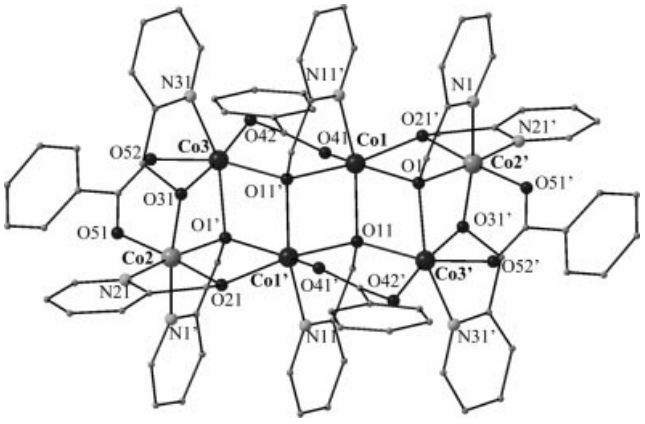


Figure 2. Partially labelled ball-and-stick presentation of the cation of **2**. H atoms are omitted for clarity. Primes are used for symmetry-related atoms.

Table 1. Selected interatomic distances [Å] and angles [°] for complex $[Co_6(O_2CMe)_4(hmp)_8](ClO_4)_2\cdot MeOH$ (**1**·MeOH).[a]

| | | | |
|---|---|---|---|
| Co(1)···Co(2) | 2.953(2) | Co(2)···Co(3) | 3.311(3) |
| Co(1)···Co(3) | 3.099(2) | Co(3)···Co(3′) | 3.189(2) |
| Co(1)–O(1) | 1.877(2) | Co(2)–O(42′) | 2.017(2) |
| Co(1)–O(11) | 1.913(2) | Co(2)–O(52) | 2.134(3) |
| Co(1)–O(31) | 1.900(2) | Co(2)–N(31) | 2.107(3) |
| Co(1)–O(51) | 1.914(2) | Co(3)–O(1) | 2.038(2) |
| Co(1)–N(1) | 1.914(3) | Co(3)–O(11) | 2.296(2) |
| Co(1)–N(11) | 1.926(3) | Co(3)–O(21) | 2.078(2) |
| Co(2)–O(11) | 2.131(2) | Co(3)–O(21′) | 2.144(2) |
| Co(2)–O(21) | 2.152(2) | Co(3)–O(41) | 2.068(2) |
| Co(2)–O(31) | 2.060(2) | Co(3)–N(21′) | 2.128(3) |
| O(1)–Co(1)–O(51) | 175.8(9) | Co(1)–O(1)–Co(3) | 104.6(1) |
| O(11)–Co(1)–N(1) | 170.6(1) | Co(1)–O(11)–Co(2) | 93.7(1) |
| O(31)–Co(1)–N(11) | 170.6(1) | Co(1)–O(11)–Co(3) | 94.4(1) |
| O(11)–Co(2)–N(31) | 155.3(1) | Co(1)–O(31)–Co(2) | 96.3(1) |
| O(21)–Co(2)–O(52) | 166.3(9) | Co(2)–O(11)–Co(3) | 96.7(1) |
| O(31)–Co(2)–O(42′) | 172.0(9) | Co(2)–O(21)–Co(3) | 103.0(1) |
| O(1)–Co(3)–O(21′) | 169.21(8) | Co(2)–O(21)–Co(3′) | 114.6(1) |
| O(11)–Co(3)–O(41) | 155.26(9) | Co(3)–O(21)–Co(3′) | 98.2(1) |
| O(21)–Co(3)–N(21′) | 151.07(9) | | |

[a] Primed atoms are related to the unprimed ones by the symmetry transformation $-x, -y + 1, -z$.

Table 2. Selected interatomic distances [Å] and angles [°] for complex $[Co_6(O_2CPh)_4(hmp)_8](ClO_4)_2\cdot 2(n\text{-hex})$ [**2**·2(*n*-hex)].[a]

| | | | |
|---|---|---|---|
| Co(1)···Co(2) | 3.117(2) | Co(2)···Co(3) | 2.932(3) |
| Co(1)···Co(3) | 3.309(2) | Co(1)···Co(1′) | 3.237(3) |
| Co(1)–O(1) | 2.305(7) | Co(2)–O(51) | 1.931(7) |
| Co(1)–O(11) | 2.067(7) | Co(2)–N(1′) | 1.941(9) |
| Co(1)–O(11′) | 2.181(7) | Co(2)–N(21) | 1.910(9) |
| Co(1)–O(21′) | 2.061(7) | Co(3)–O(1′) | 2.127(7) |
| Co(1)–O(41) | 2.057(7) | Co(3)–O(11′) | 2.129(7) |
| Co(1)–N(11′) | 2.108(8) | Co(3)–O(31) | 2.032(7) |
| Co(2)–O(1′) | 1.926(6) | Co(3)–O(42) | 1.996(7) |
| Co(2)–O(21) | 1.867(7) | Co(3)–O(52) | 2.130(7) |
| Co(2)–O(31) | 1.912(7) | Co(3)–N(31) | 2.111(9) |
| O(1)–Co(1)–O(41) | 155.2(3) | Co(1)–O(11)–Co(1′) | 99.3(3) |
| O(11)–Co(1)–N(11′) | 150.4(3) | Co(1)–O(11)–Co(3) | 114.1(3) |
| O(11′)–Co(1)–O(21′) | 167.1(3) | Co(1′)–O(1)–Co(2) | 94.5(3) |
| O(1′)–Co(2)–N(21) | 171.3(4) | Co(1′)–O(1)–Co(3) | 96.5(3) |
| O(21)–Co(2)–O(51) | 176.4(3) | Co(1′)–O(11)–Co(3) | 104.1(3) |
| O(31)–Co(2)–N(1′) | 170.6(4) | Co(1′)–O(21)–Co(2) | 105.0(3) |
| O(1′)–Co(3)–N(31) | 157.2(3) | Co(2)–O(1)–Co(3) | 92.5(3) |
| O(11′)–Co(3)–O(52) | 166.6(3) | Co(2)–O(31)–Co(3) | 96.0(3) |
| O(31)–Co(3)–O(42) | 173.3(3) | | |

[a] Primed atoms are related to the unprimed ones by the symmetry transformation $-x, -y + 2, -z + 1$.

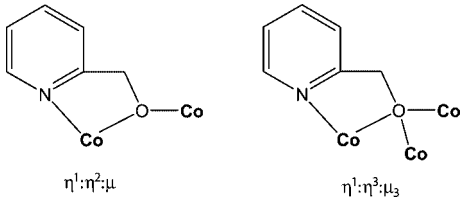


Scheme 1. The crystallographically established coordination modes of hmp$^-$ in complexes **1**, **2** and **3**.

The core $[Co^{II}_4Co^{III}_2(\mu_3\text{-}OR')_4(\mu\text{-}OR')_4]^{6+}$ is unprecedented in cobalt chemistry. Complexes **1** and **2** join a very small family of $Co^{II}_4Co^{III}_2$ clusters.[17]

 © 2007 Wiley-VCH Verlag GmbH & Co. KGaA, Weinheim 

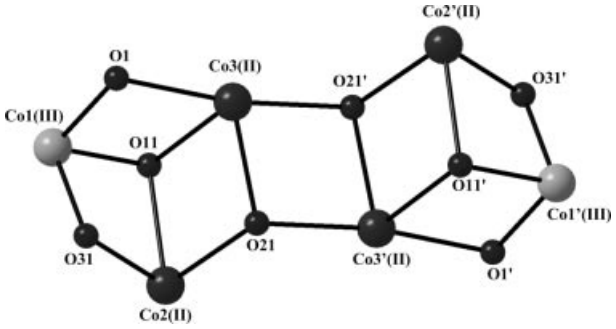


Figure 3. The $[Co^{II}_4Co^{III}_2(OR')_8]^{6+}$ core of complexes **1** and **2**.

The crystal structure of **3**·$H_2O$ reveals the formation of a linear trinuclear molecule (Figure 4). Selected interatomic distances and angles for this complex are listed in Table 3. The central metal ion, Co(1), which is located on a crystallographic inversion centre, is octahedrally coordinated by six-oxygen atoms belonging to four $hmp^-$ and two $MeCO_2^-$ ligands. The six sites on each of the distorted octahedral, terminal Co ions are occupied by the N,O-atoms [N(1), O(1), N(11), O(11)] that belong to the "chelating" part of two $hmp^-$ ligands, one N-atom [N(21)] of a terminal azido ligand and one O-atom [O(22′)] of a *syn*,*syn*-$\eta^1$:$\eta^1$:μ (2.11) $MeCO_2^-$ group. The three nitrogen atoms are in the facial configuration. The core appears to be $[Co^{II}Co^{III}_2(\mu\text{-}OR')_4]^{4+}$. Charge considerations require a formal $2Co^{III}$, $Co^{II}$ description of **3**, and the terminal metal ions are

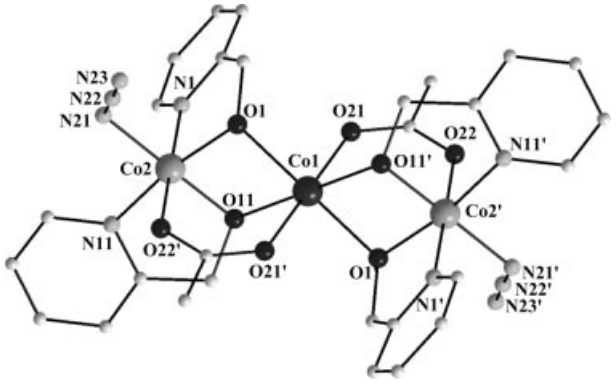


Figure 4. Molecular structure of the mixed-valence (III/II/III) complex **3** with selecting atom labelling. Primes are used for symmetry-related atoms.

clearly low-spin $Co^{III}$ ions based[16] on their Co–N,O bond lengths (all <1.95 Å) compared with those of the central Co(1) ion which has Co–O distances in the range 2.062(2)–2.097(2) Å, indicating that this is a $Co^{II}$ ion. The $hmp^-$ ions function as $\eta^1$:$\eta^2$:μ (2.21) ligands; each ligand chelates one $Co^{III}$ ion through the 2-pyridyl and the alkoxide oxygen forming a five-membered chelating ring and bridges this metal centre with the central $Co^{II}$ ion through the μ deprotonated oxygen atom (Scheme 1).

Complex **3** joins a handful of structurally characterised linear, valence-trapped $Co^{III}Co^{II}Co^{III}$ complexes[18] and an even smaller group of $Co^{II/III}$ clusters comprising both azido and carboxylate ligands.[19]

## Magnetic and EPR Studies

Magnetic susceptibility measurements were carried out on a polycrystalline sample of cluster **1** over 3–300 K and a magnetic field of 1 T (Figure 5). The $\chi_M T$ product at 300 K is 10.83 $cm^3 mol^{-1} K$, significantly higher than the spin-only value of 7.48 $cm^3 mol^{-1} K$ for four non-interacting $S$ = 3/2 ions (with $g$ = 2), and is due to the significant orbital contribution of $Co^{II}$ ions in octahedral environments. Assuming a $g_{av}$ value of 2.2, the theoretical $\chi_M T$ value is 9.08 $cm^3 mol^{-1} K$. $\chi_M T$ drops upon cooling, down to 2.12 $cm^3$ $mol^{-1}$ K at 3 K. The $(\chi_M)^{-1}$ vs. $T$ plot gives a Weiss constant of $\Theta$ = –11.5 K with $C$ = 11.2 $cm^3 mol^{-1} K$ (over the 20–300 K range). The room temperature $\chi_M T$ values of **2** at both 1 and 0.1 T are almost the same (≈ 11.0 $cm^3 mol^{-1} K$). There is a continuous decrease in $\chi_M T$ with decreasing temperature, which is more pronounced below ca. 50 K (as in **1**). The $\chi_M T$ product (1 T field) reaches the value of 2.20 $cm^3 mol^{-1} K$ at 2 K. In a 0.1 T field, however, this decrease is steeper (1.65 $cm^3 mol^{-1} K$ at 2 K). Because the data for **1** are available only at 1 T, the magnetic field effects are unknown for this compound.

Although single-ion spin-orbit coupling effects (giving a doublet ground state) could give rise to this qualitative behaviour,[17c] the low temperature $\chi_M T$ data for two hexanuclear clusters extrapolate to zero at 0 K suggesting a diamagnetic ground state and hence significant antiferromagnetic interactions. This is supported by Q-band EPR spectra for **1** at low temperature which show two features, at ca. 0 and 2 kG, which must arise from different low-lying spin

Table 3. Selected interatomic distances [Å] and angles [°] for complex $[Co_3(O_2CMe)_2(N_3)_2(hmp)_4]\cdot H_2O$ (**3**·$H_2O$).[a]

| | | | |
|---|---|---|---|
| Co(1)···Co(2) | 2.933(9) | Co(2)···Co(2′) | 5.867(9) |
| Co(1)–O(1,1′) | 2.062(2) | Co(2)–O(22′) | 1.927(2) |
| Co(1)–O(11,11′) | 2.097(2) | Co(2)–N(1) | 1.934(2) |
| Co(1)–O(21,21′) | 2.081(2) | Co(2)–N(11) | 1.935(2) |
| Co(2)–O(1) | 1.890(2) | Co(2)–N(21) | 1.946(2) |
| Co(2)–O(11) | 1.892(2) | | |
| O(1)–Co(1)–O(1′) | 180.0(5) | O(11)–Co(2)–N(21) | 177.0(9) |
| O(11)–Co(1)–O(11′) | 180.0(5) | O(22′)–Co(2)–N(1) | 176.6(8) |
| O(21)–Co(1)–O(21′) | 180.0(5) | *cis* O–Co(2)–N | 83.7(8)–93.4(9) |
| *cis* O–Co(1)–O | 87.6(7)–92.8(6) | Co(1)–O(1)–Co(2) | 95.7(8) |
| O(1)–Co(2)–N(11) | 171.0(8) | Co(1)–O(11)–Co(2) | 94.5(7) |

[a] Primed atoms are related to the unprimed ones by the symmetry transformation 1/2 – $x$, ½ – $y$, 1 – $z$.

 © 2007 Wiley-VCH Verlag GmbH & Co. KGaA, Weinheim 

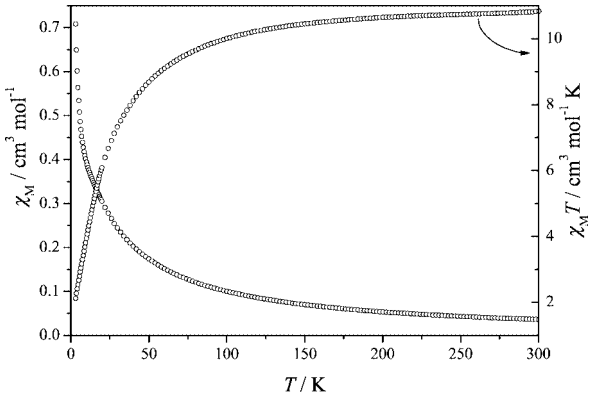


Figure 5. $\chi_M T$ vs. $T$ and $\chi_M$ vs. $T$ plots for complex **1**.

states as shown by their different temperature dependences (Figure 6). However, due to the complexity of systems comprising coupled $Co^{II}$ ions, a quantitative analysis of the susceptibility behaviour is not possible.

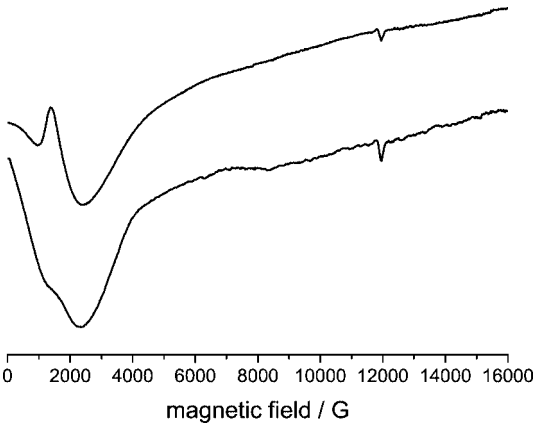


Figure 6. Q-Band (33.9 GHz) EPR spectra of a powder of **1** at 20 (top) and 5 K (bottom). The weak signal at 12000 G is most probably due to an impurity.

The room-temperature value of $\chi_M T$ for **3**·$H_2O$ at 0.1 T is 2.88 cm$^3$ mol$^{-1}$ K ($\mu_{eff}$ per $Co^{II}$ = 4.80 BM), to be compared with the spin-only ($g$ = 2) $\chi_M T$ value of 1.87 cm$^3$ mol$^{-1}$ K ($\mu_{eff}$ per $Co^{II}$ = 3.87 BM). This value is within the range observed for six-coordinate, high-spin cobalt(II) complexes.[18h,20] Because of the intrinsic orbital angular momentum in the octahedral ground state $^4T_{1g}$ (F), there is consistently a considerable orbital contribution, and effective magnetic moments for such compounds around room temperature are between 4.7 and 5.2 BM.[20] The $\chi_M T$ product decreases slowly to 2.13 cm$^3$ mol$^{-1}$ K ($\mu_{eff}$ per $Co^{II}$ = 4.13 BM) at around 25 K and then drops to 1.80 cm$^3$ mol$^{-1}$ K ($\mu_{eff}$ per $Co^{II}$ = 3.80 BM) at 3 K. This behaviour may be understood as arising from the combined effects of orbital degeneracy and zero-field splitting.[18h] The magnetic data confirm that complex **3**·$H_2O$ is in the mixed-valence state $Co^{III}$($S$ = 0) – $Co^{II}$($S$ = 3/2) – $Co^{III}$($S$ = 0) as suggested by the X-ray structural analysis.

## Conclusions and Perspectives

In summary, the initial use of the hmp$^-$/$RCO_2^-$ "blend" in Co chemistry has provided two $Co^{II}_4Co^{III}_2$ clusters with an unprecedented core and one linear $Co^{III}Co^{II}Co^{III}$ complex. The nuclearity of the mixed-valent cluster, [$Co_6$] or [$Co_3$], is controlled partly by the nature of the extra inorganic anion. Magnetic and Q-band EPR studies of the hexanuclear cobalt acetate cluster have provided preliminary useful insights into the complex interplay between single-ion properties and exchange interactions in polynuclear Co complexes. We stated in the Introduction that it was our suspicion that Co/$RCO_2^-$/hmp$^-$ chemistry might prove a rich new area for what is otherwise a well-studied metal. This work and a variety of unpublished results seem to suggest that our suspicions were correct.

## Experimental Section

**General:** All manipulations were performed under aerobic conditions using materials (Merck, Aldrich) as received. Elemental analyses (C,H,N) were performed by the University of Ioannina (Greece) Microanalytical Laboratory with an EA 108 Carlo–Erba analyzer. IR spectra (4400–450 cm$^{-1}$) were recorded from KBr pellets with a Perkin–Elmer PC 16 FTIR spectrometer. Variable-temperature magnetic susceptibility measurements were carried out at the Institute of Materials Science of the NCSR "Demokritos" on polycrystalline samples of complexes **1**–**3** in the 2.0–300 K temperature range using a Quantum Design MPMS SQUID susceptometer under magnetic fields of 1.0 and 0.1 T. Q-band (34 GHz) EPR spectra of **1** were obtained with a Bruker ESP300E spectrometer.

**Safety Note:** Perchlorate and azide salts are potentially explosive; such compounds should be synthesised and used in small quantities, and treated with utmost care at all times.

**Preparations**

**Synthesis of [$Co_6(O_2CMe)_4(hmp)_8$]($ClO_4$)$_2$·MeOH (1·MeOH):** A colourless solution of hmpH (0.10 mL, 1.00 mmol) in MeCN (5 mL) was added to a stirred pink suspension of $Co(O_2CMe)_2$·$4H_2O$ (0.26 g, 1.04 mmol) in MeCN (25 mL). The resulting purple suspension was stirred for 20 min, during which time a colourless solution of $NaClO_4$·$H_2O$ (0.14 g, 1.00 mmol) in MeOH (10 mL) was added in small portions to finally give a deep red slurry. The latter was stirred for a further 24 h, during which time all the solids were completely dissolved. The resulting deep red solution was filtered and layered with $Et_2O$ (90 mL). After 3 d dark orange-red crystals were obtained and collected by filtration, washed with cold MeOH (2 × 5 mL) and $Et_2O$ (2 × 5 mL), and dried in vacuo; the yield was 0.140 g (65% based on hmpH). The dried solid analysed as solvent-free. $C_{56}H_{60}Cl_2Co_6N_8O_{24}$ (1653.65): calcd. C 40.68, H 3.66, N 6.78; found C 40.43, H 3.81, N 6.81. Main IR data: IR (KBr): $\tilde{\nu}$ = 3428 (mb), 2920 (w), 2830 (w), 1574 (s), 1478 (m), 1434 (s), 1346 (w), 1286 (m), 1228 (w), 1092 (vs), 1044 (s), 760 (m), 728 (w), 674 (s), 628 (m), 546 (w), 494 (w) cm$^{-1}$.

**Synthesis of [$Co_6(O_2CPh)_4(hmp)_8$]($ClO_4$)$_2$·2(*n*-hex) [2·2(*n*-hex)]:** This complex was prepared in the same manner as complex **1**, except that $Co(O_2CPh)_2$ (0.31 g, 1.00 mmol) was used in place of $Co(O_2CMe)_2$·$4H_2O$, and the solution was layered with $Et_2O$/*n*-hexanes (1:1, v/v) instead of $Et_2O$. Dark orange crystals of the product were collected by filtration, washed with cold MeOH (2 × 5 mL) and

 © 2007 Wiley-VCH Verlag GmbH & Co. KGaA, Weinheim 

$Et_2O$ (2 × 5 mL), and dried in vacuo; the yield was 0.112 g (47% based on hmpH). The dried solid analysed as solvent-free. $C_{76}H_{68}Cl_2Co_6N_8O_{24}$ (1901.93): calcd. C 48.00, H 3.60, N 5.89; found C 48.17, H 3.81, N 5.94. Main IR data. IR (KBr): $\tilde{\nu}$ = 3430 (mb), 2923 (w), 2835 (w), 1573 (s), 1479 (m), 1438 (s), 1345 (w), 1284 (m), 1229 (w), 1098 (vs), 1041 (m), 763 (m), 729 (w), 674 (s), 624 (m), 543 (w), 492 (w) $cm^{-1}$.

**Synthesis of $[Co_3(O_2CMe)_2(N_3)_2(hmp)_4]\cdot H_2O$ (3·$H_2O$):** A colourless solution of hmpH (0.10 mL, 1.00 mmol) in MeCN (5 mL) was added to a stirred pink suspension of $Co(O_2CMe)_2\cdot 4H_2O$ (0.26 g, 1.04 mmol) in MeCN (25 mL). The resulting purple suspension was stirred for 20 min, during which time a colourless aqueous solution (10 mL) of $NaN_3$ (0.07 g, 1.00 mmol) was added in small portions to finally give a dark green slurry. The latter was stirred for a further 12 h and all the unreacted solids were completely dissolved. The resulting dark brown-green solution was filtered and layered with $Me_2CO$ (90 mL). After 6 d dark red crystals of the product were isolated and collected by filtration, washed with cold $Me_2CO$ (2 × 5 mL) and dried in vacuo over silica gel; the yield was 0.151 g (70% based on hmpH). The dried solid analysed as 3·$H_2O$. $C_{28}H_{32}Co_3N_{10}O_9$ (829.42): calcd. C 40.55, H 3.89, N 16.89; found C 40.33, H 4.00, N 17.24. Main IR data. IR (KBr): $\tilde{\nu}$ = 3428 (m), 2135 (vs), 1574 (s), 1478 (m), 1434 (s), 1346 (m), 1286 (m), 1044 (m), 760 (m), 728 (w), 686 (m), 628 (w), 546 (m), 494 (w) $cm^{-1}$.

**X-ray Crystallographic Studies:** Crystals of 1·MeOH, 2·2(*n*-hex), and 3·$H_2O$ were mounted in air and covered with epoxy glue. Diffraction measurements for 1·MeOH and 3·$H_2O$ were made with a Crystal Logic Dual Goniometer diffractometer using graphite-monochromated Mo-$K_\alpha$ radiation. The X-ray data set for 2·2(*n*-hex) was collected on a $P2_1$ Nicolet diffractometer upgraded by Crystal Logic using graphite-monochromated Cu-$K_\alpha$ radiation. Complete crystal data and parameters for data collection and refinement are listed in Table 4. Unit cell dimensions were determined and refined by using the angular settings of 25 automatically centred reflections in the ranges $11 < 2\theta < 23°$ (for 1·MeOH and 3·$H_2O$) and $22 < 2\theta < 54°$ [for 2·2(*n*-hex)]. Intensity data were recorded using the $\theta$–$2\theta$ scan method. Three standard reflections monitored every 97 reflections showed less than 3% variation and no decay. Lorentz, polarisation and $\Psi$-scan absorption corrections were applied using the Crystal Logic software package. For all the three structures, all hydrogen atoms were located by difference maps and were refined isotropically, except those of the methyl groups which were introduced at calculated positions as riding on bonded atoms. No H-atoms for the solvate methanol (for 1·MeOH), *n*-hexane [for 2·2(*n*-hex)] and water (for 3·$H_2O$) were included in the refinement. All non-hydrogen atoms were refined anisotropically, except of the carbon atoms of the benzoates and the solvate *n*-hexane molecules which were refined isotropically. The oxygen atoms of the perchlorate anion in 1·MeOH were found disordered and were refined over two positions with occupation factors of total sum one. All structures were solved by direct methods using SHELXS-86[21] and refined by full-matrix least-squares techniques on $F^2$ with SHELXL-97.[22]

CCDC-642412 (for 1·MeOH), -642411 [for 2·2(*n*-hex)] and -642410 (for 3·$H_2O$) contain the supplementary crystallographic data for this paper. These data can be obtained free of charge from The Cambridge Crystallographic Data Centre via www.ccdc.cam.ac.uk/data_request/cif.

Table 4. Crystal data and structure refinement for complexes $[Co_6(O_2CMe)_4(hmp)_8](ClO_4)_2\cdot$MeOH (1·MeOH), $[Co_6(O_2CPh)_4(hmp)_8](ClO_4)_2\cdot 2$(*n*-hex) [2·2(*n*-hex)], and $[Co_3(O_2CMe)_2(N_3)_2(hmp)_4]\cdot H_2O$ (3·$H_2O$).

| | 1·MeOH | 2·2(*n*-hex) | 3·$H_2O$ |
|---|---|---|---|
| Empirical formula | $C_{57}H_{64}Cl_2Co_6N_8O_{25}$ | $C_{88}H_{96}Cl_2Co_6N_8O_{24}$ | $C_{28}H_{32}Co_3N_{10}O_9$ |
| Mol. weight | 1685.64 | 2074.21 | 829.42 |
| Colour and habit | red prisms | red prisms | red prisms |
| Crystal size [mm] | 0.32 × 0.33 × 0.60 | 0.10 × 0.10 × 0.20 | 0.10 × 0.25 × 0.55 |
| Crystal system | monoclinic | triclinic | monoclinic |
| Space group | $P2_1/n$ | $P\bar{1}$ | $C1_2/c$ |
| $a$ [Å] | 10.679(6) | 12.286(5) | 24.584(8) |
| $b$ [Å] | 15.578(8) | 31.000(16) | 8.309(3) |
| $c$ [Å] | 20.572(11) | 12.336(6) | 17.228(6) |
| $\alpha$ [°] | 90 | 82.533(19) | 90 |
| $\beta$ [°] | 99.06(2) | 89.972(14) | 102.05(1) |
| $\gamma$ [°] | 90 | 83.876(17) | 90 |
| $V$ [Å$^3$] | 3380(3) | 4632(4) | 3442(2) |
| $Z$ | 2 | 2 | 8 |
| $\rho_{calcd.}$ [g cm$^{-3}$] | 1.656 | 1.487 | 1.601 |
| $T$ [°C] | 25 | 25 | 25 |
| $\lambda$ (Mo-$K_\alpha$) [Å] | 0.71073 | | 0.71073 |
| $\lambda$ (Cu-$K_\alpha$) [Å] | | 1.54180 | |
| $\mu$ [mm$^{-1}$] | 1.602 | 9.393 | 1.495 |
| $F$(000) | 1716 | 2136 | 1692 |
| $2\theta_{max}$ [°] | 50 | 90 | 50 |
| No. of reflections collected | 6126 | 8104 | 6046 |
| No. of indep. reflections/$R_{int}$ | 5954/0.0476 | 7458/0.0619 | 3025/0.0116 |
| Data with $I > 2\sigma(I)$ | 5425 | 5784 | 2750 |
| Parameters refined | 585 | 1003 | 285 |
| GOF (on $F^2$) | 1.111 | 1.018 | 1.060 |
| $R1$ [a] | 0.0396 | 0.0782 | 0.0295 |
| $wR2$ [b] | 0.1055 | 0.2070 | 0.0917 |
| Residuals [e Å$^{-3}$] | 0.457/–0.451 | 1.184/–0.558 | 0.700/–0.373 |

[a] $R1 = \Sigma(|F_o| - |F_c|)/\Sigma(|F_o|)$. [b] $wR_2 = \{\Sigma\{w[(F_o^2 - F_c^2)^2]/\Sigma[w(F_o^2)^2]\}^{1/2}$.

 © 2007 Wiley-VCH Verlag GmbH & Co. KGaA, Weinheim 

## Acknowledgments

Th. C. S., K. V. P. and S. P. P. thank European Social Fund (ESF), Operational Program for Educational and Vocational Training II (EPEAEK II) and particularly the Program PYTHAGORAS (Grant b.365.037), for funding the above work. A. K. B. thanks the Greek State Scholarship Foundation (IKY) for support through a postdoctoral grant. The British Engineering and Physical Sciences Research Council (EPSRC) is thanked for financial support.

[1] For excellent reviews, see: a) G. Christou, D. Gatteschi, D. N. Hendrickson, R. Sessoli, *MRS Bull.* **2000**, *25*, 66–71; b) D. Gatteschi, R. Sessoli, *Angew. Chem. Int. Ed.* **2003**, *42*, 268–297; c) R. Bircher, G. Chaboussant, C. Dobe, H. U. Güdel, S. I. Ochsenbein, A. Sieber, O. Waldman, *Adv. Funct. Mater.* **2006**, *16*, 209–220; d) G. Aromi, E. K. Brechin, *Struct. Bonding (Berlin)* **2006**, *122*, 1–67; e) J. R. Friedman, M. P. Sarachik, J. Tejada, R. Ziolo, *Phys. Rev. Lett.* **1996**, *76*, 3830–3833.

[2] a) R. E. P. Winpenny, in *Comprehensive Coordination Chemistry II* (Eds.: J. A. Mc Cleverty, T. J. Meyer), Elsevier, Amsterdam, **2004**, vol. 7, pp. 125–175; b) R. E. P. Winpenny, *J. Chem. Soc. Dalton Trans.* **2002**, 1–10 (Dalton Perspective); c) G. Christou, *Polyhedron* **2005**, *24*, 2065–2075.

[3] For example, see: a) G. Aromi, P. Gamez, C. Boldron, H. Kooijman, A. L. Spek, J. Reedijk, *Eur. J. Inorg. Chem.* **2006**, 1940–1944; b) A. M. Ako, I. J. Hewitt, V. Mereacre, R. Clérac, W. Wernsdorfer, C. E. Anson, A. K. Powell, *Angew. Chem. Int. Ed.* **2006**, *45*, 4926–4929; c) P. Chaudhuri, *Coord. Chem. Rev.* **2003**, *243*, 143–190; d) E. K. Brechin, *Chem. Commun.* **2005**, 5141–5153.

[4] For a review see: G. S. Papaefstathiou, S. P. Perlepes, *Comments Inorg. Chem.* **2002**, *23*, 249–274.

[5] For a comprehensive review, see: C. J. Milios, Th. C. Stamatatos, S. P. Perlepes, *Polyhedron* **2006**, *25*, 134–194.

[6] For example, see: a) C. J. Milios, A. Vinslava, P. A. Wood, S. Parsons, W. Wernsdorfer, G. Christou, S. P. Perlepes, E. K. Brechin, *J. Am. Chem. Soc.* **2007**, *129*, 8–9; b) C. J. Milios, A. Vinslava, W. Wernsdorfer, S. Moggach, S. Parsons, S. P. Perlepes, G. Christou, E. K. Brechin, *J. Am. Chem. Soc.* **2007**, *129*, 2754–2755; c) C. J. Milios, A. Vinslava, W. Wernsdorfer, A. Prescimore, P. A. Wood, S. Parsons, S. P. Perlepes, G. Christou, E. K. Brechin, *J. Am. Chem. Soc.* **2007**, *129*, 6547–6561; d) M. Belesi, X. Zong, F. Borsa, C. J. Milios, S. P. Perlepes, *Phys. Rev. B* **2007**, *75*, 064414/1–064414/7.

[7] a) G. S. Papaefstathiou, S. P. Perlepes, A. Escuer, R. Vicente, M. Font-Bardia, X. Solans, *Angew. Chem. Int. Ed.* **2001**, *40*, 884–886; b) G. S. Papaefstathiou, A. Escuer, R. Vicente, M. Font-Bardia, X. Solans, S. P. Perlepes, *Chem. Commun.* **2001**, 2414–2415; c) G. S. Papaefstathiou, A. K. Boudalis, Th. C. Stamatatos, C. J. Milios, C. G. Efthymiou, C. P. Raptopoulou, A. Terzis, V. Psycharis, Y. Sanakis, R. Vicente, A. Escuer, J.-P. Tuchagues, S. P. Perlepes, *Polyhedron* **2007**, *26*, 2089–2094.

[8] a) A. K. Boudalis, B. Donnadieu, V. Nastopoulos, J. M. Clemente-Juan, A. Mari, Y. Sanakis, J.-P. Tuchagues, S. P. Perlepes, *Angew. Chem. Int. Ed.* **2004**, *43*, 2266–2670; b) C. J. Milios, C. P. Raptopoulou, A. Terzis, F. Lloret, R. Vicente, S. P. Perlepes, A. Escuer, *Angew. Chem. Int. Ed.* **2004**, *43*, 210–212; c) Th. C. Stamatatos, D. Foguet-Albiol, C. C. Stoumpos, C. P. Raptopoulou, A. Terzis, W. Wernsdorfer, S. P. Perlepes, G. Christou, *J. Am. Chem. Soc.* **2005**, *127*, 15380–15381; d) Th. C. Stamatatos, D. Foguet-Albiol, S.-C. Lee, C. C. Stoumpos, C. P. Raptopoulou, A. Terzis, W. Wernsdorfer, S. O. Hill, S. P. Perlepes, G. Christou, *J. Am. Chem. Soc.* **2007**, *129*, 9484–9499.

[9] a) E.-C. Yang, D. N. Hendrickson, W. Wernsdorfer, M. Nakano, L. N. Zakharov, R. D. Sommer, A. L. Rheingold, M. Ledezma-Gairraud, G. Christou, *J. Appl. Phys.* **2002**, *91*, 7382–7384; b) M. Murrie, S. J. Teat, H. Stoeckli-Evans, H. U. Güdel, *Angew. Chem. Int. Ed.* **2003**, *42*, 4653–4656; c) S. J. Langley, M. Helliwell, R. Sessoli, P. Rosa, W. Wernsdorfer, R. E. P. Winpenny, *Chem. Commun.* **2005**, 5029–5031; d) A. K. Boudalis, C. P. Raptopoulou, B. Abarca, R. Ballesteros, M. Chadlaoui, J. P. Tuchagues, A. Terzis, *Angew. Chem. Int. Ed.* **2006**, *45*, 432–435; e) Y.-Z. Zhang, W. Wernsdorfer, F. Pan, Z.-H. Wang, S. Gao, *Chem. Commun.* **2006**, 3302–3304; f) M.-H. Zeng, M.-X. Yao, H. Liang, W.-X. Zhang, M.-X. Chen, *Angew. Chem. Int. Ed.* **2007**, *47*, 1832 –1835; g) A. Ferguson, A. Parkin, J. Sanchez-Benitez, K. Kamenev, W. Wernsdorfer, M. Murrie, *Chem. Commun.* **2007**, **DOI**: 10.1039/b706238a.

[10] a) E. K. Brechin, M. J. Knapp, J. C. Huffman, D. N. Hendrickson, G. Christou, *Inorg. Chim. Acta* **2000**, *297*, 389–399; b) C. A. Christmas, H.-L. Tsai, L. Pardi, J. M. Kesselman, P. K. Gantzel, R. K. Chadha, D. Gatteschi, D. F. Harvey, D. N. Hendrickson, *J. Am. Chem. Soc.* **1993**, *115*, 12483–12490.

[11] For example, see: a) C. Boskovic, E. K. Brechin, W. E. Streib, K. Folting, J. C. Bollinger, D. N. Hendrickson, G. Christou, *J. Am. Chem. Soc.* **2002**, *124*, 3725–3736; b) E. C. Sañudo, W. Wernsdorfer, K. A. Abboud, G. Christou, *Inorg. Chem.* **2004**, *43*, 4137–4144; c) L. Lecren, Y.-G. Li, W. Wernsdorfer, O. Roubeau, H. Miyasaka, R. Clérac, *Inorg. Chem. Commun.* **2005**, *8*, 626–630; d) Th. C. Stamatatos, K. A. Abboud, W. Wernsdorfer, G. Christou, *Angew. Chem. Int. Ed.* **2006**, *45*, 4134–4137.

[12] For example, see: N. Lah, I. Leban, R. Clérac, *Eur. J. Inorg. Chem.* **2006**, 4888–4894.

[13] K. Nakamoto, *Infrared and Raman Spectra of Inorganic and Coordination Compounds*, 4th ed., Wiley, New York, **1986**, pp. 251, 253, 290, 291.

[14] G. B. Deacon, R. J. Phillips, *Coord. Chem. Rev.* **1980**, *33*, 227–250.

[15] R. Coxall, S. G. Harris, D. K. Henderson, S. Parsons, P. A. Tasker, R. E. P. Winpenny, *J. Chem. Soc. Dalton Trans.* **2000**, 2349–2356.

[16] Th. C. Stamatatos, S. Dionyssopoulou, G. Efthymiou, P. Kyritsis, C. P. Raptopoulou, A. Terzis, R. Vicente, A. Escuer, S. P. Perlepes, *Inorg. Chem.* **2005**, *44*, 3374–3376.

[17] a) M. Mikuriya, M. Fukuya, *Chem. Lett.* **1998**, 421–422; b) G. Aromi, A. S. Batsanov, P. Christian, M. Helliwell, A. Parkin, S. Parsons, A. A. Smith, G. A. Timco, R. E. P. Winpenny, *Chem. Eur. J.* **2003**, *9*, 5142–5161; c) K. G. Alley, R. Bircher, O. Waldmann, S. T. Ochsenbein, H. U. Güdel, B. Moubaraki, K. S. Murray, F. Fernandez-Alonso, B. F. Abrahams, C. Boskovic, *Inorg. Chem.* **2006**, *45*, 8950–8957.

[18] a) J. A. Bertrand, J. A. Kelley, E. G. Vassian, *J. Am. Chem. Soc.* **1969**, *91*, 2394–2395; b) D. A. House, V. McKee, P. J. Steel, *Inorg. Chem.* **1986**, *25*, 4884–4889; c) V. M. Novorortsev, O. G. Ellert, T. S. Kapanadze, A. Y. Buslaev, *Koord. Khim.* **1986**, *14*, 856–861; d) C. Fukuhara, E. Asato, T. Shimoji, K. Katsura, M. Mori, K. Matsumoto, S. Ooi, *J. Chem. Soc. Dalton Trans.* **1987**, 1305–1311; e) B. Ballet, A. Bino, S. Cohen, H. Rubin, T. Zor, *Inorg. Chim. Acta* **1991**, *188*, 91–93; f) A. Golobič, B. Štefane, S. Polance, *Polyhedron* **1999**, *18*, 3661–3668; g) T. S. Billson, J. D. Crane, O. D. Fox, S. L. Heath, *Inorg. Chem. Commun.* **2000**, *3*, 718–720; h) M. Rat, R. A. de Sousa, A. Tomas, Y. Frapart, J.-P. Tuchagues, I. Artaud, *Eur. J. Inorg. Chem.* **2003**, 759–765; i) Th. C. Stamatatos, A. Bell, P. Cooper, A. Terzis, C. P. Raptopoulou, S. L. Heath, R. E. P. Winpenny, S. P. Perlepes, *Inorg. Chem. Commun.* **2005**, *8*, 533–538; j) X. He, C.-Z. Lu, C.-D. Wu, *J. Coord. Chem.* **2006**, *59*, 977–984.

[19] C. Incarvito, A. L. Rheingold, A. L. Gavrilova, C. J. Qin, B. Bosnich, *Inorg. Chem.* **2001**, *40*, 4101–4108.

[20] F. A. Cotton, G. Wilkinson, C. A. Murillo, M. Bochmann, *Advanced Inorganic Chemistry*, 6th ed., Wiley, New York, **1999**, pp. 820, 821.

[21] G. M. Sheldrick, *SHELXS-86, Program for the Solution of Crystal Structures*, University of Göttingen, Germany, **1986**.

[22] G. M. Sheldrick, *SHELXL-97, Program for the Refinement of Crystal Structures*, University of Göttingen, Germany, **1997**.

Received: May 21, 2007
Published Online: September 21, 2007

 © 2007 Wiley-VCH Verlag GmbH & Co. KGaA, Weinheim 

DOI: 10.1002/ejic.200700639

# Efficient, Ultrafast, Microwave-Assisted Syntheses of Cycloplatinated Complexes

Nicolas Godbert,[a] Teresa Pugliese,[a] Iolinda Aiello,[a] Anna Bellusci,[a] Alessandra Crispini,[a] and Mauro Ghedini*[a]

**Keywords:** Cycloplatination / Microwave synthesis / Platinum / Antitumor agents / X-ray diffraction

Cyclometallated chloridoplatinum complexes containing neutral monodentate ligands such as 2-phenylpyridine (**1a**), 2-(2′-thienyl)pyridine (**1c**) or 4-methoxypyridine (**1d**), as well as the cyclometallated benzo[*h*]quinoline chlorido complex with 4-methoxypyridine (**2d**), can be synthesised in a few minutes by irradiating the reaction mixture with microwaves. The single-crystal X-ray molecular structures of the solvato complexes **1**·dmso and **2**·dmso as well as **1c**, **1d** and **2d** are reported. The availability of this class of complexes in a few minutes offers the possibility of a combinatorial approach for the preparation of libraries of homologous compounds of potential interest for applicative purposes.
(© Wiley-VCH Verlag GmbH & Co. KGaA, 69451 Weinheim, Germany, 2007)

## Introduction

Significant research efforts are currently focused on the study of cycloplatinated complexes due to their potential antitumoural activity[1] as well as their photophysical[2] or mesomorphic[3] properties. The creation of a five-membered metallacycle and formation of the chlorido-bridged dimer $[LPt(\mu\text{-}Cl)]_2$ typically occur during standard cycloplatination reactions carried out with $K_2PtCl_4$ and a ligand HL.[4] Although cyclometallation has been extensively studied and applied, cycloplatination is not a straightforward reaction and often requires rather drastic conditions to take place.

In the last few years, "although microwave effects are still the subject of considerable current debate and controversy",[5] controlled microwave heating has been extensively used in organic synthesis to reduce reaction times and/or improve yields. Microwave-assisted reactions involving transition metals are mainly dedicated to catalytic processes[5,6] or the synthesis of coordination complexes mainly containing iridium[7] and ruthenium,[8] and there is only one example where microwave irradiation has been used to attempt cyclometallation in the synthesis of (2-arylpyridine)-iridium complexes.[9] To the best of our knowledge, cycloplatination has never been studied under microwave irradiation.

Herein we describe new synthetic protocols for the synthesis of dinuclear chlorido-bridged cycloplatinated complexes of the ligands 2-phenylpyridine and benzo[*h*]quinoline (**a** and **b**, respectively), which were selected as representative examples of species that can undergo cycloplatination with the assistance of microwaves.

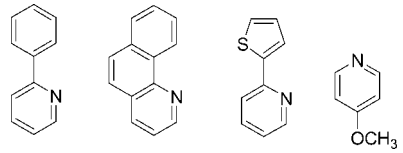


a b c d

Motivated by literature data reporting the highly cytotoxic properties of a mononuclear $Pt^{II}$ complex bearing ligand **a** both as a cyclometallated and monodentate neutral ligand against some cisplatin-resistant cell lines,[10] this article presents new synthetic strategies for the preparation of mononuclear derivatives with a similar structure that are easily obtained from their corresponding dinuclear complexes. Several new mononuclear $Pt^{II}$ complexes are obtained by both conventional and microwave-assisted syntheses and fully characterised by standard spectroscopic techniques. In addition, the molecular structures of all new synthesised complexes have been determined by single-crystal X-ray analysis.

## Results and Discussion

### Conventional Synthesis of Cycloplatinated Complexes

Cycloplatination reactions were carried out by treating ligand **a** or **b** with $K_2PtCl_4$ according to a conventional synthetic procedure. Under the reaction conditions used [24 h in 2-ethoxyethanol (EGEE) at 65 °C], the nature of the products obtained depends on the ligand/salt molar ratio. Thus, with a 1:1 ratio of ligand/$Pt^{II}$ salt the expected cyclo-

[a] Centro di Eccellenza CEMIF.CAL-LASCAMM, CR-INSTM Unità della Calabria, Dipartimento di Chimica, Università della Calabria
87036 Arcavacata di Rende (CS), Italy
Fax: +39-0984-492066
E-mail: m.ghedini@unical.it

 © 2007 Wiley-VCH Verlag GmbH & Co. KGaA, Weinheim 

platinated chlorido-bridged dimers **[1(μ-Cl)]$_2$** and **[2(μ-Cl)]$_2$** were obtained in good yields (95 and 75%, respectively), whereas with an excess of **a** (i.e. a molar ratio of 2:1 or even higher), the mononuclear cycloplatinated complex **1a**, which contains a coordinated molecule of **a**, formed almost quantitatively (95% yield). Ligand **b** gives rise exclusively to the dimeric derivative **[2(μ-Cl)]$_2$** irrespective of the ligand/salt ratio. Complexes **[1(μ-Cl)]$_2$**, **[2(μ-Cl)]$_2$** and **1a** have been reported previously,[11] although it is worthwhile noting that **1a** was either only isolated as a side product (10% yield)[12] or was obtained unexpectedly in a two-step reaction from cisplatin in rather poor overall yield.[9b]

Dissolving **[1(μ-Cl)]$_2$** or **[2(μ-Cl)]$_2$** in dmso gave the mononuclear derivatives **1**·dmso and **2**·dmso, which bear a solvent molecule as ancillary ligand.[13] The $^1$H NMR spectra of these complexes in $CDCl_3$ show the signal of the methyl protons of the coordinated solvent molecule ($\delta \approx 3.6$ ppm). Moreover, two characteristic doublets with broad $^{195}$Pt satellites ($^3J_{Pt,H}$ between 30 and 45 Hz) are observed due to the protons of the carbon atoms in the α-position with respect to the (N,C)Pt metallacycle nitrogen and carbon atoms ($\delta \approx 9.7$ and 8.4 ppm, respectively). The structures of **1**·dmso and **2**·dmso were unequivocally confirmed by single-crystal X-ray diffraction analysis (see below).

The reactivity of **[1(μ-Cl)]$_2$** and **[2(μ-Cl)]$_2$** towards the nucleophiles **a**–**d** (see above), which differ in their basicity and steric hindrance, was tested in bridge-splitting reactions to yield the corresponding monomeric adducts. Thus, refluxing **[1(μ-Cl)]$_2$** or **[2(μ-Cl)]$_2$** in 2-ethoxyethanol for 24 h with bases **a**–**d** gave complexes **1a**, **1c**, **1d** and **2d** in 95, 88, 92 and 98% yields, respectively. No complexes were formed when **[1(μ-Cl)]$_2$** and **[2(μ-Cl)]$_2$** were treated with the sterically more demanding base **b** even after longer reaction times. In particular, for **[2(μ-Cl)]$_2$**, due to the steric hindrance of the bridge itself, only the less encumbered base **d** led to the formation of a monomeric adduct **2d**.

### Microwave-Assisted Cycloplatinations

Since cycloplatinations still suffer from long reaction times of up to a week,[14] the reaction mixtures were irradiated with microwaves to try to reduce the reaction times. The Pt$^{II}$ precursor salts used in cycloplatination reactions are highly sensitive to the experimental conditions as they readily decompose at high temperature and in the presence of oxygen. In a very recent synthesis of (diimine)Pt$^{II}$ complexes,[15] the authors reported that microwave irradiation of a reaction mixture containing $K_2PtCl_4$ led to degradation to black Pt$^0$ within a few minutes after heating.

In order to overcome this limitation in the use of Pt$^{II}$ precursor salts, we decided to control the microwave heating by controlling the irradiation power during the synthesis of the new cycloplatinated species. The microwave oven was initially set to reach a maximum temperature of 65 °C after 150 W irradiation. However, this temperature was reached after only 1 min of irradiation; therefore, irradiation was automatically stopped to prevent the maximum temperature from being exceeded. Increasing the reaction time by using the oven cooling option allowed further irradiation of only 1 or 2 W instead of the expected 150 W. In order to prevent the reaction carrying on at 65 °C without microwave irradiation, the reaction vessel was cooled to room temperature in an ice bath and then re-inserted into the microwave oven to be irradiated once more. Three irradiation/cooling cycles of 1 min each were performed; the reaction times reported in Table 3 are quoted relative to the total amount of effective 150 W irradiation time. The bridged dimers **[1(μ-Cl)]$_2$** and **[2(μ-Cl)]$_2$** were obtained using a 1:1 molar ratio of ligand/metal salt according to this strategy in yields of 55–65%. These low yields are due to the formation of a small amount of black Pt$^0$.

When 2 equiv. (or more) of ligand **a** was used to reproduce the synthesis of complex **1a**, 250 W irradiation was used in order to work at a higher temperature (110 °C) than that used for the bridge dimers. This allowed quantitative conversion to the desired product **1a** in 1 min, with no sign of $K_2PtCl_4$ decomposition. Under the same experimental conditions (250 W, 110 °C), but with a smaller quantity of ligand **a**, $K_2PtCl_4$ salt decomposition was immediately observed.

As for the conventional heating synthesis, the only product isolated upon irradiation of a reaction mixture containing ligand **b** and the Pt$^{II}$ salt, irrespective of the ligand/salt ratio, is the dinuclear complex **[2(μ-Cl)]$_2$**, even after shorter reaction times (<1 min).

The microwave heating protocol was also applied to the bridge-splitting reactions between **[1(μ-Cl)]$_2$** and **[2(μ-Cl)]$_2$** and bases **a**–**d**, using 250 W of irradiation. Again, an irradiation/external cooling strategy was preferred in order to avoid temperatures higher than those previously established and to ensure that the reaction was performed under 250 W irradiation conditions. Even under these conditions only the mononuclear complexes **1a**, **1c**, **1d** and **2d** were obtained in a few minutes and in good yields (99, 74, 94 and 63% respectively). The spectroscopic characterisation of **1a**, **1c** and **1d** proved the presence of a single product in all cases. Their $^1$H NMR spectra show three characteristic doublets with broad $^{195}$Pt satellites due to the protons of the carbon atoms α to the Pt-coordinated atoms. The crude product resulting from the reaction between **d** and **[2(μ-Cl)]$_2$** contains a mixture of isomers and the $^1$H NMR spectrum of the crude product suggests a mixture of *trans*-*N*,*N* (**2d**) and *cis*-*N*,*N* (**2d′**) isomers. The clear separation of the distinctive doublets due to the protons of the carbon atoms α to the N–Pt-bonded atoms ($\delta$ = 9.82 ppm for **2d** and 9.35 ppm for **2d′**) allowed the relative ratio of the two isomers (85% of **2d** and 15% of **2d′**) to be determined. Recrystallisation of the crude reaction product from a dichloromethane/methanol solution allowed the separation of the *trans*-*N*,*N* isomer **2d**. Since this isomer is the only product formed from the reaction between **[2(μ-Cl)]$_2$** and **d** during the conventional heating routine, it can be inferred that **2d** and **2d′**, which is observed only when the reaction is performed using microwave irradiation, are the thermodynamic and kinetic products, respectively.

 © 2007 Wiley-VCH Verlag GmbH & Co. KGaA, Weinheim 

## Crystal Structure Analysis

The mononuclear complexes **1**·dmso, **2**·dmso, **1a**, **1c**, **1d** and **2d** were characterised by single-crystal X-ray diffraction analysis (Figures 1 and 2). Selected bond lengths and angles are listed in Tables 1 and 2.

Complexes **1**·dmso and **2**·dmso are formed when the dinuclear precursors are dissolved in dmso and a molecule of solvent replaces one chlorido ligand in a bridge-splitting reaction. The platinum atom in both **1**·dmso and **2**·dmso is located in a slightly distorted square-planar environment and is surrounded by the C and N atoms of the cyclometallated ligand with the coordinated solvent molecule positioned *trans* to the N atom. The Pt–S distances of 2.21–

Table 1. Selected bond lengths [Å] and angles [°] for complexes **1**·dmso and **2**·dmso.

| | **1·dmso** | **2·dmso** |
|---|---|---|
| Pt–C(11) | 2.001(4) | 2.006(3) |
| Pt–N | 2.055(3) | 2.064(3) |
| Pt–S | 2.2181(1) | 2.2074(1) |
| Pt–Cl | 2.4187(1) | 2.4032(1) |
| C(11)–Pt–N | 80.66(1) | 81.65(1) |
| C(11)–Pt–S | 98.95(1) | 98.01(9) |

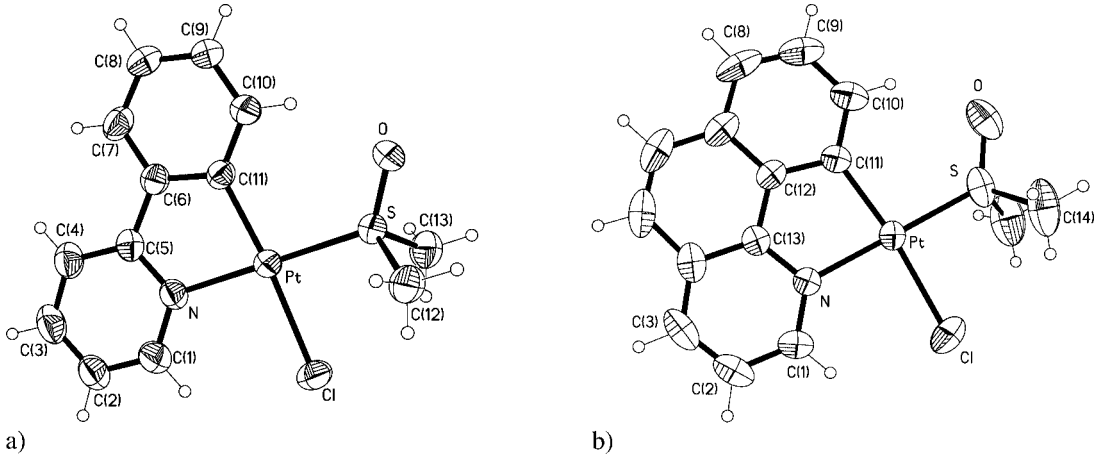


Figure 1. Molecular structures of **1**·dmso (a) and **2**·dmso (b).

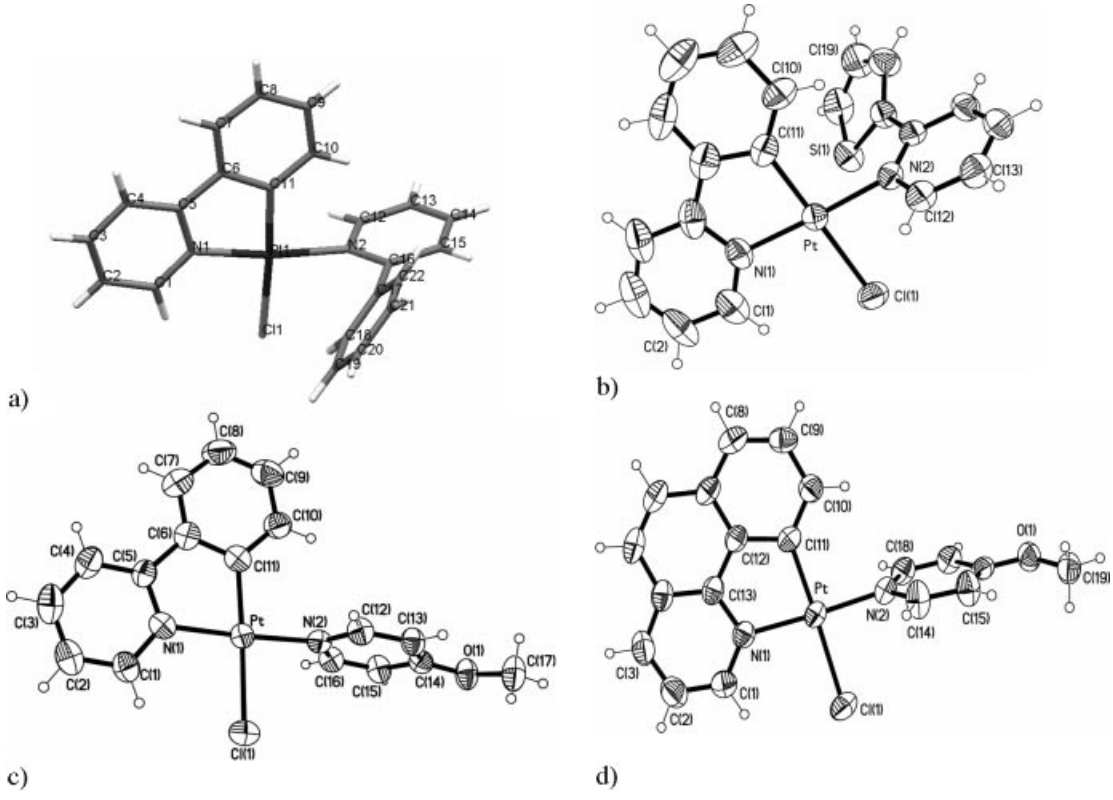


Figure 2. Molecular structures of **1a** (taken from ref.[10b]) (a), **1c** (b), **1d** (c) and **2d** (d).

 © 2007 Wiley-VCH Verlag GmbH & Co. KGaA, Weinheim 

Table 2. Selected bond lengths [Å] and angles [°] for complexes **1c**, **1d** and **2d**.

| | 1c | 1d | 2d |
|---|---|---|---|
| Pt–$C_{arom.}$ | 1.976(5), 1.981(4) | 1.968(5) | 1.981(2) |
| Pt–$N_{pyr.}$ | 2.015(4), 2.021(3) | 2.015(4) | 2.029(2) |
| Pt–$N_{base}$ | 2.027(3), 2.032(3) | 2.014(4) | 2.024(2) |
| Pt–Cl | 2.405(1), 2.424(2) | 2.413(1) | 2.390(7) |
| $C_{arom.}$–Pt–$N_{pyr.}$ | 81.53(2), 81.55(2) | 81.00(2) | 82.91(9) |
| $C_{arom.}$–Pt–$N_{base}$ | 95.02(2), 93.39(2) | 95.87(2) | 94.47(9) |
| $N_{pyr.}$–Pt–$N_{base}$ | 175.77(1), 170.49(1) | 176.77(1) | 176.93(7) |
| $C_{arom.}$–Pt–Cl | 177.95(1), 174.96(1) | 177.75(2) | 177.14(7) |
| $N_{pyr.}$–Pt–Cl | 97.36(1), 95.29(1) | 96.80(1) | 94.89(6) |
| $N_{base}$–Pt–Cl | 86.17(1), 90.28(1) | 86.34(1) | 87.78(6) |

2.22 Å are similar to those found in a search of the CSD (Cambridge Structural Database, Version 5.26) for a Pt–dmso fragment with the S atom *trans* to an N atom.

The molecular structure of **1a** has already been reported in both its monoclinic and triclinic polymorphs.[9a,10b] The crystals of **1a** isolated here were found to be the triclinic polymorph from a determination of their unit cell parameters. The molecular structures of **1c**, **1d** and **2d** reveal the formation of square-planar derivatives with the nitrogen ligands **c** and **d** bound *trans* to the nitrogen atom of the cyclometallated ligands **a** (**1c** and **1d**) and **b** (**2d**).

The dihedral angles between the two aromatic rings of the cyclometallated ligand **a** in **1c** and **1d** are 2.7(2)° and 3.2(1)° (two molecules of **1c** in the asymmetric unit) and 2.4(2)°, respectively, thereby showing a certain degree of planarity. The pyridyl ring of the $Pt^{II}$-coordinated ligands **c** and **d** is almost perpendicular to the coordination plane in all cases. The Pt–Cl bond lengths (2.39–2.42 Å) confirm the *trans* influence of the cyclometallated carbon atom, as already observed in complex **1a**.[9a] The shortest value (2.39 Å) is found in complex **2d**, where the higher electron delocalisation of the cycloplatinated ring, and its planarity, result in a stronger Pt–Cl bond than in **1d**.

Analysis of the molecular packing showed the presence of weak hydrogen bonds of the C–H···Cl type. The presence of an oxygen atom in the methoxy substituent of **d** results in the presence of additional intermolecular C–H···O interactions, with distances of 2.7–2.8 Å, in complexes **1d** and **2d**, as shown in Figure 3a, b.

## Conclusions

The results obtained from the present comparative investigations, summarised in Table 3, show that microwave irradiation is an easy, efficient and quick way to obtain mononuclear cycloplatinated complexes. Accurate simultaneous control of both temperature and irradiation power is, however, required for these sensitive cycloplatination reactions. The effective irradiation time is an important parameter to be considered when using a controlled microwave heating oven to avoid working without irradiation once the maximum set-up temperature is reached. We found that working with irradiation/external cooling cycles of a few minutes is the best way to control both parameters as it leads to less degradation of the $Pt^{II}$ starting materials in the synthesis of the dinuclear complexes **[1(μ-Cl)]$_2$** and **[2(μ-Cl)]$_2$** and the absence of decomposition in the case of the mononuclear derivatives **1a**, **1c**, **1d** and **2d**.

As the only difference between the conventional and microwave heating procedures in bridge-splitting reactions of the dinuclear compounds **[1(μ-Cl)]$_2$** and **[2(μ-Cl)]$_2$** is the reaction time, the nature of the obtained products must depend on both the electronic effects exerted by the cyclometallated fragment and the nucleophilicity of the ancillary nitrogen ligands. In particular, the bridge cleavage of **[2(μ-Cl)]$_2$** is only possible with ligand **d** (to yield the expected complex **2d**), whereas with **a** and **c**, which react easily with **[1(μ-Cl)]$_2$** to form the derivatives **1a** and **1c**, no complexes were isolated. This behaviour can be explained on the basis of the metal-chelated ring aromaticity and the π back-bonding of the cyclometallated ligand.[16] The higher electron delocalisation of the cycloplatinated ring formed by **b**, as evidenced by the stronger Pt–Cl bond in **2d** than in **1d** (Table 2), is responsible for the higher stability of the dinuclear complex **[2(μ-Cl)]$_2$**. Consequently, only the smallest and more nucleophilic ligand (**d**) is capable of reacting with **[2(μ-Cl)]$_2$** to give the corresponding mononuclear species.

The synthesis of **1a**, which is quantitative in 1 min, is a large step forward in the preparation of highly cytotoxic compounds. Furthermore, due to their structural similarities to known cytotoxic compounds, complexes **1c**, **1d** and **2d** should also be of interest for potential therapeutic applications. The availability of this class of complexes in only a

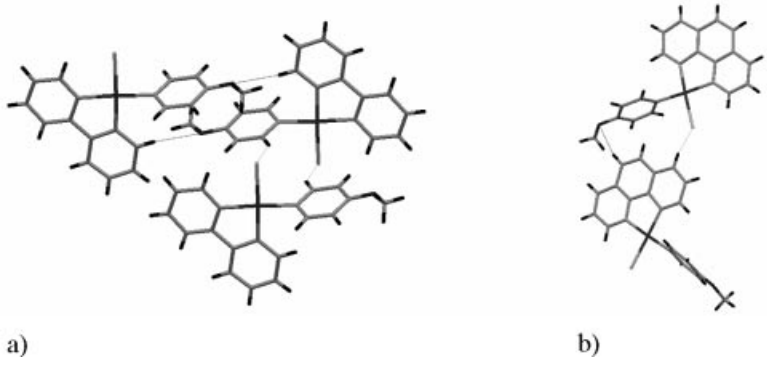


Figure 3. View of the intermolecular interactions in complexes **1d** (a) and **2d** (b).

 © 2007 Wiley-VCH Verlag GmbH & Co. KGaA, Weinheim 

Table 3. Comparative study between conventional and microwave-assisted syntheses.

| | Conventional heating | | Microwave-assisted | | | |
|---|---|---|---|---|---|---|
| | Reaction time | Yield [%] | Reaction time | Yield [%] | Power [W] | Max. temp. [°C] |
| **[1(μ-Cl)]$_2$** | 48 h | 95 | 3 min | 55 | 150 | 65 |
| **[2(μ-Cl)]$_2$** | 48 h | 75 | 3 min | 65 | 150 | 65 |
| **1a** | 24 h | 95 | 1 min | 99 | 250 | 110 |
| **1c** | 24 h | 88 | 6 min | 74 | 250 | 110 |
| **1d** | 24 h | 92 | 6 min | 94 | 250 | 110 |
| **2d** | 24 h | 98 | 6 min | 63 | 250 | 110 |

few minutes by microwave-assisted synthesis is a considerable advantage as it offers the possibility of a combinatorial approach to the preparation of families of compounds for large-scale screening studies.[17]

## Experimental Section

**General:** 2-Phenylpyridine, benzo[*h*]quinoline, 2-(2′-thienyl)pyridine, 4-methoxypyridine, potassium tetrachloroplatinate and all solvents were obtained from Aldrich and used as received. Microwave reactions were performed using a CEM Discover Synthesis Unit (CEM Corp., Matthews, NC). This instrument consists of a continuous focused microwave power delivery system with operator-selectable power output (0–300 W). The reactions were performed in glass vessels (capacity 50 mL) equipped with a condenser under atmospheric pressure. The temperature of the contents of the vessel was monitored using an optical fibre inserted through a specially designed glass-tube directly into the centre of the reaction vessel. The contents of the vessel were stirred by means of a rotating magnetic plate located below the floor of the microwave cavity and a Teflon-coated magnetic stir bar in the vessel. $^1$H NMR (500 MHz) spectra were recorded with a Bruker Avance 500 spectrometer with tetramethylsilane (TMS) as internal standard. Elemental analyses were performed with a Perkin–Elmer 2400 analyzer. The thermal behaviour was monitored with a Zeiss Axioscope polarizing microscope equipped with a Linkam CO 600 heating stage.

**[1(μ-Cl)]$_2$. Conventional Heating Synthesis:** An aqueous degassed solution (5 mL) of potassium tetrachloroplatinate (500 mg, 1.2 mmol) was added, under $N_2$, to a stirred degassed solution of 2-phenylpyridine (**a**; 185 mg, 1.2 mmol) in 2-ethoxyethanol (15 mL) and the reaction mixture heated to 80 °C for 48 h. After cooling in an ice bath, distilled water was added. The obtained yellow-green precipitate was filtered, washed with ethanol and dried under vacuum. Yield: 435 mg (95%). **Microwave-Assisted Synthesis:** The product was synthesised by treating ligand **a** (224 mg, 1.4 mmol) with potassium tetrachloroplatinate (600 mg, 1.4 mmol) in a degassed solution ($N_2$) of 2-ethoxyethanol/$H_2O$ (3:1, v/v, 20 mL) and irradiating this mixture with 150 W of microwave radiation. The temperature was prevented from rising above 65 °C by stopping the irradiation and quickly cooling the reaction mixture. Three irradiation/cooling cycles of 1 min were performed. Upon completion, the black $Pt^0$ precipitate was filtered off and distilled water added. The yellow-green precipitate obtained was washed with dichloromethane and dried under vacuum. Yield: 305 mg (55%). $C_{22}H_{16}Cl_2N_2Pt_2$ (769.44): calcd. C 34.34, H 2.10, N 3.64; found C 34.73, H 1.98, N 3.61. M.p. > 350 °C. NMR spectroscopic data are not available because **[1(μ-Cl)]$_2$** is only soluble in solvents such as dmso or dmf in which bridge splitting occurs upon dissolution to give complexes containing a solvent molecule as ancillary ligand (for example **1**·dmso).

**[2(μ-Cl)]$_2$. Conventional Heating Synthesis:** The cycloplatination reaction of benzo[*h*]quinoline (**b**) was carried out as described for the preparation of **[1(μ-Cl)]$_2$**. Yellow-green solid. Yield: 365 mg (75%). **Microwave-Assisted Synthesis:** Complex **[2(μ-Cl)]$_2$** was prepared as described for **[1(μ-Cl)]$_2$**. Yellow-green solid. Yield: 383 mg (65%). $C_{26}H_{16}Cl_2N_2Pt_2$ (817.48): calcd. C 38.20, H 1.97, N 3.43; found C 38.49, H 2.01, N 3.09. Mp > 350 °C. NMR spectroscopic data are not available for the same reason as for **[1(μ-Cl)]$_2$**.

**1·dmso:** Distilled water was added to a solution of **[1(μ-Cl)]$_2$** (380 mg, 0.5 mmol) in dmso (10 mL). The resulting yellow-green powder was filtered off, dried under vacuum and recrystallised from dichloromethane/ethanol to yield **1**·dmso quantitatively (455 mg). M.p. 208 °C. $^1$H NMR (500 MHz, $CDCl_3$, 25 °C): $\delta$ = 9.60 (d with broad $^{195}$Pt satellites, $^3J_{H,H}$ = 4.5, $^3J_{Pt,H}$ = 33 Hz, 1 H), 8.32 (d with broad $^{195}$Pt satellites, $^3J_{H,H}$ = 7.5, $^3J_{Pt,H}$ = 37.5 Hz, 1 H), 7.85 (t, $^3J_{H,H}$ = 8 Hz, 1 H), 7.71 (d, $^3J_{H,H}$ = 8 Hz, 1 H), 7.50 (d, $^3J_{H,H}$ = 7 Hz, 1 H), 7.26–7.16 (m, 3 H) 3.65 (s, 6 H) ppm. $^{13}$C NMR (500 MHz, $CDCl_3$, 25 °C): $\delta$ = 166.0, 150.1, 144.4, 140.4, 140.2, 134.1, 130.8, 125.3, 123.8, 121.9, 118.6, 47.3 ppm. $C_{13}H_{14}ClNOPtS$ (462.85): calcd. C 33.73, H 3.05, N 3.03; found C 33.95, H 2.94, N 3.25.

**2·dmso:** Distilled water was added to a solution of **[2(μ-Cl)]$_2$** (408 mg, 0.5 mmol) in dmso (10 mL). The resulting yellow-green powder was filtered off, dried under vacuum and recrystallised from dichloromethane/ethanol to yield **2**·dmso quantitatively (485 mg). M.p. 227 °C. $^1$H NMR (500 MHz, CDCl3, 25 °C): $\delta$ = 9.80 (d with broad $^{195}$Pt satellites, $^3J_{H,H}$ = 5.5, $^3J_{Pt,H}$ = 30.5 Hz, 1 H), 8.51 (d with broad $^{195}$Pt satellites, $^3J_{H,H}$ = 6.5, $^3J_{Pt,H}$ = 43.5 Hz, 1 H), 8.35 (d, $^3J_{H,H}$ = 8 Hz, 1 H), 7.81 (d, $^3J_{H,H}$ = 8.5 Hz, 1 H), 7.69 (d, $^3J_{H,H}$ = 8 Hz, 1 H), 7.70–7.56 (m, 3 H) 3.71 (s, 6 H) ppm. $^{13}$C NMR (500 MHz, $CDCl_3$, 25 °C): $\delta$ = 178.0, 154.8, 143.9, 133.7, 127.0, 126.6, 124.8, 124.5, 122.7, 121.5, 118.2, 117.5, 115.4, 47.3 ppm. $C_{15}H_{14}ClNOPtS$ (486.87): calcd. C 37.00, H 2.90, N 2.88; found C 36.76, H 1.94, N 3.01.

**1a. Conventional Heating Synthesis:** An aqueous degassed solution of potassium tetrachloroplatinate (500 mg, 1.2 mmol in 3 mL of $H_2O$) was added to a stirred degassed solution of **a** (372 mg, 2.4 mmol) in 2-ethoxyethanol (9 mL) under $N_2$ and the reaction mixture heated to 80 °C overnight. After cooling in an ice bath, distilled water was added and the yellow precipitate produced was filtered off, washed with cold ethanol and dried under vacuum. Further crystallisation from a dichloromethane/ethanol solution yielded yellow crystals of **1a**. Yield: 615 mg (95%). **Microwave-Assisted Synthesis:** The product was synthesised by treating ligand **a** (340 mg, 2.2 mmol) with potassium tetrachloroplatinate (400 mg, 1 mmol) in a degassed solution ($N_2$) of 2-ethoxyethanol/$H_2O$ (3:1, v/v, 20 mL) and irradiating this mixture with 250 W of microwave radiation for 1 min (maximum temperature reached: 110 °C). The reaction mixture was then cooled rapidly and the yellow precipitate formed was filtered off. Recrystallisation from dichloromethane/ethanol solution yielded **1a** quantitatively (591 mg). M.p. 225 °C.

 © 2007 Wiley-VCH Verlag GmbH & Co. KGaA, Weinheim 

$^1$H NMR (500 MHz, $CDCl_3$, 25 °C): $\delta$ = 9.60 (d with broad $^{195}$Pt satellites, $^3J_{H,H}$ = 5, $^3J_{Pt,H}$ = 34 Hz, 1 H), 9.23 (d with broad $^{195}$Pt satellites, $^3J_{H,H}$ = 5.5, $^3J_{Pt,H}$ = 39 Hz, 1 H), 8.08 (m, 2 H), 7.92 (td, $^3J_{H,H}$ = 8, $^3J_{H,H}$ = 2 Hz, 1 H), 7.67 (td, $^3J_{H,H}$ = 8, $^3J_{H,H}$ = 2 Hz, 1 H), 7.47 (d, $^3J_{H,H}$ = 8 Hz, 1 H) 7.35–7.26 (m, 5 H), 7.03 (td, $^3J_{H,H}$ = 7.5, $^3J_{H,H}$ = 1.5 Hz, 1 H), 6.96 (td, $^3J_{H,H}$ = 7.5, $^3J_{H,H}$ = 1.5 Hz, 1 H) 6.86 (td, $^3J_{H,H}$ = 7.5, $^3J_{H,H}$ = 1.5 Hz, 1 H), 6.17 (d with broad $^{195}$Pt satellites, $^3J_{H,H}$ = 6.5, $^3J_{Pt,H}$ = 39 Hz, 1 H) ppm. $^{13}$C NMR (500 MHz, $CDCl_3$, 25 °C): $\delta$ = 167.2, 162.3, 154.4, 151.2, 144.2, 141.1, 139.9, 138.4, 137.7, 130.82, 129.8, 129.6, 129.3, 127.8, 127.3, 123.8, 123.2, 123.1, 121.7, 118.0 ppm. $C_{22}H_{17}ClN_2Pt$ (539.91): calcd. C 48.94, H 3.17, N 5.19; found C 48.78, H 3.25, N 5.33.

**1c. Conventional Heating Synthesis:** 2-(2′-Thienyl)pyridine (**c**; 400 mg, 2.5 mmol) was added to a stirred solution of **[1(μ-Cl)]$_2$** (765 mg, 1 mmol) in 2-ethoxyethanol (15 mL) and the reaction mixture heated to 80 °C overnight. The solvent was then evaporated and the resulting solid was dissolved in dichloromethane (5 mL). Addition of ethanol (15 mL) caused the formation of a precipitate. Recrystallisation of this precipitate from dichloromethane/ethanol gave yellow crystals of **1c**. Yield: 955 mg (88%). **Microwave-Assisted Synthesis:** This product was synthesised by treating ligand **c** (27 mg, 0.17 mmol) with the chlorido-bridged dimer **[1(μ-Cl)]$_2$** (63 mg, 0.08 mmol) in degassed ($N_2$) 2-ethoxyethanol (15 mL) and irradiating this mixture at 250 W for 2 min (maximum temperature reached: 110 °C). After each irradiation step, the mixture was cooled in an ice bath and the irradiation cycle repeated three times. Distilled water was then added and the resulting yellow precipitate filtered off and recrystallised from a dichloromethane/ethanol solution. Yield: 66 mg (74%). M.p. 258 °C (dec). $^1$H NMR (500 MHz, $CDCl_3$, 25 °C): $\delta$ = 9.70 (d with broad $^{195}$Pt satellites, $^3J_{H,H}$ = 5, $^3J_{Pt,H}$ = 35 Hz, 1 H), 9.24 (d with broad $^{195}$Pt satellites, $^3J_{H,H}$ = 5, $^3J_{Pt,H}$ = 45 Hz, 1 H), 8.01 (dd, $^3J_{H,H}$ = 4, $^3J_{H,H}$ = 1.5 Hz, 1 H), 7.90–7.79 (m, 3 H) 7.62 (d, $^3J_{H,H}$ = 7.5 Hz, 1 H), 7.41 (dd, $^3J_{H,H}$ = 7.5, $^3J_{H,H}$ = 1 Hz, 1 H), 7.38 (dd, $^3J_{H,H}$ = 8, $^3J_{H,H}$ = 1 Hz, 1 H), 7.26 (m, 1 H), 7.14 (td, $^3J_{H,H}$ = 7, $^3J_{H,H}$ = 1.5 Hz, 1 H), 7.04 (td, $^3J_{H,H}$ = 7.5, $^3J_{H,H}$ = 1 Hz, 1 H), 6.98 (dd, $^3J_{H,H}$ = 5, $^3J_{H,H}$ = 4 Hz, 1 H), 6.87 (td, $^3J_{H,H}$ = 7.5, $^3J_{H,H}$ = 1 Hz, 1 H), 6.21 (d with broad $^{195}$Pt satellites, $^3J_{H,H}$ = 7, $^3J_{Pt,H}$ = 42.5 Hz, 1 H) ppm. $^{13}$C NMR (500 MHz, $CDCl_3$, 25 °C): $\delta$ = 167.4, 155.4, 154.6, 151.4, 144.1, 141.6, 138.7, 137.6, 130.7, 130.2, 130.1, 129.5, 129.4, 127.0, 126.3, 123.5, 123.4, 123.3, 121.9, 118.2 ppm. $C_{20}H_{15}ClN_2PtS$ (545.94): calcd. C 44.00, H 2.77, N 5.13; found C 44.20, H 3.05, N 5.25.

**1d. Conventional Heating Synthesis:** The preparation of **1d** was carried out as described for **1c**. Yellow solid. Yield: 903 mg (92%). **Microwave-Assisted Synthesis:** Complex **1d** was prepared as described for **1c** from **[1(μ-Cl)]$_2$** and 4-methoxypyridine (**d**). Yellow solid. Yield: 76 mg (94%). M.p. 245 °C. $^1$H NMR (500 MHz, $CDCl_3$, 25 °C): $\delta$ = 9.70 (d with broad $^{195}$Pt satellites, $^3J_{H,H}$ = 5.5, $^3J_{Pt,H}$ = 31 Hz, 1 H), 8.78 (d with broad $^{195}$Pt satellites, $^3J_{H,H}$ = 7, $^3J_{Pt,H}$ = 39.5 Hz, 2 H), 7.81 (td, $^3J_{H,H}$ = 8, $^3J_{H,H}$ = 1.5 Hz, 1 H), 7.64 (d, $^3J_{H,H}$ = 8 Hz, 1 H), 7.47 (dd, $^3J_{H,H}$ = 7.5, $^3J_{H,H}$ = 1.5 Hz, 1 H), 7.14–7.08 (m, 2 H), 6.99 (td, $^3J_{H,H}$ = 7.5, $^3J_{H,H}$ = 1.5 Hz, 1 H), 6.92 (d, $^3J_{H,H}$ = 7 Hz, 2 H), 6.44 (d with broad $^{195}$Pt satellites, $^3J_{H,H}$ = 6.5, $^3J_{Pt,H}$ = 41.5 Hz, 1 H), 3.95 (s, 3 H) ppm. $^{13}$C NMR (500 MHz, $CDCl_3$, 25 °C): $\delta$ = 171.9, 152.5, 149.1, 140.4, 130.7, 127.2, 125.4, 124.9, 124.6, 123.1, 122.9, 120.9, 119.9, 110.6, 55.45 ppm. $C_{17}H_{15}ClN_2OPt$ (493.94): calcd. C 41.35, H 3.06, N 5.67; found C 41.38, H 3.29, N 5.98.

**2d. Conventional Heating Synthesis:** Complex **2d** was prepared as described for **1c** from **[2(μ-Cl)]$_2$** and **d**. Yellow solid. Yield: 1 g (98%). **Microwave-Assisted Synthesis:** The reaction was performed as described for **1c**. The $^1$H NMR spectrum of the crude reaction product shows signals for an isomeric mixture (see text) containing **2d** (85%) and **2d′** (15%). Recrystallisation of the crude yellow solid from a dichloromethane/ethanol solution allowed the major thermodynamic isomer **2d** to be separated. Yield: 53 mg (63%). M.p. 268 °C (dec). $^1$H NMR (500 MHz, $CDCl_3$, 25 °C): $\delta$ = 9.82 (d with broad $^{195}$Pt satellites, $^3J_{H,H}$ = 5.5, $^3J_{Pt,H}$ = 35 Hz, 1 H), 8.90 (d with broad $^{195}$Pt satellites, $^3J_{H,H}$ = 7, $^3J_{Pt,H}$ = 37.5 Hz, 2 H), 8.26 (dd, $^3J_{H,H}$ = 8, $^3J_{H,H}$ = 1 Hz, 1 H), 7.74 (d, $^3J_{H,H}$ = 9 Hz, 1 H), 7.58 (d, $^3J_{H,H}$ = 7.5 Hz, 1 H), 7.55 (d, $^3J_{H,H}$ = 8.5 Hz, 1 H), 7.47 (dd, $^3J_{H,H}$ = 8, $^3J_{H,H}$ = 5.5 Hz, 1 H), 7.35 (t, $^3J_{H,H}$ = 7.5 Hz, 1 H), 6.95 (d, $^3J_{H,H}$ = 7 Hz, 2 H), 6.71 (d with broad $^{195}$Pt satellites, $^3J_{H,H}$ = 7.5, $^3J_{Pt,H}$ = 37.5 Hz, 1 H), 3.96 (s, 3 H) ppm. $^{13}$C NMR (500 MHz, $CDCl_3$, 25 °C): $\delta$ = 166.4, 156.9, 154.8, 150.3, 141.6, 139.8, 137.6, 133.6, 129.3, 129.1, 127.9, 126.4, 123.5, 121.6, 120.9, 112.0, 56.1 ppm. $C_{19}H_{15}ClN_2OPt$ (517.87): calcd. C 44.07, H 2.92, N 5.41; found C 44.38, H 3.09, N 5.71.

**X-ray Diffraction Studies:** X-ray data were collected with a Bruker-Nonius X8 Apex CCD area detector equipped with a graphite-monochromated Mo-$K_\alpha$ radiation source ($\lambda$ = 0.71073). Data reduction was performed using the SAINT programs; absorption corrections based on multiscan techniques were performed with SADABS.[18] All structures were solved by the Patterson method (SHELXS/L program in the SHELXTL-NT software package)[19] and refined by full-matrix least-squares based on $F^2$. All non-hydrogen atoms were refined anisotropically and hydrogen atoms were included as idealised atoms riding on the respective carbon atoms with C–H bond lengths appropriate to the carbon atom hybridisation. CCDC-646172 to -646176 contain the supplementary crystallographic data for this paper. These data can be obtained free of charge from The Cambridge Crystallographic Data Centre via www.ccdc.cam.ac.uk/data_request/cif.

**Crystal Data for 1·dmso:** $C_{13}H_{14}ClNOPtS$, $M_r$ = 462.85 g mol$^{-1}$, size 0.28 × 0.20 × 0.02 mm, monoclinic, space group $P2_1/c$, $a$ = 9.6290(8), $b$ = 18.9145(1), $c$ = 7.3691(6) Å, $\beta$ = 91.238(3)°, $F$(000) = 872, $V$ = 1341.80 (2) Å$^3$, $T$ = 298 K, $Z$ = 4, $D_{calcd.}$ = 2.291 g cm$^{-3}$, $\mu$ = 10.798 mm$^{-1}$, $2\theta_{max}$ = 56.6°. The structure was solved by the Patterson method and refined on $F^2$ to $R_1$ ($wR_2$) = 0.0278 (0.0609) using 2916 reflections with $I > 2\sigma(I)$. GOF = 1.056.

**Crystal Data for 2·dmso:** $C_{15}H_{14}ClNOPtS$, $M_r$ = 486.87 g mol$^{-1}$, size 0.32 × 0.16 × 0.16 mm, orthorhombic, space group $Pnma$, $a$ = 11.2795(2), $b$ = 6.9794(1), $c$ = 18.399(3) Å, $F$(000) = 920, $V$ = 1448.5 (4) Å$^3$, $T$ = 298 K, $Z$ = 4, $D_{calcd.}$ = 2.233 Mg m$^{-3}$, $\mu$ = 10.009 mm$^{-1}$, $2\theta_{max}$ = 56.6°. The structure was solved by the Patterson method and refined on $F^2$ to $R_1$ ($wR_2$) = 0.0178 (0.0359) using 1768 reflections with $I > 2\sigma(I)$. GOF = 1.072.

**Crystal Data for 1c:** $C_{20}H_{15}ClN_2PtS$, $M_r$ = 545.94 g mol$^{-1}$, size 0.32 × 0.28 × 0.16 mm, monoclinic, space group $P2_1/n$, $a$ = 17.962(2), $b$ = 9.0825(1), $c$ = 22.107(3) Å, $\beta$ = 92.111(2)°, $F$(000) = 2080, $V$ = 3604.1(8) Å$^3$, $T$ = 298 K, $Z$ = 8, $D_{calcd.}$ = 2.012 g cm$^{-3}$, $\mu$ = 8.055 mm$^{-1}$, $2\theta_{max}$ = 56.6°. The structure was solved by the Patterson method and refined on $F^2$ to $R_1$ ($wR_2$) 0.0297 (0.0685) using 7268 reflections with $I > 2\sigma(I)$. GOF = 1.029.

**Crystal Data for 1d·CHCl$_3$:** $C_{18}H_{16}Cl_4N_2OPt$, $M_r$ = 613.22 g mol$^{-1}$, size 0.40 × 0.20 × 0.02 mm, triclinic, space group $P\bar{1}$, $a$ = 9.3783(7), $b$ = 9.4050(7), $c$ = 13.2499(9) Å, $\alpha$ = 73.945(3)°, $\beta$ = 82.691(3)°, $\gamma$ = 63.670(2)°, $F$(000) = 584, $V$ = 1006.57(13) Å$^3$, $T$ = 298 K, $Z$ = 2, $D_{calcd.}$ = 2.023 g cm$^{-3}$, $\mu$ = 7.511 mm$^{-1}$, $2\theta_{max}$ = 50.7°. The structure was solved by the Patterson method and refined on $F^2$ to $R_1$ ($wR_2$) 0.0272 (0.0559) using 3192 reflections with $I > 2\sigma(I)$. GOF = 1.076.

 © 2007 Wiley-VCH Verlag GmbH & Co. KGaA, Weinheim 

**Crystal Data for 2d:** $C_{19}H_{15}ClN_2OPt$, $M_r$ = 517.87 g mol$^{-1}$, size 0.46 × 0.40 × 0.20 mm, monoclinic, space group $P2_1/n$, $a$ = 9.1327(13), $b$ = 10.1178(14), $c$ = 18.010(3) Å, $\beta$ = 90.165(6)°, $F(000)$ = 984, $V$ = 1664.2(4) Å$^3$, $T$ = 298 K, $Z$ = 4, $D_{calcd.}$ = 2.067 g cm$^{-3}$, $\mu$ = 8.599 mm$^{-1}$, $2\theta_{max}$ = 61.0°, The structure was solved by the Patterson method and refined on $F^2$ to $R_1$ ($wR_2$) 0.0203 (0.0419) using 4244 reflections with $I > 2\sigma(I)$. GOF = 1.032.

**Supporting Information** (see footnote on the first page of this article): $^1$H and $^{13}$C NMR spectra are shown in Figures S1–S6.

## Acknowledgments

Financial support from the Ministero dell'Istruzione, dell'Università e della Ricerca (MiUR) through the Centro di Eccellenza CEMIF.CAL (CLAB01TYEF) and FIRB (RBNE01P4JF) is gratefully acknowledged.

[1] a) M. D. Hall, T. W. Hambley, *Coord. Chem. Rev.* **2002**, *232*, 49–67; b) I. Kostova, *Recent Pat. Anti-Cancer Drug Discovery* **2006**, *1*, 1–22.
[2] a) M. Maestri, V. Balzani, C. Deuschel-Cornioley, A. Von Zelewsky, in *Advances in Photochemistry* (Eds.: D. Volman, G. Hammond, D. Neckers), John Wiley & Sons, New York, **1992**, vol. 17, pp. 1–68; b) M. Hissler, J. E. McGarrah, W. B. Connick, D. K. Geiger, S. D. Cummings, R. Eisenberg, *Coord. Chem. Rev.* **2000**, *208*, 115–137; c) B. L. Yin, F. Niemeyer, J. A. G. Williams, J. Jiang, A. Boucekkine, L. Toupet, H. Le Bozec, V. Guerchais, *Inorg. Chem.* **2006**, *45*, 8584–8596.
[3] a) M. Ghedini, D. Pucci, A. Crispini, G. Barberio, *Organometallics* **1999**, *18*, 2116–2124; b) C. Damm, G. Israel, T. Hegmann, C. Tschierske, *J. Mater. Chem.* **2006**, *16*, 1808–1816.
[4] a) A. D. Ryabov, *Chem. Rev.* **1990**, *90*, 403–424; b) K. Praefcke, B. Bilgin, J. Pickardt, M. Barowski, *Chem. Ber.* **1994**, *127*, 1543–1545; c) P. Steenwinkel, R. A. Gossage, G. van Koten, *Chem. Eur. J.* **1998**, *4*, 759–762; d) G. W. V. Cave, F. P. Fanizzi, R. J. Deeth, W. Errington, J. P. Rourke, *Organometallics* **2000**, *19*, 1355–1364.
[5] C. O. Kappe, *Angew. Chem. Int. Ed.* **2004**, *43*, 6250–6284.
[6] N. E. Leadbeater, *Chem. Commun.* **2005**, 2881–2902.
[7] a) T. Matsumura-Inoue, Y. Yamamoto, N. Yoshikawa, M. Terashima, Y. Yoshida, A. Fujii, K. Yoshino, *Opt. Mater.* **2004**, *27*, 187–191; b) N. Yoshikawa, S. Yamabe, N. Kanehisa, Y. Kai, H. Takashima, K. Tsukahara, *Eur. J. Inorg. Chem.* **2007**, 1911–1919.
[8] a) X. M. Xiao, J. Sakamoto, M. Tanabe, S. Yamazaki, S. Yamabe, T. Matsumura-Inoue, *J. Electroanal. Chem.* **2002**, *527*, 33–40; b) H. J. Bolink, L. Cappelli, E. Coronado, M. Gratzel, M. K. Nazeeruddin, *J. Am. Chem. Soc.* **2006**, *128*, 46–47; c) D. Martineau, M. Beley, P. C. Gros, S. Cazzanti, S. Caramori, C. A. Bignozzi, *Inorg. Chem.* **2007**, *46*, 2272–2277.
[9] a) H. Konno, Y. Sasaki, *Chem. Lett.* **2003**, *32*, 252–253; b) K. Saito, N. Matsusue, H. Kanno, Y. Hamada, H. Takahashi, T. Matsumura, *Jpn. J. Appl. Phys.* **2004**, 2733–2734.
[10] a) I. M. El-Mehasseb, M. Kodaka, T. Okada, T. Tomohiro, K. Okamoto, H. Okuno, *J. Inorg. Biochem.* **2001**, *84*, 157–158; b) T. Okada, I. M. El-Mehasseb, M. Kodaka, T. Tomohiro, K. Okamoto, H. Okuno, *J. Med. Chem.* **2001**, *44*, 4661–4667.
[11] J. Brooks, Y. Babayan, S. Lamansky, P. I. Djurovich, I. Tsyba, R. Bau, M. E. Thompson, *Inorg. Chem.* **2002**, *41*, 3055–3066.
[12] M. M. Mdleleni, J. S. Bridgewater, P. C. Watts Ford, *Inorg. Chem.* **1995**, *34*, 2334–2342.
[13] D. S. Black, G. B. Deacon, G. L. Edwards, *Aust. J. Chem.* **1994**, *47*, 217–227.
[14] N. M. Shavaleev, H. Adams, J. Best, R. Edge, S. Navaratnam, J. A. Weinstein, *Inorg. Chem.* **2006**, *45*, 9410–9415.
[15] M. Lersch, A. Krivokapic, M. Tilset, *Organometallics* **2007**, *26*, 1581–1587.
[16] A. Crispini, M. Ghedini, *J. Chem. Soc. Dalton Trans.* **1997**, 75–80.
[17] S. van Zutphen, E. A. Stone, S. van Rijt, M. S. Robillard, G. A. van der Marel, H. S. Overkleeft, H. den Dulk, J. Brouwer, J. Reedijk, *J. Inorg. Biochem.* **2005**, *99*, 2032–2038.
[18] *SMART*, *SAINT* and *SADABS*, Bruker AXS, Inc., Madison, WI, **1997**.
[19] *SHELXTL-NT – Crystal Structure Analysis Package*, version 5.1, Bruker AXS Inc., Madison, WI, USA, **1999**.

Received: June 20, 2007
Published Online: September 14, 2007

 © 2007 Wiley-VCH Verlag GmbH & Co. KGaA, Weinheim 

DOI: 10.1002/ejic.200700643

# 2-Chloro-1,3,2-diazaphospholenes – A Crystal Structural Study

**Sebastian Burck,[a] Dietrich Gudat,*[a] Kalle Nättinen,[b] Martin Nieger,[c] Mark Niemeyer,[a] and Dirk Schmid[a]**

**Keywords:** Phosphanes / Halides / X-ray diffraction / Substituent effects / Structure correlation

A series of 2-chloro-1,3,2-diazaphospholenes with different substitution patterns has been prepared from 1,4-diazabutadienes according to a general synthetic methodology. Subsequent chloride abstraction with Lewis acids affords the corresponding 1,3,2-diazaphospholenium salts. All products have been characterised spectroscopically and by single-crystal X-ray diffraction studies. A detailed analysis of trends in the structural parameters supports the interpretation that the unusual P–Cl bond lengthening in the diazaphospholenes is attributable to n(N)/σ*(P-Cl) hyperconjugation.
(© Wiley-VCH Verlag GmbH & Co. KGaA, 69451 Weinheim, Germany, 2007)

## Introduction

*P*-Functionalised 1,3,2-diazaphospholenes (**I**) are representatives of a class of N-heterocyclic phosphanes that have recently gained interest because of their unique reactivity. In particular, P–H-substituted compounds (**I**; X = H) are selective hydride-transfer reagents that allow reductive hydrogenation of element halides as well as aldehydes and aryl ketones,[1] and phosphanyl derivatives (**I**; X = $PR'_2$) react with alkenes and alkynes by diphosphination to give novel unsymmetrical 1,2-bisphosphanes.[2] This unique reactivity has, in both cases, been explained by a weakening and concomitant ionic polarisation of the P–X bonds which can be expressed in terms of bond/no-bond resonance between the canonical structures **I′** and **I′′** (Scheme 1).[3] The high weight of the ionic canonical structure **I′′** is intimately connected with the exceptional stability of the corresponding phosphenium ions **II**,[4] which are isoelectronic with imidazoyl carbenes **III**[5] and are stabilised by similar electronic factors.

Another type of functional 1,3,2-diazaphospholenes, namely *P*-chloro-substituted compounds (**I**; X = Cl),[4,6,7] are of interest not only from a synthetic point of view as precursors for the cations **II** and the aforementioned P–H and P-phosphanyl derivatives but they also provide evidence for the weakening and enhanced ionic polarisation of the exocyclic P–Cl bonds.[3] Despite the high intrinsic polarity of these bonds, these phenomena still exert a visible effect on the chemical reactivity and have, for example, been considered as crucial for the use of *P*-chlorodiazaphospholenes as organocatalysts in the P–C cross-coupling between alkyl chlorides and trimethylsilyl diphenylphosphane.[8] The P–Cl bond lengthening is also significant from a structural point of view and it has been argued that its occurrence is attributable to a high degree of aromatic stabilisation in the heterocyclic ring, which induces a concomitant spontaneous dissociation of the P–Cl bond.[4,7] Although this interpretation was subsequently discredited,[3] a precise analysis of the bonding situation in *P*-chlorodiazaphospholenes is still needed.

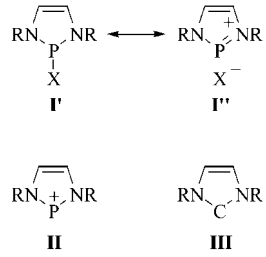


Scheme 1.

During our investigations of the chemistry of N-heterocyclic phosphanes we have developed a general synthetic method for the preparation of 2-chloro-1,3,2-diazaphospholenes and 1,3,2-diazaphospholenium ions with a wide range of substituent patterns.[1] In this work we will give a full account of this synthetic work, and we will report on the interpretation of trends in structural parameters which were obtained from X-ray diffraction studies on a comprehensive series of these compounds.

## Results and Discussion

### Syntheses and Spectroscopic Studies

Known synthetic routes to 2-chloro-1,3,2-diazaphospholenes (**I**; X = Cl) include base-induced condensations of

[a] Institut für Anorganische Chemie, Universität Stuttgart, Pfaffenwaldring 55, 70550 Stuttgart, Germany
Fax: +49-711-685-64241
E-mail: gudat@iac.uni-stuttgart.de
[b] VTT Technical Research Centre of Finland, P. O. Box 1300, Tampere, Finland
[c] Laboratory of Inorganic Chemistry, University of Helsinki, A. I. Virtasen aukio 1, Helsinki, Finland

 © 2007 Wiley-VCH Verlag GmbH & Co. KGaA, Weinheim 

$PCl_3$ with 1,4-diazabutadienes,[6] salt-elimination reactions of $PCl_3$ with 1,4-diazabutadienide dianions[7] or metathesis reactions of $PCl_3$ with 1,3,2-diazasiloles.[4] The products can be converted into diazaphospholenium salts by subsequent treatment with Lewis acids such as $AlCl_3$, $GaCl_3$, $SbCl_5$ or $Me_3SiOTf$.[3,4,9] It was shown recently that triiodide or pentachlorostannate(IV) salts of cations **II** are also accessible in one step by a redox reaction between a diazabutadiene and $PI_3$ or a mixture of $PCl_3$ and $SnCl_2$, respectively.[10] The limitations of the existing methods are that their application may be restricted to the synthesis of heterocycles with specific substitution patterns, the yields of products may be low owing to the occurrence of side reactions or difficulties in purifying the products or intermediates, or that the possible redox activity of counter anions such as $I_3^-$ or $SnCl_5^-$ may limit the use of the product in further transformations. In order to circumvent these restrictions we have developed a simple protocol for the preparation of 2-chloro-1,3,2-diazaphospholenes starting from *N*-arylated 1,4-diazabutadienes.[1] We demonstrate here that the same procedure is also applicable for the synthesis of *N*-alkylated and *C*-alkylated heterocyclic rings.

The novel *P*-chlorodiazaphospholenes **3b**,**h** and **3d**–**f** are accessible in a similar way as the previously reported derivatives **3a**,**c**,**g**[1] in a cascade reaction involving reduction of the readily available 1,4-diazabutadienes **1a**–**h** with excess lithium, quenching the resulting dianions with triethylamine hydrochloride at –78 °C, and condensation of the products formed with $PCl_3$ at the same temperature. All subsequent reaction steps can be carried out in a one-pot procedure without isolation of any intermediates. The triethylamine introduced to protonate the diazadienide dianions is reused to scavenge the hydrogen chloride liberated in the last step. As reported earlier,[9,11] protonation of the diazadienide dianions yields either α-aminoaldimines **2a**–**c**,**g**,**h** or 2,3-diamino-2-butenes **2d**–**f** depending on whether the central carbon atoms in the dianions bear hydrogen or alkyl substituents, respectively; both types of intermediates can be isolated as stable compounds if desired. The 2-chloro-1,3,2-diazaphospholenes **3b**,**d**–**f**,**h** were isolated as off-white to orange, moderately moisture-sensitive solids in good to excellent yields of 75–92% after work up. Reports of 4,5-dialkylated 1,3,2-diazaphospholenes are rare, although some derivatives have been obtained by condensation of a diaminoethene with substituted phosphorus dihalides according to a similar reaction to that reported here.[12]

Compounds **3b**,**c**,**g** were converted into the 1,3,2-diazaphospholenium salts **4b**,**c**,**g** by treatment with $Me_3SiOTf$ by analogy to a previously reported method,[3] In a similar manner, **5f** was obtained by treatment of **3f** with $GaCl_3$.[13] All phosphenium salts were isolated after work-up as air- and moisture-sensitive powders in more than 90% yield.

All phosphorus heterocycles prepared were characterised by analytical data and spectroscopic techniques. The NMR spectroscopic data of both 2-chloro-1,3,2-diazaphospholenes and phosphenium salts are unremarkable and are similar to known literature data;[1,3,4,7,10] a discussion of trends in chemical shifts (including $^{35}Cl$ and $^{15}N$ NMR spectroscopic data) has been given elsewhere[3] and is not repeated here. Methylation in the 4,5-positions of the diazaphospholene ring induces a deshielding of the $^{31}P$ NMR signals of **3d**,**e** by some 15 ppm with respect to **3a**,**c**. As expected, both the $^{31}P$ and the $^{13}C$ NMR signals of the ring carbon atoms in the 1,3,2-diazaphospholenium salts **4b**,**c** and **5f** are deshielded with respect to the appropriate signals in the neutral precursors **3b**,**c**,**f**. The salt **4b** exhibits the largest $^{31}P$ NMR shift for a 1,3,2-diazaphospholenium cation observed so far ($\delta_{^{31}P}$ = 209.4 ppm).

## Crystal Structure Studies

Suitable crystals for single-crystal X-ray diffraction studies of the 1,3,2-diazaphospholenes **3b**–**h** and the 1,3,2-diazaphospholenium salts **4b**,**c**,**g** and **5f** were obtained by crystallisation of appropriate solutions at low temperature (see Scheme 2 and Exp. Sect. for further details). The salt **5f** crystallised as a solvate with one molecule of $CH_2Cl_2$ per formula unit.

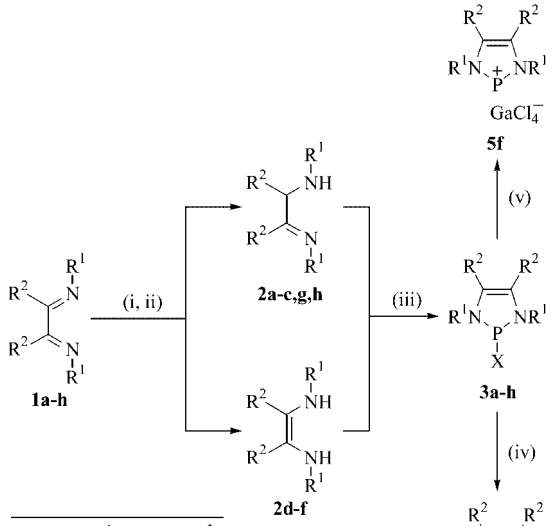


| | $R^1$ | $R^2$ |
|---|---|---|
| **1a-4a** | Mes | H |
| **1b-4b** | DMP | H |
| **1c-4c** | DIPP | H |
| **1d-3d** | Mes | Me |
| **1e-3e** | DIPP | Me |
| **1f-5f** | 2-*t*Bu$C_6H_4$ | Me |
| **1g-3g** | *t*Bu | H |
| **1h-3h** | Cy | H |

Scheme 2. Synthesis of 2-chloro-1,3,2-diazaphospholenes and 1,3,2-diazaphospholenium salts; (i) 2 Li; (ii) 2 $HNEt_3Cl$, –78 °C; (iii) $PCl_3$, –78 °C; (iv) $Me_3SiOTf$, –78 °C/–$Me_3SiCl$; (v) $GaCl_3$. (Mes = 2,4,6-$Me_3C_6H_2$, DMP = 2,6-$Me_2C_6H_3$, DIPP = 2,6-$iPr_2C_6H_3$).

The molecular structures of the *P*-chlorodiazaphospholene **3f** and the tetrachlorogallate salt **5f** are shown in Figures 1 and 2, respectively. The *tert*-butyl moieties in both

 © 2007 Wiley-VCH Verlag GmbH & Co. KGaA, Weinheim 

*N*-aryl substituents of **3f** are located on the same side of the diazaphospholene ring *trans* to the chlorine substituent, thereby suggesting that the direct steric interaction between the *tert*-butyl groups is lower than the repulsion between substituents at adjacent ring atoms. Interestingly, the arrangement of the *tert*-butyl groups in the cation of salt **5f** remains unchanged. As the distance between the phosphorus and the closest chlorine atom in the anion (3.75 Å) is close to the sum of the van der Waals radii (thus ruling out any substantial intermolecular interactions) and both nitrogen atoms still display planar coordination geometries [sum of bond angles of 359.4(6)° for N2 and 359.7(6)° for N5] it can be concluded that the steric strain between the bulky *N*-aryl substituents is negligible. The preference for the observed pseudo-$C_s$-symmetric conformation over a $C_2$-like conformation with *tert*-butyl moieties on opposite sides of the diazaphospholene ring is presumably due to the fact that it facilitates a closer stacking of molecules in the crystal.

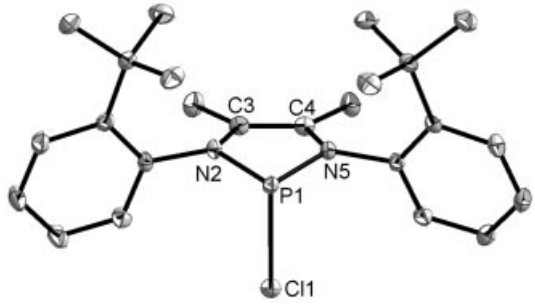


Figure 1. Molecular structure of **3f**. Thermal ellipsoids are drawn at the 50% probability level and H atoms have been omitted for clarity.

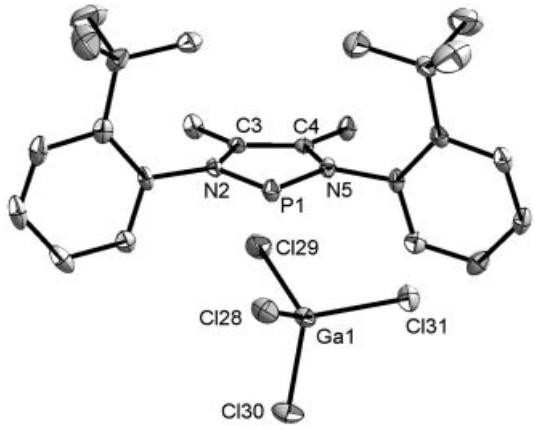


Figure 2. Molecular structure of **5f**. Thermal ellipsoids are drawn at the 50% probability level and H atoms have been omitted for clarity.

Selected bond lengths and angles of all neutral *P*-chlorodiazaphospholenes and the cations of phosphenium salts are summarised in Table 1 together with the previously reported structural data for **3a**,**g** and **4a**[3] for comparison. The five-membered rings of all *P*-chlorodiazaphospholenes feature a similar flat envelope conformation to that already found for **3a**,**g**,[3] while the rings of the cations display no significant deviations from planarity. All molecules exhibit only insignificant deviations between the two crystallographically independent P-N2/N5 and C3/4-N2/5 distances.

The endocyclic P–N and C–C bond lengths in all studied 2-chloro-1,3,2-diazaphospholenes are similar and match the values for **3a** and **3g**. The C–N bonds in **3b** and **3h** are likewise similar to those of **3a** and **3g** while the C-methylated derivatives **3d**–**f** display a small (1–2 pm) yet crystallographically significant bond lengthening. The most important variation is found for the exocyclic P–Cl bond lengths, which range from 2.243(1) Å in **3c** to 2.692(4) Å in **3g**. All distances are thus considerably longer than standard P–Cl bonds in diaminochlorophosphanes (2.13 ± 0.06 Å[14]), although the bond length in **3c**, which is the shortest P–Cl bond in a 2-chloro-1,3,2-diazaphospholene reported to date, comes quite close to the normal range. A comparison between compounds with N-Mes (**3a**,**d**) and N-DIPP (**3c**,**e**) substituents reveals that the P–Cl bonds in the latter are 3–8 pm shorter, although the reason for this effect is not obvious. The longest P–Cl bonds are found for the *N*-alkyl-substituted compounds **3g**,**h**.

Table 1. Selected bond lengths [Å] and angles [°] for the 2-chloro-1,3,2-diazaphospholenes **3a**–**h** and the cations of the 1,3,2-diazaphospholenium salts **4a**–**c**, **4g**, and **5f**.

| | $R^1$ | $R^2$ | P1–Cl1 | P1–N2 | P1–N5 | N2–C3 | N5–C4 | C3–C4 | N2–P1–N5 |
|---|---|---|---|---|---|---|---|---|---|
| **3a**[a] | Mes | H | 2.324(1) | 1.673(1) | 1.675(1) | 1.406(2) | 1.402(2) | 1.338(2) | 89.7(1) |
| **3b** | DMP | H | 2.362(1) | 1.678(2) | 1.675(2) | 1.400(2) | 1.398(2) | 1.335(3) | 89.3(1) |
| **3c** | DIPP | H | 2.243(1) | 1.684(1) | 1.679(1) | 1.408(2) | 1.402(2) | 1.333(2) | 89.4(1) |
| **3d** | Mes | Me | 2.354(1) | 1.664(2) | 1.673(1) | 1.427(2) | 1.430(2) | 1.331(2) | 89.9(1) |
| **3e** | DIPP | Me | 2.325(1) | 1.679(1) | 1.674(1) | 1.425(2) | 1.423(2) | 1.345(2) | 89.8(1) |
| **3f** | 2-*t*Bu-$C_6H_4$ | Me | 2.331(1) | 1.671(1) | 1.669(1) | 1.427(2) | 1.422(2) | 1.344(2) | 89.5(1) |
| **3g**[a] | *t*Bu | H | 2.692(4) | 1.663(1) | 1.665(1) | 1.391(1) | 1.391(1) | 1.349(1) | 90.6(1) |
| **3h** | Cy | H | 2.567(1) | 1.671(2) | 1.669(2) | 1.403(3) | 1.401(3) | 1.339(3) | 90.2(1) |
| **4a**[a] | Mes | H | – | 1.666(2) | 1.671(1) | 1.374(2) | 1.378(2) | 1.351(2) | 89.6(1) |
| **4b** | DMP | H | – | 1.664(1) | 1.664(1) | 1.373(2) | 1.373(2) | 1.351(3) | 89.5(1) |
| **4c** | DIPP | H | – | 1.677(1) | 1.675(1) | 1.365(2) | 1.371(2) | 1.356(2) | 88.9(1) |
| **4g** | *t*Bu | H | – | 1.658(2) | 1.660(2) | 1.365(3) | 1.368(3) | 1.349(4) | 90.6(1) |
| **5f**[b] | 2-*t*Bu-$C_6H_4$ | Me | – | 1.663(2) | 1.674(2) | 1.386(3) | 1.372(3) | 1.379(3) | 89.1(1) |

[a] Data from ref.[3] [b] Different crystallographic numbering scheme.

 © 2007 Wiley-VCH Verlag GmbH & Co. KGaA, Weinheim 

The P–N bond lengths in the cations of the phosphenium salts **4a**–**c**,**g** and **5f** match the values in **3a**–**h** closely, whereas the adjacent C–N bonds are approximately 3 pm longer than in the neutral compounds. The C–C bonds in the cations are also longer than in **3a**–**h**, although the difference in this case is less pronounced (approx. 1 pm) and on the verge of being significant when compared with the magnitude of the estimated standard deviations (see data in Table 1). The cation of **5f** is an exception and displays a significant lengthening of the C–C bond length, which is possibly influenced by the presence of methyl substituents at both ring carbon atoms. Apart from this effect, the variation of bond lengths in the phosphenium cations shows no clear connection with the changes in the substituent pattern.

The existence of a series of crystal structure analyses of similar compounds stimulated us to attempt a discussion of common trends in the sense of a structure correlation. This principle, which was coined by Bürgi and Dunitz,[15] states that structural changes that occur during a chemical reaction can be manifested in the ground-state structure as deviations of bond lengths and angles from "normal values" along the reaction coordinate. In the case of *P*-chlorodiazaphospholenes the extraordinary P–Cl bond lengthening, which was first reported for **3g**, can be interpreted as a consequence of spontaneous bond heterolysis that is energetically driven by the aromatisation of the cyclic phosphenium cation fragment.[4,7] Given the validity of this hypothesis, the application of the structure-correlation principle implies that a comparison of the crystal structure data of all compounds included in this study might reveal a systematic correlation between the P–Cl bond lengthening, the lengthening of the C–C double bond, and a concomitant shortening of the C–N and P–N single bonds, respectively.

Inspection of a plot of the P–Cl versus average P–N distances for the diazaphospholenes **3a**–**h** (Figure 3) reveals that the P–Cl bond lengthening indeed appears to coincide with a general shortening of the P–N bonds. A linear regression analysis reveals that this correlation is not particularly strong, and the magnitude of the correlation coefficient ($r$ = 0.78) implies the presence of some scattering which suggests that additional factors also have a major impact on both bond lengths. If one considers that the individual compounds are not isostructural but crystallise in different space groups, and thus exhibit different types of crystal packing, the observed scattering is presumably due, at least in part, to variations in intermolecular interactions (the validity of this assumption is substantiated by the observed difference in P–Cl bond lengths between pure **3g** and its toluene solvate[3]). Even though an analysis of the crystallographic data of all diaminochlorophosphanes of the type $(R_2N)_2PCl$ (except **3a**,**g**) listed in the CSD data base reveals a similar relation between the changes in P–N and P–Cl bond lengths, the two regression lines deviate substantially from each other (Figure 3). In principle, this finding underlines, in a quantitative way, the previously mentioned hypothesis of the P–Cl bond in the N-heterocyclic derivatives **3a**–**h** being much "softer" (i.e. more easily polarisable) than in diaminochlorophosphanes in general.

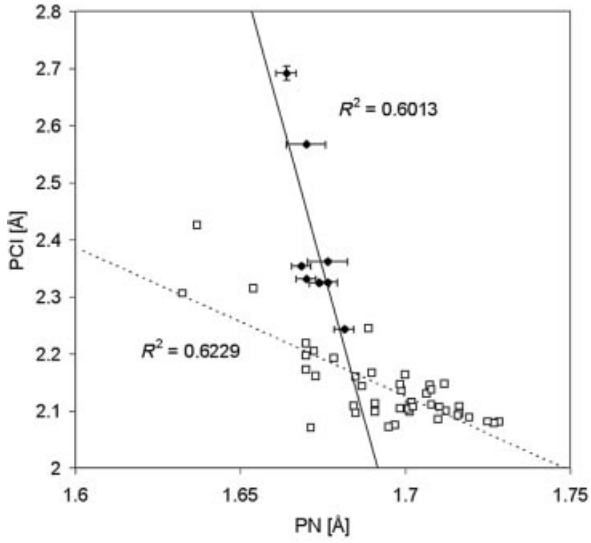


Figure 3. Plot of P–Cl distances [Å] vs. average P–N distances [Å] for **3a**–**h** (diamonds) and for all $(R_2N)_2PCl$ compounds (except **3a**,**g**) listed in the CSD data base (open squares). The solid and dashed lines represent the result of linear regression analyses. Error bars at the data points for **3a**–**h** denote a range of ±3σ, where σ is the estimated standard deviation. $R^2$ is the square of the correlation coefficient in the regression analysis.

An analysis of the trends in endocyclic P–N, N–C and C–C bond lengths in the diazaphospholenes **3a**–**h** and the salts **4a**–**c**,**g** and **5f** shows that the observed changes are essentially uncorrelated. A regression analysis of the changes in P–N and C–N distances for all compounds (Figure 4) gave a statistical correlation coefficient ($r$ = 0.41) which suggests no significant connection between both parameters. Furthermore, a positive slope for the computed regression curve indicates parallel trends of the lengths of

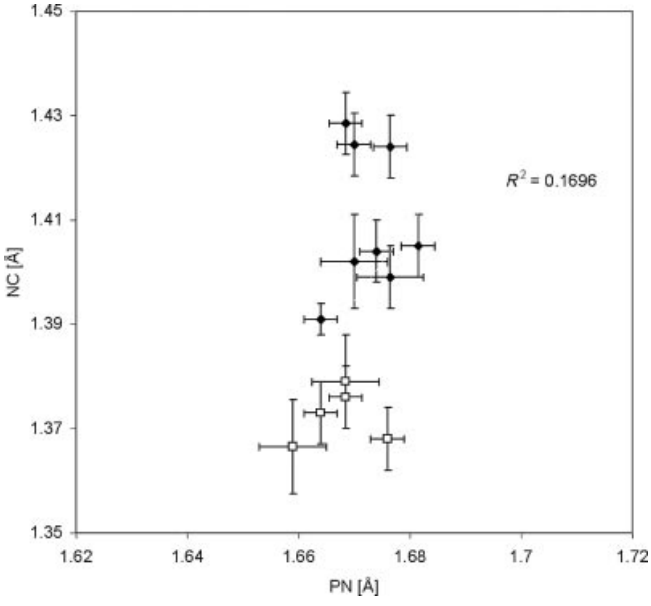


Figure 4. Plot of the average P–N distances [Å] vs. average C–N distances [Å] of **3a**–**h** (diamonds) and **4a**–**c**, **5f** (open squares). Error bars at each data point denote a range of ±3σ, where σ is the estimated standard deviation.

 © 2007 Wiley-VCH Verlag GmbH & Co. KGaA, Weinheim 

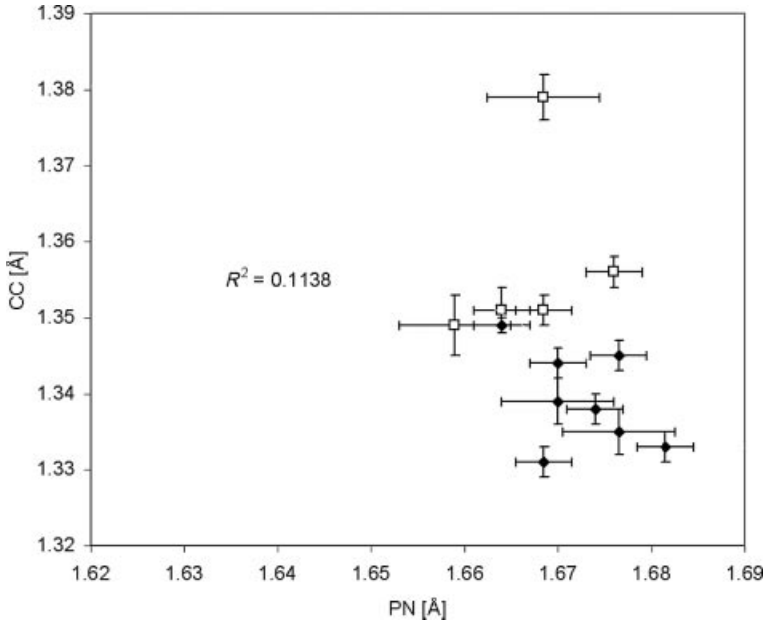


Figure 5. Plot of the average P–N distances [Å] vs. C–C distances [Å] of **3a**–**h** (diamonds) and **4a**–**c**, **5f** (open squares). Error bars at each data point denote a range of ±3σ, where σ is the estimated standard deviation.

both types of bonds, which is hardly compatible with a connection between P–Cl bond dissociation and increasing aromaticity in the ring.[4] A regression analysis of the connection between changes in P–N and C–C distances (Figure 5) indicated a statistically still weaker correlation ($r$ = 0.34), the physical interpretation of which is further complicated by the fact that the observed differences in C–C bond lengths are rather small when compared with the estimated standard deviations of the experimental data. Further regression analyses which included only data for neutral diazaphospholenes, or involved correlations between P–Cl and C–N/C–C bond lengths, gave similar or even lower values for the correlation coefficients.

On the whole, the regression analyses performed suggest a weak statistical correlation between P–Cl and P–N distances in the diazaphospholenes **3a**–**h**, whereas the variations in the endocyclic N–C and C–C bonds appear to be fairly uncorrelated. In contrast, inspection of Figures 3, 4 and 5 suggests that the data for the neutral compounds **3a**–**h** and the salts **4a**–**c**,**g** and **5f** lie in different regions of the scatter plots that are more or less well separated owing to systematic deviations in C–N and (less pronounced) C–C bond lengths between both types of compounds. All these features are very well compatible with the explanation of the bond lengthening in *P*-chlorodiazaphospholenes being due to n(N)/σ*(P-Cl) hyperconjugation, which has also been derived from earlier computational and experimental studies,[3] but do not support the interpretation as beginning P–Cl dissociation driven by increasing aromatic character of the diazaphospholene ring.

## Conclusions

We have shown that the previously reported one-pot route to 1,3,2-diazaphospholenes by reduction/protonation of 1,4-diazadienes and subsequent condensation with phosphorus trichloride offers a generally applicable and economic access to 2-chloro-1,3,2-diazaphospholenes with a wide range of substituents at both the ring nitrogen and carbon atoms. All products were obtained in high yields and purity and are suitable starting materials for further transformations.[1,3,16] In particular, subsequent Lewis acid-induced chloride abstraction permits the synthesis of N-heterocyclic phosphenium cations in overall yields that compare well with those of a recently reported one-step synthesis involving the redox reaction between a diazabutadiene and $PI_3$.[10] Systematic single-crystal X-ray diffraction studies have revealed that the P–Cl bond lengths in *P*-chlorodiazaphospholenes vary between 2.24 and 2.70 Å, with the *N*-alkyl derivatives showing systematically longer bonds than the *N*-aryl derivatives. An analysis of trends in the structural parameters underlines that the P–Cl bonds in diazaphospholenes are more easily polarised than in compounds of the type $(R_2N)_2PCl$ in general, but gives no evidence that the bond lengthening can be interpreted in terms of the onset of spontaneous bond heterolysis driven by an increase in the aromatic character of the diazaphospholene ring. This analysis supports the results of earlier experimental and computational studies which have explained this effect as being mainly the result of n(N)/σ*(P-Cl) hyperconjugation.

## Experimental Section

All manipulations were carried out under argon in flame-dried glassware. Solvents were dried prior to use according to common procedures. Compounds **1a**–**h** were synthesised according to literature procedures.[17] The synthesis of **3a**–**h** was carried out according

 © 2007 Wiley-VCH Verlag GmbH & Co. KGaA, Weinheim 

to the procedure reported in ref.[1] All other chemicals were purchased from commercial suppliers. NMR Spectra: Bruker Avance 400 ($^1$H: 400.13 MHz; $^{31}$P: 161.9 MHz; $^{13}$C: 100.4 MHz) at 30 °C; chemical shifts referred to ext. TMS ($^1$H, $^{13}$C) or 85% $H_3PO_4$ ($\Xi$ = 40.480747 MHz, $^{31}$P); positive signs of chemical shifts denote shifts to lower frequencies; coupling constants are given as absolute values; prefixes *i*-, *o*-, *m*-, *p*- denote atoms of aryl substituents. MS: Varian MAT 711, EI, 70 eV. Elemental analysis: Perkin–Elmer 2400CHSN/O analyser. Melting points were determined in sealed capillaries.

**1-[(2,6-Dimethylphenyl)imino]-2-[(2,6-dimethylphenyl)amino]ethane (2b):** Compound **1b** (18.5 g, 70 mmol) was dissolved in thf (200 mL), and lithium turnings (1.1 g, 150 mmol) were added. After stirring for 24 h the unreacted lithium was filtered off and the solution cooled to –78 °C. Triethylamine hydrochloride (15.1 g, 150 mmol) was added and the reaction mixture slowly warmed to room temperature. After the solution had become colourless all volatiles were removed in vacuo. The residue was dissolved in *n*-hexane (150 mL) and the precipitate filtered off. The solution was concentrated and the product crystallised at –20 °C. The yellow needles obtained were filtered off and dried in vacuo. Yield 12.0 g (65%), m.p. 136 °C. $^1$H NMR ($CDCl_3$): $\delta$ = 7.83 (t, $^3J_{H,H}$ = 2.1 Hz, 1 H, C*H*=N), 7.25–6.80 (m, 6 H, C*H*), 5.42 (s, 1 H, N*H*), 4.15 (d, $^3J_{H,H}$ = 2.1 Hz, 2 H, C$H_2$-N), 2.42 (s, 6 H, *o*-C$H_3$), 2.14 (s, 6 H, *o*-C$H_3$) ppm. $^{13}$C{$^1$H} NMR ($CDCl_3$): $\delta$ = 163.7 (s, *C*H=N), 150.2 (s, *i*-*C*), 146.4 (s, *i*-*C*), 128.9 (s, *m*-*C*), 128.2 (s, *o*-*C*), 128.0 (s, *m*-*C*), 126.8 (s, *p*-*C*), 123.8 (s, *o*-*C*), 121.3 (s, *p*-*C*), 52.9 (s, *C*$H_2$-N), 19.0 (s, *o*-*C*$H_3$), 18.2 (s, *o*-*C*$H_3$) ppm.

**1,4-Bis(2-*tert*-butylphenyl)-2,3-dimethyl-1,4-diazabuta-2-ene (2f):** Compound **1f** (10.4 g, 30 mmol) was dissolved in thf (300 mL), and lithium (0.5 g, 60 mmol) was added. The mixture was stirred for 24 h. The remaining lithium was filtered off, the solution cooled to –78 °C, and triethylamine hydrochloride (6.1 g, 60 mmol) was added. The reaction mixture was slowly warmed to room temperature, and all volatiles were removed in vacuo. The residue was dissolved in *n*-hexane (100 mL) and the insoluble portion filtered off. The filtrate was concentrated to 30 mL and stored at –20 °C. The yellow powder formed was filtered off and dried in vacuo. Yield 9.4 g (89%). $^1$H NMR ($CDCl_3$): $\delta$ = 7.27 (dt, $^3J_{H,H}$ = 7.8, $^4J_{H,H}$ = 1.7 Hz, 2 H, C*H*), 7.12 (dd, $^3J_{H,H}$ = 7.8, $^4J_{H,H}$ = 1.7 Hz, 2 H, C*H*), 6.83 (dt, $^3J_{H,H}$ = 7.8, $^4J_{H,H}$ = 1.7 Hz, 2 H, C*H*), 6.82 (dd, $^3J_{H,H}$ = 7.8, $^4J_{H,H}$ = 1.7 Hz, 2 H, C*H*), 5.29 (s, 2 H, N*H*), 1.91 (s, 6 H, C$H_3$), 1.37 (s, 18 H, C$H_3$) ppm. $^{13}$C{$^1$H} NMR ($CDCl_3$): $\delta$ = 143.2 (s, *i*-*C*), 138.0 (s, *o*-*C*), 126.7 (s, *o*-*C*H), 126.3 (s, *m*-*C*H), 122.2 (s, N-*C*CH$_3$), 119.9 (s, *m*-*C*H), 119.2 (s, *p*-*C*H), 34.4 (s, *C*), 30.0 [s, C(*C*H$_3$)$_3$], 15.7 (s, *C*H$_3$) ppm.

**2-Chloro-1,3-bis(2,6-dimethylphenyl)-1,3,2-diazaphospholene (3b):** Crystallisation from acetonitrile at –30 °C; colourless crystals; yield 21.2 g (92%); m.p. 184 °C. $^1$H NMR ($CDCl_3$): $\delta$ = 7.18 (m, 6 H, *m*/*p*-C*H*), 6.46 (s, 2 H, N-C*H*), 2.46 (s, 12 H, *o*-C$H_3$) ppm. $^{13}$C{$^1$H} NMR ($CDCl_3$): $\delta$ = 136.9 (d, $^2J_{P,C}$ = 4.5 Hz, *i*-*C*), 129.5 (d, $^4J_{P,C}$ = 1.3 Hz, *m*-*C*), 128.7 (s, *p*-*C*), 128.2 (s, *o*-*C*), 120.8 (d, $^2J_{P,C}$ = 8.4 Hz, N-*C*), 19.4 (d, $^4J_{P,C}$ = 2.9 Hz, *o*-*C*$H_3$) ppm. $^{31}$P{$^1$H} NMR ($CDCl_3$): $\delta$ = 149.2 (s) ppm. MS (EI): *m*/*z* (%) 330.1 (23.9) [M]$^+$, 295.2 (100.0) [M – Cl]$^+$, 190.1 (27.5) [M – $C_8H_9Cl$]$^+$. $C_{18}H_{20}ClN_2P$ (330.80): calcd. C 65.36, H 6.09, N 8.47; found C 64.55, H 6.80, N 7.84.

**2-Chloro-1,3-dimesityl-4,5-dimethyl-1,3,2-diazaphospholene (3d):** Crystallisation from dichloromethane at –20 °C, colourless crystals; yield 22.6 g (90%); m.p. 219 °C. $^1$H NMR ($CDCl_3$): $\delta$ = 6.96 (s, 4 H, *m*-C*H*), 2.30 (s, 6 H, *p*-C$H_3$), 2.28 (s, 12 H, *o*-C$H_3$), 1.82 (d, $^4J_{P,H}$ = 1.3 Hz, 6 H, C$H_3$) ppm. $^{13}$C{$^1$H} NMR ($CDCl_3$): $\delta$ = 138.7 (s, *i*-*C*), 137.0 (d, $^5J_{P,C}$ = 5.5 Hz, *p*-*C*), 131.8 (d, $^3J_{P,C}$ = 10.0 Hz, *o*-*C*), 129.7 (d, $^4J_{P,C}$ = 1.0 Hz, *m*-*C*H), 125.8 (m, N-*C*H), 21.0 (d, $^6J_{P,C}$ = 0.8 Hz, *p*-*C*H$_3$), 19.1 (d, $^4J_{P,C}$ = 1.3 Hz, *o*-*C*H$_3$), 11.1 (d, $^3J_{P,C}$ = 2.0 Hz, *C*H$_3$) ppm. $^{31}$P{$^1$H} NMR ($CDCl_3$): $\delta$ = 165.0 (s) ppm. MS (EI): *m*/*z* (%) 386.2 (21.9) [M]$^+$, 351.2 (100.0) [M – Cl]$^+$, 363.0 (19.2) [M – $CH_3Cl$]$^+$, 305.2 (2.7) [M – $C_3H_{10}Cl$]$^+$. $C_{22}H_{28}ClN_2P$ (386.90): calcd. C 68.30, H 7.29, N 7.24; found C 68.24, H 7.35, N 7.13.

**2-Chloro-1,3-bis(diisopropylphenyl)-4,5-dimethyl-1,3,2-diazaphospholene (3e):** Crystallisation from dichloromethane at –20 °C; colourless crystals; yield 8.7 g (93%); m.p. 204 °C. $^1$H NMR ($CDCl_3$): $\delta$ = 7.45–7.13 (m, 6 H, *m*/*p*-C*H*), 3.14 (sept, $^3J_{H,H}$ = 6.7 Hz, 4 H, C*H*), 1.84 (d, $^4J_{P,H}$ = 0.9 Hz, 6 H, NC-C$H_3$), 1.31 (d, $^3J_{H,H}$ = 6.7 Hz, 12 H, C$H_3$), 1.21 (d, $^3J_{H,H}$ = 6.7 Hz, 12 H, C$H_3$) ppm. $^{13}$C{$^1$H} NMR ($CDCl_3$): $\delta$ = 148.9 (d, $^4J_{P,C}$ = 5.0 Hz, *m*-*C*H), 131.0 (d, $^2J_{P,C}$ = 12.1 Hz, *i*-*C*), 129.8 (d, $^5J_{P,C}$ = 1.5 Hz, *p*-*C*H), 129.4 (s, *o*-*C*), 128.6 (s, *o*-*C*), 125.7 (s; N-*C*), 125.0 (d, $^4J_{P,C}$ = 1.0 Hz, *m*-*C*H), 28.9 (d, $^5J_{P,C}$ = 1.0 Hz, *C*H$_3$), 26.1 (d, $^5J_{P,C}$ = 1.3 Hz, *C*H$_3$), 25.0 (s, *C*H), 11.9 (d, $^3J_{P,C}$ = 3.4 Hz, NC-*C*H$_3$) ppm. $^{31}$P{$^1$H} NMR ($CDCl_3$): $\delta$ = 157.0 (s) ppm. MS (EI): *m*/*z* (%) 470.3 (15.1) [M]$^+$, 435.3 (100.0) [M – Cl]$^+$. $C_{28}H_{40}ClN_2P$ (471.07): calcd. C 71.39, H 8.56, N 5.95; found C 71.30, H 8.64, N 6.14.

**1,3-Bis(2-*tert*-butylphenyl)-2-chloro-4,5-dimethyl-1,3,2-diazaphospholene (3f):** Crystallisation from a mixture of dichloromethane/diethyl ether (2:1) at –20 °C; colourless crystals; yield 8.7 g (74%); m.p. 196 °C. $^1$H NMR ($CDCl_3$): $\delta$ = 7.72 (dd, $^3J_{H,H}$ = 7.0, $^4J_{H,H}$ = 2.0 Hz, 2 H, C*H*), 7.53 (dd, $^3J_{H,H}$ = 7.0, $^4J_{H,H}$ = 2.0 Hz, 2 H, C*H*), 7.35 (dt, $^3J_{H,H}$ = 7.0, $^4J_{H,H}$ = 2.4 Hz, 2 H, C*H*), 7.31 (dt, $^3J_{H,H}$ = 7.0, $^4J_{H,H}$ = 2.4 Hz, 2 H, C*H*), 1.81 (d, $^4J_{P,H}$ = 0.5 Hz, 6 H, C$H_3$), 1.37 (s, 18 H, C$H_3$) ppm. $^{13}$C{$^1$H} NMR ($CDCl_3$): $\delta$ = 147.8 (d, $^3J_{P,C}$ = 6.9 Hz, *o*-*C*), 135.0 (d, $^2J_{P,C}$ = 8.4 Hz, *i*-*C*), 134.0 (d, $^3J_{P,C}$ = 7.9 Hz, *o*-*C*), 129.0 (d, $^4J_{P,C}$ = 1.8 Hz, *m*-*C*), 127.8 (d, $^5J_{P,C}$ = 0.8 Hz, *p*-*C*), 126.8 (d, $^4J_{P,C}$ = 1.3 Hz, *m*-*C*), 125.8 (d, $^2J_{P,C}$ = 6.6 Hz, N-*C*), 36.0 [d, $^4J_{P,C}$ = 1.0 Hz, *C*(CH$_3$)$_3$], 32.1 (d, $^5J_{P,C}$ = 4.1 Hz, *C*H$_3$), 12.0 (d, $^3J_{P,C}$ = 3.1 Hz, *C*H$_3$) ppm. $^{31}$P{$^1$H} NMR ($CDCl_3$): $\delta$ = 161.9 (s) ppm. MS (EI): *m*/*z* (%) 414.2 (17.2) [M]$^+$, 379.2 (86.2) [M – Cl]$^+$, 174.1 (19.3) [M – $C_{12}H_{16}NPCl$]$^+$. $C_{24}H_{32}ClN_2P$ (414.96): calcd. C 69.47, H 7.77, N 6.75; found C 68.91, H 7.86, N 6.77.

**2-Chloro-1,3-dicyclohexyl-1,3,2-diazaphospholene (3h):** Crystallisation from a mixture of *n*-hexane and thf at –28 °C, colourless crystals; yield 2.46 g (43%), m.p. 148 °C. $^1$H NMR ($CDCl_3$): $\delta$ = 6.91 (s, 2 H, N-CH), 3.98–3.77 (m, 2 H, CH), 2.40–2.25 (m, 8 H, $CH_2$), 1.97–1.60 (m, 8 H, $CH_2$), 1.51–1.21 (m, 4 H, $CH_2$) ppm. $^{13}$C{$^1$H} NMR ($CDCl_3$): $\delta$ = 116.7 (d, $^2J_{P,C}$ = 8.0 Hz, N-CH), 53.5 (d, $^3J_{P,C}$ = 11.1 Hz, CH), 29.0 (d, $^4J_{P,C}$ = 9.3 Hz, $CH_2$), 28.1 (d, $^5J_{P,C}$ = 1.2 Hz, $CH_2$), 19.9 (s, $CH_2$) ppm. $^{31}$P{$^1$H} NMR ($CDCl_3$): $\delta$ = 176.5 ppm. MS (EI): *m*/*z* (%) 286.1 (14.4) [M]$^+$, 251.1 (100.0) [M – Cl]$^+$, 169.1 (7.7) [M – $C_6H_{10}Cl$]$^+$, 87.0 (44.5) [M – $C_{12}H_{20}Cl$]$^+$. $C_{14}H_{24}ClN_2P$ (286.78): calcd. C 58.71, H 8.45, N 9.79; found C 58.55, H 8.62, N 9.65. IR: $\tilde{\nu}$ = 1566 (m) cm$^{-1}$.

**1,3-Bis(2,6-dimethylphenyl)-1,3,2-diazaphospholenium Trifluoromethanesulfonate (4b):** Compound **3b** (1.32 g, 4 mmol) was dissolved in toluene (50 mL) and cooled to –78 °C. Trimethylsilyl trifluoromethanesulfonate (1.78 g, 8 mmol) was added and the solution stirred for 2 h. All volatiles were then evaporated in vacuo and the residue dissolved twice in diethyl ether (15 mL) followed by removal of the solvent. The product was dissolved in diethyl ether/dichloromethane (5 mL/10 mL) and crystallised at –20 °C. The colourless crystals were filtered off and dried in vacuo. Yield 1.26 g (95%); m.p. 236 °C. $^1$H NMR ($CD_3CN$): $\delta$ = 8.14 (s, 2 H, N-C*H*), 7.53–7.35 (m, 6 H, C*H*), 2.23 (d, $^4J_{P,H}$ = 0.6 Hz, 12 H, *o*-C$H_3$) ppm.

 © 2007 Wiley-VCH Verlag GmbH & Co. KGaA, Weinheim 

$^{13}C\{^1H\}$ NMR ($CD_3CN$): $\delta$ = 137.7 (d, $^3J_{P,C}$ = 2.5 Hz, *o-C*), 135.3 (d, $^2J_{P,C}$ = 3.6 Hz, *i-C*), 134.9 (d, $^2J_{P,C}$ = 6.7 Hz, N-*C*H), 131.6 (d, $^5J_{P,C}$ = 0.7 Hz, *p-C*), 129.9 (s, *m-C*), 17.4 (d, $^4J_{P,C}$ = 1.7 Hz, *o-C*$H_3$) ppm. $^{31}P\{^1H\}$ NMR ($CD_3CN$): $\delta$ = 209.4 (s) ppm. MS (EI): *m/z* (%) 444.0 (20.3) $[M]^+$, 295.1 (100.0) $[M - CF_3SO_3]^+$. $C_{19}H_{20}F_3N_2O_3PS$ (444.41): calcd. C 51.35, H 4.54, N 6.30; found C 52.09, H 5.10, N 6.06.

**1,3-Bis(2,6-diisopropylphenyl)-1,3,2-diazaphospholenium Trifluoromethanesulfonate (4c):** A solution of **3c** (0.89 g, 2 mmol) in toluene

Table 2. Crystallographic data, structure solution and refinement of **3b**–**f**.

| | **3b** | **3c** | **3d** | **3e** | **3f** |
|---|---|---|---|---|---|
| Empirical formula | $C_{18}H_{20}ClN_2P$ | $C_{26}H_{36}ClN_2P$ | $C_{22}H_{28}ClN_2P$ | $C_{28}H_{40}ClN_2P$ | $C_{24}H_{32}ClN_2P{\cdot}CH_2Cl_2$ |
| Formula weight | 330.78 | 442.99 | 386.88 | 471.04 | 499.86 |
| Temperature [K] | 123(2) | 123(2) | 123(2) | 173(2) | 123(2) |
| Crystal system | monoclinic | monoclinic | monoclinic | monoclinic | triclinic |
| Space group | $P2_1/c$ | $P2_1/n$ | $P2_1/c$ | $P2_1/c$ | $P\bar{1}$ |
| *a* [Å] | 14.9453(3) | 9.7599(2) | 7.7200(2) | 16.899(4) | 10.9942(3) |
| *b* [Å] | 7.2778(2) | 10.6976(2) | 18.7452(6) | 10.5903(17) | 11.0029(2) |
| *c* [Å] | 16.4943(4) | 12.3357(3) | 14.4230(4) | 16.434(3) | 12.6859(3) |
| *α* [°] | 90 | 90 | 90 | 90 | 115.005(2) |
| *β* [°] | 113.926(2) | 92.891(1) | 97.635(2) | 114.480(13) | 97.615(2) |
| *γ* [°] | 90 | 90 | 90 | 90 | 105.485(2) |
| *V* [Å$^3$] | 1639.90(7) | 1286.30(5) | 2068.69(10) | 2676.8(8) | 1286.29(5) |
| *Z* | 4 | 2 | 4 | 4 | 2 |
| $D_{calcd.}$ [g cm$^{-3}$] | 1.340 | 1.144 | 1.242 | 1.169 | 1.291 |
| Abs. coeff. [mm$^{-1}$] | 0.328 | 0.225 | 0.270 | 0.220 | 0.434 |
| *F*(000) | 696 | 476 | 824 | 1016 | 528 |
| Crystal size [mm] | 0.60 × 0.35 × 0.25 | 0.50 × 0.25 × 0.15 | 0.40 × 0.20 × 0.20 | 0.65 × 0.50 × 0.45 | 0.60 × 0.50 × 0.40 |
| *θ* range for data collection [°] | 2.98–25.03 | 2.52–24.99 | 3.05–27.48 | 2.33–28.01 | 3.07–27.48 |
| Reflections collected | 9610 | 13453 | 13602 | 6664 | 11453 |
| Unique reflections | 2881 | 4524 | 4651 | 6444 | 5698 |
| $R_{int}$ | 0.0229 | 0.0354 | 0.0348 | 0.0250 | 0.0279 |
| Data/restraints/parameters | 2881/0/203 | 4524/1/271 | 4651/0/243 | 6444/0/304 | 5698/0/282 |
| GOF on $F^2$ | 1.062 | 1.044 | 0.938 | 1.005 | 1.058 |
| $R1$ [$I > 2\sigma(I)$] | 0.0433 | 0.0257 | 0.0381 | 0.0426 | 0.0328 |
| $wR_2$ (all data) | 0.1153 | 0.0628 | 0.0906 | 0.1237 | 0.0864 |
| Largest diff. map peak/hole [e Å$^{-3}$] | 1.240/–0.271 | 0.220/–0.298 | 0.456/–0.304 | 0.496/–0.266 | 0.328/–0.302 |

Table 3. Crystallographic data, structure solution and refinement for **3h**, **4b**,**c**,**g** and **5f**.

| | **3h** | **4b** | **4c** | **4 g** | **5f** |
|---|---|---|---|---|---|
| Empirical formula | $C_{14}H_{24}ClN_2P$ | $C_{19}H_{20}F_3N_2O_3PS$ | $C_{27}H_{36}F_3N_2O_3PS$ | $C_{11}H_{20}F_3N_2O_3PS$ | $C_{24}H_{32}Cl_4GaN_2P$ |
| Formula weight | 286.77 | 444.40 | 556.61 | 348.32 | 591.01 |
| Temperature [K] | 123(2) | 123(2) | 173(2) | 123(2) | 123(2) |
| Crystal system | triclinic | orthorhombic | triclinic | orthorhombic | monoclinic |
| Space group | $P\bar{1}$ | *Pnma* | $P\bar{1}$ | *Pnma* | $P2_1/n$ |
| *a* [Å] | 6.995(2) | 10.2721(3) | 9.875(2) | 12.4780(3) | 10.1559(2) |
| *b* [Å] | 9.164(2) | 17.4393(8) | 10.708(2) | 8.5135(2) | 9.4609(2) |
| *c* [Å] | 12.244(2) | 11.7441(5) | 14.739(3) | 15.3270(4) | 28.6877(7) |
| *α* [°] | 100.67(2) | 90 | 95.172(14) | 90 | 90 |
| *β* [°] | 92.28(2) | 90 | 104.567(15) | 90 | 98.102(1) |
| *γ* [°] | 98.03(2) | 90 | 100.759(15) | 90 | 90 |
| *V* [Å$^3$] | 762.0(3) | 2103.82(15) | 1466.4(5) | 1628.21(7) | 2728.92(10) |
| *Z* | 2 | 4 | 2 | 4 | 4 |
| $D_{calcd.}$ (g cm$^{-3}$) | 1.250 | 1.403 | 1.261 | 1.421 | 1.439 |
| Abs. coeff. [mm$^{-1}$] | 0.342 | 0.278 | 0.214 | 0.337 | 1.474 |
| *F*(000) | 308 | 920 | 588 | 728 | 1216 |
| Crystal size [mm] | 0.40 × 0.30 × 0.20 | 0.50 × 0.30 × 0.15 | 0.70 × 0.35 × 0.25 | 0.40 × 0.25 × 0.15 | 0.15 × 0.15 × 0.15 |
| *θ* range for data collection [°] | 3.10–25.02 | 3.47–27.48 | 1.96–27.50 | 3.12–27.48 | 2.96–27.48 |
| Reflections collected | 8795 | 10939 | 7127 | 9671 | 14785 |
| Unique reflections | 2654 | 2463 | 6731 | 1982 | 6068 |
| $R_{int}$ | 0.0510 | 0.0337 | 0.0224 | 0.0406 | 0.0473 |
| Data/restraints/parameters | 2654/0/163 | 2463/0/141 | 6731/0/327 | 1982/0/115 | 6068/0/291 |
| GOF on $F^2$ | 1.058 | 1.017 | 1.051 | 1.075 | 0.918 |
| $R1$ [$I > 2\sigma(I)$] | 0.0369 | 0.0357 | 0.0425 | 0.0428 | 0.0358 |
| $wR_2$ (all data) | 0.0960 | 0.0950 | 0.1131 | 0.1186 | 0.0792 |
| Largest diff. map peak/hole [e A$^{-3}$] | 0.338/–0.266 | 0.262/–0.282 | 0.387/–0.378 | 0.484/–0.408 | 0.843/–0.544 |

 © 2007 Wiley-VCH Verlag GmbH & Co. KGaA, Weinheim 

(30 mL) was cooled to –78 °C and trimethylsilyl trifluoromethanesulfonate (1.08 g, 5 mmol) was added. After stirring for 2 h at room temperature all volatiles were evaporated in vacuo and the residue dissolved twice in 15 mL of diethyl ether, followed by removal of the solvent. The product was dissolved in a mixture of *n*-hexane, toluene, and dichloromethane (5 mL/5 mL/1 mL) and crystallised at –28 °C. The colourless needles were filtered off and dried in vacuo. Yield 0.78 g (73%); m.p. 259 °C. $^1$H NMR ($CDCl_3$): $\delta$ = 8.62 (d, $^3J_{P,H}$ = 0.9 Hz, 2 H, N-C*H*), 7.64 (t, $^3J_{H,H}$ = 7.8 Hz, 2 H, *p*-C*H*), 7.43 (d, $^3J_{H,H}$ = 7.8 Hz, 4 H, *m*-C*H*), 2.50 (sept, $^3J_{H,H}$ = 6.8 Hz, 4 H, C*H*), 1.36 (d, $^3J_{H,H}$ = 6.8 Hz, 12 H, C$H_3$), 1.27 (d, $^3J_{H,H}$ = 6.8 Hz, 12 H, C$H_3$) ppm. $^{13}$C{$^1$H} NMR ($CDCl_3$): $\delta$ = 144.2 (d, $^2J_{P,C}$ = 3.6 Hz, *i*-*C*), 140.2 (s, *o*-*C*), 137.1 (s, *o*-*C*), 131.5 (d, $^2J_{P,C}$ = 1.2 Hz, N-*C*H), 128.3 (s, *m*-*C*), 127.5 (s, *m*-*C*), 124.6 (s, *p*-*C*), 124.2 (s, *p*-*C*), 30.9 (s, *C*H), 30.1 (s, *C*H), 24.5 (s, *C*$H_3$), 23.0 (s, *C*$H_3$), 21.9 (s, *C*$H_3$), 20.7 (s, *C*$H_3$) ppm. $^{31}$P{$^1$H} NMR ($CDCl_3$): $\delta$ = 205.0 (s) ppm. MS (EI): *m*/*z* (%) 556.1 (12.3) $[M]^+$, 407.2 (100.0) $[M - CF_3SO_3]^+$. $C_{27}H_{36}F_3N_2O_3PS$ (556.62): calcd. C 58.26, H 6.52, N 5.03; found C 58.46, H 6.70, N 4.95.

**1,3-Di-*tert*-Butyl-1,3,2-diazaphospholenium Trifluoromethanesulfonate (4g):** M.p. 168 °C. $^1$H NMR ($CDCl_3$): $\delta$ = 8.17 (s, 2 H, N-CH), 1.69 (d, $^4J_{P,H}$ = 1.8 Hz, 18 H, $CH_3$) ppm. $^{13}$C{$^1$H} NMR ($CDCl_3$): $\delta$ = 132.9 (d, $^3J_{P,H}$ = 3.8 Hz N-C), 62.8 (d, $^2J_{P,H}$ = 7.6 Hz, 1 C), 31.4 (d, $^3J_{P,H}$ = 6.5 Hz, $CH_3$) ppm. $^{31}$P{$^1$H} NMR ($CDCl_3$): $\delta$ = 205.5. $C_{11}H_{20}F_3N_2O_3PS$ (348.32): calcd. C 36.93, H 5.79, N 8.04; found C 36.85, H 5.69, N 7.82.

**1,3-Bis(2-*tert*-butylphenyl)-4,5-dimethyl-1,3,2-diazaphospholenium Tetrachlorogallate (5f):** Compound **3f** (207 mg, 0.5 mmol) and gallium trichloride (88 mg, 0.5 mmol) were dissolved in acetonitrile (10 mL) and stirred for 5 min. Storage of the solution at –35 °C afforded colourless crystals, which were filtered off and dried in vacuo. Yield 280 mg (95%). $^1$H NMR ($CD_3CN$): $\delta$ = 7.84 (dd, $^3J_{H,H}$ = 8.2, $^4J_{H,H}$ = 1.6 Hz, 2 H, o -C*H*), 7.65 (dddd, $^3J_{H,H}$ = 8.2, $^3J_{H,H}$ = 7.3, $^4J_{H,H}$ = 1.6, $^6J_{P,H}$ = 0.9 Hz, 2 H, *m*-C*H*), 7.48 (dddd, $^3J_{H,H}$ = 7.9, $^3J_{H,H}$ = 7.3, $^4J_{H,H}$ = 1.6, $^5J_{P,H}$ = 0.9 Hz, 2 H, *p*-C*H*), 7.28 (ddd, $^3J_{H,H}$ = 7.9, $^4J_{H,H}$ = 1.6, $^5J_{H,H}$ = 0.4 Hz, 2 H, m′-C*H*), 2.21 (d, $^4J_{P,H}$ = 1.8 Hz, 6 H, C$H_3$), 1.34 (s, 18 H, C$H_3$) ppm. $^{13}$C{$^1$H} NMR ($CD_3CN$): $\delta$ = 146.9 (d, $^2J_{P,C}$ = 3.4 Hz, *i*-*C*), 144.6 (s, *o*-*C*), 132.5 (d, $^4J_{P,C}$ = 1.3 Hz, *m*-*C*H), 132.1 (s, *m*-*C*H), 132.0 (d, $^2J_{P,C}$ = 5.5 Hz, N-*C*), 130.9 (s, *m*-*C*H), 128.8 (s, *p*-*C*H), 37.3 (d, $^4J_{P,C}$ = 0.8 Hz, 1 *C*), 32.7 (d, $^5J_{P,C}$ = 2.6 Hz, *C*$H_3$), 13.8 (d, $^3J_{P,C}$ = 3.9 Hz, *C*$H_3$) ppm. $^{31}$P{$^1$H} NMR ($CD_3CN$): $\delta$ = 205.8 (s) ppm. MS (EI): *m*/*z* (%) 379.2 (100.0) $[M - GaCl_4]^+$. $C_{24}H_{32}Cl_4GaN_2P$ (591.04): calcd. C 48.77, H 5.46, N 4.74; found C 48.49, H 5.39, N 4.74.

**Crystal Structure Studies:** Single-crystal X-ray diffraction studies were carried out at low temperatures on a Nonius Kappa-CCD diffractometer or a Siemens P3 or P4 diffractometer using Mo-$K_\alpha$ radiation ($\lambda$ = 0.71073 Å). Direct methods (SHELXS-97[18]) were used for structure solution and refinement (SHELXL-97,[19] full-matrix least-squares on $F^2$). An empirical absorption correction was applied for **5f**, and H atoms were refined using a riding model. The absolute structure of **3c** was determined by refinement of Flack's *x*-parameter [*x* = 0.04(4)].[20] Important data regarding the data collection and structure solution and refinement are listed in Tables 2 and 3.

CCDC-650776 (for **3b**), -650777 (for **3c**), -650778 (for **3d**), -650770 (for **3e**), -650779 (for **3f**), -650780 (for **3h**), -650781 (for **4b**), -650771 (for **4c**), -651156 (for **4g**), and -650782 (for **5f**) contain the supplementary crystallographic data for this paper. These data can be obtained free of charge from The Cambridge Crystallographic Data Centre via www.ccdc.cam.ac.uk/data_request/cif.

## Acknowledgments

This work was financially supported by the Deutsche Forschungsgemeinschaft (DFG).

[1] a) D. Gudat, A. Haghverdi, M. Nieger, *Angew. Chem.* **2000**, *112*, 3211–3214; *Angew. Chem. Int. Ed.* **2000**, *39*, 3084–3087; b) S. Burck, D. Gudat, M. Nieger, W.-W. du Mont, *J. Am. Chem. Soc.* **2006**, *128*, 3946–3955.
[2] a) S. Burck, D. Gudat, M. Nieger, *Angew. Chem.* **2004**, *116*, 4905–4908; *Angew. Chem. Int. Ed.* **2004**, *43*, 4801–4804.
[3] D. Gudat, A. Haghverdi, H. Hupfer, M. Nieger, *Chem. Eur. J.* **2000**, *6*, 3414–3425.
[4] M. Denk, S. Gupta, R. Ramachandran, *Tetrahedron Lett.* **1996**, *37*, 9025–9028.
[5] A. J. Arduengo III, R. L. Harlow, M. Kline, *J. Am. Chem. Soc.* **1991**, *113*, 361–363.
[6] A. M. Kibardin, I. A. Litvinov, V. A. Naumanov, Y. T. Struchkov, T. V. Gryaznova, Y. B. Mikhailov, A. N. Pudovik, *Dokl. Akad. Nauk SSSR* **1988**, *298*, 369–372.
[7] C. J. Carmalt, V. Lomeli, B. G. McBurnett, A. H. Cowley, *Chem. Commun.* **1997**, 2095–2096.
[8] S. Burck, D. Förster, D. Gudat, *Chem. Commun.* **2006**, 2810–2812.
[9] a) A. H. Cowley, R. A. Kemp, J. C. Wilburn, *Inorg. Chem.* **1981**, *20*, 4289–4293; b) I. A. Litvinov, V. A. Naumov, T. V. Gryaznova, A. M. Kibardin, A. N. Pudovik, *Dokl. Akad. Nauk SSSR* **1990**, *324*, 623–625.
[10] a) G. Reeske, C. R. Hoberg, N. J. Hill, A. H. Cowley, *J. Am. Chem. Soc.* **2006**, *128*, 2800–2801; b) B. D. Ellis, C. L. B. Macdonald, *Inorg. Chim. Acta* **2007**, *351*, 329–344; c) G. Reeske, A. H. Cowley, *Inorg. Chem.* **2007**, *46*, 1426–1430.
[11] a) T. Gans-Eichler, D. Gudat, M. Nieger, *Angew. Chem.* **2002**, *114*, 1966–1969; *Angew. Chem. Int. Ed.* **2002**, *41*, 1888–1891; b) T. Gans-Eichler, D. Gudat, K. Nättinen, M. Nieger, *Chem. Eur. J.* **2006**, *12*, 1162–1173.
[12] a) A. M. Kibardin, T. V. Gryaznova, T. A. Zyablikova, Sh. K. Latypov, R. Z. Musin, A. N. Pudovik, *Zh. Obshch. Khim.* **1993**, *63*, 33–39; b) A. M. Kibardin, T. V. Gryaznova, A. N. Pudovik, *Bull. Acad. Sci. USSR Div. Chem. Sci. (Engl. Transl.)* **1987**, *36*, 1554.
[13] a) A. Dumitrescu, H. Gornitzka, W. W. Schoeller, D. Bourissou, G. Bertrand, *Eur. J. Inorg. Chem.* **2002**, 1953–1956; b) N. Burford, P. Losier, C. Macdonald, V. Kyrimis, P. K. Bakshi, T. S. Cameron, *Inorg. Chem.* **1994**, *33*, 1434–1439; c) N. Burford, P. Losier, P. K. Bakshi, T. S. Cameron, *J. Chem. Soc. Dalton Trans.* **1993**, 201–202; d) N. Burford, T. S. Cameron, J. A. C. Clyburne, K. Eichele, K. N. Robertson, S. Sereda, R. E. Wasylishen, W. A. Whitla, *Inorg. Chem.* **1996**, *35*, 5460–5467.
[14] Average and standard deviation of the result of a query in the CSD database for P–Cl distances in phosphorus compounds $(R_2N)_2P$–Cl neglecting the entries for 1,3,2-diazaphospholenes.
[15] a) *X-ray Analysis and the Structure of Organic Molecules* (Ed.: J. Dunitz), Cornell University Press Ltd., London, **1979**; b) H. B. Bürgi, J. D. Dunitz, *Acc. Chem. Res.* **1983**, *16*, 153–161; c) *Structure Correlation* (Eds.: H. B. Bürgi, J. D. Dunitz), Verlag Chemie, Weinheim, **1994**.
[16] S. Burck, D. Gudat, M. Nieger, J. Tirree, *Dalton Trans.* **2007**, 1891–1897.
[17] a) H. tom Dieck, M. Svoboda, T. Greiser, *Z. Naturforsch., Teil B* **1981**, *36*, 823–832; b) H. A. Zhong, J. A. Labinger, J. E. Bercaw, *J. Am. Chem. Soc.* **2002**, *124*, 1378–1399; c) D. J. Tempel, L. K. Johnson, R. L. Huff, P. S. White, M. Brookhart, *J. Am. Chem. Soc.* **2000**, *122*, 6686–6700.
[18] G. M. Sheldrick, *Acta Crystallogr., Sect. A* **1990**, *46*, 467–473.
[19] G. M. Sheldrick, University of Göttingen, Germany, **1997**.
[20] H. D. Flack, *Acta Crystallogr., Sect. A* **1983**, *39*, 876–881.

Received: June 21, 2007
Published Online: September 20, 2007

 © 2007 Wiley-VCH Verlag GmbH & Co. KGaA, Weinheim 

DOI: 10.1002/ejic.200700475

# Speciation of Uranyl Nitrato Complexes in Acetonitrile and in the Ionic Liquid 1-Butyl-3-methylimidazolium Bis(trifluoromethylsulfonyl)imide

**Kelly Servaes,[a] Christoph Hennig,*[b] Isabelle Billard,[c] Clotilde Gaillard,[c] Koen Binnemans,[a] Christiane Görller-Walrand,[a] and Rik Van Deun*[a]**

**Keywords:** EXAFS spectroscopy / Ionic liquids / Uranium / UV/Vis spectroscopy / X-ray absorption spectroscopy

Complex formation between the uranyl ion and nitrate ions in acetonitrile and the ionic liquid 1-butyl-3-methylimidazolium bis(trifluoromethylsulfonyl)imide ($[C_4mim][Tf_2N]$) has been studied by absorption, magnetic circular dichroism (MCD) and uranium $L_{III}$ EXAFS spectroscopy. The experimental results point to the existence of a trinitrate species $[UO_2(NO_3)_3]^-$ with $D_{3h}$ symmetry in both solvents. The atomic distances in the uranium(VI) coordination sphere for the trinitrato complex in acetonitrile are $U–O_{ax}$ = 1.77 ± 0.01 Å and $U–O_{eq}$ = 2.48 ± 0.01 Å. EXAFS data show that the uranyl ion in the ionic liquid is surrounded by six oxygen atoms in the equatorial plane at a distance of 2.49 ± 0.01 Å. The U–N distance of 2.92 ± 0.01 Å indicates a bidentate coordination of the nitrate group in both solvents. A structural comparison is made between the uranyl trinitrato complex anion $[UO_2(NO_3)_3]^-$ and the uranyl tricarbonato complex anion $[UO_2(CO_3)_3]^{4-}$. No evidence is found for the presence of uranyl nitrato complexes in aqueous solution. The optical absorption, MCD and EXAFS spectra resemble those of the hydrated free uranyl ion. There are two axial oxygen atoms at 1.77 ± 0.01 Å and five equatorial oxygen atoms at 2.41 ± 0.01 Å. These values agree well with structural parameters obtained for the uranyl aqua ion.

(© Wiley-VCH Verlag GmbH & Co. KGaA, 69451 Weinheim, Germany, 2007)

## Introduction

The molecular structure of the uranyl trinitrate complex anion $[UO_2(NO_3)_3]^-$ is well known from X-ray diffraction studies.[1–3] Dieke and Duncan first recorded the absorption spectrum of a $Cs[UO_2(NO_3)_3]$ crystal with a spectrograph and identified the so-called "fluorescent series" and "magnetic series" in the spectrum.[4,5] The magnetic circular dichroism (MCD) spectra of $[UO_2(NO_3)_3]^-$ were first described by Brint and McCaffery[6] and subsequently reinvestigated by Görller-Walrand and Colen,[7] and the electronic transitions and vibrational progressions were first identified by Denning and co-workers by measuring the σ- and π-spectra of $Cs[UO_2(NO_3)_3]$ single crystals.[8] Kaplan and co-workers observed the typical UV/Vis absorption spectrum of the $[UO_2(NO_3)_3]^-$ complex anion in ketone solvents like acetone by adding tetrabutylammonium nitrate to a solution of $UO_2(NO_3)_2$ in these solvents.[9] They noticed a good agreement between the solution spectra and those of $Cs[UO_2(NO_3)_3]$ single crystals. In contrast, these authors could not find a proof for nitrate complex formation in aqueous solution.

Extended X-ray absorption fine structure (EXAFS) spectroscopy measurements on uranyl nitrato compounds are rather scarce, although Thompson and co-workers have investigated the uranyl trinitrato unit in solid $UO_2(NO_3)_2 \cdot 6H_2O$,[10] and the uranyl nitrate dimer in solid $Him_2[\{UO_2(\mu\text{-}OH)(NO_3)_2\}_2]$ (Him = imidazolium) has been studied by Barnes et al.[11] Solvent-extraction processes of uranyl nitrate solutions have been extensively studied because of their significance for nuclear waste treatment.[12–21] These research activities include EXAFS measurements of uranyl nitrate in trimethyl phosphate, tri-*n*-butyl phosphate, triisobutyl phosphate and triphenyl phosphate, which indicate a coordination of two bidentate nitrate groups and two monodentate organophosphate ligands.[20–22] All the experimental EXAFS data obtained to date suffer from competing scattering contributions that cover the important multiple scattering features within the nitrate group. So far, trinitratouranyl species in solution have not been studied in depth by EXAFS spectroscopy, although recently there has been a strong research interest in uranyl complexes, including uranyl nitrate complexes, in ionic liquids.[23–31]

[a] Department of Chemistry, Katholieke Universiteit Leuven, Celestijnenlaan 200F, 3001 Leuven, Belgium
Fax: +32-1632-7992,
E-mail: rik.vandeun@chem.kuleuven.be
[b] Forschungszentrum Dresden-Rossendorf, Institute of Radiochemistry,
P. O. Box 510119, 01314 Dresden, Germany
Fax: +33-476-88-2505,
E-mail: hennig@esrf.fr
[c] Institut Pluridisciplinaire H. Curien, CNRS-IPHC/DRS, Chimie Nucléaire,
B. P. 28, 67037 Strasbourg Cedex 2, France

Supporting information for this article is available on the WWW under http://www.eurjic.org or from the author.

 © 2007 Wiley-VCH Verlag GmbH & Co. KGaA, Weinheim 

The speciation of uranyl complexes in solution is not always straightforward. Unlike solid-state structures, which can be determined by X-ray diffraction of single crystals, the structure of solution species can be determined only by symmetry effects, for example by optical absorption spectra, or by limited structural parameters obtained, for example, from EXAFS spectra. Various conclusions have been drawn in the past from spectroscopic results, particularly absorption, luminescence and magnetic circular dichroism spectroscopy, and in a previous paper we have demonstrated the existence of a $[UO_2Cl_4]^{2-}$ complex anion with $D_{4h}$ symmetry in acetonitrile by a combination of optical absorption spectroscopy and uranium $L_{III}$ EXAFS spectroscopy.[32] An analogous investigation by the same complementary spectroscopic techniques presented in this paper points to the existence of the uranyl trinitrato complex anion in acetonitrile and the ionic liquid 1-butyl-3-methylimidazolium bis(trifluoromethylsulfonyl)imide ([$C_4$mim][$Tf_2$N]). Furthermore, both spectroscopic techniques provide evidence for the absence of a significant degree of complex formation between the uranyl ion and nitrate ions in aqueous solution.

## Results and Discussion

The UV/Vis absorption spectrum and the MCD spectrum of uranyl nitrate in the presence of tetrabutylammonium nitrate in acetonitrile are shown in Figure 1. No further changes were observed upon increasing the nitrate concentration above the ratio $[UO_2^{2+}]/[NO_3^-]$ = 1:3, which points to a maximal coordination of the uranyl ion. The most striking feature is the increase in intensity of four bands in the long-wavelength part of the absorption spectrum (21000–24000 $cm^{-1}$) with respect to the solvated uranyl ion in acetonitrile. These lines correspond to the "magnetic series" reported by Dieke and Duncan for the single-crystal spectra of $Cs[UO_2(NO_3)_3]$, in which the coordination polyhedron of the uranyl ion has a $D_{3h}$ symmetry.[4] The transitions belonging to the magnetic series give rise to very intense, negative A-terms in the MCD spectrum (Figure 1).[7] These MCD signals originate from the electronic transition between the totally symmetric ground state $A_1'$ ($\Sigma_g^+$ in $D_{\infty h}$) to the excited state E′ ($\Delta_g$ in $D_{\infty h}$).

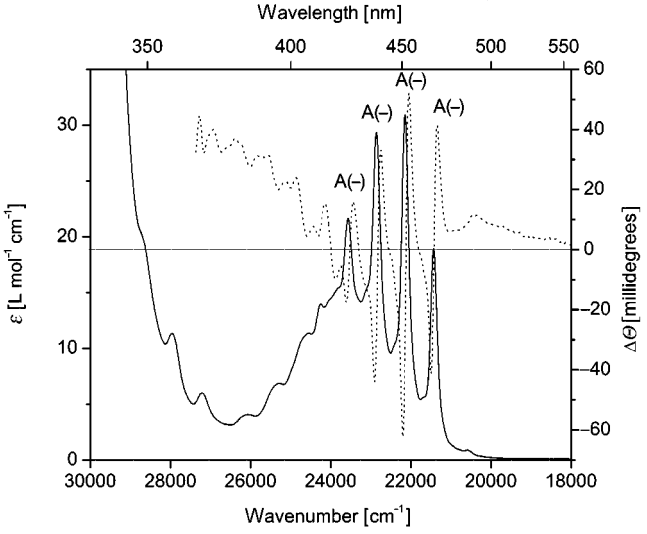


Figure 1. Optical absorption spectrum (solid line) and MCD spectrum (dotted line) of $[UO_2(NO_3)_3]^-$ in acetonitrile at room temperature. $[UO_2^{2+}]$ = 50 and $[NO_3^-]$ = 200 mM ($[UO_2^{2+}]/[NO_3^-]$ = 1:4).

The UV/Vis absorption spectrum and the MCD spectrum of uranyl nitrate in the presence of tetrabutylammonium nitrate in acetone are given as Supporting Information. These spectra are very similar to those recorded in acetonitrile. An overview of all the electronic transitions in the optical absorption spectrum of $[UO_2(NO_3)_3]^-$ in acetonitrile is given in Table 1. A detailed list of the transitions assigned for $[UO_2(NO_3)_3]^-$ in acetonitrile in $D_{3h}$ symmetry is available as Supporting Information. The presence of very intense, sharp peaks in the first part of the optical absorption spectrum is also characteristic of other complexes with $D_{3h}$ trigonal symmetry, such as $[UO_2(CO_3)_3]^{4-}$ and $[UO_2(CH_3COO)_3]^-$.[7,12,33,34]

The optical absorption spectrum and MCD spectrum of $UO_2(NO_3)_2{\cdot}6H_2O$ and $Bu_4NNO_3$ in the ionic liquid [$C_4$mim][$Tf_2$N] are given in Figure 2. The molar absorptivity in this ionic liquid solvent is of the same order of magnitude as that in acetonitrile. The absorption bands can all be assigned to transitions of the uranyl ion since [$C_4$mim][$Tf_2$N] does not absorb in this wavelength region.[35] The same typical spectroscopic features of the uranyl trinitrato complex in the range 20000–24000 $cm^{-1}$ (sharp, intense peaks in the optical absorption spectrum

Table 1. Observed electronic transitions for $[UO_2(NO_3)_3]^-$ in acetonitrile and [$C_4$mim][$Tf_2$N], assigned to $D_{\infty h}$ and $D_{3h}$ symmetry, compared with those of $Cs[UO_2(NO_3)_3]$ single crystals.[8] Energies are given in wavenumber units [$cm^{-1}$].

| Symmetry | | $[UO_2(NO_3)_3]^-$ | $[UO_2(NO_3)_3]^-$ | $Cs[UO_2(NO_3)_3]$ |
|---|---|---|---|---|
| $D_{\infty h}$ | $D_{3h}$ | Acetonitrile | [$C_4$mim][$Tf_2$N] | Single crystal[8] |
| $\Pi_g \leftarrow \Sigma_g^+$ | $E'' \leftarrow A_1'$ | 20585 | 20563 | 21090 |
| $\Delta_g \leftarrow \Sigma_g^+$ | $E'(x,y) \leftarrow A_1'$ | 21432 | 21381 | 21694 |
| $\Phi_g \leftarrow \Sigma_g^+$ | $A_1'' \leftarrow A_1'$ | – | – | 22300 |
| $(\Delta_g + \Gamma_g) \leftarrow \Sigma_g^+$ | $E'(x,y) \leftarrow A_1'$ | – | – | 23475 |
| $\Phi_g \leftarrow \Sigma_g^+$ | $A_1'' \leftarrow A_1'$ | – | – | 26640 |
| $\Phi_g \leftarrow \Sigma_g^+$ | $A_2'' \leftarrow A_1'$ | 27218 | 27167 | 27480 |

 © 2007 Wiley-VCH Verlag GmbH & Co. KGaA, Weinheim 

and very intense, negative A-terms in the MCD spectrum) as observed in acetonitrile are also observed in $[C_4mim][Tf_2N]$. Furthermore, the absorption maxima in acetonitrile and $[C_4mim][Tf_2N]$ agree well. The features in the long-wavelength part of the UV/Vis absorption spectrum and the MCD spectrum, as well as a comparison with the well-known $[UO_2(NO_3)_3]^-$ complex in ketone solvents, indicate the formation of a $[UO_2(NO_3)_3]^-$ species in $[C_4mim][Tf_2N]$. The energetic positions of the different electronic states of $[UO_2(NO_3)_3]^-$ in $[C_4mim][Tf_2N]$ are given in Table 1. A detailed assignment of the transitions of $[UO_2(NO_3)_3]^-$ in $[C_4mim][Tf_2N]$ is available as Supporting Information.

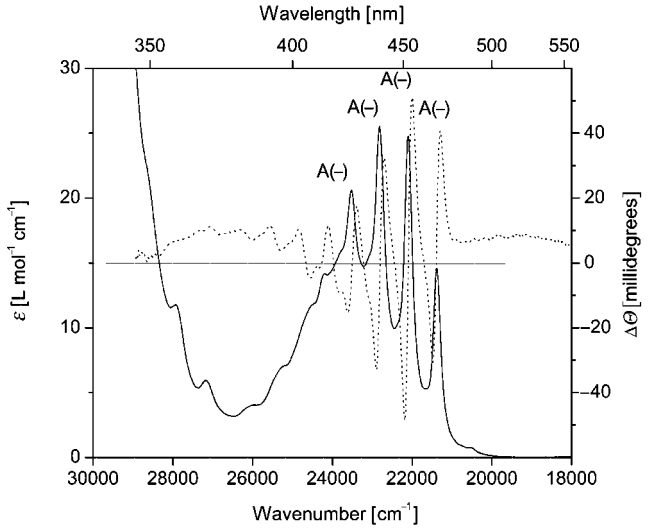


Figure 2. UV/Vis absorption spectrum (solid line) and MCD spectrum (dotted line) of $[UO_2(NO_3)_3]^-$ in $[C_4mim][Tf_2N]$ at room temperature. $[UO_2^{2+}]$ = 50 and $[NO_3^-]$ = 200 mM ($[UO_2^{2+}]/[NO_3^-]$ = 1:4).

An alternative way to obtain the trinitrato complex is to treat $UO_2$ with concentrated nitric acid in $[C_4mim][Tf_2N]$. However, nitrite ions are also formed in addition to the trinitrato complex, as evidenced by the bands in the region 25000–28500 $cm^{-1}$ in the UV/Vis absorption spectrum (given as Supporting Information). The UV/Vis spectra of nitrite ions and nitrous acid have been described by das Graças Gomes et al.[36] Nevertheless, the presence of the $[UO_2(NO_3)_3]^-$ moiety is also indicated in this case by the intense features in the long-wavelength part of the UV/Vis spectrum.

Spectroscopic measurements indicate that there is no significant complex formation between the uranyl ion and nitrate ions in aqueous solution. The optical absorption spectrum and the MCD spectrum of uranyl nitrate in water exhibit the same vibrational fine structure as that of the free uranyl ion (i.e. the hydrated uranyl ion) obtained by dissolving $UO_2(ClO_4)_2{\cdot}xH_2O$ in water (Figure 3). Moreover, no red- or blueshift of the absorption bands is observed. This similarity between the two spectra suggests that the hydrated uranyl ion is the dominant species in aqueous solution. The absorption spectra of uranyl nitrate $UO_2(NO_3)_2{\cdot}6H_2O$ in aqueous solution can be found in the Supporting Information. The typical sharp absorption bands of the uranyl trinitrato complex are absent in aqueous solution because nitrate ions form only weak complexes in this medium. The system can be characterized by three formation constants: $K_1$ = 0.5, $K_2$ = 1.0 and $K_3$ = 0.9 $L\,mol^{-1}$.[12,37] The formation constants $K_1$ and $K_2$ were determined in $NaClO_4$ medium at an ionic strength of 1.0 and $K_3$ in media of varying $HNO_3$ concentrations. The species distribution in an aqueous solution of $UO_2(NO_3)_2{\cdot}6H_2O$ (50 mM, pH = 2.4) is dominated by the uranyl aqua ion and the distribution coefficient of the nitrato species is low [94.8% $UO_2^{2+}$, 4.6% $UO_2NO_3^+$, 0.45% $UO_2(NO_3)_2$ and 0.04% $UO_2(NO_3)_3^-$]. The low-concentration nitrato species cannot be clearly distinguished by UV/Vis absorption spectroscopy. In a recent paper, Ruas and co-workers stated that the equilibrium constants for the 1:1 and 1:2 $UO_2^{2+}/NO_3^-$ complexes are low, which means that the uranyl trinitrato complex in water can be neglected in our case.[38]

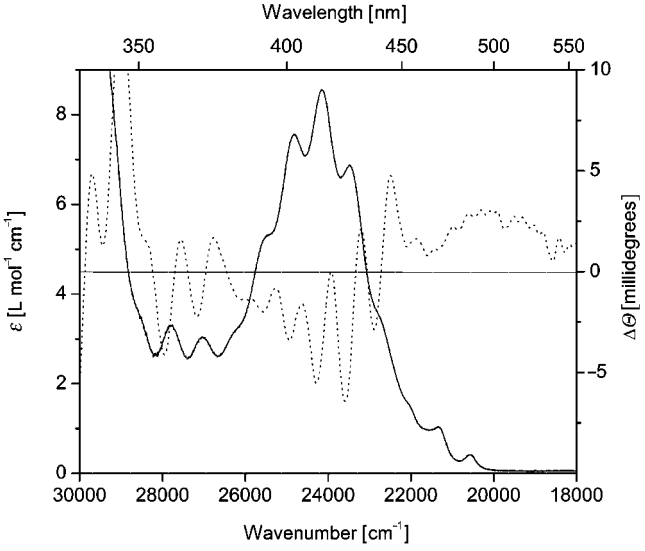


Figure 3. UV/Vis absorption spectrum (solid line) and MCD spectrum (dotted line) of $UO_2(NO_3)_2{\cdot}6H_2O$ in aqueous solution at room temperature. Uranyl concentration: 50 mM.

The UV/Vis absorption spectrum of the hydrated uranyl ion is well known,[5] although the coordination sphere of the hydrated free uranyl ion has always been a point of discussion. Models with four to six water molecules in the equatorial plane have been proposed,[39,40] although it is generally accepted that the uranyl ion is coordinated by five water molecules in the equatorial plane.[41–45]

EXAFS measurements of uranyl nitrate in the presence of tetrabutylammonium nitrate in acetonitrile as well as in $[C_4mim][Tf_2N]$ were performed to confirm the formation of a $[UO_2(NO_3)_3]^-$ species indicated by optical absorption spectroscopy. Furthermore, EXAFS can provide extra structural information, such as bond lengths, for the metal species in solution. Both the EXAFS spectra and corresponding Fourier transforms in acetonitrile and $[C_4mim][Tf_2N]$ exhibit the same structural features (Figure 4). Peaks in the Fourier transforms were not corrected

 © 2007 Wiley-VCH Verlag GmbH & Co. KGaA, Weinheim 

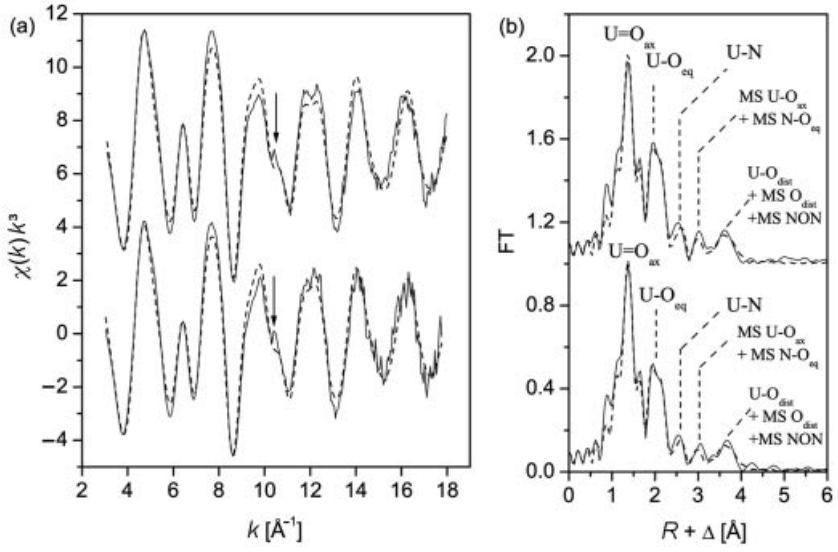


Figure 4. (a) Uranium $L_{III}$-edge $k^3$-weighted EXAFS data and (b) the corresponding Fourier transforms of $[UO_2(NO_3)_3]^-$ in acetonitrile (top) and in the ionic liquid $[C_4mim][Tf_2N]$ (bottom). Experimental data are presented as a continuous line and the theoretical curve as a dotted line. The multiple scattering path N–$O_{eq}$–N is abbreviated as MS NON. The arrow indicates a [2p4f] double-electron excitation.[57]

for the phase shift. The results of the shell-fitting procedure, including phase correction, are given in Tables 2 and 3. The coordination numbers of the equatorial oxygen atoms ($O_{eq}$) and nitrogen atoms were determined in an iterative manner by a free fit. These coordination numbers were subsequently fixed during the shell-fitting procedure in order to avoid correlation problems between $N$ and $\sigma^2$. The coordination number of the distal oxygen atoms was set equal to the coordination number of the nitrogen atoms. The fit results also indicate that three nitrate groups coordinate to uranium(VI) in a bidentate fashion, as shown in Figure 5. The U–$O_{eq}$ distance of 2.48–2.49 Å confirms the sixfold coordination of the uranyl ion as a U–$O_{eq}$ distance between 2.44 and 2.54 Å corresponds to a coordination number of six.[46] The weak peak due to nitrogen backscattering indicates a U–N distance of 2.94 Å (Figure 4). This U–N distance indicates a bidentate coordination of the $NO_3^-$ group and is in good agreement with the U–N distance in solid $Rb[UO_2(NO_3)_3]$ (2.88 Å).[3] The three coordinated nitrate ligands result in complex backscattering features mainly originating from a linear arrangement of the nitrogen atom and the distal oxygen atoms ($O_{dist}$) in each of the $NO_3^-$ ligands, with respect to the uranium atom. In this situation the scattering amplitude is greatly enhanced in the forward scattering direction due to focusing of the electron wave on the next neighbour. This effect is therefore called the "focusing effect". This focusing effect makes the distal oxygen atoms ($O_{dist}$) at a large distance of 4.16 (in acetonitrile) or 4.18 Å (in the ionic liquid $[C_4mim][Tf_2N]$) visible. A similar strong multiple scattering effect has been observed for the tricarbonato species $Ca_2[UO_2(CO_3)_3]$ in aqueous solution.[47] The amplitudes of the multiple scattering paths MS $O_{dist}$ (U–N–$O_{dist}$) and U–N–$O_{dist}$–N are much more pronounced than that of the single scattering path U–$O_{dist}$. It is interesting to note that the U–$O_{dist}$ distance in solution is slightly longer than in the solid {4.09 Å in solid $Rb[UO_2(NO_3)_3]$}.[3] The influence of the effective ligand charge on the bond lengths can be revealed by comparing uranium(VI) coordinated by nitrate and carbonate. The uranyl tricarbonato complex anion $[UO_2(CO_3)_3]^{4-}$ is isostructural with the trinitrato anion $[UO_2(NO_3)_3]^-$.[3,47] The U–$O_{eq}$ distance in the uranyl tricarbonato anion is shorter than that in the uranyl trinitrato anion (2.44 vs. 2.48–2.49 Å). Obviously, there is an influence of the U–$O_{eq}$ electron density on the U–$O_{ax}$ bond length, which results in a longer distance (1.81 Å) for the tricarbonato anion and a shorter one (1.77 Å) for the trinitrato anion.[48] The shorter U–$O_{ax}$ distance for the uranyl trinitrato anion can also be deduced from the ground-state vibrational frequencies. Thus, for the uranyl trinitrato anion the symmetric and asymmetric stretching vibrations are 884 and 956 $cm^{-1}$, respectively, compared to 808 and 856 $cm^{-1}$, respectively, for the tricarbonato anion. According to Badger's rule,[49,50] the U–$O_{ax}$ distance should therefore be smaller in the uranyl trinitrato anion.

Table 2. EXAFS structural parameters for $[UO_2(NO_3)_3]^-$ in acetonitrile.

| | $R$[a] [Å] | $N$[a] | $\sigma^2$ [Å$^2$] |
|---|---|---|---|
| U–$O_{ax}$ | 1.77 | 2[b] | 0.0012 |
| MS U–$O_{ax}$ | 3.54 | 2[b] | 0.0024 |
| U–$O_{eq}$ | 2.48 | 6.4[b] | 0.0069 |
| U–N | 2.92 | 3.1[b] | 0.0032 |
| MS N–$O_{eq}$ | 3.29 | 12.7[b] | 0.0031 |
| U–$O_{dist}$ | 4.16 | 3.1[b] | 0.0061 |
| MS $O_{dist}$ | 4.16 | 6.2[b] | 0.0061 |
| MS N–$O_{dist}$–N | 4.16 | 3.1[b] | 0.0061 |

[a] Errors in distances, $R$, are ±0.01 Å; errors in coordination numbers, $N$, are ±10%. [b] Value fixed during the shell-fitting procedure. $\Delta E$ = 3.85 eV. Weighted $F$-factor = 0.205.

 © 2007 Wiley-VCH Verlag GmbH & Co. KGaA, Weinheim 

Table 3. EXAFS structural parameters for $[UO_2(NO_3)_3]^-$ in $[C_4mim][Tf_2N]$.

| | $R$[a] [Å] | $N$[a] | $\sigma^2$ [Å$^2$] |
|---|---|---|---|
| U–$O_{ax}$ | 1.77 | 2[b] | 0.0012 |
| MS U–$O_{ax}$ | 3.54 | 2[b] | 0.0024 |
| U–$O_{eq}$ | 2.49 | 6.1[b] | 0.0076 |
| U–N | 2.92 | 2.8[b] | 0.0036 |
| MS N–$O_{eq}$ | 3.28 | 12.2[b] | 0.0054 |
| U–$O_{dist}$ | 4.18 | 2.8[b] | 0.0062 |
| MS $O_{dist}$ | 4.18 | 5.6[b] | 0.0062 |
| MS N–$O_{dist}$–N | 4.18 | 2.8[b] | 0.0062 |

[a] Errors in distances, $R$, are ±0.01 Å; errors in coordination numbers, $N$, are ±10%. [b] Value fixed during the shell-fitting procedure. $\Delta E$ = 3.85 eV. Weighted $F$-factor = 0.205.

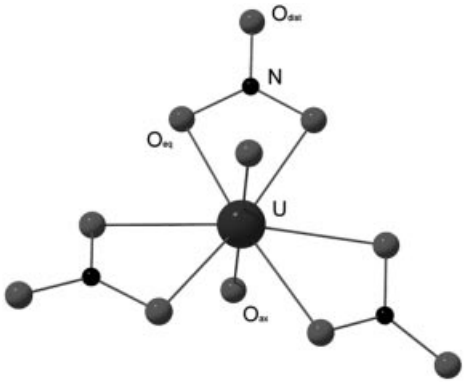


Figure 5. Ball-and-stick representation of the structure of $[UO_2(NO_3)_3]^-$.

The raw $k^3$-weighted EXAFS data of uranyl nitrate in water are shown in Figure 6. Like the optical absorption spectra, the EXAFS spectra of the aqueous solution show only the typical scattering features of the dominant hydrated uranyl ion. The largest peak in the Fourier transform represents the scattering contribution from the two axial oxygen ($O_{ax}$) atoms. The double peak at $R + \Delta$ = 1.8 Å arises from one single shell of equatorial oxygen ($O_{eq}$) atoms. This peak can be completely covered by including one single shell of equatorial oxygen atoms at 2.42 Å in the fitting procedure. The splitting of the $O_{eq}$ shell arises from a superposition of the $O_{ax}$ peak and the $O_{eq}$ peak. Due to the limited $k$-range, the Fourier transform peaks include small satellite peaks. The rather large satellite peak at high $R$-values of the $O_{ax}$ peak coincides with the $O_{eq}$ peak, which gives rise to this peak splitting.[51] Peaks in the Fourier transform were not corrected for the phase shift. The structural parameters of the EXAFS shell fitting, including phase correction, are summarized in Table 4. There are two axial oxygen atoms at 1.77 ± 0.01 Å and five equatorial oxygen atoms at 2.41 ± 0.01 Å. A fivefold coordination of the uranyl ion is characterized by a U–$O_{eq}$ distance between 2.34 and 2.42 Å.[46] These values agree well with the structural parameters obtained previously for the uranyl aqua ion in perchloric acid solution.[41,42]

Table 4. EXAFS structural parameters for uranyl nitrate in aqueous solution.

| | $R$[a] [Å] | $N$[a] | $\sigma^2$ [Å$^2$] |
|---|---|---|---|
| U–$O_{ax}$ | 1.77 | 2[b] | 0.0013 |
| MS U–$O_{ax}$ | 3.54 | 2[b] | 0.0026 |
| U–$O_{eq}$ | 2.41 | 4.9 | 0.0069 |

[a] Errors in distances, $R$, are ±0.01 Å; errors in coordination numbers, $N$, are ±10%. [b] Value fixed during the shell-fitting procedure. $\Delta E$ = 3.2 eV. Weighted $F$-factor = 0.273.

## Conclusions

We have shown that both UV/Vis absorption and EXAFS spectroscopy point unambiguously to the existence of a $[UO_2(NO_3)_3]^-$ coordination polyhedron ($D_{3h}$ sym-

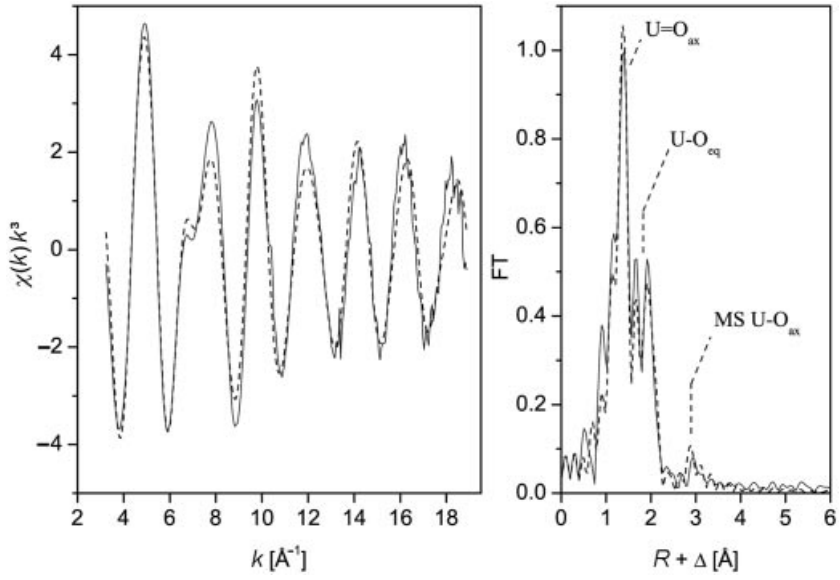


Figure 6. Uranium $L_{III}$-edge $k^3$-weighted EXAFS data (left) and the corresponding Fourier transform (right) of uranyl nitrate in aqueous solution. Experimental data are presented as a continuous line and the theoretical curve as a dotted line.

 © 2007 Wiley-VCH Verlag GmbH & Co. KGaA, Weinheim 

metry) for the uranyl nitrate complex in acetonitrile as well as in the ionic liquid [$C_4$mim][$Tf_2$N]. The sharp peaks in the long-wavelength part of the UV/Vis absorption spectra (21000–24000 $cm^{-1}$) are characteristic of a trigonal symmetry. The fit results of the EXAFS spectra and the corresponding Fourier transforms reveal the presence of six equatorial oxygen ($O_{eq}$) atoms with U–O bond lengths of 2.48–2.49 Å. The U–N distance of 2.92–2.93 Å points to a bidentate coordination of the $NO_3^-$ group. Furthermore, the distances in the equatorial plane around the uranyl ion for solution species are in good agreement with the distances in solid Rb[$UO_2(NO_3)_3$]. Only the U–$O_{dist}$ distance is slightly longer in solution. The increase in the coordination number from $N_{O_{eq}}$ = 5 (aqua ion) to $N_{O_{eq}}$ = 6 ([$UO_2(NO_3)_3]^-$) involves an increase of the U–$O_{eq}$ bond length from 2.41 to 2.48–2.49 Å. In contrast, no evidence has been found for the presence of uranyl nitrato species in aqueous solution under the given experimental conditions.

## Experimental Section

**Samples:** $UO_2(NO_3)_2{\cdot}6H_2O$ and tetrabutylammonium nitrate ($Bu_4NNO_3$) were purchased from Merck and Fluka, respectively. Dry acetonitrile was purchased from Acros. An aqueous solution of uranyl nitrate (50 mM) was prepared by dissolving $UO_2(NO_3)_2{\cdot}6H_2O$ in distilled water. The pH of this solution was 2.4. Acetonitrile was used as solvent for measurements in non-aqueous solution instead of acetone because acetonitrile is more stable than acetone in the presence of uranyl ions. Tetrabutylammonium nitrate ($Bu_4NNO_3$) was added to a solution of $UO_2(NO_3)_2{\cdot}6H_2O$ (50 mM) in acetonitrile to give uranyl/nitrate ratios of beween 1:2 and 1:4. No further changes were observed in the optical absorption spectra at [$UO_2^{2+}$]/[$NO_3^-$] ratios higher than 1:3. To obtain the spectrum of the solvated uranyl ion ("free" or "bare" uranyl ion) in acetonitrile, a solution of $UO_2(ClO_4)_2{\cdot}xH_2O$ (50 mM) was prepared as described in ref.[32] 1-Butyl-3-methylimidazolium bis(trifluoromethylsulfonyl)imide ([$C_4$mim][$Tf_2$N]) was synthesized as described in ref.[35] To reduce the water content, [$C_4$mim][$Tf_2$N] was dried in vacuo at 70 °C before preparing the solutions. $UO_2(NO_3)_2{\cdot}6H_2O$ (50 mM) and tetrabutylammonium nitrate ($Bu_4NNO_3$; 100 mM) were dissolved in [$C_4$mim][$Tf_2$N] to give a total uranyl/nitrate ratio of 1:4. The dissolution of $UO_2(NO_3)_2{\cdot}6H_2O$ and $Bu_4NNO_3$ in [$C_4$mim][$Tf_2$N] took about 3 d and resulted in a transparent, yellow solution. Initial spectroscopic measurements on mixtures of $UO_2(NO_3)_2{\cdot}6H_2O$ and $Bu_4NNO_3$ in [$C_4$mim][$Tf_2$N] did not give the typical absorption spectrum of the uranyl trinitrato complex. However, the [$UO_2(NO_3)_3]^-$ absorption bands were clearly visible when these mixtures were remeasured after several days. This indicates that the kinetics of the formation of the trinitrato complex in the ionic liquid are slow.

**Optical Spectroscopy:** UV/Vis absorption spectra in aqueous solution, acetonitrile and [$C_4$mim][$Tf_2$N] were recorded at room temperature with a Varian Cary 5000 spectrophotometer in the wavelength interval 600–300 nm. Magnetic circular dichroism (MCD) spectra were recorded with an AVIV 62DS circular dichroism spectrometer equipped with an electromagnet (magnetic field strength: 0.9 T) to provide the longitudinal magnetic field.

**EXAFS Spectroscopy:** Uranium $L_{III}$-edge EXAFS spectra were collected at the Rossendorf Beamline at the European Synchrotron Radiation Facility (ESRF, Grenoble, France).[52] The measurements were carried out in transmittance mode using argon-filled ionization chambers at ambient temperature and pressure. Higher harmonics were rejected with two platinum-coated mirrors. The measurements were performed using a double-crystal Si(111) monochromator in equidistant $k$-steps of 0.05 $Å^{-1}$ across the EXAFS region. Three scans were recorded for each sample and then averaged. An yttrium metal foil (first inflection point at 17038 eV) was used for energy calibration. The uranium $L_{III}$ threshold energy, $E_{k=0}$, was defined at 17185 eV. EXAFS data were extracted from the raw absorption spectra by standard methods, including a spline approximation for the atomic background with the program EXAFSPAK.[53] Theoretical phase and amplitude functions were calculated with FEFF 8.2.[54] The scattering phase and amplitude functions were calculated using the crystal structure of uranyl dinitrate trihydrate, $[UO_2(NO_3)_2(H_2O)_2]{\cdot}H_2O$,[55] and the rubidium uranyl salt Rb[$UO_2(NO_3)_3$].[3] The amplitude reduction factor, $S_0^2$, was found to be 0.9 from the FEFF calculation and fixed to that value in the data fits. The coordination number of the uranyl oxygen atoms ($O_{ax}$) in all fits was kept constant at two. The main multiple scattering paths, with their relative importance, are defined according to the notation in Figure 5 and given in the Supporting Information. Hudson and co-workers have indicated that the scattering contributions from paths U–$O_{ax1}$–$O_{ax2}$ and U–$O_{ax1}$–U–$O_{ax1}$ tend to cancel each other out,[56] therefore the twofold-degenerate, four-legged multiple scattering path U–$O_{ax1}$–U–$O_{ax2}$ (abbreviated as MS U–$O_{ax}$) was included in the curve fit by constraining its Debye–Waller factor, $\sigma^2$, and its effective path length to twice the values of the corresponding, freely fitted U–$O_{ax}$ single scattering path. The degeneracy of the multiple scattering paths was included in the coordination numbers $N$, therefore the degeneracy of the dominating multiple scattering paths including the distal oxygen $O_{dist}$, namely U–N–$O_{dist}$–N and U–$O_{dist}$–N (abbreviated as MS $O_{dist}$), was fixed to twice the value of the number of distal oxygen atoms present. Furthermore, the distances and Debye–Waller factor for these multiple scattering paths were linked to $R$ and $\sigma^2$ of the single scattering path U–$O_{dist}$. The number of scattering paths of the three-legged multiple scattering path U–N–$O_{eq}$ was constrained to twice the coordination number of the equatorial oxygen atoms $O_{eq}$, whereas $R$ and $\sigma^2$ were kept free in the fit. Scattering contributions of less than 5% were not considered in the fitting procedure.

**Supporting Information** (see footnote on the first page of this article): Correlation table of the irreducible representations in the different $D_{nh}$ point groups; UV/Vis absorption spectrum and data of $UO_2(NO_3)_2{\cdot}6H_2O$ in water; UV/Vis absorption spectrum and observed vibronic transitions of [$UO_2(NO_3)_3]^-$ in acetonitrile, acetone, and [$C_4$mim][$Tf_2$N]; UV/Vis absorption spectrum of $UO_2$ powder dissolved in [$C_4$mim][$Tf_2$N] with the help of $HNO_3/H_2O$; MCD and UV/Vis absorption spectra of $Bu_4NUO_2(NO_3)_3$ in a PMMA matrix; principal scattering pathways of the photoelectron in the [$UO_2(NO_3)_3]^-$ unit.

## Acknowledgments

The EXAFS measurements were performed at the Rossendorf Beamline at the ESRF. K. S. is a research assistant and R. V. D. a postdoctoral fellow of the Fund for Scientific Research, Flanders (Belgium) (FWO-Vlaanderen). This project was financed by the FWO-Vlaanderen (project G.0508.07) and by the K. U. Leuven (projects GOA03/03 and IDO/05/005). R. V. D. acknowledges financial support from the FWO-Vlaanderen ("Krediet aan Navorsers" project 1.5.099.06) and C. H. acknowledges financial support from the DFG (HE 2297/2-1).

 © 2007 Wiley-VCH Verlag GmbH & Co. KGaA, Weinheim 

[1] S. S. Malcic, L. M. Manojlovic, *Bull. Inst. Nucl. Sci. "Boris Kidrich"*, **1961**, *11*, 135–139.
[2] G. A. Barclay, T. M. Sabine, J. C. Taylor, *Acta Crystallogr.* **1965**, *19*, 205–209.
[3] A. Zalkin, L. K. Templeton, D. H. Templeton, *Acta Crystallogr., Sect. C* **1989**, *45*, 810–811.
[4] G. H. Dieke, A. B. F. Duncan, *Spectroscopic Properties of Uranium Compounds*, McGraw Hill, New York, **1965**.
[5] E. Rabinowitch, R. L. Belford, *Spectroscopy and Photochemistry of Uranyl Compounds*, Pergamon, Oxford, **1964**.
[6] P. Brint, A. J. McCaffery, *Mol. Phys.* **1973**, *25*, 311–322.
[7] C. Görller-Walrand, W. Colen, *Inorg. Chim. Acta* **1984**, *84*, 183–188.
[8] R. G. Denning, D. N. P. Foster, T. R. Snellgrove, D. R. Woodwark, *Mol. Phys.* **1979**, *37*, 1089–1107.
[9] L. Kaplan, R. A. Hildebrandt, M. Ader, *J. Inorg. Nucl. Chem.* **1956**, *2*, 153–163.
[10] H. A. Thompson, G. E. Brown Jr, G. A. Parks, *Am. Min.* **1997**, *82*, 483–496.
[11] C. E. Barnes, Y. Shin, S. Saengkerdsub, S. Dai, *Inorg. Chem.* **2000**, *39*, 862–864.
[12] J. J. Katz, G. T. Seaborg, L. R. Morss, *The Chemistry of the Actinide Elements*, Chapman and Hall, New York, **1986**.
[13] Yu. A. Zolotov, *Macrocyclic Compounds in Analytical Chemistry*, John Wiley & Sons, New York, **1997**.
[14] Yu. S. Fedorov, B. Ya. Zilberman, *Radiochemistry* **2000**, *42*, 242–246.
[15] Yu. S. Fedorov, B. Ya. Zilberman, *Radiochemistry* **1999**, *41*, 545–550.
[16] Yu. S. Fedorov, I. V. Blazheva, B. Ya. Zilberman, *Radiochemistry* **2000**, *42*, 74–78.
[17] Yu. S. Fedorov, B. Ya. Zilberman, S. M. Kulikov, I. V. Blazheva, E. N. Mishin, *Solvent Extr. Ion Exch.* **1999**, *17*, 243–257.
[18] Y. Oda, H. Funasaka, Y. Nakamura, H. Adachi, *J. Alloys Compd.* **1997**, *255*, 24–30.
[19] A. K. Mohammed, J. C. Sullivan, K. L. Nash, *Solvent Extr. Ion Exch.* **2000**, *18*, 809–820.
[20] C. Den Auwer, C. Lecouteux, M. C. Charbonnel, C. Madic, R. Guillaumont, *Polyhedron* **1997**, *16*, 2233–2238.
[21] C. Den Auwer, M. C. Charbonnel, M. T. Presson, C. Madic, R. Guillaumont, *Polyhedron* **1998**, *17*, 4507–4517.
[22] R. Chiarizia, M. P. Jensen, M. Borkowski, J. R. Ferraro, P. Thiyagarajan, K. C. Littrell, *Solvent Extr. Ion Exch.* **2003**, *21*, 1–27.
[23] K. Binnemans, *Chem. Rev.* **2007**, *107*, 2592–2614.
[24] V. A. Cocalia, K. E. Gutowski, R. D. Rogers, *Coord. Chem. Rev.* **2006**, *250*, 755–764.
[25] P. Giridhar, K. A. Venkatesan, T. G. Srinivasan, P. R. V. Rao, *J. Radioanal. Nucl. Chem.* **2005**, *265*, 31–38.
[26] M. O. Sornein, C. Cannes, C. Le Naour, G. Lagarde, E. Simoni, J. C. Berthet, *Inorg. Chem.* **2006**, *45*, 10419–10421.
[27] A. E. Bradley, C. Hardacre, M. Nieuwenhuyzen, W. R. Pitner, D. Sanders, K. R. Seddon, R. C. Thied, *Inorg. Chem.* **2004**, *43*, 2503–2514.
[28] A. Chaumont, G. Wipff, *Inorg. Chem.* **2004**, *43*, 5891–5901.
[29] C. Gaillard, A. El Azzi, I. Billard, H. Bolvin, C. Hennig, *Inorg. Chem.* **2005**, *44*, 852–861.
[30] A. E. Visser, M. P. Jensen, I. Laszak, K. L. Nash, G. R. Choppin, R. D. Rogers, *Inorg. Chem.* **2003**, *42*, 2197–2199.
[31] C. Gaillard, A. Chaumont, I. Billard, C. Hennig, A. Ouadi, G. Wipff, *Inorg. Chem.* **2007**, *46*, 4815–4826.
[32] K. Servaes, C. Hennig, R. Van Deun, C. Görller-Walrand, *Inorg. Chem.* **2005**, *44*, 7705–7707.
[33] C. Görller-Walrand, S. De Jaegere, *J. Chim. Phys.* **1972**, *4*, 726–736.
[34] S. De Houwer, C. Görller-Walrand, *J. Alloys Compd.* **2001**, *323–324*, 683–687.
[35] P. Nockemann, K. Binnemans, K. Driesen, *Chem. Phys. Lett.* **2005**, *415*, 131–136.
[36] M. das Graças Gomes, S. da S. S. Borges, L. G. F. Lopes, D. W. Franco, *Anal. Chim. Acta* **1993**, *282*, 81–85.
[37] *Gmelin Handbook*, U, Uranium suppl. vol. D1 ("Properties of uranium ions in solutions and melts"), system number 55, Springer, Berlin, **1984**.
[38] A. Ruas, O. Bernard, B. Caniffi, J.-P. Simonin, P. Turq, L. Blum, P. Moisy, *J. Phys. Chem. B* **2006**, *110*, 3435–3443.
[39] J.-C. G. Bünzli, *J. Alloys Compd.* **1993**, *192*, 266–270.
[40] S. Spencer, L. Gagliardi, N. C. Handy, A. G. Ioannou, C.-K. Skylaris, A. Willetts, A. M. Simper, *J. Phys. Chem. A* **1999**, *103*, 1831–1837.
[41] V. Vallet, U. Wahlgren, B. Schimmelpfennig, H. Moll, Z. Szabó, I. Grenthe, *Inorg. Chem.* **2001**, *40*, 3516–3525.
[42] C. Hennig, J. Tutschku, A. Rossberg, G. Bernhard, A. C. Scheinost, *Inorg. Chem.* **2005**, *44*, 6655–6661.
[43] M. Bühl, R. Diss, G. Wipff, *J. Am. Chem. Soc.* **2005**, *127*, 13506–13507.
[44] J. Neuefeind, L. Soderholm, S. Skanthakumar, *J. Phys. Chem. A* **2004**, *108*, 2733–2739.
[45] C. Görller-Walrand, W. Colen, *Chem. Phys. Lett.* **1982**, *93*, 82–85.
[46] M. R. Antonio, L. Soderholm, *The Chemistry of the Actinide and Transactinide Elements*, Springer, Dordrecht, The Netherlands, **2006**, vol. 5, pp. 3086–3198.
[47] G. Bernhard, G. Geipel, T. Reich, V. Brendler, S. Amayri, H. Nitsche, *Radiochim. Acta* **2001**, *89*, 511–518.
[48] S. P. McGlynn, J. K. Smith, W. C. Neely, *J. Chem. Phys.* **1961**, *35*, 105–116.
[49] R. G. Denning, *Struct. Bonding (Berlin)* **1992**, *79*, 215–276.
[50] J. R. Bartlett, R. P. Cooney, *J. Mol. Struct.* **1989**, *193*, 295–300.
[51] C. Hennig, K. Schmeide, V. Brendler, H. Moll, S. Tsushima, A. C. Scheinost, *Inorg. Chem.*; DOI: 10.1021/ic0619759.
[52] W. Matz, N. Schell, G. Bernhard, F. Prokert, T. Reich, J. Claußner, W. Oehme, R. Schlenk, S. Dienel, H. Funke, F. Eichhorn, M. Betzl, D. Pröhl, U. Strauch, G. Hüttig, H. Krug, W. Neumann, V. Brendler, P. Reichel, M. A. Denecke, H. Nitsche, *J. Synchrotron Radiat.* **1999**, *6*, 1076–1085.
[53] G. N. George, I. J. Pickering, *EXAFSPAK, a suite of computer programs for analysis of X-ray absorption spectra*, Stanford Synchrotron Radiation Laboratory, Stanford, **2000**.
[54] A. L. Ankudinov, B. Ravel, J. J. Rehr, S. D. Conradson, *Phys. Rev. B* **1998**, *58*, 7565–7576.
[55] R. R. Shuvalov, P. C. Burns, *Acta Crystallogr., Sect. C* **2003**, *59*, i71–i73.
[56] E. A. Hudson, P. G. Allen, L. J. Terminello, M. A. Denecke, T. Reich, *Phys. Rev. B* **1996**, *54*, 156–165.
[57] C. Hennig, *Phys. Rev. B* **2007**, *75*, 035120-1-7.

Received: May 2, 2007
Published Online: September 18, 2007

 © 2007 Wiley-VCH Verlag GmbH & Co. KGaA, Weinheim 

DOI: 10.1002/ejic.200700447

# Synthesis and Reactivity of Cobalt Complexes with Pendant Nitrogen Functional Groups

**Longjin Li,[a] Shuang Han,[b] Qiang Li,[a] Zhenxia Chen,[a] and Zhen Pang*[a]**

**Keywords:** Cyclopentadienylcobalt complexes / Carbonylcobalt complexes

Several derivatives of cyclopentadienylcobalt complexes having a pendant amino-functionalised side chain (Cp′) are described, the cyclopentadienyl ligands being (2-aminoethyl)cyclopentadienyl, (2-piperidinoethyl)cyclopentadienyl, 1-(2-piperidinoethyl)-2,3,4,5-tetraisopropylcyclopentadienyl and 2-picolylcyclopentadienyl. Chelation by the amino-functionalised side chain occurred when the Cp*-cobalt(I) dicarbonyl complexes **5**, **6**, **7** and **8** were oxidised by iodine, thereby forming the corresponding Cp*-cobalt(III) chelates **9**, **10**, **11** and **12**, respectively, through the diiodocarbonyl intermediates **5′**, **6′**, **7′** and **8′**, respectively. The stabilities of the intermediates differ greatly due to the different amino functions in the pendant side chain. Structural studies of **9**, **10** and **12** were carried out and the correlation of the I–Co–I angles and the repulsive forces from the amino-functionalised groups with the stabilities of the intermediates is discussed. The diiodocarbonyl-$\eta^5$-(2-piperidinylethyl)cyclopentadienylcobalt(III) intermediate **6′** becomes reduced to **6** by the CO released upon chelation of the former when the concentration of CO reaches about 0.088 mol L$^{-1}$. The chelated piperidine group in **10** could be easily replaced by triphenylphosphane to form the diiodotriphenylphosphanyl-$\eta^5$-(2-piperidinioethyl)cyclopentadienylcobalt(III) iodide dichloromethane solvate **13** in the presence of hydrogen iodide. A strong N–H···I hydrogen bond with an N···I distance of 3.414(14) Å and a D–H···A angle of 164.1° were found in **13**.
(© Wiley-VCH Verlag GmbH & Co. KGaA, 69451 Weinheim, Germany, 2007)

## Introduction

The cyclopentadienyl group is one of the most important ligands in organometallic chemistry.[1] Its derivatives with Lewis bases in a pendant side chain that are capable of binding to hard and soft centres in a hemilabile manner promise a rich coordination chemistry and unusual reactions at the metal centre.[2] The Lewis bases may included alkenes,[3] phosphorus atoms,[4] thioethers, ethers and ester groups.[5] N-Based Lewis bases tethered to the Cp ligand have been frequently used as hemilabile ligands. Such ligands can only weakly coordinate to late transition metal centres forming a chelate bond which can also be easily broken under mild conditions. Since the binding strength between the metal and the donor ligand can be controlled sterically or electronically, structural modification to such a pendant side chain can greatly influence the physical and chemical properties of these complexes[6] and some molecular switches, which have been designed, are based on this concept.[7,8] Furthermore, the weak coordinate bond in these complexes can be easily broken under mild condition thereby creating a vacant site on the metal and such complexes therefore have applications in catalysis. The reactivity of the active intermediate is strongly influenced by the changes in the electronic density on the metal centre and the steric nature of the chelating donor moiety. Thus, an improved understanding of the factors governing the chelation of the tethered functional group should lead to more control over the design of more efficient catalytic processes. Many complexes with a chelating pendant Lewis base tethered to a Cp ligand have be synthesised and studied.[9–22] We are interested in the chemistry of the half-sandwich type complexes with a pendant chelating functional group, especially those containing nitrogen atoms in the pendant side chain and in the factors which can influence the ability of the pendant group to chelate to the metal. In this paper we report the synthesis and reactivity of several cobalt complexes with nitrogen functionalised pendant side chain cyclopentadienyl ligands.

## Results and Discussion

Four compounds $C_5H_5CH_2CH_2NH_2$ (**1**), $C_5H_5CH_2CH_2NC_5H_{10}$ (**2**), $C_5(C_3H_7)_4HCH_2CH_2NC_5H_{10}$ (**3**) and $C_5H_5CH_2NC_5H_4$ (**4**) with a space of two carbon atoms between the nitrogen atom and cyclopentadienyl ring were all synthesized using a similar strategy, i.e. treatment of so-

[a] Department of Chemistry, Shanghai Key Laboratory of Molecular Catalysis and Innovative Materials,
Fudan University, Shanghai 200433, P. R. China
E-mail: zpang@fudan.edu.cn
[b] Department of Chemistry, Yuncheng College of Shanxi Province,
Yuncheng City, Shanxi Province 044000, P. R. China

 © 2007 Wiley-VCH Verlag GmbH & Co. KGaA, Weinheim 

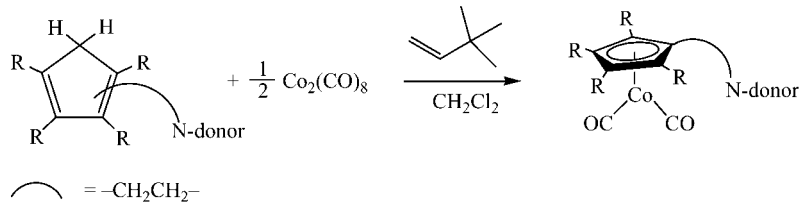


**1**, R = H, N-donor = $-NH_2$
**2**, R = H, N-donor = cyclo-$NC_5H_{10}$
**3**, R = $-CH(CH_3)_2$, N-donor = *cyclo*-$NC_5H_{10}$
**4**, R = H, N-donor = $NC_5H_4$

**5**, R = H, N-donor = $-NH_2$
**6**, R = H, N-donor = cyclo-$NC_5H_{10}$
**7**, R = $-CH(CH_3)_2$, N-donor = *cyclo*-$NC_5H_{10}$
**8**, R = H, N-donor = $NC_5H_4$

Scheme 1.

dium cyclopentadienide with a suitable halogenated alkylamine followed by standard aqueous workup. Because of the good solubility of **1** in aqueous solution, strong acidic (pH $<$ 1) and basic (pH $>$ 14) conditions must be kept during the aqueous workup in order to increase the yield. The reaction of compounds **1**–**4** with $Co_2(CO)_8$ in dichloromethane in the presence of a sacrificial olefin 3,3-dimethyl-1-butene gave the substituted dicarbonylcyclopentadienylcobalt(I) complexes **5**–**8** in moderate yields, Scheme 1.[23] If the syntheses were to be done in a higher boiling point solvent, the yields should increase.

All the dicarbonylcobalt(I) complexes show two characteristic absorption bands in their IR spectra indicating that two terminal carbonyl groups are present and that the nitrogen atoms in the side chains do not coordinate to the cobalt atoms. No chelation was observed between the cobalt(I) and the nitrogen functional group except under irradiation of light.[24] The characteristic $\nu$(CO) data are listed in Table 1.

Table 1. Characteristic CO stretching frequencies of dicarbonylcobalt(I) complex and their corresponding diiodo-monocarbonylcobalt(III) intermediates.

| Cp′(CO)$_2$Co | $\nu$(CO) [cm$^{-1}$][a] | Monocarbonyl | $\nu$(CO) [cm$^{-1}$] |
|---|---|---|---|
| **5** | 2017, 1951 | **5′** | 2068[b], 2074[c] |
| **6** | 2019, 1954 | **6′** | 2060[b], 2066[c] |
| **7** | 2003, 1943 | **7′** | 2050[a], 2046[b] |
| **8** | 2016, 1948 | **8′** | 2077[c] |

[a] Neat sample. [b] KBr pellets. [c] Dichloromethane solution.

Complexes **5**–**8** can be easily oxidised by iodine to yield the corresponding cobalt(III) complexes.[25] It has been reported that when iodine is added to an ether solution of carbonyl cyclopentadienylcobalt(I) complexes with an N-donor function in the side chain, the corresponding chelated diiodo-cobalt(III) complexes precipitate spontaneously from the reaction mixture as black microcrystals.[24a] It is believed that the chelate is formed via the diiodocarbonyl complex (vide infra) since, when the CO-free chelate precipitates, the solution is still dark purple in colour indicating the presence of the monocarbonyl species and this is supported by $^1$H NMR spectroscopic observations. In our experiment, the observations made upon the addition of iodine to the dichloromethane solutions of **5**–**8** are consistent with the literature report because they show evidence of the appearance of a strong carbonyl absorption band at higher frequencies for the solutions which is in contrast to the two carbonyl stretching frequencies observed for the precursors. This carbonyl absorption must come from the reaction intermediates **5′**–**8′** as listed in Table 1. However, in all cases, the black purple precipitate appeared immediately after the addition of iodine and the isolated precipitates also showed one carbonyl absorption band. Elemental analyses and $^1$H NMR spectroscopy indicated that the isolated products were mixtures of the CO-free chelates **9**–**12** and their corresponding diiodocarbonyl complexes **5′**−**8′**. For example, the $^1$H NMR spectrum of the precipitate obtained from the solution of iodine and **5** shows three peaks at $\delta$ = 4.22, 3.60 and 2.42 ppm. The first and third peaks result from the methylene groups between the cyclopentadienyl and amino groups in chelate **9**. The peak of 3.60 ppm could also come from the dimethylene group but it is shifted 0.12 ppm downfield compared with the similar resonance in **5**, indicating a free side chain in the $Co^{III}$ product **5′**. A carbonyl stretching frequency at 2068 cm$^{-1}$ was found for the solid but its intensity diminished at room temperature after one weak indicating the existence of the unstable **5′** and, hence, the isolated solid was initially a mixture of **5′** and **9**. The carbonyl stretching frequency of the solid product isolated from a solution of iodine and **6** or **7** was found at 2060 or 2046 cm$^{-1}$, respectively, but the signal disappeared at room temperature after about one day indicating the isolated products to be mixtures of **6′** and **10** or **7′** and **11**, respectively. Only the precipitate isolated form a solution of iodine and **8** gave the pure chelated product **12**. The stability of the reaction intermediates is therefore of the order **5′** $>$ **6′**:**7′** $>$ **8′**. The oxidising process is illustrated in Scheme 2.

The crystal structures of the chelates **9**, **10** and **12** were determined and all of them show that the tethered amino group is intramolecularly coordinated to the cobalt atom. The ORTEP diagrams and the selected structural parameters of **9**, **10** and **12** are given in Figure 1, Figure 2 and Figure 3. The Co–N bond lengths in **9**, **10** and **12** were found to be 1.979(8), 2.097(3) and 1.956(6) Å, respectively. All of these bond lengths are slightly shorter than those in related tetramethyl-substituted diiodocyclopentadienylcobalt(III) complexes, e.g. 2.115(6) Å in diiodo-$\eta^5$:$\eta^1$-[l-(2-*N*,*N*-dimethylaminoethyl)-2,3,4,5-tetramethyl cyclopenta-

 © 2007 Wiley-VCH Verlag GmbH & Co. KGaA, Weinheim 

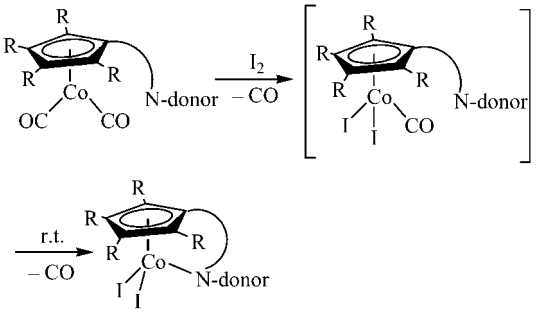


**9**, N-donor = -$NH_2$, R = H
**10**, N-donor = *cyclo*-$NC_5H_{10}$, R = H
**11**, N-donor = *cyclo*-$NC_5H_{10}$, R = -$CH(CH_3)_2$
**12**, N-donor = $NC_5H_4$, R = H

Scheme 2.

dienyl] cobalt(III) ("aminoethyl")[24a] and 2.205(2) Å in diiodo-$\eta^5$:$\eta^1$-[l-[2-(dimethylamino)phenyl]-2,3,4,5-tetramethylcyclopentadienyl]cobalt(III) ("aminophenyl").[18] Considering that the alkyl ring of piperidine is an electron-releasing substituent, the nitrogen atom in the tethered side chain in **10** should be a stronger σ donor compared with that in **9** and **12** and the chelate bond in **10** would be expected to be the strongest one among the three analogues. However, the chelate bond in **10** was found to be the longest. For easy comparison between these analogues, some structural parameters are listed in Table 2. The average lengths of the Co–I bonds in **9**, **10** and **12** are 2.5979(10), 2.5865(3) and 2.5788(16) Å, respectively − all slightly shorter than 2.622(2) Å found in "aminoethyl" and 2.604(1) Å found in "aminophenyl". The average cobalt–carbon(ring) bond lengths show the same trend but all are still in the expected range. The I–Co–I bond angles are 96.50(5), 92.70(2) and 96.68(4) degrees in **9**, **10** and **12**, respectively. The corresponding values reported for "aminoethyl" and "aminophenyl" are 94.5(1) and 91.302(12)°, respectively. The I–Co–N bond angles found in **9**, **10** and **12** are 92.07(16), 100.32(8) and 95.12(18)°, respectively. A comparison of the above structural data indicates that a large repulsive force might exist in **10** between the iodine ligands and the methylene groups in the piperidine ring adjacent to the nitrogen atom which pushes the iodine ligands away from the piperidine moiety and leads to the smallest I–Co–I angle as well as the longest Co–N bond length among the three chelates.

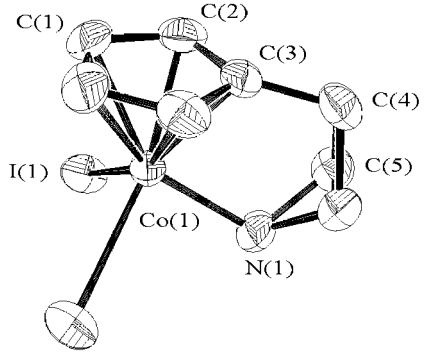


Figure 1. ORTEP diagram of **9** with the probability ellipsoids drawn at the 50% level. Hydrogen atoms have been omitted for clarity. Selected bond lengths [Å] and angles [°]: Average Co–C(ring) 2.045(1), Co(1)–N(1) 1.979(8), Co(1)–I(1) 2.5979(10), Average C–C(ring) 1.4054(4), I(1)–Co(1)–I(1A) 1 96.50(5), I(1)–Co(1)–N(1) 92.07(16), I(1A)–Co(1)–N(1) 92.07(16), Co(1)–N(1)–C(5) 110.3(7).

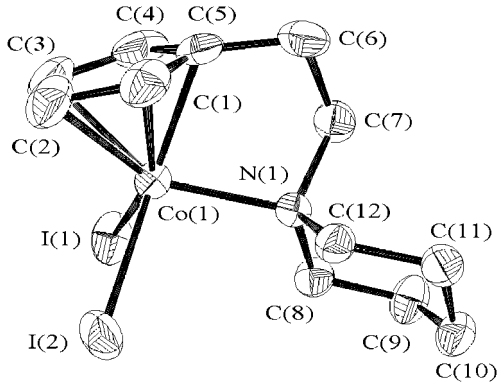


Figure 2. ORTEP diagram of **10** with the probability ellipsoids drawn at the 50% level. Hydrogen atoms have been omitted for clarity. Selected bond lengths [Å] and angles [°]: Average Co–C(ring) 2.055(6), Co(1)–N(1) 2.097(3), Co(1)–I(1) 2.6015(7), Co(1)–I(2) 2.5714(8), average C–C(ring) 1.4084(6), I(1)–Co(1)–I(2) 92.70(2), I(1)–Co(1)–N(1) 100.32(8), I(2)–Co(1)–N(1) 96.34(9), Co(1)–N(1)–C(7) 104.1(2).

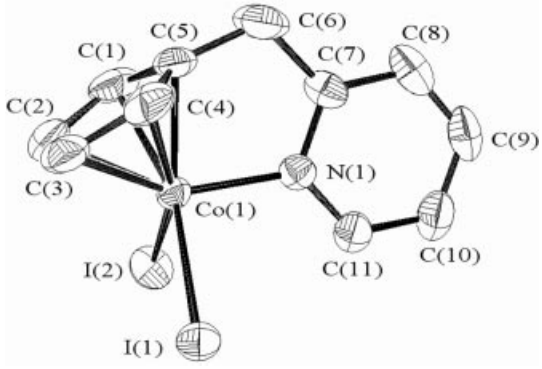


Figure 3. ORTEP diagram of **12** with the probability ellipsoids drawn at the 50% level. Hydrogen atoms have been omitted for clarity. Selected bond lengths [Å] and angles [°]: Average Co–C(ring) 2.039(8), Co(1)–N(1) 1.956(6), Co(1)–I(1) 2.5779(16), Co(1)–I(2) 2.5796(16), average C–C(ring) 1.403(14), N(1)–C(7) 1.351(10), N(1)–C(11) 1.327(10), C(7)–C(8) 1.392(12), C(8)–C(9) 1.360(14), C(9)–C(10) 1.370(14), C(10)–C(11) 1.365(12), I(1)–Co(1)–I(2) 96.68(4), I(1)–Co(1)–N(1) 95.12(18), I(2)–Co(1)–N(1) 95.12(19), Co(1)–N(1)–C(7) 116.9(5).

The COSY spectrum of **10** reveals that the methylene protons in the piperidine ring adjacent to nitrogen atom suffer large steric hindrance and retain their configuration in solution at room temperature (Figure 4). The methylene protons on the α carbon in the piperidine ring are split into two sets of signals. The signals of the protons in the *e* position at $\delta$ = 3.52 show a strong correlation with the methylene protons on the β carbon in the piperidine ring ($\delta$ = 1.72 ppm) and the signals of the protons in the *a* position at $\delta$ = 2.93 show a strong correlation with the methylene

 © 2007 Wiley-VCH Verlag GmbH & Co. KGaA, Weinheim 

Table 2. List of the structural parameters of the cyclopentadienylcobalt complexes with a nitrogen functional group in the pendant side chain.

| Chelates | I–Co−I [°] | Co–N [Å] | Co–$I_{av}$ [Å] | Co–$C(ring)_{av}$ [Å] |
|---|---|---|---|---|
| **9** | 96.50(5) | 1.979(8) | 2.5979(10) | 2.044(7) |
| **10** | 92.70(2) | 2.097(3) | 2.5865(3) | 2.055(4) |
| **12** | 96.68(4) | 1.956(6) | 2.5788(16) | 2.039(8) |
| **13** | 95.40(8) | 2.239(5) (Co–P) | 2.580(3) | 2.094(17) |
| Aminoethyl[24a] | 94.5(1) | 2.115(6) | 2.622(2) | 2.095(5) |
| Aminophenyl[15] | 91.302(12) | 2.205(2) | 2.604(1) | 2.080(3) |

protons on the ω carbon in the piperidine ring ($\delta$ = 1.22 ppm). The methylene protons on the β carbon in the piperidine are in a free-flipping motion and give rise to a broadened multiplet. We can deduce that the flipping of the methylene protons on the α carbon in the piperidine ring in **10** is prevented by steric hindrance in the chelated form. This steric hindrance results from the repulsive force of the iodine ligands which keeps the σ orbitals between cobalt and the amino nitrogen from fully overlapping and thus a longer chelate Co–N bond results. The side chains in **9** and **10** are coordinated to the cobalt in a zigzag fashion and, consequently, the latter can be expected to exist as chiral molecules. However, the very fast flip of the side chain makes the two enantiomers show only one set of signals in their $^1$H NMR spectra. Similar situations have also been found in "aminoethyl" and "aminophenyl" and by Wang et al. in the molybdenum complex $[C_5H_4CH_2CH_2NMe_2]$-$Mo(CO)_2I$.[26] In the crystal structure of **12**, an idealised mirror plane of the $Cp^*CoI_2$ fragment was found which almost coincides with the plane of the pyridine ring. The observed orientation allows the maximum overlap between the π system in pyridine and one of the two suitable d-type donor orbitals at the cobalt centre.[27] Pyridine is considered a moderate π acceptor because its LUMO is not as low in energy as, for example, that of pyrazine which is known as a good π acceptor.[28] Thus, besides the normal σ interaction, a weak π interaction between the metal and donor nitrogen is also possible. This binding pattern between the nitrogen and cobalt results in the shortest Co–N bond among the three. In the indenyl-nickel analogues reported by L. E. Groux and D. Zargarian,[30] N–C bond lengths and C–C bond lengths in the tethered pyridine moiety were found to be longer in the chelated form [average 1.354(3) Å and 1.376(3) Å, respectively] than in the non-chelated form [average 1.335(5) Å and 1.360(6) Å, respectively]. Thus a delocalisation of electron density from nickel to the pyridine π system could be assumed. The corresponding N–C bond lengths [average 1.339(10) Å] and the C–C bond lengths [average 1.372(13) Å] found in **12** are comparable with those of the chelated forms of the indenyl-nickel complexes. Comparing the slightly shorter C–C bond lengths in the Cp ring [average 1.403(14) Å] found in **12** with the corresponding data for **9** and **10** [average 1.4054(4) and 1.4084(6) Å, respectively], a possible delocalisation of electron density from cobalt to the pyridine π system is likely. The σ, π interaction between a donor atom possessing d orbitals (such as S and P from the ligand) and the metal in half-sandwich complexes is also known.[31,32] Although nitrogen does not have an available d orbital, the π system of pyridine makes the donor nitrogen atom in the tethered side chain of **12** undergo a stronger interaction with the metal compared with an S or P atom. Thus we may assert that there is a partial double bond in existence in **12** which leads to a shorter Co–N bond.

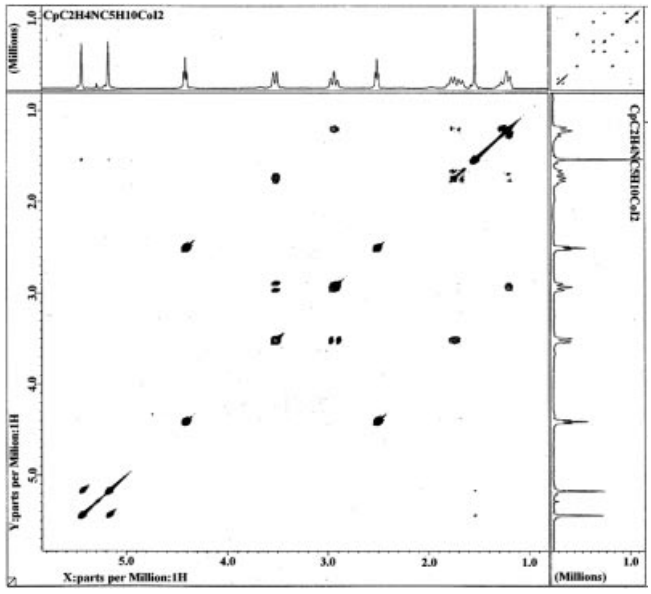


Figure 4. COSY spectrum of diiodo-$\eta^5$:$\eta^1$-(2-piperidinoethyl)cyclopentadienylcobalt(III) ($C_5H_4C_2H_4N_5H_{10}CoI_2$) (**10**) in $CDCl_3$ at 25 °C.

Since the metal–CO bond is weaker[25] for the cobalt(III) complex compared with that in the cobalt(I) complex, the amino nitrogen as a σ donor in the pendant side chain can replace the CO group in the oxidised diiodocarbonyl intermediates. Although there is greater steric hindrance around the donor atom in the piperidine moiety compared with the amino moiety, the formation of **10** was still found to be much faster than that of **9**. This phenomenon suggests that the rate of chelation might be determined by the strength of the Lewis basicity of the nitrogen atom in the donor function. However, by oxidation of **8** with iodine, pure **12** was obtained directly and we did not find a carbonyl adsorption band in the precipitate thus indicating the chelation here is the fastest among the four dicarbonyl reaction precursors. If the σ donor ability of the lone pair on the nitrogen atom in the pendant side chain were only determined by the hybridisation of the orbital, the rate of chelation in **8** should be slower than was observed in **6** or **7**. The

 © 2007 Wiley-VCH Verlag GmbH & Co. KGaA, Weinheim 

driving force for the faster rate of chelation can be attributed to the formation of a partial double bond between cobalt and nitrogen. The π interaction between cobalt(III) and nitrogen as well as the less steric hindrance and the low degree of freedom in the functionalised arm in **8** are more than enough to compensate for the lower σ donor ability of the N-based pendant function. Thus, the shortest lifetime of the diiodocarbonyl intermediate **8′** and the fastest rate of chelation observed during the oxidation process of **8** can be understood.

It has been demonstrated by Jutzi et al. that performing the reduction of diiodo cobalt(III) chelates with sodium amalgam under an atmosphere of carbon monoxide leads to the formation of dicarbonylcobalt(I) species. Without the presence of sodium amalgam, only diiodocarbonylcobalt(III) was formed in an equilibrium with the corresponding diiodo cobalt(III) chelate.[24,29] Irreversible displacement of the intramolecular coordinated ligand was only achieved under very drastic conditions. In our experiments, we found that carbon monoxide not only replaced the intramolecularly coordinated ligand but also reduced the cobalt(III) complex to a cobalt(I) complex. In a airtight reaction vessel, we observed that the reaction intermediate diiodocarbonyl-η$^5$-(2-piperidinylethyl)cyclopentadienylcobalt(III) **6′** was reduced to its corresponding dicarbonylcobalt(I) **6** by the CO released during the chelation of the tethered piperidinyl ligand as shown by the IR spectrum depicted in Figure 5. Since the decay of the adsorption of the metal–carbonyl bond at 2066 cm$^{-1}$ clearly shows the pattern of a first-order reaction and the plot of logA($\nu_{CO}$) vs. *t* has a good linear relationship ($R_2 > 0.999$) after an 882 s inducing period, the relationship between the concentration of the intermediate and time can be deduced. We estimated the initial absorbance (*t* = 0) of the diiodocarbonylcobalt(III) intermediate from the interception of the line with the ordinate by extrapolation. The carbonyl absorbance of **6** in dichloromethane was found obey the Lambert–Beer law quiet well within our experimental range. The concentration of each species at anytime can thus be calculated and such data are listed in Table 3. The reaction occurring in the IR cell can be described as shown in Scheme 3.

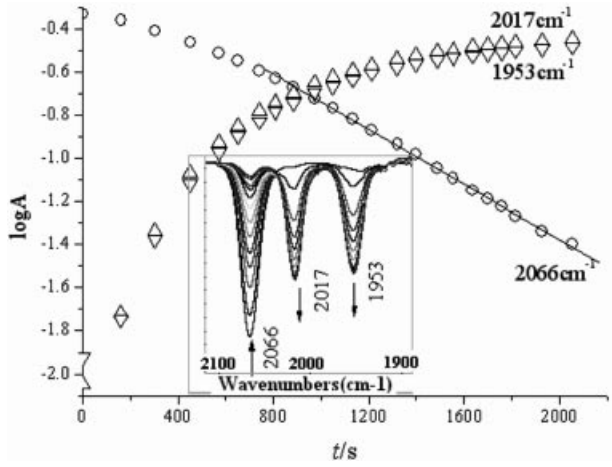


Figure 5. Reduction of diiodocarbonyl-η$^5$-(2-piperidinylethyl)cyclopentadienylcobalt(III) by carbon monoxide released via its own chelation. The inset IR spectra show the reducing *ν*(CO) of **6′** at 2066 cm$^{-1}$ and the increasing *ν*(CO) of **6** at 2017 and 1953 cm$^{-1}$, respectively.

Table 3. Changes of the carbonyl absorbance during the chelation of **6** after being oxidised by iodine in dichloromethane solution.

| *t* / s | 2066 cm$^{-1}$ *A* | 2017 cm$^{-1}$ *A* | 1953 cm$^{-1}$ *A* | CO released [mol L$^{-1}$] | CO consumed [mol L$^{-1}$] | free CO [mol L$^{-1}$] |
|---|---|---|---|---|---|---|
| 0 | 0.468 | 0.009 | 0.012 | | | |
| 161 | 0.439 | 0.019 | 0.018 | 0.174 | 0.0002 | 0.1674 |
| 304 | 0.391 | 0.046 | 0.042 | 0.188 | 0.0021 | 0.1659 |
| 451 | 0.346 | 0.086 | 0.076 | 0.202 | 0.0073 | 0.1574 |
| 571 | 0.309 | 0.119 | 0.107 | 0.214 | 0.0149 | 0.1502 |
| 651 | 0.283 | 0.142 | 0.128 | 0.222 | 0.0213 | 0.1448 |
| 742 | 0.255 | 0.166 | 0.149 | 0.23 | 0.0256 | 0.1396 |
| 808 | 0.235 | 0.183 | 0.165 | 0.236 | 0.0302 | 0.136 |
| 882 | 0.214 | 0.202 | 0.181 | 0.199 | 0.0335 | 0.0878 |
| 972 | 0.19 | 0.225 | 0.203 | 0.212 | 0.0371 | 0.0877 |
| 1050 | 0.171 | 0.24 | 0.217 | 0.222 | 0.0415 | 0.0892 |
| 1133 | 0.152 | 0.257 | 0.233 | 0.232 | 0.0444 | 0.0891 |
| 1213 | 0.135 | 0.271 | 0.249 | 0.24 | 0.0476 | 0.0893 |
| 1319 | 0.116 | 0.29 | 0.264 | 0.25 | 0.0503 | 0.088 |
| 1397 | 0.104 | 0.302 | 0.276 | 0.256 | 0.0539 | 0.0873 |
| 1487 | 0.09 | 0.313 | 0.287 | 0.262 | 0.0562 | 0.0873 |
| 1554 | 0.081 | 0.318 | 0.295 | 0.267 | 0.0583 | 0.0887 |
| 1634 | 0.071 | 0.33 | 0.301 | 0.271 | 0.0593 | 0.0863 |
| 1699 | 0.065 | 0.335 | 0.308 | 0.274 | 0.0616 | 0.0868 |
| 1757 | 0.06 | 0.342 | 0.313 | 0.277 | 0.0625 | 0.0855 |
| 1817 | 0.054 | 0.344 | 0.317 | 0.28 | 0.0639 | 0.087 |
| 1927 | 0.046 | 0.351 | 0.324 | 0.284 | 0.0643 | 0.0872 |
| 2052 | 0.04 | 0.359 | 0.331 | 0.288 | 0.0656 | 0.0867 |
| | | | | | Average: | 0.0876 |

 © 2007 Wiley-VCH Verlag GmbH & Co. KGaA, Weinheim 

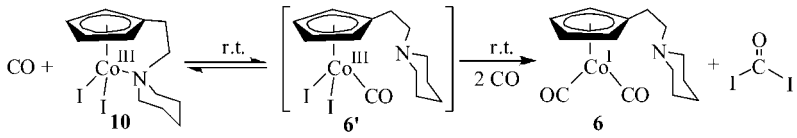


Scheme 3.

According to Scheme 3, each molecule of the diiodocarbonyl intermediate **6′** can provide one molecule of carbon monoxide after chelation. To produce each molecule of dicarbonylcobalt(I) **6** requires three molecules of carbon monoxide. The difference between the consumed molecules of diiodocarbonyl intermediate **6′** and the formed molecules of **6** is the free carbon monoxide that dissolves in solution as listed in Table 3. Based on these data, our calculations reveal that after the first 882 s induction period, the difference in the concentration of the cobalt(III) and (I) species determined by IR measurements at the same time remains a constant 0.088 mol $L^{-1}$. Since the solubility of carbon monoxide in organic solvents cannot reach such a high lever under normal conditions, bubbling carbon monoxide through a solution of a cobalt(III) chelate cannot produce an oxidation state +1. We did not observe such self-reduction in similar experiments with **5** and **8**. This can be attributed to the rate of chelation in **9** being too slow to allow a sufficiently high concentration of carbon monoxide to form in the reaction vessel and also because a small leakage of CO from the IR cell cannot be entirely prevented. On the other hand, the rate of chelation in **12** is too fast and the carbon monoxide had already escaped form the reaction solution after the iodine had been added.

It is interesting to compare the properties of the tethered functional side chains in "aminoethyl", **10** and "aminophenyl" since the stereochemical environments around the Co–N bonds are similar. The diiodomonocarbonyl precursor of "aminoethyl" reported could only exist in solution under an atmosphere of carbon monoxide whereas the diiodomonocarbonyl analogue of **10** could be isolated in the solid-state but could not be fully characterised because of its instability; completion of the chelation was observed after only about one day. The diiodomonocarbonyl analogue of "aminophenyl" was isolated from a solution after 16 h stirring at room temperature under $N_2$ and in a yield of 58%. The big difference in chelating ability is consistent with the repulsive force between the iodine ligands and the methyl (methylene) groups adjacent to the nitrogen atom. A comparison of the structural parameters of these analogues using the values of I–Co–I bond angles and the Co–N bond lengths found the largest in "aminoethyl" and the smallest in "aminophenyl".

Triphenylphosphane is known to be a better ligand for late transition metal complexes than amines. At room temperature, triphenylphosphane can replace the intramolecularly coordinated piperidine group in **10**. Since triphenylphosphane is easily oxidised by iodine to form $I_2PPh_3$ which is itself readily hydrolysed by moisture to generate hydrogen iodide and triphenylphosphane oxide, the formed diiodotriphenylphosphanyl-$\eta^5$-(2-piperidinoethyl)-cyclopentadienylcobalt(III) was thus protonated by hydrogen iodide to give the corresponding piperidinium salt **13**, crystals of which could be easily grown. From a crystal of suitable size we were able to determine the structure of **13**. The ORTEP diagram of **13** is given in Figure 6. It is interesting to find that the I–Co–I angle in **13** is 95.40(8)° and the I–Co–P angles are 91.57(14) and 92.79(14)°. Comparing the corresponding value of 92.70(2)° found in **10** suggests that the triphenylphosphane ligand experiences a smaller repulsive effect compared with the tethered intramolecular coordinated piperidine group. Triphenylphosphane is known as a ligand with a large stereochemical effect and has a cone angle of 143°.[33] However, as a strong σ donor ligand, triphenylphosphane still shows a larger *trans* effect than piperidine. The Co–C(5) bond *trans* to Co–P of 2.141(16) Å is 0.085 Å longer than the *cis* Co–C(3) bond which is 2.056(16) Å. For comparison, the Co–C(2) bond in **10** *trans* to Co–N is 2.086(4) Å, i.e. only 0.053 Å longer than the *cis* Co–C(5) bond which is 2.033(4) Å. There is one iodide counterion hydrogen bonded to the cation through N–H···I interactions with an N···I distance of 3.414(14) Å (Figure 7). This is an almost linear hydrogen bond with *d*(D–H) = 0.91 Å, *d*(H···A) = 2.53 Å and <D–H···A = 164.1°. A short contact between the iodide counterions and the hydrogen atom at C(12) adjacent to the nitrogen atom also exists and this should help the molecules pack in the crystal. To the best of our knowledge, this is one of the

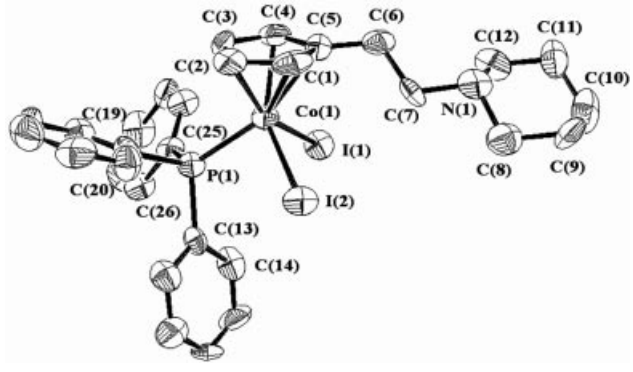


Figure 6. ORTEP diagram of **13** with the probability ellipsoids drawn at the 50% level. Hydrogen atoms, dichloromethane solvate molecule and iodide anion have been omitted for clarity. Selected bond lengths [Å] and angles [°]: Average Co–C(ring) 2.094(11), Co(1)–P(1) 2.239(5), Co(1)–I(1) 2.592(3), Co(1)–I(2) 2.568(2), average C–C(ring) 1.40(2), N(1)–C(7) 1.488(19), N(1)–C(12) 1.46(2), I(1)–Co(1)–I(2) 95.40(8), I(1)–Co(1)–P(1) 92.79(14), I(2)–Co(1)–P(1) 91.57(14), Co(1)–P(1)–C(13) 118.0(5), Co(1)–P(1)–C(19) 112.7(7), Co(1)–P(1)–C(25) 115.2(5).

 © 2007 Wiley-VCH Verlag GmbH & Co. KGaA, Weinheim 

strongest N–H···I hydrogen bonds found in the literature. A similar N–H···I hydrogen bond was found in crystals of $Me_3N{\cdot}HI$ and it was probably found to be linear with an N···I distance of 3.46(4) Å.[34] A further example can be seen in the crystal structure of the hexakis(*S*,*S*-diphenylsulfimide)cobalt(II) diiodide *S*,*S*-diphenylsulfimide acetonitrile solvate, $[Co(C_{12}H_{11}NS)_6]I_2{\cdot}C_{12}H_{11}NS{\cdot}2C_2H_3N$, in which two iodide counterions are hydrogen-bonded to the cation through N–H···I interactions, with N···I distances in the range of 3.7302(19)–3.8461(19) Å and D–H···A angles in the range of 156–172°.[35]

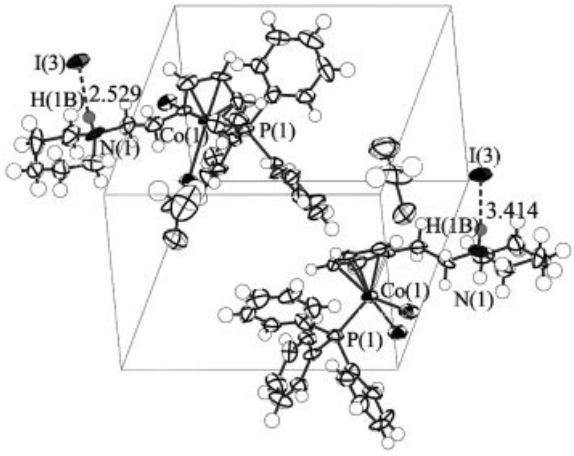


Figure 7. N–H···I hydrogen bonding in the unit cell of complex **13**.

## Conclusions

This paper reports the synthesis and reactivity of several cyclopentadienylcobalt complexes having a pendant amino-functionalised side chain. Intramolecular coordination by the pendant amino-functionalised side chain occurs when the oxidation state of the cobalt changes from +I to +III via a diiodocarbonyl intermediate. The stabilities of the intermediates differ greatly due to the different amino functions in the pendant side chains. Structural studies of chelates **9**, **10** and **12** have been carried out and these show that the Co–N bond length does not correlate with the stability of the diiodocarbonyl intermediate precursors but that there exists a correlation between the I–Co–I angles with the repulsive force from the methyl or methylene groups adjacent to the nitrogen atom. The intermediate diiodocarbonyl-$\eta^5$-(2-piperidinylethyl)cyclopentadienylcobalt(III) **6′** can be reduced to dicarbonylcyclopentadienylcobalt(I) **6** by the CO released due chelation of the former at a CO concentration of about 0.088 mol $L^{-1}$. The chelated piperidinyl group in **10** can easily be replaced by triphenylphosphane to form the diiodotriphenylphosphanyl-$\eta^5$-(2-piperidinioethyl)cyclopentadienylcobalt(III) iodide dichloromethane solvate **13** in the presence of hydrogen iodide. A strong N–H···I hydrogen bond with a N···I distance of 3.414(14) Å and a D–H···A angle of 164.1° was observed in **13**. It is one of the strongest N–H···I hydrogen bonds reported up to now.

## Experimental Section

**General:** All manipulations were carried out under an atmosphere of purified nitrogen using standard Schlenk techniques except where mentioned. All reagents were purchased from commercial sources (Acros Organics or Lancaster Synthesis Ltd) in the highest available purity and used as received. Solvents were purified by standard methods and distilled under nitrogen before use. Glassware was heated under vacuum and then flushed with $N_2$ prior to use. Alumina was heated at 300 °C under vacuum and then deactivated by addition of about 6 wt.-% of deoxygenated water before use.

Elemental analyses were performed on a Vario EL III Elemental Analyaer (Analysensysteme GmbH, Germany). IR spectra were recorded on a Nicolet Avatar-360 FTIR spectrometer in KBr pellets. A 0.2 mm NaCl IR cell was used to record the spectrum of solution samples. $^1$H NMR spectra were recorded on a Bruker Avance-DMX 500 NMR spectrometer or a JEOL ECA400 NMR spectrometer. The chemical shifts are reported in ppm relative to tetramethylsilane. Mass spectra were recorded on a Hewlett–Packard (USA) 6890/5073 gas chromatography–mass spectrometer. High resolution matrix assisted laser desorption ionisation mass spectra were recorded on an IonSpec 4.7 Tesla FTMS spectrometer at the Shanghai Institute of Organic Chemistry, Chinese Academy of Sciences, with 2,5-dihydroxybenzoic acid (DHB) serving as the absorbing matrix.

The crystal data were determined on a Bruker Smart-Apex CCD X-ray diffractometer equipped with a graphite monochromator. Data collection was performed with Mo-$K_\alpha$ radiation ($\lambda$ = 0.71073 Å) using the $\omega$-2$\theta$ scan technique to a maximum 2$\theta$ value of 26° at room temperature. The intensities were corrected for Lorentz polarisation effects and empirical absorption with the SADABS program.[36] Structures of the crystals were solved by direct methods and expanded using Fourier techniques. The non-hydrogen atoms were refined anisotropically with full-matrix least-squares methods. Hydrogen atoms were not included in the refinements. The final agreement factors are described with $R_1$ and $wR_2$ values for observed reflections. All calculations were performed on a PC computer using SHELX-97[37] the Bruker Smart program. Crystal data and experimental details for **9**, **10**, **12** and **13** are listed in Table 4 and selected bond lengths and angles are listed under the respective ORTEP diagrams.

### Synthesis of Compounds and Complexes

**2-Aminoethylcyclopentadiene (1):** Freshly distilled THF (50 mL) was added to a 250 mL Schlenk tube containing sodium sand (1.7835 g, 77.58 mmol) and the mixture was cooled in an ice-water bath. Freshly distilled cyclopentadiene (9 mL) was added dropwise and $H_2$ gas started to bubble out. After 30 min the bubbling stopped and the sodium sand had disappeared. The resultant pink solution was added by cannula to another 150 mL of Schlenk tube containing $BrCH_2CH_2NH_2{\cdot}HBr$ (4.1 g, 20.21 mmol) in THF (50 mL) which had already been cooled in an ice-water bath. The reaction mixture was then stirred at room temperature for 48 h during which time a white solid precipitated out from the solution. Water (50 mL) was added by cannula to the reaction mixture to dissolve the white precipitate. The organic layer was then separated. The aqueous phase was extracted with hexane (3 × 20 mL). The extract and the organic phase were combined and the volume was reduced to about 15 mL, cooled in an ice-water bath and acidified with aqueous HCl (concentrated HCl/water, 1:4). The separated aqueous phase was added directly to an ice-cold solution made from hexane (20 mL) and aqueous NaOH solution. The basic

 © 2007 Wiley-VCH Verlag GmbH & Co. KGaA, Weinheim 

Table 4. Crystal data and structure refinement details for **9**, **10**, **12** and **13**.

| | **9** | **10** |
|---|---|---|
| Empirical formula | $C_7H_{10}CoI_2N$ | $C_{12}H_{18}CoI_2N$ |
| *Fw* | 420.82 | 489.00 |
| *T* [K] | 293(2) | 293(2) |
| $\lambda$ [Å] | 0.71073 | 0.71073 |
| Crystal system | orthorhombic | monoclinic |
| Space group | *Pnma* | $P2_1/c$ |
| Unit cell dimensions | | |
| *a* [Å] | 7.393(2) | 14.934(4) |
| *b* [Å] | 11.708(3) | 11.805(3) |
| *c* [Å] | 11.822(3) | 16.153(4) |
| $\alpha$ [°] | 90 | 90 |
| $\beta$ [°] | 90 | 91.384(4) |
| $\gamma$ [°] | 90 | 90 |
| *V* [Å$^3$] | 1023.2(5) | 2846.9(12) |
| *Z* | 4 | 8 |
| $\rho_{calcd.}$ [mg m$^{-3}$] | 2.732 | 2.282 |
| Limiting indices | $-9 \le h \le 8$ | $-18 \le h \le 14$ |
| | $-13 \le k \le 14$ | $-12 \le k \le 14$ |
| | $-14 \le l \le 12$ | $-16 \le l \le 19$ |
| Reflections coll./unique | 4402/1062 | 12945/5599 |
| $R_{int}$ | 0.0260 | 0.0292 |
| Goodness-of-fit on $F^2$ | 1.159 | 0.791 |
| Abs. coeff. [mm$^{-1}$] | 7.653 | 5.519 |
| Crystal size [mm] | $0.15 \times 0.10 \times 0.10$ | $0.15 \times 0.10 \times 0.08$ |
| $\theta$ range for data collection [°] | 2.45 to 26.00 | 1.36 to 26.01 |
| *R* indices | $R_1 = 0.0365$ | $R_1 = 0.0275$ |
| $I > 2\sigma(I)$ | $wR_2 = 0.0927$ | $wR_2 = 0.0427$ |
| *R* indices | $R_1 = 0.0402$ | $R_1 = 0.0453$ |
| for all data[a] | $wR_2 = 0.0949$ | $wR_2 = 0.0452$ |
| Largest diff. peak/hole [e A$^{-3}$] | 1.101/–1.208 | 0.829/–0.738 |
| | **12** | **13** |
| Empirical formula | $C_{11}H_{10}CoI_2N$ | $C_{31}H_{36}Cl_2CoI_3NP$ |
| *Fw* | 468.93 | 964.11 |
| *T* [K] | 293(2) | 293(2) |
| $\lambda$ [Å] | 0.71073 | 0.71073 |
| Crystal system | triclinic | monoclinic |
| Space group | $P\bar{1}$ | *P*2(1) |
| Unit cell dimensions | | |
| *a* [Å] | 7.188(3) | 11.674(4) |
| *b* [Å] | 8.157(4) | 7.993(3) |
| *c* [Å] | 11.798(5) | 18.581(7) |
| $\alpha$ [°] | 92.976(6) | 90 |
| $\beta$ [°] | 91.282(6) | 92.043(6) |
| $\gamma$ [°] | 115.947(4) | 90 |
| *V* [Å$^3$] | 620.4(5) | 1732.7(11) |
| *Z* | 2 | 2 |
| $\rho_{calcd.}$ [mg m$^{-3}$] | 2.510 | 1.848 |
| Limiting indices | $-8 \le h \le 8$ | $-13 \le h \le 13$ |
| | $-8 \le k \le 9$ | $-9 \le k \le 9$ |
| | $-13 \le l \le 14$ | $-19 \le l \le 22$ |
| Reflections coll./unique | 2615/2164 | 7306/5608 |
| $R_{int}$ | 0.0252 | 0.0482 |
| Goodness-of-fit on $F^2$ | 0.991 | 0.927 |
| Abs. coeff. [mm$^{-1}$] | 6.326 | 3.389 |
| Crystal size [mm] | $0.15 \times 0.08 \times 0.05$ | $0.15 \times 0.10 \times 0.08$ |
| $\theta$ range for data collection [°] | 1.73 to 25.01 | 1.10 to 25.01 |
| *R* indices | $R_1 = 0.0456$ | $R_1 = 0.0641$ |
| $I > 2\sigma(I)$ | $wR_2 = 0.1126$ | $wR_2 = 0.1493$ |
| *R* indices | $R_1 = 0.0570$ | $R_1 = 0.0974$ |
| for all data[a] | $wR_2 = 0.1182$ | $wR_2 = 0.1719$ |
| Largest diff. peak/hole [e A$^{-3}$] | 1.735/–1.392 | 2.055/–1.536 |

aqueous phase (pH > 14) was extracted with hexane (3 × 20 mL). The organic phase and extract were combined, dried with anhydrous $MgSO_4$ and the solvents evaporated to give the product as an oily liquid (0.487 g, 4.46 mmol). Yield: 22.1%. The resultant oily product was identified as a 1:1 mixture of isomers. $^1$H NMR ($CDCl_3$): $\delta$ = 6.44 (d, *J* = 1.17 Hz, 1.5 H, =C*H*), 6.29 (d, *J* = 4.25 Hz, 0.5 H, =C*H*), 6.23 (s, 0.5 H, =C*H*), 6.09 (s, 0.5 H, =C*H*), 2.98 (s, 1 H, =CHC*H*−), 2.87–2.91 (m, 3 H, −C*H*), 2.56 (t, *J* = 6.7 Hz, 1 H, −C$H_2$), 2.51 (t, *J* = 6.7 Hz, 1 H, −C$H_2$) ppm. GCMS: *m*/*z* (%) = 109 (45) [M]$^+$, 80 (100) MH – $CH_2NH_2]^+$; retention times: 8.247, 8.327 min.

**(2-Piperidinoethyl)cyclopentadiene (2):** The compound was synthesised according to the reported procedure with little modification.[14] The product was purified on an alumina column. The resultant oily product was identified as a 1:1 mixture of isomers and a yield of 40% was redorded. $^1$H NMR ($CDCl_3$): $\delta$ = 6.45 (s, =C*H*), 6.42 (s, =C*H*), 6.27 (s, =C*H*), 6.19 (s, =C*H*), 6.05 (s, =C*H*), 3.59 (t, *J* = 7.34 Hz, 2 H, −C$H_2$−), 2.93 (d, *J* = 16.03 Hz, 1 H, −C*H*−), 2.69 (t, *J* = 7.35 Hz, 2 H, −C$H_2$N), 2.45 (m, 4 H, −NC$H_2$−), 1.60 (m, 4 H, −C$H_2$−), 1.46 (m, 2 H, −C$H_2$−) ppm. $^1$H NMR ([D$_6$]-acetone): $\delta$ = 6.42 (s, =C*H*), 6.21 (s, =C*H*), 6.03 (s, =C*H*), 5.94 (s, =C*H*), 5.47 (s, =C*H*), 5.11 (d, *J* = 14.41 Hz, 2 H, −C$H_2$−), 2.91 (d, *J* = 7.10 Hz, 1 H, −C*H*−), 2.50 (m, 2 H, −C$H_2$N), 2.42 (m, 4 H, −C$H_2$N), 2.12 (m, 2 H, −NC$H_2$−), 1.44 (m, 4 H, −C$H_2$−), 1.24 (m, 2 H, −C$H_2$−) ppm. $^{13}$C NMR ([D$_6$]acetone): $\delta$ = 146.58, 144.12, 133.74, 132.59, 131.37, 129.65, 125.82, 125.43, 123.92 (=*C*H), 58.52, 57.85, 56.79 (CpCH$_2$*C*H$_2$N−), 53.63 (α-N*C*H$_2$−), 42.48, 40.25, 33.29 (−*C*H$_2$−), 27.32, 26.79, 26.57 (Cp*C*H$_2$CH$_2$N−), 25.02, 23.46 (−*C*H$_2$−) ppm. GCMS: *m*/*z* (%) = 177 (25) [M]$^+$, 98 (100) [M – $C_5H_5CH_2]^+$, 80 (10) [MH – $CH_2NC_5H_{10}]^+$; retention times: 10.03, 10.15 min.

**1-(2-Piperidinoethyl)-2,3,4,5-tetraisopropylcyclopentadiene (3):** $C_5H_{10}NC_2H_4Cl$·HCl (5.174 g, 28.26 mmol) was added to an ice-cold mixture of hexane (30 mL) and aqueous KOH solution. The organic layer containing free $C_5H_{10}NC_2H_4Cl$ was separated and dried with $MgSO_4$. The volume was reduced to about 10 mL and THF (15 mL) was then added. The mixed solution was added by cannula to another 150 mL capacity Schlenk tube containing potassium tetraisopropylcyclopentadienide[19] (7.07 g, 25.8 mmol) and THF (60 mL). The resultant reaction mixture was heated to reflux for 24 h. The reaction was then quenched with water, extracted with hexane and eluted on an alumina column. A yellowish oil was obtained (3.5 g, 10.1 mmol) in a yield of 35.9%. $^1$H NMR ($CDCl_3$): $\delta$ = 3.16 (m, −C*H*C−), 2.74 (m, −C*H*C−), 2.46 (b, −C$H_2$N), 2.29 (b, −NC$H_2$), 1.87 (m, −C*H*Me$_2$), 1.62 (b, −C$H_2$−), 1.54 (b, −C$H_2$−), 1.39 (m, −CH*Me*$_2$), 1.19 (m, −CH*Me*$_2$), 1.12 (m, −CH*Me*$_2$), 1.01 (m, −CH*Me*$_2$) ppm. GCMS: *m*/*z* (%) = 345 (15) [M]$^+$.

**2-Picolylcyclopentadiene (4):** This compound was synthesised according to the reported procedure.[22] The product was separated on an alumina column. The resultant oily product was identified as 1:1 mixture of isomers. $^1$H NMR ($CDCl_3$): $\delta$ = 8.54 (t, *J* = 4.80 Hz, 1 H, =C*H*), 7.59 (m, 1 H, =C*H*), 7.17 (t, *J* = 6.88 Hz, 1 H, =C*H*), 7.11 (t, *J* = 4.60 Hz, 1 H, =C*H*), 6.44 (m, =C*H*), 6.29 (m, =C*H*), 6.23 (m, =CH), 6.10 (m, =C*H*), 3.94 (s, −C$H_2$−), 3.91 (s, −C$H_2$−), 3.00 (s, −C*H*−), 2.92 (t, −C$H_2$−) ppm.

**Dicarbonyl-η$^5$-(2-aminoethyl)cyclopentadienylcobalt(I) (5):** **1** (0.612 g, 5.61 mmol) was dissolved in $CH_2Cl_2$ (20 mL) containing 3,3-dimethyl-l-butene (5 mL) and the solution added by cannula to a $CH_2Cl_2$ solution (30 mL) containing $Co_2(CO)_8$ (0.6259 g, 1.83 mmol) at 0 °C. The deep red reaction mixture was stirred at ambient temperature and was inspected by observing the two characteristic $\nu_{CO}$ bands (2017, 1951 cm$^{-1}$) in the IR spectrum until their intensities became constant. This took about 24 h. The volume of the reaction mixture was reduced to about 2 mL under vacuum and the resultant solution was loaded on an alumina col-

 © 2007 Wiley-VCH Verlag GmbH & Co. KGaA, Weinheim 

umn and rinsed with 1:1 solvent mixture of THF and hexane. A deep red band was collected and the solvent was evaporated in vacuo. A deep red oily product was obtained (0.34 g). Yield 42.0%. $^1$H NMR ($CDCl_3$): $\delta$ = 5.02 (s, 2 H, =C*H*), 4.92 (s, 2 H, =C*H*), 3.48 (m, 4 H, $-CH_2CH_2-$) ppm. IR (neat): $\tilde{\nu}_{max}$ = 3365, 2960, 2016 (C=O), 1951 (C=O), 1598, 1439, 1366, 1261, 1090, 1023, 898, 802 cm$^{-1}$.

**Dicarbonyl-η$^5$-(2-Piperidinoethyl)cyclopentadienylcobalt(I) (6):** A similar synthetic procedure was used as described for complex **5**. Thus $Co_2(CO)_8$ (0.976 g, 2.84 mmol) and **2** (1.43 g, 8.07 mmol) were stirred together for 20 h and the resultant mixture passed down an alumina column to produce a deep red oily product (0.226 g). Yield 13.7%. $^1$H NMR ($CDCl_3$): $\delta$ = 5.04 (s, 2 H, =C*H*), 4.90 (s, 2 H, =C*H*), 2.49 (2 H, $-CH_2N-$), 2.43 (4 H, $-NCH_2-$), 2.18 (2 H, $-CH_2-$), 1.60 (4 H, $-CH_2-$), 1.45 (2 H, $-CH_2-$) ppm. IR (neat): $\tilde{\nu}_{max}$ = 3401, 2935, 2854, 2800, 2766, 2019 (C=O), 1954 (C=O), 1603, 1445, 1373, 1352, 1262, 1155, 1114, 1039, 862, 802 cm$^{-1}$.

**Dicarbonyl-η$^5$-1-(2-piperidinoethyl)-2,3,4,5-tetraisopropylcyclopentadienylcobalt(I) (7):** A similar synthetic procedure was used as described for complex **5**. Thus $Co_2(CO)_8$ (0.4944 g, 1.45 mmol) and **3** (1.00 g, 2.90 mmol) were stirred under reflux for 24 h and the resultant mixture passed down an alumina column to produce a deep red oily product (0.785 g). Yield 59.0%. $^1$H NMR ($CDCl_3$): $\delta$ = 2.44 (s, 2 H, $-CH_2N$), 2.29 (b, 4 H, $-NCH_2$), 1.91 (m, 4 H, $-CHMe_2$), 1.87 (s, 2 H, $-CH_2-$), 1.54 (b, 6 H, $-CH_2-$), 1.26 (m, 6 H, $-CHMe_2$), 1.16 (m, 12 H, $-CHMe_2$), 1.11 (m, 6 H, $-CHMe_2$) ppm. IR (neat): $\tilde{\nu}_{max}$ = 3389, 2960, 2932, 2871, 2003 (C=O), 1942 (C=O), 1466, 1381, 1367, 1261, 1155, 1108, 1041, 861, 806 cm$^{-1}$.

**Dicarbonyl-η$^5$-2-picolylcyclopentadienylcobalt(I) (8):** A similar synthetic procedure was used as described for complex **5**. Thus $Co_2(CO)_8$ (0.1755 g, 0.513 mmol) and **4** (0.1585 g, 1.01 mmol) were stirred together for 13 h and the resultant mixture passed down an alumina column to produce a deep red oily product (0.098 g). Yield 35.6%. $^1$H NMR ($CDCl_3$): $\delta$ = 8.55 (s, 1 H, =C*H*−N), 7.64 (t, 1 H, =C*H*), 7.26 (t, 1 H, =C*H*), 7.14 (t, 1 H, =C*H*), 5.09 (s, 2 H, Cp), 4.93 (s, 2 H, Cp), 3.75 (s, 2 H, $-CH_2-$) ppm. IR (neat): $\tilde{\nu}_{max}$ = 3400, 3083, 3011, 2956, 2927, 2854, 2016 (C=O), 1948 (C=O), 1591 (C=N), 1570 (C=N), 1475, 1435, 1365, 1309, 1221, 1149, 1092, 1049, 995, 920, 820, 785, 749, 616 cm$^{-1}$.

**Diiodo-η$^5$:η$^1$-(2-aminoethyl)cyclopentadienylcobalt(III) (9):** To a solution of **5** (0.087 g, 0.39 mmol) in ether (15 mL) was slowly added a solution of iodine (1.00 g, 0.394 mmol) in ether with vigorous stirring. A black-purple precipitate immediately appeared. The reaction mixture was stirred for a further 1 h. The precipitate was filtered and washed with hexane (2× 10 mL) and dried in vacuo. A red-purple solid was obtained (0.171 g). Yield: 97.7%. The solid showed a strong $\nu_{CO}$ band at 2068 cm$^{-1}$ which disappeared after about one week. The solid was dissolved in dichloromethane and layered with hexane and a crystalline product was obtained (0.148 g). Yield 90.2%. Crystals suitable for X-ray crystallographic analysis were obtained from that crop. $C_7H_{10}CoI_2N$ (420.823): calcd. H 2.39, C 19.96, N 3.33; found H 2.44, C 19.86, N 3.41. $^1$H NMR ($CDCl_3$): $\delta$ = 5.51 (t, 2 H, =C*H*), 5.27 (t, 2 H, =C*H*), 4.22 (t, *J* = 5.48 Hz, 2 H, $-CH_2N-$),2.42 (t, *J* = 6.42 Hz, 2 H, $-CH_2N-$) ppm. MS (HiRMALDI): *m*/*z* (%): 573.2 (3.0) [M + DHB – H]$^+$, 545.2 (32) [M + DHB – $CH_2NH_2$]$^+$, 438.2 (8.0) [M + $H_2O$ – H]$^+$, 293.1 (26.0) [M – I – H]$^+$. IR (KBr pellet): $\tilde{\nu}_{max}$ = 3192, 2961, 1571, 1459, 1310, 1263, 1120, 1035, 1013, 840, 734, 700.2 cm$^{-1}$. UV/Vis ($CH_3CN$): $\lambda_{max}$ ($\varepsilon$) = 247 ($7.61\times10^3$), 290 ($1.04\times10^4$), 360 ($4.03\times10^3$), 585 ($4.53\times10^2$) nm.

**Diiodo-η$^5$:η$^1$-(2-piperidinoethyl)cyclopentadienylcobalt(III) (10):** A similar synthetic procedure was used as described for complex **9**. Thus **6** (0.226 g, 0.776 mmol) in ether (15 mL) was added to iodine (0.1985 g, 0.782 mmol) in ether (15 mL) and the solution stirred overnight. The resultant green-black precipitate was washed with hexane until the washings became colourless. The solid showed a medium strong $\nu_{CO}$ band at 2059 cm$^{-1}$ which disappeared after about 12 h. The solid was dissolved in dichloromethane and filtered through a pad of celite and the solvent was then evaporated. A green-black solid was obtained (0.204 g). Yield 53.8%. Crystals suitable for X-ray crystallographic analysis were obtained from a sample dissolved in dichloromethane and layered with hexane. $C_{12}H_{18}CoI_2N$ (489.02): calcd. H 3.71, C 29.47, N 2.86; found H 3.61, C 29.58, N 2.71. $^1$H NMR ($CDCl_3$): $\delta$ = 5.46 (s, 2 H, =C*H*), 5.19 (s, 2 H, =C*H*), 4.41 (t, *J* = 6.40 Hz, 2 H, $-CH_2N-$), 3.52 (d, *J* = 13.7 Hz, 2 H, $-NCH_eH_a-$), 2.93 (t, *J* = 13.7 Hz, 2 H, $-NCH_eH_a-$), 2.51 (t, *J* = 6.40 Hz, 2 H, $-CH_2-$), 1.72 (m, 4 H, $-CH_2-$), 1.22 (m, 2 H, $-CH_2-$) ppm. $^1$H NMR ([D$_6$]acetone): $\delta$ = 5.69 (s, 2 H, =C*H*), 5.11 (s, 2 H, =C*H*), 4.49 (t, *J* = 6.40 Hz, 2 H, $-CH_2N-$), 3.61 (d, *J* = 13.3 Hz, 2 H, $-NCH_eH_a-$), 2.81 (t, *J* = 13.3 Hz, 2 H, $-NCH_eH_a-$), 2.68 (t, *J* = 6.40 Hz, 2 H, $-CH_2-$), 1.90 (m, 4 H, $-CH_2-$), 1.13 (m, 2 H, $-CH_2-$) ppm. $^{13}$C NMR ([D$_6$]acetone): $\delta$ = 112.93 ($CpCH_2-$), 83.49 (Cp), 81.38 (Cp), 65.50 ($-CH_2CH_2N-$), 61.10 (*ortho*-$NCH_2-$), 25.39 ($CpCH_2CH_2N-$), 24.32, 22.30 ($-CH_2-$) ppm. MS (HiRMALDI): *m*/*z* (%): 514.9 (12.5) [M + DHB – I – H]$^+$, 422.9 (4.0) [M + $H_2O$ – $NC_5H_{10}$]$^+$, 379.1 (23) [M + $H_2O$ – I – H]$^+$, 362.0 (10) [M – I]$^+$. IR (KBr pellet): $\tilde{\nu}_{max}$ = 3076, 2932, 2856, 2801, 1726, 1603, 1468, 1443, 1393, 1353, 1309, 1261, 1101, 1025, 802 cm$^{-1}$. UV/Vis ($CH_3CN$): $\lambda_{max}$ ($\varepsilon$) = 248 ($1.01\times10^4$), 286 ($7.06\times10^3$), 587 ($5.79\times10^2$) nm.

**Diiodo-η$^5$:η$^1$-1-(2-piperidinoethyl)-2,3,4,5-tetraisopropylcyclopentadienylcobalt(III) (11):** A similar synthetic procedure was used as described for complex **9**. Thus **7** (0.786 g, 1.71 mmol) in ether (35 mL) was added to iodine (0.4456 g, 1.76 mmol) in ether (10 mL) and the resultant mixture stirred overnight. A red-purple solid precipitated which showed a medium-strong $\nu_{CO}$ band at 2046 cm$^{-1}$. The solid was dissolved in dichloromethane and filtered through a pad of celite and the solvent subsequently removed in vacuo. A solid was obtained (0.165 g). Yield 15%. $C_{24}H_{42}CoI_2N$ (657.35): calcd. H 6.44, C 43.85, N 2.13; found H 6.96, C 44.70, N 1.91. $^1$H NMR ($CDCl_3$): $\delta$ = 1.72 (d, 6 H, $-CH_3$), 1.70 (d, 6 H, $-CH_3$), 1.53 (d, $-CH_3$), 1.50 (d, 6 H, $-CH_3$), 2.05 (m, 4 H, $Me_2CH$), 3.83 (s, 2 H, $-CH_2N-$), 3.65 (s, 4 H, $-NCH_eH_a-$), 3.32 (s, 2 H, $-NCH_eH_a-$), 3.18 (s, 4 H, $-CH_2-$), 2.37 (m, 4 H, $-CH_2-$) ppm.

**Diiodo-η$^5$:η$^1$-2-picolylcyclopentadienylcobalt(III) (12):** A similar synthetic procedure was used as described for complex **9**. Thus complex **8** (0.098 g, 0.359 mmol) in hexane (10 mL) was added to iodine (0.097 g, 0.382 mmol) in hexane (10 mL) and the mixture stirred for 24 h. The resultant dark green precipitate was separated and washed twice with hexane and dissolved in dichloromethane. The solution was filtered and the solvent removed in vacuo. A dark green solid was obtained (0.1615 g). Yield 96.0%. Crystals suitable for X-ray crystallographic analysis were obtained from a sample dissolved in dichloromethane and crystallised by layering with hexane. $C_{11}H_{10}CoI_2N$ (468.831): calcd. H 2.15, C 28.16, N 2.99; found H 2.168, C 28.29, N 2.886. $^1$H NMR ($CDCl_3$): $\delta$ = 7.97 (s, 1 H, =C*H*−N), 7.70 (t, 1 H, =C*H*), 7.16 (d, 1 H, =C*H*), 7.00 (t, 1 H, =C*H*), 5.73 (s, 2 H, Cp), 5.38 (s, 2 H, Cp), 4.09 (s, 2 H, $-CH_2-$) ppm. MS (HiRMALDI): *m*/*z* (%): 341.9 (10.0) [M – I]$^+$. IR (KBr pellet): $\tilde{\nu}_{max}$ = 3090, 2960, 2924, 2858, 1605 (C=N), 1470, 1439, 1417, 1391, 1262, 1151, 1102, 1048, 1021, 846, 764 cm$^{-1}$. UV/

 © 2007 Wiley-VCH Verlag GmbH & Co. KGaA, Weinheim 

Vis ($CH_3CN$): $\lambda_{max}$ ($\varepsilon$) = 246 ($7.51 \times 10^3$), 286 ($5.28 \times 10^3$), 405 ($6.32 \times 10^2$), 593 ($5.63 \times 10^2$) nm.

**Diiodotriphenylphosphanyl-η$^5$-(2-piperidinioethyl)cyclopentadienylcobalt(III) Iodide ($C_5H_4C_2H_4NHC_5H_{10}CoI_2PPh_3)^+I^-\cdot CH_2Cl_2$ (13):** To a stirred solution of **6** (0.120 g, 0.412 mmol) in dichloromethane (10 mL) was added iodine (0.220 g, 0.887 mmol) in dichloromethane (10 mL) and the resultant mixture was stirred for 4 h. A solution of triphenylphosphane (0.2326 g, 0.885 mmol) in dichloromethane was then added at room temperature. The reaction mixture was stirred continuously for another 24 h under room temperature. The volume of the solvent was reduced in vacuo and hexane was layered over the remaining dichloromethane solution. Brown-black needle-shaped crystals formed several days later and 0.187 g of crystallised product was separated by filtration. Crystals suitable for X-ray crystallographic analysis were obtained. Structural analysis demonstrates that a solvent molecule of dichloromethane is incorporated in the crystal lattice. The resultant product was thus formulated as $(C_5H_4C_2H_4NHC_5H_{10}CoI_2PPh_3)^+I^-\cdot CH_2Cl_2$. Based on this composition, the yield was 47% $^1$H NMR ($CDCl_3$): $\delta$ = 7.23–7.90 (m, 15 H, Ph), 5.45 (s, 2 H, =CH), 5.30 (s, 2 H, C$H_2$Cl$_2$), 4.08 (m, 2 H, −C$H_2$N−), 3.97 (m, 2 H, −NC$H_2$−), 3.93 (s, 2 H, =C*H*), 3.82 (m, 2 H, −NC$H_2$−), 3.00 (m, 2 H, −C$H_2$−), 2.63 (s, 1 H, −N*H*−), 2.34 (m, 2 H, −C$H_2$−), 1.97 (m, 4 H, −C$H_2$−) ppm. IR (KBr pellet): $\tilde{\nu}_{max}$ = 3432, 3054, 2960, 2925, 2854, 1605, 1434, 1379, 1264, 1091, 1026, 800, 741, 697 cm$^{-1}$. UV/Vis ($CH_3CN$): $\lambda_{max}$ ($\varepsilon$) = 232 ($1.65 \times 10^4$), 279 ($7.70 \times 10^3$), 585 ($8.07 \times 10^2$) nm.

**Reduction with CO:** Reaction intermediate **6′** was synthesised in situ. To a solution of **6** (0.157 g, 0.539 mmol) in dichloromethane (0.90 mL) was added iodine (0.141 g, 0.556 mmol) in dichloromethane (0.85 mL) with vigorous stirring for half a minute. The reaction mixture was then transferred to an IR cell which had been flushed with $N_2$ before use. The chamber of the IR cell was fully filled with the reaction mixture and tightly sealed with a Teflon stopper, no empty space was allowed. The first spectrum was measured 2 min after the iodine was added. The carbonyl absorption bands were monitored and the spectra were recorded. Plots of ln*A* vs. *t* for the absorbance of the monocarbonyl intermediate were linear over 2 half-lives [$\log A(2066\ cm^{-1}) = -0.0975 - 6.394 \times 10^{-4} t$, $R_2 = -0.9997$] after 882 s. From a another sample of **6** in dichloromethane, the absorbances of the carbonyl were found to be linear in the concentration range from 0.04 to 0.16 M [$A(2017\ cm^{-1}) = 0.00782 + 5.232(Co^I)$, $R_2 = 0.9999$; $A(1953\ cm^{-1}) = 0.00551 + 4.869(Co^I)$, $R_2 = 0.9999$]. The calculations of the concentrations of the diiodomonocarbonyl intermediate **6′** and the formed dicarbonyl product **6** listed in Table 3 are based on these linear relationships.

Crystallographic data have been deposited at the CCDC, 12 Union Road, Cambridge CB2 1EZ, U.K., and copies can be obtained on request, free of charge, by quoting the publication citation and the deposition numbers CCDC-615490 (for **9**), -615491 (for **10**), -615492 (for **12**) and -615489 (for **13**), respectively.

## Acknowledgments

Support for this work was provided by the National Natural Science Foundation of China, Grant No. 20471016. We also thank Prof. Linhong Weng for her excellent work on the X-ray crystallographic analysis.

[1] P. Jutzi, *J. Organomet. Chem.* **1990**, *400*, 1–17.
[2] S. Nlate, E. Herdtweck, R. A. Fischer, *Angew. Chem. Int. Ed. Engl.* **1996**, *35*, 1861–1863.
[3] a) K. H. Zimmermann, R. S. Pilato, I. T. Horvath, J. Okuda, *Organometallics* **1992**, *11*, 3935; b) A. N. Nesmeyanov, Y. T. Struchkov, V. G. Andrianov, Ml. Rybinskaya, *J. Organomet. Chem.* **1975**, *93*, C8.
[4] a) A. N. Nesmeyanov, V. V. Krivykh, M. I. Rybinskaya, *J. Organomet. Chem.* **1979**, *164*, 159; b) A. N. Nesmeyanov, V. V. Krivykh, G. A. Panosyan, P. V. Retrovskh, M. I. Rybinskaya, *J. Organomet. Chem.* **1979**, *164*, 167; c) A. N. Nesmeyanov, Y. T. Struchkov, V. G. Andrianov, M. L. Rybinskaya, *J. Organomet. Chem.* **1979**, *166*, 211.
[5] P.-H. Yeh, Z. Pang, R. F. Johnston, *J. Organomet. Chem.* **1996**, *509*, 123.
[6] a) U. Siemeling, *Chem. Rev.* **2000**, *100*, 1495; b) H. Butenschön, *Chem. Rev.* **2000**, *100*, 1527.
[7] D. A. Weinberger, T. B. Higgins, C. A. Mirkin, L. M. Liable-Sands, A. L. Rheingold, *Angew. Chem. Int. Ed.* **1999**, *38*, 2565–2568.
[8] O. Kühl, P. Lönnecke, *Inorg. Chem.* **2002**, *41*, 4315–4317.
[9] P. J. W. Deckers, B. Hessen, J. H. Teuben, *Angew. Chem. Int. Ed.* **2001**, *40*, 2516–2519.
[10] A. Mukherjee, U. Subramanyam, V. G. Puranik, T. P. Mohandas, A. Sarkar, *Eur. J. Inorg. Chem.* **2005**, 1254–1263.
[11] P. Jutzi, T. Redeker, *Eur. J. Inorg. Chem.* **1998**, 663–667.
[12] A. I. Philippoulos, N. Hadjiliadis, *Inorg. Chem.* **1997**, *36*, 1842–1849.
[13] T. Wang, C. Lai, C. Hwu, Y. Wen, *Organometallics* **1997**, *16*, 1218–1223.
[14] I. D. Kostas, *J. Organomet. Chem.* **2001**, *626*, 221–226.
[15] J. Okuda, K. H. Zimmermann, *Chem. Ber.* **1990**, *123*, 1641–1648.
[16] L. F. Groux, D. Zargarian, *Organometallics* **2003**, *22*, 3124–3133.
[17] A. Döhring, J. Göhre, P. W. Jolly, B. Kryger, J. Rust, G. P. J. Verhovnik, *Organometallics* **2000**, *19*, 388–402.
[18] M. Enders, G. Ludwig, H. Pritzkow, *Organometallics* **2001**, *20*, 827–833.
[19] K. D. Camm, S. J. Furtado, A. L. Gott, P. C. McGowan, *Polyhedron* **2004**, *23*, 2929–2936.
[20] M. S. Blais, J. C. W. Chien, M. D. Rausch, *Organometallics* **1998**, *17*, 3775–3783.
[21] O. Segnitz, M. Winter, K. Merz, R. Fischer, *Eur. J. Inorg. Chem.* **2000**, 2077–2085.
[22] Y. Xu, Y. Shen, Z. Pang, *J. Organomet. Chem.* **2004**, *689*, 823–832.
[23] J. F. Buzinkai, R. R. Schrock, *Organometallics* **1987**, *6*, 1447–1452.
[24] a) P. Jutzi, M. O. Kristen, J. Dahlhaus, B. Neumann, H.-G. Stammler, *Organometallics* **1993**, *12*, 2980–2985; b) P. Jutzi, M. O. Kristen, B. Neumann, H.-G. Stammler, *Organometallics* **1994**, *13*, 3854–3861.
[25] R. B. King, *Inorg. Chem.* **1966**, *5*, 82–87.
[26] T.-F. Wang, T.-Y. Lee, J.-W. Chou, C.-W. Ong, *J. Organomet. Chem.* **1992**, *423*, 31.
[27] a) B. E. R. Schilling, R. Hoffmann, D. L. Lichtenberger, *J. Am. Chem. Soc.* **1979**, *101*, 585–591; b) N. M. Kostic, R. F. Fenske, *J. Organomet. Chem.* **1982**, *233*, 337–351; c) P. Hofman, *Angew. Chem.* **1977**, *89*, 551.
[28] a) S. Ašperger, B. Cetina-Čižmek, *Inorg. Chem.* **1996**, *35*, 5232–5236; b) C. R. Johnson, R. E. Shepherd, *Inorg. Chem.* **1983**, *22*, 3506–3513; c) T. Uno, K. Hatano, T. Nawa, K. Nakamura, Y. Nishimura, Y. Arata, *Inorg. Chem.* **1991**, *30*, 4322–4327.
[29] J. Okuda, K.-H. Zimmermann, E. Herdtweck, *Angew. Chem. Int. Ed. Engl.* **1991**, *30*, 430.
[30] F. Laurent, L. F. Groux, D. Zargarian, *Organometallics* **2003**, *22*, 3124–3133.
[31] P. Lau, H. Braunwarth, G. Huttner, D. Günauer, K. Evertz, W. Imhof, C. Emmerich, L. Zsolnai, *Organometallics* **1991**, *10*, 3861–3873.

 © 2007 Wiley-VCH Verlag GmbH & Co. KGaA, Weinheim 

[32] M. N. Golovin, M. M. Rahman, J. E. Belmonte, W. P. Giering, *Organometallics* **1985**, *4*, 1981–1991.
[33] C. A. Tolman, *Chem. Rev.* **1977**, *77*, 313–348.
[34] G. M. Sheldrick, W. S. Sheldrick, *Acta Crystallogr., Sect. B* **1970**, *26*, 1334–1338.
[35] S. H. Dale, M. R. J. Elsegood, K. E. Holmes, P. F. Kelly, *Acta Crystallogr., Sect. C* **2005**, *61*, m34–39.
[36] G. M. Sheldrick, *SADABS*, *Program for Empirical Absorption Correction*, University of Göttingen, Göttingen, Germany, **1998**.
[37] G. Sheldrick, *SHELXL-97. Program for structure refinement*, University of Göttingen, Göttingen, Germany, **1997**.
Received: April 24, 2007
Published Online: September 20, 2007

 © 2007 Wiley-VCH Verlag GmbH & Co. KGaA, Weinheim 

DOI: 10.1002/ejic.200700597

# Displacement of Neutral Nitrogen Donors by Chloride in $AuCl_3$(3R-py) (3R-py = *meta*-Substituted Pyridine): Comparison between *meta*- and *para*-Substituted Pyridines by Kinetics and DFT Calculations

**Bruno Pitteri*[a] and Marco Bortoluzzi[a]**

**Keywords:** Gold / Kinetics / Nitrogen donors / Reaction Mechanism / DFT

The kinetics of the process $AuCl_3$(3R-py) + $Cl^- \rightarrow AuCl_4^-$ + 3R-py (3R-py = one of a number of *meta*-substituted pyridines covering a wide range of basicity) have been studied in methanol at 25 °C. The reactions obey the usual two-term rate law observed in the substitution reactions of square-planar complexes. The second-order rate constants, $k_2$, are very sensitive to the nature of the leaving group and plots of $\log k_2$ against the $pK_a$ of the conjugate acids are linear with the same slope of ca. –0.6 already found for *para*-substituted pyridines (4R-py). Until now the two groups of bases have been considered to behave in the same manner in their displacement from $Au^{III}$ and $Pt^{II}$ by various nucleophiles but, on the contrary, the reactivity of the two classes of N donors is slightly different and follows the order: 4R-py > 3R-py. This kinetic result is explained on the basis of an energetic difference between the frontier orbitals of the $AuCl_3$(3R-py) and $AuCl_3$(4R-py) derivatives.

(© Wiley-VCH Verlag GmbH & Co. KGaA, 69451 Weinheim, Germany, 2007)

## Introduction

The chemical features of (pyridine)gold(III) complexes are currently of interest from both a catalytic[1] and mechanistic point of view: in particular, the reactivity of gold(III)[2–5] in the reactions with N-donor bases has been widely studied, mainly involving pyridine and substituted pyridines (R-py) as entering or leaving groups. The same types of reactions have also been studied for platinum(II) derivatives[6–10] and it was observed that the substitution reactions (1), (2) and (3) take place with an associative mechanism, where the rate constants for the forward and the reverse reactions obey the general relationship $k_{obs} = k_1 + k_2$[nucleophile], which is usual for nucleophilic substitutions of planar four-coordinate $d^8$ metal complexes.[11]

$$AuCl_4^- + \text{R-py} \rightleftharpoons AuCl_3(\text{R-py}) + Cl^- \quad (1)$$

$$[LPtCl]^+ + \text{R-py} \rightleftharpoons [LPt(\text{R-py})]^{2+} + Cl^- \quad (2)$$

[L = 2,6-bis(methylsulfanylmethyl)pyridine,[5] bis(2-pyridylmethyl) sulfide,[7] 2,2′:6′,2′′-terpyridine,[9] biacetylbis(*N*-methyl-*N*-phenyl)-oxazone[8]]

$$LPtCl_2 + \text{R-py} \rightleftharpoons [LPt(\text{R-py})Cl]^+ + Cl^- \quad (3)$$

[L = 1,2-bis(phenylsulfanyl)ethane[6]]

The $k_1$ term is the first-order rate constant for the nucleophilic attack on the substrate by the solvent, whereas $k_2$ is the second-order rate constant for the nucleophilic attack on the substrate by the nucleophile. The $k_2$ constants are remarkably influenced by the nature of R-py, indicating that the discriminating ability of gold(III) and platinum(II) complexes is good. In both the forward and reverse reactions a linear free-energy relationship, $\log k_2 = \alpha pK_a$ + constant, occurs between the rate constant and the basicity of R-py, that is the $pK_a$ of the conjugated acid $[H(\text{R-py})]^+$. Steric retardation is observed for pyridines containing one or two *ortho* groups (usually called hindered pyridines) and these effects are in many cases approximately additive. Moreover, we studied the kinetics of the reaction $AuCl_3$(nu) + $Cl^- \rightarrow AuCl_4^-$ + nu (nu = five-membered N-donor heterocycles such as thiazole, oxazole, imidazole and their derivatives)[4] and the results were compared, under the same experimental conditions, with studies where the leaving groups are pyridines.[3] It was observed that the reactivity depends not only upon the ligand basicity but also upon the nature of the ligand in the order pyridines > five-membered heterocycles.

In recent work[5] involving reaction (1) we compared the lability of three different groups of N donors: (I) 4-substituted pyridines; (II) 4-substituted pyridines with a more extended π-system; and (III) $sp^3$ nitrogen-donor bases. The first group includes pyridine, 4-bromopyridine, 4-chloropyridine, 4-methylpyridine, 4-methoxypyridine, 4-aminopyridine and 4-(dimethylamino)pyridine, while the second group includes the derivatives of cyanopyridine, isonicotinic acid, methyl isonicotinate and 4-acetylpyridine. The lability

[a] Dipartimento di Chimica,Università "Cà Foscari" di Venezia, Calle Larga S. Marta 2137, 30123 Venezia, Italy
E-mail: pitteri@unive.it

 © 2007 Wiley-VCH Verlag GmbH & Co. KGaA, Weinheim 

of these pyridines is considerably lower than that of the third group of derivatives, i.e. the $sp^3$ ligands piperidine, cyclohexylamine and morpholine. Pyridines I and II obey the linear relationship $\log k_2 = \alpha pK_a$ + constant with $\alpha \approx -0.6$, but the reactivity of the two groups differ by about 2.3 kJ mol$^{-1}$ in the order: pyridines I > pyridines II. These differences were attributed to a ground-state stabilization due to the π back-donation from the filled orbitals of the metal atom to the antibonding orbitals of the pyridine ligands.

In some kinetic studies involving reactions (1), (2) and (3)[2,3,7,8] *meta*-substituted pyridines (3R-py) were also considered and their reactivity appeared similar to that of group I pyridines, but during our latest work regarding reaction (1),[5] trying to study *meta*-substituted pyridines like 3-methylpyridine and 3-chloropyridine, we found kinetic data that was not completely comparable with those of *para*-substituted pyridines. In order to determine whether these differences have a chemical meaning, the kinetics of the displacement of the nitrogen ligand by chloride from $AuCl_3$(3R-py) substrates in methanol at 25 °C are reported and the results are compared with those of ref.[5] The discussion is supported by ground-state DFT calculations performed on the $AuCl_3$(3R-py) and $AuCl_3$(4R-py) derivatives and the different reactivity of the coordinated *meta*- and *para*-substituted pyridines is correlated with a slight, systematic difference between the energies of the frontier orbitals of the corresponding gold(III) complexes.

## Results and Discussion

When a methanolic solution of the neutral $AuCl_3$(3R-py) substrate was allowed to react with an appropriate excess of chloride, repetitive scanning of the spectrum in the region 240–360 nm showed that the reaction evolves with time in a first-order fashion leading to the substitution of the neutral base by a chloride ion. The presence of well-maintained isosbestic points, whose position depends only upon the spectrum of the starting compound, and the comparison of the final spectrum with that of original samples of the substituted products at the same concentration, clearly indicate a single reaction stage. Addition of $LiClO_4$ indicated that primary salt effects were absent and secondary effects were negligible; thus, no further attempt to maintain a constant ionic strength was made. The reactions were studied in the presence of 0.1 mol dm$^{-3}$ $CH_3SO_3H$. Preliminary experiments showed that, at constant chloride concentration, the rate of reaction was not dependent on the concentration of acid over the range 0.02–0.2 mol dm$^{-3}$. The acid simply serves to protonate the released ligand, to prevent the reverse reaction and to force the reaction to completion. All the reactions were studied in the presence of a sufficient excess of chloride over the substrate to provide pseudo-first-order conditions. It is to be noted that these experimental conditions are the same as those used in ref.[5] The rate constants were determined in the usual way from the change in absorbance as a function of time at a conve-

Table 1. First-order rate constant, $k_{obs}$, for the reaction $AuCl_3$(3R-py) + $Cl^- \rightarrow AuCl_4^-$ + 3R-py in methanol at 25 °C (0.1 mol dm$^{-3}$ $CH_3SO_3H$).

| 3R-py | [Cl$^-$]/mol dm$^{-3}$ | $10^3 k_{obs}$/s$^{-1}$[a] | 3R-py | [Cl$^-$]/mol dm$^{-3}$ | $10^3 k_{obs}$/s$^{-1}$[a] |
|---|---|---|---|---|---|
| 3-Chloropyridine | 0.0005 | 27.7 ± 0.1 | 3-phenylpyridine | 0.001 | 1.93 ± 0.03 |
| | 0.0010 | 29.6 ± 0.1 | | 0.002 | 2.28 ± 0.01 |
| | 0.0015 | 31.5 ± 0.1 | | 0.003 | 2.81 ± 0.01 |
| | 0.0020 | 36.5 ± 0.2 | | 0.004 | 3.27 ± 0.02 |
| | 0.0025 | 38.3 ± 0.1 | | 0.005 | 3.76 ± 0.04 |
| 3-Bromopyridine | 0.0005 | 17.0 ± 0.1 | 3-hydroxymethylpyridine | 0.001 | 1.05 ± 0.01 |
| | 0.0010 | 20.2 ± 0.2 | | 0.002 | 1.26 ± 0.01 |
| | 0.0015 | 23.0 ± 0.1 | | 0.003 | 1.60 ± 0.02 |
| | 0.0020 | 28.0 ± 0.2 | | 0.004 | 1.94 ± 0.01 |
| | 0.0025 | 30.5 ± 0.1 | | 0.005 | 2.22 ± 0.03 |
| 3-Iodopyridine | 0.0005 | 10.1 ± 0.2 | 3-methoxypyridine | 0.001 | 1.39 ± 0.01 |
| | 0.0010 | 12.2 ± 0.1 | | 0.002 | 1.64 ± 0.02 |
| | 0.0015 | 14.2 ± 0.1 | | 0.003 | 2.05 ± 0.03 |
| | 0.0020 | 15.7 ± 0.2 | | 0.004 | 2.35 ± 0.04 |
| | 0.0025 | 18.1 ± 0.1 | | 0.005 | 2.68 ± 0.03 |
| 3-Fluoropyridine | 0.0005 | 17.2 ± 0.1 | 3-methylpyridine | 0.001 | 0.63 ± 0.02 |
| | 0.0010 | 19.9 ± 0.2 | | 0.002 | 0.77 ± 0.01 |
| | 0.0015 | 22.5 ± 0.1 | | 0.003 | 0.93 ± 0.03 |
| | 0.0020 | 24.9 ± 0.1 | | 0.004 | 1.08 ± 0.01 |
| | 0.0025 | 27.9 ± 0.3 | | 0.005 | 1.24 ± 0.02 |

[a] The indicated errors were obtained from the nonlinear least-squares fit of the experimental data to $D_t = D_\infty + (D_0 - D_\infty)\exp(-k_{obs}t)$ ($D_0$ = absorbance after mixing the reactants, $D_\infty$ = absorbance at completion of reaction). Each experimental measurement was repeated at least twice.

 © 2007 Wiley-VCH Verlag GmbH & Co. KGaA, Weinheim 

nient wavelength and the observed rate constants, $k_{obs}$, are collected in Table 1.

The observed rate constants, $k_{obs}$, obey the general relationship $k_{obs} = k_1 + k_2$[nucleophile], usually found for substitution in gold(III) complexes. The $k_1$ terms, which refer to the pathway in which the rate-determining step is the nucleophilic attack of the solvent followed by the rapid entry of chloride into the solvento complex,[12] are usually quite small and contribute little to the reactions. The $k_2$ terms are the second-order rate constants for the direct attack of the nucleophile, $Cl^-$, at the substrate and were determined by a linear regression of the $k_{obs}$ values vs. the chloride concentration. As expected from previous studies on gold(III) substitution reactions,[2–5] the pseudo-first-order rate constant values, $k_{obs}$, mainly depend upon the $k_2$ values, which are reported in Table 2 together with the p$K_a$ values of H[(3R-py)]$^+$ taken from ref.[13]

In Figure 1 the plots of log $k_2$ vs. p$K_a$ of the leaving 3R-py are shown, together with the data for the simple pyridine and the *para*-substituted pyridines 4R-py in the same p$K_a$ range (see ref.[5] for log $k_2$ and p$K_a$ values of these nitrogen donors).

As depicted in Figure 1, a linear relationship, log $k_2$ = αp$K_a$ + constant, is obeyed for both the *meta*-substituted (3R-py) and *para*-substituted (4R-py) pyridines, with $\alpha \approx -0.6$. Coordinated *meta*-substituted pyridines appear to be slightly less reactive than the *para*-substituted ones, even if the difference between the reactivity of the two groups of pyridines is quite small ($\Delta \approx 0.18$) and corresponds to about 1 kJ mol$^{-1}$. The chemical behaviour of the unsubstituted pyridine in its displacement by chloride from $Au^{III}$ is comparable to that of the *para*-substituted pyridines.

To explain the experimental data obtained from the kinetic measurements, ground-state DFT B3PW91 calculations were performed on $AuCl_3$(py), $AuCl_3$(3R-py) and $AuCl_3$(4R-py) derivatives. Particular interest was devoted to the frontier orbitals of the gold complexes and Table 3 reports the energy values of the HOMOs and LUMOs for all

Table 2. Second-order rate constants, $k_2$, and p$K_a$ values of [H(3R-py)]$^+$ for the reaction $AuCl_3$(3R-py) + $Cl^-$ → $AuCl_4^-$ + 3R-py in methanol at 25 °C (0.1 mol dm$^{-3}$ $CH_3SO_3H$).

| 3R-py | $k_2$/dm$^3$ mol s$^{-1}$[a] | p$K_a$ of [H(3R-py)]$^+$ |
|---|---|---|
| $AuCl_3$(3-chloropyridine) | 5.6 ± 0.6 | 2.84 |
| $AuCl_3$(3-bromopyridine) | 6.9 ± 0.4 | 2.84 |
| $AuCl_3$(3-iodopyridine) | 3.9 ± 0.1 | 3.25 |
| $AuCl_3$(3-fluoropyridine) | 5.28 ± 0.09 | 2.97 |
| $AuCl_3$(3-methylpyridine) | 0.153 ± 0.002 | 5.52 |
| $AuCl_3$(3-phenylpyridine) | 0.46 ± 0.02 | 4.80 |
| $AuCl_3$(3-hydroxymethylpyridine) | 0.30 ± 0.01 | 5.00 |
| $AuCl_3$(3-methoxypyridine) | 0.33 ± 0.01 | 4.91 |

[a] Errors were obtained from the linear regression of $k_{obs}$ values vs. chloride concentration.

Table 3. Energy values of the frontier orbitals of the $AuCl_3$(py), $AuCl_3$(3R-py) and $AuCl_3$(4R-py) complexes.

| R-py | HOMO [eV] | LUMO [eV] |
|---|---|---|
| $AuCl_3$(4-methoxypyridine) | –0.27672 | –0.14997 |
| $AuCl_3$(4-chloropyridine) | –0.28573 | –0.16001 |
| $AuCl_3$(4-methylpyridine) | –0.27872 | –0.15209 |
| $AuCl_3$(4-bromopyridine) | –0.28541 | –0.15964 |
| $AuCl_3$(pyridine) | –0.28183 | –0.15564 |
| $AuCl_3$(3-bromopyridine) | –0.28584 | –0.16068 |
| $AuCl_3$(3-methoxypyridine) | –0.27946 | –0.15314 |
| $AuCl_3$(3-chloropyridine) | –0.28629 | –0.16108 |
| $AuCl_3$(3-methylpyridine) | –0.27759 | –0.15129 |
| $AuCl_3$(3-iodopyridine) | –0.28525 | –0.15992 |
| $AuCl_3$(3-fluoropyridine) | –0.28619 | –0.16087 |
| $AuCl_3$(3-phenylpyridine) | –0.27953 | –0.15325 |
| $AuCl_3$(3-hydroxymethylpyridine) | –0.27917 | –0.15274 |

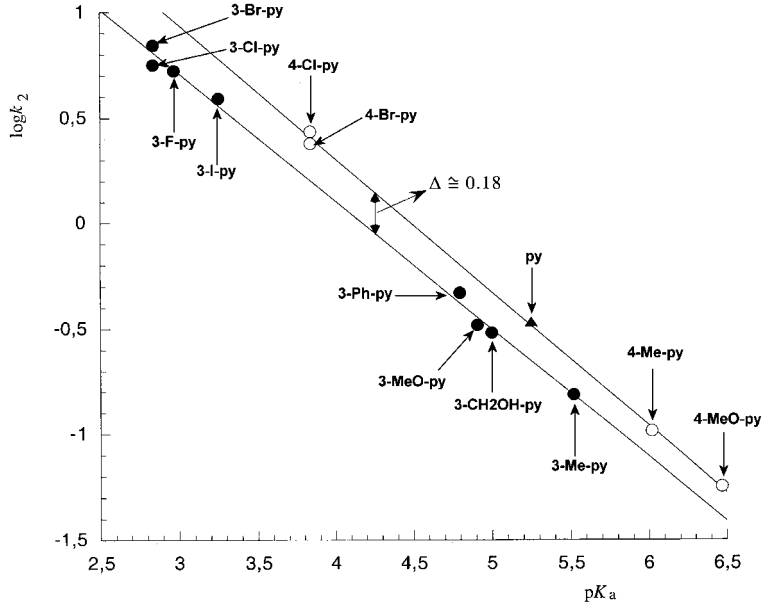


Figure 1. Plots of log $k_2$ for the reaction $AuCl_3$(R-py) + $Cl^-$ → $AuCl_4^-$ + R-py against p$K_a$ of [H(R-py)]$^+$: (▲) R-py = pyridine; (○) R-py = 4-chloropyridine, 4-methoxypyridine, 4-methylpyridine, 4-bromopyridine; (●) R-py = 3-chloropyridine, 3-bromopyridine, 3-fluoropyridine, 3-iodopyridine, 3-methylpyridine, 3-phenylpyridine, 3-hydroxymethylpyridine, 3-methoxypyridine.

 © 2007 Wiley-VCH Verlag GmbH & Co. KGaA, Weinheim 

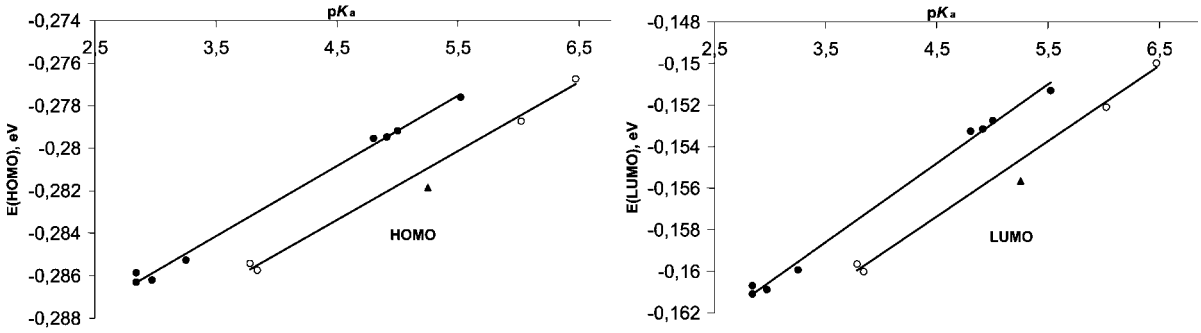


Figure 2. Plots of the (R-py) HOMO and LUMO energies against the p$K_a$ of $[H(R\text{-py})]^+$: (▲) R-py = pyridine; (○) R-py = 4-chloropyridine, 4-methoxypyridine, 4-methylpyridine, 4-bromopyridine; (●) R-py = 3-chloropyridine, 3-bromopyridine, 3-fluoropyridine, 3-iodopyridine, 3-methylpyridine, 3-phenylpyridine, 3-hydroxymethylpyridine, 3-methoxypyridine.

the considered species, while in Figure 2 the plots of HOMO and LUMO vs. p$K_a$ of the leaving 3R-py are shown.

Linear correlations between the frontier orbital energies and p$K_a$ values were found, in particular for the *para*-substituted pyridine (4R-py) derivatives where the equations are $E(\text{HOMO}) = 0.0032 \pm 0.0002\ \text{p}K_a - 0.2979 \pm 0.0008$ and $E(\text{LUMO}) = 0.0036 \pm 0.0002\ \text{p}K_a - 0.1737 \pm 0.0008$, while for the *meta*-substituted pyridine (3R-py) complexes the same equations are $E(\text{HOMO}) = 0.0031 \pm 0.0001\ \text{p}K_a - 0.2957 \pm 0.0004$ and $E(\text{LUMO}) = 0.0038 \pm 0.0001\ \text{p}K_a - 0.1719 \pm 0.0005$. As depicted in Figure 2, the gradients of the plots of the HOMO or LUMO energies vs. p$K_a$ are almost the same for both the 3R- and 4R-pyridines, while there is a significant difference (about 0.002 eV) in their intercepts. The computational results for the pyridine complex $AuCl_3$(py) are comparable to those of the $AuCl_3$(4R-py) derivatives, as was also the case with the chemical behaviour (see Figure 1). The comparison of Figure 1 and Figure 2 appears to indicate a relation between the kinetic and theoretical data, suggesting that the different reactivity of the two groups of ligands considered, 3R-py and 4R-py, could be ascribed to the different energies of the frontier orbitals depicted in Figure 2.

In the reaction studied, i.e. the nucleophilic attack of $Cl^-$ on $AuCl_3$(R-py) and the consequent displacement of the nitrogen ligand, a large role should be played by the lowest unoccupied molecular orbitals of the gold complexes and the filled atomic orbitals of the chloride ion. All the calculated LUMO energy values fall in the range –0.14997 eV to –0.16108 eV and the $AuCl_3$(3R-py) LUMOs are about 0.002 eV higher than those of the $AuCl_3$(4R-py) complexes. The three 3p atomic orbitals of $Cl^-$ have a calculated energy of –0.02709 eV, while the 3s atomic orbital corresponds to an energy value of –0.47949 eV (see Figure 3). On supposing that the observed minor reactivity of the $AuCl_3$(3R-py) complexes, compared to that of the $AuCl_3$(4R-py) derivatives, corresponds to a greater energy difference between the LUMOs of the $AuCl_3$(3R-py) species and the interacting $Cl^-$ atomic orbital, it is to be concluded that the 3s atomic orbital of the chloride ion plays an important role in the nucleophilic attack. Using a pseudo-Valence-Bond description to better explain this last conclusion regarding the reaction studied, $Cl^-$ appears to interact with the gold(III) complexes using a hybrid atomic orbital with a strong s character and, consequently, an energy value lower than those of the LUMOs of the gold complexes, as depicted in Figure 3.

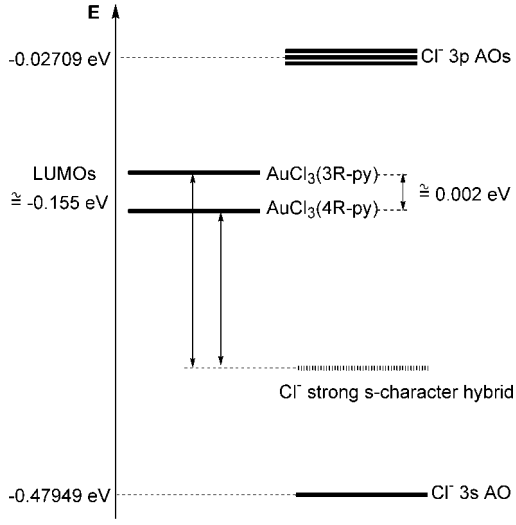


Figure 3. Plot of the $Cl^-$ 3s and 3p AOs and the $AuCl_3$(R-py) (R-py = 3R-py and 4R-py) LUMO energy levels.

## Concluding Remarks

The comparison of the results of the kinetic measurements on the process $AuCl_3(R\text{-py}) + Cl^- \rightarrow AuCl_4^- + R\text{-py}$, where R-py are *para*-substituted pyridines 4R-py and *meta*-substituted pyridines 3R-py, enabled the observation of a slightly different behaviour for these two types of pyridines, the latter type being less reactive. Moreover, by means of DFT calculations the kinetic results were correlated to a small energy difference of the frontier orbitals of the $AuCl_3$(4R-py) and $AuCl_3$(3R-py) derivatives.

 © 2007 Wiley-VCH Verlag GmbH & Co. KGaA, Weinheim 

## Experimental Section

**Materials:** Compound $KAuCl_4 \cdot 2H_2O$ was prepared from pure gold foil (99.99%). Pure reagent-grade products [LiCl, $LiClO_4$, $CH_3SO_3H$ (Aldrich)] were used without further purification. Pyridines were recrystallized or distilled before use when necessary. Anhydrous MeOH was obtained by distillation from Mg wires, but traces of water did not appear to have any appreciable effect upon the reactions. Acetone and dimethylformamide were pure reagent-grade products (Aldrich and BDH, respectively).

**Instruments:** Electronic spectra and kinetic measurements were obtained with a Perkin–Elmer Lambda 15 spectrophotometer. $^1H$ NMR spectra were obtained with Bruker Avance 300 and/or Bruker AC 200 spectrometers. COSY, NOESY and homonuclear decoupling experiments were performed to improve the characterization of the complexes. The conductivity of $1 \times 10^{-3}$ mol dm$^{-3}$ solutions in dimethylformamide at 25 °C was measured with a Radiometer CDM 83 instrument. Elemental analyses were performed by the Microanalytical Laboratory of the Faculty of Pharmaceutical Sciences of the University of Padua.

**Preparation of the Complexes:** Trichloro(3-methylpyridine)gold(III) was first characterized by Cattalini and Tobe,[3] but the preparation of the complexes of 3-fluoropyridine, 3-bromopyridine, 3-chloropyridine, 3-iodopyridine, 3-phenylpyridine, 3-(hydroxymethyl)pyridine and 3-methoxypyridine is described here for the first time. All the complexes were prepared by the following method: $KAuCl_4 \cdot 2H_2O$ (0.415 g, 1 mmol) was dissolved in water (20 mL) and an equimolar amount of the nitrogen-donor base, dissolved in a small volume of water (3 mL), was added dropwise whilst stirring. The yellow precipitate that formed almost immediately was filtered off, washed three times with water (10 mL) and dried in vacuo. The complexes were nonconductive in organic solvents. Yields were in all cases nearly quantitative (>95%). Analytical and $^1H$ NMR data are collected in Tables 4 and 5, respectively.

**Kinetics:** Reactions were initiated by adding a 0.015 mol dm$^{-3}$ acetone solution (10–20 μL) of the substrate complex, $AuCl_3$(3R-py), to a methanolic solution of chloride ion (3 mL) that had previously been brought to the reaction temperature (25 °C) in a thermostatted cell in the spectrophotometer. The concentration of the entering group was always large enough to provide pseudo-first-order conditions. After preliminary repetitive scan experiments in the range 240–360 nm to search for isosbestic points and spectral changes, the kinetics were studied by measuring the changing absorbance at a suitable wavelength (320 nm) as a function of time. Pseudo-first-order rate constants ($k_{obs}$ [s$^{-1}$]) were obtained either from the gradient of plots of $\log(D_t - D_\infty)$ vs. time or from a nonlinear least-squares fit of the experimental data to $D_t = D_\infty + (D_0 - D_\infty)\exp(-k_{obs}t)$, where $D_0$, $D_\infty$ and $k_{obs}$ are the parameters that have to be optimized ($D_0$ = absorbance after mixing the reactants, $D_\infty$ = absorbance at completion of reaction).

**Computational Details:** The computational geometry optimizations of the $AuCl_3$(3R-py) and $AuCl_3$(4R-py) complexes were performed in vacuo using the hybrid DFT B3PW91 method[14] without sym-

Table 4. Analytical data for the complexes (calcd. values in parentheses).

| Complex | C | H | N | Cl |
|---|---|---|---|---|
| $AuCl_3$(3-fluoropyridine) | 15.2 (15.0) | 1.27 (1.01) | 3.51 (3.50) | 26.5 (26.6) |
| $AuCl_3$(3-bromopyridine) | 12.8 (13.0) | 0.62 (0.87) | 3.11 (3.04) | 23.3 (23.1) |
| $AuCl_3$(3-chloropyridine) | 14.3 (14.4) | 1.10 (0.97) | 3.34 (3.36) | (34.2) (34.0) |
| $AuCl_3$(3-methylpyridine) | 18.1 (18.2) | 1.63 (1.78) | 3.72 (3.53) | 27.0 (26.8) |
| $AuCl_3$(3-iodopyridine) | 11.7 (11.8) | 0.69 (0.79) | 2.91 (2.76) | 20.7 (20.9) |
| $AuCl_4$(3-phenylpyridine) | 41.7 (41.9) | 2.11 (1.93) | 3.12 (2.97) | 22.7 (22.6) |
| $AuCl_3$(3-hydroxymethylpyridine) | 17.3 (17.5) | 1.76 (1.71) | 3.41 (3.40) | 25.9 (25.8) |
| $AuCl_3$(3-methoxypyridine) | 17.6 (17.5) | 1.51 (1.71) | 3.44 (3.39) | 26.0 (25.8) |

Table 5. $^1H$ NMR spectroscopic data for the complexes.

| Complex | $^1H$ NMR, $(CD_3)_2CO$, 298 K |
|---|---|
| $AuCl_3$(3-fluoropyridine) | $\delta$ = 9.30 (dd, 1 H, $^3J_{H,F}$ = 2.8 Hz, $^4J_{H,H}$ = 2.2 Hz, 2-H), 9.10 (d, 1 H, $^3J_{H,H}$ = 5.8 Hz, 6-H), 8.39 (ddd, 1 H, $^3J_{H,H}$ = 8.4 Hz, $^3J_{H,F}$ = 8.2 Hz, $^4J_{H,H}$ = 2.2 Hz, 4-H), 8.16 (ddd, 1 H, $^3J_{H,H}$ = 5.8 Hz, $^3J_{H,H}$ = 8.4 Hz, $^3J_{H,F}$ = 5.0 Hz, 5-H) ppm |
| $AuCl_3$(3-bromopyridine) | $\delta$ = 9.42 (d, 1 H, $^4J_{H,H}$ = 2.1 Hz, 2-H), 9.21 (dd, 1 H, $^3J_{H,H}$ = 6.0 Hz, $^4J_{H,H}$ = 1.0 Hz, 6-H), 8.67 (ddd, 1 H, $^3J_{H,H}$ = 8.4 Hz, $^4J_{H,H}$ = 2.1 Hz, $^4J_{H,H}$ = 1.0 Hz, 4-H), 8.03 (dd, 1 H, $^3J_{H,H}$ = 6.0 Hz, $^3J_{H,H}$ = 8.4 Hz, 5-H) ppm |
| $AuCl_3$(3-chloropyridine) | $\delta$ = 9.34 (d, 1 H, $^4J_{H,H}$ = 2.3 Hz, 2-H), 9.17 (dd, 1 H, $^3J_{H,H}$ = 6.0 Hz, $^4J_{H,H}$ = 1.1 Hz, 6-H), 8.55 (ddd, 1 H, $^3J_{H,H}$ = 8.3 Hz, $^4J_{H,H}$ = 2.3 Hz, $^4J_{H,H}$ = 1.1 Hz, 4-H), 8.09 (dd, 1 H, $^3J_{H,H}$ = 6.0 Hz, $^3J_{H,H}$ = 8.3 Hz, 5-H) ppm |
| $AuCl_3$(3-methylpyridine) | $\delta$ = 8.96 (s, 1 H, 2-H), 8.93 (d, 1 H, $^3J_{H,H}$ = 6.0 Hz, 6-H), 8.24 (d, 1 H, $^3J_{H,H}$ = 7.9 Hz, 4-H), 7.88 (dd, 1 H, $^3J_{H,H}$ = 6.0 Hz, $^3J_{H,H}$ = 7.9 Hz, 5-H), 2.58 (s, 3 H, $CH_3$) ppm |
| $AuCl_3$(3-iodopyridine) | $\delta$ = 9.50 (d, 1 H, $^4J_{H,H}$ = 1.8 Hz, 2-H), 9.20 (dd, 1 H, $^3J_{H,H}$ = 5.8 Hz, $^4J_{H,H}$ = 1.0 Hz, 6-H), 8.79 (ddd, 1 H, $^3J_{H,H}$ = 8.4 Hz, $^4J_{H,H}$ = 1.8 Hz, $^4J_{H,H}$ = 1.0 Hz, 4-H), 7.87 (dd, 1 H, $^3J_{H,H}$ = 5.8 Hz, $^3J_{H,H}$ = 8.4 Hz, 5-H) ppm |
| $AuCl_4$(3-phenylpyridine) | $\delta$ = 9.50 (d, 1 H, $^4J_{H,H}$ = 2.1 Hz, 2-H), 9.11 (dd, 1 H, $^3J_{H,H}$ = 6.0 Hz, $^4J_{H,H}$ = 1.0 Hz, 6-H), 8.69 (ddd, 1 H, $^3J_{H,H}$ = 6.2 Hz, $^4J_{H,H}$ = 2.1 Hz, $^4J_{H,H}$ = 1.0 Hz, 4-H), 8.09 (dd, 1 H, $^3J_{H,H}$ = 6.0 Hz, $^3J_{H,H}$ = 6.2 Hz, 5-H), 7.97–7.79 (m, 3 H, Ph), 7.75–7.52 (m, 2 H, Ph) ppm |
| $AuCl_3$(3-hydroxymethylpyridine) | $\delta$ = 9.06 (s, 1 H, 2-H), 8.99 (d, 1 H, $^3J_{H,H}$ = 6.0 Hz, 6-H), 8.35 (d, 1 H, $^3J_{H,H}$ = 7.9 Hz, 4-H), 7.95 (dd, 1 H, $^3J_{H,H}$ = 6.0 Hz, $^3J_{H,H}$ = 7.9 Hz, 5-H), 5.17 (br. s, 1 H, OH), 4.90 (s, 2 H, $CH_2$) ppm |
| $AuCl_3$(3-methoxypyridine) | $\delta$ = 8.90 (d, 1 H, $^4J_{H,H}$ = 2.4 Hz, 2-H), 8.71 (dd, 1 H, $^3J_{H,H}$ = 5.4 Hz, $^4J_{H,H}$ = 1.0 Hz, 6-H), 7.99 (ddd, 1 H, $^3J_{H,H}$ = 8.2 Hz, $^4J_{H,H}$ = 2.4 Hz, $^4J_{H,H}$ = 1.0 Hz, 4-H), 7.92 (dd, 1 H, $^3J_{H,H}$ = 8.2 Hz, $^3J_{H,H}$ = 5.4 Hz, 5-H), 4.09 (s, 3 H, $CH_3$) ppm |

 © 2007 Wiley-VCH Verlag GmbH & Co. KGaA, Weinheim 

metry constraints, in combination with the polarized, single-ζ core, triple-ζ valence 6-311G** basis set on the elements of the first rows of the periodic table and the ECP-based SDD basis set on Au and I.[15] The "restricted" formalism was applied in all calculations. All the resultant stationary points were characterized as true minima (i.e. no imaginary frequencies). A B3PW91/6-311+G** calculation (the same was used for the complexes, with the addition of sp diffuse functions) was applied to obtain the energies of the filled atomic orbitals of the chloride ion. All calculations were carried out at CINECA (Centro Italiano di Supercalcolo, Bologna, Italy) using IBM p5-575 computers with 64-bit IBM Power5 processors operating at 1.9 GHz. The software used was the Gaussian 03 program.[16]

## Acknowledgments

We sincerely thank the Ca' Foscari University of Venice for financial support (Ateneo fund 2006).

[1] a) A. S. Hasmi, J. P. Weyrauch, M. Rudolph, E. Kurpejovic, *Angew. Chem.* **2004**, *116*, 6707; b) A. S. Hasmi, J. P. Weyrauch, M. Rudolph, E. Kurpejovic, *Angew. Chem. Int. Ed.* **2004**, *43*, 6545; c) S. Wang, L. Zhang, *J. Am. Chem. Soc.* **2006**, *128*, 14274.

[2] a) L. Cattalini, M. Nicolini, A. Orio, *Inorg. Chem.* **1966**, *5*, 1674; b) L. Cattalini, A. Orio, A. Doni, *Inorg. Chem.* **1967**, *6*, 280.

[3] L. Cattalini, M. L. Tobe, *Inorg. Chem.* **1966**, *5*, 1145.

[4] B. Pitteri, M. Bortoluzzi, *Transition. Met. Chem.* **2006**, *31*, 1028.

[5] B. Pitteri, M. Bortoluzzi, *Eur. J. Inorg. Chem.* **2007**, accepted.

[6] B. Pitteri, G. Marangoni, L. Cattalini, *J. Chem. Soc. Dalton Trans.* **1994**, 3539.

[7] M. Bellicini, L. Cattalini, G. Marangoni, B. Pitteri, *J. Chem. Soc. Dalton Trans.* **1994**, 1805.

[8] B. Pitteri, G. Marangoni, L. Cattalini, *Polyhedron* **1995**, *14*, 2331.

[9] G. Annibale, L. Cattalini, L. Maresca, G. Michelon, G. Natile, *Inorg. Chim. Acta* **1974**, *10*, 211.

[10] a) B. Pitteri, G. Marangoni, F. Visentin, L. Cattalini, T. Bobbo, *Polyhedron* **1998**, *17*, 475 ; b) B. Pitteri, M. Bortoluzzi, *Polyhedron* **2006**, *25*, 2698.

[11] F. Basolo, R. G. Pearson, *Mechanism of Inorganic Reactions*, 2nd ed. Wiley, New York, **1967**.

[12] M. L. Tobe, *Comprehensive Coordination Chemistry* (Eds.: G. Wilkinson, R. D. McCleverty), Pergamon, Oxford, **1987**, vol. 1.

[13] a) D. D. Perrin, *Dissociation constants of organic bases in aqueous solutions*, Butterworths, London, **1965**; b) R. M. Smith, A. E. Martell, *Critical Stability Constants*, 2nd printing, Plenum Press, New York, **1990**, vol. 2; c) H. K. Hall, *J. Phys. Chem.* **1956**, *60*, 63.

[14] a) R. G. Parr, W. Yang, *Density-functional Theory of Atoms and Molecules*, Oxford Univ. Press, Oxford, **1989**; b) J. K. Labanowski, J. Andzelm, *Density Functional Methods in Chemistry*, Springer-Verlag, New York, **1991**; c) P. Geerlings, F. De Proft, W. Langenaker, *Chem. Rev.* **2003**, *103*, 1793; d) T. Ziegler, *Chem. Rev.* **1991**, *91*, 651; e) A. D. Becke, *J. Chem. Phys.* **1993**, *98*, 5648; f) K. Burke, J. P. Perdew, Y. Wang, in: J. F. Dobson, G. Vignale, M. P. Das (Eds.), *Electronic Density Functional Theory: Recent Progress and New Directions*, Plenum, New York, **1998**.

[15] a) A. D. McLean, G. S. Chandler, *J. Chem. Phys.* **1980**, *72*, 5639; b) R. Krishnan, J. S. Binkley, R. Seeger, J. A. Pople, *J. Chem. Phys.* **1980**, *72*, 650; c) E. R. Davidson, D. Feller, *Chem. Rev.* **1986**, *86*, 681; d) M. Dolg, in: *Modern Methods and Algorithms of Quantum Chemistry*, vol. 1 (Ed.: J. Grotendorst), John Neumann Institute for Computing, NIC series, Jülich, **2000**, pp. 479–508.

[16] M. J. Frish, G. W. Trucks, H. B. Schlegel, G. E. Scuseria, M. A. Robb, J. R. Cheeseman, J. A. Montgomery Jr, T. Vreven, K. N. Kudin, J. C. Burant, J. M. Millam, S. S. Ivengar, J. Tomasi, V. Barone, B. Mennucci, M. Cossi, G. Scalmani, N. Rega, G. A. Petersson, H. Nakatsuji, M. Hada, M. Ehara, K. Toyota, R. Fukuda, J. Hasegawa, M. Ishida, T. Nakajima, Y. Honda, O. Kitao, H. Nakai, M. Klene, X. Li, J. E. Knox, H. P. Hratchian, J. B. Cross, V. Bakken, C. Adamo, J. Jaramillo, R. Gomperts, R. E. Stratmann, O. Yazyev, A. J. Austin, R. Cammi, C. Pomelli, J. W. Ochterski, P. Y. Ayala, R. Morokuma, G. A. Voth, P. Salvador, J. J. Dannenberg, V. G. Zakrewski, S. Dapprich, A. D. Daniels, M. C. Strain, O. Farkas, D. K. Malick, A. D. Rabuck, K. Raghavachari, J. B. Foresman, J. V. Ortiz, Q. Cui, A. G. Baboul, S. Clifford, J. Cioslowski, B. B. Stefanov, G. Liu, A. Liashenko, P.Piskorz, I. Komaromi, R. L. Martin, D. J. Fox, T. Keith, M. A. Al-Laham, C. Y. Peng, A. Nanayakkara, M. Challacombe, P. M. W. Gill, B. Johnson, W. Chen, M. W. Wong, C. Gonzales, J. A. Pople, *Gaussian 03, Revision D.02*, Gaussian Inc., Wallingford CT, **2004**.

Received: June 8, 2007
Published Online: September 18, 2007

 © 2007 Wiley-VCH Verlag GmbH & Co. KGaA, Weinheim 

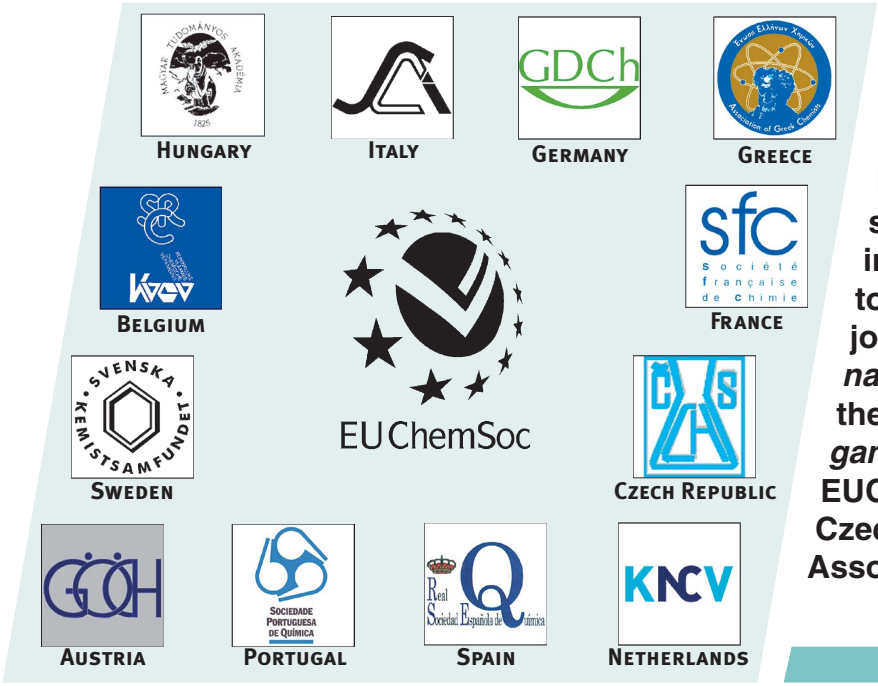


**The EUChemSoc Societies have taken the significant step into the future by merging their traditional journals, to form two leading chemistry journals, the *European Journal of Inorganic Chemistry* and the *European Journal of Organic Chemistry.* Three further EUChemSoc Societies (Austria, Czech Republic and Sweden) are Associates of the two journals.**

## COVER PICTURE

**The cover picture shows** the formation of deeply colored boronate ester polymers by three-component reactions of boronic acids with 1,2,4,5-tetrahydroxybenzene and dipyridyl compounds. The strong color of the polymers is due to efficient intrastrand charge transfer excitations from the tetraoxobenzene to the dipyridyl linker. Upon dissolution of the polymers in hot chloroform, most of the B−N connections are broken, which indicates that polymer formation is a reversible process. More details on these reactions are described in the article by K. Severin et al. on page 5177ff.

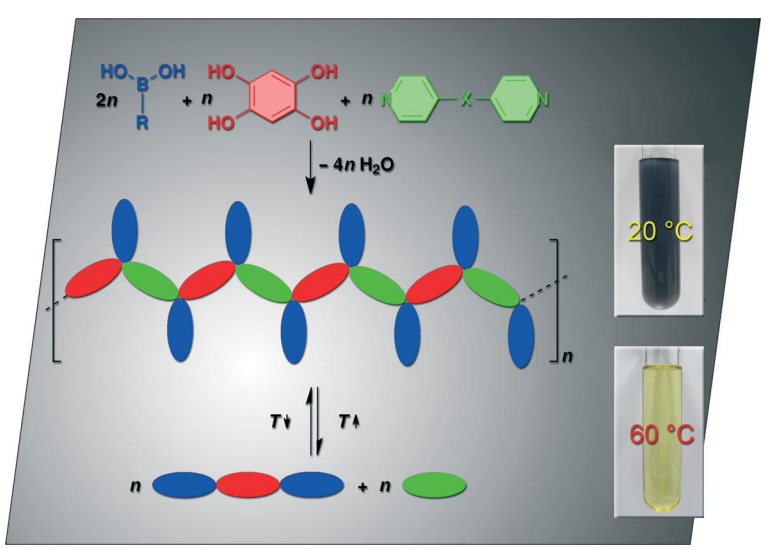


 © 2007 Wiley-VCH Verlag GmbH & Co. KGaA, Weinheim 

# CONTENTS

## SHORT COMMUNICATIONS

### Aurophilic Interactions

**P. Sevillano, O. Fuhr, O. Hampe, S. Lebedkin, C. Neiss, R. Ahlrichs, D. Fenske,* M. M. Kappes ..... 5163–5167**

Synthesis, Characterization and Quantum Mechanical Calculations of $[Au_{18}Se_8(dppthph)_6]Cl_2$

**Keywords:** luster complexes / SCS-MP2 calculations / FT-ESI mass spectrometry / Gold / Photoluminescence measurements / Selenium

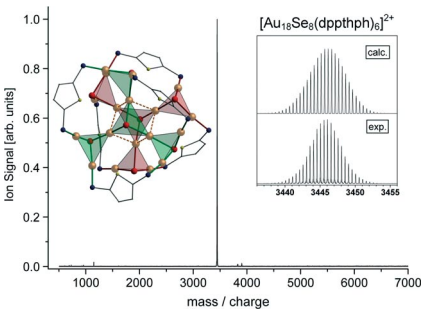


ESI MS demonstrates that in the gas phase the dimeric cation in $[Au_{18}Se_8(dppthph)_6]Cl_2$ is stabilized by six aurophilic Au···Au interactions. SCS-MP2 calculations predict a height of the Coulomb barrier for symmetric dissociation into two $[Au_9Se_2(dppthph)_3]^+$ subunits of 122 kJ/mol. In the solid state the compound crystallizes in two differently colored modifications.

### Haptotropic Rearrangement

**M. Jordan, W. Saak, D. Haase, R. Beckhaus* ..... 5168–5172**

Ring-Slipped (2,2′-Bipyridine)($\eta^3$-cyclopentadienyl)($\eta^5$-cyclopentadienyl)vanadium(II) and Its Oxidation to (2,2′-Bipyridine)bis($\eta^5$-cyclopentadienyl)vanadium(III) Tetraphenylborate

**Keywords:** Coordination modes / Vanadium / Oxidation / Metallocenes / 2,2′-Bipyridine / Haptotropic rearrangement

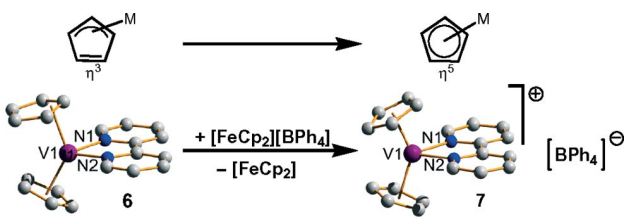


A haptotropic rearrangement of vanadocene(2,2′-bipyridine) derivatives is described. In the case of vanadium(II) an $\eta^3,\eta^5$-metallocene unit is observed, whereas the vanadium(III) complex is characterized by a classical bent $\eta^5,\eta^5$ coordination mode.

### Heteroscorpionate Ligands

**J. Elflein, F. Platzmann, N. Burzlaff* ..... 5173–5176**

One-Pot Synthesis of an Enantiopure N,N,O Scorpionate Ligand Derived from (+)-Camphor

**Keywords:** Chiral pool / Ligand design / Zinc / Rhenium / Camphor

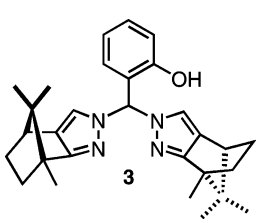


A one-pot synthesis of the new enantiopure heteroscorpionate ligand $HOPhbpm^{3cam}$ (**3**) was described. Ligand **3** was obtained by a pyridine-catalysed Peterson rearrangement, and $\kappa^2$- and $\kappa^3$-coordination of the ligand is observed. Ligand **3** was shown to form a tetrahedral zinc complex as well as an octahedral rhenium complex.

 © 2007 Wiley-VCH Verlag GmbH & Co. KGaA, Weinheim 

# FULL PAPERS

## Multicomponent Self-Assembly

The three-component reaction of aryl boronic acids with 1,2,4,5-tetrahydroxybenzene and 1,2-bis(4-pyridyl)ethylene or 4,4′-bipyridine leads to the formation of boronate ester polymers, which are deeply colored due to efficient intrastrand charge-transfer excitations.

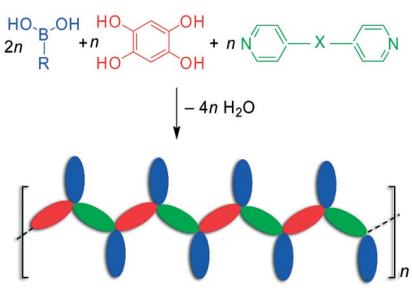


**N. Christinat, E. Croisier, R. Scopelliti, M. Cascella, U. Röthlisberger, K. Severin* ..... 5177–5181**

Formation of Boronate Ester Polymers with Efficient Intrastrand Charge-Transfer Transitions by Three-Component Reactions

**Keywords:** Boron / Charge transfer / Polymers / Self-assembly

## Oligonuclear Gallium Compounds

Metathesis of solid $GaCl_3$ with NaOEt/EtOH provided oxoalkoxide chloride complexes of gallium. Residues that were redissolved in either toluene/MeCN or toluene/pyridine gave after storage $Ga_5(\mu_5\text{-}O)(\mu\text{-}OEt)_8Cl_5$ (**1**) or $[Ga_{12}(\mu_4\text{-}O)_2(\mu_3\text{-}O)_5(\mu\text{-}OEt)_{10}Cl_{12}Py_4]Py$ (**2**), respectively, both at room temperature and in relatively high yields.

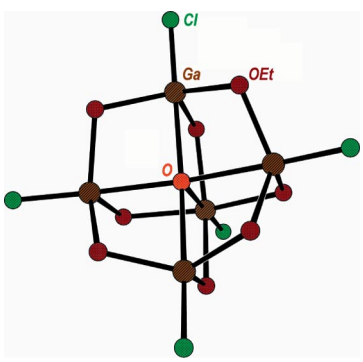


**E. V. Suslova, V. G. Kessler,* S. Gohil, N. Y. Turova ..... 5182–5188**

Oxoethoxide Chlorides – Representatives of Oligonuclear Alkoxide Complexes of Gallium: Penta- and Dodecanuclear Molecules

**Keywords:** Gallium oxides / Sol–gel precursors / Oligonuclear complexes / X-ray / Mass spectrometry

## Photoinduced Charge Separation

The recombination step of the photoinduced charge-separated state in a dyad **DII-Ir**, where the component units are separated by a bridge composed of two benzamide groups, is slowed by a factor of three with respect to a dyad **D-Ir** characterized by a bridge with a single benzamide group. The use of **DII-Ir** in the elaboration of triads with improved charge-separation properties is discussed.

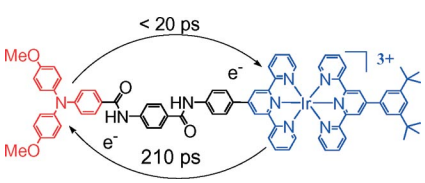


**L. Flamigni,* B. Ventura, E. Baranoff, J.-P. Collin,* J.-P. Sauvage* ... 5189–5198**

A Triphenylamine/Bis(terpyridine)$Ir^{III}$ Dyad for the Assembly of Charge-Separation Constructs with Improved Performances

**Keywords:** Charge separation / Electron transfer / Iridium / Photochemistry / Supramolecular chemistry

## Oxidation of Metal Thiolates

Oxidation of 3,3-di-*tert*-butyldithiirane 1-oxide with dimethyldioxirane (DMD) gave the title 1,2-dioxide, and its treatment with a $Pt^0$ complex provided the (disulfenato)$Pt^{II}$ complex. Oxidation of the related sulfenato–thiolato complex with DMD gave the sulfinato–thiolato complex and the same reaction in the presence of $CF_3COOH$ provided the disulfenato complex.

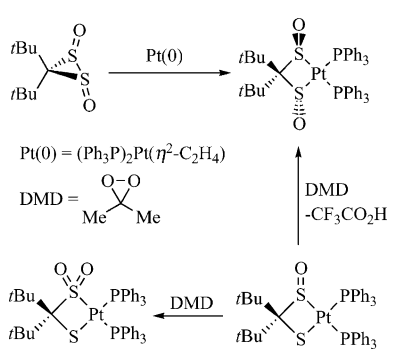


**A. Ishii,* M. Ohishi, N. Nakata ..... 5199–5206**

Preparation of 3,3-Di-*tert*-butylthiirane *trans*-1,2-Dioxide and Its Reaction with a Platinum(0) Complex To Give a (Disulfenato)platinum(II) Complex: Regioselectivity of the Oxidation of a Related (Sulfenato–thiolato)platinum(II) Complex

**Keywords:** Platinum / Dithiirane / *vic*-Disulfoxide / Oxidative addition / Oxidation

 © 2007 Wiley-VCH Verlag GmbH & Co. KGaA, Weinheim 

# CONTENTS

## Chiral Epoxidation Catalysts

**X. Sala, N. Santana, I. Serrano, E. Plantalech, I. Romero, M. Rodríguez,* A. Llobet,* S. Jansat, M. Gómez, X. Fontrodona ..... 5207–5214**

The Spectroscopic, Electrochemical and Structural Characterization of a Family of Ru Complexes Containing the $C_2$-Symmetric Didentate Chiral 1,3-Oxazoline Ligand and Their Catalytic Activity

**Keywords:** Ruthenium / N ligands / Epoxidation / Chiral ligands / Atropisomerism

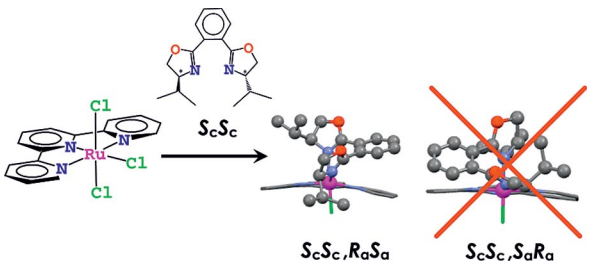


The complete characterization of a family of chiral complexes containing terpy and oxazoline ligands, where a single atropisomer is obtained as a function of the chiral ligand configuration, is presented, together with a preliminary study of their catalytic activity in olefin epoxidation.

## Communication between Co Redox Centers

**A. Arnanz, C. Moreno,* M.-L. Marcos, J. González-Velasco, S. Delgado ..... 5215–5225**

Synthesis, Characterization, Structures and Comparative Electrochemical Study of 2,4-Bis(trimethylsilylethynyl)thiophene Coordinated Carbonylcobalt Units

**Keywords:** Thiophene / Carbonylcobalt complexes / Electrochemistry

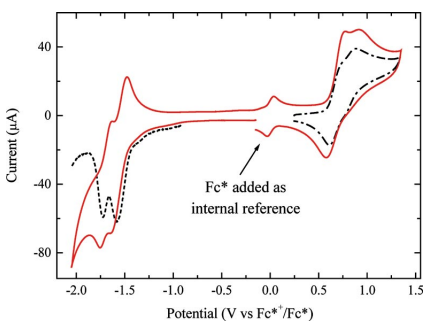


$Co_2(CO)_6$ and $Co_2(CO)_4$(dppm) derivatives of 2,4-bis(trimethylsilylethynyl)thiophene have been synthesized and characterized. A comparative electrochemical study of these complexes and those derived from 2,5-bis-(trimethylsilylethynyl)thiophene has been made.

## Gas-Sensing Materials

**L. Mi, H. Hou,* J. Xu, H. Xu, Z. Song, M. Tang, Y. Fan ..... 5226–5233**

Inclusion Complexes for Use in Room-Temperature Gas-Sensor Design

**Keywords:** Inclusion compounds / Semiconductors / Sensors / Density functional calculations / Bridging ligands

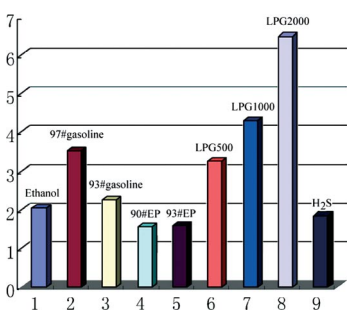


The four inclusion complexes synthesized herein show that conjugated inclusion complexes with an odd number of electrons should be useful for highly selective room-temperature gas-sensor design.

## Precursor Complexes

**X. Wang, L. Li, H. Hou,* J. Wu, Y. Fan ..... 5234–5245**

Substitution, Addition, and Recombination Reactions of Precursor Complexes with Ferrocenyl Carboxylate Units

**Keywords:** Crystal engineering / Bridging ligands / Substituent effects / Precursors

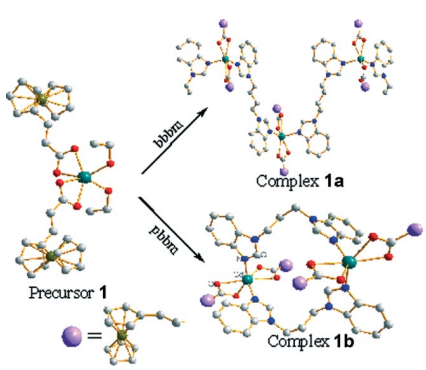


The structural integrity of the precursor complexes was maintained in the substitution or addition reactions of these complexes with ligands at room temperature, but a recombination reaction occurred under harsher refluxing conditions and four "recombinant" complexes were gained.

 © 2007 Wiley-VCH Verlag GmbH & Co. KGaA, Weinheim 

## Rhenium Olefin Complexes

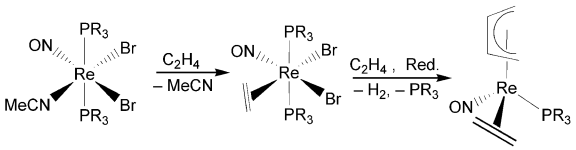


**A. Choualeb, O. Blacque, H. W. Schmalle, T. Fox, T. Hiltebrand, H. Berke* ..... 5246–5261**

Olefin Complexes of Low-Valent Rhenium

Various phosphane and nitrosyl-substituted pseudo-octahedral or pentacoordinate ethylene complexes of rhenium(+I) and (−I) were prepared. Detailed NMR and DFT analyses were used to unravel rotational isomerism of the olefinic ligands.

**Keywords:** Rhenium / Olefin complexes / Nitrosyl complexes / DFT calculation

## Amide Methanolysis

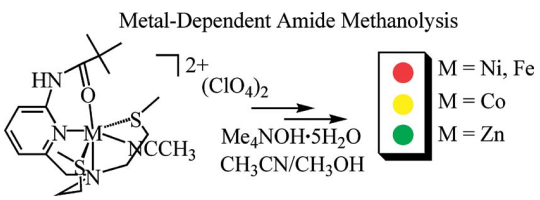


**G. K. Ingle, M. M. Makowska-Grzyka, A. M. Arif, L. M. Berreau* .... 5262–5269**

Divalent Nickel, Cobalt and Iron Complexes of an Amide-Appended $N_2S_2$ Ligand: Synthesis, Characterization and Reactivity with Hydroxide Anion

Divalent nickel, cobalt and iron complexes of an $N_2S_2$ ligand have been prepared and characterized. The amide methanolysis reactivity of these complexes upon treatment with hydroxide anion in methanol was examined. Differences in reactivity are rationalized on the basis of structural differences in the "parent" protonated complexes.

**Keywords:** N,S ligands / Amides / Metal effects / Deprotonation

## Mixed-Valent Compounds

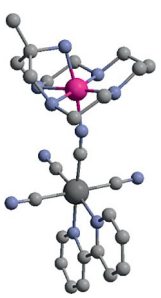

**P. V. Bernhardt,* F. Bozoglian, M. Font-Bardía, M. Martínez,* A. P. Meacham, B. Sienra, X. Solans ..... 5270–5276**

The Influence of Ligand Substitution at the Electron Donor Center in Molecular Cyano-Bridged Mixed-Valent $Co^{III}/Fe^{II}$ and $Co^{III}/Ru^{II}$ Complexes

The metal-to-metal charge-transfer energies of a new series of cyano-bridged mixed-valent $Ru^{II}/Co^{III}$ and $Fe^{II}/Co^{III}$ complexes are shown to be affected by variations to both the redox potentials of the donor and acceptor centers and the reorganizational energy brought about by replacing terminal cyano ligands with a bipyridyl ligand.

**Keywords:** Mixed-valent compounds / Cyanides / Binuclear complexes

## Encapsulated Carboxylate Ligands

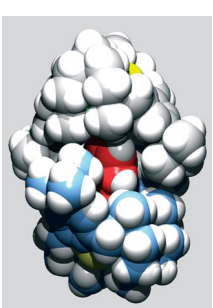

**J. Klingele, M. H. Klingele, O. Baars, V. Lozan, A. Buchholz, G. Leibeling, W. Plass, F. Meyer, B. Kersting* ..... 5277–5285**

Tetranuclear Nickel(II) Complexes Composed of Pairs of Dinuclear $LNi_2$ Fragments Linked by Acetylenedicarboxylate, Terephthalate, and Isophthalate Dianions: Synthesis, Structures and Magnetic Properties

Three tetranuclear nickel(II) complexes in which pairs of dinuclear nickel(II) complexes are linked by acetylenedicarboxylate, terephthalate, and isophthalate dianions have been prepared and structurally characterized. The $Ni^{II}_4$ complexes are well separated from each other in the solid state and allow the presence of any magnetic exchange interactions through the encapsulated dicarboxylato bridge to be determined without interference by intermolecular coupling interactions.

**Keywords:** Macrocyclic ligands / Dicarboxylato ligands / Nickel / Polynuclear complexes / Magnetic properties

 © 2007 Wiley-VCH Verlag GmbH & Co. KGaA, Weinheim 

# CONTENTS

## Chiral Dinuclear Mesocates

**S. D. Reid, C. Wilson, C. I. De Matteis, J. B. Love* ..... 5286–5293**

Using Chiral Ligand Substituents To Promote the Formation of Dinuclear, Double-Stranded Iron, Manganese, and Zinc Mesocates

**Keywords:** Ligand design / Helical structures / Ligand effects / Supramolecular chemistry / Chirality

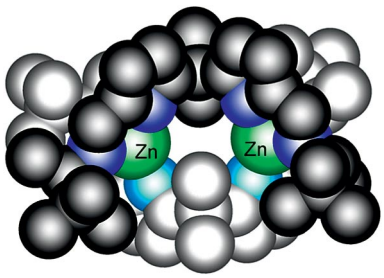


Incorporation of sterically demanding chiral imine substituents to the acyclic $N_4$-donor iminopyrrole ligand $H_2L$ disrupts the expected formation of the dinuclear, double-stranded helicates $[M_2(L)_2]$ to instead preferentially form chiral mesocates (M = Mn, Fe, Zn).

## Copper–Chalcogenide Bonding

**H. Jacobsen,*
M. J. Fink ..... 5294–5299**

Decomposition Cascades of Dicoordinate Copper(I) Chalcogenides

**Keywords:** Bond energy / Copper / Chalcogens / Density functional calculations / Dispersive interactions

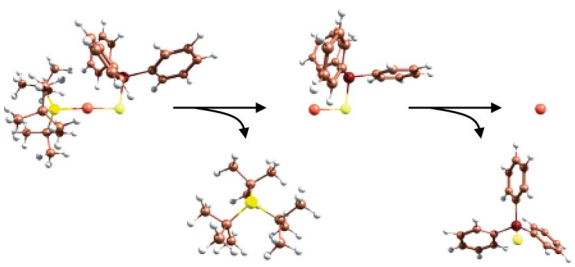

A density functional study of bond energies of various complexes that contain a copper chalcogenide core provides relates to thermal behavior and possible CVD usage of this class of compounds.

**If not otherwise indicated in the article, papers in issue 32 were published online on October 26, 2007**

 © 2007 Wiley-VCH Verlag GmbH & Co. KGaA, Weinheim 

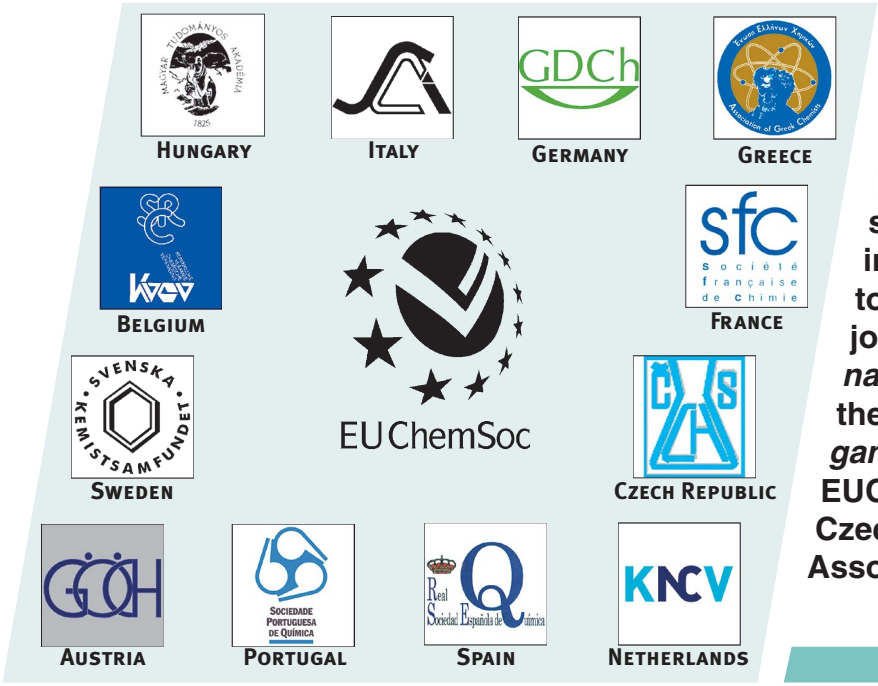


**The EUChemSoc Societies have taken the significant step into the future by merging their traditional journals, to form two leading chemistry journals, the *European Journal of Inorganic Chemistry* and the *European Journal of Organic Chemistry.* Three further EUChemSoc Societies (Austria, Czech Republic and Sweden) are Associates of the two journals.**

## COVER PICTURE

**The cover picture shows** the formation of deeply colored boronate ester polymers by three-component reactions of boronic acids with 1,2,4,5-tetrahydroxybenzene and dipyridyl compounds. The strong color of the polymers is due to efficient intrastrand charge transfer excitations from the tetraoxobenzene to the dipyridyl linker. Upon dissolution of the polymers in hot chloroform, most of the B−N connections are broken, which indicates that polymer formation is a reversible process. More details on these reactions are described in the article by K. Severin et al. on page 5177ff.

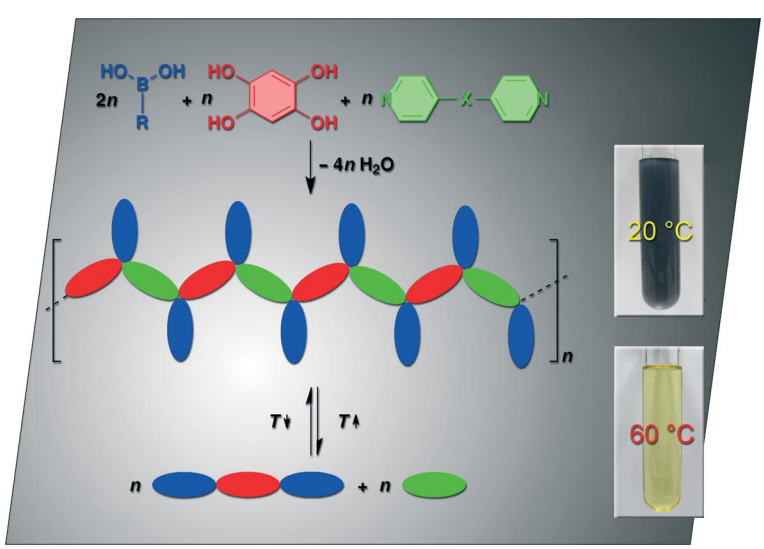


 © 2007 Wiley-VCH Verlag GmbH & Co. KGaA, Weinheim 

# SPOTLIGHTS …

## *The Mitsunobu Reaction*

T. Y. S. But, P. H. Toy*

**The Mitsunobu Reaction: Origin, Mechanism, Improvements, and Applications**

*Chem. Asian J.*
DOI: **10.1002/asia.200700182**

**Classics never fade away**: The Mitsunobu reaction is a widely used and versatile method for the dehydrative oxidation–reduction condensation of an acid/pronucleophile with an alcohol mediated by phosphine and azo reagents. The history, mechanism, and recent developments of this stereoselective workhorse condensation reaction are reviewed.

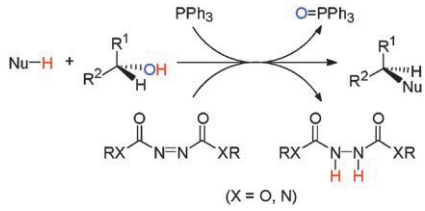


## *Photoactivation*

M. E. Hahn, J.-P. Pellois, M. Vila-Perelló, T. W. Muir*

**Tunable Photoactivation of a Post-translationally Modified Signaling Protein and its Unmodified Counterpart in Live Cells**

*ChemBioChem*
DOI: **10.1002/cbic.200700404**

**Strike a pose**… Expressed protein ligation was used to prepare caged analogues of the signaling protein Smad2 (see illustration). The function and fluorescence of the analogues could be photocontrolled in a correlated fashion. This strategy permitted the titration of the cellular levels of active phosphorylated Smad2 in its biologically relevant, full-length form.

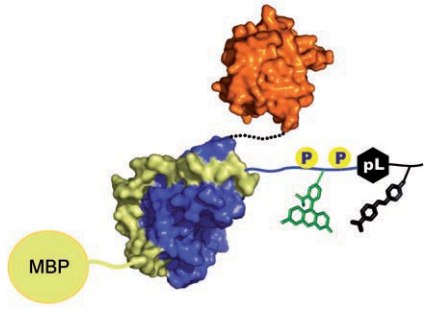


## *Lanthanide Luminescence*

A. D′Aléo, G. Pompidor, B. Elena, J. Vicat, P. L. Baldeck, L. Toupet, R. Kahn, C. Andraud,* O. Maury*

**Two-Photon Microscopy and Spectroscopy of Lanthanide Bioprobes**

*ChemPhysChem*
DOI: **10.1002/cphc.200700375**

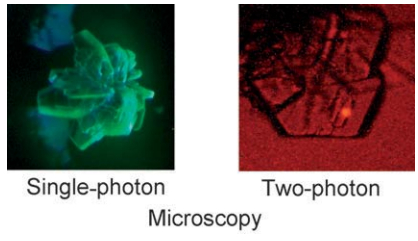


**Lanthanide bioprobes:** The first two-photon microscopy imaging experiments using tris-dipicolinate terbium complexes as a probe were carried out on derivative protein crystals. Whereas one-photon irradiation results in green luminescence of the entire crystal aggregate, two-photon excitation gives a three-dimensionally resolved spot corresponding to the confocal volume (see picture).

## *Synthetic Methods*

K. Motoshima, Y. Hiwasa, M. Yoshikawa, K. Fujimoto, A. Tai, H. Kakuta,* K. Sasaki

**Antimalarial Cation-dimers Synthesized in Two Steps from an Inexpensive Starting Material, Isonicotinic Acid**

*ChemMedChem*
DOI: **10.1002/cmdc.200700107**

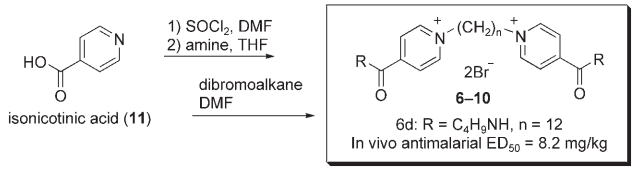


**Managing malaria**. As the area affected by malaria includes a large proportion of developing countries, there is a need for new antimalarials that can be synthesized and supplied inexpensively. In this study, bis-cation dimers, MAP series **6**–**10** synthesized from an inexpensive isonicotinic acid (**11**) in just two steps, were designed. MAP-412 (**6d**) exhibited a potent in vivo antimalarial activity.

 © 2007 Wiley-VCH Verlag GmbH & Co. KGaA, Weinheim 

EurJIC European Journal of Inorganic Chemistry

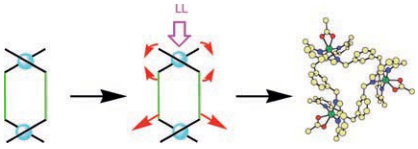


**Taken in with open arms!** Coordination chemistry is used to destabilise a linear array and turn it into a circular helicate (see figure). Changes in the geometry of the metal centre allow the product to be tailored to form dimers or circular helicates.

## *Supramolecular Chemistry*

J. Hamblin, F. Tuna, S. Bunce, L. J. Childs, A. Jackson, W. Errington, N. W. Alcock, H. Nierengarten, A. Van Dorsselaer, E. Leize-Wagner, M. J. Hannon*

**Supramolecular Circular Helicates Formed by Destabilisation of Supramolecular Dimers**

*Chem. Eur. J.*
DOI: **10.1002/chem.200700848**

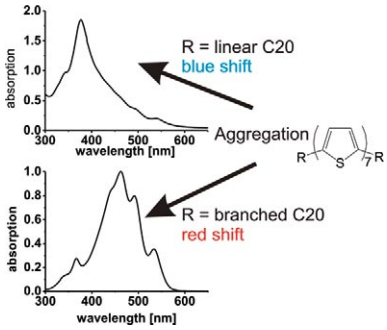


α- and α,ω-substituted oligothiophenes show a strong aggregation behaviour in solution depending on the geometry of the alkyl substituents which is reflected by a distinct blue or red shift, respectively, in the absorption spectra. A strong influence of the substituent is also found in the morphology of the aggregates and of thermal properties in the solid state.

## *Aggregation of Oligothiophenes*

S. Ellinger, A. Kreyes, U. Ziener,* C. Hoffmann-Richter, K. Landfester, M. Möller

**Aggregation Phenomena of Long α- and α,ω-Substituted Oligothiophenes – the Effect of Branched vs. Linear End-Groups**

*Eur. J. Org. Chem.*
DOI: **10.1002/ejoc.200700566**

**Outside silver, inside gold**: Gold nanoparticles are used as seeds to probe the role of plasmon excitation in the photomediated growth of silver nanoprisms. This approach generates novel core–shell nanostructures that contain a spherical (see TEM image, inset shows side view) or triangular-prism gold core with a triangular silver prism shell. The architecture of these particles can be tuned by controlling excitation wavelength and gold-core diameter.

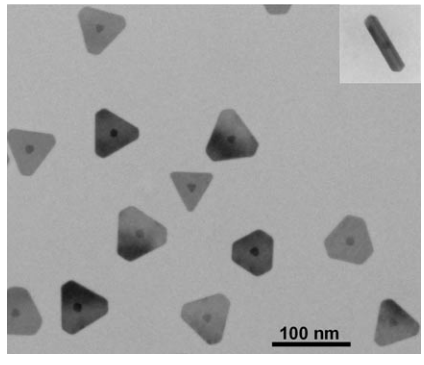


## *Core–Shell Nanostructures*

C. Xue, J. E. Millstone, S. Li, C. A. Mirkin*

**Plasmon-Driven Synthesis of Triangular Core–Shell Nanoprisms from Gold Seeds**

*Angew. Chem. Int. Ed.*
DOI: **10.1002/anie.200703185**

On these pages, we feature a selection of the excellent work that has recently been published in our sister journals. If you are reading these pages on a computer, click on any of the items to read the full article. Otherwise please see the DOIs for easy online access through Wiley InterScience.

 © 2007 Wiley-VCH Verlag GmbH & Co. KGaA, Weinheim 

DOI: 10.1002/ejic.200700870

# Synthesis, Characterization and Quantum Mechanical Calculations of $[Au_{18}Se_8(dppthph)_6]Cl_2$

**Paloma Sevillano,[a] Olaf Fuhr,[a] Oliver Hampe,[a] Sergej Lebedkin,[a] Christian Neiss,[a] Reinhart Ahlrichs,[a,b] Dieter Fenske,*[a,c] and Manfred M. Kappes[a,b]**

**Keywords:** Cluster complexes / SCS-MP2 calculations / FT-ESI mass spectrometry / Gold / Photoluminescence measurements / Selenium

The reaction of [Au(tht)Cl] (tht = tetrahydrothiophene) with 2,5-bis(diphenylphophanyl)thiophene (dppthph) and Se-$(SiMe_3)_2$ leads to the formation of $[Au_{18}Se_8(dppthph)_6]Cl_2$. This compound crystallizes in two modifications, both containing a cluster dication with nearly identical gold–selenium cores. The dication consists of two subunits only connected by six aurophilic interactions. ESI MS demonstrates that these facilitate cohesion of the cluster subunits even in the gaseous state. SCS-MP2 calculations show that the dimer is a metasable species, which is ultimately prevented from dissociation by a Coulomb barrier. In addition, photoluminescene measurements demonstrate that the small differences in the ligand shell of the cluster molecules lead to different photoluminescene properties of the two modifications. (© Wiley-VCH Verlag GmbH & Co. KGaA, 69451 Weinheim, Germany, 2007)

## Introduction

During the last years much attention has been paid to the rich chemistry of ligand-stabilized gold-containing clusters, which has been extensively studied.[1,2] In previous works, we have reported about different gold cluster compounds containing elements from the groups 15 and 16. While the compounds containing selenium bridges seem to favor species containing 10 or 18 gold atoms, with $Au_3Se$ fragments as building blocks of the larger structures,[2a–2d] the clusters containing phosphorus and arsenic bridges show more versatile arrangements containing 10, 12, 17, 18 or 19 gold atoms and different building blocks like $Au_4P_2$, $Au_4As_2$ or $Au_7P_2$ in $[Au_{12}(PPh)_2(P_2Ph_2)_2(dppm)_4Cl_2]Cl_2$, $[Au_{17}(As\mathit{n}Pr)_6(As_2\mathit{n}Pr_2)(dppm)_6]Cl_3$ and $[Au_{18}(P)_2(PPh)_4(PHPh)(dppm)_6]Cl_3$, respectively.[2e–2g] In all these compounds, the building blocks are bridged by the diphosphane ligands with the length of their carbon chains being a determining factor affecting the final geometry of the cluster compound. In this work we report the synthesis and characterization of the compound $[Au_{18}Se_8(dppthph)_6]Cl_2$ (**1**) [dppthph = 2,5-bis(diphenylphosphanyl)thiophene].

## Results and Discussion

The reaction of the gold(I) complex [Au(tht)Cl] (tht = tetrahydrothiophene), the phosphane dppthph and Se-$(SiMe_3)_2$ leads to the formation of the compound $[Au_{18}Se_8(dppthph)_6]Cl_2$ (**1**). It crystallizes in two different space groups, $P\bar{1}$ (**1a**) and $P2_12_12_1$ (**1b**), which results in crystals with different appearance and colors: yellow rectangular plates and orange highly faceted hexagonal blocks, respectively (Scheme 1).

$$[Au(tht)Cl] + dppthph + Se(SiMe_3)_2 \xrightarrow{CH_2Cl_2} [Au_{18}Se_8(dppthph)_6]Cl_2\ (\mathbf{1a}\text{ and }\mathbf{1b})$$

Scheme 1. Preparation reaction of compound **1**.

Single-crystal X-ray analysis has been carried out for **1a** and **1b**. The results are shown in Figure 1.[3] Figure 1a shows a superposition of the $[Au_{18}Se_8(dppthph)_6]^{2+}$ cations in **1a** (blue) and **1b** (orange) indicating that the Au–Se cores are nearly identical concerning bond lengths and angles. One main difference in the molecular structures of **1a** and **1b** is the different orientation of the thiophene rings of the phosphane ligands (also the orientations of the phenyl rings – not shown in Figure 1 – differ, probably due to packing effects). Figure 1b shows a labelled model of the cation in **1a**. It consists of two separate $[Au_9Se_4(dppthph)_3]^+$ subunits, each of which is formed by four corner-sharing trigonal $Au_3Se$ pyramids (red and green polyhedra). This arrangement is typical for cluster compounds of the composition $[Au_{18}E_8(dppthph)_6]^{2+}$ (E: chalcogen; dppx: bidentate phosphane).[2a,4] All gold atoms in **1a** are almost linearly coordinated (bond angles between 167.5° and 177.2°) either by two selenium atoms or by one selenium atom and one phosphorus atom of the dppthph ligands. In the inner part of the cluster there are six relatively short Au···Au distances [294.5(1)–301.1(1) pm; indicated by dashed lines in Figure 1b] between gold atoms of different subunits (Au1–Au3

[a] Institut für Nanotechnologie, Forschungszentrum Karlsruhe, Postfach 3640, 76021 Karlsruhe, Germany
[b] Institut für Physikalische Chemie, Universität Karlsruhe, 76128 Karlsruhe, Germany
[c] Institut für Anorganische Chemie, Universität Karlsruhe, 76128 Karlsruhe, Germany
Fax: +49-721-608-8440
E-mail: dieter.fenske@aoc1.uni-karlsruhe.de

 © 2007 Wiley-VCH Verlag GmbH & Co. KGaA, Weinheim 

and Au10–Au12) forming an $Au_6Se_2$ heterocubane-like motif. A view from a different angle (Figure 1c, Au···Au not drawn) shows that there is no additional chemical bond between the two $[Au_9Se_4(dppthph)_3]^+$ fragments. In contrast to all other $\{[Au_9E_4(dppx)_3]\}_2^{2+}$ cations published so far, the two subunits in **1** are not interconnected in a catenane-like way. For comparison Figure 1d shows an analogous drawing of the core of $[Au_9Se_4(dppe)_3]_2^{2+}$ [dppe = bis(diphenylphosphanyl)ethane][2a] demonstrating the catenation of the two $[Au_9Se_4(dppe)_3]^+$ cations. Because of this significant difference it was particularly intriguing to employ electrospray mass spectrometry to gain insight into the relative stability of this dication. More specifically, we wondered whether this cluster dication can be observed both in solution and in the gas phase, what the possible fragmentation pathways are {e.g. scission into two singly charged $[Au_9Se_4(dppthph)_3]^+$ ions driven by Coulomb repulsion?} and how they compare to the related cluster $[Au_{18}Se_8(dppe)_6]^{2+}$ in which the two catenated $Au_9Se_4$ subunits are further clamped together by the bidentate ligands.[2a]

Figure 2 displays a positive-ion FT-ICR mass spectrum obtained upon electrospraying a solution of **1**: The virtually only ion signal obtained is found at $m/z \approx 3446.1$. On the basis of the exact mass and the isotopomer distribution (see inset in Figure 2) it can be clearly identified as the doubly charged species $[Au_{18}Se_8(dppthph)_6]^{2+}$. The stability of this

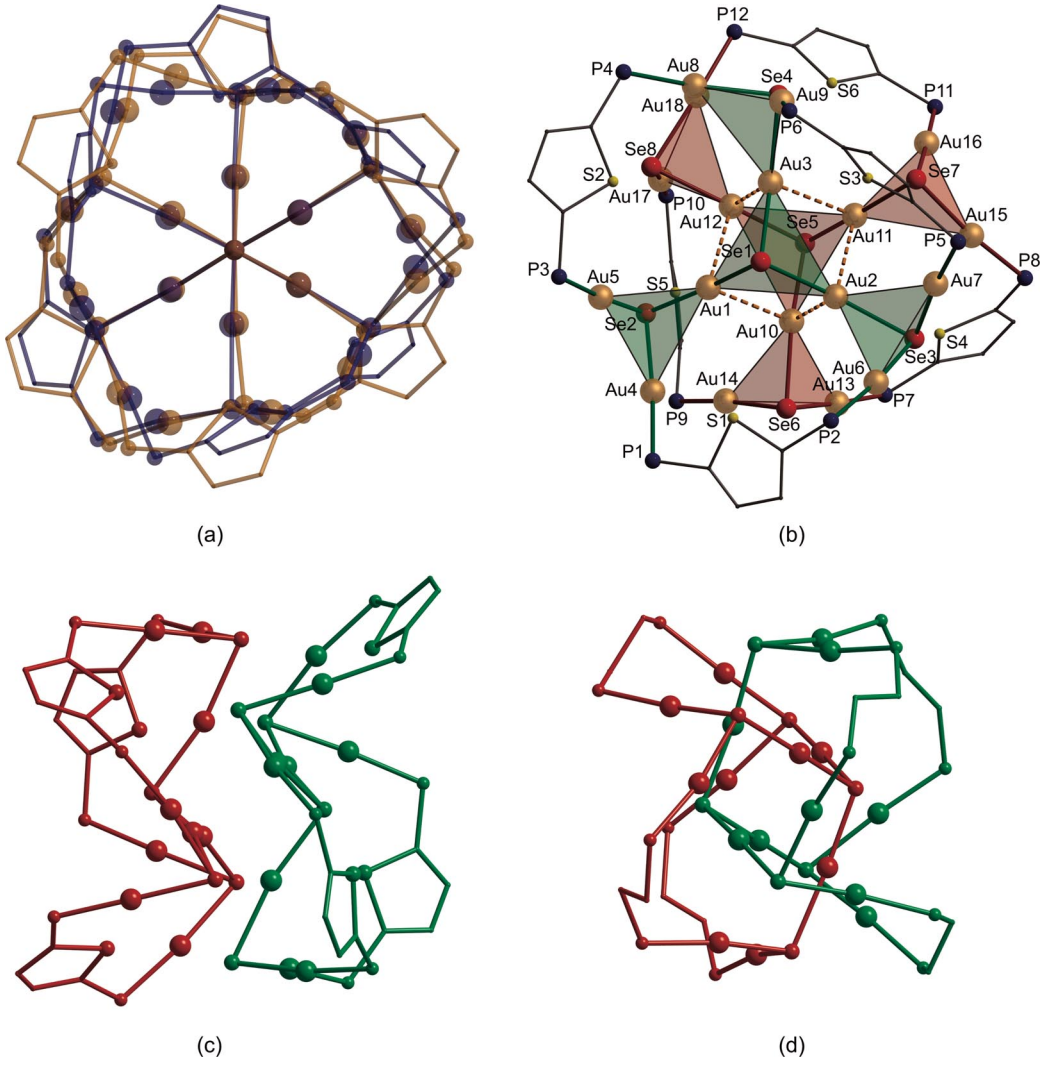


Figure 1. (a): Superposition of the cluster cores of the $[Au_{18}Se_8(dppthph)_6]^{2+}$ cations in **1a** (blue) and **1b** (orange); (b) molecular structure of the cation in **1a** (Au: gold, Se: red, P: blue, S: yellow, C: gray); (c) view of the cation in **1a** [rotated by 90° compared to Figure 1(a)] demonstrating the arrangement of the two $[Au_9Se_4(dppthph)_3]^+$ subunits (red and green); (d) view of the cation $[Au_{18}Se_8(dppe)_6]^{2+}$[2a] showing the catenane-like connection of the subunits (red and green). Selected bond lengths [pm] in the cations of **1a/1b**: Au1–Au10 299.4(1)/300.0(2), Au1–Au12 300.6(1)/299.8(2), Au2–Au10 296.8(1)/299.1(2), Au2–Au11 294.5(1)/294.9(2), Au3–Au11 301.1(1)/296.1(2), Au3–Au12 297.0(1)/294.5(2); Au1–Se1 241.9(2)/244.3(4), Au1–Se2 246.2(2)/249.3(4), Au2–Se1 243.3(2)/242.9(3), Au2–Se3 249.3(2)/248.6(3), Au3–Se1 242.7(2)/243.5(2), Au3–Se4 247.4(2)/243.1(4), Au4–Se2 242.3(2)/242.6(3), Au5–Se2 242.1(2)/244.1(4), Au6–Se3 242.1(2)/243.9(4), Au7–Se3 244.0(2)/243.3(4), Au8–Se4 244.4(2)/244.0(4), Au9–Se4 243.4(2)/245.1(3), Au10–Se5 243.2(2)/242.4(4), Au10–Se6 248.4(2)/248.5(4), Au11–Se5 242.7(2)/244.5(4), Au11–Se7 247.4(2)/250.6(4), Au12–Se5 242.2(2)/243.1(3), Au12–Se8 247.6(2)/248.3(3), Au13–Se6 244.0(2)/244.7(4), Au14–Se6 245.6(2)/241.6(4), Au15–Se7 243.6(2)/242.4(3), Au16–Se7 245.2(2)/244.5(4), Au17–Se8 245.3(2)/243.9(4), Au18–Se8 244.3(2)/243.5(4); average Au–P 225.8/225.4.

 © 2007 Wiley-VCH Verlag GmbH & Co. KGaA, Weinheim 

species was studied by means of collision-induced dissociation in the ICR cell of the FT mass spectrometer. Figure 3 shows the fragmentation mass spectra of the isolated parent ion $[Au_{18}Se_8(dppthph)_6]^{2+}$ at two different collision energies. At low collision energy – i.e. when fragmentation sets in and becomes observable – sequential loss of two dppthph ligands is observed (upper trace in Figure 3) without impairing the cluster's framework or charge. At somewhat higher collision energies (see lower trace of Figure 3) the framework of the cluster dication undergoes asymmetric scission according to Scheme 2.

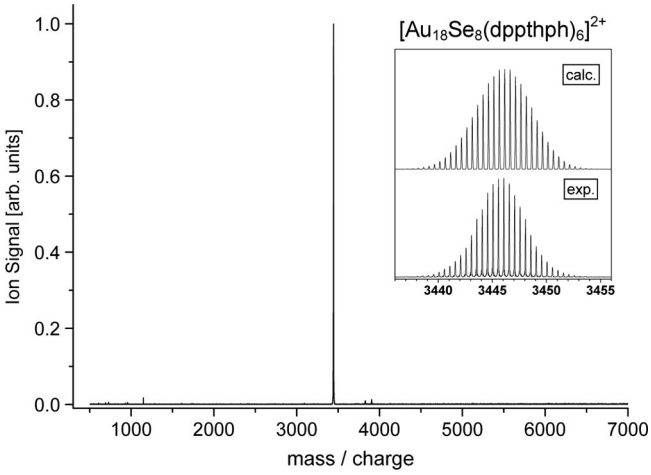


Figure 2. Positive-ion FT-ICR mass spectrum from an electrosprayed solution of **1**. The inset contrasts the experimental high-resolution signal at $m/z \approx 3446$ to the calculated isotopomer distribution for $[Au_{18}Se_8(dppthph)_6]^{2+}$.

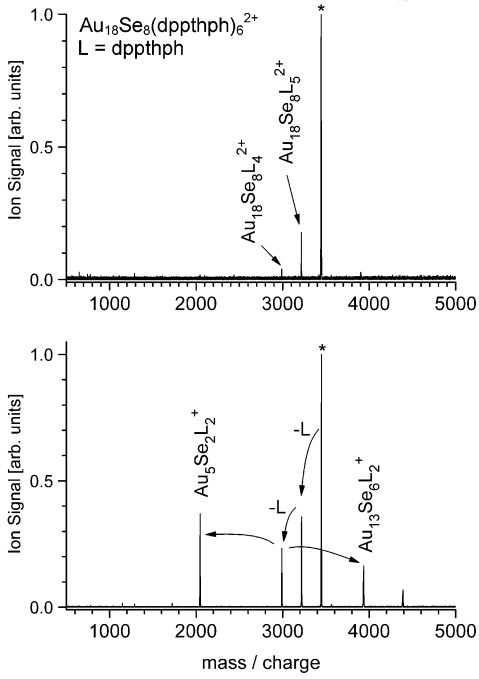


Figure 3. CID fragmentation spectra of the parent ion $[Au_{18}Se_8(dppthph)_6]^{2+}$ (marked with an asterisk) at low (upper trace) and high (lower trace) collision energies.

$$[Au_{18}Se_8(dppthph)_5]^{2+} \rightarrow [Au_{13}Se_6(dppthph)_3]^{+} + [Au_5Se_2(dppthph)_2]^{+}$$

$$[Au_{18}Se_8(dppthph)_4]^{2+} \rightarrow [Au_{13}Se_6(dppthph)_2]^{+} + [Au_5Se_2(dppthph)_2]^{+}$$

Scheme 2. Fragmentation channels observed upon collision-induced dissociation of isolated dications of **1** after loss of one and two dppthph ligands.

This is an intriguing result: Despite the two excess charges on the cluster and the known strong gold–phosphane bond,[5] loss of two neutral ligands is the primary (and therefore presumably energetically lowest-lying) fragmentation pathway before the cluster core dissociates at higher excess collision energies – presumably involving scission of the $Au_6Se_2$ heterocubane unit.

This observation and the rather small Au–Au average distance of 297 pm in the core immediately point towards a strong aurophilic interaction as discussed by, e.g., Schmidbaur[1a–1l] or Pyykkö[6] in detail. We investigated this question further by carrying out molecular electronic structure calculations. In a first attempt, the structures of the cluster **1b** (= dimer) and the monomer (= $[Au_9Se_4(dppthph)_3]^{+}$) were optimized by the density functional theory (DFT) level of theory, which predicted the cluster to be energetically unstable, with the monomers favored by 21 kJ/mol.[7] It is well known, however, that DFT is not able to describe van der Waals type interactions (to which aurophilic interactions belong) properly, and thus, DFT cannot be regarded reliable in this case.

Therefore, we investigated the bonding conditions adopting the SCS-MP2 (spin-component scaled Møller–Plesset perturbation theory of second order) level of theory as proposed by Grimme,[8] which gives more reliable results for gold cluster compounds than ordinary MP2,[9] which is known to overbind van der Waals complexes in general. In this part of the study we considered only the heterocubane core $(Au_3Se)_2^{2+}$ as illustrated in Figure 4, and computed the potential energy surface for pulling apart the two $Au_3Se^{+}$ subunits, which is also shown in Figure 4. Au–Se bond lengths and bonding angles were kept fixed to match the experimental ones.[10] With this simple model, we obtained a quite typical curve for the dissociation of multiply charged ions, revealing a Coulomb barrier height of 122 kJ/mol for symmetric dissociation with respect to the cluster. The minimum energy distance between the Se atoms is located at 476 pm and matches the experimentally observed result (crystal structure: **1a**: 478 pm, **1b**: 492 pm). The transition-state area is found to be around 680 pm. Moreover, the SCS-MP2 calculations support the finding of the DFT calculations that the dimer is only metastable with respect to the monomers, namely 102 kJ/mol, i.e. even more than predicted by DFT (albeit for a larger dication). To conclude, the observed stability of the cluster core is due to aurophilic interactions which are accompanied by a relatively high Coulomb barrier.

 © 2007 Wiley-VCH Verlag GmbH & Co. KGaA, Weinheim 

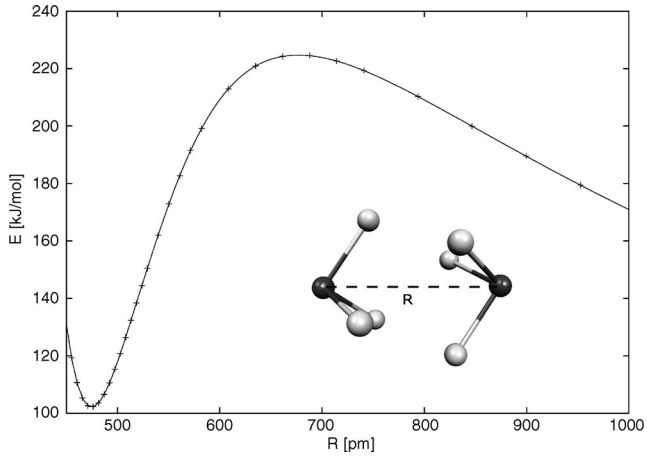


Figure 4. Potential energy surface for the symmetric dissociation and picture of the $(Au_3Se)_2^{2+}$ model complex at the SCS-MP2/QZVPP level of theory. The energy is relative to the completely separated monomers.

In accordance with the structural similarity of the two crystal modifications of **1**, we measured virtually identical FT-Raman spectra of **1a** and **1b**, particularly in the frequency range of $\geq 500\ cm^{-1}$, which is likely dominated by vibrational modes of the dppthph ligands. On the other hand, photoluminescence (PL) spectroscopy evidenced notable differences in the electronic structure and relaxation dynamics of **1a** and **1b**. Both crystals exhibited red emission under illumination in the UV/Vis spectral range, however, with distinct PL excitation (PLE) and emission spectra as shown in Figure 5. The emission maxima of **1a** and **1b** underwent uneven blueshifts from 647 and 660 nm, respectively, to 630 and 625 nm, respectively, by decreasing the temperature from 293 to 15 K (Figure 5). The PLE spectrum of **1b** is weakly structured as compared to **1a** and shows an additional shoulder at ca. 550–580 nm. The differences in the PLE spectra are consistent with the distinctly perceived colors of **1a** and **1b** (see above). PL quantum efficiency, $\phi_{PL}$, of **1a** and **1b** at ambient temperature was only $(3–4)\times10^{-2}$ and $(4–6)\times10^{-3}$, respectively, but it significantly increased by decreasing the temperature (Figure 5). The changes in $\phi_{PL}$ roughly correlate with the timescale of the PL decay (well fitted with biexponential curves). The latter occurred within tens (**1b**) and hundreds (**1a**) of nanoseconds at ambient temperature and slowed down to several microseconds at 15 K. The above deviations in the PL properties may be tentatively attributed to the different orientation of the ligands and "packing" of the cluster units in **1a** and **1b** and, correspondingly, to differences in the vibronic properties between them. In this context, the crystal modifications of **1** appear to be an interesting object for further comparative experimental and theoretical studies.

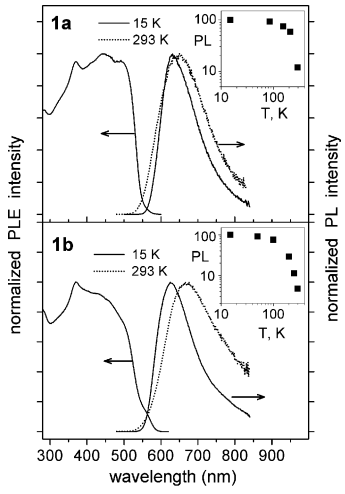


Figure 5. Normalized photoluminescence excitation (PLE) and emission (PL) spectra of crystals of **1a** (top) and **1b** (bottom) in nujol mull. The emission and excitation wavelengths for the PLE and PL spectra are 650 and 400 nm, respectively. The inserts show the temperature dependence of the integrated PL intensities.

## Conclusions

This report focuses on the aurophilic interactions in the dication $[Au_{18}Se_8(dppthph)_6]^{2+}$. In the solid state the compound $[Au_{18}Se_8(dppthph)_6]Cl_2$ crystallizes in two modifications (**1a** and **1b**) in which the cations have nearly identical cores but different orientations of the thiophene and phenyl groups in the ligand shell. This results in differences in the solid-state PL and PLE spectra of the two modifications. The dication in **1** consists of two $[Au_9Se_4(dppthph)_3]^+$ units interconnected by six aurophilic Au···Au contacts (av. distance 289 pm). These are strong enough to stabilize the dimeric cation even in the gas phase which was demonstrated by ESI MS. By SCS-MP2 calculations the height of Coulomb barrier for symmetric dissociation can be approximated as 122 kJ/mol.

## Experimental Section

**General:** All experiments regarding the synthesis were carried out under dry nitrogen. $CH_2Cl_2$ was dried with $P_2O_5$ and *n*-pentane with $LiAlH_4$. $Se(SiMe_3)_2$ was synthesized from $Me_3SiCl$ and $Na_2Se$ according to a published method.[11] [Au(tht)Cl] (tht = tetrahydrothphhene) was prepared according to standard procedures.[12]

**1:** To a solution of [Au(tht)Cl] (52 mg, 0.162 mmol) in $CH_2Cl_2$ (10 mL), dppthph (37 mg, 0.081 mmol) was added to give a colorless solution. After 30 min of stirring, $Se(SiMe_3)_2$ (0.020 mL, 0.081 mmol) was added to the former solution to give a yellow solution. This solution was layered with *n*-pentane, and a few days later yellow crystals of **1a** and orange crystals of **1b** had formed. For the spectroscopic measurements the crystals were separated manually.

**X-ray Structure Determination:** Data were collected with a STOE IPDS II diffractometer using Mo-$K_\alpha$ radiation ($\lambda$ = 0.71073 Å). Structure solution and refinement against $F^2$ were carried out using SHELXS and SHELXL software.[13] Further details are given in ref.[3]

**Mass Spectrometry:** Mass spectra were taken with a Fourier transform ion cyclotron resonance (FT-ICR) mass spectrometer (Bruker Daltonics, APEX II) equipped with a 7 T magnet and an electrospray ionization source (Analytica of Branford) with a set of home-

 © 2007 Wiley-VCH Verlag GmbH & Co. KGaA, Weinheim 

built rf ion optics for improved sensitivity. Solutions from hand-picked crystals containing **1a** in dichloromethane ($CH_2Cl_2$) were prepared and sprayed using nitrogen as nebulizing gas at a flow rate of 300 μL/h. The desolvation capillary was typically heated to about 80 °C. Collision-induced dissociation was performed employing resonant dipolar rf excitation of the parent ion to variable kinetic energies in the ICR cell and using argon as collision gas at a typical pressure of $3 \times 10^{-7}$ mbar.

**Photoluminescence Spectroscopy:** Photoluminescence spectra of nujol mulls of crystals of **1a** and **1b** were measured with a Spex Fluorolog-3 spectrometer equipped with a closed-cycle optical cryostat (Leybold) operating at 15–293 K. Emission spectra were corrected for the wavelength-dependent response of the spectrometer.[2b] An integrating sphere was applied to estimate the PL quantum efficiency of **1a** and **1b** at ambient temperature according to a procedure described in ref.[2b] Emission decay traces were recorded using an $N_2$ laser (337 nm, ≤ 4 ns) for a pulse excitation.

**Calculations:** All calculations were carried out with the TURBOMOLE program suite.[14] Geometry optimizations[15] of the cluster and the monomer were performed by adopting the TPSS[16] density functional in combination with the def2-TZVP basis sets from the TURBOMOLE library and the RI-J approximation.[17] The reported potential energy surface was scanned at the SCS-MP2 level of theory[18] with the def2-QZVPP basis sets.[19] Basis set incompleteness problems were considered by adopting counterpoise corrections (to avoid basis-set superposition errors) and basis-set extrapolation on selected points of the potential surface, but it was found that these effects approximately cancel each other for the above-mentioned basis set. A relativistic small core pseudo potential for gold was used throughout.[20]

## Acknowledgments

This work was supported by the Deutsche Forschungsgemeinschaft (Center for Functional Nanostructures), the Deutsch-Israelisches Programm (DIP), and the Fonds der Chemischen Industrie.

[1] a) H. Schmidbaur, G. Weidenhiller, O. Steigelmann, *Angew. Chem.* **1991**, *103*, 442–444; *Angew. Chem. Int. Ed. Engl.* **1991**, *30*, 433–435; b) H. Schmidbaur, O. Steigelmann, *Z. Naturforsch* **1992**, *47b*, 1721–1724; c) E. Zeller, H. Beruda, H. Schmidbaur, *Inorg. Chem.* **1993**, *32*, 3203–3204; d) N. Dufour, A. Schier, H. Schmidbaur, *Organometallics* **1993**, *12*, 2408–2410; e) E. Zeller, H. Schmidbaur, *J. Chem. Soc. Chem. Commun.* **1993**, 69–70; f) A. Blumenthal, H. Beruda, H. Schmidbaur, *J. Chem. Soc. Chem. Commun.* **1993**, 1005–1006; g) O. Steigelmann, P. Bissinger, H. Schmidbaur, *Z. Naturforsch.* **1993**, *48b*, 72–78; h) G. M. T. Cheetham, M. M. Harding, J. L. Haggitt, D. M. P. Mingos, H. R. Powell, *J. Chem. Soc. Chem. Commun.* **1993**, 1000–1001; i) E. Zeller, H. Beruda, H. Schmidbaur, *Chem. Ber.* **1993**, *126*, 2033–2036; j) H. Beruda, E. Zeller, H. Schmidbaur, *Chem. Ber.* **1993**, *126*, 2037–2040; k) H. Schmidbaur, S. Hofreiter, M. Paul, *Nature* **1995**, *377*, 503–504; l) R. E. Bachman, H. Schmidbaur, *Inorg. Chem.* **1996**, *35*, 1399–1401; m) R. C. B. Copley, D. M. P. Mingos, *J. Chem. Soc. Dalton Trans.* **1996**, 479–489; n) J. Phete, C. Maichle-Mössmer, J. Strähle, *Z. Anorg. Allg. Chem.* **1998**, *624*, 1207–1210; o) J. Phete, J. Strähle, *Z. Naturforsch.* **1999**, *54b*, 381–384.

[2] a) D. Fenske, T. Langetepe, M. M. Kappes, O. Hampe, P. Weis, *Angew. Chem.* **2000**, *112*, 1925–1928; *Angew. Chem. Int. Ed.* **2000**, *39*, 1857–1860; b) S. Lebedkin, T. Langetepe, P. Sevillano, D. Fenske, M. M. Kappes, *J. Phys. Chem. B* **2002**, *106*, 9019–9026; c) P. Sevillano, T. Langetepe, D. Fenske, *Z. Anorg. Allg. Chem.* **2003**, *629*, 207–214; d) J. Olkowska-Oetzel, P. Sevillano, A. Eichhöfer, D. Fenske, *Eur. J. Inorg. Chem.* **2004**, 1100–1106; e) P. Sevillano, O. Fuhr, M. Kattannek, P. Nava, O. Hampe, S. Lebedkin, R. Ahlrichs, D. Fenske, M. M. Kappes, *Angew. Chem.* **2006**, *118*, 3785–3791; *Angew. Chem. Int. Ed.* **2006**, *45*, 3702–3708; f) P. Sevillano, O. Fuhr, E. Matern, D. Fenske, *Z. Anorg. Allg. Chem.* **2006**, *632*, 735–738; g) P. Sevillano, O. Fuhr, O. Hampe, S. Lebedkin, E. Matern, D. Fenske, M. M. Kappes, *Inorg. Chem.* **2007**, *46*, 7294–7298.

[3] Crystallographic data: **1a**: $[Au_{18}Se_8(dppthph)_6]Cl_2 \cdot 9CH_2Cl_2$: $C_{177}H_{150}Au_{18}Cl_{20}P_{12}S_6Se_8$; triclinic, space group $P\bar{1}$, $Z = 2$; $a = 1819.2(4)$, $b = 2402.5(5)$, $c = 2499.9(5)$ pm, $\alpha = 95.37(3)$, $\beta = 91.07(3)$, $\gamma = 103.53(3)°$; $V = 10567(4) \times 10^6$ pm$^3$; $T = 180(2)$ K; $\rho_{calcd.} = 2.429$ g cm$^{-3}$, 57341 data measured of which 34770 were unique ($R_{int} = 0.0784$); 2026 parameters; $GoF = 1.017$, $wR_2 = 0.206$ (all data); $R_1 = 0.078$ [$I > 2\sigma(I)$]; largest diff. peak/hole: 4.63/–5.96 eA$^{-3}$ [the relatively high remaining electron density is located close to Au2 (95.3 pm)]; **1b**: $[Au_{18}Se_8(dppthph)_6]Cl_2 \cdot 9CH_2Cl_2$: $C_{177}H_{150}Au_{18}Cl_{20}P_{12}S_6Se_8$; orthorhombic, $P2_12_12_1$, $Z = 4$; $a = 2674.4(5)$, $b = 2861.1(6)$, $c = 3005.0(6)$ pm; $V = 22993(8) \times 10^6$ pm$^3$; $T = 180(2)$ K; $\rho_{calcd.} = 2.232$ g cm$^{-3}$, 41520 data measured of which 29252 were unique ($R_{int} = 0.0835$); 1259 parameters, 24 restrains; $GoF = 1.015$, $wR_2 = 0.195$ (all data); $R_1 = 0.071$ [$I > 2\sigma(I)$]; Flack parameter: 0.03; largest diff. peak/hole: 2.62/–2.60 eA$^{-3}$. CCDC-655627 (**1a**) and -655628 (**1b**) contain the supplementary crystallographic data for this paper. These data can be obtained free of charge from The Cambridge Crystallographic Data Centre via www.ccdc.cam.ac.uk/data_request/cif.

[4] T. Langetepe, Ph. D. Thesis, University of Karlsruhe (TH), **2001**.

[5] D. Schröder, H. Schwarz, J. Hrušák, P. Pyykkö, *Inorg. Chem.* **1998**, *37*, 624.

[6] P. Pyykkö, *Angew. Chem.* **2004**, *116*, 4512–4557; *Angew. Chem. Int. Ed.* **2004**, *43*, 4412–4456.

[7] Selected bond lengths of the optimized structure: Au···Au (within the heterocubane unit) 303.0 pm, Au–Se (within the heterocubane unit) 246.6 pm, Au–Se (from the heterocubane unit to Se outside of it) 251.3 pm; for experimental values see Figure 1.

[8] S. Grimme, *J. Chem. Phys.* **2003**, *118*, 9095–9102.

[9] S. Grimme, private communication, **2006**.

[10] Full relaxation of the core causes a collapse of the structure with the gold atoms approaching each other and the selenium atoms pushed apart. Obviously, this movement is hindered by the bulky side groups attached to the gold atoms in the full cluster.

[11] M. Schmidt, H. Ruf, *Z. Anorg. Allg. Chem.* **1963**, *321*, 270–273.

[12] R. Uson, A. Laguna, M. Laguna, *Inorg. Synth.* **1989**, *26*, 85–91.

[13] G. M. Sheldrick, *SHELXTL-97, Program for the Refinement of Crystal Structures*, University of Göttingen, **1997**.

[14] R. Ahlrichs, M. Baer, M. Haeser, H. Horn, C. Koelmel, *Chem. Phys. Lett.* **1989**, *162*, 165–169.

[15] M. v. Arnim, R. Ahlrichs, *J. Comput. Chem.* **1999**, *111*, 9183–9190.

[16] J. Tao, J. Perdew, V. N. Staroverov, G. E. Scuseria, *Phys. Rev. Lett.* **2003**, *91*, 146401.

[17] a) O. Treutler, R. Ahlrichs, *J. Chem. Phys.* **1995**, *102*, 346–354; b) F. Weigend, *Phys. Chem. Chem. Phys.* **2006**, *8*, 1057–1065; c) M. Sierka, A. Hogekamp, R. Ahlrichs, *J. Chem. Phys.* **2003**, *118*, 9136–9148.

[18] F. Weigend, M. Häser, *Theo. Chem. Acc.* **1997**, *97*, 331–340.

[19] F. Weigend, R. Ahlrichs, *Phys. Chem. Chem. Phys.* **2005**, *7*, 3297–3305.

[20] D. Andrae, U. Haeussermann, M. Dolg, H. Stoll, H. Preuss, *Theor. Chim. Acta* **1990**, *77*, 123–141.

Received: August 21, 2007
Published Online: October 11, 2007

 © 2007 Wiley-VCH Verlag GmbH & Co. KGaA, Weinheim 

DOI: 10.1002/ejic.200700904

# Ring-Slipped (2,2′-Bipyridine)($\eta^3$-cyclopentadienyl)($\eta^5$-cyclopentadienyl)-vanadium(II) and Its Oxidation to (2,2′-Bipyridine)bis($\eta^5$-cyclopentadienyl)-vanadium(III) Tetraphenylborate

**Markus Jordan,[a] Wolfgang Saak,[a] Detlev Haase,[a] and Rüdiger Beckhaus*[a]**

**Keywords:** Coordination modes / Vanadium / Oxidation / Metallocenes / 2,2′-Bipyridine / Haptotropic rearrangement

Reaction of vanadocene(II) (**4**) with 2,2′-bipyridine (**5**) leads to (2,2′-bipyridine)vanadocene(II) (**6**), exhibiting a $\eta^3$,$\eta^5$-metallocene unit, proved by X-ray diffraction. By selective one-electron oxidation employing $[Cp_2Fe]BPh_4$ salts, the cationic (2,2′-bipyridine)vanadocene(III) derivative **7** is formed. It is characterized by a classical bent bis($\eta^5$-cyclopentadienyl)vanadium(III) structure. Characteristic structural details comparing changes in the oxidation states are discussed. The ring-slip parameters are compared to those of tungsten and other vanadium complexes.
(© Wiley-VCH Verlag GmbH & Co. KGaA, 69451 Weinheim, Germany, 2007)

## Introduction

Since the synthesis and characterization of ferrocene by Fischer and Wilkinson in 1952 the cyclopentadienyl unit has become one of the most important ligands in organometallic chemistry.[1,2] In addition to the common $\eta^5$-coordination mode (a), $\eta^3$- (b), $\eta^1$- (c), ionic (d) and bridging forms (e) are known (Figure 1).[3]

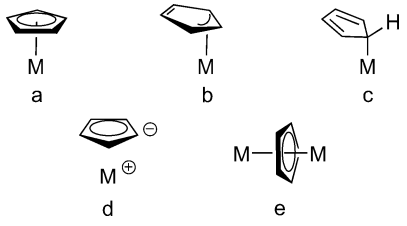


Figure 1. The most common of about ten bonding modes of the Cp ligand: (a) $\eta^5$, (b) $\eta^3$, (c) $\eta^1$, (d) ionic, (e) bridging.

Bonding modes of special interest are $\eta^3$-Cp and $\eta^1$-Cp due to their interconversion chemistry, the so-called "ring slippage".[3] Whereas the first $\eta^1$-Cp transition-metal complex was reported only three years after the characterization of ferrocene,[4] the $\eta^3$-coordination mode was discussed for several years. Generally, Cp-ligand isomerizations often play a significant role in the chemistry of their metal complexes.[5] Prominent examples of ring-slipped compounds are given in the case of complexes exhibiting an electron excess (> 18) like dicarbonyl($\eta^3$-cyclopentadienyl)($\eta^5$-cyclopentadienyl)tungsten (**1**),[6] or particularly for indenyl complexes such as those shown in Figure 2.[7]

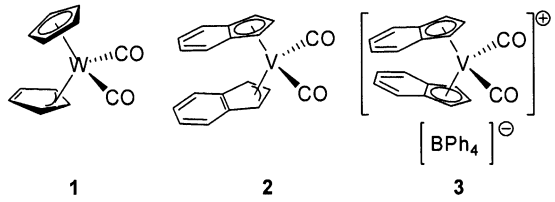


Figure 2. Prominent examples of stucturally characterized ring-slipped complexes: dicarbonyl($\eta^3$-cyclopentadienyl)($\eta^5$-cyclopentadienyl)tungsten (**1**),[6] dicarbonyl($\eta^3$-indenyl)($\eta^5$-indenyl)vanadium(II) (**2**)[7a] and the oxidized "non-slipped" form dicarbonylbis($\eta^5$-indenyl)vanadium(III) tetraphenylborate (**3**).[7b]

On the other hand, due to their electronic and steric versatility, aromatic *N*-heterocycles play an important role as classical ligands in coordination chemistry,[8] as bridging ligands in binuclear derivatives[9] and as building blocks for supramolecular compounds.[10] Beyond their capability to connect metal centres by forming ligand-to-metal bonds, they provide the opportunity of π-backbonding and thereby may affect delocalization and transport of electrons.[11] We have investigated the behaviour of bis(azine)s in the coordination sphere of low-valent titanium complexes, leading to bi-,[12] tri-,[12a,13] tetra-[12a,14] and up to octanuclear derivatives,[12a] accompanied by spontaneous C–C coupling reactions resulting from the strong reducing properties of titanium(II).[12a,13] Here we wish to report an example of the behaviour of 2,2′-bipyridine in the coordination sphere of vanadium(II) and vanadium(III). Floriani et al. described the formation of a [$Cp_2$V(2,2′-bipyridine)] derivative. However, because of the lack of structural data the authors assumed a monodentate coordination mode for the 2,2′-bipyridine ligand (17e$^-$ complex) (Figure 3).[15]

[a] Institute of Pure and Applied Chemistry, Carl von Ossietzky University,
P. O. Box 2503, 26111 Oldenburg, Germany
Fax: +49-441-798-3581
E-mail: ruediger.beckhaus@uni-oldenburg.de


WILEY InterScience DISCOVER SOMETHING GREAT
© 2007 Wiley-VCH Verlag GmbH & Co. KGaA, Weinheim

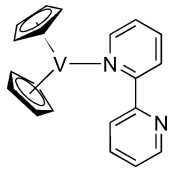


Figure 3. Assumed structure of [$Cp_2V$(2,2-bipyridine)] by Floriani et al.[15]

## Results and Discussion

First at all, we reproduced the reaction of vanadocene(II) (**4**) and 2,2′-bipyridine (**5**)[15] extended by the structural characterization of the reaction product **6**. In contrast to the proposed monodentate structure, the 2,2′-bipyridine ligand was found to act as a typical chelating unit. Additionally, one of the Cp rings exhibit an η³-coordination mode (ring slippage) (Scheme 1). Upon oxidation of complex **6** by ferrocenium tetraphenylborate, the Cp ring flips back to η⁵-coordination to form (2,2′-bipyridyl)bis(η⁵-cyclopentadienyl) vanadium(III) tetraphenylborate (**7**) (Scheme 2). A number of slip parameters were applied to these structures, and the results were compared with given examples of ring-slipped complexes such as **1** and **2**.

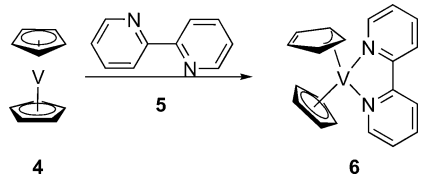


Scheme 1. Formation and structure representation of compound **6**.

### Synthesis and Characterization of (2,2′-Bipyridine)(η³-cyclopentadienyl)(η⁵-cyclopentadienyl)vanadium(II) (6)

Vanadocene(II) (**4**) and 2,2′-bipyridine (**5**) were dissolved in *n*-hexane, and the solution was stirred at room temperature overnight. The colour of the solution changed immediately from violet to black. The solution was cooled to –70 °C, and complex **6** precipitated in form of black crystals (53%).

Suitable crystals for X-ray diffraction became available by crystallization at –16 °C. Complex **6** crystallizes in the space group $R\bar{3}$; the trigonal unit cell contains 18 molecules of the compound. X-ray diffraction of these black flat prisms confirmed the bidentate chelate ligation of the 2,2′-bipyridine (**5**). However, one of the Cp rings offered only η³-coordination. This should be necessary to confirm the 18e⁻ rule in **6**. If both Cp rings were η⁵-coordinated, the complex would contain 19 electrons. With one η³-coordinated Cp ring, the preferred 17e⁻ structure of **6** was formed. The ORTEP plot (Figure 4) significantly shows the slippage of one Cp ring with respect to the other.

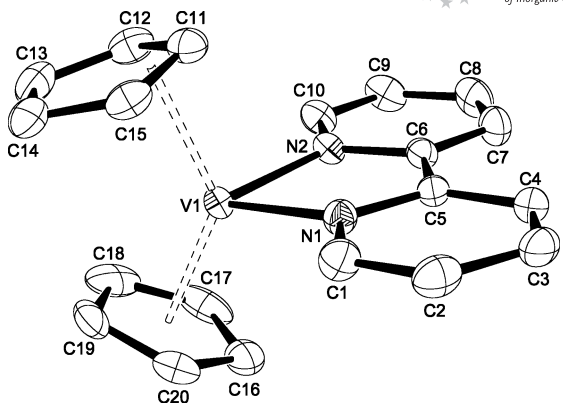


Figure 4. ORTEP plot of the solid-state molecular structure of compound **6**. Hydrogen atoms are omitted for clarity; thermal ellipsoids are drawn at the 50% probability level. Selected bond lengths [Å] and angles [°]: V1–N1 2.036(1), V1–N2 2.053(1), C5–C6 1.423(2), V1–Ct 2.01, N–V–N 76.89(5).

Furthermore the C11 atom slightly turns out of the plane formed by C12–C15 to distort the otherwise rather aromatic planar Cp ring to an envelope-like conformation. The angle $\Omega$ between plane C12–C13–C14–C15 and plane C11–C12–C15 is 8.3° and is defined by Faller, Crabtree and Habib as one of a number of slip parameters (Figure 5).[16]

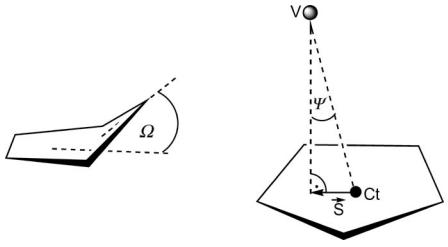


Figure 5. Graphical definition of the dihedral angle $\Omega$, the slip vector $\vec{S}$, whose norm is the slip distortion $\Delta$, and the angle slip $\Psi$, which is the angle between the plane normal and the centroid–metal vector.

This distortion seems to be typical for η³-coordinated cyclopentadienyl ligands, as can be seen in Table 1.[6,16] In contrast to that, the η⁵-coordinated Cp ring shows an angle $\Omega$ of only 1.2° between plane C17–C18–C19–C20 and plane C16–C17–C20, leading to the expected planarity of a Cp ring.

From the average of the M–C distances a further slip parameter, $\overline{\Delta M–C}$, can be calculated.[16] This parameter is a direct verification for the η³-coordinated Cp ligand. While every carbon atom is almost equidistant from the metal in η⁵-Cp, so that $\overline{\Delta M–C}$ is very small, in η³-Cp two carbons have a significantly elongated distance to the metal centre. This confirms the molecular structure of **6** in which ΔM–C of the η⁵-Cp is 0.04 Å, whereas the η³-Cp has a much higher value of 0.56 Å. Also the slip distortion $\Delta$ and the angle slip $\Psi$ (Figure 5) show clear indications for η³-coordination modes.[16]

For the 2,2′-bipyridine complex **6** and comparable derivatives (**1**,[6]**2**[7a]) selected structural ring-slip parameters are summarized in Table 1.

 © 2007 Wiley-VCH Verlag GmbH & Co. KGaA, Weinheim 

Table 1. Slip parameters (see Figure 5) for compounds **6** and **7** and similar complexes.

| Compound | | Slip parameters | | | | Ref. |
|---|---|---|---|---|---|---|
| | | $\Delta = \lvert\vec{S}\rvert$ [Å] | $\Psi$ [°] | $\overline{\Delta M–C}$ [Å] | $\Omega$ [°] | |
| **1** | [$\eta^3$] | 0.928 | 23.4 | 0.62 | 19.7 | [6,16] |
| | [$\eta^5$] | 0.076 | 2.2 | 0.10 | (4.9)[a] | |
| **2** | [$\eta^3$] | 0.798 | 20.9 | 0.56 | – | [7a] |
| | [$\eta^5$] | 0.157 | 4.6 | 0.13 | – | |
| **6** | [$\eta^3$] | 0.876 | 21.9 | 0.56 | 8.3 | [c] |
| | [$\eta^5$] | 0.063 | 1.5 | 0.04 | 1.2 | |
| **7**[b] | [$\eta^5$] | 0.110 | 3.2 | 0.03 | 0.1 | [c] |

[a] The uncertainty for this value is large. [b] Slip parameters of only one Cp were calculated because of the disordering of the others. [c] This work.

The V–N bonds of **6** are shortened relative to the only known (2,2′-bipyridine)vanadocene complex (2,2′-bipyridine)bis($\eta^5$-cyclopentadienyl)vanadium(IV) ditriflate (**8**) of Ghosh et al.,[17] but the shortening of the C5–C6 bond of the 2,2′-bipyridine (**5**) in the complex relative to the free **5**[18] is more significant (Table 2). This shortening suggests the reduced nature of the ligand in complex **6**. In the neutral vanadium(II) complex **6** and the cationic vanadium(III) derivative **7** the bipyridine ligand is nearly located in the equatorial plane (N–V–N) with a deviation of 5.35° (**6**) and 2.25° (**7**), respectively. These values are significantly lower than the corresponding value of 23.09° in [$(Cp)_2$Ti(2,2′-bipyridine)].[19]

Table 2. Selected bond lengths [Å] for **5**, **6**, **7** and **8**.

| | **5** | **6** | **7** | **8** |
|---|---|---|---|---|
| V1–N1 | – | 2.036(2) | 2.161(2) | 2.129(2) |
| V1–N2 | – | 2.053(1) | 2.165(2) | 2.128(2) |
| C5–C6 | 1.490(3) | 1.423(3) | 1.466(4) | 1.465(4) |

### Synthesis and Characterization of (2,2′-Bipyridine)bis($\eta^5$-cyclopentadienyl)vanadium(III) Tetraphenylborate (7)

Direct oxidation of **6** with ferrocenium tetraphenylborate leads to products that are insoluble in common solvents. So recrystallization of red-violet ionic complex **7** was not successful. In contrast to that, vanadocenium tetraphenylborate (**9**), prepared by the reaction of **4** with ferrocenium tetraphenylborate,[20] is passably soluble in thf. But when **5** was added directly to **9**, an amorphous powder precipitated, too.

A successful procedure is layering of an *n*-hexane solution of **5** on a thf solution of **9** to form large red-violet needles of **7**,which were suitable for X-ray diffraction, in 44% yield at the phase interface (Scheme 2). The ionic compound crystallizes in the monoclinic space group $P2_1/c$; the unit cell contains eight ion pairs and there are two independent ion pairs in the asymmetric unit. Three of four Cp rings in an asymmetric unit are disordered; however, both rings in the cation are $\eta^5$-coordinated as can be seen in the ORTEP plot in Figure 6.

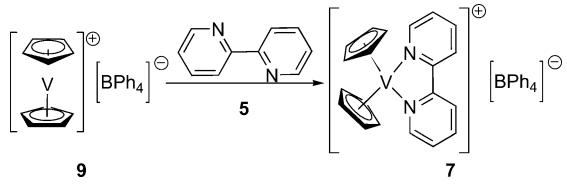


Scheme 2. Formation of compound **7**.

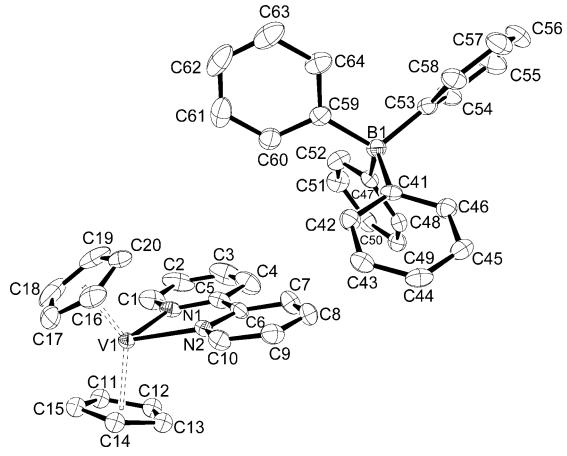


Figure 6. ORTEP plot of the solid-state molecular structure of **7** showing one ion pair of the asymmetric unit with idealized Cp rings, which are disordered in two positions and refined with isotropic coupled displacement parameters. Hydrogen atoms are omitted for clarity; thermal ellipsoids are drawn at the 50% probability level. Selected bond lengths [Å] and angles [°]: V1–N1 2.161(2), V1–N2 2.165(2), C5–C6 1.466(4), V1–Ct 1.95, B1–C 1.66, Ct–V1–Ct 135.4, N1–V1–N2 74.2.

Because of the disordering, the slip parameters for only one Cp ring, which is not disordered, were calculated (Table 1). The parameters are in good accordance with the slip parameters of the $\eta^5$-coordinated Cp rings of the other compounds in Table 1.

The V–Ct distances are insignificantly shorter than those in complex **6** (1.95 Å), but the V–N bonds as well as the connecting C5–C6 bond between the two heterocycles are lengthened relative to those in complex **6** (Table 2). In this case the heterocyclic ligand is not reduced by the metal centre. The V–N bond of **7** is a little longer relative to that in compound **8**, but the C5–C6 bond is almost equal in length (Table 2).[17]

## Conclusions

The reaction of **4** with **5** formed the 17e⁻ chelate complex (2,2′-bipyridine)($\eta^3$-cyclopentadienyl)($\eta^5$-cyclopentadienyl)-vanadium(II) (**6**) with one $\eta^3$-slipped Cp ring to avoid a 19e⁻ complex formation. Upon formal oxidation of **6**, the Cp ring flipped back to an $\eta^5$-coordination mode, forming the ionic 18e⁻ species (2,2′-bipyridine)bis($\eta^5$-cyclopentadienyl)vanadium(III) tetraphenylborate (**7**). To the best of our knowledge this is one of the rare examples of structurally characterized (cyclopentadienyl)vanadium complexes with a structurally verified $\eta^3$-ring-slippage.

 © 2007 Wiley-VCH Verlag GmbH & Co. KGaA, Weinheim 

## Experimental Section

**Reagents and General Techniques:** All operations were performed in a nitrogen atmosphere with rigorous exclusion of oxygen and moisture by using glovebox and Schlenk techniques. All chemicals used were of reagent grade or higher purity; they were purified according to standard protocols. Solvents were distilled from Na/K alloy and benzophenone under nitrogen. Chemical ionization (CI) mass spectra were taken with a Finnigan-MAT 95 spectrometer. Isobutane was used as the ionization gas. Electrospray ionization (ESI) mass spectra were recorded with a Finnigan-LCQ spectrometer. High-resolution electrospray ionization (HR-ESI) mass spectra were measured with a Micromass Premier quadrupole-time-of-flight (Q-TOF) instrument. IR spectra were recorded with a Bruker VECTOR 22 spectrometer by using KBr pellets. Elemental analyses were carried out by the Analytische Laboratorien GmbH, Lindlar (Germany). Melting points were determined by using a "Mel-Temp" by Laboratory Devices, Cambridge. 2,2′-Bipyridyl (**5**) was purchased from Merck. Vanadocene (**4**)[21] and vanadocenium tetraphenylborate (**9**)[20] were prepared according to literature procedures.

**X-ray Diffraction:** Single-crystal experiments were carried out with a STOE IPDS diffractometer with graphite-monochromated Mo-$K_\alpha$ radiation ($\lambda$ = 0.71073 Å). The structures were solved by direct phase determination and refined by full-matrix least-squares techniques against $F^2$ with the SHELXL-97 program system.[22] Crystallographic details are given in Table 3. CCDC-649843 (**6**) and -649844 (**7**) contain the supplementary crystallographic data for this paper. These data can be obtained free of charge from The Cambridge Crystallographic Data Centre via www.ccdc.cam.ac.uk/data_request/cif.

Table 3. Crystal structure data for compounds **6** and **7**.

| | **6** | **7** |
|---|---|---|
| Empirical formula | $C_{20}H_{18}N_2V$ | $C_{44}H_{38}BN_2V$ |
| Formula weight | 337.30 | 656.51 |
| Colour | black | blue-violet |
| Crystal dimensions [mm] | 0.42 × 0.31 × 0.08 | 0.45 × 0.34 × 0.13 |
| Crystal system | trigonal | monoclinic |
| Space group | $R\bar{3}$ | $P2_1/c$ |
| *A* [Å] | 19.0200(7) | 19.1779(10) |
| *B* [Å] | 19.0200(7) | 18.4200(8) |
| *C* [Å] | 23.3811(11) | 19.2887(10) |
| *α* [°] | 90 | 90 |
| *β* [°] | 90 | 95.883(8) |
| *γ* [°] | 120 | 90 |
| *V* [Å³] | 7325.1(5) | 6778.0(6) |
| *Z* | 18 | 8 |
| $D_{calcd.}$ [g cm$^{-3}$] | 1.376 | 1.287 |
| $\mu$ [mm$^{-1}$] | 0.610 | 0.328 |
| *T* [K] | 153 | 153 |
| $\theta$ range [°] | 2.62 to 26.21 | 2.12 to 26.13 |
| No. of reflections collected | 23 607 | 64 254 |
| No. of independent reflections | 3247 [*R*(int) = 0.0525] | 13 354 [*R*(int) = 0.0851] |
| No. of reflections [$I > 2\sigma(I)$] | 2474 | 7582 |
| Max., min. transmission | 0.9529 and 0.7839 | 0.9902 and 0.9525 |
| Final *R* indices [$I > 2\sigma(I)$] | *R*1 = 0.0274 *w*R2 = 0.0633 | *R*1 = 0.0440 *w*R2 = 0.0871 |
| *R* indices (all data) | *R*1 = 0.0429 *w*R2 = 0.0670 | *R*1 = 0.0934 *w*R2 = 0.0977 |

**Synthesis of (2,2′-Bipyridine)(η³-cyclopentadienyl)(η⁵-cyclopentadienyl)vanadium(II) (6):** A solution of vanadocene (**4**) (181 mg, 1 mmol) and 2,2′-bipyridine (**5**) (190 mg, 1.2 mmol) in *n*-hexane (20 mL) was stirred at room temperature overnight. The colour of the solution changed immediately from violet to black. Black crystals of **6** were obtained by cooling the solution at –70 °C for several days. They were isolated by decanting the solution, washing with cold *n*-hexane and drying in vacuo. Crystals suitable for X-ray diffraction were obtained by cooling the solution to –16 °C. Yield: 178 mg (53%). M.p.: 86 °C (dec.). MS (CI, isobutane): *m*/*z* (%) = 337.2 (46) $[M]^+$, 157.2 (100) $[(2,2'\text{-bpy-H})]^+$. IR (KBr): $\tilde{\nu}$ = 3044 (w), 1571 (s), 1504 (s), 1454 (s), 1417 (m), 1354 (w), 1301 (m), 1254 (m), 1147 (m), 1124 (w), 1082 (w), 1015 (m), 955 (m), 818 (m), 806 (m), 784 (m), 764 (m), 741 (s) cm$^{-1}$. $C_{20}H_{18}N_2V$ (337.30): calcd. C 71.21, H 5.38, N 8.30; found C 70.97, H 5.30, N 8.34.

**Synthesis of (2,2′-Bipyridine)bis(η⁵-cyclopentadienyl)vanadium(III) Tetraphenylborate (7):** A solution of vanadocenium tetraphenylborate (**9**) (61 mg, 0.116 mmol) in thf (40 mL) was layered with an *n*-hexane solution (20 mL) of 2,2′-bipyridine (**5**) (20 mg, 0.127 mmol). After two weeks, complex **7** was obtained by decanting the solution as large red-violet needles, which were suitable for X-ray diffraction. Yield: 35 mg (46%). M.p.: 220–222 °C (dec.). MS (ESI, $CH_3CN$): pos.: *m*/*z* (%) = 337.1 (100), 338.1 (18), 339.3 (2) $[Cp_2V(2,2'\text{-bipy})]^+$, 168.7 (83) $[Cp_2V(2,2'\text{-bipy})]^{2+}$; neg.: *m*/*z* (%) = 318.5 (24), 319.3 (100), 320.3 (24) $[BPh_4]^-$. HR-MS (ESI-Q-TOF, $CH_3CN$): pos.: *m*/*z* (%) = 337.0906 (100) $[Cp_2V(2,2'\text{-bipy})]^+$, 168.5456 (42) $[Cp_2V(2,2'\text{-bipy})]^{2+}$. IR (KBr): $\tilde{\nu}$ = 3053 (m), 2963 (m), 1601 (m), 1477 (m), 1442 (m), 1425 (m). 1261 (s), 1242 (s), 1155 (s), 1103 (br), 1017 (br), 945 (m), 802 (br), 769 (m), 733 (s), 703 (s), 657 (m), 610 (m) cm$^{-1}$. $C_{44}H_{38}BN_2V$ (656.51): calcd. C 80.49, H 5.83, N 4.27; found C 79.86, H 5.85, N 4.83.

## Acknowledgments

We would like to thank the Deutsche Forschungsgemeinschaft (DFG, SPP-1118) for financial support.

[1] a) E. O. Fischer, *Angew. Chem.* **1952**, *64*, 620–621; b) G. Wilkinson, J. M. Birmingham, *J. Am. Chem. Soc.* **1954**, *76*, 4281–4284; c) G. Wilkinson, *J. Organomet. Chem.* **1975**, *100*, 273–278.
[2] a) N. J. Long *Metallocenes*, Blackwell Science Oxford, **1997**; b) R. L. Halterman, A. Togni, *Metallocenes*, Wiley-VCH, Weinheim, **1998**.
[3] J. M. O'Connor, C. P. Casey, *Chem. Rev.* **1987**, *87*, 307–318.
[4] T. S. Piper, G. Wilkinson, *J. Inorg. Nucl. Chem.* **1956**, *2*, 38–45.
[5] For example CO substitution in transition-metal carbonyl complexes: F. Basolo, *Polyhedron* **1990**, *9*, 1503–1535.
[6] G. Huttner, H. H. Brintzinger, L. G. Bell, P. Friedrich, V. Bejenke, D. Neugebauer, *J. Organomet. Chem.* **1978**, *145*, 329–333.
[7] a) R. M. Kowaleski, A. L. Rheingold, W. C. Trogler, F. Basolo, *J. Am. Chem. Soc.* **1986**, *108*, 2460–2461; b) J. R. Bocarsly, C. Floriani, A. Chiesi-Villa, C. Guastini, *Inorg. Chem.* **1987**, *26*, 1871–1875.
[8] a) S. Schmatloch, U. S. Schubert, *Chem. Unserer Zeit* **2003**, *37*, 180–187; b) W. R. McWhinnie, J. D. Miller, *Adv. Inorg. Chem. Radiochem.* **1969**, *11*, 135–215.
[9] a) D. J. Berg, J. M. Boncella, R. A. Andersen, *Organometallics* **2002**, *21*, 4622–4631; b) W. Kaim, *Coord. Chem. Rev.* **2002**, *230*, 127–139; c) W. Kaim, *Angew. Chem. Int. Ed. Engl.* **1983**, *22*, 171–191.
[10] a) S. Kitagawa, R. Kitaura, S.-I. Noro, *Angew. Chem. Int. Ed.* **2004**, *43*, 2334–2375; b) M. P. Coles, D. C. Swenson, R. F. Jordan, V. G. Young Jr, *Organometallics* **1997**, *16*, 5183–5194; c) R. Robson, *J. Chem. Soc. Dalton Trans.* **2000**, 3735–3744; d) M. Fujita, N. Fujita, K. Ogura, K. Yamaguchi, *Nature* **1999**, *400*, 52–55; e) P. N. W. Baxter, J.-M. Lehn, G. Baum, D. Fen-

 © 2007 Wiley-VCH Verlag GmbH & Co. KGaA, Weinheim 

ske, *Chem. Eur. J.* **1999**, *5*, 102–112; f) B. Olenyuk, A. Fechtenkötter, P. J. Stang, *J. Chem. Soc. Dalton Trans.* **1998**, 1707–1728.
[11] a) W. Kaim, G. K. Lahiri, *Angew. Chem. Int. Ed.* **2007**, *46*, 1778–1796; b) J.-P. Launay, *Chem. Soc. Rev.* **2001**, *30*, 386–397.
[12] a) S. Kraft, R. Beckhaus, D. Haase, W. Saak, *Angew. Chem. Int. Ed.* **2004**, *43*, 1583–1587; b) I. M. Piglosiewicz, S. Kraft, R. Beckhaus, W. Haase, W. Saak, *Eur. J. Inorg. Chem.* **2005**, 938–945.
[13] a) I. Piglosiewicz, R. Beckhaus, W. Saak, D. Haase, *J. Am. Chem. Soc.* **2005**, *127*, 14190–14191; b) I. M. Piglosiewicz, R. Beckhaus, G. Wittstock, W. Saak, D. Haase, *Inorg. Chem.* **2007**, *46*, 7610–7620.
[14] S. Kraft, E. Hanuschek, R. Beckhaus, D. Haase, W. Saak, *Chem. Eur. J.* **2005**, *11*, 969–978.
[15] G. Fachinetti, S. Del Nero, C. Floriani, *J. Chem. Soc. Dalton Trans.* **1976**, 1046–1049.
[16] J. W. Faller, R. H. Crabtree, A. Habib, *Organometallics* **1985**, *4*, 929–935.
[17] P. Ghosh, A. T. Kotchevar, D. D. DuMez, S. Ghosh, J. Peiterson, F. M. Uckun, *Inorg. Chem.* **1999**, *38*, 3730–3737.
[18] M. H. Chisholm, J. C. Huffman, I. P. Rothwell, P. G. Bradley, N. Kress, W. H. Woodruff, *J. Am. Chem. Soc.* **1981**, *103*, 4945–4947.
[19] R. Gyepes, P. T. Witte, M. Horacek, I. Cisarova, K. Mach, *J. Organomet. Chem.* **1998**, *551*, 207–213.
[20] F. Calderazzo, L. Ferri, G. Pampaloni, U. Englert, *Organometallics* **1999**, *18*, 2452–2458.
[21] R. M. Kowaleski, F. Basolo, W. C. Trogler, R. W. Gedrige, T. D. Newbound, R. D. Ernst, *J. Am. Chem. Soc.* **1987**, *109*, 4860–4869.
[22] G. M. Sheldrick, *SHELXL-97, A Program for Refining Crystal Structures*, University of Göttingen, Germany, **1997**.

Received: August 31, 2007
Published Online: October 17, 2007

 © 2007 Wiley-VCH Verlag GmbH & Co. KGaA, Weinheim 

DOI: 10.1002/ejic.200700827

# One-Pot Synthesis of an Enantiopure N,N,O Scorpionate Ligand Derived from (+)-Camphor

**Johannes Elflein,[a] Florian Platzmann,[a] and Nicolai Burzlaff*[a]**

*Dedicated to Professor Horst Kisch on the occasion of his 65th birthday*

**Keywords:** Chiral pool / Ligand design / Zinc / Rhenium / Camphor

A one-pot synthesis of the new enantiopure heteroscorpionate ligand HOPhbpm$^{3cam}$ (**3**) was described. Ligand **3** was obtained in a pyridine-catalysed Peterson rearrangement starting from camphorpyrazole, thionyl chloride, and salicylaldehyde. $\kappa^2$- and $\kappa^3$-coordination of the ligand was observed, and the ligand was shown to form a tetrahedral zinc complex [Zn-$\kappa^3$-(OPhbpm$^{3cam}$)$CH_3$] (**4**) as well as an octahedral rhenium complex [Re-$\kappa^3$-(OPhbpm$^{3cam}$)$(CO)_3$] (**6**).
(© Wiley-VCH Verlag GmbH & Co. KGaA, 69451 Weinheim, Germany, 2007)

## Introduction

During the last decade, various bis(pyrazolyl)methane-based "heteroscorpionate" ligands have been recognised as very versatile ligands for bioinorganic chemistry and organometallics.[1–3] Specifically, several achiral tripodal N,N,O and N,N,S ligands were reported by Carrano and coworkers that can be obtained from 1,1′-carbonylbis(pyrazole) and functionalised aldehydes.[3–5] This cobalt-catalysed reaction, in which $CO_2$ is released, is based on some early reports from the 1970s by Peterson and Thè[6] and was recently modified by Reger to involve aldehyde and 1,1′-sulfinylbis-(pyrazole).[7] First applications of group 4 metal complexes bearing these tridentate heteroscorpionate ligands consist of catalytic ethylene and propylene polymerisation.[8]

## Results and Discussion

Recently, we reported on a rather simple concept based on prochirality that allows us to synthesise enantiopure facially binding tripod ligands from $C_2$ symmetric precursors without any additional separation of enantiomers or diastereomers.[9] $C_2$ symmetry is a feature often used in enantiopure bidentate chelating ligands.[10] In many of these, two identical enantiopure donor groups, Y*, are connected by a tetrahedral bridging atom, for example, an $sp^3$ carbon atom. Any additional group, Z, at this atom will form a prochiral centre rather than an additional stereocentre (Figure 1).[11]

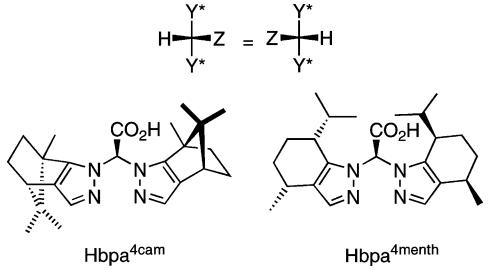


Figure 1. Prochirality in the enantiopure ligands Hbpa$^{4cam}$ and Hbpa$^{4menth}$.[9]

So far, two examples of enantiopure N,N,O tripod ligands based on this concept were published by our group, namely, bis(camphorpyrazol-1-yl)acetic acid Hbpa$^{4cam}$ and bis(menthylpyrazol-1-yl)acetic acid Hbpa$^{4menth}$ (Figure 1).[9] Other bis(pyrazolyl)methane-derived enantiopure tripod ligands were reported by Otero and coworkers recently.[12] Here we report on a one-step synthesis of an enantiopure N,N,O scorpionate ligand HOPhbpm$^{3cam}$ (**3**) derived from (+)-camphor by using a modified version of the Peterson cobalt rearrangement that does not require the cobalt catalyst.

Camphorpyrazole **1** [i.e. (4*S*,7*R*)-7,8,8-trimethyl-4,5,6,7-tetrahydro-4,7-methano-1(2)H-indazole] is an enantiopure pyrazole derived from the chiral pool that can be obtained easily and in high yield in a two-step synthesis starting from (+)-camphor.[13] Reaction of **1** with phosgene to afford 2,2′-carbonylbis(camphorpyrazole) (**2b**) was previously described in a footnote by Rebek and coworkers.[14]

[a] Institut für Anorganische Chemie und Interdisciplinary Centre for Molecular Materials (ICMM), Universität Erlangen-Nürnberg,
Egerlandstrasse 1, 91058 Erlangen, Germany
Fax: +49-9131-85-27387
E-mail: burzlaff@chemie.uni-erlangen.de
Supporting information for this article is available on the WWW under http://www.eurjic.org or from the author.

 © 2007 Wiley-VCH Verlag GmbH & Co. KGaA, Weinheim 

According to a very recent report by Artaud, phosgene can be replaced in such carbonylbis(pyrazole) syntheses by triphosgene.[15] We now found that reaction of **1** with triphosgene and triethylamine first gives the $C_1$ symmetrical isomer of 1,2′-carbonylbis(camphorpyrazole) (**2a**), which is transformed into the $C_2$ symmetrical 2,2′-carbonylbis(camphorpyrazole) (**2b**) upon standing in solution within some days (Scheme 1).

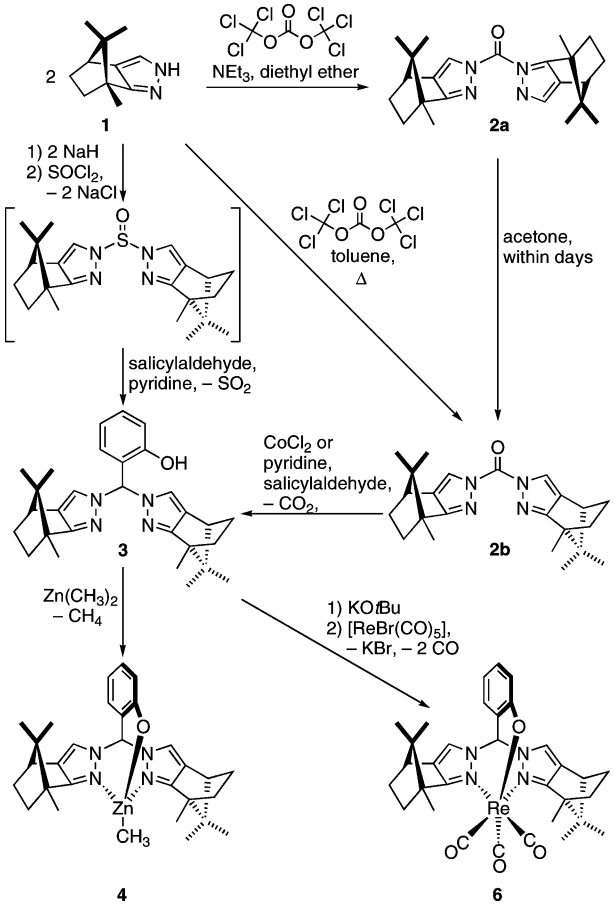


Scheme 1. Synthesis of homochiral heteroscorpionato complexes.

A reaction under reflux in toluene or benzene gives only the desired $C_2$ symmetrical 2,2′-carbonylbis(camphorpyrazole) (**2b**) in very high yield (Scheme 1). An X-ray structure determination of isomer **2b** (Figure 2) allows doubtless differentiation between the two isomers.

Furthermore, only one set of camphorpyrazole signals is observed in the $^1$H and $^{13}$C NMR spectra of **2b**, as to be expected for a $C_2$ symmetric compound, which is in contrast to the two sets of signals observed in the spectra of **2a**.

To test our concept of "prochirality-based" ligands with a new N,N,O tripod ligand, we then synthesised (*o*-hydroxyphenyl)bis(camphorpyrazol-1-yl)methane HOPhbpm$^{3cam}$ (**3**) by applying the cobalt-catalysed Peterson rearrangement of **2b** with salicylaldehyde.[16] Unfortunately, the yield of this reaction was quite erratic; this observation was also

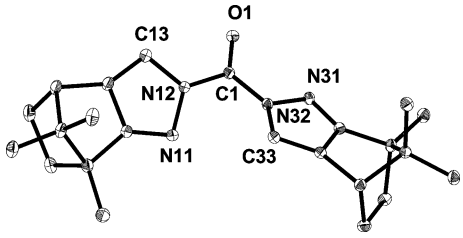


Figure 2. Molecular structure of 2,2′-carbonylbis(camphorpyrazole) (**2b**); thermal ellipsoids are drawn at the 50% probability level; hydrogen atoms are omitted for better clarity. Selected bond lengths [Å] and angles [°]: C1–O1 1.204(2), C1–N32 1.392(3), C1–N12 1.402(3), O1–C1–N32 123.93(19), O1–C1–N12 121.0(2), N32–C1–N12 115.07(18).

made by various other groups who used the Peterson rearrangement for their syntheses. We thus developed an alternative procedure for this reaction to which we were inspired by a publication of Canty and coworkers.[17] They reported on a coupling of 1,1′-carbonylbis(3,5-dimethylpyrazole) and pyridine-2-aldehyde without any cobalt catalyst.[17] Indeed, a similar reaction of **2b**, pyridine and salicylaldehyde yields the ligand (*o*-hydroxyphenyl)bis(camphorpyrazol-1-yl)methane HOPhbpm$^{3cam}$ (**3**) in reproducible yields up to 70% (Scheme 1) without the use of the cobalt catalyst. The synthetic procedure was modified further by us according to the version of Reger for the Peterson rearrangement, which we mentioned above, involving the aldehyde and 1,1′-sulfinylbispyrazole. Thereby, we finally developed a one-pot synthesis for (*o*-hydroxyphenyl)bis(camphorpyrazol-1-yl)methane HOPhbpm$^{3cam}$ (**3**) starting with the reaction of camphorpyrazole (**1**) with sodium hydride and thionyl chloride. Without any further purification, pyridine and salicylaldehyde were added to the resulting 2,2′-sulfinylbis(camphorpyrazole) to yield ligand **3** in yields up to 60%. After the reaction was scaled up, we were able to obtain up to 7 g of enantiopure ligand **3** in one run. Because of the loss of $C_2$ symmetry, the two pyrazole donors are no longer spectroscopically equivalent and two sets of signals in the $^1$H and $^{13}$C NMR spectra are exhibited.

Treatment of ligand **3** with dimethylzinc resulted in very pure monomethylzinc complex [Zn(OPhbpm$^{3cam}$)CH$_3$] (**4**) and methane without any formation of bis(ligand) complex [Zn(OPhbpm$^{3cam}$)$_2$]. In the NMR spectra, the methyl group in **4** ($^1$H NMR: $\delta$ = –0.60 ppm; $^{13}$C NMR: $\delta$ = –14.6 ppm) is observed at high field. This agrees well with the complex [Zn(bpa$^{Me_2,tBu_2}$)CH$_3$] reported recently by us and with the sterically hindered (*o*-hydroxyphenyl)bis(pyrazol-1-yl)methane zinc complex published by Carrano and coworkers.[4d,18]

In an attempt to synthesise the chlorido complex [Zn(κ$^3$-*N*,*N*,*O*-OPhbpm$^{3cam}$)Cl], colourless crystals of [Zn(κ$^2$-*N*,*N*-HOPhbpm$^{3cam}$)(Cl)$_2$] (**5**) were obtained from an acetonitrile solution.

The molecular structure (Figure 3) clearly shows κ$^2$-coordination of the ligand, similar to the achiral complex [Zn(κ$^2$-*N*,*N*-HOPhbdmpzm)(*I*)$_2$] [HOPhbdmpzm: *ortho*-(hydroxyphenyl)bis(dimethylpyrazol-1-yl)methane] recently

 © 2007 Wiley-VCH Verlag GmbH & Co. KGaA, Weinheim 

reported by Carrano and coworkers.[4d] The molecular structure of **5** is proof of the constitution of the HOPhbpm$^{3cam}$ ligand (**3**). It has to be emphasised that in this new ligand the chiral camphorpyrazolyl donors are pointing towards the zinc centre. This is different from our former ligands and makes this ligand a promising candidate for future enantioselective inductions.

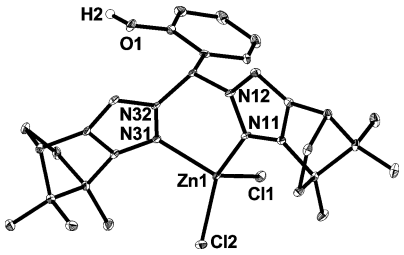


Figure 3. Molecular structure of [Zn(κ$^2$-*N*,*N*-HOPhbpm$^{3cam}$)(Cl)$_2$] (**5**); thermal ellipsoids are drawn at the 50% probability level; most hydrogen atoms are omitted for better clarity. Selected bond lengths [Å] and angles [°]: Zn–Cl1 2.2267(8), Zn–Cl2 2.2293(7), Zn–N11 2.053(2), Zn–N31 2.089(2), Zn–N31–N32 111.92(16), Zn–N11–N12 122.78(17), N11–Zn–N31 94.20(9), N11–Zn–Cl2 108.64(7), N31–Zn–Cl2 119.39(6), N11–Zn–Cl1 112.42(7), N31–Zn–Cl1 107.79(6), Cl2–Zn–Cl1 113.01(3).

Reaction of K[OPhbpm$^{3cam}$] with [ReBr(CO)$_5$] resulted in a complex [Re(OPhbpm$^{3cam}$)(CO)$_3$] (**6**). Elemental analysis, FAB MS [M + H]$^+$ peak and, pursuant to $C_1$ symmetry, three class A carbonyl vibrations at 2018, 1910 and 1881 cm$^{-1}$ indicate κ$^3$-coordination of the ligand and formation of an octahedral complex.

## Conclusions

Chiral modification of the well-established (2-hydroxyphenyl)bis(pyrazol-1-yl)methane ligands leads to the new enantiopure heteroscorpionate ligand (2-hydroxyphenyl)-bis(camphorpyrazol-1-yl)methane HOPhbpm$^{3cam}$ (**3**). This ligand provides similar coordination properties as its achiral analogues, which was proven by the synthesis of a tetrahedral monomethylzinc complex and an octahedral tricarbonylrhenium complex. The simple one-pot synthesis, starting from camphorpyrazole, thionyl chloride and salicylaldehyde, should allow broad application of this and related ligands in coordination chemistry, especially because the achiral analogues have already shown their potential for catalytic processes. Furthermore, it is obvious that in the future a broad spectrum of similar homochiral tripod ligands should be accessible by variations of this one-pot synthesis.

**Supporting Information** (see footnote on the first page of this article): Experimental details and X-ray data for **2b** and **5**.[19]

## Acknowledgments

This work was supported by the Deutsche Forschungsgemeinschaft (BU 1223/2–1 and SFB 583). We thank Dr. F. Heinemann for collecting an X-ray data set.

[1] G. Parkin, *Chem. Rev.* **2004**, *104*, 699–767.
[2] A. Otero, J. Fernańdez-Baeza, A. Antinõlo, J. Tejeda, A. Lara-Sańchez, *Dalton Trans.* **2004**, 1499–1510.
[3] C. Pettinari, R. Pettinari, *Coord. Chem. Rev.* **2005**, *249*, 663–691.
[4] a) T. C. Higgs, C. J. Carrano, *Inorg. Chem.* **1997**, *36*, 291–297; b) T. C. Higgs, C. J. Carrano, *Inorg. Chem.* **1997**, *36*, 298–306; c) T. C. Higgs, D. Ji, R. S. Czernuszewicz, B. F. Matzanke, V. Schunemann, A. X. Trautwein, M. Helliwell, W. Ramirez, C. J. Carrano, *Inorg. Chem.* **1998**, *37*, 2383–2392; d) B. S. Hammes, C. J. Carrano, *Inorg. Chem.* **1999**, *38*, 3562–3568; e) B. S. Hammes, C. J. Carrano, *Inorg. Chem.* **1999**, *38*, 4593–4600.
[5] a) T. C. Higgs, D. Ji, S. R. Czernuszewicz, K. Spartalian, C. J. O′Connor, C. Seip, C. J. Carrano, *J. Chem. Soc. Dalton Trans.* **1999**, 807–813; b) B. S. Hammes, C. J. Carrano, *J. Chem. Soc. Dalton Trans.* **2000**, 3304–3309; c) B. S. Hammes, C. J. Carrano, *Chem. Commun.* **2000**, 1635–1636; d) B. S. Hammes, C. J. Carrano, *Inorg. Chim. Acta* **2000**, *300–302*, 427–433; e) B. S. Hammes, C. J. Carrano, *Inorg. Chem.* **2001**, *40*, 919–927.
[6] a) K. I. Thé, L. K. Peterson, E. Kiehlmann, *Can. J. Chem.* **1973**, *51*, 2448–2451; b) K. I. Thé, L. K. Peterson, *Can. J. Chem.* **1973**, *51*, 422–427; c) L. K. Peterson, E. Kiehlmann, A. R. Sanger, K. I. Thé, *Can. J. Chem.* **1974**, *52*, 2367–2374.
[7] a) D. L. Reger, T. C. Grattan, K. J. Brown, C. A. Little, J. J. S. Lambda, A. L. Rheingold, R. D. Sommer, *J. Organomet. Chem.* **2000**, *607*, 120–128; b) D. L. Reger, J. R. Gardinier, M. Smith, *J. Organomet. Chem.* **2005**, *690*, 1901–1912; c) D. L. Reger, R. P. Watson, M. D. Smith, P. J. Pellechia, *J. Organomet. Chem.* **2006**, *25*, 743–755.
[8] S. Milione, C. Cuomo, A. Grassi, *Top. Catal.* **2006**, *40*, 163–172.
[9] a) I. Hegelmann, N. Burzlaff, *Eur. J. Inorg. Chem.* **2003**, 409–411; b) L. Peters, N. Burzlaff, *Polyhedron* **2004**, *23*, 245–251.
[10] Review on $C_2$ symmetry: J. K. Whitesell, *Chem. Rev.* **1989**, *89*, 1581–1590.
[11] H. Hirschmann, K. R. Hanson, *Tetrahedron* **1974**, *30*, 3649–3656.
[12] a) A. Otero, J. Fernández-Baeza, A. Antiñolo, J. Tejeda, A. Lara-Sánchez, L. Sánchez-Barba, M. Sanchez-Molina, S. Franco, I. Lopez-Solera, A. M. Rodríguez, *Eur. J. Inorg. Chem.* **2006**, 707–710; b) A. Otero, J. Fernández-Baeza, A. Antiñolo, J. Tejeda, A. Lara-Sánchez, L. Sánchez-Barba, M. Sanchez-Molina, S. Franco, I. Lopez-Solera, A. M. Rodríguez, *Dalton Trans.* **2006**, 4359–4370.
[13] a) D. D. LeCloux, C. J. Tokar, M. Osawa, R. P. Houser, M. C. Keyes, W. B. Tolman, *Organometallics* **1994**, *13*, 2855–2866; b) D. L. Jameson, R. K. Castellano, *Inorg. Synth.* **1998**, *32*, 55–57.
[14] J. Rebek, S. Wolf, A. Mossman, *J. Org. Chem.* **1978**, *43*, 180–181.
[15] E. Galardon, M. Giorgi, I. Artaud, *Dalton Trans.* **2007**, 1047–1052.
[16] To avoid extraordinarily long abbreviations, the abbreviation system for Tp and benzopyrazolylborate Tp$^{Bo}$ ligands introduced by Trofimenko was transferred to this manuscript. A superscript of 3 preceding "cam" indicates a 3,4-fusion of the camphor group to the pyrazole. This results in the abbreviation HOPhbpm$^{3cam}$ (**3**). For further details see: S. Trofimenko, *Scorpionates – The Coordination Chemistry of Polypyrazolylborate Ligands*, Imperial College Press, London, **1999**, p. 5.
[17] P. K. Byers, A. J. Canty, R. T. Honeyman, *J. Organomet. Chem.* **1990**, *385*, 417–427.
[18] I. Hegelmann, A. Beck, C. Eichhorn, B. Weibert, N. Burzlaff, *Eur. J. Inorg. Chem.* **2003**, 339–347.
[19] Crystallographic data for **2** ($C_{23}H_{30}N_4O$): crystal dimensions $0.50 \times 0.40 \times 0.30$ mm$^3$, monoclinic space group $P2_1$, $a$ = 6.7212(13) Å, $b$ = 12.544(3) Å, $c$ = 25.060(5) Å, $\beta$ = 90.32(3)°, $V$ = 2112.7(8) Å$^3$, $Z$ = 4, $\rho_{calcd.}$ = 1.190 g cm$^{-3}$, $2\Theta_{max}$ = 58.5°, Mo-$K_\alpha$ radiation, $\lambda$ = 0.71073 Å, $T$ = 100 K, 28855 reflections

 © 2007 Wiley-VCH Verlag GmbH & Co. KGaA, Weinheim 

collected, 5896 independent reflections ($R_{int}$ = 0.0834), 5474 reflections used with $I > 2\sigma$, $R$ = 0.0459, $wR$ = 0.1150. Crystallographic data for **5** ($C_{29}H_{36}Cl_2N_4OZn{\cdot}2CH_3CN$): crystal dimensions $0.23 \times 0.22 \times 0.18$ mm$^3$, triclinic space group $P1$, $a$ = 7.7111(3) Å, $b$ = 14.5669(15) Å, $c$ = 15.577(2) Å, $\alpha$ = 80.438(8)°, $\beta$ = 87.859(6)°, $\gamma$ = 80.738(5)°, $V$ = 1702.8(3) Å$^3$, $Z$ = 2, $\rho_{calcd.}$ = 1.316 g cm$^{-3}$, $2\Theta_{max}$ = 59.0°, Mo-$K_\alpha$ radiation, $\lambda$ = 0.71073 Å, $T$ = 100 K, 44677 reflections collected, 17289 independent reflections ($R_{int}$ = 0.0358), 14660 reflections used with $I > 2\sigma$, $R$ = 0.0334, $wR$ = 0.0734, Flack parameter: 0.020(6). The structures were solved by using direct methods and refined with full-matrix least-squares against $F^2$ (Siemens SHELX-97).[20] A weighting scheme was applied in the last steps of the refinement with $w = 1/[\sigma^2(F_o^2) + (aP)^2 + bP]$ and $P = [2F_c^2 + \max(F_o^2,0)]/3$. Most hydrogen atoms were included in their calculated positions and refined in a riding model. The phenol proton (**5**) was found and its coordinates were refined isotropically. Pictures were prepared with the program Diamond 2.1e.[21] CCDC-651140 (for **2b**) and -651141 (for **5**) contain the supplementary crystallographic data for this paper. These data can be obtained free of charge from The Cambridge Crystallographic Data Centre via www.ccdc.cam.ac.uk/data_request/cif.

[20] G. M. Sheldrick, *SHELX-97: Programs for Crystal Structure Analysis*, University of Göttingen, Göttingen, **1997**.

[21] K. Brandenburg, M. Berndt, *Diamond-Visual Crystal Structure Information System*, Crystal Impact GbR, Bonn, **1999**; see also: W. T. Pennington, *J. Appl. Crystallogr.* **1999**, *32*, 1028–1029.

Received: August 6, 2007
Published Online: October 11, 2007

 © 2007 Wiley-VCH Verlag GmbH & Co. KGaA, Weinheim 

DOI: 10.1002/ejic.200700723

# Formation of Boronate Ester Polymers with Efficient Intrastrand Charge-Transfer Transitions by Three-Component Reactions

Nicolas Christinat,[a] Emmanuel Croisier,[a] Rosario Scopelliti,[a][‡] Michele Cascella,[a] Ursula Röthlisberger,[a] and Kay Severin*[a]

**Keywords:** Boron / Charge transfer / Polymers / Self-assembly

The three-component reaction of aryl boronic acids with 1,2,4,5-tetrahydroxybenzene and 1,2-bis(4-pyridyl)ethylene or 4,4′-bipyridine leads to the formation of dark-purple boronate ester polymers. Crystallographic analyses show that the polymer strands have a zig–zag geometry, and the bis(dioxaborole) units are connected by dipyridyl linkers through dative B–N interactions. Upon dissolution of the polymers in hot chloroform, most of the B–N connections are broken, which indicates that polymer formation is a reversible process. A computational study provides evidence that the strong color of the polymers is due to efficient intrastrand charge-transfer excitations from the tetraoxobenzene to the dipyridyl linker.

(© Wiley-VCH Verlag GmbH & Co. KGaA, 69451 Weinheim, Germany, 2007)

## Introduction

Boronic acids are known to easily and reversibly condense with diols to form boronate esters. This type of reaction has been exploited extensively in carbohydrate chemistry where boronic acids are used as an integral part of receptors and sensors or as protecting groups.[1] The reversible formation of boronic esters has also been employed to build complex structures such as macrocycles,[2] dendrimers,[3] helicates,[4] nanotubes,[5] or porous covalent organic frameworks.[6] The labile boron–oxygen bonds are used here in a similar fashion to metal–ligand interactions in supramolecular coordination chemistry. Constitutional dynamic polymers[7] with boronate ester backbones represent another interesting class of compounds. Lavigne and coworkers showed that poly(dioxaborolane)s[8] and poly(dioxaborole)s[9] can be obtained by the condensation of diboronic acids with pentaerythritol or 1,2,4,5-tetrahydroxybenzene.[10] An interesting feature of these polymers is that hydrolytic degradation can be reversed by annealing under vacuum ("self-repairing polymers").[8] The polycondensation of diboronic acids with sugar derivatives as linkers has been investigated by the groups of Shinkai[11] and Shimizu.[12] Again it was found that the polymerization is a reversible process, which depends on the conditions.

An alternative way to generate dynamic polymers with boron centers in the backbone is the polymerization by dative B–N bonds. This was demonstrated by Wagner and coworkers who made polymers by the reaction of the borylated ferrocene [$(C_5H_4BMe_2)_2Fe$] with 4,4′-bipyridine or pyrazine[13] and by the group of Jäkle who assembled polymers with borane end groups by the reaction with 4,4′-bipyridine.[14,15] In the following we show that boronic acid–diol condensations can be used *in parallel* with dative B–N interactions to generate novel polymer architectures by three-component reactions. The resulting crystalline polymers are deeply colored due to efficient intrastrand charge-transfer transitions.

## Results and Discussion

To evaluate the possibility to generate boronate polymers with ditopic N-donor ligands, we heated a mixture of 1,2-bis(4-pyridyl)ethylene, two equivalents of 4-ethylphenylboronic acid, and one equivalent of 1,2,4,5-tetrahydroxybenzene in benzene with the use of a Dean–Stark trap. A slightly yellow solution was obtained, from which, upon cooling, a dark-purple solid (**1**) precipitated (Scheme 1). A similar behavior was observed when 4-*tert*-butylphenylboronic acid was employed: when the hot benzene solution was cooled, a dark precipitate formed (**2**).

At room temperature, products **1** and **2** were found to display low solubility in common organic solvents such as benzene, chloroform, acetonitrile, and tetrahydrofuran. Upon heating, however, it was possible to dissolve them in chloroform. This process was accompanied with a strong change in color: the dark-purple solids gave rise to weakly yellow solutions. When the hot chloroform solutions were cooled to room temperature, the purple polymers started to precipitate after a few minutes, which indicated that the color change was due to a reversible process.

[a] Institut des Sciences et Ingénierie Chimiques, École Polytechnique Fédérale de Lausanne
1015 Lausanne, Switzerland
Fax: +41-21-693-9305
E-mail: kay.severin@epfl.ch
[‡] X-ray crystal structural analysis.

 © 2007 Wiley-VCH Verlag GmbH & Co. KGaA, Weinheim 

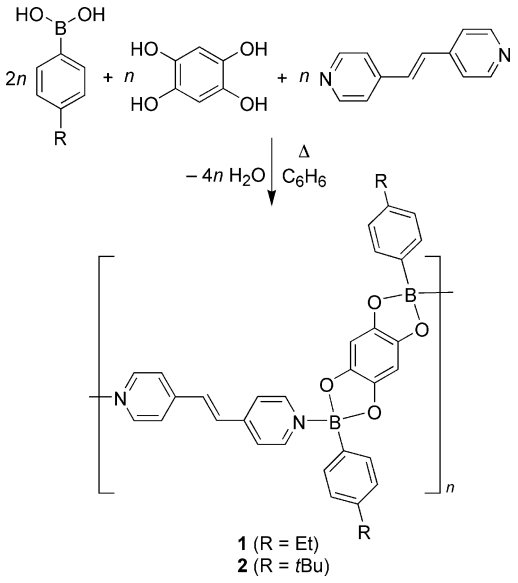


Scheme 1. Synthesis of polymers **1** and **2**.

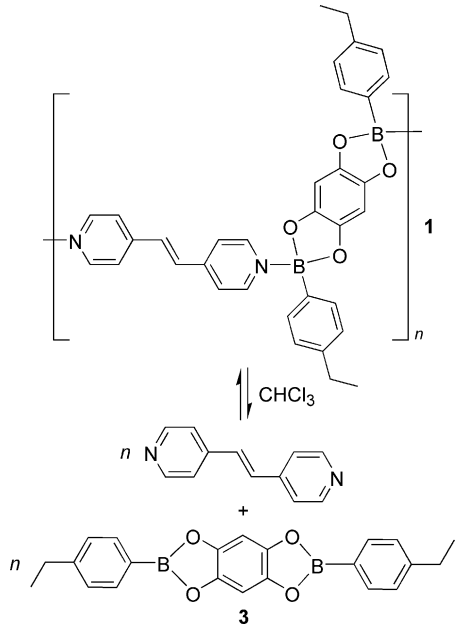


Scheme 2. When dissolved in $CHCl_3$, polymer **1** splits into 1,2-bis(4-pyridyl)ethylene and bis(dioxaborole) **3**.

A $CDCl_3$ solution of polymer **1** was analyzed by $^1H$ NMR spectroscopy, and its spectrum was nearly a superposition to those of 1,2-bis(4-pyridyl)ethylene and bis(dioxaborole) **3** ($\Delta\delta < 0.15$ ppm). The latter compound was prepared for comparison by condensing 4-ethylphenylboronic acid with 1,2,4,5-tetrahydroxybenzene.[16] The $^{11}B$ NMR spectrum of **1** showed a peak at $\delta = 28.8$ ppm, which was similar to that of **3** ($\delta = 34.6$ ppm) and very distinct from the expected signal of a tetracoordinated boron center.[17] This data suggested that the chloroform solution of polymer **1** contained mainly dissociated 1,2-bis(4-pyridyl)-ethylene and bis(dioxaborole) **3** (Scheme 2). The small differences in chemical shifts can be explained by the formation of minor amounts of B–N adducts, which are in fast equilibrium with 1,2-bis(4-pyridyl)ethylene and **3**. A related situation was observed for the ferrocene polymers prepared by Wagner et al.: upon dissolution at high temperature, the polymer was split into its monomers, $[(C_5H_4BMe_2)_2Fe]$ and 4,4′-bipyridine.[13]

The reversible formation of **1** from 1,2-bis(4-pyridyl)-ethylene and **3** allowed single crystals to be obtained from $CHCl_3$/pentane solutions, and crystallographic analysis confirmed the polymeric structure (Figure 1). The ditopic 1,2-bis(4-pyridyl)ethylene acts as a bridge between the boronate esters. The average boron–nitrogen bond length of 1.677 Å is long relative to what was observed for other crystallographically characterized adducts between $sp^2$-nitrogen donors and tetracoordinated boron centers.[18] Accordingly, the tetrahedral character (THC)[18] of the boron center is relatively low ($THC_{av}$ = 72.5%). This data is in line with the results of the NMR spectroscopic experiments, which suggest that the dative B–N bond in **1** is weak. The B–O bonds ($B–O_{av}$ 1.479 Å) are, as expected, longer than what was observed for 1,2,4,5-tetrahydroxybenzene-based bis(dioxaborole)s with trigonal planar boron (B–O 1.388–1.395 Å).[14]

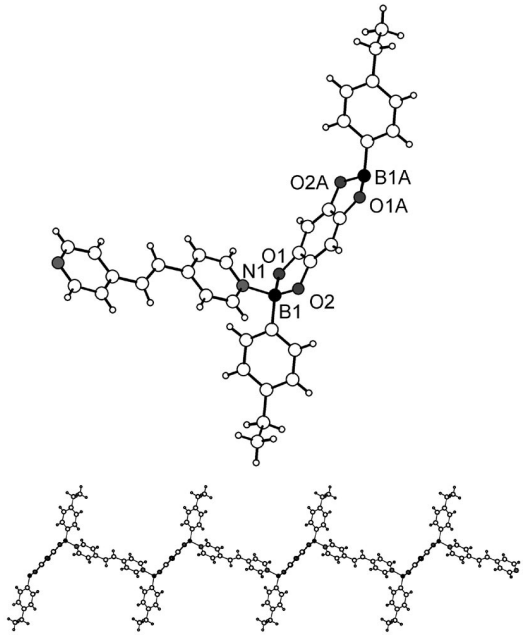


Figure 1. Molecular structure of polymer **1** in the crystal. Top: view of the repeating unit – only one of the two crystallographically independent subunits is shown; bottom: view of the polymer chain. The solvent molecule ($CHCl_3$) is not shown for clarity.

The modular nature of the three-component polymerization reactions offers structural flexibility as demonstrated by the formation of polymer **4**, which contains 4,4′-bipyridine instead of 1,2-bis(4-pyridyl)ethylene as the bridging N-donor ligand (Scheme 3). The physical properties of **4** are similar to those of **1** and **2**: the polymer has a dark-purple color and it splits into 4,4′-bipyridine and the respective boronate ester upon dissolution in hot chloroform.

 © 2007 Wiley-VCH Verlag GmbH & Co. KGaA, Weinheim 

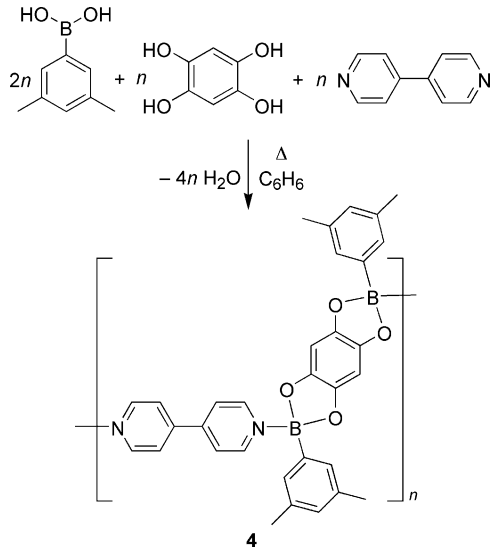


Scheme 3. Synthesis of polymer **4**.

The molecular structure of polymer **4** in the crystal is depicted in Figure 2. As it was observed for **1**, a zig–zag chain is formed. With B1–N1 1.702(5) Å, B1–O1 1.470(4) Å, and B1–O2 1.479(4) Å, the bond lengths of **4** are very similar to those of **1**. Again, the long B–N bond correlates with a low tetrahedral character of 69.5%.

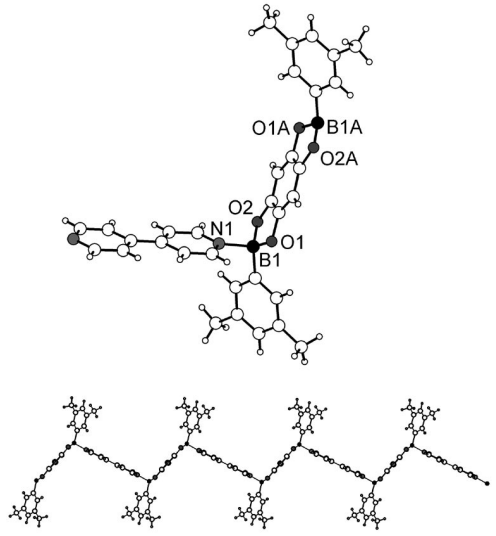


Figure 2. Molecular structure of polymer **4** in the crystal. Top: view of the repeating unit; bottom: view of the polymer chain.

The solid-state $^{11}B$ NMR spectra of polymers **1**, **2**, and **4** are in agreement with the depicted structures and show peaks around 10 ppm. An interesting difference was observed when we attempted to make a polymer from methyl boronic acid, 4,4′-bipyridine, and 1,2,4,5-tetrahydroxybenzene. Again, a dark-purple precipitate was formed (**5**), but its solid-state $^{11}B$ NMR spectrum showed two peaks at ca. 32 and ca. 9 ppm. The former peak is characteristic for a trigonal planar boron center.[16] We therefore propose that compound **5** is the monoadduct [MeB($C_6H_2O_4$)BMe(bipy)] with one trigonal and one tetragonal boron center. Apparently, the methyl boronate ester is not sufficiently Lewis acidic to promote extended polymerization.

A striking feature of polymers **1**, **2**, and **4** is their very dark-purple color. Because the color disappears upon dissolution in chloroform, it must be the fully assembled polymer, which gives rise to the strong absorption. To understand this phenomenon, we performed single-point second-order approximate coupled-cluster (CC2)[19] calculations of the electronic excitations on model systems of the acid and base pairs 1,2-bis(4-pyridyl)ethylene and 4,5-dihydroxyphenyl-4-ethylphenylborole and of their respective condensate in vacuo. Both the uncomplexed acid and base showed the first absorption peak in the near-UV region (4.2 and 3.8 eV, respectively), which is consistent with the finding that the solution containing nonassembled monomers is colorless. In contrast, the assembled acid–base complex showed one transition in the yellow-green region (2.2 eV), which is in agreement with the observed purple coloration of its crystals.

Decomposition of the optical excitation in the visible region onto a molecular orbital basis shows that it has an almost pure HOMO–LUMO π–π* character (88%). This transition corresponds to an intrastrand charge-transfer excitation from the hydroxy–phenyl ring of the dioxaborol moiety to the 1,2-bis(4-pyridyl)ethylene ring (Figure 3).[20] Charge-transfer transitions internal to the dioxaborol strand, specifically between the hydroxy–phenyl and the ethyl–phenyl rings, are not strongly affected by the presence of the pyridyl base; therefore, they do not contribute to the absorption in the visible region, and they remain confined in the UV region of the spectrum. Furthermore, it should be noted that there is no orbital contribution of boron and thus no extended conjugation as it was observed for polymers containing tricoordinate boron.[9b]

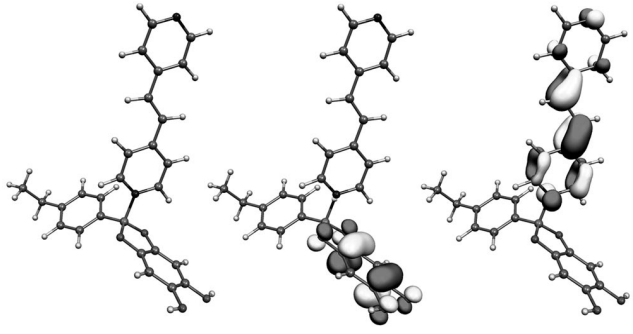

Figure 3. Left: Theoretical cluster-model of the polymeric acid–base pair. Center-right: HOMO–LUMO orbitals responsible for the charge-transfer optical transition in the yellow-green region.

## Conclusions

We showed that condensation reactions of aryl boronic acids with 1,2,4,5-tetrahydroxybenzene can be used *in parallel* with dative B–pyridyl interactions to generate novel polymer architectures by three-component reactions. The

 © 2007 Wiley-VCH Verlag GmbH & Co. KGaA, Weinheim 

resulting crystalline polymers are deeply colored due to efficient intrastrand charge-transfer transitions. An intrinsic advantage of the multicomponent assembly strategy is its modular nature, which allows structural modifications to be easily incorporated. This was evidenced by utilizing different boronic acids and dipyridyl linkers. Because of the weak B–N interaction, the polymers are not stable in solution. However, the reversible formation of the polymer backbone could be interesting from a processing point of view. Furthermore, single crystals can be grown and thus structural information can be obtained. Overall, the work further highlights the potential of boronic acids as building blocks for the generation of polymers with interesting new structures and properties.

## Experimental Section

**General:** 1,2-Bis(4-pyridyl)ethylene, 4,4′-bipyridyl, and the boronic acids were obtained from commercial sources. 1,2,4,5-Tetrahydroxybenzene was prepared as described in the literature.[21] All reactions were carried out under an atmosphere of dry nitrogen by using standard Schlenk techniques. The $^{1}H$, $^{13}C$ and $^{11}B$ spectra were recorded with a 400 MHz spectrometer by using the residual protonated solvents ($^{1}H$, $^{13}C$) as internal standards or $BF_3{\cdot}OEt_2$ ($^{11}B$) as an external standard. $^{1}H$ NMR spectra of the polymers were obtained by dissolving the samples in hot chloroform and then rapidly measuring the solutions before the polymers started to precipitate. The solid-state NMR spectra were recorded with a Bruker DRX 400 spectrometer with a 7.0-widebore magnet by utilizing a 3-mm CPMAS probehead. A solution of boric acid in $H_2O$ was used as the external standard ($\delta$ = 19.3 ppm).

**Polymer 1:** A suspension of 4-ethylphenylboronic acid (135 mg, 0.90 mmol), 1,2,4,5-tetrahydroxybenzene (64 mg, 0.45 mmol), and 1,2-bis(4-pyridyl)ethylene (82 mg, 0.45 mmol) in distilled benzene (90 mL) was heated under reflux with the use of a Dean Stark trap. After 8 h, the suspension was filtered hot, and the filtrate was cooled to room temperature. Upon cooling, a purple solid precipitated. The precipitate was filtered, washed with pentane, and dried under vacuum. Yield: 196 mg, 79%. $(C_{34}H_{30}B_2N_2O_4)_n$ (552.24)$_n$: calcd. C 73.95, H 5.48, N 5.07; found C 74.25, H 5.47, N 5.16. Crystals were obtained by slow diffusion of pentane into a solution of **1** in chloroform.

**Polymer 2:** A suspension of 4-*tert*-butylphenylboronic acid (160 mg, 0.90 mmol), 1,2,4,5-tetrahydroxybenzene (64 mg, 0.45 mmol), and 1,2-bis(4-pyridyl)ethylene (82 mg, 0.45 mmol) in distilled benzene (90 mL) was heated under reflux with the use of a Dean Stark trap. After 8 h, the suspension was filtered hot, and the filtrate was cooled to room temperature. Upon cooling, a purple solid precipitated. The precipitate was filtered, washed with pentane, and dried under vacuum. Yield: 222 mg, 81%. $(C_{38}H_{38}B_2N_2O_4)_n$ (608.34)$_n$: calcd. C 75.02, H 6.30, N 4.60; found C 75.18, H 6.39, N 4.39.

**Boronate Ester 3:** A suspension of 4-ethylphenylboronic acid (135 mg, 0.90 mmol) and 1,2,4,5-tetrahydroxybenzene (64 mg, 0.45 mmol) in distilled benzene (90 mL) was heated under reflux with the use of a Dean Stark trap. After 8 h, the suspension was filtered hot, and the filtrate was cooled to room temperature. Upon cooling, white crystals formed. The crystals were filtered, washed with pentane, and dried under vacuum. Yield: 93 mg, 58%. $^{1}H$ NMR (400 MHz, $CDCl_3$): $\delta$ = 1.29 (t, $^{3}J$ = 7 Hz, 6 H, $CH_3$), 2.73 (q, $^{3}J$ = 8 Hz, 4 H, $CH_2$), 7.31 (s, 2 H, phenyl), 7.34 (d, $^{3}J$ = 8 Hz, 4 H, phenyl), 8.00 (d, $^{3}J$ = 8 Hz, 4 H, phenyl) ppm. $^{13}C$ NMR (101 MHz, $CDCl_3$): $\delta$ = 15.45, 29.36, 98.36, 128.08, 135.15, 143.95, 149.18 ppm. $^{11}B$ NMR (128 MHz, $CDCl_3$): $\delta$ = 34.6 ($h_{1/2}$ = 870 Hz) ppm. $C_{22}H_{20}B_2O_4$ (370.01): calcd. C 71.41, H 5.45; found C 71.25, H 5.57.

**Polymer 4:** A suspension of 3,5-dimethylphenylboronic acid (135 mg, 0.90 mmol), 1,2,4,5-tetrahydroxybenzene (64 mg, 0.45 mmol), and 4,4′-bipyridyl (70 mg, 0.45 mmol) in distilled benzene (90 mL) was heated under reflux with the use of a Dean Stark trap. After 1 h, the suspension was filtered hot, and the filtrate was cooled to room temperature. Upon cooling, a purple solid precipitated. The precipitate was filtered, washed with pentane, and dried under vacuum. Yield: 176 mg, 74%. $(C_{32}H_{28}B_2N_2O_4)_n$ (526.20)$_n$: calcd. C 73.04, H 5.36, N 5.32; found C 72.62, H 5.43, N 5.45. Crystals were obtained by slow diffusion of pentane into a solution of **4** in chloroform.

**Adduct 5:** A suspension of methylboronic acid (54 mg, 0.90 mmol), 1,2,4,5-tetrahydroxybenzene (64 mg, 0.45 mmol), and 4,4′-bipyridyl (70 mg, 0.45 mmol) in distilled benzene (90 mL) was heated under reflux with the use of a Dean Stark trap. After 1 h, the suspension was filtered hot, and the filtrate was cooled to room temperature. Upon cooling, a purple solid precipitated. The precipitate was filtered, washed with pentane, and dried under vacuum. Yield: 110 mg, 71%. $C_{18}H_{16}B_2N_2O_4$ (345.95)$_n$: calcd. C 62.49, H 4.66, N 8.10; found C 62.03, H 4.46, N 7.82.

**X-ray Crystallography:** Details about the crystals and their structure refinement are listed in Table 1. Data collection was performed at 100(2) K by means of a Bruker APEX II CCD detector. Data reduction was carried out with EvalCCD.[22] Absorption correction

Table 1. Crystallographic data for polymers **1** and **4**.

| | **1**·$CHCl_3$ | **4** |
|---|---|---|
| Empirical formula | $C_{35}H_{31}B_2Cl_3N_2O_4$ | $C_{16}H_{14}BNO_2$ |
| Mol. weight / g mol$^{-1}$ | 671.59 | 263.09 |
| Crystal size / mm | 0.59 × 0.29 × 0.16 | 0.52 × 0.15 × 0.10 |
| Crystal system | triclinic | monoclinic |
| Space group | $P\bar{1}$ | $P2_1/n$ |
| $a$ / Å | 9.989(2) | 8.104(5) |
| $b$ / Å | 12.797(4) | 11.507(7) |
| $c$ / Å | 13.452(4) | 14.356(8) |
| $\alpha$ / ° | 100.01(3) | 90 |
| $\beta$ / ° | 91.234(17) | 95.82(6) |
| $\gamma$ / ° | 102.769(19) | 90 |
| Volume / Å$^3$ | 1648.3(8) | 1331.8(14) |
| $Z$ | 2 | 4 |
| Density / g cm$^{-3}$ | 1.353 | 1.312 |
| Temperature / K | 100(2) | 100(2) |
| Absorption coeff. / mm$^{-1}$ | 0.320 | 0.085 |
| $\Theta$ range / ° | 3.32 to 25.02 | 3.36 to 25.00 |
| Index ranges | –11 → 11 | –9 → 9 |
| | –15 → 15 | –13 → 13 |
| | –16 → 16 | –17 → 17 |
| Reflections collected | 28027 | 16398 |
| Independent reflections | 5765 ($R_{int}$ = 0.0729) | 2338 ($R_{int}$ = 0.1178) |
| Absorption correction | semiempirical | semiempirical |
| Max. / min. transmission | 1.0000 / 0.8119 | 1.0000 / 0.4708 |
| Data / restraints / param. | 5765 / 0 / 452 | 2338 / 0 / 181 |
| Goodness-of-fit on $F_2$ | 1.127 | 1.118 |
| Final $R$ indices [$I > 2\sigma(I)$] | $R_1$ = 0.0564 | $R_1$ = 0.0678 |
| | $wR_2$ = 0.0860 | $wR_2$ = 0.1207 |
| $R$ indices (all data) | $R_1$ = 0.1081 | $R_1$ = 0.1249 |
| | $wR_2$ = 0.1025 | $wR_2$ = 0.1408 |
| Larg. diff. peak/hole / e Å$^{-3}$ | 0.307 / –0.279 | 0.264 / –0.233 |

 © 2007 Wiley-VCH Verlag GmbH & Co. KGaA, Weinheim 

was applied to both data sets. Structure solution and refinement were performed with the SHELXTL software package, release 5.1.[23] The structures were refined by using the full-matrix least-squares on $F^2$ with all non-hydrogen atoms anisotropically defined. H atoms were placed in calculated positions by using the "riding model". CCDC-653486 and -653487 contains the supplementary crystallographic data for this paper. These data can be obtained free of charge from The Cambridge Crystallographic Data Centre via www.ccdc.cam.ac.uk/data_request/cif.

**Computational Section:** Vertical excitations for the 1,2-bis(4-pyridyl)ethylene, the (dioxaborole), and the Lewis condensate of the two species were computed at the single-point second-order approximate coupled-cluster (CC2)[17] level. Calculations were performed by using the TURBOMOLE 5.9 code,[24] within the resolution-of-the-identity (RI) approximation for the evaluation of the electron-repulsion integrals.[25] For all calculations a cc-pVDZ[26] basis set was used.

## Acknowledgments

We gratefully acknowledge the support of the Swiss National Science Foundation, the COST action D31, and the EPFL. We thank Dr. Anuji Abraham for measuring the solid-state $^{11}$B NMR spectra.

[1] a) T. D. James in *Topics in Current Chemistry Vol. 277: Creative Chemical Sensor Systems* (Ed.: T. Schrader), Springer, Berlin, **2007**, pp. 107–152; b) T. D. James in *Boronic Acids: Preparation, Applications in Organic Synthesis and Medicine* (Ed.: D. G. Hall), Wiley-VCH, Weinheim, **2005**, pp. 441–480; c) H. Fang, G. Kaur, B. Wang, *J. Fluoresc.* **2004**, *14*, 481–489; d) S. Striegler, *Curr. Org. Chem.* **2003**, *7*, 81–102; e) T. D. James, S. Shinkai in *Topics in Current Chemistry Vol. 218: Host–Guest Chemistry – Mimetic Approaches to Study Carbohydrate Recognition* (Ed.: S. Penadés), Springer, Berlin, **2001**, pp. 159–200; f) W. Wang, X. Gao, B. Wang, *Curr. Org. Chem.* **2003**, *7*, 81–102; g) T. D. James, K. R. A. S. Sandanayake, S. Shinkai, *Angew. Chem. Int. Ed. Engl.* **1996**, *35*, 1910–1922.

[2] For selected references, see: a) N. Iwasawa, H. Takahagi, *J. Am. Chem. Soc.* **2007**, *129*, 7754–7755; b) V. Barba, R. Villamil, R. Luna, C. Gogoy-Alcántar, H. Höpfl, H. I. Beltran, L. S. Zamudio-Rivera, R. Santillan, N. Farfán, *Inorg. Chem.* **2006**, *45*, 2553–2561; c) N. Christinat, R. Scopelliti, K. Severin, *Chem. Commun.* **2004**, 1158–1159; d) E. Barnea, T. Andrea, M. Kapon, M. S. Eisen, *J. Am. Chem. Soc.* **2004**, *126*, 5066–5067; e) M. Sánchez, H. Höpfl, M. E. Ochoa, N. Farfán, R. Santillan, S. Rojas-Lima, *Chem. Eur. J.* **2002**, *8*, 612–621; f) V. Barba, E. Gallegos, R. Santillan, N. Farfán, *J. Organomet. Chem.* **2001**, *622*, 259–264; g) N. Farfán, H. Höpfl, V. Barba, M. E. Ochoa, R. Santillan, E. Gómez, A. Gutiérrez, *J. Organomet. Chem.* **1999**, *581*, 70–81.

[3] N. Christinat, R. Scopelliti, K. Severin, *J. Org. Chem.* **2007**, *72*, 2192–2200.

[4] a) M. Albrecht, M. Fiege, M. Baumert, M. de Groot, R. Fröhlich, L. Russo, K. Rissanen, *Eur. J. Inorg. Chem.* **2007**, 609–616; b) H. Katagiri, T. Miyagawa, Y. Furusho, E. Yashima, *Angew. Chem. Int. Ed.* **2006**, *45*, 1741–1744.

[5] B. F. Abrahams, D. J. Price, R. Robson, *Angew. Chem. Int. Ed.* **2006**, *45*, 806–810.

[6] a) H. M. El-Kaderi, J. R. Hunt, J. L. Mendoza-Cortés, A. P. Côté, R. E. Taylor, M. O'Keeffe, O. M. Yaghi, *Science* **2007**, *316*, 268–272; b) R. W. Tilford, W. R. Gemmill, H.-C. zur Loye, J. J. Lavigne, *Chem. Mater.* **2006**, *18*, 5296–5301; c) A. P. Côté, A. I. Benin, N. W. Ockwig, M. O'Keeffe, A. J. Matzger, O. M. Yaghi, *Science* **2005**, *310*, 1166–1170.

[7] J.-M. Lehn, *Prog. Polym. Sci.* **2005**, *30*, 814–831.

[8] W. Niu, C. O'Sullivan, B. M. Rambo, M. D. Smith, J. J. Lavigne, *Chem. Commun.* **2005**, 4342–4344.

[9] a) B. M. Rambo, J. J. Lavigne, *Chem. Mater.* **2007**, *19*, 3732–3739; b) W. Niu, M. D. Smith, J. J. Lavigne, *J. Am. Chem. Soc.* **2006**, *128*, 16466–16467.

[10] For reviews on boron-containing polymers, see: a) F. Jäkle, *Coord. Chem. Rev.* **2006**, *250*, 1107–1121; b) F. Jäkle, *J. Inorg. Organomet. Polym. Mater.* **2005**, *15*, 293–307; c) K. Ma, M. Scheibitz, S. Scholz, M. Wagner, *J. Organomet. Chem.* **2002**, *652*, 11–19.

[11] a) M. Mikami, S. Shinkai, *J. Chem. Soc. Chem. Commun.* **1995**, 153–154; b) M. Mikami, S. Shinkai, *Chem. Lett.* **1995**, 603–604.

[12] I. Nakazawa, S. Suda, M. Masuda, M. Asai, T. Shimizu, *Chem. Commun.* **2000**, 881–882.

[13] a) R. E. Dinnebier, M. Wagner, F. Peters, K. Shankland, W. I. F. David, *Z. Anorg. Allg. Chem.* **2000**, *626*, 1400–1405; b) M. Grosche, E. Herdtweck, F. Peters, M. Wagner, *Organometallics* **1999**, *18*, 4669–4672; c) M. Fontani, F. Peters, W. Scheer, W. Wachter, M. Wagner, P. Zanello, *Eur. J. Inorg. Chem.* **1998**, 1453–1465.

[14] Y. Qin, C. Cui, F. Jäkle, *Macromolecules* **2007**, *40*, 1413–1420.

[15] For the functionalization of polymer side chains by dative B–N bonds, see: P. M. Iovine, M. N. Fletcher, S. Lin, *Macromolecules* **2006**, *39*, 6324–6326.

[16] For structurally related compounds, see: W. Niu, M. D. Smith, J. J. Lavigne, *Cryst. Growth & Design* **2006**, *6*, 1274–1277.

[17] H. Nöth, B. Wrackmeyer in *NMR – Basic Principles and Progress Vol. 14: NMR Spectroscopy of Boron Compounds* (Eds.: P. Diehl. E. Fluck, R. Kosfeld), Springer, Berlin, **1978**.

[18] H. Höpfl, *J. Organomet. Chem.* **1999**, *581*, 129–149.

[19] O. Christiansen, H. Koch, P. Jørgensen, *Chem. Phys. Lett.* **1995**, *243*, 409–418.

[20] For charge-transfer excitations in tetracoordinate boron compounds, see ref.[13] and: a) Y. Qin, I. Kiburu, S. Shah, F. Jäkle, *Org. Lett.* **2006**, *8*, 5227–5230; b) Y. Cui, Q.-D. Liu, D.-R. Bai, W.-L. Jia, Y. Tao, S. Wang, *Inorg. Chem.* **2005**, *44*, 601–609.

[21] P. R. Weider, L. S. Hegedus, H. Asada, S. V. D'Andreq, *J. Org. Chem.* **1985**, *50*, 4276–4281.

[22] A. J. M. Duisenberg, C. M. J. Kroon-Batenburg, A. M. M. Schreurs, *J. Appl. Crystallogr.* **2003**, *36*, 220–229.

[23] G. M. Sheldrick, *SHELXTL*, University of Göttingen, Germany, **1997**; Bruker AXS, Inc., Madison, Wisconsin, 53719, USA, **1997**.

[24] R. Ahlrichs, M. Bar, M. Haser, H. Horn, C. Kolmel, *Chem. Phys. Lett.* **1989**, *162*, 165–169.

[25] F. Weigend, M. Haser, H. Patzelt, R. Ahlrichs, *Chem. Phys. Lett.* **1998**, *294*, 143–152.

[26] D. E. Woon, T. H. Dunning, *J. Chem. Phys.* **1993**, *98*, 1358–1371.

Received: July 10, 2007
Published Online: September 12, 2007

 © 2007 Wiley-VCH Verlag GmbH & Co. KGaA, Weinheim 

DOI: 10.1002/ejic.200700635

# Oxoethoxide Chlorides – Representatives of Oligonuclear Alkoxide Complexes of Gallium: Penta- and Dodecanuclear Molecules

**Evgeniya V. Suslova,[a] Vadim G. Kessler,*[b] Suresh Gohil,[b] and Nataliya Ya. Turova[a]**

**Keywords:** Gallium oxides / Sol–gel precursors / Oligonuclear complexes / X-ray / Mass spectrometry

Metathesis of solid $GaCl_3$ with NaOEt/EtOH (1:3) provided, after separation of the NaCl precipitate, a solution containing oxoalkoxide chloride complexes of gallium. Residues from evacuation of the latter were redissolved in either toluene/MeCN (solution 1) or toluene/pyridine (solution 2). Storage of the first solution provided crystals of $Ga_5(\mu_5\text{-}O)(\mu\text{-}OEt)_8Cl_5$ (**1**), and of the second solution – $[Ga_{12}(\mu_4\text{-}O)_2(\mu_3\text{-}O)_5(\mu\text{-}OEt)_{10}Cl_{12}Py_4]Py$ (**2**), both at room temperature and in relatively high yields. Compound **1** crystallizes as a vertically contracted tetragonal pyramid with the $\mu_5$-O ligand situated in the center of the equatorial plane defined by four trigonal bipyramidal coordinated gallium atoms. The axial Ga atom has octahedral coordination. All eight edges of the pyramid are capped by μ-OEt groups, and all the chloride ligands are situated in terminal positions. Crystals of $[Ga_{12}(\mu_4\text{-}O)_2(\mu_3\text{-}O)_5(\mu\text{-}OEt)_{10}Cl_{12}Py_4]Py$ (**2**) contain two $[Ga_5(\mu_4\text{-}O)(\mu_3\text{-}O)_2(\mu\text{-}OEt)_5Cl_5Py]$ fragments connected through a cyclic $[Ga_4(\mu_3\text{-}O)_5Cl_2Py_2]$ unit with a $\mu_3$-O ligand in its center. Of the metal atoms, three possess tetrahedral, seven trigonal bipyramidal, and two octahedral coordination. The mass spectrum of **1** contains penta- and tetranuclear fragments. The spectrum of **2** contains heptameric fragments in addition to the pentanuclear fragments that are analogous to those in the spectrum of **1**. The factors leading to formation of polymeric $M(OR)_n$ and related oligonuclear oxocomplexes are discussed.

(© Wiley-VCH Verlag GmbH & Co. KGaA, 69451 Weinheim, Germany, 2007)

## Introduction

The present interest to organic derivatives of gallium is related to the possibilities of their application as precursors of a series of complex oxide materials applied as gas sensors,[1,2] luminophores,[3] and solid electrolytes, on the one hand, and $M^{II}$-doped $LaGaO_3$[4] and catalysts with zeolyte-type structures on the other hand.[5] The oligonuclear molecular complexes of gallium are also very attractive as close structural analogs, diamagnetic models, and potential reagents for tuning the magnetic moment of the oligonuclear complexes of iron(III) for applications in the field of molecular electronics.[6] It appeared extremely interesting to get closer insight into the chemistry of gallium alkoxide complexes in view of their earlier postulated rendered kinetics (slow reaction rates in ligands exchange and core rearrangements) and polymerism (coexistence of different oligomers with the same chemical composition) in contrast to kinetically unhindered iron(III) alkoxides.[7]

Among the synthetic approaches to gallium alkoxides described in the literature, a considerable emphasis has always been put on the metathesis of gallium chloride with alkali alkoxides.[8–12] Our attempts to reproduce the proposed techniques, in particular those described for the synthesis of $Ga(OEt)_3$, led consequently to rather low yields of the desired products.[13]

In the present work we report the isolation of the products of interaction of solid $GaCl_3$ with a solution of NaOEt in ethanol (taken in the stoichiometric 1:3 ratio) and their structural characterization.

## Results and Discussion

Repeated trials of the metathesis of $GaCl_3$ with sodium ethoxide in 1:3 ratio according to the techniques proposed in refs.[10–11] for the synthesis of $Ga(OEt)_3$ resulted in the following observations: (1) Alcoholysis of the solid $GaCl_3$ – a quite strong Lewis acid – resulted, to a certain extent, in the evolution of hydrogen chloride, HCl, which reacted in turn with the alcohol (a process catalyzed by $MCl_n$) with the release of water; this resulted in the presence of oxo-derivatives in the reaction products.[13] (2) The stability of gallium oxoalkoxide halides is so high that even prolonged heating of the reaction mixture at reflux was unable to achieve their decomposition (the amount of NaCl precipitate constitutes only about 80% of the theoretically calculated yield).

It is important to mention that when a toluene solution of $GaCl_3$ is applied as the reagent in metathesis (i.e., by reducing the extent of the alcoholysis side reaction[13]), the process resulted in the formation of insoluble polymeric *or-*

[a] Department of Chemistry, M. V. Lomonosov Moscow State University,
119899, Moscow, Russia
[b] Department of Chemistry, SLU,
P. O. Box 7015, 75007 Uppsala, Sweden
E-mail: Vadim.Kessler@kemi.slu.se

 WILEY InterScience DISCOVER SOMETHING GREAT © 2007 Wiley-VCH Verlag GmbH & Co. KGaA, Weinheim 

*tho*-ethoxide $Ga(OEt)_3$, which displayed a layered $[Ga(OEt)_{4/2}(OEt)]_\infty$ structure.[14] Oxo complexes are most often more soluble due to their oligonuclear molecular structure.

Preparation of a crystalline sample suitable for single-crystal X-ray studies could be achieved only with the use of polar organic solvents such as acetonitrile or pyridine. Crystals of $Ga_5(\mu_5\text{-}O)(\mu\text{-}OEt)_8Cl_5$ (**1**) were formed from solution after 5 months of storage. Crystals of **1** comprise a flattened tetragonal pyramid of metal atoms, $Ga_5$, with an octahedrally coordinated metal atom $[Ga(\mu_5\text{-}O)(\mu\text{-}OEt)_4Cl]$ in the axial position and the trigonal bipyramidal coordinated ones $[Ga(\mu_5\text{-}O)(\mu\text{-}OEt)_3Cl]$ in the equatorial plane of the pyramid. A pentadentate oxo group is situated in the center of the pyramid, and all its edges are capped by eight μ-OEt groups. Four shorter bridges are placed between the apical hexacoordinate metal atom and the equatorial metal atoms (designated as $^{(5-6)}$ in Table 1), and the other four longer bridges bind the trigonal bipyramidal coordinated Ga atoms together in the equatorial plane (designated as $^{(5-5)}$ in Table 1), see Figure 1. The bonding parameters for **1** are practically identical to those of its structural analogs – derivatives of aluminium and iron(III),[15–19] see Table 1. The only (minor) difference between the compounds presented in Table 1 lies in the position of the $\mu_5$-O group: in **1** and $Fe_5O(OEt)_8(OEt)_5$[7,16] the oxo atom lies practically within the equatorial plane [the sums of the $M^5$–($\mu_5$-O)–$M^5$ angles are 356.3 and 357.5°, respectively, which corresponds to only ca. 0.02 Å distance from the $\mu_5$-O ligand to the equatorial plane]. The same type of $\mu_5$-O ligand placement can in fact be observed for the tetragonal pyramidal isopropoxide $M_5(\mu_5\text{-}O)(\mu_3\text{-}OR)_4)(\mu\text{-}OR)_4(OR)_5$ (M = In, Sc, Y, Ln) complexes, where all metal atoms are octahedrally coordinated and the alkoxide groups, which are situated between the axial and the equatorial metal atoms, are they cap the faces of the pyramid instead of the edges.[20–25]

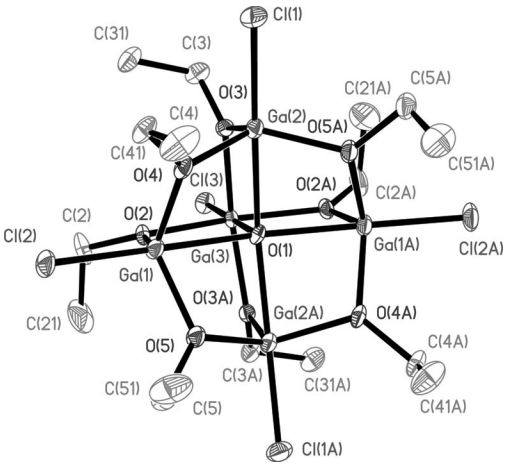


Figure 1. Molecular structure of $Ga_5(\mu_5\text{-}O)(\mu\text{-}OEt)_8Cl_5$ (**1**).

In the other molecules presented in Table 1, the sums of the equatorial angles at the $\mu_5$-O groups are ca. 331°, which corresponds to its distance to the equatorial plane of about 0.22 Å. An interesting peculiarity of all the compared structures is that the length of the bond between the $\mu_5$-O ligand and the axial, hexacoordinate, metal atom is considerably shorter than between this ligand and the pentacoordinate equatorial metal atoms, for gallium – 1.931(11) and 2.162(3) Å, respectively. This fact confirms that the central oxo atom is really involved in five bonds, and it is truly pentacoordinate. The values of the M–(μ-OC) angles in **1** (124.2–129.6°), as well as the corresponding angles for the alkoxide bridging groups in the other molecules in this fam-

Table 1. Comparison of the bonding parameters in the $[M_5(\mu_5\text{-}O)(\mu\text{-}OR)_8X_5]$ molecules ($M^6$ – octahedral coordinated, $M^5$ – trigonal bipyramidal coordinated). The molecules with closely related structures have recently been envisaged for a series of other alkoxides of iron(III) – $Fe_5O(OR)_{13}$ (R = *n*Pr, *i*Pr, *i*Bu, $CH_2CF_3$), and also $Fe_5O(O\textit{i}Pr)_{12}Cl$.[19]

| | $Ga_5O(OEt)_8Cl_5$ (**1**) | $Fe_5O(O\textit{i}Pr)_8Cl_5$,[15] $Fe_5O(OEt)_8(OEt)_5$,[7,16] $Fe_5O(OEt)_8(OSiEt)_5$[17] | $Al_5O(O\textit{i}Bu)_{13}$[18] |
|---|---|---|---|
| $M^6$–($\mu_5$-O) | 1.931 | 2.194–2.005 | 1.89 |
| $M^5$–($\mu_5$-O) | 2.162 | 2.159–2.205 | 2.08 |
| $M^6$–μ-O(R) | 1.999–2.010 | 2.021–2.062 | 1.96 |
| $M^5$–μ-O(R) $^{(5-6)}$ | 1.859–1.862 | 1.887–1.926 | 1.80 |
| $M^5$–μ-O(R) $^{(5-5)}$ | 1.873- 1.883 | 1.909–1.957 | 1.83 |
| $M^6$–X term | 2.198 (Cl) | 2.243 (Cl); 1.829 (OR), | 1.73 (OR) |
| $M^5$–X term | 2.182–2.190 (Cl) | 2.231 (Cl); 1.756–1.806 (OR) | 1.72 (OR) |
| ($\mu_5$-O)–$M^6$–μ-O(R) | 79.6–80.0 | 78.4–79.6 | 79.21 |
| ($\mu_5$-O)–$M^5$–μ-O(R) | 77.0–78.2; 160.1 | 77.9–79.1; 177.7–178.5 | 77.6–78.7 |
| μ-(R)O–$M^6$–μ-O(R) | 86.5–89.9; 159.1 | 87.7–88.0; 157.7–158.1 | 88.0; 158.4 |
| μ-(R)O–$M^5$–μ-O(R) $^{(5-6)}$ | 114.8–109.2 | 111.2–112.3; 124.43 | 110.4–115.2 |
| μ-(R)O–$M^5$–μ-O(R) $^{(5-5)}$ | 121.3–122.3 | 118.6–125.1; 117.55 | 122.6 |
| ($\mu_5$-O)–$M^6$–X term | 180.0 (Cl) | 179.0 (OR); 180 (Cl) | 180.0 |
| ($\mu_5$-O)–$M^5$–X term | 178.0–180.0 (Cl) | 177.7–178.5 (OR); 174.0(Cl) | 176.5 |
| μ-(R)O–$M^6$–X term | 100.0–100.4 (Cl) | 99.4–101.9 (OR, Cl) | 100.8 |
| μ-(R)O–$M^5$–X term | 101.1–104.9 (Cl) | 101.5 (OR); 102.40 (Cl) | 101.3 |
| $M^6$–($\mu_5$-O)–$M^5$ | 97.1–97.5 | 95.6 –96.9 | 97.3 |
| $M^5$–($\mu_5$-O)–$M^5$ | 88.60–89.55; 165.0–165.8 | 89.1–90.5; 164.8–167.2 | 89.09; 165.5 |
| $M^6$–(μ-OR)–$M^5$ | 105.0–105.8 | 95.6–96.3; 103.61–106.5 | 105.6 |
| $M^5$–(μ-OR)–$M^5$ | 108.3 | 88.8–90.5; 103.07–105.7 | 105.7 |
| $M^6$–(μ-O)–C | 128.3–129.6 | 121.3–125.2 | 128.9 |
| $M^5$–(μ-O)–C | 124.2–126.6 | 123.7–126.2 | 124.1–126.3 |

 © 2007 Wiley-VCH Verlag GmbH & Co. KGaA, Weinheim 

ily, indicate certain contribution of the $d_\pi$–$p_\pi$ interaction and predominantly $sp^2$ hybridization for the oxygen atoms according to the well-established structural correlations.[13]

According to the mass spectrometric data, molecules of **1** are present in the gas phase (Figure 2) and are relatively stable to all types of decomposition (by chemical means on evaporation and also by electron impact – the fragmentation series for the pentanuclear species is the most intense in the spectrum). The major alternative in the decomposition of **1** on evaporation is provided by the loss of a $Ga(OEt)_2Cl$ molecule, which should lead to a symmetric tetrahedral $Ga_4O(OEt)_6Cl_4$ molecule, unknown in the condensed phase, but represented by its own fragmentation series in the mass spectrum. The first ion in the series is formed by further loss of a terminal chloride ligand from this molecule, $Ga_4O(OEt)_6Cl_3^+$. It is interesting to note that the most intense ion in the mass spectrum of iron(III) ethoxide is $Fe_4O(OEt)_9^+$ [*m*/*z* (%) = 645 (100)], which possesses most probably a symmetric tetrahedral structure of the same type containing nine ethoxide ligands in addition to the oxo one.[7] Further fragmentation is associated with the loss of two more ethoxide ligands apparently with conservation of the close-packed structure (Figure 3). The formation of the close-packed structures is very characteristic of the molecular alkoxide aggregates even in the solid state and in solution.[26,27] The ionization in a mass-spectrometric experiment occurs by collision of the sample with an electron beam with the energy of 70 eV (about 675 KJ mol$^{-1}$). This transfers the molecule into a virtual state, where all metal atoms, in a molecule such as **1** that has relatively high symmetry, become equivalent. The energy is then released through ionization and loss of a fragment. The structure of the formed ion corresponds to the energy minimum for the residual fragment, which is achieved by dense packing of the metal cations and residual donor atoms.

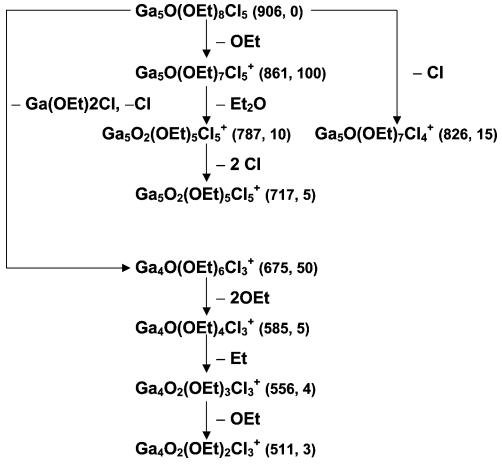


Figure 2. Mass-spectral fragmentation scheme for **1**.

The crystal structure of compound **2**, obtained from solutions of reaction products in toluene/pyridine, contains noncentrosymmetric dodecanuclear $[Ga_{12}(\mu_4\text{-}O)_2(\mu_3\text{-}O)_5(\mu\text{-}OEt)_{10}Cl_{12}Py_4]$ molecules and additional interstitial pyridine molecules in the cavities of the packing. The dodecanuclear molecules are constituted by two $[Ga_5(\mu_4\text{-}O)(\mu_3\text{-}O)_2(\mu\text{-}OEt)_5Cl_4Py]$ fragments connected to each other by a ClGaOpy unit (Figure 4). The molecule contains two octahedrally coordinated metal atoms, Ga8 and Ga9, seven trigonal bipyramidal coordinated Ga atoms – (number 1, 2, 3, 6, 10, 11, and 12), and also three tetrahedral coordinated ones. Two of the latter display a practically regular tetrahedral geometry, Ga4 and Ga7, and the third one is considerably distorted, Ga5, in the center of the molecule. Of the seven oxo groups, the two tetradentate ones, O1 and O7, have distorted tetrahedral coordination, and the four tridentate ones, O4, O6, O2, O8, are practically planar with the sums of the bonding angles of about 358°; the fifth oxo ligand, O5, in the center of the molecule has a pyramidal coordination (valence angle sum 335.6° in the $[OGa_3]$ fragment). All OEt groups are bidentate. In the center of each pentanuclear fragment one can find a planar tetragonal fragment, (Ga2–O7–Ga9–O9) and Ga1–O1–Ga8–O3), respectively.

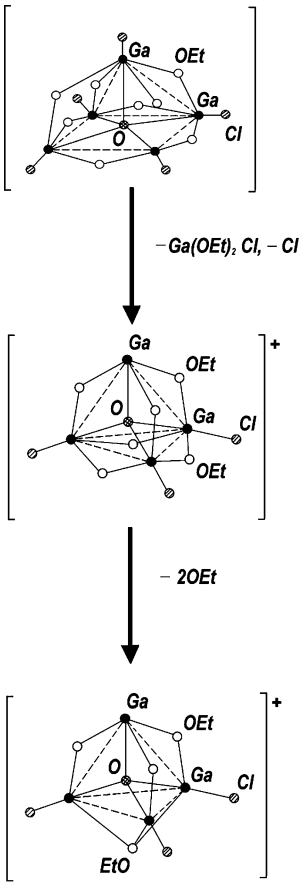


Figure 3. Partial decomposition of **1** in the gas phase.

The bond lengths of the Ga–O(oxo) fragments are independent of the coordination number of the metal atom and are determined exclusively by the bonding mode of the oxo groups. Thus, the tetradentate oxygen atoms O1 and O7 form two longer [2.037–2.367(16) Å] and two shorter bonds [1.858–2.007(16) Å]. The length of the latter is of the same order of magnitude as for the tridentate oxygen atoms O4,

 © 2007 Wiley-VCH Verlag GmbH & Co. KGaA, Weinheim 

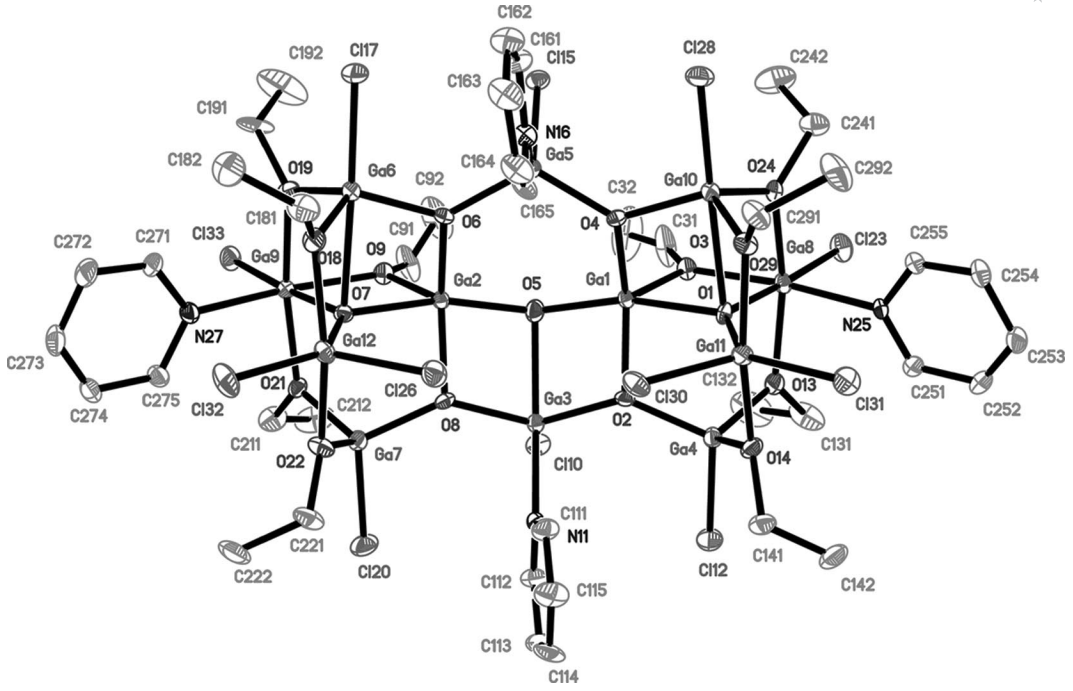


Figure 4. Molecular structure of $Ga_{12}(\mu_4\text{-}O)_2(\mu_3\text{-}O)_5(\mu\text{-}OEt)_{10}Cl_{12}Py_4$ (**2**).

O6, O2, O8–Ga [1.812–1.933(16) Å]. The only exclusion is represented by one of the bonds involving the central tridentate oxygen atom in the molecule, O5–Ga3 [2.161(18) Å]. The lengths of the Ga–(μ-OEt) bridges are within the interval 1.804–2.048(17) Å, and the distances to the terminal chloride ligands Ga–Cl is 2.113–2.236(8) Å, again independently of the coordination number of the metal atom. Only the distance to the terminal nitrogen atoms increases considerably from tetrahedral to octahedral coordination from 2.01(2) to 2.236(9) Å.

The first ions in the mass spectrum of **2** – $Ga_7O_5(OEt)_3Cl_7^+$ $Ga_7O_5(OEt)_2Cl_7^{++}$ – belong to the heptanuclear fragment and correspond to the loss of a pentanuclear core from the original molecule. The light ions correspond to those observed in the spectrum of **1**. It can be explained both by easy fragmentation of **2** into two structural fragments – pentanuclear and heptanuclear – but even possibly by partial decomposition on evaporation with formation of more volatile compound **1**.

The structure of **2** is closely related to the other chemically related oxoalkoxo complexes of aluminium and iron(III) – $[Fe_9O_3(OEt)_{21}]\cdot EtOH$,[28] $[Al_{10}O_4(OEt)_{22}]$,[29] and $[Al_{11}O_6(OnPr)_{10}(OiPr)_{10}(OR)(ROH)_2]$,[30] which have pentanuclear cores connected to each other through a common [M(μ$_3$-O)(μ-OR)] edge or through central [Al$_2$(μ$_3$-O)$_2$] or [Al(OR)(μ-O)$_2$(μ$_3$-O)$_2$][31] units (Figure 5). All the above-mentioned molecules contain tetrahedral [(μ$_4$-O)M$_4$] groups, to which an additional fifth metal atom is connected through oxo- or alkoxo bridges. In **2** these additional atoms, Ga4 and Ga7, are attached to the tetrahedral one through two μ-OR groups O13, O14 and O21, O22 and one μ$_3$-O group O2 and O8, respectively.

Gallium oxoalkoxides were synthesized in this work for the first time, but they definitely show close structural relationship to the derivatives of aluminium and iron. Easy transformations on evaporation trace a closer relationship

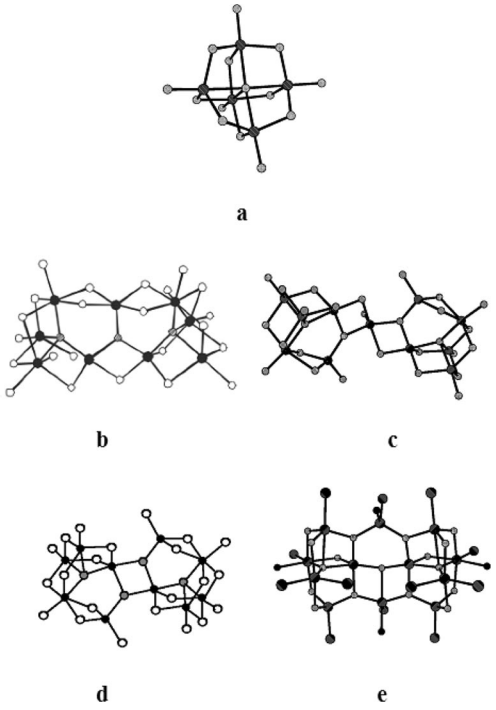


Figure 5. Comparison of the metal–ligand cores in the molecules of the penta-, nona- deca-, undeca-, and dodecanuclear oxoalkoxides: (a) $Fe_5O(OEt)_{13}$[7] or $Ga_5O(OEt)_8Cl_5$ (**1**); (b) $[Fe_9O_3(OEt)_{21}]\cdot EtOH$;[28] (c) $Al_{10}O_4(OEt)_{22}$;[29] (d) $Al_{11}O_6(OnPr)_{10}(OiPr)_{10}(OR)(ROH)_2$;[30] and (e) $Ga_{12}O_7(OEt)_{10}Cl_{12}Py_4$ (**2**).

 © 2007 Wiley-VCH Verlag GmbH & Co. KGaA, Weinheim 

to the derivatives of iron(III) and thus less kinetically hindered reactivity. The rearrangements of the gallium complexes appear to occur easily and follow the solution equilibria. It opens a way to potential new classes of gallium–iron(III) molecular aggregates, which are attractive for molecular electronic applications.[6]

## Experimental Section

All manipulations were carried out under a dry nitrogen atmosphere by using Schlenk techniques or in a glove box. Anhydrous $GaCl_3$ was purchased from Aldrich and used as received. Ethanol was dried by refluxing over $Ca(OEt)_2$ with subsequent distillation, and toluene was distillation from Na and $LiAlH_4$. Mass spectra were recorded with a JEOL JMS-SX/SX-102A mass spectrometer by applying electron beam ionization ($U$ = 70 eV) with direct-probe introduction. The reported masses of the ions were calculated for the $^{71}$Ga isotope. IR spectra were registered with a Perkin–Elmer Spectrum 100 instrument (as nujol or hexachlorobutadiene mulls). $^1$H NMR spectra were recorded in $CDCl_3$ solutions with a Bruker 400 MHz instrument at room temperature.

**Synthetic Procedure:** Sodium metal (1.22 g, 53 mmol) was dissolved in EtOH (27 mL) at room temperature. An solid $GaCl_3$ (2.85 g, 16.0 mmol) was then added to the solution. The process was strongly exothermic and accompanied by the evolution of visible amounts of HCl "mist" that was subsequently consumed by redissolution in the reaction mixture. The mixture was then heated at reflux for 5–6 h and then finally left for precipitation of NaCl (2.39 g, 41 mmol) overnight. The clear solution was removed by syringe, and the solvents were evaporated to dryness in vacuo. The residual solid was very sparingly soluble in toluene or alcohol even

Table 2. Crystal data and details of diffraction experiments for compounds **1** and **2**.

| | **1** | **2** |
|---|---|---|
| Empirical formula | $C_{16}H_{40}Cl_5Ga_5O_9$ | $C_{50}H_{80}Cl_{12}Ga_{12}N_5O_{17}$ |
| $M$ | 902.33 | 2299.24 |
| Crystal system | monoclinic | monoclinic |
| Space group | $C2/c$ | $P2_1/n$ |
| $a$ [Å] | 21.758(17) | 20.378(11) |
| $b$ [Å] | 9.519(8) | 22.127(13) |
| $c$ [Å] | 19.221(16) | 20.490(12) |
| $\alpha$ [°] | 90 | 90 |
| $\beta$ [°] | 121.733(14) | 107.176(15)3 |
| $\gamma$ [°] | 90 | 90 |
| $V$ [Å$^3$] | 3386(5) | 8827(9) |
| $Z$ | 4 | 4 |
| Independent reflections | 1696 [$R$(int) = 0.0417] | 8405 [$R$(int) = 0.0882] |
| Goodness-of-fit on $F^2$ | 0.999 | 1.019 |
| Final $R$ indices [$I > 2\sigma(I)$] | $R_1$ = 0.0645, $wR_2$ = 0.1573 | $R_1$ = 0.0691, $wR_2$ = 0.1488 |

Table 3. Selected bond lengths [Å] and angles [°] for $Ga_5O(OEt)_8Cl_5$ (**1**).[a]

| | | | | | |
|---|---|---|---|---|---|
| Ga1–O2 | 1.859(9) | Ga2–O4 | 1.883(8) | Ga3–O2 | 2.010(8) |
| Ga1–O5 | 1.873(8) | Ga2–O1 | 2.161(3) | Ga3–O2#1 | 2.010(8) |
| Ga1–O4 | 1.874(9) | Ga2–Cl1 | 2.182(4) | Ga3–Cl3 | 2.198(5) |
| Ga1–O1 | 2.162(3) | Ga3–O1 | 1.931(11) | O1–Ga2#1 | 2.161(3) |
| Ga1–Cl2 | 2.190(4) | Ga3–O3 | 1.999(7) | O1–Ga1#1 | 2.162(3) |
| Ga2–O3 | 1.862(8) | Ga3–O3#1 | 1.999(7) | O5–Ga2#1 | 1.882(8) |
| Ga2–O5#1 | 1.882(8) | | | | |
| | | | | | |
| O2–Ga1–O5 | 110.6(4) | O1–Ga2–Cl1 | 178.0(3) | Ga3–O1–Ga1#1 | 97.1(3) |
| O2–Ga1–O4 | 114.8(4) | O1–Ga3–O3 | 79.6(2) | Ga2–O1–Ga1#1 | 89.55(9) |
| O5–Ga1–O4 | 121.3(4) | O1–Ga3–O3#1 | 79.6(2) | Ga2#1–O1–Ga1#1 | 88.60(9) |
| O2–Ga1–O1 | 77.8(4) | O3–Ga3–O3#1 | 159.1(5) | Ga3–O1–Ga1 | 97.1(3) |
| O5–Ga1–O1 | 77.2(3) | O1–Ga3–O2 | 80.0(2) | Ga2–O1–Ga1 | 88.60(9) |
| O4–Ga1–O1 | 78.2(3) | O3–Ga3–O2 | 86.5(3) | Ga2#1–O1–Ga1 | 89.55(9) |
| O2–Ga1–Cl2 | 103.0(3) | O3#1–Ga3–O2 | 89.9(3) | Ga1#1–O1–Ga1 | 165.8(6) |
| O5–Ga1–Cl2 | 102.8(3) | O1–Ga3–O2#1 | 80.0(2) | Ga1–O2–Ga3 | 105.0(4) |
| O4–Ga1–Cl2 | 101.1(3) | O3–Ga3–O2#1 | 89.9(3) | Ga1–O4–Ga2 | 107.0(4) |
| O1–Ga1–Cl2 | 179.1(3) | O3#1–Ga3–O2#1 | 86.5(3) | Ga1–O5–Ga2#1 | 108.3(4) |
| O3–Ga2–O5#1 | 114.7(4) | O2–Ga3–O2#1 | 160.1(5) | C2–O2–Ga1 | 125.3(9) |
| O3–Ga2–O4 | 109.2(4) | O1–Ga3–Cl3 | 180.000(2) | C2–O2–Ga3 | 128.3(9) |
| O5#1–Ga2–O4 | 122.1(4) | O3–Ga3–Cl3 | 100.4(2) | C3–O3–Ga2 | 124.2(7) |
| O3–Ga2–O1 | 77.0(4) | O3#1–Ga3–Cl3 | 100.4(2) | C3–O3–Ga3 | 129.6(8) |
| O5#1–Ga2–O1 | 77.0(3) | O2–Ga3–Cl3 | 100.0(2) | Ga2–O3–Ga3 | 105.8(4) |
| O4–Ga2–O1 | 78.0(3) | O2#1–Ga3–Cl3 | 100.0(2) | C4–O4–Ga1 | 126.6(9) |
| O3–Ga2–Cl1 | 104.9(3) | Ga3–O1–Ga2 | 97.5(3) | C4–O4–Ga2 | 124.9(8) |
| O5#1–Ga2–Cl1 | 101.6(3) | Ga3–O1–Ga2#1 | 97.5(3) | C5–O5–Ga1 | 125.2(8) |
| O4–Ga2–Cl1 | 101.7(3) | Ga2–O1–Ga2#1 | 165.0(6) | C5–O5–Ga2#1 | 125.3(7) |

[a] Symmetry transformations used to generate equivalent atoms: #1: –x, y, $–z$ + 1/2.

 © 2007 Wiley-VCH Verlag GmbH & Co. KGaA, Weinheim 

on reflux. Its suspension in 3 mL of toluene was separated into a solution fraction and a sediment.

The sediment was treated with a mixture of MeCN (3 mL) and toluene (3 mL), which provided a dark-red solution that slowly lost its color on storage to produce colorless crystals of **1** with practically quantitative yield after 5 months. $^1$H NMR (400 MHz, $CDCl_3$): $\delta$ = 4.22 (q, $J$ = 6.5 Hz, 16 H, H-C$H_2$), 1.26 (t, $J$ = 6.0 Hz, 24 H, H-C$H_3$) ppm. $^{13}$C NMR (100 MHz, $CDCl_3$): $\delta$ = 59.6 (C-$CH_2$), 16.6 (C-$CH_3$) ppm. The presence of only one signal for each type of carbon or hydrogen atom indicates rather quick exchange under these conditions. IR (nujol): $\tilde{\nu}$ = 1302 (m), 1166.09 (m), 1093.74 (w), 1034.10 (w), 897.12 (w), 601.19 (w), 467.94 (m), 427.16 (m) cm$^{-1}$. MS: *m*/*z* (%) = 861(100) $[Ga_5O(OEt)_7Cl_5]^+$, 826 (15) $[Ga_5O(OEt)_7Cl_4]$, 787 (10) $[Ga_5O_2(OEt)_5Cl_5]^+$, 717 (5) $[Ga_5O_2(OEt)_2Cl_3]^+$, 675 (50) $[Ga_4O(OEt)_6Cl_3]^+$, 585 (5) $[Ga_4O(OEt)_4Cl_3]^+$,

Table 4. Selected bond lengths [Å] and angles [°] for $[Ga_{12}O_7(OEt)_{10}Cl_{12}Py_4]2Py$ (**2**).

| | | | | | |
|---|---|---|---|---|---|
| Ga1–O3 | 1.82(2) | Ga2–O9 | 1.897(18) | Ga11–O1 | 1.878(18) |
| Ga1–O5 | 1.861(17) | Ga2–O5 | 1.861(19) | Ga11–O14 | 2.021(18) |
| Ga1–O2 | 1.891(15) | Ga2–O8 | 1.916(16) | Ga11–O29 | 2.041(18) |
| Ga1–O4 | 1.929(15) | Ga2–O6 | 1.940(15) | Ga11–Cl30 | 2.189(9) |
| Ga1–O1 | 2.076(16) | Ga2–O7 | 2.039(18) | Ga11–Cl31 | 2.208(9) |
| Ga4–O2 | 1.816(17) | Ga7–O8 | 1.816(17) | Ga3–O2 | 1.882(16) |
| Ga4–O13 | 1.88(2) | Ga7–O21 | 1.868(18) | Ga3–O5 | 2.176(19) |
| Ga4–O14 | 1.832(19) | Ga7–O22 | 1.80(2) | Ga3–O8 | 1.865(17) |
| Ga4–Cl12 | 2.170(8) | Ga7–Cl20 | 2.174(9) | Ga3–N11 | 2.01(2) |
| Ga10–O4 | 1.880(17) | Ga6–O6 | 1.804(17) | Ga3–Cl10 | 2.184(8) |
| Ga10–O1 | 2.367(17) | Ga6–O7 | 2.350(16) | Ga12–O7 | 1.858(18) |
| Ga10–O29 | 1.810(19) | Ga6–O18 | 1.82(2) | Ga12–O22 | 2.025(19) |
| Ga10–O24 | 1.799(19) | Ga6–O19 | 1.912(19) | Ga12–O18 | 2.052(19) |
| Ga10–Cl28 | 2.192(8) | Ga6–Cl17 | 2.208(9) | Ga12–Cl26 | 2.193(9) |
| Ga8–O1 | 1.970(18) | Ga9–O7 | 2.004(18) | Ga12–Cl32 | 2.172(10) |
| Ga8–O3 | 1.992(19) | Ga9–O9 | 2.041(19) | Ga5–O4 | 1.797(17) |
| Ga8–O13 | 2.032(18) | Ga9–O21 | 1.980(16) | Ga5–O6 | 1.860(16) |
| Ga8–O24 | 1.988(18) | Ga9–O19 | 2.044(17) | Ga5–N16 | 2.01(2) |
| Ga8–N25 | 2.13(2) | Ga9–N27 | 2.10(2) | Ga5–Cl15 | 2.111(8) |
| Ga8–Cl23 | 2.219(9) | Ga9–Cl33 | 2.237(9) | | |
| | | | | | |
| O3–Ga1–O1 | 78.7(8) | N25–Ga8–Cl23 | 91.1(7) | N27–Ga9–Cl33 | 92.8 (7) |
| O5–Ga1–O1 | 163.5(8) | O9–Ga2–O7 | 81.3(8) | O1–Ga11–O29 | 81.5(7) |
| O3–Ga1–O2 | 106.0(8) | O5–Ga2–O7 | 162.5(8) | O14–Ga11–O29 | 161.9(8) |
| O2–Ga1–O4 | 144.6(8) | O9–Ga2–O8 | 104.5(7) | O1–Ga11–Cl30 | 112.1(6) |
| O5–Ga1–O2 | 81.5(8) | O8–Ga2–O6 | 146.5(8) | O14–Ga11–Cl30 | 98.0(6) |
| O3–Ga1–O4 | 104.8(8) | O5–Ga2–O8 | 81.1(8) | O29–Ga11–Cl30 | 96.5(6) |
| O3–Ga1–O5 | 114.4(9) | O9–Ga2–O6 | 104.6(8) | O1–Ga11–Cl31 | 134.7(6) |
| O5–Ga1–O4 | 101.2(8) | O5–Ga2–O9 | 113.6(8) | O14–Ga11–Cl31 | 92.2(6) |
| O2–Ga4–O14 | 112.1(8) | O5–Ga2–O6 | 101.8(7) | O29–Ga11–Cl31 | 92.0(6) |
| O2–Ga4–O13 | 111.8(8) | O22–Ga7–O8 | 108.6(8) | Cl30–Ga11-Cl31 | 113.2(4) |
| O14–Ga4–O13 | 108.0(9) | O8–Ga7–O21 | 110.8(8) | O1–Ga11–O14 | 83.1(8) |
| O2–Ga4–Cl12 | 110.5(6) | O22–Ga7–O21 | 109.8(9) | O8–Ga3–O2 | 131.9(7) |
| O14–Ga4–Cl12 | 108.1(6) | O8–Ga7–Cl20 | 110.3(6) | O2–Ga3–O5 | 73.9(7) |
| O13–Ga4–Cl12 | 106.1(6) | O22–Ga7–Cl20 | 108.5(7) | O8–Ga3–O5 | 74.4(7) |
| O4–Ga10–O1 | 77.4(6) | O21–Ga7–Cl20 | 108.8(6) | O2–Ga3–N11 | 94.7(8) |
| O29–Ga10–O4 | 113.1(8) | O6–Ga6–O7 | 76.8(6) | N11–Ga3–O5 | 150.2(9) |
| O24–Ga10–O4 | 114.5(8) | O6–Ga6–O18 | 112.8(9) | O8–Ga3–N11 | 95.3(8) |
| O29–Ga10–O1 | 74.3(7) | O6–Ga6–O19 | 116.1(8) | O2–Ga3–Cl10 | 112.1(6) |
| O24–Ga10–O1 | 72.8(7) | O18–Ga6–O7 | 73.9(7) | O5–Ga3–Cl10 | 107.2(6) |
| O29–Ga10–O24 | 112.6(9) | O19–Ga6–O7 | 77.2(7) | O8–Ga3–Cl10 | 111.2(6) |
| O29–Ga10–Cl28 | 104.6(6) | O18–Ga6–O19 | 114.2(9) | N11–Ga3–Cl10 | 102.6(7) |
| Cl28–Ga10–O1 | 178.7(5) | O6–Ga6–Cl17 | 104.9(6) | O7–Ga12–O22 | 82.5(8) |
| O24–Ga10–Cl28 | 107.2(6) | Cl17–Ga6–O7 | 178.3(5) | O7–Ga12–O18 | 80.9(8) |
| O24–Ga10–Cl28 | 103.7(6) | O18–Ga6–Cl17 | 105.4(7) | O22–Ga12–O18 | 160.4(9) |
| O1–Ga8–O3 | 77.5(8) | O19–Ga6–Cl17 | 101.8(6) | O7–Ga12–Cl26 | 108.1(6) |
| O1–Ga8–O13 | 85.2(8) | O7–Ga9–O9 | 78.7(7) | O22–Ga12–Cl26 | 95.9(7) |
| O1–Ga8–O24 | 78.8(7) | O21–Ga9–O7 | 85.1(7) | O18–Ga12–Cl26 | 99.1(6) |
| O24–Ga8–O3 | 87.7(7) | O7–Ga9–O19 | 83.0(7) | O7–Ga12–Cl32 | 138.7(6) |
| O3–Ga8–O13 | 88.1(7) | O9–Ga9–O19 | 87.8(8) | O22–Ga12–Cl32 | 94.5(7) |
| O24–Ga8–O13 | 164.0(8) | O21–Ga9–O9 | 87.5(7) | O18–Ga12–Cl32 | 91.2(6) |
| O1–Ga8–N25 | 91.4(8) | O21–Ga9–O19 | 167.8(8) | Cl32–Ga12-Cl26 | 113.1(4) |
| O3–Ga8–N25 | 168.8(9) | O7–Ga9–N27 | 90.4(9) | O4–Ga5–O6 | 120.8(7) |
| O13–Ga8–N25 | 89.8(9) | O9–Ga9–N27 | 169.1(9) | O4–Ga5–N16 | 99.0(9) |
| O24–Ga8–N25 | 91.3(9) | O21–Ga9–N27 | 91.1(8) | O6–Ga5–N16 | 97.7(9) |
| O13–Ga8–Cl23 | 100.2(6) | O19–Ga9–N27 | 91.4(9) | O4–Ga5–Cl15 | 112.4(6) |
| O1–Ga8–Cl23 | 177.3(6) | O21–Ga9–Cl33 | 97.0(6) | O6–Ga5–Cl15 | 112.4(6) |
| O24–Ga8–Cl23 | 99.6(6) | O7–Ga9–Cl33 | 176.2(6) | N16–Ga5–Cl15 | 112.5(8) |

 © 2007 Wiley-VCH Verlag GmbH & Co. KGaA, Weinheim 

556 (4) $[Ga_4O_2(OEt)_3Cl_3]^+$, 511 (3) $[Ga_4O_2(OEt)_2Cl_3]^+$. $C_{16}H_{40}Cl_5Ga_5O_9$ (902.33): calcd. C 21.29, H 4.43, Ga 38.88; found C 20.52, H 4.12, Ga 39.31.

The toluene solution was treated with pyridine (0.5 mL), which provided crystallization of a small crop (0.25 g) of crystals of **2**. Further storage of the mother liquor under septum resulted in its complete crystallization with the formation of needle-shaped crystals of [PyH][$GaCl_4$] (identified by single-crystal and powder X-ray studies). $^1$H NMR (400 MHz, $CDCl_3$): $\delta$ = 8.72 (m, 8 H, α-H-Py), 7.62 (t, $J$ = 4.7 Hz, 4 H, γ -H-Py), 7.44 (m, 8 H, β-H-Py), 4.31 (q, $J$ = 6.4 Hz, 8 H, H-C$H_2$-OEt), 4.20 (q, $J$ = 6.5 Hz, 8 H, H-C$H_2$-OEt), 3.51 (q, $J$ = 6.5 Hz, 4 H, H-C$H_2$-OEt), 1.46 (t, $J$ = 6.0 Hz, 6 H, H-C$H_3$-OEt), 1.28 (t, $J$ = 6.0 Hz, 12 H, H-C$H_3$-OEt), 0.74 (t, $J$ = 6.0 Hz, 12 H, H-C$H_3$-OEt) ppm. IR (nujol): $\tilde{\nu}$ = 1611 [vs (νPy)], 1573 [w (νPy)], 1479 (s), 1299 (w), 1218 [s (δPy)], 1156 (s), 1092 (vs), 1054 (vs), 1026 (vs, br.), 889 (vs), 887 (s), 742 (vs), 691 [vs (νGa–O)], 558 [vs, br. (νGa–O)], 452 (vs), 443 (vs), 403 (vs) cm$^{-1}$. MS: *m*/*z* (%) = 957 (20) $[Ga_7O_5(OEt)_3Cl_7]^+$, 912 (6) $[Ga_7O_5(OEt)_2Cl_7]^+$, the other ions are identical to the spectrum of **1**. $C_{50}H_{80}Cl_{12}Ga_{12}N_6O_{17}$ (2299.24): calcd. C 26.15, H 3.48, Ga 36.61; found C 25.10, H 3.02, Ga 37.62.

**X-ray Structure Determinations:** Data collection was performed with a Bruker SMART CCD 1K diffractometer at 295(2) K, with Mo-$K_\alpha$ radiation ($\lambda$ = 0.71073 Å; see Table 2 for details). The SAINTPLUS and the SHELXTL-NT program packages were used for data reduction and computations.[32] Empirical absorption correction was applied by using the Bruker SADABS program package. The structures were solved by direct methods. The coordinates of the heavy atoms were taken from the initial solution, and the non-hydrogen atoms were located in subsequent Fourier syntheses. The structures were refined by full-matrix least-squares techniques in an isotropic and then finally in an anisotropic approximation. The details on data collection and bonding parameters are presented in Tables 2, 3, and 4.

CCDC-650370 and -650371 (for **1**and **2**, respectively) contain the supplementary crystallographic data for this paper. These data can be obtained free of charge from The Cambridge Crystallographic Data Centre via www.ccdc.cam.ac.uk/data_request/cif.

## Acknowledgments

The authors express their gratitude to A. I. Yanovsky for the valuable discussions of the structure data, to the Swedish Research Council for support of this project and to the Visby Program of the Swedish Institute for the travel grant and allowance to E. V. S. and to the Russian Foundation for Basic Research (Project No. 07-03-00128) for the financial support of this work.

[1] R. Binions, C. J. Carmalt, I. P. Parkin, K. F. Pratt, G. A. Shaw, *Chem. Mater.* **2004**, *16*, 2489–2493.
[2] C. J. Carmalt, S. J. King, *Coord. Chem. Rev.* **2006**, *250*, 682–709.
[3] S. Daniele, D. Tcheboukov, L. G. Hubert-Pfalzgraf, *J. Mater. Chem.* **2002**, *12*, 2519–2524.
[4] A. S. Tas, P. J. Majewski, F. Aldinger, *J. Am. Ceram. Soc.* **2000**, *83*, 2954–2960.
[5] P. Meriaudeau, C. Naccache, *J. Mol. Catal.* **1990**, *59*, L31–L36.
[6] G. L. Abbati, L. C. Brunel, H. Casalta, A. Cornia, A. C. Fabretti, D. Gatteschi, A. K. Hassan, A. G. M. Jansen, A. L. Maniero, L. Pardi, C. Paulsen, *Chem. Eur. J.* **2001**, *7*, 1796–1807.
[7] G. A. Seisenbaeva, S. Gohil, E. V. Suslova, T. V. Rogova, N. Ya. Turova, V. G. Kessler, *Inorg. Chim. Acta* **2005**, *358*, 3506–3512.
[8] R. C. Mehrotra, R. K. Mehrotra, *Curr. Sci.* **1964**, *33*, 241–241.
[9] H. Funk, A. Paul, *Z. Anorg. Allg. Chem.* **1964**, *330*, 70–77.
[10] R. Reinmann, A. Tanner, *Z. Naturforsch., Teil B* **1965**, *20*, 524–525.
[11] J. G. Oliver, I. J. Worrall, *J. Chem. Soc. A* **1970**, 2347–2348.
[12] S. R. Bindal, P. N. Kapoor, R. C. Mehrotra, *J. Chem. Soc. A* **1969**, 863–867.
[13] N.Ya. Turova, E. P. Turevskaya, V. G. Kessler, M. I. Yanovskaya, *The Chemistry of Metal Alkoxides*, Kluwer Academic, Boston, **2002**, pp. 1–568.
[14] E. V. Suslova, N. Ya. Turova, *Russ. J. Inorg. Chem.*, in press.
[15] D. M. Reis, G. G. Nunes, E. L. Sa, G. R. Friedermann, A. S. Mangrich, D. J. Evans, P. B. Hitchcock, G. J. Leigh, J. F. Soares, *New J. Chem.* **2004**, *28*, 1168–1176.
[16] B. J. O'Keefe, S. M. Monnier, M. A. Hillmyer, W. B. Tolman, *J. Am. Chem. Soc.* **2001**, *123*, 339–340.
[17] M. Veith, F. Grätz, V. Huch, P. Gütlich, J. Ensling, *Z. Anorg. Allg. Chem.* **2004**, *630*, 2329–2336.
[18] I. Abrahams, D. C. Bradley, H. Chudzynska, M. Motevalli, R. A. Sinclair, *J. Chem. Soc. Dalton Trans.* **2002**, 259–266.
[19] M. Kusserow, J. Spandl, *Z. Anorg. Allg. Chem.* **2006**, *632*, 885–892.
[20] O. Poncelet, W. J. Sartain, L. G. Hubert-Pfalzgraf, K. Folting, K. G. Caulton, *Inorg. Chem.* **1989**, *28*, 263–267.
[21] E. P. Turevskaya, A. I. Belokon′, Z. A. Starikova, A. I. Yanovsky, E. N. Kiruschenkov, N. Ya. Turova, *Polyhedron* **2000**, *19*, 705–711.
[22] G. Westin, M. Kritikos, M. Wijk, *J. Solid State Chem.* **1998**, *141*, 168–176.
[23] M. Kritikos, M. Moustiakimov, M. Wijk, G. Westin, *J. Chem. Soc. Dalton Trans.* **2001**, 1931–1938.
[24] D. C. Bradley, H. Chudzynska, D. M. Frigo, M. E. Hammond, M. B. Hursthouse, M. A. Mazid, *Polyhedron* **1990**, *9*, 719–726.
[25] G. Westin, M. Wijk, M. Moustiakimov, M. Kritikos, *J. Sol-Gel Sci. Technol.* **1998**, *13*, 125–128.
[26] V. G. Kessler, *Chem. Commun.* **2003**, 1213–1222.
[27] V. G. Kessler, *J. Sol-Gel Sci. Technol.* **2004**, *32*, 11–18.
[28] M. Veith, F. Grätz, V. Huch, *Eur. J. Inorg. Chem.* **2001**, 367–368.
[29] A. I. Yanovsky, N. Ya. Turova, N. I. Kozlova, Yu. T. Struchkov, *Koord. Khim.* **1987**, *13*, 149–154.
[30] Z. A. Starikova, V. G. Kessler, N. Ya. Turova, D. E. Tcheboukov, E. V. Suslova, G. A. Seisenbaeva, A. I. Yanovsky, *Polyhedron* **2004**, *23*, 109–114.
[31] N. Ya. Turova, *Russ. Chem. Rev.* **2004**, *73*, 1041–1064.
[32] *SHELXTL-NT Reference Manual*, Bruker AXS, **1998**.

Received: June 19, 2007
Published Online: October 1, 2007

 © 2007 Wiley-VCH Verlag GmbH & Co. KGaA, Weinheim 

DOI: 10.1002/ejic.200700669

# A Triphenylamine/Bis(terpyridine)Ir$^{III}$ Dyad for the Assembly of Charge-Separation Constructs with Improved Performances

**Lucia Flamigni,*[a] Barbara Ventura,[a] Etienne Baranoff,[b] Jean-Paul Collin,*[b] and Jean-Pierre Sauvage*[b]**

**Keywords:** Charge separation / Electron transfer / Iridium / Photochemistry / Supramolecular chemistry

A new dyad **DII-Ir** consisting of a triphenylamine donor and a bis(terpyridine)Ir$^{III}$ acceptor separated by a bridge composed of two benzamide groups has been synthesized. The electrochemical and photophysical properties of the dyad have been compared to those of a corresponding dyad **D-Ir** characterized by a bridge connecting the donor and the acceptor consisting of a single benzamide unit. We show that, whereas the charge-separation steps are still very efficient in the long dyad (≥99 %), charge recombination is slowed by a factor of three with respect to the short dyad. This encourages the use of this dyad in the assembly of a more elaborate array DII-Ir-A, expected to overcome the disappointingly low charge-separation yield of a previously studied **D-Ir-A** short triad.

(© Wiley-VCH Verlag GmbH & Co. KGaA, 69451 Weinheim, Germany, 2007)

## Introduction

The process of producing long-lived charge-separated (CS) states is the basic event in artificial photosynthesis, which aims at efficiently converting light into chemical energy. In spite of the impressive results achieved in the last decade in multi-component arrays,[1] genuine long-lived CS states are still a valuable goal, especially when they involve less common or unexplored chromophores with respect to more conventional tetrapyrrolic or fullerene derivatives.[2] The most convenient and better tested strategy for producing genuine and indisputable CS states is that of using weakly coupled multi-component structures and of moving the electron, through a sequence of electron-transfer events, to molecular components far away from the hole. The first electron-transfer step is driven by light, whereas the following ones are ground-state electron-transfer reactions. A few years ago we started to use (terpyridine-type)Ir$^{III}$ complexes as functional assembling units of multi-component structures having either the role of electron relay[2d,3] or of photosensitizer.[4] The use of this type of complexes proved to be very valuable both for the high energy level (ca. 2.5 eV) of its excited state, a ligand-centered triplet ($^3$LC) occasionally with some charge-transfer triplet ($^3$CT) character, and for the relative ease of reduction, –0.75 V vs. SCE.[5] The high excited-state energy level prevented draining of the electronic energy of the other components due to energy transfer, and the relative ease of reduction of the complex unit provided a high driving force for the primary photoinduced electron transfer starting the sequence. By using arrays with a central bis(terpyridine)Ir$^{III}$ complex and appended porphyrins with suitable metallation to provide a good electron donor [free-base or (porphyrin)zinc complex] or a good electron acceptor [(porphyrin)gold(III) complex], respectively, we succeeded in producing a CS state with a lifetime of 450 ns and 100% yield.[2d,6]

More recently, we studied a **D-Ir-A** triad, where D is a triphenylamine electron donor, A is a naphthalenebis(imide) electron acceptor, and Ir is a bis(terpyridine)Ir$^{III}$ complex (Scheme 1).

The lifetime of the CS state with opposite charges localized at the extremities of the array, produced upon light absorption by either the D or Ir unit is remarkable, of the order of 120 μs at ambient temperature in air-free acetonitrile (100 μs in air-saturated samples), but the yield of charge separation is quite modest, of the order of 10%.[7] The reason for this inefficiency is that the intermediate CS state $D^+$-Ir$^-$-A, formed with a 100% yield by a primary electron-transfer step originating from either an excited D unit ($^1$D) or excited Ir unit ($^3$Ir), can deactivate to the ground state faster ($k = 1.4 \times 10^{10}$ s$^{-1}$) than the rate at which it undergoes a further electron-transfer step ($k = 2.4 \times 10^9$ s$^{-1}$) leading to the final CS state $D^+$-Ir-A$^-$. We reasoned that increasing the D to Ir separation from ca. 1.6 nm in the original system to a distance of ca. 2.3 nm by inserting a further benzamide linker as in **DII-Ir** (Scheme 2), could be a possible strategy to improve the final CS yield in a triad DII-Ir-A.

[a] Istituto ISOF-CNR,
Via P. Gobetti 101, 40129 Bologna, Italy
E-mail: flamigni@isof.cnr.it
[b] Laboratoire de Chimie Organo-Minérale, UMR 7177 CNRS, Université Louis Pasteur,
Institut Le Bel, 4, rue Blaise Pascal, 67070 Strasbourg, France
E-mail: jpcollin@chimie.u-strasbg.fr
sauvage@chimie.u-strasbg.fr

Supporting information for this article is available on the WWW under http://www.eurjic.org or from the author.

 © 2007 Wiley-VCH Verlag GmbH & Co. KGaA, Weinheim 

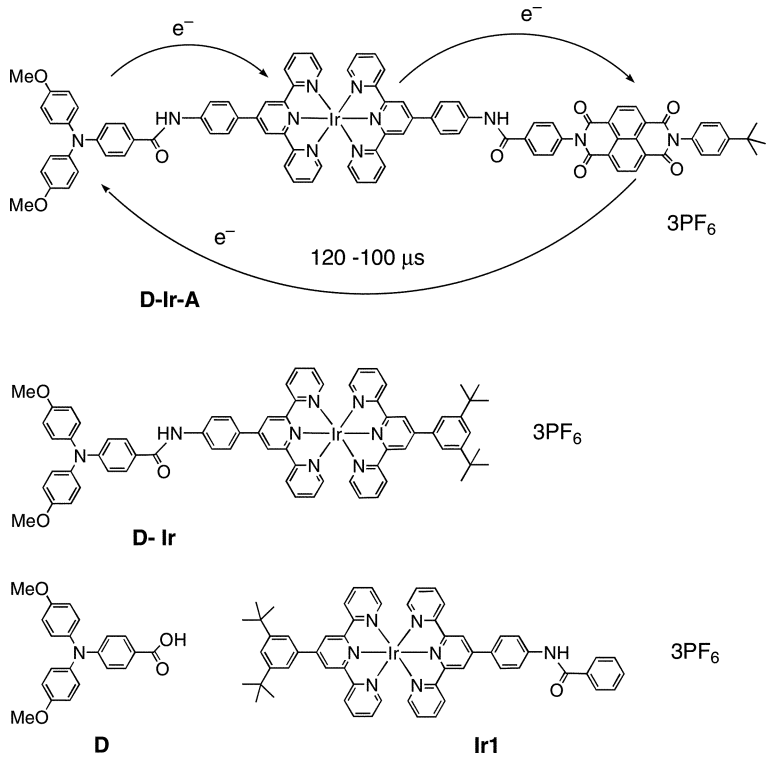


Scheme 1. Structures of the previously reported triad **D-Ir-A** and related models.

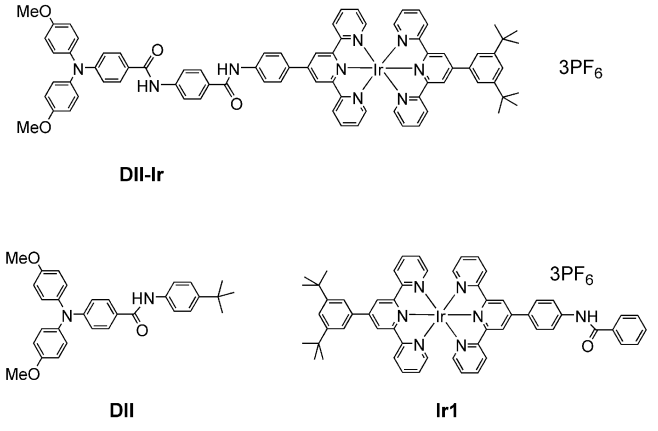


Scheme 2. Structures of the dyad **DII-Ir** and models reported in this work.

Decrease of both charge-separation ($^1$DII-Ir or DII-$^3$Ir $\rightarrow$ DII$^+$-Ir$^-$) and charge-recombination (DII$^+$-Ir$^-$ $\rightarrow$ D-Ir) rates are expected after increasing the D–Ir distance but, whereas a slight decrease in the 100% efficiency of the charge separation step can be afforded without being too detrimental to the overall CS process, a decrease in the rate of charge recombination in the dyad **DII-Ir** can have important effects on the overall charge separation over the extreme components in the derived triad DII-Ir-A. Since the synthesis of the latter requires a significant synthetic effort, we decided to verify first if the properties of the component dyad could suggest better performances for the derived triad, before undertaking the demanding synthesis of the more complex array. Therefore, the present report deals with the synthesis and photophysical properties of the dyad **DII-Ir** in order to evaluate its suitability for the construction of a triad DII-Ir-A with improved properties with respect to **D-Ir-A**.

## Results and Discussion

The systems studied in this work are the dyad **DII-Ir** and the pertinent models **DII** and **Ir1**, reported in Scheme 2. Whereas complex **Ir1** had been previously examined and its properties will be only briefly summarized, **DII** and **DII-Ir** will here be examined in detail, and their properties will be compared with those of the short counterparts **D** and **D-Ir** previously reported.[7,8] In the following discussion the terms Ir and DII (not bold) will be used to indicate the Ir metal complex (with model **Ir1**) and the donor units (with model **DII**), respectively, within the dyad.

### Synthesis

The dyad **DII-Ir** has been prepared according to the reactions shown in Scheme 3. The terpyridine **2** was prepared in two steps by homologation of the already known 4′-(4-aminophenyl)-2,2′:6′,2′′-terpyridine[9] with 4-nitrobenzoyl chloride and then by reduction of the nitro group with hydrazine in the presence of a catalytic amount of palladium on charcoal. The terpyridine **3**, bearing a triarylamine donor group linked to the terpy fragment by two amide brid-

 © 2007 Wiley-VCH Verlag GmbH & Co. KGaA, Weinheim 

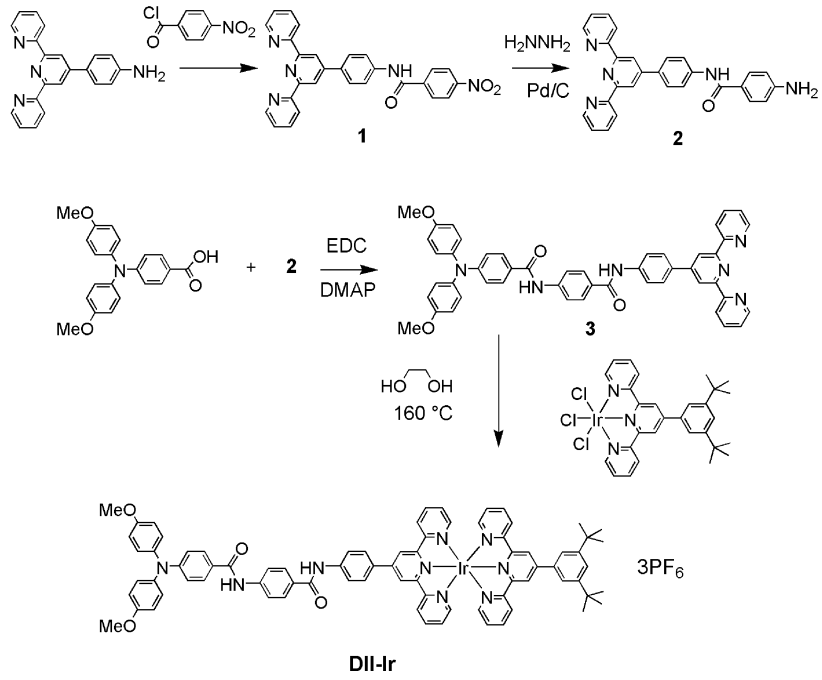


Scheme 3. Synthesis of the dyad **DII-Ir**.

ges, was prepared by condensation of the terpyridine **2** with 4-[bis(4-methoxyphenyl)amino]benzoic acid, in the presence of DMAP and EDC (peptidic coupling).[10] The dyad **DII-Ir** was obtained in 70% yield by reaction of the precursor [4′-(3,5-di-*tert*-butylphenyl)-2,2′:6′,2′′-terpyridine]-$IrCl_3$[5a] with the terpyridine **3** in ethylene glycol at 160 °C during 20 min.

## Electrochemistry

The redox characteristics of the reference compounds **Ir1** and **DII** as well as that of the dyad **DII-Ir** examined by cyclic voltammetry in $CH_3CN$ are reported with the values previously obtained for **D** and **D-Ir** in Table 1. One-electron reversible waves were observed for all the redox processes, in the dyad they were easily assigned to the corresponding individual components. A few mV of difference with respect to the short dyad **D-Ir** are observed in the redox couples of the donor group ($D^+$/D) and of the complex (terpy/terpy$^-$). Clearly, the presence of a second amide bridge in the dyad **DII-Ir** weakens even more the electronic coupling between the two redox entities.

Table 1. Cyclic voltammetry data of the reference compounds **Ir1**, **DII,** and the dyad **DII-Ir** in acetonitrile, 0.1 M $nBu_4NPF_6$, with SCE as a reference. Values for dyad **D-Ir** and model **D** are also reported.[7]

| | $E_{1/2}$ (V vs. SCE) | |
|---|---|---|
| | $D^+$/D | terpy/terpy$^-$ |
| **Ir1** | | –0.76 |
| **D** | 0.80 | |
| **D-Ir** | 0.75 | –0.75 |
| **DII** | 0.76 | |
| **DII-Ir** | 0.76 | –0.78 |

## Absorption Spectroscopy

The absorption spectra in acetonitrile of the components, their superposition, and the experimental spectrum of the array are reported in Figure 1. There is, within experimental errors, a good overlap of the experimental spectrum of **DII-Ir** with the calculated superposition of the model components in the 250–350 nm range, whereas the array spectrum differs slightly from the calculated one above 350 nm. In fact, it displays a slightly higher absorbance and a broadening on the low energy side. Quite remarkably, the broadening toward the low-energy range of the spectrum is less pronounced with respect to the short dyad **D-Ir**, characterized by an absorption extending over 500 nm, see inset of Figure 1. In order to understand this behavior we have to recall that, whereas in $(tpy)_2Ir^{3+}$-type complexes the low-energy absorption band is in general a predominantly LC transition, complexes of the $(tpy)_2Ir^{3+}$-type with benzamide sub-

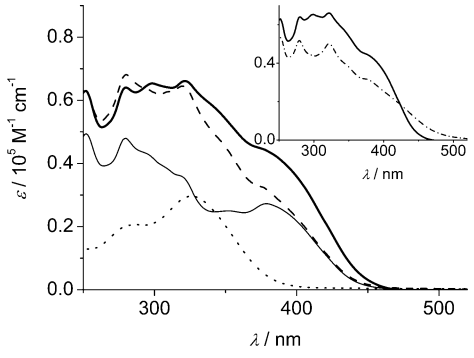


Figure 1. Absorption spectra of the model components and of the arrays. **Ir1** (thin line), **DII** (dotted line), **DII-Ir** (thick line), **Ir1 + DII** (dashed line). Inset: **DII-Ir** (thick line), **D-Ir** (dash-doted line).

 © 2007 Wiley-VCH Verlag GmbH & Co. KGaA, Weinheim 

stituents were recently demonstrated to exhibit photophysical properties at room temperature typical of a CT state, either of metal-to-ligand charge-transfer nature (MLCT) or of intraligand charge-transfer nature (ILCT).[5,11,12] The presence of an amine electron donor as a substituent can strongly enhance the ILCT nature of the transition, with the terpyridine acting as an electron acceptor and the amine as an electron donor, and further shift the absorbance to the red. From this point of view, interposition of a further amide spacer between the terpyridine acceptor and the aromatic amine donor has the effect of increasing the energy of the band, moving it further to the blue, as noticed in the inset of Figure 1 for **DII-Ir** compared to **D-Ir**.

If we ignore the small perturbation of the spectrum of the Ir unit discussed above, there is no evidence from the spectroscopic data of electronic interactions in the array with respect to the models, in agreement with the electrochemical data. This allows us to use a localized description of the individual subunits in the subsequent discussion of the photoinduced energy and electron-transfer reactions.

### Luminescence Spectroscopy

**DII** emits strongly, with a band maximum at 524 nm, slightly blueshifted with respect to the short analog **D** ($\lambda_{max}$ = 540 nm); **Ir1** emits moderately with a maximum at 570 nm (Table 2).

Table 2. Luminescence properties in air-equilibrated nitrile solvents. Acetonitrile at 295 K and butyronitrile at 77 K.

| | State | 295 K | | | 77 K | | |
|---|---|---|---|---|---|---|---|
| | | $\lambda_{max}$ [nm] | $\tau$ [ns] | $\Phi_{em}$ | $\lambda_{max}$ [nm] | $\tau$ [ns] | $E$ [eV] |
| **Ir1**[a,b] | $^3$Ir1 | 570 | 490 | $2.1\times10^{-3}$ | 510 | 80000 | 2.43 |
| **D**[b] | $^1$D | 540 | 0.450 | 0.012 | 422 | 2.6 | 2.93 |
| **D-Ir**[b] | D-$^3$Ir | | – | $\leq6\times10^{-5}$ | 515[d] | – | 2.40 |
| | $^1$D-Ir | | $<<$0.01 | $\leq6\times10^{-5}$ | – | – | |
| **DII**[c] | $^1$DII | 524 | 1.0 | 0.073 | 414 | 2.0 | 2.99 |
| **DII-Ir** | DII-$^3$Ir[a] | 570 | – | $6\times10^{-5}$ | 516 | | 2.40 |
| | $^1$DII-Ir[c] | | 0.01 | $5\times10^{-4}$ | 400[d] | | 3.10 |

[a] Excitation at 430 nm for steady state, for time-resolved determinations excitation at 373 nm. [b] From ref.[7] [c] Excitation at 330 nm for steady state, for time-resolved determinations excitation at 373 nm, 331 nm, or 355 nm. [d] Weak signal.

The luminescence spectra of the array **DII-Ir** at room temperature upon selective excitation of the Ir unit at 430 nm is compared to those of the model **Ir1** absorbing the same number of photons as the unit in the array (Figure 2, right panel). In the left panel of Figure 2 the luminescence detected in the dyad upon excitation at 330 nm, corresponding to excitation of both DII and Ir complex units (absorbing 50% each), is reported and compared to the luminescence from a solution of **DII** absorbing the same number of photons as the unit in the array. The emission of Ir and DII units in the dyad are nearly completely quenched, to ca. 3% and less than 1%, respectively, indicating the occurrence of an efficient quenching process involving both $^3$Ir and $^1$DII. It should be noticed that the weak residual luminescence in **DII-Ir** could be due to some very minor, unbound component in the dyad and not to a genuine quenched unit in the array; the definitive answer on the effective quenching of the component in the dyad can only be provided by the time-resolved experiments, discussed below.

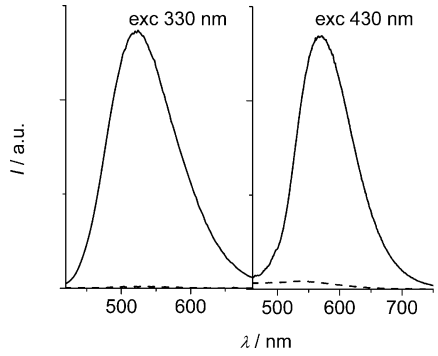


Figure 2. Room-temperature luminescence spectra in acetonitrile. Left panel: excitation at 330 nm, 50% excitation of DII and Ir components, **DII** (solid line) $A$ = 0.056, **DII-Ir** (dashed line) $A$ = 0.12. Right panel: selective excitation at 430 nm of Ir component, **Ir1** (solid line), $A$ = 0.13, **DII-Ir** (dashed line) $A$ = 0.13. The absorbance of the solutions is arranged to provide the absorption of the same number of photons in the model and in the corresponding unit in the array.

Luminescence spectra of the models **Ir1** and **DII** at 77 K in a glassy butyronitrile matrix display emission maxima at 414 and at 510 nm, respectively, with a remarkable hypsochromic shift from fluid (295 K) to rigid (77 K) solvent (see Table 2). This can be explained by a strong CT character for the $^1$DII emitting excited state which is less stabilized in a rigid medium; in the case of **Ir1**, a change in the spectral profile is also detected (compare Figures 2 and 3), indicative of a switching of the excited-state nature from a room-temperature CT to a predominantly ligand-centered state in the glass, as previously discussed.[11]

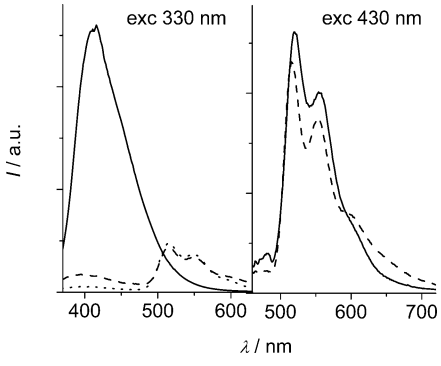


Figure 3. Luminescence spectra in butyronitrile at 77 K. Left panel: excitation at 330 nm, 50% excitation of DII and Ir components, **DII** (solid line) $A$ = 0.1, **Ir1** (dotted line) $A$ = 0.1, **DII-Ir** (dashed line) $A$ = 0.2. Right panel: selective excitation at 430 nm of Ir component, **Ir1** (solid line) $A$ = 0.08, **DII-Ir** (dashed line) $A$ = 0.08. The absorbance of the solutions is arranged to provide the absorption of the same number of photons in the model and in the corresponding unit in the array.

 © 2007 Wiley-VCH Verlag GmbH & Co. KGaA, Weinheim 

Luminescence experiments on the models and **DII-Ir** in butyronitrile glass at 77 K show that nearly no quenching of the Ir unit occurs at 77 K, whereas the DII unit is still strongly quenched also at 77 K, as evidenced in Figure 3 which compares the luminescence from **DII** and **Ir1** solutions to that from **DII-Ir** after selective excitation of the Ir complex unit at 430 nm in the right panel, or of the DII and Ir components (absorbing 50% each) at 330 nm in the left panel. With respect to the results previously reported for the short corresponding dyad **D-Ir** both at room temperature and at 77 K, in **DII-Ir** the luminescence quenching is less effective. This is in agreement with a slower electron transfer over the longer bridge connecting the donor to the Ir complex.

The luminescence lifetimes of the model **Ir1** in air-equilibrated acetonitrile solution determined by a single photon nanosecond apparatus, is 490 ns.[7] Any attempt to determine the lifetime of the Ir unit in the dyad was unsuccessful at room temperature, neither a single-photon counting technique with 0.3 ns resolution, nor a streak-camera detection with 10 ps resolution allowed any emission to be registered. Given the very low radiative rate constant of the Ir complex, $k_r \approx 5 \times 10^3$ s$^{-1}$ ($k_r = \phi/\tau$), a technique like the single-shot streak camera is not convenient for detecting such low emissions, therefore we cannot exclude for the $^3$Ir component in **DII-Ir** a lifetime shorter than 0.3 ns. Only the time-resolved absorption data discussed below will clear this point. The strong emission of **DII** was time-resolved by a picosecond streak camera after excitation at 355 nm and displays a lifetime of 1.0 ns. This luminescence is quenched in **DII-Ir** and displays a time profile very similar to the instrumental response (Figure 4) from which a lifetime of ca. 10 ps can be calculated by deconvolution with the instrumental profile. This value is in reasonable agreement with steady-state data, which indicates a reduction in the emission yield of the order of 1% in passing from the **DII** model to the dyad **DII-Ir**. In the case of the short dyad **D-Ir**, no luminescence could be detected from the D component, confirming a more efficient quenching due to electron transfer responsible for charge separation and allowing us to set an upper limit to the lifetime of $\tau << 10$ ps.

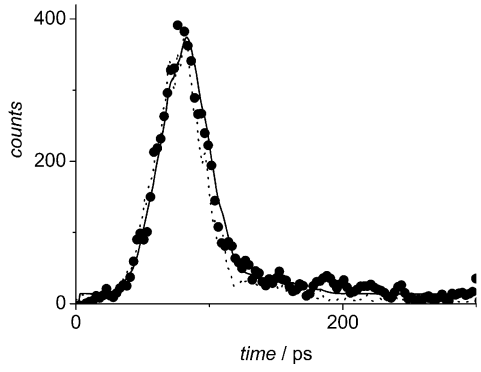


Figure 4. Luminescence registered at 520 nm from **DII-Ir** acetonitrile solution after excitation with a laser pulse (35 ps, 355 nm, 1 mJ) (full circles) with the instrumental pulse profile (dotted line) and the fitting (solid line).

Time-resolved experiments at 77 K in butyronitrile glass allowed the following parameters to be measured. The lifetime of the models **D** and **DII** are 2.6 and 2 ns, respectively, showing a slight temperature dependence. On the contrary, the lifetime of **Ir1** at 77 K is 80 μs, much longer than at room-temperature (Table 2). This has to be assigned to a switch in the nature of the excited state when the medium becomes rigid from $^3$CT, very likely of intra-ligand charge-transfer nature, to a $^3$LC, as already discussed above. In the dyad **DII-Ir**, the lifetime of Ir measured with a time-correlated single photon apparatus is 56 μs compared to the 80 μs of the model, confirming a very modest quenching in agreement with steady-state experiments. The DII unit decay in the dyad **DII-Ir** at 77 K was still extremely fast and of the same order as the exciting profile; an accurate determination of the lifetime was precluded by the strong light scattering in the glass. From the short counterpart **D-Ir** no luminescence could be detected similarly to what occurs at room temperature.

## Transient Absorption Spectroscopy

Valuable information on the products of electron transfer can be gained by transient absorption techniques. The chemically generated cation DII$^+$ (see Exp. Sect. for details) has a peak at 760 nm ($\varepsilon \approx 27400$) and a minor broad band at 590 nm, in agreement with previous reports.[13] It should be noted that at the excitation wavelength, 355 nm, both units of the **DII-Ir** dyad absorb light with the following probability (see Figure 1): 60% for Ir, 40% for D.

The end of pulse transient absorption spectra detected with picosecond resolution of optically matched solutions of the models and **DII-Ir** are reported in Figure 5. **Ir1** displays a strong absorption band with a broad maximum around 780 nm assigned to $^3$Ir1, stable on the 3 ns window of the experiment. **DII** displays a sharp band at 750 nm with a lifetime of ca. 900 ps, in reasonable agreement with the luminescence lifetime of 1.0 ns, indicating that the detected species is the singlet excited state $^1$DII.[14] The time-resolved spectrum of **DII-Ir** has a maximum at 765 nm which, for similarity with the spectrum of D$^+$-Ir$^-$ ($\lambda_{max}$ = 765 nm) and with the chemically generated spectrum of DII$^+$, is assigned to the CS state DII$^+$-Ir$^-$. No trace of the spectral features of DII, which has in fact been shown by luminescence experiments to decay with a lifetime of 10 ps, i.e. during the laser pulse, is detected. Similarly, no absorbance ascribable to $^3$Ir, which would be easily identifiable because of its broad and intense spectrum, appears at the end of the pulse. This set up the unsolved problem of the lifetime of DII-$^3$Ir species, which could not be unambiguously determined by luminescence techniques (see above). By transient absorbance experiments we can set an upper limit of 20 ps for the lifetime of DII-$^3$Ir, a longer lifetime of this species would in fact cause the appearance in the spectrum registered at the end of the pulse of the typical features of the $^3$Ir absorbance (see Figure 5) which are, on the contrary, absent. The time evolution of the spectrum, re-

 © 2007 Wiley-VCH Verlag GmbH & Co. KGaA, Weinheim 

ported in Figure 6 with the extracted time profile, allows us to derive a lifetime of the CS state of 210 ps. The absorbance decays to the baseline without leaving any residual absorbance in the longer timescale, as confirmed by nanosecond flash-photolysis experiments on **DII-Ir**. No residual absorbance in the nanosecond time scale can be detected for **DII** either, on the contrary nanosecond flash-photolysis experiments allow us to detect in **Ir1** solutions the full evolution of the $^3$Ir1 species in air-equilibrated samples which has a lifetime of 440 ns, in good agreement with the luminescence lifetime.

The singlet excited state $^1$D derived from the component **D** displayed an identical absorption spectrum but a shorter lifetime of 490 ps and, as far as the CS state is concerned, DII$^+$-Ir$^-$ has a nearly identical spectrum but a much longer lifetime than D$^+$-Ir$^-$ (70 ps).

The transient absorbance data for the models, **D-Ir** and **DII-Ir** are collected in Table 3.

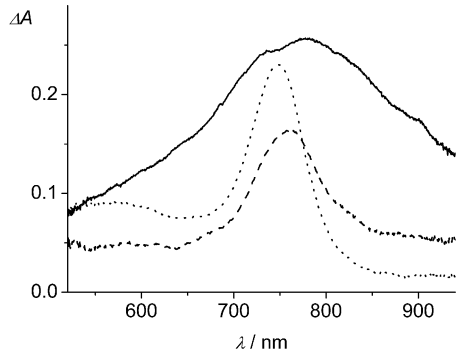


Figure 5. End of pulse absorption spectra of **Ir1** (solid line), **DII** (dotted line), and **DII-Ir** (dashed line) in acetonitrile solutions upon excitation at 355 nm (2.8 mJ/pulse, 35 ps pulse). All solutions had $A$ = 0.51 at the exciting wavelength.

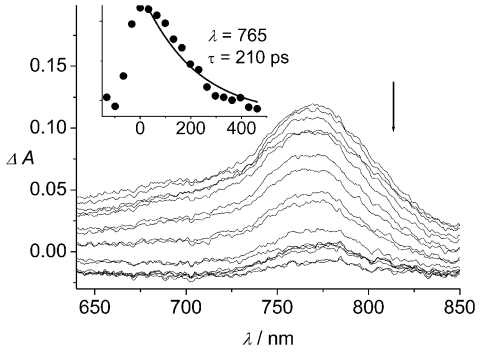


Figure 6. Time evolution of the transient spectrum of **DII-Ir** in acetonitrile (2.5 mJ, $A$ = 0.5); spectra taken with delays of 165 ps. In the inset, the time evolution of the absorbance at 765 nm and exponential fitting are shown.

Table 3. Transient absorption data at room temperature (excitation at 355 nm) in air-equilibrated acetonitrile solutions of **DII-Ir**, **D-Ir**, and models.

| | State | $\lambda_{max}$ [nm] | $\tau$ [ns] |
|---|---|---|---|
| **Ir1**[a] | $^3$Ir1 | 780 | 440 |
| **D**[a] | $^1$D | 750 | 0.49 |
| **D-Ir**[a] | D-$^3$Ir | – | <0.02 |
| | $^1$D-Ir | – | <0.02 |
| | D$^+$-Ir$^-$ | 765 | 0.070 |
| **DII** | $^1$DII$^c$ | 750 | 0.90 |
| **DII-Ir** | DII-$^3$Ir | – | <0.02 |
| | $^1$DII-Ir | | <0.02 |
| | DII$^+$-Ir$^-$ | 765 | 0.210 |

[a] From ref.[7]

## Photoinduced Processes

Scheme 4 shows the energy level diagrams of the present **DII-Ir** dyad and of the corresponding short dyad **D-Ir** [7] and can help to discuss and compare the processes in the two cases.

These diagrams can be drawn from the luminescence data collected in Table 2 and from the electrochemical data reported in Table 1. The excited-state energies are derived from the maxima of the emission at 77 K (Table 2), whereas the charge-separated state energy levels are calculated by simply adding the energy necessary to oxidize the potential donor and the energy necessary to reduce the potential acceptor in acetonitrile (Table 1) without further corrections.

Both dyads are made of an easy to oxidize D or DII component ($E_{1/2}$ = +0.75 V and $E_{1/2}$ = +0.76 V in the pertinent dyads, respectively) and of the iridium complex which can be reduced at low potentials ($E_{1/2}$ = –0.75 V in the short and $E_{1/2}$ = –0.78 V in the long dyad) yielding charge-separated states D$^+$-Ir$^-$ or DII$^+$-Ir$^-$ with an energy of 1.51 and 1.54 eV, respectively (Table 1). These are characterized by an extra electron localized on the metal complex, most probably on the ligand, and a hole on the triphenylamine donor. Charge separation is feasible both from the excited donor, $^1$DII-Ir ($^1$D-Ir) and from the excited acceptor DII-$^3$Ir (D-$^3$Ir) but the excited state quenching mechanism in the two cases will be different. When Ir is excited, a reductive quenching of its excited state will occur, i.e. the electron will move from the HOMO localized on the donor to the HOMO localized on the Ir complex, with $\Delta G^0$ = –0.9 and –0.86 eV for **D-Ir** and **DII-Ir**, respectively. When the donor is excited, an electron will move from the LUMO localized on DII to the LUMO on the Ir complex acceptor, with $\Delta G^0$ = –1.43 eV for **D-Ir** and $\Delta G^0$ = –1.56 eV for **DII-Ir**. Both types of electron transfer take place at room temperature, as testified by the quenching of the luminescent states localized on both units as shown in Figures 2 and 4.

We cannot exclude the possibility of an energy transfer from $^1$DII-Ir to DII-$^3$Ir, which is spin-forbidden but could be made possible by the strong spin-orbit coupling induced by the heavy Ir ion. The overall result would be undistinguishable from a direct electron transfer from the excited state localized on the donor; however, the 77 K experiment seems to indicate that such an energy transfer (expected to be little affected by temperature) does not take place. In the latter case in fact we would expect a sensitization of the Ir luminescence upon excitation of the DII unit at 330 nm,

 © 2007 Wiley-VCH Verlag GmbH & Co. KGaA, Weinheim 

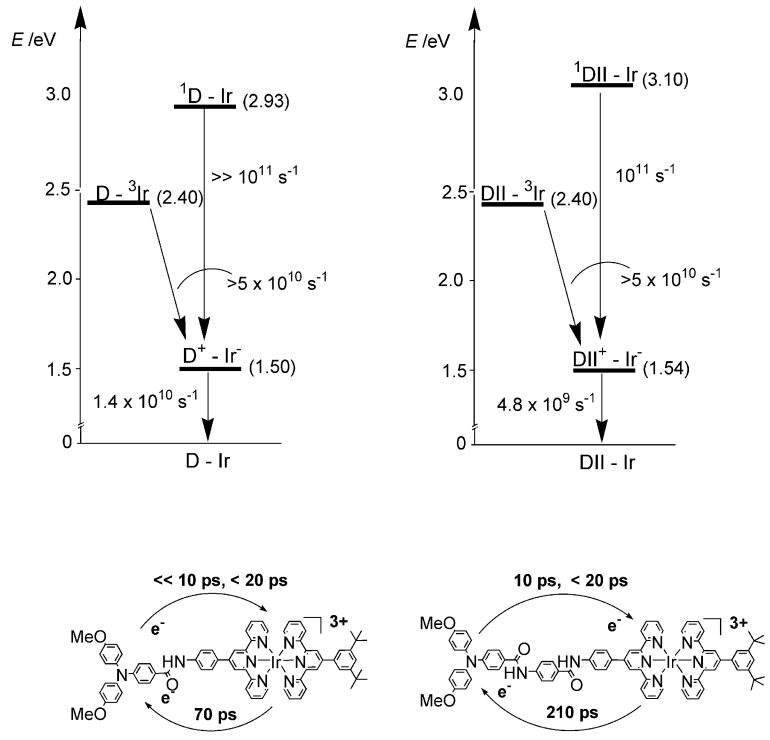


Scheme 4. Energy-level diagrams and schematic representation of the processes for **D-Ir** and **DII-Ir**.

which does not occur (see Figure 3). Therefore, the following discussion will not take the spin-forbidden energy transfer process into account.

Whereas we could measure the reaction rate of $^1$DII-Ir → DII$^+$-Ir$^-$, $k_{cs} = 10^{11}$ s$^{-1}$, corresponding to the lifetime of 10 ps, for the DII-$^3$Ir → DII$^+$-Ir$^-$ reaction we could only set a lower limit, $k_{cs} > 5 \times 10^{10}$ s$^{-1}$, based on the results of the transient absorbance (see above). In the short dyad **D-Ir**, similar results were obtained for the D-$^3$Ir → D$^+$-Ir$^-$ reaction, for which an identical lower limit of the rate constant $k_{cs} > 5 \times 10^{10}$ s$^{-1}$, corresponding to the time resolution of the transient absorbance experiment, was set. For the $^1$D-Ir → D$^+$-Ir$^-$ step, the improved time resolution of the apparatus with respect to previously reported data ($k_{cs} > 5 \times 10^{10}$ s$^{-1}$)[15] allowed us to set a limit of $k_{cs} > 10^{11}$ s$^{-1}$. The driving force of the charge-separation reactions are not very different in going from the short to the long dyad, but the distance between the donor and acceptor changes remarkably, from 1.65 to 2.3 nm. Therefore, a slower charge separation step $^1$DII-Ir → DII$^+$-Ir$^-$ compared to $^1$D-Ir → D$^+$-Ir$^-$ can be measured. On the contrary, for the charge separation starting from the excited state of the Ir metal complex, either DII-$^3$Ir → DII$^+$-Ir$^-$ or D-$^3$Ir → D$^+$-Ir$^-$, it is difficult to make comparisons since the same lower limit for the rate constant has been determined. Overall, a slight decrease in the rate of charge separation can be registered in **DII-Ir** compared to **D-Ir**; however, the yield of charge separation – $\phi_{cs} = k_{cs}/\Sigma k = k_{cs}/(k_{cs} + 1/\tau_0)$, where $\tau_0$ is the lifetime of the excited state in the models – is still of the order of 99% when starting from $^1$DII-Ir ($\tau_0$ = 1 ns) and nearly 100% when starting from DII-$^3$Ir ($\tau_0$ = 490 ns in air). Thus, the insertion of a further benzamide group between the donor and acceptor is not too detrimental to the charge-separation process at room temperature. This is different at 77 K, where the absence of quenching of the Ir component and the persistence of the quenching of the D unit in the dyad at 77 K indicate that electron transfer from DII-$^3$Ir is inefficient and only electron transfer from $^1$DII-Ir continues to be operative with a still remarkable rate of the order of 20 ps (Figure 3 and Table 2). This can be understood if one considers that the rigidity of the medium, preventing solvent molecule reorganization around the CS state, destabilizes the CS level by a value which can be quite high[16] and decreases the driving force for electron-transfer reactions originating from the DII-$^3$Ir and the $^1$DII-Ir states. Under these conditions, the lowest-lying DII-$^3$Ir (ca. 2.4 eV) is unable to transfer an electron, whereas the higher $^1$DII-Ir (ca. 3 eV) has sufficient driving force to transfer the electron also in rigid media at 77 K.

Once the charge-separated state DII$^+$-Ir$^-$ is formed, it decays to the ground state with a lifetime of 210 ps, three-times shorter than D$^+$-Ir$^-$ which has a lifetime of 70 ps. The driving force of the charge-recombination reaction is high, leading us to assume a Marcus-inverted behavior, i.e. the rate slows as the driving force increases.[17] The driving force is slightly higher for **DII-Ir** compared to **D-Ir** ($\Delta G^0$ = –1.54 eV for the long dyad against $\Delta G^0$ = –1.50 eV), but most importantly the insertion of a further benzamide group is effective in electronically decoupling the donor and acceptor units in the long dyad and decreases the charge-recombination rate. The increase from 70 to 210 ps lifetime in passing from **D-Ir** to the long **DII-Ir** dyad, suggests that

 © 2007 Wiley-VCH Verlag GmbH & Co. KGaA, Weinheim 

a newly synthesized long triad DII-Ir-A could be more efficient in producing charge separation over the terminal components. In the **D-Ir-A** triad, as discussed above, the poor efficiency of charge separation was due to the fast step ($k = 1.4 \times 10^{10}\ s^{-1}$) preferably leading $D^+$-$Ir^-$-A to the ground state rather than to the fully CS state $D^+$-Ir-$A^-$ by a further electron transfer step ($k = 2.4 \times 10^9\ s^{-1}$). The decrease of the charge recombination step in $DII^+$-$Ir^-$-A ($k = 4.8 \times 10^9\ s^{-1}$), assuming that the rest of the triad is unchanged with respect to the previously studied **D-Ir-A** triad, would allow us to reach an efficiency of charge separation of the order of 30%. This would be a noticeable improvement with respect to the yield of ca. 10% achieved in the short triad **D-Ir-A** and, if we consider that due to the increased donor–acceptor distance an even longer lifetime of the final CS would be expected in a long triad DII-Ir-A, the demanding synthesis of this structure could be undertaken with some degree of confidence in satisfactory performances.

## Conclusions

We have synthesized a new dyad **DII-Ir** made of a triphenylamine donor and of a bis(terpyridine)$Ir^{III}$ acceptor separated by a bridge composed of two benzamide groups, and we have studied the photoinduced processes. The properties of the dyad have been compared to those of a corresponding dyad **D-Ir** characterized by a bridge connecting the donor and the acceptor consisting of a single benzamide unit. We showed that, whereas the charge-separation steps are still very efficient in the long dyad (≥99%), *charge recombination is slowed by a factor of three with respect to the short dyad*. This is promising and encourages the use of this dyad in the assembly of the more elaborate array DII-Ir-A. This would simply have a further benzamide unit in the spacer connecting DII to Ir, with respect to the already studied **D-Ir-A** triad of Scheme 1 for which an unsatisfactory yield of ca. 10% of charge separation was reported. In the long triad DII-Ir-A, a lifetime of the CS state $DII^+$-$Ir^-$-A of the order of 210 ps would be expected, similar to the dyad studied here. This would decrease the competition of the recombination to the ground state with respect to the further electron-transfer step leading to full charge separation over the extreme components with an efficiency of the order of 30% with respect to the ca. 10% of the previously studied **D-Ir-A** triad. It should also be stressed that, due to the increased D–A distance, an even longer lifetime of the final CS state, with respect to the 120 μs of the short **D-Ir-A** triad, is expected.

## Experimental Section

**General:** $^1H$ NMR spectra were acquired either with a Bruker WP 200 SY, a Bruker AC300, or a Bruker AM 400 spectrometer, using the deuterated solvent as the lock and residual solvent as the internal reference ($CD_3CN$: δ = 1.96 ppm; [$D_6$]DMSO: δ = 2.52 ppm). Electron spray ionization mass spectra (ESI-MS) were recorded with a Bruker MicroTOF instrument. Cyclic voltammetry experiments were performed using an EG&G 273A potentiostat, a Pt working electrode, a Pt counter-electrode, a KCl-saturated calomel electrode (SCE) as a reference, and 0.1 M $nBu_4NPF_6$ in $CH_3CN$ as the supporting electrolyte. The typical sweep rate was 100 mV/s.

**Starting Compounds:** [4′-(3,5-Di-*tert*-butylphenyl)-2,2′:6′,2′′-terpyridine]$IrCl_3$,[5a] tpy-ph-$NH_2$,[9] 4-[bis(4-methoxyphenyl)amino]benzoic acid, **DII** and **Ir1**[7] were prepared according to the published procedures.

**1:** terpy-ph-$NH_2$ (500 mg, 1.54 mmol) was dissolved in dimethylacetamide (8 mL), after which some pyridine (2 mL) was added. Upon addition of *p*-nitrobenzoyl chloride (410 mg, 2.2 mmol, excess), the color of the solution immediately turned from pale yellow to deep yellow. After stirring at room temperature for 28 h, the reaction mixture was added dropwise to cold $Et_2O$ and was placed in the freezer for 30 min to induce precipitation. The dark yellow precipitate of **1** was filtered off and dried under vacuum. Yield: 95% (700 mg). $C_{28}H_{19}N_5O_3$ (473.48): calcd. C 71.03, H 4.04, N 14.79; found C 71.45, H 4.03, N 14.47. $^1H$ NMR ([$D_6$]DMSO, 200 MHz): δ = 10.87 (s, 1 H, NH), 8.86–8.83 (m, 6 H, 6-H, 3-H, 3′-H, 5′-H), 8.44–8.08 (m, 10 H, o1-H, m1-H, o2-H, m2-H, 4-H), 7.72–7.65 (m, 2 H, 5-H) ppm. $^{13}C$ NMR ([$D_6$]DMSO, 75 MHz): δ = 164.1, 153.5, 152.6, 149.6, 149.3, 147.6, 147.5, 140.5, 140.3, 132.0, 129.4, 127.7, 125.6, 123.6, 122.4, 120.9, 118.9 ppm. ES-MS: *m*/*z* (calcd.) = 474.16 (474.15) $[M + H]^+$.

**2:** Compound **1** (230 mg; 0.49 mmol) was suspended in refluxing MeOH/THF (1:1, v/v; 100 mL). Pd/C 5% (108 mg) was added as a solid, and a mixture of hydrazine monohydrate (0.5 mL) in MeOH (5 mL) was added dropwise over a period of 10 min. After the addition, the colorless solution was refluxed for 40 min, cooled to room temperature, filtered through Celite, and concentrated. After one night in the refridgerator, the precipitate was filtered off and washed with water, MeOH, and $Et_2O$. Compound **2** was obtained as a colorless solid. Yield: 97% (210 mg). $C_{28}H_{21}N_5O$ (443.50): calcd. C 75.83, H 4.77, N 15.79; found C 74.14, H 4.63, N 15.20. $^1H$ NMR ([$D_6$]DMSO, 200 MHz): δ = 10.02 (s, 1 H, NH), 8.79 (dd, $^4J$ = 4.7, $^5J$ = 0.8 Hz, 2 H, 6-H), 8.75 (s, 2 H, 3′-H, 5′-H), 8.70 (d, $^3J$ = 7.9 Hz, 2 H, 3-H), 8.06 (m, 2 H, 4-H), 8.00 (m, 2 H, o1-H, m1-H), 7.79 (d, $^3J$ = 8.6 Hz, 2 H, o2-H), 7.55 (ddd, $^3J$ = 7.5, $^4J$ = 4.7, $^5J$ = 1.0 Hz, 2 H, 5-H), 6.64 (d, $^3J$ = 8.6 Hz, 2 H, m2-H) ppm. $^{13}C$ NMR ([$D_6$]DMSO, 75 MHz): δ = 161.5, 152.0, 151.5, 148.8, 145.7, 145.4, 137.7, 133.8, 127.8, 125.9, 123.5, 120.9, 117.3, 117.2, 116.9, 113.7, 108.9 ppm. ES-MS: *m*/*z* (calcd.) = 444.18 (443.17) $[M + H]^+$.

**3:** DMAP (470 mg, 3.64 mmol, 3.3 equiv.) and EDC (420 mg, 2.20 mmol, 1.9 equiv.) were added to a solution of 4-[bis(4-methoxyphenyl)amino]benzoic acid (634 mg, 1.81 mmol, 1.5 equiv.) in freshly distilled $CH_2Cl_2$ (6 mL). After a few minutes of stirring, the solution was deep yellow. **2** (500 mg, 1.13 mmol) and DMF (1 mL) were added, and the reaction mixture was stirred under argon at 40 °C for 10 h. $CH_2Cl_2$ was removed under reduced pressure. Water and saturated $NaHCO_3$ solution (25 mL each) were added resulting in a pale yellow precipitate which was filtered off and washed with $NaHCO_3$ solution, water and then with a mixture of $CH_2Cl_2$/$Et_2O$ (1:1, v/v) to afford **3** as a pale yellow solid in 71% yield (626 mg, 0.81 mmol). $C_{49}H_{38}N_6O_4$ (774.86): calcd. C 75.95, H 4.94, N 10.85; found C 74.97, H 4.76, N 10.46. $^1H$ NMR ([$D_6$]DMSO, 300 MHz): δ = 10.37 (s, 1 H, NH), 10.23 (s, 1 H, NH), 8.78 (d, $^3J$ = 4.1 Hz, 2 H, 6-H), 8.70 (s, 2 H, 3′-H, 5′-H), 8.68 (d, $^3J$ = 7.9 Hz, 2 H, 3-H), 8.08–8.94 (m, 10 H, 4-H, o3-H, m3-H, o4-H, m4-H), 7.82 (d, $^3J$ = 8.9 Hz, 2 H, o5-H), 7.54 (ddd, $^3J$ = 7.5, $^3J$ = 4.9, $^4J$ = 1.1 Hz, 2 H, 5-H), 7.14 (d, $^3J$ = 9.0 Hz, 4 H, a-H), 6.98 (d, $^3J$ = 9.0 Hz, 4 H, b-

 © 2007 Wiley-VCH Verlag GmbH & Co. KGaA, Weinheim 

H), 6.74 (d, $^3J$ = 8.9 Hz, 2 H, m5-H), 3.77 (s, 6 H, $CH_3$) ppm. ES-MS: *m*/*z* (calcd.) = 775.31 (775.30) $[M + H]^+$.

**DII-Ir:** A suspension of [4′-(3,5-di-*tert*-butylphenyl)-2,2′:6′,2′′-terpyridine]$IrCl_3$ (48 mg, 0.067 mmol) and **3** (51 mg, 0.066 mmol) in ethylene glycol (15 mL) was homogenized under ultrasound during 25 min, then heated at 160 °C during 20 min under argon. The crude product was precipitated with a saturated solution of $KPF_6$, filtered off, and purified on silica ($CH_3CN/H_2O/KNO_3$, 100:0:0 to 100:7:0.7). After anion exchange, **DII-Ir** was obtained as a yellow solid. Yield: 70% (85 mg). $^1$H NMR ($CD_3CN$, 400 MHz): $\delta$ = 9.15 (s, 1 H, 1-NH), 9.10 (s, 2 H, 3′-D, 5′-D), 9.04 (s, 2 H, 3′-H, 5′-H), 8.82 (s, 1 H, 2-NH), 8.78 (dd, $^3J$ = 8.2, $^4J$ = 0.7 Hz, 2 H, 3-H), 8.73 (dd, $^3J$ = 8.2, $^4J$ = 0.7 Hz, 2 H, 3-D), 8.29–8.22 (m, 6 H, 4-H, 4-D, o3-H), 8.19 (d, $^3J$ = 8.9 Hz, 2 H, m3-H), 8.02 (d, $^3J$ = 8.8 Hz, 2 H, o4-H), 7.99 (d, $^4J$ = 1.7 Hz, 2 H, o-H), 7.90 (d, $^3J$ = 8.8 Hz, 2 H, m4-H), 7.87 (t, $^4J$ = 1.7 Hz, 1 H, p-H), 7.77–7.69 (m, 6 H, o5-H, 6-H, 6-D), 7.52–7.47 (m, 4 H, 5-H, 5-D), 7.17 (d, $^3J$ = 8.9 Hz, 4 H, a-H), 6.96 (d, $^3J$ = 8.9 Hz, 4 H, b-H), 6.7 (d, $^3J$ = 8.9 Hz, 2 H, m5-H), 3.80 (s, 6 H, $CH_3$), 1.52 (s, 18 H, *t*Bu) ppm. HR ES-MS: *m*/*z* (calcd.) = 1678.4467 (1678.4387) $[M - PF_6]^+$.

The **DII$^+$** species was generated by the addition of one drop of $Br_2$ to a solution of **DII** ($2.5 \times 10^{-4}$ M, 2 mm optical path) in acetonitrile, the calculated molar absorption coefficient assuming complete conversion of the starting **DII** was $\varepsilon$ = 27400 $M^{-1}cm^{-1}$ at 760 nm.

For the photophysical experiments, the solvents were spectrophotometric-grade acetonitrile at 295 K and butyronitrile at 77 K. If not otherwise specified, solutions were at ambient temperature and air-equilibrated. Standard 10 mm fluorescence cells were used at 295 K whereas experiments at 77 K made use of capillary tubes in a home-made quartz Dewar filled with liquid nitrogen. Because of geometrical irradiation conditions at 77 K the absolute quantum yield could not be determined, but the relative emission yields could be derived with some confidence. When necessary, solutions were bubbled for 10 min with a stream of argon in home-modified 10 mm fluorescence cells. A Perkin–Elmer Lambda 9 UV/Vis spectrophotometer and a Spex Fluorolog II spectrofluorimeter were used to acquire absorption and emission spectra. Emission quantum yields were determined after correction for the photomultiplier response, with reference to air-equilibrated (3,5-di-*tert*-butylphenyl-2,2′;6′,2′′-terpyridine)$_2$Ir$^{III}$$(PF_6)_3$ with $\phi_{em}$ = 0.022 in air-saturated acetonitrile.[5a] Luminescence lifetimes ($\tau$) were obtained with IBH single-photon counting equipment upon excitation at 373 and 331 nm from a pulsed diode source or with an apparatus based on an Nd:YAG laser (35 ps pulse duration, 355 nm, 0.5 mJ) and a Streak Camera with an overall resolution of 10 ps.[18] Transient absorbance in the picosecond range made use of a pump and probe system based on an Nd-YAG laser (Continuum PY62/10, 35 ps pulse). The third harmonic (355 nm) at a frequency of 10 Hz and an energy of ca. 3 mJ/pulse was used to excite the samples whose absorbance at the excitation wavelength was ca. 0.6. The residual 1064 nm light (ca. 40 mJ) was focused on a stirred 10 cm cell containing a mixture of $D_2O/D_3PO_4$ to produce a white light continuum which was used as analyzing light. A computer-controlled optical delay stage (Ealing) on the path of the excitation beam provided a delay between excitation and analysis. The analyzing light was split into two parts probing irradiated and un-irradiated portions, respectively, of the sample and crossed the sample cell in a nearly collinear geometry with respect to the excitation beam. The transmitted probes were fed through optical fibers into a spectrograph (Spectrapro 275, Acton) and were detected in two separate regions of a CCD detector (Princeton Instruments). The control units for the delay line, for the spectrograph and for the CCD detector were driven by customized software (Eurins) which also allowed us to acquire spectra at increasing time delays between the pump and the probe. Typically, 200–500 laser shots were collected and averaged to obtain a single spectrum at a specific time delay. Kinetic analyses were made by selecting the absorbance values of successive time-resolved spectra at the selected wavelength and by applying standard iterative procedures. More details can be found elsewhere.[19]

Nanosecond laser flash photolysis experiments were performed by a system based on an Nd-YAG laser (JK Lasers, 355 nm, 1.5–8.5 mJ, 18 ns pulse) previously described using a right-angle analysis on the excited sample.[20] Experimental uncertainties are estimated to be within 10% for lifetime determination involving simple exponential, 20% for lifetime determinations involving multiple exponentials or more complex kinetics, 15% for quantum yields, 20% for molar absorption coefficients and 3 nm for emission and absorption peaks. Molecular dimensions were estimated after MM2 energy minimization from CS Chem3D Ultra software.

**Supporting Information** (see footnote on the first page of this article): Atom numbering scheme for compounds **1**, **2**, **3**, and **DII-Ir**.

## Acknowledgments

We thank Consiglio Nazionale delle Ricerche of Italy (PM-P04-010, MACOL), Centre National de la Recherche Scientifique (France), Ministero dell'Istruzione, dell'Universita' e della Ricerca of Italy, and COST D31 for financial support.

[1] a) D. Gust, T. A. Moore, A. L. Moore, A. N. Macpherson, A. Lopez, J. M. DeGraziano, I. Gouni, E. Bittersman, G. R. Seely, F. Gao, R. A. Nieman, X. C. Ma, L. J. Demanche, S.-C. Hung, D. K. Luttrull, S.-J. Lee, P. K. Kerrigan, *J. Am. Chem. Soc.* **1993**, *115*, 11141–11152; b) K. A. Joliffe, T. D. Bell, K. P. Ghiggino, S. J. Langford, M. N. Paddon-Row, *Angew. Chem.* **1998**, *110*, 960–963; *Angew. Chem. Int. Ed. Engl.* **1998**, *37*, 916–919; c) H. Imahori, D. M. Guldi, K. Tamaki, Y. Yoshida, C. Luo, Y. Sakata, S. Fukuzumi, *J. Am. Chem. Soc.* **2001**, *123*, 6617–6628; d) H. Imahori, Y. Sekiguchi, Y. Kashiwagi, T. Sato, Y. Araki, O. Ito, H. Yamada, S. Fukuzumi, *Chem. Eur. J.* **2004**, *10*, 3184–3196.

[2] a) T. J. Meyer, *Acc. Chem. Res.* **1989**, *22*, 163–170; b) J. H. Alstrum-Acevedo, M. K. Brennaman, T. J. Mayer, *Inorg. Chem.* **2005**, *44*, 6802–6827; c) L. De Cola, V. Balzani, F. Barigelletti, L. Flamigni, P. Belser, A. von Zelewsky, M. Frank, F. Vogtle, *Inorg. Chem.* **1993**, *32*, 5228–5238; d) I. M. Dixon, J.-P. Collin, J.-P. Sauvage, L. Flamigni, *Inorg. Chem.* **2001**, *40*, 5507–5517; e) C. Chiorboli, S. Fracasso, F. Scandola, S. Campagna, S. Serroni, R. Konduri, F. M. MacDonnell, *Chem. Commun.* **2003**, *14*, 1658–1659; f) S. Chakraborty, T. J. Wadas, H. Hester, R. Schmehl, R. Eisenberg, *Inorg. Chem.* **2005**, *44*, 6865–6878; g) M. Borgström, N. Shaikh, O. Johansson, M. F. Anderlund, S. Styring, B. Åkermark, A. Magnuson, L. Hammarström, *J. Am. Chem. Soc.* **2005**, *127*, 17504–17515.

[3] a) L. Flamigni, I. M. Dixon, J.-P. Collin, J.-P. Sauvage, *Chem. Commun.* **2000**, 2479–2480; b) I. M. Dixon, J.-P. Collin, J.-P. Sauvage, F. Barigelletti, L. Flamigni, *Angew. Chem. Int. Ed.* **2000**, *39*, 1292–1295.

[4] a) L. Flamigni, G. Marconi, I. M. Dixon, J.-P. Collin, J.-P. Sauvage, *J. Phys. Chem. B* **2002**, *106*, 6663–6671; b) E. Baranoff, K. Griffiths, J.-P. Collin, J.-P. Sauvage, B. Ventura, L. Flamigni, *New J. Chem.* **2004**, *28*, 1091–1095.

[5] a) J.-P. Collin, I. M. Dixon, J.-P. Sauvage, J. A. G. Williams, F. Barigelletti, L. Flamigni, *J. Am. Chem. Soc.* **1999**, *121*, 5009–5016; b) I. M. Dixon, J.-P. Collin, J.-P. Sauvage, L. Flamigni, S. Encinas, F. Barigelletti, *Chem. Soc. Rev.* **2000**, *29*, 385–391.

 © 2007 Wiley-VCH Verlag GmbH & Co. KGaA, Weinheim 

[6] E. Baranoff, J.-P. Collin, L. Flamigni, J.-P. Sauvage, *Chem. Soc. Rev.* **2004**, *33*, 147–155.
[7] L. Flamigni, E. Baranoff, J.-P. Collin, J.-P. Sauvage, *Chem. Eur. J.* **2006**, *12*, 6592–6606.
[8] E. Baranoff, I. M. Dixon, J.-P. Collin, J.-P. Sauvage, B. Ventura, L. Flamigni, *Inorg. Chem.* **2004**, *43*, 3057–3066.
[9] P. Lainé, F. Bedioui, P. Ochsenbein, V. Marvaud, M. Bonin, E. Amouyal, *J. Am. Chem. Soc.* **2002**, *124*, 1364–1277.
[10] J. C. Sheehan, P. A. Cruickshank, G. L. Broshart, *J. Org. Chem.* **1961**, *26*, 2525–2528.
[11] L. Flamigni, B. Ventura, F. Barigelletti, E. Baranoff, J.-P. Collin, J.-P. Sauvage, *Eur. J. Inorg. Chem.* **2005**, 1312–1318.
[12] W. Leslie, A. S. Bastanov, J. A. K. Howard, J. A. G. Williams, *Dalton Trans.* **2004**, 623–631.
[13] R. I. Walter, *J. Am. Chem. Soc.* **1966**, *88*, 1923–1930.
[14] Some instability was displayed by the **DII** solution under the harsh laser energy conditions of the pump and probe experiment.
[15] Since previously reported experiments the time resolution of the luminescence experiments was improved from 20 ps to 10 ps, due to a better deconvolution procedure of the signal with the instrumental response.
[16] a) Values as high as 0.8 eV have been reported, see, for example: G. L. Gaines III, M. P. O'Neil, W. A. Swec, M. P. Niemczyk, M. R. Wasielewski, *J. Am. Chem. Soc.* **1991**, *113*, 719–721; b) L. Hammarström, F. Barigelletti, L. Flamigni, N. Armaroli, A. Sour, J.-P. Collin, J.-P. Sauvage, *J. Am. Chem. Soc.* **1996**, *118*, 11972–11973 and references cited therein.
[17] a) R. A. Marcus, N. Sutin, *Biochim. Biophys. Acta* **1985**, *811*, 265; b) R. A. Marcus, *Angew. Chem. Int. Ed. Engl.* **1993**, *32*, 1111.
[18] L. Flamigni, *J. Phys. Chem.* **1993**, *97*, 9566–9572.
[19] a) B. Ventura, A. Degli Esposti, B. Koszarna, D. T. Gryko, L. Flamigni, *New J. Chem.* **2005**, *29*, 1559–1566; b) L. Flamigni, N. Armaroli, F. Barigelletti, V. Balzani, J.-P. Collin, J.-O. Dalbavie, V. Heitz, J.-P. Sauvage, *J. Phys. Chem. B* **1997**, *101*, 5936–5943.
[20] a) L. Flamigni, *J. Phys. Chem.* **1992**, *96*, 3331–3337; b) L. Flamigni, *J. Chem. Soc. Faraday Trans.* **1994**, *90*, 2331–2336.

Received: June 28, 2007
Published Online: October 2, 2007

 © 2007 Wiley-VCH Verlag GmbH & Co. KGaA, Weinheim 

DOI: 10.1002/ejic.200700824

# Preparation of 3,3-Di-*tert*-butylthiirane *trans*-1,2-Dioxide and Its Reaction with a Platinum(0) Complex To Give a (Disulfenato)platinum(II) Complex: Regioselectivity of the Oxidation of a Related (Sulfenato–thiolato)platinum(II) Complex

**Akihiko Ishii,*[a] Masayuki Ohishi,[a] and Norio Nakata[a]**

*Dedicated to Professor Renji Okazaki on the occasion of his 70th birthday*

**Keywords:** Platinum / Dithiirane / *vic*-Disulfoxide / Oxidative addition / Oxidation

A three-membered *vic*-disulfoxide, 3,3-di-*tert*-butyldithiirane *trans*-1,2-dioxide (**8**), was synthesized by oxidation of the corresponding dithiirane 1-oxide **15** in high yield. Treatment of **8** and **15** with a platinum(0) complex, $[(Ph_3P)_2Pt(\eta^2\text{-}C_2H_4)]$, yielded the (disulfenato)$Pt^{II}$ complex **18** and the (sulfenato–thiolato)$Pt^{II}$ complex **14**, respectively, in high yields. Oxidation of the sulfenato–thiolato complex **14** with an acetone solution of dimethyldioxirane (DMD) took place at the sulfenato sulfur atom to yield the (sulfinato–thiolato)$Pt^{II}$ complex **19**, while the oxidation with $CF_3CO_3H$ occurred at the thiolato-sulfur atom leading to the disulfenato complex **18**. Oxidation of **14** with MCPBA formed both **18** and **19**. The position of oxidation on **14** with DMD was dependent on the acidity of a coexisting acid. Thus, oxidation of **14** with DMD/$CF_3CO_2H$ provided **18** and that with DMD/$PhCO_2H$ gave **19**. Oxidation of **14** with an excess amount of DMD yielded the (disulfonato)$Pt^{II}$ complex **20**.

(© Wiley-VCH Verlag GmbH & Co. KGaA, 69451 Weinheim, Germany, 2007)

## Introduction

*vic*-Disulfoxides [RS(O)S(O)R] have long been recognized as unstable intermediates in the electrophilic oxidation of disulfides[1–3] until our success in 1999 with the isolation and unambiguous structure determination of tetrathiolane 2,3-dioxide **1**, which has a –S(O)–S(O)– bond.[4,5] Since then we have reported on isolable *vic*-disulfoxides **2**–**4**.[6–10] 3-(1-Adamantyl)-3-*tert*-butyldithiirane *trans*-1,2-dioxide (**4**) is the first three-membered *vic*-disulfoxide synthesized by the oxidation of the corresponding dithiirane 1-oxide **5** with an acetone solution of dimethyldioxirane (DMD) [Equation (1)].[9] An interesting reaction of **4** is its decomposition in refluxing chloroform as shown in Scheme 1 to give sulfine **6** and sulfur monoxide (SO) by the main path. SO was trapped with thioketone **7**, generated from a minor path, to provide dithiirane 1-oxide **5** (Scheme 1). The thermal decomposition was investigated in detail experimentally and theoretically, and, for the theoretical study, 3,3-di-*tert*-butyldithiirane *trans*-1,2-oxide (**8**) was employed as the model compound of **4**.[9]

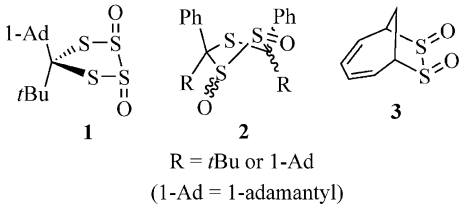


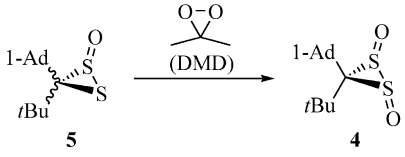


(1)

In this paper we report on the synthesis and some reactions of *vic*-disulfoxide **8**, focusing, in particular, on the platinum complex of **8** and the related compounds. While the oxidative addition of several types of sulfur–sulfur bonds in cyclic sulfur compounds to platinum(0) complexes is a topic of recent research,[11–24] it has not been clarified whether *vic*-disulfoxides bring about a similar oxidative addition to platinum(0) complexes to provide (disulfenato)$Pt^{II}$ complexes.[20] We have reported the reaction of dithiirane 1-oxides with $[(Ph_3P)_2Pt(\eta^2\text{-}C_2H_4)]$ to provide the corresponding (sulfenato–thiolato)$Pt^{II}$ complexes **9** [Equa-

[a] Department of Chemistry, Graduate School of Science and Engineering, Saitama University
Shimo-okubo, Sakura-ku, Saitama, 338-8570, Japan
Fax: +81-48-858-3700
E-mail: ishiiaki@chem.saitama-u.ac.jp

Supporting information for this article is available on the WWW under http://www.eurjic.org or from the author.

 © 2007 Wiley-VCH Verlag GmbH & Co. KGaA, Weinheim 

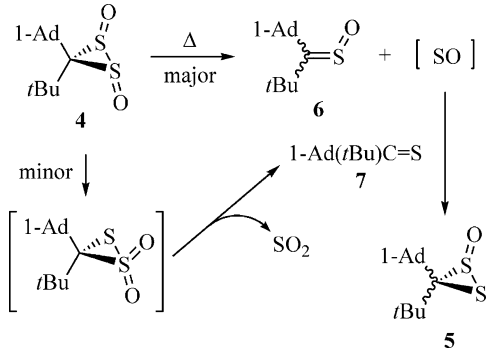


Scheme 1. Thermal decomposition of 3-(1-adamantyl)-3-*tert*-butyldithiirane *trans*-1,2-dioxide (**4**).

tion (2)].[18,19] The oxidation of (dithiolato)$M^{II}$ (M = Ni, Pd, Pt) complexes with molecular oxygen or hydrogen peroxide was studied extensively in relation to their air sensitivity.[25–39] We recently reported the regioselective oxidation of (dithiolato)$Pt^{II}$ complex **10** and its oxides with DMD under neutral conditions [Equation (3)].[24] We observed that the oxidation of the (sulfenato–thiolato)$Pt^{II}$ complex **11** led to the (sulfinato–thiolato)$Pt^{II}$ complex **12** and not the (disulfenato)$Pt^{II}$ complex **13**. This regioselectivity was rationalized in terms of the fact that the sulfenato sulfur is more reactive than the thiolato sulfur because of the back-donation of the platinum atom as Schenk proposed for the reaction of $CpRuL_2[S(O)R]$ (L = phosphane ligands) with DMD [Equation (4)].[40] In order to verify whether this regioselectivity of oxidation is true for the present system and whether the regioselectivity is influenced by the presence or absence of acid, the related (sulfenato–thiolato)$Pt^{II}$ complex **14** was prepared and subjected to an oxidation study.

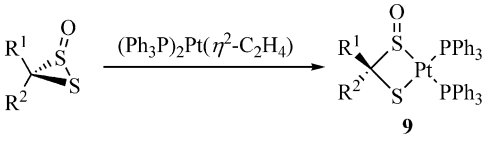


(2)

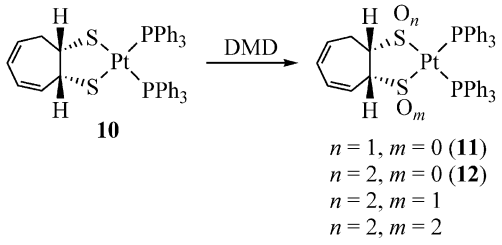


(3)

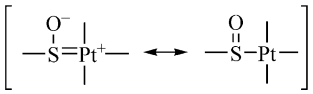

(4)

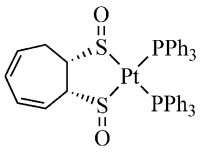


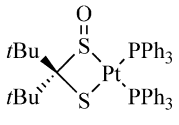


## Results and Discussion

Di-*tert*-butyldithiirane 1-oxide (**15**) was prepared by the reaction of di-*tert*-butyldiazomethane with $S_8O$ in 12% yield,[41] and was treated with DMD (5.9 molar equiv.) in dichloromethane at –20 °C. The $^1H$ NMR spectrum of the reaction mixture showed the formation of the desired 1,2-dioxide **8**, di-*tert*-butyl thioketone *S*-oxide (sulfine) (**16**), and di-*tert*-butyl ketone in a ratio of 89:10:1 (Scheme 2). The high yield of **8** indicated that the over-oxidation to give the trioxides and higher oxides hardly occurred under these conditions. The dioxide **8** was isolated by recrystallization at –20 °C in 79% yield as pale-yellow plates. The oxidation with *m*-chloroperbenzoic acid (MCPBA) (6 molar equiv.) at –20 °C proceeded slowly to give **8** in 31% yield together with sulfine **16** (6%) and the starting compound **15** (63%) ($^1H$ NMR integral ratio). In the $^1H$ NMR and $^{13}C$ NMR spectra, the two *tert*-butyl groups of 1,2-dioxide **8** are equivalent, and in the $^{13}C$ NMR spectrum, the dithiirane carbon resonated at $\delta$ = 105.9 ppm, shifted to the lower field by 19.6 ppm than that of the 1-oxide **15** ($\delta$ = 86.3 ppm).

The structure of 1,2-dioxide **8** was determined by X-ray crystallography (Figure 1). In the crystal structure of **8** the *C*2 symmetry axis runs through the center of the S–S bond and the dithiirane carbon. The S–S bond length [2.2307(11) Å] is slightly longer than that of **4** [2.242(2) Å], and the dihedral angle O–S–S–O (149.0°) is very similar to that of **4** [149.6(3)°]. The angle between the two *tert*-butyl groups widens to 122.7(2)° as observed in **4** [123.6(5)°].[9]

1,2-Dioxide **8** was stable in the crystalline state at room temperature for a long time, but decomposed gradually in chloroform at room temperature to give sulfine **16** almost quantitatively after 9 d. Heating **8** in refluxing chloroform for 2 h yielded sulfine **16** (78%), dithiirane 1-oxide **15** (14%), and thioketone **17** (4%) [Equation (5)]. The reactions depicted in Scheme 1 can be applied to explain the

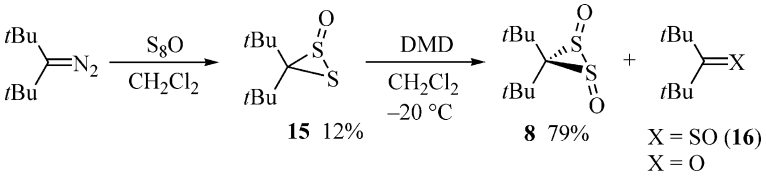


Scheme 2. Synthesis of 3,3-di-*tert*-butyldithiirane *trans*-1,2-oxide (**8**).

 © 2007 Wiley-VCH Verlag GmbH & Co. KGaA, Weinheim 

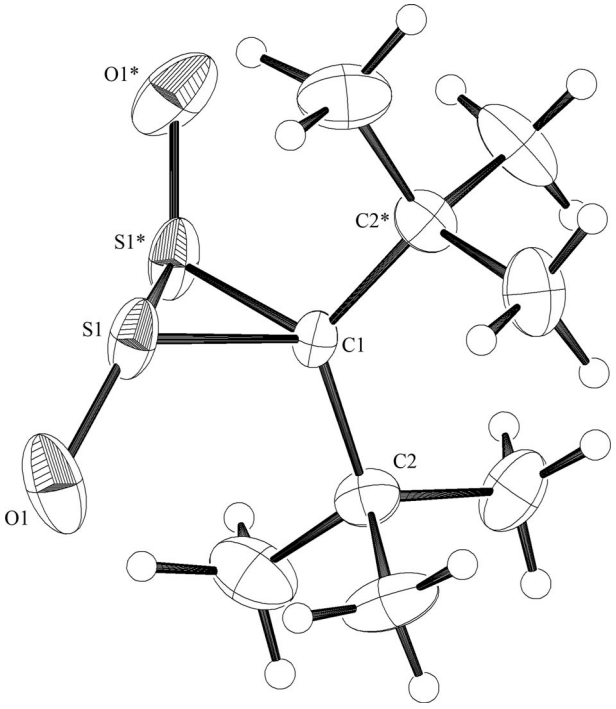


Figure 1. ORTEP drawing of 3,3-di-*tert*-butyldithiirane *trans*-1,2-dioxide (**8**) with 30% probability thermal ellipsoids. Relevant bond lengths [Å] and angles [°]: S1–O1 1.467(2), S1–C1 1.854(2), S1–S1* 2.2308(11), C1–C2 1.561(2), C1–S1 1.854(2), O1–S1–C1 115.79(10), O1–S1–S1* 113.48(9), C2–C1–C2* 122.7(2), C2–C1–S1* 110.44(10), C2–C1–S1 114.63(10), S1–C1–S1* 73.98(10).

formation mechanism of **15**–**17**. No formation of **15** and **17** on the decomposition in chloroform at room temperature may indicate that the 1,2-oxygen shift of **8** to the dithiirane 1,1-dioxide requires a larger activation energy than the extrusion of SO to give **16**, which is consistent with the theoretical consideration.[9]

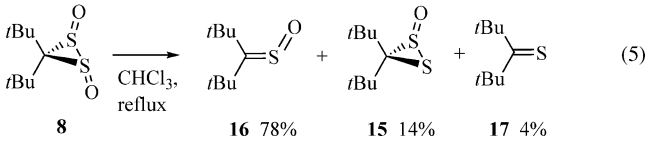


(5)

## Platinum Complexes

1,2-Dioxide **8** was treated with [$(Ph_3P)_2Pt(\eta^2\text{-}C_2H_4)$] in dichloromethane at 0 °C. The mixture containing the desired (disulfenato)Pt$^{II}$ complex **18**, sulfine **16**, and **8** was recrystallized from a mixed solvent of hexane and dichloromethane at –20 °C to give **18** as a yellow powder in 56% yield [Equation (6)]. The structure of **18** was supported by the following spectroscopic data. In the $^1$H NMR spectrum, the two *tert*-butyl groups are equivalent ($\delta$ = 1.41 ppm), indicating that the configuration of the two S=O groups in **18** is not *cis* but *trans*. In the $^{31}$P NMR spectrum a singlet accompanying the satellite signals ($^1J_{Pt,P}$ = 2596 Hz) from the $^{195}$Pt isotope is observed at $\delta$ = 15.2 ppm. This $^1J_{Pt,P}$ coupling constant value is comparable to those for phosphorus atoms *trans* to the S=O groups.[12–24] The absorption due to the S=O stretching vibration is observed at 1097 cm$^{-1}$ in the IR spectrum, which is close to those of the reported (sulfenato)Pt$^{II}$ complexes.[12–24] Recrystallization of **18** from benzene provided single crystals (yellow prisms) suitable for X-ray crystal analysis, and the structure was determined unambiguously (Figure 2).

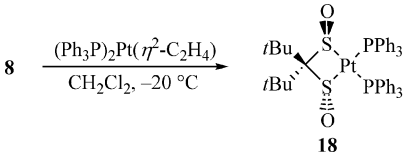


(6)

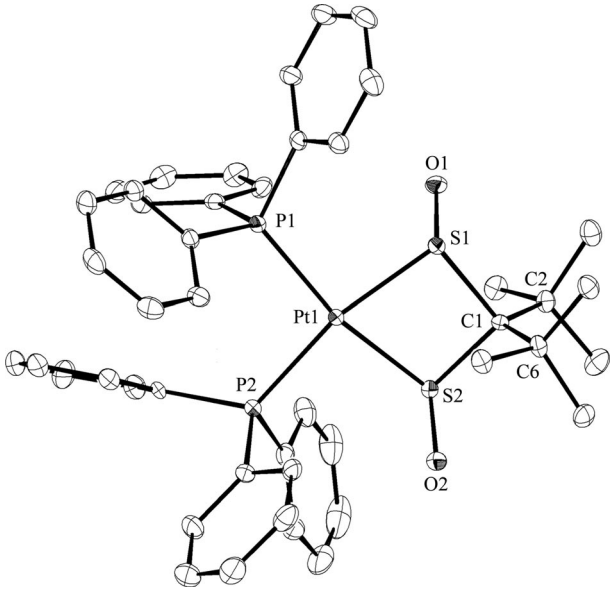


Figure 2. ORTEP drawing of (disulfenato)Pt$^{II}$ complex **18** with 30% probability thermal ellipsoids. Hydrogen atoms and the solvated molecules ($C_6H_6$) were omitted for clarity.

The (sulfenato–thiolato)Pt$^{II}$ complex **14** was prepared by the treatment of dithiirane 1-oxide **15** with [$(Ph_3P)_2Pt(\eta^2\text{-}C_2H_4)$] conducted in dichloromethane at –20 °C [Equation (7)]. The structure was determined by X-ray crystallography as depicted in Figure 3.

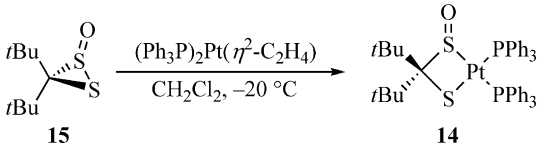


(7)

Oxidation of the sulfenato–thiolato complex **14** was investigated [Equation (8)] (Table 1). Oxidation with an equimolar amount of DMD in toluene at 0 °C yielded the (sulfinato–thiolato)Pt$^{II}$ complex **19** as the main product together with the starting complex **14**, sulfine **16**, and [$Pt(PPh_3)_2$-($S_2O_2$)][20,42] (Table 1, Entry 1). The (disulfenato)Pt$^{II}$ complex **18** was not formed at all. The structure of **19** was deter-

 © 2007 Wiley-VCH Verlag GmbH & Co. KGaA, Weinheim 

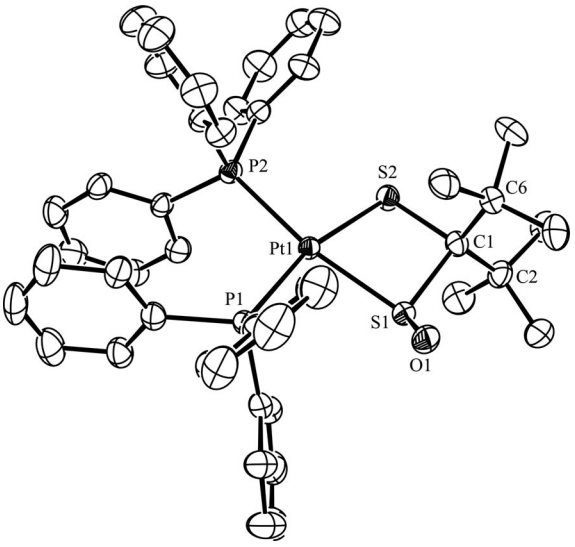


Figure 3. Molecular structure of the (sulfenato–thiolato)$Pt^{II}$ complex **14** with 30% probability thermal ellipsoids. Hydrogen atoms and solvated molecules ($CH_2Cl_2$) are omitted for clarity.

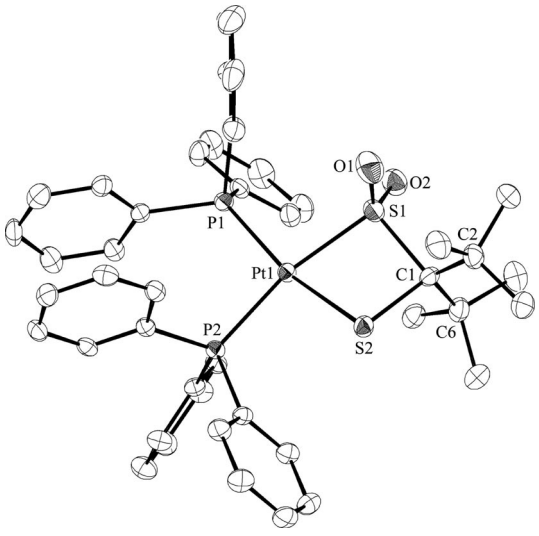


Figure 4. ORTEP drawing of (sulfinato–thiolato)$Pt^{II}$ complex **19** with 30% probability thermal ellipsoids. Hydrogen atoms and solvated molecules ($CH_2Cl_2$) are omitted for clarity.

mined from spectroscopic data. In the $^{31}P$ NMR spectrum, two doublets accompanying satellite signals from the $^{195}Pt$ isotope are observed at $\delta$ = 11.6 (d, $^2J_{P,P}$ = 18.6 Hz, $^1J_{Pt,P}$ = 2310 Hz) and 18.7 (d, $^2J_{P,P}$ = 18.6 Hz, $^1J_{Pt,P}$ = 3053 Hz). In the infrared spectrum stretching vibrations from the $SO_2$ group appear at 1067 and 1197 $cm^{-1}$. The structure of **19** was finally determined by X-ray crystallography (Figure 4).

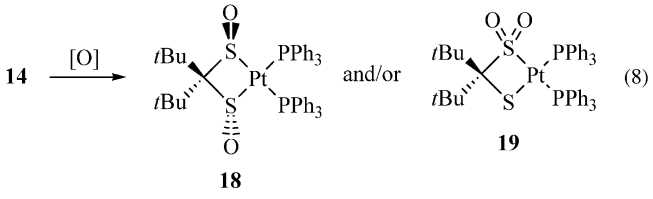


(8)

Table 1. Oxidation of (sulfenato–thiolato)$Pt^{II}$ complex **14**.

| Entry | [O] | **18** | **19** | **14**[a] | Others |
|---|---|---|---|---|---|
| 1 | DMD | 0[b] | 62[b] | 32[b] | **16** {6[b], $[Pt(PPh_3)_2(S_2O_2)]$} |
| 2 | $CF_3CO_3H$ | 9[b] | 0[b] | 73[b] | **16** (18[b]) |
| 3 | MCPBA | 6[c] | 9[c] | 29[c] | $Ph_3P{=}O$ (56[c]) |
| 4 | DMD/$CF_3CO_2H$ | 30[b] | 0[b] | 28[b] | **16** (42[b]) |
| 5 | DMD/$PhCO_2H$ | 0 | 84[c] | 0 | $Ph_3P{=}O$ (16[b]) |

[a] Recovery. [b] $^1H$ NMR integral ratio. [c] $^{31}P$ NMR peak height ratio.

Thus, it was verified that the oxidation of the (sulfenato–thiolato)$Pt^{II}$ complex **14** with DMD took place in the same regioselectivity as observed in the oxidation of **11** with DMD to give **12** [Equation (3)].

On the other hand, oxidation of **14** with $CF_3CO_3H$ gave the (disulfenato)$Pt^{II}$ complex **18** without **19** though this reaction was sluggish (a large portion of the starting complex **14** was recovered) and a substantial amount of sulfine **16** was formed as a decomposition product ($^1H$ NMR integral ratio: **18/14/16** ≈ 9:73:18) (Table 1, Entry 2). When MCPBA was employed as the oxidant both **18** and **19** were formed albeit in low yields (**18/19/14**/$Ph_3P{=}O$ ≈ 6:9:29:56) (Entry 3). The oxidation of **14** with DMD in the presence of $CF_3CO_2H$ yielded **18** together with **14** and **16** (**18/14/16** ≈ 30:28:42) (Entry 4), and that in the presence of benzoic acid gave **19** (**19**/$Ph_3P{=}O$ ≈ 81:16) (Entry 5). The change in regioselectivity as described above was explained by protonation on the sulfinyl oxygen atom with the coexisting carboxylic acid leading to a decrease in the electron density on the sulfinyl-sulfur atom [Equation (9)]. The extent of the decrease in the electron density is dependent on the strength of the acid.

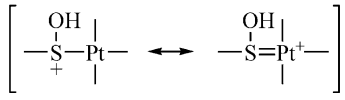


(9)

Oxidation of (sulfenato–thiolato)$Pt^{II}$ complex **14** with an excess amount of DMD (5 molar equiv.) provided the (disulfonato)$Pt^{II}$ complex **20** quantitatively [Equation (10)], the structure of which was determined by X-ray crystallography (Figure 5). The $PtO_2S_2C$ six-membered ring has a twist conformation in the crystalline state. While the two *tert*-butyl groups are equivalent in the $^{13}C$ NMR spectrum, they are nonequivalent in the $^1H$ NMR spectrum. In the $^{31}P$ NMR spectrum, a singlet with satellite signals from the $^{195}Pt$ isotope is observed at $\delta$ = 7.10 ppm ($^1J_{Pt-P}$ = 4157 Hz). Formation of a similar sulfonato complex was reported from the oxidation of the (dithiolato)$Ni^{II}$ complex with hydrogen peroxide [Equation (11)].[43] $^{31}P$ NMR spectroscopic data of $Pt^{II}$ complexes **14**, **18**–**20** are summarized in Table 2.

 © 2007 Wiley-VCH Verlag GmbH & Co. KGaA, Weinheim 

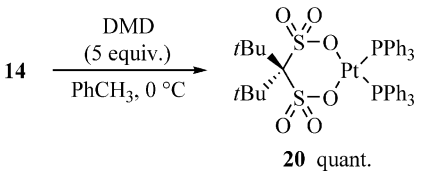


(10)

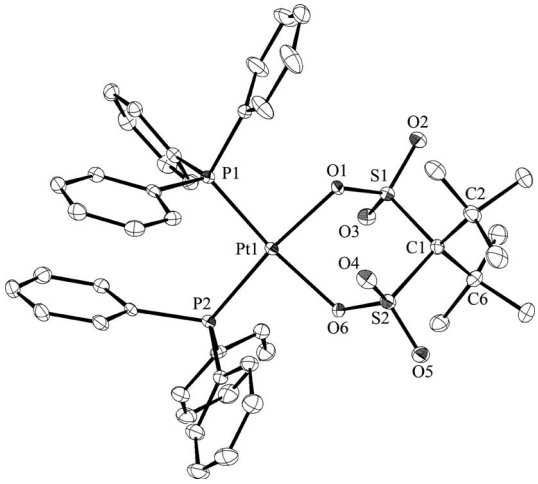


Figure 5. ORTEP drawing of (disulfonato)Pt$^{II}$ complex **20** with 30% probability thermal ellipsoids. Relevant bond lengths [Å] and angles [°]: Pt1–O1 2.090(2), Pt1–O6 2.107(2), Pt1–P1 2.2224(9), Pt1–P2 2.2375(9), O1–S1 1.503(2), S1–O2 1.438(3), S1–O3 1.442(3), S1–C1 1.877(3), C1–C6 1.617(5), C1–C2 1.623(5), C1–S2 1.888(3), S2–O4 1.436(3), S2–O5 1.439(3), S2–O6 1.512(2), O1–Pt1–O6 85.47(9), O1–Pt1–P1 88.60(7), O6–Pt1–P1 173.97(6), O1–Pt1–P2 173.25(7), O6–Pt1–P2 87.92(6), P1–Pt1–P2 98.04(3), S1–O1–Pt1 115.52(13), O2–S1–O3 115.09(15), O2–S1–O1 109.79(14), O3–S1–O1 110.15(14), O2–S1–C1 106.74(15), O3–S1–C1 109.95(15), O1–S1–C1 104.55(14), C6–C1–C2 117.8(3), C6–C1–S1 108.3(2), C2–C1–S1 109.0(2), C6–C1–S2 109.0(2), C2–C1–S2 107.3(2), S1–C1–S2 104.76(16), O4–S2–O5 115.17(16), O4–S2–O6 110.18(14), O5–S2–O6 109.26(14), O4–S2–C1 109.91(16), O5–S2–C1 106.42(15), O6–S2–C1 105.39(14), S2–O6–Pt1 116.00(13).

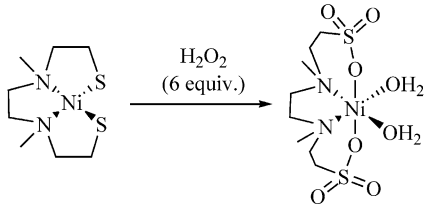


(11)

Table 2. $^{31}$P NMR spectroscopic data of Pt$^{II}$ complexes **14** and **18**–**20**.

| Compound | $\delta$ [ppm] | $^{2}J(^{31}P,^{31}P)$ [Hz] | $^{1}J(^{195}Pt,^{31}P)$ [Hz] |
|---|---|---|---|
| **18** | 15.2 | – | 2596 |
| **14** | 16.8 | 24.4 | 3306 |
| | 17.9 | 24.4 | 2338 |
| **19** | 11.6 | 18.6 | 2310 |
| | 18.7 | 18.6 | 3053 |
| **20** | 7.10 | – | 4157 |

## X-ray Crystallography of Platinum(II) Complexes 14 and 18–20

The selected bond lengths and angles of **14**, **18**, and **19** are summarized in Table 3. The sum of the four angles around the Pt atom in **14** and **18**–**20** is almost 360° and the platinum atoms keep the planarity in these complexes. The puckered angles of the four-membered rings of **18**, **14**, and **19** are 3.6°, 25.2°, and 13.0°, respectively. The S1–Pt1 and S2–Pt1 bond lengths in **18**, **14**, and **19** are not significantly influenced by the oxidation state of the sulfur atoms and lie in the narrow range 2.3065(14)–2.3421(6) Å. The P1–Pt1 and P2–Pt1 bond lengths in **18**, **14**, and **19** also fall into a narrow range [2.2943(14)–2.3347(19) Å], though the P1–Pt1 bonds *trans* to the thiolato ligands in **14** [2.2943(14) Å] and **19** [2.2956(15) Å] are slightly shorter than the others because of the weaker *trans* influence of the thiolato ligands compared with those of the sulfenato and sulfinato ligands. The P1–Pt1 [2.2224(9) Å] and P2–Pt1 [2.2375(9) Å] bond lengths in the disulfonato complex **20**, which are *trans* to the O atoms of the sulfonato ligands, are obviously shorter than the above Pt–P bond lengths.

Table 3. Selected bond lengths [Å] and bond angles [°] of **18**, **14**, and **19**.

| | **18** | **14** | **19** |
|---|---|---|---|
| S1<br>S2 | S1=SO<br>S2=SO | S1=SO<br>S2=S | S1=SO$_2$<br>S2=S |
| S1–Pt1 | 2.3134(10) | 2.3421(6) | 2.3221(16) |
| S2–Pt1 | 2.3251(10) | 2.3065(14) | 2.3163(15) |
| P1–Pt1 (*trans* to S2–Pt1) | 2.3090(10) | 2.2943(14) | 2.2956(15) |
| P2–Pt1 (*trans* to S1–Pt1) | 2.3347(10) | 2.3130(15) | 2.3012(14) |
| S1–O1, S1–O2 | 1.511(3) | 1.506(5) | 1.434(16)<br>1.464(5) |
| S2–O2 | 1.509(3) | – | – |
| S1–C1 | 1.917(3) | 1.902(6) | 1.936(6) |
| S2–C1 | 1.899(4) | 1.860(7) | 1.891(6) |
| C1–C2 | 1.577(5) | 1.586(8) | 1.571(9) |
| C1–C6 | 1.588(5) | 1.591(8) | 1.607(9) |
| S1–Pt1–P1 | 93.43(4) | 93.53(5) | 95.79(6) |
| P1–Pt1–P2 | 99.00(4) | 99.30(5) | 97.60(5) |
| P2–Pt1–S2 | 91.15(4) | 94.02(5) | 93.93(5) |
| S2–Pt1–S1 | 76.39(3)<br>(359.97)[a] | 72.94(5)<br>(359.79)[a] | 72.66(6)<br>(359.98)[a] |
| S1–Pt1–P2 | 167.50(4) | 166.78(5) | 166.60(6) |
| S2–Pt1–P1 | 165.48(3) | 165.89(6) | 167.92(5) |
| Pt1–S1–C1 | 92.38(12) | 92.2(2) | 94.66(19) |
| S1–C1–S2 | 97.79(18) | 94.5(3) | 91.8(3) |
| C1–S2–Pt1 | 92.74(12) | 94.40(18) | 96.08(19) |
| C2–C1–C6 | 120.5(3)<br>(3.6)[b] | 118.5(5)<br>(25.2)[b] | 118.4(5)<br>(13.0)[b] |

[a] Sum of the above four angles around the Pt atom. [b] Puckered angle of the four-membered ring.

The S=O bond lengths of the SO$_2$ group in **19** and **20** [1.434(16)–1.464(5) Å] are shorter than those of the sulfenato ligands in **18** [1.509(3) and 1.511(3) Å] and **14** [1.506(5) Å]. This is in accordance with those for dialkyl

 © 2007 Wiley-VCH Verlag GmbH & Co. KGaA, Weinheim 

sulfones [R–S(O)$_2$–R′, S–O 1.436 Å[44]] and sulfoxides [R–S(O)–R′, S–O 1.497 Å[44]] (R, R′ = alkyl).

The S1–C1 bond [S(O)$_2$–C bond] in **19** is elongated to a length of 1.936(6) Å, which is much longer than those of a similar type in **20** [S1–C1 1.877(3) Å and S2–C1 1.888(3) Å]. This elongation in **19** is explained by a large steric repulsion between the two oxygen atoms and the two *tert*-butyl groups as well as the $PPh_3$ ligand at the *cis* position in the four-membered ring. While ordinary S–C bond lengths in organic sulfides, sulfoxides, and sulfones become shorter in this order (1.819, 1.809, and 1.779 Å, respectively[44]), this is not true for the present, sterically congested system.

## Conclusions

We prepared a three-membered *vic*-disulfoxide, 3,3-di-*tert*-butyldithiirane *trans*-1,2-dioxide (**8**). Complexation of **8** with a platinum(0) complex yielded the (disulfenato)Pt$^{II}$ complex **18** in high yield by oxidative addition. This is the only direct method for the synthesis of (disulfenato)Pt$^{II}$ complexes. We showed that oxidation positions of (sulfenato–thiolato)Pt$^{II}$ complexes, sulfenato sulfur or thiolato sulfur, can be controlled by the acidity of the reaction media.

## Experimental Section

The melting points were determined with a Mel-Temp capillary tube apparatus and are uncorrected. $^1$H, $^{13}$C, and $^{31}$P NMR spectra were determined with Bruker AM400 or DRX400 (400, 100.7, and 162 MHz, respectively) spectrometers using $CDCl_3$ as the solvent at 25 °C, unless otherwise noted. IR spectra were recorded with a Perkin–Elmer System 2000 FT-IR spectrometer. Elemental analyses were performed by the Molecular Analysis and Life Science Center of Saitama University, where those for platinum complexes were performed with $WO_3$ as the combustion improver. An acetone solution of dimethyldioxirane (DMD) was prepared by oxidation of acetone with Oxone® (Sigma–Aldrich).[45]

**3,3-Di-*tert*-butyldithiirane 1-Oxide (15):** A solution of di-*tert*-butyldiazomethane (727.9 mg, 4.719 mmol) in dichloromethane (20 mL) was added to a solution of $S_8O$ (1.548 g, 5.691 mmol) in dichloromethane (250 mL) cooled to 0 °C. The mixture was stirred for 1 h at 0 °C and for 2 h at room temperature. Precipitates were filtered and washed with dichloromethane, and the filtrate and the washings were combined. The solvent was removed under reduced pressure, and the residue was subjected to column chromatography (silica gel: hexane/dichloromethane, 1:2) and then HPLC (hexane/dichloromethane, 3:2) to give dithiirane 1-oxide **15** as a pale-yellow oil (116.8 mg, 12%): $^1$H NMR: $\delta$ = 1.08 (s, 9 H), 1.42 (s, 9 H) ppm. $^{13}$C NMR: $\delta$ = 29.2 ($CH_3$), 31.9 ($CH_3$), 41.2 (C), 41.3 (C), 86.3 (C) ppm. IR (neat): $\tilde{\nu}$ = 1121 cm$^{-1}$. $C_9H_{18}OS_2$ (206.36): calcd. C 52.38, H 8.79; found C 52.63, H 8.82.

**3,3-Di-*tert*-butyldithiirane *trans*-1,2-Dioxide (8):** DMD (0.079 M, 17.0 mL, 1.343 mmol) was added to a solution of 3,3-di-*tert*-butyldithiirane 1-oxide (**15**) (46.8 mg, 0.227 mmol) in dichloromethane (1.5 mL) cooled to –20 °C under argon. The mixture was stirred at –20 °C for 2 h, and the solvent was removed under reduced pressure at 0 °C. The $^1$H NMR spectrum of the residue showed the formation of 1,2-dioxide **8**, di-*tert*-butyl ketone (**17**), and di-*tert*-butyl thioketone *S*-oxide (**16**) in the ratio 89:1:10. The residue was recrystallized from a mixed solvent of hexane and dichloromethane at –20 °C to give 39.9 mg (79%) of 1,2-dioxide **8** as pale-yellow plates. M.p. 85 °C (decomp.). $^1$H NMR: $\delta$ = 1.38 (s, 18 H) ppm. $^{13}$C NMR: $\delta$ = 31.1 ($CH_3$), 41.6 (C), 105.9 (C) ppm. IR (KBr): $\tilde{\nu}$ = 1063 cm$^{-1}$. $C_9H_{18}O_2S_2$ (222.36): calcd. C 48.61, H 8.16; found C 48.87, H 8.22.

**[2,2,4,4-Tetramethylpentane-3,3-dithiolato(2–)-κ*S*,κ*S*′]bis(triphenylphosphane)platinum *trans*-*S*,*S*′-Dioxide [(Disulfenato)Pt$^{II}$ Complex 18]:** A solution of [$(Ph_3P)_2Pt(\eta^2$-$C_2H_4)$] (92.9 mg, 0.124 mmol) in dichloromethane (2 mL) was added to a solution of 1,2-dioxide **8** (27.8 mg, 0.125 mmol) in dichloromethane (5 mL) cooled to 0 °C under argon. The mixture was stirred for 2 h at 0 °C, and the solvent was removed under reduced pressure. The residue was recrystallized twice from a mixed solvent of hexane and dichloromethane at –20 °C to give 66.3 mg (56%) of the (disulfenato)Pt$^{II}$ complex **18**. M.p. 125 °C (decomp.). $^1$H NMR: $\delta$ = 1.41 (s, 18 H), 7.18–7.22 (m, 12 H), 7.29–7.34 (m, 6 H), 7.38–7.43 (m, 12 H) ppm. $^{13}$C NMR: $\delta$ = 31.22 ($CH_3$), 43.97 (C), 128.08 (t, $J_{P,C}$ = 5.3 Hz, CH), 130.20 (dd, $J_{P,C}$ = 57.2, 7.4 Hz, C), 130.27 (CH), 134.21 (t, $J_{P,C}$ = 5.6 Hz, CH) ppm. $^{31}$P NMR: $\delta$ = 15.2 (s, $^1J_{Pt,P}$ = 2596 Hz for the satellite signals) ppm. IR (KBr): $\tilde{\nu}$ = 1097 cm$^{-1}$. $C_{45.5}H_{49}ClO_2P_2PtS_2$ ($C_{45}H_{48}O_2P_2PtS_2$·0.5$CH_2Cl_2$) (984.49): calcd. C 55.51, H 5.02; found C 56.17, H 5.03 (the $^1$H NMR spectrum of the same sample subjected to the elemental analysis showed the presence of 0.50 molecules of $CH_2Cl_2$ and a molecule of **18**). Single crystals suitable for X-ray crystallography were obtained by recrystallization from benzene at room temperature.

**[2,2,4,4-Tetramethylpentane-3,3-dithiolato(2–)-κ*S*,κ*S*′]bis(triphenylphosphane)platinum *S*-Oxide [(Sulfenato–thiolato)Pt$^{II}$ Complex 14]:** A solution of [$(Ph_3P)_2Pt(\eta^2$-$C_2H_4)$] (202.1 mg, 0.218 mmol) in dichloromethane (8 mL) was added to a solution of dithiirane 1-oxide **15** (45.0 mg, 0.218 mmol) in dichloromethane (3 mL) cooled to 0 °C under argon. The mixture was stirred for 2 h at 0 °C, and the solvent was removed under reduced pressure. The residue was recrystallized from a mixed solvent of hexane and dichloromethane at –20 °C to give 152.5 mg (76%) of the (sulfenato–thiolato)Pt$^{II}$ complex **14** as yellow prisms. M.p. 207 °C (decomp.). $^1$H NMR: $\delta$ = 1.12 (s, 9 H), 1.45 (br. s, 6 H), 1.62 (s, 3 H), 7.14–7.20 (m, 12 H), 7.24–7.30 (m, 6 H), 7.38–7.45 (m, 12 H) ppm. $^{13}$C NMR: $\delta$ = 29.30 ($CH_3$), 32.98 (br. s, $CH_3$), 42.60 (C), 46.30 (C), 127. 72 (t, $J_{P,C}$ = 9.9 Hz, CH), 130.01 (CH), 134.3 (m, CH) ppm (signals for aromatic quaternary carbons appear at $\delta$ = 130.425, 130.794, 130.892, and 131.297 ppm, which are not assigned). $^{31}$P NMR: $\delta$ = 16.8 (d, $^2J_{P,P}$ = 24.4 Hz and $^1J_{Pt,P}$ = 3306 Hz for the satellite signals), 17.9 (d, $^2J_{P,P}$ = 24.4 Hz and $^1J_{Pt,P}$ = 2338 Hz for the satellite signals) ppm. $C_{47}H_{52}Cl_4OP_2PtS_2$ ($C_{45}H_{48}OP_2PtS_2$·2$CH_2Cl_2$) (1095.89): calcd. C 51.51, H 4.78; found C 51.24, H 4.66.

**[2,2,4,4-Tetramethylpentane-3,3-dithiolato(2–)-κ*S*,κ*S*′]bis(triphenylphosphane)platinum *S*,*S*-Dioxide [(Sulfinato–thiolato)Pt$^{II}$ Complex 19]:** A solution of DMD (0.085 M, 0.34 mL, 0.029 mmol) was added to a solution of the (sulfenato–thiolato)Pt$^{II}$ complex **14** (27.1 mg, 0.0292 mmol) in toluene (3 mL) cooled to 0 °C under argon. The mixture was stirred for 2 h at 0 °C, and the solvent was removed under reduced pressure at 0 °C. The $^1$H NMR spectrum of the residue (28.7 mg) indicated the presence of **19**, **14**, and sulfine **16** in the ratio 62:32:6, while the $^{31}$P NMR spectrum showed signals from **19** ($\delta$ = 11.6 and 18.7 ppm) and **14** ($\delta$ = 16.8 and 18.9 ppm) together with a small amount of [$Pt(PPh_3)_2(S_2O_2)$] ($\delta$ = 6.3 ppm). The residue was recrystallized from a mixed solvent of hexane and dichloromethane at –20 °C to give 5.1 mg of an ca. 2:1 mixture of **19** and **14**. As we could not obtain **19** in the pure form, even by

 © 2007 Wiley-VCH Verlag GmbH & Co. KGaA, Weinheim 

repeated recrystallization, elemental analysis of **19** was not done. However, a single, yellow crystal suitable for X-ray analysis was obtained. $^1$H NMR: $\delta$ = 1.50 (br. s, 18 H), 7.14–7.21 (m, 12 H), 7.28–7.32 (m, 6 H), 7.38–7.44 (m, 6 H), 7.50–7.55 (m, 6 H) ppm. $^{31}$P NMR: $\delta$ = 11.6 (d, $^2J_{P,P}$ = 18.6, $^1J_{Pt,P}$ = 2310 Hz), 18.7 (d, $^2J_{P,P}$ = 18.6, $^1J_{Pt,P}$ = 3053 Hz) ppm. IR (KBr): $\tilde{\nu}$ = 1067, 1197 ($SO_2$) cm$^{-1}$.

**[2,2,4,4-Tetramethylpentane-3,3-disulfonato(2–)-κ*O*,κ*O*′]bis(triphenylphosphane)platinum [(Disulfonato)Pt$^{II}$ Complex 20]:** DMD (0.083 M, 1.25 mL, 0.10 mmol) was added dropwise to a solution of the (sulfenato–thiolato)Pt$^{II}$ complex **14** (19.3 mg, 0.021 mmol) in toluene (7 mL) at 0 °C under argon. The mixture was stirred for 2 h at 0 °C, and the solvent was removed under reduced pressure at 0 °C to give an almost pure **20** as a yellow-white solid (20.9 mg). The crude material was recrystallized from a mixed solvent of hexane and dichloromethane at –20 °C to give 7.1 mg (34%) of **20** as colorless prisms. M.p. 280 °C (decomp.). $^1$H NMR: $\delta$ = 1.52 (br. s, 9 H), 1.58 (s, 9 H), 7.20–7.26 (m, 12 H), 7.36–7.40 (m, 6 H), 7.53–7.59 (m, 12 H) ppm. $^{13}$C NMR: $\delta$ = 32.91 ($CH_3$), 42.32 (C), 126.10 (d, $J_{P,C}$ = 68.3 Hz, C), 128.47 (t, $J_{P,C}$ = 5.9 Hz, CH), 131.60 (CH), 134.58 (t, $J_{P,C}$ = 5.4 Hz, $CH_3$) ppm. $^{31}$P NMR: $\delta$ = 7.10 (s, $^1J_{Pt,P}$ = 4157 Hz) ppm. IR (KBr): $\tilde{\nu}$ = 1139, 1284 ($SO_2$) cm$^{-1}$. $C_{45}H_{48}O_6P_2PtS_2$ (1006.02): calcd. C 53.73, H 4.81; found C 54.01, H 5.04.

**X-ray Crystallography:** X-ray crystallographic analyses were performed with a Mac Science DIP3000 diffractometer (for **14**) or a Bruker AXS SMART diffractometer (for others) with a graphite-monochromated Mo-$K_\alpha$ radiation ($\lambda$ = 0.71073 Å). The structures were solved by direct methods and refined with full-matrix least-squares (SHELXL-97[46]) using all independent reflections.

**Crystal Data for 8:** $C_9H_{18}O_2S_2$, $M_r$ = 222.35 g mol$^{-1}$, yellow prism, crystal size = 0.40 × 0.40 × 0.40 mm, monoclinic, *C*2/*c*, *a* = 14.9253(13), *b* = 7.0524(6), *c* = 11.4484(9) Å, $\beta$ = 105.485(2)°, *V* = 1161.31(17) Å$^3$, $\rho_{calcd.}$ = 1.272 g cm$^{-3}$, *Z* = 4, $\mu$(Mo-$K_\alpha$) = 0.428 cm$^{-1}$. Intensity data of 1069 unique reflections were collected over the range –18 ≤ *h* ≤ 17, –8 ≤ *k* ≤ 8, –13 ≤ *l* ≤ 13 at 223 K. $R_1$ = 0.0412 [$I \geq 2\sigma(I)$, 956 reflections], $wR_2$ = 0.1062 (for all), and Gof = 1.093, 96 parameters; max./min. residual electron density: 0.253/–0.176 e Å$^{-3}$.

**Crystal Data for 18:** $C_{57}H_{60}O_2P_2PtS_2$ ($C_{45}H_{48}O_2P_2PtS_2$·2$C_6H_6$), $M_r$ = 1098.20 g mol$^{-1}$, yellow prism, crystal size = 0.25 × 0.20 × 0.12 mm, triclinic, $P\bar{1}$, *a* = 10.8885(8), *b* = 13.1343(10), *c* = 17.7604(13) Å, $\alpha$ = 81.859(2), $\beta$ = 88.115(2), $\gamma$ = 82.946(2)°, *V* = 2495.0(3) Å$^3$, $\rho_{calcd.}$ = 1.462 g cm$^{-3}$, *Z* = 2, $\mu$(Mo-$K_\alpha$) = 3.001 cm$^{-1}$. Intensity data of 9229 unique reflections were collected over the range –12 ≤ *h* ≤ 13, –15 ≤ *k* ≤ 15, –21 ≤ *l* ≤ 20 at 123 K. $R_1$ = 0.0341 [$I \geq 2\sigma(I)$, 8355 reflections], $wR_2$ = 0.0798 (for all), and Gof = 1.037, 584 parameters; max./min. residual electron density: 1.370/–0.423 e Å$^{-3}$.

**Crystal Data for 14:** $C_{47}H_{52}Cl_4OP_2PtS_2$ ($C_{45}H_{48}OP_2PtS_2$·2$CH_2Cl_2$), $M_r$ = 1095.910 g mol$^{-1}$, yellow prism, crystal size = 0.24 × 0.12 × 0.12 mm, triclinic, $P\bar{1}$, *a* = 11.6740(4), *b* = 14.6560(4), *c* = 15.3800(4) Å, $\alpha$ = 113.041(2), $\beta$ = 94.326(2), $\gamma$ = 91.289(2)°, *V* = 2410.72(12) Å$^3$, $\rho_{calcd.}$ = 1.510 g cm$^{-3}$, *Z* = 2, $\mu$(Mo-$K_\alpha$) = 3.319 cm$^{-1}$. Intensity data of 8622 unique reflections were collected over the range –14 ≤ *h* ≤ 14, –18 ≤ *k* ≤ 18, –19 ≤ *l* ≤ 18 at 298 K. $R_1$ = 0.0422 [$I \geq 2\sigma(I)$, 7676 reflections], $wR_2$ = 0.1179 (for all), and Gof = 1.037, 523 parameters; max./min. residual electron density: 0.958/–1.616 e Å$^{-3}$.

**Crystal Data for 19:** $C_{47}H_{52}Cl_4O_2P_2PtS_2$ ($C_{45}H_{48}O_2P_2PtS_2$·2$CH_2Cl_2$), $M_r$ = 1111.84 g mol$^{-1}$, yellow prism, 0.25 × 0.20 × 0.10 mm, triclinic, $P\bar{1}$, *a* = 11.6339(6), *b* = 14.6630(7), *c* = 15.1190(8) Å, $\alpha$ = 113.4220(10), $\beta$ = 94.0080(10), $\gamma$ = 93.0900(10)°, *V* = 2351.4(2) Å$^3$, $\rho_{calcd.}$ = 1.570 g cm$^{-3}$, *Z* = 2, $\mu$(Mo-$K_\alpha$) = 3.405 cm$^{-1}$. Intensity data of 8731 unique reflections were collected over the range –12 ≤ *h* ≤ 14, –17 ≤ *k* ≤ 16, –13 ≤ *l* ≤ 18 at 153 K. $R_1$ = 0.0438 [$I \geq 2\sigma(I)$, 7944 reflections], $wR_2$ = 0.1144 (for all), and Gof = 1.037, 523 parameters; max./min. residual electron density: 2.599/–1.047 e Å$^{-3}$.

**Crystal Data for 20:** $C_{47}H_{52}Cl_4O_6P_2PtS_2$ ($C_{45}H_{48}O_6P_2PtS_2$·2$CH_2Cl_2$), $M_r$ = 1175.84 g mol$^{-1}$, colorless prism, crystal size = 0.30 × 0.22 × 0.20 mm, monoclinic, $P2_1/c$, *a* = 11.9094(5), *b* = 24.2783(11), *c* = 16.9933(7) Å, $\beta$ = 98.3500(10)°, *V* = 4861.4(4) Å$^3$, $\rho_{calcd.}$ = 1.607 g cm$^{-3}$, *Z* = 4, $\mu$(Mo-$K_\alpha$) = 3.305 cm$^{-1}$. Intensity data of 9053 unique reflections were collected over the range –14 ≤ *h* ≤ 14, –28 ≤ *k* ≤ 29, –20 ≤ *l* ≤ 17 at 123 K. $R_1$ = 0.0294 ($I \geq 2\sigma(I)$, 8018 reflections), $wR_2$ = 0.0716 (for all), and Gof = 1.047, 565 parameters; max./min. residual electron density: 1.444/–0.844 e Å$^{-3}$.

CCDC-655818 (for **8**), -655819 (for **18**), -655820 (for **14**), -655821 (for **19**), and -655822 (for **20**) contain the supplementary crystallographic data. These data can be obtained free of charge from The Cambridge Crystallographic Data Centre via www.ccdc.cam.ac.uk/data_request/cif.

**Supporting Information** (see also the footnote on the first page of this article): $^{13}$C NMR spectra of **14**, **18**, and **20**, and $^1$H and $^{31}$P NMR spectra of **19** as a mixture with **14**.

## Acknowledgments

This work was supported by the Innovative Research Organization, Saitama University (A05-23 and A06-616).

[1] F. Freeman, *Chem. Rev.* **1984**, *84*, 117–135.
[2] E. L. Clenann, K. L. Stensaas, *Org. Prep. Proced. Int.* **1998**, *30*, 551–600.
[3] S. Lacombe, *Reviews on Heteroatom Chemistry* (Ed.: S. Oae), Myu, Tokyo, **1999**, vol. 21, 1–41.
[4] A. Ishii, M. Nakabayashi, J. Nakayama, *J. Am. Chem. Soc.* **1999**, *121*, 7959–7960.
[5] A. Ishii, M. Nakabayashi, Y.-N. Jin, J. Nakayama, *J. Organomet. Chem.* **2000**, *611*, 127–135.
[6] H. Oshida, A. Ishii, J. Nakayama, *Tetrahedron Lett.* **2002**, *43*, 5033–5037.
[7] H. Oshida, A. Ishii, J. Nakayama, *J. Org. Chem.* **2004**, *69*, 1695–1703.
[8] A. Ishii, S. Kashiura, H. Oshida, J. Nakayama, *Org. Lett.* **2004**, *6*, 2623–2626.
[9] A. Ishii, M. Ohishi, K. Matsumoto, T. Takayanagi, *Org. Lett.* **2006**, *8*, 91–94.
[10] A. Ishii, *J. Synth. Org. Jpn.* **2006**, *64*, 395–405.
[11] W. Weigand, S. Bräutigam, G. Mloston, *Coord. Chem. Rev.* **2003**, *245*, 167–175.
[12] W. Weigand, G. Bosl, C. Robl, W. Amrein, *Chem. Ber.* **1992**, *125*, 1047–1051.
[13] W. Weigand, R. Wünsch, *Chem. Ber.* **1996**, *129*, 1409–1419.
[14] W. Weigand, R. Wünsch, K. Polborn, G. Mloston, *Z. Anorg. Allg. Chem.* **2001**, *627*, 1518–1522.
[15] W. Weigand, R. Wünsch, C. Robl, G. Mloston, H. Nöth, M. Schmidt, *Z. Naturforsch.* **2000**, *55b*, 453–458.
[16] R. Wünsch, W. Weigand, G. Nuspl, *J. Pract. Chem.* **1999**, *341*, 768–772.
[17] W. Weigand, R. Wünsch, K. Polborn, *Inorg. Chim. Acta* **1998**, *273*, 106–110.
[18] A. Ishii, M. Saito, M. Murata, J. Nakayama, *Eur. J. Org. Chem.* **2002**, 979–982.

 © 2007 Wiley-VCH Verlag GmbH & Co. KGaA, Weinheim 

[19] A. Ishii, T. Kawai, M. Noji, J. Nakayama, *Tetrahedron* **2005**, *61*, 6693–6699.
[20] A. Ishii, M. Murata, H. Oshida, K. Matsumoto, J. Nakayama, *Eur. J. Inorg. Chem.* **2003**, 3716–3721.
[21] S. M. Aucott, H. L. Milton, S. D. Robertson, A. M. Z. Slawin, G. D. Walker, J. D. Woollins, *Chem. Eur. J.* **2004**, *10*, 1666–1676.
[22] S. M. Aucott, P. Kilian, S. D. Robertson, A. M. Z. Slawin, J. D. Woollins, *Chem. Eur. J.* **2006**, *12*, 895–902.
[23] T. Shigetomi, H. Soejima, Y. Nibu, K. Shioji, K. Okuma, Y. Yokomori, *Chem. Eur. J.* **2006**, *12*, 7742–7748.
[24] A. Ishii, S. Kashiura, Y. Hayashi, W. Weigand, *Chem. Eur. J.* **2007**, *13*, 4326–4333.
[25] C. A. Grapperhaus, M. Y. Darensbourg, *Acc. Chem. Res.* **1998**, *31*, 451–459.
[26] Y. Zhang, K. D. Ley, K. S. Schanze, *Inorg. Chem.* **1996**, *35*, 7102–7110.
[27] W. B. Connick, H. B. Gray, *J. Am. Chem. Soc.* **1997**, *119*, 11620–11627.
[28] T. M. Cocker, R. E. Bachman, *Inorg. Chem.* **2001**, *40*, 1550–1556.
[29] G. N. Schrauzer, C. Zhang, R. Chadha, *Inorg. Chem.* **1990**, *29*, 4104–4107.
[30] I. Font, R. Buonomo, J. H. Reibenspies, M. Y. Darensbourg, *Inorg. Chem.* **1993**, *32*, 5897–5898.
[31] P. J. Farmer, J.-N. Verpeaux, C. Amatore, M. Y. Darensbourg, G. Musie, *J. Am. Chem. Soc.* **1994**, *116*, 9355–9356.
[32] R. M. Buonomo, I. Font, M. J. Maguire, J. H. Reibenspies, T. Tuntulani, M. Y. Darensbourg, *J. Am. Chem. Soc.* **1995**, *117*, 963–973.
[33] M. Y. Darensbourg, T. Tuntulani, J. H. Reibenspies, *Inorg. Chem.* **1995**, *34*, 6287–6294.
[34] C. A. Grapperhaus, M. Y. Darensbourg, L. W. Sumner, D. H. Russell, *J. Am. Chem. Soc.* **1996**, *118*, 1791–1792.
[35] J. A. Bellefeuille, C. A. Grapperhaus, R. M. Buonomo, J. H. Reibenspies, M. Y. Darensbourg, *Organometallics* **1998**, *17*, 4813–4821.
[36] C. A. Grapperhaus, C. S. Mullins, P. M. Kozlowski, M. S. Mashuta, *Inorg. Chem.* **2004**, *43*, 2859–2866.
[37] T. Tuntulani, G. Musie, J. H. Reibenspies, M. Y. Darensbourg, *Inorg. Chem.* **1995**, *34*, 6279–6286.
[38] K. Sugimoto, T. Kuroda-Sowa, M. Maekawa, M. Munakata, *Bull. Chem. Soc. Jpn.* **2000**, *73*, 391–394.
[39] W. Su, R. Cao, M. Houg, D. Wu, J. Lu, *J. Chem. Soc. Dalton Trans.* **2000**, 1527–1532.
[40] W. A. Schenk, J. Frisch, W. Adam, F. Prechtl, *Inorg. Chem.* **1992**, *31*, 3329–3331.
[41] A. Ishii, T. Kawai, K. Tekura, H. Oshida, J. Nakayama, *Angew. Chem. Int. Ed.* **2001**, *40*, 1924–1926.
[42] I.-P. Lorenz, J. Kull, *Angew. Chem. Int. Ed. Engl.* **1986**, *25*, 261–262.
[43] R. K. Henderson, E. Bouwman, A. L. Spek, J. Reedijk, *Inorg. Chem.* **1997**, *36*, 4616–4617.
[44] F. H. Allen, O. Kennard, D. G. Watson, L. Brammer, A. G. Orpen, *J. Chem. Soc. Perkin Trans. 2* **1987**, S1–S19.
[45] a) W. Adam, J. Bialas, L. Hadjiarapoglou, *Chem. Ber.* **1991**, *124*, 2377; b) W. Adam, L. Hadjiarapoglou, A. Smerz, *Chem. Ber.* **1991**, *124*, 227–232.
[46] G. M. Sheldrick, *SHELXL-97, Program for Crystal Structure Refinement*, Göttingen University, Germany, **1997**.

Received: August 6, 2007
Published Online: September 26, 2007

 © 2007 Wiley-VCH Verlag GmbH & Co. KGaA, Weinheim 

DOI: 10.1002/ejic.200700368

# The Spectroscopic, Electrochemical and Structural Characterization of a Family of Ru Complexes Containing the $C_2$-Symmetric Didentate Chiral 1,3-Oxazoline Ligand and Their Catalytic Activity

**Xavier Sala,[a] Naiara Santana,[a] Isabel Serrano,[a] Elena Plantalech,[a] Isabel Romero,[a] Montserrat Rodríguez,*[a] Antoni Llobet,*[b,c] Susanna Jansat,[d] Montserrat Gómez,[d] and Xavier Fontrodona[e]**

**Keywords:** Ruthenium / N ligands / Epoxidation / Chiral ligands / Atropisomerism

The structural, spectroscopic, and electrochemical characterization and a preliminary catalytic investigation of a family of $Ru^{II}$ complexes with general formula $[Ru(Y)(terpy)(phbox\text{-}R)]^{n+}$ [where terpy is 2,2′:6′,2′′-terpyridine, phbox-R is a $C_2$-symmetric bidentate oxazoline ligand (R = Et or *i*Pr), and Y is a monodentate ligand], are discussed. The X-ray structure of $[RuCl(terpy)(phbox\text{-}i\text{Pr})]^{2+}$ has been solved and confirms, as we described recently, the predicted generation of the less hindered atropisomer, which is determined by the conformation of the stereogenic centers in the bidentate ligand. The catalytic properties of the aquo complexes have been tested in epoxidation reactions, and moderate selectivity for the epoxides is obtained for styrene and *trans*-stilbene when using $PhI(OAc)_2$ as co-oxidant.
(© Wiley-VCH Verlag GmbH & Co. KGaA, 69451 Weinheim, Germany, 2007)

## Introduction

$C_2$-Symmetric bis(1,3-oxazolines) have received an increasing amount of attention over the last few years, as can be seen from the increasing number of publications dealing with this type of ligand.[1] Since the first reports of the use of chiral oxazoline ligands in asymmetric catalysis,[2] a great variety of oxazoline-based compounds have been synthesized and successfully tested as catalysts,[3] and their coordination chemistry studied,[4] mainly because of their ease of preparation and versatility.

Atropisomerism, where chirality is generated due to rotational restriction between two isomers containing axially chiral biaryl compounds,[5,6] is a good way of obtaining efficient tools in asymmetric synthesis[6a,7] (for example the rigid molecular frameworks obtained from chiral ligands like BINAP[8]), and has found important applications in diverse areas such as liquid crystals, pharmaceuticals, nanoscale information storage, or biomimetic catalysis.[9]

Transition metal complexes bearing oxazoline ligands have shown good activities and enantioselectivities in a myriad of catalytic organic syntheses involving metals such as Cu or Fe.[10] However, the performance of oxazoline-containing ruthenium complexes as catalysts has been developed only very recently, and the number of contributions in this area is still limited.[11] Their performance as asymmetric epoxidation catalysts with clean oxidants such as $H_2O_2$, where they show good results in terms of both chemo- and enantioselectivity, has been widely studied by Beller and co-workers.[12]

Interest in polypyridylruthenium complexes stems from their multiple applications in scientific fields such as photophysics and photochemistry,[13] catalysis,[14] and bioinorganic chemistry.[15] One of the main goals for this type of complex is the design of structures that allow the fine-tuning of their redox, absorption, and emission properties. Among redox properties, and especially from a catalytic perspective, one of the major aims is the design of Ru=O functional groups and analogues capable of reversibly accepting multiple electrons and protons within a relatively narrow potential range.[16]

With all this in mind, we present here the complete characterization and catalytic activity of a family of ruthenium complexes bearing $C_2$-symmetric oxazoline ligands, including two aquo complexes that are potential pre-catalysts for redox processes involving the above mentioned Ru=O group. The chirality of the complexes prepared is determined by the stereogenic centers in the oxazoline entities

[a] Departament de Química, Universitat de Girona, Campus de Montilivi,
17071 Girona, Spain
[b] Institut Català d'Investigació Química (ICIQ),
Av. Paisos Catalans 16, 43007 Tarragona, Spain
[c] Departament de Química, Universitat Autònoma de Barcelona, Cerdanyola del Vallès, 08193 Barcelona, Spain
[d] Departament de Química Inorgànica, Universitat de Barcelona, Martí i Franquès 1–11, 08028 Barcelona, Spain
[e] Serveis Tècnics de Recerca, Universitat de Girona, Edifici P II, Campus Montilivi,
17071 Girona, Spain
Supporting information for this article is available on the WWW under http://www.eurjic.org or from the author.

 © 2007 Wiley-VCH Verlag GmbH & Co. KGaA, Weinheim 

but also by the chiral axes generated upon coordination of the ligand, which leads to atropisomeric forms.

## Results and Discussion

### Synthesis and Solid-State Structure

The complexes described here have the general formula $[Ru(Y)(terpy)(phbox\text{-}R)]^{n+}$, where phbox-R is one of the two oxazoline ligands depicted in Figure 1 and Y is a monodentate ligand [Cl, $H_2O$, MeCN, pyridine (py), or 2-hydroxypyridine (2-OH-py)]. The chlorido complexes ($R_cR_c$,$S_aR_a$)-**2a** and ($S_cS_c$,$R_aS_a$)-**2b** were obtained by reduction of $[RuCl_3(terpy)]$ (**1**) in the presence of the appropriate bidentate oxazoline ligand, and the remaining compounds were derived from these two complexes or their aquo analogs ($R_cR_c$,$S_aR_a$)-**3a** and ($S_cS_c$,$R_aS_a$)-**3b**. The nomenclature of the complexes, as explained in the Experimental Section, involves a variety of chiral configurations arising from (1) the stereogenic centers inherent to each oxazoline ligand (either *R*,*R* or *S*,*S*; see Figure 1), which are represented by the first two letters having a "c" subscript, and (2) the chiral axes generated upon coordination of the ligand to the ruthenium metal center, as symbolized by the two remaining letters of the nomenclature used, with an "a" subscript. The two latter letters correspond to the chiral axis involving the oxazolinyl ring *trans* to the terpy ligand and that involving the ring *trans* to the monodentate ligand Y, respectively. The formation of one or other isomer is determined by the configuration of the oxazoline ligand (see below).

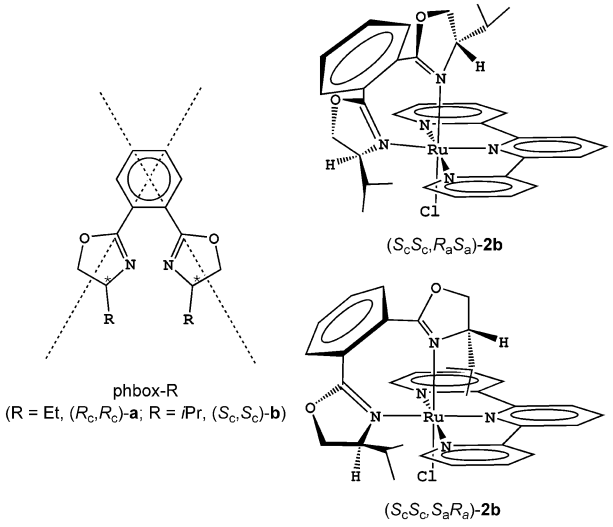


Figure 1. Atropisomers generated upon phbox-R ligand coordination.

The X-ray crystal structure for the cationic moiety of complex ($S_cS_c$,$R_aS_a$)-**2b** is shown in Figure 2; Table 1 lists selected bond lengths and angles. Further crystallographic information for this structure can be found in the Experimental Section. This cation presents a highly distorted octahedral environment around the Ru metal center, with the terpy ligand coordinating in a meridional fashion through its N atoms. Two of the remaining coordination sites are occupied by the didentate oxazoline ligand, whereas the sixth coordinative position is occupied by a chlorido ligand. The high distortion revealed in this cation is partly explained by the structural restrictions imposed by the terpy ligand coordination, which narrows the N1–Ru–N3 bond angle to 157.3°, far from the ideal value of 180° for a regular octahedral geometry.

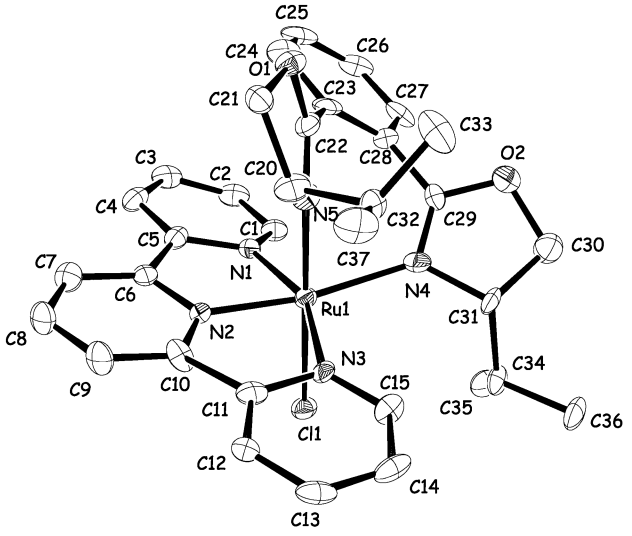


Figure 2. ORTEP plot (ellipsoids at 50% probability) of the cationic moiety of complex ($S_cS_c$,$R_aS_a$)-**2b**, including the atom numbering scheme.

Table 1. Selected bond lengths and angles for complex ($S_cS_c$,$R_aS_a$)-**2b**.

| Bond lengths [Å] | | Bond angles [°] | |
|---|---|---|---|
| Ru1–N1 | 2.042 | N1–Ru1–N2 | 79.26 |
| Ru1–N2 | 1.935 | N1–Ru1–N3 | 157.34 |
| Ru1–N3 | 2.126 | N1–Ru1–N4 | 98.95 |
| Ru1–N4 | 2.162 | N1–Ru1–N5 | 90.97 |
| Ru1–N5 | 2.035 | N2–Ru1–N3 | 78.87 |
| Ru1–Cl1 | 2.416 | N2–Ru1–N4 | 170.06 |
| | | N2–Ru1–N5 | 87.31 |
| | | N3–Ru1–N4 | 103.62 |
| | | N3–Ru1–N5 | 93.86 |
| | | N4–Ru1–N5 | 82.93 |
| | | Cl1–Ru1–N1 | 87.28 |
| | | Cl1–Ru1–N2 | 92.71 |
| | | Cl1–Ru1–N3 | 87.90 |
| | | Cl1–Ru1–N4 | 96.98 |
| | | Cl1–Ru1–N5 | 178.21 |

Coordination of the phbox-*i*Pr ligand, as described previously for analogous complexes,[17] generates a seven-membered ring which is unlikely to keep a planar conformation because of structural restrictions. The ligand is thus forced to bend in order to accommodate itself upon coordination, and this bending leads to two possible atropisomeric configurations depending on the final orientation of the central phenyl ring of the phbox-*i*Pr ligand, in other words over the N1 or N3 pyridyl rings of the terpy ligand (see Figure 1 for schematic drawings of the two possible conformations).

 © 2007 Wiley-VCH Verlag GmbH & Co. KGaA, Weinheim 

The coordination of the ligand also fixes its two oxazolinyl rings in a twisted position with regard to the central phenyl ring plane, thereby generating the two chiral axes depicted in Figure 1. The formation of one or the other atropisomer is governed by the configuration of the stereogenic centers (C20 and C31) of the oxazolinyl rings in such a way that only one atropisomer (the one that keeps the *i*Pr groups farthest away from the terpy plane) is found. The X-ray structural analysis of complex ($S_cS_c,R_aS_a$)-**2b** shows that the atropisomer generated is indeed the $S_cS_c,R_aS_a$ one, as expected for an *S*,*S* configuration of the oxazoline ligand. The N4 and N5 oxazolinyl rings of the phbox-*i*Pr ligand are rotated by 51.47° and 40.26°, respectively, with regard to the central phenyl ring, and the N5–Ru–N4 angle is 82.93°.

The terpy ligand is not perfectly planar and experiments a slight twofold bending, with the two peripheral N1 and N3 pyridyl rings pointing away from the plane of the central N2 ring (the torsion angles are 8.64° and 7.7°, respectively, which gives an overall bending of 15.53° for the ligand). The rotation of the N1 ring of the terpy ligand with regard to the central pyridyl ring in terpy places it in an almost parallel disposition with regard to the central phenyl ring of the phbox-*i*Pr ligand (the angle between these two rings is 19.91°).

Finally, the cationic moieties in the crystal interact with one another through a series of hydrogen bonds that involve the chlorido ligand of one molecule and H7 and H13 of two neighboring molecules, with contact distances of 2.65 and 2.85 Å, respectively. These interactions arrange the complex molecules such that they form pseudo-square channels in the direction of the crystallographic *b* axis, which also allow a certain degree of π-stacking between the terpy ligands of adjacent entities (see the Supporting Information for diagrams of these 3D interactions).

## Spectroscopic Properties

The UV/Vis spectra of complexes **2a**,**b**–**5a**,**b** and **6b** were recorded in dichloromethane and/or phosphate buffer solution. The main absorption wavelengths, together with their assignments, are listed in Table 2. The assignment of the spectral absorptions of $Ru^{II}$ octahedral complexes has already been well documented[18] and, accordingly, the set of highly energetic bands at wavelengths below 350 nm can be assigned to π→π* intraligand transitions. Several charge-transfer dπ(Ru)→π* MLCT absorptions in the visible region of the spectra are also present for this family of compounds. These probably involve the π antibonding orbitals of terpy as the higher aromatic character of this ligand lowers its orbitals' energies with regard to the phbox-R ligand.

No significant differences can be found in Table 2 between analogous complexes containing the phbox-Et or the phbox-*i*Pr oxazoline ligands. However, the electronic nature of the monodentate Y ligand influences the energies of the transitions involving orbitals with $d_{(Ru)}$ character to some extent. Thus, as expected, the π-donor character of the chlorido ligand increases the energy of the $d_{(Ru)}$ filled orbitals, with complexes ($R_cR_c,S_aR_a$)-**2a** and ($S_cS_c,R_aS_a$)-**2b** being the ones that show the most red-shifted MLCT bands. Complexes **5** and **6**, which contain py and 2-OH-py ligands, respectively, show absorption energies similar to those found for the corresponding aquo complexes **3a**,**b**, therefore it can be concluded that the electron-withdrawing π effects of the corresponding aromatic systems in the pyridine-type ligands are minimal. This is consistent with the rapid ligand rotation determined in solution from NMR experiments.[17]

Finally, a comparison of these complexes with structurally similar Ru complexes also containing terpy reveals that, for complexes with bidentate oxazoline ligands,[19] MLCT

Table 2. UV/Vis spectroscopic data for complexes **2a**,**b**–**5a**,**b** and **6b**.

| Compound | Solvent | $\lambda_{max}$, nm ($\varepsilon$, $M^{-1}cm^{-1}$) | Assignment |
|---|---|---|---|
| ($R_cR_c,S_aR_a$)-**2a** | $CH_2Cl_2$ | 282 (20360), 324 (26359) | π→π* |
| | | 370 (5617), 524 (5534), 570 (5202) | dπ→π* |
| ($S_cS_c,R_aS_a$)-**2b** | $CH_2Cl_2$ | 284 (23139), 322 (29822) | π→π* |
| | | 368 (6468), 530 (5342), 562 (5585) | dπ→π* |
| ($R_cR_c,S_aR_a$)-**3a** | $CH_2Cl_2$ | 282 (20215), 318 (28681) | π→π* |
| | | 475 (sh), 518 (4935) | dπ→π* |
| | phosphate buffer pH 7 | 280 (21538), 316 (25538) | π→π* |
| | | 470 (sh), 518 (4745) | dπ→π* |
| ($S_cS_c,R_aS_a$)-**3b** | $CH_2Cl_2$ | 278 (28320), 318 (29792) | π→π* |
| | | 486 (4989), 520 (4950) | dπ→π* |
| | phosphate buffer pH 7 | 264 (17983), 316 (23760) | π→π* |
| | | 467 (3296), 525 (3948) | dπ→π* |
| ($S_cS_c,R_aS_a$)-**4b** | $CH_2Cl_2$ | 280 (19150), 315 (18540), 327 (17340) | π→π* |
| | | 383 (5970), 412 (5980), 541 (4730), 567 (sh) | dπ→π* |
| ($R_cR_c,S_aR_a$)-**5a** | $CH_2Cl_2$ | 276 (22429), 318 (30269) | π→π* |
| | | 370 (sh), 475 (sh), 518 (5162) | dπ→π* |
| ($S_cS_c,R_aS_a$)-**5b** | $CH_2Cl_2$ | 278 (26080), 318 (35425) | π→π* |
| | | 370 (sh), 470 (sh), 512 (5690) | dπ→π* |
| ($S_cS_c,R_aS_a$)-**6b** | $CH_2Cl_2$ | 276 (26120), 316 (30050) | π→π* |
| | | 377 (sh), 494 (3920), 534 (sh) | dπ→π* |

 © 2007 Wiley-VCH Verlag GmbH & Co. KGaA, Weinheim 

transitions generally take place at much lower energies than those of analogous complexes having aromatic bidentate ligands,[20] thereby manifesting the increased electron-donor capacity of the oxazoline entities.

Acid-base titration was performed on complex ($S_cS_c$,$R_aS_a$)-**3b** by slow addition of NaOH to an acidic aqueous solution of the complex [Equation (1)].

$$[Ru(terpy)(phbox\text{-}iPr)(OH_2)]^{2+} \rightarrow [Ru(terpy)(phbox\text{-}iPr)(OH)]^{+} + H^{+} \quad (1)$$

The initial and final UV/Vis spectra, together with several intermediate spectra (inset), are displayed in Figure 3. The MLCT bands shift to longer wavelengths (520 and 518 nm) upon deprotonation of the aquo ligand, in agreement with the relative destabilization of the dπ(Ru) levels provoked by the anionic hydroxido ligand in a similar way to that described above for the chlorido ligand.[20d]

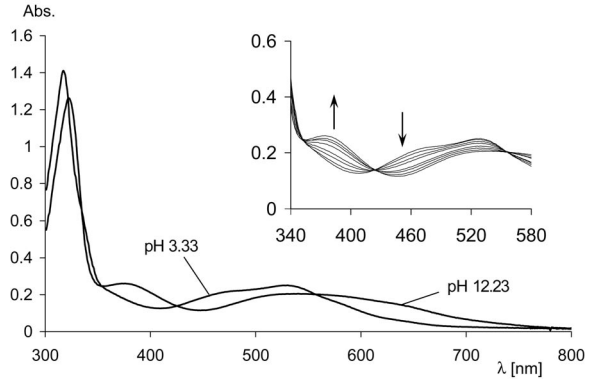


Figure 3. UV/Vis spectra of the aquo and hydroxo forms of complex ($S_cS_c$,$R_aS_a$)-**3b** at pH 3.33 and 12.23, respectively. The inset shows a detail of three of the five isosbestic points found from acid-base titration of the aquo complex with NaOH (pH values are 3.3, 8.81, 9.41, 9.60, 10.21, 10.48, 10.88, and 12.23).

The five isosbestic points at $\lambda$ = 322, 335, 352, 424, and 556 nm suggest that the aquo and hydroxo species interconvert in a net way, without generation of any side product. Addition of *p*-toluenesulfonic acid at the end of the titration regenerates the initial aquo complex. The p$K_a$ of 10.45 calculated for the deprotonation of the aquo ligand from acid-base titration is in good agreement with the value extracted from its Pourbaix diagram (see below). The complex ($R_cR_c$,$S_aR_a$)-**3a** behaves in an analogous manner, and the UV/Vis spectra of its aquo and hydroxido forms are presented as Supporting Information.

### Electrochemical and Catalytic Properties

The redox behavior of the complexes **2a**,**b**–**5a**,**b** and **6b** was studied by cyclic voltammetry. The chlorido complexes ($R_cR_c$,$S_aR_a$)-**2a** and ($S_cS_c$,$R_aS_a$)-**2b** show a simple chemically and electrochemically reversible wave in acetonitrile, which corresponds to the $Ru^{III}/Ru^{II}$ couple, at $E_{1/2}$ values of 0.70 and 0.71 V respectively. The analogous pyridine complexes ($R_cR_c$,$S_aR_a$)-**5a** and ($S_cS_c$,$R_aS_a$)-**5b** undergo an equivalent redox process at higher potential values ($E_{1/2}$ = 1.15 and 1.18 V, respectively), which is consistent with the lower electron-donating capability of the py ligand with regard to the chlorido ligand. Pyridine ligands could, in principle, produce a π-accepting effect involving the empty antibonding orbitals of the aromatic system, although this appears to be negligible for this family of complexes as inferred, as described above, from the NMR and UV/Vis spectra. The π-acceptor nature of the monodentate acetonitrile ligand is significantly manifested in ($S_cS_c$,$R_aS_a$)-**4b**, however, which presents a redox potential of 1.22 V.

The 2-OH-py complex ($S_cS_c$,$R_aS_a$)-**6b** presents a surprisingly low $E_{1/2}$ value of 0.755 V in dichloromethane. Considering the relatively long $Ru–N_{2\text{-}OH\text{-}py}$ bond length inferred from DFT calculations[17] (around 2.23 Å) one would expect a redox potential somewhat higher than those found for pyridine complexes **5a**,**b** due to the decreased σ donation. The OH group in the ring must therefore play a determinant role in the redox behavior of the complex by stabilizing the $Ru^{III}$ oxidation state through extra σ donation, probably involving deprotonation of the ligand (the p$K_a$ value for 2-OH-py is 0.75) and effective coordination of the corresponding anionic, 2-pyridonyl tautomeric form.

The cyclic voltammograms of the aqua complexes ($R_cR_c$,$S_aR_a$)-**3a** and ($S_cS_c$,$R_aS_a$)-**3b** were recorded in both dichloromethane and aqueous phosphate buffer solution. Only one redox process, corresponding to the $Ru^{IV}/Ru^{III}$ redox couple, appears in $CH_2Cl_2$ at $E_{1/2}$ = 0.98 V for both compounds. The intensity decrease or even the disappearance of the $Ru^{III}/Ru^{II}$ wave for this type of complex in dichloromethane is assigned to kinetic factors and has been described previously for similar complexes.[21] Two reversible waves, corresponding to the $Ru^{IV}/Ru^{III}$ and $Ru^{III}/Ru^{II}$ redox couples, can be observed in aqueous solution (pH 6) at $E_{1/2}$ = 0.64 and 0.46 V, respectively, for complex ($R_cR_c$,$S_aR_a$)-**3a** and at $E_{1/2}$ = 0.65 and 0.46 V, respectively, for ($S_cS_c$,$R_aS_a$)-**3b** (the cyclic voltammogram recorded for the latter is provided as Supporting Information).

The difference in the potential values of these two oxidation processes in a specific Ru-aquo complex seems to be directly related to the σ-donor and π-acceptor capacity of the ancillary ligands, as has been described by Meyer and co-workers[22a] on the basis of some empirical parameters previously calculated by Lever.[22b] As shown by the authors, two pseudo-linear relationships correlate the difference between the $E_{1/2}$ value for the two oxidation processes, $\Delta E_{1/2}$ (IV/III – III/II), with an empirical coefficient obtained from the ligands coordinated to the metal center (Figure 4). Two groups of compounds can be clearly distinguished depending on the σ-donor or π-acceptor properties of the ligands, denoted with squares and diamonds, respectively, in Figure 4.

The relatively weak π-acceptor character of the oxazoline ligand (with an empirical Lever contribution of 0.21; see the Supporting Information for a detailed description of the calculations) in complexes ($R_cR_c$,$S_aR_a$)-**3a** and ($S_cS_c$,$R_aS_a$)-**3b** places these complexes in the middle right half of the graph, far away from the central zone for two-electron processes (the aquo complexes described here are represented by a dot in Figure 4).

 © 2007 Wiley-VCH Verlag GmbH & Co. KGaA, Weinheim 

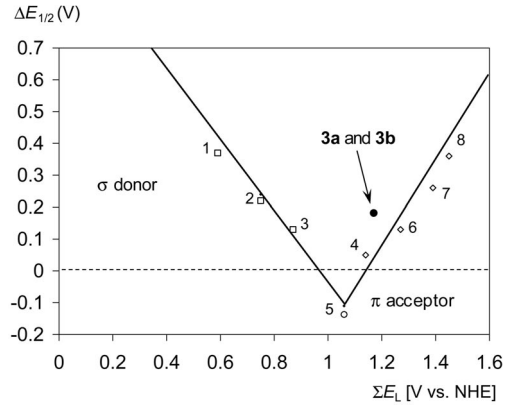


Figure 4. Meyer–Lever plot of $\Delta E_{1/2}$ vs. $\Sigma E_L$. [where $\Delta E_{1/2}$ is the difference between the $E_{1/2}$(IV/III) and $E_{1/2}$(III/II) redox potentials for the family of complexes studied]. (1) $[Ru(terpy)(acac)(OH_2)]^+$; (2) *cis*-$[Ru(terpy)(pic)(OH_2)]^+$ (pic = picolinate); (3) $[Ru(terpy)(tmen)(OH_2)]^{2+}$ (tmen = *N*,*N*,*N*,*N*-tetramethylethylenediamine); (4) $[Ru(CNC)(bpy)(OH_2)]^{2+}$ (see ref.[27]); (5) $[Ru(CNC)(n\text{BuCN})(OH_2)]^{2+}$;[27] (6) $[Ru(terpy)(bpy)(OH_2)]^{2+}$ (bpy = 2,2′-bipyridine); (7) $[Ru(bpy)_2(OH_2)(PPh_3)]^{2+}$; (8) $[Ru(terpy)(dppene)(OH_2)]^{2+}$ [dppene = *cis*-1,2-bis(diphenylphosphanyl)ethylene].

Generation of the higher oxidation state species was followed spectrophotometrically for the aquo complexes **3a**,**b**. Figure 5 shows the spectra obtained upon progressive addition of small amounts of $Ce^{IV}$ to an aqueous solution of complex ($S_cS_c$,$R_aS_a$)-**3b** at pH 1 until addition of one equivalent. The five isosbestic points observed at $\lambda$ = 270, 283, 297, 333, and 420 nm again suggest a net generation of the $Ru^{III}$ species.

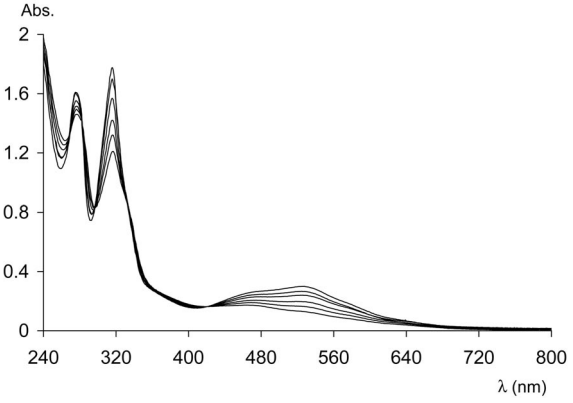


Figure 5. UV/Vis spectra registered after addition of successive amounts of $Ce^{IV}$ (up to 1 equiv.) to a 0.14 mM solution of complex ($S_cS_c$,$R_aS_a$)-**3b** in 0.1 M $HClO_4$.

Addition of a second equivalent of $Ce^{IV}$ produces a further oxidation of the complex that generates the corresponding $Ru^{IV}$-oxo species, which is almost featureless in the visible region, as has been described for analogous complexes.[20d,23] This second redox process also takes place with the presence of isosbestic points, and the manifold of spectra recorded is presented as Supporting Information together with the redox titration of complex ($R_cR_c$,$S_aR_a$)-**3a**, which follows a similar trend.

Ruthenium aquo complexes show a pH-dependence of their redox potentials due to deprotonation of the aqua ligand bonded to the metal center [Equation (2)].

$$Ru^{II}\text{-}OH_2 \underset{+H^+,+e^-}{\overset{-H^+,-e^-}{\rightleftharpoons}} Ru^{III}\text{-}OH \underset{+H^+,+e^-}{\overset{-H^+,-e^-}{\rightleftharpoons}} Ru^{IV}{=}O \quad (2)$$

This dependence is usually reflected in so-called Pourbaix diagrams, and the results obtained for complex ($S_cS_c$,$R_aS_a$)-**3b** are displayed in Figure 6.

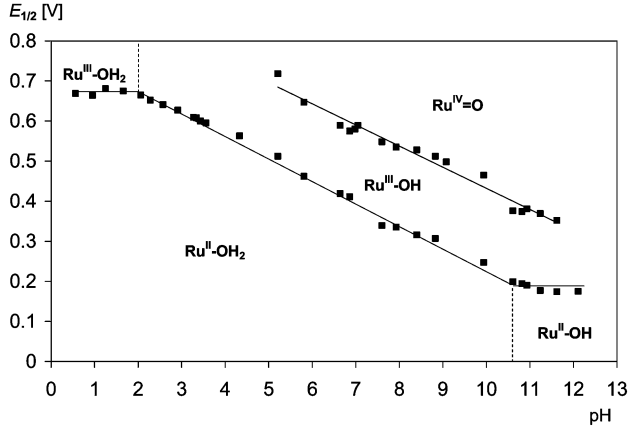


Figure 6. A plot of $E_{1/2}$ vs. pH (Pourbaix diagram) for complex ($S_cS_c$,$R_aS_a$)-**3b**. The pH/potential regions of stability for the various oxidation states and their dominant proton compositions are indicated by using abbreviations such as $Ru^{II}$–$OH_2$, for example, for $[Ru^{II}(terpy)(phbox\text{-}iPr)(H_2O)]^{2+}$. The p$K_a$ values are shown by the vertical dashed lines in the various *E*/pH regions.

The two independent one-electron redox processes that take place with simultaneous proton transfer at pH values between 5 and 10.5 are assignable to $Ru^{II}\rightarrow Ru^{III}$ and $Ru^{III}\rightarrow Ru^{IV}$ oxidations. The corresponding lines present a slope of approximately 59 mV per pH unit, as expected for a one-electron one-proton transfer; see Equation (2). At lower pH, only the $Ru^{III/II}$ couple can be observed. The diminishment or disappearance of the $Ru^{IV/III}$ redox couple in CV experiments is quite common for aquo complexes and is assumed to be caused by slow heterogeneous electron-transfer kinetics from the solution to the electrode surface.[23a,24] The stability regions for species having different proton composition are indicated in the diagram along with the p$K_a$ values for $Ru^{III}$ and $Ru^{II}$ aquo complexes, which are around 1.93 and 10.44. respectively. The latter value is fully consistent with the value determined from acid-base spectrophotometric titration, as described above.

Complex ($R_cR_c$,$S_aR_a$)-**3a** behaves in a similar way to ($S_cS_c$,$R_aS_a$)-**3b** (the corresponding Pourbaix diagram is supplied as Supporting Information). In this case, the $Ru^{IV/III}$ redox couple can be observed even at a pH lower than 4 and the p$K_a$ values for the $Ru^{III}$–$OH_2$ and $Ru^{II}$–$OH_2$ species are 2.1 and 11.1, respectively.

The redox catalytic properties of ($S_cS_c$,$R_aS_a$)-**3b** were tested in the electrochemical oxidation of target substrates such as benzyl alcohol and methyl *p*-tolyl sulfide in aqueous

 © 2007 Wiley-VCH Verlag GmbH & Co. KGaA, Weinheim 

Table 3. Alkene epoxidation catalyzed by ($S_cS_c$,$R_aS_a$)-**3b**.[a]

| Entry | Substrate | Oxidant | Substr./cat. | % Conversion | % Epoxide yield | % Bz[b] yield | Catalytic cycles |
|---|---|---|---|---|---|---|---|
| 1 | styrene | $PhI(OAc)_2$ | 200:1 | 67.3 | 36.1 | 6.1 | 71.3 |
| 2 | *trans*-stilbene | $PhI(OAc)_2$ | 150:1 | 71 | 37.4 | 4.1 | 57.9 |
| 3 | styrene | PhIO | 200:1 | 48.9 | 22.4 | 10.1 | 44.1 |
| 4 | *trans*-stilbene | PhIO | 200:1 | 74.3 | 44 | 29.6 | 87.6 |

[a] Reactions were performed at room temperature in 1,2-dichloroethane with an oxidant/substrate molar ratio of 2:1. [b] Bz stands for benzaldehyde.

neutral media. The system "0.5 mM **3b**/50 mM substrate/pH 7 phosphate buffer" at an $E_{app}$ of 0.9 V generated the respective oxidation products (benzaldehyde and sulfoxide) with good selectivities but poor yields (50% and 13% respectively), representing up to 50 and 13 catalytic cycles, after seven hours. No *ee* was observed for the sulfoxide obtained from the prochiral sulfide substrate. The electrocatalytic activity for the oxidation of benzyl alcohol is also visible in the cyclic voltammogram, with an increase in the anodic intensity at lower potential in the presence of the catalyst (see Figure S7 in the Supporting Information). The electrocatalytic oxidation of benzyl alcohol was also tested in a basic medium (0.1 M NaOH; applied potential: 0.5 V); conversions and selectivities were similar to those obtained in a neutral medium.

The catalytic activity of ($S_cS_c$,$R_aS_a$)-**3b** was also tested with regard to its ability to epoxidize alkenes. Styrene and *trans*-stilbene were chosen as substrates with PhIO and $PhI(OAc)_2$ as oxidants in 1,2-dichloroethane; the results, which were quantified by GC chromatography, are reported in Table 3. A first glance shows that the main products formed are the corresponding epoxides (styrene oxide and trans-stilbene oxide), along with minor amounts of benzaldehyde, in all cases. However, although good selectivity was achieved for the desired products, the enantioselectivity values for these reactions were low (never higher than 10% *ee*). The selectivity for the epoxide is slightly higher when $Ph(IOAc)_2$ is used as co-oxidant instead of PhIO (compare for instance entries 2 and 4 in Table 3). *trans*-Stilbene also provides better conversion and epoxide yields than styrene, probably due to the tendency of the latter to undergo double-bond cleavage and polymerization under oxidative conditions.

A potential explanation for this low enantioselectivity can be inferred from the complex structure. The approach of a prochiral substrate to the active site of the catalysts takes place in the region of the planar terpy ligand, therefore the stereogenic center in the oxazoline ligand only has a very small effect on the orientation of the substrate (see Figure 2 and the Supporting Information for different structural views of the molecular catalyst). Thus, the catalyst/substrate Interaction can occur through multiple orientations, thereby leading to racemic mixtures of reaction products.

## Conclusion

A new family of ruthenium complexes bearing terpy, oxazoline, and a monodentate ligand has been synthesized and thoroughly characterized. The catalytic activity of the aquo complexes in epoxidation catalysis has been tested. These complexes show moderate activity and chemoselectivity for the epoxide but with only low enantiomeric excesses. We are now working towards the optimization of the reaction conditions by using clean oxidants such as $H_2O_2$, and also towards a redesign of the catalysts' structures in order to achieve higher enantioselectivities.

## Experimental Section

**Materials:** All reagents used in the present work were obtained from Aldrich Chemical Co and were used without further purification. Reagent-grade organic solvents were obtained from SDS and high purity deionized water was obtained by passing distilled water through a nano-pure Mili-Q water purification system. $RuCl_3 \cdot 2H_2O$, was supplied by Johnson–Matthey Ltd. and was used as received.

**Instrumentation and Measurements:** UV/Vis spectra were recorded with a Cary 50 Scan (Varian) UV/Vis spectrophotometer in 1-cm quartz cells. pH measurements were recorded with a Micro-pH-2000 from Crison.

Cyclic voltammetry (CV) experiments were performed in a PAR 263A EG&G potentiostat or an IJ-Cambria IH-660 potentiostat, using a three-electrode cell. Glassy carbon disk electrodes (3 mm diameter) from BAS were used as the working electrode, platinum wire as the auxiliary electrode, and SSCE as the reference electrode. Cyclic voltammograms were recorded at a scan rate of 100 $mV\,s^{-1}$ under either $N_2$ or Ar. The complexes were dissolved in previously degassed solvents containing the necessary amount of supporting electrolyte to yield a 0.1 M ionic strength solution. ($n$Bu$_4$N)($PF_6$) was used as supporting electrolyte when using acetonitrile and dichloromethane as solvents. In aqueous solutions the pH was adjusted from 0 to 2 with HCl. Sodium chloride was added to keep a minimum ionic strength of 0.1 M. From pH 2 to pH 10, 0.1 M phosphate buffers were used, and from pH 10 to pH 12 dilute, $CO_2$-free NaOH was used. All $E_{1/2}$ values reported in this work were estimated from cyclic voltammetry as the average of the oxidative and reductive peak potentials ($E_{p,a} + E_{p,c}$)/2. Unless explicitly mentioned, the concentration of the complexes was approximately 1 mM.

**Catalytic Experiments:** Chemical catalysis was performed using a catalyst:substrate molar ratio of between 1:150 to 1:200, with an oxidant:substrate ration of 2:1, in 1,2-dichloroethane, with a typical catalyst concentration of 1 mM. Electrocatalytic studies at neutral pH were performed in a phosphate buffer solution, at an applied potential of 0.9 V vs. SSCE. At basic pH, a 0.1 M NaOH solution was used as solvent and the potential applied was 0.5 V vs. SSCE. The substrate:catalyst molar ratio was 100:1 in both cases. A carbon-felt electrode from SOFACEL was used as the working electrode. Evolution of the oxidized products was followed with a Shi-

 © 2007 Wiley-VCH Verlag GmbH & Co. KGaA, Weinheim 

madzu GC-17A gas chromatography apparatus after chromatography of an aliquot of the reaction mixture over alumina and further re-dissolution in a 20 mM biphenyl solution in diethyl ether, which was used as an internal standard.

**X-ray Structure Determination:** Suitable crystals of ($R_cR_c$,$S_aR_a$)-**2b** were grown by slow diffusion of diethyl ether into a dichloromethane solution of the complex at room temperature. They were obtained as black plates. The crystal was mounted on a nylon loop and intensity data were collected at low temperature [100(2) K] with a Bruker Smart Apex CCD diffractometer using graphite-monochromated Mo-$K_\alpha$ radiation ($\lambda$ = 0.71073 Å) in the $\theta$ range 2.12–28.44°. Full-sphere data collection was carried out with $\omega$ and $\phi$ scans. A total of 48274 reflections were collected, of which 7801 ($R_{int}$ = 0.1281) were unique. Programs used: data collection: Smart version 5.625 (Bruker AXS 1997-01); data reduction: Saint+ version 6.36A (Bruker AXS 2001); absorption correction: SADABS version 2.05 (Bruker AXS 2001). The structures were solved by direct methods and refined by full-matrix least-squares methods on $F^2$ with SHELXTL Version 6.12 (Bruker AXS 2001). The non-hydrogen atoms were refined anisotropically. All H-atoms were placed in geometrically optimized positions and forced to ride on the atom to which they are attached.

**Crystallographic Data for 2b:** $C_{33}H_{35}BClF_4N_5O_2Ru$, $M$ = 756.99, orthorhombic, space group $P2_12_12_1$, $a$ = 10.541(2), $b$ = 12.907(3), $c$ = 23.230(5) Å, $\alpha$ = 90.00°, $\beta$ = 90.00°, $\gamma$ = 90.00°, $V$ = 3169.5(11) Å$^3$, $Z$ = 4, $\rho_{calcd.}$ = 1.591 g cm$^{-3}$, $\mu$ = 0.645 mm$^{-1}$. Final $R_1$ = 0.0822, $wR_2$ = 0.1597 [$I > 2\sigma(I)$]. $R_1 = \Sigma||F_o| - |F_c||/\Sigma|F_o|$ and $wR_2 = [\Sigma\{w(F_o^2 - F_c^2)^2\}/\Sigma\{w(F_o^2)^2\}]^{1/2}$, where $w = 1/[\sigma^2(F_o^2) + (0.0551P)^2 + 12.3436P]$ and $P = (F_o^2 + 2F_c^2)/3$.

CCDC-635355 contains the supplementary crystallographic data for this paper. These data can be obtained free of charge from The Cambridge Crystallographic Data Center via www.ccdc.cam.ac.uk/data_request/cif.

**Preparations:** The phbox-R [R = Et, ($R_c$)-**a**; *i*Pr, ($S_c$)-**b**; see Figure 1] ligands[25] and [Ru$^{III}$Cl$_3$(terpy)] (**1**)[26] (terpy = 2,2′:6′,2″-terpyridine) were prepared according to literature procedures. The syntheses and specific spectroscopic and electrochemical data for the ruthenium complexes described in this paper {with general formula [Ru(Y)(terpy)(phbox-R)]$^{n+}$, Y = monodentate ligand, see below} have been reported previously[17] but are detailed and discussed here.

The nomenclature used for the absolute configuration of the complexes described is as follows. The first two letters refer to the absolute configuration of the oxazoline ligand and the final two letters refer to the absolute configuration of the chiral rotational axes, as detailed and exemplified in Figure 1 for the chlorido complex **2b**. Thus, the complexes discussed here are ($R_cR_c$,$S_aR_a$)-[RuCl(terpy)(phbox-et)](BF$_4$) [($R_cR_c$,$S_aR_a$)-**2a**], ($S_cS_c$,$R_aS_a$)-[RuCl(terpy)(phbox-*i*Pr)](BF$_4$) [($S_cS_c$,$R_aS_a$)-**2b**], ($R_cR_c$,$S_aR_a$)-[Ru(terpy)(phbox-et)(OH$_2$)](BF$_4$)$_2$ [($R_cR_c$,$S_aR_a$)-**3a**], ($S_cS_c$,$R_aS_a$)-[Ru(terpy)(phbox-*i*Pr)(OH$_2$)](BF$_4$)$_2$ [($S_cS_c$,$R_aS_a$)-**3b**], ($S_cS_c$,$R_aS_a$)-[Ru(terpy)(phbox-*i*Pr)(MeCN)](PF$_6$)$_2$ [($S_cS_c$,$R_aS_a$)-**4b**], ($S_cS_c$,$R_aS_a$)-[Ru(terpy)(phbox-et)(py)](PF$_6$)$_2$ [($R_cR_c$,$S_aR_a$)-**5a**], ($S_cS_c$,$R_aS_a$)-[Ru(terpy)(phbox-*i*Pr)(py)](PF$_6$)$_2$ [($S_cS_c$,$R_aS_a$)-**5b**], and ($S_cS_c$,$R_aS_a$)-[Ru(terpy)(phbox-*i*Pr)(2-OH-py)](PF$_6$)$_2$ [($S_cS_c$,$R_aS_a$)-**6b**].

**Supporting Information** (see also the footnote on the first page of this article): Additional spectroscopic and electrochemical data for the complexes described in this work.

## Acknowledgments

This research was financed by the Spanish Ministerio de Educación y Ciencia (MEC) (projects BQU2003-02884, BQU2002-04112-C02-02, and CTQ2004-01546/BQU). A. L. and M. G. are grateful to the Consell Interdepartamental de Recerca i Innovació Tecnològica (CIRIT), Generalitat de Catalunya, for financial support, and A. L. for the aid SGR2001-UG-291. A. L., M. R., and I. R. also thank Johnson Matthey for a loan of $RuCl_3 \cdot xH_2O$. E. P. and X. S. are grateful for the award of doctoral grants from CIRIT and Universitat de Girona (UdG), respectively.

[1] a) G. Desimoni, G. Faita, K. A. Jørgensen, *Chem. Rev.* **2006**, *106*, 3561–3651; b) A. Landa, A. Minkkila, G. Blay, K. A. Jørgensen, *Chem. Eur. J.* **2006**, *12*, 3472–3483; c) S. Dagorne, S. Bellemin-Laponnaz, A. Maisse-François, *Eur. J. Inorg. Chem.* **2007**, 913–925; d) H. A. McManus, P. J. Guiry, *Chem. Rev.* **2004**, *104*, 4151–4202; e) D. Rechavi, M. Lemaire, *Chem. Rev.* **2002**, *102*, 3467–3493.

[2] a) H. Brunner, U. Obermann, P. Wimmer, *J. Organomet. Chem.* **1986**, *316*, C1–C3; b) D. A. Evans, K. A. Woerpel, M. M. Hinman, M. M. Faul, *J. Am. Chem. Soc.* **1991**, *113*, 726–728; c) E. J. Corey, N. Imai, H.-Y. Zhang, *J. Am. Chem. Soc.* **1991**, *113*, 728–729.

[3] a) A. K. Ghosh, M. Packiarajan, J. Cappiello, *Tetrahedron: Asymmetry* **1998**, *9*, 1–45; b) C. Bolm, *Angew. Chem. Int. Ed. Engl.* **1991**, *30*, 542–543.

[4] M. Gómez, G. Muller, M. Rocamora, *Coord. Chem. Rev.* **1999**, *193–195*, 769–835.

[5] A. Von Zelewsky, *Stereochemistry of Coordination Compounds*, Wiley, Chichester, **1996**.

[6] a) F. Leroux, *ChemBioChem* **2004**, *5*, 644–649; b) W. C. Haase, M. Nieger, K. H. Dotz, *J. Organomet. Chem.* **2003**, *684*, 153–169; c) P. Lloyd-Williams, E. Giralt, *Chem. Soc. Rev.* **2001**, *30*, 145–157; d) M. Oki, *Top. Stereochem.* **1983**, *14*, 1–81.

[7] a) L. Pu, *Chem. Rev.* **1998**, *98*, 2405–2494; b) K. Mikami, K. Aikawa, Y. Yusa, J. J. Jodry, M. Yamanaka, *Synlett* **2002**, 1561–1578.

[8] a) R. Noyori, *Angew. Chem. Int. Ed.* **2002**, *41*, 2008–2022; b) I. Serrano, M. Rodríguez, I. Romero, A. Llobet, T. Parella, J. M. Campelo, D. Luna, J. M. Marinas, J. Benet-Buchholz, *Inorg. Chem.* **2006**, *45*, 2644–2651.

[9] a) D. S. Hesek, Y. Inoue, S. R. L. Everitt, H. Ishida, M. Kunieda, M. D. Drew, *Inorg. Chem.* **2000**, *39*, 317–324; b) D. Hesek, G. A. Hembury, M. D. Drew, S. Taniguchi, Y. Inoue, *J. Am. Chem. Soc.* **2000**, *122*, 10236–10237; c) R. A. Sheldon, *Chirotechnology*, Marcel Dekker, New York, **1993**; d) P. J. Collins, M. Hird, *Introduction to Liquid Crystals Chemistry and Physics*, Taylor & Francis, London, **1997**.

[10] See, for instance, cyclopropanation reactions in ref.[2b] and: a) N. Ostergaard, J. F. Jensen, D. Tanner, *Tetrahedron* **2001**, *57*, 6083–6088; b) T. G. Gant, M. C. Noe, E. J. Corey, *Tetrahedron Lett.* **1995**, *36*, 8745–8748. For allylic substitutions, see: c) M. A. Pericàs, C. Puigjaner, A. Riera, A. Vidal-Ferran, M. Gómez, F. Jiménez, G. Muller, M. Rocamora, *Chem. Eur. J.* **2002**, *8*, 4164–4178; d) O. Onomura, Y. Kanda, Y. Nakamura, T. Maki, Y. Matsumura, *Tetrahedron Lett.* **2002**, *43*, 3229–3231. For Diels–Alder reactions, see ref.[2c] and: e) D. A. Evans, T. Rovis, J. S. Johnson, *Pure Appl. Chem.* **1999**, *71*, 1407–1415; f) D. A. Evans, J. A. Murry, P. von Matt, R. D. Norcross, S. J. Miller, *Angew. Chem. Int. Ed. Engl.* **1995**, *34*, 798–800.

[11] For recent contributions, see: a) D. Carmona, M. P. Lamata, F. Viguri, J. Ferrer, N. Garcia, F. J. Lahoz, M. L. Martin, L. A. Oro, *Eur. J. Inorg. Chem.* **2006**, 3155–3166; b) A. J. Davenport, D. L. Davies, J. Fawcett, D. R. Russell, *J. Organomet. Chem.* **2006**, *691*, 3445–3450; c) M. Gómez, S. Jansat, G. Muller, G. Aullon, M. A. Maestro, *Eur. J. Inorg. Chem.* **2005**, 4341–4351; d) F. Nud, C. Malan, F. Spindler, C. Ruggeberg, A. T. Schmidt, H. U. Blaser, *Adv. Synth. Catal.* **2006**, *348*, 47–50; e) H. B. Am-

 © 2007 Wiley-VCH Verlag GmbH & Co. KGaA, Weinheim 

mar, J. Le Notre, M. Salem, M. T. Kaddachi, P. H. Dixneuf, *J. Organomet. Chem.* **2002**, *662*, 63–69.
[12] a) W. Mägerlein, C. Dreisbach, H. Hugl, M. K. Tse, M. Klawonn, S. Bhor, M. Beller, *Catal. Today* **2007**, *121*, 140–150; b) M. K. Tse, H. Jiao, G. Anilkumar, B. Bitterlich, F. G. Gelalcha, M. Beller, *J. Organomet. Chem.* **2006**, *691*, 4419–4433; c) M. K. Tser, S. Bhor, M. Klawonn, G. Anilkumar, H. Jiao, C. Döbler, A. Spannenberg, W. Mägerlein, H. Hugl, M. Beller, *Chem. Eur. J.* **2006**, *12*, 1855–1874; d) M. K. Tser, S. Bhor, M. Klawonn, G. Anilkumar, H. Jiao, C. Döbler, A. Spannenberg, W. Mägerlein, H. Hugl, M. Beller, *Chem. Eur. J.* **2006**, 1875–1888; e) M. K. Tse, C. Döbler, S. Bhor, M. Klawonn, W. Mägerlein, H. Hugl, M. Beller, *Angew. Chem. Int. Ed.* **2004**, *43*, 5255–5260.
[13] a) R. Ballardini, V. Balzani, A. Credi, M. T. Gandolfi, M. Venturi, *Int. J. Photoenergy* **2001**, *3*, 63; b) E. Baranoff, J.-P. Collin, J. Furusho, Y. Furusho, A. C. Laemmel, J. P. Sauvage, *Inorg. Chem.* **2002**, *41*, 1215–1222.
[14] a) S. I. Murahashi, H. Takaya, T. Naota, *Pure Appl. Chem.* **2002**, *74*, 19–24; b) T. Naota, H. Takaya, S. I. Murahashi, *Chem. Rev.* **1998**, *98*, 2599–2660; c) U. J. Jauregui-Haza, M. Dessoudeix, P. Kalck, A. M. Wilhelm, H. Delmas, *Catal. Today* **2001**, *66*, 297–302.
[15] a) S. O. Kelley, J. K. Barton, *Science* **1999**, *238*, 375–381; b) D. B. Hall, R. E. Holmlin, J. K. Barton, *Nature* **1996**, *384*, 731–735; c) C. J. Burrows, J. G. Muller, *Chem. Rev.* **1998**, *98*, 1109–1151.
[16] a) L. K. Stultz, M. H. V. Huynh, R. A. Binstead, M. Curry, T. J. Meyer, *J. Am. Chem. Soc.* **2000**, *122*, 5984–5996; b) E. L. Lebeau, T. J. Meyer, *Inorg. Chem.* **1999**, *38*, 2174–2181; c) C. M. Che, T. F. Lai, K. Y. Wong, *Inorg. Chem.* **1987**, *26*, 2289–2299; d) J. H. Muller, J. H. Acquaye, K. J. Takeuchi, *Inorg. Chem.* **1992**, *31*, 4552–4557; e) A. Gerli, J. Reedijk, M. T. Lakin, A. L. Spek, *Inorg. Chem.* **1995**, *34*, 1836–1843; f) X. Hua, M. Shang, A. G. Lappin, *Inorg. Chem.* **1997**, *36*, 3735–3740; g) M. Rodríguez, I. Romero, A. Llobet, A. Deronzier, M. Biner, T. Parella, H. Stoeckli-Evans, *Inorg. Chem.* **2001**, *40*, 4150–4156; h) M. Shiotsuki, H. Miyai, Y. Ura, T. Suzuki, T. Kondo, T. Mitsudo, *Organometallics* **2002**, *21*, 4960–4964; i) M. H. V. Huynh, L. M. Witham, J. M. Lasker, M. Wetzler, B. Mort, D. L. Jameson, P. S. White, K. J. Takeuchi, *J. Am. Chem. Soc.* **2003**, *125*, 308–309.
[17] X. Sala, E. Plantalech, I. Romero, M. Rodríguez, A. Llobet, A. Poater, M. Duran, M. Solà, S. Jansat, M. Gómez, T. Parella, H. Stoeckli-Evans, J. Benet-Buchholz, *Chem. Eur. J.* **2006**, *12*, 2798–2807.
[18] a) M. Haga, E. S. Dodsworth, A. B. P. Lever, *Inorg. Chem.* **1986**, *25*, 447–453; b) S. C. Rasmussen, S. E. Ronco, D. A. Mlsna, M. A. Billadeau, W. T. Pennington, J. W. Kolis, J. D. Petersen, *Inorg. Chem.* **1995**, *34*, 821–829; c) O. Kohle, S. Ruile, M. Gratzel, *Inorg. Chem.* **1996**, *35*, 4779–4787; d) A. Ben Altabel, S. B. Ribotta de Gallo, M. E. Folquer, N. E. Katz, *Inorg. Chim. Acta* **1991**, *188*, 67–70; e) P. A. Anderson, G. B. Deacon, K. H. Haarmann, F. R. Keene, T. J. Meyer, D. A. Reitsma, B. W. Skelton, G. F. Strouse, N. C. Thomas, T. A. Treadway, A. H. White, *Inorg. Chem.* **1995**, *34*, 6145–6157; f) K. Barqawi, A. Llobet, T. J. Meyer, *J. Am. Chem. Soc.* **1988**, *110*, 7751–7759.
[19] L. F. Szczepura, S. M. Maricich, R. F. See, M. R. Churchill, K. J. Takeuchi, *Inorg. Chem.* **1995**, *34*, 4198–4205.
[20] a) N. Chanda, S. M. Mobin, V. G. Puranik, A. Datta, M. Niemeyer, G. K. Lahiri, *Inorg. Chem.* **2004**, *43*, 1056–1064; b) C. Sens, M. Rodríguez, I. Romero, A. Llobet, T. Parella, J. Benet-Buchholz, *Inorg. Chem.* **2003**, *42*, 8385–8394; c) B. Mondal, V. G. Puranik, G. K. Lahiri, *Inorg. Chem.* **2002**, *41*, 5831–5836; d) K. J. Takeuchi, M. S. Thompson, D. W. Pipes, T. J. Meyer, *Inorg. Chem.* **1984**, *23*, 1845–1851; e) L. Roecker, W. Kutner, J. A. Gilbert, M. Simmons, R. W. Murray, T. J. Meyer, *Inorg. Chem.* **1985**, *24*, 3784–3791.
[21] a) W. F. De Giovani, A. Deronzier, *J. Electroanal. Chem.* **1992**, *337*, 285–298; b) M. Rodríguez, I. Romero, C. Sens, A. Llobet, A. Deronzier, *Electrochim. Acta* **2003**, *48*, 1047–1054.
[22] a) A. Dovletoglou, S. A. Adeyemi, T. J. Meyer, *Inorg. Chem.* **1996**, *35*, 4120–4127; b) A. B. P. Lever, *Inorg. Chem.* **1990**, *29*, 1271–1285.
[23] a) J. C. Dobson, T. J. Meyer, *Inorg. Chem.* **1988**, *27*, 3283–3291; b) A. Llobet, P. Doppelt, T. J. Meyer, *Inorg. Chem.* **1988**, *27*, 514–520; c) W. C. Cheng, W. Y. Yu, K. K. Cheung, C. M. Che, *J. Chem. Soc. Dalton Trans.* **1994**, 57–62; d) M. E. Marmion, K. J. Takeuchi, *J. Am. Chem. Soc.* **1986**, *108*, 510–511; e) S. A. Kubow, M. E. Marmion, K. J. Takeuchi, *Inorg. Chem.* **1988**, *27*, 2761–2767.
[24] a) G. E. Cabaniss, A. A. Diamantis, W. R. Murphy, R. W. Linton, T. J. Meyer, *J. Am. Chem. Soc.* **1985**, *107*, 1845–1853; b) V. J. Catalano, R. Kurtaran, R. A. Heck, A. Ohman, M. G. Hill, *Inorg. Chim. Acta* **1999**, *286*, 181–188.
[25] C. Bolm, K. Weickhard, M. Zehnder, D. Glasmacher, *Chem. Ber.* **1991**, *124*, 1173–1180.
[26] B. P. Sullivan, J. M. Calvert, T. J. Meyer, *Inorg. Chem.* **1980**, *19*, 1404–1407.
[27] E. Masllorens, M. Rodríguez, I. Romero, A. Roglans, T. Parella, J. Benet-Buchholz, M. Poyatos, A. Llobet, *J. Am. Chem. Soc.* **2006**, *128*, 5306–5307.

Received: April 4, 2007
Published Online: September 28, 2007

 © 2007 Wiley-VCH Verlag GmbH & Co. KGaA, Weinheim 

DOI: 10.1002/ejic.200700453

# Synthesis, Characterization, Structures and Comparative Electrochemical Study of 2,4-Bis(trimethylsilylethynyl)thiophene Coordinated Carbonylcobalt Units

**Avelina Arnanz,[a] Consuelo Moreno,*[a] María-Luisa Marcos,[b] Jaime González-Velasco,[b] and Salomé Delgado[a]**

**Keywords:** Thiophene / Carbonylcobalt complexes / Electrochemistry

The reaction between 2,4-dibromothiophene and trimethylsilylacetylene (TMSA) in the presence of $Pd(PPh_3)_4$, CuI and triethylamine gave rise to the formation of 2,4-bis(trimethylsilylethynyl)thiophene (**2,4T**) and 4-bromo-2-(trimethylsilylethynyl)thiophene (**2,4T′**). Complexes **1**, **2**, **3** or **1′** were obtained by direct reaction between $Co_2(CO)_8$ and **2,4T** or **2,4T′**, respectively. (Diphenylphosphanyl)methane-substituted alkyne carbonyl complexes **4**, **5**, **6** and **2′** were prepared by substitution reaction of carbonyl ligands in the presence of $Me_3NO$ at the $Co_2(CO)_6$ units of **1**, **2**, **3** and **1′**, respectively. Desilylation of the non-metallated and metallated alkynes in **4**, **5** and **6** occurred on treatment with KOH or tetrabutylammonium fluoride to give **7**, **8** and **9**. Crystals of **2′** suitable for single-crystal X-ray diffraction were grown, and the molecular structure of this compound is discussed. A comparative electrochemical study of these complexes in relation to analogous derivatives obtained from the organic ligand 2,5-bis(trimethylsilylethynyl)thiophene (**2,5T**) is reported.

(© Wiley-VCH Verlag GmbH & Co. KGaA, 69451 Weinheim, Germany, 2007)

## Introduction

Recently, the search for molecular systems that are able to transmit electronic effects between two or more remote sites efficiently has become an area of increasing endeavour.[1] The interest in this kind of complexes is due, in part, to the stabilising influence of the metal atom on reactive unsaturated carbon chains and polycarbon ligands[1,2] and, on the other hand, to their potential optoelectronic properties as non-linear optical and electroluminescent materials[3] or in the construction of molecular-scale electronic devices.[4,5] Thus, alkynyl or polyynediyl bridging ligands have been shown to be particularly efficient in allowing the passage of electronic effects between redox-active centres[6,7] and therefore the electronic properties can be modified by changing both, metal fragments and/or alkyne ligands.[4b,4d,7b,8] This electronic communication through such potential molecular wires is often evaluated by examining the redox response of electroactive groups.[5i,5j,8a,9]

In recent studies we have shown that complexes, where the redox centres are either $Co_2(CO)_6$, $Co_2(CO)_4$(dppm) or $Co_2(CO)_4$(dppa) linked by 1,3,5-tris(trimethylsilylethynyl)-benzene,[7a] 1,4-bis(trimethylsilyl)butadiyne[7b] and 2,5-bis-(trimethylsilylethynyl)thiophene (**2,5T**)[7d] ligands, present electronic communication between the metal centres. In order to study the effect of the position of the alkynyl substituents on the thiophene ring on the electronic communication between $Co_2(CO)_6$ and $Co_2(CO)_4$(dppm) moieties, we report here the synthesis, characterization and the redox properties of these units linked by the organic ligand 2,4-bis(trimethylsilylethynyl)thiophene (**2,4T**).

## Results and Discussion

### Synthesis and Spectroscopic Characterization

A similar procedure described for 2,5-bis(trimethylsilylethynyl)thiophene (**2,5T**)[10] has been used in our laboratory for the syntheses of the new ligand 2,4-bis(trimethylsilylethynyl)thiophene (**2,4T**). By the coupling reaction of 2,4-dibromothiophene with excess of TMSA [in the presence of $Pd(PPh_3)_4$, CuI and triethylamine] 2,4-bis(trimethylsilylethynyl)thiophene (**2,4T**) (33% yield) and 4-bromo-2-(trimethylsilylethynyl)thiophene (**2,4T′**) (35% yield) were obtained, both as stable yellow oils. Large amounts of a catalyst [5% mol $Pd(PPh_3)_4$ and 10% mol CuI] and higher temperature and reaction time (75 °C for 20 d) were required, causing a side reaction of the terminal acetylene, TMSA, to

[a] Departamento de Química Inorgánica, Universidad Autónoma de Madrid,
28049 Madrid, Spain
Fax: +34-91-4974833
E-mail: mconsuelo.moreno@uam.es
[b] Departamento de Química, Universidad Autónoma de Madrid, 28049 Madrid, Spain
Supporting information for this article is available on the WWW under http://www.eurjic.org or from the author.

 © 2007 Wiley-VCH Verlag GmbH & Co. KGaA, Weinheim 

afford 1,4-bis(trimethylsilyl)-1,3-butadiyne. Such side reactions were often observed in reactions with less reactive aryl bromides.[11] This synthesis needed a longer reaction time than that to obtain the analogous ligand **2,5T**, because the thiophene positions more suitable to an oxidative addition are 2 and 5. Also, from 2,6-dibromopyridine,[12] under Sonogashira coupling conditions, reasonable yields of both, the partially and fully substituted compounds containing the TMSA group were obtained. Complexes **1**, **2**, **3** or **1′** were obtained by direct reaction between $Co_2(CO)_8$ and **2,4T** or **2,4T′**, respectively.

In order to stabilise the dicobalt units, we have employed the dppm ligand (the small bite angle of dppm was expected to lead to the formation of bridged dicobalt complexes). Thus, dppm-substituted alkyne carbonyl complexes **4**, **5**, **6** and **2′** could only be prepared by substitution reaction of two or four carbonyl ligands in the presence of $Me_3NO$ at the $Co_2(CO)_6$ units of complexes **1**, **2**, **3** and **1′**, respectively (Scheme 1), because of the poor yields obtained by direct reaction between the alkyne and "$Co_2(CO)_6$(phosphane)" under thermal conditions for the analogous complexes from **2,5T**.[7d] The FT-IR spectral changes of these reactions were monitored until the $\nu_{C\equiv O}$ bands of the parent complex had disappeared.

On the basis of the isolated yield for **4** and **5**, it can be observed that the preference of the $Co_2(CO)_4$(dppm) units for coordination at the alkyne in 2-position of the thiophene ring is two times greater than that for the 4-position. This preference is also observed for the analogous complexes **1** and **2** with $Co_2(CO)_6$ units (see Exp. Sect.). Moreover, compound **5**, in $CDCl_3$ solution at room temp. for 48 h, led to **4** (**4** was never observed to yield **5**), and complex **6** decomposed to afford **4** and **5** in a 7:1 ratio [determined by thin-layer chromatography (TLC) using hexane/$CH_2Cl_2$ (5:4) as eluent]. These results can be explained by simple steric or electronic effects.

As both positions have the same substituent on the alkyne ($SiMe_3$), it can be expected that the steric demand at the end-caps are similar. Then, the preference of the $Co_2(CO)_4X$ [X = $(CO)_2$ or dppm] moieties to coordinate the alkyne in position 2 can be explained by electronic factors. In agreement with this, the electron density on the triple bond of the alkyne in position 4 is higher than on the alkyne in position 2, as judged by the $^{13}C$ NMR shifts for the alkyne C atoms; this situation should disfavor the attachment of the Co atoms to the C≡C group in position 4, since back-donation from the Co d-orbitals to the π*-MO of an electron-poor ligand is the stabilizing factor in the bonding.[13]

However, Diederich et al. obtained in the reaction of $Co_2(CO)_8$ with 1,6-bis(triisopropylsilyl)hexa-1,3,5-triyne the exclusive formation of the compound in which the carbonylcobalt fragment is coordinated to the central C≡C triple bond, which was attributed to the presence of the bulky triisopropylsilyl end-caps.[2c]

Removal of the TMS protecting group from **4** and **5** was accomplished by treatment with saturated solutions of KOH in degassed methanol at room temp. to give the terminal diyne compounds **7** and **8**, respectively, isolated as unstable red solids. Complex **9** was synthesized from **6** when stronger desilylation conditions were used (8 equiv. of $Bu_4NF$ in wet THF).

All these compounds have been characterized by spectroscopic data (IR, UV/Vis, $^1H$, $^1H\{^{31}P\}$, $^{13}C\{^1H\}$, $^{31}P\{^1H\}$ NMR, MS) and elemental analysis, details of which are given as Supporting Information, and X-ray crystallography (for **2′**).

The IR spectra of the organic ligands **2,4T** [2165 (w), 2152 (w) $cm^{-1}$] and **2,4T′** [2156 (w) $cm^{-1}$] show weak absorption bands, typically $\nu_{C\equiv C}$ stretches of the alkynyl units, in the characteristic range of diynyl complexes (two $\nu_{C\equiv C}$ stretches at ca. 2060–2200 $cm^{-1}$) and monoynyl complexes (one $\nu_{C\equiv C}$ stretch at ca. 2090–2150 $cm^{-1}$). The $^1H$ NMR spectra of both ligands show two doublet signals due to the thiophene ring protons with coupling constants that are consistent with their chemical formulations. In the $^{13}C$ NMR spectra for **2,4T** and **2,4T′**, the signals belonging to the thiophene ring ($C^3$, $C^4$, $C^5$ and $C^6$) and the alkynyl units ($C^1$, $C^2$, $C^7$ and $C^8$) can be observed, and the assignments were made on the basis of the $\delta$ values and two-dimensional NMR experiments (HMBC and HMQC).

The IR spectra of the (alkyne)cobalt complexes exhibit three strong absorptions in the carbonyl stretching region (2090–2024 $cm^{-1}$) except for compound **3** (four absorptions) due to the asymmetry of the molecule; in dppm-substituted alkyne complexes **4**–**9** and **2′** these absorptions lie at lower frequencies (2027–1950 $cm^{-1}$), and the spectral patterns are similar to those observed for previously reported (alkyne) cobalt and (substituted alkyne)cobalt complexes.[1a,1c,2c,7,14] Complexes **1**, **2**, **4** and **5** contain an uncomplexed C≡C triple bond, which gives a $\nu_{C\equiv C}$ weak absorption at ca. 2157 $cm^{-1}$. For **7** and **8** this absorption could not be observed, but a $\nu_{\equiv C-H}$ one at ca. 3301 $cm^{-1}$ is exhibited. The absence of $\nu_{C\equiv C}$ in the region of 2150 $cm^{-1}$ (for **6** and **9**) and $\nu_{\equiv C-H}$ around 3300 $cm^{-1}$ (for **9**) indicates that the alkynyl bond loses its triple-bond character and both alkyne linkages are coordinated to $Co_2(CO)_4$(dppm) units.

The NMR spectroscopic data, which have been recorded in several solvents, are consistent with the overall geometry established in the solid state for complex **2′** (Figure 1) and with the proposed structures (Scheme 1).

In $^1H$ NMR spectra, the chemical shifts for the $SiMe_3$ and C≡CH protons are found to be very sensitive to cobalt complexation on the adjacent alkyne bond, and they show a significant downfield shift with respect to the free ligands in accordance with the reduction of the C≡C triple-bond character.[15] The signals of all ring protons in the $Co_2(CO)_6$-substituted alkyne complexes are shifted downfield slightly from those of the corresponding alkynylated thiophenes, due to the strong electron-withdrawing effect of the carbonylcobalt moieties. In addition, the values of the $^1H$-$^1H$ coupling constants of $J_{HH} \approx 1.3$ Hz for the thiophene proton signals are in accordance with their non-adjacent positions (Table 1). For dppm complexes **4**–**8** and **2′** the diastereotopic protons of the $-CH_2-$ group are coupled with

 © 2007 Wiley-VCH Verlag GmbH & Co. KGaA, Weinheim 

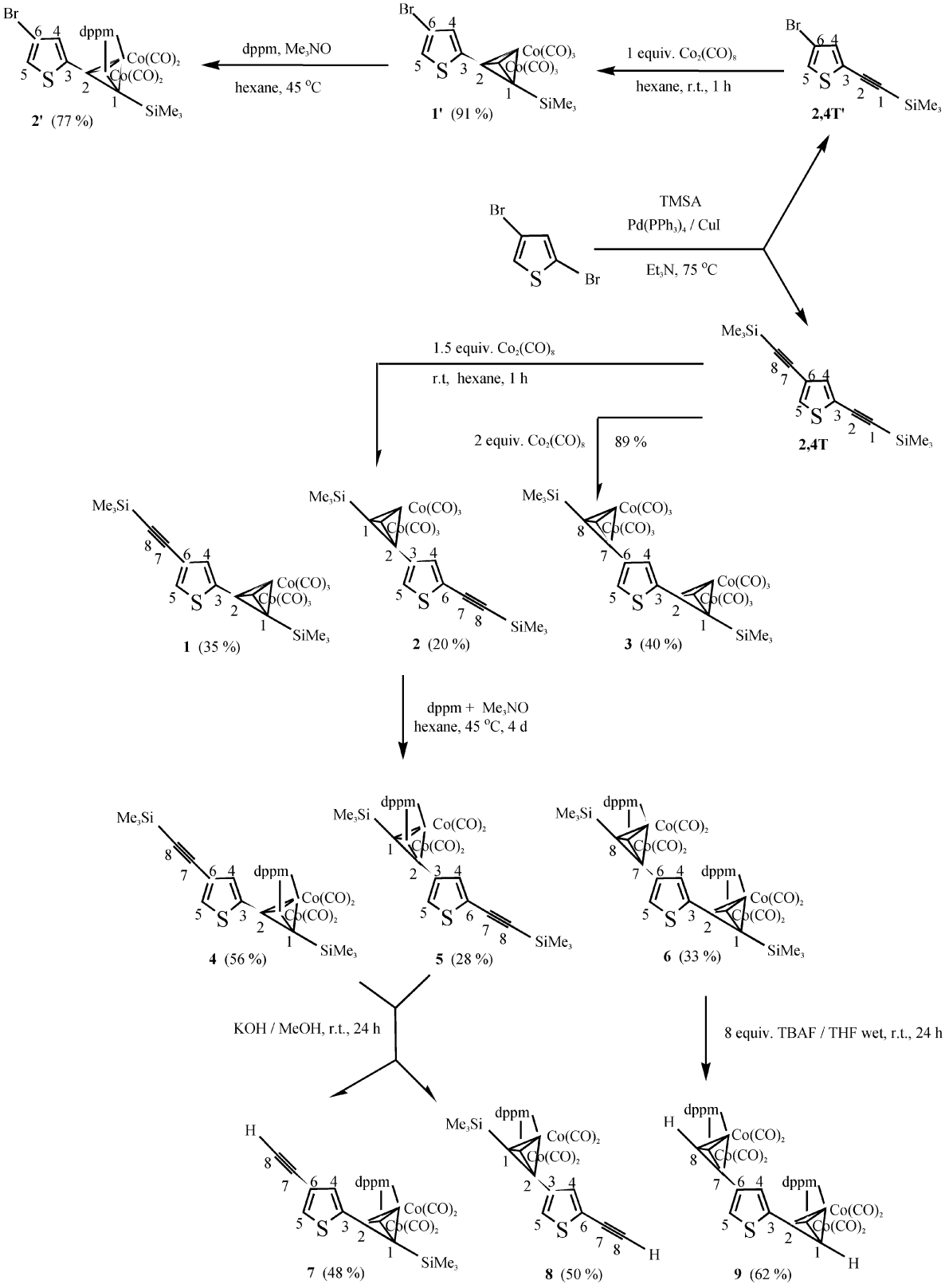


Scheme 1.

the P atoms; thus, they appear as two double triplets with $J_{HH} \approx 13.3$ Hz and $J_{PH} \approx 10.5$ Hz, except in **6**, where the inequivalent $Co_2(CO)_4$(dppm) moieties display four signals in the $^1H$ and $^1H\{^{31}P\}$ NMR spectra in $CD_2Cl_2$. Also, in **9**, the two moieties $Co_2(CO)_4$(dppm) are inequivalent, and this is reflected in the $^1H$ NMR spectrum. This spectrum

 © 2007 Wiley-VCH Verlag GmbH & Co. KGaA, Weinheim 

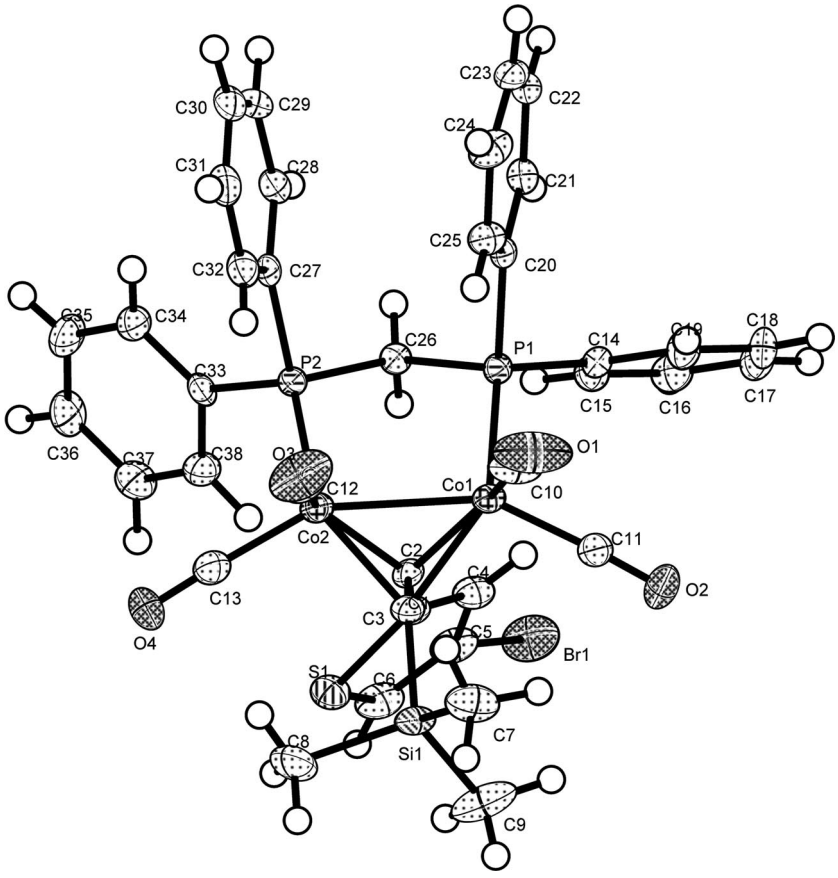


Figure 1. ORTEP diagram of **2′**, with 50% ellipsoids.

shows two resonances for the terminal "alkyne" protons, –(C–C)$_{coord}$–H in the region $\delta$ = 5.72–5.80 ppm, and they are coupled with the P atoms like in similar compounds.[7d,16] As expected,[15,17] because of the reduction in the C≡C triple-bond character, there is a downfield shift in the signal positions of these terminal protons with respect to those of the free ligand ($\delta$ = 3.32 and 2.99 ppm).

The $^{31}$P NMR spectra for **4**, **5**, **7** and **8** present a broad singlet, while for **6** and **9**, which contain two inequivalent $Co_2(CO)_4$(dppm) units, two broad singlets appear. All of them are shifted to higher frequencies (ca. 35 ppm) with respect to that of the free ligand because of the coordination.

The $^{13}$C NMR chemical shifts of the carbonyl groups in all the complexes appear as one (**1**, **2**, **3** and **1′**), two (**4**, **5**, **7**, **8** and **2′**) or four (**6** and **9**) signals at $\delta \approx 200$ and 207 ppm, suggesting that they are rapidly interchanging on the NMR scale. The carbon resonances of the free and coordinated acetylene carbon atoms can be assigned on the basis of the magnitude of the $J_{CP}$ coupling constants, chemical shifts and in comparison with analogous complexes.[1c,2c,7,18] Thus, for **4** and **5**, in $CDCl_3$ and $CD_2Cl_2$, the $C^1$, $C^2$ and $C^3$ atoms display similar triplets with $^{13}$C-$^{31}$P coupling constants of $J_{CP} \approx$ 10.1, 8.9 and 3.0 Hz, respectively. The replacement of the –$SiMe_3$ group by a proton results in a significant deshielding of the $C^1$, $C^2$, $C^7$ and $C^8$ atoms. The thiophene carbon signals appear between $\delta$ = 120 and 150 ppm (Table 2).

Compound **6** exhibits low solubility in $CDCl_3$ and $CD_2Cl_2$, and for that reason the $^{13}$C NMR spectrum was recorded in [$D_8$]THF. The unambiguous assignment of its carbon atoms has been carried out by comparison with published data of analogous compounds[7d] and by using the $^{13}$C NMR spectra of **4** and **5** in the same solvent in addition to HMQC and HMBC spectroscopy (these experiments have also been performed for the rest of the complexes) (Figure 2).

All compounds gave satisfactory mass spectrometric data; thus, the positive FAB mass spectra show the respective molecular ions or [$M^+$ – CO], as well as peaks corresponding to the consecutive loss of the CO ligands. The UV/Vis spectra of all complexes exhibit broad low-intensity absorption bands with $\lambda$ between 520 and 558 nm attributed to the d-d transitions. For **3**, **6**, and **9**, the presence of the second $Co_2(CO)_6$ or $Co_2(CO)_4$(dppm) unit results in a redshift of these absorption bands. These spectra, for complexes **4**–**9** and **2′**, are dominated by the characteristic UV bands below 380 nm associated with π-π* transitions within the phenyl groups of the bis(phosphane) ligand. In addition, strong absorptions are observed around 231, 250 and 276 nm attributed to π-π* transition associated with the thiophene ring.

 © 2007 Wiley-VCH Verlag GmbH & Co. KGaA, Weinheim 

Table 1. $^1$H NMR (300 MHz, $CDCl_3$, 25 °C, ppm) data for the compounds **1**–**9** and **2,4T**.

| | $H^4$ | $H^5$ | –C≡CH | –C–CH | –C≡C$SiMe_3$ | –C–C$SiMe_3$ |
|---|---|---|---|---|---|---|
| **2,4T** | 7.21 (d) $J_{HH}$ = 1.3 Hz | 7.32 (d) $J_{HH}$ = 1.3 Hz | – | – | 0.25 (s), 0.24 (s) | – |
| **1** | 7.22 (d) $J_{HH}$ = 1.3 Hz | 7.42 (d) $J_{HH}$ = 1.3 Hz | – | – | 0.25 (s) | 0.39 (s) |
| **2** | 7.24 (d) $J_{HH}$ = 1.4 Hz | 7.26 (s br) | | | 0.26 (s) | 0.38 (s) |
| | 7.27 (d)[a] $J_{HH}$ = 1.5 Hz | 7.31 (d)[a] $J_{HH}$ = 1.5 Hz | – | – | 0.25 (s)[a] | 0.39 (s)[a] |
| **3** | 7.31 (d) $J_{HH}$ = 1.4 Hz | 7.33 (d) $J_{HH}$ = 1.4 Hz | | | | 0.40 (s), 0.38 (s) |
| | 7.34 (d)[a] $J_{HH}$ = 1.2 Hz | 7.39 (d)[a] $J_{HH}$ = 1.2 Hz | – | – | – | 0.41 (s), 0.39 (s)[a] |
| **4** | 6.57 (d) $J_{HH}$ = 1.3 Hz | 7.28 (s br) | | | 0.28 (s) | 0.36 (s) |
| | 6.58 (d)[a] $J_{HH}$ = 1.4 Hz | 7.31 (d)[a] $J_{HH}$ = 1.4 Hz | – | – | 0.28 (s)[a] | 0.38 (s)[a] |
| | 6.52 (s br)[b] | 7.37 (s br)[b] | | | 0.24 (s)[b] | 0.36 (s)[b] |
| **5** | 6.77 (d) $J_{HH}$ = 1.4 Hz | 6.63 (d) $J_{HH}$ = 1.4 Hz | | | 0.29 (s) | 0.33 (s) |
| | 6.76 (d)[a] $J_{HH}$ = 1.5 Hz | 6.67 (d)[a] $J_{HH}$ = 1.5 Hz | – | – | 0.29 (s)[a] | 0.34 (s)[a] |
| | 6.74 (s br)[b] | 6.71 (s br)[b] | | | 0.25 (s)[b] | 0.32 (s)[b] |
| **6** | 6.68 (d) $J_{HH}$ = 1.3 Hz | 7.27 (d) $J_{HH}$ = 1.4 Hz | | | | 0.36 (s), 0.35 (s) |
| | 6.68 (d)[a] $J_{HH}$ = 1.4 Hz | 7.26 (d)[a] $J_{HH}$ = 1.4 Hz | – | – | – | 0.36 (s), 0.35 (s)[a] |
| | 6.75 (s br)[b] | 7.35 (s br)[b] | | | | 0.385 (s), 0.381(s)[b] |
| **7** | 6.67 (d) $J_{HH}$ = 1.3 Hz | 7.31 (d) $J_{HH}$ = 1.3 Hz | 2.99 (s) | – | – | 0.38 (s) |
| **8** | 6.87 (d) $J_{HH}$ = 1.4 Hz | 6.64 (d) $J_{HH}$ = 1.4 Hz | 3.32 (s) | – | – | 0.33 (s) |
| **9** | 7.43–7.15 | 7.43–7.15 | – | 5.80 (dt) $J_{HH}$ = 8.2 Hz $J_{PH}$ = 6.2 Hz 5.72 (t) $J_{PH}$ = 6.7 Hz | – | – |

[a] $CD_2Cl_2$. [b] [$D_8$]THF.

Table 2. $^{13}$C NMR (500 MHz, $CDCl_3$, 25 °C, ppm) data for the compounds **1**–**9** and **2,4T**.

| | $C^1$ | $C^2$ | $C^3$ | $C^4$ | $C^5$ | $C^6$ | $C^7$ | $C^8$ |
|---|---|---|---|---|---|---|---|---|
| **2,4T** | 99.4 (s) | 99.0 (s) | 122.2 (s) | 134.9 (s) | 130.6 (s) | 123.2 (s) | 96.5 (s) | 94.1 (s) |
| **1** | 81.0 (s br) | 93.4 (s br) | 141.9 (s) | 131.0 (s) | 130.4 (s) | 123.2 (s) | 99.2 (s) | 94.2 (s) |
| **2** | 80.0 (s br)[a] | 97.7 (s br)[a] | 139.0 (s)[a] | 134.2 (s)[a] | 125.9 (s)[a] | 124.6 (s)[a] | 96.9 (s)[a] | 100.1(s)[a] |
| **3** | 80.7 (s br) | 93.8 (s br) | 143.0 (s) | 130.3 (s) | 124.7 (s) | 139.5 (s) | 97.1 (s br) | 79.4 (s br) |
| | 81.3 (s br)[a] | 94.5 (s br)[a] | 143.1 (s)[a] | 130.8 (s)[a] | 125.2 (s)[a] | 139.9 (s)[a] | 97.7 (s br)[a] | 80.0 (s br)[a] |
| **4** | 89.7 (t) $J_{CP}$ = 10.5 Hz | 93.3 (t) $J_{CP}$ = 9.2 Hz | 147.8 (t) $J_{CP}$ = 2.7 Hz | 128.9 (s) | 128.3 (s) | 122.1 (s) | 100.4 (s) | 92.9 (s) |
| | 89.7 (t)[a] $J_{CP}$ = 10.0 Hz | 93.8 (t)[a] $J_{CP}$ = 9.4 Hz | 148.2 (t)[a] $J_{CP}$ = 3.1 Hz | 129.1 (s)[a] | 128.6 (s)[a] | 122.6 (s)[a] | 100.4 (s)[a] | 92.3 (s)[a] |
| | 88.5 (m)[b] | 93.5 (m)[b] | 147.5 (t)[b] $J_{CP}$ = 2.7 Hz | 128.8 (s)[b] | 128.3 (s)[b] | 122.3 (s)[b] | 100.3 (s)[b] | 91.9 (s)[b] |
| **5** | 87.9 (t) $J_{CP}$ = 9.9 Hz | 97.9 (t) $J_{CP}$ = 8.3 Hz | 143.7 (t) $J_{CP}$ = 3.2 Hz | 134.8 (s) | 122.1 (s) | 123.2 (s) | 97.6 (s) | 98.6 (s) |
| | 87.9 (t)[a] $J_{CP}$ = 10.0 Hz | 98.4 (t)[a] $J_{CP}$ = 8.8 Hz | 144.1 (t)[a] $J_{CP}$ = 2.9 Hz | 135.0 (s)[a] | 122.6 (s)[a] | 123.7 (s)[a] | 97.7 (s)[a] | 99.1 (s)[a] |
| | 86.8 (m)[b] | 98.0 (m)[b] | 143.6 (t)[b] $J_{CP}$ = 3.2 Hz | 134.4 (s)[b] | 122.3 (s)[b] | 123.2 (s)[b] | 97.4 (s)[b] | 97.8 (s)[b] |
| **6** | 87.9 (m)[b] | 93.3 (m)[b] | 149.5 (t)[b] $J_{CP}$ = 2.7 Hz | 120.6 (s)[b] | 126.0 (s)[b] | 145.1 (t)[b] $J_{CP}$ = 2.7 Hz | 98.2 (m)[b] | 87.2 (m)[b] |
| **7** | 89.6 (m) | 93.2 (m) | 148.3 (t) $J_{CP}$ = 3.2 Hz | 128.5 (s) 128.6 (s) | | 121.0 (s) | 79.2 (s) | 76.2 (s) |
| **8** | 88.0 (m) | 97.9 (m) | 143.9 (t) $J_{CP}$ = 2.7 Hz | 135.2 (s) | 122.3 (s) | 122.0 (s) | 77.2 (s) | 81.1 (s) |
| **9** | 74.5 (m)[a] | 83.2 (m)[a] | 147.3 (m)[a] | 121.7 (s)[a] | 128.9 (s)[a] | 143.9 (m)[a] | 89.4 (m)[a] | 75.2 (m)[a] |

[a] $CD_2Cl_2$. [b] [$D_8$]THF.

 © 2007 Wiley-VCH Verlag GmbH & Co. KGaA, Weinheim 

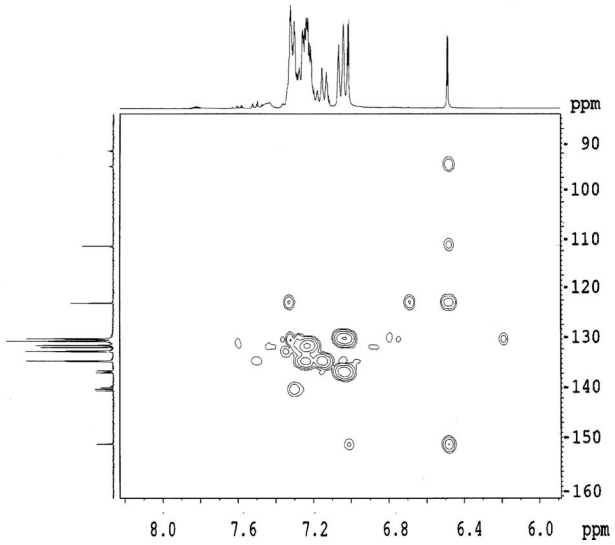


Figure 2. HMBC NMR (500 MHz, $CDCl_3$, 25 °C, ppm) spectra for complex **2′**.

Table 3. Selected bond lengths [Å] and angles [°] for **2′**.

| | | | |
|---|---|---|---|
| C(1)–C(2) | 1.358(4) | C(11)–Co(1) | 1.767(3) |
| C(1)–Si(1) | 1.853(3) | C(12)–O(3) | 1.142(4) |
| C(1)–Co(2) | 1.969(2) | C(12)–Co(2) | 1.794(3) |
| C(1)–Co(1) | 1.985(2) | C(13)–O(4) | 1.139(3) |
| C(2)–C(3) | 1.450(3) | C(13)–Co(2) | 1.781(3) |
| C(2)–Co(1) | 1.943(2) | C(26)–P(1) | 1.831(2) |
| C(2)–Co(2) | 1.975(2) | C(26)–P(2) | 1.843(2) |
| C(5)–Br(1) | 1.894(3) | Co(1)–P(1) | 2.2221(7) |
| C(10)–O(1) | 1.138(3) | Co(2)–P(2) | 2.2256(7) |
| C(10)–Co(1) | 1.797(3) | Co(1)–Co(2) | 2.4850(5) |
| C(11)–O(2) | 1.141(3) | | |
| | | | |
| C(2)–C(1)–Si(1) | 141.71(19) | C(1)–C(2)–C(3) | 136.0(2) |
| C(6)–C(5)–Br(1) | 123.7(2) | C(4)–C(5)–Br(1) | 121.5(2) |
| C(11)–Co(1)–C(2) | 97.81(11) | C(11)–Co(1)–C(10) | 99.79(14) |
| C(11)–Co(1)–C(1) | 101.12(11) | C(10)–Co(1)–C(2) | 143.70(12) |
| C(2)–Co(1)–C(1) | 40.44(10) | C(10)–Co(1)–C(1) | 104.70(12) |
| C(10)–Co(1)–P(1) | 106.82(9) | C(11)–Co(1)–P(1) | 99.37(9) |
| C(1)–Co(1)–P(1) | 138.51(7) | C(2)–Co(1)–P(1) | 101.25(7) |
| C(1)–Co(1)–Co(2) | 50.78(7) | C(2)–Co(1)–Co(2) | 51.20(7) |
| C(10)–Co(1)–Co(2) | 102.62(11) | C(11)–Co(1)–Co(2) | 147.76(8) |
| C(13)–Co(2)–C(12) | 101.48(14) | C(13)–Co(2)–C(1) | 102.53(11) |
| C(12)–Co(2)–C(1) | 98.35(11) | C(13)–Co(2)–C(2) | 102.79(11) |
| C(12)–Co(2)–C(2) | 135.73(12) | C(1)–Co(2)–C(2) | 40.28(10) |
| C(13)–Co(2)–P(2) | 98.79(9) | C(12)–Co(2)–P(2) | 111.69(9) |
| C(1)–Co(2)–P(2) | 138.56(8) | C(2)–Co(2)–P(2) | 100.46(7) |
| C(13)–Co(2)–Co(1) | 151.05(9) | C(12)–Co(2)–Co(1) | 95.39(10) |
| C(1)–Co(2)–Co(1) | 51.34(7) | C(2)–Co(2)–Co(1) | 50.06(7) |
| P(1)–Co(1)–Co(2) | 96.00(2) | P(2)–Co(2)–Co(1) | 96.55(2) |
| P(1)–C(26)–P(2) | 107.97(12) | | |

### Crystal Structure of 2′

The single-crystal X-ray structure determination of 2-{$Co_2(CO)_4$(μ-dppm)[$\mu_2$-$\eta^2$-($SiMe_3C_2$)]}-4-(Br)-$C_4H_2S$ (**2′**) confirms the structure presented in Scheme 1. Compound **2′** consists of a monosubstituted 4-bromo-2-(trimethylsilylethynyl)thiophene ligand with a dimetallic Co unit at the 2-position. The dimetallic Co moiety has two terminal carbonyl ligands on the Co atoms, bridging dppm and trimethylsilylethynyl groups. This geometry has been observed in other carbonylcobalt dimetallic complexes possessing a bridging acetylene ligand.[19] The geometric parameters for **2′** are summarized in Table 5. Table 3 contains selected bond lengths and angles. An ORTEP plot indicating the atom-labelling scheme is given in Figure 1. Complex **2′** crystallizes in the monoclinic space group $P2_1/c$, with one molecule in the asymmetric unit, but contains no crystallographic symmetry.

A highly distorted tetrahedron is formed by the coordination of the dicobalt unit with the ethynyl carbon atoms, with a Co(1)–Co(2) bond length of 2.4850(5) Å, and the average Co–C bond length was determined to be 1.968(2) Å. The Co–Co distance is comparable to those reported for the compounds 2,5-{$Co_2(CO)_4$(μ-dppm)[$\mu_2$-$\eta^2$-($SiMe_3C_2$)]}$_2C_4H_2S$[7d] and [$Co_2(CO)_4$(μ-dppm){$\mu_2$-$\eta^2$-($SiMe_3C_2$)}]$_2$($SiMe_3C{\equiv}C$)(1,3,5-$C_6H_3$)[7a] and may be considered typical for this type of clusters.[14d,20]

The coordination geometry of the Co atom is similar to a pyramid with a pentagonal-shaped base, where the Co atom is in the centre of the pyramid. The distortion of the pyramid is due to the constrained tetrahedron comprised of Co(1)–Co(2)–C(1)–C(2), as well as the bridging of the dppm ligand. The carbonyl moieties coordinate to the Co atoms in the sterically least hindered sites, thus making up the pyramid. The apex of the pyramid is one of the carbonyl groups, and the base is comprised of the carbonyl group, one of the phosphorus atoms of the dppm ligand, the two ethynyl carbon atoms, and the other Co atom. The bond lengths of the apex carbonyl groups to the Co atoms, C(10)–Co(1) and C(12)–Co(2), are 1.797(3) and 1.794(3) Å, respectively. These bond lengths are statistically not different from those of the base carbonyl groups to the Co atoms, which are 1.767(3) and 1.781 Å, for C(11)–Co(1) and C(13)–Co(2), respectively. The dihedral angle Co(1)–C(1)–C(2)–Co(2) was determined to be –84.5(7)°, whereas the dihedral angle C(1)–Co(1)–Co(2)–C(2) was determined to be –52.8(13)°. The bite angle of the dppm ligand was found to be 108.0(12)°, which is consistent with analogous bite angles of dppm in Co–Co complexes.[21]

The C(1)–C(2) bond length of the bridging ethynyl ligand, 1.358(4) Å, is consistent with reported ethynyldicobalt complexes.[22] This reflects the loss of triple-bond character as a result of coordination of the acetylenic moiety to the $Co_2$ unit. The change in hybridisation at C(1)–C(2) is also reflected in the C(1)–C(2)–C(3) angle of 136.0(2)° and the C(2)–C(1)–Si(1) angle of 141.7(19)°.

The bond lengths of the Co atoms to the phosphorus atoms of the dppm ligand are 2.222(7) Å and 2.226(7) Å for Co(1)–P(1) and Co(2)–P(2), respectively. The average P–C distances of the bridging dppm ligand, 1.835(2) Å are normal;[23] the P–C bond lengths are statistically equivalent. All other bond lengths and angles are comparable to those reported for similar structures.[7] The average carbonyl C≡O bond length was determined to be 1.140(3) Å, where all of the bond lengths are sufficiently similar. In addition, the Br–C(5) bond length is 1.894(3) Å and the C(6)–C(5)–Br and C(4)–C(5)–Br angles are 123.7(2)° and 121.5(2)°,

 © 2007 Wiley-VCH Verlag GmbH & Co. KGaA, Weinheim 

respectively. The thiophene ring is essentially planar with a root mean square deviation of 0.0045 Å. There does not appear to be any intramolecular hydrogen bonding within the molecule.

## Electrochemical Studies

The electrochemical behaviour of **1**, **2′** and **3**–**9** in $CH_2Cl_2$ solution was studied by means of cyclic voltammetry (CV) and square wave voltammetry (SWV) techniques. A preliminary study of **1** and **3**–**6** was previously published.[24] Table 4 presents data of $E_{1/2}$ [$E_{1/2} = (E_{pa} + E_{pc})/2$] for the electrochemical reduction and oxidation of **1**, **2′** and **3**–**9**. The organic ligands **2,4T** and **2,4T′** do not show any oxidation or reduction peaks in the potential range between –1.8 V and +1.5 V vs. $Fc^{*+}/Fc^{*}$ (Fc* = decamethylferrocene) in $CH_2Cl_2$.

Table 4. Electrochemical data for **1**, **2′** and **3**–**9**.[a]

| | $E_{1/2}$ for reduction | $\Delta E_{1/2}$ (red) | $E_{1/2}$ for oxidation | $\Delta E_{1/2}$ (ox) |
|---|---|---|---|---|
| **1** | –0.99[b] | | 1.24[b] | |
| **2′** | –1.54[b] | | 0.70 | |
| **3** | –1.00[b], –1.08[b] | 0.08 | 1.21[b], 1.29[b] | 0.08 |
| **4** | –1.56[b] | | 0.69 | |
| **5** | –1.60[b] | | 0.68 | |
| **6** | –1.58[b], –1.72[b] | 0.14 | 0.65, 0.77 | 0.12 |
| **7+8**[c] | –1.52[b] | | 0.69 | |
| **9** | –1.52[b], –1.64[b] | 0.12 | 0.63, 0.73 | 0.10 |

[a] In V vs. $Fc^{*+}/Fc^{*}$ in $CH_2Cl_2$ solution. Data are taken from CV and SWV at 25 °C, unless otherwise stated. [b] From CV and SWV at –30 °C. [c] Equimolecular mixture of compounds **7** and **8**.

### *Electrochemistry of 1 and 3*

CV and SWV of the $Co_2(CO)_6C_2$ derivative **1** at room temp. show chemically irreversible oxidation and reduction waves at moderate sweep rates (EC processes). Thus, when the sweep is reversed after CV reduction, no coupled anodic peak is observed, but a new small one appears at +0.12 V (irreversible). This behaviour indicates that the decomposition of $\mathbf{1}^-$ yields, among other fragments, $Co(CO)_4^-$ (oxidised at 0.12 V).[6d,7,25] The stability of $\mathbf{1}^-$ is greatly enhanced when low temperature decreases the rate of the following chemical reaction, and at –30 °C chemical reversibility is almost completely attained.

Decreasing temperature to –30 °C and increasing the sweep rate to 2 V/s allowed to observe a very small coupled reduction peak on sweep reversal after $\mathbf{1}^+$ formation. The stability of $\mathbf{1}^+$ is lower than that observed for the related cation derived from 2-[$Co_2(CO)_6\{\mu_2$-$\eta^2$-$(SiMe_3C_2)\}$]-5-($Me_3SiC{\equiv}C$)$C_4H_2S$ ($i_{pc}/i_{pa} \approx 0.55$ at –30 °C and 0.1 V/s).[7d] This result is in agreement with the higher overall π-conjugation[26] in complexes containing **2,5T** ($\lambda_{max}$ = 331 nm)[27] as compared to those of **2,4T** ($\lambda_{max}$ = 277 nm). $E_{1/2}$(ox) and $E_{1/2}$(red) for **1** are very similar to those of the corresponding **2,5T** derivative, indicating that the position of the $–C_2SiMe_3$ substituent on the thiophene ring does not have a significant influence on the electrochemical processes.

Compound **3**, with two "almost" equivalent dicobalt redox centers, shows two consecutive monoelectronic reductions and oxidations to achieve $\mathbf{3}^{2-}$ and $\mathbf{3}^{2+}$, respectively. At room temp., reduction of **3** is chemically completely irreversible; however, at –30 °C the chemical stability of the reduced species is greatly enhanced, and two distinct and almost completely reversible reduction waves are observed in CV (Figure 3). The ratio $i_{pa}/i_{pc}$ approaches 1 as the sweep rate increases. As regarding oxidation, two quasi-reversible waves are also observed, $i_{pc}/i_{pa}$ increasing as the temperature decreases.

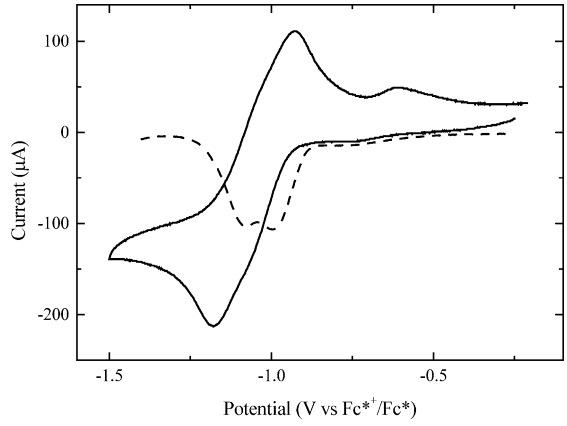


Figure 3. Cyclic (–) and square wave (- - -) voltammograms for the reduction of **3** in $CH_2Cl_2$ containing 0.15 M $TBAPF_6$ at –30 °C on a glassy carbon working electrode. CV: $v$ = 0.5 V $s^{-1}$. SWV: scan increment = 2 mV, SW amplitude = 25 mV, frequency = 15 Hz.

### *Electrochemistry of 2′ and 4–9*

Compounds **2′** and **4**–**9** contain $Co_2(CO)_4(dppm)C_2$ redox centers. The dppm ligand increases the electronic density and makes oxidations easier (less positive $E_{1/2}$) and reductions more difficult (more negative $E_{1/2}$) as observed in Table 4.

The $E_{1/2}$(ox) values are quite similar for all the compounds containing a single $Co_2(dppm)(CO)_4C_2$ redox center, independent of the nature of the other substituent on the thiophene ring (–Br in **2′**, $–C_2SiMe_3$ in **4**–**5** and $–C_2H$ in **7**–**8**) or the location of the $Co_2(dppm)(CO)_4C_2$ unit (position 2 or 4). It should be noted that **7** and **8** could not be isolated, and that an equimolecular mixture of both compounds was used for the electrochemical measurements. A single oxidation and a single reduction peak were obtained for that mixture, indicating that both compounds are oxidised and reduced at almost the same potential value. In the case of $E_{1/2}$(red), differences are not too strong among **2′**, **4**, **5** and **7+8**, but it seems that the presence of a $–C_2SiMe_3$ substituent makes reduction slightly more difficult ($E_{1/2}$ more negative), as a result of the higher electron-donating properties of the $–SiMe_3$ group as compared to –H. The bidentate ligand dppm greatly increases the chemical stability of the cations (oxidations of the compounds with one redox center are chemically completely reversible at 25 °C and 0.1 V/s) and the anions (reductions are quasi-

 © 2007 Wiley-VCH Verlag GmbH & Co. KGaA, Weinheim 

reversible at 25 °C and completely reversible a –30 °C) (Figure 4). Potential values and stability trends agree with those of related **2,5T** compounds.[7d]

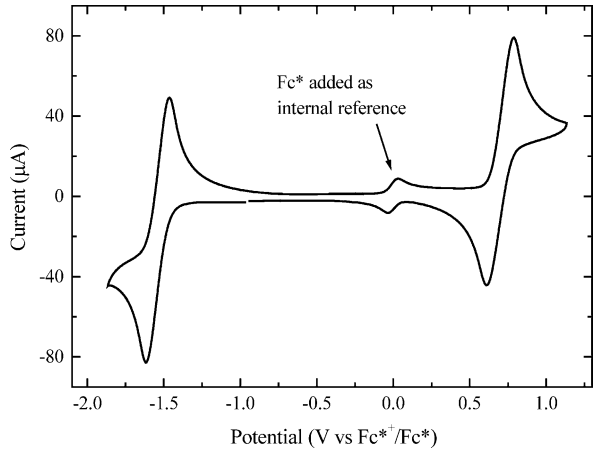


Figure 4. Cyclic voltammogram for the reduction and oxidation of **4** at –30 °C in $CH_2Cl_2$ containing 0.15 M $TBAPF_6$ on a glassy carbon working electrode at $v = 0.05\ V\,s^{-1}$.

**6** and **9** contain two $Co_2(dppm)(CO)_4C_2$ centers and show two consecutive monoelectronic oxidations and reductions. Chemical reversibility is greatly approached at –30 °C (Figure 5), allowing the determination of $E_{1/2}$. Analogous compounds, in which the ligand is **2,5T**, show a greater stability of the corresponding anions and cations, in agreement with the general trends observed in the synthesis of both sets of compounds (**2,4T** and **2,5T** derivatives) and the higher overall π-conjugation of **2,5T**, as the $C^3$–$C^4$ bond in a thiophene ring is known to have less double-bond character than the $C^2$–$C^3$ bond.[28]

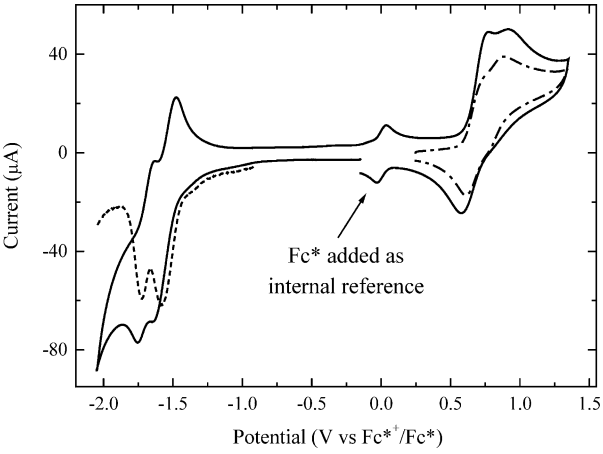


Figure 5. Voltammograms for the reduction and oxidation of **6** in $CH_2Cl_2$ containing 0.15 M $TBAPF_6$. (−) CV at –30 °C on a glassy carbon working electrode, $v = 0.1\ V\,s^{-1}$. (-·-·-) CV at 25 °C on a Pt working electrode, $v = 0.1\ V\,s^{-1}$. (- - -) SWV at –30 °C on a glassy carbon working electrode, scan increment = 2 mV, SW amplitude = 25 mV, frequency = 60 Hz.

The difference between $E_{1/2}$ of consecutive waves in compounds with two equivalent redox centers, $\Delta E_{1/2}$, is usually regarded as an estimation of the amount of electronic interaction between those centers through the bridging ligand.[9a] The two redox centers in **3**, **6** and **9** are not completely equivalent, and the observed $\Delta E_{1/2}$ could be due to intrinsic differences; however, results obtained with **4**–**5** and **7**–**8** (very scarce influence of the position of the redox center on the thiophene ring) allow to assume that most of $\Delta E_{1/2}$ is due to a low-intensity electronic interaction between the centers. The $\Delta E_{1/2}$ values observed for **3**, **6** and **9** can thus be compared to those measured for the related compounds 2,5-$[Co_2(CO)_6\{\mu_2\text{-}\eta^2\text{-}(SiMe_3C_2)\}]_2C_4H_2S$ [$\Delta E_{1/2}$(red) = 0.11 V; $\Delta E_{1/2}$(ox) = 0.24 V], 2,5-$[Co_2(CO)_4(\mu\text{-dppm})\{\mu_2\text{-}\eta^2\text{-}(SiMe_3C_2)\}]_2C_4H_2S$ [$\Delta E_{1/2}$(red) = 0.13 V; $\Delta E_{1/2}$(ox) = 0.29 V] and 2,5-$[Co_2(CO)_4(\mu\text{-dppm})\{\mu_2\text{-}\eta^2\text{-}(HC_2)\}]_2C_4H_2S$ [$\Delta E_{1/2}$(red) = 0.13 V; $\Delta E_{1/2}$(ox) = 0.20 V], respectively.[7d] All $\Delta E_{1/2}$ values (including those of the present work) indicate that a moderate electronic interaction is established through the aromatic ligand backbone, and the complexes belong to group II in the Hush–Robin–Day classification of mixed-valence compounds.[29] Data for the **2,4T** and **2,5T** derivatives show that the $\Delta E_{1/2}$(ox) values are significantly larger for the latter. This seems to indicate that the HOMO (depopulated by oxidation) of the **2,5T** derivatives shows a greater π-delocalization than the HOMO of the **2,4T** derivatives and than the LUMO (populated by reduction) in both groups, in agreement[26] with the higher conjugation observed in **2,5T** derivatives, where the $\lambda_{max}$ value is less blue-shifted relative to that of **2,4T** compounds. The differences in $\Delta E_{1/2}$ indicate a significant contribution of through-bond electronic interactions as compared to through-space ones in these compounds.

## Conclusion

The overall π-conjugation of **2,4T** derivatives is smaller than that of the analogous **2,5T** derivatives, and this results in a lower stability of the ions derived from **2,4T** and a weaker electronic communication through the aromatic ligand backbone. The derivatives of **2,4T** and **2,5T** with two redox centres belong to group II in the Hush–Robin–Day classification of mixed-valence compounds.

## Experimental Section

**Reagents and General Techniques:** All manipulations were carried out by using standard Schlenk vacuum-line and syringe techniques under oxygen-free argon. All solvents for synthetic use were dried and distilled under argon by standard procedures.[30] Column chromatography was performed by using silica gel 100 (Fluka) and preparative TLC glass plates coated with silica gel (SDS 60–17 μm, 0.25 mm thick). 2,4-Dibromothiophene (Lancaster Synthesis Inc.); $Me_3SiC{\equiv}CH$ (TMSA), $Co_2(CO)_8$, KOH (Fluka); 1,2-bis(diphenylphosphanyl)methane (dppm), CuI, a solution 1.0 M of tetrabutylammonium fluoride (TBAF) in THF (Aldrich); $NaHCO_3$, $MgSO_4$ (Panreac) and a solution of HCl (35%) (Prolabo) were used as received. Trimethylamine *N*-oxide (Aldrich) was sublimed prior to use and stored under argon. Compound $Pd(PPh_3)_4$[31] was prepared according to the literature. The $^1H$, $^1H\{^{31}P\}$, $^{13}C\{^1H\}$, $^{31}P\{^1H\}$ NMR spectra and HMQC and HMBC data were recorded with Bruker AMX-300 and -500 instruments. Chemical shifts were

 © 2007 Wiley-VCH Verlag GmbH & Co. KGaA, Weinheim 

measured relative to either an internal reference of tetramethylsilane or residual protons of the solvents. Infrared spectra were measured with a Perkin–Elmer 1650 infrared spectrometer. Elemental analyses were performed with a Perkin–Elmer 240 B microanalyser. Electronic spectra were recorded with a Unicam UV 4 UV/Vis spectrophotometer. Mass spectra were measured with a VG-Autospec mass spectrometer for FAB and EI. Spectroscopy data are available as Supporting Information. Electrochemical measurements were carried out with a computer-driven Par Mo. 273 electrochemistry system in a three-electrode cell under nitrogen in anhydrous deoxygenated $CH_2Cl_2$ containing 0.15 M tetrabutylammonium hexafluorophosphate ($TBAPF_6$) as supporting electrolyte. Cyclic and square wave voltammetry (CV and SWV, respectively) studies were carried out in a three-electrode system. Polycrystalline Pt (0.05 $cm^2$) or glassy carbon were used as working electrodes; the counter electrode was a Pt gauze and the reference electrode was a silver wire quasi-reference electrode. Decamethylferrocene (Fc*) was used as internal standard, and all potentials in this work are referenced to the $Fc^{*+}/Fc^*$ couple. Under the actual experimental conditions, $E_{1/2}$ of the ferrocene couple ($Fc^+/Fc$) was +0.55 V vs. $Fc^{*+}/Fc^*$ in $CH_2Cl_2$ solution. Coulometry of **4** was performed at 1.1 V and 1 mol of electrons per mol of **4** was found to be consumed in the oxidation process. The number of electrons involved in the remaining processes were determined by comparison of peak heights in CV.

**Synthesis of 2,4-Bis(trimethylsilylethynyl)thiophene (2,4T) and 4-Bromo-2-(trimethylsilylethynyl)thiophene (2,4T′):** To a solution of 2,4-dibromothiophene (3.0 g, 12.4 mmol) in $Et_3N$ (100 mL) was added at 0 °C $Pd(PPh_3)_4$ (0.70 g, 0.62 mmol), CuI (0.23 g, 1.24 mmol) and excess of trimethylsilylacetylene (TMSA) (12.1 g, 17.5 mL, 124 mmol). The resulting mixture was stirred first at room temperature for 0.5 h and finally at 75 °C for 20 d. The solvent was removed under reduced pressure and the residue dissolved in $Et_2O$ (100 mL) and wash with (i) a solution of HCl (10%), (ii) a saturated solution of $NaHCO_3$ and dried ($MgSO_4$). The solvent was evaporated and the residue purified by column chromatography with hexane to yield **2,4T** (1.13 g, 33% yield) and **2,4T′** (1.12 g, 35% yield) as stable yellow oils.

**Synthesis of 2-[$Co_2(CO)_6\{\mu_2$-$\eta^2$-$(SiMe_3C_2)\}$]-4-$(Me_3SiC{\equiv}C)C_4H_2S$ (1), 2-$(Me_3SiC{\equiv}C)$-4-[$Co_2(CO)_6\{\mu_2$-$\eta^2$-$(SiMe_3C_2)\}$]$C_4H_2S$ (2) and 2,4-[$Co_2(CO)_6\{\mu_2$-$\eta^2$-$(SiMe_3C_2)\}$]$_2C_4H_2S$ (3):** To a solution of **2,4T** (0.90 g, 3.26 mmol) in hexane (100 mL) was added 1.5 equiv. of $Co_2(CO)_8$. The reaction was monitored by FT-IR and $^1H$ NMR spectroscopy until the signals of the parent compounds **2,4T** and $Co_2(CO)_8$ had disappeared. After the mixture had been stirred at room temp. for 1 h, the solvent was removed under vacuum and the residue purified by thin-layer chromatography (TLC) using hexane as eluent to afford **1** (0.64 g, 35% yield) and **2** (0.36 g, 20% yield) together with **3** (1.24 g, 40% yield) as unstable solids. **3** has also been obtained as the only product in high yield (0.27 g, 89%) from **2,4T** (0.10 g, 0.36 mmol) and 2 equiv. of $Co_2(CO)_8$ and subsequent chromatography with hexane on a silica column.

**Synthesis of 2-[$Co_2(CO)_6\{\mu_2$-$\eta^2$-$(SiMe_3C_2)\}$]-4-(Br)-$C_4H_2S$ (1′):** By a similar procedure as described above, from **2,4T′** (0.75 g, 2.89 mmol) and 1 equiv. of $Co_2(CO)_8$. After the solvent had been removed under vacuum, the product was eluted with hexane on a silica column to afford **1′** (1.43 g, 91% yield) as an unstable red solid.

**Synthesis of 2-[$Co_2(CO)_4$(μ-dppm)$\{\mu_2$-$\eta^2$-$(SiMe_3C_2)\}$]-4-$(Me_3SiC{\equiv}C)C_4H_2S$ (4) and 2-$(Me_3SiC{\equiv}C)$-4-[$Co_2(CO)_4$(μ-dppm)$\{\mu_2$-$\eta^2$-$(SiMe_3C_2)\}$]$C_4H_2S$ (5):** A solution containing **1** and **2** (1.0 g, 1.78 mmol in a 1.75:1 ratio) in hexane (100 mL) was added dppm (0.68 g, 1.78 mmol) and trimethylamine *N*-oxide (0.40 g, 3.56 mmol). The reaction mixture, monitored by FT-IR spectroscopy until the $\nu_{C\equiv O}$ bands of the parent complexes had disappeared, was stirred at 45 °C for 4 d. Finally, the solvent was removed under vacuum and the residue purified by thin-layer chromatography (TLC) using hexane/$CH_2Cl_2$ (6:1) to afford **4** (0.56 g, 56% yield) and **5** (0.16 g, 28% yield) as stable dark red solids.

**Synthesis of 2,4-[$Co_2(CO)_4$(μ-dppm)$\{\mu_2$-$\eta^2$-$(SiMe_3C_2)\}]_2C_4H_2S$ (6):** The same procedure as described above was applied in the preparation of this compound from **3** (0.82 g, 0.97 mmol), dppm (1.94 mmol) and $Me_3NO$ (3.88 mmol). After the solvent had been removed under vacuum, the residue was purified by the same manner. Complex **6** (0.48 g, 33% yield) was obtained as air-stable dark green solid.

**Synthesis of 2-[$Co_2(CO)_4$(μ-dppm)$\{\mu_2$-$\eta^2$-$(SiMe_3C_2)\}$]-4-(Br)-$C_4H_2S$ (2′):** A solution of **1′** (0.27 g, 0.50 mmol) and dppm (0.50 mmol) in hexane (50 mL) was prepared. Trimethylamine *N*-oxide (0.11 g, 1.00 mmol) was added and the reaction mixture, monitored by FT-IR spectroscopy, stirred at 45 °C for 4 d. After the solvent had been removed under vacuum, the residue was purified by thin-layer chromatography (TLC) using hexane/$CH_2Cl_2$ (3:1) to afford **2′** (0.33 g, 77% yield) as stable dark red solid.

**Synthesis of 2-[$Co_2(CO)_4$(μ-dppm)$\{\mu_2$-$\eta^2$-$(SiMe_3C_2)\}$]-4-$(C{\equiv}CH)$-$C_4H_2S$ (7) and 2-$(C{\equiv}CH)$-4-[$Co_2(CO)_4$(μ-dppm)$\{\mu_2$-$\eta^2$-$(SiMe_3C_2)\}$]$C_4H_2S$ (8):** An equimolecular solution of **4** and **5** in MeOH saturated with KOH was stirred for 24 h at 25 °C. Then the solvent was removed under vacuum and the residue extracted with several portions of $Et_2O$ and purified by chromatography on a hexane-packed silica column (200 g) using hexane/$CH_2Cl_2$ (1:1) as eluent to afford **7** (48% yield) together with **8** (50% yield) as unstable solids.

**Synthesis of 2,4-[$Co_2(CO)_4$(μ-dppm)$\{\mu_2$-$\eta^2$-$(HC_2)\}]_2C_4H_2S$ (9):** To a solution of **6** (0.48 g, 0.32 mmol) in wet THF (50 mL) was added TBAF (2.56 mL, 1.0 M in THF, 2.56 mmol) and the mixture stirred at room temp. for 24 h. After the solvent had been removed under vacuum, the product was purified by chromatography on a hexane-packed silica column using hexane/$CH_2Cl_2$ (1:1) as eluent to afford **9** (0.27 g, 62% yield) as unstable dark purplish-red solid.

**X-ray Data Collection, Structure Determination and Refinement of 2′:** Dark red crystals were obtained by recrystallisation of the complex from $CH_2Cl_2$/hexane mixtures. A summary of selected crystallographic data for **2′** is given in Table 5. A red single crystal of approximate dimensions $0.25\times0.12\times0.09$ mm with prismatic shape was mounted on a glass fibre and transferred to a Bruker SMART 6K CCD area-detector three-circle diffractometer with a MAC Science Co., Ltd. rotating anode (Cu-$K_\alpha$ radiation, $\lambda$ = 1.54178 Å) generator equipped with Goebel mirrors at settings of 50 kV and 110 mA.[32] X-ray data were collected at 100 K, with a combination of several runs at different $\phi$ and $2\theta$ angles. The data were collected using 0.3° wide $\omega$ scans, crystal-to-detector distance of 4.0 cm. The raw intensity data frames were integrated with the SAINT program,[33] which also applied corrections for Lorentz and polarization effects. The substantial redundancy in data allowed empirical absorption corrections[34] to be applied using multiple measurements of symmetry-equivalent reflections. A total number of 24250 reflections were collected, and 6989 independent reflections remained after merging $R_{int}$ = 0.0358. The unit-cell parameters were obtained by full-matrix least-squares refinements of the complete data set. The structure was solved and refined using the SHELXTL/PC V 6.10 package.[35] The structure was solved by direct methods, refinement by full-matrix least squares on $F^2$ using

 © 2007 Wiley-VCH Verlag GmbH & Co. KGaA, Weinheim 

all data (negative intensities included). Weighted *R* factors ($R_w$) and all goodness-of-fit (*S*) are based on $F^2$; conventional *R* factors (*R*) are based on *F*. All non-hydrogen atoms were refined with anisotropic displacement parameters. All scattering factors and anomalous dispersions factors are contained in the SHELXTL 6.10 program library. The H-atom parameters were calculated and atoms were constrained as riding atoms with $U_{iso}$ 20% larger than those of the corresponding C atoms for the phenyl H atoms and 50% larger for the methyl H atoms. CCDC-641070 contains the supplementary crystallographic data for this paper. These data can be obtained free of charge from The Cambridge Crystallographic Data Centre via www.ccdc.cam.ac.uk/data_request/cif. Table 3 contains selected bond lengths and angles. Figure 1 presents a molecular diagram of **2′**.

Table 5. Crystal data and structure refinement for compound **2′**.

| | |
|---|---|
| Empirical formula | $C_{38}H_{33}BrCo_2O_4P_2SSi$ |
| Formula mass | 873.50 |
| Temperature | 100(2) K |
| Wavelength | 1.54178 Å |
| Crystal system | monoclinic |
| Space group | $P2_1/n$ |
| Unit-cell dimensions | $a$ = 16.5425(2) Å |
| | $b$ = 12.19370(10) Å |
| | $c$ = 19.1305(2) Å |
| | $\beta$ = 93.2610(10)° |
| Volume | 3852.65(7) Å$^3$ |
| $Z$ | 4 |
| Density (calcd.) | 1.506 Mg/m$^3$ |
| Absorption coefficient | 9.859 mm$^{-1}$ |
| $F$(000) | 1768 |
| Crystal size | 0.25 × 0.12 × 0.09 mm |
| $\theta$ range for data collection | 3.44–70.52° |
| Index ranges | $-17 \le h \le 19, -14 \le k \le 13, -21 \le l \le 22$ |
| Reflections collected | 24250 |
| Independent reflections | 6989 [$R$(int) = 0.0358] |
| Completeness to $\theta$ = 70.52° | 94.9% |
| Absorption correction | SADABS v. 2.03 |
| Refinement method | full-matrix least squares on $F^2$ |
| Data/restraints/parameters | 6989/0/574 |
| Goodness-of-fit on $F^2$ | 1.032 |
| Final $R$ indices [$I > 2\sigma(I)$] | $R_1$ = 0.0330, $wR2$ = 0.0851 |
| $R$ indices (all data) | $R_1$ = 0.0369, $wR2$ = 0.0874 |
| Largest diff. peak/hole | 1.213/–0.798 e Å$^{-3}$ |

**Supporting Information** (see footnote on the first page of this article): IR, UV/Vis, MS, $^1$H, $^{13}$C, $^{31}$P NMR spectra and elemental analysis of **1**–**9**, **1′**–**2′**, **2,4T** and **2,4T′**.

## Acknowledgments

We express our great appreciation to the Dirección General de Investigación Científica y Tecnológica, Spain (Grants No. BQU2002-02522 and CTQ2006-10940/BQU). X-ray diffraction data were collected at the Monocrystal Diffraction Laboratory SidI. Facultad de Ciencias, Universidad Autónoma de Madrid, Spain.

[1] a) R. S. Dickinson, P. J. Fraser, *Adv. Organomet. Chem.* **1974**, *12*, 323–377; b) E. Sappa, A. Tiripicchio, P. Braunstein, *Chem. Rev.* **1983**, *83*, 203–239; c) B. Happ, T. Bartik, C. Zucchi, M. C. Rossi, F. Ghelfi, G. Pályi, G. Váradi, G. Szalontai, I. T. Horváth, A. Chiesi-Villa, C. Guastini, *Organometallics* **1995**, *14*, 809–819; d) S. L. Stang, F. Paul, C. Lapinte, *Organometallics* **2000**, *19*, 1035–1043; e) P. J. Low, M. I. Bruce, *Adv. Organomet. Chem.* **2001**, *48*, 71–286; f) B. H. Danna, B. H. Robinson, J. Simpson, *J. Organomet. Chem.* **2002**, *648*, 251–269; g) N. J. Long, C. K. Williams, *Angew. Chem. Int. Ed.* **2003**, *42*, 2586–2617; h) *Carbon-Rich Organometallics Compounds* (Eds.: R. D. Adams, U. H. F. Bunz), *J. Organomet. Chem.* **2003**, *683*, 267–445; i) K. S. Schanze, E. E. Silverman, X. Zhao, *J. Phys. Chem. B* **2005**, *109*, 18451–18459; j) N. H. T. Huy, E. Perrier, L. Ricard, F. Mathey, *Organometallics* **2006**, *25*, 5176–5179.

[2] a) Y. Rubin, C. B. Knobler, F. Diederich, *J. Am. Chem. Soc.* **1990**, *112*, 4966–4968; b) T. Rappert, O. Nuernberg, H. Werner, *Organometallics* **1993**, *12*, 1359–1364; c) F. Diederich, Y. Rubin, O. L. Chapman, N. S. Goroff, *Helv. Chim. Acta* **1994**, *77*, 1441–1457; d) H. Werner, O. Gevert, P. Steinert, J. Wolf, *Organometallics* **1995**, *14*, 1786–1791; e) J. Lewis, N. J. Long, P. R. Raithby, G. P. Shields, W.-Y. Wong, M. Younus, *J. Chem. Soc. Dalton Trans.* **1997**, 4283–4288; f) R. S. Ashraf, E. Klemm, *J. Polym. Sci., Part A: Polym. Chem.* **2005**, *43*, 6445–6454.

[3] a) M. L. H. Green, S. R. Marder, M. E. Thomson, J. A. Bandy, D. Bloor, P. V. Kolinsky, R. J. Jones, *Nature* **1987**, *330*, 360–362; b) R. A. Hahn, D. Bloor, *Organic Materials for Non-Linear Optics*, The Royal Society of Chemistry, London, **1989**; c) G. D. Stuchky, S. R. Marder, J. Sohn, *Materials for Nonlinear Optics; Chemical Perspectives*, American Chemical Society, Washington, DC, **1991**; d) J. S. Miller, A. J. Epstein, *Angew. Chem. Int. Ed. Engl.* **1994**, *33*, 385–415; e) D. W. Bruce, *Inorganic Materials* (Eds.: D. W. Bruce, D. O'Hare), Wiley, Chichester, **1996**, p. 429; f) S. R. Marder, *Inorganic Materials* (Eds.: D. W. Bruce, D. O'Hare), Wiley, Chichester, **1996**, p. 121; g) M. S. Khan, M. R. A. Al-Mandhary, M. K. Al-Suti, B. Ahrens, M. F. Mahon, L. Male, P. R. Raithby, C. E. Boothby, A. Koehler, *Dalton Trans.* **2003**, 74–84; h) V. W.-W. Yam, K. M.-C. Wong, N. Zhu, *Angew. Chem. Int. Ed.* **2003**, *42*, 14001403; i) M. Haller, J. Luo, H. Li, T.-D. Kim, Y. Liao, B. H. Robinson, L. R. Dalton, A. K.-Y. Jen, *Macromolecules* **2004**, *37*, 688–690; j) R. D. Nielsen, H. L. Rommel, B. H. Robinson, *J. Phys. Chem. B* **2004**, *108*, 8659–8667; k) M. P. Cifuentes, M. G. Humphrey, J. P. Morrall, M. Samoc, F. Paul, C. Lapinte, T. Roisnel, *Organometallics* **2005**, *24*, 4280–4288; l) "Metal Complexes in Molecular Electronics – Progress and Posibilities": P. J. Low, *Dalton Trans.* **2005**, 2821–2824; m) J. G. Rodriguez, J. Esquivias, A. Lafuente, L. Rubio, *Tetrahedron* **2006**, *62*, 3112–3122.

[4] a) P. I. Dosa, C. Erben, V. S. Iyer, K. P. C. Vollhardt, I. M. Wasser, *J. Am. Chem. Soc.* **1999**, *121*, 10430–10431; b) D. T. McQuade, A. E. Pullen, T. M. Swager, *Chem. Rev.* **2000**, *100*, 2537–2574; c) N. Robertson, C. A. McGowan, *Chem. Soc. Rev.* **2003**, *32*, 96–103; d) C. J. Elsevier, J. Reedijk, P. H. Walton, M. D. Ward, *Dalton Trans.* **2003**, 1869–1880; e) J. A. Gladysz, *From sp carbon to sp$^3$ carbon double helices: How to insulate a molecular wire*, 226th ACS National Meeting, New York, United States, **2003**; f) J. A. Gladysz, *Alkene and alkyne metatheses in metal coordination spheres: From insulated molecular wires to molecular gyroscopes*, 227th ACS National Meeting, Anaheim, United States, **2004**.

[5] a) "Introduction to Molecular and Biomolecular Electronics" (Ed.: R. R. Birge), *Adv. Chem. Ser.* **1991**, *240*, 1–14; b) *Nanostructures and Mesoscopic Systems* (Eds.: W. P. Kirk, M. A. Reed), Academic Press, New York, **1992**; c) *Molecular Electronics: Science and Technology* (Ed.: A. Aviram), Confer. Proc. No. 262, American Institute of Physics, New York, **1992**; d) D. Astruc, *Electron Transfer and Radical Processes in Transition-Metal Chemistry*, VCH Publishers, New York, **1995**; e) R. P. Andres, J. D. Bielefeld, J. I. Henderson, D. B. Janes, V. R. Kolagunta, C. P. Kubiak, W. J. Mahoney, R. G. Osifchin, *Science* **1996**, *273*, 1690–1693; f) D. L. Feldheim, C. D. Keating, *Chem. Soc. Rev.* **1998**, *27*, 1–12; g) R. D. Adams, B. Qu, M. D. Smith, *Inorg. Chem.* **2001**, *40*, 2932–2934; h) M. I. Bruce, K. Costuas, J.-F. Halet, B. C. May, P. J. Low, B. K. Nicholson, B. W. Skelton, A. H. White, *J. Chem. Soc. Dalton Trans.* **2002**, 383–398; i) H. Yao, M. Sabat, R. N. Grimes, F. Fabrizi de Biani, P. Zanello, *Angew. Chem. Int. Ed.* **2003**, *42*, 1002–1005; j) H. Yao,

 © 2007 Wiley-VCH Verlag GmbH & Co. KGaA, Weinheim 

M. Sabat, R. N. Grimes, P. Zanello, F. Fabrizi de Biani, *Organometallics* **2003**, *22*, 2581–2593; k) N. Tanifuji, K. Matsuda, M. Irie, *Mol. Cryst. Liq. Cryst.* **2005**, *430*, 75–79.

[6] a) N. Le Narvor, L. Toupet, C. Lapinte, *J. Am. Chem. Soc.* **1995**, *117*, 7129–7138; b) T. Bartik, B. Bartik, M. Brady, R. Dembinski, J. A. Gladysz, *Angew. Chem. Int. Ed. Engl.* **1996**, *35*, 414–417; c) F. Coat, C. Lapinte, *Organometallics* **1996**, *15*, 477–479; d) T. S. Jung, J. H. Kim, E. K. Jang, D. H. Kim, Y.-B. Sim, B. Park, S. C. Shin, *J. Organomet. Chem.* **2000**, *599*, 232–237; e) R. D. Adams, B. Qu, *Organometallics* **2000**, *19*, 2411–2413; f) H. Jiao, J. A. Gladysz, *New J. Chem.* **2001**, *25*, 551–562.

[7] a) C. Moreno, M. L. Marcos, G. Domínguez, A. Arnanz, D. H. Farrar, R. Teeple, A. Lough, J. González-Velasco, S. Delgado, *J. Organomet. Chem.* **2001**, *631*, 19–28; b) M. L. Marcos, M. J. Macazaga, R. M. Medina, C. Moreno, J. A. Castro, J. L. Gómez, S. Delgado, J. González-Velasco, *Inorg. Chim. Acta* **2001**, *312*, 249–255; c) R. M. Medina, C. Moreno, M. L. Marcos, J. A. Castro, F. Benito, A. Arnanz, S. Delgado, J. González-Velasco, M. J. Macazaga, *Inorg. Chim. Acta* **2004**, *357*, 2069–2080; d) A. Arnanz, M. L. Marcos, C. Moreno, D. H. Farrar, A. J. Lough, J. O. Yu, S. Delgado, J. González-Velasco, *J. Organomet. Chem.* **2004**, *689*, 3218–3231.

[8] a) B. H. Robinson, J. Simpson, *Paramagnetic Organometallic Species in Activation/Selectivity Catalysis* (Ed.: M. Chanon), Kluwer Academic Publishers, Dordrecht, The Netherlands, **1989**, p. 357; b) J. Roncali, *Chem. Rev.* **1997**, *97*, 173–205; c) A. Ceccon, S. Santi, L. Orian, A. Bisello, *Coord. Chem. Rev.* **2004**, *248*, 683–724.

[9] a) A. J. Bard, L. R. Faulkner, *Electrochemical Methods: Fundamentals and Applications*, Wiley, New York, **1980**; b) G. H. Worth, B. H. Robinson, J. Simpson, *Organometallics* **1992**, *11*, 3863–3874; c) D. Osella, L. Milone, C. Nervi, M. Ravera, *Eur. J. Inorg. Chem.* **1998**, 1473–1477.

[10] a) K. Okuhara, *Bull. Chem. Soc. Jpn.* **1981**, *54*, 2045–2052; b) Y. T. Park, I. K. Seo, Y.-R. Kim, *Bull. Korean Chem. Soc.* **1996**, *17*, 480–483; c) T. X. Neenan, G. M. Whitesides, *J. Org. Chem.* **1988**, *53*, 2489–2496.

[11] a) A. S. Hay, *J. Org. Chem.* **1960**, *25*, 1275–1276; b) K. Sonogashira, *Comprehensive Organic Synthesis* (Eds.: B. M. Trost, I. Fleming), Pergamon, Oxford, **1991**, vol. 3, p. 521; c) Z. Xu, J. S. Moore, *Angew. Chem. Int. Ed. Engl.* **1993**, *32*, 246–248; d) S. Thornad, N. Krause, *J. Org. Chem.* **1998**, *63*, 8551–8553; e) K. Sonogashira, *Metal-Catalyzed Cross-Coupling Reactions* (Eds.: P. J. Stang, F. Diederich), Wiley-VCH, Weinheim, **1998**, p. 203–229; f) T. Hundertmark, A. F. Littke, S. L. Buchwald, G. C. Fu, *Org. Lett.* **2000**, *2*, 1729–1731; g) P. Siemsen, R. C. Livingston, F. Diederich, *Angew. Chem. Int. Ed.* **2000**, *39*, 2632–2657.

[12] B. H. Dana, B. H. Robinson, J. Simpson, *J. Organomet. Chem.* **2002**, *648*, 251–269.

[13] G. Cetini, O. Gambino, R. Rossetti, E. Sappa, *J. Organomet. Chem.* **1967**, *8*, 149–154.

[14] a) G. Bor, *Spectrochim. Acta* **1963**, *19*, 1209–1224; b) K. M. Nicholas, M. O. Nestle, D. Seyferth, *Transition Metal, Organometallics in Organic Synthesis* (Ed.: H. Alper), Academic Press, New York, **1978**, vol. 2, p. 2; c) J. L. Davison, *Reactions of Coordinated Ligands* (Ed.: P. S. Braterman), Plenum Press, New York, **1986**, vol. I, p. 825; d) J. Lewis, B. Lin, M. S. Khan, M. R. A. Al-Mandhary, P. R. Raithby, *J. Organomet. Chem.* **1994**, *484*, 161–167; e) W.-Y. Wong, H.-Y. Lam, S.-M. Lee, *J. Organomet. Chem* **2000**, *595*, 70–80.

[15] R. K. Harris, *Nuclear Magnetic Resonance Spectroscopy: A Physiochemical View*, Pitman, London, **1983**.

[16] a) J. Castro, A. Moyano, M. A. Pericas, A. Riera, M. A. Maestro, J. Mahía, *Organometallics* **2000**, *19*, 1704–1712; b) T. J. Snaith, P. J. Low, R. Rousseau, H. Pushmann, J. A. K. Howard, *J. Chem. Soc. Dalton Trans.* **2001**, 292–299; c) E. Champeil, S. M. Draper, *J. Chem. Soc. Dalton Trans.* **2001**, 1440–1447.

[17] S. Aime, L. Milone, R. Rossetti, P. L. Stanghellini, *Inorg. Chim. Acta* **1977**, *22*, 135–139.

[18] a) H. Lang, U. Lay, M. Weinmann, *J. Organomet. Chem.* **1992**, *436*, 265–276; b) T. Bartik, B. Happ, M. Iglewsky, H. Badmann, R. Boese, P. Heimbach, T. Hoffmann, E. Wenschuh, *Organometallics* **1992**, *11*, 1235–1241.

[19] J. C. Jeffery, R. M. S. Pereira, M. D. Vargas, M. J. Went, *J. Chem. Soc. Dalton Trans.* **1995**, 1805–1811 and references cited therein.

[20] M. I. Bruce, P. J. Low, A. Werth, B. W. Skelton, A. H. White, *J. Chem. Soc. Dalton Trans.* **1996**, 1551–1566.

[21] Average bite angle of dppm in Co–Co complexes determined to be 110.04° by analysis of data from the Cambridge Crystallographic Database.

[22] C. E. Housecroft, B. F. G. Johnson, M. S. Khan, J. Lewis, P. R. Raithby, M. E. Robson, D. A. Wilkinson, *J. Chem. Soc. Dalton Trans.* **1992**, 3171–3178.

[23] F. H. Allen, O. Kennard, D. G. Watson, L. Brammer, A. Orpen, R. Taylor, *J. Chem. Soc. Perkin Trans. 2* **1987**, S1–S18.

[24] M. L. Marcos, C. Moreno, A. Arnanz, S. Delgado, J. González-Velasco, *Portug. Electrochim. Acta* **2005**, *23*, 35–46.

[25] a) G. J. Bezems, P. H. Rieger, S. J. Visco, *J. Chem. Soc. Chem. Commun.* **1981**, 265–266; b) C. M. Arewgoda, P. H. Rieger, B. H. Robinson, J. Simpson, S. J. Visco, *J. Am. Chem. Soc.* **1982**, *104*, 5633–5640; c) D. Osella, J. Fiedler, *Organometallics* **1992**, *11*, 3875–3878; d) N. W. Duffy, J. McAdam, C. Nervi, D. Osella, M. Ravera, B. H. Robinson, J. Simpson, *Inorg. Chim. Acta* **1996**, *247*, 99–104.

[26] a) A. Sarkar, M. M. Haley, *Chem. Commun.* **2000**, 1733–1734; b) H. Tang, L. Zhu, Y. Harima, K. Yamashita, K.-K. Lee, A. Naka, M. Ishikawa, *J. Chem. Soc. Perkin Trans. 2* **2000**, 1976–1979; c) M. Can, H. Özaslan, N.-Ö. Pekmez, A. Yildiz, *Acta Chim. Slov.* **2003**, *50*, 741–750.

[27] J. Lewis, N. J. Long, P. R. Raithby, G. P. Shields, W.-Y. Wong, M. Younus, *J. Chem. Soc. Dalton Trans.* **1997**, 4283–4288.

[28] F. Fringuelli, G. Marino, A. Taticchi, G. Grandolini, *J. Chem. Soc. Perkin Trans. 2* **1974**, 332–337.

[29] a) M. B. Robin, P. Day, *Adv. Inorg. Chem. Radiochem.* **1967**, *10*, 247–422; b) G. C. Allen, N. S. Hush, *Prog. Inorg. Chem.* **1967**, *8*, 357–389.

[30] D. D. Perrin, S. L. F. Armarego, D. R. Perrin, *Purification of Laboratory Chemicals*, Pergamon Press, New York, **1980**.

[31] a) F. A. Cotton, *Inorg. Synth.* **1972**, *13*, 121; b) D. R. Coulson, *Inorg. Synth.* **1990**, *28*, 107–109.

[32] SMART, version 5.625, Area-Detector Software Package, Bruker AXS, Madison, WI, **2001**.

[33] SAINT+NT, version 6.04, Area-Detector Integration Program, Bruker AXS, Madison, WI, **2001**.

[34] G. M. Sheldrick, SADABS, version 2.03, Program for Empirical Absorption Correction, University of Göttingen, Germany, **1997**.

[35] Bruker AXS SHELXTL, version 6.10, Structure Determination Package, Bruker AXS, Madison, WI, **2000**.

Received: April 25, 2007
Published Online: September 28, 2007

 © 2007 Wiley-VCH Verlag GmbH & Co. KGaA, Weinheim 

DOI: 10.1002/ejic.200700407

# Inclusion Complexes for Use in Room-Temperature Gas-Sensor Design

Liwei Mi,[a] Hongwei Hou,*[a] Jiaqiang Xu,[b] Hong Xu,[a] Zhiyong Song,[a] Mingsheng Tang,[a] and Yaoting Fan[a]

**Keywords:** Inclusion compounds / Semiconductors / Sensors / Density functional calculations / Bridging ligands

The inclusion complex $[\{Co(bpy)(H_2O)_4\}\cdot(fcds)]_n$ (**1**), which has been constructed using the guest molecule ferrocene-1,1′-disulfonate (fcds), the bridging ligand 4,4′-bipyridine (bpy) and $d^7$ $Co^{2+}$, contains an infinite zigzag chain formed by the central $Co^{II}$ ion and the bridging bpy ligand. Guest fcds molecules lie between two adjacent zigzag chains. The highly conjugated structure of complex **1** means that it can be used as a metal-organic semiconductor, and it also shows a high response to liquefied petroleum gas (LPG) and ethanol/petroleum ether (EP) at room temperature. The inclusion complexes $[\{Co(bpp)_2(H_2O)_2\}\cdot(fcds)\cdot 4H_2O]_n$ [**2**; bpp = 1,3-bis(4-pyridyl)propane] and $[\{Zn(bpy)(H_2O)_4\}\cdot(fcds)]_n$ (**3**), on the other hand, cannot be employed as room-temperature gas sensors because they are insulators. The electrical resistivity of inclusion complex $[\{Ni(bpy)(H_2O)_4\}\cdot(fcds)]_n$ (**4**) is 621 MΩ, whereas that of $[\{Co(bpy)(H_2O)_4\}SO_4\cdot(4\text{-abaH})_2\cdot 3H_2O]_n$ (**5**) (4-abaH = 4-aminobenzoic acid) is only 137 MΩ. This means that the semi-conducting properties of such inclusion complexes depend on both the conjugated structure and the central metal ions. Furthermore, conjugated inclusion complexes with an odd number of electrons could be useful for the design of highly selective room-temperature gas sensors.

(© Wiley-VCH Verlag GmbH & Co. KGaA, 69451 Weinheim, Germany, 2007)

## Introduction

Research into low-cost, selective, sensitive and reliable room-temperature gas-sensitive materials has become increasingly important because gas management has become an issue of vital significance in these environmentally conscious times.[1] For this reason, many inorganic oxide semiconductors, such as $SnO_2$, $TiO_2$ and $WO_2$, have been used as gas sensors.[2] However, their lack of long-term stability and selectivity has prevented the widespread use of this type of sensor. Current research into state-of-the-art gas sensors is focused on metallophthalocyanine (MPC)-based semiconductors due to their high response to many gases at room temperature.[3] Undoped conventional MPCs are insulators and their semi-conducting properties are derived from their most noticeable feature, namely their highly charged conjugated electron system, the readily accessible π and π* orbitals of which allow at least partial oxidization or reduction of the macrocycle with gases such as $NO_2$ or $O_3$.[4]

Our strategy for creating room-temperature gas sensors utilizes metal-organic inclusion complexes[5] because they have already been proved to be promising materials for gas storage and molecular recognition[6] and they can easily be prepared under moderate conditions. Furthermore, metal-organic complexes usually contain highly conjugated metal organic hosts with highly charged conjugated electron systems and ionic guest molecules. We believe that both the highly conjugated systems and the central metals govern the gas-sensitive properties of inclusion complexes, which is in contrast to MPC-based gas sensors, where the π-conjugated system contributes mostly to their semiconducting properties.[7] To verify this assumption, four inclusion complexes[8] containing the guest molecule ferrocene-1,1′-disulfonate (fcds), namely $[\{Co(bpy)(H_2O)_4\}\cdot(fcds)]_n$ (**1**), $[\{Co(bpp)_2(H_2O)_2\}\cdot(fcds)\cdot 4H_2O]_n$ (**2**), $[\{Zn(bpy)(H_2O)_4\}\cdot(fcds)]_n$ (**3**), $[\{Ni(bpy)(H_2O)_4\}\cdot(fcds)]_n$ [**4**; bpy = 4,4′-bipyridine, bpp = 1,3-bis(4-pyridyl)propane], and the inclusion complex[9] $[\{Co(bpy)(H_2O)_4\}SO_4\cdot(4\text{-abaH})_2\cdot 3H_2O]_n$ (**5**; 4-abaH = 4-aminobenzonic acid), which contains the neutral molecule 4-abaH as guest, were synthesized. Complexes **1**, **4**, and **5** show some semi-conducting behavior under an adscititious voltage of 5.0 V. However, only **1** exhibits a high response to gasoline and liquefied petroleum gas at room temperature as both **2** and **3** are insulators under these conditions. Quantum chemical calculations help to reveal some of the mechanisms involved in room-temperature gas-sensor design from inclusion complexes (Scheme 1).

[a] Department of Chemistry, Zhengzhou University, Henan 450052, China
Fax: +86-371-6776-1744
E-mail: houhongw@zzu.edu.cn
[b] College of Materials and Chemical Engineering, Zhengzhou University of Light Industry, Henan 450002, China

Supporting information for this article is available on the WWW under http://www.eurjic.org or from the author.

 WILEY InterScience DISCOVER SOMETHING GREAT © 2007 Wiley-VCH Verlag GmbH & Co. KGaA, Weinheim 

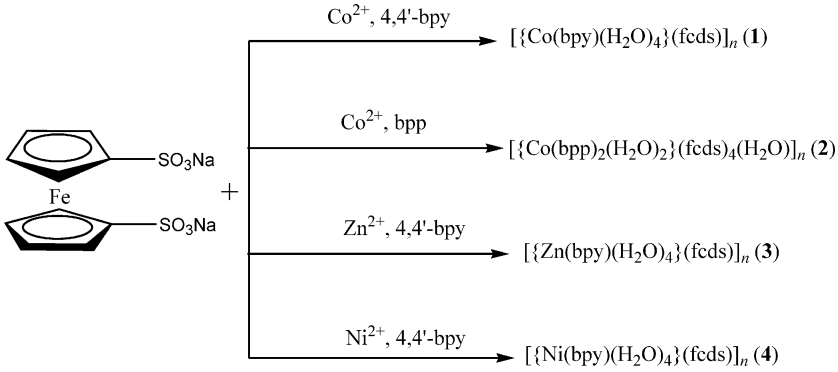


Scheme 1.

## Results and Discussion

Complex **1** was prepared by combining odd-electron divalent $Co^{2+}$ ions with highly conjugated 4,4′-bpy ligands and disodium ferrocene-1,1′-disulfonate. The molecular structure of **1** consists of two parts. The cationic component $[Co(bpy)(H_2O)_4]^{2+}$ forms an infinite zigzag chain, and fcds makes up the anionic part of **1**. As shown in Figure 1, the central cobalt ions lie at the center of a distorted octahedron formed by four oxygen atoms from water molecules

Table 1. Selected bond lengths [Å] and angles [°] for **1**–**3**.[a]

| | | | |
|---|---|---|---|
| | | **1** | |
| Co(1)–O(4)#1 | 2.0851(19) | Co(1)–O(4) | 2.0851(19) |
| Co(1)–O(5)#1 | 2.126(2) | Co(1)–O(5) | 2.126(2) |
| Co(1)–N(1) | 2.1511(19) | Co(1)–N(1)#1 | 2.1511(19) |
| O(4)#1–Co(1)–O(4) | 91.89(12) | O(4)#1–Co(1)–O(5)#1 | 90.63(8) |
| O(4)–Co(1)–O(5)#1 | 85.82(8) | O(4)#1–Co(1)–O(5) | 85.82(8) |
| O(4)–Co(1)–O(5) | 90.64(8) | O(5)#1–Co(1)–O(5) | 174.90(10) |
| O(4)#1–Co(1)–N(1) | 176.88(8) | O(4)–Co(1)–N(1) | 90.84(8) |
| O(5)#1–Co(1)–N(1) | 91.06(8) | O(5)–Co(1)–N(1) | 92.66(8) |
| O(4)#1–Co(1)–N(1)#1 | 90.84(8) | O(4)–Co(1)–N(1)#1 | 176.88(8) |
| O(5)#1–Co(1)–N(1)#1 | 92.66(8) | O(5)–Co(1)–N(1)#1 | 91.06(8) |
| N(1)–Co(1)–N(1)#1 | 86.47(11) | | |
| | | **2** | |
| Co(1)–O(4) | 2.072(4) | Co(1)–O(4)#1 | 2.072(4) |
| Co(1)–N(1)#1 | 2.205(4) | Co(1)–N(1) | 2.205(4) |
| Co(1)–N(2)#2 | 2.218(4) | Co(1)–N(2)#3 | 2.218(4) |
| O(4)–Co(1)–O(4)#1 | 180.0(2) | O(4)–Co(1)–N(1)#1 | 91.83(15) |
| O(4)#1–Co(1)–N(1)#1 | 88.17(15) | O(4)–Co(1)–N(1) | 88.17(15) |
| O(4)#1–Co(1)–N(1) | 91.83(15) | N(1)#1–Co(1)–N(1) | 180.000(2) |
| O(4)–Co(1)–N(2)#2 | 89.26(15) | O(4)#1–Co(1)–N(2)#2 | 90.74(15) |
| N(1)#1–Co(1)–N(2)#2 | 93.68(15) | N(1)–Co(1)–N(2)#2 | 86.32(15) |
| O(4)–Co(1)–N(2)#3 | 90.74(15) | O(4)#1–Co(1)–N(2)#3 | 89.26(15) |
| N(1)#1–Co(1)–N(2)#3 | 86.32(15) | N(1)–Co(1)–N(2)#3 | 93.68(15) |
| N(2)#2–Co(1)–N(2)#3 | 180.000(1) | | |
| | | **3** | |
| Zn(1)–O(4) | 2.084(2) | Zn(1)–O(4)#2 | 2.084(2) |
| Zn(1)–O(5)#2 | 2.138(3) | Zn(1)–O(5) | 2.138(3) |
| Zn(1)–N(1)#2 | 2.162(3) | Zn(1)–N(1) | 2.162(3) |
| O(4)–Zn(1)–O(4)#2 | 91.07(14) | O(4)–Zn(1)–O(5)#2 | 85.99(11) |
| O(4)#2–Zn(1)–O(5)#2 | 85.99(11) | O(4)#2–Zn(1)–O(5) | 85.99(11) |
| O(4)–Zn(1)–O(5) | 90.61(11) | O(4)–Zn(1)–N(1)#2 | 176.87(11) |
| O(5)#2–Zn(1)–O(5) | 175.16(14) | O(5)#2–Zn(1)–N(1)#2 | 92.27(11) |
| O(4)#2–Zn(1)–N(1)#2 | 91.55(10) | O(4)–Zn(1)–N(1) | 91.55(10) |
| O(5)–Zn(1)–N(1)#2 | 91.27(10) | O(5)#2–Zn(1)–N(1) | 91.27(10) |
| O(4)#2–Zn(1)–N(1) | 176.87(11) | N(1)#2–Zn(1)–N(1) | 85.88(15) |
| O(5)–Zn(1)–N(1) | 92.27(11) | | |

[a] Symmetry transformations used to generate equivalent atoms: **1**: #1 $-x - 1, y, -z - 1/2$; **2**: #1 $-x + 3, -y + 2, -z + 3$; #2 $-x + 3, -y + 2, -z + 2$; #3 $x, y, z + 1$; **3**, #1 $-x + 1/2, -y + 3/2, -z$; #2 $-x, y, -z - 1/2$; #3 $-x, -y, -z$.

 © 2007 Wiley-VCH Verlag GmbH & Co. KGaA, Weinheim 

and two nitrogen atoms from two 4,4′-bpy ligands. The coordinated water molecules form strong hydrogen bonds with the anionic part, with the shortest bond being only 1.854 Å and the longest one 3.013 Å. These bonds make the structure very stable (Tables 1 and 2).

Figure 2 shows that the cationic metal-organic and the anionic organic chains are arrange alternately along the *c* axis. The $[Co(bpy)_2(H_2O)_4]^{2+}$ chains are parallel with a distance of 8.478 Å, which gives rise to a highly conjugated structure, as proved by subsequent quantum calculations. These calculations were conducted at the density functional theory (DFT) level using the LanL2DZ basis set.[10] The results of these calculations show that the frontier molecular orbitals of **1** are primarily based on conjugated fcds [HOMO(α): 49.42%; LUMO(α): 48.75%] and the aryl groups of the bpy pillars [HOMO(α): 50.08%; LUMO(α): 50.81%], as depicted in Figure 3. This means that the whole structure of **1** is highly conjugated and that delocalization of the π-electron cloud might make the electron transfer easier. We can therefore deduce that inclusion complexes can be synthesized with semiconducting properties by a judicious choice of highly conjugated organic layers and guest molecules. The charge-transport properties of conjugated polymers in some organic semiconductors,[11] for example, are very closely associated with their π-electron clouds.[12]

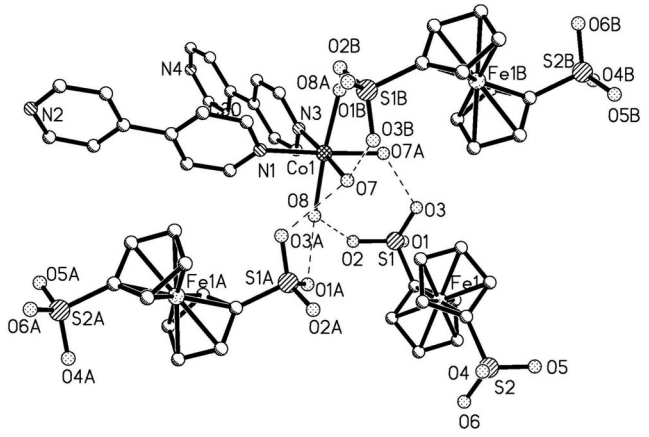


Figure 1. Building block of $[\{Co(bpy)(H_2O)_4\}\cdot(fcds)]_n$ (**1**). Hydrogen atoms have been omitted for clarity. The dotted lines represent hydrogen bonds.

Table 2. Important hydrogen bonds in **1**–**3**.[a]

| D–H | A | *d*(D–H) | *d*(D···H) | *d*(D···A) | D–H–A [°] |
|---|---|---|---|---|---|
| | | **1** | | | |
| O(4)–H(4F) | O(3)#1 | 0.65(3) | 2.14(3) | 2.790(3) | 178(4) |
| O(4)–H(4F) | S(1)#1 | 0.65(3) | 3.01(3) | 3.611(2) | 155(3) |
| O(5)–H(5E) | O(1)#2 | 0.77(3) | 2.02(3) | 2.783(3) | 179(3) |
| O(5)–H(5F) | O(2) | 0.80(3) | 1.95(3) | 2.756(3) | 174(3) |
| O(4)–H(4E) | O(3) | 0.90(4) | 1.85(4) | 2.723(3) | 166(3) |
| O(4)–H(4E) | S(1) | 0.90(4) | 2.92(4) | 3.760(3) | 156(3) |
| | | **2** | | | |
| O(4)–H(4F) | O(3)#1 | 0.88(6) | 1.84(7) | 2.703(5) | 170(6) |
| O(4)–H(4F) | S(1)#1 | 0.88(6) | 3.07(7) | 3.901(4) | 160(5) |
| O(4)–H(4E) | O(2)#2 | 0.89(2) | 1.86(3) | 2.731(5) | 164(6) |
| O(5)–H(5E) | O(1)#3 | 0.85(6) | 1.97(6) | 2.816(7) | 171(6) |
| O(5)–H(5E) | S(1)#4 | 0.85(6) | 2.94(6) | 3.701(5) | 149(5) |
| O(6)–H(6E) | O(1)#4 | 0.86(2) | 2.21(13) | 2.942(9) | 143(19) |
| O(5)–H(5F) | O(3) | 0.86(8) | 2.17(8) | 3.016(7) | 168(7) |
| O(5)–H(5F) | O(2) | 0.86(8) | 2.64(8) | 3.255(8) | 129(6) |
| O(5)–H(5F) | S(1) | 0.86(8) | 2.91(8) | 3.722(6) | 158(6) |
| O(6)–H(6E) | O(5) | 0.96(9) | 1.84(9) | 2.799(8) | 173(8) |
| | | **3** | | | |
| O(4)–H(4E) | O(2)#1 | 0.75(5) | 2.06(5) | 2.788(3) | 166(6) |
| O(4)–H(4E) | S(1)#1 | 0.75(5) | 2.90(5) | 3.611(3) | 161(5) |
| O(5)–H(5E) | O(1)#2 | 0.66(3) | 2.14(3) | 2.789(4) | 173(4) |
| O(4)–H(4F) | O(2) | 0.76(4) | 2.00(4) | 2.731(4) | 162(4) |
| O(4)–H(4F) | S(1) | 0.76(4) | 3.04(4) | 3.771(3) | 163(4) |
| O(5)–H(5F) | O(3) | 0.85(5) | 1.90(5) | 2.743(4) | 171(4) |

[a] Symmetry transformations used to generate equivalent atoms: **1**: #1 $-x-1, -y, -z$; #2 $x, -y, z-1/2$; **2**: #1 $x+1, y, z+1$; #2 $-x+2, -y+1, -z+2$; #3 $-x+1, -y+1, -z+1$; #4 $x+1, y, z$; **3**: #1 $-x, -y+1, -z$; #2 $x, -y+1, z-1/2$.

It should be noted that various gases can be detected by measuring the change of electrical conductivity induced on a suitable active layer by the absorption of gas molecules on its surface.[1a] This change in the conducting behavior of gas-sensing materials results in their use in gas sensors, although to obtain excellent gas sensors the materials must first of all be semiconductors.

The guest fcds molecules in the solid-state structure are found in the space between two adjacent $[Co(bpy)(H_2O)_4]^{2+}$-containing metal-organic layers (interlayer distance: 8.992 Å). This gives rise to numerous O–H···O hydrogen bonds, the shortest of which are only 1.854 Å. It has been reported that the sorption strength of organic compounds

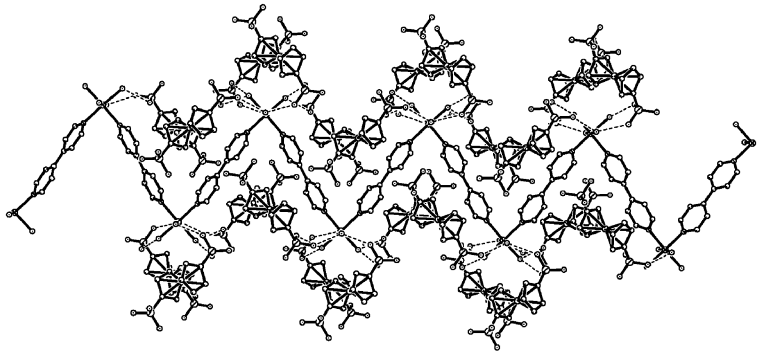

Figure 2. X-ray structure of the pillared and layered structures in solid **1**. Hydrogen atoms have been omitted for clarity.

 © 2007 Wiley-VCH Verlag GmbH & Co. KGaA, Weinheim 

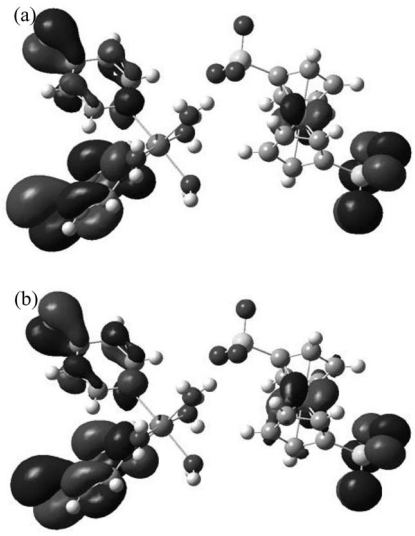


Figure 3. The frontier molecular orbitals of **1**: a) HOMO(α); b) LUMO(α).

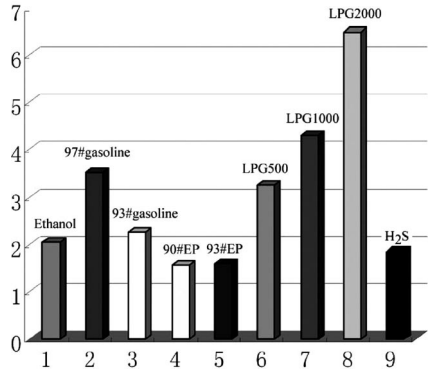


Figure 4. Selectivity of **1** to different gases at room temperature.

depends on similar weak interactions (H-bridge bonds, dispersion forces),[13] therefore the weak interactions in inclusion complexes, especially the H-bonds and π-π interactions between the aryl groups of the pyridine pillars and fcds guests, also contribute to the gas-sensing properties of these complexes. Thus, **1** should have an excellent gas response.

We measured the response of **1** to $H_2S$ (concentration: 50 ppm), ethanol (50 ppm), liquefied petroleum gas (LPG; 50, 1000, and 2000 ppm), 97# gasoline (50 ppm), 93# gasoline (50 ppm), 90# ethanol/petroleum ether (EP; 50 ppm), and 93# ethanol/petroleum ether (EP; 50 ppm) using a commercial gas-sensing measurement system containing HW-30 with no conductive binder added [90# and 97# denote the motor octane number (MON) of the gasoline]. The gas-sensitivity curve was obtained by measuring the change of conductivity at room temperature. As shown in Figure 4, complex **1** displays much higher responses to LPG, EP, gasoline, and alcohol. This behavior is different to that of metal-substituted PCs, which only show a response to highly reactive gases such as $NO_2$, $NH_3$, $Cl_2$, CO, and $N_2$.[14] For comparison, we also measured the selectivity of **1** to gases such as $NO_2$, $N_2$, CO, and $NH_3$; no response was obtained.

The experiment results show that polymeric cobalt inclusion complex **1** could be useful for identifying gases such as LPG, EP, gasoline, alcohol, and $H_2S$ due to its special crystal structure, which contains plenty of hydrogen bonds. However, complex **1** shows no response to $NO_2$, $N_2$, CO, and $NH_3$. The following possibilities must be considered regarding the difference between $NO_2$, $N_2$, CO, $NH_3$, and $H_2S$. The first is that $N_2$, CO, and $NO_2$ cannot easily coordinate to the central cobalt ion in complex **1** because this ion is coordinatively saturated by four coordinated water molecules and two nitrogen atoms from two adjacent 4,4′-bipy bridging ligands. Accordingly, complex **1** cannot be used to identify $N_2$, CO, and $NO_2$. Secondly, both $H_2S$ and $NH_3$ can easily form hydrogen bonds with complex **1**. Previous literature reports have shown that the room-temperature sensing of $H_2S$ gas is possible due to a heterocontact-type sensing mechanism,[15,16] and we believe that a similar mechanism might be functioning in our inclusion complexes. However, the sensing mechanism for $NH_3$ gas is very different to that of $H_2S$, so it is easy to understand why complex **1** can identify $H_2S$ and not $NH_3$.

There are many holes in the crystal structure of **1** which can accommodate numerous small organic gas molecules. The high response of the cobalt inclusion compound to LPG, EP, gasoline, and alcohol at room temperature might be caused by its highly conjugated structure, which possesses a large number of hydrogen bonds, although the regular arrangement of the anionic fcds-containing parts may also enhance the selectivity of this compound. Compound **1** could be reused after heating the gas sensor for a short time, although it should be noted that the selectivity of **1** is slightly lower in the reversible absorption process. This mechanism of action of an inclusion complex contrasts with that of metal-substituted PCs as the latter always contain an unsaturated central metal ion, while the divalent iron ions in our synthesized complex also lie at the center of two negative univalent cyclopentadienyl ions. MPCs could, however, serve as reactive gas sensors. Metal oxide sensor materials also respond to small gas molecules, although most of them only work at high temperature.[17]

A combined TGA-DSC analysis was carried out to study the thermal behavior of inclusion complex **1**. The experiments were performed with samples containing numerous single crystals of each compound under $N_2$/air at a heating rate of 10 °C min$^{-1}$. Crystals of **1** undergo two major weight losses at around 140 and 320 °C (Figure 5). The first weight loss between 140 and 180 °C corresponds to the removal of four coordinated water molecules (calcd. 11.40%; found 11.28%). The remaining compound remained nearly intact until 320 °C, beyond which it decomposed. This thermal behavior study shows that this complex should remain intact after heating to release testing gases such as LPG, EP, gasoline and alcohol.

 © 2007 Wiley-VCH Verlag GmbH & Co. KGaA, Weinheim 

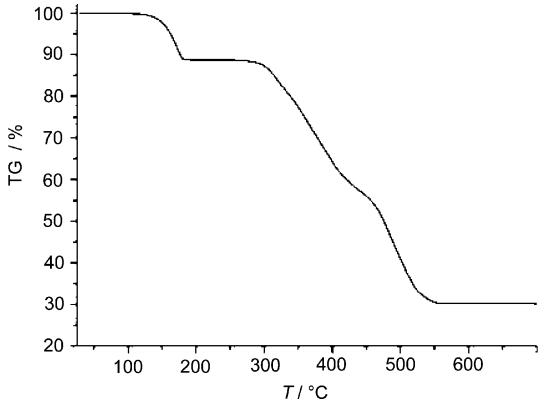


Figure 5. TGA curve of inclusion complex **1**.

Complex **2**, which contains the less conjugated ligand bpp instead of 4,4′-bpy, was synthesized under the same conditions as **1** to check that the gas-sensing properties of inclusion complexes originate from their conjugated π-electron clouds. This complex contains a different motif with double-stranded chains of loops, although it also contains the cationic component $[Co(bpp)_2(H_2O)_2]^{2+}$ and the anionic part contains fcds. As shown in Figure 6, each cobalt center is coordinated by four nitrogen atoms from four bridging bpp ligands and two oxygen atoms from two solvent water molecules. Two nitrogen atoms are nearly coplanar and two oxygen atoms occupy the axial positions. The Co–N bond lengths are 2.205, 2.205, 2.218, and 2.218 Å and all the Co–O bonds are equivalent (2.072 Å). This gives rise to a slightly distorted octahedron. The packing structure of **2** (Figure 7) shows that the double-stranded chain of loops is constructed from central $Co^{II}$ cations and bpp bridging ligands. Due to the long Co···Co distance (11.716 Å) and the distance between the middle carbon atoms of the two diametrically opposing $CH_2CH_2CH_2$ spacers (9.206 Å), the fcds guest molecules do not further bridge $Co^{II}$ cations. It should be noted that these structural factors, especially the introduction of the less conjugated ligand bpp, greatly reduce the conjugation of the whole structure, as was also confirmed by theoretical calculations. The frontier molecular orbitals of **2** (Figure 8) mainly arise from the contribution of the anionic part [HOMO(α): 99.98%; LUMO(α): 99.86%], while the aryl groups of the bpp pillars in **2** contribute very little to these orbitals [HOMO(α): 0.0024%; LUMO(α): 0.14%]. It is therefore clear that only part of **2** is highly conjugated, which means that **2** should show no gas-sensing properties. Indeed, **2** exhibits no response to gases since it shows high electronic resistivity in measurements performed under the same conditions as for **1**.

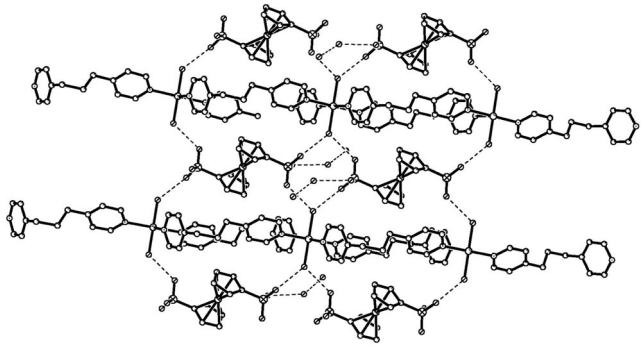

Figure 7. The 3D packing structure of **2**. Hydrogen atoms have been omitted for clarity.

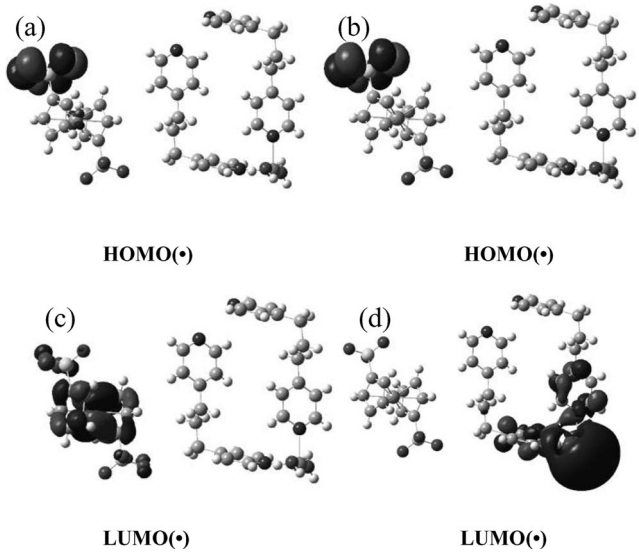


Figure 8. The frontier molecular orbitals of $[\{Co(bpp)_2(H_2O)_2\}\cdot(fcds)\cdot 4H_2O]_n$: a) HOMO(α); b) HOMO(β); c) LUMO(α); d) LUMO(β).

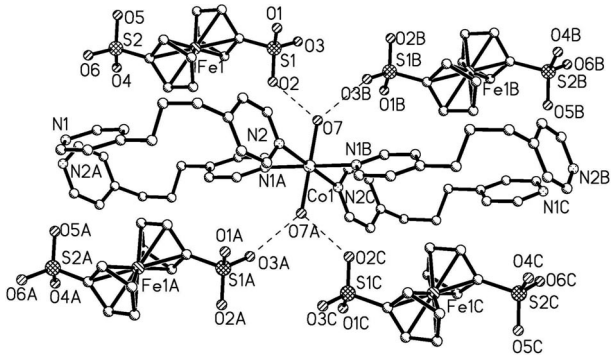


Figure 6. The molecular unit of $[\{Co(bpp)_2(H_2O)_2\}\cdot(fcds)\cdot 4H_2O]_n$ (**2**). Hydrogen atoms have been omitted for clarity.

It has been proven both experimentally and theoretically that highly conjugated molecules can be used as electron conductors.[18] The semiconducting properties of metal-organic inclusion complexes should, however, also depend on the appropriate selection of metal ions. This was further tested by the synthesis of **3**.

The molecular structure of **3** should be highly conjugated as it contains the $d^{10}$ $Zn^{2+}$ cation instead of $Co^{2+}$, highly conjugated 4,4′-bpy and fcds. This complex was synthesized under the same conditions as for **1**. The structure of **3** and its packing are shown in Figures 9 and 10, respectively. Compound **3** has essentially the same molecular structure

 © 2007 Wiley-VCH Verlag GmbH & Co. KGaA, Weinheim 

as **1** but with slightly different bond lengths and angles. The calculations also show that the aryl groups of the 4,4′-bpy pillars and the anionic parts in **3**, respectively, contribute to the frontier molecular orbitals (HOMO: 27.00 and 72.93%; LUMO: 72.66 and 27.16%). Similar to **1**, the whole crystal structure of **3** is highly conjugated. However, in contrast to **1**, **3** displays no gas-sensing properties because the experimental data show that it is an insulator. This means that a highly conjugated structure is not the governing factor in room-temperature metal-organic gas-sensor design. Obviously, the choice of central metal ion also affects the conductivity of metal-organic inclusion complexes. This was confirmed by considering the electronic structures of the central metal ions. The Co 3d orbitals in Co complexes are split due to the odd number of electrons. Cobalt is a typical divalent transition metal and Co complexes have the ability to function as electron-transfer intermediates by permitting a high electron-transfer probability.[19] However, divalent zinc complexes do not permit one-electron reduction due to their spin-coupled electronic structures and the tertiary ionization energy of zinc ions is significantly higher than that of cobalt ions, therefore **3** does not show gas-sensing properties due to its high electrical resistance.

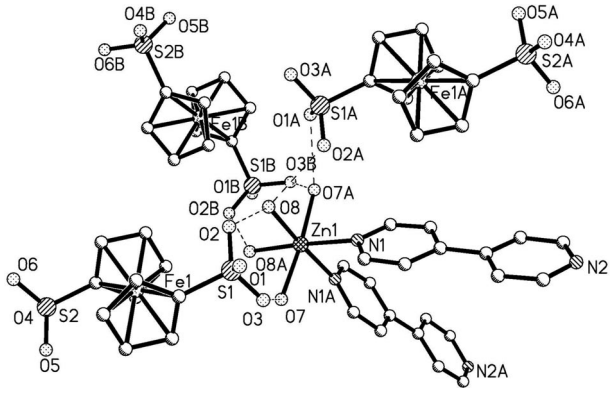


Figure 9. Coordination structure of $[\{Zn(bpy)(H_2O)_4\}\cdot(fcds)]_n$ (**3**). Hydrogen atoms have been omitted for clarity.

Complex **4**, which contains $d^8$ $Ni^{2+}$ instead of $Co^{2+}$ or $Zn^{2+}$, was prepared according to the synthetic method for **1** or **3**. Complexes **1**, **3**, and **4** show extremely similar IR spectra and complexes **1** and **3** have the same molecular structure, which led us to expect that complex **4** would also have the same structure. Elemental analyses and UV/Vis spectra for powdered samples of **1** and **4** were also recorded. The solid UV reflectance spectra of **1** and **4** are shown in Figure 11. It is clear that these compounds have similar solid-state UV spectra, therefore it is likely that **1** and **4** have the same structures expect for the central metal ions.

The gas-sensitivity test showed that the electric resistivity of **4** is 621 MΩ, lower than that of **3** but much higher than that of **1** (1.86 MΩ) as this nickel complex is likely to be low-spin.[20] A comparison of **1** with **3** and **4** showed that besides the highly conjugated systems, the central metal atoms are of significant importance for obtaining a perfect inclusion complex based gas sensor. This was further validated by the gas-sensitivity test of complex $[\{Co(bpy)(H_2O)_4\}SO_4\cdot(4\text{-abaH})_2\cdot 3H_2O]_n$ (**5**). Similar to the structure of **1**, the molecular structure of **5** is also made up of two parts, namely the cation $[Co(bpy)(H_2O)_4]^{2+}$, which forms an infinite chain with neutral 4-abaH, and the $SO_4^{2-}$ anion and lattice water. The electrical resistivity of **5** is 137 MΩ, which is lower than that of **4**, because the central metal atom in **5** is $d^7$ cobalt. Clearly, inclusion complexes with an odd number of electrons are more suitable for use as gas sensors. The electrical resistivity of **5** is higher than that of **1**, and **5** shows only a small response to $H_2S$ and liquefied petroleum gas as its anionic moiety is different to that in **1**.

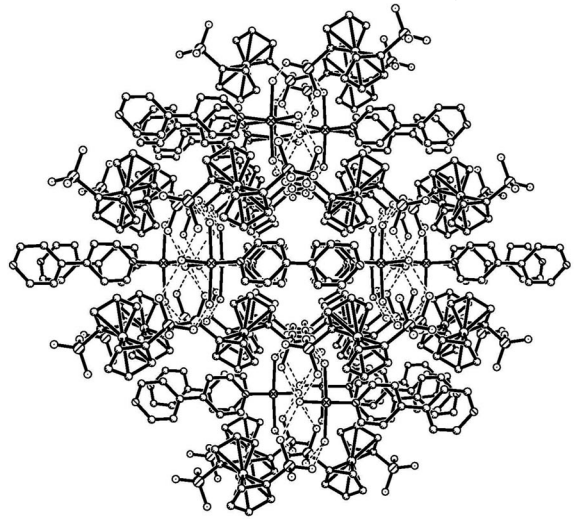

Figure 10. Crystal packing structure of **3**. Hydrogen atoms have been omitted for clarity.

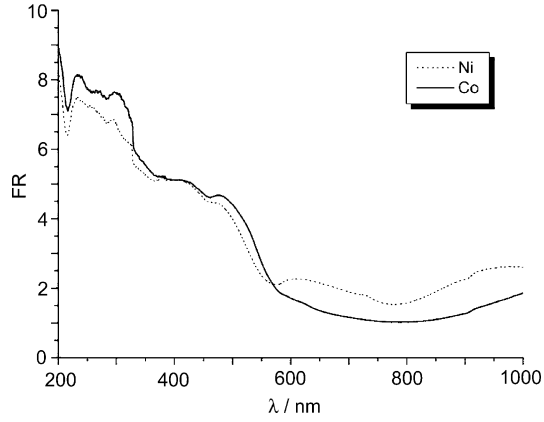


Figure 11.The solid UV reflectance spectra of **1** and **4**.

## Conclusions

The semiconducting cobalt inclusion compound **1** shows a high response to LPG, EG, and gasoline. Inclusion compounds **2** and **3** can not, however, be used as gas sensor because they are insulators. Complexes **4** and **5** have also been synthesized. A comparison of these five complexes has shown that both highly conjugated systems and the appro-

 © 2007 Wiley-VCH Verlag GmbH & Co. KGaA, Weinheim 

priate central metal ions are important factors in the design of room-temperature gas sensors containing metal-organic inclusion complexes. This study may be useful in the search for new gas-sensitive materials.

## Experimental Section

**1:** This complex was prepared by treating $CoCl_2 \cdot 6H_2O$ (0.0238 g, 0.1 mmol) with one equivalent of $Na_2fcds$ (0.0390 g, 0.1 mmol) and two equivalents of 4,4′-bipy (0.0312 g, 0.2 mmol) in a mixture of methanol (4 mL) and water (2 mL). The desired complex crystallized at room temperature as a red crystalline solid upon slow evaporation of the solvents. Yield 0.056 g (89%). $C_{20}H_{24}CoFeN_2O_{10}S_2$: calcd. C 38.05, H 3.83, N 4.44, S 10.16; found C 38.21, H 3.88, N 4.38, S 10.13. IR (KBr): $\tilde{\nu}$ = 3300 (s), 1612 (s), 1532 (s), 1418 (m), 1200 (s), 1042 (s), 1013 (m), 823 (m), 731 (m), 637 (s), 481 (s) $cm^{-1}$.

**2:** A methanol solution (3 mL) of $Na_2fcds$ (0.0390 g, 0.1 mmol) was added to a methanol solution (2 mL) of $CoCl_2 \cdot 6H_2O$ (0.0238 g, 0.1 mmol). After stirring for a while, the mixture was added to an ethanol solution of bpp (0.0396 g, 0.2 mmol) then allowed to stand in air at room temperature for a week. This procedure gave red crystals suitable for X-ray diffraction. Yield 0.037 g (41%). $C_{36}H_{48}CoFeN_4O_{12}S_2$ (907.70): calcd. C 47.64, H 5.33, N 6.17, S 7.07; found C 47.61, H 5.38, N 6.28, S 6.93. IR (KBr): $\tilde{\nu}$ = 3439 (s), 3243 (s), 2947 (m), 1615 (s), 1426 (s), 1182 (s), 1041 (s), 839 (m), 642 (s), 493 (s) $cm^{-1}$.

**3:** Complex **3** was prepared in a similar manner to **1** but with $ZnCl_2$ instead of $CoCl_2 \cdot 6H_2O$. Yield 0.052 g (81%). $C_{20}H_{24}FeN_2O_{10}S_2Zn$ (637.76): calcd. C 38.05, H 3.83, N 4.44, S 10.06; found C 37.96, H 3.86, N 4.49, S 10.09. IR (KBr): $\tilde{\nu}$ = 3453 (s), 1612 (s), 1418 (m), 1120 (s), 1067 (s), 810 (m), 659 (s), 499 (s) $cm^{-1}$.

**4:** Complex **4** was also prepared in a similar manner to **1** but with $NiCl_2 \cdot 6H_2O$ instead of $CoCl_2 \cdot 6H_2O$. Yield 0.052 g (83%). $C_{20}H_{24}FeN_2NiO_{10}S_2$ (631.09): calcd. C 38.06, H 3.83, N 4.44, S 10.16; found C 38.18, H 3.91, N 4.51, S 9.98. IR (KBr): $\tilde{\nu}$ = 3339 (s), 1612 (s), 1418 (m), 1199 (s), 1041 (s), 823 (m), 639 (s), 481 (s) $cm^{-1}$.

**Crystallographic Studies:** Diffraction intensity data for the single crystal of **1** were collected at room temperature with a Bruker Smart CCD diffractometer equipped with graphite-monochromated Mo-$K_\alpha$ radiation ($\lambda$ = 0.71073 Å). The structures were solved by direct methods and refined by full-matrix least-squares techniques on $F^2$ with anisotropic thermal parameters for all non-hydrogen atoms.[21] Hydrogen atoms were located geometrically and refined isotropically.

**Gas-Sensitivity Test:** Gas sensors were made from as-prepared single crystals of inclusion complexes **1**–**5**. The single crystals were moistured with ethanol and ground in an agate mortar to form a powdery paste. This paste was coated on an alumina tube on which a pair of Au electrodes had previously been printed and dried at room temperature in air. The gas sensitivity was measured in the static state. The tested gases ($C_2H_5OH$, HCHO, $NH_3$, and LPG, 90# gasoline, CO, $O_2$ and $N_2$) were injected into a test bottle and mixed with air. The measuring electrical circuit for the gas sensors is shown in the electronic supporting information. The resistivity of the sensor in air or a test gas can be measured by monitoring $V_{out}$. The gas sensitivity (response magnitude) in this paper was defined as $S = R_a/R_g$, where $R_a$ and $R_g$ are the resistivity of a sensor in air and in the test gas, respectively.

**Supporting Information** (see also the footnote on the first page of this article): Crystallographic data for **1**–**3**. Figure S1 shows the selectivity of **1** to different gases at room temperature, Figure S2 displays the selectivity of **1** to CO and $NH_3$ at room temperature. Figure S3 displays the frontier molecular orbital of $\{[Zn(bpy)(H_2O)_4](fcds)\}_n$, Figure S4 the IR spectra of **1**, **3** and **4**.

## Acknowledgments

This work was supported by the National Natural Science Foundation of China (grant nos. 20371042 and 20671082) and NCET.

[1] a) R. Rella, A. Serra, P. Siciliano, A. Tepore, L. Valli, A. Zocco, *Langmuir* **1997**, *13*, 6562–6567; b) J. Spadavecchia, G. Ciccarella, R. Rella, *Sens. Actuators, B* **2005**, *106*, 212–220; c) N. Pinna, G. Neri, M. Antonietti, M. Niederberger, *Angew. Chem. Int. Ed.* **2004**, *43*, 4345–4349; d) Z. L. Wang, *Adv. Mater.* **2003**, *15*, 432–436.

[2] a) N. S. Lewis, *Acc. Chem. Res.* **2004**, *37*, 663–672; b) J. W. Grate, *Chem. Rev.* **2000**, *100*, 2627–2648; c) R. W. J. Scott, S. M. Yang, N. Coombs, G. A. Ozin, D. E. Williams, *Adv. Funct. Mater.* **2003**, *13*, 225–231; d) W. Y. Li, L. N. Xu, J. Chen, *Adv. Funct. Mater.* **2005**, *15*, 851–857; e) N. Shirahata, W. Shin, N. Murayama, A. Hozumi, Y. Yokogawa, T. Kameyama, Y. Masuda, K. Koumoto, *Adv. Funct. Mater.* **2004**, *14*, 580–588; f) J. Polleux, A. Gurlo, N. Barsan, U. Weimar, M. Antonietti, M. Niederberger, *Angew. Chem. Int. Ed.* **2006**, *45*, 261–265; g) J. Q. Xu, Y. P. Chen, D. Y. Chen, J. N. Shen, *Sens. Actuators B* **2006**, *113*, 526–531.

[3] a) S. Chakane, A. Gokarna, S. V. Bhoraskar, *Sens. Actuators, B* **2003**, *92*, 1–5; b) B. Wang, X. Zuo, Y. Q. Wu, Z. M. Chen, Z. Li, *Mater. Lett.* **2005**, *59*, 3073–3077; c) R. D. Yang, B. Fruhberger, J. Park, A. C. Kummel, *Appl. Phys. Lett.* **2006**, *88*, 074104/1–074104/3.

[4] G. Guillaud, J. Simon, J. P. Germain, *Coord. Chem. Rev.* **1998**, *178–180*, 1433–1484.

[5] a) L. Fabbrizzi, F. Foti, S. Patroni, P. Pallavicini, A. Taglietti, *Angew. Chem. Int. Ed.* **2004**, *43*, 5073–5077; b) K. A. Kellersberger, J. D. Anderson, S. M. Ward, K. E. Krakowiak, D. V. Dearden, *J. Am. Chem. Soc.* **2001**, *123*, 11316–11317; c) W. Y. Sun, T. Kusukawa, M. Fujita, *J. Am. Chem. Soc.* **2002**, *124*, 11570–11571; d) T. Uemura, R. Kitaura, Y. Ohta, M. Nagaoka, S. Kitagawa, *Angew. Chem. Int. Ed.* **2006**, *45*, 4112–4114; e) H. Kim, H. Chun, G. H. Kim, H. S. Lee, K. Kim, *Chem. Commun.* **2006**, 2759–2761.

[6] a) S. A. Dalrymple, G. K. H. Shimizu, *Chem. Commun.* **2006**, 956–958; b) Y. F. Zhou, F. L. Jiang, D. Q. Yuan, B. L. Wu, R. H. Wang, Z. Z. Lin, M. C. Hong, *Angew. Chem. Int. Ed.* **2004**, *43*, 5665–5668; c) H. J. Choi, M. P. Suh, *J. Am. Chem. Soc.* **2004**, *126*, 15844–15851.

[7] a) R. M. Rosa, R. L. Szulc, R. W. C. Li, J. Gruber, *Macromol. Symp.* **2005**, *229*, 138–142; b) R. Schlaf, B. A. Parkinson, P. A. Lee, K. W. Nebesny, N. R. Armstrong, *J. Phys. Chem. B* **1999**, *103*, 2984–2992.

[8] **1**: $C_{20}H_{24}CoFeN_2O_{10}S_2$, $M$ = 631.31, monoclinic, space group $C2/c$, $a$ = 17.893(4), $b$ = 12.163(2), $c$ = 13.371(3) Å, $\beta$ = 84.7360(11)°, $V$ = 2483.09(6) Å$^3$, $Z$ = 4, $D_c$ = 1.689 Mgm$^{-3}$, $R$ = 0.0280 and $Rw$ = 0.0644; **2**: $C_{36}H_{48}CoFeN_4O_{12}S_2$, $M$ = 907.68, triclinic, space group $P\bar{1}$, $a$ = 9.5100(19), $b$ = 9.977(2), $c$ = 11.716(2) Å, $\alpha$ = 96.33(3)°, $\beta$ = 107.86(3)°, $\gamma$ = 102.96(3)°, $V$ = 1011.7(3) Å$^3$, $Z$ = 1, $D_c$ = 1.490 Mgm$^{-3}$, $R$ = 0.0601 and $Rw$ = 0.1545; **3**: $C_{20}H_{24}FeN_2O_{10}S_2Zn$, $M$ = 637.75, monoclinic, space group $C2/c$, $a$ = 17.855(4), $b$ = 12.213(2), $c$ = 13.351(3) Å, $\beta$ = 121.27(3)°, $V$ = 2488.4(9) Å$^3$, $Z$ = 4, $D_c$ = 1.702 Mgm$^{-3}$. $R$ = 0.0363 and $Rw$ = 0.0848. CCDC-612722 (for **1**), -612723 (for **2**) and -612724 (for **3**) contain the supplementary crystallographic data for this paper. These data can be obtained free of

 © 2007 Wiley-VCH Verlag GmbH & Co. KGaA, Weinheim 

charge from The Cambridge Crystallographic Data Centre via www.ccdc.cam.ac.uk/data_request/cif.
[9] H. J. Chen, *Chin. J. Struct. Chem.* **2005**, *24*, 236–240.
[10] a) M. J. Frisch, G. W. Trucks, H. B. Schlegel, G. E. Scuseria, M. A. Robb, J. R. Cheesman, J. A. Motgomery Jr., T. Vreven, K. N. Kudin, J. C. Burant, J. M. Millam, S. S. Iengar, J. Tomasi, V. Barone, B. Mennucci, M. Cossi, G. Scalmani, N. Rega, G. A. Petersson, H. Nakatsuji, M. Hada, M. Ehara, K. Toyota, R. Fukuda, J. Hasegawa, M. Ishida, T. Nakajima, Y. Honda, O. Kitao, H. Nakai, M. Klene, X. Li, J. E. Knox, H. P. Hratchian, J. B. Cross, C. Adamo, J. Jaramillo, R. Gomperts, R. E. Stratmann, O. Yazyev, A. J. Austin, R. Cammi, C. Pomelli, J. W. Ochterski, P. Y. Ayala, K. Morokuma, G. A. Voth, P. Salvador, J. J. Dannenberg, V. G. Zakrzewski, S. Dapprich, A. D. Daniels, M. C. Strain, O. Farkas, D. K. Malick, A. D. Rabuck, K. Raghavachari, J. B. Foresman, J. V. Ortiz, Q. Cui, A. G. Baboul, S. Clifford, J. Cioslowski, B. B. Stefanov, G. Liu, A. Liashenko, P. Piskorz, I. Komaromi, R. L. Martin, D. J. Fox, T. Keith, M. A. al-Laham, C. Y. Peng, A. Nanayakkara, M. Challacombe, P. M. W. Gill, B. Johnson, W. Chen, M. W. Wong, C. Gonzalez, J. A. Pople, *Gaussian 03*, Revision B.03, Gaussian, Inc., Pittsburgh, PA, **2003**; b) H. W. Hou, Y. L. Wei, Y. L. Song, L. W. Mi, M. S. Tang, L. K. Li, Y. T. Fan, *Angew. Chem. Int. Ed.* **2005**, *44*, 6067–6074; c) C. Risko, G. P. Kushto, Z. H. Kafati, J. L. Bredas, *J. Chem. Phys.* **2004**, *121*, 9031–9038.
[11] J. S. Huang, M. Kertesz, *J. Phys. Chem. B* **2005**, *109*, 12891–12898.
[12] a) A. Facchetti, M. H. Yoon, C. L. Stern, H. E. Katz, T. J. Marks, *Angew. Chem. Int. Ed.* **2003**, *42*, 3900–3903; b) C. J. Tonzola, M. M. Alam, W. Kaminsky, S. A. Jenekhe, *J. Am. Chem. Soc.* **2003**, *125*, 13548–13558; c) G. R. Hutchison, M. A. Ratner, T. J. Marks, *J. Am. Chem. Soc.* **2005**, *127*, 16866–16881.
[13] K. Bodenhöfer, A. Hierlemann, J. Seemann, G. Gauglitz, B. Koppenhoefer, W. Göpel, *Nature* **1997**, *387*, 577–582.
[14] F. Geobaldo, B. Onida, P. Rivolo, S. Borini, L. Boarino, A. Rossi, G. Amato, E. Garrone, *Chem. Commun.* **2001**, 2196–2197.
[15] L. A. Patil, D. R. Patil, *Sens. Actuators, B* **2006**, *120*, 316–323.
[16] G. H. Jain, L. A. Patil, *Sens. Actuators, B* **2007**, *123*, 246–253.
[17] J.-M. Barbe, G. Canard, S. Brandès, F. Jérôme, G. Dubois, R. Guilard, *Dalton Trans.* **2004**, 1208–1214.
[18] J. M. Seminario, A. G. Zacarias, J. M. Tour, *J. Am. Chem. Soc.* **2000**, *122*, 3015.
[19] a) S. Brooker, P. G. Plieger, B. Moubaraki, K. S. Murray, *Angew. Chem. Int. Ed.* **1999**, *38*, 408–410; b) L. M. Yan, J. M. Seminario, *J. Chem. Phys. A* **2005**, *109*, 6628–6633.
[20] a) I. M. Angulo, E. Bouwman, S. M. Lok, M. Lutz, W. P. Mul, A. L. Spek, *Eur. J. Inorg. Chem.* **2001**, *6*, 1465–1473; b) K. Kurzak, A. Gonciarz, I. Kuzniarska-Biernacka, *Pol. J. Chem.* **2005**, *79*, 47–56.
[21] a) G. M. Sheldrick, *SHELXS 97, Program for the Solution of Crystal Structures*, University of Göttingen, Germany, **1997**; b) G. M. Sheldrick, *SHELXL 97, Program for the Refinement of Crystal Structures*, University of Göttingen, Germany, **1997**.

Received: April 13, 2007
Published Online: October 2, 2007

 © 2007 Wiley-VCH Verlag GmbH & Co. KGaA, Weinheim 

DOI: 10.1002/ejic.200700542

# Substitution, Addition, and Recombination Reactions of Precursor Complexes with Ferrocenyl Carboxylate Units

Xia Wang,[a] Linke Li,[a] Hongwei Hou,*[a] Jie Wu,[a] and Yaoting Fan[a]

**Keywords:** Crystal engineering / Bridging ligands / Substituent effects / Precursors

With the use of sodium β-ferrocenylacrylate and sodium *p*-ferrocenylbenzoate as functional ligands, we synthesized mononuclear precursor complexes containing facile leaving groups or coordinatively unsaturated metal ions: $[Cd(\eta^2\text{-}OOCCH{=}CHFc)_2(C_2H_5OH)_2]$ (**1**), $\{[Cd(\eta^2\text{-}OOCC_6H_4Fc)_2(dmf)_2(H_2O)]\}$ (**2**), $\{[Cd(\eta^2\text{-}OOCC_6H_4Fc)_2(phen)(H_2O)](CH_3OH)\}$ (**3**), and $\{[Zn(OOCC_6H_4Fc)_2(phen)](H_2O)\}$ (**4**) (phen = 1,10-phenanthroline). Investigation of the four precursor ferrocenyl carboxylate complexes as building blocks resulted in ten complexes. The complexes $\{[Cd(\eta^2\text{-}OOCCH{=}CHFc)_2(bbbm)](H_2O)\}_n$ (**1a**), $\{[Cd_2(\eta^2\text{-}OOCCH{=}CHFc)_4(pbbm)_2](CH_3OH)_6(H_2O)_4\}$ (**1b**), $\{[Cd(\eta^2\text{-}OOCC_6H_4Fc)_2(py)_3](CH_3OH)_4\}$ (**2a**), $\{[Cd_2(\eta^2\text{-}OOCC_6H_4Fc)_4(btx)_2](thf)_3(CH_3OH)_2\}$ (**2b**), $\{[Cd_2(\eta^2\text{-}OOCC_6H_4Fc)_2(OOCC_6H_4Fc)_2(phen)_2(bbbm)](CH_3OH)_4(thf)_2\}$ (**3a**), and $[Zn(OOCC_6H_4Fc)_2(phen)(H_2O)]$ (**4a**) were obtained by the substitution or addition reactions of the precursor complexes under moderate conditions. As anticipated, the structural integrity of the precursor complexes can be maintained from the precursors to these complexes. We designed the structures of the complexes by controlling the number of leaving groups in the precursor complexes. In addition, a recombination may have taken place in the reactions of the precursor complexes with organic ligands under severe conditions. The "recombinant" complexes $\{[Cd_2(\eta^2\text{-}OOCCH{=}CHFc)_2(\mu_2\text{-}\eta^2\text{-}OOCCH{=}CHFc)_2(L)_2](CH_3OH)_4\}_n$ [L = 1,4-bis(imidazol-1-ylmethyl)benzene (bix), **1c**; L = btx, **1d**], $\{[Cd(\eta^2\text{-}OOCC_6H_4Fc)_2(pbbm)(H_2O)](H_2O)\}_n$ (**3b**) and $\{[Zn(OOCC_6H_4Fc)_2(bbbm)](CH_3OH)_3\}_n$ (**4b**) were also obtained under reflux conditions.
(© Wiley-VCH Verlag GmbH & Co. KGaA, 69451 Weinheim, Germany, 2007)

## Introduction

The rational design and synthesis of novel metal–organic frameworks (MOFs) have been of great research interest, not only because of their versatile intriguing architectures and topologies, but also because of their potential applications in smart optoelectronic, magnetic, microporous, and biomimetic materials.[1–13] Considerable progress has been made on the theoretical forecast and practical approaches aimed at controlling the topology structure and geometry of the network. Some structures of MOFs can, to a certain extent, be predicted by exploiting organic ligands as building blocks and elaborately by choosing metal salts to control the coordination geometry.[14–19] However, in many cases it is quite difficult to synthesize a desired MOF in a truly deliberate manner[20–22] owing to the influence of many factors, such as the coordination geometry of the central metal ion and the structural characteristics of the ligand,[23–24] solvent, and temperature.[25–27]

An approach that utilizes precursor complexes as building blocks was presented in recent years.[28–43] Precursor complexes possess specific rigid geometries and potentially extend to a multi-dimensional framework, so this kind of building block is helpful to direct the construction of a given structure.[44–51] Rather than relying on the self-assembly of fundamental building units, an alternative synthetic strategy for the construction of MOFs is to assemble precursor complexes as building blocks into predetermined structures by decoration and expansion of the basic net topologies.[52] We believe that these complexes possess the same framework of precursor complexes. Accordingly, the complexes should be easily constructed with the goal of obtaining predictable structure types from precursor complexes without framework distortion. In addition, sometimes framework distortion will occur from precursor complexes to produced complexes when the reaction conditions are relatively severe.

Nevertheless, the study of the synthesis of complexes by using precursor complexes as building units is still a challenge to chemists. With this background and as an extension of studies on the crystal engineering of coordination polymers, our group recently started a program that aims to explore the production of complexes by using the reactions of precursor complexes containing facile leaving groups or coordinatively unsaturated metal ions. Obviously, if the facile leaving groups could be replaced by appropriate ligands, complexes with the destination topology structures should be obtained by controlling the number of leaving groups in the precursor complexes under moderate reaction conditions. At the same time, complexes could also be syn-

[a] Department of Chemistry, Zhengzhou University, Zhengzhou, 450052, P. R. China
Fax: +86-371-67761744
E-mail: houhongw@zzu.edu.cn

 WILEY InterScience DISCOVER SOMETHING GREAT © 2007 Wiley-VCH Verlag GmbH & Co. KGaA, Weinheim 

thesized by the addition reaction of coordinatively unsaturated metal ions in the precursor complexes. If there were only one facile leaving group in the precursor complex, a dimer could be obtained by replacing the leaving group with a bidentate bridging ligand. If there were two leaving groups that could easily be removed in the precursor complex, the conformation of a one-dimensional polymer or a dimer could be gained by a substitution reaction with bidentate-bridging ligands. By substituting these leaving groups with monodentate ligands, we could design complexes whose structures were similar to those of the precursor complexes.[53,54] However, under severe reaction conditions, the strengths of coordination bonds become weak, and then "recombinant" complexes may be obtained. This results in the occurrence of framework distortion from precursor complexes to produced complexes. In the present work, we synthesized four mononuclear precursor complexes, from which six complexes without framework distortion were gained under moderate reaction conditions, and four complexes with framework distortion were obtained under severe conditions. Therefore, our findings demonstrate that the number of facile leaving groups in precursor complexes can control the topology structures of the desired complexes under moderate reaction conditions. Additionally, under severe conditions, the reactions of precursor complexes with ligands can lead to the formation of "recombinant" complexes.

## Results and Discussion

### The Syntheses of Precursor Complexes [Cd(η²-OOCCH=CHFc)$_2$(C$_2$H$_5$OH)$_2$] (1), {[Cd(η²-OOCC$_6$H$_4$Fc)$_2$-(dmf)$_2$(H$_2$O)]} (2), {[Cd(η²-OOCC$_6$H$_4$Fc)$_2$(phen)(H$_2$O)]-(CH$_3$OH)} (3), and {[Zn(OOCC$_6$H$_4$Fc)$_2$(phen)](H$_2$O)} (4)

As is well known, the coordinating capability of ferrocenyl carboxylate groups to metal ions is strong, and the coordination modes are also versatile, such as terminal monodentate, bidentate, and O,O′-bridging coordination modes. It makes the self-assembly of crystal engineering easily available.[55–59] Therefore, we selected sodium β-ferrocenylacrylate and sodium *p*-ferrocenylbenzoate as functional ligands to synthesize the precursor complexes. It is reported that the reaction of the two ferrocenyl carboxylate compounds with some metal salts usually produced coordination polymers.[60] As far as coordination polymers are concerned, they do not dissolve easily in common solvents, and sometimes they contain relatively few facile leaving groups or coordinatively unsaturated metal ions. Hence, coordination polymers are not the best precursor complexes. Mononuclear complexes are dissolved easily, and these complexes may contain facile leaving groups or coordinatively unsaturated metal ions, which allows complexes to be designed by substitution or addition reactions. Moreover, we believe that some coordinated solvent molecules can serve as facile leaving groups in complexes. Some N-donor chelating ligands and solvent molecules were added to the reactions of ferrocenyl carboxylate compounds with metal salts to obtain our desired precursor complexes. Accordingly, mononuclear precursor complexes **1**–**4** were obtained by treatment of FcCH=CHCOONa or FcC$_6$H$_4$COONa with the appropriate metal salts and subsidiary ligands in different solvents (Scheme 1). By using these precursor complexes as building blocks, the corresponding complexes were designed and synthesized.

### The Syntheses and Crystal Structures of {[Cd(η²-OOCCH=CHFc)$_2$(bbbm)](H$_2$O)}$_n$ (1a), {[Cd$_2$(η²-OOCCH=CHFc)$_4$(pbbm)$_2$](CH$_3$OH)$_6$(H$_2$O)$_4$} (1b), {[Cd$_2$(μ$_2$-η²-OOCCH=CHFc)$_2$(η²-OOCCH=CHFc)$_2$-(bix)$_2$](CH$_3$OH)$_4$}$_n$ (1c), and {[Cd$_2$(μ$_2$-η²-OOCCH=CHFc)$_2$-(η²-OOCCH=CHFc)$_2$(btx)$_2$] (CH$_3$OH)$_4$}$_n$ (1d)

X-ray diffraction analysis reveals that, in precursor complex **1**, the Cd$^{II}$ ion is six-coordinate with two oxygen atoms from two ethanol molecules and four oxygen atoms from two FcCH=CHCOO$^-$ units. The two ethanol molecules are facile leaving groups. So a one-dimensional polymer or a dimer can be designed by a substitution reaction of **1** with a bidentate bridging ligand under moderate reaction conditions. As anticipated, one-dimensional polymer **1a** was obtained through the reaction of **1** with bbbm [1,1-(1,4-butanediyl)bis-1*H*-benzimidazole] at room temperature. Under the same conditions, dimer **1b** was also obtained by using pbbm [1,1-(1,3-propylene)bis-1*H*-benzimidazole] instead of bbbm (Scheme 2). However, it is reported that two-dimensional ferrocenecarboxylate-containing polymer {[Cd(η²-OOCCH=CHFc)(bbbm)$_{1.5}$Cl]·1.5H$_2$O}$_n$ was obtained from the one-pot reaction of FcCH=CHCOONa, CdCl$_2$·2.5H$_2$O, and bidentate bridging ligand bbbm.[61]

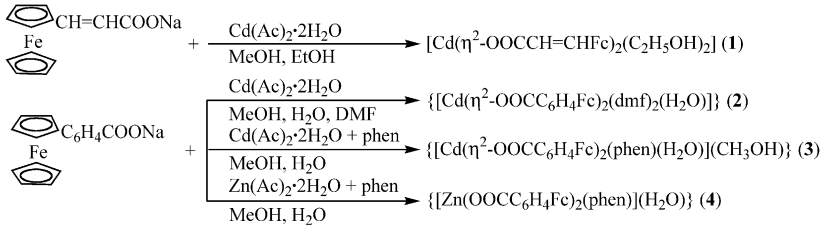


Scheme 1. The syntheses of precursor complexes **1**–**4**.

 © 2007 Wiley-VCH Verlag GmbH & Co. KGaA, Weinheim 

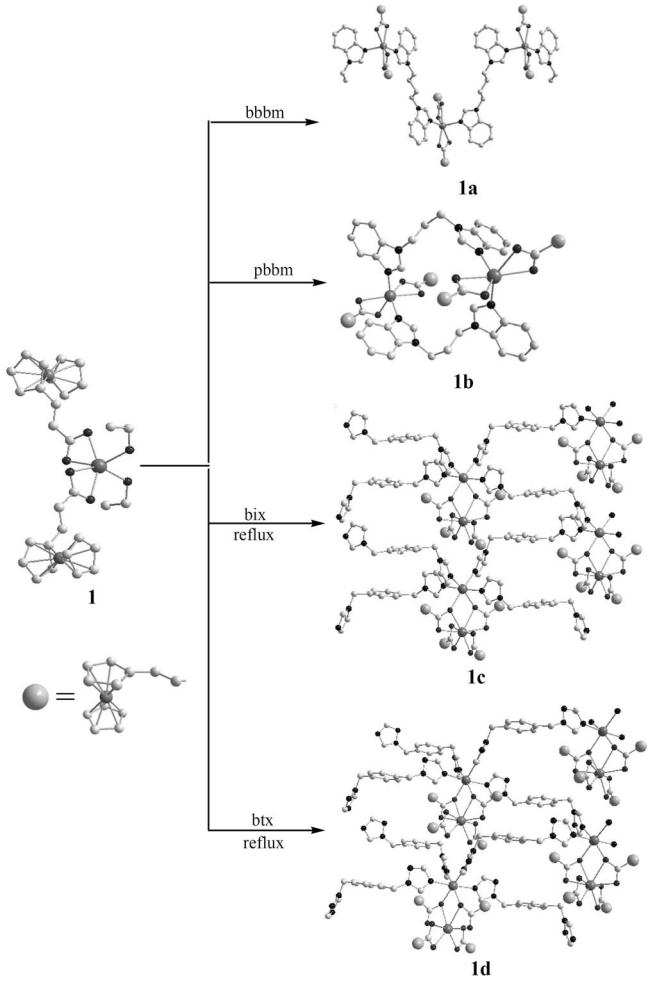


Scheme 2. The synthesis and conversion of precursor complex **1** into complexes **1a**, **1b**, **1c**, and **1d**.

Although the structures of bridging ligands bbbm and pbbm are similar, the structures of **1a** and **1b** have a distinct difference. Two benzimidazole units are connected by $–CH_2–CH_2–CH_2–CH_2–$ and $–CH_2–CH_2–CH_2–$ in ligands bbbm and pbbm, respectively. The torsion angle of C43–C44–C44A–C43A is 180.0° in **1a**, and the angle of C34–C35–C36 is 112.1° in **1b**. So, by using bbbm as a bridging ligand, one-dimensional polymers are easily formed, but dimers are easily obtained by using pbbm as a replacement to bbbm.

Polymer **1a** exhibits one-dimensional zigzag chains (as shown in Figure 1a), each $Cd^{II}$ ion is six-coordinate in a distorted octahedral environment with four oxygen atoms from two terminal chelating $\eta^2$-OOCCH=CHFc$^-$ units and two nitrogen donors from two bridging bbbm ligands. The bbbm ligands connect the $Cd^{II}$ ions by replacing the ethanol molecules, which leads to an infinite one-dimensional chain. In **1b**, two $Cd^{II}$ ions are bridged by two bridging pbbm ligands to form a dimer (Figure 1b). Each $Cd^{II}$ ion is also six-coordinate, and the coordination environment around the $Cd^{II}$ ion is similar to that of **1a**. In addition, the Cd···Cd distance in **1b** (9.603 Å) is distinctly shorter than that of **1a** (14.463 Å).

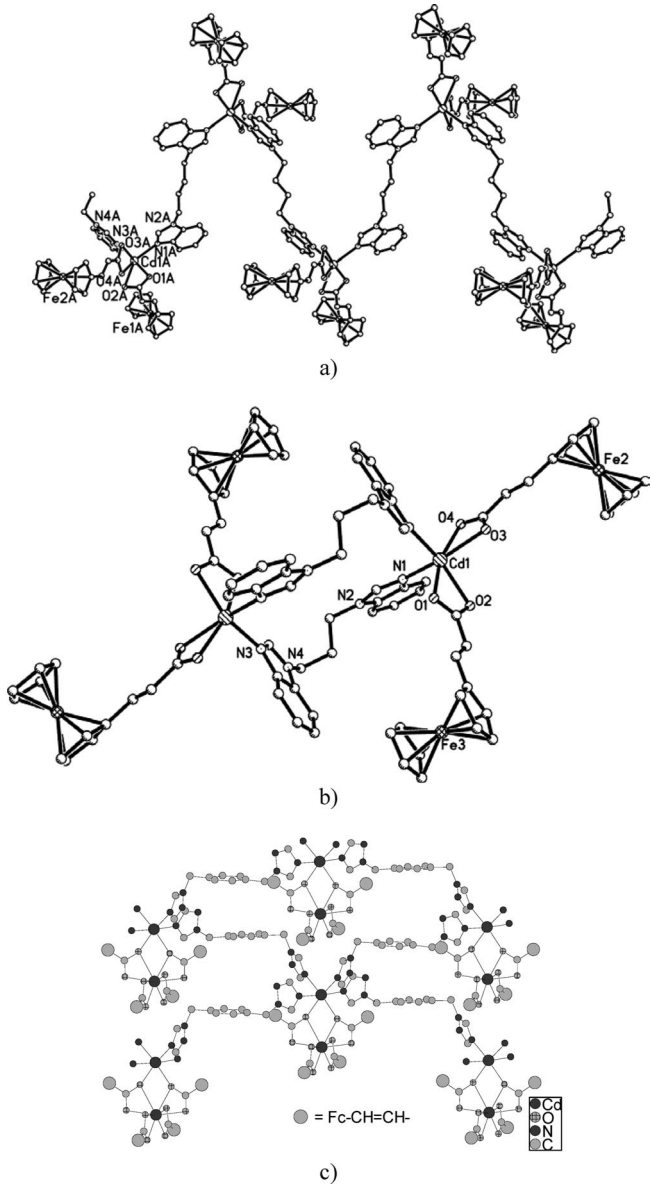


Figure 1. (a) The structure of $\{[Cd_2(\eta^2\text{-OOCCH=CHFc})_4(pbbm)_2](CH_3OH)_6(H_2O)_4\}$ (**1a**) with heteroatom numbering; (b) the structure of $\{[Cd_2(\eta^2\text{-OOCCH=CHFc})_4(pbbm)_2](CH_3OH)_6(H_2O)_4\}$ (**1b**) with heteroatom numbering; (c) two-dimensional network structure of $\{[Cd_2(\mu_2\text{-}\eta^2\text{-OOCCH=CHFc})_2(\eta^2\text{-OOCCH=CHFc})_2(btx)_2](CH_3OH)_4\}_n$ (**1d**) (hydrogen atoms and solvent molecules are omitted for clarity).

Coordination bonds in our precursor complexes are relatively stable except for those formed by the solvent molecules with metal ions under moderate reaction conditions. So the structural integrity of the precursor complexes can be maintained when the precursor complexes react with the ligands, and complexes with destination structures could be designed by using the framework of the precursor complexes, such as the formation of **1a** and **1b**. Nevertheless, the strengths of the coordination bonds become weak under severe reaction conditions (such as reflux). Some coordination bonds were easily broken. Hence, framework distortion will occur from precursor complexes to produced com-

 © 2007 Wiley-VCH Verlag GmbH & Co. KGaA, Weinheim 

plexes. As a result, "recombinant" complexes may take place under the influence of the ligands.

What will happen when precursor complex **1** is treated with bidentate bridging ligands under severe conditions? Herein, two-dimensional network polymers **1c** and **1d** were produced by the reaction of **1** with the organic bix [1,4-bis(imidazol-1-ylmethyl)benzene] or btx [1,4-bis(triazol-1-ylmethyl)benzene] ligands under reflux conditions (Scheme 2). Complexes **1c** and **1d** are produced from framework distortion of precursor complex **1**. From the structures of **1c** and **1d**, it is concluded that the phenomenon of recombination took place in the reaction of **1** with bridging ligands under severe reaction conditions.

Single-crystal X-ray analysis revealed that **1c** and **1d** are isostructural (Figure 1c), and the structures of **1c** and **1d** are distinctly different from those of **1a** and **1b**. It is interesting that the FcCH=CHCOO$^-$ units in **1c** or **1d** display two kinds of coordination modes: one coordinates with one $Cd^{II}$ ion as a chelating bidentate ligand, whereas the other bridges two adjacent $Cd^{II}$ ions as a bridging bidentate ligand. $Cd^{II}$ ions have two kinds of coordination environments in **1c** or **1d**. The coordination sphere of Cd1 is eight-coordinate and binds to four oxygen atoms from two $\eta^2$-OOCCH=CHFc units and four oxygen atoms from two $\mu_2$-$\eta^2$-OOCCH=CHFc units. However, Cd2 is six-coordinate and binds two oxygen atoms from different $\mu_2$-$\eta^2$-OOCCH=CHFc units and four nitrogen atoms from four btx or bix molecules. The neighboring two $Cd^{II}$ ions are connected by $\mu_2$-$\eta^2$-OOCCH=CHFc groups to form a binuclear unit, and all of the binuclear units are joined together by the bix or btx ligands, which leads to an infinite two-dimensional network. The Cd···Cd distances in the binuclear units of **1c** and **1d** are 3.964 and 3.983 Å, respectively, which are longer than those in reported dimeric cadmium–tetracarboxylate complexes (3.278–3.452 Å).[62–64] The Cd–N distances [from 2.290(2) to 2.352(4) Å] associated with the bridging btx and bix ligands are comparable to those found in the literature.[65–68]

### The Syntheses and Crystal Structures of {[Cd($\eta^2$-$OOCC_6H_4Fc)_2(py)_3$]($CH_3OH)_4$} (2a) and {[$Cd_2$($\eta^2$-$OOCC_6H_4Fc)_4(btx)_2$][$thf)_3(CH_3OH)_2$} (2b)

Treatment of $FcC_6H_4COONa$ with $Cd(OAc)_2{\cdot}2H_2O$ in DMF/$H_2O$ yielded precursor complex **2**. The $Cd^{II}$ ion is seven-coordinate with four oxygen atoms from two chelating $FcC_6H_4COO^-$ units, one oxygen atom from one $H_2O$ molecule, and two oxygen atoms from two DMF molecules. The $H_2O$ and DMF molecules are three leaving groups that can easily be displaced. Interestingly, the structure of complex **2** resembles a butterfly and the two coordinated $FcC_6H_4COO^-$ units are the wings. Accordingly, we thought that the syntheses of mononuclear complexes should be completed by substitution reactions of **2** with monodentate ligands. In fact, mononuclear complex **2a** with the framework of **2** was obtained through the addition of pyridine into **2** at room temperature.

It is well known that six or seven-coordinate $Cd^{II}$ is common in ferrocenyl carboxylate complexes. The $Cd^{II}$ is seven-coordinate in precursor complex **2**. So, six- or seven-coordinate $Cd^{II}$ complexes may be obtained by a substitution reaction of **2**. If the coordination number of $Cd^{II}$ in complexes is seven, the structures may form a two-dimensional network by a substitution reaction of **2** with bidentate bridging ligands under moderate reaction conditions. If the $Cd^{II}$ is six-coordinate in the obtained complexes, the structures may be binuclear or form a one-dimensional chain under the same conditions. As a matter of fact, complex **2b** was obtained by a substitution reaction of **2** with the bidentate bridging btx ligand at room temperature (Scheme 3). Because of the spatial configuration and the steric effect of btx, it is difficult to obtain a two-dimensional polymer through the reaction of **2** with btx. Relatively, a dimer or a one-dimensional polymer may be synthesized easily. Just as we thought, **2b** is a dimer, and the coordination number of the $Cd^{II}$ ion is six.

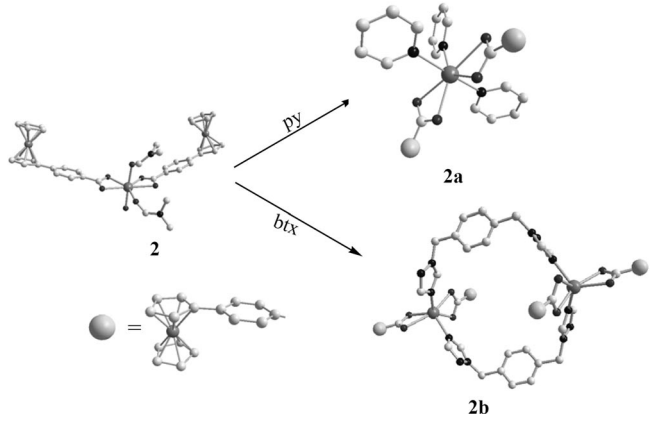


Scheme 3. The synthesis and conversion of precursor complex **2** into complexes **2a** and **2b**.

Mononuclear complex **2a** is depicted in Figure 2a, from which we can see that the $Cd^{II}$ ion is seven-coordinate, and the coordination mode of the central $Cd^{II}$ of **2a** is consistent with that of **2**. The equatorial positions are occupied by O1, O2, O1A, O2A, and N2 (the mean deviation is 0.0811 Å), and the coordination environment around the $Cd^{II}$ ion is a distorted penta bipyramid.

X-ray diffraction analysis revealed that, in **2b**, two $Cd^{II}$ ions are bridged by two bridging btx ligands to form a dimer (Figure 2b). Each $Cd^{II}$ ion coordinates with four oxygen atoms from two chelating $FcC_6H_4COO^-$ units and two nitrogen donors from two btx molecules. The Cd–O bond lengths are in the range of 2.253(5)–2.506(5) Å. In accordance with **2a**, one Cd1–$O_{carboxyl}$ distance in the bidentate mode is longer than those of **2** [from 2.360(5) to 2.454(5) Å], whereas the other distance is shorter than that of **2**. Nevertheless, treatment of $FcC_6H_4COONa$ and $Cd(OAc)_2{\cdot}2H_2O$ with bridging ligand bbp (bbp = 4,4′-trimethylene-dipyridine) generated an infinite one-dimensional ladder-like polymer {[Cd($\mu_2$-$OOCH_4C_6Fc$)($\eta^2$-

 © 2007 Wiley-VCH Verlag GmbH & Co. KGaA, Weinheim 

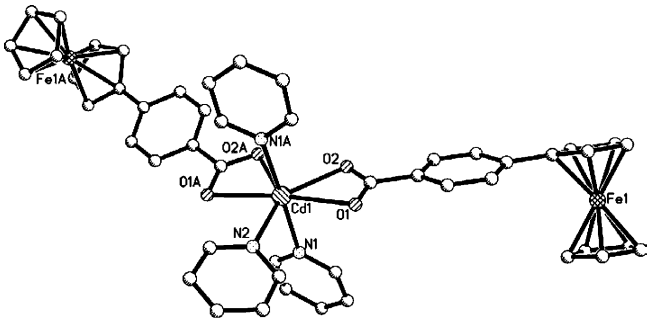


a)

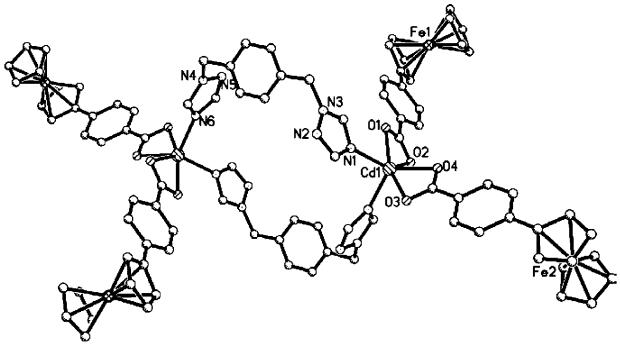


b)

Figure 2. (a) The structure of $\{[Cd(\eta^2\text{-}OOCC_6H_4Fc)_2(py)_3]\text{-}(CH_3OH)_4\}$ (**2a**) with heteroatom numbering; (b) the structure of $\{[Cd_2(\eta^2\text{-}OOCC_6H_4Fc)_4(btx)_2](thf)_3(CH_3OH)_2\}$ (**2b**) with heteroatom numbering (hydrogen atoms and solvent molecules are omitted for clarity).

$OOCH_4C_6Fc)(bbp)](CH_3OH)\}_n$ in which the neighboring $Cd^{II}$ ions are linked by the coaction of the $FcC_6H_4COO^-$ ions and the bbp ligand.[60]

### The Syntheses and Crystal Structures of $\{[Cd_2(\eta^2\text{-}OOCC_6H_4Fc)_2(OOCC_6H_4Fc)_2(phen)_2(bbbm)](CH_3OH)_4\text{-}(thf)_2\}$ (3a) and $\{[Cd(\eta^2\text{-}OOCC_6H_4Fc)_2(pbbm)(H_2O)]\text{-}(H_2O)\}_n$ (3b)

Precursor complex **3** was obtained successfully by using $FcC_6H_4COONa$ as a functional ligand and by introducing the chelate phen ligand and solvent molecule $H_2O$. There is one facile leaving group ($H_2O$ molecule) in **3**. In view of the structural features of **3**, we expected that a dimer could be obtained by using **3** as a building block and by replacing the water molecule with a bidentate bridging ligand under moderate reaction conditions. As anticipated, the reaction of **3** with bbbm resulted in dimer **3a** at room temperature. Because of the framework distortion of **3** that occurs under severe reaction conditions, one-dimensional polymer **3b** was synthesized by a recombination reaction of **3** with pbbm ligands under reflux conditions (Scheme 4).

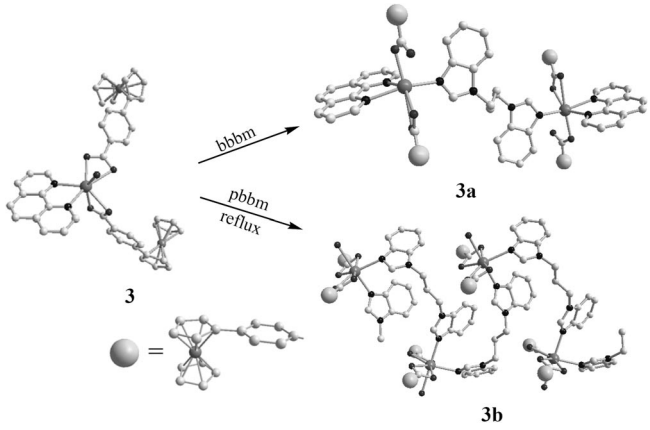


Scheme 4. The synthesis and conversion of precursor complex **3** into complexes **3a** and **3b**.

The structure of **3a** is shown in Figure 3a, and it features a six-coordinate $Cd^{II}$ ion in a distorted octahedral geometry defined by three oxygen atoms from two coordinated $FcC_6H_4COO^-$ units, two nitrogen donors from one chelating phen, and one nitrogen donor from a bridging bbbm ligand. A bbbm ligand links two $Cd^{II}$ ions to form a dimer.

By comparison with **3**, the $[Cd(\eta^2\text{-}OOCC_6H_4Fc)_2(H_2O)]$ units are bridged by pbbm to form one-dimensional quadrate-wave-like chain polymer **3b** under reflux conditions (Figure 3b). The intrachain Cd···Cd distance (9.841 Å) of **3b** is considerably shorter than that of **3a** (13.640 Å). The $Cd1\text{–}N_{phen}$ distances in dimer **3a** [2.387(7), 2.395(7) Å] are consistent with those in **3** [2.366(7), 2.390(8) Å]. Therefore, the substitution reaction of the bbbm replacing $H_2O$ in **3** has little influence on the phen group. Because of the spatial configuration and the steric effect of the ferrocene group and the pbbm ligand, the length of the $Cd1\text{–}O_{water}$ bond in polymer **3b** [2.512(8) Å] is longer than that in precursor complex **3** [2.347(7) Å].

### The Syntheses and Crystal Structures of $[Zn(OOCC_6H_4Fc)_2\text{-}(phen)(H_2O)]$ (4a) and $\{[Zn(OOCC_6H_4Fc)_2(bbbm)]\text{-}(CH_3OH)_3\}_n$ (4b)

The structure of precursor complex **4** is shown in Scheme 5. Among three $Zn\cdots O_{\eta^2\text{-}OOCC_6H_4Fc}$ distances, two of them [Zn–O1 = 1.992(4) and Zn–O4 = 1.975(4) Å] compare well with the distances found in the reported zinc carboxylate complexes[69] and another [Zn···O2 = 2.448(4) Å] is longer than the common $Zn\text{–}O_{carboxyl}$ bond length; in other words, the O2 atom coordinates to the $Zn^{II}$ ion weakly. We think the Zn···O2 bond is an uncoordinated bond.

The $Zn^{II}$ ion is usually four, five, or six-coordinate in complexes.[70] In precursor complex **4**, the $Zn^{II}$ ion is four-coordinate, thus we can obtain complexes by the addition reaction of **4** with some ligands. As a result, the addition reaction of **4** with $H_2O$ yielded complex **4a** at room temperature. Further, as the emergence of **3b**, one-dimensional

 © 2007 Wiley-VCH Verlag GmbH & Co. KGaA, Weinheim 

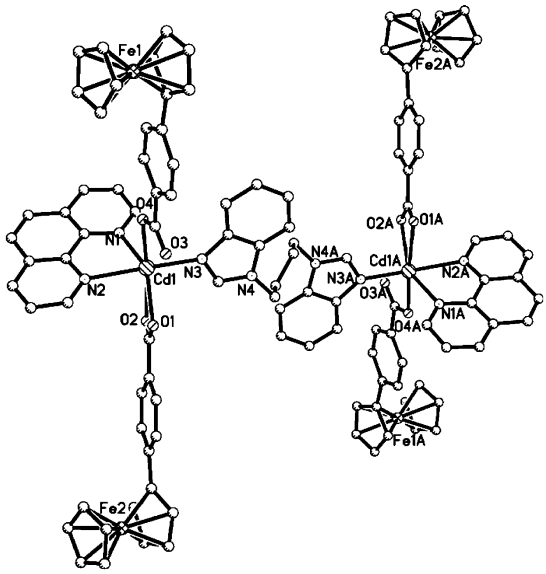


a)

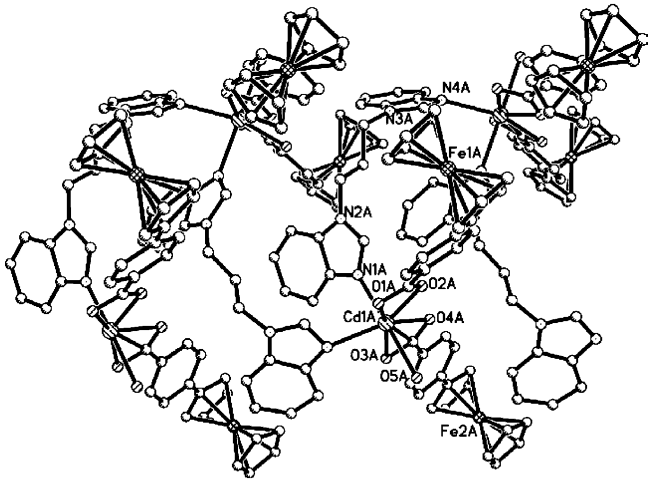


b)

Figure 3. (a) The structure of $\{[Cd_2(\eta^2\text{-}OOCC_6H_4Fc)_2(OOCC_6H_4Fc)_2(phen)_2(bbbm)](CH_3OH)_4(thf)_2\}$ (**3a**); (b) perspective view of the one-dimensional chain structure of $\{[Cd(\eta^2\text{-}OOCC_6H_4Fc)_2(pbbm)(H_2O)](H_2O)\}_n$ (**3b**) (hydrogen atoms and solvent molecules are omitted for clarity).

polymer **4b** was also synthesized by the reaction of **4** with bbbm under reflux conditions (Scheme 5).

The structure of mononuclear complex **4a** is shown in Figure 4a; the $Zn^{II}$ ion is five-coordinate in a distorted square pyramid geometry, and the O1, O5, N1, and N2 atoms are nearly located on the same plane (the mean deviation is 0.0221 Å). Because of the introduction of the $H_2O$ molecule, the distance of $Zn1\text{–}O5_{water}$ (2.088 Å) in **4a** is shorter than Zn···O2 [2.448(4) Å] in **4**. The length of $Zn\text{–}O_{carboxyl}$ in **4a** (1.953 and 2.009 Å) is in conformity with those in **4** (1.975 and 1.992 Å). Therefore, **4a** results from the addition reaction of **4** with $H_2O$. However, the recombi-

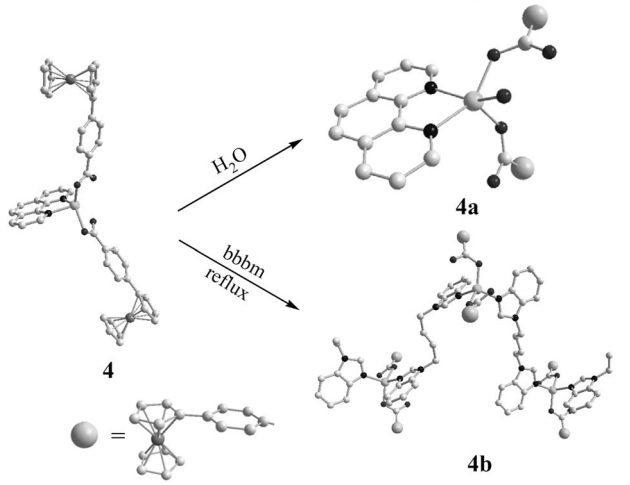


Scheme 5. The synthesis and conversion of precursor complex **4** into complexes **4a** and **4b**.

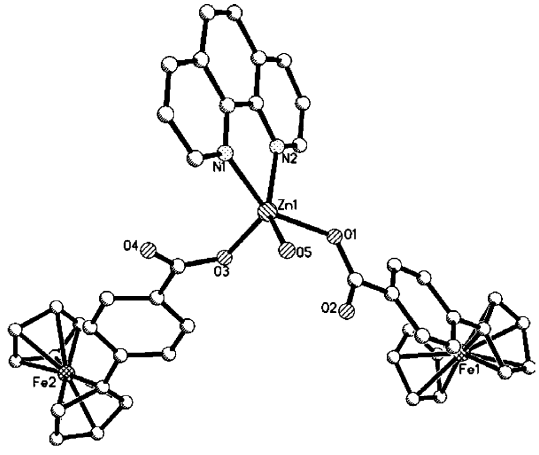


a)

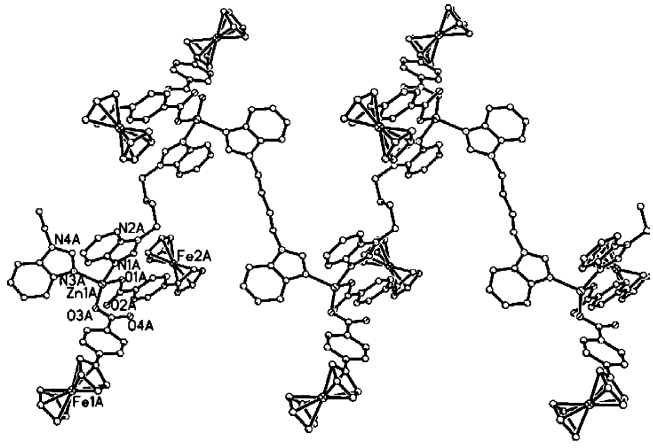


b)

Figure 4. (a) The structure of $[Zn(OOCC_6H_4Fc)_2(phen)(H_2O)]$ (**4a**) with heteroatom numbering; (b) one-dimensional chain structure of $\{[Zn(OOCC_6H_4Fc)_2(bbbm)](CH_3OH)_3\}_n$ (**4b**) (hydrogen atoms and solvent molecules are omitted for clarity).

 © 2007 Wiley-VCH Verlag GmbH & Co. KGaA, Weinheim 

nant reaction of **4** with bbbm yielded one-dimensional chain polymer **4b** (Figure 4b). Each $Zn^{II}$ ion is four-coordinate with two oxygen atoms from two monodentate coordinated $FcC_6H_4COO^-$ units and two nitrogen donors from two bbbm molecules. The torsion angle of C42–C43–C43A–C42A is 180.0°. The $Zn^{II}$ ions are connected by bbbm ligands, and the Zn···Zn distance is 12.310 Å in **4b**.

## Conclusions

The syntheses of precursor complexes **1**–**4** are necessary to obtain the desired complexes. The structural integrity of the precursor complexes can be maintained in substitution or addition reactions of the precursor complexes with ligands under moderate reaction conditions. Noteworthy is the idea that under moderate reaction conditions "the structures of the complexes are dominated by the number of facile leaving groups in the precursor complexes". Because the self-assembly of complexes lies on a delicate thermodynamic balance between enthalpy and entropy effects,[71] and the strengths of the coordination bonds become weak under severe reaction conditions, "recombinant" complexes could be obtained by the reaction of ligands and metal ions. The obtained complexes result from framework distortion of the precursor complexes. In addition, crystals of these complexes that originated from the precursor complexes could not be obtained from one-pot reactions of ferrocenyl carboxylate, metal salts, and organic ligands.

## Experimental Section

β-Ferrocenylacrylic and *p*-ferrocenylbenzoic acid and their corresponding sodium salts were prepared according to literature methods.[72,73] 1,1-(1,4-Butanediyl)bis-1*H*-benzimidazole (bbbm), 1,1-(1,3-propylene)bis-1*H*-benzimidazole (pbbm), 1,4-bis(triazol-1-ylmethyl)benzene (btx), and 1,4-bis(imidazol-1-ylmethyl)benzene (bix) were prepared according to literature methods.[74,63,75] All other staring materials were of reagent-grade quality and were obtained from commercial sources and used without further purification. Elemental analyses (C, H, and N) were carried out with a FLASH EA 1112 elemental analyzer. Infrared spectra data were recorded with a Bruker TENSOR 27 spectrophotometer with KBr pellets in the 400–4000 $cm^{-1}$ region.

**$[Cd(\eta^2\text{-}OOCCH{=}CHFc)_2(C_2H_5OH)_2]$ (1):** FcCH=CHCOONa (55.6 mg, 0.20 mmol) in methanol (8 mL) was added dropwise to a solution of $Cd(OAc)_2{\cdot}2H_2O$ (26.8 mg, 0.1 mmol) in methanol (5 mL) and ethanol (2 mL). The resulting red solution was allowed to stand at room temperature in the dark. Good quality red crystals were obtained several days later. Yield: 48.6 mg (68%). IR (KBr): $\tilde{\nu}$ = 3439 (s), 3126 (s), 2361 (m), 1634 (s), 1519 (s), 1402 (s), 1253 (m), 1102 (m), 1039 (m), 816 (m), 486 (m) $cm^{-1}$. $C_{30}H_{34}CdFe_2O_6$ (714.67): calcd. C 50.42, H 4.80; found C 50.32, H 4.86.

**$\{[Cd(\eta^2\text{-}OOCC_6H_4Fc)_2(dmf)_2(H_2O)]\}$ (2):** $FcC_6H_4COONa$ (65.6 mg, 0.2 mmol) in methanol (6 mL) was added to a solution of $Cd(OAc)_2{\cdot}2H_2O$ (26.8 mg, 0.1 mmol) in methanol (4 mL) and $H_2O$ (3 mL). A red precipitate formed immediately, and DMF (3 mL) was then added to the mixture to dissolve the precipitate. Several days later, good quality red crystals were obtained from the red solution at room temperature in the dark Yield: 53.2 mg (60%). IR (KBr): $\tilde{\nu}$ = 3422 (s), 2367 (m),1633 (s), 1539 (m), 1476 (m), 1400 (s), 1308 (m), 1108 (m), 1053 (m), 813 (m), 710 (m), 519 (m) $cm^{-1}$. $C_{40}H_{42}CdFe_2N_2O_7$ (886.86): calcd. C 54.04, H 4.89, N 3.20; found C 53.77, H 4.82, N 3.15.

**$\{[Cd(\eta^2\text{-}OOCC_6H_4Fc)_2(phen)(H_2O)](CH_3OH)\}$ (3):** A methanol (6 mL) solution of the subsidiary phen ligand (19.8 mg, 0.1 mmol) was added to an aqueous solution (2 mL) of $Cd(OAc)_2{\cdot}2H_2O$ (26.8 mg, 0.1 mmol). A methanol solution (8 mL) of $FcC_6H_4COONa$ (65.6 mg, 0.2 mmol) was then added to the above mixture. The resulting orange solution was allowed to stand at room temperature in the dark. After 1 week, good quality red crystals of **3** were obtained. Yield: 50.5 mg (53%). IR (KBr): $\tilde{\nu}$ = 3420 (m), 1584 (s), 1537 (s), 1395 (s), 1103 (m), 851 (m), 789 (m), 727 (m), 473 (m) $cm^{-1}$. $C_{47}H_{42}CdFe_2N_2O_6$ (952.91): calcd. C 58.01, H 4.05, N 2.68; found C 57.74, H 3.96, N 2.56.

**$\{[Zn(OOCC_6H_4Fc)_2(phen)](H_2O)\}$ (4)** The preparation was similar to that for **3**, except $Zn(OAc)_2{\cdot}2H_2O$ (21.9 mg, 0.1 mmol) was used instead of $Cd(OAc)_2{\cdot}2H_2O$. The resulting orange solution was allowed to stand at room temperature in the dark. After two weeks, good quality red crystals of **4** were obtained. Yield: 43.2 mg (50%). IR (KBr): $\tilde{\nu}$ = 3424 (m), 3080 (m), 1605 (s), 1547 (m), 1387 (s), 1179 (m), 1104 (m), 850 (m), 788 (m), 727 (m), 478 (m) $cm^{-1}$. $C_{46}H_{42}Fe_2N_2O_4Zn$ (863.89): calcd. C 63.94, H 4.92, N 3.20; found C 63.90, H 4.86, N 3.24.

**$\{[Cd(\eta^2\text{-}OOCCH{=}CHFc)_2(bbbm)](H_2O)\}_n$ (1a):** The crystals of complex **1** (17.9 mg, 0.025 mmol) were dissolved in THF (3 mL). A solution of bbbm (7.3 mg, 0.025 mmol) in methanol (6 mL) was added dropwise to the above solution. The resulting red solution was allowed to stand at room temperature in the dark. Good quality red crystals were obtained after several days. Yield: 14.4 mg (62%). IR (KBr): $\tilde{\nu}$ = 3421 (m), 3099 (m), 2932 (m), 1636 (s), 1541 (m), 1508 (m), 1463 (m), 1404 (s), 1291 (m), 1255 (m), 1200 (m), 1105 (m), 1043 (m), 975 (m), 748 (m), 496 (m) $cm^{-1}$. $C_{44}H_{42}CdFe_2N_4O_5$ (930.92): calcd. C 56.72, H 4.51, N 6.02; found C 56.04, H 4.51, N 5.88.

**$\{[Cd_2(\eta^2\text{-}OOCCH{=}CHFc)_4(pbbm)_2](CH_3OH)_6(H_2O)_4\}$ (1b):** The conversion of **1** to **1b** was similar to the procedures mentioned above, except pbbm (6.9 mg, 0.025 mmol) was used instead of bbbm. Three weeks later good quality red crystals were obtained from the red solution at room temperature in the dark. Yield: 17.5 mg (68%). IR (KBr): $\tilde{\nu}$ = 3423 (m), 3103 (m), 1636 (s), 1542 (m), 1510 (m), 1463 (m), 1404 (s), 1290 (m), 1254 (m), 1199 (m), 976 (m), 748 (m), 685 (m), 495 (m) $cm^{-1}$. $C_{92}H_{107}Cd_2Fe_4N_8O_{18}$ (2061.06): calcd. C 53.57, H 5.19, N 5.43; found C 53.02, H 5.08, N 5.50.

**$\{[Cd_2(\mu_2\text{-}\eta^2\text{-}OOCCH{=}CHFc)_2(\eta^2\text{-}OOCCH{=}CHFc)_2(bix)_2](CH_3OH)_4\}_n$ (1c):** A methanol solution (10 mL) of bix (6.8 mg, 0.025 mmol) was added to a THF (4 mL) solution of **1** (17.9 mg, 0.025 mmol) at room temperature. The reaction mixture was heated at refluxed for 10 min. The mixture was then allowed to set at room temperature in the dark for two weeks to afford the product as red crystals. Yield: 14.7 mg (65%). IR (KBr): $\tilde{\nu}$ = 3428 (m), 3120 (m), 1635 (s), 1545 (s), 1402 (s), 1250 (m), 1108 (m), 1027 (m), 936 (m), 824 (m), 657 (m), 496 (m) $cm^{-1}$. $C_{84}H_{88}Cd_2Fe_4N_8O_{12}$ (1809.76): calcd. C 54.49, H 4.76, N 6.05; found C 53.68, H 4.69, N 6.11.

**$\{[Cd_2(\mu_2\text{-}\eta^2\text{-}OOCCH{=}CHFc)_2(\eta^2\text{-}OOCCH{=}CHFc)_2(btx)_2](CH_3OH)_4\}_n$ (1d):** The synthesis was the same as that for **1c**, except with the use of btx (7.8 mg, 0.025 mmol) and **1** (17.9 mg, 0.025 mmol). Yield: 15.3 mg (66%). IR (KBr): $\tilde{\nu}$ = 3423 (m), 3114 (m), 1636 (s), 1547 (s), 1463 (m), 1403 (s), 1280 (m), 1255 (m), 1136

 © 2007 Wiley-VCH Verlag GmbH & Co. KGaA, Weinheim 

(s), 1010 (m), 983 (m), 872 (m), 825 (m), 675 (m), 497 (m) $cm^{-1}$. $C_{80}H_{84}Cd_2Fe_4N_{12}O_{12}$ (1853.79): calcd. C 51.78, H 4.53, N 9.06; found C 51.68, H 4.47, N 8.98.

**{[Cd(η²-OOCC$_6$H$_4$Fc)$_2$(py)$_3$](CH$_3$OH)$_4$} (2a):** Methanol (9 mL) was added to a solution of complex **2** (22.2 mg, 0.025 mmol) in pyridine (2 mL). The mixture was kept at room temperature in the dark. About one month later good quality red crystals were obtained. Yield: 13.6 mg (50%). IR (KBr): $\tilde{\nu}$ = 3428 (m), 1604 (m), 1585 (m), 1537 (m), 1398 (s), 1183 (m), 1105 (m), 1034 (m), 1007 (m), 856 (m), 818 (m), 790 (m), 707 (m), 475 (m) $cm^{-1}$. $C_{53}H_{57}CdFe_2N_3O_8$ (1088.12): calcd. C 58.46, H 5.24, N 3.86; found C 57.80, H 5.16, N 3.83.

**{[Cd$_2$(η²-OOCC$_6$H$_4$Fc)$_4$(btx)$_2$](thf)$_3$(CH$_3$OH)$_2$} (2b):** A solution of btx (7.8 mg, 0.025 mmol) in methanol (6 mL) was added to a solution of **2** (22.2 mg, 0.025 mmol) in THF (3 mL) to give a clear solution. The solution was kept at room temperature in the dark. A few days later, red crystals of **2b** were obtained. Yield: 17.0 mg (62%). IR (KBr): $\tilde{\nu}$ = 3423 (m), 3114 (m), 1588 (s), 1543 (s), 1398 (s), 1279 (s), 1135 (m), 1105 (m), 1011 (m), 731 (m), 710 (m), 674 (m), 474 (m) $cm^{-1}$. $C_{106}H_{96}Cd_2Fe_4N_{12}O_{13}$ (2194.15): calcd. C 57.97, H 4.38, N 7.66; found C 57.12, H 4.28, N 7.62.

**{[Cd$_2$(η²-OOCC$_6$H$_4$Fc)$_2$(OOCC$_6$H$_4$Fc)$_2$(phen)$_2$(bbbm)](CH$_3$OH)$_4$-(thf)$_2$} (3a):** A solution of bbbm (7.3 mg, 0.025 mmol) in methanol (6 mL) was added slowly with stirring to a solution of **3** (23.8 mg, 0.025 mmol) in THF (3 mL). One week later, good quality red crystals were obtained from the red solution at room temperature in the dark. Yield: 20.6 mg (70%). IR (KBr): $\tilde{\nu}$ = 3423 (m), 3096 (m), 1589 (s), 1543 (s), 1395 (s), 1104 (m), 849 (m), 790 (m), 747 (m), 728 (m), 710 (m), 474 (m) $cm^{-1}$. $C_{122}H_{110}Cd_2Fe_4N_8O_{14}$ (2360.38): calcd. C 62.02, H 4.66, N 4.74; found C 61.57, H 4.60, N 4.79.

**{[Cd(η²-OOCC$_6$H$_4$Fc)$_2$(pbbm)(H$_2$O)](H$_2$O)}$_n$ (3b):** A solution of pbbm (6.9 mg, 0.025 mmol) in methanol (6 mL) was added dropwise to a solution of **3** (23.8 mg, 0.025 mmol) in THF (3 mL). This reaction mixture was heated at reflux for 10 min to give a clear

Table 1. Selected bond lengths [Å] and angles [°] for complexes **1**, **1a**–**c**, **2**–**4**.

| | | | | | | | |
|---|---|---|---|---|---|---|---|
| Complex **1**[a] | | | | | | | |
| Cd1–O3 | 2.228(4) | Cd1–O1 | 2.297(3) | Cd1–O2 | 2.362(4) | O3–Cd1–O3#1 | 87.2(3) |
| O1–Cd1–O2 | 55.77(13) | O3–Cd1–O1#1 | 89.36(15) | O1#1–Cd1–O1 | 152.6(2) | O2–Cd1–O2#1 | 89.8(2) |
| O2–Cd1–O2#1 | 89.8(2) | O3#1–Cd1–O2 | 145.03(15) | O1#1–Cd1–O2 | 103.15(14) | O3–Cd1–O1 | 110.72(17) |
| Complex **2** | | | | | | | |
| Cd1–O6 | 2.293(5) | Cd1–O5 | 2.307(5) | Cd1–O7 | 2.312(4) | Cd1–O4 | 2.360(5) |
| Cd1–O2 | 2.454(5) | Cd1–O3 | 2.402(4) | Cd1–O1 | 2.408(5) | O5–Cd1–O4 | 143.63(17) |
| O5–Cd1–O2 | 78.22(16) | O3–Cd1–O2 | 165.17(17) | O7–Cd1–O4 | 90.99(17) | O1–Cd1–O2 | 53.69(16) |
| O4–Cd1–O1 | 85.31(14) | O7–Cd1–O2 | 96.12(18) | O5–Cd1–O1 | 131.04(16) | O6–Cd1–O3 | 91.6(2) |
| O4–Cd1–O3 | 54.42(15) | O3–Cd1–O1 | 139.69(15) | O6–Cd1–O2 | 80.7(2) | O6–Cd1–O1 | 90.6(2) |
| Complex **3** | | | | | | | |
| Cd1–O2 | 2.327(7) | Cd1–O5 | 2.347(7) | Cd1–O4 | 2.354(7) | Cd1–O1 | 2.505(7) |
| Cd1–N2 | 2.390(8) | Cd1–O3 | 2.524(7) | Cd1–N1 | 2.366(7) | O2–Cd1–O5 | 143.0(3) |
| N1–Cd1–O3 | 156.1(3) | N1–Cd1–N2 | 70.0(3) | O2–Cd1–O1 | 54.1(2) | O2–Cd1–N1 | 93.0(3) |
| N2–Cd1–O1 | 136.3(3) | O4–Cd1–N1 | 142.2(3) | O5–Cd1–O1 | 88.9(3) | | |
| Complex **4** | | | | | | | |
| Zn1–O4 | 1.975(4) | Zn1–O1 | 1.992(4) | Zn1–N1 | 2.097(6) | Zn1–N2 | 2.098(5) |
| N1–Zn1–N2 | 78.7(3) | O4–Zn1–O1 | 129.01(17) | O4–Zn1–N1 | 116.13(18) | O1–Zn1–N1 | 98.7(2) |
| O4–Zn1–N2 | 101.28(19) | O1–Zn1–N2 | 122.11(17) | | | | |
| Complex **1a**[b] | | | | | | | |
| Cd1–N3 | 2.264(3) | Cd1–O4 | 2.276(3) | Cd1–O2 | 2.462(4) | Cd1–O3 | 2.530(3) |
| N1–Zn1–N2 | 78.7(3) | Cd1–O1 | 2.299(4) | N3–Cd1–O4 | 115.12(12) | N3–Cd1–N1 | 103.14(11) |
| O1–Cd1–O2 | 53.21(15) | N1–Cd1–O1 | 91.71(14) | O4–Cd1–N1 | 116.91(12) | N3–Cd1–O1 | 107.16(15) |
| N1–Cd1–O2 | 144.37(13) | O4–Cd1–O2 | 81.61(12) | N3–Cd1–O3 | 84.82(11) | | |
| Complex **1b**[c] | | | | | | | |
| Cd1–N1 | 2.257(5) | Cd1–N3#1 | 2.278(5) | Cd1–O2 | 2.328(5) | Cd1–O3 | 2.335(5) |
| Cd1–O4 | 2.400(5) | Cd1–O1 | 2.407(5) | N1–Cd1–N3#1 | 98.86(19) | N1–Cd1–O2 | 98.1(2) |
| N3#1–Cd1–O2 | 138.05(19) | N1–Cd1–O3 | 151.1(2) | O3–Cd1–O4 | 55.14(19) | O2–Cd1–O3 | 89.70(18) |
| O3–Cd1–O1 | 109.9(2) | O4–Cd1–O1 | 163.65(19) | N1–Cd1–O1 | 97.2(2) | | |
| Complex **1c**[d] | | | | | | | |
| Cd1–O2 | 2.5728(19) | Cd1–O3 | 2.301(2) | Cd1–O4 | 2.599(3) | Cd1–O1 | 2.370(2) |
| Cd2–N4#2 | 2.348(3) | Cd2–N1 | 2.290(2) | Cd2–O4 | 2.321(2) | O3#1–Cd1–O3 | 164.81(10) |
| O1#1–Cd1–O1 | 88.98(10) | O1–Cd1–O2#1 | 139.20(8) | O3–Cd1–O1 | 101.50(7) | O1–Cd1–O4 | 121.30(8) |
| O1–Cd1–O2 | 50.58(7) | O3–Cd1–O4 | 51.17(7) | O3#1–Cd1–O4 | 114.02(7) | O2–Cd1–O4 | 77.28(7) |
| N1#1–Cd2–O4 | 84.14(8) | N1#1–Cd2–N1 | 176.90(12) | N1–Cd2–O4 | 98.31(8) | O4–Cd2–N4#2 | 161.68(9) |

[a] Symmetry transformations used to generate equivalent atoms: #1 $-x$, $y$, $-z$ + 1/2. [b] Symmetry transformations used to generate equivalent atoms: #1 $-x$, $y$ + 2, $-z$ + 1, #2 $-x$, $y$ + 2, $-z$. [c] Symmetry transformations used to generate equivalent atoms: #1 $-x$, $-y$, $-z$, #2 $-x$ + 1, $-y$ + 1, $-z$. [d] Symmetry transformations used to generate equivalent atoms: #1 $-x$ + 2, $y$, $-z$ + 1/2, #2 $x$ + 1/2, $y$ + 1/2, $z$, #3 $-x$ + 3/2, $y$ + 1/2, $-z$ + 1/2, #4 $x$ – 1, $y$ – 1/2, $z$, #5 $-x$ + 3/2, $-y$ + 1/2, $-z$.

 © 2007 Wiley-VCH Verlag GmbH & Co. KGaA, Weinheim 

solution. The resulting red solution was allowed to stand at room temperature in the dark. Good quality red crystals were obtained after two weeks. Yield: 14.5 mg (56%). IR (KBr): $\tilde{\nu}$ = 3421 (m), 3099 (m), 1601 (s), 1534 (s), 1461 (m), 1398 (s), 1180 (m), 1104 (m), 817 (m), 789 (m), 746 (m), 710 (m), 473 (m) $cm^{-1}$. $C_{51}H_{46}CdFe_2N_4O_6$ (1035.02): calcd. C 59.13, H 4.44, N 5.41; found C 59.08, H 4.41, N 5.36.

**$[Zn(OOCC_6H_4Fc)_2(phen)(H_2O)]$ (4a):** Complex **4** (21.6 mg, 0.025 mmol) was dissolved in THF (3 mL) whilst stirring. Methanol (6 mL) and $H_2O$ (3 mL) was added to the above solution. A few days later good quality red crystals were obtained from the red solution at room temperature in the dark. Yield: 10.0 mg (46%). IR (KBr): $\tilde{\nu}$ = 3423 (m), 3088 (m), 1606 (s), 1543 (m), 1389 (m), 1178 (m), 1104 (m), 843 (m), 790 (m), 726 (m), 520 (m), 478 (m) $cm^{-1}$. $C_{46}H_{36}Fe_2N_2O_5Zn$ (873.84): calcd. C 63.17, H 4.12, N 3.20; found C 62.86, H 4.08, N 3.22.

**$\{[Zn(OOCC_6H_4Fc)_2(bbbm)](CH_3OH)_3\}_n$ (4b):** Compound **4** (21.6 mg, 0.025 mmol) was dissolved in THF (3 mL) whilst stirring. A methanol solution (6 mL) of bbbm (7.3 mg, 0.025 mmol) was added to the above solution. The reaction mixture was heated at reflux for 15 min. Two weeks later good quality red crystals were obtained at room temperature in the dark. Yield: 16.5 mg (62%). IR (KBr): $\tilde{\nu}$ = 3423 (m), 3100 (m), 2362 (m), 1607 (s), 1555 (m), 1516 (m), 1464 (m), 1383 (s), 1297 (m), 1180 (m), 1104 (m), 823 (m), 789 (m), 745 (m), 709 (m), 518 (m), 477 (m) $cm^{-1}$. $C_{55}H_{56}Fe_2N_4O_7Zn$ (1062.11): calcd. C 62.14, H 5.27, N 5.27; found C 61.67, H 5.22, N 5.32.

**Crystal Structure Determination:** Measurements of **1**, **2**, **3**, **2b**, and **3a** were made with a Rigaku RAXIS-IV image plate area detector for study by using graphite-monochromated Mo-$K_\alpha$ ($\lambda$ = 0.71073 Å) radiation at 291(2) K with the $\omega$-2$\theta$ scan technique. The data were corrected for Lorentz and polarization factors and for

Table 2. Selected bond lengths [Å] and angles [°] for complexes **1d**, **2a**,**b**, **3a**,**b**, **4a**,**b**.

| | | | | | | | |
|---|---|---|---|---|---|---|---|
| Complex **1d**[a] | | | | | | | |
| Cd1–O2 | 2.399(4) | Cd1–O4 | 2.321(4) | Cd1–O1 | 2.501(4) | Cd1–O3 | 2.637(5) |
| Cd2–N1 | 2.352(4) | Cd2–O3 | 2.266(4) | Cd2–N6#2 | 2.340(4) | O4–Cd1–O2 | 101.81(12) |
| O3–Cd1–O3#1 | 66.0(2) | O4–Cd1–O1 | 92.32(13) | O2–Cd1–O1 | 52.88(12) | O1–Cd1–O1#1 | 168.18(17) |
| O2#1–Cd1–O1 | 138.88(12) | O4–Cd1–O3 | 51.58(12) | O2–Cd1–O3 | 122.75(14) | O3–Cd2–O3#1 | 78.7(3) |
| O1–Cd1–O3 | 76.07(13) | N6#2–Cd2–N1 | 86.17(14) | O3–Cd2–N1#1 | 163.48(17) | O3–Cd2–N1 | 88.70(17) |
| Complex **2a**[b] | | | | | | | |
| Cd1–N1 | 2.353(2) | Cd1–O2 | 2.339(2) | Cd1–N2 | 2.356(4) | Cd1–O1 | 2.593(2) |
| O2#1–Cd1–O2 | 82.94(11) | O2#1–Cd1–N1 | 95.67(9) | O2–Cd1–N1 | 87.10(9) | N1–Cd1–N1#1 | 176.32(12) |
| N1–Cd1–N2 | 88.16(6) | O2–Cd1–N2 | 138.53(6) | O2#1–Cd1–O1 | 135.04(8) | O2–Cd1–O1 | 52.73(7) |
| N1–Cd1–O1 | 89.78(9) | N2–Cd1–O1 | 86.10(5) | O1–Cd1–O1#1 | 172.20(10) | | |
| Complex **2b**[c] | | | | | | | |
| Cd1–O1 | 2.253(5) | Cd1–N6#1 | 2.280(5) | Cd1–O4 | 2.294(4) | Cd1–N1 | 2.303(6) |
| Cd1–O3 | 2.411(5) | Cd1–O2 | 2.506(5) | O1–Cd1–N6#1 | 114.03(19) | N6#1–Cd1–O3 | 88.62(19) |
| N6#1–Cd1–O4 | 123.7(2) | N1–Cd1–O3 | 91.70(19) | O1–Cd1–O2 | 54.52(16) | N6#1–Cd1–O2 | 83.64(19) |
| O4–Cd1–O3 | 55.46(16) | O1–Cd1–N1 | 86.05(19) | O4–Cd1–N1 | 117.89(18) | | |
| Complex **3a**[d] | | | | | | | |
| Cd1–O4 | 2.248(6) | Cd1–O1 | 2.304(6) | Cd1–N3 | 2.312(7) | Cd1–N1 | 2.387(7) |
| Cd1–O2 | 2.583(6) | Cd1–N2 | 2.395(7) | O4–Cd1–O1 | 127.3(3) | N1–Cd1–O2 | 92.7(2) |
| O4–Cd1–O2 | 176.0(2) | O1–Cd1–O2 | 53.6(2) | O1–Cd1–N1 | 142.1(2) | N3–Cd1–N1 | 94.6(2) |
| N2–Cd1–O2 | 81.1(2) | O1–Cd1–N2 | 86.2(2) | N1–Cd1–N2 | 70.0(3) | | |
| Complex **3b**[e] | | | | | | | |
| Cd1–O2 | 2.315(5) | Cd1–N1 | 2.354(2) | Cd1–O3 | 2.375(10) | Cd1–N4#1 | 2.397(4) |
| Cd1–O5 | 2.512(8) | Cd1–O4 | 2.474(8) | Cd1–O1 | 2.546(7) | N1–Cd1–O1 | 98.37(11) |
| O2–Cd1–N1 | 92.97(12) | O2–Cd1–N4#1 | 131.57(16) | N1–Cd1–O3 | 95.53(15) | O2–Cd1–O1 | 49.15(16) |
| N1–Cd1–N4#1 | 85.97(5) | N1–Cd1–O4 | 86.79(12) | N1–Cd1–O5 | 177.0(2) | O3–Cd1–O4 | 55.2(2) |
| O2–Cd1–O5 | 89.73(19) | O5–Cd1–O1 | 84.5(2) | O3–Cd1–O5 | 81.4(2) | | |
| Complex **4a** | | | | | | | |
| Zn1–O3 | 1.9526(14) | Zn1–O1 | 2.0095(13) | Zn1–O5 | 2.0887(16) | Zn1–N1 | 2.1102(15) |
| Zn1–N2 | 2.1593(16) | O1–Zn1–N1 | 147.87(6) | O3–Zn1–N2 | 105.76(7) | N1–Zn1–N2 | 77.41(6) |
| O5–Zn1–N1 | 90.37(6) | O3–Zn1–N1 | 113.84(6) | O3–Zn1–O1 | 97.43(6) | O3–Zn1–O5 | 107.34(8) |
| O1–Zn1–O5 | 87.03(6) | | | | | | |
| Complex **4b**[f] | | | | | | | |
| Zn1–O3 | 1.927(5) | Zn1–O1 | 1.934(6) | O3–Zn1–O1 | 132.4(3) | O3–Zn1–N1 | 103.9(2) |
| N1–Zn1–N3 | 103.2(3) | Zn1–N1 | 2.028(6) | Zn1–N3 | 2.033(6) | O1–Zn1–N1 | 96.8(3) |
| O3–Zn1–N3 | 104.9(2) | O1–Zn1–N3 | 111.5(3) | | | | |

[a] Symmetry transformations used to generate equivalent atoms: #1 $-x$, $y$, $-z$ + 1/2, #2 $x$ – 1/2, $y$ – 1/2, $z$, #3 $-x$ + 1/2, $y$ – 1/2, $-z$ + 1/2, #4 $x$ + 1/2, $y$ + 1/2, $z$. [b] Symmetry transformations used to generate equivalent atoms: #1 $-x$, $y$, $-z$ + 1/2. [c] Symmetry transformations used to generate equivalent atoms: #1 $-x$ + 1, $-y$ + 2, $-z$. [d] Symmetry transformations used to generate equivalent atoms: #1 $-x$ + 1/2, $-y$ – 1/2, $-z$ + 1. [e] Symmetry transformations used to generate equivalent atoms: #1 $x$ – 1/2, $-y$ + 1, $z$, #2 $x$ + 1/2, $-y$ + 1, $z$. [f] Symmetry transformations used to generate equivalent atoms: #1 $-x$, $-y$ + 2, $-z$ + 2, #2 $-x$ + 1, $-y$ + 2, $z$.

 © 2007 Wiley-VCH Verlag GmbH & Co. KGaA, Weinheim 

absorption by using empirical scan data. The structure was solved with the *SHELX* program, and refined by full-matrix least-squares methods based on $F^2$,[76] with anisotropic thermal parameters for the non-hydrogen atoms. The hydrogen atoms were located theoretically and not refined.

For **4**, **1a**, **1b**, **1c**, **1d**, **2a**, **3b**, **4a**, and **4b**, single-crystal X-ray diffraction was performed by using a Bruker SMART APEX CCD diffractometer equipped with graphite-monochromated Mo-$K_\alpha$ radiation ($\lambda$ = 0.71073 nm) at room temperature. The data were integrated by using the Siemens SAINT program.[77] Absorption corrections were applied. The structures were solved by direct methods and refined on $F^2$ by full-matrix least-squares with SHELXTL.[78] All non-hydrogen atoms were refined with anisotropic thermal parameters. Hydrogen atoms were located at geometrically calculated positions and refined with isotropic thermal parameters.

Selected bond lengths and bond angles are listed in Tables 1 and 2. Crystal data and experimental details for all complexes are contained in Tables 3, 4, and 5. CCDC-627164 to -627177 contain the supplementary crystallographic data for this paper. These data can be obtained free of charge from The Cambridge Crystallographic Data Centre via www.ccdc.cam.ac.uk/data_request/cif.

Table 3. Crystal data and structure refinement for complexes **1**–**4**.

| Complex | **1** | **2** | **3** | **4** |
|---|---|---|---|---|
| Formula | $C_{30}H_{34}Fe_2O_6$ Cd | $C_{40}H_{42}Fe_2N_2$ $O_7$Cd | $C_{47}H_{40}Fe_2N_2$ $O_6$Cd | $C_{46}H_{42}Fe_2N_2$ $O_4$Zn |
| *Fw* | 714.67 | 886.86 | 952.91 | 863.89 |
| *T* [K] | 291(2) | 291(2) | 291(2) | 273(2) |
| Wavelength [Å] | 0.71073 | 0.71073 | 0.71073 | 0.71073 |
| Crystal system | orthorhombic | orthorhombic | triclinic | monoclinic |
| Space group | *Pbcn* | *P*2(1)2(1)2(1) | $P\bar{1}$ | $P2_1/n$ |
| *a* [Å] | 7.6097(15) | 9.3707(19) | 13.145(3) | 20.534(8) |
| *b* [Å] | 10.596(2) | 9.5073(19) | 13.145(3) | 10.010(4) |
| *c* [Å] | 35.320(7) | 43.188(9) | 9.0832(18) | 21.134(8) |
| $\alpha$ [°] | 90 | 90 | 99.75(3) | 90 |
| $\beta$ [°] | 90 | 90 | 104.02(3) | 90.778(7) |
| $\gamma$ [°] | 90 | 90 | 83.18(3) | 90 |
| *V* [Å$^3$] | 2847.9(10) | 3847.6(13) | 1962.9(7) | 4344(3) |
| Z | 4 | 4 | 2 | 4 |
| $D_{calcd.}$ [g cm$^{-3}$] | 1.667 | 1.531 | 1.612 | 1.321 |
| *F*(000) | 1448 | 1808 | 968 | 1784 |
| $\theta$ range for data collection [°] | 1.15–27.55 | 1.89–27.51 | 1.20–25.00 | 2.45–25.03 |
| Reflections collected/unique | 6774/2576 | 12845/485 | 5646/5646 | 7617/4037 |
| Data/restraints/parameters | 2576/0/177 | 7485/0/471 | 5646/2/534 | 7617/48/551 |
| Goodness-of-fit on $F^2$ | 0.992 | 0.990 | 1.130 | 1.002 |
| Final $R_1$,[a] $wR_2$[b] | 0.0434, 0.0872 | 0.0469, 0.1090 | 0.0937, 0.2527 | 0.0574, 0.1223 |

[a] $R_1 = \Sigma||F_o| - |F_c||/\Sigma|F_o|$. [b] $wR_2 = [\Sigma w(|F_o^2| - |F_c^2|)^2/\Sigma w|F_o^2|^2]^{1/2}$. $w = 1/[\sigma^2(F_o)^2 + 0.0297P^2 + 27.5680P]$, where $P = (F_o^2 + 2F_c^2)/3$.

Table 4. Crystal data and structure refinement for complexes **1a**–**d**.

| Complex | **1a** | **1b** | **1c** | **1d** |
|---|---|---|---|---|
| Formula | $C_{44}H_{42}Fe_2N_4O_5Cd$ | $C_{92}H_{107}Fe_4N_8O_{18}$ $Cd_2$ | $C_{82}H_{86}Fe_4N_8$ $O_{11}Cd_2$ | $C_{80}H_{84}Fe_4N_{12}$ $O_{12}Cd_2$ |
| *Fw* | 930.92 | 2061.06 | 1809.76 | 1853.79 |
| *T* [K] | 291(2) | 291(2) | 291(2) | 273(2) |
| Wavelength [Å] | 0.71073 | 0.71073 | 0.71073 | 0.71073 |
| Crystal system | triclinic | triclinic | monoclinic | monoclinic |
| Space group | $P\bar{1}$ | $P\bar{1}$ | *C*2/*c* | *C*2/*c* |
| *a* [Å] | 10.0300(7) | 11.7382(19) | 24.9352(17) | 25.027(6) |
| *b* [Å] | 14.6378(10) | 12.2097(19) | 10.2209(7) | 10.104(2) |
| *c* [Å] | 16.3998(16) | 17.531(3) | 33.244(2) | 33.428(8) |
| $\alpha$ [°] | 112.2210(10) | 87.466(2) | 90 | 90 |
| $\beta$ [°] | 94.2100(10) | 88.095(3) | 106.4920(10) | 107.542(4) |
| $\gamma$ [°] | 108.3400(10) | 83.145(3) | 90 | 90 |
| *V* [Å$^3$] | 2064.4(3) | 2491.2(7) | 8124.0(10) | 8060(3) |
| Z | 2 | 1 | 4 | 4 |
| $D_{calcd.}$ [g cm$^{-3}$] | 1.498 | 1.374 | 1.475 | 1.528 |
| *F*(000) | 948 | 1059 | 3672 | 3776 |
| $\theta$ range for data collection [°] | 2.69–27.50 | 2.28–25.50 | 2.33–25.50 | 2.35–25.50 |
| Reflections collected/unique | 12995/9119 | 13348/9096 | 17502/7472 | 20556/7441 |
| Data/restraints/parameters | 9119/9/513 | 9096/75/562 | 7472/16/439 | 7441/321/455 |
| Goodness-of-fit on $F^2$ | 1.045 | 1.042 | 1.054 | 1.047 |
| Final $R_1$,[a] $wR_2$[b] | 0.0451, 0.1364 | 0.0620, 0.1700 | 0.0570, 0.1486 | 0.0638, 0.1519 |

[a] $R_1 = \Sigma||F_o| - |F_c||/\Sigma|F_o|$. [b] $wR_2 = [\Sigma w(|F_o^2| - |F_c^2|)^2/\Sigma w|F_o^2|^2]^{1/2}$. $w = 1/[\sigma^2(F_o)^2 + 0.0297P^2 + 27.5680P]$, where $P = (F_o^2 + 2F_c^2)/3$.

 © 2007 Wiley-VCH Verlag GmbH & Co. KGaA, Weinheim 

Table 5. Crystal data and structure refinement for complexes **2a**,**b**, **3a**,**b**, and **4a**,**b**.

| Complex | **2a** | **2b** | **3a** | **3b** | **4a** | **4b** |
|---|---|---|---|---|---|---|
| Formula | $C_{53}H_{57}CdFe_2N_3O_8$ | $C_{106}H_{96}Cd_2Fe_4N_{12}O_{13}$ | $C_{122}H_{110}Cd_2Fe_4N_8O_{14}$ | $C_{51}H_{46}CdFe_2N_4O_6$ | $C_{46}H_{36}ZnFe_2N_2O_5$ | $C_{55}H_{56}ZnFe_2N_4O_7$ |
| *Fw* | 1088.12 | 2194.15 | 2360.38 | 1035.02 | 873.84 | 1062.11 |
| *T* [K] | 291(2) | 291(2) | 291(2) | 291(2) | 291(2) | 291(2) |
| Wavelength [Å] | 0.71073 | 0.71073 | 0.71073 | 0.71073 | 0.71073 | 0.71073 |
| Crystal system | orthorhombic | triclinic | monoclinic | orthorhombic | monoclinic | monoclinic |
| Space group | *Pbcn* | $P\bar{1}$ | *C*2/*c* | *Pca*2(1) | $P2_1/n$ | $P2_1/n$ |
| *a* [Å] | 14.8564(16) | 10.589(2) | 34.278(7) | 10.2482(6) | 11.0675(5) | 15.2198(14) |
| *b* [Å] | 14.2892(16) | 12.554(3) | 9.1203(18) | 15.5570(9) | 12.5784(6) | 10.4325(10) |
| *c* [Å] | 23.187(3) | 20.524(4) | 36.266(7) | 34.1530(19) | 26.9840(12) | 34.029(3) |
| *α* [°] | 90 | 106.90(3) | 90 | 90 | 90 | 90 |
| *β* [°] | 90 | 95.01(3) | 106.25(3) | 90 | 90.1610(10) | 95.4730(10) |
| *γ* [°] | 90 | 96.63(3) | 90 | 90 | 90 | 90 |
| *V* [Å$^3$] | 4922.3(9) | 2572.0(9) | 10885(4) | 5445.1(5) | 3756.5(3) | 5378.4(9) |
| *Z* | 4 | 1 | 4 | 4 | 4 | 4 |
| $D_{calcd.}$ [g cm$^{-3}$] | 1.468 | 1.417 | 1.440 | 1.263 | 1.545 | 1.312 |
| *F*(000) | 2240 | 1120 | 4840 | 2112 | 1792 | 2208 |
| *θ* range for data collection [°] | 2.65–27.49 | 1.71–25.00 | 1.17–25.00 | 2.38–27.50 | 2.45–27.50 | 2.29–25.50 |
| Reflections collected/unique | 29129/5658 | 7650/7650 | 13620/8330 | 32462/10925 | 22665/8425 | 40093/10010 |
| Data/restraints/ parameters | 5658/0/308 | 7650/2/617 | 8330/3/635 | 10925/339/593 | 8425/3/513 | 10010/117/613 |
| Goodness-of-fit on $F^2$ | 1.028 | 1.062 | 1.101 | 1.036 | 1.027 | 1.031 |
| Final $R_1$,[a] $wR_2$[b] | 0.0367, 0.0913 | 0.0662, 0.1535 | 0.0899, 0.1941 | 0.1341, 0.3481 | 0.0292, 0.0704 | 0.0804, 0.2341 |

[a] $R_1 = \Sigma||F_o| - |F_c||/\Sigma|F_o|$. [b] $wR_2 = [\Sigma w(|F_o^2| - |F_c^2|)^2/\Sigma w|F_o^2|^2]^{1/2}$. $w = 1/[\sigma^2(F_o)^2 + 0.0297P^2 + 27.5680P]$, where $P = (F_o^2 + 2F_c^2)/3$.

## Acknowledgments

We thank the National Natural Science Foundation of China (Nos. 20671082 and 20371042) and NCET for support.

[1] B. Moulton, M. J. Zaworotko, *Chem. Rev.* **2001**, *101*, 1629–1658.
[2] O. R. Evans, W. Lin, *Acc. Chem. Res.* **2002**, *35*, 511–522.
[3] J. J. Perry, G. J. McManus, M. J. Zaworotko, *Chem. Commun.* **2004**, 2534–2535.
[4] M. Eddaoudi, H. Li, O. M. Yaghi, *J. Am. Chem. Soc.* **2000**, *122*, 1391–1397.
[5] S. Kitagawa, R. Kitaura, S. Noro, *Angew. Chem. Int. Ed.* **2004**, *43*, 2334–2375.
[6] L. Carlucci, G. Ciani, D. M. Proserpio, *Coord. Chem. Rev.* **2003**, *246*, 247–289.
[7] O. S. Jung, Y. J. Kim, Y. A. Lee, J. K. Park, H. K. Chae, *J. Am. Chem. Soc.* **2000**, *122*, 9921–9925.
[8] V. V. Smirnov, J. P. Roth, *J. Am. Chem. Soc.* **2006**, *128*, 3683–3695.
[9] R. Matsuda, R. Kitaura, S. Kitagawa, Y. Kubota, R. V. Belosludov, T. C. Kobayashi, H. Sakamoto, T. Chiba, M. Takata, Y. Kawazoe, Y. Mita, *Nature* **2005**, *436*, 238–241.
[10] S. R. Batten, K. S. Murray, *Coord. Chem. Rev.* **2003**, *246*, 103–130.
[11] S. R. Batten, R. Robson, *Angew. Chem. Int. Ed.* **1998**, *37*, 1460–1494.
[12] H. Jude, J. A. Krause Bauer, W. B. Connick, *Inorg. Chem.* **2004**, *43*, 725–733.
[13] F. A. Cotton, J. P. Donahue, C. A. Murillo, L. M. Perez, R. Yu, *J. Am. Chem. Soc.* **2003**, *125*, 8900–8910.
[14] L. R. MacGillivray, J. L. Atwood, *Angew. Chem. Int. Ed.* **1999**, *38*, 1018–1033.
[15] A. J. Blake, N. R. Champness, P. Hubberstey, W.-S. Li, M. A. Withersby, M. Schröder, *Coord. Chem. Rev.* **1999**, *183*, 117–138.
[16] B.-H. Ye, M.-L. Tong, X.-M. Chen, *Coord. Chem. Rev.* **2005**, *249*, 545–565.
[17] A. N. Khlobystov, A. J. Blake, N. R. Champness, D. A. Lemenovskii, A. G. Majouga, N. V. Zyk, M. Schroder, *Coord. Chem. Rev.* **2001**, *222*, 155–192.
[18] C. Janiak, *Dalton Trans.* **2003**, 2781–2804.
[19] D.-F. Sun, D. J. Collins, Y.-X. Ke, J.-L. Zuo, H.-C. Zhou, *Chem. Eur. J.* **2006**, *12*, 3768–3776.
[20] X.-D. Guo, G.-S. Zhu, Z.-Y. Li, Y. Chen, X.-T. Li, S.-L. Qiu, *Inorg. Chem.* **2006**, *45*, 4065–4070.
[21] J. Kim, B.-L. Chen, T. M. Reineke, H.-L. Li, M. Eddaoudi, D. B. Moler, M. O'Keeffe, O. M. Yaghi, *J. Am. Chem. Soc.* **2001**, *123*, 8239–8247.
[22] Y. Aoyama, K. Endo, T. Anzai, Y. Yamaguchi, T. Sawaki, K. Kobayashi, N. Kanehisa, H. Hashimoto, Y. Kai, H. Masuda, *J. Am. Chem. Soc.* **1996**, *118*, 5562–5571.
[23] M. B. Zaman, M. D. Smith, H.-C. zur Loye, *Chem. Commun.* **2001**, 2256–2257.
[24] D. L. Reger, T. D. Wright, R. F. Semeniuc, T. C. Grattan, M. D. Smith, *Inorg. Chem.* **2001**, *40*, 6212–6219.
[25] O. S. Jung, S. H. Park, K. M. Kim, H. G. Jang, *Inorg. Chem.* **1998**, *37*, 5781–5785.
[26] M. A. Withersby, A. J. Blake, N. R. Champness, P. A. Cooke, P. Hubberstey, W. S. Li, M. Schröder, *Inorg. Chem.* **1999**, *38*, 2259–2266.
[27] H.-B. Chen, H. Zhang, J.-M. Yang, Z.-H. Zhou, *Polyhedron* **2004**, *23*, 987–991.
[28] M. Fujita, M. Tominaga, A. Hori, B. Therrien, *Acc. Chem. Res.* **2005**, *38*, 369–378.
[29] M. Eddaoudi, D. B. Moler, H.-L. Li, B.-L. Chen, T. M. Reineke, M. O'Keeffe, O. M. Yaghi, *Acc. Chem. Res.* **2001**, *34*, 319–330.
[30] L. Wang, B. Zhang, J.-P. Zhang, *Inorg. Chem.* **2006**, *45*, 6860–6863.
[31] Q.-F. Xu, J.-X. Chen, W.-H. Zhang, Z.-G. Ren, H.-X. Li, Y. Zhang, J.-P. Lang, *Inorg. Chem.* **2006**, *45*, 4055–4064.
[32] N. G. Armatas, E. Burkholder, J. Zubieta, *J. Solid State Chem.* **2005**, *178*, 2430–2435.
[33] L. R. Falvello, J. C. Ginés, J. J. Carbó, A. Lledós, R. Navarro, T. Soler, E. P. Urriolabeitia, *Inorg. Chem.* **2006**, *45*, 6803–6815.

 © 2007 Wiley-VCH Verlag GmbH & Co. KGaA, Weinheim 

[34] Q.-R. Fang, G.-S. Zhu, M. Xue, Q.-L. Zhang, J.-Y. Sun, X.-D. Guo, S.-L. Qiu, S.-T. Xu, P. Wang, D.-J. Wang, Y. Wei, *Chem. Eur. J.* **2006**, *12*, 3754–3758.
[35] H. Li, M. Eddaoudi, M. O'Keeffe, *Nature* **1999**, *402*, 276–279.
[36] J. S. Seo, D. Whang, H. Lee, S. I. Jun, J. Oh, Y. J. Jeon, K. Kim, *Nature* **2000**, *404*, 982–986.
[37] B. Chen, M. Eddaoudi, S. T. Hyde, M. O'Keeffe, O. M. Yaghi, *Science* **2001**, *291*, 1021–1023.
[38] D.-F. Sun, R. Cao, Y.-Q. Sun, W.-H. Bi, D.-Q. Yuan, Q. Shi, X. Li, *Chem. Commun.* **2003**, 1528–1529.
[39] Z.-H. Zhou, J.-M. Yang, H.-L. Wan, *Cryst. Growth Des.* **2005**, *5*, 1825–1830.
[40] K. E. Christensen, L. Shi, T. Conradsson, T.-Z. Ren, M. S. Dadachov, X.-D. Zou, *J. Am. Chem. Soc.* **2006**, *128*, 14238–14239.
[41] C. Serre, F. Taulelle, G. Ferey, *Chem. Commun.* **2003**, 2755–2765.
[42] J.-H. He, J.-H. Yu, Y.-T. Zhang, Q.-H. Pan, R.-R. Xu, *Inorg. Chem.* **2005**, *44*, 9279–9282.
[43] D.-F. Li, S. Parkin, G.-B. Wang, G. T. Yee, S. M. Holmes, *Inorg. Chem.* **2006**, *45*, 2773–2775.
[44] A. Fragoso, M. L. Kahn, A. Castiñeiras, J. P. Sutter, O. Kahn, R. Cao, *Chem. Commun.* **2000**, 1547–1548.
[45] C. Benelli, A. J. Blake, E. K. Brechin, S. J. Coles, A. Graham, S. G. Harris, S. Meier, A. Parkin, S. Parsons, A. M. Seddon, R. E. P. Winpenny, *Chem. Eur. J.* **2000**, *6*, 883–896.
[46] M. Eddaoudi, J. Kim, M. O'Keeffe, O. M. Yaghi, *J. Am. Chem. Soc.* **2002**, *124*, 376–377.
[47] A. Erxleben, *Inorg. Chem.* **2001**, *40*, 208–213.
[48] M. Soler, S. K. Chandra, D. Ruiz, E. R. Davidson, D. N. Hendrickson, G. Christou, *Chem. Commun.* **2000**, 2417–2418.
[49] P. J. Hagrman, D. Hagrman, J. Zubieta, *Angew. Chem. Int. Ed.* **1999**, *38*, 2638–2684.
[50] H. Jude, J. A. Krause Bauer, W. B. Connick, *Inorg. Chem.* **2005**, *44*, 1211–1220.
[51] F. A. Cotton, L. M. Daniels, G. T. Jordan, C. A. Murillo, I. Pascual, *Inorg. Chim. Acta* **2000**, *297*, 6–10.
[52] H. Bregman, P. J. Carroll, E. Meggers, *J. Am. Chem. Soc.* **2006**, *128*, 877–884.
[53] G. H. Woehrle, J. E. Hutchison, *Inorg. Chem.* **2005**, *44*, 6149–6158.
[54] G. H. Woehrle, L. O. Brown, J. E. Hutchison, *J. Am. Chem. Soc.* **2005**, *127*, 2172–2183.
[55] J. M. Rueff, N. Masciocchi, P. Rabu, A. Sironi, A. Skoulios, *Eur. J. Inorg. Chem.* **2001**, *40*, 2843–2848.
[56] J.-C. Dai, X.-T. Wu, Z.-Y. Fu, S.-M. Hu, W.-X. Du, C.-P. Cui, L.-M. Wu, H.-H. Zhang, R.-Q. Sun, *Chem. Commun.* **2002**, 12–13.
[57] O. M. Yaghi, C. E. Davis, G.-M. Li, H.-L. Li, *J. Am. Chem. Soc.* **1997**, *119*, 2861–2868.
[58] Y.-G. Li, N. Hao, Y. Lu, E.-B. Wang, Z.-H. Kang, C.-G. Hu, *Inorg. Chem.* **2003**, *42*, 3119–3124.
[59] R. Cao, D. Sun, U. Liang, M. Hong, K. Tatsumi, Q. Shi, *Inorg. Chem.* **2002**, *41*, 2087–2094.
[60] H.-W. Hou, L.-K. Li, Y. Zhu, Y.-T. Fan, Y.-Q. Qiao, *Inorg. Chem.* **2004**, *43*, 4767–4774.
[61] L.-K. Li, Y.-L. Song, H.-W. Hou, Y.-T. Fan, Y. Zhu, *Eur. J. Inorg. Chem.* **2005**, 3238–3249.
[62] T. Allman, R. Goel, N. K. Jha, A. L. Beauchamp, *Inorg. Chem.* **1984**, *23*, 914–918.
[63] S. L. Li, T. C. W. Mak, *J. Chem. Soc. Dalton Trans.* **1995**, 1519–1524.
[64] R.-H. Wang, L. Han, F.-L. Jiang, Y.-F. Zhou, D.-Q. Yuan, M.-C. Hong, *Cryst. Growth Des.* **2005**, *5*, 129–135.
[65] X.-R. Meng, Y.-L. Song, H.-W. Hou, H.-Y. Han, B. Xiao, Y.-T. Fan, Y. Zhu, *Inorg. Chem.* **2004**, *43*, 3528–3536.
[66] Z.-Y. Wang, R.-G. Xiong, B. M. Foxman, S. R. Wilson, W.-B. Lin, *Inorg. Chem.* **1999**, *38*, 1523–1528.
[67] M. J. Plater, M. R. S. J. Foreman, T. Gelbrich, S. J. Coles, *J. Chem. Soc. Dalton Trans.* **2000**, 3065–3073.
[68] J. Tao, M.-L. Tong, X.-M. Chen, *J. Chem. Soc. Dalton Trans.* **2000**, *20*, 3669–3674.
[69] G. Li, B.-Y. Chen, L. Kell, H.-W. Hou, Y. Zhu, Y.-T. Fan, *J. Coord. Chem.* **2003**, *56*, 877–884.
[70] H.-W. Hou, L.-K. Li, G. Li, Y.-T. Fan, Y. Zhu, *Inorg. Chem.* **2003**, *42*, 3501–3508.
[71] S. Leininger, B. Olenyuk, P. J. Stang, *Chem. Rev.* **2000**, *100*, 853–908.
[72] G. D. Broadhead, J. M. Osgerby, P. L. Pauson, *J. Chem. Soc.* **1958**, 650–654.
[73] P. Hu, K.-Q. Zhao, L.-F. Zhang, *J. Si Chuan Normal. Univ. (Nat. Sci. Ed.)* **1998**, *21*, 433–435 (in Chinese).
[74] X.-J. Xie, G.-S. Yang, L. Cheng, F. Wang, *Huaxue Shiji* **2000**, *22*, 222–223.
[75] B. F. Hoskins, R. Robson, D. A. Slizys, *J. Am. Chem. Soc.* **1997**, *119*, 2952–2953.
[76] G. M. Sheldrick, *SHELXS-97: Program for the Solution and Refinement of Crystal Structures*, University of Göttingen, Germany, **1997**.
[77] *SAINT: Program for Data Extraction and Reduction*, version 6.01, Siemens Analytical X-ray Instruments Inc., Madison, WI.
[78] G. M. Sheldrick, *SHELXTL: Program for Refinement of Crystal Structures*, version 6.10, Siemens Analytical X-ray Instruments Inc., Madison, WI.

Received: May 23, 2007
Published Online: September 26, 2007

 © 2007 Wiley-VCH Verlag GmbH & Co. KGaA, Weinheim 

DOI: 10.1002/ejic.200700573

# Olefin Complexes of Low-Valent Rhenium

**Aldjia Choualeb,[a] Olivier Blacque,[a] Helmut W. Schmalle,[a] Thomas Fox,[a] Thomas Hiltebrand,[a] and Heinz Berke*[a]**

**Keywords:** Rhenium / Olefin complexes / Nitrosyl complexes / DFT calculation

Replacement of the MeCN group in the acetonitrile-*cis*-dibromo(nitrosyl)-*trans*-bis(phosphane)rhenium compounds **1a**,**b** (R = *i*Pr **a**, R = Cy **b**) with ethylene afforded the olefin derivatives [Re($\eta^2$-$H_2C{=}CH_2$)(NO)($PR_3$)$_2$Br$_2$] (**2a**,**b**) (R = *i*Pr **a**, R = Cy **b**). Compound **1a** could be converted into the dimethyl species [Re(MeCN)(NO)(P*i*Pr$_3$)$_2$Me$_2$] (**3a**) applying MeLi in toluene; the related methylation of **1b**, however, failed. Abstraction of a $Br^-$ ion from **1a**,**b** with [Na][BAr′$_4$] in acetontrile yields the air-stable salts [Re(MeCN)$_2$(NO)($PR_3$)$_2$Br]$^+$[BAr′$_4$]$^-$ (**4a**,**b**) (R = *i*Pr **a**, R = Cy **b**) and under 1 bar of $H_2$ complexes **1a**,**b** were converted into the known dihydrogen species [Re($\eta^2$-$H_2$)(NO)($PR_3$)$_2$(Br)$_2$] (**5a**,**b**) (R = *i*Pr **a**, R = Cy **b**). Reduction of [Re(MeCN)(NO)($PR_3$)$_2$Br$_2$] (**1a**,**b**) with Na/Hg under 1 bar of $C_2H_4$ afforded the butadiene complex [Re($\eta^4$-$C_4H_6$)($\eta^2$-$H_2C{=}CH_2$)(NO)($PR_3$)$_2$] (**6a**,**b**) (R = *i*Pr **a**, R = Cy **b**) via oxidative coupling of two coordinated ethylene groups followed by double β-H shift and subsequent reductive $H_2$ elimination from the formed dihydride complex. Reduction of the complexes [Re(CO)(NO)($PR_3$)$_2$Cl$_2$] (**7a**,**b**) (R = *i*Pr **a**, R = Cy **b**) with Na/Hg yields the pentacoordinate species [Re(CO)(NO)($PR_3$)$_2$($\eta^2$-$H_2C{=}CH_2$)] (**8a**,**b**) (R = *i*Pr **a**, R = Cy **b**) under the same conditions as for **6a**,**b**. Reaction of **8a** with 1 equiv. of B($C_6F_5$)$_3$ leads to the [Re(CO)$_2${NOB($C_6F_5$)$_3$}(P*i*Pr$_3$)$_2$] compound (**9a**) and to the carbonyl nitrosyl complexes [Re(CO)$_2$(NO)(P*i*Pr$_3$)$_2$] (**10a**) with evolution of ethylene. The same reaction of **8a** and **8b**, but applying 1 bar of CO, leads to exclusive formation of **9a**,**b**. Complexes **4a**, **4b**, **6b**, **8a**, **9a**, and **9b** were characterized by X-ray diffraction studies.

(© Wiley-VCH Verlag GmbH & Co. KGaA, 69451 Weinheim, Germany, 2007)

## Introduction

Over a large range of oxidation states rhenium shows generally high bond strengths to carbon donors. However, its affinity to π acceptor ligands can vary with the oxidation state of the metal center, since π back-bonding is expected to depend on the metal-d-electron count. Complexes with rhenium in high oxidation states thus show less propensity for olefin binding, a circumstance, which allows reversible olefin binding in catalytic intermediates, such as those in epoxidations,[1a] olefin metathesis reactions[1b] and in processes, which crucially involve C–H activations.[2] Compounds with rhenium in lower oxidation states are expected to more strongly bind olefins, but such rhenium centers often do not perform well in catalysis, since they frequently show reluctance to form coordinatively unsaturated species. Special ancillary ligand sets may, however, assist dissociations of other ligands. Thus, π acceptors can labilize other π acceptors sharing the metal π electron density and furthermore π donor ligands may exert a kinetic *cis* labilizing effect on *cis* ligands.[3] In this study we therefore wanted to evaluate ethylene binding to rhenium in lower oxidation states[4a] and in various ligand environments. Earlier several pseudo-octahedral or pentacoordinate olefin complexes with rhenium in low oxidation states and a partial π acceptor coordination sphere were studied for their conformational preferences in olefin rotation,[4b] photochemical isomerization processes,[4c] and in stoichiometric C–H activations,[4d] which demonstrated in various ways the basic capability of such rhenium centers to strongly interact with olefins. Our group has recently focused on the development of rhenium bisphosphane nitrosyl systems containing [Re(NO)($PR_3$)$_2$X$_2$][5] (X = halogene) and [Re(NO)$_2$($PR_3$)$_2$][6] fragments. The latter fragments were seen to react with olefins in metathesis catalyses[6] and thus demonstrated affinity to olefins. For the earlier types of fragments a high propensity for olefin uptake was extrapolated based on their capability to bind $H_2$[5] and the close relationship in binding properties of both ligands.[7] Our explorations on ethylene binding were therefore started using [Re(NO)($PR_3$)$_2$X$_2$] fragments possessing a "mixed type" ligand sphere of σ and π donors and π acceptors.

## Results and Discussion

### I. Reactions of [Re($CH_3CN$)(NO)($PR_3$)$_2$Br$_2$]

The reactions of the recently reported [Re(MeCN)(NO)($PR_3$)$_2$Br$_2$] complexes (R = *i*Pr **1a**, R = Cy **1b**)[5] with ethylene produced indeed the ethylene complexes [Re($\eta^2$-

[a] Anorganisch-chemisches Institut Universität Zürich, Winterthurerstrasse 190, 8057 Zürich, Switzerland
Fax: +41-44-6356802
E-mail: hberke@aci.uzh.ch

 © 2007 Wiley-VCH Verlag GmbH & Co. KGaA, Weinheim 

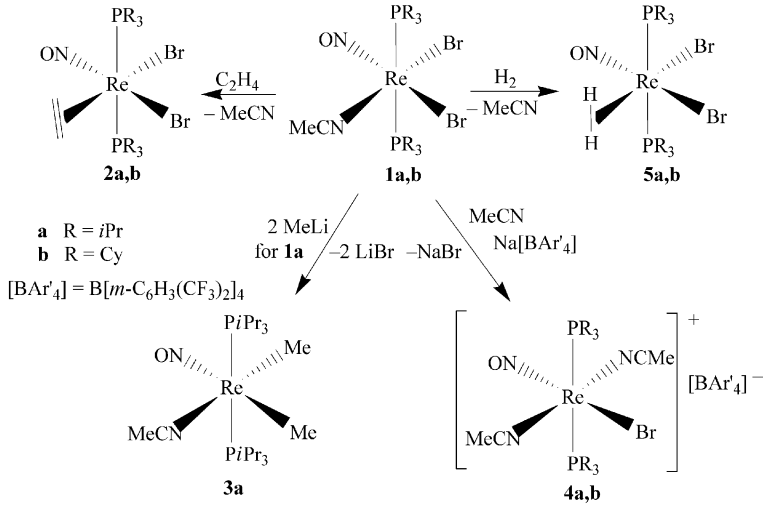


Scheme 1.

$H_2C{=}CH_2)(NO)(PR_3)_2Br_2]$ (R = *i*Pr **2a**, R = Cy **2b**) in good yields (Scheme 1). When ethylene was bubbled through the solutions of **1a**,**b** at 1 bar the color changed from light yellow to purple after 1 h for **2a** and 1.5 h for **2b**, but comparison of the $^{31}P$ NMR spectra indicated only slight changes.[5]

Complexes **2a**,**b** were characterized further by spectroscopic means (IR, $^1H$, and $^{13}C$ NMR) and the pure products showed correct elemental analyses. Studies in solution were some times more difficult for **2b**, since it exhibits low solubilities in many organic solvents. Besides a strong ν(NO) band, the solid state IR spectra of **2a**,**b** displayed ν(CH) bands in the region of 2800 to 3000 $cm^{-1}$ indicating the presence of the Re-coordinated ethylene. ν(C=C) absorptions could not be detected. The $^1H$ NMR spectrum of **2a** revealed two broad resonances at $\delta$ = 2.51 and 2.47 ppm for two chemically different types of protons of the $C_2H_4$ ligand. Apparently there is hindered rotation around the rhenium–ethylene bond with a preferred orientation of the C=C bond parallel to the P–Re–P axis, which leads to distinction of pairs of Z-protons. Even at temperatures as high as 80 °C these signals did not coalesce. In the case of complex **2b** the $^1H$ NMR signals of the olefin overlapped with those of the $PCy_3$ groups so that the hindered rotation of the olefin ligand could not be traced by $^1H$ NMR spectroscopy. However, DFT calculations (vide infra) suggest a substantial barrier of rotation for such types of bis(phosphane) complexes in general. In the $^{13}C$ NMR spectra the two carbon atoms of the $C_2H_4$ moieties are chemically equivalent and appear for **2a** and **2b** as broad triplets at $\delta$ = 39.5 ppm confirming the preferred orientation of the olefin in the P–Re–P axis. In the $^{31}P$ NMR spectra both phosphorus atoms are chemically equivalent and exhibit a singlet at $\delta$ = –13.3 ppm for **2a** and –20.3 ppm for **2b** (40 °C).

Complex **1a** reacts with 2 equiv. of MeLi in toluene to produce the corresponding dimethyl derivative [Re(NO)(MeCN)(P*i*Pr$_3$)$_2$Me$_2$] (**3a**) related to the [Re(NO)(CO)$(PR_3)_2Me_2$] complexes (R = OMe, iOPr, Me, Et) reported earlier.[8] Reaction of **2a** with only 1 equiv. of MeLi does not afford the monomethyl complex [Re(NO)(MeCN)(P*i*Pr$_3$)$_2$MeBr], rather only half an equivalent of **3a**. This could be interpreted in terms of a faster second methylation, faster than the first one. Surprisingly, all attempts to access the dimethyl rhenium species **2b** did not meet with success. A variety of inseparable products were observed indicating a complicated course of the reaction with formation of radicals.

Complex **3a** was characterized by IR, $^1H$, $^{31}P\{^1H\}$, and $^{13}C\{^1H\}$ NMR spectroscopy. Because of the liquid nature of the compound, satisfactory elemental analysis could not be obtained. The IR spectrum recorded in $CH_2Cl_2$ revealed a very strong band at 1588 $cm^{-1}$ for the NO group, as well as a weak band at 2360 $cm^{-1}$ for the coordinated MeCN ligand. Compared to **2a** the ν(NO) absorption of **3a** is shifted to lower wavenumbers by about 100 $cm^{-1}$ indicating a relatively strong π-back-bonding.[9] The $^1H$ NMR spectrum in $C_6D_6$ showed besides the signals of the *i*Pr and MeCN groups, two triplets at $\delta$ = 2.36 ppm ($J$(PH) = 2.2 Hz) and 2.29 ppm ($J$(PH) = 2.0 Hz) for the chemically inequivalent methyl groups. In the $^{13}C\{^1H\}$ NMR spectrum they give rise to broad signals at $\delta$ = 24.6 and 20.6 ppm. Complex **3a** turned out to be very air-sensitive in solution.

Abstraction of a bromide atom from **1a**,**b** using 1 equiv. of [Na][BAr′$_4$] (Ar′ = *m*-$(CF_3)_2C_6H_3$) in acetonitrile occurred within 14 h and proceeded with regiospecific replacement of the bromide *cis* to the NO group affording the [Re(MeCN)$_2$(NO)(PR$_3$)$_2$Br][BAr′$_4$] salts **4a**,**b**. The *trans*-to-NO bromide is apparently bound more strongly experiencing a push-pull stabilization of the π donor with the *trans* π acceptor. Complexes **4a**,**b** were isolated as pure yellow solids and are quite air-stable. The use of an excess of [Na][BAr′$_4$] did not lead to abstraction of the second bromide ion. Because of the cationic nature of the complexes, the solid-state IR spectra of **4a**,**b** showed ν(NO) bands shifted to higher wavenumbers in comparison with the starting materials. Bands for the two coordinated acetonitriles, which should appear in the range of 2350 to 2200 $cm^{-1}$, could not be detected. The NMR spectroscopic data of **4a**,**b** con-

 © 2007 Wiley-VCH Verlag GmbH & Co. KGaA, Weinheim 

firmed the presence of $\{Re(MeCN)_2(NO)(PR_3)_2\}$ fragments with two nitrile ligands. The $^1H$ NMR spectra displayed singlets at room temperature at $\delta = 2.89$ ppm for **4a** and at $\delta = 2.93$ ppm for **4b** attributed to the two chemically equivalent *trans* acetonitrile ligands. Singlets also appeared in the $^{31}P\{^1H\}$ NMR spectra at $\delta = 0.4$ for **4a** and –10.2 ppm for **4b**.

The molecular structures of **4a**,**b** were also determined by X-ray diffraction studies and the cations are shown in Figure 1. Complex **4b** crystallized as a $CH_2Cl_2$ solvate. The rhenium coordination was found to be pseudo octahedral with the nitrosyl ligand located *trans* to the Br atom, while the two MeCN and the phosphane groups are disposed *trans*. Selected bond lengths and angles of **4a**,**b** are summarized in Table 1. The nitrosyl groups of both compounds were found disordered with the Br ligands.

As depicted in Scheme 1, $H_2$ rapidly displaces the coordinated MeCN group in **1a**,**b** producing the corresponding dihydrogen derivatives $[Re(\eta^2\text{-}H_2)(NO)(PR_3)_2Br_2]$ (**5a**,**b**) in quantitative spectroscopic yields. Complexes **5a**,**b** were identified by $^1H$ NMR spectroscopy based on the data of their earlier preparations from the reaction of $[NEt_4][Re(NO)Br_5]$ with the corresponding phosphanes in ethanol.[5]

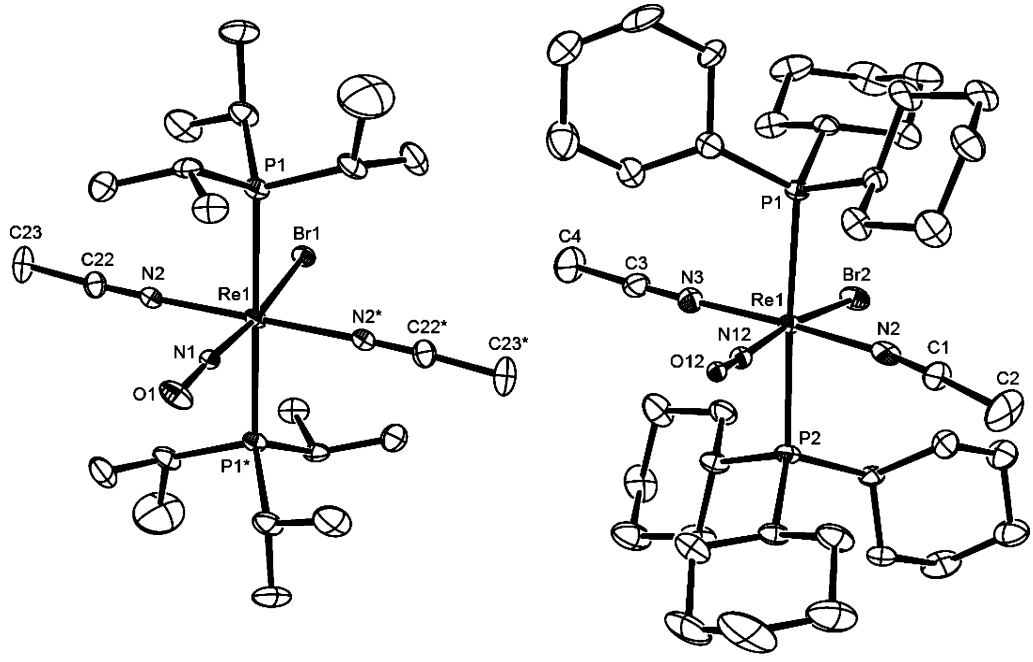


Figure 1. ORTEP drawings of the molecular structures of the cations of **4a** (left) and **4b** (right) (thermal ellipsoids are drawn at the 20 and 30% probability levels, respectively). The rhenium atom of **4a** lies on a center of inversion, only half of the molecule has been refined and the equivalent atoms (*) have been generated by the symmetry transformation $1/2 - x$, $1/2 - y$, $1/2 - z$). The resulting disorder between the NO and Br ligands, the counterions $[BAr'_4]^-$, the $CH_2Cl_2$ solvate molecule of **4b**, as well as all hydrogen atoms have been omitted for clarity.

Table 1. Selected bond lengths [Å] and angles [°] for **4a** and **4b**.

| **4a** | | **4b** | |
|---|---|---|---|
| Re(1)–P(1) | 2.5077(12) | Re(1)–P(1) | 2.5319(19) |
| Re(1)–P(1a)[a] | 2.5077(12) | Re(1)–P(2) | 2.5288(19) |
| Re(1)–N(1) | 1.830(10) | Re(1)–N(1)[b] | 1.716(7)/1.662(17) |
| Re(1)–N(2) | 2.056(3) | Re(1)–N(2) | 2.071(7) |
| Re(1)–N(2a) | 2.056(3) | Re(1)–N(3) | 2.052(6) |
| Re(1)–Br(1) | 2.4733(16) | Re(1)–Br(1)[b] | 2.5582(11)/2.486(7) |
| N(1)–O(1) | 1.208(10) | N(1)–O(1)[b] | 1.222(9)/1.178(15) |
| N(2)–C(22) | 1.129(5) | N(2)–C(1) | 1.133(10) |
| N(2a)–C(22a) | 1.129(5) | N(3)–C(3) | 1.148(10) |
| P(1)–Re(1)–P(1a) | 180 | P(1)–Re(1)–P(2) | 177.25(6) |
| N(1)–Re(1)–Br(1) | 173.7(3) | N(1)–Re(1)–Br(1) | 176.7(2) |
| N(2)–Re(1)–N(2a) | 180 | N(2)–Re(1)–N(3) | 173.5(3) |
| Re(1)–N(1)–O(1) | 173.2(12) | Re(1)–N(1)–O(1) | 173.2(6)/164(4) |
| Re(1)–N(2)–C(22) | 178.1(4) | Re(1)–N(2)–C(1) | 173.1(6) |
| Re(1)–N(2a)–C(22a) | 178.1(4) | Re(1)–N(3)–C(3) | 177.7(7) |

[a] Symmetry operation: $a = 1/2 - x$, $1/2 - y$, $1/2 - z$. [b] Split atoms due to disorder are labeled N(11), N(12), O(11), O(12), Br(1), Br(2) in the cif file.

 © 2007 Wiley-VCH Verlag GmbH & Co. KGaA, Weinheim 

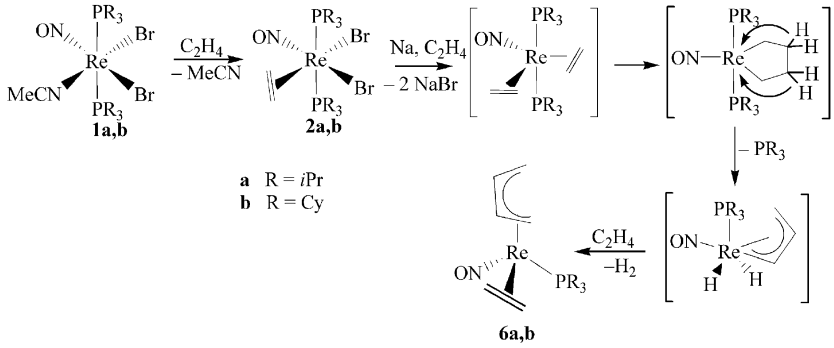


Scheme 2.

We then attempted access to olefin complexes with the rhenium center in a still lower oxidation state than +I. Reduction of **1a**,**b** with sodium amalgam in THF leads at room temperature under 1 bar of ethylene to the butadiene ethylene species $[Re(\eta^4\text{-}C_4H_6)(\eta^2\text{-}H_2C{=}CH_2)(NO)(PR_3)_2]$ (**6a**,**b**) (Scheme 2). These $Re^{-I}$ complexes were isolated as pale yellow powders in yields of 31% for **6a** and of 63% for **6b**.

In Scheme 2 a mechanism for the formation of **6a**,**b** is proposed. First generation of **2a**,**b** and then reduction to a transient $Re(ethylene)_2$ complex is suggested, which eventually converts into a metallacyclopentane structure with oxidative coupling of the two ethylene ligands.[10–12] Double β-hydride elimination and $H_2$ reductive elimination[2,13] is followed by the ethylene replacement of one phosphane ligand.

Single crystals of **6b** were obtained from a mixture of pentane/dichloromethane, 10:1 (Figure 2, Table 2). The X-ray diffraction study established the structure of **6b** in detail. The coordination sphere of **6b** can be viewed as a pseudo tetrahedron counting the butadiene as one ligand or as a pseudo square pyramid with the butadiene moiety occupying two coordination sites. According to the latter view the essentially planar $\eta^4$-butadiene, $\eta^2$-ethylene, and the NO ligand would form the base and the phosphane the apical position of the pyramid. Conformationally, the ethylene group is in parallel orientation with respect to the Re–P axis and the *cis*-butadiene ligand points with its open side toward the $PCy_3$ ligand. The ethylene and the butadiene group are disordered. The disorder could properly be resolved revealing reasonable bonding parameters. The average distance between the internal butadiene carbon atoms of 1.34(2) Å is significantly shorter by 0.09 Å than the average distances of the terminal carbon atoms of 1.43(2) Å speaking for a strong Re-butadiene back bonding with superimposition of the $\pi_3$ orbital of the butadiene moiety. For comparison, the free *cis*-butadiene bond possesses an internal C–C distance of 1.463(3) and terminal olefinic distances of 1.342(2) Å.[14,15] The Re–$C_{int}$ and Re–$C_{term}$ distances are similar and fall into the range of 2.16(3) to 2.27(2) Å emphasizing a genuine $\eta^4$ coordination mode. The Re–$C_{term}$ bond length approximately *trans* to the ethylene group is shorter by 0.09(2) Å than the Re–$C_{term}$ distance *trans* to the NO group. This can be explained via size-able differences in the *trans* influences of ethylene and the NO group with the NO ligand having the stronger effect. The hydrogen atoms of the coordinated olefins could not be located in the Fourier difference maps and they have been calculated after each refinement cycle (riding model).

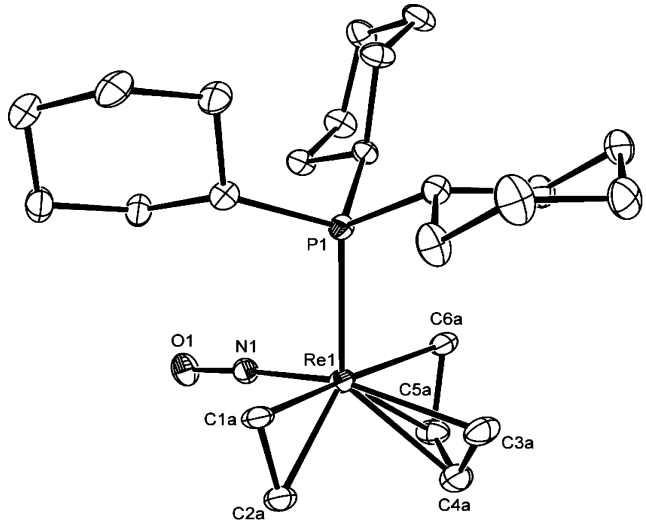


Figure 2. ORTEP drawing of the molecular structure of **6b** (thermal ellipsoids are drawn at the 30% probability level). The disorder observed between the ethylene and butadiene ligands as well as all hydrogen atoms have been omitted for clarity.

Table 2. Selected bond lengths [Å] and bond angles [°] for **6b**.

| | | | |
|---|---|---|---|
| Re(1)–N(1) | 1.770(3) | N(1)–O(1) | 1.197(4) |
| Re(1)–C(1A) | 2.285(15) | C(1A)–C(2A) | 1.434(17) |
| Re(1)–C(2A) | 2.25(2) | C(3A)–C(4A) | 1.417(17) |
| Re(1)–C(3A) | 2.235(13) | C(4A)–C(5A) | 1.344(14) |
| Re(1)–C(4A) | 2.258(9) | C(5A)–C(6A) | 1.42(2) |
| Re(1)–C(5A) | 2.18(2) | C(1B)–C(2B) | 1.43(3) |
| Re(1)–C(6A) | 2.170(18) | C(3B)–C(4B) | 1.47(2) |
| Re(1)–C(1B) | 2.30(3) | C(4B)–C(5B) | 1.34(2) |
| Re(1)–C(2B) | 2.28(3) | C(5B)–C(6B) | 1.42(2) |
| Re(1)–C(3B) | 2.272(18) | Re(1)–N(1)–O(1) | 175.8(3) |
| Re(1)–C(4B) | 2.224(11) | C(3A)–C(4A)–C(5A) | 118.2(11) |
| Re(1)–C(5B) | 2.21(3) | C(4A)–C(5A)–C(6A) | 115.4(14) |
| Re(1)–C(6B) | 2.16(3) | C(3B)–C(4B)–C(5B) | 123.4(14) |
| Re(1)–P(1) | 2.4585(10) | C(4B)–C(5B)–C(6B) | 111.3(17) |

 © 2007 Wiley-VCH Verlag GmbH & Co. KGaA, Weinheim 

Principally, butadiene can coordinate to a metal as a *cis*- or *trans*-butadiene. The *trans*-$\eta^4$-diene complexes are normally thermodynamically less stable and they may convert to the corresponding *cis*-$\eta^4$-diene complexes.[16,17] The *cis*-$\eta^4$-diene complexes are known mainly with early transition metal centers, such as in $Cp_2M(diene)$ (M = Ti, Zr, Hf),[16] as well as with Ta.[18]

Two extreme forms of butadiene *cis* coordination were found: the *cis*-$\eta^4$-1,3-diene structure and the metallacyclopent-3-ene structure. NMR spectroscopy is able to distinguish the various coordination modes of the diene ligand on the basis of their coupling constants. In the *cis* coordination the majority of diene complexes reported so far exhibit the $\eta^4$-1,3 diene structure possessing bond lengths of $C_{int}$–$C_{int} \geq C_{term}$–$C_{term}$ and M–$C_{term} \geq$ M–$C_{term}$, the dihedral angles between the planes defined by $C_{term}$, M, $C_{term}$ and $C_{term}$, $C_{int}$, $C_{int}$, $C_{term}$ atoms are generally <90°. When the dihedral angle is greater than 90° and the $C_{int}$–$C_{int}$ bond is significantly shorter than $C_{term}$–$C_{int}$, the bent metallacyclopent-3-ene structure is adopted.[12]

The $^1$H NMR and the $^{13}$C NMR spectroscopic data of **6a**,**b** indeed confirmed their *cis* butadiene structure. Also on the basis of the $^{31}$P NMR spectra, **6a**, however, exists in solution as a mixture of two stereoisomers appearing in a 3:1 ratio. Suggested by the DFT calculations modeled with a $PMe_3$ ligand (vide infra) the isomerism is anticipated to be caused by butadiene rotation. Principally the three rotamers **A**, **B**, and **C** are conceivable (Figure 3). For electronic reasons any of these rotamers are expected to have one leg of the three-legged pianostool in the diene cleft.[19] According to the calculations on a $PMe_3$ model isomer **A** is of lowest energy. **B** and **C** of this derivative lie +3.9 and +8.6 kcal/mol higher in energy. In analogy **6a** is assumed to exist in the equilibrium conformations **A** and **B**. Another point of discussion concerns the kinetics. The barrier for the interconversion of rotamer **A** and **B** apparently is low enough that room temperature thermal energy (<15 kcal/mol) can equilibrate the two isomers of **6a**, however, at a rate which is slow on the NMR time scale. By the same token the energy difference of isomers **A** and **B** of **6b** and their barrier of rotation are expected to be substantially higher than those of **6a**, since the $PCy_3$ ligand possesses a still larger cone angle than $PiPr_3$. For the latter complex the butadiene rotation is therefore considered to be "frozen out" in the energetically preferred rotamer **A**.

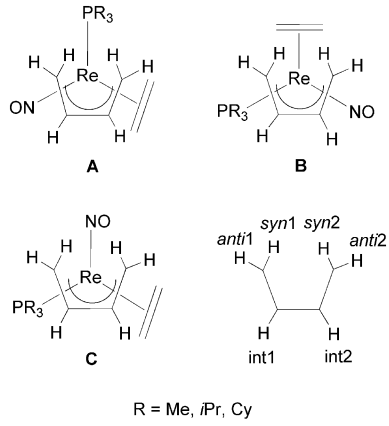


Figure 3. Projections of the rotational isomers of **6a**,**b** and **6-Me** and proton assignment for the butadiene ligand.

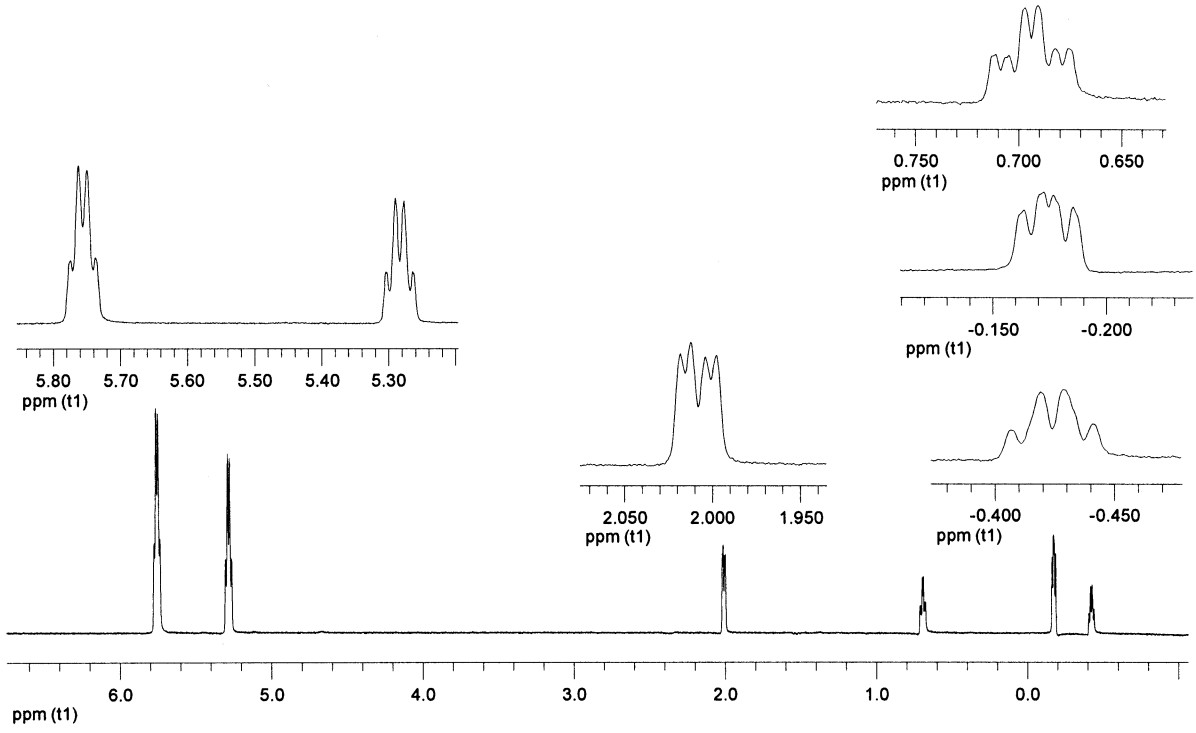


Figure 4. TOCSY for the butadiene ligand of **6b** recorded in $C_6D_6$ (r.t.) with irradiation of one *internal* CH group.

 © 2007 Wiley-VCH Verlag GmbH & Co. KGaA, Weinheim 

The $^1$H NMR spectrum of **6b** indeed points to a solution structure according to rotamer **A**, which indeed is the structure in the solid state (Figure 2). Beside the signals of the $PCy_3$ ligand, overlapping with those of the $C_2H_4$ group, the resonances of the butadiene group are attributed to two *anti*, two *syn*, and two *internal* protons. Any of the isomeric structures **A**, **B**, and **C** of **6a**,**b** possesses $C_1$ symmetry and "left/right" asymmetry of the butadiene so that the various types of butadiene protons are doubled and each butadiene proton appears at a distinct chemical shift. For **6b** this could nicely be demonstrated by a TOCSY experiment with irradiation of one *internal* CH group (Figure 4 and Table 3). For **6a**, however, the chemical shift differences between the signals of the butadiene and the ethylene groups of the rotamers **A** and **B** are very small and lead to overlap. The differences in chemical shifts between the *syn* and the *anti* protons of **6a**,**b** were found to be in the range of 0.25–1.42 ppm comparable with the $\Delta\delta$ values of $Fe(CO)_3(\eta^4\text{-}C_4H_6)$[20] and of $RhCp(\eta^4\text{-}C_4H_6)$ (1.3–2.3 ppm) (Table 3). A coupling between the *syn* protons and the phosphorus nuclei was not observed for both complexes.

Table 3. $^1$H NMR chemical shift [ppm] for the butadiene ligand of the rotamers **A** and **B** of **6a** and **A** of **6b**.

| | $H_{syn1}$ | $H_{anti1}$ | $H_{int1}$ | $H_{int2}$ | $H_{anti2}$ | $H_{syn2}$ |
|---|---|---|---|---|---|---|
| **6a(A)** | –0.21 | –0.52 | 5.72 | 5.25 | 0.56 | 1.98 |
| **6a(B)** | –0.21 | –0.72 | 5.72 | 5.25 | 0.43 | 2.06 |
| **6b(A)** | –0.17 | –0.42 | 5.76 | 5.29 | 0.70 | 2.01 |

The coupling constants $J(H_{syn1}H_{anti1})$, $J(H_{syn1}H_{int1})$, $J(H_{anti1}H_{int1})$, $J(H_{int1}H_{int2})$, $J(H_{anti2}H_{int2})$, $J(H_{syn2}H_{int2})$ of isomer **A** of **6a**,**b** and isomer **B** of **6a** are 7 and 6 Hz and $J(H_{anti2}H_{syn2})$ 4 and 3 Hz, respectively. On the basis of the couplings of the *anti* protons with the phosphorus nuclei (ca. 7 Hz) it was concluded that the butadiene units in **6a**,**b** have structures close to a *cis*-$\eta^2$-1,3-diene ligand with a minor admixture of a metallacyclo-3-pentene structure. The coordination of the ethylene group in **6a**,**b** was confirmed by $^{13}$C NMR and by NOE measurements. All ethylene protons of **6a** appear in the $^1$H NMR spectrum as chemically distinguished signals indicating hindered rotation.

## II. Reactions of $[Re(NO)(CO)(PR_3)_2Cl_2]$

In order to probe the accessibility of other $Re^{-I}$–olefin complexes, we attempted the reduction of the complexes $[Re(NO)(CO)(PR_3)_2Cl_2]$ (**7a**,**b**) (R = *i*Pr **a**, Cy **b**), related to **1a**,**b** by replacement of the olefin ligand with CO. In the presence of 1.4 bar of ethylene and otherwise under the same conditions as for the reductions of **1a**,**b**, the ethylene derivatives $[Re(NO)(CO)(\eta^2\text{-}H_2C{=}CH_2)(PR_3)_2]$ (**8a**,**b**) were obtained in good yields (Scheme 3) after reaction times of 5 d.

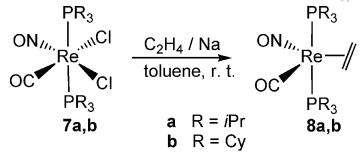


Scheme 3.

The change from yellow to orange became visible after filtration from the amalgam. The formation of **8a**,**b** was accompanied by the formation of a very small amount (about 1%) of the known dihydride complex $[Re(NO)(CO)(H_2)(PR_3)_2]$,[5] which was removed by washing of the solids with pentane. The dihydride complexes were formed in larger amounts (about 34%) when the reaction was carried out under a pressure of 10 bar of ethylene. It was concluded that the formation of the dihydride complex results from the presence of a $H_2$ impurity in the ethylene gas.

The IR spectra of **8a**,**b** reveal ν(CO) and ν(NO) absorptions, which are shifted both by more than 100 $cm^{-1}$ to lower wavenumbers compared to **7a**,**b**[8] indicating increased π-back bonding. ν(C=C) bonds are not observed, but the coordination of the ethylene group is indicated by the presence of characteristic ν(C–H) vibrations. The $^1$H NMR spectrum of **8b** is less informative with respect to a structural assignment, since the $PCy_3$ resonances cover other signals over a large area of chemical shifts. The $^1$H NMR resonances of the ethylene group of **8a** could not be detected in the room temperature spectrum, but were observed at 100 °C as a broad triplet at $\delta$ = 1.86 ppm for all chemically and magnetically inequivalent $C_2H_4$ protons.

The structures of **8a**,**b** were derived from their analytical and spectroscopic data and for **8a** it was confirmed by an exemplary X-ray diffraction study. The structure of **8a** is shown in Figure 5 and selected bond lengths and angles are given in Table 4.

The coordination geometry around the rhenium center corresponds to a distorted trigonal bipyramid with the CO and NO groups and both carbon atoms of the ethylene group located in the trigonal plane of the molecule. The two phosphane ligands occupy apical positions with a P(1)–Re(1)–P(2) angle of 178.16(3)° (Table 4). Contrary to complexes **2a**,**b** the orientation of the C=C bond is perpendicular to the P–Re–P vector, which is indicated by the dihedral angles P(1)–Re(1)–C(2) 90.37(10)°, P(1)–Re(1)–C(3) 90.73(9)°, P(2)–Re(1)–C(2) 90.75(10)°, and P(2)–Re(1)–C(3) 91.04(9)°. It is the electronically preferred orientation in $d^8$ trigonal bipyramidal structures. The C=C bond length of 1.420(8) Å is comparable to those found in other ethylene rhenium complexes.[21] The Re–N bond length of 1.799(3) Å is in accord with the values found in the literature.[22] The N1–O2 bond separation of 1.208(4) Å is in the range of 1.10 to 1.38 Å expected for a linear $NO^+$ type coordination[21–23] [Re–N–O angle of 172.7(3)°]. The positions of the hydrogen atoms of the ethylene ligand were located in a difference electron-density map and their coordinates were fixed, but their isotropic displacement parameters were freely refined.

 © 2007 Wiley-VCH Verlag GmbH & Co. KGaA, Weinheim 

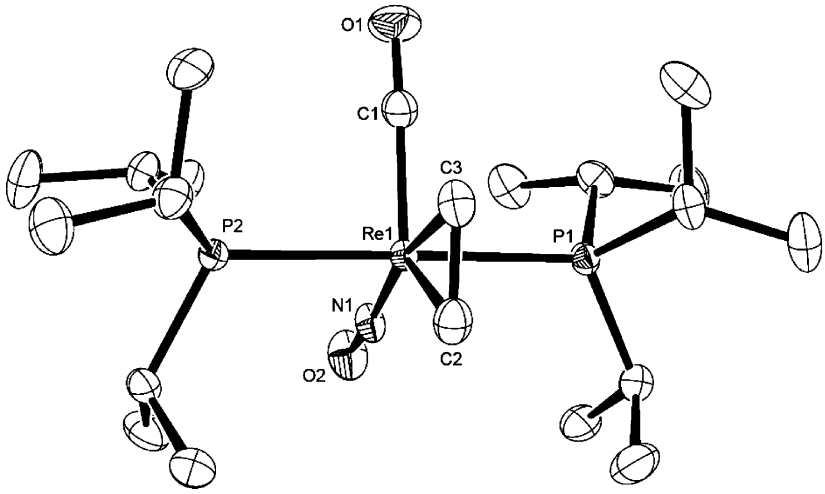


Figure 5. ORTEP drawing of the molecular structure of **8a** (thermal ellipsoids are drawn at the 50% probability level). All hydrogen atoms have been omitted for clarity.

Table 4. Selected bond lengths [Å] and bond angles [°] for **8a**.

| | | | |
|---|---|---|---|
| Re(1)–P(1) | 2.4758(9) | C(2)–Re(1)–P(1) | 90.37(10) |
| Re(1)–P(2) | 2.4744(9) | C(2)–Re(1)–P(2) | 90.75(10) |
| Re(1)–N(1) | 1.799(3) | C(3)–Re(1)–P(1) | 90.73(9) |
| Re(1)–C(1) | 1.922(4) | C(3)–Re(1)–P(2) | 91.04(9) |
| Re(1)–C(2) | 2.239(4) | N(1)–Re(1)–C(1) | 111.11(15) |
| Re(1)–C(3) | 2.282(3) | N(1)–Re(1)–C(2) | 128.67(15) |
| C(2)–C(3) | 1.420(6) | N(1)–Re(1)–C(3) | 165.26(14) |
| N(1)–O(2) | 1.208(4) | N(1)–Re(1)–P(1) | 89.32(9) |
| C(1)–O(1) | 1.151(5) | N(1)–Re(1)–P(2) | 88.84(9) |
| P(1)–Re(1)–P(2) | 178.16(3) | Re(1)–C(1)–O(1) | 176.4(3) |
| C(1)–Re(1)–C(2) | 120.22(15) | Re(1)–N(1)–O(1) | 172.7(3) |
| C(1)–Re(1)–P(1) | 89.95(11) | C(2)–C(3)–Re(1) | 70.1(2) |
| C(1)–Re(1)–P(2) | 90.75(11) | C(3)–C(2)–Re(1) | 73.3(2) |
| C(2)–Re(1)–C(3) | 36.59(14) | | |

Olefin complexes can be activated by Lewis acids to become alkene polymerization catalysts.[24–30] The olefin gets attacked by the Lewis acid forming a zwitterionic species. The metal cation and the Lewis acid attacked anionic group are covalently linked in some fashion. They have been found to represent a way to modulate ion pairing in these catalysts, thus increasing activity. One important class of these zwitterionic complexes is obtained when the counteranion is located on the alkyl group occupying the reactive wedge of the complex. These types of complexes are called Girdle-type zwitterionic compounds and have been accessed mainly through electrophilic attack of $B(C_6F_5)_3$ on suitable hydrocarbon ligands of neutral group 4 bent metallocenes.[31,32]

With the objective to generate active rhenium-based catalysts, we exemplarily attempted activation of complex **8a** with a Lewis acid. Treatment of **8a** with one equivalent of $B(C_6F_5)_3$ in toluene or benzene at room temperature did, however, not lead to the mentioned zwitterionic species $[Re^{+}(NO)(CO)(PR_3)_2CH_2CH_2B^{-}(C_6F_5)_3]$. The structures of the product showed that the $B(C_6F_5)_3$ electrophile had attacked the more Lewis basic NO site to give eventually the nitrosyl/Lewis acid adduct $\{Re(CO)_2[NOB(C_6F_5)_3](PR_3)_2\}$ (**9a**) and in addition the known complex $[Re(CO)_2(NO)(PR_3)_2]$ (**10a**) with loss of the ethylene ligand in both complexes as depicted in Scheme 4. Complex **10a** was identified

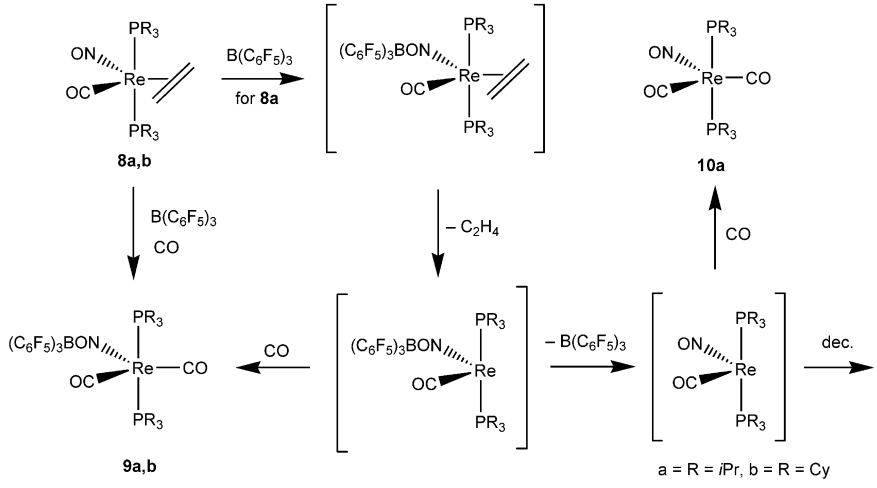


Scheme 4.

 © 2007 Wiley-VCH Verlag GmbH & Co. KGaA, Weinheim 

by its $^{31}P$ NMR spectrum ($\delta$ = 81.6 ppm) and its IR spectrum reported earlier.[8] $^{1}H$ and $^{31}P\{^{1}H\}$ NMR pursuit of the reaction confirmed generation of free ethylene and formation of **9a** and **10a** in a 1:1 ratio. Formation of the phosphane adduct $iPr_3PB(C_6F_5)_3$ was not observed.[33] Complex **9a** could be separated from **10a** in 38% yield.

Formation of **9a** with replacement of the ethylene group in **8a** by CO requires explanation of how free CO could have formed. It apparently originates from the partial decomposition of the $B(C_6F_5)_3$ adduct of **8a** to yield ethylene and CO. The presence of only low amounts of CO accounts for the low yield of **9a**.

With the objective to access **9a**,**b** in a better yield, we first prepared complex **10a**,**b** by the reaction of **8a**,**b** with CO. The reaction was very sluggish and took more than 5 d. But much to our surprise, no stable adduct formation

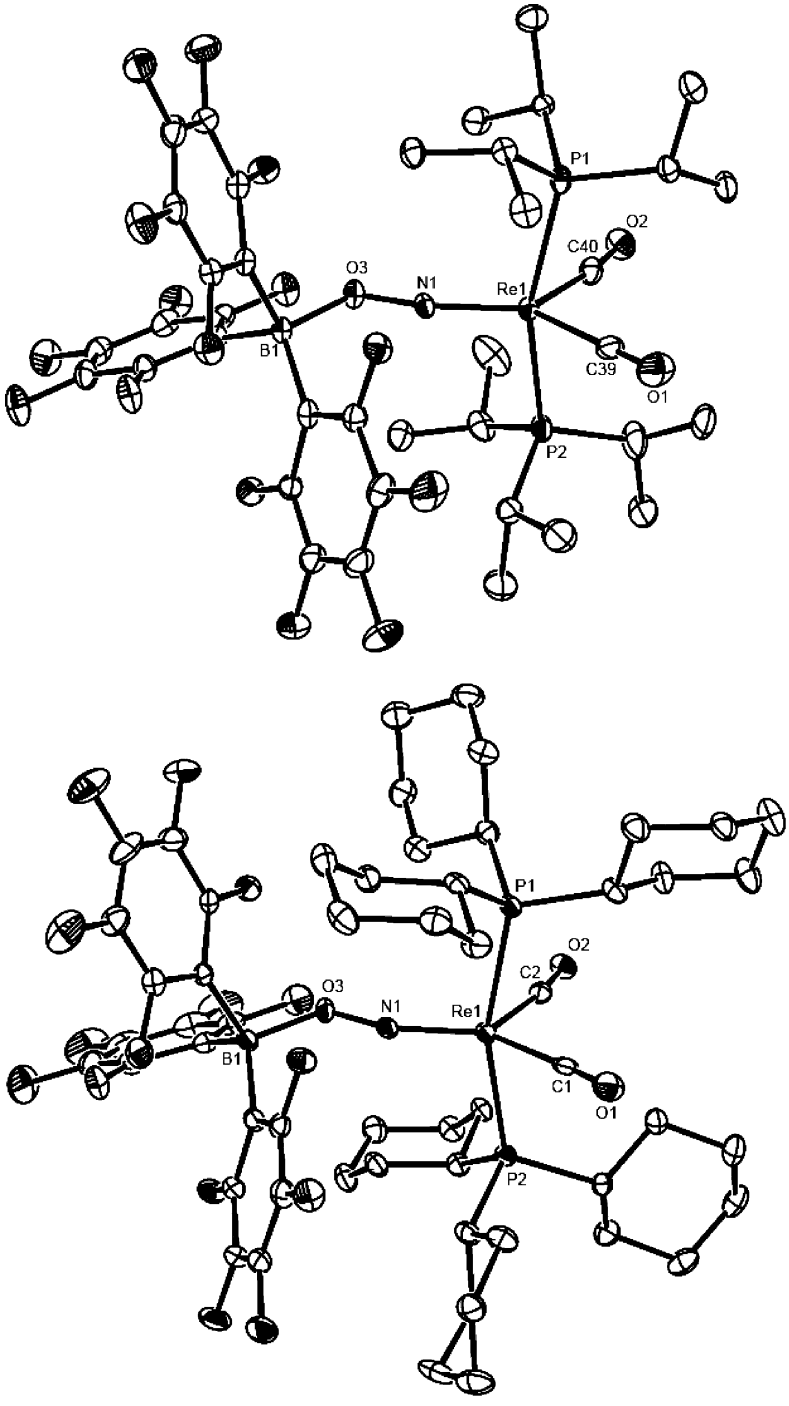


Figure 6. ORTEP drawings of the molecular structures of **9a** and **9b** (thermal ellipsoids are drawn at the 30% probability level). All hydrogen atoms have been omitted for clarity.

 © 2007 Wiley-VCH Verlag GmbH & Co. KGaA, Weinheim 

could be observed between **10a**,**b** and $B(C_6F_5)_3$. We have to assume that the additions of $B(C_6F_5)_3$ to **10a**,**b** are kinetically hindered.

When, however, **8a**,**b**, $B(C_6F_5)_3$, and CO were mixed together **9a**,**b** was produced in high yield. This observation stresses the necessity for the involvement of initial $B(C_6F_5)_3$ adducts of **8a**,**b** promoting formation of **9a**,**b** by subsequent ethylene substitution with CO (Scheme 4).

The adducts apparently release ethylene much faster than **8a**,**b** in the presence of CO to trap the unsaturated intermediates. Single crystals of **9a**,**b** were obtained from $CH_2Cl_2$/pentane solutions at –30 °C.

The molecular structures of **9a**,**b** were determined and are shown in Figure 6. The coordination geometries are distorted trigonal bipyramids. The two CO groups and the $NOB(C_6F_5)_3$ fragment are located in the trigonal plane of the molecules and the two phosphanes occupy apical positions. The phosphane ligands are bent towards the two CO groups [(P(1)–Re–P(2) 161.20(5) and 161.92(6)° for **9a** and **9b**, respectively] (Table 5). Such substantial bending of the phosphane molecules may be caused by steric "bumping" of the phosphanes and the $NOB(C_6F_5)_3$ fragment. Significant bending of the phosphanes was also observed in the hydride Lewis acid adducts $[Re(H)(NO)(NOBC_6F_5)_3(P\textit{i}Pr_3)_2]$[33] and $[Re(H)(NO)(NOBF_3)(P\textit{i}Pr_3)_2]$[5] with P(1)–Re(1)–P(2) 134.77(3) and 146.60(6)°, respectively. The electronic and steric factors favor the bending of the axial ligands towards the purely σ-donating hydride ligand and away from the nitrosyl group.[34,35] Similar to the complexes $\{Re(H)(NO)[NOB(C_6F_5)_3](P\textit{i}Pr_3)_2\}$ and $[Re(H)(NO)(NOBF_3)(P\textit{i}Pr_3)_2]$ the Re–N distances of 1.790(4) and 1.785(6) Å are only slightly affected by the coordination of $B(C_6F_5)_3$, but compared to other $\eta^1$ rhenium nitrosyl complexes the N–$OBX_3$ bond is elongated. The nitrosyl ligands are slightly bent upon $B(C_6F_5)_3$ attachment (Re(1)–N(1)–O(3) 166.2(4) and 158.6(6)°); however, it was approximately linear in the cases of $\{Re(H)(NO)[NOB(C_6F_5)_3](P\textit{i}Pr_3)_2\}$ [Re–N–O 175.0(3)°] and $[Re(H)(NO)(NOBF_3)(P\textit{i}Pr_3)_2]$ [Re–N–O 170.0(4)°]. A significant structural effect was recognized upon coordination of $BCl_3$ to a NO group in the compound $[Re(Cp)(SiMe_2Cl)(NOBCl_3)(PPh_3)]$.[36] This compound reveals a marked N–O elongation [1.47(1) Å] accompanied by a shortening of the Re–N bond [1.568(9) Å]. In **9a**,**b** the N–O bond lengths are 1.276(6) and 1.296(8) Å. Nitrosyl/Lewis acid interactions were shown to play a key role in the catalytic oxidation of alcohols,[37] as well as in catalytic hydrogenation and hydrosilylation of olefins and ketones.[33]

Table 5. Selected bond lengths [Å] and angles [°] for **9a** and **9b**.

| | **9a** | **9b** |
|---|---|---|
| Re(1)–P(1) | 2.4639(17) | 2.4840(19) |
| Re(1)–P(2) | 2.4535(17) | 2.480(2) |
| Re(1)–N(1) | 1.790(4) | 1.785(6) |
| Re(1)–C(a)[a] | 1.961(6) | 1.988(9) |
| Re(1)–C(b)[a] | 1.912(6) | 1.916(8) |
| C(a)–O(1) | 1.146(8) | 1.150(10) |
| C(b)–O(2) | 1.166(8) | 1.151(9) |
| N(1)–O(3) | 1.276(6) | 1.296(8) |
| P(1)–Re(1)–P(2) | 161.20(5) | 161.92(6) |
| C(a)–Re(1)–C(b) | 101.2(3) | 104.5(3) |
| N(1)–Re(1)–P(1) | 101.06(16) | 99.5(2) |
| N(1)–Re(1)–P(2) | 97.00(16) | 98.5(2) |
| Re(1)–N(1)–O(3) | 166.2(4) | 158.6(6) |
| N(1)–O(3)–B | 124.1(4) | 125.3(6) |

[a] C(a) and C(b) are C(39) and C(40) for **9a**, and C(1) and C(2) for **9b**.

## III. Theoretical Studies on Ethylene Complexes

As a single-faced π acceptor an olefinic ligand quite often shows barriers to free rotation around the metal–olefin bond. Generally, the C=C bond is preferentially oriented in the trigonal plane of three-coordinate complexes, is perpendicular to the plane in four-coordinate square-planar complexes, and is in plane with the trigonal plane of five-coordinate trigonal-bipyramidal complexes (Scheme 5).[38] These prevailing orientations are thought to result mostly from electronic rather than from steric effects. In $d^6$ octahedral complexes olefins do only rarely show rotational barriers, if the *cis* ligands are all the same. Barriers might appear only for cases where the π donor planes at the metal centers are electronically strongly distinguished ($R_3P$–M–$PR_3$ plane electronically more donating than the $L_1$–M–$L_3$ plane of Scheme 5). In $d^8$ trigonal bipyramidal complexes the olefin is preferentially oriented in the trigonal plane regardless of the presence of an axial $R_3P$–M–$PR_3$ arrangement. For instance in the structure of **8a** the olefin orientation is in accord with this general rule.

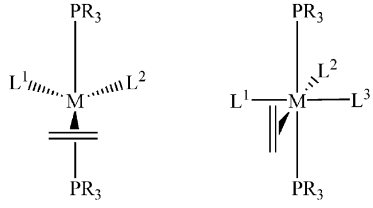


Scheme 5.

Five-coordinated $d^6$ complexes, as for instance $(\mu^2$-Cl-$[(AlMe_2)_2C\equiv)]W(CH_3)(PMe_3)_2(C_2H_4)$,[39] (bis-mesitylimido)$W(PMe_3)_2(C_2H_4)$,[40] and bis(2,6-diisopropylphenylimido)$Mo(PMe_3)_2(C_2H_4)$ show reorientation of the olefinic group.[41] In pseudo-octahedral complexes with *trans* phosphane ligands *cis* to the olefin, structures are prevailing with a parallel orientation of the olefin with respect to the P–M–P axis.[42–49] Nevertheless, some examples show the olefin lying perpendicular to the P–M–P axis.[50–53] Several of these latter examples might be governed by special effects, since they mostly possess two ethylene ligands in *trans*[50,51] or in *cis* position[52] to each other with one C=C bond parallel to the P–M–P vector and the second one perpendicular to it. To the best of our knowledge, only in the *ortho*-metallated ruthenium complex $RuH(C_2H_4)$(2-phenylpyridine)$(P\textit{i}Pr_3)_2$ has the coordinated ethylene not aligned with the P–Ru–P axis.[53]

 © 2007 Wiley-VCH Verlag GmbH & Co. KGaA, Weinheim 

The most widely accepted model for the bonding of an olefin to transition metals is that proposed by Dewar[54] and by Chatt and Duncanson.[55] This model involves formation of a σ-bond by donation of π-electrons to the metal and formation of a π-bond by back donation from the d orbitals of the metal to the olefin π*-orbital. The precise nature of this bond has been the subject of many theoretical and experimental studies.[56] In order to study the structures of **2a**, **2b**, and **8a** more thoroughly with the olefinic C=C bond lying parallel to the P–Re–P axis in the six-coordinate octahedral complexes **2a** and **2b** and in the trigonal plane of **8a** DFT calculations[57] were carried out on the model complexes $Re(PMe_3)_2X_2(NO)(C_2H_4)$ (X = Br, **2-Me**) and $Re(PMe_3)_2(CO)(NO)(C_2H_4)$ (**8-Me**).

We made use of a well-established bond partitioning scheme,[58] which divides the overall bond energy BE into various contributions from different interactions [Equation (1)], to look at the bond-forming reaction between the metal fragment and ethylene.

$$\Delta E_{int} = -[\Delta E_{elstat} + \Delta E_{Pauli} + \Delta E_{oi}] = -[\Delta E^0 + \Delta E_{oi}] \quad (1)$$

The interaction energy between both fragments $\Delta E_{int}$ is partitioned into three physically meaningful terms, namely the electrostatic interaction $\Delta E_{elstat}$, the Pauli repulsion $\Delta E_{Pauli}$, and the orbital interaction term, $\Delta E_{oi}$. When two suitable, bond-forming fragments are brought together to adapt the geometry of the final molecule, the term $\Delta E_{elstat}$ describes the classical Coulomb interaction between the unmodified and interpenetrating charge distributions of the two fragments. We further have to consider the Pauli repulsion $\Delta E_{Pauli}$, which takes into account destabilizing two-orbital four-electron interactions between occupied orbitals on both fragments. The sum of Pauli repulsion and electrostatic interaction is called the *steric interaction* $\Delta E^0$. The last term in Equation (1), $\Delta E_{oi}$ introduces the attractive orbital interaction between occupied and virtual orbitals on the two fragments, and includes polarization and charge-transfer contributions. Although $\Delta E_{int}$ values are not defined in the same way as bond dissociation enthalpies $\Delta H$, they are reasonable approximations of bond enthalpy terms, which in turn provide a good description for the bond strength.[59] The bonding analysis for **2-Me** and **8-Me** is presented in Table 6.

Table 6. Bond analysis of the [Re]–($\eta^2$-$C_2H_4$) bond for **2-Me** and **8-Me**.

| System | $\Delta E$ | $\Delta E_{Pauli}$ | $\Delta E_{elstat}$ | $\Delta E^0$ | $\Delta E_{oi}$ | $\Delta E_{int}$ |
|---|---|---|---|---|---|---|
| **2-Me** $/\!/$ | 0.0 | +225.23 | –163.13 | +62.10 | –120.86 | –58.76 |
| **2-Me** ⊥ | +23.1 | +127.25 | –90.57 | +36.68 | –59.23 | –22.55 |
| **8-Me** $/\!/$ | +10.2 | +217.96 | –159.16 | +58.79 | –111.64 | –52.84 |
| **8-Me** ⊥ | 0.0 | +194.45 | –143.07 | +51.38 | –113.15 | –61.77 |

For the three studied model complexes, both conformations with the C=C bond of ethylene parallel ($/\!/$) or perpendicular (⊥) to the P–M–P axis have been optimized without any constraints. The relative total energies confirm the structural observations since the parallel orientation is favored for **2-Me** by 23.1 kcal/mol with respect to the corresponding perpendicular conformation and the perpendicular orientation is favored for **8-Me** (by 10.2 kcal/mol with respect to the corresponding parallel conformation). The results from the bond analysis of **2-Me** show that $\Delta E_{oi}$ is the main factor determining the strength of the Re-($\eta^2$-$C_2H_4$) bond. The steric interaction term $\Delta E^0$ is dominated by the Pauli repulsion $\Delta E_{Pauli}$, and thus represents a non-bonding contribution. Despite the fact that the perpendicular orientation of ethylene reduces the steric repulsion between fragments from +62 to +37 kcal/mol (**2-Me**) the attractive orbital interaction $\Delta E_{oi}$ greatly stabilizes the parallel molecular arrangement from about 120 kcal/mol to only 59 kcal/mol for **2-Me** ⊥, respectively. In the case of the trigonal-bipyramidal complex **8-Me**, the three main contributions of **9-Me**$''$ are very similar to those for **2-Me**$''$ (differences are less than 8 kcal/mol). The major change which leads to a favored perpendicular arrangement for **8-Me** comes from the electronic contribution $\Delta E_{oi}$. Calculated $\Delta E_{oi}$ increases from 56 kcal/mol to 113 kcal/mol on going from **2-Me** ⊥ to **8-Me** ⊥, even larger than the value for **8-Me**$''$ (112 kcal/mol). For **8-Me**, both steric (+51 vs. +59 kcal/mol) and electronic terms (–113 vs. –112 kcal/mol) contribute to a better stabilization of the perpendicular arrangement.

According to the Dewar–Chatt–Duncanson model, two molecular orbitals from the metallic fragments $Re(PMe_3)_2$-(NO)(CO) or $Re(PMe_3)_2(NO)Br_2$ can compete for the formation of the π-bond by back donation to ethylene. The metal contribution to these two highest occupied molecular orbitals is mainly $d_{xz}$ and $d_{yz}$ (Scheme 6).

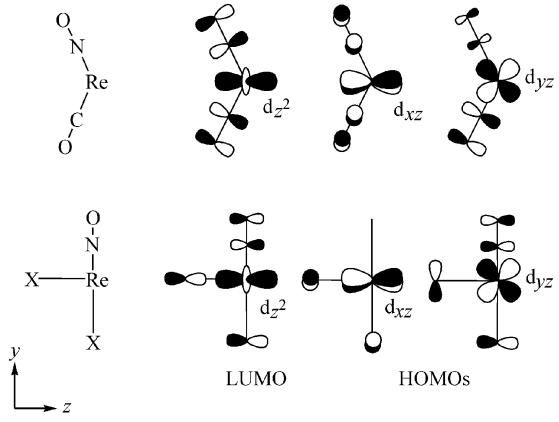


Scheme 6.

Both orbitals can interact with the olefin π*-orbital in a bonding fashion depending on the orientation of ethylene. The LUMO is mainly Re-$d_{z^2}$ and is responsible for the σ-bond by interaction with the filled $\pi_{C2H4}$ orbital. The energy levels of these crucial orbitals of the metal fragments of **2-Me** and **8-Me** in their structures of the optimized molecules are presented in Figure 7 and Table 7. In the pseudo

 © 2007 Wiley-VCH Verlag GmbH & Co. KGaA, Weinheim 

Table 7. Optimized bond angles [°] and energy levels [eV] of the metallic fragments $Re(PMe_3)_2(NO)Br_2$ of **2-Me** and $Re(PMe_3)_2(NO)(CO)$ of **8-Me**.

| System | Br–Re–Br | Br–Re–$N_{NO}$ | P–Re–Br | P–Re–P | $N_{NO}$–Re–$C_{CO}$ | LUMO | HOMO | HOMO – 1 |
|---|---|---|---|---|---|---|---|---|
| **2-Me**$''$ | 91.8 | 91.4 | 81.1 | 143.1 | | –4.677 ($d_{z^2}$) | –5.685 ($d_{xz}$) | –6.648 ($d_{yz}$) |
| **2-Me** $\perp$ | 88.9 | 89.3 | 85.9 | 168.1 | | –4.679 ($d_{z^2}$) | –5.805 ($d_{xz}$) | –6.590 ($d_{yz}$) |
| **8-Me**$''$ | | | | 159.1 | 136.8 | –3.462 ($d_{z^2}$) | –5.084 ($d_{xz}$) | –5.147 ($d_{yz}$) |
| **8-Me** $\perp$ | | | | 175.0 | 112 | –3.566 ($d_{z^2}$) | –4.488 ($d_{yz}$) | –5.820 ($d_{xz}$) |

octahedral complex **2-Me** the three ligands of the equatorial plane, two halides and one nitrosyl keep more or less their positions during ethylene rotation. The Br–Re–Br and Br–Re–$N_{NO}$ bond angles remain in the range 88.9–91.8° and P–Re–Br increases by only 5° when the ethylene lies in the $ReBr_2(NO)$ plane (Table 7). The orbitals are well separated by about 1 eV and the HOMO is mainly built from Re-$d_{xz}$ which favors the parallel orientation of ethylene with respect to the P–Re–P axis. The second occupied π-type orbital is low in energy through the bonding interaction with the nitrosyl ligand not allowing for efficient further back-bonding with the ethylene.

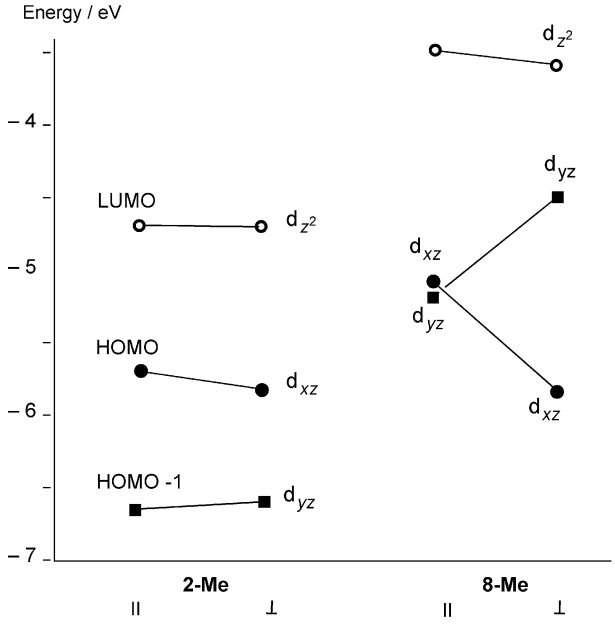


Figure 7. Energy diagram for the $d_{xz}$, $d_{yz}$, $d_{z^2}$ orbitals of the fragments $Re(PMe_3)_2(NO)(CO)$ of **2-Me** and $Re(PMe_3)_2(NO)Br_2$ of **8-Me** in their structures of the optimized molecules.

In the case of the trigonal-bipyramidal complex **8-Me**, the bending distortion of the ligands in both planes and in the opposite direction of the ethylene is easier than for **2-Me** and polarizes the $d_{xz}$ or $d_{yz}$ orbital of the metal for increased back-donation to the ethylene. Nevertheless, the degree of bending of the $PMe_3$ is limited by steric repulsions between $PMe_3$ and CO and NO and between the phosphorus ligands themselves whereas the bending of the carbonyl and nitrosyl group is only limited by electronic and steric interactions between themselves in the equatorial plane. While the P–Re–P angle decreases by 16° from 175.0 (**8-Me** $\perp$) to 159.1° (**8-Me**$''$) the $N_{NO}$–Re–$C_{CO}$ bond angle can become narrower by 25° from the parallel to the perpendicular orientation of ethylene (from 136.8 to 112°). The result is a greater destabilization of the occupied orbital built with Re-$d_{yz}$, since the overlap between Re-$d_{yz}$ and $p_y/p_z$ of the carbonyl and nitrosyl groups is reduced which becomes the HOMO of the metallic fragment. Back bonding to ethylene becomes stronger in the equatorial plane and favors the perpendicular orientation of ethylene with respect to the P–Re–P axis.

It was also challenging to provide understanding for the solution structures of the polyolefin complexes $Re(C_2H_4)(C_4H_6)(PR_3)(NO)$ **6a** and **6b**. In particular the X-ray structure of **6b** provides a good idea about the ground states of **6a** and **6b** which is pseudo tetrahedral with one ethylene group coordinated to the rhenium center in parallel orientation with respect to the Re–P axis, one *cis*-butadiene ligand bound in an $\eta^4$-coordination mode with an essentially planar carbon skeleton, one phosphane and one nitrosyl group. Complex **6a** exists in solution as a mixture of two stereoisomers **A** and **B** with either the phosphane or the olefin in the cleft of the butadiene appearing in a 3:1 ratio on the basis of the $^{31}P$ NMR spectra. Complex **6b** is expected to exclusively exist in the butadiene rotameric form **A** with the phosphane ligand oriented in the cleft of the diolefin. The potential energy surface of the model complex $Re(C_2H_4)(C_4H_6)(PMe_3)(NO)$ **6-Me** could not be fully explored, but the geometries of the global or local minima corresponding to the three possible rotational isomers **A**, **B**, and **C** were fully optimized with the help of the density functional theory (Figure 8).[60] The computed bonding energies of **6-Me** give isomer **A** as the most stable calculated structure, while **B** and **C** lie +3.9 and +8.6 kcal/mol higher in energy and thus confirm the given structural assignments for rotational isomers of **6a** and **6b**. Ethylene rotation was also checked in rotamer **A** of **6-Me**, but no other energetic minimum than the orientation parallel to the Re–P axis was found. The observed isomerism of **6a** could thus not be explained on the basis of ethylene rotational isomerism. The energy differences between structures **A** and **B** or **C** is expected to have a significant steric component and to depend on the size of the phosphane. The larger the phosphane the stronger the preference for structure **A**, since the cleft of the butadiene ligand is the only place in the molecule that provides abundant space. That would explain why **6b** with the bulky $PCy_3$ shows only isomer **A** and **6a** with the smaller $PiPr_3$ leads to rational isomerism.

 © 2007 Wiley-VCH Verlag GmbH & Co. KGaA, Weinheim 

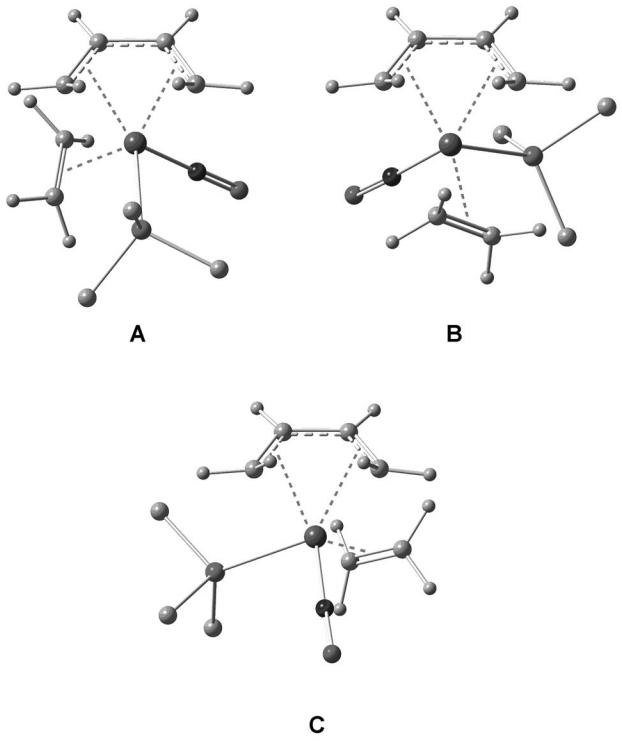


Figure 8. Optimized isomeric structures of the model complex $Re(C_2H_4)(C_4H_6)(PMe_3)(NO)$ **6-Me**.

## Conclusions

This work focused on the chemistry of new olefin rhenium complexes. The ethylene complexes **2a**,**b** were isolated in good yields by replacement of a MeCN group from **1a**,**b**. The ethylene ligand showed an unexpectedly high preference for the orientation parallel to the P–Re–P axis. Reduction of **1a**,**b** with sodium amalgam under 1 bar of ethylene affords the butadiene complexes **6a**,**b**. The salient features in bonding and the coordination geometry of **6a**,**b** have been clarified on the basis of NMR and X-ray analysis coupled with a theoretical treatment. The pentacoordinate $d^8$-olefin complexes demonstrated the olefin to be oriented in the trigonal plane of a trigonal bipyramid. This type of complex revealed a primary attack of the Lewis acid $B(C_6F_5)_3$ at the nitrosyl group rather than on the olefin, which eventually furnished $Re(CO)_2[NOB(C_6F_5)_3](PR_3)_2$ complexes with ethylene replacement in the presence of CO.

## Experimental Section

All operations were carried out under a nitrogen atmosphere using a M. Braun 150 G-B glove box. The solvents were dried with sodium/benzophenone (THF, $Et_2O$, hydrocarbons) or $P_2O_5$ ($CH_2Cl_2$, $CH_3CN$) and distilled under $N_2$ prior to use. The deuterated solvents used in the NMR experiments were dried with sodium/benzophenone ($C_6D_6$, [$D_8$]toluene, [$D_8$]THF) or $P_2O_5$ ($CD_2Cl_2$, $CD_3CN$) and vacuum transferred for storage in Schlenk flasks fitted with Teflon valves. NMR experiments were carried out with Varian Gemini 300, Varian Mercury 200, or Bruker DRX 500 spectrometers using 5-mm diameter NMR tubes equipped with Teflon valves, which allow degassing and further introduction of gases into the probe. Chemical shifts are given in ppm. $^1H$ and $^{13}C\{^1H\}$ NMR spectra were referenced to the residual proton or $^{13}C$ resonances of the deuterated solvent. $^{31}P$ chemical shifts are relative to 85% $H_3PO_4$. Microanalyses were carried out at the Anorganisch-Chemisches Institut of the University of Zürich. IR spectra were recorded with a Bio-Rad FTS-45 spectrometer. The following reagents were purchased from commercial suppliers and used without further purification: MeLi (Fluka), P*i*$Pr_3$ (STREM), ethylene (99.999% purity, MESSER or 99.9995% purity, PanGas), and $H_2$ (99.99995% purity, PanGas). Complexes **1a**,**b** were obtained according to literature procedures.[5]

**Synthesis of $[Re(NO)(P\mathit{i}Pr_3)_2(\eta^2\text{-}C_2H_4)Br_2]$ (2a):** Ethylene was bubbled through a solution of **1a** (0.100 g, 0.135 mmol) in toluene (20 mL) at room temperature for 1 h. After removal of the volatiles under vacuum, the residue was chromatographed on a $SiO_2$ column with toluene as a eluent yielding after drying in vacuo **2a** as a pale yellow powder (0.072 g, 0.1 mmol, 74%). IR (KBr): $\tilde{\nu}$ = 2963, 2920 and 2879 (s, νC–H), 1693 (vs, νNO) $cm^{-1}$. $^1H$ NMR (300.1 MHz, $C_6D_6$): $\delta$ = 3.12–2.95 (m, 6 H, $(CH_3)_2CHP$), 2.51 and 2.47 (2 br. signals, 4 H, $H_2C{=}CH_2$), 1.45–1.32 and 1.35–1.19 (2 m, 36 H, $(CH_3)_2CHP$) ppm. $^{31}P\{^1H\}$ NMR (80.9 MHz, $C_6D_6$): $\delta$ = –13.3 (s) ppm. $^{13}C\{^1H\}$ NMR (75.5 MHz, $C_6D_6$): $\delta$ = 39.5 (br., $H_2C{=}CH_2$), 26.2 (t, *J*(PC) = 11 Hz, $(CH_3)_2CHP$), 19.9 and 19.6 (2 s, $(CH_3)_2CHP$) ppm. $C_{20}H_{46}Br_2NOP_2Re$ (724.55): calcd. C 33.19, H 6.41, N 1.94; found C 33.39, H 6.52, N 1.93.

**Synthesis of $[Re(NO)(PCy_3)_2(\eta^2\text{-}C_2H_4)Br_2]$ (2b):** Complex **1b** (0.086 g, 0.088 mmol) in 100 mL of toluene was heated at 60 °C for one night. After cooling to room temperature, ethylene was bubbled through the solution for 1.5 h. The precipitate was collected and washed with cold THF (3 × 5 mL) and MeCN (3 × 5 mL) to afford **2b** as a pure pale yellow solid (0.066 g, 0.068 mmol, 78%). IR (KBr): $\tilde{\nu}$ = 2926 and 2879 (s, νC–H), 1696 (vs, νNO) $cm^{-1}$. $^1H$ NMR (300.1 MHz, $CD_2Cl_2$, 40 °C): $\delta$ = 3.00–1.32 ($H_2C{=}CH_2$ and $P(C_6H_{11})_3$) ppm. $^{31}P\{^1H\}$ NMR (80.9 MHz, $CD_2Cl_2$, 40 °C): $\delta$ = –20.3 (br. s) ppm. $^{13}C\{^1H\}$ NMR (75.5 MHz, $CD_2Cl_2$, 40 °C): $\delta$ = 39.5 (br., $H_2C{=}CH_2$), 36.5 (t, *J*(PC) = 9 Hz, $P(C_6H_{11})_3$), 29.4, 28.6 and 27.1 (3 s, $P(C_6H_{11})_3$) ppm. $C_{38}H_{70}Br_2NOP_2Re$ (964.93): calcd. C 47.30, H 7.31, N 1.45; found C 47.21, H 7.55, N 1.63.

**Synthesis of $[Re(NO)(P\mathit{i}Pr_3)_2(MeCN)Me_2]$ (3a):** To a solution of **1a** (0.081 g, 0.105 mmol) in 10 mL of toluene, cooled to –30 °C was added rapidly MeLi 1.6 M in $Et_2O$ (132 μL, 0.210 mmol). The color changed immediately from light orange to red. The mixture was stirred at –30 °C for 30 min then allowed to come to room temperature and stirred for additional 30 min. The solution was filtered through celite and the solvent was evaporated under vacuum. The extraction with pentane affords the red beet viscous complex **3a** (0.078 g, 0.128 mmol, 82%). IR ($CH_2Cl_2$): $\tilde{\nu}$ = 2360 (w, ν$MeC{\equiv}N$), 1588 (vs, νNO) $cm^{-1}$. $^1H$ NMR (300.1 MHz, $C_6D_6$): $\delta$ = 2.61–2.43 (m, 6 H, $(CH_3)_2CHP$), 2.36 (t, *J*(PH) = 2.20 Hz, 3 H, ReMe), 2.29 (t, *J*(PH) = 2.03 Hz, 3 H, ReMe), 1.97 (s, 3 H, MeCNRe), 1.32–1.22 (m, 36 H, $(CH_3)_2CHP$) ppm. $^{31}P\{^1H\}$ NMR (80.9 MHz, $C_6D_6$): $\delta$ = –15.9 (s) ppm. $^{13}C\{^1H\}$ NMR (125.8 MHz, $C_6D_6$): $\delta$ = 24.6 (t, *J*(PC) = 11 Hz, $(CH_3)_2CHP$), 20.6 (br. s, ReMe), 20.5 (br. s, ReMe), 20.2 and 20.1 (2s,$(CH_3)_2CHP$) ppm.

**Synthesis of $[Re(NO)(P\mathit{i}Pr_3)_2(MeCN)_2Br][BAr^F_4]$ (4a):** A solid $NaBAr^F_4$ (0.131 g, 0.148 mmol) was added to a solution of **1a** (0.114 g, 0.148 mmol) dissolved in 10 mL of MeCN. The mixture was stirred for 14 h at room temperature. The yellow solution was

 © 2007 Wiley-VCH Verlag GmbH & Co. KGaA, Weinheim 

filtered and the solvent was removed under vacuum. Extraction by $CH_2Cl_2$ and recrystallization from $CH_2Cl_2$/pentane at room temperature affords, after one day, yellow crystals of **4a** (0.188 g, 0.120 mmol, 81%). IR (KBr): $\tilde{\nu}$ = 1712 (vs, νNO) $cm^{-1}$. $^1H$ NMR (300.1 MHz, $CD_2Cl_2$): $\delta$ = 7.73 (m, 8 H, $BAr^F_4$), 7.56 (m, 4 H, $BAr^F_4$), 2.89 (s, 6 H, MeCNRe), 2.83–2.71 (m, 6 H, $(CH_3)_2CHP$), 1.42–1.33 (m, 36 H, $(CH_3)_2CHP$) ppm. $^{31}P\{^1H\}$ NMR (121.47 MHz, $CD_2Cl_2$): $\delta$ = 0.4 (s) ppm. $^{13}C\{^1H\}$ NMR (125.8 MHz, $CD_2Cl_2$): $\delta$ = 162.0 (q, $^1J$(BC) = 50 Hz, *ipso*-$BAr^F$), 137.7 (s, $H_3CCNRe$), 135.1 (s, *o*-$BAr^F$), 129.1 (br., *m*-$BAr^F$), 126.0 (q, $^1J$(CF) = 50 Hz, $CF_3$), 117.8 (br., *p*-$BAr^F_4$), 24.8 (t, *J*(PC) = 11 Hz, $(CH_3)_2CHP$), 19.1 (s, $(CH_3)_2CHP$), 5.2 (s, $H_3CCNRe$) ppm. $^{19}F$ NMR (125.8 MHz, $CD_2Cl_2$): $\delta$ = –64.4 ppm. $C_{54}H_{60}BBrF_{24}N_3OP_2Re$ (1561.91): calcd. C 41.95, H 3.91, N 2.72; found C 42.03, H 4.01, N 2.67.

**Synthesis of [Re(NO)(PCy$_3$)$_2$(MeCN)$_2$Br][BAr$^F_4$] (4b): 4b** (0.078 g, 0.042 mmol, 84%) was obtained by the same procedure described for **4a** by reaction of **1b** (0.050 g, 0.051 mmol) and $NaBAr^F_4$ (0.045 g, 0.051 mmol) in a mixture of THF/MeCN (15:1 mL) at room temperature after 30 h. IR (ATR): $\tilde{\nu}$ = 1703 (vs, νNO) $cm^{-1}$. $^1H$ NMR (300.1 MHz, $CD_2Cl_2$): $\delta$ = 2.94 (s, 6 H, $CH_3CN$-Re), 2.57–1.28 (m, 66 H, $P(C_6H_{11})_3$) ppm. $^{31}P\{^1H\}$ NMR (121.47 MHz, $CD_2Cl_2$): = –10.2 (s) ppm. $^{13}C\{^1H\}$ NMR (75.5 MHz, $CD_2Cl_2$): $\delta$ = 164.0 (m, *ipso*-$BAr^F$), 137.7 (s, $H_3CCNRe$), 135.2 (s, *o*-$BAr^F$), 129.4 (br., *m*-$BAr^F$), 129.0 (m, $CF_3$), 118.0 (br., *p*-$BAr^F_4$), 35.2 (t, *J*(PC) = 10 Hz, $P(C_6H_{11})_3$), 29.6, 28.9 and 26.8 (3 s, $P(C_6H_{11})_3$), 5.7 (s, $CH_3CN$-Re) ppm. $^{19}F$ NMR (125.8 MHz, $CD_2Cl_2$): $\delta$ = –63.9 ppm. $C_{72}H_{84}BBrF_{24}N_3O_2P_2Re$ (1818.28): calcd. C 47.56, H 4.65, N 2.31; found C 47.71, H 4.67, N 2.20.

**Synthesis of [Re(η$^4$-C$_4$H$_6$)(η$^2$-H$_2$C=CH$_2$)(NO)(P*i*Pr$_3$)$_2$] (6a):** In a 50 mL Young tap Schlenk tube the complex [Re(NO)(MeCN)-(P*i*Pr$_3$)$_2$Br$_2$] (**1a**) (0.100 g, 0.135 mmol) was dissolved in 20 mL of THF and 10 g of 0.7% sodium amalgam was added. Without stirring, the solution was frozen and kept under pressure of 1.4 bar of $C_2H_4$ for 5 min. The mixture was warmed to room temperature, and stirred for 3 d. Filtration over celite and removal of the solvent left a yellow residue, which was extracted with toluene and then dried. Final extraction with pentane affords a pure pale yellow powder of **6a** (0.020 g, 0.042 mmol, 31%). IR (ATR): $\tilde{\nu}$ = 2964, 2930 and 2872 (s, νC–H), 1646 (vs, νNO) $cm^{-1}$. $^1H$ NMR (500.25 MHz, $C_6D_6$): $\delta$ = 5.72 (q, *J*(HH) = 6.7 Hz, 1 H, $H_{int}C=CH_{int}$), 5.25 (q, *J*(HH) = 6.7 Hz, 1 H, $H_{int}C=CH_{int}$), 2.20 (m, 1 H, (HHC=CH*H*)Re), 2.06 (m, 0.34 H, $H_{syn2}H_{anti2}$CRe, isomer **B**), 1.98 (dd, $^3J$(HH) = 6.7, $^2J$(HH) = 3.5 Hz, 0.66 H, $H_{syn2}H_{anti2}$CRe, isomer **A**), 1.82 (m, 5 H, $(CH_3)_2CHP$ and (*HH*C=CHH)Re), 1.48 (m, 1 H, (HHC=C*H*H)Re), 1.18–0.98 and 0.95–0.87 (2 m, 18 H, $(CH_3)_2CHP$), 0.56 (td, $^3J$(HH) = $^3J$(PH) = 6.7 Hz, $^2J$(HH) = 3.5 Hz, 0.66 H, $H_{syn2}H_{anti2}$CRe, isomer **A**), 0.43 (td, $^3J$(HH) = $^3J$(PH) = 6.7 Hz, $^2J$(HH) = 3.5 Hz, 0.34 H, $H_{syn2}H_{anti2}$CRe, isomer **B**), –0.21 (m, 1 H, $H_{syn1}H_{anti1}$CRe), –0.52 (q, *J*(HH) = *J*(PH) = 6.7 Hz, 0.66 H, $H_{syn1}H_{anti1}$CRe, isomer **A**), –0.72 (q, *J*(HH) = *J*(PH) = 6.7 Hz, 0.34 H, $H_{syn1}H_{anti1}$CRe, isomer **B**) ppm. $^{31}P\{^1H\}$ NMR (121.5 MHz, $C_6D_6$): $\delta$ = 21.3 (br. s, isomer **A**), 12.9 (br. s, isomer **B**) ppm. $^{13}C\{^1H\}$ NMR (125.8 MHz, $C_6D_6$): $\delta$ = 97.5 (d, *J*(CP) = 2 Hz, $H_{int}C=CH_{int}$, isomer **B**), 96.14 (d, *J*(CP) = 2 Hz, $H_{int}C=CH_{int}$, isomer **A**), 83.0 (br. s, $H_{int}C=CH_{int}$, isomer **A**), 81.97 (br. s, $H_{int}C=CH_{int}$, isomer **B**), 34.0 (d, *J*(CP) = 5 Hz, $H_{syn1}H_{anti1}$CRe, isomer **B**), 32.8 (d, *J*(CP) = 5 Hz, $H_{syn1}H_{anti1}$CRe, isomer **A**), 30.5 (d, *J*(CP) = 6 Hz, $H_{anti2}H_{syn2}$CRe, isomer **A**), 29.7 (d, *J*(CP) = 6 Hz, $H_{anti2}H_{syn2}$CRe, isomer **B**), 29.2 (br. s, $(CH_3)_2CHP$, isomer **A**), 29.0 (br. s, $(CH_3)_2CHP$, isomer **B**), 25.5 (d, *J*(CP) = 8 Hz, (HH*C*=CHH)Re, isomer **A**), 24.9 (d, *J*(CP) = 8 Hz, (HH*C*=CHH)Re, isomer **B**), 24.7 (d, *J*(CP) = 3 Hz, (HH*C*=*C*HH)-Re, isomer **A**), 23.7 (d, *J*(CP) = 3 Hz, (HH*C*=*C*HH)Re, isomer **B**), 19.4 (s, $(CH_3)_2CHP$ isomer **A**), 19.0 (s, $(CH_3)_2CHP$, isomer **B**) ppm. $C_{15}H_{31}NOPRe$ (458.59): calcd. C 39.28, H 6.81, N 3.05; found C 39.46, H 6.93, N 3.18.

**Synthesis of [Re(η$^4$-C$_4$H$_6$)(η$^2$-H$_2$C=CH$_2$)(NO)(PCy$_3$)$_2$] (6b):** Complex **6b** (0.026 g, 0.045 mmol, 63%) was obtained by the same procedure described for **6a** by reduction of **1b** (0.070 g, 0.071 mmol) under a pressure of 1.4 bar of ethylene. IR (ATR): $\tilde{\nu}$ = 2924 and 2846 (vs, νC–H), 1643 (vs, νNO) $cm^{-1}$. $^1H$ NMR (500.25 MHz, $C_6D_6$): $\delta$ = 5.76 (q, *J*(HH) = 6.4 Hz, 1 H, $H_{int}C=CH_{int}$), 5.29 (q, $^3J$(HH) = 6.4 Hz, 1 H, $H_{int}C=CH_{int}$), 2.40–1.05 (m, 37 H, $(H_2C=CH_2)$Re and $P(C_6H_{11})_3$), 2.01 (dd, $^2J(H_{syn2}H_{anti2})$ = 3.3, *J*(HH) = 6.4 Hz, 1 H, $H_{syn2}H_{anti2}$CRe), 0.70 (td, *J*(HH) = 3.3, *J*(HH) = *J*(PH) = 6.4 Hz, 1 H, $H_{syn2}H_{anti2}$CRe), –0.17 (m, 1 H, $H_{syn1}H_{anti1}$CRe), –0.42 (q, *J*(HH) = *J*(PH) = 6.1 Hz, 1 H, $H_{syn1}H_{anti1}$CRe) ppm. $^{31}P\{^1H\}$ NMR (121.5 MHz, $C_6D_6$): $\delta$ = 10.0 (s) ppm. $^{13}C\{^1H\}$ NMR (125.8 MHz, $C_6D_6$): $\delta$ = 95.7 (s, $H_{int}C=CH_{int}$), 83.6 (s, $H_{int}C=CH_{int}$), 33.6 (d, *J*(CP) = 5 Hz, $H_{syn1}H_{anti1}$CRe), 32.2 (d, *J*(CP) = 19 Hz, $P(C_6H_{11})_3$), 31.7 (d, *J*(CP) = 13, $P(C_6H_{11})_3$, 30.5 (d, *J*(CP) = 5, $H_{anti2}H_{syn2}$CRe), 29.8 (br. s, $P(C_6H_{11})_3$, 27.9 (br. s, $P(C_6H_{11})_3$, 28.0 (d, *J*(CP) = 9 Hz, $P(C_6H_{11})_3$), 26.9 (br. s, $P(C_6H_{11})_3$), 25.3 (d, *J*(CP) = 8 Hz, (HH*C*=CHH)Re), 25.1 (d, *J*(CP) = 3 Hz, (HHC=*C*HH)Re) ppm. $C_{24}H_{43}NOPRe$ (578.78): calcd. C 49.80, H 7.48, N 2.42; found C 50.02, H 7.61, N 2.26.

**[Re(NO)(CO)(P*i*Pr$_3$)$_2$(η$^2$-C$_2$H$_4$)] (8a):** In a 60 mL Young tap Schlenk tube **7b** (0.100 g, 0.157 mmol) was dissolved in 30 mL of THF and 10 g of 0.7% sodium amalgam was added. Without stirring, the solution was frozen and kept under pressure of 1.4 bar of $C_2H_4$ for 5 min. The mixture was warmed to room temperature, and stirred for 5 d. The mixture was filtered through celite and the solvent was removed under vacuum. The orange residue was extracted with toluene and washed with cold pentane to afford pure **8a** (0.081 g, 0.136 mmol, 87%). Suitable X-ray crystals were obtained from a solution of **8a** in 3 mL of pentane at –30 °C. IR (ATR): $\tilde{\nu}$ = 2963, 2927 and 2872 (s, νC–H), 1879 (s, νCO), 1576 (s, νNO) $cm^{-1}$. $^1H$ NMR (300.1 MHz, $C_6D_6$, room temp.): $\delta$ = 2.16–1.84 (m, 6 H, $(CH_3)_2CHP$), 1.38–1.19 (m, 36 H, $(CH_3)_2CHP$) ppm. $C_2H_4$ not observed. $^1H$ NMR (300.1 MHz, [D$_8$]toluene, 100 °C): $\delta$ = 2.42–1.31 (m, $(CH_3)_2CHP$ partly overlap with signal of toluene $CH_3$), 1.86 (br. t, 4 H, $H_2C=CH_2$), 1.25–1.09 (m, 36 H, $(CH_3)_2CHP$) ppm. $^{31}P\{^1H\}$ NMR (121.5 MHz, $C_6D_6$, room temp.): $\delta$ = 13.4 (s) ppm. $^{13}C\{^1H\}$ NMR (75.5 MHz, [D$_8$]toluene, 90 °C): $\delta$ = 218.4 (t, *J*(PC) = 12 Hz, C=O), 25.1 (t, *J*(PC) = 23 Hz, $(CH_3)_2CHP$), 23.0 (br. s, $H_2C=CH_2$), 20.6 and 19.3 (2 s, $(CH_3)_2CHP$) ppm. $C_{21}H_{46}NO_2P_2Re$ (592.75): calcd. C 42.55, H 7.82, N 2.36; found C 42.69, H 8.12, N 2.35.

**[Re(NO)(CO)(PCy$_3$)$_2$(η$^2$-C$_2$H$_4$)] (8b):** Complex **8b** (0.086 g, 0.103 mmol, 90%) was obtained by the same procedure as described for **8a** via reduction of $[Re(NO)(CO)(PCy_3)_2Cl_2]$ (0.100 g, 0. 114 mmol) using 10 g of 0.7% sodium amalgam and 1.4 bar $C_2H_4$. IR (ATR): $\tilde{\nu}$ = 2925 and 2848 (s, νCO), 1883 (s, νCO), 1585 (vs, νNO) $cm^{-1}$. $^1H$ NMR (300.1 MHz, $C_6D_6$, room temp.): $\delta$ = 2.17–1.17 ($H_2C=CH_2$ and $P(C_6H_{11})_3$) ppm. $^{31}P\{^1H\}$ NMR (80.9 MHz, $C_6D_6$): $\delta$ = 5.7 (s) ppm. $^{13}C\{^1H\}$ NMR (75.5 MHz, [D$_8$]toluene, –20 °C): $\delta$ = 218.5 (t, *J*(PC) = 12 Hz, C=O), 34.4 (br., $P(C_6H_{11})_3$), 30.7, 30.3, 27.3 (3 s, $P(C_6H_{11})_3$), 23.0 (br. s, $H_2C=CH_2$) ppm. $C_{39}H_{70}NO_2P_2Re$ (833.13): calcd. C 56.22, H 8.47, N 1.68; found C 56.67, H 8.59, N 1.61.

**NMR Tube Reactions. Synthesis of [Re(η$^2$-H$_2$)(NO)(PR$_3$)$_2$Br$_2$] (R = *i*Pr 5a, R = Cy 5b):** A solution of **1a** (0.010 g, 0.013 mmol) in 0.5 mL $C_6D_6$ or **1b** (0.012 g, 0.012 mmol) in 0.5 mL of $CD_2Cl_2$ was

 © 2007 Wiley-VCH Verlag GmbH & Co. KGaA, Weinheim 

sealed under 1 bar of $H_2$. Formation of **5a**,**b** takes place immediately upon shaking of the tubes. All NMR spectroscopic data are in agreement with those previously reported.[5]

**Reaction of [Re(NO)(CO)(P*i*Pr$_3$)$_2$(η$^2$-C$_2$H$_4$)] (8a) with B(C$_6$F$_5$)$_3$ to Yield [Re(CO)$_2${NOB(C$_6$F$_5$)$_3$}(P*i*Pr$_3$)$_2$] (9a) and [Re(NO)(CO)$_2$-(PCy$_3$)$_2$] (10a):** A solution of $B(C_6F_5)_3$ (0.048 g, 0.094 mmol) in 1 mL of toluene was added dropwise with stirring to a solution of **8a** (0.056 g, 0.094 mmol) in the same solvent. The mixture was stirred further at room temperature for 22 h. The solvent was then removed in vacuo and the residue extracted with pentane and recrystallized from the same solvent at –30 °C to afford orange crystals of **9a**; yield 0.039 g, 0.036 mmol, 38%. **9a** and **10a** were identified by their IR spectra: **9a** IR (ATR): $\tilde{\nu}$ = 1968 (s, νCO),

Table 8. Summary of crystallographic data for complexes **4a**, **4b**, **6b**, **8a**, **9a**, and **9b**.

| | **4a** | **4b** | **6b** |
|---|---|---|---|
| Empirical formula | $C_{54}H_{60}BBrF_{24}N_3OP_2Re$ | $C_{72}H_{84}BBrF_{24}N_3OP_2Re{\cdot}CH_2Cl_2$ | $C_{24}H_{43}NOPRe$ |
| Molecular weight | 1561.91 | 1887.21 | 578.76 |
| Color | yellow | yellow | pale yellow |
| Crystal system | monoclinic | orthorhombic | monoclinic |
| Space group | *C*2/*c* | *Pna*2$_1$ | *P*2$_1$/*c* |
| *a* [Å] | 20.330(2) | 33.849(2) | 14.1035(9) |
| *b* [Å] | 15.0650(11) | 12.3816(11) | 11.3650(6) |
| *c* [Å] | 21.790(2) | 19.0254(18) | 17.4160(12) |
| α [°] | 90 | 90 | 90 |
| *β* [°] | 109.124(11) | 90 | 121.264(7) |
| *γ* [°] | 90 | 90 | 90 |
| *V* [Å$^3$] | 6305.4(10) | 7973.7(12) | 2386.2(3) |
| *Z* | 4 | 4 | 4 |
| $\rho_{calcd.}$ [g cm$^{-3}$] | 1.645 | 1.572 | 1.611 |
| $\mu$ [mm$^{-1}$] | 2.722 | 2.232 | 5.174 |
| Transmission range | 0.7098–0.5185 | 0.7135–0.4660 | 0.5464–0.3401 |
| Crystal size [mm] | 0.15 × 0.21 × 0.27 | 0.18 × 0.34 × 0.43 | 0.22 × 0.21 × 0.13 |
| *hkl* limiting indices | –26/25, ±19, ±28 | –38/40, ±15, ±23 | –20/17, ±16, ±24 |
| *F*(000) | 3096 | 3792 | 1168 |
| *θ* limits [°] | 2.15–28.05 | 1.75–25.92 | 2.96–30.43 |
| Number of measd. reflections | 26224 | 53039 | 51454 |
| Number of unique reflections | 7594 | 15066 | 7139 |
| Number of parameters | 415 | 960 | 272 |
| $R_1$[a] [$I > 2\sigma(I)$], all data | 0.0356, 0.0721 | 0.0467, 0.0565 | 0.0264, 0.0374 |
| $wR_2$[b] [$I > \sigma(I)$], all data | 0.0829, 0.0883 | 0.1182, 0.1237 | 0.0744, 0.0752 |
| GOF (for $F^2$) | 0.831 | 0.987 | 0.971 |
| $\Delta\rho_{max/min}$ | –1.091, 1.576 | –1.130, 1.686 | –0.670, 2.011 |
| | **8a** | **9a** | **9b** |
| Empirical formula | $C_{21}H_{46}NO_2P_2Re$ | $C_{43}H_{54}BF_{15}NO_3P_2Re$ | $C_{56}H_{66}BF_{15}NO_3P_2Re$ |
| Molecular weight | 592.74 | 1176.83 | 1345.06 |
| Color | orange | orange | orange |
| Crystal system | monoclinic | triclinic | triclinic |
| Space group | *P*2$_1$/*n* | *P*$\bar{1}$ | *P*$\bar{1}$ |
| *a* [Å] | 11.9641(13) | 11.2503(17) | 12.5747(8) |
| *b* [Å] | 14.0278(10) | 12.818(2) | 14.6063(10) |
| *c* [Å] | 15.4531(16) | 17.353(3) | 16.5491(10) |
| α [°] | 90.00 | 80.100(19) | 86.834(8) |
| *β* [°] | 100.370(13) | 85.913(19) | 88.538(8) |
| *γ* [°] | 90.00 | 75.505(18) | 67.138(7) |
| *V* [Å$^3$] | 2551.1(4) | 2385.6(7) | 2796.5(3) |
| *Z* | 4 | 2 | 2 |
| $\rho_{calcd.}$ [g cm$^{-3}$] | 1.543 | 1.638 | 1.597 |
| $\mu$ [mm$^{-1}$] | 4.904 | 2.712 | 2.324 |
| Transmission range | 0.1262–0.5018 | 0.652–0.407 | 0.666-0.845 |
| Crystal size [mm] | 0.14 × 0.48 × 0.57 | 0.27 × 0.28 × 0.44 | 0.17 × 0.13 × 0.08 |
| *hkl* limiting indices | ±16, ±19, ±21 | –15/16, –17/18, ±24 | –14/14, –17/17, ±19 |
| *F*(000) | 1200 | 1176 | 1356 |
| *θ* limits [°] | 3.20–30.39 | 2.79–30.39 | 2.83–30.39 |
| Number of measd. reflections | 29650 | 51447 | 43505 |
| Number of unique reflections | 7583 | 13094 | 15287 |
| Number of parameters | 260 | 575 | 712 |
| $R_1$[a] [$I > 2\sigma(I)$], all data | 0.0267, 0.0380 | 0.0522, 0.0635 | 0.0362, 0.0487 |
| $wR_2$[b] [$I > \sigma(I)$], all data | 0.0685, 0.0706 | 0.1412, 0.1478 | 0.1262, 0.1277 |
| GOF (for $F^2$) | 1.061 | 1.081 | 1.067 |
| $\Delta\rho_{max/min}$ | –2.543, 1.111 | –7.462, 4.098 | 1.788, –0.579 |

[a] $R_1 = \Sigma(F_o - F_c)/\Sigma F_o$; $I > 2\ \sigma(I)$. [b] $wR_2 = \{\Sigma w(F_o^2 - F_c^2)^2/\Sigma w(F_o^2)^2\}^{1/2}$.

 © 2007 Wiley-VCH Verlag GmbH & Co. KGaA, Weinheim 

1883 (s, νCO), 1458 (s, νNO) $cm^{-1}$. **10a** IR (hexane): $\tilde{\nu}$ = 1940 (s, νCO), 1852 (s, νCO), 1605 (s, νNO) $cm^{-1}$.

**Synthesis of $[Re(CO)_2\{NOB(C_6F_5)_3\}(PiPr_3)_2]$ (9a):** A solution of $B(C_6F_5)_3$ (0.064 g, 0.124 mmol) in 2 mL of toluene was added to a solution of **8a** (0.074 g, 0.124 mmol) in 15 mL of the same solvent in a Young tap Schlenk tube. Without stirring the mixture was frozen and kept under pressure of 1 bar of CO for 3 min. The mixture was warmed to room temperature and stirred for 15 min. The gas and the solvent were removed in vacuo and the orange residue was extracted with $CH_2Cl_2$ and washed several times using cold pentane to afford pure **9a** (0.126 g, 0.114 mmol, 92%). IR (ATR): $\tilde{\nu}$ = 1968 (s, νCO), 1883 (s, νCO), 1458 (s, νNO) $cm^{-1}$. $^1H$ NMR (300.1 MHz, [D$_8$]toluene): $\delta$ = 0.92–0.80 (m, 6 H, $(CH_3)_2CHP$), 1.82–1.71 (m, 36 H, $(CH_3)_2CHP$) ppm. $^{31}P\{^1H\}$ NMR (121.5 MHz, [D$_8$]toluene): $\delta$ = 32.3 (s) ppm. $^{13}C\{^1H\}$ NMR (125.8 MHz, [D$_8$]toluene): $\delta$ = 215.9 (br., C=O), 24.0 (t, $J$(PC) = 11 Hz, $(CH_3)_2CHP$), 18.6 and 18.4 (2 s, $(CH_3)_2CHP$) ppm. $C_{38}H_{42}BF_{15}NO_3P_2Re$ (1104.68): calcd. C 41.31, H 3.83, N 1.27; found C 41.75, H 3.78, N 1.30.

**Synthesis of $[Re(CO)_2\{NOB(C_6F_5)_3\}(PCy_3)_2]$ (9b):** Complex **9b** (0.088 g, 0.066 mmol, 90%) was obtained using the same procedure as described for **9a** (method B) via the reaction of **8b** (0.062 g, 0.074 mmol), $B(C_6F_5)$ (0.038 g, 0.074 mmol) under 1 bar of CO. IR (ATR): $\tilde{\nu}$ = 1974 (s, νCO), 1875 (s, νCO), 1457 (s, νN–OB) $cm^{-1}$. $^1H$ NMR (200.0 MHz, $C_6D_6$, room temp.): $\delta$ = 2.20–0.81 (m, $P(C_6H_{11})_3$) ppm. $^{31}P\{^1H\}$ NMR (80.9 MHz, $C_6D_6$): $\delta$ = 24.6 (s) ppm. $^{13}C\{^1H\}$ NMR (75.5 MHz, $C_6D_6$): $\delta$ = 211.5 (br., C=O), 37.7 (t, $J$(PC) = 13 Hz, $P(C_6H_{11})_3$, 30.5, 27.4 and 26.0 (3s, $P(C_6H_{11})_3$) ppm. $C_{56}H_{66}BF_{15}NO_3P_2Re$ (1345.07): calcd. C 50.00, H 4.94, N 1.04; found C 50.09, H 5.03, N 1.00.

**X-ray Structure Analyses of Compounds 4a, 4b, 6b, 8a, 9a, and 9b:** All six crystals were protected in hydrocarbon oil and prepared for the X-ray experiment by using a polarizing microscope. Selected crystals of **4a**, **4b**, **6b**, **8a**, **9a**, and **9b** (Table 8) were mounted on the tip of a glass fiber and immediately transferred to the goniometer of an imaging plate detector system (Stoe IPDS diffractometer). The crystals were cooled to 183(2) K and 193(2) K (**8a**) in an Oxford Cryogenic System. The crystal-to-image distances were set to 60, 70, 50, 50, 50, and 50 mm resulting in $\theta_{max}$ values of 28.05, 25.92, 30.43, 30.39, 30.39, and 30.39°. For compounds **8a**, **9a**, and **9b** rotation, and for **4a**, **4b**, and **6b** oscillation scan modes were applied. 8000 (5000 for **9a**) reflections with $I > 6\sigma(I)$ were selected for the cell parameter refinements. A total of 26224 (**4a**), 53039 (**4b**), 51454 (**6b**), 29650 (**8a**), 51447 (**9a**), and 43505 (**9b**) diffraction intensities were collected of which 7594, 15066, 7139, 7583, 13094, and 15287 were unique ($R_{int}$ = 6.52, 8.59, 6.13, 5.01, 14.04, and 8.64%) after data reduction. Numerical absorption corrections based on 12, 17, 8, 10, 15, and 7 crystal faces were applied with FACEitVIDEO and XRED.[60] The structures were solved by the Patterson (for **4a**, **6b**, **8a**, **9a**, **9b**) and by direct methods (for **4b**) using the SHELXS-97 program.[61] Interpretation of the difference electron density maps, preliminary plot generation, and checking for higher symmetry were done with PLATON[62] (1990, 1991–2005) and with the LEPAGE program.[63] All structures were refined with the program SHELXL-97[61] using anisotropic displacement parameters for heavy atoms, some exceptions in disordered structures **4a** and **4b** are given in the CIF files (see CCDC deposition numbers, see below). Positions of H-atoms were calculated after each refinement cycle (riding model). Structural plots were generated using ORTEP III.[64] For the achiral non-centrosymmetric structure of **4b** the correct space group choice ($Pna2_1$, no. 33) was confirmed by Flack's parameter $x$[65] and PLATON.[62] Refinement details are given in the "_exptl_special_details" in the respective cif files.

**Computational Details:** DFT calculations were carried out using the Amsterdam Density Functional program package ADF, release 2004.01.[57] We used the Vosko–Wilk–Nusair[66] local density approximation (LDA) and the generalized gradient approximation (GGA) with corrections for exchange and correlation according to Becke[67] and Lee–Yang–Parr,[68] respectively (BLYP). The ADF approach to DFT-GGA calculations is based on the use of Slater-type orbitals (STO) as basis functions. The valence shells of all atoms were described by double-$\xi$ basis sets augmented by one polarization function (ADF database DZP), except for rhenium for which a triple-$\xi$ basis set was applied (ADF database TZP). The frozen-core approximation was applied for the 1s electrons of carbon, oxygen, and nitrogen, for the 1s-2p electrons of phosphorus and chlorine, for the 1s-3d electrons of bromine and for the 1s-4f electrons of rhenium. Relativistic effects were taken into account in all calculations using the zero order regular approximation (ZORA).[69] The relativistic atomic potentials necessary for the relativistic calculations for each atom were calculated using the auxiliary program DIRAC, which is supplied with the ADF program package. The geometry optimizations were considered converged when the change in the maximum gradient element was smaller than $5.0 \times 10^{-4}$ Hartrees $Å^{-1}$. The other convergence criteria referring to changes in total energy, Cartesian or internal coordinates had to converge to the default values proposed by the program.

CCDC-297768 to -297771 (for **4a**, **4b**, **8a**, **9a**) and -609682 to -609683 (for **6b** and **9b**) contain the supplementary crystallographic data for this paper. These data can be obtained free of charge from the Cambridge Crystallographic Data Centre via www.ccdc.cam.ac.uk/data_request/cif.

## Acknowledgments

This work has been supported by the Swiss National Science Foundation and the Funds of the University of Zurich.

[1] a) W. R. Thiel, *Angew. Chem. Int. Ed.* **2003**, *42*, 5390; b) K. P. Gable, J. J. J. Juliette, *J. Am. Chem. Soc.* **1996**, *118*, 2625; c) A. M. LaPointe, R. R. Schrock, *Organometallics* **1995**, *14*, 1875.
[2] W. D. Jones, J. A. Maguire, G. P. Rosini, *Inorg. Chim. Acta* **1998**, *270*, 77.
[3] A. Kovacs, G. Frenking, *Organometallics* **2001**, *20*, 2510.
[4] a) J. K. Gibson, *J. Organomet. Chem.* **1998**, *558*, 51; b) L. A. Friedman, S. H. Meiere, B. C. Brooks, W. D. Harman, *Organometallics* **2001**, *20*, 1690; c) T. B. Gunnoe, W. D. Sabat, M. Harman, *Organometallics* **2000**, *19*, 728; d) A. S. Polo, M. K. Itokazu, K. M. Frin, A. O. D. Patrocinio, N. Y. M. Iha, *Coord. Chem. Rev.* **2006**, *250*, 1669; e) O. V. Ozerov, J. C. Huffman, L. A. Caulton, K. G. Watson, *Organometallics* **2003**, *22*, 2539; f) O. V. Ozerov, J. C. Huffman, L. A. Watson, M. Pink, K. G. Caulton, *J. Am. Chem. Soc.* **2007**, *129*, 6003.
[5] D. Gusev, A. Llamazares, G. Artus, H. Jacobsen, H. Berke, *Organometallics* **1999**, *18*, 75.
[6] a) C. M. Frech, O. Blacque, H. Berke, *Pure Appl. Chem.* **2006**, *78*, 1877; b) C. M. Frech, O. Blacque, H. W. Schmalle, H. Berke, C. Adlhart, P. Chen, *Chem. Eur. J.* **2006**, *12*, 3325.
[7] G. Kubas, *J. Organomet. Chem.* **2001**, *635*, 37.
[8] H. U. Hund, U. Ruppli, H. Berke, *Helv. Chim. Acta* **1993**, *76*, 963.
[9] G. Mercati, F. Morazzoni, F. Cariati, D. Giusto, *Inorg. Chim. Acta* **1978**, *29*, 165.
[10] S. J. Mclain, R. R. Schrock, *J. Am. Chem. Soc.* **1978**, *100*, 1315.

 © 2007 Wiley-VCH Verlag GmbH & Co. KGaA, Weinheim 

[11] S. J. Mclain, C. D. Wood, R. R. Schrock, *J. Am. Chem. Soc.* **1979**, *101*, 4558.
[12] F. Speiser, P. Braunstein, W. Saussine, *Acc. Chem. Res.* **2005**, *38*, 784.
[13] J. D. Fellmann, G. A. Rupprecht, R. R. Schrock, *J. Am. Chem. Soc.* **1979**, *101*, 5099.
[14] J. T. Dixon, M. J. Green, F. M. Hess, D. H. Morgan, *J. Organomet. Chem.* **2004**, *689*, 3641.
[15] D. J. Marais, N. Sheppard, B. P. Stoicheff, *Tetrahedron* **1962**, *17*, 163.
[16] H. Yasuda, Y. Kajihara, K. Mashima, K. Nagasuna, K. Lee, A. Nakamura, *Organometallics* **1982**, *1*, 388.
[17] C. Holtke, G. Erker, G. Kehr, R. Fröhlich, O. Kataeva, *Eur. J. Inorg. Chem.* **2002**, 2789.
[18] H. Yasuda, K. Tatsumi, T. Okamoto, K. Mashima, K. Lee, A. Nakamura, Y. Kai, N. Kanehisa, N. Kasai, *J. Am. Chem. Soc.* **1985**, *107*, 2410.
[19] T. A. Albright, J. K. Burdett, M. H. Whangbo, *Orbital Interactions in Chemistry*, Wiley, New York, **1985**.
[20] K. Bachmann, W. v. Philipsborn, *Org. Magn. Reson.* **1976**, *8*, 648.
[21] B. Machura, *Coordin. Chem. Rev.* **2005**, *249*, 2277.
[22] H. PtasiewiczBak, J. Leciejewicz, *Pol. J. Chem.* **1997**, *71*, 493.
[23] C. Pellecchia, A. Grassi, A. Immirzi, *J. Am. Chem. Soc.* **1993**, *115*, 1160.
[24] G. Kehr, R. Roesmann, R. Fröhlich, C. Holst, G. Erker, *Eur. J. Inorg. Chem.* **2001**, 535.
[25] P. Yang, B. C. K. Chan, M. C. Baird, *Organometallics* **2004**, *23*, 2752.
[26] H. C. Strauch, G. Erker, R. Fröhlich, M. Nissinen, *Eur. J. Inorg. Chem.* **1999**, 1453.
[27] Y. M. Sun, R. E. V. H. Spence, W. E. Piers, M. Parvez, G. P. A. Yap, *J. Am. Chem. Soc.* **1997**, *119*, 5132.
[28] T. Wondimagegn, Z. T. Xu, K. Vanka, T. Ziegler, *Organometallics* **2004**, *23*, 3847.
[29] H. Jacobsen, T. Brackemeyer, H. Berke, G. Erker, R. Fröhlich, *Eur. J. Inorg. Chem.* **2000**, 1423.
[30] Y. M. Sun, W. E. Piers, S. Rettig, *J. Chem. Commun.* **1998**, 127.
[31] J. W. Strauch, G. Erker, G. Kehr, R. Fröhlich, *Angew. Chem. Int. Ed.* **2002**, *41*, 2543.
[32] H. Jacobsen, H. Berke, S. Doring, G. Kehr, G. Erker, R. Fröhlich, O. Meyer, *Organometallics* **1999**, *18*, 1724.
[33] W. J. Huang, H. Berke, *Chimia* **2005**, *59*, 113.
[34] J. C. Peters, G. L. Hillhouse, *Polyhedron* **1994**, *13*, 1741.
[35] A. A. H. Van der Zeijden, C. Sontag, H. W. Bosch, V. Shklover, H. Berke, D. Nanz, W. v. Philipsborn, *Helv. Chim. Acta* **1991**, *74*, 1194.
[36] K. E. Lee, A. M. Arif, J. A. Gladysz, *Inorg. Chem.* **1990**, *29*, 2885.
[37] B. S. Tovrog, S. E. Diamond, F. Mares, A. Szalkiewicz, *J. Am. Chem. Soc.* **1981**, *103*, 3522.
[38] S. D. Ittel, *Adv. Organomet. Chem.* **1976**, *14*, 33.
[39] M. R. Churchill, H. J. Wasserman, *Inorg. Chem.* **1981**, *20*, 4119.
[40] U. Radius, J. Sundermeyer, H. Pritzkow, *Chem. Ber.* **1994**, *127*, 1827.
[41] P. W. Dyer, V. C. Gibson, W. Clegg, *J. Chem. Soc. Dalton Trans.* **1995**, 3313.
[42] L. D. Brown, C. F. J. Barnard, J. A. Daniels, R. J. Mawby, J. A. Ibers, *Inorg. Chem.* **1978**, *17*, 2932.
[43] P. R. Sharp, *Organometallics* **1984**, *3*, 1217.
[44] F. M. Su, C. Cooper, S. J. Geib, A. L. Rheingold, J. M. Mayer, *J. Am. Chem. Soc.* **1986**, *108*, 3545.
[45] G. R. Clark, A. J. Nielson, A. D. Rae, C. E. F. Rickard, *J. Chem. Soc. Chem. Commun.* **1992**, 1069.
[46] T. Aoshima, T. Tamura, Y. Mizobe, M. Hidai, *J. Organomet. Chem.* **1992**, *435*, 85.
[47] M. D. Butts, J. C. Bryan, X. L. Luo, G. J. Kubas, *Inorg. Chem.* **1997**, *36*, 3341.
[48] S. Y. S. Wang, D. D. VanderLende, K. A. Abboud, J. M. Boncella, *Organometallics* **1998**, *17*, 2628.
[49] H. Ishino, S. Tokunaga, H. Seino, Y. Ishii, M. Hidai, *Inorg. Chem.* **1999**, *38*, 2489.
[50] E. Carmona, J. M. Marin, M. L. Poveda, J. L. Atwood, R. D. Rogers, *J. Am. Chem. Soc.* **1983**, *105*, 3014.
[51] E. Carmona, A. Galindo, J. M. Marin, E. Gutierrez, A. Monge, C. Ruiz, *Polyhedron* **1988**, *7*, 1831.
[52] S. Komiya, A. Baba, *Organometallics* **1991**, *10*, 3105.
[53] J. Matthes, S. Grundemann, A. Toner, Y. Guari, B. Donnadieu, J. Spandl, S. Sabo-Etienne, E. Clot, H. H. Limbach, B. Chaudret, *Organometallics* **2004**, *23*, 1424.
[54] J. S. Dewar, *Bull. Soc. Chim. Fr.* **1951**, *18*, C71.
[55] J. Chatt, L. A. Duncanson, *J. Chem. Soc.* **1953**, 2939.
[56] J. Uddin, S. Dapprich, G. Frenking, B. F. Yates, *Organometallics* **1999**, *18*, 717 and references cited therein.
[57] ADF2004.01. for an overview see: G. Frenking, N. Fröhlich, *The Nature of the Bonding in Transition-Metal Compounds*, *Chem. Rev.* **2000**, *100*, *SCM*, Theoretical Chemistry, Vrije Universiteit, Amsterdam, The Netherlands, http://www.scm.com; a) F. M. Bickelhaupt, E. J. Baerends, C. F. Guerra, S. J. A. Van Gisbergen, J. G. Snijders, T. Ziegler, *J. Comput. Chem.* **2001**, *22*, 931; b) C. F. Guerra, J. G. Snijders, G. te Velde, E. J. Baerends, *Theor. Chem. Acc.* **1998**, *99*, 391.
[58] F. M. Bickelhaupt, E. J. Baerends in *Reviews of Computational Chemistry* (Eds.: D. B. Boyd, K. B. Lipkowitz), Wiley-VCH, New York, **2000**, p. 1, vol. 15.
[59] P. Coppens, L. Leiserowitz, D. Rabinovich, *Acta Crystallogr.* **1965**, *18*, 1035.
[60] *STOE-IPDS* Software package, version 2.92/1999, STOE & Cie, Darmstadt, Germany, **1999**.
[61] G. M. Sheldrick, *SHELX97*, University of Göttingen, Göttingen, Germany, **1998**.
[62] a) A. L. Spek, *Acta Crystallogr., Sect. A* **1990**, *46*, C34; b) A. L. Spek, *PLATON*, A Multipurpose Crystallographic Tool, Utrecht University, Utrecht, The Netherlands, **1998**.
[63] Y. Lepage, *J. Appl. Crystallogr.* **1987**, *20*, 264.
[64] L. J. Farrugia, *J. Appl. Cryst.* **1997**, *30*, 565.
[65] H. D. Flack, *Acta Crystallogr., Sect. A* **1983**, *39*, 876.
[66] S. H. Vosko, L. Wilk, M. Nusair, *Can. J. Phys.* **1980**, *58*, 1200.
[67] A. D. Becke, *Phys. Rev. A* **1988**, *38*, 3098.
[68] C. Yang, W. Parr, R. G. Lee, *Phys. Rev. B* **1988**, *37*, 785.
[69] a) E. van Lenthe, A. E. Ehlers, E. J. Baerends, *J. Chem. Phys.* **1999**, *110*, 8943; b) E. van Lenthe, E. J. Baerends, J. G. Snijders, *J. Chem. Phys.* **1993**, *99*, 4597; c) E. van Lenthe, E. J. Baerends, J. G. Snijders, *J. Chem. Phys.* **1994**, *101*, 9783; d) E. van Lenthe, J. G. Snijders, E. J. Baerends, *J. Chem. Phys.* **1996**, *105*, 6505; e) E. van Lenthe, R. van Leeuwen, E. J. Baerends, J. G. Snijders, *J. Quant. Chem.* **1996**, *57*, 281.

Received: June 1, 2007
Published Online: October 1, 2007

 © 2007 Wiley-VCH Verlag GmbH & Co. KGaA, Weinheim 

DOI: 10.1002/ejic.200700582

# Divalent Nickel, Cobalt and Iron Complexes of an Amide-Appended $N_2S_2$ Ligand: Synthesis, Characterization and Reactivity with Hydroxide Anion

**Gajendrasingh K. Ingle,[a] Magdalena M. Makowska-Grzyka,[a] Atta M. Arif,[b] and Lisa M. Berreau*[a]**

**Keywords:** N,S ligands / Amides / Metal effects / Deprotonation

Divalent nickel, cobalt and iron complexes {[(bmppa)-Ni($CH_3CN$)]($ClO_4$)$_2$ (**1**), [(bmppa)Co($CH_3CN$)]($ClO_4$)$_2$ (**2**), [(bmppa)Fe($CH_3CN$)]($ClO_4$)$_2$ (**3**)} of an amide-appended $N_2S_2$-donor ligand {bmppa = *N*,*N*-bis(2-methylthio)ethyl-*N*-[(6-pivaloylamido-2-pyridyl)methyl]amine} have been prepared and characterized using $^1$H NMR, IR, UV/Vis, elemental analysis and magnetic moment measurements. The complexes **2** and **3** were also characterized by X-ray crystallography. When treated with 1 equiv. of $Me_4NOH{\cdot}5H_2O$ in methanol, **1** and **2** form deprotonated amide complexes {[(bmppa$^-$)Ni]$ClO_4$ (**4**), [(bmppa$^-$)Co]$ClO_4{\cdot}H_2O$ (**5**)} which were isolated and characterized by $^1$H NMR, IR, UV/Vis, elemental analysis and magnetic moment measurements. Treatment of the $Fe^{II}$ complex **3** with 1 equiv. of $Me_4NOH{\cdot}5H_2O$ in methanol produced the free bmppa chelate ligand and a precipitate of an unidentified iron species. Heating of **5** at 50 °C in methanol for 5 d resulted in a ca. 50 % yield of amide methanolysis products and a small amount of products resulting from oxidative *N*-dealkylation of the bmppa ligand. It has been previously shown that a zinc analog of **5** undergoes quantitative amide methanolysis under milder conditions. Complex **4** does not undergo amide cleavage upon heating at 50 °C in methanol for 5 d. A rationale for the metal-dependent amide methanolysis reactivity of these complexes is proposed on the basis of structural differences in the "parent" protonated complexes.
(© Wiley-VCH Verlag GmbH & Co. KGaA, 69451 Weinheim, Germany, 2007)

## Introduction

Amide cleavage reactions are catalyzed by a variety of metal-containing enzymes. An amide hydrolase that has received considerable recent attention is peptide deformylase (PDF). In the active site of PDF, a nitrogen/sulfur-ligated iron(II) center is involved in the hydrolysis of a formamide moiety during polypeptide biosynthesis.[1–4] Notably, replacement of the $Fe^{II}$ ion with $Ni^{II}$ and $Co^{II}$ produces catalytically active enzyme.[2,3,5–8] However, with $Zn^{II}$ as the active-site metal ion, the enzyme activity is reduced by ca. 100-fold.[7,9]

To investigate the role of the metal center in PDF enzymes, Goldberg and co-workers have investigated the structural and spectroscopic properties of synthetic complexes of relevance to resting state and formato-bound forms of the enzyme.[10–14] These complexes are supported by an $N_2S$(thiolate) ligand {PATH = 2-methyl-1-[methyl(2-pyridin-2-ylethyl)amino]propane-2-thiolate}. A zinc hydroxide complex of the PATH ligand has been shown to promote the hydrolysis of phosphate and carboxy esters;[12,13] however, no reactivity with an amide substrate has been reported.

We recently reported studies of the formyl ester and formamide cleavage reactivity of a $Zn^{II}$–OH complex, [(bmnpaZn)$_2$(μ-OH)$_2$]($ClO_4$)$_2$, supported by an $N_2S_2$ ligand containing an internal hydrogen-bond donor.[15] In acetonitrile, this complex promotes the hydrolysis of methyl formate to produce methanol and a (formato)zinc complex {[(bmnpa)Zn($O_2CH$)]$ClO_4$}. In methanol, the (hydroxido)-zinc complex reacts with the alcohol to produce a (methoxido)zinc complex. Treatment of this Zn–OMe complex with formanilide results in the formation of aniline, methyl formate, and [(bmnpa)Zn($O_2CH$)]$ClO_4$. The formation of both methyl formate and the (formato)zinc complex indicated that both methanolysis and hydrolysis reactions occur in the reaction mixture.

Recently, we investigated in detail the amide methanolysis reactivity of zinc complexes of amide-appended $N_4$, $N_3S$, and $N_2S_2$ donor ligands in the presence of hydroxide anion in methanol.[16–18] The reaction pathway for amide cleavage in these systems was found to involve the initial formation of a (deprotonated amide)zinc complex which subsequently undergoes reaction with methanol to produce a reactive complex for amide methanolysis. The products generated in these amide methanolysis reactions

[a] Department of Chemistry and Biochemistry, Utah State University,
0300 Old Main Hill, Logan, UT 84322-0300, USA
Fax: +1-435-797-3390
E-mail: berreau@cc.usu.edu
[b] Department of Chemistry, University of Utah,
315 S. 1400 E., Salt Lake City, UT, 84112-0850, USA

 WILEY InterScience DISCOVER SOMETHING GREAT © 2007 Wiley-VCH Verlag GmbH & Co. KGaA, Weinheim 

are a zinc complex of a primary amine-appended chelate ligand, methyl trimethylacetate, and 1 equiv. of $Me_4NClO_4$.[16–18]

The research described herein examines how the amide methanolysis reactivity of divalent metal complexes of an amide-appended $N_2S_2$ ligand is influenced by the nature of the metal center. This work has some relevance to peptide deformylase, as we have examined the structural, spectroscopic, and amide cleavage reactivity properties of $Ni^{II}$, $Co^{II}$, and $Fe^{II}$ analogs of $[(bmppa)Zn](ClO_4)_2$ {bmppa = *N*,*N*-bis(2-methylthio)ethyl-*N*-[(6-pivaloylamido-2-pyridyl)-methyl]amine}.[16,18] To the best of our knowledge, this is the first direct comparison of amide cleavage reactivity in structurally related complexes of these metal ions. Findings of this study include: (1) similar to the chemistry of $[(bmppa)Zn](ClO_4)_2$, the $Ni^{II}$ and $Co^{II}$ analogs form deprotonated amide complexes upon treatment with hydroxide anion, whereas the $Fe^{II}$ analog decomposes to yield free bmppa ligand and unidentified iron species; and (2) of the non-zinc metals only the (deprotonated amide)$Co^{II}$ complex reacts with methanol to yield amide methanolysis products, albeit in lower yield than the zinc analog. A rationale for the metal-dependent amide methanolysis reactivity of these complexes is proposed on the basis of structural differences in the "parent" protonated complexes.

## Results and Discussion

### Synthesis and Characterization of Divalent Metal Complexes

Mononuclear divalent nickel, cobalt, and iron complexes of the bmppa ligand were prepared by treatment of the ligand with $[M(H_2O)_6](ClO_4)_2$ (M = Ni, Co, and Fe) in methanol. Recrystallization of the resulting metal complex from acetonitrile-containing solutions resulted in the isolation of $[(bmppa)M(CH_3CN)](ClO_4)_2$ (**1**: M = $Ni^{II}$; **2**: M = $Co^{II}$; **3**: M = $Fe^{II}$; Scheme 1). Each complex has been characterized by elemental analysis, $^1H$ NMR, FTIR, UV/Vis spectroscopy, mass spectrometry, and a magnetic moment measurement. For **2** and **3**, crystals suitable for single-crystal X-ray diffraction were obtained.

ORTEP drawings of the cationic portions of the X-ray structures of **2** and **3** are shown in Figure 1. Selected bond lengths and angles are given in Table 1. These complexes are nearly isostructural, with both crystallizing in the $P2_1/c$ space group. In each the divalent metal center is ligated by all of the available donor atoms of the chelate ligand and one acetonitrile solvent molecule. The geometry of the metal center in these complexes is distorted octahedral with the acetonitrile molecule positioned in the same plane as the chelate ring containing the amide moiety, thereby bisecting the S(1)–M–S(2) angle. In comparing **2** and **3**, the average M–S (**2**: 2.50 Å; **3**: 2.33 Å) and M–N (**2**: 2.10 Å; **3**: 1.99 Å) bonds are notably longer in the $Co^{II}$ derivative, whereas the M–O(1) distances differ by only ca. 0.06 Å [**2**: Co–O(1) 2.0125(15) Å; **3**: Fe–O(1) 1.956(2) Å].

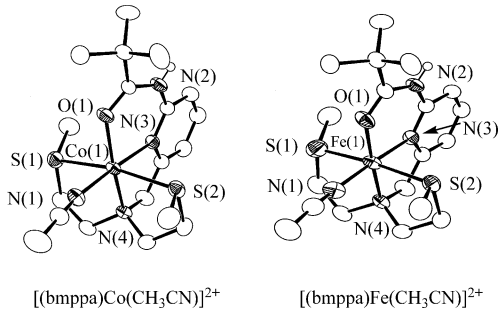


Figure 1. ORTEP drawings of the cationic portions of **2** (left) and **3** (right). Ellipsoids are plotted at the 50% probability level. All hydrogen atoms except the amide proton are not shown for clarity.

The solid-state FTIR spectral features of **1**–**3** in KBr are consistent with amide coordination. Specifically, the amide C–O stretching vibration is shifted to lower energy (ca. 1648–1633 $cm^{-1}$) as compared to the position of this vibration in the free bmppa ligand (1687 $cm^{-1}$). Solution IR spectra of **1**–**3** in acetonitrile (100 mM) have features in the region of 1700–1550 $cm^{-1}$ that are very similar to the solid-state spectra, providing evidence that amide coordination is maintained in solution. In the solid-state FTIR spectra, each complex exhibits a $\nu_{N-H}$ stretching vibration at ca. 3350–3300 $cm^{-1}$. The solution UV/Vis absorption spectral features of **1**–**3** are summarized in Table 2. All complexes show strong ligand-based absorptions at <400 nm. For **2**, a 511 nm ($\varepsilon$ = 44 $M^{-1}cm^{-1}$) transition is consistent with the $Co^{II}$ center having a six-coordinate pseudo-octahedral geometry in solution.[19] Each complex contains a high-spin pseudo-octahedral metal center, as evidenced by solution

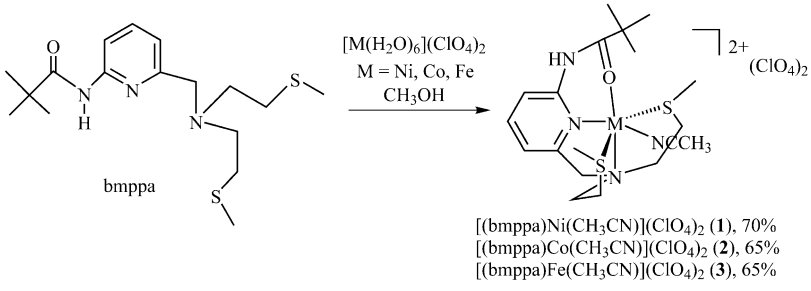


Scheme 1. Synthetic route for the preparation of divalent metal complexes of the bmppa ligand.

 © 2007 Wiley-VCH Verlag GmbH & Co. KGaA, Weinheim 

Table 1. Selected bond lengths and angles.[a]

| | 2 | 3 |
|---|---|---|
| M(1)–O(1) | 2.0125(15) | 1.956(2) |
| M(1)–N(1) | 2.0667(19) | 1.957(3) |
| M(1)–N(3) | 2.0980(17) | 1.976(2) |
| M(1)–N(4) | 2.1369(18) | 2.050(3) |
| M(1)–S(1) | 2.5092(7) | 2.3195(12) |
| M(1)–S(2) | 2.4226(7) | 2.3395(10) |
| O(1)–M(1)–N(1) | 94.42(7) | 89.95(11) |
| O(1)–M(1)–N(3) | 86.00(7) | 90.52(10) |
| N(1)–M(1)–N(3) | 175.08(8) | 177.01(12) |
| O(1)–M(1)–N(4) | 164.86(7) | 174.49(10) |
| N(1)–M(1)–N(4) | 99.06(7) | 95.21(11) |
| N(3)–M(1)–N(4) | 81.15(7) | 84.42(10) |
| O(1)–M(1)–S(1) | 90.71(5) | 92.01(8) |
| N(1)–M(1)–S(1) | 87.16(6) | 87.65(9) |
| N(3)–M(1)–S(1) | 97.73(5) | 95.28(8) |
| N(4)–M(1)–S(1) | 83.15(5) | 86.31(8) |
| O(1)–M(1)–S(2) | 99.93(5) | 94.28(8) |
| N(1)–M(1)–S(2) | 91.76(6) | 91.36(9) |
| N(3)–M(1)–S(2) | 83.34(5) | 85.66(8) |
| N(4)–M(1)–S(2) | 86.57(5) | 87.52(8) |
| S(1)–M(1)–S(2) | 169.36(2) | 173.63(4) |

[a] Estimated standard deviation in the last significant figure is given in parentheses.

magnetic moment measurements performed at 298 K using the Evans method.[20] For **1**–**3** the effective magnetic moment is higher than the spin-only value ($Ni^{II}$: 2.8 $\mu_B$; $Co^{II}$: 3.9 $\mu_B$; $Fe^{II}$: 4.9 $\mu_B$) calculated for the high-spin metal center due to spin-orbit coupling.[21]

Table 2. Selected properties of **1**–**3**.

| | 1 | 2 | 3 |
|---|---|---|---|
| UV/Vis: $\lambda$ [nm] ($\varepsilon$ [$M^{-1}cm^{-1}$])[a] | 536 (14), 867 (40), 953 (40) | 511 (44) | 754 (10) |
| $\mu_{eff}$ [$\mu_B$] | 3.0 | 4.6 | 5.0 |

[a] Spectra collected in $CH_3CN$.

Complexes **1**–**3** exhibit paramagnetically shifted $^1H$ NMR spectra. These spectra are shown in Figures 2, 3, and 4 to illustrate that each complex exhibits signals that can be identified on the basis of integrated intensity, deuterium substitution, and/or $^1H$-$^1H$ COSY experiments. When dissolved in $CD_3CN$, complex **1** (Figure 2) exhibits a *tert*-butyl methyl signal at $\delta$ = 4.6 ppm and an amide proton resonance at $\delta \approx -6$ ppm, the latter of which was assigned by deuterium substitution (with $D_2O$). In the region of $\delta \approx$ 180–10 ppm are several resonances. A sharp signal at $\delta$ = 14.2 ppm has been tentatively assigned as the γ-H of the pyridyl ring. While the remaining signals have not been conclusively assigned, we believe that the signals at $\delta \approx$ 49 and 73 ppm are for the β-H atoms of the pyridyl ring. For **2** in $CD_3CN$ (Figure 3), the *tert*-butyl methyl signal is found at $\delta \approx$ 28 ppm. The β-H and γ-H signals for this complex have been assigned on the basis of a $^1H$-$^1H$ COSY spectrum. Addition of $D_2O$ to a solution of **2** in $CD_3CN$ failed to reveal the signal of the amide hydrogen atom (by loss of the $^1H$ signal). When dissolved in $CD_3CN$, complex **3** (Figure 4) exhibits resonances in the range of $\delta \approx$ 110–0 ppm. The *tert*-butyl methyl resonance of **3** is found at $\delta$ = 4.2 ppm in dry $CD_3CN$. We tentatively assigned the β-H and γ-H signals for this complex as shown in Figure 4 on the basis of peak width and intensity. The $^1H$ NMR features of this complex exhibit a solvent dependence, with addition of a small amount of $D_2O$ (2 μL) to a water-free $CD_3CN$ solution of **3** producing an upfield shift of the *tert*-butyl resonance to $\delta \approx$ 3.4 ppm. The addition of $D_2O$ also produces changes in the spectrum in the region of $\delta$ = 20–30 ppm. Analysis of the $^1H$ NMR features of **3** as a function of solvent remains under investigation.

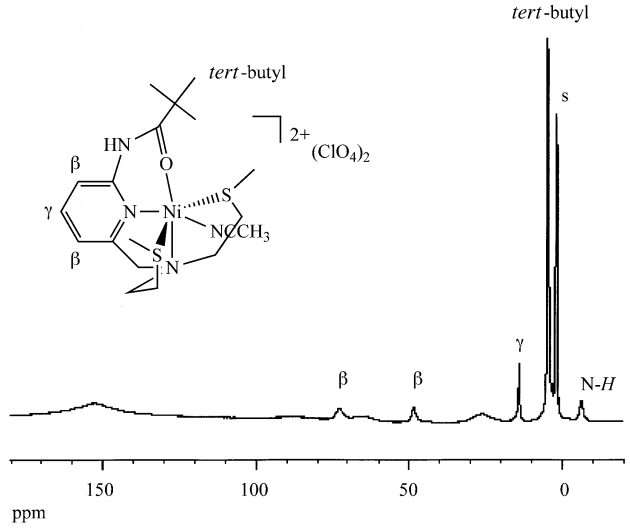


Figure 2. $^1H$ NMR spectrum of **1** in dry $CD_3CN$ at ambient temperature (s = signal of $CD_2HCN$).

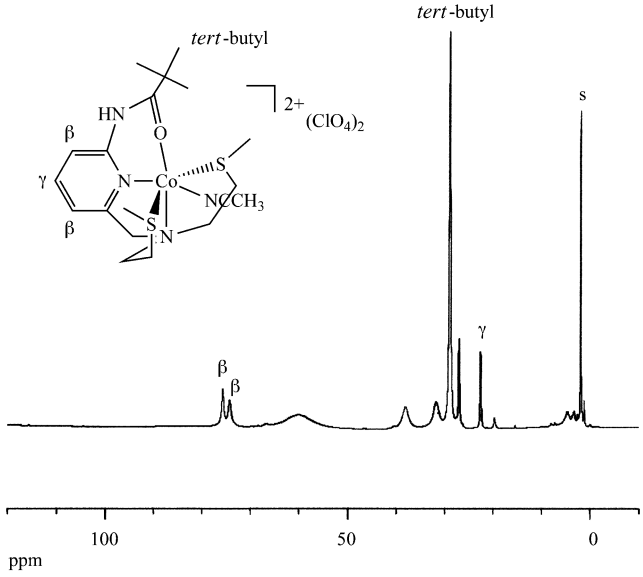


Figure 3. $^1H$ NMR spectrum of **2** in dry $CD_3CN$ at ambient temperature (s = signal of $CD_2HCN$).

 © 2007 Wiley-VCH Verlag GmbH & Co. KGaA, Weinheim 

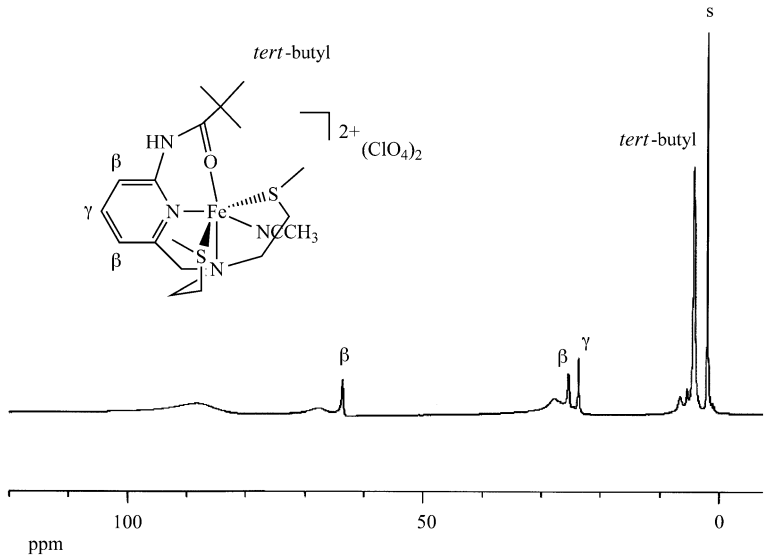


Figure 4. $^1$H NMR spectrum of **3** in dry $CD_3CN$ at ambient temperature (s = signal of $CD_2HCN$).

### Reactivity of 1–3 with Hydroxide Anion in Methanol – Isolation of Deprotonated Amide Complexes

We have previously reported that treatment of [(bmppa)Zn]$(ClO_4)_2$ with $Me_4NOH{\cdot}5H_2O$ in methanol-containing solutions results in amide methanolysis.[16,18] This reaction proceeds through the initial formation of a depronated amide complex, [(bmppa$^-$)Zn]$ClO_4$, which subsequently undergoes reaction with methanol to produce the reactive species for amide cleavage.[18] Treatment of **1** with $Me_4NOH{\cdot}5H_2O$ in methanol results in the formation of the deprotonated amide complex [(bmppa$^-$)Ni]$ClO_4$ (**4**, Scheme 2) which has been isolated and characterized by elemental analysis, FTIR, UV/Vis, $^1$H NMR spectroscopy, and a solution magnetic moment measurement. The elemental analysis data for **4** is best fit with one perchlorate anion and no coordinated solvent molecules, suggesting an overall coordination number of five for the $Ni^{II}$ center. The FTIR spectrum of **4** differs from that of [(bmppa)Ni$(CH_3CN)](ClO_4)_2$ (**1**) in that intense vibrations found in the region of ca. 1600–1635 $cm^{-1}$ for **1**, which include the $\nu(CO_{amide})$ vibration, are not present in the spectrum of **4**. Instead, a series of intense new vibrations is centered at ca. 1450 $cm^{-1}$, which is consistent with the presence of a deprotonated amide moiety.[17] The UV/Vis absorption spectral features and solution magnetic moment of **4** are given in Table 3. The absorption and $^1$H NMR (Figure 5) spectral features of **4** are different from those of **1**. In the $^1$H NMR spectrum of **4** no signal upfield of zero is present, consistent with amide deprotonation. Two prominent resonances at $\delta \approx 49$ and 73 ppm in the spectrum of **1** appear to have shifted to $\delta \approx 61$ and 64 ppm in **4**. These resonances are assigned to the β-H atoms of the pyridyl ring. It is important to note that resonance structures for the deprotonated amide moiety can be drawn wherein the anionic charge is positioned at the β-carbon atoms of the pyridyl ring, thus providing a rational for why the β-H signals shift upon deprotonation.[17] The *tert*-butyl methyl signal of **4** is shifted slightly downfield ($\delta$ = 5.6 ppm) relative to the position of the same signal of **1** ($\delta$ = 4.6 ppm). The γ-H resonances of **1** and **4** are at nearly identical chemical shifts ($\delta$ = 14.2 ppm).

Table 3. Selected properties of **4** and **5**.

| | **4** | **5** |
|---|---|---|
| UV/Vis: $\lambda$ [nm] ($\varepsilon$ [$M^{-1}cm^{-1}$])[a] | 530 (20), 835 (20), 1034 (35) | 548 (140) |
| $\mu_{eff}$ [$\mu_B$] | 3.1 | 3.7 |

[a] Spectra collected in $CH_3CN$.

Treatment of [(bmppa)Co$(CH_3CN)](ClO_4)_2$ (**2**) with $Me_4NOH{\cdot}5H_2O$ results in the formation of a brown deprotonated amide complex, [(bmppa$^-$)Co]$ClO_4{\cdot}H_2O$ (**5**). The elemental analysis of **5** is best fit with the inclusion of one water molecule in the bulk, isolated sample of the com-

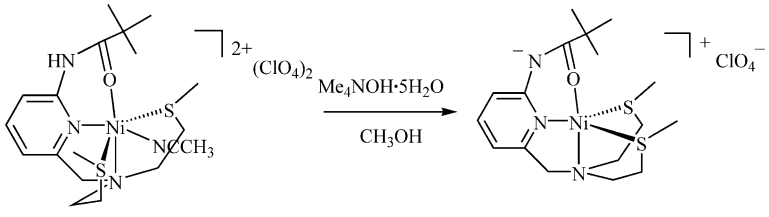


[(bmppa)Ni$(CH_3CN)](ClO_4)_2$ (**1**) [(bmppa$^-$)Ni]$ClO_4$ (**4**)

Scheme 2. Reaction of **1** with $Me_4NOH{\cdot}5H_2O$.

 © 2007 Wiley-VCH Verlag GmbH & Co. KGaA, Weinheim 

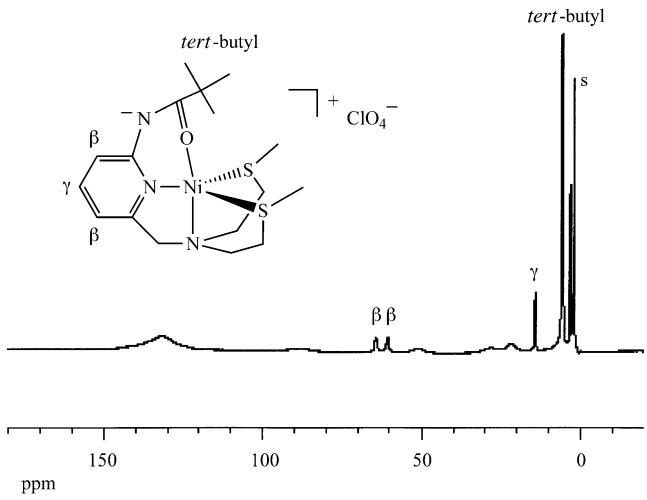


Figure 5. $^1$H NMR spectrum of **4** in dry $CD_3CN$ at ambient temperature (s = signal of $CD_2HCN$).

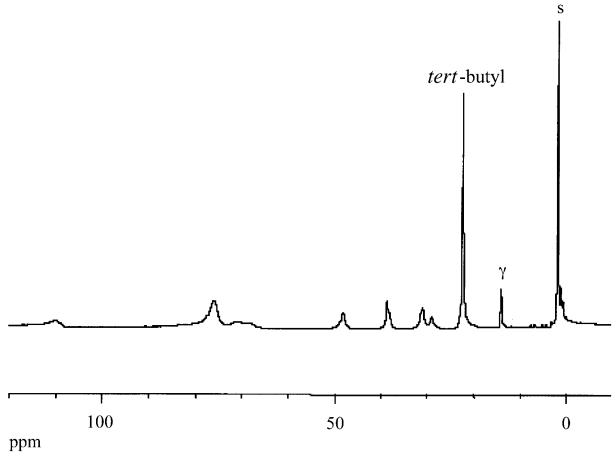


Figure 6. $^1$H NMR spectrum of **5** in dry $CD_3CN$ at ambient temperature (s = signal of $CD_2HCN$).

pound. Additional evidence for the presence of this water molecule comes from FTIR spectroscopic analysis of a crystalline sample of the complex, which revealed a $\nu_{O-H}$ vibration at 3430 $cm^{-1}$. Also present in the FTIR spectrum of **5** is an intense set of vibrations at ca. 1450 $cm^{-1}$, which is characteristic of the presence of a deprotonated amide moiety.[17] The UV/Vis absorption spectrum of **5** includes a d–d transition at 548 nm ($\varepsilon$ = 140 $M^{-1}cm^{-1}$). The intensity of this absorption band is consistent with the $Co^{II}$ center having a coordination number of five in acetonitrile.[19] On the basis of this spectroscopic data, we propose that the $Co^{II}$ center in **5** is ligated by the five available donors in the deprotonated bmppa$^-$ ligand and that the water molecule is not coordinated to the metal center. The difference in coordination number between **5** and **2** may be the reason why the $^1$H NMR features of **5** (Figure 6) are noticeably different from those of its protonated analog (Figure 3). Specifically, whereas **5** has resonances over a ca. 120 ppm region, the parent complex **2** has signals over a ca. 80 ppm region. Overall, the deprotonated amide complex exhibits generally sharper signals. In terms of specific resonances, complex **5** has a *tert*-butyl methyl resonance at $\delta \approx 22$ ppm whereas for **2** this signal is found at $\delta$ = 29 ppm. Similarly, **5** exhibits a γ-H resonance ($\delta$ = 14.2 ppm) upfield of where this signal appears in the $^1$H NMR spectrum of **2** ($\delta$ = 22.0 ppm). The magnetic moment for **5** ($\mu_{eff}$ = 3.7 $\mu_B$) is slightly below the spin-only value calculated for three unpaired electrons ($\mu_{eff}$ = 3.87 $\mu_B$). Thus far, efforts to generate X-ray quality crystals of **5** have failed, with only microcrystalline solids being isolated.

Treatment of the $Fe^{II}$ complex [(bmppa)Fe(CH$_3$CN)](ClO$_4$)$_2$ (**3**) with $Me_4NOH{\cdot}5H_2O$ in methanol under nitrogen results in the formation of a dark green precipitate in a yellow solution. Physical separation of the precipitate and the soluble components, followed by removal of the solvent from the soluble portion, yielded the free bmppa ligand in 78% yield. The green precipitate was dried under vacuum and analyzed by IR spectroscopy. This solid contains $Me_4NClO_4$ as well as unidentified iron species.

Overall, these studies revealed that, while stable divalent metal ion complexes of the deprotonated amide bmppa$^-$ ligand can be formed for $Ni^{II}$ and $Co^{II}$, an $Fe^{II}$ analog cannot be generated under similar conditions.

### Heating of 4 and 5 in Methanol

Heating of a methanol solution of the (deprotonated amide)$Ni^{II}$ complex **4** at 50 °C for 5 d, followed by removal of the $Ni^{II}$ ion using aqueous $Na_2EDTA$, produced the unaltered bmppa ligand in quantitative yield. Thus, complex **4**, which contains a deprotonated amide moiety akin to that found in [(bmppa$^-$)Zn]$ClO_4$,[17] does not undergo amide methanolysis. A rationale for the difference in reactivity between **4** and [(bmppa$^-$)Zn]$ClO_4$ involves the location of an anion binding site on the metal center. For the (deprotonated amide)$Ni^{II}$ complex, reaction with methanol could produce a pseudo-octahedral complex, wherein the methoxide is in the same plane with the coordinated amide (Figure 7). This orientation would not be productive for intramolecular amide cleavage. For the zinc derivative, we have previously proposed that the reactive species involves a tri-

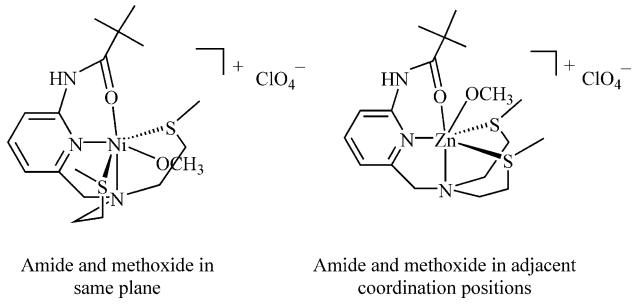


Figure 7. Proposed orientation of amide and methoxide anion in $Ni^{II}$ and $Zn^{II}$ complexes of the bmppa ligand.

 © 2007 Wiley-VCH Verlag GmbH & Co. KGaA, Weinheim 

gonal-prismatic structure, wherein the coordinated methoxide nucleophile and amide are in adjacent coordination positions (Figure 7).[17]

Heating of a methanol solution of the deprotonated amide complex **5** at 50 °C for 5 d under nitrogen, followed by removal of the $Co^{II}$ ion using aqueous $Na_2EDTA$ produced the amide methanolysis product bmapa {*N*,*N*-bis(2-methylthio)ethyl-*N*-[(6-amino-2-pyridyl)methyl]amine} in ca. 50% yield, along with unaltered bmppa ligand (ca. 43%), and a third product, *N*-(6-formylpyridin-2-yl)-2,2-dimethylpropanamide (ca. 7%).[21] The other amide methanolysis product (methyl trimethylacetate) is volatile and was not isolated or quantified. We attribute the formation of the aldehyde product to the presence of a trace amount of $O_2$ in the reaction mixture. Cobalt(II) complexes have been previously shown to undergo reaction with $O_2$ to generate reactive $Co^{III}$ peroxide or hydroperoxide complexes that mediate the *N*-dealkylation of supporting chelate ligands.[23] The production of only ca. 50% of the chelate ligand amide methanolysis product after 5 d at 50 °C contrasts with the reactivity of the zinc analog [(bmppa$^-$)Zn]-$ClO_4$, wherein a 96% yield of bmapa is obtained after heating of the complex in methanol at 40(1) °C for 48 h and removal of the $Zn^{II}$ ion. Note that control reactions have demonstrated that the bmppa ligand is unreactive in the absence of a metal ion.[16] On the basis of the structure of **2**, we speculate that a six-coordinate cobalt methoxide species may adopt either of the two structural types shown in Figure 7. If the thermodynamically more stable form is the pseudo-octahedral complex, it may rearrange with increased temperature to produce a pseudo-trigonal-prismatic geometry that is the reactive species for intramolecular amide methanolysis. Of relevance to this chemistry, we note that a trigonal-prismatic type of geometry, as is proposed for the $Zn^{II}$ cation shown in Figure 7, has been previously identified in cadmium and mercury "parent" complexes of the bmppa and beppa {*N*,*N*-bis(2-ethylthio)ethyl-*N*-[(6-pivaloylamido-2-pyridyl)methyl]amine} ligands.[16,24] These complexes undergo methanolysis of the amide when treated with 1 equiv. of base in methanol-containing solutions. In the crystal structures of the $Cd^{II}$ and $Hg^{II}$ complexes a perchlorate anion is coordinated to the metal center (Figure 8). This perchlorate interaction produces an overall distorted trigonal-prismatic geometry at the metal center. We propose that the $-OCD_3$ nucleophile (Figure 7) interacts with the metal center in a similar fashion.

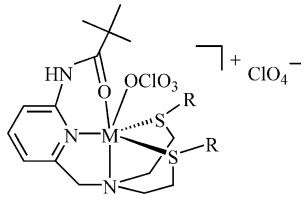


Figure 8. Structural features of cadmium and mercury "parent" complexes of amide-appended $N_2S_2$ ligands.

## Conclusions

Divalent nickel, cobalt and iron complexes of the amide-appended $N_2S_2$ donor ligand bmppa have been isolated and characterized. These "parent" complexes exhibit distorted octahedral structures and amide oxygen coordination. In the presence of base, the $Ni^{II}$ and $Co^{II}$ complexes undergo reaction to yield isolable deprotonated amide complexes that have been characterized by multiple methods. Heating of methanol solutions of these deprotonated amide complexes produces amide cleavage products only in the case of the $Co^{II}$ derivative. Notably, the reaction involving the $Co^{II}$ complex is slower than the corresponding reaction involving a zinc analog. We propose that this difference is due to the reactive zinc complex exclusively adopting a distorted trigonal-prismatic geometry, whereas the $Co^{II}$ analog may also adopt an unreactive distorted octahedral geometry. These results demonstrate the important role of metal coordination geometry preferences in influencing amide cleavage reactivity.

## Experimental Section

**General Remarks:** Reagents and solvents were purchased from commercial sources and were used as received unless otherwise noted. Solvents for glove-box use were dried according to published procedures and were degassed prior to use.[25] FTIR spectra were recorded with a Shimadzu FTIR-8400 spectrometer as KBr pellets or as $CH_3CN$ solutions (100 mM). $^1H$ and/or {$^1H$,$^1H$} COSY NMR spectra of paramagnetic $Ni^{II}$, $Co^{II}$, and $Fe^{II}$ complexes were recorded in dry $CD_3CN$ with a Bruker ARX-400 spectrometer. Chemical shifts (in ppm) are referenced to the residual solvent peak in $CD_3CN$ [$^1H$: $\delta$ = 1.94 (quint) ppm]. The chelate ligand bmppa {*N*,*N*-bis(2-methylthio)ethyl-*N*-[(6-pivaloylamido-2-pyridyl)methyl]amine} was prepared as previously reported.[26] ***Caution!*** Perchlorate salts of metal complexes with organic ligands are potentially explosive. These compounds should be handled in small quantities and with extreme caution, especially in the solid state.[27]

**[(bmppa)Ni($CH_3CN$)]($ClO_4$)$_2$ (1):** $Ni(ClO_4)_2{\cdot}6H_2O$ (0.0395 g, 0.108 mmol) dissolved in methanol (2 mL) was added to a solution of bmppa (0.0384 g, 0.108 mmol) in methanol (2 mL). The resulting purple solution was stirred at room temperature for ca. 30 min. Addition of excess of diethyl ether (ca. 60 mL) to the reaction mixture, followed by cooling at –15 °C for ca. 12 h resulted in the deposition of a purple precipitate, which was isolated and dried under vacuum. Recrystalization of this purple powder by diethyl ether diffusion into $CH_3CN/CH_3OH$ (1:1) at ambient temperature yielded purple needle crystals (0.050 g, 70%). FTIR (KBr): $\tilde{\nu}$ = 3336 ($\nu_{N-H}$), 1649, 1617, 1530, 1457, 1427, 1169, 1103, 1080 ($\nu_{ClO4}$), 796, 623 ($\nu_{ClO4}$) cm$^{-1}$. FTIR ($CH_3CN$, 100 mM, 1700–1550 cm$^{-1}$ region): $\tilde{\nu}$ = 1653, 1620 cm$^{-1}$. $C_{19}H_{32}Cl_2N_4NiO_9S_2$ (652.03): calcd. C 34.97, H 4.95, N 8.59; found C 35.15, H 4.95, N 8.65.

**[(bmppa)Co($CH_3CN$)]($ClO_4$)$_2$ (2):** This complex was prepared in an identical manner to **1**. Deep pink blocks suitable for X-ray diffraction studies were obtained from $CH_3CN/Et_2O$ (0.044 g, 65%). FTIR (KBr): $\tilde{\nu}$ = 3318 ($\nu_{N-H}$), 1635, 1612, 1528, 1452, 1422, 1099 ($\nu_{ClO4}$), 791, 619 ($\nu_{ClO4}$) cm$^{-1}$. FTIR ($CH_3CN$, 100 mM, 1700–1550 cm$^{-1}$ region): $\tilde{\nu}$ = 1653, 1648, 1619 cm$^{-1}$. $C_{19}H_{32}Cl_2CoN_4O_9S_2$ (653.03): calcd. C 34.91, H 4.94, N 8.58; found C 34.89, H 4.83, N 8.36.

 © 2007 Wiley-VCH Verlag GmbH & Co. KGaA, Weinheim 

**[(bmppa)Fe($CH_3CN$)]($ClO_4$)$_2$ (3):** Prepared in an identical manner to **1**. Recrystalization of the initially isolated yellow solid from $CH_3CN/Et_2O$ yielded green needle crystals suitable for single-crystal X-ray diffraction (0.043 g, 65%). FTIR (KBr): $\tilde{\nu}$ = 3325 (br., $\nu_{N-H}$), 1633, 1612, 1531, 1455, 1428, 1081 ($\nu_{ClO4}$), 796, 623 ($\nu_{ClO4}$) cm$^{-1}$. FTIR ($CH_3CN$, 100 mM, 1700–1550 cm$^{-1}$ region): $\tilde{\nu}$ = 1636, 1619 cm$^{-1}$. $C_{19}H_{32}Cl_2FeN_4O_9S_2$ (650.03): calcd. C 35.08, H 4.96, N 8.62; found C 34.82, H 4.95, N 8.60.

**[(bmppa$^-$)Ni]$ClO_4$ (4):** $Me_4NOH\cdot5H_2O$ (0.022 g, 0.12 mmol) dissolved in methanol (2 mL) was added to a solution of **1** (0.080 g, 0.12 mmol) in acetonitrile (3 mL). The purple solution turned a light purple/lavender color upon the addition of the base. The resulting reaction mixture was stirred under nitrogen for ca. 4 h. The solvent was then evaporated under reduced pressure. The remaining solid was dissolved in $CH_2Cl_2$ and filtered through a Celite/glass wool plug. The filtrate was concentrated under vacuum to obtain a pale purple oil. This purple oil was dissolved in a minimal amount of methanol, and the product was precipitated using an excess of diethyl ether. Upon cooling to –15 °C for ca. 48–72 h, flaky purple crystals were formed in the solution. The solvent was decanted and the product dried under reduced pressure (0.017 g, 28%). FTIR (KBr): $\tilde{\nu}$ = 3400 ($\nu_{O-H}$), 1618, 1605, 1567, 1489, 1447, 1419, 1107 ($\nu_{ClO4}$), 911, 805, 623 ($\nu_{ClO4}$) cm$^{-1}$. $C_{17}H_{28}ClN_3NiO_5S_2$ (512.69): calcd. C 39.92, H 5.52, N 8.22; found C 39.65, H 5.94, N 8.40.

**[(bmppa$^-$)Co]$ClO_4\cdot H_2O$ (5):** $Me_4NOH\cdot5H_2O$ (0.036 g, 0.20 mmol) dissolved in methanol (2 mL) was added to a solution of **2** (0.13 g, 0.20 mmol) in methanol (3 mL) . The red solution of the cobalt complex turned dark brown upon addition of the base. The resulting reaction mixture was stirred under nitrogen for ca. 6 h. The solvent was then evaporated under reduced pressure. The remaining solid was dissolved in $CH_2Cl_2$ and filtered through a Celite/glass wool plug, The filtrate was concentrated under vacuum to obtain a dark brown oil. This brown oil was dissolved in a minimal amount of acetonitrile and the product precipitated using excess diethyl ether. Upon cooling at –15 °C for 48 h, small dark brown crystals were formed in the solution. The solvent was decanted off and the product dried under reduced pressure to obtain a dark brown powder (0.066 g, 64%). FTIR (KBr): $\tilde{\nu}$ = 3433 (br., $\nu_{O-H}$), 1653, 1617, 1570, 1559, 1457, 1419, 1101 (br., $\nu_{ClO4}$), 806, 624 ($\nu_{ClO4}$) cm$^{-1}$. $C_{17}H_{28}ClCoN_3O_5S_2$ (512.93): calcd. C 39.84, H 5.51, N 8.20; found C 38.21, H 5.28, N 8.19. Trace $H_2O$ (ca. 1.0 equiv.) was present in the elemental analysis sample as indicated by an FTIR spectrum. Inclusion of this water in the calculated values produced a more satisfactory fit to the experimentally determined data. $C_{17}H_{28}N_3O_5S_2ClCo\cdot H_2O$ (530.06): calcd. C 38.49, H 5.70, N 7.93; found C 38.21, H 5.28, N 8.19.

**Reaction of 3 with $Me_4NOH\cdot5H_2O$:** $Fe(ClO_4)_2\cdot6H_2O$ (0.077 g, 0.22 mmol) dissolved in methanol (ca. 2 mL) was added to a solution of bmppa (0.077 g, 0.22 mmol) in methanol (ca. 2 mL). The resulting yellow solution was stirred under nitrogen for ca. 30 min. To this solution was added $Me_4NOH\cdot5H_2O$ (0.039 g, 0.22 mmol) dissolved in methanol (ca. 2 mL). This addition resulted in the immediate deposition of a green precipitate. The reaction mixture was stirred overnight, after which time the solvent was removed under reduced pressure, which yielded a yellow-green solid. Addition of $CH_2Cl_2$ produced a yellow solution, which was carefully transferred to another flask, and the remaining green solid was dried under vacuum. The green solid was washed with diethyl ether (3 × 2 mL), and the wash solutions were combined with the $CH_2Cl_2$ fraction and dried, which left a viscous yellow oil. The $^1$H NMR features of this oil are consistent with those of the bmppa ligand (0.060 g, 78%). The green solid contains $Me_4NClO_4$, as determined by IR spectroscopy, and unidentified iron species.

**Heating of 4 in MeOH:** $Me_4NOH\cdot5H_2O$ (0.03 g, 0.16 mmol) dissolved in methanol (5 mL) was added to a solution of **1** (0.11 g, 0.16 mmol) in methanol (15 mL) and acetonitrile (5 mL). This produced a color change from purple to reddish purple, consistent with the formation of **4**. The reaction mixture was then heated at 50 °C under nitrogen for 5 d. After cooling to room temperature, $Na_2EDTA$ (0.12 g, 0.33 mmol) dissolved in water (15 mL) was added. The pH of the solution was adjusted to 11 with aqueous NaOH, and the solution was stirred at room temperature for ca. 2 h. This aqueous solution was then extracted with $CH_2Cl_2$ (3 × 50 mL). The organic fractions were combined, dried with $Na_2SO_4$, and the solvents evaporated to dryness, which resulted in the isolation of a yellow oily product. $^1$H NMR analysis of this oil indicated the isolation of unaltered bmppa ligand in quantitative yield.

**Heating of 5 in MeOH:** Complex **2** was generated in situ by combining methanol/acetonitrile (ca. 1:1) solutions of $Co(ClO_4)_2\cdot6H_2O$ (0.099 g, 0.25 mmol) and bmppa (0.088 g, 0.25 mmol). The resulting red solution of **2** was stirred under nitrogen for ca. 30 min. To this solution $Me_4NOH\cdot5H_2O$ (0.049 g, 0.25 mmol) dissolved in methanol (5 mL) was added. This produced a color change from red to dark brown, consistent with the formation of **5**. The reaction mixture was stirred at 50 °C under nitrogen for 5 d. The reaction mixture was then cooled to room temperature and $Na_2EDTA$ (0.65 g, 1.74 mmol) dissolved in water (ca. 15 mL) added. The pH of the solution was adjusted to 11 with aqueous NaOH and the resulting mixture stirred at room temperature for ca. 2 h. The solution was extracted with $CH_2Cl_2$. All the organic fractions were collected, dried with $Na_2SO_4$, and the solvents evaporated to dryness to yield a brown oil. The $^1$H NMR spectrum of this brown oil indicated the formation of two major products and one minor product in the reaction mixture. The first major product was *N*,*N*-bis-2-(methylthio)ethyl-*N*-[(6-amino-2-pyridyl)methyl]amine (bmapa) (ca. 50%). The second major product was unaltered bmppa ligand (43%). The third minor product obtained was *N*-(6-formylpyridin-2-yl)-2,2-dimethylpropanamide[22] (ca. 7%). $^1$H NMR ($CD_3CN$, 400 MHz): $\delta$ = 9.87 (s, 1 H), 8.5 (br., NH), 8.41 (d, 1 H), 7.95 (t, 1 H), 7.66 (d, 1 H), 1.28 (s, 9 H) ppm. GC-MS: *m*/*z* (%) = 206 (9) $[M + H]^+$.

**X-ray Crystallography:** Single crystals of **2** and **3** were mounted on glass fibers with traces of viscous oil and then transferred to a NoniusKappaCD diffractometer with Mo-$K_\alpha$ radiation ($\lambda$ = 0.71073 Å) for data collection at 200(1) K. Ten frames of data were collected with an oscillation range of 1 °/frame and an exposure time of 20 s/frame. Indexing and unit-cell refinement based on all observed reflections from those ten frames indicated a monoclinic *P* lattice for both complexes. A total of 16639 reflections for **2** and 11278 reflections for **3** were indexed, integrated, and corrected for Lorentz, polarization and absorption effects using DENZO-SMN and SCALEPAC.[28] The structures were solved by a combination of direct and heavy-atom methods using SIR 97.[29] All non-hydrogen atoms were refined with anisotropic displacement coefficients. For **2** all hydrogen atoms except the amide hydrogen atom were assigned isotropic displacement coefficients $U$(H) = 1.2 $U$(*C*) or 1.5 $U(C_{methyl})$ and their coordinates were allowed to ride on their respective carbon atoms using SHELXL97.[30] The amide hydrogen atom of **2** and all the hydrogen atoms of **3** were located and refined independently. Complexes **2** and **3** crystallized in the space group $P2_1/c$. Additional details of the X-ray data collection and refinement are given in Table 4. CCDC-648591 (for **2**), and -648592 (for

 © 2007 Wiley-VCH Verlag GmbH & Co. KGaA, Weinheim 

**3**) contain the supplementary crystallographic data for this paper. These data can be obtained free of charge from the The Cambridge Crystallographic Data Centre via www.ccdc.cam.ac.uk/data_request/cif.

Table 4. Summary of X-ray data collection and refinement.[a]

| | **2** | **3** |
|---|---|---|
| Empirical formula | $C_{19}H_{32}Cl_2CoN_4O_9S_2$ | $C_{19}H_{32}Cl_2FeN_4O_9S_2$ |
| Formula mass | 654.44 | 651.36 |
| Crystal system | monoclinic | monoclinic |
| Space group | $P2_1/c$ | $P2_1/c$ |
| $a$ [Å] | 18.4261(7) | 18.3663(3) |
| $b$ [Å] | 7.81940(10) | 7.8281(1) |
| $c$ [Å] | 20.7120(8) | 20.5577(4) |
| $\alpha$ [°] | 90.0 | 90.0 |
| $\beta$ [°] | 111.9960(11) | 112.242(1) |
| $\gamma$ [°] | 90.0 | 90.0 |
| $V$ [Å$^3$] | 2766.99(15) | 2735.73(8) |
| $Z$ | 4 | 4 |
| Density (calcd.) [Mg·m$^{-3}$] | 1.571 | 1.581 |
| $T$ [K] | 200(1) | 200(1) |
| Crystal size [mm] | $0.30 \times 0.23 \times 0.15$ | $0.25 \times 0.21 \times 0.11$ |
| Diffractometer | Nonius KappaCCD | Nonius KappaCCD |
| Absorption coefficient [mm$^{-1}$] | 1.018 | 0.953 |
| $2\theta_{max}$ [°] | 67.44 | 54.96 |
| Completeness to $2\theta$ (%) | 85.7 | 99.3 |
| Reflections collected | 16639 | 11278 |
| Independent reflections | 9472 | 6227 |
| Variable parameters | 339 | 462 |
| $R1/wR_2$[b] | 0.0481/0.1182 | 0.0498/0.1155 |
| Goodness-of-fit ($F^2$) | 1.030 | 1.029 |
| Largest difference [e Å$^{-3}$] | 0.854/–0.474 | 1.047/–0.864 |

[a] Radiation used: Mo-$K_\alpha$ ($\lambda$ = 0.71073 Å). [b] $R1 = \sum ||F_o| - |F_c|| / \sum |F_o|$; $wR_2 = \{\sum[w(F_o^2 - F_c^2)^2] / [\sum (F_o^2)^2]\}^{1/2}$ where $w = 1/[\sigma^2(F_o^2) + (aP)^2 + bP]$.

## Acknowledgments

We thank the National Science Foundation (CAREER Award CHE-0094066) for funding of this research.

[1] P. T. R. Rajagopalan, X. C. Yu, D. Pei, *J. Am. Chem. Soc.* **1997**, *119*, 12418–12419.
[2] D. Groche, A. Becker, I. Schlichting, W. Kabsch, S. Schultz, A. F. V. Wagner, *Biochem. Biophys. Res. Commun.* **1998**, *246*, 342–346.
[3] A. Becker, I. Schlichting, W. Kabsch, D. Groche, S. Schultz, A. F. V. Wagner, *Nat. Struct. Biol.* **1998**, *5*, 1053–1058.
[4] E. T. Baldwin, M. S. Harris, A. W. Yem, C. L. Wolfe, A. F. Vosters, K. A. Currty, R. W. Murray, J. H. Bock, V. P. Marshall, J. I. Cialdella, M. H. Merchant, G. Choi, M. R. Deibel Jr, *J. Biol. Chem.* **2002**, *277*, 31163–31171.
[5] A. Becker, I. Schlichting, W. Kabsch, S. Schultz, A. F. Wagner, *J. Biol. Chem.* **1998**, *273*, 11413–11416.
[6] P. T. Rajagopalan, S. Grimme, D. Pei, *Biochemistry* **2000**, *39*, 779–790.
[7] S. Ragusa, S. Blanquet, T. Meinnel, *J. Mol. Biol.* **1998**, *280*, 515–523.
[8] F. Dardel, S. Ragusa, C. Lazennec, S. Blanquet, T. Meinnel, *J. Mol. Biol.* **1998**, *280*, 501–513.
[9] P. T. R. Rajagopalan, A. Datta, D. Pei, *Biochemistry* **1997**, *36*, 13910–13918.
[10] S. Chang, R. D. Sommer, A. l. Rheingold, D. P. Goldberg, *Chem. Commun.* **2001**, 2396–2397.
[11] S. Chang, V. V. Karambelkar, R. D. Sommer, A. L. Rheingold, D. P. Goldberg, *Inorg. Chem.* **2002**, *41*, 239–248.
[12] R. C. diTargiani, S. Chang, M. H. Salter, R. D. Hancock, D. P. Goldberg, *Inorg. Chem.* **2003**, *42*, 5825–5836.
[13] D. P. Goldberg, R. C. diTargiani, F. Namuswe, E. C. Minnihan, S. Chang, L. N. Zakharov, A. L. Rheingold, *Inorg. Chem.* **2005**, *44*, 7559–7569.
[14] V. V. Karambelkar, C. Xiao, Y. Zhang, A. A. Sarjeant, D. P. Goldberg, *Inorg. Chem.* **2006**, *45*, 1409–1411.
[15] R. A. Allred, K. Doyle, A. M. Arif, L. M. Berreau, *Inorg. Chem.* **2006**, *45*, 4097–4108.
[16] L. M. Berreau, M. M. Makowska-Grzyska, A. M. Arif, *Inorg. Chem.* **2000**, *39*, 4390–4391.
[17] E. Szajna, M. M. Makowska-Grzyska, C. C. Wasden, A. M. Arif, L. M. Berreau, *Inorg. Chem.* **2005**, *44*, 7595–7605.
[18] G. K. Ingle, M. M. Makowska-Grzyska, E. Szajna-Fuller, I. Sen, J. C. Price, A. M. Arif, L. M. Berreau, *Inorg. Chem.* **2007**, *46*, 1471–1480.
[19] D. R. McMillin in *Physical Methods in Bioinorganic Chemistry: Spectroscopy and Magnetism* (Ed.: L. Que Jr,), University Science Books, Sausalito, CA, **2000**, pp. 1–58.
[20] D. F. Evans, *J. Chem. Soc.* **1959**, 2003–2005.
[21] W. L. Jolly, *The Synthesis and Characterization of Inorganic Compounds*, Waveland Press, Inc., Prospect Heights, IL, **1970**.
[22] T. Mase, I. N. Houpis, A. Akao, I. Dorziotis, K. Emerson, T. Hoang, T. Iida, T. Itoh, K. Kamei, S. Kato, Y. Kato, M. Kawasaki, F. Lang, J. Lee, J. Lynch, P. Mailgres, A. Molina, T. Nemoto, S. Okada, R. Reamer, J. Z. Song, D. Tschaen, T. Wada, D. Zewge, R. P. Volante, P. J. Reider, K. Tomimoto, *J. Org. Chem.* **2001**, *66*, 6775–6786.
[23] P. Comba, S. Kuwata, G. Linti, H. Prizkow, M. Tarnai, H. Wadepohl, *Chem. Commun.* **2006**, 2074–2076 and references cited therein.
[24] M. M. Makowska-Grzyska, K. Doyle, R. A. Allred, A. M. Arif, D. C. Bebout, L. M. Berreau, *Eur. J. Inorg. Chem.* **2005**, 822–827.
[25] W. L. F. Armarego, D. D. Perrin, *Purification of Laboratory Chemicals*, 4th ed., Butterworth-Heinemann, Boston, MA, **1996**.
[26] L. M. Berreau, R. A. Allred, M. M. Makowska-Grzyska, A. M. Arif, *Chem. Commun.* **2000**, 1423–1424.
[27] W. C. Wolsey, *J. Chem. Educ.* **1973**, *50*, A335–A337.
[28] Z. Otwinowski, M. Minor, *Methods Enzymol.* **1997**, *276*, 307–326.
[29] A. Altomare, M. C. Burla, M. Camalli, G. L. Cascarano, C. Giacovazzo, A. Guagliardi, A. G. G. Moliterni, G. Polidori, R. Spagna, *J. Appl. Crystallogr.* **1999**, *32*, 115–199.
[30] G. M. Sheldrick, *SHELXL-97, Program for the Refinement of Crystal Structures*, University of Göttingen, Germany, **1997**.

Received: June 5, 2007
Published Online: September 24, 2007

 © 2007 Wiley-VCH Verlag GmbH & Co. KGaA, Weinheim 

DOI: 10.1002/ejic.200700731

# The Influence of Ligand Substitution at the Electron Donor Center in Molecular Cyano-Bridged Mixed-Valent $Co^{III}/Fe^{II}$ and $Co^{III}/Ru^{II}$ Complexes

**Paul V. Bernhardt,*[a] Fernando Bozoglian,[b] Mercè Font-Bardía,[c] Manuel Martínez,*[b] Andrew P. Meacham,[a] Beatriz Sienra,[d] and Xavier Solans[c][†]**

**Keywords:** Mixed-valent compounds / Cyanides / Binuclear complexes

In this paper we report a new variety of dinuclear cyano-bridged $Co^{III}/M^{II}$ (M = Fe or Ru) mixed-valent complexes of the general formula $[L_nCo^{III}(\mu\text{-}NC)M^{II}(CN)_x(bpy)_y]^{z+}$ (where $L_n$ represents a pentaamine macrocycle and M = Fe or Ru with $x = 4$, $y = 1$ and $z = 1$ or $x = 2$, $y = 2$ and $z = 3$)]. The incorporation of the bpy ligand in place of cyano ligands within the coordination sphere raises the $M^{III/II}$ redox potential significantly relative to the hexacyanometalate analogs we have reported previously. However, the metal-to-metal ($M^{II}$ to $Co^{III}$) charge-transfer transitions are shifted to lower energies in accordance with Hush theory as a result of a decreased reorganizational energy component, which result in them overlapping with more intense MLCT ($M^{II}$ to bpy) transitions.
(© Wiley-VCH Verlag GmbH & Co. KGaA, 69451 Weinheim, Germany, 2007)

## Introduction

In recent years we have reported on synthetic strategies leading to *molecular*, cyano-bridged, dinuclear[1–4] and trinuclear[5] $d^6$–$d^6$ heterometallic complexes; this work has been reviewed.[6] These $Co^{III}/Fe^{II}$ and $Co^{III}/Ru^{II}$ complexes each display characteristics of a *Class II* Robin and Day asymmetric, low-spin $d^6$–$d^6$ mixed-valent complex,[7] exhibiting metal-to-metal charge-transfer (MMCT, $Fe^{II}$ to $Co^{III}$ or $Ru^{II}$ to $Co^{III}$) transitions in the visible region, in addition to the transitions characteristic of the two isolated metal-complex moieties.

According to Hush theory [Equation (1)],[8] the energy of the MMCT transition ($E_{op}$) is directly related to the free energy difference ($\Delta G°$) between the $Co^{III}$–NC–$M^{II}$ and $Co^{II}$–NC–$M^{III}$ (M = Fe, Ru) forms. The $Co^{II}$–NC–$M^{III}$ form cannot be isolated as it is inherently unstable with respect to the $Co^{III}$–NC–$M^{II}$ complex so this free energy difference cannot be measured directly. However, if the two redox centers do not interact strongly then this free energy difference may be estimated from the difference between the $Co^{III/II}$ and $M^{III/II}$ redox potentials. The reorganizational energy ($\lambda$) associated with the MMCT process is also important and includes both inner sphere (bond length/angle changes) and outer sphere (solvation) terms.

$$E_{op} = \Delta G° + \lambda \quad (1)$$

In previous publications we have demonstrated how the MMCT energy of the $Co^{III}$–NC–$M^{II}$ chromophore is very sensitive to variations at both metal centers. Specifically, the ring size of the pentadentate macrocyclic ligand bound to the $Co^{III}$ ion (e.g. $L_{14}$ or $L_{15}$),[2] its geometric isomeric form (*cis* or *trans*),[3] and the donor set of the macrocycle ($N_5$ or $N_3S_2$)[4] all have an effect on the $Co^{III/II}$ redox potential, which in turn is reflected in variations in the MMCT transition energy in accordance with Hush theory. Alternatively, protonation of the terminal cyanide ligands in the hexacyanoferrate(II) moiety[9] or the substitution of the metal (Ru for Fe)[4] raises the $M^{III/II}$ (M = Fe or Ru) redox potential of the donor and the energy of the MMCT transition accordingly.

In this paper we have explored a new MMCT energy tuning strategy by replacing the hexacyanometalate(II) unit by various combinations of *cis*-$[M(CN)_4(bpy)]^{2-}$ and *cis*-$[M(CN)_2(bpy)_2]$ (M = Fe and Ru, bpy = 2,2′-bipyridyl). This change brings additional complexity to the optical properties of the system, as metal-to-ligand charge transfer (MLCT, $M^{II}$ to bpy) transitions are also possible and inherently more intense than the MMCT transitions.[10] The identification of the MMCT ($M^{II}$ to $Co^{III}$) transitions in these new mixed-valent complexes is consequently not straightforward. Nevertheless, this can be overcome when their intense electronic spectra are compared with that of the mononuclear cyano complexes of $M^{II}$ (Fe or Ru in com-

[a] Department of Chemistry, University of Queensland, Brisbane 4072, Australia
E-mail: p.bernhardt@uq.edu.au
[b] Departament de Química Inorgànica, Universitat de Barcelona, Martí i Franquès 1–11, 08028 Barcelona, Spain
E-mail: manel.martinez@qi.ub.es
[c] Departament de Mineralogia, Cristallografia i Dipòsits Minerals, Universitat de Barcelona, Martí i Franquès s/n, 08028 Barcelona, Spain
[d] Cátedra de Química Inorgánica, Facultad de Química, Universidad de la República, Avenida General Flores 2124, 11800 Montevideo, Uruguay
[†] Professor Xavier Solans passed away on September 3, 2007.
Supporting information for this article is available on the WWW under http://www.eurjic.org or from the author.

 WILEY InterScience DISCOVER SOMETHING GREAT © 2007 Wiley-VCH Verlag GmbH & Co. KGaA, Weinheim 

bination with one or two bpy ligands). This analysis brings additional information regarding the energetics of MMCT in these molecular systems.

## Results and Discussion

### Synthesis

All complexes were prepared by direct substitution of the aqua ligand on the appropriate *trans*-$[CoL_n(OH_2)]^{3+}$ complex by a single bridging cyano ligand of the $Fe^{II}$ or $Ru^{II}$ precursor. In previous papers[2,11] we have exploited a redox-catalyzed substitution reaction whereby the hexacyanoferrate(II) complex undergoes an outer sphere electron transfer cross reaction with the $Co^{III}$ partner to generate a labile $Co^{II}$ intermediate. However, given the much higher $Fe^{III/II}$ and $Ru^{III/II}$ redox potentials involved, this protocol could not be used. Despite this fact, the careful choice of stoichiometry and reaction conditions allowed the isolation of each desired complex after purification by cation chromatography. In this case the reactions are merely ligand substitutions on the $Co^{III}$ center unassisted by reduction. A detailed mechanistic study of these "uncatalyzed" processes, also applicable in some cases for the preparation of trinuclear complexes of this family, is currently underway.

### Spectroscopic Characterization

The $^1H$ NMR resonances of all the complexes of $L_{14}$ in the high-field region are indicative of retention of the so-called *trans-I* form of the $\{Co^{III}L_{14}\}$ moiety (all NH protons *syn*, see Scheme 1) which has mirror plane symmetry and hence exhibits only five chemically distinct methylene groups.[3] The $^1H$ NMR in the same region for the $\{Co^{III}L_{15}\}$ unit in the corresponding complex is consistent with the *trans-III* form (two NH protons up and two down) which has been identified in other related dinuclear complexes.[1] The low-field region of each spectrum is dominated by the aromatic bpy protons and is useful in assigning the isomeric form involving the bpy ligands for each complex. The $^1H$ NMR spectra of both [*trans*-$L_{14}Co^{III}(\mu\text{-NC})Fe^{II}(CN)_3(bpy)_{eq,ax}]^+$ and [*trans*-$L_{14}Co^{III}(\mu\text{-NC})Ru^{II}(CN)_3(bpy)_{eq,ax}]^+$ (see Figures S1a and S1b in the electronic supporting information) are virtually identical as expected from the structures shown in Figures 1 and 2. Only the two protons in 6- and 6′-positions (equivalent in the free bpy ligand) are clearly separated in the NMR spectrum and appear downfield (>9 ppm) of all other peaks because of the inductive effect of the adjacent coordinated N-atoms. The $^1H$ NMR resonances of the other bpy protons (3/3′, 4/4′ and 5/5′) overlap, despite being chemically inequivalent. The low symmetry is consistent with the *equatorial*,*axial* geometric isomeric form where one bpy N-donor (equatorial) is *trans* to a terminal cyano ligand while the other (axial) is *trans* to the unique bridging cyano ligand. The $^1H$ NMR spectrum of [*trans*-$L_{15}Co^{III}(\mu\text{-NC})Fe^{II}(CN)_3(bpy)_{eq,ax}]^+$ (Figure S1c, supporting information) in this low-field region is found indistinguishable from that of [*trans*-$L_{14}Co^{III}(\mu\text{-NC})Fe^{II}(CN)_3(bpy)_{eq,ax}]^+$ and thus the same *eq*,*ax* isomeric can be assigned. A minor band was

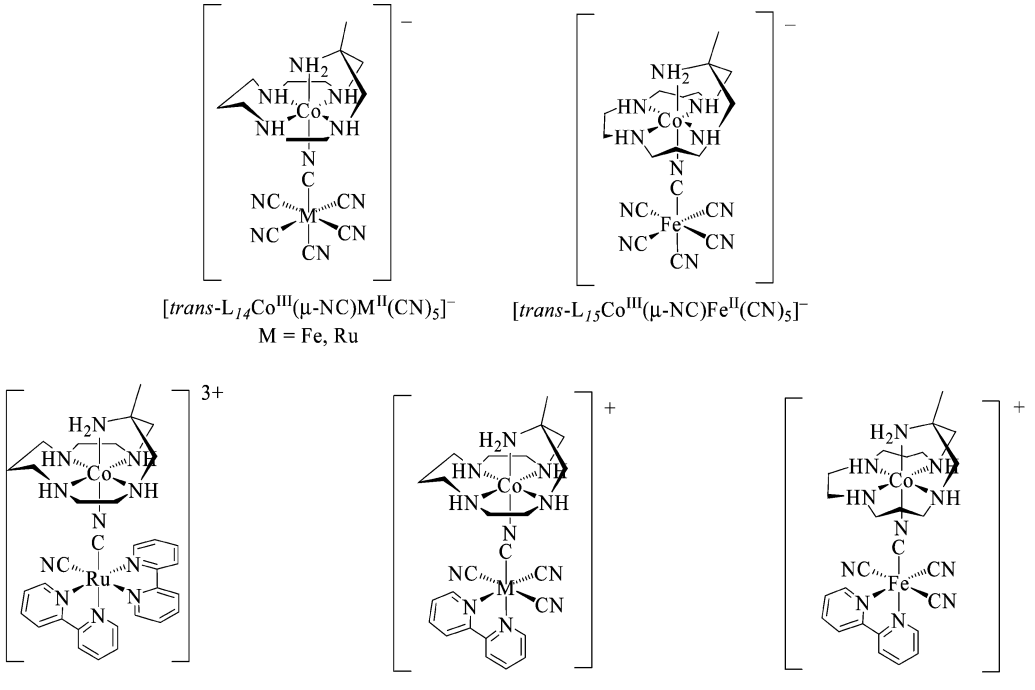


Scheme 1.

 © 2007 Wiley-VCH Verlag GmbH & Co. KGaA, Weinheim 

seen in the chromatographic purification of this complex and this is likely to be the more symmetrical *eq,eq* isomer but it was not present in sufficient quantities to characterize fully.

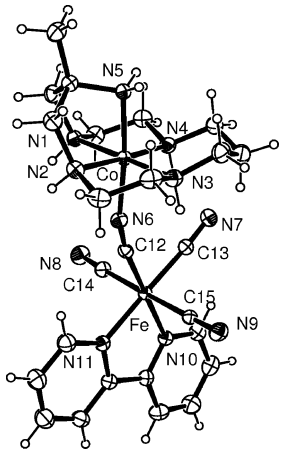


Figure 1. ORTEP drawing of the [*trans*-$L_{14}Co^{III}$(μ-NC)$Fe^{II}(CN)_3$-$(bpy)_{eq,ax}]^+$ cation (30% ellipsoids shown). Relevant bond lengths [Å] and angles [°]: Co–N(5) 1.951(2); Co–N(1) 1.958(3); Co–N(2) 1.952(3); Co–N(3) 1.960(3); Co–N(4) 1.965(3); Co–N(6) 1.897(3); Fe–N(11) 1.986(2); Fe–N(10) 1.994(2); Fe–C(12) 1.870(3); Fe–C(12)–N(6) 170.1(2); Co–N(6)–C(12) 157.5(2).

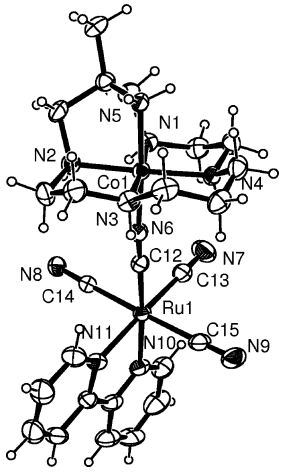


Figure 2. ORTEP drawing of the [*trans*-$L_{14}Co^{III}$(μ-NC)$Ru^{II}(CN)_3$-$(bpy)_{eq-ax}]^+$ cation (30% ellipsoids shown). Relevant bond lengths [Å] and angles [°]: Co–N(5) 1.960(5); Co–N(1) 1.940(5); Co–N(2) 1.953(5); Co–N(3) 1.945(5); Co–N(4) 1.950(6); Co–N(6) 1.906(6); Ru–N(11) 2.108(6); Ru–N(10) 2.116(5); Ru–C(12) 1.958(7); Ru–C(12)–N(6) 177.3(6); Co–N(6)–C(12) 166.7(6).

The $^1$H NMR spectrum of [*trans*-$L_{14}Co^{III}$(μ-NC)$Ru^{II}$-$(CN)(bpy)_{2,cis}]^{3+}$ (Figure S1d, supporting information) is more complex because of the presence of 4 chemically inequivalent pyridyl rings. Interestingly, a pair of high-field protons at the 6-position (from different bpy ligands) is also present, but the other two protons at the 6-position appear well upfield (7.2–7.4 ppm). This effect has also been noted previously for *cis*-$Ru(CN)_2(bpy)_2$ and $[Ru(bpy)_3]^{2+}$, and has been assigned to the shielding effect of the adjacent aromatic ring current.[12]

The IR spectra of all [*trans*-$L_nCo^{III}$(μ-NC)$M^{II}(CN)_3$-$(bpy)_{eq,ax}]^+$ ($n$ = 14 or 15, M = Fe; $n$ = 14, M = Ru) complexes are very similar in the $\tilde{\nu}_{C\equiv N}$ region, exhibiting three bands around 2060, 2080 and 2100 $cm^{-1}$. On the basis of our previous studies,[1,2,4] and those on other related cyano-bridged complexes,[13,14] the highest frequency vibration is invariably due to the bridging cyano ligand. The lowest frequency vibration is twice the intensity of the intermediate frequency band and thus is most likely due to the two equivalent (mutually *trans*) cyano ligands. The intermediate frequency band is consequently assigned to the single cyano ligand *trans* to a bpy N-donor. The IR spectrum of [*trans*-$L_{14}Co^{III}$(μ-NC)$Ru^{II}(CN)(bpy)_{2,cis}]^{3+}$ exhibits only two $\tilde{\nu}_{C\equiv N}$ bands of similar intensity. Again, the higher frequency band is assigned to the bridging cyano ligand by reference to the published IR spectrum of *cis*-$Ru(CN)_2$-$(bpy)_2$ where both ligands are terminal.[14]

## Structural Characterization

The crystal structure of [*trans*-$L_{14}Co^{III}$(μ-NC)$Fe^{II}(CN)_3$-$(bpy)_{eq,ax}]^+$ (Figure 1) shows the typical *trans-I* form of the macrocyclic $L_{14}$ ligand,[2–4] already found in the [*trans*-$L_{14}Co^{III}$(μ-NC)$Fe^{II}(CN)_5]^-$ as well as in the precursor *trans-I*-$[CoClL_{14}]^{2+}$ complexes. The bond angles and distances for the cobalt moiety on the complex do not show any significant deviation with respect to previously characterized structural analogs, and the shortest distance of the cobalt environment is, as usual, that to the cyano ligand. As for the iron $\{Fe^{II}(CN)_4(bpy)\}$ unit in the dinuclear complex, its geometry is close to octahedral with the bpy ligand in an *equatorial*,*axial* disposition, forcing the $\{Co^{III}L_{14}\}$ group to tilt severely producing a Co–N≡C angle of only 157.5°. Only for the oxidized complex [*trans*-$L_{14}Co^{III}$(μ-NC)$Fe^{III}$-$(CN)_5]$ has a tilting of this degree been observed before;[3] as a consequence the $Co^{III}$–$Fe^{II}$ distance becomes effectively shorter than in the rest of $Co^{III}/Fe^{II}$ complexes of this family.[6]

The crystal structure of [{*trans*-$L_{14}Co^{III}$(μ-NC)}$Ru^{II}$-$(CN)_3(bpy)_{eq,ax}](ClO_4)_{1/2}\cdot Cl_{1/2}\cdot 4H_2O$ was also determined. The cation geometry (Figure 2) is very similar to that of the iron analog and the only notable differences are the longer Ru coordinate bonds. There is considerable disorder in the anions both translational and over different orientations. Apart from this feature the salient features of the structure mirror those of the Fe analog.

## Electrochemistry

Electrochemistry of the four dinuclear complexes in aqueous solution identified redox couples from both metal centers. The $Co^{III/II}$ couples for [*trans*-$L_nCo^{III}$(μ-NC)$M^{II}$-$(CN)_3(bpy)_{eq,ax}]^+$ ($n$ = 14 or 15, M = Fe; $n$ = 14, M = Ru) are rather similar (Table 1) and lower than seen in [*trans*-$L_{14}Co^{III}$(μ-NC)$Ru^{II}(CN)(bpy)_{2,cis}]^{3+}$. This fact can be attributed to the electrostatic effects of the dinegatively charged $\{M(CN)_4(bpy)\}^{2-}$ moiety in the [*trans*-$L_nCo^{III}$(μ-

 © 2007 Wiley-VCH Verlag GmbH & Co. KGaA, Weinheim 

Table 1. Redox potentials and spectroscopic data for new cyano-bridged dinuclear complexes prepared. Literature values for relevant compounds of the same family have also been included.

| | $E^o$ (Ag/AgCl) / mV $Ru/Fe^{III/II}$ | $Co^{III/II}$ | $\Delta G^o$ / $cm^{-1}$ | $E_{op}$ / $cm^{-1}$ | $\lambda$ / $cm^{-1}$ |
|---|---|---|---|---|---|
| [*trans*-$L_{14}Co^{III}$(μ-NC)$Ru^{II}$(CN)$(bpy)_{2,cis}$]$^{3+}$ | 1196 | –492 | 13600 | ≈21000[a] | 7400 |
| [*trans*-$L_{14}Co^{III}$(μ-NC)$Ru^{II}(CN)_3(bpy)_{eq,ax}$]$^{+}$ | 1079 | –642 | 13900 | ≈21000[a] | 7100 |
| [*trans*-$L_{14}Co^{III}$(μ-NC)$Fe^{II}(CN)_3(bpy)_{eq,ax}$]$^{+}$ | 584 | –701 | 10400 | [b] | [c] |
| [*trans*-$L_{15}Co^{III}$(μ-NC)$Fe^{II}(CN)_3(bpy)_{eq,ax}$]$^{+}$ | 579 | –734 | 10600 | [b] | [c] |
| [*trans*-$L_{14}Co^{III}$(μ-NC)$Fe^{II}(CN)_5$]$^{-}$ | 434 | –796 | 9900 | 19600[d] | 9800 |
| [*trans*-$L_{15}Co^{III}$(μ-NC)$Fe^{II}(CN)_5$]$^{-}$ | 404 | –776 | 9500 | 18400[e] | 9000 |
| [*trans*-$L_{14}Co^{III}$(μ-NC)$Ru^{II}(CN)_5$]$^{-}$ | 954 | –733 | 13600 | 26300[f] | 12700 |

[a] Partially obscured by MLCT band. [b] Totally obscured. [c] Could not be determined. [d] Ref.[2]. [e] Ref.[1]. [f] ref.[4].

NC)$M^{II}(CN)_3(bpy)_{eq,ax}$]$^{+}$ analogs which lowers the $Co^{III/II}$ couple relative to that seen in [*trans*-$L_{14}Co^{III}$(μ-NC)$Ru^{II}$-(CN)$(bpy)_{2,cis}$]$^{3+}$ while the charge neutral {$Ru^{II}(CN)_2$-$(bpy)_2$} moiety exerts no electrostatic influence. The cyclic voltammograms of the Ru complexes are shown in Figure 3. As reported before, the $Co^{III/II}$ redox processes are fully reversible on an Hg working electrode but only quasi-reversible, or even irreversible, on glassy carbon surfaces. That is, the best responses for the $Co^{III/II}$ were obtained on Hg while the high-potential $Fe^{III/II}$ and $Ru^{III/II}$ couples (inaccessible on Hg) had to be measured with a glassy carbon electrode. Also of note are the lower $Co^{III/II}$ couples of the dinuclear hexacyanometalate complexes because of the greater (tetranegative) charge of the anionic cyano {$Fe^{II}(CN)_6$} moiety.

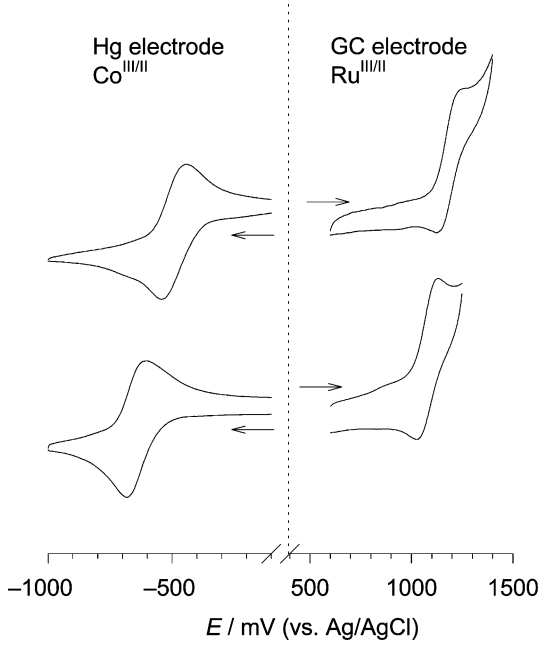


Figure 3. Cyclic voltammograms (500 mV $s^{-1}$) of [*trans*-$L_{14}Co^{III}$(μ-NC)$Ru^{II}$(CN)$(bpy)_{2,cis}$]$^{3+}$(top)and[*trans*-$L_{14}Co^{III}$(μ-NC)$Ru^{II}(CN)_3$-$(bpy)_{eq,ax}$]$^{+}$ (bottom) measured with a glassy carbon (GC) working electrode (right) or a Hg drop electrode (left). The currents have been scaled to compensate for the different electrode areas.

The $Ru^{III/II}$ and $Fe^{III/II}$ couples are both clearly influenced by the tripositively charged {$Co^{III}L_n$}$^{3+}$ moiety. Comparison with the mononuclear redox potentials of $[Fe(CN)_4(bpy)]^{-/2-}$ (380 mV),[15] $[Ru(CN)_4(bpy)]^{-/2-}$ (890 mV)[16] and *cis*-$[Ru(CN)_2(bpy)_2]^{+/0}$ (940 mV)[17] (all vs. Ag/AgCl) illustrates this point. A ca. 200 mV anodic shift is found in each case on going from the mononuclear complex to the cyano-bridged $Co^{III}/M^{II}$ complex, as for the previously studied hexacyano complexes.[1–5] Further comparisons can be made with these redox potentials of the hexacyanometalate analogs that we have already reported (Table 1). Clearly the bpy ligand destabilizes the trivalent Fe and Ru forms relative to a pair of terminal cyano ligands.

Apart from these thermodynamic measurements, there also appears to be a labilizing effect upon oxidation of the $Ru^{II}$ center. As illustrated in Figure 4, the $Ru^{III/II}$ couple of [*trans*-$L_{14}Co^{III}$(μ-NC)$Ru^{II}(CN)_3(bpy)_{eq,ax}$]$^{+}$ is irreversible at a sweep rate of 100 mV $s^{-1}$ (no cathodic peak is observed), while reversibility is restored at sweep rates higher than

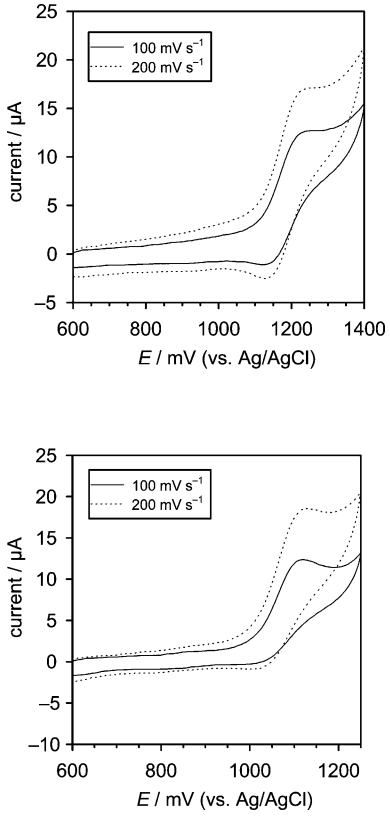


Figure 4. Sweep-rate dependence of the $Ru^{III/II}$ couple potentials for [*trans*-$L_{14}Co^{III}$(μ-NC)$Ru^{II}$(CN)$(bpy)_{2,cis}$]$^{3+}$ (top) and [*trans*-$L_{14}Co^{III}$(μ-NC)$Ru^{II}(CN)_3(bpy)_{eq,ax}$]$^{+}$ (bottom).

 © 2007 Wiley-VCH Verlag GmbH & Co. KGaA, Weinheim 

500 mV s$^{-1}$. This fact is indicative of a chemical reaction, of uncertain nature, following oxidation. The $Ru^{III/II}$ redox couple in [*trans*-$L_{14}Co^{III}$(μ-NC)$Ru^{II}$(CN)$(bpy)_{2,cis}$]$^{3+}$ appears at even higher potential yet it is reversible at all sweep rates, which rules out catalytic water oxidation as the reason for the loss of the cathodic peak in [*trans*-$L_{14}Co^{III}$(μ-NC)-$Ru^{II}(CN)_3(bpy)_{eq,ax}]^+$ (the higher potential $Ru^{III/II}$ couple should result in a greater rate of water oxidation). It seems that the chemical reaction that follows oxidation has to be related to ligand dissociation at the $Ru^{III}$ center with a first-order rate constant of ca. 15 s$^{-1}$, as determined by examination of the scan-rate dependence of the cathodic/anodic currents.[18] Electrochemical experiments run in dmf (data not shown) revealed a similar result, indicating the chemical irreversibility of the oxidation of the ruthenium center in the complex despite the absence of water. Interestingly the electrochemistry of $[Ru(CN)_4(bpy)]^{2-}$ performed under the same conditions is facile and totally reversible at sweep rates of 100 mV s$^{-1}$, which suggests a destabilizing influence of the attached $Co^{III}$ moiety. Earlier studies[19] on the bromine oxidation of $[Ru(CN)_6]^{4-}$ showed that the product is $[Ru(CN)_5(OH_2)]^{3-}$ which indicates that the intermediate $[Ru(CN)_6]^{3-}$ is unstable with respect to ligand substitution in water. Indeed the $[Ru(CN)_6]^{3-}$ ion has only recently been characterized structurally[20] and, once isolated, it decomposes rapidly upon dissolution.

### *Electronic Spectroscopy*

The energy of the MMCT transition is of interest, given the wide separation of the redox couples of the two metal centers relative to other systems we have investigated (see Table 1). The electronic spectra of [*trans*-$L_{14}Co^{III}$(μ-NC)-$Ru^{II}(CN)_3(bpy)_{eq,ax}]^+$ and [*trans*-$L_{14}Co^{III}$(μ-NC)$Ru^{II}$(CN)-$(bpy)_{2,cis}]^{3+}$ in aqueous solution show an intense MLCT ($Ru^{II}$ to bpy) peak around 400 nm which exhibits a distinct shoulder at its low-energy side (Figure 5); this shoulder is totally absent in the parent $[Ru^{II}(CN)_4(bpy)]^{2-}$ and only the MLCT band is apparent (Figure 5, dashed line). These shoulders then appear to be due to the MMCT ($Ru^{II}$ to $Co^{III}$) transitions both around 500 nm. In other systems we have already studied, such as [*trans*-$L_{14}Co^{III}$(μ-NC)$M^{II}$-$(CN)_5]^-$ (M = Fe and Ru),[2,4] the MMCT transition is dominant, as only much weaker $Co^{III}$ d–d transitions ($\varepsilon \approx 100$ M$^{-1}$ cm$^{-1}$) are seen in the visible region. Equation (1) enables the reorganization energies for each $Ru^{II}/Co^{III}$ complex to be calculated. These values are collected in Table 1.

For both $Fe^{II}$ complexes, the UV/Vis spectra show a rather broad and featureless band at 460–470 nm that may be attributed to the corresponding MLCT ($Fe^{II}$ to bpy) transition (the value being 482 nm, 2400 M$^{-1}$ cm$^{-1}$ for $[Fe^{II}$-$(CN)_4(bpy)]^{2-}$).[21] This band diminishes in intensity on addition of the oxidant $Na_2S_2O_8$ as a result of the oxidation of the iron center and two new bands (506 nm, 110 M$^{-1}$ cm$^{-1}$ and 416 nm, 940 M$^{-1}$ cm$^{-1}$) corresponding to the $[Fe^{III}(CN)_4$-$(bpy)]^-$ chromophore are evident (Figure S2, supporting information). Also, oxidation of the $Fe^{II}$ center must result in loss of the MMCT ($Fe^{II}$ to $Co^{III}$) band, but this was completely obscured by the more intense $Fe^{II}$ to bpy MLCT band so its energy is unknown.

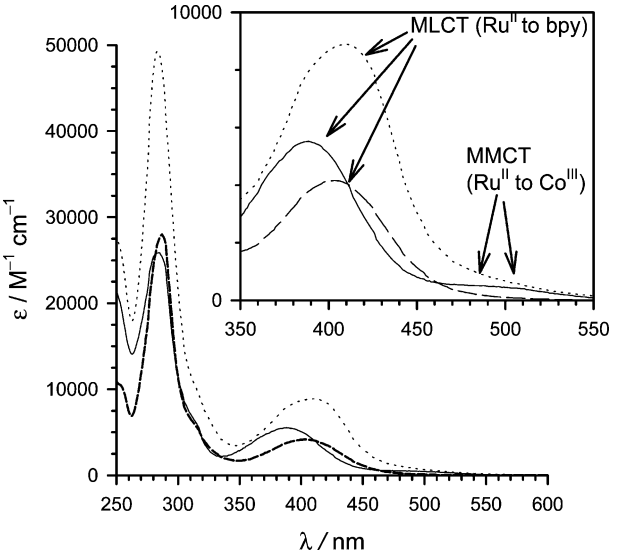


Figure 5. UV/Vis spectra of [*trans*-$L_{14}Co^{III}$(μ-NC)$Ru^{II}$(CN)-$(bpy)_{2,cis}]^{3+}$ (dotted line), [*trans*-$L_{14}Co^{III}$(μ-NC)$Ru^{II}(CN)_3$-$(bpy)_{eq,ax}]^+$ (grey solid line) and $[Ru^{II}(CN)_4(bpy)]^{2-}$ (dashed line). MLCT and MMCT bands are indicated.

Bulk electrolysis oxidation of the $Ru^{II}$–CN–$Co^{III}$ complexes was unsuccessful with decomposition occurring during the experiment. It is likely that loss of one or more cyano ligands from the $Ru^{III}$ center is the origin of this decomposition reaction by analogy with the known instability of $[Ru(CN)_6]^{3-}$.[19,20]

## Conclusions

The present study has illustrated new ways in which the MMCT energy of this extended series of molecular *Class II* mixed-valent $Co^{III}/M^{II}$ complexes can be modified through ligand exchange on the $M^{II}$ electron donor. Although partially obscured by the more intense $Ru^{II}$ to bpy MLCT transitions, the $Ru^{II}$ to $Co^{III}$ MMCT bands have been determined, while in the case of the $Fe^{II}$–CN–$Co^{III}$ systems we were unable to resolve the $Fe^{II}$ to $Co^{III}$ transitions because of their complete overlap with the more intense $Fe^{II}$ to bpy MLCT bands. In each case the substitution of a pair of *cis* cyano ligands with a single bidentate bpy ligand raises the redox potential of the $M^{II}$ donor relative to its hexacyanometalate(II) analog. Interestingly the $Co^{III/II}$ couple is inductively raised by a similar amount, leaving the free energy changes barely affected. The MMCT energy of the $Ru^{II}$–CN–$Co^{III}$ complexes is smaller because of a significant (ca. 60%) decrease in the reorganizational energy of the bpy complexes relative to the hexacyanoruthenate parent, although the variations in charge may also be a factor in addition to specific H-bonding with the number of terminal cyano ligands. We are currently exploring further synthetic

 © 2007 Wiley-VCH Verlag GmbH & Co. KGaA, Weinheim 

routes to novel di- and trinuclear mixed-valent complexes with a view to further being able to tune their optical and electrochemical properties.

## Experimental Section

**Physical Methods:** Proton NMR spectra at 400 MHz were recorded with either a Varian Mercury-400 (Serveis Científico-Tècnics de la Universitat de Barcelona) or Bruker AV400 instrument. All chemical shifts are cited relative to TMS. Cyclic voltammetry employed a BAS100B/W or EG&G 263A potentiostat and using either a glassy carbon disc working electrode, or a PAR Model 303 static Hg drop working electrode. The reference electrode was Ag/AgCl (3 M KCl) and a platinum wire counter electrode was employed. The background electrolyte was either 0.1 M $NaClO_4$ or 0.1 $NaNO_3$ as indicated. All solutions were purged with $N_2$ prior to measurement. UV/Vis spectra were measured with Analytik Jena Specord 210, HP5482A, Cary5, Cary50 and J&M TIDAS spectrophotometers. IR spectra were carried out in an FT-IR Impact 400 Nicolet spectrometer employing KBr disks or a Perkin–Elmer 1600 series spectrophotometer using an ATR assembly.

### Syntheses

**Caution:** All reactions must be carried out in a well-ventilated fume hood as liberation of HCN may occur in some of the preparations if solutions are acidified. Perchlorate salts are potentially explosive and should only be handled in small quantities, never heated in the solid state not scraped from sintered glass frits.

The precursor complexes *trans-I*-$[CoClL_{14}](ClO_4)_2$,[2] *trans-II*-$[CoClL_{15}](ClO_4)_2$,[22] $K_2[Fe(CN)_4(bpy)]\cdot 3H_2O$,[21] $K_4[Ru(CN)_6]$,[23] $K_2[Ru(CN)_4(bpy)]$[24] were prepared using published procedures. The complex *cis*-$Ru(CN)_2(bpy)_2$ was prepared by refluxing *cis*-$Ru(bpy)_2Cl_2$[25] (0.3 g) and excess KCN (0.241 g) in 50% aqueous EtOH (100 $cm^3$) for 5 h; the initial purple color changed to orange during this period. After this time the solvent was removed in vacuo (**caution** – excess cyanide present) and the resultant red/orange powder was dissolved in MeOH and purified on a Sephadex LH-20 size-exclusion column and recrystallized from MeOH/$Et_2O$. All other reagents and solvents were obtained commercially.

**[*trans*-$L_{14}Co^{III}(\mu\text{-}NC)Fe^{II}(CN)_3(bpy)_{eq,ax}](ClO_4)\cdot 4H_2O$:** A solution of *trans-I*- $[CoClL_{14}](ClO_4)_2$ (0.20 g) in water (20 $cm^3$) was adjusted to pH = 10 with NaOH and then stirred for 10 min to give the hydroxo derivative after hydrolysis of the chloro ligand. After addition of a solution of $K_2[Fe(CN)_4(bpy)]\cdot 3H_2O$ (0.22 g) in water (20 $cm^3$), the pH was raised to 6.2 with 1 M NaOH solution; any $KClO_4$ precipitate was filtered off and stirring was continued for 72 h. at 40 °C. The final solution was diluted to 1000 $cm^3$ and loaded to a $30 \times 2$ cm column of Sephadex C-25 cation-exchange resin ($Na^+$ form). Elution with 0.1 M $NaClO_4$ produced two diffuse red bands. The major second band was collected, diluted to 5 L, and reloaded onto another column of the same type. This time elution with 0.05 M $NaClO_4$ produced a narrow major band that was collected and evaporated at reduced pressure to ca. 15 $cm^3$. Standing for a few days at 5 °C produced the desired product in crystalline form (15% yield) suitable for X-ray work. $C_{25}H_{43}ClCoFeN_{11}O_8$ (775.92): calcd. C 38.7, H 5.6, N 19.8; found C 39.1, H 5.7, N 19.2. $^1H$ NMR ($D_2O$): $\delta$ = 1.35 (s, 3 H, $CH_3$), 1.80–3.70 (m, 18 H, $CH_2$), 7.50 (m, 2 H, 5/5′-pyr), 7.98 (t, 2 H, 4/4′-pyr), 8.23 (d, 2 H, 3/3′-pyr), 9.01 (d, 1 H, 6-pyr), 9.28 (d, 1 H, 6′-pyr) ppm. IR: $\tilde{\nu}_{CN}$ = 2061, 2074, 2096 $cm^{-1}$. UV/Vis ($H_2O$): $\lambda$ ($\varepsilon$, L $mol^{-1}$ $cm^{-1}$) = 458 (3380), 332 (3330) nm.

**[*trans*-$L_{15}Co^{III}(\mu\text{-}NC)Fe^{II}(CN)_3(bpy)_{eq,ax}](ClO_4)\cdot 3H_2O$:** The procedure for the preparation of the dinuclear complex is the same one as above except *trans-II*-$[CoClL_{15}](ClO_4)_2$ was used as the precursor. Elution with 0.1 M $NaClO_4$ produced two diffuse red bands. The major second one was collected, diluted to 5 L, and reloaded on another Sephadex C-25 column ($Na^+$ form). Elution with 0.05 M $NaClO_4$ produced an initial major band that was collected and evaporated at reduced pressure to ca. 15 $cm^3$. Standing in a refrigerator for a few days produced the desired product in crystalline form in a 10% yield. $C_{26}H_{43}ClCoFe_{11}O_7$ (1176.32): calcd. C 40.5, H 5.6, N 20.0; found C 40.8, H 5.9, N 21.0. $^1H$ NMR ($D_2O$): $\delta$ = 1.40 (s, 3 H, $CH_3$), 1.90–3.50 (m, 20 H, $CH_2$), 7.52 (m, 2 H, 5/5′-pyr), 8.02 (t, 2 H, 4/4′-pyr), 8.28 (d, 2 H, 3/3′-pyr), 9.10 (d, 1 H, 6-pyr), 9.32 (d, 1 H, 6′-pyr) ppm. IR: $\tilde{\nu}_{CN}$ 2052, 2080, 2106. UV/Vis ($H_2O$): $\lambda$ ($\varepsilon$, L $mol^{-1}$ $cm^{-1}$) = 470 (2500), 338 (2160) nm.

**[*trans*-$L_{14}Co^{III}(\mu\text{-}NC)Ru^{II}(CN)_3(bpy)_{eq,ax}](ClO_4)\cdot 6H_2O$:** *trans-I*-$[CoClL_{14}](ClO_4)_2$ (0.26 g) and $K_2[Ru(bpy)(CN)_4]$ (0.25 g) were refluxed in 50% aqueous MeOH (100 $cm^3$) at pH = 8. The color of the orange solution quickly darkened and developed into a brownish orange. After 6 h the solution was cooled and diluted with water to 5 L and loaded onto a Sephadex C-25 ($Na^+$ form) column and the desired product eluted with 0.1 M $NaClO_4$. Upon concentration of the eluate on a rotary evaporator an orange powder precipitated on standing. This was filtered off and then further purified via size exclusion chromatography (Sephadex LH-20, MeOH) to remove contamination by co-precipitated $NaClO_4$. The orange fraction collected from the Sephadex LH-20 column was left to slowly concentrate and the complex precipitated in a 43% yield. $C_{25}H_{45}ClCoN_{11}O_{10}Ru$ (855.15): calcd. C 35.0, H 5.5, N 18.0; found C 35.1, H 5.7, N 17.9. $^1H$ NMR ([$D_4$]MeOH): $\delta$ = 1.28 (s, 3 H, -$CH_3$), 2–3.55 (m, 16 H, -$CH_2$-), 7.052 (quint, 2 H, 5/5′-pyr), 7.97–8.03, (t, 2 H, 4/4′ pyr), 8.383–8.356 (d, 2 H, 3/3′ pyr), 9.12–9.13 (d, 1 H, 6 pyr), 9.32–9.34 (d, 1 H, 6′ pyr) ppm. IR: $\tilde{\nu}_{CN}$ 2050, 2071, 2105. UV/Vis ($H_2O$): $\lambda$ ($\varepsilon$, L $mol^{-1}$ $cm^{-1}$) = 470 (sh, 550), 389 (5500) 284 (25800) nm. Crystals of the mixed salt [*trans*-$L_{14}Co^{III}(\mu\text{-}NC)Fe^{II}(CN)_3(bpy)_{eq,ax}](ClO_4)_{1/2}\cdot Cl_{1/2}\cdot 6H_2O$ were grown from a solution of the complex in a mixture of $NaClO_4$ and NaCl.

**[*trans*-$L_{14}Co^{III}(\mu\text{-}NC)Ru^{II}(CN)(bpy)_{2,cis}](ClO_4)_3$:** *trans-I*-$[CoClL_{14}](ClO_4)_2$ (0.25 g) and *cis*-$[Ru(CN)_2(bpy)_2]$ (0.3 g) were refluxed in 50% aqueous MeOH (100 $cm^3$) at pH = 8. The color of the orange solution quickly developed in intensity. After 6 h the solution was cooled, diluted with water to 5 $dm^3$ and loaded onto a Sephadex C-25 column ($Na^+$ from). The desired product eluted as the major orange band with 0.3 M $NaClO_4$. Upon concentration of the eluate, an orange powder precipitated and was filtered off. Further purification was achieved with size exclusion chromatography (Sephadex LH-20, MeOH) to remove excess $NaClO_4$. Yield 36%. $C_{33}H_{47}Cl_3CoN_{11}O_{14}Ru$ (1088.16): calcd. C 37.04, H 4.24, N 14.40; found C 36.58, H 4.22, N 14.35. $^1H$ NMR ([$D_3$]MeCN): $\delta$ = 1.20 (s, 3H-$CH_3$), 1.4–3.5 (m, 16H-$CH_2$-), 7.26 (quint d, 2 H), 7.42 (d, 1 H), 7.61 (m, 2 H), 7.72 (td, 1 H), 7.95 (qd, 2 H), 8.11 (t quint, 2 H), 8.33 (dd, 2 H), 8.42 (t, 2 H), 9.30 (d, 1 H), 9.54 (d, 1 H) ppm. IR: $\tilde{\nu}_{CN}$ 2048, 2089. UV/Vis ($H_2O$): $\lambda$ ($\varepsilon$, L $mol^{-1}$ $cm^{-1}$) = 490 (sh, 800), 411 (8900) 283 (49300) nm.

### Crystallography

Cell constants for [{*trans*-$L_{14}Co^{III}(\mu\text{-}NC)$}$Fe^{II}(CN)_3(bpy)_{eq,ax}](ClO_4)\cdot 4H_2O$ and [{*trans*-$L_{14}Co^{III}(\mu\text{-}NC)$}$Ru^{II}(CN)_3(bpy)_{eq,ax}](ClO_4)_{1/2}Cl_{1/2}\cdot 6H_2O$ were determined by a least-squares fit to the setting parameters of 25 independent reflections measured with an Enraf–Nonius CAD4 four-circle diffractometer employing graphite-monochromated Mo-$K_\alpha$ radiation (0.71073 Å).

 © 2007 Wiley-VCH Verlag GmbH & Co. KGaA, Weinheim 

Data reduction was performed with the WINGX[26] suite of programs. Structures were solved by direct methods with SHELXS and refined by full-matrix least-squares analysis with SHELXL-97.[27] All non-H atoms were refined with anisotropic thermal parameters. Aryl, alkyl and amino H-atoms were included at estimated positions using a riding model. Water H-atoms (if any) were not located. Molecular structure diagrams were produced with ORTEP3.[28] Crystal and refinement data are summarized in Table 2, and selected bond lengths and angles appear in the captions of Figures 1 and 2.

Table 2. Crystal data.

| Formula | $C_{25}H_{43}ClCoFeN_{11}O_8$ | $C_{25}H_{47}ClCoN_{11}O_8Ru$ |
|---|---|---|
| Empirical formula | 775.93 | 825.19 |
| Crystal system | monoclinic | trigonal |
| Space group | $P2_1/c$ | $R\bar{3}$ |
| $a$ [Å] | 12.473(13) | 22.786(3) |
| $b$ [Å] | 15.579(8) | |
| $c$ [Å] | 17.929(3) | 37.01(1) |
| $\beta$ [°] | 97.53(4) | |
| $V$ [Å$^3$] | 3454(4) | 16641(5) |
| $Z$ | 4 | 18 |
| $T$ [K] | 293 | 293 |
| $D_c$ [g cm$^{-3}$] | 1.492 | 1.482 |
| $\mu$ [mm$^{-1}$] | 1.039 | 0.987 |
| $R_1$ (obsd. data) | 0.0532 | 0.0555 |
| $wR_2$ (all data) | 0.1053 | 0.1725 |

CCDC-653712 and -653713 contain the supplementary crystallographic data for this paper. These data can be obtained free of charge from The Cambridge Crystallographic Data Centre via www.ccdc.cam.ac.uk/data_request/cif.

**Supporting Information** (see also the footnote on the first page of this article): Four $^1$H NMR spectra (aromatic regions) of complexes and UV-Vis spectral changes on addition of solid $Na_2S_2O_8$ to a solution of complex [*trans*-$L_{15}Co^{III}(\mu\text{-NC})Fe^{II}(CN)_3(bpy)_{eq,ax}]^+$ in water.

## Acknowledgments

M. M. acknowledges financial support from the Departament de Universitats, Recerca i Societat de la Informació (project ACI2003-17) and the Ministerio de Educación y Ciencia (MEC) (project BQU2006-14909-C02-02). The authors also thank the Programa de Desarrollo de las Ciencias Básicas (PEDECIBA) – Química for financial support. P. V. B acknowledges financial assistance from the Australian Research Council. A. P. M gratefully acknowledges award of a fellowship from the Royal Society of Chemistry (RSC).

[1] P. V. Bernhardt, M. Martinez, *Inorg. Chem.* **1999**, *38*, 424–425.
[2] P. V. Bernhardt, B. P. Macpherson, M. Martinez, *Inorg. Chem.* **2000**, *39*, 5203–5208.
[3] P. V. Bernhardt, B. P. Macpherson, M. Martinez, *J. Chem. Soc. Dalton Trans.* **2002**, 1435–1441.
[4] P. V. Bernhardt, F. Bozoglian, B. P. Macpherson, M. Martinez, *Dalton Trans.* **2004**, 2582–2587.
[5] P. V. Bernhardt, F. Bozoglian, G. Gonzalez, M. Martinez, B. P. Macpherson, B. Sienra, *Inorg. Chem.* **2006**, *45*, 74–82.
[6] P. V. Bernhardt, F. Bozoglian, B. P. Macpherson, M. Martinez, *Coord. Chem. Rev.* **2005**, *249*, 1902–1916.
[7] M. B. Robin, P. Day, *Adv. Inorg. Chem. Radiochem.* **1967**, *10*, 247–422.
[8] N. S. Hush, *Prog. Inorg. Chem.* **1967**, *8*, 391–444.
[9] P. V. Bernhardt, F. Bozoglian, B. P. Macpherson, M. Martinez, G. Gonzalez, B. Sienra, *Eur. J. Inorg. Chem.* **2003**, 2512–2518.
[10] A. B. P. Lever, *Inorganic Electronic Spectroscopy*, Elsevier, **1984**.
[11] M. Martinez, M.-A. Pitarque, R. van Eldik, *Inorg. Chim. Acta* **1997**, *256*, 51–59.
[12] M. Maruyama, H. Matsuzawa, Y. Kaizu, *Inorg. Chim. Acta* **1995**, *237*, 159–162.
[13] K. R. Dunbar, R. A. Heintz, *Prog. Inorg. Chem.* **1997**, *19*, 283–391.
[14] C. A. Bignozzi, R. Argazzi, J. R. Schoonover, K. C. Gordon, R. B. Dyer, F. Scandola, *Inorg. Chem.* **1992**, *31*, 5260–5267.
[15] A. M. Becka, C. J. Miller, *J. Phys. Chem.* **1992**, *96*, 2657–2668.
[16] H. Adams, W. Z. Alsindi, G. M. Davies, M. B. Duriska, T. L. Easun, H. E. Fenton, J.-M. Herrera, M. W. George, K. L. Ronayne, X.-Z. Sun, M. Towrie, M. D. Ward, *Dalton Trans.* **2005**, 39–50.
[17] C. A. Bignozzi, S. Roffia, C. Chiorboli, J. Davila, M. T. Indelli, F. Scandola, *Inorg. Chem.* **1989**, *28*, 4350–4358.
[18] R. S. Nicholson, I. Shain, *Anal. Chem.* **1964**, *36*, 706–723.
[19] C. R. Johnson, R. E. Shepherd, *Inorg. Chem.* **1983**, *22*, 1117–1123.
[20] J. Bendix, P. Steenberg, I. Sotofte, *Inorg. Chem.* **2003**, *42*, 4510–4512.
[21] A. A. Schilt, R. C. Taylor, *J. Inorg. Nucl. Chem.* **1959**, *9*, 211–221.
[22] F. Benzo, P. V. Bernhardt, G. Gonzalez, M. Martinez, B. Sienra, *J. Chem. Soc. Dalton Trans.* **1999**, 3973–3979.
[23] R. A. Krause, V. Carol, *Inorg. Chim. Acta* **1986**, *113*, 161–162.
[24] C. J. Timpson, C. A. Bignozzi, B. P. Sullivan, E. M. Kober, T. J. Meyer, *J. Phys. Chem.* **1996**, *100*, 2915–2925.
[25] B. P. Sullivan, D. J. Salmon, T. J. Meyer, *Inorg. Chem.* **1978**, *17*, 3334–3341.
[26] L. J. Farrugia, *J. Appl. Crystallogr.* **1999**, *32*, 837–838.
[27] G. M. Sheldrick, *SHELX97 – Programs for Crystal Structure Analysis*, University of Göttingen, **1998**.
[28] L. J. Farrugia, *J. Appl. Crystallogr.* **1997**, *30*, 565.

Received: July 11, 2007
Published Online: September 24, 2007

 © 2007 Wiley-VCH Verlag GmbH & Co. KGaA, Weinheim 

DOI: 10.1002/ejic.200700748

# Tetranuclear Nickel(II) Complexes Composed of Pairs of Dinuclear $LNi_2$ Fragments Linked by Acetylenedicarboxylate, Terephthalate, and Isophthalate Dianions: Synthesis, Structures and Magnetic Properties

**Julia Klingele,[a] Marco H. Klingele,[a][‡] Oliver Baars,[b] Vasile Lozan,[b] Axel Buchholz,[c] Guido Leibeling,[d] Winfried Plass,[c] Franc Meyer,[d] and Berthold Kersting*[b]**

**Keywords:** Macrocyclic ligands / Dicarboxylato ligands / Nickel / Polynuclear complexes / Magnetic properties

The tetranuclear nickel(II) complexes $[(LNi^{II}_2)_2$(acetylenedicarboxylate)$][BPh_4]_2$ (**2**$[BPh_4]_2$), $[(LNi^{II}_2)_2$(terephthalate)$][BPh_4]_2$ (**3**$[BPh_4]_2$), and $[(LNi^{II}_2)_2$(isophthalate)$][BPh_4]_2$ (**4**$[BPh_4]_2$), where $L^{2-}$ represents a macrocyclic hexaaza-dithiophenolate ligand, have been synthesized and characterised by UV/Vis spectroscopy, IR spectroscopy, X-ray crystallography, and magnetic susceptibility measurements. Each dicarboxylate dianion acts as a quadridentate bridging ligand linking two bioctahedral $LNi_2$ units via $\mu_{1,3}$-bridging carboxylate functions to generate discrete $[(LNi^{II}_2)_2$(dicarboxylate)$]^{2+}$ dications with a central $LNi_2(O_2C–R–CO_2)Ni_2L$ core. The structures differ mainly in the distance between the center of the Ni···Ni axes of the isostructural $LNi_2$ units (8.841(1) Å in **2**$[BPh_4]_2$, 10.712(1) in **3**$[BPh_4]_2$, and 9.561(1) in **4**$[BPh_4]_2$) and the tilting angle between the two $Ni_2O_2$ planes (86.3° in **2**$[BPh_4]_2$, 58.2° in **3**$[BPh_4]_2$, 20.9° in **4**$[BPh_4]_2$). Magnetic susceptibility measurements on the complexes over the range 2.0–295 K reveal the presence of weak ferromagnetic exchange interactions between the $Ni^{II}$ ions within the dinuclear subunits with values for the magnetic exchange constant $J_1$ of 23.1(5), 18.1(5), and 14.2(5) $cm^{-1}$ for **2**$[BPh_4]_2$, **3**$[BPh_4]_2$, and **4**$[BPh_4]_2$, respectively ($\mathbf{H} = -2J\mathbf{S}_1\mathbf{S}_2$). The magnitude of the exchange interaction $J_2$ across the dicarboxylate bridges is in all cases less than 0.1 $cm^{-1}$, suggesting that no significant interdimer exchange coupling occurs in **2**$[BPh_4]_2$–**4**$[BPh_4]_2$.
(© Wiley-VCH Verlag GmbH & Co. KGaA, 69451 Weinheim, Germany, 2007)

## Introduction

The carboxylate group, $RCO_2^-$, can bind to transition metals in a variety of coordination modes giving rise to complexes of great structural diversity.[1] Current activities focus on the coordination chemistry of polycarboxylate ligands, as these offer great potential in the construction of polynuclear aggregates[2] and extended coordination polymers with micro- and mesoporous structures[3–6] or catalytic properties.[7] In addition, polycarboxylate ligands are of importance as spin-coupling bridging ligands[8–15] in the rapidly expanding field of molecular magnetism.[16,17] In this context, an enormous amount of literature has been generated concerning the distance dependence of magnetic exchange interactions between metal atoms linked by extended dicarboxylate ligands. Dinuclear copper complexes bridged by oxalate[18,19] and terephthalate[20–22] dianions form, by far, the largest group of such systems, and it appears that the exchange interactions depend on the M···M distance,[23] the relative orientation of the magnetic orbitals,[24] and the degree of conjugation of the organic spacer unit.[25,26]

Recently, we reported the structures and magnetic properties of an isostructural series of bioctahedral $[LM^{II}_2(OAc)]^+$ complexes, where $L^{2-}$ represents a macrodinucleating $N_6S_2$ supporting ligand (Scheme 1).[27] Intramolecular antiferromagnetic exchange interactions are present in the $Mn^{II}_2$, $Fe^{II}_2$ and $Co^{II}_2$ complexes of this series with $J$ values of –5.1, –10.6, and –2.0 $cm^{-1}$ ($\mathbf{H} = -2J\mathbf{S}_1\mathbf{S}_2$). In contrast, in the corresponding $Ni^{II}_2$ complex a ferromagnetic exchange interaction is present with $J = +6.4$ $cm^{-1}$.

In view of the increasing interest in the targeted assembly of molecular-based magnetic materials using high-spin molecules of higher nuclearity,[28–34] we considered it worthwhile to examine the possibility of linking pairs of dinuclear $[LNi^{II}_2]$ units by dicarboxylate dianions to form tetranuclear species. In the present contribution we report the synthesis and crystallographic characterization of three novel

[a] Institut für Anorganische und Analytische Chemie, Universität Freiburg,
Albertstr. 21, 79104 Freiburg, Germany
[b] Institut für Anorganische Chemie, Universität Leipzig,
Johannisallee 29, 04103 Leipzig, Germany
Fax: +49-341-973-6199
E-mail: b.kersting@uni-leipzig.de
[c] Institut für Anorganische Chemie und Analytische Chemie, Universität Jena,
Carl-Zeiss-Promenade 10, 07745 Jena, Germany
[d] Institut für Anorganische Chemie, Georg-August-Universität Göttingen,
Tammannstrasse 4, 37077 Göttingen, Germany
[‡] Present address: IoLiTec Ionic Liquids Technologies GmbH & Co. KG,
Ferdinand-Porsche-Str. 5/1, 79211 Denzlingen, Germany
Supporting information for this article is available on the WWW under http://www.eurjic.org or from the author.

 © 2007 Wiley-VCH Verlag GmbH & Co. KGaA, Weinheim 

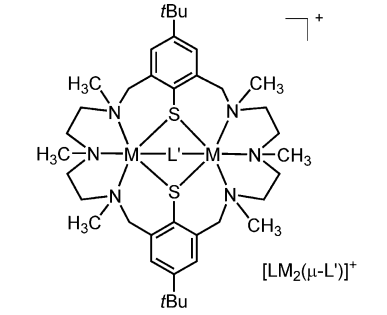


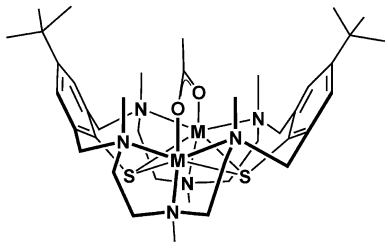

$[LM^{II}_2(OAc)]^+$ (M = $Mn^{II}$, $Fe^{II}$, $Co^{II}$, $Ni^{II}$)

Scheme 1. Dinuclear acetate-bridged complexes of the hexaazadithiophenolate ligand $L^{2-}$.

tetranuclear nickel(II) complexes of the type $[LNi^{II}_2$dicarboxylate$Ni^{II}_2L]$, where "dicarboxylate" stands for acetylenedicarboxylate, terephthalate, or isophthalate dianions. A schematic representation of these complexes is shown in Scheme 2. These novel complexes differ by the distance between the centre of the Ni···Ni axis of the isostructural $LNi_2$ subunits, their relative orientation, and the nature of the bridging ligands. The ability of the dicarboxylate dianions to mediate magnetic exchange interactions between the dinuclear subunits is examined and discussed in the light of their specific structural features.

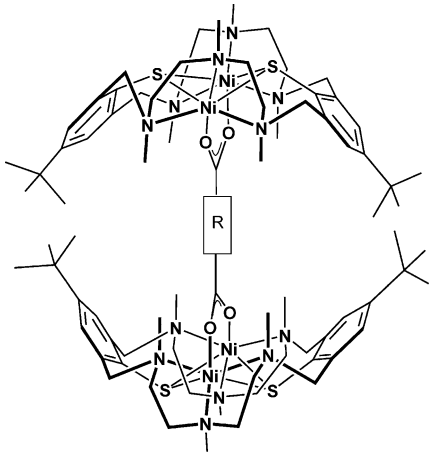


**2**, $[(LNi^{II}_2)_2$(acetylenedicarboxylate)$]^{2+}$
**3**, $[(LNi^{II}_2)_2$(terephthalate)$]^{2+}$
**4**, $[(LNi^{II}_2)_2$(isophthalate)$]^{2+}$

Scheme 2. Complexes prepared and their labels.

## Synthesis and Characterization of the Complexes

The complexes $[(LNi^{II}_2)_2$(acetylenedicarboxylato)$]^{2+}$ (**2**), $[(LNi^{II}_2)_2$(terephthalato)$]^{2+}$ (**3**), and $[(LNi^{II}_2)_2$(isophthalato)$]^{2+}$ (**4**) were readily prepared from the reaction of the dinuclear complex $[LNi^{II}_2(\mu\text{-Cl})]^+$ (**1**) and the corresponding triethylammonium dicarboxylate, prepared in situ from the acid and triethylamine in methanol in a 1:2 molar ratio, and isolated in high yield as the perchlorate or tetraphenylborate salts. The transformations are not simple substitution reactions, because simultaneous conformational changes of the supporting ligand $L^{2-}$ from the folded ($C_s$-symmetric) to the "bowl-shaped" ($C_{2v}$-symmetric) conformation take place (see Scheme 3).[35] Nonetheless, linking of two $[LNi_2]^{2+}$ fragments by the carboxylato ligands is a clean and facile step driven by the low solubility of the products.

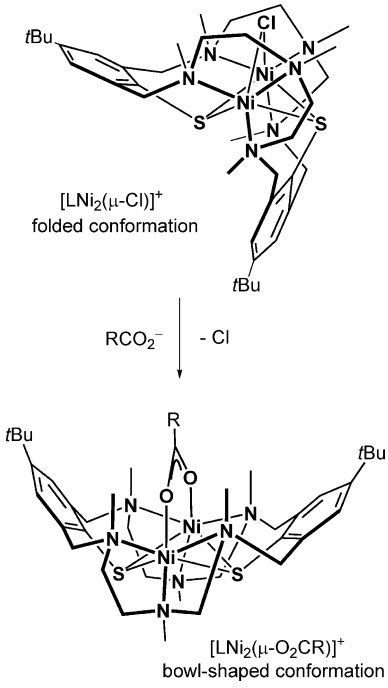


Scheme 3. Schematic representation of the two ligand conformations in the chloro- and carboxylato-bridged complexes of $(L)^{2-}$. For these conformational changes metal–ligand dissociations are required.

All compounds gave satisfactory elemental analyses and their IR spectra are marked by the prominent asymmetric and symmetric carboxylate stretching frequencies around 1580 $cm^{-1}$ and 1420 $cm^{-1}$, diagnostic of $\mu_{1,3}$-bridging carboxylate functions.[36] The UV/Vis spectra of **2**–**4** in acetonitrile display two weak bands above 500 nm typical of octahedral $Ni^{2+}$ ($d^8$, $S = 1$) ions. The observed values compare closely with those of the acetato-bridged complex $[LNi^{II}_2(OAc)]^+$,[27] indicative of a pseudo-octahedral $N_3S_2O$ coordination environment about the metal ions. This is confirmed by single-crystal X-ray crystallography.

## Description of the Crystal Structures

Crystals of $\mathbf{2}[BPh_4]_2 \cdot 2MeCN \cdot 0.5H_2O$ were obtained by slow evaporation of an acetonitrile/ethanol (1:1) solution of $\mathbf{2}[BPh_4]_2$. The crystal structure is composed of tetranuclear $[(LNi^{II}_2)_2$(acetylenedicarboxylate)$]^{2+}$ dications, tetraphen-

 © 2007 Wiley-VCH Verlag GmbH & Co. KGaA, Weinheim 

ylborate anions and acetonitrile and water solvates. Perspective drawings of the structure of **2** are depicted in Figure 1. Selected bond lengths and angles are summarized in Table 1.

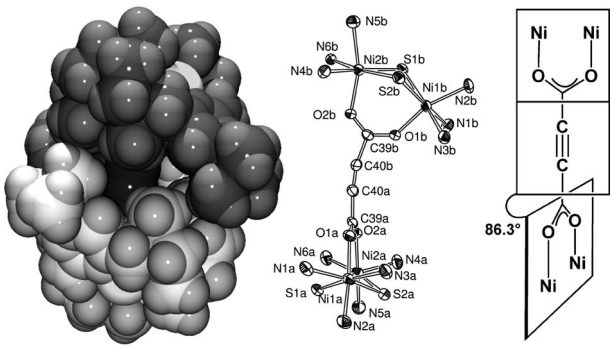


Figure 1. Left: van der Waals plot of the $[(LNi^{II}_2)_2(acetylenedicarboxylato)]^{2+}$ dication in crystals of $\mathbf{2}[BPh_4]_2{\cdot}MeCN{\cdot}0.5H_2O$. Middle: ORTEP representation of the core structure of **2** with the atom labeling Scheme. Ellipsoids are represented at the 50% probability level. Right: Mutual orientation of the $Ni_2$carboxylato planes in **2**.

The acetylenedicarboxylate dianion acts as a tetradentate bridging ligand joining two dinuclear $[LNi^{II}_2]^{2+}$ fragments through its carboxylate functions to give a tetranuclear $Ni_2(O_2CC{\equiv}CCO_2)Ni_2$ array. Each nickel atom is surrounded in a highly distorted octahedral fashion by two sulfur atoms and three nitrogen atoms from the supporting ligand, and one oxygen atom from the acetylenedicarboxylate moiety. The $Ni_2$carboxylato planes are necessarily twisted by 86.3° about the C≡C bond to relieve the unfavourable steric interactions between the bulky *t*Bu groups of the two opposing $[LNi^{II}_2]^{2+}$ subunits. The coligand is also slightly bent (C≡C 1.185(6) Å] such that the intramolecular distances between two nickel atoms of different dinuclear subunits within the tetranuclear complex range from 8.623(1) to 9.769(1) Å. The only system comparable to that of **2** is provided by the complex $[\{Mo_2(DAniF)_3\}_2(O_2CC{\equiv}CCO_2)]$, where DAniF = *N*,*N*′-di-*p*-anisylformamidinate, for which an intramolecular Mo···Mo distance of 9.537 Å has been reported.[37] There are no significant intermolecular interactions between the $Ni^{II}_4$ complexes within the lattice. The shortest intermolecular Ni···Ni distance is at 7.470(1) Å.

Table 1. Selected bond lengths [Å] and angles [°] in **2**–**4**.

| | $\mathbf{2}[BPh_4]_2{\cdot}MeCN{\cdot}H_2O$[a] | $\mathbf{3}[BPh_4]_2{\cdot}2EtOH{\cdot}MeCN_{0.5}{\cdot}H_2O$[a] | $\mathbf{4}[BPh_4]_2{\cdot}4MeCN{\cdot}EtOH$ [a] |
|---|---|---|---|
| Ni(1a)–O(1a) | 2.017(3) [1.974(3)] | 1.992(3) [1.995(3)] | 2.044(1) [1.989(2)] |
| Ni(1a)–N(1a) | 2.302(5) [2.306(4)] | 2.347(4) [2.286(4)] | 2.312(2) [2.309(2)] |
| Ni(1a)–N(2a) | 2.160(4) [2.133(4)] | 2.141(4) [2.135(4)] | 2.157(2) [2.133(2)] |
| Ni(1a)–N(3a) | 2.212(4) [2.277(4)] | 2.199(4) [2.228(4)] | 2.228(2) [2.255(2)] |
| Ni(1a)–S(1a) | 2.504(2) [2.486(2)] | 2.457(2) [2.507(2)] | 2.4750(7) [2.4981(6)] |
| Ni(1a)–S(2a) | 2.399(2) [2.408(2)] | 2.469(2) [2.486(2)] | 2.4418(6) [2.4311(6)] |
| Ni(2a)–O(2a) | 2.028(3) [2.078(3)] | 2.002(3) [2.007(3)] | 1.998(1) [2.032(1)] |
| Ni(2a)–N(4a) | 2.226(5) [2.189(4)] | 2.266(4) [2.246(4)] | 2.215(2) [2.204(2)] |
| Ni(2a)–N(5a) | 2.159(5) [2.190(4)] | 2.147(4) [2.157(4)] | 2.155(2) [2.146(2)] |
| Ni(2a)–N(6a) | 2.296(5) [2.279(4)] | 2.242(4) [2.280(4)] | 2.281(2) [2.346(2)] |
| Ni(2a)–S(1a) | 2.503(2) [2.497(2)] | 2.504(2) [2.489(2)] | 2.5099(6) [2.4567(7)] |
| Ni(2a)–S(2a) | 2.398(2) [2.446(2)] | 2.451(2) [2.460(2)] | 2.4317(6) [2.4523(6)] |
| N–O | 2.024(3) | 1.999(3) | 2.016(1) |
| Ni–N | 2.227(5) | 2.223(4) | 2.228(2) |
| Ni–S | 2.455(2) | 2.478(2) | 2.4621(6) |
| C(39a)–O(1a) | 1.261(6) [1.258(5)] | 1.257(5) [1.257(5)] | 1.255(2) [1.258(2)] |
| C(39a)–O(2a) | 1.250(6) [1.245(6)] | 1.265(5) [1.260(5)] | 1.265(2) [1.263(2)] |
| Ni(1a)···Ni(2a) | 3.469(1) | 3.460(1) | 3.475(1) |
| Ni(1b)···Ni(2b) | 3.486(1) | 3.507(1) | 3.459(1) |
| Ni(1a)···Ni(1b) | 8.623(1) | 11.028(1) | 8.120(1) |
| Ni(1a)···Ni(2b) | 9.508(1) | 10.947(1) | 10.122(1) |
| Ni(2a)···Ni(1b) | 8.757(1) | 10.833(1) | 9.909(1) |
| Ni(2a)···Ni(2b) | 9.769(1) | 11.155(1) | 11.097(1) |
| $Ni–Ni^{cent}/Ni–Ni^{cent}$[b] | 8.841(1) | 10.712(1) | 9.561(1) |
| $O–M–N_{cis}$[c] | 87.7(2) [87.3(2)] | 88.7(2) [88.2(2)] | 88.26(6) [88.12(6)] |
| $O–M–N_{trans}$[c] | 162.3(2) [162.6(2)] | 164.8(2) [164.9(2)] | 164.27(6) [164.13(6)] |
| $S–M–N_{cis}$[c] | 94.5(2) [94.7(1)] | 93.8(1) [94.2(1)] | 94.00(5) [93.94(5)] |
| $S–M–N_{trans}$[c] | 168.9(1) [169.0(1)] | 170.5(1) [169.8(1)] | 169.52(5) [169.73(5)] |
| S–M–S[c] | 78.91(6) [78.82(5)] | 80.4(1) [79.25(5)] | 79.47(2) [79.92(2)] |
| S–M–O[c] | 94.6(1) [94.4(1)] | 94.3(1) [94.1(1)] | 94.52(4) [94.49(4)] |
| N–M–N[c] | 87.8(2) [87.9(2)] | 87.6(2) [87.8(2)] | 87.61(6) [87.66(7)] |
| M–S–M[c] | 90.18(6) [90.31(5)] | 88.91(5) [89.76(5)] | 89.30(2) [89.76(6)] |
| | | | |
| $RCO_2/RCO_2$[d] | 86.3 | 58.2 | 20.9 |
| $RCO_2$/Ph[e] | – | 39.1 [19.1] | 9.6 [12.8] |

[a] Numbers in square brackets correspond to atoms labeled "b". [b] Distance between center of the Ni···Ni axes of the Ni2 units. [c] Average values. [d] Angle between the normals of the planes of the carboxylate functions. [e] Twist angle of the carboxylato planes with respect to the aromatic ring of the dicarboxylate dianion.

 © 2007 Wiley-VCH Verlag GmbH & Co. KGaA, Weinheim 

Figure 2 shows the structure of the tetranuclear nickel(II) complex **3** in crystals of **3**$[BPh_4]_2$·2EtOH·0.5MeCN·$H_2O$. Again, the terephthalato ligand acts as a bifunctional linker coordinating to two bioctahedral $[LNi^{II}_2]^{2+}$ entities via the carboxylate functions to generate a twisted $Ni_2O_2C–C_6H_4–CO_2Ni_2$ motif.

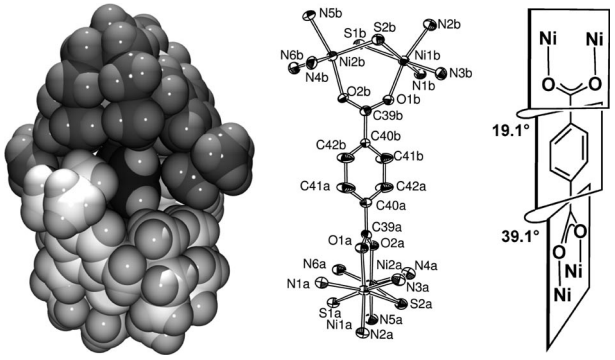


Figure 2. Left: van der Waals representation of the $[(LNi^{II}_2)_2$-(μ-terephthalato)$]^{2+}$ dication in crystals of **3**$[BPh_4]_2$·2EtOH·0.5MeCN·$H_2O$. Middle: ORTEP representation of the core structure of **3** with the atom labeling Scheme. Ellipsoids are represented at the 50% probability level. Right: Relative orientation of the $Ni_2$carboxylato planes in **3**.

The $[LNi_2]^{2+}$ subunits in **2** and **3** are structurally very similar, and the Ni–N, Ni–O, and Ni–S distances lie within very narrow ranges (Table 1). As in **2**, the *t*Bu groups of the two opposing $Ni_2$ clusters are forced to interlock to accommodate the terephthalato ligand. This causes tilting of the carboxylato planes that are rotated by 58.2° with respect to each other and by 19.1° and 39.1° with respect to the aromatic ring of the terephthalato coligand. Again, there are no intermolecular interactions between the tetranuclear complexes other than van der Waals contacts. The intramolecular Ni···Ni distances between the two dinuclear subunits are within the range 10.833(1)–11.155(1) Å (mean 10.990(1) Å]. This is a typical value for terephthalato-bridged nickel(II) complexes.[38,39]

Crystals of **4**$[BPh_4]_2$·4MeCN·EtOH are triclinic, space group $P\bar{1}$. ORTEP views of the structure of the dication **4** and the central core are provided in Figure 3. Selected bond lengths and angles are given in Table 1.

The isophthalate dianion is bonded to two $[LNi^{II}_2]^{2+}$ units through $\mu_{1,3}$-bridging carboxylate functions. The metal–ligand bond lengths within **4** reveal no anomalities and are very similar to those in **2** and **3** (Table 1). Strangely, the twisting of the carboxylato planes is less pronounced than in the previous cases. In fact, the two planes are almost coplanar with the phenyl ring of the bridging isophthalate dianion. The geometrical requirements of the isophthalate moiety with the two carboxylate functions in *meta* orientation leads to a distance of 9.561 Å between the center of the Ni···Ni axes of the dinuclear units. This value should be compared with that of 10.712 Å in **3**, where the two carboxylate functions are in *para* positions. The present coordination mode of the isophthalate dianion forming a discrete $Ni^{II}_4$ cluster is without precedence in the literature.[40–42]

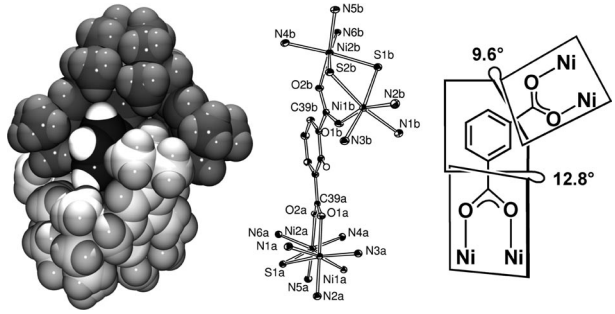


Figure 3. Left: van der Waals representation of the $[(LNi^{II}_2)_2$-(μ-isophthalato)$]^{2+}$ dication in crystals of **4**$[BPh_4]_2$·4MeCN·EtOH. Middle: ORTEP representation of the core structure of **4** with the atom labeling Scheme. Ellipsoids are represented at the 50% probability level. Right: Tilting of the $Ni_2$carboxylato planes in **4**.

In summary, all three new compounds are discrete tetranuclear nickel(II) complexes composed of pairs of bioctahedral $[LNi^{II}_2]^{2+}$ units united by a tetradentate dicarboxylate anion. The calixarene-like conformation adopted by the supporting ligand leads to an almost complete encapsulation of the $Ni_2(O_2C–R–CO_2)Ni_2$ core. As a consequence the $Ni^{II}_4$ clusters are well-separated from each other in the solid state, featuring only intermolecular van der Waals contacts. This aspect of the structures will be relevant in the following discussion of the magnetic properties of the complexes.

## Magnetic Properties

The magnetic properties of the three carboxylato-bridged complexes were examined in view of literature reports that conjugated dicarboxylate ligands are able to mediate long-range magnetic exchange interactions between paramagnetic metal ions.[43] The variable-temperature magnetic susceptibility data for **2**$[BPh_4]_2$, **3**$[BPh_4]_2$, and **4**$[BPh_4]_2$ were measured over the range 2.0–295 K using a SQUID magnetometer and an applied external magnetic field of 0.2 T. Plots of the temperature dependence of the effective magnetic moment $\mu_{eff}$ for the three compounds are shown in Figure 4. The complexes have similar magnetic properties. At room temperature, the respective values of $\mu_{eff}$ are 6.91 $\mu_B$, 6.82 $\mu_B$, and 7.13 $\mu_B$ per tetranuclear complex. With decreasing temperature the $\mu_{eff}$ values increase steadily to maximum values of 7.85 $\mu_B$ (15 K), 7.71 $\mu_B$ (15 K), and 8.03 $\mu_B$ (25 K) for **2**$[BPh_4]_2$, **3**$[BPh_4]_2$, and **4**$[BPh_4]_2$, respectively. On lowering the temperature to 2.0 K, these values decrease slightly down to 7.57 $\mu_B$, 7.02 $\mu_B$, and 5.78 $\mu_B$ at 2 K, presumably due to saturation effects or the zero-field splitting of nickel(II).

In all cases the maximum value of the effective magnetic moment is lower than expected for a spin-only value of 9.84 $\mu_B$ for $S_T = 4$ resulting from ferromagnetic coupling of four $Ni^{II}$ ($S_i = 1$, $g = 2.20$) ions. However, the values are also significantly larger than the value of 6.22 $\mu_B$ calculated for completely uncoupled spins. The overall behaviour indi-

 © 2007 Wiley-VCH Verlag GmbH & Co. KGaA, Weinheim 

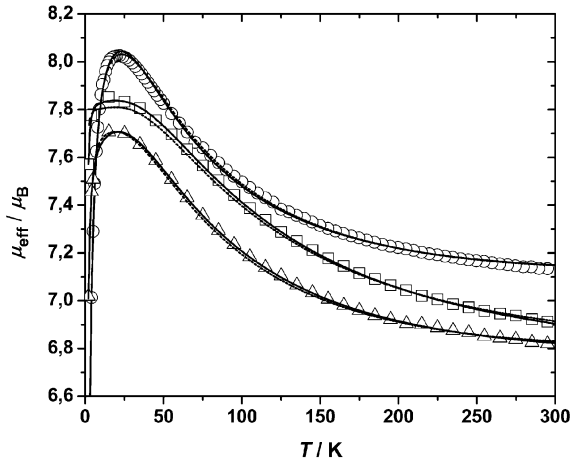


Figure 4. Temperature dependence of $\mu_{eff}$ (per tetranuclear complex) for **2**$[BPh_4]_2$ (open squares), **3**$[BPh_4]_2$ (open triangles), and **4**$[BPh_4]_2$ (open circles). The full lines represent the best theoretical fits to Equation (1). The dashed lines represent the best fits to the dimer model in Equation (3). Experimental and calculated values are provided in the electronic supporting information.

cates the presence of weak ferromagnetic exchange interactions between the $Ni^{2+}$ ions within the dinuclear subunits, but negligible, if any, coupling across the dicarboxylate bridges. The latter behaviour can be attributed to the long distance between the $Ni^{2+}$ ions spanned by the dicarboxylates. In this regard, it is worth noting that very weak exchange interactions have indeed been reported for other terephthalato- or isophthalato-bridged nickel(II) complexes.[26,44,45]

In order to determine the magnitude of the exchange interactions, the magnetic susceptibility data were simulated by using Equation (1), where $\chi_{tetra}$ and $\chi_{mono}$ refer to the molar susceptibilities of a $Ni_4$ complex and a fraction $\rho$ of a mononuclear nickel(II) impurity with Curie constant $C = Ng^2\mu_B{}^2/3kT$.

$$\chi = \chi_{tetra}(1-\rho) + 4\chi_{mono}\rho \quad (1)$$

The molar magnetic susceptibility $\chi_{tetra}$ was derived from the appropriate spin-Hamiltonian [Equation (2)] including the isotropic Heisenberg exchange, the single-ion zero-field splitting and the single-ion Zeeman interaction by a full-matrix diagonalization approach.[34]

$$H = -2J_1(\hat{S}_1 \cdot \hat{S}_2 + \hat{S}_3 \cdot \hat{S}_4) - 2J_2(\hat{S}_1 \cdot \hat{S}_3 + \hat{S}_1 \cdot \hat{S}_4 + \hat{S}_2 \cdot \hat{S}_3 + \hat{S}_2 \cdot \hat{S}_4)$$

$$H = H_{ex} + \sum_{i=1}^{4}[D_i(\hat{S}_{iz}^2 - \tfrac{1}{3}S_i(S_i+1)) + g_i\mu_B B_\tau \hat{S}_{i\tau}] \ (\tau = x, y, z) \quad (2)$$

In this model $J_1$ (= $J_{12}$ = $J_{34}$) represents the exchange interaction between the $Ni^{2+}$ ions within the dinuclear subunit, whereas $J_2$ ($J_{13}$ = $J_{14}$ = $J_{23}$ = $J_{24}$) describes the interaction across the dicarboxylate linker. In order to reduce the number of variables, the $D$ and $g$ values were considered to be identical for all of the four $Ni^{2+}$ ions.

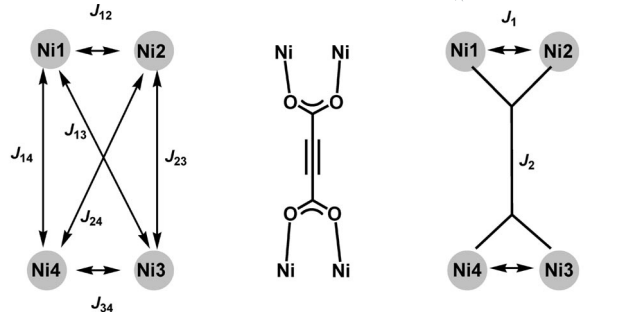


The least-squares fitting of the experimental data over the full temperature range led to $J_1$ = +23.1(5) $cm^{-1}$, $J_2$ = –0.0045(10) $cm^{-1}$, $g$ = 2.27(1), $D$ = –1.9(5) $cm^{-1}$, $\rho$ = 0.010(5)% for **2**$[BPh_4]_2$, $J_1$ = +18.1(5) $cm^{-1}$, $J_2$ = –0.0048(9) $cm^{-1}$, $g$ = 2.24(1), $D$ = –1.5(5) $cm^{-1}$, $\rho$ = 0.020(5)% for **3**$[BPh_4]_2$, and $J_1$ = +14.2(5) $cm^{-1}$, $J_2$ = –0.071(9) $cm^{-1}$, $g$ = 2.37(1), $D$ = 9.6(5) $cm^{-1}$, $\rho$ = 0.020(5)% for **4**$[BPh_4]$. The inclusion of the $D$ parameter improves the low-temperature fit significantly, but it represents by no means an accurate value since temperature-dependent magnetic susceptibility measurements are not very appropriate for the determination of $D$.[46,47] The experimentally determined $J_2$ parameters are very small and should be taken as indicative rather than definite, because they are beyond the detection limit of the technique. Nevertheless, it is clear that magnetic exchange interactions via the dicarboxylate linkers are not significant (estimated upper limit for $J_2$: $\pm$0.1 $cm^{-1}$) and that the magnetic properties of the tetranuclear systems are solely based on the exchange couplings in the binuclear $[LNi_2(O_2CR)]^+$ subunits. In this respect, we also tried to simulate the temperature dependence of the magnetic data by using an isotropic dimer model [Equation (3)] for two $Ni^{II}$ ($S$ = 1) ions based on the Hamiltonian in Equation (4).

$$\chi = 2[\chi_{dim}(1-\rho) + 2\chi_{mono}\rho] \quad (3)$$

$$H = -2JS_1S_2 + \sum_{i=1}^{2}[D_i(\hat{S}_{iz}^2 - \tfrac{1}{3}S_i(S_i+1)) + g_i\mu_B B_\tau \hat{S}_{i\tau}] \quad (\tau = x, y, z) \quad (4)$$

The magnetic data could be reproduced equally well by this approach (Figure 4), yielding $J_1$ = +23.4(5) $cm^{-1}$, $g$ = 2.26(1), $D$ = –2.2(5) $cm^{-1}$, $\rho$ = 0.010% for **2**$[BPh_4]_2$, $J_1$ = +19.3(4) $cm^{-1}$, $g$ = 2.23(1), $D$ = –4.8(5) $cm^{-1}$, $\rho$ = 0.035% for **3**$[BPh_4]_2$, and $J_1$ = +15.5(5) $cm^{-1}$, $g$ = 2.35, $D$ = 12.0(5) $cm^{-1}$, $\rho$ = 0.03% for **4**$[BPh_4]$. Again, this analysis establishes a weak ferromagnetic coupling between the two $Ni^{II}$ ions. All of these values are in excellent agreement with those reported for the dinuclear nickel(II) complexes $[LNi^{II}_2(OAc)][BPh_4]$ and $[LNi^{II}_2(OBz)][BPh_4]$,[48] providing further support for the absence of significant interdimer exchange coupling in **2**$[BPh_4]_2$–**4**$[BPh_4]_2$.

There has been much interest in the distance-dependence of superexchange interactions between paramagnetic transition metal ions bridged by extended organic spacer ligands.[22,23] In this regard a large number of dicarboxylato-bridged copper(II) dimers with Cu···Cu separations of 5 to 15 Å have been prepared and their magnetic properties have

 © 2007 Wiley-VCH Verlag GmbH & Co. KGaA, Weinheim 

been determined.[22,23] In general, the magnetic exchange interactions decrease rapidly with increasing M···M separations and the experimentally determined $J$ values approach the values predicted by the Coffman Buettner relation ($|J| \leq 1$ cm$^{-1}$ for $d$(M···M) $\geq 9$ Å).[23,49] Cano et al. have shown that this finding also applies to other paramagnetic metal ions,[26] and the *inter*dimer exchange couplings of the present complexes ($|J| \leq 0.1$ cm$^{-1}$, $d$($Ni_2$···$Ni_2$) 8.623–11.155 Å) are in good agreement with the reported trend. There seems to be no dependence of the *inter*dimer coupling on the mutual orientation of the $Ni_2O_2$ planes, which is in line with our previous observations.[50]

## Conclusions

In summary, we presented the synthesis and characterization of the first members of a new class of tetranuclear nickel(II) complexes in which pairs of dinuclear $Ni_2$-aminethiophenolate complexes are linked by acetylenedicarboxylate, terephthalate and isophthalate groups. The complexes are readily prepared and exist as stable and discrete complexes in solution and in the solid state as ascertained by various spectroscopic methods and X-ray crystallography. The magnetic properties of these compounds reveal the presence of weak ferromagnetic exchange interactions between the $Ni^{II}$ ions of the dinuclear subunits and negligible coupling across the dicarboxylate bridges. A dependence of the *inter*dimer coupling on the mutual orientation of the $Ni_2O_2$ planes was not observed. High-spin molecules of this sort are presumably only accessible with shorter bridging ligands such as oxalate or squarate dianions. These studies are underway.

## Experimental Section

**General Remarks:** Solvents and reagents were of reagent grade quality and used as received unless otherwise specified. [$LNi^{II}_2$(μ-Cl)]$ClO_4$ was prepared according to a literature procedure.[51] Melting points were determined in open glass capillaries and are uncorrected. IR spectra were measured on a Bruker VECTOR 22 FT-IR spectrophotometer as KBr pellets, electronic absorption spectra on a Jasco V-570 UV/Vis/Near IR spectrophotometer. Temperature-dependent magnetic susceptibility measurements on powdered solid samples were carried out on a SQUID magnetometer (MPMS Quantum Design) over the temperature range 2.0–295 K. The measurements were performed at applied magnetic fields of 0.20 and 0.50 T. For all three compounds, the magnetic behaviour does not change with field. The observed susceptibility data were corrected for underlying diamagnetism using Pascal's constants.

**Derivation of the Magnetic Susceptibility Expression for Tetranuclear Ni Complexes:** The complete matrix of $H$ can be calculated by writing out the coupled states and determining the matrix elements by elementary operations with angular momenta operators.[52,53] The resulting Hamiltonian matrix is diagonalized numerically for given values of $J_1$, $J_2$, $g$ and $D$. The slope of $E$ vs. $B$ is calculated at the desired field; this slope is the magnetic moment for the $i^{th}$ energy level. The molar paramagnetic susceptibility, $\chi$, of the system is then calculated as a function of temperature using Equation (1), where $\chi_{tetra}$ and $\chi_{mono}$ refer to the molar susceptibilities of the tetranuclear complex [Equation (5)] and the fraction $\rho$ of a mononuclear nickel(II) impurity with Curie constant $C = Ng^2\mu_B{}^2/3kT$ [Equation (6)]. $\chi_{dim}$ is the molar susceptibility of the binuclear subunit. A least-squares program then compares calculated and observed susceptibility curves and changes the parameters to get the best fit.[34]

$$\chi_{tetra} = \frac{N}{B_0}\frac{\sum_i(-\partial E_i/\partial B)\exp(-E_i/kT)}{\sum_i \exp(-E_i/kT)} \quad (5)$$

$$\chi_{mono} = \frac{Ng^2\mu_B^2}{3kT}\left(\frac{2}{2}\left(\frac{2}{2}+1\right)\right) \quad (6)$$

**Safety note! Caution:** *Perchlorate salts of transition metal complexes are hazardous and may explode. Only small quantities should be prepared and handled with great care.*

**[($LNi^{II}_2$)$_2$(acetylenedicarboxylato)][$ClO_4$]$_2$ (2[$ClO_4$]$_2$):** Triethylamine (50 mg, 0.50 mmol) was added to a solution of acetylenedicarboxylic acid (28.5 mg, 0.250 mmol) in methanol (30 mL). [$LNi^{II}_2$Cl]$ClO_4$ (**1**[$ClO_4$]) (461 mg, 0.500 mmol) was added to this solution with constant stirring. A green precipitate resulted immediately. Additional $LiClO_4 \cdot 3H_2O$ (160 mg, 1.00 mmol) was added to ensure complete precipitation of the product. After stirring for 1 d, the green precipitate was collected by filtration, washed several times with cold methanol and dried in the air. Yield 335 mg (71%), m.p. 302–303 °C (decomp.). IR (KBr): $\tilde{\nu}$ = 3439 (m), 2963 (s), 2869 (s), 2249 (w), 2018 (w), 1596 [s, $\nu_{asym}(RCO_2^-)$], 1463 (s), 1424 (w), 1394 [w, $\nu_{sym}(RCO_2^-)$], 1355 (s), 1264 (m), 1235 (m), 1202 (w), 1170 (w), 1154 (m), 1096 [vs, $\nu_3(ClO_4^-)$], 1039 (s), 1001 (w), 984 (w), 932 (m), 912 (m), 881 (m), 826 (s), 819 (m), 809 (m), 766 (w), 754 (w), 682 (m), 624 [vs, $\nu_4(ClO_4^-)$] (s), 602 (w), 564 (w), 545 (w), 535 (w), 493 (w), 441 (w), 417 cm$^{-1}$ (w).

**[($LNi^{II}_2$)$_2$(acetylenedicarboxylato)][$BPh_4$]$_2$ (2[$BPh_4$]$_2$):** A solution of $NaBPh_4$ (342 mg, 1.00 mmol) in ethanol (50 mL) was added to a solution of **2**[$ClO_4$]$_2$ (188 mg, 0.100 mmol) in acetonitrile (150 mL). The reaction mixture was allowed to stir for 1 h, before the volume of the solution was reduced in vacuo to about 50 mL. The green product was filtered, washed with ethanol and dried in the air to give 190 mg (82%) of **2**[$BPh_4$]$_2$ as a green, air-stable, microcrystalline powder, m.p. 279–280 °C (decomp.). IR (KBr (cm$^{-1}$)): $\tilde{\nu}$ = 3434 (s), 3122 (w), 3054 (s), 3030 (s), 2963 (s), 2867 (s), 2808 (m), 1945 (w), 1880 (w), 1815 (w), 1763 (w), 1597 [s, $\nu_{asym}(CO_2^-)$], 1461 (s), 1425 (m), 1392 [m, $\nu_{sym}(CO_2^-)$], 1355 (s), 1308 (m), 1264 (m), 1235 (m), 1202 (w), 1170 (w), 1154 (m), 1133 (w), 1078 (s), 1058 (s), 1039 (s), 999 (w), 930 (w), 911 (w), 882 (w), 824 (m), 733 [s, $\nu(BPh_4^-)$], 705 [s, $\nu(BPh_4^-)$], 681 (m), 627 (m), 612 (m), 563 (w), 544 (w), 492 (w), 470 (w), 414 (w). UV/Vis ($CH_2Cl_2$): $\lambda_{max}$ ($\varepsilon$) = 656 (32), 1091 nm (82 M$^{-1}$cm$^{-1}$). $C_{128}H_{168}B_2N_{12}Ni_4O_4S_4$ (2323.44): calcd. C 66.17, H 7.29, N 7.23, S 5.52; found C 65.85, H 7.31, N 7.20, S 5.68. Single crystals of **2**[$BPh_4$]$_2$·2MeCN·0.5$H_2O$ suitable for an X-ray structure analysis were grown by slow evaporation of an ethanol/acetonitrile solution of **2**[$BPh_4$]$_2$. These crystals slowly lose solvent molecules of solvent of crystallization at ambient temperature and turn dull.

**[($LNi_2$)$_2$(terephthalato)][$ClO_4$]$_2$ (3[$ClO_4$]$_2$):** Triethylamine (50 mg, 0.50 mmol) was added to a solution of terephthalic acid (41.5 mg, 0.250 mmol) in methanol (30 mL). A solution of [$LNi^{II}_2$Cl]$ClO_4$ (**1**[$ClO_4$]) (461 mg, 0.500 mmol) in methanol (50 mL) was slowly added resulting in the immediate formation of a green precipitate. After the addition was complete, further $LiClO_4 \cdot 3H_2O$ (160 mg,

 © 2007 Wiley-VCH Verlag GmbH & Co. KGaA, Weinheim 

1.00 mmol) dissolved in methanol (2 mL) was added, and stirring was continued for additional 3 h. The pale-green product was collected by filtration, washed several times with cold methanol to remove any soluble impurities, and dried in the air. Yield 358 mg (74%), m.p. 317–318 °C (decomp.). IR (KBr): $\tilde{\nu}$ = 3443 (m), 2962 (s), 2868 (s), 2020 (w), 1719 (w), 1584 [s, $\nu_{asym}(RCO_2^-)$], 1463 (s), 1423 (m), 1392 [s, $\nu_{sym}(RCO_2^-)$], 1364 (m), 1309 (w), 1292 (w), 1265 (w), 1234 (m), 1201 (w), 1170 (w), 1153 (w), 1097 [vs, $\nu_3(ClO_4^-)$], 1060 (s), 1040 (s), 1017 (w), 1001 (w), 982 (w), 931 (m), 913 (m), 881 (m), 825 (s), 807 (m), 752 (m), 694 (w), 669 (w), 623 [s, $\nu_4(ClO_4^-)$], 601 (w), 564 (w), 538 (m), 493 (w), 446 (w), 437 (w), 417 $cm^{-1}$ (w).

**[(LNi$_2$)$_2$(terephthalato)][BPh$_4$]$_2$ (3[BPh$_4$]$_2$):** A solution of $NaBPh_4$ (342 mg, 1.00 mmol) in ethanol (100 mL) was added to a warm solution of **3**[$ClO_4$]$_2$ (194 mg, 0.100 mmol) in acetonitrile (150 mL). The reaction mixture was allowed to stir for 1 h. Upon concentration of the solution a green microcrystalline precipitate formed, which was filtered, washed with ethanol and dried in the air for 2 d yielding 214 mg (90%) of **3**[$BPh_4$]$_2$ as a green powder, m.p. > 365 °C. IR (KBr): $\tilde{\nu}$ = 3436 (s), 3053 (s), 3032 (s), 3121 (w), 2962 (s), 2866 (s), 2807 (m), 1940 (w), 1879 (w), 1812 (w), 1762 (w), 1583 [s, $\nu_{asym}(CO_2^-)$], 1460 (s), 1424 (s), 1390 [s, $\nu_{sym}(CO_2^-)$], 1364 (s), 1308 (m), 1265 (m), 1233 (m), 1201 (w), 1170 (w), 1152 (m), 1112 (w), 1076 (s), 1059 (s), 1041 (s), 1001 (w), 982 (w), 929 (m), 912 (m), 882 (m), 823 (s), 734 [s, $\nu(BPh_4^-)$], 704 [s, $\nu(BPh_4^-)$], 668 (w), 629 (m), 612 (s), 563 (w), 538 (m), 491 (w), 471 (w), 416 $cm^{-1}$ (w). UV/Vis ($CH_2Cl_2$): $\lambda_{max}$ ($\varepsilon$) = 651 (27), 1118 nm (62 $M^{-1}cm^{-1}$). $C_{132}H_{172}B_2N_{12}Ni_4O_4S_4$ (2375.51): calcd. C 66.74, H 7.30, N 7.08, S 5.40; found C 66.50, H 7.16, N 7.09, S 5.66. Single crystals of **3**·[$BPh_4$]$_2$·2EtOH·0.5MeCN·$H_2O$ suitable for an X-ray crystal structure analysis were grown by slow evaporation of a solution of **3**[$BPh_4$]$_2$ dissolved in ethanol/acetonitrile (1:1).

**[(LNi$_2$)$_2$(isophthalate)][ClO$_4$]$_2$ (4[ClO$_4$]$_2$):** Triethylamine (51 mg, 0.50 mmol) and solid [$LNi^{II}_2Cl[ClO_4]$ (**1**[$ClO_4$]) (461 mg, 0.500 mmol) was added to a solution of isophthalic acid (41.5 mg, 0.250 mmol) in MeOH (30 mL) with stirring at ambient temperature. The resulting green suspension was stirred overnight. A methanol solution (5 mL) of $LiClO_4·3H_2O$ (320 mg, 2.00 mmol) was added and stirring was continued for another 3 h. The green precipitate was filtered, washed with cold ethanol, and dried in the air. Yield 368 mg (76%), m.p. 331–332 °C (decomp.). IR (KBr): $\tilde{\nu}$ = 3426 (m), 2962 (s), 2869 (s), 1716 (w), 1607 (s) [$\nu_{as}(RCO_2^-)$], 1573 (s), 1462 (s), 1422 [m, $\nu_s(RCO_2^-)$], 1394 (s), 1364 (m), 1308 (w), 1265 (w), 1233 (w), 1202 (w), 1153 (m), 1096 [vs, $\nu_3(ClO_4^-)$], 1078 (s), 1041 (s), 1000 (w), 982 (w), 931 (w), 913 (w), 881 (w), 825 (m), 818 (m), 808 (w), 739 (w), 713 (w), 624 [m, $\nu_4(ClO_4^-)$], 564 (w), 540 (w), 491 (w), 463 (w), 452 (w), 428 (w), 413 (w), 405 $cm^{-1}$ (w). UV/Vis ($CH_3CN$): $\lambda_{max}$ ($\varepsilon$) = 265 (14869), 304 (12212), 330 (9902), 640 (49), 1141 nm (76 $M^{-1}cm^{-1}$).

**[(LNi$_2$)$_2$(isophthalate)][BPh$_4$]$_2$ (4[BPh$_4$]$_2$):** This salt was prepared in much the same way as described for **2**[$BPh_4$]: To a suspension of **4**[$ClO_4$]$_2$ (201 mg, 0.100 mmol) in acetonitrile (50 mL) was added a solution of $NaBPh_4$ (342 mg, 1.00 mmol) in ethanol (50 mL). After the resulting mixture was stirred for 2 h, the suspension was filtered, washed with ethanol, and dried in the air. Yield 225 mg (95%), m.p. 334–335 °C (decomp.). IR (KBr): $\tilde{\nu}$ = 3448 (w), 3053 (m), 3030 (m), 2962 (s), 2865 (s), 1815 (w), 1603 [s, $\nu_{asym}(RCO_2^-)$], 1564 (s), 1460 (s), 1426 [m, $\nu_{sym}(RCO_2^-)$], 1381 (s), 1307 (w), 1265 (m), 1233 (w), 1201 (w), 1152 (w), 1078 (m), 1059 (m), 1041 (m), 999 (w), 929 (w), 911 (w), 882 (w), 824 (m), 734 [s, $\nu(BPh_4^-)$], 704 [s, $\nu(BPh_4^-)$], 627 (m), 612 (m), 563 (w), 534 (w), 466 (w), 428 $cm^{-1}$ (w). UV/Vis ($CH_3CN$): $\lambda_{max}$ ($\varepsilon$) = 304 (13511), 330 (10913), 648 (61), 1106 nm (87 $M^{-1}cm^{-1}$). $C_{132}H_{172}B_2N_{12}Ni_4O_4S_4$ (2375.51): calcd. C 66.74, H 7.30, N 7.08, S 5.40; found C 65.31, H 7.36, N 6.78, S 5.31. Single crystals of **4**[$BPh_4$]$_2$·4MeCN·EtOH suitable for an X-ray crystal structure analysis were grown by slow evaporation of a solution of **4**[$BPh_4$]$_2$ in ethanol/acetonitrile.

**Collection and Reduction of X-ray Data:** Suitable single crystals of **2**[$BPh_4$]$_2$·MeCN·0.5$H_2O$, **3**[$BPh_4$]$_2$·2EtOH·$MeCN_{0.5}$·$H_2O$ and **4**[$BPh_4$]$_2$·4MeCN·EtOH were selected and mounted on the tip of a glass fibre using perfluoropolyether oil. The data sets were collected at 210(2) K using a Bruker SMART CCD diffractometer or a STOE IPDS-2T diffractometer. Graphite-monochromated Mo-$K_\alpha$ radiation ($\lambda$ = 0.71073 Å) was used throughout. The data were pro-

Table 2. Crystallographic data for complexes **2**[$BPh_4$]·MeCN·$H_2O$, **3**[$BPh_4$]$_2$·2EtOH·$MeCN_{0.5}$·$H_2O$, and **4**[$BPh_4$]$_2$·4MeCN·EtOH.

| Compound | **2**[$BPh_4$]·MeCN·$H_2O$ | **3**[$BPh_4$]$_2$·2EtOH·$MeCN_{0.5}$·$H_2O$ | **4**[$BPh_4$]$_2$·4MeCN·EtOH |
|---|---|---|---|
| Formula | $C_{130}H_{173}B_2N_{13}Ni_4O_5S_4$ | $C_{137}H_{187.5}B_2N_{12.5}Ni_4O_7S_4$ | $C_{142}H_{190}B_2N_{16}Ni_4O_5S_4$ |
| $M_r$ [g/mol] | 2382.51 | 2506.20 | 2585.80 |
| Space group | $P\bar{1}$ | $P\bar{1}$ | $P\bar{1}$ |
| $a$ [Å] | 14.325(3) | 15.929(3) | 13.115(2) |
| $b$ [Å] | 18.128(4) | 16.817(3) | 17.965(2) |
| $c$ [Å] | 26.297(5) | 25.687(5) | 29.867(1) |
| $\alpha$ [°] | 78.20(3) | 97.73(3) | 84.74(1) |
| $\beta$ [°] | 80.86(3) | 100.44(3) | 80.21(1) |
| $\gamma$ [°] | 75.11(3) | 94.28(3) | 76.94(1) |
| $V$ [Å$^3$] | 6419(2) | 6671(2) | 6745(1) |
| $Z$ | 2 | 2 | 2 |
| $d_{calcd.}$ [g/cm$^3$] | 1.249 | 1.248 | 1.273 |
| Crystal size [mm] | 0.25 × 0.25 × 0.25 | 0.25 × 0.25 × 0.25 | 0.30 × 0.30 × 0.30 |
| $\mu$(Mo-$K_\alpha$) [mm$^{-1}$] | 0.699 | 0.677 | 0.672 |
| 2$\theta$ limits [°] | 2.36–56.64 | 2.46–56.64 | 6.38–55.96 |
| Measured reflections | 59137 | 61365 | 63201 |
| Independent reflections | 30293 | 31445 | 32119 |
| Observed reflections[a] | 11268 | 12048 | 22292 |
| Number of parameters | 1457 | 1441 | 1562 |
| $R1$[b] ($R1$ all data) | 0.0530 (0.1657) | 0.0544 (0.1596) | 0.0375 (0.0644) |
| $wR_2$[c] ($wR_2$ all data) | 0.1386 (0.1871) | 0.1368 (0.1675) | 0.0782 (0.0839) |
| Max., min. peaks [e/Å$^3$] | 1.777, –0.760 | 1.249, –0.747 | 0.871, –0.524 |

[a] Observation criterion: $I > 2\sigma(I)$. [b] $R1 = \Sigma||F_o| - |F_c||/\Sigma|F_o|$. [c] $wR_2 = \{\Sigma[w(F_o^2 - F_c^2)^2]/\Sigma[w(F_o^2)^2]\}^{1/2}$.

 © 2007 Wiley-VCH Verlag GmbH & Co. KGaA, Weinheim 

cessed with the programs SAINT (**2**, **3**)[54] or STOE X-AREA (for **4**)[55] and corrected for absorption.[56] Selected details of the data collection and refinement are given in Table 2. The structures were solved by direct methods[57] and refined by full-matrix least-squares techniques on the basis of all data against $F^2$ using SHELXL-97.[58] PLATON was used to search for higher symmetry.[59] H atoms were placed at calculated positions and refined as riding atoms with isotropic displacement parameters. All non-hydrogen atoms were refined anisotropically, except for those of some disordered solvate molecules.

Some of the solvate molecules in **2**, **3**, and **4** were found to be severely disordered and/or only partially occupied. In the crystal structure of **2**$[BPh_4]_2$·MeCN·$H_2O$ one *t*Bu group and the MeCN and $H_2O$ solvate molecules were found to be disordered over two sites. The respective orientations were refined using a split atom model to give site occupancy factors of 0.51(2)/0.49(2) (for C(32a)–C(34a) and C(32c)–C(34c)), 0.62(2)/0.38(2) (for N(7)C(41a)C(42a) and N(7)C(41b)C(42b), and 0.78(2)/0.22(2) (for O(5a) and O(5b)), respectively. The C, N, and O atoms of the solvate molecules could only be refined isotropically, and geometric constraints using SADI instructions were required to keep the structure of the MeCN molecule reasonable. Water and acetonitrile hydrogen atoms were not included in the refinement. The solvate molecules in **3**$[BPh_4]_2$·2EtOH·0.5MeCN·$H_2O$ were found to be severely disordered. It was not possible to resolve this disorder, and geometric constraints using SADI instructions had to be used to maintain the structure of the solvate molecules reasonable. The occupancy factors of two EtOH and the MeCN were reduced to 0.5. The C, N, and O atoms of all solvate molecules were refined isotropically. Finally, the EtOH molecule in **4** was also found to be disordered over two sites. The disorder was refined by using a split atom model with restrained C–O and C–C distances applying SADI instructions to give site occupancies of 0.59(2) for O(3)C(54A)C(55) and 0.41(2) O(3)C(54B)C(55), respectively. Graphics were produced with Ortep3[60] for Windows.

CCDC-654069 (for **2**), -654070 (for **3**), and -654071 (for **4**) contain the supplementary crystallographic data for this paper. These data can be obtained free of charge from the Cambridge Crystallographic Data Centre via www.ccdc.cam.ac/data_request/cif.

**Supporting Information** (see also the footnote on the first page of this article): Experimental and calculated magnetic susceptibility data for all compounds.

## Acknowledgments

We sincerely thank the Deutsche Forschungsgemeinschaft (DFG) (priority program 1137 "Molecular Magnetism") for funding of this work.

[1] F. A. Cotton, G. Wilkinson, C. A. Murillo, M. Bochmann, *Advanced Inorganic Chemistry*, 6th ed., John Wiley & Sons, Weinheim, **1999**, p. 486.
[2] a) F. A. Cotton, J. P. Donahue, C. A. Murillo, *J. Am. Chem. Soc.* **2003**, *125*, 5436–5450; b) F. A. Cotton, J. P. Donahue, C. A. Murillo, L. M. Perez, *J. Am. Chem. Soc.* **2003**, *125*, 5486–5492.
[3] a) M. Eddaoudi, D. B. Moler, H. Li, B. Chen, T. M. Reineke, M. O'Keefe, O. M. Yaghi, *Acc. Chem. Res.* **2001**, *34*, 319–330; b) M. Eddaoudi, J. Kim, J. B. Wachter, H. K. Chae, M. O'Keefe, O. M. Yaghi, *J. Am. Chem. Soc.* **2001**, *123*, 4368–4369; c) J. L. C. Rowsell, A. R. Milward, K. S. Park, O. M. Yaghi, *J. Am. Chem. Soc.* **2004**, *126*, 5666–5667; d) T. J. Barton, L. M. Bull, W. G. Klemperer, D. A. Loy, B. McEnaney, M. Misono, P. A. Monson, G. Pez, G. W. Scherer, J. C. Vartuli, O. M. Yaghi, *Chem. Mater.* **1999**, *11*, 2633–2656.
[4] C. N. R. Rao, S. Natarajan, A. Choudhury, S. Neeraj, A. A. Ayi, *Acc. Chem. Res.* **2001**, *34*, 80–87.
[5] B. Moulton, M. J. Zaworotko, *Chem. Rev.* **2001**, *101*, 1629–1658.
[6] S. Kitagawa, R. Kitaura, S. Noro, *Angew. Chem.* **2004**, *116*, 2388–2430; *Angew. Chem. Int. Ed.* **2004**, *43*, 2334–2375.
[7] S. Kitagawa, S. Noro, T. Nakamura, *Chem. Commun.* **2006**, 701–707.
[8] O. Kahn, *Molecular Magnetism*, VCH, Weinheim, **1993**.
[9] *Magneto-Structural Correlation in Exchange Coupled Systems* (Eds.: R. D. Willet, D. Gatteschi, O. Kahn), NATO ASI Series, Redidel, Dordrecht, **1985**.
[10] J. S. Miller, A. J. Epstein, *Angew. Chem.* **1994**, *106*, 399–432; *Angew. Chem. Int. Ed. Engl.* **1994**, *33*, 385–418.
[11] M. Julve, J. Faus, M. Verdaguer, A. Gleizes, *J. Am. Chem. Soc.* **1984**, *106*, 8306–8308.
[12] a) J. J. Girerd, O. Kahn, M. Verdaguer, *Inorg. Chem.* **1980**, *19*, 274–276; b) E. Bakalbassis, P. Bergerat, O. Kahn, S. Jeannin, Y. Jeannin, Y. Dromzee, M. Guillot, *Inorg. Chem.* **1992**, *31*, 625–631; c) O. Kahn, C. J. Martinez, *Science* **1998**, *279*, 44–48.
[13] L. Deakin, A. M. Arif, J. S. Miller, *Inorg. Chem.* **1999**, *38*, 5072–5077.
[14] P. S. Mukherjee, T. K. Maji, G. Mostafa, J. Ribas, M. S. E. Fallah, N. R. Chaudhuri, *Inorg. Chem.* **2001**, *40*, 928–931.
[15] D. Gatteschi, R. Sessoli, A. Cornia, *Chem. Commun.* **2000**, 725–732.
[16] D. Gatteschi, R. Sessoli, *Angew. Chem.* **2003**, *115*, 278–309; *Angew. Chem. Int. Ed.* **2003**, *42*, 268–297.
[17] O. Sato, J. Tao, Y.-Z. Zhang, *Angew. Chem.* **2007**, *119*, 2200–2236; *Angew. Chem. Int. Ed.* **2007**, *46*, 2152–2187.
[18] T. R. Felthouse, E. J. Laskowski, D. N. Hendrickson, *Inorg. Chem.* **1977**, *16*, 1077–1089.
[19] a) M. Julve, M. Verdaguer, A. Gleizes, M. Philoche-Levisalles, O. Kahn, *Inorg. Chem.* **1984**, *23*, 3808–3818; b) S. Alvarez, M. Julve, M. Verdaguer, *Inorg. Chem.* **1990**, *29*, 4500–4507.
[20] M. Verdaguer, J. Gouteron, S. Jeannin, Y. Jeannin, O. Kahn, *Inorg. Chem.* **1984**, *23*, 4291–4296.
[21] a) E. G. Bakalbassis, C. A. Tsipis, J. Mrozinski, *Inorg. Chem.* **1985**, *24*, 4231–4233; b) E. G. Bakalbassis, J. Mrozinski, C. A. Tsipis, *Inorg. Chem.* **1986**, *25*, 3684–3690; c) C. E. Xanthopoulos, M. P. Sigalas, G. A. Katsoulos, C. A. Tsipis, A. Terzis, M. Mentzafos, A. Hountas, *Inorg. Chem.* **1993**, *32*, 5433–5436.
[22] P. Chaudhuri, K. Oder, K. Wieghardt, S. Gehring, W. Haase, B. Nuber, J. Weiss, *J. Am. Chem. Soc.* **1988**, *110*, 3657–3658.
[23] R. E. Coffman, G. R. Buettner, *J. Phys. Chem.* **1979**, *83*, 2387–2392.
[24] K. S. Burger, P. Chaudhuri, K. Wieghardt, B. Nuber, *Chem. Eur. J.* **1995**, *1*, 583–589.
[25] C. Erasmus, W. Haase, *Spectrochim. Acta, Ser. A* **1994**, *50*, 2189–2195.
[26] J. Cano, G. De Munno, J. L. Sanz, R. Ruiz, J. Faus, F. Lloret, M. Julve, A. Caneschi, *J. Chem. Soc. Dalton Trans.* **1997**, 1915–1923.
[27] Y. Journaux, T. Glaser, G. Steinfeld, V. Lozan, B. Kersting, *Dalton Trans.* **2006**, 1738–1748.
[28] *Magnetism: Molecules to Materials* (Eds.: J. S. Miller, M. Drillon), Wiley-VCH, Weinheim, **2001**.
[29] E. Coronado, P. Delhaes, D. Gatteschi, J. S. Miller, Eds., *Molecular Magnetism: From Molecular Assmblies to Devices*, NATO ASI Series, Kluwer, Dordrecht, The Netherlands, **1995**, vol. 321.
[30] S. P. Watton, P. Fuhrmann, L. E. Pence, A. Caneschi, A. Cornia, G. L. Abbati, S. J. Lippard, *Angew. Chem.* **1997**, *109*, 2917–2919; *Angew. Chem. Int. Ed. Engl.* **1997**, *36*, 2774–2776.
[31] J. Larionova, M. Gross, M. Pilkington, H. Andres, H. Stoeckli-Evans, H. U. Güdel, S. Decurtins, *Angew. Chem.* **2000**, *112*, 1667–1672; *Angew. Chem. Int. Ed.* **2000**, *39*, 1605–1609.

 © 2007 Wiley-VCH Verlag GmbH & Co. KGaA, Weinheim 

[32] A. L. Dearden, S. Parsons, R. E. P. Winpenny, *Angew. Chem.* **2001**, *113*, 155–158; *Angew. Chem. Int. Ed.* **2001**, *40*, 151–154.
[33] S. Demeshko, G. Leibeling, S. Dechert, F. Meyer, *Dalton Trans.* **2006**, 3458–3465.
[34] B. Kersting, G. Steinfeld, D. Siebert, *Chem. Eur. J.* **2001**, *7*, 4253–4258.
[35] M. Gressenbuch, B. Kersting, *Eur. J. Inorg. Chem.* **2007**, 90–102.
[36] K. Nakamoto, *Infrared and Raman Spectra of Inorganic and Coordination Compounds*, John Wiley & Sons, New York, **1986**.
[37] F. A. Cotton, J. P. Donahue, C. Lin, C. A. Murillo, *Inorg. Chem.* **2001**, *40*, 1234–1244.
[38] E. G. Bakalbassis, A. P. Bozopoulos, J. Mrozinski, P. J. Rentzeperis, C. A. Tipsis, *Inorg. Chem.* **1988**, *27*, 529–532.
[39] C. S. Hong, J. H. Yoon, J. H. Lim, H. H. Ko, *Eur. J. Inorg. Chem.* **2005**, 4818–4821.
[40] S. K. Shakhatreh, E. G. Bakalbassis, I. Bruedgam, H. Hartl, J. Mrozinski, C. A. Tsipis, *Inorg. Chem.* **1991**, *30*, 2801–2806.
[41] C. Ma, C. Chen, Q. Liu, F. Chen, D. Liao, L. Li, L. Sun, *Eur. J. Inorg. Chem.* **2004**, 3316–3325.
[42] S. A. Bourne, J. J. Lu, A. Mondal, B. Moulton, M. J. Zaworotko, *Angew. Chem.* **2001**, *113*, 2169–2171; *Angew. Chem. Int. Ed.* **2001**, *40*, 2111–2114.
[43] S. Bayly, J. A. McCleverty, M. D. Ward, D. Gatteschi, F. Totti, *Inorg. Chem.* **2000**, *39*, 1288–1293.
[44] L. Li, D. Liao, Z. Jiang, S. Yan, *Inorg. Chem.* **2002**, *41*, 421–424.
[45] Z. L. Deng, J. Shi, Z. H. Jiang, D. Z. Liao, S. P. Yan, G. L. Wang, H. G. Wang, R. J. Wang, *Polyhedron* **1992**, *11*, 885–887.
[46] T. Beissel, T. Glaser, F. Kesting, K. Wieghardt, B. Nuber, *Inorg. Chem.* **1996**, *35*, 3936–3947.
[47] K. K. Nanda, A. W. Addison, N. Paterson, E. Sinn, L. K. Thompson, U. Sakaguchi, *Inorg. Chem.* **1998**, *37*, 1028–1036.
[48] J. Hausmann, M. H. Klingele, V. Lozan, G. Steinfeld, D. Siebert, Y. Journaux, J. J. Girerd, B. Kersting, *Chem. Eur. J.* **2004**, *10*, 1716–1728.
[49] S. K. Hoffmann, W. Hilczer, J. Goslar, *Appl. Magn. Reson.* **1994**, *7*, 289–321.
[50] V. Lozan, P. Solntsev, K. V. Domasevitch, B. Kersting, *Eur. J. Inorg. Chem.* **2007**, 3217–3226.
[51] B. Kersting, G. Steinfeld, *Chem. Commun.* **2001**, 1376–1377.
[52] E. Sinn, *Coord. Chem. Rev.* **1970**, *5*, 313–347.
[53] P. W. Atkins, *Molecular Quantum Mechanics*, 2nd ed., Oxford University Press, Oxford, **1983**.
[54] SAINT+ V6.02, Bruker AXS, Madison, WI, **1999**.
[55] XAREA, Stoe & Cie, Darmstadt, Germany, **2001**.
[56] SADABS, An empirical absorption correction program part of the SAINTPlus NT version 5.10 package, BRUKER AXS, Madison, WI, **1998**.
[57] G. M. Sheldrick, *Acta Crystallogr., Sect. A* **1990**, *46*, 467–473.
[58] G. M. Sheldrick, *SHELXL-97*, Computer program for crystal structure refinement, University of Göttingen, Göttingen, Germany, **1997**.
[59] A. L. Spek, *PLATON - A Multipurpose Crystallographic Tool*, Utrecht University, Utrecht, The Netherlands, **2000**.
[60] L. J. Farrugia, *J. Appl. Crystallogr.* **1997**, *30*, 565.

Received: July 16, 2007
Published Online: October 1, 2007

 © 2007 Wiley-VCH Verlag GmbH & Co. KGaA, Weinheim 

DOI: 10.1002/ejic.200700804

# Using Chiral Ligand Substituents To Promote the Formation of Dinuclear, Double-Stranded Iron, Manganese, and Zinc Mesocates

**Stuart D. Reid,[a] Claire Wilson,[a] Cristina I. De Matteis,[b] and Jason B. Love*[c]**

**Keywords:** Ligand design / Helical structures / Ligand effects / Supramolecular chemistry / Chirality

The synthesis and structures of dinuclear manganese, iron, and zinc complexes of chiral di-iminodipyrromethane ligands (L) are reported. Schiff base condensation reactions between 5,5′-diformyl-2,2′-dipyrromethane and the chiral amines (–)-(*R*)-CH(Me)*t*Bu and (+)-(*R*)-CH(Me)Ph result in the straightforward synthesis of the new, chiral ligands $H_2L^2$ and $H_2L^3$, respectively. Salt elimination reactions between $K_2L$ and divalent Mn and Fe halides, and protonolysis reactions between $ZnMe_2$ and $H_2L$ result in the formation of the new dinuclear complexes $[M_2(L)_2]$. Investigation of the structures of these compounds in solution and in the solid state reveal that chiral mesocates are formed for L = $L^2$, whereas for L = $L^3$, a racemic mixture of helicates is present.

(© Wiley-VCH Verlag GmbH & Co. KGaA, 69451 Weinheim, Germany, 2007)

## Introduction

Dinuclear metallohelicates are often viewed as the simplest and most fundamental of chiral supramolecular architectures.[1] The clockwise (*P*) or counter-clockwise (*M*) helical rotation intrinsic to these compounds is inherited from the homochiral mechanical coupling of Δ or Λ chiral metal centres,[2] i.e. ΔΔ or ΛΛ configurations, respectively, while heterochiral coupling (ΔΛ) results in the assembly of the achiral mesocate or box diastereomer. The significance of chirality throughout the natural and physical sciences has prompted increased efforts in supramolecular chemistry to develop simple methodologies that discriminate between the formation of helicate and mesocate diastereomers, and, ultimately, between (*M*) and (*P*) enantiomers of metallohelicates. Racemic mixtures of metallohelicates can be separated by fractional crystallisation or by chromatographic techniques,[3] but a second chiral entity, such as a chiral anion or other templating agents,[4] and/or chiral ligands,[5–7] are necessary to direct the selective synthesis of single enantiomer helicates. The preferential, and diastereoselective, synthesis of mesocates instead of helicates appears controlled by a variety of factors, such as the modification (chiral or not) of the spacer unit between the two donor compartments,[8–10] the variation of the metal,[11–13] and the incorporation of a guest molecule.[14]

We identified previously the donor-extended dipyrromethane $H_2L^1$ (Scheme 1) as a ligand that is suitable for use in the synthesis of neutral, dinuclear metallohelicates due to the rigidity of the iminopyrrole chelates, the preference of iminopyrrole to pyrrole–pyrrole chelation in the potassium salt of the *meso*-$CPh_2$ analogue, $\{K_2[t\text{BuN=CH-}(C_4H_2N)_2CPh]_2\}$,[15] and the presence of the $sp^3$-hybridized hinge group between the two donor compartments. Indeed, divalent Mn, Fe, Co and Zn transition metal complexes of $L^1$ are isolated as the unusually volatile, double-stranded, dinuclear helicates $[M_2(L^1)_2]$ which are isostructural and display distinctive cleft motifs as a result of offset face-to-face π-stacking interactions between iminopyrrole groups

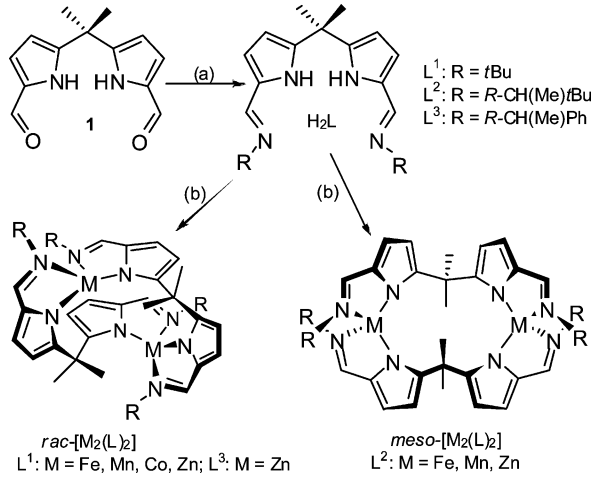


Scheme 1. Synthesis of the dinuclear, double-stranded, helicates and mesocates, $[M_2(L)_2]$. Reagents and conditions: (a) $L^2$: (*R*)-[*t*Bu(Me)HC]$NH_2$, $K_2CO_3$, EtOH; $L^3$: (*R*)-[Ph(Me)HC]$NH_2$, *p*-$C_6H_4MeSO_3H$, MeOH, (b) M = Mn, Fe, Co: (i) KH, THF, (ii) $MX_2$, THF, M = Zn: $ZnMe_2$, toluene, Δ.

[a] School of Chemistry, University of Nottingham, Nottingham, NG7 2RD, UK
[b] School of Pharmacy, Centre for Biomolecular Sciences, University of Nottingham, Nottingham, NG7 2RD, UK
[c] School of Chemistry, University of Edinburgh, Edinburgh, EH9 3JJ, UK
Fax: +44-131-6504743
E-mail: jason.love@ed.ac.uk

 WILEY InterScience DISCOVER SOMETHING GREAT © 2007 Wiley-VCH Verlag GmbH & Co. KGaA, Weinheim 

of opposing ligand strands; this interaction is observed both in the solid state and in solution at low temperature.[16,17] Herein, we demonstrate that the introduction of chiral imine substituents, derived from chiral primary amines, to these ligands can result in the diastereoselective formation of unusual chiral mesocates,[10] and not the expected enantiopure helicates.

## Results and Discussion

### Synthesis of $[M_2(L)_2]$ Complexes

We have shown previously that the Schiff base condensation reaction between the dialdehyde **1** and *t*BuNH$_2$ in the presence of $K_2CO_3$ results in the formation of the imine-functionalised dipyrromethane ligand $H_2L^1$ in good yield.[16] By using a similar synthetic protocol, the new, chiral ligand $H_2L^2$ [R = (*R*)-CH(Me)*t*Bu] was prepared in good yield (Scheme 1), and was isolated as a volatile, yellow oil that was best purified by vacuum sublimation at 130 °C/$10^{-2}$ mbar. While the synthesis of $H_2L^3$ [R = (*R*)-CH(Me)-Ph] according to this route proved problematic, Schiff base formation was found to be assisted by the addition of a catalytic amount of *p*-toluenesulfonic acid; $H_2L^3$ was isolated as a very viscous orange oil from hot hexanes. The conversion of the dialdehyde **1** into the Schiff base ligands $H_2L$ is supported by the appearance of characteristic imine resonances at $\delta$ = 7.76 and 7.78 ppm in the $^1$H NMR spectra of $H_2L^2$ and $H_2L^3$, respectively, coupled with the loss of the aldehyde proton resonance at $\delta$ = 9.29 ppm in **1**.

The salt elimination reactions between $K_2L^2$, prepared in situ by the reaction between $H_2L^2$ and KH in THF, and $MnCl_2$ and $FeBr_2$ were carried out, and resulted in the respective formation of yellow $[Mn_2(L^2)_2]$ and orange $[Fe_2(L^2)_2]$ as crystalline solids in moderate isolated yields. The 1:1 metal/ligand ratios were supported by elemental analysis, and the formulation of these complexes as dinuclear by electron-impact mass spectrometry (EIMS), in which the molecular ion of $[Mn_2(L^2)_2]$ was observed at *m*/*z* (%) = 898 (14) [M$^+$], and that for $[Fe_2(L^2)_2]$ at *m*/*z* (%) = 900 (21) [M$^+$]. The solution magnetic susceptibilities were determined using Evans' method and found to be $\mu_{eff}$ = 8.06 and 7.28 $\mu_B$ for the Mn and Fe complexes, respectively. These data support the presence of two, spin-isolated tetrahedral Mn ($S$ = 5/2, $\mu_{calcd.}$ = 8.37 $\mu_B$) and Fe ($S$ = 2, $\mu_{calcd.}$ = 6.93 $\mu_B$) paramagnets; these magnetic moments are similar to those observed for the related helicate complexes $[Mn_2(L^1)_2]$ and $[Fe_2(L^1)_2]$, and suggest that neither direct M–M bonding nor magnetic superexchange pathways are present to enable spin coupling.[16] The protonolysis reaction between $ZnMe_2$ and $H_2L^2$ in toluene formed the dinuclear zinc complex $[Zn_2(L^2)_2]$ in good yield. As with the $Mn_2$ and $Fe_2$ complexes above, the 1:1 metal/ligand ratio was supported by elemental analysis, although in this case the complex was found to be solvated by dichloromethane, and EIMS displayed a molecular ion at *m*/*z* (%) = 918 (8) [M$^+$].

### Solid-State Structures of $[M_2(L^2)_2]$

An X-ray crystallographic study on single crystals of the Mn, Fe, and Zn complexes was undertaken in order to determine their structures in the solid state. The $[M_2(L^2)_2]$ complexes were found to have similar structures, with the Mn and Fe compounds isomorphous, and, surprisingly, were not the expected helicates, but were instead dinuclear, double-stranded mesocates that result from opposing ΔΛ configurations at the metal atoms. The solid-state structure of *meso*-$[Zn_2(L^2)_2]$ is shown in Figure 1 as ORTEP and space-filled diagrams, with the space-filled structure of the

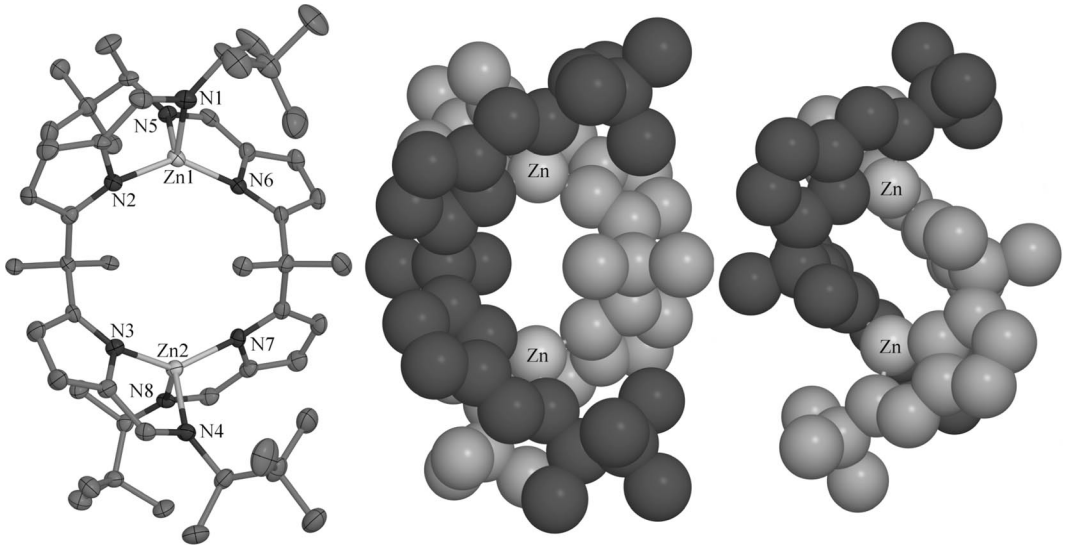


Figure 1. Solid-state structure of the mesocate $[Zn_2(L^2)_2]$ (left). For clarity, only one molecule from the asymmetric unit is shown, all hydrogen atoms are omitted, and thermal displacement ellipsoids are drawn at 50% probability; space-filled diagrams of *meso*-$[Zn_2(L^2)_2]$ (centre) and *rac*-$[Zn_2(L^1)_2]$ (right) are included for comparison.

 © 2007 Wiley-VCH Verlag GmbH & Co. KGaA, Weinheim 

helicate analogue, *rac*-$[Zn_2(L^1)_2]$, included for visual comparison; selected bond lengths and angles are described in Table 1 and crystal data in Table 2.

Table 1. Selected bond lengths [Å] and angles [°] of *meso*-$[M_2(L^2)_2]$ complexes, M = Mn, Fe, Zn.

| | M = Mn | M = Fe | M = Zn |
|---|---|---|---|
| M–M | 5.32 | 5.29 | 5.39 |
| M1–N1 | 2.199(4) | 2.096(6) | 2.090(4) |
| M1–N2 | 2.067(4) | 2.024(6) | 1.984(4) |
| M1–N5 | 2.167(4) | 2.134(6) | 2.080(4) |
| M1–N6 | 2.082(4) | 2.005(6) | 1.973(4) |
| N1–M1–N2 | 82.79(15) | 84.8(3) | 85.02(16) |
| N1–M1–N5 | 102.78(16) | 102.1(2) | 103.05(15) |
| N1–M1–N6 | 119.81(14) | 117.9(3) | 120.64(16) |
| N2–M1–N5 | 120.20(16) | 117.8(2) | 119.53(16) |
| N2–M1–N6 | 145.31(14) | 144.6(2) | 140.38(16) |
| N5–M1–N6 | 82.50(15) | 85.4(2) | 85.84(16) |

In each structure, the metal atoms adopt distorted tetrahedral geometries with exceptionally obtuse angles (>140°) towards the intrametallic cavity of the mesocate, as defined by N2–M1–N6. These angles contrast to those observed for other dinuclear mesocates which are generally more acute, for example, the (diphenylmethane-linked iminopyridyl)dicopper complex, $[Cu_2\{CH_2(p\text{-}C_6H_4N{=}CH\text{-}o\text{-}C_5H_4N)_2\}_2]$, displays an N–Cu–N angle of 134.65(16)°,[13] and similarly, the internal N–Zn–N angle in the dizinc mesocate $[Zn_2\{(\text{-}CH_2N{=}CH\text{-}o\text{-}C_6H_4NSO_2C_6H_4Me\text{-}p)_2\}_2]$ measures 110.0(5)°; in this latter complex, however, there does exist a larger angle *exo* to the molecular cleft of 134.2(4)°.[12] The internal angles in the *meso*-$[M_2(L^2)_2]$ complexes are also significantly more obtuse than those of the corresponding helicates, *rac*-$[M_2(L^1)_2]$: 136.59(9)° (M = Mn), 137.35(9)° (Fe), 132.08(11)° (Zn). The M–N(pyrrole) and M–N(imine) bond lengths in the *meso*-$[M_2(L^2)_2]$ complexes are similar to those in *rac*-$[M_2(L^1)_2]$, and are consistent with the transition metals in their divalent oxidation states. The intrametallic M···M separations in *meso*-$[M_2(L^2)_2]$ (5.3–5.4 Å) are significantly longer than those observed for the *rac*-$[M_2(L^1)_2]$ complexes: 4.75 Å (M = Mn), 4.69 Å (Fe), 4.69 Å (Zn), and this lack of metal–metal bonding supports the above magnetochemical analysis.

## Solution Structures

The possible presence of both helicate and mesocate diastereomers in solution was assessed using $^1$H NMR spectroscopy. It was reasoned that the addition of chiral imine substituents located at the termini of the ligand would have no effect on the $D_2$ symmetry of the helicate, whereas that of the mesocate diastereomer would reduce from $C_{2h}$ to $C_2$ (Figure 2).

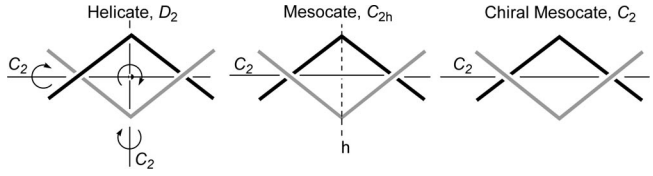


Figure 2. Effect of chiral ligand substituents on the symmetries of *rac*- and *meso*-$[M_2(L)_2]$.

The $^1$H NMR spectrum of $[Fe_2(L^2)_2]$ showed clean, paramagnetically shifted resonances that could be tentatively assigned by integration to the majority of the ligand protons, and was possibly indicative of a reduction in symmetry. However, the $^1$H NMR spectrum of $[Zn_2(L^2)_2]$, recorded in $C_6D_6$ (Figure 3), was more informative, and can be assigned to either a 50:50 mixture of diastereomers of the *rac*-helicate, i.e. (*R**,*R**)-(*M*)-$[Zn_2(L^2)_2]$ and (*R**,*R**)-(*P*)-$[Zn_2(L^2)_2]$, or the chiral mesocate (*R**,*R**)-*meso*-$[Zn_2(L^2)_2]$ as two sets of resonances are observed for each ligand proton environment. To differentiate between these two possibilities, $^1$H NMR NOE spectra were recorded (Figure 3), and show that irradiation of the single *meso*-methyl resonance at $\delta$ =

Table 2. Crystallographic data for the complexes *meso*-$[M_2(L^2)_2]$ (M = Mn, Fe, Zn).

| | $[Mn_2(L^2)_2]\cdot 0.75$(hexane) | $[Fe_2(L^2)_2]\cdot 0.5$(hexane) | $[Zn_2(L^2)_2]$ |
|---|---|---|---|
| Empirical formula | $C_{54.5}H_{86.5}Mn_2N_8$ | $C_{53}H_{83}Fe_2N_8$ | $C_{50}H_{76}N_8Zn_2$ |
| $M_r$ | 963.70 | 943.97 | 919.42 |
| Cell setting, space group | monoclinic, $P2_1$ | monoclinic, $P2_1$ | monoclinic, $P2_1$ |
| $a$ [Å] | 12.651(2) | 12.6987(15) | 13.9099(21) |
| $b$ [Å] | 18.971(3) | 18.764(2) | 20.317(3) |
| $c$ [Å] | 13.773(2) | 13.680(2) | 18.746(3) |
| $\beta$ [°] | 107.297(3) | 106.080(2) | 111.249(2) |
| $V$ [Å$^3$] | 3156(2) | 3132.1(11) | 4937.5(7) |
| $Z$ | 2 | 2 | 4 |
| $D_x$ [Mg m$^{-3}$] | 1.014 | 1.001 | 1.237 |
| $\mu$ [mm$^{-1}$] | 0.436 | 0.498 | 1.013 |
| $T_{min}$, $T_{max}$ | 0.552, 1.000 | 0.787, 1.00 | 0.82, 1.000 |
| $R[F^2 > 2\sigma(F^2)]$ | 0.0702 | 0.0819 | 0.0529 |
| $wR(F^2)$ | 0.1968 | 0.2310 | 0.1283 |
| $S$ | 1.028 | 1.056 | 0.990 |
| $\Delta\rho_{max}$, $\Delta\rho_{min}$ [e Å$^{-3}$] | 0.665, –0.404 | 1.037, –0.408 | 1.235, –0.538 |
| Flack parameter | –0.03(2) | 0.04(3) | 0.010(9) |
| CCDC- | 651323 | 651322 | 651321 |

 © 2007 Wiley-VCH Verlag GmbH & Co. KGaA, Weinheim 

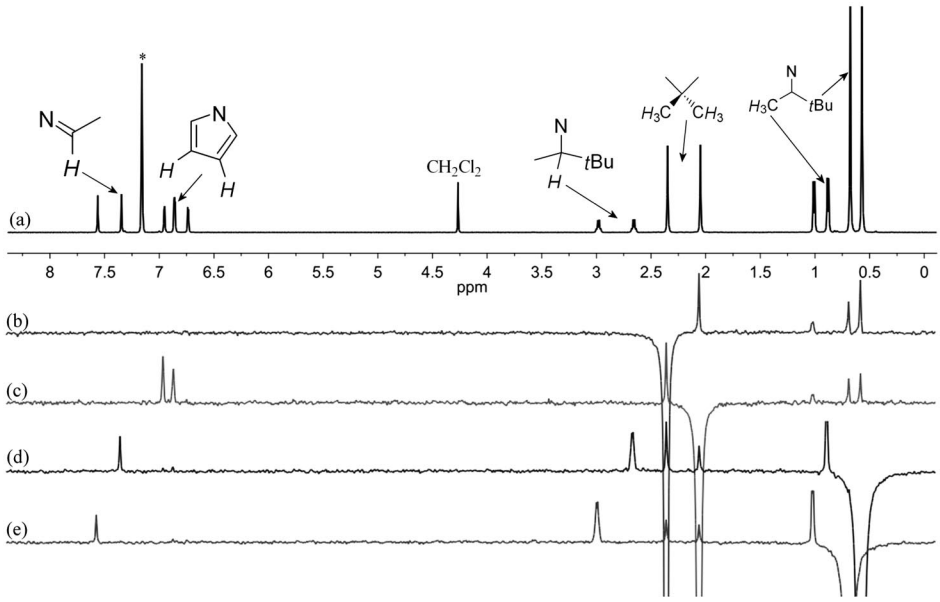


Figure 3. $^1$H NMR NOE experiments for $[Zn_2(L^2)_2]$ in $C_6D_6$ (*) at 298 K: (a) full $^1$H NMR spectrum; (b)/(c) irradiation of *meso*-$CH_3$ groups; (d)/(e) irradiation of terminal *t*Bu groups.

2.34 ppm results in positive NOE with the other *meso*-methyl resonance at $\delta$ = 2.04 ppm, and vice versa. In the helicate, the *meso*-methyl protons are identical by symmetry, and no NOE would be expected between the two (*R**,*R**)-(*M*) and (*R**,*R**)-(*P*) diastereomers as they are magnetically and chemically different; hence, it is clear that the complex $[Zn_2(L^2)_2]$ is a mesocate in solution. This is further corroborated by the observation of positive NOEs for both *meso*-methyl protons on the irradiation of separate *tert*-butyl protons. In the solid state, the *meso*-methyl groups of $[Zn_2(L^2)_2]$ occupy non-equivalent positions inside (*endo*) and outside (*exo*) the intrametallic cleft. It is evident that this structure is also adopted in solution, as positive NOEs between the *meso*-methyl protons at $\delta$ = 2.04 ppm and the pyrrolic protons at $\delta$ = 6.95 and 6.86 ppm are observed, while no NOE between the other *meso*-methyl and the pyrrolic protons is seen, i.e. only the *meso*-methyl protons with resonance at $\delta$ = 2.04 ppm have through-space proximity to the pyrrolic protons and so can be assigned as the *exo*-Me group.

## Helicate Formation

The reaction between $H_2L^3$ and $ZnMe_2$ was carried out to further assess the effect of chiral imine substituents on mesocate and helicate formation, and resulted in the formation of the dinuclear complex $[Zn_2(L^3)_2]$ in good yield; ligand $H_2L^3$ incorporates (*R*)-CH(Me)Ph imine substituents that have the same absolute configuration as those in $H_2L^2$. While we have been unable to determine the solid-state structure of $[Zn_2(L^3)_2]$ by single-crystal X-ray diffraction, the $^1$H NMR spectrum of the crude material in $C_6D_6$ (Figure 4a) was recorded, and was found to be similar to that of *meso*-$[Zn_2(L^2)_2]$ in which two pairs of resonances are observed for each ligand proton environment. However, it was noticed that the crude solid $[Zn_2(L^3)_2]$ was only partially soluble in $Et_2O$, and that after extraction with $Et_2O$, the $^1$H NMR spectrum of the residual solids had changed (Figure 4b) to one in which the two sets of proton resonances were now of unequal intensity (5:1 integral ratio); elemental analysis of these solids supported the 1:1 metal/ligand ratio expected for a dinuclear complex. As such, and in contrast to the complexes of $L^2$, it is clear that a racemic mixture of the two helical diastereomers, (*R**,*R**)-(*M*)-$[Zn_2(L^3)_2]$ and (*R**,*R**)-(*P*)-$[Zn_2(L^3)_2]$, has been formed, and that the two diastereomers can be partially separated by solvent extraction.

It is evident that upon elaboration of the ligand terminus, i.e. changing the imine substituent from *t*Bu to (*R*)-CH(Me)Ph to (*R*)-CH(Me)*t*Bu, there is a change in the gross structures of the dinuclear complexes, from double-stranded metallohelicates to mesocates, and that the effect of ligand variation is extremely subtle. Modifications to ligands that are capable of supporting helical structures have been shown previously to result in changes to the gross molecular structure. For example, variation of the stereo-controlling units between dicatecholate groups can result in the formation of triple-stranded mesocates in preference to helicates.[7,8] In these systems, however, it is likely that host-guest solvate interactions are the primary factor in favouring helicate or mesocate structures.[14] It has also been found that increasing the steric bulk from H to Et at the *ortho* positions of the phenyl spacers in double-stranded dicopper iminopyridine complexes promotes a helical twist at the methylene position, and so results in a change from a mixture of *meso* and *rac* diastereomers to purely *rac*-helicates. In the case of the above $[M_2(L)_2]$ complexes, it is

 © 2007 Wiley-VCH Verlag GmbH & Co. KGaA, Weinheim 

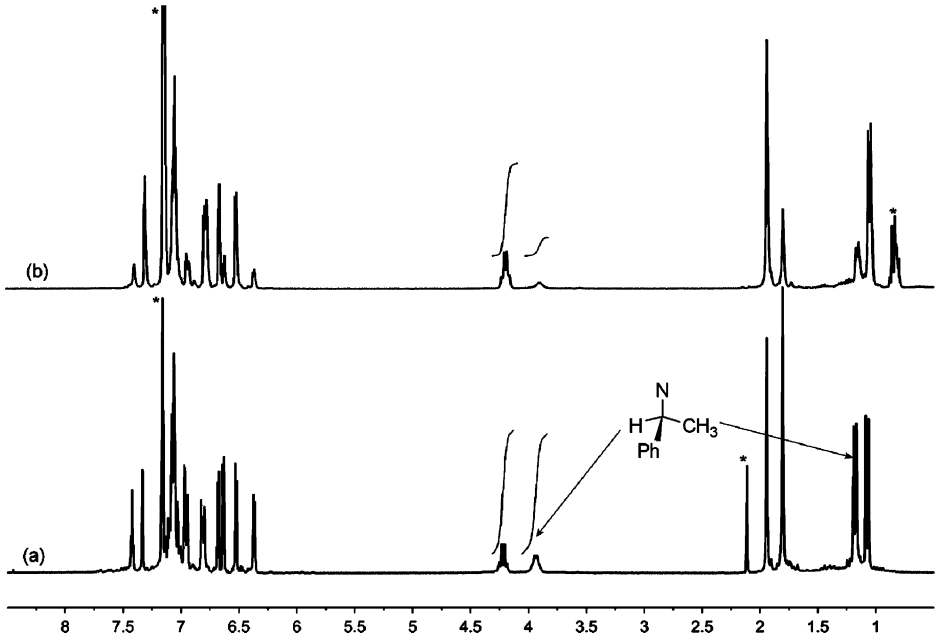


Figure 4. $^1$H NMR spectra of (a) crude $[Zn_2(L^3)_2]$, and (b) $Et_2O$-washed $[Zn_2(L^3)_2]$, in $C_6D_6$ (* $C_6D_6$, toluene and hexanes impurities).

unusual that the use of the chiral ligand substituent CH(Me)*t*Bu at the ligand terminus has resulted in a helicate to mesocate interconversion, as the addition of chiral terminal groups to the ligand usually results in the preferential formation of one helical enantiomer.[5] Furthermore, to the best of our knowledge, there is only a single reported example of a chiral dinuclear mesocate, formed as a result of reaction between an enantiopure tetradentate binaphthoxydiimine ligand and $Cu(OAc)_2$.[10] In this latter case, however, the formation of the chiral mesocate was found to depend on the length of the alkyl chain between the two N-O donor sets, with a shorter alkyl chain length resulting in the preferential formation of an enantiopure trinuclear circular helicate.

It is difficult to account for the favoured formation of the mesocate complexes over the helicates on addition of the bulky chiral imine substituent CH(Me)*t*Bu. However, it is clear that this preference is metal-independent, as Mn, Fe, and Zn helicates are formed using $L^1$, while only mesocates are formed with $L^2$ for the same metals. While it is possible that the salt elimination synthetic methodology could impart diastereoselectivity through host–guest or solvate interactions,[14] this appears unlikely as helicates of $L^1$ are also formed using transamination routes in nonpolar solvents.[16] To try to gain a better understanding of the factors behind the formation of helicates vs. mesocates, molecular-mechanics-based conformational analysis and geometry optimisations were carried out to determine the difference in energy between the helicate and mesocate structures of each of the three Fe complexes $[Fe_2(L)_2]$, where L = $L^1$, $L^2$ and $L^3$. The Fe complexes were chosen because of the availability of crystallographically determined helicate and mesocate Fe complex structures.[16]

## Molecular Mechanics Calculations

Energy differences between the helicate and mesocate structures for each of the Fe complexes were calculated using the Extensible and Systematic Force Field (ESFF) molecular mechanics method, which has been parameterized for all elements up to radon in the Periodic Table.[18] The conformational space of the substituents was explored using dihedral angle driving calculations where rotation around the substituent(C)–imine(N) bond was carried out in 60° increments, followed by energy minimisation of all resulting conformations. The crystallographic structures of the helicate $[Fe_2(L^1)_2]$ and the mesocate $[Fe_2(L^2)_2]$ were used as templates for generating the required pairs of structures. Inspection of the crystal structures of the helicate $[Fe_2(L^1)_2]$ and the mesocate $[Fe_2(L^2)_2]$ indicated that the bond lengths in the pyrrole rings corresponded, as expected, to partial double bonds. The bond lengths of the imine moieties, and the adjoining bond to the pyrrole ring, were more akin to double and single bonds, respectively. These bond types were therefore used in the ESFF calculations, and atom types were assigned accordingly.

The lowest energy structures arising from the dihedral angle driving calculations were identified, and the energy differences between the mesocate and helicate structures determined. While the differences in global minimum energy obtained were small ($<10$ kcal mol$^{-1}$) and insufficient to account for the observed differences in product distributions, it is notable that for $L^1$ ($\Delta E$ = 6.51 kcal mol$^{-1}$) and $L^3$ ($\Delta E$ = 4.75 kcal mol$^{-1}$), the helicate structure is of lower energy, whilst in the case of $L^2$ ($\Delta E$ = –1.26 kcal mol$^{-1}$) the mesocate structure is of lower energy; as such, these calculated energies correlate to the products observed experimentally.

 © 2007 Wiley-VCH Verlag GmbH & Co. KGaA, Weinheim 

Although only weak effects, it is therefore likely that the steric demand and relative conformation of the imine substituents are contributory factors towards the preferential formation of the helicate or mesocate structures.

## Conclusions

In this work we have shown that the incorporation of the bulky chiral imine substituent (*R*)-CH(Me)*t*Bu at the termini of the tetradentate ligand $H_2L^2$ disrupts the expected formation of the dinuclear, double-stranded helicates $[M_2(L)_2]$ to form preferentially the *meso* diastereomers $[M_2(L^2)_2]$; use of the sterically less demanding (*R*)-CH(Me)-Ph substituent results in racemic mixtures of the diastereotopic helicates, $[Zn_2(L^3)_2]$. The solid-state structures of the mesocates are retained in solution and can be differentiated from the helicates using $^1$H NMR NOE spectroscopy. In the solid state, the M···M separations are considerably longer in the mesocate structures than those of the helicate analogues, and a more obtuse N–M–N angle is subtended towards the intrametallic cleft. This transformation from helicate to mesocate is independent of the metals employed, and provides straightforward methodology to charge-neutral, chiral mesocates. However, the fundamental reasons behind preferential mesocate formation remain unclear, as, while molecular mechanics calculations suggest that the steric influence of the imine-substituent is influential, there remains insufficient thermodynamic distinction between helicate and mesocate structures.

## Experimental Section

**General Remarks:** Unless otherwise stated, all reactions were carried out using standard Schlenk techniques under nitrogen or argon or in a nitrogen-filled Vacuum Atmospheres OmniLab glovebox. Solvents were dried (hexanes, pentane, $Et_2O$ and THF were passed through activated alumina towers;[19] dichloromethane was distilled from $CaH_2$) and stored over molecular sieves (4 Å); all other solvents were used as purchased. Deuteriated benzene was refluxed in the presence of K, vacuum-distilled, and freeze-pump-thaw-degassed three times. The dipyrromethane $Me_2C(C_4H_4N)_2$,[20] and the dialdehyde synthon 5,5′-CHO-$Me_2C(C_4H_4N)_2$ (**1**)[15] were prepared according to literature procedures. $MnCl_2{\cdot}4H_2O$ was dried according to literature methods.[21] The $^1$H NMR and $^{13}$C{H} NMR spectra were recorded with a Bruker DPX-300 spectrometer operating at 300.13 and 75.47 MHz, respectively; residual protiosolvent served as an internal reference for the former. Combustion analyses were carried out by Mr. Stephen Boyer at the London Metropolitan University and EIMS by Dr. Ali Abdul-Sada of the University of Sussex.

**Crystallography. General Methods and Solution and Refinement Details:** Single-crystal diffraction data were collected using graphite-monochromated Mo-$K_\alpha$ X-radiation with either a Bruker SMART1000 {$[Fe_2(L^2)_2]$} or SMART APEX {$[Mn_2(L^2)_2]$, $[Zn_2(L^2)_2]$} CCD area detector diffractometer equipped with an Oxford Cryostream cooling device. All data were collected at 150 K. Details of the individual data collections and refinements are given in Table 2. Structures were solved with SHELXS-97 using heavy-atom methods for $[Mn_2(L^2)_2]$ and direct methods for $[Fe_2(L^2)_2]$ and $[Zn_2(L^2)_2]$. All structures were refined by least-squares full-matrix refinement against $F^2$ using SHELXL-97,[22] and all fully occupied non-H atoms refined with anisotropic atomic displacement parameters (adps). Hydrogen atoms were geometrically placed and refined as part of a riding model. $[Mn_2(L^2)_2]$ showed disorder in the two chiral C(Me)*t*Bu groups C20 and C26 which were modelled over two sites with occupancies 0.60 and 0.40 in both cases. C45 was modelled over two sites with occupancies 0.60 and 0.40. Geometric and rigid-bond restraints were applied in all cases, and partially occupied atom sites were refined with isotropic adps. The chiral C(Me)*t*Bu groups C1 and C45 showed large adps with no disorder model, so were refined with isotropic adps. The poorly defined solvent was accounted for by SQUEEZE and found to be 73 electrons/cell and was assigned as 1.5 molecules of hexane. $[Fe_2(L^2)_2]$ showed disorder in the two chiral C(Me)*t*Bu groups C20 and C45 which were modelled over two sites with occupancies 0.60 and 0.40, and 0.50 and 0.50, respectively. Geometric and rigid-bond restraints were applied in all cases, and partially occupied atom sites were refined with isotropic adps. The poorly defined solvent was accounted for by SQUEEZE and found to be 57 electrons/cell and was assigned as one molecule of hexane. $[Zn_2(L^2)_2]$ contained two molecules per asymmetric unit, and showed disorder in carbon C96 which was modelled over two sites with occupancies 0.45 and 0.55. CCDC-651321 to -651323 contain the supplementary crystallographic data for this paper. These data can be obtained free of charge from The Cambridge Crystallographic Data Centre via www.ccdc.cam.ac.uk/data_request/cif.

**Molecular Modeling Calculations:** Molecular mechanics energy calculations were carried out using the Extensible and Systematic Force Field (ESFF), as implemented within the Discover programme.[23] Modification, visualisation and analysis of molecular structures were carried out using the Insight II molecular graphics software.[23] Low-energy structures were obtained by conformational analysis and energy minimisation of the helicate and mesocate geometries of all three Fe complexes $[Fe_2(L)_2]$, where L = $L^1$, $L^2$ and $L^3$. The starting geometries for these complexes were obtained by either using or modifying the crystallographically determined Fe complex structures. For the helicate geometries, the crystal structure of $[Fe_2(L^1)_2]$ was used as a backbone structure, and the substituent altered using the Builder module within Insight II. For the mesocate geometries, the crystal structure of $[Fe_2(L^2)_2]$ was used as a backbone structure, and the CH(Me)*t*Bu substituents altered. In all cases the stereochemistry of the substituents were confirmed as (*R*). Conformational analysis was carried out by rotating around the C(substituent)–N(imine) bond, as defined in Figure 5, and subsequent geometry optimisation of the resulting conformations. The dihedral drive calculation involved rotation of the C1–N2–C3–C4 dihedral angle in each of the four substituents, from –180° to +180° in 60° increments, followed by unrestrained energy

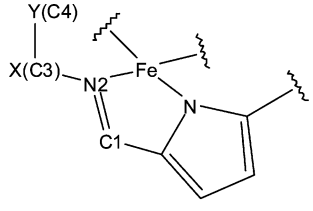


$L^1$: X = $C(CH_3)_2$, Y = $CH_3$
$L^2$: X = $CH(CH_3)$, Y = *t*Bu
$L^3$: X = $CH(CH_3)$, Y = Ph

Figure 5. Dihedral angle (C1–N2–C3–C4) rotated during conformational analysis calculations.

 © 2007 Wiley-VCH Verlag GmbH & Co. KGaA, Weinheim 

minimisation of each of the 2401 conformations arising. ESFF partial atomic charges and atom types were assigned; in particular the NH atom type was assigned for the pyrrole nitrogen atom. Minimisations were carried out using steepest descents, followed by conjugate gradient and Newton–Raphson methods, until the convergence criterion (maximum derivative = 0.001) was reached.

**Synthesis of $H_2L^2$:** (–)-(*R*)-3,3-Dimethyl-2-butylamine (4.83 g, 47.7 mmol) and $K_2CO_3$ (5.00 g) were added to a stirred solution of **1** (5.00 g, 21.7 mmol) in EtOH (100 mL). The resulting slurry was stirred for 24 h, after which the mixture was filtered and the precipitate washed once with EtOH (10 mL). The combined filtrate and washings were dried at reduced pressure, the resulting viscous red oil extracted with $CH_2Cl_2$ (10 mL) and transferred to a sublimation tube. The oil was sublimed twice at 130 °C/$10^{-2}$ mbar to yield $H_2L^2$ as a pale yellow oil, 6.46 g, 75%. $^1$H NMR ($C_6D_6$, 298 K): $\delta$ = 9.81 (br. s, 2 H, NH), 7.76 (s, 2 H, CH=N), 6.31 (d, $J$ = 3.6 Hz, 2 H, pyrrole H), 5.95 (d, $J$ = 3.6 Hz, 2 H, pyrrole H), 2.75 (q, $J$ = 6.5 Hz, 2 H, chiral CH), 1.08 (s, 6 H, *meso* $CH_3$), 1.04 (d, $J$ = 7.7 Hz, 6 H, chiral $CH_3$), 0.92 (s, 18 H, chiral $CMe_3$) ppm. $^{13}$C{$^1$H} NMR ($C_6D_6$, 298 K): $\delta$ = 149.7 (s, CH=N), 142.5 (s, $C_q$), 130.6 (s, $C_q$), 114.1 (s, CH), 106.8 (s, CH), 75.7 (s, chiral CH), 36.1 (s, $C_q$), 34.7 (s, $C_q$), 28.8 (s, *meso* $CH_3$), 27.2 (s, chiral $CMe_3$), 18.2 (s, chiral $CH_3$) ppm. ESMS: $m/z$ (%) = 397 (100) [$M^+$].

**Synthesis of $H_2L^3$:** (+)-(*R*)-Phenylethylamine (5.06 mL, 39.6 mmol) and *p*-toluenesulfonic acid (342 mg, 1.80 mmol) were added to a stirred solution of **1** (4.15 g, 18.0 mmol) in MeOH (100 mL). The resulting orange solution was stirred for 1 h and then concentrated to dryness at reduced pressure. The orange residues were extracted with hot hexanes (15 mL), filtered though a plug of Celite and the volatiles removed at low pressure for 24 h to yield $H_2L^3$ as a viscous orange oil, 5.02 g, 64%. $C_{29}H_{32}N_4$ (436.59): calcd. C 79.76, H 7.40, N 12.83; found C 79.68, H 7.87, N 12.57. $^1$H NMR ($C_6D_6$, 298 K): $\delta$ = 8.87 (br. s, 2 H, NH), 7.78 (s, 2 H, CH=N), 7.38 (d, $J$ = 7.1 Hz, 4 H, phenyl H), 7.10 (m, 6 H, phenyl H), 6.27 (s, $J$ = 3.6 Hz, 2 H, pyrrole H), 5.91 (s, $J$ = 3.6 Hz, 2 H, pyrrole H), 4.23 (q, $J$ = 6.6 Hz, 2 H, chiral CH), 1.49 (d, $J$ = 6.6 Hz, 6 H, chiral $CH_3$), 1.07 (s, 6 H, *meso* $CH_3$) ppm. $^{13}$C{$^1$H} NMR ($C_6D_6$, 298 K): $\delta$ = 150.0 (s, CH=N), 145.9 (s, $C_q$), 142.6 (s, $C_q$), 130.2 (s, $C_q$), 128.6 (s, CH), 127.1 (s, CH), 127.0 (s, CH), 114.6 (s, CH), 106.6 (s, CH), 69.5 (s, chiral CH), 35.7 (s, $C_q$), 28.2 (s, *meso* $CH_3$), 24.9 (s, chiral $CH_3$) ppm.

**Synthesis of $[Mn_2(L^2)_2]$:** A solution of $H_2L^2$ (586 mg, 1.48 mmol) in THF (10 mL) was added to a stirred slurry of KH (178 mg, 4.43 mmol) in THF (10 mL). Effervescence occurred immediately and the resulting slurry was stirred for 1 h, after which the ligand salt was added dropwise to a slurry of $MnCl_2$ (186 mg, 1.48 mmol) in THF (10 mL). The resultant yellow slurry was heated at 80 °C for 24 h, after which the mixture was filtered though Celite, and the yellow filtrate concentrated to dryness under reduced pressure. The yellow solid was extracted into hexanes (5 mL) and cooled to deposit 109 mg, 16% of $[Mn_2(L^2)_2]$ as a yellow crystalline solid. Crystals suitable for X-ray diffraction were grown by slow cooling a hexane solution to –30 °C. $C_{50}H_{76}Mn_2N_8$ (899.08): calcd. C 67.31, H 8.54, N 12.46; found C 67.39, H 8.42, N 12.45. EIMS: $m/z$ (%) = 898 (14) [$M^+$], 841 (53) [$M^+$ – *t*Bu], 450 (43) [$MnL^2$], 43 (100) [*t*Bu – Me]. $\mu_{eff}$ ($C_6D_6$) = 8.06 $\mu_B$.

**Synthesis of $[Fe_2(L^2)_2]$:** To a stirred slurry of KH (154 mg, 3.83 mmol) in THF (10 mL) was added a solution of $H_2L^2$ (507 mg, 1.28 mmol) in THF (10 mL). Effervescence occurred immediately and the resulting slurry was stirred for 1 h, after which the ligand salt was added dropwise to a stirred slurry of $FeBr_2$ (291 mg, 1.35 mmol) in THF (10 mL). The resultant red-brown slurry was heated at 80 °C for 24 h, after which the mixture was filtered, and the red filtrate concentrated to dryness under reduced pressure. The resultant orange solid was extracted into $Et_2O$ (5 mL) and cooled to –20 °C to deposit 276 mg, 48% of $[Fe_2(L^2)_2]$ as an orange crystalline solid. Crystals suitable for X-ray diffraction were grown by slow cooling a hexane solution to –30 °C. $C_{50}H_{76}Fe_2N_8$ (900.90): calcd. C 66.65, H 8.52, N 12.44, found C 66.46, H 8.52, N 12.29. $^1$H NMR ($C_6D_6$, 298 K): $\delta$ = 58.7 (s, 2 H) = 48.2 (s, 2 H), 8.6 (s, 2 H), 6.5 (br. s, 6 H), 4.8 (s, 6 H), –0.9 (s, 2 H), –2.4 (s, 18 H), –3.8 (s, 18 H) ppm. EIMS: $m/z$ (%) = 900 (21) [$M^+$], 843 (11) [$M^+$ – *t*Bu], 396 (48) [$L^2$], 339 (100) [$L^2$ – *t*Bu]. $\mu_{eff}$ ($C_6D_6$) = 7.28 $\mu_B$.

**Synthesis of $[Zn_2(L^2)_2]\cdot(CH_2Cl_2)$:** A solution of $ZnMe_2$ (2.0 M) in toluene (1 mL) was added to a stirred solution of $H_2L^2$ (574 mg, 1.45 mmol) in toluene (15 mL). Effervescence occurred immediately and the solution turned pale orange. The reaction mixture was heated at 80 °C under reduced pressure for 24 h, after which the solvents were evaporated under reduced pressure and the residues extracted with $CH_2Cl_2$ (2 mL). Pentane (10 mL) was then added until cloud point, and the solution was cooled, resulting in the deposition of 352 mg, 53% of $[Zn_2(L^2)_2]\cdot(CH_2Cl_2)$ as a pale yellow, crystalline solid. Crystals suitable for X-ray diffraction were grown by diffusion of pentane into a $CH_2Cl_2$ solution. $C_{50}H_{76}N_8Zn_2\cdot CH_2Cl_2$ (1004.9): calcd. C 60.96, H 7.82, N 11.15; found C 61.19, H 8.09, N 11.04. $^1$H NMR ($C_6D_6$, 298 K): $\delta$ = 7.55 (s, 1 H, CH=N), 7.33 (s, 1 H, CH=N), 6.95 (d, $J$ = 3.6 Hz, 1 H, pyrrole H), 6.86 (d, $J$ = 3.8 Hz, 2 H, pyrrole H), 6.73 (d, $J$ = 3.7 Hz, 1 H, pyrrole H), 4.24 (s, 1 H, $CH_2Cl_2$), 2.97 (q, $J$ = 6.8 Hz, 1 H, CH), 2.64 (q, $J$ = 6.6 Hz, 1 H, CH), 2.34 (s, 3 H, *meso* $CH_3$), 2.04 (s, 3 H, *meso* $CH_3$), 1.00 (d, $J$ = 6.8 Hz, 3 H, $CH_3$), 0.87 (d, $J$ = 6.6 Hz, 3 H, $CH_3$), 0.67 (s, 9 H, $CMe_3$), 0.56 (s, 9 H, $CMe_3$) ppm. $^{13}$C{$^1$H} NMR ($C_6D_6$, 298 K): $\delta$ = 159.5 (s, CH) = 158.3 (s, $C_q$), 158.2 (s, $C_q$), 158.0 (s, CH), 134.2 (s, $C_q$), 120.4 (s, CH), 120.1 (s, CH), 113.1 (s, CH), 112.5 (s, CH), 72.8 (s, CH), 68.3 (s, CH), 53.1 (s, $CH_2Cl_2$), 39.1 (s, $C_q$), 34.8 (s, $C_q$) ppm. 34.7 (s, $C_q$), 31.9 (s, *meso* $CH_3$), 26.8 (s, $CMe_3$), 26.7 (s, $CMe_3$), 23.3 (s, *meso* $CH_3$), 16.6 (s, $CH_3$), 15.8 (s, $CH_3$). EIMS: $m/z$ (%) = 918 (8) [$M^+$], 863 (26) [$M^+$ – *t*Bu], 49 (100) [*t*Bu – 8 H].

**Synthesis of $[Zn_2(L^3)_2]$:** A solution of $ZnMe_2$ (2.0 M) in toluene (0.5 mL) was added dropwise to a stirred solution of $H_2L^3$ (393 mg, 0.9 mmol) in toluene (10 mL). Gas evolved immediately and the resulting yellow-brown solution was heated at 80 °C for 24 h, after which the orange-yellow solution was dried at reduced pressure and the pale yellow solids inspected by $^1$H NMR spectroscopy. $^1$H NMR ($C_6D_6$, 298 K): $\delta$ = 7.60 (s, 2 H, CH=N), 7.34 (s, 2 H, CH=N), 7.3–6.7 (m, 20 H, phenyl H), 6.68 (d, $J$ = 3.5 Hz, 2 H, pyrrole H), 6.63 (d, $J$ = 3.5 Hz, 2 H, pyrrole H), 6.51 (d, $J$ = 3.5 Hz, 2 H, pyrrole H), 6.36 (d, $J$ = 3.5 Hz, 2 H, pyrrole H), 4.22 (q, $J$ = 7.1 Hz, 2 H, chiral CH), 3.92 (q, $J$ = 6.2 Hz, 2 H, chiral CH), 1.93 (s, 6 H, *meso* $CH_3$), 1.80 (s, 6 H, *meso* $CH_3$), 1.19 (d, $J$ = 7.0 Hz, 6 H, chiral $CH_3$), 1.08 (d, $J$ = 7.0 Hz, 6 H, chiral $CH_3$) ppm. The yellow solids were then extracted into $Et_2O$ (5 mL) and cooled. The resulting slurry was filtered and the liquors concentrated to dryness to yield 112 mg, 25%, of $[Zn_2(L^3)_2]$ as yellow solids. $C_{58}H_{60}N_8Zn_2$ (999.93): calcd. C 69.67, H 6.05, N 11.21; found C 69.54, H 6.15, N 11.15.

## Acknowledgments

The authors thank the EPSRC (UK), The Royal Society, and the Universities of Nottingham and Edinburgh for their support.

 © 2007 Wiley-VCH Verlag GmbH & Co. KGaA, Weinheim 

[1] J. W. Steed, J. L. Atwood, *Supramolecular Chemistry*, John Wiley & Sons, Chichester, UK, **2000**; C. Provent, A. F. Williams, in *Perspectives in Supramolecular Chemistry*, vol. 5 (Ed.: J.-P. Sauvage), John Wiley & Sons, Chichester, UK, **1999**, p. 135; J.-M. Lehn, *Supramolecular chemistry: concepts and perspectives*, VCH, Weinheim, **1995**; J.-M. Lehn, A. Rigault, J. Siegel, J. Harrowfield, B. Chevrier, D. Moras, *Proc. Natl. Acad. Sci. USA* **1987**, *84*, 2565; M. Albrecht, *Chem. Soc. Rev.* **1998**, *27*, 281; M. Albrecht, *Chem. Eur. J.* **2000**, *6*, 3485; M. Albrecht, *Chem. Rev.* **2001**, *101*, 3457; M. Albrecht, I. Janser, R. Froehlich, *Chem. Commun.* **2005**, 157; V. Amendola, L. Fabbrizzi, P. Pallavicini, *Coord. Chem. Rev.* **2001**, *216–217*, 435; D. L. Caulder, K. N. Raymond, *Acc. Chem. Res.* **1999**, *32*, 975; E. C. Constable, *Compr. Supramol. Chem.* **1996**, *9*, 213; M. J. Hannon, L. J. Childs, *Supramol. Chem.* **2004**, *16*, 7; M. D. Ward, J. A. McCleverty, J. C. Jeffery, *Coord. Chem. Rev.* **2001**, *222*, 251; R. Ziessel, *Coord. Chem. Rev.* **2001**, *216–217*, 195; T. Bark, A. Von Zelewsky, *Chimia* **2000**, *54*, 589; U. Knof, A. von Zelewsky, *Angew. Chem. Int. Ed.* **1999**, *38*, 303.

[2] S. Alvarez, D. Avnir, *Dalton Trans.* **2003**, 562.

[3] R. Krämer, J.-M. Lehn, A. D. Cian, J. Fischer, *Angew. Chem. Int. Ed. Engl.* **1993**, *32*, 703; R. C. Scarrow, D. L. White, K. N. Raymond, *J. Am. Chem. Soc.* **1985**, *107*, 6540; N. C. Fletcher, R. T. Brown, A. P. Doherty, *Inorg. Chem.* **2006**, *45*, 6132; M. J. Hannon, I. Meistermann, C. J. Isaac, C. Blomme, J. R. Aldrich-Wright, A. Rodger, *Chem. Commun.* **2001**, 1078; J. M. C. A. Kerckhoffs, J. C. Peberdy, I. Meistermann, L. J. Childs, C. J. Isaac, C. R. Pearmund, V. Reudegger, S. Khalid, N. W. Alcock, M. J. Hannon, A. Rodger, *Dalton Trans.* **2007**, 734; W. Schuh, H. Kopacka, K. Wurst, P. Peringa, *Eur. J. Inorg. Chem.* **2002**, 2202; A. Thompson, D. Dolphin, *J. Org. Chem.* **2000**, *65*, 7870; G. Rapenne, B. T. Patterson, J.-P. Sauvage, F. R. Keene, *Chem. Commun.* **1999**, 1853; B. Hasenknopf, J.-M. Lehn, *Helv. Chim. Acta* **1996**, *79*, 1643.

[4] N. C. Habermehl, P. M. Angus, N. L. Kilah, L. Norén, A. D. Rae, A. C. Willis, S. B. Wild, *Inorg. Chem.* **2006**, *45*, 1445; R. M. Yeh, K. N. Raymond, *Inorg. Chem.* **2006**, *45*, 1130; R. M. Yeh, M. Ziegler, D. W. Johnson, A. J. Terpin, K. N. Raymond, *Inorg. Chem.* **2001**, *40*, 2216.

[5] M. Meyer, B. Kersting, R. E. Powers, K. N. Raymond, *Inorg. Chem.* **1997**, *36*, 5179; B. Kersting, K. Meyer, R. E. Powers, K. N. Raymond, *J. Am. Chem. Soc.* **1996**, *118*, 7221; A. Orita, T. Nakano, D. L. An, K. Tanikawa, K. Wakamatsu, J. Otera, *J. Am. Chem. Soc.* **2004**, *126*, 10389; O. Mamula, A. von Zelewsky, *Coord. Chem. Rev.* **2003**, *242*, 87; G. Baum, E. C. Constable, D. Fenske, C. E. Housecroft, T. Kulke, *Chem. Eur. J.* **1999**, *5*, 1862; G. Baum, E. C. Constable, D. Fenske, T. Kulke, *Chem. Commun.* **1997**, 2043; T. E. Wood, N. D. Dalgleish, E. D. Power, A. Thompson, X. Chen, Y. Okamoto, *J. Am. Chem. Soc.* **2005**, *127*, 5740; T. E. Wood, A. C. Ross, N. D. Dalgleish, E. D. Power, A. Thompson, X. Chen, K. Okamoto, *J. Org. Chem.* **2005**, *70*, 9967; H.-L. Kwong, H.-L. Yeung, W.-S. Lee, W.-T. Wong, *Chem. Commun.* **2006**, 4841.

[6] M. Albrecht, S. Dehn, G. Raabe, R. Frölich, *Chem. Commun.* **2005**, 5690; M. Albrecht, S. Schmid, M. deGroot, P. Weis, R. Frölich, *Chem. Commun.* **2003**, 2526; R. Prabaharan, N. C. Fletcher, *Dalton Trans.* **2003**, 2558; M. A. Masood, E. J. Enemark, T. D. P. Stack, *Angew. Chem. Int. Ed.* **1998**, *37*, 928; Y. Wang, H. Fu, F. Shen, X. Sheng, A. Peng, Z. Gu, H. Ma, J. S. Ma, J. Yao, *Inorg. Chem.* **2007**, *46*, 3548; S. G. Telfer, G. Bernardinelli, A. F. Williams, *Chem. Commun.* **2001**, 1498; S. G. Telfer, R. Kuroda, *Chem. Eur. J.* **2005**, *11*, 57; S. G. Telfer, T. Sato, R. Kuroda, *Angew. Chem. Int. Ed.* **2004**, *43*, 581; S. G. Telfer, T. Sato, R. Kuroda, J. Lefebvre, D. B. Leznoff, *Inorg. Chem.* **2004**, *43*, 421.

[7] E. J. Enemark, T. D. P. Stack, *Angew. Chem. Int. Ed. Engl.* **1995**, *34*, 996.

[8] I. Janser, M. Albrecht, K. Hunger, S. Burk, K. Rissanen, *Eur. J. Inorg. Chem.* **2006**, 244; M. Albrecht, I. Janser, H. Houjou, R. Fröhlich, *Chem. Eur. J.* **2004**, *10*, 2839; M. Albrecht, S. Kotila, *Angew. Chem. Int. Ed. Engl.* **1995**, *34*, 2135.

[9] L. J. Childs, M. Pascu, A. J. Clarke, N. W. Alcock, M. J. Hannon, *Chem. Eur. J.* **2004**, *10*, 4291.

[10] T. Maeda, Y. Furusho, M. Shiro, T. Takata, *Chirality* **2006**, *18*, 691.

[11] Y.-P. Cai, C.-Y. Su, C.-L. Chen, Y.-M. Li, B.-S. Kang, A. S. C. Chan, W. Kaim, *Inorg. Chem.* **2003**, *42*, 163; J. Fielden, D.-L. Long, C. Evans, L. Cronin, *Eur. J. Inorg. Chem.* **2006**, 3930; T. K. Ronson, H. Adams, T. Riis-Johannessen, J. C. Jeffery, M. D. Ward, *New J. Chem.* **2006**, *30*, 26.

[12] A. M. Garcia-Deibe, J. S. Matalobos, M. Fondo, M. Vazquez, M. R. Bermejo, *Inorg. Chim. Acta* **2004**, *357*, 2561.

[13] J. Keegan, P. E. Kruger, M. Nieuwenhuyzen, N. Martin, *Cryst. Growth Des.* **2002**, *2*, 329.

[14] J. Xu, T. J. Parac, K. N. Raymond, *Angew. Chem. Int. Ed.* **1999**, *38*, 2878.

[15] J. B. Love, A. J. Blake, C. Wilson, S. D. Reid, A. Novak, P. B. Hitchcock, *Chem. Commun.* **2003**, 1682.

[16] S. D. Reid, A. J. Blake, W. Köckenberger, C. Wilson, J. B. Love, *Dalton Trans.* **2003**, 4387.

[17] S. D. Reid, A. J. Blake, C. Wilson, J. B. Love, *Inorg. Chem.* **2006**, *45*, 636.

[18] S. Shi, L. Yan, Y. Yang, J. Fisher-Shaulsky, T. Thacher, *J. Comput. Chem.* **2003**, *24*, 1059.

[19] A. B. Pangborn, M. A. Giardello, R. H. Grubbs, R. K. Rosen, F. J. Timmers, *Organometallics* **1998**, *15*, 1518.

[20] B. J. Littler, M. A. Miller, C.-H. Hung, R. W. Wagner, D. F. O'Shea, P. D. Boyle, J. S. Lindsey, *J. Org. Chem.* **1999**, *64*, 1391.

[21] P. Boudjouk, J.-H. So, *Inorg. Synth.* **1992**, *29*, 108.

[22] *SHELXTL*, version 6.10, Bruker AXS Inc., Madison, Wisconsin, U.S.A., **2000**.

[23] *Discover 3.0.0* and *Insight II*, Molecular Simulations Inc., now owned by Accelrys, San Diego, California, USA.


Received: June 21, 2007
Published Online: September 24, 2007

 © 2007 Wiley-VCH Verlag GmbH & Co. KGaA, Weinheim 

DOI: 10.1002/ejic.200700743

# Decomposition Cascades of Dicoordinate Copper(I) Chalcogenides

Heiko Jacobsen*[a][‡] and Mark J. Fink[b]

**Keywords:** Bond energy / Copper / Chalcogens / Density functional calculations / Dispersive interactions

Cu–E, Si–E, and Cu–P bond energies of $R_3PCuESiR_3$ and $CuESiR_3$ complexes (E = O, S, Se) have been investigated using PBE density-functional calculations, and including empirical corrections for dispersive interactions (DFT-D). The bond energies have been used to investigate likely pathways of molecular decomposition. The energy profile for thermal decomposition is to a large degree independent of the nature of the phosphane ligands and silyl groups. Oxides, sulfides, and selenides have qualitatively the same thermal decomposition profile. Thermal decomposition is not likely to produce copper chalcogenide units CuE, but elemental copper Cu instead. Consideration of intermolecular van der Waals attraction suggests that the linear geometry of system $t$Bu$_3$PCuOSiPh$_3$ as found in the crystal is most likely due to crystal packing and intermolecular forces.

(© Wiley-VCH Verlag GmbH & Co. KGaA, 69451 Weinheim, Germany, 2007)

## 1. Introduction

Copper(I) oxide and chalcogenide complexes find extensive usage in a broad variety of applications ranging from catalysis[1] over photovoltaic devices[2,3] to metallaprotein models.[4] In addition, this class of compounds displays a rich chemistry with a great diversity of stoichiometries and geometries, which is governed by the ability of the group 16 element to adopt either terminal or bridging coordination modes. Variations in the ligand framework around the copper center lead to polymeric or oligomeric cluster compounds,[5] structures with a cyclic $Cu_2E_2$ core,[6] and monomeric complexes.[7]

Copper also plays a major role in meeting the challenges of ever increasing requirements for electrical performance of on-chip wiring, because it is a key element of the interconnection network on a chip of high-performance semiconductor components.[8] One key technique in the design of such devices is chemical vapor deposition (CVD), and with the synthesis of new copper complexes that can be used in CVD applications, coordination chemistry is stretching the limits of micro-electronics technology.[9]

Recently, we reported the synthesis and characterization of the first triad of monomeric dicoordinate copper(I) chalcogenide complexes $t$Bu$_3$PCuESiPh$_3$ (**1**, E = O; **2**, E = S; **3**, E = Se).[10] The X-ray analyses of the copper silylchalcogenolates reveal significant structural structure differences originating from the nature of the chalcogen atom E. The oxygen atom in complex **1** has a linear coordination geometry in contrast to the highly bent sulfur and selenium analogs, **2** and **3**.

In a first theoretical analysis of dicoordinate copper(I) chalcogenides we have performed a detailed analysis of the structure and bonding of representative $H_3PCuESiH_3$ and $CuESiH_3$ model complexes.[11] In the present work, we focus on the thermochemistry of Cu–P, Cu–E, and Si–E bonds in this class of compounds. It is hoped that elucidation of possible decomposition cascades will provide valuable insight into the CVD applicability of copper chalcogenides. In addition, we provide an analysis and rationale of the unexpected molecular geometry of $t$Bu$_3$PCuOSiPh$_3$ **1** as found in the solid state.

## 2. Results and Discussion

The Cu–P, Cu–E, and Si–E bond energies for a variety of dicoordinate copper(I) chalcogenides have been investigated. The compound numbering of our model complexes is illustrated in Scheme 1.

Bond energies for Cu–P, Cu–E, and E–Si bonds have been estimated from dissociation enthalpies in the gas phase. For calculations of the bond-dissociation enthalpies at 0 K, $\Delta H^0$, reactants and products have been considered to adopt the geometry and electronic structure of their ground states. The decomposition pathways considered in this work are outlined on Scheme 2.

**2.1 The Copper–Phosphane Bond:** We begin our discussion with a detailed analysis of the Cu–P bond. The bond properties of the phosphane ligand have received considerable attention in the literature, and various concepts

[a] KemKom,
Libellenweg 2, 25917 Leck, Nordfriesland, Germany
E-mail: jacobsen@kemkom.com
[b] Department of Chemistry, Tulane University,
6400 Freret St., New Orleans, LA 70118, USA
[‡] Current address: Department of Chemistry, Tulane University,
6400 Freret St., New Orleans, LA 70118, USA
E-mail: jheiko@tulane.edu

Supporting information for this article is available on the WWW under http://www.eurjic.org or from the author.

 © 2007 Wiley-VCH Verlag GmbH & Co. KGaA, Weinheim 

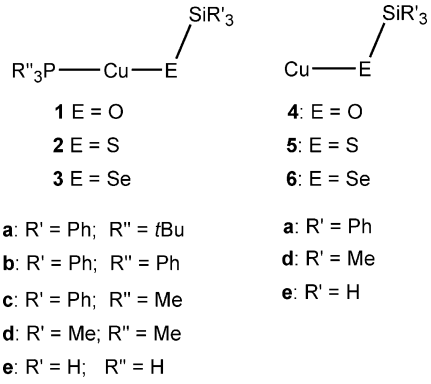


Scheme 1.

like the Tolman angle,[12] basicity parameters[13] or the lone-pair energy of the phosphane donor[14] find extensive use to predict and reason the bonding behavior of phosphanes toward transition-metal fragments. Here, we shall look at bond-dissociation enthalpies $\Delta H^0$, and we will make use of a partitioning of the so called bond-snapping energy $BE_{snap}$[15] into orbital contributions $\Delta E_{int}$ and steric terms $\Delta E^0$. The bond-snapping energy describes the interaction of two suitably prepared fragments, having the right geometry of the final molecule and an electron configuration that allows for bond formation. We model the Cu–P as donor–acceptor bond, and Cu–E and Si–E bonds as covalent bonds formed in the coupling of two radical fragments. In this work, $BE_{snap}$ contains an additional contribution due to dispersive interactions $E_{disp}$ between the phosphane ligands and the silyl groups, and the breakdown that is used here is given in Equation (1).

$$BE_{snap} = -[\Delta E^0 + \Delta E_{int} + E_{disp}] \quad (1)$$

We have drawn on this analysis extensively in our previous work on copper chalcogenide complexes,[11] and in addition we refer the reader to the literature[16] for a detailed account of the energy decomposition scheme employed in this work.

Bond-dissociation enthalpies $\Delta H^0$ and bond-snapping energies $BE_{snap}$ are collected in Table 1. Also included are the individual contributions to $BE_{snap}$ due to steric interaction $\Delta E^0$, orbital interaction $\Delta E_{int}$, and dispersive interaction $E_{disp}$.

Table 1. Energy terms (in kJ/mol) for the Cu–P bond of various copper(I) chalcogenides.

| | $\Delta E^0$ | $\Delta E_{int}$ | $E_{disp}$ | $BE_{snap}$ | $\Delta H^0$ |
|---|---|---|---|---|---|
| **1a** | –59 | –203 | –8 | 270 | 268 |
| **1b** | –17 | –221 | –13 | 251 | 250 |
| **1c** | –59 | –182 | –3 | 244 | 245 |
| **1d** | –48 | –178 | –1 | 227 | 213 |
| **1e** | –17 | –171 | 0 | 188 | 173 |
| **2a** | –38 | –194 | –10 | 242 | 235 |
| **2b** | –4 | –207 | –14 | 225 | 220 |
| **2c** | –40 | –172 | –4 | 216 | 212 |
| **2d** | –29 | –165 | –1 | 195 | 183 |
| **2e** | 1 | –155 | 0 | 154 | 140 |
| **3a** | –30 | –195 | –11 | 236 | 233 |
| **3b** | 0 | –199 | –11 | 210 | 209 |
| **3c** | –32 | –176 | –6 | 214 | 212 |
| **3d** | –23 | –165 | –1 | 189 | 177 |
| **3e** | 5 | –153 | 0 | 148 | 136 |

The bond-dissociation enthalpies follow the expected trend O > S ≈ Se; the $\Delta H^0$ values for the oxygen compounds are about 30 kJ/mol larger than those for the heavier chalcogenides. Within a series of chalcogenide compounds, the bond-dissociation enthalpies span a range of about 130 kJ/mol, where the P*t*Bu$_3$ compounds define the higher end, and the PH$_3$ complexes the lower end of the scale. Overall, the values are in good agreement with bond-dissociation enthalpies at 0 K. Discrepancies arise due to the fact that the geometric preparation energy[15] has not been accounted for, but the overall agreement justifies the derivation of trends based on a more detailed analysis of the bond-snapping energy $BE_{snap}$.

When we consider the individual components of the bond-snapping energy, we notice that the steric interaction $\Delta E^0$ constitutes a bonding rather than repulsive interaction. This indicates that attractive electrostatic interaction outweighs the contribution of the Pauli repulsion. The magnitude of the stabilizing steric interaction terms of the phosphane ligands PR$_3$″ can be ordered in terms of the R″ group as *t*Bu > Me > Ph > H. This trend correlates well with the accepted basicity of the phosphane ligands.[13] When the silyl group carries methyl rather than phenyl substituents, both the PR$_3$′′ ligand and the SiR$_3$ group compete for electrostatic interaction with the chalcogenide–metal core CuE. As a consequence, $\Delta E^0$ for the PMe$_3$ ligand is reduced

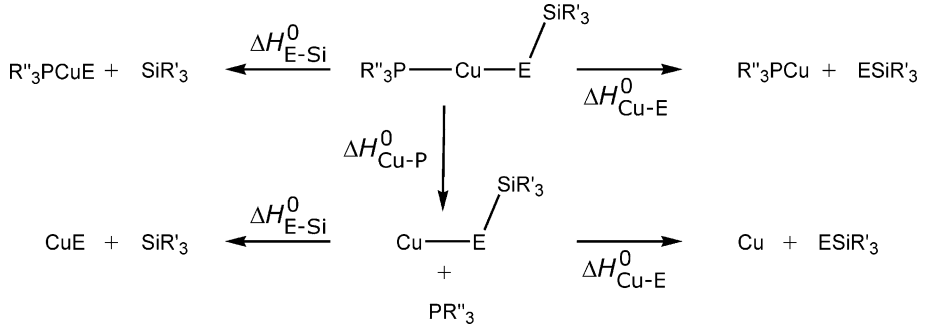


Scheme 2.

 © 2007 Wiley-VCH Verlag GmbH & Co. KGaA, Weinheim 

(compare entries **1c** and **1d**, **2c** and **2d**, **3c** and **3d** in Table 1).

The major contribution to $BE_{snap}$ arises from the orbital interaction energy $\Delta E_{int}$. If we extend the basicity arguments and restrict the interaction between a phosphane ligand and a copper–chalcogenide core to electron donation only, the phosphane lone-pair energies provide a measure of the ligand donor strength, and thus a measure of $\Delta E_{int}$. We then would expect the same qualitative ranking found for the steric interaction to be reciprocated in the orbital interaction: *t*Bu > Me > Ph > H. Inspection of the data in Table 1, however, indicates that the triphenylphosphane ligand unexpectedly shows the strongest orbital interaction.

By now, it is well recognized that the bond between the phosphane ligands and transition-metal fragments contains a sizeable contribution due to π-backdonation,[17] and an early DFT investigation of $(CO)_5Cr(PH_3)$ reports a metal–phosphane bond strength of 144 kJ/mol, with a contribution of about 25% attributed to π-backdonation.[18] Employing orbital-based arguments, the amount of backdonation between [P] and [CuE] fragments is qualitatively represented by the $HOMO_{[CuE]}$–$LUMO_{[P]}$ gap. An orbital analysis of model system has revealed the fact that Cu–E $\pi_{dp}$-antibonding orbitals are among the set of highest occupied molecular orbitals of the copper-chalcogenide core, and that backdonation from Cu-based d orbitals to σ* orbitals of the phosphane ligand strengthens the Cu–P bond.[11]

An inspection of the frontier-orbital energies of the phosphane ligands and copper–chalcogenide cores corroborates the trends in Cu–P bonding indicated thus far, and also provides an explanation for the unusually high $\Delta E_{int}$ contribution of the $PPh_3$ ligand. HOMO and LUMO energies for the CuE cores **4a**, **5a**, and **6a** and for the phosphanes $PR_3''$, R'' = *t*Bu, Ph, Me, H, are depicted in Figure 1.

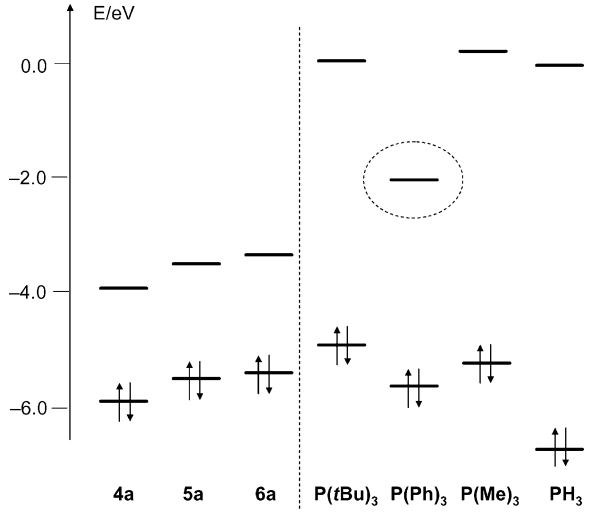


Figure 1. Frontier-orbital energies for copper–chalcogenide fragments (left) and phosphane ligands (right). The LUMO of $PPh_3$ is at an unexpectedly low energy level (dotted circle).

Trends in basicities correlate well with relative $HOMO_{[P]}$ energies. The LUMO of triphenylphosphane is at exceptionally low energy, which causes a reduced $HOMO_{[CuE]}$–$LUMO_{[P]}$ gap, and consequently enhances the backdonation. This observation accounts for the unexpectedly strong orbital interaction of triphenylphosphane.

When assessing the Cu–P bond strength, it is instructive to compare the Cu–P bond strength for the Cu atom to that for CuE cores. The Cu–P bond strength in $H_3P$–Cu is calculated to amount to 104 kJ/mol.[19] In contrast, the Cu–P bond-snapping energies $BE_{snap}$ in **1a**, **2a**, and **3a** are stronger by 69, 36, and 32 kJ/mol, respectively. The presence of the chalcogen atom significantly strengthens the Cu–P bond. This is due to backdonation out of filled Cu–E $\pi_{dp}$-antibonding orbital into empty σ* orbitals of the phosphane ligand.

Dispersive interactions $E_{disp}$ provide additional bond stabilization of up to 14 kJ/mol for systems with sterically demanding phosphane ligands and large silyl groups. We will return to the importance of dispersive interactions at a later point in our discussion.

**2.2 Bonds Involving Chalcogen Atoms:** The bond-dissociation enthalpies $\Delta H^0$ of Cu–E and E–Si bonds are displayed in Figure 2. The Cu–E, and E–Si bond strengths follow the expected trend O > S > Se. The silicon–oxygen bond is a strong bond with a dissociation energy of 536 kJ/mol,[20]

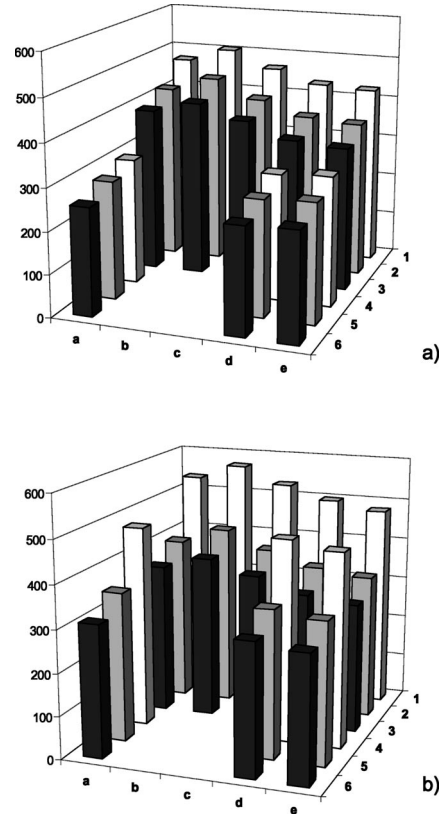


Figure 2. Bond-dissociation enthalpies $\Delta H^0$ (in kJ/mol) of copper–chalcogen bonds (Cu–E; Figure 2, a) and silicon–chalcogen bonds (Si–E; Figure 2, b).

 © 2007 Wiley-VCH Verlag GmbH & Co. KGaA, Weinheim 

and the O–Si bond-dissociation enthalpies for the copper chalcogenides fall all around this value. When we compare Cu–E bond energies of systems with phosphane ligands (**1**, **2**, **3**) with bond energies of systems without phosphane ligands (**4**, **5**, **6**), we find that coordination of a $PR_3$ significantly enhances the Cu–E bond strength. For example, if we consider the "real" systems **1a**, **2a**, **3a**, the copper–chalcogenide Cu–E bonds are stronger by 174 kJ/mol (E = O), 141 kJ/mol (E = S) and 138 kJ/mol (E = Se), in comparison to the "phosphane-free" systems **4a**, **5a**, and **6a**.

Not only does the presence of a chalcogen atom strengthen the Cu–P bond, as discussed above, but the presence of a phosphane ligand also induces a stabilization of the Cu–E bond. This synergistic effect is caused by enhanced π-backbonding from the copper center to the phosphane ligand. As mentioned before, Cu–E $\pi_{dp}$-antibonding orbitals are among the set of highest occupied molecular orbitals of the Cu–E core. Backdonation from Cu-based d orbitals to σ* orbitals of the phosphane ligand not only strengthens the Cu–P bond, but at the same reduces the antibonding Cu–E interaction and thus strengthens the Cu–E bond.

The Si–E bonding interaction too is enhanced due to the presence of an additional phosphane ligand. This secondary intrinsic effect amounts to 22 kJ/mol (E = O), 10 kJ/mol (E = S) and 9 kJ/mol (E = Se) for model compounds with $PH_3$ ligands and $SiH_3$ groups. For real systems with P*t*$Bu_3$ ligands and $SiPh_3$ groups, this effect is more pronounced and yields a secondary intrinsic stabilization energies of 59 kJ/mol (E = O), 43 kJ/mol (E = S) and 41 kJ/mol (E = Se), respectively.

If we compare relative Si–E and Cu–E bond strengths, we find that for systems without $PR_3$ ligands, the Si–E bonds are always stronger than the Cu–E bonds. The average energy differences are about 165 kJ/mol for oxygen complexes, but only about 65 kJ/mol and 50 kJ/mol for sulfur and selenium compounds, respectively. When we turn to phosphane complexes, we find modifications in this general trend due to the fact that the presence of phosphorus ligand significantly enhances the Cu–E bond strength. For the O complexes the energy difference between Si–O and Cu–O bonds decreases to about 60 kJ/mol, still in favor of the silicon–oxygen bond. For the heavier chalcogen atoms, the relative bond strengths between Si–E and Cu–E bonds is now inverted; and the S and Se complexes all have Cu–E bonds that are stronger than Si–E bonds by about 25 and 35 kJ/mol, respectively.

When we investigate the influence of the R′ and R′′ ligands on the strength of the Cu–E and Si–E bonds, we find that for phosphane systems these bond energies vary within a range of about 80 kJ/mol. For complexes without an additional phosphane ligand, we find that independent of the nature of the R′ group, for a given chalcogen element the values for Cu–E and Si–E bond-dissociation enthalpies are approximately the same.

**2.3 Decomposition Cascades:** We are now at a point that we can discuss possible decomposition pathways of dicoordinate copper(I) chalcogenides, Scheme 3.

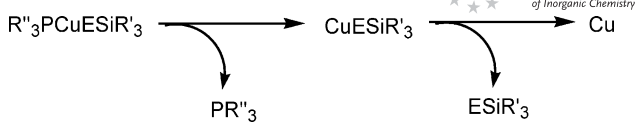


Scheme 3.

For all complexes investigated in the present work, the Cu–P bond always constitutes the weakest link. Thus, thermal decomposition of a dicoordinate copper(I) chalcogenide (DCC) is most likely initiated by dissociation of the phosphane ligand; a process that results in formation of a monocoordinate copper(I) chalcogenide (MCC). For this type of compounds, contrary to DCCs, the Cu–E bond is always weaker than the Si–E bond. Therefore, the second step in thermal decomposition most likely involves cleavage of the Cu–E bond. Thermal decomposition is not likely to produce copper chalcogenide units CuE, but elemental copper Cu instead. Furthermore, the energy profile for thermal decomposition is to a large degree independent of the nature of the phosphane ligands and silyl groups. Oxides, sulfides, and selenides all have qualitatively the same thermal decomposition profile. In addition, sulfides and selenides display approximately the same quantitative thermodynamics.

**2.4 The Structure of *t*$Bu_3$PCuOSi$Ph_3$ in the Gas Phase and in the Solid State:** X-ray crystallography has shown that the Cu atoms in the copper silylchalcogenolates *t*$Bu_3$PCuE-$SiPh_3$ (**1**, E = O; **2**, E = S; **3**, E = Se) have either a linear or a near-linear coordination geometry in all three complexes. Interestingly, the O atom in complex **1** is also linear, which is in contrast to the highly bent S and Se analogs, compounds **2** and **3**, respectively.[10] Our initial calculations on $H_3$PCuE$SiH_3$ model compounds have indicated that the unusual geometry of the oxygen compound **1** is not caused by intermolecular orbital interactions such as extended π-delocalization, but are the result of a fine balance of electrostatic interaction and Pauli repulsion.[11] In the last section of this work, we will address the unusual solid-state structure of *t*$Bu_3$PCuE$SiPh_3$ (**1a**) in more detail.

Our geometry optimization of **1a**, the gas-phase analog of the solid-state structure **1**, resulted in a bent geometry with an angle ∠(Cu–O–Si) of 117°. In addition, we optimized a linear structure **1a**′ by fixing the angle ∠(Cu–O–Si) at 180°. In the gas phase, the linear structure is 23 kJ/mol higher in energy compared to the bent ground state geometry, and an energy partitioning for the linearization process is outlined in Figure 3.

When complex **1a** takes on a linear, rather than a bent geometry, the distance between the P and Si centers of the sterically demanding peripheral ligands increases from 493 pm to 556 pm, and Pauli repulsion is reduced. As a consequence, the linear geometry is favored in terms of the steric interaction $\Delta E^0$. However, the orbital interactions $\Delta E_{int}$ as well as dispersive interaction are stronger in a bent arrangement, and as a consequence, the linear structure **1a**′ is higher in energy.

Our calculations indicate that the dispersive interactions $E_{disp}$ lead to an increase in bond energy in **1a** and therefore

 © 2007 Wiley-VCH Verlag GmbH & Co. KGaA, Weinheim 

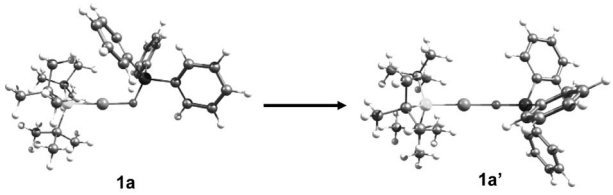


$\Delta E^0$ = –40 kJ/mol; $\Delta E_{int}$ = 56 kJ/mol; $\Delta E_{disp}$ = 7 kJ/mol; $\Delta E$ = 23 kJ/mol

Figure 3. Bond linearization of $t$Bu$_3$PCuOSiPh$_3$ in the gas phase.

to a larger barrier to planarity. We attribute this increase to an enhanced long-range $1/r^6$-induced dipole-induced dipole attraction. van der Waals forces not only incorporate short-range exponential repulsion arising from Pauli orthogonalization, but long-range dispersive attraction as well. Due to the large separation of the sterically demanding ligands, the long-range attraction outweighs the short-range repulsion, and nonbonded interactions strengthen, but not weaken, the Cu–P, Cu–E, and Si–E bonds.

Although the barrier to planarity is increased due to *intramolecular* dispersive attraction, in the crystal there exists the possibility of *intermolecular*, long-range dispersive interaction, which might lower the barrier to planarity or even favor a linear coordination geometry over a bent arrangement.

Compound **1** crystallizes in the highly symmetric space group $P\bar{3}$, in which the linear P–Cu–O–Si skeleton lies exactly on a crystallographic threefold rotation axis. The crystal packing for **1** is displayed in Figure 4; also indicated are neighboring phosphane ligands and silyl groups that give rise to dispersive stabilization.

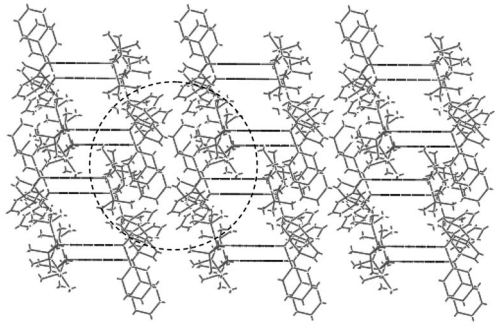

**1a**(bent, solid state) → **1a'**(linear, solid state) $\Delta E_{disp}$ = –28 kJ/mol

Figure 4. Crystal packing of $t$Bu$_3$PCuOSiPh$_3$. Neighboring phosphane ligands and silyl groups from different molecular units undergo dispersive interaction (dotted circle).

We have calculated intermolecular dispersion energies for the linear geometry **1a**′ based on the crystal structure of **1**. The dispersion forces in the solid state for a bent geometry **1a** were modeled after the crystal structure of the sulfur analog, and if we compare the dispersive lattice energies we find that the linear arrangement is favored over a packing of a bent molecular unit by 28 kJ/mol per molecule. The energetic stabilization of a linear arrangement due to packing forces slightly outweighs the preparation energy required to distort the bent structure and we conclude that the unusual molecular structure of $t$Bu$_3$PCuOSiPh$_3$ as observed in the solid state results from crystal packing, and is not an indication of unusual intermolecular bonding.

Molecular structures as obtained from crystal structure analysis are not always good representations for the geometry of the isolated and unperturbed molecule. If the potential energy surface of internal molecular coordinates is shallow and does not display a pronounced minimum, intermolecular dispersive forces as well as intermolecular electrostatic interaction[21] might significantly influence the geometry of the molecular unit in the solid state.

## 3. Conclusion

As stated in the introduction, one of the main goals of the present work was to elucidate the CVD applicability of copper chalcogenides, and in conclusion of this work, we shall summarize our findings with respect to this question. We found that the energy profile for thermal decomposition is to a large degree independent of the nature of the phosphane ligands and silyl groups. We also found that oxides, sulfides, and selenides have qualitatively the same thermal decomposition profile.

A minor aspect of the current work was the analysis and rationalization of the unexpected molecular geometry of $t$Bu$_3$PCuESiPh$_3$ as found in the solid state. Consideration of intermolecular van der Waals attraction suggests that the linear geometry of system $t$Bu$_3$PCuOSiPh$_3$ as found in the crystal is most likely due to crystal packing and intermolecular forces.

## 4. Computational Details

Density-functional calculations have been carried out using the Amsterdam Density Functional ADF suite of programs, version ADF2006.01.[22] The calculation were based on the local-density approximation with Slater exchange[23] and VWN-V correlation.[24] Gradient corrections as proposed by Perdew, Burke and Enzerhof[25] have been added self-consistently.

Molecular orbitals were expanded in an uncontracted set of Slater-type orbitals (STOs). For H and C the basis used was of double-ζ quality, whereas for O, Si, P, S, and Se a triple-ζ basis has been employed, and both basis sets were augmented with one set of polarization functions (ADF basis sets III and IV, respectively). The transition metal was described by a triple-ζ basis augmented with two sets of polarization functions (ADF basis set V). The core shells (C, O: 1s; Si, P, S, Cu: 1s2s2p; Se: 1s2s2p3s3p3d) were treated by the frozen-core approximation, and an auxiliary set of s, p, d, f and g STOs was used to fit the molecular density and to represent the Coulomb and exchange potentials accurately in each SCF cycle.[26]

Geometries have been optimized according to the method developed by Versluis and Ziegler.[27] Frequencies for molecules with R′ = R′′ = H have been calculated analytically,[28] and served as basis for zero-point-energy corrections. Empirical corrections for intramolecular dispersive forces between $SiR_3'$ groups and $PR_3''$ ligands have been included for geometry optimization and energy calculations (DFT-D).[29]

 © 2007 Wiley-VCH Verlag GmbH & Co. KGaA, Weinheim 

Intermolecular dispersive interactions in the crystal have been calculated with the Generalized Lattice Utility Program GULP.[30] These calculations employ an undamped dispersion potential of the form suggested by Tang and Toennies.[31]

The consistency of the density functional calculations has been checked by single point calculations using other pure and hybrid density functionals, as well as different basis sets. These calculations are documented in the Supporting Information.

**Supporting Information** (see also the footnote on the first page of this article): Cartesian coordinates and final energies for optimized complexes. Results of consistency calculations.

## Acknowledgments

We gratefully acknowledge Prof. L. Cavallo for granting access to the MoLNaC Computing Facilities at Dipartimento di Chimica, Università di Salerno.

[1] R. Grigg, D. M. Cooper, S. Holloway, S. McDonald, E. Millington, M. A. B. Sarker, *Tetrahedron* **2005**, *81*, 8677–8685; V. Percec, C. Grigoras, *J. Poly. Sci., Part A* **2005**, *43*, 3920–3931; A. Corma, A. E. Palomares, F. Rey, F. Márquez, *J. Catal.* **1997**, *170*, 140–149; J. Linder, M. A. V. Garcia, A. Achdev, J. Schwank, *J. Chem. Soc. Chem. Commun.* **1989**, 1833–1835.
[2] T. Komuro, H. Kawaguchi, K. Tatsumi, *Inorg. Chem.* **2002**, *41*, 5083–5090.
[3] W. Hirpo, S. Dhingra, A. C. Sutorik, M. G. Kanatzidis, *J. Am. Chem. Soc.* **1993**, *115*, 1597–1599; K. K. Banger, J. A. Hollingsworth, J. D. Harris, J. Cowan, W. E. Buhro, A. F. Hepp, *Appl. Organomet. Chem.* **2002**, *16*, 617–627; R. P. Raffaelle, S. L. Castro, A. F. Hepp, S. G. Bailey, *Prog. Photovolt. Res. Appl.* **2002**, *10*, 433–439; B. J. Stanbery, *Crit. Rev. Solid State Mater. Sci.* **2002**, *27*, 73–117.
[4] D. R. Winge, C. T. Dameron, G. N. George, I. J. Pickering, I. G. Dance, *Bioinorg. Chem. Copper* **1993**, 110–123.
[5] I. G. Dance, M. L. Scudder, L. J. Fitzpatrick, *Inorg. Chem.* **1985**, *24*, 2547–2550.
[6] X.-Y. Liu, F. Mota, P. Alemany, J. J. Novoa, S. Alvarez, *Chem. Commun.* **1998**, 1149–1150.
[7] D. T. T. Tran, N. J. Taylor, J. F. Corrigan, *Angew. Chem. Int. Ed.* **2000**, *39*, 935–937; D. T. T. Tran, J. F. Corrigan, *Organometallics* **2000**, *19*, 5202–5208.
[8] K. Maex, M. R. Baklanov, D. Shamiryan, F. Iacopi, S. H. Brongersma, Z. S. Yanovitskaya, *J. Appl. Phys.* **2003**, *93*, 8793–8841.
[9] P. Doppelt, *Coord. Chem. Rev.* **1998**, *178*, 1785–1809; Y. B. Dong, M. D. Smith, R. C. Layland, H. C. zur Loye, *Inorg. Chem.* **1999**, *38*, 5027–5033.
[10] I. Medina, H. Jacobsen, J. T. Mague, M. J. Fink, *Inorg. Chem.* **2006**, *45*, 8844–8846.
[11] H. Jacobsen, M. J. Fink, *Inorg. Chim. Acta* **2007**, *360*, 3511–3517.
[12] C. A. Tolman, *Chem. Rev.* **1977**, *77*, 313–348.
[13] S. Joerg, R. S. Drago, J. Sales, *Organometallics* **1998**, *17*, 589–599.
[14] H. M. Senn, D. V. Deubel, P. E. Blöchl, A. Togni, G. Frenking, *J. Mol. Struct. THEOCHEM* **2000**, *506*, 233–242.
[15] H. Jacobsen, T. Ziegler, *Comments Inorg. Chem.* **1995**, *17*, 301–307.
[16] F. M. Bickelhaupt, E. J. Baerends, *Rev. Comput. Chem.* **2000**, *15*, 1–86.
[17] G. Frenking, K. Wichmann, N. Fröhlich, C. Loschen, M. Lein, J. Frunzke, V. M. Rayón, *Coord. Chem. Rev.* **2003**, *238*, 55–82.
[18] H.-B. Kraatz, H. Jacobsen, T. Ziegler, P. M. Boorman, *Organometallics* **1993**, *12*, 76–80.
[19] G. A. Bowmaker, M. Pabst, N. Rösch, H. Schmidbauer, *Inorg. Chem.* **1993**, *32*, 880–887.
[20] K. M. Downard, J. H. Bowie, R. N. Hayes, *Aust. J. Chem.* **1990**, *43*, 511–520.
[21] H. Jacobsen, T. Brackemeyer, H. Berke, G. Erker, R. Fröhlich, *Eur. J. Inorg. Chem.* **2000**, 1423–1428
[22] G. te Velde, F. M. Bickelhaupt, S. J. A. van Gisbergen, C. Fonseca Guerra, E. J. Baerends, J. G. Snijders, T. Ziegler, *J. Comput. Chem.* **2001**, *22*, 931–967; C. Fonseca Guerra, J. G. Snijders, G. te Velde, E. J. Baerends, *Theor. Chem. Acc.* **1998**, *99*, 391–403. ADF2006.01, SCM, Theoretical Chemistry, Vrije Universiteit, Amsterdam, The Netherlands.
[23] J. C. Slater, *Phys. Rev.* **1951**, *81*, 385–390.
[24] S. H. Vosko, L. Wilk, M. Nusair, *Can. J. Phys.* **1980**, *58*, 1200–1211.
[25] J. P. Perdew, K. Burke, M. Ernzerhof, *Phys. Rev. Lett.* **1996**, *77*, 3865–3868; J. P. Perdew, K. Burke, M. Ernzerhof, *Phys. Rev. Lett.* **1997**, *78*, 1396.
[26] E. J. Baerends, D. E. Ellis, P. Ros, *Chem. Phys.* **1973**, *2*, 41–51.
[27] L. Versluis, T. Ziegler, *J. Chem. Phys.* **1988**, *88*, 322–328.
[28] S. K. Wolff, *Int. J. Quantum Chem.* **2005**, *104*, 645–659; H. Jacobsen, A. Berces, D. P. Swerhone, T. Ziegler, *Comput. Phys. Commun.* **1997**, *100*, 263–276; A. Berces, R. M. Dickson, L. Y. Fan, H. Jacobsen, D. P. Swerhone, T. Ziegler, *Comput. Phys. Commun.* **1997**, *100*, 247–262; H. Jacobsen, A. Berces, D. P. Swerhone, T. Ziegler, *ACS Symp. Ser.* **1996**, *629*, 154–163.
[29] S. Grimme, *J. Comput. Chem.* **2004**, *25*, 1463–1473. J. M. Ducere, L. Cavallo, manuscript in preparation.
[30] J. D. Gale, *J. Chem. Soc. Faraday Trans.* **1997**, *93*, 629–637; J. D. Gale, A. L. Rohl, *Mol. Simul.* **2003**, *29*, 291–341; J. D. Gale, *Z. Kristallogr.* **2005**, *220*, 552–554.
[31] K. T. Tang, J. P. Toennies, *J. Chem. Phys.* **1984**, *80*, 3726–3741.

Received: July 13, 2007
Published Online: October 1, 2007

 © 2007 Wiley-VCH Verlag GmbH & Co. KGaA, Weinheim

**The EUChemSoc Societies have taken the significant step into the future by merging their traditional journals, to form two leading chemistry journals, the *European Journal of Inorganic Chemistry* and the *European Journal of Organic Chemistry.* Three further EUChemSoc Societies (Austria, Czech Republic and Sweden) are Associates of the two journals.**

## COVER PICTURE

**The cover picture shows** that consecutive protonation of the pyridine N and imine N atoms of 4-pyridinealdazine (PCA) in the complex [Re(4,4′-$CO_2$Me-bpy)$(CO)_3$(PCA)]$^+$ (bpy = 2,2′-bipiridine) lead to bell-shaped curves for both the absorbance and the emission intensity vs. pH; the latter property can be employed to devise novel luminescent pH sensors of the *on-off-on* type. Details are discussed in the article by N. E. Katz et al. on p. 5323ff.

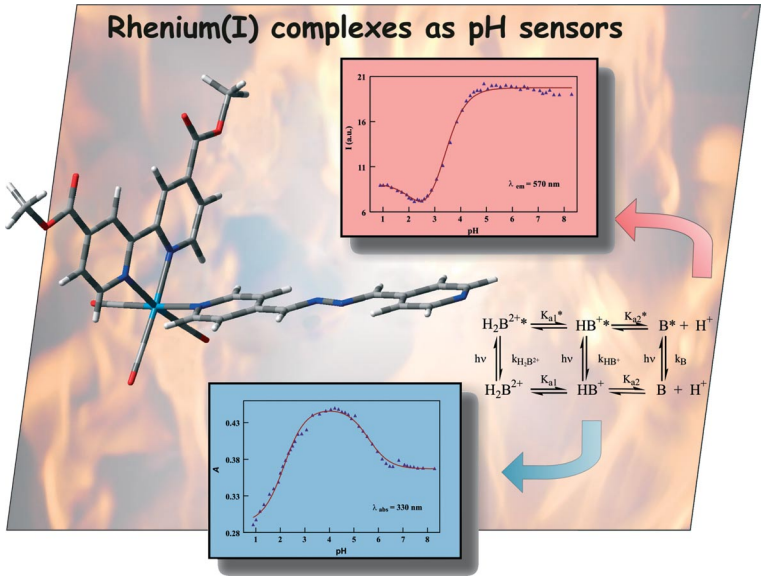


 © 2007 Wiley-VCH Verlag GmbH & Co. KGaA, Weinheim

**The EUChemSoc Societies have taken the significant step into the future by merging their traditional journals, to form two leading chemistry journals, the *European Journal of Inorganic Chemistry* and the *European Journal of Organic Chemistry.* Three further EUChemSoc Societies (Austria, Czech Republic and Sweden) are Associates of the two journals.**

## COVER PICTURE

**The cover picture shows** that consecutive protonation of the pyridine N and imine N atoms of 4-pyridinealdazine (PCA) in the complex [Re(4,4′-$CO_2$Me-bpy)$(CO)_3$(PCA)]$^+$ (bpy = 2,2′-bipiridine) lead to bell-shaped curves for both the absorbance and the emission intensity vs. pH; the latter property can be employed to devise novel luminescent pH sensors of the *on-off-on* type. Details are discussed in the article by N. E. Katz et al. on p. 5323ff.

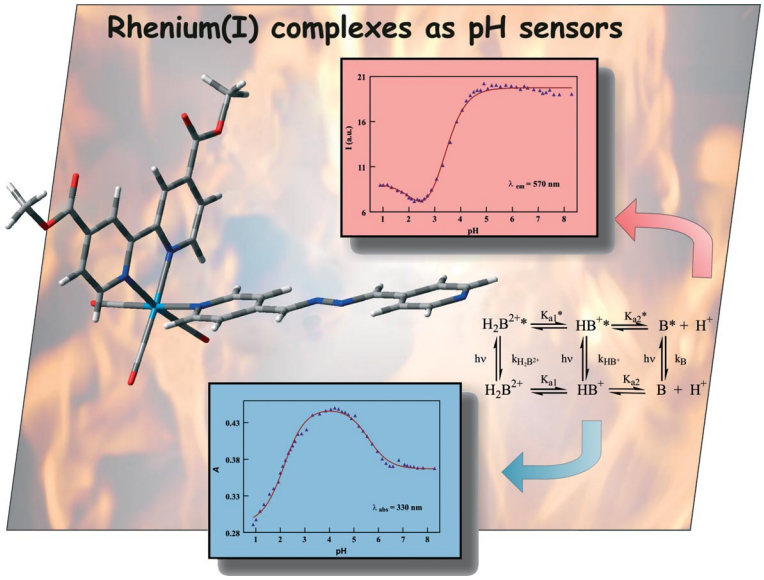


 © 2007 Wiley-VCH Verlag GmbH & Co. KGaA, Weinheim 

# CONTENTS

## SHORT COMMUNICATION

### B−C Bond Activation

**M. Kowalewski, B. Krumm, P. Mayer, A. Schulz,* A. Villinger ..... 5319−5322**

Transition-Metal-Free Boron−Carbon Bond Activation: Insertion of an NNP Fragment into a Boron−Carbon Bond

**Keywords:** Azaphosphole / Diazadiphosphetidine / Insertion / Lewis acids / Boranes / X-ray elucidation

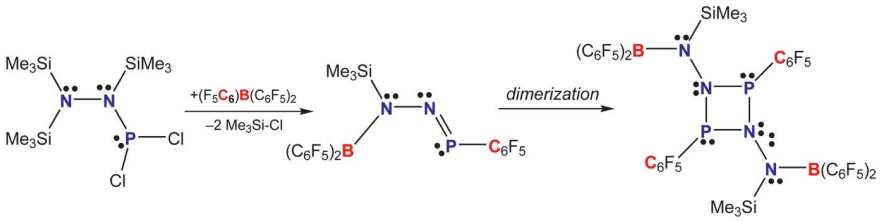


A formal NNP fragment insertion into a B−C bond was achieved by the reaction of $(Me_3Si)_2N-N(SiMe_3)-PCl_2$ with $B(C_6F_5)_3$. A novel diazadiphosphetidine with a phosphorus(III) atom attached to a pentafluorophenyl group was isolated and fully characterized.

## FULL PAPERS

### Donor−Acceptor Systems

**M. Cattaneo, F. Fagalde, N. E. Katz,* C. D. Borsarelli, T. Parella ..... 5323−5332**

pH-Induced Luminescence Changes of Chromophore-Quencher Tricarbonylpolypyridylrhenium(I) Complexes with 4-Pyridinealdazine

**Keywords:** Donor-acceptor systems / Rhenium / Photochemistry / Molecular devices / Mixed-valent compounds

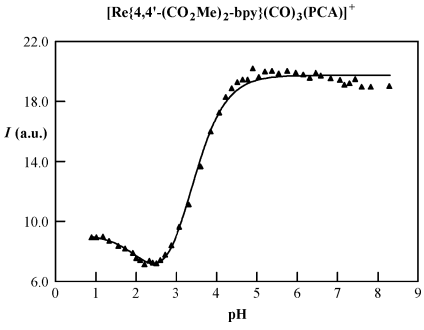


New emissive mono- and dinuclear chromophore-quencher tricarbonylpolypyridylrhenium(I) complexes containing 4-pyridinealdazine (PCA) are prepared and characterized by spectroscopic, electrochemical, and photophysical techniques. Consecutive protonation of the pyridinyl nitrogen atom and the imine nitrogen atom of PCA leads to bell-shaped curves for both the absorbance and emission intensities vs. pH for some of these complexes; this latter property can be employed to devise novel luminescent pH sensors of the on-off-on type.

### Asymmetric Dimolybdenum Complex

**K. Pal, S. Sarkar* ..... 5333−5344**

Synthesis, Structure and a DFT/TDDFT Study of a Diimido-Bridged Asymmetric Dimolybdenum Complex

**Keywords:** Mixed-valence compounds / Molybdenum / Cyclic voltammetry / Electronic structure / Density functional calculations

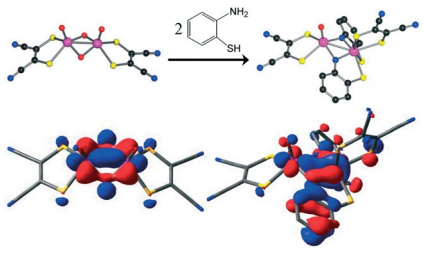


The two Mo centers in an asymmetric dimeric mixed-valence molybdenum complex containing oxidomolybdenum and desoxomolybdenum entities have formal oxidation states that result from a combination of $Mo^{VI}$ and $Mo^{IV}$, as confirmed by IR, EPR, and CV investigations and the results of DFT-TDDFT calculations.

 © 2007 Wiley-VCH Verlag GmbH & Co. KGaA, Weinheim 

## Metathesis Catalysts

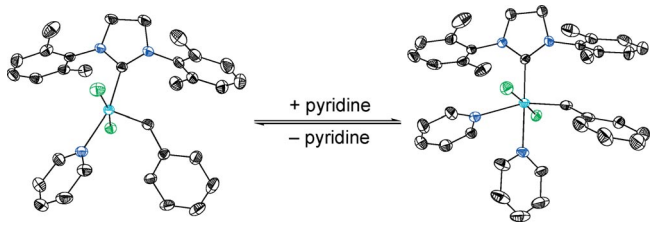


**W.-Z. Zhang, R. He,***
**R. Zhang ..... 5345–5352**

Benzylideneruthenium Complexes Bearing Pyridine-Based Ligands and Their Influence on the Formation of Mono- or Bis-(pyridine) Complexes

**Keywords:** Metathesis / Ruthenium / N ligands / Ligand effects / Homogeneous catalysis

Benzylideneruthenium complexes bearing one or two pyridine-based ligands are synthesized and the influence of these ligands on the formation and interconversion of these complexes is discussed based on X-ray crystallographic and mass spectrometric evidence. Color code: black = C, blue = N, green = Cl, cyan = Ru.

## $ZnBr_2$(pyrimidine) Compounds

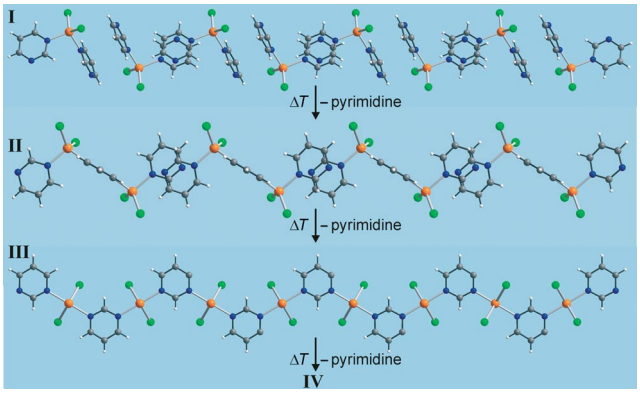


**C. Näther,* G. Bhosekar, I. Jeß .....**
**..... 5353–5359**

Synthesis, Crystal Structures and Thermal Properties of New $ZnBr_2$(pyrimidine) Coordination Compounds

**Keywords:** Coordination compounds / Synthesis / Crystal structure / Thermal reactivity

Four new $ZnBr_2$(pyrimidine) coordination polymers were prepared, either in solution or by thermal decomposition reactions, and the thermal reactivity and thermodynamic stability of these compounds were investigated.

## Mixed-Metal Aggregates

The reaction between the $Ni_2$ assembly on a formylphenolate template with a coordinated terminal water molecule and a capping imidazolidine ligand and $N_3^-$ or $ClO_4^-$ anions leads to two different types of products. The metallacrown-type coordination of the $Na^+$ cations results in new $NaNi_2$ complexes engaged in ferromagnetic interactions.

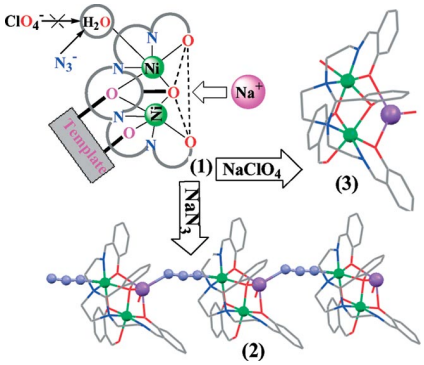


**A. R. Paital, M. Mikuriya, D. Ray* ..... 5360–5368**

New Mixed-Metal Aggregates Derived From Dinickel Complexes on a 2-Formylphenolate Template: Counteranion Dependent Formation of 1D Chain and Discrete $NaNi_2$ Complexes

**Keywords:** Mixed-metal complexes / Imidazolidine / Dinuclear $Ni^{II}$ complexes / Crystal structure / Magnetic properties

## Thiolatocopper(I) Complexes

A series of mono- and polynuclear thiolatocopper(I) complexes exhibiting various coordination spheres is structurally characterized. The steric demands of the thiolato ligand have a clear effect on the coordination features with little influence of the reaction conditions. As low as the two-coordinate Cu centers were obtained, which represent structural models of the active site of copper metallochaperones.

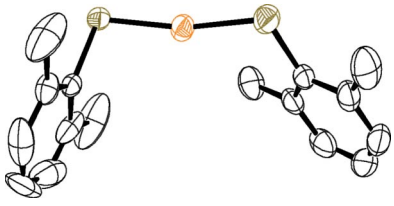

**S. Zeevi, E. Y. Tshuva* ..... 5369–5376**

Synthesis and X-ray Characterization of Mono- and Polynuclear Thiolatocopper(I) Complexes: The Effect of Steric Bulk on Coordination Number and Nuclearity

**Keywords:** Copper / S ligands / Cluster compounds / Coordination modes / Metallochaperones

 © 2007 Wiley-VCH Verlag GmbH & Co. KGaA, Weinheim 

# CONTENTS


## Chiral Cobalt Complexes

**C. P. Pradeep, P. S. Zacharias, S. K. Das* ..... 5377–5389**

Enantiopure Mono- and Mixed-Valence Multinuclear Cobalt Complexes from Amino Alcohol Based Ligands

**Keywords:** Chiral complexes / Cobalt / Chiral amino alcohols / Supramolecular chemistry / Ligand-controlled nuclearity

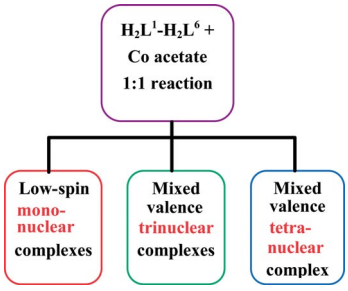


Chiral amino alcohol based tridentate Schiff bases, derived from 5-OMe-, 5-H-, and 5-$NO_2$-substituted salicylaldehydes and (*S*)-(+)-2-phenylglycinol and (*S*)-(−)-2-amino-3-phenyl-1-propanol, were found to act as versatile ligands in their coordination behavior towards cobalt ions and gave a range of optically active complexes like mononuclear low-spin $Co^{III}$ complexes, mixed-valence trinuclear $Co^{III}-Co^{II}-Co^{III}$ complexes, and a mixed-valence tetranuclear $(Co^{III})_3Co^{II}$ complex.

## C–C Coupling

**V. P. Ananikov,* D. G. Musaev, K. Morokuma ..... 5390–5399**

Critical Effect of Phosphane Ligands on the Mechanism of Carbon–Carbon Bond Formation Involving Palladium(II) Complexes: A Theoretical Investigation of Reductive Elimination from Square-Planar and T-Shaped Species

**Keywords:** C–C coupling / Palladium / Catalysis / Steric effect / Electronic effect / Phosphane ligands

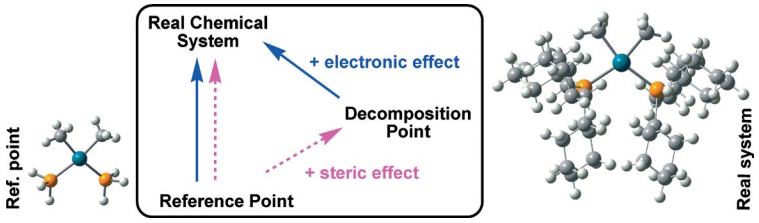


Relative reactivity in carbon–carbon bond formation involving a four-coordinated pathway follows the order: L = $PPh_3$ > $PH_3$ > $PCy_3$ > $PMe_3$. However, for reductive elimination involving T-shaped complexes by the ligand predissociation pathway, relative reactivity changes in the order: L = $PCy_3$ > $PPh_3$ > $PH_3$ > $PMe_3$.

## Artificial Nucleases

**X.-Q. Chen, X.-J. Peng,* J.-Y. Wang, Y. Wang, S. Wu, L.-Z. Zhang, T. Wu, Y.-K. Wu ..... 5400–5407**

Efficient Increase of DNA Cleavage Activity of a Diiron(III) Complex by a Conjugating Acridine Group

**Keywords:** DNA cleavage / Iron complex / Diiron(III) complex / Intercalator / Acridine

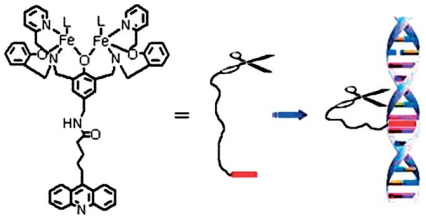

As a result of the binding interaction between DNA and an acridine moiety, a 14-fold promotion in the cleavage activity of a diiron(III) complex can be brought about.

## Tetranuclear Palladium Complexes

**J. J. Fernández,* A. Fernández, D. Vázquez-García, M. López-Torres, A. Suárez, N. Gómez-Blanco, J. M. Vila* ..... 5408–5418**

Tetranuclear Complexes of $Pd^{II}$ with Tridentate [*C*,*N*,*O*] and [*O*,*N*,*O*] Ligands: Synthesis, Reactivity and Structural Isomerism

**Keywords:** Palladium / Cyclometallation / Metallacycles / Tridentate [*C*,*N*,*O*] ligands / C–H activation

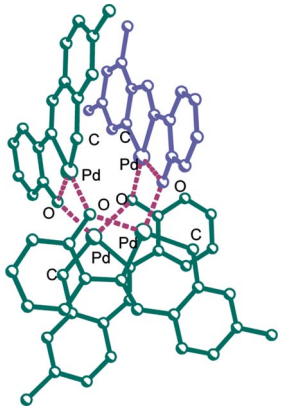

Palladium(II) compounds with tridentate [*C*,*N*,*O*] ligands display tetranuclear structures regardless of whether they are cyclometallated. A new type of tetranuclear palladacyle bearing two different metallated moieties was found.


 © 2007 Wiley-VCH Verlag GmbH & Co. KGaA, Weinheim 

## Luminescent Lanthanide Complexes

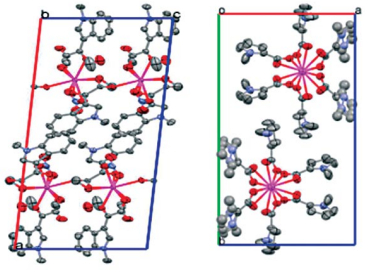

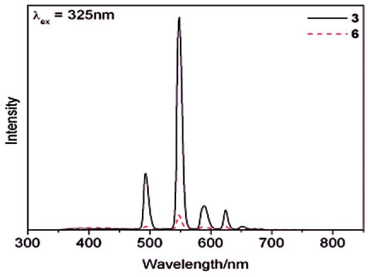


Luminescence studies on six lanthanide complexes with two pyrrole-derivatized carboxylic acid ligands show that modification of the ligands can tune the triplet energy levels of the ligands to match the $^5D_0$ energy level of $Eu^{3+}$ and the $^5D_4$ energy level of $Tb^{3+}$, which improves the energy transfer efficiency from the antenna to the $Eu/Tb^{3+}$ ions.

**G.-L. Law, K.-L. Wong, K.-K. Lau, H.-L. Tam, K.-W. Cheah, W.-T. Wong* ..... 5419–5425**

Synthesis, Crystal Structures, and Photophysical Properties of Lanthanide Complexes Containing Pyrrole-Derivatized Carboxylate Ligands

**Keywords:** Lanthanide / Luminescence / Terbium / Europium / Pyrrole

## Water Clusters

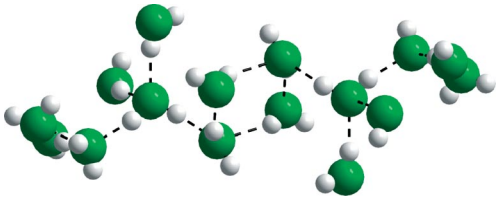

Porous metal–organic framework structures are built from a podand ligand and transition metal ions under ambient conditions to form infinite chains of metallacycles. Discrete high-nuclearity water clusters have been identified inside the voids in these structures.

**S. Neogi, E. C. Sañudo, P. K. Bharadwaj* ..... 5426–5432**

Transition-Metal Porous Coordination Polymers with a Podand Ligand: Structure of Discrete Water Clusters and Variable-Temperature Magnetism

**Keywords:** Water clusters / Coordination polymers / Metal–organic frameworks / Podand ligands / Magnetism

## Versatility of Thiosemicarbazones

The [α-diphenylethanedione bis(4-ethylthiosemicarbazonato)]palladium(II) complex and the dichloridobis(5-ethoxy-4-ethyl-5,6-diphenyl-4,5-dihydro-2*H*-[1,2,4]-triazine-3-thione)zinc(II) complex, obtained by metal-induced cyclization, have been prepared and characterized by X-ray analysis.

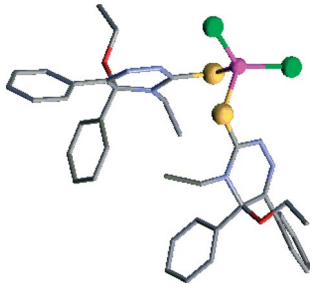

**A. I. Matesanz, C. Pastor, P. Souza* ..... 5433–5438**

Synthesis, Characterization and X-ray Structures of [α-Diphenylethanedione bis-(4-ethylthiosemicarbazonato]palladium(II) and 1,2,4-Triazine-3-thione–Zinc(II) Complexes Obtained by Metal-Induced Cyclization

**Keywords:** Thiosemicarbazones / Cocrystals / Palladium(II) / Zinc(II) / X-ray diffraction

## Metal Phosphonates

Four heterometal phosphonates, $NaM[O_3PCH(OH)CO_2]$ (M = Mn, Fe, Co, Zn), with a 3D framework were synthesized hydrothermally, and their structures were determined by single-crystal X-ray diffraction. Their thermal stabilities and their magnetic and luminescent properties are also described.

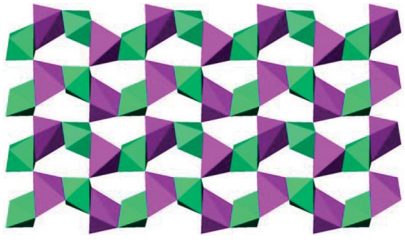

**Z. Lai, R. Fu, S. Hu, X. Wu* ..... 5439–5446**

Syntheses, Crystal Structures, Thermal Stabilities, and Magnetic and Luminescent Properties of 3D Heterometal Phosphonates: $NaM[O_3PCH(OH)CO_2]$ (M = Mn, Fe, Co, Zn)

**Keywords:** Crystal structure / Phosphorus / Luminescence / Magnetism / Thermal stability

 © 2007 Wiley-VCH Verlag GmbH & Co. KGaA, Weinheim 

# CONTENTS

## Oxalate−Selenate Hybrids

**M.-L. Feng, J.-G. Mao* ..... 5447−5454**

Luminescent Organically Templated Lanthanide Oxalate−Selenate Hybrids

**Keywords:** Hydrothermal syntheses / Lanthanides / Selenium / Crystal structures / Luminescent properties

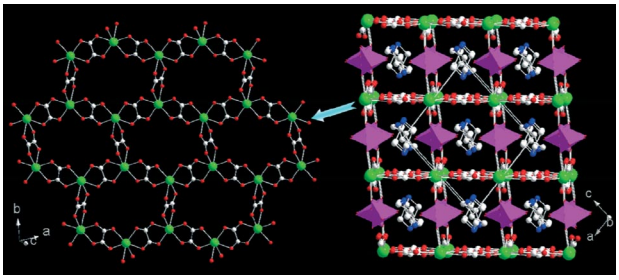

Two series of novel organically templated lanthanide(III) oxalate−selenate hybrids were prepared and structurally characterized. Their structures range from 2D layers to 3D networks. They exhibit strong luminescent emission bands in the visible or near IR region.

**If not otherwise indicated in the article, papers in issue 33 were published online on November 12, 2007**

 © 2007 Wiley-VCH Verlag GmbH & Co. KGaA, Weinheim 

# SPOTLIGHTS …

## *Polyoxometalates*

S.-T. Zheng, M.-H. Wang, G.-Y. Yang*

**Extended Architectures Constructed from Sandwich Tetra-Metal-Substituted Polyoxotungstates and Transition-Metal Complexes**

*Chem. Asian J.*
DOI: **10.1002/asia.200700166**

**All joined up**: Hydrothermal synthesis produces three unprecedented coordination polymers constructed from sandwich tetra-transition-metal-substituted polyoxotungstates and transition-metal complexes. These compounds were structurally characterized by X-ray diffraction analysis and exhibit reversible water-sorption capabilities.

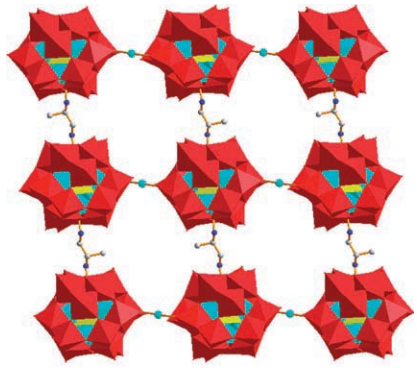

## *Biosynthesis*

A. C. Stewart, I. J. Clifton, R. M. Adlington, J. E. Baldwin,* P. J. Rutledge*

**A Cyclobutanone Analogue Mimics Penicillin in Binding to Isopenicillin N Synthase**

*ChemBioChem*
DOI: **10.1002/cbic.200700176**

**Switching β-lactam for cyclobutanone** creates a new class of penicillin-like ring system, in which the β-lactam nitrogen atom is replaced by carbon. But how similar really is the structure of this new carbocyclic ring system to a penicillin? By cocrystallising the cyclobutanone analogue of isopenicillin N with isopenicillin N synthase (the central enzyme in penicillin biosynthesis), we have addressed this question.

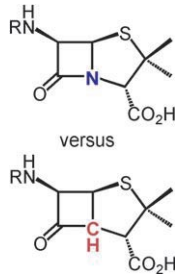


## *Ionic Liquids*

T. Köddermann, D. Paschek, R. Ludwig*

**Molecular Dynamic Simulations of Ionic Liquids: A Reliable Description of Structure, Thermodynamics and Dynamics**

*ChemPhysChem*
DOI: **10.1002/cphc.200700552**

**Move with the force:** A new force field for simulating imidazolium-based ionic liquids [$C_n$mim][$NTf_2$] (see figure) reproduces with good agreement the experimental values for the heats of vaporization, shear viscosities and NMR rotational correlation times. The results suggest that the inaccuracies arising from previous methods are due to the overestimation of the Lennard–Jones interactions.

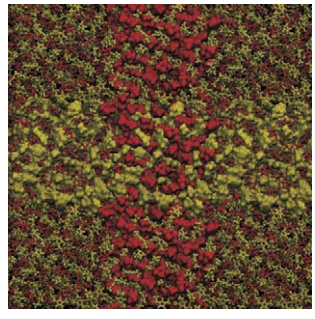

## *Structural Biology*

J. Kondo, K. Pachamuthu, B. François, J. Szychowski, S. Hanessian,* E. Westhof*

**Crystal Structure of the Bacterial Ribosomal Decoding Site Complexed with a Synthetic Doubly Functionalized Paromomycin Derivative: a New Specific Binding Mode to an A-Minor Motif Enhances in vitro Antibacterial Activity**

*ChemMedChem*
DOI: **10.1002/cmdc.200700113**

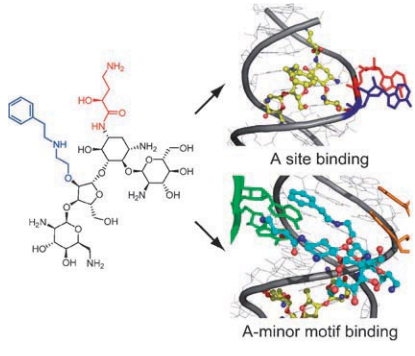


**The synthetic paromomycin** analogue with the L-haba group and an ether chain with an *O*-phenethylaminoethyl group could specifically bind to ribosomes in two different modes: 1) the classical binding to the A site and 2) binding to an A-minor motif participating in the recognition of the codon–anticodon helix or in the intersubunit bridges.

 © 2007 Wiley-VCH Verlag GmbH & Co. KGaA, Weinheim 

# … ON OUR SISTER JOURNALS

EurJIC European Journal of Inorganic Chemistry

## *Phosphane Ligands*

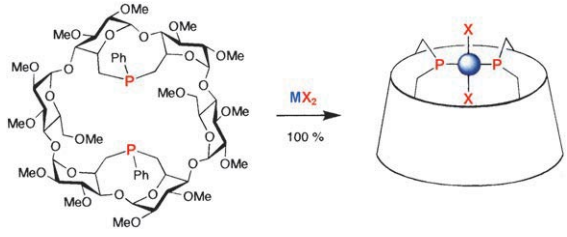


**Tailor-made for *trans* chelation:** A remarkably rigid diphosphane has been obtained by capping the entrance of a cyclodextrin with two "PPh" units. When treated with Group 10 metal halides, this ligand not only behaves exclusively as a chelating ligand, but also selectively forms *trans* complexes (see picture).

L. Poorters, D. Armspach,* D. Matt,* L. Toupet, S. Choua, P. Turek

**Synthesis and Properties of TRANSDIP, a Rigid Chelator Built upon a Cyclodextrin Cavity: Is TRANSDIP an Authentic *trans*-Spanning Ligand?**

*Chem. Eur. J.*
DOI: **10.1002/chem.200700831**

## *Light-Harvesting Devices*

The wider spectral profile of fullerene dyads with 1,2,4-triethynylbenzene branching units when compared to their 1,3,5-triethynylbenzene analogues clearly points out improved light-harvesting capabilities.

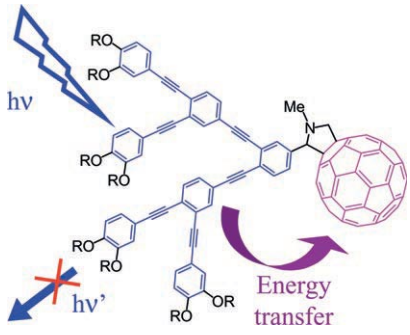


J. N. Clifford, A. Gégout, S. Zhang, R. Pereira de Freitas, M. Urbani, M. Holler, P. Ceroni,* J.-F. Nierengarten,* N. Armaroli*

**Fullerene Derivatives Substituted with Differently Branched Phenyleneethynylene Dendrons: Synthesis, Electronic and Excited State Properties**

*Eur. J. Org. Chem.*
DOI: **10.1002/ejoc.200700689**

## *Anion–π Interactions*

**A fluoride sandwich**: A cylindrophane macrocycle framed with cyanuric acid rings selectively complexes fluoride ion by a combination of anion–π interactions and ion-pair-reinforced hydrogen bonds. This compound is the first example of a purpose-designed host that exploits anion–π bonding.

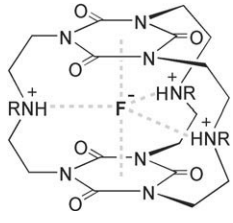


M. Mascal,* I. Yakovlev, E. B. Nikitin, J. C. Fettinger

**Fluoride-Selective Host Based on Anion–π Interactions, Ion Pairing, and Hydrogen Bonding: Synthesis and Fluoride-Ion Sandwich Complex**

*Angew. Chem. Int. Ed.*
DOI: **10.1002/anie.200704005**

On these pages, we feature a selection of the excellent work that has recently been published in our sister journals. If you are reading these pages on a computer, click on any of the items to read the full article. Otherwise please see the DOIs for easy online access through Wiley InterScience.

 © 2007 Wiley-VCH Verlag GmbH & Co. KGaA, Weinheim 

DOI: 10.1002/ejic.200700895

# Transition-Metal-Free Boron–Carbon Bond Activation: Insertion of an NNP Fragment into a Boron–Carbon Bond

**Markus Kowalewski,[a] Burkhard Krumm,[a] Peter Mayer,[a] Axel Schulz,*[b,c] and Alexander Villinger[b]**

*Dedicated to the memory of Nils Wiberg*

**Keywords:** Azaphosphole / Diazadiphosphetidine / Insertion / Lewis acids / Boranes / X-ray elucidation

The influence and reactivity of fluorine-containing Lewis acids such as neat $BF_3$, $BF_3{\cdot}OEt_2$, and $B(C_6F_5)_3$ on $Me_3SiCl$ elimination in $(Me_3Si)_2N–N(SiMe_3)–PCl_2$ was investigated. The reaction with $B(C_6F_5)_3$ resulted in the formation of a novel diazadiphosphetidine with a phosphorus(III) atom attached to a pentafluorophenyl group, which can be regarded as a formal NNP fragment insertion into a B–C bond.

(© Wiley-VCH Verlag GmbH & Co. KGaA, 69451 Weinheim, Germany, 2007)

## Introduction

The $GaCl_3$-assisted elimination in silylated dichloro(hydrazino)phosphane,[1–3] $(Me_3Si)_2N–N(SiMe_3)–PCl_2$, followed by a formal [3+2] cycloaddition[4] represents an elegant approach to the formation of triazadiphospholes and tetrazaphospholes, which was introduced only recently (Scheme 1). As this reaction sequence only occurs when $GaCl_3$ is added into a solution of $(Me_3Si)_2N–N(SiMe_3)–PCl_2$ (**1**) in common organic solvents (e.g. $CH_2Cl_2$, benzene, etc.), this new reaction type was named a $GaCl_3$-assisted [3+2] cycloaddition. The ambivalent $(Me_3Si)_2N–N(SiMe_3)–PCl_2$ displays both dipolarophile and/or 1,3-dipole characteristics. $GaCl_3$ is required to release the hidden dipolarophile and/or 1,3-dipole by decreasing the activation barrier to $Me_3SiCl$ elimination. In this context, we studied the influence of fluorine-containing Lewis acids such as neat $BF_3$, $BF_3{\cdot}OEt_2$, and $B(C_6F_5)_3$ on the $Me_3SiCl$ elimination in

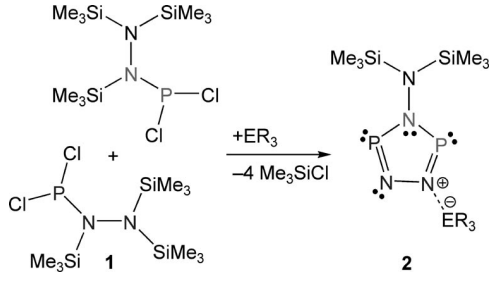


Scheme 1. Lewis acid assisted [3+2] cycloaddition with ambivalent dichloro(hydrazino)phosphane (**1**) to yield a triazadiphosphole [$ER_3$ = $GaCl_3$, $B(C_6F_5)_3$].

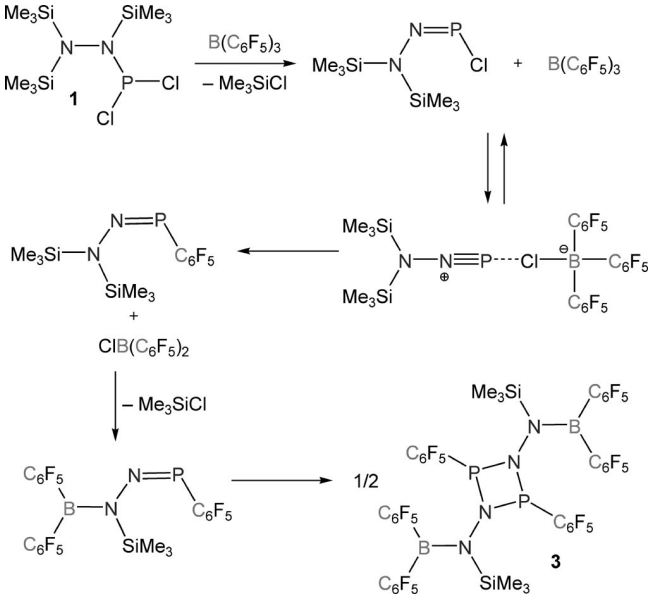


Scheme 2. Proposed mechanism of the $B(C_6F_5)_3$-assisted 1,2-elimination of $Me_3SiCl$ in **1** followed by an unusual insertion of a NNP fragment into a B–C bond, which finally results in the formation of **3**.

[a] LMU München, Department Chemie und Biochemie
Butenandt-Str. 5–13, 81377 München, Germany
[b] Universität Rostock, Institut für Chemie
Albert-Einstein-Str. 3a, 18059 Rostock, Germany
Fax: +49-381-4986382
E-mail: axel.schulz@uni-rostock.de
Homepage: www.chemie.uni-rostock.de/ac/schulz
[c] Leibniz-Institut für Katalyse e.V. an der Universität Rostock,
Albert-Einstein-Str. 29a, 18059 Rostock, Germany
Supporting information for this article is available on the WWW under http://www.eurjic.org or from the author.

 © 2007 Wiley-VCH Verlag GmbH & Co. KGaA, Weinheim 

$(Me_3Si)_2N–N(SiMe_3)–PCl_2$. Herein, we detail the reactivity of these fluorine-containing Lewis acids towards $(Me_3Si)_2$-N–$N(SiMe_3)$–$PCl_2$, which proceeds in the case of $B(C_6F_5)_3$, by the first reported example of an unusual NNP fragment insertion into a boron–carbon bond (Scheme 2).

## Results and Discussion

Absolutely no reaction was observed when a large excess of neat $BF_3$ (b.p. –100 °C, ca. 15 mL) was added to **1** at –110 °C. Also, after further stirring of this reaction mixture for 5 h at –100 °C no $Me_3SiCl$ elimination could be observed; only the starting material was isolated after removal of $BF_3$. Obviously, thermal activation is needed to trigger $Me_3SiCl$ elimination. Hence, **1** was treated with $BF_3$ in diethyl ether at ambient temperature. This reaction led to complete decomposition. Compounds $[N_2H_5]^+[BF_4]^-$,[5] $Me_3SiF$, and $PFCl_2$ could be identified amongst the decomposition products.

These failures prompted us to utilize the sterically demanding fluorine-containing Lewis acid $B(C_6F_5)_3$. Again, no reaction was observed when **1** was added to a solution of $B(C_6F_5)_3$ in $CH_2Cl_2$ at ambient temperature. Only upon heating of this solution in a sealed tube up to 70 °C did slow $Me_3SiCl$ elimination occur, which was completed after 3 d of stirring as shown by $^{31}P$ NMR spectroscopic studies (**1**: $^{31}P$ NMR: $\delta$ = 166.6 ppm disappeared).

Contrary to the reaction of **1** with $GaCl_3$, the reaction with $B(C_6F_5)_3$ yielded two products: (1) a highly soluble $B(C_6F_5)_3$ adduct of the expected trizadiphosphole (**2**) (NMR yield 24%, Scheme 1, multiplets in the $^{31}P$ NMR spectrum at $\delta$ = 317.4 and 286.4 ppm; cf. $GaCl_3$ adduct: 317.2 and 292.1 ppm)[1] and (2) a new species (NMR yield 42%, $^{31}P$ NMR: $\delta$ = 253 ppm). Surprisingly, upon cooling of the above reaction mixture down to 5 °C, a large amount of beautiful orange crystals of the new species was obtained (isolated yield 29%). Single-crystal X-ray studies revealed a surprising 2,4-bis(pentafluorophenyl)-1,3-bis[*N*-trimethylsilyl-*N*-bis(pentafluorophenyl)boranyl]amino[1,3,2,4]diazadiphosphetidine (**3**) as the product (Scheme 2, Figure 1).

Pure dry **3** is stable at temperature up to 400 °C (m.p. 225 °C), is neither heat nor shock sensitive, and decomposes even only slowly in water and on air indicating a good kinetic protection by the bulky $C_6F_5$ groups. It should be mentioned that **3** is almost insoluble in any common solvent at ambient temperature.

X-ray elucidation of the orange crystals revealed a four-membered P–N heterocatenated ring (**3**) with two P–$C_6F_5$ and two N–R [R = $N(SiMe_3)(B(C_6F_5)_2)$] centers, and its formation can be described as a dimerization of monomeric R–N–N=P–$C_6F_5$, which is formed by $Me_3SiCl$ elimination (Figure 1 and Scheme 2) followed by an intriguing transfer of one pentafluorophenyl group (see below). Compound **3** crystallizes in cubes in the triclinic space group $P\bar{1}$ with one unit per cell. The asymmetric unit of **3** consists of only half of the molecule. The entire molecule can be generated by an inversion center sited on the centroid of the $P_2N_2$ four-membered ring. Moreover, this molecule is found to be disordered. Two different positions, which displays the existence of two conformers, are found for both P–$C_6F_5$ moieties with an occupation of 61.5 (**A**) and 38.5% (**B**). Both positions correspond to a rotation about the N–N axis with an angle of 109.2° between both rings. In both conformers the $P_2N_2$ ring is ideally planar [∠ P2–N2–P2′–N2′ = 0.0° (**A**), ∠ P1–N2–P1′–N2′ = 0.0° (**B**)].

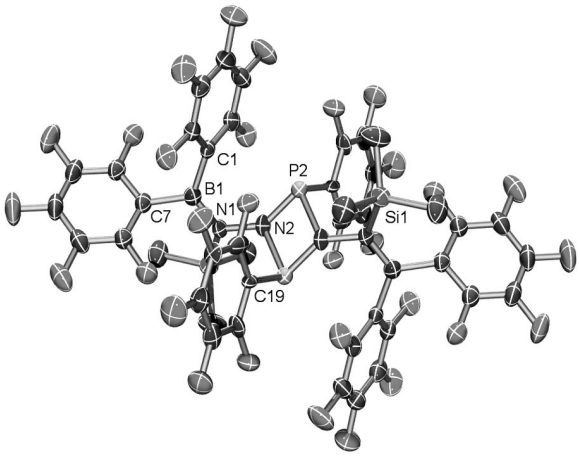


Figure 1. ORTEP drawing of the molecular structure of **3** (conformer **A**) in the crystal. Thermal ellipsoids with 50% probability at 200 K (hydrogen atoms omitted for clarity). Selected bond lengths [Å] and angles [°]: P2–N2 1.664(2), P2–N2′ 1.793(2), P2–C13 1.913(3), P2–P2′ 2.649(2), Si1–N1 1.818(2), N1–B1 1.400(3), N1–N2 1.442(3); N2–P2–N2′ 80.0(1), N2–P2–C13 105.2(2), N2–P2–P2′ 41.78(7), B1–N1–N2 117.4(2), B1–N1–Si1 125.4(2), N2–N1–Si1 115.4(1), N1–N2–P2 131.8(2), P2–N2–P2′ 100.0(1), N1–B1–C7 122.2(2), C1–B1–C7 114.3(2).

$^{31}P$ MAS NMR studies proved the existence of two conformers in the solid state (Figure S1),[6] which is indicated by two resonances at $\delta$ = 264.0 (isomer **A**, Figures 1 and 2) and 240.7 ppm (isomer **B**, Figure 2). Interestingly, we were able to assign these two resonances on the basis of the excellent agreement between theoretically and experimentally obtained values of the $^{31}P$ NMR chemical shift tensor (see Supporting Information).[6a]

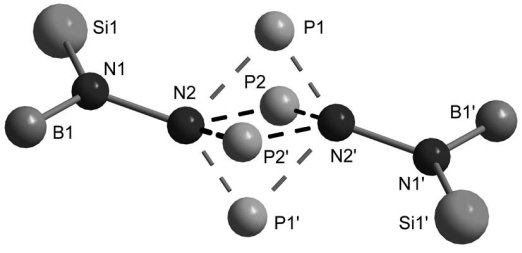


Figure 2. Illustration of the disorder problem in **3**. Conformer **A** corresponds to the N2–P2–N2′–P2′ plane, **B** to the N2–P1–N2′–P1′. All H, C, and F atoms are omitted for clarity.

Conformer **A** is shown in Figure 1, and it displays a *trans* arrangement of the two $C_6F_5$ groups attached to the P atoms, which is also found in conformer **B**. As expected for tricoordinated phosphorus(III) species, two rather long and two short P–N distances are found [*d*(P2–N2) = 1.664(2) Å,

 © 2007 Wiley-VCH Verlag GmbH & Co. KGaA, Weinheim 

*d*(P2–N2′) = 1.793(2) Å (**A**); *d*(P1–N2) = 1.631(2) Å, *d*(P1–N2′) = 1.838(3) Å (**B**)]. Comparison with the sum of the covalent radii [$d_{cov}$(N–P) = 1.8 Å, $d_{cov}$(N=P) = 1.6 Å] indicates partial π bonding for the shorter P–N distance in both conformers [1.664(2) and 1.631(2) Å]. A large and a small angle are found for the $P_2N_2$ ring [∠ N2–P2–N2′ = 80.0(1)°, ∠ P2–N2–P2′ = 100.0(1)° (**A**); ∠ N2–P1–N2′ = 79.5(1)°, ∠ P1–N2–P1′ = 100.5(1)° (**B**)]. Selected structural data of both conformers are summarized in Tables S2 and S3.[6b]

The complete mechanism for the formation of a triazadiphosphole (**2**) according to Scheme 1 is still unknown although 1,2-elimination of $Me_3SiCl$ was experimentally proven as the initial step.[3] When $B(C_6F_5)_3$ is used as the Lewis acid two things are worthy to be discussed: (1) a large thermal activation (3 d at 70 °C) is needed to trigger $Me_3SiCl$ elimination (cf. $GaCl_3$ reaction: 1 h at 20 °C) and (2) the formation of a different species, a diazadiphosphetidine (**3**), as the main product beside **2** is observed (Schemes 1 and 2).

Presumably, after the initial elimination of $Me_3SiCl$, free borane can attack the second chlorine atom attached to the phosphorus atom of the iminophosphane chloride, which leads to chlorine/$C_6F_5$ exchange (Scheme 2). The intermediate $ClB(C_6F_5)_2$ reacts under $Me_3SiCl$ elimination to give monomeric **3**. Reactions of $ClB(C_6F_5)_2$ with $Me_3Si$-substituted amines are known,[7] for example, $ClB(C_6F_5)_2$ treated with $HN(SiMe_3)_2$ yields $HN(SiMe_3)[B(C_6F_5)_2]$ or $HN[B(C_6F_5)_2]_2$ depending on the stoichiometry. Moreover, the $ClB(C_6F_5)_3^-$ anion is well known.[8] Finally, dimerization results in the formation of diazadiphosphetidine **3**. For kinetic reasons, the formation of **3** is favored when $B(C_6F_5)_3$ is used, whereas only **2** is observed when $GaCl_3$ is used as the Lewis acid. The overall reaction of **1** with $B(C_6F_5)_3$ can be regarded as the insertion of $Me_3Si$–NNP (covalent azide analogue containing one phosphorus atom) into one B–C bond, followed by a final dimerization process or a formal [3+2] addition of the borane to $Me_3SiNNP$, which is generated in situ after elimination of two molecules $Me_3SiCl$. It should be emphasized that both reactions according to Schemes 1 and 2 can be reproduced.

Transfer reactions involving the $C_6F_5$ group are well known in transition-metal chemistry,[9] and they are often responsible for catalyst poisoning.[10] Such transition-metal-induced $C_6F_5$ transfer reactions often follow after the formation of intermediates, and they are stabilized by F···M agostic interactions with a cationic transition-metal center (M).[11] The latter interaction often leads to C–F activation, which may even result in M–F bond formation by C–F bond cleavage. Metal-free C–F bond activation is also known, for example, when secondary phosphanes such as $(Me_3C_6H_2)_2PH$ are treated with $B(C_6F_5)_3$ to yield $(Me_3C_6H_2)_2PH(C_6F_4)BF(C_6F_5)_2$.[12] Shifts of the $C_6F_5$ group are known to possess large activation barriers, for example, a large activation barrier for a 1,2-shift of a $C_6F_5$ group has already been observed by Metzler and Denk in a silylene–borane adduct, which slowly rearranges to a stable silylborane with a half-life of about one month.[13]

To estimate the thermodynamics of the formation of **2** and **3** and to obtain insight into the bond-formation process, computations were carried out at the B3LYP/6-31G(d,p) level of theory.[6d,6e,14] The calculated energy for the formation of triazadiphosphole (**2**) is an exothermic and an exergonic process for all of the Lewis acids studied [Scheme 1; $\Delta_{298}G^0$ = –317.3, –331.2, –348.6, and –304.2 kJ mol$^{-1}$ for $BF_3$, $BCl_3$, $BBr_3$, and $B(C_6F_5)_3$, respectively]. The latter value can be compared with the formation of **3** for which a smaller energy release was calculated ($\Delta_{298}G^0$ = –258.0 kJ mol$^{-1}$). The formation of the monomeric species [according to **1** + $B(C_6F_5)_3$ → ½**3** + 2$Me_3SiCl$] is associated with an energy gain of –135.8 kJ mol$^{-1}$, whereas dimerization is slightly endergonic with 13.6 kJ mol$^{-1}$. It is interesting to note that monomeric **3** is observed with a large intensity in the mass spectrum besides the dimer.

As expected, according to NBO analysis (natural bond orbital)[6d,6e,15] the NP bonds within the $P_2N_2$ ring of **3** are purely σ in character and are strongly polarized (N: 77%, P: 23%) with a partial charge of +1.28*e* at the phosphorus atom and –0.95*e* at the nitrogen atom. We calculate a charge of –0.86*e* at the exocyclic nitrogen atom and a positive charge of +0.87*e* and +1.93*e* at the boron and silicon atoms, respectively.

## Conclusion

The formation of **3** represents the first example of the insertion of a NNP fragment into a B–C bond. In this context, our results offer a new perspective on the insertion and activation of boron–carbon bonds. Moreover, **3** is the first example of a structurally characterized diazadiphosphetidine with phosphorus(III) attached to a perfluoro group.

## Experimental Section

**3:** To a stirred solution of dichloro[*N*,*N*′,*N*′-tris(trimethylsilyl)hydrazino]phosphane (1.75 g, 5 mmol) in dichloromethane (10 mL) was slowly added a solution of tris(pentafluorophenyl)borane (2.82 g, 5.5 mmol) in dichloromethane (10 mL) by syringe at ambient temperature. The yellowish solution was heated in a sealed tube under reflux for 3 d at 70 °C, which resulted in an orange suspension. After cooling to room temperature, the solution was concentrated to a total volume of 10 mL and stored at 0 °C overnight to afford an orange, microcrystalline powder. Dichloromethane (10 mL) was added, and the orange residue was filtered (F4) and washed several times by repeated back distillations of the solvent. The product was dried in vacuo to yield 0.94 g (29%) of **3** as an orange solid. M.p. 225 °C. FTIR (KBr): $\tilde{\nu}$ = 2992 (vw), 2964 (vw), 2908 (vw), 1648 (m), 1519 (s), 1480 (s), 1397 (m), 1366 (m), 1312 (m), 1285 (m), 1259 (m), 1150 (m), 1089 (m), 1043 (w), 1017 (w), 976 (s), 928 (w), 854 (s), 778 (m), 722 (w), 669 (w), 629 (w), 503 (w) cm$^{-1}$. FTIR (ATR): $\tilde{\nu}$ = 2992 (vw), 2966 (vw), 2912 (vw), 1647 (m), 1516 (s), 1466 (s), 1395 (m), 1365 (m), 1311 (m), 1284 (m), 1257 (m), 1204, w, 1147 (m), 1139 (m), 1084 (m), 1044 (w), 1016 (w), 970 (s), 928 (w), 910 (w), 838 (s), 776 (m), 761 (w), 748 (w), 721 (w), 670 (w), 658, w, 628 (w), 618 (w) cm$^{-1}$. Raman (200 mW, 25 °C): 2994 (2), 2967 (2), 2911 (6), 2546 (1), 1649 (10), 1520 (2),

 © 2007 Wiley-VCH Verlag GmbH & Co. KGaA, Weinheim 

1401 (8), 1363 (7), 1309 (2), 1309 (2), 1288 (2), 1141 (2), 1118 (3), 1094 (2), 1021 (2), 982 (1), 848 (2), 819 (2), 785 (2), 771 (2), 658 (2), 621 (2), 596 (6), 527 (8), 501 (7), 446 (8), 397 (8), 363 (4) $cm^{-1}$. $^{31}P\{^1H\}$ NMR (121.5 MHz, $CD_2Cl_2$, 25 °C): $\delta$ = 253 (br.) ppm. $^{31}P$ MAS NMR (25 °C, $\omega_{rot}$ = 20 kHz): $\delta$ = 240.7 (s), 264.0 (s) ppm. MS (EI, 70 eV, >5%): *m/z* (%) = 168 (26.2) [$C_6F_5$], 277 (26.8), 345 (19.5) [$B(C_6F_5)_2$], 365 (28.0), 629 (58.4) [½ **3**Me], 644 (100) [½ **3**], 1288 (30.6) [**3**]. $C_{42}H_{18}N_4B_2F_{30}P_2Si_2$ (1288.3): calcd. C 39.16, H 1.41, N 4.35; found C 40.62, H 1.00, N 4.22.

Crystals suitable for single-crystal X-ray studies were obtained by cooling the reaction solution slowly to 5 °C. An X-ray quality crystal of **3** was selected in silicon oil at ambient temperature and was cooled to 200(2) K during measurement. The data for compound **3** was collected with a Nonius Kappa CCD diffractometer by using graphite-monochromated Mo-$K_\alpha$ radiation ($\lambda$ = 0.71073). The structure was solved by direct methods and refined by full-matrix least-squares procedures (SHELXL-97).[16] All non-hydrogen atoms were refined anisotropically; hydrogen atoms were included in the refinement at calculated positions by using a riding model. The P($C_6F_5$) unit was split over two positions and the occupancy of each part (**A** and **B**) refined. For the carbon atoms of the split $C_6F_5$ rings, rigid group refinement was performed. A second X-ray study from a different experiment gave the same result (see Supporting Information). CCDC-653980 contains the supplementary crystallographic data for this paper. These data can be obtained free of charge from the Cambridge Crystallographic Data Centre via www.ccdc.cam.ac.uk/data_request/cif.

**Supporting Information** (see footnote on the first page of this article): Full experimental details and characterization data, X-ray crystallographic refinement data, selected bond lengths and angles, and computational details of **3**.

## Acknowledgments

Financial support by the Deutsche Forschungsgemeinschaft (SCHU 1170/4-1) is gratefully acknowledged. We thank Dr. Jörn Schmedt auf der Günne for recording the MAS NMR spectra.

[1] S. Herler, A. Villinger, J. Weigand, P. Mayer, A. Schulz, *Angew. Chem.* **2005**, *117*, 7968–7971; *Angew. Chem. Int. Ed.* **2005**, *44*, 7790–7793.
[2] P. Mayer, A. Schulz, A. Villinger, *Chem. Commun.* **2006**, 1236–1238.
[3] G. Fischer, S. Herler, P. Mayer, A. Schulz, A. Villinger, J. Weigand, *Inorg. Chem.* **2005**, *44*, 1740–1751.
[4] a) R. Huisgen in *1,3-Dipolar Cycloaddition Chemistry* (Ed.: A. Padwa), Wiley, New York, **1984**, pp. 1–176; b) A. Padwa in *Comprehensive Organic Synthesis* (Ed.: B. M. Trost), Pergamon, Oxford, **1991**, vol. 4, pp. 1069–1109; c) for a review of asymmetric 1,3-dipolar cycloaddition reactions, see K. V. Gothelf, K. A. Jorgensen, *Chem. Rev.* **1998**, *98*, 863–909; d) for a review of synthetic applications, see J. Mulzer, *Org. Synth. Highlights* **1991**, 77–95.
[5] M. Kowalewski, P. Mayer, A. Schulz, A. Villinger, *Acta Crystallogr. Sect. E* **2006**, *62*, i248–i249.
[6] See the Supporting Information: a) chemical shifts ($^{31}P\{^1H\}$, $^{31}P$ MAS) and assignment was carried out on the basis of the excellent agreement between theoretically (utilizing the two structures obtained from X-ray elucidation) and experimentally obtained shifts ($\delta[^{31}P]$); b) crystal data; c) full description of the experimental data, technique and details; d) computational details [B3LYP/6-31G(d,p)]; e) summary of the NBO analysis for **3**: (i) partial charges, (ii) hybridization effects, and (iii) polarization.
[7] J. R. Galsworthy, M. L. H. Green, V. C. Williams, A. N. Chernega, *Polyhedron* **1998**, *17*, 119–124.
[8] B. E. Bosch, G. Erker, R. Fröhlich, O. Meyer, *Organometallics* **1997**, *16*, 5449–5456.
[9] T. Wondimagegn, Z. Xu, K. Vanka, T. Ziegler, *Organometallics* **2005**, *24*, 2076–2085 and references cited therein.
[10] a) P. Arndt, U. Jäger-Fiedler, M. Klahn, W. Baumann, A. Spannenberg, V. V. Burlakow, U. Rosenthal, *Angew. Chem. Int. Ed.* **2006**, *45*, 4195–4198; b) J. D. Scollard, D. H. McConville, S. J. Rettig, *Organometallics* **1997**, *16*, 1810–1812.
[11] For example: a) P. Arndt, W. Baumann, A. Spannenberg, U. Rosenthal, V. V. Burlakow, V. Shur, *Angew. Chem. Int. Ed.* **2003**, *42*, 1414–1418; b) T. J. Woodman, M. Thornton-Pett, M. Bochmann, *Chem. Commun.* **2001**, 329–330; c) L. H. Doerrer, A. J. Graham, D. Haussinger, M. L. H. Green, *J. Chem. Soc. Dalton Trans.* **2000**, 813–820.
[12] G. C. Welch, R. R. San Juan, J. D. Masuda, D. W. Stephan, *Science* **2006**, *314*, 1124–1126.
[13] N. Metzler, M. Denk, *Chem. Commun.* **1996**, 2657–2658.
[14] Single-point calculations were computed with a tight conversion criterion by using the program package Gaussian 98; for computational details see the Supporting Information. M. J. Frisch, G. W. Trucks, H. B. Schlegel, G. E. Scuseria, M. A. Robb, J. R. Cheeseman, V. G. Zakrzewski, J. A. Montgomery, Jr., R. E. Stratmann, J. C. Burant, S. Dapprich, J. M. Millam, A. D. Daniels, K. N. Kudin, M. C. Strain, O. Farkas, J. Tomasi, V. Barone, M. Cossi, R. Cammi, B. Mennucci, C. Pomelli, C. Adamo, S. Clifford, J. Ochterski, G. A. Petersson, P. Y. Ayala, Q. Cui, K. Morokuma, D. K. Malick, A. D. Rabuck, K. Raghavachari, J. B. Foresman, J. Cioslowski, J. V. Ortiz, B. B. Stefanov, G. Liu, A. Liashenko, P. Piskorz, I. Komaromi, R. Gomperts, R. L. Martin, D. J. Fox, T. Keith, M. A. Al-Laham, C. Y. Peng, A. Nanayakkara, C. Gonzalez, M. Challacombe, P. M. W. Gill, B. Johnson, W. Chen, M. W. Wong, J. L. Andres, C. Gonzalez, M. Head-Gordon, E. S. Replogle, J. A. Pople, *Gaussian 98 Revision A6*, Gaussian Inc., Pittsburgh, PA, **1998**.
[15] a) E. D. Glendening, A. E. Reed, J. E. Carpenter, F. Weinhold, *NBO Version 3.1*; b) J. E. Carpenter, F. Weinhold, *J. Mol. Struct. (Theochem)* **1988**, *169*, 41–62; c) F. Weinhold, J. E. Carpenter, *The Structure of Small Molecules and Ions*, Plenum, New York, **1988**, p. 227; d) F. Weinhold, C. Landis, *Valency and Bonding: A Natural Bond Orbital Donor-Acceptor Perspective*, Cambridge University, Cambridge, **2005** and references cited therein.
[16] a) *SIR97: A New Tool for Crystal Structure Determination and Refinement*: A. Altomare, M. C. Burla, M. Camalli, G. L. Cascarano, C. Giacovazzo, A. Guagliardi, A. G. G. Moliterni, G. Polidori, R. Spagna, *J. Appl. Crystallogr.* **1999**, *32*, 115–119; b) G. M. Sheldrick *SHELXS-97, Program for Refinement of Crystal Structures*, University of Göttingen, Göttingen, Germany, **1997**.

Received: August 7, 2007
Published Online: October 25, 2007

 © 2007 Wiley-VCH Verlag GmbH & Co. KGaA, Weinheim 

DOI: 10.1002/ejic.200700860

# pH-Induced Luminescence Changes of Chromophore-Quencher Tricarbonylpolypyridylrhenium(I) Complexes with 4-Pyridinealdazine

**Mauricio Cattaneo,[a] Florencia Fagalde,[a] Néstor E. Katz,*[a] Claudio D. Borsarelli,[b] and Teodor Parella[c]**

**Keywords:** Donor-acceptor systems / Rhenium / Photochemistry / Molecular devices / Mixed-valent compounds

The new chromophore-quencher tricarbonylrhenium(I) complexes $[Re(4,4'\text{-}X_2\text{-bpy})(CO)_3(PCA)]^+$, $[(4,4'\text{-}X_2\text{-bpy})(CO)_3Re(\mu\text{-PCA})Re(CO)_3(4,4'\text{-}X_2\text{-bpy})]^{2+}$, and $[(4,4'\text{-}X_2\text{-bpy})(CO)_3Re^{I}(\mu\text{-PCA})Ru^{II}(NH_3)_5]^{3+}$ (X = Ph or $CO_2Me$ and PCA = 4-pyridinealdazine) have been synthesized as their $PF_6^-$ salts and characterized by spectroscopic, electrochemical, and photophysical techniques. In contrast to previously reported species with X = Me or H, these complexes emit at room temperature in $CH_3CN$. The recovery of luminescence can thus be ascribed to the change of energy levels induced by adding electron-withdrawing substituents to the 2,2′-bipyridine ring, since the emissive $Re^{II}(X_2bpy^-)$ excited state becomes much lower in energy than the $Re^{II}(PCA^-)$ non-emissive excited state. For the mononuclear and symmetric dinuclear rhenium(I) complexes with X = $CO_2Me$, consecutive protonation of both the pyridinyl and imine N atoms of PCA in aqueous solution leads to unusual bell-shaped curves for both the absorption and the emission intensities vs. pH because of opposite effects on the electronic delocalization of PCA. This latter property can be employed to devise novel luminescent pH sensors of the on-off-on type. The corresponding unsymmetrical dinuclear complexes $[(4,4'\text{-}X_2\text{-bpy})(CO)_3Re^{I}(\mu\text{-PCA})Ru^{III}(NH_3)_5]^{4+}$ have been obtained in situ by oxidizing the $[Re^{I},Ru^{II}]$ precursors in $CH_3CN$ solution. Spectral and electrochemical measurements with these complexes lead to the values of the metal-to-metal electronic coupling elements.

(© Wiley-VCH Verlag GmbH & Co. KGaA, 69451 Weinheim, Germany, 2007)

## Introduction

Tricarbonylpolypyridylrhenium(I) complexes of the type *fac*-$[Re(\alpha\text{-diimine})(CO)_3L]^+$ (L = auxiliary monodentate ligand) have very interesting properties, such as relatively high thermal and photochemical stabilities, high redox potentials, and luminescence in the visible region that have led to their applications as light switches,[1] ion sensors,[2] intercalating agents for nucleic acids,[3] probes for biological molecules,[4] and models in fundamental studies of energy- and electron-transfer reactions relevant to solar energy conversion.[5] Tuning the physicochemical properties of these complexes by changing the nature of the diimine and/or L offers a high degree of versatility for the design of new supramolecular systems that may perform useful specific functions.[5r]

We have recently described the novel chromophore-quencher tricarbonylrhenium(I) complexes $[Re(4,4'\text{-}X_2\text{-bpy})(CO)_3(PCA)]^+$ and $[(4,4'\text{-}X_2\text{-bpy})(CO)_3Re(\mu\text{-PCA})Re(CO)_3(4,4'\text{-}X_2\text{-bpy})]^{2+}$ (bpy = 2,2′-bipyridine, X = $CH_3$ or H, and PCA = 4-pyridinealdazine).[6,7] Emission from the lowest-energy metal-to-ligand charge-transfer excited state $^3MLCT$ $[d_\pi(Re)\rightarrow\pi^*(X_2bpy)]$ is completely quenched in these complexes by the presence of PCA in the mononuclear species at room temperature in $CH_3CN$. Quenching of luminescence has been observed before in tricarbonylpolypyridylrhenium(I) complexes with electron-acceptor ligands (L) such as *N*-methyl-4,4′-bipyridinium ($MQ^+$), *N*-benzyl-4,4′-bipyridinium ($BzQ^+$), or *N*-(4-pyridyl)-β-(*N*-methylpyridinium-3-yl)acrylamide ($pyAm\text{-}Mepy^+$).[8] In the case of L = PCA, the emission was also found to be quenched in aqueous solution at high pH values, and when the pH was lowered until one of the imine N atoms of PCA became protonated, alteration of the ligand conjugation brought about a recovery of luminescence. We thus concluded that these complexes can be employed as luminescent pH sensors.[7]

In this work, we have prepared and studied the new complexes $[Re(4,4'\text{-}X_2\text{-bpy})(CO)_3(PCA)]^+$, $[(4,4'\text{-}X_2\text{-bpy})(CO)_3Re(\mu\text{-PCA})Re(CO)_3(4,4'\text{-}X_2\text{-bpy})]^{2+}$, and $[(4,4'\text{-}X_2\text{-bpy})(CO)_3Re^{I}(\mu\text{-PCA})Ru^{II/III}(NH_3)_5]^{3+/4+}$ (X = Ph and $CO_2Me$), thereby completing the previously studied series. We expected that introducing substituted bipyridines with strongly electron-withdrawing groups would have different

[a] Instituto de Química Física, Facultad de Bioquímica, Química y Farmacia, Universidad Nacional de Tucumán,
Ayacucho 491 (T4000INI), San Miguel de Tucumán, Argentina
Fax: +54-381-424-8169
E-mail: nkatz@fbqf.unt.edu.ar
[b] Instituto de Ciencias Químicas, Facultad de Agronomía y Agroindustrias, Universidad Nacional de Santiago del Estero, Av. Belgrano (S) 1912 (G4200ABT), Santiago del Estero, Argentina
[c] Servei de RMN, Universitat Autònoma de Barcelona, Bellaterra, 08193 Barcelona, Spain

 © 2007 Wiley-VCH Verlag GmbH & Co. KGaA, Weinheim 

effects on the emission properties. Indeed, we found that the emission is recovered at high pH values, and protonation changes in the PCA ligand can now be employed to devise novel luminescent switches of the on-off-on type. The effect of pH on the emission properties of the previously reported complex $[Re(bpy)(CO)_3(4,4'\text{-bpy})]^+$ (4,4′-bpy = 4,4′-bipyridine)[9] was also studied in order to compare the behavior of complexes containing an auxiliary ligand with one protonation site (4,4′-bpy) with that of those containing an auxiliary ligand with two protonation sites (PCA). Finally, dinuclear unsymmetrical complexes with $[Ru(NH_3)_5]^{n+}$ as electron donor ($n$ = 2) or acceptor ($n$ = 3) groups have been prepared and characterized in relation to intramolecular electron transfer in the Marcus inverted region.[10]

The structures of the ligands, along with the atom numbering for NMR assignments, are shown in Scheme 1; the structures of the complexes are shown in Scheme 2.

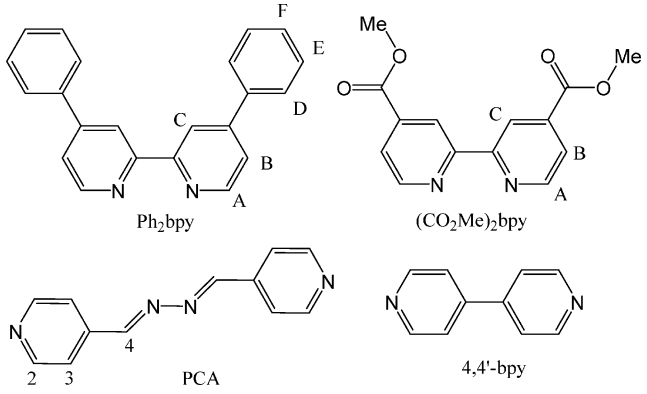


Scheme 1. Ligands.

## Results and Discussion

### Syntheses, Solubilities, and IR and NMR Spectral Characterizations

The synthetic methods used to obtain the new mono- and dinuclear tricarbonylpolypyridylrhenium complexes described in this work are slightly different from those previously developed in our laboratory.[6,7,11,12] All the complexes are soluble in acetonitrile, dichloromethane, and acetone and their purity was confirmed by chemical analysis, CV, and IR, NMR, and UV/Vis spectroscopy. The ester complexes are soluble in water and are stable for several days in neutral solutions at low concentrations ($\leq 10^{-4}$ M), whereas the phenyl complexes are not soluble in water, even with $Cl^-$ as the counterion. The solubility of rhenium(I) complexes in water has a direct impact on their applications in radiopharmaceuticals.[7] The values of the carbonyl stretching frequencies ($\nu_{CO}$) in the IR spectra of complexes **1** and **2** (2032 and 1918 $cm^{-1}$, respectively) are almost the same as those reported for related complexes of the type *fac*-$[Re(4,4'\text{-}X_2\text{-bpy})(CO)_3(L)]PF_6$,[6,7,11,12] whereas the values of the carbonyl stretching frequencies in the IR spectra of complexes **5** and **6** (2037 and 1927 $cm^{-1}$, respectively) are slightly higher than those of **1** and **2**, thereby indicating a stronger π-backbonding effect from Re to the bipyridine rings substituted with moderately strong electron-withdrawing groups, as reported previously for complexes such as *fac*-$[Re(4,4'\text{-}X_2\text{-bpy})(CO)_3(L)]PF_6$ {X = $C(O)NEt_2$, $CO_2Et_2$ and L = py-PTZ [10-(4-picolyl)phenothiazine]}.[13] All these values of $\nu_{CO}$ are consistent with a facial configuration of the carbonyl groups of local $C_{3v}$ symmetry. Both the mono- and dinuclear species were completely characterized by NMR spectroscopy (see Experimental Section).

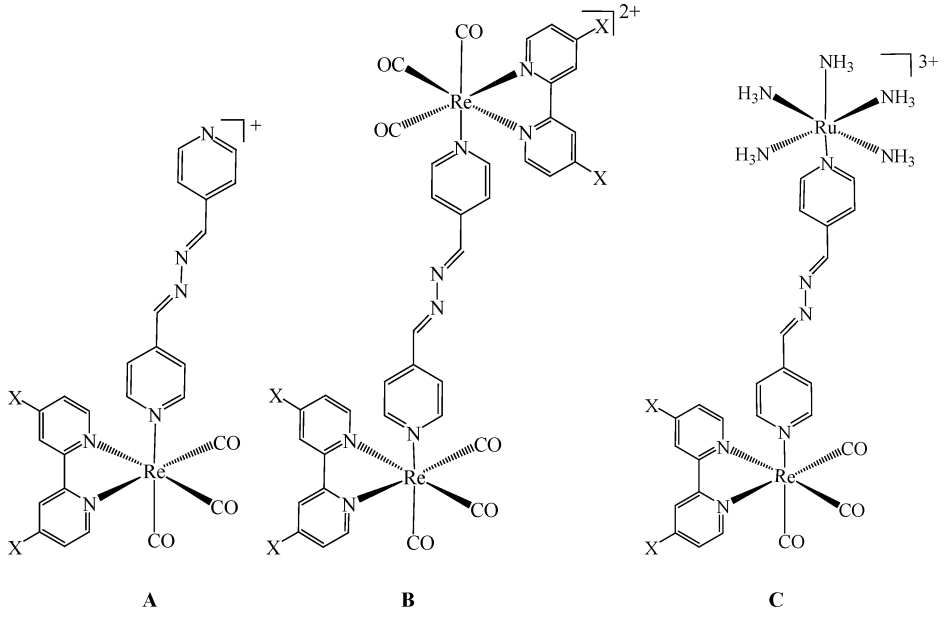


Scheme 2. **A**: Complexes **1** (X = Ph) and **5** (X = $CO_2Me$); **B**: Complexes **2** (X = Ph) and **6** (X = $CO_2Me$); **C**: Complexes **3** (X = Ph) and **7** (X = $CO_2Me$).

 © 2007 Wiley-VCH Verlag GmbH & Co. KGaA, Weinheim 

Six signals are observed for the protons of coordinated PCA in the mononuclear complexes due to coordination of only one of the pyridinyl N atoms to one rhenium center. For the dinuclear complexes, only three signals are observed for the protons of PCA due to the symmetry imposed by coordination of both pyridinyl nitrogen atoms of PCA to two rhenium centers. As a general trend, metal coordination induces slight displacements of the chemical shifts of the PCA moiety in all complexes to higher fields with respect to the values in the free ligands. Diffusion coefficients ($D$) were also determined to gain more insight into their overall molecular size.[14] The $D$ values (in $CD_3CN$ at 25 °C) of the mononuclear species **1** and **5** are $10.00 \times 10^{-10}$ and $10.23 \times 10^{-10}$ $m^2 s^{-1}$, respectively, and for the dinuclear species **2** and **6** $7.94 \times 10^{-10}$ and $8.31 \times 10^{-10}$ $m^2 s^{-1}$, respectively. These changes of 25% in the $D$ value between the mono- and dinuclear species strongly agree with the corresponding increase in molecular weights (about 75%) and hydrodynamic radius (7.2 and 7.0 Å for the mononuclear species **1** and **5** and 9.0 and 8.7 Å for the dinuclear complexes **2** and **6**, respectively). Furthermore, the characteristic $^{15}N$ chemical shifts of the nitrogen atoms from the different ligands provide direct experimental evidence for the existence of an Re–N bond. Thus, the $^{15}N$ chemical shifts of the two pyridinyl nitrogen atoms of PCA in the mononuclear species appear at $\delta \approx +323$ (free N) and +238 ppm (N bonded to Re), whereas a single resonance appears at $\delta \approx +238$ ppm in the dinuclear complexes. Figure 1 shows the $^1H$ NMR spectrum of complex **2** as a representative example.

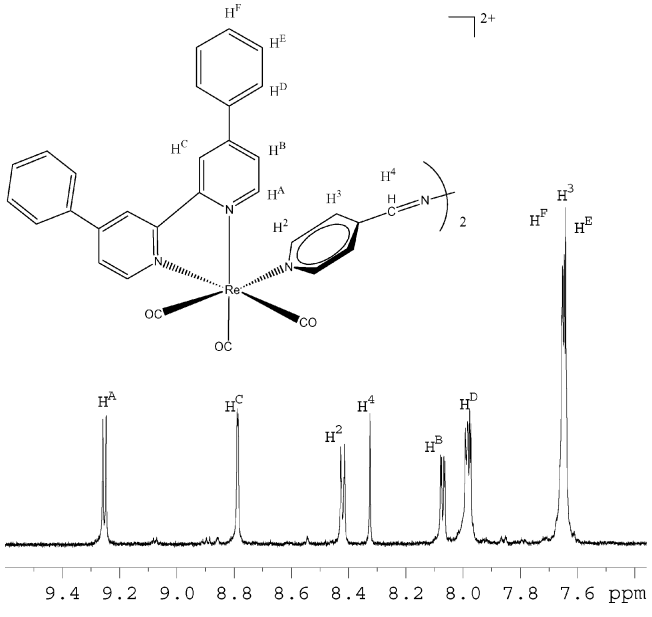


Figure 1. $^1H$ NMR spectrum of complex **2** in $CD_3CN$ at 500.13 MHz.

## UV/Vis Spectra

Table 1 shows the spectroscopic data for complexes **1**–**8** in $CH_3CN$. Characteristic spin-allowed intraligand $\pi \rightarrow \pi^*$ transitions of the polypyridyl ligands give rise to intense UV absorptions between 200 and 330 nm.[6,7,9] The mononuclear complexes **1** and **5** present minimum-energy absorptions at $\lambda_{max}$ = 346 and 352 nm, respectively, which can be assigned, as observed previously in the analogous complexes $[Re(X_2bpy)(CO)_3(L)]^+$ ($\lambda_{max}$ = 330–380 nm),[6,7] to overlapping metal-to-ligand charge transfers (MLCT) of the type $d_\pi(Re) \rightarrow \pi^*(X_2bpy)$ and $d_\pi(Re) \rightarrow \pi^*(PCA)$. These same bands are redshifted to $\lambda_{max}$ = 350 and 355 nm, respectively, in the homodinuclear $Re^I$–$Re^I$ complexes **2** and **6**, as reported previously for symmetric dinuclear complexes of the type $[(X_2bpy)(CO)_3Re(L)Re(CO)_3(X_2bpy)]^{2+}$.[6,7,9] Figure 2 shows the UV/Vis spectrum of complex **6** as a representative example. It is noteworthy that both the $\pi \rightarrow \pi^*$ transitions of $X_2bpy$ as well as the MLCT $d_\pi(Re) \rightarrow \pi^*(X_2bpy)$ transitions are shifted to longer wavelengths when increasing the electron-accepting strength of the substituent X, as already reported for similar species.[9,13,15] On the other hand, when comparing the effect of ligands L in complexes of the type $[Re(bpy)(CO)_3L]^+$, a

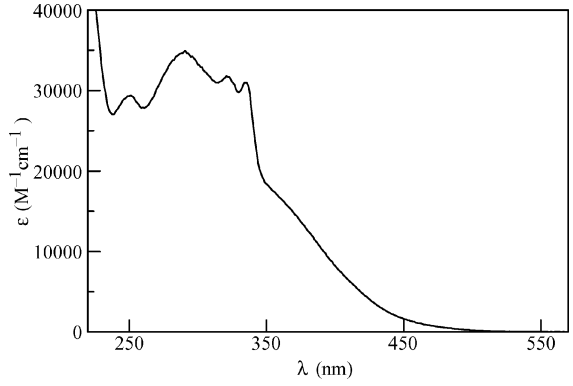


Figure 2. UV/Vis spectrum of $[\{4,4'\text{-}(MeO_2C)_2\text{-}bpy\}(CO)_3Re(\mu\text{-}PCA)Re(CO)_3\{4,4'\text{-}(MeO_2C)_2\text{-}bpy\}]^{2+}$ (**6**) in $CH_3CN$.

Table 1. UV/Vis spectroscopic data (in $CH_3CN$) at 22 °C.

| Complex | $\lambda_{max}$ [nm] ($10^{-3}$ $\varepsilon_{max}$ [$M^{-1} cm^{-1}$]) |
|---|---|
| $[Re(Ph_2bpy)(CO)_3(PCA)]^+$ (**1**) | 346 (18.6), 330 (29.1), 284 (57.6) |
| $[(Ph_2bpy)(CO)_3Re(\mu\text{-}PCA)Re(CO)_3(Ph_2bpy)]^{2+}$ (**2**) | 350 (26.8), 330 (40.4), 284 (76.5) |
| $[(Ph_2bpy)(CO)_3Re^I(\mu\text{-}PCA)Ru^{II}(NH_3)_5]^{3+}$ (**3**) | 560 (14.6), 350 (20.2), 330 (30.8), 283 (60.4) |
| $[(Ph_2bpy)(CO)_3Re^I(\mu\text{-}PCA)Ru^{III}(NH_3)_5]^{4+}$ (**4**) | 496 (4.7), 350 (24.4), 330 (36.4), 281 (66.6) |
| $[Re\{4,4'\text{-}(MeO_2C)_2\text{-}bpy\}(CO)_3(PCA)]^+$ (**5**) | 352 (9.2), 335 (18.8), 320 (21.8), 290 (27.0) |
| $[\{4,4'\text{-}(MeO_2C)_2\text{-}bpy\}(CO)_3Re(\mu\text{-}PCA)Re(CO)_3\{4,4'\text{-}(MeO_2C)_2\text{-}bpy\}]^{2+}$ (**6**) | 355 (17.5), 335 (31.0), 321 (31.8), 291 (34.9) |
| $[\{4,4'\text{-}(MeO_2C)_2\text{-}bpy\}(CO)_3Re^I(\mu\text{-}PCA)Ru^{II}(NH_3)_5]^{3+}$ (**7**) | 560 (13.6), 355 (10.9), 334 (20.9), 320 (23.3), 284 (28.8) |
| $[\{4,4'\text{-}(MeO_2C)_2\text{-}bpy\}(CO)_3Re^I(\mu\text{-}PCA)Ru^{III}(NH_3)_5]^{4+}$ (**8**) | 501 (2.0), 355 (13.6), 335 (24.5), 321 (26.6), 280 (30.6) |

 © 2007 Wiley-VCH Verlag GmbH & Co. KGaA, Weinheim 

blueshift of the (Re→bpy) MLCT band can be observed with increasing electron-withdrawing power of L; in effect, the values of $\lambda_{max}$ in $CH_3CN$ decrease in the order 4-Etpy ($\lambda_{max}$ = 352 nm)[16] > 4,4′-bpy ($\lambda_{max}$ = 340 nm)[9] > PCA ($\lambda_{max}$ = 332 nm),[7] thus pointing to an increasing stabilization of the $d_\pi$(Re) energy levels.

With respect to the UV/Vis spectra of the unsymmetrical dinuclear complexes **3**, **4**, **7**, and **8**, we can assign the bands in the $Re^{I}$–$Ru^{II}$ complexes **3** and **7** at $\lambda_{max}$ = 350 and 560 nm to $d_\pi(Re)\rightarrow\pi^*(X_2bpy, PCA)$ and $d_\pi(Ru)\rightarrow\pi^*(PCA)$ MLCT transitions, respectively. For the $Re^{I}$–$Ru^{III}$ complexes **4** and **8**, which were prepared in situ by oxidation of **3** and **7**, respectively, with bromine, the bands at $\lambda_{max}$ = 560 nm disappear completely, and the new bands that appear at $\lambda_{max}$ = 497 and 501 nm, respectively, whose values were obtained by Gaussian deconvolution, as shown in Figure 3 for complex **4**, can be assigned to $Re^{I}\rightarrow Ru^{III}$ MMCT transitions, with some contribution from $PCA\rightarrow Ru^{III}$ LMCT bands, as discussed previouly for the analogous species with $Me_2$bpy and bpy.[6,7]

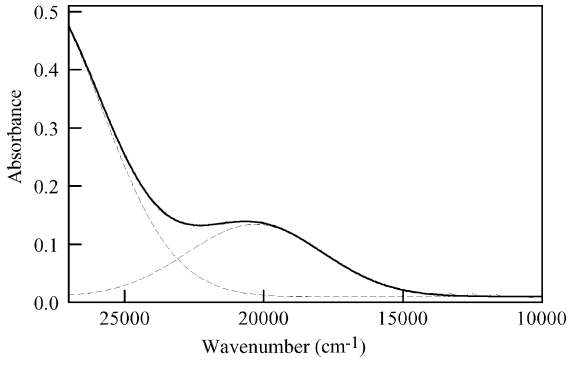


Figure 3. Gaussian deconvolution of the visible bands of the mixed-valent complex $[(Ph_2bpy)(CO)_3Re^{I}(\mu\text{-}PCA)Ru^{III}(NH_3)_5]^{4+}$ (**4**; approx. $3\times10^{-5}$ M) obtained by $Br_2$ oxidation (in $CH_3CN$) of the dinuclear complex **3**.

Figure 4 shows the results of a controlled-potential electrolysis of complex **3** in $CH_3CN$ at 800 mV. The results obtained are consistent with those obtained upon bromine oxidation. In effect, the $d_\pi(Ru)\rightarrow\pi^*(PCA)$ MLCT band at $\lambda_{max}$ = 560 nm disappears completely, and a new MMCT band (combined with an LMCT band) appears near 500 nm. When reverting the oxidation process in the spectroelectrochemical experiment, the intensity of the $d_\pi(Ru)\rightarrow\pi^*(PCA)$ MLCT band at $\lambda_{max}$ = 560 nm is not recovered completely, which is consistent with the results obtained upon $Sn^{2+}$ reduction. We consider that, besides mere electron transfer, the formation of a *cis* isomer is possibly favored on oxidation.

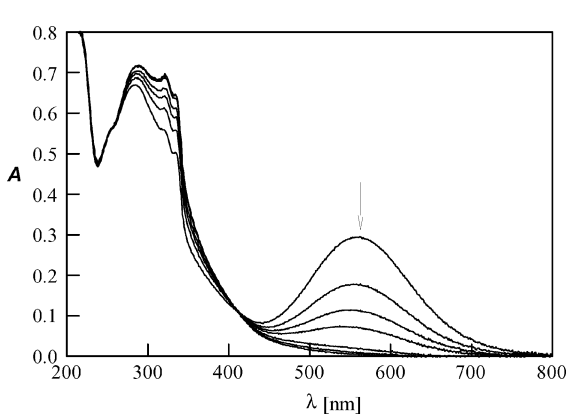


Figure 4. Controlled potential electrolysis of a $CH_3CN$ solution of $[(Ph_2bpy)(CO)_3Re^{I}(\mu\text{-}PCA)Ru^{II}(NH_3)_5]^{3+}$ (**3**; approx. $2\times10^{-5}$ M) at 800 mV in an OTTLE cell. The arrow indicates increasing times: $t$ = 0, 1, 2, 3, 4, 8, and 10 min.

## Photophysical Properties

In contrast to the previously reported complexes with $Me_2$bpy and bpy,[6,7] the complexes studied in this work emit in $CH_3CN$ solution at room temperature. The shape and position of the emission maxima are typical of $Re^{II}$-(diimine$^-$) MLCT excited states.[13] Table 2 shows the data obtained at 22 °C for the emission maxima, lifetimes, and emission quantum yields for complexes **1**, **2**, **5**, and **6**. The same lifetimes were obtained both by laser flash photolysis and by pulsed luminescence decay in argon-saturated solutions, thereby indicating that the luminescence properties are not due to impurities. Furthermore, the reported chemical analyses and the spectral and electrochemical data point to a high degree of purity of the complexes under study. The observed quantum yields, which were calculated and corrected by taking into account the refractive indices of the solvents and absorbance differences, as described in the literature,[17] are much lower (by a factor of about $10^2$) than those reported for related complexes with the same chromophore,[13] which can be attributed to intramolecular luminescence quenching induced by the presence of the PCA ligand.[6,7] This quenching was attributed in the $Me_2$bpy derivative to crossing to a neighboring $[(X_2bpy)(CO)_3Re^{II}$-$(PCA^-)]^+$ excited state, as confirmed by laser flash photolysis and low-temperature emission measurements.[6] The radiative rate constants $k_r$ (approx. $10^3$–$10^4$ $s^{-1}$), on the other hand, are lower than those expected (approx. $10^5$ $s^{-1}$) for $Re^{I}$ complexes of the type $[Re(bpy)(CO)_3X]$ (X = substituted pyridine).[13] Energy transfer from $^3$MLCT (Re→bpy) to PCA to give an excited intraligand triplet state ($^3$PCA*) that decays non-radiatively to the ground state may be the cause of these low values of $k_r$. In support of this argument, it should be noted that changes in photophysical properties brought about by MLCT or intraligand excited states placed very close to the luminescent excited state have al-

Table 2. Photophysical data (in $CH_3CN$) of complexes of the type $[Re(4,4'\text{-}X_2\text{-}bpy)(CO)_3(PCA)]^+$ and $[(4,4'\text{-}X_2\text{-}bpy)(CO)_3Re$-$(\mu\text{-}PCA)Re(CO)_3(4,4'\text{-}X_2\text{-}bpy)]^{2+}$ at 22 °C.

| X | Complex | $\lambda_{em}$ [nm] | $\Phi_{em}$[a] | $\tau$ [ns] |
|---|---|---|---|---|
| Ph | **1** | 552 | 0.0010 | 690 |
| | **2** | 552 | 0.0045 | 865 |
| $CO_2Me$ | **5** | 570 | 0.0004 | 132 |
| | **6** | 565 | 0.0017 | 187 |

[a] Calculated as described previously.[7,17]

 © 2007 Wiley-VCH Verlag GmbH & Co. KGaA, Weinheim 

ready been observed in related complexes.[18] Moreover, a recent review by Schmehl et al. gives a detailed discussion of similar systems in which reversible energy transfer between a long-lived $^3$IL state and a $^3$MLCT state leads to longer lived $^3$MLCT emission.[19] In complex **2**, laser flash photolysis showed the emergence of a transient with $\lambda_{max}$ = 380 nm, which is typical of the absorption of the radical anion of bpy ligands, as shown in Figure 5, together with emission bleaching at $\lambda_{max}$ = 550 nm. The lifetime ($\tau$) is 865 ns, which is about two orders of magnitude higher than the lifetime of the excited state of $[Re(Me_2bpy)(CO)_3(PCA)]^+$. These findings are consistent with formation of an $Re^{II}(Ph_2bpy^-)$ excited state. The mononuclear complex $[Re(Ph_2bpy)(CO)_3(PCA)]^+$ has a lower lifetime ($\tau$ = 690 ns) but with a similar transient spectrum. We conclude that, since $Ph_2bpy$ is a much better π-acceptor than $Me_2bpy$ and bpy, the energy of the emissive $Re^{II}(Ph_2bpy^-)$ excited state becomes much lower than that of the non-emissive $Re^{II}(PCA^-)$ excited state, with consequent recovery of luminescence at room temperature. As shown in Table 2, the quantum yields and lifetimes for the complexes containing $(CO_2Me)_2bpy$ are lower than those of the $Ph_2bpy$ complexes. Luminescence in the series of complexes $[Re(4,4'\text{-}X_2\text{-}bpy)(CO)_3(PCA)]^+$ and $[(4,4'\text{-}X_2\text{-}bpy)(CO)_3Re(\mu\text{-}PCA)Re(CO)_3(4,4'\text{-}X_2\text{-}bpy)]^{2+}$ can thus be finely tuned by changing the nature of X: when X = Me or H, the emission is almost completely quenched,[6,7] whereas when X = Ph or $CO_2Me$, emission is partially recovered because of the less effective intramolecular quenching by PCA.

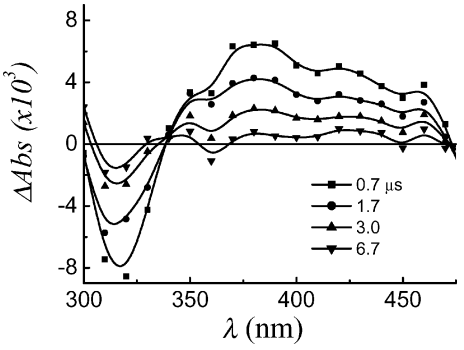


Figure 5. Transient spectra of $[(Ph_2bpy)(CO)_3Re(\mu\text{-}PCA)Re(CO)_3(Ph_2bpy)]^{2+}$ (**2**) in deaerated $CH_3CN$ solution at 22 °C.

## Protonation Equilibria

These studies were carried out with complexes **1**, **2**, **5**, and **6** since the heterodinuclear complexes **3**, **4**, **7**, and **8** have very low stability in aqueous solutions, as already reported for analogous complexes.[7] Table 3 shows the acidity constants obtained from the spectrophotometric and spectrofluorometric titrations of all the measured complexes. Complexes **1** and **2** were measured in a 1:4 mixture of $CH_3CN/H_2O$ because of their poor solubility in water. The effect of the organic solvent could be to lower all p$K_a$ values with respect to those in aqueous solution. In water, complexes **5** and **6** emit very weakly between $\lambda_{max}$ = 565 nm at pH 8.5 and $\lambda_{max}$ = 575 nm at pH 1.5 ($\lambda_{ex}$ = 380 nm). When performing the experiment at constant ionic strength, a decrease in pH brings about not only an increased emission from the Re→$X_2$bpy MLCT excited state but also a noticeable isomerization/hydrolysis process of the PCA and $(CO_2Me)_2bpy$ ligands, which becomes enhanced at extreme pH values. Evidence for ligand isomerization has been presented before,[6,7] and evidence of ester hydrolysis emerges when comparing the final spectra, obtained after several hours, with the spectra of the corresponding complexes of carboxylic acid substituted bipyridines. On the other hand, more accurate values of the protonation constants could be obtained when the protonation studies were done with larger volumes of solution since the decomposition processes were negligible during the time taken for the measurements. This latter method has therefore been used for reporting the values in Table 3, except for the reference complex $[Re(bpy)(CO)_3(4,4'\text{-}bpy)]^+$, which proved to be very stable in aqueous solutions.

Consistent and reproducible values of p$K_a$ for both ground and excited states could only be obtained for the mononuclear complex **5** starting from basic aqueous solutions. Both the absorbance and luminescence data can be fitted with a three-species diagram involving protonation equilibria of the ground and excited states of PCA complexes, as shown in Scheme 3. Two ground-state p$K_a$ values were detected by fitting the UV/Vis absorptivity changes with pH at $\lambda$ = 330 nm, as shown in Figure 6(a). The first of these (p$K_{a1}$ = 2.15) corresponds to one of the imine N atoms of coordinated PCA and the second one (p$K_{a2}$ = 5.59) corresponds to the free pyridine N atom of coordinated PCA. This latter value is 0.4 units larger than the

Table 3. Values of p$K_a$ for the ground and excited states of complexes **1**, **2**, **5**, and **6** at 22 °C in aerated aqueous solution.

| Complex | p$K_a$ | p$K_a$* |
|---|---|---|
| $[Re(Ph_2bpy)(CO)_3(PCA)]^+$ (**1**)[a] | p$K_{a1}$ < 1<br>p$K_{a2}$ = 5.08 ± 0.23 | p$K_{a1}$* < 1 |
| $[(Ph_2bpy)(CO)_3Re(\mu\text{-}PCA)Re(CO)_3(Ph_2bpy)]^{2+}$ (**2**)[a] | p$K_{a1}$ < 1 | p$K_{a1}$* < 1 |
| $[Re\{4,4'\text{-}(MeO_2C)_2\text{-}bpy\}(CO)_3(PCA)]^+$ (**5**)[b] | p$K_{a1}$ = 2.15 ± 0.03<br>p$K_{a2}$ = 5.59 ± 0.06 | p$K_{a1}$* = 2.34 ± 0.17<br>p$K_{a2}$* = 3.33 ± 0.05 |
| $[\{4,4'\text{-}(MeO_2C)_2\text{-}bpy\}(CO)_3Re(\mu\text{-}PCA)Re(CO)_3\{4,4'\text{-}(MeO_2C)_2\text{-}bpy\}]^{2+}$ (**6**)[c] | p$K_a$ < 1 | not detected |
| $[Re(bpy)(CO)_3(4,4'\text{-}bpy)]^{+}$[c] | p$K_a$ = 3.70 ± 0.07 | p$K_{a1}$* = 4.03 ± 0.05 |

[a] In $CH_3CN/H_2O$ (1:4). [b] Data obtained from bulk experiments. [c] Data obtained from experiments at constant ionic strength ($I$ = 0.1 M).

 © 2007 Wiley-VCH Verlag GmbH & Co. KGaA, Weinheim 

value for the free ligand, probably because of the $Re^{I}\rightarrow$PCA π-backbonding effect. Both p$K_a$ values are very similar to those corresponding to the previously studied complex $[Re(bpy)(CO)_3(PCA)]^+$ (p$K_{a1}$ = 1.98 and p$K_{a2}$ = 5.41),[7] thereby indicating little influence of the nature of the substituent X on the basicity of coordinated PCA.

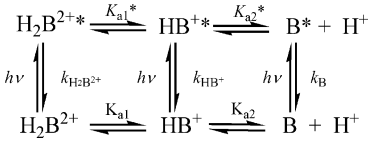


Scheme 3. Three-species diagram for the protonated equilibria of the ground and excited states of PCA complexes. B is the non-protonated species.

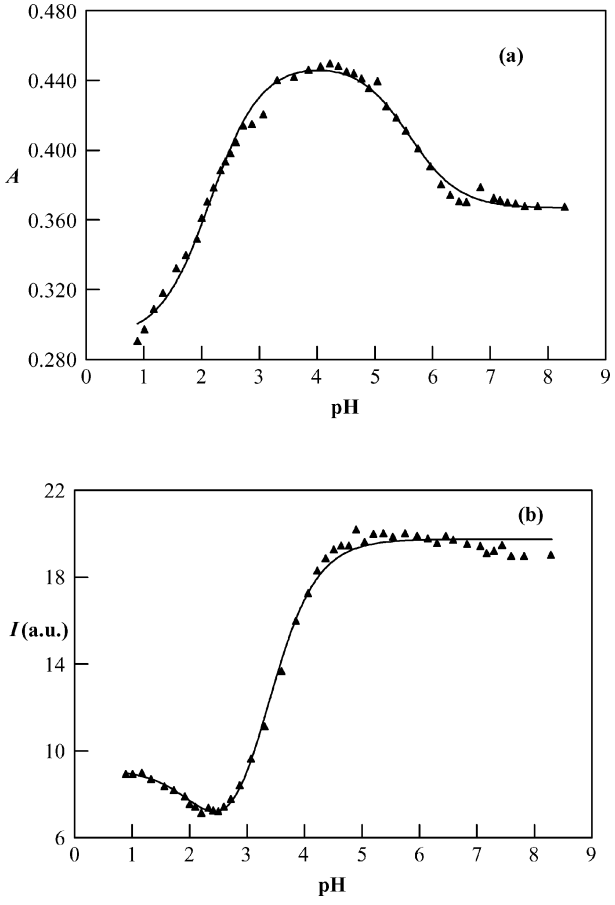


Figure 6. Variation of (a) absorbance $A$ (at $\lambda$ = 330 nm) and (b) emission intensity (at $\lambda_{ex}$ = 380 nm and $\lambda_{em}$ = 570 nm) for $[Re\{4,4'\text{-}(MeO_2C)_2\text{-}bpy\}(CO)_3(PCA)]^+$ (**5**) in aqueous buffer, with pH. The lines indicate the best fits using a three-species model in each case.

As found before in related unsubstituted bpy complexes,[7] protonation of the pyridine N atom of PCA leads to an absorbance increase at $\lambda$ = 330 nm due to an increased $d_\pi$(Re)-π*(PCA) coupling. The MLCT band corresponding to this transition is expected to fall in this region.[6] Protonation of the imine N atom of PCA leads instead to an absorbance decrease at $\lambda$ = 330 nm because the energy of the lowest-lying π* orbital of PCA is increased and $d_\pi$(Re)-π*(PCA) coupling is consequently diminished. The result is a bell-shaped curve which can be reproduced in an inverted way when fitting the emission intensities at different pH values. This is in contrast to similar carbonylrhenium complexes, where only sigmoid curves have been observed.[2,7] As shown in Figure 6(b), complex **5** presents two adjustable excited-state p$K_a$* values: the first one, p$K_{a1}$* = 2.34, corresponds to the imine N atom of coordinated PCA and the second one, p$K_{a2}$* = 3.33, corresponds to the free pyridine N atom of coordinated PCA. No better fitting could be obtained between pH = 5 and 9, and in any case the observed deviations from the fits are within the experimental uncertainties of the intensity measurements. The first basicity constant of the excited state is higher than that of the ground state (by around 0.2 p$K$ units), as expected for tricarbonylrhenium(I) complexes,[2] but lower than that of the complex $[Re(bpy)(CO)_3(PCA)]^+$ (by around 0.4 units),[7] thereby evidencing the effect of decreasing the electron density on PCA as a result of including a more electron-accepting bipyridine ligand. Strikingly, the value of p$K_{a2}$* is 2.26 units lower than that of the ground state, which points to the fact that since more electron density has been delocalized in the excited state, $[(CO_2Me)_2bpy^{-}(CO)_3\text{-}Re^{II}(PCA)]^+$, to the substituted bpy ligand, less electron density is available at the remote N atom of the coordinated PCA ligand, and possibly evidencing some contribution of the p$K_a$ of the carboxylate-substituted bpy that results from hydrolysis of the ester-substituted bpy.

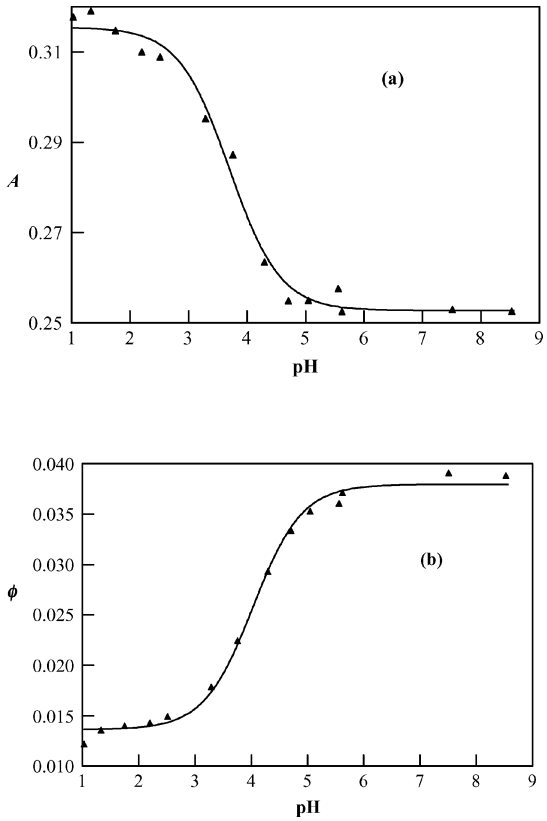


Figure 7. Variation of (a) absorbance $A$ (at $\lambda$ = 350 nm) and (b) emission quantum yield $\Phi_{em}$ (at $\lambda_{ex}$ = 350 nm and $\lambda_{em}$ = 552 nm) for $[Re(bpy)(CO)_3(4,4'\text{-bpy})]^+$ in aqueous buffer, with pH. The lines indicate the best fits using a two-species model in each case.

 © 2007 Wiley-VCH Verlag GmbH & Co. KGaA, Weinheim 

There is only one protonation site possible in the model complex $[Re(bpy)(CO)_3(4,4'\text{-bpy})]^+$, namely the free pyridyl N atom. As shown in Figure 7, a value of the ground-state $pK_a$ of 3.70, which agrees with those reported for polypyridylruthenium complexes, is obtained by fitting absorbance changes with pH.[20] However, we obtain a $pK_a^*$ value of 4.03 for the excited state when fitting the emission quantum yields with pH. This value is higher than that of the ground state by 0.33 units and points to much less electron density being delocalized onto the unsubstituted bpy ligand in the excited state.

We conclude that when the free pyridine N atom of coordinated PCA is protonated, the π* excited state of PCA decreases in energy, and the emission is partially quenched, as observed before for $MQ^+$,[8] but when the imine N atom of coordinated PCA is protonated, the π* excited state of PCA increases in energy, due to alteration of the ligand conjugation, and emission is recovered again. In effect, when decreasing the pH from 4 to 1, the band assigned to the π-π* transition of PCA at $\lambda_{max}$ = 290 nm is shifted to lower wavelengths, thereby indicating a proton-induced energy increase of the π* levels of PCA. The mononuclear species **5** can therefore be used as a novel luminescent pH sensor of the on-off-on type.

## Electrochemistry

Table 4 shows the electrochemical data for the studied complexes. The redox potentials for the $Re^{II}/Re^{I}$ couple of the mononuclear $Re^{I}$ species **1**, the $Re^{I}$–$Re^{I}$ dinuclear species **2**, and the $Re^{I}$–$Ru^{II}$ dinuclear species **3** are very similar, with $E_{1/2}$ values between 1.8 and 1.9 V, with some degree of irreversibility, as expected for carbonyl(diimine)rhenium(I) complexes.[6,7,11,12] The redox potentials for the $Re^{II}/Re^{I}$ couple in complexes **5**, **6**, and **7** are higher than 2.0 V and could not be detected. The PCA ligand is reduced irreversibly at $E_{peak} \approx -0.8/-1.0$ V in all complexes except **7**. The first reduction of $X_2$bpy appears at $E_{peak} \approx -1.2$ V, while a second irreversible reduction at $E_{peak} \approx -1.4$ V can be attributed to an $Re^{I/0}$ couple, as reported previously for the related $Me_2$bpy complex.[6]

The voltammetric wave that appears in the asymmetric $Re^{I}$–$Ru^{II}$ dinuclear complexes **3** and **7** at $E_{1/2}$ = 0.46 and 0.48 V, respectively, which is absent in the mononuclear rhenium complexes, can be readily assigned to the $Ru^{III}/Ru^{II}$ couple by comparison with similar complexes.[6,7] The high $\Delta E_p$ values (92–134 mV) suggest redox-induced ligand isomerization processes, and experimental evidence of redox-induced ligand isomerization has been described previously.[6] Varying the sweep rate gave no better $\Delta E$ values at higher sweep rates. The differences between the redox potentials of both metallic couples in **3** and **7** are: $\Delta E_{1/2} = E_{1/2}(Re^{II}/Re^{I}) - E_{1/2}(Ru^{III}/Ru^{II})$ = 1.52 and 1.54 V, respectively.

## Intramolecular Electron Transfer

The reorganization energy, $\lambda$, for the intramolecular electron transfer through the PCA bridge can be calculated from the Marcus–Hush equations and the experimental

Table 4. Electrochemical data (in $CH_3CN$) at 22 °C.[a]

| Complex | Process | $E_{1/2}$ [V] ($\Delta E_p$ [mV]) | $E_{peak}$ [V] |
|---|---|---|---|
| $[\{4,4'\text{-}(Ph)_2\text{-bpy}\}(CO)_3Re(PCA)]^+$ (**1**) | $Re^{2+/+}$ | | 1.85 |
| | $PCA^{0/-}$ | | –0.98 |
| | $Ph_2bpy^{0/-}$ | –1.14 (51) | |
| | $Re^{+/0}$ | –1.28 (94) | |
| $[\{\{4,4'\text{-}(Ph)_2\text{-bpy}\}(CO)_3Re\}_2PCA]^{2+}$ (**2**) | $Re^{2+/+}$ | | 1.86 |
| | $PCA^{0/-}$ | | –0.78 |
| | $Ph_2bpy^{0/-}$ | | –1.18 |
| | $Re^{+/0}$ | –1.27 (97) | |
| $[\{4,4'\text{-}(Ph)_2\text{-bpy}\}(CO)_3Re^{I}(\mu\text{-PCA})Ru^{II}(NH_3)_5]^{3+}$ (**3**) | $Re^{2+/+}$ | 1.77 (166) | |
| | $Ru^{3+/2+}$ | 0.48 (134) | |
| | $PCA^{0/-}$ | | –0.95 |
| | $Ph_2bpy^{0/-}$ | | –1.16 |
| | $Re^{+/0}$ | | –1.31 |
| $[\{4,4'\text{-}(MeO_2C)_2\text{-bpy}\}(CO)_3Re(PCA)]^+$ (**5**) | $Re^{2+/+}$ | | >2 |
| | $PCA^{0/-}$ | | –0.81 |
| | $(MeO_2C)_2bpy^{0/-}$ | –0.96 (172) | |
| | $Re^{+/0}$ | | –1.32 |
| $[\{\{4,4'\text{-}(MeO_2C)_2\text{-bpy}\}(CO)_3Re\}_2PCA]^{2+}$ (**6**) | $Re^{2+/+}$ | | >2 |
| | $PCA^{0/-}$ | | –0.81 |
| | $(MeO_2C)_2bpy^{0/-}$ | –0.96 (172) | |
| | $Re^{+/0}$ | | –1.32 |
| $[\{4,4'\text{-}(MeO_2C)_2\text{-bpy}\}(CO)_3Re^{I}(\mu\text{-PCA})Ru^{II}(NH_3)_5]^{3+}$ (**7**) | $Re^{2+/+}$ | | >2 |
| | $Ru^{3+/2+}$ | 0.46 (92) | |
| | $PCA^{0/-}$ | | –0.64 |
| | $(MeO_2C)_2bpy^{0/-}$ | | –1.01 |
| | $Re^{+/0}$ | | –1.22 |

[a] All CV data were obtained at a scan rate of 200 mV $s^{-1}$.

 © 2007 Wiley-VCH Verlag GmbH & Co. KGaA, Weinheim 

data of the MMCT transition in the heterodinuclear complexes **4** and **8**[21] to be approximately 0.9 eV, a value similar to that obtained previously for the analogous complexes with $Me_2$bpy and bpy.[6,7] The values determined for the metal–metal electronic coupling elements ($H_{AB} = 8.8 \times 10^2$ and $6.2 \times 10^2$ $cm^{-1}$ for the Ph and $CO_2Me$ derivatives, respectively) are consistent with those obtained previously for mixed-valent symmetric and unsymmetrical dinuclear complexes of PCA.[6,7] These complexes might be considered as prototypes for simulating primary charge separations in the inverted region.

## Conclusions

Continuing our previous studies on proton-induced luminescence of chromophore-quencher tricarbonylpolypyridylrhenium(I) complexes, we have shown in this work that quenching of luminescence in these complexes can not only be turned on and off by changing the substituents on the 2,2′-bipyridine acceptor group but also by changing the acidity of their aqueous solutions. In particular, the mononuclear complex $[Re\{4,4'\text{-}(MeO_2C)_2\text{-}bpy\}(CO)_3(PCA)]^+$ can be employed as a novel luminescent pH sensor of the on-off-on type rather than the recently reported luminescent off-on-off switches based on polypyridylruthenium complexes.[22]

## Experimental Section

**Materials and Techniques:** All chemicals used were p.a. grade. $CH_3CN$ was distilled from $P_4O_{10}$. Tetrakis(*n*-butyl)ammonium hexafluorophosphate (TBAH) was recrystallized from ethanol three times and dried at 150 °C for 72 h. IR spectra were recorded (as KBr pellets) with an FTIR Perkin–Elmer Spectrum RX-I spectrophotometer. UV/Vis spectra were recorded with a Varian Cary 50 spectrophotometer for solutions in 1-cm cells. Redox titrations were performed stoichiometrically by adding aliquots of a stock solution of $Br_2$ in $CH_3CN$ which had previously been standardized by known procedures.[20] Reductions were carried out by adding solid $SnCl_2$ to $CH_3CN$ solutions of the oxidized complexes. Electrochemical measurements were performed in $CH_3CN$ (0.1 M TBAH) with a BAS Epsilon electrochemical equipment. A standard three-electrode compartment cell was used, with Ag/AgCl (3 M KCl) as a reference electrode, vitreous C as a working electrode, and Pt wire as an auxiliary electrode. All redox potentials ($E_{1/2}$) are referenced to Ag/AgCl. Spectroelectrochemical measurements were performed in an OTTLE (optically transparent thin layer electrolysis) type cell from BAS. Emission studies were performed with a Shimadzu RF-5301 PC spectrofluorometer in 1-cm fluorescence cells. Laser-flash photolysis (LFP) experiments were carried out with a Q-switched Nd:YAG laser (Continuum Minilite II) generating 355-nm pulses (fwhm: 10 ns; 5 mJ per pulse). The signals were recorded with a Luzchem m-LFP 112 system and fed into a transient Tektronik TDS 3032B recorder. Time-resolved luminescence detection was carried out with a home-made system composed of an *f*/4 monochromator (PTI-101, 1200 blazes) coupled with a red-extended PMT (Hamamatsu R928) placed at right angles to the excitation laser pulse. The output of the detector was fed to the Tektronix TDS3032B digital oscilloscope linked to an on-line PC for data transfer and analysis. Typically, about 100–200 laser cycles with the excitation laser operating at 15 Hz were averaged in order to obtain the decay times with a suitable signal-to-noise ratio. NMR spectra were recorded in $CD_3CN$ with an Avance Bruker 500.13 MHz spectrometer. Full $^1H$, $^{13}C$, and $^{15}N$ chemical shift assignments were performed by collecting 2D COSY, 2D $^1H$-$^{13}C$ HSQC, 2D $^1H$-$^{13}C$ HMBC, 2D $^1H$-$^{15}N$ HMBC, and 2D NOESY (mixing time: 500 ms) experiments. Diffusion NMR coefficients were measured at 25 °C using the LEDBP pulse sequence (diffusion time: 150 ms) with sample spinning at 20 Hz to minimize convection effects.[14] Argon was bubbled through the solutions for 15 min prior to electrochemical and photophysical measurements. Chemical analyses for C, H, and N were done at INQUIMAE, University of Buenos Aires, Argentina, with an estimated error of ±0.5%.

**Preparation of PCA and 4,4′-$(MeO_2C)_2$-bpy:** The ligands 4-pyridinealdazine and 4,4′-bis(methoxycarbonyl)-2,2′-bipyridine were prepared as described previously.[23,24]

**Preparation of $[Re(Ph_2bpy)(CO)_3(PCA)]PF_6 \cdot H_2O$ (1) and $[(Ph_2bpy)(CO)_3Re(\mu\text{-}PCA)Re(CO)_3(Ph_2bpy)](PF_6)_2$ (2):** These salts were prepared by a procedure similar to that reported in the literature.[6,7] In a typical experiment, $[Re(CO)_5Cl]$ (181 mg, 0.50 mmol) and 4,4′-diphenyl-2,2′-bipyridine (154 mg, 0.50 mmol) were heated at reflux in toluene (20 mL) for 1 h. It was cooled and then precipitated with hexane (40 mL). The solid obtained after additional cooling was collected, washed with hexane and diethyl ether, and dried in vacuo. The resulting complex $[Re(Ph_2bpy)(CO)_3Cl]$ (272 mg, 0.443 mmol) and $Ag(CF_3SO_3)$ (114 mg, 0.443 mmol) were heated at reflux in thf (40 mL) for 30 min. PCA (139 mg, 0.664 mmol) was then added to the reaction mixture and heating at reflux was continued for 2 h. After removal of AgCl by filtration, the solvent was removed in a rotary evaporator to give a yellow oil. This oil was dissolved in 80 mL of 3:1 (v:v) $MeOH/H_2O$, 2 g of $NH_4PF_6$ dissolved in 20 mL of water was added, and the mixture was put in the freezer. The yellow precipitate that formed was filtered and washed with copious amounts of $H_2O$ and three times with portions of diethyl ether. This solid was dissolved in a minimum amount of 1:4 (v/v) acetonitrile/dichloromethane, adsorbed onto a silica gel (Kieselgel 60) column and eluted with the same solvent. The yellow fractions (the first is complex **2** and the second is complex **1**) were concentrated to dryness, redissolved in acetone, and precipitated with hexane. **1:** Yield: 66 mg (14%). $C_{37}H_{28}F_6N_6O_4PRe$ (951.84): calcd. C 46.7, H 2.97, N 8.83; found C 46.5, H 2.74, N 8.10. IR (KBr): $\tilde{\nu}$ = 2032 (s), 1918 (s), 1615 (m), 1542 (w), 1474 (m), 1413 (m), 1235 (w), 840 (s), 766 (m), 739 (w), 695 (w), 627 (w), 558 (m) $cm^{-1}$. $^1H$ NMR (500.13 MHz, $CD_3CN$, 25 °C): $\delta$ = 9.24 (d, $J$ = 5.8 Hz, 2 H, $H^A$), 8.78 (d, $J$ = 1.8 Hz, 2 H, $H^C$), 8.68 (dd, $J$ = 1.6, 4.5 Hz, 2 H, $H^2$, 8.44 (s, 1 H, $H^4$), 8.42 (s, 1 H, $H^{4'}$), 8.41 (dd, $J$ = 5.4, 1.7 Hz, 2 H, $H^{2'}$), 8.06 (dd, $J$ = 1.8, 5.8 Hz, 2 H, $H^B$), 7.97 (m, 4 H, $H^D$), 7.68 (m, 4 H, $H^3$ and $H^{3'}$), 7.62 (m, 6 H, $H^E$ and $H^F$) ppm. $^{13}C$ NMR (125.6 MHz $CD_3CN$, 25 °C): $\delta$ = 123.0 ($C^3$), 123.5 ($C^C$), 125.7 ($C^{3'}$), 127.0 ($C^B$), 128.7 ($C^D$), 130.5 ($C^E$), 132.1 ($C^F$), 136.2 (C), 141.4 (C), 145.0 (C), 151.6 ($C^2$), 153.7 ($C^A$), 153.8 ($C^{2'}$), 154.9 (C), 157.3 (C), 158.4 ($C^{4'}$), 161.4 ($C^4$), 190.0 ($C^{CO\,trans}$), 197.1 ($C^{CO\,cis}$) ppm. $^{15}N$ NMR (50.69 MHz $CD_3CN$, 25 °C; chemical shifts extracted from the $^1H$-$^{15}N$ HMBC spectrum): $\delta$ = 234.8 ($N^{A'}$), 239.3 ($N^{1'}$), 322.1 ($N^1$), 374.3 ($N^{5'}$), 379.7 ($N^5$) ppm. **2:** Yield: 48 mg (12%). $C_{62}H_{42}F_{12}N_8O_6P_2Re_2$ (1657.4): calcd. C 44.9, H 2.55, N 6.76; found C 44.8, H 2.51, N 6.37. IR (KBr): $\tilde{\nu}$ = 2032 (s), 1918 (s), 1615 (m), 1542 (w), 1474 (m), 1413 (m), 1236 (w), 840 (s), 766 (m), 739 (w), 696 (w), 627 (w), 558 (m) $cm^{-1}$. $^1H$ NMR (500.13 MHz, $CD_3CN$, 25 °C): $\delta$ = 9.25 (d, $J$ = 6.0 Hz, 4 H, $H^A$), 8.79 (d, $J$ = 1.7 Hz, 4 H, $H^C$), 8.42 (dd, $J$ = 1.7, 5.2 Hz, 4 H, $H^2$),

 © 2007 Wiley-VCH Verlag GmbH & Co. KGaA, Weinheim 

8.32 (s, 2 H, $H^4$), 8.07 (dd, $J$ = 5.6, 1.6 Hz, 4 H, $H^B$), 7.98 (dd, $J$ = 5.6, 1.6 Hz, 8 H, $H^D$), 7.68–7.64 (m, $J$ = 1.7, 5.2 Hz, 16 H, $H^3$, $H^F$ and $H^E$) ppm. $^{13}$C NMR (125.6 MHz $CD_3CN$, 25 °C): $\delta$ = 122.6 ($C^C$), 124.8 ($C^3$), 126.0 ($C^B$), 128.2 ($C^D$), 129.8 ($C^F$), 131.3 ($C^E$), 135.6 (C), 143.3 (C) 152.8 (C), 153.2 ($C^2$), 154.4 ($C^A$), 156.1 (C), 157.1 ($C^4$), 191.6 ($C^{CO}$*trans*), 196.3 ($C^{CO}$*cis*) ppm. The $^1$H NMR spectrum is shown in Figure 1.

**Preparation of [($Ph_2$bpy)(CO)$_3$Re$^I$(μ-PCA)Ru$^{II}$($NH_3$)$_5$]($PF_6$)$_3$·6$CH_2Cl_2$ (3):** Complex **1** (30 mg, 0.032 mmol) was stirred in acetone (10 mL) under argon for 30 min and [Ru($NH_3$)$_5$($H_2O$)]($PF_6$)$_2$ (16 mg, 0.032 mmol), prepared as described in the literature,[25] was then added. The mixture was stirred under argon in the dark for 2 h. Diethyl ether (100 mL) was added to precipitate the complex, which was re-dissolved in a minimum amount of acetone. Dichloromethane (40 mL) and diethyl ether (40 mL) were added to re-precipitate the complex, which was filtered and washed with dichloromethane, diethyl ether, and water. It was finally dissolved in acetonitrile and purified by chromatography on Sephadex LH-20, using acetonitrile as the eluting solvent. The first, blue fraction was collected, concentrated to dryness, re-dissolved in acetone, precipitated with dichloromethane, filtered, washed with dichloromethane and diethyl ether, and dried in vacuo over $P_4O_{10}$. Yield: 30 mg (66%). $C_{43}H_{53}Cl_{12}F_{18}N_{11}O_3P_3ReRu$ (1919.6): calcd. C 26.9, H 2.8, N 8.0; found C 26.6, H 2.8, N 8.5.

**Preparation of [($Ph_2$bpy)(CO)$_3$Re$^I$(μ-PCA)Ru$^{III}$($NH_3$)$_5$]$^{4+}$ (4):** This heterodinuclear ion was generated in situ by adding bromine to an acetonitrile solution of **3** or by electrochemical oxidation. The oxidation progress was monitored by measuring the absorbance changes in the 200–1100 nm range.

**Preparation of [Re{4,4′-($MeO_2C$)$_2$-bpy}(CO)$_3$(PCA)]$PF_6$·$H_2O$ (5) and [(4,4′-($MeO_2C$)$_2$-bpy)(CO)$_3$Re(μ-PCA)Re(CO)$_3${4,4′-($MeO_2C$)$_2$-bpy}]($PF_6$)$_2$ (6):** [Re(CO)$_5$Cl] (181 mg, 0.50 mmol) and 4,4′-bis-(methoxycarbonyl)-2,2′-bipyridine (136 mg, 0.50 mmol) were heated at reflux in toluene (20 mL) for 1 h. Precipitation was achieved by adding hexane (20 mL) to the cooled solution. The red solid obtained after additional cooling was collected, washed with hexane and diethyl ether, and dried in vacuo. The resulting complex [Re{4,4′-($MeO_2C$)$_2$-bpy}(CO)$_3$Cl] (280 mg, 0.485 mmol) and Ag($CF_3SO_3$) (114 mg, 0.443 mmol) were heated at reflux in thf (40 mL) for 30 min. PCA (153 mg, 0.728 mmol) was then added to the reaction mixture and heating at reflux was continued for 2 h. After removal of AgCl by filtration, the solvent was removed in a rotary evaporator to give an orange oil. This oil was dissolved in 40 mL of 3:1 (v/v) MeOH/$H_2O$, 2 g of $NH_4PF_6$ dissolved in 10 mL of water was added, and the mixture was put in the freezer. The yellow precipitate that formed was filtered and washed with copious amounts of $H_2O$ and three times with portions of diethyl ether. It was then dissolved in a minimum amount of 1:4 (v/v) acetonitrile/dichloromethane, adsorbed onto a silica gel (Kieselgel 60) column and eluted with the same solvent. The yellow fractions (the first is complex **6** and the second is complex **5**) were concentrated to dryness, redissolved in acetone, and precipitated with hexane. **5:** Yield: 107 mg (24%). $C_{29}H_{24}F_6N_6O_8PRe$ (915.72): calcd. C 38.0, H 2.6, N 9.2; found C 37.9, H 2.1, N 9.0. IR (KBr): $\tilde{\nu}$ = 2037 (s), 1927 (s), 1735 (s), 1616 (m), 1560 (w), 1440 (m), 1408 (m), 1327 (m), 1308 (m), 1266 (m), 1232 (m), 1134 (w), 981 (w), 843 (s), 785 (w), 766 (m), 722 (w), 644 (w), 558 (m) cm$^{-1}$. $^1$H NMR (500.13 MHz, $CD_3CN$, 25 °C): $\delta$ = 9.40 (dd, $J$ = 5.7, 0.7 Hz, 2 H, $H^A$), 8.91 (dd, $J$ = 1.6, 0.7 Hz, 2 H, $H^C$), 8.70 (dd, $J$ = 1.7, 4.5 Hz, 2 H, $H^2$), 8.45 (s, 1 H, $H^4$), 8.42 (s, 1 H, $H^{4'}$), 8.30 (dd, $J$ = 5.2, 1.6 Hz, 2 H, $H^{2'}$), 8.22 (dd, $J$ = 1.6, 5.6 Hz, 2 H, $H^B$), 7.69 (dd, $J$ = 1.7, 4.5 Hz, 2 H, $H^3$), 7.64 (dd, $J$ = 1.6, 5.2 Hz, 2 H, $H^{3'}$), 4.02 (s, 6 H, Me) ppm. $^{13}$C NMR (125.6 MHz $CD_3CN$, 25 °C): $\delta$ = 54.3 (C of Me), 123.0 ($C^3$), 125.3 (C), 125.7 ($C^{3'}$), 129.0 ($C^B$), 141.4 (C), 142.7 (C), 145.0 (C), 151.6 (C), 153.8 (C), 153.8 ($C^{2'}$), 156.1 ($C^2$), 157.6 ($C^{4'}$), 158.3 (C), 161.4 ($C^4$), 164.4 (C) ppm. $^{15}$N NMR (50.69 MHz $CD_3CN$, 25 °C; chemical shifts extracted from the $^1$H-$^{15}$N HMBC spectrum): $\delta$ = 248.0 ($N^{A'}$), 237.2 ($N^{1'}$),322.9 ($N^1$), 373.0 ($N^{5'}$), 375.5 ($N^5$) ppm. **6:** Yield: 48 mg (12%). $C_{46}H_{34}F_{12}N_8O_{14}P_2Re_2$ (1585.2): calcd. C 34.9, H 2.2, N 7.1; found C 34.7, H 2.1, N 6.8. IR (KBr): $\tilde{\nu}$ = 2037 (s), 1927 (s), 1735 (s), 1618 (m), 1560 (w), 1440 (m), 1408 (m), 1327 (m), 1307 (m), 1266 (m), 1232 (m), 1134 (w), 981 (w), 843 (s), 785 (w), 766 (m), 722 (w), 644 (w), 558 (m) cm$^{-1}$. $^1$H NMR (500.13 MHz, $CD_3CN$, 25 °C): $\delta$ = 9.37 (dd, $J$ = 5.6, 0.6 Hz, 4 H, $H^A$), 8.88 (dd, $J$ = 1.7, 0.6 Hz, 4 H, $H^C$), 8.27 (dd, $J$ = 1.7, 5.2 Hz, 4 H, $H^2$), 8.27 (s, 2 H, $H^4$), 8.20 (dd, $J$ = 5.6, 1.6 Hz, 4 H, $H^B$), 7.57 (dd, $J$ = 1.7, 5.2 Hz, 4 H, $H^3$), 4.00 (s, 12 H, Me) ppm. $^{13}$C NMR (125.6 MHz $CD_3CN$, 25 °C): $\delta$ = 54.2 ($C^{Me}$), 125.3 ($C^C$), 125.7 (C), 129.0 (C), (C), 142.7 (C), 144.6 ($C^3$), 153.9 ($C^2$), 156.0 ($C^A$), 157.5 ($C^4$), 158.5 (C), 164.4 (C), 191.6 ($C^{CO}$*trans*), 196.3 ($C^{CO}$*cis*) ppm. $^{15}$N NMR (50.69 MHz $CD_3CN$, 25 °C; chemical shifts extracted from the $^1$H-$^{15}$N HMBC spectrum): $\delta$ = 250.5 ($N^{A'}$), 238.1 ($N^1$), 377.6 ($N^5$) ppm.

**Preparation of [{4,4′-($MeO_2C$)$_2$-bpy}(CO)$_3$Re$^I$(μ-PCA)Ru$^{II}$($NH_3$)$_5$]-($PF_6$)$_3$·$CH_2Cl_2$ (7):** Complex **5** (50 mg, 0.056 mmol) was stirred in acetone (10 mL) under argon for 30 min, and [Ru($NH_3$)$_5$-($H_2O$)]($PF_6$)$_2$ (28 mg, 0.056 mmol), prepared as described in the literature,[25] was added. The mixture was stirred continuously under argon in the dark for 2 h. Diethyl ether (100 mL) was then added to precipitate the complex, which was redissolved in a minimum amount of acetone. Dichloromethane (60 mL) and diethyl ether (60 mL) were added to re-precipitate the complex, which was filtered and washed with dichloromethane, diethyl ether, and water. It was finally dissolved in acetonitrile and purified by chromatography on Sephadex LH-20 using acetonitrile as the eluting solvent. The first, blue fraction was collected, concentrated to dryness, redissolved in acetone, precipitated with dichloromethane, filtered, washed with dichloromethane and diethyl ether, and dried in vacuo over $P_4O_{10}$. Yield: 55 mg (71%). $C_{31}H_{39}Cl_2F_{18}N_{11}O_7P_3ReRu$ (1470.8): calcd. C 25.3, H 2.7, N 10.5; found C 25.1, H 2.7, N 10.8.

**Preparation of [{4,4′-($MeO_2C$)$_2$-bpy}(CO)$_3$Re$^I$(μ-PCA)Ru$^{III}$-($NH_3$)$_5$]$^{4+}$ (8):** This heterodinuclear ion was generated in situ by adding bromine to an acetonitrile solution of **7** or by electrochemical oxidation. The oxidation progress was monitored by measuring the absorbance changes in the 200–1100 nm range.

**Preparation of [Re(bpy)(CO)$_3$(4,4′-bpy)]$PF_6$ (9):** This complex was available from previous studies.[11]

**Protonation Studies:** For p$K_a$ determinations, pH titrations by spectrophotometric and spectrofluorometric techniques were performed with two kinds of experiments. In the first one, Britton and Robinson's buffer, which consists of a mixture of 0.04 M acetic acid, 0.04 M phosphoric acid, and 0.04 M boric acid with variable amounts of a solution of 0.2 M NaOH, was used, and the ionic strength was fixed at 0.1 M with a solution of NaCl. The complexes were dissolved in aqueous solutions of 0.1 M NaCl and stirred for about 5 h until the filtered solution showed a final average absorbance of about 0.4. Each sample was prepared just before measurement with 2 mL of buffer and 2 mL of a stock solution of the complex. The pH value of each fraction was then determined with a Metrohm pH-meter. Reversal of the pH values of the extreme fractions was done by adding 3 M HCl or 3 M NaOH. In each titration, 12–15 points were recorded. In the second experiment, the ionic strength was not regulated. Only one solution (approx. 30 mL) was used, with Britton and Robinson's buffer, which con-

 © 2007 Wiley-VCH Verlag GmbH & Co. KGaA, Weinheim 

sists of 0.02 M acetic acid, 0.02 M phosphoric acid and 0.02 M boric acid with a small amount of 3 M NaOH solution up to pH = 10. The complex was dissolved by adding a drop of acetonitrile and rapidly mixing with the buffer solution. 3 M HCl (40–60 μL) was added to lower the pH to 1.5. In each titration, 40–50 points were recorded. Both methods gave consistent results. Luminescence and absorption measurements were performed with air-saturated solutions. We used a previously reported technique to fit the obtained data for all complexes.[7] The experimental data were fitted with the PSI Plot software. The fits were all satisfactory, giving consistent and reasonable values of p$K_a$ and p$K_a$*.

## Acknowledgments

We thank the Universidad Nacional de Tucumán (UNT), the Consejo Nacional de Investigaciones Científicas y Técnicas (CONICET), and the Agencia Nacional de Promoción Científica y Tecnológica (ANPCyT), all from Argentina, for financial support. The Deutscher Akademischer Austauschdienst (DAAD) is gratefully acknowledged for the donation of the Bioanalytical Systems equipment. F. F., N. E. K., and C. D. B are members of the Research Career from CONICET, Argentina. M. C. thanks CONICET for a graduate fellowship and specially his father for being an exemplary person.

[1] A. S. Polo, M. K. Itokazu, K. M. Frin, A. O. de Toledo Patrocínio, N. Y. Murakami Iha, *Coord. Chem. Rev.* **2006**, *250*, 1669–1680.
[2] B. Higgins, B. A. DeGraff, J. N. Demas, *Inorg. Chem.* **2005**, *44*, 6662–6669, and references cited therein.
[3] H. D. Stoeffler, N. B. Thornton, S. L. Temkin, K. S. Schanze, *J. Am. Chem. Soc.* **1995**, *117*, 7119–7128.
[4] K. K.-W. Lo, K. H.-K. Tsang, K.-S. Sze, *Inorg. Chem.* **2006**, *45*, 1714–1722.
[5] a) M. Wrighton, D. L. Morse, *J. Am. Chem. Soc.* **1974**, *96*, 998–1003; b) T. D. Westmoreland, K. S. Schanze, P. E. Neveux Jr, E. Danielson, B. P. Sullivan, P. Chen, T. J. Meyer, *Inorg. Chem.* **1985**, *24*, 2596–2597; c) K. Kalyanasundaram, *J. Chem. Soc. Faraday Trans.* **1986**, *2*, 2401–2415; d) P. Chen, T. D. Westmoreland, E. Danielson, K. S. Schanze, D. Anthon, P. E. Neveux Jr, T. J. Meyer, *Inorg. Chem.* **1987**, *26*, 1116–1126; e) P. Chen, E. Danielson, T. J. Meyer, *J. Phys. Chem.* **1988**, *92*, 3708–3711; f) A. Juris, S. Campagna, I. Bidd, J.-M. Lehn, R. Ziessel, *Inorg. Chem.* **1988**, *27*, 4007–4011; g) B. P. Sullivan, *J. Phys. Chem.* **1989**, *93*, 24–26; h) W. Kaim, H. E. A. Kramer, C. Vogler, J. Reiker, *J. Organomet. Chem.* **1989**, *367*, 107–115; i) L. Wallace, D. C. Jackman, D. P. Rillema, J. W. Merkert, *Inorg. Chem.* **1995**, *34*, 5210–5214; j) S. Berger, A. Klein, W. Kaim, J. Fiedler, *Inorg. Chem.* **1998**, *37*, 5664–5671; k) L. C. Abbott, C. J. Arnold, T.-Q. Ye, K. C. Gordon, R. N. Perutz, R. E. Hester, J. N. Moore, *J. Phys. Chem. A* **1998**, *102*, 1252–1260; l) M. Feliz, G. Ferraudi, *Inorg. Chem.* **1998**, *37*, 2806–2810; m) D. R. Striplin, G. A. Crosby, *Coord. Chem. Rev.* **2001**, *211*, 163–175; n) D. M. Dattelbaum, M. K. Itokazu, N. Y. Murakami Iha, T. J. Meyer, *J. Phys. Chem. A* **2003**, *107*, 4092–4095; o) O. S. Wenger, L. M. Henling, M. W. Day, J. R. Winkler, H. B. Gray, *Inorg. Chem.* **2004**, *43*, 2043–2048; p) I. E. Pomestchenko, D. E. Polyansky, F. N. Castellano, *Inorg. Chem.* **2005**, *44*, 3412–3421; q) K. K. W. Lo, K. H. K. Tsang, W. K. Hui, N. Zhu, *Inorg. Chem.* **2005**, *44*, 6100–6110; r) M. Ghirotti, C. Chiorboli, M. T. Indelli, F. Scandola, M. Casanova, E. Iengo, E. Alessio, *Inorg. Chim. Acta* **2007**, *360*, 1121–1130.
[6] M. Cattaneo, F. Fagalde, N. E. Katz, A. M. Leiva, R. Schmehl, *Inorg. Chem.* **2006**, *45*, 127–136.
[7] M. Cattaneo, F. Fagalde, N. E. Katz, *Inorg. Chem.* **2006**, *45*, 6884–6891.
[8] a) T. D. Westmoreland, H. LeBozec, R. W. Murray, T. J. Meyer, *J. Am. Chem. Soc.* **1983**, *105*, 5952–5954; b) P. Chen, E. Danielson, T. J. Meyer, *J. Phys. Chem.* **1988**, *92*, 3708–3711; c) P. Chen, M. Curry, T. J. Meyer, *Inorg. Chem.* **1989**, *28*, 2271–2280; d) R. Duesing, G. Tapolsky, T. J. Meyer, *J. Am. Chem. Soc.* **1990**, *112*, 5378–5379; e) N. E. Katz, S. L. Mecklenburg, T. J. Meyer, *Inorg. Chem.* **1995**, *34*, 1282–1284.
[9] G. Tapolsky, R. Duesing, T. J. Meyer, *Inorg. Chem.* **1990**, *29*, 2285–2297.
[10] R. A. Marcus, N. Sutin, *Biochem. Biophys. Acta* **1985**, *811*, 265–322.
[11] F. Fagalde, N. E. Katz, *J. Coord. Chem.* **2001**, *54*, 367–377.
[12] M. G. Mellace, F. Fagalde, N. E. Katz, *Polyhedron* **2003**, *22*, 369–374.
[13] L. Sacksteder, A. P. Zipp, E. A. Brown, J. Streich, J. N. Demas, B. A. DeGraff, *Inorg. Chem.* **1990**, *29*, 4335–4340.
[14] N. Esturau, F. Sánchez-Ferrando, C. Roumestand, M. A. Delsuc, J. A. Gavin, T. Parella, *J. Magn. Reson.* **2001**, *153*, 48–55.
[15] L. Worl, R. Duesing, P. Chen, L. Della Ciana, T. J. Meyer, *J. Chem. Soc. Dalton Trans.* **1991**, 849–858.
[16] J. K. Hino, L. Della Ciana, W. J. Dressick, B. P. Sullivan, *Inorg. Chem.* **1992**, *31*, 1072–1080.
[17] J. V. Caspar, T. J. Meyer, *J. Am. Chem. Soc.* **1983**, *105*, 5583–5590.
[18] D. J. Stufkens, A. Vlček Jr, *Coord. Chem. Rev.* **1998**, *177*, 127–179, and references cited therein.
[19] X. Wang, A. Del Guerzo, R. H. Schmehl, *J. Photochem. Photobiol. C* **2004**, *5*, 55–77.
[20] F. Fagalde, N. E. Katz, *J. Chem. Soc. Dalton Trans.* **1993**, 571–575.
[21] C. Creutz, *Prog. Inorg. Chem.* **1983**, *30*, 1–73.
[22] F. Gao, H. Chao, F. Zhon, B. Peng, L.-N. Ji, *Inorg. Chem. Commun.* **2007**, *10*, 170–173.
[23] D. M. Ciurtin, Y.-B. Dong, M. D. Smith, T. Barclay, H.-C. zur Loye, *Inorg. Chem.* **2001**, *40*, 2825–2834.
[24] F. H. Case, *J. Am. Chem. Soc.* **1946**, *68*, 2574–2577.
[25] J. E. Sutton, H. Taube, *Inorg. Chem.* **1981**, *20*, 3125–3134.

Received: August 17, 2007
Published Online: October 31, 2007

 © 2007 Wiley-VCH Verlag GmbH & Co. KGaA, Weinheim 

DOI: 10.1002/ejic.200700628

# Synthesis, Structure and a DFT/TDDFT Study of a Diimido-Bridged Asymmetric Dimolybdenum Complex

**Kuntal Pal[a] and Sabyasachi Sarkar*[a]**

*In memory of Professor Frank Albert Cotton*

**Keywords:** Mixed-valence compounds / Molybdenum / Cyclic voltammetry / Electronic structure / Density functional calculations

The homobimetallic complex $(Bu_4N)_2$[MoO(mnt)Mo{*o*-aminobenzothiolato(3–)-*N*,*S*}$_2$(mnt)] (**2**; mnt = 1,2-dicyanoethylenedithiolate) has been synthesized as a dark green solid by treating $(Bu_4N)_2[Mo_2O_4(mnt)_2]$ (**1**) with *o*-aminothiophenol in $CH_3CN$. An X-ray crystal structure analysis of **2** reveals that it possesses an asymmetric structure where one Mo has a distorted octahedral geometry and the other a square-pyramidal geometry. The basal plane of the two Mo centers makes an angle of 26.41°, which is nearly one quarter of 90°. The shape of the ν(Mo=O) band in the IR spectrum of **2** suggests that these Mo atoms may have different oxidation states. The different reactivity of **1** with *o*-aminothiophenol and 2-aminoethanethiol was followed by EPR spectroscopy, and analysis of the different end-products from these reactions supports the proposal that **2** is a mixed-valence compound containing $Mo^{VI}$ and $Mo^{IV}$ centers. The electronic structures of **1** and **2** have been calculated at the DFT level of theory to analyse the effect of a deviation of the basal plane on the metal–metal bond in **2**. The cyclic voltammetric responses of **1** and **2** have been measured to correlate the data with the computational results. TDDFT calculations have been performed on **1** and **2** in the gas phase and also in a solvent medium to assign the transitions corresponding to the peaks found in the respective experimental electronic absorption spectra of these complexes.

(© Wiley-VCH Verlag GmbH & Co. KGaA, 69451 Weinheim, Germany, 2007)

## Introduction

Terminal oxido- or sulfido-coordinated higher-valent Mo complexes with dithiolene as co-ligand are good models for molybdenum-based enzymes.[1,2] Hexacoordinate $Mo^{VI}$ complexes[3] generally adopt a distorted octahedral geometry with *cis* dioxido or oxido-sulfido groups, whereas related $Mo^{IV}$ complexes generally adopt a square-pyramidal geometry[4] with a terminal Mo=O group or trigonal biprismatic geometry with a terminal Mo–SR (thiolato) moiety.[5] Molybdenum(V) complexes[6] are generally stabilized by di-$\mu_2$-oxido or mono-$\mu_2$-oxido bridging groups and have the general formula $\{M_2X_2Y_2\}^{2+}$, where X (terminal group) and Y (bridging group) are a combination of O and S atoms. The stability of di-$\mu_2$-oxido-bridged dimeric $Mo^V$ complexes arises from a strong Mo($d_{xy}$)–Mo($d_{xy}$) σ bond[7,8] supplemented by pπ bonding between the bridging ligand atoms and the two Mo atoms, which remain almost in the same plane. Imidomolybdenum complexes, which are isoelectronic to oxido complexes, are also known,[9,10] and two Lewis structures have been proposed for the Mo–N binding mode of the imido group to Mo (Scheme 1).[11] In the first, the nitrogen atom acts as a four-π-electron donor and Mo–N–R angle is close to 180°, whereas in the second the nitrogen atom acts as a two-electron donor and the Mo–N–R linkage is bent. The majority of monomeric Mo-imido complexes have a linear imido linkage and most imido-bridged Mo complexes have a bent imido linkage.

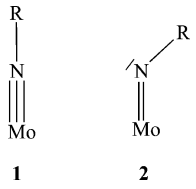


**1** **2**

Scheme 1. Two possible binding modes of the imido group at an Mo center.

Dialkyldithiocarbamato (dtc)-coordinated dimeric $Mo^V$ complexes with terminal and/or bridging imido linkages have been synthesized from the corresponding oxido and/or sulfido complexes[9] by substitution reactions. Most $Mo^{VI}$-imido complexes[10] have a linear Mo–N–R linkage. The re-

[a] Department of Chemistry, Indian Institute of Technology Kanpur,
Kanpur 208016, India
Fax: +91-512-2597265
E-mail: abya@iitk.ac.in

Supporting information for this article is available on the WWW under http://www.eurjic.org or from the author.

 © 2007 Wiley-VCH Verlag GmbH & Co. KGaA, Weinheim 

action of a dtc-coordinated oxido-$Mo^{VI}$ complex with 2-aminothiophenol has been reported to produce the intermediate imido complex $[Mo^{VI}(dtc)_2(NC_6H_4S)(OCH_3)]$,[11] which reacts further to give $[Mo^{V}O(dtc)(\mu_2\text{-}NC_6H_4S)_2\text{-}Mo^{V}(dtc)]$ on heating in the solid state under vacuum. The chemistry of oxidomolybdenum complexes varies with the co-ligand, which ranges from dtc to dithiolene-type ligands such as 1,2-dicyanoethenedithiolate (mnt).[12] Although both these co-ligands are sulfur donor bidentate ligands they differ in the bite angle on coordination to the Mo center. In this article we report the reaction of 2-aminothiophenol with a symmetrical di-$\mu_2$-oxido $Mo^{V}$ dithiolene complex to form an asymmetric dimeric dimolybdenum mnt-coordinated complex. The di-$\mu_2$-oxido groups are replaced by imido coordination arising from coordination of the deprotonated 2-aminothiophenol to asymmetric oxidomolybdenum and desoxomolybdenum centers. The reaction is followed by EPR spectroscopy to understand its course, and DFT and TDDFT calculations of the synthesized complex have been carried out to correlate its spectral properties with electronic structure.

## Results and Discussion

### Synthesis and IR Studies

The dithiolene-coordinated dimeric $Mo^{V}$ complex $[Bu_4N]_2[Mo_2O_4(mnt)_2]$ (**1**) has been reported recently.[6a] One of the di-$\mu_2$-oxido groups in **1** is readily protonated in the presence of a weak acid and the conjugate base of the acid then coordinates to the metal center to give linear mono $\mu_2$-oxido-bridged dimeric $Mo^{V}$ complexes with the general formula $[Mo_2O_3(mnt)_2(X)_2]^-$ [X = SPh (**1a**), Cl (**1b**), and Br (**1c**)].[6a] It has been shown that **1a**–**c**, which possess an $\{Mo_2O_3\}^{2+}$ core, hydrolyze back to **1** in the presence of traces of moisture via an EPR-active monomeric $[MoO(mnt)(X)(OH)]^-$ species. This EPR-active intermediate is readily dimerized to a stable di-$\mu_2$-oxido-bridged form due to the presence of two monodentate ligands in adjacent equatorial positions. Our goal was to synthesize a monomeric $Mo^{V}$ species with three S donor atoms (two from a dithiolene ligand and one from an SR group) to mimic the half-reduced state of sulfite oxidase.[13] The vacant fourth site in the equatorial plane of the expected square-based pyramidal Mo complex could be filled by an N-donor therefore we decided to use 2-aminothiophenol and 2-aminoethanethiol, both of which provide one S and one N atom. Both these ligands are in a zwitterionic form in solution, like an amino acid, although 2-aminoethanethiol, unlike 2-aminothiophenol, lacks $\pi$ delocalization. Treatment of **1**, **1a**, **1b**, or **1c** with 2-aminothiophenol in dichloromethane causes the color of the solution to change to light green, which suggests the formation of a new species, although addition of petroleum ether allowed only **1** to be isolated. The light-green species is EPR-active and the isolation of only **1** from such a reaction mixture clearly suggests that the 2-aminothiophenolato-coordinated $Mo^{V}$ monomer (EPR active) is in equilibrium with **1** in solution and that addition of the second solvent shifts the equilibrium towards **1**. The use of a more polar solvent such as acetonitrile led to a similar reactivity, whereas employing more drastic reaction conditions changed the course of the reaction. Thus, refluxing **1** with 2-aminothiophenol in acetonitrile yielded **2**. Unlike dtc-coordinated Mo complexes, however, **1** does not react with aniline or substituted anilines.

Addition of a solution of 2-aminoethanethiol in methanol to an acetonitrile solution of **1** caused a color change of the reaction mixture from yellow to dark-orange and finally to green, followed by immediate precipitation of yellow $[Mo^{VI}O_2(SCH_2CH_2NH_2)]$[14] in 48% yield. Further workup yielded 46% of $[(Bu_4N)_2][Mo^{IV}O(mnt)_2]$ from the mother liquor (Scheme 2). Reaction of $[Mo^{VI}O_2(mnt)_2]^{2-}$ with 2-aminothiphenol or 2-aminoethanethiol yielded $[Mo^{IV}O(mnt)_2]^{2-}$ quantitatively, with no formation of any imido-coordinated complex.[15] Similar reactions of these aminothiols with dtc-coordinated $Mo^{VI}$ complexes have shown a different chemistry.[10]

On the basis of the total charge and the diamagnetic nature of **2**, the possible formal oxidation states of the two Mo(1)/Mo(2) centers are either +5/+5 or +6/+4. This question can be resolved by considering the Mo=O stretching vibration of this unsymmetrical complex as the $\nu$(Mo=O) vibration in molybdenum complexes is sensitive to the formal oxidation state of Mo. Thus, this vibration in pentacoordinate bis-dithiolene $Mo^{IV}$ complexes[16] generally appears below 940 $cm^{-1}$, whereas in related $Mo^{V}$ species it

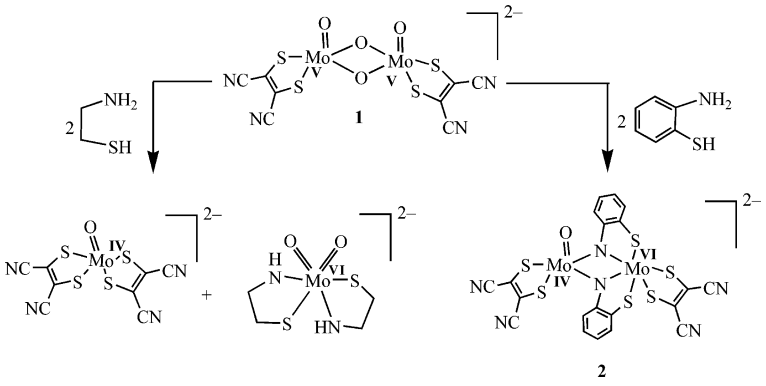


Scheme 2. Reaction of $(Bu_4N)_2[Mo^{V}_2O_4(mnt)_2]$ (**1**) with 2-aminothiophenol and 2-aminoethanethiol.

 © 2007 Wiley-VCH Verlag GmbH & Co. KGaA, Weinheim 

Table 1. Values of ν(Mo=O) [$cm^{-1}$] for selected Mo complexes.

| Complexes | ν(Mo=$O_t$)[a] | Ref. |
|---|---|---|
| $[Mo_2O(mnt)_2\{o\text{-aminobenzothiolato}(3-)\text{-}N,S\}_2]^{2-}$ | 937 | this work |
| $[Mo^{IV}O(mnt)_2]^{2-}$ | 932 | [3c] |
| $[Mo^{IV}O(mnt)(Bu_2bpy)]$ | 939 | [4d] |
| $[Mo^{V}{}_2O_4(mnt)_2]^{2-}$ | 977 | this work |
| $[Mo^{V}{}_2O_2(mnt)_2(\mu\text{-SPh})_2(\mu\text{-OR})]^{-1}$ (R = Me, Et, *i*Pr) | 951, 958, 961 | [6a] |
| $[Mo^{V}{}_2O_2(mnt)_2(\mu\text{-O})(\mu\text{-SPh})(\mu\text{-Br})]^{-2}$ | 960 | [6a] |
| $[Mo^{V}{}_2O_2(mnt)_2(\mu\text{-O})(\mu\text{-SPh})(\mu\text{-CH}_3SO_3)]^{-2}$ | 957 | [6a] |
| $[Mo^{V}{}_2O_2(mnt)_2(\mu\text{-O})(\mu\text{-SEt})(\mu\text{-CH}_3SO_3)]^{-2}$ | 952 | [6a] |

[a] t = terminal.

appears above 950 $cm^{-1}$ (Table 1). The appearance of ν(Mo=O) at 937 $cm^{-1}$ in **2** therefore indicates that the Mo(2) center is formally in the $Mo^{IV}$ state, which fixes the oxidation state of Mo(1) as +6.

## EPR Studies

The reaction leading to **2** involves the initial formation of an EPR-active $Mo^{V}$ species. This intermediate could not be identified in the case of 2-aminoethanthiol as rapid precipitation of yellow $[Mo^{VI}O_2(SCH_2CH_2NH_2)]$[14] from the reaction mixture took place with the formation of an equivalent amount of $[(Bu_4N)_2][Mo^{IV}O(mnt)_2]$.[14] Such a behavior can be explained by a disproportionation reaction where removal of the oxidized part of the product as a solid drives the reaction quickly to completion. In contrast, a similar reaction with 2-aminothiophenol led to the formation of an EPR-active $Mo^{V}$ signal (Figure 1) which was stable for hours, thereby indicating the inability of the complex formed to undergo a disproportionation reaction.

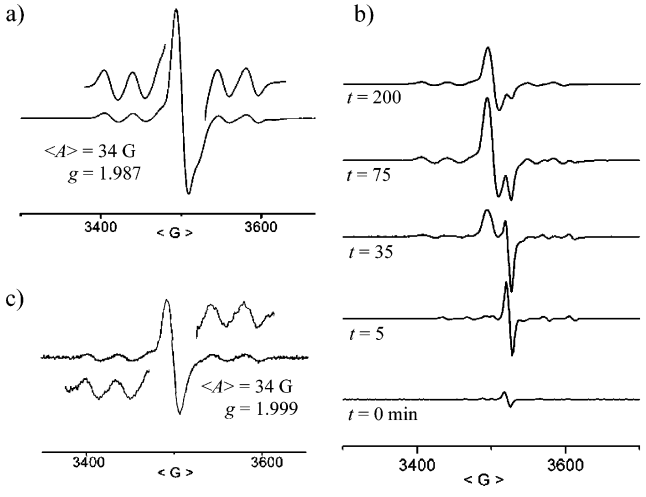


Figure 1. EPR spectra of the reaction of $(Bu_4N)_2[Mo^{V}{}_2O_4(mnt)_2]$ (**1**) with 2-aminothiophenol in acetonitrile at room temperature: a) at the initial stage (5 min), $<A>$ = 34 G, $g$ = 1.987; b) EPR signal at different time intervals showing the appearance of another EPR active species ($<A>$ = 34 G, $g$ = 1.999); c) after 24 h.

Attempts to isolate this species were unsuccessful and only the starting complex **1** was obtained. We were able to identify the formation of an intermediate $Mo^{V}$ species ($<g>$ = 1.987; Figure 1, a) in the initial stages of the reaction which was stable for a long time and only disappeared on heating the solution. This EPR signal is associated with another EPR $Mo^{V}$ signal ($<g>$ = 1.999; Figure 1), although this second signal remains even after the disappearance of the main EPR signal (Figure 1, c). The broad nature of the EPR signal (13 G) prevented us from identifying any superhyperfine interaction arising from nearby protons. Changing the reaction medium to a less polar solvent like dichloromethane did not help to reduce the line width. In the frozen state (liquid nitrogen), the EPR spectrum shows a tetragonally distorted line shape with ($A_{\parallel}$ = 45 G, $g_{\perp}$ = 1.990, $g_{\parallel}$ = 1.955, $g_{average}$ = 1.979; see electronic supporting information). For a square-planar-based Mo complex where the metal is coordinated to the sulfur atoms of mnt and the nitrogen of *o*-aminothiophenol, the fourth corner is presumably occupied by a hydroxido ligand, as shown in Scheme 3. The proton associated with this hydroxido group is positioned in such a way that it interacts with the unpaired electron of $Mo^{V}$ in the $d_{xy}$ orbital. Such super hyperfine splittings generally appear in the 2–7 G range for a $Mo^{V}$–OH interaction.[17a,17b] In the present case the broad nature of the EPR signal [component line width (peak separation) = 30 G] prevents us from identifying any H-related superhyperfine splitting. The retention of a weak $Mo^{V}$ signal at $<g>$ = 1.999 could be associated with the formation of a side product. This EPR signal also loses its intensity on prolonged standing and finally disappears.

A green tarry product, which is soluble in dichloromethane but not in benzene or toluene, was obtained from the mother liquor after removal of the solvent. This solubility difference suggests that the by-product does not contain a neutral complex with an $\{Mo(NS)_3\}$ core.[17] If this product were to contain a $Mo^{V}$ monomeric tris-chelated by-product like $[Mo^{V}(abt)_3]^{-}$ type complex[17] then the appearance of a more delocalized $<g>$ value near to 2 would be likely and the core of the complex would probably be $\{MoS_6\}$ or $\{Mo(NS)_3\}$, or a combination of these two.[17] Further characterization of this species is currently underway. It is important to note that **2** could only be isolated in good yield after refluxing the reaction mixture for 20 h; shorter reaction times led to the isolation of large amounts of unreacted **1**. These observations can be interpreted as follows. Complex **1** reacts initially with 2-aminothiophenol by opening the oxido-bridged dimeric structure, which results in the

 © 2007 Wiley-VCH Verlag GmbH & Co. KGaA, Weinheim 

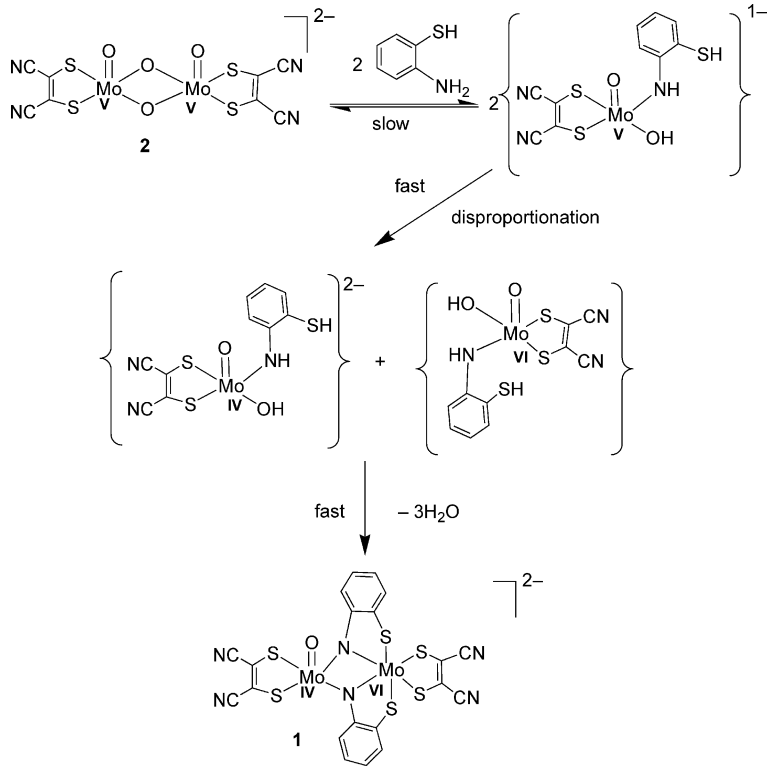


Scheme 3. Proposed mechanism for the formation of $(Bu_4N)_2[Mo^{IV}O(mnt)Mo^{VI}(mnt)\{o\text{-aminobenzothiolato}(3-)\text{-}N,S\}_2]$ (**2**) from the reaction of $(Bu_4N)_2[Mo^{V}_2O_4(mnt)_2]$ (**1**) with 2-aminothiophenol via an EPR-active intermediate species.

appearance of a $Mo^V$ signal and a complex with an $\{Mo^V(O)(S)_2(RNH)(OH)\}$ core, which disproportionates to $\{Mo^{IV}(O)(S)_2\}$ and $\{Mo^{VI}(O)(S)_2\}$ moieties upon heating (Scheme 3). These intermediates interact with the dangling SH groups that result from weak oxido coordination to $Mo^{VI}$. This leads to complete deprotonation of the $RNH^-$ groups (finally releasing three equivalents of $H_2O$), which becomes a bridging $RN^{2-}$ ($sp^2$-hybridized, isoelectronic to $O^{2-}$) ligand (Scheme 3).

The reaction of **1** with $HSCH_2CH_2NH_2$ in $CH_3CN$ initially gives a green solution, which turns orange upon precipitation of a yellow complex. This complex was identified as $[Mo^{VI}O_2(SCH_2CH_2NH_2)]$ by subsequent comparison with literature data[14] and its formation is accompanied by that of $[Bu_4N]_2[Mo^{IV}O(mnt)_2]$.[3c] Both complexes were isolated in a 1:1 ratio, thus confirming the disproportionation of EPR-active $Mo^V$ into $Mo^{IV}$ and $Mo^{VI}$ species. In this case the absence of a phenyl ring means that there is no π interaction, which may speed up the disproportionation reaction. The discrete monomeric intermediates further rearrange in a ligand-exchange reaction to yield $Mo^{IV}$ monoxido and $Mo^{VI}$ dioxido complexes.[3c]

## Structural Descriptions

The structure of **1** has been reported previously.[6a] An ORTEP view of the anion of **2** is shown in Figure 2 and selected bond lengths and angles are listed in Table 2. Compound **1** is a symmetrical dimeric $Mo^V$ complex in which each molybdenum center of the anion of **1** possesses a pentacoordinate square-pyramidal geometry where the basal plane contains two S donor atoms from one mnt ligand and two bridging oxido groups. One terminal oxido group in the axial position completes the square-pyramidal geometry. The Mo atoms lie around 0.73 Å above their respective basal planes (S1–S2–O3–O4 and S3–S4–O3–O4, Figure 2). The two Mo atoms are bonded by a metal–metal σ bond with a relatively short bond length of 2.582 Å. The average Mo–$O_t$ bond lengths are 1.68 Å and the two mnt ligands are nearly symmetrically bonded to two Mo atoms, with a mean Mo–S distance of 2.433 Å.

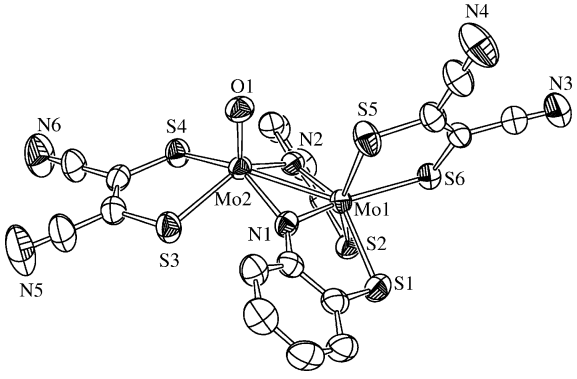


Figure 2. Crystal structure (ORTEP view with 50% thermal ellipsoids) showing the atom numbering scheme (except carbon atoms) for the anion of **2**. Hydrogen atoms have been omitted for clarity.

 © 2007 Wiley-VCH Verlag GmbH & Co. KGaA, Weinheim 

Table 2. Selected bond lengths and angles for the anion of $(Bu_4N)_2$-$[Mo^{IV}O(mnt)Mo^{VI}(mnt)\{o\text{-aminobenzothiolato}(3^-)\text{-}N,S\}_2]$ (**2**).

| | | | |
|---|---|---|---|
| Mo(1)–N(1) | 1.925(4) | Mo(2)–O(1) | 1.681(3) |
| Mo(1)–N(2) | 1.940(4) | Mo(2)–N(1) | 2.022(4) |
| Mo(1)–S(1) | 2.4379(16) | Mo(2)–N(2) | 2.008(4) |
| Mo(1)–S(2) | 2.4396(15) | Mo(2)–S(3) | 2.4170(18) |
| Mo(1)–S(5) | 2.4263(15) | Mo(2)–S(4) | 2.4310(14) |
| Mo(1)–S(6) | 2.4786(16) | Mo(1)–Mo(2) | 2.6854(11) |
| N(1)–C(8) | 1.386(6) | N(2)–C(6) | 1.396(6) |
| N(1)–Mo(1)–N(2) | 95.05(16) | N(1)–Mo(2)–N(2) | 90.06(15) |
| Mo(1)–N(1)–Mo(2) | 85.72(16) | Mo(1)–N(2)–Mo(2) | 85.70(16) |
| N(1)–Mo(1)–S(1) | 78.21(12) | N(2)–Mo(1)–S(1) | 149.40(11) |
| N(1)–Mo(1)–S(2) | 120.14(12) | N(2)–Mo(1)–S(2) | 77.63(12) |
| N(1)–Mo(1)–S(5) | 82.56(12) | N(2)–Mo(1)–S(5) | 106.27(12) |
| N(1)–Mo(1)–S(6) | 156.70(11) | N(2)–Mo(1)–S(6) | 105.25(12) |
| S(1)–Mo(1)–S(2) | 80.18(5) | S(2)–Mo(1)–S(6) | 76.20(5) |
| S(1)–Mo(1)–S(5) | 102.43(6) | S(2)–Mo(1)–S(5) | 156.92(5) |
| S(1)–Mo(1)–S(6) | 89.47(6) | S(5)–Mo(1)–S(6) | 80.88(5) |
| O(1)–Mo(2)–S(3) | 109.29(13) | O(1)–Mo(2)–S(4) | 104.33(12) |
| O(1)–Mo(2)–N(1) | 109.56(16) | O(1)–Mo(2)–N(2) | 110.26(16) |
| N(1)–Mo(2)–S(3) | 80.84(11) | N(2)–Mo(2)–S(4) | 140.21(11) |
| S(3)–Mo(2)–S(4) | 81.87(5) | O(1)–Mo(2)–Mo(1) | 109.01(12) |

Complex **2** is asymmetric (Figure 2). The asymmetric unit of **2** contains two tetrabutylammonium cations and one anionic dimeric Mo complex. Interestingly, the two Mo centers in **2** have different coordination environments: the first one is a desoxo [Mo(1)] moiety whereas the other [Mo(2)] is an oxidomolybdenum moiety. Mo(1) has a distorted octahedral geometry and is coordinated to three bidentate ligands, whereas Mo(2) has a square-pyramidal geometry with one terminal oxido group at its axial position. The basal plane ($N^1$–$N^2$–$S^3$–$S^4$) of this square pyramid contains two imido N atoms from an aminothiophenolato ligand and two S atoms from a dithiolene ligand. The Mo(2)–O distance is 1.681 Å. Two metal centers are bridged (denoted by br) by two $RN^{2-}$ (bent imido linkage, Scheme 1) units where each N is in a trigonal planar geometry ($sp^2$ hybridization) and the average $N_{br}$–$C_{C_6H_4SN}$ distance is 1.393 Å, which indicates a strong π delocalization of the Mo d electron throughout the benzene ring of the bridging ligand via the bridging N atom. The Mo(2)–$N_{br}$ distances (2.008 and 2.022 Å) are longer than the Mo(1)–$N_{br}$ distances (1.940 and 1.925 Å), which imposes an asymmetry in the bonding at the two metal centers. The choice of the XY coordinate plane for a distorted octahedral geometry or a basal plane for comparison with the basal plane of the Mo(2) center (square-pyramidal geometry) is very difficult for such an asymmetric molecule. However, we can consider that the $N_1$, $N_2$, $S_1$, and $S_6$ donor atoms contribute to the XY coordinate plane or basal plane in this octahedral geometry due to the metal–metal bond formation. The basal plane of Mo(1) ($N_1$–$N_2$–$S_1$–$S_6$) makes an angle 26.41° (Figure 3) with the basal plane (XY coordinate plane) of the Mo(2) center (mean plane of the N1, N2, S1, and S6 donor atoms), which is nearly a quarter of 90°. The Mo–Mo bond is somewhat longer (2.685 Å) than that for **1**. The metal–metal bond length in most bridged bimetallic system depends on the size of the bridging atoms and for N atoms it should be shorter than O atoms (Mo–Mo distance is 2.58 Å for **1**), although the reverse is observed here. This is probably due to the overlap of the corresponding σ- and π-bonding orbitals. The Mo–Mo bond lengths in a series of dithiolene-coordinated dimeric Mo complexes are listed in Table 3.

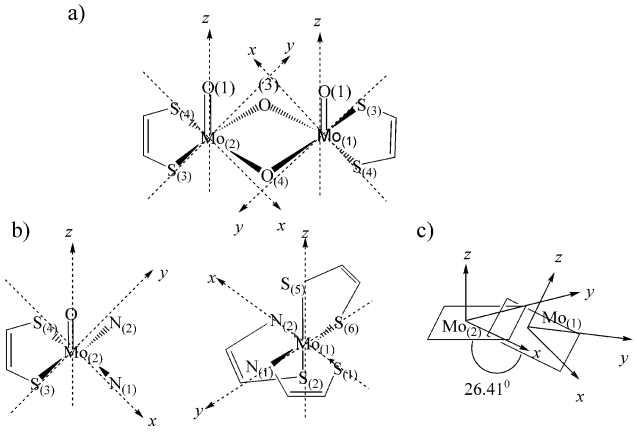


Figure 3. View of the basal plane containing the Mo center in $(Bu_4N)_2[Mo^V_2O_4(mnt)_2]$ (**1**) (a) and $(Bu_4N)_2[Mo^{IV}O(mnt)$-$Mo^{VI}(mnt)\{o\text{-aminobenzothiolato}(3\text{–})\text{-}N,S\}_2]$ (**2**; b and c).

Most dtc-coordinated diimido-bridged dimeric $Mo^V$ complexes with an $\{Mo^V_2O_2(\mu\text{-}NR)_2\}^{2+}$ core are structurally symmetrical[9] like **1**, whereas diimido-bridged dimeric $Mo^V$ complexes like $[Mo^VO(dtc)(\mu_2\text{-}NC_6H_4S)_2Mo^V(dtc)]$[10] are asymmetric. The desoxomolybdenum center in this compex is very close to trigonal prismatic whereas in **2** the

Table 3. Mo–Mo bond lengths of selected mnt-coordinated dimeric Mo complexes.

| Complex | Bridging atoms | Mo–Mo [Å] | Ref. |
|---|---|---|---|
| $[Bu_4N]_2[Mo^V_2O_4(mnt)_2]$ | O, O | 2.581 | [6a] |
| $[Bu_4N]_2[Mo^V_2O_2(mnt)_2(\mu\text{-}O)(\mu\text{-}SPh)(\mu\text{-}Br)]$ | O, $S_{SPh}$ | 2.670 | [6a] |
| $[Bu_4N]_2[Mo^V_2O_2(mnt)_2(\mu\text{-}O)(\mu\text{-}SPh)(\mu\text{-}CH_3SO_3)]$ | O, $S_{SPh}$ | 2.730 | [6a] |
| $[Bu_4N]_2[Mo^V_2O_2(mnt)_2(\mu\text{-}O)(\mu\text{-}SEt)(\mu\text{-}CH_3SO_3)]$ | O, $S_{SEt}$ | 2.731 | [6a] |
| $[Bu_4N][Mo^V_2O_2(mnt)_2(\mu_2\text{-}SPh)_2(\mu\text{-}OMe)]$ | $S_{SPh}$, $S_{SPh}$ | 2.856 | [6a] |
| $(Bu_4N)_2[Mo^{IV}O(mnt)Mo^{VI}$ (mnt)$\{o\text{-aminobenzothiolato}(3\text{–})\text{-}N,S\}_2]$ | $N_{C_6H_4S}$, $N_{C_6H_4S}$ | 2.685 | this work |
| $[Mo^V_2O(dtc)_2(\mu_2\text{-}N\text{-}C_6H_4S)_2]$ | $N_{C_6H_4S}$, $N_{C_6H_4S}$ | 2.659 | [10a] |
| $[Mo^V_2O_2(\mu_2\text{-}N\text{-}p\text{-tol})_2(dtc)_2]$ | N-*p*-tol, N-*p*-tol | 2.629 | [9] |
| $[Mo^V_2O_2(\mu_2\text{-}NPh)_2(dtc)_2]$ | NPh, NPh | 2.645 | [9] |
| $[Mo^V_2O_2(\mu_2\text{-}N\text{-}C_6H_4Me\text{-}o)_2(dtc)_2]$ | N-$C_6H_4$Me-*o*, N-$C_6H_4$Me-*o* | 2.633 | [9] |
| $[Mo^V_2O_2(N\text{-}C_6H_4Me\text{-}o)_2(\mu_2\text{-}N\text{-}C_6H_4Me\text{-}o)_2(dtc)_2]$ | N-$C_6H_4$Me-*o*, N-$C_6H_4$Me-*o* | 2.632 | [9] |
| $[Mo^V_2O(dtc)_3(\mu_2\text{-}NPh)_2][BF_4]$ | NPh, NPh | 2.654 | [9] |

 © 2007 Wiley-VCH Verlag GmbH & Co. KGaA, Weinheim 

same center adopts a distorted octahedral geometry. This difference is due to the small bite angle of the dtc ligand compared to mnt. The trigonal-prismatic distortion may have a different bonding scheme that does not affect the Mo–Mo bond length as much as in the corresponding symmetric systems. The average Mo–S bond lengths of all these complexes are very similar although the Mo–Mo bond length in **2** is slightly longer (Table 3) than in dtc-coordinated diimido-bridged dimeric $Mo^{V}$ complexes.

### Electronic Structure Calculations

The results of the IR and EPR studies and the difference in reactivity of **1** with 1,2-aminothiophenol and 1,2-aminoethanethiol strongly support that compound **2** may possess a mixed-valent $\{M_2\}$ unit. In view of the different nature of the two Mo centers in **2**, we decided to calculate the ground-state electronic structures of **1** and **2** at the DFT (B3LYP) level of theory to determine the energies and compositions of their molecular orbitals (MOs). In both cases the initial geometry was taken from the crystal structure and the geometry was optimized in the gas phase. Additional single-point calculations taking into account a solvent effect were also performed. Selected frontier molecular orbitals, together with their percentage contributions estimated from a Mulliken population analysis calculated in acetonitrile medium, are shown in Figure 4. The assignment of the type of each MO was made on the basis of its composition and by visual inspection of its localized orbital. The coordinate frames for both compounds were assigned by a visual inspection of the $d_{z^2}$ and $d_{xy}$ orbitals and this assignment was found to agree with previous assignments.[7,8] Because of the presence of two different coordinate frames in one molecule that differ from planarity, two additional single-point calculations were carried out using two different coordinate frames (as described in Figure 3) to calculate the percentage contribution of the atomic orbital to the MOs. A table comparing selected bond lengths obtained from the crystal structure and the gas-phase-optimized geometry is given as supporting information. The percentage contributions of the atomic orbitals to selected MOs for **1** and **2** are listed in Table 4.

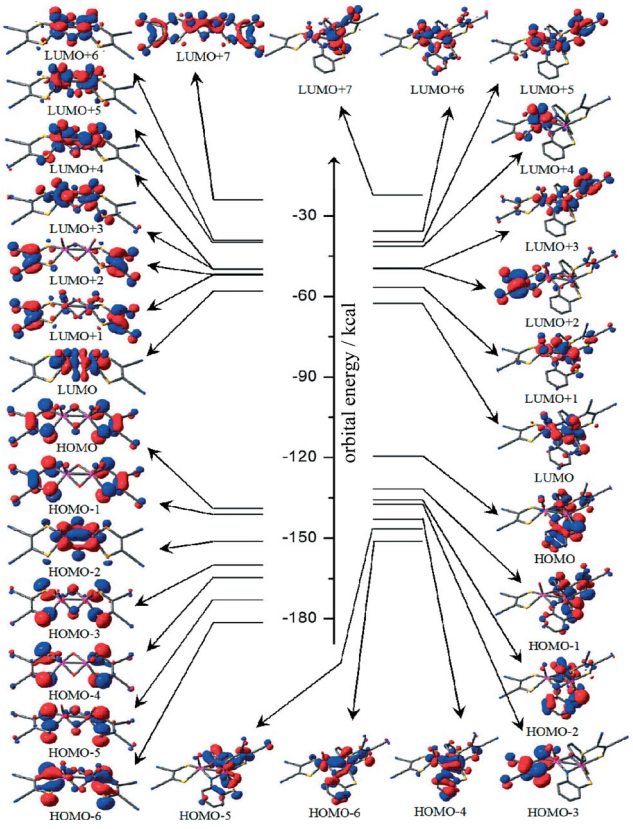


Figure 4. Pictorial representation of the molecular orbitals with levels energy (kcal mol$^{-1}$; seven highest-occupied and eight lowest-unoccupied) of $(Bu_4N)_2[Mo^{V}_2O_4(mnt)_2]$ (**1**) (left) and $(Bu_4N)_2$-$[Mo^{IV}O(mnt)Mo^{VI}(mnt)\{o\text{-aminobenzothiolato}(3-)\text{-}N,S\}_2]$ (**2**) (right) calculated in acetonitrile.

Figure 4 shows the frontier orbitals of **1** and **2** that control the electronic transitions and electrochemical behaviors of these complexes. The two highest molecular orbitals (HOMO and HOMO–1) for **1** have a large contribution

Table 4. Percentage contributions of atomic orbitals to selected molecular orbitals of $(Bu_4N)_2[Mo^{V}_2O_4(mnt)_2]$ (**1**) and $(Bu_4N)_2[Mo^{IV}O$-$(mnt)Mo^{VI}(mnt)\{o\text{-aminobenzothiolato}(3-)\text{-}N,S\}_2]$ (**2**), calculated in acetonitrile.

| MO | 1 | 2 |
|---|---|---|
| LUMO+7 | Ligand π* + metal $d_{z^2}$ | Ligand S π* |
| LUMO+6 | [33% $d_{yz}$ {Mo(1)} + 32% $d_{yz}$ {Mo(2)} + O] π | [33% $d_{xz}$ {Mo(1)} +29% $d_{xz}$ {Mo(2)}] π |
| LUMO+5 | [37% $d_{xz}$ {Mo(1)} + 38% $d_{xz}$ {Mo(2)} + O] π | [25% $d_{z^2}$ {Mo(2)} + ligand] π* |
| LUMO+4 | [36% $d_{yz}$ {Mo(1)} + 35% $d_{xz}$ {Mo(2)} + O] π | [56% $d_{yz}$ {Mo(2)} + Pz (O)] π* |
| LUMO+3 | [32% $d_{xy}$ {Mo(1)} + 32% $d_{xy}$ {Mo(2)} + O] π | [20% $d_{xy}$ {Mo(1)} + 12% $d_{xy}$ {Mo(2)}] σ* + ligand π |
| LUMO+2 | (N≡C–C=C–C≡N) π* of mnt | (N≡C–C=C–C≡N) π* of mnt |
| LUMO+1 | (N≡C–C=C–C≡N) π* of mnt | [38% $d_{xz}$ {Mo(1)} + 14% $d_{xy}$ {Mo(2)}] σ* + ligand π |
| LUMO | [32% $d_{xy}$ {Mo(1)} + 32% $d_{xy}$ {Mo(2)}] σ*+ O π* | [50% $d_{yz}$ {Mo(1)} + 9% $d_{xy}$ {Mo(2)}] σ* + ligand π |
| HOMO | (S–C=C–S) π* | Sπ of mnt and aminothiophenolate at Mo(1) |
| HOMO–1 | (S–C=C–S) π* | (S–C=C–S) π* of mnt + S π of aminothiophenolate at Mo(1) |
| HOMO–2 | [38% $d_{xy}$ {Mo(1)} + 38% $d_{xy}$ {Mo(2)}] σ + O π | (S–C=C–S) π* of mnt at Mo(2) |
| HOMO–3 | S π* mnt + O π* of bridge oxido | S π of aminothiophenolate at Mo(2) |
| HOMO–4 | S π* of mnt | [10% $d_{xy}$ {Mo(1)} + 6% $d_{xz}$ {Mo(1)} + 5% $d_{yz}$ {Mo(1)} + 18% $d_{xy}$ {Mo(2)}] σ |
| HOMO–5 | S π* of mnt | (S–C=C–S) π* of mnt + S π of aminothiophenolate + C=C π* at Mo(1) |
| HOMO–6 | S π* of mnt | (S–C=C–S) π* of mnt + S π of aminothiophenolate + C=C π* at Mo(1) |

 © 2007 Wiley-VCH Verlag GmbH & Co. KGaA, Weinheim 

from the π* antibonding orbital of the dithiolene ligands (mnt). The next lowest lying and deeply buried occupied orbital (HOMO–2) is formed from a σ-bonding interaction between the $d_{xy}$ orbitals of two Mo centers (each with 32%) and the O π orbital of the bridging oxygen atoms. HOMO–3 to HOMO–6 have only a π orbital contribution from the S atoms of two dithiolene ligands. The LUMO is formed from an antibonding interaction between the $d_{xy}$ orbitals of two Mo centers (38% each) and the O π orbitals of the bridging oxygen atoms. The next two highest energy virtual orbitals (LUMO+1 and LUMO+2) have contributions from the C–CN π antibonding orbital of mnt. The rest of the metal d orbitals involved in lateral π overlap are empty and in a high energy state. The Mo–Mo σ bond of most symmetric dimeric di-$\mu_2$-oxido $Mo^V$ ($d^1$ system) complexes is formed by the head-on overlap of the $d_{xy}$ orbitals of each Mo center. This is also the case for complex **1**, where the HOMO–2 and LUMO correspond to the σ bonding and antibonding molecular orbitals, respectively, and are formed by the usual overlap of two $d_{xy}$ orbitals from each metal center.

The situation for **2** is somewhat more complicated because of its unsymmetrical nature and the fact that the two metal centers have different geometries. These metals are bridged by an $RN^{2-}$ anion and hence should have different bonding. The HOMO, HOMO–1, and HOMO–2 are ligand (mnt and 2-aminothiophenolate) S π based orbitals, and a deeply buried HOMO–4 shows the bonding interaction between the two Mo centers, which originated from the overlap of the $d_{xy}$ orbital of Mo(2) (18%) and a mixture of three d orbitals ($d_{xy}$, $d_{xz}$, and $d_{yz}$) of Mo(1) (8%, 6%, and 5% respectively; Table 4). The total contribution of the metal d orbitals is 37%. The higher energy LUMO, LUMO+1, and LUMO+3 (Figure 4, Table 4) show antibonding interactions with Mo(2) ($d_{xy}$) and Mo(1) ($d_{xy}$, $d_{yz}$, and $d_{xz}$), whereas LUMO+2 has a maximum contribution from the N≡C–C=C–C≡N π* antibonding orbital. Based on the total metal contribution to HOMO–4 the extent of bonding for the σ bond is 37%, and based on the full contribution of the Mo(2) ($d_{xy}$) orbital (considering only a σ-bonding interaction between the two metal centers), the extent of σ-bonding overlap of the $d_{xy}$, $d_{yz}$, and $d_{xz}$ orbitals of Mo(1) is approximately 50, 25, and 25% respectively.

Cotton and co-workers[18] have established the formation of a maximum of four M–M bonds (σ, 2π, δ) for any $\{M_2\}$ unit where both the metal centers contribute atomic orbitals of the same symmetry to give maximum overlap and form a particular metal–metal bond, although the possible formation of five M–M bonds has also been reported recently.[19] The formation of an M→M′ dative bond with different orbitals ($Md_{z^2}$, $M'd_{x^2-y^2}$) in heterobimetallic systems involves the *xy*-coordination frame of the respective metal center as orthogonal to each other.[20] The complex $[Mo_2(O\textit{i}Pr)_4(dmpe)_2]$ is an interesting example with dissimilar coordination of two metal centers.[21] The strength of the multiple Mo–Mo bonds in this complex is maximum for a perfectly eclipsed configuration of the basal planes and tends to zero for a fully staggered configuration. This has been related to the extent of π and δ overlap, which is itself dependent on the twist angle.[22] However, the situation may differ for a σ bond when the angle between the basal planes of the two metal centers is about one quarter of 90°, as we observed for **2**. None of the five d orbitals of a metal center in the $\{M_2\}$ moiety can be transformed to another center by rotating the coordinate frame by an angle of one quarter of 90°. This deviation from planarity of the coordination framework of two metal centers will minimize the extent of overlap of their respective d orbitals. This deviation is 26.41° for complex **2**, which forbids a perfect σ overlap between the Mo(2) $d_{xy}$ and Mo(1) $d_{xy}$ orbitals. However, a partial symmetry is allowed for the overlap of Mo(2) ($d_{xy}$) and Mo(1) ($d_{xy}$, $d_{yz}$, $d_{xz}$) orbitals for a direct Mo–Mo interaction where the two bonding electrons come from $Mo(2)^{IV}$ (MO energy level diagram shown in Figure 3). The extent of bonding is only about 35% accounted for by σ donation from a metal d orbital, therefore the Mo–Mo distance is longer then expected (according to the size of the bridging atom). This bond also involves some degree of π interaction, as reflected by the Mo(1)–$N_{br}$ bond length being shorter than Mo(2)–$N_{br}$ and high delocalization of the metal centers with the ligand π orbitals throughout the molecule. Thus, the interaction of two asymmetric metal center fragments can be viewed as a donor–acceptor interaction where partial σ overlap between one donor and three acceptor orbitals (or a hybrid of three metal d orbitals) as well as a π (ligand) donor/acceptor interaction supplement the resulting bond; this explains the diamagnetism of **2**. Under such circumstances, it is difficult to assign the exact oxidation states of the two Mo centers in **2**, although assigning the formal oxidation state of Mo(1) center as +6 and the Mo(2) center as +4 is a good approximation that solves the problem of electron bookkeeping and supports the experimental results.

A population analysis (Mulliken and NBO) of the partial atomic charges for complexes **1** and **2** was carried out using the same method and basis set. The partial atomic charge distributions of selected atoms are listed in Table 5. The overall charge distribution is symmetric in **1** and asymmetric in **2**. The atomic charge distribution of the S atoms is nearly zero for both **1** and **2**, and the N and O atoms both

Table 5. Calculated gas-phase Mulliken and NBO atomic charges of the $\{Mo_2O_4S_6\}^{2-}$ core of **1** and the $\{Mo_2N_2S_6O\}^{2-}$ core of **2**.

| | **1** | | **2** | |
|---|---|---|---|---|
| Atom | Mulliken | NBO | Mulliken | NBO |
| Mo(1) | 0.62 | 1.14 | 0.13 | 0.35 |
| Mo(2) | 0.62 | 1.14 | 0.59 | 0.96 |
| S1 | 0.16 | –0.09 | 0.23 | –0.01 |
| S2 | 0.16 | –0.09 | 0.27 | 0.01 |
| S3 | 0.16 | –0.09 | 0.19 | 0.08 |
| S4 | 0.16 | –0.09 | 0.20 | 0.06 |
| S5 | – | – | 0.33 | 0.07 |
| S6 | – | – | 0.34 | 0.01 |
| O1 | –0.44 | –0.52 | –0.44 | –0.49 |
| O2 | –0.44 | –0.52 | – | – |
| N1/O3 | –0.62 | –0.72 | –0.86 | –0.58 |
| N2/O4 | –0.62 | –0.72 | –0.83 | –0.58 |

 © 2007 Wiley-VCH Verlag GmbH & Co. KGaA, Weinheim 

carry negative charges. The two Mo centers in **1** have the same positive atomic partial charges whereas the charge distribution at the two metal centers in **2** is unequal and is lower than **1** [Mulliken for **2** Mo(1): 0.13, Mo(2): 0.59; NBO Mo(1): 0.35, Mo(2): 0.96]. Although the formal oxidation state of Mo(2) is +4, which is less than that (+6) of Mo(1), the Mo(2) center has a greater positive charge. This may be due to the presence of a highly electron-withdrawing Mo=O moiety at Mo(2). Similarly, the presence of all-thiol ligation in Mo(1) clearly reflects the high delocalization of the ligand π orbitals, which reduces its positive atomic partial charge.

### Cyclic Voltammetry

The cyclic voltammograms (CVs) of **1** (Figure 5) and **2** (Figure 6) were recorded in a $10^{-3}$ M solution in acetonitrile at 298 K at a scan rate of 100 mV $s^{-1}$. The potential was measured using a glassy carbon electrode with Ag/AgCl as reference electrode with 0.1 M tetrabutylammonium perchlorate as supporting electrolyte. The CV of **1** shows one irreversible oxidation at 1.22 V and one quasi-reversible reduction at –1.56 V. The CV of **2** shows two irreversible ligand oxidations at 0.85 and 1.08 V and a fully reversible reduction at –1.16 V.

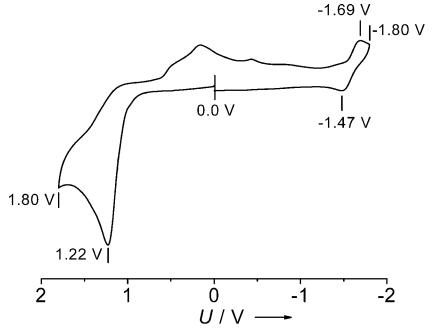


Figure 5. Cyclic voltammogram of $(Bu_4N)_2[Mo^V_2O_4(mnt)_2]$ (**1**) in acetonitrile. Scan rate: 100 mV $s^{-1}$, *U* stands for voltage.

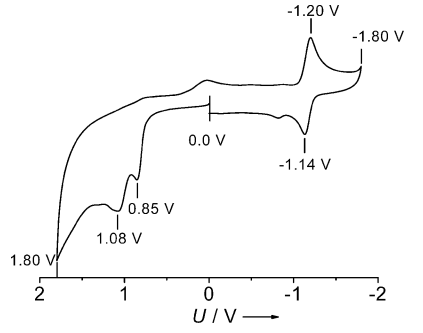


Figure 6. Cyclic voltammogram of $(Bu_4N)_2[Mo^{IV}O(mnt)$-$Mo^{VI}(mnt)\{o$-aminobenzothiolato(3–)-*N*,*S*$\}_2]$ (**2**) in acetonitrile. Scan rate: 100 mV $s^{-1}$, *U* stands for voltage.

The CV responses can easily be explained by the nature of the HOMOs and LUMOs. Thus, the irreversible oxidation of **1** is due to oxidation of the mnt ligand because the HOMO of **1** is a ligand S π* orbital of mnt. The two irreversible oxidations observed for **2** are associated with two types of ligand oxidation because the HOMO, as the potential electron donor, is predominately populated by the S π* orbitals of mnt and the 2-aminothiophenolato ligand. The quasi-reversible reduction of one of the $Mo^V$ centers is viewed as the population of an electron on the LUMO, which is formed by the antibonding interaction of two metal $d_{xy}$ orbitals. In the LUMO of **2** the Mo(2) $d_{xz}$ orbital is predominantly populated and a fully reversible reduction of $Mo^{VI}$ center is possible. This reversibility clearly indicates that the one-electron reduction of **2** does not significantly affect the Mo–Mo bond because of the high delocalization by σ donation and π acceptance through the bridging ligands between the two Mo centers of the respective fragments and also through the benzene rings of the bridging ligands. The one-electron reduction of **1** makes this system unstable because the addition of this electron to the σ* antibonding orbital reduces the bond order and directly affects the Mo–Mo bond. The less negative potential for reduction of the Mo center of **2** compared to **1** correlates nicely with the smaller HOMO–LUMO gap found for **2** by the DFT calculations.

### Optical Absorption Spectra

The electronic spectra of complexes **1** and **2** were recorded in acetonitrile. Complex **1** shows only one peak at 353 nm, whereas complex **2** shows two peaks at 338 and 439 nm in the UV region. Two other low energy bands observed for **2** in the visible region at around 580 and 648 nm, with almost equal intensity, are absent in **1**. The absorption spectra of **1** and **2** are shown in Figure 7. The metal-mnt complexes and the free $Na_2$mnt ligand show an absorption band at around 364 nm due to an intraligand charge-transfer transition. The electronic spectra of complexes **1** and **2** were also measured in other solvents with different polarities (dichloromethane and dmf; see electronic supporting information). No remarkable changes in the position of the maximum absorption wavelength ($\lambda_{max}$), the optical absorption coefficient, or the overall nature of the absorption spectra of **1** and **2** were observed on changing the solvent polarity.

TD-DFT calculations on **1**, **2**, and the free ligand $[\{S_2C_2(CN)_2\}^{2-}]$ were carried out at the G03/B3LYP level in the gas phase and with a solvent effect (COSMO) on the gas phase optimized geometry to assign the experimentally observed low-lying electronic transitions in the visible region. The time-dependent DFT approach (TD-DFT) is a rigorous method for calculating vertical electronic excitation spectra. The solvent dielectric constant and radius were considered as being those of acetonitrile. The free mnt ion is not soluble in acetonitrile and its experimental spectrum was therefore recorded in methanol, thus the solvent effect was calculated for the solvents acetonitrile and methanol. Singlet excited states were calculated based on the singlet ground-state geometry. The lowest 40 singlet excited states with oscillator strengths greater than 0.01 ($f > 0{:}01$)

 © 2007 Wiley-VCH Verlag GmbH & Co. KGaA, Weinheim 

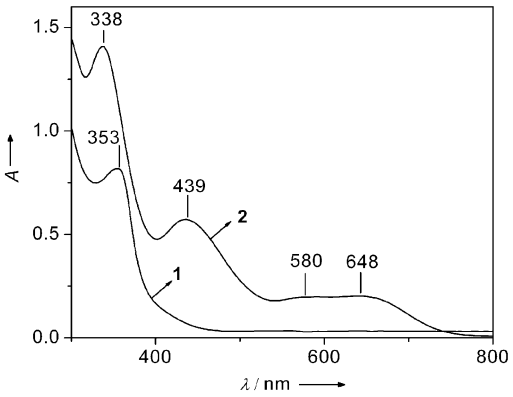


Figure 7. Electronic absorption spectrum of a $5 \times 10^{-5}$ M solution of $(Bu_4N)_2[Mo^V_2O_4(mnt)_2]$ (**1**) and $(Bu_4N)_2[Mo^{IV}O(mnt)Mo^{VI}(mnt)\{o\text{-aminobenzothiolato}(3-)\text{-}N,S\}_2]$ (**2**) in acetonitrile.

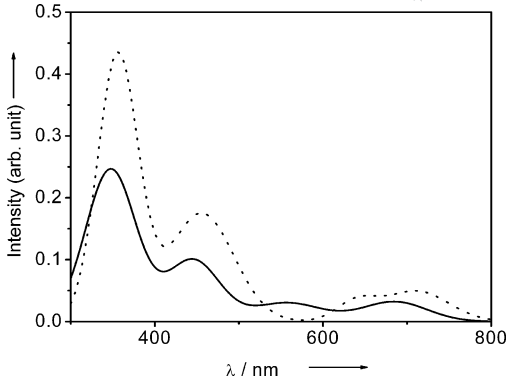


Figure 9. Computed absorption spectrum of $(Bu_4N)_2[Mo^{IV}O(mnt)\text{-}Mo^{VI}(mnt)\{o\text{-aminobenzothiolato}(3-)\text{-}N,S\}_2]$ (**2**) in the gas phase (solid line) and in acetonitrile (dotted line).

were considered for TD-DFT calculations, and the singlet excited states were fitted to Gaussian line shapes. The simulated CT spectra were prepared by fitting each excited state energy to a Gaussian curve with a full-width-at-half-maximum of 45 nm for complex **1** and 63 nm for complex **2**. A table containing the low-energy excitation wavelengths and oscillator strengths (OS) for compounds **1**, **2**, and the free ligand in the gas phase and in acetonitrile is provided as supporting information. The computed electronic spectra of **1** and **2** in the gas phase and in acetonitrile are shown in Figures 8 and 9 respectively. According to the TD-DFT calculations the free ligand mnt has only one absorption band in the visible region at around 427 nm in the gas phase and around 415 nm in both solvents. The calculated band in these three different media shows a blue shift with respect to the experimental value (approx. 364 nm) and this band is due to the intraligand charge transfer from S–C=C–S π* (HOMO) to NC–C=C–CN (LUMO) π*.

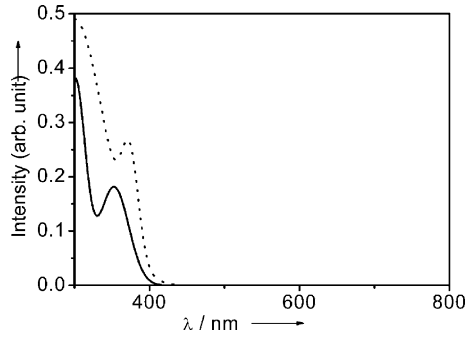


Figure 8. Computed absorption spectrum of $(Bu_4N)_2[Mo^V_2O_4(mnt)_2]$ (**1**) in the gas phase (solid line) and in acetonitrile (dotted line).

One intense charge-transfer band was found at 368 nm in the gas phase and at 370 nm in the solvent phase for complex **1**. The experimentally observed peak at 364 nm can be assigned as either a ligand S–C=C–S π* (HOMO) to ligand NC–C=C–CN (LUMO+3) internal charge-transfer transition or an intraligand charge-transfer transition. Another high energy charge-transfer band was computed in the lower UV region. This is responsible for the higher energy transition ($\lambda < 300$, experimentally observed) which is due to an MLCT transition from HOMO–2 to LUMO+6. Unfortunately, the solvent absorption prevented us from recording the experimental absorption spectrum in the region below 300 nm.

The single electron in the $d_{xy}$ ($Mo^V$) orbital, which is engaged in metal–metal bond formation, is deeply buried and does not take part in any electronic transition in the visible region, although it does appear in the very high energy region ($\lambda < 300$). The other empty d orbitals are highly destabilized by π interactions and this may be the reason why **1** does not show any MLCT or LMCT transition in the 300–1000-nm region.

The most intense absorption bands at 335 nm in the gas phase and 342 nm in the solvent phase for **2** match well with the experimentally observed absorption band at 338 nm. This can be assigned as the sum of major overlapping HOMO–2 to LUMO+5 and LUMO+6, HOMO–5 to LUMO+3, and HOMO–5 to LUMO+3 electronic transitions with ligand S π to metal d orbital charge transfer character (LMCT). The second LMCT band is at 429 nm in the gas phase and at 451 nm in the solvent phase in the visible region, which is compatible with the experimentally found absorption at 439 nm. There are also some slightly lower intensity transitions found within ±30 nm of the 439 nm band. The experimentally observed band at 439 nm can therefore be assigned as a multiple LMCT band originating from different types of ligand S π* antibonding orbital to metal antibonding d orbital transitions. Because of the multiple nature of the charge-transfer transitions appearing in a very close region, this absorption is broad in nature and its half width is larger than that of the peak at 338 nm. The two experimentally observed low energy and less intense peaks around 648 and 580 nm are broad in nature. The calculated absorption peaks found in this region at three different wavelengths (683, 617, and 549 nm) in the gas phase are shifted to 705, 636, and 554 nm, respectively, in the solvent phase and have almost the same intensity. These three peaks give rise to two absorptions at 683 and

 © 2007 Wiley-VCH Verlag GmbH & Co. KGaA, Weinheim 

at 558 nm in the gas phase and at 705 and at 563 nm in the solvent phase, respectively. Thus, the experimentally found peak at 580 nm is due to a charge-transfer transition from two different types of ligand S π* antibonding orbitals to metal antibonding d orbitals (HOMO to LUMO+1 and HOMO–1 to LUMO). The peak at 648 nm (experimental) can be assigned as a ligand S π orbital to metal antibonding d orbital (HOMO to LUMO) transition. The simulated spectra of **1** and **2** show a shift of the wavelength of some charge-transfer bands between the solvent model and the gas phase, although the experimental absorption spectra recorded in solvents with different polarities show no such shifts.

## Conclusions

Most known higher valent (+4, +5, and +6) dimeric Mo complexes are symmetrical with respect to the two molybdenum centers, therefore complex **2** is unique in that it features one oxido and one desoxo Mo moiety bridged by a common ligand that imparts a different coordination framework around each Mo center. Such structural asymmetry, the presence of an Mo–Mo bond between the two Mo centers, extended π delocalization throughout the molecule, the position of the $\nu_{(Mo=O)}$ absorption, and a detailed EPR study support the presence of a mixed-valent $\{Mo_2(RN)_2\}$ unit in **2**. The individual Mo centers [Mo(1) and Mo(2)] in **2** may have nearly +6 and +6 oxidation states. The redox chemistry observed in the CVs for both **1** and **2** has been correlated with the theoretical results, and the observed electronic absorption spectra have been analyzed by TD-DFT calculations. Analysis of the bonding by DFT calculations has shown a new bonding feature in the asymmetric dimeric complex **2**. The plausibility of a σ-type overlap involving one d orbital from one metal center and a hybrid orbital of three d orbitals from the other metal center in a dimeric molecule has been investigated in a situation where the deviation of the angle between the respective basal planes is around 26°. While checking such a possibility the overlap of one donor metal d orbital and three acceptor metal d orbitals to form a molybdenum–molybdenum bond is invoked. The possibility of influencing such bonding by changing the donor or the acceptor is currently being explored.

## Experimental Section

**Starting Materials and Physical Methods:** All reactions were carried out in air and under ambient conditions. $Bu_4NBr$, 2-aminothiophenol, and 2-aminoethanethiol were obtained from Aldrich and NaCN and ammonium heptamolybdate from S. D. Fine chemicals Ltd. India. $Na_2[S_2C_2(CN)_2]$ ($Na_2$mnt) was prepared according to a literature method.[12] Solvents and reagents were distilled and dried by standard procedures. IR spectra were recorded as CsI pellets with a Bruker Vertex 70 FT-IR spectrophotometer. Elemental analyses for carbon, hydrogen, nitrogen, and sulfur were obtained with a Perkin–Elmer 2400 microanalyser. Electronic spectra were recorded with a Cintra 10 UV/Vis spectrophotometer. Low-temperature (frozen state, 77 K) EPR spectra were recorded with a Varian E-109 (X-band) spectrometer in dual cavity mode and the EPR parameters were calculated from the measured spectra using DPPH ($g$ = 2.0023) as calibrant. Room-temperature solution spectra were recorded with a Bruker EMX X-band EPR spectrometer using DPPH ($g$ = 2.0023) as calibrant and the EPR parameters were calculated using the Bruker WINEPR system. Samples for room-temperature solution EPR spectra were prepared under argon and then transferred into a flat quartz cell fitted with a gas-tight septum. Cyclic voltammetric measurements were performed with a BASi Epsilon-EC Bioanalytical systems, Inc. instrument. Cyclic voltammograms of $10^{-3}$ M acetonitrile solutions of the compounds were recorded with a glassy carbon working electrode and 0.1 M $Bu_4NClO_4$ as supporting electrolyte; all experiments employed an Ag/AgCl reference electrode and platinum auxiliary electrode. All electrochemical experiments were performed under argon at 298 K.

**Synthesis of $(Bu_4N)_2[Mo^{IV}O(mnt)Mo^{VI}(mnt)\{o$-aminobenzothiolato-(3–)-*N*,*S*$\}_2]$ (2):** $(Bu_4N)_2[Mo_2O_4(mnt)_2]$ (1020 mg, 1 mmol) was dissolved in 15 mL of dry acetonitrile and 2-aminothiophenol (2 mL, 2 mmol) was added dropwise with constant stirring, whereupon the color of the solution changed from yellow to bright green. The mixture was refluxed for 6–8 h, after which time the color of the solution had changed to dark green. The reaction mixture was cooled to room temperature. A microcrystalline product was isolated directly from this solution upon addition of 2-propanol and diethyl ether (840.0 mg 69%). The compound was recrystallized from acetonitrile, 2-propanol and diethyl ether. $C_{52}H_{80}Mo_2N_8OS_6$ (1217.54): calcd. C 51.53, H, 6.58, N 9.21, S, 15.78; found C 51.48, H 6.82, N 9.35, S 15.75. FT-IR (CsI): $\tilde{\nu}$ = 939 $cm^{-1}$ (vs, Mo=O). UV/Vis: $\lambda_{CH_2Cl_2}$ ($\varepsilon$) = 338 nm (22659 $M^{-1}cm^{-1}$), 439 (10819), 586 (3713), 645 (3796).

**Reaction of $(Bu_4N)_2[Mo_2O_4(mnt)_2]$ with $HSCH_2CH_2NH_2$:** $(Bu_4N)_2[Mo_2O_4(mnt)_2]$ (1020 mg, 1 mmol) was dissolved in 15 mL of dry acetonitrile then a solution of 2-aminoethanethiol (0.16 g, 2 mmol) in 5 mL of methanol was added with constant starring, whereupon the color of the solution changed from yellow to dark orange and finally to brownish green with precipitation of an orange solid. The reaction mixture was allowed to stand for a few hours to complete the precipitation and was then filtered. The filtrate was washed with 2-propanol and finally with diethyl ether and dried under vacuum (A; 408 mg, 46%). Addition of 2-propanol and diethyl ether to the filtrate resulted in the precipitation a dark-green crystalline product, which was washed with 2-propanol and diethyl ether and dried under vacuum (B; 134 mg, 48%).

**Analysis for A:** The analytical and spectrochemical data were identical to those for $[Bu_4N]_2[Mo^{IV}O(mnt)_2]$.[3c]

**Analysis for B:** The analytical and spectrochemical data were identical to those for $[Mo^{VI}O_2(SCH_2CH_2NH_2)]$.[14]

**X-ray Structure Determination:** Suitable crystals of $(Bu_4N)_2[Mo^{IV}O(mnt)Mo^{VI}(mnt)\{o$-aminobenzothiolato(3–)-*N*,*S*$\}_2]$ (**2**) were obtained from the crystallization procedures described in the synthesis. A single crystal of **2** was glued to a glass fiber and mounted on a Bruker Smart Apex diffractometer equipped with a CCD area detector and data were collected using graphite-monochromated Mo-$K_\alpha$ radiation ($\lambda$ = 0.71069 Å) at low temperature (100 K). An empirical absorption correction was applied using the SADABS program. Cell constants were obtained from the least-squares refinement of three-dimensional centroids by recording narrow $\omega$ rotation frames until completion of almost all reciprocal space in the stated $\theta$ range. The data were collected with SMART 5.628 (Bruker, 2003), and were integrated with the Bruker SAINT

 © 2007 Wiley-VCH Verlag GmbH & Co. KGaA, Weinheim 

program. A total of 20591 reflections were collected ($\theta$ = 1.91 to 28.41°), of which 14704 reflections were unique {$R_{int}$ = 0.0320 [$I > 2\sigma(I)$]}. The space group of this compound was determined based on the lack of systematic absences and intensity statistics. The structure was solved using SIR97[23] and refined using SHELXL-97[24] in the space group $P\bar{1}$. Full-matrix least-squares/difference Fourier cycles were performed to locate the remaining non-hydrogen atoms. All non-hydrogen atoms were refined with anisotropic displacement parameters. The final $R$ factor was 6.81% ($wR2$ = 13.30%). Some of carbon atoms of the butyl group of one of the tetrabutylammonium cation were found to be disordered over two positions and were refined with the free part instruction using SHELXL-97. The crystal structure was produced with ORTEP.[25] Selected crystallographic data parameters for **2** are listed in Table 6.

Table 6. Crystallographic data parameters of $(Bu_4N)_2[Mo^{IV}O(mnt)Mo^{VI}(mnt)\{o\text{-aminobenzothiolato}(3-)\text{-}N,S\}_2]$ (**2**).

| | |
|---|---|
| Empirical formula | $C_{52}H_{80}Mo_2N_8OS_6$ |
| Formula weight | 1217.54 |
| Crystal system | triclinic |
| Space group | $P\bar{1}$ |
| Temperature [K] | 100 |
| $Z$ | 2 |
| $a$ [Å] | 11.258(5) |
| $b$ [Å] | 12.616(5) |
| $c$ [Å] | 22.559(5) |
| $\alpha$ [°] | 85.984(5) |
| $\beta$ [°] | 76.962(5) |
| $\gamma$ [°] | 80.766 |
| $V$ [Å$^3$] | 3079(2) |
| $D_{calcd}$ [Mg m$^{-3}$] | 1.313 |
| $F(000)$ | 1272 |
| Absorption [mm$^{-1}$] | 0.651 |
| Theta range [°] | 1.9–28.41 |
| Reflections collected | 20591 |
| Reflections unique | 14704 |
| GOF ($F^2$) | 0.993 |
| $R_1$[a] ($wR_2$[b]) | 0.068 (0.1330) |

[a] $R_1 = \Sigma||F_o| - |F_c||/\Sigma|F_o|$. [b] $wR_2 = \{\Sigma[w(F_o^2 - F_c^2)^2]/\Sigma[w(F_o^2)^2]\}^{1/2}$.

CCDC-274974 (for **2**) contains the supplementary crystallographic data for this paper. These data can be obtained free of charge from The Cambridge Crystallographic Data Center via www.ccdc.cam.ac.uk/data_request/cif.

**Computational Details:** All calculations were performed with the Gaussian 03 package (revision B.04).[26] Molecular orbitals were visualized using Gauss View. Geometry optimizations, single point calculations, and population analysis of the molecular orbitals were carried out at the density functional theory (DFT) level with Becke's three-parameter hybrid exchange functional,[27] the non-local correlation provided by the Lee, Yang, and Parr expression, and the Vosko, Wilk, and Nuair 1980 correlation functional (III) local (B3LYP) 6-31g*+ basis set[28] were used for H, C, N, O, and S atoms. The LANL2DZ[29] basis set and LANL2 pseudo-potentials of Hay and Wadt[30] were used for the Mo atom. The initial geometry of the anions of **1** and **2** were taken from the crystal structure[6a] and each geometry was optimized without any symmetry constraints. The initial geometry of the $[S_2C_2(CN)_2]^{2-}$ ($mnt^{2-}$) was modeled using the same geometrical parameters as in the Mo complex. The optimized minima were characterized by harmonic vibration frequency calculations where minima have no imaginary frequency. For the medium effect, additional single-point energy calculations and time-dependent DFT (TD-DFT) calculations were carried out on the gas phase optimized geometries with the same method, same basis set, and the conductor like screening model[31] (COSMO). The solvent chosen was acetonitrile. The lowest 40 singlet excited states were considered for TD-DFT calculations.

**Supporting Information** (see also the footnote on the first page of this article): Table showing a comparison of selected bond lengths obtained from the crystal structure and gas-phase optimized geometry; experimental and computed UV/Vis absorption spectra; the HOMO and LUMO of $[S_2C_2(CN)_2]^{2-}$; a table containing low-energy excitation wavelengths and oscillator strengths (OS) for **1**, **2** and $[S_2C_2(CN)_2]^{2-}$; and EPR spectra.

## Acknowledgments

Thanks are due to Council of Scientific and Industrial Research (CSIR) for providing a doctoral fellowship (to K. P.) and to the Department of Science and Technology (DST), New Delhi for funding.

[1] a) K. V. Rajagopalan, in *Molybdenum and Molybdenum-Containing Enzymes*, 1st ed. (Ed.: M. P. Coughlan), Pergamon Press, Oxford, **1980**; b) R. S. Pilato, E. I. Stiefel, in *Bioinorganic Catalysis*, 2nd ed. (Eds.: J. Reedijk, E. Bouwman), Marcel Dekker, New York, **1999**, pp. 81–152; c) M. Dixon, E. C. Webb, C. J. R. Throne, K. F. Tipton, *Enzymes*, 3rd ed., Academic Press, New York, **1979**.

[2] E. I. Stiefel, *Dithiolene Chemistry*, in *Progress in Inorganic Chemistry* (Ed.: K. D. Karlin), John Wiley & Sons, New York, **2004**, vol. 52.

[3] a) E. I. Stiefel, *Prog. Inorg. Chem.* **1977**, *22*, 1–223; b) E. I. Stiefel, *Molybdenum(VI)*, in *Comprehensive Coordination Chemistry* (Eds.: G. Wilkinson, R. D. Gillard, J. A. McCleverty), Pergamon, Oxford, **1987**, pp. 1375–1420; c) C. G. Young, *Molybdenum*, in *Comprehensive Coordination Chemistry II* (Eds.: J. A. McCleverty, T. J. Meyer, A. G. Wedd), Pergamon, Oxford, pp. 444–445; d) S. K. Das, P. K. Chaudhury, D. Biswas, S. Sarkar, *J. Am. Chem. Soc.* **1994**, *116*, 9061; e) B. S. Lim, M. W. Willer, M. Miao, R. H. Holm, *J. Am. Chem. Soc.* **2001**, *123*, 8343; f) N. Ueyama, H. Oku, M. Kondo, T. A. Okamura, N. Yoshinaga, A. Nakamura, *Inorg. Chem.* **1996**, *35*, 643; g) J. P. Donahue, C. R. Goldsmith, U. Nadiminti, R. H. Holm, *J. Am. Chem. Soc.* **1998**, *120*, 12869.

[4] a) C. D. Garner, J. M. Charnock, *Molybdenum(IV)*, in *Comprehensive Coordination Chemistry* (Eds.: G. Wilkinson, R. D. Gillard, J. A. McCleverty), Pergamon, Oxford, **1987**, pp. 1329–1374; b) C. G. Young, *Molybdenum*, in *Comprehensive Coordination Chemistry II* (Eds.: J. A. McCleverty, T. J. Meyer, A. G. Wedd), Pergamon, Oxford, **1987**, pp. 470–471; c) J. H. Enemark, J. A. J. Cooney, J.-J. Wang, R. H. Holm, *Chem. Rev.* **2004**, *104*, 1175–1200; d) H. Sugimoto, K. Sieren, H. Tsukube, K. Tanaka, *Eur. J. Inorg. Chem.* **2003**, *14*, 2633–2638.

[5] a) C. D. Garner, J. M. Charnock, *Molybdenum(III), (IV), and (V)*, in *Comprehensive Coordination Chemistry II* (Eds.: G. Wilkinson, R. D. Gillard, J. A. McCleverty), Pergamon, Oxford, **1987**, pp. 1329–1374; b) D. Coucouvanis, *Adv. Inorg. Chem.* **1998**, *45*, 1–73; c) C. G. Young, I. P. McInerney, M. A. Bruck, J. H. Enemark, *Inorg. Chem.* **1990**, *29*, 412–416; d) K. Nagrajan, H. K. Joshi, P. K. Chaudhuri, K. Pal, J. A. Cooney, J. H. Enemark, S. Sarkar, *Inorg. Chem.* **2004**, *43*, 4532–4533; e) A. Majumdar, K. Pal, S. Sarkar, *J. Am. Chem. Soc.* **2006**, *128*, 4196–4197; f) B. S. Lim, R. H. Holm, *J. Am. Chem. Soc.* **2001**, *123*, 1920–1930; g) K.-M. Sung, R. H. Holm, *J. Am. Chem. Soc.* **2001**, *123*, 1931–1943; h) B. S. Lim, J. P. Donahue, R. H. Holm, *Inorg. Chem.* **2000**, *39*, 263–273; i) B. S. Lim, K.-M. Sung, R. H. Holm, *J. Am. Chem. Soc.* **2000**, *122*, 7410–7411; j) J. Jiang, R. H. Holm, *Inorg. Chem.* **2004**, *43*, 1302–1310; k) K.-M. Sung, R. H. Holm, *Inorg. Chem.* **2000**, *39*, 1275–1281.

 © 2007 Wiley-VCH Verlag GmbH & Co. KGaA, Weinheim 

[6] a) K. Pal, R. Maiti, P. K. Chaudhury, S. Sarkar, *Inorg. Chim. Acta* **2007**, *360*, 2721–2733; b) L. Richard, C. Martin, R. Wiest, *Inorg. Chem.* **1975**, *14*, 2300; c) F. A. Cotton, W. H. Ilsley, *Inorg. Chim. Acta* **1982**, *59*, 213; d) M. G. B. Drew, A. Kay, *J. Chem. Soc. A* **1971**, *89*, 1846; e) V. R. Ott, D. S. Swieter, F. A. Schultz, *Inorg. Chem.* **1977**, *16*, 2538; f) F. A. Schultz, V. R. Ott, D. S. Rolison, D. C. Bravard, J. W. McDonald, W. E. Newton, *Inorg. Chem.* **1978**, *17*, 1758.
[7] a) F. A. Cotton, *Inorg. Chem.* **1965**, *4*, 334; b) F. A. Cotton, *J. Less Common Met.* **1977**, *54*, 3.
[8] A. B. Blake, F. A. Cotton, J. S. Wood, *J. Am. Chem. Soc.* **1964**, *86*, 3024.
[9] T. A. Coffey, G. D. Forster, G. Hogarth, *J. Chem. Soc. Dalton Trans.* **1995**, 2337.
[10] a) M. Minelli, R. L. Kuhlman, S. J. Shaffer, M. Y. Chiang, *Inorg. Chem.* **1992**, *31*, 3891; b) M. Minelli, M. R. Carson, D. W. Whisenhunt, J. L. Hubbard Jr, *Inorg. Chem.* **1990**, *29*, 442; c) M. Minelli, M. R. Carson, D. W. Whisenhunt, W. Imhof Jr, G. Huttner, *Inorg. Chem.* **1990**, *29*, 4801.
[11] a) E. A. Maatta, B. L. Haymore, R. A. D. Wentworth, *Inorg. Chem.* **1980**, *19*, 1055; b) L. O. Atovmyan, V. V. Tkachen, S. A. Shchepinov, *Sov. J. Coord. Chem. (Engl. Transl.)* **1978**, *4*, 460; c) K. L. Wall, K. Folting, J. C. Huffman, R. A. D. Wentworth, *Inorg. Chem.* **1983**, *22*, 1756.
[12] a) G. Bahr, B. Schleltzer, *Chem. Ber.* **1955**, *88*, 1771; b) G. Bahr, *Angew. Chem.* **1956**, *68*, 525; c) E. I. Stiefel, L. E. Bennett, Z. Dori, T. H. Crawford, C. Simo, H. B. Gray, *Inorg. Chem.* **1970**, *9*, 281; d) A. Davison, R. H. Holm, *Inorg. Synth.* **1967**, *10*, 8.
[13] a) L. G. Howell, I. Fridovich, *J. Biol. Chem.* **1968**, *243*, 5941–5947; b) D. L. Kessler, K. V. Rajagopalan, *J. Biol. Chem.* **1972**, *247*, 6566–6573; c) D. L. Kessler, K. V. Rajagopalan, *Biochim. Biophys. Acta* **1974**, *370*, 399–409; d) J. L. Johnson, K. V. Rajagopalan, *J. Clin. Invest.* **1978**, *58*, 543–550; e) S. P. Kramer, J. L. Johnson, A. A. Ribeiro, D. S. Mullington, K. V. Rajagopalan, *J. Biol. Chem.* **1987**, *262*, 16357; f) G. N. George, I. J. Pickering, C. Kisker, *Inorg. Chem.* **1999**, *38*, 2539–2540; g) C. Kisker, H. Schindelin, A. Pacheco, W. A. Wehbi, R. M. Garrett, K. V. Rajagopalan, J. H. Enemark, D. C. Rees, *Cell* **1997**, *91*, 973–983; h) H. K. Joshi, J. A. Cooney, F. E. Inscore, N. E. D. Gruhn, L. Lichtenberger, J. H. Enemark, *Proc. Natl. Acad. Sci. USA* **2003**, *100*, 3719–3724.
[14] A. Kay, P. C. H. Mitchell, *J. Chem. Soc. A* **1970**, 2421–2428.
[15] P. K. Chaudhury, K. Nagarajan, A. Kumar, R. Maiti, S. K. Das, S. Sarkar, *Indian J. Chem. Sect. A* **2003**, *42*, 2223.
[16] C. G. Young, *Molybdenum*, in *Comprehensive Coordination Chemistry II* (Eds.: J. A. McCleverty, T. J. Meyer, A. G. Wedd), Pergamon, Oxford, pp. 461.
[17] a) E. I. Stiefel, in *Molybdenum and Molybdenum-Containing Enzymes*, 1st ed. (Ed.: M. P. Coughlan), Pergamon Press, Oxford, **1980**, pp. 80–64; b) Book of Abstracts, *Second International Conference on the Chemistry and Uses of Molybdenum*, New Collage, Oxford, England, 30 Aug.–03 Sept., **1976**, pp. 265–269; c) K. Yamanouchi, J. H. Enmark, *Inorg. Chem.* **1978**, *17*, 2911–2917; d) J. K. Garner, N. Pariyadath, J. L. Corbin, E. I. Stiefel, *Inorg. Chem.* **1978**, *17*, 897–904.
[18] a) F. A. Cotton, *J. Chem. Educ.* **1983**, *60*, 713–720; b) F. A. Cotton, *Chem. Soc. Rev.* **1975**, *4*, 27; c) F. A. Cotton, *Acc. Chem. Res.* **1978**, *11*, 225; d) F. A. Cotton, S. M. Morehouse, *Inorg. Chem.* **1965**, *4*, 1377–1381; e) F. A. Cotton, R. A. Walton, *Multiple Bonds between Metal Atoms*, 2nd ed., Clarendon Press, Oxford, **1993**; f) F. A. Cotton, G. Wilkinson, C. A. Murillo, M. Bochmann, *Advanced Inorganic Chemistry*, 6th ed., John Wiley & Sons, **1999**.
[19] a) L. Gagliardi, B. O. Roos, *Nature* **2005**, *433*, 845–851; b) T. Nguyen, A. D. Sutton, M. Brynda, J. C. Fettinger, G. J. Long, P. P. Power, *Science* **2005**, *310*, 844–847.
[20] a) T. Yamaguchi, F. Yamazaki, T. Ito, *J. Am. Chem. Soc.* **2001**, *123*, 734–744; b) C. Mealli, F. Pichierri, L. Randaccio, E. Zangrando, M. Krumm, D. Holtenrich, B. Lippert, *Inorg. Chem.* **1995**, *34*, 3418–3424.
[21] a) M. H. Chisholm, J. C. Huffman, G. William, *J. Am. Chem. Soc.* **1987**, *109*, 2514–2515; b) B. E. Bursten, W. F. Schneider, *Inorg. Chem.* **1989**, *28*, 3293–3296; c) M. H. Chisholm, J. C. Huffman, R. J. Tatz, *J. Am. Chem. Soc.* **1984**, *106*, 5385–5386.
[22] a) F. A. Cotton, P. E. Fanwick, J. W. Fitch, H. D. Glicksman, R. A. Walton, *J. Am. Chem. Soc.* **1979**, *101*, 1752–1757; b) S. A. Best, T. J. Smith, R. A. Walton, *Inorg. Chem.* **1978**, *17*, 99–104.
[23] A. Altomare, M. C. Burla, M. Camalli, G. L. Cascarano, C. Giacovazzo, A. Guagliardi, A. G. G. Moliterni, G. Polidori, R. Spagna, *J. Appl. Crystallogr.* **1999**, *32*, 115–119.
[24] G. M. Sheldrick, *SHELX97: A Program for Crystal Structure Analysis* (release 97-2), University of Göttingen, Germany, **1997**.
[25] L. J. Farrugia, *J. Appl. Crystallogr.* **1997**, *30*, 565.
[26] *Gaussian 03*, Revision B.05, M. J. Frisch, G. W. Trucks, H. B. Schlegel, G. E. Scuseria, M. A. Robb, J. R. Cheeseman, J. A. Montgomery Jr, T. Vreven, K. N. Kudin, J. C. Burant, J. M. Millam, S. S. Iyengar, J. Tomasi, V. Barone, B. Mennucci, M. Cossi, G. Scalmani, N. Rega, G. A. Petersson, H. Nakatsuji, M. Hada, M. Ehara, K. Toyota, R. Fukuda, J. Hasegawa, M. Ishida, T. Nakajima, Y. Honda, O. Kitao, H. Nakai, M. Klene, X. Li, J. E. Knox, H. P. Hratchian, J. B. Cross, C. Adamo, J. Jaramillo, R. Gomperts, R. E. Stratmann, O. Yazyev, A. J. Austin, R. Cammi, C. Pomelli, J. W. Ochterski, P. Y. Ayala, K. Morokuma, G. A. Voth, P. Salvador, J. J. Dannenberg, V. G. Zakrzewski, S. Dapprich, A. D. Daniels, M. C. Strain, O. Farkas, D. K. Malick, A. D. Rabuck, K. Raghavachari, J. B. Foresman, J. V. Ortiz, Q. Cui, A. G. Baboul, S. Clifford, J. Cioslowski, B. B. Stefanov, G. Liu, A. Liashenko, P. Piskorz, I. Komaromi, R. L. Martin, D. J. Fox, T. Keith, M. A. Al-Laham, C. Y. Peng, A. Nanayakkara, M. Challacombe, P. M. W. Gill, B. Johnson, W. Chen, M. W. Wong, C. Gonzalez, J. A. Pople, Gaussian, Inc., Pittsburgh PA, **2003**.
[27] a) A. D. Becke, *J. Chem. Phys.* **1993**, *98*, 5648; b) C. Lee, W. Yang, R. G. Par, *Phys. Rev. B* **1988**, *37*, 785.
[28] G. A. Patersson, M. A. Al-Laham, *J. Chem. Phys.* **1991**, *94*, 6081.
[29] P. J. Hay, W. R. Wadt, *J. Chem. Phys.* **1985**, *82*, 299.
[30] a) P. J. Hey, W. R. Wadt, *J. Chem. Phys.* **1985**, *82*, 270–283; b) W. R. Wadt, P. J. Hey, *J. Chem. Phys.* **1985**, *82*, 284–298.
[31] a) P. E. Smith, R. M. Brunne, A. E. Mark, W. F. Gunsteren, *J. Phys. Chem.* **1993**, *97*, 2009–2014; b) G. Löffler, H. Schreiber, O. Steinhauser, *J. Mol. Biol.* **1997**, *270*, 520–534; c) F. Ogliaro, S. P. de Visser, S. Cohen, P. K. Sharma, S. Shaik, *J. Am. Chem. Soc.* **2002**, *124*, 2806–2814.

Received: June 17, 2007
Published Online: October 9, 2007

 © 2007 Wiley-VCH Verlag GmbH & Co. KGaA, Weinheim 

DOI: 10.1002/ejic.200700631

# Benzylideneruthenium Complexes Bearing Pyridine-Based Ligands and Their Influence on the Formation of Mono- or Bis(pyridine) Complexes

**Wen-Zhen Zhang,[a] Ren He,*[a] and Rong Zhang[a]**

**Keywords:** Metathesis / Ruthenium / N ligands / Ligand effects / Homogeneous catalysis

Benzylideneruthenium complexes bearing the N-heterocyclic carbene (NHC) ligand 1,3-bis(2,6-dimethylphenyl)-4,5-dihydroimidazol-2-ylidene ($H_2$IMe) and one or two pyridine-based ligands have been prepared by treating [$RuCl_2$(=CHPh)($H_2$IMe)($PPh_3$)] with the corresponding pyridine derivative. X-ray crystallographic and mass spectrometric evidence is used to investigate the interconversion between mono- and bis(pyridine) complexes and the influence of the pyridine ligand on the formation of these complexes. The catalytic activity of these complexes has been tested in the ring-closing metathesis (RCM) reaction of diallylmalononitrile and the cross metathesis (CM) reaction of acrylonitrile with terminal olefins.

(© Wiley-VCH Verlag GmbH & Co. KGaA, 69451 Weinheim, Germany, 2007)

## Introduction

Alkylideneruthenium complexes, which exhibit remarkable air and water stability and significant functional-group tolerance, have been applied extensively as efficient metathesis catalysts in organic synthesis and polymer chemistry.[1] In particular, the second-generation Grubbs catalyst,[2] which contains a saturated NHC ligand instead of one of the $PCy_3$ ligands of the first-generation Grubbs catalyst,[3] exhibits a dramatically enhanced catalytic activity.[4] Further substitution of the $PCy_3$ ligand in the second-generation Grubbs catalyst with pyridine or 3-bromopyridine has resulted in the successful development of fast-initiating catalysts **I**[5] and **II**[6] (Figure 1). The alkylidene complex **IV**, analogous to complex **II**, is also a fast initiator of olefin metathesis.[7]

With regard to catalysts **I**–**IV**, bis(pyridine) complexes are considered to be formed preferentially to mono(pyridine) complexes. The solid-state structures of bis(pyridine) complexes **I** and **IV** have been confirmed by X-ray crystallography, although Grubbs has also observed that the mono(pyridine) complex [$RuCl_2$(=CHPh)($H_2$IMes)($C_5H_5N$)] can be formed by recrystallizing complex **I** and then drying it under vacuum. This implies that the six-coordinate bis(pyridine) complex **I** can easily lose pyridine under vacuum to give the five-coordinate mono(pyridine) complex.[5]

Five-coordinate benzylidenemono(pyridine)ruthenium complexes can be obtained exclusively under certain circumstances. Thus, the reaction of complex **I** with NaI affords the benzylidenediiodidoruthenium complex **V** with a single pyridine ligand rather than the corresponding bis(pyridine) complex, probably due to the relatively large size of the iodido ligands and the lower electrophilicity at the metal center.[5] Fogg has reported that modification of the anionic ligands of [$RuCl_2$(=CHPh)(IMes)($Py)_2$] with aryloxido ligands also results in a series of five-coordinate benzylidenemono(pyridine)ruthenium catalysts (**VII**–**XI**).[8] X-ray crystallographic analysis of complex **VII** clearly showed mono(pyridine) coordination, presumably because of steric hindrance.[8a] Similarly, Buchmeiser et al. have reported that treatment of [$RuCl_2$(=CHPh)($Mes_2$-THP)($PCy_3$)] ($Mes_2$-THP = 1,3-dimesityltetrahydropyrimidin-2-ylidene) with an excess of pyridine gives the mono(pyridine) complex **VI**, which they tentatively attributed to the increased donor capability and steric hindrance of the $Mes_2$-THP ligand compared to $H_2$IMes.[9] Accordingly, the steric and electronic properties of the NHC and anionic ligands around the metal center have a pronounced effect on the formation of mono- or bis(pyridine) complexes. The influence of the pyridine ligand on the formation of mono- or bis(pyridine) complexes has rarely been investigated, however.

Herein we describe the synthesis, X-ray crystallographic structures and mass spectrometric behavior of benzylideneruthenium complexes containing various pyridine ligands and the interconversion between mono- and bis(pyridine) complexes. These studies provide some insight into how the pyridine ligands influence the formation of mono- or bis(pyridine) complexes. Additionally, the catalytic ac-

[a] State Key Laboratory of Fine Chemicals, Dalian University of Technology (DUT),
158 Zhongshan Rd., 116012 Dalian, China
Fax: +86-411-83633080
E-mail: beyoudutmost@yahoo.com.cn

Supporting information for this article is available on the WWW under http://www.eurjic.org or from the author.

 © 2007 Wiley-VCH Verlag GmbH & Co. KGaA, Weinheim 

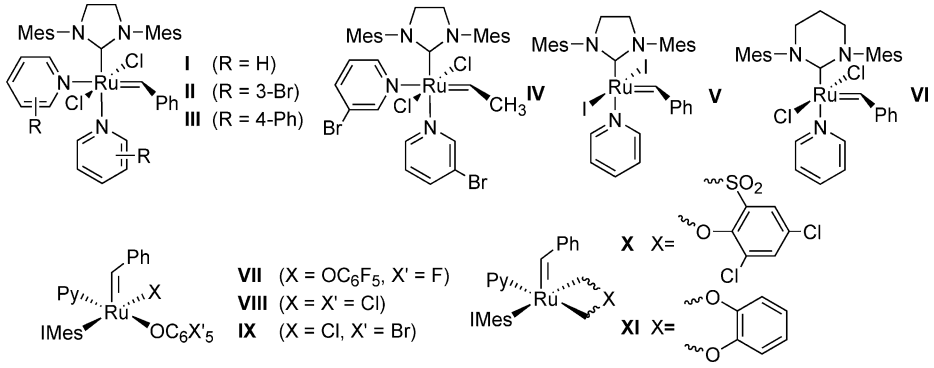


Figure 1. Benzylidenebis- and -mono(pyridine)ruthenium complexes used as metathesis catalysts (IMes = 1,3-dimesitylimidazol-2-ylidene; Mes = 2,4,6-trimethylphenyl).

tivity of these complexes is tested in the ring-closing metathesis (RCM) reaction of diallylmalononitrile and the cross metathesis (CM) reaction of acrylonitrile with terminal olefins.

## Results and Discussion

### Synthesis and X-ray Crystallography

Benzylideneruthenium complexes **2**–**5** were prepared in good yield by treating $[RuCl_2(=CHPh)(H_2IMe)(PPh_3)]$ (**1**) [10] with the corresponding pyridine derivative according to the procedure described by Grubbs (Scheme 1).[5,6] Complex **1**, which bears a $PPh_3$ ligand instead of the $PCy_3$ ligand of the second-generation Grubbs catalyst, was used in this reaction because dissociation of the $PPh_3$ ligand in complex **1** proved to be easier than that of $PCy_3$ in the Grubbs catalyst.[11] Complex **2**, which contains a more labile ligand, was found to be unsuitable as a precursor for the synthesis of other complexes containing pyridine-based ligands because of the difficulty in separating the two complexes.

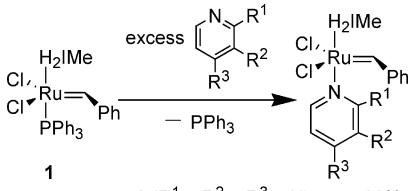


Scheme 1. Synthesis of mono(pyridine) complexes.

Complexes **2** and **3** are easily accessible, although the synthesis of complexes **4** and **5**, which contain an *ortho*-substituted pyridine ligand to weaken the coordination of the pyridine ligand to the ruthenium atom and accelerate initiation through steric hindrance, proved time-consuming and relatively difficult to perform. The reaction of complex **1** with 2,6-dimethylpyridine, quinoline, or 2-bromopyridine failed to yield the corresponding complexes, probably due to an excessive weakening of the coordinating ability of these pyridine-based ligands.

The $^1H$ NMR spectroscopic and mass spectrometric data of complexes **2**–**5** suggested that they are mono(pyridine) complexes. Complexes **2**, **4**, and **5** were investigated by X-ray crystallography to confirm their five-coordinate mono(pyridine) structure. Crystals suitable for X-ray analysis were obtained by slow diffusion of pentane into saturated chloroform/hexane (for complexes **2** and **5**) or dichloromethane/hexane (for complex **4**) solutions of the complexes. Crystals of complex **3** suitable for X-ray analysis could not be obtained. The crystal structures of complexes **2**, **4**, and **5** are shown in Figures 2, 3, and 4, respectively. Selected bond lengths and angles are summarized in Table 1, and crystal data and other details of the structure analysis are given in the Experimental Section.

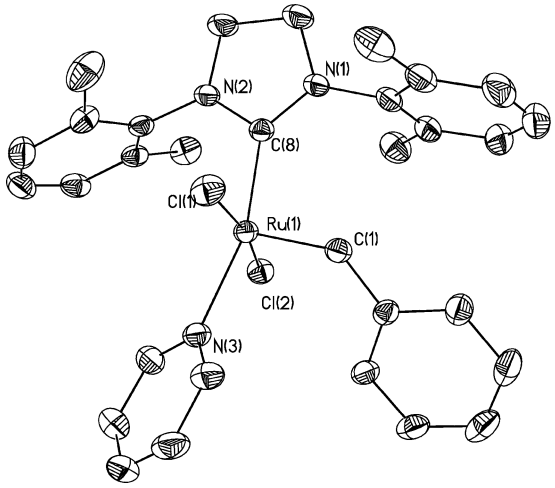


Figure 2. Molecular structure of **2** with thermal ellipsoids drawn at the 30% probability level. Hydrogen atoms have been omitted for clarity.

X-ray analysis confirmed that complexes **2**, **4**, and **5** are five-coordinate mono(pyridine) complexes. The coordination geometries of these complexes are distorted square pyramids with the two chlorido ligands and the pyridine and NHC ligands in a mutually *trans* arrangement and the apical positions occupied by the benzylidene ligands. The

 © 2007 Wiley-VCH Verlag GmbH & Co. KGaA, Weinheim 

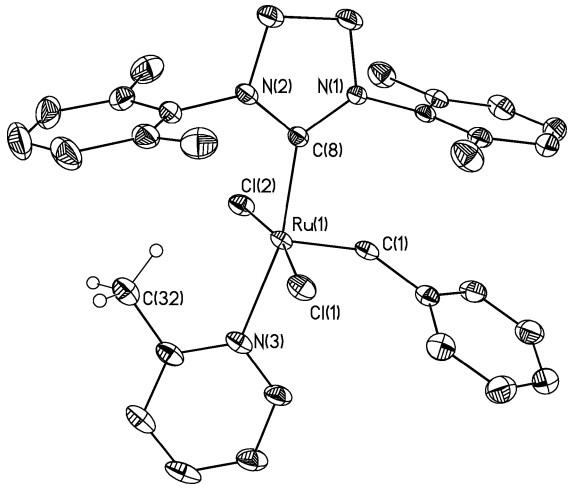


Figure 3. Molecular structure of **4** with thermal ellipsoids drawn at the 30% probability level. Most hydrogen atoms have been omitted for clarity.

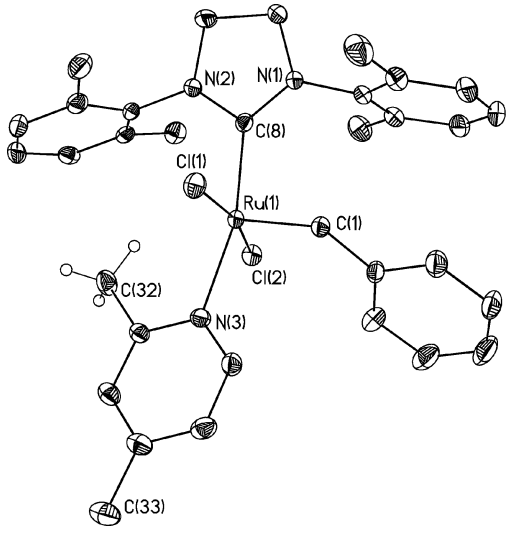


Figure 4. Molecular structure of **5** with thermal ellipsoids drawn at the 30% probability level. Most hydrogen atoms have been omitted for clarity.

Ru–N(3) bonds of **4** [2.165(3) Å] and **5** [2.160(3) Å] are longer than that of **2** [2.156(2) Å], which suggests a weaker interaction between the ruthenium atom and the pyridine ligands in complexes **4** and **5** due to the steric hindrance of the *ortho*-methyl group. The fact that the Ru–C(8) (N-heterocyclic carbene) bonds of **4** [2.042(3) Å] and **5** [2.043(3) Å] are longer than that of **2** [2.025(3) Å] is likely due to the relatively moderate *trans* effects of *ortho*-substituted pyridines, which also reflects the trend of the Ru–N(3) bond lengths. Complex **5** has slightly shorter Ru–N(3) and longer Ru–C(8) bond than complex **4**, which can be attributed to the electron-donating effect of the *para*-methyl group in the 2,4-dimethylpyridine ligand. The dihedral angles between the NHC ring and the pyridine ring of **4** (11.7°) and **5** (23.0°) are narrower than that of **2** (42.1°), and the C(8)–Ru–N(3) angles of **4** [165.45(14)°] and **5** [165.62(14)°] are slightly wider than that of **2** [163.82(10)°], both of which might be due to the steric demands of the *ortho*-methyl group in the pyridine ligand of complexes **4** and **5**. Accordingly, it can be concluded that the steric demand of the *ortho*-methyl group in the pyridine ligand plays a crucial role in the formation of five-coordinate mono(pyridine) complexes **4** and **5**.

Additionally, the ruthenium centers in complexes **4** and **5** do not appear to have the agostic interactions that are known to stabilize four-coordinate 14-electron ruthenium(II) complexes as the closest Ru···C [other than C(1) and C(8); 3.04 Å for **4** and 3.03 Å for **5**] and Ru···H distances (other than $H_{carbene}$; 2.37 Å for **4** and **5**) are all too long for an agostic interaction.[12]

## Interconversion between Mono- and Bis(pyridine) Complexes

As described by Grubbs, the bis(pyridine) complex **6** can also change into the mono(pyridine) complex **2** upon loss of one pyridine ligand under vacuum, and complex **2** can easily reconvert into complex **6** in the presence of an excess of pyridine (Scheme 2). For instance, a crystal of complex

Table 1. Selected bond lengths [Å] and angles [°] for complexes **2** and **4**–**7**.

| | **2** | **4** | **5** | **6** | **7** |
|---|---|---|---|---|---|
| Ru–C(1) | 1.829(3) | 1.836(4) | 1.838(4) | 1.867(6) | 1.860(5) |
| Ru–C(8) | 2.025(3) | 2.042(3) | 2.043(4) | 2.053(6) | 2.060(5) |
| Ru–N(3) | 2.156(2) | 2.165(3) | 2.160(3) | 2.205(5) | 2.207(4) |
| Ru–N(4) | | | | 2.367(5) | 2.359(4) |
| Ru–Cl(1) | 2.3844(7) | 2.3749(10) | 2.3873(12) | 2.4275(16) | 2.4379(14) |
| Ru–Cl(2) | 2.3636(7) | 2.4081(10) | 2.3864(11) | 2.3912(17) | 2.3740(13) |
| C(8)–Ru–C(1) | 97.42(12) | 95.06(15) | 94.91(17) | 94.1(2) | 94.8(2) |
| C(8)–Ru–N(3) | 163.82(10) | 165.45(14) | 165.62(14) | 178.95(19) | 177.52(18) |
| C(8)–Ru–N(4) | | | | 101.91(19) | 101.92(17) |
| C(8)–Ru–Cl(1) | 89.51(8) | 91.44(10) | 88.29(12) | 88.22(17) | 90.08(15) |
| C(8)–Ru–Cl(2) | 93.58(8) | 92.68(10) | 95.60(12) | 90.75(17) | 88.02(15) |
| C(1)–Ru–N(3) | 98.33(11) | 99.48(14) | 97.70(16) | 86.7(2) | 87.54(19) |
| C(1)–Ru–N(4) | | | | 161.2(2) | 161.98(19) |
| C(1)–Ru–Cl(1) | 90.57(9) | 102.06(13) | 88.70(15) | 83.81(19) | 84.78(17) |
| C(1)–Ru–Cl(2) | 97.46(9) | 88.09(13) | 101.14(15) | 100.39(19) | 98.15(17) |
| Cl(1)–Ru–Cl(2) | 170.94(3) | 168.67(4) | 169.04(4) | 175.74(6) | 176.62(5) |

 © 2007 Wiley-VCH Verlag GmbH & Co. KGaA, Weinheim 

**6** suitable for X-ray analysis can be obtained by slow diffusion of pentane into a chloroform/hexane solution of complex **2** (10 mg) and pyridine (0.1 mL, approx. 75 equiv.). Figure 5 illustrates the molecular structure of complex **6**, and Table 1 summarizes selected bond lengths and angles. Crystal data and other details of the structure analysis are presented in the Experimental Section.

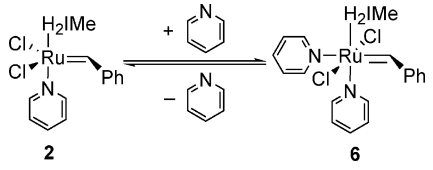


Scheme 2. Interconversion between mono(pyridine) complex **2** and bis(pyridine) complex **6**.

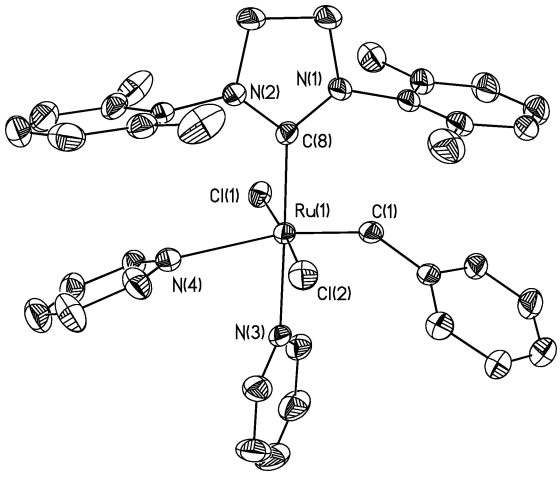


Figure 5. Molecular structure of **6** with thermal ellipsoids drawn at the 30% probability level. Hydrogen atoms have been omitted for clarity.

Complex **6** has a pseudo-octahedral geometry with the two chlorido ligands in a *trans* arrangement and two pyridine ligands in a mutually *cis* arrangement and *trans* to the NHC and the benzylidene ligand, respectively. The Ru–C, Ru–N, and Ru–Cl bonds in complex **6** are all longer than in complex **2**, presumably due to the increased steric demand and relatively lower electrophilicity at the metal center when another pyridine ligand is introduced *trans* to the benzylidene ligand. Similarly, the C(8)–Ru–N(3) and Cl(1)–Ru–Cl(2) angles are widened to 178.95(19)° and 175.74(6)°. The Ru–N(4) [2.367(5) Å] bond in complex **6** is 0.16 Å longer than Ru–N(3) [2.205(5) Å], which implies that the pyridine ligand *trans* to the benzylidene ligand is more likely to dissociate than the pyridine ligand *trans* to the NHC ligand. Removal of the pyridine ligand *trans* to the benzylidene ligand in bis(pyridine) complex **6** can therefore be easily carried out to form mono(pyridine) complex **2** under certain circumstances, for example under vacuum or in solution. The pyridine ligand in complex **2** is relatively difficult to remove because the Ru–N(3) interaction is strengthened, whereas the steric environment and relatively higher electrophilicity at the metal center allow for the association of one pyridine ligand at the coordination site *trans* to the benzylidene ligand.

Interestingly, treatment of complex **1** with an excess of isoquinoline gives the six-coordinate bis(isoquinoline) complex **7** even after drying the product under vacuum for 24 h (Scheme 3). Crystals of complex **7** suitable for X-ray analysis were obtained by slow diffusion of pentane into a saturated chloroform/hexane solution of the complex. As shown in Figure 6 and Table 1, the molecular structure of complex **7** is similar to that of complex **6**. The Ru–N(4) [2.359(4) Å] bond is 0.15 Å longer than Ru–N(3) [2.207(4) Å], which means that the isoquinoline ligand *trans* to the benzylidene ligand is more likely to dissociate than the isoquinoline ligand *trans* to the NHC ligand. The Ru–N(4) bond of **7** [2.359(4) Å] is shorter than that of **6** [2.367(5) Å], which suggests that the interaction between the ruthenium atom and the isoquinoline ligand *trans* to the benzylidene ligand in complex **7** is stronger than the interaction between the ruthenium atom and the pyridine ligand *trans* to the benzylidene ligand in complex **6**. Additionally, the saturated vapor tension of isoquinoline is lower than that of pyridine, which means that bis(isoquinoline) complex **7** cannot be converted into the corresponding five-coordinate mono(isoquinoline) complex under vacuum. However, this conversion can easily be carried out under other conditions, for example in solution.

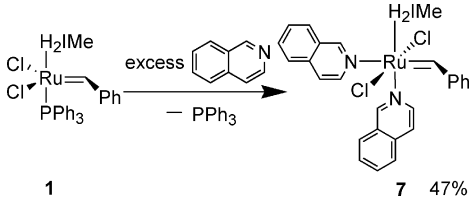


Scheme 3. Synthesis of bis(isoquinoline) complex **7**.

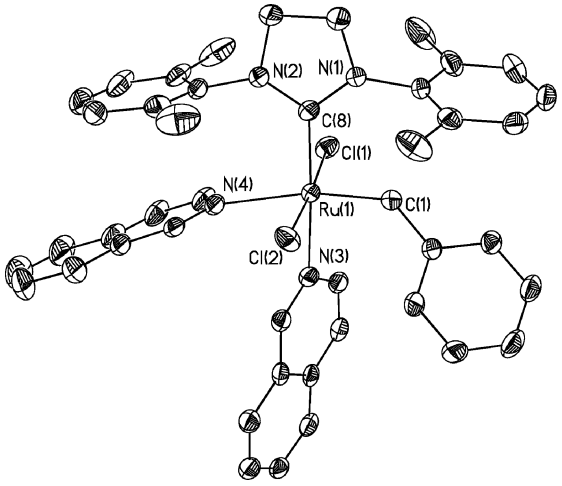


Figure 6. Molecular structure of **7** with thermal ellipsoids drawn at the 30% probability level. Hydrogen atoms have been omitted for clarity.

## Mass Spectrometric Study

Tandem mass spectrometry[13] can be performed when the complexes are delivered to the ionization source in

 © 2007 Wiley-VCH Verlag GmbH & Co. KGaA, Weinheim 

$CH_2Cl_2/CH_3CN$ solution and the collision cone voltages are changed sequentially. All mass spectra are available as Supporting Information. At collision cone voltages of 3 V the $[M - Cl + CH_3CN]^+$ cations are found as base peaks for complexes **2** and **3**, which indicates that the pyridine ligands are still bound to the metal center. However, the base peak for complex **4** is the $[M - Cl - py + 2\ CH_3CN]^+$ cation under the same conditions, which means that 2-methylpyridine has dissociated from the metal center and $CH_3CN$ has occupied the vacant coordination site. The different behaviors of these complexes show the different labilities of their ligands. Thus, the 2-methylpyridine ligand in complex **4** dissociates more easily than the pyridine ligands in complexes **2** and **3**. The dissociation of all pyridine ligands in complexes **2**–**4** was found to be easier than that of $PPh_3$ in complex **1**, which is consistent with the different initiation rates determined by NMR spectroscopy or UV/Vis kinetic studies.[6]

The mono(isoquinoline) species $[M - Cl - quinoline + CH_3CN]^+$ was found as the base peak for the bis(isoquinoline) complex **7** (collision cone voltage: 3 V), which suggests that one of the isoquinoline ligands in complex **7** is prone to dissociate under these conditions.

When complex **1** is delivered to the ionization source in $CH_2Cl_2$/pyridine solution, the bis(pyridine) species $[M - Cl - PPh_3 + 2\ pyridine]^+$ is detected, whereas, when complex **4** is delivered to the ionization source in $CH_2Cl_2$/2-methylpyridine/$CH_3CN$ solution, no bis(pyridine) species is found and the $[M - Cl + CH_3CN]^+$ cation is the base peak. This suggests that a bis(pyridine) complex can be formed in the presence of excess pyridine, whereas a bis(2-methylpyridine) complex cannot be formed even in the presence of an excess of 2-methylpyridine, probably due to steric hindrance from the *ortho*-methyl group.

### Metathesis Activity

The catalytic activities of complexes **2**–**5** and **7** were tested in the RCM reaction of diallylmalononitrile and the CM reaction of acrylonitrile with terminal olefins (Scheme 4).[14]

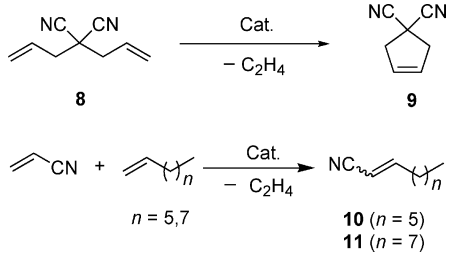


Scheme 4. RCM of diallylmalononitrile and CM of acrylonitrile with terminal olefins.

Studies by Grubbs have suggested that the catalyst efficiency during metathesis of cyano-containing olefin is related to dissociation rate of the ligands.[6] As shown in Tables 2 and 3, complex **4** has a higher catalytic activity than the other complexes as either dissociation of the sterically hindered 2-methylpyridine ligand is rapid and/or rebinding of it is slow.

Table 2. RCM reaction of diallylmalononitrile.[a]

| Catalyst | Cat. [mol-%] | Time [h] | Conversion [%][b] |
|---|---|---|---|
| **1** | 5 | 12 | 44 |
| **2** | 1 | 1 | 70 |
| **3** | 0.5 | 1 | 95 |
| **4** | 0.5 | <0.5 | 99 |
| **4** | 0.2 | 1 | 96 |
| **5** | 0.5 | 1 | 93 |
| **5** | 0.2 | 1 | 90 |
| **7** | 0.5 | 1 | 79 |

[a] 0.1 M diallylmalononitrile in $CH_2Cl_2$ at 40 °C. [b] Conversion was determined by GC and confirmed by $^1H$ NMR spectroscopy.

Table 3. CM reaction between acrylonitrile and α-olefins.[a]

| Catalyst | *n* | Yield [%][b] | *E*/*Z*[c] |
|---|---|---|---|
| **2** | 5 | 56 | 1:3.2 |
| **3** | 5 | 75 | 1:2.1 |
| **4** | 5 | 81 | 1:2.8 |
| **5** | 5 | 70 | 1:3.0 |
| **7** | 5 | 57 | 1:2.9 |
| **2** | 7 | 67 | 1:3.0 |
| **3** | 7 | 83 | 1:1.9 |
| **4** | 7 | 95 | 1:2.9 |
| **5** | 7 | 76 | 1:3.0 |
| **7** | 7 | 49 | 1:3.1 |

[a] 0.1 M acrylonitrile (1.0 equiv.) in $CH_2Cl_2$, α-olefin (2.0 equiv.), catalyst (2 mol-%), 40 °C, 12 h. [b] Yield of isolated product. [c] Ratios determined by $^1H$ NMR spectroscopy.

Addition of 10 equiv. of pyridine (relative to complex **2**) to the mixture of the RCM reaction of **8** catalyzed by complex **2** (Table 2) did not alter the conversion, which suggests that the catalytic activity of bis(pyridine) complex **6** is the same as that of mono(pyridine) complex **2**. The 16-electron mono(pyridine) complex **2** loses a pyridine ligand to form the 14-electron catalytically active intermediate, therefore the process whereby the 18-electron bis(pyridine) complex **6** converts into the 16-electron mono(pyridine) complex **2** must occur so fast that it can be neglected.

## Conclusions

Benzylideneruthenium complexes containing pyridine-based ligands have been prepared by treating complex **1** with various pyridine ligands. The steric demands of these pyridine ligands play a crucial role in the formation of mono- or bis(pyridine) complexes: *ortho*-substituted pyridine ligands form five-coordinate mono(pyridine) complexes whereas pyridine ligands without *ortho* substituents form both six-coordinate bis(pyridine) complexes and five-coordinate mono(pyridine) complexes. The bis- and mono(pyridine) complexes can interconvert under certain circumstances by loss or association of the pyridine ligand *trans* to the benzylidene ligand. This interconversion has very little effect on the catalytic activities of these complexes. The *ortho* substituents of the pyridine ligands can weaken the

 © 2007 Wiley-VCH Verlag GmbH & Co. KGaA, Weinheim 

interaction between the ruthenium center and the ligands due to steric hindrance and therefore accelerate the dissociation of these ligands, which enhances the initiation of the catalysts. Complex **4**, which bears a 2-methylpyridine ligand, exhibits the highest catalytic activity for the RCM reaction of diallylmalononitrile and the CM reaction of acrylonitrile with terminal olefins, of complexes **2**–**5** and **7**.

## Experimental Section

**General Procedures:** Oxygen- and/or moisture-sensitive materials were manipulated using standard Schlenk techniques under dry nitrogen. NMR spectra were recorded with a Varian Inova instrument (400 MHz for $^1$H, 160 MHz for $^{31}$P, 100 MHz for $^{13}$C). High-resolution mass spectra were recorded with a Q-TOF mass spectrometer (Micromass, England) equipped with a Z-spray ionization source. GC analyses were performed with a Hewlett–Packard HP 6890 equipped with an FID and an HP-5 column. Pyridine, 3-bromopyridine, 2-methylpyridine, 2,4-dimethylpyridine, and acrylonitrile were freshly distilled before use. Ruthenium complex **1**[9] and diallylmalononitrile[15] were prepared according to literature procedures. Dichloromethane was dried with $CaH_2$, distilled, and stored under nitrogen, whereas thf, toluene, and hexane were dried and distilled from Na/benzophenone. All other reagents were of analytical grade, were purchased commercially, and used as received, unless noted otherwise.

**[$RuCl_2$(=CHPh)($H_2$IMe)($C_5H_5N$)] (2):** Pyridine (10.0 mL, 0.124 mol) was added to complex **1** (1.10 g, 1.37 mmol) in a 150-mL Schlenk flask; no additional solvent was required. The reaction mixture was stirred at room temperature for 10 min, during which time a color change from red-brown to green was observed. Hexane (120 mL) was then added at room temperature and a green solid precipitated. This precipitate was filtered, washed four times with 10 mL of hexane, and dried in vacuo for 6 h to afford **2** as a green powder (0.79 g, 93% yield). $^1$H NMR (400 MHz, $CDCl_3$): $\delta$ = 19.12 (s, 1 H, Ru=C*H*Ph), 8.64 (br. s, 2 H, pyridine), 7.79–6.93 (multiple peaks, 14 H, pyridine, *ortho* C*H*, *para* C*H*, *meta* C*H*, 2,6-dimethylphenyl aromatic C*H*), 4.13 (s, 4 H, NC$H_2$C$H_2$N), 2.67 (br. s, 6 H, *ortho* C$H_3$), 2.32 (br. s, 6 H, *ortho* C$H_3$) ppm. $^{13}$C NMR ($CDCl_3$, 100 MHz): $\delta$ = 307.32 (m, Ru=*C*HPh), 220.41 [s, Ru–*C*(N)$_2$], 152.23, 150.44, 136.70, 136.08, 130.64, 130.29, 129.65, 129.04, 128.41, 128.13, 124.04, 123.80, 48.32, 22.85, 18.69 ppm.

**[$RuCl_2$(=CHPh)($H_2$IMe)(3-Br-$C_5H_4N$)] (3):** 3-Bromopyridine (6.0 mL, 62.1 mmol) was added to complex **1** (1.90 g, 2.37 mmol) in a 150-mL Schlenk flask; no additional solvent was required. The reaction mixture was stirred at room temperature for 20 min, during which time a color change from red-brown to green was observed. Hexane (120 mL) was then added at room temperature and a green solid precipitated. The flask was sealed under nitrogen and allowed to stand at 0 °C overnight. The green precipitate was then filtered, washed four times with 10 mL of hexane, and dried in vacuo for 6 h to afford **3** as a green powder (1.53 g, 92% yield). $^1$H NMR (400 MHz, $CDCl_3$): $\delta$ = 19.05 (s, 1 H, Ru=C*H*Ph), 8.74 (br. s, 1 H, pyridine), 8.59 (br. s, 1 H, pyridine), 7.90–7.04 (multiple peaks, 13 H, pyridine, *ortho* C*H*, *para* C*H*, *meta* C*H*, 2,6-dimethylphenyl aromatic C*H*), 4.13 (s, 4 H, NC$H_2$C$H_2$N), 2.63 (br. s, 6 H, *ortho* C$H_3$), 2.36 (br. s, 6 H, *ortho* C$H_3$) ppm. $^{13}$C NMR ($CDCl_3$, 100 MHz): $\delta$ = 316.34 (m, Ru=*C*HPh), 216.63 [s, Ru–*C*(N)$_2$], 152.73, 151.48, 148.13, 138.80, 134.57, 132.23, 132.13, 130.33, 130.26, 128.85, 128.09, 127.04, 124.57, 120.78, 51.46, 20.58, 18.93 ppm. $C_{31}H_{32}BrCl_2N_3Ru$ (698.5): calcd. C 53.31, H 4.62, N 6.02; found C 53.12, H 4.59, N 6.07.

**[$RuCl_2$(=CHPh)($H_2$IMe)(2-Me-$C_5H_4N$)] (4):** 2-Methylpyridine (6.0 mL, 60.8 mmol) was added to complex **1** (0.50 g, 0.62 mmol) in a 150-mL Schlenk flask; no additional solvent was required. The reaction mixture was stirred at room temperature for 12 h, during which time a color change from red-brown to green was observed. Hexane (100 mL) was then added at room temperature and a green solid precipitated. The flask was sealed under nitrogen and allowed to stand at 0 °C overnight. The green precipitate was then filtered, washed four times with 10 mL of hexane, and dried in vacuo for 6 h to afford **4** as a green powder (0.33 g, 84% yield). $^1$H NMR (400 MHz, $CDCl_3$): $\delta$ = 19.64 (s, 1 H, Ru=C*H*Ph), 8.49 (br. s, 1 H, pyridine), 8.01 (br. s, 1 H, pyridine), 7.57–7.02 (multiple peaks, 7 H, pyridine, *ortho* C*H*, *para* C*H*, *meta* C*H*), 6.82 (br. s, 4 H, 2,6-dimethylphenyl aromatic C*H*), 6.55 (br. s, 2 H, 2,6-dimethylphenyl aromatic C*H*), 4.16 (s, 2 H, NC$H_2$C$H_2$N), 3.95 (s, 2 H, NC$H_2$C$H_2$N), 2.76 (br. s, 9 H, pyridine C$H_3$, *ortho* C$H_3$), 2.25 (s, 6 H, *ortho* C$H_3$) ppm. $^{13}$C NMR ($CDCl_3$, 100 MHz): $\delta$ = 312.64 (m, Ru=*C*HPh), 218.09 [s, Ru–*C*(N)$_2$], 159.53, 151.74, 151.34, 140.53, 139.08, 137.94, 137.75, 137.28, 136.59, 130.91, 130.33, 129.35, 128.99, 128.76, 128.67, 128.33, 128.04, 127.80, 127.62, 126.49, 125.17, 121.32, 120.93, 51.76, 50.85, 31.58, 20.34, 18.41 ppm.

**[$RuCl_2$(=CHPh)($H_2$IMe)(2,4-$Me_2$-$C_5H_3N$)] (5):** 2,4-Dimethylpyridine (2.0 mL, 17.2 mmol) was added to complex **1** (0.14 g, 0.17 mmol) in a 150-mL Schlenk flask; no additional solvent was required. The reaction mixture was stirred at room temperature for 2 h, during which time a color change from red-brown to green was observed. Hexane (100 mL) was then added at room temperature and a green solid precipitated. The green precipitate was filtered, washed four times with 10 mL of hexane, and dried in vacuo for 6 h to afford **5** as a green powder (0.10 g, 89% yield). $^1$H NMR (400 MHz, $CDCl_3$): $\delta$ = 19.61 (s, 1 H, Ru=C*H*Ph), 7.99 (br. s, 1 H, pyridine), 7.57–6.38 (multiple peaks, 13 H, pyridine, *ortho* C*H*, *para* C*H*, *meta* C*H*, 2,6-dimethylphenyl aromatic C*H*), 4.16 (s, 2 H, NC$H_2$C$H_2$N), 3.95 (s, 2 H, NC$H_2$C$H_2$N), 2.75 (br. s, 9 H, pyridine C$H_3$, *ortho* C$H_3$), 2.24 (s, 6 H, *ortho* C$H_3$), 2.12 (s, 3 H, pyridine C$H_3$) ppm. $^{13}$C NMR ($CDCl_3$, 100 MHz): $\delta$ = 312.49 (m, Ru=*C*HPh), 218.38 [s, Ru–*C*(N)$_2$], 158.75, 151.24, 148.08, 140.46, 139.07, 137.86, 130.80, 130.15, 129.23, 128.89, 128.69, 128.53, 128.20, 126.01, 122.41, 51.63, 50.71, 31.51, 21.48, 20.45, 18.34 ppm.

**[$RuCl_2$(=CHPh)($H_2$IMe)($C_9H_7N$)$_2$] (7):** Isoquinoline (1.0 mL, 8.4 mmol) was added to complex **1** (0.30 g, 0.37 mmol) in a 150-mL Schlenk flask, then 5 mL of toluene was added as solvent. The reaction mixture was stirred at room temperature for 1 h, during which time a color change from red-brown to green was observed. Hexane (100 mL) was then added at room temperature and a green solid precipitated. The green precipitate was filtered, washed four times with 10 mL of hexane and dried in vacuo for 6 h to afford **7** as a green powder (0.14 g, 47% yield). $^1$H NMR (400 MHz, $CDCl_3$): $\delta$ = 19.18 (s, 1 H, Ru=C*H*Ph), 9.32 (s, 1 H, isoquinoline), 8.92 (s, 1 H, isoquinoline), 8.59 (s, 1 H, isoquinoline), 8.50 (s, 1 H, isoquinoline), 8.16–6.99 (multiple peaks, 21 H, isoquinoline, *ortho* C*H*, *para* C*H*, *meta* C*H*, 2,6-dimethylphenyl aromatic C*H*), 4.14 (s, 4 H, NC$H_2$C$H_2$N), 2.63 (br. s, 6 H, *ortho* C$H_3$), 2.35 (s, 6 H, *ortho* C$H_3$) ppm. $^{13}$C NMR ($CDCl_3$, 100 MHz): $\delta$ = 314.44 (m, Ru=*C*HPh), 218.31 [s, Ru–*C*(N)$_2$], 155.17, 152.80, 151.31, 150.52, 148.40, 144.56, 143.12, 138.17, 136.16, 135.73, 135.40, 131.45, 130.31, 130.13, 129.56, 128.94, 128.04, 127.90, 127.41, 127.22, 126.64, 126.46, 126.17, 121.18, 120.91, 120.40, 51.80, 20.45, 18.82 ppm.

**X-ray Crystallographic Studies:** Crystals suitable for X-ray diffraction were mounted on glass fibers. Data collection was performed

 © 2007 Wiley-VCH Verlag GmbH & Co. KGaA, Weinheim 

with a Bruker Smart APEX CCD diffractometer using graphite-monochromated Mo-$K_\alpha$ radiation ($\lambda$ = 0.71073 Å) at 273 K (for complex **2**) or 180 K. The diffraction frames were integrated using the SAINT package. The structures were solved by direct methods using the program SHELXS-97. Structure refinements by full-matrix least squares on $F^2$ were carried out with the program SHELXL-97. All non-hydrogen atoms of the complexes were assigned anisotropic displacement parameters. The hydrogen atoms were constrained to idealized geometries and assigned isotropic displacement parameters equal to 1.2-times the $U_{iso}$ values of their respective parent atoms. Crystal data and other details of the structure analyses are presented in Table 4. CCDC-635304 (**2**), -645279 (**6**), -642416 (**4**), -642417 (**5**), and -642415 (**7**) contain the supplementary crystallographic data for this paper. These data can be obtained free of charge from The Cambridge Crystallographic Data Center via www.ccdc.cam.ac.uk/data_request/cif.

**Tandem Mass Spectrometry:** The samples were delivered to the ionization source in $CH_2Cl_2$/$CH_3CN$ solution. The complexes were dissociated by collision-induced dissociation (CID) in the collision cell of a Micromass Q-Tof with a capillary voltage of 2300 V, an extraction cone voltage of 2 V, and a sample cone voltage of 10 V. The desolvation temperature was set to 190 °C and the source temperature to 100 °C. Nitrogen was used as both drying and nebulizing gas with flow rates of 450 and 50 L h$^{-1}$, respectively. The CID spectra were obtained by selecting the precursor ion of interest with the quadrupole and then collision with argon gas in the CID cell and finally mass analysis by Tof. The collision-cell pressure was maintained at 6 psi. Fragment ions were obtained upon adjusting the collision cone voltage of the mass spectrometer to higher values (for example 19 V).

**General Procedure for Ring-Closing Metathesis:** In a typical experiment, catalyst **4** (2.5 mg, 3.9 μmol) and diallylmalononitrile (117 mg, 0.8 mmol) were weighed into a dried, two-necked flask equipped with a reflux condenser, and 8 mL of solvent was then added. The resulting mixture was then stirred under the conditions given in Table 2. After completion of the reaction, the mixture was filtered through a short pad of silica gel and the solvent removed in vacuo. Conversion was measured by GC-FID and confirmed by NMR spectroscopy. Compound **8**: $^1$H NMR (400 MHz, $CDCl_3$): $\delta$ = 5.90 (ddt, $J$ = 7.2, 10.4, 16.8 Hz, 2 H, $CH_2$=C*H*$CH_2$), 5.45 [dd, $J$ = 0.8, 10.4 Hz, 2 H, (*Z*) C$H_2$=CH$CH_2$], 5.41 [dd, $J$ = 0.8, 16.8 Hz, 2 H, (*E*) C$H_2$=CH$CH_2$], 2.69 (d, $J$ = 7.2 Hz, 4 H, $CH_2$=CHC$H_2$) ppm. HRMS (EI): calcd. for $C_9H_{10}N_2$ [M]$^+$ 146.0844; found 146.0851. Compound **9**: $^1$H NMR (400 MHz, $CDCl_3$): $\delta$ = 5.81 (s, 2 H, $CH_2$C*H*=C*H*$CH_2$), 3.22 (s, 4 H, C$H_2$CH=CHC$H_2$) ppm. HRMS (EI): calcd. for $C_7H_6N_2$ [M]$^+$ 118.0531; found 118.0532.

**General Procedure for the Cross Metathesis Reaction of Acrylonitrile with α-Olefins:** In a typical experiment, catalyst **4** (16.4 mg, 25.9 μmol) was weighed into a dried, two-necked flask equipped with a reflux condenser, then 1-octene (290 mg, 2.6 mmol) and acrylonitrile (67 mg, 1.3 mmol) in $CH_2Cl_2$ (13 mL) were added. The resulting mixture was then stirred under the conditions listed in Table 3. After completion of the reaction, the mixture was filtered through a short pad of silica gel and the solvent removed in vacuo. The crude mixture was purified by chromatography on silica gel to yield the product (140 mg, 81%); the (*E*)/(*Z*) ratio was determined by $^1$H NMR spectroscopy to be 1:2.8. Compound **10**: $^1$H NMR (400 MHz, $CDCl_3$): $\delta$ = 6.69 [dt, $J$ = 6.8, 16.4 Hz, 1 H, (*E*) $CH_2$C*H*=CHCN], 6.47 [dt, $J$ = 7.6, 10.8 Hz, 1 H, (*Z*) $CH_2$C*H*=CHCN], 5.30 [d, $J$ = 16.4 Hz, 1 H, (*E*) $CH_2$CH=C*H*CN], 5.28 [d, $J$ = 10.8 Hz, 1 H, (*Z*) $CH_2$CH=C*H*CN], 2.39 [q, $J$ = 7.6 Hz, 2 H, (*Z*) C$H_2$CH=CHCN], 2.19 [q, $J$ = 6.8 Hz, 2 H, (*E*) C$H_2$CH=CHCN], 1.26–1.31 (m, 8 H), 0.86 (t, $J$ = 6.8 Hz, 3 H) ppm. Compound **11**: $^1$H NMR (400 MHz, $CDCl_3$): $\delta$ = 6.71 [dt, $J$ = 6.8, 16.4 Hz, 1 H, (*E*) $CH_2$C*H*=CHCN], 6.49 [dt, $J$ = 7.6,

Table 4. Crystallographic data for complexes **2** and **4**–**7**.

| | **2**·$CHCl_3$ | **4**·2$CH_2Cl_2$ | **5**·3.25$CHCl_3$ | **6**·2$CHCl_3$·0.5$H_2O$ | **7**·0.25$CHCl_3$·0.25$H_2O$ |
|---|---|---|---|---|---|
| Empirical formula | $C_{32}H_{34}Cl_5N_3Ru$ | $C_{34}H_{39}Cl_6N_3Ru$ | $C_{36.25}H_{40}Cl_{11.75}N_3Ru$ | $C_{38}H_{41}Cl_8N_4O_{0.50}Ru$ | $C_{44.25}H_{42.25}Cl_{2.75}N_4O_{0.25}Ru$ |
| Formula mass | 738.94 | 803.45 | 1035.32 | 946.42 | 832.65 |
| Color | green | green | green | green | green |
| Crystal dimensions [mm] | 0.33 × 0.14 × 0.13 | 0.70 × 0.40 × 0.20 | 0.50 × 0.25 × 0.13 | 0.52 × 0.50 × 0.40 | 0.74 × 0.60 × 0.31 |
| Crystal system | triclinic | monoclinic | triclinic | triclinic | monoclinic |
| Space group | *P*1 | $P2_1/c$ | *P*1 | *P*1 | $P2_1/c$ |
| $a$ [Å] | 10.1262(2) | 11.1997(3) | 9.3780(2) | 9.9107(3) | 12.1217(3) |
| $b$ [Å] | 11.0684(2) | 15.4394(4) | 12.5870(3) | 12.3197(3) | 18.3008(5) |
| $c$ [Å] | 14.8361(2) | 21.0496(6) | 19.7469(5) | 17.1758(4) | 19.8541(5) |
| $\alpha$ [°] | 96.5600(10) | 90 | 93.6080(10) | 93.665(2) | 90 |
| $\beta$ [°] | 94.6810(10) | 103.032(2) | 100.3410(10) | 90.712(2) | 104.8440(10) |
| $\gamma$ [°] | 92.1950(10) | 90 | 94.8690(10) | 90.316(2) | 90 |
| $V$ [Å$^3$] | 1644.54(5) | 3546.08(17) | 2277.53(9) | 2092.62(9) | 4257.38(19) |
| $Z$ | 2 | 4 | 2 | 2 | 4 |
| $T$ [K] | 273(2) | 180(2) | 180(2) | 180(2) | 180(2) |
| $D_{calcd.}$ [g cm$^{-3}$] | 1.492 | 1.505 | 1.510 | 1.502 | 1.300 |
| $\mu$ [mm$^{-1}$] | 0.909 | 0.923 | 1.063 | 0.920 | 0.576 |
| $F$(000) | 752 | 1640 | 1045 | 962 | 1717 |
| $\theta$ range [°] | 2.35 to 29.07 | 2.29 to 25.00 | 1.63 to 25.00 | 2.63 to 25.00 | 2.06 to 25.00 |
| Index ranges ($h$, $k$, $l$) | ±13, ±15, ±20 | ±13, ±18, –23 to 25 | ±11, ±14, ±23 | –9 to11, ±14, ±20 | ±14, ±21, ±23 |
| Reflections collected | 18548 | 19876 | 18924 | 15278 | 45627 |
| Independent reflections/$R_{int}$ | 8678/0.0311 | 6219/0.0384 | 7949/0.0284 | 7301/0.0328 | 7481/0.0409 |
| Obsd reflections [$I > 2\sigma(I)$] | 6776 | 4944 | 6743 | 5600 | 6241 |
| Data/restraints/parameters | 8678/0/370 | 6219/0/397 | 7949/0/496 | 7301/3/464 | 7481/0/505 |
| $R1$/$wR2$ [$I > 2\sigma(I)$] | 0.0432/0.1058 | 0.0437/0.1167 | 0.0508/0.1548 | 0.0693/0.1972 | 0.0622/0.1994 |
| $R1$/$wR2$ (all data) | 0.0596/0.1157 | 0.0591/0.1257 | 0.0612/0.1638 | 0.0902/0.2136 | 0.0740/0.2078 |
| GOF (on $F^2$) | 1.034 | 1.048 | 1.086 | 1.059 | 1.098 |
| Largest diff peak/hole [e Å$^{-3}$] | 1.520/–0.641 | 1.075/–1.184 | 1.452/–0.996 | 1.682/–1.455 | 1.502/–0.794 |

 © 2007 Wiley-VCH Verlag GmbH & Co. KGaA, Weinheim 

10.8 Hz, 1 H, (*Z*) $CH_2CH$=CHCN], 5.32 [d, *J* = 16.4 Hz, 1 H, (*E*) $CH_2CH$=C*H*CN], 5.30 [d, *J* = 10.8 Hz, 1 H, (*Z*) $CH_2CH$=C*H*CN], 2.42 [q, *J* = 7.6 Hz, 2 H, (*Z*) $CH_2CH$=CHCN], 2.22 [q, *J* = 6.8 Hz, 2 H, (*E*) $CH_2CH$=CHCN], 1.26–1.31 (m, 12 H), 0.89 (t, *J* = 6.8 Hz, 3 H) ppm.

**Supporting Information** (see footnote on the first page of this article): Tandem mass spectra of all complexes.

## Acknowledgments

We thank Dr. Cheng He for X-ray crystallographic analysis and Prof. Xiao-Bing Lu, Dr. Xiao Jiang, Dr. Xiao-Gang Li, and Dr. Ping Liu for helpful discussions.

[1] a) T. M. Trnka, R. H. Grubbs, *Acc. Chem. Res.* **2001**, *34*, 18–29; b) R. H. Grubbs, *Tetrahedron* **2004**, *60*, 7117–7140; c) A. Fürstner, *Angew. Chem.* **2000**, *112*, 3140–3172; *Angew. Chem. Int. Ed.* **2000**, *39*, 3012–3043; d) D. Astruc, *New J. Chem.* **2005**, *29*, 42–56; e) E. Colacino, J. Martinez, F. Lamaty, *Coord. Chem. Rev.* **2007**, *251*, 726–764.

[2] M. Scholl, S. Ding, C. W. Lee, R. H. Grubbs, *Org. Lett.* **1999**, *1*, 953–956.

[3] P. Schwab, R. H. Grubbs, J. W. Ziller, *J. Am. Chem. Soc.* **1996**, *118*, 100–110.

[4] a) M. S. Sanford, M. Ulman, R. H. Grubbs, *J. Am. Chem. Soc.* **2001**, *123*, 749–750; b) M. S. Sanford, J. A. Love, R. H. Grubbs, *J. Am. Chem. Soc.* **2001**, *123*, 6543–6554.

[5] M. S. Sanford, J. A. Love, R. H. Grubbs, *Organometallics* **2001**, *20*, 5314–5318.

[6] J. A. Love, J. P. Morgan, T. M. Trnak, R. H. Grubbs, *Angew. Chem. Int. Ed.* **2002**, *41*, 4035–4037.

[7] a) S. E. Lehman Jr, K. B. Wagener, *Organometallics* **2005**, *24*, 1477–1482; b) J. E. Williams, M. J. Harner, M. B. Sponsler, *Organometallics* **2005**, *24*, 2013–2015.

[8] a) J. C. Conrad, D. Amoroso, P. Czechura, G. P. A. Yap, D. E. Fogg, *Organometallics* **2003**, *22*, 3634–3636; b) J. C. Conrad, H. H. Parnas, J. L. Snelgrove, D. E. Fogg, *J. Am. Chem. Soc.* **2005**, *127*, 11882–11883; c) S. Monfette, D. E. Fogg, *Organometallics* **2006**, *25*, 1940–1944; d) J. C. Conrad, K. Camm, D. E. Fogg, *Inorg. Chim. Acta* **2006**, *359*, 1967–1973.

[9] D. Wang, L. Yang, U. Decker, M. Findeisen, M. R. Buchmeiser, *Macromol. Rapid Commun.* **2005**, *26*, 1757–1762.

[10] W.-Z. Zhang, C.-X. Bai, X.-B. Lu, R. He, *J. Organomet. Chem.* **2007**, *692*, 3563–3567.

[11] J. A. Love, M. S. Sanford, M. W. Day, R. H. Grubbs, *J. Am. Chem. Soc.* **2003**, *125*, 10103–10109.

[12] a) M. S. Sanford, L. M. Henling, M. W. Day, R. H. Grubbs, *Angew. Chem. Int. Ed.* **2000**, *39*, 3451–3453; b) S. Takahashi, S. Hikichi, M. Akita, Y. Moro-oka, *Organometallics* **1999**, *18*, 2571–2573; c) D. J. Huang, K. Folting, K. G. Caulton, *J. Am. Chem. Soc.* **1999**, *121*, 10318–10322.

[13] For representative examples of mass spectrometric studies on ruthenium catalysts, ruthenium-catalyzed olefin metathesis reactions, and tandem mass spectrometry in the gas phase, see: a) C. Adlhart, C. Hinderling, H. Baumann, P. Chen, *J. Am. Chem. Soc.* **2000**, *122*, 8204–8214; b) C. Adlhart, P. Chen, *Angew. Chem. Int. Ed.* **2002**, *41*, 4484–4487; c) P. Chen, *Angew. Chem. Int. Ed.* **2003**, *42*, 2832–2847; d) P. Chen, M. H. Chisholm, J. C. Gallucci, X.-Y. Zhang, Z.-P. Zhou, *Inorg. Chem.* **2005**, *44*, 2588–2595.

[14] W.-Z. Zhang, R. Zhang, R. He, *Tetrahedron Lett.* **2007**, *48*, 4203–4205.

[15] E. Díez-Barra, A. de la Hoz, A. Moreno, P. Sánchez-Verdú, *J. Chem. Soc. Perkin Trans. 1* **1991**, 2589–2592.

Received: June 18, 2007
Published Online: October 8, 2007

 © 2007 Wiley-VCH Verlag GmbH & Co. KGaA, Weinheim 

DOI: 10.1002/ejic.200700701

# Synthesis, Crystal Structures and Thermal Properties of New $ZnBr_2$(pyrimidine) Coordination Compounds

**Christian Näther,*[a] Gaurav Bhosekar,[a] and Inke Jeß[a]**

**Keywords:** Coordination compounds / Synthesis / Crystal structure / Thermal reactivity

Four new bromidozinc(II) coordination compounds with pyrimidine as a ligand were prepared, either in solution or by thermal decomposition reactions, and the thermal reactivity and thermodynamic stability of these compounds were investigated. These results are compared with those for the corresponding $ZnI_2$(pyrimidine) compounds. The ligand-rich 1:2 compound dibromidobis(pyrimidine-*N*)zinc(II) (**I**) crystallizes in the monoclinic space group $P2_1/n$. In this structure the zinc atoms are coordinated by two bromido ligands and two pyrimidine ligands within distorted tetrahedra. On heating, compound **I** is transformed into the ligand-deficient 2:3 intermediate bis(dibromido)bis(pyrimidine-*N*)($\mu_2$-pyrimidine-*N*,*N*′)dizinc(II) (**II**), which crystallizes in the monoclinic space group *C*2/*c*. The crystal structure consists of two $ZnBr_2$(pyrimidine) subunits, which are connected by an additional pyrimidine ligand through μ-*N*,*N*′ coordination. Thermal decomposition of compound **II** leads to the formation of the ligand-deficient 1:1 compound dibromido($\mu_2$-pyrimidine-*N*,*N*′)zinc(II) (**III**), which crystallizes in the orthorhombic space group *Pmma*. In compound **III**, the zinc atoms are coordinated by four bromine atoms and two pyrimidine ligands within distorted octahedra. The $ZnBr_2$ units are connected through common edges into chains, which are linked by the pyrimidine ligands into layers. On heating, compound **III** is transformed into the ligand-deficient 2:1 compound $(ZnBr_2)_2$(pyrimidine) (**IV**), which decomposes to give $ZnBr_2$. Solvent-mediated conversion experiments in solution show that not all of the compounds can be prepared by treating $ZnBr_2$ and pyrimidine in the molar ratio given by the formula of the final product.
(© Wiley-VCH Verlag GmbH & Co. KGaA, 69451 Weinheim, Germany, 2007)

## Introduction

Investigations on coordination polymers, inorganic–organic hybrid compounds and metal–organic frameworks are attracting increasing interest[1] because of the potential applications of these systems as electric, magnetic, optical or porous materials.[2] Most of these compounds are normally prepared in solution, where different stable and metastable species exist in equilibrium. In view of this, mixtures of compounds are often obtained during the synthesis, and some specific target compounds cannot be prepared at all. Recently we have demonstrated that thermal decomposition of ligand-rich precursor materials is a suitable alternative method for the convenient synthesis of new coordination compounds.[3] In this method, ligand-rich precursors are heated, leading to ligand-deficient coordination compounds by stepwise liberation of the ligands. One advantage of this method is that the equilibrium is shifted irreversibly in the direction of the ligand-deficient coordination compounds, and thus new compounds which are metastable or unstable in solution can be discovered and prepared as phase-pure solids.

Recently we have reported on new iodidozinc(II) coordination compounds with pyrimidine as a ligand.[4] Altogether, seven different compounds were obtained, including three polymorphic modifications (Figure 1). The ligand-rich 1:2 compound **1** decomposes in several steps, in which ligand-deficient compounds **2**, **3** and **4** [2:3 (**2**), 1:1 (**3**) and 2:1 (**4**)] are formed as intermediates. Detailed analysis of the crystal structures of these compounds clearly indicates a strong correlation between the crystal structures of the reactants and the products for the first two thermal reactions. Slight changes in the reaction conditions lead to the formation of a further 1:1 compound of composition $[ZnI_2(pyrimidine)]_4(acetonitrile)_{0.25}$ (**5**). On heating, compound **5** loses acetonitrile and decomposes to give a new 1:1 polymorphic modification **6**. Compound **6** undergoes a polymorphic phase transition to yield the new compound **7**, which is finally transformed into the 1:1 compound **3**. Solvent-mediated conversion experiments clearly show that compound **3** represents the thermodynamically most stable form at room temperature, whereas **5**, **6** and **7** are metastable. Our results clearly show that different stable and metastable species are in equilibrium and that product formation in such thermal decomposition reactions depends on the actual structure of the ligand-rich precursor compound.

[a] Institut für Anorganische Chemie, Universität zu Kiel, Olshausenstr. 40 (Otto-Hahn-Platz 6–7), 24098 Kiel
Fax: +49-431-880-1520
E-mail: cnaether@ac.uni-kiel.de
Supporting information for this article is available on the WWW under http://www.eurjic.org or from the author.

 © 2007 Wiley-VCH Verlag GmbH & Co. KGaA, Weinheim 

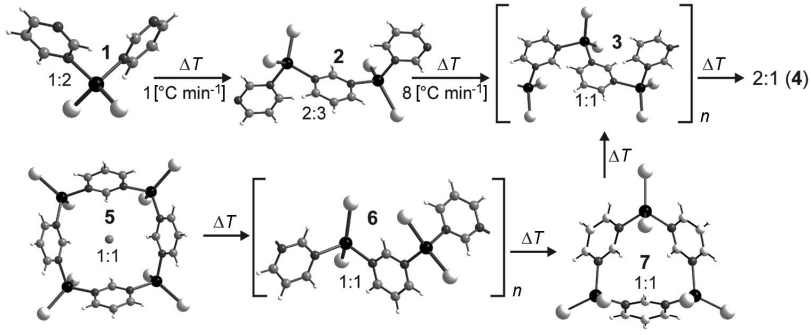


Figure 1. Schematic presentation of the thermal reactions of $ZnI_2$(pyrimidine) coordination compounds.[4]

In order to gain more insight into such reactions, we have investigated the corresponding compounds with $ZnBr_2$ and pyrimidine. Here we report on the results of these investigations.

## Results and Discussion

### Crystal Structures

The ligand-rich 1:2 compound **I** crystallizes in the monoclinic space group $P2_1/n$ with four formula units in the unit cell and all atoms in general positions. The crystal structure of **I** is isomorphous to $ZnI_2$(pyrimidine)$_2$.[4] In the crystal structure, there are discrete complexes, in which the zinc atoms are coordinated by two bromine atoms and two nitrogen atoms of the pyrimidine ligands within distorted tetrahedra (Figure 2: top and Table 1). The pyrimidine ligands of adjacent complexes are stacked in the direction of the crystallographic *a* axis, which indicates π–π interactions (Figure 2: bottom).

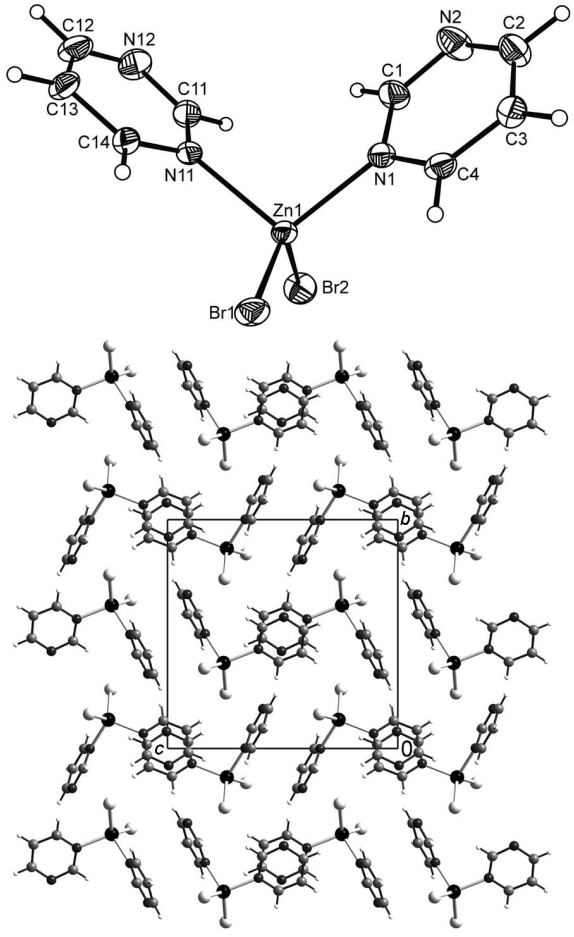


Figure 2. Crystal structure of compound **I** with a view of the coordination sphere of the zinc cations with labelling and displacement ellipsoids drawn at the 50% probability level (top) and a view of the crystal structure in the direction of the crystallographic *a* axis (bottom).

The ligand-deficient 2:3 intermediate **II** crystallizes in the monoclinic space group $C2/c$ with eight formula units in the unit cell. This compound is isomorphous to $(ZnI_2)_2$(pyrimidine)$_3$.[4] In the crystal structure discrete $[(ZnBr_2)_2$(pyrimidine)$_3]$ units are found, which are located in special positions (Figure 3: top). Each zinc atom is coordinated by two bromine atoms and two nitrogen atoms, one on a terminal and one on a bridging pyrimidine ligand (Figure 3: top and Table 1). The zinc atoms are bridged by a pyrimidine ligand with μ-*N*,*N*′ coordination. The terminal pyrimidine rings are stacked in the direction of the crystallographic *b* axis, indicating π–π interactions (Figure 3: bottom).

The ligand-deficient 1:1 compound **III** crystallizes in the orthorhombic space group *Pmma* with two formula units in the unit cell. The zinc and the bromine atoms as well as the pyrimidine ligands are located on crystallographic mirror planes. This compound is not isomorphous to the corresponding iodido analogue $ZnI_2$(pyrimidine).[4] In this structure the zinc atoms are coordinated by four bromine atoms and two nitrogen atoms of pyrimidine ligands within slightly distorted octahedra (Figure 4: top and Table 1). The zinc atoms are connected by the pyrimidine ligands into zigzag chains, which elongate in the direction of the crystallographic *a* axis (Figure 4: middle). The zinc octahedra are additionally connected through common Br edges into corrugated layers, which are located in the *ab* plane (Figure 4: bottom).

 © 2007 Wiley-VCH Verlag GmbH & Co. KGaA, Weinheim 

Table 1. Bond lengths [Å] and angles [°] for compounds **I**, **II** and **III**.[a]

| | | | |
|---|---|---|---|
| Compound **I** | | | |
| Zn1–N1 | 2.063(3) | Zn1–N11 | 2.081(3) |
| Zn1–Br2 | 2.3489(6) | Zn1–Br1 | 2.3500(5) |
| N1–Zn1–Br2 | 110.55(9) | N11–Zn1–Br2 | 105.50(9) |
| N1–Zn1–Br1 | 106.94(9) | N1–Zn1–N11 | 102.79(11) |
| Br2–Zn1–Br1 | 124.12(2) | N11–Zn1–Br1 | 104.78(8) |
| Compound **II** | | | |
| Zn1–N11 | 2.070(4) | Zn1–Br2 | 2.3333(8) |
| Zn1–N1 | 2.091(4) | Zn1–Br1 | 2.3523(8) |
| N11–Zn1–N1 | 101.21(16) | N11–Zn1–Br1 | 104.80(12) |
| N11–Zn1–Br2 | 110.28(13) | N1–Zn1–Br1 | 105.97(11) |
| N1–Zn1–Br2 | 110.37(11) | Br2–Zn1–Br1 | 122.10(3) |
| Compound **III** | | | |
| Zn1–N1 | 2.178(3) | Zn1–Br1 | 2.6287(3) |
| Zn1–N1B | 2.178(3) | Zn1–Br1D | 2.6287(3) |
| Zn1–Br1B | 2.6287(3) | Zn1–Br1C | 2.6287(3) |
| Br1–Zn1E | 2.6287(3) | Br1–Zn1–Br1D | 89.056(12) |
| N1–Zn1–N1B | 180.00(17) | N1–Zn1–Br1C | 89.93(6) |
| N1–Zn1–Br1B | 90.07(6) | N1B–Zn1–Br1C | 90.07(6) |
| N1B–Zn1–Br1B | 89.93(6) | Br1B–Zn1–Br1C | 89.056(12) |
| N1–Zn1–Br1 | 89.93(6) | Br1–Zn1–Br1C | 90.944(12) |
| N1B–Zn1–Br1 | 90.07(6) | Br1D–Zn1–Br1C | 180.0 |
| Br1B–Zn1–Br1 | 180.0 | C1–N1–Zn1 | 122.3(3) |
| N1–Zn1–Br1D | 90.07(6) | C2–N1–Zn1 | 120.8(3) |
| N1B–Zn1–Br1D | 89.93(6) | Br1B–Zn1–Br1D | 90.944(12) |

[a] Symmetry transformations used to generate equivalent atoms: A: $-x + 3/2, -y, z$; B: $-x + 1, -y, -z$; C: $x, y - 1, z$; D: $-x + 1, -y + 1, -z$.

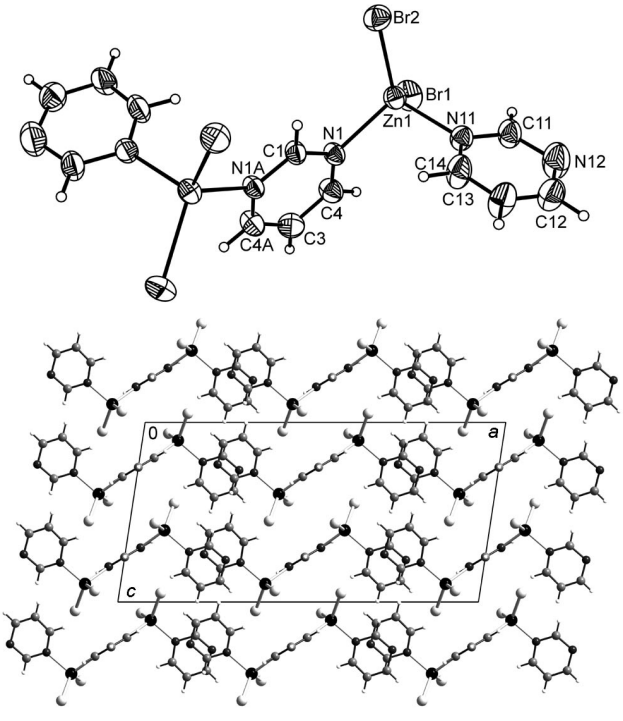


Figure 3. Crystal structure of compound **II** with a view of the coordination sphere of the zinc cations with labelling and displacement ellipsoids drawn at the 50% probability level (top; symmetry codes: A = $-x, y, -z + 3/2$) and a view of the crystal structure in the direction of the crystallographic *b* axis (bottom).

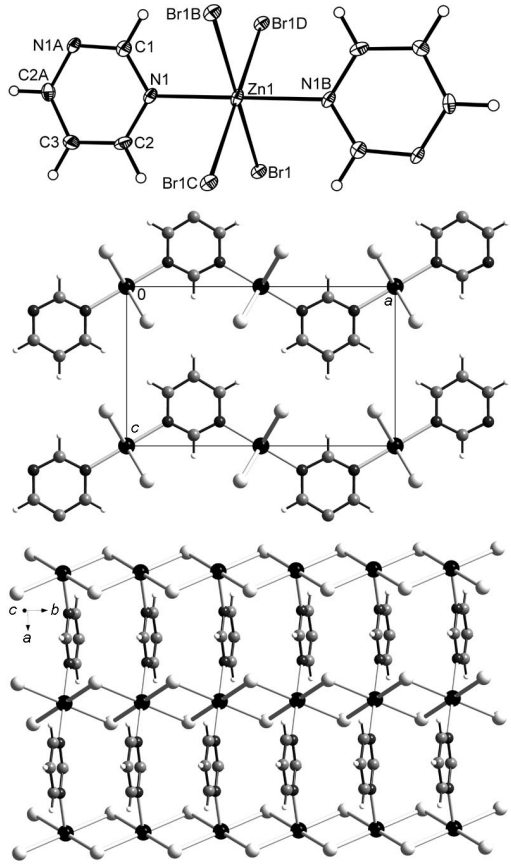


Figure 4. Crystal structure of compound **III** with a view of the coordination sphere of the zinc cations with labelling and displacement ellipsoids drawn at the 50% probability level (top; symmetry codes: A: $-x + 1, -y, -z$; B: $x, y - 1, z$; C: $-x + 1, -y + 1, -z$) and a view of the structure in the direction of the crystallographic *b* axis (bottom).

## Thermoanalytical Investigations

Five mass steps are observed for compound **1** on heating, of which the first four steps are accompanied by endothermic events in the DTA curve (Figure 5). From the MS trend scan curve it is evident that only pyrimidine ligands ($m/z$ = 80) are liberated in the first four steps and the DTG curve shows that not all of the steps are well resolved. The experimental mass loss in each of the first four TG steps is in good agreement with that calculated for the removal of half of the pyrimidine ligands in each step ($\Delta m_{theo}$ –1/2 pyrimidine = –10.4%) (Figure 5). Thus, it can be inferred that in these steps a ligand-deficient 2:3, 1:1 and 2:1 compound is formed, which finally decomposes to give $ZnBr_2$, which vaporizes on further heating.

In order to determine the nature of the thermal decomposition products, additional thermogravimetric measurements were performed in which the heating was stopped after each step. The residues thus obtained were investigated by X-ray powder diffraction (Figure 6) and elemental analysis; the results are presented in the Experimental Section.

 © 2007 Wiley-VCH Verlag GmbH & Co. KGaA, Weinheim 

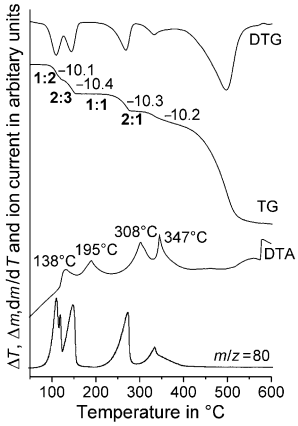


Figure 5. DTA, TG, DTG and MS trend scan curves for compound **I** [heating rate: 4 °C min$^{-1}$; $m/z$ = 80 (pyrimidine)]; given are the mass changes [%] and the peak temperatures $T_p$ [°C].

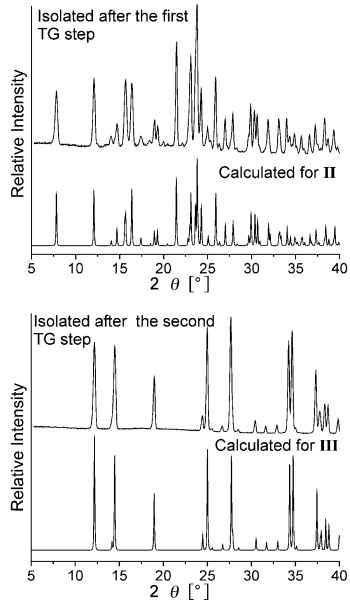


Figure 6. Experimental X-ray powder diffraction pattern of the residue obtained after the first (top) and second (bottom) TG step in the thermal decomposition of the ligand-rich 1:2 compound **I**, accompanied by the calculated X-ray powder diffraction patterns for compounds **II** and **III**.

The experimental X-ray powder diffraction patterns of the residues formed in the first and second TG steps are in excellent agreement with those calculated for compounds **II** and **III**, clearly indicating that in the first TG step the ligand-deficient 2:3 intermediate **II** is formed, and then it is transformed into the ligand-deficient 1:1 compound **III** on further heating (Figure 5 and Figure 6). In addition, the results of an elemental analysis of the residues agrees with the expected results for a 2:3 and 1:1 compound (Experimental Section). These results show that both compounds are obtained as phase-pure solids even though the first TG step is not well resolved. It is interesting to note that the powder pattern of the residue formed in the third step matches well with that of the pattern of a solid obtained by stirring a crystalline suspension of $ZnBr_2$ and pyrimidine in *n*-hexane for several days. This result indicates that the ligand-deficient compound **IV** can also be prepared in solution.

The elemental analysis of the residue formed in the third TG step corresponds to a new compound of 2:1 stoichiometry of composition $(ZnBr_2)_2$(pyrimidine) (**IV**). As expected, the experimental X-ray powder diffraction pattern of this compound is completely different from that calculated for compounds **II** and **III** and for $ZnBr_2$ (Figure 7).

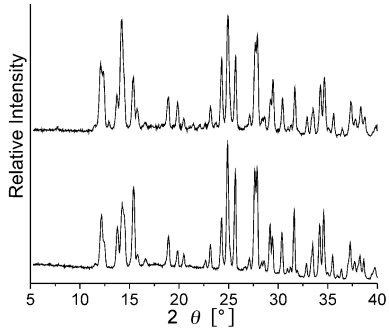


Figure 7. Experimental X-ray powder diffraction pattern of the residue obtained after the third TG step during the thermal decomposition of the ligand-rich 1:2 compound **I** (top) and the experimental X-ray powder diffraction pattern for compound **IV** obtained from solution (bottom).

## Investigations on the Stability of the Compounds in Solution and in the Solid State

The stability of compounds **I**, **II** and **III** as solids was investigated by time-dependent X-ray powder diffraction. These investigations show that compounds **II** and **III** are stable over several days, whereas the ligand-rich 1:2 compound **I** decomposes even at room temperature within a few days to give compound **III**.

The stability of these compounds was further investigated in solution by solvent-mediated conversion experiments. In these experiments the metal salt and ligand are mixed in different stoichiometric ratios by using acetonitrile as a solvent. These crystalline suspensions were stirred for a week in order to obtain the thermodynamically most stable form. Afterwards the products were investigated by X-ray powder diffraction (Table 2). These experiments clearly showed that all compounds are stable and can also be prepared in solution. However, it is to be noted that not all of these compounds can be prepared simply by mixing the reactants stoichiometrically as given by the formula. Thus, the reaction of $ZnBr_2$ and pyrimidine in 2:3 mol ratio results in the formation of the 1:1 compound **III**, whereas

Table 2. Result of the crystallization experiments in different solvents as a function of the molar ratio between metal and ligand (pyrimidine).

| $ZnBr_2$/Ligand | 1:4 | 1:3 | 1:2 | 2:3 | 1:1 | 2:1 |
|---|---|---|---|---|---|---|
| Compound | **I** (1:2) | | **II** (2:3) | **III** (1:1) | | **IV**(2:1) |

 © 2007 Wiley-VCH Verlag GmbH & Co. KGaA, Weinheim 

the reaction in a 1:2 mol ratio leads to the formation of the 2:3 compound **II** (Table 2). This indicates that for the preparation of the ligand-rich compounds, an excess of the ligand must always be used. The ligand-deficient compound **IV** is difficult to prepare, because in many cases it is contaminated with compound **III** or $ZnBr_2$ (Table 2).

### Comparison of $ZnX_2$(pyrimidine) Coordination Compounds (X = Cl, I)

As mentioned earlier, for the corresponding coordination compounds with $ZnI_2$ a variety of compounds and polymorphic modifications were found.[4] The different polymorphic modifications were detected when the pseudopolymorphic 1:1 compound $[ZnI_2(pyrimidine)]_4(acetonitrile)_{0.25}$ was decomposed, which was prepared by fast precipitation under kinetic control from a solution of $ZnI_2$ and pyrimidine in acetonitrile by adding an antisolvent in which the compound is insoluble. In view of this observation, several attempts were made to prepare the corresponding acetonitrile solvate of the bromide compound. However, this always resulted in the formation of the ligand-deficient 1:1 compound **III**. From $ZnI_2$ and pyrimidine, two metastable polymorphic modifications of the 1:1 compound could also be prepared by performing the crystallization under kinetic control.[4] Similar attempts to prepare such forms of the bromide compound by nucleation-controlled crystallization[5] did not result in any polymorphic modifications. It must also be noted that the reaction of $ZnCl_2$ with pyrimidine leads only to one compound of composition $ZnCl_2$(pyrimidine),[6] which shows that the number of possible compounds in the $ZnX_2$(pyrimidine) [X = I, Br, Cl] system decreases from iodine to chlorine.

Differences between the $ZnI_2$ and $ZnBr_2$ coordination compounds are also found in the thermal reactivity of the ligand-rich 1:2 compounds, which are isotypic. On slow heating $ZnI_2(pyrimidine)_2$ (**1**) is transformed directly into the ligand-deficient 1:1 compound $ZnI_2$(pyrimidine) (**3**), without the formation of the ligand-deficient 2:3 intermediate **2**. Compound **2** can only be obtained by thermal decomposition if fast heating rates are used, which shows that kinetics plays an important role in product formation. In contrast, thermal decomposition of $ZnBr_2(pyrimidine)_2$ (**I**) leads directly to the formation of the 2:3 compound $(ZnBr_2)_2(pyrimidine)_3$, regardless of the actual heating rate.

In this context, it must be mentioned that for the decomposition reaction of the discrete units in $ZnI_2(pyrimidine)_2$ (**1**), via the oligomeric units in $(ZnI_2)_2(pyrimidine)_3$ (**2**), to the chains in $ZnI_2$(pyrimidine) (**3**), a smooth reaction pathway can be found (Figure 8: left).[4] In contrast, only for the reaction of $ZnBr_2(pyrimidine)_2$ (**I**) to give $(ZnBr_2)_2(pyrimidine)_3$ (**II**) a smooth reaction pathway is found, whereas for the transformation of the 2:3 intermediate **II** into the ligand-deficient 1:1 compound **III**, large translational and rotational changes are needed and thus no smooth reaction pathway can be expected (Figure 8: right).

## Conclusions

In this contribution we have presented four new coordination compounds based on $ZnBr_2$ and pyrimidine, which can be prepared by thermal decomposition from the ligand-rich compound $ZnBr_2$(pyrimidine). These compounds can also be prepared in solution; however, the ligand-rich compounds are only accessible if an excess of ligand is used. The reaction of $ZnBr_2$ and pyrimidine in a ratio given by the formula of the final compound does not lead to compounds **I** and **II**. This phenomenon is frequently observed in the preparation of such compounds, and therefore new compounds can be easily overlooked if the synthesis is performed only in solution. In contrast, by thermal decomposition of the ligand-rich compounds, all ligand-deficient compounds can be detected in a single measurement. A comparison of the thermal properties of these bromido complexes with those of the corresponding iodidozinc(II) and chloridozinc(II) coordination compounds reveals several differences, which include the influence of the actual heating rate on product formation, the mechanism of such reactions and the possibility of the preparation of thermodynamically metastable compounds and different polymorphic modifications.

## Experimental Section

**Synthesis of Compound I:** $ZnBr_2$ (112.59 mg, 0.5 mmol) and pyrimidine (240.24 mg, 3.0 mmol) were mixed in acetonitrile (0.5 mL).

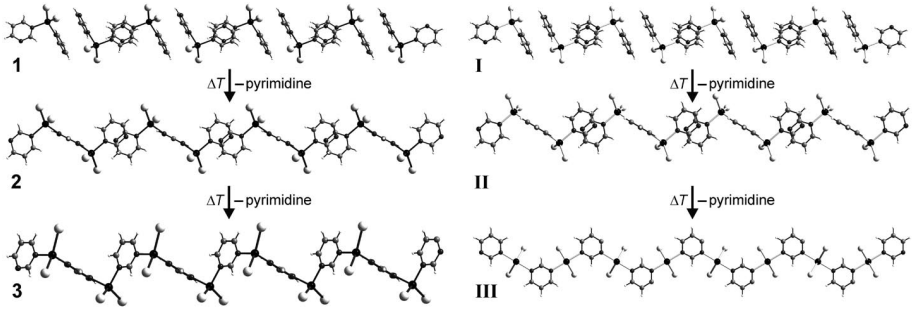


Figure 8. Structural relationships between the crystal structures of the $ZnI_2$(pyrimidine) (left) and $ZnBr_2$(pyrimidine) coordination polymers.

 © 2007 Wiley-VCH Verlag GmbH & Co. KGaA, Weinheim 

Afterwards, diethyl ether (1.0 mL) was added to the clear solution for precipitation. Yield: 133.6 mg (69.36%) based on $ZnBr_2$. $C_8H_8Br_2N_4Zn$ (385.37): calcd. C 24.93, H 2.09, N 14.54; found C 25.02, H 2.18, N 14.63. IR (KBr): $\tilde{\nu}$ = 1591 (s), 1561 (m), 1471 (m), 1406 (s), 1369 (w), 1237 (w), 1174 (m), 1082 (m), 1016 (m), 817 (w), 705 (m), 688 (m), 643 (m) $cm^{-1}$. Single crystals were prepared by the reaction of $ZnBr_2$ (56.29 mg, 0.25 mmol) and pyrimidine (120.12 mg, 1.5 mmol) in acetonitrile (0.5 mL). Slow evaporation of the solvent from the clear solution yields colourless crystals in about a week.

**Synthesis of Compound II:** $ZnBr_2$ (112.59 mg, 0.5 mmol) and pyrimidine (80.08 mg, 1.0 mmol) were mixed in acetonitrile (0.5 mL). Afterwards, diethyl ether (1.0 mL) was added to the clear solution for precipitation. Yield: 161.9 mg (93.77%) based on $ZnBr_2$. $C_{12}H_{12}Br_4N_6Zn_2$ (690.66): calcd. C 20.87, H 1.75, N 12.17; found C 21.00, H 1.72, N 12.14. IR (KBr): $\tilde{\nu}$ = 3121 (w), 3095 (w), 3064 (m), 1594 (s), 1560 (s), 1472 (s), 1409 (s), 1228 (w), 1173 (m), 1081 (s), 1017 (m), 814 (m), 705 (s), 644 (m) $cm^{-1}$. Single crystals were prepared by the reaction of $ZnBr_2$ (112.59 mg, 0.5 mmol) and pyrimidine (80.08 mg, 1.0 mmol) in a mixture of acetonitrile (2.0 mL) and water (0.3 mL). Slow evaporation of the solvent yielded colourless crystals in about 4 d.

**Synthesis of Compound III:** $ZnBr_2$ (112.59 mg, 0.5 mmol) and pyrimidine (40.04 mg, 0.5 mmol) were mixed in acetonitrile (0.5 mL). Afterwards diethyl ether (1.0 mL) was added for precipitation. Yield: 129.3 mg (84.71%). $C_4H_4Br_2N_2Zn$ (305.28): calcd. C 15.74, H 1.32, N 9.18; found C 15.87, H 1.29, N 9.09. IR (KBr): $\tilde{\nu}$ = 3121 (w), 3075 (w), 1595 (s), 1569 (m), 1465 (s), 1402 (s), 1356 (w), 1220 (m), 1180 (m), 1145 (w), 1081 (s), 1028(m), 933 (w), 801 (m), 688 (s), 661(s) $cm^{-1}$. Single crystals were prepared by the reaction of $ZnBr_2$ (22.51 mg, 0.1 mmol) and pyrimidine (8.08 mg, 0.1 mmol) in water (0.3 mL). Slow evaporation of the solvent yielded colourless crystals in about one week.

**Synthesis of Compound IV:** This compound was difficult to obtain in solution, because in most cases it was contaminated with compound **III**. From several reactions with different stoichiometric ratios of $ZnBr_2$ and pyrimidine, we obtained only one batch which was phase-pure. Its X-ray powder diffraction pattern is shown in Figure 7. However, the pure compound can be prepared in quantitative yield by thermal decomposition of compound **I**, **II** or **III**. $C_4H_4Br_4N_2Zn_2$ (530.46): calcd. C 9.06, H 0.76, N 5.28; found C 9.13, H 0.81, N 5.35. IR (KBr): $\tilde{\nu}$ = 3106 (w), 3082 (w), 1684 (w), 1596 (s), 1569 (m), 1465 (s), 1403 (s), 1220 (m), 1180 (s), 1082 (s), 1028 (s), 801 (m), 689 (s), 660 (s) $cm^{-1}$.

**Elemental Analysis of the Residues Obtained in the Thermal Decomposition of Compound I**

(A) Isolated after the first heating step (compound **II**) $C_{12}H_{12}Br_4N_6Zn_2$ (690.66): calcd. C 20.87, H 1.75, N 12.17; found C 20.94, H 1.69, N 12.20. (B) Isolated after the second heating step (compound **III**) $C_4H_4N_2Br_2Zn$ (305.28): calcd. C 15.74, H 1.32, N 9.18; found C 15.86, H 1.28, N 9.08. (C) Isolated after the third heating step (compound **IV**) $C_4H_4Br_4N_2Zn_2$ (530.46): calcd. C 9.06, H 0.76, N 5.28; found C 8.48, H 1.47, N 4.98.

**Single Crystal Structure Analysis:** All investigations were performed with an Imaging Plate Diffraction System (IPDS-1) from STOE & CIE. Structure solutions were performed with direct methods by using SHELXS-97,[7] and structure refinements were performed against $F^2$ with SHELXL-97.[7] For all structures a numerical absorption correction was applied by using X-Red[8] and X-Shape.[8] All non-hydrogen atoms were refined with anisotropic displacement parameters. All hydrogen atoms were positioned with idealized geometry and were refined with fixed isotropic displacement parameters [$U_{eq}$(H) = 1.2·$U_{eq}$(C)] by using a riding model with $d_{C–H}$ = 0.95 Å. Details of the structural determination are given in Table 3 and in the Supporting Information.

CCDC-651854 (**I**), -651855 (**II**) and -651856 (**III**) contain the supplementary crystallographic data for this paper. These data can be obtained free of charge from The Cambridge Crystallographic Data Centre via www.ccdc.cam.ac.uk/data_request/cif.

**X-ray Powder Diffraction:** X-ray powder diffraction experiments were performed by using a STOE STADI P transmission powder diffractometer with Cu-$K_\alpha$-radiation ($\lambda$ = 154.0598 pm), which is equipped with a position-sensitive detector (scan range: 5°–45°) from STOE & CIE.

**Differential Thermal Analysis, Thermogravimetry and Mass Spectrometry:** The heating-rate-dependent DTA-TG measurements were performed under a nitrogen atmosphere (purity: 5.0) with

Table 3. Crystal data and results of the structural refinement for compounds **I**, **II** and **III**.

| Compound | **I** | **II** | **III** |
|---|---|---|---|
| Chemical formula | $C_8H_8Br_2N_4Zn$ | $C_{12}H_{12}Br_4N_6Zn_2$ | $C_4H_4N_2Br_2Zn$ |
| Formula weight | 385.37 | 690.66 | 305.28 |
| Crystal system | monoclinic | monoclinic | orthorhombic |
| Space group | $P2_1/n$ | $C2/c$ | $Pmma$ |
| $a$ [Å] | 7.6087(6) | 22.8319(19) | 12.2327(14) |
| $b$ [Å] | 12.4580(8) | 7.7361(5) | 3.7481(3) |
| $c$ [Å] | 12.5606(10) | 11.4845(9) | 7.2659(6) |
| $\beta$ [°] | 91.854 (10)° | 98.656(10) | – |
| Volume [Å$^3$] | 1189.99 (15) | 2005.4(3) | 333.14(5) |
| $Z$ | 4 | 8 | 2 |
| Calculated density [g cm$^{-3}$] | 2.151 | 2.288 | 3.043 |
| $\mu$ [mm$^{-1}$] | 8.751 | 10.369 | 15.578 |
| $2\theta$ range [°] | 2.30 to 28.03 | 2.78 to 28.03 | 2.80 to 28.04 |
| Measured reflections | 11267 | 9201 | 3127 |
| Unique reflections | 2778 | 2394 | 478 |
| Observed reflections [$I > 2\sigma(I)$] | 2341 | 1809 | 441 |
| $R_1$[a] [$I > 2\sigma(I)$] | 0.0360 | 0.0413 | 0.0268 |
| $wR_2$[b] [all data] | 0.0968 | 0.1168 | 0.0697 |
| GOF | 1.026 | 1.024 | 1.100 |
| Residual electron density [e Å$^{-3}$] | 0.778/–0.918 | 0.908/–0.759 | 1.106/–1.128 |

[a] $R_1 = \Sigma \, ||F_o| - |F_c|| / \Sigma |F_o|$. [b] $wR_2 = \{\Sigma[w(F_o^2 - F_c^2)^2] / \Sigma[w(F_o^2)^2]\}^{1/2}$.

 © 2007 Wiley-VCH Verlag GmbH & Co. KGaA, Weinheim 

$Al_2O_3$ crucibles in a STA-409CD instrument from Netzsch. The DTA-TG-MS measurements were performed with the same instrument, which is connected to a quadrupole mass spectrometer from Balzers by a Skimmer coupling from Netzsch. The MS measurements were performed in analog and trend scan mode in $Al_2O_3$ crucibles in a dynamic nitrogen atmosphere (purity: 5.0) by using heating rates of 4 °C min$^{-1}$. All measurements were performed with a flow rate of 75 mL min$^{-1}$ and were corrected for buoyancy and current effects. The instrument was calibrated by using standard reference materials.

**Elemental Analysis:** CHN analysis has been performed with a EURO EA Elemental Analyzer, fabricated by EURO VECTOR Instruments and Software.

**Supporting Information** (see footnote on the first page of this article): Tables with bond lengths and angles and details of the structure determinations. Experimental and calculated X-ray powder diffraction patterns for compounds **I**–**III**. IR and Raman spectra of compounds **I**–**III**.

## Acknowledgments

We gratefully acknowledge the financial support by the State of Schleswig-Holstein and the Deutsche Forschungsgemeinschaft (Projekt No.: NA 720/1–1). We thank Professor Dr. Wolfgang Bensch for the facility to use his experimental equipment.

[1] a) A. Y. Robin, K. M. Fromm, *Coord. Chem. Rev.* **2006**, *250*, 2127–2157; b) P. J. Hagrman, D. Hagrman, J. Zubieta, *Angew. Chem. Int. Ed.* **1999**, *38*, 2638–2684; c) S. L. James, *Chem. Soc. Rev.* **2003**, *5*, 276–288; d) R. Robson in *Comprehensive Supramolecular Chemistry*, Pergamon, New York, **1996**, ch. 22, p. 733; e) R. Robson, B. F. Abrahams, S. R. Batten, R. W. Grable, B. F. Hoskins, J. Liu in *Supramolecular Architecture*, ACS publications, Washington DC, **1992**, ch. 19; f) S. R. Batten, R. Robson, *Angew. Chem.* **1998**, *110*, 1558–1595; *Angew. Chem. Int. Ed. Engl.* **1998**, *37*, 1460–1494; g) P. J. Hagrman, D. Hagrman, J. Zubieta, *Angew. Chem.* **1999**, *111*, 2798–2848; *Angew. Chem. Int. Ed.* **1999**, *38*, 2638–2684; h) A. J. Blake, N. R. Champness, P. Hubberstey, W.-S. Li, M. A. Withersby, M. Schröder, *Coord. Chem. Rev.* **1999**, *183*, 117–138; i) D. Braga, L. Maini, M. Polito, L. Scaccianoce, G. Cojazzi, F. Grepioni, *Coord. Chem. Rev.* **2001**, *216*–217; j) M. Kosal, J. Chou, S. Wilson, K. Suslick, *Nat. Mater.* **2002**, *1*, 118–121; k) O. M. Yaghi, H. Li, C. Davis, D. Richardson, T. L. Groy, *Acc. Chem. Res.* **1998**, *31*, 474–484.

[2] a) S. Kitagawa, K. Uemura, *Chem. Soc. Rev.* **2005**, *34*, 109–119; b) P. Horcajada, C. Serre, M. Vallet-Regi, M. Sebban, F. Taulelle, G. Ferey, *Angew. Chem. Int. Ed.* **2006**, *45*, 5974–5978; c) B. Paul, C. Näther, B. Walfort, K. M. Fromm, B. Zimmermann, H. Lang, C. Janiak, *Cryst. Eng. Commun.* **2005**, *7*, 309–319; d) M. Eddaoudi, J. Kim, N. Rosi, D. Vodak, J. Wachter, M. O'Keefe, O. M. Yaghi, *Science* **2002**, *295*, 469–472; e) J. L. C. Rowsell, O. M. Yaghi, *Microporous Mesoporous Mater.* **2004**, *73*, 3–14; f) H. K. Chae, D. Y. Siberio-Perez, J. Kim, Y. B. Go, M. Eddaoudi, A. J. Matzger, M. O'Keefe, O. M. Yaghi, *Nature* **2004**, *427*, 523–527; g) S. Noro, S. Kitagawa, M. Kondo, K. Seki, *Angew. Chem. Int. Ed.* **2000**, *39*, 2081–2084; h) M. Latroche, S. Surblé, C. Serre, C. Mellot-Draznieks, P. L. Llewellyn, J.-H. Lee, J.-S. Chang, S. H. Jhung, G. Férey, *Angew. Chem. Int. Ed.* **2006**, *45*, 8227–8231; i) S. R. Batten, K. Murray, *Coord. Chem. Rev.* **2003**, *246*, 103–130; j) B. Moulton, J. Lu, R. Hajndl, S. Hariharan, M. J. Zaworotko, *Angew. Chem. Int. Ed.* **2002**, *41*, 2821–2824; k) L.-X. Dai, *Angew. Chem. Int. Ed.* **2004**, *43*, 5726–5729; l) C. Janiak, *Dalton Trans.* **2003**, 2781–2804.

[3] a) G. Bhosekar, I. Jeß, C. Näther, *Inorg. Chem.* **2006**, *43*, 6508–6515; b) C. Näther, I. Jeß, *Inorg. Chem.* **2006**, *45*, 7446–7454; c) C. Näther, I. Jeß, *Inorg. Chem.* **2003**, *42*, 2968–2976; d) C. Näther, I. Jeß, N. Lehnert, D. Hinz-Hübner, *Solid State Sci.* **2003**, *5*, 1343–1357; e) C. Näther, I. Jeß, *J. Solid State Chem.* **2002**, *169*, 103–112; f) C. Näther, J. Greve, *J. Solid State Chem.* **2003**, *176*, 259–265; g) C. Näther, I. Jeß, *Eur. J. Inorg. Chem.* **2004**, 2868–2876; h) C. Näther, M. Wriedt, I. Jeß, *Inorg. Chem.* **2003**, *42*, 2391–2397.

[4] C. Näther, G. Bhosekar, I. Jeß, *Inorg. Chem.* **2007**, in press.

[5] J. Breu, W. Seidl, D. Huttner, F. Kraus, *Chem. Eur. J.* **2002**, *8*, 4454–4460.

[6] J. Pickardt, B. Staub, *Z. Naturforsch.* **1996**, *51b*, 947–951.

[7] G. M. Sheldrick, *SHELXS-97 and SHELXL-97*, University of Göttingen, Germany, **1997**.

[8] *X-Shape, Version 1.03 and X-Red, Version 1.11*, STOE & CIE GmbH, Darmstadt, Germany, **1998**.

Received: July 4, 2007
Published Online: October 11, 2007

 © 2007 Wiley-VCH Verlag GmbH & Co. KGaA, Weinheim 

DOI: 10.1002/ejic.200700694

# New Mixed-Metal Aggregates Derived From Dinickel Complexes on a 2-Formylphenolate Template: Counteranion Dependent Formation of 1D Chain and Discrete $NaNi_2$ Complexes

**Alok Ranjan Paital,[a] Masahiro Mikuriya,[b] and Debashis Ray*[a]**

**Keywords:** Mixed-metal complexes / Imidazolidine / Dinuclear $Ni^{II}$ complexes / Crystal structure / Magnetic properties

The combination of 2-formylphenol (Hfp) and the dinucleating ligand $H_3L$ {2-(2′-hydroxyphenyl)-1,3-bis[4-(2-hydroxyphenyl)-3-azabut-3-enyl]-1,3-imidazolidine} with $Ni(NO_3)_2 \cdot 6H_2O$ leads to the self-assembly of a $Ni_2$ complex capable of showing anion dependent $Na^+$ coordination. The terminal aqua coordinated $[Ni_2(fp)L(H_2O)] \cdot 3H_2O$ (**1**·$3H_2O$) neutral fragment, formed in the absence of any $Na^+$ source, produces a 1D chain complex $[\{Ni_2(fp)L(N_3)(Na)(H_2O)\} \cdot 5H_2O]_n$ (**2**·$5H_2O)_n$ and a discrete $NaNi_2$ complex $[Ni_2(fp)L(Na)(H_2O)_2] \cdot ClO_4 \cdot H_2O$ (**3**·$ClO_4$·$H_2O$) through its weak oxophilic interaction with a $Na^+$ cation of the coordinated trisphenolate unit of $L^{3-}$ as observed in metallacrowns. In complexes **2** and **3**, the $Ni^{II}$ ions are coupled ferromagnetically to yield $S = 2$ ground states. The magnetic data can be modeled by using the Van Vleck equation incorporating intermolecular interactions.

(© Wiley-VCH Verlag GmbH & Co. KGaA, 69451 Weinheim, Germany, 2007)

## Introduction

Mixed-metal aggregates, involving intimate association of $Na^+$ ions with transition-metal clusters,[1] have recently drawn attention because of their interesting structural and magnetic properties and also because of their contribution towards the understanding of molecular recognition in biological systems.[2] Structural characterization of $Na^+$- and $Ca^{2+}$-bound $Mn_4$ clusters has shown promise in recent times for their relevance in understanding the oxygen-evolving center of photosystem II (PS II).[3] Salicylaldimines[4] and its substituted analogues[5] are known to exhibit simultaneous coordination of transition and alkali metal ions. In recent years, we and others were interested in the multinucleating properties of the ligand $H_3L$ {2-(2′-hydroxyphenyl)-1,3-bis[4-(2-hydroxyphenyl)-3-azabut-3-enyl]-1,3-imidazolidine, Scheme 1} for various reasons, which include their importance in bioinorganic chemistry, molecular magnetism, and catalysis.[6–11]

During the course of these investigations, we observed that under certain conditions, complexation reactions with $Mn^{III}$, $Fe^{III}$, $Co^{III}$, or $Cu^{II}$ leads to the hydrolysis of the imidazolidine ring[12–14] and even the destruction of the imine bond.[15] The instability of some of the dinuclear $Ni^{II}$ complexes of a related ligand was also reported.[16] While investigating the use of 2-formylphenol (Hfp) as a hydrolysis-inhibiting template ligand in nickel phenolate chemistry of $H_3L$, we recently observed that hydrolysis can be prevented by use of the appropriate *o*-formylphenols as coligands, namely 2-formylphenol (Hfp, Scheme 1, right) and 2,6-diformyl-4-methylphenol (Hdfp).[17] The terminal single-water–coordinated, neutral complex $[Ni_2L(fp)(H_2O)] \cdot 3H_2O$ (**1**·$3H_2O$) was synthesized on the formylphenolate template as reported recently.[17] The substitution reaction of the coordinated water molecule was tested in a reaction with $NaN_3$ and provides a 1D chain complex $\{[Ni_2L(fp)(N_3)(Na)(H_2O)] \cdot 5H_2O\}_n$ (**2**·$5H_2O)_n$ that links $Ni_2$ neutral fragments by $(H_2O)NaN_3$ units. The role of the anion, which has the potential to remove the terminal water molecule coordinated to one of the nickel ions, for the metallacrown-ether-like coordination of the $Na^+$ cation through the coordinated trisphenolate unit of $L^{3-}$ is further verified by a second reaction of **1** with $NaClO_4 \cdot H_2O$ that forms $[Ni_2L(fp)(Na)(H_2O)_2] \cdot ClO_4 \cdot H_2O$ (**3**·$ClO_4$·$H_2O$). In complex **3**, as the coordinated water molecule cannot be substituted by bulky perchlorate anion because of steric effects, it remains uncoordinated. These reactions constitute rare examples in which simultaneous incorporation of both

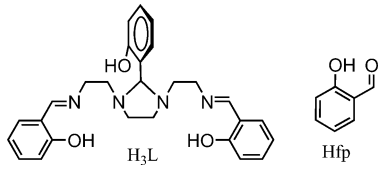


Scheme 1.

[a] Department of Chemistry, Indian Institute of Technology, Kharagpur 721302, India
Fax: +91-3222-82252
E-mail: dray@chem.iitkgp.ernet.in
[b] School of Science and Technology, Kwansei Gakuin University, 2-1 Gakuen 669-1337, Japan

Supporting information for this article is available on the WWW under http://www.eurjic.org or from the author.


WILEY InterScience DISCOVER SOMETHING GREAT
© 2007 Wiley-VCH Verlag GmbH & Co. KGaA, Weinheim

cation and anion in a charge neutral complex is observed. The oxophilic nature of $Na^+$ allows its coordination to the trisphenolate unit first, after which anions are either incorporated or remain uncoordinated in order to provide 1D chain or discrete $NaNi_2$ complexes, respectively. The typical arrangement of $L^{3-}$ around the $Ni^{II}$ ions in **1** leads to the formation of a [–O–Ni–O–Ni–O–] moiety disposed so as to provide three *facial* oxygen donors that form distorted square-pyramidal and trigonal coordination environments around $Na^+$ cation, which is different from the most common octahedral coordination.[8,18]

Herein, we report the synthesis, crystallographic characterization, and magnetic properties of two different $Na^+$-bound $Ni_2$ complexes assembled on formylphenolate templates and with a coordinated capping dinucleating $L^{3-}$ ligand. The anion-dependent binding of $Na^+$ ions leads to a novel 1D $Ni_2(O_3)$–Na–$N_3$–$Ni_2(O_3)$ chain and a discrete $NaNi_2$ complex.

## Results and Discussion

### Syntheses, Reactivity, and Spectroscopic Characterizations

The ligand $H_3L$ {2-(2′-hydroxyphenyl)-1,3-bis[4-(2-hydroxyphenyl)-3-azabut-3-enyl]-1,3-imidazolidine} was prepared according to a literature procedure.[19] The aqua $Ni_2$ complex **1** was prepared on a 2-formylphenolate ($fp^-$) template by using $Ni(NO_3)_2{\cdot}6H_2O$ and $H_3L$ in MeOH solvent under refluxing conditions following a standardized procedure reported by us.[17] In that report we noticed that in solution, $H_3L$ is unstable during reactions with nickel(II) salts and crystals of the hydrogen-bonded dimer of the mononuclear complex cations $[Ni(HL')]_2^{2+}$ were produced in low yield ($H_2L'$ is the hexadentate proligand formed from the imidazolidine ring hydrolysis of $H_3L$).[17] Since the 2-formylphenolate ($fp^-$) moiety is generated from the hydrolysis of $L^{3-}$, the ligand decomposition could be inhibited in the presence of the former as a template. The process of ligand hydrolysis, however, is inhibited completely if Hfp is mixed beforehand with a solution of $Ni(NO_3)_2{\cdot}4H_2O$, which presumably leads to the formation of intermediate **A** (Scheme 2). This results in the formation of complex **1** after addition of $H_3L$, where the deprotonated 2-formylphenolate ($fp^-$) behaves as a tridentate bridging ligand that stabilizes the $Ni^{II}_2$ complex. In the present work, we have studied the anion-dependent metalloligand behavior of **1** towards the binding of the sodium ion. A general procedure was followed for the synthesis of complexes **2** and **3** by using two sources of $Na^+$ such as $NaN_3$ and $NaClO_4{\cdot}H_2O$ in MeCN at room temperature in air. The reaction of complex **1** with $NaN_3$ in a 1:1 or 1:2 molar ratio in $CH_3CN$/MeOH (1:1) solvent mixture with stirring in air gives a green microcrystalline complex **2** in 78% yield (Scheme 2).

Addition of excess $NaN_3$ could not displace the formylphenolate template from **1** to produce any azido-bridged dinickel complex. The reaction of complex **1** with $NaClO_4{\cdot}H_2O$ in $CH_3CN$/EtOH (1:1) whilst stirring in air at room temperature yields **3** as a green microcrystalline com-

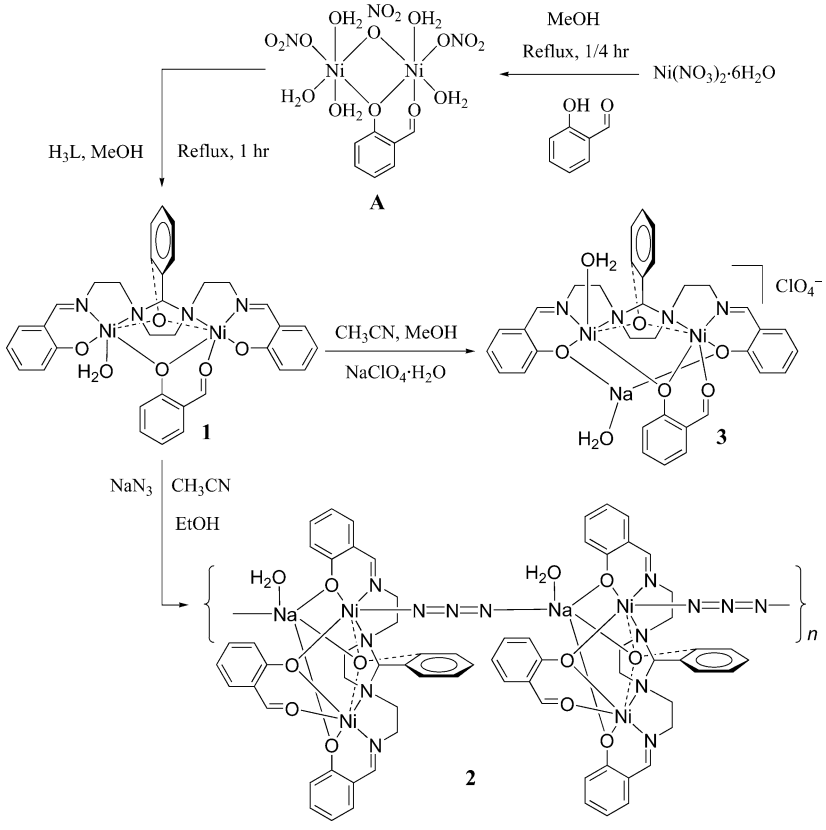


Scheme 2.

 © 2007 Wiley-VCH Verlag GmbH & Co. KGaA, Weinheim 

plex in 75% yield. Both of these reactions show that oxophilic $Na^+$ ions could be attached at the trisphenolate metaloligand site of the $Ni_2L$ fragment and that charge neutrality is maintained by anions. All the compounds are insoluble in water and separate directly from the reaction mixture, and were thoroughly washed with water before characterization. The formulation of all the complexes is consistent with elemental and metal analysis and solution electrical conductivity data in $CH_3CN$. The molar conductivity values ($\Lambda_M$) are 16 and 130 $\Omega^{-1}cm^2\,mol^{-1}$ (28 °C) and are consistent with the charge neutral and 1:1 electrolyte behavior of **2** and **3**, respectively. FTIR and UV/Vis spectral analyses also confirm the formation of **2** and **3**.

### Infrared Spectroscopy

The FTIR spectra of **2** and **3** show strong absorption bands at 1639 and 1642 $cm^{-1}$, respectively, which are characteristic of the coordinated C=N functionality of the ligand $L^{3-}$, and these values are slightly lowered in energy relative to that of the free ligand $H_3L$. Broad medium bands spanning the 3600 to 3200 $cm^{-1}$ range with maxima at 3411 and 3421 $cm^{-1}$ are observed, which can be assigned to ν(OH) stretching vibrations from both the metal-ion-coordinated and lattice water molecules in complexes **2** and **3**, respectively. Both the asymmetric and symmetric stretching vibrations are in this range. Strong bands at 1598 and 1600 $cm^{-1}$ are observed, which correspond to ν(C=O) of the coordinated functionality of $fp^-$ in complexes **2** and **3**, respectively. In addition, complex **2** shows a very strong sharp band at 2074 $cm^{-1}$ for the $\nu_{as}(N_3^-)$ stretching band.[20] The FTIR spectrum of complex **3** contains the characteristic vibration at 1121 $cm^{-1}$ for the uncoordinated tetrahedral perchlorate anion.[21]

### Electronic Spectroscopy

Hexacoordination of the metal centers in **2** and **3** is also retained in solution as evidenced by the UV/Vis absorption spectra. The light green solution of complex **2** shows three broad electronic absorption bands at 932 ($\nu_1$, $\varepsilon$ = 90 $M^{-1}cm^{-1}$), 783 ($\nu_2$, $\varepsilon$ = 35 $M^{-1}cm^{-1}$) and 603 nm ($\nu_3$, $\varepsilon$ = 60 $M^{-1}cm^{-1}$). These can be assigned to the $^3A_{2g}(F)\rightarrow{}^3T_{2g}(F)$, $^3A_{2g}(F)\rightarrow{}^1E_{1g}(D)$, and $^3A_{2g}(F)\rightarrow{}^3T_{1g}(F)$ ligand-field transitions in accord with $d^8$ ions in near octahedral coordination environments.[22] Apart from these, two other bands at 375 ($\varepsilon$ = 12605 $M^{-1}cm^{-1}$) and 271 nm ($\varepsilon$ = 17235 $M^{-1}cm^{-1}$) are observed, which arise from charge-transfer transitions. Similarly, for complex **3**, bands at 922 ($\varepsilon$ = 85 $M^{-1}cm^{-1}$), 783 ($\varepsilon$ = 30 $M^{-1}cm^{-1}$), and 510 nm ($\varepsilon$ = 55 $M^{-1}cm^{-1}$) are observed as a result of d–d transitions assigned to $^3A_{2g}(F)\rightarrow{}^3T_{2g}(F)$, $^3A_{2g}(F)\rightarrow{}^1E_{1g}(D)$, and $^3A_{2g}(F)\rightarrow{}^3T_{1g}(F)$ transitions, respectively. Apart from these, two other bands at 375 ($\varepsilon$ = 12870 $M^{-1}cm^{-1}$) and 295 nm ($\varepsilon$ = 14485 $M^{-1}cm^{-1}$) are observed for the charge-transfer transitions. The band arising from the $^3A_{2g}(F)\rightarrow{}^3T_{1g}(P)$ transition is probably hidden under the intense absorption bands in the near ultraviolet region of the spectrum at 375 nm.

### Description of Structures

Green blocklike single crystals suitable for X-ray structure determination were obtained by slow evaporation of $CH_3CN$ and $CH_3CN$/EtOH (1:1) solutions of **2** and **3**, respectively, after a week. Atom labeling scheme and molecular views (ORTEP) of the complexes are shown in Figures 1–9. Selected interatomic distances and angles are collected in Table 1 and Table 2.

Table 1. Selected interatomic distances [Å] and angles [°] for complex **2**.

| | | | |
|---|---|---|---|
| Ni1–O1 | 1.989(8) | O1–Ni1–N2 | 174.0(4) |
| Ni1–N1 | 2.025(10) | N1–Ni1–N2 | 83.0(4) |
| Ni1–O4 | 2.041(7) | O4–Ni1–N2 | 95.1(3) |
| Ni1–O2 | 2.070(6) | O2–Ni1–N2 | 90.2(3) |
| Ni1–O5 | 2.099(8) | O5–Ni1–N2 | 91.7(3) |
| Ni1–N2 | 2.176(9) | N4–Ni2–O3 | 90.7(3) |
| Ni2–N4 | 1.997(8) | N4–Ni2–O4 | 173.8(3) |
| Ni2–O3 | 2.012(7) | O3–Ni2–O4 | 92.1(3) |
| Ni2–O4 | 2.082(6) | N4–Ni2–N5 | 91.5(4) |
| Ni2–N5 | 2.083(12) | O3–Ni2–N5 | 91.9(4) |
| Ni2–O2 | 2.103(7) | O4–Ni2–N5 | 93.8(4) |
| Ni2–N3 | 2.196(9) | N4–Ni2–O2 | 97.6(3) |
| Na1–O3 | 2.264(9) | O3–Ni2–O2 | 88.2(3) |
| Na1–O1 | 2.301(9) | O4–Ni2–O2 | 77.1(3) |
| Na1–N7 | 2.364(19) | N5–Ni2–O2 | 170.9(4) |
| Na1–O2 | 2.377(8) | N4–Ni2–N3 | 83.3(3) |
| Na1–O6 | 2.513(16) | O3–Ni2–N3 | 171.8(3) |
| | | O4–Ni2–N3 | 93.3(3) |
| Ni1–O4–Ni2 | 99.2(3) | N5–Ni2–N3 | 93.8(4) |
| Ni1–O2–Ni2 | 97.6(3) | O2–Ni2–N3 | 87.0(3) |
| O1–Ni1–N1 | 91.0(4) | O3–Na1–O1 | 127.9(4) |
| O1–Ni1–O4 | 90.9(3) | O3–Na1–N7 | 114.1(5) |
| N1–Ni1–O4 | 175.6(4) | O1–Na1–N7 | 118.0(5) |
| O1–Ni1–O2 | 90.5(3) | O3–Na1–O2 | 76.2(3) |
| N1–Ni1–O2 | 105.2(3) | O1–Na1–O2 | 76.1(3) |
| O4–Ni1–O2 | 78.7(3) | N7–Na1–O2 | 122.3(5) |
| O1–Ni1–O5 | 88.9(3) | O3–Na1–O6 | 91.9(5) |
| N1–Ni1–O5 | 88.3(4) | O1–Na1–O6 | 83.0(5) |
| O4–Ni1–O5 | 87.8(3) | N7–Na1–O6 | 96.7(7) |
| O2–Ni1–O5 | 166.5(3) | O2–Na1–O6 | 140.9(6) |

### *$\{[Ni_2(fp)L(N_3)(Na)(H_2O)]\cdot5H_2O\}_n$ $(2\cdot5H_2O)_n$*

The molecular structure of **2** in Figure 1 reveals a dinuclear asymmetric unit that is similar to that in complex **1** with the coordination of azide to the $Ni^{II}$ ion instead of water. One $Na^+$ cation sits on the *facial* trisphenolate unit of the $Ni_2L$ fragment, and $N_3^-$ anion maintains the charge neutrality within the molecule. In all other respects, the asymmetric unit of **2** has a similar structural description as that of **1** and also exhibits similar metric parameters. The asymmetric units in **2** are interconnected through end-to-end[23] azide bridges between Ni2 and Na1, and the 1D chain[24] in complex $\{[Ni_2L(fp)(Na)(N_3)(H_2O)]\cdot5H_2O\}_n$ $(2\cdot5H_2O)_n$ is propagated (Figure 2).

 © 2007 Wiley-VCH Verlag GmbH & Co. KGaA, Weinheim 

Table 2. Selected interatomic distances [Å] and angles [°] for complex **3**.

| | | | |
|---|---|---|---|
| Ni1–O4 | 2.009(5) | O2–Ni1–O5 | 169.2(2) |
| Ni1–N1 | 2.018(7) | O1–Ni1–O5 | 89.5(3) |
| Ni1–O2 | 2.026(5) | O4–Ni1–N2 | 96.0(2) |
| Ni1–O1 | 2.067(5) | N1–Ni1–N2 | 83.9(3) |
| Ni1–O5 | 2.069(7) | O2–Ni1–N2 | 91.9(2) |
| Ni1–N2 | 2.118(7) | O1–Ni1–N2 | 172.0(2) |
| Ni2–O3 | 2.006(5) | O5–Ni1–N2 | 92.0(3) |
| Ni2–N4 | 2.006(7) | O3–Ni2–N4 | 90.1(3) |
| Ni2–O4 | 2.057(5) | O3–Ni2–O4 | 91.9(2) |
| Ni2–O2 | 2.058(5) | N4–Ni2–O4 | 177.8(3) |
| Ni2–N3 | 2.189(7) | O3–Ni2–O2 | 91.2(2) |
| O6–Ni2 | 2.154(6) | N4–Ni2–O2 | 102.4(2) |
| Na1–O1 | 2.498(8) | O4–Ni2–O2 | 78.6(2) |
| Na1–O3 | 2.570(7) | O3–Ni2–O6 | 90.0(2) |
| | | N4–Ni2–O6 | 87.0(3) |
| Ni1–O2–Ni2 | 96.3(2) | O4–Ni2–O6 | 92.0(2) |
| Ni1–O4–Ni2 | 96.9(2) | O2–Ni2–O6 | 170.6(2) |
| O4–Ni1–N1 | 175.3(3) | O3–Ni2–N3 | 173.0(2) |
| O4–Ni1–O2 | 80.5(2) | N4–Ni2–N3 | 83.1(3) |
| N1–Ni1–O2 | 104.2(3) | O4–Ni2–N3 | 94.9(2) |
| O4–Ni1–O1 | 91.9(2) | O2–Ni2–N3 | 88.7(2) |
| N1–Ni1–O1 | 88.4(2) | O6–Ni2–N3 | 91.2(3) |
| O2–Ni1–O1 | 88.0(2) | O7–Na1–O1 | 110.4(6) |
| O4–Ni1–O5 | 89.1(2) | O7–Na1–O3 | 109.4(6) |
| N1–Ni1–O5 | 86.2(3) | O1–Na1–O3 | 107.1(3) |

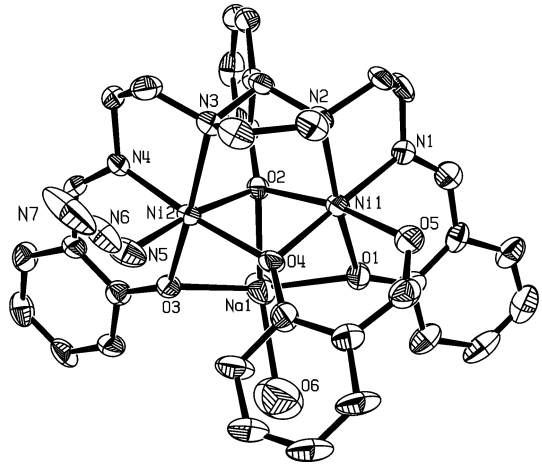


Figure 1. ORTEP representation of an asymmetric unit of $[Ni_2L(fp)(Na)(N_3)(H_2O)]$ (**2**) at the 50% probability level. Hydrogen atoms are omitted for clarity. Only independent non-carbon atoms are labeled.

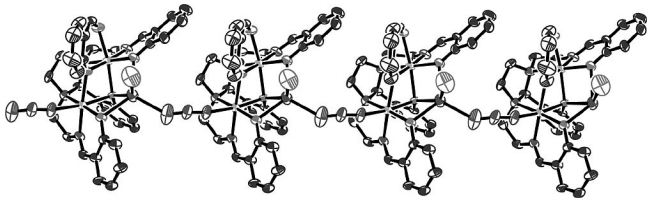

Figure 2. ORTEP representation of $\{[Ni_2L(fp)(Na)(N_3)(H_2O)]\cdot 5H_2O\}_n$ (**2**·$5H_2O$)$_n$ at the 50% probability level. Hydrogen atoms are omitted for clarity.

Complex **2** (Figure 1) is an aggregate of two $Ni^{II}$ ions linked together by the $N_4O_3$ heptadentate ligand $L^{3-}$ (Scheme 1). The bridging function is accomplished by the central imidazolidine group (NCN group) and phenoxide moiety (one μ-O atom) of $L^{3-}$, while the imine N atom and the phenoxide O donor at each side of the ligand occupy two additional coordination sites of each $Ni^{II}$ center. An exogenous bidentate 2-formylphenolate ($fp^-$) ligand contributes to the bridging within the complex through the phenolate O donor and introduces asymmetry by binding to only one Ni atom through its carbonyl moiety. Hexacoordination around the other Ni ion is then achieved through the binding of an azide ion. The two Ni atoms are thus coordinated in distorted octahedral $N_2O_4$ and $N_3O_3$ environments; the two octahedra share the edge defined by the bridging phenolate oxygen atoms (Scheme S1). The planes intersecting at this edge form an angle of 153.37° as a result of the folding imposed by the imidazolidine ring [N2···N3 distance of 2.272(5) Å]. The geometric restrictions resulting from $L^{3-}$ also lead to different Ni–O–Ni angles, 97.6(3)° and 99.2(3)° for the endogenous and exogenous phenolate oxygen atoms, respectively. The intramolecular Ni···Ni distance is 3.139(4) Å relative to 3.056 Å in complex **1**, which clearly indicates that this distance is increased as a result of 1D chain formation. The imidazolidine nitrogen atoms [Ni–$N_{imd}$ (imd = imidazolidine) distances of 2.176(9) and 2.196(9) Å] are further away from $Ni^{II}$ than the imine nitrogen atoms [Ni–$N_{im}$ (im = imine) distances of 1.997(8) and 2.025(10) Å]. The O–Ni–O angles [78.7(3) and 77.1(3)°] within the metallacyclic $Ni_2(\mu\text{-}O)_2$ diamond core indicate distortions of the metal ion octahedra. The degree of distortion from an ideal octahedral (90°) geometry is reflected in the *cisoid* [105.2(3)–77.1(3)°] and the *transoid* [175.6(4)–166.5(3)°] angles. The bridging Ni–O(phenolate) distances (av. 2.073 Å) are longer than the terminal distances (av. 2.005 Å). The terminal Ni–O(carbonyl) and Ni–N(azide) distances are 2.099(8)° and 2.083(12) Å, respectively. The particular arrangement of $L^{3-}$ around the $Ni^{2+}$ ions leads to the formation of a [–O–Ni–O–Ni–O–] moiety (Figure 3 left) disposed so as to provide three facial donors that form an isosceles triangular face in order to favorably interact with the sodium ion through one oxygen atom of each of the phenolate groups [$d$(Na–$O_{Ph}$) = 2.264(9)–2.377(8) Å] (Scheme 3 left). These distances fall within the ranges observed for other metallacrowns or metallacryptates.[25] The sodium ion is found in an overall five-coordinate geometry ($NO_4$ donors); the three phenolate O atoms, a water O atom [$d$(Na–O6) = 2.513(16) Å], and a bridging azido N atom [$d$(Na–N7) = 2.364(19) Å]. Its coordination geometry can be viewed as a distorted square-pyramid in which the azido ligand is located in the apical position (Figure 3 right).

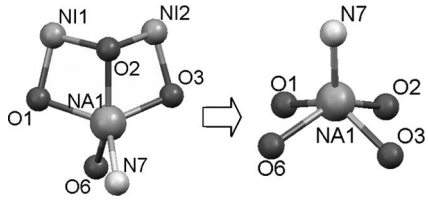


Figure 3. Left: the $NaNO_4Ni_2$ core in **2**; right: the square-pyramidal coordination environment around the $Na^+$ ion.

 © 2007 Wiley-VCH Verlag GmbH & Co. KGaA, Weinheim 

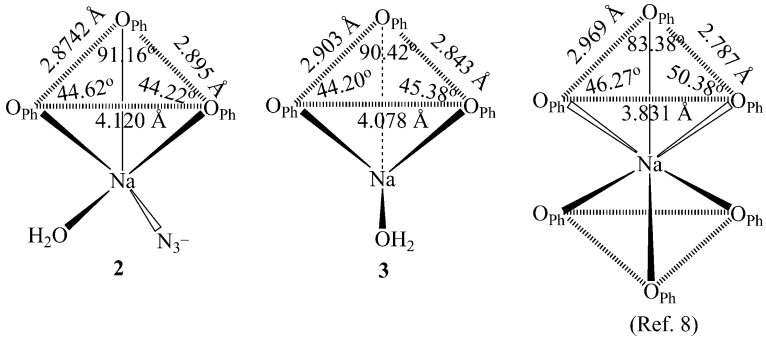


Scheme 3. Different coordination environments around $Na^I$. Left: the coordination of a trisphenolate isosceles triangular face within a $NaNO_4$ core in **2**; middle: the same $O_3$ triangular face within a $NaO_4$ core in **3**; right: the relative orientation of two such faces in a $NaO_6$ core in a reported $Cu_4$ complex (ref.[8]).

The staggered face-to-face orientation of two such triangular faces of the O donors of each ligand in $Cu_2L(N_3)$ is responsible for trapping the $Na^+$ cation in a distorted octahedral geometry, as reported earlier[8] (Scheme 3 right). Thus, the 1,3-bridging mode of the azido group between Ni and Na prevents any formation of a $Ni_4$-type cluster and leads to a 1D network with a Ni2···Na1 distance of 6.108 Å. The torsion angle around Ni2–N5–N7–Na1 is –89.09°, which indicates a *cis* bridging of $N_3^-$ in a *gauche* conformation (Figure 4). The crystal-packing diagram along the crystallographic *a* axis is depicted in Figure S1.

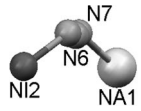


Figure 4. The *gauche* conformation of the $N_3$ bridge between Na and Ni.

The coordinated and lattice water molecules in **2** form an intermolecular hydrogen-bonded 2D network (Figure 5). Three of the five water molecules of crystallization [containing the O7, O8, O11 atoms] are involved in a zigzag intermolecular hydrogen-bonding network – the O6 atoms coordinated to the $Na^+$ ions connect two adjacent rows of azide-bridged 1D molecular chains made up of Ni2···Na1 units through a hydrogen-bonding network along the crystallographic *b* axis (Figure 6). The interatomic distances within this network are 2.78(3), 3.07(3), 2.70(3), and 2.82(3) Å, respectively, for the O6···O11, O11···O7, O7···O8, and O8···O6 interactions. The O7 atom is further hydrogen bonded with the template carbonyl oxygen atom O5 [O5···O7, 2.867(17) Å], which generates another network along the *a* axis (Figure 7). The remaining two water molecules of crystallization show strong hydrogen bonding [O9···O10, 2.43(4) Å], and O9 is further hydrogen bonded with the azide N7 nitrogen atom with a distance of 2.985(5) Å.

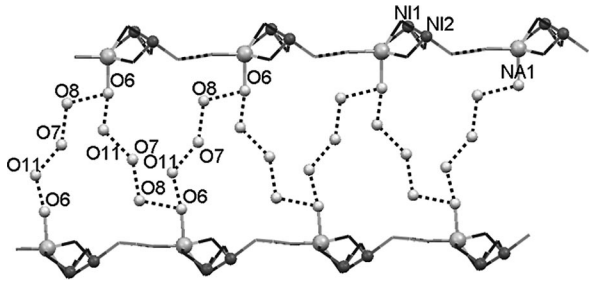


Figure 6. The hydrogen-bonded 1D water chain running along the crystallographic *b* axis between the two azido-bridged 1D molecular chains in **2**.

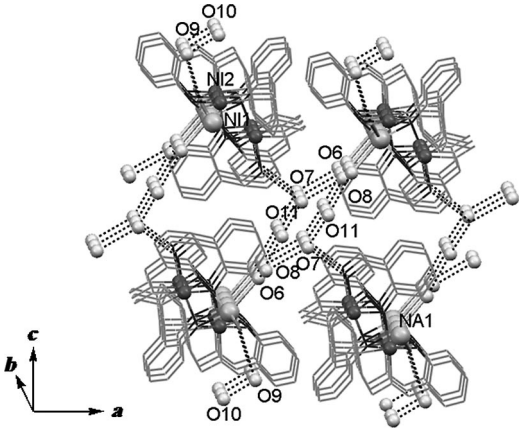


Figure 5. The intermolecular hydrogen-bonded 2D network viewed along an arbitary axis in **2**.

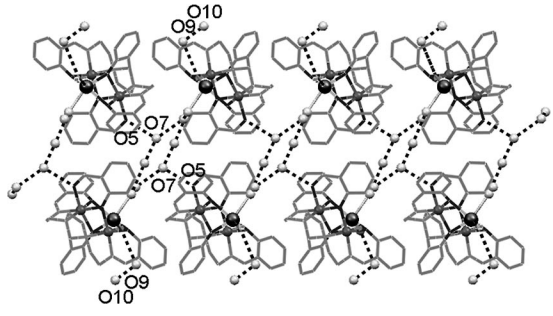


Figure 7. The hydrogen-bonded 1D chain connecting the $NaNi_2$ units along the crystallographic *a* axis in **2**. Ni: dark gray; O: light gray; Na: black.

 © 2007 Wiley-VCH Verlag GmbH & Co. KGaA, Weinheim 

### *[$Ni_2$(fp)LNa($H_2O$)$_2$]·$ClO_4$·$H_2O$ (3·$ClO_4$·$H_2O$)*

The molecular structure of **3** reveals a $[Ni_2L(fp)Na(H_2O)_2]^+$ complex cation and a $ClO_4^-$ anion with one water molecule of crystallization. Complex **3** (Figure 8) is a dinuclear aggregate of $Ni^{II}$ ions bridged and chelated by the ligand $L^{3-}$ in the same manner as in complex **2**, with the exception that one $Na^+$ cation is coordinated to two terminal phenolate oxygen atoms and one water molecule of crystallization.

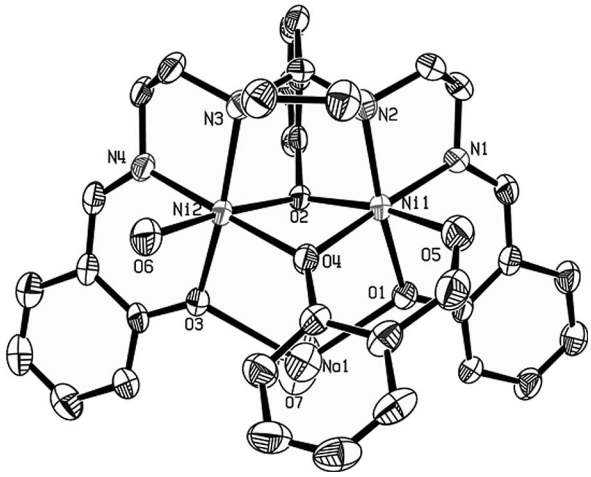


Figure 8. ORTEP representation of $[Ni_2L(fp)(Na)(H_2O)_2]^+$ (**3**) at the 40% probability level. Hydrogen atoms are omitted for clarity. Only independent non-carbon atoms are labeled.

An exogenous 2-formylphenolate ($fp^-$) ligand contributes to the bridging in the complex through the phenolate O donor and introduces asymmetry into the complex by binding to only one Ni atom through its carbonyl moiety. The Ni–O(carbonyl) distance of 2.069(7) Å is typical for this type of linkage, as in Ni–O(urea).[26] Hexacoordination around the other Ni ion is achieved through the binding of a molecule of water. Each Ni atom is thus coordinated in a distorted octahedral $N_2O_4$ environment; the two octahedra share the edge defined by the bridging phenolate oxygen atoms (Scheme S1). The planes intersecting at this edge form an angle of 152.46°, as a result of the folding imposed by imidazolidine ring [N2···N3 distance of 2.296(5) Å]. The O–Ni–O angles [80.5(2) and 78.6(2)°] within the metallacyclic $Ni_2(\mu\text{-}O)_2$ diamond core indicate distortions of the metal ion octahedra. The degree of distortion from an ideal octahedral (90°) geometry is reflected in the *cisoid* [104.2(3)–78.6(2)°] and the *transoid* [177.8(3)–169.2(2)°] angles. The Ni–$O_{Ph}$ bond lengths are in the range 2.006(5)–2.154(6) Å. The bridging Ni–O(phenolate) distances (av. 2.037 Å) are comparable with the terminal distances (av. 2.036 Å). The terminal Ni–O(carbonyl) and Ni–O(water) distances are 2.069(7) Å and 2.154(6) Å, respectively. The geometric restrictions resulting from $L^{3-}$ also lead to different Ni–O–Ni angles [96.3(2)° and 96.9(2)° for endogenous and exogenous phenolate oxygen atoms, respectively]. The intramolecular Ni···Ni distance is 3.042 Å and is comparable to 3.056 Å in complex **1**. The imidazolidine N atoms [Ni–$N_{imd}$ distances of 2.118(7) and 2.189(7) Å] are further away from $Ni^{II}$ than the imine N atoms [Ni–$N_{im}$ distances of 2.006(7) and 2.018(7) Å]. The $O_4$ coordination environment around the $Na^+$ cation is a distorted tetrahedral with O–Na–O bond angles within the range 107.1(3)–110.4(6)°. The particular arrangement of $L^{3-}$ around the metal ions provides three facial donors that form an isosceles triangular face such that they can favorably interact with the $Na^+$ ion (Scheme 3, middle), which is loosely held by the terminal phenolate O atoms of the $Ni_2L$ fragment as evidenced from the Na–$O_{Ph}$ bond lengths of 2.498(8) and 2.570(7) Å, which are comparable to the Na–$O_{water}$ distance of 2.496(18) Å in **2**.

The central endogenous phenolate oxygen atom is 3.310 Å away from the $Na^+$ cation, which is longer than 2.388(9) Å in **2**. The oxygen atom (O6) of the coordinated water molecule to $Ni^{II}$ is engaged in hydrogen bonding with the oxygen atom (O8) of the lattice water molecule and one of the oxygen atoms (O11) of the perchlorate anion with distances of 2.698 [O6···O8] and 3.028 Å [O6···O11], respectively (Figure 9). A crystal-packing diagram along the *b* axis is depicted in Figure S2.

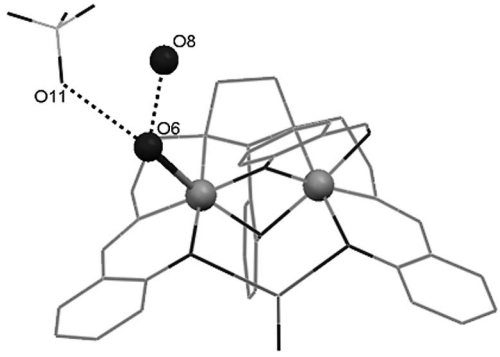


Figure 9. Intramolecular hydrogen bonding between the coordinated water molecule and the anion and the lattice water molecule viewed along an arbitary axis.

## Magnetic Properties

### *{[$Ni_2$(fp)L($N_3$)(Na)($H_2O$)]·5$H_2O$}$_n$ (2·5$H_2O$)$_n$*

The magnetic exchange within the 1D polymeric motif of complex **2** was investigated by means of bulk magnetization methods. Measurements were collected under a constant magnetic field of 0.5 T in the temperature range 4.5–300 K. The effective magnetic moment at 300 K of the 1D chain is 4.66 $\mu_B$ per molecule of the above complex; this value is 4.72 $\mu_B$ at 4.5 K. The plots of $\chi_M$ and $\mu_{eff}$ as a function of *T* for this complex are represented in Figure 10 ($\chi_M$ is the molar paramagnetic susceptibility and $\mu_{eff}$ is effective magnetic moment). At room temperature, $\chi_M$ is slightly higher than that expected for a pair of independent $Ni^{II}$ ions with a *g* value of 2.29, and it increases upon cooling, with a more pronounced slope as the temperature approaches zero. This behavior clearly shows that the intramolecular coupling is ferromagnetic. The magnetic data were fitted by consider-

 © 2007 Wiley-VCH Verlag GmbH & Co. KGaA, Weinheim 

ing the intermolecular interactions. The model involves the use of a $\chi_M = f(T)$ expression [Equation (1)] derived from the Van Vleck equation.

$$\chi_M = \frac{2Ng^2\beta^2}{k(T-\theta)}\left[\frac{5+\exp(-4J/kT)}{5+3\exp(-4J/kT)+\exp(-6J/kT)}\right] \quad (1)$$

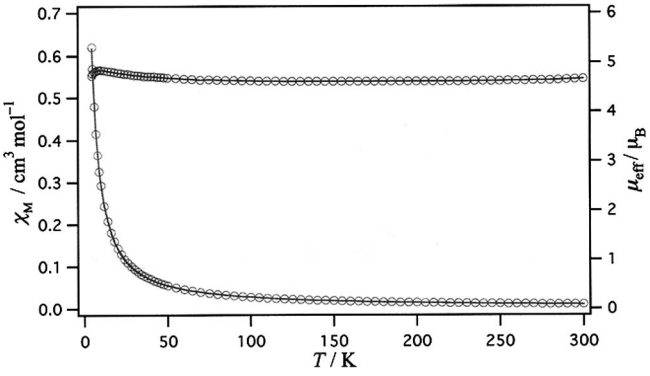


Figure 10. Plot of the temperature dependence of $\chi_M$ and $\mu_{eff}$ for **2**.

The parameters for this fit are $J = 2.02\ cm^{-1}$, $g = 2.29$, and $\theta = -1.7$ K. The small and ferromagnetic intramolecular coupling may be ascribed to the Ni–O–Ni angles formed by the phenolate bridges [between 97.6(3) and 99.0(3)°], which are within the range predicted for ferromagnetic interactions between the two nickel(II) ions, or to the imidazolidine –NCN– bridge, which also has been shown to facilitate ferromagnetic Ni···Ni exchange interaction.[17] The weak interdimer antiferromagnetic coupling is mediated by the Ni–$\mu_{1,3}$-$N_3$–Na···Ni bridges.

### *[$Ni_2$(fp)L(Na)($H_2O$)$_2$]·$ClO_4$·$H_2O$ (3·$ClO_4$·$H_2O$)*

The magnetic exchange within the binuclear motif of complex **3** was investigated by means of bulk magnetization methods. Measurements were made under a constant magnetic field of 0.5 T in the temperature range 4.5–300 K. The effective magnetic moment at 300 K of the binuclear complex **3** is 4.54 $\mu_B$ per molecule of the above complex; this value is 4.99 $\mu_B$ at 4.5 K. The temperature dependence of the magnetic moment was analyzed by the same $\chi_M = f(T)$ expression [Equation (1)] as that for complex **2**. The plots of $\chi_M$ and $\mu_{eff}$ as a function of $T$ for this complex are represented in Figure 11. The parameters for this fit are $J = 3.04\ cm^{-1}$, $g = 2.24$, and $\theta = -0.87$ K. This behavior clearly shows that the intramolecular coupling is ferromagnetic in nature.

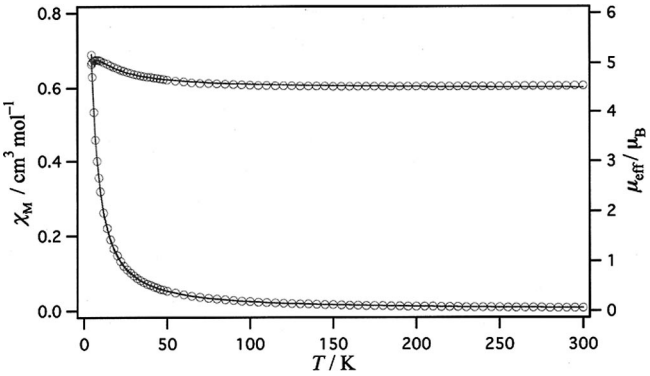


Figure 11. Plot of the temperature dependence of $\chi_M$ and $\mu_{eff}$ for **3**.

## Concluding Remarks

As part of the interesting metal–ligand chemistry of $L^{3-}$, we have previously shown that reaction of $H_3L$ with $Ni^{II}$ on 2-formylphenolate as a template leads to the high yield formation of the terminal aqua coordinated neutral metalloligand [$Ni_2$(fp)L($H_2O$)]·3$H_2O$ (**1**·3$H_2O$) in the absence of any $Na^+$ source. Now we have shown that reaction of complex **1** with two different sodium salts produces counteranion–controlled, new, mixed-metal 1D chains {[$Ni_2$(fp)L($N_3$)(Na)($H_2O$)]·5$H_2O$}$_n$ (**2**·5$H_2O$)$_n$ and discrete $NaNi_2$ complexes [$Ni_2$(fp)L(Na)($H_2O$)$_2$]·$ClO_4$·$H_2O$ (**3**·$ClO_4$·$H_2O$) through the metallacrown-like coordination of $Na^+$ ions to the trisphenolate face of the $Ni_2L$ fragments. Magnetic measurements indicate that complexes **2** and **3** exhibit ferromagnetic superexchange between the $Ni^{II}$ centers to yield $S = 2$ ground states. We are currently working to exploit the asymmetry induced by the external template bridges in this reaction system to obtain heterometallic complexes.

## Experimental Section

**Materials and Physical Measurements:** The chemicals used were obtained from the following sources: triethylenetetramine, sodium azide, and nickel nitrate hexahydrate from S.D. Fine Chem. (India) and 2-hydroxy benzaldehyde from SRL (India). All other chemicals and solvents were reagent grade materials and were used as received, without further purification. The elemental analyses (C, H, N) were performed with a Perkin–Elmer model 240C elemental analyzer. FTIR spectra were recorded with a Perkin–Elmer RX1 spectrophotometer. The solution electrical conductivity and electronic spectra were obtained by using a Unitech type U131C digital conductivity meter with a solute concentration of about $10^{-3}$ M and a Shimadzu UV 3100 UV/Vis/NIR spectrophotometer, respectively. The room temperature magnetic susceptibilities in the solid state were measured with a home-built Gouy balance fitted with a Polytronic d.c. power supply. The experimental magnetic susceptibilities were corrected for the diamagnetic response by using Pascal's constants. Magnetic measurements were carried out on polycrystalline samples (ca. 70 mg)with a Quantum Design MPMS-5S SQUID magnetometer operating at a constant magnetic field of 5000 G between 4.5–300 K. The experimental magnetic moment was corrected for the diamagnetic contribution from the sample holder and the diamagnetic response from the sample, which was evaluated from Pascal's constants.

**General:** All experimental procedures were carried out in air at room temperature. The ligand $H_3L$ {2-(2′-hydroxyphenyl)-1,3-bis[4-(2-hydroxyphenyl)-3-azabut-3-enyl]-1,3-imidazolidine} was prepared according to a literature procedure.[19] Complex **1** was synthesized by a literature procedure.[17]

 © 2007 Wiley-VCH Verlag GmbH & Co. KGaA, Weinheim 

Table 3. Crystallographic data for complexes $(\mathbf{2}\cdot 5H_2O)_n$ and $\mathbf{3}\cdot ClO_4\cdot H_2O$.

| | | |
|---|---|---|
| Molecular formula | $C_{34}H_{44}N_7O_{11}NaNi_2$ | $C_{34}H_{38}N_4O_{12}ClNaNi_2$ |
| Molecular weight | 867.13 | 870.51 |
| Crystal system | monoclinic | monoclinic |
| Space group | $P2_1/a$ | $P2_1/a$ |
| $a$ [Å] | 19.069(2) | 11.920(1) |
| $b$ [Å] | 9.036(1) | 17.536(2) |
| $c$ [Å] | 22.108(3) | 17.639(4) |
| $\beta$ [°] | 101.97(2) | 91.79(2) |
| $U$ [Å$^3$] | 3726.6(8) | 3685.4(10) |
| $D_c$ [g cm$^{-3}$] | 1.524 | 1.558 |
| $Z$ | 4 | 4 |
| $F$(000) | 1760 | 1776 |
| Crystal size [mm] | $0.32\times0.28\times0.26$ | $0.28\times0.26\times0.22$ |
| $\mu$ [mm$^{-1}$] | 1.091 | 1.174 |
| $\theta$ range [°] | 1.88–24.97 | 1.15–24.97 |
| $R_1$,[a] $wR_2$ [$I>2\sigma(I)$] | 0.0933, 0.2506 | 0.0810, 0.2142 |
| Goodness-of-fit on $F^2$ | 0.954 | 1.069 |
| Final difference map max, min [e Å$^{-3}$] | 0.875, –1.019 | 0.999, –1.147 |

[a] $R_1 = \Sigma(||F_o| - |F_c||)/\Sigma|F_o|$; $wR_2 = [\Sigma w(|F_o| - |F_c|)^2/\Sigma w(F_o)^2]^{1/2}$; $w = 0.75/[\sigma^2(F_o) + 0.0010F_o^2]$.

**$\{[Ni_2L(fp)(N_3)(Na)(H_2O)]\cdot 5H_2O\}_n$ $(\mathbf{2}\cdot 5H_2O)_n$:** A methanolic solution of $NaN_3$ (0.033 g, 0.52 mmol) was added dropwise to a $CH_3CN$ solution (50 mL) of complex **1** (0.4 g, 0.52 mmol) over 15 min, and the mixture was stirred for 1 h. The resulting solution was filtered and left undisturbed so that the solvents could slowly evaporate. After 4 d, a green crystalline product was obtained (≈78% yield). The solid was isolated, washed with cold methanol, and dried under vacuum over $P_4O_{10}$. $C_{34}H_{44}N_7NaNi_2O_{11}$ (867.17): calcd. C 47.09, H 5.11, N 11.30; found C 46.89, H 5.24, N 11.18%. Molar conductance (MeCN solution): $\Lambda_M = 16\ \Omega^{-1}cm^2mol^{-1}$. UV/Vis spectrum ($CH_3CN$): $\lambda_{max}$ ($\varepsilon_{max}$, $M^{-1}cm^{-1}$) = 932 (90), 783 (35), 603 (60), 375 (12605), 271 (17235) nm. Selected IR bands (KBr): $\tilde{\nu}$ = 3411 (br.), 2074 (s), 1639 (s), 1598 (s), 1535 (m), 1486 (m), 1447 (s), 1400 (m), 1341 (m), 1291 (m), 1150 (w), 760 (m) cm$^{-1}$.

**$[Ni_2L(fp)(Na)(H_2O)_2]\cdot ClO_4\cdot H_2O$ $(\mathbf{3}\cdot ClO_4\cdot H_2O)$:** A methanolic solution of $NaClO_4\cdot H_2O$ (0.073 g, 0.52 mmol) was added dropwise to a $CH_3CN$ solution (50 mL) of **1** (0.4 g, 0.52 mmol) over 15 min, and the mixture was stirred for 1 h. The resulting solution was filtered and left undisturbed so that the solvents could slowly evaporate. After 7 d, a green crystalline product was obtained (≈75% yield). The solid was isolated, washed with cold methanol, and dried under vacuum over $P_4O_{10}$. $C_{34}H_{38}ClN_4NaNi_2O_{12}$ (870.51): calcd. C 46.91, H 4.39, N 6.43; found C 46.86, H 4.22, N 6.34. Molar conductance (MeCN solution): $\Lambda_M = 130\ \Omega^{-1}cm^2mol^{-1}$. UV/Vis spectrum ($CH_3CN$): $\lambda_{max}$ ($\varepsilon_{max}$, $M^{-1}cm^{-1}$) = 922 (85), 783 (30), 510 (55), 375 (12870), 295(14485) nm. Selected IR bands (KBr): ν = 3421 (br.), 1642 (s), 1628 (s), 1600 (s), 1540 (m), 1484 (m), 1461 (m), 1445 (s), 1290 (m), 1121 (s), 758 (m) cm$^{-1}$.

**X-ray Crystallographic Procedures for 2 and 3:** Information concerning X-ray data collection and structure refinement of the compound is summarized in Table 3. The intensity data of the complexes **2** and **3** were collected on Nonius CAD4 X-ray diffractometer that uses graphite monochromated Mo-$K_\alpha$ radiation ($\lambda$ = 0.71073 Å) by ω-scan method. Data were collected at 293 K. For complex **2**, total of 6680 reflections were recorded with Miller indices, $h_{min}$ = 0, $h_{max}$ = 22, $k_{min}$ = 0, $k_{max}$ = 10, $l_{min}$ = –26, $l_{max}$ = 25. For complex **3**, a total of 6724 reflections were recorded with Miller indices, $h_{min}$ = 0, $h_{max}$ = 14, $k_{min}$ = 0, $k_{max}$ = 20, $l_{min}$ = –20, $l_{max}$ = 20. In the final cycles of full-matrix least-squares on $F^2$ all non-hydrogen atoms were assigned anisotropic thermal parameters. The positions of the H atoms bonded to C atoms were calculated (C–H distance 0.97 Å). The structure was solved using the programme SHELX-97[27] and refined by full-matrix least-squares methods with use of the programme SHELX-97.[28] CCDC-628157 and -628158 for complexes **2** and **3** contain the supplementary crystallographic data for this paper. These data can be obtained free of charge from The Cambridge Crystallographic Data Centre via www.ccdc.cam.ac.uk/data_request/cif.

**Supporting Information** (see footnote on the first page of this article): The distorted octahedral $N_2O_4$ and $N_3O_3$ environments around the Ni centres in complexes **2** and **3** and the packing diagrams of complexes **2** and **3** are presented.

## Acknowledgments

We are thankful to the Council of Scientific and Industrial Research, New Delhi, India for the financial support, and M. M. acknowledges the financial support by the "Open Research Center" Project for Private Universities: matching fund subsidy and Grants-in-Aid for Scientific Research No. 19550074 from the Ministry of Education, Culture, Sports, Science and Technology, Govt. of Japan.

[1] a) E. E. Moushi, T. C. Stamatatos, W. Wernsdorfer, V. Nastopoulos, G. Christou, A. J. Tasiopoulos, *Angew. Chem. Int. Ed.* **2006**, *45*, 7722–7725; b) E. E. Moushi, C. Lampropoulos, W. Wernsdorfer, V. Nastopoulos, G. Christou, A. J. Tasiopoulos, *Inorg. Chem.* **2007**, *46*, 3795–3797; c) M. Murugesu, W. Wernsdorfer, K. A. Abboud, E. K. Brechin, G. Christou, *Dalton Trans.* **2006**, 2285–2287; d) G. AromÌ, A. R. Bell, M. Helliwell, J. Raftery, S. J. Teat, G. A. Timco, O. Roubeau, R. E. P. Winpenny, *Chem. Eur. J.* **2003**, *9*, 3024–3032; e) D. M. J. Doble, C. H. Benison, A. J. Blake, D. Fenske, M. S. Jackson, R. D. Kay, W.-S. Li, M. Schröder, *Angew. Chem. Int. Ed.* **1999**, *38*, 1915–1918.

[2] C. Y. Huang, S. G. Rhee, P. B. Chock, *Annu. Rev. Biochem.* **1982**, *51*, 935–971.

[3] I. J. Hewitt, J.-K. Tang, N. T. Madhu, R. Clérac, G. Buth, C. E. Ansona, A. K. Powell, *Chem. Commun.* **2006**, 2650–2652.

[4] a) O. F. Schall, K. Robinson, J. L. Atwood, G. W. Gokel, *J. Am. Chem. Soc.* **1991**, *113*, 7434–7435; b) C. Chen, D. Huang, X. Zhang, F. Chen, H. Zhu, Q. Liu, C. Zhang, D. Liao, L. Li, L. Sun, *Inorg. Chem.* **2003**, *42*, 3540–3548; c) D. Cunningham, P. McArdle, M. Mitchell, N. N. Chonchubhair, M. O'Gara, *Inorg. Chem.* **2000**, *39*, 1639–1649.

 © 2007 Wiley-VCH Verlag GmbH & Co. KGaA, Weinheim 

[5] S. K. Dey, N. Mondal, M. S. E. Fallah, R. Vicente, A. Escuer, X. Solans, M. Font-Bardía, T. Matsushita, V. Gramlich, S. Mitra, *Inorg. Chem.* **2004**, *43*, 2427–2434.
[6] M. Bera, W. T. Wong, G. Aromí, D. Ray, *Eur. J. Inorg. Chem.* **2005**, 2526–2535.
[7] P. K. Nanda, G. Aromí, D. Ray, *Chem. Commun.* **2006**, 3181–3183.
[8] P. K. Nanda, G. Aromí, D. Ray, *Inorg. Chem.* **2006**, *45*, 3143–3145.
[9] M. Fondo, A. M. García-Deibe, M. Corbella, E. Ruiz, J. Tercero, J. Sanmartín, M. R. Bermejo, *Inorg. Chem.* **2005**, *44*, 5011–5020.
[10] M. Fondo, N. Ocampo, A. M. García-Deibe, M. Corbella, M. R. Bermejo, J. Sanmartín, *Dalton Trans.* **2005**, 3785–3794.
[11] M. Fondo, A. M. Garcia-Deibe, J. Sanmartin, M. R. Bermejo, L. Lezama, T. Rojo, *Eur. J. Inorg. Chem.* **2003**, 3703–3706.
[12] M. Bera, U. Mukhopadhyay, D. Ray, *Inorg. Chim. Acta* **2005**, *358*, 437–443.
[13] M. Bera, K. Biradha, D. Ray, *Inorg. Chim. Acta* **2004**, *357*, 3556–3562.
[14] P. K. Nanda, D. Mandal, D. Ray, *Polyhedron* **2006**, *25*, 702–710.
[15] P. K. Nanda, M. Bera, G. Aromí, D. Ray, *Polyhedron* **2006**, *25*, 2791–2799.
[16] M. Fondo, N. Ocampo, A. M. Garcia-Deibe, R. Vicente, M. Corbella, M. R. Bermejo, J. Sanmartin, *Inorg. Chem.* **2006**, *45*, 255–262.
[17] A. R. Paital, W. T. Wong, G. Aromí, D. Ray, *Inorg. Chem.* **2007**, *46*, 5727–5733.
[18] a) L. Balazs, H. J. Breunig, E. Lork, C. I. Rat, *Appl. Organomet. Chem.* **2005**, *19*, 1263–1267; b) G. L. Abbati, L.-C. Brunel, H. Casalta, A. Cornia, A. C. Fabretti, D. Gatteschi, A. K. Hassan, A. G. M. Jansen, A. L. Maniero, L. Pardi, C. Paulsen, U. Segre, *Chem. Eur. J.* **2001**, *7*, 1796–1807; c) R. W. Saalfrank, N. Low, B. Demleitner, D. Stalke, M. Teichert, *Chem. Eur. J.* **1998**, *4*, 1305–1311.
[19] E. Wong, S. Liu, T. Lugger, F. E. Hahn, C. Orvig, *Inorg. Chem.* **1995**, *34*, 93–101.
[20] M. Monfort, I. Resino, M. S. E. Fallah, J. Ribas, X. Solans, M. Font-Bardia, H. Stoeckli-Evans, *Chem. Eur. J.* **2001**, *7*, 280–287.
[21] a) M. Bera, W. T. Wong, G. Aromi, J. Ribas, D. Ray, *Inorg. Chem.* **2004**, *43*, 4787–4789; b) K. Nakamoto, *Infrared and Raman Spectra of Inorganic and Coordination Compounds*, 5th ed., Wiley & Sons, New York, **1997**.
[22] a) D. Nicholls in *Comprehensive Inorganic Chemistry* (Eds.: J. C. Bailar, H. J. Emeleus, R. Nyholm, A. F. Trotman-Dickenson), Pergamon, Oxford, **1973**, ch. 3, p. 1152; b) S. Mukhopadhyay, D. Ray, *Ind. J. Chem.* **1995**, *34A*, 466–468; c) T. Koga, H. Furutachi, T. Nakamura, N. Fukita, M. Ohba, K. Takahashi, H. Ōkawa, *Inorg. Chem.* **1998**, *37*, 989–996; d) M. Konrad, F. Meyer, A. Jacobi, P. Kircher, P. Rutsch, L. Zsolnai, *Inorg. Chem.* **1999**, *38*, 4559–4566.
[23] a) A. M. Madalan, M. Noltemeyer, M. Neculai, H. W. Roesky, M. Schmidtmann, A. Müller, Y. Journaux, M. Andruh, *Inorg. Chim. Acta* **2006**, *359*, 459–467; b) L. Fabrizzi, P. Pallavicini, L. Parodi, A. Perrotti, N. Sardone, A. Taglietti, *Inorg. Chim. Acta* **1996**, *244*, 7–9; c) A. Escuer, C. J. Harding, Y. Dussart, J. Nelson, V. McKee, R. Vicente, *J. Chem. Soc. Dalton Trans.* **1999**, 223–228.
[24] a) J. Ribas, A. Escuer, M. Monfort, R. Vicente, R. Cortés, L. Lezama, T. Rojo, *Coord. Chem. Rev.* **1999**, *193–195*, 1027–1068; b) M. Monfort, J. Ribas, X. Solans, M. Font-Bardia, *Inorg. Chem.* **1996**, *35*, 7633–7638; c) C. S. Hong, Y. Do, *Angew. Chem. Int. Ed.* **1999**, *38*, 193–195; d) R. Vicente, A. Escuer, J. Ribas, M. S. E. Fallah, X. Solans, M. Font-Bardia, *Inorg. Chem.* **1995**, *34*, 1278–1281.
[25] a) L. Y. Wang, S. Igarashi, Y. Yukawa, Y. Hoshino, O. Roubeau, G. Aromí, R. E. P. Winpenny, *Dalton Trans.* **2003**, 2318–2324; b) B. R. Gibney, H. Wang, J. W. Kampf, V. L. Pecoraro, *Inorg. Chem.* **1996**, *35*, 6184–6193.
[26] H. E. Wages, K. L. Taft, S. J. Lippard, *Inorg. Chem.* **1993**, *32*, 4985–4987.
[27] G. M. Sheldrick, *SHELXS-97, Program for the Solution of Crystal Structures*, University of Göttingen, Germany, **1997**.
[28] G. M. Sheldrick, *SHELXS-97, Program for the Refinement of Crystal Structures*, University of Göttingen, Germany, **1997**.

Received: July 3, 2007
Published Online: October 12, 2007

 © 2007 Wiley-VCH Verlag GmbH & Co. KGaA, Weinheim 

EurJIC European Journal of Inorganic Chemistry



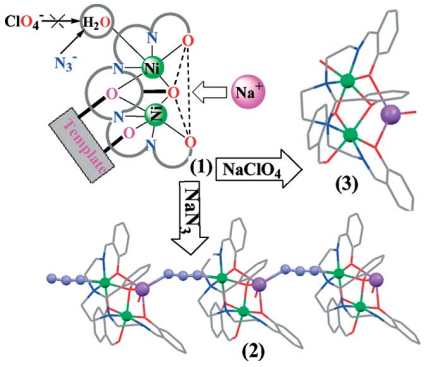


The reaction between the $Ni_2$ assembly on a formylphenolate template with a coordinated terminal water molecule and a capping imidazolidine ligand and $N_3^-$ or $ClO_4^-$ anions leads to two different types of products. The metallacrown-type coordination of the $Na^+$ cations results in new $NaNi_2$ complexes engaged in ferromagnetic interactions.

**A. R. Paital, M. Mikuriya, D. Ray* ..... 5360–5369**

New Mixed-Metal Aggregates Derived From Dinickel Complexes on a 2-Formylphenolate Template: Counteranion Dependent Formation of 1D Chain and Discrete $NaNi_2$ Complexes

**Keywords:** Mixed-metal complexes / Imidazolidine / Dinuclear $Ni^{II}$ complexes / Crystal structure / Magnetic properties

 © 2007 Wiley-VCH Verlag GmbH & Co. KGaA, Weinheim 

DOI: 10.1002/ejic.200700710

# Synthesis and X-ray Characterization of Mono- and Polynuclear Thiolatocopper(I) Complexes: The Effect of Steric Bulk on Coordination Number and Nuclearity

**Shiri Zeevi[a] and Edit Y. Tshuva*[a]**

**Keywords:** Copper / S ligands / Cluster compounds / Coordination modes / Metallochaperones

We have synthesized a number of $Cu^{I}$ complexes of thiophenolato ligands with different alkyl substituents in the *ortho* positions in a single-step procedure starting from a readily available copper(I) precursor to evaluate the coordination preferences of the metal atom. In most cases similar reaction conditions led to the formation of two complexes: a mononuclear complex and a polynuclear cluster, as evident from X-ray crystallography. One dinuclear complex formed has the unique geometry of an $L_2Cu_2(\mu\text{-}L)_2$ core that has not previously been observed for related systems. The steric bulk around the metal atom has a clear effect on the coordination sphere of the complex obtained. Ligands with no *ortho* substituents and those with one substituent with a size varying from methyl to *tert*-butyl all lead to the formation of three-coordinate complexes for the mononuclear species, and clusters of different sizes where larger substituents lead to larger cages and all copper centers are three-coordinate as well. The introduction of two methyl substituents (one in each *ortho* position) leads to either a mononuclear two-coordinate copper complex or a polynuclear cluster where two copper centers are three-coordinate and three are two-coordinate.

(© Wiley-VCH Verlag GmbH & Co. KGaA, 69451 Weinheim, Germany, 2007)

## Introduction

The recent discovery of a number of proteins from the family of copper metallochaperones, and their structural identification by X-ray crystallography, has refocused attention on copper(I) chemistry.[1–14] These proteins have a conserved motif of MTCXXC (single-letter abbreviation of amino acids, where X represents any amino acid), and binding to the copper(I) center is achieved through the two cysteine residues, with a potential third ligand in some cases. This coordination sphere, namely a low coordination number and soft thiolato ligands, favors the valence state of copper(I) over copper(II) and thus lowers the oxidation potential, which means that the possibly harmful redox behavior of copper is avoided as is any interference with other beneficial redox processes.

Numerous studies have been reported on copper(II) chemistry, including those directed towards modeling various copper protein active sites.[15–18] Herein we focus on understanding the structure and coordination preferences of thiolatocopper(I) complexes of monodentate ligands and evaluating the conditions required to obtain two-coordinate copper centers.[19–32] Hence, thiophenolato ligands with varying steric demands were employed, leading to complexes with different coordination spheres around the copper center (Scheme 1).

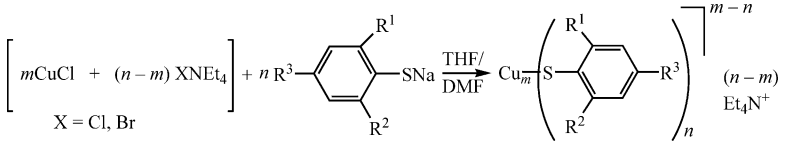


a b / c

**1**: $R^1 = R^2 = H$; $R^3 = t$Bu; $n = 3$ $m = 1$
**2**: $R^1 = i$Pr; $R^2 = R^3 = H$; $n = 3$ $m = 1$ / $n = 4$ $m = 2$
**3**: $R^1 = t$Bu; $R^2 = R^3 = H$; $n = 3$ $m = 1$ / $n = 6$ $m = 4$
**4**: $R^1 = R^2 = Me$; $R^3 = H$; $n = 2$ $m = 1$ / $n = 6$ $m = 5$

Scheme 1.

[a] Department of Inorganic Chemistry, The Hebrew University of Jerusalem,
91904 Jerusalem, Israel
Fax: +972-2-658-4282
E-mail: tshuva@chem.ch.huji.ac.il

 © 2007 Wiley-VCH Verlag GmbH & Co. KGaA, Weinheim 

## Results and Discussion

Our reaction conditions were aimed at obtaining two-coordinate copper(I) complexes as structural models for the active site of copper metallochaperones.[4,33] Thus, our straightforward and single-step synthetic procedure generally involved mixing of the commercially available copper(I) precursor CuCl with approximately 1 equiv. of $Et_4NX$ (X = Cl, Br) in thf or dmf and stirring overnight at room temp., followed by addition of 1.5–2 equiv. of the thiolato ligand which had previously been stirred with an excess of NaH overnight, and stirring the resulting mixture for 24 h. Crystallization from a suitable solvent gave single crystals suitable for X-ray crystallography. In most cases the mononuclear complex obtained was accompanied by a polynuclear cluster, which was crystallized under similar reaction conditions, occasionally in the same flask. The complexes formed do not necessarily feature the stoichiometry employed between the copper(I) salt, ligand (**1a**–**4a**), and counterion, and the net reaction stoichiometry of the different complexes formed is presented in Scheme 1. We will begin our discussion with the series of mononuclear complexes obtained (**1b**–**4b**), followed by a description of the clusters (**2c**–**4c**).

### Mononuclear Complexes

Treatment of the sodium salt of **1a** with the copper(I) precursor in thf (Scheme 1) gave a colorless solution. Crystallization from thf at –30 °C gave colorless crystals that were analyzed by crystallography despite their significant disorder. The structure of one anion of the product $[Et_4N]_2[Cu\{S(p\text{-}tBuC_6H_4)\}_3]$ (**1b**), out of several found in the asymmetric unit, is presented in Figure 1, and selected bond lengths and angles for this molecule are summarized in Table 1. All molecules in the asymmetric unit are very similar to one another in terms of general structure and bond characteristics.

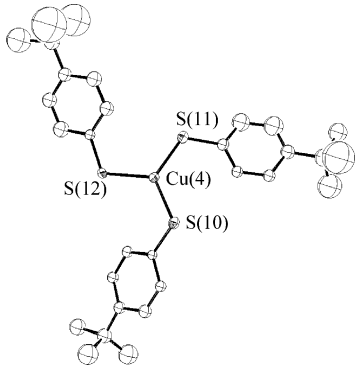


Figure 1. ORTEP drawing of one dianion in $[Et_4N]_2[Cu\{S(p\text{-}tBuC_6H_4)\}_3]$ (**1b**) showing 50% probability ellipsoids. H atoms, solvent molecules, counterions, and disorder have been omitted for clarity.

The structure features a three-coordinate copper(I) center with a highly planar-trigonal geometry, as shown by the sum of the angles around the metal atom (360.0°). Three thiolato ligands bind to the metal atom with two $Et_4N^+$ counterions stabilizing the copper(I) state. All Cu–S bond lengths (2.24–2.26 Å) are similar, thereby indicating one average bond type of mostly covalent nature. A somewhat broader range is observed for the S–Cu–S angles (117–124°), with a mean value of 120° in agreement with the trigonal geometry. These values are also in agreement with those obtained for other related three-coordinate $Cu^I$ complexes of thiophenolato ligands without *ortho* substituents.[21–23] These latter complexes were obtained under different reaction conditions, the main difference being the significantly lower ligand to metal stoichiometry employed in our case. This suggests that the coordination number of three is favored for the copper(I) center in this system.

Table 1. Selected bond lengths [Å] and angles [°] for a representative dianion of **1b**–**3b**.

| | | | |
|---|---|---|---|
| $[Cu\{S(p\text{-}tBuC_6H_4)\}_3]^{2-}$ in **1b** | | | |
| Cu(4)–S(10) | 2.257(3) | S(10)–Cu(4)–S(11) | 124.17(11) |
| Cu(4)–S(11) | 2.234(3) | S(11)–Cu(4)–S(12) | 117.49(12) |
| Cu(4)–S(12) | 2.244(3) | S(12)–Cu(4)–S(10) | 118.33(12) |
| $[Cu\{S(o\text{-}iPrC_6H_4)\}_3]^{2-}$ in **2b** | | | |
| Cu(1)–S(1) | 2.251(1) | S(1)–Cu(1)–S(2) | 118.78(4) |
| Cu(1)–S(2) | 2.271(1) | S(2)–Cu(1)–S(3) | 115.37(4) |
| Cu(1)–S(3) | 2.239(1) | S(3)–Cu(1)–S(1) | 125.68(4) |
| $[Cu\{S(o\text{-}tBuC_6H_4)\}_3]^{2-}$ in **3b** | | | |
| Cu(1)–S(1) | 2.232(2) | S(1)–Cu(1)–S(2) | 122.89(6) |
| Cu(1)–S(2) | 2.244(2) | S(2)–Cu(1)–S(3) | 115.06(7) |
| Cu(1)–S(3) | 2.291(2) | S(3)–Cu(1)–S(1) | 121.67(7) |

We were now interested in exploring the influence of steric effects on the coordination number of the complex formed, and found that increasing the bulk by adding an *ortho*-isopropyl group, or even a larger -*tert*-butyl group, does not have a significant influence on the outcome as regards the coordination parameters of the copper(I) complex obtained. Thus, treating the sodium salt of **2a** or **3a** with the copper(I) precursor in dmf under similar reaction conditions (Scheme 1) gave colorless solutions from which $[Et_4N]_2[Cu\{S(o\text{-}iPrC_6H_4)\}_3]$ (**2b**) and $[Et_4N]_2[Cu\{S(o\text{-}tBuC_6H_4)\}_3]$ (**3b**) were crystallized, respectively, by slow diffusion of thf/hexane at room temperature. The X-ray structures of **2b** and **3b** are presented in Figures 2 and 3, respectively, and selected bond lengths and angles are summarized in Table 1.

Both **2b** and **3b** feature a similar anionic three-coordinate copper(I) complex with a $D_{3h}$-symmetric core, which is reduced to the $C_3$ symmetry of the entire anion by the ligand structure. Two anions surrounded by two $Et_4N^+$ cations each are present in the asymmetric unit of each structure. The bond lengths and angles are in a similar range to those of **1b** (Table 1) and most of the previously reported three-coordinate (thiophenolato)copper(I) structures.[21–23,34] The high planarity of the core is only very slightly reduced by the substituents' bulk, with the sum of the S–Cu–S angles being 359.8° for **2b** and 359.6° for **3b**, which indicates little influence of the steric groups.

 © 2007 Wiley-VCH Verlag GmbH & Co. KGaA, Weinheim 

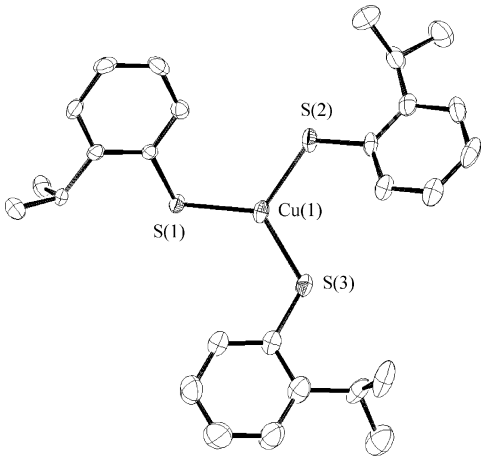


Figure 2. ORTEP drawing of one dianion of $[Et_4N]_2[Cu\{S(o\text{-}iPrC_6H_4)\}_3]$ (**2b**) showing 50% probability ellipsoids. H atoms, solvent molecules, and counterions have been omitted for clarity.

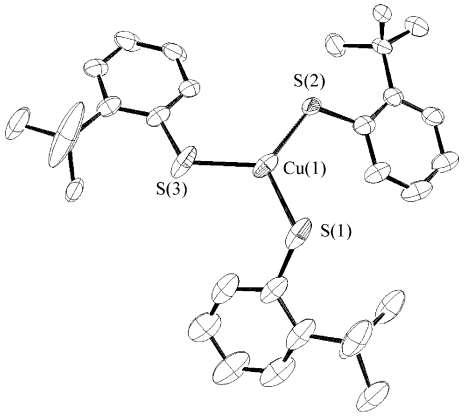


Figure 3. ORTEP drawing of one dianion of $[Et_4N]_2[Cu\{S(o\text{-}t BuC_6H_4)\}_3]$ (**3b**) showing 50% probability ellipsoids. H atoms, solvent molecules, and counterions have been omitted for clarity.

The H···S distance between the hydrogen atom in the second *ortho* position and the nearest sulfur atom in the structures of **2b** and **3b** (Scheme 2) is between 2.7 and 3.0 Å, which suggests that an additional bulky substituent at this position should interfere with the trigonal structure and may lead to a different coordination sphere.[19] Indeed, treatment of the copper(I) precursor with the sodium salt of ligand **4a** (Scheme 1) according to the same procedure as for **1a**–**3a** gave a colorless solution from which single crystals formed upon diffusion of a thf/hexane solution at room temperature. The X-ray structure of the anion of product $[Et_4N][Cu\{S(o,o'\text{-}Me_2C_6H_3)\}_2]$ (**4b**) is presented in Figure 4, and selected bond lengths and angles are summarized in Table 2.

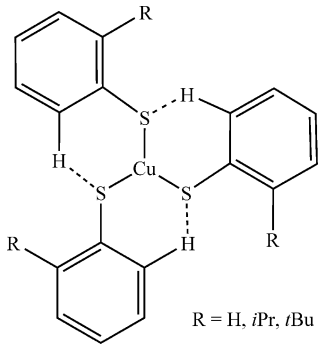


Scheme 2.

Table 2. Selected bond lengths [Å] and angles [°] for the anion of **4b**.

| $[Cu\{S(o,o\text{-}Me_2C_6H_3)\}_2]^-$ | | | |
|---|---|---|---|
| Cu(1)–S(1) | 2.127(1) | S(1)–Cu(1)–S(2) | 165.22(7) |
| Cu(1)–S(2) | 2.111(3) | C(1)–S(1)–Cu(1)–S(2) | 166.1 |
| | | C(1)–S(1)–S(2)–C(9) | 42.1 |

The structure features a two-coordinate copper(I) anionic center with one $Et_4N^+$ counterion. The position of S(2) at 70% probability gives an S–Cu–S angle of 165.2°, which deviates quite substantially from linearity. The short Cu–S bond lengths of 2.11–2.13 Å[19,20] are in accordance with strong covalent-type bonds. Interestingly, a comparison of the X-ray structure of **4b** with the two previously reported two-coordinate thiolatocopper(I) complexes[19,20] showed two distinctive features for **4b**, namely the above-mentioned substantial deviation of the S–Cu–S angle from

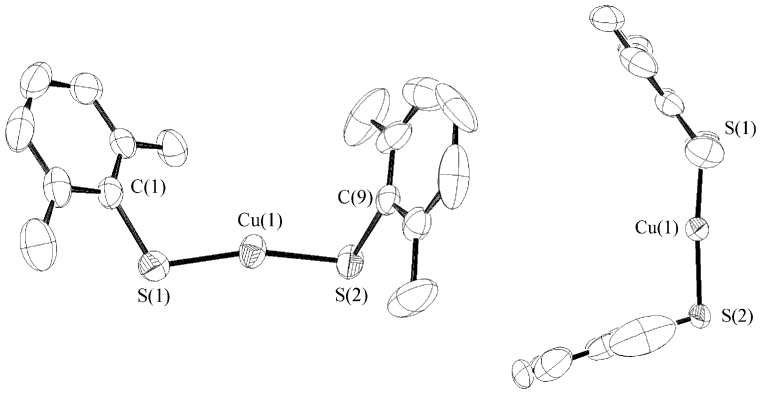


Figure 4. ORTEP drawing of the $[Cu\{S(o,o'\text{-}Me_2C_6H_3)\}_2]^-$ anion in **4b** showing 50% probability ellipsoids. H atoms, the counterion, and disorder have been omitted for clarity.

 © 2007 Wiley-VCH Verlag GmbH & Co. KGaA, Weinheim 

linearity and the fact that the aromatic rings of the ligands both face in the same direction as the Cu–S bonds in this solid-state structure.

Complex **4b** may thus be considered as a basic structural model of copper metallochaperone proteins, which feature a two-coordinate copper(I) center bound to two thiolato ligands.[4,33] It has been suggested that additional coordination of a third ligand to the copper atom may take place in the natural systems,[4,9,10,35,36] and further support for this notion comes from the S–Hg–S angle observed in the X-ray structure of Atx1 (167°).[4] This actually means that **3b** bears a high coordination resemblance to the active site of Atx1, resulting from its simple steric demands and crystal packing, without the protein folding surroundings.

### Polynuclear Clusters

Complex **1b** was the only product that we were able to identify in several reactions with ligand **1a**, both according to X-ray crystallography and NMR spectroscopy (see above). In contrast, all other bulkier ligands (**2a**–**4a**; Scheme 1) allowed the identification of trace amounts of a polynuclear complex under conditions similar to those applied for formation of the mononuclear complexes **2b**–**4b**, although with a small difference in the applied stoichiometric ratio of ligand/metal in some cases. Thus, another type of colorless single crystals was obtained from the same reaction flask where **2b** had been crystallized following the reaction of the sodium salt of **2a** with the copper(I) precursor in a ligand/metal ratio of about 1.5:1. The X-ray structure of these crystals indicated the formation of the dinuclear complex $[Et_4N]_2[Cu_2\{\mu\text{-}S(o\text{-}i\text{Pr}C_6H_4)\}_2\{S(o\text{-}i\text{Pr}C_6H_4)\}_2]$ (**2c**; Figure 5); selected bond lengths and angles are summarized in Table 3.

Complex **2c** features a $C_2$-symmetric $Cu_2SC^{Ar}_4$ core where the two copper(I) centers are each three-coordinate with very high planarity, as shown by the value of 360.0° for the sum of the S–Cu–S angles around each metal center. Two thiolato ligands are terminal and two bridge the two metal atoms, thereby preserving the 2:1 ligand/metal ratio, with a total of two $Et_4N^+$ counterions. Two of the aromatic rings of the thiolato ligands face in the same direction, giving rise to a nonpropeller-type geometry. The Cu–S bond lengths of the bridging ligand (2.30–2.34 Å) are longer than those of the terminal ones (2.18–2.19 Å), as expected, and similar values are observed between each bridging ligand and the copper centers, thus indicating a similar average bond for the symmetrical core. Naturally, one S–Cu–S angle for each metal atom (90.4–91.0°) is more acute than the other two (123.9–145.0°) to accommodate the four-membered ring of the Cu–S–Cu–S core. Additionally, the steric demands of the ring also contribute to rather acute Cu–S–Cu angles (mean value of 67.5°). The Cu···Cu distance is 2.584 Å, with no evidence of a metal–metal interaction. To the best of our knowledge, this is the first example of a dinuclear thiolatocopper(I) complex where both copper atoms are three-coordinate.

Table 3. Selected bond lengths [Å] and angles [°] for the dianion of **2c**.

| $[Cu_2\{\mu\text{-}S(o\text{-}i\text{Pr}C_6H_4)\}_2\{S(o\text{-}i\text{Pr}C_6H_4)\}_2]^{2-}$ | | | |
|---|---|---|---|
| Cu(1)–S(1) | 2.340(1) | S(1)–Cu(1)–S(2) | 91.00(4) |
| Cu(1)–S(2) | 2.300(1) | S(2)–Cu(1)–S(3) | 145.05(4) |
| Cu(1)–S(3) | 2.180(1) | S(3)–Cu(1)–S(1) | 123.94(4) |
| Cu(2)–S(1) | 2.338(1) | S(1)–Cu(2)–S(2) | 90.44(4) |
| Cu(2)–S(2) | 2.325(1) | S(2)–Cu(2)–S(4) | 127.56(4) |
| Cu(2)–S(4) | 2.188(1) | S(4)–Cu(2)–S(1) | 142.00(4) |
| Cu(1)···Cu(2) | 2.584 | Cu(1)–S(1)–Cu(2)–S(2) | 46.9 |

Under similar conditions to those that led to **3b** as discussed above (Scheme 1), both in terms of reaction procedure and crystallization conditions, formation of another type of light yellow crystals was observed. X-ray analysis revealed their structure to be $[Et_4N]_2[Cu_4\{\mu\text{-}S(o\text{-}t\text{Bu}C_6H_4)\}_6]$ (**3c**), as shown in Figure 6; selected bond lengths and angles are summarized in Table 4.

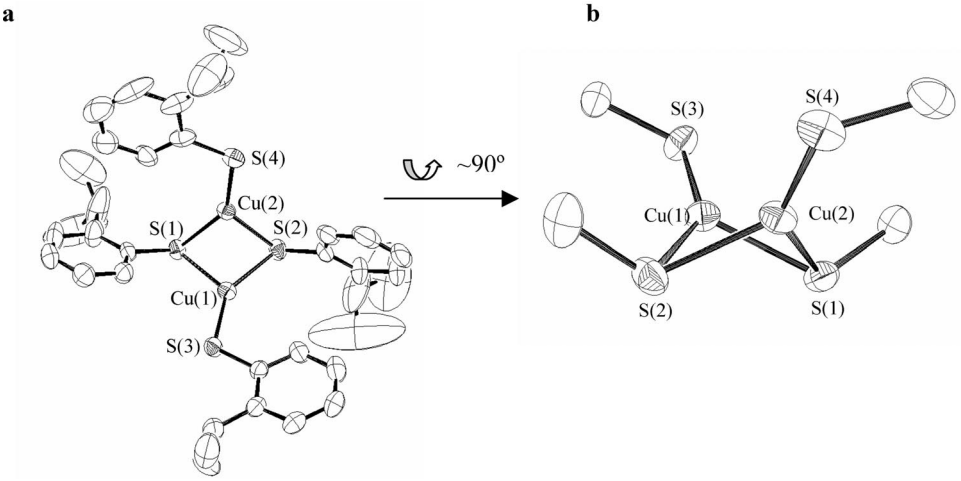


Figure 5. ORTEP drawings of the $[Cu_2\{\mu\text{-}S(o\text{-}i\text{Pr}C_6H_4)\}_2\{S(o\text{-}i\text{Pr}C_6H_4)\}_2]^{2-}$ dianion of **2c** (50% probability ellipsoids) showing the full structure (a) and a structure where the aromatic rings of the ligands have been omitted for clarity (b). H atoms, counterions, and solvent molecules have also been omitted for clarity in both structures.

 © 2007 Wiley-VCH Verlag GmbH & Co. KGaA, Weinheim 

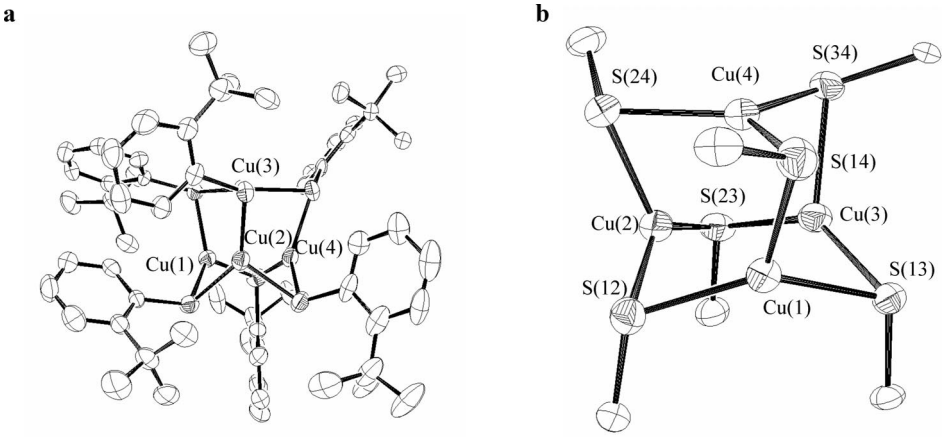


Figure 6. ORTEP drawing of the $[Cu_4\{\mu\text{-}S(o\text{-}t\text{Bu}C_6H_4)\}_6]^{2-}$ dianion in **3c** showing 50% probability ellipsoids: (a) full structure; (b) the aromatic rings of the ligands have been omitted for clarity. H atoms and counterions have also been omitted for clarity in both cases.

Table 4. Selected bond lengths [Å] and angles [°] for the dianion of **3c**.

| $[Cu_4\{\mu\text{-}S(o\text{-}t\text{Bu}C_6H_4)\}_6]^{2-}$ | | | |
|---|---|---|---|
| Cu(1)–S(12) | 2.241(2) | S(12)–Cu(1)–S(13) | 138.50(9) |
| Cu(1)–S(13) | 2.307(2) | S(13)–Cu(1)–S(14) | 102.80(9) |
| Cu(1)–S(14) | 2.332(3) | S(14)–Cu(1)–S(12) | 118.26(9) |
| Cu(2)–S(12) | 2.321(2) | S(12)–Cu(2)–S(23) | 137.95(9) |
| Cu(2)–S(23) | 2.236(3) | S(23)–Cu(2)–S(24) | 122.7(1) |
| Cu(2)–S(24) | 2.296(2) | S(24)–Cu(2)–S(12) | 99.00(9) |
| Cu(3)–S(13) | 2.256(2) | S(13)–Cu(3)–S(23) | 138.13(9) |
| Cu(3)–S(23) | 2.317(3) | S(23)–Cu(3)–S(34) | 100.69(8) |
| Cu(3)–S(34) | 2.315(2) | S(34)–Cu(3)–S(13) | 120.69(9) |
| Cu(4)–S(14) | 2.279(3) | S(14)–Cu(4)–S(24) | 121.6(1) |
| Cu(4)–S(24) | 2.295(3) | S(24)–Cu(4)–S(34) | 118.5(1) |
| Cu(4)–S(34) | 2.270(3) | S(34)–Cu(4)–S(14) | 119.79(9) |
| Cu(1)···Cu(2) | 2.766 | | |
| Cu(1)···Cu(3) | 2.715 | | |
| Cu(2)···Cu(3) | 2.716 | | |

The structure features an adamantane-like tetrahedron of metal atoms enveloped by a disordered octahedron of six $\mu_2$-thiolato ligands.[22–24,27–30,37–39] Each of the six ligand units in the tetranuclear copper(I) cluster bridges the edges of the tetrahedral array of copper atoms, and each copper center is three-coordinate with high planarity of the trigonal geometry (sum of the angles around the copper center of 359.6–359.9°), with a total of two $Et_4N^+$ counterions. The high $T_d$ symmetry of the core is reduced by the substituted aromatic ligands and their position, where the aromatic rings on two of the bound thiolato ligands for three of the four copper atoms [Cu(1), Cu(2), and Cu(3); Figure 6] face in opposite directions rather than giving the propeller-type geometry observed for Cu(4).[24] The ranges of Cu–S bond lengths (2.24–2.33 Å) and S–Cu–S angles (99–138°, with a mean value of 119.0°)[24] are somewhat broader than the equivalent values obtained for **1b**–**3b**, and the Cu···Cu distances (2.71–2.78 Å) provide no significant structural evidence for a copper–copper interaction. The Cu–S–Cu angles lie in a somewhat narrower range (72.0–74.6°). The Cu–S bond lengths, Cu···Cu distances, S–Cu–S angles, and Cu–S–Cu angles are also all similar to those obtained for other $Cu_4S_6$ clusters of ligands having no significant steric bulk, including both aliphatic thiolato ligands[22,27,30] and thiophenolato ligands having no *ortho* substituents,[23,24,29] which are commonly obtained from $Cu^{II}$ precursors with higher ligand/metal stoichiometric ratios. In addition, these values deviate only slightly from the ideal values of 2.64 Å for a Cu···Cu distance and 2.29 Å for a Cu–S distance in such cores,[22,23] which suggests that the *ortho* substituents do not have much effect on the metal–sulfur core.

The disubstituted ligand **4a** (Scheme 1) also leads to a polynuclear structure upon treatment of its sodium salt with the copper(I) precursor under the reaction conditions used for the synthesis of **4b**. The pentanuclear complex $[Et_4N][Cu_5\{\mu\text{-}S(o,o'\text{-}Me_2C_6H_3)\}_6]$ (**4c**) crystallized from dichloromethane at –30 °C as pale-yellow single crystals suitable for X-ray crystallography. The structure of this complex is presented in Figure 7 and selected bond lengths and angles are summarized in Table 5.

The structure features a trigonal bipyramid of copper atoms within a trigonal antiprism of $\mu_2$-thiolato ligands, with a $D_3$-symmetrical core.[25,31,32] A single $Et_4N^+$ cation counters the cluster charge. Three of the five copper atoms in the cluster of **4c** are two-coordinate and two are three-coordinate. The three-coordinate centers have a trigonal geometry with a somewhat reduced planarity (sum of the angles around the metal atom 358.7°). All six thiolato ligands are bridging, with Cu–S distances of 2.24–2.29 Å that are rather similar to the ones obtained for previous three-coordinate structures. The shorter distances to the two-coordinate metal atoms (2.17–2.19 Å) are only slightly shorter than those obtained for **4b**. The S–Cu–S angles range from 112 to 130° for the three-coordinate copper atoms, which is only a slightly broader range than that obtained for **1b**–**3b**. The S–Cu–S angles for the two-coordinate copper atoms are 164–166°, similar to the value obtained for **4b**, and again deviate significantly from linearity. The mean value of the Cu–S–Cu angles (75.5°) is somewhat higher than that

 © 2007 Wiley-VCH Verlag GmbH & Co. KGaA, Weinheim 

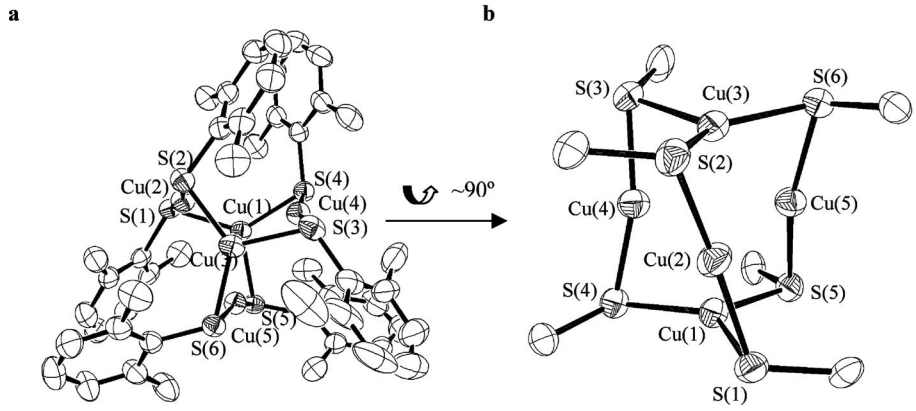


Figure 7. ORTEP drawing of the $[Cu_5\{\mu\text{-}S(o\text{-}t\text{Bu}C_6H_4)\}_6]^-$ anion of **4c** showing 50% probability ellipsoids: (a) full structure; (b) aromatic rings of the ligands have been omitted for clarity. H atoms, counterions, and solvent molecules have also been omitted for clarity in both cases.

Table 5. Selected bond lengths [Å] and angles [°] for the anion of **4c**.

| $[Cu_5\{\mu\text{-}S(o,o\text{-}Me_2C_6H_3)\}_6]^-$ | | | |
|---|---|---|---|
| Cu(1)–S(1) | 2.2583(9) | S(1)–Cu(1)–S(4) | 130.76(4) |
| Cu(1)–S(4) | 2.242(1) | S(4)–Cu(1)–S(5) | 111.71(4) |
| Cu(1)–S(5) | 2.2866(9) | S(5)–Cu(1)–S(1) | 116.23(4) |
| Cu(3)–S(2) | 2.256(1) | S(2)–Cu(3)–S(3) | 112.88(4) |
| Cu(3)–S(3) | 2.284(1) | S(3)–Cu(3)–S(6) | 115.47(4) |
| Cu(3)–S(6) | 2.247(1) | S(6)–Cu(3)–S(2) | 130.29(4) |
| Cu(2)–S(1) | 2.1775(9) | S(1)–Cu(2)–S(2) | 166.54(4) |
| Cu(2)–S(2) | 2.170(1) | S(3)–Cu(4)–S(4) | 163.91(4) |
| Cu(4)–S(3) | 2.174(1) | S(5)–Cu(5)–S(6) | 162.74(4) |
| Cu(4)–S(4) | 2.173(1) | | |
| Cu(5)–S(5) | 2.1805(9) | | |
| Cu(5)–S(6) | 2.191(1) | | |
| Cu(1)···Cu(2) | 2.674 | | |
| Cu(1)···Cu(3) | 3.885 | | |
| Cu(2)···Cu(4) | 3.351 | | |

observed for the smaller cluster in **3c**. The Cu···Cu distances range between 2.67 and 3.88 Å, with no significant structural evidence for a metal–metal interaction. The $Cu_5S_6$-type cluster observed for **4c** is less common but is nonetheless similar in its general geometry to other previously reported $Cu_5S_6$ core structures that have been obtained mainly from $Cu^{II}$ precursors with aliphatic thiolato ligands exhibiting no significant steric bulk, with higher ligand/metal stoichiometric ratios.[20,25,31,32]

## Conclusions

We have obtained a series of mononuclear thiolatocopper(I) complexes accompanied by a series of polynuclear clusters obtained from the same ligands under similar reaction conditions. Clearly, increasing the steric bulk around the metal atom by adding a second substituent in the position *ortho* to the thiol group reduces the coordination number. Generally, the preferred coordination number of the metal atom obtained with ligands inducing small steric effects is three, regardless of the stoichiometric ratio employed. This coordination number was obtained with a ligand having no *ortho* substituents as well as with a range of ligands singly *ortho*-substituted, namely, with H to *t*Bu *ortho* groups, both in the mononuclear complexes and in all of the copper atoms in the polynuclear structures obtained from these ligands. Two-coordinate copper(I) centers have only been observed with the dimethylthiophenolato ligand, which has two *ortho* substituents, both in the mononuclear complex and for three of the copper centers in the pentanuclear cluster. Additionally, if we consider the steric effects produced by the ligands to follow the order 2 *ortho*-Me groups > 1 *ortho*-*t*Bu group > 1 *ortho*-*i*Pr group > 0 *ortho* substituents (H atoms), when exploring the clusters obtained taking this order into consideration we find that the larger the steric bulk the larger the cage that is formed under the conditions employed, with the smallest dinuclear structure exhibiting a unique geometry that has not been observed previously with related ligands. Tuning steric effects can therefore have a major influence on the coordination sphere of the copper(I) complexes obtained.

## Experimental Section

4-*tert*-Butylthiophenol (**1a**; 97%), 2-isopropylthiophenol (**2a**; tech. 90%), 2,6-dimethylthiophenol (**4a**; 95%), and tetraethylammonium bromide (98%) were purchased from Aldrich Chemical Company Inc. and used without further purification. 2-*tert*-Buthylthiophenol (**3a**; tech. 80%) was purchased from Alfa Aesar Inc. and used without further purification. Tetraethylammonium chloride (98%) was purchased from Sigma Inc. and used without further purification. Copper chloride (CuCl) was purchased from Fluka Inc. and used without further purification. All syntheses that required a conditions were performed in an M. Braun dry box or under nitrogen using Schlenk line techniques. Anhydrous dmf was purchased from Aldrich Chemical Company Inc. and used without further purification. All other solvents were distilled from K or K/benzophenone under nitrogen and stored in the dry box. X-ray diffraction data were obtained with a Bruker Smart Apex diffractometer. CCDC-647993 to -647999 contain the supplementary crystallographic data

 © 2007 Wiley-VCH Verlag GmbH & Co. KGaA, Weinheim 

for this paper. These data can be obtained free of charge from The Cambridge Crystallographic Data Center via www.ccdc.cam.ac.uk/data_request/cif. NMR spectroscopic data were recorded with an AMX-300 or AMX-400 Bruker spectrometer. Elemental analysis was performed in the microanalytical laboratory of our institute. Reliable elemental analysis for complexes of coordination number higher than two could not be performed due to their enhanced susceptibility to oxidation.

**$[Et_4N]_2[Cu\{S(p\text{-}tBuC_6H_4)\}_3]$ (1b):** A suspension of sodium hydride (0.58 mmol) in 2 mL of thf was added to a solution of **1a** (0.25 mmol) in thf (2 mL) at room temp. under nitrogen. Copper(I) chloride (0.13 mmol) in thf (2 mL) was added to a solution of tetraethylammonium bromide (0.13 mmol) in thf (2 mL) at room temp. under nitrogen and the two solutions were stirred separately in sealed flasks for 24 h. The solution containing the ligand was then added to the solution containing the copper salt and the reaction mixture was stirred overnight. The thf was removed under reduced pressure, and colorless crystals of **1b** (33 mg, 49%) were obtained from thf at –30 °C. $^1$H NMR (300 MHz, $CDCl_3$, $Me_4Si$, 25 °C): $\delta$ = 7.2 (d, $J$ = 8.3 Hz, 6 H, Ar), 6.9 (d, $J$ = 8.3 Hz, 6 H, Ar), 3.2 (q, $J$ = 7.2 Hz, 16 H, $NCH_2CH_3$), 1.2 (s, 27 H, $t$Bu), 1.2 (tt, $J$ = 7.2, 1.8 Hz, 24 H, $NCH_2CH_3$) ppm. **Crystal Data:** Complex **1b** was crystallized from thf at –30 °C. The asymmetric unit contains five anions and ten cations and is disordered. $C_{46}H_{79}CuN_2S_3$, $M$ = 819.83, triclinic, $a$ = 20.317(3), $b$ = 25.894(3), $c$ = 27.231(3) Å, $\alpha$ = 109.280(2), $\beta$ = 101.349(2), $\gamma$ = 96.776(2)°, $V$ = 12997(3) Å$^3$, $T$ = 173(2) K, space group $P\bar{1}$, $Z$ = 10, $\mu$(Mo-$K_\alpha$) = 0.569 mm$^{-1}$, 146212 reflections measured, 56251 unique ($R_{int}$ = 0.1079). $R(F_o^2)$ for [$I > 2\sigma(I)$] = 0.2100, $Rw$ for [$I > 2\sigma(I)$] = 0.4616.

**$[Et_4N]_2[Cu\{S(o\text{-}iPrC_6H_4)\}_3]$ (2b):** Complex **2b** was synthesized in analogy to **1b** by treating a solution of **2a** (0.28 mmol) previously stirred with sodium hydride (0.46 mmol) in dmf with a solution of copper chloride (0.19 mmol) previously stirred with tetraethylammonium chloride (0.21 mmol) in dmf. Colorless crystals of **2b** (17 mg, 23%) were obtained from hexane and thf by slow diffusion at room temp. $^1$H NMR (300 MHz, $CDCl_3$, $Me_4Si$, 25 °C): $\delta$ = 7.7 (dd, $J$ = 7.5, 1.5 Hz, 3 H, Ar), 7.0 (dd, $J$ = 7.4, 1.8 Hz, 3 H, Ar), 6.8 (dt, $J$ = 7.3, 1.7 Hz, 3 H, Ar), 6.7 (dt, $J$ = 7.2, 1.8 Hz, 3 H, Ar), 4.0 [sept, $J$ = 6.9 Hz, 3 H, $CH(CH_3)_2$], 3.1 (q, $J$ = 7.3 Hz, 16 H, $NCH_2CH_3$), 1.2 [d, $J$ = 6.9 Hz, 18 H, $CH(CH_3)_2$], 1.2 (tt, $J$ = 7.28, 1.5 Hz, 24 H, $NCH_2CH_3$) ppm. **Crystal Data:** Complex **2b** was crystallized from hexane and thf by slow diffusion at room temp. The asymmetric unit contains two anions and four cations. $C_{43}H_{73}CuN_2S_3$, $M$ = 777.75, orthorhombic, $a$ = 24.386(2), $b$ = 24.543(2), $c$ = 15.3518(14) Å, $V$ = 9188.4(14) Å$^3$, $T$ = 100(2) K, space group $P2(1)2(1)2$, $Z$ = 8, $\mu$(Mo-$K_\alpha$) = 0.640 mm$^{-1}$, 98306 reflections measured, 18045 unique ($R_{int}$ = 0.0521). $R(F_o^2)$ for [$I > 2\sigma(I)$] = 0.0488, $Rw$ for [$I > 2\sigma(I)$] = 0.1290.

**$[Et_4N]_2[Cu\{S(o\text{-}tBuC_6H_4)\}_3]$ (3b): 3b** was synthesized in analogy to **1b** by treating a solution of **3a** (0.49 mmol) previously stirred with sodium hydride (0.62 mmol) in dmf with a solution of copper chloride (0.23 mmol) previously stirred with tetraethylammonium chloride (0.26 mmol) in dmf. Colorless crystals of **3b** (70 mg, 52%) were obtained from hexane and thf by slow diffusion at room temp. $^1$H NMR (300 MHz, $CDCl_3$, $Me_4Si$, 25 °C): $\delta$ = 7.6 (br. s, 3 H, Ar), 7.1 (br. s, 3 H, Ar), 6.7 (s, 6 H, Ar), 3.2 (q, $J$ = 7.2 Hz, 16 H, $NCH_2CH_3$), 1.5 (s, 27 H, $t$Bu), 1.16 (tt, $J$ = 7.2, 1.8 Hz, 24 H, $NCH_2CH_3$) ppm. **Crystal Data:** Complex **3b** was crystallized from hexane and thf by slow diffusion at room temp. The asymmetric unit contains two anions, four cations, and solvent. $C_{46}H_{79}CuN_2S_3$·0.5thf, $M$ = 855.88, monoclinic, $a$ = 16.607(4), $b$ = 25.473(6), $c$ = 23.608(5) Å, $\beta$ = 102.922(4)°, $V$ = 9734(4) Å$^3$, $T$ = 100(1) K, space group $Ia$, $Z$ = 8, $\mu$(Mo-$K_\alpha$) = 0.611 mm$^{-1}$, 53563 reflections measured, 21026 unique ($R_{int}$ = 0.0406). $R(F_o^2)$ for [$I > 2\sigma(I)$] = 0.0749, $Rw$ for [$I > 2\sigma(I)$] = 0.1903.

**$[Et_4N][Cu\{S(o,o'\text{-}Me_2C_6H_3)\}_2]$ (4b):** Complex **4b** was synthesized in analogy to **1b** by treating a solution of **4a** (0.51 mmol) previously stirred with sodium hydride (0.70 mmol) in thf with a solution of copper chloride (0.30 mmol) previously stirred with tetraethylammonium chloride (0.32 mmol) in thf. Colorless crystals of **4b** (57 mg, 48%) were obtained from hexane and thf by slow diffusion at room temp. $C_{24}H_{38}CuNS_2$ (468.25): calcd. C 61.56, H 8.18, N 2.99; found C 62.01, H 8.44, N 3.10. $^1$H NMR (400 MHz, $CDCl_3$, $Me_4Si$, 25 °C): $\delta$ = 6.9 (d, $J$ = 7.4 Hz, 4 H, Ar), 6.7 (t, $J$ = 7.4 Hz, 2 H, Ar), 2.7 (q, $J$ = 7.3 Hz, 8 H, $NCH_2CH_3$), 2.5 (s, 12 H, $CH_3$), 1.0 (tt, $J$ = 7.3, 1.7 Hz, 12 H, $NCH_2CH_3$) ppm. **Crystal Data:** Complex **4b** was crystallized from hexane and thf by slow diffusion at room temp. The asymmetric unit contains one anion, one cation and one disordered S atom. $C_{24}H_{38}CuNS_2$, $M$ = 468.21, monoclinic, $a$ = 11.0173(8), $b$ = 14.5458(11), $c$ = 15.5467(12) Å, $\beta$ = 101.0680(10)°, $V$ = 2445.1(3) Å$^3$, $T$ = 173(2) K, space group $P2_1/c$, $Z$ = 4, $\mu$(Mo-$K_\alpha$) = 1.074 mm$^{-1}$, 27240 reflections measured, 5808 unique ($R_{int}$ = 0.0554). $R(F_o^2)$ for [$I > 2\sigma(I)$] = 0.0564, $Rw$ for [$I > 2\sigma(I)$] = 0.1269.

**$[Et_4N]_2[Cu_2\{\mu\text{-}S(o\text{-}iPrC_6H_4)\}_2\{S(o\text{-}iPrC_6H_4)\}_2]$ (2c):** Complex **2c** was synthesized similarly to **2b** by treating a solution of **2a** (0.28 mmol) previously stirred with sodium hydride (0.46 mmol) in dmf with a solution of copper chloride (0.19 mmol) previously stirred with tetraethylammonium chloride (0.21 mmol) in dmf. Colorless crystals of **2c** (approx. 10 mg, 10%) were obtained from hexane and thf by slow diffusion at room temp. **Crystal Data:** Complex **2c** was crystallized from hexane and thf by slow diffusion at room temp. The asymmetric unit contains one anion and two cations. $C_{52}H_{84}Cu_2N_2S_4$, $M$ = 992.53, monoclinic, $a$ = 15.1590(9), $b$ = 17.7437(10), $c$ = 20.2433(12) Å, $\beta$ = 90.9740(10)°, $V$ = 5442.0(6) Å$^3$, $T$ = 173(2) K, space group $P2_1/c$, $Z$ = 4, $\mu$(Mo-$K_\alpha$) = 0.969 mm$^{-1}$, 59897 reflections measured, 11892 unique ($R_{int}$ = 0.0291). $R(F_o^2)$ for [$I > 2\sigma(I)$] = 0.0702, $Rw$ for [$I > 2\sigma(I)$] = 0.1970.

**$[Et_4N]_2[Cu_4\{\mu\text{-}S(o\text{-}tBuC_6H_4)\}_6]$ (3c):** Complex **3c** was synthesized similarly to **3b** by treating **3a** (0.34 mmol) previously stirred with sodium hydride (0.66 mmol) in dmf with copper chloride (0.39 mmol) previously stirred with ammonium chloride (0.39 mmol) in dmf solution. Pale-yellow crystals of **3c** (approx. 8 mg, 10%) were obtained from hexane and thf by slow diffusion at room temp. **Crystal Data:** Complex **3c** was crystallized from hexane and thf by slow diffusion at room temp. The asymmetric unit contains one anion and two cations. $C_{76}H_{118}Cu_4N_2S_6$, $M$ = 1506.24, monoclinic, $a$ = 18.4258(14), $b$ = 29.451(2), $c$ = 21.0690(16) Å, $\beta$ = 101.9630(10)°, $V$ = 11185.0(15) Å$^3$, $T$ = 100(2) K, space group $Ia$, $Z$ = 4, $\mu$(Mo-$K_\alpha$) = 0.890 mm$^{-1}$, 59102 reflections measured, 24286 unique ($R_{int}$ = 0.0730). $R(F_o^2)$ for [$I > 2\sigma(I)$] = 0.0879, $Rw$ for [$I > 2\sigma(I)$] = 0.2423.

**$[Et_4N][Cu_5\{\mu\text{-}S(o,o\text{-}Me_2C_6H_3)\}_6]$ (4c):** Complex **4c** was synthesized similarly to **4b** by treating a solution of **4a** (0.38 mmol) previously stirred with sodium hydride (0.70 mmol) in thf with a solution of copper chloride (0.27 mmol) previously stirred with tetraethylammonium bromide (0.28 mmol) in thf. Pale-yellow crystals of **4c** (approx. 8 mg, 10%) were obtained from $CH_2Cl_2$ at –30 °C. **Crystal Data:** Complex **4c** was crystallized from $CH_2Cl_2$ and traces of toluene at –30 °C. The asymmetric unit contains one anion, one cation and solvents. $C_{56}H_{74}Cu_5NS_6$·$C_7H_8$·$CH_2Cl_2$, $M$ = 1448.28, orthorhombic, $a$ = 20.7894(12), $b$ = 21.0811(12), $c$ = 15.0306(9) Å, $V$ = 6587.4(7) Å$^3$, $T$ = 173(2) K, space group $Pna2_1$, $Z$ = 4, $\mu$(Mo-$K_\alpha$)

 © 2007 Wiley-VCH Verlag GmbH & Co. KGaA, Weinheim 

= 1.898 $mm^{-1}$, 72115 reflections measured, 14359 unique ($R_{int}$ = 0.0402). $R(F_o^2)$ for [$I > 2\sigma(I)$] = 0.0367, $Rw$ for [$I > 2\sigma(I)$] = 0.0844.

## Acknowledgments

We thank the Allon Foundation and the Human Frontier Science Program for financial support. We also thank Dr. Shmuel Cohen for solution of the X-ray structures.

[1] S. J. Lippard, *Science* **1999**, *284*, 748–749.
[2] L. A. Finney, T. V. O'Halloran, *Science* **2003**, *300*, 931–936.
[3] T. V. O'Halloran, V. C. Culotta, *J. Biol. Chem.* **2000**, *275*, 25057–25060.
[4] A. C. Rosenzweig, *Acc. Chem. Res.* **2001**, *34*, 119–128.
[5] T. L. Poulos, *Nat. Struct. Biol.* **1999**, *6*, 709–711.
[6] D. L. Huffman, T. V. O'Halloran, *Annu. Rev. Biochem.* **2001**, *70*, 677–701.
[7] E. D. Harris, *Annu. Rev. Nutr.* **2000**, *20*, 291–310.
[8] E. Luk, L. T. Jensen, V. C. Culotta, *J. Biol. Inorg. Chem.* **2003**, *8*, 803–809.
[9] F. Arnesano, L. Banci, I. Bertini, S. Ciofi-Baffoni, *Eur. J. Inorg. Chem.* **2004**, 1583–1593.
[10] K. A. Markossian, B. I. Kurganov, *Biochemistry (Moscow)* **2003**, *68*, 827–837.
[11] S. A. Koch, M. M. O. Pena, D. J. Thiele, *Chem. Biol.* **1997**, *4*, 549–560.
[12] A. L. Lamb, A. S. Torres, T. V. O'Halloran, A. C. Rosenzweig, *Nat. Struct. Biol.* **2001**, *8*, 751–755.
[13] A. L. Lamb, A. K. Wernimont, R. A. Pufahl, V. C. Culotta, T. V. O'Halloran, A. C. Rosenzweig, *Nat. Struct. Biol.* **1999**, *6*, 724–729.
[14] A. K. Wernimont, D. L. Huffman, A. L. Lamb, T. V. O'Halloran, A. C. Rosenzweig, *Nat. Struct. Biol.* **2000**, *7*, 766–771.
[15] L. Mirica, X. Ottenwaelder, T. D. P. Stack, *Chem. Rev.* **2004**, *104*, 1013–1046.
[16] D. B. Rorabacher, *Chem. Rev.* **2004**, *104*, 651–698.
[17] S. Mandal, G. Das, R. Singh, R. Shukla, P. K. Bharadwaj, *Coord. Chem. Rev.* **1997**, *160*, 191–235.
[18] C. Belle, W. Rammal, J.-L. Pierre, *J. Inorg. Biochem.* **2005**, *99*, 1929–1936.
[19] S. A. Koch, R. Fikar, M. Millar, T. O'Sullivan, *Inorg. Chem.* **1984**, *23*, 121–122.
[20] K. Fujisawa, S. Imai, N. Kitajima, Y. Moro-oka, *Inorg. Chem.* **1998**, *37*, 168–169.
[21] C. D. Garner, J. R. Nicholson, W. Clegg, *Inorg. Chem.* **1984**, *23*, 2148–2150.
[22] D. Coucouvanis, C. N. Murphy, S. K. Kanodia, *Inorg. Chem.* **1980**, *19*, 2993–2998.
[23] K. Fujisawa, S. Imai, S. Suzuki, Y. Moro-oka, Y. Miyashita, Y. Yamada, K. Okamoto, *J. Inorg. Biochem.* **2000**, *82*, 229–238.
[24] I. G. Dance, G. A. Bowmaker, G. R. Clark, J. K. Seadon, *Polyhedron* **1983**, *2*, 1031–1043.
[25] G. A. Bowmaker, G. R. Clark, J. K. Seadon, I. G. Dance, *Polyhedron* **1984**, *3*, 535–544.
[26] T. Okamura, N. Ueyama, A. Nakamuram, E. W. Ainscough, A. M. Brodie, J. M. Waters, *J. Chem. Soc. Chem. Commun.* **1993**, 1658–1660.
[27] M. Baumgartner, H. Schmalle, C. Baerlocher, *J. Solid State Chem.* **1993**, *107*, 63–75.
[28] E. H. Griffith, G. W. Hunt, E. L. Amma, *J. Chem. Soc. Chem. Commun.* **1976**, 432–433.
[29] M. Baumgartner, W. Bensch, P. Hug, E. Dubler, *Inorg. Chim. Acta* **1987**, *136*, 139–147.
[30] M. Baumgartner, H. Schmalle, E. Dubler, *Polyhedron* **1990**, *9*, 1155–1164.
[31] G. A. Bowmaker, L. Tan, *Aust. J. Chem.* **1979**, *32*, 1443–1452.
[32] I. G. Dance, *J. Chem. Soc. Chem. Commun.* **1976**, 68–69.
[33] M. Ralle, S. Lutsenko, N. J. Blackburn, *J. Biol. Chem.* **2003**, *278*, 23163–23170.
[34] R. Kivekas, *Acta Chem. Scand.* **1995**, *49*, 305–306.
[35] L. Banci, I. Bertini, S. Ciofi-Baffoni, X.-C. Su, G. P. M. Borrelly, N. J. Robinson, *J. Biol. Chem.* **2004**, *279*, 27502–27510.
[36] R. A. Pufahl, C. P. Singer, K. L. Peariso, S.-J. Lin, P. J. Schmidt, C. J. Fahrni, V. C. Culotta, J. E. Penner-Hahn, T. V. O'Halloran, *Science* **1997**, *278*, 853–856.
[37] I. G. Dance, J. C. Calabrese, *Inorg. Chim. Acta* **1976**, *19*, L41–L42.
[38] C. P. Huber, M. L. Post, O. Siiman, *Acta Crystallogr., Sect. B* **1978**, *34*, 2629–2632.
[39] J. R. Nicholson, I. L. Abrahams, W. Clegg, C. D. Garner, *Inorg. Chem.* **1985**, *24*, 1092–1096.

Received: July 8, 2007
Published Online: October 16, 2007

 © 2007 Wiley-VCH Verlag GmbH & Co. KGaA, Weinheim 

DOI: 10.1002/ejic.200700834

# Enantiopure Mono- and Mixed-Valence Multinuclear Cobalt Complexes from Amino Alcohol Based Ligands

**Chullikkattil P. Pradeep,[a] Panthapally S. Zacharias,[a] and Samar K. Das*[a]**

**Keywords:** Chiral complexes / Cobalt / Chiral amino alcohols / Supramolecular chemistry / Ligand-controlled nuclearity

Chiral amino alcohol based tridentate Schiff bases, derived from 5-OMe-, 5-H-, and 5-$NO_2$-substituted salicylaldehydes and (*S*)-(+)-2-phenylglycinol and (*S*)-(–)-2-amino-3-phenyl-1-propanol, were found to act as versatile ligands in their coordination behavior towards cobalt and gave a range of complexes like mononuclear low-spin $Co^{III}$ complexes, mixed-valence trinuclear $Co^{III}$–$Co^{II}$–$Co^{III}$ complexes, and a mixed-valence tetranuclear $(Co^{III})_3Co^{II}$ complex on 1:1 molar ratio reaction with $Co(CH_3COO)_2{\cdot}4H_2O$ in methanol at room temperature. The steric and electronic properties of these ligands are found to control the overall geometry and nuclearity of the resulting complexes. 5-OMe-Substituted ligands ($\mathbf{H_2L^1}$ and $\mathbf{H_2L^2}$) gave mononuclear low-spin $Co^{III}$ complexes $[CoL^1(HL^1)]{\cdot}0.25DMF$ (**1**) and $[CoL^2(HL^2)]{\cdot}0.25DMF$ (**2**). Single-crystal X-ray structure analysis of complex **2** revealed that the relevant complex crystallizes with four mononuclear units in the asymmetric unit ($Z' = 4$), and these units self-assemble through O–H···O hydrogen-bonding interactions resulting in the formation of homochiral supramolecular helices in the crystal lattice. The 5-H- and 5-$NO_2$-substituted ligands ($\mathbf{H_2L^3}$, $\mathbf{H_2L^4}$, $\mathbf{H_2L^5}$) afforded mixed-valence trinuclear $Co^{III}$–$Co^{II}$–$Co^{III}$ complexes $[Co(CoL^3{}_2)_2{\cdot}H_2O]{\cdot}2DMF{\cdot}2H_2O$ (**3**), $[Co(CoL^4{}_2)_2{\cdot}H_2O]{\cdot}2DMF{\cdot}H_2O$ (**4**), and $[Co(CoL^5{}_2)_2{\cdot}DMF]{\cdot}2DMF{\cdot}H_2O$ (**5**), respectively. Crystal structure analyses of complexes **3** and **5** revealed rare trinuclear geometries of these complexes, in which two terminal octahedral low-spin $Co^{III}$ complexes act as chelating ligands for a central high-spin $Co^{II}$ center through alkoxide bridging. For steric reasons, the central cobalt adopts a highly distorted geometry in these complexes viz. distorted trigonal bipyramidal in complex **3** and distorted square planar in complex **5**. The ligand $\mathbf{H_2L^6}$ gave an interesting tetranuclear mixed-valence complex, $H[Co(CoL^6{}_2)_3]{\cdot}H_2O$ (**6**), in which three octahedral low-spin $Co^{III}$ complexes act as ligands for a central high-spin $Co^{II}$ center in distorted trigonal prismatic geometry. Interestingly, the three types (mononuclear: **1**, **2**; trinuclear: **3**, **4**, **5**; tetranuclear: **6**) of complexes showed large variations in their nuclearity and overall geometry despite the fact that the experimental conditions for all these complexes were identical. This fact highlights the influence of different substitutions on ligands in determining the final geometry of the resulting complexes in these reactions. Complexes **1**–**6** were characterized by elemental and routine spectral analyses. Compounds **2**, **3**, **5**, and **6** have been unequivocally characterized by single-crystal X-ray structure determinations as well. Chiral properties of these complexes were confirmed by circular dichroism (CD) spectral studies.

(© Wiley-VCH Verlag GmbH & Co. KGaA, 69451 Weinheim, Germany, 2007)

## Introduction

Synthesis of enantiopure metal complexes having predetermined properties is an important task in modern chemistry; one successful approach towards this goal being the use of well designed chiral ligands.[1] The quest for the development of improved chiral ligand systems necessitates the identification of novel and versatile chiral sources, in addition to the traditional chiral pools such as natural amino acids.[2] Presently, chiral amino alcohols have emerged as a promising chiral source for the preparation of asymmetric catalysts, chiral auxiliaries, and biologically relevant compounds.[3] Schiff bases of chiral amino alcohols are widely employed in catalysis and complexes of these ligands with various metal ions have been successfully employed as catalysts for a number of asymmetric transformations.[4] A thorough understanding of the coordination properties of such ligands will, therefore, be of great importance in designing more efficient systems. Structural studies including single-crystal X-ray crystallography can reveal the collective as well as complex roles of various structure-directing elements (such as steric and electronic effects) of the ligand systems in determining the overall geometry, and hence properties, of the resulting complexes. However, the number of structurally characterized amino alcohol based chiral complexes is surprisingly limited in the literature.[5]

[a] School of Chemistry, University of Hyderabad, Hyderabad 500046, India
Fax: +91-40-2301-2460
E-mail: skdsc@uohyd.ernet.in

Supporting information for this article is available on the WWW under http://www.eurjic.org or from the author.

 © 2007 Wiley-VCH Verlag GmbH & Co. KGaA, Weinheim 

At the same time, identification of new cobalt-containing proteins in recent years (e.g., nitrile hydratase, methionine aminopeptidase etc.) points to the need to acquire a much wider knowledge of the coordination properties of cobalt in various ligand environments, especially chiral environments.[6] Chiral amino alcohol based Schiff bases, with their phenolic and alcoholic donor groups and potential for steric and electronic fine-tuning, are suitable candidates for bioinorganic modeling studies as well. In our efforts to understand the structure-directing effects of chiral amino alcohol based ligands on the coordination properties of biologically and catalytically relevant metal ions,[7] we report here the syntheses, crystal structures, and properties of some fascinating enantiopure cobalt complexes **1**–**6**, derived from chiral amino alcohol based Schiff bases $\mathbf{H_2L^1}$–$\mathbf{H_2L^6}$ (Scheme 1).

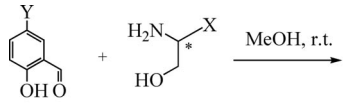


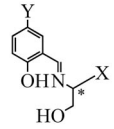


$\mathbf{H_2L''}$

| $\mathbf{H_2L''}$ | X | Y |
|---|---|---|
| $\mathbf{H_2L^1}$ | Ph | OMe |
| $\mathbf{H_2L^2}$ | $CH_2Ph$ | OMe |
| $\mathbf{H_2L^3}$ | Ph | H |
| $\mathbf{H_2L^4}$ | $CH_2Ph$ | H |
| $\mathbf{H_2L^5}$ | $CH_2Ph$ | $NO_2$ |
| $\mathbf{H_2L^6}$ | Ph | $NO_2$ |

| | |
|---|---|
| $[CoL^1(HL^1)]\cdot 0.25DMF$ | **1** |
| $[CoL^2(HL^2)]\cdot 0.25DMF$ | **2** |
| $[Co(CoL^3{}_2)_2\cdot H_2O]\cdot 2DMF\cdot 2H_2O$ | **3** |
| $[Co(CoL^4{}_2)_2\cdot H_2O]\cdot 2DMF\cdot H_2O$ | **4** |
| $[Co(CoL^5{}_2)_2\cdot DMF]\cdot 2DMF\cdot H_2O$ | **5** |
| $H[Co(CoL^6{}_2)_3]\cdot H_2O$ | **6** |

Scheme 1.

We have described herein how the steric and electronic properties of substituents 'X' and 'Y' on the ligand backbone (see Scheme 1) affect the overall geometry and nuclearity of this series of compounds **1**–**6** in identical experimental conditions. It was found that, the 5-OMe-substituted ligands ($\mathbf{H_2L^1}$ and $\mathbf{H_2L^2}$) furnished mononuclear low-spin $Co^{III}$ complexes $[CoL^1(HL^1)]\cdot 0.25DMF$ (**1**) and $[CoL^2(HL^2)]\cdot 0.25DMF$ (**2**). The 5-H- and 5-$NO_2$-substituted ligands ($\mathbf{H_2L^3}$, $\mathbf{H_2L^4}$, $\mathbf{H_2L^5}$) are responsible for the isolation of mixed-valence trinuclear $Co^{III}$–$Co^{II}$–$Co^{III}$ complexes $[Co(CoL^3{}_2)_2\cdot H_2O]\cdot 2DMF\cdot 2H_2O$ (**3**), $[Co(CoL^4{}_2)_2\cdot H_2O]\cdot 2DMF\cdot H_2O$ (**4**), and $[Co(CoL^5{}_2)_2\cdot DMF]\cdot 2DMF\cdot H_2O$ (**5**) respectively. Interestingly, the combination of X = Ph and Y = $NO_2$ ($\mathbf{H_2L^6}$) afforded a tetranuclear mixed-valence compound $H[Co(CoL^6{}_2)_3]\cdot H_2O$ (**6**) in which three mononuclear low-spin $Co^{III}$ complexes act as ligands for a central high-spin $Co^{II}$ center that is in distorted trigonal prismatic geometry. The following sections describe and analyze the above-mentioned observations in detail.

## Results and Discussion

### Synthesis and Characterization of Chiral Ligands $H_2L^1$–$H_2L^6$

The chiral ligands (Scheme 1) were synthesized in good yields by the Schiff base condensation of 1 equiv. of salicylaldehyde/substituted salicylaldehyde with 1 equiv. of the respective chiral amino alcohol in methanol solutions at room temperature. The IR spectra of all the ligands show broad peaks in the range of 3210–3500 $cm^{-1}$ because of the phenolic and alcoholic OH groups. Peaks observed around 1600, 1490, and 1450 $cm^{-1}$ are most probably due to aromatic C=C stretching vibrations. These Schiff bases exhibit a $\nu$(C=N) band in the range of 1626–1649 $cm^{-1}$ and the peaks in the range 1028–1070 $cm^{-1}$ are assigned to alcoholic C–O stretching. $\nu_{asym}$ and $\nu_{sym}$ stretches of the –$NO_2$ group present in ligands $\mathbf{H_2L^5}$ and $\mathbf{H_2L^6}$ appear at 1545, 1350 and 1543, 1346 $cm^{-1}$ respectively.[8]

The electronic absorption spectra of the chiral Schiff base ligands $\mathbf{H_2L^1}$–$\mathbf{H_2L^6}$ in acetonitrile solvent exhibit characteristic absorption bands at about 320 and 255 nm, which are assigned to transitions of the intramolecularly hydrogen-bonded salicylidenimino chromophore. These ligands also show circular dichroism (CD) spectra that have multiple Cotton effects corresponding to the electronic absorption maxima (see Figure S2 in the electronic supporting information for a representative CD and an electronic spectral curve for the ligand $\mathbf{H_2L^1}$). The negative sign of these observed Cotton effect bands can be correlated with the absolute configuration of the respective amino alcohol moiety.[9]

### Synthesis of Complexes 1–6

Complexes **1**–**6** were synthesized by reacting one molar equivalent of the corresponding Schiff base ligand with one molar equivalent of cobalt acetate tetrahydrate in methanol solutions at room temperature. The red-brown solutions thus obtained were evaporated completely and subsequently extracted with dichloromethane (DCM). The DCM solutions on evaporation gave dark red-brown solids that were recrystallized from dimethylformamide (DMF) solutions. Coordination of the imine nitrogen to the metal center is seen in the $\nu$(C=N) IR band of the complexes in the range 1651–1641 $cm^{-1}$. In some complexes, this value is found to be slightly higher than that of the uncoordinated Schiff base. Although this is uncommon, it has been reported in the literature.[10] The strong band at ca. 1540 $cm^{-1}$ is characteristic of the phenolic C–O stretching mode acquiring partial double bond character through conjugation with the imine system in chelate rings. The C=C stretch appears at ca. 1600 $cm^{-1}$ as a shoulder band. Elemental analytical data of the complexes did not conform to a general molecular formula. Based on elemental and other characterization data, described in the following sections, it was found that complexes **1**–**6** showed variations in their nuclearity and overall geometry despite the fact that the experimental con-

 © 2007 Wiley-VCH Verlag GmbH & Co. KGaA, Weinheim 

ditions were identical. It was also found that all the complexes contain at least one $Co^{III}$ center in their molecular structure, probably formed by the oxidation of $Co^{II}$ acetate used in the syntheses. Atmospheric oxygen is the possible oxidizing agent here, and this oxidation is facilitated by the alkoxide and phenoxide groups present on the ligands. $\mathbf{H_2L^1}$ and $\mathbf{H_2L^2}$ gave mononuclear low-spin $Co^{III}$ complexes, while ligands $\mathbf{H_2L^3}$, $\mathbf{H_2L^4}$, and $\mathbf{H_2L^5}$ gave mixed-valence trinuclear $Co^{III}$–$Co^{II}$–$Co^{III}$ complexes. The ligand $\mathbf{H_2L^6}$ gave an interesting tetranuclear cobalt complex with rather uncommon trigonal prismatic geometry around the central cobalt. Tetradentate Schiff base–oxovanadium complexes having electron-donating or -withdrawing groups at the 5-position of the salicylaldehyde moieties are reported to show similar structural diversity, where the 5-MeO-substituted complex is monomeric and the 5-H- and 5-$NO_2$-substituted complexes are found to be polymeric.[11]

In order to rule out the possibility that the observed changes in nuclearity of complexes **1**–**6** might have been caused by slight changes in the experimental conditions rather than the influence of ligand substitutions, the synthetic reactions of complexes **1**–**6** were carefully reproduced many times and in each case the reported products were obtained in good yields as the main product, confirming that the substitution on the ligand backbone is mainly responsible for the observed changes in nuclearity.

## Electronic and Circular Dichroism Spectra of Complexes 1–6

The electronic and circular dichroism spectra of complexes **1**–**6** were recorded in acetonitrile solutions. The electronic spectra show two weak bands in the 650–700 nm and 520–535 nm ranges. These bands are tentatively assigned to $^1A_{1g} \rightarrow {}^1T_{1g}$ and $^1A_{1g} \rightarrow {}^1T_{2g}$ ligand field transitions respectively, characteristic of an octahedral $Co^{III}$ center.[12] It appears that the relatively high intensities of these d-d

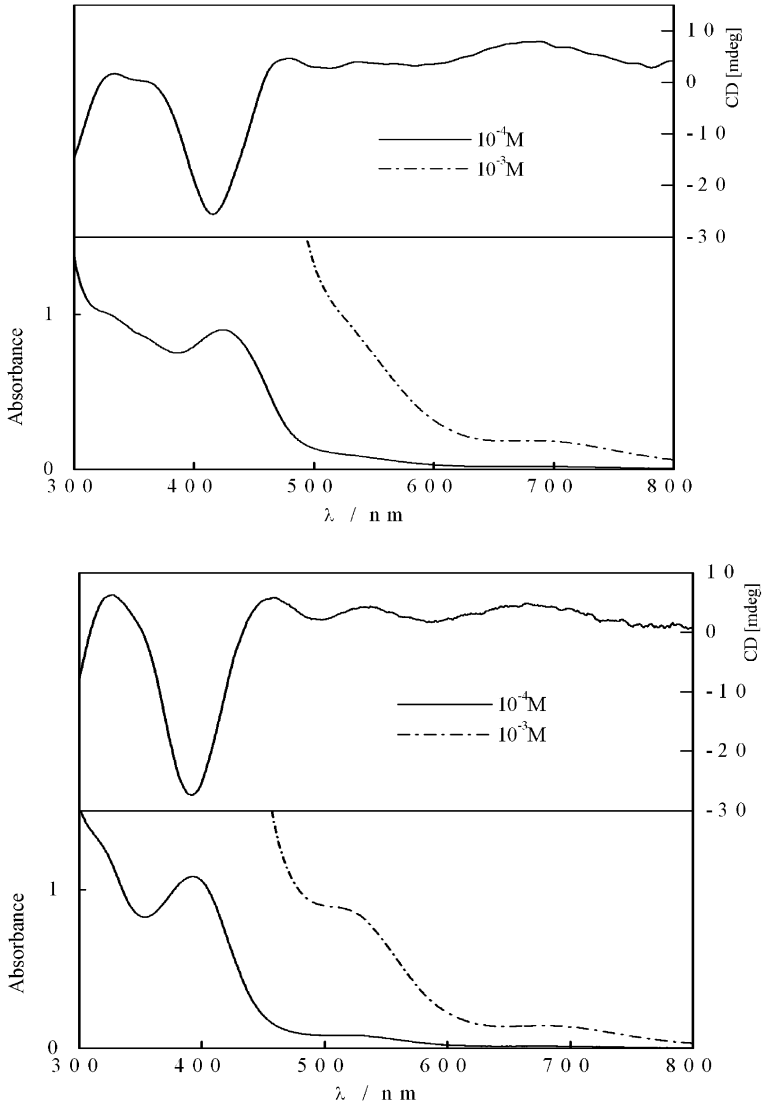


Figure 1. The electronic and circular dichroism spectra of complexes **1** (top) and **3** (bottom).

 © 2007 Wiley-VCH Verlag GmbH & Co. KGaA, Weinheim 

bands are due to strong tail-from-charge transfer transitions. The intense band observed around 400 nm is assigned to phenolate $(O^{-})p_{\pi} \rightarrow Co^{III}$ charge-transfer transition (LMCT). The other intense transitions in the spectra are assigned to intraligand charge-transfer transitions (ILCT). The transitions due to $Co^{II}$ centers are not observed in mixed-valence complexes **3**–**6**, probably because these transitions might have been obscured by the intense absorptions due to $Co^{III}$ centers of these complexes.[13] Two representative electronic absorption spectra are shown in Figure 1.

A general blueshift in band positions is observed for these complexes with electron-withdrawing substituents on ligands. This blueshift originating from the electron-withdrawing nature of the substituents has been observed previously in some similar complexes.[14]

The circular dichroism spectra of these complexes show bands corresponding to their respective electronic absorptions. The visible bands due to the d-d transitions are positive, while the charge transfer transitions appear as negative Cotton effects. The electronic and CD spectra of complexes **1**–**6** are similar despite their structural changes. The appearance of $Co^{III}$ d-d bands for all six complexes confirms the presence of at least one $Co^{III}$ center in each of the complexes. The representative CD curves are presented in Figure 1.

### Magnetic Properties

The magnetic susceptibility measurements of complexes **1**–**6** were performed on powdered samples at room temperature. Complexes **1** and **2** were found to be diamagnetic, as expected for a low-spin $Co^{III}$ state. Magnetic moments in the range of 3.4–5.1 BM were observed for complexes **3**–**6**, which indicate the presence of a high-spin $Co^{II}$ center ($S$ = 3/2) with three unpaired electrons in these complexes. The magnetic properties of polynuclear complexes are extremely sensitive to structural modifications. The $Co^{II}$ center present in these complexes (**3**–**6**) is found to exist in a variety of structural environments ranging from distorted trigonal bipyramidal in **3** to distorted trigonal prismatic in complex **6**. Therefore, the large spread of the observed $\mu_{eff}$ values for these complexes is attributed to their geometric distortions that influence the magnitude of the ligand field splitting. The observed low effective magnetic moment for complex **3** (3.4 B.M.) implies that the orbital contribution to the spin-only value (3.87 B.M.) is fairly small in this complex.

### Crystal Structure of Complex 2

Single crystals of complex **2** suitable for X-ray crystallography were grown from DMF solutions by slow evaporation method. The complex crystallizes in the chiral space group orthorhombic $P2_12_12_1$. The asymmetric unit consists of four mononuclear cobalt complexes and one solvent DMF molecule. The cobalt complexes are almost octahedral in shape and their tridentate ONO donor Schiff base ligand binds the metal in a meridional manner. The molecular geometry and the atom-labeling scheme for a representative mononuclear unit are given in Figure 2 (see Table S4 in the electronic supporting information for selected bond lengths and bond angles for this complex). Although the respective hydrogen atoms are not located in the difference Fourier maps, it is assumed that in each mononuclear unit one of the ligands is doubly deprotonated while the second

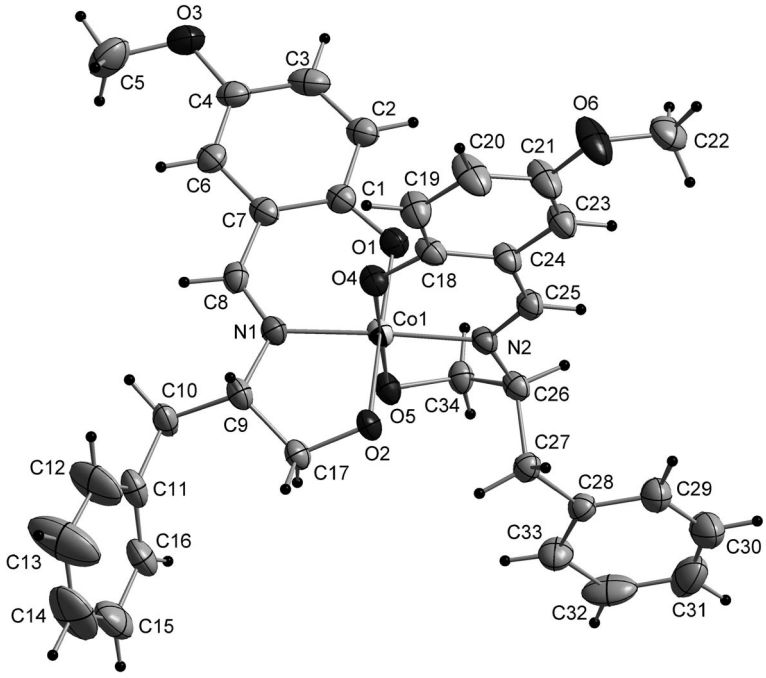


Figure 2. Molecular structure of a representative mononuclear unit of complex **2** showing atom-labeling scheme. Thermal ellipsoids are represented by their 30% probability level.

 © 2007 Wiley-VCH Verlag GmbH & Co. KGaA, Weinheim 

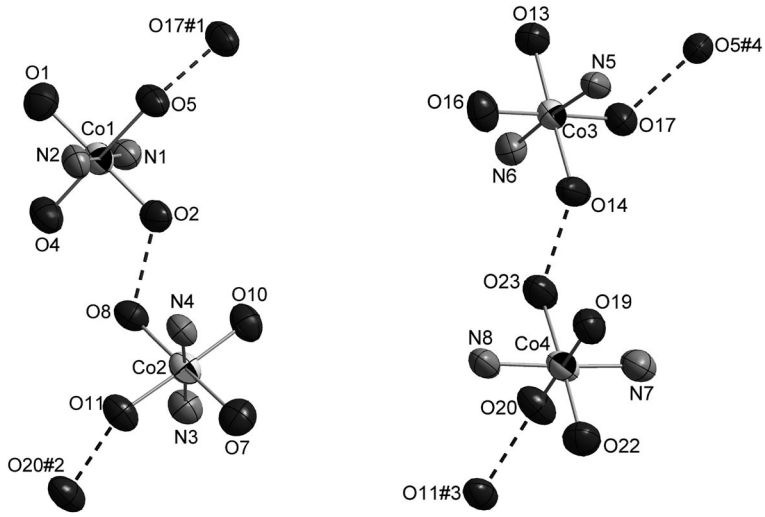


(a) (b)

Figure 3. O–H···O hydrogen-bonding interaction pattern in the asymmetric unit of complex **2** resulting in hydrogen-bonded dimers.

one is singly deprotonated. It is observed that in each mononuclear unit one of the Co–$O_{alk}$ bond lengths is considerably longer than the other [for example Co1–O2 1.906(5) Å while Co1–O5 1.944(4) Å], probably for the above-mentioned reason. This conclusion is also consistent with the overall charge balance of the system. The average Co–$O_{phe}$ [1.882(5) Å], Co–$O_{alk}$ [1.932(5) Å], and Co–$N_{imi}$ [1.902(6) Å] bond lengths are within the range reported for low-spin $Co^{III}$ complexes.[15] The room-temperature magnetic-moment measurements showed that the complex is diamagnetic, also indicating a low-spin $Co^{III}$ complex.

The four mononuclear cobalt complexes present in the asymmetric unit self-assemble through intermolecular O–H···O interactions resulting in the formation of homochiral supramolecular helices in the crystal lattice (Figures 3 and 4).

Each mononuclear complex contains two alcoholic oxygen atoms, one of which is protonated and the other deprotonated. The protonated alcoholic oxygen atom acts as the hydrogen-bond donor while the deprotonated alcoholic oxygen atom acts as the acceptor. The four mononuclear complexes can be labeled as Co1, Co2, Co3, and Co4 (Figure S4, supporting information). The complexes Co1 and Co2 are interconnected by a strong hydrogen bond between alcoholic oxygen atoms O2 and O8 [O2···O8 2.442(6) Å] and exist as a hydrogen-bonded dimer as shown in Figure 3 (a). Similarly, the mononuclear units Co3 and Co4 also exist as a dimer (Figure 3, b), formed by the hydrogen-bonding interactions between alcoholic oxygen atoms O14 and O23 [O14···O23 2.386(7) Å]. These independent dimers are further linked to each other through two O–H···O interactions [O5···O17 2.464(6) Å and O11···O20 2.425(6) Å] resulting in supramolecular hydrogen-bonded homochiral helices in the relevant crystal lattice, as presented in Figure 4. The resulting O–H···O interactions are strong, as evident from the rather short O···O distances.

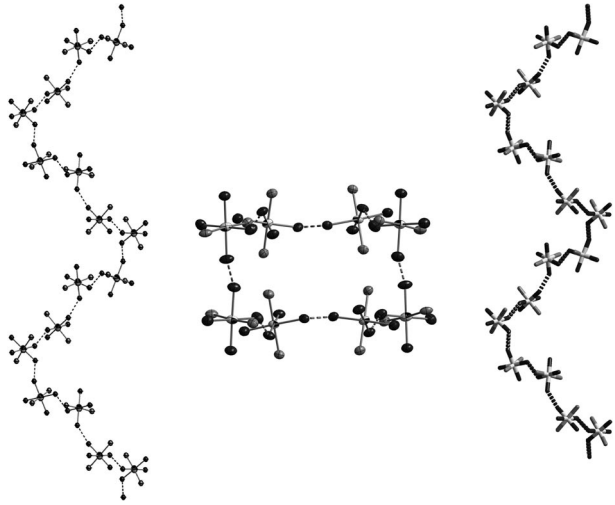

Figure 4. View illustrating intermolecular O–H···O hydrogen-bonding interactions among adjacent molecules that lead to the formation of supramolecular homochiral helices in the crystal lattice of complex **2**. Left: ball-and-stick representation. Right: wire frame representation of the helix. Middle: view down the crystallographic *b* axis showing the helical groove.

One full turn of the helix contains eight mononuclear complexes (Figure 4, left and right), that is, each hydrogen-bonded dimer (Figure 3) in the asymmetric unit repeats twice in one helical turn. The pitch distance is found to be 25.508 Å. The path of the helix can be traced by following the hydrogen bonds counter-clockwise around the twofold screw axis of the helix. The complex is chiral and the crystal contains only one enantiomer of the complex. This local

 © 2007 Wiley-VCH Verlag GmbH & Co. KGaA, Weinheim 

chirality translates into the formation of only left-handed helices on the supramolecular level. Figure 4 clearly depicts the hydrogen-bonding pattern in the asymmetric unit and the mode of propagation of helices in the crystal lattice.

### Crystal Structure of Complex 3

The single crystals of complex **3** suitable for X-ray analysis were grown from DMF solutions by a slow evaporation method. The complex crystallizes in noncentrosymmetric triclinic space group $P\bar{1}$. X-ray analysis shows that the asymmetric unit of complex **3** contains one trinuclear cobalt complex, two solvent DMF molecules, and two water molecules. The molecular structure, with atom-labeling scheme of the complex, is shown in Figure 5. The relevant crystallographic parameters are given in Table 1 (see Table S5 in the supporting information for selected bond lengths and angles observed in complex **3**).

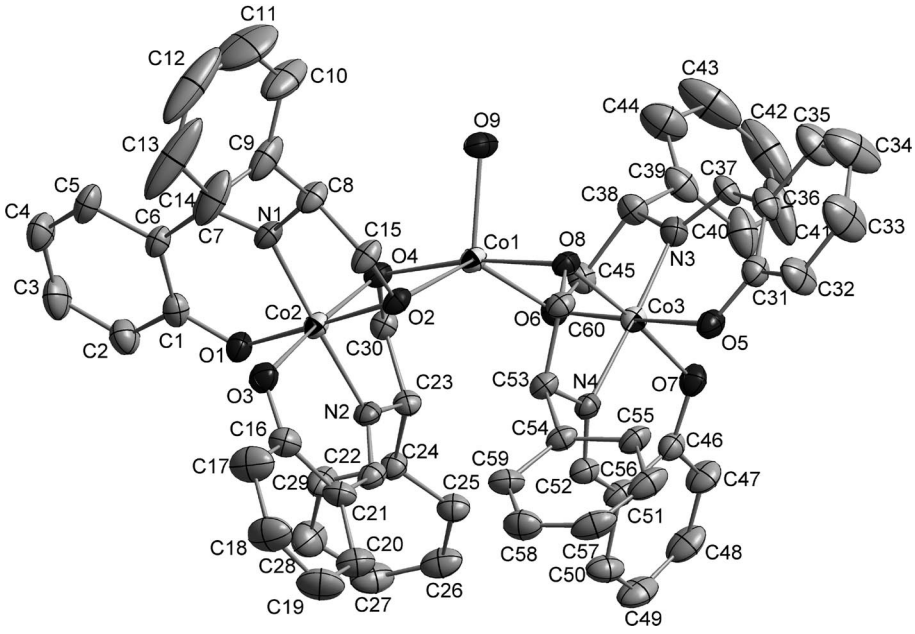


Figure 5. Molecular structure of complex **3** showing atom-labeling scheme. Hydrogen atoms and solvent molecules are omitted for clarity. Thermal ellipsoids are represented by their 30% probability level.

Table 1. Summary of X-ray collection data.

| Complex | **2** | **3** | **5** | **6** |
|---|---|---|---|---|
| Empirical formula | $C_{139}H_{147}Co_4N_9O_{25}$ | $C_{66}H_{72}Co_3N_6O_{13}$ | $C_{73}H_{79}Co_3N_{11}O_{20}$ | $C_{90}H_{75}Co_4N_{12}O_{25}$ |
| Formula mass | 2579.38 | 1334.09 | 1607.26 | 1960.34 |
| Crystal system | orthorhombic | triclinic | monoclinic | tetragonal |
| Space group | $P2_12_12_1$ | $P\bar{1}$ | $P2_1$ | $P4_12_12$ |
| $\lambda$ [Å] | 0.71073 | 0.71073 | 0.71073 | 0.71073 |
| $a$ [Å] | 21.5421(11) | 11.4737(7) | 12.352(11) | 18.5054(5) |
| $b$ [Å] | 25.5084(13) | 12.4004(8) | 24.736(19) | 18.5054(5) |
| $c$ [Å] | 25.6047(13) | 13.2286(8) | 13.085(5) | 46.257(3) |
| $\alpha$ [°] | | 105.0090(10) | | |
| $\beta$ [°] | | 92.7810(10) | 90.22(6) | |
| $\gamma$ [°] | | 93.7460(10) | | |
| $V$ [Å$^3$] | 14069.9(12) | 1809.87(19) | 3998(5) | 15840.7(11) |
| $Z$ | 4 | 1 | 2 | 4 |
| $\mu$ [mm$^{-1}$] | 0.532 | 0.739 | 0.690 | 0.459 |
| $\rho_{calcd.}$ [g cm$^{-3}$] | 1.218 | 1.224 | 1.335 | 0.822 |
| $T$ [°C] | 25 | 25 | 25 | 25 |
| Scan type | $\omega$ | $\omega$ | $\omega$ | $\omega$ |
| Independent reflections | 147193 ($R_{int}$ = 0.098) | 18905 ($R_{int}$ = 0.023) | 9308 ($R_{int}$ = 0.158) | 183227 ($R_{int}$ = 0.124) |
| Observed reflections | 27690 | 13920 | 9304 | 19330 |
| Number of parameters | 1598 | 735 | 909 | 591 |
| Goodness-of-fit | 0.99 | 1.03 | 1.02 | 0.92 |
| $R_1$, $wR_2$ [$I > 2\sigma(I)$] | 0.078, 0.183 | 0.072, 0.179 | 0.083, 0.176 | 0.082, 0.209 |
| Largest diff. peak and hole [e Å$^{-3}$] | 1.05 and –0.33 | 0.80 and –0.32 | 0.57 and –0.61 | 0.97 and –0.42 |
| Absolute structure parameter | –0.001(16) | 0.036(17) | –0.02(3) | –0.02(2) |

 © 2007 Wiley-VCH Verlag GmbH & Co. KGaA, Weinheim 

In the trinuclear geometry of complex **3**, the two terminal cobalt centers are distorted octahedral with $N_2O_4$ coordination sphere. The doubly deprotonated Schiff base ligands act as tridentate donors and bind the cobalt ions in a meridional fashion. The square base of the octahedron is made up of two phenoxo oxygen atoms and two alkoxide oxygen atoms, about which the two imine nitrogen atoms are situated at *trans* positions. The average Co–$N_{imi}$ [1.909(5) Å for Co2 and 1.904(6) Å for Co3], Co–$O_{phe}$ [1.880(5) Å for Co2 and 1.900(5) Å for Co3], and Co–$O_{alk}$ [1.914(5) Å for Co2 and 1.904(4) Å for Co3] distances observed are consistent with the corresponding values observed in related octahedral $Co^{III}$ complexes.[15] The observed distortions from ideal octahedral geometry are caused by the small bite angle of the Schiff base group [N2–Co2–O4 83.6(2)° for Co2 and N4–Co3–O8 83.9(2)° for Co3].

These two terminal octahedral cobalt complexes act as chelating ligands to the central cobalt Co1 through alkoxide oxygen bridging. The central cobalt is five-coordinated with an $\{O_5\}$ coordination sphere. The five coordination sites are satisfied by four bridging alkoxide oxygen atoms and a water molecule. The geometry around Co1 can be considered as distorted trigonal bipyramidal in which the axial Co–O bond lengths Co1–O4 and Co1–O8 [av. 2.113(5) Å] are significantly longer than the other three Co–O bonds, which are considered as equatorial bonds [av. 1.994(5) Å]. The distortion along the axial direction is also obvious from the O4–Co1–O8 angle of 170.38(17)°. The $\tau$ value for the central cobalt, as explained by Addison et al.,[16] is calculated to be 0.66, as shown in Scheme 2, confirming a distorted trigonal bipyramidal (tbp) geometry around it ($\tau$ = 1 for ideal trigonal bipyramidal geometry, $\tau$ = 0 for ideal square-pyramidal geometry). This distortion from ideal tbp geometry can be rationalized by the formation of two constrained four-membered rings around Co1 (Figure 5) as a result of the alkoxide oxygen bridging. Steric factors caused by the bulky terminal cobalt centers may also contribute to the observed distortions. The two four-membered rings attached to the central cobalt are inclined to each other at an angle of 54°.

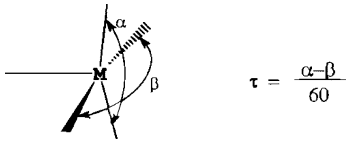


$$\tau = \frac{\alpha - \beta}{60}$$

Scheme 2.

The Co–O bond lengths [av. 2.042(5) Å] around the central cobalt Co1 are significantly longer than those around the terminal cobalt ions, indicating that the central cobalt is divalent while the terminal ones are trivalent. The variations in $Co^{III}$–O and $Co^{II}$–O bond lengths can be expected because the Shannon radius of $Co^{II}$ (0.885 Å) is larger than that of $Co^{III}$ (0.75 Å).[17] The trimer is therefore formulated as a $Co^{III}$–$Co^{II}$–$Co^{III}$ mixed-valence complex, as shown in Figure 5. This assignment is also supported by the fact that there should be two $Co^{3+}$ ions and one $Co^{2+}$ ion in complex **3** to balance the net charge of $8^-$ created by four doubly deprotonated ligands in the molecule.

The average Co···Co separation is found to be 3.011(11) Å in complex **3**, which is considerably smaller than the Co···Co separations [3.821[18a], 3.872,[18b] and 3.066[18c] Å] found in similar mixed-valence trinuclear cobalt complexes. The Co2–Co1–Co3 angle is found to be 136.33(3)°.

There are hydrogen-bonding interactions among the coordinated water molecule and the solvent DMF molecules in the molecular structure of complex **3**. The two DMF molecules are connected to the coordinated water molecule through O–H···O hydrogen-bonding interactions. The relevant O···O distances are O9···O10#1 2.591(9) Å and O9···O11#2 2.610(10) Å where #1 = $x$, 1 + $y$, –1 + $z$ and #2 = $x$, 1 + $y$, $z$ (see Figure S5, electronic supporting information, for hydrogen-bonding in compound **3**).

## Crystal Structure of Complex 5

X-ray analysis on a single crystal of compound **5** indicates that the asymmetric unit of complex **5** contains one trinuclear cobalt complex, two solvent DMF molecules, and one solvent water molecule. The complex crystallizes in the monoclinic space group $P2_1$. Crystallographic details are presented in Table 1.

Quite similar to the structure of complex **3**, the molecular structure of complex **5** also consists of a trinuclear cobalt geometry, as shown in Figure 6. The two terminal cobalt complexes in this molecule are in distorted octahedral $N_2O_4$ coordination sphere and have doubly deprotonated amino alcohol Schiff base ligand $\mathbf{H_2L^5}$ satisfying the coordination sites around the cobalt in a meridional manner. The deviations of bond angles from ideal octahedral values are within ±7° (see supporting information, Table S6). The average Co–$N_{imi}$ [1.887(10) Å for Co2 and 1.912(9) Å for Co3], Co–$O_{phe}$ [1.884(8) Å for Co2 and 1.895(8) Å for Co3], and Co–$O_{alk}$ [1.898(8) Å for Co2 and 1.901(7) Å for Co3] distances observed for the terminal cobalt centers are consistent with corresponding values observed in related octahedral $Co^{III}$ systems.[15]

The two terminal octahedral Co complexes act as chelating units for the central cobalt Co1 through alkoxide oxygen bridging. As expected, the central cobalt is five-coordinated, the fifth coordination site being occupied by a solvent DMF molecule. Two four-membered rings are formed around Co1 as a result of the chelation through alkoxide oxygen atoms by the two terminal cobalt octahedral complexes. Because of this, Co1 assumes a highly distorted geometry, which is almost intermediate between trigonal bipyramidal (tbp) and square-pyramidal (sp), as evidenced by the $\tau$ value of 0.40 (see Scheme 2).[16] It can be concluded from this value that the distortion is more towards square-pyramidal in this case. The two four-membered rings attached to the central cobalt are inclined to each other at an angle of 44°.

 © 2007 Wiley-VCH Verlag GmbH & Co. KGaA, Weinheim 

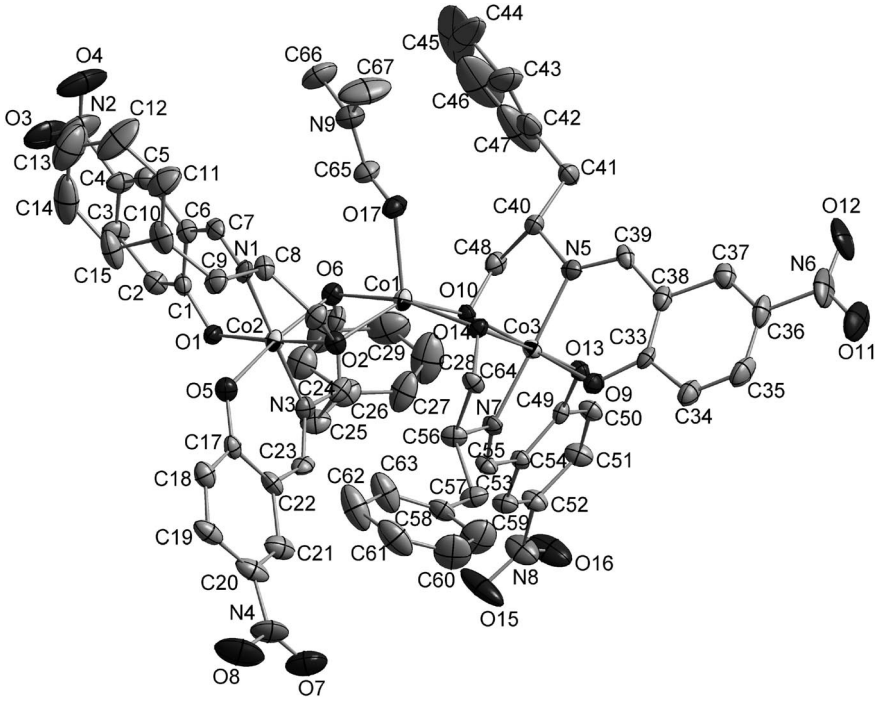


Figure 6. Molecular structure of complex **5** showing atom-labeling scheme. Hydrogen atoms and solvent molecules are omitted for clarity. Thermal ellipsoids are represented by their 30% probability level.

As in the case of complex **3**, the bond lengths around the central cobalt Co1 are significantly longer than those around the terminal cobalt centers in complex **5** as well, indicating that the central cobalt is divalent while the terminal ones are trivalent. The average Co–O distance for Co1 is 2.039(9) Å. Based on the bond length analysis, charge balance, and magnetic moment measurement studies, the trimer in complex **5** can be regarded as a $Co^{III}$–$Co^{II}$–$Co^{III}$ mixed-valence complex.

Similar to complex **3**, the Co···Co separations of 2.992(3) Å [Co2···Co1] and 2.969(3) Å [Co3···Co1] are found to be smaller than the Co···Co separations reported for similar mixed-valence systems.[18] The Co2–Co1–Co3 angle is 140.01(8)°.

### Crystal Structure of Complex 6

The single crystals of complex **6** suitable for X-ray analysis were grown by slow evaporation of DMF solutions. The complex crystallizes in the chiral tetragonal space group $P4_12_12$. The molecular structure and atom-labeling scheme of the complex are presented in Figure 7.

The asymmetric unit contains half of the complex molecule and a solvent water molecule. The crystal structure reveals an interesting tetranuclear geometry for complex **6**, in which three mononuclear cobalt complexes act as chelating ligands for a central cobalt ion. The terminal cobalt complexes are almost octahedral in shape, having two ONO donor Schiff base ligands satisfying the coordination sites of each cobalt in a meridional style.

The central cobalt Co1 is six-coordinated. The coordination polyhedron exhibits, surprisingly, a distorted trigonal

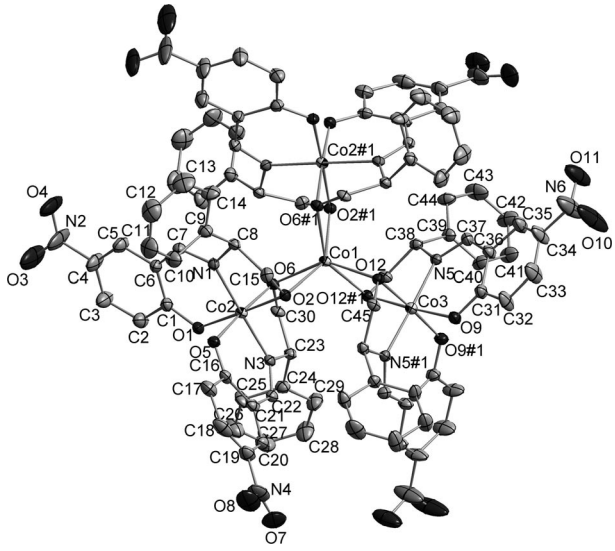


Figure 7. Molecular structure of complex **6** showing atom-labeling scheme. Symmetry-generated atoms are mostly unlabeled. Hydrogen atoms and solvent water molecule are omitted for clarity. Thermal ellipsoids are represented by their 20% probability level.

prismatic (tp) geometry, which is rather scarce for polynuclear cobalt complexes. Four chelating alkoxide oxygen atoms [O2, O6, O12, and O12#1] from cobalt centers Co2 and Co3 form the square base for the trigonal prism. The oxygen atoms O2#1 and O6#1 from the third cobalt center Co2#1, occupy the remaining two vertices to complete the trigonal prismatic coordination sphere around the central Co1 as shown in Figure 8.

 © 2007 Wiley-VCH Verlag GmbH & Co. KGaA, Weinheim 

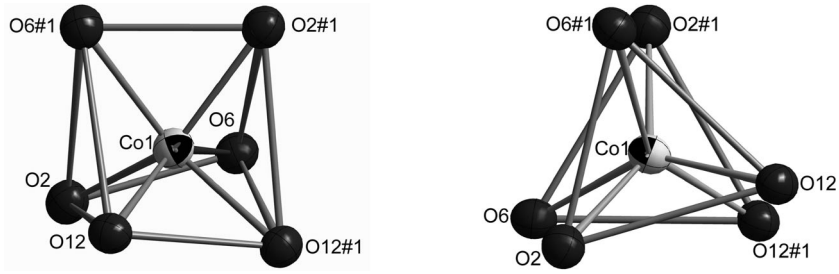


Figure 8. Left: coordination sphere depicting the distorted trigonal prismatic geometry around the central cobalt in complex **6**. Right: view down the trigonal faces of the coordination sphere showing distortion from ideal trigonal prismatic geometry.

The two trigonal faces of the trigonal prism (made up of oxygen atoms O2, O6#1, O12 and O2#1, O12#1, O6) are not equilateral and the square base also shows distortion from ideal geometry. The torsion angle involving opposing corners and the centroids of the trigonal faces are 17.39°, 17.39°, and 16.50° (see Figure 8, right). The distortion from the ideal trigonal prismatic geometry is possibly due to the severe steric overcrowding caused by the three bulky cobalt complexes that act as ligands for the central cobalt ion.

The average Co–$N_{imi}$ [1.897(5) Å for Co2, Co2#1 and 1.875(4) Å for Co3], Co–$O_{phe}$ [1.899(4) Å for Co2, Co2#1 and 1.899(4) Å for Co3], and Co–$O_{alk}$ [1.885(4) Å for Co2, Co2#1 and 1.883(4) Å for Co3] distances observed for terminal cobalt complexes are comparable to the corresponding values observed in related octahedral $Co^{III}$ systems[15] (see supporting information for selected bond lengths and bond angles (Table S7) for complex **6**). The average Co–O bond length of 2.148(3) Å around Co1 is found to be considerably longer than those around the terminal cobalt atoms. By the same argument given in the case of complexes **3** and **5**, it can be assumed that the central cobalt is in 2+ oxidation state. The steric crowding might have caused an additional increase in length of these bonds compared to those in complexes **3** and **5**.

Oxidation state assignment in complex **6** is also supported by the magnetic moment measurements and electronic spectroscopic studies. The electronic spectrum of the complex is similar to the mononuclear $Co^{III}$ complexes **1** and **2**, which indicates the presence of $Co^{III}$ units in the complex. Also the complex shows a net magnetic moment of 5.1 B.M. at room temperature, corresponding to the presence of a high-spin $Co^{II}$ center. If all the tridentate ligands are doubly deprotonated in the molecule, there will be an excess of one negative charge in the complex. It is assumed that this extra negative charge might have been compensated for by one proton (probably because of single deprotonation of one of the ligands) at an unknown position in the complex. A similar situation is reported in the literature for a mononuclear $Co^{III}$ complex with a similar ligand system.[19]

Calculations using the CALC VOID option in PLATON[20] showed a potential solvent access area of 8601.5 $Å^3$ (54.3%) per unit cell of the complex. This fact is also supported by the relatively low $\rho_{calcd}$ value of 0.822 $g\,cm^{-3}$ observed by the X-ray analysis. This void is created as a result of intermolecular C–H···O hydrogen-bonding interactions of the complex with its surrounding molecules, generating a three-dimensional hydrogen-bonded network in the crystal lattice (Figure 9). In these interactions, the oxygen atoms O3, O7, and O10 of the $–NO_2$ group act as the hydrogen-bond acceptor while the aromatic carbon atoms C28, C3, and C11 act as the donors. The relevant hydrogen-bonding

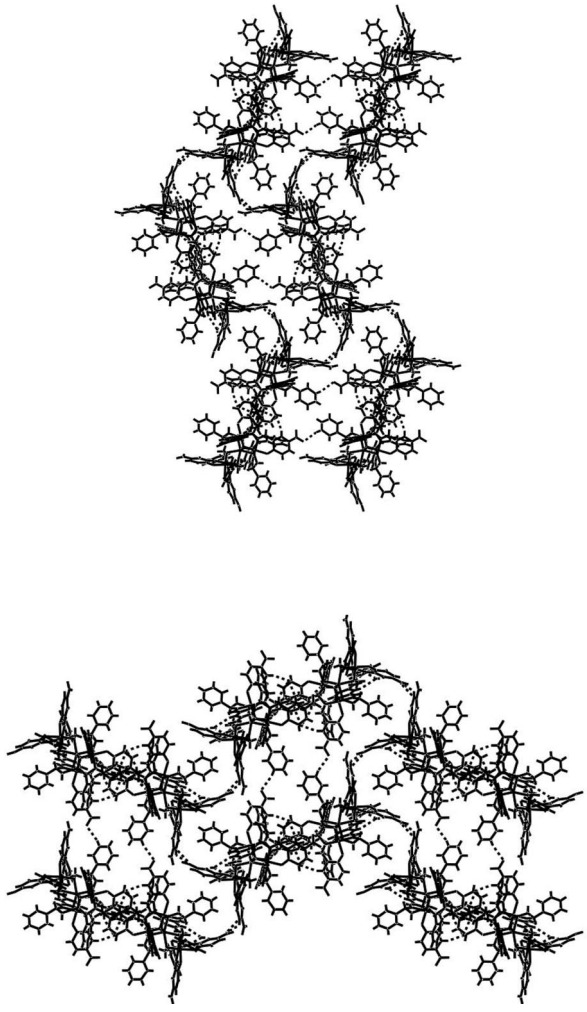

Figure 9. Packing diagrams of complex **6** showing the intermolecular C–H···O hydrogen-bonding interactions that lead to the formation of voids in the crystal lattice. View along the *a* axis (top) and view along the *b* axis (bottom).

 © 2007 Wiley-VCH Verlag GmbH & Co. KGaA, Weinheim 

parameters are given in the supporting information (Table S8). The extension of hydrogen-bonding interactions in a three-dimensional manner thus leads to porosity in the crystal lattice with an overall solvent access area of above 50% in the unit cell. This area is partly occupied by solvent water molecules. The solvent water oxygen O13 is involved in C–H···O hydrogen-bonding interactions with the complex molecule carbons C20 and C22.

## Conclusions

Many interesting observations are made in this study using simple chiral Schiff base ligands and cobalt acetate. The basic coordination sites and geometries of the ligands $H_2L^1$ to $H_2L^6$ are kept the same, changing the substitution on the salicylaldehyde part and the length of the amino alcohol side chain. It is found that these changes control the overall coordination geometries of the resulting cobalt complexes even though the experimental conditions were identical. Complexes of ligands with unsubstituted and 5-nitro-substituted salicylaldehydes prefer multinuclear arrangement while the methoxy-substituted derivatives prefer mononuclear arrangement. In complexes **1**–**6**, the ligands contain both phenolic and alcoholic OH groups. Although both phenol and alkoxy groups can act as bridging functionalities, in these complexes the phenolic oxygen atoms do not act as a bridging group. In complexes **3**–**6** only alkoxide oxygen atoms were found to act as a bridging group. We can assume that the bridging ability of alkoxide oxygen atoms predominates in these complexes probably because of factors like steric and overall crystal packing effects.

In the multinuclear complexes studied here, the high-spin cobalt(II) adopts geometries ranging from distorted trigonal bipyramidal (tbp) and distorted square-pyramidal (sp) to distorted trigonal prismatic (tp). One of the reasons for such distortions may be steric effects caused by the bulky octahedral cobalt(III) complexes acting as ligands. These new edge-sharing octahedral-tbp/sp/tp-octahedral complexes **3**–**6** are complementary to the previous reports of edge-sharing octahedral-tetrahedral-octahedral and face-sharing all-octahedral trinuclear complexes.[21] From the present study, it is also clear that alkoxide oxygen atoms are capable of stabilizing high-spin cobalt(II) ions in a variety of rare geometrical arrangements.

High-spin $Co^{II}$ has a definite preference for octahedral over trigonal prismatic geometry. The previously reported trigonal prismatic complexes of $Co^{II}$ are mostly made up of rigid multidentate ligands.[22] The structure of complex **6** demonstrates that even bulky coordination complexes can stabilize such a geometry around high-spin $Co^{II}$, despite its preference for octahedral geometry. The extensive hydrogen-bonding interactions and the crystal-packing forces might have played some role in dictating such a geometry around the central cobalt in complex **6**.

The nitro-substituted ligands $H_2L^5$ and $H_2L^6$ gave both tri- and tetranuclear complexes. Here the steric effect of the lengthy side arm might have played a crucial role in dictating the said geometries. The lengthy $CH_2Ph$ group creates more steric crowding around the central cobalt in complex **5**, unlike the Ph-substituted derivative in complex **6**, thus preventing another octahedral complex from approaching and coordinating to it.

The crystal structures of complexes **3** and **5** belong to the limited number of structurally characterized trinuclear cobalt complexes with mixed oxidation states. There are two main reported classes of trinuclear cobalt complexes of mixed-spin states. One includes mixed-valence trinuclear complexes of the form $Co^{III}$($S$ = 0)–$Co^{II}$($S$ = 3/2)–$Co^{III}$ ($S$ = 0),[13,18f] and another, mixed-spin trinuclear complexes of the form $Co^{II}$ ($S$ = 1/2)–$Co^{II}$ ($S$ = 3/2)–$Co^{II}$ ($S$ = 1/2).[23] The trinuclear complexes **3**–**5** discussed here belong to the former category.

Finally, it has been shown that the tridentate chiral Schiff base ligands $H_2L^1$–$H_2L^6$ are very versatile in their coordination behavior towards cobalt and can readily form stable mono-, tri-, and tetranuclear chiral complexes with interesting structural features. Besides the isolation, characterization, and analysis of properties of chiral mono-, tri-, and tetranuclear cobalt complexes, we have demonstrated that the introduction of a different substitution on the ligand backbone can result in unexpected structural modifications of resulting complexes.

## Experimental Section

**General Information:** Microanalytical (C,H,N) data were obtained with a FLASH EA 1112 Series CHNS Analyzer. A Shimadzu 3101-PC UV/Vis/NIR spectrophotometer was used to record the electronic spectra. Infrared spectra were recorded by using KBr pellets with a Jasco-5300 FTIR spectrophotometer. $^1$H NMR spectra in $CDCl_3$ solutions were recorded with a Bruker DRX-400 spectrometer, using $Si(CH_3)_4$ as an internal standard. Room temperature solid-state magnetic susceptibilities were measured by using a Sherwood Scientific magnetic susceptibility balance. The CD spectra were measured in solution phase with a JASCO J-810 spectropolarimeter. Salicylaldehyde, 5-nitrosalicylaldehyde, 5-methoxysalicylaldehyde, (*S*)-(+)-2-phenylglycinol, and (*S*)-(–)-2-amino-3-phenyl-1-propanol were purchased from Lancaster (India) and used as received. Solvents used for UV/Vis and CD analyses were of HPLC grade and procured from E. Merck (India). All other chemicals were of analytical grade and were used without further purification.

**Synthesis of Chiral Schiff Bases $H_2L^1$–$H_2L^6$:** The synthesis and characterization of chiral Schiff bases $H_2L^3$, $H_2L^4$, $H_2L^5$, and $H_2L^6$ have been reported elsewhere.[7]

**$H_2L^1$:** (*S*)-(+)-2-Phenylglycinol (0.137 g, 1 mmol) and 5-methoxysalicylaldehyde [2-hydroxy-5-methoxybenzaldehyde] (0.152 g, 1 mmol) were stirred together in methanol (15 mL) for 3 h at room temperature. The resulting yellow solution was filtered and the filtrate was kept open at room temperature for slow evaporation. A yellow solid, thus obtained, was washed with hexane and dried at room temperature. Yield 0.25 g, 92%. $C_{16}H_{17}NO_3$ (271.31): calcd. C 70.83, H 6.32, N 5.16; found C 70.77, H 6.25, N 5.11. IR (KBr): $\tilde{\nu}$ = 3485, 2860, 1635, 1589, 1491, 1272, 1157, 1068, 1028, 902, 831, 790, 761, 700, 534, 457 cm$^{-1}$. $^1$H NMR (400 MHz, $CDCl_3$): $\delta$ = 3.77 (s, 3 H, $OCH_3$), 3.92–3.94 (d, $J$ = 6.5 Hz, 2 H, $CH_2$), 4.46–4.49 (t, $J$ = 6.44 Hz, 1 H, CH), 6.78–6.94 (m, 3 H, Ar), 7.26–7.39

 © 2007 Wiley-VCH Verlag GmbH & Co. KGaA, Weinheim 

(m, 5 H, Ar), 8.45 (s, 1 H, HC=N) ppm. UV/Vis ($CH_3CN$): $\lambda_{max}$ ($\varepsilon$, $M^{-1}cm^{-1}$) = 343 (5039), 258 (10309) nm. CD ($CH_3CN$, $10^{-4}$ M): $\lambda_{max}$ (mdeg) = 343 (–12.70), 258 (–19.80) nm.

**$H_2L^2$:** (*S*)-(–)-2-Amino-3-phenyl-1-propanol (0.151 g, 1 mmol) and 5-methoxysalicylaldehyde (0.152 g, 1 mmol) were stirred together in methanol (15 mL) for 3 h at room temperature. The resulting yellow solution was filtered and the filtrate was kept open for slow evaporation. A yellow semi-solid was obtained and washed with hexane and dried at room temperature. Yield: 0.26 g, 90%. $C_{17}H_{19}NO_3$ (285.34): calcd. C 71.56, H 6.71, N 4.91; found C 71.3, H 6.56, N 5.01. IR (KBr): $\tilde{\nu}$ = 3422, 1635, 1591, 1493, 1379, 1334, 1271, 1224, 1159, 1037, 908, 821, 761, 702 $cm^{-1}$. $^1H$ NMR (400 MHz, $CDCl_3$): $\delta$ = 2.8–3.0 (m, 2 H, $CH_2$), 3.51 (m, 1 H, CH), 3.73 (s, 3 H, $OCH_3$), 3.77–3.82 (m, 2 H, $CH_2$-OH), 6.57–6.95 (m, 3 H, Ar), 7.13–7.27 (m, 5 H, Ar), 8.03 (s, 1 H, HC=N) ppm. UV/Vis ($CH_3CN$): $\lambda_{max}$ ($\varepsilon$, $M^{-1}cm^{-1}$) = 343 (5025), 258 (7916), 230 (20892) nm. CD ($CH_3CN$, $10^{-4}$ M): $\lambda_{max}$ (mdeg) = 343 (–11.6), 258 (–19.2) nm.

**$H_2L^5$:** (*S*)-(–)-2-Amino-3-phenyl-1-propanol (0.151 g, 1 mmol) and 5-nitrosalicylaldehyde (0.167 g, 1 mmol) were stirred together in methanol (15 mL) for 3 h at room temperature. The resulting yellow solution was filtered and the filtrate was kept for 2 d in an open beaker for slow evaporation. The yellow precipitate of **$H_2L^5$** thus obtained was washed with hexane and dried at room temperature. Yield 0.27 g, 90%. $C_{16}H_{16}N_2O_4$ (300.31): calcd. C 63.99, H 5.37, N 9.33; found C 64.05, H 5.29, N 9.18. IR (KBr): $\tilde{\nu}$ = 3470, 1649, 1618, 1543, 1487, 1446, 1404, 1346, 1226, 1134, 1064, 941, 904, 835, 756, 729, 700, 630 $cm^{-1}$. $^1H$ NMR (400 MHz, $CDCl_3$): $\delta$ = 2.97 (m, 2 H, $CH_2$-Ph), 3.65 (m, $^1H$, CH), 3.86 (m, 2 H, $CH_2$-OH), 6.92 (d, 1 H, Ar, *ortho* to OH), 7.2 (m, 5 H, Ar), 8.04 (s, 1 H, HC=N), 8.06 (d, 1 H, Ar, *ortho* to $NO_2$), 8.15 (m, 1 H, Ar, *ortho* to $NO_2$) ppm. UV/Vis ($CH_3CN$): $\lambda_{max}$ ($\varepsilon$, $M^{-1}cm^{-1}$) = 401 (6950), 325 (9931), 260 (17447), 240 (17111) nm. CD ($CH_3CN$, $10^{-4}$ M): $\lambda_{max}$ (mdeg) = 401 (–2.66), 320 (–4.66), 260 (–5.85), 240 (–3.85) nm.

**Synthesis of Cobalt Complexes 1–6:** All six cobalt complexes **1**–**6**, reported here, were prepared according to the following general procedure.

$(CH_3COO)_2Co{\cdot}4H_2O$ (0.249 g, 1 mmol) was added to a methanolic solution (25 mL) of the respective chiral ligand (1 mmol). The mixture was stirred at room temperature in air overnight. The resultant dark red-brown solution was evaporated to dryness using a rotavapor and a vacuum pump. The solid thus obtained was extracted with dichloromethane and evaporated to give a red-brown microcrystalline solid, which was recrystallized from a solution of DMF.

**$[CoL^1(HL^1)]{\cdot}0.25DMF$ (1):** Yield 0.23 g, 74%. $C_{32}H_{31}CoN_2O_6{\cdot}0.25C_3H_7NO$ (616.81): calcd. C 63.77, H 5.35, N 5.11; found C 64.06, H 5.29, N 5.23. IR (KBr): $\tilde{\nu}$ = 2928, 1635, 1539, 1469, 1423, 1298, 1259, 1219, 1157, 1033, 947, 819, 769, 702, 528, 418 $cm^{-1}$. UV/Vis ($CH_3CN$): $\lambda_{max}$ ($\varepsilon$, $M^{-1}cm^{-1}$): 255 (35880), 315 (7686), 418 (3803), 535 (423), 700 (88) nm. CD ($CH_3CN$, $10^{-4}$ M): $\lambda_{max}$ (mdeg): 275 (–21.6), 417 (–26.13), 535 (4.14), 692 (8.05) nm.

**$[CoL^2(HL^2)]{\cdot}0.25DMF$ (2):** Yield 0.22 g, 69%. $C_{34}H_{35}CoN_2O_6{\cdot}0.25C_3H_7NO$ (644.86): calcd. C 64.72, H, 5.74, N, 4.89; found C 64.48, H 5.39, N 4.44. IR (KBr): $\tilde{\nu}$ = 3414, 3028, 2924, 1635, 1537, 1464, 1385, 1304, 1255, 1217, 1157, 1084, 1035, 814, 744, 700, 532, 466 $cm^{-1}$. UV/Vis ($CH_3CN$): $\lambda_{max}$ ($\varepsilon$, $M^{-1}cm^{-1}$) = 255 (35471), 315 (7544), 420 (3914), 535 (435), 700 (96) nm. CD ($CH_3CN$, $10^{-4}$ M): $\lambda_{max}$ (mdeg) = 292 (–9.15), 415 (–10.14), 520 (0.62), 685 (6.40) nm.

**$[Co(CoL^3_2)_2{\cdot}H_2O]{\cdot}2DMF{\cdot}2H_2O$ (3):** Yield 0.26 g, 77%. $C_{66}H_{72}Co_3N_6O_{13}$ (1334.11): calcd. C 59.42, H 5.44, N 6.30; found C 59.05, H 5.15, N 6.11. IR (KBr): $\tilde{\nu}$ = 3416, 3051, 2918, 2854, 1633, 1597, 1533, 1493, 1454, 1439, 1385, 1344, 1317, 1253, 1195, 1147, 1124, 1095, 1028, 945, 896, 831, 752, 704, 650, 628, 592, 534 $cm^{-1}$. UV/Vis ($CH_3CN$): $\lambda_{max}$ ($\varepsilon$, $M^{-1}cm^{-1}$) = 252 (87930), 317 (13220), 398 (9402), 525 (867), 690 (138) nm. CD ($CH_3CN$, $10^{-4}$ M): $\lambda_{max}$ (mdeg) = 262 (–24.88), 282 (–18.84), 394 (–27.62), 535 (4.19), 668 (4.55) nm. Room temp. magnetic moment = 3.4 B.M.

**$[Co(CoL^4_2)_2{\cdot}H_2O]{\cdot}2DMF{\cdot}H_2O$ (4):** Yield 0.26 g, 76%. $C_{70}H_{78}Co_3N_6O_{12}$ (1372.20): calcd. C 61.27, H 5.73, N 6.12; found C 61.69, H 5.53, N 5.98. IR (KBr): $\tilde{\nu}$ = 3024, 2916, 1635, 1599, 1535, 1448, 1388, 1315, 1195, 1147, 1082, 956, 844, 748, 700, 580, 524, 468 $cm^{-1}$. UV/Vis ($CH_3CN$): $\lambda_{max}$ ($\varepsilon$, $M^{-1}cm^{-1}$) = 251 (76170), 322 (10950), 394 (8070), 526 (1284), 705 (400) nm. CD ($CH_3CN$, $10^{-4}$ M): $\lambda_{max}$ (mdeg) = 280 (–4.19), 394 (–13.27), 516 (0.22), 675 (3.48) nm. Room temp. magnetic moment = 4.35 B.M.

**$[Co(CoL^5_2)_2{\cdot}DMF]{\cdot}2DMF{\cdot}H_2O$ (5):** Yield 0.28 g, 70%. $C_{73}H_{79}Co_3N_{11}O_{20}$ (1607.27): calcd. C 54.55, H 4.95, N 9.59; C 54.78, H 4.83, N 9.13. IR (KBr): $\tilde{\nu}$ = 2922, 1647, 1601, 1545, 1473, 1386, 1313, 1097, 947, 831, 754, 702, 659, 489 $cm^{-1}$. UV/Vis ($CH_3CN$): $\lambda_{max}$ ($\varepsilon$, $M^{-1}cm^{-1}$) = 240 (72860), 317 (21190), 385 (50960), 520 (1013), 650 (350) nm. CD ($CH_3CN$, $10^{-4}$ M): $\lambda_{max}$ (mdeg) = 259 (–12.26), 390 (–13.17), 522 (1.96), 660 (4.83) nm. Room temp. magnetic moment = 4.25 B.M.

**$H[Co(CoL^6_2)_3]{\cdot}H_2O$ (6):** Yield 0.22 g, 68%. $C_{90}H_{75}Co_4N_{12}O_{25}$ (1960.36): calcd. C 55.14, H 3.86, N, 8.57; found C 55.01, H 3.92, N 8.23. IR (KBr): $\tilde{\nu}$ = 3566, 2924, 1647, 1602, 1548, 1473, 1383, 1313 (nitro), 1132, 1101, 1026, 951, 827, 756, 696, 655, 540 $cm^{-1}$. UV/Vis ($CH_3CN$): $\lambda_{max}$ ($\varepsilon$, $M^{-1}cm^{-1}$) = 243 (120830), 315 (38660), 387 (92940), 520 (1560), 650 (478) nm. CD ($CH_3CN$, $10^{-4}$ M): $\lambda_{max}$ (mdeg) = 262 (–45.73), 383 (–40.37), 530 (8.25), 660 (11.00) nm. Room temp. magnetic moment = 5.1 B.M.

**X-ray Crystallography:** A summary of the crystallographic data for compounds **2**, **3**, **5**, and **6** is given in Table 1. Data for complexes **2**, **3**, and **6** were collected at room temperature with a Bruker SMART APEX CCD area detector system [$\lambda$(Mo-$K_\alpha$) = 0.71073 Å], graphite monochromator, 2400 frames were recorded with an $\omega$-scan width of 0.3°, crystal-detector distance 60 mm, collimator 0.5 mm. The data were reduced using SAINTPLUS[24] and a multiscan absorption correction using SADABS[24] was performed. The structures were solved by direct methods and refined on $F^2$ by full-matrix least-squares procedures using SHELX-97 programs.[25] Hydrogen atoms were introduced on calculated positions and included in the refinement riding on their respective parent atoms. The absolute configurations for the complex molecules were successfully determined by refining the respective Flack parameters.[26] In the case of complex **2**, all the non-hydrogen atoms are refined anisotropically. The hydrogen atoms associated with some of the alcoholic oxygen atoms were not located in the difference Fourier maps. For complex **3**, all the non-hydrogen atoms except that of the uncoordinated solvent molecules are refined anisotropically. Some of the benzene rings show disorder and some restraints were applied. Hydrogen atoms were not located in association with coordinated and solvent water molecules. For complex **6**, the $R_{int}$ value was considerably higher (0.1235). Such a high $R_{int}$ value is attributed to the long *c* axis [46.257(3) Å] and the subsequent difficulty in neatly resolving adjacent reflections and to the low diffraction power of the relevant crystal characterized by a large fraction of weak intensities. Also this particular complex contains a large amount of void space. All the non-hydrogen atoms except the water oxygen are refined anisotropically. The hydrogen atoms associated with the sol-

 © 2007 Wiley-VCH Verlag GmbH & Co. KGaA, Weinheim 

vent water molecule are not located in the difference Fourier maps. Single crystals of complex **5** were grown by slow evaporation of a dimethylformamide solution. Unit cell determination and the data collection were performed on an Enraf–Nonius Mach3 single-crystal diffractometer using graphite-monochromated Mo-$K_\alpha$ radiation ($\lambda$ = 0.71073 Å). An empirical absorption correction was applied to the data based on the $\psi$-scans of three reflections.[27] Programs of WinGX[28] were used for data reduction and absorption correction. The structure was solved by direct methods and refined on $F^2$ by full-matrix least-squares procedures using the SHELX-97 program.[25] All the non-hydrogen atoms except the uncoordinated solvent molecules were refined anisotropically. Some benzene rings show disorder and some restraints were applied. Hydrogen atoms were not located in association with water molecule oxygen atom. A high $R_{int}$ value (0.1510) observed in this case is probably due to the low diffraction power of the crystal characterized by a large fraction of weak intensities.

CCDC-651783 (for **2**), -651784 (for **3**), -651785 (for **5**), and -651786 (for **6**) contain the supplementary crystallographic data for this paper. These data can be obtained free of charge from The Cambridge Crystallographic Data Center via www.ccdc.cam.ac.uk/data_request/cif.

**Supporting Information** (see also the footnote on the first page of this article): Detailed synthesis and characterization of the Schiff bases (ligands) $\mathbf{H_2L^1}$–$\mathbf{H_2L^6}$; representative $^1$H NMR spectrum of $\mathbf{H_2L^6}$; representative UV and CD spectra of $\mathbf{H_2L^1}$; crystal structure description of the ligand $\mathbf{H_2L^5}$; additional figures for crystal structures of the complexes; tables (selected bond lengths and angles) for compounds **2**, **3**, **5**, and **6**; a table for hydrogen-bonding parameters for compound **6**; a table for summary of electronic spectra and room temperature magnetic moments for compounds **1**–**6**.

## Acknowledgments

We thank the Department of Science and Technology, Government of India, for financial support (Project No.: SR/SI/IC-18/2002). The National X-ray Diffractometer facility at the University of Hyderabad by the Department of Science and Technology, Government of India, is gratefully acknowledged. We are grateful to University Grants Commitee (UGC), New Delhi, for providing the infrastructure facility at the University of Hyderabad under a University with Potential for Excellence grant. C. P. P. thanks University Grants Commitee (UGC), New Delhi, for a fellowship.

[1] a) A. Von Zelewsky, O. Mamula, *J. Chem. Soc. Dalton Trans.* **2000**, 219–231; b) U. Knof, A. Von Zelewsky, *Angew. Chem. Int. Ed.* **1999**, *38*, 302–322; c) C. Provent, A. F. Williams, *Transition Metals in Supramolecular Chemistry* (Ed.: J. P. Sauvage), John Wiley and Sons, New York, **1999**, pp. 135–191; d) R. Büchner, J. S. Field, H. Raymond, *Inorg. Chem.* **1997**, *36*, 3952–3956; e) V. H. Houlding, V. M. Miskowski, *Coord. Chem. Rev.* **1991**, *111*, 145–152; f) J. Zyss, C. Dhenaut, T. Chauvan, I. Ledoux, *Chem. Phys. Lett.* **1993**, *206*, 409–414; g) N. J. Long, *Angew. Chem. Int. Ed. Engl.* **1995**, *34*, 37–56.

[2] a) M. A. Alam, M. Nethaji, M. Ray, *Angew. Chem. Int. Ed.* **2003**, *42*, 1940–1942; b) X.-W. Liu, N. Tang, Y.-H. Chang, M.-Y. Tan, *Tetrahedron: Asymmetry* **2004**, *15*, 1269–1273; c) C.-T. Yang, M. Vetrichelvan, X. Yang, B. Moubaraki, K. S. Murray, J. J. Vittal, *Dalton Trans.* **2004**, 113–121; d) P. Deschamps, P. P. Kulkarni, B. Sarkar, *Inorg. Chem.* **2003**, *42*, 7366–7368; e) C.-T. Yang, B. Moubaraki, K. S. Murray, J. J. Vittal, *Dalton Trans.* **2003**, 880–889.

[3] a) J. L. Vicario, D. Badía, L. Carrillo, E. Reyes, J. Etxebarria, *Curr. Org. Chem.* **2005**, *9*, 219–235; b) G. Lu, Y.-M. Li, X.-S. Li, A. S. C. Chan, *Coord. Chem. Rev.* **2005**, *249*, 1736–1744; c) L. Pu, H.-B. Yu, *Chem. Rev.* **2001**, *101*, 757–824; d) D. J. Ager, I. Prakash, D. R. Schaad, *Chem. Rev.* **1996**, *96*, 835–876.

[4] Titanium catalysts: a) M. Hayashi, Y. Miyamoto, T. Inoue, N. Oguni, *J. Org. Chem.* **1993**, *58*, 1515–1522; b) Á. Gama, L. Z. Flores-López, G. Aguirre, M. Parra-Hake, R. Somanathan, T. Cole, *Tetrahedron: Asymmetry* **2005**, *16*, 1167–1174; c) Q. Tian, C. Jiang, Y. Li, C. Jiang, T. You, *J. Mol. Catal. A: Chem.* **2004**, *219*, 315–317; d) V. Banphavichit, W. Mansawat, W. Bhanthumnavin, T. Vilaivan, *Tetrahedron* **2004**, *60*, 10559–10568; e) J. R. Petersen, J. M. Hoover, W. S. Kassel, A. L. Rheingold, A. R. Johnson, *Inorg. Chim. Acta* **2005**, *358*, 687–694. Vanadium catalysts: f) C. Bolm, F. Bienewald, *Angew. Chem. Int. Ed. Engl.* **1995**, *34*, 2640–2642; g) S. A. Blum, R. G. Bergman, J. A. Ellmann, *J. Org. Chem.* **2003**, *68*, 150–155; h) Á. Gama, L. Z. Flores-López, G. Aguirre, M. Parra-Hake, L. H. Hellberg, R. Somanathan, *ARKIVOC* **2003**, *11*, 4–15; i) A. Barbarini, R. Maggi, M. Muratori, G. Sartori, R. Sartorio, *Tetrahedron: Asymmetry* **2004**, *15*, 2467–2473. Copper catalysts: j) T. Aratani, Y. Yoneyoshi, T. Nagase, *Tetrahedron Lett.* **1975**, *16*, 1707–1710; k) Z. Li, G. Liu, Z. Zheng, H. Chen, *Tetrahedron* **2000**, *56*, 7187–7191; l) C. Jiang, Z. Ming, Q. Tan, D. Qian, T. You, *Enantiomer* **2002**, *7*, 287–293; m) M. Itagaki, K. Hagiya, M. Kamitamari, K. Masumoto, K. Suenobu, Y. Yamamoto, *Tetrahedron* **2004**, *60*, 7835–7843. Other metal ion catalysts: n) H.-L. Kwong, L.-S. Cheng, W.-S. Lee, *J. Mol. Catal. A: Chem.* **1999**, *150*, 23–29; o) R. Tümerdem, G. Topal, Y. Turgut, *Tetrahedron: Asymmetry* **2005**, *16*, 865–868; p) P. Västilä, J. Wettergren, H. Adolfsson, *Chem. Commun.* **2005**, 4039–4041; q) J. K. Park, H. G. Lee, C. Bolm, B. M. Kim, *Chem. Eur. J.* **2005**, *11*, 945–950; r) S. Malfait, L. Pélinski, J. Brocard, *Tetrahedron: Asymmetry* **1996**, *7*, 653–656.

[5] a) R. Fleischer, H. Wunderlich, M. Braun, *Eur. J. Org. Chem.* **1998**, 1063–1070; b) J. Hartung, S. Drees, M. Greb, P. Schmidt, I. Svoboda, H. Fuess, A. Murso, D. Stalke, *Eur. J. Org. Chem.* **2003**, 2388–2408; c) L. Cai, H. Mahmoud, Y. Han, *Tetrahedron: Asymmetry* **1999**, *10*, 411–427; d) K. Yanagi, M. Minobe, *Acta Crystallogr., Sect. C: Cryst. Struct. Commun.* **1987**, *43*, 2060–2063; e) K. Yanagi, M. Minobe, *Acta Crystallogr., Sect. C: Cryst. Struct. Commun.* **1987**, *43*, 1045–1048; f) Y. Yuan, J. Yao, J. Lu, Y. Zhang, R. Gu, *Inorg. Chem. Commun.* **2005**, *8*, 1014; g) S. G. Telfer, T. Sato, R. Kuroda, J. Lefebvre, D. B. Leznoff, *Inorg. Chem.* **2004**, *43*, 421–429.

[6] P. V. Bernhardt, G. A. Lawrance in *Comprehensive Coordination Chemistry II*, (Eds: J. A. McCleverty, T. J. Meyer), Elsevier-Pergamon, Oxford, **2004**, vol. 6, pp. 1–145.

[7] a) C. P. Pradeep, T. Htwe, P. S. Zacharias, S. K. Das, *New J. Chem.* **2004**, *28*, 735–739; b) C. P. Pradeep, P. S. Zacharias, S. K. Das, *Polyhedron* **2005**, *24*, 1410–1416; c) C. P. Pradeep, P. S. Zacharias, S. K. Das, *J. Chem. Sci.* **2005**, *117*, 133–137; d) C. P. Pradeep, P. S. Zacharias, S. K. Das, *Eur. J. Inorg. Chem.* **2005**, 3405–3408; e) C. P. Pradeep, *Acta Crystallogr., Sect. E: Struct. Rep. Online* **2005**, *61*, o3825–o3827; f) C. P. Pradeep, P. S. Zacharias, S. K. Das, *J. Chem. Sci.* **2006**, *118*, 311–317.

[8] R. M. Silverstein, F. X. Webster, *Spectroscopic Identification of Organic Compounds*, John Wiley & Sons Inc., New York, **1998**.

[9] a) H. E. Smith, J. R. Neergaard, E. P. Burrows, F.-M. Chen, *J. Am. Chem. Soc.* **1974**, *96*, 2908–2916; b) H. E. Smith, B. G. Padilla, J. R. Neergaard, F.-M. Chen, *J. Org. Chem.* **1979**, *44*, 1690–1695.

[10] T. Głowiak, L. Jerzykiewicz, J. M. Sobczak, J. J. Ziółkowski, *Inorg. Chim. Acta* **2003**, *356*, 387–392.

[11] M. Tsuchimoto, R. Kasahara, K. Nakajima, M. Kojima, S. Ohba, *Polyhedron* **1999**, *18*, 3035–3039.

[12] a) M. S. Shongwe, S. K. M. Al-Hatmi, H. M. Marques, R. Smith, R. Nukada, M. Mikuriya, *J. Chem. Soc. Dalton Trans.* **2002**, 4064–4069; b) Y.-S. Xie, X.-T. Liu, M. Zhang, K.-J. Wei, Q.-L. Liu, *Polyhedron* **2005**, *24*, 165–171.

[13] H. Kobayashi, K. Ohki, I. Tsujikawa, K. Osaki, N. Uryû, *Bull. Chem. Soc. Jpn.* **1976**, *49*, 1210–1220.

 © 2007 Wiley-VCH Verlag GmbH & Co. KGaA, Weinheim 

[14] a) R. J. P. Williams, *J. Chem. Soc.* **1955**, 137–145; b) R. N. Mukherjee, O. A. Rajan, A. Chakravorty, *Inorg. Chem.* **1982**, *21*, 785–790; c) J. W. Pyrz, A. L. Roe, L. J. Stern, L. Que Jr, *J. Am. Chem. Soc.* **1985**, *107*, 614–620.
[15] a) A. Böttcher, T. Takeuchi, K. I. Hardcastle, T. J. Meade, H. B. Gray, D. Cwikel, M. Kapon, Z. Dori, *Inorg. Chem.* **1997**, *36*, 2498–2504; b) M. Dey, C. P. Rao, P. K. Saarenketo, K. Rissanen, E. Kolehmainen, P. Guionneau, *Polyhedron* **2003**, *22*, 3515–3521.
[16] A. W. Addison, T. N. Rao, J. Reedijk, J. V. Rijn, G. C. Verschoor, *J. Chem. Soc. Dalton Trans.* **1984**, 1349–1356.
[17] R. D. Shannon, *Acta Crystallogr., Sect. A: Found. Crystallogr.* **1976**, *32*, 751–767.
[18] a) T. S. Billson, J. D. Crane, O. D. Fox, S. L. Heath, *Inorg. Chem. Commun.* **2000**, *3*, 718–720; b) V. Gama, R. T. Henriques, M. Almeida, L. Veiros, M. J. Calhorda, A. Meetsma, J. L. de Boer, *Inorg. Chem.* **1993**, *32*, 3705–3711; c) B. Ballet, A. Bino, S. Cohen, H. Rubin, T. Zor, *Inorg. Chim. Acta* **1991**, *188*, 91–93; d) J. A. Bertrand, J. A. Kelley, E. G. Vassian, *J. Am. Chem. Soc.* **1969**, *91*, 2394–2395; e) D. A. House, V. McKee, P. J. Steel, *Inorg. Chem.* **1986**, *25*, 4884–4889; f) C. Fukuhara, E. Asato, T. Shimoji, K. Katsura, M. Mori, K. Matsumoto, S. Ooi, *J. Chem. Soc. Dalton Trans.* **1987**, 1305–1311; g) K. Okamoto, S. Aizawa, T. Konno, H. Einaga, J. Hidaka, *Bull. Chem. Soc. Jpn.* **1986**, *59*, 3859–3864; h) M. J. Heeg, E. L. Blinn, E. Deutsch, *Inorg. Chem.* **1985**, *24*, 1118–1120; i) F. A. Cotton, R. Hügel, R. Eiss, *Inorg. Chem.* **1968**, *7*, 18–23; j) D. Mandal, M. Mikuriya, H.-K. Fun, D. Ray, *Inorg. Chem. Commun.* **2007**, *10*, 657–660.
[19] R. L. De, K. Samanta, K. Maiti, E. Keller, *Inorg. Chim. Acta* **2001**, *316*, 113–116.
[20] A. L. Spek, *PLATON, A Multipurpose Crystallographic Tool*, Utrecht University, The Netherlands, **2002**.
[21] a) T. C. Higgs, K. Spartalian, C. J. O'Connor, B. F. Metzanke, C. J. Carrano, *Inorg. Chem.* **1998**, *37*, 2263–2272; b) U. Auerbach, C. Stockheim, T. Weyhermuller, K. Wieghardt, B. Nuber, *Angew. Chem. Int. Ed. Engl.* **1993**, *32*, 714–716; c) T. Beissel, T. Glaser, F. Kesting, K. Wieghardt, B. Nuber, *Inorg. Chem.* **1996**, *35*, 3936–3947; d) T. Beissel, F. Birkelbach, E. Bill, T. Glaser, F. Kesting, C. Krebs, T. Weyhermuller, K. Wieghardt, C. Butzlaff, A. X. Trautwein, *J. Am. Chem. Soc.* **1996**, *118*, 12376–12390.
[22] a) P. B. Donaldson, P. A. Tasker, N. W. Alcock, *J. Chem. Soc. Dalton Trans.* **1977**, 1160–1165; b) D. Funkemeier, R. Mattes, *J. Chem. Soc. Dalton Trans.* **1993**, 1313–1319; c) R. L. Paul, A. J. Amoroso, P. L. Jones, S. M. Couchman, Z. R. Reeves, L. H. Rees, J. C. Jeffery, J. A. McCleverty, M. D. Ward, *J. Chem. Soc. Dalton Trans.* **1999**, 1563–1568.
[23] V. Kasempimolporn, H. Ōkawa, S. Kida, *Bull. Chem. Soc. Jpn.* **1979**, *52*, 1928–1931.
[24] Bruker, *SADABS, SMART, SAINTPLUS and SHELXTL*, Bruker AXS Inc., Madison, WI, USA, **2000**.
[25] G. M. Sheldrick, *SHELX-97*, *Program for Crystal Structure Solution and Refinement*, University of Göttingen, Germany, **1997**.
[26] H. D. Flack, *Acta Crystallogr., Sect. A: Found. Crystallogr.* **1983**, *39*, 876–881.
[27] A. C. T. North, D. C. Philips, F. S. Mathews, *Acta Crystallogr., Sect. A: Found. Crystallogr.* **1968**, *24*, 351–359.
[28] L. J. Farrugia, *J. Appl. Crystallogr.* **1999**, *32*, 837–838.

Received: August 8, 2007
Published Online: October 12, 2007

 © 2007 Wiley-VCH Verlag GmbH & Co. KGaA, Weinheim 

DOI: 10.1002/ejic.200700850

# Critical Effect of Phosphane Ligands on the Mechanism of Carbon–Carbon Bond Formation Involving Palladium(II) Complexes: A Theoretical Investigation of Reductive Elimination from Square-Planar and T-Shaped Species

**Valentine P. Ananikov,*[a,b] Djamaladdin G. Musaev,[b] and Keiji Morokuma[b]**

**Keywords:** C–C coupling / Palladium / Catalysis / Steric effect / Electronic effect / Phosphane ligands

A theoretical ONIOM study has been carried out to understand the influence of phosphane ligands on the structure of Pd complexes and their reactivity in C–C bond formation. The calculations were performed for Me–Me reductive elimination with the ligands L = $PPh_3$, $PCy_3$, $PMe_3$, $PH_3$, and vinyl–vinyl, Ph–Ph, ethynyl–ethynyl, vinyl–Me, vinyl–Ph and vinyl–ethynyl couplings with L = $PPh_3$ for $[PdR_2L_n]$ complexes ($n$ = 1, 2). The calculations revealed critical changes in the reactivity of palladium complexes depending on the mechanism and ligand type. In the case of the standard four-coordinate pathway ($n$ = 2) the relative reactivity in carbon–carbon bond formation follows the order: L = $PPh_3$ > $PH_3$ > $PCy_3$ > $PMe_3$. However, for reductive elimination involving T-shaped complexes by the ligand predissociation pathway ($n$ = 1), the relative reactivity changes in the order: L = $PCy_3$ > $PPh_3$ > $PH_3$ > $PMe_3$. The theoretical study suggested that the steric effect of phosphane ligands has the largest impact on the structure of the initial palladium complexes, while the electronic effect is most influential on the transition states of C–C coupling in these complexes.
(© Wiley-VCH Verlag GmbH & Co. KGaA, 69451 Weinheim, Germany, 2007)

## 1. Introduction

Palladium-catalyzed reactions have had a major impact on developing new synthetic methods for C–C and C–X bond formation.[1–4] On several reactions it was established that the choice of an appropriate phosphane ligand for the palladium complex plays a crucial role in creating and optimizing new catalytic methodologies.[1,2] Utilization of organic chlorides (aryl chlorides, etc.)[5] in cross-coupling reactions is an outstanding recent example of tuning catalytic activity by steric and electronic effects of ligands. The key finding was to carry out the cross-coupling reaction with very electron-rich ligands.[6,7] Undoubtedly, further development of the field strongly depends on our understanding of reaction mechanisms and rationalization of the influence of phosphane ligands, especially on the reactivity of the intermediate metal complexes involved in these catalytic transformations.[8,9]

Different approaches, including IR frequencies, NMR chemical shifts and coupling constants, electronic density distribution, etc.,[10,11] have been developed to characterize steric and electronic effects of phosphane ligands on the ground-state geometry of transition-metal complexes. An attempt has been made to correlate structural and energetic properties of Pt and Pd complexes with steric and electronic properties of phosphane ligands.[12] In contrast to ground-state properties, predicting the reactivity of transition-metal complexes is a much more challenging problem. A recent study has suggested the MESP (Molecular Electrostatic Potential) approach to characterize the electron-donating ability of phosphane ligands.[13] A later work criticized this approach and concluded that MESP is unsubstantiated for characterizing the donating ability of phosphanes.[14] However, a further analysis again provided some evidence that MESP could be a good measure of the electron-donating ability of phosphanes.[15,16] Finally, a recent review on the subject made uncertain conclusions concerning the usage of modern theoretical methods to deal with the problem.[16] This example clearly emphasizes the complexity of the question and indicates the necessity of a clarifying study in this fascinating field.

[a] N. D. Zelinsky Institute of Organic Chemistry, Russian Academy of Sciences,
Leninsky Prospect 47, Moscow 119991, Russia
Fax: +7-4951355328
E-mail: val@ioc.ac.ru
[b] Cherry L. Emerson Center for Scientific Computation and Department of Chemistry, Emory University,
Atlanta, Georgia 30322, USA
Supporting information for this article is available on the WWW under http://www.eurjic.org or from the author.

 WILEY InterScience DISCOVER SOMETHING GREAT © 2007 Wiley-VCH Verlag GmbH & Co. KGaA, Weinheim 

A very important question concerns the nature of transition-metal complexes involved in the reductive elimination reaction. In a number of experimental reports it has been proposed that phosphane ligand dissociation accelerates C–C and C–X bond formation on Pd and Pt complexes (via T-shaped intermediates).[17,18] A computational study performed for the C–H reductive elimination reaction from Pt complexes with model $PH_3$ and $PMe_3$ ligands has suggested, however, that direct reductive elimination without ligand dissociation is preferred for four-coordinate complexes.[19] The study raises a question concerning the relative reactivity of four-coordinate vs. three-coordinate complexes in C–C bond formation.

The above discussion reveals a rather complex picture of C–C bond formation on transition-metal complexes with strong dependence on the complex type, substituents and ligand environment, which may not find a concise explanation based on available mechanistic knowledge. So far, only simple $PH_3$ and $PMe_3$ ligands were mostly utilized in theoretical studies of C–C bond-formation reactions.[20–25] However, detailed investigation of the systems with real-size ligands is required to link available experimental data with computations.

In the present study we have evaluated the effect of phosphane ligands on C–C bond formation from $Pd^{II}$ complexes (Scheme 1) through the reductive elimination mechanism (**1** → **2-TS** → **3**) involving four-coordinate initial complexes as well as the dissociative pathway (**4** → **5-TS** → **3**) involving three-coordinate species. We have calculated the most frequently used triphenylphosphane ligand ($PPh_3$) and trialkylphosphanes ($PMe_3$ and $PCy_3$) with different bulkiness of the organic groups. For comparative purpose, we have also calculated the $PH_3$ model ligand widely used in earlier theoretical studies.

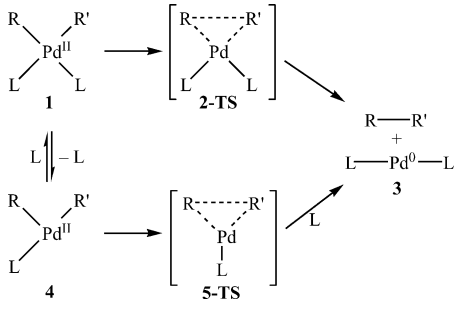


Scheme 1. Carbon–carbon coupling through four-coordinate and three-coordinate mechanisms; R, R′ = $CH_3$, $CH{=}CH_2$, $C_6H_5$, C≡CH; L = $PH_3$, $PMe_3$, $PPh_3$, $PCy_3$.

## 2. Computational Procedure

All calculations were performed by utilizing the two-layer ONIOM approach.[26,27] In the ONIOM partitioning the studied $[MR_2(PR'_3)_2]$ complexes (L = $PR'_3$) were divided into two layers: the first layer includes the ligands R, metal center and phosphorus atoms, and the second layer includes the substituents at the phosphane ligands (R′). A graphical representation of the partitioning scheme is given in Scheme 2.

The first layer was treated at the high B3LYP/BSI level. The basis set BSI consists of the SDD basis set[28] for the metal atom and the 6-311G(d) basis set[29] for the other atoms. The second layer was treated at the relatively low HF/Lanl2mb level. Therefore, this two-layer ONIOM approach used in the present study was denoted as ONIOM-(B3LYP/BSI:HF/Lanl2mb) and it was utilized for geometry optimization and frequency calculations throughout the paper, unless otherwise mentioned. Single-point energy calculations were carried out at the ONIOM(B3LYP/BSI:B3-LYP/Lanl2dz) level by using ONIOM(B3LYP/BSI:HF/Lanl2mb)-optimized geometry: this approach was denoted as ONIOM(B3LYP/BSI:B3LYP/Lanl2dz)//ONIOM(B3LYP/BSI:HF/Lanl2mb).

In the ONIOM studies the normal-coordinate analysis has been performed for all stationary points to characterize the nature of TSs and equilibrium structures and to calculate Gibbs free energies (298.15 K, 1 atm, rigid rotor harmonic oscillator approximation). All calculations were performed without symmetry constraints with the Gaussian 03 program.[30] The reliability of the chosen theory level in geometry optimization and energy calculations has been confirmed by a special study (see Supporting Information).

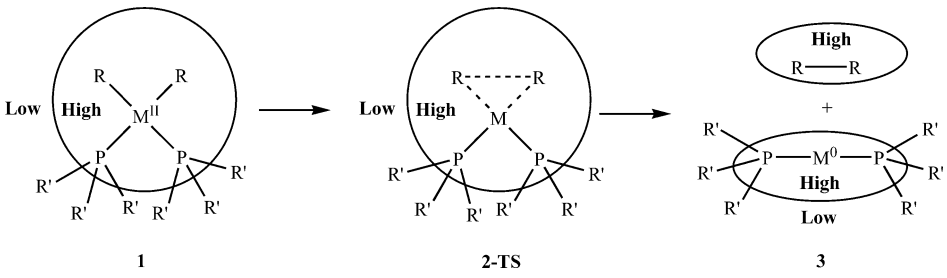


Scheme 2. Model (the first layer, in circle) and real systems used in the ONIOM calculations, which are treated at high and low levels, respectively.

 © 2007 Wiley-VCH Verlag GmbH & Co. KGaA, Weinheim 

Table 1. Calculated relative energies of the stationary points **1**–**5-TS** on the $\Delta E$, $\Delta H$ and $\Delta G$ energy surfaces[a,b] [kcal/mol] at 298.15 K and 1 atm; system **A** at the B3LYP/BSI level, systems **B**–**J** at the ONIOM(B3LYP/BSI:B3LYP/Lanl2dz)//ONIOM(B3LYP/BSI:HF/Lanl2mb) level.

| System | M | L | $R^1$ | $R^2$ | **1** | **2-TS** | **3** | **4** | **5-TS** |
|---|---|---|---|---|---|---|---|---|---|
| **A** | Pd | $PH_3$ | Me | Me | 0.0/0.0/0.0 | 25.2/24.2/23.6 | –31.4/–30.4/–41.7 | 17.2/15.0/2.4 | 29.3/26.9/15.7 |
| **B** | Pd | $PMe_3$ | Me | Me | 0.0/0.0/0.0 | 30.0/29.1/26.4 | –32.4/–31.5/–46.3 | 20.7/18.8/3.5 | 33.0/30.8/16.5 |
| **C** | Pd | $PPh_3$ | Me | Me | 0.0/0.0/0.0 | 23.1/22.2/17.9 | –39.2/–38.5/–54.7 | 13.9/12.1/–6.3 | 26.2/24.2/6.6 |
| **D** | Pd | $PCy_3$ | Me | Me | 0.0/0.0/0.0 | 28.8/27.4/25.1 | –39.2/–39.6/–56.5 | 13.3/10.6/–7.2 | 24.9/21.9/4.8 |
| **E** | Pd | $PPh_3$ | $CH=CH_2$ | $CH=CH_2$ | 0.0/0.0/0.0 | 3.7/3.0/2.8 | –44.2/–43.7/–59.4 | 12.0/10.5/–6.6 | 15.0/13.0/–3.0 |
| **F** | Pd | $PPh_3$ | Ph | Ph | 0.0/0.0/0.0 | 9.7/8.8/9.3 | –43.2/–43.3/–59.6 | 10.8/9.4/–10.3 | 14.8/12.7/–4.6 |
| **G** | Pd | $PPh_3$ | C≡CH | C≡CH | 0.0/0.0/0.0 | 13.3/12.0/10.2 | –24.1/–24.4/–40.0 | 22.2/20.7/3.7 | 29.4/27.1/10.0 |
| **H** | Pd | $PPh_3$ | $CH=CH_2$ | Me | 0.0/0.0/0.0 | 11.8/11.1/10.4 | –40.2/–39.8/–56.3 | 12.4/10.5/–6.8 | 19.2/17.1/0.9 |
| **I** | Pd | $PPh_3$ | $CH=CH_2$ | Ph | 0.0/0.0/0.0 | 7.5/6.7/6.7 | –42.5/–42.3/–59.4 | 11.9/10.5/–7.1 | 15.4/13.4/–2.4 |
| **J** | Pd | $PPh_3$ | $CH=CH_2$ | C≡CH | 0.0/0.0/0.0 | 8.4/7.4/6.7 | –31.5/–31.8/–48.4 | 14.5/12.8/–4.0 | 21.4/19.0/2.8 |

[a] The values are provided in the order *E*/*H*/*G*. [b] In the five-coordinate species **4** and **5-TS** the ligand in *trans* position to $R^1$ was dissociated.

Table 2. Calculated selected bond lengths [Å] and angles [°] for the studied complexes; system **A** at the B3LYP/BSI level, systems **B**–**G** at the ONIOM(B3LYP/BSI:HF/Lanl2mb) level.[a,b]

| System | M | L | $R^1$, $R^2$ | Structure | M–C1[c] | M–C2[c] | M–P1[d] | M–P2[d] | C1–C2[c] | C1–M–C2[c] | P1–M–P2[d] | Tilt angle[e] |
|---|---|---|---|---|---|---|---|---|---|---|---|---|
| **A** | Pd | $PH_3$ | Me | **1** | 2.100 | 2.100 | 2.367 | 2.367 | 2.778 | 82.8 | 102.2 | 0.8 |
| | | | | **2-TS** | 2.198 | 2.198 | 2.384 | 2.384 | 2.071 | 56.2 | 111.4 | 52.0 |
| | | | | **4** | 2.047 | 2.038 | 2.410 | – | 2.791 | 86.2 | – | – |
| | | | | **5-TS** | 2.117 | 2.167 | 2.304 | – | 2.084 | 58.2 | – | – |
| **B** | Pd | $PMe_3$ | Me | **1** | 2.132 | 2.132 | 2.322 | 2.322 | 2.774 | 81.2 | 107.2 | 0.1 |
| | | | | **2-TS** | 2.196 | 2.196 | 2.331 | 2.331 | 2.117 | 57.6 | 118.7 | 59.8 |
| | | | | **4** | 2.053 | 2.046 | 2.373 | 86.2 | 2.802 | 86.2 | – | – |
| | | | | **5-TS** | 2.117 | 2.161 | 2.290 | 58.4 | 2.290 | 58.4 | – | – |
| **C** | Pd | $PPh_3$ | Me | **1** | 2.123 | 2.113 | 2.370 | 2.376 | 2.770 | 81.6 | 103.2 | 1.9 |
| | | | | **2-TS** | 2.190 | 2.190 | 2.367 | 2.367 | 2.113 | 57.7 | 122.1 | 60.7 |
| | | | | **4** | 2.057 | 2.046 | 2.383 | – | 2.788 | 85.6 | – | – |
| | | | | **5-TS** | 2.125 | 2.164 | 2.306 | – | 2.072 | 57.8 | – | – |
| **D** | Pd | $PCy_3$ | Me | **1** | 2.127 | 2.127 | 2.432 | 2.432 | 2.642 | 76.8 | 110.1 | 9.2 |
| | | | | **2-TS** | 2.193 | 2.197 | 2.385 | 2.411 | 2.109 | 57.4 | 120.3 | 67.6 |
| | | | | **4** | 2.060 | 2.044 | 2.392 | – | 2.771 | 84.9 | – | – |
| | | | | **5-TS** | 2.124 | 2.159 | 2.318 | – | 2.061 | 57.5 | – | – |
| **E** | Pd | $PPh_3$ | $CH=CH_2$ | **1** | 2.074 | 2.061 | 2.374 | 2.392 | 2.614 | 78.4 | 104.4 | 3.2 |
| | | | | **2-TS** | 2.091 | 2.086 | 2.369 | 2.383 | 2.559 | 57.7 | 108.7 | 5.8 |
| | | | | **4** | 2.016 | 1.991 | 2.389 | – | 2.760 | 87.1 | – | – |
| | | | | **5-TS** | 2.031 | 2.031 | 2.362 | – | 2.151 | 64.0 | – | – |
| **F** | Pd | $PPh_3$ | Ph | **1** | 2.095 | 2.076 | 2.384 | 2.405 | 2.694 | 80.5 | 104.6 | 8.5 |
| | | | | **2-TS** | 2.129 | 2.137 | 2.401 | 2.385 | 1.981 | 55.3 | 108.7 | 16.6 |
| | | | | **4** | 2.029 | 2.011 | 2.386 | – | 2.751 | 85.8 | – | – |
| | | | | **5-TS** | 2.049 | 2.066 | 2.352 | – | 2.126 | 62.2 | – | – |
| **G** | Pd | $PPh_3$ | C≡CH | **1** | 2.010 | 1.999 | 2.356 | 2.372 | 2.724 | 85.6 | 104.4 | 0.3 |
| | | | | **2-TS** | 2.014 | 2.018 | 2.388 | 2.375 | 1.809 | 53.3 | 109.0 | 1.4 |
| | | | | **4** | 1.981 | 1.920 | 2.333 | – | 2.815 | 92.3 | – | – |
| | | | | **5-TS** | 1.961 | 1.948 | 2.373 | – | 1.957 | 60.1 | – | – |

[a] Length of the formed carbon–carbon bond in organic products R–R: 1.529 (**3_A** to **3_D**), 1.456 (**3_E**), 1.485 (**3_F**), 1.365 (**3_G**); length of the Pd–P bond in the $PdL_2$ product complexes: 2.289 (**3_A**), 2.286 (**3_B**), 2.295 (**3_C**, **3_E** to **3_G**), 2.315 (**3_D**). [b] The imaginary frequencies [$i$ $cm^{-1}$] for the transition states **2-TS_A** to **2-TS_G**, respectively: 481, 450, 432, 434, 373, 328, 435; for the transition states **5-TS_A** to **5-TS_G**, respectively: 425, 426, 441, 451, 278, 251, 370. [c] C1 and C2 belong to $R^1$ and $R^2$, respectively. [d] P1 is *trans* to C1 and P2 is *trans* to C2. [e] Absolute value of the angle between the P1–M–P2 and C1–M–C2 planes.

The calculated relative energies ($\Delta E$, $\Delta H$, $\Delta G$) of reactants, intermediates, transition states and products are summarized in Table 1, while their most important structural parameters are listed in Table 2. The optimized structures of Me–Me reductive elimination reactions are shown in Figures 1 and 2, and those of the coupling of unsaturated organic groups are given in Figure S1 (see Supporting Information).

 © 2007 Wiley-VCH Verlag GmbH & Co. KGaA, Weinheim 

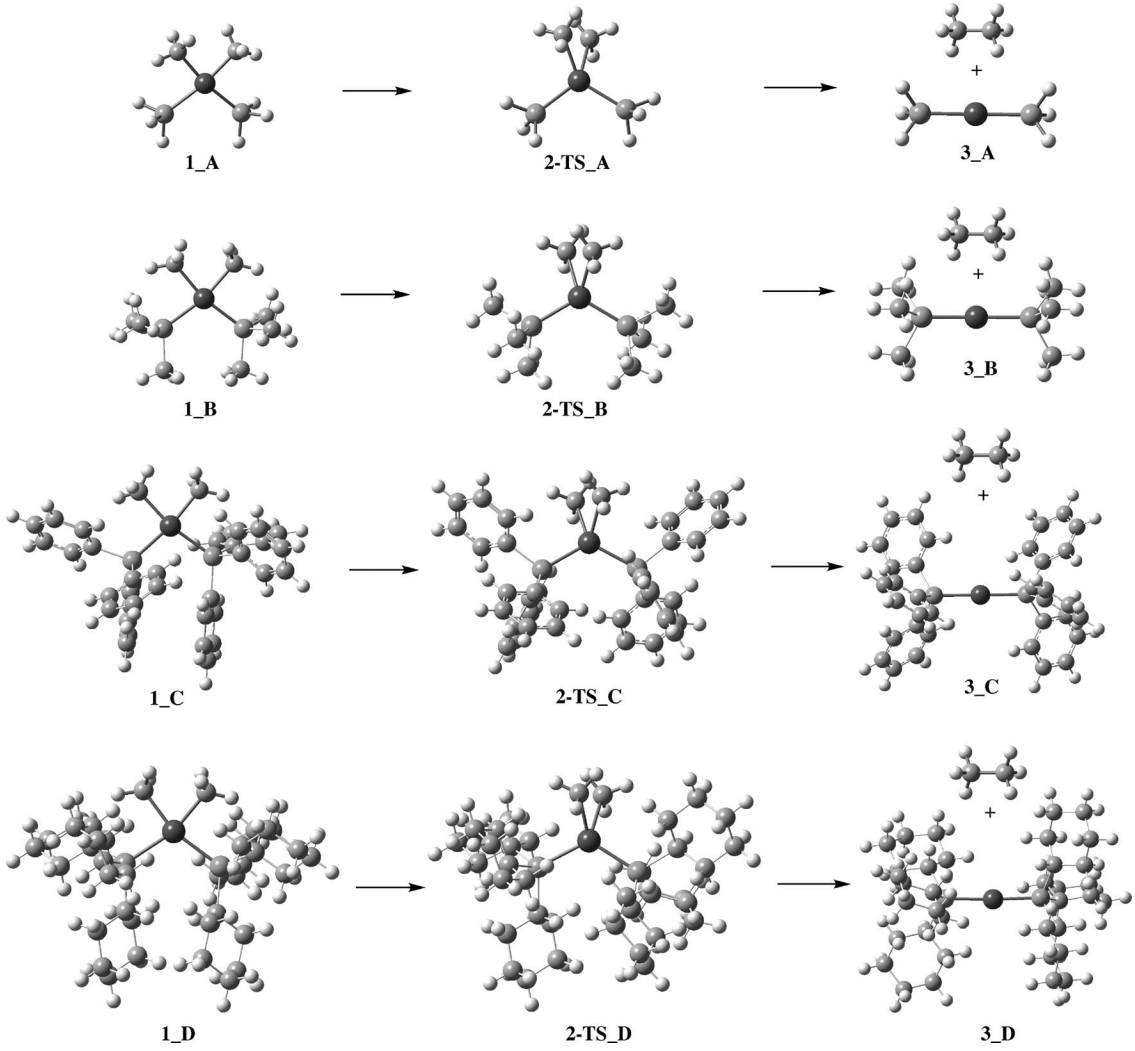


Figure 1. Optimized structures of the initial complexes, transition states and products of the Me–Me coupling from $[Pd(CH_3)_2L_2]$ with different ligands. Their important geometry parameters are given in Table 2 and the energetic data is listed in Table 1.

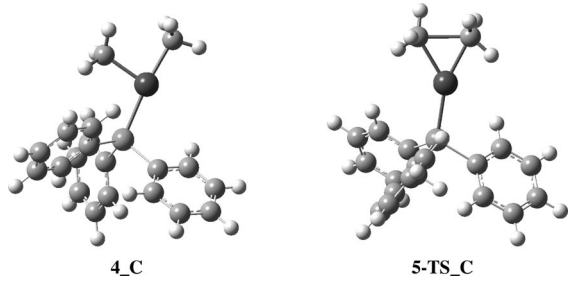


Figure 2. Optimized structures **4_C** and **5-TS_C**. Their important geometry parameters are given in Table 2 and the energetic data is listed in Table 1.

## 3. Results

First, we analyze the effect of the phosphane ligand on the geometry of the $[Pd(CH_3)_2L_2]$ complexes, followed by a discussion of the potential-energy surfaces of Me–Me coupling for both (four- and three-coordinate) pathways of the reductive elimination reaction. Finally, C–C bond formation between the unsaturated organic groups (vinyl, phenyl and ethynyl) and unsymmetrical couplings will be considered with the triphenylphosphane ligand.

### A. Effect of Phosphane Ligands on the Geometry of the $[Pd(CH_3)_2L_2]$ Complexes (1_A to 1_D)

In this section we analyze how sensitive the geometry parameters of the initial metal complexes are to the nature of the phosphane ligands. Both Pd–C and Pd–P bonds will be involved in the comparison. The shortest Pd–C distance was calculated for the L = $PH_3$ case, and substituted phosphane ligands increased the Pd–C distance by 0.018–0.032 Å (Table 2). The following trend in Pd–C bond length was obtained for the ligands studied (in Å):[31] **1_B** (2.132; L = $PMe_3$) > **1_D** (2.127; L = $PCy_3$) > **1_C** (2.118; L = $PPh_3$) > **1_A** (2.100; L = $PH_3$).

Alkyl-substituted phosphanes gave longer Pd–C bonds relative to L = $PPh_3$ and $PH_3$. The longest Pd–C bond was calculated for L = $PMe_3$ having the smaller substituent size

 © 2007 Wiley-VCH Verlag GmbH & Co. KGaA, Weinheim 

as compared to L = $PCy_3$. However, rather small changes in the bond length do not provide the necessary basis for further analysis. The calculations agree with available experimental data; according to the X-ray studies, M–$C_{methyl}$ distances span a range of 2.08–2.16 Å and are not much sensitive to the identity of the phosphane ligand.[32] Indeed, the influence of the crystal-packing effect may diminish the small differences in M–C bond lengths caused by the ligand effect.

The following trend in Pd–P bond length was calculated for the studied ligands (in Å):[31] **1_D** (2.432; L = $PCy_3$) > **1_C** (2.373; L = $PPh_3$) > **1_A** (2.367; L = $PH_3$) > **1_B** (2.322; L = $PMe_3$)

Longer Pd–P bonds for L = $PCy_3$ can be explained by the bulkiness of this ligand. The presence of large steric repulsions in the case of $PCy_3$ is also evident from increased P–Pd–P angles and decreased C–Pd–C angles, as compared to the other ligands (Table 2). Despite the obvious geometry changes caused by the $PCy_3$ ligand, the overall trend cannot be easily rationalized. Similar conclusions can be drawn upon analysis of experimental geometries determined in X-ray studies.[32]

### B. Effect of the Organic Group on the Geometry of the $[PdR_2(PPh_3)_2]$ Complexes (1_E to 1_J)

The structures **1_E** to **1_G** with unsaturated organic ligands and L = $PPh_3$ (Table 2) can be compared with similar compounds for L = $PH_3$ studied earlier.[23] Introducing Ph substituents into the phosphane ligand increased on average the length of the Pd–C bonds by 0.01–0.03 Å, while the trends in the Pd–P distances and P–Pd–P angles were less pronounced; the average changes were <0.02 Å and <1°, respectively.

It is important to point out that the conformational flexibility of $PPh_3$ caused some deviations towards an asymmetric ligand environment. In fact, Pd–C1 and Pd–C2 bonds, as well as Pd–P1 and Pd–P2 bonds, within the same complex (**1_E** to **1_G**, as well as **1_C**) differ by 0.01–0.02 Å (Table 2). The expected relationship of the shorter Pd–C bond *trans* to the longer Pd–P bond in these complexes originates from the *trans* effect (Table 2). It should be pointed out that experimental X-ray studies have also reported unsymmetrical ligand environments with similar differences in the bond lengths.[32] Finally, in agreement with the discussion in section A, no clear trends between the geometry parameters of the initial complexes and the nature of phosphane ligands can be outlined.

### C. Effect of Phosphane Ligands on the Energetics of Reductive Elimination from the Four-Coordinate $[Pd(CH_3)_2L_2]$ Complexes (1_A to 1_D)

The investigated reductive elimination reactions occur by a concerted mechanism (Figure 1). In such a case, movement along the reaction coordinate involves elongation of Pd–C bonds and an increase in P–Pd–P angles, as well as shortening of C–C bonds and a decrease in C–Pd–C angles. Optimized geometry parameters for the initial complexes and transition states reflect these structural changes (Table 2).

According to the calculated barriers ($\Delta H^{\neq}$), the reactivity of the studied complexes in the reductive elimination reaction decreases in the order (Table 1): **1_C** (L = $PPh_3$) > **1_A** (L = $PH_3$) > **1_D** (L = $PCy_3$) > **1_B** (L = $PMe_3$).

Therefore, the lowest reactivity in C–C bond formation was predicted for the complex with the $PMe_3$ ligand, while the complex with the $PPh_3$ ligand should be the most reactive. All reactions are exothermic; energy gain upon product formation follows the trend: **1_C**, **1_D** > **1_A**, **1_B** (Table 1).[33] The calculated $\Delta E$ and $\Delta H$ values are nearly identical, with a difference of <1.5 kcal/mol. In terms of $\Delta G$ the reactions are highly exoergic (due to the entropy contribution as well), and the activation barriers are slightly decreased (Table 1).[34]

The calculated reactivity order can not be easily understood on the basis of the known properties of the ligands. In order to estimate the electronic and steric effects of the ligand on reaction energetics, we have applied decomposition analysis based on ONIOM calculations at different levels (Scheme 3). The system with the simplest ligand (L = $PH_3$) computed at the MO level was used as a reference point. From the reference point we cannot directly estimate the desired steric and electronic effects in the real chemical system (L = $PR'_3$) calculated at the ONIOM(MO:MO) level. However, the analysis can be simplified by carrying out ONIOM(MO:MM) calculations on the real systems, for the decomposition point, which includes only the steric effect of substituents R′. The difference between the reference and decomposition points provides information about the steric effect in the studied system, while the electronic effect can be revealed by comparing the real system and the decomposition point (Scheme 3).

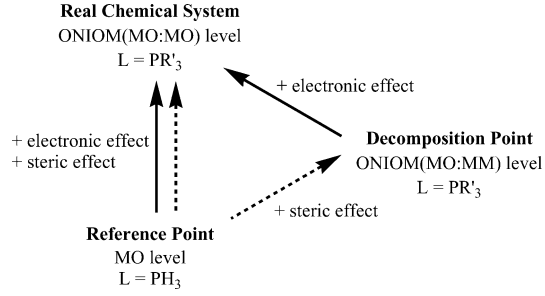


Scheme 3. ONIOM decomposition analysis to evaluate steric and electronic effects of phosphane ligands in the studied complexes.

For the decomposition point, we have carried out single-point ONIOM(B3LYP/BSI:UFF) calculations with the UFF molecular mechanics force field as the low level (Table 3). Comparison of ONIOM(B3LYP/BSI:UFF) energies for L = $PMe_3$, $PPh_3$, $PCy_3$ with the B3LYP/BSI energy for L = $PH_3$, reveals a small and noncharacteristic change for the $PMe_3$ ligand, while the activation barriers for the $PPh_3$ and $PCy_3$ ligands are decreased by 4–7 kcal/mol (see Tables 1 and 3). This trend is in good qualitative agreement

 © 2007 Wiley-VCH Verlag GmbH & Co. KGaA, Weinheim 

with the steric bulkiness of the ligands: $PCy_3$, $PPh_3 > PMe_3 \approx PH_3$.[35]

Table 3. Calculated $\Delta E$ relative energies of the stationary points **1**, **2-TS** and **3** at the ONIOM(B3LYP/BSI:UFF)//ONIOM(B3LYP/BSI:HF/Lanl2mb) level [kcal/mol].

| System | M | L | $R^1$, $R^2$ | **1** | **2-TS** | **3** |
|---|---|---|---|---|---|---|
| B | Pd | $PMe_3$ | Me | 0.0 | 26.8 | –32.9 |
| C | Pd | $PPh_3$ | Me | 0.0 | 17.8 | –46.7 |
| D | Pd | $PCy_3$ | Me | 0.0 | 20.7 | –43.8 |

In the present metal complexes, the steric effect includes repulsion between the phosphane ligands and between the phosphane and $CH_3$ ligands. These steric repulsions destabilize both the initial complex **1** and the transition state **2-TS**. The decrease in the activation barrier ($\Delta E^{\neq}$) at the ONIOM(B3LYP/BSI:UFF) level suggests that the initial complex **1** is more destabilized by the steric repulsions relative to the transition state **2-TS**.[36] This energy trend is in excellent agreement with geometry parameters, because in the transition state both P–Pd–P and P–Pd–$C_{cis}$ angles become larger. The energy gain ($\Delta E$) calculated at the ONIOM(B3LYP/BSI:UFF) level is almost the same for the $PMe_3$ ligand and significantly higher for the $PPh_3$ and $PCy_3$ ligands relative to the ONIOM(B3LYP/BSI:B3LYP/Lanl2dz) level (see Tables 1 and 3, respectively), which is also evident from minimizing steric repulsions in **3**.

Now we can consider the influence of the electronic effect. In the present system the interaction between the phosphane ligand and the metal center affects both the initial complex and the transition state. The nature of the electronic effect can be revealed by comparative analysis of the ONIOM(B3LYP/BSI:UFF) energy surface, which includes only the steric effect, and the ONIOM(B3LYP/BSI:B3LYP/Lanl2dz) energy surface, which includes both electronic and steric effects. Comparison of the ONIOM(B3LYP/BSI:-UFF) and ONIOM(B3LYP/BSI:B3LYP/Lanl2dz) energies [both evaluated by using the same ONIOM(B3LYP/BSI:HF/Lanl2mb) optimized geometries] has shown that for L = $PMe_3$, $PPh_3$, $PCy_3$, inclusion of the electronic effects increased the activation barriers by 3–8 kcal/mol (see Tables 1 and 3, respectively). This suggests that electronic effects may have more influence on the transition state than on the initial complex.[37] It appears that the weak metal–carbon bond in the transition state is more sensitive to the electronic effect than the relatively strong bond of the initial complex.

### D. Reductive Elimination from the Three-Coordinate $[Pd(CH_3)_2L]$ Complexes (4_A to 4_D) by the Phosphane Ligand Predissociation Mechanism

Another pathway of C–C bond formation may involve phosphane ligand dissociation **1** → **4** followed by **4** → **5-TS** reductive elimination (Scheme 1). Reassociation of the phosphane ligand after releasing the organic product results in the same product, **3**.[38] An example of the optimized structures of **4_C** and **5-TS_C** is shown in Figure 2. Complex **4_C** affords T-shaped geometry with nonequivalent Pd–C bonds, which is shifted towards Y-shaped geometry upon moving to **5-TS_C**. However, the transition-state structure did not become symmetric as was evident from different Pd–C1 and Pd–C2 bond lengths (Table 2) and P–Pd–C angles.[39] Similar geometry changes were also observed for the other three-coordinate structures considered in the present study. Comparing corresponding **2-TS** and **5-TS** geometries, one may clearly notice an earlier character for **5-TS** (shorter Pd–C bonds and longer C–C bonds for **5-TS**, see Table 2).

In agreement with geometry trends, phosphane ligand predissociation significantly lowers activation energies of the reductive elimination process. The calculated **4** → **5-TS** activation barriers on the $\Delta E$, $\Delta H$ and $\Delta G$ surfaces have similar values in the range 11–13 kcal/mol for all of the studied complexes (**4_A** to **4_D**), which are much smaller than **1** → **2-TS** activation barriers of $\Delta H^{\neq}$ = 22–29 kcal/mol (**1_A** to **1_D**). Therefore, if monoligated $[PdR_2L]$ species **4** would be involved as the initial complexes (in such a case ligand predissociation is not required) in the C–C reductive elimination, the reaction would be faster and less sensitive to the ligand effects. In the case of four-coordinate initial complexes the activation barriers **1** → **5-TS** should be considered to estimate the relative reactivity order (because **4** is higher in energy than **1** on the $\Delta H$ surface), which follows the trend (see Table 1): L = $PCy_3$ > $PPh_3$ > $PH_3$ > $PMe_3$.

As evident from Table 1, the potential surface is dramatically influenced by the value of the Pd–P bond energy (energy difference between **4** and **1**). The calculated Pd–P bond energy (in $\Delta H$) for the first phosphane ligand dissociation from the $[Pd(CH_3)_2L_2]$ complexes **1_A** to **1_D** decreases in the order: $PMe_3$ (18.8 kcal/mol) > $PH_3$ (15.0 kcal/mol) > $PPh_3$ (12.1 kcal/mol) > $PCy_3$ (10.6 kcal/mol).

Comparison of the $PH_3$ and $PMe_3$ ligands (both having relatively small steric effects) indicates that electron donation from the ligand to the metal center increases the Pd–P bond energy in the present complexes. However, for the more bulky $PCy_3$ ligand, the steric repulsions in **1** decrease the Pd–P bond energy and facilitate phosphane ligand dissociation. As a result, carbon–carbon bond formation through the **1** → **4** → **5-TS** → **3** pathway for L = $PCy_3$ is energetically even less demanding than that through the **1** → **2-TS** → **3** pathway for L = $PPh_3$ ($\Delta H^{\neq}$ = 21.9 and 22.2 kcal/mol, respectively). The entropy contribution should provide additional energetic favor to the dissociation pathway on the $\Delta G$ surface.[34]

### E. Reductive Elimination of Unsaturated Vinyl, Phenyl and Ethynyl Groups from the Four-Coordinate $[PdR_2(PPh_3)_2]$ Complexes (1_E to 1_G) and the Three-Coordinate $[PdR_2PPh_3]$ Complexes (4_E to 4_G)

Vinyl–vinyl, phenyl–phenyl and ethynyl–ethynyl couplings on $Pd^{II}$ centers with the $PPh_3$ ligand also proceeded through the concerted transition states (Figure S1, Supporting Information). However, these reductive elimination re-

 © 2007 Wiley-VCH Verlag GmbH & Co. KGaA, Weinheim 

actions require the overcoming of smaller activation barriers (Table 1). According to the calculated $\Delta H^{\neq}$ values, the reactivity in C–C bond formation among the present complexes follows the trend: **1_E** (vinyl–vinyl) > **1_F** (Ph–Ph) > **1_G** (ethynyl–ethynyl) > **1_C** (Me–Me). The formation of buta-1,3-diene (**3_E**) and biphenyl (**3_F**) is exothermic by $\Delta H \approx$ –43 kcal/mol; the formation of buta-1,3-diyne (**1_G**) is less exothermic with $\Delta H$ = –24.4 kcal/mol.[40]

The Pd–P bond energy increases in the order ($\Delta H$ [kcal/mol]): **1_F** (9.4) < **1_E** (10.5) << **1_G** (20.7) for the vinyl, phenyl and ethynyl complexes, respectively (Table 1). The higher bond energy in the case **1_G** is consistent with the shorter Pd–P bond in this compound (Table 2). Therefore, according to the calculated energetics (Table 1), vinyl–vinyl and Ph–Ph couplings are likely to involve the three-coordinate reaction pathway (**1** → **4** → **5-TS** → **3**), while ethynyl–ethynyl coupling should follow the standard pathway with four-coordinate species (**1_G** → **2-TS_G** → **3_G**). The calculated energetic trend is in excellent agreement with available experimental studies showing that $[Pd(CH_3)_2L_2]$ complexes are rather stable in solution, whereas analogous diphenylpalladium complexes are unstable.[17d,41] It has also been shown that replacement of Me groups by Ph groups in the $PMe_xPh_{3-x}$ ligands increases the rate of C–C bond formation within the catalytic cross-coupling cycle.[1d]

### F. Unsymmetrical Coupling of Methyl–Vinyl, Phenyl–Vinyl and Ethynyl–Vinyl Groups from the Four-Coordinate $[PdR^1R^2(PPh_3)_2]$ Complexes (1_H to 1_J) and the Three-Coordinate $[PdR^1R^2PPh_3]$ Complexes (4_H to 4_J)

Reductive elimination of Me and vinyl groups by the four-coordinate pathway (**1_H** → **2-TS_H** → **3_H**) requires overcoming the activation barrier of $\Delta H^{\neq}$ = 11.1 kcal/mol and is exothermic by $\Delta H$ = –39.8 kcal/mol (Table 1). These values are intermediate between the vinyl–vinyl ($\Delta H^{\neq}$ = 3.0 kcal/mol, $\Delta H$ = –43.7 kcal/mol) and Me–Me ($\Delta H^{\neq}$ = 22.2 kcal/mol, $\Delta H$ = –38.5 kcal/mol) couplings. Thus, the following relative reactivity should be expected: vinyl–vinyl > vinyl–Me > Me–Me. The same relationship was calculated for the other studied unsymmetrical couplings: the vinyl–Ph coupling is intermediate between the vinyl–vinyl and Ph–Ph couplings, and the vinyl–ethynyl coupling is intermediate between the vinyl–vinyl and ethynyl–ethynyl couplings (Table 1).

Remarkably, this tendency remains valid for the three-coordinate pathway,[42] although the difference in activation barriers was rather small (**4** → **5-TS**; $\Delta H$ [kcal/mol]): vinyl–vinyl (2.5) > vinyl–Me (6.6) > Me–Me (12.1); vinyl–vinyl (2.5) > vinyl–Ph (2.9) > Ph–Ph (3.3); vinyl–vinyl (2.5) > vinyl–ethynyl (6.2) > ethynyl–ethynyl (6.4).

Geometry parameters are in line with the energy data and follow the trends discussed above; optimized geometry parameters are listed in Table S1 (see Supporting Information).

## 4. Discussion

It was shown that geometry parameters of initial $[PdR_2L_2]$ complexes are not very sensitive to the nature of the phosphane ligands. Therefore, electronic and steric properties derived from the initial metal complexes or from the free ligands should be used with care for predicting the reactivity of transition-metal complexes. Moreover, the calculations have shown that the influence of the conformational changes on geometry may be of the same order of magnitude as the ligand effects.

Applying ONIOM decomposition analysis, we have found that the steric effect of phosphane ligands mostly influences the initial $Pd^{II}$ complex, while the electronic effect has the greatest impact on the transition state. The larger steric effect of R′ decreases the activation barriers of C–C reductive elimination. The electronic effect changes the reactivity in the opposite manner: inclusion of the electronic effect increases the activation barriers.

In sections 2C and 2D we have analyzed the four-coordinate and three-coordinate pathways separately; here we provide a joint analysis of both pathways to predict the overall reactivity in the studied system. The reductive elimination reaction from $Pd^{II}$ complexes by the four-coordinative pathway follows the trend: L = $PPh_3$ > $PH_3$ > $PCy_3$ > $PMe_3$. However, in the case of the three-coordinate pathway the complex with the tricyclohexylphosphane ligand becomes more reactive: L = $PCy_3$ > $PPh_3$ > $PH_3$ > $PMe_3$.[43] The relative reactivity through these two pathways is determined by the strength of the metal–phosphorus bond. The calculated Pd–P bond dissociation enthalpy for $[Pd(CH_3)_2L_2]$ decreases in the order: L = $PMe_3$ > $PH_3$ > $PPh_3$ > $PCy_3$. Easy dissociation of the $PCy_3$ ligand favors C–C coupling by the three-coordinate pathway. Considering both potential energy surfaces, for L = $PCy_3$ the reaction is most likely to undergo the three-coordinate predissociation pathway involving T-shaped complexes, for L = $PH_3$ and L = $PMe_3$ the classical four-coordinate pathway, and for L = $PPh_3$ both pathways should be accessible.

The results of theoretical studies of C–H reductive elimination from platinum complexes with $PH_3$ and $PMe_3$ ligands[19] are in excellent agreement with our study of C–C bond formation on Pd; for these ligands the four-coordinate pathway should be preferred. At the same time, this indicates that for studies of the ligand effect, $PH_3$ and $PMe_3$ are unreliable models of $PPh_3$ and $PCy_3$. Explicit consideration of substituents is required to obtain agreement with experiment.

Coupling of different organic groups from $[PdR_2(PPh_3)_2]$ complexes was predicted to be in the following reactivity order: vinyl–vinyl > Ph–Ph > ethynyl–ethynyl > Me–Me for the four-coordinate pathway and vinyl–vinyl, Ph–Ph > Me–Me > ethynyl–ethynyl for the three-coordinate pathway. The Pd–P bond dissociation enthalpy depends on the nature of the organic group being eliminated that is attached to the palladium atom as was calculated for the series of $[PdR_2(PPh_3)_2]$ complexes: R = Me, ethynyl > Ph, vinyl. Therefore, vinyl–vinyl and Ph–Ph couplings are

 © 2007 Wiley-VCH Verlag GmbH & Co. KGaA, Weinheim 

likely to proceed by the three-coordinate predissociation pathway; however, ethynyl–ethynyl coupling can start directly from the four-coordinate complex.

Special note should be made concerning the solvent effect. Using PCM calculations it was reported that the solvent effect does not change in a substantial manner the potential energy surfaces of four-coordinate reductive elimination pathways involving neutral metal complexes.[22] In case of the predissociation pathway, the solvent could coordinate to a vacancy in the metal center. However, taking into account that most organic solvents (toluene, benzene, dichloromethane, chloroform, hexanes, etc.) are weakly coordinated to a metal center, this process is unlikely to introduce principal changes to the mechanism.[44]

## 5. Conclusions

The study has clearly shown that the ligand effect on C–C bond formation should be considered in view of the reaction mechanism, otherwise it may be a source of inconsistencies or even erroneous conclusions. The influence of steric and electronic factors depends on the nature of reacting species and the ligand environment as well as the type of organic groups being eliminated.

The calculations revealed that different ligands may involve different mechanisms of the C–C reductive elimination reaction. Among the ligands studied, $PCy_3$ should be used to facilitate the T-shaped pathway by the predissociation mechanism and increase the reactivity. The $PMe_3$ ligand should be utilized for stabilizing the four-coordinate complexes and decrease the reactivity in reductive elimination reactions. The $PPh_3$ ligand represents a more universal choice, since it showed good reactivity for both mechanisms.

According to the calculated activation barriers, the relative reactivity orders were found for a series of C–C coupling reactions involving various organic groups. Particularly, for the four-coordinate pathway: vinyl–vinyl > vinyl–Ph > vinyl–ethynyl > Ph–Ph > vinyl–Me > ethynyl–ethynyl > Me–Me; and for the three-coordinate pathway: vinyl–vinyl > vinyl–Ph > vinyl–ethynyl, Ph–Ph > vinyl–Me, ethynyl–ethynyl > Me–Me. The relative reactivity orders for both pathways coincide, except that rather small activation barriers in the latter case did not allow us to draw a clear distinction for some reactions.

Finally, we would like to point out that ONIOM calculations provide reliable results not only for the evaluation of geometries and energy data, but also for analyzing electronic and steric effects. ONIOM partitioning to high and low levels gives a flexible tool to define a region of interest, whose steric and electronic properties are analyzed.

**Supporting Information** (see footnote on the first page of this article): Testing the reliability of geometry optimization (Section 1). Testing the reliability of energy calculations (Section 2). Optimized structures of the initial complexes, transition states and products for vinyl–vinyl, Ph–Ph and ethynyl–ethynyl coupling from $[PdR_2(PPh_3)_2]$ (Figure S1); their important geometry parameters are given in Table 2 and the energetic data is listed in Table 1. The calculated selected bond lengths [Å] and angles [°] for the systems **H**–**J** at the ONIOM(B3LYP/BSI:HF/Lanl2MB) level (Table S1).

## Acknowledgments

V. P. A. acknowledges the Visiting Fellowship at the Cherry L. Emerson Center of Emory University.

[1] a) J. Tsuji, *Transition Metal Reagents and Catalysts: Innovations in Organic Synthesis*, John Wiley & Sons, Chichester, **2000**; b) *Handbook of organopalladium chemistry for organic synthesis* (Ed.: E. Negishi), John Wiley & Sons, New York, Chichester, **2002**, vol. 1, pp. 215–994; c) M. Beller, C. Bolm, *Transition Metals for Organic Chemistry*, Wiley-VCH: Weinheim, **1998**; d) *Metal-catalyzed Cross-coupling Reactions* (Eds.: F. Diederich, P. J. Stang), Wiley-VCH, Weinheim, **1998**.

[2] a) I. P. Beletskaya, A. V. Cheprakov, "Metal complexes as catalysts for C-C cross-coupling reactions", in *Comprehensive Coordination Chemistry II* (Eds.: J. A. McCleverty, T. J. Meyer), Elsevier Ltd., Oxford, **2004**, vol. 9, pp. 305–368; b) N. Miyaura, A. Suzuki, *Chem. Rev.* **1995**, *95*, 2457; c) N. Miyaura, *J. Organomet. Chem.* **2002**, *653*, 54; d) V. Farina, V. Krishnamurthy, W. J. Scott, "The Stille Reaction", in *Organic Reactions*, John Wiley & Sons Inc., New York, **1997**, vol. 50; e) K. Kugami, M. Kosugi, *Top. Curr. Chem.* **2002**, *219*, 87.

[3] a) A. Togni, H. Grützmacher (Eds.), *Catalytic Heterofunctionalization*, Wiley-VCH, Weinheim, **2001**; b) M. Beller, J. Seayad, A. Tillack, H. Jiao, *Angew. Chem. Int. Ed.* **2004**, *43*, 3368; c) I. Beletskaya, C. Moberg, *Chem. Rev.* **2006**, *106*, 2320; d) F. Alonso, I. P. Beletskaya, M. Yus, *Chem. Rev.* **2004**, *104*, 3079.

[4] a) J. Louie, J. F. Hartwig, *Tetrahedron Lett.* **1995**, *36*, 3609; b) A. S. Guram, R. A. Rennels, S. L. Buchwald, *Angew. Chem. Int. Ed. Engl.* **1995**, *34*, 1348; c) J. F. Hartwig, *Inorg. Chem.* **2007**, *46*, 1936; d) J. P. Wolfe, S. Wagaw, J.-F. Marcoux, S. L. Buchwald, *Acc. Chem. Res.* **1998**, *31*, 805.

[5] From the chemical and industrial points of view readily available and cheap organic chlorides are the best starting materials for catalytic C–C and C–X bond formation. Not surprisingly, activation of organic chlorides is one of the most actively studied areas of transition-metal catalysis.

[6] For a recent review, see: S. P. Nolan, O. Navarro, "C–C Bond Formation by Cross-Coupling" in *Comprehensive Organometallic Chemistry III* (Eds.: D. M. P. Mingos, R. H. Crabtree), Elsevier Ltd., Oxford, **2007**, vol. 11, pp. 1–37.

[7] Selected representative examples: a) S. D. Walker, T. E. Barder, J. R. Martinelli, S. L. Buchwald, *Angew. Chem. Int. Ed.* **2004**, *43*, 1871; b) A. F. Littke, C. Dai, G. Fu, *J. Am. Chem. Soc.* **2000**, *122*, 4020; c) J. P. Stambuli, R. Kuwano, J. F. Hartwig, *Angew. Chem. Int. Ed.* **2002**, *41*, 4746; d) A. Zapf, A. Ehrentraut, M. Beller, *Angew. Chem. Int. Ed.* **2000**, *39*, 4153; e) V. P. W. Bohm, C. W. K. Gstottmayr, T. Weskamp, W. A. Herrmann, *J. Organomet. Chem.* **2000**, *595*, 186; f) A. Zapf, M. Beller, *Chem. Eur. J.* **2000**, *6*, 1830; g) J. P. Wolfe, R. A. Singer, B. H. Yang, S. L. Buchwald, *J. Am. Chem. Soc.* **1999**, *121*, 9550; h) X. Bei, H. W. Turner, W. H. Weinberg, A. S. Guram, *J. Org. Chem.* **1999**, *64*, 6797; i) C. Zhang, J. Huang, M. L. Trudell, S. P. Nolan, *J. Org. Chem.* **1999**, *64*, 3804; j) A. F. Littke, G. Fu, *Angew. Chem. Int. Ed.* **1998**, *37*, 3387.

[8] Theoretical studies of the mechanism of cross-coupling reactions with $PH_3$ and $PMe_3$ model ligands: a) R. Alvarez, O. N. Faza, A. R. de Lera, D. J. Cardenas, *Adv. Synth. Catal.* **2007**, *349*, 887; b) A. A. C. Braga, G. Ujaque, F. Maseras, *Organometallics* **2006**, *25*, 3647; c) A. A. C. Braga, N. H. Morgon, G. Ujaque, F. Maseras, *J. Am. Chem. Soc.* **2005**, *127*, 9298; d) R. Alvarez, O. N. Faza, C. S. López, A. R. de Lera, *Org. Lett.* **2006**, *8*, 35; e) A. Ariafard, Z. Lin, I. J. S. Fairlamb, *Organometallics* **2006**, *25*, 5788; f) E. Napolitano, V. Farina, M. Persico, *Organometallics* **2003**, *22*, 4030.

 © 2007 Wiley-VCH Verlag GmbH & Co. KGaA, Weinheim 

[9] Representative theoretical studies of C–halogen bond activation related to cross-coupling reactions: a) M. Ahlquist, P.-O. Norrby, *Organometallics* **2007**, *26*, 550; b) M. Ahlquist, P. Fristrup, D. Tanner, P.-O. Norrby, *Organometallics* **2006**, *25*, 2066; c) L. J. Goossen, D. Koley, H. L. Hermann, W. Thiel, *Organometallics* **2005**, *24*, 2398; d) T. R. Cundari, J. Deng, *J. Phys. Org. Chem.* **2005**, *18*, 417; e) H. M. Senn, T. Ziegler, *Organometallics* **2004**, *23*, 2980; f) A. Sundermann, J. M. L. Martin, *Chem. Eur. J.* **2001**, *7*, 1703.

[10] Selected references: a) C. A. Tolman, *Chem. Rev.* **1977**, *77*, 313; b) W. Strohmeier, F.-J. Muller, *Chem. Ber.* **1967**, *100*, 2812; c) W. Strohmeier, F.-J. Muller, *Z. Naturforsch., Teil B* **1967**, *22*, 451; d) G. M. Bodner, M. Gaul, *J. Organomet. Chem.* **1975**, *101*, 63; e) G. M. Bodner, *Inorg. Chem.* **1975**, *14*, 2694; f) T. A. Mastryukova, M. I. Kabachnik, *Russ. Chem. Rev.* **1969**, *38*, 795; g) W. A. Henderson, C. A. Streuli, *J. Am. Chem. Soc.* **1960**, *82*, 5791; h) A. L. Fernandez, C. Reyes, A. Prock, W. P. Giering, *Organometallics* **1998**, *17*, 2503; i) A. L. Fernandez, T. Y. Lee, C. Reyes, A. Prock, W. P. Giering, C. M. Haar, S. P. Nolan, *J. Chem. Soc. Perkin Trans. 2* **1999**, 2631; j) D. R. Anton, R. H. Crabtree, *Organometallics* **1983**, *2*, 621; k) L. Perrin, E. Clot, O. Eisenstein, J. Loch, R. H. Crabtree, *Inorg. Chem.* **2001**, *40*, 5806; l) K. D. Cooney, T. R. Cundari, N. W. Hoffman, K. A. Pittard, M. D. Temple, Y. Zhao, *J. Am. Chem. Soc.* **2003**, *125*, 4318; m) S. Otto, A. Roodt, *Inorg. Chim. Acta* **2004**, *357*, 1; n) M. Yamanaka, A. Shiga, *J. Theor. Comput. Chem.* **2005**, *4*, 345.

[11] Reviews: a) K. A. Bunten, L. Z. Chen, A. L. Fernandez, A. J. Poe, *Coord. Chem. Rev.* **2002**, *233*, 41; b) D. White, N. J. Coville, "Quantification of Steric Effects in Organometallic Chemistry" in *Advances in Organometallic Chemistry*, Elsevier, New York, **1994**, vol. 36, pp. 95–158; c) T. L. Brown, K. J. Lee, *Coord. Chem. Rev.* **1993**, *128*, 89.

[12] a) C. M. Haar, S. P. Nolan, W. J. Marshall, K. G. Moloy, A. Prock, W. P. Giering, *Organometallics* **1999**, *18*, 474; b) D. C. Smith Jr, C. M. Haar, E. D. Stevens, S. P. Nolan, J. W. Marshall, K. G. Moloy, *Organometallics* **2000**, *19*, 1427.

[13] C. H. Suresh, N. Koga, *Inorg. Chem.* **2002**, *41*, 1573.

[14] W. P. Giering, A. Prock, A. L. Fernandez, *Inorg. Chem.* **2003**, *42*, 8033.

[15] C. H. Suresh, *Inorg. Chem.* **2006**, *45*, 4982.

[16] O. Kuhl, *Coord. Chem. Rev.* **2005**, *249*, 693.

[17] a) B. S. Williams, K. I. Goldberg, *J. Am. Chem. Soc.* **2001**, *123*, 2576; b) D. M. Crumpton-Bregel, K. I. Goldberg, *J. Am. Chem. Soc.* **2003**, *125*, 9442; c) W. J. Marshall, V. V. Grushin, *Organometallics* **2003**, *22*, 1591; d) A. Gillie, J. K. Stille, *J. Am. Chem. Soc.* **1980**, *102*, 4933; e) P. Dierkes, P. W. N. M. van Leeuwen, *J. Chem. Soc. Dalton Trans.* **1999**, 1519; f) G. Mann, D. Baranano, J. F. Hartwig, A. L. Rheingold, I. A. Guzei, *J. Am. Chem. Soc.* **1998**, *120*, 9205; g) J. E. Marcone, G. K. Moloy, *J. Am. Chem. Soc.* **1998**, *120*, 8527.

[18] P. Espinet, A. M. Echavarren, *Angew. Chem. Int. Ed.* **2004**, *43*, 4704.

[19] a) K. L. Bartlett, K. I. Goldberg, T. Borden, *J. Am. Chem. Soc.* **2000**, *122*, 1456; b) K. L. Bartlett, K. I. Goldberg, T. Borden, *Organometallics* **2001**, *20*, 2669.

[20] For representative studies, see: a) K. Tatsumi, R. Hoffmann, A. Yamamoto, J. K. Stille, *Bull. Chem. Soc. Jpn.* **1981**, *54*, 1857; b) J. L. Low, W. A. Goddard, *J. Am. Chem. Soc.* **1986**, *108*, 6115; c) J. L. Low, W. A. Goddard, *Organometallics* **1986**, *5*, 609; d) N. Koga, K. Morokuma, *Organometallics* **1991**, *10*, 946; e) M. R. A. Blomberg, P. E. M. Siegbahn, U. Nagashima, J. Wennerberg, *J. Am. Chem. Soc.* **1991**, *113*, 424; f) P. E. M. Siegbahn, M. R. A. Blomberg, *J. Am. Chem. Soc.* **1992**, *114*, 10548; g) S. Sakaki, M. Ieki, *J. Am. Chem. Soc.* **1993**, *115*, 2373; h) S. Sakaki, M. Ogawa, Y. Musashi, T. Arai, *Inorg. Chem.* **1994**, *33*, 1660; i) S. Sakaki, N. Mizoe, Y. Musashi, B. Biswas, M. Sugimoto, *J. Phys. Chem. A* **1998**, *102*, 8027; j) G. S. Hill, R. J. Puddephatt, *Organometallics* **1998**, *17*, 1478; k) Z. Cao, M. B. Hall, *Organometallics* **2000**, *19*, 3338; l) S. A. Macgregor, G. W. Neave, C. Smith, *J. Chem. Soc. Faraday Trans.* **2003**, *124*, 111.

[21] For general reviews, see: a) A. Didieu, *Chem. Rev.* **2000**, *100*, 543; b) D. G. Musaev, K. Morokuma, *Top. Catal.* **1999**, *7*, 107; c) P. E. M. Siegbahn, M. R. A. Blomberg, in *Theoretical Aspects of Homogeneous Catalysis, Applications of Ab initio Molecular Orbital Theory* (Eds.: P. W. N. M. van Leeuwen, J. H. van Lenthe, K. Morokuma), Kluwer Academic Publishers, Dordrecht, The Netherlands, **1995**; d) N. Koga, K. Morokuma, *Chem. Rev.* **1991**, *91*, 823.

[22] Vinyl–vinyl coupling: a) V. P. Ananikov, D. G. Musaev, K. Morokuma, *J. Am. Chem. Soc.* **2002**, *124*, 2839; b) V. P. Ananikov, D. G. Musaev, K. Morokuma, *Organometallics* **2001**, *20*, 1652.

[23] Coupling of $sp^3$, $sp^2$ and sp carbon atoms: V. P. Ananikov, D. G. Musaev, K. Morokuma, *Organometallics* **2005**, *24*, 715.

[24] Theoretical study of reductive elimination of organic molecules from palladium(II) complexes with chelate ligands: E. Zuiderma, P. W. N. M. van Leeuwen, C. Bo, *Organometallics* **2005**, *24*, 3703.

[25] An example of the ligand effect studied for gold(I) complexes: a) O. D. Häberlen, S. C. Chung, N. Rösch, *Int. J. Quantum Chem.* **1994**, *28*, 595; b) O. D. Häberlen, N. Rösch, *J. Phys. Chem.* **1993**, *97*, 4970.

[26] a) S. Dapprich, I. Komáromi, K. S. Byun, K. Morokuma, M. J. Frisch, *J. Mol. Struct. (Theochem)* **1999**, *462*, 1; b) T. Vreven, K. Morokuma, *J. Comput. Chem.* **2000**, *21*, 1419.

[27] V. P. Ananikov, R. Szilagyi, K. Morokuma, D. G. Musaev, *Organometallics* **2005**, *24*, 1938.

[28] a) P. Schwerdtfeger, M. Dolg, W. H. Schwarz, G. A. Bowmaker, P. D. W. Boyd, *J. Chem. Phys.* **1989**, *91*, 1762; b) D. Andrae, U. Haubermann, M. Dolg, H. Stoll, H. Preuss, *Theor. Chim. Acta* **1990**, *77*, 123; c) A. Bergner, M. Dolg, W. Küchle, H. Stoll, H. Preuss, *Mol. Phys.* **1993**, *80*, 1431.

[29] R. Krishnan, J. S. Binkley, R. Seeger, J. A. Pople, *J. Chem. Phys.* **1980**, *72*, 650.

[30] M. J. Frisch, G. W. Trucks, H. B. Schlegel, G. E. Scuseria, M. A. Robb, J. R. Cheeseman, J. A. Montgomery, Jr., T. Vreven, K. N. Kudin, J. C. Burant, J. M. Millam, S. S. Iyengar, J. Tomasi, V. Barone, B. Mennucci, M. Cossi, G. Scalmani, N. Rega, G. A. Petersson, H. Nakatsuji, M. Hada, M. Ehara, K. Toyota, R. Fukuda, J. Hasegawa, M. Ishida, T. Nakajima, Y. Honda, O. Kitao, H. Nakai, M. Klene, X. Li, J. E. Knox, H. P. Hratchian, J. B. Cross, V. Bakken, C. Adamo, J. Jaramillo, R. Gomperts, R. E. Stratmann, O. Yazyev, A. J. Austin, R. Cammi, C. Pomelli, J. W. Ochterski, P. Y. Ayala, K. Morokuma, G. A. Voth, P. Salvador, J. J. Dannenberg, V. G. Zakrzewski, S. Dapprich, A. D. Daniels, M. C. Strain, O. Farkas, D. K. Malick, A. D. Rabuck, K. Raghavachari, J. B. Foresman, J. V. Ortiz, Q. Cui, A. G. Baboul, S. Clifford, J. Cioslowski, B. B. Stefanov, G. Liu, A. Liashenko, P. Piskorz, I. Komaromi, R. L. Martin, D. J. Fox, T. Keith, M. A. Al-Laham, C. Y. Peng, A. Nanayakkara, M. Challacombe, P. M. W. Gill, B. Johnson, W. Chen, M. W. Wong, C. Gonzalez, J. A. Pople, *Gaussian 03*, rev. C1, Gaussian, Inc., Wallingford, CT, **2004**,.

[31] The averaged value for **1_C** has been used (see Table 2); see discussion below concerning an asymmetric ligand environment.

[32] a) J. C. Thomas, J. C. Peters, *J. Am. Chem. Soc.* **2003**, *125*, 8870; b) S. M. Reid, J. T. Mague, M. J. Fink, *J. Am. Chem. Soc.* **2001**, *123*, 4081; c) J. Ledford, C. S. Shultz, D. P. Gates, P. S. White, J. M. DeSimone, M. Brookhart, *Organometallics* **2001**, *20*, 5266; d) A. S. Abu-Surrah, T. Debaerdemaeker, W. Huhn, B. Rieger, M. Klinga, T. Repo, M. Leskela, *Acta Crystallogr., Sect. C* **2000**, *56*, e42; e) W. De Graaf, J. Boersma, W. J. J. Smeets, A. L. Spek, G. Van Koten, *Organometallics* **1989**, *8*, 2907; f) J. M. Wisner, T. J. Bartczak, J. A. Ibers, J. J. Low, W. A. Goddard III, *J. Am. Chem. Soc.* **1986**, *108*, 347; g) J. M. Wisner, T. J. Bartczak, J. A. Ibers, *Organometallics* **1986**, *5*, 2044; h) see also ref.[12] and discussion therein.

[33] In the present study we do not consider the intermediate σ or π complexes, which may lie on the potential energy surface

 © 2007 Wiley-VCH Verlag GmbH & Co. KGaA, Weinheim 

between **2-TS** and **3**. Stationary point **3** is of most practical importance, since it corresponds to the product-releasing stage of the catalytic reactions. Numerous studies on the structure and stability of σ or π complexes are already available in the literature (see, for example refs.[20–23]).

[34] It should be noted that gas-phase calculations may overestimate the entropy contribution. For that reason we mainly involve the Δ*H* surface in the discussion. Although, it is clearly established that the dissociation process in solution is more favorable on the Δ*G* surface.

[35] An exact quantitative estimation is unlikely to be obtained in this simple comparison scheme.

[36] An opposite case (if TS is more destabilized than the initial complex) would lead to an increase in the activation energy.

[37] An important issue, which should also be considered for the precise evaluation of the electronic and steric effects by this method, is the quality of the force field (for instance, in terms of the correct reproduction of nonbonded repulsions, etc.). The ONIOM(B3LYP:UFF) level covers a broad range of systems and was utilized in the present study; however, further clarification may be required to investigate the scope of this approach in more detail.

[38] In this case intermediate σ or π complexes may undergo a ligand-substitution reaction (see also ref.[33]).

[39] Values of the P–Pd–C1 and P–Pd–C2 angles [°]: 160.0, 138.0 (**5-TS_A**); 163.1, 138.5 (**5-TS_B**); 160.9, 141.3 (**5-TS_C**); 159.4, 143.1 (**5-TS_D**). Steric bulkiness of the ligands decreases the difference between these angles: 26.0 (**5-TS_A**); 24.6 (**5-TS_B**); 19.6 (**5-TS_C**); 16.3 (**5-TS_D**).

[40] Similar reaction and activation energy changes were predicted for the complexes with $PH_3$ ligands analyzed in detail earlier (see ref.[23]). Therefore, we do not concentrate on the differences between the organic groups, the phosphane ligand effect will be considered instead.

[41] A. Moravskiy, J. K. Stille, *J. Am. Chem. Soc.* **1981**, *103*, 4182.

[42] In the calculations of the three-coordinate pathway we assume dissociation of the phosphane ligand *trans* to the vinyl group, because the Pd–P bond was calculated to be relatively weaker for that case.

[43] Under experimental conditions these pathways may be switched by addition of an excess of phosphane ligand (to retard ligand dissociation from the Pd complex and favor the four-coordinate pathway) or by using low-ligated palladium species (to facilitate the three-coordinate pathway).

[44] Due to the high *trans* effect of the σ-bonded carbon ligand the solvent molecule most likely will dissociate prior to C–C reductive elimination, which in such a case will undergo the same **4** → **5-TS** → **3** pathway. If the solvent molecule remains coordinated, this will correspond to an intermediate case between the strongly bound phosphane ligand (**1** → **2-TS** → **3** pathway) and the three-coordinate pathway (**4** → **5-TS** → **3**).

Received: August 15, 2007
Published Online: October 12, 2007

 © 2007 Wiley-VCH Verlag GmbH & Co. KGaA, Weinheim 

DOI: 10.1002/ejic.200700383

# Efficient Increase of DNA Cleavage Activity of a Diiron(III) Complex by a Conjugating Acridine Group

Xiao-Qiang Chen,[a] Xiao-Jun Peng,*[a] Jing-Yun Wang,[b] Yan Wang,[b] Song Wu,[b] Li-Zhu Zhang,[a] Tong Wu,[a] and Yun-Kou Wu[a]

**Keywords:** DNA cleavage / Iron complex / Diiron(III) complex / Intercalator / Acridine

A new diferric complex, $Fe_2L_b$, in which a DNA intercalator (acridine) is linked to a precursor diferric complex ($Fe_2L_a$), has been designed and synthesised as a hydrolytic cleaving agent of DNA. Compared with $Fe_2L_a$ (without the DNA intercalator) ($L_a$: 2,6-bis{[(2-hydroxybenzyl)(pyridin-2-yl)methylamino]methyl}-4-methylphenol), $Fe_2L_b$ [$L_b$: 5-(acridin-9-yl)-*N*-(3,5-bis{[(2-hydroxybenzyl)(pyridin-2-yl)methylamino]-methyl}-4-hydroxybenzyl)pentanamide] leads to a 14-fold increase in the cleavage efficiency of plasmid DNA due to the binding interaction between DNA and the acridine moiety. The interaction has been demonstrated by UV/Vis absorption, CD spectroscopy, viscidity experiments and thermal denaturation studies. The hydrolytic mechanism is supported by evidence from T4 DNA ligase assay, reactive oxygen species (ROS) quenching and BNPP [bis(4-nitrophenyl) phosphate, a DNA model] cleavage experiments. The pH dependence of the BNPP cleavage by $Fe_2L_a$ in aqueous buffer media shows a bell-shaped pH–$k_{obs}$ profile with an optimum point around a pH of 7.0 which is in good agreement with the maximum point of the pH-dependent relative concentration curve of active species from the pH titration experiments. The determination of the initial rates at a pH of 7.36 as a function of substrate concentration reveals saturation kinetics with Michaelis–Menten-like behaviour and $Fe_2L_a$ shows a rate acceleration increase of $4.7 \times 10^6$ times in the hydrolysis of BNPP.
(© Wiley-VCH Verlag GmbH & Co. KGaA, 69451 Weinheim, Germany, 2007)

## Introduction

Mimicking the activities of nucleases is currently an attractive research area in molecular biology and therapy owing to its essential role in artificial restriction enzyme and conformational probes of nucleic acids.[1–4] A number of oxidative cleavage reagents have been used with great success in DNA footprinting[5] for locating base mismatches and loop regions,[6] for locating conformational variations in DNA[7] and as chemotherapeutic agents.[8] However, these oxidative cleavage agents require the addition of an external agent (e.g., light or hydrogen peroxide) to initiate cleavage. Furthermore, oxidative cleavage is mediated by reactive oxygen species (ROS) which can cause other severe cytotoxic effects. These drawbacks of the oxidative reagents hinder their potential applications in vivo. For eliminating the possibility of significant cytotoxic side effect of ROS, pathways that result in DNA cleavage by hydrolysis mechanisms have been considered to be preferable. However, the phosphodiester bonds of DNA are exceptionally resistant to hydrolysis under physiological conditions and it is a great challenge to find new catalysts to enhance the hydrolysis.[9–11] In the past decade, a variety of metal complexes which can promote the hydrolysis of DNA and phosphodiesters have been reported, including complexes based on $Cu^{II}$, $Zn^{II}$, $Co^{III}$ and lanthanide ions.[12–21] Furthermore, many elegant dinuclear complexes have been developed as structural or functional models of the enzymes.[22] Compared with mononuclear complexes, dinuclear complexes have the higher activity as a result of the cooperative interaction of metal ions in stabilising the transition state of phosphodiester cleavage.

Among the physiologically relevant metal ions, iron has been much less studied in the hydrolytic reaction[23–25] due to the fact that Fe-dependent DNA cleavage is often involved in oxygen free radical processes such as the Fenton reaction. In fact, purple acid phosphatases (PAP), comprising diiron active centers can catalyse the hydrolysis of certain phosphate esters, including nucleoside di- and triphosphates and aryl phosphates under weakly acidic conditions.[26] On the other hand, many efforts have so far been made to enhance the reactivity of metal complexes cleaving DNA. One of these strategies is the conjunction of metal complexes and intercalating groups to increase the DNA affinity of cleavage agents.[27–29] Tecilla et al. synthesised a series of $Zn^{II}$ complex-intercalator conjugates, the struc-

[a] State Key Laboratory of Fine Chemicals, Dalian University of Technology,
158 Zhongshan Road, Dalian 116012, P. R. China
Fax: +86-411-88993906
E-mail: pengxj@dlut.edu.cn
[b] Department of Bioscience and Biotechnology, Dalian University of Technology,
Dalian 116023, P. R. China
Supporting information for this article is available on the WWW under http://www.eurjic.org or from the author.

 WILEY InterScience DISCOVER SOMETHING GREAT © 2007 Wiley-VCH Verlag GmbH & Co. KGaA, Weinheim 

tures of which feature a *cis*,*cis*-triaminocyclohexane chelating subunit linked to an anthraquinone moiety through alkyl spacers with different lengths and reactivity studies showed that the length of the spacer which tethers the intercalating unit to the catalytic group is a key element in the cleavage activity.[28] An earlier complex was reported by Lawrence and co-workers, who appended acridine to a pentadentate N5 ligand and used it as a cofactor for $Fe^{II}$-promoted DNA oxidative cleavage.[29] However, examples of dinuclear complexes appended to the intercalating groups as hydrolytic agents are surprisingly rare.

In our work, the new diferric complex $Fe_2L_b$ is derived from $L_b$ (Scheme 1), the structure of which features a binuclear $Fe^{III}$ complex subunit linked an acridine moiety through a long spacer. The intercalating role of acridine has been confirmed by UV/Vis absorption, CD spectroscopy, viscidity experiments and thermal denaturation studies. The hydrolytic role of the diiron(III) subunit has also been confirmed from the efficient cleavage of the BNPP [bis(4-nitrophenyl) phosphate]. Furthermore, the conjugate can effectively promote the hydrolysis of plasmid DNA.

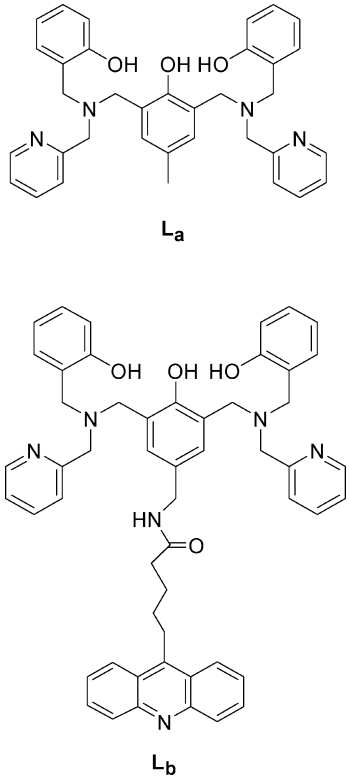


Scheme 1. Molecular structures of ligands used.

## Results and Discussion

### Synthesis and Characterisation

$L_a$ was prepared according to a procedure previously described by Neves et al.[30] $L_b$ was synthesised according to the reaction sequences depicted in Scheme S1. The previous report by Tecilla and co-workers has shown that the flexible spacer is very important in enhancing the activity of the conjugate toward DNA cleavage. Consequently, 5-(acridin-9-yl)pentanoic acid was chosen to link with the dinuclear metal moiety through an imide bond.[28] The acid was synthesised according to the method provided by Nadukkudy et al.[31] The compound 2-[3,5-bis(chloromethyl)-4-hydroxybenzyl]isoindole-1,3-dione, reported in our earlier publications,[32] was incubated with 2-{[(pyridin-2-ylmethyl)-amino]methyl}phenol in the presence of triethylamine to yield the intermediate **2**. After deprotection of **2** with hydrazine hydrate in ethanol at room temperature, the amine obtained was then linked to the acridinium subunit by an amide bond to afford the ligand $L_b$ in a yield of 50%. The diiron(III) complex $[Fe^{III}_2(BBPMP)(\mu\text{-}OAc)_2]$ with acetate bridging groups using $L_a$ as a ligand has been previously reported by Neves and co-works.[30] In accordance with this report, we initially obtained two complexes with acetate bridging groups using $L_a$ and $L_b$. Unfortunately, the solubilities in water were too low to carry out DNA experiments. Based on the modified synthesis, the complexes $Fe_2L_a$ and $Fe_2L_b$ were obtained and both have high solubility in water. Attempts to obtain the structures of $Fe_2L_a$ and $Fe_2L_b$ by X-ray diffraction were not successful although $Fe_2L_a$ and $Fe_2L_b$ were characterised by elemental analysis and spectroscopic methods (see Figures S1–S11 in the electronic supporting information). The binuclear structures of the complexes were supported by the calculated isotopic distributions which are in agreement with those measured using high-resolution ESI-MS (Figures S2 and S6–S9, supporting information). For $Fe_2L_a$, the observed species at $m/z$ ($z$ = 1) = 731.1150 corresponds to the singly-charged diiron species $[Fe^{III}_2(L_{a-3H})(OCH_3)_2]^+$. The six positive charges due to the two $Fe^{3+}$ ions and the five negative charges due to three phenolates ($L_a$–3 H) and the two methoxy ligands (from the exchange of ligand during ESI-MS using $CH_3OH$ as flowing phase) result in a single positively charged species. A similar analysis can also be applied to $Fe_2L_b$.

### pBR322 DNA Cleavage by Binuclear $Fe^{III}$ Complexes

In the absence of any added reductant or oxidant, when plasmid DNA pBR322 (0.02 $\mu g\,\mu L^{-1}$, 32 μM bp) is incubated at 37 °C for 1 h in 20 mM HEPES at pH 7.0 with $Fe_2L_a$ or $Fe_2L_b$, activity can already be observed with less than 50 μM of the catalysts and DNA becomes converted from supercoiled (form I) to nicked (form II) to an extent which depends on the concentration of the dinuclear complexes (Figure 1). A comparison between the activity of $Fe_2L_a$ and $Fe_2L_b$ provided clear evidence for the important role of the acridine subunit in promoting the efficiency of cleavage, while just 5 μM $Fe_2L_b$ is required to cleave 81% of supercoiled DNA after 1 h at 37 °C, the concentration of $Fe_2L_a$ necessary to provide the same effect is more than 20 μM. From Figures 2 and 3 it may also be seen that the relative amount of supercoiled plasmid DNA decreases upon increasing the incubation time. Through exponential decay fitting, the rate constant of the supercoiled DNA

 © 2007 Wiley-VCH Verlag GmbH & Co. KGaA, Weinheim 

cleavage for 20 μM $Fe_2L_b$ was determined to be $1.0 \times 10^{-2}$ $s^{-1}$ (Figure S12) which corresponds to a half-life of a minute. The rate constant represents a 14-fold increase in the cleavage efficiency when compared with the $Fe_2L_a$ species ($7.1 \times 10^{-4}$ $s^{-1}$, Figure S13). A similar rate acceleration (15-fold) was also reported by Tecilla et al. with a Zn-triaminocyclohexane complex tethered to an anthraquinone intercalator.[28] In order to verify the impact of the intercalation, we carried out the cleavage experiments in the presence of the mixture of acridine (5 μM) and $Fe_2L_a$ (5 μM). As shown in Figure S14, the extent of DNA cleavage by the mixture of acridine and $Fe_2L_a$ is similar to $Fe_2L_a$ and the activity is much less than for $Fe_2L_b$ (covalently linked with acridine). Furthermore, the kinetic experiment using the mixture show cleavage rate for form I is $6.9 \times 10^{-4}$ $s^{-1}$ (Figure S15–S16) which is also similar to $Fe_2L_a$ ($7.1 \times 10^{-4}$ $s^{-1}$). In contrast, the rate constant of $Fe_2L_b$ is much larger ($1.0 \times 10^{-2}$ $s^{-1}$). All of this evidence indicates that conjugation between the acridinium group and the diiron(III) subunit is necessary to get a fast cleavage rate.

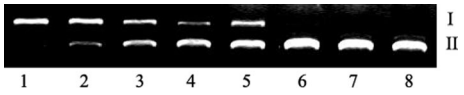


Figure 1. Agarose gel electrophoresis of pBR322 plasmid DNA treated with $Fe_2L_a$ (lane 2–4) and $Fe_2L_b$ (lane 5–8) for 1 h in an HEPES buffer (20 mM, pH 7.0) at 37 °C. Lane 1: control DNA, lane 2: $Fe_2L_a$ 10 μM, lane 3: $Fe_2L_a$ 20 μM, lane 4: $Fe_2L_a$ 50 μM, lane 5: $Fe_2L_b$ 5 μM, lane 6: $Fe_2L_b$ 10 μM, lane 7: $Fe_2L_b$ 20 μM, lane 8: $Fe_2L_b$ 50 μM.

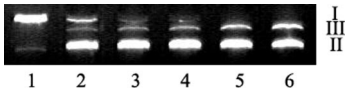


Figure 2. Time-dependence of pBR322 plasmid DNA cleavage by 20 μM $Fe_2L_a$ in an HEPES buffer (20 mM, pH 7.0) at 37 °C. Lane 1: control, lane 2: $Fe_2L_a$ 30 min, lane 3: 1 h, lane 4: 2 h, lane 5: 4 h, lane 6: 16 h.

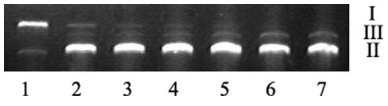


Figure 3. Time-dependence of pBR322 plasmid DNA cleavage by 20 μM $Fe_2L_b$ in an HEPES buffer (20 mM, pH 7.0) at 37 °C. Lane 1: control, lane 2: $Fe_2L_b$ 5 min, lane 3: 10 min, lane 4: 15 min, lane 5: 20 min, lane 6: 30 min, lane 7: 50 min.

The DNA cleaving systems based on mono-ferric complexes mostly involve the $Fe^{II}$ ion and DNA cleavage by these systems, such as Fe-bleomycin and the Fenton agent, occur by an oxidative mechanism. The $Fe^{III}$-based agents so far reported are relatively few although $Fe^{III}$ is present in the active site of some phosphatases. Two $Fe^{III}$ complexes with high hydrolytic activity in DNA cleavage have been reported and both of them are binuclear. The first complex $Fe_2$(HPTB), described by Schnaith, Que and co-workers in 1994[25] showed a surprising reactivity: in the presence of the complex at a concentration of 10 μM at 25 °C and a pH of 8.0, the supercoiled form was completely degraded immediately after mixing. However, the cleavage system was very complicated because high activity depended on "oxidative" conditions, i.e. the presence of $H_2O_2$ or $O_2$ and a reductant (dithiothreitol or ascorbate). No rate constant was reported which might result from the fact that the cleavage occurred with the initial burst of activity and the extent of cleavage did not increase after lengthening the reaction time. The second diiron(III) complex $Fe_2$(DTPB) was investigated by Liu and co-workers.[23] In the presence of such a complex at 37 °C, a pH of 7.0 and a concentration of 100 μM, the supercoiled DNA was degraded with a rate constant of $2.0 \times 10^{-3}$ $s^{-1}$ and the cleavage did not depend on the presence of $O_2$. Compared with $Fe_2$(DTPB), the activity of $Fe_2L_a$ seems somewhat lower ($7.1 \times 10^{-4}$ $s^{-1}$) at 20 μM. However, for $Fe_2L_b$ with a rate constant of $1.0 \times 10^{-2}$ $s^{-1}$ at a concentration as low as 20 μM, the cleavage efficiency is evidently better than for $Fe_2$(DTPB).

## Complex–DNA Interaction

The DNA binding ability of $Fe_2L_b$ was studied using UV spectroscopy by following the absorbance intensity changes of the acridine group at 253 nm. Upon addition of increasing amounts of DNA to the complex, 48% hypochromism was observed (Figure 4) which indicates the interaction between acridine group and DNA. From the plot of [DNA]/($\varepsilon_a - \varepsilon_f$) vs. [DNA], the intrinsic binding constant of the complex with DNA was calculated to be $(5.0 \pm 0.1) \times 10^5$ $M^{-1}$. The moderate binding for this complex is comparable to those observed for many other acridine derivatives.[33]

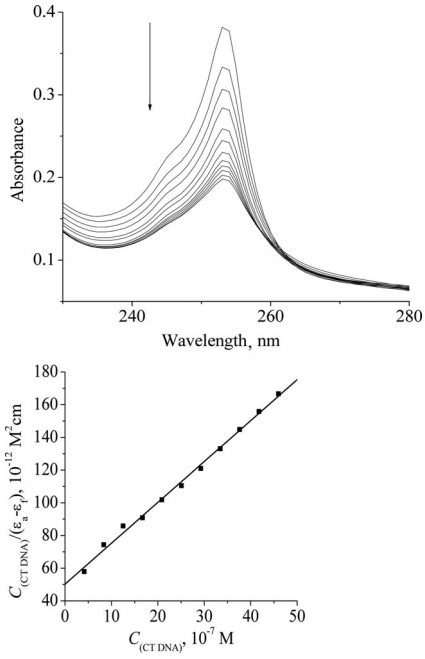


Figure 4. Top: absorption spectra of $Fe_2L_b$ ($0.67 \times 10^{-5}$ M) in the presence of increasing amounts of CT DNA ($6.27 \times 10^{-4}$ M) at 25 °C. Bottom: plot of [DNA]/($\varepsilon_a - \varepsilon_f$) vs. [DNA].

 © 2007 Wiley-VCH Verlag GmbH & Co. KGaA, Weinheim 

As a means for further clarifying the binding of the binuclear complex, viscosity measurements were carried out on calf thymus DNA by varying the concentration of the complex. Acridine, a classical intercalator, causes a moderated increase in the viscosity of the DNA solution due to the separation of base pairs at intercalation sites and hence an increase in overall DNA length (Figure 5). In contrast, $Fe_2L_a$ causes a decrease in DNA solution viscosity under the same conditions which can be attributed to the binding between $Fe_2L_a$ and DNA through charge affinity leading to a distortion of the DNA structure. Compared with $Fe_2L_a$, $Fe_2L_b$ further decreases the viscosity of DNA and the result suggests that the cooperation between the diiron complex and the acridine subunit makes distortion of the DNA more intense. The thermal denaturation studies show that the addition of $Fe_2L_b$ to the calf thymus DNA could raise $T_m$ from (78.3 ± 0.2) °C to (80.0 ± 0.5) °C but no change was observed in the case of $Fe_2L_a$ (Figure S17). The CD spectra also show the difference in the interaction between $Fe_2L_a$ and $Fe_2L_b$ with CT DNA (Figure S18): Incubation of DNA and $Fe_2L_a$ caused the intensities of both the positive and negative ellipticity bands to decrease, while incubation of DNA and $Fe_2L_b$ caused the intensities of the negative ellipticity band to increase and the positive ellipticity band blue-shift. This suggests the acridine moiety has a significant effect on the conformational changes of DNA.

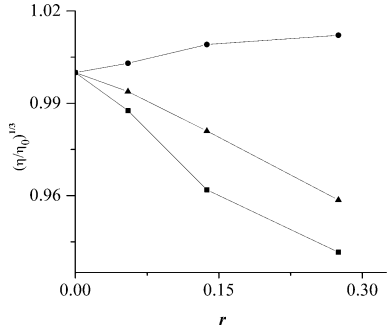


Figure 5. Effect of increasing the amounts of the compounds on the relative specific viscosity of calf thymus DNA. Viscosity is presented as $[\eta/\eta_0]^{1/3}$ in accord with the theory of Cohen and Eisenberg (1969). ● acridine + CT DNA, ▲ $Fe_2L_a$ + CT DNA, ■ $Fe_2L_b$ + CT DNA. $r = C_{compound}/C_{DNA}$.

## Cleavage Mechanism Analysis

The earlier two diiron(III) complexes $Fe_2$(DTPB) and $Fe_2$(HPTB), described respectively by Liu[23] and by Que,[25] have shown the yielding linearised DNA can be quantitatively relegated by confirming the occurrence of a hydrolytic mechanism. In our cases, the linearised DNA has also been relegated by T4 ligase (Figure 6), although the relegation is not complete. In some cases, the hydrolytic products either did not end at the required 5′-phosphate and 3′-OH (ribose) termini or the complex sometimes bound to the termini of cleaved DNA. These reasons would result in the relegation being incomplete or even failing completely.[34,35] To explore the effects of molecular oxygen on the degradation of DNA by the complexes, reactions were also performed under anaerobic conditions (Figure S19) and the results showed that $Fe_2L_a$ and $Fe_2L_b$ still effectively cleaved pBR322 DNA with little inhibition. In contrast, the oxidative cleaving system $Fe(EDTA)^{2-}$/DTT showed very strong oxygen dependence. Another general way to discriminate the hydrolytic mechanism from the oxidative mechanism is the examination of the DNA cleavage in the presence of reactive oxygen species (ROS) scavengers. Figure 7 indicates little effect on the cleavage efficiency of DNA with $Fe_2L_b$ when DMSO or $NaN_3$ are added and superoxide dismutase (SOD) can even promote the cleavage efficiency. The experimental results suggest that hydroxyl radical, singlet oxygen and superoxide are not involved in the diiron DNA cleavage system. Additionally, the possibility of hydroxyl radical formation in the presence of $Fe_2L_a$ can also be evaluated by monitoring the changes in absorbance at 552 nm for the dye rhodamine B. Degradation of the dye can provide a direct measure of the concentration of the hydroxyl radical formed.[36] In the presence of $Fe_2L_a$, no obvious decrease in absorbance of the dye was detected over the time of the experiment (Figure S20) even after $H_2O_2$ was added, indicating that the hydroxyl radical is not formed under these conditions. An oxidative pathway can therefore be ruled out in the cleavage of DNA by diiron(III) complexes and, evidently, the cleavage occurs through a hydrolytic mechanism.

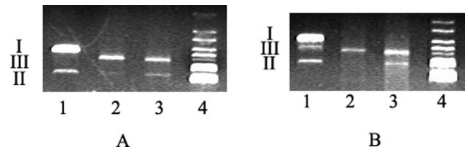


Figure 6. Ligation of pBR322 DNA cleaved by $Fe_2L_a$ and $Fe_2L_b$. A, lane 1: supercoiled (upper) and nicked (lower) pBR322 DNA, lane 2: linearised pBR322 DNA cleaved by $Fe_2L_a$, lane 3: ligation of linearised pBR322 DNA by T4 DNA ligase, lane 4: λ DNA-EcoT14 I digest markers. B, lane 1: supercoiled (upper) and nicked (lower) pBR322 DNA, lane 2: linearised pBR322 DNA cleaved by $Fe_2L_b$, lane 3: ligation of linearised pBR322 DNA by T4 DNA ligase, lane 4: λ DNA-EcoT14 I digest markers.

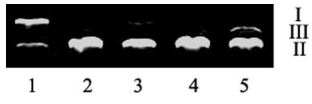


Figure 7. Agarose gel electrophoresis of pBR322 plasmid DNA treated with complex $Fe_2L_b$ in various inhibitors of ROS. Incubation time: 1 h (37 °C). Lane 1: control, lane 2: $Fe_2L_b$ 50 μM, lane 3: $Fe_2L_b$ 50 μM + 1 mM DMSO, lane 4: $Fe_2L_b$ 50 μM + 1 mM $NaN_3$, lane 5: $Fe_2L_b$ 50 μM + 10 U of SOD.

## Hydrolysis of BNPP Catalysed by $Fe_2L_a$

Cleavage experiments of phosphodiesters were also carried out to further verify the hydrolytic activity of diiron complexes. In these kinds of experiments, BNPP is often used as a DNA model compound in the assessment of phosphodiesterase activity. For ensuring the solubility of the binary of the catalyst-substrate compound, the mixed solu-

 © 2007 Wiley-VCH Verlag GmbH & Co. KGaA, Weinheim 

tion including DMSO (10 vol.-%) was used. The reaction was monitored by following the increase in the absorbance at 400 nm which indicates the release of NP from BNPP. The determination of the initial rates at a pH of 7.36 as a function of substrate concentration revealed saturation kinetics with Michaelis–Menten-like behaviour (Figure 8). A linearisation after Lineweaver–Burke gave the following kinetics values: $K_M = (3.1 \pm 0.1) \times 10^{-3}$ M, $V_{max} = (3.1 \pm 0.6) \times 10^{-9}$ mol L$^{-1}$ s$^{-1}$, and the catalytic constant $k_{cat} = V_{max}/[Fe_2L_a]_0 = (5.2 \pm 0.2) \times 10^{-5}$ s$^{-1}$. The second-order rate constant, $k_{BNPP}$ (= $k_{cat}/K_M$) for BNPP is $(1.7 \pm 0.1) \times 10^{-2}$ M$^{-1}$ s$^{-1}$ and the substrate binding constant $K_b = 1/K_M = (3.2 \pm 0.1) \times 10^2$ M$^{-1}$. From the kinetic data obtained under these conditions, a rate acceleration toward BNPP of ca. $(4.7 \pm 0.2) \times 10^6$ times was found. The rate is comparable to that observed for other binuclear transition metal-based complexes.[17]

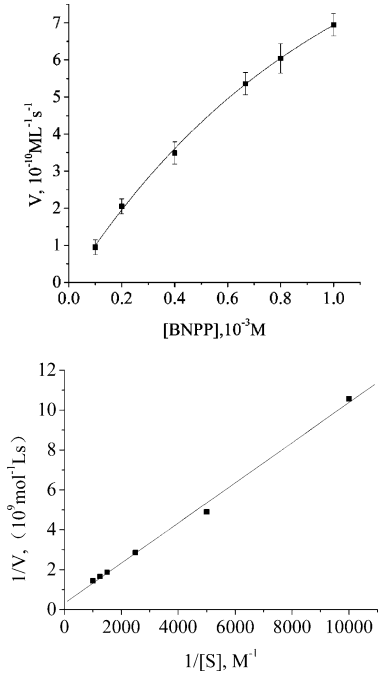


Figure 8. Top: saturation kinetic experiments for the cleavage of BNPP by $Fe_2L_a$ at a pH of 7.36 and 50 °C. $I$ = 0.10 M ($NaNO_3$), $[Fe_2L_a]_0$ = 0.06 mM, [HEPES buffer] = 50 mM, 10 vol.-% DMSO solution. Bottom: Lineweaver–Burke plot.

It was noted that the pH dependence of the catalytic activity between pH values of 5.9 and 8.5 shows a bell-shaped profile (Figure 9) with an optimum point at about pH 7.0. On the other hand, potentiometric titration of $Fe_2L_a$ shows two successive titratable protons in a 1:9 DMSO/$H_2O$ solvent mixture (Figure 10). Sigmoidal fitting gives the p$K_a$ values of 5.3 and 8.5, respectively. From the titration curve, we propose a processes according to the equilibria represented by Equations (1) and (2).

$$\underset{\mathbf{a}}{[Fe_2L_a(H_2O)(H_2O)]} \rightleftharpoons \underset{\mathbf{b}}{[Fe_2L_a(H_2O)(OH)]} + H^+ \quad (1)$$

$$\underset{\mathbf{b}}{[Fe_2L_a(H_2O)(OH)]} \rightleftharpoons \underset{\mathbf{c}}{[Fe_2L_a(OH)(OH)]} + H^+ \quad (2)$$

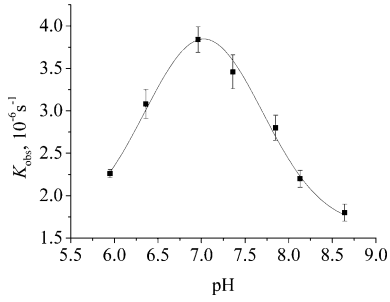


Figure 9. Dependence of the reaction rate on the pH under the following conditions: 10 vol.-% DMSO solution, 50 °C, $[Fe_2L_a] = 6.0 \times 10^{-5}$ mol L$^{-1}$, [BNPP] = $2 \times 10^{-4}$ mol L$^{-1}$, [buffer] = $5.0 \times 10^{-2}$ mol L$^{-1}$ (buffer: MES or HEPES), $I$ = 0.1 mol L$^{-1}$ ($NaNO_3$).

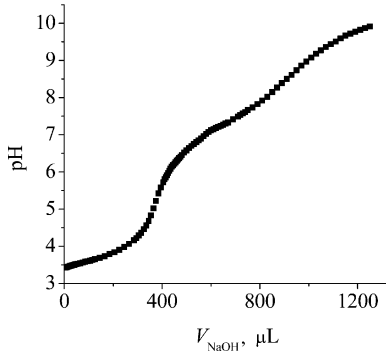


Figure 10. Potentiometric titration of $Fe_2L_a$ ($2.0 \times 10^{-4}$ M) with an increasing amount of 0.01 M NaOH in DMSO/$H_2O$ (1:9).

The distribution curves (Figure 11) of the deprotonated products of $Fe_2L_a$ in a 1:9 DMSO/$H_2O$ mixture display maximum monohydroxo species concentrations at a pH of 6.9 which is in good agreement with the optimum point for the catalytic activity at a pH of 7.0. These results indicate that the b species is the active species for the cleavage of phosphodiesters. As proposed previously [equilibria (1) and (2)], monohydroxo species can provide a labile Fe–$OH_2$ bond for phosphodiester binding and another $Fe^{III}$ bound hydroxide group for nucleophilic attack on the phosphorus atom. The decrease in the reactivity at pH > 7.0 most probably arises from the presence of the fully deprotonated form c, in which the tendency of the $OH^-$ ion from the Fe–OH group to leave becomes reduced even though a more concentrated $OH^-$ solution can increase the nucleophilic reactivity.

 © 2007 Wiley-VCH Verlag GmbH & Co. KGaA, Weinheim 

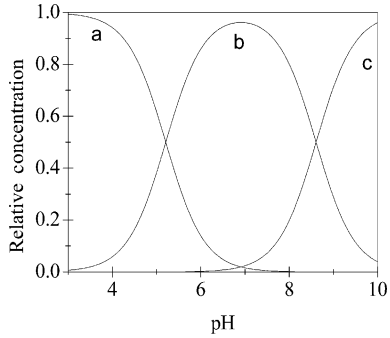


Figure 11. The distribution curves of the protonated products of $Fe_2L_a$ in DMSO/$H_2O$ (1:9). (**a**: the binuclear $Fe^{III}$ complex with two water molecules bound to the metal centre; **b**: the monohydroxo species and **c**: the dihydroxo one).

## Conclusions

In summary, we have designed and synthesised a new diiron complex $Fe_2L_b$ with an acridine group as an intercalator of DNA. The cleavage experiments indicate that the intercalative function can lead to a 14-fold increase in the cleavage efficiency. Furthermore, the hydrolytic mechanism studies demonstrate the potential of binuclear ferric complexes as catalyst models for artificial nucleases. In future work, we plan to link diiron(III) complexes with recognisable functional groups in the hope of realising the sequence-selective cleavage of DNA.

## Experimental Section

**General:** When necessary, reactions and manipulations were carried out under an atmosphere of nitrogen. All reagents and solvents were analytical reagent grade and were used without further purification unless otherwise noted. UV/Vis spectra were recorded with a Lambda 35 UV/Vis spectrometer. ESI–MS spectra and high-resolution mass spectra were recorded on an HP 1100 MSD and an HPLC-Q-Tof MS (Micro) instrument, respectively. NMR spectra were recorded with a 400-MHz Varian INOVA system. IR spectra were obtained by using an FTIR-430 spectrometer. Elemental analyses were performed on a Vario EL III instrument. The potentiometric titration was performed on a PHS-3C pH meter. Viscosity measurements were recorded with a NXE-1B viscometer. Circular dichroism spectra of DNA were obtained with a JASCO J-20 automatic recording spectropolarimeter. The ImageMaster VDS system (Pharmacia Biotech) was used for electrophoresis experiments.

### Syntheses

Bis(4-nitrophenyl) phosphates (BNPP) were prepared and purified following a modified literature method.[37]

**2-(4-Hydroxy-3,5-bis{[(2-hydroxybenzyl)pyridin-2-ylmethylamino]-methyl}benzyl)isoindole-1,3-dione (2) (Scheme S1):** A solution of 2-[3,5-bis(chloromethyl)-4-hydroxybenzyl]isoindole-1,3-dione (0.61 g, 3.0 mmol), 2-{[(pyridin-2-yl)methylamino]methyl}phenol (1.40 g, 6.5 mmol) and $Et_3N$ in $CH_2Cl_2$ was stirred at ambient temperature for 2 d. The reaction mixture was then diluted with $CH_2Cl_2$ and washed with brine. The organic phase was dried with $Na_2SO_4$ and the solvent was removed by evaporation. Purification on silica gel using EtOAc as eluent gave the desired product (71%). $^1$H NMR ($CDCl_3$): $\delta$ = 8.60 (d, $J$ = 4.4 Hz, 2 H, Py-H), 7.84 (m, 2 H, Py-H), 7.65–7.70 (m, 4 H, $PhCH_2Ph$-H), 7.26 (d, $J$ = 6 Hz, 4 H, Py-H), 7.23 (t, $J$ = 4.4 Hz, 2 H, Py-H), 7.10 (t, $J$ = 7.2 Hz, 2 H,H-Ph), 7.02 (d, $J$ = 7.2 Hz, 2 H, Ph-H), 6.72–6.76 (t, $J$ = 7.2 Hz, 4 H, Ph-H), 4.71 (s, 2 H, Ph−$CH_2$−Pht), 3.83 (s, 4 H, N−$CH_2$−Py), 3.80 (s, 4 H, N−$CH_2$−Ph), 3.77 (s, 4 H, N−$CH_2$−Ph) ppm. ESI-MS: $m/z$ 706.3 $[M + H]^+$, HRMS calcd. for $C_{43}H_{39}N_5O_5$ 706.3029, found 706.3022.

**4-Aminomethyl-2,6-bis{[(2-hydroxybenzyl)pyridin-2-ylmethylamino]-methyl}phenol (3):** Compound **2** (0.52 g, 7.4 mmol) was suspended in EtOH (10 mL) and hydrazine hydrate (0.22 g, 4.5 mmol) was added. The solution was heated to reflux for 2 h and stirred at ambient temperature overnight and the solvent was then evaporated under reduced pressure. The resultant solid was treated with 2 M HCl then extracted with $CH_2Cl_2$ and dried with $Na_2SO_4$. Evaporation of the solvent yielded 0.36 g (85%) of the product. $^1$H NMR ($CD_3COCD_3$,): $\delta$ = 8.61–8.64 (m, 2 H, Py−H), 7.79 (dt, $J$ = 7.7, 1.8 Hz, 2 H, Py−H), 7.32–7.38 (m, 4 H, Py−H), 7.07–7.14 (m, 6 H, Ph−H), 6.71–6.76 (m, 4 H, Ph−H), 4.30 (s, 2 H, Ph−$CH_2$−N), 3.87 (s, 4 H, N−$CH_2$−Py), 3.80 (s, 4 H, N−$CH_2$−Ph), 3.77 (s, 4 H, N−$CH_2$−Ph) ppm. ESI-MS: $m/z$ 576.3 $[M + H]^+$. HR-MS calcd. for $C_{35}H_{37}N_5O_3$ 576.2975, found 576.2980.

**5-(Acridin-9-yl)pentanoic Acid (4):**[31] Diphenylamine (1.69 g, 0.01 mol), hexanedioic acid (4.38 g, 0.03 mol) and anhydrous $ZnCl_2$ (6.8 g, 0.05 mol) were mixed well and heated at 230 °C for 20 h. $H_2SO_4$ (20 mL, 20 vol.-%) was then added to the reaction mixture which was subsequently heated to reflux for 4 h. The mixture was cooled and neutralised using aqueous $NH_3$ (25 vol.-%) solution. A solid product precipitated. After purification by silica gel column chromatography [eluted by a mixture (1:1) of EtOAc and petroleum ether], the pure compound was obtained. $^1$H NMR ($CD_3COCD_3$,): $\delta$ = 8.40 (d, $J$ = 8.8 Hz, 2 H, Acr-H), 8.15 (d, $J$ = 8.8 Hz, 2 H, Acr−H), 7.84 (t, $J$ = 7.6 Hz, 2 H, Acr−H), 7.64 (t, $J$ = 7.4 Hz, 2 H, Acr−H), 3.68 (t, $J$ = 7.2 Hz, 2 H, $CH_2$Acr), 2.3 (t, $J$ = 6.4 Hz, 2 H, $CH_2$COOH), 1.75 [m, 4 H, −$(CH_2)_2$−] ppm. ESI-MS $m/z$: 278.0 $[M - H]^-$.

**5-(Acridin-9-yl)-*N*-(3,5-bis{[(2-hydroxybenzyl)(pyridin-2-yl)methylamino]methyl}-4-hydroxybenzyl)pentanamide ($L_b$):** 5-(Acridin-9-yl)-pentanoic acid (0.126 g, 0.45 mmol) was heated to reflux in $SOCl_2$ (1 mL) for 2 h and the excess $SOCl_2$ was removed under reduced pressure. The dry solid was redissolved in dry acetonitrile (2 mL) and cooled in an ice bath. Compound **3** (0.22 g, 0.38 mmol) and triethylamine (0.5 mL) were added to the acetonitrile solution which was stirred under argon overnight as the temperature gradually returned to room temperature. Removing the solvent and purification on a column of silica gel using MeCN/$H_2O$ (95:5) as the eluent gave 0.16 g (50%) of the desired product. $^1$H NMR ($CD_3Cl$): $\delta$ = 8.56 (d, $J$ = 4.8 Hz, 2 H, Py−H), 8.35 (d, $J$ = 8.8 Hz, 2 H, Acr−H), 8.2 (d, $J$ = 8.8 Hz, 2 H, Acr−H), 7.77 (t, $J$ = 7.6 Hz, 2 H, Acr−H), 7.60 (t, $J$ = 7.8 Hz, 2 H, Py−H), 7.53 (t, $J$ = 7.6 Hz, 2 H, Acr−H), 7.15–7.21 (m, 4 H, Py−H), 7.10 (t, $J$ = 7.6 Hz, 2 H, Ph−H), 6.96 (s, 2 H, Ph−H), 6.92 (d, $J$ = 8 Hz, 2 H, Ph−H), 6.79 (d, $J$ = 6.4 Hz, 2 H, Ph−H), 6.93 (t, $J$ = 7.6 Hz, 2 H, Ph−H), 6.36 (br., 1 H, −NHCO−), 4.27 (d, $J$ = 5.2 Hz, 2 H, NH−$CH_2$−Ph), 3.77 (s, 4 H, N−$CH_2$−Py), 3.71 (s, 4 H, N−$CH_2$−Ph), 3.65 (s, 4 H, N−$CH_2$−Ph), 3.61 (t, $J$ = 7.2 Hz, 2 H, $CH_2$−Acr), 2.34 (t, $J$ = 7.2 Hz, 2 H, $CH_2$−CONH), 1.95–1.99 (m, 2 H, −$CH_2CH_2$−), 1.82–1.84 (m, 2 H, −$CH_2CH_2$−) ppm. ESI-MS $m/z$ 837.5 $[M + H]^+$, HRMS calcd. for $C_{53}H_{52}N_6O_4$ 837.4128, found 837.4135.

**Synthesis of the Binuclear Complexes $Fe_2L_aCl_3{\cdot}3H_2O$ ($Fe_2L_a$) and $Fe_2L_bCl_3{\cdot}4H_2O$ ($Fe_2L_b$):** $L_a$ (0.05 g, 0.09 mmol) and 2 equiv.

 © 2007 Wiley-VCH Verlag GmbH & Co. KGaA, Weinheim 

$FeCl_3 \cdot 6H_2O$ (0.049 g, 0.18 mmol) were dissolved in $H_2O$ and heated at 50 °C for 1 h to obtain a dark blue solution and the solution was then concentrated under reduced pressure. The target product $Fe_2L_a$ was the obtained as a solid residue. $C_{35}H_{39}Cl_3Fe_2N_4O_6$ ($Fe_2L_aCl_3 \cdot 3H_2O$): calcd. C 50.66, H 4.74, N 6.75; found C 50.64, H 4.49, N 6.81. High-Resolution ESI-MS ($CH_3OH$ as flowing phase) (Figure S1–S2) *m/z*: $[Fe^{III}Fe^{III}(L_{a-3H})(OCH_3)(OCH_3)]^+$ 731.1150; $[Fe^{III}Fe^{III}$ ($L_a$–3 H) $(OCH_3)]^{2+}$, 350.1511. IR (KBr) (Figure S3): $\tilde{\nu}$ = 3427–3066 (br., s), O–H of water and C–H of aromatic ring; 2922 (m) and 2855 (m), C–H of methane; 1609 (s) and 1475 (s), C=C of aromatic ring; 1264 (s), C–O of phenol; 759 $cm^{-1}$ (s), C–H of aromatic ring. UV/Vis ($H_2O$): $\lambda_{max}$ ($\varepsilon_m$, L $mol^{-1}$ $cm^{-1}$) (Figure S4): 260 (shoulder, 20000) attributed to the π–π* transition of the ligand; 531 nm(4400) attributed to the iron(III)−ligand charge transfer. Similarly, spectroscopic data of $Fe_2L_b$ were obtained. $C_{53}H_{57}Cl_3Fe_2N_6O_8$ ($Fe_2L_bCl_3 \cdot 4H_2O$): calcd. C 56.63, H 5.11, N 7.48; found C 56.92, H 4.45, N 7.62. High-Resolution ESI-MS ($CH_3OH$ as flowing phase) (Figure S5–S9) *m/z*: $[Fe^{III}Fe^{III}$ ($L_b$–3 H) $(OCH_3)H]^{3+}$ 325.6591; $[Fe^{III}Fe^{III}$ ($L_b$–3 H) $(OH)]^{2+}$ 480.9854; $[Fe^{III}Fe^{III}$ ($L_b$–3 H) (OH)(HCl)$]^{2+}$ 498.9745; $[Fe^{III}Fe^{III}$ ($L_b$–3 H) $(OCH_3)$(HCl)$]^{2+}$ 505.9684; $[Fe^{III}Fe^{III}$ ($L_b$–3 H) (OAc)(HCl)$]^{2+}$ 520.9583. IR (KBr) (Figure S10): $\tilde{\nu}$ = 3417–3000 (br., s), O–H of water and C–H of aromatic ring; 2925 (m) and 2857 (m), C–H of methane; 1635 (s) and 1478 (s), C=C of aromatic ring; 1265 (strong), C–O of phenol; 759 $cm^{-1}$ (strong), C–H of aromatic ring. UV/Vis ($H_2O$): $\lambda_{max}$ ($\varepsilon_m$, L $mol^{-1}$ $cm^{-1}$) (Figure S11): 253 (56300) and 354 (13300) attributed to the π–π* transition of ligand; 531 nm (2980) attributed to the iron(III)−ligand charge transfer.

**pBR322 DNA Cleavage Experiments by the Binuclear Metal Complexes:** DNA cleavage experiments were performed using pBR 322 (Takara) in a 20 mM HEPES buffer, pH 7.0, with incubating DNA (0.4 μg) at 37 °C in the presence and absence of the metal complex for the specified time. The cleavage reactions were stopped by addition of 3 μL of a loading buffer (0.25% bromphenol blue, 25% glycerol, 1 mM EDTA, 2% SDS). The electrophoresis of DNA cleavage products was performed on 1% agarose gel. The gels were run at 130 V for 45 min in a 0.01 M pH 7.0 TAE buffer. The resolved bands were visualised by ethidium bromide staining and were then quantified. A correction factor of 1.22 was utilised to account for the decreased ability of ethidium bromide to intercalate into form I DNA compared with forms II and III.[38]

**Cleavage of pBR322 in the Presence of ROS Scavengers:** Scavengers of reactive oxygen intermediates (DMSO, $NaN_3$ and SOD) were added alternatively to the reaction mixtures. Cleavage was initiated by the addition of $Fe_2L_b$ and stopped by 3 μL of a loading buffer (0.25% bromphenol blue, 25% glycerol, 1 mM EDTA, 2% SDS). Further analysis was conducted using the standard procedures described above.

**Absorption Titration of $Fe_2L_b$ Binding to DNA:** The solutions of CT DNA gave a UV absorbance ratio at 260 and 280 nm, $A_{260}/A_{280} > 1.8$, indicating that the DNA was sufficiently free of protein.[39] The concentrated stock solution of CT DNA (stored at 4 °C and not used for more than 6 d) was prepared and the concentration of DNA in the nucleotide phosphate was determined by UV absorbance at 260 nm after a 1:10 dilution. The molar absorption coefficient of CT DNA was taken as 6600 $M^{-1}$ $cm^{-1}$.[39] A solution (3 mL) of $0.67 \times 10^{-5}$ M $Fe_2L_b$ in water was incubated for 30 min at 25 °C. With addition of increasing amounts of 2 μL aliquots of DNA ($6.27 \times 10^{-4}$ M), the influence of volume was found to be negligible. The binding constant was determined using the following equation: $C_{DNA}/(\varepsilon_a - \varepsilon_f) = C_{DNA}/(\varepsilon_b - \varepsilon_f) + 1/K_b(\varepsilon_b - \varepsilon_f)$, where $\varepsilon_a$, $\varepsilon_f$, and $\varepsilon_b$ correspond to $A_{obsd}$/[complex], the extinction coefficient for the free iron complex and the extinction coefficient for the iron complex in the fully bound form, respectively. The intrinsic binding constant $K_b$ was given by the ratio of the slope to intercept through the plot of $C_{DNA}/(\varepsilon_a - \varepsilon_f)$ vs. $C_{DNA}$.

**Viscosity Measurements:** Viscosity experiments were carried out on a NXE-1B viscometer at 25 °C. The concentration of DNA was 280 μM in the nucleotide phosphate and the flow times were determined with a manually operated timer. Data were presented as $[\eta/\eta_0]^{1/3}$ vs. [complex]/[DNA] ($\eta$ is the viscosity of DNA solution in the presence of the compound and $\eta_0$ is the viscosity of DNA alone).

**Ligation Experiment on the DNA Fragments:** Enzymatic assays were performed using T4 DNA ligase to determine whether the cleaved products were consistent with hydrolysis of the phosphodiester linkages in DNA. First, the linearised DNA was isolated from the pBR 322 DNA cleavage products by $Fe_2L_a$ or $Fe_2L_b$. Then, the following reaction was carried out for relegation: 1.5 μL of 10× ligation buffer, 10 μL of linearised pBR 322 DNA, 1 μL of T4 ligase (2 units), and 2.5 μL of $H_2O$ were mixed and incubated at 16 °C for 24 h. The ligation products were monitored by the electrophoresis and visualised by staining in an ethidium bromide solution.

**Anaerobic Reactions:** Deoxygenated water was prepared by four freeze-pump-thaw cycles. Before each cycles the water was equilibrated with nitrogen to assist the deoxygenating process. The deoxygenated water was stored under a nitrogen atmosphere prior to use. All anaerobic stock solutions were prepared in Schlenk tubes under nitrogen using the deoxygenated water. Reaction mixtures were prepared by the addition of the appropriate volumes of the stock solutions to the tubes and were incubated in a nitrogen-filled glovebag.

**Thermal Denaturation of DNA:** In 0.01 M $Na_2HPO_4$ buffer (pH 7.0), the absorption values of DNA as well the mixture of DNA and dinuclear $Fe^{III}$ complexes at 260 nm were recorded by increasing the temperature in 5 °C increments from 55 °C to 95 °C in a thermostatic bath where the controls were the buffer and the buffers in the absence and presence of the diiron complex, the concentration of which was the same as that in the sample.

**CD Spectra Measurements:** Circular dichroism spectra of DNA were obtained on a JASCO J-20 automatic recording spectropolarimeter operating at 25 °C. The region between 200 and 300 nm was scanned for each sample.

**Kinetic Measurements:** The kinetic measurements were performed at 50 °C in buffered solutions of a 1:9 mixture of DMSO/water. 2-(Morpholino)ethanesulfonic acid (MES) and 2-[4-(2-hydroxyethyl)-piperazin-1-yl]ethanesulfonic acid (HEPES) were used as buffers. The ionic strength was fixed to 0.1 M with sodium nitrate. In a typical experiment, aqueous buffer solution (1.5 mL) was mixed with complex $Fe_2L_a$ stock solution (in water) (0.9 mL) and DMSO (0.3 mL) in a temperature-controlled spectrometric cell. After the mixture was equilibrated for 15 min, BNPP stock solution (in water) was added (0.3 mL) and data collection was started immediately. The cleavage of BNPP was measured by following the increase in the absorption of 4-nitrophenolate (NP) at 400 nm. NP concentrations were determined using the molar extinction coefficients for NP of 2500, 4500, 9000, 12800, 16800, 17900, 19900 $M^{-1}$ $cm^{-1}$ at pH values of 5.95, 6.36, 6.96, 7.36, 7.85, 8.13 and 8.64, respectively. The activities of the complexes were determined by the method of initial rates. At least three independent measurements were made.

**Potentiometric Titration of $Fe_2L_a$:** To an aqueous solution of $Fe_2La$ ($2.0 \times 10^{-4}$ M) containing 10 vol.-% DMSO was added a solution of

 © 2007 Wiley-VCH Verlag GmbH & Co. KGaA, Weinheim 

0.01 M NaOH dropwise. Each data point was obtained by adding 2–20 μL of NaOH solution at 25 °C.

**Supporting Information** (see also the footnote on the first page of this article): Synthesis of $L_b$ (Scheme S1). High-Resolution ESI-MS spectrum of $Fe_2L_a$ (Figure S1, S2). IR spectra of $Fe_2L_a$ (Figure S3). Absorption spectra of 60 μM $Fe_2L_a$ (Figure S4). High-Resolution ESI-MS spectrum of $Fe_2L_b$ (Figure S5–S9). IR spectra of $Fe_2L_b$ (Figure S10). Absorption spectra of 60 μM $Fe_2L_b$ (Figure S11). Time course of DNA cleavage by 20 μM $Fe_2L_b$ (Figure S12). Time course of DNA cleavage by 20 μM $Fe_2L_a$ (Figure S13). Agarose gel electrophoresis of pBR322 DNA treated with $Fe_2L_a$, the mixture of acridine and $Fe_2L_a$, $Fe_2L_b$ (Figure S14). Time-dependence of DNA cleavage by the mixture of 20 μM $Fe_2L_a$ and 20 μM acridine (Figure S15). Time course of DNA cleavage by the mixture of 20 μM $Fe_2L_a$ and 20 μM acridine (Figure S16). Thermal Denaturation studies of DNA (Figure S17). The CD spectra of CT DNA with complexes (Figure S18). Anaerobic and aerobic cleavage of pBR322 DNA by diiron(III) complexes and $Fe(EDTA)^{2-}$/DTT (Figure S19). Quantification of hydroxyl radicals by following the degradation of rhodamine B (Figure S20).

## Acknowledgments

This work was supported by the Ministry of Education of China and National Natural Science Foundation of China (projects 20376010 and 20472012).

[1] K. E. Erkkila, D. T. Odom, J. K. Barton, *Chem. Rev.* **1999**, *99*, 2777–2796.
[2] K. Lang, J. Mosinger, D. M. Wagnerova, *Coord. Chem. Rev.* **2004**, *248*, 321–350.
[3] H. T. Chifotides, K. R. Dunbar, *Acc. Chem. Res.* **2005**, *38*, 146–156.
[4] A. Sreedhara, J. A. Cowan, *J. Biol. Inorg. Chem.* **2001**, *6*, 337–347.
[5] W. K. Pogozelski, T. J. McNeese, T. D. Tuilius, *J. Am. Chem. Soc.* **1995**, *117*, 6428–6433.
[6] C. J. Burrows, S. E. Rokita, *Acc. Chem. Res.* **1994**, *27*, 295–301.
[7] M. D. Kuwabara, D. S. Sigman, *Biochemistry* **1987**, *26*, 7234–7238.
[8] J. Stubbe, J. W. Kozarich, *Chem. Rev.* **1987**, *87*, 1107–1136.
[9] J. Rammo, R. Hettich, A. Roigk, H. J. Schneider, *Chem. Commun.* **1996**, 105–107.
[10] M. Yashiro, A. Ishikuno, M. Komiyama, *J. Chem. Soc., Chem. Commun.* **1995**, 1793–1794.
[11] M. P. Fitzsimons, J. K. Barton, *J. Am. Chem. Soc.* **1997**, *119*, 3379–3380.
[12] M. W. Göbel, *Angew. Chem. Int. Ed. Engl.* **1994**, *33*, 1141–1143.
[13] F. H. Fry, A. J. Fischmann, M. J. Belousoff, L. Spiccia, J. Brugger, *Inorg. Chem.* **2005**, *44*, 941–950.
[14] R. Ren, P. Yang, W. J. Zheng, Z. C. Hua, *Inorg. Chem.* **2000**, *39*, 5454–5463.
[15] S. Matsuda, A. Ishikubo, A. Kuzuya, M. Yashiro, M. Komiyama, *Angew. Chem. Int. Ed.* **1998**, *37*, 3284–3286.
[16] O. Iranzo, A. Y. Kovalevsky, J. R. Morrow, J. P. Richard, *J. Am. Chem. Soc.* **2003**, *125*, 1988–1993.
[17] J. Chen, X. Y. Wang, Y. G. Zhu, J. Lin, X. L. Yang, Y. Z. Li, Y. Lu, Z. J. Guo, *Inorg. Chem.* **2005**, *44*, 3422–3430.
[18] N. H. Williams, J. Chin, *Chem. Commun.* **1996**, 131–132.
[19] N. H. Williams, W. Cheung, J. Chin, *J. Am. Chem. Soc.* **1998**, *120*, 8079–8087.
[20] P. E. Jurek, A. M. Jurek, A. E. Martell, *Inorg. Chem.* **2000**, *39*, 1016–1020.
[21] C. A. Chang, B. H. Wu, B. Y. Kuan, *Inorg. Chem.* **2005**, *44*, 6646–6654.
[22] N. H. Williams, B. Takasaki, M. Wall, J. Chin, *Acc. Chem. Res.* **1999**, *32*, 485–493.
[23] C. L. Liu, S. W. Yu, D. F. Li, Z. R. Liao, X. H. Sun, H. B. Xu, *Inorg. Chem.* **2002**, *41*, 913–922.
[24] F. Verge, C. Lebrun, M. Fontecave, S. Menage, *Inorg. Chem.* **2003**, *42*, 499–507.
[25] L. H. Schnaith, R. S. Hanson, L. Que Jr, *Proc. Natl. Acad. Sci. USA* **1994**, *91*, 569–573.
[26] B. Vincent, G. L. Olivier-Lilley, B. A. Averill, *Chem. Rev.* **1990**, *90*, 1447–1467.
[27] K. D. Copeland, M. P. Fitzsimons, R. P. Houser, J. K. Barton, *Biochemistry* **2002**, *41*, 343–356.
[28] E. Boseggia, M. Gatos, L. Lucatello, F. Mancin, S. Moro, M. Palumbo, C. Sissi, P. Tecilla, U. Tonellato, G. Zagotto, *J. Am. Chem. Soc.* **2004**, *126*, 4543–4549.
[29] G. Roelfes, M. E. Branum, L. Wang, L. Que Jr, B. L. Feringa, *J. Am. Chem. Soc.* **2000**, *122*, 11517–11518.
[30] A. Neves, M. A. de Brito, I. Vencato, V. Drago, K. Griesar, W. Haase, *Inorg. Chem.* **1996**, *35*, 2360–2368.
[31] V. E. Nadukkudy, S. Muthusami, R. Danaboyina, *Synth. Commun.* **1999**, *29*, 4007–4014.
[32] F. Shi, H. Y. Li, X. J. Peng, R. Zhang, X. Q. Chen, J. L. Fan, L. C. Sun, *Chin. Chem. Lett.* **2004**, *15*, 1407–1410.
[33] J. Joseph, E. Kuruvilla, A. T. Achuthan, D. Ramaiah, G. B. Schuster, *Bioconjugate Chem.* **2004**, *15*, 1230–1235.
[34] M. Scarpellini, A. Neves, R. Hörner, A. J. Bortoluzzi, B. Szpoganics, C. Zucco, R. A. N. Silva, V. Drago, A. S. Mangrich, W. A. Ortiz, W. A. C. Passos, M. C. B. de Oliveira, H. Terenzi, *Inorg. Chem.* **2003**, *42*, 8353–8365.
[35] C. Sissi, F. Mancin, M. Gatos, M. Palumbo, P. Tecilla, U. Tonellato, *Inorg. Chem.* **2005**, *44*, 2310–2317.
[36] A. Sreedhara, J. D. Freed, J. A. Cowan, *J. Am. Chem. Soc.* **2000**, *122*, 8814–8824.
[37] A. Williams, A. N. Richard, *J. Chem. Soc. B* **1971**, 1973–1979.
[38] R. P. Hertzberg, P. B. Dervan, *J. Am. Chem. Soc.* **1982**, *104*, 313–315.
[39] M. E. Reichmann, S. A. Rice, C. A. Thomas, P. Doty, *J. Am. Chem. Soc.* **1954**, *76*, 3047–3053.

Received: April 8, 2007
Published Online: October 16, 2007

 © 2007 Wiley-VCH Verlag GmbH & Co. KGaA, Weinheim 

DOI: 10.1002/ejic.200700478

# Tetranuclear Complexes of $Pd^{II}$ with Tridentate [*C*,*N*,*O*] and [*O*,*N*,*O*] Ligands: Synthesis, Reactivity and Structural Isomerism

**Jesús J. Fernández,*[a] Alberto Fernández,[a] Digna Vázquez-García,[a] Margarita López-Torres,[a] Antonio Suárez,[a] Nina Gómez-Blanco,[a] and José M. Vila*[b]**

**Keywords:** Palladium / Cyclometallation / Metallacycles / Tridentate [*C*,*N*,*O*] ligands / C–H activation

Treatment of the Schiff base ligand 2,3,4-$(MeO)_3C_6H_2C(H)=N[2\text{-}(OH)\text{-}5\text{-}t\text{Bu}C_6H_3]$ (**a**) with palladium(II) acetate in toluene gave the cyclometallated complex $[Pd\{2,3,4\text{-}(MeO)_3C_6HC(H)=N(2\text{-}O\text{-}5\text{-}t\text{Bu}C_6H_3)\}]_4$ (**1a**) with the tridentate ligand [*C*,*N*,*O*]. The complex showed a tetranuclear arrangement of the cyclometallated monomers with a $P_4O_4$ core. Reaction of $2,6\text{-}(Me)_2C_6H_3C(H)=N[2\text{-}(OH)C_6H_4]$ (**b**) and $2,5\text{-}(Me)_2C_6H_3C(H)=N[2\text{-}(OH)C_6H_4]$ (**c**) with palladium(II) acetate under similar conditions yielded the tetranuclear complexes $[Pd\{6\text{-}Me\text{-}2\text{-}CH_2C_6H_3C(H)=N(2\text{-}OC_6H_4)\}]_4$ (**1b**) and $[Pd\{5\text{-}Me\text{-}2\text{-}CH_2C_6H_3C(H)=N(2\text{-}OC_6H_4)\}]_4$ (**1c**), respectively, in which the tridentate [*C*,*N*,*O*] ligand is bound through the aliphatic methyl carbon. Treatment of $2,4\text{-}(Me)_2C_6H_3C(H)=N[2\text{-}(OH)C_6H_4]$ (**d**) with palladium(II) acetate yielded a mixture of isomers, $[Pd\{4\text{-}Me\text{-}2\text{-}CH_2C_6H_3C(H)=N\text{-}(2\text{-}OC_6H_4)\}]_n[Pd\{2,4\text{-}(Me)_2C_6H_2C(H)=N(2\text{-}OC_6H_4)\}]_{4-n}$ ($n$ = 0–4), also bearing a tetranuclear structure. However, the tetramer was assembled by two types of mononuclear Pd(ligand) building blocks: the ligand is coordinated through the aliphatic methyl carbon in one and through the aromatic *ortho* carbon in the other. The crystal structure of one such isomer confirmed the spectroscopic data. Treatment of $2\text{-}(OH)\text{-}4,6\text{-}(MeO)_2C_6H_2C(H)=N[2\text{-}(OH)C_6H_4]$ (**e**) and $2\text{-}(OH)C_6H_4\text{-}C(H)=N[2\text{-}(OH)C_6H_4]$ (**f**) with palladium(II) acetate yielded the tetranuclear complexes $[Pd\{2\text{-}O\text{-}4,6\text{-}(MeO)_2C_6H_2C(H)=N(2\text{-}OC_6H_4)\}]_4$ (**1e**) and $[Pd\{2\text{-}OC_6H_4C(H)=N(2\text{-}OC_6H_4)\}]_4$ (**1f**), respectively, after double deprotonation of the ligand, which coordinates to the metal through the two phenoxy oxygen atoms and the imine nitrogen atom in these complexes. Reaction of compounds **1a**–**1f** with tertiary phosphanes in acetone gave mono- and dinuclear complexes, after cleavage of the tetranuclear structure. In these complexes, the tertiary phosphane is bonded *trans* to the nitrogen atom. The crystal structures for **1a**, **1c**, **1e**, **1d/1d′** are reported; they show the characteristic $Pd_4O_4$ core.

(© Wiley-VCH Verlag GmbH & Co. KGaA, 69451 Weinheim, Germany, 2007)

## Introduction

Cyclometallated compounds have been extensively surveyed,[1–5] and they exhibit a good number of applications related to organic as well as to organometallic compounds, metallomesogens and catalytic materials;[6–13] they also promote unusual coordination environments.[14] The more common cyclometallated complexes encountered in the literature are the palladium(II) five-membered ring species after activation of aromatic $C(sp^2)$ atoms. Analogous compounds containing alkyl $C(sp^3)$–Pd bonds are also known although these are more scarce.[15–19]

On the other hand, the building of supramolecular assemblies has also attracted much attention in the past years,[20–24] and among these, examples containing square-planar palladium(II) units have been of great interest in view of their potential applications.[25] Nevertheless, few examples of supramolecular species with cyclometallated building blocks have been reported,[26–31] many of which correspond to tetrameric assemblies derived from palladium(II) cyclometallated complexes with [*C*,*N*,*X*] (*X* = *O*, *S*) tridentate ligands. Thus, for the [*C*,*N*,*S*] species, thiosemicarbazones give tetranuclear structures with an eight-membered $Pd_4S_4$ core,[32–34] and tetranuclear cluster complexes derived from benzothiazolines[35,36] are also known. As for the [*C*,*N*,*O*] derivatives,[37–40] they also exhibit an analogous tetranuclear structure with a $Pd_4O_4$ core. In order to attain neutrality the ligand is usually deprotonated in the complex, at the hydrazine nitrogen atom, at the benzothiazoline nitrogen atom or at the phenol oxygen atom. Even when there is no metal–carbon bond formation, the tetranuclear structure is reached only after deprotonation, as has been reported for a coordination compound derived from a [*N*,*N*,*S*] ligand.[41]

The purpose of this paper is twofold: first, to study the activation of aromatic carbon atoms against aliphatic carbon atoms by checking the bonding possibilities of *N*-phenol Schiff base ligands, and secondly, to determine the

[a] Departamento de Química Fundamental, Universidad de La Coruña,
15071 La Coruña, Spain
Fax: +34-981-167065
E-mail: qiluaafl@udc.es
[b] Departamento de Química Inorgánica, Universidad de Santiago de Compostela,
15782 Santiago de Compostela, Spain
Fax: +34-981-595012
E-mail: qideport@usc.es

 WILEY InterScience DISCOVER SOMETHING GREAT © 2007 Wiley-VCH Verlag GmbH & Co. KGaA, Weinheim 

structural particularity of the resulting complexes in terms of their polynuclear nature.

## Results and Discussion

The ligands employed provide several coordination approaches as a function of the substitution pattern of the phenyl ring. Thus, only **a**, **c**, **d** and **f** have available aromatic $sp^2$ carbon atoms suitable for metallation, as well as MeO, Me and OH substituents liable to carbon–metal and oxygen–metal bond formation. On the other hand, **b** and **e** may bind to the metal only through the MeO or OH groups; accordingly, different alternatives of palladation were found. Hence, in **a** the metal atom was found to be bonded exclusively through the C-6 atom, with no sign of metallation of the C-2 methoxy group, resulting in the formation of a five-membered palladated ring. For **b** and **c**, either the C-2 Me group or the C-6 Me group was metallated to render a six-membered palladated ring in each case. Metallation of the C-6 carbon atom in ligand **c** was not observed, quite possibly because of the steric hindrance imposed by the neighbouring C-5 Me group. The reaction of ligand **d** with palladium acetate provided a mixture of products, one rendering metallation at the aromatic C-6 atom, and another one at the aliphatic C-2 Me group, yielding $–CH_2–$Pd bond formation. Most outstanding for the tetranuclear structure of the **d** species was that, as opposed to the [*C*,*N*,*S*] or [*C*,*N*,*O*] tetramers previously reported where the four cyclometallated moieties were identical, the present case poses an unprecedented example of a tetranuclear structure with two distinct palladated groups having five and six-membered metallated rings. As for **e** and **f**, *C*-metallation was not accomplished in any instance; the deprotonation of both phenoxy groups favoured the coordination of the ligands as [*O*,*N*,*O*]. In all the cases depicted above the resulting products after palladation of the ligands were tetranuclear compounds, irrespective of the metallated atom, including the [*O*,*N*,*O*] bonded ligands.

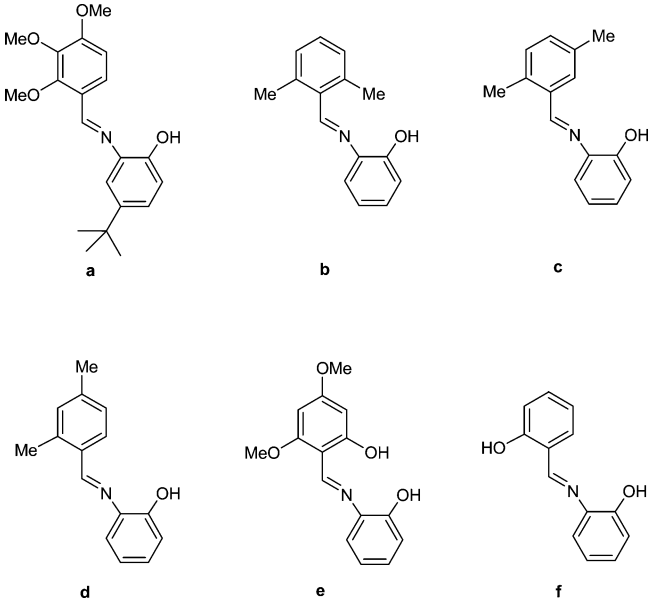


For the convenience of the reader the compounds and reactions are shown in Schemes 1, 2, 3 and 4. The compounds described in this paper were characterized by elemental analysis (C, H, N), by IR and $^1H$, $^{31}P\{^1H\}$ NMR spectroscopy, and, in part, by FAB mass spectrometry and single-crystal X-ray diffraction (Experimental Section).

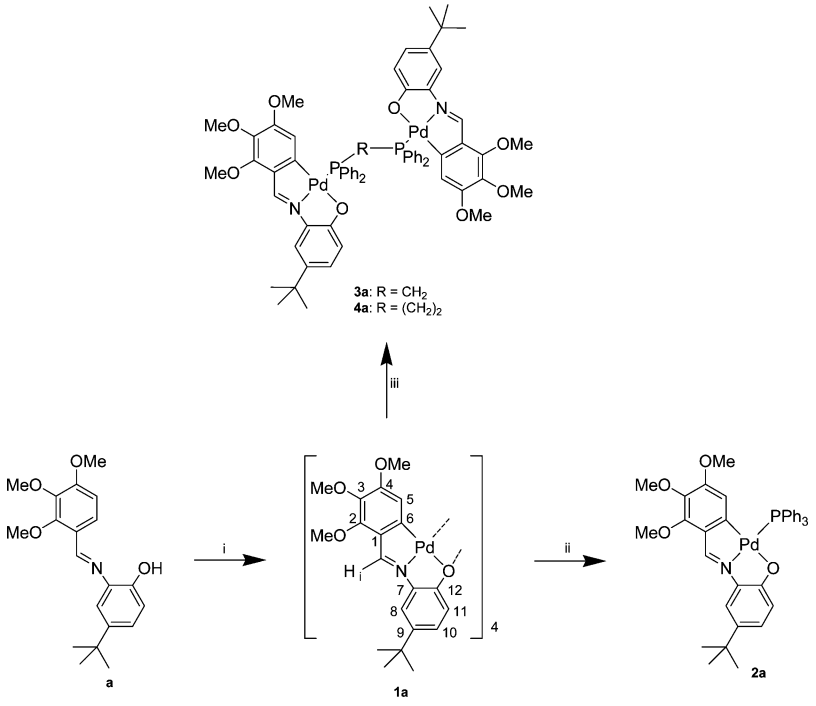


Scheme 1. (i) $Pd(AcO)_2$, (toluene); (ii) $PPh_3$ (acetone, 1:4 molar ratio); (iii) diphosphane (acetone, 1:2 molar ratio).

 © 2007 Wiley-VCH Verlag GmbH & Co. KGaA, Weinheim 

The reaction of **a** with palladium(II) acetate in toluene at 60 °C gave [Pd{2,3,4-$(MeO)_3C_6HC(H)$=N(2-O-5-$t$Bu$C_6H_3$)}]$_4$ (**1a**) as an air-stable solid, which was fully characterized. The IR spectrum showed the shift of the ν(C=N) stretch toward lower wavenumbers from the free ligand value, because of nitrogen coordination of the imine,[42,43] and the absence of the ν(O–H) stretch, as compared to the ligand (3427 cm$^{-1}$), in accordance with loss of the –OH proton. In the $^1$H NMR spectrum the *H*C=N and 5-H resonances were high-field shifted, as compared to the uncoordinated ligand, by 1.43 and 0.9 ppm, respectively; the low $\delta$ values in these cases were due to the structure of the complexes, which puts the *H*C=N and 5-H protons in the proximity of the shielding zone of the phenyl rings of a neighbouring metallated ligand.[32,33,37,39] Likewise, absence of the O*H* resonance in the $^1$H NMR spectrum confirmed deprotonation.

The FAB mass spectra showed the cluster of peaks characteristic of the [MH]$^+$ fragment centred at 1792 uma; the isotopic pattern was in good agreement with the tetrameric formulation.

### Crystal Structure of 1a

Suitable crystals were grown by slowly evaporating chloroform from a solution. Crystal data are given in Table 1. The ORTEP illustration of complex **1a**·$H_2O$ is shown in Figure 1. The core of the tetrameric molecule consists of an eight-membered ring of alternating palladium and oxygen atoms. Each palladium atom is bonded to the ligand through an aryl carbon, a C=N nitrogen, and a phenoxy oxygen atom, and also to a bridging oxygen atom of a neighbouring cyclometallated ligand monomer, in a slightly distorted square-planar arrangement. The mean deviations from the least-squares plane are: Pd1, C1, N1, O1, O9, 0.0215 Å; Pd2, C21, N2, O5, O13, 0.0208 Å; Pd3, C41, N3, O5, O9, 0.0166 Å; Pd4, C69, N4, O1, O13, 0.0300 Å. The bond lengths at palladium are within the expected values.[37–40] The resulting cluster has approximate $C_2$ symmetry; the $C_2$ axis is perpendicular to and bisects Pd1···Pd2 and Pd3···Pd4. The Pd1···Pd2 and Pd3···Pd4 distances of 3.378(1) and 3.412(1) Å, respectively, preclude any Pd–Pd interactions. Two of the quasi-planar Pd ligand units are parallel and almost orthogonal to the other two parallel monomer moieties.

Treatment of **1a** with triphenylphosphane or diphosphanes (dppm, dppe) gave the mononuclear [Pd{2,3,4-$(MeO)_3$-$C_6HC(H)$=N(2-O-5-$t$Bu$C_6H_3$)}($PPh_3$)] (**2a**) or dinuclear [{Pd(2,3,4-{MeO}$_3C_6HC${H}=N{2-O-5-$t$Bu$C_6H_3$})}$_2$(μ-$PPh_2CH_2PPh_2$)] (**3a**) and [{Pd(2,3,4-{MeO}$_3C_6HC${H}=N{2-O-5-$t$Bu$C_6H_3$})}$_2${μ-$PPh_2(CH_2)_2PPh_2$}] (**4a**) species, as air-stable solids, which were fully characterized (Experimental Section), with opening of the polynuclear structure after P–$O_{bridging}$ bond cleavage; the Pd–$O_{chelating}$ bond remained intact in all cases. The $^1$H NMR spectrum of **2a** showed the resonances of the 5-H and *H*C=N protons as doublets, coupled to the $^{31}$P nucleus of the phosphane ligand ($J_{H,P}$ = 3.4 and 10.7 Hz, respectively), and the $^{31}$P{$^1$H} NMR spectrum showed the phosphorus resonance as a singlet at $\delta$ = 34.2 ppm; these findings were in agreement with an arrangement in which the phosphorus atom is *trans* to the nitrogen atom.[44–47] The *H*C=N proton resonance, at $\delta$ = 8.14 ppm, showed a smaller high-field shift than that in compound **1a**, as compared to the free ligand, in agreement with the opening of the polynuclear structure.[39] Only one singlet was observed in the $^{31}$P{$^1$H} NMR spectra of **3a** and **4a** for the two equivalent phosphorus nuclei.

The reaction of **b** and **c** with palladium(II) acetate in toluene at 60 °C gave the tetranuclear complexes [Pd{6-Me-2-$CH_2C_6H_3C(H)$=N(2-$OC_6H_4$)}]$_4$ (**1b**) and [Pd{5-Me-2-

Table 1. Selected bond lengths [Å] and angles [°] for complex **1a**.

| | | | |
|---|---|---|---|
| Pd1–C1 | 1.958(14) | Pd3–C41 | 1.966(13) |
| Pd1–N1 | 1.967(10) | Pd3–N3 | 1.953(10) |
| Pd1–O1 | 2.144(9) | Pd3–O5 | 2.047(8) |
| Pd1–O9 | 2.045(8) | Pd3–O9 | 2.134(8) |
| Pd2–C21 | 1.965(13) | Pd4–C61 | 1.953(13) |
| Pd2–N2 | 1.951(10) | Pd4–N4 | 1.961(10) |
| Pd2–O5 | 2.122(8) | Pd4–O1 | 2.034(8) |
| Pd2–O13 | 2.052(9) | Pd4–O13 | 2.138(9) |
| Pd1–Pd2 | 3.3776(14) | Pd3–Pd4 | 3.4120(14) |
| C1–Pd1–N1 | 82.6(6) | N3–Pd3–C41 | 82.4(5) |
| C1–Pd1–O9 | 96.6(5) | C41–Pd3–O5 | 96.8(4) |
| N1–Pd1–O1 | 81.6(4) | N3–Pd3–O9 | 81.8(4) |
| O9–Pd1–O1 | 99.3(3) | O5–Pd3–O9 | 99.1(3) |
| C21–Pd2–N2 | 82.8(5) | C61–Pd4–N4 | 82.2(5) |
| C21–Pd2–O13 | 96.8(5) | C61–Pd4–O1 | 96.0(5) |
| N2–Pd2–O5 | 81.5(4) | N4–Pd4–O13 | 81.7(4) |
| O13–Pd2–O5 | 99.0(3) | O1–Pd4–O13 | 100.0(3) |
| Pd4–O1–Pd1 | 115.4(4) | Pd3–O5–Pd2 | 116.0(4) |
| Pd1–O9–Pd3 | 119.0(4) | Pd2–O13–Pd4 | 114.5(4) |

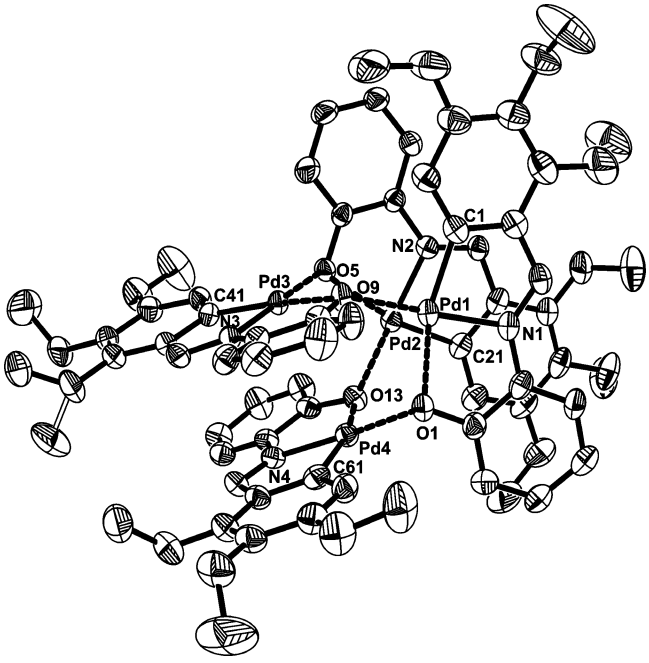


Figure 1. Molecular structure of [Pd{2,3,4-$(MeO)_3C_6HC(H)$=N(2-O-5-$t$Bu$C_6H_3$)}]$_4$ (**1a**). $t$Bu groups have been omitted for clarity. Ellipsoids drawn at 40% level.

 © 2007 Wiley-VCH Verlag GmbH & Co. KGaA, Weinheim 

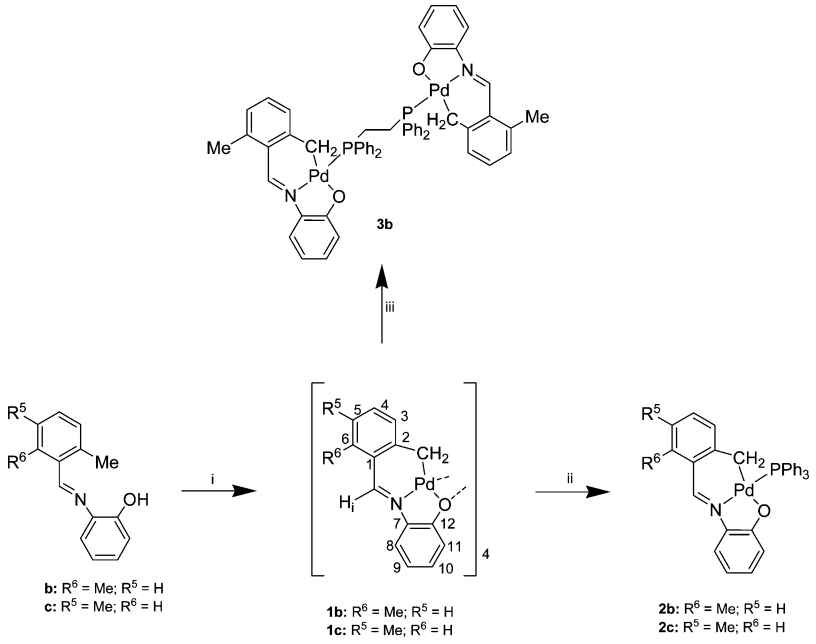


Scheme 2. (i) $Pd(AcO)_2$, (toluene); (ii) $PPh_3$ (acetone, 1:4 molar ratio); (iii) diphosphane (acetone, 1:2 molar ratio).

$CH_2C_6H_3C(H)=N(2\text{-}OC_6H_4)\}]_4$ (**1c**), respectively, as air-stable solids which were fully characterized (Experimental Section). Bonding of the metal was attained through a methyl group in both cases; the integration for the multiplet signals in the $^1H$ NMR spectrum of **1c** showed that the C-6 atom was not metallated. The spectroscopic data was in agreement with nitrogen coordination of the C=N group and deprotonation of the phenoxy group, vide supra (Scheme 2, see the Experimental Section). The resonances at $\delta \approx 3.5$ ppm and $\delta \approx 2.5$ ppm were assigned to the AB system of the two nonequivalent methylene protons ($J_{H,H}$ = 13.6 and 14.1 Hz for **1b** and **1c**, respectively). Their diastereotopic nature follows from the tetrameric structure of the complex, which renders both methylene protons, on either side of the metallated moiety, magnetically nonequivalent (see the crystal structure of **1c**). The singlet resonance at $\delta$ = 2.28 ppm (**1b**) and $\delta$ = 2.44 ppm (**1c**) were assigned to the nonmetallated methyl groups. An interesting feature in the $^1H$ NMR spectrum of **1c** is the presence of weak signals, four low-intensity doublets ascribed to the 11-H and $CH_2$ protons were identified, which could be indicative of the presence of other species in solution. However, we were unable to isolate the minor components of the mixture by column chromatography or by any other methods. The $^1H$ NMR spectrum of **1c** recorded at 323 K displayed the same weak signals with no appreciable difference in either the chemical shift or in the relative intensities. When **1c** was treated with triphenylphosphane to give the mononuclear complex **2c**, vide infra, only the signals corresponding to this complex appeared in its spectrum; this seems to suggest that the weak resonances mentioned above could be due to a different grouping of the cyclometallated monomer fragments in the polynuclear structure, which when cleaved only yields **2c** in solution. The presence of weak and poorly resolved signals has been observed earlier in a similar complex.[37]

The synthesis of **1c** is one of the rare examples where activation of an aliphatic carbon, rather than an aromatic carbon, is preferred for metallation.[15–19] This is particularly interesting because activation of the aliphatic carbon implies the formation of a six-membered chelate ring as opposed to the more stable five-membered one.

## Crystal Structure of 1c

Suitable crystals were grown by slowly evaporating chloroform from a solution. Crystal data are given in Table 2. The ORTEP illustration of complex **1c** is shown in Figure 2. Compound **1c** shows as tetranuclear structure with a $Pd_4O_4$ core similar to that described for **1a**; the most noticeable difference being the metallated carbon, which in this case was an $sp^3$ $CH_2$ carbon as opposed to the aromatic $sp^2$ carbon atom in **1a**. The coordination geometry about the palladium atoms is slightly distorted square-planar. The mean deviations from the least-squares plane are: Pd1, C14, N1, O1, O2, 0.0271 Å; Pd2, C34, N2, O2, O1#1, 0.0342 Å. The bond lengths and angles are in the range of those previously reported.[16,18,37–40] Another central feature of this complex is the planar disposition of the six-membered cyclometallated ring.

Several structures of cyclometallated complexes derived from Schiff bases in which the ligand is coordinated through a $CH_2$ carbon have been described previously; however, with the exception of a recent example reported by us,[48] in the remaining cases the six-membered cyclo-

 © 2007 Wiley-VCH Verlag GmbH & Co. KGaA, Weinheim 

Table 2. Selected bond lengths [Å] and angles [°] for complex **1c**.

| | | | |
|---|---|---|---|
| Pd1–C14 | 1.985(9) | Pd2–C34 | 1.997(10) |
| Pd1–N1 | 1.976(6) | Pd2–N2 | 1.967(7) |
| Pd1–O1 | 2.123(5) | Pd2–O2 | 2.124(5) |
| Pd1–O2 | 2.077(6) | Pd2–O1#1 | 2.057(6) |
| Pd1–Pd1#1 | 3.2441(12) | Pd2–Pd2#1 | 3.2241(12) |
| N1–Pd1–C14 | 95.1(3) | N2–Pd2–C34 | 95.3(4) |
| N1–Pd1–O1 | 82.1(2) | N2–Pd2–O2 | 82.0(2) |
| C14–Pd1–O2 | 89.6(3) | C34–Pd2–O1#1 | 88.8(3) |
| O2–Pd1–O1 | 93.2(2) | O1#1–Pd2–O2 | 93.9(2) |
| Pd1–O2–Pd2 | 119.3(3) | Pd2#1–O1–Pd1 | 120.3(3) |

Symmetry transformations used to generate equivalent atoms: # 1 – *x* – 1/2, –*y* + 1/2, *z*

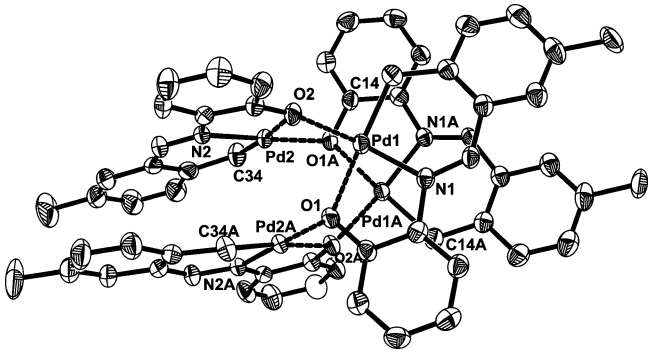


Figure 2. Molecular structure of [Pd{5-Me-2-$CH_2C_6H_3C(H)$=N(2-$OC_6H_4$)}]$_4$ (**1c**). Ellipsoids drawn at the 40% level.

metallated ring showed a nonplanar geometry with a boat-like structure.[16,18,49–53] We believe that in **1c** the tetranuclear structure brings close two of the cyclometallated ligands, thus imposing planarity of the ring in order to avoid mutual steric repulsion.

Treatment of **1b** and **1c** with triphenylphosphane yielded the mononuclear complexes **2b** and **2c**, respectively, upon cleavage of the P–$O_{bridging}$ bond. The $^1$H NMR spectra showed a doublet resonance assigned to the two equivalent $CH_2$ protons, consequent on splitting of the tetranuclear structure, coupled to the $^{31}$P nucleus, $\delta$ = 2.96 ppm ($^3J_{P,H}$ = 5.8 Hz) and $\delta$ = 2.93 ppm ($^3J_{P,H}$ = 5.8 Hz) for **2b** and **2c**, respectively.

The reaction of **1b** with the tertiary diphosphane $Ph_2P(CH_2)_2PPh_2$ (dppe) gave the dinuclear cyclometallated complex, [{Pd(6-Me-2-$CH_2C_6H_3C${H}=N{2-$OC_6H_4$})}$_2${μ-$PPh_2(CH_2)_2PPh_2$}] (**3b**), which was fully characterized. The $^1$H NMR spectrum showed only one set of signals for the two cyclometallated moieties, and a singlet at $\delta$ = 33.2 ppm in the $^{31}$P{$^1$H} NMR spectrum was assigned to the two equivalent phosphorus nuclei.

Treatment of **d** with palladium(II) acetate, under the same conditions as those used for the synthesis of **1a**–**1c**, yielded a mixture of isomers, [Pd{4-Me-2-$CH_2C_6H_3C$-(H)=N(2-$OC_6H_4$)}]$_n$ and [Pd{2,4-$(Me)_2C_6H_2C$(H)=N(2-$OC_6H_4$)}]$_{4-n}$ ($n$ = 0–4), featuring dissimilar cyclometallated units arising from the different metallation site chosen by the metal: aromatic sp$^2$ phenyl carbon atoms or aliphatic sp$^3$ methyl carbon atoms. The $^1$H NMR spectrum in $CDCl_3$ showed extended overlapping of the signals as expected for a complex mixture, as an outcome of which only five partially overlapped doublets, of the ten required, were assigned to the $CH_2$ protons at $\delta \approx$ 3.5–4.0 ppm. The signals corresponded to the isomers bearing a metallated methyl group, [Pd{4-Me-2-$CH_2C_6H_3C$(H)=N(2-$OC_6H_4$)}]$_n$[Pd{2,4-$(Me)_2C_6H_2C$(H)=N(2-$OC_6H_4$)}]$_{4-n}$ ($n$ = 1, 3, 4) and two isomers with $n$ = 2, depending on whether the two cyclometallated monomers [Pd{4-Me-2-$CH_2C_6H_3C$(H)=N(2-$OC_6H_4$)}] were opposite or adjacent in the tetranuclear arrangement (a sixth isomer is possible when metallation is through the C-6 carbon atom: [Pd{2,4-$(Me)_2C_6H_2C$-(H)=N(2-$OC_6H_4$)}($PPh_3$)]$_4$). Surprisingly, the $^1$H NMR spectrum recorded in a donor solvent such as [$D_6$]dmso showed two singlet signals at $\delta$ = 8.82 ppm and $\delta$ = 8.41 ppm assigned to two chemically different *H*C=N protons, putting forward the existence of only two species in the solution in the aftermath of the tetranuclear structure break-up caused by coordination of the solvent, which yielded the mononuclear fragments [Pd{4-Me-2-$CH_2C_6$-$H_3C$(H)=N(2-$OC_6H_4$)}([$D_6$]dmso)], **1d**(dmso), and [Pd{2,4-$(Me)_2C_6H_2C$(H)=N(2-$OC_6H_4$)}([$D_6$]dmso)], **1d′**(dmso), with C(sp$^3$)–Pd and C(sp$^2$)–Pd bonds, respectively (see Scheme 3). Hence, only one singlet was observed for the $CH_2$ protons at 3.26 ppm, as opposed to the AB system in the tetranuclear structure, vide supra. The relative molar ratio of the complexes in solution was 1:0.5 [**1d**(dmso)/**1d′**(dmso)]. Regardless of the reaction time and temperature used in the synthesis, the final relative molar ratio remained unchanged.

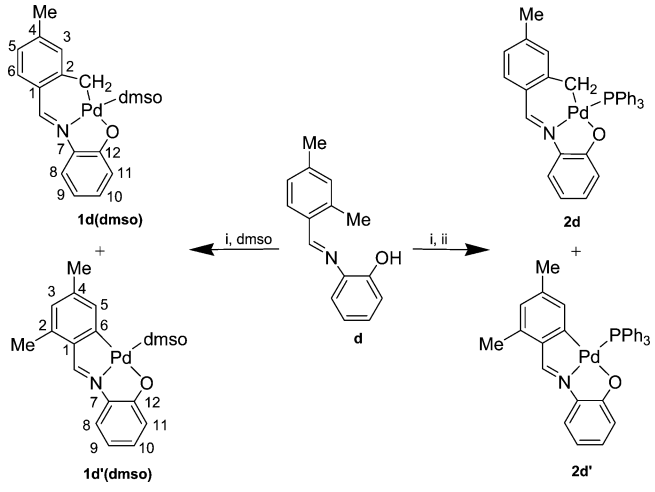


Scheme 3. (i) $Pd(AcO)_2$, (toluene); (ii) $PPh_3$ (acetone, 1:4 molar ratio).

We suggest that in nondonor solvents such as chloroform the [Pd{4-Me-2-$CH_2C_6H_3C$(H)=N(2-$OC_6H_4$)}] and [Pd{2,4-$(Me)_2C_6H_2C$(H)=N(2-$OC_6H_4$)}] building blocks were randomly arranged into tetranuclear moieties. Therefore, four isomers were present in the solution (vide supra), in addition to the two "pure" complexes [Pd{4-Me-2-$CH_2C_6H_3C$(H)=N(2-$OC_6H_4$)}]$_4$ and [Pd{2,4-$(Me)_2C_6H_2C$-(H)=N(2-$OC_6H_4$)}]$_4$. However, when the mixture was dissolved in a donor solvent the tetranuclear structure was cleaved, and the two distinct mononuclear moieties could

 © 2007 Wiley-VCH Verlag GmbH & Co. KGaA, Weinheim 

be isolated. Another approach to the separation of the mononuclear isomers was treatment of the complex mixture with triphenylphosphane in acetone, which yielded complexes [Pd{4-Me-2-$CH_2C_6H_3C(H)=N(2\text{-}OC_6H_4)$}$(PPh_3)$] (**2d**) and [Pd{2,4-$(Me)_2C_6H_2C(H)=N(2\text{-}OC_6H_4)$}$(PPh_3)$] (**2d′**), which were fully characterized (Experimental Section). The above-mentioned assumption was confirmed by the crystal structure of one of the isomers.

### Crystal Structure of the Mixture of [Pd{4-Me-2-$CH_2C_6H_3C(H)=N(2\text{-}OC_6H_4)$}]$_3$[Pd{2,4-$(Me)_2$-$C_6H_2C(H)=N(2\text{-}OC_6H_4)$}]

Crystal data are given in Table 3, and the ORTEP illustration is shown in Figure 3. A single crystal was isolated from a chloroform solution of the mixture of isomers and its resolved crystal and molecular structure showed the characteristic tetranuclear arrangement described for **1a** and **1c** bearing a central $Pd_4O_4$ core. Each palladium atom was coordinated to the ligand **d** through the C=N nitrogen, and to two phenoxy oxygen atoms, one of the latter two pertaining to a neighbouring metallated unit. However, the fourth coordination position was occupied by the C46 aromatic carbon for the Pd3 atom and by the C67 methylene carbon atom for Pd4. The ligand coordinated to Pd1 was found to be disordered, the major component (70%) corresponded to a ligand coordinated through the C7A methylene carbon and the minor component through the C6B aromatic carbon. The ligand coordinated to Pd2 was also disordered (50% for each component) and coordinated through the C26B aromatic or the C27A aliphatic carbon atoms, respectively, for each component.

Table 3. Selected bond lengths [Å] and angles [°] for complex **1d/d′**.

| | | | |
|---|---|---|---|
| Pd1–C7A | 1.941(10) | Pd3–C46 | 1.948(5) |
| Pd1–N1 | 1.962(5) | Pd3–N3 | 1.954(4) |
| Pd1–C6B | 1.99(3) | Pd3–O1 | 2.067(4) |
| Pd1–O4 | 2.052(4) | Pd3–O3 | 2.142(4) |
| Pd1–O1 | 2.140(4) | Pd4–C67 | 1.976(6) |
| Pd2–C26B | 1.926(16) | Pd4–N4 | 1.978(5) |
| Pd2–N2 | 1.976(4) | Pd4–O2 | 2.063(4) |
| Pd2–C27A | 2.006(10) | Pd4–O4 | 2.124(4) |
| Pd2–O3 | 2.034(3) | | |
| Pd2–O2 | 2.136(4) | | |
| Pd1–Pd2 | 3.4385(9) | Pd3–Pd4 | 3.2368(9) |
| C7A–Pd1–N1 | 90.8(3) | C46–Pd3–N3 | 81.8(2) |
| N1–Pd1–C6B | 86.0(6) | C46–Pd3–O1 | 98.7(2) |
| C7A–Pd1–O4 | 92.3(3) | N3–Pd3–O3 | 80.93(15) |
| C6B–Pd1–O4 | 97.1(6) | O1–Pd3–O3 | 98.64(14) |
| N1–Pd1–O1 | 81.93(18) | C67–Pd4–N4 | 93.9(2) |
| O4–Pd1–O1 | 95.02(17) | C67–Pd4–O2 | 89.8(2) |
| C26B–Pd2–N2 | 75.7(5) | N4–Pd4–O4 | 82.40(18) |
| N2–Pd2–C27A | 96.4(3) | O2–Pd4–O4 | 93.96(15) |
| C26B–Pd2–O3 | 106.7(5) | Pd3–O1–Pd1 | 123.8(2) |
| C27A–Pd2–O3 | 86.3(3) | Pd4–O2–Pd2 | 119.15(19) |
| N2–Pd2–O2 | 81.65(18) | Pd2–O3–Pd3 | 116.79(17) |
| O3–Pd2–O2 | 95.74(15) | Pd1–O4–Pd4 | 115.5(2) |

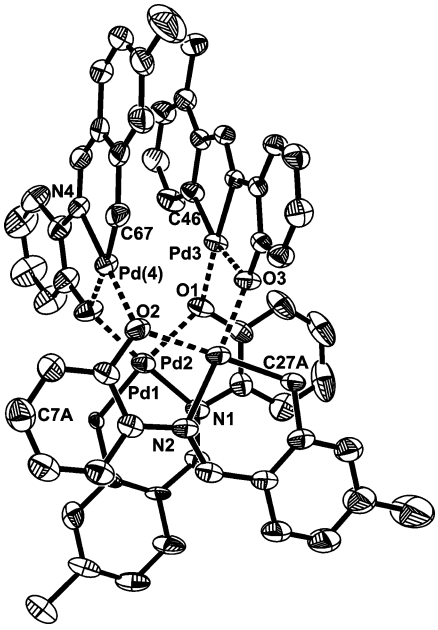


Figure 3. Molecular structure of the mixture of [Pd{4-Me-2-$CH_2C_6H_3C(H)=N(2\text{-}OC_6H_4)$}]$_n$ and [Pd{2,4-$(Me)_2C_6H_2C(H)=N(2\text{-}OC_6H_4)$}]$_{4-n}$ ($n$ = 3). Minor components of the disordered structure have been omitted for clarity. Ellipsoids drawn at the 40% level.

The reaction of **e** and **f** with palladium(II) acetate in toluene gave the non-cyclometallated complexes [Pd{2-O-4,6-$(MeO)_2C_6H_2C(H)=N(2\text{-}OC_6H_4)$}]$_4$ (**1e**) and [Pd{2-$OC_6H_4C(H)=N(2\text{-}OC_6H_4)$}]$_4$ (**1f**) as yellow and red air-stable solids, respectively. The IR spectroscopic data was in good agreement with nitrogen coordination of the imine,[42,43] and absence of the ν(O–H) bands, indicated double deprotonation of the ligands; the latter was confirmed by the absence of the O*H* resonances in the $^1$H NMR spectra. While the $^1$H NMR spectrum for **1e** showed a high-field shift of the *H*C=N resonance ($\delta$ = 1.19 ppm), similar to that observed for **1a**–**1c**, the *H*C=N resonance for

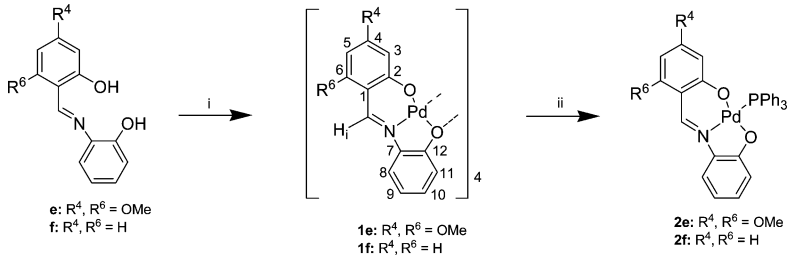


Scheme 4. (i) $Pd(AcO)_2$, (toluene); (ii) $PPh_3$ (acetone, 1:4 molar ratio).

 © 2007 Wiley-VCH Verlag GmbH & Co. KGaA, Weinheim 

**1f** appeared at $\delta$ = 8.94 ppm (shifted by 0.24 ppm), putting forward that the *H*C=N proton was not in the shielding area of the phenyl ring of an adjacent metallated ligand, probably because of cleavage of the tetranuclear structure caused by the coordination of [$D_6$]dmso used as the NMR solvent (vide supra). The IR, NMR and mass spectra of these complexes did not definitely establish their tetranuclear nature; nevertheless, resolution of the molecular structure of **1e** evidenced the tetrameric arrangement of the palladated fragments (Scheme 4).

Whereas for ligand **e** coordination is only possible through the phenoxy oxygen atoms, ligand **f** holds two coordination sites, the C-6 carbon and the phenoxy oxygen atoms; however, regardless of the reaction conditions used, the cyclometallated complex was not obtained in any case.

### Crystal Structure of 1e·2$CH_2Cl_2$

Suitable crystals were grown by slowly evaporating dichloromethane from a solution. Crystal data are given in Table 4, and the ORTEP illustration of complex **1e** is shown in Figure 4. The molecular structure of **1e**·2$CH_2Cl_2$ showed a [Pd(ligand)]$_4$ tetrameric structure, in which each palladium atom was coordinated in a slightly distorted square-planar geometry through the two deprotonated phenoxy oxygen atoms, the C=N nitrogen and an oxygen atom from another Pd(ligand) unit. The mean deviations from the least-squares plane are: Pd1, O1, O2, O14, N1, 0.0091 Å; Pd2, O5, O6, O10, N2, 0.0015 Å; Pd3, O2, O9, O10, N3, 0.0285 Å; Pd4, O6, O13, O14, N4, 0.0074 Å. The core was formed by an eight-membered $Pd_4O_4$ ring of similar geometry to those described above. Each palladium atom belongs to two fused five- and six-membered rings, which are planar, and coplanar with the two phenol rings. The four units are arranged as parallel pairs in two sets at nearly right angles. Bond lengths and angles are within the expected values.[16,18,37–40]

Table 4. Selected bond lengths [Å] and angles [°] for complex **1e**.

| | | | |
|---|---|---|---|
| Pd1–O1 | 1.965(4) | Pd3–O9 | 1.953(4) |
| Pd1–O2 | 2.013(4) | Pd3–O10 | 2.008(4) |
| Pd1–O14 | 2.074(4) | Pd3–O2 | 2.076(3) |
| Pd1–N1 | 1.940(4) | Pd3–N3 | 1.940(4) |
| Pd2–O5 | 1.953(4) | Pd4–O13 | 1.953(4) |
| Pd2–O6 | 1.999(3) | Pd4–O14 | 2.031(3) |
| Pd2–O10 | 2.068(4) | Pd4–O6 | 2.057(4) |
| Pd2–N2 | 1.940(4) | Pd4–N4 | 1.933(4) |
| Pd1–Pd2 | 3.0695(8) | Pd3–Pd4 | 3.1011(7) |
| N1–Pd1–O1 | 95.05(16 | N3–Pd3–O9 | 95.33(16) |
| N1–Pd1–O2 | 83.87(16) | N3–Pd3–O10 | 83.96(16) |
| O1–Pd1–O14 | 87.81(15) | O9–Pd3–O2 | 86.65(14) |
| O2–Pd1–O14 | 93.25(14) | O10–Pd3–O2 | 94.10(14) |
| N2–Pd2–O5 | 94.98(17) | N4–Pd4–O13 | 95.28(16) |
| N2–Pd2–O6 | 84.50(16) | N4–Pd4–O14 | 83.89(16) |
| O5–Pd2–O10 | 87.90(14) | O13–Pd4–O6 | 86.32(15) |
| O6–Pd2–O10 | 92.62(14) | O14–Pd4–O6 | 94.51(14) |
| Pd1–O2–Pd3 | 121.28(17) | Pd3–O10–Pd2 | 120.78(18) |
| Pd2–O6–Pd4 | 116.87(17) | Pd4–O14–Pd1 | 118.98(17) |

The reaction of **1e** and **1f** with triphenylphosphane yielded the mononuclear complexes [Pd{2-O-4,6-(MeO)$_2$-$C_6H_2C$(H)=N(2-$OC_6H_4$)}($PPh_3$)] (**2e**) and [Pd{2-$OC_6H_4$C-(H)=N(2-$OC_6H_4$)}($PPh_3$)] (**2f**) after cleavage of the tetranuclear structure, as air-stable solids, which were fully characterized. The $^{31}$P NMR spectroscopic data were in accordance with an arrangement in which the phosphorus atom is *trans* to the nitrogen atom. Contrary to the case of five-membered ring palladacycles, the 3-H protons and (in **2e**) the C-4 MeO group were not affected by shielding from the phosphane phenyl rings; expansion of the metallated ring to six members places these nuclei away form the appropriate shielding zone.

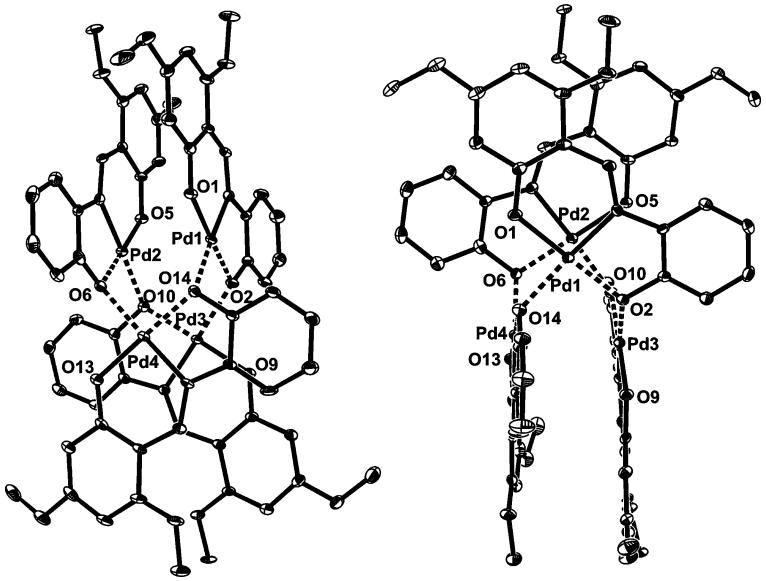


Figure 4. Molecular structure of [Pd{2-O-4,6-(MeO)$_2C_6H_2C$(H)=N(2-$OC_6H_4$)}]$_4$, (**1e**). Ellipsoids drawn at the 40% level.

 © 2007 Wiley-VCH Verlag GmbH & Co. KGaA, Weinheim 

## Conclusions

We have shown that Schiff base ligands derived from 2-aminophenol offer different bonding modes to palladium(II) because of the various donor atoms they possess, behaving as tridentate [*C*,*N*,*O*] or [*O*,*N*,*O*] ligands. In all cases, tetranuclear compounds were formed upon reaction of the ligand with the metal salt through metallation of a substituted phenyl ring. As with the tridentate [*C*,*N*,*S*] thiosemicarbazones, formation of the central eight-membered $Pd_4O_4$ core seems to favour tetranuclear clusters, as opposed to the dinuclear moieties obtained from didentate [*C*,*N*] Schiff bases. Where choice was possible, five-membered ring metallacycles were preferred over six-membered ones; nevertheless, the latter may be obtained when substituents hinder attack of the metal atom on the phenyl ring. In the case of ligand **d**, where metallation may proceed through a phenyl or a methyl carbon atom, mixed five- and six-membered palladated moieties build up the tetrameric structure, thus constituting an unprecedented example of a tetranuclear cyclopalladated compound.

## Experimental Section

**General Procedures:** Solvents were purified by standard methods.[54] Chemicals were reagent grade. The phosphanes $PPh_3$, $Ph_2PCH_2PPh_2$ (dppm) and $Ph_2P(CH_2)_2PPh_2$ (dppe) were purchased from Aldrich Chemie. Microanalyses were carried out with a Carlo Erba Elemental Analyzer, Model 1108. IR spectra were recorded by using Nujol mulls or KBr discs with a Perkin–Elmer 1330 and a Mattson spectrophotometer. NMR spectra were obtained in $CDCl_3$ solutions and referenced to $SiMe_4$ [$^1H$, or 85% $H_3PO_4$ $^{31}P\{^1H\}$]; they were recorded with a Bruker AC-2005 spectrometer. All chemical shifts were reported downfield from the standards. The FAB mass spectra were recorded by using a Quatro mass spectrometer with a Cs ion gun; 3-nitrobenzyl alcohol (3-NBA) was used as the matrix.

**Syntheses**

**2,3,4-$(MeO)_3C_6H_2C(H)=N[2-(OH)-5-tBuC_6H_3]$ (a):** 2,3,4-$(MeO)_3C_6H_2COH$ (1.000 g, 6.06 mmol) was added to a solution of 2-amino-4-*tert*-butylphenol (1.188 g, 6.06 mmol) in dry chloroform (50 $cm^3$). The solution was heated under reflux in a Dean–Stark apparatus for 4 h. After cooling to room temperature the chloroform was removed, and a brown solid was obtained. Yield: 1850 mg, 89%. $C_{20}H_{25}NO_4$ (343.18): calcd. C 69.9, H 7.3, N 4.1; found C 68.5, H 7.0, N 3.8. IR: $\tilde{\nu}$ = 3427 (m, $\nu_{O-H}$), 1589 (s, $\nu_{C=N}$) $cm^{-1}$. $^1H$ NMR (200 MHz, $CDCl_3$): $\delta$ = 1.13 (s, 9 H, *t*Bu), 3.92, 3.95, 4.02 (s, 9 H, MeO), 6.80 (d, $^3J_{H5,H6}$ = 8.3 Hz, 1 H, 5-H), 7.92 (d, $^3J_{H5,H6}$ = 8.3 Hz, 1 H, 6-H), 6.95 (d, $^2J_{H,H}$ = 8.3 Hz, 11 H), 7.4 (m, 2 H, 8-H, 10-H), 8.76 (s, 1 H, OH) (resonance taken from a spectrum recorded in [$D_6$]dmso), 8.97 (s, 1 H, $H_i$) ppm. FAB-MS: *m*/*z* = 344 $[MH]^+$.

Schiff base ligands **b**–**d** were prepared similarly as brown solids.

**2,6-$(Me)_2C_6H_3C(H)=N[2-(OH)C_6H_4]$ (b):** Yield: 1214 mg, 89%. $C_{15}H_{15}NO$ (225.12): calcd. C 79.9, H 6.7, N 6.2; found C 68.5, H 7.0, N 3.8. IR: $\tilde{\nu}$ = 3396 (m, $\nu_{O-H}$), 1621 (s, $\nu_{C=N}$) $cm^{-1}$. $^1H$ NMR (200 MHz, $CDCl_3$) $\delta$ = 2.64 (s, 6 H, Me), 7.2 (m, 7 H), 9.1 (s, 1 H, $H_i$), 10.8 (br, 1 H, OH) ppm.

**2,5-$(Me)_2C_6H_3C(H)=N[2-(OH)C_6H_4]$ (c):** Yield: 1188 mg, 88%. $C_{15}H_{15}NO$ (225.12): calcd. C 79.9, H 6.7, N 6.2; found C 79.8, H 6.7, N 6.1. IR: $\tilde{\nu}$ = 3375 (s, $\nu_{O-H}$), 1608 (sh, $\nu_{C=N}$) $cm^{-1}$. $^1H$ NMR (200 MHz, $CDCl_3$): $\delta$ = 2.41, 2.59 (s, 6 H, Me), 6.95 (dt, $^3J_{H,H}$ = 7.5 Hz, $^4J_{H,H}$ = 1.2 Hz, 1 H), 7.06 (dd, $^3J_{H,H}$ = 8.0 Hz, $^4J_{H,H}$ = 1.2 Hz, 1 H), 7.3 (m, 5 H), 7.91 (s, 6-H), 8.9 (s, 1 H, $H_i$), 9.8 (br, 1 H, OH) ppm.

**2,4-$(Me)_2C_6H_3C(H)=N[2-(OH)C_6H_4]$ (d):** Yield: 1589 mg, 97%. $C_{15}H_{15}NO$ (225.12): calcd. C 79.9, H 6.7, N 6.2; found C 79.4, H 6.4, N 6.1. IR: $\tilde{\nu}$ = 3043 (m, $\nu_{O-H}$), 1619 (s, $\nu_{C=N}$) $cm^{-1}$. $^1H$ NMR (200 MHz, $CDCl_3$): $\delta$ = 2.40, 2.61 (s, 6 H, Me), 6.5 (br, 1 H, OH), 6.94 (t, $^3J_{H,H}$ = 7.6 Hz, 1 H), 7.3 (m, 5 H), 7.91 (d, $^3J_{H6,H5}$ = 7.8 Hz, 1 H, 6-H), 8.97 (s, 1 H, $H_i$) ppm.

Schiff base **e** was prepared similarly as a yellow solid.

**2-(OH)-4,6-$(MeO)_2C_6H_2C(H)=N[2-(OH)C_6H_4]$ (e):** Yield: 1523 mg, 93%. $C_{15}H_{15}NO_4$ (273.10): calcd. C 65.9, H 5.5, N 5.1; found C 65.8, H 5.5, N 5.1. IR: $\tilde{\nu}$ = 3430 (m, $\nu_{O-H}$), 3385 (sh), 1625 (sh, m, $\nu_{C=N}$) $cm^{-1}$. $^1H$ NMR (200 MHz, $CDCl_3$): $\delta$ = 3.85, 3.84 (s, 6 H, MeO), 5.6 (br, 1 H, OH), 5.9, 6.1 (s, 2 H, 3-H, 5-H), 7.0 (m, 4 H), 8.9 (s, 1 H, $H_i$), 10.8 (br, 1 H, OH) ppm.

Schiff base **f** was prepared similarly as a red solid.

**2-$(OH)C_6H_4C(H)=N[2-(OH)C_6H_4]$ (f):** Yield: 1176 mg, 92%. $C_{13}H_{11}NO_2$ (213.08): calcd. C 73.2, H 5.2, N 6.6; found C 73.1, H 5.0, N 6.3. IR: $\tilde{\nu}$ = 3500 (m, $\nu_{O-H}$), 1630 (m, $\nu_{C=N}$) $cm^{-1}$. $^1H$ NMR (200 MHz, $CDCl_3$): $\delta$ = 5.7 (br, 1 H, OH), 7.2 (m, 8 H), 8.7 (s, 1 H, $H_i$), 12.2 (br, 1 H, OH) ppm.

**$[Pd\{2,3,4-(MeO)_3C_6HC(H)=N(2-O-5-tBuC_6H_3)\}]_4$ (1a):** A pressure tube containing 2,3,4-$(MeO)_3C_6H_2C(H)=N[2-(OH)-5-tBuC_6H_3]$ (0.456 mg, 1.33 mmol), palladium acetate (0.300 g, 1.33 mmol) and dry toluene (20 $cm^3$) was sealed under argon. The resulting mixture was heated at 60 °C for 24 h. After cooling to room temperature the solution was filtered through Celite to remove the small amount of black palladium formed. The solvent was removed under vacuum to give a red oil, which was recrystallized from dichloromethane/hexane to give the desired product as a red solid. Yield: 1191 mg, 50%. $C_{80}H_{92}N_4O_{16}Pd_4$ (1791.28): calcd. C 53.6, H 5.2, N 3.1; found C 53.0, H 5.1, N 3.1. IR: $\tilde{\nu}$ = 1571 (sh, m, $\nu_{C=N}$) $cm^{-1}$. $^1H$ NMR (200 MHz, $CDCl_3$): $\delta$ = 1.24 (s, 9 H, *t*Bu), 3.38, 3.81, 4.03 (s, 9 H, MeO), 5.81 (s, 1 H, 5-H), 6.75 (d, $^4J_{H8,H10}$ = 2.2 Hz, 1 H, 8-H), 6.99 (dd, $^3J_{H10,H11}$ = 8.8 Hz, $^4J_{H8,H10}$ = 2.2 Hz, 1 H, 10-H), 7.35 (d, 1 H, 11-H), 7.54 (s, 1 H, $H_i$) ppm. FAB-MS: *m*/*z* = 1792 $[MH]^+$, 896 $[M/2]^+$.

Compound **1b** was prepared similarly as a brown solid.

**$[Pd\{6-Me-2-CH_2C_6H_3C(H)=N(2-OC_6H_4)\}]_4$ (1b):** Yield: 98 mg, 30%. $C_{60}H_{52}N_4O_4Pd_4$ (1318.75): calcd. C 54.4, H 4.3, N 4.2; found C 53.9, H 4.1, N 4.1. IR: $\tilde{\nu}$ = 1583 (s, $\nu_{C=N}$) $cm^{-1}$. $^1H$ NMR (200 MHz, $CDCl_3$): $\delta$ = 2.28 (s, 3 H, Me), 2.60, 3.49 (d, $J_{gem(H,H)}$ = 13.6 Hz, 2 H, -$CH_2$-), 6.51 (dt, $^3J_{H9,H8}$ = 8.3 Hz, $^3J_{H10,H9}$ = 7.2 Hz, $^4J_{H11,H9}$ = 1.3 Hz, 1 H, 9-H), 6.80 (d, $^3J_{H5,H4}$ = 7.6 Hz, 1 H, 5-H), 6.86 (m, 2 H, 8-H, 4-H), 7.04 (d, $^3J_{H4,H3}$ = 7.4 Hz, 1 H, 3-H), 7.5 (dt, $^3J_{H10,H9}$ = 7.2 Hz, $^3J_{H11,H10}$ = 8.3 Hz, $^4J_{H10,H8}$ = 1.3 Hz, 1 H, 10-H), 7.84 (dd, $^3J_{H11,H10}$ = 8.3 Hz, $^4J_{H11,H9}$ = 1.3 Hz, 1 H, 11-H), 8.13 (s, 1H, $H_i$) ppm. FAB-MS: *m*/*z* = 331 $[(M/4)H]^+$.

Compound **1c** was prepared similarly as a red solid.

**$[Pd\{5-Me-2-CH_2C_6H_3C(H)=N(2-OC_6H_4)\}]_4$ (1c):** Yield: 40 mg, 45%. $C_{60}H_{52}N_4O_4Pd_4$ (1318.75): calcd. C 54.4, H 4.3, N 4.2; found C 54.2, H 4.3, N 4.1. IR: $\tilde{\nu}$ = 1582 (s, $\nu_{C=N}$) $cm^{-1}$. $^1H$ NMR (200 MHz, $CDCl_3$): $\delta$ = 2.44 (s, 3 H, Me), 2.45 (d, $J_{gem(H,H)}$ = 14.1 Hz, 1 H, -$CH_2$-), 3.59 (d, $J_{gem(H,H)}$ = 14.1 Hz, 1 H, -$CH_2$-), 6.50 (dt, $^3J_{H9,H8}$ = 7.8 Hz, $^4J_{H11,H9}$ = 0.9 Hz, 1 H, 9-H), 6.8 (m, 3 H), 7.2 (m, 3 H), 7.13 (s, 1 H, $H_i$), 7.74 (dd, $^3J_{H11,H10}$ = 8.3 Hz, $^4J_{H11,H9}$ = 0.9 Hz, 1 H, 11-H) ppm.

 © 2007 Wiley-VCH Verlag GmbH & Co. KGaA, Weinheim 

**[Pd{4-Me-2-$CH_2C_6H_3C(H)=N(2-OC_6H_4)$}]$_n$[Pd{2,4-$(Me)_2C_6H_2C(H)=N(2-OC_6H_4)$}]$_{4-n}$ ($n$ = 0–4):** The mixture was prepared by following a procedure similar to that used for **1a**, but with reaction times of 5 h, 24 h and 3 d and reaction temperatures of 40, 60 and 80 °C. The components of the mixture could not be separated by column chromatography or by other methods. Yield: 30 mg, 30%. $C_{60}H_{52}N_4O_4Pd_4$ (1318.75): calcd. C 54.4, H 4.3, N 4.2; found C 54.3, H 4.3, N 4.0. IR: $\tilde{\nu}$ = 1598 (s, $\nu_{C=N}$) cm$^{-1}$. $^1$H NMR (200 MHz, $CDCl_3$): $\delta$ = 3.62 (d, $J_{gem(H,H)}$ = 13.5 Hz, 1 H, -$CH_2$-), 3.53 (d, $J_{gem(H,H)}$ = 14.0 Hz, 1 H, -$CH_2$-), 3.83 (d, $J_{gem(H,H)}$ = 13.0 Hz, 1 H, -$CH_2$-), 3.84 (d, $J_{gem(H,H)}$ = 14.0 Hz, 1 H, -$CH_2$-), 3.92 (d, $J_{gem(H,H)}$ = 13.7 Hz, 1 H, -$CH_2$-) ppm. $^1$H NMR (200 MHz, [D$_6$]dmso): $\delta$ = 2.14 (s, 3 H, Me), 2.34, 2.35 (s, 6 H, Me′), 3.26 (s, 2 H, -$CH_2$-), 8.41 (s, 1 H, H$_i$), 8.82 (s, 1 H, H$_i$) ppm.

Compound **1e** was prepared similarly as a yellow solid.

**[Pd{2-O-4,6-$(MeO)_2C_6H_2C(H)=N(2-OC_6H_4)$}]$_4$ (1e):** Yield: 117 mg, 75%. $C_{60}H_{52}N_4O_{16}Pd_4$ (1510.75): calcd. C 47.7, H 3.5, N 3.7; found C 47.5, H 3.4, N 3.5. IR: $\tilde{\nu}$ = 1612 (s, $\nu_{C=N}$) cm$^{-1}$. $^1$H NMR (200 MHz, $CDCl_3$): $\delta$ = 3.70, 3.82 (s, 6 H, MeO), 5.57, 5.73 (d, H5, $^4J_{H5,H3}$ = 1.9 Hz, 2 H, 3-H), 6.59 (t, $^3J_{H9,H8}$ = 7.5 Hz, 1 H, 9-H), 7.09 (m, 2 H, 8-H, 10-H), 7.71 (s, 1 H, H$_i$), 8.33 (d, $^3J_{H11,H10}$ = 8.3 Hz, 1 H, 11-H) ppm.

Compound **1f** was prepared similarly as a red solid. Different reaction times (5 h, 24 h and 5 d) were used with similar yields.

**[Pd{2-$OC_6H_4C(H)=N(2-OC_6H_4)$}]$_4$ (1f):** Yield: 118 mg, 86%. $C_{52}H_{36}N_4O_8Pd_4$ (1270.75): calcd. C 49.2, H 2.8, N 4.4; found C 48.9, H 2.8, N 4.3. IR: $\tilde{\nu}$ = 1609 (s, $\nu_{C=N}$) cm$^{-1}$. $^1$H NMR (200 MHz, [D$_6$]dmso): $\delta$ = 7.17 (m, $^3J_{H10,H11}$ = 8.3 Hz, $^3J_{H10,H9}$ = 7.0 Hz, $^4J_{H10,H8}$ = 1.3 Hz, 1 H, 10-H), 7.30 (m, $^3J_{H,H}$ = 8.0 Hz, $^3J_{H,H}$ = 6.8 Hz, $^4J_{H,H}$ = 1.3 Hz, 1 H), 7.34 (dd, H8, $^3J_{H9,H8}$ = 8.3 Hz, 1 H), 7.57 (dd, $^3J_{H,H}$ = 8.7 Hz, $^4J_{H,H}$ = 1.3 Hz, 1 H), 7.60 (m, $^4J_{H,H}$ = 1.3 Hz, 1 H, 9-H), 7.93 (m, $^3J_{H,H}$ = 8.6 Hz, $^3J_{H,H}$ = 6.8 Hz, $^4J_{H,H}$ = 1.8 Hz, 1 H), 8.18 (dd, $^3J_{H,H}$ = 8.0 Hz, $^4J_{H,H}$ = 1.8 Hz, 1 H), 8.33 (dd, 1 H, 11-H), 8.94 (1 H, H$_i$) ppm. FAB-MS: $m/z$ = 637 [M/2]$^+$.

**[Pd{2,3,4-$(MeO)_3C_6HC(H)=N(2-O-5-tBuC_6H_3)$}($PPh_3$)] (2a):** $PPh_3$ (6.99 mg, 0.026 mmol) was added to a suspension of **1a** (12 mg, 0.006 mmol) in acetone (15 cm$^3$). The mixture was stirred for 12 h, and the solvent was removed to give a violet solid, which was recrystallized from acetone/hexane. Yield: 15 mg, 80%. $C_{38}H_{38}NO_4PPd$ (710.11): calcd. C 64.3, H 5.4, N 1.9; found C 64.3, H 5.3, N 1.8. IR: $\tilde{\nu}$ = 1544 (s, $\nu_{C=N}$) cm$^{-1}$. $^1$H NMR (200 MHz, $CDCl_3$): $\delta$ = 1.27 (s, 9 H, *t*Bu), 2.92, 3.73, 3.98 (s, 9 H, MeO), 5.49 (d, $^4J_{H5,P}$ = 3.4 Hz, 1 H, 5-H), 6.45 (d, $^3J_{H10,H11}$ = 8.7 Hz, 1 H, 11-H), 6.96 (dd, $^3J_{H10,H11}$ = 8.7 Hz, $^4J_{H8,H10}$ = 1.9 Hz, 1 H, 10-H), 7.05 (d, $^4J_{H8,H10}$ = 1.9 Hz, 1 H, 8-H), 8.14 (d, $^4J_{H_i,P}$ = 10.7 Hz, 1 H, H$_i$) ppm. $^{31}$P{$^1$H} NMR (80.96 MHz, $CDCl_3$): $\delta$ = 34.2 (s) ppm.

Compounds **2b**–**2f** were prepared similarly as red or brown (**2b**) solids.

**[Pd{6-Me-2-$CH_2C_6H_3C(H)=N(2-OC_6H_4)$}($PPh_3$)] (2b):** Yield: 10 mg, 60%. $C_{33}H_{29}NOPPd$ (592.98): calcd. C 66.8, H 4.9, N 2.4; found C 66.5, H 4.7, N 2.3. IR: $\tilde{\nu}$ = 1581 (s, $\nu_{C=N}$) cm$^{-1}$. $^1$H NMR (200 MHz, $CDCl_3$): $\delta$ = 2.55 (s, 3 H, Me), 2.96 (d, $^3J_{CH_2,P}$ = 5.8 Hz, 2 H, -$CH_2$-), 6.43 (t, $^3J_{H10,H9}$ = 7.3 Hz, 1 H, 10-H), 6.52 (t, $^4J_{H5,CH_2}$ = 4.4 Hz, 1 H, 2-H), 6.92 (m, 3 H), 7.09 (t, $^3J_{H,H}$ = 7.8 Hz, 1 H), 8.69 (d, $^4J_{H_i,P}$ = 12.7 Hz, 1 H, H$_i$) ppm. $^{31}$P{$^1$H} NMR (80.96 MHz, $CDCl_3$): $\delta$ = 33.4 (s) ppm.

**[Pd{5-Me-2-$CH_2C_6H_3C(H)=N(2-OC_6H_4)$}($PPh_3$)] (2c):** Yield: 29 mg, 60%. $C_{33}H_{29}NOPPd$ (592.98): calcd. C 66.8, H 4.9, N 2.4; found C 66.4, H 4.8, N 2.3. IR: $\tilde{\nu}$ = 1581 (s, $\nu_{C=N}$) cm$^{-1}$. $^1$H NMR (200 MHz, $CDCl_3$): $\delta$ = 2.28 (s, 3 H, Me), 2.93 (d, $^3J_{CH_2,P}$ = 5.8 Hz, 2 H, -$CH_2$-), 6.43 (t, $^3J_{H10,H9}$ = 7.5 Hz, 1 H, 10-H), 6.66 (d, $^3J_{H3,H4}$ = 7.8 Hz, 1 H, 3-H), 6.89 (m, 2 H, 4-H, 11-H), 7.09 (t, $^3J_{H9,H8}$ = 7.5 Hz, $^4J_{H11,H9}$ = 1.5 Hz, 1 H, 9-H), 7.25 (d, $^3J_{H9,H8}$ = 7.5 Hz, 1 H, 8-H), 7.27 (s, 1 H, 6-H), 8.32 (d, $^4J_{H_i,P}$ = 12.7 Hz, 1 H, H$_i$) ppm. $^{31}$P{$^1$H} NMR (80.96 MHz, $CDCl_3$): $\delta$ = 33.8 (s) ppm. FAB-MS: $m/z$ = 592 [M]$^+$.

Compounds **2d** and **2d′** were prepared by a similar procedure to the one described for **2a** using as starting material the mixture of isomers **1d/1d′**. The compounds were obtained as a mixture [in a 1:0.5 (**2d/2d′**) molar ratio] from which the pure compounds could not be isolated by column chromatography or by other methods.

**[Pd{4-Me-2-$CH_2C_6H_3C(H)=N(2-OC_6H_4)$}($PPh_3$)] (2d) and [Pd{2,4-$(Me)_2C_6H_2C(H)=N(2-OC_6H_4)$}($PPh_3$)] (2d′):** Yield: 23 mg, 50%. $C_{33}H_{29}NOPPd$ (592.98): calcd. C 66.8, H 4.9, N 2.4; found C 66.3, H 4.7, N 2.3. IR: $\tilde{\nu}$ = 1581 (s, $\nu_{C=N}$) cm$^{-1}$. $^1$H NMR (200 MHz, $CDCl_3$): $\delta$ = 2.67 (s, 6 H, Me′), 2.25 (s, 3 H, Me), 2.93 (d, $^3J_{CH_2,P}$ = 5.8 Hz, 2 H, -$CH_2$-), 5.67 (d, $^4J_{H5,P}$ = 3.4 Hz, 1 H, 5′-H), 8.20 (d, $^4J_{H_i,P}$ = 10.3 Hz, 1 H, H$_i$′), 8.32 (d, $^4J_{H_i,P}$ = 12.7 Hz, 1 H, H$_i$) ppm. $^{31}$P{$^1$H} NMR (80.96 MHz, $CDCl_3$): $\delta$ = 34.6 (**2d′**), 33.8 (s) (**2d**) ppm.

**[Pd{2-O-4,6-$(MeO)_2C_6H_2C(H)=N(2-OC_6H_4)$}($PPh_3$)] (2e):** Yield: 29 mg, 60%. $C_{33}H_{28}NO_4PPd$ (639.97): calcd. C 61.9, H 4.4, N 2.2; found C 61.5, H 4.1, N 2.0. IR: $\tilde{\nu}$ = 1611 (s, $\nu_{C=N}$) cm$^{-1}$. $^1$H NMR (200 MHz, $CDCl_3$): $\delta$ = 3.67, 3.88 (s, 6 H, MeO), 5.63, 5.78 (d, $^4J_{H5,H3}$ = 2.2 Hz, 2 H, 3-H, 5-H), 6.64 (t, $^3J_{H10,H9}$ = 7.5 Hz, 1 H, 10-H), 6.90 (d, $^3J_{H11,H10}$ = 7.5 Hz, 1 H, 11-H), 7.03 (t, 1 H, 9-H), 7.72 (d, $^3J_{H9,H8}$ = 8.3 Hz, 1 H, 8-H), 9.12 (d, $^4J_{H_i,P}$ = 18.1 Hz, 1 H, H$_i$) ppm. $^{31}$P{$^1$H} NMR (80.96 MHz, $CDCl_3$): $\delta$ = 23.4 (s) ppm. FAB-MS: $m/z$ = 639 [M]$^+$.

**[Pd{2-$OC_6H_4C(H)=N(2-OC_6H_4)$}($PPh_3$)] (2f):** Yield: 25 mg, 66%. $C_{31}H_{24}NO_2PPd$ (579.92): calcd. C 64.2, H 2.4, N 4.2; found C 64.3, H 2.3, N 4.0. IR: $\tilde{\nu}$ = 1603 (s, $\nu_{C=N}$) cm$^{-1}$. $^1$H NMR (200 MHz, $CDCl_3$): $\delta$ = 6.61 (d, $^3J_{H5,H4}$ = 8.5 Hz, 1 H, 5-H), 6.7 (m, 2 H, 3-H, 10-H), 6.92 (dd, $^3J_{H11,H10}$ = 8.3 Hz, $^3J_{H11,H9}$ = 1.2 Hz, 1 H, 11-H), 7.08 (dt, $^3J_{H10,H9}$ = 6.9 Hz, $^3J_{H9,H8}$ = 8.3 Hz, 1 H, 9-H), 7.22 (dt, $^3J_{H5,H4}$ = 8.6 Hz, $^3J_{H4,H3}$ = 6.8 Hz, $^3J_{H4,H2}$ = 1.8 Hz, 1 H, 4-H), 7.74 (dd, $^3J_{H9,H8}$ = 8.3 Hz, $^4J_{H10,H8}$ = 1.4 Hz, 1 H, 8-H), 8.61 (dd, $^4J_{H_i,P}$ = 17.1 Hz, 1 H, H$_i$) ppm. $^{31}$P{$^1$H} NMR (80.96 MHz, $CDCl_3$): $\delta$ = 23.3 (s) ppm. FAB-MS: $m/z$ = 579 [M]$^+$.

Compounds **3a** and **4a** were obtained as violet solids by a similar procedure, but with a 1:2 complex **1a**/ diphosphane molar ratio.

**[{Pd(2,3,4-{MeO}$_3$C$_6$HC{H}=N{2-O-5-*t*BuC$_6$H$_3$})}$_2$(μ-$PPh_2CH_2PPh_2$)] (3a):** Yield: 19 mg, 60%. $C_{65}H_{68}N_2O_8P_2Pd_2$ (1280.03): calcd. C 60.9, H 5.3, N 2.2; found C 60.2, H 5.2, N 2.1. IR: $\tilde{\nu}$ = 1544 (s, $\nu_{C=N}$) cm$^{-1}$. $^1$H NMR (200 MHz, $CDCl_3$): $\delta$ = 1.32 (s, 9 H, *t*Bu), 2.89, 3.70, 3.95 (s, 9 H, MeO), 5.39 (d, $^4J_{H5,P}$ = 4.3 Hz, 1 H, 5-H), 6.46 (d, $^3J_{H10,H11}$ = 9.2 Hz, 1 H, 11-H), 7.1 (m, 2 H, 10-H, 8-H), 7.99 (d, $^4J_{H_i,P}$ = 10.7 Hz, 1 H, H$_i$) ppm. $^{31}$P{$^1$H} NMR (80.96 MHz, $CDCl_3$): $\delta$ = 25.6 (s) ppm.

**[{Pd(2,3,4-{MeO}$_3$C$_6$HC{H}=N{2-O-5-*t*BuC$_6$H$_3$})}$_2${μ-$PPh_2(CH_2)_2PPh_2$}] (4a):** Yield: 21 mg, 65%. $C_{66}H_{70}N_2O_8P_2Pd_2$ (1294.06): calcd. C 61.3, H 5.4, N 2.1; found C 61.1, H 5.3, N 2.0. IR: $\tilde{\nu}$ = 1544 (s, $\nu_{C=N}$) cm$^{-1}$. $^1$H NMR (200 MHz, $CDCl_3$): $\delta$ = 1.30 (s, 9 H, *t*Bu), 2.85, 3.72, 3.97 (s, 9 H, MeO), 5.38 (s, 1 H, 5-H), 6.51 (d, $^3J_{H10,H11}$ = 8.7 Hz, 1 H, 11-H), 7.01 (dd, $^3J_{H10,H11}$ = 8.7 Hz, $^4J_{H8,H10}$ = 1.9 Hz, 1 H, 10-H), 7.09 (d, $^4J_{H8,H10}$ = 1.9 Hz, 1 H, 11-H) ppm. $^{31}$P{$^1$H} NMR (80.96 MHz, $CDCl_3$): $\delta$ = 35.0 (s) ppm.

Compound **3b** was obtained following a similar procedure as a brown solid.

 © 2007 Wiley-VCH Verlag GmbH & Co. KGaA, Weinheim 

Table 5. Crystal and structure refinement data.

| | **1a**·$H_2O$ | **1c** | **1d/d′** | **1e**·$4CH_2Cl_2$ |
|---|---|---|---|---|
| Chemical formula | $C_{80}H_{94}N_4O_{17}Pd_4$ | $C_{60}H_{52}N_4O_4Pd_4$ | $C_{60}H_{52}N_4O_4Pd_4$ | $C_{64}H_{60}Cl_8N_4O_{16}Pd_4$ |
| Formula weight | 1809.19 | 1318.66 | 1318.66 | 1850.36 |
| $T$ [°C] | 293(2) | 293(2) | 293(2) | 120(2) |
| $\lambda$ | 0.71073 | 0.71073 | 0.71073 | 0.71073 |
| Crystal system | monoclinic | orthorhombic | triclinic | monoclinic |
| Space group | *C*2/*c* | *Fdd*2 | $P\bar{1}$ | *C*12/*c*1 |
| $a$ [Å] | 23.371(1) | 9.311(2) | 12.334(3) | 31.233(6) |
| $b$ [Å] | 23.254(1) | 27.305(6) | 13.728(3) | 17.500(3) |
| $c$ [Å] | 30.721(1) | 39.281(8) | 17.537(5) | 27.541(5) |
| $\alpha$ [°] | | | 75.770(4) | |
| $\beta$ [°] | 94.635(1) | | 81.472(4) | 113.864(3) |
| $\gamma$ [°] | | | 81.208(4) | |
| $V$ [Å$^3$] | 16641(1) | 9986(4) | 2825(1) | 13766(4) |
| $Z$ | 8 | 8 | 2 | 8 |
| $\mu$ [mm$^{-1}$] | 1.444 | 1.472 | 1.300 | 1.408 |
| $2\theta_{max}$ [°] | 56.58 | 52.88 | 52.88 | 52.92 |
| Refln. collected | 53553 | 2611 | 31767 | 77225 |
| Refln. independent | 19987 ($R_{int}$ = 0.068) | 2210 ($R_{int}$ = 0.035) | 11533 ($R_{int}$ = 0.031) | 14150 ($R_{int}$ = 0.088) |
| $R_1$[a] | 0.0598 | 0.0311 | 0.0432 | 0.0401 |
| $wR_2$[b] | 0.1891 | 0.0808 | 0.1332 | 0.0969 |

[a] $R_1 = \Sigma||F_o| - |F_c||/\Sigma|F_o|$, $[F > 4\sigma(F)]$. [b] $wR_2 = [\Sigma[w(F_o^2 - F_c^2)^2/\Sigma w(F_o^2)^2]^{1/2}$, all data.

**[{Pd(6-Me-2-$CH_2C_6H_3C\{H\}$=N{2-$OC_6H_4$})}$_2${μ-$PPh_2(CH_2)_2PPh_2$}] (3b):** Yield: 23 mg, 70%. $C_{56}H_{50}N_2O_2P_2Pd_2$ (1057.80): calcd. C 63.6, H 4.8, N 2.6; found C 63.6, H 4.7, N 2.6. IR: $\tilde{\nu}$ = 1581 (s, $\nu_{C=N}$) cm$^{-1}$. $^1$H NMR (200 MHz, $CDCl_3$): $\delta$ = 2.55 (s, 3 H, Me), 2.90 (d, $^3J_{CH_2,P}$ = 9.1 Hz, 2 H, -$CH_2$-), 6.43 (t, $^3J_{H10,H9}$ = 6.8 Hz, 1 H, 10-H), 6.74 (t, $^4J_{H_3,CH_2}$ = 2.3 Hz, 1 H, 3-H), 6.84 (dd, $^3J_{H,H}$ = 8.3 Hz, $^4J_{H,H}$ = 0.9 Hz, 1 H), 6.94 (d, $^3J_{H,H}$ = 4.9 Hz, 1 H), 7.10 (dt, $^3J_{H,H}$ = 8.3 Hz, $^4J_{H,H}$ = 1.4 Hz, 1 H), 8.71 (m, 1 H, $H_i$) ppm. $^{31}P\{^1H\}$ NMR (80.96 MHz, $CDCl_3$): $\delta$ = 33.2 (s) ppm.

**X-ray Crystallographic Study:** Three-dimensional, room temperature X-ray data were collected with a Siemens Smart CCD diffractometer by the $\omega$ scan method with graphite-monochromated Mo-$K_\alpha$ radiation (Table 5). All the measured reflections were corrected for Lorentz and polarisation effects and for absorption by semiempirical methods based on symmetry-equivalent and repeated reflections. The structures were solved by direct methods and refined by full-matrix least-squares on $F^2$. Hydrogen atoms were included in calculated positions and refined in riding mode. The C60 atom of **1a** was disordered over two positions with occupancies of approximately 50%. The C1–C9 and C21–C28 carbon atoms, corresponding to the benzal phenyls of two of the cyclometallated ligands in complex **1d/d′** were found to be disordered over two positions (with occupancies of approximately 70% [C1–C9] and 50% [C21–C28] for the major components). The refinement was carried out by taking into account the minor components. Refinement converged at a final $R$ = 0.0598, 0.0311, 0.0432 and 0.0401 (for complexes **1a**, **1c**, **1d/d′** and **1e**, respectively, observed data, $F$) and $wR_2$ = 0.1891, 0.0808, 0.1332 and 0.0909 (for complexes **1a**, **1c**, **1d/d′** and **1e**, respectively, unique data, $F^2$), with allowance for thermal anisotropy of all non-hydrogen atoms. The structure solution and refinement were carried out by using the program package SHELX-97.[55]

CCDC-608700 (for **1a**), -608701 (for **1c**), -608702 (for **1d/d′**) and -608703 (for **1e**) contain the supplementary crystallographic data for this paper. These data can be obtained free of charge from The Cambridge Crystallographic Data Centre via www.ccdc.cam.ac.uk/data_request/cif.

## Acknowledgments

We thank the Ministerio de Educación y Ciencia (Project CTQ2006-15621-C02-01/BQU) for financial support.

[1] I. Omae in *Organometallic Intramolecular-Coordination Compounds*, Elsevier Science Amsterdam–New York, **1986**.
[2] V. V. Dunina, O. A. Zalevskaya, V. M. Potapov, *Russ. Chem. Rev.* **1984**, *571*, 250.
[3] G. R. Newkome, W. E. Puckett, W. K. Gupta, G. E. Kiefer, *Chem. Rev.* **1986**, *86*, 451–489.
[4] A. D. Ryabov, *Chem. Rev.* **1990**, *90*, 403–424.
[5] M. Pfeffer, *Recl. Trav. Chim. Pays-Bas* **1990**, *109*, 567–576.
[6] M. Pfeffer, J. P. Sutter, M. A. Rottevel, A. de Cian, J. Fischer, *Tetrahedron* **1992**, *48*, 2427–2440.
[7] A. D. Ryabov, R. van Eldik, G. Le Borgne, M. Pfeffer, *Organometallics* **1993**, *12*, 1386–1393.
[8] B. S. Wild, *Coord. Chem. Rev.* **1997**, *166*, 291–311.
[9] S. Y. M. Chooi, P. H. Leung, C. C. Lim, K. F. Mok, G. H. Quek, K. Y. Sim, M. K. Tan, *Tetrahedron: Asymmetry* **1992**, *3*, 529–532.
[10] P. Espinet, M. A. Esteruelas, L. A. Oro, J. L. Serrano, E. Sola, *Coord. Chem. Rev.* **1992**, *17*, 215–274.
[11] C. Navarro-Ranninger, I. López-Solera, J. Rodríguez, J. L. García-Ruano, P. R. Raithby, J. R. Masaguer, C. Alonso, *J. Med. Chem.* **1993**, *36*, 3795–3801.
[12] C. Navarro-Ranninger, I. López-Solera, V. M. Gonzalez, J. M. Pérez, A. Alvarez-Valdés, A. Martin, P. R. Raithby, J. R. Masaguer, C. Alonso, *Inorg. Chem.* **1996**, *35*, 5181–5187.
[13] A. Bose, C. H. Saha, *J. Mol. Catal.* **1989**, *49*, 271–283.
[14] J. M. Vila, M. T. Pereira, J. M. Ortigueira, J. J. Fernández, A. Fernández, M. López-Torres, H. Adams, *Organometallics* **1999**, *18*, 5484–5487.
[15] A. Zucca, M. A. Cinellu, M. V. Pinna, S. Stoccoro, G. Minghetti, M. Manassero, M. Sansoni, *Organometallics* **2000**, *19*, 4295–4304.
[16] P. L. Alsters, P. F. Engel, M. P. Hogerheide, M. Copijn, A. L. Speck, G. van Koten, *Organometallics* **1993**, *12*, 1831–1844.
[17] J. Albert, R. M. Ceder, M. Gómez, J. Granell, J. Sales, *Organometallics* **1992**, *11*, 1536–1541.

 © 2007 Wiley-VCH Verlag GmbH & Co. KGaA, Weinheim 

[18] J. Albert, J. Granell, J. Sales, X. Solans, M. Font-Altaba, *Organometallics* **1986**, *5*, 2567–2568.
[19] D. J. Cárdenas, A. M. Echavarren, A. Vegas, *Organometallics* **1994**, *13*, 882–889.
[20] J. M. Lehn, *Supramolecular Chemistry*, VCH, Weinheim, **1995**.
[21] L. Fabbrizzi, A. Poggi, *Transition Metals in Supramolecular Chemistry, Vol. 448*, Kluwer Academic Publishers, Dordrecht, **1994**.
[22] M. Eddaoudi, D. B. Moler, H. Li, B. Chen, T. M. Reineke, M. O'Keefe, O. M. Yaghi, *Acc. Chem. Res.* **2001**, *34*, 319–330.
[23] A. J. Blake, N. R. Champness, P. Hubberstey, W. S. Li, M. A. Withersby, M. Schröder, *Coord. Chem. Rev.* **1999**, *183*, 117–138.
[24] P. J. Hagrman, D. Hagrman, J. Zubieta, *Angew. Chem. Int. Ed.* **1999**, *38*, 2638–2684.
[25] J. W. Canary, B. C. Gibb in *Progress in Inorganic Chemistry, Vol. 45* (Ed. K. D. Karlin), Wiley, New York, **1997**, p. 1.
[26] M. López-Torres, A. Fernández, J. J. Fernández, A. Suárez, S. Castro-Juiz, J. M. Vila, M. T. Pereira, *Organometallics* **2001**, *20*, 1350–1353.
[27] J. R. Hall, S. J. Loeb, G. K. H. Shimizu, G. P. A. Yap, *Angew. Chem. Int. Ed.* **1998**, *37*, 121–123.
[28] R. F. Carina, A. F. Williams, G. Bernardinelli, *Inorg. Chem.* **2001**, *40*, 1826–1832.
[29] C. Fernández-Rivas, D. J. Cárdenas, B. Martín-Matute, A. Monge, E. Gutiérrez-Puebla, M. A. Echevarren, *Organometallics* **2001**, *20*, 2998–3006.
[30] C. López, A. Caubet, R. Bosque, X. Solans, M. Font-Bardía, *J. Organomet. Chem.* **2002**, *645*, 146–151.
[31] J. Vicente, M. C. Lagunas, E. Bleuel, M. C. Ramírez de Arellano, *J. Organomet. Chem.* **2002**, *648*, 62–71.
[32] J. M. Vila, M. T. Pereira, J. M. Ortigueira, M. López-Torres, D. Lata, M. Graña, A. Suárez, J. J. Fernández, A. Fernández, *J. Chem. Soc. Dalton Trans.* **1999**, 4193–4201.
[33] D. Vázquez-García, A. Fernández, J. J. Fernández, M. López-Torres, A. Suárez, J. M. Ortigueira, J. M. Vila, H. Adams, *J. Organomet. Chem.* **2000**, *595*, 199–207.
[34] A. G. Quiroga, J. M. Perez, I. Lopez-Solera, J. R. Masaguer, A. Luque, P. Roman, A. Edwards, C. Alonso, C. Navarro-Ranninger, *J. Med. Chem.* **1998**, *41*, 1399–1408.
[35] T. Kawamoto, I. Nagasawa, H. Kuma, Y. Kushi, *Inorg. Chem.* **1996**, *35*, 2427–2432.
[36] T. Kawamoto, I. Nagasawa, H. Kuma, Y. Kushi, *Inorg. Chim. Acta* **1997**, *265*, 163–167.
[37] C. López, A. Caubet, S. Pérez, X. Soláns, M. Font-Bardía, *J. Organomet. Chem.* **2003**, *681*, 82–90.
[38] C. Chen, Y. Liu, S. Peng, S. Liu, *J. Organomet. Chem.* **2004**, *689*, 1806–1815.
[39] A. Fernández, D. Vázquez-García, J. J. Fernández, M. López-Torres, A. Suárez, S. Castro-Juiz, J. M. Vila, *New J. Chem.* **2002**, *26*, 398–404.
[40] H. Yang, M. A. Khan, K. M. Nicholas, *J. Chem. Soc., Chem. Commun.* **1992**, 210–212.
[41] F. Hueso-Urena, N. A. Illan-Cabeza, M. N. Moreno-Carretero, A. L. Penas-Chamorro, R. Faure, *Inorg. Chem. Commun.* **1999**, *2*, 323–326.
[42] H. Onoue, I. Moritani, *J. Organomet. Chem.* **1972**, *43*, 431–436.
[43] H. Onoue, K. Minami, K. Nakagawa, *Bull. Chem. Soc. Jpn.* **1970**, *43*, 3480–3485.
[44] R. Bosque, J. Granell, J. Sales, M. Fon-Bardiá, X. Solans, *J. Organomet. Chem.* **1993**, *453*, 147–154.
[45] J. M. Vila, M. Gayoso, M. T. Pereira, M. López-Torres, G. Alonso, J. J. Fernández, *J. Organomet. Chem.* **1993**, *445*, 287–294.
[46] J. M. Vila, M. Gayoso, M. T. Pereira, A. Romar, J. J. Fernández, M. Thornton-Pett, *J. Organomet. Chem.* **1991**, *401*, 385–394.
[47] J. Granell, J. Sales, M. Fon-Bardiá, X. Solans, *Organometallics* **1995**, *14*, 1393–1404.
[48] A. Amoedo, L. Adrio, J. M. Antelo, J. Martínez, M. T. Pereira, A. Fernández, J. M. Vila, *Eur. J. Inorg. Chem.* **2006**, 3016–3021.
[49] J. Barro, J. Granell, D. Sainz, J. Sales, *J. Organomet. Chem.* **1993**, *456*, 147–154.
[50] C. López, S. Pérez, X. Soláns, M. Font-Bardía, *J. Organomet. Chem.* **2002**, *650*, 258–267.
[51] J. Albert, J. M. Cadena, A. González, J. Granell, X. Solans, M. Font-Bardía, *Chem. Commun.* **2003**, 528–529.
[52] G. De Mundo, M. Ghedini, F. Neve, *Inorg. Chim. Acta* **1995**, *239*, 155–158.
[53] C. Chen, Y. Liu, S. Peng, S. Liu, *Organometallics* **2005**, *24*, 1075–1081.
[54] D. D. Perrin, W. L. F. Armarego, D. L. Perrin, *Purification of Laboratory Chemicals*, 3rd ed., Pergamon, London, **1998**.
[55] G. M Sheldrick, *SHELX-97, An Integrated System for Solving and Refining Crystal Structures from Diffraction Data*, University of Göttingen, Germany, **1997**.

Received: May 2, 2007
Published Online: October 4, 2007

 © 2007 Wiley-VCH Verlag GmbH & Co. KGaA, Weinheim 

DOI: 10.1002/ejic.200700584

# Synthesis, Crystal Structures, and Photophysical Properties of Lanthanide Complexes Containing Pyrrole-Derivatized Carboxylate Ligands

Ga-Lai Law,[a] Ka-Leung Wong,[b] Kok-Kin Lau,[a] Hoi-Lam Tam,[c] Kok-Wai Cheah,[c] and Wing-Tak Wong*[a]

**Keywords:** Lanthanide / Luminescence / Terbium / Europium / Pyrrole

Two pyrrole-deriviatized carboxylic acids [$\mathbf{L^1}$ = 1-methylpyrrole-2-carboxylate] and [$\mathbf{L^2}$ = *N*-methyl-3-indoleglyoxylate] were used as ligands to prepare six lanthanide coordination compounds $[(\mathbf{L^1})_3Ln]_n$ (Ln = Eu, **1**; Gd, **2**; Tb, **3**) and $[(\mathbf{L^2})_n$-$Ln(NO_3)(MeOH)_2]_n$ (Ln = Eu, **4**; Gd, **5**; Tb, **6**). These complexes have been synthesized and structurally characterized by single-crystal X-ray diffraction. The phosphorescence behavior of the ligands in the $Gd^{3+}$ complexes show that modification of the ligands can tune the triplet energy levels of the ligands so that they match the $^5D_0$ energy level of $Eu^{3+}$ and the $^5D_4$ energy level of $Tb^{3+}$; thus, the energy transfer efficiency from antenna to $Eu^{3+}$ and $Tb^{3+}$ is improved, and the $Eu^{3+}$ and $Tb^{3+}$ emission intensity is enhanced. This concept can be applied towards improving the luminescent properties of $Ln^{3+}$ complexes by the modification of coordinating ligands.
(© Wiley-VCH Verlag GmbH & Co. KGaA, 69451 Weinheim, Germany, 2007)

## Introduction

One topic of current interest in materials research is the synthesis of lanthanide complexes because of their promising photoluminescent properties. The major advantages of lanthanide complexes as luminescent materials are the long emission lifetimes and narrow bandwidths.[1–3] Because lanthanide f–f transitions are Laporte forbidden, the direct excitation of electrons in lanthanide-metal ions is very inefficient; thus, the resulting emissions from lanthanide-metal ions are very weak.[4–6] One way to improve the weak luminescence properties of lanthanide ions is to use sensitizing chromophores or antennae as ligands in lanthanide-metal complexes.[7–8] Through complexation with a chromophore, the luminescence of the lanthanide ions can be enhanced greatly (by more than $10^4$ fold).[9] This enhancement is mainly because direct excitation of the lanthanide ions can be avoided. In other words, luminescence in lanthanide–ligand complexes results from the electronic excitation of the coordinated chromophore followed by ligand-to-lanthanide energy transfer.

The choice of ligand for complexation plays a key role in constructing efficient luminescent lanthanide complexes. Two common requirements for selecting a ligand for coordination with lanthanide ions are the metal binding strength and ultraviolet (UV) absorption properties of the ligand. Among several categories of organic ligands, aromatic carboxylate ligands are one of the most common groups that fulfil the above two basic requirements. Aromatic carboxylate ligands are frequently used as sensitizing agents for enhancing the luminescence in the lanthanide species because they can chelate the lanthanide-metal ions tightly through their anionic carboxylate groups and strongly absorb UV radiation; the energy absorbed is subsequently transferred to the lanthanide-metal centre.[10–11]

Herein we report six lanthanide–organic complexes that incorporate two types of carboxylic acid ligands 1-methylpyrrole-2-carboxylate ($\mathbf{L^1}$) and *N*-methyl-3-indoleglyoxylate ($\mathbf{L^2}$) (Figure 1). These ligands are complexed with lanthanide(III) nitrate salts to form [Ln(1-methylpyrrole-2-carboxylate)$_3$(MeOH)$_2$($H_2O$)] (Ln = Eu, Gd, and Tb for **1**, **2**, and **3**, respectively) and $[Ln_2$(*N*-methyl-3-indoleglyoxylate$)_6$-$(MeOH)_4]_n$ (Ln = Eu, Gd, and Tb for **4**, **5** and **6**, respectively). Both of $\mathbf{L^1}$ and $\mathbf{L^2}$ show strong antenna effects with high quantum efficiency, and two molecular structures (**1** and **4**) of the newly synthesized complexes have been elucidated in this work.

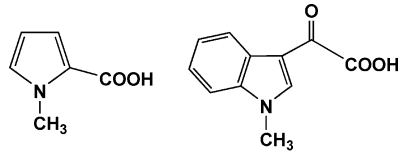


$\mathbf{L^1}$ $\mathbf{L^2}$

Figure 1. The molecular structures of $\mathbf{L^1}$ and $\mathbf{L^2}$.

[a] Department of Chemistry, The University of Hong Kong, Pokfulam, Hong Kong
Fax: +852-2547-2933
E-mail: wtwong@hkucc.hku.hk
[b] Department of Biology and Chemistry, City University of Hong Kong,
TatChee Avenue, Kowloon Tong, Hong Kong
[c] Department of Physics, Hong Kong Baptist University, Kowloon Tong, Hong Kong
Supporting information for this article is available on the WWW under http://www.eurjic.org or from the author.

 © 2007 Wiley-VCH Verlag GmbH & Co. KGaA, Weinheim 

## Results and Discussion

### Crystal Structures of 1 and 4

The X-ray diffraction analysis reveals that **1** and **4** adopt a highly symmetrical, polymeric structure in which the europium metal ions form the skeleton. All europium ions in the two europium complexes adopt a nine-coordinate geometry. In **1**, each europium ion is bidentately coordinated by three bidentate carboxylate ligands and monodentately coordinated by another three tridentate, bridging carboxylate ligands. Two of the three tridentate, bridging carboxylate ligands are bidentately chelated to an adjacent europium ion, and the remaining tridentate, bridging carboxylate ligand is bidentately coordinated to another adjacent europium ion (Figure 2). Each europium ion can be described as a nine-coordinate, twisted tricapped trigonal prism, in which the top plane is formed by O(1), O(4), and O(6) atoms, whereas the bottom plane is defined by the other equivalent, but offset in position, O(1), O(4), and O(6) atoms. The O(2), O(3), and O(5) atoms cap three quadrilateral faces of the trigonal prism. The packing diagram of **1** is shown in Figure 3.

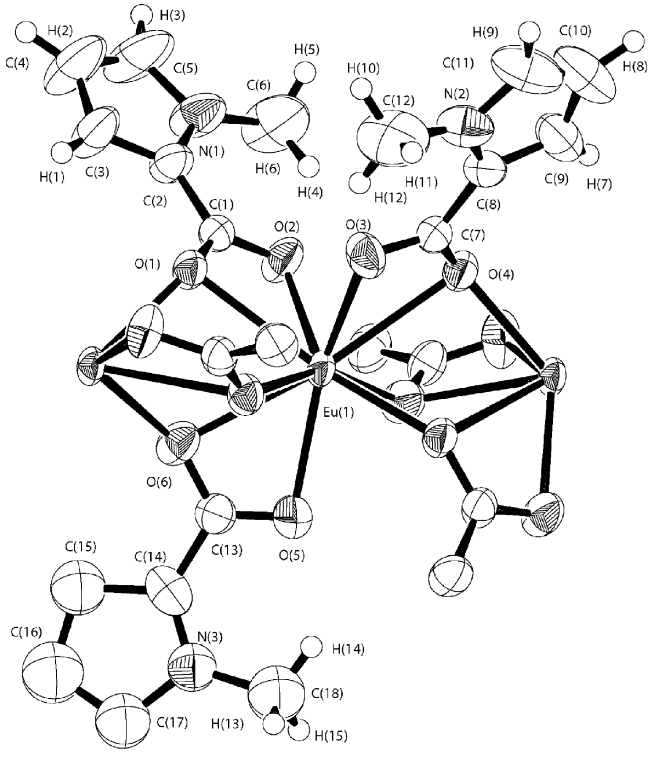


Figure 2. ORTEP drawing of **1**.

The Eu–Eu bond length and Eu–Eu–Eu bond angle in **1** are 3.793 Å and 178.38°, respectively. The bond length is much shorter and the bond angle is much larger than those in $[Eu_2(Benzoate)_6(MeOH)_4]_n$ (4.915 Å and 165.7°). The Eu–O bond lengths in **1** range from 2.400(3) to 2.727(3) Å, which are longer than those of $[Eu_2(Benzoate)_6(MeOH)_4]_n$ [2.309(6) to 2.535(6) Å].[11] The average Eu–O bond length (2.410 Å) for the carboxylate O atoms chelated by only one

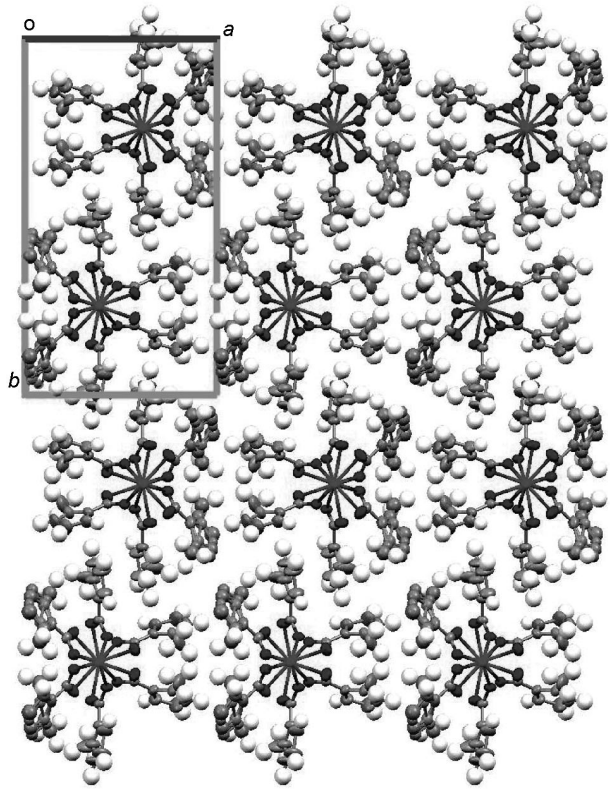


Figure 3. Packing diagram for **1** projected down the *c* axis.

europium ion is shorter than the average Eu–O bond length (2.672 Å) for the carboxylate O atoms chelated by two europium ions, which is obviously because of steric hindrance. The average C–O(CO) distance and O(CO)–C–O(CO) angle are 1.268 Å and 119.6,° respectively. The average C–O–Eu bond angle (88.1°) for the carboxylate O atoms chelated by two europium ions is much smaller than the average C–O–Eu bond angle (101.3°) for the carboxylate O atoms chelated by only one europium ion. The average O(CO)–Eu–O(CO) bond angle is 50.77°.

Recrystallization of the europium complex that contained the glyoxylate ligand gave light yellow, plate-like crystals of **4**, which were studied by X-ray diffraction crystallography. The perspective view of **4** is shown in Figure 4. The packing diagram of **4** projecting down the *a* axis is shown in Figure 5. Summaries of the crystallographic data and experimental parameters for **1** and **4** are supplied in the Supporting Information along with selected bond lengths and angles.

Complex **4** is a polymeric chain, in which europium ions constitute the skeleton. As shown in Figure 4, each europium ion in **4** is nine-coordinate, with five oxygen atoms from three glyoxylate ligands, two oxygen atoms from one nitrate molecule and two oxygen atoms from two methanol solvent molecules. The presence of an additional carbonyl group in glyoxylate ligands relative to that in carboxylate ligands results in an unusual coordination between the glyoxylate ligands and the lanthanide ions. In the structure

 © 2007 Wiley-VCH Verlag GmbH & Co. KGaA, Weinheim 

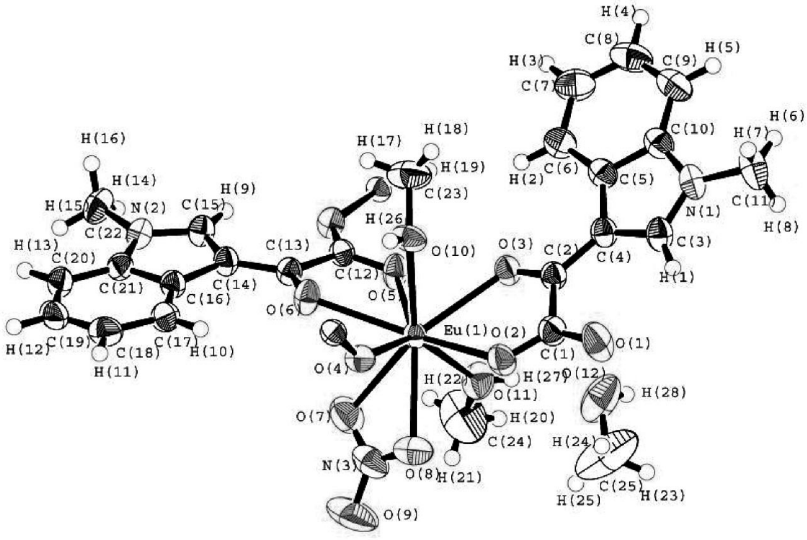


Figure 4. ORTEP drawing of **4**.

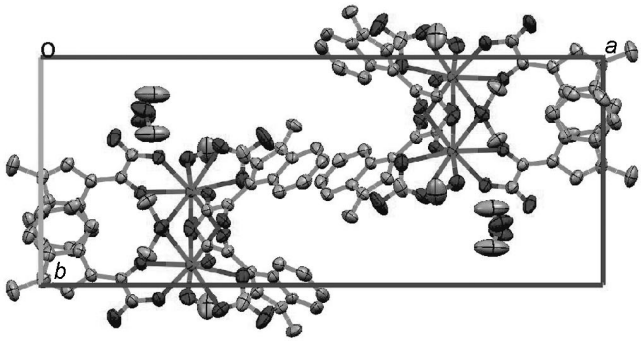


Figure 5. Packing diagram of **4** projected down the *a* axis.

of **4**, each europium ion is coordinated to two carbonyl oxygen atoms of two glyoxylate ligands and three carboxylic oxygen atoms of three glyoxylate ligands. In other words, two carboxylate groups of two or three glyoxylate ligands coordinate as bidentate bridges between two europium ions, whereas the carboxylate group of the remaining glyoxylate ligand coordinates as bidentate bridges between one europium ion and one hydrogen atom of a MeOH molecule. The Eu–Eu bond length and Eu–Eu–Eu bond angle in **4** (6.322 Å and 116.21°, respectively) are much longer and smaller than those in $[Eu_2(Benzoate)_6(MeOH)_4]_n$ (4.915 Å and 165.7°, respectively).[11] The longer Eu–Eu bond in **4** probably results from the greater steric hindrance associated with the *N*-methyl-3-indoleglyoxylate group than the benzoate group. The average Eu–O(carboxyl), Eu–O(carbonyl), Eu–O(MeOH), and Eu–O(nitrate) bond lengths in **4** are 2.405, 2.479, 2.474, and 2.496 Å, respectively. The average C–O (carboxyl and Eu-coordinated) bond length and O(carbonyl)–Eu–O(carboxyl) bond angle are 1.252 Å and 64.3°, respectively. There are four different hydrogen bonds in **4**. Two hydrogen bonds form between the hydrogen atom of one of the coordinated MeOH molecules and the two carboxylic oxygen atoms of one of the coordinated glyoxylate ligands [O(10)–H(26)···O(4) 2.62(5) Å and O(10)–H(26)···O(5)$^{i}$ 1.99(5) Å; i: $x$, 3/2 – $y$, 1/2 + $z$]. The third hydrogen bond is formed between the hydrogen atom of the free MeOH molecule and the non-coordinated carboxylic oxygen atom of one of the glyoxylate ligands [O(12)–H(28)···O(1)$^{ii}$ 1.95(7) Å; ii: $x$, 1/2 – $y$, 1/2 + $z$]. The fourth hydrogen bond is formed between the non-coordinated MeOH molecule and one of the coordinated MeOH molecules [O(11)–H(27)···O(12) 2.01(6) Å].

The different number of carbonyl groups in $\mathbf{L^1}$ and $\mathbf{L^2}$ (Figure 1) should result in structural differences in the corresponding lanthanide complexes. Ligand $\mathbf{L^1}$ has only one carbonyl group so is expected to form $Ln^{3+}$ complexes with four-membered rings, whereas $\mathbf{L^2}$ has two carbonyl groups so is expected to form $Ln^{3+}$ complexes with five-membered rings (Figure 4 and Figure 5).

## Photophysical Properties of 1–6

The UV/Vis absorption behavior of ligands $\mathbf{L^1}$ and $\mathbf{L^2}$ and their lanthanide complexes are shown in Figure 6 and Figure 7. The three absorption bands observed for **1**–**3** (see the arrows in Figure 6: ca. 32258 $cm^{-1}$, ca. 28986 $cm^{-1}$, and ca. 23256 $cm^{-1}$) and one band observed for **4**–**6** (Figure 7, ca. 30480 $cm^{-1}$) are similar to the peaks observed in the UV/Vis spectra of the ligands. By comparison of the UV/Vis spectra for **1**–**6** with that of the ligands, the bands can be attributed to benzyl π–π* transitions, which undergo red shifts of approximately 1000 $cm^{-1}$ upon complexation.[12] Moreover, a very close resemblance is observed between the UV/Vis absorption spectra of **1**–**6** and analogous lanthanide complexes that are coordinated by equivalent ligands.

 © 2007 Wiley-VCH Verlag GmbH & Co. KGaA, Weinheim 

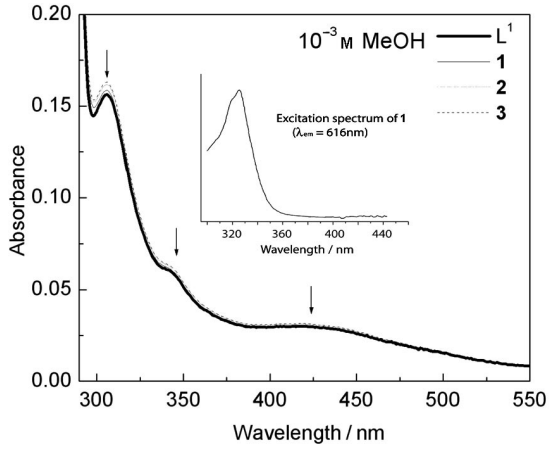


Figure 6. UV/Vis absorption spectra of $\mathbf{L^1}$ and of their complexes **1**–**3**, and the excitation spectra of complex **1** (inset).

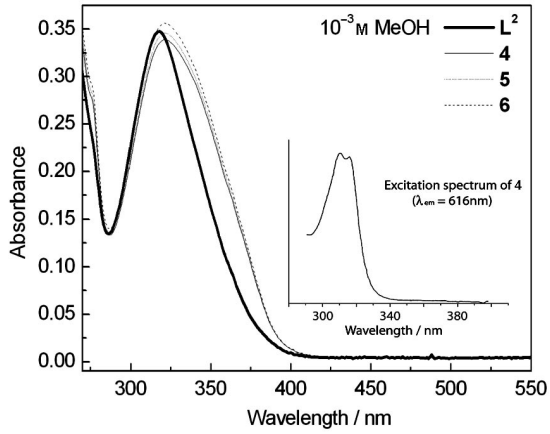


Figure 7. UV/Vis absorption spectra of $\mathbf{L^2}$ and of their complexes **4**–**6**, and the excitation spectra of complex **4** (inset).

The high degree of similarity in the UV/Vis absorption bands of **1**–**6** and those of analogous lanthanide complexes that incorporate equivalent ligands implies that they are likely to have similar or the same ligand–metal coordination modes, and hence similar or the same coordination structure. The slight band broadening observed in the absorption spectra of the complexes **4**–**6** upon complexation is induced by the steric effect of the ligands, which are not equivalent in **4**–**6** (Figure 7).

The luminescence properties of the ligands and of their lanthanide complexes were measured in the solid state at room temperature (Figures 8 and S1). The intense, linear broad emission band ($\lambda_{ex}$ = 325 nm) characteristic of ligands $\mathbf{L^1}$ and $\mathbf{L^2}$ are shown in the Supporting Information (Figure S1). The emission bands observed for $\mathbf{L^1}$ and $\mathbf{L^2}$ at ca. 400 and 410 nm, respectively, are attributed to the benzyl π–π* relaxation ($S_1 \rightarrow S_0$). The four structured, narrow emission bands at 480, 545, 580, and 620 nm for Tb complexes **3** and **6** and bands at 594, 620, 650 and 700 nm for Eu complexes **1** and **4** are assigned to an electronic energy transition between the $^5D_4 \rightarrow {}^7F_J$ ($J$ = 6, 5, 4, 3) states. The transitions $^5D_0 \rightarrow {}^7F_J$ ($J$ = 1, 2, 3, 4) are shown in the linear process for two types for Tb and Eu complexes.[13] There are great variations between the emission intensity in the Tb and Eu complexes. The matching of the triplet states in these lanthanide systems is an important criteria for the energy transfer from the ligand to the lanthanide (Figure 9 and Figure 10).

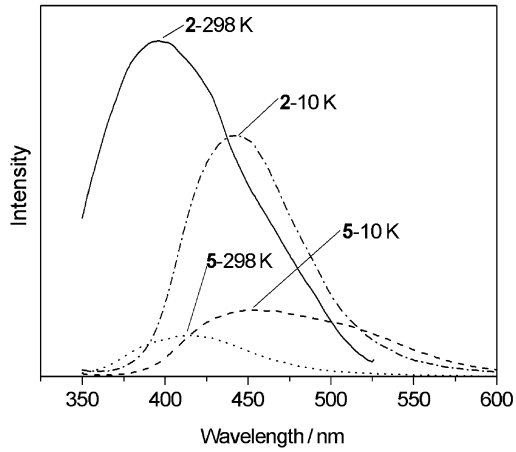


Figure 8. Solid-state emission spectra for Gd complexes **2** and **5** (298 K and 10 K), $\lambda_{ex}$ = 325 nm.

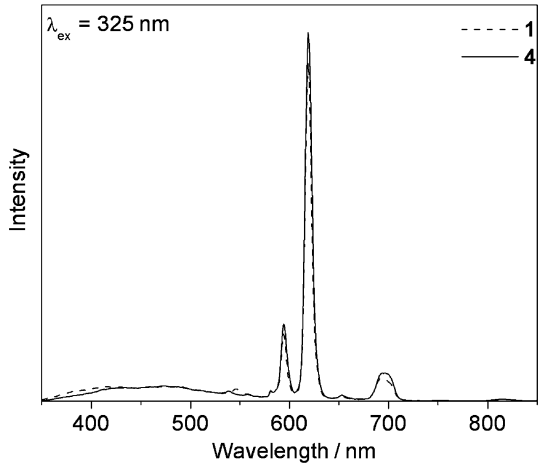


Figure 9. Solid-state normalized emission spectra for Eu complexes **1** and **4** (10 K), $\lambda_{ex}$ = 325 nm.

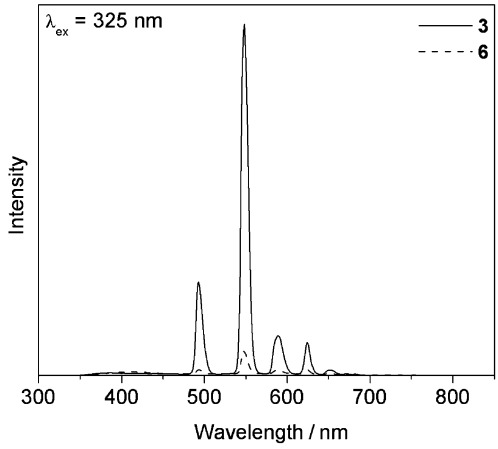


Figure 10. Solid-state normalized emission spectra for Tb complexes **3** and **6** (10 K), $\lambda_{ex}$ = 325 nm.

 © 2007 Wiley-VCH Verlag GmbH & Co. KGaA, Weinheim 

Table 1. The solid-state luminescence lifetime ($\tau$) and quantum yield ($\Phi$) of the ligands and lanthanide complexes at 10 K. ($\lambda_{ex}$ = 337 nm, **L¹** $\lambda_{em}$ = 405 nm, **L²** $\lambda_{em}$ = 410 nm, **1** and **4** $\lambda_{em}$ = 616 nm, **2** and **5** $\lambda_{em}$ = ca. 450 nm, **3** and **6** $\lambda_{em}$ = 545 nm).

| | **L¹** | **L²** | **1** | **2**[a] | **3** | **4** | **5**[a] | **6** |
|---|---|---|---|---|---|---|---|---|
| $\tau$ [ms] | $9.1\times10^{-6}$ | $17.6\times10^{-6}$ | 1.29 | $7.67\times10^{-3}$ | 1.14 | 0.86 | $5.53\times10^{-3}$ | 1.33 |
| $\Phi$[b] | – | – | 0.23 | – | 0.18 | 0.21 | – | 0.06 |

[a] The phosphorescence lifetimes of in **2** and **5** ($\mathbf{T_1}\rightarrow \mathbf{S_0}$) are measured at 10 K.[15] [b] Quantum yield obtained by comparison with sodium salicylate (as standard).[16–17]

The lowest energy level of $Gd^{3+}$ ($^6P_{7/2}$) is much higher than energy levels of the ligands; therefore, it is assumed that there are no energy transitions between the ligand and metal.[14] The phosphorescence of these Gd complexes was measured under cold conditions (10 K) in the solid state (see Figure 8).

The luminescence lifetimes were recorded to verify the fluorescence and phosphorescence at 10 K. The emission lifetimes on a nanosecond scale ($S_1 \rightarrow S_0$) were measured at ca. 400 and 415 nm for **L¹** and **L²**, respectively, and on a microsecond scale ($T_1 \rightarrow S_0$) at ca. 440 and 470 nm for **L¹** and **L²**, respectively. The details of the luminescence lifetimes are shown in Table 1.

In line with the foregoing experimental results, the schematic energy level diagram, which includes the triplet state energy levels of the Gd complexes, and the energy transfer process are shown in Figure 11. Given that the energy level $^5D_4$ for Tb is ca. 20500 $cm^{-1}$, the energy gap between the ligand triplet state and the metal centre is greater than 2000 $cm^{-1}$ in Tb complexes of ligand **L¹** , which is too high to allow an effective back transfer. In contrast, the triplet state energy levels in the Gd complexes of **L²** are too close to $^5D_4$, so is too low to prevent thermally competitive back energy transfer from the $^5D_4$ to the ligand triplet state; Hence, only a weak green f–f emission band was observed.[18]

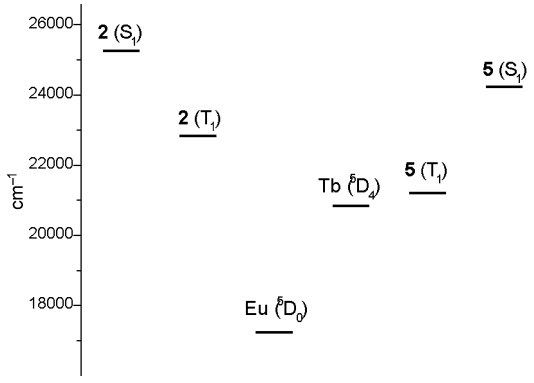


Figure 11. The lowest triplet-state energy levels of the ligands in the Gd complexes (**2** and **5**) and the resonance energy level of $Eu^{3+}$ and $Tb^{3+}$ ions.[19]

The energy gap between the ligand triplet states and the europium is greater than 2000 $cm^{-1}$, which is similar to the Tb complexes described above; however, the energy level of the $^5D_0$ state for Eu is ca. 17500 $cm^{-1}$, which is 3000 $cm^{-1}$ lower than the Tb ($^5D_4$) energy level. According to the Lativa empirical rules,[19] an optimal ligand-to-metal transfer process for $Eu^{3+}$ requires more than 2500 $cm^{-1}$. Comparison of the energy for the triplet states of **2** (22837 $cm^{-1}$) and **5** (21173 $cm^{-1}$) with that for the $^5D_0$ state for Eu (17240 $cm^{-1}$) suggests that the europium complexes exhibit better luminescence properties than the terbium complexes because the energy transfer from the ligands is better converted.[21]

## Conclusions

Two series of lanthanide complexes coordinated with aromatic chromophore-containing pyrrole-derivatized carboxylate ligands were successfully synthesized and characterized by MS and FT-IR spectroscopic analyses. The solid-state molecular structures of some of these complexes were also precisely determined by X-ray crystallography. The X-ray diffraction studies reveal that the lanthanide complexes that incorporate bidentate carboxylate ligands (1-methylpyrrole-2-carboxylic acid and *N*-methyl-3-indoleglyoxylic acid) could attain highly symmetrical polymeric structures without any coordination with luminescence-quenching solvent or water molecules. Several europium and terbium complexes were found to be capable of exhibiting solid-state luminescence of high intensity, long lifetimes and high efficiency.

## Experimental Section

**General Remarks**: All solvents were purified and dried by standard methods prior to use.[20] All chemicals, unless otherwise stated, were purchased commercially and used as received. Ligands 1-methylpyrrole-2-carboxylic acid (**L¹**) and *N*-methyl-3-indoleglyoxylic acid (**L²**) were acquired from commercial sources. Sodium hydroxide (1.0 equiv.) was added to a solution of **L¹** and **L²** (1.0 equiv.) in MeOH (20 mL). After stirring the solution for about 1 h at room temperature, lanthanide(III) nitrate hexahydrate (Ln = Eu, Gd and Tb) (1.0 equiv.) was added to the reaction mixture. The resulting reaction mixture was then stirred at room temperature for another 24 h. The precipitate that was formed was isolated by suction filtration and purified by washing with $CH_2Cl_2$ and MeOH. The purified product was finally isolated as a powder.

**[(1-Methylpyrrole-2-carboxylate)$_3$Eu]$_n$ (1):** 1-Methylpyrrole-2-carboxylic acid (150 mg) was used as the chelating ligand, and the purified product was isolated as a dark brown powder. Yield: 349 mg (56%). MS (ESI, MeOH): *m*/*z* = 526 [$M^+$ + 2], 525 [$M^+$ + 1], 524 [$M^+$], 523 [$M^+$ – 1]. IR (KBr): $\tilde{\nu}$ = 1560 and 1545 [asymmetric $\nu(COO^-)$], 1458 [symmetric $\nu(COO^-)$] $cm^{-1}$. $C_{18}H_{18}EuN_3O_6$ (534.2): calcd. C 41.23, H 3.46, N 8.01; found C 41.22, H 3.45, N 8.05.

 © 2007 Wiley-VCH Verlag GmbH & Co. KGaA, Weinheim 

**[(1-Methylpyrrole-2-carboxylate)$_3$Gd]$_n$ (2):** 1-Methylpyrrole-2-carboxylic acid (150 mg) was used as the chelating ligand, and the purified product was isolated as a dark brown powder. Yield: 360 mg (57%). MS (ESI, MeOH): *m*/*z* = 534 [$M^+$ + 4], 533 [$M^+$ + 3], 532 [$M^+$ + 2], 531 [$M^+$ + 1], 530 [$M^+$], 529 [$M^+$ – 1], 528 [$M^+$ – 2]. IR (KBr): $\tilde{\nu}$ = 1560 and 1545 [asymmetric $\nu(COO^-)$], 1458 and 1425 [symmetric $\nu(COO^-)$] cm$^{-1}$. $C_{18}H_{18}GdN_3O_6$ (529.6): calcd. C 40.82, H 3.43, N 7.93; found C 40.83, H 3.46, N 7.91

**[(1-Methylpyrrole-2-carboxylate)$_3$Tb]$_n$ (3):** 1-Methylpyrrole-2-carboxylic acid (150 mg) was used as the chelating ligand, and the purified product was isolated as a dark brown powder. Yield: 318 mg (50%). MS (ESI, MeOH): *m*/*z* = 531 [$M^+$], 530 [$M^+$ – 1], 529 [$M^+$ – 2]. IR (KBr): $\tilde{\nu}$ = 1541 [asymmetric $\nu(COO^-)$], 1466 and 1429 [symmetric $\nu(COO^-)$] cm$^{-1}$. $C_{18}H_{18}N_3O_6Tb$ (521.2): calcd. C 40.69, H 3.41, N 7.91; found C 40.66, H 3.46, N 7.90.

**[(*N*-Methyl-3-indoleglyoxylate)$_2$Eu(NO$_3$)(MeOH)$_2$]$_n$ (4):** *N*-Methyl-3-indoleglyoxylic acid (200 mg) was used as the chelating ligand, and the purified product was isolated as a bright greenish-yellow powder. Yield: 346 mg (52%). MS (ESI, MeOH): *m*/*z* = 683 [$M^+$ + 1], 682 [$M^+$], 681 [$M^+$ – 1], 680 [$M^+$ – 2]. IR (KBr): $\tilde{\nu}$ = 3700–2700 [$\nu$(O–H)(coordinated MeOH)], 1636 [$\nu$(C=O)], 1576 [asymmetric $\nu(COO^-)$], 1466 [$\nu$(N–O)(coordinated)], 1437 and 1405 [symmetric $\nu(COO^-)$], 1254 [$\nu$(N–O)(coordinated)], 1091 [$\nu$(N–O)(coordinated)] cm$^{-1}$. $C_{25}H_{28}EuN_3O_{12}$ (714.4): calcd. C 42.03, H 3.95, N 5.88; found C 42.01, H 3.96, N 5.87.

**[(*N*-Methyl-3-indoleglyoxylate)$_2$Gd(NO$_3$)(MeOH)$_2$]$_n$ (5):** *N*-Methyl-3-indoleglyoxylic acid (200 mg) was used as the chelating ligand, and the purified product was isolated as a bright greenish-yellow powder. Yield: 342 mg (51%). MS (ESI, MeOH): *m*/*z* = 691 [$M^+$ + 3], 690 [$M^+$ + 2], 689 [$M^+$ + 1], 688 [$M^+$], 687 [$M^+$ – 1], 686 [$M^+$ – 2], 685 [$M^+$ – 3]. IR (KBr): $\tilde{\nu}$ = 3700–2700 [$\nu$(O–H)(coordinated MeOH)], 1637 [$\nu$(C=O)], 1576 [asymmetric $\nu(COO^-)$], 1466 [$\nu$(N–O)(coordinated)], 1431 and 1405 [symmetric $\nu(COO^-)$], 1252 [$\nu$(N–O)(coordinated)], 1091 [$\nu$(N–O)(coordinated)] cm$^{-1}$. $C_{25}H_{28}GdN_3O_{12}$ (719.7): calcd. C 41.72, H 3.92, N 5.84; found C 41.73, H 3.96, N 5.81.

**[(*N*-Methyl-3-indoleglyoxylate)$_2$Tb(NO$_3$)(MeOH)$_2$]$_n$ (6):** *N*-Methyl-3-indoleglyoxylic acid (200 mg) was used as the chelating ligand, and the purified product was isolated as a bright greenish-yellow powder. Yield: 323 mg (48%). MS (ESI, MeOH): *m*/*z* = 689 [$M^+$], 688 [$M^+$ – 1], 687 [$M^+$ – 2]. IR (KBr): $\tilde{\nu}$ = 3700–2700 [$\nu$(O–H)(coordinated MeOH)], 1637 [$\nu$(C=O)], 1574 [asymmetric $\nu(COO^-)$], 1466 [$\nu$(N–O)(coordinated)], 1431 and 1405 [symmetric $\nu(COO^-)$], 1253 [$\nu$(N–O)(coordinated)], 1090 [$\nu$(N–O)(coordinated)] cm$^{-1}$. $C_{25}H_{28}N_3O_{12}Tb$ (721.4): calcd. C 41.62, H 3.91, N 5.82; found C 41.63, H 3.96, N 5.81.

**Crystallography Data:** Single crystals that were suitable for X-ray crystallographic analyses of complexes **1** and **4** were mounted in glass capillaries. Diffraction data were collected at room temperature with a Bruker AXS SMART CCD diffractometer equipped with graphite-monochromated Mo-$K_\alpha$ radiation ($\lambda$ = 0.71073 Å). Crystallographic collection data and structure refinements are summarized in Table 2. Intensity data were also corrected for Lorentz and polarisation effects, and an approximation of absorption correction by inter-image scaling was applied. The space groups of both crystals were determined from a combination of Laue symmetry checks, and their systematic absences were confirmed by successful refinement of the structures. The structures were solved by direct methods, SIR 92[22] or SHELXS 97,[23] along with Fourier-difference techniques. Structural refinements were made on *F* by full-matrix least-squares analysis. The hydrogen atoms of the organic moieties were generated in their idealized position. All calculations were performed on a personal computer by using the program package CrystalStructure.[24] CCDC-600404 and -641121 contain the supplementary crystallographic data for this paper. These data can be obtained free of charge from The Cam-

Table 2. Crystal data and structure refinement parameters for **1** and **4**.

| | **1** | **4** |
|---|---|---|
| Empirical formula | $C_{18}H_{18}EuN_3O_6$ | $C_{25}H_{28}EuN_3O_{12}$ |
| Formula weight | 524.32 | 714.47 |
| Crystal color, habit | light yellow, rod | light yellow, plate |
| Crystal dimensions [mm] | 0.04 × 0.05 × 0.42 | 0.08 × 0.32 × 0.46 |
| Crystal system | monoclinic | monoclinic |
| Lattice type | primitive | primitive |
| Space group | $P2_1/c$ (#14) | $P2_1/c$ (#14) |
| *a* [Å] | 12.273(2) | 25.764(6) |
| *b* [Å] | 21.604(4) | 10.352(2) |
| *c* [Å] | 7.586(1) | 10.735(2) |
| $\beta$ [°] | 97.47(1)° | 94.720(10) |
| *V* [Å$^3$] | 1994.3(6) | 2853.4(10) |
| *Z* | 4 | 4 |
| $D_{calcd.}$ [g cm$^{-3}$] | 1.746 | 1.663 |
| $2\theta_{max}$ [°] | 55 | 55 |
| *F*(000) | 1032 | 1432 |
| $\mu$ (Mo-$K_\alpha$) [cm$^{-1}$] | 31.77 | 22.6 |
| Number of reflections measured | 24400 | 17621 |
| Number of unique reflections | 4567 | 6717 |
| $R_{int.}$ | 0.024 | 0.039 |
| Number of observed reflections [$I > 2\sigma(I)$] | 3068 | 5249 |
| Number of parameters | 268 | 408 |
| $R$[a] | 0.025 | 0.028 |
| $R_w$[b] | 0.029 | 0.062 |
| Goodness of fit (GOF)[c] | 1.051 | 1.042 |
| Max. shift / error | 0 | 0.02 |

[a] $R = [\Sigma(||F_o| - |F_c||)] / \Sigma|F_o|$. [b] $R_w = [\Sigma w(|F_o| - |F_c|)^2 / \Sigma w|F_o|^2]^{1/2}$. [c] GOF = $[\Sigma w(|F_o| - |F_c|)^2 / (N_{obs} - N_{param})]^{1/2}$.

 © 2007 Wiley-VCH Verlag GmbH & Co. KGaA, Weinheim 

bridge Crystallographic Data Centre via www.ccdc.cam.ac.uk/data_request/cif.

**Photophysical Measurements:** The UV/Vis absorption spectra were recorded by using a HP UV-8453 spectrophotometer to measure the range between 200 and 1100 nm in MeOH ($10^{-3}$ M). The solution-state excitation spectra were recorded by using a Perkin–Elmer LS 50B Luminescence spectrophotometer that was equipped with a R928 photomultiplier tube, and the spectra were corrected for detector response and stray background light. The solid samples were housed in an Oxford (CC1104) instruments closed-cycle cryostat pulsed by cryodrive (Edwards 1.5) for luminescence spectra collected at 10 K. The temperature was adjusted from 10 K to 300 K by using a programmable intelligent temperature controller (Oxford IT502). A He–Cd laser (Kimmon IK5352R-D) at 325 nm with a maximum power of 5 mW was used. The excitation light was modulated at 20 Hz by using a mechanical chopper (Stardford SR540). The emitted light from the sample was then collected and detected by using a 25-mm focal length double monochromator with a thermoelectrically cooled photomultiplier tube (PMT) (Hamamatsu R363–10) as the detector. For lifetime measurements, the 337-nm pulsed line from a nitrogen laser was used as the excitation light. The sample was pulsed by this light source with a 4-ns pulse width. The decay-time spectra were examined by a HP5452A 500 MHz oscilloscope.[15]

**Supporting Information** (see footnote on the first page of this article): Selected bond lengths and angles for **1** and **4**; solid-state emission spectra of the ligands $\mathbf{L^1}$ and $\mathbf{L^2}$.

## Acknowledgments

The authors acknowledge the financial support of the Hong Kong Research Grants Council, City University of Hong Kong and the University of Hong Kong. G. L. L. acknowledges the receipt of a postgraduate studentship administered by the University of Hong Kong, and K. L. W. acknowledges the Research Scholarship Enhancement Scheme of the City University of Hong Kong.

[1] S. P. Fricker, *Chem. Soc. Rev.* **2006**, *6*, 524–533.
[2] A. Beerby, L. M. Bushby, D. Maffeo, J. A. G. Williams, *J. Chem. Soc. Dalton Trans.* **2002**, 48–54.
[3] K.-L. Wong, W.-M. Kwok, W.-T. Wong, D. L. Phillips, K.-W. Cheah, *Angew. Chem. Int. Ed.* **2004**, *43*, 4659–4662.
[4] G. F. de Sá, O. L. Malta, C. Mello Donegá, A. M. Simas, R. L. Longo, P. A. Santa-Cruz, E. F. da Silva Jr., *Coord. Chem. Rev.* **2000**, *196*, 165–195.
[5] H. C. Aspinal, *Chem. Rev.* **2002**, *102*, 1807–1850.
[6] A. de Bettencourt-Dias, A. Poloukhtine, *J. Phys. Chem. B* **2006**, *110*, 25638–25645; S. Visaanathan, A. de Bettencourt-Dias, *Inorg. Chem.* **2006**, *45*, 10138–10146; D. Parker, R. S. Dickins, H. Puschmann, C. Crossland, J. A. K. Howard, *Chem. Rev.* **2002**, *102*, 1977–2010.
[7] J. Zhang, P. D. Badger, S. J. Geib, S. Petoud, *Angew. Chem. Int. Ed.* **2005**, *44*, 2508–2512.
[8] J.-C. G. Bunzli, C. Piguet, *Chem. Rev.* **2002**, *102*, 1897–1928.
[9] H. Tsukube, S. Shinoda, *Chem. Rev.* **2002**, *102*, 2389–2404.
[10] I. Lukeš, J. Kotek, P. Vojtıšek, P. Hermann, *Coord. Chem. Rev.* **2001**, *216–217*, 287–312.
[11] W. P.-W. Lai, W.-T. Wong, B. K.-F. Li, K.-W. Cheah, *New J. Chem.* **2002**, *26*, 576–581.
[12] A. W.-H. Lam, W.-T. Wong, S. Gao, G.-H. Wen, X.-X. Zhang, *Eur. J. Inorg. Chem.* **2003**, 149–163.
[13] J. Sztucki, W. Stręk, *Chem. Phys.* **1990**, *143*, 347–357.
[14] J.-C. G. Bunzli, "Spectroscopic Properties of Rare Earths" in *Optical Materials* (Ed.: G. K. Liu), Springer-Verlag, Berlin, **2002**.
[15] L. D. Carlos, J. A. Fernandes, R. A. Sá Ferreira, O. L. Malta, I. S. Gonçalves, P. Ribeiro-Claro, *Chem. Phys. Lett.* **2005**, *413*, 22–24.
[16] R. Pavithran, M. L. P. Reddy, S. A. Junior, R. O. Freire, G. B. Rocha, P. P. Lima, *Eur. J. Inorg. Chem.* **2005**, 4129–4137.
[17] M. Latva, H. Takalo, V. M. Mukkala, C. Matachescu, J. C. Rodríguez-Ubis, J. Kankare, *J. Lumin.* **1997**, *75*, 149–169.
[18] G. R. Choppin, D. R. Peterman, *Coord. Chem. Rev.* **1998**, *174*, 283–299.
[19] M. Shi, F. Li, T. Yi, D. Zhang, H. Hu, C. Huang, *Inorg. Chem.* **2005**, *44*, 8929–8936.
[20] A. Dadabhoy, S. Faulkner, P. G. Sammes, *J. Chem. Soc., Perkin Trans. 2* **2002**, 348–357.
[21] D. D. Perrin, W. L. F. Armarego, *Purification of Laboratory Chemicals*, Pergamon, Oxford, 4th ed., **1996**.
[22] *SIR 92*: A. Altomare, G. Cascarano, C. Giacovazzo, A. Guagliardi, M. C. Brula, G. Polidori, M. Camalli, *J. Appl. Crystallogr.* **1994**, *27*, 435.
[23] G. M. Sheldrick, *SHELXS 97*, University of Göttingen, Germany, **1997**.
[24] *CrystalStructure*, Single Crystal Structure Analysis Software, version 3.5.1, Rigaku/MSC Corporation, Rigaku/MSC, 9009 New Trails Drive, The Woodlands, Texas, USA, Rigaku, Akishima, Tokyo, Japan, **2003**; D. J. Watkin, C. K. Prout, J. R. Carruthers, P. W. Betteridge, *Crystals*, Chemical Crystallography Lab., Oxford, UK, **1996**, issue 10.

Received: June 5, 2007
Published Online: October 17, 2007

 © 2007 Wiley-VCH Verlag GmbH & Co. KGaA, Weinheim 

DOI: 10.1002/ejic.200700586

# Transition-Metal Porous Coordination Polymers with a Podand Ligand: Structure of Discrete Water Clusters and Variable-Temperature Magnetism

**Subhadip Neogi,[a] E. Carolina Sañudo,[b] and Parimal K. Bharadwaj*[a]**

**Keywords:** Water clusters / Coordination polymers / Metal–organic frameworks / Podand ligands / Magnetism

The podand ligand tris(4-carboxy-2-phenoxyethyl)amine ($ptaH_3$) readily reacts with $Co^{II}$, $Mn^{II}$ and $Ni^{II}$ salts at room temperature to afford porous coordination polymers, $\{Co(ptaH)\cdot 5H_2O\}_n$ (**1**), $\{[Mn(ptaH)(H_2O)]\cdot 4H_2O\}_n$ (**2**), and $\{[Ni(ptaH)(4H_2O)]\cdot 6H_2O\}_n$, (**3**). Crystallographic studies performed on these systems reveal that their structures are based on infinite chains of interlinked metallacycles. The bridging carboxylate groups extend the open framework structures, with oval-shaped voids. Supramolecularly assembled water clusters of different sizes, whose structures are proportionate with the size and shape of the MOFs, fill these voids. While discrete $(H_2O)_{10}$ clusters are present in **1** and **2**, both $(H_2O)_2$ and $(H_2O)_{16}$ clusters occupy the voids in **3**. Magnetic susceptibility measurements, in the temperature range 2–300 K, on **1** and **2** reveal that the metal centers are antiferromagnetically coupled in each case.
(© Wiley-VCH Verlag GmbH & Co. KGaA, 69451 Weinheim, Germany, 2007)

## Introduction

Supramolecular association of water molecules in diverse environments has been a subject of considerable current interest.[1–5] This is because the key to test and calibrate theoretical studies in order to understand the properties of bulk water is the precise structural data of hydrogen-bonded small water clusters in diverse environments. The advantage of clusters is the possibility to simply vary the size and to investigate the development of properties of the condensed phase in a step by step manner. Bulk water exhibits a fascinating array of properties, some of which are considered anomalous, and this is due to tremendous fluctuations in H-bonding interactions and rearrangement dynamics among the water molecules in a group. However, this diversity of H-bonding interactions is very crucial in the biological world as it can enforce a delicate balance[6] between several possible conformations of enzymes essential for expressing their functional behavior. In the abiological world, the degree of structuring of the water clusters can influence the structure of metal–organic open frameworks (MOF), where both water–MOF and water–water interactions can be the driving force that affects the overall structure. It follows, therefore, that an understanding of the formation of water clusters is important from the perspective of stabilization and functioning of biomolecules, as well as the structure of MOFs. In addition, they are of relevance in the study[7] of cloud and ice formation, solution chemistry, among others.

MOF structures of paramagnetic metal ions are particularly interesting as these may give rise to a series of novel framework structures with potential applications in the fields of molecular magnetism[8] and materials chemistry.[9] A commonly used strategy in building such extended network structures is to employ bridging ligands that are capable of transmitting magnetic interactions in addition to propagating the network.

We have initiated a research program to synthesize porous coordination polymers with the ultimate goal(s) of having new materials for magnetism, supramolecular storage of guest molecules, and catalysis among other applications. We describe here the formation of three MOFs with $Mn^{II}$, $Co^{II}$, and $Ni^{II}$ metal ions and a tripodal ligand,[10] with an aromatic carboxylate group at each terminal. The position of the carboxylate groups in the ligand excludes the formation of a homoleptic metal complex and favors the binding of more than one metal ion, which leads to a carboxylate-bridged MOF structure. This ligand, therefore, allows us to study the magnetic behavior of the MOF formed, as well as the structure of the water clusters present in the voids.

## Results and Discussion

The MOFs once isolated are found to be stable in air and insoluble in water or any common organic solvent. All the compounds show strong IR absorption bands between 1350 and 1550 $cm^{-1}$ characteristic[10] of coordinated carboxylate groups.

[a] Department of Chemistry, Indian Institute of Technology, Kanpur 208016, India
[b] Departament de Química Inorgànica, Universitat de Barcelona, Diagonal 647, 08028 Barcelona, Spain
E-mail: pkb@iitk.ac.in
Supporting information for this article is available on the WWW under http://www.eurjic.org or from the author.

 © 2007 Wiley-VCH Verlag GmbH & Co. KGaA, Weinheim 

The structure of **1** consists of $Co^{II}$ ions, a partially deprotonated $ptaH^{2-}$ ligand, and water molecules. Hexacoordination of the metal is fulfilled by four carboxylate groups from four different ligand units (Scheme 1). Here, two carboxylate groups donate both their O atoms, one carboxylate group donates one O atom (the other O atom is donated to a different $Co^{II}$ ion), while the fourth carboxylate is protonated and donates a single O atom. This leads to a 2D coordination polymer built from metallacycles that extend along the crystallographic *a* axis (Figure 1). The bridging carboxylate group extends the structure in the third dimension. The position of the H atom attached to the carboxylate group could not be located in the difference maps. In this structure, Co–O(carboxylate) bond lengths span the range 2.018(2)–2.179(2) Å and compare well with the distances found in other octahedral $Co^{II}$–carboxylate structures.[11] Bond angles around the metal do not deviate significantly from the ideal octahedral coordination geometry. The overall structure of **1** is quite similar to the Cd complex reported by us previously.[10c] However, subtle differences remain between the two structures.

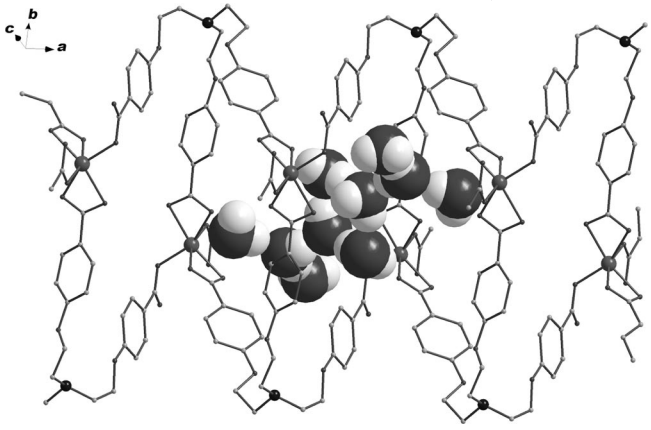


Figure 1. Perspective view of the decameric water cluster in the metallacyclic cavity in **1**.

The coordination mode of $Mn^{II}$ in **2** is slightly different from that of **1**. Each $Mn^{II}$ ion is bonded to four carboxylate groups from four different $ptaH^{2-}$ units and to one water

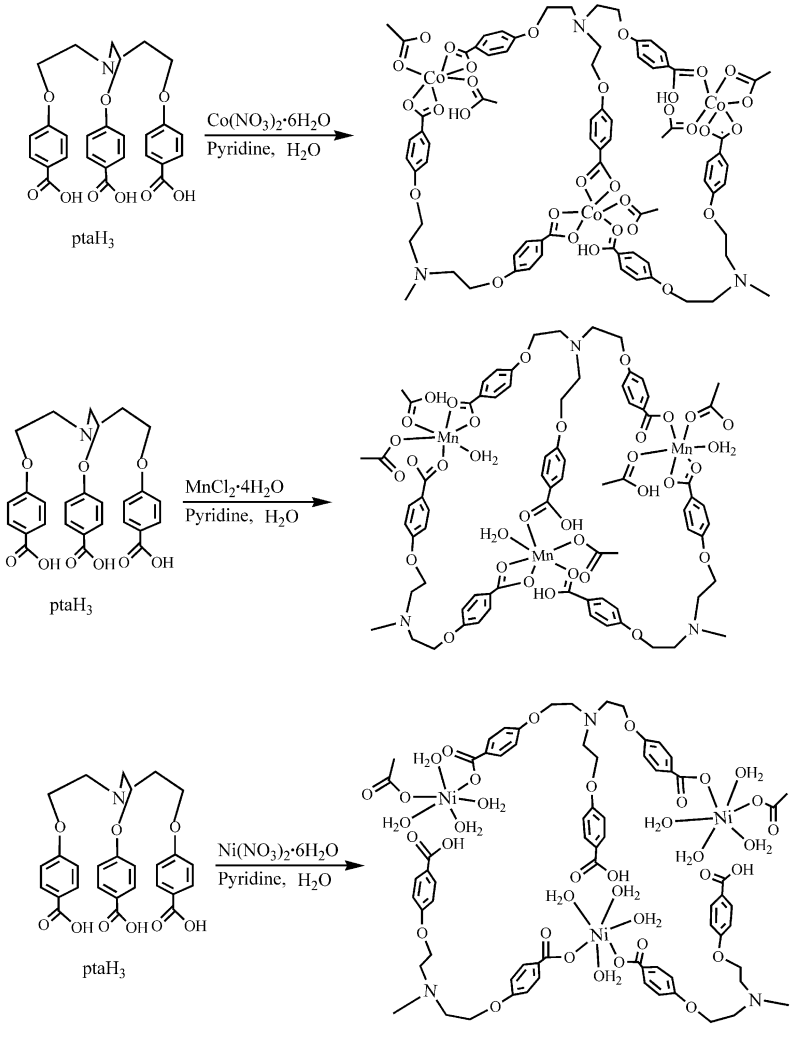


Scheme 1. Bonding scheme for the compounds **1**, **2** and **3**.

 © 2007 Wiley-VCH Verlag GmbH & Co. KGaA, Weinheim 

molecule. While one carboxylate group donates both its O atoms, the remaining three donate one O atom each, and the sixth coordination position is occupied by an $H_2O$ molecule (Scheme 1). As in **1**, the metallacycles propagate along the crystallographic *a* axis (Figure 2).

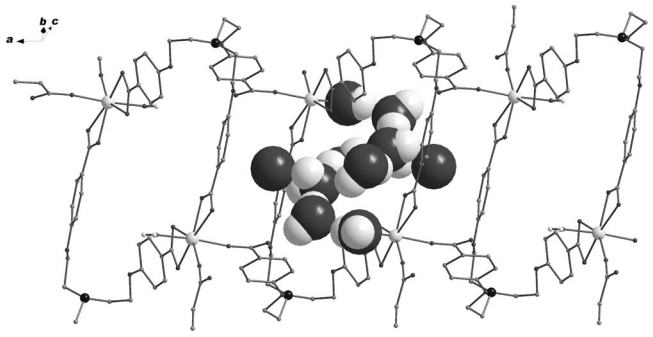

Figure 2. The oval-shaped cavity in **2** with embedded discrete $(H_2O)_{10}$ cluster.

In **3**, only two arms of $ptaH^{2-}$ are bonded to the $Ni^{II}$ ions, while the third arm is free. Each metal ion is hexacoordinate, with ligation from two carboxylate O atoms from two different ligands and four water molecules to form a coordination polymeric chain extending along the crystallographic *a* axis. Two metal-bound water molecules from one polymeric chain is H-bonded to the uncoordinated carboxylate group of another chain to form an overall 2D structure (Figure 3) with cavities that are much larger than those present in **1** and **2**. As in the previous cases, the H atom attached to one of the carboxylate groups of the ligand could not be located in the difference maps.

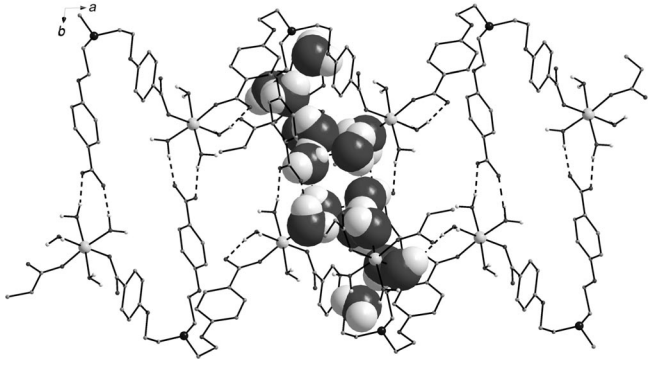

Figure 3. A view of the hexadecameric water cluster inside the H-bonded interlinked metallacycles in **3**. Only the H atoms attached to the water molecules are shown for clarity.

In **1**, the metallacycles have two different dimensions. In the first, two $Co^{II}$ ions exhibit a distance of 9.37 Å, while the distance between two bridgehead nitrogen atoms is 18.92 Å. For the adjacent matallacycle, these dimensions are 10.71 and 18.38 Å, respectively. Similarly, in **2**, in one metallacycle, the $Mn^{II}\cdots Mn^{II}$ distance is 9.98 Å, while the N···N distance is 18.67 Å. For the adjacent metallacycle, these distances are 11.15 and 17.81 Å, respectively. It follows, therefore, that the cavity in **1** is narrower than that of **2**. This difference is reflected in the structures of the $(H_2O)_{10}$ clusters present in the cavities of the two MOFs.

The $(H_2O)_{10}$ cluster in **1** can be viewed as that derived from a cyclic tetramer connected by acyclic trimers at the two opposite ends (Figure 4a). The tetrameric unit is quasiplanar, similar to that predicted theoretically[12] and found in several crystal hydrates.[13] The Ow···Ow distances (2.84–2.76 Å) and O···H–O angles (158.5–169.1°) suggest strong H-bonding interactions between the water molecules. The atoms Ow1, Ow2, Ow1′ and Ow2′ act as H-bond donors to the available carboxylate O atoms with Ow···O (carboxylate) distances in the range 2.76–2.82 Å (Table 1), which maintain strong water–MOF interactions as well. The distance between Ow5 and Ow5′ is within H-bonding distance (2.79 Å). However, these atoms are related by a center of symmetry, and their corresponding H atoms are oriented either towards or away from each other and are not considered to be H-bonded. The H···H separation of 1.07 Å is, however, shorter than the shortest intermolecular H···H separation (1.949 Å) found in the polymorph A of 1,2,3,5-

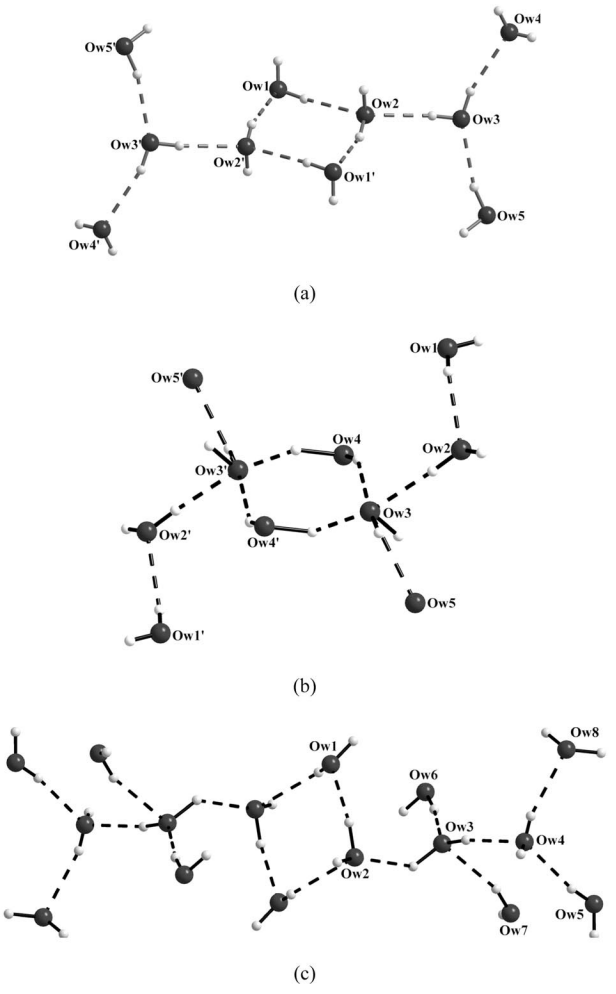


Figure 4. Closer views of the water clusters in (a) **1**, (b) **2**, and (c) **3**, showing the atom numbering scheme.

 © 2007 Wiley-VCH Verlag GmbH & Co. KGaA, Weinheim 

tetra-*O*-acetyl-β-D-ribofuranose[14a] or in a $Zn^{II}$ complex[14b] that crystallizes in presence of nitrobenzene as the guest. The repulsive interaction associated with this short distance is compensated by strong nonbonding water–MOF interactions.

Table 1. Non-bonding distances [Å] and angles [°] for the water clusters in **1**–**3**.

| | | | |
|---|---|---|---|
| **1** | | | |
| Ow1···Ow2 | 2.84(4) | Ow3···Ow5 | 2.78(3) |
| Ow1···Ow2′ | 2.76(4) | Ow1···O9 | 2.76(3) |
| Ow2···Ow3 | 2.79(4) | Ow2···O2 | 2.82(4) |
| Ow3···Ow4 | 2.77(3) | Ow4···O8 | 2.93(4) |
| Ow1···Ow2···Ow1′ | 101.4(9) | Ow2–H···Ow1′ | 161.9(1) |
| Ow1···Ow2···Ow3 | 119.3(9) | Ow3–H···Ow2 | 169.1(2) |
| Ow1′···Ow2···Ow3 | 136.2(9) | Ow3–H···Ow4 | 158.5(2) |
| Ow2···Ow3···Ow4 | 115.2(9) | Ow5–H···Ow3 | 165.5(6) |
| Ow2···Ow3···Ow5 | 107.7(8) | Ow1–H···O9 | 160.6(3) |
| Ow4···Ow3···Ow5 | 135.8(9) | Ow2–H···O2 | 160.6(2) |
| Ow1–H···Ow2 | 168.4(2) | Ow4–H···O8 | 152.3(2) |
| **2** | | | |
| Ow1···Ow2 | 2.75(8) | Ow1···O9 | 2.75(9) |
| Ow2···Ow3 | 2.73(2) | Ow2···O9 | 2.73(7) |
| Ow3···Ow4 | 2.62(3) | | |
| Ow3···Ow4′ | 2.88(3) | | |
| Ow3···Ow5 | 2.56(5) | | |
| Ow1···Ow2···Ow3 | 110.1(5) | Ow2–H···Ow3 | 171.0(5) |
| Ow2···Ow3···Ow4 | 92.6(6) | Ow4–H···Ow3 | 143.3(8) |
| Ow2···Ow3···Ow4′ | 153.7(7) | Ow4′–H···Ow3 | 136.9(7) |
| Ow2···Ow3···Ow5 | 95.9(1) | Ow3–H···Ow5 | 125.4(2) |
| Ow4···Ow3···Ow4′ | 76.9(5) | Ow1–H···O9 | 168.9(4) |
| Ow1–H···Ow2 | 156.3(4) | Ow2–H···O9 | 162.4(1) |
| **3** | | | |
| Ow1···Ow2 | 2.76(9) | Ow1···O8 | 2.76(7) |
| Ow1···Ow2′ | 2.73(7) | Ow2···O5 | 2.82(9) |
| Ow2···Ow3 | 2.82(6) | Ow4···O3 | 2.67(7) |
| Ow3···Ow4 | 2.71(1) | Ow5···O9 | 2.82(8) |
| Ow3···Ow6 | 2.78(6) | Ow6···O6 | 2.67(8) |
| Ow3···Ow7 | 2.96(9) | Ow7···O9 | 2.57(8) |
| Ow4···Ow5 | 2.71(8) | Ow8···O3 | 2.72(8) |
| Ow4···Ow8 | 2.72(9) | Ow9···O5 | 2.75(6) |
| Ow9···Ow10 | 2.72(5) | Ow10···O5 | 2.80(6) |
| Ow1···Ow2.Ow1′ | 92.8(2) | Ow1–H···Ow2′ | 148.5(2) |
| Ow2···Ow1···Ow2′ | 87.2(1) | Ow3–H···Ow2 | 134.7(2) |
| Ow2···Ow3···Ow4 | 111.9(2) | Ow8–H···Ow4 | 169.3(2) |
| Ow2···Ow3···Ow6 | 112.8(2) | Ow9–H···Ow10 | 169.7(3) |
| Ow2···Ow3···Ow7 | 133.5(2) | Ow3–H···Ow4 | 158.07(2) |
| Ow3vOw4···Ow5 | 110.8(1) | Ow4–H···Ow5 | 159.6(2) |
| Ow3···Ow4···Ow8 | 108.5(2) | Ow6–H···Ow3 | 171.3(2) |
| Ow1–H···Ow2 | 147.6(3) | Ow7–H···Ow3 | 162.7(2) |
| Ow1–H···O8 | 156.7(2) | Ow7–H···O9 | 163.5(2) |
| Ow2–H···O5 | 168.6(2) | Ow8–H···O3 | 162.2(2) |
| Ow4–H···O3 | 170.0(3) | Ow9–H···O5 | 161.6(2) |
| Ow5–H···O9 | 175.9(2) | Ow10–H···O5 | 159.2(2) |
| Ow6–H···O6 | 172.4(2) | | |

The water decamer in **2** has a different structure. The cyclic tetramer is connected to two dimers at opposite ends, where two single water molecules are also H-bonded (Figure 4b). This cluster of water molecules requires more space than those present in **1** and therefore **2** has a larger void space. The water molecules are quite strongly H-bonded to each other as evident from the O···O distances (2.54–2.87 Å) and O···H–O angles (136.9- 171.0°). It is to be noted here that the H atoms attached to Ow5 could not be located in the difference maps. As in the case of **1**, Ow5 and Ow5′ are within H-bonding distance (2.43 Å). Since they are related by a center of symmetry, they are not considered to be H-bonded following the same argument as that made for **1**. This cluster is H-bonded to available carboxylate O atoms with Ow···O distances in the range 2.73–2.75 Å. Buck et al. had suggested[15] that the minimum energy conformation for the decamer is an octameric cube with two water molecules fused at one of the edges, while a more recent calculation showed that two fused parallel pentamers to be the energetically most stable from.[16] Whereas few water decamers[17] with different structures have been identified in metal–ligand hybrids or purely organic crystals, decamers in the form of two fused parallel cyclic pentamers with staggered conformation have been characterized[18] in organic hosts. The structures of the $(H_2O)_{10}$ clusters in **1** and **2** are different from any of these and result from strong water–MOF and water–water interactions.

The large H-bonded cavity in **3** can accommodate higher nuclearity clusters. Eight water molecules from each asymmetric unit are supramolecularly connected to centrosymmetrically related eight more molecules to form a $(H_2O)_{16}$ cluster that occupies the void between two polymeric chains (Figure 3). The structure can be described as a tetrameric core to which two hexameric units are attached at opposite ends. A $(H_2O)_{16}$ cluster in a $Cu^{II}$-containing MOF was identified earlier[19] to resemble the shape and size of the void for optimum MOF–water interactions. Theoretical calculations on the $(H_2O)_{16}$ cluster[20] show a number of local minima, including fused cubes derived from the $D_{2d}$ and $S_4$ forms of the $(H_2O)_8$ unit as well as five-membered rings, two of which also contain one six-membered ring. A closer view of the $(H_2O)_{16}$ cluster in **3** (Figure 4c) shows a wide variation in the O···O nonbonding distances (2.96–2.71 Å) relative to 2.759 Å in ice $I_h$ or 2.85 Å in liquid water.[21] The O···O···O angles also vary widely (133.5–87.2°) with an average value of 110.3°. The shape of the cavity in **3** closely follows the shape of the water cluster to maximize the strength as well as the number of interactions with the MOF.

Thermal gravimetric analysis of compound **1** in air shows that weight loss begins at 60 °C, and the loss of 13.6%, which corresponds to the loss of all water molecules (calculated 13.72%), takes place above 200 °C, and soon after, the compound decomposes. The thermogravimetric curve of **2** shows a plateau, and weight loss begins at 60 °C, and the loss of 13.7%, which corresponds to the loss of all water molecules (calculated 13.80%), takes place beyond 200 °C. Complete breakdown of the structure takes place at about 270 °C. Thermal gravimetric analysis of **3** in air shows that the removal of water occurs in stages, beginning at 50 °C, and the loss of 24%, which corresponds to the loss of all water molecules (calculated 24.1%), takes place above 150 °C. Complete decomposition is achieved above approximately 240 °C.

 © 2007 Wiley-VCH Verlag GmbH & Co. KGaA, Weinheim 

## Magnetic Studies

Since paramagnetic transition metal ions are present with carboxylate bridges in both **1** and **2**, magnetic susceptibility studies were performed on **1** and **2**. Variable-temperature magnetic susceptibility data were collected for **1** in the temperature range 2–300 K with an applied magnetic field of 0.5 T. The susceptibility increases smoothly with decreasing temperature (Figure 5a), and the change in susceptibility as a function of temperature follows the Curie–Weiss law at temperatures above 200 K. The value of the Curie constant (3.38 $cm^3 K mol^{-1}$) is consistent with hexacoordinate high-spin $Co^{II}$ ions (2.8–3.4 $cm^3 K mol^{-1}$) [22]; the Curie–Weiss constant has a negative value of –23.71 K, which indicates antiferromagnetic interactions between the metal centers. When analyzing the $\chi T$ versus $T$ plot, the decrease observed is due to the depopulation of the $J$ = 5/2 state and the preferential population of the $J$ = 1/2 state, in addition to any possible interaction between the $Co^{II}$ ions. The $\chi T$ value of 3.14 $cm^3 K mol^{-1}$ per $Co^{II}$ ion at 300 K is in agreement with the expected value for a distorted octahedral $Co^{II}$ ion with strong spin-orbit coupling. As the temperature decreases, so does the value for $\chi T$, until at 2 K, it reaches the value of 1.26 $cm^3 K mol^{-1}$ per $Co^{II}$ ion. This value is significantly smaller than that expected for isolated $Co^{II}$ centers (1.875 $cm^3 K mol^{-1}$). The magnetization versus field plot (Figure 5b) saturates at a value of 2.06 at 5.0 T, as expected, which is significantly lower than that predicted by the Brillouin law ($Co^{II}$ ion with spin-orbit coupling $S_{eff}$ = 1/2 and $g$ = 4.33[21]); this further supports a weak antiferromagnetic coupling between the $Co^{II}$ ions in **1**. In the 3D network, the $Co^{II}$ ions are grouped in pairs, bridged by two *syn*-, *anti*-carboxylate arms of the $ptaH^{2-}$ ligands. This type of bonding leads to weak antiferromagnetic interactions,[23] as observed in **1**.

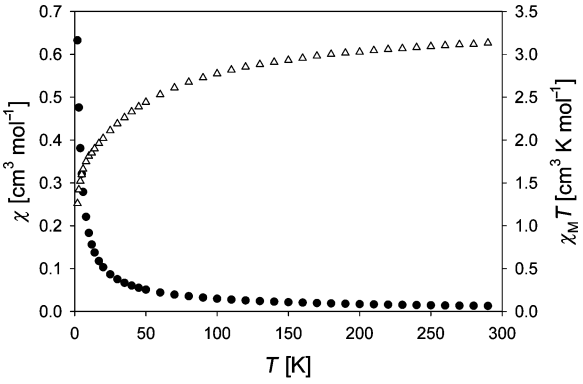


(a)

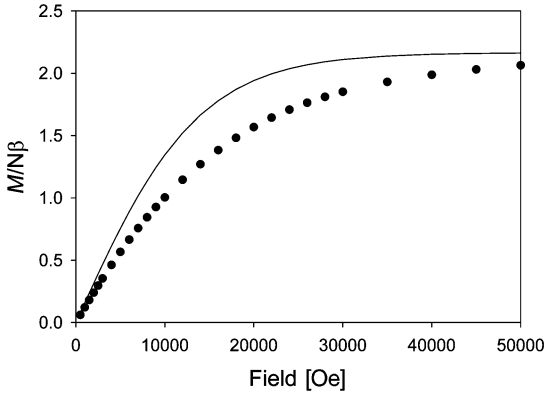


(b)

Figure 5. (a) Temperature dependence of the magnetic susceptibility of **1**. $\chi$ is shown as circles, $\chi T$ is shown as triangles. (b) Magnetization plot for compound **1**. The solid line is the Brillouin function for a $Co^{II}$ ion with spin-orbit coupling.

Figure 6 shows the temperature dependence of the magnetic susceptibility of compound **2** at an applied DC field of 0.3 T in the temperature range 2–300 K and at 200 G below 25 K. In the solid-state structure of **2**, the $Mn^{II}$ ions are arranged in dimers, which, in turn, are organized into a 3D network by the ligands. The dimers are held at an average distance of 10 Å by the $ptaH^{2-}$ ligand, and thus, from a magnetic point of view, the sample has been treated as isolated $[Mn^{II}]_2$ units. The $\chi T$ product at 300 K has a value of 9.2 $cm^3 K mol^{-1}$, slightly above that expected for two noninteracting $Mn^{II}$ ions (4.375 $cm^3 K mol^{-1}$ per $Mn^{II}$, $S$ = 5/2). As the temperature decreases, the $\chi T$ product decreases very slowly to a value of 8.0 $cm^3 K mol^{-1}$ at 50 K and then sharply decreases to 1.1 $cm^3 K mol^{-1}$ at 2 K, which indicates weak antiferromagnetic coupling between the manganese centers, leading to $S$ = 0. The magnetization at 2 K rises continuously with the field to a value of 2.8 at 5 T, without reaching saturation, and confirms the $S$ = 0 value predicted from the susceptibility versus $T$ data. A simple Van Vleck equation[24] for a dimeric $S$ = 5/2 system was used to fit the experimental data. A good agreement between the experimental and calculated data was obtained for $J$ = –0.70 $cm^{-1}$ and $g$ = 2.07, with a TIP of $120 \times 10^{-6}$ $cm^3 mol^{-1}$ over the entire temperature range. The fit is shown in Figure 5 as a solid line. The weakness of the coupling is easily explained, given the very long Mn–Mn separation: the only possible exchange pathways are two *syn*-, *anti*-carboxylate groups from the ligand unit that hold the $Mn^{II}$ ions 3.86 Å apart. Only very weak coupling can be expected under these conditions, as confirmed by the experimental data. We have recorded FTIR spectra of all three compounds (see Supporting Information) to characterize the vibrational stretching frequency of the O–H bond of the water clusters. In each case, a broad peak appears that centers around 3420 $cm^{-1}$, which can be attributed to the water cluster. The IR spectrum of ice[13] shows the O–H stretching band at 3220 $cm^{-1}$, while this stretching vibration in liquid water[13] appears at 3490 and 3280 $cm^{-1}$. This suggests that the water clusters in **1**–**3** show O–H stretching vibrations similar to that of liquid water. This broad band significantly reduces on heating the compounds under vacuum (0.1 mm), which suggests that the water molecules escape from the lattice. Deliberate exposure to water vapor does not lead to reabsorption of water into the

 © 2007 Wiley-VCH Verlag GmbH & Co. KGaA, Weinheim 

lattice as monitored by FTIR spectroscopy. Powder X-ray diffraction patterns of the compounds before and after desolvation show major changes in the peak positions as well as in their intensities. Therefore, loss of water from the lattice leads to the breakdown of the framework structure, which supports the thermal analysis results.

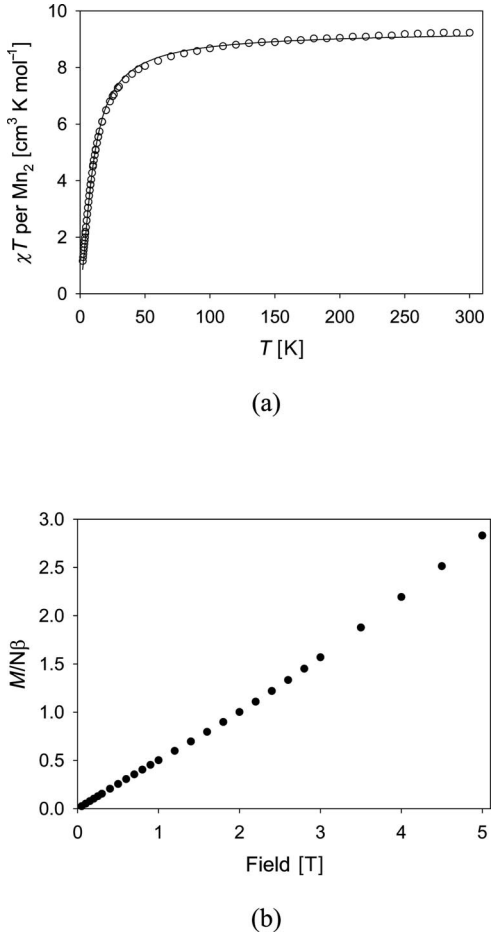


Figure 6. (a) Temperature dependence of the magnetic susceptibility of **2**. (b) Magnetization versus field plot at 2 K for compound **2**.

## Conclusions

In conclusion, we have characterized three different MOF structures of transition-metal ions with the tripodal ligand. The large voids present in the MOFs contain supramolecularly bound water molecules of different nuclearity. The size and shape of these water clusters closely follow the available volume of the void spaces. These water clusters act as a "glue" to reinforce the coordination polymeric chains and to extend the open framework structures. Variable-temperature magnetic susceptibility measurements on **1** and **2** reveal that the metal centers are *anti*-ferromagnetically coupled.

## Experimental Section

**Materials:** The metal salts were obtained from Aldrich and used as received. All other chemicals were procured from S. D. Fine Chemicals, India. All solvents were purified prior to use.

**Physical Measurements:** Spectroscopic data were collected as follows: IR (KBr disk, 400–4000 $cm^{-1}$) Perkin–Elmer Model 1320; X-ray powder pattern (Cu-$K_\alpha$ radiation at a scan rate of 3°/min, 293 K) Siefert ISODEBYEFLEX-2002 X-ray generator; thermogravimetric analysis (heating rate of 5 °C/min) Perkin–Elmer Pyris 6. Microanalyses for the compounds were obtained from the Central Drug Research Institute, Lucknow, India. Magnetic data were collected at the Unitat de Mesures Magnètiques at the Universitat de Barcelona by using crushed crystals of the sample on a Quantum Design MPMS-XL SQUID magnetometer equipped with a 5 T magnet. Diamagnetic corrections were calculated using Pascal's constants, and an experimental correction for the sample holder was applied.

**Synthesis**

The ligand tris(4-carboxy-2-phenoxyethyl)amine ($ptaH_3$) was prepared following the method described previously.[10c]

**{[Co(ptaH)]·5H$_2$O}$_n$ (1):** The tripodal ligand $ptaH_3$ (0.13 g, 0.25 mmol) was dissolved in a thf solution (10 mL) containing tetraethyl ammonium hydroxide (1.2 mL). To this, an aqueous solution of $Co(NO_3)_2{\cdot}6H_2O$ (0.15 g, 0.51 mmol) was added dropwise, and the reaction mixture stirred for 2 h at room temperature. Rectangular pink crystals suitable for X ray diffraction were obtained after 7 d on slow evaporation of the filtrate. Yield approximately 60%. $C_{27}H_{35}CoNO_{14}$: calcd. C 49.39, H 5.37, N 2.13; found C 49.97, H 5.16, N 2.34.

**{[Mn(ptaH)(H$_2$O)]·4H$_2$O}$_n$ (2):** The tripodal ligand $ptaH_3$ (0.13 g, 0.25 mmol) was dissolved in thf (10 mL) containing tetraethyl ammonium hydroxide solution (1.2 mL) whilst continuously stirring at room temperature. To this, an aqueous solution of $MnCl_2{\cdot}4H_2O$ (0.10 g, 0.50 mmol) was added, and the reaction mixture stirred for 2 h at room temperature. The resulting clear solution was allowed to evaporate at room temperature. Colorless, parallelepiped crystals of **2** were recovered after 10 d. Yield approximately 55%. $C_{27}H_{35}MnNO_{14}$: calcd. C 49.70, H 5.40, N 2.14; found C 50.18, H 5.17, N 2.65.

**{[Ni(ptaH)(4H$_2$O)]·6H$_2$O}$_n$ (3):** Compound **3** was isolated as dark green rectangular crystals following a similar method to that described for **1**, by using $Ni(NO_3)_2{\cdot}6H_2O$ in place of $Co(NO_3)_3{\cdot}6H_2O$ at room temperature. Yield approximately 60%. $C_{27}H_{45}NNiO_{19}$ (746.36): calcd. C 43.45, H 6.08, N 1.87; found C 43.68, H 6.21, N 2.04.

**X-ray Structural Studies:** Single-crystal X-ray data on **1**–**3** were collected at 100 K with a Bruker SMART APEX CCD diffractometer by using graphite-monochromated Mo-$K_\alpha$ radiation ($\lambda$ = 0.71073 Å), and the structures were solved and refined as described earlier.[8a] The H-bonding distances and angles for the water clusters in **1**–**3** are summarized in Table 1, and the crystal and refinement data are collected in Table 2. CCDC-646841 to -646843 for **1**–**3** contain the supplementary crystallographic data for this paper. These data can be obtained free of charge from The Cambridge Crystallographic Data Centre via www.ccdc.cam.ac.uk/data_request/cif.

**Supporting Information** (see footnote on the first page of this article): IR, TGA, X-ray powder diffraction patterns are presented. Additional figures showing structures of compounds **1**–**3** are also included.

 © 2007 Wiley-VCH Verlag GmbH & Co. KGaA, Weinheim 

Table 2. Crystal and structure refinement data for **1**–**3**.

| | | | |
|---|---|---|---|
| Empirical formula | $C_{27}H_{35}NO_{14}Co$ (**1**) | $C_{27}H_{35}NO_{14}Mn$ (**2**) | $C_{27}H_{45}NO_{19}Ni$ (**3**) |
| Formula weight | 656.49 | 652.50 | 746.35 |
| Temperature | 100(1)K | 100(1)K | 100(1)K |
| Radiation, wavelength | Mo-$K_\alpha$, 0.71073 Å | Mo-$K_\alpha$, 0.71073 Å | Mo-$K_\alpha$, 0.71073 Å |
| Crystal system | triclinic | triclinic | triclinic |
| Space group | $P\bar{1}$ | $P\bar{1}$ | $P\bar{1}$ |
| $a$ [Å] | 10.2111(9) | 10.743(5) | 11.203(2) |
| $b$ [Å] | 11.3529(10) | 12.614(5) | 11.605(2) |
| $c$ [Å] | 12.2940(11) | 12.659(5) | 13.237(2) |
| $\alpha$ [°] | 93.265(2) | 104.354(5) | 91.782(5) |
| $\beta$ [°] | 97.981(2) | 114.121(5) | 92.255(5) |
| $\gamma$ [°] | 94.308(2) | 94.527(5) | 98.886(5) |
| $V$ [Å$^3$] | 1404.1(2) | 1484.9(11) | 1697.8(12) |
| $Z$ | 2 | 2 | 2 |
| $\rho_{calcd.}$ [Mg/m$^3$] | 1.553 | 1.459 | 1.460 |
| $\mu$ [mm$^{-1}$] | 0.686 | 0.515 | 0.653 |
| $F(000)$ | 686 | 682 | 788 |
| Reflections collected | 9243 | 9741 | 11411 |
| Independent reflections | 6077 | 5514 | 6386 |
| Refinement method | Full-matrix least squares on $F^2$ | Full-matrix least squares on $F^2$ | Full-matrix least squares on $F^2$ |
| GOF | 1.143 | 1.046 | 1.146 |
| Final $R$ indices [$I > 2\sigma(I)$] | $R1$ = 0.049, $wR2$ = 0.093 | $R1$ = 0.079, $wR2$ = 0.116 | $R1$ = 0.060, $wR2$ = 0.098 |
| $R$ indices (all data) | $R1$ = 0.058, $wR2$ = 0.109 | $R1$ = 0.097, $wR2$ = 0.171 | $R1$ = 0.082, $wR2$ = 0.124 |

## Acknowledgments

P. K. B. acknowledges financial support from the Department of Science and Technology, New Delhi, India (grant No.SR/S5/NM-38/2003). S. N. thanks the CSIR, India for a Senior Research Fellowship. E. C. S acknowledges financial support from the Spanish Government (Grant CTQ2006/03949BQU and for a Juan de la Cierva fellowship).

[1] a) M. Mascal, L. Infantes, J. Chisholm, *Angew. Chem. Int. Ed.* **2006**, *45*, 32; b) L. Infantes, J. Chisholm, S. Motherwell, *CrystEngCommun.* **2003**, *5*, 480; c) J. Chisholm, E. Pidcock, J. Streek, L. Infantes, S. Motherwell, F. H. Allen, *CrystEngCommun* **2006**, *1*, 11; d) L. Infantes, L. Fábián, W. D. S. Motherwell, *CrystEngCommun.* **2007**, *1*, 65.

[2] a) A. Michaelides, S. Skoulika, E. G. Bakalbassis, J. Mrozinski, *Cryst. Growth Des.* **2003**, *3*, 487; b) B. Sreenivasulu, J. J. Vittal, *Angew. Chem. Int. Ed.* **2004**, *43*, 5769.

[3] K. Raghuraman, K. K. Katti, L. J. Barbour, N. Pillarsetty, C. L. Barnes, K. V. Katti, *J. Am. Chem. Soc.* **2003**, *125*, 6955.

[4] a) A. Müller, E. Krickemeyer, H. Bögge, M. Schmidtmann, B. Botar, M. O. Talismanova, *Angew. Chem. Int. Ed.* **2003**, *42*, 2085; b) L. E. Cheruzel, M. S. Pometun, M. R. Cecil, M. S. Mashuta, R. J. Wittebort, R. M. Buchanan, *Angew. Chem. Int. Ed.* **2003**, *42*, 5452.

[5] a) B.-Q. Ma, H.-L. Sun, S. Gao, *Angew. Chem. Int. Ed.* **2004**, *43*, 1374; b) A. Nangia, *Water Clusters in Crystal Hydrates*, Encyclopedia of Supramolecular Chemistry, **2007**, p.1.

[6] A. Ben-Naim, *Biophys. Chem.* **2002**,*101*, 309.

[7] K. Koga, H. Tanaka, X. C. Zen, *Nature* **2000**, *408*, 564.

[8] a) O. Kahn, *Molecular Magnetism*, Wiley-VCH, New York, **1993**; b) J. S. Miller, A. J. Epstein, *Angew. Chem. Int. Ed. Engl.* **1994**, *33*, 385; c) M. Ohba, H. Okawa, *Coord. Chem. Rev.* **2000**, *198*, 313; d) A. J. Tasiopoulos, A. Vinslava, W. Wernsdorfer, K. A. Abboud, G. Christou, *Angew. Chem. Int. Ed.* **2004**, *43*, 2117.

[9] a) S. Kitagawa, R. Kitaura, S.-I. Noro, *Angew. Chem. Int. Ed.* **2004**, *43*, 2334;. b) J. L. C. Rowsell, O. M. Yaghi, *Angew. Chem. Int. Ed.* **2005**, *44*, 4670; c) C. J. Kepert, M. J. Rosseinsky, *Chem. Commun.* **1999**, 375; d) M. Dincă, A. Dailly, Y. Liu, C. M. Brown, D. A. Neumann, J. R. Long, *J. Am. Chem. Soc.* **2006**, *128*, 16876; e) G. Férey, C. Mellot-Draznieks, C. Serre, F. Millange, J. Dutour, S. Surblé, I. Margiolaki, *Science* **2005**, *309*, 2040; f) C.-D. Wu, W. Lin, *Angew. Chem. Int. Ed.* **2005**, *44*, 1958.

[10] a) S. Neogi, G. Savitha, P. K. Bharadwaj, *Inorg. Chem.* **2004**, *43*, 3771; b) S. Neogi, P. K. Bharadwaj, *Inorg. Chem.* **2005**, *44*, 816; c) S. Neogi, P. K. Bharadwaj, *Cryst. Growth Des.* **2006**, *6*, 433; d) S. Neogi, P. K. Bharadwaj, *Polyhedron* **2006**, *25*, 1491.

[11] R. H. Groeneman, L. R. MacGillivray, J. L. Atwood, *Inorg. Chem.* **1999**, *38*, 208.

[12] a) S. Pal, N. B. Sankaran, A. Samanta, *Angew. Chem. Int. Ed.* **2003**, *42*, 1741; b) S. Supriya, S. Manikumari, P. Raghavaiah, S. K. Das, *New J. Chem.* **2003**, *27*, 218.

[13] J. D. Cruzan, L. B. Braly, K. Liu, M. G. Brown, J. G. Loeser, R. J. Saykally, *Science* **1996**, *271*, 59.

[14] a) P. Bombicz, M. Czugler, R. Tellgren, A. Kálmán, *Angew. Chem. Int. Ed.* **2003**, *42*, 1957; b) S. Das, P. K. Bharadwaj, *Inorg. Chem.* **2006**, *45*, 5257.

[15] U. Buck, F. Huisken, *Chem. Rev.* **2000**, *100*, 3863.

[16] S. Maheswary, N. Patel, N. Sathyamurthy, A. D. Kulkarni, S. R. Gadre, *J. Phys. Chem. A* **2001**, *105*, 10525.

[17] a) N.-H. Hu, Z.-G. Li, J.-W. Xu, H.-Q. Jia, J.-J. Niu, *Cryst. Growth Des.* **2007**, *7*, 15; b) M. Estrader, J. Ribas, V. Tangoulis, X. Solans, M. F. Bardia, M. Maestro, C. Diaz, *Inorg. Chem.* **2006**, *45*, 8239; c) M. Yoshizawa, T. Kusukawa, M. Kawano, T. Ohhara, I. Tanaka, K. Kurihara, N. Nimura, M. Fujita, *J. Am. Chem. Soc.* **2005**, *127*, 2798; d) R. D. Bergougnant, A. Y. Robin, K. M. Fromm, *Cryst. Growth Des.* **2005**, *5*, 1691; e) L. J. Barbour, G. W. Orr, J. L. Atwood, *Nature* **1998**, *393*, 671.

[18] a) O. Ermer, J. Neudörfl, *Chem. Eur. J.* **2001**, *7*, 4961; b) S. K. Ghosh, P. K. Bharadwaj, *Eur. J. Inorg. Chem.* **2006**, 1341.

[19] S. K. Ghosh, P. K. Bharadwaj, *Inorg. Chem.* **2004**, *43*, 6887.

[20] K. D. Jordan, C. J. Tsai, *J. Phys. Chem.* **1993**, *97*, 5208.

[21] a) D. Eisenberg, W. Kauzmann, *The Structure and Properties of Water, Oxford University Press*, Oxford, **1969**; b) N. H. Fletcher, *The Chemical Physics of Ice*, Cambridge University Press, Cambridge, **1970**.

[22] R. L. Carlin *Magnetochemistry*, Springer-Verlag, Berlin, Heidelberg, **1986**.

[23] J. M. Rueff, N. Masciocchi, P. Rabu, A. Sironi, A. Skoulios, *Eur. J. Inorg. Chem.* **2001**, 2843.

[24] C. J. O'Connor, *Prog. Inorg. Chem* **1982**, *29*, 203.

Received: June 5, 2007
Published Online: October 2, 2007

 © 2007 Wiley-VCH Verlag GmbH & Co. KGaA, Weinheim 

DOI: 10.1002/ejic.200700619

# Synthesis, Characterization and X-ray Structures of [α-Diphenylethanedione bis(4-ethylthiosemicarbazonato)]palladium(II) and 1,2,4-Triazine-3-thione–Zinc(II) Complexes Obtained by Metal-Induced Cyclization

**Ana I. Matesanz,[a] Cesar Pastor,[b] and Pilar Souza*[a]**

**Keywords:** Thiosemicarbazones / Cocrystals / Palladium(II) / Zinc(II) / X-ray diffraction

The new cyclic 5-ethoxy-4-ethyl-5,6-diphenyl-4,5-dihydro-2*H*-[1,2,4]-triazine-3-thione ligand (HTa3T-Et) has been obtained by an intramolecular cyclization reaction of α-diphenylethanedione bis(4-ethylthiosemicarbazone) ($H_2$BbTSC-Et). The cyclization may be promoted either by hydroxylic solvents or by $Zn^{II}$ ions. Thus, the reaction of $H_2$BbTSC-Et with $ZnCl_2$ led to the formation of $[Zn(HTa3T\text{-}Et)_2Cl_2]$ containing not the ligand $H_2$BbTSC-Et but the cyclic HTa3T-Et ligand that forms during the reaction. On the other hand, crystallization of $H_2$BbTSC-Et from DMSO/EtOH produces a cocrystal containing the open-chain $H_2$BbTSC-Et ligand together with the cyclic HTa3T-Et molecules, which are linked to a DMSO molecule by hydrogen bonds. However, reaction of the cocrystal with $Pd^{II}$ ions yields a planar tetracoordinate complex in which only the $H_2$BbTSC-Et ligand, in the deprotonated form, is present. The preparation and molecular structures of these compounds are discussed.

(© Wiley-VCH Verlag GmbH & Co. KGaA, 69451 Weinheim, Germany, 2007)

## Introduction

Thiosemicarbazones (TSCs) are a versatile type of ligand because of the number of donor atoms they possess, among which sulfur is of paramount importance in the metal–ligand linkage; moreover, their configurational flexibility creates the possibility of a variety of coordination modes.[1–3] Thiosemicarbazone derivatives have raised considerable interest in chemistry and biology because of the antibacterial, antiviral and antitumor activity that many of them have shown.[4,5] In some cases, the highest activity is associated with a metal complex rather than the free thiosemicarbazone.[6]

It is well known that thiosemicarbazones derived from 1,2-dicarbonyl compounds easily cyclize during the synthesis process, especially when hydroxylic solvents are used or when solutions in such solvents are allowed to crystallize over several days.[7] In all cases, this cyclization leads to 1,2,4-triazine-3-thione ligands (Scheme 1); these ligands are very versatile and are able to form mono-, di- and polynuclear metal complexes as a result of two different coordination modes: as a monodentate, neutral ligand with coordination through the sulfur atom or as an anionic bidentate ligand with coordination through the sulfur and nitrogen atoms.[8]

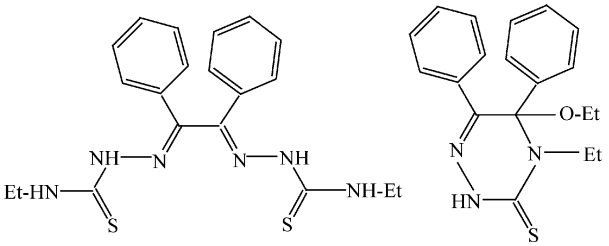


$H_2$BbTSC-Et HTa3T-Et

Scheme 1. Structures for the open-chain $H_2$BbTSC-ET and the cyclic HTa3T-Et ligands.

Compounds containing the 1,2,4-triazine moiety have been found in natural products and some of these have important applications in various fields. For example, 1,2,4-triazine-3,5-diones represent aza analogues of pyrimidine nucleic acid bases, some neutral antibiotics are derivatives of pyrimido[5,4-*e*]-1,2,4-triazine, and 4-amino-6-*tert*-butyl-3-methylthio-1,2,4-triazine-5-one and 4-amino-3-methyl-6-phenyl-1,2,4-triazine-5-one are used as agricultural chemicals.[9]

As part of our systematic investigation on the coordination chemistry of thiosemicarbazone derivatives,[10,11] we recently reported a paper that focuses on the structure–antitumor activity relationships of a series of palladium and platinum α-diphenylethanedione bis(thiosemicarbazone) derivatives. In all compounds studied there, the ligands unambiguously show the bis(thiosemicarbazone) form.[12] To extend

[a] Departamento de Química Inorgánica, Facultad de Ciencias, Universidad Autónoma de Madrid,
C/ Francisco Tomás y Valiente 7, 28049 Madrid, Spain
Fax: +34-914974833
E-mail: pilar.souza@uam.es
[b] Servicio Interdepartamental de Apoyo a la Investigación, Facultad de Ciencias, Universidad Autónoma de Madrid,
C/ Francisco Tomás y Valiente, 7, 28049 Madrid, Spain

 © 2007 Wiley-VCH Verlag GmbH & Co. KGaA, Weinheim 

our studies, particularly with respect to the coordination properties of $H_2$BbTSC-Et and the stereochemistry and molecular structure of the complexes, we planned to synthesize new metal derivatives. It was possible, after numerous attempts at crystallization of the $H_2$BbTSC-Et ligand, to obtain good quality crystals suitable for X-ray analysis from DMSO/EtOH solution. These proved to be cocrystals containing, together with $H_2$BbTSC-Et, the cyclic derivative formed by an intramolecular cyclization reaction. To the best of our knowledge, this is the first report of the isolation of a bis(thiosemicarbazone) molecule and the cyclized form as single crystals. Interestingly, the reaction of the new cocrystal isolated with palladium(II) ions gave the mononuclear $N_2S_2$-tetracoordinate bis(thiosemicarbazone) complex instead the binuclear $CNS_2$-tetracoordinate complex recently reported by us.[12]

Some of the different routes published that undergo the cyclization of thiosemicarbazones use a metallic salt ($Zn^{2+}$, $Cu^{2+}$ and $Fe^{3+}$). On this basis and in order to search for novel cyclized compounds, we also report here the reaction of $H_2$BbTSC-Et with $ZnCl_2$. The reaction yields a new zinc(II) compound containing, in neutral form, the cyclic ligand 5-ethoxy-4-ethyl-5,6-diphenyl-4,5-dihydro-2*H*-[1,2,4]-triazine-3-thione (HTa3T-Et, see Scheme 1).

## Results and Discussion

### Synthesis of the Ligands

The preparation of crude $H_2$BbTSC-Et was carried out according to ref.[12] Analytical and spectroscopic properties are consistent with those reported.

Attempted slow recrystallization of $H_2$BbTSC-Et from DMSO/EtOH resulted in the isolation of a cocrystal $H_2$BbTSC-Et/HTa3T-Et in a 1:1 ratio that also contains DMSO molecules. The structural data suggests that some $H_2$BbTSC-Et molecules may be transformed into the final 1,2,4-triazine-3-thione ligand by an intramolecular cyclization reaction, similar to that described by Alsop et al.[13] The cyclization with concomitant insertion of ethanol and elimination of 4-ethylthiosemicarbazide seems to be favoured when hydroxylic solvents are used or when solutions in such solvents are allowed to crystallize over several days.

### Structures of the Ligands

The structure of the cocrystal $H_2$BbTSC-Et/HTa3T-Et consists of one $H_2$BbTSC-Et molecule and one cyclic triazine molecule HTa3T-Et together with one dimethylsulfoxide molecule of crystallization (Figure 1). Selected bond lengths and angles are given in Table 1.

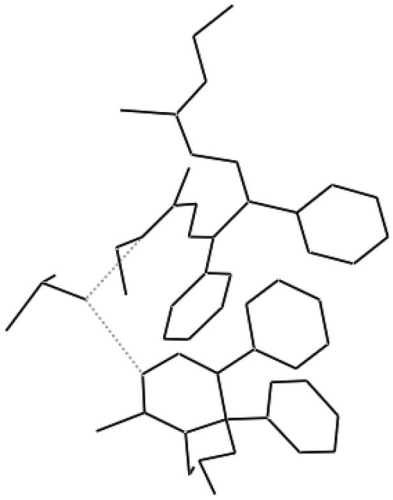

Figure 1. Structure of the cocrystal $H_2$BbTSC-Et/HTa3T-Et.

Table 1. Selected bond lengths [Å] for $H_2$BbTSC-Et and $H_2$BbTSC-Et/HTa3T-Et.

| $H_2$BbTSC-Et | | $H_2$BbTSC-Et/HTa3T-Et | |
|---|---|---|---|
| S1–C3 | 1.678(2) | S1–C3 | 1.681(3) |
| S2–C6 | 1.676(2) | S2–C6 | 1.689(3) |
| N1–C2 | 1.459(3) | N1–C2 | 1.467(4) |
| N1–C3 | 1.317(3) | N1–C3 | 1.313(4) |
| N2–N3 | 1.356(2) | N2–N3 | 1.362(4) |
| N2–C3 | 1.369(3) | N2–C3 | 1.371(4) |
| N3–C4 | 1.286(3) | N3–C4 | 1.290(3) |
| N4–C5 | 1.291(3) | N4–C5 | 1.294(4) |
| N4–N5 | 1.360(2) | N4–N5 | 1.360(3) |
| N5–C6 | 1.368(3) | N5–C6 | 1.375(4) |
| N6–C6 | 1.317(3) | N6–C6 | 1.325(4) |
| N6–C7 | 1.456(3) | N6–C7 | 1.460(4) |
| | | S3–C23 | 1.679(3) |
| | | N7–C22 | 1.470(4) |
| | | N7–C23 | 1.344(4) |
| | | N7–C25 | 1.490(4) |
| | | N8–N9 | 1.359(4) |
| | | N8–C23 | 1.354(4) |
| | | N9–C24 | 1.281(4) |

The crystal and molecular structures with the numbering schemes of the $H_2$BbTSC-Et and HTa3T-Et molecules are shown in Figure 2.

The $H_2$BbTSC-Et molecule consists of two distinct essentially planar sections, which are pivoted about the C5–C4 "backbone" of the ligand, with a C15–C5–C4–C9 torsion angle of 79.4(3)°. Within each planar section, the C–N and N–N bond lengths, intermediate between the ideal values of corresponding single and double bonds, are indicative of a delocalized system. The existence of the thiosemicarbazone groups in the thione form, in the solid state, is evidenced by the C–S bond lengths of 1.681(3) and 1.689(3) Å, which are close to a formal C=S bond length.[13]

The HTa3T-Et molecule is a triazine–thione formed from an intramolecular reaction during the recrystallization process. This six-membered heterocyclic $C_3N_3$ ring is close to planar [torsional angles: C25–N7–C23–N8 10.0(4)°, N9–N8–C23–N7 1.5(4)°, N8–N9–C24–C25 –0.4(4)°]. Although

 © 2007 Wiley-VCH Verlag GmbH & Co. KGaA, Weinheim 

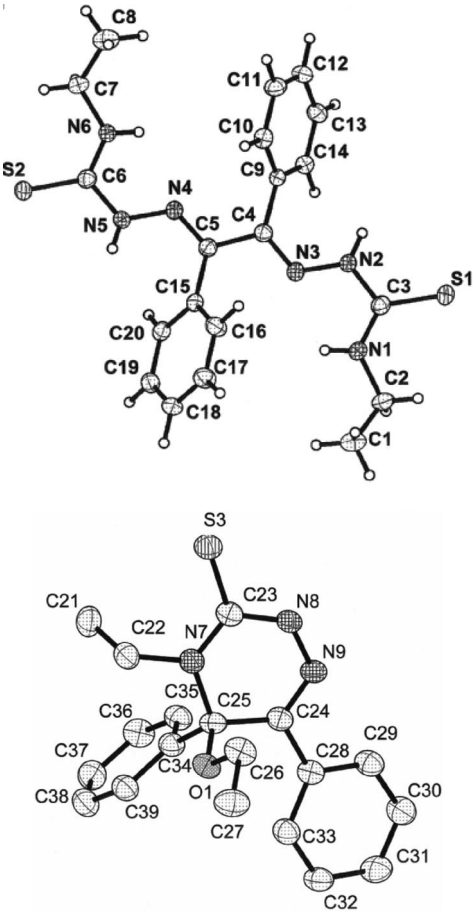


Figure 2. Molecular structure of the $H_2$BbTSC-Et (top) and HTa3T-Et (below) molecules, which shows the atom numbering scheme.

the C–S bond length of 1.679(3) Å is in the range of a C=S bond, some electronic delocalization occurs in the ring formed. Thus, while the bond length for N9–C24 of 1.281(4) Å is consistent with a C=N bond, both N8–C23 and N7–C23 bonds [1.354(4) and 1.344(4) Å, respectively] are considerably shorter than the predicted length of 1.47 Å for a C–N bond. Further, the N8–N9 bond with a length of 1.359(4) Å is significantly shorter than the predicted N–N bond length of 1.45 Å. On the other hand, the N7–C25 bond [1.490(4) Å] is slightly longer than the predicted C–N bond, and the C24–C25 bond [1.523(4) Å] is slightly shorter than the predicted length 1.54 Å for a C–C bond.[14]

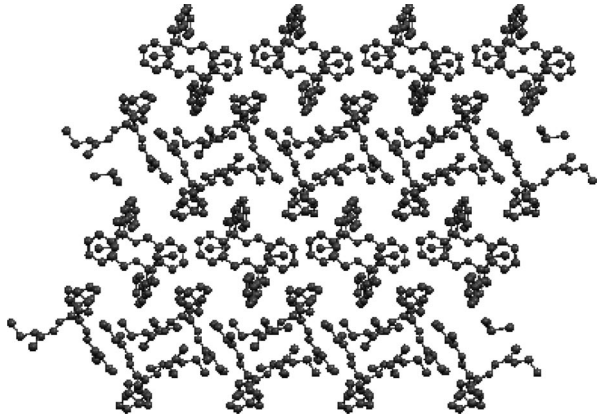

Figure 3. View of cocrystal $H_2$BbTSC-Et/HTa3T-Et along the *b* axis.

Within the crystal, the two independent molecules are linked to a DMSO molecule by N–H···O bonds. The crystal packing along the *b* axis (Figure 3) shows parallel alternating lines of $H_2$BbTSC-Et and HTa3T-Et molecules.

## Synthesis and Structure of the Complex [Pd(BbTSC)]

We have recently verified that the reaction of crude $H_2$BbTSC-Et with $Li_2PdCl_4$ in methanol undergoes *ortho*-metallation to give a dinuclear bis(thiosemicarbazone) complex.[12] Thus, we decided to investigate the coordinating properties of the cocrystal $H_2$BbTSC-Et/HTa3T-Et to palladium(II). The analytical and spectroscopic data of the isolated compound are in agreement with the formula [Pd(BbTSC)], in which the $H_2$BbTSC ligand is in the doubly deprotonated form. Green single crystals were obtained on recrystallization from DMSO, and the X-ray diffraction study confirmed the proposed formulae.

An ORTEP representation of [Pd(BbTSC)] together with the atom labelling scheme is shown in Figure 4, and selected bond lengths and angles are given in Table 2. This neutral $Pd^{II}$ complex crystallizes in the monoclinic *C*2/*c* space group with $Z = 4$ as discrete $C_{20}H_{22}N_6S_2Pd$·DMSO molecules.

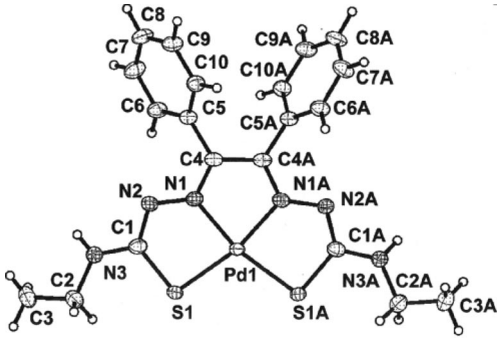


Figure 4. Molecular structure of [Pd(BbTSC)].

On the basis of other α-diketone bis(thiosemicarbazones),[15] the mode of coordination for this complex is as expected; two iminic nitrogen atoms and two thiolato sulfur atoms bond to palladium on the loss of the hydrogen atoms of N2 and N2A from both thiosemicarbazone moieties to give an approximately planar, four-coordinate complex. Thus, the coordination of the bis(thiosemicarbazone) results in the formation of three five-membered chelate rings (PdSCNN, PdNCCN and PdNNCS).

A careful examination of the bond length data shows that the Pd–$N_{iminic}$ and Pd–S distances are comparable with those reported for other thiosemicarbazone palladium(II) complexes with strong Pd–N coordination.[10] Since the Pd–S bonds are significantly longer than the Pd–N bonds, the coordination geometry around the metal ion is more trape-

 © 2007 Wiley-VCH Verlag GmbH & Co. KGaA, Weinheim 

Table 2. Selected bond lenghs [Å] and angles [°] for [Zn(HTa3T-Et)$_2$Cl$_2$] and [Pd(BbTSC)].

| [Zn(HTa3T-Et)$_2$Cl$_2$] | | [Pd(BbTSC)] | |
|---|---|---|---|
| S1–C1 | 1.7113(19) | S1–C1 | 1.771(3) |
| N1–C1 | 1.329(2) | N1–C4 | 1.325(4) |
| N1–C2 | 1.490(2) | N2–C1 | 1.332(4) |
| N2–C1 | 1.342(2) | N3–C1 | 1.334(4) |
| N3–C3 | 1.281(3) | N3–C2 | 1.462(4) |
| N2–N3 | 1.376(2) | N1–N2 | 1.351(4) |
| Zn1–Cl1 | 2.2380(5) | Pd1–N1 | 1.982(3) |
| Zn1–Cl1A | 2.2379(5) | Pd1–N1A | 1.982(3) |
| Zn1–S1 | 2.3694(5) | Pd1–S1 | 2.2792(8) |
| Zn1–S1A | 2.3693(5) | Pd1–S1A | 2.2792(8) |
| Cl1A–Zn1–Cl1 | 124.74(3) | N1A–Pd1–N1 | 82.38(15) |
| Cl1A–Zn1–S1A | 111.374(17) | N1–Pd1–S1A | 166.84(8) |
| Cl1A–Zn1–S1 | 102.003(17) | N1–Pd1–S1 | 84.47(8) |
| Cl1–Zn1–S1 | 111.376(17) | N1A–Pd1–S1A | 84.46(8) |
| Cl1–Zn1–S1A | 102.000(17) | N1A–Pd1–S1 | 166.84(8) |
| S1A–Zn1–S1 | 103.79(3) | S1A–Pd1–S1 | 108.69(4) |

zoid than square. The overall impression from the values of the bond lengths and angles in the vicinity of the palladium atom is that the ligand cavity is too small to accommodate the $Pd^{2+}$ ion ideally. Thus, the N–Pd–N bond angles are less than 90°, and the sulfur ends of the ligand arms are pushed outwards beyond the natural position that would be adopted by the planar ligand, with S–Pd–S bond angles of ca. 109°.

The loss of the protons originally bonded to N2 and N2A atoms produces a negative charge delocalized in the ligand system, which is consistent with the C–N distances (intermediate between formal single and double bonds) and C–S distances (see Table 2). This substantiates the displacement of the tautomeric equilibrium to the thiol form in the ligand.

The terminal uncoordinated nitrogen atoms are involved in intermolecular hydrogen bonds with the oxygen atoms of the solvent molecules; the contact distances and angles are N3···O1 2.897(4) Å and N–H–O 162(4)°.

### Synthesis and Structure of the Complex [Zn(HTa3T-Et)$_2$Cl$_2$]

The reaction of crude $H_2$BbTSC-Et ligand with $ZnCl_2$ in ethanol led to the formation of the crystalline yellow [Zn(HTa3T-Et)$_2$Cl$_2$] complex. The analytical, spectroscopic, and X-ray diffraction data (see Experimental Section) revealed that $H_2$BbTSC-Et is transformed into cyclic 5-ethoxy-4-ethyl-5,6-diphenyl-4,5-dihydro-2*H*-[1,2,4]-triazine-3-thione (HTa3T-Et) during the complexation reaction. An analogous cyclization of 2-pyridinformamide 4-ethylthiosemicarbazone that is promoted by the presence of silver(I) ions was reported recently by Castiñeiras et al.[16]

The mother liquor was allowed to stand at 4 °C. After several days, crystalline pale yellow needles were isolated, which were identified as the free ligand $H_2$BbTSC-Et by X-ray diffraction analysis. Its molecular structure essentially shows the same structural characteristics as that of the open-chain molecule in the cocrystal $H_2$BbTSC-Et/HTa3T-Et. Selected bond lengths and angles are given in Table 1.

The crystal packing (Figure 5) shows parallel pseudochains of molecules, and the absence of any solvent of crystallization indicates possible existence of noncovalent interactions between the individual bis(thiosemicarbazone) molecules. A closer look reveals π–π stacking interactions between successive thiosemicarbazone moieties (3.62 Å). These extended intermolecular interactions are responsible for holding the crystal together.

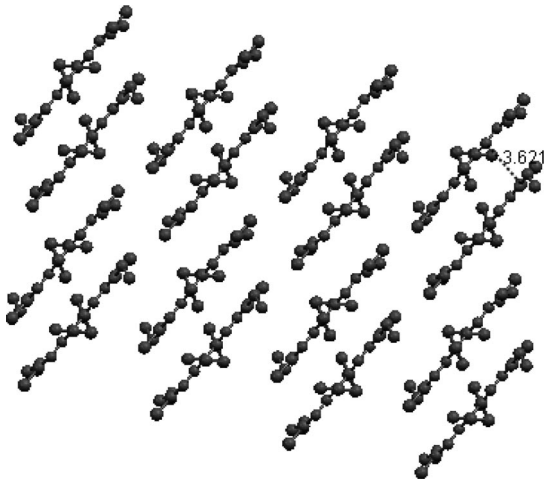


Figure 5. Side view of $H_2$BbTSC-Et, which shows the parallel disposition of the molecules as a result of π–π stacking.

An ORTEP representation of [Zn(HTa3T-Et)$_2$Cl$_2$] together with the atom labelling scheme is shown in Figure 6, and selected bond lengths and angles are given in Table 2.

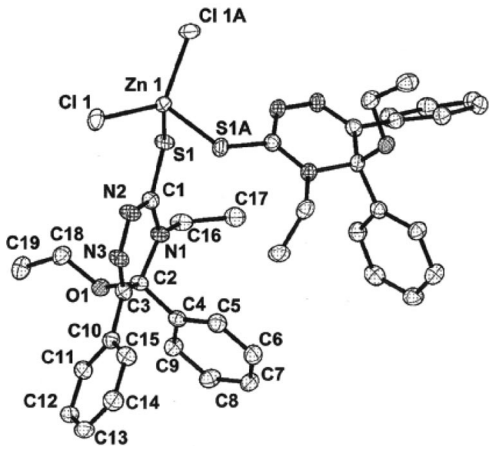


Figure 6. Molecular structure of [Zn(HTa3T-Et)$_2$Cl$_2$] (H atoms were omitted for clarity).

This neutral complex crystallizes in the orthorhombic *Fdd*2 space group with $Z = 8$. The zinc atom is tetracoordinated by two chlorido ligands and two sulfur atoms from the neutral monodentate ligands HTa3T-Et. The largest angular distortion from ideal tetrahedral geometry is shown by Cl1A–Zn–Cl1 [124.74(3)°]. Although the chlorido ligands participate in the hydrogen bonding, the distances Zn–Cl [2.238 Å] fall in the range of the shortest lengths for

 © 2007 Wiley-VCH Verlag GmbH & Co. KGaA, Weinheim 

terminal Zn–Cl bonds.[17] The Zn–S and C–S distances [2.369 and 1.711 Å, respectively] are similar to those found in other complexes with thiocarbonyl sulfur atoms.[18] The 4-ethyl substituent on the N1 atom reduces the possibilities for hydrogen bonding. Thus, only two intramolecular N2–H···Cl bonds are present in the complex.

An analysis of the relative disposition of the complex molecules in the crystal structure highlights the importance of aromatic–aromatic edge-to-face interactions in the packing that takes place when the crystal is formed.[19,20] The perpendicular (ca. 96°) distance between C–H and the plane of π system is ca. 2.88 Å.

## Conclusions

The investigations show that the synthesis of bis(thiosemicarbazone) derivatives from α-diketones with alkyl substituents can be complicated by the formation of cyclized products. Typically, the α-bis(thiosemicarbazones) are made by heating a thiosemicarbazide under reflux with an α-diketone in an alcoholic solvent with an acid catalyst. Although it is well known that such solvents favour cyclization, we have not found the cyclic 1,2,4-triazine-3-thione form in our previous studies. However, slow recrystallization of the $H_2$BbTSC-Et from DMSO/EtOH affords a cocrystal composed of a 1:1 ratio of open-chain $H_2$BbTSC-Et and cyclic 1,2,4-triazine-3-thione. The formation of the cocrystal could be favoured by the presence of DMSO molecules since they each form two hydrogen bonds with the terminal nitrogen atom of one thiosemicarbazone moiety (hindering the cyclization) and with the hydrazinic nitrogen atom of the other thiosemicarbazone moiety (favouring the cyclization).

The intramolecular cyclization reaction may also be promoted by the presence of the salt $ZnCl_2$. Thus, we have achieved the isolation of a $Zn^{II}$–1,2,4-triazine-3-thione complex in which the zinc atom is tetracoordinated by two chlorido ligands and two sulfur atoms from the neutral monodentate cyclic ligands. Although the different steps involved in this process are not completely understood, it has been assumed that the metal ion plays an important role in this process, probably because of both inductive and stereochemical effects, as do the solvent and the counterion of the metal.

However, reaction of the cocrystal with $Li_2PdCl_4$ yields a planar tetracoordinate complex in which the bis(4-ethylthiosemicarbazone) ligand in the deprotonated form is present. In this case, the clear preference for a planar environment of the $Pd^{II}$ ion assists the stabilization of the bis(thiosemicarbazone) form.

In summary, the conversion of $H_2$BbTSC-Et to the cyclic 1,2,4-triazine-3-thione form is relatively rapid in hydroxylic solvents, and when a metallic salt is present, the formation of the metal complex stabilizes one of the forms according to its structural preferences. Thus, the cyclization of the $H_2$BbTSC-Et ligand can be controlled by selection of the appropriate metal salt and reaction conditions. Moreover, in this case, the presence of either the phenyl rings, which allow extensive delocalization, or the $^4$N substitution appears to facilitate the cyclization of the $H_2$BbTSC-Et ligand.

## Experimental Section

**Materials:** Solvents were purified and dried according to standard procedures. 4-Ethylthiosemicarbazide, 1,2-diphenylethanedione, lithium chloride, palladium(II) chloride and zinc chloride were commercially available from Aldrich.

**Preparation of the Ligands:** $H_2$BbTSC-Et was synthesized according to ref.[11]. Yield: 0.35 g (77%). Analytical and spectroscopic properties are consistent with those reported. Attempted slow recrystallization of $H_2$BbTSC-Et from DMSO/EtOH resulted in the isolation of a cocrystal, which is composed of a 1:1 ratio of $H_2$BbTSC-Et and cyclic HTa3T-Et according to its crystal and molecular structure.

**[Zn(HTa3T-Et)$_2$Cl$_2$]:** The reaction of $ZnCl_2$ (0.3 mmol) in ethanol (40 mL) with $H_2$BbTSC-Et (0.3 mmol), over 5 h whilst stirring and refluxing, led to the formation of a yellow solution, which was filtered and allowed to evaporate at room temperature overnight to give a yellow crystalline solid. The product was identified as the [Zn(HTa3T-Et)$_2$Cl$_2$] complex, which does not contain the $H_2$BbTSC-Et ligand but the cyclic HTa3T-Et molecule. Single prismatic crystals suitable for X-ray diffraction were selected directly from the reaction vessel. Yield: 0.17 g (71%). MS (FAB$^+$ with mNBA matrix): *m/z* (%) = 816.1 [M + H]$^+$, 340.1 (100) [HTa3T – Et + H]$^+$. IR (KBr): $\tilde{\nu}$ = 3252 (s, NH), 1574 (s, CN), 854 (w, CS-thioamide IV band). $^1$H NMR ([D$_6$]DMSO): $\delta$ = 9.72 (s, 1 H, $^2$NH), 7.72–7.20 (m, 6 H, Ph), 3.64–3.59 (m, 3 H, $CH_2CH_3$), 3.35–3.33 (m, 3 H, $OCH_2CH_3$), 1.30–1.25 (t, $J$ = 3.0 Hz, 2 H, $CH_2CH_3$), 1.20–1.15 (t, $J$ = 2.0 Hz, 2 H, $OCH_2CH_3$) ppm. After filtering the $Zn^{II}$ complex, the mother liquor was allowed to stand at 4 °C, and after several days, pale yellow needles of the free ligand $H_2$BbTSC-Et suitable for X-ray analysis were obtained. Analytical and spectroscopic properties are consistent with those previously reported.[11]

**[Pd(BbTSC-Et)]:** The reaction of cocrystal $H_2$BbTSC-Et/HTa3T-Et (1 mmol) with a methanol solution of lithium tetrachloropalladate prepared in situ from palladium(II) chloride (1.2 mmol) and lithium chloride (4.4 mmol), over 5 h at room temperature while stirring, led to a dark green solution, which was filtered. From the solution, a dark green solid was isolated by slow evaporation of the solvent, which could then be recrystallized from DMSO to give green crystals suitable for X-ray analysis. On the basis of the molecular structure of [Pd(BbTSC-Et)], the coordinated doubly deprotonated ligand was unambiguously identified as $H_2$BbTSC-Et. Yield: 0.15 g (30%). $C_{20}H_{22}N_6S_2Pd$·DMSO (595.08): calcd. C 44.40, H 4.70, N 14.10, S 16.15; found C 44.00, H 5.00, N 13.50, S 15.40%. IR (KBr): $\tilde{\nu}$ = 3237, 3187 (s, NH), 1547 (s, CN), 842 (w, CS-thioamide IV band) cm$^{-1}$. $^1$H NMR ([D$_6$]DMSO): $\delta$ = 8.10 (t, $J$ = 4.0 Hz, 1 H, $^4$NH), 7.17–7.11 (m, 6 H, Ph), 3.26 (m, 2 H, $CH_2CH_3$), 1.23 (m, 3 H, $CH_2CH_3$).

**Physical Measurements:** Elemental analyses were performed on a LECO CHNS-932 microanalyzer. Fast atom bombardment (FAB) mass spectra were performed with a VG AutoSpec spectrometer (nitrobenzyl alcohol matrix). $^1$H NMR spectra ([D$_6$]DMSO) were recorded with BRUKER AMX-300 spectrometer. All cited physical measurements were obtained from the Servicio Interdepartamental de Investigación (SIDI) of the Universidad Autónoma de Madrid.

 © 2007 Wiley-VCH Verlag GmbH & Co. KGaA, Weinheim 

Table 3. Crystal data and structure refinement for $H_2$BbTSC-Et, $H_2$BbTSC-Et/HTa3T-Et, [Zn(HTa3T-Et)$_2$Cl$_2$] and [Pd(BbTSC)].

| | $H_2$BbTSC-Et | $H_2$BbTSC-Et /HTa3T-Et | [Zn(HTa3T-Et)$_2$Cl$_2$] | [Pd(BbTSC)] |
|---|---|---|---|---|
| Formula | $C_{20}H_{24}N_6S_2$ | $C_{41}H_{51}N_9O_2S_4$ | $C_{38}H_{42}Cl_2N_6O_2S_2Zn$ | $C_{22}H_{28}N_6OPdS_3$ |
| $M$ | 412.57 | 830.15 | 815.17 | 595.08 |
| System | triclinic | monoclinic | orthorhombic | monoclinic |
| Space group | $P\bar{1}$ | $P2_1/c$ | $Fdd2$ | $C2/c$ |
| $a$ [Å] | 9.5938(11) | 19.1014(9) | 22.1376(5) | 12.3451(6) |
| $b$ [Å] | 9.8145(12) | 11.3471(5) | 28.2782(8) | 22.2996(11) |
| $c$ [Å] | 12.0817(15) | 20.9504(10) | 12.6602(2) | 9.1162(5) |
| $\alpha$ [°] | 98.752(4) | 90 | 90 | 90 |
| $\beta$ [°] | 106.338(4) | 105.820(3) | 90 | 95.758(3) |
| $\gamma$ [°] | 96.281(4) | 90 | 90 | 90 |
| $V$ [Å$^3$] | 1065.0(2) | 4368.9(4) | 7925.4(3) | 2496.9(2) |
| $\lambda$ [Å] | 1.54178 | 1.54178 | 1.54178 | 1.54178 |
| $T$ [K] | 100(2) | 100(2) | 100(2) | 100(2) |
| $Z$ | 2 | 4 | 8 | 4 |
| $D_c$ [g cm$^{-3}$] | 1.287 | 1.262 | 1.366 | 1.583 |
| $F$(000) | 436 | 1760 | 3392 | 1216 |
| $\mu$ [mm$^{-1}$] | 2.402 | 2.359 | 3.412 | 8.562 |
| $R_1$ (all data) | 0.0535 | 0.0829 | 0.0254 | 0.0401 |
| $R_1$ [$I > 2\sigma(I)$] | 0.0425 | 0.0503 | 0.0251 | 0.0315 |
| $wR_2$(all data) | 0.1215 | 0.1327 | 0.0645 | 0.0806 |
| $wR_2$[$I > 2\sigma(I)$] | 0.1104 | 0.1166 | 0.0642 | 0.0760 |
| GOF | 1.036 | 1.019 | 1.122 | 1.023 |

Infrared spectra (KBr discs) were recorded with a Bomen–Michelson spectrophotometer (4000–400 cm$^{-1}$).

**X-ray Crystallographic Studies:** A summary of the crystal data, experimental details and refinement results is listed in Table 3. The X-ray measurement was performed on a Bruker SMART 6 K CCD area-detector three-circle diffractometer with a rotating anode generator (Cu-$K_\alpha$ radiation, $\lambda$ = 1.54178 Å) equipped with Goebel mirrors at settings of 50 kV and 110 mA. X-ray data were collected at 100 K. The software package SHELXTL version 6.10 was used for space group determination, structure solution and refinement. The structures were solved by direct methods, completed with difference Fourier syntheses, and refined with full-matrix least-squares techniques against $F^2$ by using SHELXL-97.

CCDC-649679 (ligand $H_2$BbTSC-Et), -649677 (cocrystal $H_2$BbTSC-Et/HTa3T-Et), -649678 {compound [Zn(HTa3T-Et)$_2$Cl$_2$]} and -634275 {compound [Pd(BbTSC-Et)]} contain the supplementary crystallographic data for this paper. These data can be obtained free of charge from The Cambridge Crystallographic Data Centre via www.ccdc.cam.ac.uk/data_request/cif.

## Acknowledgments

We are grateful to Ministerio de Sanidad y Consumo, Instituto de Salud Carlos III (PI040354) of Spain for financial support.

[1] D. X. West, A. E. Liberta, S. B. Padhye, R. C. Chikate, P. B. Sonawane, A. S. Kumbhar, R. G. Yerande, *Coord. Chem. Rev.* **1993**, *123*, 49–71.
[2] J. S. Casas, M. S. García-Tasende, J. Sordo, *Coord. Chem. Rev.* **2000**, *209*, 197–261.
[3] A. Amoedo, L. A. Adrio, J. M. Antelo, J. Martínez, M. T. Pereira, A. Fernández, J. M. Vila, *Eur. J. Inorg. Chem.* **2006**, *15*, 3016–3021.
[4] Y. Yu, J. Wong, D. B. Lovejoy, D. S. Kalinowski, D. R. Richardson, *Clin. Cancer Res.* **2006**, *12*, 6876–6883.
[5] P. Genova, T. Varadinova, A. I. Matesanz, D. Marinova, P. Souza, *Toxicol. Appl. Pharmacol.* **2004**, *197*, 107–112.
[6] D. X. West, A. E. Liberta, S. B. Padhye, P. B. Chikate, P. B. Sonawane, A. S. Kumbhar, R. G. Yerande, *Coord. Chem. Rev.* **1993**, *123*, 49–71.
[7] M. Christlieb, J. R. Dilworth, *Chem. Eur. J.* **2006**, *12*, 6194–6206.
[8] E. Lopez-Torres, M. Mendiola, *Polyhedron* **2005**, *24*, 1435–1444.
[9] J. G. Haasnoot, *Coord. Chem. Rev.* **2000**, *200–202*, 131–185.
[10] A. I. Matesanz, J. M. Pérez, P. Navarro, J. M. Moreno, E. Colacio, P. Souza, *J. Inorg. Biochem.* **1999**, *76*, 29–37.
[11] A. I. Matesanz, P. Souza, *J. Inorg. Biochem.* **2007**, *101*, 245–253.
[12] A. I. Matesanz, P. Souza, *J. Inorg. Biochem*. **2007**, *101*, 1354–1361.
[13] L. Aslop, A. R. Cowley, J. R. Dilworth, P. S. Donnelly, J. M. Peach, J. T. Rider, *Inorg. Chim. Acta* **2005**, *358*, 2770–2780.
[14] P. Souza, A. Arquero, A. Garcia-Onrubia, V. Fernández, A. M. Leiva, U. Müller, *Z. Naturforsch., Teil B* **1989**, *44*, 946–950.
[15] P. J. Blower, T. C. Castle, A. R. Cowley, J. R. Dilworth, P. S. Donnelly, E. Labisbal, F. E. Sowrey, S. J. Teat, M. Went, *Dalton Trans.* **2005**, 4416–4425.
[16] A. Castiñeiras, I. García-Santos, S. Dehnen, P. Sevillano, *Polyhedron* **2006**, *25*, 3653–3660.
[17] N. C. Kasuga, K. Sekino, M. Ishikawa, A. Honda, M. Yokoyama, S. Nakano, N. Shimada, C. Koumo, K. Nomiya, *J. Inorg. Biochem.* **2003**, *96*, 298–310.
[18] P. Souza, L. Sanz, V. Fernández, A. Arquero, E. Gutierrez, A. Monge, *Z. Naturforsch., Teil B* **1991**, *46*, 767–774.
[19] J. W. Steed, D. R. Turner, K. Wallace, *Core Concepts in Supramolecular Chemistry and Nanochemistry*, VCH, Weinheim, **2007**, p. 23.
[20] P. Gamez, J. Reedijk, *Eur. J. Inorg. Chem.* **2006**, *1*, 29–42.

Received: June 14, 2007
Published Online: October 16, 2007

 © 2007 Wiley-VCH Verlag GmbH & Co. KGaA, Weinheim 

DOI: 10.1002/ejic.200700623

# Syntheses, Crystal Structures, Thermal Stabilities, and Magnetic and Luminescent Properties of 3D Heterometal Phosphonates: $NaM[O_3PCH(OH)CO_2]$ (M = Mn, Fe, Co, Zn)

**Zhuzhi Lai,[a] Ruibiao Fu,[a] Shengmin Hu,[a] and Xintao Wu*[a]**

**Keywords:** Crystal structure / Phosphorus / Luminescence / Magnetism / Thermal stability

Four heterometal 2-hydroxyl(phosphono)carboxylates, $NaM[O_3PCH(OH)CO_2]$ [M = Mn (**1**), Fe (**2**), Co (**3**), Zn (**4**)], were synthesized hydrothermally. Single-crystal X-ray diffraction data reveal that they are isostructural and crystallize in the orthorhombic space group *Pbca* (No. 61) with $a$ = 10.1365(16)–10.4557(5) Å, $b$ = 9.6890(9)–9.8265(4) Å, $c$ = 10.7942(19)–10.9353(1) Å, $V$ = 1060.2(3)–1123.22(7) Å$^3$, and $Z$ = 8. Each $[MO_6]$ (M = Mn, Fe, Co, Zn) octahedron contacts three neighboring $[NaO_5]$ pyramids through two edges and one corner to form a Na/MO layer. The layers are further connected by $O_3PCH(OH)CO_2^{3-}$ groups into an interesting 3D heterometallic framework. Thermogravimetric and powder X-ray diffraction analysis indicate that solids **1**–**4** are thermally stable up to 350, 250, 340, and 350 °C, respectively. Magnetic measurements show the presence of antiferromagnetic interaction for $M^{II}$ ions (M = Mn, Fe, Co) in compounds **1**–**3**. These solids exhibit bright cyan (for **1**, **2**, and **4**) or purple (for **3**) luminescence after induced by fluorescent whitener, and the luminescence can be irreversibly transformed into bright yellow (for **1** and **4**) or red (for **3**) simply by annealing treatment at 300 °C.

(© Wiley-VCH Verlag GmbH & Co. KGaA, 69451 Weinheim, Germany, 2007)

## Introduction

The design and construction of new inorganic–organic hybrid materials based on metal phosphonates is of current interest owing to their potential applications as catalysts, ion-exchangers, small molecular sensors, and nonlinear optics.[1] During the past two years, phosphonic acids containing a second functional group such as hydroxy, amine, carboxyl, and pyridyl, were successfully introduced as bridging ligands for the isolation of new metal phosphonates with intriguing structures and properties.[2–5] This is mainly due to the additional functional groups that can improve the solubility and crystallinity of metal phosphonates, which results in the growth of suitable single crystals for X-ray structural analysis. Then, an instinctive strategy of attaching two additional functional groups to the phosphonic acid was performed to obtain several novel solids, such as $M_x[Fe(O_2CCH_2)_2NCH_2PO_3]_6{\cdot}nH_2O$ (M = Na, K, Rb), with a maple leaf lattice and lanthanide phosphonates possessing homochiral porous frameworks as well as blue, red, or near IR luminescence.[6] In this regard, we focused on utilizing 2-hydroxy(phosphono)acetic acid (Hpaa) containing three functional groups (–OH,–COOH, and–$PO_3H_2$) to construct four-layered hybrid materials that are antiferromagnetic and one 3D polar open-framework with nonlinear optical activity and high thermal stability.[7] On one hand, there are few reports on heterometal phosphonates with multifunctional phosphonic acids as bridging groups.[6a,8] On the other hand, Hpaa would adopt numerous coordination modes through 6 active oxygen donors to bond a maximum of 15 metal atoms. Therefore, a series of experiments was carried out to search for new heterometallic polymers with Hpaa as bridging ligands. In this paper, we report the syntheses, structures, and properties (including thermal stability, magnetism, and luminescence) of four new heterometal phosphonates with a 3D framework, namely, $NaM[O_3PCH(OH)CO_2]$ (M = Mn: **1**; Fe: **2**; Co: **3**; Zn, **4**).

## Results and Discussion

### Syntheses and Characterization

**$Na_2L$** is a commercial fluorescent whitener; if it exists in the initial reaction mixture, the products are denoted as **1a**–**4a** and if not as **1b**–**4b**. Initially, the usage of **$Na_2L$** is to grow suitably sized single crystals of the metal phosphonates, because $M^{2+}$(M = Mn, Fe, Co, Zn) ions can be easily precipitated by **$Na_2L$**, which prevents the formation of large amounts of $NaM[O_3PCH(OH)CO_2]$ (M = Mn, Fe, Co, Zn). $NH_4Cl$ may serve as a structure-directing agent to grow suitable single crystals. When NaF is treated with acetic acid, HF is produced, which can increase the solubility of

[a] State Key Laboratory of Structural Chemistry, Fujian Institute of Research on the Structure of Matter, Chinese Academy of Science,
Fuzhou, Fujian 350002, China
E-mail: wxt@fjirsm.ac.cn

Supporting information for this article is available on the WWW under http://www.eurjic.org or from the author.

 © 2007 Wiley-VCH Verlag GmbH & Co. KGaA, Weinheim 

these compounds and result in the growth of single crystals for X-ray structural analysis. Single crystals of these compounds can also be obtained without the salts or acetic acid. However, their size and quality are not suitable for single-crystal XRD.

Experimental powder XRD patterns of **1a**–**4a** are all consistent with those simulated from single-crystal X-ray data of compounds **1**–**4**, which indicates that final products **1a**–**4a** are homogeneous phases, and elemental analyses of **1a** and **3a** are in accord with the calculated values. Furthermore, the IR spectra of **1a** and **3a** are consistent with those of **2b** and **4b** and do not include absorption bands around 1198 and 1182 $cm^{-1}$, which are assigned to the asymmetric stretching vibrations of the sulfonate group (Supporting Information, Figure S1).[9] These results indicate that crystals of **1a** and **3a** that have been repeatedly rinsed with distilled water under ultrasonic treatment contain few residual $Na_2L$.

As shown in Figure S1 (Supporting Information), the IR spectra of **1a**, **2b**, **3a**, and **4b** have a medium band in the range of 3003–3049 $cm^{-1}$, which originates from the O–H stretching vibration of the hydroxy group. Additionally, a very strong band around 1590 $cm^{-1}$ and a medium band near 1373 $cm^{-1}$ are attributed to the carboxylate group. It is interesting that the P=O stretching vibration appears around 1176 $cm^{-1}$, which exhibits a redshift of about 24 $cm^{-1}$ relative to those in [M{$HO_3PCH(OH)CO_2$}] (M = Mn, Fe, Co, Zn) and $(NH_4)Zn[O_3PCH(OH)CO_2]$.[7] Both diffuse reflectance spectra of compounds **3** and **3**–**300** have a broad and strong absorption band around 539 nm, which corresponds to the d–d transition of the $Co^{II}$ ion (Supporting Information, Figure S2); the π–π* transitions of the C=O moiety for compounds **3** and **3**–**300** appear at 232 and 217 nm, respectively.

### Structural Descriptions

Single-crystal XRD patterns revealed that compounds **1**–**4** are isostructural and feature a 3D heterometallic framework. In addition, all experimental powder XRD patterns of compounds **1**–**4** are in agreement with those simulated from single-crystal X-ray data of solid **1** (Figure 1). Therefore, only the structure of **1** will be discussed in detail as a representative. The asymmetric unit of **1** consists of one $Mn^{II}$ ion, one $Na^{I}$ ion, and one $O_3PCH(OH)CO_2^{3-}$ group (Figure 2). The $O_3PCH(OH)CO_2^{3-}$ group is chelated to the $Mn^{II}$ ion through one phosphonate oxygen atom (O2a) and one carboxylate oxygen atom (O5) to form a Mn–O–C–C–P–O six-membered chelating ring; the $Mn^{II}$ ion is also chelated by another equivalent $O_3PCH(OH)CO_2^{3-}$ group through the hydroxy group (O4c) and another carboxylate oxygen donor (O6) into a Mn–O–C–C–O five-membered chelating ring, which results in an obvious small bond angle [O4c–Mn1–O6 = 67.20(11)°]. This is similar to those in [M{$HO_3PCH(OH)CO_2$}] (M = Mn, Fe, Co, Zn).[7a] As a

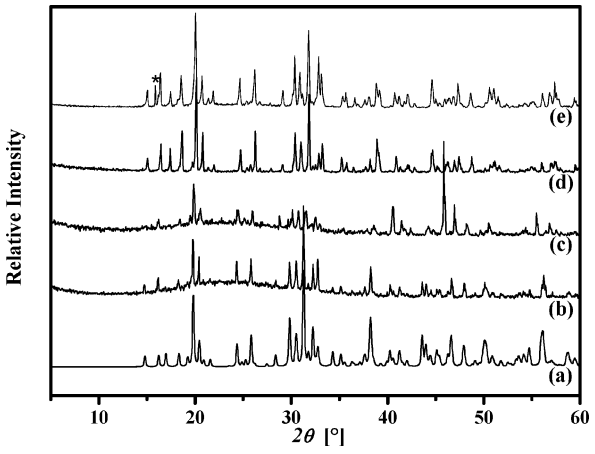


Figure 1. (a) The simulated XRD pattern of compound **1**; (b)–(e) experimental powder XRD patterns for compounds **1**–**4**, respectively. (*) The additional peak at about 15° may result from the background.

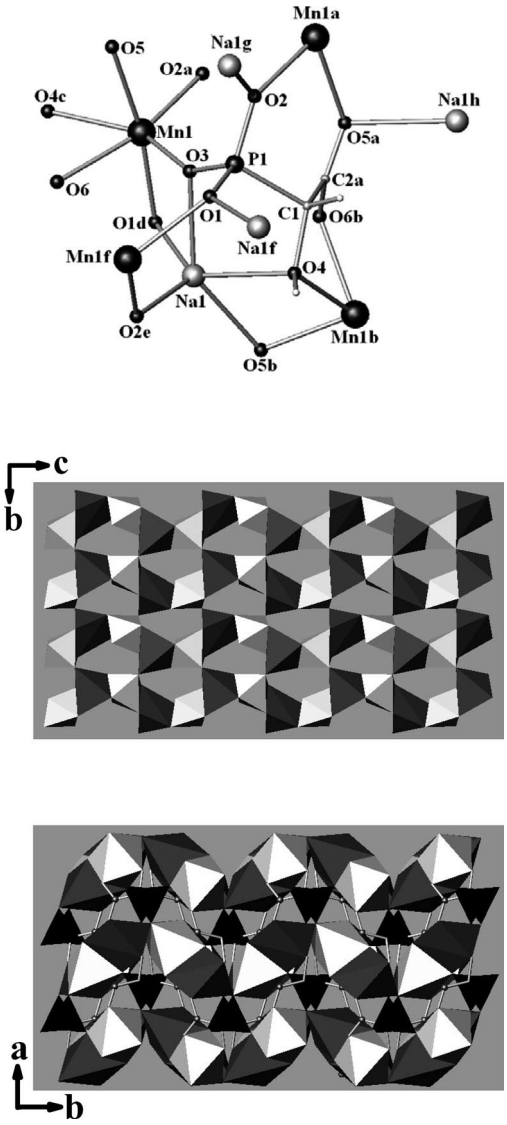


Figure 2. (Top) Ball–stick view of the coordination geometries of sodium, manganese, and phosphorus in compound **1**; (middle) polyhedral representation of the Na/MnO layer; and (bottom) 3D framework in compound **1**. White octahedron: [$MnO_6$], gray pyramid: [$NaO_5$], black tetrahedron: [$CPO_3$].

 © 2007 Wiley-VCH Verlag GmbH & Co. KGaA, Weinheim 

result, the $Mn^{II}$ ion is located in a distorted [$MnO_6$] octahedral coordination geometry, which is completed by another two phosphonate oxygen atoms from two different equivalent $O_3PCH(OH)CO_2^{3-}$ groups (O1d and O3). The values of the Mn–O bond lengths are in the range of 2.198(3)–2.343(3) Å, whereas the $Na^I$ geometry is a [$NaO_5$] pyramid, defined by three phosphonates oxygen atoms, one carboxylate oxygen donor, and one hydroxy group from four equivalent $O_3PCH(OH)CO_2^{3-}$ groups. The Na–O distances range from 2.349(3) to 2.485(3) Å. Except for O6b, which is only coordinated to one $Mn^{II}$ ion, another oxygen atom of $O_3PCH(OH)CO_2^{3-}$ bonds one $Mn^{II}$ ion and one $Na^I$ ion. So, the $O_3PCH(OH)CO_2^{3-}$ group exhibits a new octadentate mode to combine four $Mn^{II}$ ions and four $Na^I$ ions. This is obviously different from the tetradentate mode in $(NH_4)Zn[O_3PCH(OH)CO_2]$ and the tridentate mode in $M[HO_3PCH(OH)CO_2]$ (M = Mn, Fe, Co, Zn).[7]

Each [$MnO_6$] octahedron shares two edges and one corner with neighboring three [$NaO_5$] pyramids, respectively, to form a Na/MnO layer consisting of six-membered rings (6MRs), and the Na/MnO layers are further bridged by $O_3PCH(OH)CO_2^{3-}$ groups and strong hydrogen bonds between –OH and –COO [O4–H2···O6$_{(x, -y-1/2, z+1/2)}$ = 2.632(4) Å] into an interesting 3D organic–inorganic hybrid framework.

## Thermal Stabilities

Thermogravimetric analyses (TGA) of compounds **1**–**4** illustrate that under an atmosphere of nitrogen gas there is little weight loss for these compounds up to 410, 380, 390, and 370 °C, respectively (Figure 3). Thereupon, sharp weight-loss stages appear due to the decomposition of their frameworks. Furthermore, after solids **1**–**4** are annealed at 350, 250, 340 and 350 °C, respectively, their powder XRD patterns are all essentially in agreement with those simulated by single-crystal XRD data, which unambiguously indicate little change in their frameworks (Supporting Information, Figures S3–S6).

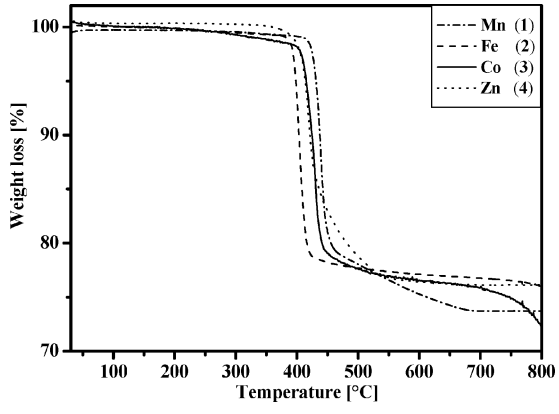


Figure 3. TGA curves of compounds **1**–**4**.

## Magnetic Properties

The temperature dependence of the $\chi_m T$ product, magnetic susceptibility ($\chi_m$) and inverse magnetic susceptibility ($1/\chi_m$) for compounds **1**–**3** at 5 kOe from 2 K to room temperature are shown in Figure S7 (Supporting Information).

The molar magnetic susceptibility of compound **1** increases with decreasing temperature and reaches a maximum at 5 K. At 305 K, the effective magnetic moment per manganese atom (5.70 $\mu_B$) is consistent with the expected spin-only value of 5.92 $\mu_B$ ($g$ = 2, $S$ = 5/2), and also according to the reported magnetic moments of $Mn^{II}$ ranging from 5.2 to 5.9 $\mu_B$.[7] Upon cooling, $\chi_m T$ product decreases slowly from 305 to 50 K. Thereupon, $\chi_m T$ decreases more quickly to 1.41 emu K mol$^{-1}$ at 2 K. In the temperature range of 2–305 K, the magnetic susceptibility follows the Curie–Weiss law [$\chi_m^{-1}$ = 1.82(5) + 0.2401(3)$T$] ($r$ = 0.9999), with $C$ = 4.16 emu K mol$^{-1}$ and $\theta$ = –7.6 K. The above results demonstrate antiferromagnetic interaction of the $Mn^{II}$ ions.[7a,10]

The effective magnetic moment per $Fe^{II}$ ion (5.25 $\mu_B$) for compound **2** at 307 K is slightly higher than the expected spin-only value of 4.90 $\mu_B$ ($g$ = 2, $S$ = 2).[10] With decreasing temperature, the effective magnetic moment decreases slowly down to 100 K (5.17 $\mu_B$) and then rapidly to 2.75 $\mu_B$ at 2 K. Between 2 and 305 K, the magnetic susceptibility also fits well with the Curie–Weiss law [$\chi_m^{-1}$ = 1.28(2) + 0.2859(1)$T$] ($r$ = 0.99999), with $C$ = 3.50 emu K mol$^{-1}$ and $\theta$ = –4.49 K. The decrease in the value of $\chi_m T$ with decreasing temperature and negative $\theta$ value indicate antiferromagnetic interaction of the $Fe^{II}$ ions.[7a,10]

Unlike those of compounds **1** and **2**, the $\chi_m T$ product of **3** decreases gradually from 2.86 emu K mol$^{-1}$ at 303 K down to 0.63 emu K mol$^{-1}$ at 2 K. From the above-mentioned equation, at 303 K the effective magnetic moment per cobalt atom ($\mu_{eff}$ = 4.78 $\mu_B$) is obviously higher than the reported spin-only value of 3.87 $\mu_B$. However, the value lies in the range of 4.4–5.2 $\mu_B$ owing to orbital contribution at room temperature.[10] In the range of 10–303 K, the magnetic susceptibility is consistent with the Curie–Weiss law [$\chi_m^{-1}$ = 4.87(9) + 0.3362(6)$T$] ($r$ = 0.9999), with $C$ = 2.97 emu K mol$^{-1}$ and $\theta$ = –14.5 K. The decrease in the value of $\chi_m T$ with decreasing temperature and negative $\theta$ value suggests antiferromagnetic interaction of the $Co^{II}$ ion.[7a,10] In addition, the magnetic susceptibility and thermal dependence of the $\chi_m T$ product are almost in agreement with those of pristine solid after polycrystalline **3** was previously heated at 300 or 340 °C for 2 h in an air atmosphere (Supporting Information, Figure S8). This result indicates little change in the valence of cobalt during the annealing treatment.

## Luminescent Properties

The solid-state luminescent properties of solids **1**–**4** were investigated under ambient temperature. Compounds **1b**–**4b** show no luminescence under our experimental conditions. In contrast, compounds **1a**–**4a** display bright blue-green (for **1a**, **2a** and **4a**) or purple (for **3a**) emission (Figure 4). The maximum band of **3a** is 434 nm, which exhibits a 11, 22, and 20-nm blueshift relative to those of compounds **1a**,

 © 2007 Wiley-VCH Verlag GmbH & Co. KGaA, Weinheim 

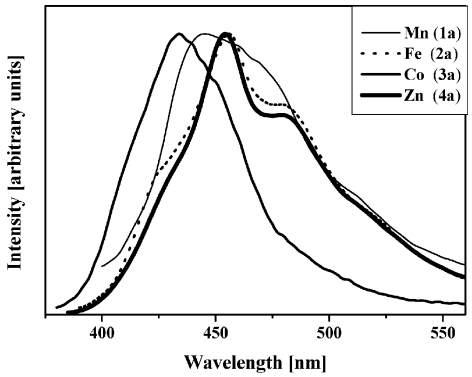


Figure 4. Normalized fluorescent emission spectra of **1a**–**4a** at room temperature in the solid state.

**2a** and **4a**, respectively. The blueshift is due to self-absorption through d–d transition of the $Co^{II}$ ion in the range of 428–654 nm. These emissions cannot be attributed to MLCT (metal-to-ligand charge transfer) and LMCT (ligand-to-metal charge transfer) in nature, and may probably be assigned to the intraligand n–π* transition for two reasons: (1) a bright blue-green emission with $\lambda_{max}$ = 460 nm can also be observed from a solution of $(H_2O_3P)$-$CH(OH)(CO_2H)$ and (2) all maximum bands of corresponding excitation spectra for solids **1a**–**4a** and $(H_2O_3P)$-$CH(OH)(CO_2H)$ solution fall in the range of 360–377 nm (Supporting Information, Figure S9, S10).[5] The lifetimes for $\lambda_{ex,em}$ = 380,450 nm of **1a** and $\lambda_{ex,em}$ = 368,460 nm of **2a** are 1.67(2) and 2.08(4) ns, respectively, which matches

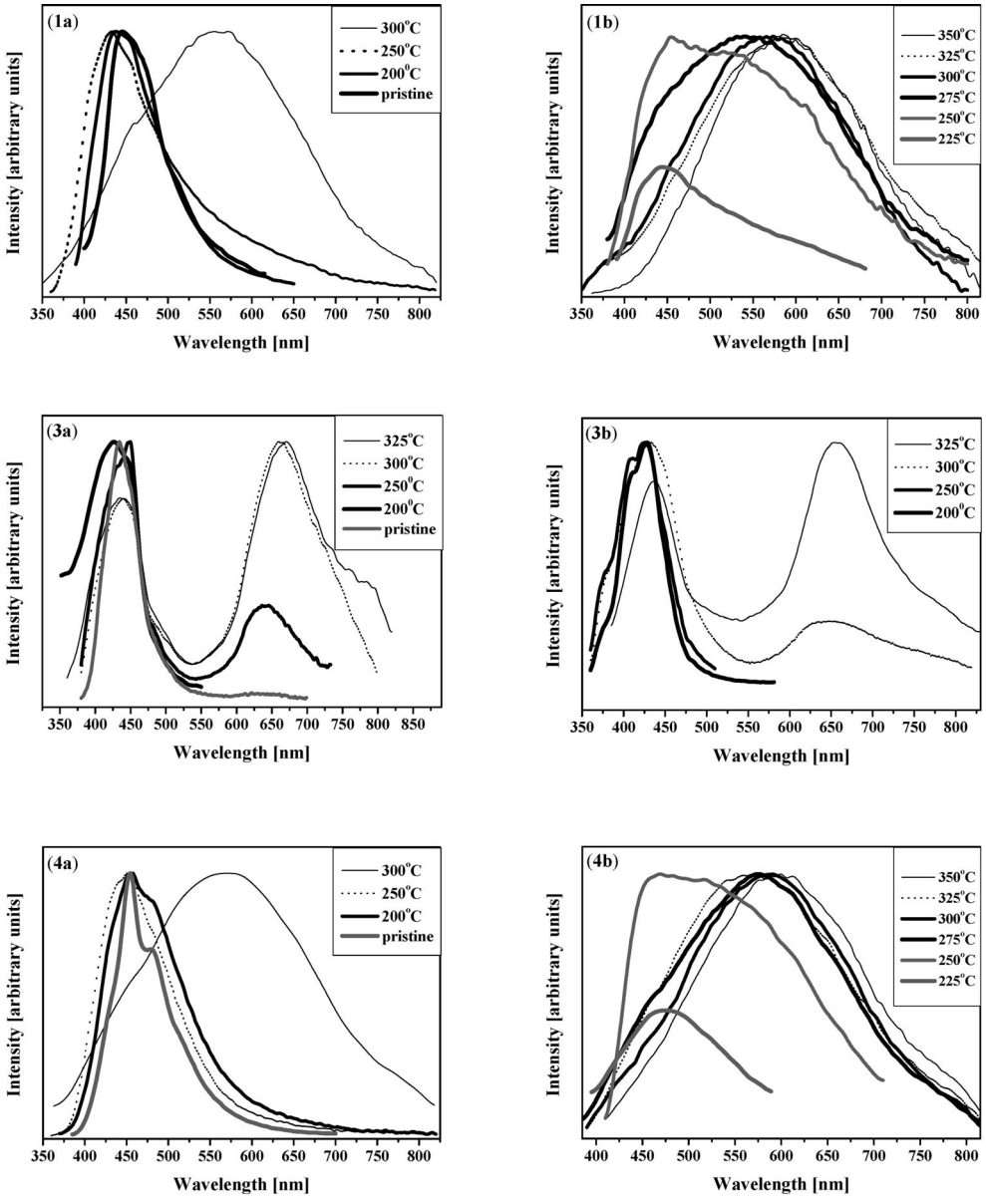


Figure 5. Room-temperature solid-state normalized fluorescent emission spectra of pristine **1a**, **1b**, **3a**, **3b**, **4a**, and **4b** − compounds were previously annealed at different temperatures.

 © 2007 Wiley-VCH Verlag GmbH & Co. KGaA, Weinheim 

that of Hpaa [2.69(5) ns for $\lambda_{ex,em}$ = 370,462 nm], whereas solid **3a** has a very short lifetime [0.35(2) ns, for $\lambda_{ex,em}$ = 352,430 nm]. Preliminary experimental results revealed that the luminescent intensities of **1a** and **3a** are about 16 and 27% of that of $\mathbf{Na_2L}$, respectively. Furthermore, it is surprising that if **3b** is previously immersed in dilute $\mathbf{Na_2L}$ solution for 6 d and then rinsed with distilled water under ultrasonic treatment repeatedly, it can also give off bright-purple luminescence similar to that of **3a** (Supporting Information, Figure S10). This phenomenon is also observed for **1b**. The above results indicate that $\mathbf{Na_2L}$ would induce intrinsic luminescence of **1**–**4**. However, the mechanism of how $\mathbf{Na_2L}$ induces the luminescence is still unknown. Furthermore, solid **3a** can also emit bright-purple luminescence if $\mathbf{Na_2L}$ is reduced to 0.01 mmol in the synthetic mixture, which indicates that the luminescent properties may not depend on the amount of $\mathbf{Na_2L}$ in the synthetic mixture. In addition, annealing treatment at 225 °C (for **1b** and **4b**) or 200–250 °C (for **3b**) can also induce weak blue-green (for **1b** and **4b**) and bright-purple (for **3b**) luminescence.

Another attractive feature of compounds **1**, **3**, and **4** is their irreversible transformation of luminescent color through annealing treatment (Figure 5). Both **1a** and **4a** will give off bright-yellow luminescence ($\lambda_{max}$ = 571 nm) with a broad profile if they are previously annealed at 300 °C. The full width at half maximum heights (FWHM) of **1a** and **4a** are 239 and 258 nm, respectively. Because d–d transition for the $Co^{II}$ ion would absorb blue and green light with a maximum at 539 nm, **3a** can emit both purple and red emissions after annealing treatment, which is different to those of **1a** and **4a**. The intensities of purple and red emissions for **3a** will be tuned with different annealing temperature. For example, if **3a** is previously annealed at 250 °C, it displays bright purplish red luminescence, and the intensity ratio between the two peak bands at 449 and 636 nm is –2.6. After **3a** is annealed at 300 °C, red luminescence is intensified to reduce the ratio between the two maximum bands at 440 and 659 nm to –0.78, resulting in bright-red emission. Noteworthy is that the luminescent spectra of **3a** that was previously annealed at 250 and 300 °C are similar to the absorption spectra of chlorophyll a and b, respectively, which indicates that **3a** is an attractive candidate to be used in light conversion agriculture materials [light conversion agriculture material has the function of converting a light spectrum (like UV, green light) into blue and red light so as to promote the growth of vegetables].

Similar transformations of luminescent color with annealing treatment can also be observed on solids **1b**, **3b**, and **4b**. Because the $Mn^{II}$ ion is an important luminescent activator that gives off red emission, it seems that the transformation of luminescent colors for solids **1**, **3**, and **4** are not related to the transition-metal centers.[11] So, the IR spectra of solids **3** and **4** with different annealing temperatures were recorded to investigate the changes in the $O_3PCH(OH)CO_2^{3-}$ anion (Supporting Information, Figures S12, S13). However, all IR spectra are in agreement with those of the pristine solids. A suitable single crystal of **3** was carefully selected and annealed at 300 °C, and X-ray single-crystal diffraction revealed that the bond lengths of C=O and P–O in compound **3**–**300** are slightly shorter than those in pristine **3**, which results in the slight contraction of the unit-cell volume. This is in accord with the π–π* transition of C=O of compound **3**–**300**, which shows about a 15-nm blueshift relative to that of pristine **3** for strengthening the C=O band after the annealing treatment. Such slightly irreversible changes in the $O_3PCH(OH)CO_2^{3-}$ anion may cause the transformations of luminescent colors from blue-green to yellow (for **1**, **4**) or from purple to red (for **3**). In addition, the corresponding excitation spectra exhibit broad profiles in the range of 250–400 nm, which may be assigned to intraligand π–π* as well as n–π* transitions (Supporting Information, Figures S14–S19).

Furthermore, lifetimes for blue emission of solids **1** and **4** range from 1.6(1) to 3.21(7) ns, which are shorter than those of yellow emission [3.3(2)–6.3(4) ns] (Figures 6 and 7). For compound **3**, the lifetimes for purple and red luminescence are in the range of 0.35(4)–0.90(2) and 1.8(1)–2.7(2) ns, respectively (Figures 8 and 9).

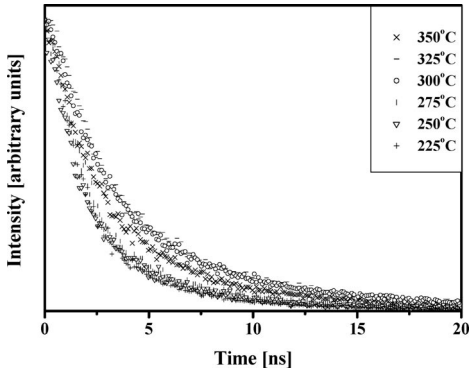


Figure 6. Room-temperature solid-state fluorescent intensity as a function of time for **1b** previously annealed at 225 ($\lambda_{ex,em}$ = 365, 445 nm), 250 ($\lambda_{ex,em}$ = 365, 420 nm), 275 ($\lambda_{ex,em}$ = 365, 458 nm), 300 ($\lambda_{ex,em}$ = 365, 575 nm), 325 ($\lambda_{ex,em}$ = 367, 580 nm), and 350 °C ($\lambda_{ex,em}$ = 370, 580 nm), respectively.

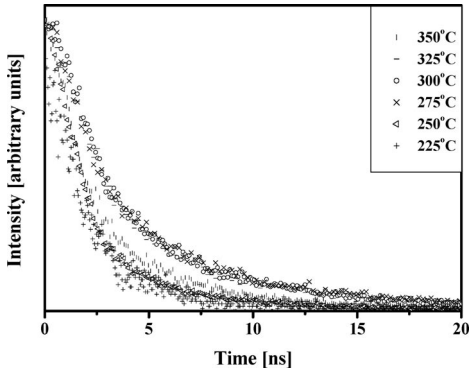


Figure 7. Room-temperature solid-state fluorescent intensity as a function of time for **4b** previously annealed at 225 ($\lambda_{ex,em}$ = 370, 478 nm), 250 ($\lambda_{ex,em}$ = 365, 460 nm), 275 ($\lambda_{ex,em}$ = 368, 573 nm), 300 ($\lambda_{ex,em}$ = 330, 588 nm), 325 ($\lambda_{ex,em}$ = 362, 562 nm), and 350 °C ($\lambda_{ex,em}$ = 365, 584 nm), respectively.

 © 2007 Wiley-VCH Verlag GmbH & Co. KGaA, Weinheim 

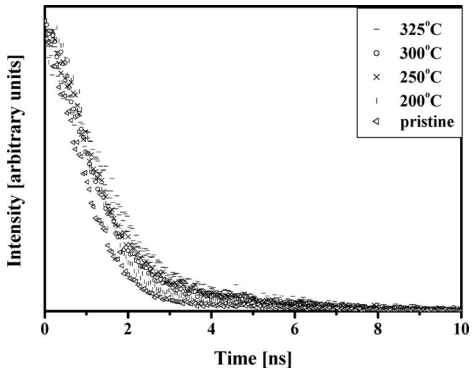


Figure 8. Room-temperature solid-state fluorescent intensity as a function of time for **3a** ($\lambda_{ex,em}$ = 352, 430 nm) as well as **3a** previously annealed at 200 ($\lambda_{ex,em}$ = 350, 428 nm), 250 ($\lambda_{ex,em}$ = 330, 445 nm), 300 ($\lambda_{ex,em}$ = 340, 440 nm), and 325 °C ($\lambda_{ex,em}$ = 362, 436 nm), respectively.

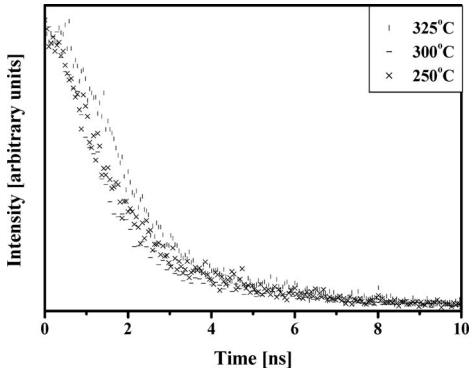


Figure 9. Room-temperature solid-state fluorescent intensity as a function of time for **3a** previously annealed at 250 ($\lambda_{ex,em}$ = 360, 640 nm), 300 ($\lambda_{ex,em}$ = 340, 660 nm), and 325 °C ($\lambda_{ex,em}$ = 365, 668 nm), respectively.

## Conclusions

In summary, the hydrothermal syntheses, crystal structures, and properties (including thermal stability, magnetism, and luminescence) of four new heterometal 2-hydroxyl-(phosphono)carboxylates were described. Solids **1**, **3**, and **4** are the first phosphonate-based compounds that possess intrinsic blue-green or purple luminescence properties induced by fluorescent whitener (**$Na_2L$**) or heat treatment. The luminescent colors can be irreversibly transformed into yellow or red emission by simple annealing treatment. These properties make them of interest for potential application as emitters in displaying technology, as well as advanced anticounterfeiting technical products.

## Experimental Section

**Materials and Instrumentation:** Hydroxy(phosphono)acetic acid solution was obtained from Changzhou City Jianghai Chemical Factory as water treatment agent (48.0 wt.-%). All other chemicals were obtained from commercial sources and used without further purification. Compounds **1**–**4** were synthesized in 25-mL Teflon-lined stainless steel vessels under autogenous pressure. The reactants were stirred homogeneously before heating. Elemental analyses were carried out with a Vario EL III element analyzer. Infrared spectra were obtained with a Nicolet Magna 750 FTIR spectrometer. The diffuse reflectance spectra of compounds **3** and **3**–**300** (polycrystalline **3** was previously annealed at 300 °C for 2 h in an air atmosphere) were recorded with a Perkin–Elmer Lambda 35 UV/Vis spectrometer. Fluorescent properties of solids **1**–**4** were investigated with FLS920 and LifeSpec-ps at ambient temperature. Thermogravimetric analysis was performed with a NETZSCH STA449C under nitrogen gas flow at a heating rate of 10 °C min$^{-1}$ (for **1** and **4**) or 15 °C min$^{-1}$ (for **2** and **3**) from room temperature to 800 °C. Powder X-ray diffraction (XRD) patterns were acquired with a DMAX-2500 diffractometer by using Cu-$K_\alpha$ radiation in an ambient environment. Magnetic properties of compounds **1**–**3** were measured with a Quantum Design PPMS at a magnetic field of 5000 Oe from 2 K to room temperature.

**$NaMn[O_3PCH(OH)CO_2]$ (1):** A mixture of $Mn(CH_3COO)_2{\cdot}4H_2O$ (0.2536 g, 1.035 mmol), disodium 4,4′-bis(2-sulfonatostiryl)biphenyl (**$Na_2L$**; 0.5821 g, 1.035 mmol), $NH_4Cl$ (2.2102 g, 41.32 mmol), NaF (0.0904 g, 2.153 mmol), $(H_2O_3P)CH(OH)(CO_2H)$ solution (0.5 mL, 2 mmol), and $H_2O$ (10.0 mL) was heated at 140 °C for 96 h. The final mixture was repeatedly rinsed with distilled water under ultrasonic treatment to obtain pure colorless crystals of **1**. Experimental powder XRD pattern of the product was in agreement with that simulated from single-crystal X-ray data, which indicated a homogeneous phase. The yield was 67% (0.1594 g) based on $Mn(CH_3COOH)_2{\cdot}4H_2O$. Final pH value of this reaction mixture was 3.72. $C_2H_2MnNaO_6P$ (230.94): calcd. C 10.40, H 0.87; found C 10.63, H 1.24. IR (KBr pellet): $\tilde{\nu}$ = 999 (w), 999 (vs, $\upsilon as_{CO}$), 999 (s), 3049 (m, $\upsilon_{O-H}$), 2929 (w, $\upsilon_{C-H}$), 2786 (w), 2733 (w), 2625 (w), 2520 (w), 1589 (vs, $\upsilon as_{CO}$), 1423 (s, $\delta_{C-H}$), 1373 (m, $\upsilon s_{CO}$), 1273 (m, $\delta_{C-H}$), 1176 (s, $\upsilon_{P=O}$), 1144 (s, $\upsilon_{P-O}$), 1095 (vs, $\upsilon_{P-O}$), 1056 (w, $\upsilon_{P-O}$), 995 (m, $\upsilon_{P-O}$), 983 (w), 847 (w), 796 (m), 767 (w, $\upsilon_{C-P}$), 748 (w, $\upsilon_{C-P}$), 665 (w), 588 (m), 542 (m), 494 (s) cm$^{-1}$. Crystals of **1** can also be obtained in the absence of **$Na_2L$** and $NH_4Cl$ as follows: A mixture of $Mn(CH_3COO)_2{\cdot}4H_2O$ (0.1225 g, 0.4998 mmol), NaF (0.3500 g, 8.335 mmol), $(H_2O_3P)CH(OH)(CO_2H)$ solution (1.0 mL, 4 mmol), acetic acid (2.0 mL), and $H_2O$ (8.0 mL) was heated at 120 °C for 144 h. The final mixture was also rinsed with distilled water under ultrasonic treatment many times to obtain pure colorless crystals of **1**. Experimental powder XRD pattern of the product was in accord with that simulated from single-crystal X-ray data, which indicated a homogeneous phase.

**$NaFe[O_3PCH(OH)CO_2]$ (2):** A mixture of $FeCl_2{\cdot}4H_2O$ (0.1014 g, 0.5100 mmol), $NH_4Cl$ (2.5 g, 47 mmol), NaF (0.4 g, 9.5 mmol), $(H_2O_3P)CH(OH)(CO_2H)$ solution (0.7 mL, 3 mmol), and $H_2O$ (10.0 mL) was heated at 140 °C for 96 h. The final mixture was repeatedly rinsed with distilled water under ultrasonic treatment to obtain pure colorless crystals of **2**. Experimental powder XRD pattern of the product was in agreement with that simulated from single-crystal X-ray data, which indicated a homogeneous phase. The yield was 33% (0.0383 g) based on $FeCl_2{\cdot}4H_2O$. Final pH value of this reaction mixture was 3.79. $C_2H_2FeNaO_6P$ (231.85): calcd. C 10.36, H 0.87; found C 10.32, H 1.16. IR (KBr pellet): $\tilde{\nu}$ = 3026 (m, $\upsilon_{O-H}$), 2931 (w, $\upsilon_{C-H}$), 2786 (w), 2733 (w), 2625 (w), 2524 (w), 1591 (vs, $\upsilon as_{CO}$), 1426 (s, $\delta_{C-H}$), 1374 (s, $\upsilon s_{CO}$), 1275 (s, $\delta_{C-H}$), 1177 (s, $\upsilon_{P=O}$), 1148 (s, $\upsilon_{P-O}$), 1088 (vs, $\upsilon_{P-O}$), 1056 (w, $\upsilon_{P-O}$), 993 (s, $\upsilon_{P-O}$), 985 (s), 845 (m), 806 (m), 773 (w, $\upsilon_{C-P}$), 753 (w, $\upsilon_{C-P}$), 665 (m), 594 (m), 549 (m), 490 (s) cm$^{-1}$. Crystals of **2** can also be obtained with **$Na_2L$** in an initial mixture as follows: A mixture of $FeCl_2{\cdot}4H_2O$ (0.1001 g, 0.5035 mmol), **$Na_2L$** (0.2801 g, 0.4980 mmol), NaF (0.4001 g, 9.528 mmol), $(H_2O_3P)CH(OH)(CO_2H)$ solution (1 mL, 4 mmol), acetic acid (2.0 mL), and

 © 2007 Wiley-VCH Verlag GmbH & Co. KGaA, Weinheim 

$H_2O$ (8.0 mL) was heated at 120 °C for 144 h The final mixture was also rinsed with distilled water under ultrasonic treatment many times to obtain pure crystals of **2** Experimental powder XRD pattern of the product was also in agreement with that simulated from single-crystal X-ray data, which indicated a homogeneous phase.

**$NaCo[O_3PCH(OH)CO_2]$ (3):** A mixture of $Co(CH_3COO)_2{\cdot}4H_2O$ (0.249 g, 1.00 mmol), **$Na_2L$** (0.5843 g, 1.039 mmol), NaF (0.1657 g, 3.946 mmol), $(H_2O_3P)CH(OH)(CO_2H)$ solution (0.7 mL, 3 mmol), acetic acid (2.0 mL), and $H_2O$ (8.0 mL) was heated at 140 °C for 96 h. The final mixture was repeatedly rinsed with distilled water under ultrasonic treatment to obtain pure red crystals of **3**. Experimental powder XRD pattern of the product was in agreement with that simulated from single-crystal X-ray data, which indicated a homogeneous phase. The yield was 93% (0.2172 g) based on $Co(CH_3COOH)_2{\cdot}4H_2O$. Final pH value of this reaction mixture was 3.80. $C_2H_2CoNaO_6P$ (234.93): calcd. C 10.23, H 0.86; found C 10.26, H 1.22. IR (KBr pellet): $\tilde{\nu}$ = 3003 (m, $\upsilon_{O-H}$), 2936 (m, $\upsilon_{C-H}$), 2787 (w), 2729 (w), 2619 (w), 2521 (w), 1595 (vs, $\upsilon as_{CO}$), 1428 (s, $\delta_{C-H}$), 1373 (m, $\upsilon s_{CO}$), 1273 (m, $\delta_{C-H}$), 1177 (s, $\upsilon_{P=O}$), 1151 (s, $\upsilon_{P-O}$), 1090 (vs, $\upsilon_{P-O}$), 1054 (w, $\upsilon_{P-O}$), 987 (vs, $\upsilon_{P-O}$), 846 (m), 813 (m), 777 (w, $\upsilon_{C-P}$), 756 (w, $\upsilon_{C-P}$), 671 (m), 660 (m), 593 (m), 557 (m), 492 (s) $cm^{-1}$. Crystals of **3** can also be obtained in the absence of **$Na_2L$** as follows: A mixture of $Co(CH_3COO)_2{\cdot}4H_2O$ (0.249 g, 1.00 mmol), NaF (0.2001 g, 4.765 mmol), $(H_2O_3P)$-$CH(OH)(CO_2H)$ solution (0.5 mL, 2 mmol), acetic acid (0.5 mL), and $H_2O$ (8.0 mL) was heated at 120 °C for 144 h. The final mixture was also rinsed with distilled water under ultrasonic treatment many times to obtain pure red crystals of **3**. Experimental powder XRD pattern of the product was also in agreement with that simulated from single-crystal X-ray data, which indicated a homogeneous phase.

**$NaZn[O_3PCH(OH)CO_2]$ (4):** A mixture of $Zn(CH_3COO)_2{\cdot}2H_2O$ (0.11 g, 0.501 mmol), NaF (0.35 g, 8.3 mmol), $(H_2O_3P)CH$-$(OH)(CO_2H)$ solution (1.0 mL, 4 mmol), acetic acid (2.0 mL), and $H_2O$ (8.0 mL) was heated at 140 °C for 96 h. The final mixture was repeatedly rinsed with distilled water under ultrasonic treatment to obtain pure crystals of **4**. Experimental powder XRD pattern of the product was in agreement with that simulated from single-crystal X-ray data, which indicated a homogeneous phase. The yield was 46% (0.0490 g) based on $Zn(CH_3COO)_2{\cdot}2H_2O$. Final pH value of this reaction mixture was 2.84. $C_2H_2NaO_6PZn$ (241.37): calcd. C 9.95, H 0.84; found C 9.95, H 1.24. IR (KBr pellet): $\tilde{\nu}$ = 3023 (m, $\upsilon_{O-H}$), 2935 (w, $\upsilon_{C-H}$), 2792 (w), 2737 (w), 2625 (w), 2524 (w), 1591 (vs, $\upsilon as_{CO}$), 1433 (s, $\delta_{C-H}$), 1376 (s, $\upsilon s_{CO}$), 1277 (m, $\delta_{C-H}$), 1179 (s, $\upsilon_{P=O}$), 1154 (s, $\upsilon_{P-O}$), 1083 (vs, $\upsilon_{P-O}$), 1062 (w, $\upsilon_{P-O}$), 994 (s, $\upsilon_{P-O}$), 985 (w), 848 (m), 808 (m), 776 (w, $\upsilon_{C-P}$), 755 (w, $\upsilon_{C-P}$), 673 (m), 663 (m), 594 (m), 558 (m), 500 (s), 490 (s) $cm^{-1}$. Crystals of **4** can also be obtained with **$Na_2L$** in an initial mixture as follows: A mixture of $Zn(CH_3COO)_2{\cdot}2H_2O$ (0.2195 g, 1.000 mmol), NaF (0.2001 g, 4.765 mmol), **$Na_2L$** (0.5602 g, 0.9960 mmol), $(H_2O_3P)$-$CH(OH)(CO_2H)$ solution (0.5 mL, 2 mmol), acetic acid (0.5 mL), and $H_2O$ (8.0 mL) was heated at 140 °C for 96 h. The final mixture was rinsed with distilled water under ultrasonic treatment many times to obtain pure crystals of **4**. Experimental powder XRD pattern of the product was also in agreement with that simulated from single-crystal X-ray data, which indicated a homogeneous phase.

**Single-Crystal X-ray Diffraction:** X-ray data were collected at 293(2) K with a Siemens SMART-CCD diffractometer (for **1**), a Rigaku Mercury CCD/AFC diffractometer (for **2**–**4**), and a Saturn 70 CCD diffractometer (for **3**–**300**) by using graphite-monochromated Mo-$K_\alpha$ radiation [$\lambda$(Mo-$K_\alpha$) = 0.71073 Å]. Data of compound **1** were reduced and absorption corrected with SMART and SADABS software, respectively, whereas data of compounds **2**–**4** and **3**–**300** were reduced with CrystalClear v1.3. These structures were solved by direct methods and refined by full-matrix least-squares techniques on $F^2$ by using SHELXTL-97.[12] All non-hydrogen atoms were treated anisotropically. The positions of hydrogen atoms were located from difference Fourier map and assigned with fixed isotropic thermal parameter. Crystal data are summarized in Table 1. CCDC-629750 to -629753 for compounds **1**–**4**, respectively, contain the supplementary crystallographic data for this paper. These data can be obtained free of charge from The Cambridge Crystallographic Data Centre via www.ccdc.cam.ac.uk/data_request/cif.

**Relative Luminescent Intensity:** Coin-like tablets of solids **1a**, **3a**, and **$Na_2L$** with about 1.3-cm diameter and 0.1-cm thickness were prepared at room temperature. First, a tablet of **$Na_2L$** was excited at 372 nm to obtain the emission spectrum, and then all the experimental conditions (including optical set up, focalization point, illuminated cross-section, sample holder, and emission and excitation slits width) were held constant and a tablet of solid **1a** was excited at 376 nm to obtain the emission spectrum. Second, a tablet of **$Na_2L$** was excited at 410 nm to obtain the emission spectrum, and then all the experimental conditions (including optical set up, focalization point, illuminated cross-section, sample holder, and emis-

Table 1. Crystallographic data for compounds **1**–**4**.

| Complex | **1** | **2** | **3** | **3-300** | **4** |
|---|---|---|---|---|---|
| Formula | $C_2H_2MnNaO_6P$ | $C_2H_2FeNaO_6P$ | $C_2H_2CoNaO_6P$ | $C_2H_2CoNaO_6P$ | $C_2H_2ZnNaO_6P$ |
| FW | 230.94 | 231.85 | 234.93 | 234.93 | 241.37 |
| Space group | *Pbca* | *Pbca* | *Pbca* | *Pbca* | *Pbca* |
| *a* [Å] | 10.4557(5) | 10.266(3) | 10.1998(9) | 10.181(3) | 10.1365(16) |
| *b* [Å] | 9.8265(4) | 9.743(3) | 9.6890(9) | 9.673(3) | 9.6893(15) |
| *c* [Å] | 10.9353(1) | 10.862(3) | 10.7943(10) | 10.784(3) | 10.7942(19) |
| *V* [Å$^3$] | 1123.22(7) | 1086.3(5) | 1066.76(17) | 1062.1(5) | 1060.2(3) |
| *Z* | 8 | 8 | 8 | 8 | 8 |
| *T* [K] | 293(2) | 293(2) | 293(2) | 293(2) | 293(2) |
| $D_{calcd.}$ [g cm$^{-3}$] | 2.731 | 2.835 | 2.926 | 2.938 | 3.024 |
| $\mu$ [mm$^{-1}$] | 2.682 | 3.119 | 3.566 | 3.582 | 4.984 |
| GOF on $F^2$ | 1.168 | 1.101 | 1.185 | 1.111 | 1.307 |
| $R_{int}$ | 0.0230 | 0.0190 | 0.0368 | 0.0208 | 0.0500 |
| $R1$[a] [$I > 2\sigma(I)$] | 0.0455 | 0.0202 | 0.0341 | 0.0173 | 0.0444 |
| $wR2$[b] [all data] | 0.1189 | 0.0493 | 0.0643 | 0.0446 | 0.0832 |

[a] $R1 = \Sigma(||F_o| - |F_c||)/\Sigma |F_o|$. [b] $wR2 = \{\Sigma w[(F_o^2 - F_c^2)]/\Sigma w[(F_o^2)^2]\}^{0.5}$.

 © 2007 Wiley-VCH Verlag GmbH & Co. KGaA, Weinheim 

sion and excitation slits width) were held constant and a tablet of solid **3a** was excited at 352 nm to obtain the emission spectrum.

**Annealing Treatment:** In an oven, polycrystallines of **1**–**4** were heated in air from room temperature to the required temperature over 30 min and then held at that temperature for 120 min. The crystals were then naturally cooled to ambient temperature.

**Supporting Information** (see also the footnote on the first page of this article): Tables of selected bond lengths and angles and plots consisting of IR, PXRD, magnetic, and luminescent data.

## Acknowledgments

This research was supported by grants from the State Key Laboratory of Structure Chemistry, Fujian Institute of Research on the Structure of Matter, Chinese Academy of Sciences (CAS), the National Ministry of Science and Technology of China (2007CB815301 and 2006CB932900), the National Science Foundation of China (20733003 and 20673118), the Science Foundation of CAS, and Fujian Province for Research Funding Support (KJCX2-YW-M05, 2005HZ01-1, 2007J0171, 2006J0014 and 2006F3132).

[1] a) A. Clearfield, "Metal Phosphonate Chemistry" in *Progress in Inorganic Chemistry* (Eds.: A. D. Karlin), John Wiley & Sons, New York, **1998**, vol. 47, pp. 371–510; b) A. Clearfield in *New Developments in Ion Exchange Materials* (Eds.: M. Abe, T. Kataoka, T. Suzuki), Kodansha, Ltd., Tokyo, **1991**; c) I. O. Benítez, B. Bujoli, L. J. Camus, C. M. Lee, F. Odobel, D. R. Talham, *J. Am. Chem. Soc.* **2002**, *124*, 4363–4370; d) G. E. Fanucci, J. Krzystek, M. W. Meisel, L.-C. Brunel, D. R. Talham, *J. Am. Chem. Soc.* **1998**, *120*, 5469–5479; e) C. Y. Ortiz-Avila, C. Bhardwaj, A. Clearfield, *Inorg. Chem.* **1994**, *33*, 2499–2500; f) T. E. Mallouk, J. A. Gavin, *Acc. Chem. Res.* **1998**, *31*, 209–217; g) L. C. Brousseau III, T. E. Mallouk, *Anal. Chem.* **1997**, *69*, 679–687; h) O. R. Evans, W. Lin, *Acc. Chem. Res.* **2002**, *35*, 511–522; i) K. Maeda, *Microporous Mesoporous Mater.* **2004**, *73*, 47–54; j) A. Clearfield, Z. Wang, *J. Chem. Soc. Dalton Trans.* **2002**, 2937–2947; k) A. Clearfield, *Curr. Opinion. Sol. State Mater. Res.* **2002**, *6*, 495–506.

[2] a) B. Liu, P. Yin, X. Y. Yi, S. Gao, L. M. Zheng, *Inorg. Chem.* **2006**, *45*, 4205–4213; b) B. Liu, Y. Z. Li, L. M. Zheng, *Inorg. Chem.* **2005**, *44*, 6921–6923; c) X. Y. Yi, B. Liu, R. Jiménez-Aparicio, F. A. Urbanos, S. Gao, W. Xu, J. S. Chen, Y. Song, L. M. Zheng, *Inorg. Chem.* **2005**, *44*, 4309–4314; d) P. Yin, S. Gao, Z. M. Wang, C. H. Yan, L. M. Zheng, X. Q. Xin, *Inorg. Chem.* **2005**, *44*, 2761–2765.

[3] a) J. A. Groves, S. R. Miller, S. J. Warrender, C. Mellot-Draznieks, P. Lightfoota, P. A. Wright, *Chem. Commun.* **2006**, 3305–3307; b) J. Kratochvil, M. Necas, V. Petricek, J. Pinkas, *Inorg. Chem.* **2006**, *45*, 6562–6564; c) R. Vivani, F. Costantino, U. Costantino, M. Nocchetti, *Inorg. Chem.* **2006**, *45*, 2388–2390; d) S. S. Bao, G. S. Chen, Y. Wang, Y. Z. Li, L. M. Zheng, Q. H. Luo, *Inorg. Chem.* **2006**, *45*, 1124–1129; e) S. Bauer, H. Mu1ller, T. Bein, N. Stock, *Inorg. Chem.* **2005**, *44*, 9464–9470; f) J. A. Groves, P. A. Wright, P. Lightfoot, *Inorg. Chem.* **2005**, *44*, 1736–1739; g) B. P. Yang, J. G. Mao, *Inorg. Chem.* **2005**, *44*, 566–571; h) J. A. Groves, S. R. Miller, S. J. Warrender, C. Mellot-Draznieks, P. Lightfoota, P. A. Wright, *Chem. Commun.* **2006**, 3305–3307; i) C. Serre, J. A. Groves, P. Lightfoota, A. M. Z. Slawin, P. A. Wright, N. Stock, T. Bein, M. Haouas, F. Taulelle, G. Férey, *Chem. Mater.* **2006**, *18*, 1451–1457; j) K. Abu-Shandi, H. Winkler, C. Janiak, *Z. Anorg. Allg. Chem.* **2006**, *632*, 629–633; k) K. Abu-Shandi, C. Janiak, *Z. Naturforsch., Teil B* **2005**, *60*, 1250–1254.

[4] a) X. M. Zhang, J. J. Hou, W. X. Zhang, X. M. Chen, *Inorg. Chem.* **2006**, *45*, 8120–8125; b) J. Svoboda, V. Zima, L. Beneš, K. Melánová, M. Vlček, *Inorg. Chem.* **2005**, *44*, 9968–9976; c) M. M. Gómez-Alcantara, M. A. G. Aranda, P. Olivera-Pastor, P. Beran, J. L. García-Muñoz, A. Cabeza, *Dalton Trans.* **2006**, 577–585.

[5] a) X. M. Gan, B. M. Rapko, J. Fox, I. Binyamin, S. Pailloux, E. N. Duesler, R. T. Paine, *Inorg. Chem.* **2006**, *45*, 3741–3745; b) S. Comby, R. Scopelliti, D. Imbert, L. Charbonnière, R. Ziessel, J. C. G. Bu1nzli, *Inorg. Chem.* **2006**, *45*, 3158–3160.

[6] a) D. Cave, F. C. Coomer, E. Molinos, H. H. Klauss, P. T. Wood, *Angew. Chem. Int. Ed.* **2006**, *45*, 803–806; b) Q. Yue, J. Yang, G. H. Li, G. D. Li, J. S. Chen, *Inorg. Chem.* **2006**, *45*, 4431–4439; c) J. L. Song, J. G. Mao, *Chem. Eur. J.* **2005**, *11*, 1417–1424; d) Y. Gong, W. Tang, W. B. Hou, Z. Y. Zha, C. W. Hu, *Inorg. Chem.* **2006**, *45*, 4987–4995; e) D. K. Cao, Y. Z. Li, Y. Song, L. M. Zheng, *Inorg. Chem.* **2005**, *44*, 3599–3604; f) D. K. Cao, Y. Z. Li, L. M. Zheng, *Inorg. Chem.* **2005**, *44*, 2984–2985.

[7] a) R. B. Fu, S. C. Xiang, H. S. Zhang, J. J. Zhang, X. T. Wu, *Cryst. Growth Des.* **2005**, *5*, 1795–1799; b) R. B. Fu, H. S. Zhang, L. S. Wang, S. M. Hu, Y. M. Li, X. H. Huang, X. T. Wu, *Eur. J. Inorg. Chem.* **2005**, 3211–3213.

[8] P. Vojtíšek, P. Cígler, J. Kotek, J. Rudovský, P. Hermann, I. Lukeš, *Inorg. Chem.* **2005**, *44*, 5591–5599.

[9] J. M. Kesselman-Truttmann, S. J. Hug, *Environ. Sci. Technol.* **1999**, *33*, 3171–3176.

[10] a) F. Sanz, C. Parada, J. M. Rojo, C. Ruiz-Valero, *Chem. Mater.* **2001**, *13*, 1334–1340; b) R. l. Carlin, *Magneto-Chemistry*, Springer, New York, **1986**.

[11] a) Y. B. Dong, G. X. Jin, M. D. Smith, R. Q. Huang, B. Tang, H. C. zur Loye, *Inorg. Chem.* **2002**, *41*, 4909–4914; b) X. D. Guo, G. S. Zhu, Q. R. Fang, M. Xue, G. Tian, J. Y. Sun, X. T. Li, S. L. Qiu, *Inorg. Chem.* **2005**, *44*, 3850–3855; c) J. Tao, M. L. Tong, J. X. Shi, X. M. Chen, S. W. Ng, *Chem. Commun.* **2000**, 2043–2044; d) M. García-Hipólito, O. Alvarez-Fregoso, E. Martínez, C. Falcony, M. A. Aguilar-Frutis, *Optic. Mater.* **2002**, *20*, 113–118; e) J. Wang, S. B. Wang, Q. Su, *J. Mater. Chem.* **2004**, *14*, 2569–2574.

[12] G. M. Sheldrick, *SHELXT 97: Program for Crystal Structure Refinement*, University of Göttingen, Germany, **1997**.

Received: June 15, 2007
Published Online: October 8, 2007

 © 2007 Wiley-VCH Verlag GmbH & Co. KGaA, Weinheim 

DOI: 10.1002/ejic.200700744

# Luminescent Organically Templated Lanthanide Oxalate–Selenate Hybrids

Mei-Ling Feng[a,b] and Jiang-Gao Mao*[a]

**Keywords:** Hydrothermal syntheses / Lanthanides / Selenium / Crystal structures / Luminescent properties

Hydrothermal reactions of lanthanide nitrates with selenic acid, sodium oxalate, and organic amines led to two series of new organically templated lanthanide oxalate–selenate hybrids with 2D-layer or 3D-network structures, namely, $Ln_2(SeO_4)_2(C_2O_4)(H_2O)_4$·pip (Ln = Eu **1**; Tb **2**; Dy **3**; Er **4**; Yb **5**) (pip = piperazine) and $[H_2pip]_2[Ln_2(SeO_4)_2(C_2O_4)_3]$·$H_2O$ (Ln = Er **6**; Yb **7**; Lu **8**; Y **9**). Their structures were established by X-ray single-crystal diffraction. Isostructural compounds **1**–**5** feature a 2D inorganic–organic hybrid neutral layer of $Ln_2(SeO_4)_2(C_2O_4)(H_2O)_4$. The neutral piperazine molecules are located at the interlayer spaces and interconnect with the inorganic skeleton through hydrogen bonds. Compounds **6**–**9** are isostructural and possess 3D pillared layered architectures composed of lanthanide oxalate layers bridged by selenate anions (the pillar). The template cations are located at the tunnels of the structure. Compounds **1**, **2**, and **3** display emission bands in the red-, green-, and pink-light regions, respectively, and these compounds have lifetimes of 0.178, 0.962, and 0.276 ms, respectively. Compounds **6** and **7** both exhibit emission bands in the near-IR region.
(© Wiley-VCH Verlag GmbH & Co. KGaA, 69451 Weinheim, Germany, 2007)

## Introduction

Recent studies on the preparations of new compounds possessing inorganic open frameworks with guest organic entities have revealed the diversity of such materials in terms of structure topology and composition, particularly in the presence of organic amines as structure-directing agents, which usually occupy the structural voids and are well isolated from the inorganic skeleton.[1–3] The main interest in this class of compounds stems from their potential applications in the areas of catalysis, sorption, and separation processes.[3–5] So far, a remarkable variety of such materials has been reported and most of the reports are based on metal phosphates.[6] Recently, this research field has been extended to the oxido anions of group 16 elements such as metal sulfates.[7] Selenium exists in many different oxidation states and various forms such as $H_2SeO_3$, $HSeO_3^-$, $SeO_3^{2-}$, $Se_2O_5^{2-}$, and $SeO_4^{2-}$.[8] As for the oxido anions of $Se^{IV}$, a few organically templated transition-metal selenites with various structural types have been reported.[9–11] 3D open-framework $[NH_2(CH_2)_4NH_2]_{0.5}[M(HSeO_3)(Se_2O_5)]$ (M = Zn, Co, Ni) with a diamondoid network containing both hydrogenselenite and diselenite anions were reported by Rao et al.[12] A series of organically templated or organically bonded copper(II), indium(III), and gallium(III) selenites were prepared in our laboratory recently.[13] Both organically templated and linked vanadium and $Mo^{VI}$ selenites were isolated.[14–16] However, reports on organically templated metal selenates are still relatively rare hitherto, in particular lanthanide ones. The oxido anions of Se differ from those of S in their most stable oxidation states and their redox behaviors.[17] The most stable oxidation state of S is +6 as in $SO_4^{2-}$, whereas that of Se is +4 as in $SeO_3^{2-}$ or $Se_2O_5^{2-}$. The reduction potential of the $XO_4^{2-}/XO_3^{2-}$ couple is 0.03 V in alkaline medium for Se and 0.119 V for S, which has strong effects on the thermal stabilities of their metal compounds. It is, therefore, difficult to stabilize a metal selenate framework under the hydrothermal conditions especially in the presence of reducing amine templates.[18a] So far the organically templated 1D cadmium(II) selenate $[H_2en][Cd(HSeO_4)_2(H_2O)_2]$, layered lanthanide(III) selenates $[H_2en]_{0.5}[Ln(SeO_4)_2(H_2O)_2]$ (Ln = La, Nd, or Pr) and $[H_2pip]_{0.5}[La(SeO_4)_2]$·$0.5H_2O$, and 3D lanthanum(III) selenate $[H_2en][La_2(SeO_4)_4(H_2O)_3]$·$H_2O$ were isolated by Rao et al.[18] The organically templated lithium[19] and zinc selenates[20] were been reported. Several organically templated uranyl selenates were obtained by the Krivovichev group.[21] Very recently, the organically templated indium selenates $[H_2en]_{0.5}[In(SeO_4)(C_2O_4)(H_2O)_2]$ and $[H_2en][InF_3(SeO_4)]$ were prepared in our laboratory.[13b]

Lanthanide compounds are of special interest due to their unique luminescent properties.[22,23] It is assumed that organically templated lanthanide selenates with a rigid second ligand such as oxalate would have novel structural architecture and good luminescent properties.[24] The combination of two types of ligands (selenate and oxalate) may

[a] State Key Laboratory of Structural Chemistry, Fujian Institute of Research on the Structure of Matter, Chinese Academy of Sciences,
Fuzhou 350002, P. R. China
[b] Graduate School of the Chinese Academy of Sciences,
Beijing 100039, P. R. China
Fax: +86-591-83714946
E-mail: mjg@ms.fjirsm.ac.cn
Supporting information for this article is available on the WWW under http://www.eurjic.org or from the author.

 © 2007 Wiley-VCH Verlag GmbH & Co. KGaA, Weinheim 

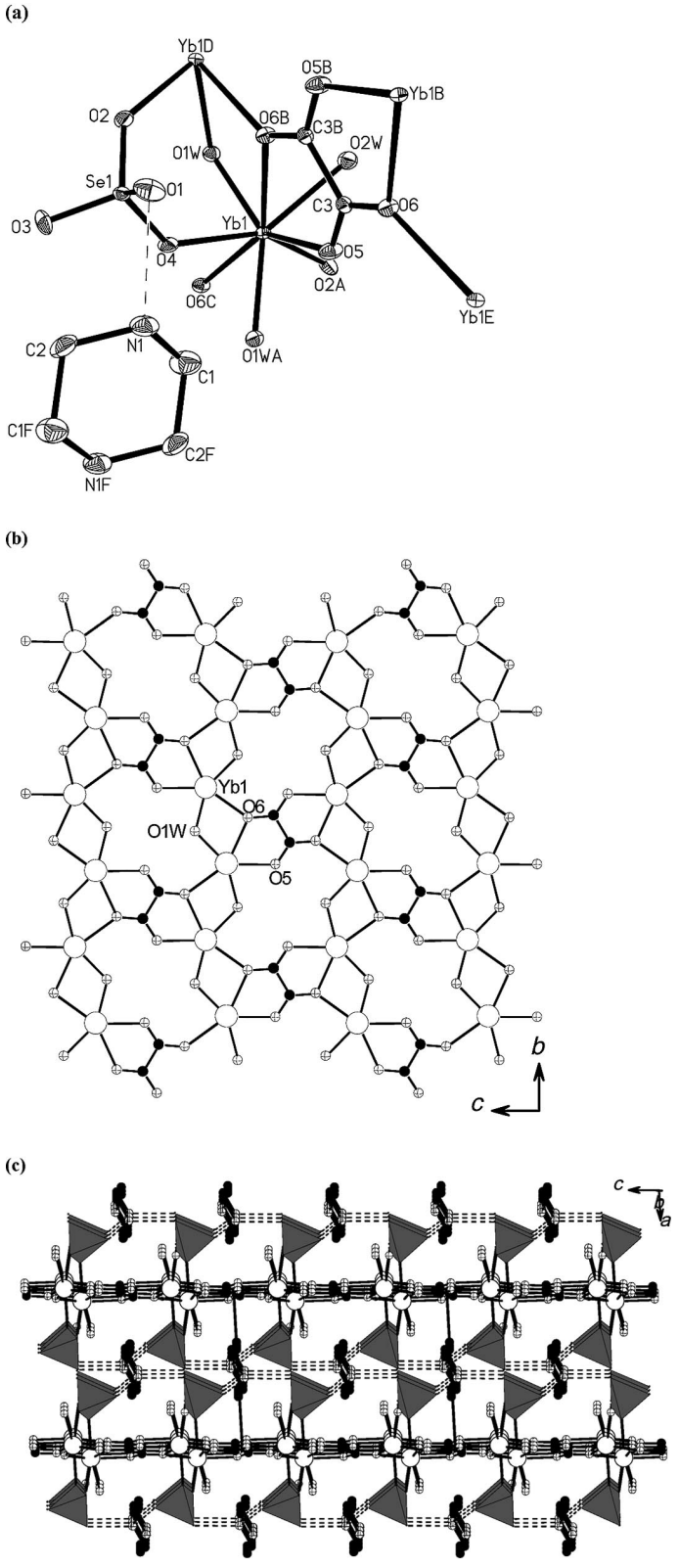


Figure 1. (a) ORTEP drawing of the selected unit of **5**. Thermal ellipsoids are drawn at the 50% probability level. Hydrogen atoms are omitted for clarity. Symmetry codes for generated atoms: a) $-x$, $y + 1/2$, $-z + 3/2$; b) $-x$, $-y$, $-z + 1$; c) $x$, $-y + 1/2$, $z + 1/2$; d) $-x$, $y - 1/2$, $-z + 3/2$; e) $x$, $-y + 1/2$, $z - 1/2$; f) $-x - 1$, $-y + 1$, $-z + 1$. Hydrogen bonds are drawn as dotted lines; (b) 2D ytterbium(III) oxalate layer in compound **5** parallel to the *bc* plane. The Yb, O, and C atoms are drawn as white, crossed, and black circles, respectively; (c) view of the structure of **5** down the *b* axis. The Yb, O, C, and N atoms are drawn as white, crossed, black, and octanded circles, respectively. The selenate tetrahedra are shaded in medium grey. Hydrogen bonds are drawn as dotted lines.

 © 2007 Wiley-VCH Verlag GmbH & Co. KGaA, Weinheim 

enhance the energy transfer efficiency from ligands to lanthanide ions and improve the luminescent properties of the lanthanide compounds due to the so-called "antenna effect".[24a–24c,25] Furthermore, the coordination of both types of ligands with the lanthanide ion may reduce or eliminate aqua ligands that usually quench the luminescence of the $Ln^{III}$ ions.[24a,24b] Our current research efforts in this aspect resulted in two series of new luminescent organically templated lanthanide(III) oxalate–selenate hybrids with 2D-layer and 3D-network structures, namely, $Ln_2(SeO_4)_2(C_2O_4)(H_2O)_4$·pip (pip = piperazine; Ln = Eu **1**; Tb **2**; Dy **3**; Er **4**; Yb **5**) and $[H_2pip]_2[Ln_2(SeO_4)_2(C_2O_4)_3]$·$H_2O$ (Ln = Er **6**; Yb **7**; Lu **8**; Y **9**). Herein we report their syntheses, crystal structures, and luminescent properties.

## Results and Discussion

Compounds **1**–**9** represent first members of organically templated lanthanide(III) oxalate–selenate hybrids. $Ln_2(SeO_4)_2(C_2O_4)(H_2O)_4$·pip (Ln = Eu **1**; Tb **2**; Dy **3**; Er **4**; Yb **5**) have a layered structure, whereas $[H_2pip]_2[Ln_2(SeO_4)_2(C_2O_4)_3]$·$H_2O$ (Ln = Er **6**; Yb **7**; Lu **8**; Y **9**) feature a pillared layered structure. It should be noted that the synthetic conditions for the two series of compounds are almost the same except for the amount of $Na_2C_2O_4$ used. $Ln_2(SeO_4)_2(C_2O_4)(H_2O)_4$·pip (Ln = Eu **1**; Tb **2**; Dy **3**; Er **4**; Yb **5**) were obtained when the $Ln/C_2O_4$ molar ratio was about 3:1. When the amount of $Na_2C_2O_4$ was doubled, $[H_2pip]_2[Ln_2(SeO_4)_2(C_2O_4)_3]$·$H_2O$ (Ln = Er **6**; Yb **7**; Lu **8**; Y **9**) were isolated, and the open frameworks of the compounds were dominated by lanthanide oxalates. Therefore, the amount of second metal linker plays an important role in the chemical compositions and crystal structures of the inorganic–organic hybrids formed.

Compounds **1**–**5** are isostructural; hence, only the structure of **5** will be discussed in detail as a representative example. As shown in Figure 1a, the asymmetric unit of **5** consists of 14 independent non-hydrogen atoms, 11 of which belong to the neutral framework (one Yb atom, one Se atom, one C atom, six O atoms, and two aqua ligands) and the remaining three for the organic amine (one N atom and two C atoms). The ytterbium(III) ion is eight-coordinate and is chelated by two $SeO_4^{2-}$ anions in a monodentate fashion, one oxalate anion in a bidentate chelating fashion and one in a unidentate fashion, and three aqua ligands. One of the aqua ligands (O1W) bridges two $Yb^{III}$ ions. The Yb–O1W distance [2.204(3) and 2.259(3) Å] is significantly shorter than the Yb–O2W (terminal) bonds [2.425(3) Å] (Table 1). The other Yb–O ($C_2O_4^{2-}$ and $SeO_4^{2-}$) bond lengths vary from 2.275(3) to 2.514(3) Å (Table 1), which are comparable to those reported in other ytterbium(III) selenates and oxalates.[26a,26b] The oxalate anion is hexadentate: it chelates two $Yb^{III}$ ions (O5, O6) by forming two Yb–O–C–C–O five-membered rings and also it bridges two other $Yb^{III}$ ions. The O6 atom is bidentate, whereas the O5 atom is unidentate. The selenate anion is bidentate bridging.

The interconnection of the $Yb^{III}$ ions by chelating and bridging oxalate anions and as well as bridging O1W led to a 2D layer of ytterbium(III) oxalate parallel to the *bc* plane (Figure 1b), which is different from the lanthanide oxalates with 1D-chain and 3D-porous network structures previously reported.[24b,24c] Four-membered rings (Yb–O1W–Yb–O6) and 12-membered rings composed of four $Yb^{III}$ ions, two carboxylate groups, and two aqua ligands are present within the 2D layer. The selenate groups hang above and below the central lanthanide oxalate layer and form a 2D neutral layer of $Yb_2(SeO_4)_2(C_2O_4)(H_2O)_4$. The interlayer distance is 9.3 Å. The piperazine molecules are located at the interlayer spaces and form hydrogen bonds with the noncoordinating selenate oxygen atoms [N1···O1 2.736(5) and N1···O3 (symmetry code: $x$, $-y + 1/2$, $z - 1/2$) 2.757(5)] (Figure 1c and Table 1).

The use of more oxalate anions in the preparation afforded $[H_2pip]_2[Ln_2(SeO_4)_2(C_2O_4)_3]$·$H_2O$ (Ln = Er **6**, Yb **7**, Lu **8**, and Y **9**) with a 3D pillared layered structure. Their 3D pillared layered architectures are built from 2D lanthanide oxalate layers bridged by selenate anions (the pillar) (Figure 2c). The structure of the $Er^{III}$ compound will be described in detail as an example. The asymmetric unit of **6** consists of 22 independent non-hydrogen atoms, 15 of which belong to the anionic framework (1 Er atom, 1 Se atom, 3 C atoms, and 10 O atoms), 6 for the template cation (2 N atoms and 4 C atoms), and 1 for a lattice water molecule (Figure 2a). The erbium(III) ion is eight-coordinate and is chelated by two $SeO_4^{2-}$ anions in a monodentate

Table 1. Selected bond lengths [Å] for compounds **1**, **3**, **5**, **6**, and **9**.[a]

| Ln–O | **1** (Eu) | **3** (Dy) | **5** (Yb) | Ln–O | **6** (Er) | **9** (Y) |
|---|---|---|---|---|---|---|
| Ln1–O1W | 2.274(3) | 2.243(3) | 2.204(3) | Ln1–O3#1 | 2.297(3) | 2.300(3) |
| Ln1–O1W#1 | 2.331(3) | 2.297(3) | 2.259(3) | Ln1–O2 | 2.298(3) | 2.302(3) |
| Ln1–O2#1 | 2.352(3) | 2.321(3) | 2.275(3) | Ln1–O5#2 | 2.334(3) | 2.340(3) |
| Ln1–O4 | 2.403(3) | 2.359(3) | 2.301(3) | Ln1–O7 | 2.344(3) | 2.352(3) |
| Ln1–O5 | 2.441(3) | 2.407(3) | 2.359(3) | Ln1–O8#2 | 2.362(3) | 2.373(3) |
| Ln1–O2W | 2.508(3) | 2.470(3) | 2.425(3) | Ln1–O6 | 2.374(3) | 2.379(3) |
| Ln1–O6#2 | 2.538(3) | 2.518(3) | 2.500(3) | Ln1–O9 | 2.393(3) | 2.403(3) |
| Ln1–O6#3 | 2.568(3) | 2.544(3) | 2.514(3) | Ln1–O10#3 | 2.429(3) | 2.441(3) |
| Hydrogen bonds: | | | | | | |
| N1···O1 | 2.754(6) | 2.747(5) | 2.736(5) | | | |
| N1···O3#4 | 2.775(6) | 2.763(5) | 2.757(5) | | | |

[a] Symmetry transformations used to generate equivalent atoms: For **1**, **3**, and **5**: #1 $-x$, $y + 1/2$, $-z + 3/2$; #2 $-x$, $-y$, $-z + 1$; #3 $x$, $-y + 1/2$, $z + 1/2$; #4 $x$, $-y + 1/2$, $z - 1/2$. For **6** and **9**: #1 $x + 1/2$, $-y + 1/2$, $z - 1/2$; #2 $x - 1/2$, $-y + 1/2$, $z - 1/2$; #3 $-x$, $-y$, $-z + 1$.

 © 2007 Wiley-VCH Verlag GmbH & Co. KGaA, Weinheim 

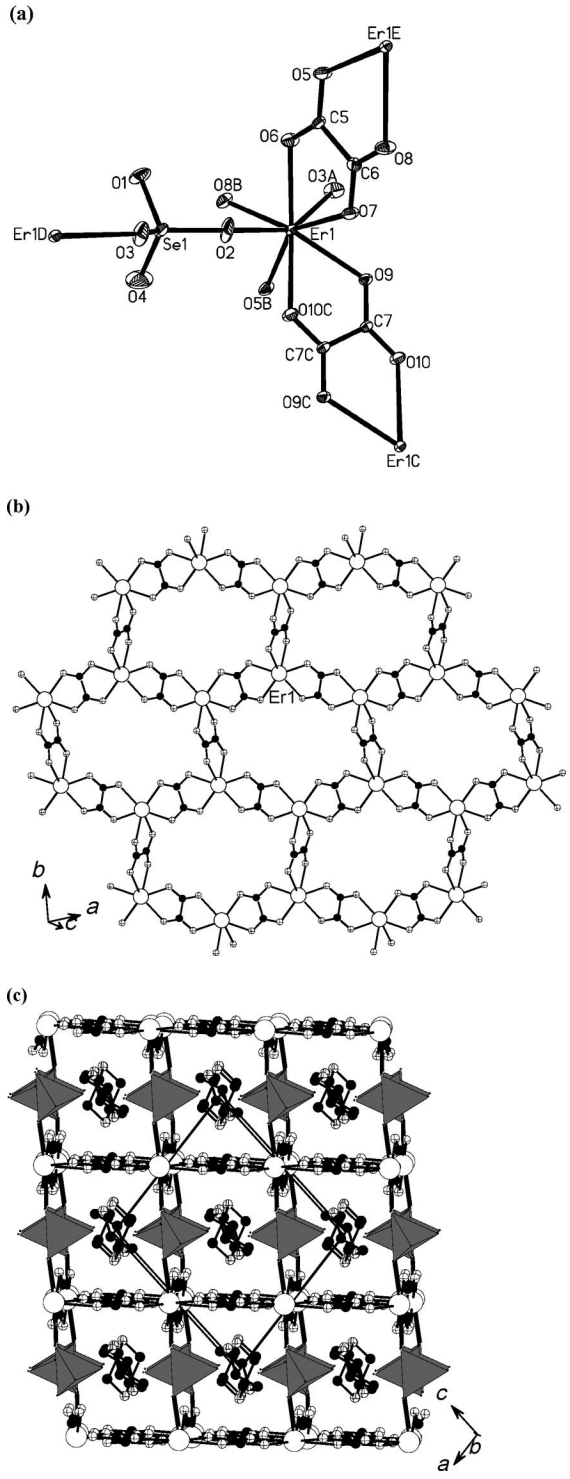


Figure 2. (a) ORTEP drawing of the selected unit in compound **6**. Thermal ellipsoids are drawn at the 50% probability level. Symmetry codes for generated atoms: a) $x + 1/2, -y + 1/2, z - 1/2$; b) $x - 1/2, -y + 1/2, z - 1/2$; c) $-x, -y, -z + 1$; d) $x - 1/2, -y + 1/2, z + 1/2$; e) $x + 1/2, -y + 1/2, z + 1/2$. The template cation and the lattice water molecule are omitted for clarity; (b) A (–202) erbium(III) oxalate layer in compound **6**. The Er, O, and C atoms are drawn as white, crossed, and black circles, respectively; (c) view of the structure of **6** down the *b* axis. The Er, O, C, and N atoms are drawn as white, crossed, black, and octanded circles, respectively. The selenate tetrahedra are shaded in medium grey.

fashion and three oxalate anions all in a bidentate chelating fashion. The Er–O distances fall in the range of 2.297(3)–2.429(3) Å (Table 1), which are comparable to those reported for other erbium(III) selenates and oxalates.[26b,26c] The selenate anion is bidentate and bridges two $Er^{III}$ ions. Different from that in compounds **1**–**5**, each oxalate anion in compound **6** is tetradentate and forms two Er–O–C–C–O five-membered chelating rings.

The interconnection of the $Er^{III}$ ions through the chelating and bridging oxalate anions results in the formation of a (–202) erbium(III) oxalate layer. Different from the lanthanide oxalate layers in compounds **1**–**5**, the erbium(III) oxalate layer in **6** is based on 24-membered rings composed of 6 $Er^{III}$ ions and 6 carboxylate groups (Figure 2b). The lattice water molecule is located at the center of the above ring. The above layers of lanthanide oxalates are further cross-linked by selenate anions into a 3D pillared layered architecture with large tunnels running along the *b* axis (Figure 2c). The tunnel is formed by 16-membered rings composed of 4 $Er^{III}$ ions, 2 selenate anions, and 2 carboxylate groups. The solvent accessible volume in compound **6** is 38.1% according to calculations performed by using the PLATON program.[27] The doubly protonated piperazine cations are located at the above tunnels. No hydrogen bonds are found between the template cations and oxygen atoms from the framework (Figure 2c).

The IR spectra of compounds **1**–**9** clearly exhibit the characteristic vibration bands for the selenate (893–696 and 586–416 $cm^{-1}$) and oxalate groups (1654–1627 and 1384–1315 $cm^{-1}$). The broad bands in the range of 3609–2461 $cm^{-1}$ correspond to the stretching vibrations of water molecules and organic amines in all compounds.

The TGA curves of compounds **1**–**3** and **5**–**9** are shown in Figure S1 (see the Supporting Information). The TGA curves of compounds **1**–**3** and **5** are similar and display three main steps of weight loss (Figure S1a). Compound **1** was used as an example. The first step in the 160–306 °C range corresponds to the release of the four aqua ligands and neutral piperazine molecule, the observed weight loss of 17.7% is close to the calculated value of 18.9%. The second step covering from 306–560 °C can be assigned to the partial decomposition of the selenate and oxalate anions. The third step in the range of 560–1000 °C represents further combustion of the compound. The total weight loss at 1000 °C is 54.1%, and on the basis of the slope of the TGA curves, the decomposition is not complete. The thermal decomposition mechanism of the metal selenate is very complicated; the selenate anion was reported to decompose into $SeO_2$ and $O_2$, and the final residues are probably a mixture of metal oxide and metal selenide.[18a] The TGA diagrams of compounds **6**–**9** are similar and display three main weight losses (Figure S1b). Compound **6** is used as an example. The first step began at 60 °C and was completed at 140 °C, which corresponds to the release of the lattice water molecule. The observed weight loss of 1.72% is very close to the calculated value (1.67%). The second step covered from 140 °C to 434 °C, which corresponds to the release of the piperazine cations and the par-

 © 2007 Wiley-VCH Verlag GmbH & Co. KGaA, Weinheim 

tial decomposition of the selenate and oxalate anions. The third step is the further combustion of the compound. The total weight loss at 1000 °C is 61.8%, and on the basis of the slope of the TGA curves, the decomposition is not complete. Similar to those in **3**, the final residues are expected to be mainly a mixture of metal oxide and metal selenide.[18a]

## Luminescent Properties

The solid-state luminescent properties of compounds **1**–**7** and the ligands ($Na_2C_2O_4$ and $H_2SeO_4$) were investigated at room temperature. Compounds **4** and **5** and the ligands do not show observable emission bands under our experimental conditions. The emission spectra of compounds **1**, **2**, **3**, **6**, and **7** are given in Figure 3. Compound **1** shows the characteristic emission bands for the $Eu^{III}$ ion in the visible region under excitation at 363 nm (Figure 3a). They are due to $^5D_0 \rightarrow {}^7F_J$ ($J$ = 0, 1, 2, 3, and 4) transitions: 577 nm ($^5D_0 \rightarrow {}^7F_0$); 585, 589, and 600 nm ($^5D_0 \rightarrow {}^7F_1$); 608, 611, 618, 620, and 625 nm ($^5D_0 \rightarrow {}^7F_2$); 654 nm (weak, $^5D_0 \rightarrow {}^7F_3$), and 688, 694, 698, 701, and 703 nm ($^5D_0 \rightarrow {}^7F_4$).[28] The splitting of the $^5D_0 \rightarrow {}^7F_1$, $^5D_0 \rightarrow {}^7F_2$, and $^5D_0 \rightarrow {}^7F_4$ transition bands is due to the "crystal field effect" of the $Eu^{III}$ ion in a $C_1$ symmetry, which led to the complete degeneracy of the $^7F_J$ ($J$ = 1 and 2) and the partial degeneracy of the $^7F_4$ states. The most intense transition is $^5D_0 \rightarrow {}^7F_2$ in the red light region. The Eu ($^5D_0$) lifetime ($\lambda_{ex,em}$ = 363, 618 nm) of **1** was measured to be 0.178 ms. Compound **2** displays the characteristic emission bands for the $Tb^{III}$ ion under excitation at 354 nm (Figure 3b). The emission bands can be assigned to $^5D_4 \rightarrow {}^7F_J$ ($J$ = 6, 5, 4, and 3) transitions of the $Tb^{III}$ ion: 484 nm ($^5D_4 \rightarrow {}^7F_6$), 541 and 546 nm ($^5D_4 \rightarrow {}^7F_5$), 589 nm ($^5D_4 \rightarrow {}^7F_4$), and 626 nm ($^5D_4 \rightarrow {}^7F_3$).[29] The Tb ($^5D_4$) lifetime for compound **2** under

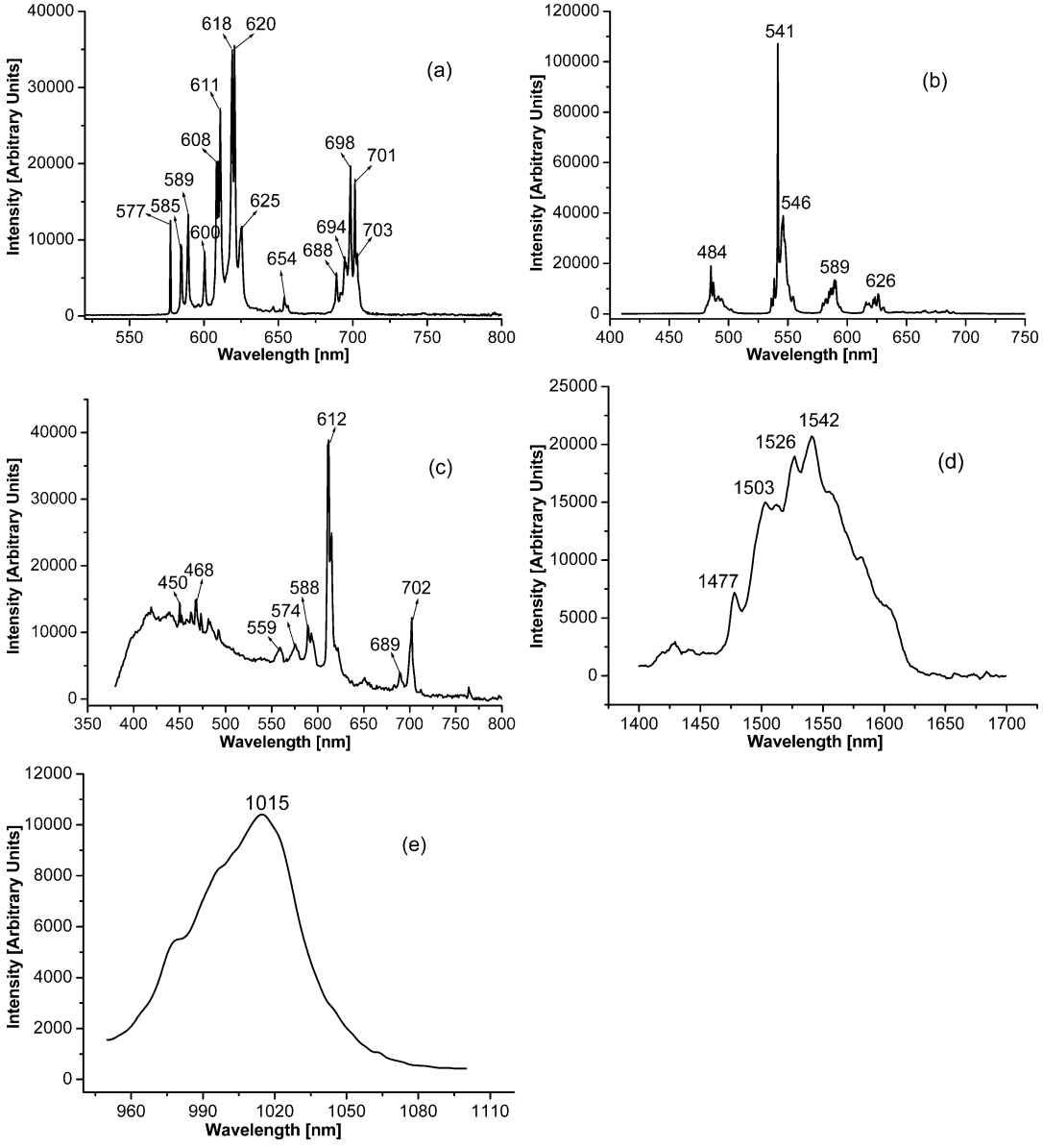


Figure 3. Solid-state emission spectra for (a) **1**; (b) **2**; (c) **3**; (d) **6**; and (e) **7** at room temperature.

 © 2007 Wiley-VCH Verlag GmbH & Co. KGaA, Weinheim 

$\lambda_{ex,em}$ = 354, 548 nm is 0.962 ms. Compound **3** displays both broad and sharp emission bands that are characteristic for $Dy^{III}$ ions when excited at 285 nm (Figure 3c). The broad emission bands at about 450 and 468 nm can be assigned to the $^4F_{9/2}\rightarrow{}^6H_{15/2}$ transition, the weak emission bands at 559, 574, and 588 nm are due to the $^4F_{9/2}\rightarrow{}^6H_{13/2}$ transition, and the emission bands at 612 and 702 nm can be assigned to the $^4F_{9/2}\rightarrow{}^6H_{11/2}$ and $^4F_{9/2}\rightarrow{}^6H_{9/2}$ transitions of the $Dy^{III}$ ion.[29,30] The $^4F_{9/2}\rightarrow{}^6H_{15/2}$ and $^4F_{9/2}\rightarrow{}^6H_{13/2}$ transitions were split into several sub-bands, which may result from the Stark sublevel splitting of the $^6H_{15/2}$ and $^6H_{13/2}$ energy levels by the ligand field.[29] The Dy ($^4F_{9/2}$) lifetime for $\lambda_{ex,em}$ = 285, 612 nm is about 0.276 ms. The emission spectrum of **6** exhibits emission bands in the near-IR region ($\lambda_{ex}$ = 520 nm, Figure 3d). The emission bands at 1477, 1503, 1526, and 1542 nm can all be attributed to the $^4I_{13/2}\rightarrow{}^4I_{15/2}$ transition of the $Er^{III}$ ion.[24b,31,32] The splitting of the $^4I_{13/2}\rightarrow{}^4I_{15/2}$ transition bands is probably due to the ligand field effect of erbium(III) located at a site with a $C_1$ symmetry. Compound **7** shows only a broad fluorescence emission band centered at 1015 nm in the near-IR region ($\lambda_{ex}$ = 937 nm, Figure 3e), which is assigned to the $^2F_{5/2}\rightarrow{}^2F_{7/2}$ transition for the $Yb^{III}$ ion.[33] No emission bands in the near-IR region were observed for compounds **4** and **5**, which is probably due to the quenching effect of the luminescence state by high-frequency vibrating aqua ligands.[24a,24b] Therefore, the luminescence of the inorganic–organic hybrids formed can be significantly enhanced if more rigid oxalate anions are incorporated into the frameworks of the lanthanide selenates.

## Conclusions

In summery, through the introduction of the rigid linker oxalate as the second metal linker, novel organically templated lanthanide oxalate–selenates with 2D and 3D structures were hydrothermally synthesized. Furthermore, the introduction of the rigid linker oxalates into the lanthanide(III) selenates can afford new inorganic–organic hybrids with novel structures and enhanced luminescent properties. Compounds **1**, **2**, and **3** are respectively capable of producing red-, green-, and pink light in electroluminescent devices, whereas **6** and **7** are luminescent materials in the near IR region. We believe that a wide range of other new lanthanide open frameworks and microporous materials can be developed by self-assembly or structurally directed synthesis by using a similar technique.

## Experimental Section

**Materials and Methods:** All chemicals were purchased from commercial sources and used without further purification. Elemental analyses were performed with a Vario EL III elemental analyzer. IR spectra were recorded with a Magna 750 FTIR spectrometer photometer as KBr pellets in the range of 4000–400 $cm^{-1}$. Thermogravimetric analyses were carried out with a NETZSCH STA 449C unit at a heating rate of 10 °C $min^{-1}$ under a nitrogen atmosphere. X-ray powder diffraction (XRD) patterns (Cu-$K_\alpha$) were collected in a sealed glass capillary with a XPERT-MPD $\theta$–$2\theta$ diffractometer. Photoluminescence analyses were performed with an Edinburgh FLS920 fluorescence spectrometer.

**General Method for the Preparation of $Ln_2(SeO_4)_2(C_2O_4)(H_2O)_4\cdot$pip (Ln = Eu 1; Tb 2; Dy 3; Er 4; Yb 5):** A mixture of $H_2SeO_4$ solution (40%, 0.24 mL, 0.93 mmol), piperazine·$6H_2O$ (0.105 g, 0.54 mmol), $Na_2C_2O_4$ (0.018 g, 0.13 mmol), and $Ln(NO_3)_3\cdot6H_2O$ (0.32 mmol) in distilled water (2 mL) was sealed in an autoclave equipped with a Teflon liner (23 mL) and then heated at 100 °C for 5 d. The initial and final pH values of the solution did not show appreciable change and were close to 5.0

**1:** Prepared by the general method. Brick-shaped crystals. Yield: 0.052 g (48% based on $C_2O_4^{2-}$). IR (KBr): $\tilde{\nu}$ = 3583 (s), 3359 (s), 2963 (w), 2835 (w), 2731 (w), 2461 (w), 1627 (s), 1453 (m), 1315 (m), 1090 (m), 1008 (m), 974 (w), 886 (s), 863 (w), 848 (s), 806 (w), 711 (s), 585 (m), 538 (m), 444 (w), 423 (s) $cm^{-1}$. $C_6H_{18}Eu_2N_2O_{16}Se_2$ (836.06): calcd. C 8.62, H 2.17, N 3.35; found C 8.51, H 2.25, N 3.20.

**2:** Prepared by the general method. Brick-shaped crystals. Yield: 0.049 g (45% based on $C_2O_4^{2-}$). IR (KBr): $\tilde{\nu}$ = 3591 (s), 3357 (s), 2961 (w), 2834 (w), 2730 (w), 2478 (w), 1654 (w), 1629 (s), 1453 (m), 1317 (s), 1212 (w), 1091 (m), 1008 (w), 974 (w), 889 (s), 866 (w), 851 (m), 812 (w), 727 (s), 696 (w), 586 (m), 535 (m), 448 (w), 425 (s) $cm^{-1}$. $C_6H_{18}N_2O_{16}Se_2Tb_2$ (849.98): calcd. C 8.48, H 2.13, N 3.30; found C 8.16, H 2.55, N 3.14.

**3:** Prepared by the general method. Brick-shaped crystals. Yield: 0.048 g (43% based on $C_2O_4^{2-}$). IR (KBr): $\tilde{\nu}$ = 3596 (s), 3358 (s), 2961 (w), 2835 (w), 2731 (w), 2479 (w), 1633 (s), 1454 (m), 1318 (s), 1212 (w), 1092 (m), 1008 (m), 974 (w), 889 (s), 866 (w), 851 (s), 814 (w), 734 (s), 697 (w), 586 (m), 536 (m), 449 (s), 426 (s) $cm^{-1}$. $C_6H_{18}Dy_2N_2O_{16}Se_2$ (857.14): calcd. C 8.41, H 2.12, N 3.27; found C 8.30, H 2.16, N 3.22.

**4:** Prepared by the general method. Brick-shaped crystals. Yield: 0.013 g (12% based on $C_2O_4^{2-}$). IR (KBr): $\tilde{\nu}$ = 3607 (s), 3394 (s), 2961 (w), 2787 (w), 2479 (w), 1633 (s), 1454 (w), 1320 (m), 1212 (w), 1092 (w), 1008 (w), 974 (w), 891 (s), 867 (w), 853 (m), 816 (w), 740 (m), 697 (w), 587 (m), 533 (m), 452 (w), 429 (s) $cm^{-1}$. $C_6H_{18}Er_2N_2O_{16}Se_2$ (866.65): calcd. C 8.32, H 2.09, N 3.23; found C 8.24, H 2.76, N 3.15.

**5:** Prepared by the general method. Brick-shaped crystals. Yield: 0.023 g (20% based on $C_2O_4^{2-}$). IR (KBr): $\tilde{\nu}$ = 3609 (s), 3379 (s), 2963 (w), 2834 (w), 2788 (w), 2473 (w), 1632 (s), 1454 (m), 1320 (s), 1211 (w), 1093 (m), 1008 (m), 974 (w), 893 (s), 868 (m), 855 (m), 826 (w), 753 (s), 695 (w), 587 (m), 535 (m), 454 (w), 426 (s) $cm^{-1}$. $C_6H_{18}N_2O_{16}Se_2Yb_2$ (878.21): calcd. C 8.21, H 2.07, N 3.19; found C 8.23, H 2.10, N 3.17.

**General Method for the Preparation of $[H_2pip]_2[Ln_2(SeO_4)_2(C_2O_4)_3]\cdot H_2O$ (Ln = Er 6; Yb 7; Lu 8; Y 9):** The synthetic procedure for the preparation of compounds **6**–**9** was similar to that of compounds **1**–**5** except that the amount of $Na_2C_2O_4$ used was doubled. The initial and final pH values of the solution were close to 5.5.

**6:** Prepared by the general method. Prism-shaped crystals. Yield: 0.043 g (46% based on $C_2O_4^{2-}$). IR (KBr): $\tilde{\nu}$ = 3435 (s), 3040 (w), 1630 (s), 1421 (w), 1384 (w), 1315 (m), 1080 (w), 1005 (w), 882 (s), 856 (s), 798 (m), 789 (m), 583 (m), 499 (m), 460 (m), 420 (w) $cm^{-1}$. $C_{14}H_{26}Er_2N_4O_{21}Se_2$ (1078.83): calcd. C 15.59, H 2.43, N 5.20; found C 15.64, H 2.49, N 5.21.

**7:** Prepared by the general method. Prism-shaped crystals. Yield: 0.029 g (31% based on $C_2O_4^{2-}$). IR (KBr): $\tilde{\nu}$ = 3435 (m), 3218 (w), 2973 (w), 1632 (s), 1422 (w), 1315 (m), 1081 (w), 883 (s), 856 (s),

 © 2007 Wiley-VCH Verlag GmbH & Co. KGaA, Weinheim 

798 (m), 788 (m), 583 (s), 499 (s), 461 (m) $cm^{-1}$. $C_{14}H_{26}N_4O_{21}Se_2Yb_2$ (1090.39): calcd. C 15.36, H 2.40, N 5.12; found C 14.93, H 2.93, N 4.93.

**8:** Prepared by the general method. Prism-shaped crystals. Yield: 0.030 g (32% based on $C_2O_4^{2-}$). IR (KBr): $\tilde{\nu}$ = 3435 (s), 3219 (w), 3042 (w), 1632 (s), 1423 (w), 1316 (s), 1081 (w), 883 (s), 868 (s), 856 (s), 798 (m), 788 (m), 583 (m), 498 (m), 460 (m), 417 (w) $cm^{-1}$. $C_{14}H_{26}Lu_2N_4O_{21}Se_2$ (1094.25): calcd. C 15.33, H 2.39, N 5.11; found C 14.85, H 2.86, N 4.92.

**9:** Prepared by the general method. Prism-shaped crystals. Yield: 0.027 g (34% based on $C_2O_4^{2-}$). IR (KBr): $\tilde{\nu}$ = 3449 (m), 3219 (w), 3038 (w), 1631 (s), 1453 (w), 1423 (w), 1315 (s), 1080 (m), 882 (s), 857 (s), 798 (s), 789 (s), 584 (m), 499 (m), 459 (m), 416 (w) $cm^{-1}$. $C_{14}H_{26}N_4O_{21}Se_2Y_2$ (922.13): calcd. C 18.19, H 2.84, N 6.06; found C 18.14, H 2.88, N 6.04.

On the basis of X-ray powder diffraction studies, compounds **1**–**9** were obtained as pure phases. The measured patterns are in good agreement with those simulated from single-crystal structures (see Figure S2, Supporting Information).

**X-ray Crystallography:** Data collection for compounds **1**, **2**, **4**, **7**, and **8** were performed with Siemens Smart CCD and compounds **3**, **5**, **6**, and **9** with a Rigaku Mercury CCD diffractometer both equipped with graphite-monochromated Mo-$K_\alpha$ radiation ($\lambda$ = 0.71073 Å). Lattice parameter measurements indicate that compounds **1**–**5** are isostructural as are compounds **6**–**9**; hence, full data collections for only compounds **1**, **3**, **5**, **6**, and **9** were performed. Intensity data were collected by the narrow frame method at 293 K and corrected for Lorentz and polarization effects as well as for absorption by the SADABS program.[34] All structures were solved by direct methods and refined by full-matrix least-squares cycles in SHELX-97.[34] All non-hydrogen atoms were refined with anisotropic thermal parameters. Hydrogen atoms attached to C and N atoms and for aqua ligands in compounds **1**, **3**, and **5** were located at geometrically calculated positions and refined with isotropic thermal parameters. Hydrogen atoms for water molecules in compounds **6** and **9** were not included in the refinements. Crystallographic data and structural refinement parameters for compounds **1**–**4** are summarized in Table 2 and for compounds **5**–**9** in Table 3. Important bond lengths for compounds **1**, **3**, **5**, **6**, and **9** are listed in Table 1.

CCDC-644791 (for **1**), -644792 (for **3**), -644793 (for **5**), -644794 (for **6**), and -644795 (for **9**) contain the supplementary crystallographic data for this paper. These data can be obtained free of charge from The Cambridge Crystallographic Data Centre via www.ccdc.cam.ac.uk/data_request/cif.

**Supporting Information** (see footnote on the first page of this article): TGA curves for compounds **1**–**3** and **5**–**9** and X-ray powder diffraction patterns for compounds **1**–**9**.

Table 2. Crystal data and structure refinements for compounds **1**–**4**.

| Compound | **1** | **2** | **3** | **4** |
|---|---|---|---|---|
| Formula | $C_6H_{18}Eu_2N_2O_{16}Se_2$ | $C_6H_{18}N_2O_{16}Se_2Tb_2$ | $C_6H_{18}Dy_2N_2O_{16}Se_2$ | $C_6H_{18}Er_2N_2O_{16}Se_2$ |
| *Fw* | 836.06 | 849.98 | 857.14 | 866.65 |
| Space group | $P2_1/c$ | $P2_1/c$ | $P2_1/c$ | $P2_1/c$ |
| *a* [Å] | 9.4382(5) | 9.430 | 9.389(3) | 9.342 |
| *b* [Å] | 7.4745(4) | 7.440 | 7.406(3) | 7.375 |
| *c* [Å] | 12.8140(7) | 12.750 | 12.732(5) | 12.676 |
| $\beta$ [°] | 93.4230(10) | 93.30 | 93.336(4) | 93.178 |
| *V* [Å$^3$] | 902.36(8) | 892 | 883.9(5) | 872 |
| *Z* | 2 | 2 | 2 | 2 |
| $D_{calcd.}$ [g cm$^{-3}$] | 3.077 | 3.194 | 3.220 | 3.340 |
| $\mu$ [mm$^{-1}$] | 11.007 | 12.141 | 12.594 | 13.986 |
| GOF on $F^2$ | 1.115 | | 1.148 | |
| $R_1$, $wR_2$ [$I>2\sigma(I)$][a] | 0.0217, 0.0520 | | 0.0185, 0.0461 | |
| $R_1$, $wR_2$ (all data) | 0.0239, 0.0532 | | 0.0198, 0.0467 | |

[a] $R_1 = \Sigma||F_o| - |F_c||/\Sigma|F_o|$, $wR_2 = \{\Sigma w[(F_o)^2 - (F_c)^2]^2/\Sigma w[(F_o)^2]^2\}^{1/2}$.

Table 3. Crystal data and structure refinements for compounds **5**–**9**.

| Compound | **5** | **6** | **7** | **8** | **9** |
|---|---|---|---|---|---|
| Formula | $C_6H_{18}N_2O_{16}Se_2Yb_2$ | $C_{14}H_{26}Er_2N_4O_{21}Se_2$ | $C_{14}H_{26}N_4O_{21}Se_2Yb_2$ | $C_{14}H_{26}Lu_2N_4O_{21}Se_2$ | $C_{14}H_{26}N_4O_{21}Se_2Y_2$ |
| *Fw* | 878.21 | 1078.83 | 1090.39 | 1094.25 | 922.13 |
| Space group | $P2_1/c$ | $P2_1/n$ | $P2_1/n$ | $P2_1/n$ | $P2_1/n$ |
| *a* [Å] | 9.309(3) | 8.754(3) | 8.680 | 8.700 | 8.7749(10) |
| *b* [Å] | 7.333(2) | 15.873(4) | 15.780 | 15.863 | 15.8803(17) |
| *c* [Å] | 12.643(4) | 9.466(3) | 9.520 | 9.372 | 9.5077(9) |
| $\beta$ [°] | 93.169(5) | 99.887(3) | 99.665 | 100.166 | 99.855(6) |
| *V* [Å$^3$] | 861.7(4) | 1295.8(6) | 1284 | 1273 | 1305.3(2) |
| *Z* | 2 | 2 | 2 | 2 | 2 |
| $D_{calcd.}$ [g cm$^{-3}$] | 3.385 | 2.765 | 2.795 | 2.805 | 2.346 |
| $\mu$ [mm$^{-1}$] | 15.100 | 9.347 | 10.088 | 10.489 | 7.317 |
| GOF on $F^2$ | 1.030 | 1.093 | | | 1.063 |
| $R_1$, $wR_2$ [$I>2\sigma(I)$][a] | 0.0183, 0.0465 | 0.0231, 0.0578 | | | 0.0337, 0.0825 |
| $R_1$, $wR_2$ (all data) | 0.0210, 0.0474 | 0.0260, 0.0596 | | | 0.0411, 0.0865 |

[a] $R_1 = \Sigma||F_o| - |F_c||/\Sigma|F_o|$, $wR_2 = \{\Sigma w[(F_o)^2 - (F_c)^2]^2/\Sigma w[(F_o)^2]^2\}^{1/2}$.

 © 2007 Wiley-VCH Verlag GmbH & Co. KGaA, Weinheim 

## Acknowledgments

We thank the Nation Nature Science Foundation of China (No. 20573113, 20371047, and 20521101), NSF of Fujian Province (No. E0420003), and Key Project of Chinese Academy of Sciences (No. KJCX2-YW-H01) for the financial support.

[1] G. Férey, A. K. Cheetham, *Science* **1999**, *283*, 1125.
[2] D. J. Chesnut, D. Hagrman, P. J. Zapf, R. P. Hammond Jr, R. LaDuca, R. C. Haushalter, J. Zubieta, *Coord. Chem. Rev.* **1999**, *190–192*, 737.
[3] A. K. Cheetham, G. Férey, T. Loiseau, *Angew. Chem. Int. Ed.* **1999**, *38*, 3268.
[4] P. B. Moore in *Crystallochemical Aspects of the Phosphate Minerals* (Eds.: J. Niagru, P. B. Moore), Springer, Berlin, **1984**.
[5] a) S. H. Feng, R. R. Xu, *Acc. Chem. Res.* **2001**, *34*, 239; b) J. H. Yu, R. R. Xu, *Acc. Chem. Res.* **2003**, *36*, 481.
[6] a) C. N. R. Rao, S. Natarajan, A. Choudhury, S. Neeraj, A. A. Ayi, *Acc. Chem. Res.* **2001**, *34*, 80; b) Y. C. Liao, C. H. Lin, S. L. Wang, *J. Am. Chem. Soc.* **2005**, *127*, 9986; c) F. Millange, R. I. Walton, N. Guillou, T. Loiseau, D. O'Hare, G. Férey, *Chem. Commun.* **2002**, 826; d) H. S. Park, I. Bull, L. M. Peng, G. Y. J. Victer, C. P. Grey, J. B. Parise, *Chem. Mater.* **2004**, *16*, 5350.
[7] a) G. Paul, A. Choudhury, C. N. R. Rao, *J. Chem. Soc. Dalton Trans.* **2002**, 3589; b) G. Paul, A. Choudhury, C. N. R. Rao, *Angew. Chem. Int. Ed.* **2002**, *41*, 4297; c) J. N. Behera, G. Paul, A. Choudhury, C. N. R. Rao, *Chem. Commun.* **2004**, 456; d) C. N. R. Rao, J. N. Behera, D. Meenakshi, *Chem. Soc. Rev.* **2006**, *35*, 375.
[8] a) J. Q. Dumm, P. W. Brown, *J. Am. Ceram. Soc.* **1997**, *80*, 2488; b) F. Chen, P. C. Burns, R. C. Ewing, *J. Nucl. Mater.* **1999**, *275*, 81.
[9] W. T. A. Harrison, M. L. F. Phillips, J. Stanchfield, T. M. Nenoff, *Angew. Chem. Int. Ed.* **2000**, *39*, 3808.
[10] A. Choudhury, U. Kumar D, C. N. R. Rao, *Angew. Chem. Int. Ed.* **2002**, *41*, 158.
[11] a) I. Pasha, A. Choudhury, C. N. R. Rao, *Solid State Sci.* **2003**, *5*, 257; b) F. Millange, C. Serre, T. Cabourdin, J. Marrot, G. Férey, *Solid State Sci.* **2004**, *6*, 229.
[12] D. Udayakumar, C. N. R. Rao, *J. Mater. Chem.* **2003**, *13*, 1635.
[13] a) M. L. Feng, A. V. Prosvirin, J. G. Mao, K. R. Dunbar, *Chem. Eur. J.* **2006**, *12*, 8312; b) M. L. Feng, X. L. Li, J. G. Mao, *Cryst. Growth Des.* **2007**, *7*, 770.
[14] a) I. Pasha, A. Choudhury, C. N. R. Rao, *Inorg. Chem.* **2003**, *42*, 409; b) H. Nakano, T. Ozeki, A. Yagasaki, *Inorg. Chem.* **2001**, *40*, 1816.
[15] a) Z. Shi, D. Zhang, S. Feng, G. Li, Z. Dai, W. Fu, X. Chen, J. Hua, *J. Chem. Soc. Dalton Trans.* **2002**, 1873; b) Z. Dai, X. Chen, Z. Shi, D. Zhang, G. Li, S. Feng, *Inrog. Chem.* **2003**, *42*, 908; c) Z. Dai, Z. Shi, G. Li, D. Zhang, W. Fu, H. Jin, W. Xu, S. Feng, *Inrog. Chem.* **2003**, *42*, 7396.
[16] a) U. Kortz, M. G. Savelieff, F. Y. A. Ghali, L. M. Khalil, S. A. Maalouf, D. I. Sinno, *Angew. Chem. Int. Ed.* **2002**, *41*, 4070; b) M. L. Feng, J. G. Mao, *Eur. J. Inorg. Chem.* **2004**, 3712.
[17] N. N. Greenwood, A. Earnshaw, *Chemistry of the Elements*, 2nd ed., Butterworth-Heinemann, Oxford, **2001**.
[18] a) I. Pasha, A. Choudhury, C. N. R. Rao, *J. Solid State Chem.* **2003**, *174*, 386; b) J. N. Behera, A. A. Ayi, C. N. R. Rao, *Chem. Commun.* **2004**, 968; c) D. Udayakumar, M. Dan, C. N. R. Rao, *Eur. J. Inorg. Chem.* **2004**, 1733.
[19] J. Plocek, D. Havlicek, I. Nemec, I. Cisarova, Z. Micka, *J. Solid State Chem.* **2003**, *170*, 308.
[20] M. L. Feng, J. G. Mao, *J. Solid State Chem.* **2004**, *177*, 3529.
[21] a) S. V. Krivovichev, V. Kahlenberg, *J. Am. Chem. Soc.* **2005**, *127*, 1072; b) S. V. Krivovichev, V. Kahlenberg, *Eur. J. Inorg. Chem.* **2005**, 1653; c) S. V. Krivovichev, V. Kahlenberg, *Z. Anorg. Allg. Chem.* **2005**, *631*, 2352.
[22] a) S. R. Batten, R. Robson, *Angew. Chem. Int. Ed.* **1998**, *37*, 1460; b) H. Tsukube, S. Shinoda, *Chem. Rev.* **2002**, *102*, 2389; c) M. Lwamoto, H. Furukawa, Y. Mine, F. Uemura, S. I. Mikuriya, S. Kagawa, *J. Chem. Soc. Chem. Commun.* **1986**, 1272.
[23] a) C. Benelli, D. Gatteschi, *Chem. Rev.* **2002**, *102*, 2369; b) C. Piguet, G. Bernardinelli, G. Hopfgartner, *Chem. Rev.* **1997**, *97*, 2005; c) G. Bernardinelli, G. Hopfgartner, S. Petoud, O. Schaad, *J. Am. Chem. Soc.* **1996**, *118*, 6681; d) N. Sabbatini, M. Guardigli, J. M. Lehn, *Coord. Chem. Rev.* **1993**, *123*, 201; e) J. Kido, Y. Okamoto, *Chem. Rev.* **2002**, *102*, 2357; f) H. Zhao, M. J. Bazile, J. R. Galán-Mascarós, K. R. Dunbar, *Angew. Chem. Int. Ed.* **2003**, *42*, 1015; g) C. Reinhard, H. U. Gudel, *Inorg. Chem.* **2002**, *41*, 1048.
[24] a) J. L. Song, C. Lei, J. G. Mao, *Inorg. Chem.* **2004**, *43*, 5630; b) J. L. Song, J. G. Mao, *Chem. Eur. J.* **2005**, *11*, 1417; c) S. M. Ying, J. G. Mao, *Cryst. Growth Des.* **2006**, *6*, 964; d) C. N. R. Rao, S. Natarajan, R. Vaidhyanathan, *Angew. Chem. Int. Ed.* **2004**, *43*, 1466; e) H. Steinfink, G. D. Brunton, *Inorg. Chem.* **1970**, *9*, 112; f) F. Fourcade-Cavillou, J.-C. Trombe, *Solid State Sci.* **2002**, *4*, 1199; g) S. Romero, A. Mosset, J. C. Trombe, *J. Solid State Chem.* **1996**, *127*, 256.
[25] a) F. S. Richardson, *Chem. Rev.* **1982**, *82*, 541; b) W. D. Horrocks, D. R. Sudnik, *J. Am. Chem. Soc.* **1979**, *101*, 334; c) C. H. Evans, *Biochemistry of the Elements Vol. 8: Biochemistry of the Lanthanides*, Plenum, New York, **1990**; d) J. Legendziewicz, *J. Appl. Spectrosc.* **1995**, *62*, 189.
[26] a) L. D. Iskhakova, S. M. Ovanisyan, *Zh. Neorg. Khim.* **1995**, *40*, 1768; b) L. A. Kahwa, F. R. Fronczek, J. Selbin, *Inorg. Chim. Acta* **1984**, *82*, 167; c) R. E. Morris, A. P. Wilkinson, A. K. Cheetham, *Inorg. Chem.* **1992**, *31*, 4774.
[27] A. L. Spek, *Platon: A Multi-Purpose Crystallographic Tool*, Utrecht University, Utrecht, The Netherlands, **2001**.
[28] a) S. Comby, D. Imbert, A. S. Chauvin, J. C. G. Bunzli, L. J. Charbonniere, R. F. Ziessel, *Inorg. Chem.* **2004**, *43*, 7369; b) E. Guillet, D. Imbert, R. Scopelliti, J. C. G. Bunzli, *Chem. Mater.* **2004**, *16*, 4063; c) I. Billard, S. Mekki, C. Gaillard, P. Hesemann, G. Moutiers, C. Mariet, A. Labet, J. C. G. Bunzli, *Eur. J. Inorg. Chem.* **2004**, 1190.
[29] J. Xia, B. Zhao, H. S. Wang, W. Shi, Y. Ma, H. B. Song, P. Cheng, D. Z. Liao, S. P. Yan, *Inorg. Chem.* **2007**, *46*, 3450.
[30] Y. G. Huang, B. L. Wu, D. Q. Yuan, Y. Q. Xu, F. L. Jiang, M. C. Hong, *Inorg. Chem.* **2007**, *46*, 1171.
[31] a) G. A. Hebbink, L. Grave, L. A. Woldering, D. N. Reinhoudt, F. C. J. M. van Vegel, *J. Phys. Chem. A* **2003**, *107*, 2483; b) S. Faulkner, S. J. A. Pope, *J. Am. Chem. Soc.* **2003**, *125*, 10526; c) S. J. A. Pope, A. M. Kenwright, V. A. Boote, S. Faulkner, *Dalton Trans.* **2003**, 3780.
[32] W. K. Wong, H. Liang, J. Guo, W. Y. Wong, W. K. Lo, K. F. Li, K. W. Cheah, Z. Zhou, W. T. Wong, *Eur. J. Inorg. Chem.* **2004**, 829.
[33] L. N. Sun, J. B. Yu, H. J. Zhang, Q. G. Meng, E. Ma, C. Y. Peng, K. Y. Yang, *Microporous Mesoporous Mater.* **2007**, *98*, 156.
[34] a) G. M. Sheldrick, *Program SADABS*, University of Göttingen, **1995**; b) *CrystalClear (v. 1.3.5)*, Rigaku Corp., Woodlands, TX, **1999**; c) G. M. Sheldrick, *SHELXTL: Crystallographic Software Package (v. 5.1)*, Bruker-AXS, Madison, WI, **1998**.

Received: July 14, 2007
Published Online: October 12, 2007

 © 2007 Wiley-VCH Verlag GmbH & Co. KGaA, Weinheim 

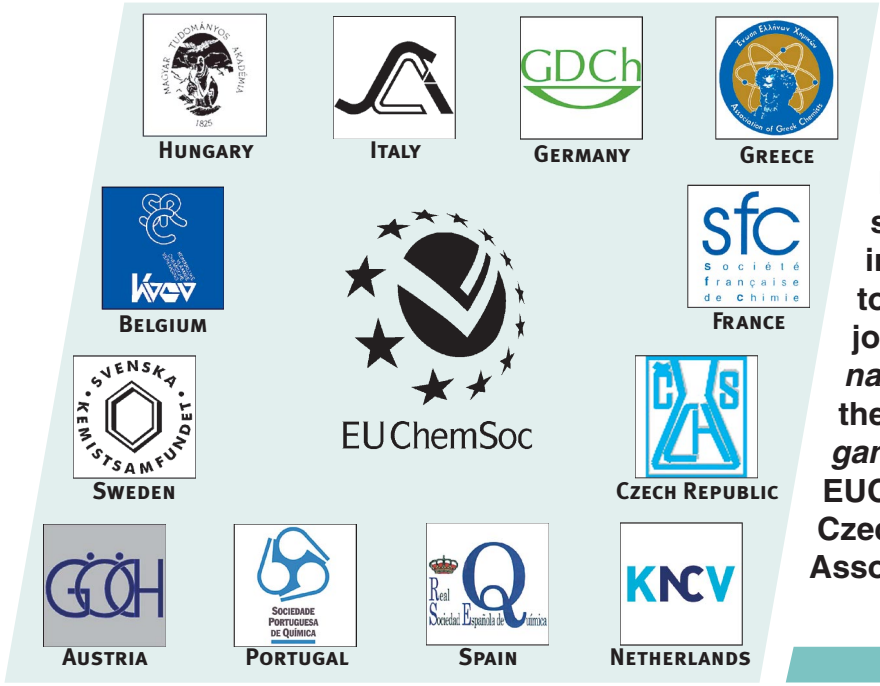


**The EUChemSoc Societies have taken the significant step into the future by merging their traditional journals, to form two leading chemistry journals, the *European Journal of Inorganic Chemistry* and the *European Journal of Organic Chemistry*. Three further EUChemSoc Societies (Austria, Czech Republic and Sweden) are Associates of the two journals.**

## COVER PICTURE

**The cover picture shows** two spotlights illuminating the structure of the first sandwich complex featuring an all-heavy group 14 element-consisting $Si_4$-cyclic ligand, namely, a derivative of ($\eta^5$-cyclopentadienyl)($\eta^4$-tetrasilacyclobutadiene)cobalt [($\eta^4$-$R_4Si_4$)-CoCp] (R = SiMe*t*Bu$_2$). The Me and *t*Bu groups on the Si substituents, as well as the H atoms on the Cp ring, are removed for simplicity. The title compound was smoothly prepared by a ligand exchange reaction between the tetrasilacyclobutadiene dianion salt $K^+_2$·[$R_4Si_4$]$_2$ and [$CpCoI_2$-($PPh_3$)]. Systematic comparison of the complex [($\eta^4$-$R_4Si_4$)CoCp] and its carbon analogue [$\eta^4$-($Me_3Si$)$_4C_4$]CoCp revealed important structural distinctions between the two complexes that result from the different ring sizes of the cyclobutadiene ligands $\eta^4$-$R_4E_4$ (R = SiMe*t*Bu$_2$, E = Si vs. R = $SiMe_3$, E = C). Details of the synthesis of the novel Co complex, as well as of its structural and electronic peculiarities, are discussed in the Short Communication by A. Sekiguchi et al. on p. 5471ff.

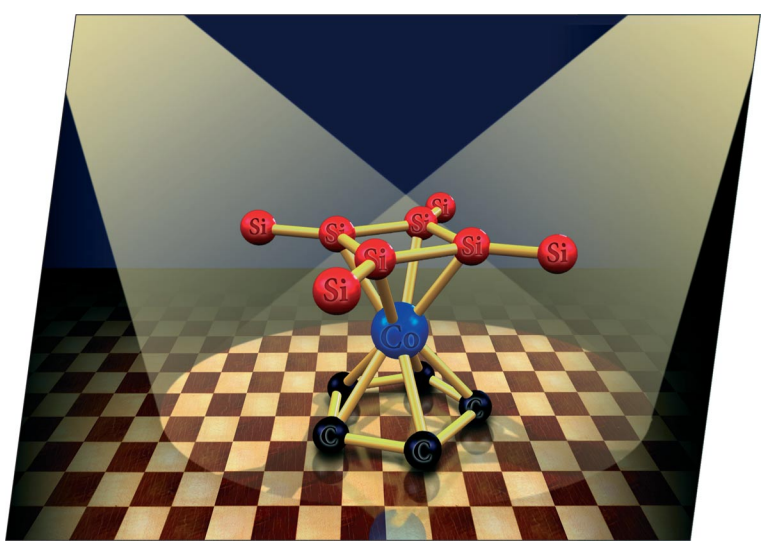


 © 2007 Wiley-VCH Verlag GmbH & Co. KGaA, Weinheim 

# CONTENTS

## SHORT COMMUNICATION


### Sandwich Complex with $\eta^4$-$Si_4R_4$

**K. Takanashi, V. Ya. Lee, M. Ichinohe, A. Sekiguchi* ..... 5471–5474**

($\eta^5$-Cyclopentteadienyl)($\eta^4$-tetrasila- and $\eta^4$-trisilagermacyclobutadiene)cobalt: Sandwich Complexes Featuring Heavy Cyclobutadiene Ligands

**Keywords:** Cobalt / Cyclobutadiene ligand / Cyclopentadienyl ligand / Germanium / Silicon


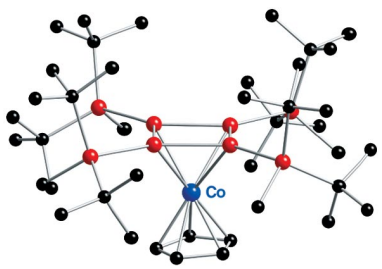


($\eta^5$-Cyclopentadienyl)($\eta^4$-tetrasila-cyclobutadiene)cobalt complex **2**

($\eta^5$-Cyclopentadienyl)($\eta^4$-tetrasila- and $\eta^4$-trisilagermacyclobutadiene)cobalt sandwich complexes [($\eta^4$-$R_4Si_4$)CoCp] (**2**) and [($\eta^4$-$R_4Si_3Ge$)CoCp] (**4**) (R = SiMe*t*$Bu_2$) were synthesized by reaction of the dipotassium salts of tetrasilacyclobutadiene dianion $K^+_2$·$[R_4Si_4]^{2-}$ (**1**) and trisilagermacyclobutadiene dianion $K^+_2$·$[R_4Si_3Ge]^{2-}$ (**3**) with $[CpCoI_2(PPh_3)]$. The structures of the new Co complexes were confirmed by X-ray analysis.

## FULL PAPERS


### Metal–Organic Frameworks

**I. Senkovska, J. Fritsch, S. Kaskel* ..... 5475–5479**

New Polymorphs of Magnesium-Based Metal–Organic Frameworks $Mg_3(ndc)_3$ (ndc = 2,6-Naphthalenedicarboxylate)

**Keywords:** Metal–organic frameworks / Magnesium / 2,6-Naphthalenedicarboxylic acid / Solvent effects / Gas adsorption


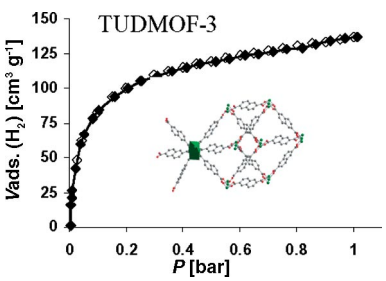


Two new magnesium 2,6-naphthalenedicarboxylate (ndc) metal–organic frameworks, $[Mg_3(ndc)_3(dif)_4]$ (**1**) (dif = *N*,*N*-diisopropylformamide) and $[Mg_3(ndc)_3(dmf)_2(CH_3OH)(H_2O)](dmf)$ (**2** = TUDMOF-3) (dmf = *N*,*N*-dimethylformamide), have been synthesised. TUDMOF-3 has a permanent porosity with a Langmuir surface area of 632 $m^2\ g^{-1}$, a specific pore volume of 0.21 $cm^3\ g^{-1}$ and a hydrogen storage capacity of 1.23 wt.-% (77 K, 1 bar). Compound **1** is not porous.


### Hybrid Mesostructures

**S.-R. Zhai, S. S. Park, M. Park, M. H. Ullah, C.-S. Ha* ..... 5480–5488**

Direct Synthesis of Zr-Containing Hybrid Periodic Mesoporous Organosilicas with Tunable Zirconium Content

**Keywords:** Silicates / Template synthesis / Orangic–inorganic hybrid composites / Mesoporous materials


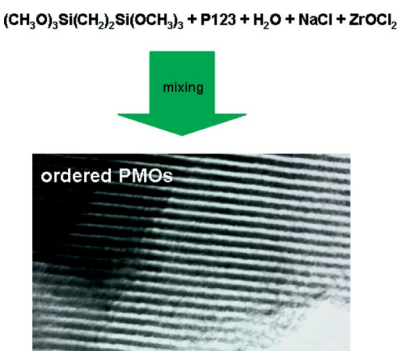


Highly ordered Zr-containing periodic mesoporous organosilicas (ZrPMO) were successfully synthesized, for the first time, by employing a $ZrOCl_2$/NaCl combination as the promoting agent; the addition of extra amounts of acid was not needed throughout the synthetic process.

 © 2007 Wiley-VCH Verlag GmbH & Co. KGaA, Weinheim 

## Contrast Agents

The propylene bridge in the skeleton of the $H_5EPTPACH_2OH$ ligand optimizes the water-exchange rate of the $[Gd(EPTPA\text{-}CH_2OH)(H_2O)]^{2-}$ complex, for efficiency as a MRI contrast agent, as a result of the steric compression imposed around its water binding site, as shown by solution relaxometric characterization. The hydroxymethyl substituent group is useful for conjugation of the reporter group. However, these changes, relative to those incurred by the DTPA chelate, significantly decrease its thermodynamic and kinetic stability.

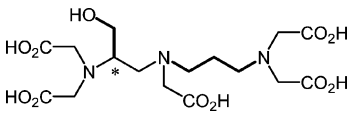


**S. Torres, J. A. Martins,* J. P. André,* G. A. Pereira, R. Kiraly, E. Brücher, L. Helm, É. Tóth, C. F. G. C. Geraldes* ..... 5489–5499**

$H_5EPTPACH_2OH$: Synthesis, Relaxometric Characterization and $^1H$ NMR Spectroscopic Studies on the Solution Dynamics of Its $Ln^{III}$ Complexes

**Keywords:** Lanthanides / Contrast agents / MRI / Microscopic protonation scheme / Stability constants

## Isomerism of Copper Complexes

The preference for axial or equatorial positioning of the bridging atoms and of the amine or pyridine N centers of tridentate ligands L in $LCu^{II}(\mu\text{-}X)_2Cu^{II}L$ complexes was probed experimentally and by DFT calculations. Their preference for either a *syn* or *anti* configuration in an equatorial/equatorial situation was also evaluated.

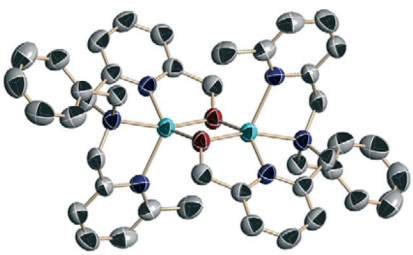

**J. Manzur,* A. Vega,* A. M. García, C. Acuña, M. Sieger, B. Sarkar, M. Niemeyer, F. Lissner, T. Schleid, W. Kaim* ..... 5500–5510**

Coordination Alternatives in Dinuclear Bis(pyridin-2-ylalkyl)benzylaminecopper(II) Complexes with $OH^-$, $RO^-$, $F^-$, or $Cl^-$ Bridges: Experimental Structures and DFT Preferences

**Keywords:** Copper / EPR spectroscopy / Isomerism / N ligands / Structure

## Coordination Oligomers/Polymers

Reactions of three preformed $Cu^{II}$/bdmpp complexes [bdmpp = 2,6-bis(3,5-dimethyl-1*H*-pyrazol-1-yl)pyridine] with 4,4′-bipy, dicyanamide (dca), azide, and $MCl_2$ (M = Cu, Co, Ni) lead to a series of homo- and heterometallic coordination oligomers and polymers. Their structures and redox properties were investigated.

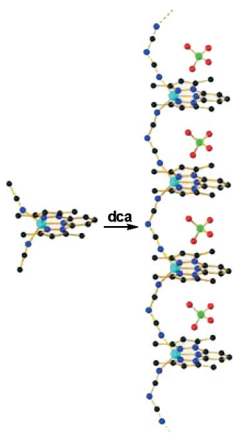


**G.-F. Liu, Z.-G. Ren, H.-X. Li, Y. Chen, Q.-H. Li, Y. Zhang, J.-P. Lang* ..... 5511–5522**

Homo- and Heterometallic Coordination Oligomers and Polymers Derived from the Preformed Complexes $[Cu(bdmpp)(MeCN)_2](ClO_4)_2$, $[Cu(bdmpp)(N_3)_2]$, and $[Cu(bdmpp)(N_3)(\mu\text{-}N_3)]_2$ [bdmpp = 2,6-bis(3,5-dimethyl-1*H*-pyrazol-1-yl)pyridine]: Syntheses, Structures, and Redox Properties

**Keywords:** Copper / Structures / Oligomers / Polymers / Redox properties

## Water-Soluble Ruthenium Complexes

A series of [tris(pyrazolyl)borato]ruthenium complexes bearing the water-soluble cage phosphane 1,3,5-triaza-7-phosphaadamantane (PTA) and its boranyl adduct $PTA(BH_3)$, including the water-soluble hydride $[TpRuH(PTA)_2]$, have been synthesised and characterised. Cyclic voltammetric studies in MeCN and dmso generally show reversible $Ru^{II/III}$ oxidation waves and the values of $E_{1/2}^{ox}$ reflect the electron-donating character of the ligands, whose Lever electrochemical parameter ($E_L$) is estimated for the first time.

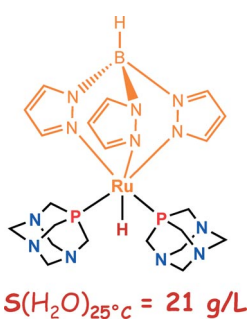


**S. Bolaño, J. Bravo,* J. Castro, M. Mar Rodríguez-Rocha, M. F. C. Guedes da Silva, A. J. L. Pombeiro,* L. Gonsalvi, M. Peruzzini* ..... 5523–5532**

Synthesis, Reactivity, X-ray Crystal Structures and Electrochemical Behaviour of Water-Soluble [Tris(pyrazolyl)borato]-ruthenium(II) Complexes of 1,3,5-Triaza-7-phosphaadamantane (PTA)

**Keywords:** Electrochemistry / Water-soluble complexes / Pyrazolylborates / Ruthenium / N ligands

 © 2007 Wiley-VCH Verlag GmbH & Co. KGaA, Weinheim 

# CONTENTS

## 3d–4f Coordination Polymers

**A. M. Madalan, K. Bernot, F. Pointillart, M. Andruh,* A. Caneschi* ..... 5533–5540**

First $Ni^{II}$–$Ln^{III}$ Coordination Polymers Constructed by Using $[Ni(bpca)_2]$ as a Building Block [Hbpca = bis(2-pyridylcarbonyl)amine]: Synthesis, Crystal Structures and Magnetic Properties

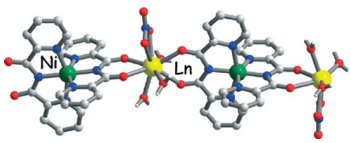


Three new heterobimetallic 1D coordination polymers have been obtained by assembling the $[Ni(bpca)_2]$ complex, as a building block, with lanthanide cations: $[\{Ln(O_2NO)(H_2O)_3\}\{Ni(bpca)_2\}](NO_3)_2 \cdot 3H_2O$ (Ln Gd **1**; Tb **2**; Dy **3**). Their static and dynamic magnetic properties were investigated and discussed.

**Keywords:** Nickel / Lanthanides / Heterobimetallic coordination polymers / Magnetic properties

## Ditungsten(III) Complexes

**O. Coutelier, R. M. Gauvin,* G. Nowogrocki, J. Trébosc, L. Delevoye, A. Mortreux* ..... 5541–5547**

A New Donor-Stabilized Ditungsten Amido Alkoxido Species: Synthesis, Crystal Structure, Fluxionality, and Grafting onto Silica

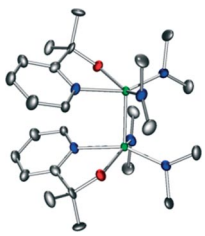

A new dimeric tungsten(III) complex containing amido and chelating pyridine–alkoxido ligands was synthesized through protonolysis of $[W_2(NMe_2)_6]$ by 2-(2-pyridyl)propan-2-ol and fully characterized. Grafting of this compound onto silica has been investigated by elemental analysis, DRIFTS, and solid-state NMR spectroscopy.

**Keywords:** Tungsten / Metal-metal multiple bonds / Ligand design / Grafting / Silica / Alkyne metathesis

## Copper–Thiolate Clusters

**B. K. Maiti, K. Pal, S. Sarkar* ..... 5548–5555**

Flexible $Cu^{I}$–Thiolate Clusters with Relevance to Metallothioneins

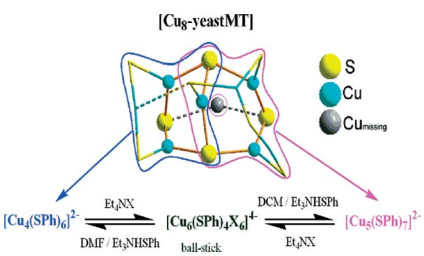


The structural diversity in some Cu–thiol small clusters with relevance to the chemistry of Cu-containing metallothioneins was investigated. Solvent polarity and the copper/thiol ratio may change the local cluster geometry, which causes flexibility of the copper–sulfur bond. These small clusters have superposition motifs in bigger clusters such as $Cu_8$-yeastMT.

**Keywords:** Metallothioneins / Flexibility / Coordination modes / Copper / Sulfur / Photoluminescence

## Au–Au Interactions

**F. Balzano, A. Cuzzola, P. Diversi,* F. Ghiotto, G. Uccello-Barretta ..... 5556–5562**

Cationic Gold(I) Phosphanyl Thiolates: Aurophilic Interactions in the Solid State and in Solution

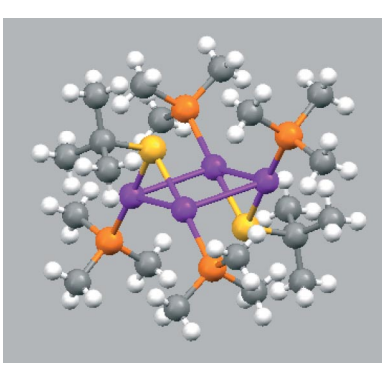

Cationic gold(I) phosphane alkanethiolates of the formula $[Au_2(StBu)(phosphane)_2][BF_4]$ were investigated in solution by MS and NMR spectroscopy. These compounds are dimeric in the solid state and are bound through aurophilic interactions; some of these compounds maintain the integrity of the Au–Au bonds in solution depending on the nature of the phosphane.

**Keywords:** Gold / Sulfur / Thiolates / Aurophilicity / Aggregation / ESI MS / NMR spectroscopy

 © 2007 Wiley-VCH Verlag GmbH & Co. KGaA, Weinheim 

## Organohydroborate

Based upon single-crystal X-ray diffraction analysis, the potassium salt of the 9-BBN hydroborate anion has a tetrameric structure when associated with toluene, methyl THF, or a mixture of toluene/THF, and THF/diethyl ether. While with the chelating solvent DME, it has a dimeric structure.

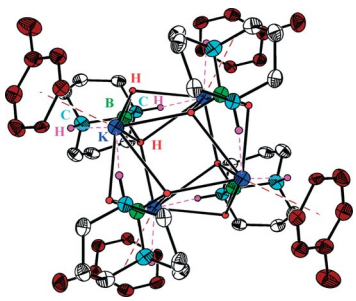


**X. Chen, S. Liu, B. Du, E. A. Meyers, S. G. Shore* ..... 5563–5570**

The Structure of Potassium and Tetramethylammonium Salts of the Cyclic Organohydroborate Anion $[H_2BC_8H_{14}]^-$ with Different Solvent Ligands

**Keywords:** Agostic interactions / X-ray diffraction / Organohydroborate / Potassium salts

## Hybrid Materials

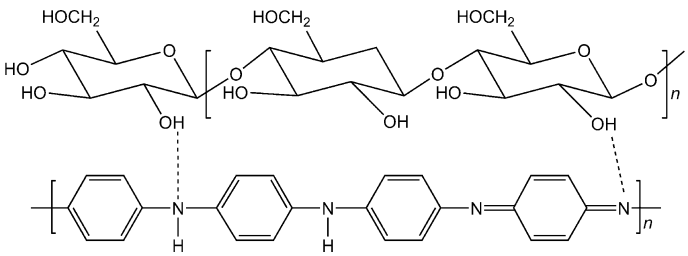


Conducting polymer/cellulose fibre composites, using polypyrrole and polyaniline, have been successfully prepared. By utilising the redox active nature of the conducting polymer coatings, silver nanoparticles have been deposited on the surface of the composite fibres. This additionally gives rise to fibres with antimicrobial properties.

**F. M. Kelly,* J. H. Johnston, T. Borrmann, M. J. Richardson ..... 5571–5577**

Functionalised Hybrid Materials of Conducting Polymers with Individual Fibres of Cellulose

**Keywords:** Polypyrrole / Polyaniline / Cellulose / Fibres / Conductivity / Antimicrobial activity

## Olefin Metathesis Catalysts

The use of Ru-based NHC-arene complexes as alternatives to the Grubbs-type catalysts used in olefin metathesis is described.

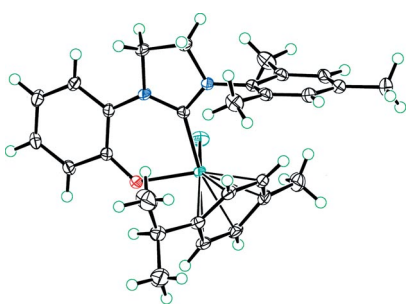

**N. Ledoux,* B. Allaert, F. Verpoort ..... 5578–5583**

Ruthenium-Based NHC-Arene Systems as Ring-Opening Metathesis Polymerisation Catalysts

**Keywords:** Carbene ligands / Homogeneous catalysis / Olefin polymerisation / Ruthenium

## Catalytic Ethylene Oligomerization

A series of iron, cobalt and nickel complexes bearing 2-arylimino-9-phenyl-1,10-phenanthrolines has been synthesized, characterized and evaluated for ethylene oligomerization. Most of the complexes show good catalytic activity for ethylene oligomerization, with the cobalt catalysts being more active than their iron analogues.

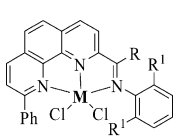


**M** = Fe, Co, Ni

**S. Jie, S. Zhang, W.-H. Sun* ..... ..... 5584–5598**

2-Arylimino-9-phenyl-1,10-phenanthrolinyl-iron, -cobalt and -nickel Complexes: Synthesis, Characterization and Ethylene Oligomerization Behavior

**Keywords:** Nitrogen ligands / Late transition metals / Iron / Ethylene / Oligomerization

 © 2007 Wiley-VCH Verlag GmbH & Co. KGaA, Weinheim 

# CONTENTS

## Octaruthenium Grids on HOPG

**D.-L. Shieh, Y.-S. Lin, K.-B. Shiu, J.-L. Lin* ..... 5599–5603**

Orientation and Arrangement of Octaruthenium Supramolecules with Alkyl Chains on Graphite

**Keywords:** Supramolecular chemistry / Scanning tunneling microscopy / Ruthenium

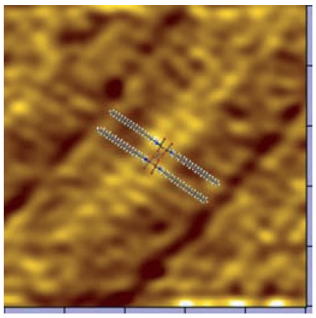

{[$Ru_2(CO)_4(NH_2C_{16}H_{33})_2$]($\mu$-$O_2CCO_2$)}$_4$ / HOPG

The self-assemblies of octaruthenium grid-type supramolecules, [$Ru_2(CO)_4(NH_2C_{16}H_{33})_2$]($\mu$-$O_2CCO_2$)$_4$, on highly oriented pyrolytic graphite (HOPG) in air and in phenyloctane were studied by scanning tunneling microscopy (STM).

# REMOVAL

**L.-Y. Li, Q. Yuan, L. Liao,* C.-H. Yan, J. Chen ..... 5605**

Removal: "Ultra-Simple Synthesis of Ordered Mesoporous $\gamma$-Alumina: High Thermal Stability and Catalytic Activity"

**If not otherwise indicated in the article, papers in issue 34 were published online on November 20, 2007**

 © 2007 Wiley-VCH Verlag GmbH & Co. KGaA, Weinheim 

# CONTENTS

## SHORT COMMUNICATION


### Sandwich Complex with $\eta^4$-$Si_4R_4$

**K. Takanashi, V. Ya. Lee, M. Ichinohe, A. Sekiguchi* ..... 5471–5474**

($\eta^5$-Cyclopentadienyl)($\eta^4$-tetrasila- and $\eta^4$-trisilagermacyclobutadiene)cobalt: Sandwich Complexes Featuring Heavy Cyclobutadiene Ligands

**Keywords:** Cobalt / Cyclobutadiene ligand / Cyclopentadienyl ligand / Germanium / Silicon


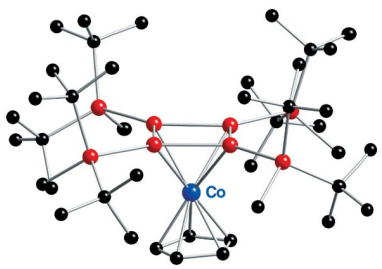


($\eta^5$-Cyclopentadienyl)($\eta^4$-tetrasila-cyclobutadiene)cobalt complex **2**


($\eta^5$-Cyclopentadienyl)($\eta^4$-tetrasila- and $\eta^4$-trisilagermacyclobutadiene)cobalt sandwich complexes [($\eta^4$-$R_4Si_4$)CoCp] (**2**) and [($\eta^4$-$R_4Si_3Ge$)CoCp] (**4**) (R = SiMe*t*$Bu_2$) were synthesized by reaction of the dipotassium salts of tetrasilacyclobutadiene dianion $K^+_2$·$[R_4Si_4]^{2-}$ (**1**) and trisilagermacyclobutadiene dianion $K^+_2$·$[R_4Si_3Ge]^{2-}$ (**3**) with $[CpCoI_2(PPh_3)]$. The structures of the new Co complexes were confirmed by X-ray analysis.


## FULL PAPERS


### Metal–Organic Frameworks

**I. Senkovska, J. Fritsch, S. Kaskel* ..... 5475–5479**

New Polymorphs of Magnesium-Based Metal–Organic Frameworks $Mg_3(ndc)_3$ (ndc = 2,6-Naphthalenedicarboxylate)

**Keywords:** Metal–organic frameworks / Magnesium / 2,6-Naphthalenedicarboxylic acid / Solvent effects / Gas adsorption


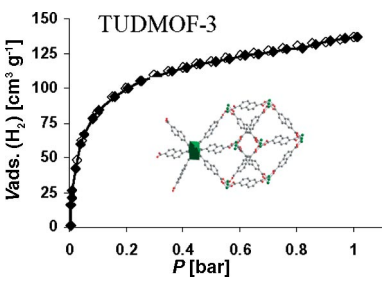



Two new magnesium 2,6-naphthalenedicarboxylate (ndc) metal–organic frameworks, $[Mg_3(ndc)_3(dif)_4]$ (**1**) (dif = *N*,*N*-diisopropylformamide) and $[Mg_3(ndc)_3(dmf)_2(CH_3OH)(H_2O)]$(dmf) (**2** = TUDMOF-3) (dmf = *N*,*N*-dimethylformamide), have been synthesised. TUDMOF-3 has a permanent porosity with a Langmuir surface area of 632 $m^2$ $g^{-1}$, a specific pore volume of 0.21 $cm^3$ $g^{-1}$ and a hydrogen storage capacity of 1.23 wt.-% (77 K, 1 bar). Compound **1** is not porous.

### Hybrid Mesostructures

**S.-R. Zhai, S. S. Park, M. Park, M. H. Ullah, C.-S. Ha* ..... 5480–5488**

Direct Synthesis of Zr-Containing Hybrid Periodic Mesoporous Organosilicas with Tunable Zirconium Content

**Keywords:** Silicates / Template synthesis / Orangic–inorganic hybrid composites / Mesoporous materials


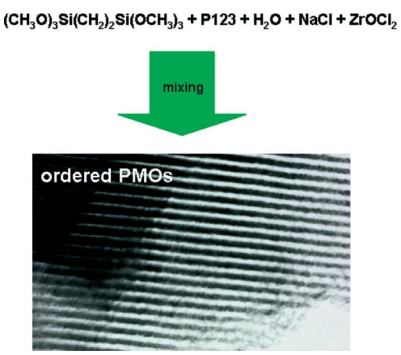



Highly ordered Zr-containing periodic mesoporous organosilicas (ZrPMO) were successfully synthesized, for the first time, by employing a $ZrOCl_2$/NaCl combination as the promoting agent; the addition of extra amounts of acid was not needed throughout the synthetic process.


 © 2007 Wiley-VCH Verlag GmbH & Co. KGaA, Weinheim 

## Contrast Agents

The propylene bridge in the skeleton of the $H_5EPTPACH_2OH$ ligand optimizes the water-exchange rate of the $[Gd(EPTPA\text{-}CH_2OH)(H_2O)]^{2-}$ complex, for efficiency as a MRI contrast agent, as a result of the steric compression imposed around its water binding site, as shown by solution relaxometric characterization. The hydroxymethyl substituent group is useful for conjugation of the reporter group. However, these changes, relative to those incurred by the DTPA chelate, significantly decrease its thermodynamic and kinetic stability.

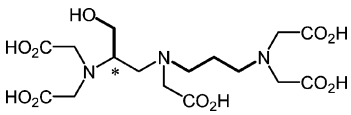


**S. Torres, J. A. Martins,* J. P. André,* G. A. Pereira, R. Kiraly, E. Brücher, L. Helm, É. Tóth, C. F. G. C. Geraldes* ..... 5489–5499**

$H_5EPTPACH_2OH$: Synthesis, Relaxometric Characterization and $^1H$ NMR Spectroscopic Studies on the Solution Dynamics of Its $Ln^{III}$ Complexes

**Keywords:** Lanthanides / Contrast agents / MRI / Microscopic protonation scheme / Stability constants

## Isomerism of Copper Complexes

The preference for axial or equatorial positioning of the bridging atoms and of the amine or pyridine N centers of tridentate ligands L in $LCu^{II}(\mu\text{-}X)_2Cu^{II}L$ complexes was probed experimentally and by DFT calculations. Their preference for either a *syn* or *anti* configuration in an equatorial/equatorial situation was also evaluated.

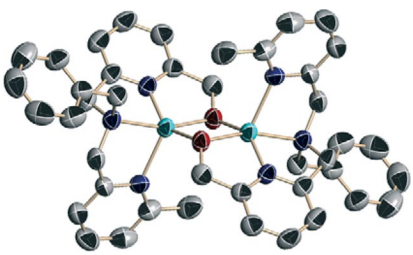

**J. Manzur,* A. Vega,* A. M. García, C. Acuña, M. Sieger, B. Sarkar, M. Niemeyer, F. Lissner, T. Schleid, W. Kaim* ..... 5500–5510**

Coordination Alternatives in Dinuclear Bis(pyridin-2-ylalkyl)benzylaminecopper(II) Complexes with $OH^-$, $RO^-$, $F^-$, or $Cl^-$ Bridges: Experimental Structures and DFT Preferences

**Keywords:** Copper / EPR spectroscopy / Isomerism / N ligands / Structure

## Coordination Oligomers/Polymers

Reactions of three preformed $Cu^{II}$/bdmpp complexes [bdmpp = 2,6-bis(3,5-dimethyl-1*H*-pyrazol-1-yl)pyridine] with 4,4′-bipy, dicyanamide (dca), azide, and $MCl_2$ (M = Cu, Co, Ni) lead to a series of homo- and heterometallic coordination oligomers and polymers. Their structures and redox properties were investigated.

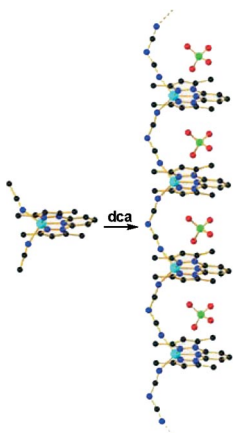


**G.-F. Liu, Z.-G. Ren, H.-X. Li, Y. Chen, Q.-H. Li, Y. Zhang, J.-P. Lang* ..... 5511–5522**

Homo- and Heterometallic Coordination Oligomers and Polymers Derived from the Preformed Complexes $[Cu(bdmpp)(MeCN)_2](ClO_4)_2$, $[Cu(bdmpp)(N_3)_2]$, and $[Cu(bdmpp)(N_3)(\mu\text{-}N_3)]_2$ [bdmpp = 2,6-bis(3,5-dimethyl-1*H*-pyrazol-1-yl)pyridine]: Syntheses, Structures, and Redox Properties

**Keywords:** Copper / Structures / Oligomers / Polymers / Redox properties

## Water-Soluble Ruthenium Complexes

A series of [tris(pyrazolyl)borato]ruthenium complexes bearing the water-soluble cage phosphane 1,3,5-triaza-7-phosphaadamantane (PTA) and its boranyl adduct $PTA(BH_3)$, including the water-soluble hydride $[TpRuH(PTA)_2]$, have been synthesised and characterised. Cyclic voltammetric studies in MeCN and dmso generally show reversible $Ru^{II/III}$ oxidation waves and the values of $E_{1/2}^{ox}$ reflect the electron-donating character of the ligands, whose Lever electrochemical parameter ($E_L$) is estimated for the first time.

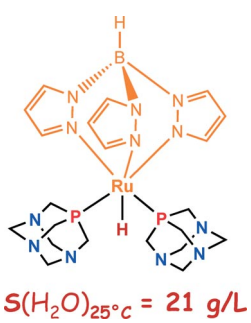


**S. Bolaño, J. Bravo,* J. Castro, M. Mar Rodríguez-Rocha, M. F. C. Guedes da Silva, A. J. L. Pombeiro,* L. Gonsalvi, M. Peruzzini* ..... 5523–5532**

Synthesis, Reactivity, X-ray Crystal Structures and Electrochemical Behaviour of Water-Soluble [Tris(pyrazolyl)borato]-ruthenium(II) Complexes of 1,3,5-Triaza-7-phosphaadamantane (PTA)

**Keywords:** Electrochemistry / Water-soluble complexes / Pyrazolylborates / Ruthenium / N ligands

 © 2007 Wiley-VCH Verlag GmbH & Co. KGaA, Weinheim 

# CONTENTS

## 3d–4f Coordination Polymers

**A. M. Madalan, K. Bernot, F. Pointillart, M. Andruh,* A. Caneschi* ..... 5533–5540**

First $Ni^{II}$–$Ln^{III}$ Coordination Polymers Constructed by Using $[Ni(bpca)_2]$ as a Building Block [Hbpca = bis(2-pyridylcarbonyl)amine]: Synthesis, Crystal Structures and Magnetic Properties

**Keywords:** Nickel / Lanthanides / Heterobimetallic coordination polymers / Magnetic properties

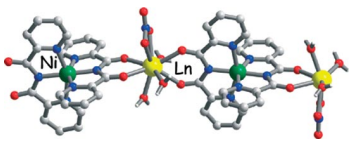


Three new heterobimetallic 1D coordination polymers have been obtained by assembling the $[Ni(bpca)_2]$ complex, as a building block, with lanthanide cations: $[\{Ln(O_2NO)(H_2O)_3\}\{Ni(bpca)_2\}](NO_3)_2 \cdot 3H_2O$ (Ln Gd **1**; Tb **2**; Dy **3**). Their static and dynamic magnetic properties were investigated and discussed.

## Ditungsten(III) Complexes

**O. Coutelier, R. M. Gauvin,* G. Nowogrocki, J. Trébosc, L. Delevoye, A. Mortreux* ..... 5541–5547**

A New Donor-Stabilized Ditungsten Amido Alkoxido Species: Synthesis, Crystal Structure, Fluxionality, and Grafting onto Silica

**Keywords:** Tungsten / Metal-metal multiple bonds / Ligand design / Grafting / Silica / Alkyne metathesis

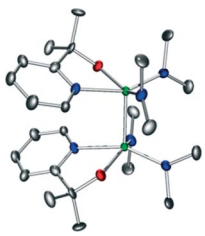

A new dimeric tungsten(III) complex containing amido and chelating pyridine–alkoxido ligands was synthesized through protonolysis of $[W_2(NMe_2)_6]$ by 2-(2-pyridyl)propan-2-ol and fully characterized. Grafting of this compound onto silica has been investigated by elemental analysis, DRIFTS, and solid-state NMR spectroscopy.

## Copper–Thiolate Clusters

**B. K. Maiti, K. Pal, S. Sarkar* ..... 5548–5555**

Flexible $Cu^{I}$–Thiolate Clusters with Relevance to Metallothioneins

**Keywords:** Metallothioneins / Flexibility / Coordination modes / Copper / Sulfur / Photoluminescence

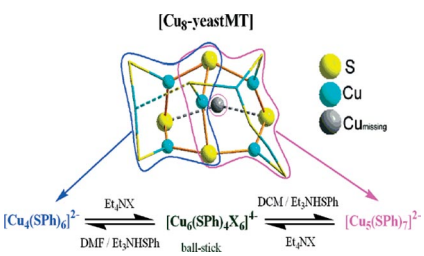


The structural diversity in some Cu–thiol small clusters with relevance to the chemistry of Cu-containing metallothioneins was investigated. Solvent polarity and the copper/thiol ratio may change the local cluster geometry, which causes flexibility of the copper–sulfur bond. These small clusters have superposition motifs in bigger clusters such as $Cu_8$-yeastMT.

## Au–Au Interactions

**F. Balzano, A. Cuzzola, P. Diversi,* F. Ghiotto, G. Uccello-Barretta ..... 5556–5562**

Cationic Gold(I) Phosphanyl Thiolates: Aurophilic Interactions in the Solid State and in Solution

**Keywords:** Gold / Sulfur / Thiolates / Aurophilicity / Aggregation / ESI MS / NMR spectroscopy

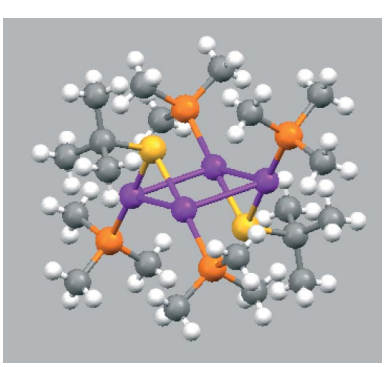

Cationic gold(I) phosphane alkanethiolates of the formula $[Au_2(StBu)(phosphane)_2][BF_4]$ were investigated in solution by MS and NMR spectroscopy. These compounds are dimeric in the solid state and are bound through aurophilic interactions; some of these compounds maintain the integrity of the Au–Au bonds in solution depending on the nature of the phosphane.

 © 2007 Wiley-VCH Verlag GmbH & Co. KGaA, Weinheim 

## Organohydroborate

Based upon single-crystal X-ray diffraction analysis, the potassium salt of the 9-BBN hydroborate anion has a tetrameric structure when associated with toluene, methyl THF, or a mixture of toluene/THF, and THF/diethyl ether. While with the chelating solvent DME, it has a dimeric structure.

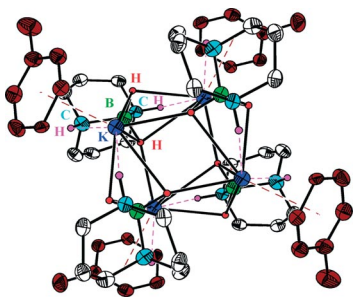


**X. Chen, S. Liu, B. Du, E. A. Meyers, S. G. Shore* ..... 5563–5570**

The Structure of Potassium and Tetramethylammonium Salts of the Cyclic Organohydroborate Anion $[H_2BC_8H_{14}]^-$ with Different Solvent Ligands

**Keywords:** Agostic interactions / X-ray diffraction / Organohydroborate / Potassium salts

## Hybrid Materials

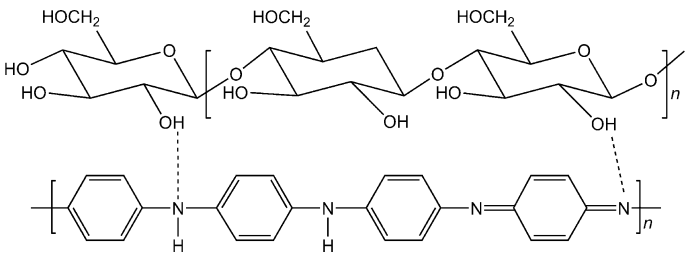


Conducting polymer/cellulose fibre composites, using polypyrrole and polyaniline, have been successfully prepared. By utilising the redox active nature of the conducting polymer coatings, silver nanoparticles have been deposited on the surface of the composite fibres. This additionally gives rise to fibres with antimicrobial properties.

**F. M. Kelly,* J. H. Johnston, T. Borrmann, M. J. Richardson ..... 5571–5577**

Functionalised Hybrid Materials of Conducting Polymers with Individual Fibres of Cellulose

**Keywords:** Polypyrrole / Polyaniline / Cellulose / Fibres / Conductivity / Antimicrobial activity

## Olefin Metathesis Catalysts

The use of Ru-based NHC-arene complexes as alternatives to the Grubbs-type catalysts used in olefin metathesis is described.

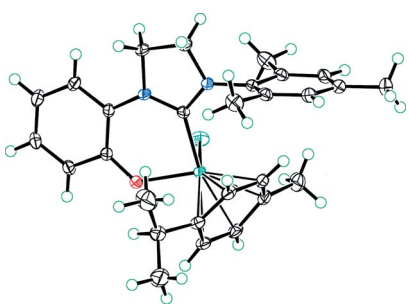

**N. Ledoux,* B. Allaert, F. Verpoort ..... 5578–5583**

Ruthenium-Based NHC-Arene Systems as Ring-Opening Metathesis Polymerisation Catalysts

**Keywords:** Carbene ligands / Homogeneous catalysis / Olefin polymerisation / Ruthenium

## Catalytic Ethylene Oligomerization

A series of iron, cobalt and nickel complexes bearing 2-arylimino-9-phenyl-1,10-phenanthrolines has been synthesized, characterized and evaluated for ethylene oligomerization. Most of the complexes show good catalytic activity for ethylene oligomerization, with the cobalt catalysts being more active than their iron analogues.

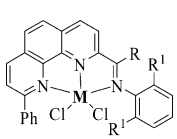


**M** = Fe, Co, Ni

**S. Jie, S. Zhang, W.-H. Sun* ..... ..... 5584–5598**

2-Arylimino-9-phenyl-1,10-phenanthrolinyl-iron, -cobalt and -nickel Complexes: Synthesis, Characterization and Ethylene Oligomerization Behavior

**Keywords:** Nitrogen ligands / Late transition metals / Iron / Ethylene / Oligomerization

 © 2007 Wiley-VCH Verlag GmbH & Co. KGaA, Weinheim 

# CONTENTS

## Octaruthenium Grids on HOPG

**D.-L. Shieh, Y.-S. Lin, K.-B. Shiu, J.-L. Lin* ..... 5599–5603**

Orientation and Arrangement of Octaruthenium Supramolecules with Alkyl Chains on Graphite

**Keywords:** Supramolecular chemistry / Scanning tunneling microscopy / Ruthenium

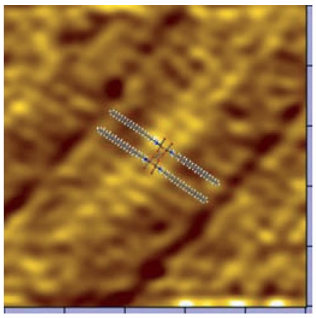

{[$Ru_2(CO)_4(NH_2C_{16}H_{33})_2$]($\mu$-$O_2CCO_2$)}$_4$ / HOPG

The self-assemblies of octaruthenium grid-type supramolecules, [$Ru_2(CO)_4(NH_2C_{16}H_{33})_2$]($\mu$-$O_2CCO_2$)$_4$, on highly oriented pyrolytic graphite (HOPG) in air and in phenyloctane were studied by scanning tunneling microscopy (STM).

# REMOVAL

**L.-Y. Li, Q. Yuan, L. Liao,* C.-H. Yan, J. Chen ..... 5605**

Removal: "Ultra-Simple Synthesis of Ordered Mesoporous $\gamma$-Alumina: High Thermal Stability and Catalytic Activity"

**If not otherwise indicated in the article, papers in issue 34 were published online on November 20, 2007**

 © 2007 Wiley-VCH Verlag GmbH & Co. KGaA, Weinheim 

# SPOTLIGHTS …

## *Micro Flow Synthesis*

A. Nagaki, Y. Tomida, H. Usutani, H. Kim, N. Takabayashi, T. Nokami, H. Okamoto, J.-i. Yoshida*

**Integrated Micro Flow Synthesis Based on Sequential Br–Li Exchange Reactions of *p*-, *m*-, and *o*-Dibromobenzenes**

*Chem. Asian J.*
DOI: **10.1002/asia.200700231**

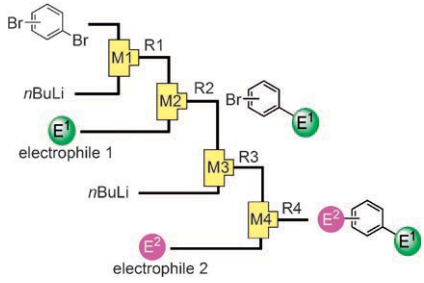


**On… and on… and on…** A variety of *p*-, *m*-, and *o*-disubstituted benzenes can be synthesized based on the Br–Li exchange reaction of the corresponding dibromobenzene by using a micro flow system. This method allows the use of much higher temperatures than are required for conventional macro batch systems.

## *Inhibitors*

A. Barazza, M. Götz, S. A. Cadamuro, P. Goettig, M. Willem, H. Steuber, T. Kohler, A. Jestel, P. Reinemer, C. Renner, W. Bode, L. Moroder*

**Macrocyclic Statine-Based Inhibitors of BACE-1**

*ChemBioChem*
DOI: **10.1002/cbic.200700383**

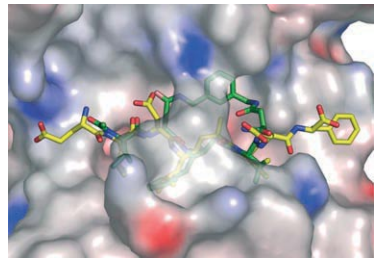

**Hitting BACE**. A 23-membered macrocyclic inhibitor of BACE-1 containing statine as a transition state analogue in the ring structure (green) was found to bind with the peptide backbone in an extended conformation to the active-site cleft, in a manner almost identical to that of a substrate-derived linear hydroxyethylene-octapeptide (yellow), without steric clashes with the flap domain.

## *Acid/Base Chemistry*

S.-C. Park, J.-K. Kim, C.-W. Lee, E.-S. Moon, H. Kang*

**Acid–Base Chemistry at the Ice Surface: Reverse Correlation Between Intrinsic Basicity and Proton-Transfer Efficiency to Ammonia and Methyl Amines**

*ChemPhysChem*
DOI: **10.1002/cphc.200700489**

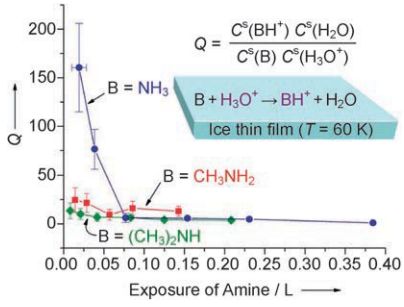


**On thin ice**: A surface-sensitive mass spectrometric method quantifies the efficiency of proton transfer from the hydronium ion to amine molecules (B) at the ice surface. The proton-transfer efficiency defined by reaction quotient $Q$ (see figure), exhibits the order $NH_3 > (CH_3)NH_2 = (CH_3)_2NH$, which opposes the trend of amine basicity in the gas phase or aqueous solution.

## *Bioconjugates*

A. K. Petrus, A. R. Vortherms, T. J. Fairchild,* R. P. Doyle*

**Vitamin $B_{12}$ as a Carrier for the Oral Delivery of Insulin**

*ChemMedChem*
DOI: **10.1002/cmdc.200700239**

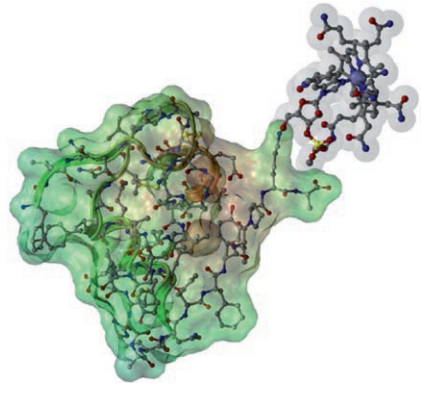

**The noninvasive delivery of insulin** continues to be a major goal for the treatment of diabetes mellitus. Oral–enteric administration would make insulin delivery easier and more effective, as higher patient compliance and improved glycemic control are likely; yet the oral–enteric pathway has been unfeasible owing to insulin's susceptibility to proteolytic degradation and inefficient enteric uptake. Herein we show that a noninvasive oral delivery route for insulin is possible through the vitamin $B_{12}$ uptake pathway. In diabetic rat models, insulin–$B_{12}$ conjugates can significantly lower blood glucose levels when administered orally.


© 2007 Wiley-VCH Verlag GmbH & Co. KGaA, Weinheim

EurJIC European Journal of Inorganic Chemistry

## *Conducting Polymers*

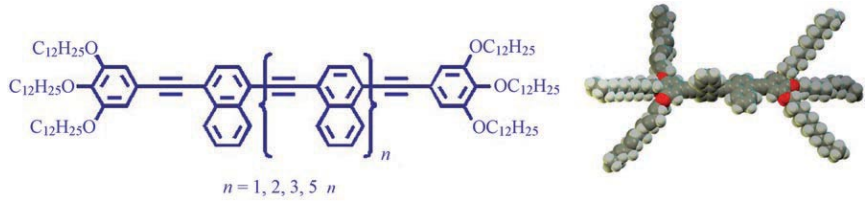


**Spare the rod but don't spoil the triplet!** Increasing the length of supposedly highly conjugated molecular rods does not necessarily lead to a lowering of their spectroscopic triplet energies. The synthesis and characterization of molecular rods, such as depicted, is also described.

A. C. Benniston,* A. Harriman,*
D. B. Rewinska, S. Yang, Y.-G. Zhi

**On the Conjugation Length for Oligo(ethynylnaphthalene)-Based Molecular Rods**

*Chem. Eur. J.*
DOI: **10.1002/chem.200701235**

## *DNA*

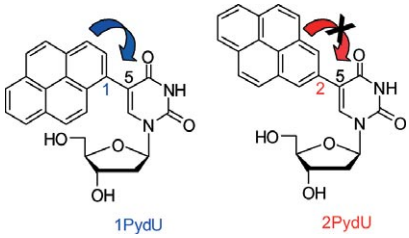


Electronically coupled or not? The position of the chromophore attachment in pyrene-modified uridines is critical for the optical properties of this nucleoside label.

C. Wanninger-Weiß,
H.-A. Wagenknecht*

**Synthesis of 5-(2-Pyrenyl)-2′-deoxyuridine as a DNA Modification for Electron-Transfer Studies: The Critical Role of the Position of the Chromophore Attachment**

*Eur. J. Org. Chem.*
DOI: **10.1002/ejoc.200700818**

## *Electrocatalysis*

**Getting rid of copper**: A class of ternary Pt–Cu–Co electrocatalysts for the reduction of oxygen in polymer electrolyte membrane fuel cells shows unprecedented activity improvements over state-of-the-art Pt catalysts. The active phase of the catalysts is synthesized by selective electrochemical dissolution (dealloying, see picture) of Cu-rich alloy-particle precursors, resulting in Pt-enriched core–shell particles.

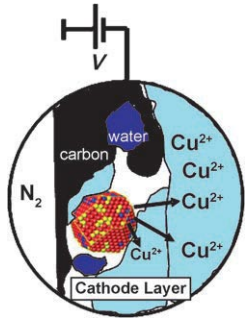


R. Srivastava, P. Mani, N. Hahn,
P. Strasser*

**Efficient Oxygen Reduction Fuel Cell Electrocatalysis on Voltammetrically Dealloyed Pt–Cu–Co Nanoparticles**

*Angew. Chem. Int. Ed.*
DOI: **10.1002/anie.200703331**

On these pages, we feature a selection of the excellent work that has recently been published in our sister journals. If you are reading these pages on a computer, click on any of the items to read the full article. Otherwise please see the DOIs for easy online access through Wiley InterScience.

 © 2007 Wiley-VCH Verlag GmbH & Co. KGaA, Weinheim 

DOI: 10.1002/ejic.200701046

# ($\eta^5$-Cyclopentadienyl)($\eta^4$-tetrasila- and $\eta^4$-trisilagermacyclobutadiene)cobalt: Sandwich Complexes Featuring Heavy Cyclobutadiene Ligands

**Kazunori Takanashi,[a] Vladimir Ya. Lee,[a] Masaaki Ichinohe,[a] and Akira Sekiguchi*[a]**

**Keywords:** Cobalt / Cyclobutadiene ligand / Cyclopentadienyl ligand / Germanium / Silicon

($\eta^5$-Cyclopentadienyl)($\eta^4$-tetrasilacyclobutadiene)cobalt {[($\eta^4$-$R_4Si_4$)CoCp], **2**} and ($\eta^5$-cyclopentadienyl)($\eta^4$-trisilagermacyclobutadiene)cobalt {[($\eta^4$-$R_4Si_3Ge$)CoCp], **4**} (R = SiMe*t*Bu$_2$) were synthesized by reaction of the dipotassium salts of tetrasilacyclobutadiene dianion $K^+_2$·$[R_4Si_4]^{2-}$ (**1**) and trisilagermacyclobutadiene dianion $K^+_2$·$[R_4Si_3Ge]^{2-}$ (**3**) with $[CpCoI_2(PPh_3)]$. Alternatively, **4** was prepared by the reaction of **3** with $[Cp_2Co]^+$·$[PF_6]^-$. X-ray crystallographic analysis of **2** confirmed its sandwich-type structure, manifesting a nearly square-planar $Si_4$ ring and diagnostic perhaptocoordination of both ligands, $\eta^4$-tetrasilacyclobutadiene and $\eta^5$-cyclopentadienyl, to the Co atom.
(© Wiley-VCH Verlag GmbH & Co. KGaA, 69451 Weinheim, Germany, 2007)

## Introduction

Sandwich complexes, known since the revolutionary discovery of ferrocene in 1951[1a,1b] and the determination of its novel structure in 1952,[1c,1d] constitute one of the most important classes of organotransition metal complexes. Accordingly, such sandwich complexes, particularly those featuring cyclopentadienyl and cyclobutadiene ligands, attracted a great deal of interest from both the fundamental and industrial organometallic chemistry communities.[2] For example, ($\eta^5$-cyclopentadienyl)[$\eta^4$-tetrakis(trimethylsilyl)cyclobutadiene]cobalt [$\eta^4$-$(Me_3Si)_4C_4$]CoCp (**A**)[3] represents such an important sandwich complex that found an interesting synthetic application as a convenient precursor for the 6π-electron aromatic derivative of the dilithium salt of the cyclobutadiene dianion.[3c,3d] The novel field of transition metal complexes with cyclic polyene ligands incorporating the heavier Group 14 elements represents another organometallic challenge that is very attractive from the viewpoint of their unique electronic structures and possible practical applications.[4] Thus, a series of transition metal complexes with heavy cyclopentadienyl ligands has been synthesized by Tilley,[4a–4g] whereas Kira recently reported the preparation of a (silacyclobutadiene)Co complex[4m] and Tokitoh reported the synthesis of sila-, germa- and stannaarene complexes of Cr, Mo and Ru.[4h–4l] We have also contributed to the field, utilizing tetrasilacyclobutadiene[4n,4o] and heavy cyclopentadienyl[4h] as a novel ligand for transition metal complexes. Thus, we succeeded in the synthesis of two types of carbonyl(tetrasilacyclobutadiene) transition metal complexes, $K^+$·[($\eta^4$-$R_4Si_4$)$Co(CO)_2]^-$ (**B**)[4n] and [($\eta^4$-$R_4Si_4$)$Fe(CO)_3$] (**C**)[4o] (R = SiMe*t*Bu$_2$) (Scheme 1), which show a stronger π-donating ability of the tetrasilacyclobutadiene ligand compared with that of its carbon counterpart. However, to the best of our knowledge, sandwich complexes in which the ring of one of the ligands entirely consists of heavier Group 14 elements are still unknown. In this paper, we report the synthesis and structural characterization of the first sandwich cyclopentadienyl complexes, featuring $\eta^4$-tetrasilacyclobutadiene and $\eta^4$-trisilagermacyclobutadiene ligands.

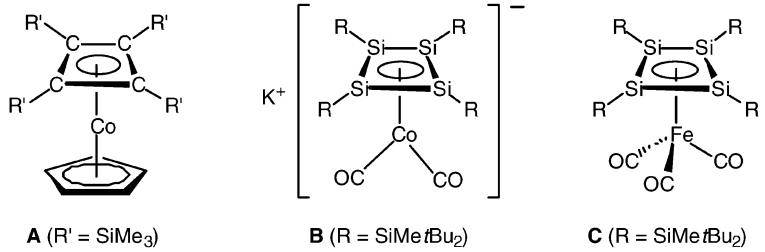


**A** (R' = $SiMe_3$) **B** (R = SiMe*t*Bu$_2$) **C** (R = SiMe*t*Bu$_2$)

Scheme 1. Cyclobutadiene complex **A** and tetrasilacyclobutadiene complexes **B** and **C**.

[a] Department of Chemistry, Graduated School of Pure and Applied Sciences, University of Tsukuba
Tsukuba, Ibaraki 305-8571, Japan
Fax: +81-29-853-4314
E-mail: sekiguch@chem.tsukuba.ac.jp

 © 2007 Wiley-VCH Verlag GmbH & Co. KGaA, Weinheim 

## Results and Discussion

Reaction of the dipotassium salt of tetrasilacyclobutadiene dianion derivative $K^+_2{\cdot}[R_4Si_4]^{2-}$ (R = SiMe*t*Bu$_2$) (**1**)[5] with [CpCoI$_2$(PPh$_3$)] in THF produced the corresponding sandwich complex, ($\eta^5$-cyclopentadienyl)[$\eta^4$-tetrakis(di-*tert*-butylmethylsilyl)tetrasilacyclobutadiene]cobalt {[($\eta^4$-$R_4Si_4$)CoCp], **2**}, accompanied by elimination of PPh$_3$ (Scheme 2). Complex **2** was isolated as air- and moisture-sensitive orange crystals in 36% yield by recrystallization from hexane. Both the $^1$H and $^{13}$C NMR spectra of **2** display only one set of signals for the Me and *t*Bu groups of the *t*Bu$_2$MeSi substituents because of the free rotation about the vertical axis passing through the Si$_4$ ring center and the Co atom. The cyclopentadienyl carbon signals are observed in the normal region at $\delta$ = 80.3 ppm. The endocyclic silicon atoms of the Si$_4$ ring resonate at $\delta$ = 0.4 ppm; this value being shifted upfield compared with typical values of sp$^2$-Si atoms.[6] Our GIAO computations well reproduced such chemical shift, giving a value of $\delta$ = –4.7 ppm for the model complex [($\eta^4$-R′$_4$Si$_4$)CoCp] (**2′**) (R′ = SiMe$_3$).[7] Such general tendency of the great shielding of skeletal Si atoms of the tetrasilacyclobutadiene ligand upon its complexation to transition metal atoms, previously observed by us for other transition metal complexes, could be most reasonably achieved in terms of the strong 3d(Co)→π*(Si$_4$) π back donation. Utilizing the same synthetic procedure, we also prepared the Si$_3$Ge hybrid heavy cyclobutadiene complex ($\eta^5$-cyclopentadienyl)[$\eta^4$-tetrakis(di-*tert*-butylmethylsilyl)trisilagermacyclobutadiene]cobalt {[$\eta^4$-$R_4Si_3Ge$]CoCp, **4**} (yield 41%) by reaction of the dipotassium salt of the trisilagermacyclobutadiene dianion derivative $K^+_2{\cdot}[R_4Si_3Ge]^{2-}$ (R = SiMe*t*Bu$_2$) (**3**)[8] with [CpCoI$_2$(PPh$_3$)] in THF. Alternatively, **4** was synthesized (yield 62%) by the reaction of **3** with $[Cp_2Co]^+{\cdot}[PF_6]^-$, accompanied by the elimination of CpK, similar to the case of complex **B**.[4n] Although highly air- and moisture-sensitive, **4** is thermally very stable up to 287 °C. The structure of **4** was established by NMR spectral and X-ray diffraction data. Thus, **4** exhibits three sets of signals for the Me and *t*Bu groups in both $^1$H and $^{13}$C NMR spectra, as expected. The $^{29}$Si NMR spectrum of **4** shows a total of five signals ($\delta$ = –13.7, 22.0, 24.1, 32.1 and 43.5 ppm), of which the most upfield ($\delta$ = –13.7 ppm) and the most downfield ($\delta$ = 43.5 ppm) signals were attributed to the endocyclic Si atoms with the latter signal corresponding to Si atoms bound to the Ge atom.

The X-ray crystal structure of **2** is represented in Figure 1. The bond lengths between the skeletal silicon and cobalt atoms in **2** range from 2.3862(7) to 2.3990(7) Å, which is in the range reasonably expected for a tetrahaptocoordinated tetrasilacyclobutadiene ligand, being similar to those in the previously reported complex $K^+{\cdot}[(\eta^4\text{-}R_4Si_4)Co(CO)_2]^-$ (**B**) [2.3935(7)–2.4225(7) Å].[4n] The endocyclic silicon–silicon bond lengths in **2** spread over the narrow range of 2.2718(10)–2.2725(9) Å, which is just in between the typical values of an Si–Si single (2.34 Å) and an Si=Si double (2.15 Å) bond.[9] The difference between the longest and shortest endocyclic silicon–silicon bond in **2** ($\Delta$ = 0.0007 Å) is smaller than that in ($\eta^4$-$R_4Si_4$)Fe(CO)$_3$ (**C**) ($\Delta$ = 0.0192 Å),[4o] primarily because of the different degree of steric interaction between the bulky *t*Bu$_2$MeSi substituents on the tetrasilacyclobutadiene ring and cyclopentadienyl (in **2**) or carbonyl (in **C**) ligands. The latter reason affects also the orientation of the *t*Bu$_2$MeSi groups in **2** to minimize their mutual steric interaction: they are arranged in a clockwise manner with the silyl substituents' Si atoms being nearly coplanar with the Si$_4$ ring plane [the up and down deviations of the Si atoms from the Si$_4$ mean plane are 0.0198(7) and 0.0043(7) Å, respectively]. On the other hand, the small Me groups of the *t*Bu$_2$MeSi substituents in **C**[4o] are uniformly directed toward the carbonyl ligands. Remarkably, the tetrasilacyclobutadiene ligand in **2** possesses an almost regular square-planar geometry, with the sum of the interior bond angles being 360.0°, which corresponds to a negligible folding of 1.1°. The crystal structure of **4** was also unambiguously determined by X-ray crystallography to confirm its sandwich composition; however, a precise structural determination was prevented by the positional disorder between the skeletal Si and Ge atoms.

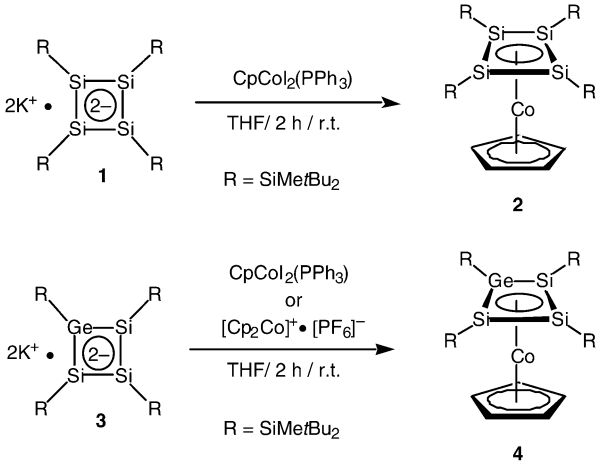


Scheme 2. Synthesis of heavy cyclobutadiene complexes **2** and **4**.

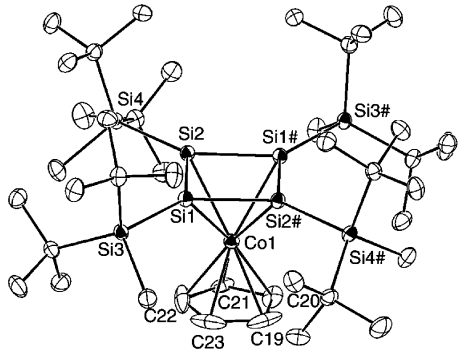


Figure 1. ORTEP drawing of **2** (30% probability level, hydrogen atoms are not shown). Selected bond lengths [Å]: Si1–Si2 2.2725(9), Si1–Si2# 2.2718(10), Si1–Co1 2.3862(7), Si2–Co1 2.3990(7), Si1–Si3 2.3784(9), Si2–Si4 2.3846(8). Selected bond angles [°]: Si2–Si1–Si2# 90.08(3), Si1–Si2–Si1# 89.92(3). Dihedral angle [°]: Si1–Si2–Si1#/Si1–Si2#–Si1# 1.10(2).

 © 2007 Wiley-VCH Verlag GmbH & Co. KGaA, Weinheim 

In order to gain a deeper insight into the structures of these novel sandwich complexes, we performed computations on the $Me_3Si$-substituted model [($\eta^4$-R′$_4Si_4$)CoCp] (R′ = $SiMe_3$) (**2′**) and the complex [$\eta^4$-$(Me_3Si)_4C_4$]CoCp (**A**). The structural parameters for experimental compounds **2** and **A**[3d] and those of calculated **2′** and **A** are summarized in Table 1. The structural features of **2** were fairly well reproduced in the calculated structure **2′**, except for the location of the silyl substituents' Si atoms. Thus, whereas these Si atoms in **2** are nearly coplanar with the $Si_4$ ring, in the optimized structure of **2′** they are tilted towards the Co atom from the $Si_4$ mean plane by 0.236–0.261 Å. In contrast, the silyl substituents' Si atoms in the calculated structure of **A** are bent away from the Co atom, being situated 0.294–0.330 Å above the $C_4$ ring. Such a distinction in the position of the silyl substituents in the calculated structures of **2′** and **A** would be reasonably explained by the difference in the ring size of cyclobutadienes $R_4E_4$ (E = Si, C; R = $SiMe_3$), implying different extents of the effective π($R_4E_4$)–3d(Co) orbitals' interaction depending on the size of the carbon 2pπ- and silicon 3pπ-orbitals, as schematically illustrated in Figure 2. The experimentally observed in-plane positions of the silyl substituents in **2** are due to the balance between the two opposite tendencies: favorable orbital interactions and unfavorable steric repulsion between the bulky silyl substituents and Cp ligand.

Table 1. Geometrical parameters of the experimental (**2** and **A**) and calculated (**2′** and **A**) structures of the cyclobutadiene cobalt complexes [($\eta^4$-$R_4E_4$)CoCp] (E = Si, C).

| | **2** (E = Si) experimental | **2′** (E = Si) calculated | **A** (E = C)[a] experimental | **A** (E = C) calculated |
|---|---|---|---|---|
| E–Co [Å] | 2.3862(7) | 2.389 | 1.989(2) | 1.980 |
| | 2.3990(7) | 2.390 | 1.992(2) | 1.983 |
| | | 2.392 | 1.995(2) | 1.986 |
| | | 2.395 | 2.012(2) | 1.987 |
| Endocyclic E–E [Å] | 2.2718(10) | 2.262 | 1.480(3) | 1.481 |
| | 2.2725(9) | 2.262 | 1.481(3) | 1.482 |
| | | 2.264 | 1.486(3) | 1.482 |
| | | 2.264 | 1.486(3) | 1.482 |
| Si substituent– | +0.0198(7) | –0.236 | +0.3954(8) | +0.330 |
| $E_4$-mean plane [Å][b] | –0.0043(7) | –0.257 | +0.3798(7) | +0.314 |
| | | –0.260 | +0.0010(7) | +0.295 |
| | | –0.261 | –0.0798(8) | +0.294 |

[a] From ref.[3d] [b] Positive and negative values correspond to the location of Si substituents above and below the $E_4$ mean plane, respectively.

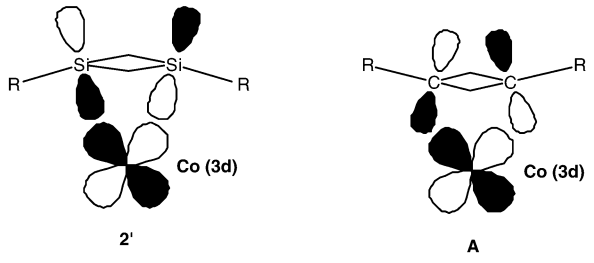


Figure 2. Systematic illustration of the interaction between the $R_4E_4$ (E = Si, C; R = $SiMe_3$) pπ- and Co 3d-orbitals in calculated **2′** and **A**.

## Conclusions

New sandwich complexes featuring heavy cyclobutadiene ligands ($\eta^5$-cyclopentadienyl)($\eta^4$-tetrasilacyclobutadiene)-cobalt {[($\eta^4$-$R_4Si_4$)CoCp], **2**} and ($\eta^5$-cyclopentadienyl)($\eta^4$-trisilagermacyclobutadiene)cobalt {[($\eta^4$-$R_4Si_3Ge$)CoCp], **4**} (R = $SiMe$*t*$Bu_2$) were synthesized by the reaction of the corresponding dipotassium salts of the tetrasilacyclobutadiene dianion $K^+_2$·$[R_4Si_4]^{2-}$ (**1**) and the trisilagermacyclobutadiene dianion $K^+_2$·$[R_4Si_3Ge]^{2-}$ (**3**) with [$CpCoI_2(PPh_3)$]. The systematic comparison between **2** and its carbon analog, ($\eta^5$-cyclopentadienyl)[$\eta^4$-tetrakis(trimethylsilyl)cyclobutadiene]cobalt {[$\eta^4$-$(Me_3Si)_4C_4$]CoCp (**A**)}, showed significant structural differences between them caused by the difference in the ring size of the cyclobutadiene ligand $R_4E_4$ (R = $SiMe$*t*$Bu_2$, E = Si vs. R = $SiMe_3$, E = C).

## Experimental Section

**Starting Materials:** The dipotassium salt of the tetrasilacyclobutadiene dianion, $K^+_2$·$[R_4Si_4]^{2-}$ (R = $SiMe$*t*$Bu_2$) (**1**), was prepared according to a published experimental procedure.[5] The dipotassium salt of the trisilagermacyclobutadiene dianion, $K^+_2$·$[R_4Si_3Ge]^{2-}$ (R = $SiMe$*t*$Bu_2$) (**3**), was also synthesized in a similar manner.[8] The cobalt complex [$CpCoI_2(PPh_3)$] was synthesized according to a literature procedure,[10] whereas complex $[Cp_2Co]^+$·$[PF_6]^-$ was commercially available and purchased from Tokyo Kasei Co.

**($\eta^5$-Cyclopentadienyl)[$\eta^4$-tetrakis(di-*tert*-butylmethylsilyl)tetrasilacyclobutadiene]cobalt {[$\eta^4$-(*t*$Bu_2$MeSi)$_4Si_4$]CoCp} (2):** The dipotassium salt of the tetrasilacyclobutadiene dianion, $K^+_2$·$[R_4Si_4]^{2-}$ (R = $SiMe$*t*$Bu_2$) (**1**) (104 mg, 0.094 mmol), and [$CpCoI_2(PPh_3)$] (55 mg, 0.095 mmol) were placed in a reaction tube with a magnetic stirring bar. Oxygen-free dry THF (2 mL) was introduced by vacuum transfer, and the reaction mixture was stirred at room temperature to give an orange solution within 1 h. Then the solvent was removed in vacuo, and dry hexane was introduced. After inorganic salt was removed by centrifugation, the residue was recrystallized from hexane (1 mL) at –30 °C to give **2** (29 mg, 36%) as orange crystals; m.p. 290–292 °C. $^1$H NMR (400 MHz, $C_6D_6$): $\delta$ = 0.30 (s, 12 H, *t*$Bu_2$*Me*Si), 1.22 (s, 72 H, *tBu*$_2$MeSi), 5.33 (s, 5 H, $C_5H_5$) ppm. $^{13}$C NMR (100.6 MHz, $C_6D_6$): $\delta$ = –3.6, 21.5, 30.4, 80.3 ppm. $^{29}$Si NMR (79.5 MHz, $C_6D_6$): $\delta$ = 0.4 (skeletal Si), 22.2 (substituents Si) ppm. UV/Vis (THF): $\lambda$ ($\varepsilon$) = 294 (23000), 347 (6100), 407 (3200) nm. $C_{41}H_{89}CoSi_8$ (865.78): calcd. C 56.88, H 10.36; found C 57.26, H 10.30.

**($\eta^5$-Cyclopentadienyl)[$\eta^4$-tetrakis(di-*tert*-butylmethylsilyl)trisilagermacyclobutadiene]cobalt {[$\eta^4$-(*t*$Bu_2$MeSi)$_4Si_3$Ge]CoCp} (4) by Reaction of $K^+_2$·$[R_4Si_3Ge]^{2-}$ (R = $SiMe$*t*$Bu_2$) and [$CpCoI_2(PPh_3)$]:** The dipotassium salt of the trisilagermacyclobutadiene dianion, $K^+_2$·$[R_4Si_3Ge]^{2-}$ (R = $SiMe$*t*$Bu_2$) (**3**) (129 mg, 0.112 mmol), and [$CpCoI_2(PPh_3)$] (65 mg, 0.112 mmol) were placed in a reaction tube with a magnetic stirring bar. Oxygen-free dry THF (2 mL) was introduced by vacuum transfer, and the reaction mixture was stirred at room temperature to give an orange solution within 1 h. Then the solvent was removed in vacuo, and dry hexane was introduced. After inorganic salt was removed by centrifugation, the residue was recrystallized from hexane (1 mL) at –30 °C to give **4** (42 mg, 41%) as orange crystals; m.p. 287 °C. $^1$H NMR (400 MHz, $C_6D_6$): $\delta$ = 0.26 (s, 3 H, *t*$Bu_2$*Me*Si), 0.30 (s, 3 H, *t*$Bu_2$*Me*Si), 0.32 (s, 6 H, *t*$Bu_2$*Me*Si), 1.18 (s, 18 H, *tBu*$_2$MeSi), 1.19 (s, 18 H, *tBu*$_2$MeSi), 1.23 (s, 18 H, *tBu*$_2$MeSi), 1.24 (s, 18 H, *tBu*$_2$MeSi), 5.29 (s, 5 H, $C_5H_5$) ppm. $^{13}$C NMR (100.6 MHz, $C_6D_6$): $\delta$ = –3.7 (2 C), –3.5, –2.9,

 © 2007 Wiley-VCH Verlag GmbH & Co. KGaA, Weinheim 

21.2, 21.26, 21.31, 21.9, 30.2, 30.32, 30.34, 30.4, 79.7 ppm. $^{29}$Si NMR (79.5 MHz, $C_6D_6$): $\delta$ = –13.7 (1 skeletal Si), 22.0 (2 Si), 24.1, 32.1 (substituents Si), 43.5 (2 skeletal Si) ppm. UV/Vis (THF): $\lambda$ ($\varepsilon$) = 295 (14000), 410 (2100), 464 (770) nm. $C_{41}H_{89}CoGeSi_7$ (910.28): calcd. C 54.10, H 9.85; found C 53.79, H 9.74.

**($\eta^5$-Cyclopentadienyl)[$\eta^4$-tetrakis(di-*tert*-butylmethylsilyl)trisilagermacyclobutadiene]cobalt {[$\eta^4$-(*t*Bu$_2$MeSi)$_4$Si$_3$Ge]CoCp} (4) by Reaction of K$^+_2$·[R$_4$Si$_3$Ge]$^{2-}$ (R = SiMe*t*Bu$_2$) and [Cp$_2$Co]$^+$·[PF$_6$]$^-$:** The dipotassium salt of the trisilagermacyclobutadiene dianion, K$^+_2$·[R$_4$Si$_3$Ge]$^{2-}$ (R = SiMe*t*Bu$_2$) (**3**) (129 mg, 0.112 mmol), and [Cp$_2$Co]$^+$·[PF$_6$]$^-$ (38 mg, 0.114 mmol) were placed in a reaction tube with a magnetic stirring bar. Oxygen-free dry toluene (2 mL) was introduced by vacuum transfer, and the reaction mixture was stirred at room temperature to give an orange solution within 0.5 h. Then the solvent was removed in vacuo, and dry hexane was introduced. After inorganic salt was removed by centrifugation, the residue was recrystallized from hexane to give **4** (63 mg, 62%) as orange crystals.

**X-ray Diffraction Studies and Crystal Data for 2:** A single crystal of **2** suitable for X-ray diffraction study was grown from a hexane solution. The diffraction data were collected with a MacScience DIP2030 image plate diffractometer equipped with a rotation anode using graphite-monochromatized Mo-$K_\alpha$ radiation ($\lambda$ = 0.71070 Å) at 150 K. The structure was solved by direct methods using the SIR-92 program[11] and refined by full-matrix least-squares methods using the SHELXL-97 program.[12] Crystal data: $C_{41}H_{89}CoSi_8$, $M$ = 865.77, orthorhombic, *Pccn*, $a$ = 19.1700(5), $b$ = 15.8280(9), $c$ = 17.1620(10) Å, $V$ = 5207.3(4) Å$^3$, $Z$ = 4, $D_{calcd.}$ = 1.104 g/cm$^3$, $R$ = 0.0437 ($wR$ = 0.1259 for all data) for 6260 reflections with $I > 2\sigma(I)$, $GOF$ = 0.924. CCDC-659562 contains the supplementary crystallographic data for this paper. These data can be obtained free of charge from The Cambridge Crystallographic Data Centre via www.ccdc.cam.ac.uk/data_request/cif.

## Acknowledgments

This work was supported by the Ministry of Education, Science, Sports, and Culture of Japan through a Grant-in-Aid for Scientific Research Program (Nos. 17655014, 17550029, 19020012, 19022004, 19029006, 19105001).

[1] a) T. J. Kealy, P. L. Pauson, *Nature* **1951**, *168*, 1039; b) S. A. Miller, J. A. Tebboth, J. F. Tremaine, *J. Chem. Soc.* **1952**, 632; c) G. Wilkinson, M. Rosenblum, M. C. Whiting, R. B. Woodward, *J. Am. Chem. Soc.* **1952**, *74*, 2125; d) E. Ruch, E. O. Fischer, *Z. Naturforsch* **1952**, *7b*, 676.

[2] Reviews on cyclobutadiene and cyclopentadienyl complexes of transition metals and main group elements: a) A. Efraty, *Chem. Rev.* **1977**, *77*, 691; b) P. K. Baker, H. Silgram, *Trends Organomet. Chem.* **1999**, *3*, 21; c) P. Jutzi, N. Burford, *Chem. Rev.* **1999**, *99*, 969; d) P. H. M. Budzelaar, J. J. Engelberts, J. H. van Lenthe, *Organometallics* **2003**, *22*, 1562; e) D. Seyferth, *Organometallics* **2003**, *22*, 2.

[3] ($\eta^4$-Cyclobutadiene)($\eta^5$-cyclopentadienyl)cobalt {[$\eta^4$-(Me$_3$Si)$_4$-C$_4$]CoCp} (**A**): a) H. Sakurai, J. Hayashi, *J. Organomet. Chem.* **1974**, *70*, 85; b) J. R. Fritch, K. P. C. Vollhardt, M. R. Thompson, V. W. Day, *J. Am. Chem. Soc.* **1979**, *101*, 2768; c) A. Sekiguchi, T. Matsuo, M. Tanaka, H. Watanabe, *J. Am. Chem. Soc.* **2000**, *122*, 5652; d) A. Sekiguchi, T. Matsuo, M. Tanaka, H. Watanabe, M. Nakamoto, *Russ. Chem. Bull., Int. Ed.* **2004**, *53*, 1109; e) A. Sekiguchi, T. Matsuo, *Synlett* **2006**, 2683.

[4] Transition metal complexes featuring heavy cyclopentadienyl ligands: a) W. P. Freeman, T. D. Tilley, A. L. Rheingold, R. L. Ostrander, *Angew. Chem. Int. Ed. Engl.* **1993**, *32*, 1744; b) W. P. Freeman, T. D. Tilley, A. L. Rheingold, *J. Am. Chem. Soc.* **1994**, *116*, 8428; c) J. M. Dysard, T. D. Tilley, *J. Am. Chem. Soc.* **1998**, *120*, 8245; d) J. M. Dysard, T. D. Tilley, *J. Am. Chem. Soc.* **2000**, *122*, 3097; e) J. M. Dysard, T. D. Tilley, *Organometallics* **2000**, *19*, 2671; f) J. M. Dysard, T. D. Tilley, *Organometallics* **2000**, *19*, 4720; g) W. P. Freeman, J. M. Dysard, T. D. Tilley, A. L. Rheingold, *Organometallics* **2002**, *21*, 1734; h) V. Ya. Lee, R. Kato, A. Sekiguchi, A. Krapp, G. Frenking, *J. Am. Chem. Soc.* **2007**, *129*, 10340. Heavy arene ligands: i) N. Nakata, N. Takeda, N. Tokitoh, *Angew. Chem. Int. Ed.* **2003**, *42*, 115; j) A. Shinohara, N. Takeda, T. Sasamori, T. Matsumoto, N. Tokitoh, *Organometallics* **2005**, *24*, 6141; k) Y. Mizuhata, T. Sasamori, N. Takeda, N. Tokitoh, *J. Am. Chem. Soc.* **2006**, *128*, 1050; l) N. Tokitoh, N. Nakata, A. Shinohara, N. Takeda, T. Sasamori, *Chem. Eur. J.* **2007**, *13*, 1856. Heavy cyclobutadiene ligands: m) Y. Kon, K. Sakamoto, C. Kabuto, M. Kira, *Organometallics* **2005**, *24*, 1407; n) K. Takanashi, V. Ya. Lee, T. Matsuno, M. Ichinohe, A. Sekiguchi, *J. Am. Chem. Soc.* **2005**, *127*, 5768; o) K. Takanashi, V. Ya. Lee, M. Ichinohe, A. Sekiguchi, *Angew. Chem. Int. Ed.* **2006**, *45*, 3269 [a parent complex ($\eta^4$-H$_4$C$_4$)Fe(CO)$_3$ was synthesized by Pettit et al.: G. F. Emerson, L. Watts, R. Pettit, *J. Am. Chem. Soc.* **1965**, *87*, 131]. Recent review on the application of heavy cyclic polyenes as novel ligands for transition metal complexes: p) V. Ya. Lee, A. Sekiguchi, *Angew. Chem. Int. Ed.* **2007**, *46*, 6596.

[5] V. Ya. Lee, K. Takanashi, T. Matsuno, M. Ichinohe, A. Sekiguchi, *J. Am. Chem. Soc.* **2004**, *126*, 4758.

[6] The $^{29}$Si NMR chemical shifts of the doubly bonded Si atoms incorporated in the four-membered ring were reported to be in the range $\delta$ = 141.4–182.7 ppm: a) M. Kira, T. Iwamoto, C. Kabuto, *J. Am. Chem. Soc.* **1996**, *118*, 10303; b) N. Wiberg, H. Auer, H. Nöth, J. Knizek, K. Polborn, *Angew. Chem. Int. Ed.* **1998**, *37*, 2869; c) A. Sekiguchi, T. Matsuno, M. Ichinohe, *J. Am. Chem. Soc.* **2001**, *123*, 12436; d) see ref.[4o]; e) see ref.[5]

[7] All computations were performed with the GAUSSIAN 03W program package (revision D.01) at the B3PW91/6-31G(d) level for all atoms: M. J. Frisch, G. W. Trucks, H. B. Schlegel, G. E. Scuseria, M. A. Robb, J. R. Cheeseman, J. A. Montgomery, Jr., T. Vreven, K. N. Kudin, J. C. Burant, J. M. Millam, S. S. Iyengar, J. Tomasi, V. Barone, B. Mennucci, M. Cossi, G. Scalmani, N. Rega, G. A. Petersson, H. Nakatsuji, M. Hada, M. Ehara, K. Toyota, R. Fukuda, J. Hasegawa, M. Ishida, T. Nakajima, Y. Honda, O. Kitao, H. Nakai, M. Klene, X. Li, J. E. Knox, H. P. Hratchian, J. B. Cross, V. Bakken, C. Adamo, J. Jaramillo, R. Gomperts, R. E. Stratmann, O. Yazyev, A. J. Austin, R. Cammi, C. Pomelli, J. W. Ochterski, P. Y. Ayala, K. Morokuma, G. A. Voth, P. Salvador, J. J. Dannenberg, V. G. Zakrzewski, S. Dapprich, A. D. Daniels, M. C. Strain, O. Farkas, D. K. Malick, A. D. Rabuck, K. Raghavachari, J. B. Foresman, J. V. Ortiz, Q. Cui, A. G. Baboul, S. Clifford, J. Cioslowski, B. B. Stefanov, G. Liu, A. Liashenko, P. Piskorz, I. Komaromi, R. L. Martin, D. J. Fox, T. Keith, M. A. Al-Laham, C. Y. Peng, A. Nanayakkara, M. Challacombe, P. M. W. Gill, B. Johnson, W. Chen, M. W. Wong, C. Gonzalez, J. A. Pople, *Gaussian 03W*, revision D.01, Gaussian, Inc., Wallingford, CT, **2004**.

[8] The synthesis of the dipotassium salt of the trisilagermacyclobutadiene dianion K$^+_2$·[R$_4$Si$_3$Ge]$^{2-}$ (R = SiMe*t*Bu$_2$) will be reported elsewhere.

[9] M. Kaftory, M. Kapon, M. Botoshansky, in *The Chemistry of Organic Silicon Compounds* (Eds.: Z. Rappoport, Y. Apeloig), Wiley, Chichester, **1998**, vol. 2, part 1, chapter 5.

[10] R. B. King, *Inorg. Chem.* **1966**, *5*, 82.

[11] A. Altomare, G. Cascarano, C. Giacovazzo, A. Guagliardi, M. C. Burla, G. Polidori, M. Camalli, *J. Appl. Crystallogr.* **1994**, *27*, 435.

[12] G. M. Sheldrick, *SHELXL-97, Program for Crystal Structure Refinement*, University of Göttingen, Germany, **1997**.

Received: September 26, 2007
Published Online: November 8, 2007

 © 2007 Wiley-VCH Verlag GmbH & Co. KGaA, Weinheim 

DOI: 10.1002/ejic.200700728

# New Polymorphs of Magnesium-Based Metal–Organic Frameworks $Mg_3(ndc)_3$ (ndc = 2,6-Naphthalenedicarboxylate)

**Irena Senkovska,[a] Julia Fritsch,[a] and Stefan Kaskel*[a]**

**Keywords:** Metal–organic frameworks / Magnesium / 2,6-Naphthalenedicarboxylic acid / Solvent effects / Gas adsorption

Two new magnesium 2,6-naphthalenedicarboxylate (ndc) metal–organic frameworks, $[Mg_3(ndc)_3(dif)_4]$ (**1**) (dif = *N*,*N*-diisopropylformamide) and $[Mg_3(ndc)_3(dmf)_2(CH_3OH)(H_2O)](dmf)$ (**2** = TUDMOF-3) (dmf = *N*,*N*-dimethylformamide), have been synthesised under solvothermal conditions from $Mg(NO_3)_2{\cdot}6H_2O$ and pure 2,6-naphthalenedicarboxylic acid. According to single-crystal X-ray crystallographic studies, complex **1** crystallises in the space group $P2_1/n$ [$a$ = 14.769(3) Å, $b$ = 13.325(3) Å, $c$ = 17.998(4) Å, $\beta$ = 108.67(2)°] and complex **2** in the space group $P\bar{1}$ [$a$ = 11.1116(11) Å, $b$ = 12.6229(13) Å, $c$ = 17.800(2) Å, $\alpha$ = 88.568(14)°, $\beta$ = 83.833(13)°, $\gamma$ = 70.167(11)°]. The structures of compounds **1** and **2** consist of trinuclear magnesium clusters connected to six dicarboxylate ligands; for **2**, the clusters act as distorted octahedral nodes to give a 3D network. In contrast, the trinuclear clusters in **1** act as pseudo-planar-hexagonal nodes to give a 2D network assembly. According to nitrogen and hydrogen physisorption measurements at 77 K for compounds **1** and **2**, TUDMOF-3 has a permanent porosity with a Langmuir surface area of 632 $m^2 g^{-1}$, a specific pore volume of 0.21 $cm^3 g^{-1}$ and a hydrogen storage capacity of 1.23 wt.-% at 77 K and 1 bar, whereas compound **1** is not porous.

(© Wiley-VCH Verlag GmbH & Co. KGaA, 69451 Weinheim, Germany, 2007)

## Introduction

Metal–organic frameworks (MOFs) are compounds in which organic multifunctional molecules act as linkers to interconnect metal ion or multinuclear complex (cluster) nodes into a 3D network of predefined topology.[1–6] MOFs are a relatively new class of microporous materials that show promise for diverse applications because of their high porosity, tunable pore size and functionality.[7–10]

2,6-Naphthalenedicarboxylate (ndc) is an adequate molecular linker for the construction of coordination polymers because of its rigidity and stability. Recently, several interesting examples of MOF structures containing ndc were discovered: $[Al(OH)(ndc)(H_2O)]$ (MIL-69),[11] $[M(ndc)(H_2O)]$ (M = Mn, Zn or Cd),[12,13] $[Yb_2(ndc)_3(H_2O)_3]$,[14] $[M_2(OH)_2(ndc)]$ (M = Zn or Co),[15,16] $[M_2(ndc)_3(dmf)_4](H_2O)_m$ (M = Eu, Tb or Ce),[17] $[M(ndc)(H_2O)_m]$ (M = Ni or Co),[13,16] $Zn_6(ndc)_5(OH)_2(dmf)_6$ (MOF-48)[18] and $Zn_4O(ndc)_3$ (IRMOF-8).[10] The MOFs based on light metals such as Li, Mg and Al have recently received more attention. Constructing light-metal-based MOFs should allow the formation of lightweight materials that can be useful in gas storage applications.[19]

In a previous paper, we have reported a Mg-ndc-based MOF, $[Mg_3(ndc)_3(dmf)_4]$ (TUDMOF-2), and have shown that the pore size of the $Mg_3(ndc)_3$ networks can be adjusted by using different solvents (dmf, def).[20] In fact, TUDMOF-2 has the same network topology as $[Mg_3(ndc)_3(def)_4]$,[21] but the smaller solvent molecules induce the widening of pores, which leads to a larger specific surface area (SSA). In order to verify this concept, we have studied other solvents with smaller and larger diameters (Scheme 1).

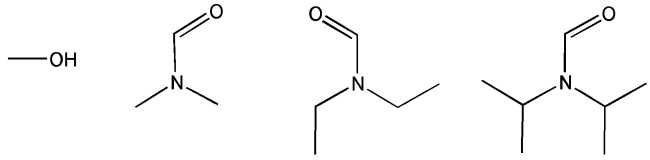


Scheme 1. The solvents used for pore size adjustment in $Mg_3(ndc)_3$.

In the following, we describe the structure of two new magnesium carboxylates, $[Mg_3(ndc)_3(dif)_4]$ (**1**) and $[Mg_3(ndc)_3(dmf)_2(CH_3OH)(H_2O)](dmf)$ (**2** = TUDMOF-3) (*Technical University Dresden Metal–Organic Framework No. 3*), which are also constructed from Mg clusters and 2,6-naphthalenedicarboxylate linkers.

## Results and Discussion

### Synthesis and Structural Characterisation of 1 and 2

The solvothermal reaction of $Mg(NO_3)_2{\cdot}6H_2O$ and $H_2ndc$ in dif at 383 K results in the formation of yellow

[a] Department of Inorganic Chemistry, Dresden University of Technology
Mommsenstr. 6, 01069 Dresden, Germany
Fax: +49-351-46337287
E-mail: Stefan.Kaskel@chemie.tu-dresden.de

 © 2007 Wiley-VCH Verlag GmbH & Co. KGaA, Weinheim 

crystals of **1**. For the same reaction carried out in dmf/$CH_3OH$ (1:1) solution, colourless crystals of **2** were obtained.

Complex **1** crystallises in the monoclinic space group $P2_1/n$ and contains two crystallographically independent magnesium atoms (Mg1 and Mg2). Mg1 and one of the two independent $ndc^{2-}$ anions are located at a general position. Mg2 and the middle of the central C–C bond in the naphthalene system in the second anion are positioned on crystallographic centres of inversion. The three magnesium atoms in **1** form a perfectly linear $[Mg_3(\mu_3\text{-}O)_2(\mu_2\text{-}O)_4]$ unit with $C_1$ symmetry (Figure 1a).

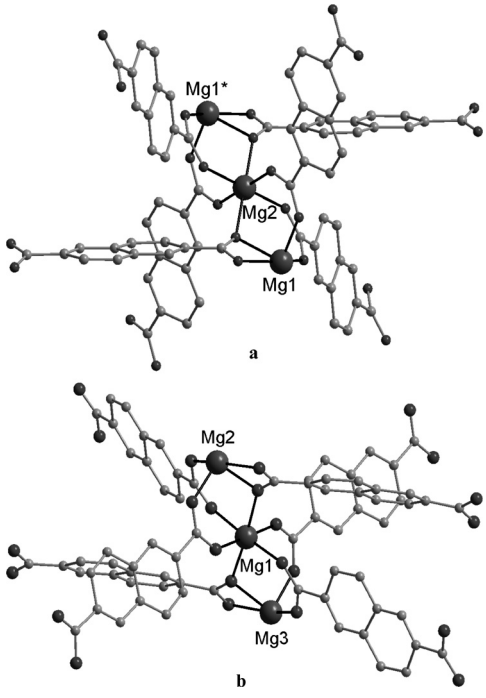


Figure 1. Trinuclear Mg carboxylate clusters and representation of the inorganic six-coordinate SBUs in **1** (a) and in **2** (b). Symmetry operation (*): $-x$, $-y$, $-z$.

The $[Mg_3(\mu_3\text{-}O)_2(\mu_2\text{-}O)_4]$ unit can be regarded as a secondary building unit (SBU). This trinuclear unit is a successful SBU, through which many interesting structures have been constructed in the past decade.[14,22–25] It should be noted that the trinuclear SBU is the most important Mg cluster, because the same structural motif was found in all Mg MOFs with a rigid 3D framework and permanent porosity reported so far.[20,21,25–29] Obviously, this SBU plays a key role in the formation of 3D networks in magnesium coordination polymers and a study of the multinuclear magnesium complexes assumes considerable importance.

The trinuclear magnesium clusters in **1** are connected by rigid organic linkers (ndc). The ndc ligands in compound **1** adopt two coordination modes that connect two Mg atoms: a bidentate bridging mode and an asymmetric chelating bridging mode. Consequently, a 2D layered MOF with triangular meshes and a $3^6$ topology is formed (Figure 2b). The Mg–O(carboxylate) distances for the terminal Mg1 atoms are in the range 1.997(3)–2.180(3) Å, whereas the Mg–O(carboxylate) distances for the central Mg2 atom are between 2.046(3) and 2.123(3) Å.

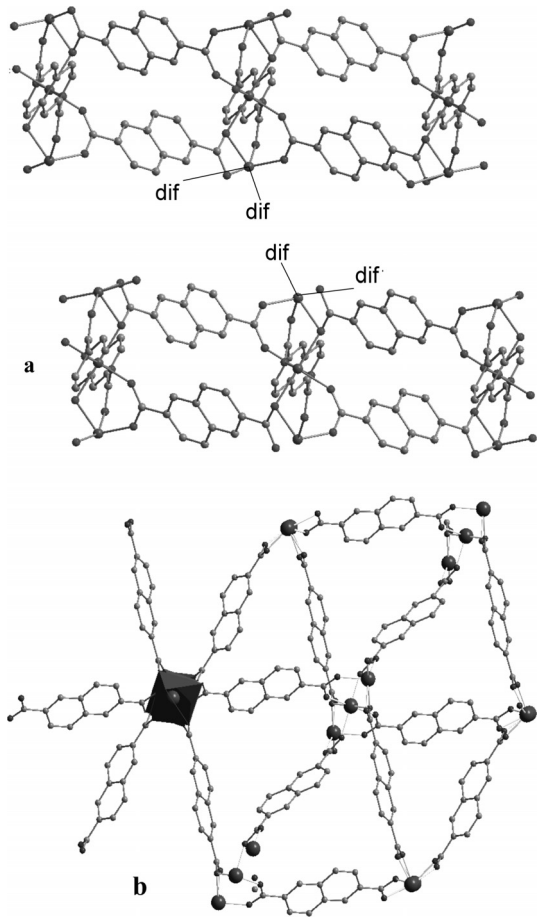


Figure 2. (a) The layer structure of **1** viewed along the crystallographic $b$ axis (the dif molecules are presented schematically); (b) the $3^6$ 2D layer network of **1** (coordinated dif molecules are not shown).

The thickness of the layer, given by the Mg–Mg distance between the terminal Mg atoms in the same SBU, is 7.15(1) Å, and the distance between two adjacent layers, given by the Mg–Mg distance between the terminal Mg atoms in neighbouring SBUs, is 9.48(1) Å (Figure 2a).

Two of the four dif molecules coordinated to a trinuclear cluster protrude into the triangular cavities, whereas the other two dif molecules fill the space between the layers, thereby separating two adjacent layers; therefore, the existence of the 2D network can be explained by the dif-induced steric hindrance that prevents the formation of coordinative bonds between adjacent SBUs and in this way prevents the formation of the 3D network too.

Single-crystal X-ray diffraction analysis reveals that compound **2** has essentially the same SBU (Figure 1b); the difference is that all three Mg atoms are located at a general position, and the SBU has no higher symmetry. Consequently, the cluster loses the perfect linearity and the Mg2–Mg1–Mg3 angle in this case is 176.75(1)°. The Mg2–O(carboxylate) distances range from 2.022(3) to 2.205(3) Å,

 © 2007 Wiley-VCH Verlag GmbH & Co. KGaA, Weinheim 

the Mg3–O(carboxylate) distances are between 1.967(3) and 2.188(3) Å, and the central Mg1–O(carboxylate) distances are between 2.038(4) and 2.118(4) Å.

The eight six-coordinate SBUs in **2** are interlinked through the $ndc^{2-}$ anions to form a highly distorted cubic network (Figure 3). One methanol and one dmf molecule are bound to Mg3 and one water and one dmf molecule are bound to Mg2 to give six-coordinate magnesium atoms. The solvent molecules in **2** can be removed to give a porous network having open magnesium sites. A summary of crystal data and structure refinement is provided in Table 2.

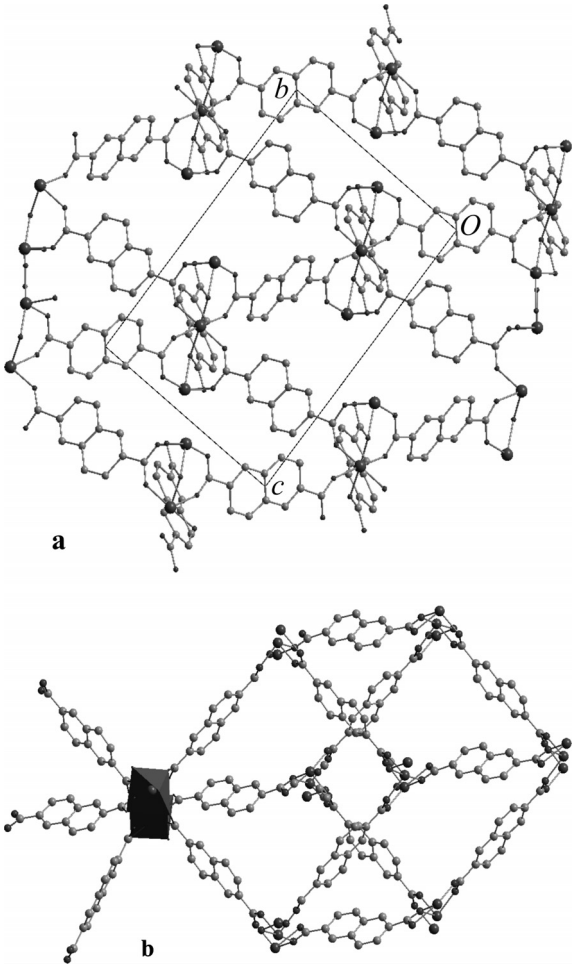


Figure 3. Extended structure of **2**: (a) viewed along the crystallographic *a* axis; (b) the 3D distorted cubic network cell of **2** (solvent molecules are omitted in both cases).

## Thermogravimetric Analysis

The thermogravimetric analysis (TGA) of **1** shows continuous weight loss in the temperature range from 330 to 790 K. The weight loss of 42.1% observed from 330 to 680 K can be attributed to the loss of four coordinated dif molecules (expected weight loss: 41.94%). The linker starts to decompose at 680 K.

A weight loss for **2** occurs between 398 and 693 K corresponding to the loss of dmf, $CH_3OH$ and $H_2O$ solvent molecules (observed: 28.0%, calculated: 27.35%), followed by the decomposition of the ligand in the temperature range 758–918 K. The weight loss is consistent with the elemental analysis and the empirical formula deduced from the single-crystal X-ray crystallographic analysis.

## Evacuated Frameworks and Sorption Properties

All materials were evacuated under vacuum and heated to 423 K. The desolvated $Mg_3(ndc)_3$ framework of $[Mg_3(ndc)_3(dmf)_2(CH_3OH)(H_2O)](dmf)$ is hereafter denoted as **2a**. The powder XRD pattern of **2** changes after removal of the guest molecules relative to that of the as-synthesised product (Figure 4a). A similar behaviour of the framework was observed for TUDMOF-2. But in the case of TUDMOF-3 the original framework of **2** could not be regenerated through a treatment of **2a** with dmf or a dmf/$CH_3OH$ mixture. According to XRD analysis (Figure 4b), a new unknown structure can by identified as a result of the resolvation. This compound has no porosity.

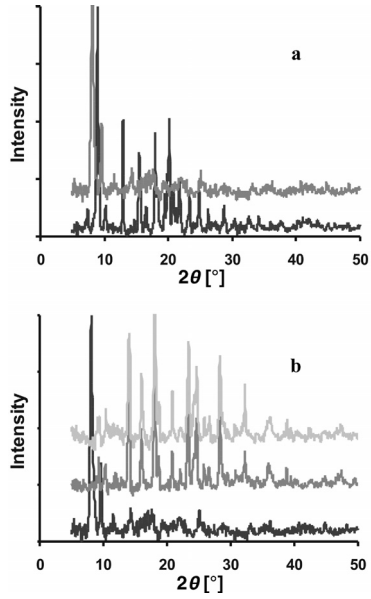


Figure 4. X-ray powder diffraction patterns (a) for **2** as synthesised (black) and **2** desolvated (grey); (b) for **2** desolvated (black), **2** resolvated with dmf (dark grey) and **2** resolvated with dmf/$CH_3OH$ (1:1) (light grey).

Gas-sorption properties of **1** and **2** were examined by measuring $N_2$ and $H_2$ adsorption isotherms at 77 K. Significant differences between **1** and **2** were observed in the gas-adsorption properties. The $N_2$ isotherms for **2** display typical type-I adsorption characteristics (Figure 5a).

 © 2007 Wiley-VCH Verlag GmbH & Co. KGaA, Weinheim 

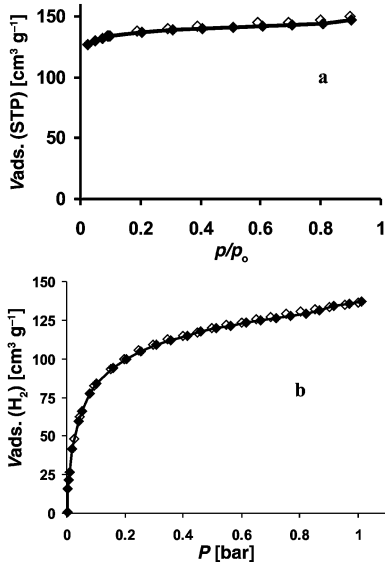


Figure 5. (a) The $N_2$ adsorption (solid symbols) and desorption (empty symbols) isotherms of **2** at 77 K; (b) $H_2$ adsorption (solid symbols) and desorption (empty symbols) isotherms of **2** at 77 K.

The Brunauer–Emmett–Teller (BET) surface areas of the solvent-free frameworks of **2** were estimated to be 418 $m^2 g^{-1}$ at 0.3 $p/p_0$. The sorption isotherm was also fitted to a Langmuir equation; the resulting specific surface area is 623 $m^2 g^{-1}$. The micropore volume obtained from nitrogen adsorption at 77 K and 0.2 $p/p_0$ is 0.21 $cm^3 g^{-1}$. The hydrogen adsorption isotherm for **2** measured at 77 K is given in Figure 5b. The maximum $H_2$ uptake of **2** is 1.23 wt.-% at 1 bar. Compound **1** is essentially nonporous; it has only a low $N_2$ adsorption capacity and a type-II adsorption isotherm.

### The Role of Solvent

It was shown that the use of def, dmf or dmf/$CH_3OH$ mixtures as solvents in the solvothermal reaction of $Mg(NO_3)_2 \cdot 6H_2O$ and $H_2$ndc leads to the formation of three different porous compounds, $Mg_3(ndc)_3(def)_4$, $Mg_3(ndc)_3(dmf)_4$ (TUDMOF-2) or $[Mg_3(ndc)_3(dmf)_2(CH_3OH)(H_2O)](dmf)$ (TUDMOF-3), respectively. The networks formed have identical topology, but the minor structural differences (lattice constants) influence the sorption properties of the materials. Several reactions were carried out to elucidate the influence of the solvent mixture composition on the formation of the different compounds. $Mg(NO_3)_2$ and $H_2$ndc were treated at 110 °C for 24 h with varying proportions of def (or dmf) and $CH_3OH$ (or $C_2H_5OH$) (Table 1). The products were identified by powder X-ray diffraction analysis.

In the case of solvent mixtures containing def and dmf, the resulting product is a compound incorporating only one type of solvent. In the case of mixed-solvent solutions containing dmf and methanol, TUDMOF-3 was obtained as the main product. If dmf or def is mixed with ethanol (1:1), then the compound containing only formamide is obtained.

Table 1. The role of solvent in defining the product from the solvothermal reaction of $Mg(NO_3)_2$ and $H_2$ndc at 383 K.

| Solvent | Solvent ratio [%] | Product |
|---|---|---|
| def | 100 | $Mg_3(ndc)_3(def)_4$ |
| dmf | 100 | $Mg_3(ndc)_3(dmf)_4$ |
| dmf + $C_2H_5OH$ | 50:50 | $Mg_3(ndc)_3(dmf)_4$ |
| def + $C_2H_5OH$ | 50:50 | $Mg_3(ndc)_3(def)_4$ |
| dmf + $CH_3OH$ | 50:50 | $[Mg_3(ndc)_3(dmf)_2(CH_3OH)(H_2O)](dmf)$ |
| dmf + def | 25:75 | $Mg_3(ndc)_3(def)_4$ |
| dmf + def | 50:50 | $Mg_3(ndc)_3(dmf)_4$ |
| dmf + def | 75:25 | $Mg_3(ndc)_3(dmf)_4$ |

Furthermore, the hydrothermal treatment of TUDMOF-2 or $Mg_3(ndc)_3(def)_4$ in def or dmf, respectively, did not convert one into the other; thus, a given network retains its structure irrespective of the postsynthetic solvothermal treatment.

## Conclusion

In summary, TUDMOF-3 has the same network topology as TUDMOF-2, but the occlusion of smaller solvent molecules induces significant structural changes resulting in a different space group and higher specific surface area. On the other hand, the larger solvent molecule in **1**, dif, hinders the formation of a 3D network, resulting in a 2D double-layered structure. The solvent plays a key role in the construction of the networks and predetermines the formation of a certain product. The selection of the solvent or solvent mixture demonstrates the potential for pore size adjustment in metal–organic frameworks.

## Experimental Section

**General Remarks:** All reagents and solvents (reagent-grade) were used as received. Elemental analyses (C, H, N) were performed by the Elemental Analysis Service, Institute of Organic Chemistry, Dresden University of Technology. Powder X-ray diffraction (PXRD) data were collected by using a Stoe STADI P powder diffractometer with Cu-$K_{\alpha 1}$ radiation. Thermogravimetric analyses (TGA) were carried out by using a Netzsch STA 409 thermal analyser with heating in air at 10 K $min^{-1}$ to 1273 K. Physisorption isotherms were measured at 77 K with a Quantachrome Autosorb1C apparatus. High-purity gases were used (nitrogen: 99.999%, hydrogen: 99.999%). Prior to the measurement, the samples were evacuated for 16 h at 423 K. The specific surface areas and porosity parameters were derived from the $N_2$ adsorption data.

**X-ray Crystallography:** Single-crystal X-ray diffraction data for complexes **1** and **2** were recorded with a STOE IPDS I image plate diffractometer by using Mo-$K_\alpha$ radiation. The structures were solved by direct methods with the help of SHELXS-86[30] and refined by full-matrix least-squares techniques with SHELXL-97.[31] Non-hydrogen atoms were refined with anisotropic temperature parameters. The hydrogen atoms of the $CH_3$ groups and aromatic

 © 2007 Wiley-VCH Verlag GmbH & Co. KGaA, Weinheim 

hydrogen atoms were positioned geometrically and refined by using a riding model; the remaining hydrogen atoms were located from the difference Fourier maps. Further details of the structural analysis are summarised in Table 2. CCDC-650990 (for **1**) and -650991 (for **2**) contain the supplementary crystallographic data for this paper. These data can be obtained free of charge from the Cambridge Crystallographic Data Centre via www.ccdc.cam.ac.uk/data_request/cif.

Table 2. Crystallographic data for compounds **1** and **2**.

| Compound | **1** | **2** |
|---|---|---|
| Chemical formula | $C_{64}H_{78}Mg_3N_4O_{16}$ | $C_{46}H_{45}Mg_3N_3O_{17}$ |
| Mol. mass | 1232.23 | 984.78 |
| Space group | $P2_1/n$ | $P\bar{1}$ |
| $a$ [Å] | 14.769(3) | 11.1116(11) |
| $b$ [Å] | 13.325(3) | 12.6229(13) |
| $c$ [Å] | 17.998(4) | 17.800(2) |
| $\alpha$ [°] | 90 | 88.568(14) |
| $\beta$ [°] | 108.67(2) | 83.833(13) |
| $\gamma$ [°] | 90 | 70.167(11) |
| $V$ [Å$^3$] | 3355.3(12) | 2334.8(4) |
| $Z$ | 2 | 2 |
| Reflns. collected/independent | 14802/4255 | 12566/5605 |
| Reflns. observed [$I > 2\sigma(I)$] | 2308 | 3026 |
| GoF on $F^2$ | 1.005 | 0.944 |
| $R$, $wR$ [$I > 2\sigma(I)$] | 0.0659, 0.1115 | 0.0535, 0.1207 |
| Max., min. peaks [e Å$^{-3}$] | 0.221, –0.221 | 0.076, –0.066 |

### Preparation and Characterisation

**$[Mg_3(ndc)_3(dif)_4]$ (1):** 2,6-Naphthalenedicarboxylic acid (0.16 g, 0.75 mmol) was dissolved in dif (10 mL). $Mg(NO_3)_2{\cdot}6H_2O$ (0.26 g, 1.0 mmol) was added to this solution. The mixture was filled into a 40-mL Teflon liner and was heated in an autoclave at 383 K for 20 h. It was then cooled to room temperature at a rate of 0.05 K min$^{-1}$ to produce large crystals of **1**, which were suited for X-ray analysis. Yield: 0.10 g (32.5%). $Mg_3C_{64}H_{78}N_4O_{16}$ (1232.23): calcd. C 62.38, H 6.38, N 4.55; found C 62.10, H 6.37, N 4.52.

**$[Mg_3(ndc)_3(dmf)_2(CH_3OH)(H_2O)](dmf)$ (2):** A mixture of $Mg(NO_3)_2{\cdot}6H_2O$ (0.52 g, 2.0 mmol) and 2,6-naphthalenedicarboxylic acid (0.32 g, 1.4 mmol) in dmf (20 mL) and $CH_3OH$ (20 mL) was filled into a 250-mL Teflon liner. The mixture was heated in an autoclave at 383 K for 24 h, then cooled to room temperature at a rate of 0.05 K min$^{-1}$. The resulting colourless crystals were collected, washed with methanol and dried under argon to give **2**. Yield: 0.36 g (73.5%). $Mg_3C_{46}H_{45}N_3O_{17}$ (984.78): calcd. C 56.10, H 4.61, N 4.27; found C 55.46, H 4.62, N 4.22.

## Acknowledgments

This work was supported by the German Ministry of Science and Education (BMBF: FK 03X0011B).

[1] S. Kaskel, *Handbook of Porous Solids* **2002**, *2*, 1190–1249.
[2] J. L. C. Rowsell, O. M. Yaghi, *Microporous Mesoporous Mater.* **2004**, *73*, 3–14.
[3] M. Eddaoudi, D. B. Moler, H. Li, B. Chen, T. M. Reineke, M. O'Keeffe, O. M. Yaghi, *Acc. Chem. Res.* **2001**, *34*, 319–330.
[4] O. M. Yaghi, M. O'Keeffe, N. W. Ockwig, H. K. Chae, M. Eddaoudi, J. Kim, *Nature* **2003**, *423*, 705–714.
[5] A. K. Cheetham, C. N. R. Rao, R. K. Feller, *Chem. Commun.* **2006**, 4780–4795.
[6] O. M. Yaghi, *Nat. Mater.* **2007**, *6*, 92–93.
[7] U. Mueller, M. Schubert, F. Teich, H. Puetter, K. Schierle-Arndt, J. Pastre, *J. Mater. Chem.* **2006**, *16*, 626–636.
[8] S. Kitagawa, R. Kitaura, S.-I. Noro, *Angew. Chem. Int. Ed.* **2004**, *43*, 2334–2375.
[9] C. Janiak, *Dalton Trans.* **2003**, 2781–2804.
[10] M. Eddaoudi, J. Kim, N. Rosi, D. Vodak, J. Wachter, M. O'Keeffe, O. M. Yaghi, *Science* **2002**, *295*, 469–472.
[11] T. Loiseau, C. Mellot-Draznieks, H. Muguerra, G. Ferey, M. Haouas, F. Taulelle, *C. R. Chim.* **2005**, *8*, 765–772.
[12] K. O. Kongshaug, H. Fjellvag, *Solid State Sci.* **2002**, *4*, 443–447.
[13] F. A. A. Paz, J. Klinowski, *J. Solid State Chem.* **2004**, *177*, 3423–3432.
[14] F. A. A. Paz, J. Klinowski, *Chem. Commun.* **2003**, 1484–1485.
[15] K. O. Kongshaug, H. Fjellvag, *J. Solid State Chem.* **2004**, *177*, 1852–1857.
[16] M. Kurmoo, H. Kumagai, *Mol. Cryst. Liq. Cryst. Sci. Technol., Sect. A* **2002**, *376*, 555–565.
[17] Z. Wang, C.-M. Jin, T. Shao, Y.-Z. Li, K.-L. Zhang, H.-T. Zhang, X.-Z. You, *Inorg. Chem. Commun.* **2002**, *5*, 642–648.
[18] D. T. Vodak, M. E. Braun, J. Kim, M. Eddaoudi, O. M. Yaghi, *Chem. Commun.* **2001**, 2534–2535.
[19] J. L. C. Rowsell, O. M. Yaghi, *Angew. Chem. Int. Ed.* **2005**, *44*, 4670–4679.
[20] I. Senkovska, S. Kaskel, *Eur. J. Inorg. Chem.* **2006**, 4564–4569.
[21] M. Dinca, J. R. Long, *J. Am. Chem. Soc.* **2005**, *127*, 9376–9377.
[22] K. O. Kongshaug, H. Fjellvag, *Solid State Sci.* **2003**, *5*, 303–310.
[23] Y. Wang, B. Bredenkotter, B. Rieger, D. Volkmer, *Dalton Trans.* **2007**, 689–696.
[24] S. M. Hawxwell, H. Adams, L. Brammer, *Acta Crystallogr., Sect. B* **2006**, *62*, 808–814.
[25] M. Eddaoudi, H. Li, O. M. Yaghi, *J. Am. Chem. Soc.* **2000**, *122*, 1391–1397.
[26] J. A. Rood, B. C. Noll, K. W. Henderson, *Main Group Chem.* **2006**, *5*, 21–30.
[27] S. Ma, J. A. Fillinger, M. W. Ambrogio, J.-L. Zuo, H.-C. Zhou, *Inorg. Chem. Commun.* **2007**, *10*, 220–222.
[28] V. Chandrasekhar, R. Azhakar, J. F. Bickley, A. Steiner, *Chem. Commun.* **2005**, 459–461.
[29] J. A. Rood, B. C. Noll, K. W. Henderson, *Inorg. Chem.* **2006**, *45*, 5521–5528.
[30] *SHELXS-86: Program for Crystal Structure Determination*, v. **1986**.
[31] *SHELXL-97: Program for Crystal Structure Refinement*, v. **1993/1997**.

Received: July 10, 2007
Published Online: October 25, 2007

 © 2007 Wiley-VCH Verlag GmbH & Co. KGaA, Weinheim 

DOI: 10.1002/ejic.200700775

# Direct Synthesis of Zr-Containing Hybrid Periodic Mesoporous Organosilicas with Tunable Zirconium Content

**Shang-Ru Zhai,[a] Sung Soo Park,[a] Mina Park,[a] M. Habib Ullah,[a] and Chang-Sik Ha*[a]**

**Keywords:** Silicates / Template synthesis / Orangic–inorganic hybrid composites / Mesoporous materials

Highly ordered Zr-containing periodic mesoporous organosilicas (ZrPMO) with different Zr/Si ratios were successfully synthesized, for the first time, by employing a $ZrOCl_2$/NaCl combination as the promoting agent and by simply adjusting the molar ratio of the zirconium species to the organosilica precursor; no addition of mineral acids was necessary. The effect of preparation parameters on the structural and textural properties were carefully investigated by using different ratios of NaCl/Si and Zr/Si. It was found that both salts are essential for this system and highly ordered ZrPMOs can be prepared within fairly wide Si/Zr ratios (5–100) while keeping the NaCl/Si ratio constant. To prove the effectiveness of this synthetic pathway with a higher Zr incorporation, ZrPMO materials were also synthesized under strongly acidic conditions for the purpose of comparison. The synthesized ZrPMO materials were thoroughly characterized by ICP-AES, SAXS, $N_2$ sorption, TEM, SEM, $^{13}C$ CP/$^{29}Si$ MAS NMR spectroscopy, XPS, and TGA. Elemental analyses show that the amount of Zr incorporated into ZrPMO, which was synthesized under mild conditions, is greater than that obtained in a strongly acidic environment, and the Zr content, with a Si/Zr ratio up to 12, is close to that in the initial gel composition. A plausible assembly mechanism based on the synergistic effect of both "nonhydrolyzable" (NaCl) and "hydrolyzable" ($ZrOCl_2$) inorganic salts was discussed in detail, where the "salting out" effect and self-generated acidity from both inorganic salts, respectively, are believed to be key factors for the formation of ordered SBA-15-type ZrPMO materials under the synthetic conditions.

(© Wiley-VCH Verlag GmbH & Co. KGaA, 69451 Weinheim, Germany, 2007)

## Introduction

Since its first synthesis in 1999,[1–3] periodic mesoporous organosilica (PMO) materials have attracted increasing research attention in the field of ordered mesoporous materials. These novel hybrid materials, characterized with the high organic content incorporated within the framework, were synthesized by the hydrolysis and condensation of bis(trialkoxysilyl)alkylsilanes such as $(R'O)_3Si\text{-}R\text{–}Si(R'O)_3$ with the aid of structure-directing agents.[1–4] The fascinating properties featured by these materials include highly ordered structures and uniform pore-size distributions within a framework formed by a homogeneous distribution of organic fragments and inorganic oxide. In comparison with their inorganic counterparts, these hybrid mesostructures offer unique advantages and enormous possibilities that are closely associated with the characteristics of the organic polymers, such as tunable interfacial and physicochemical properties, by simply varying the organic bridging groups embedded within the mesoporous framework. With the aforementioned advantages, PMO materials are promising candidates in the fields of catalysis, selective adsorption, chromatography, low-*k* devices, or host–guest chemistry.

At present, PMO materials with various framework bridging groups ranging from small aliphatic spacers to aromatic and large heterocyclic ones were successfully synthesized.[5–15] Recently, the synthesis of bi- and multifunctional PMOs has become a hot research topic in this field, because proper selection of these groups allows one to design functional nanocomposites for specific catalytic and environmental applications.[16–21] The synthesis of these materials has been carried out by using cationic, anionic, and nonionic oligomeric and copolymeric surfactants under basic or acidic conditions.

Although the development of PMOs has opened new opportunities in the field of mesoporous materials, there is still a lack of application of these materials to the field of catalysis. Thus, unlike in the case of inorganic mesostructured materials upon which many different heteroatoms have been supported in the hope to discover catalytic properties, only a few examples have been reported on the functionalization of PMOs with the use of heterometallic atoms. Most of them use the organic functionality as a ligand to bind the

[a] National Research Laboratory of Nano-Information Materials, Department of Polymer Science and Engineering, Pusan National University,
Pusan 609-735, Korea
Fax: +82-51-514-4331
E-mail: csha@pusan.ac.kr

Supporting information for this article is available on the WWW under http://www.eurjic.org or from the author.

 WILEY InterScience DISCOVER SOMETHING GREAT © 2007 Wiley-VCH Verlag GmbH & Co. KGaA, Weinheim 

metallic atoms,[22,23] but these procedures are only appropriate for a small amount of metal atom–organic functionality pairs. The second strategy used for synthesizing these metal-functionalized PMOs involves direct synthetic procedures through the isomorphic substitution of the silicon atoms by the metal species of interest. In most cases, however, this procedure has only successfully been applied to the heterogenization of limited metal species in the synthesis of hexagonally packed PMO materials by using cationic surfactants.[24–32] For instance, aluminum was incorporated within the mesoporous framework of ethanesilicas by a direct synthetic method with the use of cationic surfactants under basic conditions.[24–26] The resultant hybrid mesostructures showed a high hydrothermal stability that can be attributed to the presence of hydrophobic ethane bridging groups distributed within the whole framework. Furthermore, this highly hydrophobic character improved the catalytic behavior in alkylation reactions in comparison with that shown by AlMCM-41 materials.[24] Likewise, titanium, chromium, vanadium, and other species have also been incorporated into the structure of ethane-bridged PMO materials, and these obtained materials showed a good degree of incorporation of the metal functionality.[27–33] In these works, it was reported that Ti-containing PMO materials are highly hydrophobic and fairly efficient in the epoxidation of α-pinene,[27] epoxidation of propene into propene oxide in the vapor phase,[28] and ammoxidation of ketones to oximes.[29] Apparently, the enhanced catalytic efficiency was directly associated with the framework hydrophobicity of these hybrid catalysts. Among these limited reports,[24–33] however, only one paper was devoted to the synthesis of SBA-15-type PMO from titanocene dichloride by using copolymeric surfactant under acidic conditions, and these hybrid catalysts showed good performance in the epoxidation of 1-octene with hydroperoxides.[33] Currently, there is a quest for large-pore hybrid PMO materials from the point of view of immobilization or transformation of bulky molecules; therefore, these results have prompted us to take a step forward in the synthesis of metal-functionalized PMO materials with large pore diameters.

In the present study, we report an effective and convenient synthetic pathway to zirconium-functionalized periodic mesoporous organosilicas (PMOs) by employing a $ZrOCl_2$/NaCl combination as the promoting agent under acid-free conditions. This is, to the best of our knowledge, the first example of SBA-15-type ZrPMO with tunable Zr content synthesized by simply adjusting the molar ratio of Zr/Si while retaining another NaCl/Si ratio constant. The resultant materials were characterized and have excellent structural ordering, narrow pore-size distributions, and hybrid organic–inorganic frameworks; meanwhile, these characterization results indicate that both inorganic salts are essential to the formation of ordered ZrPMO materials. More desirably, this novel synthetic system is more advantageous in comparison to the HCl-assisted synthetic pathway either from the point of view of zirconium incorporation or the structural properties of the obtained ZrPMO materials.

## Results and Discussion

### Effect of Both NaCl/Si and Zr/Si Molar Ratios

As reported, since its first synthesis in 1998,[34] SBA-15-type materials have been extensively studied.[35] However, it is difficult to synthesize Zr-incorporated SBA-15 silicas with a high amount of Zr loading, because the Zr–O–Si bonds are easily dissociated; this is due to the hydrolysis of zirconium precursors under the strongly acidic hydrothermal preparation conditions. However, by decreasing the acidity of the synthetic system to balance the hydrolysis rate of Zr precursors with that of the silicon precursors, the interaction between the Zr–OH and Si–OH species in the synthesis gels could be effectively enhanced, which would result in a higher amount of Zr ion incorporated in the framework of SBA-15-type materials. Therefore, by following our previous studies,[7,36] this paper reports an effective direct synthesis of a higher amount of Zr incorporated in the SBA-15-like PMO materials by employing a $ZrOCl_2$/NaCl combination as the promoting agent under acid-free conditions, and the Zr content loaded in the PMO materials is tunable by simply adjusting the Si/Zr molar ratios from 5 to 100 in the synthesis gels while keeping the NaCl/Si ratio constant.

To prove the importance of the salt combination during the synthesis, the effect of both NaCl/Si and Si/Zr ratios were thoroughly investigated. With Si/Zr = 10 for all samples, the variation of the SAXS patterns as a function of the NaCl/Si ratios is illustrated in Figure 1. Well-defined SAXS patterns are clearly observed for those samples synthesized with NaCl/Si ratios varied from 1–6, similar to those recorded for all SBA-15-type materials as described by Zhao et al.[34,35] The SAXS patterns of these samples exhibit at least three well-resolved peaks, which can be indexed to the (100), (110), and (200) reflections of the hexagonal space group *p6mm*. Among these samples, however, the optimal structural ordering of the hexagonal mesostructure was obtained for the sample synthesized with a NaCl content around NaCl/Si = 4, which is evidenced by the reflection intensity that decreased as the NaCl/Si ratios increased or decreased relative to this point. This observation is reminiscent of the previous results for large-pore PMOs, which proved that highly ordered mesostructures were successfully prepared in the presence of a large amount of Na(K)Cl salts.[7,37]

Therefore, the ratio of NaCl/Si was fixed at 4 in the following experiments that allowed the study of the effects of the Si/Zr molar ratios on the synthesis; Figure 2 shows the SAXS patterns of samples synthesized with different Si/Zr ratios varied from 5–100. With only one exception from that prepared without zirconium salt, all other patterns of the extracted PMOs exhibit very sharp reflections, which clearly indicates a high degree of structural ordering. Likewise, the reflections can be indexed as (100), (110), and (200) peaks according to the 2D hexagonal symmetry of the materials.[34] The results strongly reveal the effectiveness of this synthetic method irrespective of the fairly wide range of Zr/Si ratios, which is somewhat similar to the studies

 © 2007 Wiley-VCH Verlag GmbH & Co. KGaA, Weinheim 

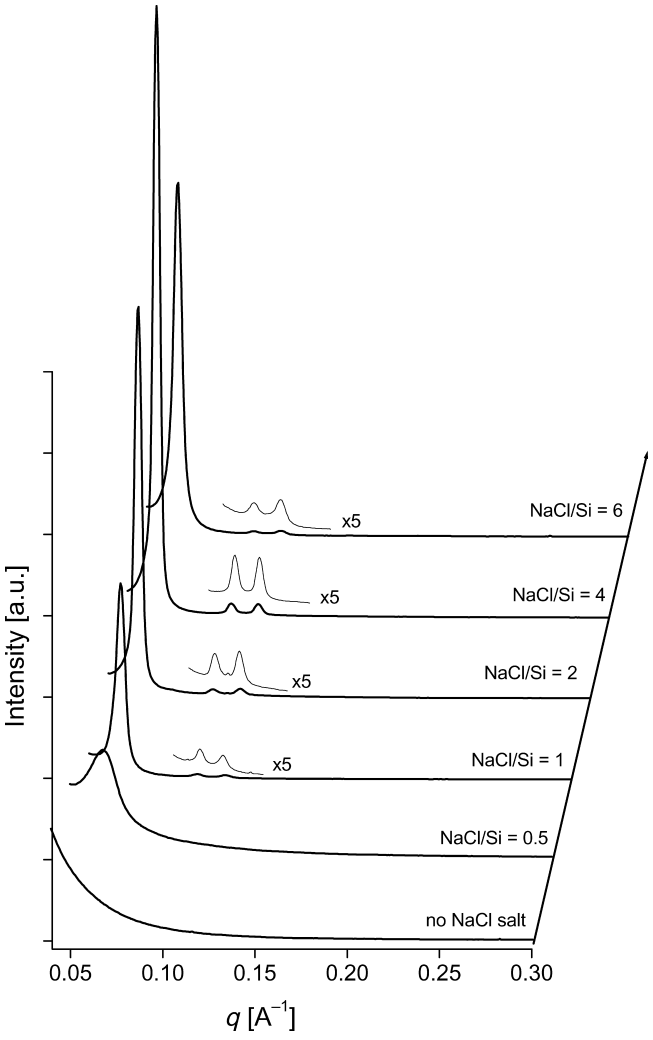


Figure 1. SAXS patterns of samples prepared at different NaCl/Si ratios while keeping Si/Zr = 10.

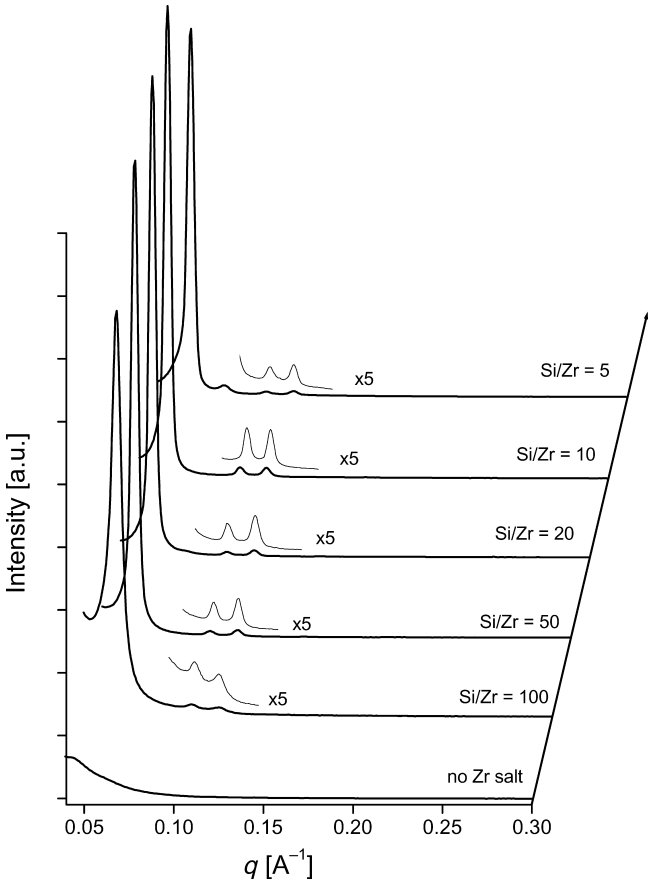


Figure 2. SAXS patterns of materials synthesized by using different Si/Zr molar ratios while fixing NaCl/Si = 4.

reported recently where highly ordered SBA-15-like PMO materials were facilely prepared within a wide composition range by employing a KCl-assisted low-acid-concentration synthetic pathway.[37] By combining the SAXS data (Figures 1 and 2), we can clearly see that the combination of $ZrOCl_2$/NaCl is indispensable for this synthesis, that is, highly ordered PMO materials are easily achievable with a variable zirconium salt amount while keeping the NaCl/Si ratio constant; this fascinating observation has never been reported for large-pore PMO materials templated by block copolymer surfactants.

To further prove the important effect of this salt combination on the structural ordering of the resultant materials, a series of samples were also synthesized by using various acid concentrations for comparison purpose, where the zirconium salt amount with Si/Zr = 10 is constant through all experiments. Figure 3 shows that the samples synthesized with 0.4 and 1.0 M HCl exhibit a single peak together with a broad shoulder and another one from 0.2 M HCl only possesses a very broad peak. Such reflection patterns are often observed for wormhole-like mesostructures, in agreement with our previous results that disordered PMOs were commonly obtained under strong acidic conditions without the assistance of NaCl.[7] In contrast, the fact that a highly ordered sample can be easily synthesized by using the $ZrOCl_2$/NaCl pair without the addition of any mineral acids further indicates that this salt combination is very effective for the assembly of ordered organosilica–surfactant nanocomposites, even though the amount of zirconium salt added in the reaction gels is quite small; a plausible formation mechanism will be discussed below.

The zirconium contents in the PMO materials synthesized by using both salt pair and HCl solutions were determined by ICP-AES and XPS techniques, and the results are summarized in Table 1. The former technique provides the elemental analysis of the bulk sample, whereas the latter gives the surface composition information. The atomic ratios of Si/Zr in the solids synthesized by using $ZrOCl_2$/NaCl were found to be slightly larger than that in the synthesis gels. These results might be due to variations in zirconium leaching during the extraction processes by using acidified ethanol. It was reported that this phenomenon is common to directly synthesized metal-incorporated hybrid frameworks where the complete removal of surfactant is relatively more difficult due to the enhanced interaction between the surfactant and the metal species.[38,39] However, the zirconium content in the above-described materials is consider-

 © 2007 Wiley-VCH Verlag GmbH & Co. KGaA, Weinheim 

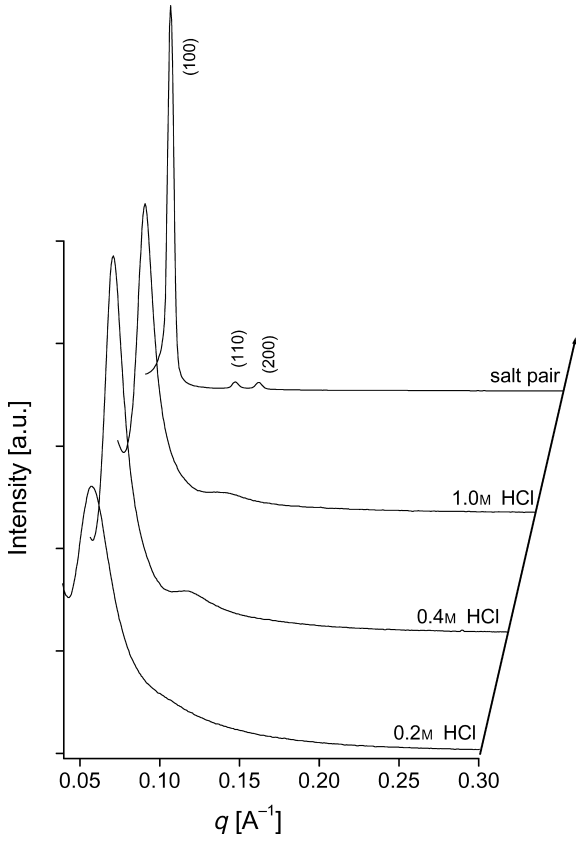


Figure 3. SAXS patterns of PMO materials synthesized by using different HCl concentrations, here the Si/Zr molar ratio is 10 for all samples.

ably higher than that of the samples synthesized with HCl solutions especially for those obtained with 0.4 or 1.0 M HCl, which is in agreement with the reported observations.[39] Noticeably, this synthetic pathway, that is, the use of $ZrOCl_2$/NaCl as the promoting agent, is not only more effective for the formation of highly ordered PMO materials but also more favorable for zirconium incorporation than the HCl-assisted synthesis, which can be considered the main advantage of this route.

In addition, the surface Si/Zr atomic ratios are, for representative materials synthesized from the $ZrOCl_2$–NaCl pair, significantly larger than that used in the synthesis (see Table 1). This is expected by taking into account that zirconium species may be mainly incorporated into the hybrid frameworks, and consequently, zirconium atoms are preferentially located at the interior pore surfaces.[40] In Figure 4, the O 1s, Zr 3d, and Si 2p core-level spectra for the sample

Table 1. Elemental analysis and structural parameters of ZrPMOs synthesized from different pathways.

| Si/Zr (gel) | Si/Zr ICP | XPS (solid) | Surface area[a] [$m^2 g^{-1}$] | Pore volume[b] [$cm^3 g^{-1}$] | Pore size[c] [nm] | Micropore volume[d] [$cm^3 g^{-1}$] |
|---|---|---|---|---|---|---|
| 100 | 106.4 | –[h] | 740 | 0.83 | 8.5 | 0.14 |
| 50 | 54.5 | 107.5 | 770 | 0.86 | 7.3 | 0.15 |
| 20 | 22.8 | 46.9 | 772 | 0.81 | 7.0 | 0.18 |
| 10 | 12.6 | 25.4 | 1048 | 1.19 | 5.9 | 0.17 |
| 10[e] | 21.5 | –[h] | 475 | 0.50 | 5.7 | 0.13 |
| 10[f] | 35.8 | –[h] | 707 | 0.48 | 6.2 | 0.26 |
| 10[g] | 86.2 | –[h] | 635 | 0.64 | 6.5 | 0.15 |

[a] Multipoint surface area calculated at relative pressure of $P/P_0$ = 0.05–0.25. [b] Total pore volume determined by the $N_2$ amount adsorbed at the highest $P/P_0$ (0.99). [c] Calculated by the conventional BJH method. [d] Calculated by the *t*-plot method with the use of experimental points at a relative pressure of $P/P_0$ = 0.10–0.20. [e] Synthesized by using 0.2 M HCl. [f] Synthesized by using 0.4 M HCl. [g] Synthesized by using and 1.0 M HCl. [h] Not determined.

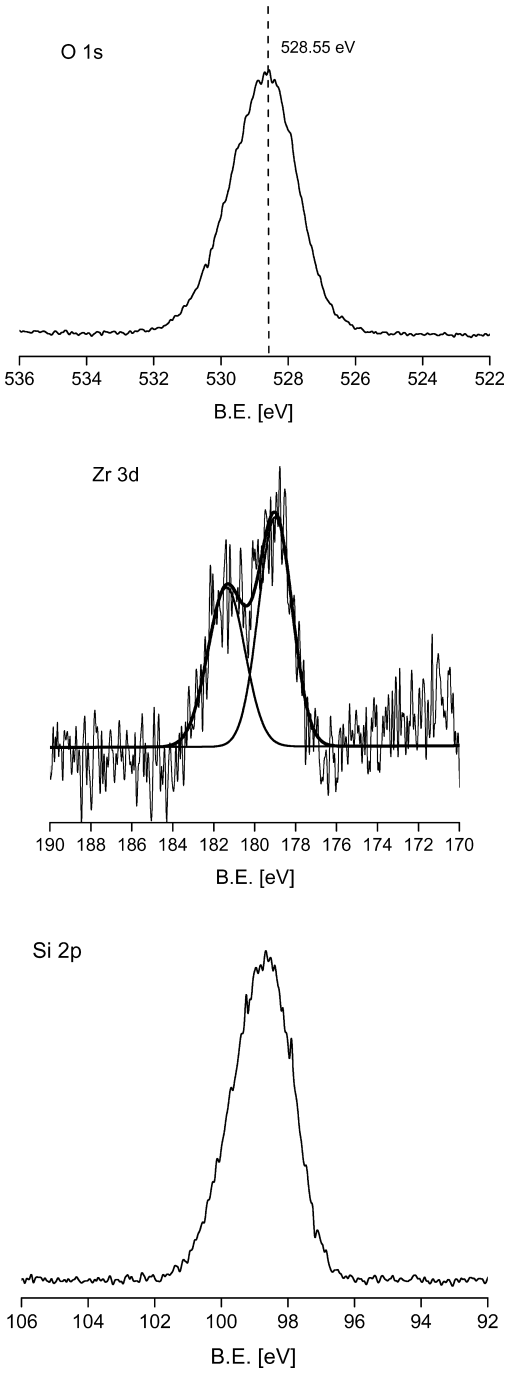


Figure 4. O 1s, Zr 3d, and Si 2p core-level spectra for the sample synthesized by using a $ZrOCl_2$–NaCl combination with Si/Zr = 10.

 © 2007 Wiley-VCH Verlag GmbH & Co. KGaA, Weinheim 

synthesized by using the salt pair with Si/Zr = 10 are presented as an example. The binding energy (BE) of O 1s (528.55 eV) was 1.65 eV lower than that given by oxygen in $ZrO_2$ (530.2 eV), and the binding energy of Zr 3d (179.1 eV) in this PMO material was also distinctly lower than that in $ZrO_2$ (181.9 eV). This significant shift indicated that no segregated oxide phase of zirconium was present,[40,41] which clearly supports the incorporation of zirconium into the hybrid framework. It should be noted, however, that the BE values for O 1s, Zr 3d, and Si 2p (98.65 eV) of this sample is considerably lower than that of the Zr-incorporated inorganic frameworks reported before,[40,41] which may be associated with the unique hybrid character of this PMO material. To the best of our knowledge, this is the first example of a preparation of highly ordered SBA-15-type ZrPMO materials with tunable framework zirconium content by the addition of inorganic salts and under such mild synthetic conditions.

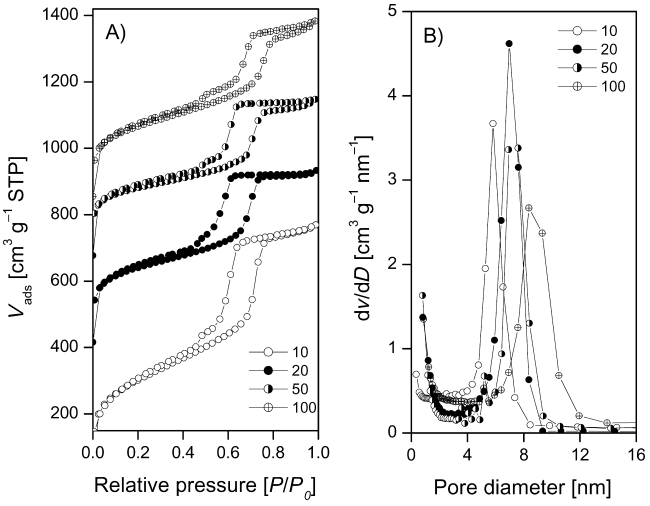


Figure 5. (A) Nitrogen adsorption isotherms and (B) BJH pore-size distributions of ZrPMO materials prepared by using the $ZrOCl_2$–NaCl combination with various Si/Zr molar ratios (as shown inset in the figures).

## Physical Properties

Figure 5 shows the nitrogen adsorption isotherms of the typical ZrPMO materials synthesized with different Si/Zr ratios by the $ZrOCl_2$–NaCl-assisted pathway. All samples exhibit a high degree of structural ordering, as indicated by the distinct capillary condensation step of the respective adsorption isotherm. This strongly suggests the presence of uniform cylindrical pores in these materials, in accordance with the 2D hexagonal pore structures revealed by the SAXS analysis and those reported results for SBA-15-like PMO or siliceous materials prepared under strongly acidic conditions.[7,34,42] Correspondingly, the pore-size distributions calculated from the adsorption branch clearly display a uniform pore structure for all samples (Figure 5B). The specific structural parameters derived from this sorption analysis such as total pore volumes, micropore volumes, pore sizes, and BET surface areas are summarized in Table 1. Noticeably, all ZrPMOs possess the typical structural properties of SBA-15-type materials such as large surface area and pore volume and a considerable amount of micropores,[34,42] and these textural features are comparable to those excellent SBA-15-like PMO or silica materials prepared from other synthesis systems.[7,34] Besides, it is interesting to note that a distinct relationship between the structural properties and preparation conditions can be drawn among these samples, that is, the specific surface areas and pore sizes clearly decrease and increase, respectively, with the Si/Zr ratios. All of these parameters indicate that the structural ordering, textural properties, and the incorporation of zirconium into the ZrPMO materials can be easily achieved by using different Si/Zr ratios by the synthesis pathway.

Consistent with the results of the SAXS and the physisorption measurements, respectively, the transmission electron microscopy (TEM) images of the representative samples viewed along different directions show well-ordered hexagonal arrays of 2D mesoporous channels (Figure 6), which further confirms that these samples are of *p6mm* hexagonal structure. Actually, no distinct difference can be found between this observation and that for P123-templated PMOs synthesized under various conditions such as such salt-assisted acidic synthesis[7,37] or the true-liquid-crystal-templating (TLCT) approach,[43] which strongly indicates the outstanding promoting effects of the salt pair in this synthetic system though the zirconium salt amount is very small; the function of both salts is entirely similar to that of reported Na(K)Cl/HCl combinations used for the synthesis of highly ordered mesostructures templated by block copolymers.[7,35,44,45]

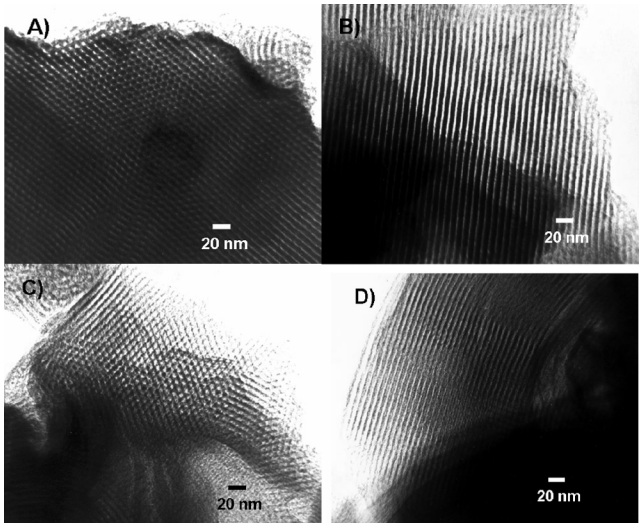


Figure 6. TEM micrographs of the samples synthesized by using the $ZrOCl_2$–NaCl pair with Si/Zr = 10 (A, B) and 100 (C, D).

The representative scanning electron microscopy (SEM) images for the ZrPMO materials synthesized with different Si/Zr ratios are shown in Figure S1 (Supporting Information). Clearly, no characteristic morphologies can be

 © 2007 Wiley-VCH Verlag GmbH & Co. KGaA, Weinheim 

found for all samples and irregular particles or aggregates are dominant through all the images, even though the particle/cluster size looks like it decreases with increasing Si/Zr ratios. Noticeably, these results are vastly different from those reported for SBA-15-type materials prepared under strongly acidic conditions, as described by Zhao et al., where wheat-like fibers composed of short rod-like particles were commonly observed.[34,42] This may be closely associated with the different preparation conditions (e.g. acidity, temperature, shear flow, ionic strength, etc.), which can exert a great impact on the hydrolysis and condensation kinetics of silica sources and therefore the morphological properties of the final mesophases.[34,46]

As far as this synthetic system is concerned, however, possibly there is no favorable orientation growth effect during the assembly process because of the fairly mild synthetic conditions. Under such conditions, the sol–gel kinetics of the organosilica precursor are so slow that the induction time for precipitation is too long to have a favorable effect on the macroscopic morphologies, even though this synthetic system is enough for the formation of ordered mesoporous frameworks. Actually, another observation directly confirmed the mildness of this synthesis system, that is, only less-ordered materials were obtained without stirring during the assembly process (see Figure S2); meanwhile, no distinct morphological variation was observed between both samples obtained with or without stirring during the synthesis (Figure S3). This result indicates that the shear flow is of great importance for the formation of highly ordered ZrPMO materials in this system due to the mild synthetic conditions, which is greatly different from the earlier work carried out in strongly acidic solutions.[47]

### Framework Properties

The $^{13}C$ cross-polarization (CP) and $^{29}Si$ MAS NMR spectra were used to clarify the basic structural information in these ZrPMO samples prepared with different Si/Zr ratios from the $ZrOCl_2$–NaCl-assisted synthesis. Interestingly, it was indeed found that there were no distinct differences in the spectra results between these samples, which indicates that the ethylene-bridging groups were completely intact in all samples, even though their framework compositions were different due to the variable zirconium content (see Table 1). For specific examples, Figure 7 shows the $^{13}C$ and $^{29}Si$ NMR spectra of two representative ZrPMO samples synthesized with Si/Zr = 10 and 100, respectively. In the case of the $^{13}C$ CP NMR spectra, a prominent peak is observed at 4.8 ppm for all samples, which is attributed to the ethylene carbon atoms covalently linked to the Si atoms in the framework.[7,8,43] Besides this, another three weak peaks at $\delta$ = 17.6, 57.8, and 70.1 ppm for the extracted samples can be assigned to the tiny amount of ethoxy ($-OC_2H_5$) groups exchanged during the extraction process and residual copolymer surfactant, respectively. However, in comparison with the sample prepared with Si/Zr = 100, a distinct peak due to the residual P123 is observed for the sample with a lower Si/Zr ratio of 10, though a similar extraction process was used for both samples. This result might be attributed to the presence of a relatively large amount of zirconium ions in the framework, which results in surfactant molecules that are more difficult to remove even under the identical extraction conditions.[38]

In addition, the $^{29}Si$ MAS NMR spectra of all samples exhibit two distinct signals at –56.5 and –64.0 ppm, which are attributable to the $T^2$ [C-*Si*(OH)$(OSi)_2$] and $T^3$ [C-*Si*$(OSi)_3$] silica species, respectively. Another very weak signal at –48.7 ppm due to the $T^1$ [C-*Si*$(OH)_2$(OSi)] silica environment is also observed. The strong intensity for the $T^2$ and $T^3$ signals indicates the formation of relatively condensed organosilicate frameworks for these samples; actually, there is no apparent difference between these materials and those prepared under strongly acidic conditions.[7,43]

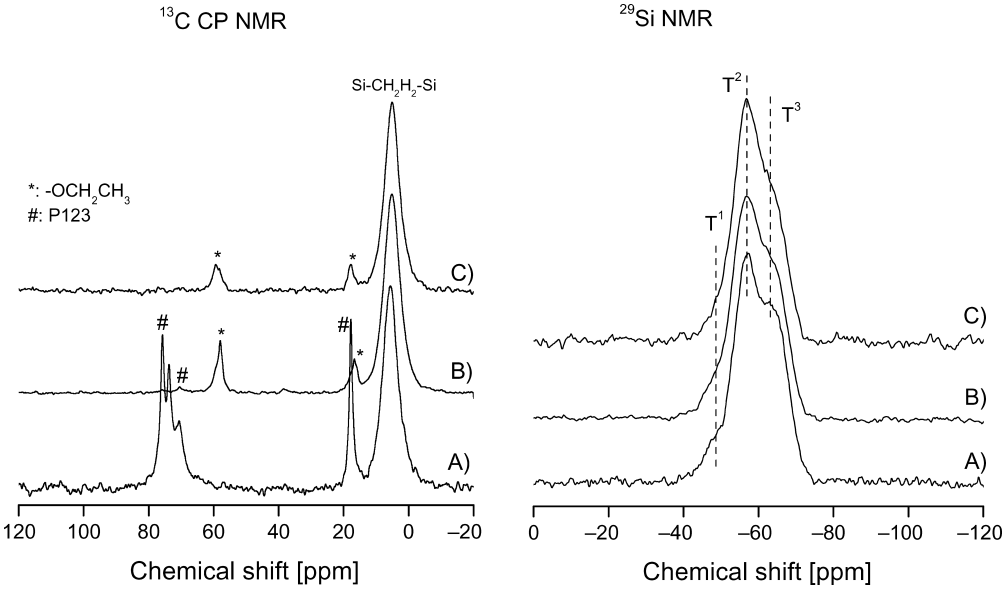


Figure 7. Solid-state $^{13}C$ CP and $^{29}Si$ MAS NMR spectra of the samples: (A) as-synthesized ZrPMO and (B) extracted ZrPMO obtained with Si/Zr = 10 by the salt-pair-assisted synthesis; (C) extracted ZrPMO prepared by using the similar method with Si/Zr = 100.

 © 2007 Wiley-VCH Verlag GmbH & Co. KGaA, Weinheim 

The absence of $SiO_4$ species such as $Q^3$ [*Si*(OH)$(OSi)_3$] and $Q^4$ [*Si*$(OSi)_4$], which produce signals between –90 and –120 ppm, indicates that no carbon–silicon bond cleavage of the BTME precursors occurred during this mild synthesis. These combined analyses clearly demonstrate that all of the Si atoms in these ZrPMO materials are bonded covalently to carbon atoms. It should be noted, however, that no significant changes in the $^{29}Si$ NMR spectra due to the different zirconium content incorporated into the framework can be seen for these samples. This is also an indication that the local environment of silica species in these hybrid materials is totally irregular in nature, which is similar to the previous results reported for Zr-incorporated SBA-15 silicas.[39,48]

Thermogravimetric analysis (TGA) conducted in flowing air and the derivative plots of as-synthesized and extracted ZrPMO synthesized with Si/Zr = 10 by the synthetic pathway are depicted in Figure 8. For both profiles, the weight loss below 120 °C is due to the removal of the physically adsorbed water or ethanol exchanged during the extraction process. A main weight loss (ca. 38%) in the range of 180–450 °C is observed for the as-synthesized one, which can be mainly assigned to the decomposition/combustion of the copolymer surfactant molecules.[39] After extraction, however, the weight loss (ca. 7%) observed in the same region appears too large to be attributed solely to the residual P123 surfactant, that is, there should be some contribution from the framework ethylene groups, which is consistent with the reported results[43,49] and the aforementioned $^{13}C$ CP NMR spectroscopic analysis that only a tiny amount of residual surfactant molecules were detected. However, it should be pointed out that the decompositions of the ethylene bridging groups is not only limited to this region, the weight loss over the range of 260–650 °C should be principally attributed to their removal under the present working conditions.[43]

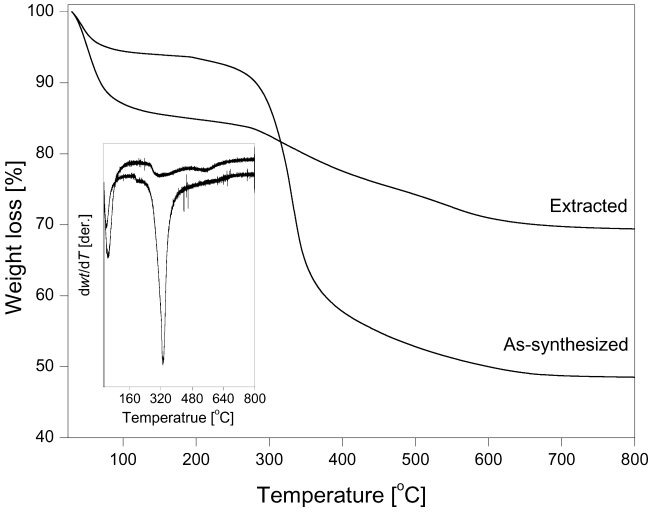


Figure 8. TG and DTG (inset) profiles of as-synthesized and solvent-extracted ZrPMO material prepared with Si/Zr = 10 by using this synthetic pathway.

**Plausible Mechanism**

Our results obtained by SAXS, $N_2$ sorption, XPS, TEM, and NMR spectroscopic techniques show that, even though no additional acid was added in the synthesis, highly ordered ZrPMO materials with a tunable zirconium content could be facilely prepared by using the $ZrOCl_2$/NaCl-assisted synthetic strategy by simply adjusting the amount of $ZrOCl_2$ in the synthesis gels. In practice, inorganic salts can play an important role in the synthesis of mesoporous materials especially for those nonionic surfactant-templating pathways, and recently a review article from Zhao et al. comprehensively detailed the effect of inorganic salts on the morphologies and structural properties of mesoporous silicates templated by nonionic surfactants.[35]

As far as the triblock copolymer-templating system (P123, F127, etc) is concerned, however, in most cases the inorganic additives are only nonhydrolyzable salts like sodium or potassium species, and the syntheses were still carried out under strongly acidic conditions.[7,44] In contrast, a combination of both "nonhydrolyzable" and "hydrolyzable" salts such as NaCl and $ZrOCl_2$ was used in this study under acid-free conditions. This synthetic pathway has never been reported for P123-templated PMOs, even though the NaCl/KCl-assisted acidic pathways have been frequently employed for the preparation of large-pore PMO materials.[7,37,45] It is well-established that both salts can respectively act as a well-understood micelle-promoting agent[35,44] (lower the critical micelle concentration and temperature of copolymer surfactant) and "catalyst"[39,50] for the hydrolysis and condensation of the silica precursors that were promoted by the self-generated acidity from the hydrolysis of inorganic $ZrOCl_2$. Indeed, the self-adjusted acidity, even though the zirconium salt amount (atomic ratio Si/Zr $\geq$ 10) added in the reaction gels is very small, is enough for the sol–gel processing of the bridged organosilanes due to their easier hydrolysis and condensation features in comparison with the conventional silica sources like tetraethoxysilane (TEOS) or tetramethoxysilane (TMOS).[51] Under such mild synthetic conditions, the induction time for precipitation is reasonably longer than that of the synthesis carried out under strongly acidic conditions, as described before, which might be responsible for the featureless morphologies of the final SBA-15-like ZrPMO products, even though their well-ordered framework channels could be easily assembled in this mild environment. As a matter of fact, this formation mechanism in nature is somewhat similar to the reported "acid–base pair" concept for those mesoporous nonsiliceous materials templated by copolymer surfactants, in which the appropriate acidity self-generated from the inorganic precursors is a key factor for the whole synthesis.[52,53] Likewise, in this work the organosilica precursor and $ZrOCl_2$ can be considered the so-called "base" and "acid", respectively. It is proposed that the hydrolyzed zirconyl cations may take the place of protons and adhere to either the hydrophilic side of the polymer micelle or the silanol group to form cationic species, which participate in the self-assembly process. Therefore, zirconium ions can be

 © 2007 Wiley-VCH Verlag GmbH & Co. KGaA, Weinheim 

effectively incorporated into the organosilicate frameworks due to the easiness of Zr–O–Si formation in this mild environment.[39,42] During this process, the presence of NaCl, a known micelle-promoting agent for copolymer P123, can change the ionic strength of the synthesis gels and favorably facilitate the formation of ordered ZrPMO materials, which has no direct interaction with the species involved in the self-assembly of the micelle and organosilica precursor.[39,46] Both salts have been found to be essential for the synthesis of highly ordered ZrPMO materials with large pore diameters.

## Conclusions

A new synthetic pathway was developed to incorporate zirconium ions into SBA-15-type PMO materials with excellent mesostructural ordering and tunable zirconium content by simply adjusting the $ZrOCl_2$ amount of the $ZrOCl_2$–NaCl salt combination, which was used as the promoting agent through the synthetic process and thus no additional mineral acids was necessary. A simple "neutralization" concept based on the chemical properties of the components of this synthesis system was discussed, in which the organosilica precursor and hydrolyzable $ZrOCl_2$ salt can be considered as the "base" and "acid", respectively. With this mechanism, the acidity self-generated by the zirconium salt is of great importance for the hydrolysis of the organosilica source. Simultaneously, the addition of NaCl can effectively enhance the interaction between the copolymer micelles and hydrolyzed species and facilitate the assembly of well-ordered ZrPMO materials. In comparison with those studies conducted under strongly acid conditions, this synthetic method is environmentally friendly and efficient in incorporating zirconium ions into the framework of the hybrid mesoporous materials. Actually, this synthetic pathway can also be applied to the preparation of other heteroatom-containing PMO materials, a series of Al-, Sn-, Fe-, and Cr-incorporated SBA-15-type mesostructures have been successfully prepared by using the corresponding inorganic chloride salts and will be reported in the near future.

## Experimental Section

**Chemicals:** All chemicals [zirconyl chloride octahydrate ($ZrOCl_2{\cdot}8H_2O, \geq 99\%$)] used as a zirconium source for the synthesis of zirconium-functionalized hybrid materials, triblock copolymer surfactant (Pluronic 123, molecular weight = 5800, $EO_{20}$-$PO_{70}EO_{20}$), and bis(trimethoxysilyl)ethane [$(CH_3O)_3SiCH_2CH_2Si(OCH_3)_3$, BTME, 96%] were purchased from Aldrich-Sigma Chemical Inc. All chemicals were used as received without further purification. Millipore water was used in all experiments.

**Synthesis of ZrPMO Materials:** Highly ordered ethylene-bridged ZrPMO materials can be successfully synthesized from BTME by using a $ZrOCl_2$–NaCl salt combination as the promoting agent for the assembly process, and there is no requirement for additional mineral acids. In a typical synthesis, P123 (1.5 g) and a predetermined amount of $ZrOCl_2{\cdot}8H_2O$ and NaCl were dissolved in deionized water (50 g) and stirred for 4 h at 40 °C. Then, BTME (1.96 mL) was added to the solution and stirred for 24 h at the same temperature, which was taken as the reaction temperature in the following text. The molar compositions of the synthesis are BTME/P123/$H_2O$/NaCl/$ZrOCl_2{\cdot}8H_2O$ = 1:0.034:400:0–8:0–0.4. The mother solution along with the precipitate was then transferred to an autoclave and hydrothermally treated for 48 h at 80 °C. The ZrPMO materials were finally obtained after filtration and two times extraction with HCl acidified ethanol (v/v, 3:100) at 60 °C for 6 h to remove the template.

**Characterization:** Small-angle X-ray scattering (SAXS) measurements were performed by using a synchrotron X-ray source of Pohang Accelerator Laboratory (PAL, Korea): Co-$K_\alpha$ ($\lambda$ = 1.608 Å) radiation with an energy range of 4–16 keV. Transmission electron microscopy (TEM) images were obtained with a JEOL2010 electron microscope with an acceleration voltage of 200 kV. Scanning electron microscopy (SEM) images were recorded with a JEOL 6400 microscope operating at 20 kV. Nitrogen adsorption isotherms were obtained with a Quantachrome's Quadrasorb SI analyzer at –196 °C. Before the measurements, the samples were degassed at 120 °C for 12 h in vacuo. The Brumauer–Emmett–Teller (BET) surface area was calculated by using experimental points at a relative pressure of $P/P_0$ = 0.05–0.25. The total pore volume was calculated by the $N_2$ amount adsorbed at the highest $P/P_0$ for each sample ($P/P_0$ = 0.99). The pore-size distribution was calculated by the conventional Barrett-Joyner-Halenda (BJH) method. The micropore area and volume were calculated by the *t*-plot method by using experimental points at a relative pressure of $P/P_0$ = 0.10–0.20. $^{13}C$ cross polarization (CP) and $^{29}Si$ MAS NMR spectra were obtained with a Bruker DSX400 spectrometer at room temperature with a 4 mm zirconia rotor spinning at 6 kHz (resonance frequencies of 79.5 and 100.6 MHz for $^{29}Si$ and $^{13}C$ CPMAS NMR, respectively; 90° pulse width of 5 μs, contact time 2 ms, recycle delay 3 s for both $^{29}Si$ and $^{13}C$ CP MAS NMR). Thermogravimetric analysis (TGA) was performed with a Perkin–Elmer Pyris Diamond TG instrument at a heating rate of 10 °C min$^{-1}$ in air. The zirconium content of the prepared ZrPMO materials was determined by ICP-Atomic Emission Spectroscopy (ICP-AES) by using a Plasma 400 (Perkin–Elmer) spectrometer equipped with Cetac6000AT+ ultrasonic nebulizer. To study the surface elements of the materials in their existing state, X-ray photoelectron spectroscopy (XPS) measurements were carried out with a PHI-1600ESCA System XPS spectrometer (Perkin–Elmer, USA) by using nonmonochromatic Mg-$K_\alpha$ radiation, operated at 15 kV and under $10^{-7}$ Pa pressure with photoelectron energy set at 1254 eV. The elements on the surface were quantified by using the peak areas.

**Supporting Information** (see footnote on the first page of this article): SEM images of the ZrPMO samples synthesized by using $ZrOCl_2$–NaCl with different Si/Zr molar ratios, SAXS patterns and SEM images of the samples synthesized.

## Acknowledgments

This work was financially supported by the Korea Science and Engineering Foundation (KOSEF) through the National Research Laboratory Program funded by the Ministry of Science and Technology, MOST (MOST; M10300000369-06J0000-36910), the SRC/ERC Program of MOST/KOSEF (R11-2000-070-080020), and the Brain Korea 21 Project. SAXS measurements at Pohang Accelerator Laboratory, Korea, are acknowledged.

 © 2007 Wiley-VCH Verlag GmbH & Co. KGaA, Weinheim 

[1] S. Inagaki, S. Guan, Y. Fukushima, T. Ohsuna, O. Terasaki, *J. Am. Chem. Soc.* **1999**, *121*, 9611–9614.
[2] B. J. Melde, B. T. Holland, C. F. Balandford, A. Stein, *Chem. Mater.* **1999**, *11*, 3302–3308.
[3] T. Asefa, M. J. MacLachlan, N. Coombs, G. A. Ozin, *Nature* **1999**, *402*, 867–871.
[4] F. Hoffmann, M. Cornelius, J. Morell, M. Fröba, *Angew. Chem. Int. Ed.* **2006**, *45*, 3216–3251.
[5] T. Asefa, M. J. MacLachlan, H. Grondey, N. Coombs, G. A. Ozin, *Angew. Chem. Int. Ed.* **2000**, *39*, 1808–1811.
[6] A. Sayari, S. Hamoudi, Y. Yang, I. L. Moudrskovski, J. R. Ripmeester, *Chem. Mater.* **2000**, *12*, 3857–3863.
[7] W. P. Guo, J. Y. Park, M. O. Oh, H. W. Jeong, W. J. Cho, I. Kim, C. S. Ha, *Chem. Mater.* **2003**, *15*, 2295–2298.
[8] X. Y. Bao, X. S. Zhao, X. Li, P. A. Chia, J. Li, *J. Phys. Chem. B* **2004**, *108*, 4684–4689.
[9] Y. Xia, W. Wang, R. Mokaya, *J. Am. Chem. Soc.* **2005**, *127*, 790–798.
[10] J. Morell, G. Wolter, M. Fröba, *Chem. Mater.* **2005**, *17*, 804–808.
[11] J. Liu, Q. H. Yang, L. Zhang, D. Jiang, X. Shi, H. Q. Yang, H. Zhong, C. Li, *Adv. Funct. Mater.* **2007**, *17*, 569–576.
[12] S. Inagaki, S. Guan, T. Ohsuna, O. Terasaki, *Nature* **2002**, *416*, 314–317.
[13] A. Sayari, W. Wang, *J. Am. Chem. Soc.* **2005**, *127*, 12194–12195.
[14] M. P. Kapoor, Q. H. Yang, S. Inagaki, *J. Am. Chem. Soc.* **2002**, *124*, 15176–15177.
[15] O. Olkhovyk, M. Jaroniec, *J. Am. Chem. Soc.* **2005**, *127*, 60–61.
[16] O. Olkhovyk, M. Jaroniec, *Ind. Eng. Chem. Res.* **2007**, *46*, 1745–1751.
[17] T. Asefa, M. Kruk, M. J. MacLachlan, N. Coombos, H. Gronden, M. Jaroniec, G. A. Ozin, *J. Am. Chem. Soc.* **2001**, *123*, 8520–8530.
[18] Q. H. Yang, J. Liu, J. Yang, *J. Catal.* **2004**, *228*, 265–272.
[19] M. A. Wahab, I. Imae, Y. Kawakami, C. S. Ha, *Chem. Mater.* **2005**, *17*, 2165–2174.
[20] D. M. Jiang, Q. H. Yang, J. Yang, L. Zhang, G. R. Zhu, W. Su, C. Li, *Chem. Mater.* **2005**, *17*, 6154–6160.
[21] J. Morell, M. Güngerich, G. Wolter, J. Jiao, M. Hunger, P. J. Klar, M. Fröba, *J. Mater. Chem.* **2006**, *16*, 2809–2818.
[22] C. Baleizao, B. Gigante, D. Das, M. Alvaro, H. Garcia, A. Corma, *Chem. Commun.* **2003**, 1860–1861.
[23] A. Corma, D. Das, H. Garcia, A. Leyva, *J. Catal.* **2005**, *229*, 322–331.
[24] Q. Yang, Y. Li, L. Zhang, J. Yang, C. Li, *J. Phys. Chem. B* **2004**, *108*, 7934–7937.
[25] B. J. Hughes, J. B. Guilbaud, M. Allix, Y. Z. Khimyak, *J. Mater. Chem.* **2005**, *15*, 4728–4733.
[26] W. P. Guo, X. S. Zhao, *Microporous Mesoporous Mater.* **2005**, *85*, 32–38.
[27] M. P. Kapoor, A. Bhaumik, S. Inagaki, K. Kuraoka, T. Yazawa, *J. Mater. Chem.* **2002**, *12*, 3078–3083.
[28] M. P. Kapoor, A. Sinha, S. Seelan, S. Inagaki, S. Taubota, H. Yoshida, M. Haruta, *Chem. Commun.* **2002**, 2902–2903.
[29] A. Bhaumik, M. P. Kapoor, S. Inagaki, *Chem. Commun.* **2003**, 470–471.
[30] W. Cho, J. W. Park, C. S. Ha, *Mater. Lett.* **2004**, *58*, 3551–3554.
[31] S. Shylesh, A. P. Singh, *Microporous Mesoporous Mater.* **2006**, *94*, 127–138.
[32] S. Shylesh, Ch. Srilakshmi, A. P. Singh, B. G. Anderson, *Microporous Mesoporous Mater.* **2007**, *99*, 334–344.
[33] J. A. Melero, J. Eglesias, J. M. Arsuaga, J. Sainz-pardo, P. de Frutos, S. Blazquez, *J. Mater. Chem.* **2007**, *17*, 377–385.
[34] D. Y. Zhao, J. L. Feng, Q. S. Huo, N. Melosh, G. H. Fredrickson, B. F. Chmelka, G. D. Stucky, *Science* **1998**, *279*, 548–552.
[35] Y. Wan, Y. F. Shi, D. Y. Zhao, *Chem. Commun.* **2007**, 897–926.
[36] X. G. Cui, W. C. Zin, C. S. Ha, *Mater. Lett.* **2005**, *18*, 2257–2261.
[37] S. Z. Qiao, C. Z. Yu, Q. H. Hu, Y. G. Jin, X. S. Zhao, G. Q. Lu, *Microporous Mesoporous Mater.* **2006**, *91*, 59–69.
[38] S. Shylesh, P. P. Samuel, A. P. Singh, *Microporous Mesoporous Mater.* **2007**, *100*, 250–258.
[39] S. Y. Chen, L. Y. Jang, S. Cheng, *Chem. Mater.* **2004**, *16*, 4174–4180.
[40] J. M. Liu, S. J. Liao, G. D. Jiang, X. L. Zhang, L. Petrik, *Microporous Mesoporous Mater.* **2006**, *95*, 306–311.
[41] A. Infantes Molina, J. Mérida Robles, P. Maireles Torres, E. Finocchio, G. Busca, E. Rodríguez Castellón, J. L. G. Fierro, A. Jiménez López, *Microporous Mesoporous Mater.* **2004**, *75*, 23–32.
[42] M. Selvaraj, S. Kawi, *Chem. Mater.* **2007**, *19*, 509–519.
[43] H. Zhu, D. J. Jones, J. Zajac, J. Rozière, R. Dutartre, *Chem. Commun.* **2001**, 2568–2569.
[44] C. Z. Yu, B. Z. Tian, B. Fan, G. D. Stucky, D. Y. Zhao, *Chem. Commun.* **2001**, 2726–2727.
[45] X. F. Zhou, S. Z. Qiao, N. Hao, X. Wang, C. Z. Yu, L. Wang, D. Y. Zhao, G. Q. Lu, *Chem. Mater.* **2007**, *19*, 1870–1876.
[46] C. Z. Yu, J. Fan, B. Z. Tian, D. Y. Zhao, G. D. Stucky, *Adv. Mater.* **2002**, *14*, 1742–1745.
[47] A. Sayari, B. H. Han, Y. Yang, *J. Am. Chem. Soc.* **2004**, *126*, 14348–14349.
[48] F. X. Li, F. Yu, Y. Li, R. Li, K. Xie, *Microporous Mesoporous Mater.* **2007**, *101*, 250–255.
[49] R. M. Grudzien, B. E. Grabicka, S. Pinkus, M. Jaroniec, *Chem. Mater.* **2006**, *18*, 1722–1725.
[50] P. Shah, A. V. Ramaswamy, K. Lazar, V. Ramaswamy, *Microporous Mesoporous Mater.* **2007**, *100*, 210–226.
[51] X. Y. Bao, X. S. Zhao, S. Z. Qiao, S. K. Bhatia, *J. Phys. Chem. B* **2004**, *108*, 16441–16450.
[52] B. Z. Tian, X. Y. Liu, B. Tu, C. Z. Yu, J. Fan, L. M. Wang, S. H. Xie, G. D. Stucky, D. Y. Zhao, *Nat. Mater.* **2003**, *2*, 159–163.
[53] Y. Wan, H. F. Yang, D. Y. Zhao, *Acc. Chem. Res.* **2006**, *39*, 423–432.

Received: July 23, 2007
Published Online: October 17, 2007

 © 2007 Wiley-VCH Verlag GmbH & Co. KGaA, Weinheim 

DOI: 10.1002/ejic.200700435

# $H_5EPTPACH_2OH$: Synthesis, Relaxometric Characterization and $^1H$ NMR Spectroscopic Studies on the Solution Dynamics of Its $Ln^{III}$ Complexes

**Susana Torres,[a] José A. Martins,*[a] João P. André,*[a] Giovannia A. Pereira,[b] Robert Kiraly,[c] Ernö Brücher,[c] Lothar Helm,[d] Éva Tóth,[e] and Carlos F. G. C. Geraldes*[b]**

**Keywords:** Lanthanides / Contrast agents / MRI / Microscopic protonation scheme / Stability constants

The synthesis and characterization of a new metal chelator, 4-(*S*)-hydroxymethyl-3,6,10-tri(carboxymethyl)-3,6,10-triazadodecanedioic acid ($H_5EPTPACH_2OH$), is reported. Protonation constants for the ligand $H_5EPTPACH_2OH$ and for the previously reported $H_5EPTPAC16$ have been determined by potentiometry, which reveals that both ligands display slightly higher protonation constants relative to that of the ligand $DTPA^{5-}$. The stability constant for the $[Gd(EPTPACH_2OH)(H_2O)]^{2-}$ complex has also been determined by potentiometry. The obtained value ($\log K_{GdL} = 16.7$) is two orders of magnitude lower than that for the $[Gd(EPTPA)(H_2O)]^{2-}$ complex, which indicates the destabilizing effect of the pendant hydroxymethyl group at the EPTPA backbone. The microscopic protonation scheme has been deduced from the pH dependence of the $^1H$ NMR spectra of both $H_5EPTPACH_2OH$ and $H_5EPTPAC16$ ligands. The first two protonations occur exclusively at the backbone nitrogen atoms – the first protonation occurs preferentially at the more basic central nitrogen atom. The second proton distributes preferentially between the two terminal nitrogen atoms with the favoring of the trimethylene nitrogen atom over the ethylene nitrogen atom. The $Ln^{III}$ complexes of the ligand $H_5EPTPACH_2OH$ have been prepared and their solution dynamics studied by $^1H$ NMR spectroscopy. Two sets of resonances of very different intensities from two isomeric complexes have been observed. Relaxometric investigations ($^{17}O$ NMR and $^1H$ NMRD) demonstrate that the $[Gd(EPTPACH_2OH)(H_2O)]^{2-}$ complex displays an accelerated water-exchange rate ($k_{ex} = 87.6 \times 10^6\ s^{-1}$) that is close to the theoretically derived optimal value. However, the kinetic stability of this complex in phosphate-buffered solutions towards $Zn^{2+}$ transmetallation is quite low, but higher than that of the corresponding methyl derivative.

(© Wiley-VCH Verlag GmbH & Co. KGaA, 69451 Weinheim, Germany, 2007)

## Introduction

Magnetic resonance imaging (MRI) uses radiofrequency waves and a strong magnetic field to provide remarkably clear and detailed pictures of internal organs and tissues. The development of this imaging modality parallels the emergence of a new class of metallopharmaceutics, known as contrast agents (CAs).[1,2] Contrast agents are primarily $Gd^{III}$ complexes because this metal ion has seven unpaired electrons and a slow electronic relaxation rate.[3]

In fact, the image-enhancing capability of the commercially available poly(aminocarboxylate)-based chelates is only a few percent of the maximum value predicted by the Solomon–Bloembergen–Morgan theory.[4,5] In order to attain maximum relaxivities, the rotational correlation time ($\tau_r$), proton-exchange rate ($k_{ex}$), and electronic spin relaxation rates ($T_e$) have to be optimized simultaneously.[4,5]

The covalent attachment of $Gd^{III}$ chelates to slow-tumbling macromolecules (linear polymers,[6] carbohydrates,[7] proteins,[8] and dendrimers[9]) and the formation of host–guest noncovalent interactions between $Gd^{III}$ chelates and macromolecules[10] are successful strategies to increase $\tau_r$. An alternative way to achieve this goal is through self-assembly of amphiphilic $Gd^{III}$ chelates[11] or through the inclusion of lipophilic $Gd^{III}$ chelates in liposomes[12] or other lipid-based colloidal systems.[13]

In spite of the efforts to optimize the rotational correlation time of slow-tumbling $Gd^{III}$ complexes, the relaxivity

[a] Centro de Química, Campus de Gualtar, Universidade do Minho,
4710-057 Braga, Portugal
Fax: +351-253-678-983
E-mail: jmartins@quimica.uminho.pt
jandre@quimica.uminho.pt
[b] Departamento de Bioquímica, Faculdade de Ciências e Tecnologia, Universidade de Coimbra, Apartado 3126,
3001-401 Coimbra, Portugal
Fax: +351-239-853-607
E-mail: geraldes@ci.uc.pt
[c] Department of Inorganic and Analytical Chemistry, University of Debrecen,
4010 Debrecen, Hungary
[d] Laboratoire de Chimie Inorganique et Bioinorganique, Ecole Polytechnique Fédérale de Lausanne, EPFL-BCH,
1015 Lausanne, Switzerland
[e] Centre de Biophysique Moléculaire, CNRS,
Rue Charles Sadron, 45071 Orléans, France
Supporting information for this article is available on the WWW under http://www.eurjic.org or from the author.

 © 2007 Wiley-VCH Verlag GmbH & Co. KGaA, Weinheim 

enhancement achieved may be limited if the water-exchange rate ($k_{ex}$) is not simultaneously optimized. When the water-exchange rate is too fast, the protons are not effectively relaxed. Conversely, the coordination site is needlessly occupied by a relaxed water molecule. Most $Gd^{III}$ complexes investigated to date as potential contrast agents have very slow water-exchange rates ($k_{ex} \approx 10^6\ s^{-1}$), far from its optimal value (about $k_{ex} = 10^8\ s^{-1}$).

The water exchange in $Gd^{III}$ complexes is essentially determined by two factors, both of which can, to some extent, be controlled by design.[14] The first and most easily controlled factor is the electron density on the central lanthanide ion. Electron deficiency on the metal ion results in slow dissociation of the bound water molecule as a result of the enhanced electrostatic attraction responsible for the shortening of the lanthanide–water bond. Therefore, ligands containing anionic groups (e.g. carboxylates) are responsible for a fast water exchange, whereas neutral ligands (e.g. amides or alcohols) would favor slower water exchange. Another way of obtaining $Gd^{III}$ complexes with fast water exchange rates is related to the design of ligands that display an increased steric hindrance around the water coordination site. Muller and co-workers have reported a reduction in the time of residence of the bound water molecule ($\tau_M$; $\tau_M = 1/k_{ex}$) for a series of $Gd^{III}$–DTPA complexes bearing diverse substituents on the C4 carbon atom of the ethylene bridge: Gd(*S*)-C4-Me-DTPA ($\tau_M^{310}$ = 91 ns), Gd(*S*)-C4-*n*Bu-DTPA ($\tau_M^{310}$ = 82 ns), Gd(*S*)-C4-*i*Bu-DTPA ($\tau_M^{310}$ = 108 ns), Gd(*S*)-C4-*i*Pr-DTPA ($\tau_M^{310}$ = 98 ns), and Gd-C4-diMe-DTPA ($\tau_M^{310}$ = 57 ns) relative to that of the parent $Gd^{III}$–DTPA complex ($\tau_M^{310}$ = 143 ns).[15] The same effect has been reported by the same authors for $Gd^{III}$–DTPA complexes bearing ethoxybenzyl,[16] benzyl,[17] and (4,4-diphenylcyclohexyl)phosphonooxymethyl[18] substituents on the C4 carbon atom of the ethylene bridge. A comparative study of the four possible regioisommerically benzyl-functionalized $Gd^{III}$–DTPA complexes showed that substitution at C4 (next to the ethylene bridge terminal nitrogen atom) and C7 (central acetate) yields higher steric hindrance of the coordinated water molecule (with a corresponding higher increase in the water-exchange rate) than substitution at C5 (next to the ethylene bridge central nitrogen atom) and C2 (terminal acetate).[19] However, substitution at C5 and C4 are the most effective in sterically reducing the accessibility of $Zn^{2+}$ to the ligand, and thus are the most protective against transmetallation by this ion.[19]

Merbach et al. also demonstrated that the insertion of an extra methylene group to the backbone or to a pendant arm in macrocyclic tetraacetate complexes and to DTPA-derived complexes causes steric compression around the water-binding site, with a corresponding increase in the bound-water-exchange rate ($k_{ex}$) by a factor of one or two orders of magnitude for $[Gd(DTTA\text{-}prop)(H_2O)]^{2-}$ and $[Gd(EPTPA\text{-}bz\text{-}NO_2)(H_2O)]^{2-}$, respectively.[20] In solution, lanthanide(III) complexes of $H_4DOTA$-like ligands are typically present as a mixture of two diastereoisomers: the square antiprismatic (SAP) or M ("major") and the twisted square-antiprismatic (TSAP) or m ("minor") isomer.[21] Studies revealed that these isomers display different $\tau_M$ values.[22] The neighborhood of the water molecule in a TSAP isomer is more sterically crowded, and therefore the water molecule exchanges 10–100 times faster than in a SAP isomer. Therefore, $Gd^{III}$ complexes displaying, in solution, exclusively the TSAP isomer could potentially lead to high relaxivity CAs.

In this paper, we report the synthesis and characterization of the ligand 4-(*S*)-hydroxymethyl-3,6,10-tris(carboxymethyl)-3,6,10-triazadodecanedioic acid (**1**, $H_5EPTPA\text{-}CH_2OH$) and of its $Ln^{III}$ complexes and compare the properties of this ligand with that of its hexadecanoyl ester derivative (**2**, $H_5EPTPAC16$)[23] [Figure 1]. The protonation constants were determined for both ligands by potentiometry, and their microscopic protonation scheme was obtained with NMR pH titrations. For ligand **1**, the stability constant of the $Gd^{III}$ complex was also obtained by potentiometry, and the solution dynamics of several $Ln^{III}$ complexes was studied by $^1H$ NMR spectroscopy. $^{17}O$ NMR and NMRD measurements have been performed on the $[Gd(EPTPACH_2OH)(H_2O)]^{2-}$ complex, thus allowing us to determine the parameters that govern its relaxivity. Its stability towards $Zn^{2+}$ transmetallation was also tested.

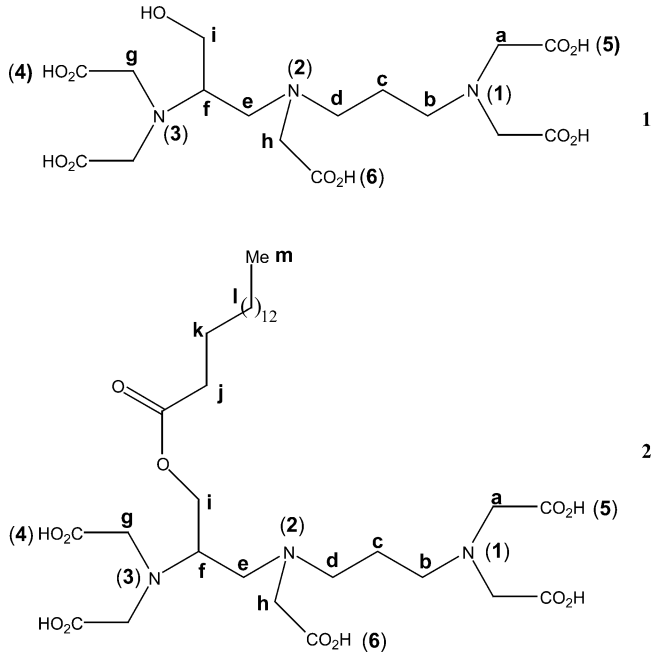


Figure 1. Chemical structures of the ligands $H_5EPTPACH_2OH$ (**1**) and $H_5EPTPAC16$ (**2**). Arbitrary numbers and labelling is shown for convenience of the $^1H$ NMR assignment.

## Results and Discussion

### Synthesis of the Ligands

We have recently reported a new synthetic path to metal chelators based on the EPTPA skeleton bearing a hydroxymethyl group on the ethylenediamine unit. The substi-

 © 2007 Wiley-VCH Verlag GmbH & Co. KGaA, Weinheim 

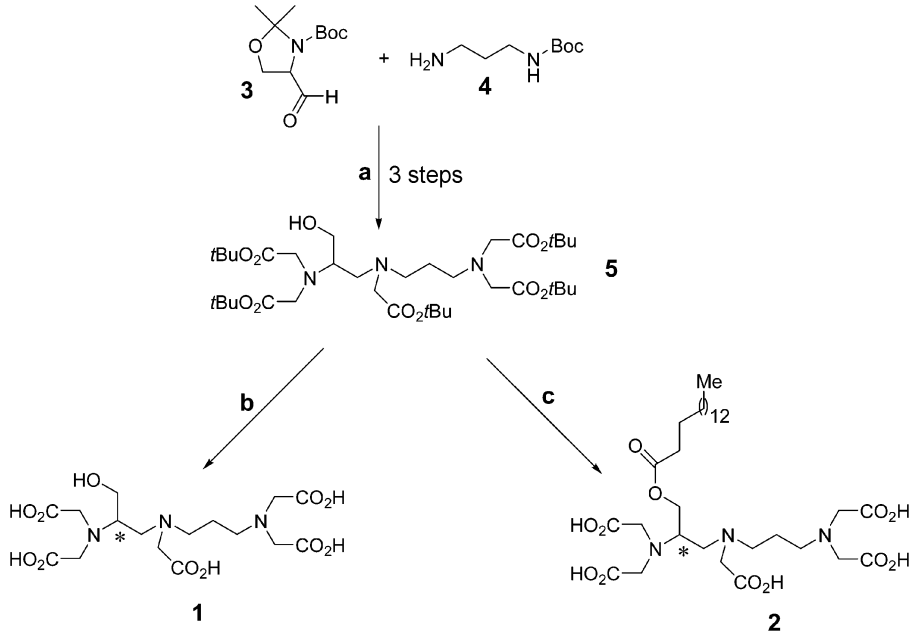


Scheme 1. (a) ref.[22] (b) 6M HCl/EtOH (1:1). (c) ref.[23]

tution of an ethylene by a propylene bridge on the DTPA skeleton is aimed at imposing steric compression around the water binding site, and therefore, to lead to $Gd^{III}$ complexes with fast water-exchange rates. The hydroxymethyl "handle" is ideal for conjugation of the key protected intermediate **5** (Scheme 1) to organic moieties for targeting and/or $\tau_r$ optimization purposes. As *proof of concept* we have recently reported the synthesis and characterization the new micellar contrast agent $[Gd(EPTPAC16)(H_2O)]^{2-}$.[23]

Acidic deprotection of the fully protected intermediate **5** affords in quantitative yields the new chelator $H_5$EPTPA-$CH_2OH$ (**1**) [Scheme 1]. The synthesis started with the unnatural *R* enantiomer of serine (D-Serine), and it is reasonable to assume that the synthetic route devised is not likely to have led to racemization or inversion of configuration on the stereogenic center. Ligand **1** displays a stereogenic center that is assumed to have an absolute *S* configuration. The apparent inversion of configuration *R*→*S* reflects only a change in the assignment of priority of one of the groups attached to the stereogenic center. The enantiomer excess could have been determined for the fully protected intermediate **5** through, for example, the MTPA ester method.[24] Although the enantiomeric excess was not measured, the obtained $[\alpha]_D$ values of –31.9 ($c$ = 1.0, $H_2O$, pH = 1.40) and –6.3 ($c$ = 1.0, $H_2O$, pH = 9.8) confirm that the fully deprotected compound **1** is optically active. The dramatic difference in the measured $[\alpha]_D$ values under acidic and basic conditions probably reflects the rigidity of the ligand in acidic media, which results from intramolecular hydrogen bonding.

## Potentiometric Determination of Protonation and Stability Constants

The protonation constants of the ligands EPTPA-$CH_2OH^{5-}$ and $EPTPAC16^{5-}$ were determined by pH potentiometric titrations (Figure 2). The protonation constants of the two ligands, $pK_i = \log K_i^H$, where $K_i^H$ is defined as in Equation (1), are listed and compared to those of similar ligands and DTPA in Table 1 (standard deviations are shown in parenthesis).

$$K_i^H = [H_iL]/[H_{i-1}L][H^+];\ i = 0,1,2,3,4,5 \quad (1)$$

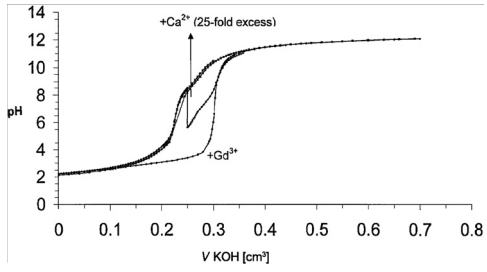


Figure 2. Potentiometric pH titration curves for the ligand EPTPA-$CH_2OH^{5-}$ in the absence and in the presence of $Ca^{II}$ or $Gd^{III}$ [$c$(EPTPACH$_2$OH) = 2.055 mM, $c$(KOH) = 0.2461 M, metal/ligand ratio = 1:1, $I$ = 1.0 M KCl, $T$ = 25 °C].

Both $EPTPACH_2OH^{5-}$ and $EPTPAC16^{5-}$ ligands display a slightly higher protonation constant for the first protonation step than that for the ligand $DTPA^{5-}$[25], as observed previously for the unsubstituted ligand $EPTPA^{5-}$[26] and the backbone substituted EPTPA-bz-$NO_2^{5-}$[20c] (see Table 1). Such an increase in the protonation constants relative to those for $DTPA^{5-}$ also occurs for the subsequent protonation steps for all the backbone substituted ligands, including the two studied in this work. This general increase in the protonation constants upon replacement of one ethylene group in the backbone of $DTPA^{5-}$ by one trimethylene group results from reduced electrostatic repulsion between the protonated amino groups on lengthening of the chain between them.[26] The most pronounced increase is ob-

 © 2007 Wiley-VCH Verlag GmbH & Co. KGaA, Weinheim 

Table 1. Protonation constants for the ligands $H_5EPTPACH_2OH$ (**1**) (25 °C, $I$ = 1.0 M KCl) and $H_5EPTPAC16$ (**2**) (25 ± 0.2 °C, $I$ = 0.1 M) and stability constants for the $Gd^{III}$–$EPTPACH_2OH$ complex (25 °C, $I$ = 1.0 M KCl). Data for other ligands are included for comparison.

| | $H_5DTPA$[25] | $H_5EPTPA$-bz-$NO_2$[20c] | $H_5EPTPA$[26] | $H_5EPTPACH_2OH$[a] | $H_5EPTPAC16$[a] |
|---|---|---|---|---|---|
| p$K_1$ | 10.41 | 10.86(±0.01) | 10.60 | 10.65(±0.08) | 11.04(±0.01) |
| p$K_2$ | 8.37 | 8.91(±0.02) | 8.92 | 8.39(±0.09) | 8.91(±0.02) |
| p$K_3$ | 4.09 | 4.70(±0.02) | 5.12 | 4.43(±0.09) | 5.41(±0.03) |
| p$K_4$ | 2.51 | 3.25(±0.02) | 2.80 | 2.78(±0.10) | 5.02(±0.02) |
| p$K_5$ | 2.04 | 2.51(±0.03) | [c] | 2.75(±0.08) | 2.66(±0.08) |
| log $K_{GdL}$ | 22.50 | 19.20 (±0.02) | 22.77[b] | 16.7(±0.05) | [c] |
| log $K_{GdHL}$ | 1.80 | 3.40(±0.02) | [c] | 3.64(±0.04) | [c] |

[a] This work. [b] In ref.[20c] the corrected values for $[Gd(EPTPA)(H_2O)]^{2-}$ were found: log $K_{GdL}$ = 18.75(±0.07) by direct titration and log $K_{GdL}$ = 17.5 (±0.3) by competition with EDTA. [c] Not determined.

served for the third and fourth protonation steps for the ligand $EPTPAC16^{5-}$. This agrees with the fact that polyamines with increasing chain length usually display increasing protonation constants.[27]

The first protonation constant for the ligands $EPTPA^{5-}$ and $EPTPACH_2OH^{5-}$ is practically the same (within experimental error). The protonation constants for the other protonation steps are slightly lower for $EPTPACH_2OH^{5-}$ than those observed for $EPTPA^{5-}$. The first four protonation constants of the ligand $EPTPAC16^{5-}$ are higher than those of the nonconjugated ligand $EPTPACH_2OH^{5-}$. A rather pronounced effect is observed for the fourth protonation constant of $EPTPAC16^{5-}$ – its value is two orders of magnitude higher than the corresponding value for $EPTPA\text{-}CH_2OH^{5-}$.

The stability and the protonation constants of the metal complexes are expressed in Equation (2) and Equation (3).

$$K_{ML} = [ML]/[M][L] \quad (2)$$

$$K_{MH_iL} = [MH_iL]/[MH_{i-1}L][H^+];\ i = 1,2 \quad (3)$$

These thermodynamic stability constants, obtained by pH potentiometry for the $Gd^{III}$–$EPTPACH_2OH$ system (Figure 2), are also listed in Table 1 and compared to those for the Gd complexes of similar ligands and DTPA. The species distribution diagram for the system $Gd^{III}/EPTPA\text{-}CH_2OH/(H^+)$, represented in Figure 3, indicates that above pH 5, there is no free $Gd^{III}$ in a solution containing a 1:1 molar ratio of $Gd^{III}$ and ligand. The unprotonated complex $[Gd(EPTPACH_2OH)(H_2O)]^{2-}$ is the only species present at physiological pH 7.4. For the ligand $EPTPAC16^{5-}$, the observation of precipitation in the system for pH values below 4 precluded the determination of the stability constants of its $Gd^{III}$ complex.

The value previously determined for the complex $[Gd(EPTPA)(H_2O)]^{2-}$ (log $K_{GdL}$ = 22.77) from a competition study with $EDTA^{4-}$[26] is about the same as that measured for $[Gd(DTPA)(H_2O)]^{2-}$. This value did not seem reasonable because of the fact that EPTPA complexes form one six-membered chelates, which are less stable than the five-membered rings observed for the DTPA analogues. We therefore would have expected a lower stability for the EPTPA complexes. This was indeed demonstrated by Merbach et al.,[20c] who found, for $[Gd(EPTPA)(H_2O)]^{2-}$, a

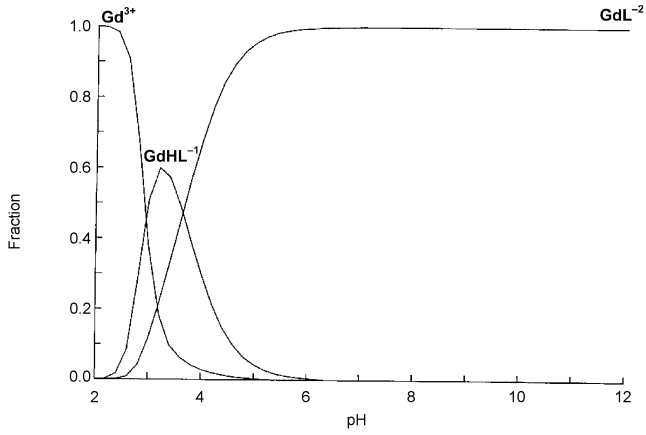


Figure 3. Species distribution curves for a 2 mM $Gd^{III}/EPTPA\text{-}CH_2OH/(H^+)$ system containing a 1:1 molar ratio of $Gd^{III}$ to ligand ($I$ = 1.0 M KCl, $T$ = 25 °C). Fraction is relative to 2 mM total $Gd^{III}$ species.

value log $K_{GdL}$ = 18.75(±0.07) by direct titration and log $K_{GdL}$ = 17.5(±0.3) by competition with EDTA. The value log $K_{GdL}$ = 16.7 ± 0.05 obtained in the present study for the thermodynamic stability constant of the complex $[Gd(EPTPACH_2OH)(H_2O)]^{2-}$ is two orders of magnitude lower than the corrected value for $[Gd(EPTPA)(H_2O)]^{2-}$ and even lower than the value for the complex $[Gd(EPTPA\text{-}bz\text{-}NO_2)(H_2O)]^{2-}$,[20c] which indicates the destabilizing effect of the $CH_2OH$ substituent group at the EPTPA backbone. All these substitutions occur at the C4 position (position b, see Figure 1) of the EPTPA backbone, which might not be optimal for the stability of the complex; however, this depends on the type of substituent. It has been shown that substitution at the EPTPA backbone with a phenyl group has a stabilizing effect on the $[Gd(EPTPA)(H_2O)]^{2-}$ structure towards $Zn^{2+}$ transmetallation; the effect is much higher when the substitution is at C9 than at C4 (positions b and f, respectively, see Figure 1), but substitution with a methyl group at C9 or C4 has no stabilizing effect on the parent compound.[28]

The present results, summarized in Table 1, show that the stability of the $Ln^{III}$ complexes of the EPTPA derivatives decreases when the sum of the protonation constants of the free ligand increases, which is the opposite of the usual

 © 2007 Wiley-VCH Verlag GmbH & Co. KGaA, Weinheim 

trend found for many polyamino–polycarboxylic acids.[29] The trend can be explained by the presence of an extra $CH_2$ group in the ligand backbone, which increases the basicity of the adjacent nitrogen donor atoms, but reduces the stability of the six-membered chelate ring formed.

## NMR pH Titrations

The macroscopic protonation constants obtained by potentiometry give no information on the microscopic sequence of protonation of the ligand sites. This protonation sequence can be obtained by $^1H$ NMR pH titration, where the chemical shifts of the ligand methylene protons are determined as a function of the pH, since the protonation of a basic site of a poly(aminocarboxylate) ligand results in a deshielding of the adjacent nonlabile methylene protons.[30] Changes in chemical shifts can quantitatively indicate the site of protonation.[30,31]

The $^1H$ NMR pH titration curves for some of the protons of the ligands $H_5EPTPACH_2OH$ and $H_5EPTPAC16$ are shown in Figure 4. The corresponding resonances were assigned at different pH values on the basis of signal multiplicities, the signal crossovers, and COSY spectra in the whole pH range studied. These titration curves display sharp changes at different pH values, which relate to the protonation states of the ligand. Since there is fast exchange on the NMR time scale among the various protonated species ($H_nL$), the observed shift of a given proton is given by the average of the shifts of the various species ($\delta_{H_nL}$) weighted by their molar fractions ($x_n$); $\delta_{obs} = \Sigma x_n \cdot \delta_{H_nL}$.[30] The procedure used to obtain the protonation fractions at each ligand site has been described in detail.[31] In summary, the shifts of the protonated species ($\delta_{H_nL}$), obtained by fitting the experimental pH titration curves by using the potentiometric protonation constants, were used to calculate the protonation fractions (%) at the nitrogen [$f_N = f_{(1)}$, $f_{(2)}$, $f_{(3)}$] and oxygen [$f_O = f_{(4)}$, $f_{(5)}$, $f_{(6)}$] atoms (labelled in Figure 1) of each ligand protonation state $H_nL$ (integer $n$ = 1, 2, 3,... is the number of moles of acid added per mole of ligand). It was assumed that the protonation shifts at the various sites are additive, with a total shift ($\Delta\delta$) given by the expression $\Delta\delta = \Sigma C_N \cdot f_N + \Sigma C_{N'} \cdot f_N + \Sigma C_O \cdot f_O$, where $C_N$ = 0.75 ppm, $C_{N'}$ = 0.35 ppm and $C_O$ = 0.20 ppm are pH-independent shielding constants valid for linear poly(aminocarboxylate) ligands.[30]

The values of $f_N$ [$f_{(1)}$, $f_{(2)}$, $f_{(3)}$] and $f_O$ [$f_{(4)}$, $f_{(5)}$, $f_{(6)}$] were calculated for the $H_nL$ species of the two ligands and compared with those reported for $H_5EPTPA$[26] (see Table S3 in the Supporting Information). The first two protonations occur in all cases exclusively at the backbone nitrogen atoms [$f_O = f_{(4)}$, $f_{(5)}$, $f_{(6)} = 0$]. The $f_i$ values for $n$ = 1 show that the first protonation is very similar for the three ligands, where the more basic central nitrogen atom [$N_{(2)}$] is protonated preferentially to the terminal ones, as was also found for DTPA.[26,30,31] For $n$ = 2, there is a preference for the protonation of the terminal nitrogen atoms over that of the central nitrogen atom in all ligands. However, the protonation of the two terminal nitrogen atoms is quite distinct in the three asymmetric ligands EPTPA and the two derivatives studied in this work. The protonation of the trimethylene nitrogen atom [$N_{(1)}$] is favored over that of the ethylene nitrogen atom [$N_{(3)}$] for $n$ = 1–3, because of the increased separation in the positive charges in $N_{(1)}$–$N_{(2)}$ relative to $N_{(2)}$–$N_{(3)}$ and possibly also because of the stabilization of a six-membered ring by hydrogen bonding between $N_{(1)}$ and $N_{(2)}$. The protonation of $N_{(3)}$ is less favored in the two EPTPA derivatives than in EPTPA because of the steric effect of the C4-substituents in the ethylenediamine moiety. The forms with the protonated terminal nitrogen atoms are stabilized by internal hydrogen bonding with the corresponding carboxylate groups, which leads to increased values for the second and third protonation constants relative to those for DTPA.[26,30,31] These internal hydrogen bonds also lead to preferential protonation of the carboxylate groups bound to the less protonated nitrogen atoms, as shown by the $f_i$ values, which could be obtained for $n > 2$.

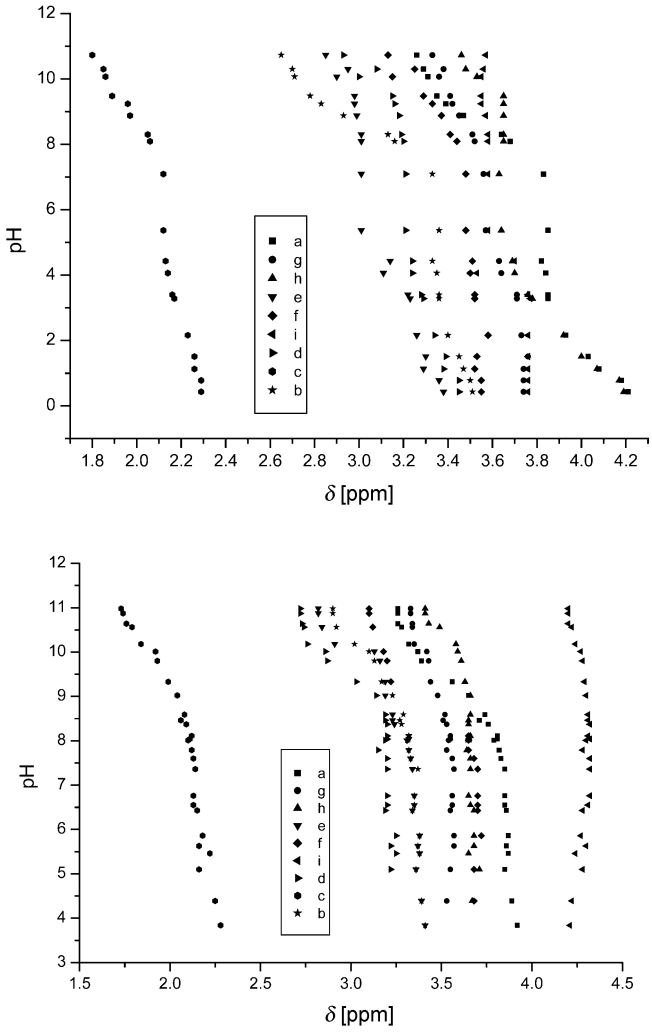


Figure 4. Variation of the $^1H$ NMR chemical shifts versus pH for the ligands $H_5EPTPACH_2OH$ (top) and $H_5EPTPAC16$ (bottom) [see Figure 1 for the labelling of protons].

 © 2007 Wiley-VCH Verlag GmbH & Co. KGaA, Weinheim 

### $^1$H NMR Study of [Ln(EPTPACH$_2$OH)]$^{2-}$ Complexes

The $^1$H NMR spectra of the [Ln(EPTPACH$_2$OH)]$^{2-}$ complexes, both diamagnetic (Ln = La, Lu, Y) and paramagnetic (Ln = Pr, Nd, Sm, Eu, Tb, Dy, Yb), were obtained in $D_2O$ at pH 7.0 as a function of temperature (7, 25, 60 and 80 °C; see Figure S1 in the Supporting Information for some typical spectra). The diamagnetic spectra (illustrated in Figure S1a by the $Y^{III}$ complex) are quite crowded and were not fully assigned. The presence of high and low intensity resonances could be seen throughout the whole spectrum for all the diamagnetic complexes. The COSY spectrum of [Y(EPTPACH$_2$OH)]$^{2-}$ (Figure S2a, Supporting Information) contains two sets of five cross peaks of high and low intensity, which correspond to the five AB quartets characteristic of the methylene protons of the five bound acetate groups of EPTPA in two isomeric complexes of high and low populations. The signals for the $Lu^{III}$ and $Y^{III}$ complexes did not broaden significantly at high temperatures. This is not the case for the $La^{III}$ complex, whose signals becomes very broad at high temperature, as found for the $La^{III}$- and $Lu^{III}$–DTPA complexes, in which the central nitrogen racemization process is quite effective, and therefore, the spectra of the two asymmetric conformers present is effectively averaged.[32,33]

All the $^1$H NMR spectra of the paramagnetic complexes studied also show high and low intensity resonances. This is best seen in the sharper spectra of the early-$Ln^{III}$ series (see Figure S1b,c,d), which confirms the presence of two isomeric complexes, one of much higher population than the other. The major complex, whose spectrum exhibits 21 resonances of high intensity, has a smaller spread of proton paramagnetic shifts than that of the low intensity resonances of the minor complex. The presence of one resonance per nonexchangeable ligand proton shows that racemization of the central nitrogen through the wagging of the attached acetate group does not occur. Again, a different result is observed for the spectra of the paramagnetic $Ln^{III}$–DTPA complexes, where racemization of the central nitrogen through a wagging motion of its bound acetate group averages the spectra of the two asymmetric conformers present in solution.[34,35]

All the paramagnetic spectra were too complex to be assigned, even with the help of observable COSY cross peaks (Figure S2b,c). The signals from the major isomer were not significantly broadened at high temperatures, in contrast to those from the minor isomer. This is most clearly observed for the spectrum of the $Sm^{III}$ complex (Figure S1c), with a major/minor ratio of 25:4, in which the broadening of the three high-frequency doublets (7.66, 7.27, and 6.85 ppm) at 40 °C makes the couplings unobservable. Further, of the three low-frequency multiplets, the one at –2.02 ppm is selectively broadened at 40 °C. The major and minor isomers observed in the [Ln(EPTPACH$_2$OH)]$^{2-}$ complexes result from the conformational properties of the ligand backbone. While the six-membered ring formed by the $Ln^{III}$–propylenediamine chelate is locked in a chair conformation,[36] the ethylenediamine moiety can adopt a δ or λ conformation in its five-membered ring chelate. One of these conformations places the $CH_2OH$ substituent in a more stable, less-crowded position than that in the other conformation. The $CH_2OH$ substituent prevents the central acetate wagging motion and also slows down the δ/λ backbone interconversion process that averages the spectra of the major (M) and minor (m) complexes. The selective broadening of the signals of minor complex that results from this dynamic process is a consequence of the equilibrium constant $K_{eq}$ = [m]/[M] << 1 being unfavorable to the m species, which leads to relative kinetic constants $k$(m→M) >> $k$(M→m).

### $^{17}$O NMR, $^1$H NMRD and EPR Measurements

The water-exchange rate was determined for the $Gd^{III}$–EPTPACH$_2$OH$^{5-}$ complex from a variable-temperature $^{17}$O NMR spectroscopic study. Additionally, the magnetic field dependence of the longitudinal water proton relaxivities ($r_1$) [nuclear magnetic relaxation dispersion − NMRD − curves] at different temperatures and EPR spectra were measured on the same complex with the objective of determining the parameters that describe water exchange, rotation, electronic relaxation, and proton relaxivity.

The obtained experimental NMRD data (Figure 5) and the $^{17}$O NMR chemical shifts ($\Delta\omega_r$), longitudinal ($1/T_{1r}$) and transverse ($1/T_{2r}$) relaxation rates (Figure 6) were analyzed simultaneously by using the Solomon–Bloembergen–Morgan (SBM) theory (for the equations used in the data analysis, see the Supporting Information). It was assumed that [Gd(EPTPACH$_2$OH)(H$_2$O)]$^{2-}$ had one inner-sphere water molecule ($q$ = 1), as in the [Gd(EPTPA)(H$_2$O)]$^{2-}$ and [Gd(EPTPA-bz-NO$_2$)(H$_2$O)]$^{2-}$ complexes.[20c] The parameters obtained in the fit are shown in Table 2, and Figures 5 and 6 show the corresponding fitted curves obtained for the NMRD and $^{17}$O NMR spectroscopic data. The ratio of the rotational correlation times of the Gd–O and Gd–H vectors, $\tau_{rO}$ and $\tau_{rH}$, respectively, fluctuated during the fits around its theoretical lower limit of 0.65 (based on geometrical considerations) and has been fixed to that value.[37] Some parameters given in Table 2 have been adjusted in preliminary fits and fixed in the final fitting procedure. Other parameters were fixed in the fit to typical values from the literature:[4,5] the $^{17}$O scalar coupling constant $A/\hbar$ = $-3.2 \times 10^6$ rad s$^{-1}$, the relative diffusion coefficient between the complex and water molecules $D_{GdH}^{298} = 25 \times 10^{10}$ m$^2$ s$^{-1}$ and the corresponding activation energy $E_{DGdH}$ = 25 kJ mol$^{-1}$, the distance of closest approach between the $Gd^{III}$ ion and the outer-sphere water molecules $a_{GdH}$ = 3.6 Å, the distances between $Gd^{III}$ and the coordinated water oxygen atom $r_{GdO}$ = 2.50 Å and protons $r_{GdH}$ = 3.10 Å, the quadrupolar coupling constant for the bound water $^{17}$O $\chi(1+\eta^2/3)^{1/2}$ = 7.68 MHz,[38] and the empirical constant for the outer-sphere contribution to the $^{17}$O chemical shift $C_{os}$ = 0.1.[20c] The values obtained for the activation parameters for water exchange, $\Delta H^{\ddagger}$ and $\Delta S^{\ddagger}$, and for the activation energies, $E_v$ and $E_R$, are very close to those obtained for the [Gd(EPTPA)(H$_2$O)]$^{2-}$ and [Gd(EPTPA-bz-NO$_2$)(H$_2$O)]$^{2-}$ complexes (Table 2).[20c]

 © 2007 Wiley-VCH Verlag GmbH & Co. KGaA, Weinheim 

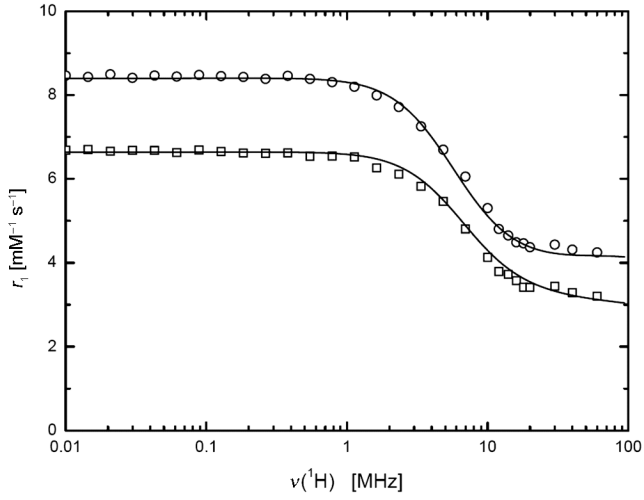


Figure 5. $^1$H NMRD profiles at 25 °C (circles) and 37 °C (squares) for $[Gd(EPTPACH_2OH)(H_2O)]^{2-}$. The lines represent curves from results of a simultaneous fit of NMRD and $^{17}$O NMR spectroscopic data.

Table 3 compares the values for the parameters that determine relaxivity – the water-exchange rate ($k_{ex}^{298}$), the rotational correlation time of the complex ($\tau_{rO}^{298}$) and the electron spin relaxation parameters ($\Delta^2$ and $\tau_V^{298}$) – obtained for $[Gd(EPTPACH_2OH)(H_2O)]^{2-}$ with the corresponding values for $Gd^{III}$ complexes with other ligands containing the EPTPA structure and with DTPA.[20c,23,39] The 20 MHz proton relaxivities obtained for those systems are also compared.[26] The water-exchange rate of $[Gd(EPTPA\text{-}CH_2OH)(H_2O)]^{2-}$, $k_{ex}^{298} = 87.6 \times 10^6$ s$^{-1}$, is consistent with values obtained for analogous chelates that form between $Gd^{III}$ and EPTPA-based ligands and is close to the theoretically derived optimal value ($k_{ex}^{298} \approx 10^8$ s$^{-1}$[20c]). In all these compounds, steric compression around the water binding site leads to accelerated water exchange relative to DTPA-based $Gd^{III}$ complexes.[20c,23] However, it is interesting to observe that, while the inclusion of substituents on the C4 carbon atom of the ethylene bridge of a series of $Gd^{III}$–DTPA complexes leads to a 3–5 fold increase in $k_{ex}^{298}$ relative to that of the parent complex $[Gd(DTPA)(H_2O)]^{2-}$,[15–18] similar substitution on the C4 carbon atom of the ethylene bridge of a series of $Gd^{III}$–EPTPA complexes leads to a 2–4 fold decrease in $k_{ex}^{298}$ relative to that of the parent complex $[Gd(EPTPA)(H_2O)]^{2-}$;[20c,23] $[Gd(EPTPA)(H_2O)]^{2-}$ has a $k_{ex}^{298}$ value that is 100 times larger than that of $[Gd(DTPA)(H_2O)]^{2-}$. Another study has also shown that substitution by a methyl group at C4, and specially at C9 (propylene bridge), in the parent complex gives the highest $k_{ex}$ values, but substitution by a bulkier phenyl group at both positions decreases the water-exchange rates to values only 3 times larger than that for $Gd^{III}$–DTPA.[28]

With regard to rotational dynamics, the rotational correlation time obtained for $[Gd(EPTPACH_2OH)(H_2O)]^{2-}$ is comparable to the values for other small $Gd^{III}$ complexes, where the relative values increase, as expected, with their molecular weights. Therefore, the 20 MHz proton relaxivity

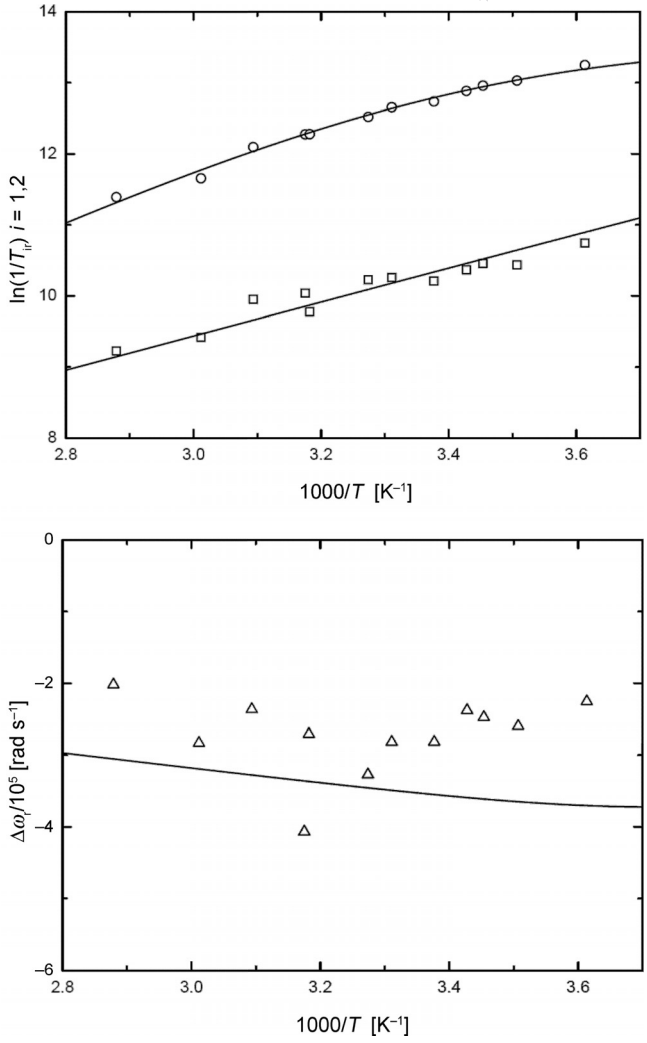


Figure 6. Temperature dependence of transverse and longitudinal $^{17}$O relaxation rates (top) and $^{17}$O chemical shifts (bottom) for $[Gd(EPTPACH_2OH)(H_2O)]^{2-}$ at $B$ = 4.7 T. The lines represent curves from results of a simultaneous fit of NMRD and $^{17}$O NMR spectroscopic data.

Table 2. Parameters obtained for the $[Gd(EPTPACH_2OH)(H_2O)]^{2-}$ chelate from the analysis of $^{17}$O NMR and NMRD data (parameters in italics have been fixed in the final fit).

| Parameter | |
|---|---|
| $k_{ex}^{298}$ [$10^6$ s$^{-1}$] | 87.6 ± 16.3 |
| $\Delta H^{\ddagger}$ [kJ mol$^{-1}$] | 30.5 ± 4.1 |
| $\Delta S^{\ddagger}$ [J mol$^{-1}$ K$^{-1}$] | +9.4 ± 10 |
| $A/\hbar$[$10^6$ rad s$^{-1}$] | *–3.2* |
| $\tau_{rO}^{298}$ [ps] | 116.2 |
| $E_R$ [kJ mol$^{-1}$] | 19.8 ± 1.3 |
| $\tau_V^{298}$ [ps] | 8.8 ± 0.7 |
| $E_v$ [kJ mol$^{-1}$] | *1.0* |
| $\Delta^2$ [$10^{20}$ s$^{-2}$] | 0.89 ± 0.10 |
| $D_{GdH}^{298}$ [$10^{-10}$ m$^2$ s$^{-1}$] | *25* |
| $E_{DGdH}$[kJ mol$^{-1}$] | *25* |
| $\tau_{rH}^{298}/\tau_{rO}^{298}$ | *0.65* |

$r_1$ of the EPTPA-based $Gd^{III}$ complexes, shown in Table 3, is determined by the (relatively fast) rotational correlation time, as is usual for all small complexes.

 © 2007 Wiley-VCH Verlag GmbH & Co. KGaA, Weinheim 

Table 3. Relaxivity (at 20 MHz and 25 °C) and parameters determining relaxivity for selected $Gd^{III}$ complexes.

| Complex | $k_{ex}^{298}$ [$10^6$ $s^{-1}$] | $\tau_{rO}^{298}$ [ps] | $\Delta^2$ [$10^{20}$ $s^{-2}$] | $\tau_V^{298}$[ps] | $r_1$ [$mM^{-1}$ $s^{-1}$] |
|---|---|---|---|---|---|
| $[Gd(DTPA)(H_2O)]^{2-}$[39] | 3.3 | 58 | 0.46 | 25 | 3.89[26][c] |
| $[Gd(EPTPA)(H_2O)]^{2-}$[20c] | 330 | 75 | 0.76 | 22.4 | 3.85[26][d] |
| $[Gd(EPTPACH_2OH)(H_2O)]^{2-}$[a] | 87.6 | 116.2 | 0.4 | 22 | 4.37 |
| $[Gd(EPTPA\text{-}bz\text{-}NO_2)(H_2O)]^{2-}$[20c] | 150 | 122 | 0.89 | 8.8 | 4.73 |
| $[Gd(EPTPAC16)(H_2O)]^{2-}$[23][b] | 170 | $\tau_{rH}$ = 200 | 0.08 | 44 | 9.11 |

[a] This work. [b] Monomer form. [c] At 37.0 ± 0.1 °C and pH = 7.6 ± 0.1. [d] At 37.0 ± 0.1 °C and pH = 7.5 ± 0.1.

In our combined analysis of the $^{17}O$ NMR and NMRD data, we used the simple Solomon–Bloembergen–Morgan (SBM) theory, which is known to give only a rough approximation for electron spin relaxation rates $1/T_{1e}$ and $1/T_{2e}$.[40–42] We will therefore not discuss the parameters linked to it ($\tau_v$, $\Delta^2$). X-band EPR spectra of the $[Gd(EPTPACH_2OH)(H_2O)]^{2-}$ complex in aqueous solution at 298 K gave an approximately Lorentzian line centered at a magnetic field corresponding to $g_L \approx 2.0$, with an experimental peak-to-peak linewidth $\Delta H_{pp}$ = 23.64 ± 0.05 mT. The value for the linewidth was independent of the concentration of the complex in the range studied. The corresponding transverse electronic relaxation rate ($1/T_{2e}$) was calculated using Equation (4), in which the symbols have their usual meaning.[43]

$$\frac{1}{T_{2e}} = \frac{g_L \mu_B \pi \sqrt{3}}{h} \Delta H_{pp} \quad (4)$$

The calculated transverse electron spin relaxation rate of $(1/T_{2e})_{exp} = 2.265 \times 10^{10}$ $s^{-1}$ (at $B$ = 0.34 T) is about three times larger than $(1/T_{2e})_{calc} = 7.14 \times 10^9$ $s^{-1}$, the value calculated by using Morgan's equation (A20, Supporting Information) with $\Delta^2$ and $\tau_V^{298}$ obtained from the simultaneous fitting of the $^{17}O$ NMR and $^1H$ NMRD data (Table 3). X-band experimental EPR values of $1/T_{2e}$ have been systematically found to be larger than those calculated for many $Gd^{III}$ complexes, which confirms the deficiencies of SBM theory.[31,43,44,45] The use of a more recent description of electron spin relaxation needs, however, EPR measurements to be made over a wide temperature range and with different frequencies.[46]

### Transmetallation Kinetics

The kinetic stability of $[Gd(EPTPACH_2OH)(H_2O)]^{2-}$ in solution towards transmetallation with $Zn^{2+}$ was evaluated by the time dependence of the decrease in the water proton longitudinal relaxation rate ($R_1^p$) of phosphate-buffered solutions containing $Zn^{2+}$.[47] Precipitation as phosphates of the $Gd^{3+}$ ions released as a result of substitution by $Zn^{2+}$ leads to a decrease in $R_1^p$ that is proportional to the amount of released $Gd^{3+}$ ions. In the absence of $Zn^{2+}$, the stability of the $Gd^{3+}$ complex in the phosphate buffer depends on the buffer concentration, and is much higher at 10 mM than at 67 mM (Figure 7). The kinetic stability in the concentrated buffer is similar to the behavior observed for $[Gd(4\text{-Me-EPTPA})(H_2O)]^{2-}$.[28] In the presence of $Zn^{2+}$, the decrease in $R_1^p$ is much faster, which indicates a fast and extensive transmetallation process (Figure 7). The rate and extent of this process increases with buffer concentration. However, at higher buffer concentrations, the kinetic stability of $[Gd(EPTPACH_2OH)(H_2O)]^{2-}$ towards $Zn^{2+}$ transmetallation is higher than that of $[Gd(4\text{-Me-EPTPA})(H_2O)]^{2-}$, but is still much lower than that of C9- and C4 phenyl-substituted $[Gd(EPTPA)(H_2O)]^{2-}$ derivatives.[28]

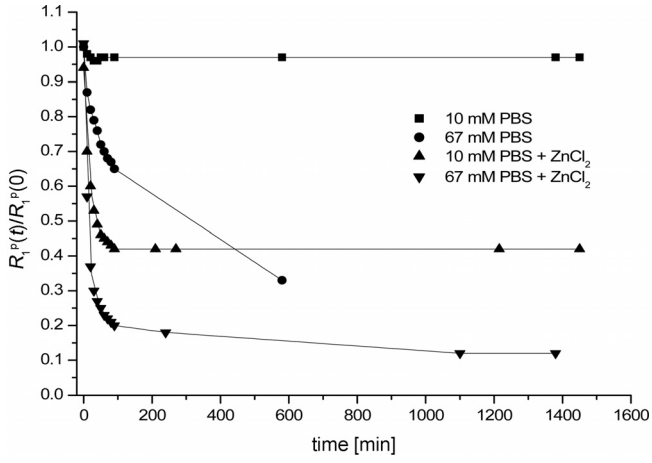


Figure 7. Time evolution of the proton relaxation rate of 2.5 mM $[Gd(EPTPACH_2OH)(H_2O)]^{2-}$ (20 MHz, 310 K, pH 7.1) in (■) 10 mM PBS, (●) 67 mM PBS, (▲) 10 mM PBS and 2.5 mM of $ZnCl_2$, and (▼) 67 mM PBS and 2.5 mM of $ZnCl_2$.

## Conclusions

We have devised a new synthetic route to the ligand 4-(*S*)-hydroxymethyl-3,6,10-tri(carboxymethyl)-3,6,10-triazadodecanoic acid, $H_5EPTPACH_2OH$. The fully protected precursor compound **5** is a versatile block for conjugation to biological moieties for targeting purposes and/or optimization of $\tau_r$, as demonstrated before.[23] The hydroxymethyl group allows the construction of potentially responsive contrast agents through enzymatic activation of cleavable bonds such as ester, phosphodiester, and glycosidic bonds. Moreover, although we have not attempted to functionalize the complex of the deprotected ligand **1**, we envisage that this could be an interesting approach to the (enzymatic) synthesis of conjugates that cannot resist the usual harsh deprotection conditions.

 © 2007 Wiley-VCH Verlag GmbH & Co. KGaA, Weinheim 

Potentiometry studies reveal that the ligand displays slightly higher protonation constants relative to those for the ligand $DTPA^{5-}$, which is consistent with the fact that polyamines with increasing chain length usually display increasing protonation constants. NMR pH titrations give some insight into the ligand microscopic protonation scheme. The first protonation occurs at the more basic central nitrogen atom preferentially over the terminal ones, as was also found for $DTPA^{5-}$. In the second protonation step, there is a preference for the terminal trimethylene and ethylene nitrogen atoms over the central nitrogen atom. Moreover, protonation at the ethylene nitrogen atoms is less favored because of the steric effect of the C4 substituents.

The stability constant (log $K_{GdL}$ = 16.7) for the $[Gd(EPTPACH_2OH)(H_2O)]^{2-}$ complex is two orders of magnitude lower than that for the $[Gd(EPTPA)(H_2O)]^{2-}$ complex, which indicates the destabilizing effect of the $CH_2OH$ group on the EPTPA backbone.

$^1H$ NMR studies of the $Ln^{III}$ chelates of these ligands in aqueous solution unambiguously show two sets of high and low intensity resonances, despite being too complex to be assigned, which confirms the presence of two isomeric complexes, one of much higher population than the other.

The water-exchange rate obtained for $[Gd(EPTPA-CH_2OH)(H_2O)]^{2-}$ is close to the theoretically derived optimal value that gives the highest proton relaxivities of $Gd^{III}$-based contrast agents. Despite the optimization of the water-exchange rate, the corresponding proton relaxivities are limited by a far from optimal rotational correlation time.

This ligand offers the possibility for conjugation of slowly rotating moieties through the hydroxymethyl handle, therefore this allows the design of $Gd^{III}$-based contrast agents with simultaneous optimization of the water-exchange rate and rotational correlation time. This approach has been previously applied to the synthesis of the $[Gd(EPTPAC16)(H_2O)]^{2-}$ complex.[23]

The kinetic stability of $[Gd(EPTPACH_2OH)(H_2O)]^{2-}$ in phosphate-buffered solutions towards $Zn^{2+}$ transmetallation is quite low, but higher than that of $[Gd(4\text{-}Me\text{-}EPTPA)(H_2O)]^{2-}$.[28]

## Experimental Section

**Materials and Equipment:** Chemicals of the highest analytical grade were purchased from Sigma–Aldrich and were used without further purification. Solvents used were of reagent grade and purified by the usual methods. Reactions were monitored by TLC on Kieselgel 60 $F_{254}$ (Merck) and products were detected by examination under UV light (254 nm) and by adsorption of iodine vapor. $^1H$ and $^{13}C$ NMR spectra (assigned by 2D DQF-COSY and HMQC techniques) were recorded with a Varian Unity Plus 300 NMR spectrometer operating at 299.938 MHz and 75.428 MHz for $^1H$ and $^{13}C$, respectively. For $^1H$ and $^{13}C$ NMR spectra recorded in $D_2O$, chemical shifts ($\delta$) are given in ppm relative to sodium 3-(trimethylsilyl)propanesulfonate (TSP) as internal reference ($^1H$, $\delta$ = 0.0 ppm) and *tert*-butanol as external reference ($^{13}C$, $CH_3$ $\delta$ = 30.29 ppm). $^{13}C$ NMR spectra were proton broad-band decoupled by using a GARP-1 modulated decoupling scheme. Mass spectrometry measurements were performed with an APEX III FT-ICR MS (Bruker Daltonics, Billerica, MA), equipped with a 7-T actively shielded magnet. Ions were generated by using an Apollo API electrospray ionization (ESI) source (Bruker Daltonics, Billerica, MA). Samples were prepared by applying a spray solution of 50:49.5:0.5 (v/v/v) water/methanol/formic acid at a v/v ratio of 1 to 5%. Data acquisition and data processing were performed with the XMASS software, version 6.1.2 (Bruker Daltonics).

### Synthesis and Characterization

**Compounds 2, 3, 4 and 5:** The synthesis of compounds **2**, **3**, **4**, and **5** was described previously by us.[23]

**Compound 1:** Purified compound **5** (2.32 g, 5.98 mmol) was stirred overnight at room temperature with 6 M HCl/EtOH (1:1, 40 $cm^3$) to afford the title compound in a quantitative yield. As the precursor, fully protected compound **5** was of analytical purity, as demonstrated before,[23] no further purification of the deprotected final compound **1** was judged necessary. $^1H$ NMR (300 MHz, $H_2O$, pH = 5.26): $\delta$ = 2.14 (m, 2 H, $NCH_2CH_2CH_2$), 2.99–3.72 [m br., 9 H, overlapping signals from $NCH_2CH_2CH_2$; $OHCH_2NCHCH_2N$], 3.60 (s, 4 H, terminal acetate protons linked to the ethylene bridge), 3.65 (s, 2 H, central acetate protons), 3.87 (s, 4 H, terminal acetate protons linked to the propylene bridge) ppm. $^{13}C$ (5.6 MHz, $D_2O$): $\delta$ = 23.12 ($NCH_2CH_2CH_2N$), 54.11, 55.86, 56.30 and 57.78 (signals from $NCH_2CH_2CH_2N$ and from $HOCH_2CHCH_2$), 56.70 [$N(CH_2CO_2H)_2$], 60.07 [$N(CH_2CO_2H)_2$], 61.73 ($NCH_2CO_2H$, central acetate), 63.68 ($NCHCH_2N$), 173.32, 175.92 and 180.22 ($CO_2H$) ppm. HRMS ($ESI^+$): calcd. for $C_{16}H_{28}N_3O_{11}$ $[M + H]^+$ 438.1725680; found 438.1718352.

### Protonation and Stability Constants Determined by Potentiometry

Ligand protonation constants were determined at constant ionic strengths [1.0 M KCl for $H_5EPTPACH_2OH$ and 0.1 M $(CH_3)_4NCl$ for $H_5EPTPAC16$]. The ligand solutions (5 $cm^3$ $H_5EPTPACH_2OH$ and 3 $cm^3$ $H_5EPTPAC16$), stirred continuously, were titrated in a thermostatted cell (25 ± 0.2 °C) under a constant stream of $N_2$ by using 0.25 M ($H_5EPTPACH_2OH$) and 0.05 M ($H_5EPTPAC16$) standardized solutions of KOH as the titrants in a Metrohm Dosimat 776 and 665 automatic burette. Combined glass electrodes (Metrohm 6.0234.100 and C14/02-Sc, Ag/AgC1 reference electrode in 3 M KCl; Moeller Scientific Glass Instruments, Switzerland) connected to a Radiometer pHM93 reference pH meter and Metrohm 692 pH/ion meter were used to measure the pH. Protonation constants were determined at 0.002 M and 0.003 M ligand concentrations from two-two parallel titrations. The exact concentration of the $H_5EPTPACH_2OH$ stock solution was also determined potentiometrically. During the ligand titration, after the observation of the first equivalent point, a 25-fold excess of $Ca^{II}$ ions were injected into the sample. The large excess of $Ca^{II}$ liberated the protons that remained on the ligand, and a second equivalent point was observable. The two ligand equivalent protons between the two equivalent points can be determined (see Figure 2). For determination of the stability constants of the [Gd(EPTPACH2OH)-$(H_2O)]^{2-}$ complex, solutions containing the ligand and $Gd^{III}$ in equimolar concentrations were titrated directly with KOH. The hydrogen ion concentration was calculated from the measured pH values by using the correction method suggested by Irving et al.[48] Data treatment and processing was done with the program PSEQUAD.[49]

### NMR pH Titrations

Solutions of the ligands (11.8 mM) for NMR pH titrations were made in $D_2O$ (99.8%), and the pD was adjusted with DCl or $CO_2$-free NaOD. The final pD values were measured on a HANNA

 © 2007 Wiley-VCH Verlag GmbH & Co. KGaA, Weinheim 

8417 pH meter with a HI1310 combined electrode (HANNA instruments, Italy) and converted to pH values by using the isotopic correction pH = pD – 0.4.[50] $^1$H NMR (1D and 2D COSY) spectra for the pH titrations were carried out with a Varian Unity Plus 300 NMR spectrometer operating at 299.938 MHz at a probe temperature of 25 ± 0.5 °C. Chemical shifts ($\delta$) are given in ppm relative to TSP as internal reference.

**$^1$H NMR of [Ln(EPTPACH$_2$OH)]$^{2-}$:** To an aqueous solution of the ligand (pH = 5.0) was added dropwise an aqueous solution of the corresponding $LnCl_3$ in a1:1 mol ratio. The pH was kept at about 5.0 by the addition of aqueous KOH, and the solution was stirred at room temperature for 1 h. The pH was then adjusted to 7.0 by the addition of KOH (aqueous solution). The solution was concentrated under reduced pressure. The solutions for NMR measurements were obtained by dissolution of the solid complexes obtained previously in $D_2O$ ($V$ = 1 cm$^3$) to obtain 30 mM concentrations. Proton 1D and 2D COSY spectra of the solutions of the diamagnetic ($La^{III}$, $Lu^{III}$, and $Y^{III}$) and paramagnetic ($Pr^{III}$, $Nd^{III}$, $Sm^{III}$, $Eu^{III}$, $Tb^{III}$, $Dy^{III}$, and $Yb^{III}$) complexes were obtained at 7, 25, 60, and 80 °C with Varian Unity Plus 300 (299.938 MHz) and Varian Unity 500 (499.826 MHz) NMR spectrometers.

**$^{17}$O NMR, NMRD and EPR Experiments**

**Sample Preparation:** The $Gd^{III}$ chelate of EPTPACH$_2$OH (for $^{17}$O NMR and NMRD) was prepared by mixing equimolar amounts of $GdCl_3$ and the ligand. A slight excess (5%) of ligand was used, and the pH of the stock solution was adjusted by adding aqueous NaOH (0.1 M). The solution was allowed to react for 1 h at room temperature. The absence of free metal was checked in each sample by testing with xylenol orange.[51] $^{17}$O-enriched water ($^{17}$O: 11.4%) was added to the solutions for the $^{17}$O measurements to improve the sensitivity. The final solution concentration was 25.39 mmol kg$^{-1}$ at pH 6.89. For the NMRD experiments, 6.99 mM solutions at pH 6.18 were used.

**$^{17}$O NMR Experiments:** Variable-temperature $^{17}$O NMR measurements were performed with a Bruker Avance-200 (4.7 T, 27.1 MHz) spectrometer, and a BVT-3000 temperature-control unit was used to stabilize the temperature that was measured by a substitution technique. The samples were sealed in glass spheres that fitted into 10-mm o.d. NMR tubes to eliminate susceptibility corrections to the chemical shifts.[52,53] Longitudinal relaxation rates $1/T_1$ were obtained by the inversion recovery method, and transverse relaxation rates $1/T_2$ by the Carr–Purcell–Meiboom–Gill spin-echo technique. As an external reference, acidified water of pH 3.4 was used.

**NMRD Measurements:** The measurements were performed by using a Stelar Spinmaster FFC NMR relaxometer (0.01–20 MHz) equipped with a VTC90 temperature control unit. At higher fields, the $^1$H relaxivity measurements were performed with Bruker Minispecs mq30 (30 MHz), mq40 (40 MHz), and mq60 (60 MHz) instruments. In each case, the temperature was measured by a substitution technique. Variable-temperature measurements were performed at 25 and 37 °C.

**EPR Spectroscopy:** The X-band (0.34 T, 9.4 GHz) EPR spectra were recorded with a Bruker ESP 300E spectrometer. The spectra were recorded at 25 °C on a quartz flat cell at four different concentrations (23 mM, 10 mM, 5 mM, 1 mM) of aqueous [Gd(EPTPACH2OH)(H$_2$O)]$^{2-}$, pH 6.8 The frequency was calibrated with diphenyl picrylhydrazyl (dpph), and the magnetic field with $Mn^{II}$ in MgO. The transverse electronic relaxation rates, $1/T_{2e}$, were calculated from the EPR linewidths according to Reuben.[54]

**Transmetallation:** Transmetallation by $Zn^{2+}$ ions was evaluated by the decrease in the water proton longitudinal relaxation rate, at 310 K and 20 MHz (Bruker Minispec mq20), of phosphate-buffered solutions (PBS, pH 7.1, 10 mM or 67 mM) containing 2.5 mM of [Gd(EPTPACH$_2$OH)(H$_2$O)]$^{2-}$ and 2.5 mM of $ZnCl_2$.[47] The water longitudinal relaxation rate was also measured on PBS-buffered solutions (pH 7.1, 10 mM and 67 mM) containing 2.5 mM of [Gd(EPTPACH$_2$OH)(H$_2$O)]$^{2-}$.[28]

**Data Analysis:** The simultaneous least-squares fittings of the $^{17}$O NMR and NMRD relaxation data were performed with the Visualiseur/Optimiseur programs on a Matlab platform version 6.5.[55]

**Supporting Information** (see footnote on the first page of this article): Equations used for the determination of the relaxivity parameters from the analysis of NMRD and $^{17}$O NMR spectroscopic data; Tables used for the determination of the microscopic protonation scheme of the ligands, which contain the pH dependence of the proton chemical shifts for H$_5$EPTPACH$_2$OH (Table S1) and H$_5$EPTPAC16 (Table S2), Table detailing the calculated percent protonation fractions of the different basic sites of H$_5$EPTPACH$_2$OH and H$_5$EPTPAC16 for different values of $n$ (for identification of $f_n$ sites see Figure 1) and listing the reported values for H$_5$EPTPA (Table S3), Tables containing the frequency dependence of the water proton relaxivities of [$Gd^{III}$(EPTPACH$_2$OH)(H$_2$O)]$^{2-}$ at two temperatures (Table S4), and the variable temperature reduced transverse and longitudinal $^{17}$O relaxation rates and chemical shifts of [Gd(EPTPACH$_2$OH)(H$_2$O)]$^{2-}$ solution at 4.7 T (Table S5); 300 MHz $^1$H NMR spectra of [Ln(EPTPACH$_2$OH)]$^{2-}$ complexes in $D_2O$ (30 mM, pH 7.0, $T$ = 25 °C): a) $Nd^{III}$ complex, b) $Eu^{III}$ complex, c) $Sm^{III}$ complex, d) $Y^{III}$ complex (Figure S1) and 500 MHz $^1$H COSY spectra of [Ln(EPTPACH$_2$OH)]$^{2-}$ complexes in $D_2O$ (30 mM, pH 7.0, $T$ = 25 °C), from top to bottom: $Y^{III}$ complex, $Nd^{III}$ complex, $Sm^{III}$ complex (Figure S2).

## Acknowledgments

This work was financially supported by the Foundation of Science and Technology (FCT), Portugal (project POCTI/QUI/47005/2002 and the Ph.D. grants SFRH/BD/11222/2002 to S. T. and SFRH/BD/9685/2002 to G. A. P.), by FEDER, and by Swiss National Science Foundation (L. H.). This work was carried out in the frame of the EC COST Actions D38 "Metal-Based Systems for Molecular Imaging Applications" and the EU Network of Excellence European Molecular Imaging Laboratory (EMIL, LSCH-2004-503569).

[1] R. B. Lauffer, *Chem. Rev.* **1987**, *87*, 901–927.
[2] S. Aime, M. Botta, M. Fasano, E. Terreno, *Chem. Soc. Rev.* **1998**, *27*, 19–29.
[3] P. Caravan, J. J. Ellison, T. J. McMurry, R. B. Lauffer, *Chem. Rev.* **1999**, *99*, 2293–2352.
[4] É. Tóth, L. Helm, A. E. Merbach, *Top. Curr. Chem.* **2002**, *221*, 61–101.
[5] *The Chemistry of Contrast Agents in Medical Magnetic Resonance Imaging* (Eds.: É. Tóth, A. E. Merbach), Wiley, Chichester, **2001**.
[6] a) É. Tóth, L. Helm, K. E. Kellar, A. E. Merbach, *Chem. Eur. J.* **1999**, *5*, 1202–1211; b) F. A. Dunand, É. Tóth, R. Hollister, A. E. Merbach, *J. Biol. Inorg. Chem.* **2001**, *6*, 247–255; c) M. G. Duarte, M. H. Gil, J. A. Peters, J. M. Colet, L. Vander Elst, R. N. Muller, C. F. G. C. Geraldes, *Bioconjugate Chem.* **2001**, *12*, 170–177.
[7] a) D. M. Corsi, L. V. Elst, N. Muller, H. van Bekkum, J. A. Peters, *Chem. Eur. J.* **2001**, *7*, 64–71; b) J. P. André, C. F. G. C. Geraldes, J. A. Martins, A. E. Merbach, M. I. M. Prata, A. C. Santos, J. J. P. de Lima, É. Tóth, *Chem. Eur. J.* **2004**, *10*, 5804–5816; c) P. Baía, J. P. André, C. F. G. C. Geraldes, J. A. Martins, A. E. Merbach, É. Tóth, *Eur. J. Inorg. Chem.* **2005**, 2110–2119.

 © 2007 Wiley-VCH Verlag GmbH & Co. KGaA, Weinheim 

[8] a) S. Aime, M. Fasano, E. Terreno, M. Botta in *The Chemistry of Contrast Agents in Medical Magnetic Resonance Imaging* (Eds.: É. Tóth, A. E. Merbach), Wiley, Chichester, **2001**, p. 193; b) S. Aime, M. Botta, S. G. Crich, G. Giovenzana, G. Palmisano, M. Sisti, *Bioconjugate Chem.* **1999**, *10*, 192–199; c) S. Aime, M. Botta, M. Fasano, G. S. Crich, E. Terreno, *J. Biol. Inorg. Chem.* **1996**, *1*, 312–319.

[9] a) É. Tóth, D. Pubanz, S. Vauthey, L. Helm, A. E. Merbach, *Chem. Eur. J.* **1996**, *2*, 1607–1615; b) L. H. Bryant Jr, M. W. Brechbiel, C. Wu, J. W. M. Bulte, V. Herynek, J. A. Frank, *J. Magn. Reson. Imaging* **1999**, *9*, 348–352; c) G. M. Nicolle, É. Tóth, H. Schmitt-Willich, B. Radüchel, A. E. Merbach, *Chem. Eur. J.* **2002**, *8*, 1040–1048; d) S. Laus, A. Sour, R. Ruloff, É. Tóth, A. E. Merbach, *Chem. Eur. J.* **2005**, *11*, 3064–3076.

[10] a) S. Aime, M. Botta, M. Fasano, S. G. Crich, E. Terreno, *J. Biol. Inorg. Chem.* **1996**, *1*, 312–319; b) P. Caravan, N. J. Cloutier, M. T. Greenfield, S. A. McDermid, S. U. Dunham, J. W. M. Bulte, J. C. Amedio Jr, R. J. Looby, R. M. Supkowski, W. De W. Horrocks Jr, T. J. McMurry, *J. Am. Chem. Soc.* **2002**, *124*, 3152–3162; c) S. Aime, M. Botta, S. G. Crich, G. B. Giovenzana, R. Pagliarin, M. Piccinini, M. Sisti, E. Terreno, *J. Biol. Inorg. Chem.* **1997**, *2*, 470–479.

[11] a) J. P. André, É. Tóth, H. Fisher, A. Seelig, H. R. Mäcke, A. E. Merbach, *Chem. Eur. J.* **1999**, *5*, 2977–2983; b) G. M. Nicolle, É. Tóth, K. P. Eisenwiener, H. R. Mäcke, A. E. Merbach, *J. Biol. Inorg. Chem.* **2002**, *7*, 757–769; c) K. Kimpe, T. N. Parac-Vogt, S. Laurent, C. Piérart, L. Vander Elst, R. N. Muller, K. Binnemans, *Eur. J. Inorg. Chem.* **2003**, *16*, 3021–3027.

[12] a) S. L. Fossheim, A. K. Fahlvik, J. Klaveness, R. N. Muller, *Magn. Reson. Imaging* **1999**, *17*, 83–89; b) V. Weissig, J. Babich, V. Torchilin, *Colloid Surf. B-Biointerfaces* **2000**, *18*, 293–299; c) C. Gløgård, G. Stensrud, R. Hovland, S. L. Fossheim, J. Klaveness, *Int. J. Pharm.* **2002**, *233*, 131–140; d) K.-E. Løkling, S. L. Fossheim, J. Klaveness, R. Skurtveit, *J. Control. Release* **2004**, *98*, 87–95.

[13] a) S. Morel, E. Terreno, E. Ugazio, S. Aime, M. R. Gasco, *Eur. J. Pharm. Biopharm.* **1998**, *45*, 157–163; b) C. Gløgård, G. Stensrud, J. Klaveness, *Int. J. Pharm.* **2003**, *253*, 39–48.

[14] M. Woods, S. Zhang, A. D. Sherry, *Curr. Med. Chem.: Immunol. Endocr. Metab. Agents* **2004**, *4*, 349–369.

[15] S. Laurent, F. Botteman, L. V. Elst, R. N. Muller, *Magn. Reson. Mater. Phys. Biol. Med.* **2004**, *16*, 235–245.

[16] L. V. Elst, F. Maton, S. Laurent, F. Seghi, F. Chapelle, R. N. Muller, *Magn. Reson. Med.* **1997**, *38*, 604–614.

[17] S. Laurent, L. V. Elst, S. Houzé, N. Guérit, R. N. Muller, *Helv. Chim. Acta* **2000**, *83*, 394–406.

[18] R. N. Muller, B. Radüchel, S. Laurent, J. Platzek, C. Piérart, P. Mareski, L. Vander Elst, *Eur. J. Inorg. Chem.* **1999**, 1949–1955.

[19] S. Laurent, F. Botteman, L. V. Elst, R. N. Muller, *Helv. Chim. Acta* **2004**, *87*, 1077–1089.

[20] a) R. Ruloff, É. Tóth, R. Scopelliti, R. Tripier, H. Handel, A. E. Merbach, *Chem. Commun.* **2002**, 2630–2631; b) L. Burai, É. Tóth, A. E. Merbach, *Chem. Commun.* **2003**, 2680–2681; c) S. Laus, R. Ruloff, É. Tóth, A. E. Merbach, *Chem. Eur. J.* **2003**, *9*, 3555–3566.

[21] S. Aime, M. Botta, M. Fasano, M. P. M. Marques, C. F. G. C. Geraldes, D. Pubanz, A. E. Merbach, *Inorg. Chem.* **1997**, *36*, 2059–2068.

[22] a) F. A. Dunand, R. S. Dickins, D. Parker, A. E. Merbach, *Chem. Eur. J.* **2001**, *7*, 5160–5167; b) M. Woods, Z. Kovacs, S. Zhang, A. D. Sherry, *Angew. Chem. Int. Ed.* **2003**, *42*, 5889–5892; c) J. Rudovský, P. Cígler, J. Kotek, P. Hermann, P. Vojtíšek, I. Lukeš, J. A. Peters, L. V. Elst, R. N. Muller, *Chem. Eur. J.* **2005**, *11*, 2373–2384.

[23] S. Torres, J. A. Martins, J. P. André, C. F. G. C. Geraldes, A. E. Merbach, É. Tóth, *Chem. Eur. J.* **2006**, *12*, 940–948.

[24] J. C. Amedio Jr, P. J. Bernard, M. Fountain, G. V. Wagenen Jr, *Synth. Commun.* **1999**, *29*, 2377–2391.

[25] *IUPAC Stability Constants*, Academic Software, and K. J. Powell, Release 1.05, Yorks, LS21 2PW (UK), **1999**.

[26] Y.-M. Wang, C.-H. Lee, G.-C. Liu, R.-S. Sheu, *J. Chem. Soc. Dalton Trans.* **1998**, 4113–4118.

[27] J. D. Clark, D. Q. Perrin, *Q. Rev.* **1964**, *18*, 295–320.

[28] S. Laurent, L. V. Elst, A. Vroman, R. N. Muller, *Helv. Chim. Acta* **2007**, *90*, 562–573.

[29] G. R. Choppin, *J. Less-Common Met.* **1985**, *112*, 193–205.

[30] J. L. Sudmeier, C. N. Reilley, *Anal. Chem.* **1964**, *36*, 1698–1706.

[31] C. F. G. C. Geraldes, A. M. Urbano, M. C. Alpoim, A. D. Sherry, K. T. Kuan, R. Rajagopalan, F. Maton, R. N. Muller, *Magn. Reson. Imaging* **1995**, *13*, 401–420.

[32] E. N. Rizkalla, G. R. Choppin, W. P. Cacheris, *Inorg. Chem.* **1993**, *32*, 582–586.

[33] J. A. Peters, *Inorg. Chem.* **1988**, *27*, 4686–4691.

[34] B. G. Jenkins, R. B. Lauffer, *J. Magn. Reson.* **1988**, *80*, 328–336.

[35] B. G. Jenkins, R. B. Lauffer, *Inorg. Chem.* **1988**, *27*, 4730–4738.

[36] S. Cortes, E. Brücher, C. F. G. C. Geraldes, A. D. Sherry, *Inorg. Chem.* **1990**, *29*, 5–9.

[37] F. A. Dunand, A. Borel, A. E. Merbach, *J. Am. Chem. Soc.* **2002**, *124*, 710–716.

[38] O. V. Yazyev, L. Helm, *J. Chem. Phys.* **2006**, *125*, 545031-8.

[39] D. H. Powell, O. M. N. Dhubhghaill, D. Pubanz, L. Helm, Y. S. Lebedev, C. Schlaepfer, A. E. Merbach, *J. Am. Chem. Soc.* **1996**, *118*, 9333–9346.

[40] L. Helm, *Prog. NMR Spect.* **2006**, *49*, 45–64.

[41] P. H. Fries, E. Belorizky, *J. Chem. Phys.* **2005**, *123*, 124510-1.

[42] J. Kowalewski, D. Kruk, G. Parigi in *Advances in Inorganic Chemistry* (Eds.: R. Van Eldik, I. Bertini), Elsevier, San Diego, **2005**.

[43] J. Kotek, P. Lebdušková, P. Hermann, L. V. Elst, R. N. Muller, C. F. G. C. Geraldes, T. Maschmeyer, I. Lukeš, J. A. Peters, *Chem. Eur. J.* **2003**, *9*, 5899–5915.

[44] A. Borel, É. Tóth, L. Helm, A. Janóssy, A. E. Merbach, *Phys. Chem. Chem. Phys.* **2000**, *2*, 1311–1317.

[45] L. Burai, É. Tóth, G. Moreau, A. Sour, R. Scopelliti, A. E. Merbach, *Chem. Eur. J.* **2003**, *9*, 1394–1404.

[46] S. Rast, A. Borel, L. Helm, E. Belorizky, P. H. Fries, A. E. Merbach, *J. Am. Chem. Soc.* **2001**, *123*, 2637–2644.

[47] S. Laurent, L. V. Elst, F. Copoix, R. N. Muller, *Invest. Radiol.* **2001**, *36*, 115–122.

[48] H. M. Irving, M. G. Miles, L. Pettit, *Anal. Chim. Acta* **1967**, *38*, 475–488.

[49] L. Zékány, I. Nagypál in *Computational Methods for Determination of Formation Constants* (Ed.: D. J. Leggett), Plenum, N. Y., **1985**, p. 291.

[50] P. K. Glasoe, F. A. Long, *J. Phys. Chem.* **1960**, *64*, 188–190.

[51] G. Brunisholz, M. Randin, *Helv. Chim. Acta* **1959**, *42*, 1927–1938.

[52] A. D. Hugi, L. Helm, A. E. Merbach, *Helv. Chim. Acta* **1985**, *68*, 508–521.

[53] I. Solomon, *Phys. Rev.* **1955**, 559–565.

[54] J. Reuben, *J. Phys. Chem.* **1971**, *75*, 3164–3167.

[55] F. Yerly, *VISUALISEUR 2.3.4*, and *OPTIMISEUR 2.3.4*, Lausanne (Switzerland), **1999**.


Received: April 20, 2007
Published Online: October 19, 2007

 © 2007 Wiley-VCH Verlag GmbH & Co. KGaA, Weinheim 

DOI: 10.1002/ejic.200700637

# Coordination Alternatives in Dinuclear Bis(pyridin-2-ylalkyl)-benzylaminecopper(II) Complexes with $OH^-$, $RO^-$, $F^-$, or $Cl^-$ Bridges: Experimental Structures and DFT Preferences

**Jorge Manzur,*[a] Andrés Vega,*[b] Ana María García,[a] Carolina Acuña,[a] Monika Sieger,[c] Biprajit Sarkar,[c] Mark Niemeyer,[c] Falk Lissner,[c] Thomas Schleid,[c] and Wolfgang Kaim*[c]**

**Keywords:** Copper / EPR spectroscopy / Isomerism / N ligands / Structure

The compounds $[L^1Cu(\mu\text{-}OH)_2CuL^1](ClO_4)_2$ (**1**), $[L^2Cu(\mu\text{-}OH)_2CuL^2](ClO_4)_2$ (**2**), $[L^3Cu(\mu\text{-}OH)_2CuL^3](ClO_4)_2$ (**3**), $[L^3Cu(\mu\text{-}OMe)_2CuL^3](ClO_4)_2$ (**4**), $[L^3Cu(\mu\text{-}F)_2CuL^3](BF_4)_2$ (**5**), $[L^4Cu(\mu\text{-}Cl)_2CuL^4](ClO_4)_2$ (**6**), and $[Cu(\mu\text{-}L^5)_2Cu](ClO_4)_2$ (**7**), where $L^1$ = bis(pyridin-2-ylmethyl)benzylamine, $L^2$ = (6-methylpyridin-2-ylmethyl)(pyridin-2-ylmethyl)benzylamine, $L^3$ = bis(6-methylpyridin-2-ylmethyl)benzylamine, $L^4$ = (pyridin-2-ylethyl)(pyridin-2-ylmethyl)benzylamine, and $L^5$ = (6-oxidomethylpyridin-2-ylmethyl)(6-methylpyridin-2-ylmethyl)benzylamine, were structurally characterized and studied by low-temperature EPR spectroscopy. The formation of compound **5** involved fluoride abstraction from $BF_4^-$ and that of **7** involved $O_2$-assisted C–H (methyl) activation/monooxygenation of $L^3$. Whereas the dications of **1**–**4** and **7** possess a square-pyramidal configuration at the copper(II) centers with hydroxide or alkoxide bridges in equatorial positions, the dications of **5** and **6** exhibit equatorial/axial arrangements for the bridging halide ions. In the dication of **5**, the tridentate ligand binds in a meridional fashion and includes two adjacent five-membered chelate rings. Such a situation has been observed previously only with chloride, alkoxide, or aqua bridges. In contrast to the *syn* configuration of the dication of **2**, the dications of complexes **1**, **3**, **4**, and **7** adopt an *anti* configuration with respect to the binding of $L^n$. The dications of **1**, **2**, and **7** have the pyridinyl or 6-methylpyridinyl groups in the axial position, whereas those of **3** and **4** feature the tertiary amine N atom at that site. DFT calculations of various configurations of the dications of **1**–**6** reproduce the experimentally observed structural alternatives in complexes **1**–**4**, but they do not predict the axial/equatorial structure of **5** as the lowest-energy configuration. The systematic overestimation of repulsive forces and thus of distances by DFT may result in an underestimation of the π-π interaction between the largely coplanar *mer*-$L^3$ ligands separated by about 3.6 Å in **5**, which probably affects its structure. By incorporating these and previous results, the *syn* versus *anti*, equatorial/equatorial versus equatorial/axial, and axial pyridine versus axial amine structural alternatives are discussed.

(© Wiley-VCH Verlag GmbH & Co. KGaA, 69451 Weinheim, Germany, 2007)

## Introduction

Bis(hydroxido)-bridged dicopper(II) complexes are among the most typical products from reactions between copper(I) compounds and molecular oxygen.[1–8] The reactions of $Cu^I$ with $O_2$ have found interest in synthesis because of their potential use in the hydroxylation of aromatic and other organic compounds.[9] In $O_2$ transport proteins[10] and oxygenation or oxidoreductase enzymes,[11,12] however, the formation of bis(hydroxido)dicopper(II) products is usually avoided to ensure reversibility. Among the most widely used copper coligands in this context are the tridentate bis(pyridin-2-ylalkyl)amines,[2,3,6,7a] which can be modified in terms of their steric bulk, electronic effects, and alkyl chain lengths, which thus allows tridentate coordination in both facial[2a,2b,13] and meridional fashions.[2b–2d] In contrast, the equally popular[6] tris(pyrazolyl)borate,[4] tris(pyrazolyl)methane,[7b] and triazacyclononane ligands[5] are restricted to facial coordination.

The formation of copper(II) [or copper(III)][6] species after the interaction of $O_2$ and $Cu^I$ is accompanied by the typical structural peculiarities of the $d^9$ (or $d^8$) configuration, that is, the tendency to form approximately square-

[a] Universidad de Chile, Facultad de Ciencias Físicas y Matemáticas, Departamento de Ciencia de los Materiales, Casilla 2777, Santiago, Chile
Fax: +56-2-699-4119
E-mail: jmanzur@dqb.uchile.cl
[b] Universidad Nacional Andres Bello, Facultad de Ecología y Recursos Naturales, Departamento de Ciencias Químicas, República 275, Santiago, Chile
Fax: +56-2-6618269
E-mail: andresvega@unab.cl
[c] Institut für Anorganische Chemie, Universität Stuttgart, Pfaffenwaldring 55, 70550 Stuttgart, Germany
Fax: +49-711-685-64165
E-mail: kaim@iac.uni-stuttgart.de

Supporting information for this article is available on the WWW under http://www.eurjic.org or from the author.

 WILEY InterScience DISCOVER SOMETHING GREAT © 2007 Wiley-VCH Verlag GmbH & Co. KGaA, Weinheim 

pyramidal structures with significantly different equatorial (*e*) and axial (*a*) binding sites.[6] Because tridentate chelating ligands restrict rapid interconversion, there are clear structural alternatives for doubly bridged dicopper(II) systems, viz., the *e*/*e* or *e*/*a* situations (Scheme 1a). Whereas the *e*/*e* conformation typically shows a rather symmetrical bridging arrangement with $Cu^{II}$–OH distances of about 1.93 Å,[2a,2b,3–5,7a,13] the much longer axial bonds extend to 2.25–2.30 Å for the few *e*/*a* examples described so far.[2b–2d,14] These isolated examples were formulated as containing six-membered chelate rings with relaxed N–Cu–N bite angles of about 90°.[2b–2d] Examples with smaller chelate rings were restricted to chlorido-, alkoxido-, and aqua-bridged species.[7a,15]

In a detailed analysis of the original assertion of a bis(hydroxido)-bridged dicopper(II) complex with an *e*/*a* arrangement, [2b] Lee and Holm showed[14] that bridging by two fluoride ions abstracted from $PF_6^-$ − perhaps by a $Cu/O_2/H_2O$-assisted process − may instead account for the observed configuration. In addition, these authors reported the formation of small amounts of a dicopper(II) complex doubly bridged by a tetradentate anionic monooxygenated ligand generated by the activation of benzylic $CH_2$.[14]

For the more common[16] $[L^nCu(\mu\text{-}X)_2CuL^n]^{2+}$ systems with *e*/*e* configurations of the bridging ligands, two further kinds of structural alternatives are established: the axial ligands may be arranged in an *anti* or *syn* orientation relative to the $Cu(\mu\text{-}X)_2Cu$ plane (Scheme 1b),[7a] and the unsymmetrical tridentate bis(pyridin-2-ylalkyl)amine ligands may bind with the pyridine or the amine N atoms in the axial position (Scheme 1c).[2a]

In this contribution we describe seven additional examples of these kinds of $[L^nCu(\mu\text{-}X)_2CuL^n]^{2+}$ complexes, which may shed light on the structural alternatives delineated above. Of the compounds $[L^1Cu(\mu\text{-}OH)_2CuL^1](ClO_4)_2$ (**1**), $[L^2Cu(\mu\text{-}OH)_2CuL^2](ClO_4)_2$ (**2**), $[L^3Cu(\mu\text{-}OH)_2CuL^3](ClO_4)_2$ (**3**), $[L^3Cu(\mu\text{-}OMe)_2CuL^3](ClO_4)_2$ (**4**), $[L^3Cu(\mu\text{-}F)_2CuL^3](BF_4)_2$ (**5**), $[L^4Cu(\mu\text{-}Cl)_2CuL^4](ClO_4)_2$ (**6**) and $[Cu(\mu\text{-}L^5)_2Cu](ClO_4)_2$ (**7**), where $L^1$ = bis(pyridin-2-ylmethyl)benzylamine, $L^2$ = (6-methylpyridin-2-ylmethyl)(pyridin-2-ylmethyl)benzylamine, $L^3$ = bis(6-methylpyridin-2-ylmethyl)benzylamine, $L^4$ = (pyridin-2-ylethyl)(pyridin-2-ylmethyl)benzylamine, and $L^5$ = (6-oxidomethylpyridin-2-ylmethyl)(6-methylpyridin-2-ylmethyl)benzylamine, complexes **1**–**3** and **7** were obtained from treatment of in situ generated copper(I) precursors $[L^nCu(L')]^+$ with air (L′: solvent). The ligands except for $L^5$ were described in the literature,[7a,17] as were some of the copper(I) precursors.[17] An additional copper(I) compound, $[L^3Cu(PPh_3)](BF_4)$, is described here for comparison with the recently

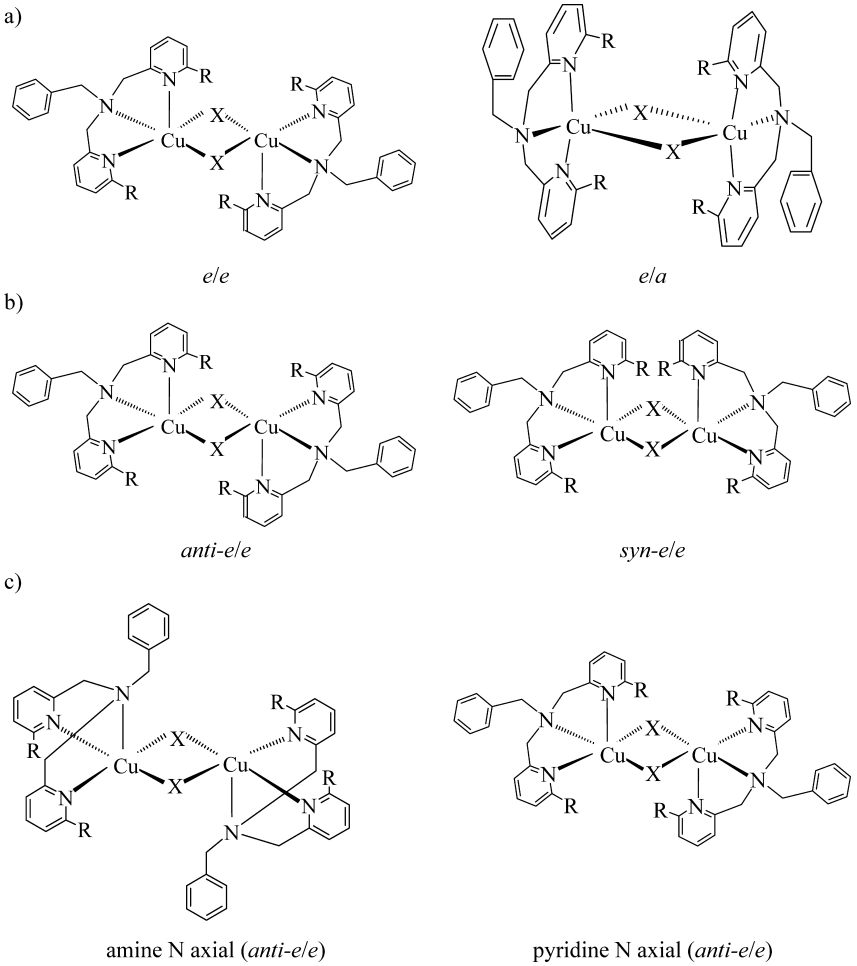


Scheme 1.

 © 2007 Wiley-VCH Verlag GmbH & Co. KGaA, Weinheim 

reported $[L^3CuL']$($BF_4$) species, where L′ = $CH_3CN$ or CO.[17] Whereas the oligomethylene chain length in the ligands controls the chelate ring sizes,[18] the 6-methyl substitution at the pyridin-2-yl ring has been reported to decrease its donor ability and slow down the reaction rate due to steric repulsion.[17] Within the $L^1$, $L^2$, and $L^3$ ligand series, substitution at the pyridin-2-yl rings was increased while the five-membered chelate rings were maintained, which thus resulted in a largely planar ligand geometry relative to some previously studied systems.[2b,2d] In the course of these studies we not only encountered the well-established[14,19] fluoride abstraction from $BF_4^-$ to yield an unusual structure for **5**, we also observed small amounts of dimeric product complex **7**, which contained a tetradentate anionic monooxygenated ligand $L^5$, from the reaction involving $L^3$. In contrast to a previous observation,[14] however, the attack had not occurred at the connecting benzylic methylene functionality, but at the α-*methyl* group of the pyridine ring. Such CH activation by $Cu/O_2$ resembles enzymatic processes[14,20] and is studied in the context of synthetic transformations;[9] an alkylperoxidocopper(II) complex resulting from the attack on an α-picolyl methyl group was reported recently.[9e]

To investigate the metal–metal interaction (coupling) and the possible dissociation of the dinuclear complexes in solution,[2b] we studied compounds **1**–**6** by EPR spectroscopy. The dications of compounds **1**–**6** were subjected to DFT calculations of various coordination alternatives in order to confirm their configurational preferences and to understand the stereochemically relevant factors involved.

## Results and Discussion

### Synthesis

Bis(hydroxido)-bridged dicopper(II) complexes **1**–**3** were typically obtained as final products from reactions between in situ generated copper(I) complexes of the ligands after exposure to atmospheric conditions [Equation (1)]. One $Cu^I$ compound, $[L^3Cu(PPh_3)](BF_4)$, was isolated for NMR spectroscopic analysis and structural characterization (cf. below).

$$4\ L^nCu^+ + O_2 + 2\ H_2O \rightarrow 2\ [L^nCu(\mu\text{-}OH)_2CuL^n]^{2+} \quad (1)$$

The lability of the bis(hydroxido)-bridged dicopper(II) complexes in certain solvents allowed simple conversion of **3** into bis(methoxido)-bridged **4** containing the $[L^3Cu(\mu\text{-}OMe)_2CuL^3]^{2+}$ dication. The use of the $[Cu(CH_3CN)_4]$-($BF_4$) precursor led to bis(fluorido)-bridged **5** by well-established[14,19] $F^-$ abstraction from tetrafluoroborate, where the remaining $BF_3$ can act as a Lewis acidic partner for amines. This reactivity has been observed even with $PF_6^-$, a supposedly more inert anion.[14] Both the unambiguous crystallographic signature of $F^-$ versus $OH^-$ and the much more pronounced asymmetry of the central four-membered ring is typical for bis(fluorido)- versus bis(hydroxido)-bridged dicopper(II) complexes (cf. below).[14] Otherwise, halide-bridged complexes such as **6** can be obtained by using the corresponding copper salt. In the absence of an available halide ion for bridging, a secondary reaction may occur that presumably involves the metal-assisted monooxygenation of a partially activated C–H bond. These reactions proceed in low yields.[14] However, whereas Lee and Holm found a product with a monooxygenated benzylic $CH_2$ group from a pyridyl–amine linkage,[14] we observed the monooxygenation of a $CH_3$ group in the α position of the pyridine. The resulting complex **7** thus contains two anionic, tetradentate (6-oxidomethylpyridin-2-ylmethyl)(6-methylpyridin-2-ylmethyl)benzylamine bridges. CH activation by $Cu/O_2$ is currently studied in the context of synthetic transformations[9] and within attempts to elucidate the mechanisms of corresponding enzymes,[20] that is, tyrosinases,[21] for aromatic CH groups and dopamine β monoxygenase or peptidylglycine α-hydroxylating monooxygenase (PHM) for nonaromatic CH groups.[22] These reactions may proceed via mononuclear ($Cu^{II}$-superoxido)[23] or dinuclear ($Cu^{II}$-peroxido)[6,9e] precursor intermediates to yield the reactive copper–oxyl ($O^{\cdot-}$) species that effects the necessary H abstraction before rebound.[24]

### Structure Description

The crystallographic data of the systems studied by X-ray diffraction are summarized in Tables 5 and 6.

Despite the poor data quality, the structure results (bond lengths and angles; Tables 1 and 2) for $[L^3Cu(PPh_3)](BF_4)$ indicate that the corresponding complex cation possesses an intermediate structure between those of $[L^3Cu(CH_3CN)]^+$ and $[L^3Cu(CO)]^+$.[17] This reflects the moderately lower π-acceptor ability of $PPh_3$ relative to that of CO. The overall structure of this complex (Figure 1) remains that of a highly distorted tetrahedron,[17] which can be alternatively described as a trigonal pyramid with the more weakly bonded amine N atom at the apex.

Among the bis(hydroxido)-bridged dicopper(II) complexes with nearly square-pyramidal configurations ($\tau < 0.20$),[25] compounds **1**–**3** (Figures 2, 3, and 4; Table 1) exhibit the familiar *e/e* configuration[2a,2b,3–5,7a] for the rather symmetrically bonded hydroxide bridges. However, whereas **1** and **3** show *anti*-positioned axial (6-methyl)pyridin-2-yl ligands, the 6-methylpyridin-2-yl axial ligands in **2** were found in a *syn* configuration and face each other with the smallest distance between the methyl-substituted ring C6′ and C6′′ carbon atoms measuring 3.57 Å (Figure 3). The least-squares planes defined by the apical rings (N1′, C2′, C3′, C4′, C5′, C6′ and N1′′, C2′′, C3′′, C4′′, C5′′, C6′′) are not completely parallel; they adopt a small dihedral angle of 4.2(1)°. The distances between the centroids of each ring and the neighboring planes are 3.44 and 3.50 Å, respectively.

The preference of the sterically more demanding 6-methylpyridin-2-yl group for the axial position is not unexpected, and the tendency of unactivated pyridines to adopt this position has been reconfirmed recently.[2a] However, with strong donor substituents such as OR or $NR_2$ in the *para*

 © 2007 Wiley-VCH Verlag GmbH & Co. KGaA, Weinheim 

Table 1. Selected bond lengths [Å] and angles [°] for compounds **1**·$CH_3COCH_3$, **2**·$H_2O$, and **3**.

| **1**[a] | | **2**[b] | | | | **3**[c] | |
|---|---|---|---|---|---|---|---|
| Cu–O1 | 1.921(4) | Cu′–O1′ | 1.952(5) | Cu′–N2′ | 2.054(6) | Cu–O1A | 1.891(11) |
| Cu–O1A | 1.947(4) | Cu′–O1″ | 1.948(5) | Cu″–N2″ | 2.043(5) | Cu–O1 | 1.905(12) |
| Cu–N1 | 1.983(5) | Cu″–O1′ | 1.919(4) | Cui–N3i | 2.013(6) | Cu–N1 | 2.041(12) |
| Cu–N2 | 2.058(4) | Cu″–O1″ | 1.960(5) | Cu″–N3″ | 1.993(6) | Cu–N2 | 2.288(13) |
| Cu–N3 | 2.280(5) | Cu′–N1′ | 2.279(7) | Cu′–Cu″ | 2.955(1) | Cu–N3 | 2.018(11) |
| Cu–CuA | 2.922(1) | Cu″–N1″ | 2.332(6) | | | Cu–CuA | 3.009(3) |
| N1–Cu–N2 | 83.4(2) | N3′–Cu′–N2′ | 83.6(3) | N1″–Cu″–O1″ | 94.8(2) | N1–Cu–N2 | 79.6(5) |
| N1–Cu–N3 | 101.4(2) | N3″–Cu″–N2″ | 84.4(2) | N3″–Cu″–O1′ | 97.9(2) | N1–Cu–N3 | 100.1(5) |
| N2–Cu–N3 | 77.3(2) | N3′–Cu′–N1′ | 96.8(3) | N3″–Cu″–O1″ | 167.2(2) | N2–Cu–N3 | 77.6(5) |
| N1–Cu–O1 | 97.6(2) | N3″–Cu″–N1″ | 97.6(2) | N2″–Cu″–O1′ | 173.8(2) | N1–Cu–O1 | 93.2(5) |
| N2–Cu–O1 | 176.2(2) | N2′–Cu′–N1′ | 76.0(3) | N2″–Cu″–O1″ | 95.5(2) | N2–Cu–O1 | 107.9(5) |
| N3–Cu–O1 | 106.0(2) | N2″–Cu″–N1″ | 76.0(2) | N1′–Cu′–O1′ | 98.1(2) | N3–Cu–O1 | 166.4(5) |
| N3–Cu–O1A | 93.7(2) | N3′–Cu′–O1′ | 164.1(2) | N1′–Cu′–O1″ | 111.2(3) | N3–Cu–O1A | 91.3(5) |
| N2–Cu–O1A | 96.2(2) | N3′–Cu′–O1″ | 99.3(2) | Cu′–O1′–Cu″ | 99.5(2) | N2–Cu–O1A | 120.3(6) |
| N1–Cu–O1A | 164.4(2) | N2′–Cu′–O1′ | 94.6(2) | Cu′–O1″–Cu″ | 98.2(2) | N1–Cu–O1A | 159.0(5) |
| O1–Cu–O1A | 81.9(2) | N2′–Cu′–O1″ | 171.6(3) | O1′–Cu′–O1″ | 80.4(2) | O1–Cu–O1A | 75.1(6) |
| Cu–O1–CuA | 98.1(2) | N1″–Cu″–O1′ | 109.2(2) | O1′–Cu″–O1″ | 80.9(2) | Cu–O1–CuA | 104.9(6) |

[a] A: –*x*, –*y* + 2, –*z*. [b] The symbols ′ and ″ refer to two crystallographically nonequivalent molecule halves. [c] A: 0.5 – *x*,1.5 – *y*,1 – *z*.

Table 2. Selected bond lengths [Å] and angles [°] for compounds **4**–**7**.

| **4**[a] | | **5**[b] | | **6**[c] | | **7**[d] | |
|---|---|---|---|---|---|---|---|
| Cu–O1A | 1.930(2) | Cu–F1 | 1.878(1) | Cu–N1 | 1.994(4) | Cu–O1A | 1.948(3) |
| Cu–O1 | 1.933(2) | Cu–F1A | 2.268(1) | Cu–N2 | 2.088(4) | Cu–O1 | 1.962(3) |
| Cu–N1 | 2.040(2) | Cu–N1 | 2.016(2) | Cu–N3 | 2.008(4) | Cu–N1 | 2.186(4) |
| Cu–N2 | 2.254(2) | Cu–N2 | 2.011(2) | Cu–Cl1 | 2.298(1) | Cu–N2 | 2.102(3) |
| Cu–N3 | 2.019(2) | Cu–N3 | 2.031(2) | Cu–Cl1A | 2.791(1) | Cu–N3 | 1.923(3) |
| Cu–CuA | 3.0520(7) | Cu–CuA | 3.134(1) | Cu–CuA | 3.714(1) | Cu–CuA | 2.9067(10) |
| N1–Cu–N2 | 80.61(9) | N1–Cu–N2 | 84.12(7) | N1–Cu–N2 | 90.7(2) | N1–Cu–N2 | 80.42(13) |
| N1–Cu–N3 | 98.11(9) | N1–Cu–N3 | 163.79(7) | N1–Cu–N3 | 172.0(2) | N1–Cu–N3 | 114.15(15) |
| N2–Cu–N3 | 78.45(9) | N2–Cu–N3 | 81.90(7) | N2–Cu–N3 | 81.3(2) | N2–Cu–N3 | 81.75(14) |
| N1–Cu–O1 | 94.47(9) | N1–Cu–F1 | 97.02(6) | N1–Cu–Cl1 | 93.5(1) | N1–Cu–O1 | 112.90(13) |
| N2–Cu–O1 | 105.44(9) | N2–Cu–F1 | 169.10(6) | N2–Cu–Cl1 | 166.3(1) | N2–Cu–O1 | 162.24(13) |
| N3–Cu–O1 | 167.31(9) | N3–Cu–F1 | 98.27(6) | N3–Cu–Cl1 | 94.5(1) | N3–Cu–O1 | 81.98(13) |
| N3–Cu–O1A | 91.69(9) | | | N1–Cu–Cl1A | 95.3(1) | N3–Cu–O1A | 144.81(14) |
| N2–Cu–O1A | 107.91(9) | | | N2–Cu–Cl1A | 105.9(1) | N2–Cu–O1A | 105.63(12) |
| N1–Cu–O1A | 168.22(9) | | | N3–Cu–Cl1A | 85.8(1) | N1–Cu–O1A | 101.03(13) |
| O1–Cu–O1A | 75.62(8) | F1–Cu–F1A | 82.26(5) | Cu–Cl1–CuA | 93.2(1) | O1–Cu–O1A | 83.95(12) |
| Cu–O1–CuA | 104.38(8) | Cu–F1–CuA | 97.74(5) | Cl1–Cu–Cl1A | 86.8(1) | Cu–O1–CuA | 96.05(12) |

[a] A: –*x*, 2 – *y*, –*z*. [b] A: 1 – *x*, 1 – *y*, 1 – *z*. [c] A: 1 – *x*, 1 – *y*, 1 – *z*. [d] A: 2 – *x*, –*y*, 1 – *z*.

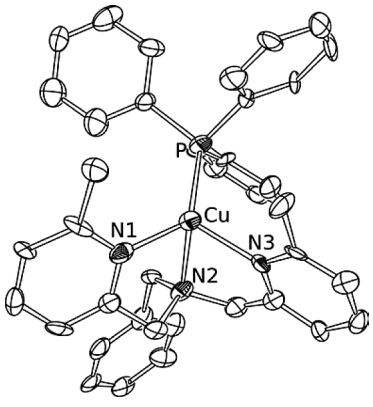


Figure 1. Molecular structure of the cation in the crystal of $[L^3Cu(PPh_3)](BF_4)$. Selected bond lengths [Å] and angles [°]: Cu–P 2.178(4), Cu–N1 2.007(11), Cu–N2 2.202(10), Cu–N3 2.074(10); P–Cu–N1 129.1(3), P–Cu–N2 119.2(3), P–Cu–N3 116.9(3), N1–Cu–N2 80.9(4), N1–Cu–N3 112.8(4), N2–Cu–N3 78.0(4).

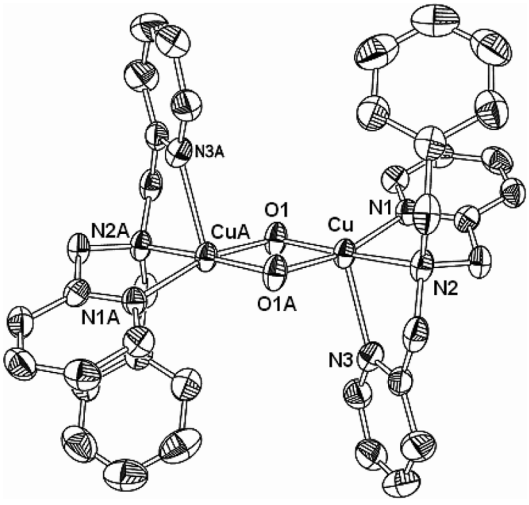


Figure 2. Molecular structure of the dication in the crystal of $[L^1Cu(\mu\text{-}OH)_2CuL^1](ClO_4)_2\cdot 2Me_2CO$ (**1**).

 © 2007 Wiley-VCH Verlag GmbH & Co. KGaA, Weinheim 

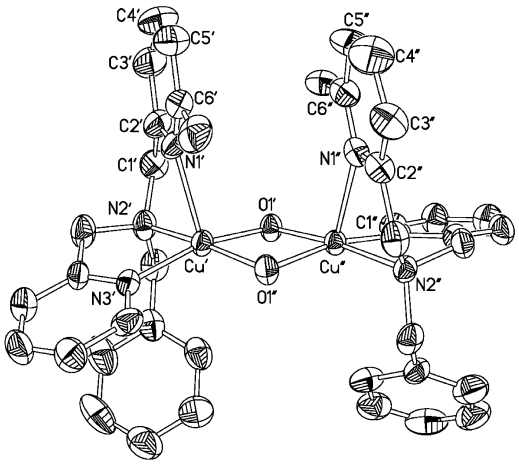


Figure 3. Molecular structure of the dication in the crystal of $[L^2Cu(\mu\text{-}OH)_2CuL^2](ClO_4)_2 \cdot H_2O$ (**2**).

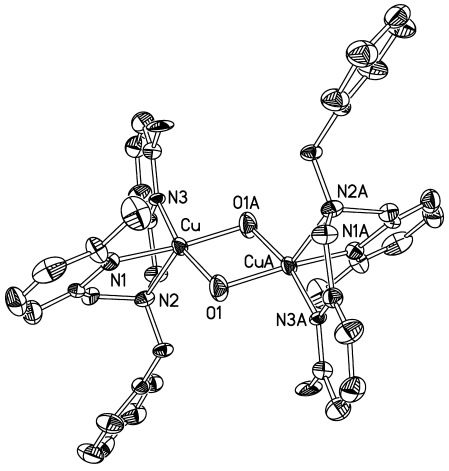


Figure 4. Molecular structure of the dication in the crystal of $[L^3Cu(\mu\text{-}OH)_2CuL^3](ClO_4)_2$ (**3**).

position, the pyridines may prefer the equatorial coordination, leaving the axial binding site for the trialkylamine N atom.[2a] The *syn* configuration for **2** is reminiscent of that of a 6-trifluoromethyl-substituted analogue,[7a] which suggests that there is an attractive interaction.

The related hydroxido- and methoxido-bridged structures **3** and **4** (Figures 4 and 5, respectively) are very similar in their *anti* configurations, which are almost superimposable. The Cu–O distances are a bit shorter for **3** [1.891(2), 1.905(2) Å] than for **4** [1.930(2), 1.933(2) Å]. The methoxy carbon atoms of the OMe groups lie at opposite sides of the central $Cu_2O_2$ plane in **4** and are almost coplanar. The C–O vector defines an angle of only 7.9° with the plane.

As pointed out before,[2d] bis(chlorido)-bridged dicopper(II) complexes can readily adopt the *e/a* arrangement for the bridges with long axial Cu–Cl distances of about 2.8 Å. A previous study of $[L^1Cu(\mu\text{-}Cl)_2CuL^1](ClO_4)_2$ (**8**) showed[7a] that this also holds when two five-membered chelate rings are formed in the $L^n$Cu moiety. Compound

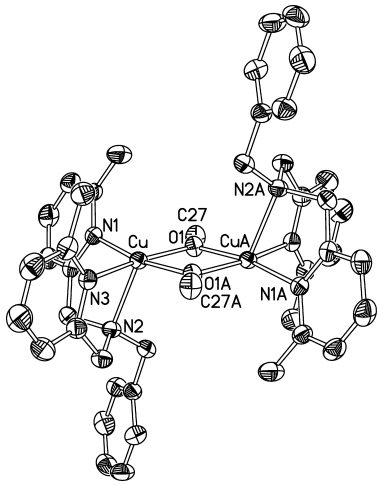


Figure 5. Molecular structure of the dication in the crystal of $[L^3Cu(\mu\text{-}OMe)_2CuL^3](ClO_4)_2$ (**4**).

**6**, $[L^4Cu(\mu\text{-}Cl)_2CuL^4](ClO_4)_2$, described here shows that the same kind of structure is obtained after lengthening either one of the alkyl chains that connects the amine N atom or the pyridin-2-yl moiety from $CH_2$ to $CH_2CH_2$ (Figure 6, Table 2).

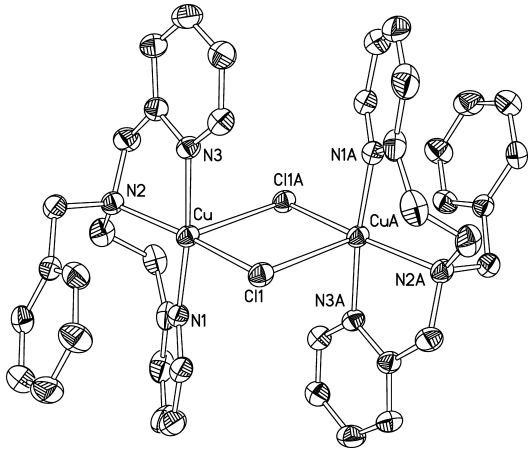


Figure 6. Molecular structure of the dication in the crystal of $[L^4Cu(\mu\text{-}Cl)_2CuL^4](ClO_4)_2$ (**6**).

In contrast to $\mu\text{-}Cl^-$, $\mu\text{-}OR^-$, and $\mu\text{-}OH_2$, the smaller $\mu\text{-}OH^-$ bridges typically favor the *e/e* configuration in dinuclear $[(\eta^3\text{-}L)Cu(\mu\text{-}OH)_2Cu(\eta^3\text{-}L)]^{2+}$ complexes. The tridentate ligands will then coordinate in a facial mode. This rule is not only confirmed by the revision of the initially assigned hydroxido-bridged complex with the *e/a* configuration[2b] to a fluorido-bridged species,[14] but it is also corroborated by the examples presented here, viz., an *e/e* configuration for **3** and **4** but an *e/a* configuration for fluorido-bridged **5** (Figure 7). Nevertheless, the latter is surprising because meridional binding of tridentate ligands such as $L^3$ is less favorable due to the necessity to form two adjacent five-membered chelate rings (Table 2).

 © 2007 Wiley-VCH Verlag GmbH & Co. KGaA, Weinheim 

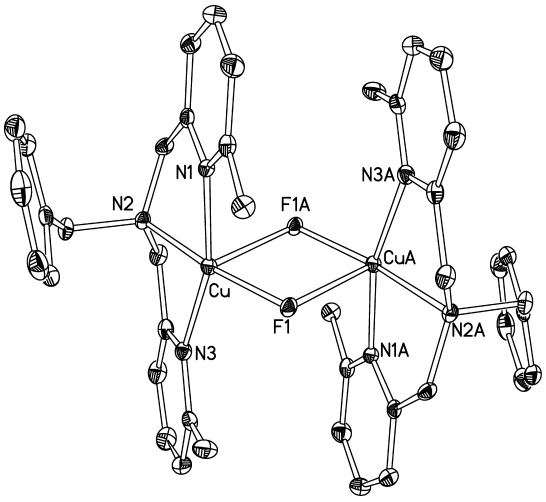


Figure 7. Molecular structure of the dication in the crystal of $[L^3Cu(\mu\text{-}F)_2CuL^3](BF_4)_2{\cdot}2CH_2Cl_2$ (**5**).

According to the five-membered chelate ring situation, the N–Cu–N angles in **5** have decreased to about 83° and the *trans*-N1–Cu–N3 angle to 163.79(7)°. Measuring 169.10(6)°, the other *trans*-N2–Cu–F1 angle is distinctly more linear, as is the N1–Cu–N3 angle for the *mer*-coordinated $L^4$ in compound **6**, which measures 172.0(2)°. All Cu–N bond lengths in **5** lie around 2.02 Å; the typically weaker bonding to the amine N atom is compensated for by its preferred central position in *mer*-$L^3$. In contrast, the difference between the short equatorial Cu–F bond length and the typically[14] long axial Cu–F distance is almost 0.4 Å. The molecular dication of **5** has inversion symmetry (Figure 7), and the central $Cu_2F_2$ ring approaches a rectangular geometry because the bond lengths differ widely but the Cu–F1–CuA and F1–Cu–F1A angles [97.74(5) and 82.26(5)°, respectively] do not strongly deviate from 90°. Measuring 3.134(1) Å, the Cu–CuA distance is longer than the corresponding distances in the *e*/*e*-configured hydroxido

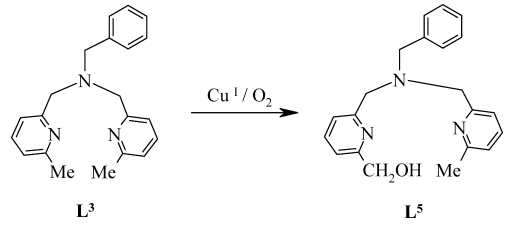


Scheme 2.

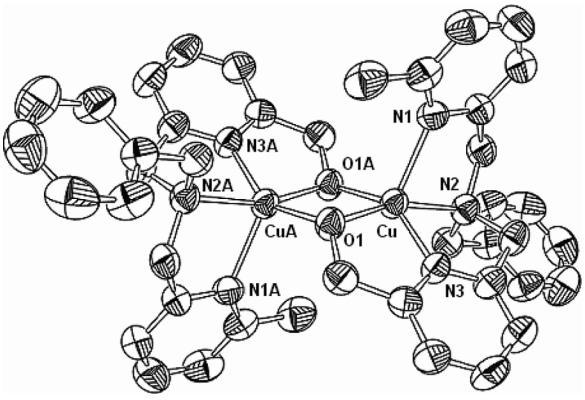


Figure 8. Molecular structure in the crystal of $[Cu(\mu\text{-}L^5)_2Cu]$ (**7**).

Table 3. Relative energies (most stable isomer = 0 kcal mol$^{-1}$) calculated for the different coordination alternatives of compounds **1**–**6**, **8**, and $[L^2Cu(\mu\text{-}OMe)_2CuL^2]^{2+}$.[a]

| Compound number | Bridge configuration | Orientation | Axial ligand | Relative energy [kcal mol$^{-1}$] |
|---|---|---|---|---|
| **1** | *e*/*e* | *anti* | **Pyridine-N** | **0.1** |
| | *e*/*e* | *anti* | Amine-N | 0 |
| | *e*/*e* | *syn* | Pyridine-N | 0.9 |
| | *e*/*e* | *syn* | Amine-N | 2.8 |
| | *e*/*a* | *syn* | OH | 16.7 |
| **2** | *e*/*e* | *anti* | Pyridine-N | 0.3 |
| | *e*/*e* | *anti* | Amine-N | 2.1 |
| | *e*/*e* | *syn* | **Pyridine-N** | **0.1** |
| | *e*/*e* | *syn* | Amine-N | 0 |
| | *e*/*a* | *syn* | OH | 17.9 |
| **3** | *e*/*e* | *anti* | Pyridine-N | 9.5 |
| | *e*/*e* | *anti* | **Amine-N** | **0** |
| | *e*/*e* | *syn* | Pyridine-N | 9.7 |
| | *e*/*e* | *syn* | Amine-N | 0.3 |
| | *e*/*a* | *syn* | OH | 23.8 |
| **4** | *e*/*e* | *anti* | Pyridine-N | 12.5 |
| | *e*/*e* | *anti* | **Amine-N** | **0** |
| | *e*/*e* | *syn* | Pyridine-N | 15.2 |
| | *e*/*e* | *syn* | Amine-N | 1.0 |
| | *e*/*a* | *syn* | OMe | 2.4 |
| $[L^2Cu(\mu\text{-}MeO)_2][CuL^2]^{2+}$ | *e*/*e* | *anti* | Pyridine-N | 3.6 |
| | *e*/*e* | *anti* | **Amine-N** | **0** |
| | *e*/*e* | *syn* | Pyridine-N | 4.2 |
| | *e*/*e* | *syn* | Amine-N | 5.9 |
| | *e*/*a* | *syn* | OMe | 19.7 |
| **5** | *e*/*e* | *anti* | Pyridine-N | 0 |
| | *e*/*e* | *anti* | Amine-N | 0.1 |
| | *e*/*e* | *syn* | Pyridine-N | 0.8 |
| | *e*/*e* | *syn* | Amine-N | 1.1 |
| | ***e*/*a*** | *syn* | **F** | **6.3** |
| **6** | *e*/*e* | *anti* | Pyridine-N | 10.6 |
| | *e*/*e* | *anti* | Amine-N | 8.0 |
| | *e*/*e* | *syn* | Pyridine-N | 9.8 |
| | *e*/*e* | *syn* | Amine-N | 47.5 |
| | ***e*/*a*** | *syn* | **Cl** | **0** |
| **8** | *e*/*e* | *anti* | Pyridine-N | 1.7 |
| | *e*/*e* | *anti* | Amine-N | 7.8 |
| | *e*/*e* | *syn* | Pyridine-N | 0.9 |
| | *e*/*e* | *syn* | Amine-N | 9.2 |
| | ***e*/*a*** | *syn* | **Cl** | **0** |

[a] *e*/*e*: equatorial/equatorial; *e*/*a*: equatorial/axial; in bold: experimentally observed geometry.

 © 2007 Wiley-VCH Verlag GmbH & Co. KGaA, Weinheim 

derivatives **1**–**3** (<3.01 Å), but much smaller than those in the chlorido-bridged **6** [3.714(1) Å] and **8** [3.566(1) Å],[7a] and that reported for a complex involving nonplanar, six-membered chelate rings (3.271 Å).[2d] In fact, the virtually planar $L^3Cu^{II}$ moieties in **5** are arranged in a parallely stacked structure (dihedral angle of 4.5°) with partially overlapping pyridyl-ring π systems and oppositely oriented methyl groups. The interplanar distance of about 3.6 Å (vs. 3.35 Å in graphite) indicates a π–π interaction that probably induces and stabilizes[2b] the structure. π–π interactions have been implicated before in similar complexes,[2b] and relatively long interplanar distances are typical for nitrogen-containing aromatic molecules.[26] The aromatic rings of the benzyl substituents in **5** also overlap with the pyridyl rings (dihedral angle of 21.4°) with interplanar distances (e.g. 3.068 Å for N1–C21) that allow such π–π interactions. In total, a π–π–π arrangement (pyridyl, pyridyl, benzyl) results that is reminiscent of a recently described dicopper(I) complex involving phenylphosphane and bipyrimidine π systems.[27]

Complex **7** in which the $L^3$ ligand has undergone monooxygenation at a picolyl methyl group and then deprotonation to yield tetradentate anionic $L^5$ (Scheme 2) shows the familiar *anti* configuration of the *e*/*e* arrangement, with the nonmonooxygenated 6-methylpyridyl group in the axial position (Figure 8). Because of the restriction by tetrachelation, the square planar configuration is slightly more distorted ($\tau = 0.28$) than in the other cases ($\tau < 0.20$). Table 3 summarizes the experimentally observed coordination situations, and the following discussion is concerned with the possible predictability of such structural preferences.

### DFT Calculations for the $[L^nCu(\mu\text{-}X)_2CuL^n]^{2+}$ Dications

The variety of structural alternatives for these complexes (Scheme 1, Table 3) and their realization under different conditions have prompted us to undertake a DFT calculation study to rationalize the experimental results and to explore the predictive potential of the method. Table 3 summarizes the energies calculated for the different stereoisomers, and the DFT-calculated structure parameters are found in Table S1 (Supporting Information).

As can be expected just by considering steric hindrance, dicopper(II) complexes sharing an edge of the two square-based pyramids favor the *anti* arrangement for the apical ligands. For the dication of **1**, $[L^1Cu(\mu\text{-}OH)_2CuL^1]^{2+}$, the *anti*-*e*/*e* structure with pyridine or amine nitrogen atoms in the apical position should be expected. The X-ray structure shows a pyridyl *anti*-*e*/*e* geometry for this complex (as a perchlorate salt). DFT results predict this isomer to be 0.006 eV higher in energy than the most stable *anti*-*e*/*e* amine configuration. Both these isomers are practically of the same energy, so packing could play an important role in determining the observed crystal structure. The *syn*-*e*/*e* isomers for the complex are 0.041 and 0.121 eV higher in energy that the most stable configuration. The *e*/*a* isomer was computed to be 0.723 eV less stable than the *anti*-*e*/*e* pyridyl isomer. Interestingly, the *anti*-*e*/*e* pyridyl configuration is preserved when complex **2** is crystallized as an aqua solvate instead of the acetone solvate described in the text, where the packing interactions must be completely different.

Replacement of one α-hydrogen atom on one of the pyridyl groups of $L^1$ by a methyl group leads to $L^2$. The dication of **2**, $[L^2Cu(\mu\text{-}OH)_2CuL^2]^{2+}$, crystallizes in the *syn*-*e*/*e* pyridyl geometry (with perchlorate counteranions); this was also observed for the trifluoromethyl derivative of $L^2$.[7a] DFT calculations for **2** show that the energy of the *syn*-*e*/*e* pyridyl isomer lies just 0.002 eV above that of the most stable *syn*-*e*/*e* amine alternative. The *anti* configurations are a bit higher in energy, whereas the energy of the *e*/*a* isomer lies about 0.7 eV above that of the most stable isomer. The observed structure may result from $CX_3\cdots$ring interactions that could occur in the *syn* configuration between the substituted pyridine rings. The replacement of the other α-hydrogen atom by a methyl group to give $[L^3Cu(\mu\text{-}OH)_2CuL^3]^{2+}$ (dication of **3**) has a strong effect on the relative energies. In this complex, the *anti*-*e*/*e* amine configuration is computed to be the most stable isomer, and this result coincides with the X-ray determined structure for the perchlorate salt.

Changing the hydroxy bridge into a methoxy one leads to $[L^2Cu(\mu\text{-}OMe)_2CuL^2]^{2+}$[7a] and $[L^3Cu(\mu\text{-}OMe)_2CuL^3]^{2+}$ (dication of **4**), where again the *anti*-*e*/*e* amine form is calculated to be the most stable isomer, and this is confirmed by the X-ray diffraction results. Moreover, the computed energy differences between the most stable isomer and the others are now larger, which suggests that the incorporation of a methyl group on the bridge produces enhanced repulsion.

The complexes $[L^3Cu(\mu\text{-}F)_2CuL^3]^{2+}$ (dication of **5**), $[L^4Cu(\mu\text{-}Cl)_2CuL^4]^{2+}$ (dication of **6**), and $[L^1Cu(\mu\text{-}Cl)_2CuL^1]^{2+}$ (dication of **8**) were studied to test the effect of halide bridges. Their experimental structures correspond to the *e*/*a* isomer. The most stable isomer computed for the dication of **5** is the *anti*-*e*/*e* pyridyl form. Although this result does not fit the experimental observations (*e*/*a* isomer), the difference in energy of this isomer relative to the most stable one at 0.275 eV is noticeably diminished in comparison to the hydroxy or methoxy analogues, where the energy differences between the *e*/*e* and *e*/*a* configurations are of the order of 1 eV. The computational results for the dications of **6** and **8** show that the most stable isomers possess *e*/*a* configurations, which is in agreement with the experimental results.

In conclusion, the DFT method makes a clear distinction between the *e*/*e* and *e*/*a* configurations. Although the calculated energy differences are not very large in the case of some *syn*- and *anti*-*e*/*e* isomers, the DFT method has correctly reproduced the experimentally favored complex configurations except in the case of the dication of **5** where additional, highly distance-dependent π–π interactions are obviously underestimated[26,27] because of the systematic overestimation of distances.

 © 2007 Wiley-VCH Verlag GmbH & Co. KGaA, Weinheim 

### EPR Spectroscopy

The EPR method is suited to study intramolecular spin–spin interactions of copper(II) ions in dinuclear complexes and to investigate their possible dissociation into mononuclear species in solution.[2b] We therefore studied the compounds by this method in the solid state and in frozen solutions at 110 K (Figure 9, Table 4).

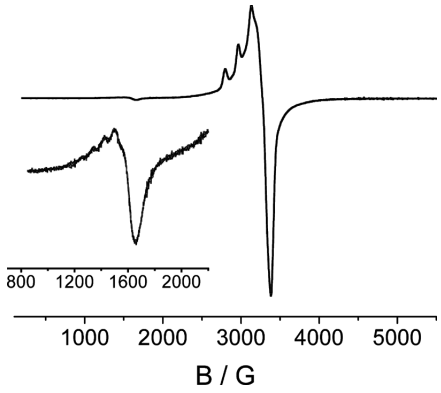


Figure 9. EPR signal of compound $[L^4Cu(\mu\text{-}Cl)_2CuL^4](ClO_4)_2$ (**6**) with half-field component (insert).

Table 4. EPR parameters of complexes in $CH_2Cl_2/CH_3CN$ (*x*/*y*) at 110 K.

| Complex | (*x*/*y*) | $g_\parallel$ | $g_\perp$ | $g_{av}$ | $A_\parallel$[a] |
|---|---|---|---|---|---|
| **1** | 2/1 | | | 2.10[b]<br>4.10[b,c] | |
| **3** | 4/1 | 2.260 | 2.050 | 2.120<br>4.27[b–d] | 15.0 |
| **4** | 4/1 | 2.270 | 2.057 | 2.128<br>4.26[b–d] | 14.6 |
| **5** | 1/0 | 2.270 | 2.056 | 2.127<br>4.21[b–d] | 15.6 |
| **6** | 4/1 | 2.206<br>4.91[c] | 2.040<br>4.21[c] | 2.075<br>4.44[c] | 17.6<br>8.3[c] |
| **8** | 5/1 | 2.224<br>4.86[c] | 2.015<br>4.16[c,e] | 2.085<br>4.39[c] | 17.7<br>8.7[c] |

[a] In mT. [b] Unresolved signal. [c] Half-field signal. [d] Weak signal. [e] $A_\perp$ = 2.0 mT.

The complexes show typical[2] EPR signals for $Cu^{II}(\mu\text{-}X)_2Cu^{II}$ cores in both cases with the spectra in frozen solutions being better resolved (Figure 9). Under both sets of conditions we could observe half-field transitions for certain compounds, especially for the halide-bridged species possessing a pronounced asymmetry of the Cu(μ-X)Cu core and possible triplet ground states.[7a] The fact that both solid samples and frozen solutions exhibit the half-field signals for the triplet excited states suggests that the dinuclear arrangement remains largely intact in the chosen $CH_2Cl_2/CH_3CN$ solvent mixtures. Preliminary UV/Vis spectroscopic experiments have shown that association and ligand substitution equilibria can occur in media such as alcohols. The differences between the complexes are rather small except for the somewhat higher $A_\parallel$ ($^{63,65}Cu$) and lower *g* values for the chloride-bridged species **6** and **8** (Table 4). The increased copper–halide covalency and the higher spin-orbit coupling contributions from $Cl^-$ are held responsible for these differences.

## Conclusions

During this study of $[L^nCu(\mu\text{-}X)_2CuL^n)]^{2+}$ complex dications, we encountered a remarkable structural variety (Table 3). Nevertheless, DFT calculations were able to confirm the preferred configuration of most of these structures by their computed relative energies except in the case of the $F^-$-bridged complex **5**, where the systematic overestimation of repulsive forces and thus of distances led to wrong predictions as a result of underestimated π–π interactions. Whereas some effects such as the preference of the more weakly basic halide ligands for the axial position are easily rationalized, the differences between the *anti* and *syn* orientations or the preferred N donor for the axial position are not readily obvious. Karlin and coworkers noted that "such structural differences or variations may need to be considered to explain certain aspects of […] reactivity patterns",[2a] and therefore, a detailed computational approach may provide increased efficiency in the design and development of ligands for broader interest such as in metal/$O_2$-induced CH activation;[9] an example encountered accidentally is presented here as doubly monooxygenated complex **7**.

## Experimental Section

**Instrumentation:** EPR spectra in the X band were recorded with a Bruker System EMX. $^1H$ NMR spectra were recorded in $CDCl_3$ with a Bruker AMX-300 NMR spectrometer. IR spectra were obtained with a Bruker Vector 22 instrument.

**Syntheses of Ligands:** The ligands $L^1$ = bis(pyridin-2-ylmethyl)benzylamine, $L^2$ = (6-methylpyridin-2-ylmethyl)(pyridin-2-ylmethyl)-benzylamine, $L^3$ = bis(6-methylpyridin-2-ylmethyl)benzylamine, and $L^4$ = (pyridin-2-ylethyl)(pyridin-2-ylmethyl)benzylamine were prepared according to the literature[7a,17] by reaction of the appropriate secondary amine with benzyl bromide in $CH_3CN$ as the solvent.

#### Synthesis of Copper Complexes

***Caution*:** *Perchlorate complexes are potentially explosive and should be handled with care.*

**$[L^3Cu(PPh_3)](BF_4)$:** To a solution of $L^3$ (55 mg, 0.173 mmol) in $CH_2Cl_2$ (10 mL) was added $[Cu(CH_3CN)_3(PPh_3)]BF_4$ (83 mg, 0.155 mmol). The mixture was stirred at room temperature overnight. After reducing the solvent 3 mL, a bright yellow product precipitated in 79% yield (89 mg) by adding hexane/toluene (1:1). Crystals were obtained by recrystallization from $CH_2Cl_2$ at –20 °C. Single crystals were covered with a layer of viscous hydrocarbon oil (Paratone N, Exxon), attached to a glass fiber, and instantly placed in a low-temperature $N_2$ stream. $^1H$ NMR (300 MHz, $CD_3CN$): δ = 2.62 (s, 6 H), 3.56 (s, 2 H), 3.67 (AB-m, 4 H), 7.08 (br., 2 H), 7.21–7.33 (m, 15 H), 7.37–7.54 (m, 7 H), 7.80 (pt, *J* = 7.7 Hz, 2 H) ppm. $C_{39}H_{38}BCuF_4N_3P$ (730.07): calcd. C 64.16, H 5.25, N 5.76; found C 63.92, H 5.93, N 5.12.

**$[L^3Cu(CH_3CN)](BF_4)$:** To a solution of $L^3$ (100 mg, 0.315 mmol) in $CH_2Cl_2$ (10 mL) was added $[Cu(CH_3CN)_4]BF_4$ (100 mg,

 © 2007 Wiley-VCH Verlag GmbH & Co. KGaA, Weinheim 

0.318 mmol). The mixture was stirred for 2 h at room temperature. After reducing the solvent to 2 mL and adding hexane a partially crystalline and highly air-sensitive precipitate was obtained and dried. Yield: 69 mg (43%). $^1$H NMR (300 MHz, $CD_3CN$): $\delta$ = 2.71 (s, 6 H), 3.81 (AB-m, 4 H), 3.93 (s, 2 H), 7.11 (d, $J$ = 8 Hz, 2 H), 7.25–7.40 (m, 7 H), 7.68 (pt, $J$ = 7.7 Hz, 2 H) ppm.

**$[L^1Cu(\mu\text{-}OH)_2CuL^1](ClO_4)_2\cdot 2CH_3COCH_3$ ($1\cdot 2CH_3COCH_3$):** To a suspension of $[Cu(CH_3CN)_4](ClO_4)$ (654 mg, 2 mmol) in acetone (10 mL) was added an acetone solution of the ligand (579 mg, 2 mmol) under an atmosphere of nitrogen. The mixture was stirred for 30 min to give a yellow solution, and then the flask was opened to the atmosphere. The solution turned blue, and the solid product separated with time. Crystals suitable for X-ray diffraction studies were obtained by recrystallization from boiling acetone. Yield: 697 mg (66%). IR (KBr pellet): $\tilde{\nu}$ = 3570 (sharp, shoulder), 3450 (br., OH), 1604, 1574, 1481, 1444 (sharp, py), 1100 (vs, $ClO_4^-$) cm$^{-1}$.$C_{44}H_{52}Cl_2Cu_2N_6O_{12}$ (1054.9): calcd. C 50.1, H 5.0, N 8.0, Cu 12.0; found C 48.8, H 4.9, N 8.1, Cu 12.3.

**$[L^2Cu(\mu\text{-}OH)_2CuL^2](ClO_4)_2\cdot H_2O$ ($2\cdot H_2O$):** To a suspension of $[Cu(CH_3CN)_4](ClO_4)$ (654 mg, 2 mmol) in $CH_2Cl_2$ (10 mL) was added a dichloromethane solution of the ligand (607 mg, 2 mmol) under an atmosphere of nitrogen. The mixture was stirred for 30 min after which the flask was opened to the atmosphere. After several hours a blue solid separated. Recrystallization from boiling ethanol gave crystals suitable for X-ray diffraction studies. Yield: 460 mg (45%). IR (KBr pellet): $\tilde{\nu}$ = 3600 (sharp, shoulder), 3500 (br., OH), 1603, 1577, 1473, 1458 (sharp, py), 1100 (vs, $ClO_4^-$) cm$^{-1}$. $C_{40}H_{46}Cl_2Cu_2N_6O_{11}$ (1020.9): calcd. C 48.8, H 4.7, N 8.5, Cu 12.9; found C 48.2, H 4.6, N 8.5, Cu 13.4.

**$[L^3Cu(\mu\text{-}OH)_2CuL^3](ClO_4)_2$ (3):** To a suspension of $[Cu(CH_3CN)_4](ClO_4)$ (654 mg, 2 mmol) in $CH_2Cl_2$ (10 mL) was added a dichloromethane solution of the ligand (635 mg, 2 mmol) under an atmosphere of nitrogen. The mixture was stirred for 30 min after which the flask was opened to the atmosphere. Blue crystals of **3** suitable for X-ray studies were obtained by slow evaporation of the solvent. Yield: 448 mg (45%). IR (KBr pellet): $\tilde{\nu}$ = 3560 (sharp, shoulder), 3500 (br., OH), 1610, 1579, 1469, 1441 (sharp, py), 1095 (vs, $ClO_4^-$) cm$^{-1}$. $C_{42}H_{48}Cl_2Cu_2N_6O_{10}$ (994.9): calcd. C 50.7, H 4.9, N 8.5, Cu 12.8; found C 52.1; H 4.8; N 8.2; Cu 13.1.

**$[L^3Cu(\mu\text{-}OMe)_2CuL^3](ClO_4)_2$ (4):** This compound was obtained by recrystallization of compound **3** in boiling methanol. IR (KBr pellet): $\tilde{\nu}$ = 1609, 1578, 1468, 1441 (sharp, py), 1090 (vs, $ClO_4^-$) cm$^{-1}$. $C_{44}H_{52}Cl_2Cu_2N_6O_{10}$ (1022.9): calcd. C 51.6, H 5.1, N 8.2, Cu 12.4; found C 50.8, H 5.0, N 7.9, Cu 12.6.

**$[L^3Cu(\mu\text{-}F)_2CuL^3](BF_4)_2\cdot 2CH_2Cl_2$ ($5\cdot 2CH_2Cl_2$):** To a cooled (–20 °C) solution of $[L^3Cu(CH_3CN)]BF_4$ (89 mg, 0.175 mmol) in $CH_2Cl_2$ (5 mL) was added $O_2$-saturated $CH_2Cl_2$ solution (5 mL). The initially bright-yellow solution turned deep green spontaneously. The mixture was stirred for 1 h at –20 °C. Removal of the solvent gave a deep green residue that was recrystallized from $CH_2Cl_2$ at –10 °C to afford a green product. Yield: 30 mg (36%). $C_{44}H_{50}B_2Cl_4Cu_2F_{10}N_6$ (1143.42): calcd. C 47.68, H 4.69, N 8.20; found C 45.71, H 4.64, N 8.67.

**$[L^4Cu(\mu\text{-}Cl)_2CuL^4](ClO_4)_2$ (6):** This complex was obtained by the reaction of a 1:1 mixture of copper(II) perchlorate hexahydrate (370 mg) and anhydrous copper(II) chloride (135 mg) with the $L^4$ ligand in methanol. Recrystallization from boiling methanol afforded crystals suitable for X-ray diffraction. Yield: 442 mg (44%). IR (KBr pellet): $\tilde{\nu}$ = 1610, 1570, 1485, 1448 (sharp, py), 1100 (vs, $ClO_4^-$) cm$^{-1}$. $C_{40}H_{42}Cl_4Cu_2N_6O_8$ (1003.7): calcd. C 47.8, H 4.2, N 8.4, Cu 12.7; found C 47.1, H 4.0, N 8.3, Cu 12.5.

**$[Cu(\mu\text{-}L^5)_2Cu](ClO_4)_2$ (7):** Evaporation of the residual solution resulting from the synthesis of compound **3** gave a blue-green syrup that was dissolved in acetonitrile. Slow evaporation of this solution gave a small amount of green crystals identified as compound **7** by X-ray diffraction.

**X-ray Data Collection and Refinement Details:** Single crystals of the compounds were glued to the tip of glass capillaries and then

Table 5. Crystallographic and refinement details for compounds $[L^3Cu(PPh_3)](BF_4)$, $1\cdot 2CH_3COCH_3$, $2\cdot H_2O$, and **3**.

| | $[L^3Cu(PPh_3)](BF_4)$ | $1\cdot 2CH_3OCH_3$ | $2\cdot H_2O$ | **3** |
|---|---|---|---|---|
| Formula | $C_{39}H_{38}BCuF_4N_3P$ | $C_{44}H_{52}Cl_2Cu_2N_6O_{12}$ | $C_{40}H_{46}Cl_2Cu_2N_6O_{11}$ | $C_{42}H_{48}Cl_2Cu_2N_6O_{10}$ |
| *Fw* | 730.04 | 1054.91 | 984.82 | 994.85 |
| Crystal system | monoclinic | triclinic | orthorhombic | monoclinic |
| Space group | $P2_1/c$ | $P\bar{1}$ | $P2_12_12_1$ | $C2/c$ |
| *a* [Å] | 16.225(7) | 10.530(1) | 12.1372(7) | 18.979(5) |
| *b* [Å] | 9.925(4) | 11.019(1) | 16.777(1) | 8.7256(18) |
| *c* [Å] | 23.327(9) | 11.390(1) | 22.710(1) | 27.449(6) |
| *α* [°] | 90 | 67.289(2) | 90 | 90 |
| *β* [°] | 105.79(1) | 87.113(2) | 90 | 104.854(8) |
| *γ* [°] | 90 | 86.747(2) | 90 | 90 |
| Volume [Å$^3$] | 3615(3) | 1216.6(3) | 4624.2(5) | 4393.7(17) |
| *Z* | 4 | 1 | 4 | 4 |
| *F*(000) | 1512 | 546 | 2028 | 2072 |
| $D_{calcd.}$ [g cm$^{-3}$] | 1.341 | 1.440 | 1.413 | 1.519 |
| Crystal size [mm] | 0.5 × 0.05 × 0.01 | 0.45 × 0.13 × 0.05 | 0.50 × 0.34 × 0.16 | 0.38 × 0.18 × 0.02 |
| *T* [K] | 173 | 293 | 293 | 293 |
| 2*θ* range | 3.15 to 27.04 | 3.88 to 50.20 | 3.02 to 50.16 | 1.53 to 25.04 |
| *μ* [mm$^{-1}$] | 0.701 | 1.049 | 1.097 | 1.156 |
| Index ranges | $-19 \le h \le 20$ | $-12 \le h \le 12$ | $-14 \le h \le 14$ | $-22 \le h \le 22$ |
| | $-10 \le k \le 12$ | $-13 \le k \le 13$ | $-20 \le k \le 19$ | $-10 \le k \le 10$ |
| | $-27 \le l \le 26$ | $-13 \le l \le 13$ | $-26 \le l \le 27$ | $-32 \le l \le 32$ |
| No. reflections collected | 4214 | 4272 | 8211 | 3887 |
| No. reflections observed | 2355 | 2737 | 6010 | 2768 |
| *R*, $R_w$[a] | 0.1184, 0.2100 | 0.0738, 0.1676 | 0.0728, 0.1926 | 0.1625, 0.3581 |
| Final difference [e Å$^{-3}$] | 0.530, –0.548 | 0.665, –0.552 | 0.852, –0.743 | 1.043, –1.531 |

[a] $R = \Sigma||F_o| - |F_c||/\Sigma|F_o|$. $R_w = [\Sigma w(|F_o| - |F_c|)^2/\Sigma w(F_o)^2]^{1/2}$, where $w = 1/\sigma^2(F_o)$. $\lambda$(Mo-$K_\alpha$) = 0.71073 Å.

 © 2007 Wiley-VCH Verlag GmbH & Co. KGaA, Weinheim 

Table 6. Crystallographic and refinement details for compounds **4**, **5**·2$CH_2Cl_2$, **6**, and **7**.

| | **4** | **5**·2$CH_2Cl_2$ | **6** | **7** |
|---|---|---|---|---|
| Formula | $C_{44}H_{52}Cl_2Cu_2N_6O_{10}$ | $C_{44}H_{50}B_2Cl_4Cu_2F_{10}N_6$ | $C_{40}H_{42}Cl_4Cu_2N_6O_8$ | $C_{42}H_{44}Cl_2Cu_2N_6O_{10}$ |
| *Fw* | 1022.92 | 1141.83 | 1003.70 | 990.83 |
| Crystal system | monoclinic | monoclinic | monoclinic | monoclinic |
| Space group | $P2_1/n$ | $P2_1/n$ | $P2_1/c$ | $P2_1/n$ |
| *a* [Å] | 10.8139(11) | 11.9814(3) | 9.1595(8) | 10.4493(11) |
| *b* [Å] | 16.8512(18) | 13.4624(3) | 17.762(2) | 17.0095(18) |
| *c* [Å] | 13.4087(14) | 15.7738(4) | 12.557(1) | 12.8309(13) |
| *α* [°] | 90 | 90 | 90 | 90 |
| *β* [°] | 109.745(2) | 112.168(1) | 91.305(2) | 109.945(2) |
| *γ* [°] | 90 | 90 | 90 | 90 |
| Volume [Å$^3$] | 2299.8(4) | 2356.22(10) | 2042.5(3) | 2143.7(4) |
| *Z* | 2 | 4 | 2 | 2 |
| *F*(000) | 1060 | 1168 | 1028 | 1020 |
| $D_{calcd.}$ [g cm$^{-3}$] | 1.477 | 1.614 | 1.632 | 1.535 |
| Crystal size [mm] | 0.30 × 0.20 × 0.17 | 0.46 × 0.2 × 0.06 | 0.27 × 0.24 × 0.12 | 0.42 × 0.20 × 0.07 |
| *T* [K] | 293 | 293 | 293 | 293 |
| 2*θ* range | 2.02 to 25.10 | 3.88 to 28.28 | 3.98 to 50.16 | 2.07 to 25.07 |
| *μ* [mm$^{-1}$] | 1.104 | 1.21 | 1.365 | 1.182 |
| Index ranges | $-12 \le h \le 12$ | $-15 \le h \le 15$ | $-10 \le h \le 10$ | $-12 \le h \le 12$ |
| | $-20 \le k \le 20$ | $-17 \le k \le 17$ | $-21 \le k \le 21$ | $-20 \le k \le 20$ |
| | $-15 \le l \le 15$ | $-20 \le l \le 19$ | $-14 \le l \le 14$ | $-15 \le l \le 15$ |
| No. reflections collected | 4087 | 5784 | 3610 | 3808 |
| No. reflections observed | 3323 | 4850 | 2557 | 2661 |
| $R$, $R_w$[a] | 0.0438, 0.1067 | 0.0375, 0.0805 | 0.0593, 0.1452 | 0.0573, 0.1498 |
| Final difference [e Å$^{-3}$] | 0.633, –0.209 | 0.487, –0.477 | 0.817, –0.487 | 0.566, –0.285 |

[a] $R = \Sigma||F_o| - |F_c||/\Sigma|F_o|$. $R_w = [\Sigma w(|F_o| - |F_c|)^2/\Sigma w(F_o)^2]^{1/2}$, where $w = 1/\sigma^2(F_o)$. $\lambda$(Mo-$K_\alpha$) = 0.71073 Å.

mounted on either a Bruker SMART-APEX[28a] (**1**–**4**, **6**, **7**), or a Bruker-Nonius Kappa CCD diffractometer [{$L^3$Cu(PPh$_3$)}(BF$_4$) and **5**]. Intensity data for **1**–**4**, **6**, and **7** were collected by using 10 s by frame (except for **4** where 30 s was used), separated by 0.3°. Data integration and cell refinement was made by using SAINTPLUS.[28b] The structures were solved by direct methods with the use of XS and XL in SHELXTL,[28c] or the program system SHELXL-97 in connection with absorption correction.[28d] Anisotropic thermal parameters were included for all non-hydrogen atoms. H atoms were placed geometrically and refined by using a riding model, including free rotation of methyl groups and variable isotropic displacement parameters. Final *R* values and important bond parameters are listed in Tables 1, 2, 5, and 6.

Analysis of the raw data for complex **3** clearly suggested that the crystal had two identifiable components, related by a 180° rotation around <–1,–2,0>. Data reduction using both components shows one major component (mean $I/\sigma$ = 2.0) and a minor one (mean $I/\sigma$ = 0.5). A rather small amount of reflections (≈5%) corresponds to overlapped data. Structure solution and structure refinement were finally performed considering just the major component.

During the last stages of refinement some disorder of the perchlorate anions for complexes **1**, **2**, **3**, **4**, and **6** was obvious. This was modeled by using partially occupied positions, which were first refined and then held constant for the final refinement.

**DFT Calculations:** DFT calculations were carried out by using the Amsterdam Density Functional package[29a] developed by Baerends and coworkers.[29b–29f] The local density approximation for electron correlation was treated with the Vosko–Wilk–Nusair parametrization.[30a] The nonlocal corrections of Becke[30b,30c] and Perdew[30d,30e] (BP86) were added to the exchange and correlation energies, respectively. The numerical integration procedure applied for the calculations was developed by te Velde et al.[29f] The standard ADF STO TZP basis set was used.[29a] The frozen-core approximation[30f] was considered for Cu, 3p; Cl, 2p; F, O, N, and C, 1s. Geometry optimization and single point calculations were done for $[Cu_2L_2X_2]^{2+}$ by considering a unrestricted singlet state involving $C_i$ or $C_2$ symmetry as constraints for *anti* and *syn* models, respectively.

CCDC-647370 to -647377 contain the supplementary crystallographic data for this paper. These data can be obtained free of charge from The Cambridge Crystallographic Data Centre via www.ccdc.cam.ac.uk/data_request/cif.

**Supporting Information** (see footnote on the first page of this article): Selected DFT optimized distances and angles for model complexes **1**–**6**, **8**, and $[L^2Cu(\mu\text{-MeO})_2CuL^2]^{2+}$, bond lengths and angles for [$L^3$Cu(PPh$_3$)](BF$_4$).

## Acknowledgments

This work was performed within the Collaborative Research Centre SFB 706 (Selective Catalytic Oxidations Using Molecular Oxygen; Stuttgart) and funded by the German Research Foundation, the Fonds der Chemischen Industrie (FCI) and by FONDECYT (project No. 1050484).

[1] a) W. H. Crawford, H. W. Richardson, J. R. Wasson, D. J. Hodgson, W. E. Hatfield, *Inorg. Chem.* **1976**, *15*, 2107; b) O. Kahn, *Molecular Magnetism*, VCH, Weinheim, **1993**; c) E. Ruiz, P. Alemany, S. Alvarez, J. Cano, *Inorg. Chem.* **1997**, *36*, 3683; d) E. Ruiz, P. Alemany, S. Alvarez, J. Cano, *J. Am. Chem. Soc.* **1997**, *119*, 1297.

[2] a) J. Shearer, C. X. Zhang, L. N. Zakharov, A. L. Rheingold, K. D. Karlin, *J. Am. Chem. Soc.* **2005**, *127*, 5469; b) I. Sanyal, M. Mahroof-Tahir, M. S. Nasir, P. Ghosh, B. I. Cohen, Y. Gultneh, R. W. Cruse, A. Farooq, K. D. Karlin, S. Liu, J. Zubieta, *Inorg. Chem.* **1992**, *31*, 4322; c) K. D. Karlin, Q.-F. Gan, A. Farooq, S. Liu, J. Zubieta, *Inorg. Chem.* **1990**, *29*, 2549; d) K. D. Karlin, Y. Gultneh, J. C. Hayes, J. Zubieta, *Inorg. Chem.*

 © 2007 Wiley-VCH Verlag GmbH & Co. KGaA, Weinheim 

**1984**, *23*, 519; e) K. D. Karlin, S. Kaderli, A. D. Zuberbühler, *Acc. Chem. Res.* **1997**, *30*, 139; f) L. Quant Hatcher, K. D. Karlin, *J. Biol. Inorg. Chem.* **2004**, *9*, 669.

[3] a) T. Osako, K. Ohkubo, M. Taki, Y. Tachi, S. Fukuzumi, S. Itoh, *J. Am. Chem. Soc.* **2003**, *125*, 11027; b) T. Osako, Y. Ueno, Y. Tachi, S. Itoh, *Inorg. Chem.* **2003**, *42*, 8087; c) S. Itoh, S. Fukuzumi, *Bull. Chem. Soc. Jpn.* **2002**, *75*, 2081; d) Y. Tachi, K. Aita, S. Teramae, F. Tani, Y. Naruta, S. Fukuzumi, S. Itoh, *Inorg. Chem.* **2004**, *43*, 4558.

[4] a) N. Kitajima, *Adv. Inorg. Chem.* **1992**, *39*, 1; b) N. Kitajima, Y. Moro-oka, *Chem. Rev.* **1993**, *94*, 737; c) M. Suzuki, H. Furutachi, H. Otawa, *Coord. Chem. Rev.* **2000**, *200–202*, 105.

[5] a) W. B. Tolman, *Acc. Chem. Res.* **1997**, *30*, 227; b) E. A. Lewis, W. B. Tolman, *Chem. Rev.* **2004**, *104*, 1047.

[6] L. M. Mirica, X. Ottenwaelder, T. D. P. Stack, *Chem. Rev.* **2004**, *104*, 1013.

[7] a) D. Rojas, A. M. Garcia, A. Vega, Y. Moreno, D. Venegas-Yazigi, M. T. Garland, J. Manzur, *Inorg. Chem.* **2004**, *43*, 6324; b) W. Kaim, C. Titze, T. Schurr, M. Sieger, M. Lawson, J. Jordanov, D. Rojas, A. M. Garcia, J. Manzur, *Z. Anorg. Allg. Chem.* **2005**, *631*, 2568.

[8] a) S. Schindler, *Eur. J. Inorg. Chem.* **2000**, 2311; b) M. Schatz, V. Raab, S. P. Foxon, G. Brehm, S. Schneider, M. Reiher, M. C. Holthausen, J. Sundermeyer, S. Schindler, *Angew. Chem.* **2004**, *116*, 4460; *Angew. Chem. Int. Ed.* **2004**, *43*, 4360.

[9] a) P. Gamez, P. G. Aubel, W. L. Driessen, J. Reedijk, *Chem. Soc. Rev.* **2001**, *30*, 376; b) S. Itoh, H. Kumei, M. Taki, S. Nagatomo, T. Kitagawa, S. Fukuzumi, *J. Am. Chem. Soc.* **2001**, *123*, 6708; c) E. Pidcock, H. V. Obias, M. Abe, H.-C. Liang, K. D. Karlin, E. I. Solomon, *J. Am. Chem. Soc.* **1999**, *121*, 1299; d) G. Battaini, E. Monzani, A. Perotti, C. Para, L. Casella, L. Santagostini, M. Gullotti, R. Dillinger, C. Näther, F. Tuczek, *J. Am. Chem. Soc.* **2003**, *125*, 4185; e) M. Mizuno, K. Honda, J. Cho, H. Furatachi, T. Tosha, T. Matsumoto, S. Fujinami, T. Kitagawa, M. Suzuki, *Angew. Chem.* **2006**, *118*, 7065; *Angew. Chem. Int. Ed.* **2006**, *45*, 6911; f) B. Schönecker, T. Zheldakova, Y. Liu, M. Kötteritzsch, W. Günther, H. Görls, *Angew. Chem.* **2003**, *115*, 3361; *Angew. Chem. Int. Ed.* **2003**, *42*, 3240; g) P. Spuhler, M. C. Holthausen, *Angew. Chem.* **2003**, *115*, 6143; *Angew. Chem. Int. Ed.* **2003**, *42*, 5961; h) E. Spodine, J. Manzur, *Coord. Chem. Rev.* **1992**, *119*, 171.

[10] K. E. van Holde, K. I. Miller, H. Decker, *J. Biol. Chem.* **2001**, *276*, 15563.

[11] a) J. P. Klinman, *Chem. Rev.* **1996**, *96*, 2541; b) B. J. Brazeau, B. J. Johnson, C. M. Wilmot, *Arch. Biochem. Biophys.* **2004**, *428*, 22.

[12] E. I. Solomon, P. Chen, M. Metz, S. K. Lee, A. E. Palmer, *Angew. Chem. Int. Ed.* **2001**, *40*, 4570.

[13] a) S. A. Leaver, C. A. Kilner, M. A. Halcrow, *Acta Crystallogr., Sect. C: Cryst. Struct. Commun.* **2004**, *60*, m1; b) H. Hayashi, S. Fujinami, S. Nagatomo, S. Ogo, M. Suzuki, A. Uehara, Y. Watanabe, T. Kitagawa, *J. Am. Chem. Soc.* **2000**, *122*, 2124.

[14] S. C. Lee, R. H. Holm, *Inorg. Chem.* **1993**, *32*, 4745.

[15] O. Svajlenova, J. Vanco, J. Marek, *Acta Crystallogr. Sect. C: Cryst. Struct. Commun.* **2004**, *60*, m275.

[16] a) W. E. Hatfield, *Comments, Inorg. Chem.* **1981**, *1*, 105; b) T. Rojo, M. I. Arriortua, J. Ruiz, J. Darriet, G. Villeneuve, D. Beltran-Porter, *J. Chem. Soc. Dalton Trans.* **1987**, 285 and references cited therein; c) F. Calderazzo, F. Marchetti, G. Dell'Amico, G. Pelizzi, A. Colligiani, *J. Chem. Soc. Dalton Trans.* **1980**, 1419.

[17] T. Osako, S. Terada, T. Tosha, S. Nagatomo, H. Furutachi, S. Fujinami, T. Kitagawa, M. Suzuki, S. Itoh, *Dalton Trans.* **2005**, 3514.

[18] K. D. Karlin, S. E. Sherman, *Inorg. Chim. Acta* **1982**, *65*, L39.

[19] a) J. Reedijk, *Comments, Inorg. Chem.* **1982**, *1*, 379; b) I. B. Gorrell, G. Parkin, *Inorg. Chem.* **1990**, *29*, 2452; c) H. Casellas, A. Pevec, B. Ozlevcar, P. Gamez, J. Reedijk, *Polyhedron* **2005**, *24*, 1549.

[20] W. Kaim, B. Schwederski, *Bioinorganic Chemistry*, Wiley, Chichester, **1994**, ch. 10.

[21] H. Decker, T. Schweikardt, F. Tuczek, *Angew. Chem.* **2006**, *118*, 4658; *Angew. Chem. Int. Ed.* **2006**, *45*, 4546.

[22] S. T. Prigge, B. A. Eipper, R. E. Mains, L. M. Amzel, *Science* **2004**, *304*, 864.

[23] C. Würtele, E. Gaoutchenova, K. Harms, M. C. Holthausen, J. Sundermeyer, S. Schindler, *Angew. Chem.* **2006**, *118*, 3951; *Angew. Chem. Int. Ed.* **2006**, *45*, 3867.

[24] a) P. Chen, D. E. Root, C. Campochiaro, K. Fujisawa, E. I. Solomon, *J. Am. Chem. Soc.* **2003**, *125*, 466; b) S.-K. Lee, S. DeBeer George, W. E. Antholine, B. Hedman, K. O. Hodgson, E. I. Solomon, *J. Am. Chem. Soc.* **2002**, *124*, 6180.

[25] a) A. W. Addison, T. N. Rao, J. Reedijk, J. van Rijn, C. G. Verschoor, *J. Chem. Soc. Dalton Trans.* **1984**, 1349; b) A. Schmuck, K. Seppelt, *Chem. Ber.* **1989**, *122*, 803.

[26] C. Janiak, *J. Chem. Soc. Dalton Trans.* **2000**, 3885.

[27] M. Sieger, C. Vogler, A. Klein, A. Knödler, M. Wanner, J. Fiedler, S. Zalis, T. L. Snoeck, W. Kaim, *Inorg. Chem.* **2005**, *44*, 4637.

[28] a) *SMART-APEX*, X-ray Diffraction System, Bruker, **1998**; b) *SAINTPLUS Version 6.02*, Bruker AXS, Madison, WI, **1999**; c) *SHELXTL Version 5.1*, Bruker AXS, Madison, WI, **1998**; d) G. M. Sheldrick, *SHELX-97: Program for Crystal Structure Solution and Refinement*, University of Göttingen, Göttingen, **1997**; e) W. Herrendorf, H. Bärnighausen, *Program HABITUS*, Karlsruhe, Germany, **1993**.

[29] a) ADF2002.01, *Theoretical Chemistry*, Vrije Universiteit, Amsterdam, The Netherlands, SCM (http://www.scm.com); b) E. J. Baerends, D. E. Ellis, P. Ros, *Chem. Phys.* **1973**, *2*, 41; c) G. te Velde, E. J. Baerends, *J. Comput. Phys.* **1992**, *99*, 84; d) C. Fonseca Guerra, J. G. Snijders, G. te Velde, E. J. Baerends, *Theo. Chim. Acc.* **1998**, *99*, 391; e) F. M. Bickelhaupt, E. J. Baerends, *Rev. Comput. Chem.* **2000**, *15*, 1; f) G. te Velde, F. M. Bickelhaupt, C. Fonseca Guerra, S. J. A. van Gisbergen, E. J. Baerends, J. G. Snijders, T. Ziegler, *J. Comput. Chem.* **2001**, *22*, 931.

[30] a) S. D. Vosko, L. Wilk, M. Nusair, *Can. J. Chem.* **1990**, *58*, 1200; b) A. D. Becke, *J. Chem. Phys.* **1986**, *84*, 4524; c) A. D. Becke, *Phys. Rev. A* **1988**, *38*, 3098; d) J. P. Perdew, *Phys. Rev. B* **1986**, *33*, 8822; e) J. P. Perdew, *Phys. Rev. B* **1986**, *34*, 7406; f) L. Verluis, T. Ziegler, *J. Chem. Phys.* **1988**, *88*, 322.

Received: June 20, 2007
Published Online: October 30, 2007

 © 2007 Wiley-VCH Verlag GmbH & Co. KGaA, Weinheim 

DOI: 10.1002/ejic.200700657

# Homo- and Heterometallic Coordination Oligomers and Polymers Derived from the Preformed Complexes $[Cu(bdmpp)(MeCN)_2](ClO_4)_2$, $[Cu(bdmpp)(N_3)_2]$, and $[Cu(bdmpp)(N_3)(\mu\text{-}N_3)]_2$ [bdmpp = 2,6-bis(3,5-dimethyl-1*H*-pyrazol-1-yl)pyridine]: Syntheses, Structures, and Redox Properties

**Guang-Fei Liu,[a] Zhi-Gang Ren,[a] Hong-Xi Li,[a] Yang Chen,[a] Qiu-Hong Li,[a] Yong Zhang,[a] and Jian-Ping Lang*[a,b]**

**Keywords:** Copper / Structures / Oligomers / Polymers / Redox properties

Reactions of three $Cu^{II}$ complexes of 2,6-bis(3,5-dimethyl-1*H*-pyrazol-1-yl)pyridine (bdmpp), $[Cu(bdmpp)(MeCN)_2](ClO_4)_2$ (**1**), $[Cu(bdmpp)(N_3)_2]\cdot 1.5H_2O$ (**2**·$1.5H_2O$), and $[Cu(bdmpp)(N_3)(\mu\text{-}N_3)]_2\cdot 2MeOH$ (**3**·2MeOH), with 4,4′-bipy, dicyanamide (dca), azide, and $MCl_2$ (M = Cu, Co, Ni) yield a series of homo- and heterometallic coordination oligomers and polymers, $[\{Cu(bdmpp)(ClO_4)\}_2(\mu\text{-}4,4'\text{-bipy})](ClO_4)_2$ (**4**), $\{[Cu(bdmpp)(\mu\text{-dca})](ClO_4)\}_n$ (**5**), $\{[Cu(bdmpp)(\mu\text{-}N_3)](ClO_4)\cdot MeCN\}_n$ (**6**), $[\{Cu(N_3)(bdmpp)\}_2(\mu\text{-}N_3)_2Cu(N_3)_2]$ (**7**), and $[\{Cu(\mu\text{-}N_3)(bdmpp)(\mu\text{-}N_3)M(\mu\text{-}N_3)(X)\}_2\cdot eMeCN]_n$ (**8**: M = Co, X = $N_3$, *e* = 0; **9**: M = Ni, X = Cl; *e* = 4). Compounds **1**–**9** have been characterized by elemental analysis, IR spectroscopy, and single-crystal X-ray crystallography. Compound **4** has a centrosymmetric dimeric dication structure in which two $[Cu(bdmpp)(ClO_4)]^+$ fragments are bridged by one 4,4′-bipy. Compounds **5** and **6** have a 1D linear or spiral chain extending along the *b* axis in which each $[Cu(bdmpp)]^{2+}$ fragment is linked through bridging dca or azide anions, respectively. Compound **7** has a trinuclear sandwich structure in which two molecules of **2** link a $Cu(N_3)_2$ species through two end-on bridging azide anions. Compounds **8** and **9** have a similar 1D chain structure extending along the *c* axis in which $[Cu(\mu\text{-}N_3)(bdmpp)(\mu\text{-}N_3)M(\mu\text{-}N_3)(X)]_2$ (M = Co, Ni) molecules are linked by end-to-end azide anions (**8**) or end-on azide anions (**9**). In addition, the electrochemical properties of **1**–**9** in DMF were investigated by cyclic voltammetry. (© Wiley-VCH Verlag GmbH & Co. KGaA, 69451 Weinheim, Germany, 2007)

## Introduction

In past decades, design and construction of coordination oligomers and polymers from metal complex or cluster precursors has attracted considerable attention because of their structural diversity[1–11] and their potential applications in advanced materials.[12–20] From the viewpoint of the "design", a suitable metal complex or cluster precursor may possess one of the following requirements. Firstly, that some ligands around the metal center or cluster core are labile and readily replaced by other strong donor ligands. Secondly, that some ligands in the complex or cluster are potential multilinkers to interconnect with other metal centers or cluster cores. Thirdly, that the coordination is unsaturated for at least one metal atom of the complex or cluster. Many preformed clusters match these requirements and have been employed to serve as excellent precursors for the formation of a number of cluster-based supramolecules.[3–6,8–11,21–24] In contrast to the cluster precursors, employment of the preformed metal complexes for the formation of homo- or heterometallic coordination oligomers or polymers is less explored.

Recently we have been engaged in the construction of coordination oligomers and polymers from preformed mononuclear complexes and metal sulfide clusters.[11,21–26] One useful approach is to introduce the bulky ligands that block some of the coordination sites of the metal center, which may cause it to form the unsaturated coordination geometry. Among numerous bulky ligands, the tridentate ligand 2,6-bis(3,5-dimethyl-1*H*-pyrazol-1-yl)pyridine (bdmpp) attracted our attention. This ligand has been employed to react with metal ions to form various complexes.[27–30] Some metal/bdmpp complexes did show unsaturated coordination geometry around the metal center.[27–30] However, these compounds have not been used as precursors to further assemble coordination oligomers and polymers. To this end, we prepared three $Cu^{II}$/bdmpp complexes, $[Cu(bdmpp)(MeCN)_2](ClO_4)_2$ (**1**), $[Cu(bdmpp)(N_3)_2]\cdot 1.5H_2O$ (**2**·$1.5H_2O$), and $[Cu(bdmpp)(N_3)(\mu\text{-}N_3)]_2\cdot 2MeOH$ (**3**·2MeOH), in high yields. Compounds **1**–**3** match the above-mentioned requirements and could be used as pre-

[a] School of Chemistry and Chemical Engineering, Suzhou University,
Suzhou 215123, Jiangsu, People's Republic of China
Fax: +86-512-65880089
E-mail: jplang@suda.edu.cn
[b] State Key Laboratory of Coordination Chemistry, Nanjing University,
Nanjing 210093, Jiangsu, People's Republic of China

 © 2007 Wiley-VCH Verlag GmbH & Co. KGaA, Weinheim 

cursors to form a family of homo- and heterometallic coordination oligomers and polymers: $[\{Cu(bdmpp)(ClO_4)\}_2(\mu\text{-}4,4'\text{-bipy})](ClO_4)_2$ (**4**), $\{[Cu(bdmpp)(\mu\text{-dca})](ClO_4)\}_n$ (**5**), $\{[Cu(bdmpp)(\mu\text{-}N_3)](ClO_4)\cdot MeCN\}_n$ (**6**), $[\{Cu(N_3)(bdmpp)\}_2(\mu\text{-}N_3)_2Cu(N_3)_2]$ (**7**), and $[\{Cu(\mu\text{-}N_3)(bdmpp)(\mu\text{-}N_3)M(\mu\text{-}N_3)(X)\}_2\cdot e MeCN]_n$ (**8**: M = Co, X = $N_3$, $e$ = 0; **9**: M = Ni, X = Cl; $e$ = 4). Furthermore, we have employed cyclic voltammetry (CV) to investigate the electrochemical behaviors of **1**–**9** in order to understand the changes of the redox properties of the assembled oligomers and polymers relative to their precursors. In this paper, we report their syntheses, crystal structures, and redox properties.

## Results and Discussion

Reaction of $[Cu(MeCN)_4](ClO_4)_2$ with equimolar bdmpp in MeCN resulted in a green solution. Slow diffusion of $Et_2O$ into the solution led to the formation of green blocks of **1** in 85% yield (Scheme 1). On the other hand, treatment of $CuCl_2\cdot 2H_2O$ with $NaN_3$ and bdmpp in 1:2:1 and 1:4:1 (molar ratio) in MeOH followed by slow evaporation of solvents gave rise to **2**·1.5$H_2O$ and **3**·2MeOH in 75% and 72% yields, respectively. The formation of **2**·1.5$H_2O$ and **3**·2MeOH depended on the molar ratio of $CuCl_2\cdot 2H_2O$ and $NaN_3$ during the reaction. As discussed later in this paper, when the lower ratio (1:2) was used, the Cu atom was apt to adopt a less saturated coordination (five-coordinate) and **2**·1.5$H_2O$ was thus formed. When the higher ratio (1:4 or more) was used, the Cu atom was more apt to adopt a saturated coordination (six-coordinate) and **3**·2MeOH was formed.

As discussed later in this paper, the $Cu^{II}$ atom in **1** is chelated by one bdmpp and coordinated by two labile MeCN molecules. When the two MeCN molecules are replaced by strong bridging donor ligands, the $Cu^{II}$ center may have up to three more coordination sites available and its trigonal-bipyramidal coordination geometry may be turned to square-planar, square-pyramidal, or octahedral. The remaining $[Cu(bdmpp)]^{2+}$ fragment along with bridging ligands may serve as multiconnecting nodes to form novel oligomers and polymers. Among the potential bridging donor ligands, we chose 4,4′-bypyridine (4,4′-bipy), sodium dicyanamide, and sodium azide for this purpose.

Treatment of **1** with equimolar 4,4′-bipy followed by a similar procedure used in the isolation of **1** produced blue crystals of **4** in 63% yield, while reactions of **1** with equimolar sodium dicyanamide or sodium azide followed by a similar workup gave rise to green crystals of **5** and deep green crystals of **6** in 75% and 80% yields, respectively (Scheme 1). It is noted that in these cases, the two MeCN molecules coordinated at the Cu center of **1** were replaced and the $[Cu(bdmpp)]^{2+}$ fragment was retained, even though the coordination geometry of the Cu atom was changed during the reactions. The different outcomes from the aforementioned three reactions deserve comment. Compared with the dca and $N_3^-$ ligands, 4,4′-bipy seems somewhat bulky and rigid. The replacement of the two MeCN molecules of the cation of **1** by 4,4′-bipy only afforded a dinuclear complex **4**. The less rigid ligand, dca or $N_3^-$, removed the two MeCN molecules of the cation of **1** and linked the $[Cu(bdmpp)]^{2+}$ fragments through end-to-end μ-1,5-bridging mode (dca) or μ-1,3-bridging mode ($N_3^-$), forming polymeric species **5** and **6**, respectively.

In the cases of **2** and **3**, both complexes may also work as precursors for oligomers and polymers as they have two terminal azides that could link other metal ions. Accordingly, reactions of **2** with a mixture of $CuCl_2\cdot 2H_2O$ and $NaN_3$ in a molar ratio of 1:1:4 produced the homometallic

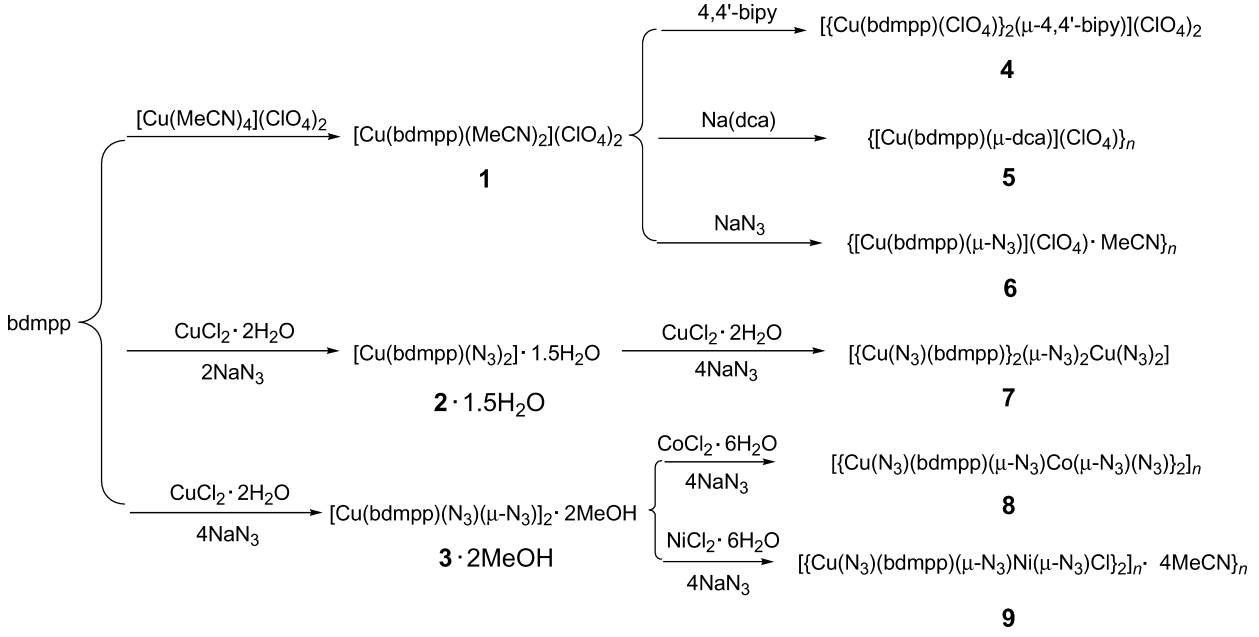


Scheme 1. Reactions of bdmpp with $[Cu(MeCN)_4](ClO_4)_2$ and $CuCl_2\cdot 2H_2O/NaN_3$; reactions of **1** with 4,4′-bipy, Na(dca), and $NaN_3$; reactions of **2** with $CuCl_2\cdot 2H_2O$ and $NaN_3$; and reactions of **3** with $MCl_2\cdot 6H_2O$ (M = Cu, Co, Ni) and $NaN_3$.

 © 2007 Wiley-VCH Verlag GmbH & Co. KGaA, Weinheim 

oligomer **7** in 67% yield, while those of **3** with a mixture of $MCl_2·6H_2O$ (M = Co, Ni) and $NaN_3$ in a molar ratio of 1:1:4 followed by a similar workup afforded two heterometallic polymers, **8** and **9**, in 50% and 49% yields, respectively (Scheme 1). In these cases, **2** or **3** only used their terminal azides to link the possible $Cu(N_3)_2$ or $[M(\mu\text{-}N_3)(X)]_2$ (M = Co, X = $N_3$; M = Ni, X = Cl) species. The coordination geometry for each Cu center in **2** or **3** is retained.

Solids **1**–**9** were relatively air- and moisture-stable, and were soluble in DMF and DMSO. The elemental analysis was consistent with the chemical formula of **1**–**9**. The IR spectrum of **1** showed a sharp $\nu$(CN) at 2249 $cm^{-1}$, suggesting the presence of terminal acetonitrile molecules. In the IR spectra of **2**·1.5$H_2O$, **3**·2MeOH, and **6**–**9** the strong absorptions at 2040/2068 (**2**·1.5$H_2O$), 2045 (**3**·2MeOH), 2041 (**7**), and 2029 (**8**) $cm^{-1}$ may be attributed to the asymmetric stretching frequencies of the terminal azide groups while those at 2073 (**3**·2MeOH), 2054/2066 (**6**), 2066 (**7**), 2066 (**8**), and 2069 (**9**) $cm^{-1}$ may be assigned to be the asymmetric stretching vibrations of end-on or end-to-end bridging azide groups.[31] In the IR spectrum of **5**, a band at 2179 $cm^{-1}$ was assigned to be the stretching vibration of the dca ligand with a bidentate $\mu_{1,5}$ coordination.[25] In the IR spectra of **1** and **4**–**6**, strong and broad peaks at 1122/1087/1060 (**1**), 1093/1024 (**5**), and 1144/1118/1084 (**6**) $cm^{-1}$ are the characteristic Cl–O stretching vibrations of the free perchlorate anions while that at 1087 $cm^{-1}$ (**4**) may be assigned to be a unidentate perchlorato ligand. The identities of **1**–**9** were further confirmed by X-ray crystallography.

Compound **1** crystallizes in the orthorhombic space group *Pbca* and the asymmetric unit consists of one $[Cu(bdmpp)(MeCN)_2]^{2+}$ dication and two $ClO_4^-$ anions. Unlike the most reported fashion of the square-pyramidal geometry,[30] the five-coordinate copper(II) atom in **1** adopts a distorted trigonal-bipyramidal geometry, which is coordinated by three N atoms from the bdmpp ligand and two N atoms from the acetonitrile molecules (Figure 1). N(1) and N(5) are located in apical positions, while N(3),

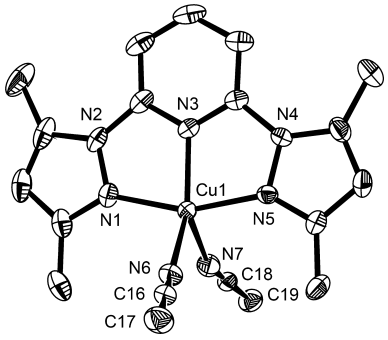


Figure 1. Perspective view of the $[Cu(bdmpp)(MeCN)_2]^{2+}$ dication of **1** with 50% thermal ellipsoids. All hydrogen atoms are omitted for clarity.

Table 1. Selected bond lengths [Å] and angles [°] of **1**–**3**.[a]

| | | | |
|---|---|---|---|
| | Compound **1** | | |
| Cu(1)–N(1) | 1.981(3) | Cu(1)–N(6) | 2.054(3) |
| Cu(1)–N(3) | 1.947(2) | Cu(1)–N(7) | 2.162(3) |
| Cu(1)–N(5) | 1.967(2) | | |
| N(1)–Cu(1)–N(3) | 78.95(10) | N(5)–Cu(1)–N(6) | 97.30(10) |
| N(3)–Cu(1)–N(5) | 79.52(10) | N(1)–Cu(1)–N(7) | 97.72(10) |
| N(5)–Cu(1)–N(1) | 158.43(11) | N(3)–Cu(1)–N(7) | 122.33(10) |
| N(1)–Cu(1)–N(6) | 98.58(10) | N(5)–Cu(1)–N(7) | 94.80(10) |
| N(3)–Cu(1)–N(6) | 140.88(10) | N(6)–Cu(1)–N(7) | 96.77(11) |
| | Compound **2** | | |
| Cu(1)–N(1) | 2.0192(19) | Cu(1)–N(6) | 1.9373(18) |
| Cu(1)–N(3) | 1.9721(17) | Cu(1)–N(9) | 2.186(2) |
| Cu(1)–N(5) | 2.0124(19) | | |
| N(1)–Cu(1)–N(3) | 78.09(7) | N(6)–Cu(1)–N(9) | 102.39(9) |
| N(3)–Cu(1)–N(5) | 78.37(8) | N(1)–Cu(1)–N(6) | 100.50(8) |
| N(5)–Cu(1)–N(1) | 156.18 | N(3)–Cu(1)–N(6) | 152.30(7) |
| N(3)–Cu(1)–N(9) | 105.27(8) | N(5)–Cu(1)–N(6) | 98.62(8) |
| N(5)–Cu(1)–N(9) | 93.64(9) | N(1)–Cu(1)–N(9) | 95.98(9) |
| | Compound **3** | | |
| Cu(1)–N(1) | 2.090(4) | Cu(1)–N(9) | 2.107(5) |
| Cu(1)–N(3) | 2.021(4) | Cu(1)–N(6A) | 2.149(4) |
| Cu(1)–N(5) | 2.096(4) | Cu(1)–N(6) | 2.038(4) |
| N(1)–Cu(1)–N(3) | 77.42(16) | N(5)–Cu(1)–N(9) | 91.19(17) |
| N(3)–Cu(1)–N(5) | 76.80(15) | N(6)–Cu(1)–N(9) | 95.50(17) |
| N(5)–Cu(1)–N(1) | 153.63(16) | N(1)–Cu(1)–N(6A) | 92.54(16) |
| N(1)–Cu(1)–N(6) | 102.65(16) | N(3)–Cu(1)–N(6A) | 88.57(15) |
| N(3)–Cu(1)–N(6) | 166.20(16) | N(5)–Cu(1)–N(6A) | 92.26(15) |
| N(5)–Cu(1)–N(6) | 103.70(16) | N(6)–Cu(1)–N(6A) | 77.63(17) |
| N(1)–Cu(1)–N(9) | 87.10(17) | N(9)–Cu(1)–N(6A) | 172.88(17) |
| N(3)–Cu(1)–N(9) | 98.28(17) | | |

[a] Symmetry code: A: $-x$, $-y + 2$, $-z$.

 © 2007 Wiley-VCH Verlag GmbH & Co. KGaA, Weinheim 

N(6), and N(7) are in equatorial positions. The two Cu–N (MeCN) bonds are longer than the three Cu–N (bdmpp) bonds (Table 1), suggesting that the two MeCN molecules may be easily replaced by other strong donor ligands.

Compounds **2**·1.5$H_2O$ and **3**·2MeOH crystallize in the monoclinic space group $P2_1/n$ and the asymmetric unit of **2** contains one discrete [Cu(bdmpp)$(N_3)_2$] molecule and one and a half of the water solvent molecules, while that of **3** has half of the [Cu(bdmpp)(μ-$N_3$)$(N_3)$]$_2$ molecule and one methanol solvent molecule. In the structure of **2**, Cu(1) adopts a distorted square-pyramidal geometry (Figure 2). The basal plane is defined by N(1), N(3), and N(5) from the bdmpp ligand and N(6) from a terminal azide. The apical site is occupied by N(9) of the other terminal azide. The axial Cu(1)–N(9) of 2.186(2) Å is slightly longer than the basal Cu–N bonds (Table 1), but shorter than that found in [$Cu_2$(terpy)$_2$-μ-$(N_3)_2(N_3)_2Cu_3$-μ-$(N_3)_4(N_3)_2$] [terpy = 2,2′:6′,2′′-terpyridine, 2.288(3) Å].[20] It is noted that Cu(1) displaces 0.3613 Å out of the N(1)–N(3)–N(5)–N(6) least-squares plane, which causes the *trans* angles in the basal plane to deviate significantly from 180°.

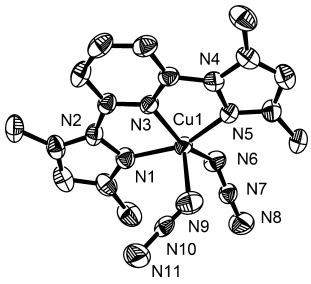


Figure 2. Molecular structure of **2** with 50% thermal ellipsoids. All hydrogen atoms are omitted for clarity.

As shown in Figure 3, **3** consists of two [Cu(bdmpp)-$(N_3)$]$^+$ fragments that are bridged by a pair of end-on bridging $N_3^-$ anions, forming a centrosymmetric dimetallocyclic $Cu_2N_2$ core structure. The $Cu_2N_2$ core is symmetric and the Cu(1)···Cu(1A) contact is 3.263(13) Å, which excludes any metal–metal interaction. Each Cu atom adopts a distorted octahedral geometry, where N(1), N(3), and N(5) of the bdmpp ligand and N(6) of the bridge azide occupy the equatorial sites, and N(6A) and N(9) from one bridging and one terminal azide sit at the two apical sites. The Cu atom lies 0.1024 Å out of the equatorial plane. The average Cu–$N_{apical}$ bond [2.128(4) Å] is slightly longer than the average Cu–$N_{equatorial}$ bond [2.075(4) Å] (Table 1).

Compound **4** crystallizes in the triclinic space group $P\bar{1}$ and the asymmetric unit contains half of the [{Cu(bdmpp)$(ClO_4)$}$_2$(μ-4,4′-bipy)]$^{2+}$ dication and one $ClO_4^-$ anion. The centrosymmetric structure of the dication contains two [Cu(bdmpp)$(ClO_4)$]$^+$ fragments bridged by one 4,4′-bipy ligand (Figure 4). As indicated in Table 2, Cu(1) in each [Cu(bdmpp)$(ClO_4)$]$^+$ fragment takes a distorted square-pyramidal geometry, coordinated by N(1), N(3), and N(5) from the bdmpp ligand and N(6) from 4,4′-bipy, which are in equatorial positions, and O(1) from one

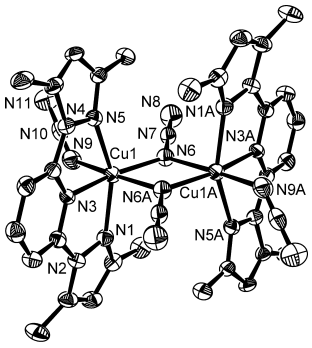


Figure 3. Molecular structure of **3** with 50% thermal ellipsoids. All hydrogen atoms are omitted for clarity.

$ClO_4^-$, which occupies the apical site. Cu(1) sits over the basal plane with out-of-plane displacement of 0.1688 Å. The Cu(1)–N bond lengths are similar to those of **2**, while the Cu(1)–O bond length [2.2856(18) Å] is comparable to that observed in complexes containing square-pyramidally coordinated $Cu^{II}$ [Cu(pr2pz)$(ClO_4)_2$] [pr2pz = 1,2-bis[5-methyl-3-(2-methylpropyl)amino-1*H*-pyrazol-1-yl]ethane, 2.451(3) Å].[32]

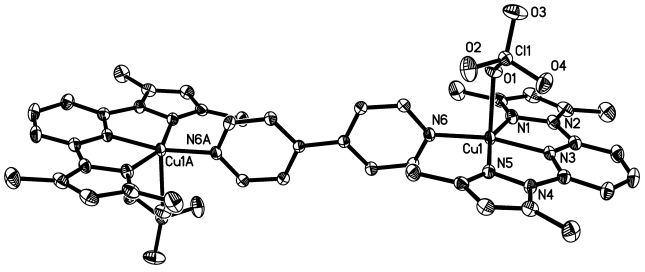


Figure 4. Perspective view of the [{Cu(bdmpp)$(ClO_4)$}$_2$(μ-4,4′-bipy)]$^{2+}$ dication of **4** with 50% thermal ellipsoids. All hydrogen atoms are omitted for clarity.

Compound **5** crystallizes in the monoclinic space group $C2/c$ and the asymmetric unit consists of one [Cu(bdmpp)(μ-dca)]$^+$ cation and one $ClO_4^-$ anion. Like that of the Cu center of **1**, Cu(1) in the cation of **5** adopts a distorted trigonal-bipyramidal geometry, coordinated by N(3) of the bdmpp ligand and N(6) and N(8A) atoms of μ-dca (in equatorial positions), and N(1) and N(5) of the bdmpp ligand (in apical positions) (Figure 5). The bond lengths and angles around Cu(1) in **5** (Table 2) are similar to those observed in **1**. Topologically, the [Cu(bdmpp)]$^{2+}$ fragment in **5** works as a two-connecting node, which is linked to two equivalent nodes through Cu-μ-dca-Cu bridges to form a 1D [Cu(bdmpp)(μ-dca)]$_n^{n+}$ chain extending along the *b* axis. It is worth noting that the bdmpp ligands covering the chain are parallel to each other and have the same direction. Two neighboring bdmpp ligands linked by one dca may be visualized as a molecular clip with a diameter of 7.4952(3) Å [Cu(1)···Cu(1A) contact]. Thus, the structure of **5** may be best described as a unique 1D chain of clips, each of which "clamps" one $ClO_4^-$ anion inside it.

 © 2007 Wiley-VCH Verlag GmbH & Co. KGaA, Weinheim 

Table 2. Selected bond lengths [Å] and angles [°] of **4**–**6**.[a]

| | | | |
|---|---|---|---|
| | | Compound **4** | |
| Cu(1)–N(1) | 2.004(2) | Cu(1)–N(6) | 1.975(2) |
| Cu(1)–N(3) | 1.944(2) | Cu(1)–O(1) | 2.2856(18) |
| Cu(1)–N(5) | 2.026(2) | | |
| N(1)–Cu(1)–N(3) | 79.55(9) | N(5)–Cu(1)–N(6) | 99.35(8) |
| N(3)–Cu(1)–N(5) | 79.10(8) | N(1)–Cu(1)–O(1) | 89.49(8) |
| N(5)–Cu(1)–N(1) | 158.06(8) | N(3)–Cu(1)–O(1) | 98.36(7) |
| N(1)–Cu(1)–N(6) | 100.44(8) | N(5)–Cu(1)–O(1) | 98.55(7) |
| N(3)–Cu(1)–N(6) | 167.73(8) | N(6)–Cu(1)–O(1) | 93.90(8) |
| | | Compound **5** | |
| Cu(1)–N(1) | 1.991(3) | Cu(1)–N(6) | 2.059(3) |
| Cu(1)–N(3) | 1.974(3) | Cu(1)–N(8A) | 2.075(3) |
| Cu(1)–N(5) | 2.008(3) | | |
| N(1)–Cu(1)–N(3) | 78.56(11) | N(5)–Cu(1)–N(8A) | 94.84(12) |
| N(3)–Cu(1)–N(5) | 78.09(11) | N(1)–Cu(1)–N(6) | 95.80(11) |
| N(5)–Cu(1)–N(1) | 156.63(11) | N(3)–Cu(1)–N(6) | 131.78(11) |
| N(1)–Cu(1)–N(8A) | 100.51(12) | N(5)–Cu(1)–N(6) | 98.94(12) |
| N(3)–Cu(1)–N(8A) | 128.69(11) | N(6)–Cu(1)–N(8A) | 99.51(12) |
| | | Compound **6** | |
| Cu(1)–N(1) | 1.995(2) | Cu(1)–N(8A) | 2.448(3) |
| Cu(1)–N(3) | 1.949(2) | Cu(1)–N(6) | 1.932(2) |
| Cu(1)–N(5) | 2.013(2) | | |
| N(3)–Cu(1)–N(5) | 79.33(8) | N(5)–Cu(1)–N(6) | 100.51(9) |
| N(1)–Cu(1)–N(3) | 79.30(8) | N(1)–Cu(1)–N(8A) | 88.02(9) |
| N(5)–Cu(1)–N(1) | 158.46(8) | N(3)–Cu(1)–N(8A) | 90.49(10) |
| N(1)–Cu(1)–N(6) | 99.76(9) | N(5)–Cu(1)–N(8A) | 94.82(9) |
| N(3)–Cu(1)–N(6) | 167.43(8) | N(6)–Cu(1)–N(8A) | 102.3(10) |

[a] Symmetry codes for **5**: A: $x$, $y - 1$, $z$; for **6**: A: $-x + 1/2$, $y - 1/2$, $-z + 1/2$.

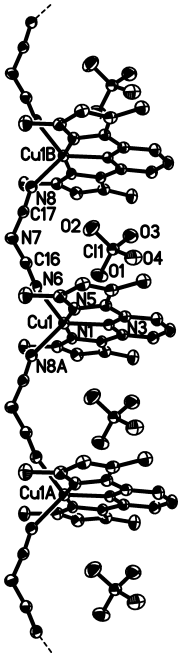


Figure 5. View of a section of the chain of **5** (extending along the *b* axis) with 50% thermal ellipsoids. All hydrogen atoms are omitted for clarity.

Compound **6** crystallizes in the monoclinic space group $P2_1/n$, and the asymmetric unit consists of one $[Cu(bdmpp)(\mu\text{-}N_3)]^+$ cation, one $ClO_4^-$ anion, and one MeCN solvent molecule. The $[Cu(bdmpp)]^{2+}$ fragment of **6** again acts as a two-connecting node, which is connected to the equivalent nodes through end-to-end bridging $N_3^-$ to form a 1D spiral chain extending along the *b* axis (Figure 6). The average chain-to-chain separation is 3.9 Å, and there are no evident interactions between the cationic chains and the counteranions and MeCN solvent molecules. For the $[Cu(bdmpp)(\mu\text{-}N_3)]^+$ cation of **6**, the Cu(1) atom adopts a similar coordination geometry to that of **2**, coordinated by N(1), N(3), and N(5) of the bdmpp ligand, and N(6) of one azide anion (in equatorial sites) and N(8A) of the other azide anion (in apical site). As listed in Table 2, one end-to-end bridging Cu(1)–N(8A) bond [2.448(2) Å] is 0.5 Å longer than the other one [Cu(1)–N(6)], which may be due to the requirement for the formation of the spiral chain. Other bond lengths and angles around Cu(1) in **6** are comparable to those of the corresponding ones of **2**.

Compound **7** crystallizes in the triclinic space group $P\bar{1}$ and the asymmetric unit contains half of the $[\{Cu(bdmpp)(N_3)\}_2(\mu\text{-}N_3)_2Cu(N_3)_2]$ molecule. The molecular structure of **7** is shown in Figure 7 and the selected bond lengths and angles are listed in Table 3. In this structure, the framework of **2** is almost retained. Two molecules of **2** link a $Cu(N_3)_2$ species through two end-on bridging azide anions to form a sandwich structure. Alternatively, the structure may be viewed as a centrosymmetric sandwich structure, in which one planar $[Cu(N_3)_2(\mu\text{-}N_3)_2]^{2-}$ anion is placed in between two planar $[Cu(bdmpp)(N_3)]^+$ cations through a pair of Cu-μ-$N_3$-Cu bridges. The skeleton planes of the two bdmpp ligands are almost parallel but with opposite orientations, and their separation is about 6.3 Å. In

 © 2007 Wiley-VCH Verlag GmbH & Co. KGaA, Weinheim 

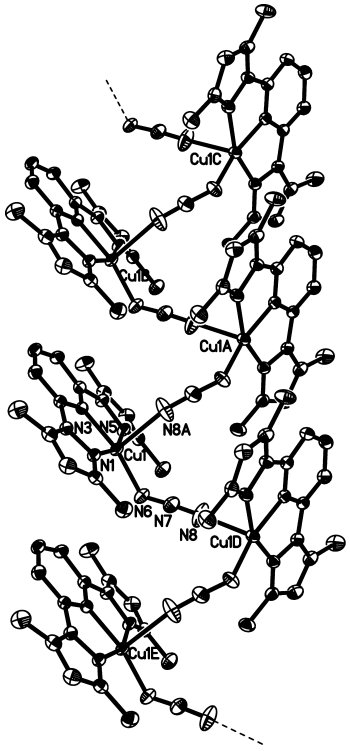


Figure 6. View of a section of the chain of **6** (extending along the *b* axis) with 50% thermal ellipsoids. All hydrogen atoms are omitted for clarity.

the $[Cu(bdmpp)(N_3)]^+$ cations, Cu(1) or Cu(1A) has a square-pyramidal geometry. The Cu(1)–N (bdmpp) and Cu(1)–N (terminal $N_3^-$) bond lengths are similar to those of **2**. The end-on bridging Cu(1)–N(9) bond is slightly longer than the corresponding bond of **2** and shorter than that of **6**. For the $[Cu(N_3)_2(\mu\text{-}N_3)_2]^{2-}$ anion, Cu(2) has a typical square-planar geometry, coordinated by two terminal and two end-on bridging azide anions. The bridging Cu(2)–N(9) bond [2.343(2) Å] is 0.38 Å longer than the terminal Cu(2)–N(12) bond.

Compounds **8** and **9** crystallize in the triclinic space group $P\bar{1}$ and the asymmetric unit contains half of the $[Cu(\mu\text{-}N_3)(bdmpp)(\mu\text{-}N_3)M(\mu\text{-}N_3)(X)]_2$ molecule (**8**: M = Co, X = $N_3$; **9**: M = Ni, X = Cl) and two MeCN solvent molecules for **9**. Compounds **8** and **9** have a 1D chain structure (extending along the *c* axis) in which $[Cu(\mu\text{-}N_3)(bdmpp)(\mu\text{-}N_3)M(\mu\text{-}N_3)(X)]_2$ molecules are linked by

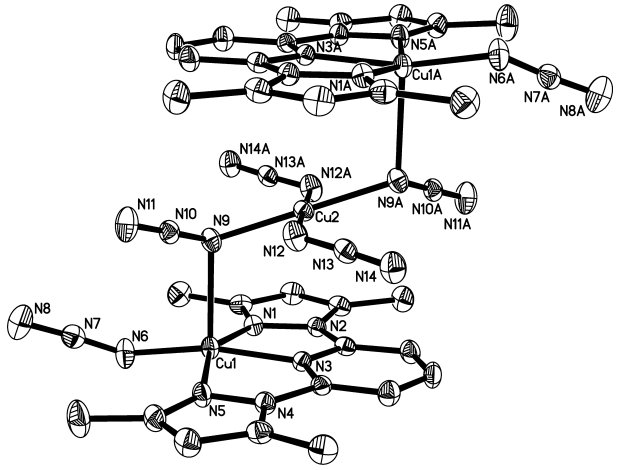


Figure 7. Perspective view of **7** with 50% thermal ellipsoids. All hydrogen atoms are omitted for clarity.

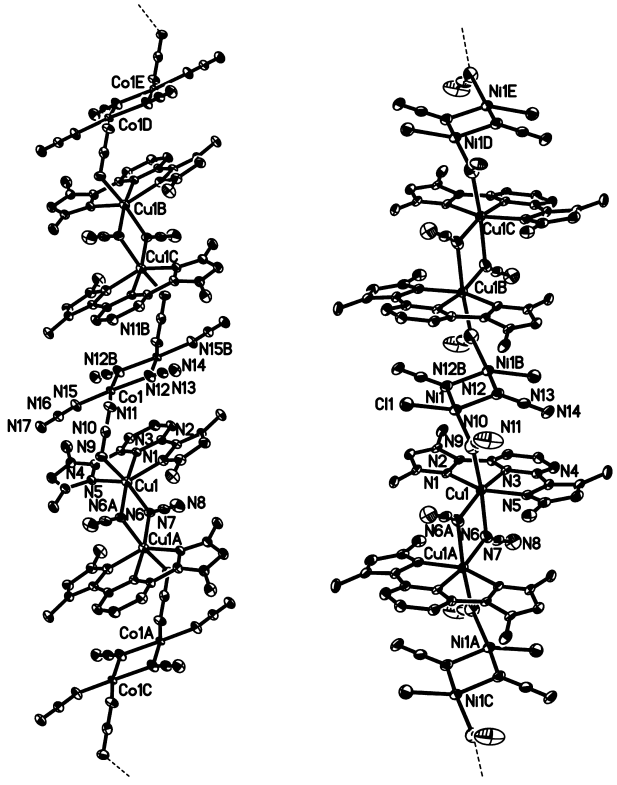


Figure 8. View of a section of the chain of **8** (left) and **9** (right) (extending along the *c* axis) with 50% thermal ellipsoids. All hydrogen atoms are omitted for clarity.

Table 3. Selected bond length [Å] and angles [°] of **7**.[a]

| | | | |
|---|---|---|---|
| Cu(1)–N(6) | 1.918(2) | Cu(1)–N(9) | 2.343(2) |
| Cu(1)–N(3) | 1.964(2) | Cu(1)–N(1) | 2.046(2) |
| Cu(1)–N(5) | 2.045(2) | Cu(2)–N(12) | 1.961(2) |
| Cu(2)–N(9) | 2.003(2) | | |
| N(6)–Cu(1)–N(5) | 102.27(10) | N(6)–Cu(1)–N(9) | 100.88(10) |
| N(6)–Cu(1)–N(3) | 166.43(10) | N(3)–Cu(1)–N(9) | 92.50(9) |
| N(3)–Cu(1)–N(5) | 78.45(9) | N(5)–Cu(1)–N(9) | 95.66(9) |
| N(6)–Cu(1)–N(1) | 98.50(10) | N(1)–Cu(1)–N(9) | 94.75(9) |
| N(3)–Cu(1)–N(1) | 77.92(9) | N(12)–Cu(2)–N(9A) | 90.91(10) |
| N(5)–Cu(1)–N(1) | 154.52(9) | N(12)–Cu(2)–N(9) | 89.09(10) |

[a] Symmetry code: A: $-x + 1, -y, -z + 1$.

 © 2007 Wiley-VCH Verlag GmbH & Co. KGaA, Weinheim 

end-to-end azide anions (**8**) (Figure 8, left) or end-on azide anions (**9**) (Figure 8, right). Each $[Cu(\mu\text{-}N_3)(bdmpp)(\mu\text{-}N_3)\text{-}M(\mu\text{-}N_3)(X)]_2$ molecule consists of one centrosymmetric $[Cu(bdmpp)(\mu\text{-}N_3)]_2^{2+}$ dication and one centrosymmetric $[(\mu\text{-}N_3)M(\mu\text{-}N_3)(X)]_2^{2-}$ dianion linked by one end-to-end azide (**8**) or one end-on azide (**9**). The structure of the dication in **3** is almost kept in the structures of **8** and **9**. Each Cu atom in **8** or **9** adopts a distorted octahedral geometry, coordinated by three N atoms from one bdmpp ligand and three N atoms from one end-to-end and two end-on azides (**8**) or three end-on azides (**9**). In this case, the end-to-end bridging Cu(1)–N(9) bond of **8** is even shorter than the end-on bridging Cu(1)–N(9) in **9** (Table 4). Other bond lengths and angles around Cu in **8** or **9** are similar to those of the corresponding ones of **3**. The Cu(1)···Cu(1A) separation is 3.2105(14) Å for **8** and 3.3779(13) Å for **9**.

Within the dianion of **8**, each Co atom is coordinated by one terminal, one end-to-end bridging, and two bridging azides, forming a square-planar geometry. The Co(1)···Co(1B) contact is 3.1234(13) Å while the Cu(1)···Co(1) contact between the dication and dianion is 4.4064(13) Å. The mean Co(1)–N bond length [1.966(4) Å] is similar to that found in $[PPh_4][Co(N_3)_3Cl]$[33] [Co–N 1.946(3) Å]. However, in the structure of the anion of **9**, each Ni atom also adopts a square-planar geometry, coordinated by one terminal Cl atom and three end-on bridging azides. The Ni(1)···Ni(1B) contact is 3.091(2) Å while the Cu(1)···Ni(1) contact between the dication and dianion is 3.5670(12) Å. The terminal Ni(1)–Cl(1) bond [2.2499(19) Å] is longer than that found in [(L)NiKCl·3THF] [L = *N*,*N*′-bis(2,6-diisopropylphenyl)-2,6-pyridinedicarboxamido, 2.1688(17) Å],[34] while the Ni–N bond is slightly longer than that in $[L^1Ni(N_3)]$ [$L^1$ = $Me_2NCH_2CH_2N(Me)C_6H_4OH$, 1.905(7) Å].[35]

The electrochemical behaviors of **1**–**9** have been investigated by cyclic voltammetry (CV) in DMF containing 0.1 M tetraethylammonium perchlorate (TEAP). The electrochemical data are summarized in Table 5. Under similar experimental conditions, the electrochemical studies of the free ligand using the cyclic voltammetry showed no electrochemical activity within the scanned potential window. Thus, the electrochemical waves observed in the cyclic voltammograms of **1**–**9** are only metal-based.

All the complexes show the quasireversible redox process with a potential of about 0.00 V in the cathode and about

Table 4. Selected bond lengths [Å] and angles [°] of **8** and **9**.[a]

| | | | |
|---|---|---|---|
| | Compound **8** | | |
| Cu(1)–N(6A) | 2.030(4) | Cu(1)–N(9) | 2.235(4) |
| Cu(1)–N(5) | 2.089(4) | Co(1)–N(15) | 1.919(4) |
| Cu(1)–N(3) | 2.094(4) | Co(1)–N(11) | 1.958(5) |
| Cu(1)–N(1) | 2.104(4) | Co(1)–N(12) | 1.990(4) |
| Cu(1)–N(6) | 2.140(4) | Co(1)–N(12B) | 1.997(5) |
| N(3)–Cu(1)–N(6A) | 168.11(16) | N(6)–Cu(1)–N(6A) | 79.37(18) |
| N(5)–Cu(1)–N(3) | 74.76(16) | N(5)–Cu(1)–N(6) | 96.79(17) |
| N(6)–Cu(1)–N(1A) | 108.23(18) | N(6)–Cu(1)–N(9) | 167.97(16) |
| N(5)–Cu(1)–N(1) | 146.19(15) | N(15)–Co(1)–N(11) | 99.5(2) |
| N(3)–Cu(1)–N(1) | 73.94(16) | N(15)–Co(1)–N(12) | 166.9(2) |
| N(5)–Cu(1)–N(6A) | 105.04(17) | N(11)–Co(1)–N(12) | 91.59(19) |
| N(3)–Cu(1)–N(6) | 88.83(15) | N(15)–Co(1)–N(12B) | 92.21(19) |
| N(1)–Cu(1)–N(6) | 95.05(17) | N(11)–Co(1)–N(12B) | 168.31(18) |
| N(9)–Cu(1)–N(6A) | 88.68(16) | N(12)–Co(1)–N(12B) | 76.8(2) |
| N(5)–Cu(1)–N(9) | 87.56(17) | Cu(1)–N(6)–Cu(1B) | 100.63(18) |
| N(3)–Cu(1)–N(9) | 103.15(15) | Co(1)–N(12)–Co(1B) | 103.2(2) |
| N(1)–Cu(1)–N(9) | 87.35(17) | | |
| | Compound **9** | | |
| Cu(1)–N(3) | 1.999(4) | Cu(1)–N(9) | 2.253(7) |
| Cu(1)–N(6A) | 2.010(5) | Ni(1)–N(9) | 1.963(5) |
| Cu(1)–N(5) | 2.061(4) | Ni(1)–N(12B) | 1.976(4) |
| Cu(1)–N(1) | 2.089(4) | Ni(1)–N(12) | 1.986(4) |
| Cu(1)–N(6) | 2.345(7) | Ni(1)–Cl(1) | 2.2499(19) |
| N(3)–Cu(1)–N(5) | 78.26(15) | N(5)–Cu(1)–N(6) | 89.97(16) |
| N(5)–Cu(1)–N(6A) | 101.12(17) | N(1)–Cu(1)–N(6) | 92.60(16) |
| N(3)–Cu(1)–N(1) | 77.35(14) | N(9)–Cu(1)–N(6) | 173.88(18) |
| N(1)–Cu(1)–N(6A) | 103.48(17) | N(9)–Ni(1)–N(12B) | 154.3(2) |
| N(3)–Cu(1)–N(6A) | 165.3(2) | N(9)–Ni(1)–N(12) | 94.3(2) |
| N(5)–Cu(1)–N(1) | 155.29(14) | N(12)–Ni(1)–N(12B) | 77.5(2) |
| N(3)–Cu(1)–N(9) | 99.16(17) | N(9)–Ni(1)–Cl(1) | 101.29(19) |
| N(9)–Cu(1)–N(6A) | 95.5(3) | Cl(1)–Ni(1)–N(12B) | 96.34(14) |
| N(5)–Cu(1)–N(9) | 92.56(18) | N(12)–Ni(1)–Cl(1) | 152.95(14) |
| N(1)–Cu(1)–N(9) | 87.43(17) | Ni(1)–N(9)–Cu(1) | 115.4(3) |
| N(3)–Cu(1)–N(6) | 86.81(17) | Ni(1)–N(12)–Ni(1B) | 102.5(2) |
| N(6)–Cu(1)–N(6A) | 78.5(3) | Cu(1)–N(6)–Cu(1) | 101.5(3) |

[a] Symmetry codes for **8**: A: $-x + 1, -y, -z$; B: $-x + 1, -y, -z + 1$; for **9**: A: $-x + 1, -y + 2, -z + 1$; B: $-x + 1, -y + 2, -z$.

 © 2007 Wiley-VCH Verlag GmbH & Co. KGaA, Weinheim 

Table 5. Electrochemical data of complexes **1**–**9**.[a]

| Complexes | **1** | **2** | **3** | **4** | **5** | **6** | **7** | **8** | **9** |
|---|---|---|---|---|---|---|---|---|---|
| $E_I$ [V] | –0.01 | –0.06 | –0.05 | 0.02 | 0.09 | 0.02 | 0.01 | –0.09 | –0.02 |
| $E_I'$ [V] | 0.18 | 0.24 | 0.33 | 0.21 | 0.24 | 0.22 | 0.56 | 0.22 | 0.59 |
| $E_{1/2}$ [V] | 0.09 | 0.15 | 0.19 | 0.09 | 0.07 | 0.10 | 0.12 | 0.15 | 0.30 |
| $\Delta E_I$ [V] | 0.19 | 0.30 | 0.38 | 0.19 | 0.15 | 0.20 | 0.55 | 0.31 | 0.61 |
| $E_{II}$ [V] | –0.42 | –0.59 | –0.57 | –0.48 | –0.42 | –0.54 | –0.63 | –0.52 | –0.66 |
| $E_{II}'$ [V] | 0.04 | – | – | 0.06 | –0.03 | – | –0.20 | –0.18 | –0.18 |
| $E_{1/2}$ [V] | –0.23 | – | – | –0.23 | –0.19 | – | –0.42 | –0.35 | –0.47 |
| $\Delta E_{II}$ [V] | 0.46 | – | – | 0.57 | 0.39 | – | –0.43 | 0.34 | 0.48 |
| $E_{III}$ [V] | | | – | – | – | – | –1.26 | –1.28 | –1.03 |
| $E_{III}'$ [V] | – | – | – | – | – | – | 0.13 | 0.02 | –0.12 |

[a] Measured by CV at scan rate of 0.1 V/s; 1.0 mM in DMF containing 0.1 M TEAP for all complexes with a concentration of $1 \times 10^{-3}$ M. Condition: working electrode, Pt plate ($2 \times 2$ mm$^2$); counter electrode, Pt wire; reference electrode, SCE.

0.22 V in the anode (except 0.33 V for **3**, 0.56 V for **7**, and 0.59 V for **9**) (Figure 9), corresponding to the change from $Cu^{II}$ species to $Cu^{I}$ species. When the CV measurements were performed at different scan rates such as 0.05, 0.1, 0.2, and 0.5 V/s, it was found that the ratio of cathodic to anodic peak current was close to unity, especially for a lower scan rate, suggesting this first step is a quasireversible reduction process.[36] The second reduction waves in the range of –0.40 to –0.70 V for **1**, **4**, **5**, **7**, **8**, and **9** are quasireversible and due to the formation of $Cu^{I}$ species followed by the deposition of $Cu^0$ onto the electrode surface as judged by the appearance on the reverse scan of a greater anodic peak current at the corresponding potential $E_{II}'$ than that of the cathode.[37] The separation between the potentials of the first redox couple for all complexes is $\Delta E_I$ = 0.15 V or greater and the weak peak current at $E_{II}$ indicates that a geometrical reorganization, hindered to a large extent by the low flexibility of the coordination sphere, is involved in the reduction process.[36] After several cycles, the color of solutions of these complexes became light and more metal particles were found on the electrode surface. These facts were the evidence of the decomposition of the complexes during the CV measurement.

Compared to the second reduction wave of their precursor **1**, those of **4** and **6** are very weak and the potential shift negative (Figure 9a), while the second reduction electrochemical response and potential of **5** are almost the same as **1**. These facts indicate that the stronger binding of azide and 4,4′-bipy ligands to the metal center and the coordination sphere is more stable than that of dca and acetonitrile ligands.

The large difference of $\Delta E_I$ value (0.55 V for **7** and 0.61 V for **9**) between the the potentials of the first redox couple is consistent with the stronger spin–spin interaction of metals. Further reductions at $E_{III}$ = –1.26 V for **7**, –1.28 V for **8**, and –1.03 V for **9** are almost totally irreversible, which may be due to the deposition of $Cu^0$ (planar Cu), $Co^0$, and $Ni^0$ onto the electrode surface as judged by the appearance of a sharp anodic peak at $E_{III}'$ = 0.18, 0.02, and –0.12 V for **7**, **8**, and **9**, corresponding to the redissolution of $Cu^0$, $Co^0$, and $Ni^0$, respectively.

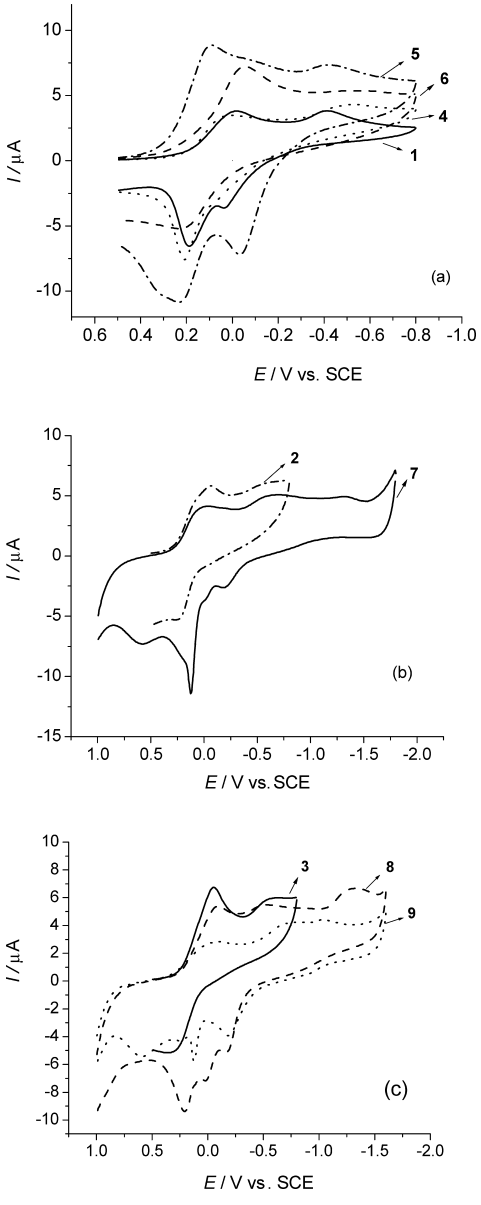


Figure 9. Cyclic voltammograms of complexes **1**–**9**.

 © 2007 Wiley-VCH Verlag GmbH & Co. KGaA, Weinheim 

## Conclusions

In this paper, we demonstrated our new approaches to the assembly of a set of homometallic or heterometallic coordination oligomers and polymers from reactions of preformed complexes **1**–**3** with different linkers 4,4′-bipy, dca, and azide as well as $M^{2+}$ (M = Cu, Co, Ni). In the structures of **4**–**6**, the $[Cu(bdmpp)]^{2+}$ fragment of **1** was retained, even though the copper coordination geometry was changed during the reactions. Compound **4** forms a 4,4′-bipy-bridged dimer structure, while **5** and **6** show a 1D dca-bridged chain of clips and a 1D spiral azido-bridged chain, respectively. In this structure of **7**, the structure of **2** was kept and two molecules of **2** connect a $Cu(N_3)_2$ species through two end-on bridging azide anions to form a sandwich structure. In the structure of **8** or **9**, the structure of **3** was retained, and the $[Cu(bdmpp)(\mu\text{-}N_3)(\mu\text{-}N_3)]_2$ molecules of **3** interconnect with the $[M(\mu\text{-}N_3)(X)]_2$ molecules through end-to-end azides (**8**) or end-on azides (**9**) to form a 1D chain structure. Electrochemical studies on **1**–**9** revealed that one quasireversible redox wave was observed at higher potential for all these complexes, while, **1**, **4**, **5**, **7**, **8**, and **9** showed the second quasireversible redox wave at lower potentials. It is concluded that though the assembled products retain the $[Cu(bdmpp)]^{2+}$ fragment of **1** or the whole molecule **2** or **3**, their electrochemical properties are influenced by the bridging ligands around the Cu center of the fragment or other metal ions introduced in their frameworks. The interesting topological structures of **4**–**9** make **1**–**3** very promising precursors for the synthesis of homo- and heterometallic coordination oligomers and polymers. We are currently extending this work by studies on the synthesis of novel homo- or heterometallic coordination oligomers and polymers from reactions of **1**–**3** with other polydentate donor ligands such as 5,10,15,20-tetra(4-pyridyl)-21*H*,23*H*-porphyrin and 2,4,6-tri(4-pyridyl)-1,3,5-triazine, and other main group metals ($Pb^{2+}$, $Bi^{3+}$) and transition metals ($Zn^{2+}$, $Cd^{2+}$, $Hg^{2+}$, etc.).

## Experimental Section

**General Remarks:** Compounds bdmpp[38] and $[Cu(MeCN)_4](ClO_4)_2$[39] were prepared according to the literature method. All other reagents were used as purchased. The IR spectra were recorded with a Varian 1000 FTIR spectrometer as KBr disk (4000–400 $cm^{-1}$). The elemental analyses for C, H, and N were performed on an EA1110 CHNS elemental analyzer. Cyclic voltammetry was carried out at 0.1 V/s under oxygen-free conditions using a three-electrode cell with platinum film electrode as working electrode, platinum wire as counter electrode, and SCE as reference electrode. In DMF solution, tetraethylammonium perchlorate (TEAP) was used as the supporting electrolyte.

**$[Cu(bdmpp)(MeCN)_2](ClO_4)_2$ (1):** bdmpp (0.027 g, 0.1 mmol) was added to a blue solution containing $[Cu(MeCN)_4](ClO_4)_2$ (0.043 g, 0.1 mmol) in MeCN (10 mL). The resulting green solution was stirred for about 0.5 h and then filtered. Diethyl ether (20 mL) was layered onto the filtrate to form green blocks of **1** (0.052 g, 85% based on bdmpp) in several days. IR (KBr disc): $\tilde{\nu}$ = 3137 (m), 2249 (m), 1614 (s), 1566 (s), 1486 (s), 1392 (s), 1320 (s), 1295 (s), 1144 (s), 1106 (s), 1059 (s), 995 (s), 795 (m), 743 (m), 622 (s) $cm^{-1}$. $C_{19}H_{23}Cl_2CuN_7O_8$ (611.88): calcd. C 37.30, H 3.79, N 16.02; found C 37.46, H 3.56, N 15.90.

**$[Cu(bdmpp)(N_3)_2]\cdot 1.5H_2O$ ($2\cdot 1.5H_2O$):** $NaN_3$ (0.013 g, 0.2 mmol) was added to a blue solution containing $CuCl_2\cdot 2H_2O$ (0.017 g, 0.1 mmol) in MeOH (5 mL) and $H_2O$ (5 mL). The solution turned deep brown instantly and bdmpp (0.027 g, 0.1 mmol) was added. The resulting deep green solution was stirred for about 0.5 h and then filtered. Slow evaporation of solvents from the solution for 2 weeks produced deep green crystals of $\mathbf{2}\cdot 1.5H_2O$ (0.033 g, 75% based on bdmpp). IR (KBr disc): $\tilde{\nu}$ = 3144 (w), 2924 (w), 2068 (vs), 2040 (vs), 1614 (vs), 1562 (s), 1488 (vs), 1418 (s), 1392 (s), 1319 (s), 1139 (m), 1054 (m), 986 (m), 799 (m), 740 (m), 675 (w) $cm^{-1}$. $C_{15}H_{20}CuN_{11}O_{1.5}$ (441.94): calcd. C 40.77, H 4.56, N 34.86; found C 40.46, H 4.42, N 34.91.

**$[Cu(bdmpp)(N_3)(\mu\text{-}N_3)]_2\cdot 2MeOH$ ($3\cdot 2MeOH$):** Compound $\mathbf{3}\cdot 2MeOH$ (0.032 g, 72% based on bdmpp) was isolated as deep green crystals from the reaction of $CuCl_2\cdot 2H_2O$ (0.017 g, 0.1 mmol), $NaN_3$ (0.026 g, 0.4 mmol), and bdmpp (0.027 g, 0.1 mmol) in $MeOH/H_2O$ followed by a similar workup to that used in the isolation of **2**. IR (KBr disc): $\tilde{\nu}$ = 3129 (w), 2073 (vs), 2045 (vs), 1614 (s), 1564 (m), 1487 (s), 1389 (m), 1318 (m), 1294 (m), 1141 (w), 1084 (w), 1054 (m), 848 (m), 791 (w), 742 (w), 558 (w) $cm^{-1}$. $C_{32}H_{42}Cu_2N_{22}O_2$ (893.98): calcd. C 43.00, H 4.74, N 34.47; found C 43.16, H 4.52, N 34.52.

**$[\{Cu(bdmpp)(ClO_4)\}_2(\mu\text{-}4,4'\text{-bipy})](ClO_4)_2$ (4):** 4,4′-bpy (0.016 g, 0.1 mmol) was added to a green solution containing **1** (0.061 g, 0.1 mmol) in MeCN (10 mL). The mixture was stirred for 10 min, the color of the solution then turned blue, and the solution was filtered. Layering $Et_2O$ (15 mL) onto the filtrate afforded blue blocks of **4** (0.038 g, 63% based on **1**). IR (KBr disc): $\tilde{\nu}$ = 3135 (w), 2996 (w), 1617 (s), 1594 (m), 1564 (m), 1486 (s), 1432 (m), 1390 (m), 1322 (m), 1122 (m), 1087 (s), 1060 (s), 992 (m), 790 (w), 744 (w), 624 (m) $cm^{-1}$. $C_{40}H_{42}Cl_4Cu_2N_{12}O_{16}$ (1215.76): calcd. C 39.51, H 3.48, N 13.82; found C 40.02, H 3.42, N 13.94.

**$\{[Cu(bdmpp)(\mu\text{-dca})](ClO_4)\}_n$ (5):** Compound **5** (0.037 g, 75% based on **1**) was isolated as green crystals from the reaction of **1** (0.061 g, 0.1 mmol) and Na(dca) (0.009 g, 0.1 mmol) followed by a similar workup to that used in the isolation of $\mathbf{2}\cdot 1.5H_2O$. IR (KBr disc): $\tilde{\nu}$ = 3130 (w), 2964 (m), 2179 (s), 1618 (s), 1566 (m), 1488 (s), 1370 (m), 1320 (m), 1261 (s), 1093 (s), 1024 (s), 800 (s), 744 (w), 624 (m) $cm^{-1}$. $C_{17}H_{17}ClCuN_8O_4$ (496.38): calcd. C 41.14, H 3.45, N 22.57; found C 41.26, H 3.22, N 22.44.

**$\{[Cu(bdmpp)(\mu\text{-}N_3)](ClO_4)\cdot MeCN\}_n$ (6):** Compound **6** (0.041 g, 80% based on **1**) was isolated as deep green crystals from the reaction of **1** (0.061 g, 0.1 mmol) and $NaN_3$ (0.007 g, 0.1 mmol) followed by a similar workup to that used in the isolation of $\mathbf{2}\cdot 1.5H_2O$. IR (KBr disc): $\tilde{\nu}$ = 3107 (w), 2065 (vs), 2054 (s), 1613 (s), 1565 (m), 1482 (s), 1430 (m), 1391 (m), 1316 (m), 1144 (s), 1118 (s), 1084 (s), 991 (m), 793 (w), 743 (w), 625 (m) $cm^{-1}$. $C_{17}H_{20}ClCuN_9O_4$ (513.41): calcd. C 39.77, H 3.93, N 24.55; found C 39.64, H 3.76, N 24.72.

**$[\{Cu(N_3)(bdmpp)\}_2(\mu\text{-}N_3)_2Cu(N_3)_2]$ (7):** $NaN_3$ (0.026 g, 0.4 mmol) and $CuCl_2\cdot 2H_2O$ (0.017 g, 0.1 mmol) were added to a deep green solution containing **2** (0.044 g, 0.1 mmol) in MeCN (10 mL). The solution was stirred for 20 min; it then darkened and was filtered. Diethyl ether (20 mL) was layered onto the filtrate to form dark brown blocks of **7** (0.033 g, 67% based on **2**) in several days. IR (KBr disc): $\tilde{\nu}$ = 3430.6 (m), 3142 (w), 2066 (vs), 2041 (s), 1614 (s), 1562 (m), 1486 (s), 1418 (m), 1392 (m), 1318 (m), 1139 (m), 1084

 © 2007 Wiley-VCH Verlag GmbH & Co. KGaA, Weinheim 

(m), 1053 (m), 986 (w), 799 (w), 740 (w) $cm^{-1}$. $C_{30}H_{34}Cu_3N_{28}$ (977.47): calcd. C 37.04, H 3.52, N 40.32; found C 37.16, H 3.36, N 39.96.

**[{Cu(μ-$N_3$)(bdmpp)(μ-$N_3$)Co(μ-$N_3$)($N_3$)}$_2$]$_n$ (8):** Compound **8** (0.056 g, 50% based on **3**) was isolated as dark green crystals from the reaction of **3** (0.089 g, 0.1 mmol), $CoCl_2·6H_2O$ (0.048 g, 0.2 mmol), and $NaN_3$ (0.052 g, 0.8 mmol) followed by a similar workup to that used in the isolation of **7**. IR (KBr disc): $\tilde{\nu}$ = 3432 (w), 3133 (w), 2963 (m), 2066 (vs), 2029 (s), 1608 (s), 1562 (m), 1473 (s), 1388 (m), 1372 (m), 1293 (m), 1261 (s), 1096 (m), 1031 (m), 986 (w), 793 (s), 741 (w) $cm^{-1}$. $C_{30}H_{34}Co_2Cu_2N_{34}$ (1115.85): calcd. C 32.29, H 3.07, N 42.68; found C 32.12, H 3.32, N 42.24.

**[{Cu(μ-$N_3$)(bdmpp)(μ-$N_3$)Ni(μ-$N_3$)Cl}$_2$·4MeCN]$_n$ (9):** Compound **9** (0.062 g, 49% based on **3**) was isolated as dark green crystals from

Table 6. Crystallographic data for **1**, **2**·1.5$H_2O$, **3**·2MeOH, **4**, and **5**.

| Compounds | **1** | **2**·1.5$H_2O$ | **3**·2MeOH | **4** | **5** |
|---|---|---|---|---|---|
| Formula | $C_{19}H_{23}Cl_2CuN_7O_8$ | $C_{15}H_{20}Cu_1N_{11}O_{1.5}$ | $C_{32}H_{42}Cu_2N_{22}O_2$ | $C_{40}H_{42}Cl_4Cu_2N_{12}O_{16}$ | $C_{17}H_{17}ClCuN_8O_4$ |
| $M_r$ | 611.88 | 441.94 | 893.98 | 1215.76 | 496.38 |
| Temperature [K] | 193(2) | 153(2) | 153(2) | 153(3) | 153(3) |
| Crystal system | orthorhombic | monoclinic | monoclinic | triclinic | monoclinic |
| Space group | *Pbca* | $P2_1/n$ | $P2_1/n$ | $P\bar{1}$ | $C2/c$ |
| *a* [Å] | 12.626(3) | 11.201(2) | 8.9002(18) | 7.6768(15) | 24.4394(9) |
| *b* [Å] | 14.821(3) | 11.629(2) | 12.487(3) | 8.9909(18) | 7.4925(3) |
| *c* [Å] | 27.060(5) | 14.927(3) | 17.473(4) | 17.265(3) | 21.4748(8) |
| *α* [°] | | | | 99.49(3) | |
| *β* [°] | | 103.89(3) | 99.65(3) | 91.54(3) | 95.100(10) |
| *γ* [°] | | | | 91.46(3) | |
| *V* [Å$^3$] | 5063.6(18) | 1887.4(6) | 1914.5 | 1174.4(4) | 3912.8(3) |
| *Z* | 8 | 2 | 2 | 1 | 8 |
| $D_{calcd}$ [g/cm$^3$] | 1.605 | 1.552 | 1.551 | 1.719 | 1.685 |
| *F*(000) | 2504 | 908 | 924 | 620 | 2024 |
| *μ* [mm$^{-1}$] | 1.132 | 1.193 | 1.175 | 1.219 | 1.298 |
| Total reflections | 45277 | 18050 | 18303 | 11618 | 17961 |
| Unique reflections | 4618 ($R_{int}$ = 0.0460) | 4313 ($R_{int}$ = 0.0328) | 3494 ($R_{int}$ = 0.0756) | 5351 ($R_{int}$ = 0.0184) | 4469 ($R_{int}$ = 0.0457) |
| Obsd. reflections | 4492 | 3870 | 2876 | 4970 | 3770 |
| Parameters | 340 | 285 | 271 | 364 | 285 |
| $R_1$[a] | 0.0445 | 0.0346 | 0.0682 | 0.0347 | 0.0614 |
| $wR_2$[b] | 0.1208 | 0.0998 | 0.1379 | 0.1129 | 0.1713 |
| *S*[c] | 1.015 | 1.064 | 1.088 | 1.074 | 1.072 |
| Residual peaks [e/Å$^3$] | 0.490, –0.416 | 0.523, –0.522 | 0.573, –0.452 | 0.697, –0.831 | 1.283, –2.402 |

[a] $R_1 = \Sigma||F_o| - |F_c||/\Sigma|F_o|$. [b] $wR_2 = \{w\Sigma(|F_o| - |F_c|)^2/\Sigma w|F_o|^2\}^{1/2}$. [c] $S = \{\Sigma w(|F_o| - |F_c|)^2/(n - p)\}^{1/2}$, where *n* is the number of reflections and *p* is the total number of parameters refined.

Table 7. Crystallographic data for **6**–**9**.

| Compounds | **6** | **7** | **8** | **9** |
|---|---|---|---|---|
| Formula | $C_{17}H_{20}ClCuN_9O_4$ | $C_{30}H_{34}Cu_3N_{28}$ | $C_{30}H_{34}Co_2Cu_2N_{34}$ | $C_{38}H_{46}Cl_2Cu_2N_{32}Ni_2$ |
| $M_r$ | 513.41 | 977.47 | 1115.85 | 1266.47 |
| Temperature [K] | 193(2) | 193(2) | 153(2) | 153(2) |
| Crystal system | monoclinic | triclinic | triclinic | triclinic |
| Space group | $P2_1/n$ | $P\bar{1}$ | $P\bar{1}$ | $P\bar{1}$ |
| *a* [Å] | 12.821(3) | 8.6789(17) | 9.3824(19) | 11.852(2) |
| *b* [Å] | 7.2431(14) | 10.594(2) | 9.4618(19) | 11.868(2) |
| *c* [Å] | 23.237(5) | 10.760(2) | 13.615(3) | 11.910(2) |
| *α* [°] | | 90.38(3) | 106.55(3) | 102.21(3) |
| *β* [°] | 98.38(3) | 102.31(3) | 97.90(3) | 112.52(3) |
| *γ* [°] | | 95.51(3) | 104.33(3) | 112.14(3) |
| *V* [Å$^3$] | 2134.9(7) | 961.7(3) | 1094.0(4) | 1303.5(5) |
| *Z* | 4 | 1 | 1 | 1 |
| $D_{calcd}$ [g/cm$^3$] | 1.597 | 1.688 | 1.694 | 1.613 |
| *F*(000) | 1052 | 497 | 564 | 646 |
| *μ* [mm$^{-1}$] | 1.194 | 1.711 | 1.774 | 1.684 |
| Total reflections | 19889 | 9259 | 10626 | 12272 |
| Unique reflections | 3901 ($R_{int}$ = 0.0740) | 3485($R_{int}$ = 0.0285) | 4944 ($R_{int}$ = 0.0644) | 5838 ($R_{int}$ = 0.0628) |
| Obsd. reflections | 3700 | 3017 | 3779 | 4060 |
| Parameters | 294 | 281 | 311 | 349 |
| $R_1$[a] | 0.0360 | 0.0348 | 0.0600 | 0.0636 |
| $wR_2$[b] | 0.0922 | 0.0831 | 0.1817 | 0.1711 |
| *S*[c] | 1.062 | 1.084 | 1.009 | 1.082 |
| Residual peaks [e/Å$^3$] | 0.459, –0.429 | 0.340, –0.428 | 1.463, –2.114 | 1.404, –1.343 |

[a] $R_1 = \Sigma||F_o| - |F_c||/\Sigma|F_o|$. [b] $wR_2 = \{w\Sigma(|F_o| - |F_c|)^2/\Sigma w|F_o|^2\}^{1/2}$. [c] $S = \{\Sigma w(|F_o| - |F_c|)^2/(n - p)\}^{1/2}$, where *n* is the number of reflections and *p* is the total number of parameters refined.

 © 2007 Wiley-VCH Verlag GmbH & Co. KGaA, Weinheim 

the reaction of **3** (0.089 g, 0.1 mmol), $NiCl_2·6H_2O$ (0.048 g, 0.2 mmol), and $NaN_3$ (0.052, 0.8 mmol) followed by a similar workup to that used in the isolation of **7**. IR (KBr disc): $\tilde{\nu}$ = 3433 (m), 3129 (w), 2963 (m), 2085 (s), 2069 (vs), 1613 (s), 1566 (m), 1485 (s), 1420 (m), 1392 (m), 1318 (m), 1261 (s), 1179 (m), 1095 (m), 1024 (s), 988 (m), 801 (s), 740 (w), 670 (w) $cm^{-1}$. $C_{38}H_{46}Cl_2Cu_2N_{32}Ni_2$ (1266.47): calcd. C 36.04, H 3.66, N 35.39; found C 35.82, H 3.52, N 35.33.

**X-ray Structure Determinations:** X-ray-quality crystals of **1**, **2**·1.5$H_2O$, **3**·2MeOH, and **4**–**9** were obtained directly from the above preparations. Measurements of **1**, **3**·2MeOH, **6**, and **7** were made on a Rigaku Mercury CCD X-ray diffractometer by using graphite-monochromated Mo-$K_\alpha$ ($\lambda$ = 0.71070 Å). Single crystals were mounted with grease at the top of a glass fiber and cooled to 193 K in a liquid $N_2$ stream. Cell parameters were refined using the program CrystalClear (Rigaku and MSC, version 1.3, 2001). The collected data were reduced using the program CrystalClear (Rigaku and MSC, version 1.3, 2001) while an absorption correction (multiscan) was applied. Measurements of **2**·1.5$H_2O$, **4**, **5**, **8**, and **9** were made on a Rigaku *R*-axis Spider diffractometer with graphite-monochromated Mo-$K_\alpha$ radiation ($\lambda$ = 0.71073 Å) at 153 K. Data reductions and absorption corrections were performed with the SAINT and SADABS software packages.

All the structures were solved by direct methods and refined on $F^2$ by full-matrix least-squares methods with the SHELXTL-97 program.[40] In the case of **2**·1.5$H_2O$, one water solvent molecule was found to be disordered over two orientations with an occupancy ratio of O(1)/O(1′) = 0.533/0.467. the other water solvent molecule was modeled with an occupancy factor of 0.5. For **4**, one $ClO_4^-$ anion was found to be split over two orientations by rotation around the Cl(2)–O(5) bond, which were refined with occupancy factors of 0.455:0.545 for O(6)/O(6′), O(7)/O(7′), and O(8)/O(8′). All non-hydrogen atoms were refined anisotropically. The H atoms of the water solvent molecules in **2**·1.5$H_2O$ and that of the hydroxy group of the methanol solvent molecule in **3** were located from the Fourier maps. All other H atoms on C atoms were placed in geometrically idealized positions C–H 0.98 Å for methyl groups; C–H 0.95 Å for phenyl groups and pyrazole ring; and constrained to ride on their parent atoms with $U_{iso}$(H) = 1.2$U_{eq}$(C) for phenyl groups and pyrazole ring and $U_{iso}$(H) = 1.5$U_{eq}$(C) for methyl groups. A summary of the key crystallographic information for **1**, **2**·1.5$H_2O$, **3**·2MeOH, and **4**–**9** is given in Tables 6 and 7.

CCDC-651925 (for **1**), -651926 (for **2**·1.5$H_2O$), -651927 (for **3**·2MeOH), -651928 (for **4**), -651929 (for **5**), -651930 (for **6**), -651931 (for **7**), -651932 (for **8**), and -651933 (for **9**) contain the supplementary crystallographic data for this paper. These data can be obtained free of charge from The Cambridge Crystallographic Data Center via http://www.ccdc.cam.ac.uk/data_request/cif.

## Acknowledgments

This work was supported by the National Natural Science Foundation (No. 20525101), the Natural Science Foundation of Jiangsu Province (No. BK2004205), the Specialized Research Fund for the Doctoral Program of Higher Education (No. 20050285004), and the State Key Laboratory of Coordination Chemistry of Nanjing University and the Qin-Lan Project of Jiangsu Province in China.

[1] R. Robson, B. F. Hoskins, *J. Am. Chem. Soc.* **1990**, *112*, 1546–1554.
[2] P. J. Stang, B. Olenyuk, *Acc. Chem. Res.* **1997**, *30*, 502–518.
[3] F. A. Cotton, C. Lin, C. A. Murillo, *Acc. Chem. Res.* **2001**, *34*, 759–771.
[4] M. Eddaoudi, D. B. Moler, H. L. Li, B. Chen, T. M. Reineke, M. O'Keeffe, O. M. Yaghi, *Acc. Chem. Res.* **2001**, *34*, 319–330.
[5] H. D. Selby, B. K. Roland, Z. P. Zheng, *Acc. Chem. Res.* **2003**, *36*, 933–944.
[6] H. T. Chifotides, K. R. Dunbar, *Acc. Chem. Res.* **2005**, *38*, 146–156.
[7] L. M. C. Beltran, J. R. Long, *Acc. Chem. Res.* **2005**, *38*, 325–334.
[8] Y. V. Mironov, N. G. Naumov, K. A. Brylev, Q. A. Efremova, V. E. Fedorov, K. Hegetschweiler, *Angew. Chem. Int. Ed.* **2004**, *43*, 1297–1300.
[9] Z. H. Yan, C. S. Day, A. Lachgar, *Inorg. Chem.* **2005**, *44*, 4499–4505.
[10] B. F. Abrahams, M. G. Haywood, R. Robson, *Chem. Commun.* **2004**, 938–939.
[11] J. P. Lang, Q. F. Xu, Z. N. Chen, B. F. Abrahams, *J. Am. Chem. Soc.* **2003**, *125*, 12682–12683.
[12] N. B. O'Brien, T. O. Marier, I. C. Paul, R. S. Drago, *J. Am. Chem. Soc.* **1973**, *95*, 6640–6645.
[13] J. P. Costes, J. P. Laurent, J. M. M. Sanchez, J. S. Varela, M. Ahlgren, M. Sundberg, *Inorg. Chem.* **1997**, *36*, 4641–4646.
[14] Z. Q. Xu, L. K. Thompson, C. J. Matthews, D. O. Miller, A. E. Goeta, J. A. K. Howard, *Inorg. Chem.* **2001**, *40*, 2446–2449.
[15] N. M. Shavaleev, Z. R. Bell, G. Accorsi, M. D. Ward, *Inorg. Chim. Acta* **2003**, *351*, 159–166.
[16] X. Z. Li, L. N. Zhu, C. Q. Li, D. Z. Liao, *Inorg. Chem. Commun.* **2006**, *9*, 1297–1300.
[17] Q. M. Wang, X. T. Wu, W. J. Zhang, T. L. Sheng, P. Lin, J. M. Li, *Inorg. Chem.* **1999**, *38*, 2223–2226.
[18] B. Vangdal, J. Carranza, F. Lloret, M. Julve, J. Sletten, *J. Chem. Soc. Dalton Trans.* **2002**, 566–574.
[19] J. Carranza, C. Brennan, J. Sletten, F. Lloret, M. Julve, *J. Chem. Soc. Dalton Trans.* **2002**, 3164–3170.
[20] J. D. Woodward, R. V. Backov, K. A. Abboud, D. Dai, H. J. Koo, M. H. Whangbo, M. W. Meisel, D. R. Talham, *Inorg. Chem.* **2005**, *44*, 638–648.
[21] J. P. Lang, Q. F. Xu, R. X. Yuan, B. F. Abrahams, *Angew. Chem. Int. Ed.* **2004**, *43*, 3917–3921.
[22] J. P. Lang, C. M. Jiao, S. B. Qiao, W. H. Zhang, B. F. Abrahams, *Inorg. Chem.* **2005**, *44*, 3664–3668.
[23] Q. F. Xu, J. X. Chen, W. H. Zhang, Z. G. Ren, H. X. Li, Y. Zhang, J. P. Lang, *Inorg. Chem.* **2006**, *45*, 4055–4064.
[24] J. X. Chen, W. H. Zhang, X. Y. Tang, Z. G. Ren, H. X. Li, Y. Zhang, J. P. Lang, *Inorg. Chem.* **2006**, *46*, 7671–7680.
[25] J. P. Lang, Q. F. Xu, W. H. Zhang, H. X. Li, Z. G. Ren, J. X. Chen, Y. Zhang, *Inorg. Chem.* **2006**, *45*, 10487–10496.
[26] Q. Y. Li, W. H. Zhang, H. X. Li, X. Y. Tang, J. P. Lang, Y. Zhang, X. Y. Wang, G. Song, *Chin. J. Chem.* **2006**, *24*, 1716–1720.
[27] M. A. Halcrow, *Coord. Chem. Rev.* **2005**, *249*, 2880–2908.
[28] G. Zoppellaro, A. Geies, V. Enkelmann, M. Baumgarten, *Eur. J. Org. Chem.* **2004**, 2367–2374.
[29] S. A. Willison, H. Jude, R. M. Antonelli, J. M. Rennekamp, N. A. Eckert, J. A. K. Bauer, W. B. Connick, *Inorg. Chem.* **2004**, *43*, 2548–2555.
[30] N. K. Solanki, E. J. L. McInnes, D. Collison, C. A. Kilner, J. E. Davies, M. A. Halcrow, *J. Chem. Soc. Dalton Trans.* **2002**, 1625–1630.
[31] K. Nakamoto, *Infrared and Raman Spectra of Inorganic and Coordination Compounds, Part B: Applications in Coordination, Organometallic, and Bioinorganic Chemistry*, 5th ed., Wiley, New York, **1997**, pp. 124–126.
[32] A. M. Schuitema, P. G. Aubel, I. A. Koval, M. Engelen, W. L. Driessen, J. Reedijk, M. Lutz, A. L. Spek, *Inorg. Chim. Acta* **2003**, *355*, 374–385.
[33] K. Steiner, W. Willing, U. Müller, K. Dehnicke, *Z. Anorg. Allg. Chem.* **1987**, *55*, 7–15.

 © 2007 Wiley-VCH Verlag GmbH & Co. KGaA, Weinheim 

[34] J. C. Wasilke, G. Wu, X. H. Bu, G. Kehr, G. Erker, *Organometallics* **2005**, *24*, 4289–4297.
[35] N. Mondal, S. Mitra, V. Gramilich, S. O. Ghodsi, K. M. A. Malik, *Polyhedron* **2001**, *20*, 135–141.
[36] J. Losada, I. Del Peso, L. Beyer, *Inorg. Chim. Acta* **2001**, *321*, 107–115.
[37] S. Torelli, C. Belle, I. Gautier-Luneau, J. L. Pierre, E. Saint-Aman, J. M. Latour, L. L. Pape, D. Luneau, *Inorg. Chem.* **2000**, *39*, 3526–3536.
[38] D. L. Jameson, K. A. Goldsby, *J. Org. Chem.* **1990**, *55*, 4992–4994.
[39] I. Csoregh, P. Kierkegaard, R. Norrestam, *Acta Crystallogr., Sect. B: Struct. Sci.* **1975**, *31*, 314–317.
[40] G. M. Sheldrick, *SHELXS-97and SHELXL-97. Program for the refinement of crystal structures*, University of Göttingen, Germany, **1997**.

Received: June 26, 2007
Published Online: October 17, 2007

 © 2007 Wiley-VCH Verlag GmbH & Co. KGaA, Weinheim 

DOI: 10.1002/ejic.200700672

# Synthesis, Reactivity, X-ray Crystal Structures and Electrochemical Behaviour of Water-Soluble [Tris(pyrazolyl)borato]ruthenium(II) Complexes of 1,3,5-Triaza-7-phosphaadamantane (PTA)

**Sandra Bolaño,[a] Jorge Bravo,*[a] Jesus Castro,[a] M. Mar Rodríguez-Rocha,[a] M. Fátima C. Guedes da Silva,[b,c] Armando J. L. Pombeiro,*[b] Luca Gonsalvi,[d] and Maurizio Peruzzini*[d]**

**Keywords:** Electrochemistry / Water-soluble complexes / Pyrazolylborates / Ruthenium / N ligands

A series of chloridoruthenium(II) complexes bearing the tripodal ligand tris(pyrazolyl)borate (Tp), the water-soluble cage phosphane 1,3,5-triaza-7-phosphaadamantane (PTA) and its *N*-boranyl adduct PTA($BH_3$), together with $PPh_3$, have been synthesised. The corresponding monohydrido complexes have also been obtained by treating the chlorides with NaOMe. The X-ray crystal structures of [TpRuCl(PTA)($PPh_3$)] (**2**) and [TpRuCl(PTA)$_2$] (**3**) are also described. Cyclic voltammetry (CV) studies in MeCN and dmso generally show reversible $Ru^{II/III}$ oxidation waves and the values of $E_{1/2}^{ox}$ reflect the electron-donating character of the ligands [Tp (each arm) > PTA > PTA($BH_3$)], whose Lever electrochemical parameter ($E_L$) has been estimated for the first time.

(© Wiley-VCH Verlag GmbH & Co. KGaA, 69451 Weinheim, Germany, 2007)

## Introduction

Whereas the chemistry of (cyclopentadienido)- and (pentamethylcyclopentadienido)ruthenium derivatives has been covered in the literature both broadly and in more detail,[1] less attention has been devoted to the corresponding hydrotris(pyrazolyl)borate (Tp) complexes, which have thus received increasing attention in recent years.[2] TpRu complexes containing a variety of co-ligands, particularly N-donors such as diamines, MeCN, pyridine, cycloocta-1,5-diene (cod) and hemilabile phosphanylamine ligands, were first reported about a decade ago,[3,4] the main interest residing in the application of such compounds as active catalysts for the dimerisation of terminal acetylenes or the coupling of phenylacetylene with benzoic acid or allyl alcohols.[4a,5] Tertiary phosphanes have also been used as co-ligands,[6] and complexes such as [TpRuX($PPh_3$)$_2$] (X = Cl or H)[6a,6e,6h] and [TpRu(MeCN)($PPh_3$)$_2$]$BF_4$[6e] have been shown to be quite efficient catalyst precursors for such reactions.[5,6e,7] Recent intriguing applications of TpRu complexes have been reported by Gunnoe and co-workers and include the use of [TpRuX($PMe_3$)$_2$] (X = non-dative heteroatomic ligands such as OH, OMe, OPh or NHPh) for the catalytic H/D exchange between water and deuterated arenes,[8] and the spectacular catalytic hydroarylation of α-alkenes promoted by [TpRuPh(CO)(MeCN)] to give alkylarenes with good preference for the linear isomers over the branched ones.[9] Extension of this hydroarylation protocol to multiple C–X (X = O, S) bonds has also been demonstrated.[10] The hydration of nitriles to amides catalysed by the hydride [TpRuH($PPh_3$)(MeCN)] has also been reported and is considered to be assisted by formation of an Ru–H···H–OH dihydrogen-bonding interaction in the transition state, which lowers the reaction barrier for the hydration step.[11]

The coordination properties of the Tp anion and substituted derivatives have been described in detail by Trofimenko, who has discussed their analogies and differences with cyclopentadienido ligands.[2,12] A good example of this is the comparison between [TpRuCl($PPh_3$)$_2$] and [CpRuCl($PPh_3$)$_2$],[13] where the higher reactivity of the former towards ligand substitution has been ascribed to both the higher nucleophilicity imparted to the metal atom by Tp, which labilises the Ru–Cl bond, and the higher steric constraint caused by the bulkier tris(pyrazolyl) framework. Another aspect of this class of tripodal ligands, which is recognized as being beneficial in their catalytic application, is their hemilability and the consequent easy change of hapticity from $\kappa^3$- to $\kappa^2$-coordination.[14]

[a] Departamento de Química Inorgánica, Facultade de Química, Universidade de Vigo,
Campus Universitario, 36310 Vigo, Spain
E-mail: jbravo@uvigo.es
[b] Centro de Química Estrutural, Complexo I, Instituto Superior Técnico, TU-Lisbon,
Av. Rovisco Pais, 1049-001 Lisboa, Portugal
E-mail: pombeiro@ist.utl.pt
[c] Universidade Lusófona de Humanidades e Tecnologias,
Av. Campo Grande 376, 1749-024 Lisboa, Portugal
[d] Istituto di Chimica del Composti Organometallici, Consiglio Nazionale delle Ricerche (ICCOM-CNR),
Via Madonna del Piano 10, 50019 Sesto Fiorentino (Firenze), Italy
E-mail: mperuzzini@iccom.cnr.it

 © 2007 Wiley-VCH Verlag GmbH & Co. KGaA, Weinheim 

We have been interested for some years in the organometallic reactivity and application in catalysis of water-soluble phosphanes such as 1,3,5-triaza-7-phosphaadamantane (PTA),[15] and we recently communicated the synthesis of its *N*-$BH_3$ adduct [PTA($BH_3$)].[16] To the best of our knowledge, no examples of TpRu complexes bearing monodentate water-soluble phosphanes are known in the literature.[17] Herein we describe the synthesis of a series of novel $TpRu^{II}$ chlorido and hydrido complexes bearing various combinations of PTA, PTA($BH_3$) and $PPh_3$ as ancillary ligands, together with the X-ray crystal structure determinations of selected complexes. The cyclic voltammetric behaviour of the TpRu complexes is also reported as it provides interesting information on the donor abilities of the ligands.

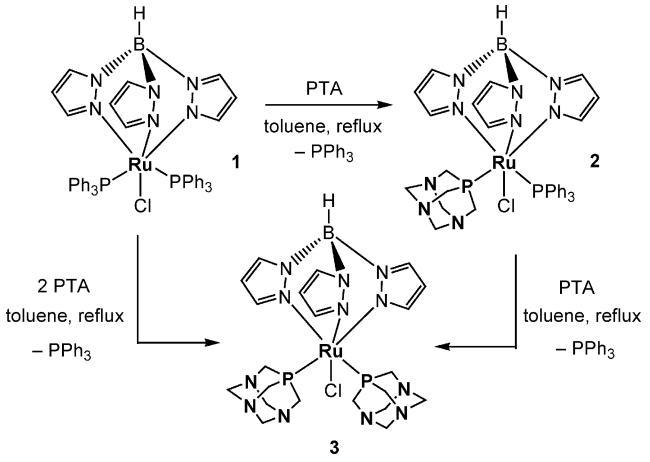


Scheme 1.

## Results and Discussion

### Synthesis and Characterisation of TpRu Complexes with PTA and PTA($BH_3$)

The novel [tris(pyrazolyl)borato]ruthenium(II) complexes [TpRuCl(PTA)($PPh_3$)] (**2**) and [TpRuCl($PTA)_2$] (**3**) were prepared in good yields by treating [TpRuCl($PPh_3)_2$] with PTA in refluxing toluene in the molar ratio 1:1 or 1:2, respectively. Alternatively, compound **3** can be synthesised by treating **2** with PTA in refluxing toluene (Scheme 1).

A similar reaction with the *N*-boranyl adduct of PTA [PTA($BH_3$)] gives the complexes [TpRuCl($PPh_3$){PTA-($BH_3$)}] (**4**) and [TpRuCl{PTA($BH_3)_2$}] (**5**). Alternatively, the TpRu complexes **4** and **5**, which contain the boronated PTA ligand, may be prepared in a straightforward manner by direct boronation of **2** and **3** in thf with excess $BH_3$·thf at room temperature. Whereas the reaction proceeds smoothly for **2** in a 1:1 ratio to give compound **4** in good yield, an excess of $BH_3$·thf has to be added to **3** in order to obtain **5** (Scheme 2) as the only product of the reaction (see below).

Whilst monitoring the reaction of **3** with increasing amounts of $BH_3$·thf by $^{31}P\{^1H\}$ NMR spectroscopy, we observed, in addition to the signals corresponding to complex **5**, the appearance of two new doublets ($\delta$ = –18.4 and –29.6 ppm, $^2J_{P,P}$ = 35.7 Hz), which progressively disappear as the singlet due to **5** increases in intensity. Although we did not attempt to isolate the complex first formed from **3**, the two doublets may be reasonably attributed to the formation of the intermediate mixed species [TpRuCl-(PTA){PTA($BH_3$)}] (**5′**).

Monitoring of the reaction between **2** (or **3**) and excess $BH_3$·thf by $^{31}P\{^1H\}$ NMR spectroscopy in situ does not provide evidence for the formation of boronated species other than **5**. The absence of NMR signals ascribable to ruthenium complexes containing polyboronated ligands [PTA($BH_3)_x$, $x$ = 2, 3][16a] raises the question as to whether the *N*,*N*-diboronated PTA skeleton may still represent a valid P-type ligand for metal coordination.

Good analytical data were obtained for all complexes **2**–**5**, which were isolated as fairly air-stable yellow solids. Their solubility in common solvents depends strongly on

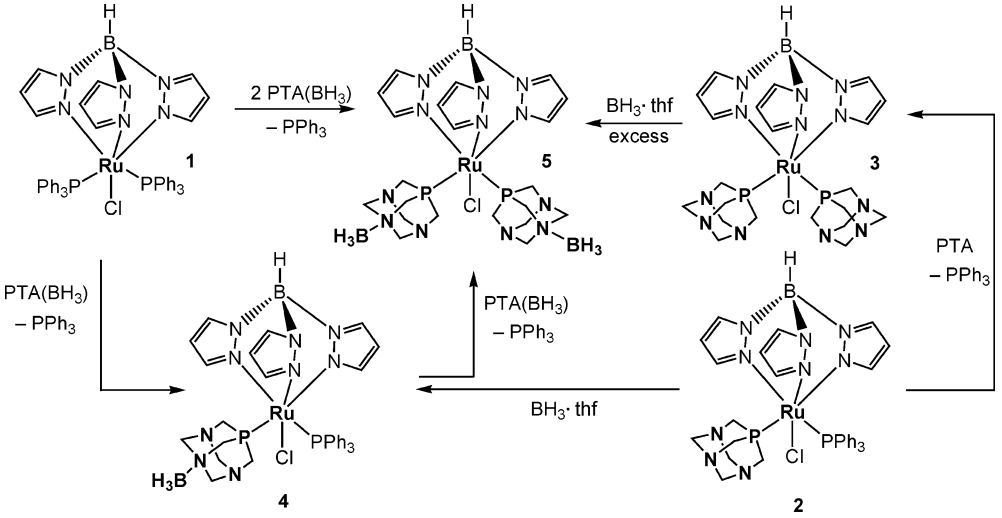


Scheme 2.

 © 2007 Wiley-VCH Verlag GmbH & Co. KGaA, Weinheim 

the nature of the phosphanes contained in the complexes. Thus, **2** is soluble in most common polar organic solvents but only slightly soluble in water ($S_{25°C}$ = 2.1 mg mL$^{-1}$), whereas replacement of the second $PPh_3$ ligand by PTA makes **3** water-soluble ($S_{25°C}$ = 18 mg mL$^{-1}$). Solutions of **3** in $D_2O$ are stable at room temperature for several days, as indicated by the corresponding $^{31}P\{^1H\}$ NMR spectrum, which displays a singlet at $\delta$ = –26.1 ppm that remains unchanged. A new, slightly deshielded singlet slowly appears at $\delta$ = –24.0 ppm upon heating to 60 °C, and these two signals reach comparable intensities at this temperature after 6 d. This new signal may be safely attributed to aquation of the chlorido derivative to give the cationic aquo complex $[TpRu(H_2O)(PTA)_2]Cl$ (**3′**) (Scheme 3). Ligand substitution in related Ru(PTA) complexes, such as the antitumour compounds $[(\eta^6\text{-arene})RuCl_2(PTA)]$[18] and the corresponding Cp analogue, $[CpRuCl(PTA)(PPh_3)]$,[19] has also been reported. Quantitative formation of the same aquo cation takes place at 60 °C upon mixing $D_2O$ solutions of $TlPF_6$ and **3** (NMR-tube experiment). No attempt was made to isolate the aquo complex in the solid state.

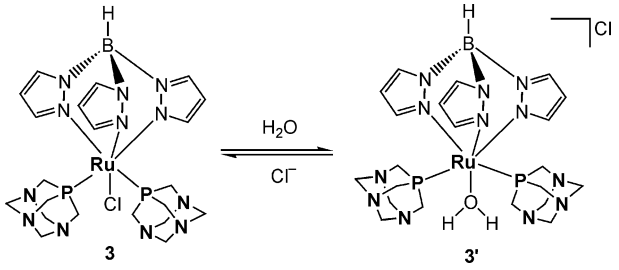


Scheme 3.

Boronation of PTA decreases the solubility of the complexes, making **4** sparingly soluble in halogenated solvents and acetone and insoluble in water. Complex **5**, which bears two boronated $PTA(BH_3)$ ligands, is practically insoluble in common organic solvents except dmso.

All complexes were fully characterised by elemental analysis and conventional spectroscopic techniques (IR and NMR) and, in the case of compounds **2** and **3**, crystals suitable for an X-ray analysis were obtained (see below). The IR spectra of compounds **2**–**5** show the characteristic $\nu_{BH}$ band of the Tp ligand at 2475–2508 cm$^{-1}$. Complexes **4** and **5** also exhibit three absorptions between 2267 and 2376 cm$^{-1}$ due to the stretching modes of the *N*-coordinated borane ($BH_3$) unit. The $^1H$ NMR spectra of compounds **2**–**5** confirm the presence of the Tp ligand, showing the characteristic signals of the pyrazolyl protons in the range $\delta$ = 5.68–8.17 ppm. As expected, the complexity of the Tp signal depends on the degree of symmetry of the molecule due to homo- or heterophosphane substitution, and the same trend was observed in the $^{13}C$ NMR spectra, which were fully assigned (see Experimental Section) with the help of $^1H$,$^{13}C$-HSQC and DEPT-135 NMR experiments.

The $^{31}P\{^1H\}$ NMR spectrum of **2** shows two doublets at $\delta$ = –34.2 and 46.9 ppm ($^2J_{P,P}$ = 33.1 Hz) corresponding to the phosphorus resonances of PTA and $PPh_3$, respectively. Compound **3** presents a singlet at $\delta$ = –28 ppm corresponding to the P nuclei of both PTA ligands. Compounds **4** and **5** give a similar pattern, with two doublets at $\delta$ = –25.3 and 44.0 ppm ($^2J_{P,P}$ = 32.6 Hz) for compound **4** and a singlet at $\delta$ = –19.5 ppm for compound **5**, which is shifted downfield due to the influence of the $BH_3$ group. The presence of an $N_{PTA}$-coordinated borane unit is further confirmed by broad signals in the $^1H$ NMR spectra between $\delta$ = 0.74 and 1.54 ppm that integrate for three (**4**) or six protons (**5**), respectively.

## Single-Crystal X-ray Structure Determination for Complexes 2 and 3

Suitable crystals of **2** and **3** were grown from dilute toluene solutions. Selected bond lengths and angles are summarised in Table 1, while thermal ellipsoid representations of the solid-state structures of one of the molecules in the asymmetric unit of $[TpRuCl(PTA)(PPh_3)]$ (**2**) and $[TpRuCl(PTA)_2]$ (**3**), along with the atomic numbering schemes, are depicted in Figures 1 and 2, respectively.

Table 1. Selected bond lengths [Å] and angles [°] for **2** and **3**.[a]

| **3** | | **2** | | |
|---|---|---|---|---|
| | | | Molecule 1 | Molecule 2 |
| Ru–N(13) | 2.100(4) | Ru–$N_{Tp}$ | 2.098(7) | 2.087(7) |
| Ru–N(11$^i$) | 2.148(3) | Ru–$N_{Tp}$ | 2.121(7) | 2.110(7) |
| Ru–N(11) | 2.148(3) | Ru–$N_{Tp}$ | 2.131(7) | 2.149(7) |
| Ru–P | 2.2676(10) | Ru–$P_{PTA}$ | 2.288(2) | 2.288(2) |
| Ru–P$^i$ | 2.2675(10) | Ru–P | 2.326(2) | 2.332(2) |
| Ru–Cl | 2.4186(16) | Ru–Cl | 2.422(2) | 2.418(2) |
| N–$C_{PTA}$ (av.) | 1.464(6) | N–$C_{PTA}$ (av.) | 1.466(9) | 1.465(9) |
| P–$C_{PTA}$ (av.) | 1.846(4) | P–$C_{PTA}$ (av.) | 1.851(8) | 1.843(8) |
| N(11$^i$)–Ru–N(11) | 81.24(17) | $N_{Tp}$–Ru–$N_{Tp}$ | 81.0(2) | 81.2(3) |
| N(13)–Ru–N(11$^i$) | 88.37(11) | $N_{Tp}$–Ru–$N_{Tp}$ | 88.4(2) | 88.3(3) |
| N(13)–Ru–N(11) | 88.37(11) | $N_{Tp}$–Ru–$N_{Tp}$ | 86.9(2) | 86.4(2) |
| N(13)–Ru–P | 92.22(8) | $N_{Tp}$–Ru–$P_{PTA}$ | 88.52(17) | 88.81(17) |
| N(11$^i$)–Ru–P | 90.26(9) | $N_{Tp}$–Ru–$P_{PTA}$ | 89.40(18) | 89.04(18) |
| N(11)–Ru–P | 171.47(9) | $N_{Tp}$–Ru–$P_{PTA}$ | 170.03(18) | 170.0(2) |
| N(13)–Ru–P$^i$ | 92.22(8) | $N_{Tp}$–Ru–P | 94.44(17) | 94.08(18) |
| N(11$^i$)–Ru–P$^i$ | 171.47(9) | $N_{Tp}$–Ru–P | 172.60(19) | 173.10(18) |
| N(11)–Ru–P$^i$ | 90.26(9) | $N_{Tp}$–Ru–P | 91.80(18) | 91.95(19) |
| P–Ru–P$^i$ | 98.22(5) | $P_{PTA}$–Ru–P | 97.89(8) | 97.85(8) |
| N(13)–Ru–Cl | 174.57(12) | $N_{Tp}$–Ru–Cl | 172.45(17) | 172.01(18) |
| N(11$^i$)–Ru–Cl | 87.51(8) | $N_{Tp}$–Ru–Cl | 89.79(19) | 85.68(19) |
| N(11)–Ru–Cl | 87.51(8) | $N_{Tp}$–Ru–Cl | 85.53(19) | 89.5(2) |
| P–Ru–Cl | 91.34(3) | $P_{PTA}$–Ru–Cl | 92.04(8) | 91.99(8) |
| P$^i$–Ru–Cl | 91.34(3) | P–Ru–Cl | 92.94(8) | 93.69(8) |

[a] Symmetry transformations used to generate equivalent atoms: i: *x*, 3/2 – *y*, *z*.

In keeping with the solution characterisation, both compounds consist of discrete molecules where the ruthenium(II) ion exhibits a distorted octahedral geometry with three contiguous coordination positions occupied by the $\kappa^3$-*N*,*N*′,*N*′′ tridentate Tp ligand. One chlorido ligand and two mutually *cis*- oriented phosphane ligands (two *P*-bonded PTA ligands for **3** and one *P*-bonded PTA and one triphenylphosphane ligand for **2**) complete the coordination polyhedron around the ruthenium atom. The nitrogen-donor atoms of the Tp ligand occupy one of the faces of the octahedron, with the shorter Ru–N bond corresponding

 © 2007 Wiley-VCH Verlag GmbH & Co. KGaA, Weinheim 

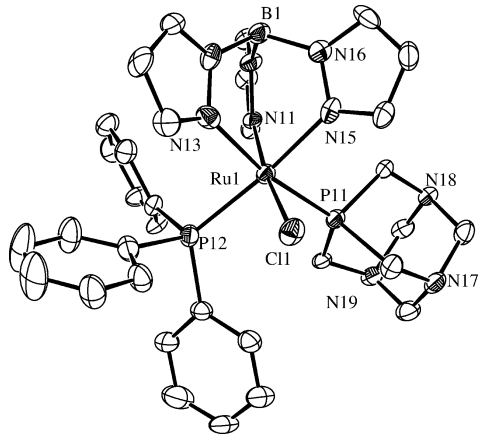


Figure 1. ORTEP view and atom-numbering scheme for **2**, showing thermal ellipsoids at the 30% probability level. Hydrogen atoms have been omitted for clarity.

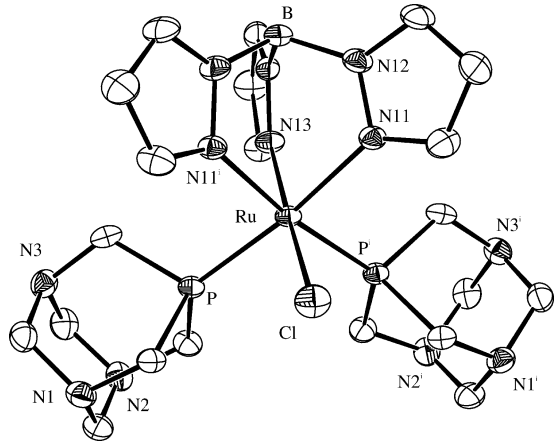


Figure 2. ORTEP view and atom-numbering scheme for **3**, showing thermal ellipsoids at the 30% probability level. Hydrogen atoms have been omitted for clarity.

to that *trans* to the chlorido ligand. The Ru–N bonds *trans* to phosphorus atoms in **3** are identical on symmetry grounds and differ by 0.01 and 0.03 Å in the two molecules of **2**. These values are analogous to those found for other Tp–$Ru^{II}$ complexes.[20]

The average Ru–Cl bond length (2.42 Å) is similar to previously published values.[4d,6a,6b,7,21] The Ru–$P_{PTA}$ bond lengths in **3** and **2** are 2.267(1) and 2.288(2) Å, respectively, and are similar to those found for other PTA complexes with ruthenium.[19,21a,22] The angles around the metal atom deviate by less than 4° from the theoretical value of 90° except in two cases. One of these is the P–Ru–P angle, which opens to 98.22(5)° in **3** and 97.87(8)° in **2** despite the fact that the cone angle of $PPh_3$ (approx. 147°) is larger than that of PTA (approx. 102°).[15,22b,23] The other exception involves the N–Ru–N chelate angles of the Tp ligand in the same plane as the phosphorus atoms, which are narrower as a consequence of the variation of the P–Ru–P angles and have values of 81.24(17)° for **3** and 81.1(2)° (av.) for **2**. The *trans* angles diverge from the theoretical value of 180° due to the chelate requirements of the Tp ligand and the steric effects of the phosphane ligands already discussed for the *cis* angles. Thus, the N–Ru–Cl angles have values of between 172.0(1) and 174.6(1)° and the P–Ru–N angles range from 172.0(2) to 173.1(2)°.

## Electrochemical Studies

Electrochemical studies on the present TpRu complexes were carried out to collect information about the donor properties of PTA and its *N*-boranyl adduct. The electrochemical behaviour of $[TpRuCl(PPh_3)_2]$ (**1**) was also investigated in order to compare these properties with triphenylphosphane. In spite of the increasing amount of attention being paid to this class of water-soluble ligands,[15] electrochemical studies on their coordination complexes have rarely been carried out and, to the best of our knowledge, are limited to Darensbourg's analysis of electrocatalysed $H_2$ production by models of iron hydrogenases incorporating PTA and electrophilically activated PTA analogues[24] and to a recent study on (cyclopentadienido)-ruthenium complexes related to the present TpRu species by online electrochemistry and electrospray mass spectrometry (EC/ESI-MS).[25]

The electrochemical behaviour of ruthenium(II) complexes **1**–**5** was studied in MeCN and dmso. Cyclic voltammetry (CV) in 0.2 M $[Bu_4N][BF_4]$ at a Pt disc electrode in both solvents shows a reversible, one-electron oxidation wave assigned to the $Ru^{II} \rightarrow Ru^{III}$ oxidation (wave I, at the half-wave oxidation potential values, ${}^{I}E_{1/2}{}^{ox}$, given in Table 2). Hence, it concerns the $Ru^{II/III}$ redox couple, as has been commonly recognized[26–30] for other $Ru^{II/III}$ complexes and also for the complexes $[CpRuCl(L)(L')]$ (L = PTA, $PPh_3$).[25] The occurrence of a one-electron oxidation was confirmed by exhaustive controlled potential electrolysis (CPE) in MeCN at a potential slightly anodic to that of the peak potential, which led to the consumption of nearly 1 F per mol of complex, with conversion of the oxidation wave to the corresponding reduction one at the same half-wave redox potential.

Table 2. Cyclic voltammetric data for the ruthenium complexes **1**–**5**.[a]

| Complex | MeCN | | dmso | |
|---|---|---|---|---|
| | ${}^{I}E_{1/2}{}^{ox}$ | ${}^{II}E_{p}{}^{ox}$, ${}^{III}E_{p}{}^{ox}$ | ${}^{I}E_{1/2}{}^{ox}$ | ${}^{II}E_{p}{}^{ox}$ |
| $[TpRuCl(PPh_3)_2]$ (**1**) | 0.70[b] | 1.98[c] | 0.74 | 1.11 |
| $[TpRuCl(PPh_3)(PTA)]$ (**2**) | 0.70 | 1.26[d] | 0.70 | 1.13[e] |
| $[TpRuCl(PTA)_2]$ (**3**) | 0.66 | 1.23[f] | 0.61 | 1.14 |
| $[TpRuCl(PPh_3)\{PTA(BH_3)\}]$ (**4**) | 0.80 | 1.75, 1.87[g] | 0.77 | – |
| $[TpRuCl\{PTA(BH_3)\}_2]$ (**5**) | 0.89[h] | 1.15, 1.23[g] | 0.79 | 1.14 |

[a] Potentials in V (±0.02) vs. SCE, measured at 0.2 $V s^{-1}$. [b] The reversible oxidation wave with a lower current intensity observed at ${}^{I}E_{1/2}{}^{ox}$ = 1.00 V is ascribed to $[(\kappa^2\text{-Tp})RuCl(MeCN)(PPh_3)_2]$. [c] Upon scan reversal, a cathodic reversible wave is detected at 1.26 V. [d] Upon scan reversal, a cathodic reversible wave is detected at 0.89 V. [e] Upon scan reversal, a cathodic reversible wave is detected at 0.85 V. [f] Upon scan reversal, a cathodic reversible wave is detected at 1.03 V. [g] Poorly defined. [h] The reversible oxidation wave with a lower current intensity observed at ${}^{I}E_{1/2}{}^{ox}$ = 0.75 V is assigned to $[TpRuCl(MeCN)\{PTA(BH_3)\}]$.

 © 2007 Wiley-VCH Verlag GmbH & Co. KGaA, Weinheim 

A low-intensity reversible oxidation wave was also observed at a slightly higher or lower $E_{1/2}^{ox}$ value with respect to wave I for complexes [TpRuCl($PPh_3$)$_2$] (**1**; Figure 3) and [TpRuCl{PTA($BH_3$)}$_2$] (**5**), respectively, in MeCN. This additional process was assigned to oxidation of the complexes generated in situ by partial ligand displacement by MeCN, which should result in the formation of the acetonitrile adducts [($\kappa^2$-Tp)RuCl(MeCN)($PPh_3$)$_2$] or [TpRuCl(MeCN)-{PTA($BH_3$)}] (see below). This partial ligand displacement appears to occur more extensively in dmso since wave I of the complexes in this solvent usually exhibits a much lower peak current intensity and CPE involves a charge consumption much lower than 1 F per mol of complex. This behaviour can be explained by considering the replacement of one of the coordinating arms of $\kappa^3$-Tp (thus becoming $\kappa^2$-Tp) by dmso (see below) and formation of complexes that exhibit oxidation potentials about 0.4 V above those of the starting complexes (wave I). In fact, a second irreversible oxidation wave (wave II) with a higher current intensity than that of wave I is observed close to the solvent/electrolyte discharge in dmso at an $E_p^{ox}$ value that is 0.35–0.53 V more anodic than that of $^{I}E_{1/2}^{ox}$ (Table 2). This second oxidation wave could also involve a ligand-centred oxidation since free PTA presents an irreversible oxidation wave at 1.05 V vs. SCE.

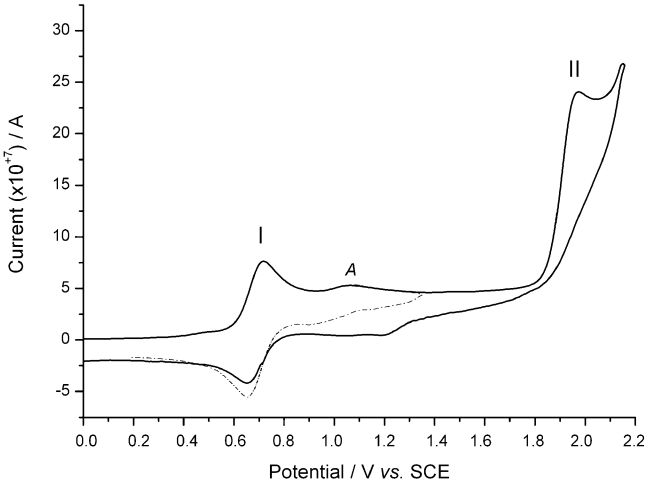


Figure 3. Cyclic voltammograms of [TpRuCl($PPh_3$)$_2$] (**1**) (0.7 mM) in 0.2 M [$Bu_4N$][$BF_4$]/MeCN at a platinum disc ($d$ = 0.5 mm) working electrode and at a scan rate of 0.2 V s$^{-1}$. Wave A is assigned to [($\kappa^2$-Tp)RuCl(MeCN)($PPh_3$)$_2$] (see text). The dotted line represents the cathodic scan following the oxidation waves I and A.

In the cyclic voltammograms in MeCN wave I is also followed at a higher potential by a second (and in a couple of cases also by a third) irreversible oxidation wave (Table 2) which is also believed to be ligand- rather than metal-centred. In fact, the $Ru^{III/IV}$ redox potential would be expected (see below) at a much higher potential (> 2.4 V vs. SCE) and, for example, the potassium salt of Tp in MeCN exhibits irreversible oxidation waves at 1.61 and 1.96 V. Such oxidation waves were not investigated further.

The values of the $Ru^{II/III}$ oxidation potential ($^{I}E_{1/2}^{ox}$) of our complexes should reflect the electron-donor character of the ligands, which thus can be ordered as follows: PTA > $PPh_3$ > PTA($BH_3$). This character can even be measured by applying the redox potential parametrisation approach proposed by Lever[26] for octahedral complexes, based on the linear relationship [Equation (1)] in which the redox potential of a complex (in V vs. NHE) is related to electrochemical parameters determined by the ligands and the metal redox centre. In this equation $\Sigma E_L$ is the sum of the values of the $E_L$ ligand parameter for all the ligands and $S_M$ and $I_M$ are the slope and intercept, respectively (dependent upon the metal, redox couple, spin state and stereochemistry).

$$E_{1/2}^{ox} = S_M \cdot (\Sigma E_L) + I_M \quad (1)$$

Application of Equation (1) to the complexes under study (with the $^{I}E_{1/2}^{ox}$ oxidation potentials converted to V vs. NHE) with known values of $I_M$ (0.04 V vs. NHE) and $S_M$ (0.97) for the $Ru^{II}/Ru^{III}$ redox centre, as well as $E_L$ for the $Cl^-$ and $PPh_3$ ligands (–0.24 and 0.39, respectively)[26] allowed us to tentatively estimate, for the first time, the $E_L$ parameter for Tp (in complex **1**), PTA (in complexes **2** and **3**) and its *N*-boranyl adduct, PTA($BH_3$) (in complexes **4** and **5**) as an average of two (for Tp) or four (for the other ligands) values for each ligand (measured in both MeCN and dmso). The estimated $E_L$ values (Table 3) are as follows: 0.14 V (for each coordinated arm of Tp), 0.34 (PTA) and 0.45 [PTA($BH_3$)] V vs. NHE. This order confirms the ordering above for the net electron-donor ability of such ligands on the basis of the oxidation potentials of their complexes.

Table 3. $E_L$ ligand parameter values estimated in this study.[a]

| Ligand | $E_L$ [V] vs. NHE |
|---|---|
| Tp | 014[b] |
| PTA | 0.34 |
| PTA($BH_3$) | 0.45 |

[a] From Lever's equation [Equation (1)]. [b] Per ligating pyrazolyl arm.

Remarkably, Tp appears to be a net electron-donor similar to $HCpz_3$ [hydrotris(pyrazolyl)methane], for which an identical $E_L$ value has been estimated.[31] However, each pyrazolyl arm of Tp is a slightly weaker electron donor than pyrazole itself ($E_L$ = 0.20 V vs. NHE). Application of Equation (1), using the estimated $E_L$ values, to the above-mentioned unassigned low-intensity oxidation waves at 1.00 and 0.77 V vs. SCE (in MeCN solutions of complexes **1** and **5**), allowed us to tentatively identify the corresponding complexes as [($\kappa^2$-Tp)RuCl(MeCN)($PPh_3$)$_2$] and [TpRuCl(MeCN){PTA($BH_3$)}], which have predicted $E_{1/2}^{ox}$ values of 0.96 and 0.74 V, respectively. The former complex is derived from displacement of one pyrazolyl arm of Tp in **1** by MeCN, whereas the latter complex results from substitution of one PTA($BH_3$) ligand by acetonitrile.

Since *S*-bonded dmso ($E_L$ = 0.57 V)[32] behaves as a considerably weaker net electron-donor than each ligating arm of Tp ($E_L$ = 0.14 V as estimated above) and the corresponding $\Delta E_L$ difference is 0.43 V, coordinative displacement of one pyrazolyl group of Tp (conversion from a tri- to a di-

 © 2007 Wiley-VCH Verlag GmbH & Co. KGaA, Weinheim 

hapto ligand) by dmso would result in an increase of the oxidation potential of the complex by a value of $0.43\,S_M$ [Equation (1)], i.e. 0.42 V. This difference is comparable to those observed between the oxidation potentials of the second and first waves (Table 2) in dmso ($\Delta E^{ox}$ in the 0.35–0.53 V range), thereby suggesting the occurrence of such a displacement reaction. This implies that the oxidation waves observed at potentials higher than those of wave I ($Ru^{II/III}$ redox pair) should not be assigned to the $Ru^{III/IV}$ oxidation. Indeed, the estimated $Ru^{III/IV}$ oxidation potentials (approx. 2.4 V vs. SCE), by application of a proposed version of Lever's relationship in which $S_M = 1.03$ and $I_M = 1.68$ V vs. NHE,[28] are much higher than the experimentally measured ones.

### Synthesis and Characterisation of Water-Soluble TpRu Hydrides

The hydrido[tris(pyrazolyl)borato]ruthenium(II) complex [TpRuH($PPh_3$)(PTA)] (**6**) was prepared by chloride metathesis upon treatment of **2** with an excess of NaOMe in MeOH at room temperature. Attempts to prepare this hydride according to the more standard method[33] using $NaBH_4$ as hydride source failed due to partial boronation of PTA. Similarly, the reaction of **2** with $LiHBEt_3$ or $LiAlH_4$ did not afford reproducible results and generally resulted in extensive decomposition. Attempts to prepare the bis(PTA) hydride [TpRuH($PTA)_2$] (**7**) by using NaOMe or similar reagents proved unsuccessful, although treatment of complex **6** with PTA in refluxing toluene was an excellent method to prepare **7**. Further reaction of **6** with $BH_3$·thf provides a straightforward method to synthesise the new PTA-boronated hydrido complex [TpRuH($PPh_3$){PTA-($BH_3$)}] (**8**). A summary of these reactions is shown in Scheme 4.

The hydrides **6**–**8**, which were isolated as pale-yellow solids in moderate yields, decompose slowly in air; thus, they were stored under argon. The complexes are soluble in halogenated solvents but slowly revert to the corresponding chloro complexes. The IR spectra of all hydride compounds, apart from the characteristic $\nu_{BH}$ band of the Tp ligand (2456–2464 $cm^{-1}$), show a medium-intensity absorption at 1920–1940 $cm^{-1}$ attributed to $\nu_{RuH}$.

The $^1H$ NMR spectra of compounds **6**–**8** confirm the presence of the Tp ligand by showing the characteristic signals of the pyrazole hydrogen atoms of the Tp group. Again, the number of these signals reflects the number of identical co-ligands attached to the metal centre. The $^1H$ NMR spectra of complexes **6** and **8** show a high-field-shifted doublet of doublets, each centred at $\delta \approx -14$ ppm, due to coupling to two different phosphorus atoms, which is highly diagnostic for the presence of a terminal hydrido ligand, whereas complex **7** displays a triplet at $\delta \approx -16$ ppm corresponding to the single hydrido ligand coupled to the two magnetically equivalent PTA P atoms ($^2J_{P,H} = 30.6$ Hz). A triplet with similar NMR parameters has been reported for the related hydride [CpRuH($PTA)_2$] ($\delta = -14.46$ ppm, $^2J_{P,H} = 36.0$ Hz).[21a,22d]

In agreement with the proposed formulation, the $^{31}P\{^1H\}$ and $^{13}C\{^1H\}$ NMR spectra of hydrides **6**–**8** show similar patterns to the chlorido complexes and do not require additional comment.

Interestingly, while the solubility of the mixed PTA/$PPh_3$ hydride **6** in water is rather modest ($S_{25\,°C} = 2.0$ mg $mL^{-1}$), the bis(PTA) hydride **7** is readily soluble in water ($S_{25\,°C} = 21$ mg $mL^{-1}$), where it does not decompose even upon standing at room temperature for a week.

Water-soluble transition metal hydrides are still uncommon species[34] despite the increased attention recently paid to catalytic applications in water or aqueous biphasic systems and the growing interest in synthesising metal hydrides that combine good water solubility with thermal robustness and tolerance to highly polar substrates. As **6** seems to fulfil these latter requirements, it appears to be a good candidate for further studies and applications in aqueous-phase hydrogenation catalysis. Current work in our laboratories is

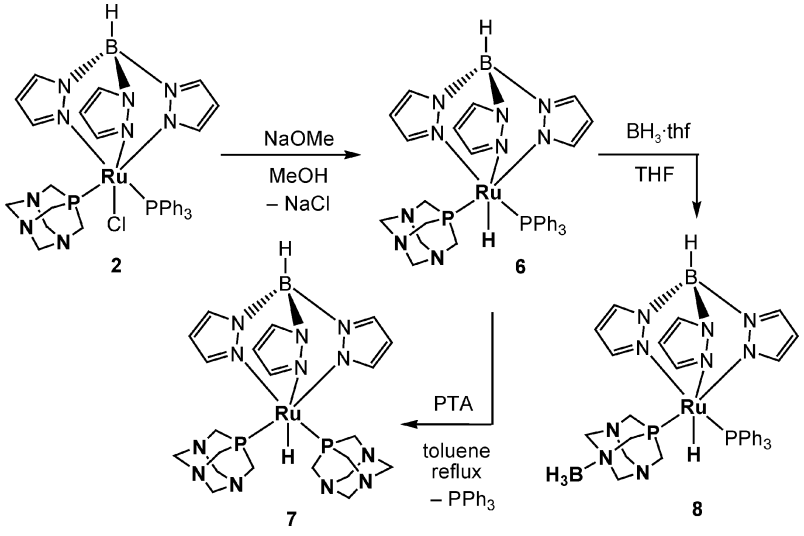


Scheme 4.

 © 2007 Wiley-VCH Verlag GmbH & Co. KGaA, Weinheim 

aimed at investigating the scope of **6** in catalysis and at preparing new water-soluble transition metal hydrides based on PTA and related systems.

## Conclusions

A series of chloridoruthenium(II) complexes bearing the anionic tripodal tris(pyrazolyl)borato (Tp) ligand and the water-soluble cage phosphane PTA, or its boronated version PTA($BH_3$), have been synthesised and characterised by spectroscopic methods and X-ray diffraction analysis of selected complexes {[TpRuCl(PTA)($PPh_3$)] and [TpRuCl-($PTA)_2$]}. Electrochemical CV studies have indicated the occurrence of partial $\kappa^3$ to $\kappa^2$ dechelation of Tp in some cases, and have allowed us to measure the values of $E_{1/2}^{ox}$, which reflect the electron-donor character of the ligands [Tp (each arm) > PTA > $PPh_3$ > PTA($BH_3$)]; the Lever electrochemical parameter $E_L$ has also been estimated for the first time (except for $PPh_3$).

A series of TpRu hydrides containing PTA and PTA($BH_3$) have been prepared and characterised. The hydride [TpRuH($PTA)_2$], which has been prepared in good yield, shows good solubility in water and high thermal stability. Further studies are in progress to determine the activities of the complexes obtained as hydrogenation catalysts in aqueous and biphasic systems and to evaluate their biological activity towards selected cell lines and their role in medicinal chemistry.[35]

## Experimental Section

**General Methods:** All experimental manipulations were carried out under argon using standard Schlenk techniques. Once isolated, the complexes were found to be relatively stable in air, but were stored for precaution under an inert gas. All solvents were purified by conventional procedures[36] and distilled prior to use. The ligands PTA,[37] PTA($BH_3$),[16a] KTp[12a] and the complex [TpRuCl-($PPh_3)_2$][6a] (**1**) were prepared according to published methods. Other reagents were purchased from commercial sources in the highest available purity and used as received. IR spectra (KBr disc) were recorded with a Bruker Vector IFS 28 FT spectrophotometer. NMR spectra [$^1$H, $^{31}$P($^1$H), $^{13}$C($^1$H)] were obtained at room temperature (25 °C) with a Bruker ARX-400 spectrometer operating at frequencies of 400, 161 and 100 MHz, respectively; the spectra were recorded in $CDCl_3$, [$D_6$]dmso, $D_2O$ or $CD_2Cl_2$ solution using the solvent as internal reference. $^1$H and $^{13}$C{$^1$H} NMR signals are referenced to internal TMS and those of $^{31}$P{$^1$H} to 85% $H_3PO_4$; downfield shifts ($\delta$ in ppm) are considered positive. The $^1$H,$^1$H-COSY, $^1$H,$^{13}$C-HSQC 2D-NMR experiments were performed with the same instrument using standard programs and processing routines. Microanalyses were carried out with a Fisons EA-1108 elemental analyzer.

**Synthesis of [TpRuCl(PTA)($PPh_3$)] (2):** Solid PTA (180 mg, 1.14 mmol) was added to a stirred suspension of [TpRuCl($PPh_3)_2$] (**1**; 1000 mg, 1.14 mmol) in 20 mL of toluene, and the reaction mixture was refluxed for 40 min. The resultant yellow solution was filtered through Celite while hot to remove impurities. The yellow filtrate was reduced under vacuum to about 3 mL, and a yellow microcrystalline solid was precipitated upon addition of diethyl ether (5 mL). This precipitate was collected on a sintered glass frit and washed with diethyl ether (3 × 10 mL) before being dried in vacuo. Yield: 740 mg (84%). $S_{25\,°C}$ = 2.1 mg mL$^{-1}$. $C_{33}H_{37}BClN_9P_2Ru$ (769.0): calcd. C 51.54, H 4.85, N 16.39; found C 51.50, H 4.87, N 16.35. IR (KBr pellet): $\nu_{BH}$ = 2475 cm$^{-1}$ (w). $^1$H NMR ($CDCl_3$, 400 MHz): $\delta$ = 3.88 (m, 6 H, PC$H_2$N), 4.20–4.46 (m, NC$H_2$N, 6 H), 5.68 [t, $^3J_{H,H}$ = 2.3 Hz, 1 H, HB-($C_3H_3N_2)_3$], 5.77 [td, $^3J_{H,H}$ = 2.2, $^5J_{H,P}$ = 1.0 Hz, 1 H, HB-($C_3H_3N_2)_3$], 5.98 [d, $^3J_{H,H}$ = 2.1 Hz, 1 H, HB($C_3H_3N_2)_3$], 6.21 [td, $^3J_{H,H}$ = 2.2, $^5J_{H,P}$ = 1.0 Hz, 1 H, HB($C_3H_3N_2)_3$], 6.62 [d, $^3J_{H,H}$ = 2.1 Hz, 1 H, HB($C_3H_3N_2)_3$], 7.22–7.30 (m, 3 H, P$Ph_3$), 7.30–7.37 (m, 6 H, P$Ph_3$), 7.52–7.63 [m, 6 H, P$Ph_3$, 3 H, HB($C_3H_3N_2)_3$], 8.17 [d, $^3J_{H,H}$ = 2.1 Hz, 1 H, HB($C_3H_3N_2)_3$] ppm. $^{13}$C{$^1$H} NMR ($CDCl_3$, 100 MHz): $\delta$ = 51.9 (d, $^1J_{C,P}$ = 13.4 Hz, P$CH_2$N), 73.4 (d, $^3J_{C,P}$ = 5.6 Hz, N$CH_2$N), 105.2 [d, $^4J_{C,P}$ = 2.1 Hz, HB($C_3H_3N_2)_3$], 105.7 [d, $^4J_{C,P}$ = 2.1 Hz, HB($C_3H_3N_2)_3$], 105.8 [s, HB($C_3H_3N_2)_3$], 127.5–130.0 (*C* $PPh_3$), 133.4–136.6 (*C* $PPh_3$), 135.3 [s, HB-($C_3H_3N_2)_3$], 135.5 [s, HB($C_3H_3N_2)_3$], 135.9 [s, HB($C_3H_3N_2)_3$], 143.5 [s, HB($C_3H_3N_2)_3$], 144.2 [s, HB($C_3H_3N_2)_3$], 146.6 [s, HB-($C_3H_3N_2)_3$] ppm. $^{31}$P{$^1$H} NMR ($CDCl_3$, 161 MHz): $\delta$ = –34.2 (d, $^2J_{P,P}$ = 33.1 Hz, $P_{PTA}$), 46.9 (d, $^2J_{P,P}$ = 33.1 Hz, $P_{PPh_3}$) ppm.

**Synthesis of [TpRuCl($PTA)_2$] (3). Method A:** Solid PTA (90 mg, 0.57 mmol) was added to a stirred suspension of **1** (200 mg, 0.23 mmol) in 10 mL of toluene, and the reaction mixture was refluxed for 4 h. The resulting yellow precipitate was filtered and washed with diethyl ether (3 × 5 mL) and ethanol (3 × 5 mL) before being dried in vacuo. Yield: 128 mg (84%). **Method B:** Solid PTA was added (20 mg, 0.13 mmol) to a yellow solution of **2** (100 mg, 0.13 mmol) in hot toluene (10 mL), and the reaction mixture was stirred and refluxed for 3 h. The resulting yellow precipitate was filtered and washed with diethyl ether (3 × 5 mL) and ethanol (3 × 5 mL) before being dried in vacuo. Yield: 71 mg (83%). $S_{25\,°C}$ = 18 mg mL$^{-1}$. $C_{21}H_{34}BClN_{12}P_2Ru$ (663.87): calcd. C 37.99, H 5.16, N 25.32; found C 37.96, H 5.19, N 25.21. IR [KBr pellets]: $\nu_{BH}$ 2508 cm$^{-1}$ (w). $^1$H NMR ($CDCl_3$, 400 MHz): $\delta$ = 4.13 (s, 12 H, PC$H_2$N), 4.44, 4.54 (AB system, $^2J_{AB}$ = 14.0 Hz, 12 H, NC$H_2$N), 6.19 [br., $^3J_{H,H}$ = 2.4 Hz, 3 H, HB($C_3H_3N_2)_3$], 7.13 [d, $^3J_{H,H}$ = 1.5 Hz, 1 H, HB($C_3H_3N_2)_3$], 7.62 [d, $^3J_{H,H}$ = 2.1 Hz, 2 H, HB($C_3H_3N_2)_3$], 7.72 [d, $^3J_{H,H}$ = 2.3 Hz, 1 H, HB($C_3H_3N_2)_3$], 7.92 [d, $^3J_{H,H}$ = 1.7 Hz, 2 H, HB($C_3H_3N_2)_3$] ppm. $^{13}$C{$^1$H} NMR ($CDCl_3$, 100 MHz): $\delta$ = 53.9 (d, $^1J_{C,P}$ = 7.1 Hz, P$CH_2$N), 73.4 (d, $^3J_{C,P}$ = 3.2 Hz, N$CH_2$N), 105.8, 106.3, 135.4, 136.7, 143.2, 146.9 [all s, HB($C_3H_3N_2)_3$] ppm. $^{31}$P{$^1$H} NMR ($CDCl_3$, 161 MHz): $\delta$ = –28.3 ppm (s); ($D_2O$, 161 MHz): $\delta$ = –26.1 ppm (s).

**Synthesis of [TpRuCl($PPh_3$){PTA($BH_3$)}] (4). Method A:** Solid PTA($BH_3$) (97 mg, 0.57 mmol) was added to a stirred suspension of **1** (500 mg, 0.57 mmol) in 15 mL of toluene, and the reaction mixture was gently refluxed for 40 min. The yellow solution was filtered through Celite while hot, and the yellow filtrate was concentrated under vacuum to about 4 mL. Addition of diethyl ether (5 mL) gave **4** as a yellow microcrystalline solid, which was filtered and washed with diethyl ether (3 × 10 mL) before being dried in vacuo. Yield: 295 mg (66%). **Method B:** $BH_3$·thf was added with a syringe (0.4 mL, 0.4 mmol) to a suspension of **2** (300 mg, 0.39 mmol) in 20 mL of thf. The yellowish mixture was stirred at room temperature for 1 h before being filtered through Celite. The filtrate was concentrated under vacuum to about 4 mL, and diethyl ether (5 mL) was added to give a yellow solid, which was washed with diethyl ether (3 × 5 mL) and ethanol (3 × 5 mL) before being dried in vacuo. Yield: 262 mg (86%). $C_{33}H_{40}B_2ClN_9P_2Ru$ (782.83): calcd. C 50.63, H 5.15, N 16.10; found C 50.59, H 5.21, N 16.03. IR (KBr pellet): $\nu_{BH(Tp)}$ = 2478 cm$^{-1}$ (m); $\nu_{BH\{PTA(BH_3)\}}$ = 2364 (s), 2314 (m), 2267 (m). $^1$H NMR ($CDCl_3$, 400 MHz): $\delta$ = 0.90–1.44

 © 2007 Wiley-VCH Verlag GmbH & Co. KGaA, Weinheim 

(br., 3 H, B$H_3$), 3.35–4.50 (m, 12 H, C$H_{2\{PTA(BH_3)\}}$), 5.78 [br. s, 1 H, HB($C_3H_3N_2$)$_3$], 5.80 [br. s, 1 H, HB($C_3H_3N_2$)$_3$], 6.21 [br. s, 1 H, HB($C_3H_3N_2$)$_3$], 6.63 [br. s, 1 H, HB($C_3H_3N_2$)$_3$], 7.21–7.50 (m, 15 H, P$Ph_3$), 7.62 [br. s, 2 H, HB($C_3H_3N_2$)$_3$], 7.65 [d, $^3J_{H,H}$ = 2.1 Hz, 1 H, HB($C_3H_3N_2$)$_3$], 8.09 [br. s, 1 H, HB($C_3H_3N_2$)$_3$] ppm. $^{13}C\{^1H\}$ NMR ($CDCl_3$, 100 MHz): $\delta$ = 49.1 (d, $^1J_{C,P}$ = 15.5 Hz, P$CH_2$N), 49.7 (d, $^1J_{C,P}$ = 14.8 Hz, P$CH_2$N), 55.2 (d, $^1J_{C,P}$ = 10.6 Hz, P$CH_2$N), 71.1 (d, $^3J_{C,P}$ = 5.6 Hz, N$CH_2$N), 77.7 (N$CH_2$N; partially masked by the $CDCl_3$ resonance), 105.6 [d, $^4J_{C,P}$ = 2.1 Hz, HB($C_3H_3N_2$)$_3$], 105.8 [d, $^4J_{C,P}$ = 2.1 Hz, HB($C_3H_3N_2$)$_3$], 106.3 [s, HB($C_3H_3N_2$)$_3$], 128.0–135.0 (*C* PPh$_3$), 135.7 [s, HB($C_3H_3N_2$)$_3$], 135.8 [s, HB($C_3H_3N_2$)$_3$], 136.4 [s, HB($C_3H_3N_2$)$_3$], 143.8 [s, HB($C_3H_3N_2$)$_3$], 144.3 [s, HB($C_3H_3N_2$)$_3$], 147.0 [s, HB($C_3H_3N_2$)$_3$] ppm. $^{31}P\{^1H\}$ NMR ($CDCl_3$, 161 MHz): $\delta$ = –25.34 (d, $^2J_{P,P}$ = 32.6 Hz, $P_{PTA(BH_3)}$), 43.98 (d, $^2J_{P,P}$ = 32.6 Hz, $P_{PPh_3}$) ppm.

**Synthesis of [TpRuCl{PTA(BH$_3$)}$_2$] (5). Method A:** Solid PTA(BH$_3$) (49 mg, 0.29 mmol) was added to a stirred suspension of **1** (100 mg, 0.11 mmol) in 10 mL of toluene, and the mixture was heated to reflux for 4 h. Workup as described above gave a yellow precipitate, which was collected by filtration through a sintered glass frit and washed with diethyl ether (3 × 5 mL) before being dried in vacuo. Yield: 50 mg (57%). **Method B:** 3 equiv. of BH$_3$·thf (0.4 mL, 0.4 mmol) was added with a syringe to a yellow suspension of **3** (100 mg, 0.15 mmol) in thf (15 mL) whilst stirring. The mixture was stirred at room temperature for 1 h. After removing the volatiles in vacuo, the resulting yellowish solid was washed with diethyl ether (3 × 5 mL) and dried in vacuo. Yield: 81 mg (75%). $C_{21}H_{40}B_3ClN_{12}P_2Ru$ (721.5): calcd. C 36.47, H 5.83, N 24.31; found C 36.25, H 5.85, N 24.39. IR (KBr pellet): $\nu_{BH(Tp)}$ = 2482 cm$^{-1}$ (m); $\nu_{BH\{PTA(BH_3)\}}$ = 2376 (s), 2318 (m), 2275 (m). $^1H$ NMR ([D$_6$]dmso, 400 MHz): $\delta$ = 0.74–1.54 (br., 6 H, B$H_3$), 3.29–4.46 (m, 24 H, C$H_{2\{PTA(BH_3)\}}$), 6.29 [d, $^3J_{H,H}$ = 2.3 Hz, 3 H, HB($C_3H_3N_2$)$_3$], 7.53 [d, $^3J_{H,H}$ = 1.5 Hz, 1 H, HB($C_3H_3N_2$)$_3$], 7.86 [d, $^3J_{H,H}$ = 2.2 Hz, 2 H, HB($C_3H_3N_2$)$_3$], 7.94 [br. s, 3H HB($C_3H_3N_2$)$_3$] ppm. $^{13}C\{^1H\}$ NMR ([D$_6$]dmso, 100 MHz): $\delta$ = 49.5 (d, $^1J_{C,P}$ = 7.4 Hz, P$CH_2$N), 55.2 (d, $^1J_{C,P}$ = 6.4 Hz, P$CH_2$N), 69.4 (br. s, N$CH_2$N), 76.4 (br. s, N$CH_2$N), 105.6 (s, 2 C), 106.9 (s, 1 C), 135.5 (s, 2 C), 137.0 (s, 2 C), 143.3 (s, 1 C), 148.0 [s, 1 C, HB($C_3H_3N_2$)$_3$] ppm. $^{31}P\{^1H\}$ NMR ([D$_6$]dmso, 161 MHz): $\delta$ = –19.5 ppm (s).

**Synthesis of [TpRuH(PPh$_3$)(PTA)] (6):** Solid **2** (200 mg, 0.26 mmol) was added in small portions to a vigorously stirred solution of sodium methoxide prepared by dissolving sodium (30 mg, 1.3 mmol) in 40 mL of methanol, and the reaction mixture was stirred at room temperature for 1.5 h. The mixture was then filtered through Celite to give a yellow solution, which was reduced under vacuum and worked up as above. The yellow solid obtained was washed with ethanol (3 × 5 mL). Yield (90 mg, 47%). $S_{25\,°C}$ = 2.0 mg mL$^{-1}$. $C_{33}H_{38}BN_9P_2Ru$ (734.55): calcd. C 53.96, H 5.21, N 17.16; found C 53.92, H 5.18, N 17.05. IR (KBr pellet): $\nu_{BH}$ = 2456 cm$^{-1}$ (m); $\nu_{RuH}$ = 1920 (w). $^1H$ NMR ($CD_2Cl_2$, 400 MHz): $\delta$ = –14.89 (dd, $^2J_{H,P}$ = 31.2, $^2J_{H,P}$ = 25.4 Hz, 1 H, Ru*H*), 3.35–3.70 (m, 6 H, PC$H_2$N), 4.00–4.31 (m, NC$H_2$N, 6 H), 5.55 [t, $^3J_{H,H}$ = 1.9 Hz, 1 H, HB($C_3H_3N_2$)$_3$], 6.10 [t, $^3J_{H,H}$ = 1.9 Hz, 1 H, HB($C_3H_3N_2$)$_3$], 6.15 [t, $^3J_{H,H}$ = 1.90 Hz, 1 H, HB($C_3H_3N_2$)$_3$], 6.37 [br. s, 1 H, HB($C_3H_3N_2$)$_3$], 7.16–7.41 [m, 15 H, P$Ph_3$, 1 H, HB($C_3H_3N_2$)$_3$], 7.51 [d, $^3J_{H,H}$ = 2.2 Hz, 1 H, HB($C_3H_3N_2$)$_3$], 7.61 [d, $^3J_{H,H}$ = 2.2 Hz, 1 H, HB($C_3H_3N_2$)$_3$], 7.76 [s, 1 H, HB($C_3H_3N_2$)$_3$], 7.83 [d, $^3J_{H,H}$ = 2.2 Hz, 1 H, HB($C_3H_3N_2$)$_3$] ppm. $^{13}C\{^1H\}$ NMR ($CD_2Cl_2$, 100 MHz): $\delta$ = 55.6 (d, $^1J_{C,P}$ = 13.4 Hz, P$CH_2$N), 73.3 (d, $^3J_{C,P}$ = 5.6 Hz, N$CH_2$N), 104.5 [d, $^4J_{C,P}$ = 2.1 Hz, HB($C_3H_3N_2$)$_3$], 104.9 [d, $^4J_{C,P}$ = 2.1 Hz, HB($C_3H_3N_2$)$_3$], 105.2 [s, HB($C_3H_3N_2$)$_3$], 127.4–134.7 (*C* PPh$_3$), 134.8 [s, HB($C_3H_3N_2$)$_3$], 135.1 [s, HB($C_3H_3N_2$)$_3$], 135.3 [s, HB($C_3H_3N_2$)$_3$], 144.7 [s, HB($C_3H_3N_2$)$_3$], 145.4 [s, HB($C_3H_3N_2$)$_3$], 147.5 [d, $^4J_{C,P}$ = 2.8 Hz, HB($C_3H_3N_2$)$_3$] ppm. $^{31}P\{^1H\}$ NMR ($CDCl_2$, 161 MHz): $\delta$ = –24.4 (d, $^2J_{P,P}$ = 34.7 Hz, $P_{PTA}$), 69.5 (d, $^2J_{P,P}$ = 34.7 Hz, $P_{PPh_3}$) ppm.

**Synthesis of [TpRuH(PTA)$_2$] (7):** Solid PTA (32 mg, 0.20 mmol) was added to a solution of **6** (150 mg, 0.20 mmol) in 10 mL of warm toluene, and the mixture was refluxed for 2 h before being filtered through Celite while hot. Workup of the yellow filtered solution as described above gave the hydride **7** as a yellow precipitate, which was collected by filtration through a sintered glass frit and washed with diethyl ether (3 × 5 mL) and ethanol (3 × 5 mL) before being dried in vacuo. Yield: 40 mg (40%). $S_{25\,°C}$ = 21 mg mL$^{-1}$. $C_{21}H_{35}BN_{12}P_2Ru$ (629.42): calcd. C 40.07, H 5.60, N 26.70; found C 39.92, H 5.55, N 26.63. IR (KBr pellet): $\nu_{BH}$ = 2464 cm$^{-1}$ (w); $\nu_{RuH}$ = 1866 (w). $^1H$ NMR ($CD_2Cl_2$, 400 MHz): $\delta$ = –15.96 (t, $^2J_{P,H}$ = 30.6 Hz, 1 H, Ru*H*), 3.75, 3.89 (AB system, $^2J_{AB}$ = 15.0 Hz, 12 H, PC$H_2$N), 4.31, 4.40 (AB system, $^2J_{AB}$ = 13.0 Hz, 12 H, NC$H_2$N), 6.08 [br. s, 2 H, HB($C_3H_3N_2$)$_3$], 6.26 [br. s, 1 H, HB($C_3H_3N_2$)$_3$], 7.53 [br. s, 1 H, HB($C_3H_3N_2$)$_3$], 7.57 [br. s, 2 H, HB($C_3H_3N_2$)$_3$], 7.63 [br. s, 2 H, HB($C_3H_3N_2$)$_3$], 7.75 [br. s, 1 H, HB($C_3H_3N_2$)$_3$] ppm. $^{31}P\{^1H\}$ NMR ($CD_2Cl_2$, 161 MHz): $\delta$ = –16.8 (s) ppm.

**Synthesis of [TpRuH(PPh$_3$){[PTA(BH$_3$)}] (8):** A slight excess of BH$_3$·thf (0.2 mL, 0.2 mmol) was added with a syringe to a yellow suspension of **6** (100 mg, 0.14 mmol) in 10 mL of thf and the mixture was stirred at room temperature for 1 h. The resulting solution was filtered through Celite to remove impurities and the filtrate was concentrated to dryness under vacuum. The yellow solid obtained was washed with diethyl ether (3 × 5 mL) and ethanol (3 × 5 mL) before being dried under vacuum. Yield: 58 mg (55%). $C_{33}H_{41}B_2N_9P_2Ru$ (748.39): calcd. C 57.96, H 5.52, N 16.84; found C 57.89, H 5.62, N 16.79. IR (KBr pellet): $\nu_{BH(Tp)}$ = 2464 cm$^{-1}$ (w); $\nu_{BH\{PTA(BH_3)\}}$ = 2368 (m), 2319 (m), 2271 (w); $\nu_{RuH}$ = 1940 (m). $^1H$ NMR ($CD_2Cl_2$, 400 MHz): $\delta$ = –14.58 (dd, $^2J_{H,P}$ = 32.5, $^2J_{H,P}$ = 24.6 Hz, 1 H, Ru*H*), 0.60–1.59 (br., 3 H, B$H_3$), 3.03–4.17 (m, 12 H, C$H_2$), 5.58 [br. s, 1 H, HB($C_3H_3N_2$)$_3$], 6.11 [br. s, 1 H, HB($C_3H_3N_2$)$_3$], 6.19 [br. s, 1 H, HB($C_3H_3N_2$)$_3$], 6.40 [br. s, 1 H, HB($C_3H_3N_2$)$_3$], 7.15–7.40 [m, 15 H, P$Ph_3$, 1 H, HB($C_3H_3N_2$)$_3$], 7.53 [d, $^3J_{H,H}$ = 2.0 Hz, 1 H, HB($C_3H_3N_2$)$_3$], 7.63 [d, $^3J_{H,H}$ = 2.0 Hz, 1 H, HB($C_3H_3N_2$)$_3$], 7.71 [br. s, 1 H, HB($C_3H_3N_2$)$_3$], 7.87 [d, $^3J_{H,H}$ = 2.0 Hz, 1 H, HB($C_3H_3N_2$)$_3$] ppm. $^{31}P\{^1H\}$ NMR ($CD_2Cl_2$, 161 MHz): $\delta$ = –15.7 (d, $^2J_{P,P}$ = 35.6 Hz, $P_{PTA(BH_3)}$), 68.6 (d, $^2J_{P,P}$ = 35.6 Hz, $P_{PPh_3}$) ppm.

**Electrochemical Studies:** The electrochemical experiments were performed with an EG&G PAR 273A potentiostat/galvanostat connected to a computer through a GPIB interface. Cyclic voltammograms were obtained for 0.2 M solutions of [Bu$_4$N][BF$_4$] in MeCN or dmso at a platinum disc working electrode (0.5 mm diameter) probed by a Luggin capillary connected to a silver wire pseudo-reference electrode; a Pt auxiliary electrode was also employed. Controlled-potential electrolyses (CPE) were carried out in electrolyte solutions with the above-mentioned composition in a two-compartment, three-electrode cell separated by a glass frit and equipped with platinum gauze working and counter electrodes. A Luggin capillary, probing the working electrode, was connected to a silver wire pseudo-reference electrode. The CPE experiments were monitored regularly by cyclic voltammetry (CV), thus assuring that no significant potential drift occurred during the electrolyses. The electrochemical experiments were performed under $N_2$ at room temperature. The potentials of the complexes were measured by CV in the presence of the couple [Fe($\eta^5$-$C_5H_5$)$_2$]$^{0/+}$ as the internal standard ($E_{1/2}^{ox}$ = 0.45 V vs. SCE both in MeCN and dmso)[38] and the

 © 2007 Wiley-VCH Verlag GmbH & Co. KGaA, Weinheim 

Table 4. Crystal data and structure refinement.

| | **2** | **3** |
|---|---|---|
| Empirical formula | $C_{66}H_{74}B_2Cl_2N_{18}P_4Ru_2$ | $C_{21}H_{34}BClN_{12}P_2Ru$ |
| Formula mass | 1537.97 | 663.87 |
| Temperature [K] | 293(2) | 293(2) |
| Wavelength [Å] | 0.71073 | 0.71073 |
| Crystal system | triclinic | orthorhombic |
| Space group | $P\bar{1}$ | *Pnma* |
| *a* [Å] | 10.1826(11) | 19.135(2) |
| *b* [Å] | 20.161(2) | 15.873(2) |
| *c* [Å] | 22.728(3) | 10.7859(13) |
| *α* [°] | 95.022(2) | 90 |
| *β* [°] | 101.080(2) | 90 |
| *γ* [°] | 90.104(3) | 90 |
| *V* [Å$^3$] | 4560.5(9) | 3275.9(7) |
| *Z* | 2 | 4 |
| $D_{calcd.}$ [Mg m$^{-3}$] | 1.120 | 1.346 |
| Absorption coefficient [mm$^{-1}$] | 0.502 | 0.689 |
| *F*(000) | 1576 | 1360 |
| Crystal size [mm] | 0.25 × 0.45 × 0.48 | 0.48 × 0.47 × 0.35 |
| θ range for data collection [°] | 1.30–28.09 | 2.13–28.01 |
| Index ranges | $-11 \le h \le 13$; $-22 \le k \le 26$; $-29 \le l \le 29$ | $-24 \le h \le 22$; $-13 \le k \le 20$; $-14 \le l \le 14$ |
| Reflections collected | 22493 | 16403 |
| Independent reflections | 16330 [*R*(int) = 0.0701] | 3907 [*R*(int) = 0.0644] |
| Reflections observed [$I > 2\sigma(I)$] | 6854 | 2754 |
| Data completeness | 0.734 | 0.953 |
| Absorption correction | SADABS | SADABS |
| Max/min transmission | 1.0000/0.8263 | 1.000/0.604 |
| Refinement method | Full-matrix least squares on $F^2$ | Full-matrix least squares on $F^2$ |
| Data/restraints/parameters | 16330/0/847 | 3907/0/184 |
| Goodness-of-fit on $F^2$ | 0.842 | 1.012 |
| Final *R* indices [$I > 2\sigma(I)$] | $R_1$ = 0.0737 $wR_2$ = 0.1496 | $R_1$ = 0.0524 $wR_2$ = 0.1302 |
| *R* indices (all data) | $R_1$ = 0.1376 $wR_2$ = 0.1785 | $R_1$ = 0.0779 $wR_2$ = 0.1370 |
| Largest diff. peak/hole [e Å$^{-3}$] | 1.333/–1.846 | 1.105/–1.218 |

redox potential values are normally quoted relative to the SCE. However, for the application of the Lever equation [Equation (1)] they were converted to V vs. NHE by adding 0.245 V.

**Crystallographic Studies:** Data were collected with a Siemens Smart CCD area-detector diffractometer with graphite-monochromated Mo-$K_\alpha$ radiation. Absorption correction was carried out using SADABS.[39] The crystallographic calculations were performed with the Oscail program.[40] The structures were solved by Patterson methods and refined by a full-matrix least-squares procedure based on $F^2$.[41] Non-hydrogen atoms were refined with anisotropic displacement parameters. Hydrogen atoms were included in idealised positions and refined with isotropic displacement parameters. In both cases the Squeeze program[42] was used to correct the reflection data for diffuse scattering due to disordered solvent. Atomic scattering factors and anomalous dispersion corrections for all atoms were taken from the International Tables for X-ray Crystallography.[43] Further details of crystal data and structural refinement are given in Table 4. CCDC-651193 (**2**) and -651192 (**3**) contain the supplementary crystallographic data for this paper. These data can be obtained free of charge from The Cambridge Crystallographic Data Centre via www.ccdc.cam.ac.uk/data_request/cif.

## Acknowledgments

The authors would like to thank the EC for promoting this scientific activity through the FP6 Research Training Network AQUACHEM (contract MCRTN-2003-503864). Thanks are also expressed to "Firenze Hydrolab", a project sponsored by a Ente Cassa di Risparmio di Firenze, and to the Fundação para a Ciência e a Tecnologia (Portugal) and its POCI 2010 programme (FEDER funded), for financial support. S. B. thanks the Xunta de Galicia for a Parga Pondal contract. M. R.-R. thanks the Xunta de Galicia for a postgraduate grant.

[1] a) R. H. Crabtree, *The Organometallic Chemistry of the Transition Metals*, 2nd ed., J. Wiley, New York, **1994**; b) G. O. Spessard, G. L. Miessler, *Organometallic Chemistry*, Prentice-Hall, Upper Saddle River, NJ, **1997**.

[2] S. Trofimenko, *Chem. Rev.* **1993**, *93*, 943–980, and references cited therein.

[3] C. Slugovc, R. Schmid, K. Kirchner, *Coord. Chem. Rev.* **1999**, *185/186*, 109–126.

[4] a) C. Gemel, G. Trimmel, C. Slugovc, S. Kremel, K. Mereiter, R. Schmid, K. Kirchner, *Organometallics* **1996**, *15*, 3998–4004; b) C. Gemel, P. Wiede, K. Mereiter, V. N. Sapunov, R. Schmid, K. Kirchner, *J. Chem. Soc. Dalton Trans.* **1996**, 4071–4076; c) G. Trimmel, C. Slugovc, P. Wiede, K. Mereiter, V. N. Sapunov, R. Schmid, K. Kirchner, *Inorg. Chem.* **1997**, *36*, 1076–1083; d) C. Slugovc, P. Wiede, K. Mereiter, R. Schmid, K. Kirchner, *Organometallics* **1997**, *16*, 2768–2769; e) F. A. Jalón, A. Otero, A. Rodríguez, *J. Chem. Soc. Dalton Trans.* **1995**, 1629–1633.

[5] C. Slugovc, D. Doberer, C. Gemel, R. Schmid, K. Kirchner, B. Winkler, F. Stelzer, *Monatsh. Chem.* **1998**, *129*, 221–233.

[6] a) N. W. Alcock, I. D. Burns, K. S. Claire, A. F. Hill, *Inorg. Chem.* **1992**, *31*, 2906–2908; b) C. Gemel, G. Kickelbick, R. Schmid, K. Kirchner, *J. Chem. Soc. Dalton Trans.* **1997**, 2113–2117; c) C. Slugovc, V. Sapunov, P. Wiede, K. Mereiter, R. Schmid, K. Kirchner, *J. Chem. Soc. Dalton Trans.* **1997**, 4209–4216; d) N.-Y. Sun, S. J. Simpson, *J. Organomet. Chem.* **1992**, *434*, 341–349; e) W.-C. Chan, C.-P. Lau, Y.-Z. Chen, Y.-Q. Fang, S.-M. Ng, G. Jia, *Organometallics* **1997**, *16*, 34–44; f)

 © 2007 Wiley-VCH Verlag GmbH & Co. KGaA, Weinheim 

M. A. Halcrow, B. Chaudret, S. Trofimenko, *J. Chem. Soc. Chem. Commun.* **1993**, 465–467; g) B. Moreno, S. Sabo-Etienne, B. Chaudret, A. Rodríguez-Fernández, F. A. Jalón, S. Trofimenko, *J. Am. Chem. Soc.* **1995**, *117*, 7441–7451; h) M. Jiménez-Tenorio, M. A. Jiménez Tenorio, M. C. Puerta, P. Valerga, *Inorg. Chim. Acta* **1997**, *259*, 77–84.

[7] C. Slugovc, K. Mereiter, E. Zobetz, R. Schmid, K. Kirchner, *Organometallics* **1996**, *15*, 5275–5277.

[8] Y. Feng, M. Lail, K. A. Barakat, T. R. Cundari, T. B. Gunnoe, J. L. Petersen, *J. Am. Chem. Soc.* **2005**, *127*, 14174–14175.

[9] a) M. Lail, B. N. Arrowood, T. B. Gunnoe, *J. Am. Chem. Soc.* **2003**, *125*, 7506–7507; b) K. A. Pittard, J. P. Lee, T. R. Cundari, T. B. Gunnoe, J. L. Petersen, *Organometallics* **2004**, *23*, 5514–5523; c) M. Lail, C. M. Bell, D. Conner, T. R. Cundari, T. B. Gunnoe, J. L. Petersen, *Organometallics* **2004**, *23*, 5007–5020; d) N. A. Foley, M. Lail, T. B. Gunnoe, T. R. Cundari, J. L. Petersen, *J. Am. Chem. Soc.* **2007**, *129*, 6765–6781.

[10] J. P. Lee, K. A. Pittard, T. R. Cundari, T. B. Gunnoe, J. L. Petersen, *Organometallics* **2006**, *25*, 1500–1510.

[11] W. K. Fung, X. Huang, M. L. Man, S. M. Ng, M. Y. Hung, Z. Lin, C. P. Lau, *J. Am. Chem. Soc.* **2003**, *125*, 11539–11544.

[12] a) S. Trofimenko, *J. Am. Chem. Soc.* **1966**, *88*, 1842–1844; b) S. Trofimenko, *J. Am. Chem. Soc.* **1967**, *89*, 3904–3905; c) S. Trofimenko, *Chem. Rev.* **1972**, *72*, 497–509.

[13] For reviews on the chemistry of $[CpRuCl(PPh_3)_2]$ and derivatives, see: a) M. A. Bennett, K. Khan, E. Wenger, *Comprehensive Organometallic Chemistry II*, vol. 7 (Eds.: E. W. Abel, F. G. A. Stone, G. Wilkinson), Pergamon, Oxford, **1995**; b) S. G. Davies, J. P. McNally, A. J. Smallridge, *Adv. Organomet. Chem.* **1990**, *30*, 1–76.

[14] See, for example: E. Clot, O. Eisenstein, W. D. Jones, *Proc. Natl. Acad. Sci.* **2007**, *104*, 6939–6944.

[15] A. D. Phillips, L. Gonsalvi, A. Romerosa, F. Vizza, M. Peruzzini, *Coord. Chem. Rev.* **2004**, *248*, 955–993.

[16] a) S. Bolaño, A. Albinati, J. Bravo, L. Gonsalvi, M. Peruzzini, *Inorg. Chem. Commun.* **2006**, *4*, 360–363; b) *N*-boronation of PTA has also been reported by Frost et al.: B. J. Frost, C. A. Mebi, P. J. Gingrich, *Eur. J. Inorg. Chem.* **2006**, 1182–1189.

[17] Water-soluble complexes of the related tripodal tris(pyrazolyl) methanesulfonate ligand ($SO_3Cpz_3$) are known. See, for example: E. C. Alegria, L. M. Martins, M. Haukka, A. J. Pombeiro, *Dalton Trans.* **2006**, 4954–4961.

[18] C. Scolaro, A. Bergamo, L. Brescacin, R. Delfino, M. Cocchietto, G. Laurenczy, T. J. Geldbach, G. Sava, P. J. Dyson, *J. Med. Chem.* **2005**, *48*, 4161–4171.

[19] C. Lidrissi, A. Romerosa, M. Saoud, M. Serrano-Ruiz, L. Gonsalvi, M. Peruzzini, *Angew. Chem. Int. Ed.* **2005**, *44*, 2568–2572.

[20] See, for example: G. Albertin, S. Antoniutti, M. Bortoluzzi, J. Castro-Fojo, S. García-Fontán, *Inorg. Chem.* **2004**, *43*, 4511–4522, and references cited therein.

[21] a) D. N. Akbayeva, L. Gonsalvi, W. Oberhauser, M. Peruzzini, F. Vizza, P. Brueggeller, A. Romerosa, G. Sava, A. Bergamo, *Chem. Commun.* **2003**, 264–265; b) B. Buriez, I. D. Burns, A. F. Hill, A. J. P. White, D. J. Williams, J. D. E. T. Wilton-Ely, *Organometallics* **1999**, *18*, 1504–1516; c) C. Slugovc, K. Mauthner, M. Kacetl, K. Mereiter, R. Schmid, K. Kirchner, *Chem. Eur. J.* **1998**, *4*, 2043–2050; d) C. Slugovc, V. N. Sapunov, P. Wiede, K. Mereiter, R. Schmid, K. Kirchner, *J. Chem. Soc. Dalton Trans.* **1997**, 4209–4216; e) D. C. Wilson, J. H. Nelson, *J. Organomet. Chem.* **2003**, *682*, 272–289; f) S. Hartmann, R. F. Winter, B. M. Brunner, B. Sarkar, A. Knodler, I. Hartenbach, *Eur. J. Inorg. Chem.* **2003**, 876–891; g) S. Pavlik, C. Gemel, C. Slugovc, K. Mereiter, R. Schmid, K. Kirchner, *J. Organomet. Chem.* **2001**, *617/618*, 301–310; h) S. Pavlik, K. Mereiter, M. Puchberger, K. Kirchner, *J. Organomet. Chem.* **2005**, *690*, 5497–5507; i) S. Pavlik, K. Mereiter, M. Puchberger, K. Kirchner, *Organometallics* **2005**, *24*, 3561–3575; j) S. Pavlik, M. Puchberger, K. Mereiter, K. Kirchner, *Eur. J. Inorg. Chem.* **2006**, 4137–4142; k) Y. Takahashi, M. Akita, S. Hikichi, Y. Moro-oka, *Inorg. Chem.* **1998**, *37*, 3186–3194.

[22] a) C. A. Mebi, R. P. Nair, B. J. Frost, *Organometallics* **2007**, *26*, 429–438; b) A. Romerosa, T. Campos-Malpartida, C. Lidrissi, M. Saoud, M. Serrano-Ruiz, M. Peruzzini, J. A. Garrido-Cárdenas, F. García-Maroto, *Inorg. Chem.* **2006**, *45*, 1289–1298; c) C. A. Mebi, B. J. Frost, *Organometallics* **2005**, *242*, 339–346; d) B. J. Frost, C. A. Mebi, *Organometallics* **2004**, *23*, 5317–5323; e) S. Bolaño, L. Gonsalvi, F. Zanobini, F. Vizza, V. Bertolasi, A. Romerosa, M. Peruzzini, *J. Mol. Catal. A* **2004**, *224*, 61–70; f) A. Romerosa, M. Saoud, T. Campos-Malpartida, C. Lidrissi, M. Serrano-Ruiz, M. Peruzzini, J. A. Garrido, F. García-Maroto, *Eur. J. Inorg. Chem.* **2007**, 2803–2812.

[23] C. A. Tolman, *J. Am. Chem. Soc.* **1970**, *92*, 2956–2965.

[24] R. Mejia-Rodriguez, D. Chong, J. H. Reibenspies, M. P. Soriaga, M. Y. Darensbourg, *J. Am. Chem. Soc.* **2004**, *126*, 12004–12014.

[25] V. Gutkin, J. Gun, P. V. Prikhodchenko, O. Lev, L. Gonsalvi, M. Peruzzini, A. Romerosa, T. Campos Malpartida, C. Lidrissi, *J. Electrochem. Soc.* **2007**, *154*, F7–F15.

[26] A. B. P. Lever, *Inorg. Chem.* **1990**, *29*, 1271–1285.

[27] N. A. Bokach, M. Haukka, P. Hirva, M. F. C. Guedes da Silva, V. Yu. Kukushkin, A. J. L. Pombeiro, *J. Organomet. Chem.* **2006**, *691*, 2368–2377.

[28] E. Reisner, V. B. Arion, A. Eichinger, N. Kandler, G. Geister, A. J. L. Pombeiro, B. K. Keppler, *Inorg. Chem.* **2005**, *44*, 6704–6716.

[29] E. Reisner, V. B. Arion, M. F. C. Guedes da Silva, R. Lichtenecker, A. Eichinger, B. K. Keppler, V. Yu. Kukushkin, A. J. L. Pombeiro, *Inorg. Chem.* **2004**, *43*, 7083–7093.

[30] A. J. L. Pombeiro, *Eur. J. Inorg. Chem.* **2007**, 1473–1482.

[31] E. C. B. Alegria, L. M. D. R. S. Martins, M. F. C. Guedes da Silva, A. J. L. Pombeiro, *J. Organomet. Chem.* **2005**, *690*, 1947–1958.

[32] M. F. C. Guedes da Silva, A. J. L. Pombeiro, S. Geremia, E. Zangrando, M. Calligaris, A. V. Zinchenko, V. Yu. Kukushkin, *J. Chem. Soc. Dalton Trans.* **2000**, 1363–1371.

[33] See, for example: a) M. Jiménez-Tenorio, M. D. Palacios, M. C. Puerta, P. Valerga, *Organometallics* **2005**, *24*, 3088–3098; b) M. A. Jiménez Tenorio, M. Jiménez Tenorio, M. C. Puerta, P. Valerga, *J. Chem. Soc. Dalton Trans.* **1998**, 3601–3607.

[34] a) S. Ogo, N. Makihara, Y. Kaneko, Y. Watanabe, *Organometallics* **2001**, *20*, 49034910; b) T. Abura, S. Ogo, Y. Watanabe, S. Fukuzumi, *J. Am. Chem. Soc.* **2003**, *125*, 4149–4154.

[35] For application of PTA complexes in medicinal chemistry, see: a) W. H. Ang, P. J. Dyson, *Eur. J. Inorg. Chem.* **2006**, 4003–4018; b) A. Dorcier, W. H. Ang, S. Bolaño, L. Gonsalvi, L. Juillerat-Jeannerat, G. Laurenczy, M. Peruzzini, A. D. Phillips, F. Zanobini, P. J. Dyson, *Organometallics* **2006**, *25*, 4090–4096 and references cited therein.

[36] D. D. Perrin, W. Armarego, *Purification of Laboratory Chemicals*, 3rd ed. Butterworth and Heinemann, Oxford, **1988**.

[37] a) D. J. Daigle, A. B. Pepperman, G. Boudreaux, *J. Heterocycl. Chem.* **1974**, *11*, 1085–1086; b) D. J. Daigle, *Inorg. Synth.* **1998**, *32*, 40–45.

[38] A. J. L. Pombeiro, M. F. C. Guedes da Silva, M. A. N. D. A. Lemos, *Coord. Chem. Rev.* **2001**, *219–221*, 53–80.

[39] G. M. Sheldrick, *SADABS: An empirical absorption correction program for area detector data*, University of Göttingen, Germany, **1996**.

[40] P. McArdle, *J. Appl. Crystallogr.* **1995**, *28*, 65–67.

[41] G. M. Sheldrick, *SHELX-97: A program for the solution and refinement of crystal structures*, University of Göttingen, Germany, **1997**.

[42] A. L. Spek, *Acta Crystallogr., Sect A* **1990**, *46*, C34–C36.

[43] *International Tables for X-ray Crystallography*, Kluwer, Dordrecht, **1992**, vol. C.

Received: June 29, 2007
Published Online: October 17, 2007

 © 2007 Wiley-VCH Verlag GmbH & Co. KGaA, Weinheim 

DOI: 10.1002/ejic.200700717

# First $Ni^{II}$–$Ln^{III}$ Coordination Polymers Constructed by Using $[Ni(bpca)_2]$ as a Building Block [Hbpca = bis(2-pyridylcarbonyl)amine]: Synthesis, Crystal Structures and Magnetic Properties

**Augustin M. Madalan,[a] Kevin Bernot,[b,c] Fabrice Pointillart,[b] Marius Andruh,*[a] and Andrea Caneschi*[b]**

**Keywords:** Nickel / Lanthanides / Heterobimetallic coordination polymers / Magnetic properties

Three new heterobimetallic 1D coordination polymers have been obtained by assembling the $[Ni(bpca)_2]$ complex, as a building block, with lanthanide cations: $[\{Ln(O_2NO)(H_2O)_3\}\{Ni(bpca)_2\}](NO_3)_2{\cdot}3H_2O$ (Ln Gd **1**; Tb **2**; Dy **3**). The three compounds are isostructural and their structure consists of infinite cationic chains with $Ln^{III}$ ions connected by $[Ni(bpca)_2]$ complexes acting as bridging bis-bidentate ligands. The charge of the chains is counterbalanced by uncoordinated nitrate ions. The $Ln^{III}$ ions display a coordination number of nine: four oxygen atoms from the carbonyl groups of the bpca ligands belonging to two $\{Ni(bpca)_2\}$ moieties, two oxygen atoms from a chelating nitrato ion and three water molecules. The magnetic investigation of the gadolinium derivative **1** revealed very weak intrachain $Ni^{II}$–$Gd^{III}$-ferromagnetic interactions ($\theta$ = +0.15 K). The weak intrachain-exchange interactions, as well as the bad magnetic isolation of the chains in the crystals, preclude the single-chain magnet behaviour of compounds **2** and **3**. The out-of-phase, $\chi''$, signal observed with compounds **2** and **3** can be ascribed to the magnetic slow relaxation of the lanthanide ions ($Tb^{III}$, $Dy^{III}$).

(© Wiley-VCH Verlag GmbH & Co. KGaA, 69451 Weinheim, Germany, 2007)

## Introduction

The interest in the 3d–4f combined coordination chemistry is strongly related to the tremendous development of molecular magnetism.[1] In the early 1990s $Cu^{II}$ and $Gd^{III}$ ions were extensively employed in making heterometallic complexes, because the exchange interaction between the two ions was found to be ferromagnetic in most cases.[2] Numerous $Cu^{II}$–$Ln^{III}$-polynuclear complexes, ranging from discrete entities to coordination polymers with various dimensionalities and network topologies, were synthesized.[3] In spite of the large spin carried by the $Gd^{III}$ ion ($S$ 7/2), the critical temperatures for the classical molecule-based magnets were found to be very low.[4] The main reason for this is the rather weak exchange interaction between $Cu^{II}$ and $Gd^{III}$. More recently, the interest of chemists moved towards lanthanides exhibiting a high anisotropy, as a prerequisite for designing single-molecule magnets (SMMs) and single-chain magnets (SCMs). The best candidates are terbium(III), dysprosium(III) and holmium(III). Indeed, several SMMs based upon 3d and 4f ($Tb^{III}$, $Dy^{III}$, $Ho^{III}$) ions were reported recently.[5] Moreover, it has been shown that even mononuclear $Tb^{III}$ and $Dy^{III}$ complexes fulfil the conditions to exhibit a slow relaxation of the magnetization.[6] Single-chain magnets constructed from anisotropic lanthanides ions are known as well.[7]

Several synthetic strategies are currently employed to obtain 3d–4f complexes:[1,3] (i) self-assembly processes involving metallo-ligands (building-blocks) and assembling $Ln^{3+}$ cations; (ii) the clever use of dissymmetric bi- or tricompartmental ligands, which are able to interact selectively with the two different metal ions; (iii) the employment of preformed 3d–4f complexes as nodes, by connecting them with various spacers; and (iv) one-pot procedures.

The coordination of the bis(2-pyridylcarbonyl)amine anion, $pbca^-$, to various metal ions generates numerous bischelated complexes, $[M^{II}(bpca)_2]$ and $[M^{III}(bpca)_2]^+$, which can act as ligands towards a second metal ion forming oligonuclear complexes[8] and coordination polymers.[9] Mixed valence $Fe^{II}/Fe^{III}$ chains have also been obtained by assembling low-spin $[Fe(bpca)_2]^+$ or similar cations containing methyl-substituted bpca ligands with $Fe^{2+}$ ions. These compounds exhibit single-chain magnetic behaviour.[10]

[a] University of Bucharest, Faculty of Chemistry, Inorganic Chemistry Laboratory,
Str. Dumbrava Rosie nr. 23, 020464 Bucharest, Romania
[b] L.A.M.M., Department of Chemistry and INSTM Research Unit, Università di Firenze,
Via della Lastruccia 3, 50019 Sesto Fiorentino, Italy
[c] Sciences Chimiques de Rennes, UMR 6226 CNRS-INSA Rennes, Equipe Matériaux Inorganiques: Chimie Douce et Réactivité, INSA Rennes,
20 Avenue des Buttes de Coësmes, CS 14315, 35043 Rennes Cedex, France

Supporting information for this article is available on the WWW under http://www.eurjic.org or from the author.

 © 2007 Wiley-VCH Verlag GmbH & Co. KGaA, Weinheim 

Because of their strongly oxophilic character, the lanthanide cations easily interact with the oxygen atoms from the carbonyl groups of the bpca ligands coordinated to the first metal ion to form 3d–4f-heterometallic complexes. In this paper we report on the first one-dimensional coordination polymers constructed from $[Ni(bpca)_2]$ building blocks and $Ln^{3+}$ ions.

## Results and Discussion

### Structures

Three new compounds, with the general formula $[\{Ln(O_2NO)(H_2O)_3\}\{Ni(bpca)_2\}](NO_3)_2{\cdot}3H_2O$, were obtained by self-assembly processes involving neutral $[Ni(bpca)_2]$ building blocks and $Ln^{3+}$ ions (Ln Gd, **1**; Tb, **2**; Dy, **3**). The crystallographic investigation revealed that the three complexes are isostructural (Table 1). Therefore, only the crystal structure of the dysprosium derivative will be described here.

The structure of **3** consists of infinite cationic chains with $Dy^{3+}$ ions connected by $[Ni(bpca)_2]$ complexes acting as bridging bis-bidentate ligands (Figure 1). The charge of the chains is counterbalanced by uncoordinated nitrate ions. The nickel ions are hexacoordinated by the two bpca ligands, as in similar complexes.[9] The Ni–N(amide) distances [2.024(3) and 2.027(3) Å] are slightly shorter than the Ni–N(py) ones [2.110(3), 2.106(3), 2.115(3) and 2.131(3) Å]. So the coordination polyhedron of the nickel ion is slightly compressed.

The dysprosium ion displays a coordination number of nine: four oxygen atoms from the carbonyl groups of the bpca ligands belonging to two $\{Ni(bpca)_2\}$ moieties, two oxygens from a chelating nitrato ion and three water molecules. The Dy–O distances vary between 2.336(3) and 2.481(3) Å. The short distances correspond to the dysprosium–aqua bonds. The distance between the metallic centres within a chain is Dy···Ni 5.865 Å. Other relevant bond lengths are collected in Table 2.

The analysis of the packing diagrams shows that all the chains run along the crystallographic *b* axis. At the supramolecular level, the chains interact through graphite-like π–π contacts (3.38–3.62 Å), which are established between the phenyl rings arising from the bpca ligands from neighbouring chains, resulting in a 3D supramolecular array (Figure 2).

The supramolecular interactions between chains are reinforced by hydrogen-bond networks perpendicular to the direction of the chains. The formation of these hydrogen-bond 2D arrays involves all the coordinated and uncoordinated water molecules and nitrate ions. A detailed view of this network is presented in Figure 3. It is interesting to note that some of the crystallization water molecules self-organize by hydrogen bonds into $(H_2O)_4$ clusters (O2S···O3S···O2S′···O3S′, Figure 3).

Table 1. Crystallographic data, details of data collection and structure refinement parameters for compounds **1**–**3**.

| Compound | **1** | **2** | **3** |
|---|---|---|---|
| Chemical formula | $C_{24}H_{28}GdN_9NiO_{19}$ | $C_{24}H_{28}N_9NiO_{19}Tb$ | $C_{24}H_{28}DyN_9NiO_{19}$ |
| $M$ [g mol$^{-1}$] | 962.48 | 964.15 | 967.73 |
| Temperature [K] | 293(2) | 293(2) | 173(2) |
| Wavelength [Å] | 0.71073 | 0.71073 | 0.71073 |
| Crystal system | monoclinic | monoclinic | monoclinic |
| Space group | $P2_1/c$ | $P2_1/c$ | $P2_1/c$ |
| $a$ [Å] | 9.1179(11) | 9.1261(10) | 9.0747(3) |
| $b$ [Å] | 23.3192(32) | 23.287(2) | 23.3593(7) |
| $c$ [Å] | 16.4804(15) | 16.4972(11) | 16.3107(5) |
| $\alpha$ [°] | 90 | 90 | 90 |
| $\beta$ [°] | 95.350(10) | 95.441(10) | 95.177(2) |
| $\gamma$ [°] | 90 | 90 | 90 |
| $V$ [Å$^3$] | 3488.8(6) | 3490.1(6) | 3443.41(19) |
| $Z$ | 4 | 4 | 4 |
| $D_c$ [g cm$^{-3}$] | 1.808 | 1.812 | 1.867 |
| $F(000)$ | 1868 | 1872 | 1924 |
| $\mu$ [mm$^{-1}$] | 2.515 | 2.642 | 2.795 |
| Goodness-of-fit on $F^2$ | 0.995 | 0.955 | 1.012 |
| Final $R_1$, $wR_2$ [$I > 2\sigma(I)$] | 0.0719, 0.1413 | 0.0520, 0.0947 | 0.0356, 0.0718 |
| $R_1$, $wR_2$ (all data) | 0.1845, 0.1780 | 0.1404, 0.1164 | 0.0647, 0.0810 |

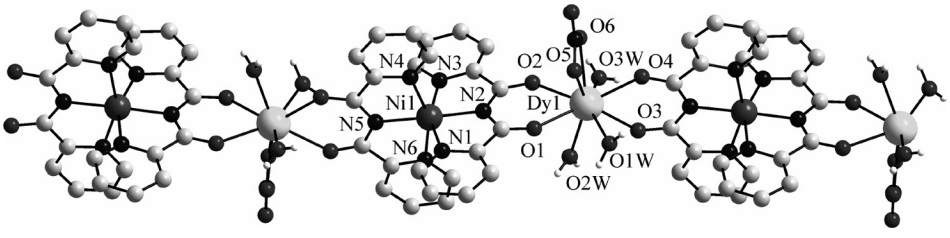


Figure 1. View of a cationic chain in crystal **3**, along with the atom-labelling scheme.

 © 2007 Wiley-VCH Verlag GmbH & Co. KGaA, Weinheim 

Table 2. Selected bond lengths [Å] and angles for compounds **1**–**3**.

| **1** | | **2** | | **3** | |
|---|---|---|---|---|---|
| Ni1–N1 | 2.118(8) | Ni1–N1 | 2.113(4) | Ni1–N1 | 2.110(3) |
| Ni1–N2 | 2.025(7) | Ni1–N2 | 2.023(3) | Ni1–N2 | 2.024(3) |
| Ni1–N3 | 2.110(7) | Ni1–N3 | 2.102(4) | Ni1–N3 | 2.106(3) |
| Ni1–N4 | 2.125(7) | Ni1–N4 | 2.117(4) | Ni1–N4 | 2.115(3) |
| Ni1–N5 | 2.024(7) | Ni1–N5 | 2.028(3) | Ni1–N5 | 2.027(3) |
| Ni1–N6 | 2.126(7) | Ni1–N6 | 2.128(4) | Ni1–N6 | 2.131(3) |
| Gd1–O1 | 2.436(6) | Tb1–O1 | 2.429(3) | Dy1–O1 | 2.406(2) |
| Gd1–O2 | 2.407(6) | Tb1–O2 | 2.398(3) | Dy1–O2 | 2.397(2) |
| Gd1–O3 | 2.429(6) | Tb1–O3 | 2.428(3) | Dy1–O3 | 2.422(2) |
| Gd1–O4 | 2.424(6) | Tb1–O4 | 2.419(3) | Dy1–O4 | 2.404(2) |
| Gd1–O5 | 2.472(8) | Tb1–O5 | 2.460(5) | Dy1–O5 | 2.473(3) |
| Gd1–O6 | 2.494(8) | Tb1–O6 | 2.491(4) | Dy1–O6 | 2.481(3) |
| Gd1–O1W | 2.403(6) | Tb1–O1W | 2.389(3) | Dy1–O1W | 2.349(3) |
| Gd1–O2W | 2.398(7) | Tb1–O2W | 2.386(4) | Dy1–O2W | 2.336(3) |
| Gd1–O3W | 2.394(7) | Tb1–O3W | 2.363(4) | Dy1–O3W | 2.341(3) |

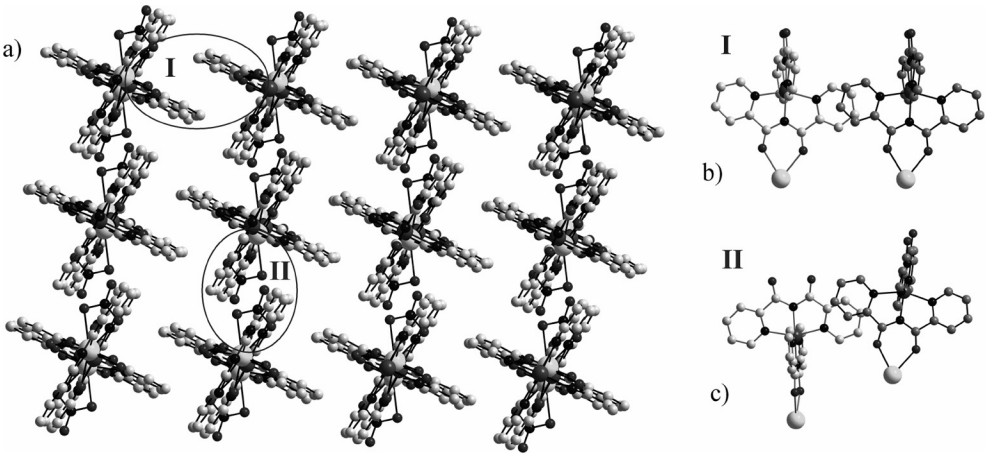


Figure 2. View of the packing diagram in crystal **3** along the *b* axis [(a) the uncoordinated nitrate ions and water molecules were omitted for clarity], and details of the π–π stacking interactions established between the phenyl rings arising from the bpca ligands from neighbouring chains [(b) and (c)].

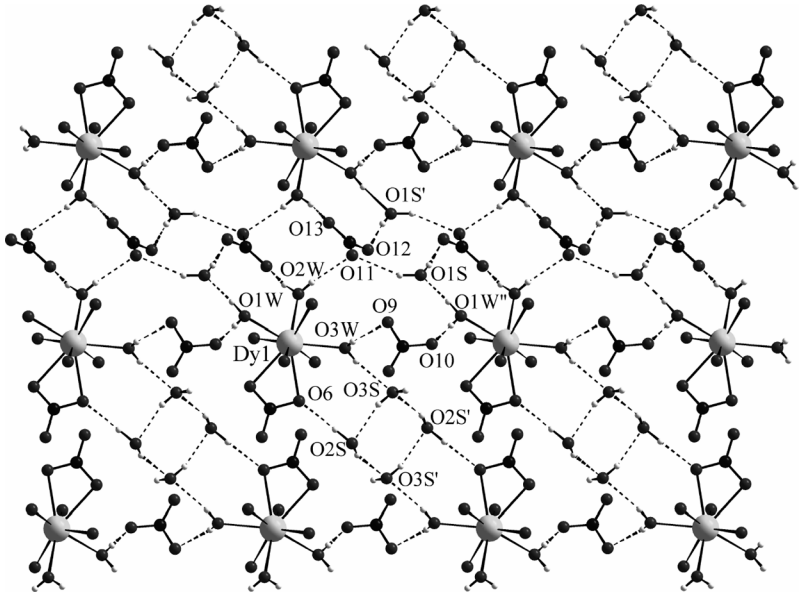


Figure 3. View of the hydrogen-bond network in crystal **3**: O1W–H2W···O1S 1.77(5) Å (*x*, *y*, *z*); O1W–H1W···O10 1.90(5) Å (–1 + *x*, *y*, *z*); O1S–H2S···O11 2.18(5) Å (–1 + *x*, *y*, *z*); O1S–H1S···O12 1.95(6) Å (1 – *x*, 1 – *y*, –*z*); O2W–H3W···O11 2.06(4) Å (*x*, *y*, *z*); O2W–H4W···O13 1.94(5) Å (1 – *x*, 1 – *y*, –*z*); O3W–H6W···O9 2.10(7) Å (*x*, *y*, *z*); O3W–H5W···O3S 2.07(6) Å (*x*, *y*, *z*); O3S–H5S···O2S 1.97(8) Å (*x*, *y*, *z*); O2S–H3S···O6 2.01(8) Å (*x*, *y*, *z*); O2S–H4S···O3S 2.13(4) Å (2 – *x*, 1 – *y*, 1 – *z*).

 © 2007 Wiley-VCH Verlag GmbH & Co. KGaA, Weinheim 

The collective effect of the supramolecular interactions plays a certain role in the magnetic properties of these compounds (vide infra).

### Magnetic Properties

In the present study we focused on the following lanthanides as partners for the nickel(II) ion: gadolinium, terbium, dysprosium. The reasons for this are the following: (i) the nature and magnitude of the $Ni^{II}$–$Gd^{III}$-exchange interaction can, in principle, be easily determined since $Gd^{III}$, with an $^8S_{7/2}$ ground term, has no orbital contribution to the magnetic moment and the Heisenberg–Dirac–Van Vleck Hamiltonian can be employed;[11] and (ii) terbium(III) and dysprosium(III) are expected to bring a strong anisotropy to the magnetic moment and, consequently, one important condition to eventually observe the slow relaxation of the magnetization is fulfilled. The nickel(II) ion itself exhibits an anisotropy as a consequence of the zero-field splitting effects.

These compounds are also potentially very appealing from a dynamic point of view. In fact monodimensional compounds based on both 3d and 4f ions are quite recent[12] and to the best of our knowledge none of these display single-chain magnet (SCM) behaviour. As reminded in the introduction, SCMs based either on 3d or 4f ions are already known, but each of these categories of chains has its own drawbacks.

On the one hand, transition ions are obviously good candidates to build SCMs as they generally give rise to strong magnetic-exchange interactions in the system. Hence $Co^{II}$, $Ni^{II}$, $Mn^{III}$, $Fe^{III}$ based SCMs are known.[13] But these ions are slightly anisotropic and this precludes more spectacular slow relaxation. On the other hand, some of the lanthanide cations such as the $Tb^{III}$ and $Dy^{III}$ are highly anisotropic. As the $g_{//}$ values are very large and the $g_{\perp}$ almost vanished, they can be considered as almost perfect Ising ions. However, the magnetic interaction between the 4f ions is rather weak as their magnetic orbitals are highly shielded by the 5s, 5p and 6s ones. In fact, reported 4f-based SCMs also involve organic radicals providing the required strong intrachain-magnetic interaction. Hence these chains are not strictly based on 4f ions but have to be considered as 2p–4f magnetic chains.[7] Finally, a huge amount of work reports quite strong magnetic-exchange interactions between transition and lanthanide ions in molecular complexes.[1–3] Therefore, combining 3d or 4f ions in the same one-dimensional edifice could offer the possibility to enhance the magnetic slow relaxation process in SCMs.

### Static Magnetic Properties

#### *{[{Gd($O_2$NO)($H_2O$)$_3$}{Ni(bpca)$_2$}]($NO_3$)$_2$·3$H_2O$}$_n$ (1)*

The thermal variation of the $\chi_M T$ product is shown in Figure 4. It has a constant value equal to 8.99 $cm^3\,K\,mol^{-1}$ from 300 to about 70 K and then it increases slightly. Below 25 K, the $\chi_M T$ product decreases rapidly to reach a value of 7.40 $cm^3\,K\,mol^{-1}$ at 3 K. The value of $\chi_M T$ at room temperature (8.99 $cm^3\,K\,mol^{-1}$) is close to the expected value of 8.96 $cm^3\,K\,mol^{-1}$ for the two isolated $Gd^{III}$ ($S$ 7/2, $g$ 2.00) and $Ni^{II}$ ($S$ 1, $g$ 2.08) complexes. The experimental and calculated magnetizations from 0–6 T are shown in Figure 5. The value of the magnetization at 6 T is 8.6 $\mu_B$, close to the expected saturated value of 9 $\mu_B$ for one $Gd^{III}$ and one $Ni^{II}$ ion; even if the curve is not flat. The calculated magnetization is obtained from a classical Brillouin function for two magnetically isolated $Gd^{III}$ ($S$ 7/2, $g$ 2.00) and $Ni^{II}$ ($S$ 1, $g$ 2.08)[9b] ions.

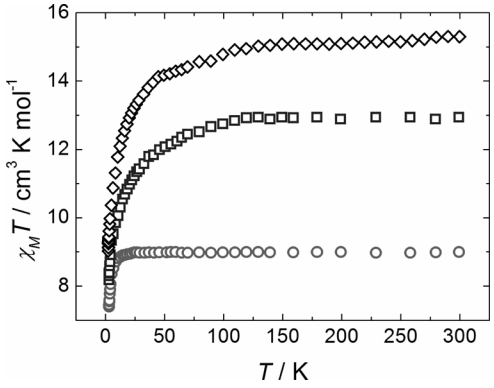


Figure 4. Thermal variation of the $\chi_M T$ product in the temperature range 3–300 K for **1** (gray circles), **2** (dark-gray squares) and **3** (diamonds).

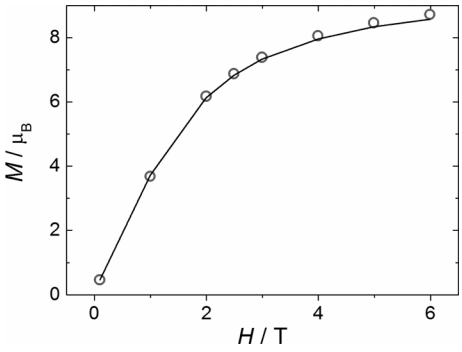


Figure 5. Experimental (gray circles) and calculated Brillouin-function (full black line) magnetizations of **1** over the field range 0–6 T.

The experimental and calculated magnetizations are quasi-superimposed (Figure 5), the magnetic-exchange interaction is indeed supposed to be very weak between the $Ni^{II}$ and $Gd^{III}$ ions through the $bpca^-$ ligand. At high field the calculated magnetization is lower than the experimental one leading to a possible very weak ferromagnetic interaction. The $Gd^{III}$ ion is the only truly isotropic lanthanide ion ($g$ 2.00) and can thus be easily modelled. The ferromagnetic-exchange interaction is confirmed by the weak but positive Curie–Weiss constant $\theta$ +0.15 K, extracted from

 © 2007 Wiley-VCH Verlag GmbH & Co. KGaA, Weinheim 

the fit of the high temperature region of the $\chi^{-1}$ vs. $T$ curve (Figure S1). On the other hand the decrease at low temperatures, out of the fitted region, can be attributed to two phenomena: (i) antiferromagnetic-intermolecular-exchange interactions from the short contacts between two nearest nitrate anions bonded to a $Gd^{III}$ ion leading to the formation of a hydrogen-bond network (Figure 3) and π–π interactions between the phenyl rings of the $bpca^-$ ligands (Figure 2); and (ii) zero-field splitting of the $Ni^{II}$ ions.

### *{[{Tb(O$_2$NO)(H$_2$O)$_3$}{Ni(bpca)$_2$}](NO$_3$)$_2$·3H$_2$O}$_n$ (2) and {[{Dy(O$_2$NO)(H$_2$O)$_3$}{Ni(bpca)$_2$}](NO$_3$)$_2$·3H$_2$O}$_n$ (3)*

The thermal variation of the $\chi_M T$ product and the magnetization curves are shown for the two compounds in Figure 4 and S2, respectively. The values at 300 K are 12.94 $cm^3 K mol^{-1}$ for **2** and 15.30 $cm^3 K mol^{-1}$ for **3**. These experimental values are close to the expected values of 12.90 $cm^3 K mol^{-1}$ and 15.25 $cm^3 K mol^{-1}$, respectively, calculated from the equation $\chi_M T$ $(Ng^2_{Ni}\beta/3k)[S_{Ni}(S_{Ni}+1)]$ + $(Ng^2_{Ln}\beta^2/3k)[J_{Ln}(J_{Ln}+1)]$, with one Ln $Tb^{III}$ ($J$ 6, $g_J$ 3/2) or one Ln $Dy^{III}$ ($J$ 15/2, $g_J$ 4/3)[1a] associated with one $Ni^{II}$ ion ($S$ 1, $g$ 2.08). Both curves show a plateau on cooling until 150 K and then decrease in a monotonous manner. At 3 K the $\chi_M T$ product has a value of 8.30 $cm^3 K mol^{-1}$ and 9.60 $cm^3 K mol^{-1}$ for the $Tb^{III}$ and $Dy^{III}$ derivatives, respectively.

The $Tb^{III}$ ion is a non-Kramer ion having a $^7F_6$ ground state whereas the $Dy^{III}$ ion is a Kramer ion with a $^6H_{15/2}$ ground state.[11] Including them in a one-dimensional compound is of interest as it brings great anisotropy to the system and can give rise to SCM behaviour.[7] However, the fitting of the magnetic data of such a sample is complicated by the strong spin-orbit coupling affecting the lanthanide ions. In particular, the ground state is split into Stark sublevels under the influence of the crystal field.[1b] The crystal-field effects are of the order of 100 $cm^{-1}$ for lanthanides. Consequently when the temperature decreases, the depopulation of these sublevels leads to a deviation from the Curie law leading to a variation of the $\chi_M T$ product even in the absence of any exchange interaction. One can consider that at low temperature only the non-Kramers ground state (for $Tb^{III}$ ion) or Kramers doublet (for $Dy^{III}$ ion) are populated because the energy state separation between the ground state and the first exited state is greater than 1500 $cm^{-1}$.[11] The magnetic properties can thus be modelled using an effective spin $S_{eff}$ 1 (for $Tb^{III}$ ion) and $S_{eff}$ 1/2 (for $Dy^{III}$ ion) with a very anisotropic $g_{eff}$ value. Below 150 K, the decrease of the $\chi_M T$ product for both compounds is therefore attributed to the depopulation of the Stark sublevels of the $Ln^{III}$ ions and not to a magnetic-exchange interaction. This phenomenon hampers the observation of an eventual magnetic-exchange interaction between the $Ni^{II}$ and the $Ln^{III}$ ions. However, some of us, in a previous work on a trinuclear compound of formula {[Ni(bpca)$_2$][Dy(hfac)$_3$](CHCl$_3$)} (noted **4**),[8c] have demonstrated that a weak ferromagnetic-exchange interaction between the $Ni^{II}$ and the $Dy^{III}$ ions through the $bpca^-$ ligand can occur. Moreover previous investigations on similar compounds have shown that with these types of compounds $Dy^{III}$- and $Tb^{III}$-based complexes display magnetic-exchange interactions of the same nature.[1a]

The magnetic analysis of the $Gd^{III}$ derivative gives us evidence of a weak ferromagnetic exchange interaction with the $Ni^{II}$ ion, and hence we found it reasonable to consider that the $Ln^{III}$ and the $Ni^{II}$ ions are weakly ferromagnetically coupled in **2** and **3**. Given the structural configuration of these compounds, we believe that the interchain interactions should be considered as the principal cause of the low temperature decrease of $\chi_M T$. The low value of the intrachain-magnetic interaction, together with the numerous pathways expected to alter the good isolation of the chain, do not allow for a fit of the $\chi_M T$ vs. $T$ curve with a ferromagnetic-chain model.

### Dynamic Magnetic Properties

For the reasons stated above we focus our *ac* analysis on the $Tb^{III}$ (Figure S3) and $Dy^{III}$ (Figure 6) derivatives. In the absence of an external field a small frequency dependence is visible on either the in or out-of-phase signals ($\chi'$ and $\chi''$, respectively). Even if weak, these signals differ notably from the noise of the susceptometer. However, both derivatives display a low $\chi''/\chi'$ ratio, with most of the susceptibility coming from the in-phase component of the magnetization. We thus found it unreasonable to attribute this frequency dependence to a magnetic slow relaxation.

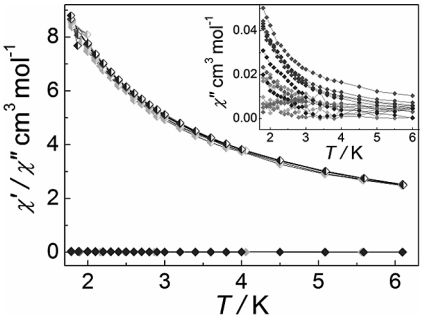


Figure 6. Temperature dependence of the in-phase (half filled symbols) and out-of-phase (filled symbols) susceptibility for **2** (from 100 to 20000 Hz). In the inset the out-of-phase susceptibility is enlarged.

Different reasons may explain the absence of a divergence of the $\chi_M T$ product at low temperature, together with the non-relevant $\chi''$ signal. The first and obvious one is the very weak intrachain-magnetic interaction. As described thanks to the study of **1**, the interaction is very low (Curie–Weiss constant $\theta$ +0.15 K) in these chains. However, no 3D ordering is visible here. This is in contrast with what has been observed in other reported chains.[12] Another reason is the bad magnetic isolation of the chains. The π-stacking interactions (Figure 2) between the chains and the extended network created by the hydrogen bonds (Figure 3) strongly alter the ratio between the intra- and interchain interac-

 © 2007 Wiley-VCH Verlag GmbH & Co. KGaA, Weinheim 

tions. This hampers the apparition of a single-chain magnetic behaviour.

In order to further explain the properties of these two chains we want to compare them to the previously cited {[Ni(bpca)$_2$][Dy(hfac)$_3$](CHCl$_3$)} (**4**) compound. This complex is a field dependant SMM, in the sense that its slow relaxation is switched on by a small external field. It thus displays a field dependence at the maximum of the $\chi''$ values. In fact it exhibits a low $\chi''/\chi'$ ratio in the zero-external field, which is a consequence of a fast zero-field tunnelling of the magnetization. Recent results on phthalocyaninate derivatives of lanthanide[6] have shown that this fast tunnelling can be suppressed by applying a small static field. Surprisingly it was found that **2** and **3** do not behave in the same way and do not show any field dependence of the out-of-phase susceptibility.

A last consideration can be made thanks to a close analysis of the molecular structure of **3** and **4**. This latter complex is very similar to the chain. Its inner core formed by the [Ni(bpca)$_2$] moiety is highly similar to that of the chain. The major deviations in the Ni$^{II}$–N$_x$ distances and angles are about 0.02 Å and 2°, respectively. From the magnetic point of view the similarity in the compression of the octahedron around the nickel ion allows us to assume that the anisotropy is equal in **3** and **4**. The main differences between the two compounds are obviously in the environment of the Dy$^{III}$ ions. The {[Ni(bpca)$_2$][Dy(hfac)$_3$](CHCl$_3$)} complex is made up of Dy$^{III}$ coordinated to three hfac$^-$ entities and two oxygen atoms from the bpca$^-$ ligand, which can be considered to be in a *cis* position. This arrangement gives a coordination polyhedron with two quasi-quadrilateral faces composed of four oxygen atoms [torsion angle (O10–O9–O15–O13) 176.6°, (O14–O16–O11–O12) 11.43°]. The coordination polyhedron is close to a square antiprism, a $D_{4d}$ site symmetry.

On the contrary the coordination polyhedron of Dy$^{III}$ in **3** has a different symmetry. Indeed the torsion angle between the four oxygen atoms sharing the possible quadrilateral face is (O2–O1–O6–O5) 165.7°, which is now quite far from the expected 180°. Hence the coordination polyhedron, even if slightly distorted, is close to a 4-capped square antiprism, having a $C_{4v}$ site symmetry.[14]

Ishikawa and coworkers have shown how the magnetic slow relaxation of 4f systems is strongly related to the symmetry of the lanthanide polyhedron.[15] Unfortunately quantitative analyses were only performed for the $D_{3h}$ symmetry. But by the same manner, it seems reasonable to consider that in our case the passage from a $D_{4d}$ to a $D_{2d}$ symmetry affects the dynamic properties of the Dy(hfac)$_3$ moiety. In fact, the crystal field potentials for these two site symmetries are quite different.[16] This may be, together with the above hypotheses, an explanation for the absence of a slow relaxation in **2** and **3**. Over the investigated temperature range we are not able to assign unambiguously the origin of the out-of-phase signal. Given the very low interaction between the magnetic centres along the chain, it seems reasonable to think that the magnetic slow relaxation of the lanthanide ion is one of the origins of the $\chi''$ signal.

## Conclusions

Compounds **1**, **2** and **3** are examples of 3d–4f molecular chains in which the magnetic intrachain interactions are quite weak. This, together with their bad magnetic isolation, hampers the apparition of a magnetic slow relaxation in **2** and **3**. However, we can learn something from these compounds. On comparing them with **4**, the absence of any field dependence of the out-of-phase susceptibility in **2** and **3** may highlight the role played by the symmetry of the lanthanide polyhedron. The use of the lanthanide precursor in an appropriate symmetry environment may be an additional key to favour the slow relaxation of the lanthanide ion in 4f-based compounds. To the best of our knowledge, compounds **1**–**3** are the first coordination polymers constructed by using [M(bpca)$_2$] complexes as building blocks.

## Experimental Section

**Syntheses:** The [Ni(bpca)$_2$] complex was obtained according to ref.[9b] The compounds [{Gd(O$_2$NO)(H$_2$O)$_3$}{Ni(bpca)$_2$}](NO$_3$)$_2$·3H$_2$O (**1**), [{Tb(O$_2$NO)(H$_2$O)$_3$}{Ni(bpca)$_2$}](NO$_3$)$_2$·3H$_2$O (**2**) and [{Dy(O$_2$NO)(H$_2$O)$_3$}{Ni(bpca)$_2$}](NO$_3$)$_2$·3H$_2$O (**3**) were obtained by the same manner: [Ni(bpca)$_2$] (0.05 mmol) was dissolved in a mixture of CHCl$_3$/CH$_3$OH (1:1, 5 mL) and added to a methanolic solution (3 mL) containing Gd(NO$_3$)$_3$·6H$_2$O (0.05 mmol) for **1**, Tb(NO$_3$)$_3$·6H$_2$O (0.05 mmol) for **2** and Dy(NO$_3$)$_3$·5H$_2$O (0.05 mmol) for **3**, respectively. After 2–3 min the combination of the components produced very fine needle-like light-brown crystals. These same solutions, containing the crystalline precipitates, were allowed to stand at room temp. for 1–2 d, which resulted in the dissolution of the precipitates, and further standing for 2 d led to the occurrence of the prismatic light-brown crystals of **1**, **2** and **3**, by slow evaporation.

**Gd(O$_2$NO)(H$_2$O)$_3$}{Ni(bpca)$_2$}](NO$_3$)$_2$·3H$_2$O (1):** Yield 82%. IR data (KBr): $\tilde{\nu}$ = 3375 (s, broad), 1675 (s), 1596 (m), 1563 (m), 1470 (w), 1447 (w), 1382 (vs), 1345 (s), 1283 (m), 1114 (w), 1090 (w), 1043 (w), 1018 (w), 833 (vw), 799 (w), 757 (m), 713 (w), 628 (m), 544 (vw), 517 (w), 418 (w) cm$^{-1}$. C$_{24}$H$_{28}$GdN$_9$NiO$_9$ (962.48): calcd. C 29.92, H 2.91, N 13.09; found C 30.4, H 2.7, N 12.9.

**[{Tb(O$_2$NO)(H$_2$O)$_3$}{Ni(bpca)$_2$}](NO$_3$)$_2$·3H$_2$O (2):** Yield 85%. IR data (KBr): $\tilde{\nu}$ = 3367 (s, broad), 1675 (s), 1597 (m), 1563 (m), 1471 (w), 1449 (w), 1384 (vs), 1347 (s), 1291 (m), 1150 (w), 1093 (w), 1044 (w), 1018 (w), 833 (vw), 811 (vw), 758 (m), 718 (w), 633 (m), 519 (w), 420 (w) cm$^{-1}$. C$_{24}$H$_{28}$N$_9$NiO$_9$Tb (964.15): calcd. C 29.87, H 2.90, N 13.07; found C 29.3, H 3.1, N 12.8.

**[{Dy(O$_2$NO)(H$_2$O)$_3$}{Ni(bpca)$_2$}](NO$_3$)$_2$·3H$_2$O (3):** Yield 91%. IR data (KBr): $\tilde{\nu}$ = 3356 (s, broad), 1674 (s), 1597 (m), 1561 (m), 1473 (m), 1451 (m), 1384 (vs), 1297 (m), 1150 (vw), 1094 (w), 1046 (w), 1017 (w), 833 (vw), 811 (vw), 759 (m), 720 (w), 634 (m), 519 (w), 420 (w) cm$^{-1}$. C$_{24}$H$_{28}$DyN$_9$NiO$_9$ (967.73): calcd. C 29.76, H 2.89, N 13.02; found C 29.3, H 2.9, N 13.1.

**X-ray Structure Determinations:** X-ray diffraction measurements were performed with a Bruker-Nonius Kappa CCD diffractometer using graphite-monochromated Mo-$K_\alpha$ radiation ($\lambda$ = 0.71073 Å). The structures were solved by direct methods and refined by full-matrix least-squares techniques based on $F^2$. The non-H atoms were refined with anisotropic displacement parameters. Calculations were performed using the SHELX-97 crystallographic software package.

 © 2007 Wiley-VCH Verlag GmbH & Co. KGaA, Weinheim 

CCDC-653381 -653383 contain the supplementary crystallographic data for this paper. These data can be obtained free of charge from The Cambridge Crystallographic Data Centre via www.ccdc.cam.ac.uk/data_request/cif.

**Magnetic Measurements:** All magnetic measurements were performed using pellets in order to avoid orientation of these very anisotropic materials. The *dc*-magnetic susceptibility measurements were performed with a Cryogenic S600 SQUID magnetometer between 2 and 300 K in an applied magnetic field of 0.1 T for temperatures in the range 2–50 K and 1 T for temperatures between 50 and 300 K. These measurements were all corrected for the diamagnetic contribution as calculated with Pascal's constants. The *ac*-magnetic susceptibility measurements were performed on the same samples using a homemade *ac*-probe operating in the range 100–25000 Hz.[17]

**Supporting Information** (see also the footnote on the first page of this article): Temperature dependence of $\chi^{-1}$ for compound **1** (Figure S1), magnetization versus field curves for compounds **2** and **3** (Figure S2), Temperature dependence of the in- and out-of-phase susceptibilities for compound **3** (Figure S3).

## Acknowledgments

We acknowledge the financial support from the Italian Ministero dell'Università e della Ricerca (MURST) (FIRB and PRIN grants), from the The European Commission (EC) through the Human Potential Program RTNQUELMOLNA (MRTN-CT-2003-504880), from the Molecular Approach to Nanomagnets and Multifunctional Materials, Network of Excellence (MAGMANet) (NMP3-CT-2005-515767) and from the Romanian CEEX Program (grant D11-17). F. P. thanks the Deutsche Forschungsgemeinschaft (DFG) (SPP1137) for his post-doctoral fellowship. Prof. R. Sessoli is acknowledged for stimulating discussions.

[1] a) C. Benelli, D. Gatteschi, *Chem. Rev.* **2002**, *102*, 2369 and references cited therein; b) J.-P. Sutter, M. L. Kahn, *Magnetism: Molecules to Materials*, (Ed.: J. S. Miller, M. Drillon), Wiley-VCH, Weinheim, **2005**, vol. V, p. 161.

[2] a) A. Bencini, C. Benelli, A. Caneschi, R. L. Carlin, A. Dei, D. Gatteschi, *J. Am. Chem. Soc.* **1985**, *107*, 8128; b) C. Benelli, A. Caneschi, D. Gatteschi, O. Guillou, L. Pardi, *Inorg. Chem.* **1990**, *29*, 1751; c) M. Andruh, I. Ramade, E. Codjovi, O. Guillou, O. Kahn, J. C. Trombe, *J. Am. Chem. Soc.* **1993**, *115*, 1822; d) J.-P. Costes, F. Dahan, A. Dupuis, J.-P. Laurent, *Inorg. Chem.* **1996**, *35*, 2400; e) J.-P. Costes, F. Dahan, A. Dupuis, J.-P. Laurent, *Inorg. Chem.* **1997**, *36*, 3429; f) J.-P. Costes, F. Dahan, A. Dupuis, *Inorg. Chem.* **2000**, *39*, 5994.

[3] a) M. Sakamoto, K. Manseki, H. Okawa, *Coord. Chem. Rev.* **2002**, *219–221*, 379; b) R. E. P. Winpenny, *Chem. Soc. Rev.* **1998**, *27*, 447; c) ·L. Cahill, D. L. T. de Lill, M. Frisch, *CrystEngComm* **2007**, *9*, 15; d) R. Gheorghe, P. Cucos, M. Andruh, J.-P. Costes, B. Donnadieu, S. Shova, *Chem. Eur. J.* **2006**, *12*, 187, and references cited therein; e) M. Andruh, *Chem. Commun.* **2007**, 2565.

[4] a) F. Bartolome, J. Bartolome, R. L. Oushoorn, O. Guillou, O. Kahn, *J. Magn. Magn. Mater.* **1995**, *140–144*, 1711; b) M. Evanghelisti, F. Bartolome, J. Bartolome, M. L. Kahn, O. Kahn, *J. Magn. Magn. Mater.* **1999**, *196–197*, 584.

[5] a) S. Osa, T. Kido, N. Matsumoto, N. Re, A. Pochaba, J. Mroziński, *J. Am. Chem. Soc.* **2004**, *126*, 420; b) C. M. Zaleski, E. C. Depperman, J. W. Kampf, M. L. Kirk, V. L. Pecoraro, *Angew. Chem. Int. Ed.* **2004**, *43*, 3012; c) A. Mishra, W. Wernsdorfer, K. A. Abboud, G. Christou, *J. Am. Chem. Soc.* **2004**, *126*, 15648; d) A. Mishra, W. Wernsdorfer, S. Parsons, G. Christou, E. K. Brechin, *Chem. Commun.* **2005**, 2086; e) J.-P. Costes, F. Dahan, W. Wernsdorfer, *Inorg. Chem.* **2006**, *45*, 5; f) M. Murugesu, A. Mishra, W. Wernsdorfer, K. A. Abboud, G. Christou, *Polyhedron* **2006**, *25*, 613; g) C. M. Zaleski, J. W. Kampf, T. Mallah, M. L. Kirk, V. L. Pecoraro, *Inorg. Chem.* **2007**, *46*, 1954; h) F. Mori, T. Nyui, T. Ishida, T. Nogami, K.-Y. Choi, H. Nojiri, *J. Am. Chem. Soc.* **2006**, *128*, 1440; i) M. Ferbinteanu, T. Kajiwara, K.-Y. Choi, H. Nojiri, A. Nakamoto, N. Kojima, F. Cimpoesu, Y. Fujimura, S. Takaishi, M. Yamashita, *J. Am. Chem. Soc.* **2006**, *128*, 9008; j) C. Aronica, G. Pilet, G. Chastanet, W. Wernsdorfer, J.-F. Jacquot, D. Luneau, *Angew. Chem. Int. Ed.* **2006**, *45*, 4659; k) J. Tang, I. Hewitt, N. T. Madhu, G. Chastanet, W. Wernsdorfer, C. E. Anson, C. Benelli, R. Sessoli, A. K. Powell, *Angew. Chem. Int. Ed.* **2006**, *45*, 1729.

[6] a) N. Ishikawa, M. Sugita, W. Wernsdorfer, *Angew. Chem. Int. Ed.* **2005**, *44*, 2931; b) N. Ishikawa, M. Sugita, T. Ishikawa, S. Koshihara, Y. Kaizu, *J. Phys. Chem. B* **2004**, *108*, 11265; c) N. Ishikawa, M. Sugita, T. Ishikawa, S. Koshihara, Y. Kaizu, *J. Am. Chem. Soc.* **2003**, *125*, 8694.

[7] a) K. Bernot, L. Bogani, A. Caneschi, D. Gatteschi, R. Sessoli, *J. Am. Chem. Soc.* **2006**, *128*, 7947; b) L. Bogani, C. Sangregorio, R. Sessoli, D. Gatteschi, *Angew. Chem. Int. Ed.* **2005**, *44*, 5817; c) K. Bernot, L. Bogani, R. Sessoli, D. Gatteschi, *Inorg. Chim. Acta* **2007**, doi:10.1016/j.ica.2006.12.002.

[8] a) T. Kajiwara, T. Ito, *J. Chem. Soc. Dalton Trans.* **1998**, 3351; b) T. Kajiwara, R. Sensui, T. Naguchi, A. Kamiyama, T. Ito, *Inorg. Chim. Acta* **2002**, *337*, 299; c) F. Pointillart, K. Bernot, R. Sessoli, D. Gatteschi, *Chem. Eur. J.* **2007**, *13*, 1602.

[9] a) A. Kamiyama, T. Naguchi, T. Kajiwara, T. Ito, *Angew. Chem. Int. Ed.* **2000**, *39*, 3130; b) A. Kamiyama, T. Naguchi, T. Kajiwara, T. Ito, *Inorg. Chem.* **2002**, *41*, 507.

[10] a) T. Kajiwara, M. Nakano, Y. Kaneko, S. Takaishi, T. Ito, M. Yamashita, A. Igashira-Kamiyama, H. Nojiri, Y. Ono, N. Kojimq, *J. Am. Chem. Soc.* **2005**, *127*, 101150; b) Y. Kaneko, T. Kajiwara, H. Yamane, M. Yamashita, *Polyhedron* **2007**, *26*, 2074; c) H. Tanaka, T. Kajiwara, Y. Kaneko, S. Takaishi, M. Yamashita, *Polyhedron* **2007**, *26*, 2105.

[11] O. Kahn, *Molecular Magnetism*, VCH, Weinheim, **1993**.

[12] a) B. Yan, Z. Chen, S. Wang, S. Gao, *Chem. Lett.* **2001**, 350; b) B. Yan, H.-D. Wang, Z.-D. Chen, *Polyhedron* **2001**, *20*, 591; c) S. Tanase, M. Andruh, A. Müller, C. Schmidtmann, C. Mathonière, G. Rombaut, *Chem. Commun.* **2001**, 1084; d) S. Gao, G. Su, T. Yi, B.-Q. Ma, *Phys. Rev. B* **2001**, *63*, 054431; e) B. Yan, H.-D. Wang, Z.-D. Chen, *Inorg. Chem. Commun.* **2000**, *3*, 653; f) B. Yan, Z. Chen, *Helv. Chim. Acta* **2001**, *84*, 817; g) H.-Z. Kou, S. Gao, C.-H. Li, D.-Z. Liao, B.-C. Zhou, R.-J. Wang, Y. Li, *Inorg. Chem.* **2002**, *41*, 4756; h) A. Figuerola, C. Diaz, M. S. El Fallah, J. Ribas, M. Maestro, J. Mahia, *Chem. Commun.* **2001**, 1204; i) A. Figuerola, C. Diaz, J. Ribas, V. Tangoulis, C. Sangregorio, D. Gatteschi, M. Maestro, J. Mahia, *Inorg. Chem.* **2003**, *42*, 5274; j) A. Figuerola, C. Diaz, J. Ribas, V. Tangoulis, J. Granell, F. Lloret, J. Mahia, M. Maestro, *Inorg. Chem.* **2003**, *42*, 641; k) H.-Z. Kou, B. C. Zhou, R. J. Wang, *Inorg. Chem.* **2003**, *42*, 7658; l) A. Figuerola, J. Ribas, D. Casanova, M. Maestro, S. Alvarez, C. Diaz, *Inorg. Chem.* **2005**, *44*, 6949; m) A. Figuerola, J. Ribas, X. Solans, M. Font-Bardia, M. Maestro, C. Diaz, *Eur. J. Inorg. Chem.* **2006**, 1846; n) B. Du, E. Ding, E. A. Meyers, S. G. Shore, *Inorg. Chem.* **2001**, *40*, 3637; o) B. Du, E. Ding, E. A. Meyers, S. G. Shore, *Inorg. Chem.* **2000**, *39*, 4639; p) D. W. Knoeppel, J. Liu, E. A. Meyers, S. G. Shore, *Inorg. Chem.* **1998**, *37*, 4828; q) D. W. Knoeppel, S. G. Shore, *Inorg. Chem.* **1996**, *35*, 1747; r) D. W. Knoeppel, S. G. Shore, *Inorg. Chem.* **1996**, *35*, 5328; s) R. Gheorghe, M. Andruh, J.-P. Costes, B. Donnadieu, *Chem. Commun.* **2003**, 2778; t) J.-P. Costes, G. Novitchi, S. Shova, F. Dahan, B. Donnadieu, J. P. Tuchagues, *Inorg. Chem.* **2004**, *43*, 7792; u) H. Zhao, N. Lopez, A. Prosvirin, H. T. Chifotides, K. R. Dunbar, *Dalton Trans.* **2007**, 878.

 © 2007 Wiley-VCH Verlag GmbH & Co. KGaA, Weinheim 

[13] C. Coulon, H. Miyasaka, R. Clérac, *Struct. Bonding (Berlin)* **2006**, *122*, 163 and references cited therein.
[14] R. B. King, *J. Am. Chem. Soc.* **1969**, *91*, 7211.
[15] a) M. Sugita, N. Ishikawa, T. Ishikawa, S. Koshihara, Y. Kaizu, *Inorg. Chem.* **2006**, *45*, 1299; b) N. Ishikawa, M. Sugita, T. Okubo, N. Tanaka, T. Lino, Y. Kaizu, *Inorg. Chem.* **2003**, *42*, 2440.
[16] a) B. R. Judd, *Phys. Rev.* **1962**, *127*, 750; b) G. S. Ofelt, *J. Chem. Phys.* **1962**, *37*, 511.
[17] S. Midollini, A. Orlandini, P. Rosa, L. Sorace, *Inorg. Chem.* **2005**, *44*, 2060.

Received: July 9, 2007
Published Online: October 17, 2007

 © 2007 Wiley-VCH Verlag GmbH & Co. KGaA, Weinheim 

DOI: 10.1002/ejic.200700732

# A New Donor-Stabilized Ditungsten Amido Alkoxido Species: Synthesis, Crystal Structure, Fluxionality, and Grafting onto Silica

**Olivier Coutelier,[a] Régis M. Gauvin,*[a] Guy Nowogrocki,[a] Julien Trébosc,[a] Laurent Delevoye,[a] and André Mortreux*[a]**

**Keywords:** Tungsten / Metal-metal multiple bonds / Ligand design / Grafting / Silica / Alkyne metathesis

A new dimeric tungsten(III) complex containing amido and chelating pyridine–alkoxido ligands was synthesized through protonolysis of $[W_2(NMe_2)_6]$ by 2-(2-pyridyl)propan-2-ol and fully characterized by X-ray diffraction and infrared and NMR spectroscopy. Intramolecular exchange processes were studied by variable-temperature NMR spectroscopy. The compound was grafted onto dehydroxylated silica by protonolysis of an amido–tungsten bond, and the structure of the supported species was investigated by infrared and solid-state (bidimensional) NMR spectroscopy. The reactivity of the molecular and grafted species toward alkynes was probed.
(© Wiley-VCH Verlag GmbH & Co. KGaA, 69451 Weinheim, Germany, 2007)

## Introduction

The recent focus on alkene metathesis following the Nobel prize award to Y. Chauvin, R. R. Schrock, and R. Grubbs has emphasized that the corresponding reaction involving carbon-carbon triple bonds, namely alkyne metathesis,[1] is still a field offering significant challenges.[2] Selectivity of this reaction suffers from side reactions such as trimerization into substituted benzene derivatives, coupling into cyclopentadiene analogues, or polymerization yielding polyacetylenes. The latter reaction is most particularly encountered with terminal alkynes, where the acidity of the terminal C–H induces the rapid formation of polymerization propagating species. Development of new catalysts for this transformation is therefore of considerable interest. Inspired by Schrock's systems based on $[(t\text{BuO})_3W{\equiv}C\text{-}t\text{Bu}]$ and $[(t\text{BuO})_3W{\equiv}W(Ot\text{Bu})_3]$,[3] as well as by our findings on the dramatic influence of quinuclidine as a Lewis base additive in this reaction,[4] we have recently disclosed a new catalytic system that relies on the hemilability concept.[5] Indeed, use of $[W_2(OC(Me)_2CH_2OMe)_6]$ (**2**), in which methoxy donor groups are incorporated within the alkoxido fragments, has led to unprecedented activity for the metathesis of phenylacetylene and 1-heptyne (Scheme 1).[6] The use of alkoxido ligands bearing donor groups thus seems to be a promising approach to develop efficient and selective catalytic systems. In this view, we have chosen to focus on an alkoxido ligand bearing a pyridyl function.[7] Furthermore, Basset and Moore have both reported silica-grafted catalysts displaying high activity and

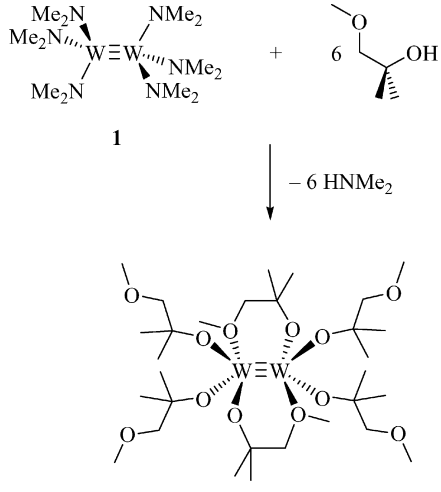


Scheme 1. Synthesis and reactivity of **2**.

[a] Unité de Catalyse et de Chimie du Solide, UMR 8181 CNRS, ENSCL,
B. P. 90108, 59652 Villeneuve d'Ascq Cedex, France
Fax: +33-3-20436585
E-mail: regis.gauvin@ensc-lille.fr
andre.mortreux@ensc-lille.fr
Supporting information for this article is available on the WWW under http://www.eurjic.org or from the author.

 © 2007 Wiley-VCH Verlag GmbH & Co. KGaA, Weinheim 

selectivity.[8] On the other hand, we have recently shown that the grafting onto silica of compounds inactive as homogeneous catalysts can afford heterogeneous catalysts active toward terminal alkynes.[9] As the supporting of organometallic species plays a significant role in this chemistry, this prompted us to probe the effect of grafting on other (potential) catalysts.

The present contribution describes our results on the synthesis, solid- and liquid-state structural investigations of a ditungsten complex bearing a bidentate pyridylalkoxido ligand, and on its grafting onto dehydroxylated silica to generate binuclear supported species.

## Results and Discussion

### Synthesis and Characterization of Complex $[W_2(L)_2(NMe_2)_4]$ (3)

The reaction of **1** with 12 equivalents of 2-(2-pyridyl)propan-2-ol, (L)H in toluene at room temperature affords a deep red solution, from which, after stripping off the volatiles and washing with pentane, $[W_2(L)_2(NMe_2)_4]$ (**3**) is obtained as a red-orange solid in 40% yield (Scheme 2). NMR follow-up of the reaction in $C_6D_6$ in the presence of excess (L)H shows that the reaction does not proceed further, despite extended reaction times and more elevated temperatures. In the presence of six equivalents of (L)H, **1** reacts to afford mainly the monosubstituted complex $[W_2(L)(NMe_2)_5]$, on the basis of $^1$H NMR spectroscopic data (see electronic supporting information). The addition of six further equivalents of (L)H to the reaction mixture leads to the selective formation of **3** after 12 h. This differs from the reaction of **1** with *tert*-butyl alcohol, which affords under similar conditions the hexakis(alkoxido) dinuclear complex through complete alcoholysis of the dimethylamido ligands. This is most probably due to the strong binding of the chelating pyridine, which prevents coordination of the bulky alcohol, most probably a prerequisite for the protonolysis of the tungsten–amido bond.

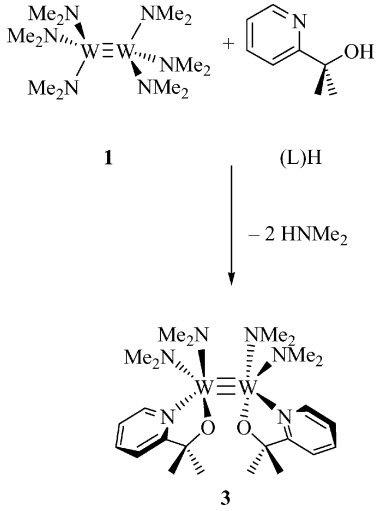


Scheme 2. Synthesis of **3**.

Single crystals suitable for X-ray analysis have been grown in pentane where **3** is slightly soluble. The molecular structure of **3** is depicted in Figure 1. Selected bond lengths and angles are summarized in Table 1.

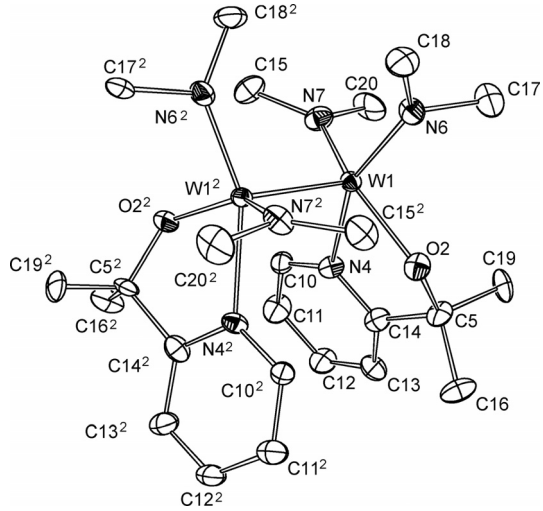


Figure 1. ORTEP representation of **3** with the thermal ellipsoids at 50% of probability. H atoms are omitted for clarity.

Table 1. Selected bond lengths (Å) and angles (°) for complex **3**.

| | | | |
|---|---|---|---|
| W1–W1² | 2.3351(5) | W1–N7 | 1.986(6) |
| W1–N4 | 2.263(5) | W1–N6 | 1.975(6) |
| W1–O2 | 2.021(5) | | |
| N6–W1–N7 | 101.3(2) | O2–W1–N4 | 71.63(18) |
| N6–W1–O2 | 91.7(3) | N6–W1–W1² | 104.05(16) |
| N7–W1–O2 | 144.22(19) | N7–W1–W1² | 101.79(16) |
| N6–W1–N4 | 155.7(2) | O2–W1–W1² | 107.14(13) |
| N7–W1–N4 | 84.13(19) | N4–W1–W1² | 97.81(13) |

Each tungsten of the dimer adopts a distorted square-planar coordination [the sum of angles is 348.8(5)°], composed of two dimethylamido and one chelating pyridylalkoxido ligands. The two tungsten-based fragments are connected by a $C_2$ axis, which intersects the compound at the center of the W–W triple bond. The configuration adopted by the compound is classical for $M_2L_8$ compounds.[10] The two $WL_4$ entities are eclipsed, thus minimizing steric repulsions (Figure 2). The bond lengths are classical: the W1–W1² bond length of 2.3351(5) Å is within the expected range[11] {see for example 2.332(1) in $[W_2(OCHMe_2)_6(py)_2]$[12] or 2.3340(5) in $[W_2(OCH_2tBu)_6(py)_2]$[13]}. The pyridine nitrogen to tungsten bond length [2.263(5) Å] is comparable to that observed in similar complexes.[12,13] The tungsten–amido [1.986(6) and 1.975(6) Å] and tungsten–alkoxido [2.021(5) Å] bond lengths are unexceptional. The two nitrogen amido are planar [sum of angles at N6 and N7 of 359.99(9) and 359.35(8)°, respectively], and the $NMe_2$ fragments are aligned with the W–W triple bond [C18–N6–W1–W1² and C15–N7–W1–W1² dihedral angles of 8.1(7) and 4.5(6)°, respectively]. Thus, proximal methyl groups (C15 and C18) are located over the W–W bond, while distal methyl groups point in the opposite direction.

 © 2007 Wiley-VCH Verlag GmbH & Co. KGaA, Weinheim 

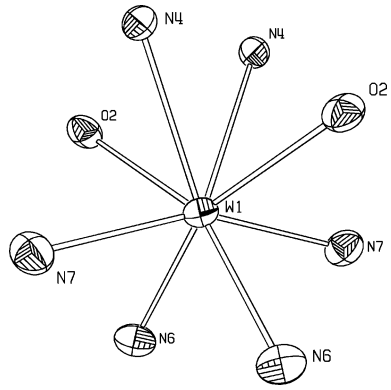


Figure 2. View of the central skeleton of **3** looking down the W1–W1[2] axis.

Room temperature $^1$H NMR spectroscopic data is consistent with the presence of a single type of [N–O] ligand, indicating that the $C_2$ symmetry observed in the solid-state is retained in solution. The pyridyl *ortho* C–H gives rise to a characteristic doublet of triplets in the low field region ($\delta$ = 9.06 ppm). The two diastereotopic methyl groups resonate at $\delta$ = 1.75 and 1.04 ppm. At room temperature, the spectrum comprises three signals for the $NMe_2$ groups at $\delta$ = 4.73, 3.70, and 2.28 ppm, as broad peaks of intensities 6, 12, and 6 H, respectively. This is consistent with two types of $NMe_2$ groups, and is characteristic of hindered rotation around the W–N bond.[14] In order to shed light on the dynamic processes at hand, variable-temperature NMR studies have been carried out (Figure 3). Two different processes involving the two types of $NMe_2$ ligands have been observed (Table 2).

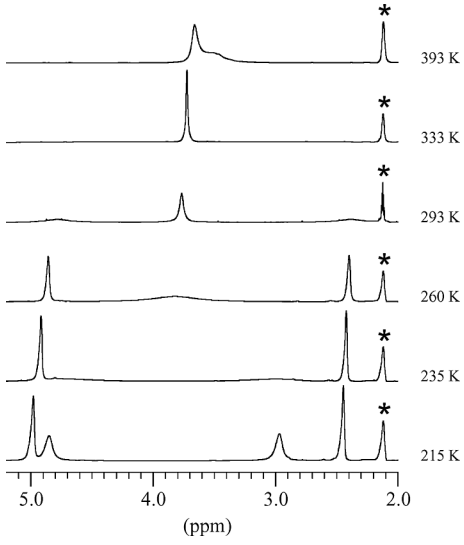


Figure 3. Variable-temperature $^1$H NMR spectra of complex **3** in the *N*-methyl group region ([D$_8$]toluene, 400 MHz; * denotes solvent peak).

On the basis of the literature data,[16] the shielded and deshielded signals within each of these pairs can be respectively assigned to the distal and proximal methyl groups.

Table 2. Variable-temperature NMR studies on **3**: coalescing pairs of signals and corresponding activation energies ([D$_8$]toluene).

| $\delta$ [ppm] | $T_c$ [K] | $\Delta G^{\neq}$ [kJ mol$^{-1}$][15] |
|---|---|---|
| 4.98, 2.44 | 333 (±5) | 60.4 (±0.1) |
| 4.86, 2.96 | 245 (±5) | 44.4 (±0.1) |

This was confirmed by the low-temperature NOESY correlation spectrum, which also allowed us to assign the pairs of signals at $\delta$ = 4.98 and 2.44 ppm and at $\delta$ = 4.86 and 2.96 ppm to the $NMe_2$ group in *cis* and *trans* position to the pyridine, respectively, on the basis of interactions with the pyridine *ortho* CH. This is in agreement with the relative energetic barriers: the $NMe_2$ group *cis* to the pyridine, [$\Delta G^{\neq}$ = 60.4 (±0.1) kJ mol$^{-1}$] is located in a more congested environment (pyridine and $NMe_2$ groups) than the *trans* $NMe_2$ [$\Delta G^{\neq}$ = 44.4 (±0.1) kJ mol$^{-1}$].

Complex **3** is inactive toward 4-nonyne in the absence of additive. In situ protonolysis with four equivalents of alcohol was attempted to generate $[W_2(OR)_4(L)_2]$ species, bearing in mind the high reactivity of alkoxido species $[W_2(OR)_6]$ in alkyne metathesis. A series of alcohols was screened: *tert*-butyl alcohol, 1-adamantanol, phenol, and 3-quinuclidinol. Only the latter afforded an active catalyst, although a high temperature (363 K) was necessary to reach the thermodynamic equilibrium mixture (1 h). This may be related to this alcohol's coordinative ability through its nitrogen atom. However, further characterization efforts are necessary at this stage to confirm that the amido–tungsten bond protonolysis took place. Moreover, regarding the potential of catalysts bearing this [N,O] ligand in alkyne metathesis, the strongly basic pyridine may hinder the alkyne substrate coordination, a step necessary to cleave the $W_2$ dimer and generate a catalytically active alkylidine species.

## Grafting of Complex 3 Onto Partially Dehydroxylated Silica

These results on the alcoholysis of the W–$NMe_2$ bond producing a metathesis active system prompted us to study the effect of the grafting of **3** onto an inorganic support, since surface hydroxy groups are frequently compared to ROH moieties.[17] Partially dehydroxylated silica was used as a support for the grafting of **3**. Bearing only isolated silanol groups as protic sites on its surface, silica treated under vacuum at 700 °C behaves as a bulky silanol ligand when reacted with organometallic reagents, affording well-defined single site catalysts.[18] Moreover, metal amido species have been grafted with success onto inorganic supports.[8b,19] More precisely, W–$NMe_2$ groups readily react with surface silanols to afford covalent ≡Si–O–W bonds, as shown by the studies on the grafting of **1** onto silica.[8] Grafting of **3** onto $SiO_2$-700 proceeds at room temperature in pentane. During the reaction course, the supernatant color fades from dark to clear orange, while the suspended solid turns to dark red. After three pentane washings and drying at 80 °C for 3 h under a $10^{-6}$ mbar vacuum, **4** is obtained as an ochre powder (Scheme 3). When carrying out

 © 2007 Wiley-VCH Verlag GmbH & Co. KGaA, Weinheim 

the reaction between **3** and suspended partially dehydroxylated silica in $C_6D_6$, the only new compound observed by $^1H$ NMR was $HNMe_2$. No pyridyl alcohol ligand (L)H was detected, which is consistent with the protonolysis of the W–$NMe_2$ bond by ≡SiOH as the preferred grafting mode. Elemental analysis indicates a tungsten content of 10.53 wt.-%. The molar ratios N/W and C/W, respectively of 2.46 and 12.23, are close to values expected for ≡Si–O–[$W_2(L)_2(NMe_2)_3$] (2.50 and 11, respectively), which is in agreement with a clean reaction of complex **3** with isolated surface silanols forming a single W–O–Si bond.

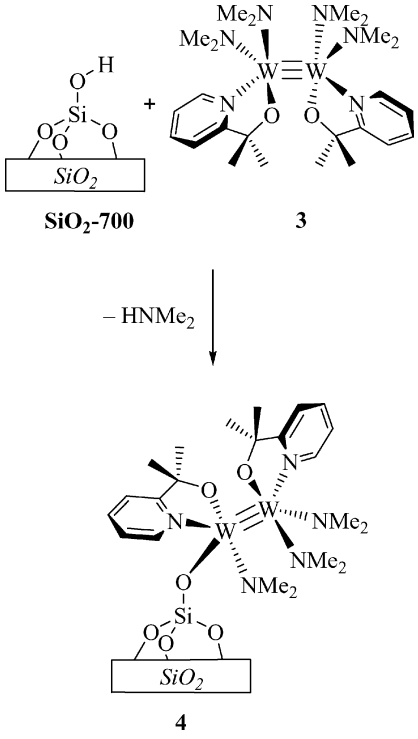


Scheme 3. Grafting of **3** onto partially dehydroxylated silica.

Diffuse reflectance infrared spectroscopic studies on **4** indicate that the silica silanol groups have been entirely consumed, as evidenced from the disappearance of the $\nu_{OH}$ signal at 3747 $cm^{-1}$ [Figure 4, (c)]. This indicates that surface saturation has been reached during the grafting. Moreover, the spectrum of **4** comprises peaks accounting for aromatic C–H bonds (3065 and 3081 $cm^{-1}$) and aliphatic C–H bonds (2974–2769 $cm^{-1}$), as well as aromatic ring-related signals at 1607 and 1568 $cm^{-1}$. For these signals, the similarity with the spectroscopic features of **3** (1600 and 1567 $cm^{-1}$) indicates minor changes within the coordination sphere of the metal.

Solid-state NMR studies on **4** have been carried out to get a better understanding of the grafted species structure. The $^1H$ MAS NMR spectrum comprises peaks analogous to those observed in the $^1H$ solution NMR of **3** (Figure 5). Deconvolution of the spectrum is presented in Figure 6c. Aromatic protons resonate at $\delta$ = 7.2 and 9.3 ppm, the latter being assigned to C–Hs in the *ortho* position of the pyridine

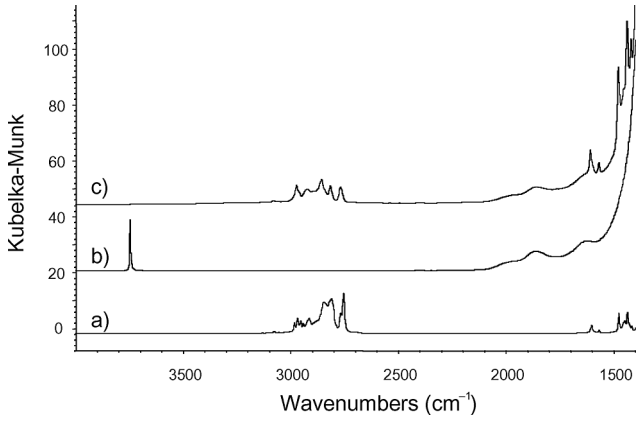


Figure 4. DRIFT spectra of a) **3**, b) $SiO_2$-700, c) **4**.

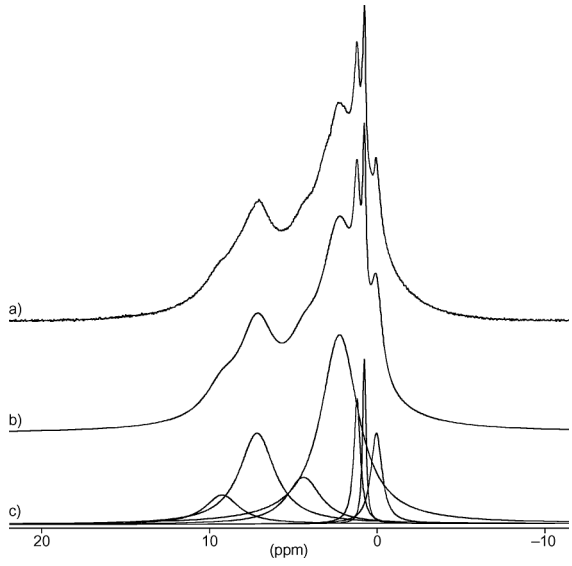


Figure 5. (a) $^1H$ MAS spectrum of **4** (400.1 MHz); (b) and (c) calculated spectrum and deconvolution results.

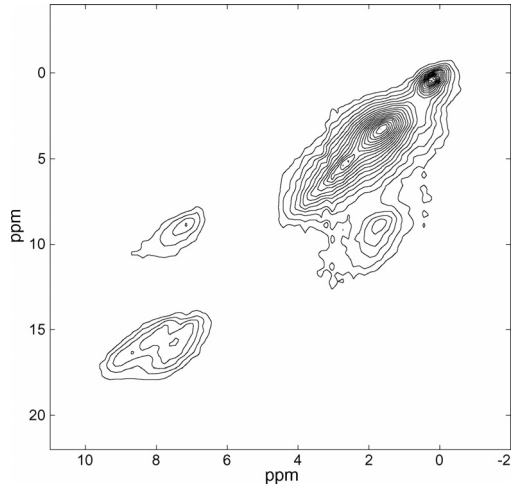


Figure 6. $^1H$ 2D double-quantum MAS spectrum of **4** using excitation/reconversion pulse train of one rotor period (50 μs) (800.13 MHz, 20 kHz spinning speed, pulse radio frequency 80 kHz).

 © 2007 Wiley-VCH Verlag GmbH & Co. KGaA, Weinheim 

fragment ($C^6H$). Assignment of the signals observed between 4.4 and 0.1 ppm is less straightforward. On the basis of the comparison to the signals of **3**, the peaks at $\delta$ = 4.4 and 2.3 ppm can be unambiguously assigned to NMe groups. Moreover, as a comparison, the $^1$H MAS NMR spectrum of ≡Si–O–[$W_2(NMe_2)_5$] comprises three signals at 4.2, 3.2, and 2.5 ppm.[9] The other three signals at 1.2, 0.8, and 0.1 ppm are assigned to either NMe or diastereotopic CMe groups.[20] The high number of signals is in line with the lowering of the symmetry and increased rotation barriers due to the increased bulk resulting from the silica surface.

The use of a high-field NMR spectrometer (18.8 T, 800 MHz for $^1$H resonance) could not significantly improve the resolution of the $^1$H MAS NMR spectrum due to signal artifacts related to probe background signal overlapping the 0–4 ppm region. However, we have been able to run a Double Quanta MAS experiment[21] on this instrument in order to gain further insight on the structure of the grafted species of **4**. In Figure 6 is presented the spectrum resulting from the double-quantum correlation experiment using one rotor period mixing time for Back-to-Back (BABA) excitation. This technique gives the means to probe proximities between protons for which dipolar coupling is strong. Moreover, it efficiently filters out the artifacts stemming from probe background. The 2QMAS spectrum exhibits the least mobile sites that still experience sufficient dipolar coupling to correlate.

The aromatic protons give rise to two off-diagonal patterns at 9–8 ppm, assigned to the *ortho* pyridine protons based on the characteristic chemical shift, and at 8–7 ppm, for other aromatic protons. These correlations are in line with spatial proximities between these types of CHs. The broad distribution for the *ortho* pyridine protons indicates that these are present in different types of sites. This is consistent with the non-symmetric structure of the surface species and with the presence of the silica surface as a ligand, which can significantly affect the chemical shift of these nuclei in a non-homogeneous way. The other main off-diagonal interaction observed on the spectrum implies nuclei resonating around 7.3 ppm and 1.6 ppm. This corresponds to the interaction between the non-*ortho* pyridine protons and one or more CMe groups, most probably within the same [N,O] framework, an assignment in agreement with the chemical shifts of these signals. Accordingly, when comparing distances in the X-ray crystal structure (Figure 1 and Table 1), the C13-*H*–C16-*H* distance is of 2.332 Å, which is similar to the C13-*H*–C12-*H* distance (2.336 Å). Off-diagonal correlations for the $NMe_2$ groups are not observed on the 2D spectrum. The more rigid character of the [N,O] chelating ligand implies that the $CMe_2$ groups are less mobile than the $NMe_2$ groups, which thereby enhances the dipolar interactions, and thus increases their sensitivity to the double quantum correlation experiment compared to the dimethylamido protons. When using the two rotor periods BABA excitation, and thus probing longer interaction ranges, another off-diagonal correlation was observed between signals at 9 ppm and 1.6 ppm (Figure 7). This corresponds to *ortho* pyridine protons interacting with a C*Me* group, and, more precisely, with the same CMe which correlates with the non-*ortho* pyridine protons (this interaction is of course also visible on the spectrum). This correlation most probably implies protons located on two different [N,O] ligands on the same grafted species. Indeed, on the X-ray structure of **3**, the C10-*H*–C16$^2$-*H* distance is of 2.510 Å (inter-ligand interaction), much shorter than C10-*H*–C16-*H* or C10-*H*–C19-*H* distances of 5.434 and 4.730 Å, respectively (intra-ligand interaction).

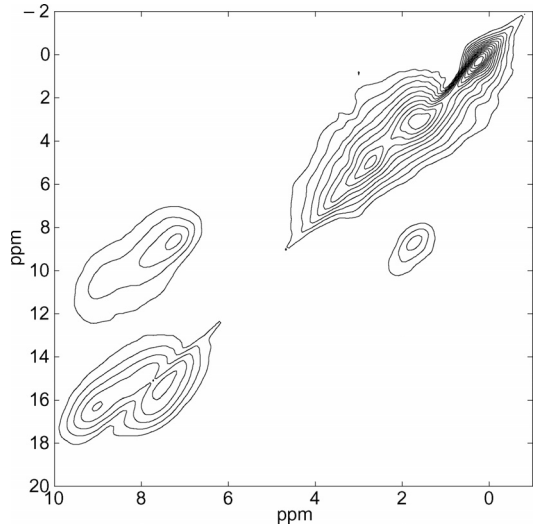


Figure 7. $^1$H 2D double quantum MAS spectrum of **4** using excitation/reconversion pulse train of two rotor periods (100 μs) (800.13 MHz, 20 kHz spinning speed, pulse RF = 80 kHz).

$^{13}$C CP MAS NMR signals are reminiscent of those of the molecular precursor (Figure 8). Signals of the pyridine carbons appear at 171.8, 150.0, 135.9, and 119.3 ppm. The $CMe_2$ groups give rise to signals at $\delta$ = 84.1 and 81.7 ppm for two different types of *C*$Me_2$, and to a broad signal centered at $\delta$ = 30.5 ppm for the methyl groups. Two other peaks are observed at $\delta$ = 57.9 and 48.2 ppm, a range corresponding to WN*Me* groups. Indeed, the $^{13}$C CP MAS NMR spectrum of ≡Si–O–[$W_2(NMe_2)_5$] comprises three peaks at $\delta$ = 58.2, 47.8, and 37.6 ppm.[9] Other WN*Me* signals may be hidden under the broad peak centered at $\delta$ =

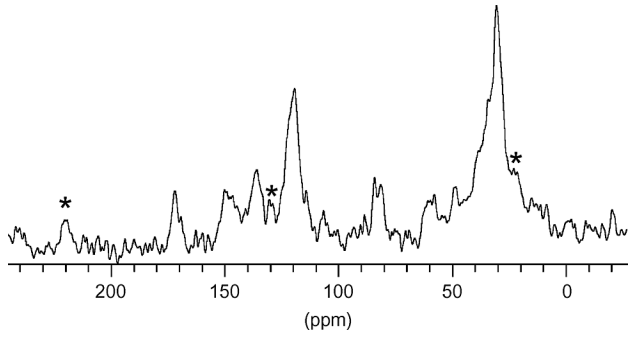


Figure 8. $^{13}$C CP MAS spectrum of **4** (100.6 MHz; * denotes rotation peaks).

 © 2007 Wiley-VCH Verlag GmbH & Co. KGaA, Weinheim 

30.5 ppm. Again, the high number of C*Me* and N*Me* signals is consistent with the low symmetry of the grafted species.

The reactivity of **4** toward alkyne metathesis was probed. Unfortunately, this material proved to be inactive toward 4-nonyne, giving no metathesis products in detectable quantities under the conditions used for **3** (see above).

## Conclusions

The synthesis of a dinuclear tungsten(III) complex bearing pyridylalkoxido and amido ligands has been accomplished through alcoholysis of the hexakis-amido ditungsten derivative. The controlled grafting of this compound has been successfully carried out, as shown by several characterization techniques. The reactivity spectrum of the molecular compound and of its grafted analogue in alkyne metathesis is narrow; only the coordination complex displays (modest) activity, under very specific conditions. The blocking of a coordination site by the pyridine nitrogen may be at the origin of the lack of reactivity of the $W_2$ core, by preventing access to reactive sites of the metallic species (W–N and W≡W bonds). Thus, in this case, the hemilabile character of the studied ligand may not be sufficient to perform its ascribed role, as in the case of the methoxy-substituted derivatives. Future efforts in catalyst design are in progress, aimed at introducing less coordinating functions on the alkoxide ligands.

## Experimental Section

**General Procedures:** All experiments were performed under argon using standard Schlenk techniques or in a M-Braun glove-box, with rigorous exclusion of traces of moisture and air. THF, benzene, toluene, and hexane were purified by distillation from sodium/benzophenone ketyl and were stored over activated 4-Å molecular sieves. $[W_2(NMe_2)_6]$ was synthesized by following the literature procedure.[22] The silica support (Aerosil 380 silica, Degussa, specific area 380 $m^2 g^{-1}$) was heated under $10^{-6}$ mbar at 500 °C for 15 h then at 700 °C for 4 h. Elemental analyses were performed in the Service Central d'Analyses du CNRS (tungsten) and in the LSEO, University of Bourgogne (C,H,N). DRIFT spectra were recorded with a Nicolet Protégé 460 equipped with an MCT detector and a Harrick analysis chamber, with a resolution of 4 $cm^{-1}$. NMR liquid-phase spectra were recorded with Bruker Avance 300 and Avance 400 spectrometers at 298 K, unless specified otherwise. NMR (solid-state) spectra were recorded with a Bruker Avance 400 ($^1$H: 400.1 MHz, $^{13}$C: 100.6 MHz) and Avance II 800 ($^1$H: 800.13 MHz). The $^1$H-$^{13}$C CP experiments were obtained at a spinning frequency of 10 kHz, with a recycle delay of 5 s and 10240 scans were collected. For the CP step, a ramped radio-frequency (RF) field centered at 50 kHz was applied on protons, while the carbon RF field was matched to obtain an optimum signal. The contact time was set to 1.5 ms for the $^{13}$C CP experiment. 2D Double Quantum Magic-Angle Spinning spectra were performed at 20 kHz spinning speed on a 18.8 T Avance II Bruker spectrometer (Larmor frequency 800.13 MHz). 2Q coherences were created using the BABA[21] scheme with mixing times of one (50 μs) or two (100 μs) rotor periods and an 80 kHz RF field. Chemical shifts for $^1$H and $^{13}$C NMR spectra are reported relative to TMS. Gas chromatography analyses were performed with a Chrompack CP9001 gas chromatograph under $N_2$ flow with a CPSil 8 CB column (15 m length, 0.32 mm diameter, 0.25 μm film thickness). Deconvolution was performed using the dmfit program.[23]

**Synthesis of $[W_2\{(2\text{-pyr})C(Me_2)_2O\}_2(NMe_2)_4]$ (3):** To a solution of $[W_2(NMe_2)_6]$ (101 mg, 0.16 mmol) in toluene (10 mL) was added a solution of 2-(2-pyridyl)propan-2-ol (260 mg, 1.9 mmol) in toluene (5 mL). The reaction mixture was stirred for 16 h at room temperature during which the solution turned deep red. All volatile compounds were removed under vacuum and the resulting red solid was heated to 60 °C under vacuum ($10^{-2}$ mbar). The red residue was washed with a small portion of pentane where it is only slightly soluble. The product was obtained as a red powder in 40% yield. Crystals suitable for X-ray analysis were grown in pentane. $C_{24}H_{44}N_6O_2W_2$ (816.3): calcd. C 35.31, H 5.43; found C 35.27, H 5.81. $^1$H NMR (300 MHz, [D$_6$]benzene): $\delta$ = 9.04 [dt, $^3J$(H-H) = 5.4, $^4J$(H-H) = 0.7 Hz, 2 H, 6-H pyr], 6.52 [dt, $^3J$(H-H) = 7.6, $^4J$(H-H) = 1.5 Hz, 2 H, 4-H pyr], 6.28 [ddd, $^3J$(H-H) = 7.1, $^3J$(H-H) = 5.6, $^4J$(H-H) = 1.3 Hz, 2 H, 5-H pyr], 6.20 [dt, $^3J$(H-H) = 7.8, $^4J$(H-H) = 1.0 Hz, 2 H, 3-H pyr], 4.73 (s, broad, 6 H, N$^1$*Me*Me), 3.70 (s, 12 H, N$^2$Me$_2$), 2.28 (s, broad, 6 H, N$^1$Me*Me*), 1.75 (s, 6 H, C*Me*Me), 1.04 (s, 6 H, CMe*Me*) ppm. $^{13}$C{$^1$H} NMR (100 MHz, [D$_8$]toluene, 283 K): $\delta$ = 171.60 (C-2 pyr), 150.11 (C-3 pyr), 135.38 (C-4 pyr), 121.05 (C-5, pyr), 118.26 (C-6 pyr), 80.90 (*C*Me$_2$), 57.78 (broad, NMe), 51.38 (broad, NMe), 43.23 (broad, NMe), 38.60 (C*Me*), 33.36 (C*Me*) ppm. IR [diffuse reflectance]: $\tilde{\nu}$ = 3103 (w), 3078 (w), 3055 (w), 3029 (w), 3001 (w), 2983 (m), 2969 (m), 2955 (m), 2942 (m), 2916 (m), 2846 (s), 2810 (s), 2768 (m), 2755 (s), 2708 (w), 1652 (w), 1631 (w), 1600 (w), 1567 (w), 1546 (w), 1542 (w), 1533 (w), 1475 (m), 1448 (m), 1435 (m), 1414 (w), 1395 (w), 1369 (m), 1347 (m), 1294 (m), 1273 (m), 1245 (s), 1214 (w), 1185 (s), 1155 (s), 1122 (s), 1099 (m), 1078 (m), 1053 (s), 1018 (m), 995 (s), 964 (s), 958 (s), 947 (s), 909 (w), 886 (m), 874 (w), 805 (w), 777 (s), 758 (s), 739 (w), 696 (w), 672 (w), 648 (m), 614 (s), 561 (s), 553 (m), 546 (m), 538 (m), 531 (w), 524 (m), 511 (w), 500 (w), 495 (w), 487 (w) $cm^{-1}$.

**Synthesis of Material 4:** To a suspension of $SiO_2$-700 (116 mg) in pentane (4 mL) was added a solution of **3** (35 mg, $43.10^{-6}$ mol) in pentane (4 mL). The silica rapidly turned to deep red-brown while the supernatant gradually lost its color. After overnight stirring at room temperature, the red-brown solid was separated by filtration, washed with pentane (3 × 8 mL), and dried under vacuum ($10^{-6}$ mbar) to afford 149 mg of **4** as a deep red-brown powder. Elemental analysis (%): C 8.41, H 1.20, N 1.97, W 10.53. IR (diffuse reflectance): $\tilde{\nu}$ = 3081 (w), 3065 (w), 2974 (m), 2923 (m), 2896 (m), 2858 (m), 2816 (m), 2769 (m), 2711 (w), 1607 (m), 1568 (m), 1477 (m), 1568 (m), 1477 (s), 1419 (s), 1375 (s), 1355 (s) $cm^{-1}$. $^1$H MAS (400 MHz): $\delta$ = 9.4 (sh), 7.07, 4.3, 2.07, 1.20, 0.00 ppm. $^{13}$C CP-MAS (100.6 MHz): $\delta$ = 171.8, 150.0, 135.9, 130.4, 119.3, 84.1, 81.7, 57.9, 48.4, 30.5 ppm.

**Catalytic Investigations:** A Schlenk tube was charged with 4-nonyne (1.45 mmol), decane (0.1 mL), and toluene (5 mL), affording solution **A**, and was then heated to 363 K. A second Schlenk tube was charged with **3** (0.0254 mmol), alcohol (0.101 mmol), toluene (1 mL), and was stirred at room temperature for 10 min affording solution **B**. Solution **B** was then injected to solution **A** at 363 K. The reaction was stopped after 1 h by injection of methanol and exposition to air. Conversion and selectivity were measured by GC analysis using decane as the internal standard. Alcohols used for these tests were *tert*-butyl alcohol, 3-quinuclidinol, 1-adamandanol, and phenol.

 © 2007 Wiley-VCH Verlag GmbH & Co. KGaA, Weinheim 

**X-ray Structural Analysis of 3:** Crystal and refinement data are summarized in Table 3. X-ray data were collected with a Bruker SMART CCD area-detector diffractometer with Mo-$K_\alpha$ radiation ($\lambda$ = 0.71073 Å) at $T$ = 100 K. The structure was solved by direct methods.[24] Refinement against $F^2$ was performed by SHELX-97 with anisotropic temperature factors for non-hydrogen atoms and protons at geometrically calculated positions as riding atoms. Residuals in the final Fourier-difference map are probably due to imperfect absorption corrections.

Table 3. Crystallographic data for **3**.

| | |
|---|---|
| Empirical formula | $C_{24}H_{44}N_6O_2W_2$ |
| Formula mass | 816.35 |
| Crystal system | orthorhombic |
| Space group | *Aba*2 |
| *a* [Å] | 10.953(2) |
| *b* [Å] | 14.556(3) |
| *c* [Å] | 18.172(4) |
| *V* [Å $^3$] | 2897.3(10) |
| *Z* | 4 |
| $D_{calcd.}$ [g cm$^{-3}$] | 1.872 |
| $\mu$(Mo-$K_\alpha$) [mm$^{-1}$] | 7.964 |
| *F*(000) | 1576 |
| 2$\theta$ range [°] | 4.48–53.98 |
| Measured reflections | 10234 |
| Unique reflections | 3055 |
| Parameters/restraints | 160/1 |
| Final *R*1 | 0.0250 |
| Final *wR*2 | 0.0571 |
| Goodness of fit | 0.880 |

CCDC-652385 (for **3**) contains the supplementary crystallographic data for this paper. These data can be obtained free of charge from the Cambridge Crystallographic Data Centre via www.ccdc.cam.ac.uk/data_request/cif.

**Supporting Information** (see also the footnote on the first page of this article): $^1$H NMR spectrum (room temp., $C_6D_6$) of intermediate $[W_2(L)(NMe_2)_5]$ obtained from the reaction of **1** with six equivalents of (L)H.

## Acknowledgments

We thank the Centre National de la Recherche Scientifique (CNRS) and the Institut Universitaire de France (IUF) for their financial support and for a Ph. D. grant (to O. C.), and Bertrand Revel, Centre Commun de Mesures RMN, Université des Sciences et Technologies de Lille (USTL), for his assistance with NMR spectroscopy. Nord/Pas de Calais Region, Europe (FEDER), CNRS, French Ministry of Science, USTL and Ecole Nationale Supérieure de Chimie de Lille (ENSCL) are thanked for funding the Bruker 800 MHz spectrometer.

[1] a) A. Fürstner, P. W. Davies, *Chem. Commun.* **2005**, 2307–2320; b) A. Mortreux, O. Coutelier, *J. Mol. Catal., A* **2006**, *254*, 96–104; c) W. Zhang, J. S. Moore, *Adv. Synth. Catal.* **2007**, *349*, 93–120.
[2] R. R. Schrock, *Adv. Synth. Catal.* **2007**, *349*, 25.
[3] a) R. R. Schrock, M. L. Liestmann, L. G. Sturgeoff, *J. Am. Chem. Soc.* **1982**, *104*, 4291–4293; b) S. A. Krouse, R. R. Schrock, *Macromolecules* **1989**, *22*, 2569–2576.
[4] O. Coutelier, A. Mortreux, *Adv. Synth. Catal.* **2006**, *348*, 2038–2042.
[5] P. Braunstein, F. Naud, *Angew. Chem. Int. Ed.* **2001**, *40*, 680–699.
[6] a) O. Coutelier, G. Nowogrocki, A. Mortreux, *Abstracts of the 16th International Symposium on Olefin Metathesis and Related Chemistry*, Poznan, **2005**; b) O. Coutelier, J.-F. Paul, A. Mortreux, *Adv. Synth. Catal.*, accepted.
[7] For examples of complexes bearing bidentate pyridylalkoxido ligands, see: a) I. Kim, Y. Nishihara, R. F. Jordan, R. D. Rogers, A. L. Rheingold, G. P. A. Yap, *Organometallics* **1997**, *16*, 3314–3323; b) W. A. Herrmann, J. Fridgen, G. M. Lobmaier, M. Spiegler, *New J. Chem.* **1999**, *23*, 5–7; c) S. Bellemin-Laponnaz, K. S. Coleman, J. A. Osborn, *Polyhedron* **1999**, *18*, 2533–2536.
[8] a) M. Chabanas, A. Baudouin, C. Copéret, J.-M. Basset, *J. Am. Chem. Soc.* **2001**, *123*, 2062–2063; b) H. Weissman, K. N. Plunkett, J. S. Moore, *Angew. Chem. Int. Ed.* **2006**, *45*, 585–588.
[9] R. M. Gauvin, O. Coutelier, E. Berrier, A. Mortreux, L. Delevoye, J.-F. Paul, A.-S. Mamède, E. Payen, *Dalton Trans.* **2007**, 3127–3130.
[10] M. H. Chisholm, *Acc. Chem. Res.* **1990**, *23*, 419–425.
[11] M. H. Chisholm, *Polyhedron* **1983**, *2*, 681–722.
[12] M. Akiyama, M. H. Chisholm, F. A. Cotton, M. W. Extine, D. A. Haitko, D. Little, P. E. Fanwick, *Inorg. Chem.* **1979**, *18*, 2266–2270.
[13] J. T. Barry, J. C. Bollinger, M. H. Chisholm, K. C. Glasgow, J. C. Huffman, E. A. Lucas, E. B. Lubkovsky, W. E. Streib, *Organometallics* **1999**, *18*, 2300–2308.
[14] See for example: a) F. A. Cotton, B. R. Stults, J. M. Troup, M. H. Chisholm, M. Extine, *J. Am. Chem. Soc.* **1975**, *97*, 1242–1243; b) H. Schultz, K. Folting, J. C. Huffman, W. E. Streib, M. H. Chisholm, *Inorg. Chem.* **1993**, *32*, 6056–6066.
[15] H. Günther, *La Spectroscopie de RMN*, 5th ed., Masson, Paris, France, **1993**.
[16] M. H. Chisholm, F. A. Cotton, *Acc. Chem. Res.* **1978**, *11*, 356–362.
[17] F. J. Feher, T. A. Budzichowski, *Polyhedron* **1995**, *14*, 3239–3253.
[18] C. Copéret, M. Chabanas, R. P. Saint-Arroman, J.-M. Basset, *Angew. Chem. Int. Ed.* **2003**, *42*, 156–181.
[19] For examples of grafting of amido complexes onto inorganic supports, see: a) Q. Zhuang, K. Tanaka, M. Ichikawa, *J. Chem. Soc. Chem. Commun.* **1990**, 1477–1478; b) S. Grasser, C. Haessner, K. Koehler, F. Lefebvre, J.-M. Basset, *Phys. Chem. Chem. Phys.* **2003**, *5*, 1906–1911; c) F. Blanc, J. Thivolle-Cazat, J.-M. Basset, C. Copéret, A. S. Hock, Z. J. Tonzetich, R. R. Schrock, *J. Am. Chem. Soc.* **2007**, *129*, 1044–1045.
[20] The peak observed at $\delta$ = 0.1 ppm cannot be assigned to silicon grease, which was not used at any point in our syntheses, and for which no $^{13}$C NMR signal is detected.
[21] I. Schnell, S. P. Brown, H. Y. Low, H. Ishida, H. W. Spiess, *J. Am. Chem. Soc.* **1998**, *120*, 11784–11795.
[22] M. H. Chisholm, J. D. Martin, J. E. Hill, I. P. Rothwell, *Inorg. Synth.* **1992**, *29*, 137–140.
[23] D. Massiot, F. Fayon, M. Capron, I. King, S. Le Calvé, B. Alonso, J.-O. Durand, B. Bujoli, Z. Gan, G. Hoatson, *Magn. Reson. Chem.* **2002**, *40*, 70–76.
[24] a) *SMART Software Users Guide*, version 5.0, Bruker Analytical X-ray Systems, Inc., Madison, WI, USA, **1999**; b) *SAINT Software Users Guide*, version 6.0, Bruker Analytical X-ray Systems, Inc., Madison, WI, USA, **1999**; c) G. M. Sheldrick, *SADABS*, Bruker Analytical X-ray Systems, Inc., Madison, WI, USA, **1999**; d) G. M. Sheldrick, *SHELXTL*, version 5.10, Bruker Analytical X-ray Systems, Inc., Madison, WI, USA, **1999**.

Received: July 11, 2007
Published Online: October 17, 2007

 © 2007 Wiley-VCH Verlag GmbH & Co. KGaA, Weinheim 

DOI: 10.1002/ejic.200700784

# Flexible $Cu^{I}$–Thiolate Clusters with Relevance to Metallothioneins

**Biplab K. Maiti,[a] Kuntal Pal,[a] and Sabyasachi Sarkar*[a]**

**Keywords:** Metallothioneins / Flexibility / Coordination modes / Copper / Sulfur / Photoluminescence

Simple Cu–thiolate chemistry was developed to demonstrate the presence of copper clusters with $\{Cu_4S_6\}$, $\{Cu_5S_7\}$ and $\{Cu_6S_4\}$ cores in relevance to copper-containing metallothioneins. The new hexanuclear tricoordinate triply bridging thiolatocopper(I) clusters $[NEt_4]_4[Cu_6(SPh)_4Cl_6]$ (**1**) and $[NEt_4]_4[Cu_6(SPh)_4Br_6]$ (**2**) were synthesized from the soup of polymeric $[Cu^{I}SPh]_n$ and quaternary ammonium halide. These complexes readily converted into $[Et_4N]_2[Cu_5(SPh)_7]$ (**3**) and $[Et_4N]_2[Cu_4(SPh)_6]$ (**4**) in the presence of excess amounts of thiol. All are structurally characterized by single-crystal X-ray crystallography and these smaller clusters may be inscribed into the structurally characterized larger cluster $\{Cu_8S_{10}\}$ obtained from synthetic copper yeast metallothioneins. Like Cu–MT proteins, all these clusters show photoluminescence around 560 nm on excitation at 350 nm, and these emission spectra are completely quenched by molecular oxygen. Variable copper stoichiometry and the interconversion of only monodentate thiolate ligands in these clusters convey the importance of flexibility, which is relevant to metallothioneins.
(© Wiley-VCH Verlag GmbH & Co. KGaA, 69451 Weinheim, Germany, 2007)

## Introduction

Intracellular copper is transiently associated with small copper-binding proteins as copper chaperones that distribute copper to specific intracellular destinations and to metallothioneins (MT). MT is a class of low molecular weight cysteine rich proteins that generally shuffle essential metal ions like copper and zinc in biosystems, and they are present in all animal phyla as well as in certain fungi, plants and cyanobacteria.[1–7] The protection of cells against toxic metal ions through the process of sequestration is another role played by these proteins. MT proteins from varied species showed to share a particular set of sequence-specific characters with the consensus sequence -CxCxxxxCxC- and -CxCxxxxxCxC- motifs.[8] These four cysteine units may thus be used to complex copper ions besides other cysteine moieties located differently in apo-MT proteins. In Cu–MT coordination chemistry, the $Cu^{I}$/protein stoichiometry is varied because of the diverse functions of copper, such as acquisition, metabolism, storage and transport. Among these, in vitro synthesized N.crassa MT was shown to provide flexible polypeptide folds that may be influenced by the variable coordination number of copper, which results from metal–thiolate clusters with varied stoichiometries, such as $Cu_4(CysS)_7$($Cu_4$–NcMT) or $Cu_6(CysS)_7$($Cu_6$–NcMT).[8] A neuronal growth inhibitory factor, metallothionein-3, was shown to contain the $Cu_4(CysS)_9$ ($Cu_4$-humanMT-3) cluster located in the N-terminal β-domain of the protein, which can further be loaded with copper to yield a $Cu_6(CysS)_9$ cluster.[9] The isolation of a synthesized $Cu_8(CysS)_{10}$($Cu_8$-yeastMT) cluster is thought to crystallize from a solution of $Cu_7$-yeastMT, which leaves the $Cu_6$ cluster in solution.[10] In contrast to zinc, which normally retains a tetrahedral coordination, the ready adaptation of $Cu^{I}$ to diagonal, trigonal or tetrahedral coordination geometries has made the chemistry of Cu–MT diverse and interesting. In the large $Cu_8$–$S_{10}$ cluster, the only two diagonal Cu binding sites are thought to be responsible for trafficking copper in biological systems, and this ability is attributable to the labile bonding of these two copper atoms.[10,11] Prediction of the formulation of the copper–thiolate cluster is also hindered by the ability of the sulfur atom of the cysteinyl moiety to link the bridging ligand in a $\mu_2$-S or $\mu_3$-S fashion. Furthermore, the possibility of a large degree of folding in the protein may account for the structural interplay of these copper clusters. Among the common $Cu_n$ clusters ($n$ = 4,[12] 6,[8,9] 7[13] and 8[10,11]) known to be present in Cu–MT, the varied ligation number of the thiolate ion ($CysS_m$, $m$ = 4 to 11) contributes to the diverse stoichiometry that one can anticipate in Cu–MT clusters. Accordingly, many examples of monodentate thiolatocopper(I) clusters have been reported so far by X-ray crystallography[14–16] [$CuS_2$,[17] $CuS_3$,[18,19] $Cu_2S_2$,[20] $Cu_3S_3$,[21] $Cu_4S_4$,[22] $Cu_4S_6$,[18,23–26] $Cu_5S_6$,[27,28] $Cu_5S_7$,[29] $Cu_6S_4$ (in this work) $Cu_7S_8$,[30] $Cu_8S_8$[31] and $Cu_{12}S_{12}$[32]].

[a] Department of Chemistry, Indian Institute of Technology Kanpur,
Kanpur 208016, India
Fax: +91-512-2597265
E-mail: abya@iitk.ac.in
Supporting information for this article is available on the WWW under http://www.eurjic.org or from the author.


© 2007 Wiley-VCH Verlag GmbH & Co. KGaA, Weinheim

On the basis of this principle, we allowed the free assembly of discrete copper(I)–thiolate clusters from the soup of polymeric $[Cu^ISPh]_n$[33] and quaternary ammonium halide in the presence or absence of an excess amount of thiolate ions. We report herein the first synthesis of the hexanuclear tricoordinate triply bridging thiolatocopper(I) clusters $[NEt_4]_4[Cu_6(SPh)_4Cl_6]$ (**1**) and $[NEt_4]_4[Cu_6(SPh)_4Br_6]$ (**2**). They were characterized by X-ray crystallography as well as by spectroscopic methods, including UV/Vis and luminescence, and their ready interconversion with $[Et_4N]_2[Cu_5(SPh)_7]$ (**3**) and $[Et_4N]_2[Cu_4(SPh)_6]$ (**4**). All these smaller clusters may be inscribed into the structurally characterized larger cluster $\{Cu_8S_{10}\}$ obtained from the synthesized copper yeast metallothioneins. From a synthetic analogue approach, the present study is based on the filling of this gap to achieve this specific cluster arrangement.

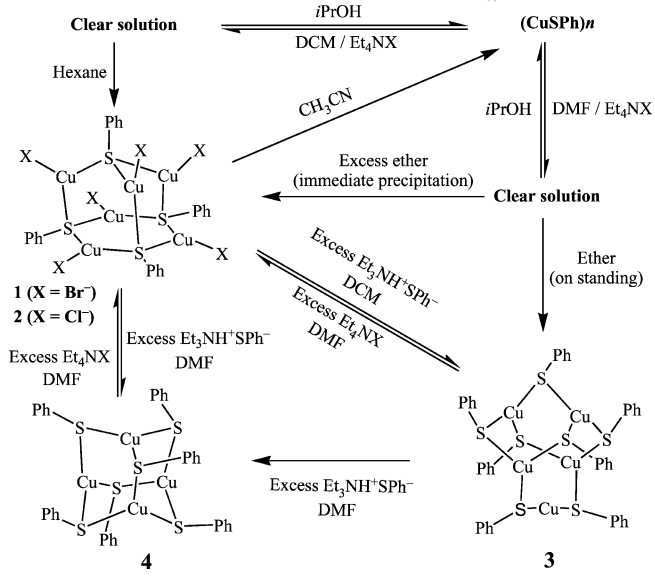


Scheme 1. The facile interconversion of $Cu_4$-, $Cu_5$- and $Cu_6$ clusters.

## Results and Discussion

### Synthesis

$Cu^I$–thiolate clusters are known and earlier synthetic strategies generally involved the use of $Cu^{II}$ ions to exploit the reducing power of the thiolate group used as a ligand. This synthetic protocol led to the formation of a mixture of products such as $[Me_4N]_2$ salt of **3** and **4**[34] and both were crystallized out. In another procedure, the use of $Cu^I$ as the source material was made and this was treated with KSPh in acetonitrile and the $[PPh_4]_2$ salt of **4**[18] was isolated. Alternatively, $[PPh_4]_2[Cu(SPh)_3]$[18] was treated with $[Cu(CH_3CN)_4]ClO_4{\cdot}2H_2O$ in boiling acetonitrile to synthesize the same compound, but the yield of the product in these procedures was not reported. In the present work, our intention was to understand the solubility of the Cu–thiolate polymer in the form of isolable discrete cluster anions as quaternary ammonium ion salts in the presence or absence of an excess amount of thiolate ions. The hexanuclear copper(I)–thiolate complexes having $Cu_6S_4X_6$ (X = $Cl^-$ and $Br^-$) (Scheme 1) were synthesized by treating $(CuSPh)_n$[33] with the respective quaternary ammonium halide salt ($Et_4NX$) in a 1:1 molar ratio of CuSPh/$Et_4NX$ to produce **1** and **2** as block-shaped colourless crystals in high yield.

By changing the reaction medium and by performing the reaction in the presence of available thiolate ions, the synthesis of **3** and **4** and the mutual interconversion of all four (**1**–**4**) of these discrete clusters was followed by electronic spectroscopy as shown in Figure S1 (Supporting Information). Our attempt to increase the ligation of the thiolate ions by metathesis of **1** or **2** by anticipating the formation of $\{Cu_6(SPh)_{10}\}$ in light of attaining maximum thiolate ligation similar to those reported in the MT proteins was thwarted by the isolation of **3** and **4** instead. Compound **3** was synthesized by the reaction of CuSPh with $Et_4NCl$ in a 1:1 molar ratio in DMF as bright-yellow needle-shaped crystals in high yield. It is noteworthy that **3** crystallized out of solution on standing after the addition of diethyl ether. In contrast, the addition of an excess amount of diethyl ether caused rapid precipitation of the $Cu_6$ cluster instead. The reactions of **1** or **2** with excess amounts of thiolate ions afforded solvent-dependent formation of **3** and **4** in almost quantitative yields. In less polar solvents, such as DCM, the reaction of **1** or **2** with an excess amount of thiolate afforded **3**, whereas in more polar solvents, such as DMF, the reaction led to the formation of **4**. It was found that the transformation of **1** into **3** was very facile in the reverse direction. The reversal of **4** to **1** or **2** may also readily be achieved by the addition of an excess amount of countercation in DMF, but **3** may be converted irreversibly into **4** in DMF. Compounds **1** and **2** in $CH_3CN$, and in any other protic solvent, decompose with the precipitation of insoluble $(CuSPh)_n$[33] and the release of $[Et_4N]X$ (X = Cl and Br) into the solution. The interconversion between these compounds is dependent on the solvent used and on the Cu/S ratio. The Cu/S ratio in Cu–MT may be affected by the surrounding environment or even by a variation in the cysteine content of the peptide; however, it is important to note that the availability of Cu is the key factor affecting the stoichiometry of the Cu/S clusters in MT. All these compounds, when present in solution, are susceptible to aerial oxidation, which leads to decomposition. Even in the solid state, surface oxidation of **1** or **2** is noticed on exposure to air, and the surface turns from pure white to white with a greenish tinge. EPR response of this reaction clearly indicates that EPR inactive $Cu^I$ is oxidized to EPR active $Cu^{II}$.

### Description of Structures

Suitable diffraction quality single crystals of all the reported complexes were made according to the procedure described in the corresponding synthesis section. Details of the crystallographic data collection and refinement parameters are provided in Table 3.

 © 2007 Wiley-VCH Verlag GmbH & Co. KGaA, Weinheim 

Crystals of chloro and bromo compounds **1** and **2**, respectively, are isostructural, triclinic, $P\bar{1}$ and have the same number of formula units ($Z = 2$) in each unit cell of very similar dimensions. Complexes **1** and **2** exhibit a $Cu_6S_4X_6$ core (Figure 1), which is constructed from the aggregation of six $Cu^I$ centres, six halide (Cl or Br) atoms and four S (benzenethiolate) atoms.

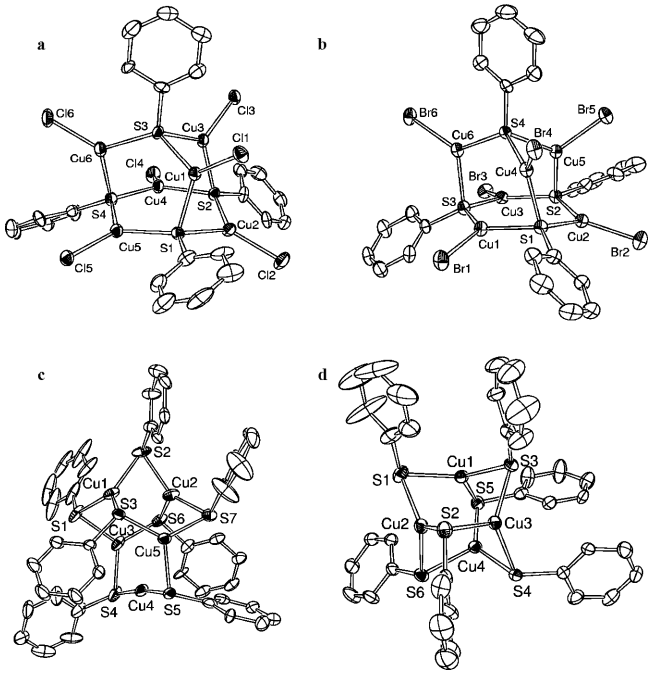


Figure 1. The structure (ORTEP view) of the complex anion of (a) **1**; (b) **2**; (c) **3** and (d) **4**. The atomic numbering scheme is shown and the thermal ellipsoids are drawn at the 50% probability level; hydrogen atoms have been omitted for clarity.

Compounds **1** or **2** can be divided into two segments to form one $Cu_3S_3X_3$ unit (bottom segment) and one $Cu_3SX_3$ unit (top segment) (atoms labelled with superscript b and t, respectively). These two units are bound by the S atom of the thiolate that bridges two Cu atoms in $Cu^b{}_3S^b{}_3$ and is bound to the Cu atom in $Cu^t{}_3S^t$. The top $S^t$Ph ligand is directed axially and is perpendicular to the virtual $Cu^t{}_3$ plane. Each copper atom in the top is three coordinate and forms bonds from one S atom and one halogen atom in the same segment and one S atom from the bottom segment. In this way, a core is formed that comprises a fused six-membered $Cu_3S_3$ ring: one for the bottom (almost planar hexagon) and three for the side faces (pseudochair configuration). Each copper atom in the bottom is three coordinate with bonds from two S atoms and one halogen atom in the same segment, and these $S^b$Ph ligands are around the equatorial girdle and form a virtual $Cu^b{}_3$ plane. The two $Cu_3$ triangle bases are oriented face-to-face and are rotated by ca. 45°. Each copper centre in the cluster adopts an approximately trigonal planar geometry, and it is coordinated to two thiolate ligands and a halide ion. The mean angle at the coordinated copper is 119.75(7)° for **1** and 119.95(6)° for **2**, which suggests an almost trigonal planar geometry of the copper centre in these complexes. Each sulfur atom of the phenylthiolate ligand within the cluster adopts an approximate tetrahedral geometry that coordinates three trigonally coordinated copper atoms (triply bridging thiolate ligand). The Cu–S bond lengths [mean 2.2465(17) Å for **1** and mean 2.2502(18) Å for **2**][35] are dependent on the coordination number of the copper atom and distinct ranges can be distinguished: 2.14–2.17 Å for two coordinate[29,36] copper atoms, 2.22–2.23 Å for three coordinate[18,23–26,37] copper atoms and 2.33–2.48 Å for four coordinate[38–40] copper atoms, and the Cu···Cu separations range from 2.8622(12) to 4.0699(13) Å for **1** and from 2.8242(13) to 4.0557(13) Å for **2**. Bond lengths and angles are listed in Table 1.

The type of $Cu_4S_6$ and $Cu_5S_7$ core[18,23,26,29] observed for **3** and **4** (Figure 1), respectively, were structurally characterized previously for monodentate S donor ligands in $[Cu_4(SPh)_6]^{2-}$ and $[Cu_5(SPh)_7]^{2-}$ with $[Me_4N]$ and $[PPh_4]$ salts, and the dimension of these cores as $[Et_4N]$ salts are detailed in Table 3. Complexes **1**, **2** and **4** possess tricoordinated copper; in **1** and **2** $\mu_3$-SPh bridging exists, whereas in **4**, $\mu_2$-SPh bridging is present. Unlike **1**, **2** or **4**, compound **3** possesses both tri- and bicoordinated copper but with only a $\mu_2$-SPh bridging ligand. Similar to **1** or **2**, the Cu–S bonds in Cu–thiolate bridges in **3** or **4** range from 2.159 to 2.309 Å. This may be compared with the Cu–S–Cys bonds in the range from 2.145 to 2.395 Å found in the structurally characterized $Cu_8(CysS)_{10}$ ($Cu_8$-yeastMT) cluster.[10] The $Cu_8(CysS)_{10}$ ($Cu_8$-yeastMT) cluster[10] can be described as two groupings of four copper atoms; both groups have a flattened tetrahedron structure and two of the eight copper atoms are diagonally coordinated and the six others are trigonally coordinated with doubly and triply bridging cysteine moieties, as highlighted in Figure 2.

Structurally characterized clusters **1**, **2**, **3** and **4** may be inscribed within the structurally characterized $Cu_8(CysS)_{10}$ ($Cu_8$-yeastMT) cluster in Figure 2 and comparison of the Cu–S distance in **1**, **2**, **3**, **4** and $Cu_8(CysS)_{10}$ ($Cu_8$-yeastMT) cluster are listed in Table 2. In Figure 2, cluster **4** is placed on the left side (Cu1, Cu2, Cu3 and Cu4) of the larger cluster, $Cu_8(CysS)_{10}$ and **3** are placed on the right side (Cu4, Cu5, Cu6, Cu7 and Cu8) of the larger cluster $Cu_8(CysS)_{10}$, and both share one common copper atom (Cu4). The Cu1 atom of the larger cluster is bonded with S1 and S3 but Cu1 in **4** is tricoordinated with an extra bond to S5. The bicoordinated Cu1 in $Cu_8$-yeastMT is directly related to its labile nature in displaying copper trafficking properties. The two diagonally coordinated copper ions (Cu1 and Cu8) are more labile than other copper atoms in $Cu_8(CysS)_{10}$. In this respect, $Cu_6$ clusters **1** or **2** are more important. In Figure 2, the six copper ions in $Cu_8(CysS)_{10}$ [(Cu2, Cu4 and Cu6) and (Cu3, Cu7 and a missing Cu as shown encircled)] can be described as grouped into two set of three, both of which have planar triangle geometry and linked by sulfur. A closer inspection shows that for $Cu_8$-yeastMT, middle part of the skeleton have similar structural motif of **1** or **2** as shown in Figure 2.

 © 2007 Wiley-VCH Verlag GmbH & Co. KGaA, Weinheim 

Table 1. Bond lengths (Å) and angles (°) of **1** and **2**.

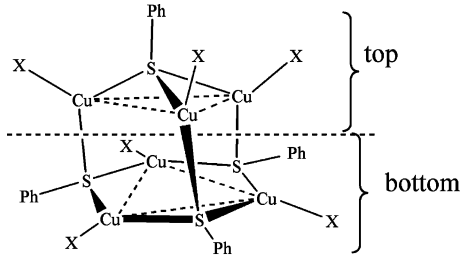


X = Cl (1) and Br (2)

| Parameter | Range (average) of **1** | Range (average) of **2** |
|---|---|---|
| Within top segment[a] | | |
| Cu–S | 2.244–2.258 (2.251) | 2.243–2.251 (2.245) |
| Cu···Cu | 2.862–3.860 (3.504) | 2.833–3.819 (3.484) |
| Cu–S–Cu | 79–118 (105) | 78–117 (103) |
| Cu–Cu–Cu | 44–69 (60) | 44–69 (60) |
| Within bottom segment[a] | | |
| Cu–S | 2.244–2.258 (2.251) | 2.243–2.251 (2.245) |
| Cu···Cu | 2.862–3.860 (3.504) | 2.833–3.819 (3.484) |
| Cu–S–Cu | 79–118 (105) | 78–117 (103) |
| Cu–Cu–Cu | 44–69 (60) | 44–69 (60) |
| Interaction from top to bottom[a] | | |
| Cu–S | 2.236–2.268 (2.250) | 2.230–2.265 (2.247) |
| S–Cu–S | 103–118 (113) | 105–122 (115) |

[a] See above schematic representation.

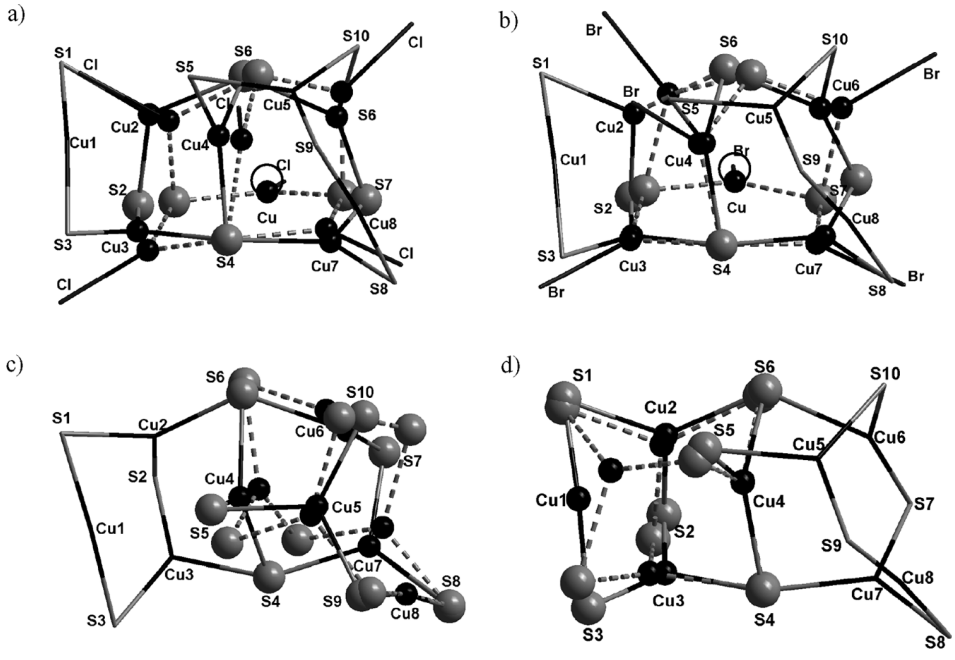


Figure 2. Ball & stick models: (a) superposition of the $\{Cu_6S_4\}$ framework (broken line) of complex anion **2** and the $\{Cu_6S_4\}$ core (represented Cu2–S2–Cu3–S4–Cu4–S6–Cu6–S7–Cu7 and one missing copper position marked in circle) of $Cu_8$-yeastMT; (b) superposition of the $\{Cu_6S_4\}$ framework (broken line) of complex anion **1** and the $\{Cu_6S_4\}$ core (represented Cu2–S2–Cu3–S4–Cu4–S6–Cu6–S7–Cu7 and one missing copper position marked in circle) of $Cu_8$-yeastMT; (c) superposition of the $\{Cu_5S_7\}$ framework (broken line) of complex anion **3** and the $\{Cu_5S_7\}$ core (represented Cu4–S4–S5–Cu5–S9–S10–Cu6–S6–Cu7–S7–Cu8–S8) of $Cu_8$-yeastMT; (d) superposition of the $\{Cu_4S_6\}$ framework (broken line) of complex anion **4** and the $\{Cu_4S_6\}$ core (represented Cu1–S1–Cu2–S2–Cu3–S3–S4–Cu4–S5–S6) of $Cu_8$-yeastMT.

 © 2007 Wiley-VCH Verlag GmbH & Co. KGaA, Weinheim 

Table 2. Comparison of Cu–S distances in **1**, **2**, **3**, **4** and $Cu_8$–MT.

| Parameter | **1** | **2** | **3** | **4** | $Cu_8$–MT |
|---|---|---|---|---|---|
| Bridging mode of S | $\mu_3$-SR | $\mu_3$-SR | $\mu_2$- & $\mu_3$-SR | $\mu_2$-SR | $\mu_2$- & $\mu_3$-SR |
| Coordination at Cu centre | $S_2Cl$ | $S_2Br$ | $S_2$ & $S_3$ | $S_3$ | $S_2$ & $S_3$ |
| Cu–S | 2.244–2.258 Å | 2.243–2.251 Å | 2.160– 2.297 Å | 2.245–2.306 Å | 2.139–2.395 Å |

### Electronic and Photoluminescent Spectra

Complexes **1** and **2** are colourless and display featureless electronic spectra with a strong absorption in the UV region. As shown in Figure 3, the UV/Vis absorption spectrum of **1** in DCM showed a strong absorption centred at $\lambda_{max}$ = 272 nm ($\varepsilon$ = 27800 $M^{-1}cm^{-1}$). Likewise, the absorption spectrum for complex **2** is similar: $\lambda_{max}$ = 266 nm ($\varepsilon$ = 33100 $M^{-1}cm^{-1}$).

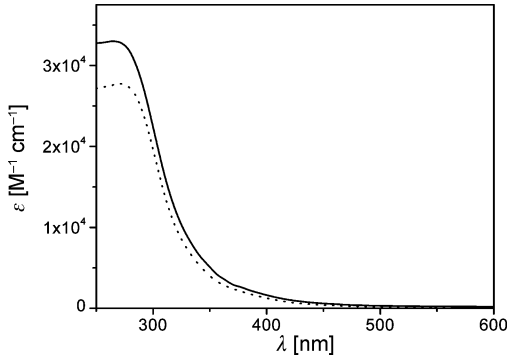


Figure 3. Absorption spectra of complex **1** (broken line) and **2** (solid line) at room temperature in DCM.

Excitation spectra of solid samples of hexanuclear copper(I) complexes **1** and **2** are shown in Figure 4. Compound **2** exhibits a broad excitation band centred at $\lambda_{ex}$ = 346 nm with a weak shoulder at 425 nm, whereas an intense band is observed at $\lambda_{ex}$ = 346 nm for corresponding solid complex **1**.

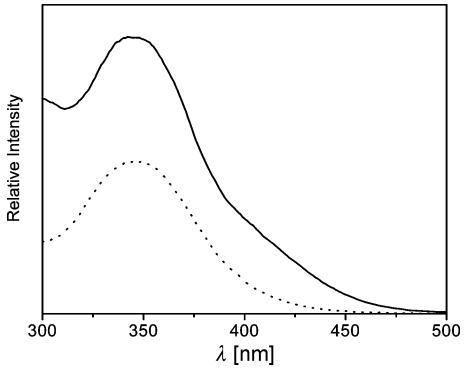


Figure 4. Excitation spectra of **1** (broken line) and **2** (solid line) at room temperature in the solid state.

Photoluminescence is a powerful tool to investigate the structural information of Cu–MTs because of the characteristic luminescence properties of the $Cu^I$–thiolate clusters. Complexes **1** to **4** display photoluminescence like other copper–sulfur clusters.[41,42] Compounds **1**, **2** and **3** each exhibit an intense emission band in the range 555–573 nm (excitation at 350 nm), whereas under identical conditions, a very weak emission at 572 nm (excitation at 350 nm) was observed from **4** (Figure 5). Possible assignment of transition is considered as: (1) ligand-to-metal CT (LMCT), (2) the halide-to-metal CT (XMCT), (3) transition in Cu cluster (CC–MOs), (4) halide-to-ligand CT (XLCT) and (5) $Cu^I$ d–s transition.

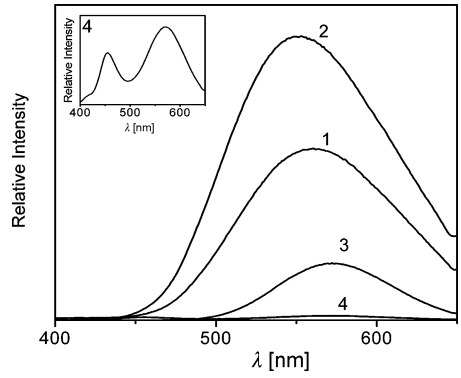


Figure 5. Emission spectra of **1** (560 nm), **2** (555 nm), **3** (573 nm) and **4** (572 nm) at room temperature in the solid state (excitation at 350 nm); inset: the emission spectra of **4** in relatively enlarged scale of intensity.

From a structural viewpoint, cluster **1** and **2** ($Cu_6$ cluster) both have long Cu···Cu separations (>2.8 Å). So, transition in Cu clusters (CC–MOs) does not contribute in the emission spectra. However, the charge-transfer emission band depends on the metal coordination ligand. Given the strong electron-donating ability of the thiolate ligand, it is expected that the origin of the emission is due to thiolate–copper(I) (LMCT) transition. Contributions like XMCT and XLCT may be minor, if they exist. The emission spectrum of **4** shows two bands at 436 nm and 572 nm. The low-energy emission band is attributed to thiolate–copper(I) (LMCT) transition and the high-energy band to CC origin (the Cu···Cu separation <2.8 Å). Compound **3** exhibits an emission band at 573 nm, which may originate from LMCT states in accord with the electron-donating ability of the thiolate ligands. The observed differential emission intensity must be based on the cluster size and the Cu/S stoichiometry. The loss in intensity of **1** than **2** is due to some oxidation of $Cu^I$ to $Cu^{II}$ during (see latter) isolation in atmospheric air. The Cu–MT proteins have been found to exhibit significant luminescence,[43–45] which is related to the $Cu^I$–thiolate chromophore and Cu–S protein emission lies from 580–700 nm at room temperature. Like Cu–MT proteins, clusters **1**–**4** show photoluminescence in the region around 560 nm on excitation at 350 nm (Figure 5). Interestingly, such emission property can help to identify the Cu/thiol stoichiometry in apo-NcMT proteins.[8] However, with the option of varying the ability of

 © 2007 Wiley-VCH Verlag GmbH & Co. KGaA, Weinheim 

complexation of $Cu^I$ with the overall sulfahydryl groups present in such proteins, the intensity of the emission spectra may be deceptive to extract the actual stoichiometry of the Cu–MT proteins. The difference in Cu/MT stoichiometry in such reconstitution by using apo-NcMT and Zn–NcMT is noteworthy to reflect the possibility in the use of different sulfahydryl groups based on the flexibility of the MT. Complex **1** is found to be more oxygen sensitive and even in the solid its white surface slowly developed a greenish tinge and displayed the appearance of EPR-active $Cu^{II}$ concomitant to the quenching of the emission around 560 nm (Figure 6).

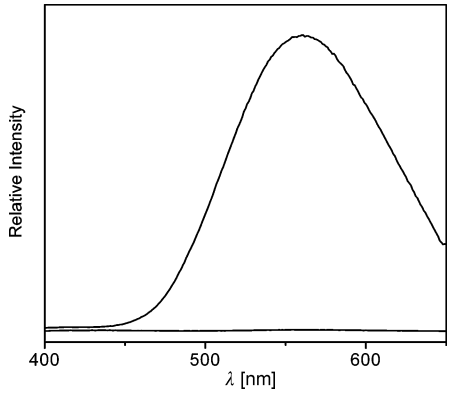


Figure 6. Emission spectra of **1** in the solid state at room temperature: (a) freshly prepared; (b) after 24 h exposure to air.

## Conclusions

We demonstrated the facile interconversion of Cu–SPh clusters with different stoichiometries in relation to the flexibility of MT proteins. The structural variations in these synthesized clusters in solution clearly demonstrate their ability to shuffle copper ions interplaying the overall coordinating ability of the copper cluster, which is not dependent on the nature of the bridging thiolate ion.[46–48] It is to be noted that in the synthesized $Cu_8$-yeastMT cluster[10] or in $Cu_7$-saccharomyces cerevisiae,[12] the presence of the $Cu_6$ cluster is predicted because of the loose coordination of the terminal copper ions. Interestingly, the Cu–S–Cys bond (2.144 Å) between Cu44 and Cys7 is one of the shortest Cu–S–Cys bonds present in the $Cu_8$-yeastMT cluster,[10] but this bond is readily broken and loses the Cu44 ion in solution. This is due to the exposure of this end of the cluster to solvent where this copper can be readily dissociated in solution.[10] We also demonstrated that such copper ion shuffling is possible with a change in solvent under ambient conditions. The Cu/S ratio in Cu–MT can be affected by the surrounding environment or even be variations in the cysteine content; however, it is important to note that the availability of Cu is the key factor affecting the stoichiometry of the Cu/S clusters in MT. The well-known complexity of copper(I)–thiolates is greatly enhanced when moving towards the cysteine rich copper-metallothioneins, whose flexibility is not only due to the lability of the metal–sulfur bond but also to the mobility of the peptide chain.[10] Thus, variation in the folding in this class of proteins may be related to the uptake and release of a copper ion. The different degree of incorporation of copper ions as observed in identifying $Cu_4$ clusters in direct interaction with copper ions with an apo-MT is in contrast with the formation of a $Cu_6$ cluster formed by the displacement of a zinc ion from Zn–MT[8,49–52] and directly related to structural variations influenced by the coordination of zinc ions subsequent to their displacement by copper ions.

## Experimental Section

**General:** All the reactions were carried out under an inert atmosphere and under ambient conditions. $Et_4NBr$, $Et_4NCl$ and thiophenol were obtained from standard commercial sources. Solvents were distilled and dried by standard procedure. Elemental analyses for carbon, hydrogen, nitrogen and sulfur analysis were recorded with a Perkin–Elmer 2400 microanalyzer. Electronic spectra were recorded with a Cintra 10 UV/Vis spectrophotometer. The emission spectra were recorded with a fluorolog fluorescence spectrophotometer. EPR spectra were measured with a Varian E-109 and with a Bruker EMX X-band EPR spectrometer at room temperature in solid sample. NMR spectra were recorded with a JEOL JNM-LA 400 FT–NMR machine. $[Cu^ISPh]_n$ was prepared by a literature procedure.[33]

**$[Et_4N]_4[Cu_6(SPh)_4Cl_6]$ (1):** To a suspension of polymeric $[Cu^ISPh]_n$ (0.34 g, 2 mmol) in DMF (25 mL) was added $Et_4NCl$ (0.49 g, 3 mmol). The mixture was stirred at room temperature to afford a clear-yellow solution within 10 min. An excess amount of diethyl ether (≈ 100 mL) was added to precipitate the light yellow product and this was separated by filtration, washed with 2-propanol to remove any unreacted $Et_4NCl$ followed by diethyl ether and vacuum dried. Compound **1** was crystallized by dissolving it in DCM and by adding hexane and was isolated as colourless blocks. The crystal when free from solvent is very susceptible to loose coordinated solvent molecules, which results in opacity and brittle crystals. Freshly isolated transparent crystals on dissolution in DMSO decomposed to release $Et_4NCl$ and the solvent in the lattice. Yield: 0.38 g (75%). $^1H$ NMR (400 MHz, [D$_6$]DMSO): $\delta$ = 1.154 (t, $J$ = 7.1 Hz, 3 H, $CH_3$), 3.199 (q, $J$ = 7.1 Hz, 2 H, $CH_2$), 5.731 (s, 2 H) ppm. NMR showed the presence of $CH_2Cl_2$; proton integration provided roughly $1.5CH_2Cl_2$ per molecule of the complex. $C_{56}H_{100}Cl_6Cu_6N_4S_4$ (1551.69): calcd. C 43.31, H 6.44, N 3.61, S 8.25; found C 43.45, H 6.62, N 3.57, S 8.23.

**$[Et_4N]_4[Cu_6(SPh)_4Br_6]$ (2)**

**Method 1:** A procedure similar to that described for the synthesis of **1** was carried out with $Et_4NBr$ (0.66 g, 3 mmol) in place of $Et_4NCl$ to afford a light yellow precipitate. Compound **2** crystallized from DCM/hexane as colourless blocks. Yield: 0.48 g (80%).

**Method 2:** To a solution of **3** (0.34 g, 0.25 mmol) in DMF (25 mL) was added an excess amount of $Et_4NBr$. The mixture was stirred to afford a light yellow solution within 15 min. An excess amount of diethyl ether (≈ 100 mL) was added to precipitate the crude product. This was separated by filtration and washed with 2-propanol to free it from excess $Et_4NBr$. The product was crystallized from DCM/hexane as colourless blocks. The ready loss of solvent for this complex is similar to that observed with **1**. Yield: 0.31 g (65%). $^1H$ NMR (400 MHz, [D$_6$]DMSO): $\delta$ = 1.145 (t, $J$ = 7.1 Hz, 3 H, $CH_3$), 3.192 (q, $J$ = 7.1 Hz, 2 H, $CH_2$), 5.734 (s, 2 H) ppm. NMR showed the presence of $CH_2Cl_2$ and integration provided $1.5CH_2Cl_2$ per molecule of **2**. $C_{56}H_{100}Br_6Cu_6N_4S_4$ (1818.38): calcd. C 36.96, H 5.5, N 3.08, S 7.04; found C 37.02, H 5.68, N 2.99, S 7.01.

 © 2007 Wiley-VCH Verlag GmbH & Co. KGaA, Weinheim 

**$[Et_4N]_2[Cu_5(SPh)_7]$ (3)**

**Method 1:** To a solution of **2** (0.45 g, 0.25 mmol) in DCM (25 mL) was added a mixture of HSPh (1 mL) and $Et_3N$ (0.5 mL). The mixture was stirred at room temperature to afford a light-yellow solution. Into this solution was added hexane (15 mL) and on standing overnight at 0 °C bright-yellow crystals had separated out. These were separated by filtration, washed with hexane and dried in vacuo. Yield: 0.27 g (68%).

**Method 2:** To a suspension of $[Cu^{I}SPh]_n$ (0.34 g, 2 mmol) in DMF (25 mL) was added $Et_4NCl$ (0.49 g, 3 mmol). The mixture was stirred at room temperature to afford a clear-yellow solution. Into this solution was added diethyl ether (≈15 mL) and on standing at 0 °C overnight bright-yellow crystals had separated out. Product **3** was separated by filtration, washed with 2-propanol, ether and dried in vacuo. Yield: 0.23 g (62%). $C_{58}H_{75}Cu_5N_2S_7$ (1342.44): calcd. C 51.85, H 5.59, N 2.09, S 16.69; found C 51.82, H 5.57, N 2.06, S 16.66.

**$[Et_4N]_2[Cu_4(SPh)_6]\cdot 0.5C_3H_8O$ (4):** To a solution of **2** (0.45 g, 0.25 mmol) in DMF (25 mL) was added a mixture of HSPh (1 mL) and $Et_3N$ (0.5 mL). The mixture was stirred for 15 min at room temperature to afford a light-yellow solution. Into this solution was added 2-propanol (40 mL) and on standing at 0 °C overnight pale-yellow crystals had separated out. The crystals were separated by filtration, washed with diethyl ether and dried in vacuo. Yield: 0.30 g (70%). $^1$H NMR (400 MHz, [D$_6$]DMSO): $\delta$ = 1.068 (t, $J$ = 5.6 Hz, 3 H, $CH_3$), 3.095 (q, $J$ = 7.1 Hz, 2 H, $CH_2$), 6.7498 (m, 2 H, *p*-Ph), 7.316 (d, $J$ = 6.9 Hz, 2 H, *o*-Ph) ppm. $^{13}$C NMR (100 MHz, [D$_6$]-DMSO): $\delta$ = 7.011 (-$CH_3$), 25.440 (α-C of *i*PrOH), 51.429 (-$CH_2$-), 121.203 (*p*-Ph), 126.781 (*m*-Ph), 132.557 (*o*-Ph), 145.449 (1C-Ph) ppm. On the basis of the integration of the protons from the phenyl and alkyl groups of the main complex, the extra alkyl protons found were assigned to the *i*PrOH molecules present in the lattice. $C_{53.5}H_{74}Cu_4N_2O_{0.5}S_6$ (1199.72): calcd. C 53.51, H 6.17, N 2.33, S 16.00; found C 53.48, H 6.12, N 2.36, S 16.09.

**X-ray Crystallography:** Suitable diffraction quality crystals were obtained from the crystallization procedures described in each synthesis. The crystals used in the analyses were glued to a glass fibre and mounted on a BRUKER SMART APEX diffractometer. The instrument was equipped with CCD area detector and data were collected by using graphite-monochromated Mo-$K_\alpha$ radiation ($\lambda$ = 0.71069 Å) at low temperature (100 K). All empirical absorption corrections were applied by using the SADABS program. Cell constants were obtained from the least-squares refinement of three-dimensional centroids through the use of CCD recording of narrow $\omega$ rotation frames, completing almost all-reciprocal space in the stated $\theta$ range. All data were collected with SMART 5.628 (BRUKER, 2003), and were integrated with the BRUKER SAINT program. The structure was solved by using SIR97 and refined with the use of SHELXL-97.[53] The space group of those compounds was determined on the basis of the lack of systematic absence and intensity statistics. Full-matrix least-squares/difference Fourier cycles were performed which located the remaining non-hydrogen atoms. All non-hydrogen atoms were refined with anisotropic displacement parameters. Each complex (**1**, **2** and **3**) possesses only one molecule in their respective asymmetric unit. In the asymmetric unit of compound **4**, there are two independent $Cu_4$ units. The additional symmetry for **4** was checked through PLATON.[54,55] Single crystals of complex **4** were grown from three different batches but all these possess similar crystallographic asymmetric unit. Some of the carbon atoms of ethyl groups of tetraethylammonium cation were disordered for **1**, **2**, **3** and **4** and refined with free part instruction by using SHELXL-97. The structures of **1**, **2** and **4** suffered from disordered and unidentified solvent (DCM/Hexane for **1**, **2** and 2-propanol for **4**) in the lattice, which was not included in the refinement but was taken care of by the SQUEEZE-procedure (from PLATON).[54,55] The volumes occupied by the solvent were 1049.5, 1115.6 and 214.4 Å$^3$, respectively; the numbers of electrons per unit cell deduced by SQUEEZE were 139, 146 and 26. All hydrogen atoms were placed in idealized calculated positions and allowed to ride on their corresponding carbon atoms with fixed isotropic contributions. Further information on crystal data, data collection and structure refinement are summarized in Table 3. Disordered solvent molecule of **1** and **2** were squeezed by using PLATON and details of squeeze results were appended to the crystallographic data file. CCDC-616824 to -616827 contain the supplementary crystallographic data for this paper. These data can be obtained free of charge from The Cambridge Crystallographic Data Centre via www.ccdc.cam.ac.uk/data_request/cif.

**Supporting Information** (see footnote on the first page of this article): UV/Vis and NMR spectra of synthesized complexes.

Table 3. Crystallographic data[a] and refinement details for complexes of **1**, **2**, **3** and **4**.

| Complexes | **1** | **2** | **3** | **4** |
|---|---|---|---|---|
| Formula | $C_{56}H_{100}Cl_6Cu_6N_4S_4$ | $C_{56}H_{100}Br_6Cu_6N_4S_4$ | $C_{58}H_{75}Cu_5N_2S_7$ | $C_{52}H_{70}Cu_4N_2S_6$ |
| Formula weight | 1551.69 | 1818.38 | 1342.44 | 1169.72 |
| Crystal system | triclinic | triclinic | triclinic | triclinic |
| Space group | $P\bar{1}$ | $P\bar{1}$ | $P\bar{1}$ | $P\bar{1}$ |
| $T$ [K] | 100(2) | 100(2) | 100(2) | 100(2) |
| $Z$ | 2 | 2 | 2 | 4 |
| $a$ [Å] | 13.77(5) | 14.145(5) | 12.374(5) | 17.072(5) |
| $b$ [Å] | 18.100(5) | 18.065(5) | 13.047(5) | 18.633(5) |
| $c$ [Å] | 18.109(5) | 18.333(5) | 20.828(5) | 18.648(5) |
| $\alpha$ [°] | 100.936(5) | 100.416(5) | 93.545(5) | 109.482(5) |
| $\beta$ [°] | 107.023(5) | 107.354(5) | 106.841(5) | 91.779(5) |
| $\gamma$ [°] | 95.100(5) | 95.409(5) | 112.367(5) | 93.123(5) |
| $V$ [Å$^3$] | 4186(2) | 4343(2) | 2919.4(18) | 5576(3) |
| $D_{calcd.}$ [g cm$^{-3}$] | 1.231 | 1.390 | 1.527 | 1.393 |
| $\mu$ [mm$^{-1}$] | 1.818 | 4.328 | 2.081 | 1.764 |
| $\theta$ range [°] | 2.00–28.30 | 2.07–28.35 | 2.07–28.35 | 2.17–28.33 |
| GOF ($F_2$) | 1.117 | 0.939 | 1.091 | 1.119 |
| $R_1$[b] | 0.0659 | 0.070 | 0.0727 | 0.0711 |
| $wR_2$[c] | 0.1496 | 0.1692 | 0.1474 | 0.1419 |

[a] Mo-$K_\alpha$ radiation. [b] $R_1 = \sum||F_o| - |F_c||/\sum|F_o|$. [c] $wR_2 = \{\sum[w(F_o^2 - F_c^2)^2]/\sum[w(F_o^2)^2]\}^{1/2}$.

 © 2007 Wiley-VCH Verlag GmbH & Co. KGaA, Weinheim 

## Acknowledgments

B. K. M. and K. P. gratefully acknowledge doctoral fellowships from the UGC and the CSIR, New Delhi, respectively; S. S. thanks DST, New Delhi for funding.

[1] J. D. Otvos, I. M. Armitage, *Proc. Natl. Acad. Sci. USA* **1980**, *77*, 7094.
[2] D. R. Winge, K. A. Miklossy, *J. Biol. Chem.* **1982**, *257*, 3471.
[3] K. B. Nielson, D. R. Winge, *J. Biol. Chem.* **1984**, *259*, 4941.
[4] M. J. Stillman, A. J. C. Law, W. Cai, A. J. Zelazowski, *Experientia Suppl.* **1987**, *52*, 203.
[5] J. H. R. Kägi, Y. Kojima, *Experientia Suppl.* **1987**, *52*, 25.
[6] Y. J. Li, U. Weser, *Inorg. Chem.* **1992**, *31*, 5526.
[7] M. J. Stillman, *Coord. Chem. Rev.* **1995**, *144*, 461A.
[8] P. A. Cobine, R. T. McKay, K. Zangger, C. T. Dameron, I. M. Armitage, *Eur. J. Biochem.* **2004**, *271*, 4213.
[9] B. Roschitzki, M. Vašák, *J. Biol. Inorg. Chem.* **2002**, *7*, 611.
[10] V. Calderone, B. Dolderer, H. J. Hartmann, H. Echner, C. Luchinat, C. D. Bianco, S. Mangani, U. Weser, *Proc. Natl. Acad. Sci. USA* **2005**, *102*, 51.
[11] H. J. Hartmann, U. Weser, *Biochim. Biophys. Acta* **1988**, *953*, 1.
[12] Z. Xiao, F. Loughlin, G. N. George, G. J. Howlett, A. G. Wedd, *J. Am. Chem. Soc.* **2004**, *126*, 3081.
[13] I. Bertini1, H. Hartmann, T. Klein, G. Liu1, C. Luchinat, U. Weser, *Eur. J. Biochem.* **2000**, *267*, 1008.
[14] I. G. Dance, *Polyhedron* **1986**, *5*, 1037.
[15] P. J. Blower, J. R. Dilworth, *Coord. Chem. Rev.* **1987**, *76*, 121.
[16] G. Henkel, B. Krebs, *Chem. Rev.* **2004**, *104*, 801.
[17] K. Fujisawa, S. Imai, N. Kitajima, Y. Moro-oka, *Inorg. Chem.* **1998**, *37*, 168.
[18] D. Coucouvanis, C. N. Murphy, S. K. Kanodia, *Inorg. Chem.* **1980**, *19*, 2993.
[19] C. D. Garner, J. R. Nicholson, W. Clegg, *Inorg. Chem.* **1984**, *23*, 2148.
[20] R. K. Chadha, R. Kumar, D. G. Tuck, *Can. J. Chem.* **1987**, *65*, 1336.
[21] I. G. Dance, L. J. Fitzpatrick, M. L. Scudder, *J. Chem. Soc. Chem. Commun.* **1983**, 546.
[22] E. Block, H. Kang, G. Ofori-Okai, J. Zubieta, *Inorg. Chim. Acta* **1990**, *167*, 147.
[23] M. Baumgartner, W. Bencsh, P. Hug, E. Dubler, *Inorg. Chim. Acta* **1987**, *136*, 139.
[24] J. R. Nicholson, I. L. Abrahams, W. Clegg, C. D. Garner, *Inorg. Chem.* **1985**, *24*, 1092.
[25] I. G. Dance, J. C. Calabrese, *Inorg. Chim. Acta* **1976**, *19*, L41.
[26] G. A. Bowmaker, G. R. Clark, I. G. Dance, *Polyhedron* **1983**, *2*, 1031.
[27] G. A. Bowmaker, G. R. Clark, J. K. Seadon, I. G. Dance, *Polyhedron* **1984**, *3*, 535.
[28] I. G. Dance, *J. Chem. Soc. Chem. Commun.* **1976**, 68.
[29] I. G. Dance, *Aust. J. Chem.* **1978**, *31*, 2195.
[30] M. Baumgartner, H. Schmalle, E. Dubler, *Polyhedron* **1990**, *9*, 1155.
[31] I. Schroeter-Schmid, J. Z. Straehle, *Z. Naturforsch., Teil B* **1990**, *45*, 1537.
[32] E. Block, M. Gernon, H. Kang, G. Ofori-Okai, J. Zubieta, *Inorg. Chem.* **1989**, *28*, 1263.
[33] I. G. Dance, P. J. Guerney, A. D. Rae, M. L. Scudder, *Inorg. Chem.* **1983**, *22*, 2883.
[34] The syntheses of **3** and **4** were earlier reported by different methods, but mixtures of both **3** and **4** or poor diffraction-quality crystals were obtained. See refs.[18,23–26,29]
[35] B. L. Hathaway, *Comprehensive Coordination Chemistry* (Ed.: G. Wilkinson), Pergamon, Oxford, England, **1987**, vol. 5, p. 533.
[36] I. G. Dance, *J. Chem. Soc. Chem. Commun.* **1976**, 68.
[37] Compounds **1**, **2** in this work.
[38] B. K. Maiti, K. Pal, S. Sarkar, *Inorg. Chem. Commun.* **2004**, *7*, 1027.
[39] A. N. M. Lanfredi, A. Tiripicchio, A. Camus, N. Marsich, *J. Chem. Soc. Dalton Trans.* **1989**, 753.
[40] R. V. Parish, Z. Salehi, R. G. Pritchard, *Angew. Chem. Int. Ed. Engl.* **1997**, *36*, 251.
[41] P. C. Ford, E. Cariati, J. Bourassa, *Chem. Rev.* **1999**, *99*, 3625.
[42] V. W. W. Yam, K. K. W. Lo, *Chem. Soc. Rev.* **1999**, *28*, 323.
[43] A. R. Green, M. J. Stillman, *Inorg. Chim. Acta* **1994**, *226*, 275.
[44] M. Beltramini, K. Lerch, *FEBS Lett.* **1981**, *127*, 201.
[45] G. Meloni, P. Faller, M. Vasák, *J. Biol. Chem.* **2007**, *282*, 16068.
[46] I. J. Pickering, G. N. George, C. T. Dameron, B. Kurz, D. R. Winge, I. G. Dance, *J. Am. Chem. Soc.* **1993**, *115*, 9498.
[47] T. A. Smith, K. Lerch, K. O. Hodgson, *Inorg. Chem.* **1986**, *25*, 4611.
[48] G. N. George, J. Byrd, D. R. Winge, *J. Biol. Chem.* **1988**, *263*, 8199.
[49] M. Beltramini, K. Lerch, *Biochemistry* **1983**, *22*, 2043.
[50] M. Beltramini, G. M. Giacometti, B. Salvato, G. Giacometti, K. Muenger, K. Lerch, *Biochem. J.* **1989**, *260*, 189.
[51] A. R. Green, A. Presta, Z. Gasyna, M. J. Stillman, *Inorg. Chem.* **1994**, *33*, 4159.
[52] K. Fujisawa, S. Imai, S. Suzuki, Y. Moro-oka, Y. Miyashita, Y. Yamada, K. Okamoto, *J. Inorg. Biochemistry* **2000**, *82*, 229.
[53] G. M. Sheldrick, *SHELXL-97: Program for Crystal Structure Refinement*, University of Göttingen, Germany, **1997**.
[54] A. L. Spek, *PLATON*, University of Utrecht, The Netherlands, **2001**.
[55] A. L. Spek, *Acta Crystallogr., Sect. A* **1990**, *46*, 194.

Received: July 24, 2007
Published Online: October 25, 2007

 © 2007 Wiley-VCH Verlag GmbH & Co. KGaA, Weinheim 

DOI: 10.1002/ejic.200700798

# Cationic Gold(I) Phosphanyl Thiolates: Aurophilic Interactions in the Solid State and in Solution

**Federica Balzano,[a] Angela Cuzzola,[a] Pietro Diversi,*[a] Fabio Ghiotto,[b] and Gloria Uccello-Barretta[a]**

**Keywords:** Gold / Sulfur / Thiolates / Aurophilicity / Aggregation / ESI MS / NMR spectroscopy

The aggregation states in solution of gold(I) cationic complexes of the formula $[Au_2(StBu)(L_2)][BF_4]$ (L = $PMe_3$, $PEt_3$, $PtBu_3$, $PPh_3$; $L_2$ = dppm, dppe) were studied by MS (ESI) and DOSY spectroscopy. These compounds are tetranuclear in the solid state with a core of four gold centres bound together by aurophilic interactions and bridging thiolato groups. Some of these tetranuclear systems are maintained intact in solution depending on the phosphane steric properties or denticity.

(© Wiley-VCH Verlag GmbH & Co. KGaA, 69451 Weinheim, Germany, 2007)

## Introduction

It is well known that many gold(I) complexes in the solid state adopt structures in which polynuclear systems are stabilized by the presence of relatively short Au···Au distances (aurophilic interactions).[1] In particular, cationic gold(I) phosphanyl thiolates $[Au_2(SR)(L_2)][BF_4]$ (L = phosphane), prepared by Bruce and coworkers by chemical oxidation of the corresponding neutral phosphanyl thiolates [Au(SR)(L)], exist in the solid state as oligomers; most of these structures have a core of four gold atoms associated by aurophilic interactions.[2] It is not clear if such structures survive in solution or are cleaved to give dinuclear species (there is no conclusive evidence on this point in the literature) (Figure 1). We recently prepared a series of related compounds with the formula $[Au_2(SR)(L_2)][BF_4]$ (R = $CMe_3$, $CH_2CMe_3$, $CH_2CHMe_2$, $CPh_3$; L = $PMe_3$, $PMe_2Ph$, $PMePh_2$, $PPh_3$) and $[Au_2(SR)(dppe)][BF_4]$ [dppe = 1,2-bis(diphenylphosphanyl)ethane] by following the synthetic strategy of Bruce.[3] In the solid state, the aurophilic interactions build up a structure of four gold atoms with pairs of atoms bound by bridging thiolato ligands, which, at least in the cases studied by X-ray analysis, are generally arranged in an almost perfect square or in an unprecedented zig–zag sequence in the case of $[Au_2(StBu)(dppe)][BF_4]$. The correct formulation for these complexes in the solid state is therefore $[Au_4(SR)_2(L_4)][BF_4]_2$.

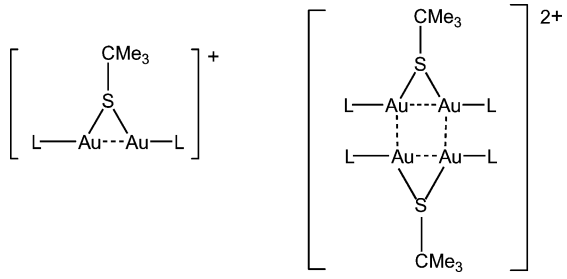


Figure 1. Di- and tetranuclear structural formulae of **2**.

It would be certainly important for a better understanding of the properties and the reactivities of these systems to establish whether the aurophilic interactions unsupported by bridging thiolato groups exist only in the solid state or may survive in the presence of a solvent. Indeed, because of the low energy of such interactions (5–15 kcal mol$^{-1}$),[2e] an equilibrium dimer/monomer can be postulated, which is possibly influenced by the nature of the solvent (polarity, chemical affinity for the metal centre, etc.) and/or the nature of the phosphane and/or thiolato ligands.

In the literature there is only a limited number of studies estimating the presence of aurophilic interactions in solution, and most of them concern $Au^I$–$Au^I$ intramolecular contacts often assisted by the presence of a bidentate phosphane.[4] In these cases, the authors demonstrated the partial survival of the Au–Au bonding interactions by using $^1H$ and $^{31}P$ VT NMR, UV/Vis and EXAFS spectroscopy. There are a few scattered reports also for the study of the intermolecular interactions in solution: the complexes $[Au_2(dppm)(CH_2)_2S(O)NMe_2][BF_4]$ [dppm = 1,1-bis(diphenylphosphanyl)methane], $[Au_2(dmpm)(CH_2)_2S(O)$-

[a] Dipartimento di Chimica e Chimica Industriale dell'Università di Pisa,
Via Risorgimento 35, 56126 Pisa, Italy
E-mail: div@dcci.unipi.it
[b] Scuola Normale Superiore,
Piazza dei Cavalieri 7, 56126 Pisa, Italy

 © 2007 Wiley-VCH Verlag GmbH & Co. KGaA, Weinheim 

$NMe_2][BF_4]$ [dmpm = 1,1-bis(dimethylphenylphosphanyl)-methane][5] and $\{[(PPh_3)Au]_2Cl\}[SbF_6]$,[6] all of which crystallize as dimers because of the formation of two $Au^I$–$Au^I$ intermolecular bonds, were shown by electronic spectroscopy to maintain at least in part their dimeric structure. Recently, diphosphane gold complexes with Au–Au contacts were studied by EXAFS spectroscopy.[4a]

In consideration of the above, to obtain information on the aggregation state in dissolved cationic phosphanyl thiolates, we began a study of the homogeneous series of gold(I) derivatives with the formula $[Au_2(StBu)(L_2)][BF_4]$ (L = $PMe_3$ **2a**, $PEt_3$ **2b**, $PtBu_3$ **2c**, $PPh_3$ **2d**; $L_2$ = dppm **2e**, dppe **2f**) by using MS (ESI) and DOSY (Diffusion Ordered SpectroscopY). MS (ESI) was recently used for the characterization of supramolecular organometallic assemblies.[7] DOSY NMR techniques, although very promising,[8a,8b] have not attracted much attention so far[8c,8d] for applications in organometallic and inorganic chemistry in solution. Here we report some conclusions obtained during these studies.

## Results and Discussion

### Synthesis

Complexes **2a**–**f** were all prepared by chemical oxidation of corresponding thiolates **1a**–**f** with $[FeCp_2]BF_4$. Compounds **1b**,**c**, **1e**, **2b**,**c** and **2e** have not been reported before, and their preparation and characterization can be found in the Experimental Section. The X-ray structures of **2d**[9] and **2f**[3b] are reported in the literature; for the other thiolates with monodentate phosphanes we assume that they exist in the solid state in the usual four-membered square planar arrangement.

### Mass Spectrometry Studies

The analyses were carried out in methanol solution. As explained above, the gold(I) complexes here investigated may exist in solution as monocationic dinuclear species and/or as dicationic tetranuclear species. The analysis of the isotopic cluster of the molecular ion is crucial to assess the cationic charge: in fact the $[Au_4(StBu)_2(PR_3)_4]^{2+}$ ion, in addition to the peak corresponding to $m/z$ = M/2, presents other minor peaks at $m/z$ = M/2 + $n$/2 ($n$ = 1, 2, 3, etc.) due to the minor isotopes of carbon, sulfur and hydrogen), whereas $[Au_2(StBu)(PR_3)_2]^+$ shows signals at M/2+$n$ ($n$ = 0, 1, 2, 3, etc.). Figures 2–6 report the MS (ESI) spectrum of each complex with the corresponding attributions and the enlargement of the isotopic cluster of the molecular ion.

In the case of **2a**, the isotopic cluster (Figure 2b) is rather resolved and allows us to conclude that the dicationic tetranuclear structure observed in the solid state is largely maintained in solution. The MS–MS spectrum of the molecular ion does not give further information on the aggregation state. However it is interesting to note that, under more severe experimental conditions [declustering potential (*DP*) at 120 V], the isotopic cluster of the molecular peak reveals that the dinuclear species arose at the expense of the tetranuclear species (Figure 2c). The $Au_6$ species responsible for the peak at $m/z$ = 921 most probably formed in the ionization step.

In the case of **2b**, the isotopic cluster is poorly resolved (Figure 3b). It is therefore difficult to draw specific conclusions, but in consideration of the NMR spectroscopic results (vide infra) we suggest that only the dinuclear specie is present in solution. The $m/z$ = 1005 peak may be derived from the aggregation of the dinuclear species during the ionization process. The MS–MS spectrum does not give any additional evidence.

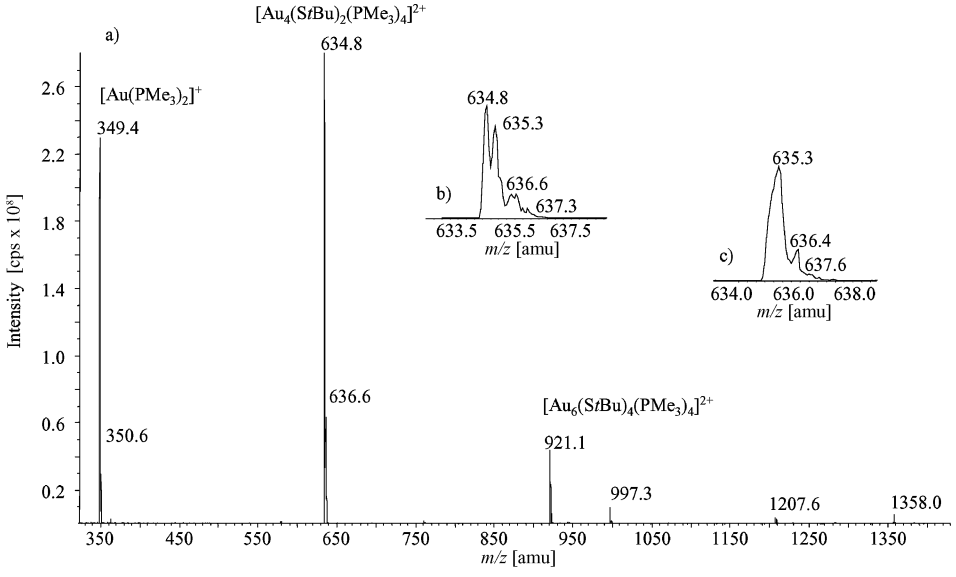


Figure 2. a) MS (ESI+) of **2a**; b) enlargement of the isotopic cluster at $m/z$ = 635 at *DP* = 20 V and c) at *DP* = 120 V.

 © 2007 Wiley-VCH Verlag GmbH & Co. KGaA, Weinheim 

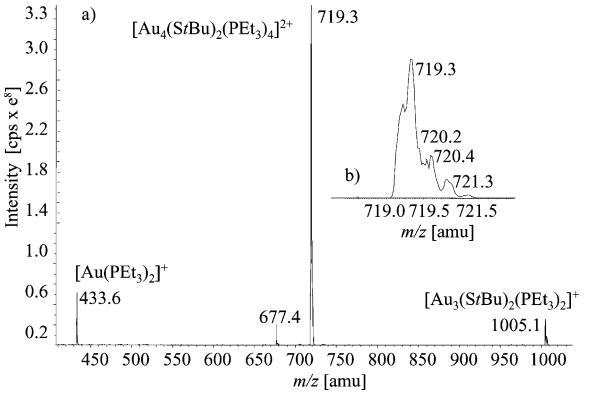


Figure 3. a) MS (ESI+) of **2b**; b) enlargement of the isotopic cluster at *m*/*z* = 719.3.

Alternatively, the mass spectrum recorded for **2c** shows a fairly well-resolved isotopic cluster (Figure 4b), which indicates that only the monocharged dinuclear species is present. The peak at *m*/*z* = 1174 is due to an adduct probably formed during the ionization process.

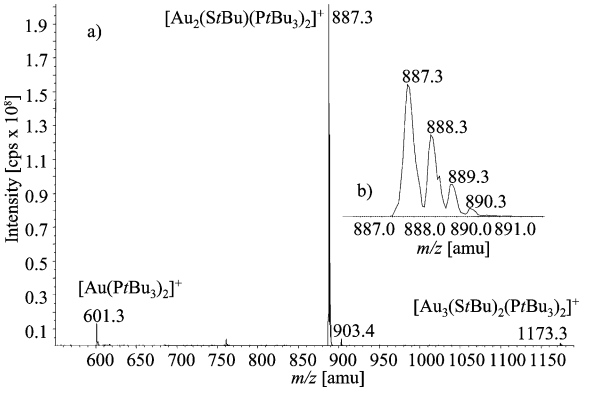


Figure 4. a) MS (ESI+) of **2c**; b) enlargement of the isotopic cluster at *m*/*z* = 887.3.

Similar conclusions can be drawn for **2d** from the analysis of its mass spectrum (Figure 5).

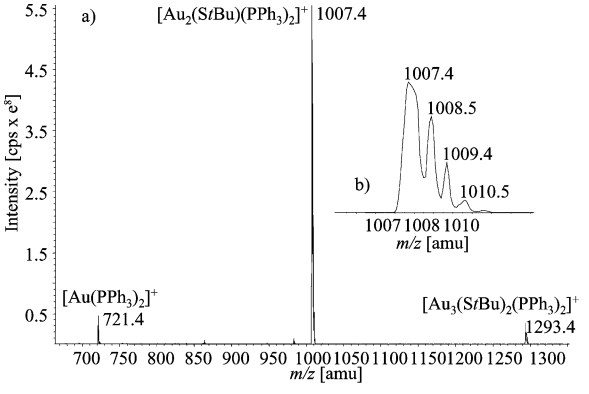


Figure 5. a) MS (ESI+) of **2d**; b) enlargement of the isotopic cluster at *m*/*z* = 1007.4.

Finally, complexes **2e**,**f** containing diphosphanes are present in solution as tetranuclear dications, as was predictable because the diphosphane holds the two dinuclear units firmly together. In the particular case of **2f**, the isotopic cluster is poorly resolved (Figure 6b) and the MS–MS spectrum of the ion at *m*/*z* = 881 shows a small peak at *m*/*z* = 1167 (Figure 6c). Because a species with more gold atoms than the precursor ion is unlikely to form on fragmentation, the presence of a fragment ion at greater *m*/*z* values confirms the tetranuclear nature of **2f**.

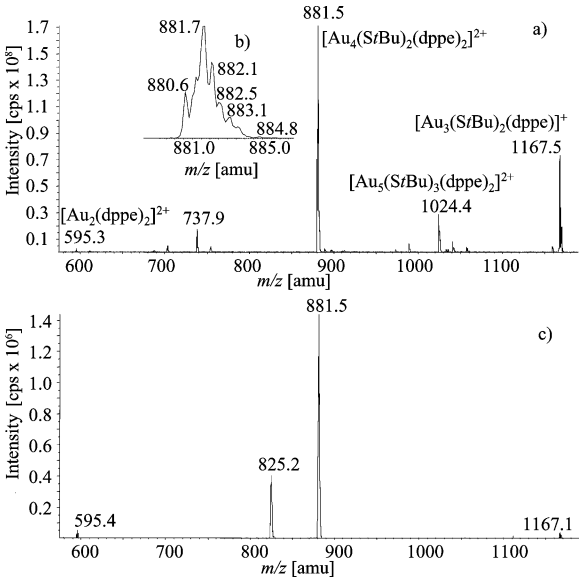


Figure 6. a) MS (ESI+) of **2f**; b) enlargement of the isotopic cluster at *m*/*z* = 881.7; c) MS–MS spectrum of the ion at *m*/*z* = 881.

From these data it is clear that the ability of **2a**–**2d** to maintain totally or partially the aurophilic interactions in solution seems to depend largely on the steric hindrance of the phosphane (then on its cone angle, which is in the order $PMe_3 < PEt_3 < PPh_3 < PtBu_3$).[10] In the case of **2e** and **2f** it is the chelating phosphane, in addition to the thiolato ligand, that binds together the four gold atoms, independently of the survival of the aurophilic interactions.

## NMR Spectroscopy

The average diffusion coefficients can be related to hydrodynamic radii $r_H$ by means of the Stokes–Einstein equation [Equation (1)].

$$D = \frac{kT}{c\pi\eta r_H} \quad (1)$$

where $k$ is the Boltzmann constant, $T$ is the absolute temperature, $\eta$ the viscosity and $c$ is a numerical factor, which usually approximates to 6 for large-size molecules.

A more accurate estimation of hydrodynamic radius $r'_H$ can be obtained[11] by Equation (2), where the $c$ factor is expressed as a function of the solvent-to-solute ratio of ra-

 © 2007 Wiley-VCH Verlag GmbH & Co. KGaA, Weinheim 

dii on the basis of the model proposed by Wirtz and coworkers[12] and where $r_{solv}$ is the van der Waals radius of the solvent.

$$D = \frac{kT\left[1+0.695\left(\frac{r_{solv}}{r_H'}\right)^{2.234}\right]}{6\pi\eta r_H'} \quad (2)$$

Valentini et al.[13] used DOSY measurements to determine the diffusion coefficients of some iron and palladium compounds, whose structures in the solid state were known. They obtained the hydrodynamic radii by using the Stokes–Einstein equation and compared these results to the radii of greatest steric hindrance obtained from crystallographic parameters, $r_R$ (rotating the molecule around its geometric centre), and they found very good consistency. The technique was also exploited for the characterization of intermediates in organometallic reactions involving copper,[14] ruthenium,[15] platinum[8b] and zirconium[16] complexes. Finally, some papers report the use of this methodology to study the aggregation state in solution of organolithium[17] and ruthenium complexes.[8c,11]

Several correction factors[17b,18] for the equation, both semiempirical and theoretical have been proposed, by taking into account the dimensions and the nonspherical form of the particle, concentration and so on, but they have been used only rarely as an internal standard is preferred. Some authors[8,19] suggested the use of tetramethylsilane (TMS) as an internal standard to avoid the problems derived from the change in the viscosity due to the variation of the concentration after the addition of the solute to be analyzed and from the temperature.

The spectra were generally performed in deuterated dichloromethane, but in some cases also in methanol and acetone in order to study the influence of the solvent. As the internal standard for viscosity we adopted TMS and all diffusion coefficients were corrected with respect to it.

To test the reliability of the method, our preliminary study was directed towards thiolato phosphanyl compounds **1a**–**f**, as there is no evidence of aurophilic interactions in the solid state and presumably all the more so in solution (Table 1).

Table 1. $D$ ($\times 10^{10}$ m$^2$s$^{-1}$) and $r$ [Å] values for **1a**–**f** in $CD_2Cl_2$ at 298 K.

| | $D$ | $r_H$[a] | $r'_H$[b] | $r$[c] | $r$[d] |
|---|---|---|---|---|---|
| [Au(S*t*Bu)(PMe$_3$)] (**1a**) | 14.6 | 3.4 | 4.2 | 4.8 | 4.8 |
| [Au(S*t*Bu)(PEt$_3$)] (**1b**) | 12.6 | 4.0 | 4.7 | 5.4 | 5.1 |
| [Au(S*t*Bu)(P*t*Bu$_3$)] (**1c**) | 12.2 | 4.1 | 4.8 | 5.5 | 5.2 |
| [Au(S*t*Bu)(PPh$_3$)] (**1d**) | 10.4 | 4.9 | 5.4 | 6.1 | 6.2 |
| [Au$_2$(S*t*Bu)$_2$(dppm)] (**1e**) | 7.3 | 7.0 | 7.4 | – | 6.8 |
| [Au$_2$(S*t*Bu)$_2$(dppe)] (**1f**) | 7.2 | 7.0 | 7.4 | 7.4[e] | – |

[a] Calculated by using Equation (1), $c$ = 6, $T$ = 298 K, $\eta$ ($CD_2Cl_2$, 298 K) = $0.433 \times 10^{-3}$ kg m$^{-1}$ s$^{-1}$. [b] Calculated by using Equation (2). [c] Calculated from X-ray structure data. [d] Calculated from the minimized gas-phase structure (PM3/AM1). [e] See ref.[3]

The values of the hydrodynamic radii, calculated by employing Equation (1) with $c$ = 6, were all lower with respect to those obtained from X-ray or PM3 calculations. In the case of **1f**, which is known to be stable in solution as dissociative processes are unlikely, excellent agreement was obtained by the introduction of the Wirtz correction [Equation (2), Table 1), that is, by considering the solvent-to-solute ratio of the radii. However, the corrected hydrodynamic radii of neutral monophosphane derivatives **1a**–**d** were also slightly lower, which suggests a dissociative equilibrium. Actually, like traditional NMR measurements, DOSY techniques, in the presence of rapid exchange, show only one peak resulting from the weighted average of the signals of each species involved. Because it is well known that gold(I) compounds are often involved in rapid phosphane exchange reactions,[20] it is probable that this is the reason for the observed discrepancy between the observed and calculated radii.

We then proceeded with the NMR investigation of the series of cationic clusters **2a**–**f**. X-ray structures in the solid state are known only for [Au$_4$(S*t*Bu)$_2$(dppe)$_2$][BF$_4$]$_2$[3] (which we assume remains tetranuclear in solution) and for [Au$_4$(S*t*Bu)$_2$(PPh$_3$)$_4$][BF$_4$]$_2$;[10] for the other complexes we used data from published structures of similar model compounds or alternatively we performed PM3 calculations using the ArgusLab program.[21] As the only limitation we assumed that the S–Au–P angle had to be as close as possible to 180°. Analysis of the models of **2a**–**d** shows that the radii of greatest steric hindrance of the di- and tetranuclear species do not differ too much (ca 1 or 2 Å), as the only difference in size between the two species is in the third dimension with the assumption that the other two remain roughly constant. In spite of that, the NMR spectroscopic results shown in Table 2 are fairly consistent and point to the same conclusions reached by MS (ESI) spectrometry: the corrected hydrodynamic radius of **2a** is consistent with a tetranuclear species, whereas for **2b** it is intermediate between that of the dinuclear and the tetranuclear species, which indicates that both structures are present in solution (probably involved in rapid equilibrium).

For dppm and dppe derivatives **2e**,**f**, as expected, the radii are nicely consistent with those predicted for the tetranuclear species. Complexes **2c**,**d** gave, in contrast, even smaller $r'_H$ values than those predicted for the dinuclear species from the X-ray structure data, so they probably undergo some dissociation of the phosphane (as is likely from the literature concerning phosphane gold(I) phosphanyl derivatives and from basicity considerations in particular) or even further disruption of the remaining Au–Au interactions.

Finally, to acquire information on the influence of the solvent on the equilibrium involving di- and tetranuclear species, we made some measurements in deuterated methanol and acetone for comparison with the results obtained in dichloromethane. We chose to study triethylphosphane derivative **2b**, which, as reported above, was found to exist as a mixture of the di- and tetranuclear species, and dppe complex **2f** for comparison (Table 3).

The results for complex **2b** in acetone are fairly consistent with a dinuclear monocation formulation, which most probably means that the equilibrium observed in dichloro-

 © 2007 Wiley-VCH Verlag GmbH & Co. KGaA, Weinheim 

Table 2. $D$ ($\times 10^{10}$ m$^2$s$^{-1}$) and $r$ [Å] for **2a**–**f** in $CD_2Cl_2$ at 298 K.

| | D | $r_H$[a] | $r'_H$[b] | $r$[c] $Au_2$ | $r$[c] $Au_4$ | $r$[d] $Au_2$ | $r$[d] $Au_4$ | Aggregation degree |
|---|---|---|---|---|---|---|---|---|
| $[Au_2(StBu)(PMe_3)_2][BF_4]$ (**2a**) | 8.7 | 5.8 | 6.3 | 4.8 | 6.0 | 4.8 | 5.9 | tetranuclear |
| $[Au_2(StBu)(PEt_3)_2][BF_4]$ (**2b**) | 9.3 | 5.5 | 6.0 | 5.4 | 7.3 | 5.7 | 7.2 | di- and tetranuclear |
| $[Au_2(StBu)(PtBu_3)_2][BF_4]$ (**2c**) | 9.1 | 5.6 | 6.1 | 6.8 | 7.9 | 6.8 | 7.8 | dinuclear |
| $[Au_2(StBu)(PPh_3)_2][BF_4]$ (**2d**) | 7.6 | 6.7 | 7.1 | 8.1[e] | 9.1[e] | 8.4 | 8.9 | dinuclear |
| $[Au_2(StBu)(dppm)][BF_4]$ (**2e**) | 6.1 | 8.3 | 8.6 | – | 8.4 | – | 8.6 | tetranuclear |
| $[Au_2(StBu)(dppe)][BF_4]$ (**2f**) | 6.1 | 8.2 | 8.6 | – | 9.1 | – | – | tetranuclear |

[a] Calculated by using Equation (1), $c = 6$, $\eta$ ($CD_2Cl_2$, 298 K) = $0.433 \times 10^{-3}$ kg m$^{-1}$ s$^{-1}$. [b] Calculated by using Equation (2). [c] Calculated from X-ray structure data under the assumption of a spherical shape. [d] Calculated from the minimized gas-phase structure (PM3). [e] See ref.[9]

Table 3. $D$ ($\times 10^{10}$ m$^2$s$^{-1}$) and $r_H$ [Å] values for **2b** and **2f** in $(CD_3)_2CO$ and $CD_3OD$.

| | Solvent | D | $r_H$[a] | $r'_H$[b] | $r$ $Au_2$[c] | $r$ $Au_4$[d] |
|---|---|---|---|---|---|---|
| $[Au_2(StBu)(dppe)][BF_4]$ (**2f**) | $(CD_3)_2CO$ | 8.1 | 8.9 | 9.2 | | 9.1 |
| $[Au_2(StBu)(dppe)][BF_4]$ (**2f**) | $CD_3OD$ | 5.1 | 7.9 | 8.1 | | 9.1 |
| $[Au_2(StBu)(PEt_3)_2][BF_4]$ (**2b**) | $(CD_3)_2CO$ | 14.7 | 4.9 | 5.4 | 5.4–5.7 | |
| $[Au_2(StBu)(PEt_3)_2][BF_4]$ (**2b**) | $CD_3OD$ | 9.1 | 4.4 | 4.8 | 5.4–5.7 | |

[a] Calculated by using Equation (1), $c = 6$, $T = 298$ K, $\eta_{MeOH}$ (298 K) = $0.544 \times 10^{-3}$ kg m$^{-1}$ s$^{-1}$, $\eta_{acetone}$ (298 K) = $0.306 \times 10^{-3}$ kg m$^{-1}$ s$^{-1}$. [b] Calculated by using Equation (2). [c] Calculated from the minimized gas-phase structure (PM3). [d] From X-ray data.[21]

methane is completely shifted towards the rupture of the unsupported aurophilic bonds. In methanol, **2b** shows a hydrodynamic radius that is even lower with respect to that expected for a dinuclear species; thus, some other dissociative process favoured by the polar protic solvent can be invoked. Actually, methanol seems to promote other dissociative processes even in the case of complex **2f**, which, however, maintains its tetranuclear structure in acetone as in dichloromethane.

## Conclusions

Table 4 shows our conclusions on the aggregation state of the cationic gold complexes $[Au_2(StBu)(L_2)][BF_4]$ (**2a**–**2f**) on the basis of MS and NMR experiments.

Table 4. Evaluation of the degree of aggregation of **2a**–**f** in solution by MS (ESI) and DOSY techniques.

| Complex | MS (MeOH) | DOSY ($CD_2Cl_2$) | Phosphane cone angle [°] |
|---|---|---|---|
| **2a** | tetranuclear | tetranuclear | 118 |
| **2b** | dinuclear | di- and tetranuclear | 132 |
| **2c** | dinuclear | dinuclear | 182 |
| **2d** | dinuclear | dinuclear | 145 |
| **2e** | tetranuclear | tetranuclear | – |
| **2f** | tetranuclear | tetranuclear | – |

In spite of the fact that DOSY spectroscopy and MS (ESI) are performed under rather different conditions (concentration, solvent, etc.), the results are on the whole highly consistent. The main conclusion is that some of the complexes of **2** exist in a tetranuclear form even in dilute solutions, which shows that aurophilic interactions, although not as strong as covalent bonds, are able to maintain the solid state architecture even in solution. Another conclusion seems to be that the survival in solution of the aurophilic interactions depends upon the steric hindrance of the phosphane, because the greater the cone angle, the greater the repulsion between the two monocharged unities connected by aurophilic interactions, and, as a consequence, the dinuclear is preferred to the tetranuclear structure. Moreover, apart from diphosphane derivatives **2e**,**f**, the aurophilic interactions are maintained (at least partially) only when relatively small ligands (trimethyl- and triethylphosphane) are present. Obviously the solvent plays an important role: the polarity and the affinity for gold may determine the aggregation state, as shown by triethylphosphane derivative **2b**, which completely loses its tetranuclear structure in a polar solvent like acetone and methanol, whereas it maintains the dimeric structure in part in the less-polar solvent dichloromethane.

Finally, this work, in addition to the existing literature, shows that NMR and MS techniques may be very useful in the assessment of the degree of aggregation in solution of coordination systems, and they can provide better understanding of the reactivity of species that may exist in a supramolecular aggregation.

## Experimental Section

**Chemicals:** All manipulations and reactions were carried out under an atmosphere of nitrogen or argon by using standard techniques. All solvents were used without any further purification. $[Au(SCMe_3)]_n$ was prepared according to the literature.[22]

**Physical Measurements:** $^1$H and $^{31}$P NMR spectra were recorded with a Varian Gemini 200 instrument working at 200 MHz. DOSY experiments were performed with a Varian INOVA600 spectrometer operating at 600 MHz for $^1$H by using a 5 mm broadband inverse probe with $z$ axis gradient; and the sample temperature was maintained at 25 °C. They were carried out by using a stimulated echo sequence with self-compensating gradient schemes, a spectral width of 8000 Hz and 64 K data points. Typically, a value of 100 ms was used for $\Delta$, 1.0 ms for $\delta$ and g was varied in 30 steps (16 transients each) to obtain an approximately 90–95% decrease in the resonance intensity at the largest gradient amplitudes. The base-

 © 2007 Wiley-VCH Verlag GmbH & Co. KGaA, Weinheim 

lines of all arrayed spectra were corrected prior to processing the data. After data acquisition, each FID was apodized with 1.0 Hz line broadening and Fourier transformed. The data were processed with the DOSY macro (involving the determination of the resonance heights of all the signals above a preestablished threshold and the fitting of the decay curve for each resonance to a Gaussian function) to obtain pseudo-two-dimensional spectra with NMR chemical shifts along one axis and calculated diffusion coefficients along the other. Centesimal analysis were carried out in the microanalysis laboratory of Dipartimento di Scienze Farmaceutiche dell'Università di Pisa. The mass spectra were obtained with an Applied Biosystems-MDS Sciex API 4000 triple quadrupole mass spectrometer (Concord, ON, Canada), equipped with Turbo-V Ion-Spray (TIS) source. The operative parameters are as follows: ion-spray voltage (IS), 5.0 kV; gas source 1 (GS1), 25; gas source 2 (GS2), 25; turbo temperature (TEM), 0 °C; entrance potential (EP), 10 V; declustering potential (*DP*), 20 V; scan range, 300–1500 *m*/*z*. MS–MS product ions were produced by collision-induced dissociation (CID) of selected precursor ions in the LINAC collision cell (Q2) and mass-analyzed in the second mass filter (Q3). Additional experimental conditions for MS–MS product ions spectra included: collision (CAD) gas, nitrogen; CAD gas pressure, 4 m Pa; collision energy (CE), ramp from 5 to 130 eV (step = 2); collision cell exit potential (CXP), 15 V. Each sample for MS (ESI) was prepared diluting 1:100 with methanol a 5 mg mL$^{-1}$ dichloromethane solution of the target compound and was infused by a syringe pump Harvard Mod. 22 (Harvard Apparatus, Holliston, MA, USA). Melting points were obtained by using a Mel Temp II (Laboratory Devices, USA) equipped with a mercury thermometer as detector of the temperature.

**Reaction of [Au(S*t*Bu)]$_n$ with L (L = PMe$_3$, PEt$_3$, P*t*Bu$_3$, PPh$_3$). Formation of [Au(S*t*Bu)(L)] (1a–d):** The complexes were all prepared according to the literature method.[3] Compounds **1b**,**c** have not been described before.

**Complex 1a:** MS (ESI+): *m*/*z* (%) = 349 (45) $[Au(PMe_3)_2]^+$, 363 (15) $[Au(StBu)(PMe_3) + H]^+$, 635 (100) $[Au_4(StBu)_2(PMe_3)_4]^{2+}$, 761 (15) not assigned, 921 (29) $[Au_3(StBu)_2(PMe_3)_2]^+$, 997 (15) $[Au_3(StBu)_2(PMe_3)_3]^+$.

**Complex 1b:** Small silver flakes from pentane solution. Yield: 0.153 g (80%). M.p. 43 °C. $^1$H NMR (200 MHz, $CD_2Cl_2$, 25 °C): $\delta$ = 1.19 (dt, $^2J_{P,H}$ = 18.3 Hz, $^3J_{H,H}$ = 7.7 Hz, 6 H, $PCH_2$), 1.45 (s, 9 H, $SCMe_3$), 1.83 (dq, $^3J_{P,H}$ = 9.3 Hz, $^3J_{H,H}$ = 7.7 Hz, 9 H, $PCCH_3$) ppm. $^1$H NMR (200 MHz, $C_6D_6$, 25 °C): $\delta$ = 0.63 (dt, $^2J_{P,H}$ = 18.3 Hz, $^3J_{H,H}$ = 7.7 Hz, 9 H, $PCH_2$), 0.90 (dq, $^3J_{P,H}$ = 9.3 Hz, $^3J_{H,H}$ = 7.7 Hz, 6 H, $PCCH_3$), 1.93 (s, 9 H, $SCMe_3$) ppm. $^{31}$P NMR (200 MHz, $CD_2Cl_2$, 25 °C): $\delta$ = 38.64 (s) ppm. $^{31}$P NMR (200 MHz, $C_6D_6$, 25 °C): $\delta$ = 38.36 (s) ppm. $C_{10}H_{24}AuPS$ (404.31): calcd. C 29.71, H 5.98; found C 29.77, H 5.92.

**Complex 1c:** White microcrystals from toluene/pentane solution. Yield: 1.040 g (70%). M.p. 154 °C. $^1$H NMR (200 MHz, $CD_2Cl_2$, 25 °C): $\delta$ = 1.46 (s, 9 H, $SCMe_3$), 1.51 (d, $^3J_{P,H}$ = 13.2 Hz, 27 H, $PCMe_3$) ppm. $^1$H NMR (200 MHz, $C_6D_6$, 25 °C): $\delta$ = 1.93 (s, 9 H, $SCMe_3$), 1.07 (d, $^3J_{P,H}$ = 13.2 Hz, 27 H, $PCMe_3$) ppm. $^{31}$P NMR (200 MHz, $CD_2Cl_2$, 25 °C): $\delta$ = 92.58 (s) ppm. $^{31}$P NMR (200 MHz, $C_6D_6$, 25 °C): $\delta$ = 91.46 (s) ppm. MS (ESI+): *m*/*z* (%) = 361 (15) not assigned, 489 (62) $[Au(StBu)(PtBu_3)_4 + H]^+$, 512 (16) $[Au(StBu)(PtBu_3)_4 + Na]^+$, 548 (27) not assigned, 887 (100) $[Au_2(StBu)(PtBu_3)_2]^+$. $C_{16}H_{36}AuPS$ (488.47): calcd. C 39.34, H 7.43; found C 39.12, H 7.38.

**Reaction of [Au(S*t*Bu)]$_n$ with L$_2$ (L$_2$ = dppm, dppe). Formation of [Au$_2$(S*t*Bu)$_2$(L$_2$)] (1e,f):** Complexes **1f**,**e** were prepared according to a literature procedure described for **1f**.[3]

**Complex 1e:** Pale yellow microcrystals from toluene/pentane solution. Yield: 0.444 g (93%). $^1$H NMR (200 MHz, $CDCl_3$, 25 °C): $\delta$ = 1.52 (s, 18 H, $SCMe_3$), 2.38 (s, 2 H, $PCH_2$), 7.2–7.8 (br. m, 20 H, $PPh_2$) ppm. $^1$H NMR (200 MHz, $CD_2Cl_2$, 25 °C): $\delta$ = 1.46 (s, 18 H, $SCMe_3$), 3.62 (s, 2 H, $PCH_2$), 7.3–7.8 (br. m, 20 H, $PPh_2$) ppm. $^{31}$P NMR (200 MHz, $CDCl_3$, 25 °C): $\delta$ = 30.11 (s), 28.27 (s) ppm. $C_{33}H_{40}Au_2P_2S_2$ (956.69): calcd. C 41.43, H 4.21; found C 41.40, H 4.16.

**Complex 1f:** MS (ESI+): *m*/*z* (%) = 881 $[Au_4(StBu)_2(dppe)_2]^{++}$ (100%), 993 $[Au_2(StBu)_2(dppe) + Na]^+$ (25), 1024 $[Au_5(StBu)_3(dppe)_2]^{++}$ (58), 1033 (not assigned, 23), 1167 $[Au_3(StBu)_2(dppe)]^+$ (25).

**Reaction of [Au(S*t*Bu)(L)] (L = PMe$_3$, PEt$_3$, P*t*Bu$_3$, PPh$_3$) with [FeCp$_2$][BF$_4$]. Formation of [Au$_2$(S*t*Bu)(L$_2$)][BF$_4$] (2a–d):** All complexes were prepared according to the literature.[3]

**Complex 2a:** MS (ESI+): *m*/*z* (%) = 349 (85) $[Au(PMe_3)_2]^+$, 635 (100) $[Au_4(StBu)_2(PMe_3)_4]^{2+}$, 921 (14) $[Au_6(StBu)_4(PMe_3)_4]^{2+}$. MS–MS 635: *m*/*z* (%)= 273 (65) $[Au(PMe_3)]^+$, 349 (62) $[Au(PMe_3)_2]^+$, 579 (100) $[Au_4(SH)_2(PMe_3)_4]^{2+}$ or $[Au_2(SH)(PMe_3)_2]^+$, 635 (30) $[Au_4(StBu)_2(PMe_3)_4]^{2+}$.

**Complex 2b:** White microcrystals from dichloromethane solution. Yield: 0.157 g (71%). $^1$H NMR (200 MHz, $CD_2Cl_2$, 25 °C): $\delta$ = 1.59 (s, 18 H, $SCMe_3$), 1.23 (dt, $^2J_{P,H}$ = 19.1 Hz, $^3J_{H,H}$ = 7.7 Hz, 24 H, $PCH_2$), 1.94 (dq, $^3J_{P,H}$ = 9.9 Hz, $^3J_{H,H}$ = 7.7 Hz, 36 H, $PCCH_3$) ppm. $^1$H NMR (200 MHz, $C_6D_6$, 25 °C): $\delta$ = 1.55 (s, 18 H, $SCMe_3$), 0.88 (dt, $^2J_{P,H}$ = 19.1 Hz, $^3J_{H,H}$ = 7.7 Hz, 24 H, $PCH_2$), 1.61 (dq, $^3J_{P,H}$ = 9.9 Hz, $^3J_{H,H}$ = 7.7 Hz, 36 H, $PCCH_3$) ppm. $^{31}$P NMR (200 MHz, $CD_2Cl_2$, 25 °C): $\delta$ = 37.93 (s) ppm. $^{31}$P NMR (200 MHz, $C_6D_6$, 25 °C): $\delta$ = 38.36 (s) ppm. MS (ESI+): *m*/*z* (%) = 433 (14) $[Au(PEt_3)_2]^+$, 719 (100) $[Au_4(StBu)_2(PEt_3)_4]^{2+}$, 1005 $[Au_3(StBu)_2(PEt_3)_2]^+$. MS–MS 719: *m*/*z* (%) = 315 (100) $[Au(PEt_3)]^+$, 433 (67) $[Au(PEt_3)_2]^+$, 663 (72) $[Au_4(SH)_2(PEt_3)_4]^{2+}$ or $[Au_2(SH)(PEt_3)_2]^+$, 719 (6) $[Au_4(StBu)_2(PEt_3)_4]^{2+}$. $C_{16}H_{39}Au_2BF_4P_2S$: calcd. C 23.84, H 4.88; found C 23.65, H 4.76.

**Complex 2c:** Light grey microcrystals from dichloromethane solution. Yield: 0.810 g (88%). $^1$H NMR (200 MHz, $CD_2Cl_2$, 25 °C): $\delta$ = 1.61 (s, 18 H, $SCMe_3$), 1.54 (d, $^3J_{P,H}$ = 13.9 Hz, 108 H, P*t*Bu) ppm. $^{31}$P NMR (200 MHz, $CD_2Cl_2$, 25 °C): $\delta$ = 92.74 (s) ppm. MS (ESI+): *m*/*z* (%) = 601 (6) $[Au(PtBu_3)_2]^+$, 887 (100) $[Au_2(StBu)(PtBu_3)_2]^+$, 1173 (6) $[Au_3(StBu)_2(PtBu_3)_2]^+$. MS–MS 887: *m*/*z* (%) = 231 (16) $[Au(PH_3)]^+$, 287 (52) $[Au(PH_2tBu)]^+$, 343 (49) $[Au(PHtBu_2)]^+$, 399 (43) $[Au(PtBu_3)]^+$, 489 (16) not assigned, 493 (14) $[Au_2(SH)(PH_3)_2]^+$, 549 (54) $[Au_2(SH)(PH_3)(PH_2tBu)]^+$, 572 (32) not assigned, 606 (32) $[Au_2(SH)(PH_3)(PHtBu_2)]^+$, 629 (25) not assigned, 647 (16) not assigned, 662 (100) $[Au_2(SH)(PH_3)(PtBu_3)]^+$, 685 (67) not assigned, 703 (83) not assigned, 718 (84) $[Au_2(SH)(PH_2tBu)(PtBu_3)]^+$, 741 (31) not assigned, 759 (36) not assigned, 775 (54) $[Au_2(SH)(PHtBu_2)(PtBu_3)]^+$, 831 (46) $[Au_2(SH)(PtBu_3)_2]^+$, 887 (22) $[Au_2(StBu)(PtBu_3)_2]^+$. $C_{28}H_{63}Au_2BF_4P_2S$ (974.56): calcd. C 34.51, H 6.52; found C 34.63, H 6.71.

**Complex 2d:** MS (ESI+): *m*/*z* (%) = 721 $[Au(PPh_3)_2]^+$, 1007 (100) $[Au_2(StBu)(PPh_3)_2]^+$, 1293 (7%) $[Au_3(StBu)(PPh_3)_2]^+$. MS–MS 1007: *m*/*z* (%) = 185 (25) $[PPh_2]^+$, 459 (85) $[Au(PPh_3)]^+$, 721 (100) $[Au(PPh_3)_2]^+$, 951 (35) $[Au_2(SH)(PEt_3)_2]^+$, 1008 (15) $[Au_2(StBu)(PPh_3)_2 + H]^+$.

**Reaction of [Au$_2$(S*t*Bu)$_2$(L$_2$)] (L$_2$ = dppm, dppe) with [FeCp$_2$][BF$_4$]. Formation of [Au$_4$(S*t*Bu)$_2$(L$_2$)$_2$][BF$_4$]$_2$ (2e,f):** The complexes were prepared according to the literature.[3]

**Complex 2e:** Yellow microcrystals from dichloromethane solution. Yield: 0.235 g (87%). $^1$H NMR (200 MHz, $CD_2Cl_2$, 25 °C): $\delta$ =

 © 2007 Wiley-VCH Verlag GmbH & Co. KGaA, Weinheim 

1.54 (s, 18 H, $SCMe_3$), 4.35 (t, $^2J_{P,H}$ = 12.0 Hz, 4 H, $PCH_2$), 7.2–7.6 (br. m, 40 H, $PPh_2$) ppm. $^{31}P$ NMR (200 MHz, $CD_2Cl_2$, 25 °C): $\delta$ = 31.28 (br. s), 34.18 (br. s) ppm. MS (ESI+): *m/z* (%) = 581 (9) $[Au_2(dppm)_2]^{2+}$, 867 (100) $[Au_4(StBu)_2(dppm)_2]^{2+}$, 1019 (95) not assigned, 1153 (50) $[Au_3(StBu)_2(dppm)]^+$. MS–MS 867: *m/z* (%) = 185 (30) $[PPh_2]^+$, 397 (31) not assigned, 795 (100) not assigned, 811 (35) $[Au_4(SH)_2(dppm)_2]^{2+}$, 840 (9) $[Au_4(SH)(StBu)(dppm)_2]^{2+}$, 868 (13) $[Au_4(StBu)_2(dppm)_2]^{2+}$. $C_{58}H_{62}Au_4B_2F_8P_4S_2$ (1908.63): calcd. C 36.50, H 3.27; found C 36.88, H 3.19.

**Complex 2f:** MS (ESI+): *m/z* (%) = 595 $[Au_2(dppe)_2]^{2+}$, 738 (9) not assigned, 881 (100) $[Au_4(StBu)_2(dppe)_2]^{2+}$, 1024 (17) $[Au_5(StBu)_3(dppe)_2]^{2+}$, 1167 (42) $[Au_3(StBu)_2(dppe)]^+$. MS–MS 882: *m/z* (%) = 596 (2) $[Au_2(dppe)_2]^{2+}$, 825 (30) $[Au_4(SH)_2(dppe)_2]^{2+}$, 882 (100) $[Au_4(StBu)_2(dppe)_2]^{2+}$, 1167 (2) $[Au_3(StBu_3)_2(dppe)]^+$.

## Acknowledgments

We thank Ceramvetro Gold s.r.l., Florence (Italy) for the generous gift of gold. The work was supported by the Istituto di Chimica dei Composti Organometallici del Consiglio Nazionale delle Ricerche (ICCOM-CNR).

[1] a) F. Scherbaum, A. Grohmann, B. Huber, C. Krüger, H. Schmidbaur, *Angew. Chem. Int. Ed. Engl.* **1988**, *27*, 1602; b) H. Schmidbaur, *Gold. Bull.* **1990**, *23*, 11–21; c) H. Schmidbaur, *Chem. Soc. Rev. (London)* **1995**, *24*, 391–401; d) H. Schmidbaur, *Gold Bull.* **2000**, *33*, 3–10.

[2] a) J. Chen, T. Jiang, G. Wei, A. A. Mohamed, C. Homrighausen, J. A. Krause Bauer, A. E. Bruce, M. R. M. Bruce, *J. Am. Chem. Soc.* **1999**, *121*, 9225–9226; b) A. A. Mohamed, A. E. Bruce, M. R. M. Bruce, *Met.-Based Drugs* **1999**, *6*, 233–238; c) A. A. Mohamed, H. E. Abdou, J. Chen, A. E. Bruce, M. R. M. Bruce, *Comments Inorg. Chem.* **2002**, *23*, 321–334; d) A. A. Mohamed, J. Chen, A. E. Bruce, M. R. M. Bruce, J. A. Krause Bauer, D. T. Hill, *Inorg. Chem.* **2003**, *42*, 2203–2205; e) J. Chen, A. A. Mohamed, H. E. Abdou, J. A. Krause Bauer, J. P. Fackler Jr, A. E. Bruce, M. R. M. Bruce, *Chem. Commun.* **2005**, 1575–1577; f) a related tetragold neutral thiolate was reported: W. J. Hunks, M. C. Jennings, R. J. Puddephatt, *Inorg. Chem.* **2000**, *39*, 2699–2702.

[3] a) P. Diversi, F. Balzano, A. Cuzzola, F. Ghiotto, G. Uccello Barretta, P. Salvadori, *Atti del XXII Convegno SCI 2006, INO-P-91*, Firenze, September 2006; b) A. Battisti, O. Bellina, P. Diversi, S. Losi, F. Marchetti, P. Zanello, *Eur. J. Inorg. Chem.* **2007**, 865–875.

[4] a) R. Narayanaswamy, M. A. Young, E. Parkhurst, M. Ouellette, M. E. Kerr, D. M. Ho, R. C. Elder, A. E. Bruce, M. R. M. Bruce, *Inorg. Chem.* **1993**, *32*, 2506–2517; b) A. Pintado-Alba, H. de la Riva, M. Nieuwhuyzen, D. Bautista, P. R. Raithby, H. A. Sparkes, S. J. Teat, J. M. Lopez-de-Luzuriaga, M. C. Lagunas, *Dalton Trans.* **2004**, 3459–3467; c) H. de la Riva, A. Pintado-Alba, M. Nieuwenhuyzen, C. Hardacre, M. C. Lagunas, *Chem. Commun.* **2005**, 4970–4972; d) T. L. Stott, M. O. Wolf, B. O. Patrick, *Inorg. Chem.* **2005**, *44*, 620–627; e) A. Deák, T. Megyes, G. Tárkányi, P. Király, L. Biczók, G. Pálimkás, P. J. Stang, *J. Am. Chem. Soc.* **2006**, *128*, 12668–12670.

[5] D. F. Feng, S. S. Tang, C. W. Liu, I. J. B. Lin, *Organometallics* **1997**, *16*, 901–909.

[6] A. Hamel, N. W. Mitzel, H. Schmidbaur, *J. Am. Chem. Soc.* **2001**, *123*, 5106–5107.

[7] a) P. Wang, G. R. Newkome, C. Wesdemiotis, *Int. J. Mass Spectrom.* **2006**, *255–256*, 86–92; b) S. Watase, T. Kitamura, N. Kanehisa, M. Shizuma, M. Nakamoto, Y. Kai, S. Yanagida, *Chem. Lett.* **2003**, *32*, 1070–1071.

[8] a) P. S. Pregosin, P. G. Anil Kumar, I. Fernandez, *Chem. Rev.* **2005**, *105*, 2977–2998; b) Y. Cohen, L. Avram, L. Frish, *Angew. Chem. Int. Ed.* **2005**, *44*, 520–554; c) C. Zuccaccia, G. Bellachioma, G. Cardaci, A. Macchioni, *Organometallics* **2000**, *19*, 4663–4665; d) T. Megyes, H. Jude, T. Grosz, I. Bakò, T. Radnai, G. Tarkanyi, G. Palinkas, P. J. Stang, *J. Am. Chem. Soc.* **2005**, *127*, 10731–10738.

[9] A. Sladek, H. Schmidbaur, *Chem. Ber.* **1995**, *128*, 907–909.

[10] a) C. A. Tolman, *Chem. Rev.* **1977**, *77*, 313–348; b) Md. M. Rahman, H. Ye Liu, A. Prock, W. P. Giering, *Organometallics* **1987**, *6*, 650–658.

[11] D. Zuccaccia, A. Macchioni, *Organometallics* **2005**, *24*, 3476–3486.

[12] a) A. Gierer, K. Z. Wirtz, *Naturforsch., Teil A* **1953**, *8*, 522; b) A. Spernol, K. Z. Wirtz, *Naturforsch., Teil A* **1953**, *8*, 532.

[13] M. Valentini, P. S. Pregosin, H. Ruegger, *Organometallics* **2000**, *19*, 2551–2555.

[14] A. Pichota, P. S. Pregosin, M. Valentini, M. Worle, D. Seebach, *Angew. Chem. Int. Ed.* **2000**, *39*, 153–156.

[15] M. Valentini, P. S. Pregosin, H. Ruegger, *J. Chem. Soc. Dalton Trans.* **2000**, 4507–4510.

[16] a) N. E. Schlörer, E. J. Cabrita, S. Berger, *Angew. Chem. Int. Ed.* **2002**, *41*, 107–109; b) S. Beck, A. Geyer, H. H. Brintzinger, *Chem. Commun.* **1999**, 2477–2478.

[17] a) I. Keresztes, P. G. Williard, *J. Am. Chem. Soc.* **2000**, *122*, 10228–10229; b) I. Fernandez, E. Martinez-Viviente, F. Breher, P. S. Pregosin, *Eur. J. Inorg. Chem.* **2005**, *11*, 1495–1506.

[18] J. T. Edward, *J. Chem. Educ.* **1970**, *47*, 261–270.

[19] E. J. Cabrita, S. Berger, *Magn. Reson. Chem.* **2001**, *39*, S 142–148.

[20] a) M. J. Mays, P. A. Vergnano, *J. Chem. Soc. Dalton Trans.* **1979**, 1112–1115; b) C. B. Colburn, W. E. Hill, C. A. McAuliffe, R. V. Parish, *J. Chem. Soc. Chem. Commun.* **1979**, 218–219; c) S. Al-Baker, W. E. Hill, *J. Chem. Soc. Dalton Trans.* **1986**, 1297–1300.

[21] M. A. Thompson, *ArgusLab 4.0.1*, Planaria Software LLC, Seattle, WA http://www.arguslab.com.

[22] G. A. Bowmaker, B. C. Dobson, *J. Chem. Soc. Dalton Trans.* **1981**, 267–270.

Received: July 27, 2007
Published Online: October 24, 2007

 © 2007 Wiley-VCH Verlag GmbH & Co. KGaA, Weinheim 

DOI: 10.1002/ejic.200700836

# The Structure of Potassium and Tetramethylammonium Salts of the Cyclic Organohydroborate Anion $[H_2BC_8H_{14}]^-$ with Different Solvent Ligands

**Xuenian Chen,[a] Shengming Liu,[a] Bin Du,[a] Edward A. Meyers,[a] and Sheldon G. Shore*[a]**

**Keywords:** Agostic interactions / X-ray diffraction / Organohydroborate / Potassium salts

Solvated potassium salts of the 9-BBN hydroborate anion have been prepared and their structures have been determined by single-crystal X-ray diffraction analyses. A tetrameric complex $\{LK[(\mu\text{-}H)_2BC_8H_{14}]\}_4$ is formed when L is toluene, MeTHF, toluene/THF, THF/$Et_2O$ mixtures. The basic framework consists of a distorted $K_4B_4$ cube in which potassium and boron are at alternate corners of the cube linked by bridging hydrogen atoms and α-C–H hydrogen atoms from the 9-BBN hydroborate that appear to form agostic interactions with potassium. There are two types of bridging hydrogen atoms: one is connected to three potassium atoms and one boron atom in a $\mu_4$-coordination arrangement, and the other one is connected to two potassium atoms and one boron atom in a $\mu_3$-coordination arrangement. There are four $\mu_4$-hydrogen arrangements in the structure. They are located inside of the $K_4B_4$ cube. The four $\mu_3$-hydrogen arrangements are located outside of the distorted $K_4B_4$ cube. The coordination number of potassium is 8 with the three $\mu_4$-, two $\mu_3$-bridging hydrogen atoms, two α-C–H hydrogen atoms, and one oxygen atom of the solvent, L (there is a weak $\pi\text{-}\eta^6$ interaction when the solvent is toluene). On the other hand, in the chelating solvent DME, a dimeric structure is formed in which the inner part is planar with potassium and boron located at alternate corners. The potassium is connected to four $\mu_3$-bridging hydrogen atoms, two apparent agostic α-C–H bonding hydrogen atoms, and four oxygen atoms of two DME molecules. Its coordination number is 10 including the agostic interactions. The structure of the uncoordinated $[H_2BC_8H_{14}]^-$ anion is observed in the tetramethylammonium salt.
(© Wiley-VCH Verlag GmbH & Co. KGaA, 69451 Weinheim, Germany, 2007)

## Introduction

Alkali metal (cyclooctane-1,5-diyl) dihydroborates (9-BBN hydriborate anion) have been readily prepared through the reaction of 9-borabicyclo[3.3.1]nonane dimer (9-BBN) with alkali metal hydrides in ether solvents[1] [reaction (1)]. These organohydroborates have been employed as chelating ligands through B–H–M bridges to produce a variety of complexes with transition metals,[2] lanthanides,[3,4] and actinides.[5]

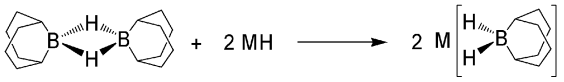


(1)

In the divalent lanthanide complexes $[K(MeTHF)_3]_2\{Ln[(\mu\text{-}H)_2BC_8H_{14}]_4\}$ (MeTHF = 2-methyltetrahydrofuran, Ln = Eu, Yb),[3] four types of interaction between hydrogen and the metal atoms are reported (Scheme 1). The interactions **1a** and **1b** represent the commonly observed metal–hydrogen–boron bridge bond and metal-agostic hydrogen interactions observed in transition and lanthanide metal complexes of the 9-BBN hydroborate ion. The interactions **1c** and **1d** are observed in the complexes $[K(MeTHF)_3]_2\{Ln[(\mu\text{-}H)_2BC_8H_{14}]_4\}$.[3]

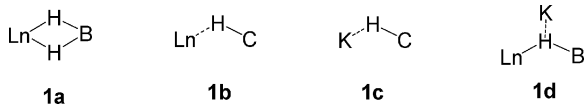


Scheme 1.

These observations provide the impetus to determine if interactions such as **1a**–**c**, and analogs of **1d** exist in the potassium salt of the anion $[(\mu\text{-}H)_2BC_8H_{14}]^-$. Thus investigation of the structure of the potassium salt of the 9-BBN hydroborate anion $[H_2BC_8H_{14}]^-$ was carried out. It was found that the structure of the potassium salt is a tetramer when crystallized as a toluene solvate. To compare the effect of solvate on the molecular character of $K[(\mu\text{-}H)_2BC_8H_{14}]$, crystals were also grown from MeTHF, DME, and mixed solvents. The structure of $[NMe_4][H_2BC_8H_{14}]$ was also determined since that of the uncoordinated 9-BBN hydroborate is apparently previously unreported.

## Results and Discussion

### 1. Preparation

The solvate-free potassium salt of 9-BBN hydroborate was prepared by the literature method.[1] Samples were dis-

[a] Department of Chemistry, the Ohio State University, 100W 18th Ave, Columbus, OH 43210, USA
Fax: +1-614-292-1685
E-mail: shore@chemistry.ohio-state.edu
Supporting information for this article is available on the WWW under http://www.eurjic.org or from the author.

 © 2007 Wiley-VCH Verlag GmbH & Co. KGaA, Weinheim 

Table 1. Crystallographic data for **1**, **2**, **3** and **4**.

| | **1** | **2** | **3** | **4** |
|---|---|---|---|---|
| Empirical formula | $C_{12}H_{28}BN$ | $C_{60}H_{96}B_4K_4$ | $C_{54}H_{96}B_4K_4O_2$ | $C_{32}H_{72}B_2K_2O_8$ |
| Formula weight (amu) | 197.16 | 1017.01 | 976.95 | 684.72 |
| Temperature [°C] | –73 | –123 | –73 | –53 |
| Crystal system | monoclinic | tetragonal | monoclinic | monoclinic |
| Space group | *C*2/*c* | I4(1)/a | *C*2/*c* | *C*2 |
| *a* [Å] | 19.6161(5) | 22.918(5) | 27.728(6) | 15.798(1) |
| *b* [Å] | 7.179(2) | 22.918(5) | 11.388(3) | 18.848(1) |
| *c* [Å] | 18.675(5) | 11.410(3) | 22.428(5) | 15.592(1) |
| *α* [°] | 90 | 90 | 90 | 90 |
| *β* [°] | 100.12(3) | 90 | 126.22(3) | 113.52(1) |
| *γ* [°] | 90 | 90 | 90 | 90 |
| *V* [Å$^3$] | 2589.0(12) | 5993(2) | 5713(2) | 4256.6(4) |
| *Z* | 8 | 4 | 4 | 4 |
| $D_{calcd.}$ [g cm$^{-3}$] | 1.012 | 1.127 | 1.136 | 1.068 |
| $\mu$ [mm$^{-1}$] | 0.056 | 0.332 | 0.348 | 0.262 |
| 2$\theta$ range [°] | 4.44–55.06 | 5.02–52.04 | 4.50–54.88 | 3.54–49.92 |
| Index ranges | $-25 \le h \le 25$, $-9 \le k \le 9$, $-24 \le l \le 24$ | $-28 \le h \le 28$, $-28 \le k \le 28$, $-13 \le l \le 14$ | $-35 \le h \le 35$, $-14 \le k \le 14$, $-29 \le l \le 28$ | $-18 \le h \le 18$, $-22 \le k \le 22$, $-18 \le l \le 18$ |
| Reflections collected | 11135 | 19051 | 12535 | 13963 |
| Independent reflection | 2978 | 2908 | 6507 | 7392 |
| $R_{int}$ | 0.0274 | 0.0278 | 0.0222 | 0.0285 |
| Completeness to $\theta$ [%] | 99.7 | 98.6 | 99.6 | 99.8 |
| Max/min transmission | 0.9933,0.9894 | 0.9519,0.9040 | 0.9242,0.8879 | 0.9743,0.9422 |
| Data/restraints/parameter | 2978/0/239 | 2908/0/284 | 6507/0/395 | 7392/1/431 |
| $R_1$ [$I > 2.0\sigma(I)$] [a] | 0.0406 | 0.0369 | 0.0491 | 0.0523 |
| $wR_2$ (all data) [b] | 0.1098 | 0.0961 | 0.1398 | 0.1431 |
| Goodness-of-fit on $F^2$ | 1.066 | 1.055 | 1.015 | 1.013 |
| Largest difference peak and hole [e Å$^{-3}$] | 0.244, –0.165 | 0.123, –0.185 | 0.416, –0.527 | 0.188, –0.182 |

[a] $R_1 = \Sigma||F_o| - |F_c||/\Sigma|F_o|$. [b] $wR_2 = [\Sigma w(F_o^2 - F_c^2)^2/\Sigma w(F_o^2)^2]^{1/2}$.

solved in the solvents toluene, 2-methyltetrahydrofuran (MeTHF), DME, a 1:1 mixture of toluene and THF, and a 1:1 mixture of THF and ether to form the corresponding solutions of the potassium salt. From these solutions, crystals suitable for X-ray diffraction analysis were obtained by slowly evaporating the solvent. The tetramethylammonium salt of 9-BBN hydroborate was prepared by a metathesis reaction between $K[H_2BC_8H_{14}]$ and $[NMe_4]Cl$ in THF and characterized by proton NMR, elemental analysis and single-crystal X-ray diffraction analyses. Crystal data are given in Table 1.

## 2. Structures

### *2.1 Structure of [NMe$_4$][H$_2$BC$_8$H$_{14}$] (1)*

The reported lithium salts of 9-BBN hydroborates, $[(OEt_2)Li(H_2BC_8H_{14})]_2$, $[(THF)_2Li(H_2BC_8H_{14})]_2$, and $[(THF)_{0.5}(TMEDA)_{0.5}Li(H_2BC_8H_{14})]_2$ [DMEDA = $(CH_3)_2N(CH_2)_2N(CH_3)_2$] have been shown to be the dimers.[6] Interaction between alkali metal and the bridging hydrogen atoms and α-C–H hydrogen atoms occurs in these complexes. Sodium 9-BBN hydroborates, to the best of our knowledge, are unreported. Potassium 9-BBN hydroborates were reported earlier,[1] but without X-ray structures. In addtition to our earlier reported studies of the potassium 9-BBN hydroborate complexes of Yb and Eu,[3,4] we have examined and report here the structures of several potassium 9-BBN hydroborate solvates and that of the solvent free anion.

In order to obtain a structure of a simple 9-BBN anion not coordinated to a cation, the tetramethylammonium salt of 9-BBN hydroborate was prepared. The structure of the $[NMe_4][H_2BC_8H_{14}]$ (**1**) is relatively simple, that of an ionic complex with separated $[NMe_4]^+$ cation and $[H_2BC_8H_{14}]^-$ anion. The structure of the anion is shown in Figure 1. This allows us to observe changes in the structure of the anion when it is coordinated to potassium in compounds **2**, **3** and **4** and a detailed discussion follows later. In the cation, average values are C–N 1.496(2) Å, C–H 0.97(2) Å, C–N–C 109.5(6)°, N–C–H 107.3(7)° and H–C–H 111.5(15)°.

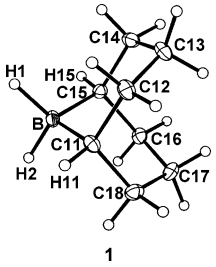


1

Figure 1. The structure of **1**, showing 25% probability thermal ellipsoids. Coordinates and isotropic temperature factors of all hydrogen atoms were allowed to vary and are drawn with arbitrary thermal ellipsoids.

 © 2007 Wiley-VCH Verlag GmbH & Co. KGaA, Weinheim 

### *2.2 Structure of {(Tol) K[(μ-H)$_2$BC$_8$H$_{14}$]}$_4$ (2)*

The gross features of the structure of **2** (Figure 2, a) consist of a foundation that is a distorted $K_4B_4$ cube, with potassium and boron at alternate corners (Figure 2, b). The distances of K–B10, K–B10A, and K–B10B, three edges of the distorted cube, are 3.083(2), 3.749(2), and 3.033(2) Å. Angles B10–K–B10A, B10–K–B10B, and B10A–K–B10B are 92.7(1)°, 106.0(1)°, and 91.5(1)°, while the angles K–B10–K0A, K–B10–K0C, and K0A–B10–K0C are 85.7(1)°, 86.6(1)°, and 75.6(1)°. There are two types of bridging hydrogen atoms: four, four coordinate $\mu_4$-H that reside in the cube and four three coordinate $\mu_3$-H that are situated outside the cube (Figure 2, c). The unit may also be described as a cluster with its centroid at coordinates (0.5, 0.75, 0.625) and a fourfold axis of rotary-inversion along the crystal c-direction.

Potassium is also $\eta^6$-π coordinated to toluene and is involved in agostic interactions with two α-CH hydrogen atoms of the 9-BBN hydroborate ligands. The four $\mu_3$ external bridging hydrogen atoms are located over four of the faces of the $K_4B_4$ cube and are close to being coplanar. In contrast, the four $\mu_4$ bridging hydrogen atoms inside the cube are at the corners of a tetrahedron. This tetrahedron is inverted with and rotated approximately 60° with respect to the potassium tetrahedron, but maintains the same orientation as the boron tetrahedron (Figure 2, d). The potassium is bonded to three $\mu_4$-H bridging hydrogen atoms and two $\mu_3$-H bridging hydrogen atoms. The K–H distance with four-coordinate hydrogen atoms are 2.610(13), 2.750(13), and 2.917(13) Å, compared to those with three coordinate hydrogen atoms, 2.653(13) and 2.762(13) Å.

It is of interest that the cubic arrangement is also observed in the tetrameric sodium hydroborate complexes $[(NaBMe_3H)_4OEt_2]$[7] and $NaBH_4$·TMTA (TMTA = trimethyltriazacyclononane).[8] But it is worth noting that in $NaBH_4$·TMTA, the $BH_4$ group supplies only one hydrogen atom for bridging to three Na centers, while the 9-BBN hydroborate ligand in complex **2** provides two bridging hydrogen atoms one of which is coordinated to three K atoms as $\mu_4$-bridging hydrogen atoms and the other is coordinated

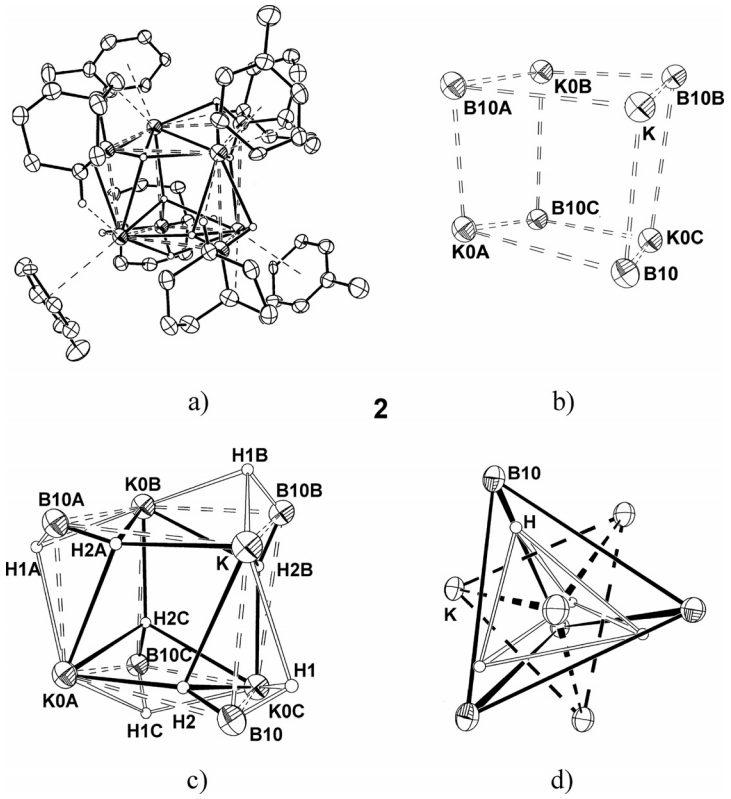


Figure 2. a) The structure of **2**, showing 25% probability thermal ellipsoids. Bridging hydrogen atoms and α-hydrogen atoms are drawn with arbitrary thermal ellipsoids. All other hydrogen atoms omitted for clarity. b) The distorted $K_4B_4$ cube of the structure of **2**. Distances [Å]: K–B10 3.083(2); K–B10A 3.749(2); K–B10B, 3.033(2); angles [°]: B10–K–B10A 92.7(1), B10–K–B10B 106.0(1), B10A–K–B10B 91.5(1), K–B10–K0A 85.7(1), K–B10–K0C 86.6(1), K0A–B10–K0C 75.6(1). The twofold rotation axis along the *c*-direction relates K to K0A, K0B to K0C, B10 to B10A, B10B to B10C. The K atoms are calculated to be 2.67 Å from the centroid and the B atoms 3.01 Å. c) The interactions between the potassium and the $\mu_4$- and $\mu_3$-coordination bridging hydrogen atoms in the structure of **2**. Distances [Å]: K–H1 2.653(13), K–H1B 2.762(13), K–H2 2.917(13), K–H2A 2.610(13), K–H2B 2.750(13) and B10–H1 1.259(14), B10–H2 1.234(14). d) The relationship among the three tetrahedrons. Four $\mu_4$-hydrogen atoms at distances [Å]: H2–H2A 2.99(2), H2–H2B 3.39(2), H2–H2C 3.39(2); angles [°]: H2–H2B–H2A 63.8(5), H2–H2C–H2A 63.8(5), H2–H2C–H2B 52.5(4); four potassium atoms at distances [Å]: K–K0A 4.673(2), K–K0B 4.196(2), K–K0C 4.196(2); angles [°]: K–K0C–K0A 56.2(1), K–K0B–K0A 56.2(1), K–K0C–K0B 67.7(1); four boron atoms at distances [Å]: B10B–B10A 4.964(2), B10–B10B 4.886(2), B10–B10C 4.886(2); angles [°]: B10–B10B–B10A 59.5(1), B10–B10C–B10A 59.5(1), B10–B10C–B10B 61.1(1).

 © 2007 Wiley-VCH Verlag GmbH & Co. KGaA, Weinheim 

to two K atoms as $\mu_3$-bridging hydrogen atoms. The coordination geometries of the $\mu_4$-bridging hydrogen atoms in complex **2** are very similar to those in the $Na_4H_4$ unit in the complexes $(NaBMe_3H)_4OEt_2$ and tetrameric $NaBH_4$·TMTA.[7,8]

In complex **2**, the potassium also interacts with two α-C–H hydrogen atoms by apparent agostic interaction (Figure 2, a). These occur between the K atom and H11 and H15 with distances of K–H11, 2.716(16) and K–H15, 2.769(16) Å, which are comparable to the distances of potassium with bridging hydrogen atoms, K–H1 [2.653(14), 2.762(14) Å] and K–H2 [2.917(14), 2.610(14) Å, 2.750(14) Å].

In the molecular structure of complex **2** (Figure 2, a), the toluene molecule is disordered with fractional occupancies of 0.581(5) for part (A) and 0.419(5) for part (B). They interact in $\eta^6$-π coordination with potassium with the K–C distances ranging from 3.267(8) to 3.407(12) Å. Though long known experimentally and much studied theoretically, alkali metal-π (arene) interactions have recently taken on a new significance with the suggestion that intramolecular cationic interactions with (electron-rich) aromatic centers can influence protein structures.[9] Such interaction can best be described as an induced dipole interaction[10] with K–C distances for the $\eta^6$-bound toluene molecules in the range 3.267(8)–3.407(12) Å.[11,12] These distances are comparable to those found in the group of K-$\eta^6$-toluene in corresponding complexes. The interactions between K and $\eta^6$-toluene as well as with two α-C–H hydrogen atoms also contribute to the stabilization of the tetrameric species of **2** in addition to the potassium to BH contacts.

### *2.3 Structure of [(THF)$_2$(Tol)$_2$K$_4$]{H$_2$BC$_8$H$_{14}$}$_4$ (3)*

The structure of **3** was obtained from a single crystal grown in a mixed solvent of THF and toluene in approximately 1:1 ratio (Figure 3, a). It is a tetrameric structure with two THF and two toluene ligands coordinated to four potassium atoms. [One of the 9-BBN ligands is disordered with occupancies for part B1 = 0.743(3) and 0.247(3) for part B3. Only the B1 anion is drawn in the figures.] The arrangement of 9-BBN hydroborate anions coordinated to potassium is different than that in structure **2**. The $K_4B_4$ cube is much more distorted. Though the $\mu_3$- and $\mu_4$-types of bridging hydrogen atoms exist in the structure of **3**, the geometrical arrangement differs from that in structure **2**. Four $\mu_4$-bridging hydrogen atoms are still located inside of the $K_4B_4$ distorted cube, which is similar to that in structure **2**. However, four $\mu_3$-bridging hydrogen atoms are associated with only two faces (Figure 3, b).

This arrangement differs from that of **2**, in which four $\mu_3$-bridging hydrogen atoms are located at four faces (Figure 2, c). Thus the twelve K–B edges of the distorted $K_4B_4$ cube are divided into two types, four with an average length 3.702(4) Å and eight shorter ones with an average length of 3.020(4) Å. The centroid of this structure is at (0.5, 0.40699, 0.25) and it possesses a twofold axis parallel to the *b*-axis of the crystal (Figure 3, b) in a manner similar to that of structure **2**. The distances of potassium and bridging hydrogen atoms fall in the normal range with the longest 2.82(2) Å and the shortest 2.60(3) Å. In addition, potassium also appears to interact with two α-C–H hydrogen atoms by agostic interaction to complete its coordination sphere. The potassium α-C–H hydrogen distances: K1–H15 2.80(2), and K2–H11 2.75(2) Å are comparable to those in structure **2**.

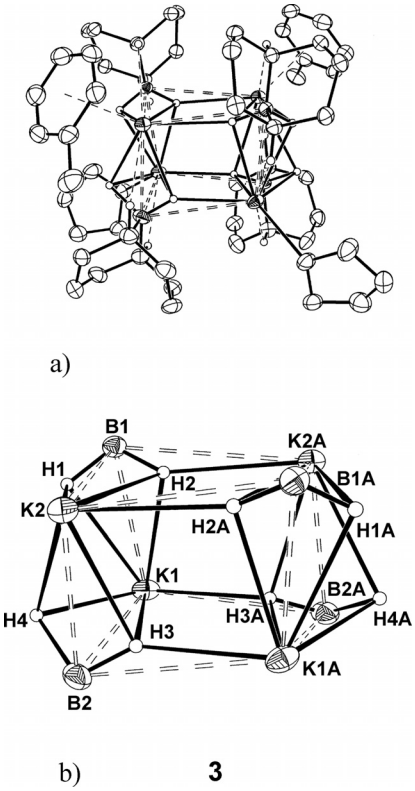


Figure 3. a) The structure of **3**, showing 25% probability thermal ellipsoids. Bridging hydrogen atoms and α-hydrogen atoms are drawn with arbitrary thermal ellipsoids. All other hydrogen atoms omitted for clarity. b) The interactions between the potassium and $\mu_4$- and $\mu_3$-bridging hydrogen atoms in the structure of **3**. Distances [Å]: K1–B2A 3.636(4), K2–B1A 3.768(5), K1–B1 2.987(2), K1–B2 3.038(4), K2–B1 3.026(2), K2–B2 3.028(4), K1–H1 2.63(2), K1–H2 2.71(4), K1–H3 2.71(2), K1–H4 2.75(3), K2–H1 2.67(2), K2–H2 2.82(2), K2–H3 2.71(2), K2–H4 2.60(3); angles [°]: B1–K1–B2 97.29(8), B1–K1–B2A 103.3(1), B2–K1–B2A 96.1(1), B1–K2–B2 96.66(9), B1–K2–B1A 90.9(1), B2–K2–B1A 99.5(1), K1–B1–K2 82.63(6), K1–B1–K2A 77.7(1), K2–B1–K2A 87.5(1), K1–B2–K2 81.76(9), K1–B2–K1A 81.8(1), K2–B2–K1A 79.4(1).

### *2.4 Structure of [(DME) K(H$_2$BC$_8$H$_{14}$)]$_2$ (4)*

The molecular structure of **4** is a dimer. In the asymmetric unit there are two half-molecular fragments that produce two similar molecules through symmetry operations. In one molecule a twofold axis passes through K1 and K3 and is perpendicular to B12–B12A. In the other a twofold axis passes through B1 and B2 and is perpendicular to K2–K2A. One molecule is displayed in Figure 4 in which K1, K3, B12, and B12A are shown. Distances B12–K1 and B12–K3 are 3.156(5) and 3.125(5) Å; angles K1–B12–K3, B12–K1–B12A, and B12–K3–B12A are 82.73(9), 96.6(2), and 97.9(2)°. The K1–K3 distance, 4.151(2) Å, is compar-

 © 2007 Wiley-VCH Verlag GmbH & Co. KGaA, Weinheim 

able to those in structure **2**. Each potassium atom is bound to four oxygen atoms from the DME ligands, four bridging hydrogen atoms, and two α-C–H hydrogen atoms by agostic interaction. All bridging hydrogen atoms are bound to one boron atom and two potassium atoms as $\mu_3$-hydrogen atoms. The K1–H121 distance of 2.98(4) Å is comparable to 2.68(3) Å of the K1–H111, 2.91(4) Å of K1–H112, here the hydrogen atoms come from the K–H–B bridges. The K1–O11 and K1–O12 distances are 2.765(4) and 2.808(3) Å which are comparable to ordinary K–O bond lengths.[3] Thus the coordination number of K appears to be 10. Corresponding values for the second molecule present in the structure are given in the electronic supporting information.

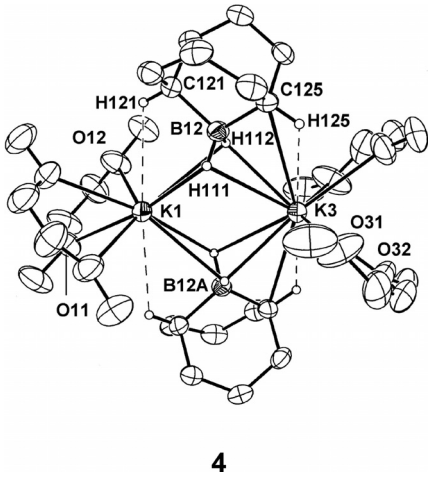


**4**

Figure 4. The structure of **4**, showing 25% probability thermal ellipsoids. Bridging hydrogen and α-hydrogen atoms are drawn with arbitrary thermal ellipsoids. All other hydrogen atoms omitted for clarity. The interaction between the potassium and the four oxygen atoms from the two DME and six hydrogen atoms including the four $\mu_3$-bridging hydrogen atoms, and the two α-C–H hydrogen atoms by agostic interaction. Distances [Å]: K1–O11 2.808(3), K1–O12 2.765(4), K1–H111 2.68(3), K1–H112 2.91(4), K1–H121 2.98(4).

Table 2 compares bond parameters of **1**, **2**, **3**, **4** and the 9-BBN dimer $(C_8H_{14}B)(\mu\text{-}H)_2(BC_8H_{14})$.[13] For the compounds bond parameters are not noticeably different with the exception of the B–H distance in **4** which is still within $2\sigma$ of the corresponding bond length in the other 9-BBN hydroborate ligands. That the $[H_2BC_8H_{14}]^-$ anion readily functions as a ligand in forming bridge bonds with potassium in the dimeric and tertrameric molecules can be related to the fact that these bond parameters are virtually unchanged in the formation of the dimeric and tetrameric complexes (see electronic supporting information for details). This also appears to be true for the dimeric 9-BBN hydroborate complexes of lithium.[6]

That with the solvent DME a dimer is formed rather than a tetramer is related to the fact that the DME is bidentate with its two oxygen atoms coordinating to potassium, thereby occupying an additional coordination site than the monodentate ether ligands thus blocking possible further association through a K–H–B bridge. Compared to the 9-BBN dimer, the obvious difference is that the angle of H–B–H, 87(2)°, is about 20° smaller than those in **1**, **2**, **3** and **4**.[14] This smaller HBH angle in the 9-BBN dimer and other diboranes probably relates to the significantly smaller size of boron compared to the alkali metals.[15]

Table 2. The comparison of bond parameters that involve the boron atom in complexes **1**, **2**, **3**, **4** and 9-BBN dimer {all data are average value and the standard deviations of the average values are calculated either by $[\Sigma(l_i - l)^2/n(n-1)]^{1/2}$ or $1/n(\Sigma\sigma_i^2)^{1/2}$, the larger value being reported}.

| | Distances [Å] | | Angles [°] | | |
|---|---|---|---|---|---|
| | B–H | B–C | H–B–H | H–B–C | C–B–C |
| **1** (ion pair) | 1.195 (10) | 1.626(3) | 107.5(9) | 111.2(4) | 104.98(8) |
| **2** (tetramer) | 1.247 (12) | 1.627(3) | 108.7(9) | 110.8(7) | 104.89(13) |
| **3** (tetramer) | 1.16(2) | 1.628(19) | 106.6(22) | 111.9(21) | 103.9(9) |
| **4** (dimer) | 1.08(8) | 1.629(9) | 106(2) | 112(1) | 103.9(5) |
| 9-BBN dimer | 1.25(2) | 1.567(2) | 87(2) | | 111.8(3) |

### *2.5 Structures of [(MeTHF) K($H_2BC_8H_{14}$)]$_4$ (5), [($OEt_2$) K($H_2BC_8H_{14}$)]$_4$ (6a) and [(THF)$_2$($OEt_2$)$_2$$K_4$]-{$H_2BC_8H_{14}$}$_4$ (6b)*

Poor quality crystals of **5** were grown from 2-methyltetrahydrofuran (MeTHF) and of **6** from mixtures of THF and diethyl ether (see chapter X-ray Structure Determination and the electronic supporting information for details). The structure of molecule **5** is similar to that of **2**. The K–K distances in **5** range from 4.050(6) to 4.506(6) Å. They are comparable to those in structure **2**. The formation of the tetramer is believed to be mainly dependent on the interaction between potassium and bridging hydrogen atoms. When the solvent is a monodentate ligand or a π donor the tetrameric structure is formed. The potassium is bound to one oxygen atom from 2-methyltetrahydrofuran (MeTHF) and seven hydrogen atoms including three $\mu_4$-hydrogen atoms, two $\mu_3$-hydrogen atoms, and two α-C–H hydrogen atoms by agostic interactions. The K–H distances range from 2.64(6) to 2.86(7) Å. They are not significantly different whether the hydrogen is from $\mu_4$-hydrogen atoms or $\mu_3$-hydrogen atoms, even from α-C–H hydrogen atoms by agostic interaction.

There are two independent molecules **6a** and **6b** in the unit cell for the structure of a single crystal obtained from the mixed solvent of ether and THF. The structure of **6a** contains four ether molecules, while the structure of **6b** contains two ether molecules and two THF molecules coordinated to potassium atoms, respectively. Both structures are tetramers and the inner part is the distorted $K_4B_4$ cube and the structural descriptions are similar to those of **2** and **3**.

## Summary

The solid-state structure of an alkali metal 9-BBN hydroborate is dependent on the alkali metal size and other coordinating ligands. The 9-BBN hydroborate salts of lithium are dimeric structures with ether or THF ligands. The coordination number of lithium is 5 or 6 with bridging hydrogen atoms, α-C–H hydrogen atoms in agostic interactions, and oxygen atoms of ether or THF in the structure of those

 © 2007 Wiley-VCH Verlag GmbH & Co. KGaA, Weinheim 

complexes.[6] However, the 9-BBN hydroborate salts of potassium, form tetrameric structures in the non-coordinating solvent toluene, the single dentate coordinating solvents MeTHF, THF, ether, and/or their 1:1 mixtures. The coordination number is 8 with three $\mu_4$-, two $\mu_3$-bridging hydrogen atoms, two α-C–H hydrogen atoms and one oxygen atom of solvent (or the weak $\eta^6$ interaction with the π system of toluene). The chelating ligand DME prevents formation of the tetramer of 9-BBN hydroborate salt instead the dimer, **4**, is formed in which the coordination number of potassium is 10 with four $\mu_3$-bridging, two α-C–H hydrogen atoms and four oxygen atoms of the DME ligand.

The striking structural feature of the tetrameric structure of the potassium salts of 9-BBN hydroborate is that the $K_4B_4$ core is a much distorted cube. Similar arrangements occur in complexes $(NaBMe_3H)_4OEt_2$[7] and $NaBH_4$·TMTA,[8] which have only one bridging hydrogen. In contrast to a very distorted $K_4B_4$ cube in the potassium salts of 9-BBN hydroborate, a much more regular $M_4O_4$ cube is a typical structure for alkali metal alkoxides $[MOR]_4$.[16] In the systems studied, interaction between B–H hydrogen atoms and α-C–H hydrogen atoms with potassium is a question of interest. Evidences for such interactions have been given by single-crystal X-ray diffraction and infrared and NMR spectroscopy.[17] The spectra we obtained were too complicated to decipher with confidence. But low temperature single-crystal X-ray diffraction, is suggestive of such an interaction.

The tetramethylammonium salt of 9-BBN hydroborate provides the structure of the anion $[H_2BC_8H_{14}]^-$.

## Experimental Section

**General Comments:** All manipulations were carried out on a standard high vacuum line or in a dry box under nitrogen. Toluene, 2-methyltetrahydrofuran, tetrahydrofuran, DME, and ether were dried with sodium/benzophenone and freshly distilled prior to use. Celite was dried by heating at 150 °C under dynamic vacuum for 5 h. Potassium hydride (Aldrich) was received as an oil slurry, washed with hexane, vacuum dried, and stored in the drybox. $C_8H_{14}B(\mu\text{-}H)_2BC_8H_{14}$, and $NMe_4Cl$ were purchased from Aldrich and used as received. Solvent-free $K[H_2BC_8H_{14}]$ was prepared by literature procedures.[1] Elemental analyses were performed by Galbraith Laboratories, Inc. of Knoxville, TN, U.S.A. NMR spectra were recorded with a Bruker AM-250 spectrometer. $^1H$ NMR spectra were obtained at 250.1 MHz, and referenced to residual solvent protons. $^{11}B$ NMR spectra were obtained at 80.3 MHz, and externally referenced to $BF_3$·$OEt_2$ in $C_6D_6$ ($\delta$ = 0.00 ppm). Infrared spectra were recorded with a Mattson–Polaris FT-IR spectrometer with 2 $cm^{-1}$ resolution.

**X-ray Structure Determination:** Single-crystal X-ray diffraction data were collected with a Nonius Kappa CCD diffraction system, which employs graphite-monochromated Mo-$K_\alpha$ radiation ($\mu$ = 0.71073 Å). A single crystal of a complex, **1** to **6**, was mounted on the tip of a glass fiber coated with Fomblin oil (a pentafluoro polyether). Unit cell parameters were obtained by indexing the peaks in the first 10 frames and refined employing the whole data set. All frames were integrated and corrected for Lorentz and polarization effects using the DENZO-SMN package (Nonius BV, 1999).[18] The empirical absorption correction was applied with the SORTAV program[19] provided by *MaXus* software.[20] The positions of the heavy atom K were revealed by the Patterson method. The structures were refined using the SHELXTL-97 (difference electron density calculations and full-matrix least-squares refinements) structure solution package.[21] Data merging was performed using the data preparation program supplied by SHELXTL-97. Other calculations was made using WinGX (version 1.70.01), which includes Platon, Parst programs.[22] After all non-hydrogen atoms were located and refined anisotropically, hydrogen atom positions were calculated assuming standard geometries. All hydrogen atoms of both the organohydroborate ring and the tetramethylammonium group in **1**, all hydrogen atoms of the organohydroborate ring in **2**, and bridge hydrogen atoms and α-hydrogen atoms of the organohydroborate ring in **3** to **6** were located on difference maps and their positional and isotropic thermal parameters were refined. This is the commonly accepted procedure for locating hydrogen atoms by X-ray diffraction and distances are probably within a 0.1 Å if the atom bound to hydrogen is not a heavy fifth or sixth row element.

In **2** the toluene molecule is disordered [fractional occupancies 0.587(6), 0.413(6)] with average ring distances <C–C> 1.39(2) and 1.38(5) Å, respectively, and for the ordered 9-BBN group <C–C> 1.535(2) Å. In **3**, one 9-BBN group is ordered, <C–C> 1.534(2) Å. A second 9-BBN group is disordered [fractional occupancies 0.745(4) and 0.255(4)] with <C–C> 1.535(5), 1.53(1) Å, respectively. All agostic contacts have been calculated only with respect to the ordered 9-BBN group. In **4** there is no apparent disorder and for the three independent 9-BBN groups present <C–C> 1.523(5), 1.523(2), and 1.520(2) Å. The crystals grown for compounds **5** and **6** were of poor quality. Crystals of **5** were merohedrally twinned and disordered while many atoms in the THF and ether ligands of **6** were split and large difference electron density residuals remained after all atoms had been located. The data for these compounds has been relegated to the supporting information.

CCDC-620329 to -620334 contain the supplementary crystallographic data for this paper. These data can be obtained free of charge from The Cambridge Crystallographic Data Center via www.ccdc.cam.ac.uk/data_request/cif.

**Preparation of $[NMe_4][H_2BC_8H_{14}]$ (1):** $K[H_2BC_8H_{14}]$ (0.162 g, 1.0 mmol) and $NMe_4Cl$ (0.110 g, 1.0 mmol) were put into a flask in the dry box. The flask was degassed and about 10 mL of THF was condensed into the flask. The system was warmed and stirred at room temperature for 3 h to produce **1** and a KCl precipitate. Then the mixture was filtered to remove the KCl solid. THF solution was concentrated at room temperature and colorless X-ray quality crystals 0.180 g (0.91 mmol, 91.3% yield) formed. $^{11}B$ NMR (250 MHz, [$D_8$]toluene, 25 °C, $BF_3$·$OEt_2$): $\delta$ = –15.0 (t) ppm. $^1H$ NMR (250 MHz, [$D_8$]toluene, 25 °C, TMS): $\delta$ = 2.36 (s, 12 H, Me), 2.27–0.658 (m, α-, β-, γ-H of $H_2BC_8H_{14}$ unit) ppm. $^1H\{^{11}B\}$ NMR (250 MHz, [$D_8$]toluene, 25 °C, TMS): $\delta$ = 1.34 (s, $\mu$-H of $H_2BC_8H_{14}$ unit) ppm. IR (KBr): $\tilde{\nu}$ = 3108 (w), 3074 (m), 2975 (w), 2920 (sh), 2873 (vs), 2826 (s), 1960 (w), 1849 (s), 1828 (sh), 1794 (m), 1733 (w), 1699 (m), 1651 (m), 1557 (m), 1539 (m), 1425 (vs), 1401 (sh), 1341 (s), 1315 (sh, w), 1284 (m), 1261 (m), 1203 (m), 1168 (w), 1111 (m), 1067 (m), 1041 (m), 1014 (vs), 928 (m), 888 (m), 865 (w), 828 (sh), 805 (vs), 734 (m), 463 (m) $cm^{-1}$. $C_{12}H_{28}BN$ {$[N(CH_3)_4]$ $(H_2BC_8H_{14})$} (197.17): C 73.09, H 14.31, N 6.09; found C 73.18, H 14.70, N 5.84.

**Preparation of $\{(Tol)K[(\mu\text{-}H)_2BC_8H_{14}]\}_4$ (2):** Solvent-free $K[H_2BC_8H_{14}]$ (0.2 g) was dissolved in toluene to produce a $K[H_2BC_8H_{14}]$ solution. After it was filtered, the solution was con-

 © 2007 Wiley-VCH Verlag GmbH & Co. KGaA, Weinheim 

centrated at room temperature to afford colorless X-ray quality crystal of complex **2**. $^{11}$B NMR (250 MHz, [D$_8$]THF, 25 °C, $BF_3{\cdot}OEt_2$): $\delta$ = –15.5 (t) ppm. $^{11}$B{$^1$H} NMR (250 MHz, [D$_8$]THF, 25 °C, $BF_3{\cdot}OEt_2$): $\delta$ = –15.5 (s) ppm. $^1$H NMR (250 MHz, [D$_8$]-THF, 25 °C, TMS): $\delta$ = 7.13 (m, $C_6H_5$ of toluene), 2.30–0.89 (m, $CH_3$ of toluene and β-, γ-*H* of $H_2BC_8H_{14}$ unit), 0.62 (s, α-*H* of $H_2BC_8H_{14}$ unit) ppm. $^1$H{$^{11}$B} NMR (250 MHz, [D$_8$]THF, 25 °C, TMS): $\delta$ = 0.80 (s, μ-*H* of $H_2BC_8H_{14}$ unit) ppm. $^{11}$B NMR (250 MHz, [D$_8$]toluene, 25 °C, $BF_3{\cdot}OEt_2$): $\delta$ = –17.2 (t) ppm. $^{11}$B{$^1$H} NMR (250 MHz, [D$_8$]toluene, 25 °C, $BF_3{\cdot}OEt_2$): $\delta$ = –17.2 (s) ppm. $^1$H NMR (250 MHz, [D$_8$]toluene, 25 °C, TMS): $\delta$ = 2.34–0.88 (m, $CH_3$ of toluene and β-, γ-*H* of $H_2BC_8H_{14}$ unit), 0.32 (s, α-*H* of $H_2BC_8H_{14}$ unit) ppm. $^1$H{$^{11}$B}NMR (250 MHz, [D$_8$]toluene, 25 °C, TMS): $\delta$ = 0.18 (s, $\mu$-*H* of $H_2BC_8H_{14}$ unit) ppm. IR (KBr): $\tilde{\nu}$ = 2979 (m), 2946 (s, sh), 2915 (vs), 2862 (vs), 2829 (vs), 2808 (vs,sh), 2680 (w), 2647 (w), 2614 (w), 2361 (w), 2320 (w), 2236 (w,sh), 2198 (m,sh), 2158 (s), 2125 (s), 2077 (s), 1977 (s,sh), 1957 (s), 1487 (m), 1455 (m), 1384 (w), 1229 (s), 1160 (m), 1076 (m), 1037 (w), 984 (w), 939 (w), 901 (w), 829 (w), 794 (w), 683 (w), 613 (w), 526 (w), 472 (w), 420 (m) cm$^{-1}$. {[K(C$_7$H$_8$)$_{0.05}$(H$_2$BC$_8$H$_{14}$)]$_4$}: $C_{8.35}H_{16.4}B_1K_1$ (166.73): calcd. C 60.15, H 9.91; found C 59.96, H 9.59.

**Preparation of [(DME)K(H$_2$BC$_8$H$_{14}$)]$_2$ (4):** Solvent-free K[H$_2$BC$_8$H$_{14}$] (0.2 g) was dissolved in DME to produce a K[H$_2$BC$_8$H$_{14}$] solution. After it was filtered, the solution was concentrated at room temperature to afford colorless X-ray quality crystal of complex **4**: $^{11}$B NMR (250 MHz, [D$_8$]THF, 25 °C, $BF_3{\cdot}OEt_2$): $\delta$ = –16.2 (t) ppm. $^{11}$B{$^1$H} NMR (250 MHz, [D$_8$]THF, 25 °C, $BF_3{\cdot}OEt_2$): $\delta$ = –16.2 (s) ppm. $^1$H NMR (250 MHz, [D$_8$]-THF, 25 °C, TMS): $\delta$ = 3.44 (s, $CH_2$ of DME), 3.28 (s, $CH_3$ of DME), 1.80–1.45 (m, β-, γ-*H* of $H_2BC_8H_{14}$ unit), 0.60 (s, α-*H* of $H_2BC_8H_{14}$ unit) ppm. $^1$H{$^{11}$B} NMR (250 MHz, [D$_8$]THF, 25 °C, TMS): $\delta$ = 0.78 (s, $\mu$-*H* of $H_2BC_8H_{14}$ unit) ppm. $^{11}$B NMR (250 MHz, [D$_8$]toluene, 25 °C, $BF_3{\cdot}OEt_2$): $\delta$ = –17.2 (t) ppm. $^{11}$B{$^1$H} NMR (250 MHz, [D$_8$]toluene, 25 °C, $BF_3{\cdot}OEt_2$): $\delta$ = –17.2 (s) ppm. $^1$H NMR (250 MHz, [D$_8$]toluene, 25 °C, TMS): $\delta$ = 3.07–3.02 (m, $CH_2$ and $CH_3$ of DME), 2.32–1.83 (m, β-, γ-*H* of $H_2BC_8H_{14}$ unit), 0.38 (s, α-*H* of $H_2BC_8H_{14}$ unit) ppm. $^1$H{$^{11}$B} NMR (250 MHz, [D$_8$]toluene, 25 °C, TMS): $\delta$ = 0.27 (s, μ-*H* of $H_2BC_8H_{14}$ unit) ppm. IR (KBr): $\tilde{\nu}$ = 2979 (m), 2946 (s, sh), 2915 (vs), 2863 (vs), 2828 (vs), 2807 (vs,sh), 2679 (w), 2647 (w), 2614 (w), 2319 (w), 2236 (w,sh), 2198 (m,sh), 2158 (s), 2125 (s), 2079 (s), 2040 (s,sh), 1977 (s,sh), 1957 (s), 1485 (m), 1450 (m), 1385 (w), 1337 (w), 1229 (s), 1159 (m), 1076 (m), 1037 (w), 939 (w), 903 (w), 829 (w), 794 (w), 731 (w), 682 (w), 527 (w), 473 (w), 421 (m) cm$^{-1}$. {[K(H$_2$BC$_8$H$_{14}$)]$_2$}: $C_8H_{16}B_1K_1$ (162.12): calcd. C 59.26, H 9.95; found C 58.81, H 10.07.

Crystals of **3**, **5**, and **6** were obtained employing the same method as for the preparation of **2** and **4** by using the corresponding solvent or a mixture of solvents. Provided here are their structures without chemical analysis because they have very similar structures with **2**.

**Supporting Information** (see also the footnote on the first page of this article): Details of structural information for complexes **1**–**6** include crystallographic data and figures for **5** and **6**, BBN unit disorder in **3**, coordination environment of potassium in **4**, and the comparison of distances and angles of BBN in the coordinated arrangement in **2** and the non-coordinated arrangement in **1** are presented.

## Acknowledgments

This work was supported by the National Science Foundation through the Grant CHE 02-13491.

[1] a) R. Köster, G. Seidel, *Inorg. Chem.* **1983**, *22*, 198; b) H. C. Brown, B. Singaram, P. C. Mathew, *J. Org. Chem.* **1981**, *46*, 2712.
[2] a) X. Chen, S. Liu, C. E. Plečnik, F.-C. Liu, G. Fraenkel, S. G. Shore, *Organometallics* **2003**, *22*, 275; b) F. Lacrroix, C. E. Plečnik, S. Liu, F.-C. Liu, E. A. Meyers, S. G. Shore, *J. Organomet. Chem.* **2003**, *687*, 69; c) N. N. Ho, R. Bau, C. E. Plečnik, S. G. Shore, X. Wang, A. J. Schultz, *J. Organomet. Chem.* **2002**, *654*, 216; d) E. R. Ding, F.-C. Liu, S. Liu, E. A. Meyers, S. G. Shore, *Inorg. Chem.* **2002**, *41*, 5329; e) C. E. Plečnik, F.-C. Liu, S. Liu, J. Liu, E. A. Meyers, S. G. Shore, *Organometallics* **2001**, *20*, 3599; f) S. Liu, F.-C. Liu, G. Renkes, S. G. Shore, *Organometallics* **2001**, *20*, 5717; g) F.-C. Liu, C. E. Plečnik, S. Liu, J. Liu, E. A. Meyers, S. G. Shore, *J. Organomet. Chem.* **2001**, *627*, 109; h) F.-C. Liu, J. Liu, E. A. Meyers, S. G. Shore, *J. Am. Chem. Soc.* **2000**, *122*, 6106; i) F.-C. Liu, B. Du, J. Liu, E. A. Meyers, S. G. Shore, *Inorg. Chem.* **1999**, *38*, 3228; j) F.-C. Liu, J. Liu, E. A. Meyers, S. G. Shore, *Inorg. Chem.* **1999**, *38*, 2169; k) J. Liu, E. A. Meyers, S. G. Shore, *Inorg. Chem.* **1998**, *37*, 496; l) F.-C. Liu, J. Liu, E. A. Meyers, S. G. Shore, *Inorg. Chem.* **1998**, *37*, 3293; m) G. T. Jordan IV, F.-C. Liu, S. G. Shore, *Inorg. Chem.* **1997**, *36*, 5597; n) G. T. Jordan IV, S. G. Shore, *Inorg. Chem.* **1996**, *35*, 1087.
[3] X. Chen, S. Lim, C. E. Plečnik, S. Liu, D. Bin, E. A. Meyers, S. G. Shore, *Inorg. Chem.* **2005**, *44*, 6052.
[4] X. Chen, S. Lim, C. E. Plečnik, S. Liu, D. Bin, E. A. Meyers, S. G. Shore, *Inorg. Chem.* **2004**, *43*, 692.
[5] P. Zanella, F. Ossola, M. Porchia, A. Chiesi-Villa, G. Rossetto, C. Guastini, *J. Organomet. Chem.* **1987**, *323*, 295.
[6] J. Knizek, H. Nöth, *J. Organomet. Chem.* **2000**, *614–615*, 168.
[7] a) N. A. Bell, H. M. M. Shearer, C. B. Spencer, *Acta Crystallogr. Sect. C* **1983**, *39*, 694; b) N. A. Bell, H. M. M. Shearer, C. B. Spencer, *J. Chem. Soc. Chem. Commun.* **1980**, 711.
[8] H.-H. Giese, T. Habereder, H. Nöth, W. Ponikwar, S. Thomas, M. Warchhold, *Inorg. Chem.* **1999**, *38*, 4188.
[9] a) G. K. Fukin, S. V. Linderman, J. K. Kochi, *J. Am. Chem. Soc.* **2002**, *124*, 8329; b) S. K. Burley, G. A. Petsko, *FEBS Lett.* **1986**, *203*, 139.
[10] G. A. Bowmaker, H. Schmidbauer, *Organometallics* **1990**, *9*, 1813.
[11] a) Intercalation of atomic potassium into a graphite (0001) surface gave a layer spacing of 5.35 Å (i.e. 2 × K–Cl): N. J. Wu, A. Ignatiev, *Phys. Rev. B* **1983**, *28*, 7288; b) The interlayer spacing of graphite is 3.35 Å: N. J. Wu, A. Ignatiev, *Phys. Rev. B* **1982**, *25*, 2983; c) L. Pauling, *The Nature of the Chemical Bond*, 3rd ed., Cornell University Press, Ithaca, NY, **1960**.
[12] a) G. R. Giesbrecht, J. C. Gordon, D. L. Clark, C. A. Hijar, B. L. Scott, J. G. Watkin, *Polyhedron* **2003**, *22*, 153; b) G. Bai, H. W. Roesky, M. Noltemeyer, H.-G. Schmit, *J. Chem. Soc. Dalton Trans.* **2002**, 2437; c) G. Bai, H. W. Roesky, M. Noltemeyer, H.-G. Schmit, *Organometallics* **2002**, *21*, 2789; d) I. Korobkov, G. Aharonian, S. Gambarotta, G. P. A. Yap, *Organometallics* **2002**, *21*, 4899; e) G. C. Forbes, A. R. Kennedy, B. A. Mulvey, R. E. Roberts, R. B. Rowlings, *Organometallics* **2002**, *21*, 5115; f) S. Chitsaz, B. Neumüller, *Organometallics* **2001**, *20*, 2338; g) N. Beswick, M. A. Choi, A. D. Hopkins, M. McPartlin, M. A. Paver, D. S. Wright, *Chem. Commun.* **1998**, 261; h) H.-J. Gosink, F. Nief, L. Ricard, F. Mathey, *Inorg. Chem.* **1995**, *34*, 1306; i) C. J. Schaverien, J. B. V. Mechelen, *Organometallics* **1991**, *10*, 1704.
[13] N. C. Webb, M. R. Becker, *J. Chem. Soc. B* **1967**, 1317.
[14] D. J. Brauer, C. Krüger, *Acta Crystallogr. Sect. B* **1973**, *29*, 1684.
[15] a) D. S. Jones, W. N. Lipscomb, *Acta Crystallogr. Sect. A* **1970**, *26*, 196; b) H. W. Smith, W. N. Lipscomb, *J. Chem. Phys.* **1965**, *43*, 1060.
[16] a) J. Schmidt-Bäse, U. Klingebiel, *Chem. Ber.* **1989**, *122*, 815; b) K. Dippel, N. K. Kewehols, P. G. Jones, U. Klingebiel, D. Z. Schmidt, *Naturforsch., Teil B* **1987**, *42*, 1253; c) P. G. Williard,

 © 2007 Wiley-VCH Verlag GmbH & Co. KGaA, Weinheim 

J. M. Sabrno, *Tetrahedron Lett.* **1985**, *26*, 3931; d) M. M. Shearer, C. B. Spencer, *Acta Crystallogr. Sect. B* **1980**, *36*, 2046; e) M. M. Shearer, C. B. Spencer, *Chem. Commun. (London))* **1966**, 194.

[17] a) M. Brookhart, M. L. H. Green, L.-L. Wong, *Prog. Inorg. Chem.* **1988**, *36*, 1; b) R. H. Crabtree, D. G. Hamilton, *Adv. Organometallics Chem.* **1988**, *28*, 299; c) M. Brookhart, M. L. H. Green, *J. Organomet. Chem.* **1983**, *250*, 395.

[18] Z. Otwinowsky, W. Minor, Processing of X-ray Diffraction Data Collected in Oscillation Mode; In *Methods in Enzymology, vol. 276: Macromolecular Crystallography, Part A* (Eds.: C. W. Carter, R. M. Sweet Jr, ), Academic Press, New York, **1997**, pp. 307–326.

[19] a) R. H. Blessing, *Acta Crystallogr. Sect. A* **1995**, *51*, 33; b) R. H. Blessing, *J. Applied Crystallogr.* **1997**, *30*, 421.

[20] S. Mackay, C. J. Gilmore, C. Edwards, M. Tremayne, N. Stuart, K. Shankland, *MaXus*: *A Computer Program for the Solution and Refinement of Crystal Structures from Diffraction Data*; University of Glasgow, Scotland, Nonius BV, Delft, The Netherlands, and MacScience Co. Ltd., Yokohama, Japan, **1998**.

[21] G. M. Sheldrick, *SHELXTL-97*: *A Structure Solution and Refinement Program*; University of Göttingen, Germany, **1998**.

[22] a) L. J. Farrugia, *J. Appl. Cryst.* **1999**, *32*, 837–838; b) A. L. Spek, *J. Appl. Cryst.* **2003**, *36*, 7–13; c) M. Nardeli, *J. Appl. Cryst.* **1995**, *28*, 659.

Received: June 9, 2007
Published Online: October 17, 2007

 © 2007 Wiley-VCH Verlag GmbH & Co. KGaA, Weinheim 

DOI: 10.1002/ejic.200700608

# Functionalised Hybrid Materials of Conducting Polymers with Individual Fibres of Cellulose

**Fern M. Kelly,*[a] James H. Johnston,[a] Thomas Borrmann,[a] and Michael J. Richardson[a]**

**Keywords:** Polypyrrole / Polyaniline / Cellulose / Fibres / Conductivity / Antimicrobial activity

Polypyrrole and polyaniline conducting polymer composites with individual fibres of cellulose have been successfully prepared and characterised. For this, individual Kraft paper pulp fibres have been fully encapsulated with polypyrrole and polyaniline by direct polymerisation of the respective monomers using ferric chloride and ammonium persulfate as the oxidants. These novel conducting polymer/cellulose fibre composite materials exhibit the inherent properties of both components. They include the electrical and chemical properties of polypyrrole and polyaniline and the strength, flexibility and available surface areas of the cellulose fibre. This allows for interesting opportunities for the development of new added-value products in the paper and packaging industries. Additionally, by utilising the redox active surface of the fibre's polymer coating, silver ions have been reduced to silver metal, thereby producing cellulose/conducting polymer/silver composites. Silver and its compounds have long been identified for their bactericidal effects and thus antimicrobial properties are imparted to the hybrid materials. This gives rise to applications requiring the inhibition of microbial growth. The chemical and physical characterisation of such products has been carried out using scanning electron microscopy (SEM), cyclic voltammetry, X-ray photoelectron spectroscopy (XPS) energy dispersive spectroscopy (EDS) and electrical conductivity measurements, and additionally the testing of their antimicrobial activity.
(© Wiley-VCH Verlag GmbH & Co. KGaA, 69451 Weinheim, Germany, 2007)

## 1. Introduction

Inherently conducting polymers have been widely investigated since their introduction in the 1970's due to their excellent electrical and optical properties.[1] Electrical conductivity arises from the conjugation of π electrons formed by the overlapping of carbon *p* orbitals along the polymer-chain backbone which allows for the efficient transfer of electrons along the polymer backbone.[2] High electrical conductivity can be achieved by doping the conductive polymer with an appropriate agent, which can be either electron-rich (*n*-dopant) or -poor (*p*-dopant) in comparison to the polymer.

Two of the most commonly studied conductive polymers are polypyrrole (PPy) and polyaniline (PAn). This is due to their high electrical conductivity, good environmental stability, chemical properties (oxidation/reduction) and relative ease of synthesis. However, due to their poor mechanical properties and processability industrial application has been cautious. Improvement of the properties of conducting polymers is achievable by creating hybrid materials, in which textile fibres are coated with conducting polymers. In doing so, the hybrids possess the tensile strength, flexibility and relatively high surface area associated with the fibre whilst retaining the desired chemical and electrical properties of the polymer.[3]

Previous studies have shown that individual synthetic organic polymer fibres, such as Nylon and Lycra, may be successfully coated with conducting polymers.[4–6] These materials have applications as chemical and bio-mechanical sensors. This paper conversely presents individual natural fibres of cellulose (Kraft paper pulp) that have been successfully coated by PPy and PAn, using ferric chloride or ammonium persulfate to facilitate polymerisation. As the surface morphology of nylon and other synthetic polymer fibres is much smoother and more uniform than cellulose, the surface of a conducting polymer/nylon fibre, which similarly encapsulates the fibre substrate, is also smoother than that of the PPy/cellulose and PAn/cellulose composite fibres. The chemical and physical properties of the conducting polymer coating and the bonding between the conducting polymer coating and cellulose fibre substrate have been characterised accordingly. The resultant cellulose fibre/conducting polymer hybrids have applications on their own (e.g. antistatic and chemical sensing papers), or can also be incorporated into other host materials (conventional polymer sheeting and extrusions) thereby adding new functionality due to the polymer coated fibres.

Additionally, by utilising the redox active surface of the fibre's polymer coating, silver metal nanoparticles may be incorporated into the composite. Electrochemical deposition of metals on electrodes by conducting polymers such

[a] School of Chemical and Physical Sciences, Victoria University of Wellington,
P. O. Box 600, Wellington, New Zealand
Fax: +64-4-463-5237
E-mail: Fern.Kelly@vuw.ac.nz

 © 2007 Wiley-VCH Verlag GmbH & Co. KGaA, Weinheim 

as PPy and PAn has been well studied.[7–13] Electroless deposition for the recovery of metals has also been reported in which polymer films are oxidised by metal ions of relatively high oxidation potential, effectively reducing the metal to its neutral form. Silver,[14–16] gold[17] and palladium[18–19] have proved successful in this procedure.

This paper outlines an electroless deposition method of metal recovery, whereby silver from solution is reduced, from $Ag^+$ to $Ag^0$, by an oxidised form of the polymer coating. The removal of silver ions from aqueous media indicates the potential application of conducting polymer composites for the recovery of noble metals or in wastewater treatment. Furthermore, through the incorporation of silver, the fibre/polymer composites possess an inhibitory action against bacterial growth. Thus, future applications of such materials may include antimicrobial papers. To the best of our knowledge, this is the first report of the preparation and characterisation of cellulose/conducting polymer/silver hybrid materials.

## 2.Results and Discussion

### 2.1 Conducting Polymer/Cellulose Hybrid Materials

Neat Kraft paper fibres are white, approximately 2.5 to 3.0 mm in length and with a fibre diameter of approximately 30 to 40 μm. The fibres have a relatively smooth surface (Figure 1), but at higher magnifications individual micro-fibrils (indicated by arrows) unwinding from the parent fibre can be observed. Composites based on PPy yielded black fibres of Kraft paper, with each fibre being individually coated with the PPy polymer. The surface morphology of a cellulose fibre/PPy composite is shown in Figure 2. With increasing magnification, it is seen that the PPy coating comprises small uniform spheres about 100 to 150 nm in diameter which are fused together to fully encapsulate the fibre. The polymer coating closely follows the original morphology of the fibres such that even individual fibrils of the parent paper fibre are entirely encapsulated, but remain discernible.

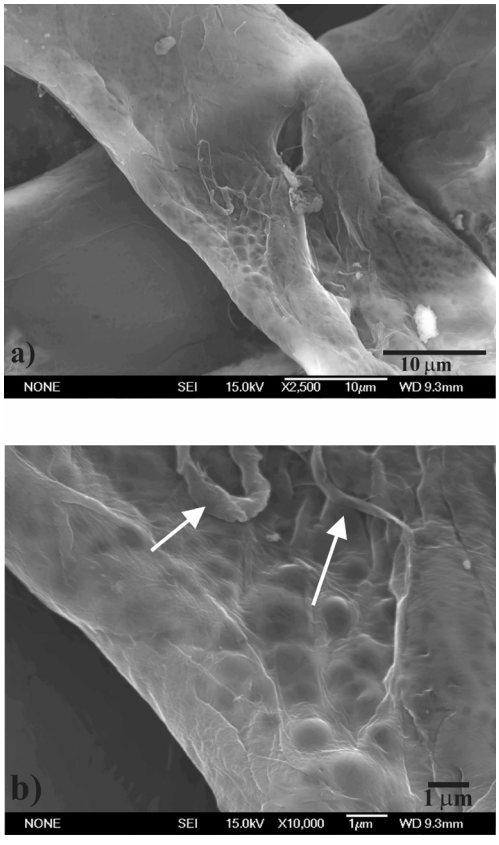


Figure 1. a) Neat cellulose fibres, 2500 times magnification; b) indicating unwinding micro-fibrils, 10000 times magnification.

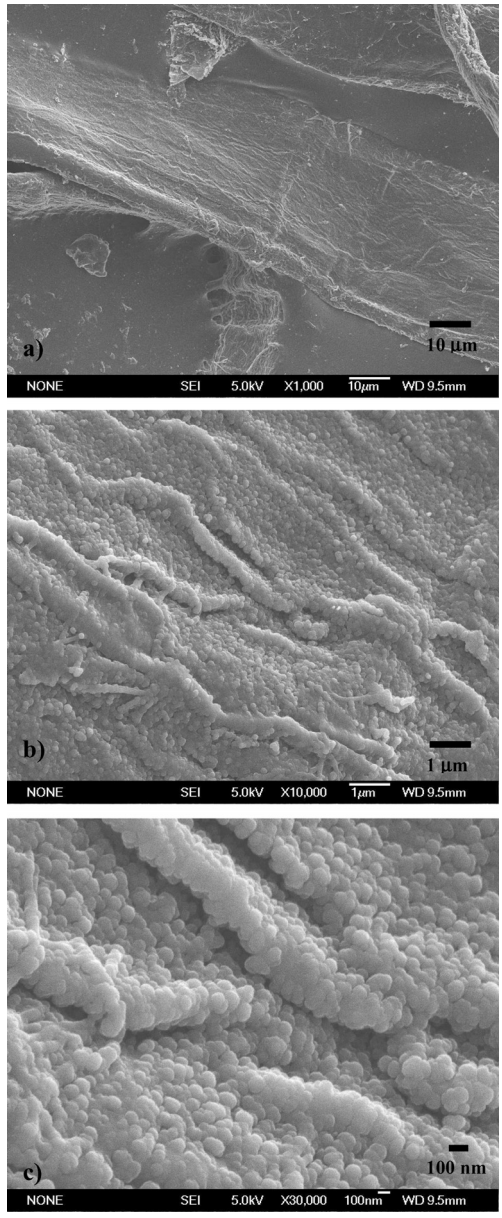


Figure 2. a)–c) Electron microscope images showing increasing magnifications of a paper fibre/polypyrrole composite ($FeCl_3$ as oxidant).

 © 2007 Wiley-VCH Verlag GmbH & Co. KGaA, Weinheim 

When ferric chloride was employed as the oxidising agent in the preparation of fibre/PAn composites, the polymer coating resulted in the emeraldine salt form. Conversely, when the oxidant utilised was ammonium persulfate the resulting PAn coating was in the emeraldine base form. These results were implied by the respective green and blue colours observed and confirmed by UV/Vis spectroscopy. Composites of PAn similarly exhibit a polymer coating wherein the fibres are fully encapsulated yet the underlying morphology and micro-fibrils remain similarly clearly distinguishable. The average size of the polymer spheres of PAn is observed to be smaller than those of PPy, approximately 50 to 100 nm in diameter (Figure 3).

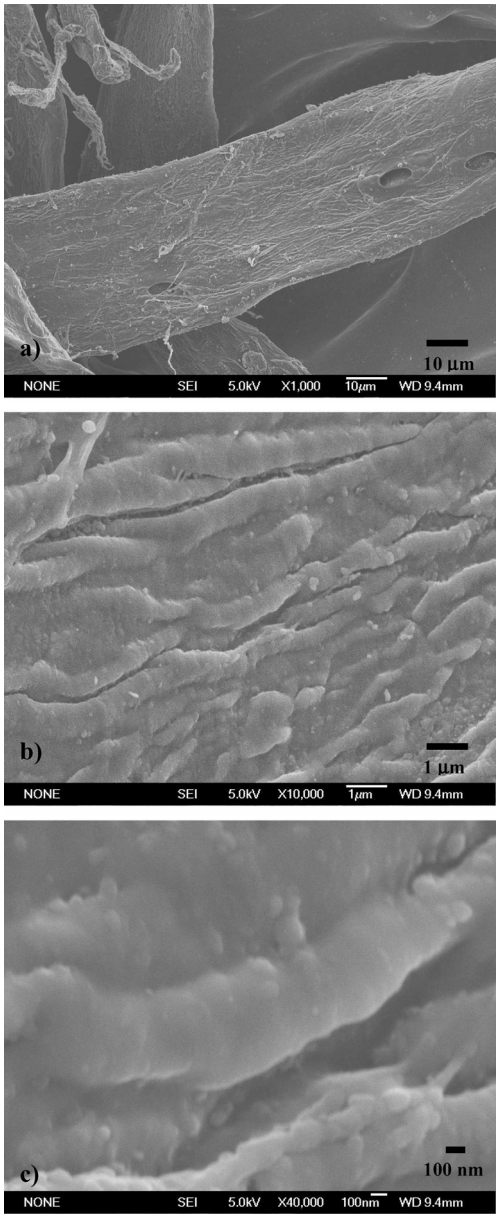


Figure 3. a)–c) Electron microscope images showing increasing magnifications of a paper fibre/polyaniline composite ($FeCl_3$ as oxidant).

## 2.2 Cyclic Voltammetry

Cyclic voltammetry was used to determine the electrochemical transitions of the fibre composites and to ascertain their thermodynamic stability. The cyclic voltammograms for the cellulose/polymer composites, despite being dissimilar from their corresponding electrochemically synthesised free polymers, still showed transitions from reduced to oxidised forms. This demonstrates that the important redox feature of conducting polymers was retained in the preparation of the composites.

When the scan rate of the cyclic voltammograms for the free polymer was altered, from 10 to 50 $mV s^{-1}$, the positions of the peaks representing the electrochemical transitions remain unchanged. This implies that the polymers themselves are thermodynamically stable and the kinetics of the redox transitions are faster than the scan speeds used in the measurements. It also indicates that there is only one method of electron transport in the free polymer.

When repeating these measurements for the fibre/polymer composites, the position of the redox peaks relating to the respective electrochemical transitions change as the scan speed is altered (Figure 4). Additionally, the transition peaks from emeraldine to pernigraniline and the reverse are not observed. This may indicate two things.[20–21] Firstly, the specific transition that yields the redox peak in the particular voltammogram is either not thermodynamically stable or the kinetics of the redox transition are slower than the scan rates. Secondly, contact between the fibres and the electrode may not be ideal. However, the first explanation is preferred as the expected colours and changes in the UV/Vis spectra for the transition from emeraldine (blue) to pernigraniline (purple) are indeed observed.

As both the substrate and the polymer are themselves thermodynamically stable, the change in peak position relating to these electrochemical transitions with changing scan speeds also implies that there is chemical bonding between the polymer and the underlying fibre with a complex electron interaction. The interaction between the substrate and the coating presumably gives rise to alternative and slower pathways for the electron transfer in the redox processes taking place in the fibre/polymer composite.

## 2.3 X-ray Photoelectron Spectrometry

The nature of the chemical bond between the cellulose-fibre substrate and polymer coating, inferred by cyclic voltammetry is further elucidated by XPS. Previous studies have suggested that the bond between polymer and cellulose substrates exists in the form of hydrogen bonding.[22,23] For cellulose composites with PAn and PPy, this implies that there is an interaction between nitrogen-bound hydrogen atoms (NH) on the polymer chain backbone and the lone pairs of electrons of the surface hydroxy (OH) groups of cellulose. This bonding may be in conjunction with, or may be substituted by, bonding between the hydrogen (H) of the surface OH groups of cellulose and the free electron pair of nitrogen (N) atoms in the polymer backbone.

 © 2007 Wiley-VCH Verlag GmbH & Co. KGaA, Weinheim 

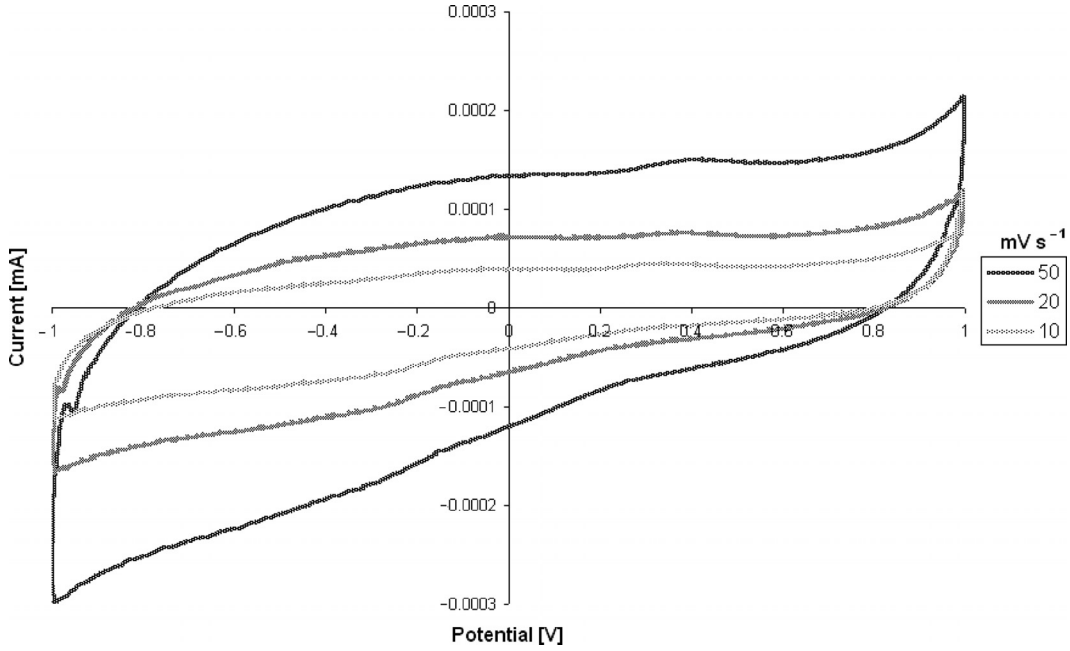


Figure 4. Cyclic voltammograms of paper/polyaniline composite ($FeCl_3$ as the oxidant) at different scan speeds.

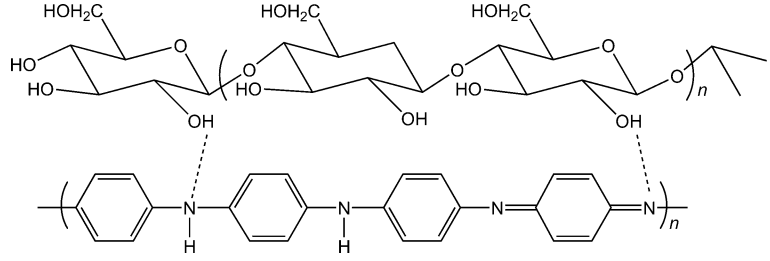


Figure 5. Possible bonding of cellulose to polyaniline.

XPS analyses carried out reinforce the suggestion that the chemical bonding is, in fact, hydrogen bonding between the nitrogen lone pairs of the polymer coating with the OH groups of the underlying cellulose substrate (Figure 5). This is shown by the oxygen XPS spectrum for the cellulose/PAn composite (Figure 6, b), in which there are distinct changes when compared to the same spectra for free cellulose fibres (Figure 6, a).

Of specific importance, is the appearance of a shoulder associated directly with C–OH bonding to N in the O 1s spectrum for the cellulose/PAn composite (Figure 6, b). The shift in the primary O 1s peak relating to C–OH bonds, from 533.3 to 530.6 eV for cellulose and the PAn-coated analogue, respectively, further indicates the presence of a chemical interaction between OH and N. The binding of the hydroxyl groups of cellulose to nitrogen lone pairs of PAn would result in lowering the binding energy of the oxygen from which the attached hydrogen atoms are being delocalised. This is supported by studies on oxygen binding for cellulose published by Wagner et al.[24]

The XPS spectrum for nitrogen for the cellulose/PAn composite was poorly resolved. However, the position and line width of the peak is comparable to that provided by Rodrigues et al.[25] for the N 1s spectrum of PAn bound to

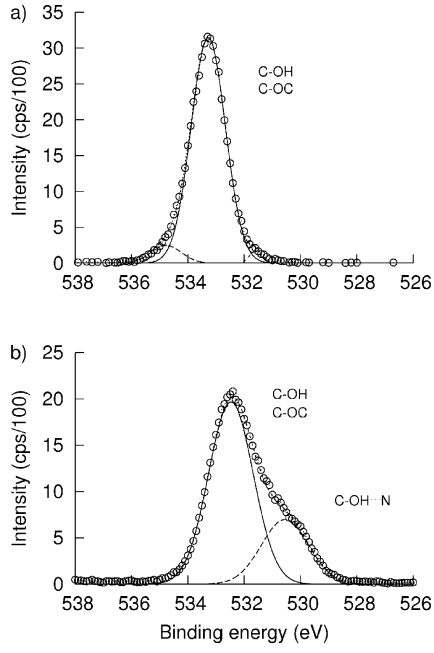


Figure 6. XPS spectra for (a) O 1s for cellulose; (b) O 1s for cellulose/polyaniline composite.

 © 2007 Wiley-VCH Verlag GmbH & Co. KGaA, Weinheim 

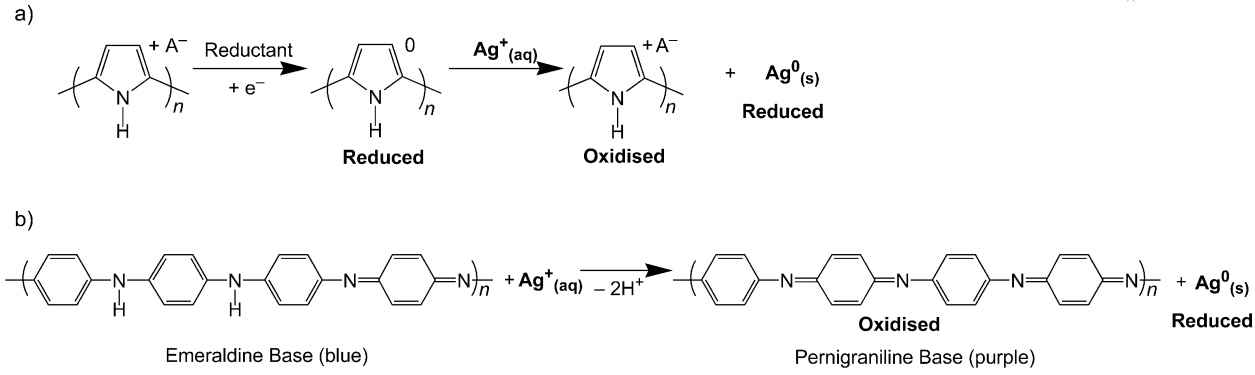


Figure 7. Chemical reduction of $Ag^+$ to $Ag^0$ by polypyrrole (a) and polyaniline (b).

lignin. On this basis it can be assumed that both imine and amine groups are present on the composite surface and that the mode of bonding is similar, whereby PAn binds from the nitrogen lone pairs through to the OH groups of cellulose rather than OH groups of lignin.

### 2.4 Fibre/Conducting Polymer/Silver Composites

A scheme of the reduction processes of silver ions by PPy and PAn, respectively, is shown in Figure 7. Under ambient conditions, PPy exists in an oxidised form due to atmospheric oxygen. Thus, PPy composites were first reduced by treatment with the reducing agent sodium borohydride. Upon addition of silver nitrate PPy is re-oxidised, therefore chemically reducing ionic silver to silver metal, which is deposited on the surface of the polymer.

Under ambient conditions PAn exists in its half-oxidised, emeraldine, form. Thus, by placing emeraldine base PAn/fibre composites directly into a silver nitrate solution, the polymer surface is oxidised to pernigraniline base, effectively reducing silver ions on the polymer surface to metallic silver. The redox reaction was noted by a colour change of the fibres from blue (emeraldine base) to purple (pernigraniline base).

Energy dispersive spectroscopy (EDS) was employed to determine the chemical composition of the surface of the fibre/polymer/silver composites. Figure 8 presents a secondary electron SEM image together with EDS representative of silver (lower levels of silver denoted with black, high levels of silver denoted with grey) for fibre/PAn/silver composites. As indicated by these images, a uniform coating of silver exists across the surface of the fibre polymer composites. The same is observed for the fibre/PPy composites.

SEM imaging of silver composites at higher magnifications shows the silver is present as individual nanoparticles (Figure 9). The greater spatial resolution of the SEM images shows that, although silver metal is distributed evenly across the polymer surface, the coating is not complete as implied by the lesser resolution of the EDS elemental maps.

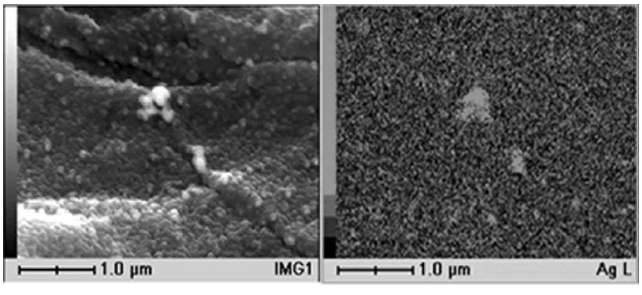


Figure 8. EDS overlay of C and Ag for cellulose fibre/polypyrrole/silver composite.

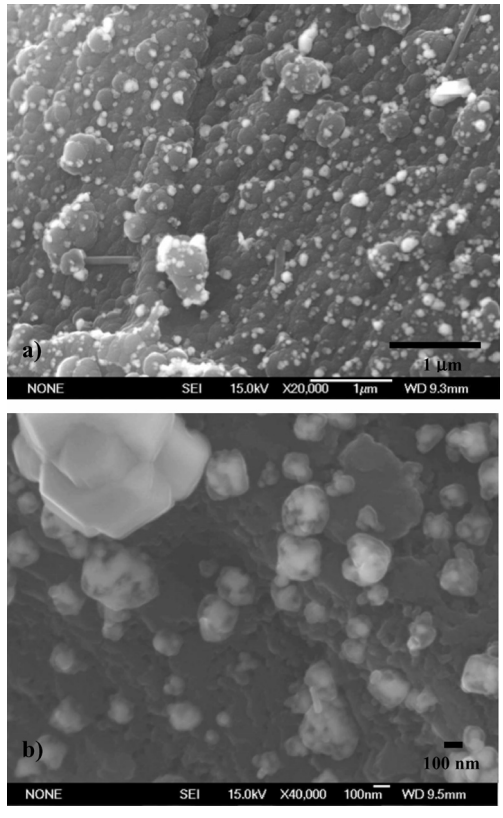


Figure 9. a)–b) Individual particulates of silver on the surface of a cellulose fibre/polypyrrole/silver composite at increasing magnification.

### 2.5 Electrical Conductivity

The Van der Pauw method was used to measure the electrical conductivities of the cellulose fibre/polymer hybrids

 © 2007 Wiley-VCH Verlag GmbH & Co. KGaA, Weinheim 

produced. The calculated conductivities ranged from $5.6 \times 10^{-4}$ S cm$^{-1}$ to $6.0 \times 10^{-4}$ S cm$^{-1}$ for PAn composites and $2.1 \times 10^{-3}$ S cm$^{-1}$ to $2.6 \times 10^{-1}$ S cm$^{-1}$ for PPy composites. The conductivity of single cellulose fibres has been measured as $0.1 \times 10^{-6}$ S cm$^{-1}$ at 50% relative room humidity.[26] Thus, this considerable increase in electrical conductivity from insulating to weak semiconductivity is indeed significant. Therefore, substantial opportunities exist for the development and application of conducting papers and packaging products from these materials. By incorporation into plastic materials the electrical conductivity (antistatic), redox properties (chemical sensing) and tensile strength can be imparted to the host plastic.

Interestingly, an increase in conductivity was not observed for the silver-coated composites. This may be attributed to silver being deposited on the surface in the form of individual nanoparticles (Figure 9) with poor electrical contact between particles. Conductivities were in fact seen to be lower for silver-coated composites compared to their polymer counterparts (Table 1). Contributing to the apparent decrease in conductivity may be the removal of the $Cl^-$ dopant and/or the lesser conductivity of the oxidised form of the underlying polymer due to a reduction in the electron transfer along the polymer backbone due to the chemical reduction of silver onto its surface.

Table 1. Electrical conductivities of merino cellulose fibre/polymer composites.

| Description | Conductivity [S cm$^{-1}$] | Potential oxidation state of polymer |
|---|---|---|
| PPy/Cellulose | $2.6 \times 10^{-1}$ | reduced |
| PPy/Cellulose/Ag | $3.8 \times 10^{-4}$ | oxidised |
| PAn/Cellulose | $6.0 \times 10^{-4}$ | emeraldine |
| PAn/Cellulose/Ag | $3.6 \times 10^{-9}$ | pernigraniline |

### 2.6 Antimicrobial Testing

For all samples, the silver-coated composites actively inhibited the growth of *Staphylococcus aureus* microbes and hence tested positive for their antimicrobial activity. White, hazy areas indicate bacterial growth, whereas the more transparent circles surrounding the fibre/polymer/silver composites, in the agar, indicate bacterial-free regions, i.e. zones of inhibition (Figure 10).

Silver is thought to migrate from the surface of the fibre composite inhibiting the growth of microbes in its path. The extent of silver-induced antimicrobial activity is directly proportional to ionic silver concentration.[27] Hence, the greater the silver ion concentration, the greater the antimicrobial efficacy will be. The release rate of unbound, free silver ions may therefore be correlated with the antimicrobial activity of the composite materials. As the zone of inhibition is similar for the fibre/PAn/silver and fibre/PPy/silver composites it can be assumed that the concentrations of silver across the surface of the composites are relatively similar. The release mechanism, which is deemed to be the same for all composites investigated, will theoretically be the limiting factor. This will also determine the effective lifetime of the antimicrobial activity. As the silver is strongly tethered to the polymer/fibre surface, this activity period will be desirably long.

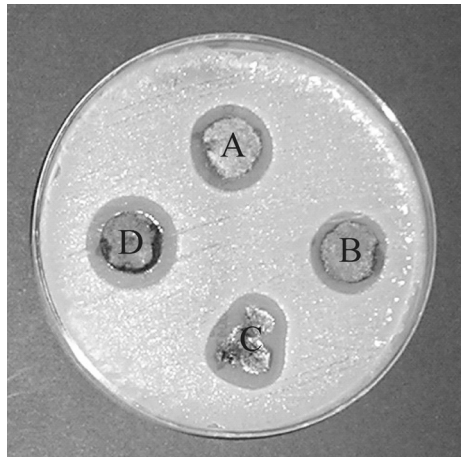


Figure 10. Zones of inhibition of *Staphlococcus aureus* microbial growth; cellulose fibre/polypyrrole/silver composites (A and B), cellulose fibre/polyaniline/silver composites (C and D).

## 3. Conclusions

New hybrid materials of cellulose fibres with conducting polymers have been successfully produced, in which individual Kraft fibres have been fully encapsulated by PPy and PAn spheres fused together in a continuous sheet to coat the fibres in their entirety. The bond between the fibre substrate and polymer coating is believed to be hydrogen bonding between the respective polymer (NH, N) and the OH groups of the cellulose on the fibre surface. The electrical conductivity of the prepared hybrid materials increased substantially from that of Kraft paper pulp, with conductivities as high as $2.6 \times 10^{-1}$ S cm$^{-1}$. Fibre/conducting polymer/silver composites were also successfully produced by utilising the redox capability of the polymer surface. The conductivities for the silver analogues decreased compared with the fibre/polymer hybrids. This is likely due to poor electrical contact between adjacent silver nanoparticles, as indicated by findings from scanning electron microscopy, and the lesser conductivity of the underlying oxidised polymer. Silver composites tested positive in their antimicrobial activity against *Staphylococcus aureus*. The conducting polymer/cellulose fibre composite products and their silver analogues can be used in plastics and packaging materials, whereby the unique properties of the composites, such as redox, electrical conductivity and antimicrobial properties, can be imparted to these materials thereby adding important functionality to them.

## 4. Experimental Section

### 4.1. Reagents and Equipment

Kraft paper pulp, produced from bleached *P. radiata*, was obtained from Carter Holt Harvey NZ. All chemicals employed were of ana-

 © 2007 Wiley-VCH Verlag GmbH & Co. KGaA, Weinheim 

lytical grade and used as received unless otherwise stated. Pyrrole (Pyr, 97%) and aniline (Ani, 99%) monomer were purchased from Aldrich Chemicals, as were *p*-dodecyl benzyl sulfonate and ferric chloride. Aniline and pyrrole were distilled twice prior to use. Ammonium persulfate was obtained from Koch-Light Laboratories Ltd.

The morphology of the fibre/polymer/silver hybrids were characterised utilising a JEOL 6500 F field-emission gun scanning electron microscope. The redox properties of the conducting polymer/fibre composites were measured by cyclic voltammetry, comprising an Amel 7050 potentiostat and Junior Assist software. Fibre composites were attached to the electrode using Parafilm®. After soaking in the degassed conductive potassium perchlorate/perchloric acid (pH = 2) solution for 30 min the connection was tightened, ensuring ample contact between the sample and the electrode, and measurements were carried out. X-ray photoelectron spectroscopy (XPS) measurements were carried out using a Kratos Axis Ultra system with an aluminium filament operating at 10 mA and 15 kV using the $K_\alpha$ line. The pass energy for the survey scans was 160 eV and 10 eV for the narrow scans, and the sample area 300 × 700 μm. The binding energies were calibrated using the C–C 1s photoelectron peak at 285.0 eV. Conducting polymer-coated cellulose fibres were pressed into discs, using IR pellet-making apparatus, and their direct current (DC) electrical conductivity analysed by the Van der Pauw method for determining the conductivity for pressed discs and irregularly shaped samples.

### 4.2 Preparation of Conducting Polymer/Cellulose Fibre Hybrid Materials

Conducting polymer/cellulose fibre hybrids, using individual fibres of Kraft pulp, were prepared by the following method: Kraft pulp (0.5 g of 1 $cm^2$ pieces) was mixed with distilled water (100 $cm^3$) in a blender to give a fully dispersed suspension of individual pulp fibres. The resultant suspension was filtered by Büchner filtration and the fibres re-dispersed, with stirring, in a solution of pyrrole or aniline monomer (0.5 M) and *p*-dodecylbenzyl sulfonate (0.05 M) in water (200 $cm^3$). Stirring for approximately 1 h allowed for the monomer to be absorbed onto the surface of individual cellulose fibres. Then the fibres were filtered and washed with further monomer solution (0.5 M, 100 $cm^3$) and added to the oxidant, ferric chloride or ammonium persulfate (0.5 M, 100 $cm^3$). Polymerisation ensued, noted by a change in colour from orange to dark green to black, over a time period of approximately 5 min. However, the solution was left for a further 3 h to ensure complete polymerisation.

The resultant conducting polymer-coated cellulose fibres were filtered and washed on a 100 μm sieves with water and then subjected to repeated sonication with ethanol. This procedure was repeated several times in order to remove any excess and unbound polymer. Then the hybrid fibres were washed with hydrochloric acid (1.0 M) to effect doping with $Cl^-$ ions, followed by further washing with water. The resulting fibres were air-dried to give individual conducting polymer-coated cellulose fibres, which were black in colour.

### 4.3. Preparation of Fibre/Conducting Polymer/Silver Composites

A silver coating was deposited on the surface of the polymer-coated fibres by chemical reduction of $Ag^+$ to $Ag^0$. In the case of PPy/fibre composites, the polymer coating was first reduced in the presence of excess reducing agent ($NaBH_4$, 2.0 M in triethylene glycol dimethyl ether), and the resulting fibres filtered and washed quickly with water to remove residual reductant. Then the reduced polymer fibres were suspended in $AgNO_3$ (0.1 M, 100 $cm^3$), allowed to react with the $Ag^+$ ions and then washed, filtered and sonicated in ethanol to remove excess $Ag^+$ and $Ag^0$.

A reducing agent was unnecessary for the reduction of silver on the surface of PAn/fibre composites. PAn composites in the form of emeraldine base were added directly to $AgNO_3$ (0.1 M, 100 $cm^3$). The redox reaction ensued in which emeraldine base was oxidised to pernigraniline, thus simultaneously reducing $Ag^+$ to $Ag^0$ at the surface of the coated fibre (see part b of Figure 7, section 2.4). The oxidation reaction was noted by a colour change from blue (emeraldine base) to purple (pernigraniline base). The resultant fibres were similarly washed with distilled water, filtered and then sonicated in ethanol to remove excess silver.

## Acknowledgments

Funding support from the Polymer and Electronics Research Centre (PERC), University of Auckland and the Curtis-Gordon Research Scholarship in Chemistry are gratefully acknowledged.

[1] H. Stubb, E. Punkka, J. Paloheimo, *Mater. Sci. Rep.* **1993**, *10*, 85–140.
[2] S. N. Bhadani, M. Kumari, S. K. Sen Gupta, G. C. Sahu, *J. Appl. Polym. Sci.* **1997**, *64*, 1073–1077.
[3] E. Hakansson, A. Kaynak, T. Lin, S. Nahavandi, T. Jones, E. Hu, *Synth. Met.* **2004**, *144*, 21–28.
[4] G. E. Collins, L. J. Buckley, *Synth. Met.* **1996**, *78*, 93–101.
[5] D. C. Trivedi, S. K. Dhawan, *Polym. Adv. Technol.* **1993**, *4*, 335–340.
[6] J. Wu, D. Zhou, C. O. Too, G. G. Wallace, *Synth. Met.* **2005**, *155*, 698–701.
[7] S. Holdcroft, B. L. Funt, *J. Electroanal. Chem.* **1988**, *240*, 89–103.
[8] R. J. Nichols, D. Schröer, H. Meyer, *Electrochim. Acta* **1995**, *40*, 1479–1485.
[9] M. Hepel, Y.-M. Chen, R. Stephenson, *J. Electrochem. Soc.* **1996**, *143*, 498–505.
[10] Y. C. Liu, B. J. Hwang, *Thin Solid Films* **1999**, *339*, 233–239.
[11] D. K. Sarkar, X. J. Zhou, A. Tannous, M. Louie, K. T. Leung, *Solid State Commun.* **2003**, *125*, 365–368.
[12] V. D. Jović, T. Trišović, B. M. Jović, M. Vojnović, *J. Electroanal. Chem.* **1996**, *408*, 149–155.
[13] N. L. Pickup, J. S. Shapiro, D. K. Y. Wong, *Anal. Chim. Acta* **1998**, *364*, 41–51.
[14] A. Q. Zhang, C. Q. Cui, J. Y. Lee, F. C. Loh, *J. Electrochem. Soc.* **1995**, *142*, 1097–1104.
[15] S. Ivanov, V. Tsakova, *Electrochim. Acta* **2005**, *50*, 5616–5623.
[16] E. T. Kang, Y. P. Ting, K. G. Neoh, K. L. Tan, *Synth. Met.* **1995**, *69*, 477–478.
[17] Y. Ohnishi, S. Yoshimoto, M. Kato, *Synth. Met.* **2004**, *144*, 265–269.
[18] S. W. Huang, K. G. Neoh, C. W. Shih, D. S. Lim, E. T. Kang, H. S. Han, *Synth. Met.* **1998**, *96*, 117–122.
[19] V. W. Lim, E. T. Kang, K. G. Neoh, *Synth. Met.* **2001**, *123*, 107–115.
[20] A. J. Bard, L. R. Faulkner, *Electrochemical Methods: Fundamentals and Applications*, Chaps. 2 and 5, Wiley, **1980**.
[21] R. A. Jeong, G. J. Lee, H. S. Kim, K. Ahn, K. Lee, K. H. Kim, *Synth. Met.* **1998**, *98*, 9–15.
[22] J. H. Johnston, J. Moraes, T. Borrmann, *Synth. Met.* **2005**, *153*, 65–68.
[23] J. Moraes, *Master of Science* Thesis, Victoria University of Wellington, **2004**.
[24] C. D. Wagner, D. A. Zatko, R. H. Raymond, *Anal. Chem.* **1980**, *52*, 1445–1451.
[25] P. C. Rodrigues, M. Muraro, C. M. Garcia, G. P. Souza, M. Abbate, W. H. Schreiner, M. A. Gomes, *Eur. Polym. J.* **2001**, *37*, 2217–2223.
[26] G. R. Lowe Jr, G. A. Baum, *Tappi J.* **1979**, *62*, 87–89.
[27] W. Bender, P. Stutte, *ACS Symp. Ser.* **2001**, *792*, 218–242.

Received: June 12, 2007
Published Online: October 23, 2007

 © 2007 Wiley-VCH Verlag GmbH & Co. KGaA, Weinheim 

DOI: 10.1002/ejic.200700665

# Ruthenium-Based NHC-Arene Systems as Ring-Opening Metathesis Polymerisation Catalysts

Nele Ledoux,*[a] Bart Allaert,[a] and Francis Verpoort[a]

**Keywords:** Carbene ligands / Homogeneous catalysis / Olefin polymerisation / Ruthenium

The availability of starting materials, the complexity of the preparative routes and the cost to make the catalyst are key in the development of industrially relevant olefin metathesis catalysts. With this in mind, new synthetic routes, which lead to alternatives for the classic ruthenium benzylidene complexes and circumvent the need for patented Grubbs intermediates were explored. The research presented herein focuses on the coordination of "saturated" N-heterocyclic carbene (NHC) ligands to Ru dimer [(*p*-cymene)$RuCl_2$]$_2$. As the coordination of the standard NHC ligand $H_2$IMes (1,3-dimesityl-4,5-dihydroimidazol-2-ylidene) was found to be unattainable, bidentate NHC analogues were synthesized instead. These are *O*-hydroxyaryl-substituted NHCs, capable of binding with the metal centre through the oxygen atom as well as through the carbene carbon atom. Their chelating properties improved the stability of the corresponding ruthenium arene complexes, which allowed more successful isolation.
(© Wiley-VCH Verlag GmbH & Co. KGaA, 69451 Weinheim, Germany, 2007)

## Introduction

Olefin metathesis is a fundamental catalytic process and stands among the most prominent ways to build carbon–carbon bonds.[1–6] The reaction consists of the cleavage and reformation of alkene double bonds with a simultaneous exchange of substituents. Cross metathesis (CM),[7,8] ring-closing metathesis (RCM),[9] ring-opening metathesis polymerisation (ROMP)[10] and acyclic diene metathesis polymerisation (ADMET),[11] illustrate the versatility of the olefin metathesis reaction. Thanks to the continuous improvement of its initiators and a sharpened comprehension of its reaction mechanism,[12–30] the olefin metathesis transformation has been upgraded to a very practical, efficient and flexible synthetic methodology. Olefin metathesis now allows cleaner, more efficient and less expensive industrial production of polymers, fine chemicals, pesticides and pharmaceutical intermediates. Despite the recent advances, the search for commercially relevant catalyst systems remains challenging. When thinking of commercial applications, one should not only focus on catalyst activity, selectivity or stability, as highly developed initiators are sometimes too expensive for applications on an industrial scale. Other important aspects are the availability of the starting materials, the complexity of the preparative routes and the cost to make the catalyst. In addition, it is often relevant to search for patent-free synthetic strategies. Up to now, most synthetic pathways toward Grubbs 2nd generation complexes, of which catalyst **1** is the most popular, proceed through bis(phosphane) benzylidene systems.[31,32] A more direct pathway with the use of moderate reaction conditions and readily available starting materials is quite desirable. This also involves the need for alternative means to introduce the alkylidene moiety, which avoid the quite cumbersome preparative routes by diazo compounds.[33] In this context, the Ru dimer [(*p*-cymene)$RuCl_2$]$_2$ (**2**) is air and moisture stable, and it is an easy to handle precursor that is an ideal starting material for the synthesis of allenylidene or vinylidene catalysts to be used for metathesis.[34–44] In order to find a resembling alternative for the classic Grubbs catalyst **1**, it would be necessary to coordinate $H_2$IMes (1,3-dimesityl-4,5-dihydroimidazol-2-ylidene) to Ru dimer **2**. Whereas several groups claim to have synthesized [(*p*-cy-

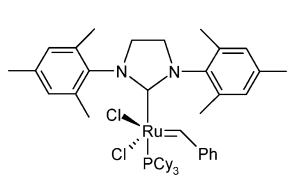

1

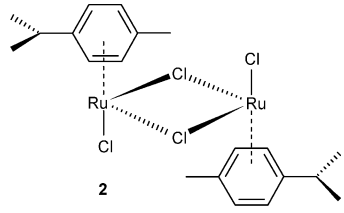

2

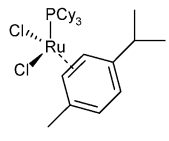

3

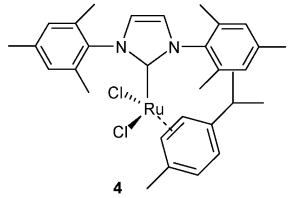

4

[a] Department of Inorganic and Physical Chemistry, Laboratory of Organometallic Chemistry and Catalysis, Ghent University, Krijgslaan 281 (S-3), 9000 Ghent, Belgium
Fax: +32-9-264-4983
E-mail: nele.ledoux@gmail.com


WILEY InterScience DISCOVER SOMETHING GREAT
© 2007 Wiley-VCH Verlag GmbH & Co. KGaA, Weinheim

mene)($H_2$IMes)Ru$Cl_2$] in situ, it was never isolated, nor fully characterized.[45,46] Driven by the fascinating challenge to find alternative synthetic strategies, we herein describe the endeavour we undertook to contribute to this quest.

## Results and Discussion

Whereas the coordination of IMes (1,3-dimesitylimidazol-2-ylidene) to Ru dimer **2** proceeds readily by standard synthetic strategies (complex **4**),[38,47] analogous binding of $H_2$IMes was found to be more problematic. Regardless of the reaction conditions applied, a mixture of Ru complexes was obtained (Scheme 1). Only when the chloroform adduct $H_2$IMes(H)($CCl_3$) was used as a carbene precursor could a small rate of N-heterocyclic carbene (NHC) coordination be evidenced through $^{13}$C NMR spectroscopy. A $^{13}$C NMR resonance was found at $\delta$ = 202.5 ppm, which is characteristic for the carbene carbon atom coordinated to the metal centre. However, $^1$H NMR spectroscopic analysis of the reaction products revealed that desired complex **5** was only formed as a minor product together with undefined hydridic species. $^1$H NMR spectroscopic resonances were found at $\delta$ = –3.64, –3.98, –5.09 and –5.62 ppm.

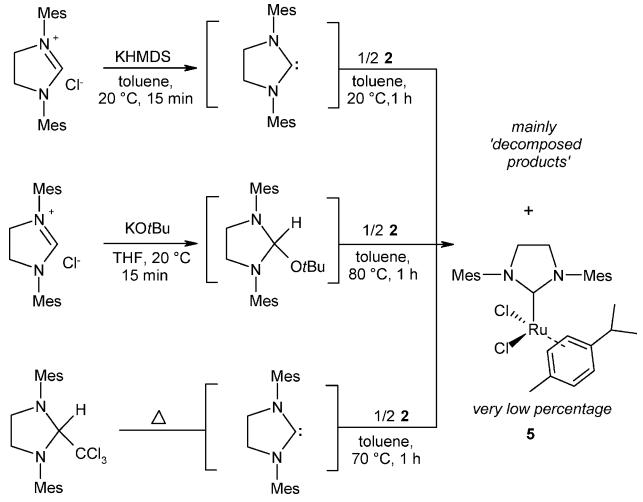


Scheme 1. Synthesis of [(*p*-cymene)($H_2$IMes)Ru$Cl_2$].

Because the failure in our efforts to isolate **5** was assigned to a lack of stability of the complex, a bidentate analogue of the NHC ligand was synthesized. The chelating properties of a bidentate NHC were expected to ameliorate the complex stability through a "chelate effect". The synthesis of 1-(mesityl)-3-(2-hydroxyphenyl)-4,5-dihydroimidazolium chloride salt (**6**) was straightforward following a procedure outlined by Grubbs et al.[48] In order to effectuate ligand coordination, the NHC precursor was treated with 2 equiv. of base; that is, 1 equiv. to liberate the free carbene and 1 equiv. to deprotonate the phenolic group. After 15 min of reaction time, Ru dimer **2** was added to the reaction mixture. As expected, the ligand bound to the metal centre in a chelating manner (Scheme 2). Because of the pseudotetrahedral arrangement of the ligands, a stereogenic centre was created at the Ru centre, leading to the existence of two stereoisomers. Complex **7** shows high stability and can be handled in air without any sign of decomposition. To explore its thermal stability, a solution of **7** (16.5 mg, 0.030 mmol) and coronene (internal standard, 9.0 mg, 0.030 mmol) in deuterated chlorobenzene ($C_6D_5Cl$, 0.50 mL) was followed over time at 100 °C by using $^1$H NMR spectroscopy. After 48 h, no sign of decomposition was observed. At 120 °C, the complex fully decomposed within 4 h.

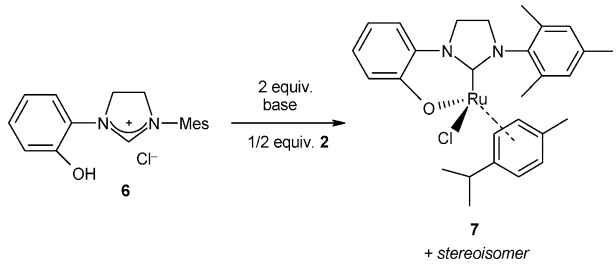


Scheme 2. Synthesis of NHC-arene complex **7**.

Dark-red crystals of **7** suitable for X-ray structure analysis were grown by slow evaporation of a toluene/$CH_2Cl_2$ solution, and its molecular structure is represented in Figure 1. The molecular species consists of a *p*-cymene ligand showing $\eta^6$-bonding, an anionic chloride ligand and a bidentate (C,O) chelating NHC ligand. The isopropyl group on the arene ligand is a little distorted away from the metal centre as a result of steric factors.

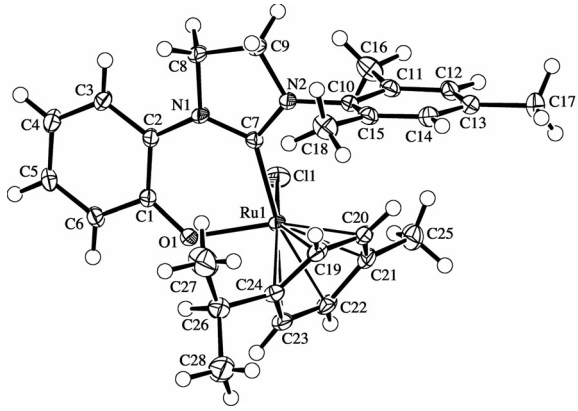

Figure 1. The molecular structure of **7**; ellipsoids show 50% probability.

The catalytic activity of **7** was evaluated in the ROMP of the highly strained monomer norbornene and compared to the activity of Ru dimer **2**, complex **3** and **4** (Table 1). Our results reveal that **7** displays very poor activity in metathesis reactions; only 20% of norbornene polymerised during a reaction time of 3 h at 85 °C (Table 1, Entry 4). It has been described in the literature that for this catalyst type decomplexation of the arene ligand is the prior requirement for the generation of catalytic activity.[49–52] The complex must be coordinatively unsaturated for a substrate to enter the coordination sphere of the metal. In other words, for the catalyst to become active, a ligand has to dissociate to generate a vacant site. However, the high stability of complex **7** indicates that arene ligand dissociation is greatly restrained.

 © 2007 Wiley-VCH Verlag GmbH & Co. KGaA, Weinheim 

Table 1. ROMP of 2-norbornene.[a]

| Entry | Catalyst | Conversion [%] | Mn (*103) | PDI | *cis* [%] |
|---|---|---|---|---|---|
| 1 | **2** | 84 | 198 | 2.1 | 45 |
| 2 | **3** | ≈100 | 85 | 2.9 | 16 |
| 3 | **4** | ≈100 | 339 | 2.8 | 49 |
| 4 | **7** | 20 | 108 | 3.8 | 57 |
| 5 | **7** + phenylacetylene | 33 | 228 | 3.0 | 52 |
| 6 | **7** + TMSD | 21 | 588 | 3.0 | 75 |
| 7 | **8** | 17 | 1954 | 2.0 | 81 |
| 8 | **9** | 16 | 1112 | 2.6 | 78 |
| 9 | **10** | 4 | – | – | – |
| 10 | **10** + phenylacetylene | 7 | 32 | 3.1 | 42 |
| 11 | **10** + TMSD | 10 | 65 | 4.5 | 65 |
| 12 | **11** | 14 | 932 | 2.1 | 61 |

[a] Catalyst/norbornene, 1:2500, cat. conc. = 0.41 mM, 85 °C, solvent = 0.5 mL of $CH_2Cl_2$ to dissolve the catalyst + 10 mL of toluene, reaction time = 3 h. A correction factor of 0.5*Mn was applied for characterizing the PNBs by gel permeation chromatography.[53] The *cis* fraction was determined by $^1$H NMR spectroscopy: $\delta$ = 5.36 CH=CH *trans*, 5.22 CH=CH *cis*.

With the aim to generate the vinylidene moiety in situ, an excess amount of phenylacetylene (20 equiv.) was added to the catalyst (Table 1, Entry 5). Only a minor activity enhancement was observed. Also, the addition of (trimethylsilyl)diazomethane (TMSD), which is known to activate [(*p*-cymene)($PCy_3$)$RuCl_2$] (**3**) with the in situ formation of [$RuCl_2$(=$CHSiMe_3$)($PCy_3$)][49,54] did not significantly enhance the catalytic activity (Table 1, Entry 6). In a dissociative ligand substitution pathway, dissociation of the *p*-cymene moiety is a prerequisite for the generation of an empty coordination site where the alkylidene moiety can be introduced. As a result of the exceptional stability of the complex, which is accompanied by a low dissociation tendency of the arene ligand, the addition of a terminal alkyne or a diazo compound was found to have only a minor effect. Furthermore, we observed that in contrast to complexes of type **3** or **4**, which become more active towards metathesis upon UV irradiation,[35,51,55] the ROMP-catalyzed by **7** is not photoinduced, as no change in the outcome was seen when reactions were carried out in the dark or under constant irradiation with UV light (shortwave UV: 254 nm, longwave UV: 365 nm).

The addition of an excess amount of ethereal HCl to **7** caused protonation of the phenolic oxygen atom, therefrom affording complex **8** as a bright orange solid (Scheme 3). The OH proton was found at $\delta$ = 10.08 ppm as a broad $^1$H NMR ($C_6D_6$) spectroscopic signal. Through breaking of the chelate, the complex was expected to lose part of its extreme stability and become more reactive. Entry 7 in Table 1 shows that a loss of catalytic activity was observed instead! Also, cationic counterpart **9** exhibited poor ROMP activity (Table 1, Entry 8). As expected, losing the chelate effect induced a significantly decreased stability of complex **8**. The complex was found to decompose rapidly in solution. Even as a solid stored under inert atmosphere the complex was unstable and slowly changed colour from orange to green (time course of two weeks). NMR spectroscopic analysis of the decomposition product indicated that both NHC and *p*-cymene ligand were still coordinated to the Ru centre. Therefore, we suggest that **8** suffers from a tendency to undergo *ortho* metallation with the 2-hydroxyphenyl amino side group.[46,56–58]

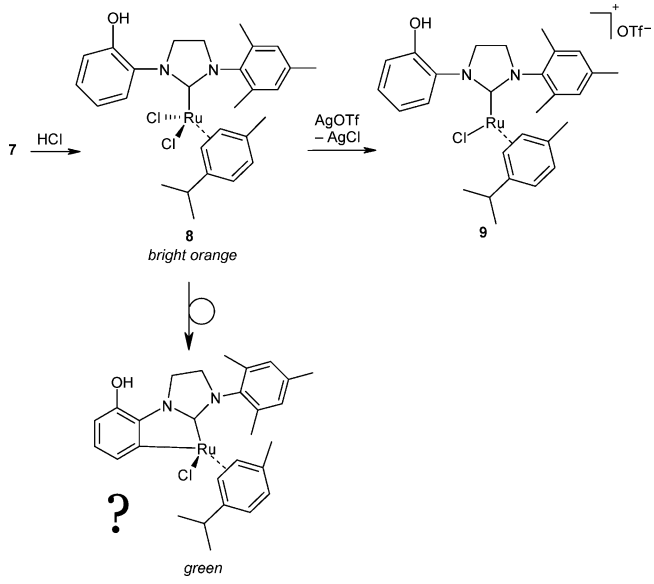


Scheme 3. Losing the chelate effect.

Anticipating that this *ortho* metallation might be avoided by a small modification in the NHC framework, a methyl unit was introduced at the carbon atom in the *ortho* position of the 2-hydroxyphenyl group. Coordination of the new bidentate NHC afforded air- and moisture-stable complex **10**. Also, this complex is a poor initiator for metathesis and the addition of a terminal alkyne or TMSD group only slightly increases the polymer yield (Table 1, Entries 9–11).

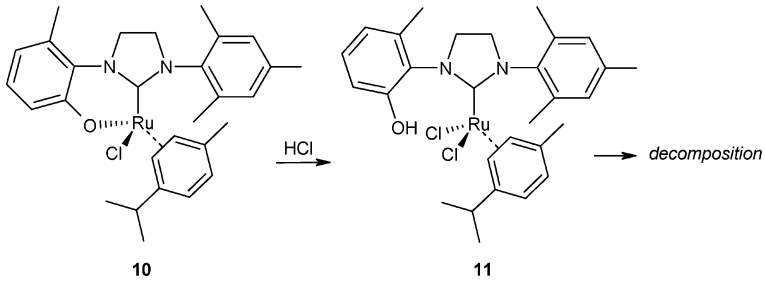


Scheme 4. Modified complexes **10** and **11**.

 © 2007 Wiley-VCH Verlag GmbH & Co. KGaA, Weinheim 

Again, HCl was added to "break" the chelate to afford complex **11**. Thereupon the catalytic activity in the ROMP of 2-norbornene was slightly enhanced (Table 1, Entry 12). In spite of the small ligand modification (*ortho* methylation), also this complex was found to slowly decompose. A solution of **11** in $CH_2Cl_2$ changed colour from orange to dark green during a time course of 1 h. Unfortunately, a complex mixture of products was obtained, and we were not able to identify the decomposition products (Scheme 4).

## Conclusions

From these results, it is clear that complexes of the type [(*p*-cymene)(L)$RuCl_2$] (with L = $H_2$IMes or resembling NHC) are not very reactive, and they too unstable for practical use. Likely due to stability problems, we were unable to isolate complex [(*p*-cymene)($H_2$IMes)$RuCl_2$] (**5**). Similar complexes **8** and **11** were successfully isolated, but only when an uncommon synthetic strategy was followed. The NHCs were first introduced as bidentate ligands, which greatly enhanced the stability of the complex through the chelate effect. Subsequent treatment with hydrochloric acid caused a breaking of the chelate O–Ru bond and formation of complexes [(*p*-cymene)(NHC)$RuCl_2$] bearing monodentate NHCs. Upon loss of the chelate effect, a dramatic decrease in the stability of the complex was observed; as a result, complexes **8** and **11** could not be kept for more than a few days even when stored as a solid under an inert atmosphere. In solution, both complexes decomposed very rapidly, which drastically restricted their catalytic value. To adequately compete with the Grubbs catalysts, it is unquestionable that better activity and stability levels have to be reached. Therefore, our attention has now been drawn to other synthetic methods that first introduce an alkylidene moiety and then, in a second reaction step, realize the coordination of an NHC ligand. We hope to be able to report on these results in the near future.

## Experimental Section

**General:** All reactions and manipulations involving organometallic compounds were conducted in oven-dried glassware under an argon atmosphere by using standard Schlenk techniques. Solvents were dried with appropriate drying agents and distilled prior to use. $^1$H and $^{13}$C NMR spectroscopic measurements were performed with a Varian Unity-300 spectrometer. Ru dimer **2**,[59] $H_2$IMes(H)($CCl_3$),[60] the bidentate NHC salts[47] and complex **3**[35] were prepared according to literature procedures. (Trimethylsilyl)diazomethane (TMSD) was purchased from Aldrich as a solution in hexane. We were unable to do elemental analysis on complexes **9** and **11** because of the lack of stability of these compounds. For these two complexes, we hope that characterisation through $^1$H NMR and $^{13}$C NMR spectroscopy is sufficient.

**Synthesis of the Complexed**

**[(*p*-cymene)$RuCl_2$(IMes)] (4):** The synthesis of complex **4** was previously reported by Nolan et al. to result from the reaction of Ru dimer with free IMes carbene.[38] We herein describe a slightly altered synthetic strategy, which avoids the isolation and handling of the air- and moisture-sensitive free carbene. To a dry Schlenk flask charged with 1,3-bis(2,4,6-trimethylphenyl)imidazolium chloride (0.490 g, 1.44 mmol) and dry toluene (5 mL) was added LiHMDS (0.5 M in toluene, 2.88 mL, 1 equiv.). The resulting suspension was stirred at room temperature for 15 min. Ru dimer **2** (0.43 g, 0.70 mmol) was then added as a solid, and the mixture was stirred at room temperature for an additional 45 min. The solution was filtered to remove residual salts, and the filtrate was concentrated under vacuum. The residue was dissolved in a small amount of $CH_2Cl_2$ (1 mL) and precipitated upon addition of hexane (25 mL). The orange solid was filtered off and vacuum dried. Yield: 0.67 g, 78%. NMR spectroscopic data are similar to those reported by Nolan et al.: $^1$H NMR (300 MHz, $CDCl_3$): $\delta$ = 6.95 (s, 4 H, Mes-3,5-H), 6.90 (s, 2 H, NC*H*C*H*N), 5.03 (d, $J$ = 5.5 Hz, 2 H, *p*-cymene aryl-H), 4.63 (d, $J$ = 5.5 Hz, 2 H, *p*-cymene aryl-H), 2.51 (m, 1 H, *p*-cymene C*H*($CH_3$)$_2$), 2.35 (s, 6 H, mesityl *p*-C$H_3$), 2.23 (s, 6 H, mesityl *o*-C$H_3$), 1.79 (s, 3 H, *p*-cymene C$H_3$), 1.07 [d, $J$ = 6.8 Hz, 6 H, *p*-cymene CH(C$H_3$)$_2$] ppm. $^{13}$C NMR (75 MHz, $CDCl_3$): $\delta$ = 6.95 172.0 (N*C*N), 139.0, 138.9, 130.1, 128.9, 125.4, 103.1, 96.0, 87.0, 85.9, 30.4 [*p*-cymene *C*H($CH_3$)$_2$], 22.9, 22.7, 21.4, 19.3, 18.24, 18.0 ppm.

**NHC-Arene Complex 7:** The NHC precursor 1-mesityl-3-(2-hydroxyphenyl)-4,5-dihydroimidazolium chloride (0.765 g, 2.41 mmol) was treated with a solution of potassium hexamethyldisilazide (KHMDS; 0.5 M in toluene, 9.66 mL, 4.83 mmol, 2 equiv.) over 15 min at room temperature. A suspension of Ru dimer **2** (0.70 g, 1.14 mmol) in toluene was added, and the resulting mixture was stirred for an additional 1.5 h at room temperature. The toluene solution was filtered and washed with $CH_2Cl_2$ (2 × 10 mL). After evaporation of the filtrate, cold acetone was added while stirring. Subsequent filtration allowed the isolation of the pure red-pink catalyst, which was thoroughly dried. Yield: 0.58 g, 46%. $^1$H NMR (300 MHz, $CDCl_3$): $\delta$ = 6.93–7.02 (m, 3 H, aryl CH), 6.79 (t, $^3J_{H,H}$ = 7.3 Hz, 1 H, aryl CH), 6.71 (d, $^3J_{H,H}$ = 7.9 Hz, 1 H, aryl CH), 6.43 (t, $^3J_{H,H}$ = 7.3 Hz, 1 H, aryl CH), 5.52 (d, $J$ = 4.6 Hz, 1 H, *p*-cymene aryl-H), 5.26 (d, $J$ = 4.6 Hz, 1 H, *p*-cymene aryl-H), 5.09 (d, $J$ = 3.4 Hz, 1 H, *p*-cymene aryl-H), 4.43 (pseudo q, $J_{app}$ = ca. 10.5 Hz, 1 H, NC$H_2$C$H_2$N), 4.18 (pseudo q, $J_{app}$ = ca. 10.5 Hz, 1 H, NC$H_2$C$H_2$N), 4.02 (pseudo q, $J_{app}$ = ca. 10.5 Hz, 1 H, NC$H_2$C$H_2$N), 3.92 (pseudo q, $J_{app}$ = ca. 10.5 Hz, 1 H, NC$H_2$C$H_2$N), 3.69 (d, $J$ = 3.2 Hz, 1 H, *p*-cymene aryl-H), 2.50 (s, 3 H, mesityl C$H_3$), 2.42 (s, 3 H, mesityl C$H_3$), 2.41 [m, 1 H, *p*-cymene C*H*($CH_3$)$_2$], 2.33 (s, 3 H, mesityl C$H_3$), 1.58 (s, 3 H, *p*-cymene C$H_3$), 0.96 [d, $^3J_{H,H}$ = 6.7 Hz, 3 H, *p*-cymene CH(C$H_3$)$_2$], 0.83 [d, $^3J_{H,H}$ = 6.7 Hz, 3 H, *p*-cymene CH(C$H_3$)$_2$] ppm. $^{13}$C NMR (75 MHz, $CDCl_3$): $\delta$ = 202.7 (N*C*N), 157.4 (*C*-O), 139.7 (NHC aryl-C), 139.0 (NHC aryl-C), 138.0 (NHC aryl-C), 136.2 (NHC aryl-C), 130.9 (NHC aryl-C), 130.5 and 130.3 (NHC aryl-C), 128.9 and 128.8 (NHC aryl-C), 124.92 and 124.86 (NHC aryl-C), 121.3 and 121.2 (NHC aryl-C), 116.3 and 116.2 (NHC aryl-C), 113.9 and 113.8 (NHC aryl-C), 101.1 (*p*-cymene aryl-C), 95.2 (*p*-cymene aryl-C), 94.7 (*p*-cymene aryl-C), 93.1 (*p*-cymene aryl-C), 83.8 (*p*-cymene aryl-C), 79.4 (*p*-cymene aryl-C), 51.1 (*C*$H_2$C$H_2$), 48.7 (CH$_2$*C*H$_2$), 30.2 and 30.1 [p-cymene *C*H($CH_3$)$_2$], 23.3 (*C*$H_3$), 21.3 and 21.1 (*C*$H_3$), 20.0 and 19.8 (*C*$H_3$), 18.6 and 18.5 (*C*$H_3$), 18.3 and 18.1 (*C*$H_3$) ppm. *Some carbon atoms have a double peak in the spectrum, which indicates the presence of two diastereomers in roughly an equal ratio.* $C_{28}H_{33}ClN_2ORu$ (550.11): C 61.14, H 6.05, N 5.09; found C 61.39, H 6.08, N 5.12.

**NHC-Arene Complex 8:** Complex **7** (0.125 g, 0.227 mmol) was dissolved in $CH_2Cl_2$ (5 mL). An excess amount of HCl (1 N in $Et_2O$, 1 mL) was added, and the resulting mixture was stirred at room temperature for 5 min. Solvents were evaporated and hexane

 © 2007 Wiley-VCH Verlag GmbH & Co. KGaA, Weinheim 

(25 mL) was added to precipitate complex **8** as a bright orange solid. Yield: 0.12 g, 93%. $^1$H NMR (300 MHz, $CDCl_3$): $\delta$ = 8.02 (d, $J$ = 7.5 Hz, 1 H, aryl C*H*), 7.10 (s, 1 H, aryl C*H*), 7.03 (s, 1 H, aryl C*H*), 6.96 (m, 1 H, aryl C*H*), 6.89 (m, 2 H, aryl C*H*), 5.70 (br. s, 2 H, *p*-cymene aryl-*H*), 5.32 (br. s, 2 H, *p*-cymene aryl-*H*), 4.34 (m, 2 H, NC$H_2$C$H_2$N), 4.10 (m, 1 H, NC$H_2$C$H_2$N), 3.98 (m, 1 H, NC$H_2$C$H_2$N), 2.86 [sept, $J$ = 5.5 Hz, 1 H, *p*-cymene C*H*($CH_3$)$_2$], 2.58 (s, 3 H, mesityl C$H_3$), 2.38 (s, 3 H, mesityl C$H_3$), 2.35 (s, 3 H, mesityl C$H_3$), 1.75 (s, 3 H, *p*-cymene $CH_3$), 1.02 [m, 6 H, *p*-cymene CH(C$H_3$)$_2$] ppm. *Signals of the aromatic p-cymene protons appear as broad signals due to internal rotation of the ligand.* $^1$H NMR (300 MHz, $C_6D_6$): $\delta$ = 10.08 (br. s, 1 H, O*H*) ppm. $^{13}$C NMR (75 MHz, $CDCl_3$): $\delta$ = 203.0 (N*C*N), 146.1 (*C*-OH), 139.8 (NHC aryl-C), 138.8 (NHC aryl-C), 137.4 (NHC aryl-C), 135.5 (NHC aryl-C), 130.4 (NHC aryl-C), 129.5 (NHC aryl-C), 129.2 (NHC aryl-C), 125.1 (NHC aryl-C), 121.7 (NHC aryl-C), 118.9 (NHC aryl-C), 117.7 (NHC aryl-C), 105.0 (br., *p*-cymene aryl-C), 97.3 (br., *p*-cymene aryl-C), 92.1 (br., *p*-cymene aryl-C), 82.3 (br., *p*-cymene aryl-C), 52.0 (N*C*$H_2$C$H_2$N), 49.7 (N*C*$H_2$C$H_2$N), 30.4 [*p*-cymene *C*H($CH_3$)$_2$], 23.6 (*C*$H_3$), 21.3 (*C*$H_3$), 21.2 (*C*$H_3$), 19.8 (*C*$H_3$), 18.9 (*C*$H_3$), 18.5 (*C*$H_3$) ppm. $C_{28}H_{34}Cl_2N_2ORu$ (586.57): calcd. C 57.34, H 5.84, N 4.78; found C 56.62, H 5.79, N 4.54.

**Cationic NHC-arene Complex 9:** Silver triflate (0.049 g, 0.19 mmol) was added to a solution of **8** (0.109 g, 0.19 mmol) in $CH_2Cl_2$ (5 mL). The reaction mixture was stirred for 15 min at room temperature. The solution was filtered to remove AgCl, and the solvent was evaporated to almost complete dryness. The addition of hexane (10 mL) led to precipitation of the desired cationic complex as a bright orange solid, which was filtered off and dried in vacuo. Yield: 0.13 g, 96%. $^1$H NMR (300 MHz, $CDCl_3$): $\delta$ = 7.51 (d, $J$ = 5.1 Hz, 1 H, aryl C*H*), 7.08 (s, 1 H, aryl C*H*), 7.02 (m, 4 H), 5.75 (br. s, 2 H, *p*-cymene aryl-*H*), 5.43 (br. s, 2 H, *p*-cymene aryl-*H*), 4.53 (m, 1 H, NC$H_2$C$H_2$N), 4.28 (m, 1 H, NC$H_2$C$H_2$N), 4.09 (m, 2 H, NC$H_2$C$H_2$N), 2.59 (s, 3 H, mesityl C$H_3$), 2.47 [m, 1 H, *p*-cymene C*H*($CH_3$)$_2$], 2.36 (s, 3 H, mesityl C$H_3$), 2.33 (s, 3 H, mesityl C$H_3$), 1.63 (s, 3 H, *p*-cymene $CH_3$), 0.95 [m, 6 H, *p*-cymene CH(C$H_3$)$_2$] ppm. $^{13}$C NMR (75 MHz, $CDCl_3$): $\delta$ = 204.4 (N*C*N), 144.2 (*C*-OH), 139.9 (NHC aryl-C),138.8 (NHC aryl-C), 136.8 (NHC aryl-C), 135.5 (NHC aryl-C), 130.6 (NHC aryl-C), 129.4 (NHC aryl-C), 129.0 (NHC aryl-C), 125.7 (NHC aryl-C), 123.5 (NHC aryl-C), 118.4 (NHC aryl-C), 117.8 (NHC aryl-C), 91.8 (br., *p*-cymene aryl-C), 83.2 (br., *p*-cymene aryl-C), 52.1 (N*C*$H_2$C$H_2$N), 49.6 (N*C*$H_2$C$H_2$N), 30.6 [*p*-cymene *C*H($CH_3$)$_2$], 23.0 (*C*$H_3$), 21.2 (*C*$H_3$), 21.1 (*C*$H_3$), 19.9 (*C*$H_3$), 18.7 (*C*$H_3$), 18.2 (*C*$H_3$) ppm.

**NHC-Arene Complex 10:** In an analogous procedure as for complex **7**, 1-mesityl-3-(2-hydroxy-6-methylphenyl)-4,5-dihydroimidazolium chloride (0.284 g, 0.86 mmol), KHMDS (0.5 M in toluene, 3.43 mL) and Ru dimer **2** (0.25 g, 0.41 mmol) afforded complex **10** as an orange-red solid. Yield: 0.15 g, 32%. $^1$H NMR (300 MHz, $CDCl_3$): $\delta$ = 7.02 (m, 2 H, aryl C*H*), 6.84 (t, $J$ = 6.9 Hz, 1 H, aryl C*H*), 6.73 (d, $J$ = 7.3 Hz, 1 H, aryl C*H*), 6.46 (m, 1 H, aryl C*H*), 5.56 (d, $J$ = 6.3 Hz, 1 H, *p*-cymene aryl-*H*), 5.29 (br. s, 1 H, *p*-cymene aryl-*H*), 5.11 (d, $J$ = 5.0 Hz, 1 H, *p*-cymene aryl-*H*), 4.43 (pseudo q, $J$ = 10.5 Hz, 1 H, NC$H_2$C$H_2$N), 4.18 (pseudo q, $J$ = 10.1 Hz, 1 H, NC$H_2$C$H_2$N), 4.04–3.92 (m, 2 H, NC$H_2$C$H_2$N), 3.71 (br. s, 1 H, *p*-cymene aryl-*H*), 2.53 (s, 3 H, mesityl C$H_3$), 2.45 (s, 6 H, 2-hydroxy-6-methylphenyl and mesityl C$H_3$), 2.41 [m, 1 H, *p*-cymene C*H*($CH_3$)$_2$], 2.36 (s, 3 H, mesityl C$H_3$), 1.61 (s, 3 H, *p*-cymene $CH_3$), 0.98 [d, $J$ = 7.0 Hz, 3 H, *p*-cymene CH(C$H_3$)$_2$], 0.85 [d, $J$ = 6.8 Hz, 3 H, *p*-cymene CH(C$H_3$)$_2$] ppm. $^{13}$C NMR (75 MHz, $CDCl_3$): $\delta$ = 201.5 (N*C*N), 156.1 (*C*-OH), 138.6 (NHC aryl-C), 137.8 (NHC aryl-C), 136.8 (NHC aryl-C), 134.9 (NHC aryl-C), 129.5 (NHC aryl-C), 129.2 (NHC aryl-C), 127.5 (NHC aryl-C), 123.8 (NHC aryl-C), 120.0 (NHC aryl-C), 114.9 (NHC aryl-C), 112.6 (NHC aryl-C), 99.5 (br., *p*-cymene aryl-C), 97.6 (*p*-cymene aryl-C), 93.9 (br., *p*-cymene aryl-C), 91.9 (*p*-cymene aryl-C), 82.4 (br., *p*-cymene aryl-C), 78.0 (*p*-cymene aryl-C), 49.8 (N*C*$H_2$C$H_2$N), 47.4 (N*C*$H_2$C$H_2$N), 28.9 [*p*-cymene *C*H($CH_3$)$_2$], 22.1 (*C*$H_3$), 20.0 (*C*$H_3$), 19.8 (*C*$H_3$), 18.6 (*C*$H_3$), 17.3 (*C*$H_3$), 16.9 (*C*$H_3$) ppm. $C_{29}H_{35}ClN_2ORu$ (564.14): calcd. C 61.74, H 6.25, N 4.97; found C 61.48, H 6.12, N 4.56.

**NHC-Arene Complex 11:** Analogous to **8**, complex **11** was obtained as an orange solid in good yield (83%). Characterisation through $^1$H NMR spectroscopy was troublesome as the aromatic *p*-cymene protons and the backbone protons on the NHC appeared as very broad signals due to internal rotation of the ligands. $^1$H NMR (300 MHz, $CDCl_3$): $\delta$ = 7.19 (m, 1 H, aryl C*H*), 7.07 (br. s, 1 H, aryl C*H*), 7.03 (s, 1 H, aryl C*H*), 6.88 (m, 1 H, aryl C*H*), 6.58 (m, 2 H, aryl C*H*), 5.49–5.36 and 5.19 (br. signals, 4 H, *p*-cymene aryl-*H*), 4.26–3.92 (br. m, 4 H, NC$H_2$C$H_2$N), 2.69–0.88 (several signals) ppm. $^1$H NMR (300 MHz, $C_6D_6$): $\delta$ = 10.14 (br. s, 1 H, O*H*) ppm. $^{13}$C NMR (75 MHz, $CDCl_3$): $\delta$ = 202.2 (N*C*N), 151.2 (*C*-OH), 138.2 (NHC aryl-C), 136.5 (NHC aryl-C), 134.9 (NHC aryl-C), 131.1 (NHC aryl-C), 129.4 (NHC aryl-C), 128.2 (NHC aryl-C), 124.3 (NHC aryl-C), 119.4 (NHC aryl-C), 118.1 (NHC aryl-C), 116.9 (NHC aryl-C), 98.1 (br., *p*-cymene aryl-C), 95.0 (br., *p*-cymene aryl-C), 93.4 (br., *p*-cymene aryl-C), 80.9 (br., *p*-cymene aryl-C), 53.8 (br., N*C*$H_2$C$H_2$N), 29.3 [*p*-cymene *C*H($CH_3$)$_2$], 22.4 (*C*$H_3$), 21.7 (*C*$H_3$), 21.0 (*C*$H_3$), 20.4 (*C*$H_3$), 19.6 (*C*$H_3$), 19.1 (*C*$H_3$) ppm.

**Catalytic Reactions**

**ROMP of 2-Norbornene:** In a typical ROMP experiment (see Table 1), the catalyst (0.004248 mmol) in $CH_2Cl_2$ (0.5 mL) was transferred into a 15-mL vessel followed by the addition of 2-norbornene (1 g, 2500 equiv.) and toluene (10 mL). The reaction was then stirred at 85 °C for 3 h. To stop the polymerisation, a 2-ethyl vinyl ether/BHT(2,6-di-*tert*-butyl-4-methylphenol) solution in $CHCl_3$ was added. The reaction mixture was then poured into MeOH (50 mL) to precipitate the polymer. The polymer was isolated upon filtration and analysed gravimetrically by $^1$H NMR spectroscopy and GPC (gel permeation chromatography).

CCDC-652147 contains the supplementary crystallographic data for this paper. These data can be obtained free of charge from The Cambridge Data Centre via www.ccdc.cam.ac.uk/data_request/cif.

## Acknowledgments

The authors gratefully acknowledge the FWO-Flanders and the research Fund of Ghent University for generous financial support during the preparation of this manuscript. We wish to thank Olivier F. Grenelle and Dr. Marc G. Proot of Chevron Technology, Ghent, for elemental analyses and *dr* determination and Anthony Linden of the Institute of Organic Chemistry, University of Zürich, for collecting the crystallographic data set.

[1] R. H. Grubbs, *Tetrahedron* **2004**, *60*, 7117–7140.
[2] A. Fürstner, *Angew. Chem. Int. Ed.* **2000**, *39*, 3012–3043.
[3] M. Schuster, S. Blechert, *Angew. Chem. Int. Ed.* **1997**, *36*, 2036–2056.
[4] R. H. Grubbs, *Adv. Synth. Catal.* **2007**, *349*, 34–40.
[5] K. J. Ivin, J. C. Mol, *Olefin Metathesis and Metathesis Polymerizations*, Academic, San Diego, **1997**.
[6] R. H. Grubbs, *Handbook of Metathesis*, Wiley-VCH, Weinheim, **2003**.

 © 2007 Wiley-VCH Verlag GmbH & Co. KGaA, Weinheim 

[7] S. J. Connon, S. Blechert, *Angew. Chem. Int. Ed.* **2003**, *42*, 1900–1923.
[8] A. K. Chatterjee, T.-L. Choi, D. P. Sanders, R. H. Grubbs, *J. Am. Chem. Soc.* **2003**, *125*, 11360–11370.
[9] R. H. Grubbs, S. J. Miller, G. C. Fu, *Acc. Chem. Res.* **1995**, *28*, 446–452.
[10] C. W. Bielawski, R. H. Grubbs, *Prog. Polym. Sci.* **2007**, *32*, 1–29.
[11] J. E. Schwendeman, A. C. Church, K. B. Wagener, *Adv. Synth. Catal.* **2002**, *344*, 597–613.
[12] E. L. Dias, S. T. Nguyen, R. H. Grubbs, *J. Am. Chem. Soc.* **1997**, *119*, 3887–3897.
[13] S. F. Vyboishchikov, M. Bühl, W. Thiel, *Chem. Eur. J.* **2002**, *8*, 3962–3975.
[14] S. Fomine, S. M. Vargas, M. A. Tlenkopatchev, *Organometallics* **2003**, *22*, 93–99.
[15] F. Bernardi, A. Bottoni, G. P. Miscione, *Organometallics* **2003**, *22*, 940–947.
[16] W. J. van Rensburg, P. J. Steynberg, W. H. Meyer, M. M. Kirk, G. S. Forman, *J. Am. Chem. Soc.* **2004**, *126*, 14332–14333.
[17] C. Adlhart, P. Chen, *J. Am. Chem. Soc.* **2004**, *126*, 3496–3510.
[18] M. Jordaan, P. van Helden, C. G. C. E. Sittert, H. C. M. Vosloo, *J. Mol. Catal. A* **2006**, *254*, 145–154.
[19] L. Cavallo, *J. Am. Chem. Soc.* **2002**, *124*, 8965–8973.
[20] B. F. Straub, *Adv. Synth. Catal.* **2007**, *349*, 204–214.
[21] M. Ulman, R. H. Grubbs, *Organometallics* **1998**, *17*, 2484–2489.
[22] M. S. Sanford, J. Love, R. H. Grubbs, *J. Am. Chem. Soc.* **2001**, *123*, 6543–6554.
[23] M. S. Sanford, M. Ulman, R. H. Grubbs, *J. Am. Chem. Soc.* **2001**, *123*, 749–750.
[24] B. F. Straub, *Angew. Chem. Int. Ed.* **2005**, *44*, 5974–5978.
[25] M. A. O. Volland, C. Adlhart, C. A. Kiener, P. Chen, P. Hofmann, *Chem. Eur. J.* **2001**, *7*, 4621–4632.
[26] P. E. Romero, W. E. Piers, *J. Am. Chem. Soc.* **2005**, *127*, 5032–5033.
[27] C. Adlhart, C. Hinderling, H. Baumann, P. Chen, *J. Am. Chem. Soc.* **2000**, *122*, 8204–8214.
[28] A. G. Wenzel, R. H. Grubbs, *J. Am. Chem. Soc.* **2006**, *128*, 16048–16049.
[29] A. Correa, L. Cavallo, *J. Am. Chem. Soc.* **2006**, *128*, 13352–13353.
[30] P. E. Romero, W. E. Piers, *J. Am. Chem. Soc.* **2007**, *129*, 1698–1704.
[31] M. Scholl, T. M. Trnka, J. P. Morgan, R. H. Grubbs, *Tetrahedron Lett.* **1999**, *40*, 2247–2250.
[32] J. Huang, E. D. Stevens, S. P. Nolan, J. L. Peterson, *J. Am. Chem. Soc.* **1999**, *121*, 2674–2678.
[33] P. Schwab, R. H. Grubbs, J. W. Ziller, *J. Am. Chem. Soc.* **1996**, *118*, 100–110.
[34] K. J. Harlow, A. F. Hill, J. D. E. T. Wilton-Eley, *J. Chem. Soc. Dalton Trans.* **1999**, 285–291.
[35] A. Fürstner, M. Liebl, C. W. Lehmann, M. Picquet, R. Kunz, C. Bruneau, D. Touchard, P. H. Dixneuf, *Chem. Eur. J.* **2000**, *6*, 1847–1857.
[36] M. Picquet, D. Touchard, C. Bruneau, P. H. Dixneuf, *New J. Chem.* **1999**, *23*, 141–143.
[37] A. Fürstner, M. Picquet, C. Bruneau, P. H. Dixneuf, *Chem. Commun.* **1998**, 1315–1316.
[38] L. Jafarpour, J. Huang, E. D. Stevens, S. P. Nolan, *Organometallics* **1999**, *18*, 3760–3763.
[39] L. Jafarpour, S. P. Nolan, *J. Organomet. Chem.* **2001**, *617–618*, 17–27.
[40] H. Katayama, F. Ozawa, *Coord. Chem. Rev.* **2004**, *248*, 1703–1715.
[41] H. Katayama, F. Ozawa, *Organometallics* **1998**, *17*, 5190–5196.
[42] H. Katayama, F. Ozawa, *Chem. Lett.* **1998**, 67–68.
[43] J. Louie, R. H. Grubbs, *Angew. Chem. Int. Ed.* **2001**, *40*, 247–249.
[44] I. Dragutan, V. Dragutan, *Platin. Met. Rev.* **2006**, *50*, 81–94.
[45] L. Delaude, A. Demonceau, A. F. Noels, *Chem. Commun.* **2001**, 986–987.
[46] L. Delaude, M. Szypa, A. Demonceau, A. F. Noels, *Adv. Synth. Catal.* **2002**, *344*, 749–756.
[47] C. Lo, R. Cariou, C. Fischmeister, P. H. Dixneuf, *Adv. Synth. Catal.* **2007**, *349*, 546–550.
[48] A. W. Waltman, R. H. Grubbs, *Organometallics* **2004**, *23*, 3105–3107.
[49] A. Demonceau, A. W. Stumpf, E. Saive, A. F. Noels, *Macromolecules* **1997**, *30*, 3127–3136.
[50] T. Karlen, A. Ludi, A. Mühlebach, P. Bernhard, C. Pharisa, *J. Polym. Sci. Part A: Polym. Chem.* **1995**, *33*, 1665–1674.
[51] A. Hafner, A. Mühlebach, P. A. van der Schaaf, *Angew. Chem. Int. Ed.* **1997**, *360*, 2121–2124.
[52] A. Fürstner, L. Ackermann, *Chem. Commun.* **1999**, 95–96.
[53] C. W. Bielawski, D. Benitez, T. Morita, R. H. Grubbs, *Macromolecules* **2001**, *34*, 8610–8618.
[54] R. Castarlenas, D. Sémeril, A. F. Noels, A. Demonceau, P. H. Dixneuf, *J. Organomet. Chem.* **2002**, *663*, 235–238.
[55] L. Delaude, A. Demonceau, A. F. Noels, *Chem. Commun.* **2001**, 986–987.
[56] P. B. Hitchcock, M. F. Lappert, P. L. Pye, S. Thomas, *J. Chem. Soc. Dalton Trans.* **1979**, 1929–1942.
[57] T. M. Trnka, J. P. Morgan, M. S. Sanford, T. E. Wilhelm, M. Scholl, T.-L. Choi, S. Ding, M. W. Day, R. H. Grubbs, *J. Am. Chem. Soc.* **2003**, *125*, 2546–2558.
[58] S. H. Hong, A. Chlenov, M. W. Day, R. H. Grubbs, *Angew. Chem. Int. Ed.* **2007**, *46*, 5148–5151.
[59] M. A. Bennett, T. N. Huang, T. W. Matheson, A. K. Smith, *Inorg. Synth.* **1985**, *21*, 75.
[60] H. Türkmen, B. Cetinkaya, *J. Organomet. Chem.* **2006**, *691*, 3749–3759.

Received: June 27, 2007
Published Online: October 19, 2007

 © 2007 Wiley-VCH Verlag GmbH & Co. KGaA, Weinheim 

DOI: 10.1002/ejic.200700690

# 2-Arylimino-9-phenyl-1,10-phenanthrolinyl-iron, -cobalt and -nickel Complexes: Synthesis, Characterization and Ethylene Oligomerization Behavior

Suyun Jie,[a] Shu Zhang,[a] and Wen-Hua Sun*[a]

**Keywords:** Nitrogen ligands / Late transition metals / Iron / Ethylene / Oligomerization

A series of 2-imino-9-phenyl-1,10-phenanthrolines **1**–**6** has been prepared and investigated as new tridentate N3 ligands in coordination with metal chlorides. Their iron(II) (**1a**–**6a**), cobalt(II) (**1b**–**6b**), and nickel(II) (**1c**–**6c**) complexes have been synthesized and characterized by elemental and spectroscopic analysis in conjunction with single-crystal X-ray diffraction studies. Some of the iron complexes show good activities in the selective dimerization of ethylene upon treatment with MAO or MMAO, while the cobalt complexes show higher activities than their iron analogues and lead to the formation of $C_6$ and $C_8$ oligomers. The nickel complexes display high catalytic activities toward ethylene oligomerization in the presence of $Et_2AlCl$ and an auxiliary ligand ($PPh_3$).

(© Wiley-VCH Verlag GmbH & Co. KGaA, 69451 Weinheim, Germany, 2007)

## Introduction

Ethylene oligomerization is an important catalytic process for the production of linear α-olefins as basic chemicals.[1] The catalysts currently used in industrial processes include alkylaluminum compounds, a combination of alkylaluminum compounds and early transition metal complexes, nickel(II) complexes,[1a] and monoanionic [P,O] nickel-based catalysts (SHOP).[2] In the past decade, research on late transition metal complexes as catalysts for ethylene oligomerization and polymerization has attracted considerable attraction in both academic and industrial circles due to the possibility of their forming highly active and selective catalysts.[3–5] This was stimulated by the pioneering work by Brookhart's group,[6] who discovered that cationic α-diiminonickel complexes are effective catalysts for ethylene oligomerization and polymerization. Since this initial investigation of tetracoordinate nickel complexes, more attention has been paid recently to pentacoordinate complexes of nickel incorporating tridentate ligands such as N^N^O,[7] N^P^N,[8] P^N^N,[9] P^N^P,[9a] and N^N^N,[10–15] as well as their iron and cobalt analogues.

The discovery of highly active iron- and cobalt-based olefin polymerization catalysts was made possible by the design of bis(imino)pyridines as tridentate ligands by the Brookhart and Gibson groups,[16] who carried out detailed investigations of metal complexes bearing bis(imino)pyridine ligands by modifying the substituents on the aryl ring linked to the imino group and checking their influence on the catalytic activity and the resulting oligomerization or polymerization products.[4] Extensive research into alternative models of iron and cobalt complexes ligated with new types of tridentate $N_3$ ligands did not result in highly active precursors for ethylene oligomerization or polymerization.[17] Nevertheless, tridentate $N_3$ ligands are still of great interest for the preparation of late transition metal complexes as catalysts for ethylene oligomerization and polymerization[10–15,17–20] as the selective synthesis of short ethylene oligomers, particularly α-olefins, is of industrial importance.

The variation of catalyst models by designing new organic compounds that can be used as tridentate ligands has been targeted by our group for the production of highly active catalysts of iron and cobalt,[11,15,19,20] as well as nickel.[11–14] Some of these complexes have shown promising catalytic activities toward ethylene oligomerization and polymerization, such as highly active iron catalysts bearing 2-imino-1,10-phenanthrolines[19] and 2-(2-benzimidazolyl)-2-[1-(arylimino)ethyl]pyridines[15b] along with bimetallic iron complexes bearing 2-methyl-2,4-bis(6-iminopyridin-2-yl)-1*H*-1,5-benzodiazepines;[15a] their cobalt analogues also showed good activities.[15a,15b,20] Similarly to the bis(imino)pyridine catalytic systems,[4] we found that the above iron-based catalysts are generally more active than their cobalt analogues, although the exceptional cobalt complexes ligated by 2,9-bis(imino)-1,10-phenanthrolines showed better activity than their iron analogues.[11] Moreover, all the corresponding nickel complexes showed good catalytic activity for ethylene oligomerization,[11,12,14a] as did our more recent nickel complexes bearing 2-(benzimidazol-2-yl)-1,10-phenanthrolines.[13]

Along with the decisive influence of the ligands, especially the steric and electronic effects of substituents, on the

[a] Key Laboratory of Engineering Plastics and Beijing National Laboratory for Molecular Sciences, Institute of Chemistry, Chinese Academy of Sciences,
Beijing 100080, China
Fax: +86-10-6261-8239
E-mail: whsun@iccas.ac.cn


WILEY InterScience® DISCOVER SOMETHING GREAT
© 2007 Wiley-VCH Verlag GmbH & Co. KGaA, Weinheim

catalytic activities and products, the nature of the metal also greatly affects catalytic behavior. Metal complexes containing 2-imino-1,10-phenanthrolines generally show good to high catalytic activities for ethylene oligomerization and polymerization.[12,19,20] A high steric bulk of the ligands was recognized to be critical for a high catalytic activity of diiminonickel complexes for ethylene polymerization,[6] whereas, in comparison with 2-imino-1,10-phenanthrolinyl metal complexes,[12,19,20] the additional imino group in metal complexes bearing 2,9-diimino-1,10-phenanthrolines[11] has a negative effect as the additional imino group is assumed to coordinate to the active species, which results in a deactivated species. In order to check the effect of steric hindrance, 2-imino-9-phenyl-1,10-phenanthroline complexes have been targeted as precursors for ethylene oligomerization.

Herein we report the synthesis of 2-acetyl- and 2-benzoyl-9-phenyl-1,10-phenanthrolines and their subsequent transformation into 2-imino-9-phenyl-1,10-phenanthrolines for use as ligands. These compounds keep the same coordinative framework as 2-imino-1,10-phenanthrolines but with an additional phenyl group at the 9-position. Their late transition metal (Fe, Co, and Ni) complexes are synthesized and characterized and the catalytic properties of these complexes for ethylene oligomerization are evaluated under various reaction conditions. The effects of ligand environment and reaction conditions on the activity and the distribution of oligomers obtained are investigated systematically.

## Results and Discussion

### Preparation of Ketones I and II

2-Cyano-1,10-phenanthroline and 2-acetyl-1,10-phenanthroline were prepared according to the literature procedures.[19a,21] 2-Acetyl-9-phenyl-1,10-phenanthroline (ketone I) was synthesized by attaching a phenyl group at the phenanthroline ring using 2-acetyl-1,10-phenanthroline as the starting material (Scheme 1). The carbonyl group of 2-acetyl-1,10-phenanthroline was first protected with ethylene glycol and the 2-(2-methyl-1,3-dioxolan-2-yl)-1,10-phenanthroline formed in this condensation reaction was purified on an alumina column.[22] A solution of 1.7 equivalents of phenyllithium in diethyl ether was added dropwise to a suspension of 2-(2-methyl-1,3-dioxolan-2-yl)-1,10-phenanthroline in toluene under nitrogen at low temperature (0 °C) and the reaction mixture was maintained for an additional 3 h at 0 °C.[23] This procedure gave 2-(2-methyl-1,3-dioxolan-2-yl)-9-phenyl-1,10-phenanthroline by elimination of lithium hydride.[24] 2-(2-Methyl-1,3-dioxolan-2-yl)-9-phenyl-1,10-phenanthroline was purified as a yellow oil on a silica column and then refluxed in acetone in the presence of *p*-toluenesulfonic acid to cleave the 1,3-dioxolane moiety. The desired product (2-acetyl-9-phenyl-1,10-phenanthroline) precipitated from the solution and was obtained by filtration as a pale-yellow solid.

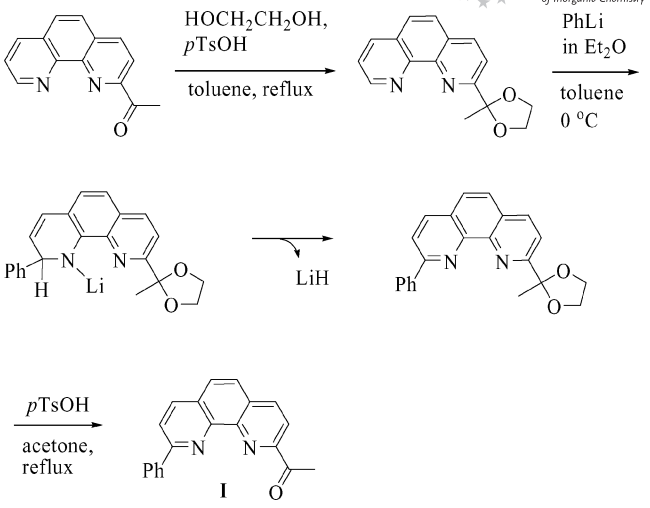


Scheme 1. Synthesis of ketone I.

2-Benzoyl-9-phenyl-1,10-phenanthroline (ketone II) was prepared in a one-step reaction between 2-cyano-1,10-phenanthroline and three equivalents of phenyllithium (Scheme 2). Thus, a solution of phenyllithium in diethyl ether was added dropwise to a suspension of 2-cyano-1,10-phenanthroline in toluene at –78 °C, then the mixture was slowly warmed to room temperature and stirred overnight. The reaction proceeds by initial addition of phenyllithium to the nitrile group[25] followed by a Ziegler alkylation.[24] Subsequent hydrolysis gave the benzoyl-substituted product. The resultant mixture was extracted with dichloromethane and the organic phase was purified on a silica column. The desired compound (2-benzoyl-9-phenyl-1,10-phenanthroline) was obtained as a slightly yellow solid in acceptable yield.

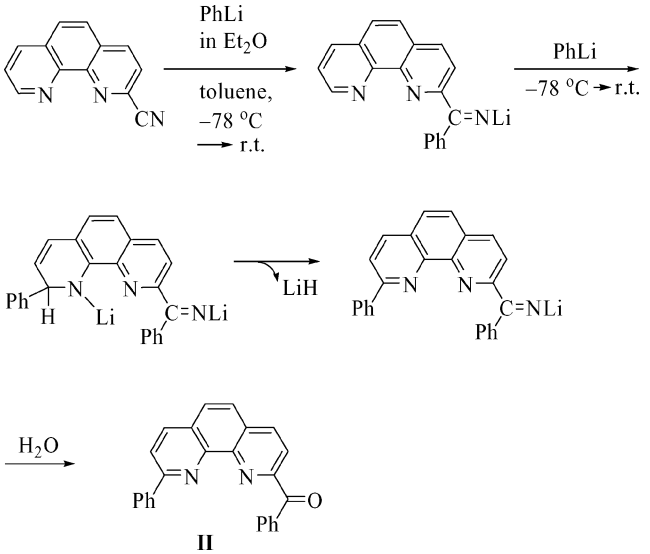


Scheme 2. Synthesis of ketone II.

 © 2007 Wiley-VCH Verlag GmbH & Co. KGaA, Weinheim 

### Synthesis and Characterization of Ligands 1–6 and Complexes 1a–6a, 1b–6b, and 1c–6c

The 2-imino-9-phenyl-1,10-phenanthrolinyl ligands **1**–**6** were prepared by condensing ketones I or II with the corresponding substituted anilines in the presence of *p*-toluenesulfonic acid in toluene or tetraethyl silicate (Scheme 3). The ligands were obtained in high yield and were characterized by IR, $^1$H, and $^{13}$C NMR spectroscopy as well as elemental analysis. The iron complexes **1a**–**6a** were readily prepared by mixing the corresponding ligand with one equivalent of $FeCl_2{\cdot}4H_2O$ in thf at room temperature under nitrogen (Scheme 3). The resulting complexes precipitated from the reaction solution and were separated as air-stable green or brown solids. Similarly, the cobalt complexes **1b**–**6b** and nickel complexes **1c**–**6c** were synthesized by treating the corresponding ligand with one equivalent of $CoCl_2$ or $NiCl_2{\cdot}6H_2O$ in anhydrous ethanol at room temperature. The methyl ketimine cobalt complexes **1b**–**3b** were obtained as green powders, whereas the phenyl ketimine complexes **4b**–**6b** were red-brown. The corresponding nickel complexes **1c**–**6c** were obtained as orange or yellow powders. All complexes were well characterized by FT-IR spectroscopy and elemental analysis. A comparison of the IR spectra of the complexes and their corresponding ligands shows that the C=N stretching vibrations of the iron, cobalt, and nickel complexes are shifted to lower wavenumber and their peak intensities greatly reduced, thereby indicating a coordinative interaction between the imino nitrogen atom and the central metal. Some samples for elemental analysis were prepared as crystals, therefore the analytical results show the incorporation of solvent molecules. The structures of ligand **2**, iron complex **2a**, cobalt complexes **1b**, **4b**, and **6b**, and nickel complexes **1c** and **5c** in the solid state were confirmed by single-crystal X-ray diffraction analysis.

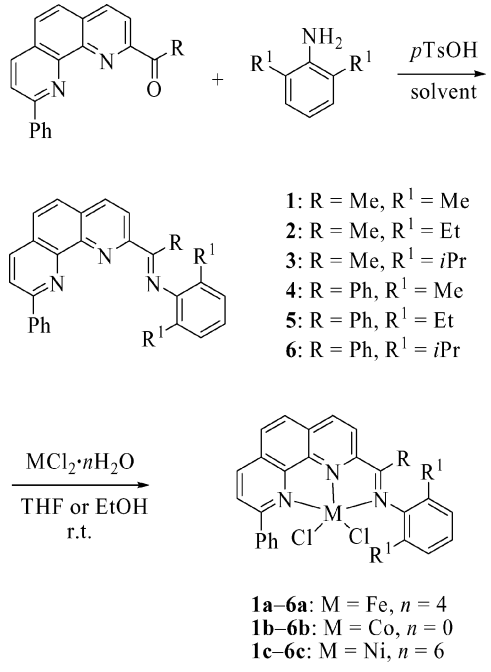


Scheme 3. Synthesis of ligands **1**–**6** and complexes **1a**–**6a**, **1b**–**6b**, and **1c**–**6c**.

### Crystal Structures

Single crystals of ligand **2** suitable for X-ray diffraction analysis were grown by recrystallization from a dichloromethane/hexane (1:5, v/v) solution. The molecular structure is shown in Figure 1. The imino nitrogen atom is disposed *trans* to the phenanthroline nitrogen atoms with a typical C=N double bond length of 1.270(2) Å. The phenyl ring on C1 is nearly coplanar with the plane of the phenanthroline moiety (dihedral angle: 6.2°), whereas the aryl ring on the imino nitrogen atom is approximately perpendicular to the plane of the phenanthroline moiety and the phenyl plane on C1 (dihedral angles: 92.1 and 89.6°, respectively).

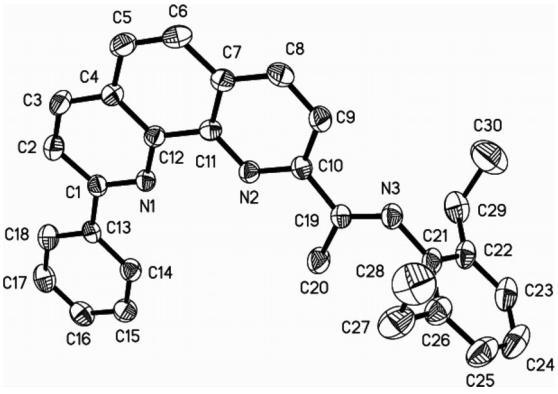


Figure 1. Molecular structure of ligand **2** with all hydrogen atoms omitted for clarity. Selected bond lengths [Å] and bond angles [°]: N1–C1 1.330(2), N1–C12 1.355(3), N2–C11 1.356(3), N2–C10 1.327(2), N3–C19 1.270(2), N3–C21 1.422(3); C19–N3–C21 121.62(2), N3–C19–C10 117.6(2), N3–C19–C20 125.0(2).

Single crystals of complex **2a** suitable for X-ray diffraction analysis were obtained by slow diffusion of diethyl ether into its methanol solution under nitrogen. The asymmetric unit of complex **2a** contains the halves of two independent molecules, as shown in Figure 2. The coordination geometry around the iron center can be described as a distorted trigonal bipyramid in which N2 of the phenanthroline group and two chlorides form the equatorial plane. The two independent molecules have slightly different bond lengths and bond angles, as shown in Table 1. The iron center deviates slightly (0.0469 Å) from the equatorial plane in both molecules, and the phenyl ring on C1 or C1A and the plane of the phenanthroline moiety make the same dihedral angle (53.5°), which is very different from that in the corresponding ligand **2** (6.2°). The plane of the phenanthroline moiety is nearly perpendicular to the equatorial plane [86.8° in (a) and 88.4° in (b)]. The dihedral angles between the phenyl ring on C1 or C1A and the equatorial plane are also the same (139.1°) for the two molecules, while the angles between the aryl ring on the imino nitrogen atom and the

 © 2007 Wiley-VCH Verlag GmbH & Co. KGaA, Weinheim 

equatorial plane are very different [56.8° in (a) and 78.9° in (b)]. The Fe–N bond in the equatorial plane in each molecule is clearly shorter than the two axial Fe–N bonds, and the axial Fe–N(phenanthroline) bond is about 0.1 Å longer than the Fe–N(imino) bond. The phenyl group on C1 results in a longer Fe–N1 bond length [av. 2.392(3) Å] than that of a related 2-acetyl-1,10-phenanthroline complex [2.271(3) Å].[19a] The two Fe–Cl bond lengths differ by about 0.1 Å. Although the two imino C=N bonds are slightly different [1.293(5) Å in (a) and 1.271(5) Å in (b)], they are both typical of an imino C=N double bond. The C=N bond length in molecule (b) is almost identical to that in ligand **2** [1.270(2) Å].

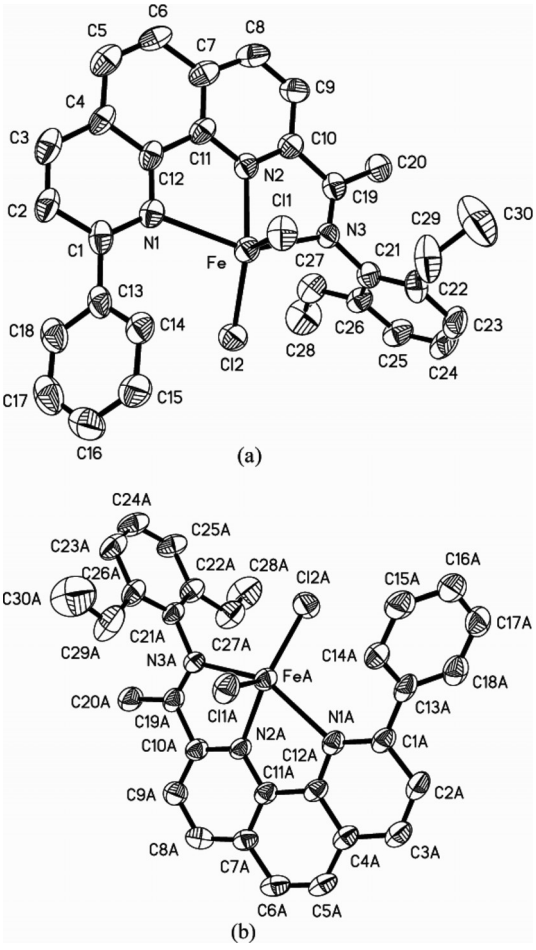


Figure 2. Molecular structure of complex **2a** showing the two crystallographically independent molecules of the asymmetric unit. Water molecules and all hydrogen atoms have been omitted for clarity.

Single crystals of cobalt complexes **1b**, **4b**, and **6b** were grown by slow diffusion of hexane into their solutions in dichloromethane. Their molecular structures are shown in Figures 3, 4, and 5, respectively, and selected bond lengths and angles are collected in Table 2. The coordination geometry around the cobalt center in these complexes can be described as a distorted trigonal bipyramid with N2 of the phenanthrolinyl group and two chlorides forming the equatorial plane.

Table 1. Selected bond lengths [Å] and angles [°] for complex **2a**.

| | | | |
|---|---|---|---|
| Fe–N1 | 2.391(3) | FeA–N1A | 2.393(3) |
| Fe–N2 | 2.101(3) | FeA–N2A | 2.104(3) |
| Fe–N3 | 2.298(3) | FeA–N3A | 2.283(3) |
| Fe–Cl1 | 2.3405(1) | FeA–Cl1A | 2.3456(1) |
| Fe–Cl2 | 2.2492(1) | FeA–Cl2A | 2.2469(1) |
| N3–C19 | 1.293(5) | N3A–C19A | 1.271(5) |
| N2–Fe–N1 | 73.77(1) | N2A–FeA–N1A | 73.18(1) |
| N2–Fe–N3 | 73.18(1) | N2A–FeA–N3A | 72.89(1) |
| N1–Fe–N3 | 145.86(1) | N1A–FeA–N3A | 144.89(1) |
| N1–Fe–Cl1 | 93.70(8) | N1A–FeA–Cl1A | 94.32(8) |
| N2–Fe–Cl1 | 98.23(9) | N2A–FeA–Cl1A | 98.71(9) |
| N3–Fe–Cl1 | 99.19(8) | N3A–FeA–Cl1A | 99.43(9) |
| N1–Fe–Cl2 | 104.73(9) | N1A–FeA–Cl2A | 105.71(9) |
| N2–Fe–Cl2 | 141.53(9) | N2A–FeA–Cl2A | 143.73(9) |
| N3–Fe–Cl2 | 95.87(9) | N3A–FeA–Cl2A | 96.35(9) |
| Cl1–Fe–Cl2 | 120.09(5) | Cl1A–FeA–Cl2A | 117.38(5) |

The cobalt atom in complex **1b** deviates slightly (–0.0517 Å) from the equatorial plane composed by N2, Cl1, and Cl2 and the axial Co–N bonds form an angle of 149.22(1)° (N1–Co–N3). The phenyl ring on C1 and the plane of the phenanthroline moiety form a dihedral angle of 41.0°, and the plane of the phenanthroline moiety is almost perpendicular to the equatorial plane (dihedral angle: 93.2°). The dihedral angles between the phenyl ring on C1 and the equatorial plane and the aryl ring on the imino nitrogen atom and the equatorial plane are 134.0° and 133.7°, respectively. The two axial Co–N distances [2.313(4) and 2.279(4) Å] are much longer than the Co–N bond [2.035(4) Å] in the equatorial plane and the two Co–Cl linkages differ by 0.06 Å. The imino N3–C19 bond length is 1.289(6) Å, which is typical of a C=N double bond.

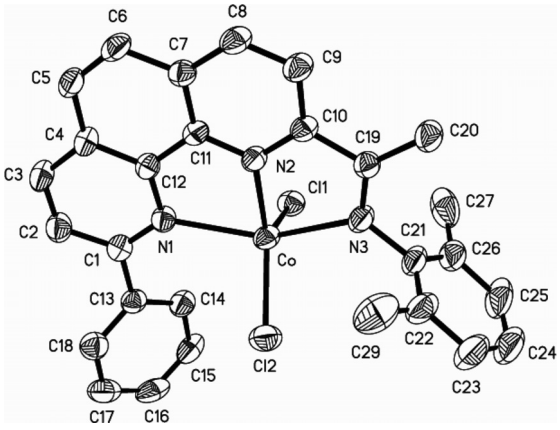


Figure 3. Molecular structure of complex **1b**. Water molecules and all hydrogen atoms have been omitted for clarity.

The central cobalt atom in the phenyl ketimine complex **4b** also deviates slightly (0.0196 Å) from the equatorial plane containing N2, Cl1, and Cl2. The bond lengths and angles around the cobalt center are very similar to those in **1b**, although the phenyl ring on C1 and the plane of the phenanthroline moiety make a dihedral angle (16.4°) that is very different from that in **1b** (41.0°). The phenyl ring on

 © 2007 Wiley-VCH Verlag GmbH & Co. KGaA, Weinheim 

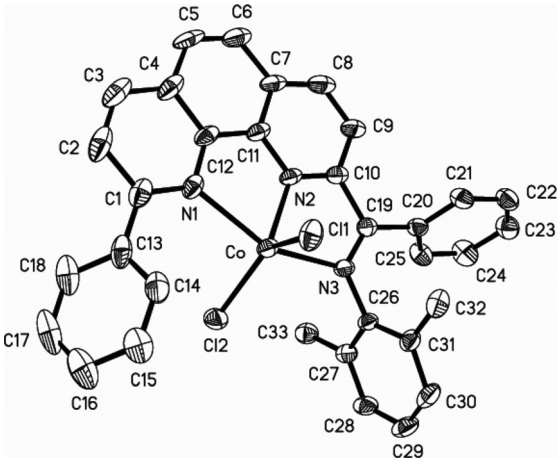


Figure 4. Molecular structure of complex **4b** showing one $CH_2Cl_2$ molecule. All hydrogen atoms have been omitted for clarity.

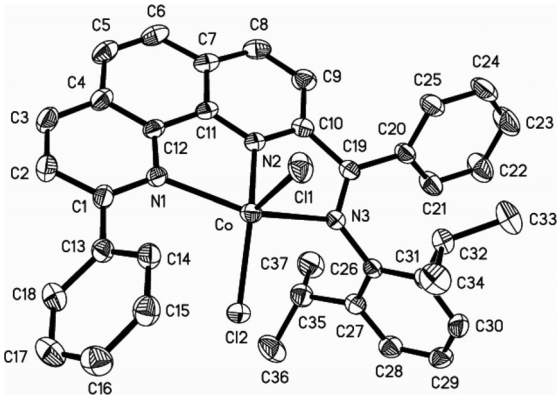


Figure 5. Molecular structure of complex **6b** showing one $CH_2Cl_2$ molecule. All hydrogen atoms have been omitted for clarity.

C1, the plane of the phenanthroline moiety, the phenyl ring on the imino carbon atom, and the aryl ring on the imino nitrogen atom are all approximately perpendicular to the equatorial plane, with dihedral angles of 80.1°, 88.9°, 91.5°, and 86.0°, respectively.

The central cobalt atom in the phenyl ketimine complex **6b**, which contains bulkier isopropyl groups at the *ortho* positions of the aryl ring at the imino nitrogen atom, deviates slightly more (0.1829 Å) from the equatorial plane containing N2, Cl1, and Cl2 than in the other complexes. This complex also has a smaller N2–Co–Cl1 bond angle [97.27(8)°] and larger N2–Co–Cl2 bond angle [140.69(8)°]. The two axial Co–N bonds also make a slightly smaller angle of 143.99(9)° (N1–Co–N3). In contrast to the other complexes, the phenyl ring on C1 is nearly coplanar to the plane of the phenanthroline moiety, with a dihedral angle of 3.3° that is much smaller than in other analogues and even smaller than in ligand **2** (6.2°). The dihedral angles between the phenyl ring on C1, the plane of the phenanthroline moiety, the phenyl ring on the imino carbon, and the aryl ring on the imino nitrogen and the equatorial plane [82.8°, 80.4°, 88.9°, and 89.2°, respectively] are similar to those in **4b**. The axial Co–N1(phenanthroline) bond in **6b** is 0.19 Å shorter than the Co–N3(imino) bond, which is very different from the situation in other cobalt analogues (about 0.04 Å in **1b** and **4b**). One possible reason for this is that the bulkier isopropyl groups at the *ortho* positions of the aryl ring bound to the imino nitrogen take up more space and lead to a shortening of the Co–N1 bond [2.180(2) Å] and a lengthening of the Co–N3 bond [2.372(2) Å]. This steric effect also leads to a shortening of the imino N3–C19 bond [1.255(4) Å].

Single crystals of nickel complexes **1c** and **5c** were obtained by layering hexane on their corresponding dichloromethane solutions. X-ray diffraction analysis revealed that they display a distorted trigonal bipyramidal geometry in which the central nickel atom is coordinated to three nitrogen atoms from the ligand and two halides. Similar to their iron and cobalt analogues, one nitrogen atom (N2) of the phenanthrolinyl group and two chlorides compose the equatorial plane; the imino nitrogen (N3) and another nitrogen (N1) of the phenanthrolinyl group occupy the two axial coordination sites. Their molecular structures are shown in Figures 6 and 7, respectively, and selected bond lengths and angles are collected in Table 2.

Table 2. Selected bond lengths [Å] and bond angles [°] in complexes **1b**, **1c**, **4b**, **5c**, and **6b**.

| | **1b** (M = Co) | **1c** (M = Ni) | **4b** (M = Co) | **5c** (M = Ni) | **6b** (M = Co) |
|---|---|---|---|---|---|
| M–N1 | 2.313(4) | 2.300(7) | 2.299(3) | 2.219(3) | 2.180(2) |
| M–N2 | 2.035(4) | 1.962(6) | 2.034(3) | 1.970(4) | 2.012(2) |
| M–N3 | 2.279(4) | 2.238(6) | 2.257(3) | 2.220(3) | 2.372(2) |
| M–Cl1 | 2.2923(2) | 2.274(3) | 2.2745(1) | 2.2988(1) | 2.2192(1) |
| M–Cl2 | 2.2357(2) | 2.217(3) | 2.2404(1) | 2.2234(1) | 2.1917(9) |
| N3–C19 | 1.289(6) | 1.275(9) | 1.278(4) | 1.276(5) | 1.255(4) |
| N1–M–N2 | 76.16(15) | 78.4(3) | 76.64(12) | 78.32(1) | 77.62(1) |
| N2–M–N3 | 74.00(15) | 76.0(3) | 74.01(1) | 75.40(1) | 70.50(9) |
| N1–M–N3 | 149.22(1) | 154.1(2) | 149.77(1) | 152.86(1) | 143.99(9) |
| N1–M–Cl1 | 97.95(11) | 95.46(2) | 94.07(8) | 91.79(1) | 103.79(7) |
| N1–M–Cl2 | 99.72(1) | 92.28(2) | 96.22(8) | 98.16(1) | 103.95(7) |
| N2–M–Cl1 | 104.94(1) | 101.4(2) | 100.88(8) | 99.41(1) | 97.27(8) |
| N2–M–Cl2 | 133.77(1) | 120.9(2) | 131.09(8) | 129.52(1) | 140.69(8) |
| N3–M–Cl1 | 96.80(1) | 93.11(2) | 98.37(8) | 99.04(1) | 96.55(7) |
| N3–M–Cl2 | 95.48(1) | 97.66(2) | 97.55(8) | 93.33(1) | 90.89(7) |
| Cl1–M–Cl2 | 121.12(6) | 137.71(1) | 128.01(5) | 131.07(6) | 119.62(4) |

 © 2007 Wiley-VCH Verlag GmbH & Co. KGaA, Weinheim 

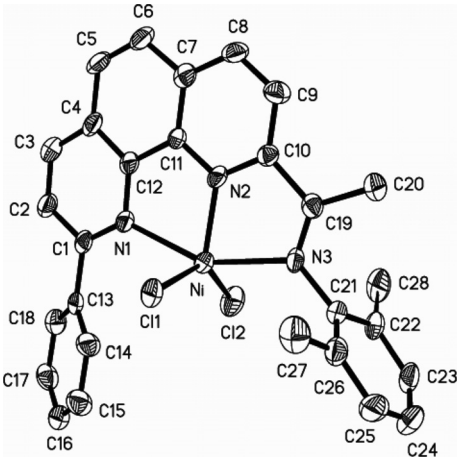


Figure 6. Molecular structure of complex **1c** showing one $CH_2Cl_2$ molecule. All hydrogen atoms have been omitted for clarity.

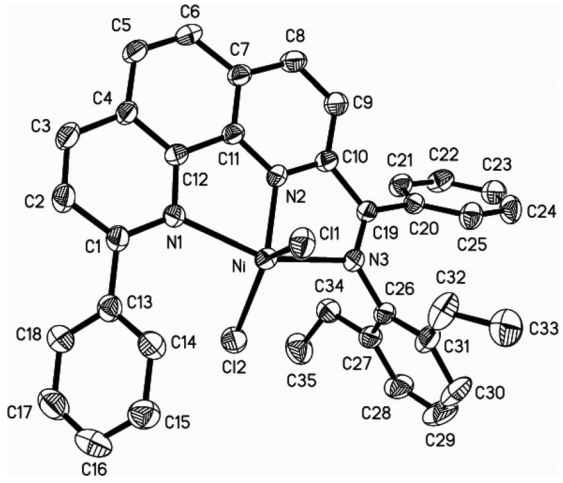


Figure 7. Molecular structure of complex **6b** showing two $CH_2Cl_2$ molecules. All hydrogen atoms have been omitted for clarity.

The central nickel atom in **1c** deviates by 0.0128 Å from the equatorial plane containing N2, Cl1, and Cl2 and the two axial Ni–Cl bonds make an axial angle (N1–Ni–N3) of 154.1(2)°. Both the equatorial plane and the plane of the phenyl group on the imino nitrogen are almost perpendicular to the plane of the phenanthroline moiety (dihedral angles of 84.8° and 87.8°, respectively). The plane of the pendant phenyl group on C1 makes a dihedral angle of 33.6° with the plane of the phenanthroline moiety and 51.2° with the equatorial plane. Similarly to a related phenanthrolinylnickel complex, the Ni–N bond in the equatorial plane is clearly shorter than the axial Ni–N bonds, although the presence of a phenyl group on C1 leads to an elongation of the Ni–N1 bond [2.300(7) Å vs. 2.157(3) Å];[12] the two Ni–Cl bond lengths are essentially identical. Despite showing typical character of a C=N double bond, the imino N3–C19 bond [1.275(9) Å] is slightly shorter than that in a related phenanthrolinylnickel complex [1.284(4) Å],[12] whereas much larger Cl1–Ni–Cl2 [137.71(1)°] and smaller N2–Ni–Cl1 [120.9(2)°] bond angles are observed after addition of a phenyl group at the 9-position of phenanthroline [110.62(4)° and 153.12(8)°, respectively, in the related nickel complex].[12]

Despite several similarities with **1c**, complex **5c** also has its own structural characteristics due to the presence of a phenyl group at the imino carbon instead of a methyl group. Thus, the central nickel atom deviates 0.0102 Å from the equatorial plane containing N2, Cl1, and Cl2, and the introduced phenyl group forms a dihedral angle of 5.7° with the plane of the phenanthroline moiety and is almost perpendicular to the equatorial plane (dihedral angle of 82.2°). The equatorial plane is still almost perpendicular to the plane of the phenanthroline moiety (dihedral angle of 87.5°), whereas the dihedral angle between the plane of the phenyl group on the imino nitrogen and the plane of the phenanthroline moiety decreases significantly to 7.2°. The plane of the pendant phenyl group on C1 makes a decreased dihedral angle of 8.0° with the plane of the phenanthroline moiety and an increased dihedral angle of 79.9° with the equatorial plane. All bond lengths and angles in **5c** are similar to those in **1c**.

## Ethylene Oligomerization

### *Ethylene Oligomerization with Iron Complexes 1a–6a*

The iron(II) complexes **1a**–**6a** were first investigated as ethylene oligomerization catalysts at 1 atm of ethylene pressure (Table 3), although the results were not satisfactory as almost no absorption of ethylene was observed with diethylaluminum chloride as co-catalyst. Activation with methylaluminoxane (MAO) gave a low catalytic activity for methyl-substituted complexes **1a** and **4a**, although ethyl-substituted complexes **2a** and **5a** were found to be less active and isopropyl-substituted complexes **3a** and **6a** completely inactive. Modified methylaluminoxane (MMAO) was found to be a more effective co-catalyst than MAO with a similar effect of the ligand environment on the catalytic activity. Thus, for complexes bearing the same substituents on the aryl ring of the imino nitrogen, phenyl ketimine (R = Ph) complexes **4a**–**6a** showed a relatively higher catalytic activity than the corresponding methyl ketimine (R = Me) complexes **1a**–**3a**. Complex **4a** exhibited the highest activity of $2.64 \times 10^5$ g mol$^{-1}$(Fe) h$^{-1}$, with 1-butene as the main product. Under the same reaction conditions, the variation of $R^1$ on the aryl ring of the imino nitrogen was found to have a strong influence on the catalytic activity. Thus, increasing the bulkiness of $R^1$ in both methyl and phenyl ketimine complexes caused the catalytic activity to decrease dramatically (methyl > ethyl > isopropyl), and in all cases essentially only dimerization was achieved, with a high selectivity for 1-butene.

The iron(II) complexes **1a**–**6a** were studied for ethylene oligomerization at 10 atm of ethylene pressure in the presence of MAO or MMAO; much higher catalytic activities were observed than those obtained at 1 atm (Table 3). With MAO as a co-catalyst the highest activity of $1.94 \times 10^6$ g mol$^{-1}$(Fe) h$^{-1}$ was obtained with complex **4a**. In general, however, under similar conditions, these complexes

 © 2007 Wiley-VCH Verlag GmbH & Co. KGaA, Weinheim 

Table 3. Ethylene oligomerization with complexes **1a**–**6a**.[a]

| Entry | Cat. | Co-cat. | *P* [atm][b] | *T* [°C][c] | Activity[d] | % Oligomer distribution[e] $C_4/\Sigma C$ | $C_6/\Sigma C$ | % Selectivity for 1-$C_4$[e] |
|---|---|---|---|---|---|---|---|---|
| 1 | **1a** | MAO | 1 | 20 | 0.259 | 100 | – | 96.1 |
| 2 | **2a** | MAO | 1 | 20 | 0.059 | 100 | – | 100 |
| 3 | **3a** | MAO | 1 | 20 | – | – | – | – |
| 4 | **4a** | MAO | 1 | 20 | 0.295 | 100 | – | 100 |
| 5 | **5a** | MAO | 1 | 20 | 0.052 | 100 | – | 100 |
| 6 | **6a** | MAO | 1 | 20 | – | – | – | – |
| 7 | **1a** | MMAO | 1 | 20 | 4.78 | 100 | – | 100 |
| 8 | **2a** | MMAO | 1 | 20 | 1.63 | 100 | – | 100 |
| 9 | **3a** | MMAO | 1 | 20 | 0.199 | 100 | – | 100 |
| 10 | **4a** | MMAO | 1 | 20 | 26.4 | 100 | – | 100 |
| 11 | **5a** | MMAO | 1 | 20 | 5.13 | 100 | – | 100 |
| 12 | **6a** | MMAO | 1 | 20 | 0.275 | 100 | – | 100 |
| 13 | **1a** | MAO | 10 | 40 | 40.8 | 99.2 | 0.8 | 99.8 |
| 14 | **2a** | MAO | 10 | 40 | 29.1 | 98.7 | 1.3 | 99.8 |
| 15 | **3a** | MAO | 10 | 40 | 0.621 | 100 | – | 100 |
| 16 | **4a** | MAO | 10 | 40 | 194 | 99.2 | 0.8 | 99.9 |
| 17 | **5a** | MAO | 10 | 40 | 51.6 | 98.6 | 1.4 | 100 |
| 18 | **6a** | MAO | 10 | 40 | 0.409 | 100 | – | 100 |
| 19 | **1a** | MMAO | 10 | 40 | 269 | 99.4 | 0.6 | 100 |
| 20 | **2a** | MMAO | 10 | 40 | 47.9 | 100 | – | 100 |
| 21 | **3a** | MMAO | 10 | 40 | 1.90 | 100 | – | 100 |
| 22 | **4a** | MMAO | 10 | 40 | 211 | 99.1 | 0.9 | 100 |
| 23 | **5a** | MMAO | 10 | 40 | 54.3 | 98.7 | 1.3 | 100 |
| 24 | **6a** | MMAO | 10 | 40 | 0.465 | 100 | – | 100 |

[a] General conditions: cat.: 5 μmol; Al/Fe: 500; solvent (toluene): 30 mL for 1 atm and 100 mL for 10 atm; reaction time: 30 min. [b] Ethylene pressure. [c] Reaction temperature. [d] $10^4$ g mol$^{-1}$(Fe) h$^{-1}$. [e] Weight percentage determined by GC.

were found to be much less active than the corresponding 2-imino-1,10-phenanthrolinyliron complexes,[19] probably due to the presence of a phenyl group at the 9-position of the 1,10-phenanthroline ligand, which hinders the insertion of ethylene. MMAO was found to be more effective than MAO at 10 atm of ethylene pressure, and the methyl-substituted complexes **1a** [$2.69 \times 10^6$ g mol$^{-1}$(Fe) h$^{-1}$] and **4a** [$2.11 \times 10^6$ g mol$^{-1}$(Fe) h$^{-1}$] displayed the highest activity. The isopropyl-substituted complexes **3a** and **6a** always showed lower catalytic activity, probably because the bulkier isopropyl groups at the *ortho* positions of the aryl ring at the imino nitrogen affect the active species by preventing the coordination of an ethylene molecule at the metal center. A similar trend to that obtained at 1 atm as regards the effect of ligand environment on the catalytic activities and catalytic products was obtained for both the MAO and MMAO catalytic systems.

### *Ethylene Oligomerization with Cobalt Complexes 1b–6b*

Complex **5b** was studied as a model for ethylene oligomerization under varying conditions at 1 atm of ethylene pressure (Table 4). No catalytic activity was observed with diethylaluminum chloride (Al/Co = 100 or 200) as co-catalyst at 20 °C, whereas in the presence of MAO or MMAO (Al/Co = 500) the catalytic activity increased remarkable and the products mainly consisted of butene and hexene, with a high selectivity for 1-butene (>96%). The catalytic system **5b**/MAO showed a higher activity than **5b**/MMAO, although both gave a similar distribution of oligomers and a similar selectivity for 1-butene (entries 1 and 4, Table 4). MAO was therefore chosen as a co-catalyst during the subsequent investigations at 1 and 10 atm of ethylene pressure. The **5b**/MAO system showed the lowest activity, with a butene content in the oligomeric products of more than 90%, at an Al/Co molar ratio of 100 (entry 2, Table 4). Increasing the Al/Co molar ratio in the range 200–2000 led to an increase in the activity to $6.42 \times 10^5$ g mol$^{-1}$(Co) h$^{-1}$ at a Al/Co molar ratio of 500 and then a gradual decrease. The distribution of oligomers and the selectivity for 1-butene hardly changed.

The reaction temperature was found to have a remarkable influence on the catalytic activity and the distribution of oligomers. The highest activity was achieved at 20 °C and a slightly lower activity was obtained, although with a higher amount of butene produced (91.0%), at lower temperature (0 °C; entry 8, Table 4). An elevated reaction temperature also resulted in a decrease of the catalytic activity and butene content; for instance, **5b**/MAO showed an activity of $8.74 \times 10^4$ g mol$^{-1}$(Co) h$^{-1}$ with a 72.5% butene content at 80 °C (entry 11, Table 4). No significant difference was observed between methyl- and ethyl-substituted complexes for both methyl and phenyl ketimine complexes. However, the isopropyl-substituted complexes **3b** and **6b** displayed lower catalytic activities and gave a smaller amount of butene and higher amount of hexene than the corresponding methyl- or ethyl-substituted complexes. In contrast to bis(imino)pyridine,[4] 2-benzimidazolyl-6-iminopyridine,[15b] 2-quinoxalinyl-6-iminopyridine,[15c] and 2-imino-1,10-phenanthroline systems,[19,20] these cobalt complexes display much higher catalytic activities than their corresponding iron analogues under similar reaction conditions.

 © 2007 Wiley-VCH Verlag GmbH & Co. KGaA, Weinheim 

Table 4. Ethylene oligomerization with complexes **1b**–**6b**.[a]

| Entry | Cat. | *P* [atm][b] | Al/Co | *T* [°C][c] | Activity[d] | % Oligomer distribution[e] | | | % Selectivity for 1-$C_4$[e] |
|---|---|---|---|---|---|---|---|---|---|
| | | | | | | $C_4/\Sigma C$ | $C_6/\Sigma C$ | $\geq C_8/\Sigma C$ | |
| 1[f] | **5b** | 1 | 500 | 20 | 5.93 | 77.1 | 16.2 | 6.7 | 96.1 |
| 2 | **5b** | 1 | 100 | 20 | 0.76 | 90.7 | 5.9 | 3.4 | 98.0 |
| 3 | **5b** | 1 | 200 | 20 | 2.33 | 86.3 | 10.6 | 3.1 | 97.0 |
| 4 | **5b** | 1 | 500 | 20 | 6.42 | 78.5 | 15.2 | 6.3 | 96.7 |
| 5 | **5b** | 1 | 1000 | 20 | 5.70 | 77.8 | 15.1 | 7.1 | 97.4 |
| 6 | **5b** | 1 | 1500 | 20 | 5.42 | 76.0 | 16.7 | 7.3 | 96.1 |
| 7 | **5b** | 1 | 2000 | 20 | 4.31 | 82.2 | 14.8 | 3.0 | 98.2 |
| 8 | **5b** | 1 | 500 | 0 | 3.64 | 91.0 | 7.6 | 1.4 | 98.4 |
| 9 | **5b** | 1 | 500 | 40 | 5.05 | 81.1 | 16.0 | 2.9 | 95.9 |
| 10 | **5b** | 1 | 500 | 60 | 1.41 | 72.4 | 19.2 | 8.4 | 97.2 |
| 11 | **5b** | 1 | 500 | 80 | 0.874 | 72.5 | 16.6 | 10.9 | 96.3 |
| 12 | **1b** | 1 | 500 | 20 | 6.85 | 94.3 | 5.7 | – | 97.0 |
| 13 | **2b** | 1 | 500 | 20 | 6.71 | 91.9 | 5.4 | 2.7 | 97.9 |
| 14 | **3b** | 1 | 500 | 20 | 5.23 | 80.0 | 16.5 | 3.5 | 95.4 |
| 15 | **4b** | 1 | 500 | 20 | 5.58 | 84.4 | 14.8 | 0.8 | 96.4 |
| 16 | **6b** | 1 | 500 | 20 | 2.85 | 55.2 | 28.1 | 16.7 | 94.3 |
| 17 | **1b** | 10 | 500 | 30 | 43.2 | 92.1 | 7.6 | 0.3 | 99.8 |
| 18 | **2b** | 10 | 500 | 30 | 40.6 | 95.7 | 4.0 | 0.3 | 99.7 |
| 19 | **3b** | 10 | 500 | 30 | 65.2 | 75.7 | 23.0 | 1.3 | 99.7 |
| 20 | **4b** | 10 | 500 | 30 | 49.0 | 84.5 | 13.4 | 2.1 | 99.8 |
| 21 | **5b** | 10 | 500 | 30 | 73.3 | 80.5 | 16.8 | 2.7 | 99.7 |
| 22 | **6b** | 10 | 500 | 30 | 28.0 | 46.7 | 34.0 | 19.3 | 100 |

[a] General conditions: cat.: 5 μmol; co-cat.: MAO; solvent (toluene): 30 mL for 1 atm and 100 mL for 10 atm; reaction time: 30 min. [b] Ethylene pressure. [c] Reaction temperature. [d] $10^5$ g mol$^{-1}$(Co) h$^{-1}$. [e] Weight percentage determined by GC. [f] Co-cat.: MMAO.

When the ethylene pressure was increased from 1 to 10 atm the catalytic activity of each complex increased greatly, with a very high selectivity for 1-butene. Complex **5b** was found to have the highest activity [$7.33 \times 10^6$ g mol$^{-1}$(Co) h$^{-1}$; entry 21, Table 4]. For methyl ketimine complexes, methyl-substituted **1b** and ethyl-substituted **2b** showed comparable catalytic activities and a similar distribution of oligomers, whereas isopropyl-substituted **3b** showed a higher activity and gave a larger amount of hexene than **1b** or **2b**. A slightly higher amount of hexene was obtained for the corresponding phenyl ketimine complexes than with the methyl ketimine complexes. Complex **6b**, which contains bulkier isopropyl groups on the aryl ring of the imino nitrogen, was found to be slightly less active and produce a wider distribution of oligomers ($C_4$ to $C_{22}$, along with a small amount of polyethylene waxes) than **4b** or **5b** (entry 22, Table 4).

### *Ethylene Oligomerization with Nickel Complexes 1c–6c*

Complex **5c** was investigated for ethylene oligomerization in the presence of different co-catalysts at 1 atm of ethylene pressure. Unlike the nickel complexes ligated by other 1,10-phenanthroline derivatives,[11–13] almost no catalytic activity was observed with **5c** in the presence of MAO. When MMAO was used as a co-catalyst, however, slightly better activity was obtained and only butene was generated, with a high selectivity for 1-butene (entry 3, Table 5). However, $Et_2AlCl$ was found to be more effective as a co-catalyst for nickel complexes, although the selectivity for 1-butene was slightly lower. For example, at an Al/Ni molar ratio of 300, **5c**/$Et_2AlCl$ showed an activity of $1.43 \times 10^4$ g mol$^{-1}$(Ni) h$^{-1}$, with a selectivity of 78.5% for 1-butene, at 1 atm of ethylene pressure (entry 5, Table 5).

The addition of $PPh_3$ as an auxiliary ligand to nickel-based catalytic systems has been demonstrated to improve catalytic activity and prolong catalyst lifetime,[7a,12,26] although the mechanism is still not clear. However, in the presence of MAO, the addition of $PPh_3$ had no effect and the system still had no activity. For the catalytic system **5c**/MMAO, the addition of 10 equiv. of $PPh_3$ resulted in an increase in catalytic activity but a drastic decrease in the selectivity for 1-butene (entry 4, Table 5).

The effect of varying the amount of $PPh_3$ added on the catalytic activity and the selectivity for 1-butene was investigated with the catalytic system **5c**/$Et_2AlCl$ at 1 atm of ethylene pressure. Addition of two equivalents of $PPh_3$ improved the catalytic activity to $9.63 \times 10^4$ g mol$^{-1}$(Ni) h$^{-1}$, with a small amount of hexene generated, whereas the selectivity for 1-butene decreased from 78.5% to 27.1% (entry 6, Table 5). Increasing the amount of $PPh_3$ ($\leq$20) led to a further enhancement of catalytic activity and a further decrease of selectivity for 1-butene. The addition of 20 equivalents of $PPh_3$ gave the highest activity [$6.82 \times 10^5$ g mol$^{-1}$(Ni) h$^{-1}$] and the lowest selectivity (8.5%; entry 10, Table 5). Further increasing the amount of $PPh_3$ to 30 equivalents reduced the catalytic activity and increased the selectivity for 1-butene.

The effect of reaction temperature on the catalytic activity was also studied in the presence of 10 equivalents of $PPh_3$. When keeping the other conditions constant, the optimum catalytic activity was obtained at 20 °C; both increasing and decreasing the reaction temperature led to a lower catalytic activity and higher selectivity for 1-butene.

 © 2007 Wiley-VCH Verlag GmbH & Co. KGaA, Weinheim 

Table 5. Ethylene oligomerization with complexes **1c**–**6c**.[a]

| Entry | Cat. | Equiv. of $PPh_3$[b] | $P$ [atm][c] | $T$ [°C][d] | $t$ [min][e] | Activity[f] | % Oligomer distribution[g] | | % Selectivity for |
|---|---|---|---|---|---|---|---|---|---|
| | | | | | | | $C_4/\Sigma C$ | $C_6/\Sigma C$ | 1-$C_4$[g] |
| 1[h] | **5c** | – | 1 | 20 | 30 | – | – | – | – |
| 2[h] | **5c** | 10 | 1 | 20 | 30 | – | – | – | – |
| 3[i] | **5c** | – | 1 | 20 | 30 | 0.048 | 100 | – | 92.8 |
| 4[i] | **5c** | 10 | 1 | 20 | 30 | 0.128 | 100 | – | 41.6 |
| 5 | **5c** | – | 1 | 20 | 30 | 0.143 | 100 | – | 78.5 |
| 6 | **5c** | 2 | 1 | 20 | 30 | 0.963 | 97.8 | 2.2 | 27.1 |
| 7 | **5c** | 5 | 1 | 20 | 30 | 2.29 | 98.1 | 1.9 | 24.0 |
| 8 | **5c** | 10 | 1 | 20 | 30 | 3.31 | 98.1 | 1.9 | 15.9 |
| 9 | **5c** | 10 | 1 | 20 | 60 | 3.71 | 96.5 | 3.5 | 3.5 |
| 10 | **5c** | 20 | 1 | 20 | 30 | 6.82 | 97.7 | 2.3 | 8.5 |
| 11 | **5c** | 30 | 1 | 20 | 30 | 2.75 | 98.8 | 1.2 | 27.2 |
| 12 | **5c** | 10 | 1 | 0 | 30 | 1.14 | 99.2 | 0.8 | 34.6 |
| 13 | **5c** | 10 | 1 | 0 | 60 | 1.91 | 98.4 | 1.6 | 16.3 |
| 14 | **5c** | 10 | 1 | 40 | 30 | 2.36 | 97.2 | 2.8 | 22.7 |
| 15 | **5c** | 10 | 1 | 60 | 30 | 1.58 | 95.4 | 4.6 | 20.2 |
| 16 | **1c** | 10 | 1 | 20 | 30 | 3.74 | 98.0 | 2.0 | 17.5 |
| 17 | **1c** | 10 | 1 | 20 | 60 | 3.49 | 96.7 | 3.3 | 4.3 |
| 18 | **2c** | 10 | 1 | 20 | 30 | 3.29 | 97.3 | 2.7 | 15.9 |
| 19 | **2c** | 10 | 1 | 20 | 60 | 4.67 | 97.0 | 3.0 | 5.8 |
| 20 | **3c** | 10 | 1 | 20 | 30 | 3.33 | 97.5 | 2.5 | 14.0 |
| 21 | **3c** | 10 | 1 | 20 | 60 | 3.68 | 96.1 | 3.9 | 3.2 |
| 22 | **4c** | 10 | 1 | 20 | 30 | 3.47 | 97.8 | 2.2 | 15.2 |
| 23 | **4c** | 10 | 1 | 20 | 60 | 4.71 | 95.7 | 4.3 | 2.8 |
| 24 | **6c** | 10 | 1 | 20 | 30 | 5.88 | 97.5 | 2.5 | 10.6 |
| 25 | **6c** | 10 | 1 | 20 | 60 | 3.89 | 96.4 | 3.6 | 6.6 |
| 26 | **5c** | – | 10 | 30 | 30 | 2.26 | 98.9 | 1.1 | 97.1 |
| 27 | **5c** | 10 | 10 | 30 | 30 | 5.87 | 100 | – | 93.0 |
| 28 | **5c** | 20 | 10 | 30 | 30 | 51.7 | 97.5 | 2.5 | 36.5 |
| 29 | **1c** | 20 | 10 | 30 | 30 | 36.8 | 98.1 | 1.9 | 36.2 |
| 30 | **2c** | 20 | 10 | 30 | 30 | 61.5 | 98.7 | 1.3 | 50.2 |
| 31 | **3c** | 20 | 10 | 30 | 30 | 39.6 | 98.9 | 1.1 | 63.4 |
| 32 | **4c** | 20 | 10 | 30 | 30 | 39.1 | 98.1 | 1.9 | 38.9 |
| 33 | **6c** | 20 | 10 | 30 | 30 | 57.7 | 98.4 | 1.6 | 34.9 |

[a] General conditions: cat.: 5 μmol; co-cat.: $Et_2AlCl$; Al/Ni: 300; solvent (toluene): 30 mL for 1 atm and 100 mL for 10 atm. [b] $PPh_3$ was added as an auxiliary ligand. [c] Ethylene pressure. [d] Reaction temperature. [e] Reaction time. [f] $10^5\ g\,mol^{-1}(Ni)\,h^{-1}$. [g] Weight percentage determined by GC. [h] Co-cat.: MAO; Al/Ni: 500. [i] Co-cat.: MMAO; Al/Ni: 500.

In general, an induction time of 10–20 min is observed after the addition of $PPh_3$, and a lower temperature led to a longer induction time and catalyst lifetime. For instance, the catalytic activity of **5c** at 0 or 20 °C after 60 min was found to be higher than that after 30 min, although a lower selectivity for 1-butene was obtained with a slightly larger amount of hexene produced after 60 min, which indicates that the isomerization reaction of 1-butene to 2-butene takes place at the same time as the oligomerization reaction. Generally, phenyl ketimine complexes display slightly higher activities than methyl ketimine complexes bearing the same substituents on the aryl ring of the imino nitrogen. The catalytic properties of methyl ketimine complexes after 30 min were found to be not greatly affected by the substituents on the aryl ring of the imino nitrogen, and complexes **1c**–**3c** showed comparable catalytic activity and similar selectivity for 1-butene. However, when the reaction time was prolonged to 60 min a higher catalytic activity and slightly higher selectivity for 1-butene were achieved with ethyl-substituted **2c** than with methyl-substituted **1c** and isopropyl-substituted **3c**. For phenyl ketimine complexes, isopropyl-substituted **6c** showed the highest activity of $5.88\times10^5\ g\,mol^{-1}(Ni)\,h^{-1}$ after 30 min and methyl-substituted **4c** showed the highest activity of $4.71\times10^5\ g\,mol^{-1}(Ni)\,h^{-1}$ after 60 min (entry 23 and 24, Table 5).

The catalytic activity and selectivity for 1-butene of **5c** increased to $2.26\times10^5\ g\,mol^{-1}(Ni)\,h^{-1}$ and 97.1%, respectively (entry 26, Table 5) at 10 atm of ethylene pressure without $PPh_3$, whereas at 1 atm the catalytic activity and the selectivity for 1-butene did not change greatly when 10 equivalents of $PPh_3$ was introduced into the catalytic system (entry 27, Table 5), which means that both the $PPh_3$/Ni molar ratio and the concentration of $PPh_3$ in the reaction solution affect the catalytic properties. When the amount of $PPh_3$ was increased to 20 equivalents the catalytic activity of **5c** increased to $5.17\times10^6\ g\,mol^{-1}(Ni)\ h^{-1}$, with a lower selectivity for 1-butene (36.5%; entry 28, Table 5). Five other nickel complexes were therefore also investigated in the presence of 20 equivalents of $PPh_3$ at 10 atm of ethylene pressure. A higher catalytic activity and selectivity for 1-butene was obtained for each complex than at 1 atm, and the highest activity of $6.15\times10^6\ g\,mol^{-1}(Ni)\,h^{-1}$ was achieved with **2c**, with a selectivity of 50.2% for 1-butene.

 © 2007 Wiley-VCH Verlag GmbH & Co. KGaA, Weinheim 

In general, the selectivity for 1-butene increases with increasing ethylene pressure, probably due to a competition between chain transfer and chain isomerization, and a higher ethylene concentration thus favors the formation of 1-butene due to rapid chain transfer rather than chain isomerization.[27]

## Conclusions

A series of iron, cobalt, and nickel complexes bearing 2-imino-9-phenyl-1,10-phenanthroline ligands have been synthesized, characterized, and evaluated as catalyst precursors in ethylene oligomerization. Some iron complexes show good catalytic activities, with high selectivity for ethylene oligomerization [**1a**/MMAO: $2.69 \times 10^6$ g mol$^{-1}$(Fe) h$^{-1}$], upon treatment with MAO or MMAO. Unexpectedly, in contrast to previous results with other tridentate $N_3$ catalytic systems, the cobalt complexes generally show much higher activities and broader oligomer distributions than the corresponding iron analogues. The ligand environment and the reaction parameters play an important role in influencing both the catalytic activity and the oligomer distributions for iron and cobalt complexes. The highest activity of up to $7.33 \times 10^6$ g mol$^{-1}$(Co) h$^{-1}$ for ethylene oligomerization has been obtained with the catalytic system **5b**/MAO at 10 atm of ethylene pressure. $Et_2AlCl$ is a more effective co-catalyst for nickel complexes, and the addition of $PPh_3$ significantly improves the catalytic activity and prolong the catalyst lifetime. The addition of 20 equiv. of $PPh_3$ leads to higher catalytic activities at 10 atm of ethylene pressure.

## Experimental Section

**General:** All manipulations of air- and moisture-sensitive compounds were carried out under an atmosphere of nitrogen using standard Schlenk techniques. Melting points were measured with a digital electrothermal apparatus without calibration. IR spectra were recorded with a Perkin–Elmer FT-IR 2000 spectrometer for KBr discs in the range 4000–400 cm$^{-1}$. $^1$H and $^{13}$C NMR spectra were recorded with a Bruker DMX-300 or DMX-400 instrument with TMS as the internal standard. Elemental analyses were performed with a Flash EA1112 microanalyzer. GC analyses were performed with a Varian CP-3800 gas chromatograph equipped with a flame ionization detector and a 30-m (0.2-mm i.d., 0.25-μm film thickness) CP-Sil 5 CB capillary column. The yield of oligomers was calculated by referencing to the mass of solvent on the basis of the prerequisite that the mass of each fraction is approximately proportional to its integrated area in the GC trace.

Toluene, diethyl ether and thf were refluxed over sodium-benzophenone and distilled under nitrogen prior to use. Diethylaluminum chloride was purchased from Acros Chemicals. Methylaluminoxane (MAO, 1.46 M in toluene) and modified methylaluminoxane (MMAO-3A, 7% aluminum in heptane solution) were purchased from Akzo Corp (USA). All other chemicals were obtained commercially and used without further purification unless otherwise stated.

**Synthesis of 2-Acetyl-9-phenyl-1,10-phenanthroline (I)**

**2-(2-Methyl-1,3-dioxolan-2-yl)-1,10-phenanthroline:** A mixture of 2-acetyl-1,10-phenanthroline (2.230 g, 10.0 mmol), glycol (3.254 g, 52.4 mmol) and *p*-toluenesulfonic acid (206 mg) was refluxed in toluene (100 mL) for 18 h until no further formation of water was observed in a Dean–Stark trap. The solvent was then removed under reduced pressure and the residue was eluted with petroleum ether/ethyl acetate (1:2, v/v) on an alumina column. The second eluting fraction was collected and concentrated to give a slightly yellow solid in 50.0% yield (1.333 g). M.p. 119–121 °C. FT-IR (KBr disc): $\tilde{\nu}$ = 3054, 2993, 2980, 2938, 2900, 1619, 1589, 1552, 1505, 1490, 1476, 1445, 1391, 1376, 1256, 1232, 1204, 1147, 1129, 1106, 1029, 1009, 953, 855, 789, 752, 675 cm$^{-1}$. $^1$H NMR (400 MHz, $CDCl_3$): $\delta$ = 9.24 (d, $J$ = 4.4 Hz, 1 H, phen), 8.25 (d, $J$ = 8.4 Hz, 1 H, phen), 8.22 (d, $J$ = 8.4 Hz, 1 H, phen), 7.93 (d, $J$ = 8.4 Hz, 1 H, phen), 7.77 (s, 2 H, phen), 7.61 (dd, $J_1$ = 8.0 Hz, $J_2$ = 4.4 Hz, 1 H, phen), 4.18 (t, $J$ = 6.4 Hz, 2 H, $CH_2$), 4.01 (t, $J$ = 6.4 Hz, 2 H, $CH_2$), 1.98 (s, 3 H, $CH_3$) ppm. $^{13}$C NMR (100 MHz, $CDCl_3$): $\delta$ = 161.5, 150.5, 146.4, 145.8, 136.8, 136.0, 129.0, 128.1, 126.7, 126.3, 122.9, 119.5, 109.2, 65.2, 25.6 ppm. $C_{16}H_{14}N_2O_2$ (266.29): calcd. C 72.16, H 5.30, N 10.52; found C 72.18, H 5.23, N 11.00.

**2-Acetyl-9-phenyl-1,10-phenanthroline (I):** A phenyllithium solution was prepared by slowly adding a solution of bromobenzene (0.9 mL, 8.50 mmol) in diethyl ether (20 mL) to two equiv. of lithium (118 mg, 17.0 mmol) in diethyl ether (30 mL) at room temperature under nitrogen. The phenyllithium solution was then added dropwise to a suspension of 2-(2-methyl-1,3-dioxolan-2-yl)-1,10-phenanthroline (1.333 g, 5.00 mmol) in toluene (40 mL) at 0 °C and the initial yellow suspension turned dark brown. The resultant solution was stirred under nitrogen at 0 °C for an additional 3 h, then the reaction was quenched by slow addition of water (100 mL) and the mixture stirred. The yellow organic layer was separated and the aqueous layer was extracted several times with $CH_2Cl_2$. The organic phases were combined and dried with anhydrous sodium sulfate. After evaporation of the solvent the residue was purified on a silica column to give the pure product as a yellow oil. This oil was dissolved in 50 mL of acetone containing *p*-toluenesulfonic acid (170 mg) as a catalyst and refluxed for 15 h. The desired product was precipitated from the solution and collected by filtration as a pale-yellow solid in 47.5% yield (710 mg). M.p. 184–186 °C. FT-IR (KBr disc): $\tilde{\nu}$ = 3103, 3026, 2916, 1694, 1633, 1620, 1597, 1565, 1537, 1495, 1367, 1285, 1219, 1190, 1120, 1034, 1011, 888, 817, 766, 741, 678, 566 cm$^{-1}$. $^1$H NMR (300 MHz, $CDCl_3$): $\delta$ = 8.44 (d, $J$ = 7.2 Hz, 2 H, Ph), 8.34 (d, $J$ = 3.0 Hz, 2 H, phen), 8.30 (d, $J$ = 8.4 Hz, 1 H, phen), 8.17 (d, $J$ = 8.4 Hz, 1 H, phen), 7.88 (d, $J$ = 8.7 Hz, 1 H, phen), 7.78 (d, $J$ = 8.7 Hz, 1 H, phen), 7.59 (t, $J$ = 7.2 Hz, 2 H, Ph), 7.50 (t, $J$ = 7.2 Hz, 1 H, Ph), 3.14 (s, 3 H, $COCH_3$) ppm. $^{13}$C NMR (75 MHz, $CDCl_3$): $\delta$ = 200.3, 156.6, 152.3, 145.4, 144.8, 138.5, 136.5, 130.4, 129.3, 128.4, 128.1, 127.3, 127.0, 125.3, 119.7, 119.6, 25.2 ppm. $C_{20}H_{14}N_2O$ (298.34): calcd. C 80.52, H 4.73, N 9.39; found C 80.00, H 4.77, N 9.36.

**Synthesis of 2-Benzoyl-9-phenyl-1,10-phenanthroline (II):** A phenyllithium solution was prepared by slowly adding a solution of bromobenzene (3.2 mL, 30.5 mmol) in diethyl ether (20 mL) to two equiv. of lithium (439 mg, 63.2 mmol) in diethyl ether (30 mL) at room temperature under nitrogen. This phenyllithium solution was then added dropwise to a suspension of 2-cyano-1,10-phenanthroline (2.053 g, 10.0 mmol) in toluene (50 mL) at –78 °C and the mixture was slowly warmed to room temperature. After stirring for 12 h at room temperature, the reaction was quenched by slow addition of water (100 mL) and the mixture stirred. The red organic layer was separated and the aqueous layer was extracted several times with $CH_2Cl_2$. The organic phases were combined and dried with anhydrous sodium sulfate. After evaporation of the solvent the residue was purified on a silica column to give the pure product

 © 2007 Wiley-VCH Verlag GmbH & Co. KGaA, Weinheim 

as a yellow solid in 21.3% yield (1.245 g). M.p. 162–164 °C. FT-IR (KBr disc): $\tilde{\nu}$ = 3060, 3034, 1645, 1616, 1595, 1575, 1545, 1505, 1486, 1446, 1420, 1364, 1319, 1288, 1183, 1152, 1093, 1023, 944, 878, 865, 768, 716, 692 $cm^{-1}$. $^1H$ NMR (300 MHz, $CDCl_3$): $\delta$ = 8.93 (d, $J$ = 7.2 Hz, 2 H, Ph), 8.55–8.39 (m, 4 H), 8.30 (d, $J$ = 8.4 Hz, 1 H, phen), 8.16 (d, $J$ = 8.4 Hz, 1 H, phen), 7.89 (d, $J$ = 8.7 Hz, 1 H, phen), 7.81 (d, $J$ = 8.7 Hz, 1 H, phen), 7.72–7.62 (m, 3 H, Ph), 7.56–7.49 (m, 3 H, Ph) ppm. $^{13}C$ NMR (100 MHz, $CDCl_3$): $\delta$ = 191.4, 156.5, 153.4, 145.9, 144.6, 138.8, 136.7, 136.6, 132.7, 132.5, 129.8, 129.6, 128.6, 128.3, 127.8, 127.5, 127.3, 125.4, 122.6, 119.6 ppm. $C_{25}H_{16}N_2O$ (360.41): calcd. C 83.31, H 4.47, N 7.77; found C 82.94, H 4.45, N 7.73.

**Synthesis of Ligand 1:** A mixture of 2-acetyl-9-phenyl-1,10-phenanthroline (225 mg, 0.75 mmol), 2,6-dimethylaniline (184 mg, 1.50 mmol), and *p*-toluenesulfonic acid (80 mg) in toluene (20 mL) was refluxed for 24 h under $N_2$. The solvent was then evaporated under reduced pressure and the residue was eluted with petroleum ether/ethyl acetate (20:1, v/v) on an alumina column. The second fraction was collected and concentrated to give a yellow solid in 34.6% yield (105 mg). M.p. 190–192 °C. FT-IR (KBr disc): $\tilde{\nu}$ = 3041, 3018, 2914, 1635, 1605, 1590, 1546, 1506, 1485, 1467, 1362, 1293, 1204, 1118, 1091, 855, 761, 739, 687 $cm^{-1}$. $^1H$ NMR (300 MHz, $CDCl_3$): $\delta$ = 8.80 (d, $J$ = 8.4 Hz, 1 H, phen), 8.45 (d, $J$ = 7.5 Hz, 2 H, Ph), 8.34 (d, $J$ = 8.7 Hz, 2 H, phen), 8.18 (d, $J$ = 8.4 Hz, 1 H, phen), 7.85 (d, $J$ = 3.9 Hz, 2 H, phen), 7.56 (t, $J$ = 7.5 Hz, 2 H, Ph), 7.47 (t, $J$ = 7.5 Hz, 1 H, Ph), 7.11 (d, $J$ = 7.5 Hz, 2 H, Ar), 6.97 (t, $J$ = 7.5 Hz, 1 H, Ar), 2.62 (s, 3 H, $COCH_3$), 2.09 (s, 6 H, 2 Me) ppm. $^{13}C$ NMR (75 MHz, $CDCl_3$): $\delta$ = 168.0, 156.9, 155.8, 149.0, 146.0, 145.1, 139.2, 137.1, 136.5, 129.8, 129.6, 128.9, 127.9, 127.8, 127.5, 127.3, 126.1, 125.3, 123.1, 120.6, 119.9, 18.0, 16.7 ppm. $C_{28}H_{23}N_3$ (401.50): calcd. C 83.76, H 5.77, N 10.47; found C 83.69, H 5.76, N 10.40.

**Synthesis of Ligand 2:** Ligand **2** was prepared from 2-acetyl-9-phenyl-1,10-phenanthroline (446 mg, 1.50 mmol) and 2,6-diethylaniline (491 mg, 3.20 mmol) as a yellow solid in 44.2% yield (284 mg) in a similar manner to that described for ligand **1**. M.p. 181–183 °C. FT-IR (KBr disc): $\tilde{\nu}$ = 3060, 3037, 2960, 2929, 2868, 1639, 1608, 1589, 1546, 1507, 1486, 1452, 1418, 1369, 1296, 1258, 1194, 1119, 1099, 862, 828, 762, 740, 686 $cm^{-1}$. $^1H$ NMR (300 MHz, $CDCl_3$): $\delta$ = 8.80 (d, $J$ = 8.4 Hz, 1 H, phen), 8.45 (d, $J$ = 7.5 Hz, 2 H, Ph), 8.33 (d, $J$ = 8.4 Hz, 2 H, phen), 8.17 (d, $J$ = 8.4 Hz, 1 H, phen), 7.80 (d, $J$ = 3.9 Hz, 2 H, phen), 7.56 (t, $J$ = 7.5 Hz, 2 H, Ph), 7.47 (t, $J$ = 7.5 Hz, 1 H, Ph), 7.16 (d, $J$ = 7.2 Hz, 2 H, Ar), 7.07 (t, $J$ = 7.2 Hz, 1 H, Ar), 2.64 (s, 3 H, $COCH_3$), 2.42 (q, $J$ = 7.2 Hz, 4 H, 2 Et), 1.16 (t, $J$ = 7.2 Hz, 6 H, 2 Et) ppm. $^{13}C$ NMR (75 MHz, $CDCl_3$): $\delta$ = 167.7, 156.9, 155.9, 148.0, 146.0, 145.1, 139.2, 137.1, 136.5, 131.1, 129.8, 129.6, 128.9, 127.8, 127.5, 127.3, 126.1, 126.0, 123.4, 120.5, 119.8, 24.7, 17.0, 13.8 ppm. $C_{30}H_{27}N_3$ (429.56): calcd. C 83.88, H 6.34, N 9.78; found C 83.66, H 6.40, N 9.60.

**Synthesis of Ligand 3:** Ligand **3** was prepared from 2-acetyl-9-phenyl-1,10-phenanthroline (298 mg, 1.00 mmol) and 2,6-diisopropylaniline (448 mg, 2.50 mmol) as a yellow solid in 53.1% yield (243 mg) in a similar manner to that described for ligand **1**. M.p. 256–258 °C. FT-IR (KBr disc): $\tilde{\nu}$ = 3061, 2962, 2924, 2865, 1635, 1607, 1589, 1579, 1546, 1507, 1486, 1462, 1436, 1420, 1381, 1366, 1294, 1247, 1189, 1117, 1097, 860, 780, 761, 741, 685 $cm^{-1}$. $^1H$ NMR (400 MHz, $CDCl_3$): $\delta$ = 8.82 (d, $J$ = 8.4 Hz, 1 H, phen), 8.45 (d, $J$ = 7.6 Hz, 2 H, Ph), 8.33 (dd, $J_1$ = 8.4 Hz, $J_2$ = 4.7 Hz, 2 H, phen), 8.17 (d, $J$ = 8.4 Hz, 1 H, phen), 7.88 (d, $J$ = 4.0 Hz, 2 H, phen), 7.56 (t, $J$ = 7.6 Hz, 2 H, Ph), 7.47 (t, $J$ = 7.6 Hz, 1 H, Ph), 7.21 (d, $J$ = 7.6 Hz, 2 H, Ar), 7.13 (t, $J$ = 7.6 Hz, 1 H, Ar), 2.86 (sept, $J$ = 6.8 Hz, 2 H, 2 *i*Pr), 2.66 (s, 3 H, $COCH_3$), 1.19 (d, $J$ = 6.6 Hz, 6 H, *i*Pr), 1.17 (d, $J$ = 6.5 Hz, 6 H, *i*Pr) ppm. $^{13}C$ NMR (75 MHz, $CDCl_3$): $\delta$ = 167.7, 156.9, 155.8, 146.7, 146.0, 145.2, 139.2, 137.1, 136.5, 135.8, 129.9, 129.7, 129.0, 127.8, 127.5, 127.3, 126.1, 123.7, 123.1, 120.6, 119.9, 28.3, 23.3, 23.0, 17.3 ppm. $C_{32}H_{31}N_3$ (457.61): calcd. C 83.99, H 6.83, N 9.18; found C 84.00, H 6.84, N 8.98.

**Synthesis of Ligand 4:** 2-Benzoyl-9-phenyl-1,10-phenanthroline (760 mg, 2.10 mmol), 2,6-dimethylaniline (585 mg, 4.80 mmol), and *p*-toluenesulfonic acid (100 mg) were combined with tetraethyl silicate (5 mL) in a flask. The flask was equipped with a condenser and a Dean–Stark trap and the mixture was heated at about 130 °C for 36 h under $N_2$. Tetraethyl silicate was then removed under reduced pressure and the residue was eluted with petroleum ether/ethyl acetate (6:1, v/v) on an alumina column. The second fraction was collected and concentrated to give a yellow solid in 38.4% yield (376 mg). M.p. 142–144 °C. FT-IR (KBr disc): $\tilde{\nu}$ = 3055, 2943, 1616, 1589, 1577, 1544, 1505, 1484, 1441, 1368, 1319, 1290, 1207, 1088, 1024, 969, 858, 773, 765, 740, 716, 694 $cm^{-1}$. $^1H$ NMR (400 MHz, $CDCl_3$): $\delta$ = 8.87 (d, $J$ = 8.4 Hz, 1 H, phen), 8.37 (d, $J$ = 8.4 Hz, 1 H, phen), 8.26–8.24 (m, 3 H), 8.11 (d, $J$ = 8.4 Hz, 1 H, phen), 7.82 (s, 2 H, phen), 7.57 (d, $J$ = 8.0 Hz, 2 H, Ph), 7.46 (m, 4 H, Ph), 7.38 (t, $J$ = 7.2 Hz, 2 H, Ph), 6.96 (d, $J$ = 7.2 Hz, 2 H, Ar), 6.86 (t, $J$ = 7.2 Hz, 1 H, Ar), 2.12 (s, 6 H, 2 Me) ppm. $^{13}C$ NMR (100 MHz, $CDCl_3$): $\delta$ = 166.1, 155.9, 155.7, 148.2, 145.7, 144.7, 138.5, 136.3, 136.0, 135.4, 129.6, 129.2, 129.1, 128.9, 128.3, 127.9, 127.3, 127.0, 126.8, 126.7, 125.5, 125.2, 122.7, 121.7, 118.9, 18.2 ppm. $C_{33}H_{25}N_3$ (463.57): calcd. C 85.50, H 5.44, N 9.06; found C 85.14, H 5.47, N 8.94.

**Synthesis of Ligand 5:** Ligand **5** was prepared from 2-benzoyl-9-phenyl-1,10-phenanthroline (570 mg, 1.58 mmol) and 2,6-diethylaniline (498 mg, 3.27 mmol) as a yellow solid in 72.8% yield (556 mg) in a similar manner to that described for ligand **4**. M.p. 187–189 °C. FT-IR (KBr disc): $\tilde{\nu}$ = 3060, 3034, 2962, 2918, 1618, 1586, 1542, 1504, 1485, 1440, 1363, 1294, 1200, 1090, 965, 869, 763, 697 $cm^{-1}$. $^1H$ NMR (400 MHz, $CDCl_3$): $\delta$ = 8.85 (d, $J$ = 8.0 Hz, 1 H, phen), 8.37–8.22 (m, 4 H), 8.09 (d, $J$ = 8.0 Hz, 1 H, phen), 7.80 (s, 2 H, phen), 7.58 (s, 2 H, Ph), 7.45–7.36 (m, 6 H, Ph), 7.01–6.97 (m, 3 H, Ar), 2.61 (q, $J$ = 7.2 Hz, 2 H, Et), 2.34 (q, $J$ = 7.2 Hz, 2 H, Et), 1.16 (t, $J$ = 7.2 Hz, 6 H, 2 Et) ppm. $^{13}C$ NMR (100 MHz, $CDCl_3$): $\delta$ = 165.7, 156.2, 156.1, 147.6, 146.1, 145.1, 138.9, 136.7, 136.4, 135.4, 131.1, 130.3, 129.6, 129.2, 128.7, 128.5, 127.7, 127.5, 127.3, 127.2, 125.8, 125.5, 123.4, 122.1, 119.2, 24.5, 13.5 ppm. $C_{35}H_{29}N_3$ (491.62): calcd. C 85.51, H 5.95, N 8.55; found C 85.03, H 5.94, N 8.48.

**Synthesis of Ligand 6:** Ligand **6** was prepared from 2-benzoyl-9-phenyl-1,10-phenanthroline (394 mg, 1.09 mmol) and 2,6-diisopropylaniline (433 mg, 2.44 mmol) as a yellow solid in 74.0% yield (420 mg) in a similar manner to that described for ligand **4**. M.p. 170–171 °C. FT-IR (KBr disc): $\tilde{\nu}$ = 3063, 2958, 2860, 1611, 1588, 1544, 1506, 1487, 1463, 1430, 1358, 1291, 1194, 1091, 966, 858, 777, 757, 701 $cm^{-1}$. $^1H$ NMR (300 MHz, $CDCl_3$): $\delta$ = 8.84 (d, $J$ = 8.4 Hz, 1 H, phen), 8.38–8.24 (m, 4 H), 8.11 (d, $J$ = 8.4 Hz, 1 H, phen), 7.82 (s, 2 H, phen), 7.62 (m, 2 H, Ph), 7.49–7.39 (m, 6 H, Ph), 7.04 (m, 3 H, Ar), 3.00 (sept, $J$ = 6.8 Hz, 2 H, 2 *i*Pr), 1.19 (d, $J$ = 6.8 Hz, 6 H, *i*Pr), 0.97 (d, $J$ = 6.8 Hz, 6 H, *i*Pr) ppm. $^{13}C$ NMR (100 MHz, $CDCl_3$): $\delta$ = 164.9, 155.9, 145.7, 144.6, 138.5, 136.3, 136.0, 135.2, 134.5, 130.3, 129.1, 128.7, 128.4, 128.2, 128.1, 127.2, 127.1, 126.9, 126.7, 125.4, 123.2, 122.4, 121.8, 111.8, 28.1, 23.7, 21.6 ppm. $C_{37}H_{33}N_3$ (519.68): calcd. C 85.51, H 6.40, N 8.09; found C 84.91, H 6.36, N 7.84.

**Synthesis of Iron Complexes 1a–6a. General Procedure:** The ligand (0.20 mmol) and one equiv. of $FeCl_2{\cdot}4H_2O$ (0.20 mmol) were

 © 2007 Wiley-VCH Verlag GmbH & Co. KGaA, Weinheim 

placed in a Schlenk tube, which was purged three times with nitrogen and then charged with thf. The reaction mixture was then stirred at room temperature for 9 h. The resulting precipitate was filtered, washed with diethyl ether, and dried in vacuo. All the iron(II) complexes were isolated in high yield.

**Complex 1a:** Isolated as a green powder in 98.4% yield (104 mg). FT-IR (KBr disc): $\tilde{\nu}$ = 3059, 2953, 2918, 2867, 1615, 1590, 1555, 1504, 1491, 1468, 1451, 1435, 1374, 1299, 1205, 865, 792, 772, 745, 702 $cm^{-1}$. $C_{28}H_{23}Cl_2FeN_3 \cdot 1/2CH_2Cl_2$ (570.72): calcd. C 59.98, H 4.24, N 7.36; found C 59.61, H 4.34, N 7.28.

**Complex 2a:** Isolated as a green powder in 95.9% yield (107 mg). FT-IR (KBr disc): $\tilde{\nu}$ = 3063, 2966, 2929, 2872, 1617, 1584, 1558, 1504, 1490, 1442, 1374, 1289, 1243, 1205, 1193, 1152, 1141, 1060, 859, 786, 759, 744, 701 $cm^{-1}$. $C_{30}H_{27}Cl_2FeN_3$ (556.31): calcd. C 64.77, H 4.89, N 7.55; found C 64.26, H 4.59, N 7.50.

**Complex 3a:** Isolated as a green powder in 66.2% yield (78 mg). FT-IR (KBr disc): $\tilde{\nu}$ = 3062, 2969, 2926, 2865, 1611, 1590, 1557, 1501, 1490, 1463, 1440, 1374, 1330, 1286, 1247, 1185, 1152, 1138, 870, 786, 748, 701 $cm^{-1}$. $C_{32}H_{31}Cl_2FeN_3$ (584.36): calcd. C 65.77, H 5.35, N 7.19; found C 65.15, H 5.32, N 6.95.

**Complex 4a:** Isolated as a gray-green powder in 86.9% yield (103 mg). FT-IR (KBr disc): $\tilde{\nu}$ = 3056, 2922, 1620, 1588, 1549, 1489, 1445, 1368, 1300, 1212, 1155, 1001, 863, 774, 744, 703 $cm^{-1}$. $C_{33}H_{25}Cl_2FeN_3 \cdot H_2O$ (608.34): calcd. C 65.15, H 4.47, N 6.91; found C 65.12, H 4.11, N 6.85.

**Complex 5a:** Isolated as a brown powder in 79.8% yield (99 mg). FT-IR (KBr disc): $\tilde{\nu}$ = 3061, 2966, 2874, 1594, 1553, 1490, 1444, 1368, 1291, 1261, 1107, 1059, 1000, 868, 781, 702 $cm^{-1}$. $C_{35}H_{29}Cl_2FeN_3$ (618.38): calcd. C 67.98, H 4.73, N 6.80; found C 67.94, H 4.78, N 6.57.

**Complex 6a:** Isolated as a green powder in 86.6% yield (112 mg). FT-IR (KBr disc): $\tilde{\nu}$ = 3031, 2959, 2866, 1620, 1587, 1550, 1488, 1459, 1436, 1364, 1319, 1274, 1206, 995, 872, 850, 704 $cm^{-1}$. $C_{37}H_{33}Cl_2FeN_3$ (646.43): calcd. C 68.75, H 5.15, N 6.50; found C 68.42, H 5.23, N 6.59.

**Synthesis of Cobalt Complexes 1b–6b and Nickel Complexes 1c–6c. General Procedure:** The ligand (0.20 mmol) and one equiv. of $CoCl_2$ or $NiCl_2 \cdot 6H_2O$ (0.20 mmol) were placed in a Schlenk tube along with anhydrous ethanol. The reaction mixture was then stirred at room temperature for 9 h. The resulting precipitate was filtered, washed with diethyl ether, and dried in vacuo. All the complexes were isolated in high yield.

**Complex 1b:** Isolated as a green powder in 65.6% yield (70 mg). FT-IR (KBr disc): $\tilde{\nu}$ = 3063, 2945, 2914, 1619, 1585, 1557, 1504, 1490, 1451, 1437, 1374, 1290, 1256, 1206, 1142, 989, 919, 865, 791, 772, 745, 700, 653, 609 $cm^{-1}$. $C_{28}H_{23}Cl_2CoN_3 \cdot H_2O$ (549.36): calcd. C 61.22, H 4.59, N 7.65; found C 61.46, H 4.34, N 7.24.

**Complex 2b:** Isolated as a green powder in 80.3% yield (91 mg). FT-IR (KBr disc): $\tilde{\nu}$ = 3061, 2969, 2924, 2865, 1613, 1582, 1557, 1501, 1489, 1463, 1441, 1375, 1330, 1288, 1185, 1153, 869, 786, 749, 700 $cm^{-1}$. $C_{30}H_{27}Cl_2CoN_3$ (559.39): calcd. C 64.41, H 4.86, N 7.51; found C 64.25, H 4.92, N 7.27.

**Complex 3b:** Isolated as a green powder in 85.6% yield (103 mg). FT-IR (KBr disc): $\tilde{\nu}$ = 3450, 3062, 2964, 2932, 2875, 1618, 1585, 1558, 1504, 1490, 1441, 1375, 1290, 1193, 859, 787, 760, 745, 701 $cm^{-1}$. $C_{32}H_{31}Cl_2CoN_3$ (587.45): calcd. C 65.43, H 5.32, N 7.15; found C 64.48, H 5.55, N 6.61.

**Complex 4b:** Isolated as a red-brown powder in 80.2% yield (95 mg). FT-IR (KBr disc): $\tilde{\nu}$ = 3057, 2919, 1612, 1597, 1555, 1490, 1445, 1371, 1317, 1289, 1213, 999, 863, 774, 748, 721, 703 $cm^{-1}$. $C_{33}H_{25}Cl_2CoN_3 \cdot CH_2Cl_2$ (678.34): calcd. C 60.20, H 4.01, N 6.19; found C 60.25, H 4.02, N 6.28.

**Complex 5b:** Isolated as a red-brown powder in 77.6% yield (84 mg). FT-IR (KBr disc): $\tilde{\nu}$ = 3063, 2963, 2934, 2875, 1613, 1596, 1552, 1498, 1490, 1442, 1371, 1319, 1288, 1108, 995, 872, 782, 751, 720, 701 $cm^{-1}$. $C_{35}H_{29}Cl_2CoN_3 \cdot CH_2Cl_2$ (706.40): calcd. C 61.21, H 4.42, N 5.95; found C 60.68, H 4.28, N 5.63.

**Complex 6b:** Isolated as a red-brown powder in 78.4% yield (103 mg). FT-IR (KBr disc): $\tilde{\nu}$ = 3058, 3032, 2959, 2924, 2865, 1619, 1599, 1552, 1489, 1437, 1370, 1319, 1274, 1207, 1100, 995, 873, 850, 759, 718, 652 $cm^{-1}$. $C_{37}H_{33}Cl_2CoN_3 \cdot CH_2Cl_2$ (734.45): calcd. C 62.14, H 4.80, N 5.72; found C 62.17, H 4.82, N 5.54.

**Complex 1c:** Isolated as an orange powder in 89.3% yield (95 mg). FT-IR (KBr disc): $\tilde{\nu}$ = 3445, 3056, 1611, 1587, 1556, 1503, 1489, 1453, 1376, 1294, 1204, 1148, 862, 793, 773, 745, 702 $cm^{-1}$. $C_{28}H_{23}Cl_2N_3Ni \cdot 1/2CH_2Cl_2$ (573.57): calcd. C 59.68, H 4.22, N 7.33; found C 59.89, H 4.44, N 7.20.

**Complex 2c:** Isolated as an orange powder in 89.7% yield (100 mg). FT-IR (KBr disc): $\tilde{\nu}$ = 3442, 3062, 2958, 2871, 1616, 1584, 1559, 1502, 1489, 1442, 1377, 1302, 1292, 1192, 1060, 859, 787, 762, 744, 701 $cm^{-1}$. $C_{30}H_{27}Cl_2N_3Ni \cdot 1/2CH_2Cl_2$ (601.62): calcd. C 60.89, H 4.69, N 6.98; found C 60.46, H 4.96, N 6.67.

**Complex 3c:** Isolated as an orange powder in 76.5% yield (90 mg). FT-IR (KBr disc): $\tilde{\nu}$ = 3426, 3060, 2967, 2865, 1609, 1586, 1558, 1489, 1443, 1378, 1330, 1293, 1185, 1151, 869, 787, 761, 749, 702 $cm^{-1}$. $C_{32}H_{31}Cl_2N_3Ni \cdot CH_2Cl_2$ (672.14): calcd. C 58.97, H 4.95, N 6.25; found C 58.44, H 5.02, N 6.20.

**Complex 4c:** Isolated as a yellow powder in 96.0% yield (114 mg). FT-IR (KBr disc): $\tilde{\nu}$ = 3388, 1618, 1592, 1554, 1486, 1445, 1378, 1290, 1212, 1057, 1038, 1004, 868, 778, 754, 723, 703 $cm^{-1}$. $C_{33}H_{25}Cl_2N_3Ni \cdot H_2O$ (611.19): calcd. C 64.85, H 4.45, N 6.88; found C 65.09, H 4.16, N 6.82.

**Complex 5c:** Isolated as a orange powder in 90.6% yield (113 mg). FT-IR (KBr disc): $\tilde{\nu}$ = 3061, 2963, 1597, 1558, 1489, 1443, 1377, 1291, 1209, 1148, 1108, 1065, 1040, 1004, 867, 784, 706 $cm^{-1}$. $C_{35}H_{29}Cl_2N_3Ni \cdot 1/2CH_2Cl_2$ (663.69): calcd. C 64.24, H 4.56, N 6.33; found C 64.50, H 4.75, N 6.60.

**Complex 6c:** Isolated as an orange powder in 75.1% yield (98 mg). FT-IR (KBr disc): $\tilde{\nu}$ = 3440, 3057, 2962, 2866, 1621, 1595, 1554, 1490, 1439, 1377, 1322, 1293, 1207, 1151, 1101, 1024, 872, 784, 763, 707 $cm^{-1}$. $C_{37}H_{33}Cl_2N_3Ni \cdot 1/2CH_2Cl_2$ (691.75): calcd. C 65.11, H 4.95, N 6.07; found C 65.01, H 5.04, N 5.85.

**General Procedure for Ethylene Oligomerization at 1 atm of Ethylene Pressure:** A flame-dried, three-necked flask was loaded with the catalyst precursor and purged three times with nitrogen. Ethylene was then charged in the flask along with freshly distilled toluene and the mixture stirred for 10 min under 1 atm of ethylene pressure. The reaction temperature was controlled with a water bath and the required amount of co-catalyst was then injected with a syringe. The reaction mixture was stirred for the required time and then the reaction was quenched by addition of 5% aqueous hydrogen chloride. The contents and distributions of oligomers were determined by GC.

**General Procedure for Ethylene Oligomerization at 10 Atm of Ethylene Pressure:** A 250-mL stainless steel reactor equipped with a mechanical stirrer and a temperature controller was heated in vacuo for at least 2 h at above 80 °C, then cooled to the required reaction temperature under ethylene atmosphere and charged with toluene, the desired amount of co-catalyst, and a toluene solution of the

 © 2007 Wiley-VCH Verlag GmbH & Co. KGaA, Weinheim 

Table 6. Crystal data and structure refinement for **1b**, **2**, **2a**, and **4b**.

| | **1b** | **2** | **2a** | **4b** |
|---|---|---|---|---|
| CCDC number | 650187 | 650185 | 650186 | 650188 |
| Formula | $C_{28}H_{23}Cl_2CoN_3O$ | $C_{30}H_{27}N_3$ | $C_{30}H_{27}C_{12}FeN_3O_{0.5}$ | $C_{33}H_{25}Cl_2CoN_3{\cdot}CH_2Cl_2$ |
| Formula weight | 547.32 | 429.55 | 564.30 | 678.32 |
| Temperature [K] | 293(2) | 294(2) | 293(2) | 294(2) |
| Wavelength [Å] | 0.71073 | 0.71073 | 0.71073 | 0.71073 |
| Crystal system | monoclinic | triclinic | triclinic | triclinic |
| Space group | $C2/c$ | $P\bar{1}$ | $P\bar{1}$ | $P\bar{1}$ |
| $a$ [Å] | 25.9027(8) | 7.869(2) | 13.3880(6) | 8.6610(14) |
| $b$ [Å] | 16.9116(6) | 11.840(3) | 14.0560(6) | 9.5741(15) |
| $c$ [Å] | 16.5805(5) | 13.547(4) | 14.9754(6) | 19.014(3) |
| $\alpha$ [°] | 90 | 105.675(5) | 83.065(3) | 81.376(2) |
| $\beta$ [°] | 128.031(2) | 94.203(5) | 86.114(3) | 88.499(3) |
| $\gamma$ [°] | 90 | 99.069(5) | 78.191(3) | 86.065(3) |
| $V$ [Å$^3$] | 5721.0(3) | 1191.1(6) | 2735.6(2) | 1555.0(4) |
| $Z$ | 8 | 2 | 4 | 2 |
| $D_{calcd.}$ [g cm$^{-3}$] | 1.271 | 1.198 | 1.370 | 1.449 |
| $\mu$ [mm$^{-1}$] | 0.810 | 0.071 | 0.772 | 0.925 |
| $F(000)$ | 2248 | 456 | 1168 | 694 |
| Crystal size [mm] | 0.26 × 0.20 × 0.15 | 0.24 × 0.15 × 0.12 | 0.20 × 0.14 × 0.12 | 0.25 × 0.12 × 0.08 |
| $\theta$ range [°] | 2.46–28.32 | 1.82–26.49 | 1.37–28.36 | 1.08–26.45 |
| Limiting indices | –34 ≤ h ≤ 34 | –9 ≤ $h$ ≤ 5 | –17 ≤ h ≤ 17 | –10 ≤ h ≤ 7 |
| | –22 ≤ k ≤ 22 | –14 ≤ $k$ ≤ 14 | –18 ≤ k ≤ 18 | –10 ≤ k ≤ 11 |
| | –21 ≤ l ≤ 22 | –16 ≤ $l$ ≤ 15 | –19 ≤ l ≤ 19 | –23 ≤ l ≤ 19 |
| % Completeness to $\theta$ | 99.1 ($\theta$ = 28.32°) | 97.7 ($\theta$ = 26.49°) | 98.8 ($\theta$ = 28.36°) | 97.7 ($\theta$ = 26.45°) |
| Absorption correction | empirical | empirical | empirical | empirical |
| No. of parameters | 334 | 302 | 667 | 379 |
| Goodness-of-fit on $F^2$ | 0.931 | 0.981 | 0.734 | 1.018 |
| $R1$ [$I > 2\sigma(I)$] | 0.0672 | 0.0538 | 0.0494 | 0.0522 |
| $wR2$ | 0.1895 | 0.1183 | 0.1191 | 0.1208 |
| Largest diff. peak/hole [e Å$^{-3}$] | 0.915/–0.349 | 0.121/–0.171 | 0.381/–0.374 | 0.491/–0.499 |

Table 7. Crystal data and structure refinement for **1c**, **5c**, and **6b**.

| | **1c** | **5c** | **6b** |
|---|---|---|---|
| CCDC number | 650190 | 650191 | 650189 |
| Formula | $C_{28}H_{23}Cl_2N_3Ni{\cdot}CH_2Cl_2$ | $C_{35}H_{29}Cl_2N_3Ni{\cdot}2CH_2Cl_2$ | $C_{37}H_{33}Cl_2CoN_3{\cdot}CH_2Cl_2$ |
| Formula weight | 616.03 | 791.07 | 734.42 |
| Temperature [K] | 293(2) | 293(2) | 293(2) |
| Wavelength [Å] | 0.71073 | 0.71073 | 0.71073 |
| Crystal system | monoclinic | triclinic | triclinic |
| Space group | $P2_1/c$ | $P\bar{1}$ | $P\bar{1}$ |
| $a$ [Å] | 18.870(4) | 9.2599(4) | 9.2300(18) |
| $b$ [Å] | 9.7077(19) | 9.6246(4) | 10.254(2) |
| $c$ [Å] | 15.550(3) | 20.9828(9) | 17.912(4) |
| $\alpha$ [°] | 90 | 97.054(2) | 96.51(3) |
| $\beta$ [°] | 96.26(3) | 95.194(2) | 90.33(3) |
| $\gamma$ [°] | 90 | 98.629(2) | 92.04(3) |
| $V$ [Å$^3$] | 2831.6(10) | 1823.54(13) | 1683.2(6) |
| $Z$ | 4 | 2 | 2 |
| $D_{calcd.}$ [g cm$^{-3}$] | 1.445 | 1.441 | 1.449 |
| $\mu$ [mm$^{-1}$] | 1.086 | 1.003 | 0.860 |
| $F(000)$ | 1264 | 812 | 758 |
| Crystal size [mm] | 0.26 × 0.19 × 0.11 | 0.31 × 0.22 × 0.20 | 0.30 × 0.18 × 0.12 |
| $\theta$ range [°] | 2.17–25.01 | 0.98–28.35 | 1.14–26.47 |
| Limiting indices | –19 ≤ $h$ ≤ 22 | –12 ≤ $h$ ≤ 12 | –11 ≤ $h$ ≤ 11 |
| | –11 ≤ $k$ ≤ 1 | –10 ≤ $k$ ≤ 12 | –12 ≤ $k$ ≤ 10 |
| | –18 ≤ $l$ ≤ 18 | –27 ≤ $l$ ≤ 27 | –17 ≤ $l$ ≤ 22 |
| % Completeness to $\theta$ | 100.0 ($\theta$ = 25.01°) | 98.7 ($\theta$ = 28.35°) | 97.4 ($\theta$ = 26.47°) |
| Absorption correction | empirical | empirical | empirical |
| No. of parameters | 334 | 424 | 415 |
| Goodness-of-fit on $F^2$ | 1.00 | 0.87 | 1.038 |
| $R1$ [$I > 2\sigma(I)$] | 0.0917 | 0.0614 | 0.0452 |
| $wR2$ | 0.1527 | 0.1661 | 0.1048 |
| Largest diff. peak/hole [e Å$^{-3}$] | 0.360/–0.407 | 0.540/–0.531 | 0.697/–0.629 |

 © 2007 Wiley-VCH Verlag GmbH & Co. KGaA, Weinheim 

catalyst precursor; the total volume was 100 mL. The reactor was sealed and pressurized to 10 atm of ethylene pressure at the required reaction temperature, and the ethylene pressure was maintained with a feed of ethylene. After the required time the pressure was released. A small amount of the reaction solution was collected and the reaction quenched by addition of 5% aqueous hydrogen chloride. The organic layer was analyzed by GC to determine the composition and mass distribution of the oligomers obtained. Finally, the remaining reaction solution was quenched with 5% hydrochloric acid in ethanol.

**X-ray Crystallography:** Single-crystal X-ray diffraction studies for **1b**, **1c**, **2a**, and **5c** were carried out with a Bruker P4 diffractometer with graphite-monochromated Mo-$K_\alpha$ radiation ($\lambda$ = 0.71073 Å) at 293(2) K. Intensity data for crystals of **2**, **4b** and **6b** were collected with a Bruker SMART 1000 CCD diffractometer with graphite-monochromated Mo-$K_\alpha$ radiation ($\lambda$ = 0.71073 Å). Cell parameters were obtained by global refinement of the positions of all collected reflections. Intensities were corrected for Lorentz and polarization effects and empirical absorption. The structures were solved by direct methods and refined by full-matrix least-squares on $F^2$. All non-hydrogen atoms were refined anisotropically. All hydrogen atoms were placed in calculated positions. Structure solution and refinement were performed with the SHELXL-97 package.[28] Crystallographic data and processing parameters for **1b**, **1c**, **2**, **2a**, **4b**, **5c**, and **6b** are summarized in Tables 6 and 7.

CCDC-650185 to -650191 contain the supplementary crystallographic data for this paper, which could be obtained free of charge from the Cambridge Crystallographic Data Centre via www.ccdc.cam.ac.uk/data_request/cif.

## Acknowledgments

This project was supported by the National Natural Science Foundation of China (grant nos. 20473099 and 20674089). We thank Mr. Saliu Alao Amolegbe (a CAS-TWAS Postgraduate Fellow from Nigeria) for English corrections.

[1] a) D. Vogt, *Applied Homogeneous Catalysis with Organometallic Compounds* (Eds.: B. Cornils, W. A. Herrmann), VCH, Weinheim, **2002**, vol. 1, p. 240–253; b) A. M. Al-Jarallah, J. A. Anabtawi, M. A. B. Siddiqui, A. M. Aitani, A. W. Al-Sa'doun, *Catal. Today* **1992**, *14*, 1–121.

[2] a) W. Keim, F. H. Kowaldt, R. Goddard, C. Krüger, *Angew. Chem. Int. Ed. Engl.* **1978**, *17*, 466–467; b) W. Keim, *Angew. Chem. Int. Ed. Engl.* **1990**, *29*, 235–244; c) P. Braunstein, Y. Chauvin, S. Mercier, L. Saussine, A. D. Cian, J. Fisher, *J. Chem. Soc. Chem. Commun.* **1994**, 2203–2204; d) J. Heinicke, M. He, A. Dal, H.-F. Klein, O. Hetche, W. Keim, U. Flörke, H.-J. Haupt, *Eur. J. Inorg. Chem.* **2000**, 431–440.

[3] a) G. J. P. Britovsek, V. C. Gibson, D. F. Wass, *Angew. Chem. Int. Ed.* **1999**, *38*, 428–447; b) S. D. Ittel, L. K. Johnson, M. Brookhart, *Chem. Rev.* **2000**, *100*, 1169–1203; c) V. C. Gibson, S. K. Spitzmessor, *Chem. Rev.* **2003**, *103*, 283–316; d) W. Zhang, W. Zhang, W.-H. Sun, *Prog. Chem.* **2005**, *17*, 310–319; e) S. Jie, S. Zhang, W.-H. Sun, *Petrochem. Tech. (Shiyou Huagong)* **2006**, *35*, 295–300.

[4] a) C. Bianchini, G. Giambastiani, I. G. Rios, G. Mantovani, A. Meli, A. M. Segarra, *Coord. Chem. Rev.* **2006**, *250*, 1391–1418 and references therein; b) V. C. Gibson, C. Redshaw, G. A. Solan, *Chem. Rev.* **2007**, *107*, 1745–1776 and references therein.

[5] a) F. Speiser, P. Braunstein, L. Saussine, *Acc. Chem. Res.* **2005**, *38*, 784–793; b) W.-H. Sun, D. Zhang, S. Zhang, S. Jie, J. Hou, *Kinet. Catal.* **2006**, *47*, 278–283.

[6] a) L. K. Johnson, C. M. Killian, M. Brookhart, *J. Am. Chem. Soc.* **1995**, *117*, 6414–6415; b) D. P. Gates, S. A. Svejda, E. Oñate, C. M. Killian, L. K. Johnson, P. S. White, M. Brookhart, *Macromolecules* **2000**, *33*, 2320–2334.

[7] a) X. Tang, W.-H. Sun, T. Gao, J. Hou, J. Chen, W. Chen, *J. Organomet. Chem.* **2005**, *690*, 1570–1580; b) Q.-Z. Yang, A. Kermagoret, M. Agostinho, O. Siri, P. Braunstein, *Organometallics* **2006**, *25*, 5518–5527.

[8] F. Speiser, P. Braunstein, L. Saussine, *Dalton Trans.* **2004**, 1539–1545.

[9] a) J. Hou, W.-H. Sun, S. Zhang, H. Ma, Y. Deng, X. Lu, *Organometallics* **2006**, *25*, 236–244; b) C. Zhang, W.-H. Sun, Z.-X. Wang, *Eur. J. Inorg. Chem.* **2006**, *23*, 4895–4902.

[10] a) D. M. Dawson, D. A. Walker, M. Thornton-Pett, M. Bochmann, *J. Chem. Soc. Dalton Trans.* **2000**, 459–466; b) S. Al-Benna, M. J. Sarsfield, M. Thornton-Pett, D. Ormsby, P. J. Maddox, P. Bres, M. Bochmann, *J. Chem. Soc. Dalton Trans.* **2000**, 4247–4257; c) F. A. Kunrath, R. F. de Souza, O. L. Casagrande Jr, N. R. Brooks, V. G. Young Jr, *Organometallics* **2003**, *22*, 4739–4743; d) N. Ajellal, M. C. A. Kuhn, A. D. G. Boff, M. Hörner, C. M. Thomas, J.-F. Carpentier, O. L. Casagrande Jr, *Organometallics* **2006**, *25*, 1213–1216.

[11] L. Wang, W.-H. Sun, L. Han, H. Yang, Y. Hu, X. Jin, *J. Organomet. Chem.* **2002**, *658*, 62–70.

[12] W.-H. Sun, S. Zhang, S. Jie, W. Zhang, Y. Li, H. Ma, J. Chen, K. Wedeking, R. Fröhlich, *J. Organomet. Chem.* **2006**, *691*, 4196–4203.

[13] M. Zhang, S. Zhang, P. Hao, S. Jie, W.-H. Sun, P. Li, X. Lu, *Eur. J. Inorg. Chem.* **2007**, 3816.

[14] a) P. Hao, S. Zhang, W.-H. Sun, Q. Shi, S. Adewuyi, X. Lu, P. Li, *Organometallics* **2007**, *26*, 2439–2446; b) S. Adewuyi, G. Li, S. Zhang, W. Wang, P. Hao, W.-H. Sun, N. Tang, J. Yi, *J. Organomet. Chem.* **2007**, *692*, 3532–3541.

[15] a) S. Zhang, I. Vystorop, Z. Tang, W.-H. Sun, *Organometallics* **2007**, *26*, 2456–2460; b) S. Zhang, W.-H. Sun, X. Kuang, I. Vystorop, J. Yi, *J. Organomet. Chem.* **2007**, *692*, 5307–5316; c) W.-H. Sun, P. Hao, S. Zhang, Q. Shi, W. Zuo, X. Tang, *Organometallics* **2007**, *26*, 2720–2734; d) W.-H. Sun, P. Hao, G. Li, S. Zhang, W. Wang, J. Yi, M. Asma, N. Tang, *J. Organomet. Chem.* **2007**, *692*, 4506–4518.

[16] a) B. L. Small, M. Brookhart, A. M. A. Bennett, *J. Am. Chem. Soc.* **1998**, *120*, 4049–4050; b) B. L. Small, M. Brookhart, *J. Am. Chem. Soc.* **1998**, *120*, 7143–7144; c) G. J. P. Britovsek, V. C. Gibson, B. S. Kimberley, P. J. Maddox, S. J. McTavish, G. A. Solan, A. J. P. White, D. J. Williams, *Chem. Commun.* **1998**, 849–850; d) G. J. P. Britovsek, M. Bruce, V. C. Gibson, B. S. Kimberley, P. J. Maddox, S. Mastroianni, S. J. McTavish, C. Redshaw, G. A. Solan, S. Stromberg, A. J. P. White, D. J. Williams, *J. Am. Chem. Soc.* **1999**, *121*, 8728–8740.

[17] a) G. J. P. Britovsek, V. C. Gibson, O. D. Hoarau, S. K. Spitzmesser, A. J. P. White, D. J. Williams, *Inorg. Chem.* **2003**, *42*, 3454–3465; b) V. C. Gibson, S. K. Spitzmesser, A. J. P. White, D. J. Williams, *Dalton Trans.* **2003**, 2718–2727; c) R. Cowdell, C. J. Davies, S. J. Hilton, J.-D. Maréchal, G. A. Solan, O. Thomas, J. Fawcett, *Dalton Trans.* **2004**, 3231–3240.

[18] a) G. J. P. Britovsek, S. P. D. Baugh, O. Hoarau, V. C. Gibson, D. F. Wass, A. J. P. White, D. J. Williams, *Inorg. Chim. Acta* **2003**, *345*, 279–291; b) Y. Nakayama, Y. Baba, H. Yasuda, K. Kawakita, N. Ueyama, *Macromolecules* **2003**, *36*, 7953–7958; c) C. J. Davies, S. J. Hilton, G. A. Solan, W. Stannard, J. Fawcett, *Polyhedron* **2005**, *24*, 2017–2026; d) J. D. A. Pelletier, Y. D. M. Champouret, J. Cadarso, L. Clowes, M. Ganete, K. Singh, V. Thanarajasingham, G. A. Solan, *J. Organomet. Chem.* **2006**, *691*, 4114–4123.

[19] a) W.-H. Sun, S. Jie, S. Zhang, W. Zhang, Y. Song, H. Ma, J. Chen, K. Wedeking, R. Fröhlich, *Organometallics* **2006**, *25*, 666–677; b) S. Jie, S. Zhang, W.-H. Sun, X. Kuang, T. Liu, J. Guo,16961 *J. Mol. Catal. A: Chem.* **2007**, *269*, 85–96; c) S. Zhang, S. Jie, Q. Shi, W.-H. Sun, *J. Mol. Catal. A: Chem.* **2007**, *276*, 174–183.

 © 2007 Wiley-VCH Verlag GmbH & Co. KGaA, Weinheim 

[20] S. Jie, S. Zhang, K. Wedeking, W. Zhang, H. Ma, X. Lu, Y. Deng, W.-H. Sun, *C. R. Chim.* **2006**, *9*, 1500–1509.
[21] E. J. Corey, A. L. Borror, T. Foglia, *J. Org. Chem.* **1965**, *30*, 288–290.
[22] A. J. Showler, P. A. Darley, *Chem. Rev.* **1967**, *67*, 427–440.
[23] C. Dietrich-Buchecker, B. Colasson, D. Jouvenot, J.-P. Sauvage, *Chem. Eur. J.* **2005**, *11*, 4374–4386.
[24] K. Ziegler, H. G. Gellert, *Justus Liebigs Ann. Chem.* **1950**, *567*, 179–185.
[25] J. Einhorn, J. L. Luche, *Tetrahedron Lett.* **1986**, *26*, 501–504.
[26] a) C. Carlini, M. Isola, V. Liuzzo, A. M. R. Galletti, G. Sbrana, *Appl. Catal. A* **2002**, *231*, 307–320; b) J. C. Jenkins, M. Brookhart, *Organometallics* **2003**, *22*, 250–256; c) W.-H. Sun, W. Zhang, T. Gao, X. Tang, L. Chen, Y. Li, X. Jin, *J. Organomet. Chem.* **2004**, *689*, 917–929.
[27] a) C. M. Killian, L. K. Johnson, M. Brookhart, *Organometallics* **1997**, *16*, 2005–2007; b) S. A. Svejda, M. Brookhart, *Organometallics* **1999**, *18*, 65–74.
[28] G. M. Sheldrick, *SHELXL-97*, *Program for the Refinement of Crystal Structures*, University of Göttingen, Germany, **1997**.
Received: July 2, 2007
Published Online: October 24, 2007

 © 2007 Wiley-VCH Verlag GmbH & Co. KGaA, Weinheim 

DOI: 10.1002/ejic.200700757

# Orientation and Arrangement of Octaruthenium Supramolecules with Alkyl Chains on Graphite

**Dong-Lin Shieh,[a] Yi-Shiue Lin,[a] Kom-Bei Shiu,[a] and Jong-Liang Lin*[a]**

**Keywords:** Supramolecular chemistry / Scanning tunneling microscopy / Ruthenium

The self-assemblies of octaruthenium grid-type supramolecules, $\{[Ru_2(CO)_4(NH_2C_{16}H_{33})_2](\mu\text{-}O_2CCO_2)\}_4$, on highly oriented pyrolytic graphite (HOPG) in air and in 1-phenyloctane were studied by scanning tunneling microscopy (STM). The surface supramolecules are arranged into rows in which the metal cores are linearly packed and the alkyl chains are parallel to the surface. With the aid of theoretical calculations in the framework of density functional theory, the electronic origin of the tunneling in the measured STM images is discussed.
(© Wiley-VCH Verlag GmbH & Co. KGaA, 69451 Weinheim, Germany, 2007)

## Introduction

Nanoscience and nanotechnology have great potential for making a significant impact on our society. The design and fabrication of nanoscaled structures with functional properties have attracted considerable attention recently. A host of devices can be miniaturized by shrinking them in size (top-down approach). An alternative is a bottom-up approach based on assembly of building units at the molecular level. Self-organization and self-assembly are a well-established phenomenon and are critically important in living organisms as well as chemistry and material science.[1] Supramolecules formed through coordination chemistry exhibit versatile structures (square, triangle, cage, etc.) and ample metal-based or ligand-based functionality.[2,3] The incorporated electronic, magnetic, photochemical, photophysical, redox, and/or catalytic properties can lead to applications in molecular recognition, electrochemical sensing, information storage, catalysis, and so on. In addition, the well-defined cavities of the supramolecules create the possibilities of host–guest and inclusion chemistries.[4] As particle or device size diminishes, the ratio of surface area to volume increases and surface properties play a crucial role. Recently, ordered assemblies of supramolecules with transition-metal cyclic structures on surfaces were reported, such as grid-type Co, Zn, and Fe complexes on HOPG,[5] octaruthenium and tetraruthenium complexes on HOPG,[6] Pt complexes with shapes of rectangle, square, and cage on Au(111),[7] and square Pt complexes on chloride-covered Cu(100).[8] From a technological point of view, several key parameters need to be precisely controlled for these complexes, including physical and chemical properties, surface distribution, and molecular orientation of adsorbates.[4] A monolayer film structure is a combined result of the interactions between adsorbed molecules and the substrate and between adsorbed molecules themselves, which can be controlled by hydrogen bonding, dipole–dipole coupling, steric effects, and so on. $Cu^{II}$ salicyclic aldehyde complexes and aldimine derivative complexes show different adsorption layer lattices on HOPG,[9] that is, a film structure is modified by ligand substitution. Ligand substitution or only introduction of specific functional groups at given positions in the ligand moieties opens a pathway to control not only two-dimensional film structure but also the molecular orientation in the films.[5a] Recently, we reported that $\{[Ru_2(CO)_4(PMe_3)_2](\mu\text{-}O_2CCO_2)\}_4$, an octaruthenium supramolecule with a square shape (Figure 1, structure **1**), forms two kinds of two-dimensional, well-ordered assemblies on HOPG in air. One of the assemblies is composed of supramolecules containing Ru–Ru bonds perpendicular to the surface and the $PMe_3$ groups as outermost parts. In the other assembly, the supramolecules adopt an orientation with the Ru–Ru bonds parallel to the surface and the CO groups as outermost parts. The identification of the layer structure was based on the direct comparison of the dimensions of the octaruthenium supramolecule with the size of the bright lobes observed in the STM images. In the present study, we demonstrate the formation of a two-dimensional assembly of $\{[Ru_2(CO)_4(NH_2(CH_2)_{15}CH_3)_2](\mu\text{-}O_2CCO_2)\}_4$ on HOPG (Figure 1, structure **2**), in which the supramolecules are arranged in rows and the Ru–Ru bonds are parallel to the substrate surface. The possible tunneling origin for the observed images of the octaruthenium molecules is discussed with the aid of density functional theory calculations.

[a] Department of Chemistry, National Cheng Kung University, 1, Ta Hsueh Road, Tainan, Taiwan 701, Republic of China
Fax: +886-6-2740552
E-mail: jonglin@mail.ncku.edu.tw
Supporting information for this article is available on the WWW under http://www.eurjic.org or from the author.

 © 2007 Wiley-VCH Verlag GmbH & Co. KGaA, Weinheim 

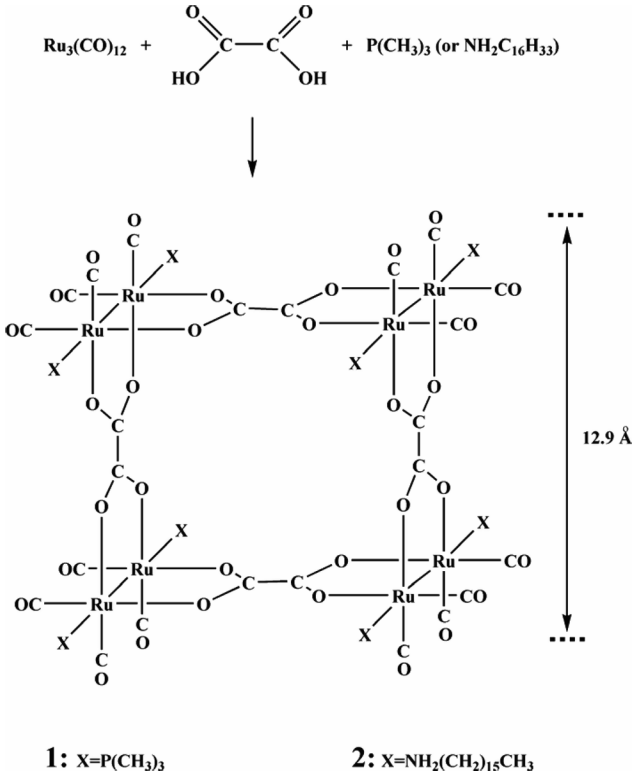


Figure 1. Formation of the grid-type octaruthenium complexes.

## Results and Discussion

Figure 2a presents a $15.0 \times 15.0$ nm$^2$ STM image of **2** on HOPG, assembled in $CH_2Cl_2$ and measured in air with a positive sample bias of 0.25 V in constant current mode (0.098 nA). This image shows a structure constituted by parallel rows. The width of each row is approximately 49.0 Å, with a linear bright region in the center area. The row width is close to the length (48 Å) of **2** calculated from one $CH_3$ end group to the other one on the opposite side across the metal cores on the basis of the theoretically optimized structure of **2** with zig–zag hydrocarbon chains. Figure 2b compares the *I–V* curve measured at the bright area in Figure 2a to the typical *I–V* curve of the pure HOPG plane. In the former case, the flat *I–V* feature about the zero bias voltage shows the presence of a bandgap. The measurements of the tunneling current at every bias were made three times and averaged to improve the signal-to-noise ratio. In some areas of **2**-covered HOPG, edges of islands formed by the ordered arrangement of the supramolecules can be observed. Figure 3a is a $600 \times 600$ nm$^2$ STM image, measured with a sample bias of –0.07 V and a tunneling current of 0.049 nA in air; it shows a step separating two terraces. On the basis of the tunneling image and the *I–V* spectrum measured around point A in the lower area (not shown), the dark terrace is attributed to a clean graphite surface. The row-like feature of Figure 2a is also observed in the high-resolution STM images taken in the bright terrace of Figure 3a, as shown in Figure S1 (Supporting Information). The line profile across the step (from point A to B) shows that the height difference between the two terraces is approximately 17 Å (Figure 3b), which is close to the height of the molecule, ca. 15.9 Å [sum of the oxygen nucleus-to-nucleus distance (12.9 Å, as indicated in Figure 1) and the van der Waals radii of two oxygen atoms (ca. 3 Å)]. These geometric similarities, the row width corresponding to the molecular length and the island height corresponding to the molecular height, indicate that the adsorbed supramolecules adopt an orientation with their long hydrocarbon chains and Ru–Ru bonds parallel to the surface. For an adsorbed molecule of **2** with this orientation, there are four coordinated CO molecules in contact with the surface.

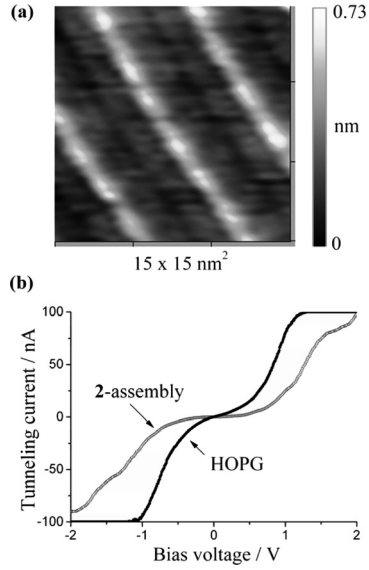


Figure 2. (a) STM image measured with a positive sample bias voltage of 0.25 V and a tunneling current of 0.098 nA in air of the assembly of **2** on HOPG. The width of the rows corresponds to the length of the molecule; (b) comparison of the *I–V* curves of clean and **2**-covered HOPG surfaces.

Because the formation of the layer structure of **2** on HOPG must depend on the interactions between **2** and the HOPG surface as well as on the interactions between molecules of **2**, a model compound, $\{[Ru_2(CO)_4(NH_3)(NH_2\text{-}C_8H_{17})](\mu\text{-}O_2CCO_2)\}_4$, on HOPG was calculated to address the bonding nature of **2**. In these calculations, the HOPG surface is represented by a sheet of carbon atoms fixed at the graphite lattice positions, with the edge carbon atoms coordinately saturated with H atoms. The total atom number (500 atoms) was confined by the software package in computation; therefore, only the model compound was studied instead of **2**. For the two adsorption systems of Figure 4a, b in which the adsorbed molecules have a 10° directional difference, the energy discrepancy is only 3 kcal mol$^{-1}$. This small difference in energy can be attributed to the weak van der Waals interaction between the molecule and the surface, which is not strongly dependent on the adsorption sites. The optimized 2.9 Å distance between the graphite surface and the O atom of the terminal CO (Figure 4a) is consistent with the sum of the van der Walls radii of C and O.

 © 2007 Wiley-VCH Verlag GmbH & Co. KGaA, Weinheim 

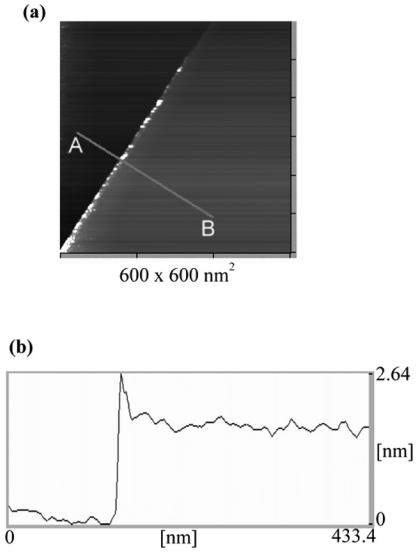


Figure 3. (a) A $600 \times 600$ nm$^2$ STM image measured in air with a sample bias voltage of –0.07 V and a tunneling current of 0.049 nA of a step separating a bright terrace representing a **2**-covered area and a dark terrace representing an uncovered area of HOPG; (b) the line profile from A to B shows that the height between the two terraces is ca. 17 Å.

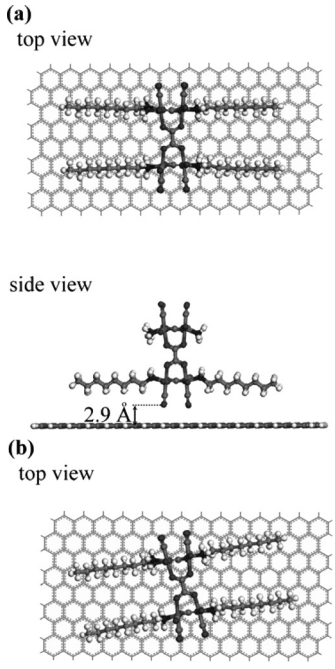


Figure 4. Optimized adsorption structures of a $\{[Ru_2(CO)_4(NH_3)(NH_2C_8H_{17})][\mu\text{-}O_2CCO_2]\}_4$ model compound in different directions (10° difference); structure (b) has an energy that is only 3 kcal mol$^{-1}$ higher.

To check the effect of the presence of solvent molecules on the adsorption structure and 2D array of **2** on HOPG, the assembly of **2** on HOPG was assembled and probed by STM in 1-phenyloctane. In a recent STM study of hexadehydrotribenzo[12]annulene derivatives (DBA) on HOPG, it was found that the structure of the DBA networks on HOPG is dramatically influenced by the presence of different solvent molecules.[10] The STM image of the ordered layer structure of **2** on HOPG measured in 1-phenyloctane with a +1.9 V sample bias voltage and a tunneling current of 0.049 nA is presented in Figure 5a. The molecules of **2** are packed into rows with a width of ca. 46.5 Å, similar to that observed in air. Figure 5b is a magnified image of the center region of Figure 5a, with a superimposed structure of **2** to show the matched length.

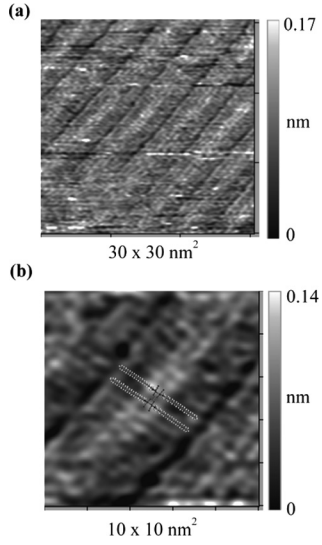


Figure 5. (a) A 30 nm × 30 nm STM image measured with a sample bias voltage of 1.9 V and a tunneling current of 0.049 nA in 1-phenyloctane of the assembly of **2** on HOPG; (b) magnified graph of the center region of (a) with a superimposed molecule of **2**.

To further address the origin of the tunneling, the molecular orbitals from the HOMO to HOMO-10 and from the LUMO to LUMO+9 of **2** were calculated in the framework of density functional theory (LDA-PWC). HOMO-*n* denotes the orbital below the HOMO by n energy levels; LUMO+*n* denotes the orbital above the LUMO by n energy levels. The wavefunctions from the HOMO to HOMO-3 of **2** and their relative energies are shown in Figure 6. The orbitals from the HOMO-4 to HOMO-10 are displayed in Figure S2 (Supporting Information). The orbitals from the HOMO to HOMO-3 mainly comprise Ru $4d_{z^2}$, N $2p_z$, and C $2p_z$ of the CO group and O $2p_z$ of the CO and $O_2CCO_2$ groups. The orbitals from the HOMO-4 to HOMO-7 contain the components of Ru 4d, N 2p, and O 2p of the CO and $O_2CCO_2$ groups. Ru 4d and O 2p of the CO and $O_2CCO_2$ groups contribute to the orbitals from HOMO-8 to HOMO-10. Figure 7 and Figure S3 (Supporting Information) show that the predominant contributions of the orbitals from the LUMO to LUMO+4 are C 2p and O 2p of the bridging $O_2CCO_2$ group. The orbitals from the LUMO+5 to LUMO+9 mainly consist of Ru 4d, C 2p, and O 2p of the terminal CO group. Our DFT calculations (LDA-PWC and GGA-PBE) show that the HOMO–LUMO gap of **2** is ca. 1.2 V. The self-assembled layer of **2** on HOPG in air was imaged at a small bias voltage of +0.25 V (Figure 1a). Different mechanisms were proposed for STM images of adsorbed molecules measured at low

 © 2007 Wiley-VCH Verlag GmbH & Co. KGaA, Weinheim 

bias voltages, in the gap between the HOMO and LUMO states, including work function modulation, resonant tunneling, and weak mixing of states of the molecule and substrate through molecule–substrate interaction.[11] In the case of the STM image of **2** assembled and measured in 1-phenyloctane, a +1.9 V sample bias was used. With an assigned HOMO–LUMO energy gap of 1.2 V and the assumption that the substrate Fermi level is located at the midpoint in the gap, the calculated energy levels from the LUMO to LUMO+9 are all below the Fermi level at a positive bias of 1.9 V, that is, these states become accessible for electron tunneling from HOPG to the molecules.

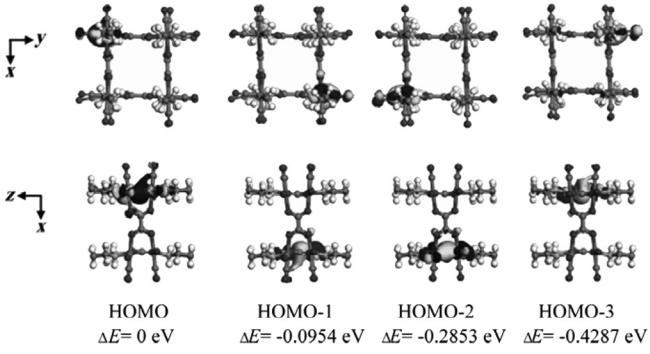


Figure 6. Individual molecular orbitals of **2** from the HOMO to HOMO-3 and their relative energies. $NH_2C_2H_5$ is used to replace $NH_2C_{16}H_{33}$ to save space.

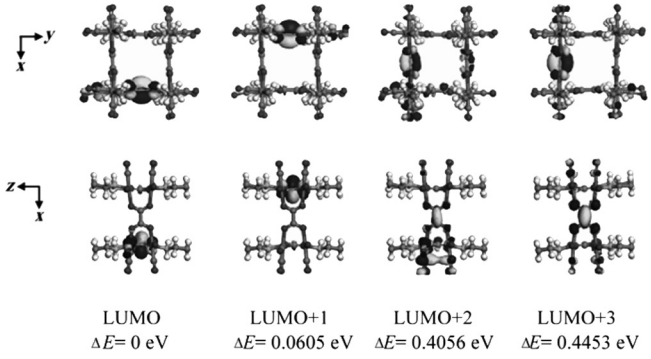


Figure 7. Individual molecular orbitals of **2** from the LUMO to LUMO+3 and their relative energies. $NH_2C_2H_5$ is used to replace $NH_2C_{16}H_{33}$ to save space.

## Conclusions

Grid-type octaruthenium complex **2** consisting of CO and $NH_2C_{16}H_{33}$ terminal ligands and a $O_2CCO_2$ bridging ligand was designed, synthesized, and studied with STM. Molecules of **2** on HOPG form an ordered assembly in which the molecules are arranged into rows, and they adopt an orientation with their Ru–Ru bonds and hydrocarbon chains parallel to the surface.

## Experimental Section

**Synthesis of $[Ru_2(CO)_4(NH_2C_{16}H_{33})_2](\mu\text{-}O_2CCO_2)_4$:** Freshly prepared $[Ru_3(CO)_{12}]$, oxalic acid·$2H_2O$, and THF were added in a pressure Schlenk tube. The mixture was heated to 120 °C while magnetically stirred for 6 h. To avoid the back-reaction, the gases evolved were drawn off from time to time. *n*-Hexadecylamine was then added. The solution was stirred for 2 h more, and then the solvents were removed under vacuum to afford a solid residue. Recrystallization from $CH_2Cl_2$/MeOH gave $[Ru_2(CO)_4(NH_2C_{16}H_{33})_2](\mu\text{-}O_2CCO_2)_4$. Yield: 83%. $^1H$ NMR (300 MHz, $CD_2Cl_2$): $\delta$ = 0.86 (t, $J$ = 6.4 Hz, 24 H, terminal $CH_3$), 1.54 (m, 16 H, $CH_2CH_3$), 2.32 (s, $NH_2$), 2.91 (t, $J$ = 7.1 Hz, 16 H, $CH_2NH_2$), 1.25 (m, 208 H, $104 \times CH_2$). IR ($CH_2Cl_2$): $\tilde{\nu}$ = 1591 (CO), 1979 (CO), 2030 (CO) $cm^{-1}$. $C_{152}H_{280}N_8O_{32}Ru_8$ (3540.47): calcd. C 51.6, H 8.0, N 3.2; found C 51.4, H 8.0, N 3.2.

**$[Ru_2(CO)_4(NH_2C_{16}H_{33})_2](\mu\text{-}O_2CCO_2)_4$ Film Preparation for STM Investigation:** The 2D layer structure of $[Ru_2(CO)_4(NH_2C_{16}H_{33})_2](\mu\text{-}O_2CCO_2)_4$ on HOPG was investigated in air and in 1-phenyloctane. The film formation procedures for these two STM studies were different. In the former case, a drop of $[Ru_2(CO)_4(NH_2C_{16}H_{33})_2](\mu\text{-}O_2CCO_2)_4$ in $CH_2Cl_2$ (0.01 M) was deposited on a freshly cleaved surface of HOPG (ZYB quality), which was placed in the middle of a glass container with a small amount of $CH_2Cl_2$ left on the bottom, and then the container was sealed immediately. After 6 h, the HOPG was taken out of the container and the $CH_2Cl_2$ was allowed to vaporize before STM images were recorded. It was found that **2** with the long alkyl chains $[-(CH_2)_{15}CH_3]$ needed much more time, relative to molecules of **1** reported previously, to pack into an ordered assembly by diffusion and adjustment of their relative positions in the interface of the solvent ($CH_2Cl_2$) and HOPG. In the case of **2** in 1-phenyloctane, a drop of 1-phenyloctane solution saturated with $[Ru_2(CO)_4(NH_2C_{16}H_{33})_2](\mu\text{-}O_2CCO_2)_4$ was placed on a freshly cleaved HOPG surface, which allowed the formation of an assembly of **2**. After 6 h, the surface was scanned by STM. Electrochemically etched W tips were used for the STM studies (Seiko Instruments, SPA 400) at constant current mode. All the STM images were collected with $256 \times 256$ data points.

**Molecular Orbital Calculations:** The optimized molecular structure as well as the orbitals and energies of $[Ru_2(CO)_4(NH_2C_{16}H_{33})_2](\mu\text{-}O_2CCO_2)_4$ were calculated in the framework of density functional theory by using the DMol$^3$ package, in which the Perdew–Wang local exchange and correlation function (LDA-PWC) and double-numerical basis set were employed. The calculations were spin-unrestricted and did not include a relativistic effect for the core electrons. In addition, another method, the generalized gradient approximation of Perdew, Burke, and Ernzerhof to the exchange and correlation functional (GGA-PBE), was also employed to calculate the supramolecular orbitals and their corresponding energies. A consistent HOMO–LUMO energy gap was obtained with both methods.

**Supporting Information** (see footnote on the first page of this article): Additional STM image and the HOMO- and LUMO-related orbitals of **2**.

## Acknowledgments

This research was financially supported by the National Science Council of the Republic of China (NSC 95-2113-M-006-017-MY2).

[1] a) J. U. Lane, J. L. Atwood, J. E. D. Davies, D. D. MacNicol, F. Vögtle (Eds.), *Comprehensive Supramolecular Chemistry*, Pergamon, Oxford, **1996**, vol. 9; b) G. F. Swiegers, T. J. Malefetse, *Chem. Rev.* **2000**, *100*, 3483–3538; c) G. M. Whitesides, M. Boncheva, *Proc. Natl. Acad. Sci. USA* **2002**, *99*, 4769–4774.

 © 2007 Wiley-VCH Verlag GmbH & Co. KGaA, Weinheim 

[2] a) N. L. S. Yue, M. C. Jennings, R. J. Puddephatt, *Inorg. Chem.* **2005**, *44*, 1125–1131; b) M. P. Martin-Redondo, L. Scoles, B. T. Sterenberg, K. A. Udachin, A. J. Carty, *J. Am. Chem. Soc.* **2005**, *127*, 5038–5039; c) F. A. Cotton, C. A. Murillo, X. Wang, R. Yu, *Inorg. Chem.* **2004**, *43*, 8394–8403; d) D. C. Caskey, R. K. Shoemaker, J. Michl, *Org. Lett.* **2004**, *6*, 2093–2096; e) J. Forniés, J. Gómez, E. Lalinde, M. T. Moreno, *Chem. Eur. J.* **2004**, *10*, 888–898; f) S. J. Lee, J. S. Kim, W. Lin, *Inorg. Chem.* **2004**, *43*, 6579–6588; g) K. Kumazawa, Y. Yamanoi, M. Yoshizawa, T. Kusukawa, M. Fujita, *Angew. Chem. Int. Ed.* **2004**, *43*, 5936–5940; h) P. Angaridis, J. F. Berry, F. A. Cotton, C. A. Murillo, X. Wang, *J. Am. Chem. Soc.* **2003**, *125*, 10327–10334; i) Y. K. Kryschenko, S. R. Seidel, A. M. Arif, P. J. Stang, *J. Am. Chem. Soc.* **2003**, *125*, 5193–5198; j) Z. Qin, M. C. Jennings, R. J. Puddephatt, *Inorg. Chem.* **2002**, *41*, 3967–3974.

[3] a) S. Alvarez, *Dalton Trans.* **2005**, 2209–2233; b) Y. X. Ke, D. J. Collins, H. C. Zhou, *Inorg. Chem.* **2005**, *44*, 4154–4156; c) M. Fujita, M. Tominaga, A. Hori, B. Therrien, *Acc. Chem. Res.* **2005**, *38*, 369–378; d) D. L. Reger, R. F. Semeniuc, M. D. Smith, *Inorg. Chem.* **2003**, *42*, 8137–8139; e) U. Radhakrishnan, M. Schweiger, P. J. Stang, *Org. Lett.* **2001**, *3*, 3141–3143; f) C. J. Kuehl, T. Yamamoto, S. R. Seidel, P. J. Stang, *Org. Lett.* **2002**, *4*, 913–915; g) B. J. Holliday, C. A. Mirkin, *Angew. Chem. Int. Ed.* **2001**, *40*, 2022–2043.

[4] B. J. Holliday, C. A. Mirkin, *Angew. Chem. Int. Ed.* **2001**, *40*, 2022–2043.

[5] a) A. Semnov, J. P. Spatz, M. Möller, J.-M. Lehn, B. Sell, D. Schubert, C. H. Weidle, U. S. Schubert, *Angew. Chem. Int. Ed.* **1999**, *38*, 2547–2550; b) U. Ziener, J.-L. Lehn, A. Mourran, M. Möller, *Chem. Eur. J.* **2002**, *8*, 951–957; c) M. S. Alam, S. Strömsdörfer, V. Dremov, P. Müller, J. Kortus, M. Ruben, J.-M. Lehn, *Angew. Chem. Int. Ed.* **2005**, *44*, 7869–7900; d) A. Mourran, U. Ziener, M. Möller, E. Breuning, M. Ohkita, J.-M. Lehn, *Eur. J. Inorg. Chem.* **2005**, 2641–2647; e) M. Ruben, J. Rojo, F. J. Romero-Salguero, L. H. Uppadine, J.-M. Lehn, *Angew. Chem. Int. Ed.* **2004**, *43*, 3644–3662.

[6] D.-L. Shieh, K.-B. Shiu, J.-L. Lin, *Eur. J. Inorg. Chem.* **2004**, 2223–2227.

[7] Q.-H. Yuan, L.-J. Wan, H. Jude, P. T. Stang, *J. Am. Chem. Soc.* **2005**, *127*, 16279–16286.

[8] C. Safarowsky, L. Merz, A. Rang, P. Broekmann, B. A. Hermann, C. A. Schalley, *Angew. Chem. Int. Ed.* **2004**, *43*, 1291–1294.

[9] P. Zell, F. Mögele, U. Ziener, B. Rieger, *Chem. Commun.* **2005**, 1294–1296.

[10] K. Tahara, S. Furukawa, H. Uji-i, T. Uchino, T. Ichikawa, J. Zhang, W. Mamdouh, M. Sonoda, F. C. De Schryver, S. De Feyter, Y. Tobe, *J. Am. Chem. Soc.* **2006**, *128*, 16613–16625.

[11] a) J. K. Spong, H. A. Mizes, L. J. LaComb Jr, M. M. Dovek, J. E. Frommer, J. S. Foster, *Nature* **1990**, *338*, 137–139; b) W. Mizutani, M. Shigeno, M. Ono, K. Kajimura, *Appl. Phys. Lett.* **1990**, *56*, 1974–1976; c) Z. Klusek, W. Kolowski, *J. Electron Spectrosc. Relat. Phenom.* **2000**, *107*, 63–72; d) A. J. Fisher, P. E. Blöchl, *Phys. Rev. Lett.* **1993**, *70*, 3263–3266.

Received: July 18, 2007
Published Online: October 24, 2007

 © 2007 Wiley-VCH Verlag GmbH & Co. KGaA, Weinheim 

10.1002/ejic.200701198

# Removal: "Ultra-Simple Synthesis of Ordered Mesoporous γ-Alumina: High Thermal Stability and Catalytic Activity"

**Le-Yue Li,[a] Quan Yuan,[b] Lei Liao,*[a] Chun-Hua Yan,[b] and Jun Chen[a]**

**Removal of Article from Wiley InterScience:** The article "Ultra-Simple Synthesis of Ordered Mesoporous γ-Alumina: High Thermal Stability and Catalytic Activity", published online on September 4, 2007 in Wiley InterScience (www.interscience.wiley.com) (DOI: 10.1002/ejic.200700645), has been removed.

The article was fraudulently submitted to the *European Journal of Inorganic Chemistry* without the approval of the authors named on the article, using false authorship details. The article was stolen in draft form from the computer network of the authors Chun-Hua Yan and Quan Yuan. No person at Wuhan University was involved in any way in the incident.

The Editor of the *European Journal of Inorganic Chemistry*, Dr. Karen Hindson, the authors and Wuhan University are satisfied with the severity of the punitive measures imposed upon the perpetrator of this fraud by the Ethics Commission of the College of Chemistry and Molecular Engineering of Peking University.

*The Authors/The Editor*

Received: October 31, 2007
Published Online: November 16, 2007

[a] State Key Lab of Advanced Technology for Materials Synthesis and Processing, Department of Chemistry, Wuhan University, Wuhan 430070, China
Fax: +86-27-68754112
E-mail: ll43420024@hotmail.com
[b] Beijing National Laboratory for Molecular Sciences, State Key Lab of Rare Earth Materials Chemistry and Applications & PKU-HKU Joint Lab in Rare Earth Materials and Bioinorganic Chemistry, Peking University, Beijing, China

 © 2007 Wiley-VCH Verlag GmbH & Co. KGaA, Weinheim 

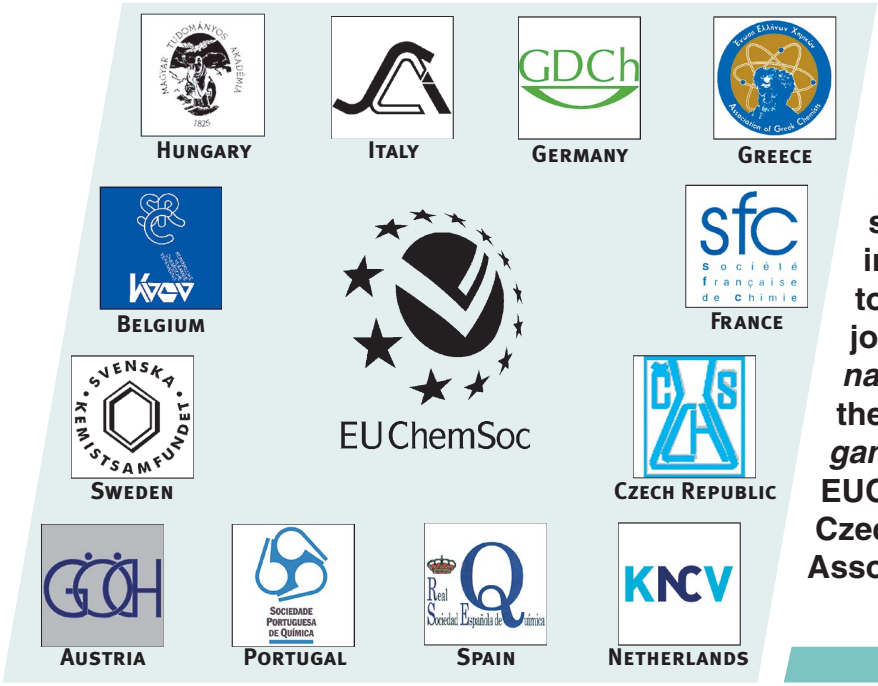


**The EUChemSoc Societies have taken the significant step into the future by merging their traditional journals, to form two leading chemistry journals, the *European Journal of Inorganic Chemistry* and the *European Journal of Organic Chemistry.* Three further EUChemSoc Societies (Austria, Czech Republic and Sweden) are Associates of the two journals.**

## COVER PICTURE

**The cover picture shows** the insertion of a $Pt^0$ complex fragment into the S−S bond of a 1,2,4-trithiolane 1-*S*-oxide. Reactions of $Pt^0$ complexes with small sulfur-containing heterocycles have become more and more popular in order to generate and stabilize reactive sulfur-containing species. The reaction presented leads to three- and four-membered platinacycles by ring contraction with expulsion of the reactive thiocarbonyl derivatives. The postulated mechanism for the fragmentation of 1,2,4-trithiolane 1-*S*-oxide, as well as the molecular structures, give a reasonable explanation for the observed selectivity. Details are discussed in the article by W. Weigand, G. Mloston et al. on p. 5627 ff. We thank Dr. Jaroslaw Romanski for decorating our Christmas tree (background) for this year and designing the cover picture.

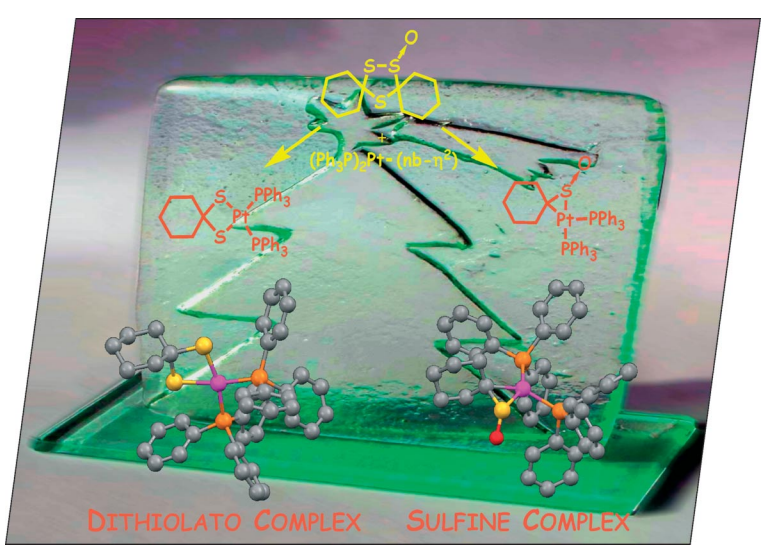


 © 2007 Wiley-VCH Verlag GmbH & Co. KGaA, Weinheim 

# CONTENTS

## SHORT COMMUNICATION


### Silver Coordination Oligomer

**Y. Wang, U. Englert* ..... 5623–5625**

The First Linear Coordination Oligomer Linked by 4,4′-Bipyridine

**Keywords:** Coordination polymers / Chain structures / Polycations / Oligomers / X-ray diffraction


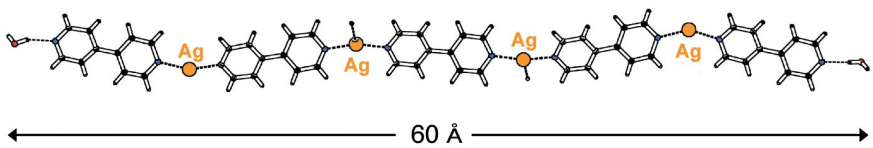



Quite long, but no polymers yet! Coordination oligomers $[Ag_4(bipy)_5]^{4+}$ and $[Ag_2(bipy)_3]^{2+}$ were trapped in the same salt. A change in the counteranion was sufficient to induce polymerization.


## FULL PAPERS


### Pt Chemistry

**H. Petzold, S. Bräutigam, H. Görls, W. Weigand,* J. Romanski, G. Mloston* ..... 5627–5632**

Oxidation of Spirocyclohexyl-1,2,4-trithiolane and Complexation Reaction with $[Pt(\eta^2\text{-nb})(PPh_3)_2]$

**Keywords:** Insertion reactions / 1,2,4-Trithiolanes / Platinum / S ligands / Thioketone complexes


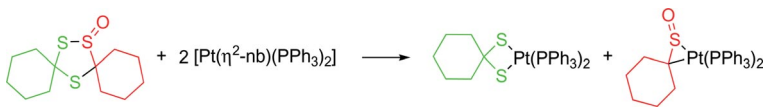



Insertion of a $Pt^0$ complex fragment into the S–S bond of a 1,2,4-trithiolane as well as into that of its 1-*S* and 4-*S*-oxide is presented. Subsequent ring contraction with expulsion of reactive thiocarbonyl derivatives leads to three- and four-membered platinacycles that include thiolato and sulfenato structures. The postulated mechanism and the molecular structures give a reasonable explanation for the observed selectivity.



### Heteroleptic Ruthenium(II) Complexes

**A. I. Philippopoulos,* A. Terzis, C. P. Raptopoulou, V. J. Catalano, P. Falaras ..... 5633–5644**

Synthesis, Characterization, and Sensitizing Properties of Heteroleptic $Ru^{II}$ Complexes Based on 2,6-Bis(1-pyrazolyl)pyridine and 2,2′-Bipyridine-4,4′-dicarboxylic Acid Ligands

**Keywords:** 2,6-Bis(1-pyrazolyl)pyridine / Heteroleptic $Ru^{II}$ complexes / Dye-sensitized solar cells / Ruthenium / Protonation


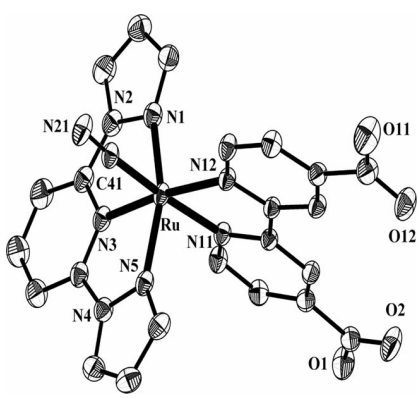



The synthesis and characterization of a series of novel heteroleptic ruthenium(II) complexes bearing the 2,6-bis(1-pyrazolyl)-pyridine (bpp) and 2,2′-bipyridine-4,4′-dicarboxylic acid ($dcbpyH_2$) ligands, as well as their performance as dye sensitizers in nanocrystalline solar cells for the conversion of visible light into electricity, is presented. These complexes efficiently sensitize nanostructured $TiO_2$ films and the resulting photoelectrodes incorporated in solid-state DSSCs show enhanced overall power conversion efficiency, which strongly depends on their molecular structure and their degree of protonation.



### (Guanidine)zinc Catalysts

**J. Börner, S. Herres-Pawlis,* U. Flörke, K. Huber ..... 5645–5651**

[Bis(guanidine)]zinc Complexes and Their Application in Lactide Polymerisation

**Keywords:** Guanidine / D,L-Lactide / N ligands / Ring-opening polymerization / Zinc


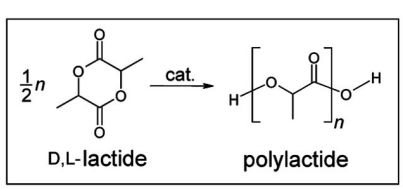


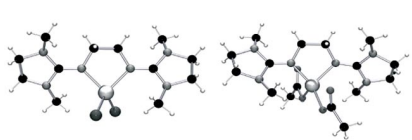


The first examples of aliphatic [bis(guanidine)]zinc complexes $[Zn(DMEG_2e)Cl_2]$, $[Zn(DMEG_2e)(CH_3COO)_2]$ and $[Zn(DMEG_2e)_2](CF_3SO_3)_2$ containing $N^1,N^2$-bis(1,3-dimethylimidazolidin-2-ylidene)ethane-1,2-diamine have been synthesised and fully characterised. These compounds are able to catalyse the polymerisation of D,L-lactide. PLAs with molecular weights ($M_w$) up to 59000 g/mol could be obtained.

## Ca-Mediated Styrene Polymerization

Increase of the steric bulk in the 2- and 7-positions of the fluorenyl ligands in several new organocalcium initiators led to a considerable improvement in the stereoselectivity for styrene polymerization. Syntheses, structures and polymerization results are discussed.

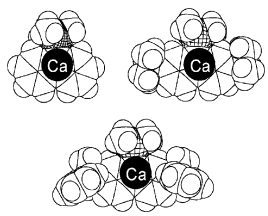


**D. F.-J. Piesik, K. Häbe, S. Harder* ..... 5652–5661**

Ca-Mediated Styrene Polymerization: Tacticity Control by Ligand Design

**Keywords:** Alkaline-earth metals / Calcium / Polymerization catalysis / Fluorene ligands / Polystyrene

## Modified Polyoxoanions

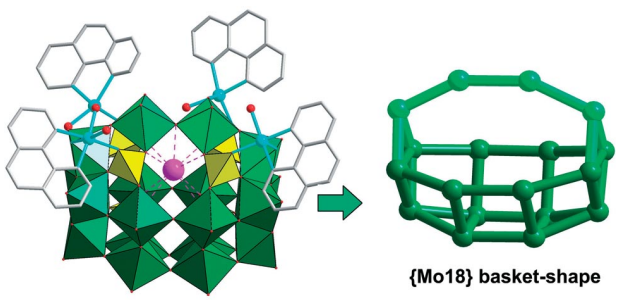


A basket-like mixed-valent polyoxoanion $[Sr⊂P_6Mo_4^{V}Mo_{14}^{VI}O_{73}]^{10-}$ modified with $\{Cu(phen)(H_2O)_x\}$ ($x = 1-3$) fragments was hydrothermally synthesized and structurally characterized. The compound shows good electrocatalytic activity to reduce hydrogen peroxide.

**K. Yu, Y.-G. Li,* B.-B. Zhou,* Z.-H. Su, Z.-F. Zhao, Y.-N. Zhang ..... 5662–5669**

A Basket-Like $[Sr⊂P_6Mo^{V}_4Mo^{VI}_{14}O_{73}]^{10-}$ Polyoxoanion Modified with $\{Cu(phen)(H_2O)_x\}$ ($x = 1-3$) Fragments: Synthesis, Structure, Magnetic, and Electrochemical Properties

**Keywords:** Polyoxometalate / Organic–inorganic hybrid / Basket-like / Electrocatalysis

## Magnetostructural Correlation

Three end-on azido dinuclear $Mn^{II}$ complexes based on tripyridyl ligands show intramolecular ferromagnetic superexchange. Clearer magnetostructural correlation for end-on azido-bridged $Mn^{II}$ complexes was obtained.

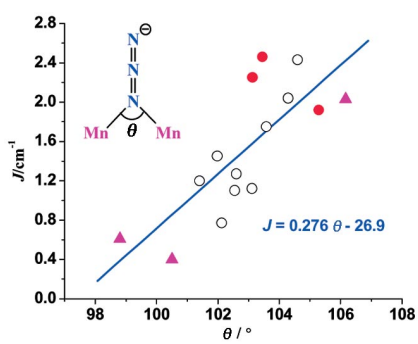


**M.-M. Yu, Z.-H. Ni, C.-C. Zhao, A.-L. Cui, H.-Z. Kou* ..... 5670–5676**

Synthesis and Magnetic Study of $\mu_{1,1}$-Azido-Bridged Dinuclear Manganese(II) Complexes Based on Tripyridyl Ligands

**Keywords:** Manganese / Dinuclear complexes / Crystal structures / Magnetic properties / Azido bridge

## Dimetallic Hydroformylation Catalysts

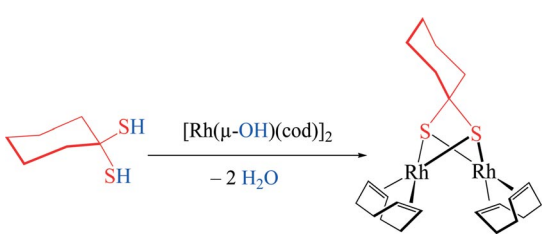


The *gem*-dithiolato-bridged dinuclear compound $[Rh_2(\mu\text{-}S_2Chxn)(cod)_2]$ was obtained in a straightforward manner from 1,1-dimercaptocyclohexane and $[Rh(\mu\text{-}OH)(cod)]_2$. This compound is an efficient catalyst precursor in the presence of P-donor ligands for the hydroformylation of oct-1-ene under mild conditions. The *trans*-dinuclear species $[Rh_2(\mu\text{-}S_2Chxn)(CO)_2(PPh_3)_2]$ was isolated from the catalytic solutions

**M. A. F. Hernandez-Gruel, G. Gracia-Arruego, A. B. Rivas, I. T. Dobrinovitch, F. J. Lahoz, A. J. Pardey, L. A. Oro,* J. J. Pérez-Torrente* ..... 5677–5683**

Novel *gem*-Dithiolato-Bridged Rhodium Hydroformylation Catalysts: Bridging the Gap in Dinuclear Rhodium Thiolate Chemistry

**Keywords:** Homogeneous catalysis / Hydroformylation / Dinuclear complexes / *gem*-Dithiolato ligands / Rhodium

 © 2007 Wiley-VCH Verlag GmbH & Co. KGaA, Weinheim 

# CONTENTS

## Fluoride/Amide Exchange

**P. L. Shutov, S. S. Karlov,* K. Harms, M. V. Zabalov, J. Sundermeyer,* J. Lorberth, G. S. Zaitseva .... 5684–5692**

*ortho*-Directed Metathetical Fluoride/Amide Exchange in (Pentafluorophenyl)-amides

**Keywords:** Fluorinated ligands / Amides / Nucleophilic substitution / Density functional calculations

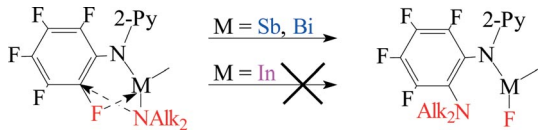


Metathetical fluoride/amide exchange has been examined in pentafluoro(2-pyridyl)-anilides of Sb, Bi, and In by synthetic and X-ray studies and density functional calculations. The tendency for this rearrangement increases with an increase of the covalent radius and decreases with an increase of the coordination number of the central atom.

## The Spin-Crossover Metastable State

**V. Legrand, S. Pillet, C. Carbonera, M. Souhassou, J.-F. Létard, P. Guionneau, C. Lecomte* .... 5693–5706**

Optical, Magnetic and Structural Properties of the Spin-Crossover Complex [Fe(btr)(NCS)]·HO in the Light-Induced and Thermally Quenched Metastable States

**Keywords:** Iron(II) / Photoswitching / Structural analysis / Photomagnetism / Spin crossover

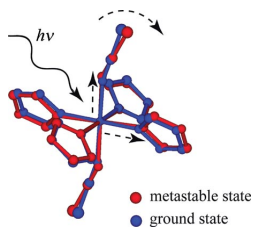


The light-induced and thermally induced structural reorganization of the spin-crossover complex $[Fe(btr)_2(NCS)_2]\cdot H_2O$ are discussed together with photomagnetic and optical reflectivity results.

## Hydrodesulfurization (HDS)

**A. Nova, F. Novio, P. González-Duarte*, A. Lledós,* R. Mas-Ballesté ..... 5707–5719**

C–S Bond Activation and Partial Hydrogenation of Thiophene by a Dinuclear Trihydride Platinum Complex

**Keywords:** C–S activation / Desulfurization / Thiophene / Hydride ligands / Platinum / Reaction mechanisms

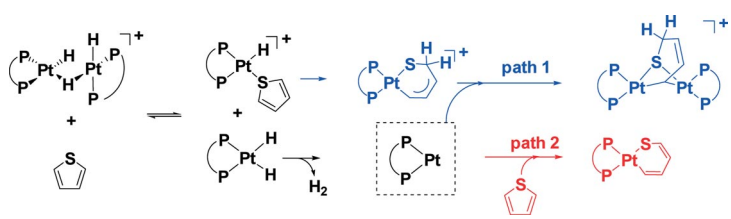


Hydrodesulfurization reactions with transition metals: the reaction of $[(dppp)_2Pt_2H_3]$-$ClO_4$ with thiophene achieves activation of the C–S bond. The corresponding mechanism has been interpreted on the basis of DFT calculations. The reactivity of the complexes obtained in this reaction has led to the characterization of new platinum species.

## Zeolite-Y-Encapsulated Complexes

**M. R. Maurya,* B. Singh, P. Adão, F. Avecilla, J. Costa Pessoa ... 5720–5734**

Zeolite-Encapsulated Copper(II) Complexes of Pyridoxal-Based Tetradentate Ligands for the Oxidation of Styrene, Cyclohexene and Methyl Phenyl Sulfide

**Keywords:** Zeolites / Copper(II) complexes / Heterogeneous catalysis / Oxidation reactions

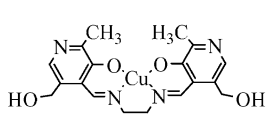


[Cu(pydx-en)] (**1**)

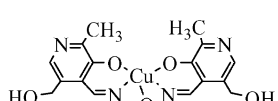


[Cu(pydx-1,3-pn)(MeOH)] (**2**)

[Cu(pydx-en)] (**1**) and [Cu(pydx-1,3-pn)-(MeOH)] (**2**) have been encapsulated in the supercages of zeolite-Y and used as catalysts for the oxidation of styrene, cyclohexene and methyl phenyl sulfide.

 © 2007 Wiley-VCH Verlag GmbH & Co. KGaA, Weinheim 

## Phase Transition in $Pt(bpy)Cl_2$

Luminescence of the red form of $Pt(bpy)Cl_2$ has been measured as a function of hydrostatic pressure. The band maximum is shifted by $-147\ cm^{-1}\,kbar^{-1}$. Strong discontinuities in the optical properties at 17.7 kbar were interpreted in terms of a crystallographic phase transition from the red to a denser yellow form of $Pt(bpy)Cl_2$. First-principles calculations based on density functional theory were used to study this transformation.

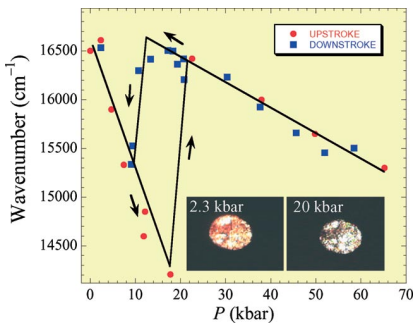


**R. Valiente,* J. M. García-Lastra, P. García-Fernández, S. García-Revilla, O. S. Wenger ..... 5735–5742**

Red-to-Yellow Pressure-Induced Phase Transition in Pt(bpy)Cl: Spectroscopic Study Supported by DFT Calculations

**Keywords:** Phase transition / High-pressure chemistry / DFT calculations / Platinum(II) / Metal–metal interactions

## Platinum(II) Complexes with O-Donors

Acidolysis of the complexes $[Pt(CH_3)(terpy)]Y$ (Y = $PF_6$, $CH_3SO_3$, $CF_3SO_3$, $ClO_4$, $BF_4$; terpy = 2,2′:6′,2′′-terpyridine) with $CH_3SO_3$ affords the corresponding methanesulfonato derivatives $[Pt(OSO_2CH_3)(terpy)]Y$. A mixture of the methanesulfonato and nitrato complexes is obtained when Y = $NO_3$, whereas the reaction of $[Pt(CH_3)(terpy)](CF_3SO_3)$ with triflic acid gives the aqua species $[Pt(terpy)(H_2O)](SO_3CF_3)_2$. The new hydroxido-bridged dimers $[Pt_2(\mu\text{-}OH)(terpy)_2](X)$ [X = $(ClO_4)_3$, $(PF_6)_2(CF_3SO_3)$] are isolated and their X-ray crystal structures determined.

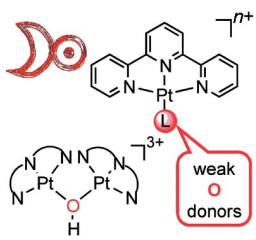


**G. Annibale,* P. Bergamini, V. Bertolasi, M. Bortoluzzi, M. Cattabriga, B. Pitteri ..... 5743–5751**

The Relative Coordinating Ability of Some Weak O-Donor Anions and Water Towards the $[Pt(terpy)]^{2+}$ (terpy = 2,2′:6′,2′′-terpyridine) Center – X-ray Crystal Structures of $[Pt(terpy)(H_2O)](CF_3SO_3)_2$ and $[Pt_2(\mu\text{-}OH)(terpy)_2](PF_6)_2(CF_3SO_3)$

**Keywords:** Platinum / Bridging ligands / N ligands / O ligands

## Octahedral Organotin Compounds

The compounds $L_2SnR_2$ [L = *N*-(3,5-dichlorosalicylidene)aniline; R = $CH_3$ (**1**), R = $CH_2Ph$ (**2**)] and $L'_2SnR_2$ [**3**: L′ = *N*-(3-*tert*-butylsalicylidene)aniline, R = $CH_2Ph$] have been synthesized and characterized. The X-ray crystal structure of compound **2** showed an octahedral geometry with the alkyl groups in a *trans* relationship. Cationic species generated therefrom promoted ethylene oligomerization under mild conditions.

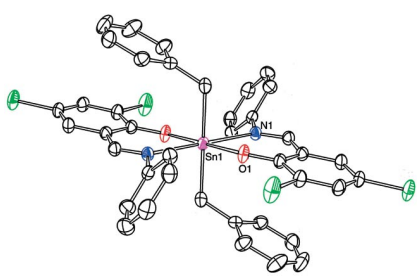


**L. Annunziata, D. Pappalardo,* C. Tedesco, C. Pellecchia ..... 5752–5759**

Octahedral Alkylbis(phenoxy-imine)tin(IV) Complexes: Effect of Substituents on the Geometry of the Complexes and Their Reactivity Toward Ionizing Species and Ethylene

**Keywords:** Tin / N,O ligands / Cations / Ethylene / Oligomerization

**INDEX 2007 ..... 5763–5773**

*The editorial staff and the publishers thank all readers, authors, referees, and advertisers for their interest and support over the past year and wish them all a happy new year.*

**If not otherwise indicated in the article, papers in issue 35 were published online on November 28, 2007**

 © 2007 Wiley-VCH Verlag GmbH & Co. KGaA, Weinheim 

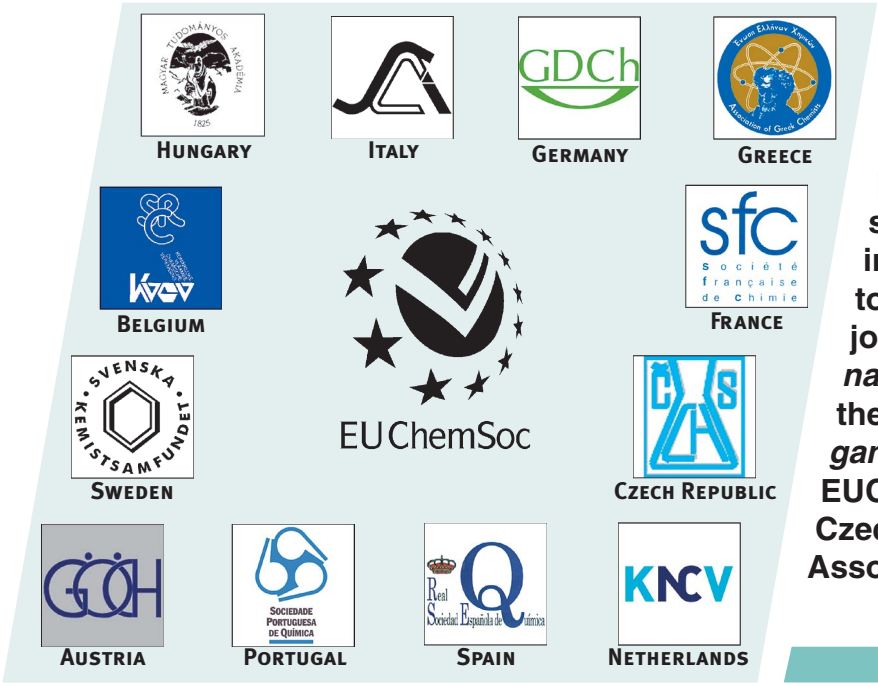


**The EUChemSoc Societies have taken the significant step into the future by merging their traditional journals, to form two leading chemistry journals, the *European Journal of Inorganic Chemistry* and the *European Journal of Organic Chemistry.* Three further EUChemSoc Societies (Austria, Czech Republic and Sweden) are Associates of the two journals.**

## COVER PICTURE

**The cover picture shows** the insertion of a $Pt^0$ complex fragment into the S−S bond of a 1,2,4-trithiolane 1-*S*-oxide. Reactions of $Pt^0$ complexes with small sulfur-containing heterocycles have become more and more popular in order to generate and stabilize reactive sulfur-containing species. The reaction presented leads to three- and four-membered platinacycles by ring contraction with expulsion of the reactive thiocarbonyl derivatives. The postulated mechanism for the fragmentation of 1,2,4-trithiolane 1-*S*-oxide, as well as the molecular structures, give a reasonable explanation for the observed selectivity. Details are discussed in the article by W. Weigand, G. Mloston et al. on p. 5627 ff. We thank Dr. Jaroslaw Romanski for decorating our Christmas tree (background) for this year and designing the cover picture.

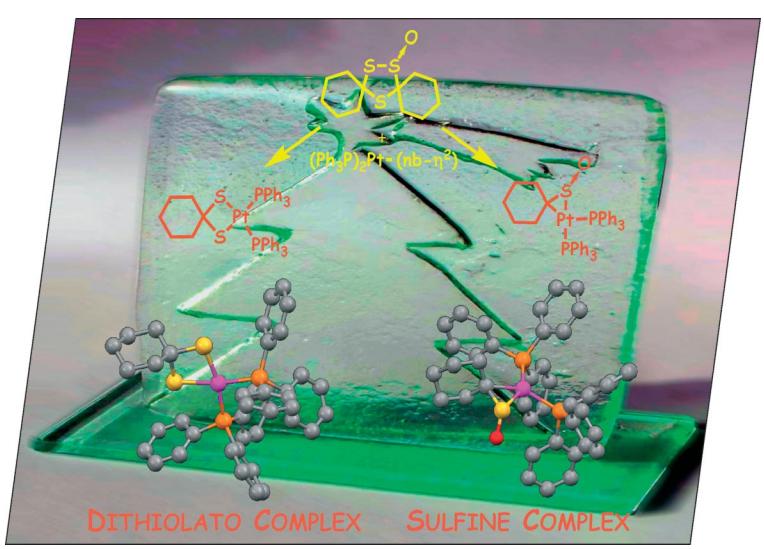


 © 2007 Wiley-VCH Verlag GmbH & Co. KGaA, Weinheim 

# SPOTLIGHTS …

## *Allylations*

J. T. Mohr, B. M. Stoltz*

**Enantioselective Tsuji Allylations**

*Chem. Asian J.*
DOI: **10.1002/asia.200700183**

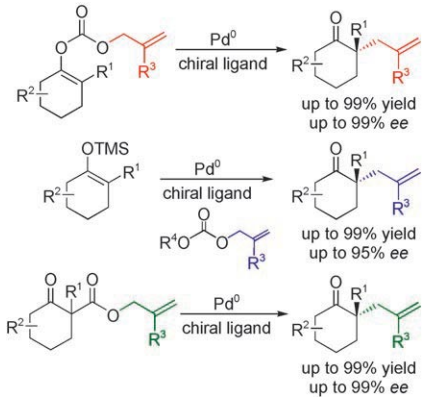


**A fresh take**: Several variants of the Tsuji allylation reactions have been rendered enantioselective in recent years. These important developments have provided valuable methods for the synthesis of enantioenriched cycloalkanone building blocks. The use of these asymmetric reactions in total synthesis has also been reported. TMS = trimethylsilyl.

## *Protein Evolution*

V. Stein, I. Sielaff, K. Johnsson, F. Hollfelder*

**A Covalent Chemical Genotype–Phenotype Linkage for in vitro Protein Evolution**

*ChemBioChem*
DOI: **10.1002/cbic.200700459**

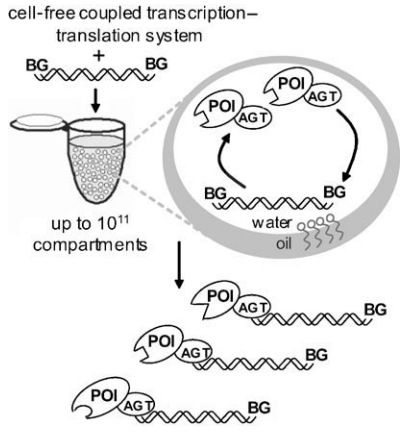


**Display model**. Proteins fused to $O^6$-alkylguanine alkyltransferase (AGT) were expressed in vitro and conjugated to their coding DNA via $O^6$-benzylguanine, a suicide inhibitor of AGT. The potential of this display system is demonstrated for several proteins in model selection experiments. Enrichments of up to 100-fold and DNA recovery rates of up to 2.4% are achieved per round of selection.

## *CO Adsorption*

M. Heinen, Y.-X. Chen, Z. Jusys, R. J. Behm*

**Room Temperature $CO_{ad}$ Desorption/Exchange Kinetics on Pt Electrodes—A Combined In Situ IR and Mass Spectrometry Study**

*ChemPhysChem*
DOI: **10.1002/cphc.200700425**

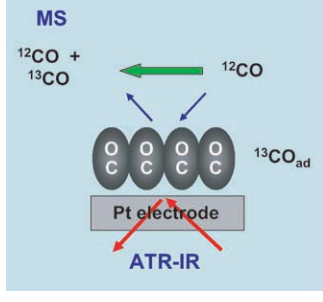


**Desorption and exchange of CO**: The exchange of a saturated $^{13}CO$ adlayer by gas-phase $^{12}CO$ is monitored by in situ attenuated total reflection infrared spectroscopy (ATR–IR) spectroscopy and online mass spectrometry (see figure). First-order exchange and the dependence of the exchange rate on the partial pressure of $^{12}CO$ indicate $CO_{ad}$ desorption at room temperature and a desorption-controlled exchange mechanism.

## *Structure–Activity Relationships*

B. R. Hearn,* K. Sundermann, J. Cannoy, D. V. Santi

**Semisynthesis and Cytotoxicity of Hypothemycin Analogues**

*ChemMedChem*
DOI: **10.1002/cmdc.200700128**

Evaluation of the hypothemycin cytotoxicity SAR identifies the C4′–C8′ region of the macrocyclic lactone as relatively intolerant of structural modifications. Manipulation of the 4-position of the resorcylic acid, however, provides new opportunities to improve solubility and pharmacokinetic properties as this site may be modified without negatively impacting cytotoxicity.

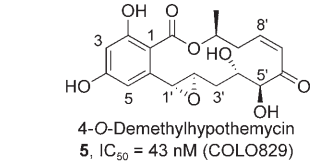

4-*O*-Demethylhypothemycin
**5**, $IC_{50}$ = 43 nM (COLO829)

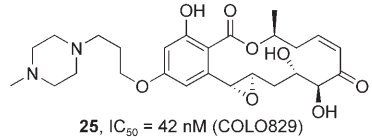

**25**, $IC_{50}$ = 42 nM (COLO829)


© 2007 Wiley-VCH Verlag GmbH & Co. KGaA, Weinheim

EurJIC European Journal of Inorganic Chemistry

## *Mass Spectrometry*

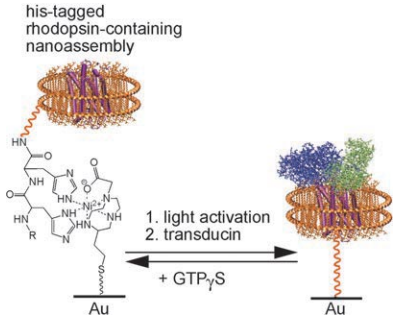


**Delicate probing**: When nanodisc assemblies are used to present membrane proteins on a biochip surface, interactions of these proteins can be studied by mass spectrometry. The method is illustrated with the protein rhodopsin, which is immobilized to a self-assembled monolayer by way of a his-tagged membrane scaffold protein. Upon activation of rhodopsin with light, the protein complex transducin binds and can be detected using SAMDI mass spectrometry.

V. L. Marin, T. H. Bayburt, S. G. Sligar,* M. Mrksich*

**Functional Assays of Membrane-Bound Proteins with SAMDI-TOF Mass Spectrometry**

*Angew. Chem. Int. Ed.*
DOI: **10.1002/anie.200702694**

## *Responsive Ligands*

Tetrathiafulvalene–imine–pyridine assemblies have been synthesized and shown to generate both electrochemical and colorimetric responses upon lead binding.

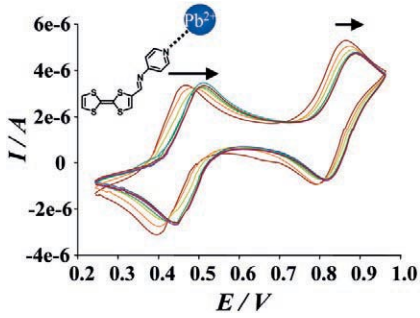


J.-Y. Balandier, A. Belyasmine, M. Sallé*

**Tetrathiafulvalene–Imine–Pyridine Assemblies for $Pb^{2+}$ Recognition**

*Eur. J. Org. Chem.*
DOI: **10.1002/ejoc.200700705**

## *Asymmetric Catalysis*

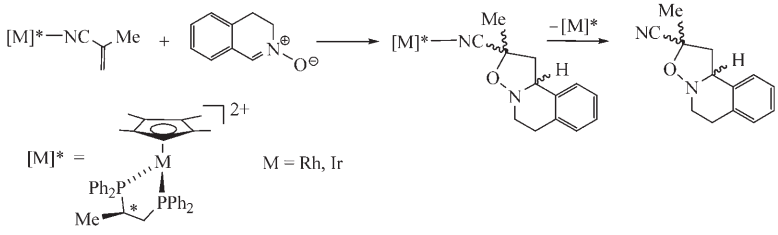


**Performance enhancement**: By taking advantage of the knowledge of the relative abundance and stereochemistry of the active metallic intermediates present in the catalytic system (see scheme), a moderate enantioselectivity can be improved to achieve an excellent level of selection. In addition, such studies provide explanations for unexpected trends, the relationship between the configuration at the metal to the stereochemical outcome, and the efficient reutilization of the catalyst.

D. Carmona,* M. P. Lamata, F. Viguri, R. Rodríguez, F. J. Lahoz, L. A. Oro

**Half-Sandwich Rhodium (and Iridium) Complexes as Enantioselective Catalysts for the 1,3-Dipolar Cycloaddition of 3,4-Dihydroisoquinoline *N*-Oxide to Methacrylonitrile**

*Chem. Eur. J.*
DOI: **10.1002/chem.200701140**

On these pages, we feature a selection of the excellent work that has recently been published in our sister journals. If you are reading these pages on a computer, click on any of the items to read the full article. Otherwise please see the DOIs for easy online access through Wiley InterScience.

 © 2007 Wiley-VCH Verlag GmbH & Co. KGaA, Weinheim 

DOI: 10.1002/ejic.200701042

# The First Linear Coordination Oligomer Linked by 4,4′-Bipyridine

Yutian Wang[a] and Ulli Englert*[a]

**Keywords:** Coordination polymers / Chain structures / Polycations / Oligomers / X-ray diffraction

A unique coordination oligomer derived from bridging 4,4′-bipyridine (bipy) ligands was synthesized and characterized. Long linear $[Ag_4(bipy)_5]^{4+}$ tetracations, shorter $[Ag_2(bipy)_3]^{2+}$ dications and 4-aminobenzoate anions represent the major constituents. When silver nitrate was added to solutions of this salt, polymerization in high yield occurred.
(© Wiley-VCH Verlag GmbH & Co. KGaA, 69451 Weinheim, Germany, 2007)

## Introduction

The optical, catalytic or magnetic properties of coordination polymers make them candidates for a plethora of potential applications.[1] The broad interest in this subject is reflected in an increasing number of publications during the last decade.[2] Active research is devoted to the structural chemistry of metal-containing polymers: about 11% of the structurally characterized organometallic and coordination compounds are polymeric.[3,4] 4,4′-Bipyridine (bipy) plays an important role among the organic linkers between metal cations. The relevance of this ligand for the construction of coordination polymers was recently reviewed by Biradha et al.[5] We encountered single-crystal to single-crystal reactions in surprisingly dynamic coordination polymers involving 4,4′-bipyridine.[6,7] To date, about 800 metal-containing derivatives of this organic ligand have been studied by diffraction methods; a large majority of these compounds contain bridging bipyridine molecules, but structures with a terminal bipy connected to a single metal cation through only one of the N donors have also been described.[8] Chemists intuitively associate polymers with oligomers as obvious intermediates; to the best of our knowledge, no linear coordination oligomer based on 4,4′-bipyridine, that is, no complex of finite nuclearity containing more than two metal atoms linked by this ligand, has ever been structurally characterized.[9] In this contribution, we wish to report the synthesis and characterization of the first oligocation based on bridging and terminal 4,4′-bipy ligands.

## Results and Discussion

Silver mono- or dicarboxylates and difunctional N donor ligands such as ethylendiamine,[10–12] 4,4′-bipyridine[13–21] or 1,2-diaminocyclohexane[22,23] have been reported to form polycationic $[Ag(ligand)^+]_\infty$ chains that are potentially cross-linked through weaker interactions such as argentophilic contacts or long Ag–O bonds. In contrast to this predictable behaviour, the reaction between silver 4-aminobenzoate and 4,4′-bipyridine results in the unexpected and unprecedented formation of **1**, which is a rather complex solid. Single-crystal X-ray diffraction showed that

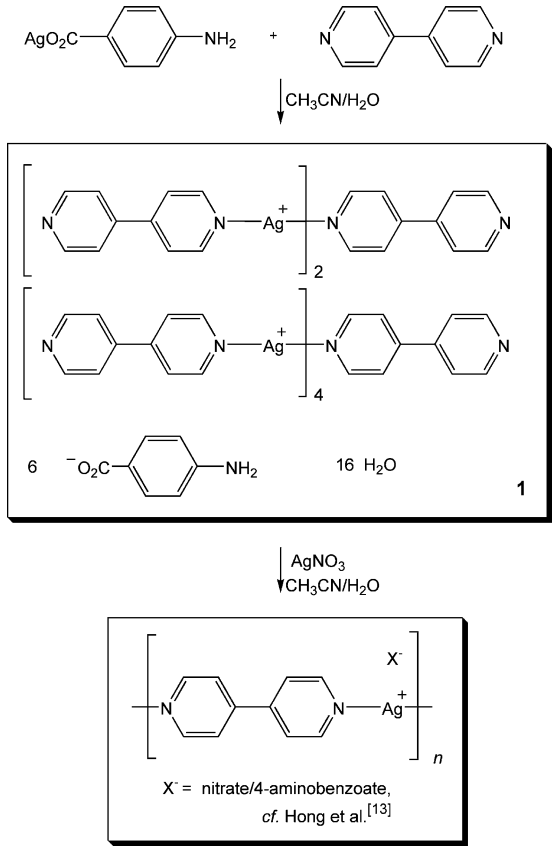


Scheme 1. Synthesis of **1** and polymerization upon addition of $AgNO_3$.

[a] Institut für Anorganische Chemie, RWTH Aachen,
Landoltweg 1, 52074 Aachen, Germany
Fax: +49-241-8092288
E-mail: ullrich.englert@ac.rwth-aachen.de
Supporting information for this article is available on the WWW under http://www.eurjic.org/ or from the author.

 © 2007 Wiley-VCH Verlag GmbH & Co. KGaA, Weinheim 

its building blocks comprise a dication $[Ag_2(bipy)_3]^{2+}$, a tetracation $[Ag_4(bipy)_5]^{4+}$, 6 4-aminobenzoate anions and 16 water molecules (Scheme 1).

The two cationic residues in the asymmetric unit are represented in Figure 1a,b: Ag–N bonds lead to the expected almost linear coordination of the $Ag^I$ centres, and deviations due to additional considerably longer and weaker interactions between the silver centres and the aqua or carboxylato oxygen atoms are also apparent. Five of the $Ag^I$ centres interact with two O donor ligands, whereas the sixth $Ag^I$ centre interacts with only one O donor ligand; the distances of these interactions fall in the range between 2.45 and 2.69 Å. Among the 16 water molecules in the asymmetric unit of **1**, 4 play a special role. Not only do they coordinate to the silver cations, but they also form hydrogen-bonding bridges with the dangling ends of the oligocations; the uncoordinated N atoms of the terminal bipy ligands act as acceptors. The long $[Ag_4(bipy)_5]^{4+}$ cations are crosslinked by bridging carboxylato oxygen atoms from two anions (Figure 1c).

The crosslinked longer residues and the discrete shorter cationic residues in **1** extend along the crystallographic *c* direction with stacking distances of approximately 3.5 Å. Matching torsion angles between the aryl rings along both polymer chains ensure a largely coplanar arrangement along the stacking direction (Figure 2).

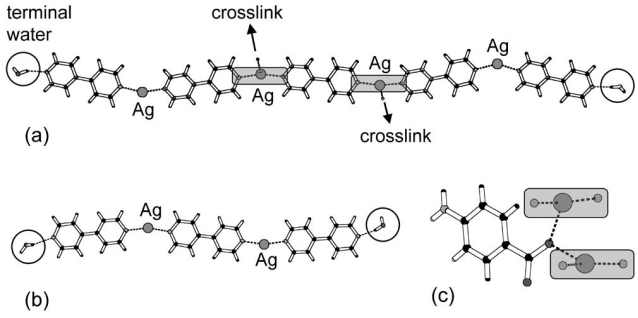


Figure 1. Tetracation $[Ag_4(bipy)_5]^{4+}$ (a) and dication $[Ag_2(bipy)_3]^{2+}$ (b) in **1**; the water molecules that are hydrogen bonded to the terminal pyridyl rings interact with metal centres in neighbouring residues through rather long coordinative bonds [Ag–O min 2.617(3), max 2.678(4) Å]; Ag···O interactions are not shown. (c) Geometry of a carboxylate crosslink between adjacent tetracations; the two symmetrically independent Ag···Ag distances are 3.2811(11) and 3.3773(11) Å.

Hydrogen bonding in **1** is limited by the number of H donors: The 16 water molecules and the 6 amino groups result in a total of 44 potential donor hydrogen atoms; the structure comprises a larger number of suitable classical acceptor sites, namely those associated with the 12 carboxylato and 16 water oxygen atoms, in addition to the 4 bipy N atoms. Of the 44 donor H atoms, 40 find an electronegative acceptor atom in reasonable geometry, and the remaining four, all of them aryl-bonded amino hydrogen atoms, point towards the centres of the aromatic rings in the adjacent anions. A detailed analysis of short interresidue contacts in **1** is provided in the Supporting Information.

As outlined above, 4 of the 16 water molecules in the asymmetric unit of **1** simultaneously participate in two different interactions with the ionic residues of the structure and both are hydrogen bonded and weakly metal coordinated. DSC and thermogravimetric studies show that the water molecules from **1** are released in two steps and in a 3:1 ratio upon heating. It is tempting to associate the second dehydration step with the loss of the more tightly bonded water molecules that terminate the oligocations.

## Conclusions

Compound **1** was obtained in high yields and should not simply be regarded as a singular novel structure. Solutions of the compound show the chemical reactivity expected for oligomers. The residues contributing to the formation of **1**, namely, 4-aminobenzoate, $Ag^I$ cations and the 4,4′-bipyridine ligand, in the additional presence of nitrate anions, take part in a different and less spectacular reaction described recently by Hong et al.[13] These authors obtained a one-dimensional coordination polymer of composition $\{[Ag(4,4'\text{-bipy})(H_2O)](aba)_{0.5}(NO_3)_{0.5}\cdot(H_2O)_{0.5}\}_\infty$ with infinite polycationic chains. The nature of the anions is decisive for the outcome of the reaction. When silver nitrate is added to a solution of oligomeric compound **1** in acetonitrile/water (Scheme 1), the above-mentioned coordination polymer precipitates almost quantitatively. The oligocations in **1** do not represent a dead end; rather, they are intermediates on the way to polymers that can be trapped under a favourable combination of counteranions.

## Experimental Section

Silver 4-aminobenzoate [Ag(aba)] was prepared from potassium benzoate and silver nitrate. Satisfactory microanalytical data were

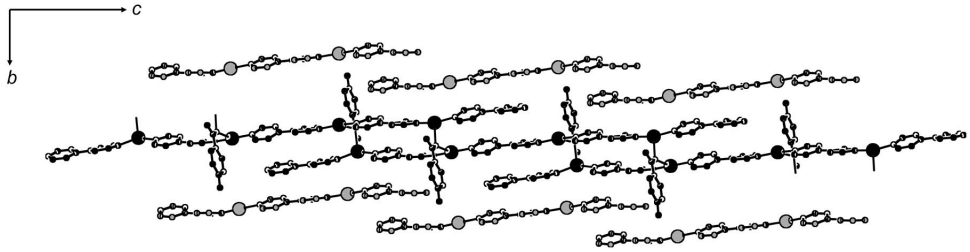


Figure 2. Arrangement of the anion-crosslinked tetracations (black) and the discrete dications (grey) in the crystal structure of **1**; the remaining four anions and the water molecules are omitted.

 © 2007 Wiley-VCH Verlag GmbH & Co. KGaA, Weinheim 

obtained. The structure of this salt was determined by Amiraslanov et al.[24]

**1:** A solution of 4,4′-bipyridine (0.124 g, 0.8 mmol) in $CH_3CN$ (5 mL) was added to a solution of Ag(aba) (0.146 g, 0.6 mmol) in acetonitrile/water (1:1), and the mixture was stirred for 30 min at room temperature and then filtered. After 2 d of slow evaporation at room temperature, light-yellow crystals suitable for X-ray diffraction precipitated. Yield: 0.225 g [75%, based on Ag(aba)]. Compound **1** is stable when exposed to light. $C_{122}H_{132}Ag_6N_{22}O_{28}$ (3001.72): calcd. C 48.82, H 4.43, N 10.27; found C 48.68, H 4.46, N 10.20. $^1$H NMR (400 MHz; $CD_3CN/D_2O$, 1:1): $\delta$ = 6.72 (m, 6×2 H, 4-aminobenzoate), 7.68 (m, 6×2 H, 4-aminobenzoate), 7.81 (m, 8×4 H, 4,4′-bipyridine), 8.67 (m, 8×4 H, 4,4′-bipyridine) ppm. The spectrum confirms the composition of the bulk and the expected integration result of 24 H (6 anions) versus 64 H (8 bipyridine moieties).

Compound **1** was dehydrated in two steps, and the second step was close to decomposition. Around 100 °C, a weight loss of 7.8% (calculated for the loss of 12 $H_2O$ 7.2%) occurred and around 120 °C, a weight loss of 2.6% (calculated for the loss of 4 $H_2O$ 2.4%) occurred (Supporting Information).

The IR spectrum of **1** and that of the coordination polymer reported by Hong et al.[13] differ significantly in the region between 1420 and 1350 $cm^{-1}$. In contrast to the polymer, **1** does not contain $NO_3^-$ anions.

**Single-Crystal X-ray Structure Determination:** Data were collected with a Bruker Smart APEX CCD detector (Mo-$K_\alpha$ radiation, $\lambda$ = 0.71073 Å, graphite monochromator) with a D8 goniometer. Temperature was controlled with an Oxford Cryosystems Series 800 instrument. Intensities were integrated with SAINT[25] and corrected for absorption with SADABS.[26] Structures were solved by direct methods (SHELXS-97)[27] and refined on $F^2$ with SHELXL-97.[28]

**Crystal Data for 1:** Monoclinic space group $P2_1$, $a$ = 18.2356(11) Å, $b$ = 14.0626(8) Å, $c$ = 23.6767(14) Å, $\beta$ = 95.988(2)°, $V$ = 6038.5(6) Å$^3$, $Z$ = 2; $T$ = 130 K; refinement of 1604 parameters based on 29526 independent out of totally 70319 reflections converged at $R_1$ = 0.0506, $wR_2$ = 0.0994, $GOF$ = 1.000. In view of the inversion twinning [Flack parameter[29] 0.539(15)] encountered for the crystal documented here, intensity data on a second crystal were collected and a Flack parameter of 0.351(18) was obtained. CCDC-657268 contains the supplementary crystallographic data for this paper. These data can be obtained free of charge from The Cambridge Crystallographic Data Centre via www.ccdc.cam.ac.uk/data_request/cif.

**Supporting Information** (see footnote on the first page of this article): Crystal data and structure refinement, Ag coordination and intermolecular interactions, thermal analysis, polymerization and photographs of crystals.

## Acknowledgments

We thank Dr. A. Fischer and D. Peters-Groth, Grünenthal GmbH Aachen, for thermal analyses and Cand. Chem. Y. Zhao for assistance with the structural study. The DFG is acknowledged for a fellowship to Y. W.

[1] C. Janiak, *Dalton Trans.* **2003**, 278.
[2] A. Y. Robin, K. M. Fromm, *Coord. Chem. Rev.* **2006**, *250*, 2127.
[3] According to the CSD (cf. ref.[4]), V.5.28, including the update of Jan 2007, ca. 18000 structures out of ca. 170000 error-free organometallic and coordination compounds with 3D coordinates were polymeric.
[4] F. Allen, *Acta Crystallogr., Sect. B* **2002**, *58*, 380.
[5] K. Biradha, M. Sarkar, L. Rajput, *Chem. Commun.* **2006**, 4169.
[6] C. Hu, U. Englert, *Angew. Chem. Int. Ed.* **2005**, *44*, 2281.
[7] C. Hu, U. Englert, *Angew. Chem. Int. Ed.* **2006**, *45*, 3457.
[8] A search in the CSD (see refs.[3,4]) resulted in 61 error-free terminal bipy structures without disorder for which 3D coordinates were available.
[9] Dinuclear compounds involving both bridging and terminal 4,4′-bipy ligands were described in the following publications: a) X.-J. Lin, Z. Shen, Y.-Z. Li, H. Uno, Y. Song, H.-J. Xu, X.-Z. You, *J. Coord. Chem.* **2005**, *58*, 1139; b) J. T. Sampanthar, J. J. Vittal, *J. Chem. Soc. Dalton Trans.* **1999**, 1993; c) S. Gao, J.-W. Liu, L.-H. Huo, H. Zhao, S. W. Ng, *Acta Crystallogr., Sect. E* **2004**, *60*, m1590; d) M. Aoyagi, K. Biradha, M. Fujita, *Bull. Chem. Soc. Jpn.* **2000**, *73*, 1369. Cyclic oligomers have been described: The CSD (see refs.[3,4]) compiles 15 examples of molecular squares $M_4(bipy)_4$, and an $Os_6(bipy)_6$ ring has been characterized by Y. L. Cho, H. Uh, S.-Y. Chang, H.-Y. Chang, M.-G. Choi, I. Shin, K.-S. Jeong, *J. Am. Chem. Soc.* **2001**, *123*, 1258.
[10] H.-L. Zhu, X.-J. Sun, D.-Q. Wang, *Z. Kristallogr. New Cryst. Struct.* **2003**, *218*, 30.
[11] Z. L. You, L. Yang, Y. Zou, W. J. Zeng, W. S. Liu, H. L. Zhu, *Acta Crystallogr., Sect. C* **2004**, *60*, m117.
[12] A. Usman, H. K. Fun, S. Chantrapromma, H. L. Zhu, X. J. Wang, *Acta Crystallogr., Sect. C* **2003**, *59*, m97.
[13] R. Wang, M. C. Hong, J. Luo, F. Jiang, L. Han, Z. Lin, R. Cao, *Inorg. Chim. Acta* **2004**, *357*, 103.
[14] L. Ye, Y. Wu, *Acta Crystallogr., Sect. E* **2005**, *61*, m1894.
[15] J. T. Sampanthar, J. J. Vittal, *Cryst. Eng.* **2000**, *3*, 117.
[16] M.-L. Tong, X.-M. Chen, S. W. Ng, *Inorg. Chem. Commun.* **2000**, *3*, 436.
[17] D. Sun, R. Cao, Y. Sun, W. Bi, X. Li, Y. Wang, Q. Shi, X. Li, *Inorg. Chem.* **2003**, *42*, 7512.
[18] G. A. Bowmaker, Effendy, K. C. Lim, B. W. Skelton, D. Sukarianingsih, A. T. White, *Inorg. Chim. Acta* **2005**, *358*, 4342.
[19] D.-Q. Zhang, W.-H. Zhang, Q.-F. Xu, J.-P. Lang, S. W. Ng, *Acta Crystallogr., Sect. E* **2004**, *60*, 1256.
[20] F. Li, T. Li, D. Yuan, L. Lv, R. Cao, *Inorg. Chem. Commun.* **2006**, *9*, 691.
[21] Y. Wang, U. Englert, unpublished results.
[22] J.-C. Lee, H. Takahashi, Y. Matsui, *Z. Kristallogr. New Cryst. Struct.* **2005**, *220*, 493.
[23] I. Kalf, M. Braun, Y. Wang, U. Englert, *CrystEngComm* **2006**, *8*, 916.
[24] R. Amiraslanov, B. T. Usubaliev, G. N. Nadzhafov, A. A. Musaev, E. M. Movsumov, K. S. Mamedov, *Zh. Strukt. Khim.* **1980**, *21*, 112.
[25] Bruker AXS, *SAINT+: Program for Reduction of Data Collected on Bruker CCD Area Detector Diffractometer V. 6.02*, Bruker AXS Inc., Madison, USA, **1999**.
[26] G. M. Sheldrick, *SADABS: Program for Empirical Absorption Correction of Area Detector Data*, University of Göttingen, **1996**.
[27] G. M. Sheldrick, *SHELXS97: Program for Crystal Structure Solution*, University of Göttingen, **1997**.
[28] G. M. Sheldrick, *SHELXL97: Program for Crystal Structure Refinement*, University of Göttingen, **1997**.
[29] H. D. Flack, *Acta Crystallogr., Sect. A* **1983**, *39*, 876.

Received: September 25, 2007
Published Online: November 8, 2007

 © 2007 Wiley-VCH Verlag GmbH & Co. KGaA, Weinheim 

DOI: 10.1002/ejic.200700890

# Oxidation of Spirocyclohexyl-1,2,4-trithiolane and Complexation Reaction with $[Pt(\eta^2\text{-nb})(PPh_3)_2]$

**Holm Petzold,[a] Silvio Bräutigam,[a] Helmar Görls,[a] Wolfgang Weigand,*[a] Jaroslaw Romanski,[b] and Grzegorz Mloston*[b]**

**Keywords:** Insertion reactions / 1,2,4-Trithiolanes / Platinum / S ligands / Thioketone complexes

Oxidation of spirocylcohexyl-1,2,4-trithiolane **1** yielded the 4-*S*- and 1-*S*-oxide, **2** and **3**, respectively. The complexation reactions of **1**–**3** with $[Pt(\eta^2\text{-nb})(PPh_3)_2]$ (**4**; nb = norbornene) have been studied. The formed dithiolato, thioketone, thiolatosulfenato and sulfine complexes **5**–**8** have been isolated and characterized by $^1$H-, $^{31}$P NMR and IR spectroscopy and by mass spectrometry. The mechanism of the reaction is discussed. The reaction proceeds by insertion of the $Pt^0$ complex fragment into the sulfur–sulfur bond and subsequent ring contraction by extrusion of a thioketone or sulfine. Comparison of the molecular structures of the oxidized complexes **7** and **8** with the nonoxidized complex **5** shows elongation of the sulfenato–platinum bond and elongation of the platinum–phosphorus bond in the corresponding *trans* position. The product formed suggests that, in this system, formation of thiolato–platinum bonds is energetically favoured to sulfenato–platinum bonds. The structures of **5**, **7** and **8** were established by X-ray crystallography.
(© Wiley-VCH Verlag GmbH & Co. KGaA, 69451 Weinheim, Germany, 2007)

## Introduction

1,2,4-Trithiolanes form a class of sulfur-rich five-membered heterocycles, which have attracted considerable attention in recent times. The parent compound as well as some 3,5-dialkyl-1,2,4-trithiolanes are naturally occurring substances.[1] On the other hand, 3,3,5,5-tetrasubstituted derivatives are easily formed as interception products of the reaction of intermediate thiocarbonyl *S*-sulfides (thiosulfines) with dipolarophilic thioketones.[2]

It is well known that the heating of these heterocycles in solution or in the gas phase (Flash Vacuum Pyrolysis, FVP) results in a cycloreversion reaction leading to thiosulfines (existing in an equilibrium with isomeric dithiiranes) and the corresponding thioketones.[3,4] In this way, 1,2,4-trithiolanes are used as a convenient source of in situ formed thiosulfines, which subsequently can be trapped by other dipolarophiles.[4] Very recently 1,2,4-trithiolanes have been used for syntheses of mimics for the active site of [Fe-only]-hydrogenase.[5,6] Along with the parent 1,2,4-trithiolane, there are also some oxidized species found in marine organisms.[7] In a recent investigation, the parent as well as the 3,3,5,5-tetramethyl-1,2,4-trithiolane were oxidized, and the diverse oxides were obtained and characterized. The study showed that the oxidation reactions with *m*-chloroperbenzoic acid (*m*-CPBA) result in the formation of a mixture of 1-*S*- and 4-*S*-oxides in comparable amounts.[8] Over the last years, reactions of cyclic disulfanes, thiosulfinates and thiosulfonates with $Pt^0$ have been described, which result in dithiolato, sulfenato thiolato, sulfinato thiolato, as well as thiosulfonato $Pt^{II}$ complexes. Except for the latter compound, all the compounds were formed by oxidative addition of $Pt^0$ complexes to the S–S(O)$_n$ moiety ($n$ = 0–2).[9–13] 1,2,4-Trithiolanes and their 1-*S*-oxides undergo reactions with $Pt^0$ complexes.[9,13]

Here we present a systematic investigation of the reactivity of the 1,2,4-trithiolane **1** and of its 4-*S*- and 1-*S*-oxide, **2** and **3**, respectively, with $[Pt(\eta^2\text{-nb})(PPh_3)_2]$ (**4**; nb = norbornene).

## Results and Discussion

The spirocyclohexyl-1,2,4-trithiolane **1** was oxidized by using *m*-CPBA. After separation by means of column chromatography, two main products were obtained as pure compounds (Scheme 1), along with some starting material and a mixture of two higher oxides.[14] The $^{13}$C NMR spectrum of the first eluted fraction shows 12 different signals. The signals at $\delta$ = 95.5 and 82.3 ppm are assigned to the quaternary C atoms C3 and C5. The second eluted fraction shows only six different signals, and for C3 and C5, only one signal at $\delta$ = 84.6 ppm is found. The elemental analysis and the found molecular peak in the mass spectra confirm

[a] Institut für Anorganische und Analytische Chemie, Friedrich-Schiller Universität Jena,
August-Bebel Str. 2, 07743 Jena, Germany
Fax: +49-3641-948102
E-mail: c8wewo@uni-jena.de
[b] Section of Heteroorganic Compounds, University of Łódź,
Narutowicza 68, 90-136 Łódź, Poland
Fax: +48-42-6781609
E-mail: gmloston@uni.lodz.pl
Supporting information for this article is available on the WWW under http://www.eurjic.org or from the author.

 © 2007 Wiley-VCH Verlag GmbH & Co. KGaA, Weinheim 

the formula $C_{12}H_{20}S_3O$; hence, the minor product is the 1-*S*-oxide **3** and the major product must be the 4-*S*-oxide **2**. The amount of the isolated 4-*S*-oxide **2** is nearly four times that of the 1-*S*-oxide **3**. Both products are crystalline; they are therefore more manageable than the tetramethyl derivatives.[8] The tendency to form the 4-*S*-oxide over the 1-*S*-oxide is well known for the unsubstituted 1,2,4-trithiolane and 3,3,5,5-tetramethyl-1,2,4-trithiolane.[7,8] In contrast, for the more bulkily substituted derivatives, such as tetraphenyl[13] and 3,5-di-*tert*-butyl-3,5-diphenyl derivatives,[15] exclusive oxidation at S1 and S2 is observed.

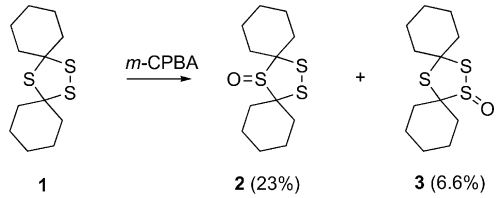


Scheme 1. Oxidation of spirocyclohexyl-1,2,4-trithiolane **1**.

Treatment of spirocyclohexyl-1,2,4-trithiolane **1** with 2 equiv. [Pt(η²-nb)($PPh_3$)$_2$] (**4**) in toluene at 50 °C yielded a 1:1 mixture of two complexes (Scheme 2) in the crude product according to the $^{31}$P NMR spectrum. This spectrum showed the existence of two spin systems, one $A_2$ spin system with a $^1J$(P,Pt) value of 2971 Hz and an AB spin system with a $^2J$(P,P) value of 16 Hz and $^1J$(P,Pt) values of 4600 Hz and 2838 Hz. The first spin system is typical for complexes of the type [Pt($PPh_3$)$_2$($S_2CR_2$)] and is assigned to the dithiolato complex **5**; fractional crystallization gave the pure complex **5** in 64% yield with respect to 2 equiv. **4**. The results of the X-ray analysis are shown in Figure 1. The complex has a distorted quadratic planar geometry with a small S–Pt–S angle of 75.54(2) °. The S–Pt bond lengths of 2.3123(7) and 2.3231(7) Å are slightly longer than the P–Pt bond lengths of 2.2874(7) and 2.2820(6) Å. The structure is comparable to those reported for the similar complexes.[10,16]

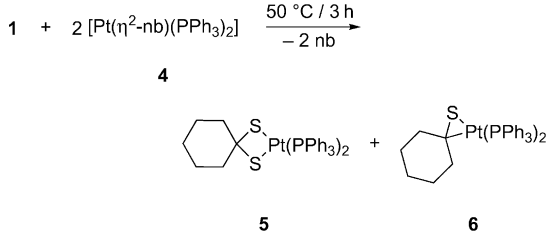


Scheme 2. Reaction of 1,2,4-trithiolane **1** with platinum complex **4**.

The second spin system observed in the $^{31}$P NMR spectrum is assigned to the thioketone complex **6**. An independent synthesis from cyclohexanonethione and [Pt(η²-nb)($PPh_3$)$_2$] yielded a sample whose identity was confirmed to be **6** by TLC and $^{31}$P NMR spectroscopy. The fragmentation of **1** found is similar to that reported for the reaction of bulkily substituted 1,2,4-trithiolanes with $Fe_2(CO)_9$.[5]

Similar treatment of the 4-*S*-oxide **2** with excess [Pt(η²-nb)($PPh_3$)$_2$] gave a 1:1 mixture of the thioketone complex **6**

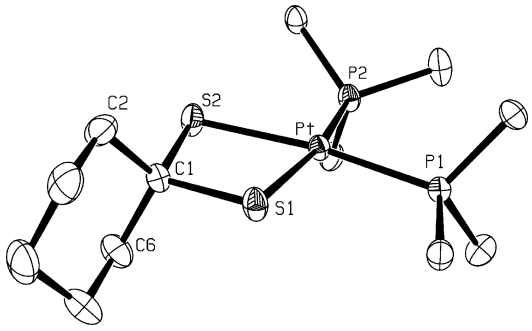


Figure 1. ORTEP[26] drawing of the molecular structure of the dithiolato complex **5** (for clarity, hydrogen atoms are omitted and the phenyl groups are represented only by their *ipso*-carbon atoms). Selected bond lengths (Å) and angles (°): Pt–P2 2.2874(7); Pt–P1 2.2820(6); Pt–S1 2.3123(7); Pt–S2 2.3231(7); S1–C1 1.847(3); S2–C1 1.836(3); P2–Pt–P1 99.89(2); S1–Pt–S2 75.54(2).

and a second complex **7** (Scheme 3). The pure complex **7** was isolated in 52% yield with respect to 2 equiv. **4** in a manner similar to that described for the dithiolato complex **5**. The $^{31}$P NMR spectrum of **7** shows an AB spin system with a $^2J$(P,P) value of 16 Hz and $^1J$(P,Pt) values of 3324 Hz and 2343 Hz. Elemental analysis and mass spectroscopy confirm the molecular formula of $C_{42}H_{40}OP_2PtS_2$. In the IR spectrum, a strong broad band is found at $\tilde{\nu}$ = 995 cm$^{-1}$, which is typical for sulfenato ligands bound to platinum(II).[11d,13] Finally, X-ray analysis unambiguously confirms the expected structure of the sulfenato thiolato complex **7**. The molecular structure of **7** is shown in Figure 2.

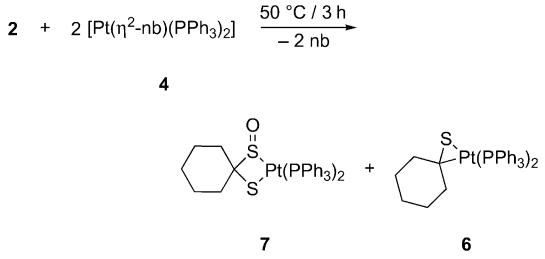


Scheme 3. Reaction of spirocyclohexyl-1,2,4-trithiolane 4-*S* oxide **2** with **4**.

The complex has a distorted sqare–planar geometry. The sulfur–platinum bond length (S1–Pt) is 2.3174(6) Å and is in the range of those found in the dithiolato complex **5**. A similar bond length relative to that in **5** is observed for the phosphorus–platinum bond P2–Pt [2.2944(6) Å] in the *trans* position. In contrast, the sulfur–platinum bond S2–Pt to the sulfenato ligand is slightly elongated by 0.01 Å. The higher *trans* influence of the sulfenato ligand results in an elongation the P1–Pt bond by approximately 0.04 Å. This observation is in a good agreement with the smaller value observed for the $^1J$(P,Pt) constant. The sulfur–oxygen bond in the sulfenato ligand [1.503(2) Å] is slightly longer than those reported for similar sterically crowded complexes.[12]

Complex **4** reacted with the 1-*S* oxide **3** at room temperature in a few minutes to yield a 1:1 mixture of the dithiolato complex **5** and a new product **8**, which shows an AB spin system with a $^2J$(P,P) value of 24 Hz and $^1J$(P,Pt) values of

 © 2007 Wiley-VCH Verlag GmbH & Co. KGaA, Weinheim 

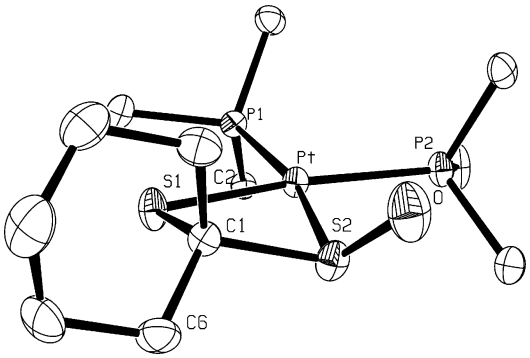


Figure 2. ORTEP[26] drawing of the molecular structure of the sulfenato thiolato complex **7** (for clarity, hydrogen atoms are omitted and the phenyl groups are represented only by their *ipso*-carbon atoms). Selected bond lengths (Å) and angles (°): Pt–P2 2.2944(6); Pt–P1 2.3193(6); Pt–S1 2.3174(6); Pt–S2 2.3336(6); S1–C1 1.837(2); S2–C1 1.858(2); S2–O 1.503(2); P2–Pt–P1 100.01(2); S1–Pt–S2 74.33(2).

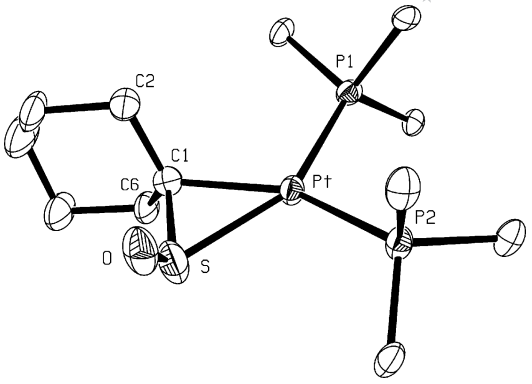


Figure 3. ORTEP[26] drawing of the molecular structure of the sulfine complex **8** [for clarity, hydrogen atoms and O1A are omitted and the phenyl groups are represented only by their *ipso*-carbon atoms]. Selected bond lengths (Å) and angles (°): Pt–P2 2.3038(16); Pt–P1 2.2867(16); Pt–S1 2.3338(18); Pt–C1 2.126(6); S1–C1 1.770(6); S1–O1 1.436(8); S1–O1A 1.321(13); P2–Pt–P1 105.29(6); S1–Pt–C1 46.48(17).

3817 Hz and 3075 Hz in the $^{31}P$ NMR spectrum (Scheme 4). In the mass spectrum, the molecular peak is found at $m/z$ = 850, and the elemental analysis confirms the molecular formula $C_{42}H_{40}OP_2PtS$. On the basis of these data, structure **8** can be assigned to the isolated complex. The result is in good agreement with that observed in the reaction between 3,3,5,5-tetraphenyl-1,2,4-trithiolane 1-*S*-oxide and $[Pt(\eta^2\text{-}C_2H_4)(PPh_3)_2]$.[13] Recrystallization from a thf/pentane mixture yielded crystals that were suitable for X-ray analysis. The results are shown in Figure 3.

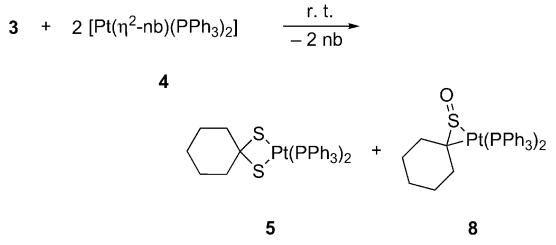


Scheme 4. Reaction of spirocyclohexyl-1,2,4-trithiolane 1-*S* oxide **3** with **4**.

The sulfine fragment incorporated in complex **8** is coordinated by an $\eta^2$ mode and the complex has a distorted square-planar coordination sphere. The structure is comparable with that reported for the 9*H*-fluorene-9-thione-*S*-oxide complex.[17] The P1–Pt bond located in the *trans* position to the oxidized sulfur atom has a length of 2.2867(16) Å and the value for this bond length falls at the higher end of the range (2.25–2.30 Å) found for thioketone complexes.[9,10,18,19] In contrast to that found in the structure of **6**, the sulfur–platinum bond in **8** is remarkably longer [2.3338(18) Å] than those found in thioketone complexes (2.27–2.29 Å).[9,10,18,19] In the registered spectra of the crude product, there is no indication for the formation of **6** or **7**.

Taking this into account, the reactions of 1,2,4-trithiolane **1** and of the oxides **2** and **3** likely proceed in the first step by insertion of the $Pt^0$ complex fragment into the sulfur–sulfur bond of the 1,2,4-trithiolane ring.[9,11b,13] Ring contraction of the six-membered platinacycles formed, by expulsion of a thioketone or sulfine, leads to the four-membered platinacycles **5** and **7**, respectively. The former thioether sulfur atom is bonded to the platinum atom. In the last step, the thioketone or sulfine is complexed by a second equivalent of **4** to yield **6** or **8**, respectively. The exclusive formation of **5** and **8** in the reaction of the 1-*S*-oxide **3** with **4** suggests the favoured formation of thiolato ligands instead of sulfenato ligands in this system.

## Conclusions

In summary, the reactions of spirocylcohexyl-1,2,4-trithiolane **1** and of its 4-*S*- and 1-*S*-oxide, **2** and **3**, respectively, proceed by insertion of the $Pt^0$ complex fragment into the sulfur–sulfur bond and subsequent ring contraction by expulsion of a thioketone or sulfine. The reactions yield the thioketone complex **6** and dithiolato complex **5**, as well as their mono *S*-oxides **8** and **7**. Comparison of the molecular structures of the oxidized and nonoxidized complexes shows an elongation of the sulfenato–platinum bond as well as the elongation of the platinum–phosphorus bond in the corresponding *trans* position. Selective extrusion of a sulfine instead of the thioketone in the case of **3** suggests that the formation of thiolato–platinum bonds is energetically favoured over sulfenato–platinum bonds.

## Experimental Section

**General:** Melting points were determined with an AXIOLAB microscope with a TMHS 600 heating plate and are uncorrected. $^1H$-, $^{31}P$- and $^{13}C$ NMR spectra were determined with BRUKER DRX 400 or BRUKER DRX 200 spectrometers at 30 °C; chemical shifts are referred to the protons of the solvent or 85% $H_3PO_4$. $^{31}P$- and $^{13}C$ NMR spectra are proton decoupled. IR spectra were recorded with a PERKIN ELMER System 2000 FT-IR spectrome-

 © 2007 Wiley-VCH Verlag GmbH & Co. KGaA, Weinheim 

ter. Mass spectra were recorded with a FINNIGAN MAT SSQ 710 mass spectrometer. Elemental analyses were determined with a LECO CHNS-932. All reactions were performed under argon, and solvents were dried by using sodium/benzophenone. Starting materials 7,14,15-trithia-dispiro[5.1.5.2]pentadecane (**1**)[20] and the $Pt^0$ complex **4**[18] were prepared according to the literature procedures.

**Oxidation of Spirocyclohexyl-1,2,4-trithiolane 1:** *m*-CPBA (70%, 1.2 g, 5.4 mmol) dissolved in $CH_2Cl_2$ (10 mL) was added in small portions to a solution of spirocyclohexyl-1,2,4-trithiolane **1** (1 g, 3.8 mmol) in $CH_2Cl_2$ (20 mL) at 0 °C. The reaction mixture was stirred for an additional 2 h and subsequently washed with a diluted aqueous solution of $NaHCO_3$. The organic layer was separated, dried with $Na_2SO_4$, and reduced to dryness, and the residue was subjected to column chromatography to yield the 1-*S*-oxide **3** and the 4-*S*-oxide **2**, as well as a mixture of higher oxides.

**Spirocyclohexyl-1,2,4-trithiolane 1-*S*-Oxide 3:** Colourless crystals. Yield: 70 mg (6.6%). M.p. 46 °C. $^1$H NMR (200 MHz, $CDCl_3$): $\delta$ = 2.25–2.1 (m, 4 H), 2.1–1.9 (m, 4 H), 1.8–1.3 (m, 12 H) ppm. $^{13}$C NMR (50 MHz, $CDCl_3$): $\delta$ = 95.5 (q-C), 82.3 (q-C), 49.5, 43.6, 36.8, 32.4, 26.8, 26.1, 25.6, 25.0, 24.2, 23 ppm. IR (KBr): $\tilde{\nu}$ = 2920 (s), 1447 (s), 1098 [s, (S=O)] $cm^{-1}$. $C_{12}H_{20}OS_3$ (277.49): calcd. C 52.13, H 7.29, S 34.79; found C 52.15, H 6.59, S 35.01.

**Spirocyclohexyl-1,2,4-trithiolane 4-*S*-Oxide 2:** Colourless crystals. Yield: 240 mg (23%). M.p. 115 °C. $^1$H NMR (200 MHz, $CDCl_3$): $\delta$ = 2.09 (m), 1.90 (dt), 1.78 (m), 1.63 (m), 1.33 (m) ppm. $^{13}$C NMR (50 MHz, $CDCl_3$): $\delta$ = 84.6 (q-C), 33.7, 28.2, 25.2, 24.6, 23.1 ppm. IR (KBr): $\tilde{\nu}$ = 2931 (s), 1443 (s), 1067 [s, (S=O)] $cm^{-1}$. $C_{12}H_{20}OS_3$ (277.49): calcd. C 52.13, H 7.29, S 34.79; found C 52.06, H 7.21, S 34.92.

**Reaction of Spirocyclohexyl 1,2,4-Trithiolane 1 with [Pt($\eta^2$-nb)-($PPh_3$)$_2$] (4):** A portion of spirocyclohexyl-1,2,4-trithiolane **1** (30 mg, 0.11 mmol) was added to a solution of **4** (120 mg, 0.15 mmol) in toluene (10 mL). The solution immediately turned red and was stirred for an additional 3 h at 50 °C. The formation of the dithiolato complex **5** and the thioketone complex **6** in a 1:1 ratio was monitored by TLC. The solvent was reduced to dryness, and the crude product was washed with diethyl ether. The residue was dissolved in thf (10 mL) and filtered through silica gel. The solvent was reduced (to 5 mL), and the mixture was stored in a flask with pentane (10 mL). After 1 d, the dithiolato complex **5** was obtained. Yellow crystals. Yield: 40 mg (64%). M.p. 275 °C dec. $^1$H NMR (400 MHz, $CD_2Cl_2$): $\delta$ = 7.44 (m, 12 H), 7.30 (m, 6 H), 7.20 (m, 12 H), 1.86 (m, 4 H), 1.44 (m, 4 H), 1.25 (m, 2 H) ppm. $^{13}$C NMR (100 MHz, $CD_2Cl_2$): $\delta$ = 135.0 (t, $J_{C,P}$ = 5.5 Hz), 131.0 (m), 130.5, 127.9 (t, $J_{C,P}$ = 5.2 Hz), 68.1 (s, $^2J_{C,Pt}$ = 58 Hz), 50.5 (s, $^3J_{C,Pt}$ = 23 Hz), 25.9, 23.3 ppm. $^{31}$P{$^1$H} NMR (81 MHz, $CDCl_3$): $\delta$ = 24.76 (s, $^1J_{P,Pt}$ = 2971 Hz) ppm. IR (KBr): $\tilde{\nu}$ = 3073, 3052, 2925, 2850, 1967 (w), 1903 (w), 1820 (w), 1628 (s br.), 1480, 1434 (s), 1185, 1095 (s), 1028, 1014, 998, 743 (s), 693 (s), 542/525/515/497 ($PC_3$) $cm^{-1}$. MS (FAB): *m*/*z* (%) = 865 (0.5) $[M]^+$, 752 (1) $[M - (S{=}C(CH_2)_5)]^+$, 718 $[(Ph_3P)_2Pt]^+$, 307 (100). $C_{42}H_{40}P_2PtS_2$ (865.92): calcd. C 58.26, H 4.66, S 7.41; found C 58.26, H 4.74, S 7.19.

**Reaction of Spirocyclohexyl 1,2,4-trithiolane 4-*S*-Oxide 2 with [Pt($\eta^2$-nb)($PPh_3$)$_2$] (4):** The reaction was carried out in a manner similar to that with the unoxidized spirocyclohexyl 1,2,4-trithiolane **1**, except with spirocyclohexyl-1,2,4-trithiolane 4-*S*-oxide **2** (31 mg, 0.11 mmol). TLC as well as $^{31}$P NMR spectroscopy of the crude product showed the formation of a 1:1 mixture of **6** and **7**. In analogy to **5** the sulfenato thiolato complex **7** was isolated by chromatography and subsequent crystallization. Yellow crystals. Yield: 35 mg (52%). M.p. 222 °C dec. $^1$H NMR (200 MHz, $CDCl_3$): $\delta$ = 7.50–7.18 (m, 30 H), 1.98–1.3 (m, 10 H) ppm. $^{31}$P{$^1$H} NMR (81 MHz, $CDCl_3$): $\delta$ = 21.0 (d, $^2J_{P,P}$ = 16, $^1J_{P,Pt}$ = 3324 Hz), 19.8 (d, $^2J_{P,P}$ = 16, $^1J_{P,Pt}$ = 2343 Hz) ppm. IR (KBr): $\tilde{\nu}$ = 3054, 2927, 2852, 1969 (w), 1818 (w), 1632 (s br.), 1481, 1435 (s), 1185, 1096 (s), 1019, 998, 995 (br.)/955 (br.) (S=O), 744 (s), 693 (s), 539/523/513/497 ($PC_3$) $cm^{-1}$. MS (FAB): *m*/*z* (%) = 882 (4), 767 (24) $[M - (S{=}C(CH_2)_5)]^+$, 718 (20) $[(Ph_3P)_2Pt]^+$. $C_{42}H_{40}OP_2PtS_2$ (881.92): calcd. C 57.20, H 4.57, S 7.27; found C 56.71, H 4.61, S 7.02.

**Reaction of Spirocyclohexyl-1,2,4-trithiolane 1-*S*-Oxide 3 with [Pt($\eta^2$-nb)($PPh_3$)$_2$] (4):** A portion of spirocyclohexyl 1,2,4-trithiolane 1-*S*-oxide **3** (25 mg, 0.09 mmol) was added to a solution of **4** (120 mg, 0.15 mmol) in toluene (10 mL) at room temperature. The colour of the reaction mixture became slightly yellow, and after some minutes, a solid precipitated. The formation of the dithiolato complex **5** and the sulfine complex **8** was confirmed by TLC. The solvent was evaporated, and residue was subjected to column chromatography (THF/hexane, 1:2, $SiO_2$). The first substantial fraction was assigned to the dithiolato complex **5**, and second fraction contained the sulfine complex **8**; this fraction was collected to yield the pure sulfine complex **8**. White crystals. Yield: 25 mg (40%). M. p. 193 °C dec. $^1$H NMR (200 MHz, $CDCl_3$): $\delta$ = 7.33 (m, 6 H), 7.24 (m, 12 H), 7.15 (m, 12 H), 2.43 (d, $J_{H,H}$ = 13 Hz), 1.57 (m, 1 H), 1.49 (m, 3 H), 1.41 (m, 2 H), 1.09 (m, 1 H), 1.05 (m, 1 H), 0.84 (m, 1 H) ppm. $^{13}$C NMR (100 MHz, $CD_2Cl_2$): $\delta$ = 134.2 (m, *ipso*-C), 134.0 (m, Ph-C), 129.8 (s, Ph-C), 128.4 (s, Ph-C), 127.8 (m, Ph-C), 83.4 [d, $^2J$(C,P) = 53 Hz], 33.0 (s br.), 32.4 (d, $J_{C,P}$ = 6 Hz), 29.1 (d, $J_{C,P}$ = 8 Hz), 28.7, 26.6 ppm. $^{31}$P{$^1$H} NMR (81 MHz, $CDCl_3$): $\delta$ = 27.4 (d, $^2J_{P,P}$ = 24, $^1J_{P,Pt}$ = 3817 Hz), 26.4 (d, $^2J_{P,P}$ = 24, $^1J_{P,Pt}$ = 3075 Hz) ppm. IR (KBr): $\tilde{\nu}$ = 3072, 3053, 2923, 2847, 1968 (w), 1900 (w), 1816 (w), 1634 (s br.), 1480, 1434 (s), 1183, 1095 (s), 1027, 1011, 997, 983 (S=O), 743 (s), 695 (s), 538/521/510/497 (PC3) $cm^{-1}$. MS (FAB): *m*/*z* (%) = 850 (15), 719 (100) $[(Ph_3P)_2Pt]^+$. $C_{42}H_{40}OP_2PtS$ (849.86): calcd. C 59.36, H 4.74, S 3.77; found C 59.23, H 4.86, S 3.43.

**Synthesis of the Cyclohexanethione Complex 6:** Cyclohexanon diethyl ketal (1 g, 5.8 mmol) was dissolved in nonane (30 mL). A stream of hydrogen sulfide was passed through the reaction mixture, and a few drops of concentrated sulfuric acid were added. The mixture became red. After 30 min, the excess hydrogen sulfide was removed by passing a stream of argon through. Solid $NaHCO_3$ was added, and the organic layer was washed with water and dried with $Na_2SO_4$. The nonane was distilled off under reduced pressure, and cyclohexanthione was trapped in a cooling trap as a solution in nonane. Complex **4** (80 mg, 0.1 mmol) in toluene (10 mL) was added to this solution. The solvent was evaporated, and the residue was washed with diethyl ether, dissolved in thf (15 mL) and filtered over silica gel. The solvent was reduced (to 3 mL), and the mixture was stored in a flask with pentane (20 mL). After some days, pure thioketone complex **6** crystallized. White crystals. Yield: 50 mg (60%). M.p. 234 °C dec. $^1$H NMR (400 MHz, $CDCl_3$): $\delta$ = 7.39–7.30 (m, 12 H), 7.24–7.11 (m, 18 H); 1.6–1.4 (m, 9 H), 0.87 (m, 1 H) ppm. $^{13}$C NMR (100 MHz, $CDCl_3$): $\delta$ = 135.4–133.4 (m), 133.8 (m), 129.2 (m), 127.3 (m), 86.3 (d, $^2J_{C,P}$ = 55 Hz), 43.8, 33.1 (d, $^3J_{C,P}$ = 8.5, $^2J_{C,Pt}$ = 45 Hz), 27.4 ppm. $^{31}$P{$^1$H} NMR (81 MHz, $CDCl_3$): $\delta$ = 28.2 (d, $^2J_{P,P}$ = 16, $^1J_{P,Pt}$ = 4600 Hz), 27.0 (d, $^2J_{P,P}$ = 16, $^1J_{P,Pt}$ = 2838 Hz) ppm. IR (KBr): $\tilde{\nu}$ = 3052, 2921, 2844, 1964 (w), 1626 (br.), 1479, 1434 (s), 1183, 1094 (s), 1027, 1014, 998, 742, 695 (s), 542/521/511/497 ($PC_3$) $cm^{-1}$. MS (FAB): *m*/*z* (%) = 719 (1) $[M - (S{=}C(CH_2)_5)]^+$. $C_{42}H_{40}P_2PtS$ (833.86): calcd. C 60.49, H 4.83, S 3.85; found C 60.19, H 4.82, S 3.67.

**Crystal Structure Determination:** The intensity data for the compounds were collected on a Nonius KappaCCD diffractometer by

 © 2007 Wiley-VCH Verlag GmbH & Co. KGaA, Weinheim 

using graphite-monochromated Mo-$K_\alpha$ radiation. Data were corrected for Lorentz and polarization effects and for absorption effects.[21–23] The structures were solved by direct methods (SHELXS[24]) and refined by full-matrix least-squares techniques against $F_o^2$ (SHELXL-97[25]). All hydrogen atoms of the structures were included at calculated positions with fixed thermal parameters. With the exception of the carbon atom C1 in compound **8**, all non-disordered, non-hydrogen atoms were refined anisotropically.[25] The oxygen atom in complex **8** had a 50:50 occupancy disorder over two positions, we therefore will not discuss the S–O bond length for the compound. Ortep-3 for Windows[26] was used for the structure representations.

**Crystal Data for 5:** $C_{42}H_{40}P_2PtS_2$, $M_r$ = 865.89 g mol$^{-1}$, colourless prism, size 0.02 × 0.02 × 0.02 mm, triclinic, space group $P\bar{1}$, $a$ = 10.4720(2), $b$ = 11.4799(3), $c$ = 16.6495(3) Å, $\alpha$ = 75.337(1), $\beta$ = 73.691(1), $\gamma$ = 82.905(1)°, $V$ = 1855.49(7) Å$^3$, $T$ = –90 °C, $Z$ = 2, $\rho_{calcd.}$ = 1.550 g cm$^{-3}$, $\mu$(Mo-$K_\alpha$) = 40.09 cm$^{-1}$, multiscan, trans$_{min}$: 0.5208, trans$_{max}$: 0.6615, $F$(000) = 864, 13452 reflections in $h$(–13/13), $k$(–14/14), $l$(–21/20), measured in the range 2.11° ≤ $\Theta$ ≤ 27.31°, completeness $\Theta_{max}$ = 98.9%, 8262 independent reflections, $R_{int}$ = 0.0189, 7656 reflections with $F_o > 4\sigma(F_o)$, 424 parameters, 0 restraints, $R_{1obs}$ = 0.0233, $wR_{2obs}$ = 0.0560, $R_{1all}$ = 0.0269, $wR_{2all}$ = 0.0579, GOOF = 1.015, largest difference peak and hole: 0.968/–1.061 e Å$^{-3}$.

**Crystal Data for 7:** $C_{42}H_{40}OP_2PtS_2$, $M_r$ = 881.89 g mol$^{-1}$, colourless prism, size 0.02 × 0.02 × 0.01 mm, triclinic, space group $P\bar{1}$, $a$ = 10.5086(2), $b$ = 11.3733(2), $c$ = 16.6699(4) Å, $\alpha$ = 76.040(1), $\beta$ = 74.247(1), $\gamma$ = 83.006(1)°, $V$ = 1857.50(7) Å$^3$, $T$ = –90 °C, $Z$ = 2, $\rho_{calcd.}$ = 1.577 g cm$^{-3}$, $\mu$ (Mo-$K_\alpha$) = 40.08 cm$^{-1}$, multiscan, trans$_{min}$: 0.6680, trans$_{max}$: 0.7621, $F$(000) = 880, 13298 reflections in $h$(–13/13), $k$(–14/14), $l$(–21/20), measured in the range 2.02° ≤ $\Theta$ ≤ 27.46°, completeness $\Theta_{max}$ = 99.4%, 8451 independent reflections, $R_{int}$ = 0.0184, 8026 reflections with $F_o > 4\sigma(F_o)$, 433 parameters, 0 restraints, $R_{1obs}$ = 0.0223, $wR_{2obs}$ = 0.0545, $R_{1all}$ = 0.0244, $wR_{2all}$ = 0.0556, GOOF = 1.023, largest difference peak and hole: 0.939/–1.383 e Å$^{-3}$.

**Crystal Data for 8:** $C_{42}H_{40}OP_2PtS$, $M_r$ = 849.83 g mol$^{-1}$, colourless prism, size 0.05 × 0.05 × 0.05 mm, orthorhombic, space group *Pbca*, $a$ = 16.0302(3), $b$ = 16.2448(4), $c$ = 27.5941(6) Å, $V$ = 7185.7(3) Å$^3$, $T$ = –90 °C, $Z$ = 8, $\rho_{calcd.}$ = 1.571 g cm$^{-3}$, $\mu$ (Mo-$K_\alpha$) = 40.85 cm$^{-1}$, multiscan, trans$_{min}$: 0.4608, trans$_{max}$: 0.5615, $F$(000) = 3392, 43387 reflections in $h$(–20/17), $k$(–17/21), $l$(–33/35), measured in the range 2.61° ≤ $\Theta$ ≤ 27.54°, completeness $\Theta_{max}$ = 99.2%, 8219 independent reflections, $R_{int}$ = 0.1025, 4772 reflections with $F_o > 4\sigma(F_o)$, 429 parameters, 0 restraints, $R_{1obs}$ = 0.0528, $wR_{2obs}$ = 0.0948, $R_{1all}$ = 0.1191, $wR_{2all}$ = 0.1134, GOOF = 0.987, largest difference peak and hole: 2.072/–3.542 e Å$^{-3}$.

CCDC-655294 (**5**), -655295 (**7**), and -655296 (**8**) contain the supplementary crystallographic data for this paper. These data can be obtained free of charge from The Cambridge Crystallographic Data Centre via www.ccdc.cam.ac.uk/data_request/cif.

**Supporting Information** (see footnote on the first page of this article): The IR spectra of complexes **5**–**8** are included.

## Acknowledgments

Financial support for this work was provided by the Freistaat Thüringen and DAAD (PKZ D/04/11451, H. P.). G. M. and J. R. acknowledge financial support by the Rector of the University of Łódź (Grant No. 505/712).

[1] a) G. S. Nielsen, L. M. Larsen, L. Poll, *J. Agric. Food Chem.* **2003**, *51*, 1970–1976; b) C.-K. Shu, M. L. Hagerdon, B. D. Mookherjee, C.-T. Ho, *J. Agric. Food Chem.* **1985**, *33*, 438–442; c) R. Gmelin, R. Susilo, G. R. Fenwick, *Phytochemistry* **1981**, *20*, 2521–2523; d) M. Boelens, L. M. Van der Linde, P. J. De Valois, H. M. Van Dort, H. J. Takken, *J. Agric. Food Chem.* **1974**, *22*, 1071–1076; e) H. W. Brinkman, H. Copier, J. J. M. De Leuw, S. B. Tjan, *J. Agric. Food Chem.* **1972**, *20*, 177–181.

[2] a) K. Okuma, *Sulfur Rep.* **2002**, *23*, 209–241; b) G. Mloston, H. Heimgartner in *Targets in Heterocyclic Systems – Chemistry and Properties* (Eds.: O. A. Attanasi; D. Spinelli) , Italian Society of Chemistry, Rome, **2006**, vol. 10, ch. 2.3.

[3] G. Mloston, J. Romanski, H. P. Reisenauer, G. Maier, *Angew. Chem.* **2001**, *113*, 401–404; *Angew. Chem. Int. Ed.* **2001**, *40*, 393–396.

[4] a) R. Huisgen, J. Rapp, *Tetrahedron* **1997**, *53*, 939–960; b) G. Maier, H. P. Reisenauer, J. Romanski, H. Petzold, G. Mloston, *Eur. J. Org. Chem.* **2006**, 3721–3729.

[5] J. Windhager, H. Görls, H. Petzold, G. Mloston, G. Linti, W. Weigand, *Eur. J. Inorg. Chem.* **2007**, 4462–4471.

[6] a) L. C. Song, Z. Y. Yang, Y. J. Hua, H. T. Wang, Y. Liu, Q.-M. Hu, *Organometallics* **2007**, *26*, 2106–2110; b) J. Windhager, M. Rudolph, S. Braeutigam, H. Goerls, W. Weigand, *Eur. J. Inorg. Chem.* **2007**, 2748–2760.

[7] S. J. Wratten, D. J. Falkner, *J. Org. Chem.* **1976**, *41*, 2465–2467.

[8] H. Petzold, S. Bräutigam, H. Görls, W. Weigand, U. Uhlemann, R. Geßner, W. Kiefer, J. Popp, A. Majchrzak, G. Mloston, *Inorg. Chim. Acta* **2004**, *357*, 1897–1908.

[9] a) W. Weigand, R. Wünsch, C. Robl, G. Mloston, H. Nöth, M. Schmidt, *Z. Naturforsch., Teil B* **2000**, *55*, 453–458.

[10] H. Petzold, S. Bräutigam, H. Görls, W. Weigand, M. Celeda, G. Mloston, *Chem. Eur. J.* **2006**, *12*, 8090–8095.

[11] a) T. Shigetomi, H. Soejima, Y. Nibu, K. Shioji, K. Okuma, Y. Yokomori, *Chem. Eur. J.* **2006**, *12*, 7742–7748; b) W. Weigand, S. Bräutigam, G. Mloston, *Coord. Chem. Rev.* **2003**, *245*, 167–175; c) A. Ishii, M. Murata, H. Oshida, K. Matsumoto, J. Nakayama, *Eur. J. Inorg. Chem.* **2003**, 3716–3721; d) W. Weigand, R. Wünsch, *Chem. Ber.* **1996**, *129*, 1409–1419; e) A. Ishii, M. Ohishi, N. Nakata, *Eur. J. Inorg. Chem.* **2007**, 5199–5206.

[12] A. Ishii, M. Saito, M. Murata, J. Nakayama, *Eur. J. Org. Chem.* **2002**, 979–982.

[13] W. Weigand, R. Wünsch, K. Polborn, G. Mlostoń, *Z. Anorg. Allg. Chem.* **2001**, *627*, 1518–1522.

[14] The $^{13}$C NMR spectrum of this isolated fraction shows two different sets of 12 signals for each compound. The signals for the quaternary ring carbon atoms appear at 103.5/93.1 and 91.4/86.7 ppm. Attempts to separate the two compounds were in vain.

[15] a) H. Oshida, A. Ishii, J. Nakayama, *J. Org. Chem.* **2004**, *69*, 1695–1703; b) H. Oshida, A. Ishii, J. Nakayama, *Tetrahedron Lett.* **2002**, *43*, 5033–5037.

[16] a) A. Shaver, R. D. Lai, P. H. Bird, W. Wickramasinghe, *Can. J. Chem.* **1985**, *63*, 2555–2558; b) V. W.-W. Yam, P. K.-Y. Yeung, K.-K. Cheung, *J. Chem. Soc. Chem. Commun.* **1995**, 267–269; c) S.-W. A. Fong, T. S. A. Hor, *J. Chem. Soc. Dalton Trans.* **1999**, 639–651.

[17] J. W. Gosselink, G. van Koten, K. Vrieze, B. Zwanenburg, B. H. M. Lammerink, *J. Organomet. Chem.* **1979**, *179*, 411–419.

[18] H. Petzold, H. Görls, W. Weigand, *J. Organomet. Chem.* **2007**, *692*, 2736–2742.

[19] H. Petzold, H. Görls, W. Weigand, J. Romanski, G. Mloston, *Heteroat. Chem.* **2007**, *18*, 584–590.

[20] F. Asinger, M. Thiel, G. Lipfert, *Justus Liebigs, Ann. Chem.* **1959**, *627*, 195–201.

[21] *COLLECT*, Data Collection Software; Nonius B. V., Netherlands, **1998**.

[22] Z. Otwinowski, W. Minor, "Processing of X-ray Diffraction Data Collected in Oscillation Mode" in *Methods in Enzy-*

 © 2007 Wiley-VCH Verlag GmbH & Co. KGaA, Weinheim 

*mology*, Vol. 276, Macromolecular Crystallography, Part A (Ed.: C. W. Carter, R. M. Sweet), Academic Press **1997**, pp. 307–326.
[23] *SORTAV*: R. H. Blessing, *Acta Crystallogr., Sect. A* **1995**, *51*, 33–38.
[24] G. M. Sheldrick, *Acta Crystallogr., Sect. A* **1990**, *46*, 467–473.
[25] G. M. Sheldrick, *SHELXL-97 (Release 97–2)*, University of Göttingen, Germany, **1997**.
[26] *Ortep-3 for Windows*: L. J. Farrugia, *J. Appl. Crystallogr.* **1997**, *30*, 565.

Received: August 28, 2007
Published Online: November 13, 2007

 © 2007 Wiley-VCH Verlag GmbH & Co. KGaA, Weinheim 

DOI: 10.1002/ejic.200700287

# Synthesis, Characterization, and Sensitizing Properties of Heteroleptic $Ru^{II}$ Complexes Based on 2,6-Bis(1-pyrazolyl)pyridine and 2,2′-Bipyridine-4,4′-dicarboxylic Acid Ligands

**Athanassios I. Philippopoulos,*[a][‡] Aris Terzis,[b] Catherine P. Raptopoulou,[b] Vincent J. Catalano,[c] and Polycarpos Falaras*[a]**

**Keywords:** 2,6-Bis(1-pyrazolyl)pyridine / Heteroleptic $Ru^{II}$ complexes / Dye-sensitized solar cells / Ruthenium / Protonation

Starting from the $Ru(bpp)Cl_3$ precursor (**1**), a family of novel heteroleptic $Ru^{II}$ complexes of the general formulae [Ru(bpp)(dcbpyH)(X)] [X = $Cl^-$ (**2a**), $NCS^-$, (**3**)] and Na[Ru(bpp)(dcbpy)(CN)] (**4**) with the ligands 2,6-bis(1-pyrazolyl)pyridine (bpp) and 2,2′-bipyridine-4,4′-dicarboxylic acid ($dcbpyH_2$) has been synthesized, spectroscopically characterized, and attached to nanocrystalline $TiO_2$ electrodes to be tested as solar cell sensitizers. Addition of HCl to (**2a**) led to the corresponding cationic derivative $[Ru(bpp)(dcbpyH_2)Cl]Cl$ (**2b**). All complexes were characterized by FT-IR, FT-Raman, UV/Vis, $^1H$ NMR spectroscopy, elemental analysis, and mass spectrometry. Complex **4** and the previously reported $[Ru(bdmpp)(dcbpyH_2)Cl](PF_6)$ (**5**) [bdmpp is 2,6-bis(3,5-dimethyl-1-pyrazolyl)pyridine] were characterized by single-crystal X-ray diffraction. The photo-electochemical properties of the dyes **2**–**4** were investigated and the efficiency of the corresponding dye-sensitized solar cells was compared to the sensitizing performance of the *cis*-$[Ru(dcbpyH)_2(NCS)_2](NBu_4)_2$ (**N719**) dye.

(© Wiley-VCH Verlag GmbH & Co. KGaA, 69451 Weinheim, Germany, 2007)

## Introduction

During the last decade, nanocrystalline titania films sensitized by transition-metal complexes have been extensively used for the conversion of light to electricity, because of their high efficiency (approximately 10%) and low cost.[1] The so-called dye-sensitized solar cells (DSSCs) consist of a photoanode, a sensitizer chemically adsorbed on the surface of a mesoporous oxide layer, and a counter electrode sandwiching an electrolyte containing the redox couple (usually the $I^-/I_3^-$ system in an organic medium).[2] Undoubtedly one of the most important parts of the cell is the sensitizer, mainly a ruthenium(II) polypyridine complex bearing suitable anchoring groups (carboxylic or phosphonic) for efficient grafting to the oxide surface via ester-type bond formation.[3] These dyes have to fulfill many other requirements like intense absorption in the visible region, efficient electron injection to the conduction band of the semiconductor, high stability of the sensitizer molecule, and reversibility of its redox chemistry.[4] Also, the electron transfer from the excited state of the dye to the semiconductor ($TiO_2$) should be very fast in comparison with decay to the ground state of the dye. Broad spectral response covering the entire visible range extending to the near-IR region is one of the most important prerequisites of a potential molecular sensitizer.

There is now a significant scientific effort for the development of efficient sensitizers with improved spectroscopic-photovoltaic characteristics for solar cell applications. Thus, a series of homoleptic $[Ru(L)_3]^{2+}$ and heteroleptic $[Ru(L^1)(L^2)(L^3)]^{2+}$, $[Ru(L^1)(L^2)(NCS)_2]$ (L = substituted bipyridyl with appropriate anchoring groups) ruthenium(II) complexes have been prepared.[5,6] So far one of the best sensitizers is *cis*-$[Ru(dcbpyH_2)_2(NCS)_2]$, known as N3, with a solar to electricity efficiency as high as 11.04%.[7] Moreover, a cell with extra pure monoprotonated *cis*-$[Ru(dcbpyH)_2(NCS)_2](NBu_4)_2$ (**N719** sensitizer), equipped with an antireflecting coating, gave an overall conversion efficiency of 11.18%. Use of modified ligands endowed with hydrophobic groups[8] and supramolecular functionalities has been proved to facilitate dye/redox couple interaction and dye regeneration.[9] On the basis of a judicious substitution of the bidentate by a tridentate ligand, a tris(isothiocyanato)-(4,4′,4′′-tricarboxy-2,2′:6,2′′-terpyridine)ruthenium(II) complex, so called black dye,[10] with a conversion efficiency of 10.4%, was proved to exhibit similar photovoltaic properties to the N3 dye. To further explore this possibility, 2,6-bis(3,5-dimethyl-1-pyrazolyl)pyridine

[a] NSCR "Demokritos", Institute of Physical Chemistry, Aghia Paraskevi Attikis, 15310 Greece
Fax: +30-210-6511766
E-mail: papi@chem.demokritos.gr
[b] NSCR "Demokritos", Institute of Material Science, Aghia Paraskevi Attikis, 15310 Greece
[c] Department of Chemistry, University of Nevada, Reno, NV 89557, USA
[‡] Current address: Inorganic Chemistry Laboratory, Department of Chemistry, National and Kapodistrian University of Athens, Panepistimiopolis, Zografou 15771, Greece
Fax: +30-210-7274782
E-mail: atphilip@chem.uoa.gr

 © 2007 Wiley-VCH Verlag GmbH & Co. KGaA, Weinheim 

(bdmpp)[11] (Scheme 1), a tridentate analogue to the terpyridine ligand, has been introduced in a $Ru^{II}$ metal center.[12]

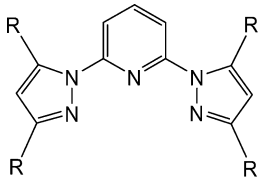


bpp: R = H; bdmpp: R = Me

Scheme 1. Structural formula of the ligands bpp and bdmpp.

In this respect, in our laboratory, we set out to synthesize ruthenium(II) molecular sensitizers using both the bdmpp and $dcbpyH_2$ ligands. Such a synthesis allows us to study the properties of the complexes and evaluate their influence on the performance of the corresponding dye-sensitized solar cells. As a result, the heteroleptic complexes $[Ru(bdmpp)(dcbpyH_2)(X)](PF_6)$ have been synthesized and successfully examined for the sensitization process.[13] In a more systematic approach towards this aim, i.e. the preparation of alternatives for the N3 and the corresponding black dye, in this paper, we report the synthesis and spectroscopic characterization of a series of neutral [Ru(bpp)(dcbpyH)(X)] (X = $Cl^-$, $NCS^-$) (**2a**, **3**), cationic $[Ru(bpp)(dcbpyH_2)Cl]Cl$ (**2b**), and anionic Na[Ru(bpp)-(dcbpy)(CN)] (**4**) ruthenium(II) complexes containing the tridentate ligand 2,6-bis(1-pyrazolyl)pyridine. Furthermore, their photo-electrochemical properties have been studied in sandwich-type solid-state nanocrystalline $TiO_2$ cells using a composite polymer redox electrolyte, namely PEO/$TiO_2$/$I^-$/$I_3^-$,[14] (PEO = polyethylene oxide, MW = $2 \times 10^6$) and compared to those of the corresponding $[Ru(bdmpp)(dcbpyH_2)-(X)](PF_6)$.[13]

## Results and Discussion

### Syntheses

The complexes **1**–**4** were synthesized by a route analogous to that reported previously.[13] The synthetic procedure for the preparation of complexes **1**–**2a** is shown in Scheme 2. Reaction of the precursor $Ru(bpp)Cl_3$ (**1**)[15] with the 2,2′-bipyridine-4,4′-dicarboxylic acid ligand in refluxing ethanol/water (1:1, v/v) and in the presence of $Et_3N$ (acting as both reducing and deprotonating agent) afforded selectively the heteroleptic neutral complex [Ru(bpp)(dcbpyH)-Cl] (**2a**), which was isolated as a red-brown microcrystalline solid in 97% yield. It is a stable solid that does not decompose after heating at 215 °C. Its structure is similar to that reported for the [Ru(bmipy)(dcbpyH)I] [bmipy = 2,6-bis(1-methylbenzimidazol-2-yl)pyridine compound,[16] taking into consideration, that both octahedral complexes bear a tridentate (coordinated via nitrogen atoms), a halide, and a deprotonated (dcbpyH) 2,2′-bipyridine-4,4′-dicarboxylic acid] ligands around the $Ru^{II}$ metal center.

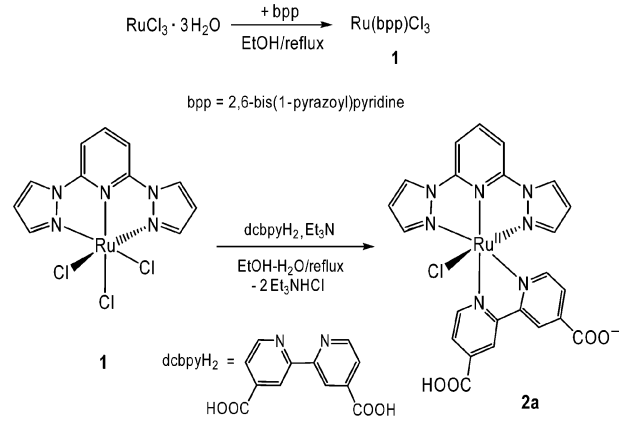


Scheme 2. Stepwise formation of complexes **1**, **2a**.

In a boiling methanol/water solution (1:1, v/v) containing an excess of the amphidentate thiocyanate ligand, complex **2a** undergoes metathesis reaction resulting in the isothiocyanato complex [Ru(bpp)(dcbpyH)(NCS)] (**3**), that was isolated as an orange-red solid in 89% yield [Equation (1)]. This complex shows a remarkable thermal stability and decomposes without melting at 261–262 °C.

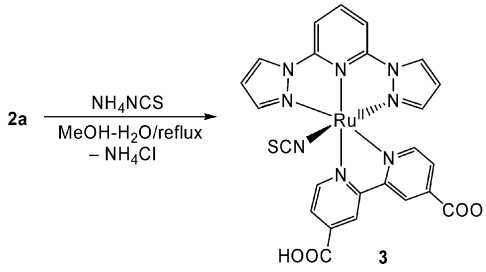


(1)

Monitoring of the reaction by FT-IR and $^1H$ NMR spectroscopy revealed that the reaction was completed after 4 h of heating. Elemental analysis data for complexes **2a** and **3** are consistent with the calculated composition of the proposed structure. This is also supported by FT-IR spectroscopy (see corresponding section concerning IR spectroscopy) and by derivatization, i.e. formation of the $[Ru(bpp)(dcbpyH_2)Cl]Cl$ complex (**2b**), where both carboxylate groups are protonated (vide infra).

In addition, compound **2a** reacts in the presence of an excess of NaCN, under the same conditions, to give the cyano complex Na[Ru(bpp)(dcbpy)(CN)] (**4**) as an orange solid in 67.5% yield [Equation (2)]. Complex **4** decomposes upon melting at 249 °C.

Addition of an aqueous solution of HCl (excess), to **2a** is accompanied by protonation of the carboxylate ($–COO^-$) group of the bidentate ligand (dcbpyH), affording quantitatively the $[Ru(bpp)(dcbpyH_2)Cl]Cl$ dye (**2b**), as a brown-black solid [Equation (3)].[17] It is a stable solid that does not decompose after heating at 240 °C.

Following a simple purification step, i.e. crystallization of the crude products, all complexes have been obtained in high yield as air stable and analytically pure solids. Therefore, the use of time-consuming column chromatography

 © 2007 Wiley-VCH Verlag GmbH & Co. KGaA, Weinheim 

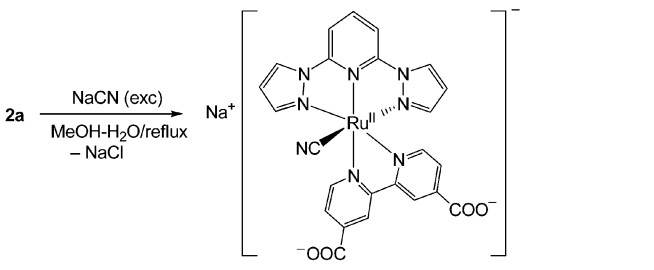


(2)

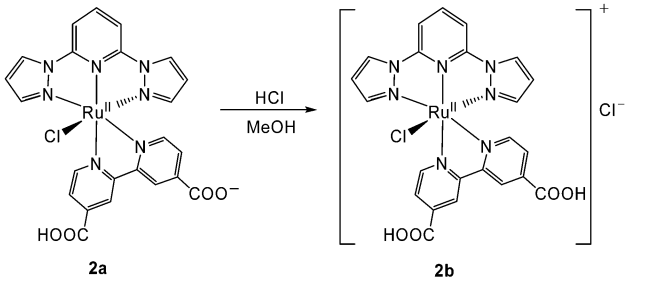


(3)

purification is avoided. In addition, in the case of complex **3**, only the N-bonded isomer was isolated (see IR-Raman section).[18] This is very important, since ruthenium bipyridine complexes with thiocyanate ligands typically yield an isomeric mixture of N- and S-bonded isomers.[15,19] Compounds **2**–**3** were found to be soluble in dimethylformamide (DMF), dimethyl sulfoxide (DMSO), and slightly soluble in methanol. The corresponding complex **4** dissolves very well in water and is less soluble in DMSO. The composition of the ruthenium(II) complexes **2a**–**4** was confirmed by elemental analyses and their spectroscopic properties were examined by FT-IR, FT-Raman, UV/Vis and $^1H$ NMR spectroscopy. The molecular composition of all compounds was further confirmed by mass spectrometric data (electrospray). The molecular structure of **4**·7.5$H_2O$·0.5$CH_3CN$ was determined by single-crystal X-ray diffraction (vide infra). Also the corresponding [Ru(bdmpp)(dcbpy$H_2$)Cl]-($PF_6$) sensitizer **5**[13b] was characterized by X-ray crystallography and the crystallographic data were compared with those of **4**.

## Characterization

### *IR-Raman Spectroscopic Data*

The IR spectra of complexes **2a** and **3** are almost identical in the region of 4000–400 $cm^{-1}$ as expected for isostructural compounds, except for the presence of a strong NCS band (in complex **3**) at 2109 $cm^{-1}$ which is assigned to the $\nu_{as}$(NCS) mode. This band appears at a position close to that of related ruthenium(II) complexes for which N-bonding of the NCS group has been confirmed.[20] The presence of a less intense band at 815 $cm^{-1}$ is assigned to the $\nu_s$(C=S) stretching vibration.[21] The Raman band that is characteristic of the $\nu_{as}$(NCS) vibration appears at 2112 $cm^{-1}$, slightly shifted compared to the value observed by IR spectroscopy (Table 1). Both complexes exhibited a broad and medium intensity absorption band at 1718 and 1717 $cm^{-1}$ respectively which is assigned to the ν(C=O) stretching vibration. This band has a slightly higher frequency than that of [Ru(bdmpp)(dcbpy$H_2$)Cl]($PF_6$) (1715 $cm^{-1}$)[13b] and [Ru(bdmpp)(dcbpy$H_2$)(NCS)]($PF_6$) (1713 $cm^{-1}$) respectively[13a] which may be attributed to the higher electron density at the $Ru^{II}$ center of complexes bearing the methyl-substituted pyrazolyl-pyridine ligand bdmpp. The bands at 1628 and 1627 $cm^{-1}$ respectively, overlapping with the bpy bands[3c,19] at 1609 and 1610 $cm^{-1}$, are tentatively assigned to the antisymmetric carboxylate vibration $\nu_{as}(CO_2^-)$.[22] The cationic complex **2b** displays the ν(C=O) stretching vibration at 1718 $cm^{-1}$, while the ν(C–O) mode is present as a medium intensity band at 1230 $cm^{-1}$.[5a]

The absence of IR bands above 1700 $cm^{-1}$ in the anionic complex **4** indicates that no protonated C=O group is present. Instead, there is a very strong and broad band at 1600 $cm^{-1}$ which is assigned to the antisymmetric stretching vibration of $\nu_{as}(CO_2^-)$. The strong band at 1377 $cm^{-1}$ can probably be assigned to the symmetric vibration mode $\nu_s(CO_2^-)$ of the carboxylate group.[23] The presence of a terminal cyanido ligand in **4** is indicated by a medium intensity ν(CN) IR absorption band at 2077 $cm^{-1}$ and thus corroborates the molecular structure of **4** determined by X-ray crystallography (vide infra). This band appears at a position close to that of the cyanide ion in NaCN (ν(CN) = 2085 $cm^{-1}$). The ν(CN) frequency of **4** is comparable with those of similar ruthenium complexes $Na_4$[Ru(dcbpy)$_2$-(CN)$_2$] (2077 and 2059 $cm^{-1}$),[24] [Ru(ttp)(L)(CN)]($PF_6$)[25]

Table 1. Selected Raman and FT-IR spectroscopic data [$cm^{-1}$] of complexes **2**–**4**.

| Complexes | ν(N=C) | ν(C=O) | $\nu_{as}(CO_2)$ | ν(C=C) | ν(C=C) | ν(C=N) | $\nu_s(CO_2^-)$ | ν(C–O) |
|---|---|---|---|---|---|---|---|---|
| **2a** (IR) | – | 1718 (m) | 1628 (m)[a] | 1609 (s) | 1539 (m) | 1481 (vs) | 1369 (m) | 1237 (m) |
| (Raman) | – | – | – | 1612 | – | – | 1368 | – |
| **2b** (IR) | – | 1718 (m) | – | 1610 (s) | 1539 (m) | 1483 (vs) | – | 1230 (m) |
| (Raman) | – | 1718 (m) | – | 1612 | – | – | – | 1224 (w) |
| **3** (IR) | 2109 (vs) | 1717 (m) | 1627 (m)[a] | 1610 (s) | 1543 (m) | 1482 (vs) | 1371 (m) | 1233 (m) |
| (Raman) | 2122 (s) | – | – | 1613 | – | – | – | – |
| **4** (IR) | 2077 (m) | – | 1600 (vs) | – | 1543 (m) | 1479 (vs) | 1377 (m) | 1234 (w) |
| (Raman) | 2076 (w) | – | 1610 (vs) | – | 1542 (m) | 1476 (m) | 1367 (vs) | 1226 (m) |

[a] The IR bands at 1628 and 1627 $cm^{-1}$, overlap with that of the bpy ring modes ν(C=C) at 1609 and 1610 $cm^{-1}$.

 © 2007 Wiley-VCH Verlag GmbH & Co. KGaA, Weinheim 

[ttp = 4′-p-tolyl-2,2′:6′,2′′-terpyridine, L = bpy, ν(CN) = 2079 $cm^{-1}$; L = Phen, ν(CN) = 2075 $cm^{-1}$], and *cis*-[($Et_2$-dcbpy)$_2$Ru(CN)$_2$] [ν(CN) = 2085 and 1996 $cm^{-1}$], respectively.[26] Also it compares well with the stretching vibration of the osmium complex [Os($H_2$teterpy)(CN)$_3$](TBA)$_2$ [ν(CN) = 2076 $cm^{-1}$, $H_3$teterpy = 2,2′:6′,2′′-terpyridine-4,4′,4′′-tricarboxylic acid, TBA = tetrabutylammonium].[27] In addition, the Raman spectrum of complex **4** in crystalline form gave very well resolved bands indicative of the high purity of this material, confirming the presence of the characteristic ν(CN) mode as a medium intensity band at 2076 $cm^{-1}$.

Moreover, the Raman spectrum of **2b** reveals at low frequency a medium intensity band for the $\nu_s$(Ru–Cl) stretching mode at 335 $cm^{-1}$. This value compares well with that mentioned for [$RuCl_4$(MeCN)$_2$](N$Et_4$).[28]

### *NMR Spectroscopic Studies*

The $^1$H NMR spectra of all complexes show a similar pattern in the aromatic region, indicating that substitution of the chlorido ligand by pseudohalides takes place without significant changes in the octahedral geometry at the ruthenium atom. In all cases signal assignment is based on integration, splitting patterns, chemical shifts, $^1$H-$^1$H COSY experiments, and literature values concerning similar systems.[13,16]

The $^1$H NMR spectra of complexes **2**–**4** were recorded in $(CD_3)_2SO$ at ambient temperature and Figure 1 presents the characteristic spectrum of complex **2a**. In this solvent, the compound **2a** undergoes substitution of the chlorido ligand, because of its labile nature,[29] as evidenced in the $^1$H NMR spectrum of **2a** which shows the formation of new resonance signals next to the expected ones, after 14 h standing. For this reason, only data from freshly prepared samples provides a basis for proper interpretation. The aromatic region of the spectrum of complex **2a** displays six sharp (four doublets and two singlets) and well-resolved resonance signals at $\delta$ = 10.09 (H$^{21}$), 9.26 (H$^{18}$), 9.01 (H$^{15}$), 8.25 (H$^{20}$), 7.53 (H$^{12}$), and 7.35 (H$^{13}$) ppm respectively, attributable to the six protons of the 2,2′-bipyridine-4,4′-dicarboxylic acid ligand. In addition, the $^1$H NMR spectrum of **2a**, shows a multiplet signal at $\delta$ = 8.45 ppm for the three pyridyl hydrogen atoms ($C_6H_3$ moiety, H$^{5-7}$). Two doublet signals at $\delta$ = 9.28 (H$^{1,11}$), 7.40 (H$^{3,9}$) ppm and a pseudotriplet resonance at $\delta$ = 6.70 ppm (H$^{2,10}$) are due to the chemical equivalent pyrazolyl hydrogen atoms.

The low field singlet at $\delta$ = 10.09 ppm is assigned to the H$^{21}$ proton of dcbpyH that is close to the coordinated chlorine atom. This singlet signal is upfield shifted by 0.55 and 0.29 ppm respectively, compared to the isothiocyanato complex **3** and the cyano complex **4**. Both the H$^{18}$ and H$^{15}$ singlet resonances of complexes **3** and **4** are shifted upfield compared to the precursor (**2a**) by 0.22 (0.46) and 0.21 (0.39) ppm, respectively.

### *Electronic Spectra*

The UV/Vis absorption spectra of freshly prepared complexes **2**–**4** measured in DMSO are shown in Figure 2 and the corresponding electronic spectroscopic data are summarized in Table 2.

The high energy bands in the 294 to 313 nm range are assigned to π-π* charge-transfer transitions localized on bipyridine ligands.[30] The absorption bands in the visible region can be assigned to the metal-to-ligand charge transfer transition bands ($^1$MLCT), as mentioned for other Ru$^{II}$ polypyridyl complexes.[31] The UV/Vis spectra of **2** and **3** are similar displaying a broad band that consists of three absorption bands in the visible region at 480, 434, 384 (**2a**),

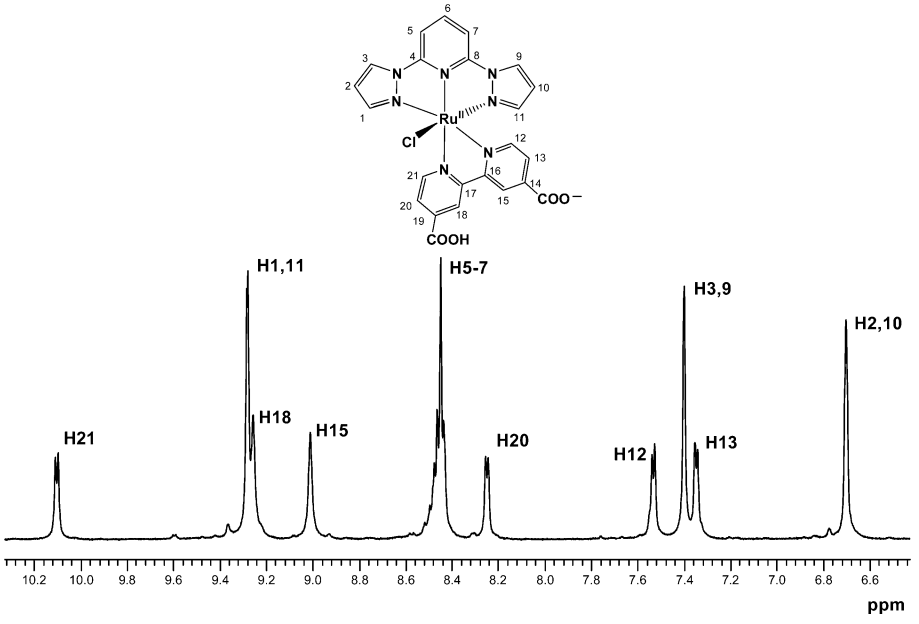


Figure 1. $^1$H NMR spectrum of complex [Ru(bpp)(dcbpyH)Cl] (**2a**) in $(CD_3)_2SO$ at ambient temperature. A numbering scheme showing our tentative assignment for NMR peaks is included.

 © 2007 Wiley-VCH Verlag GmbH & Co. KGaA, Weinheim 

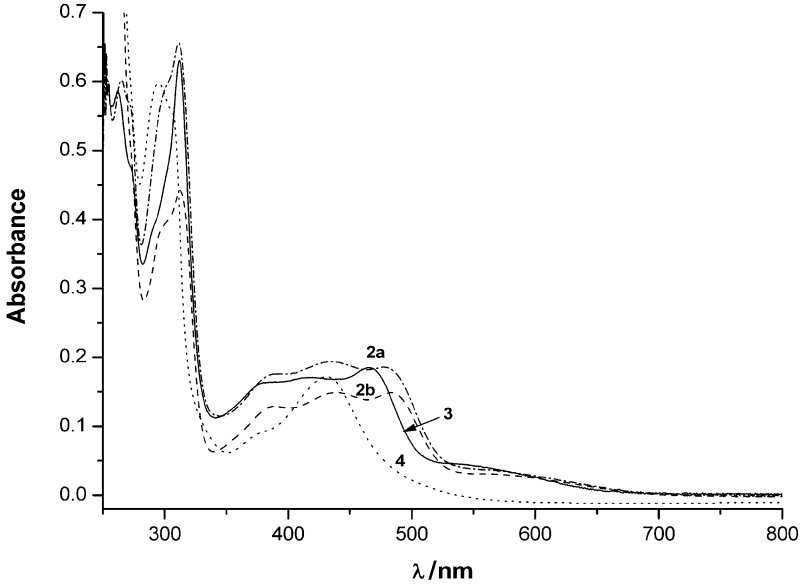


Figure 2. UV/Vis absorption spectra of **2a** (-.-), **2b** (···), **3** (—), and **4** (---) in dimethyl sulfoxide at 298 K.

Table 2. Electronic spectroscopic data of the complexes **2**–**4** measured in DMSO solution at 289 K.

| Complexes | Absorption data [$\lambda_{max}$ [nm] ($\varepsilon$, $10^3$ $M^{-1}$ $cm^{-1}$)] | | | |
|---|---|---|---|---|
| **2a** | 312 (25.5) | 384 (6.8) | 434 (7.3) | 480 (7.5) |
| **2b** | 313 (49.9) | 388 (14.6) | 438 (16.8) | 483 (16.8) |
| **3** | 312 (29.4) | 376 (7.5) | 418 (7.9) | 466 (8.6) |
| **4** | 307 (11.5) | – | 377 (1.9) | 430 (3.6) |

483, 438, 388 (**2b**), and 466, 418, 376 (**3**) nm, respectively. The visible spectrum of sensitizer **4** displays a broad band at 430 nm. The complexes **2a**, **3**, **4** maximum absorption wavelengths are blue shifted in the order $Cl^-$, $NCS^-$, $CN^-$, consistent with a decrease of electron density on the metal, as previously reported for ruthenium(II) dyes.[32] It is also worth mentioning that the absorption spectra of **2a**, **2b**, and **3** show a broad band at approximately 570 nm (530 nm for **3**), that expands in the near-IR region, up to 700 nm (approximately 610 nm for **3**). This behavior is very important for the photosensitization process as it permits harvesting and transformation of the less energetic photons.[10a] On the other hand, the $^1$MLCT bands of the cationic complex **2b** with fully protonated –COOH groups in the bipyridine ligand are slightly shifted toward the red compared to **2a** (from 480, 433, and 384 nm to 483, 438, and 388 nm).[33] It has to be mentioned that comparing complexes **2a** and **2b,** the extinction coefficient increases significantly. This behavior has also been verified by recording the spectra of the two dyes in amine-free dimethylformamide solution, where a similar increase of the extinction coefficient ($\varepsilon$) by about 25% was observed. This can be attributed to the different structure of the two complexes (**2a** is an internal salt while **2b** is a typical inorganic salt). In addition, for both complexes in DMF, a hypsochromic shift was observed ($\lambda_{max}$ = 456 nm for **2a** and $\lambda_{max}$ = 468 nm for **2b**). Finally, detailed analysis has shown that our complexes present no emission at ambient temperature in DMSO (**2a**–**3**) and aqueous solutions (**4**), respectively. The same result was confirmed with degassed solvents. Additionally, no emission signal was observed for dyes **2a**–**3** chemically attached on the surface of $TiO_2$ films. Indeed, emissive ruthenium(II) complexes incorporating the 2,6-bis(1-pyrazolyl)pyridine ligand have not been reported to date. This is mainly attributed to the fact that these complexes are expected to have low-lying triplet ligand field excited states ($^3$LF) that facilitate rapid nonradiative decay therefore decreasing the probability of radiative emission.[34] On the contrary luminescent complexes with terpy ligands of the type $[Ru(terpy)(bpy)L]^{2+}$ are well known, which are generally weak emitters at room temperature.[35] Accordingly, no room-temperature emission was observed for the *cis*-[2,2′-bipyridine-5,5′-$(CO_2H)_2$]$_2$Ru$(X)_2$ (X = $Cl^-$, $CN^-$, $NCS^-$) complexes.[36]

### *X-ray Diffraction Studies*

The solid-state structure of complex **4** was determined by single-crystal X-ray diffraction. For comparison reasons, the molecular structure of its analogue, the $Ru^{II}$ complex $[Ru(bdmpp)(dcbpyH_2)Cl](PF_6)$ (**5**), is described. The molecular structures of **4** and **5** are depicted in Figures 3 and 4, respectively.

Both complexes reveal distorted octahedral geometry around the ruthenium metal ion. Distortion results from the constrained bite angle of the chelating tridentate of 156.15(3)° and 156.5(3)° for N(1)–Ru–N(5), respectively. Also deviation from an octahedral geometry is evidenced from the short bite angle N(11)–Ru–N(12) of 77.68°(12) and 78.6°(3), respectively, as observed in [Ru(bdmpp)-(bpy)Cl]Cl·1.25$CHCl_3$,[37] [N(11)–Ru–N(21) 79.8°(5)], and in *cis*-$[Ru(dcbpyH_2)_2(NCS)_2]$·5.0DMSO,[38] [N(11)–Ru–N(21) 79.8°(5), N(31)–Ru–N(41) 79.1°(5)]. As a result of the constrained bite angle of the 2,6-bis(1-pyrazolyl)pyridine ligands, the ruthenium–nitrogen bond to the pyridine nitrogen [complex **4**, Ru–N(3) 1.987(3) Å; complex **5**,

 © 2007 Wiley-VCH Verlag GmbH & Co. KGaA, Weinheim 

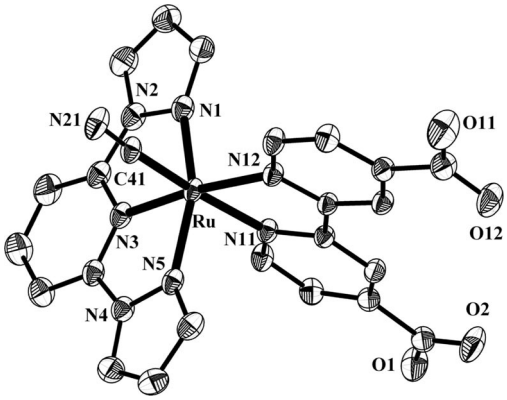


Figure 3. A perspective view of the anion **4**·7.5$H_2O$·0.5$CH_3CN$ in the solid state. Thermal ellipsoids are set at the 50% probability level. Hydrogen atoms and solvate (water and acetonitrile) molecules have been omitted for clarity. Selected bond lengths [Å] and bond angles [°] of **4**·7.5$H_2O$·0.5$CH_3CN$: Ru–N(1) 2.096(4), Ru–N(3) 1.987(3), Ru–N(5) 2.061(4), Ru–N(11) 2.109(3), Ru–N(12) 2.080(3), Ru–C(41) 1.999(4), N(1)–Ru–N(3) 77.8(14), N(1)–Ru–N(11) 95.0(13), N(1)–Ru–N(12) 106.6(13), Ru–C(41)–N(21) 176.1(4).

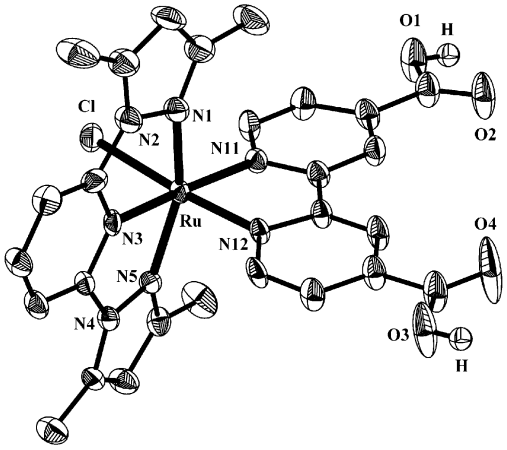


Figure 4. A perspective view of the cation **5**·2$CH_3CN$·0.5$CH_3OH$ (50% probability of thermal ellipsoids). Hydrogen atoms on the carboxylate moieties of the dcbpy$H_2$ are shown only. The remaining H-atoms and the solvate (water and acetonitrile) molecules have been omitted for clarity. Selected bond lengths [Å] and bond angles [°] of **5**·2$CH_3CN$·0.5$CH_3OH$: Ru–N(1) 2.086(8), Ru–N(3) 1.987(7), Ru–N(5) 2.069(7), Ru–N(11) 2.065(7), Ru–N(12) 2.024(7), Ru–Cl 2.403(3), N(1)–Ru–N(3) 79.0(3), N(1)–Ru–N(11) 99.5(3), N(12)–Ru–Cl 174.9(2), N(1)–Ru–Cl 86.9(2).

1.987(6) Å] is shorter than those belonging to the pyrazolyl substituents [complex **4**, Ru–N(1) 2.096(4) Å, Ru–N(5) 2.061(4) Å; complex **5**, 2.085(8) Å, 2.096(4) Å]. The ligands bpp and bdmpp chelate meridionally via the three nitrogen atoms, i.e. N(1), N(3), and N(5), forming a plane with one nitrogen [N(12) or N(11), respectively] of the functionalized 2,2′-bipyridine ligand. The second nitrogen atom [N(11) or N(12), respectively] of the dcbpy$H_2$ and the chlorido (cyanido) ligand occupies the axial positions. The Ru–Cl bond length of **5**·2$CH_3CN$·0.5$CH_3OH$ [2.403(2) Å] lies in the expected range for related $Ru^{II}$ complexes, [Ru(bdmpp)(bpy)Cl]Cl·1.25$CHCl_3$, [Ru–Cl 2.419(3) Å],[37] [Ru(bdmpp)($Me_2$bpy)Cl]($PF_6$)·1.25$CHCl_3$ [Ru–Cl 2.445(2) Å],[37] [Ru(dcbpy$H_2$)(cymene)Cl][$NO_3$] [Ru–Cl 2.3966(10) Å].[34] Likewise, the Ru–C41 bond length of the cyanido ligand in **4**·7.5$H_2O$·0.5$CH_3CN$ [1.999(4) Å] lies in the range observed for other anionic [Ru(CN)(py)(pc)]($NBu_4$) [pc = phthalocyanine, Ru–C 2.01(2) Å],[39] and cationic ruthenium cyano complexes [Ru(terpy)(phen)(CN)]($PF_6$) [Ru–C 2.004(3) Å].[40] The coordination geometry around the $Na^+$ cation is distorted octahedron comprised of water solvate molecules, whereas no interactions less than 3 Å are observed between the $Na^+$ and the oxygen atoms of the carboxylate groups. The separations of the oxygen atoms of the water molecules to the $Na^+$ cation lay in the range 2.249(9)–2.968(26) Å. In the structure of **4**, intermolecular distances in the range 2.752–3.268 Å between the solvate water molecules and the carboxylato oxygen atoms as well as the cyano nitrogen atom, result in an interesting hydrogen-bonding pattern, which contributes to the further stability of the lattice structure. The cations of **5** are doubly hydrogen bonded through the protonated carboxylate moieties of the dcbpy$H_2$ ligand giving rise to the formation of dimers [HO3···O2′ (1 – *x*, –*y*, 1 – *z*) 1.905 Å, O3···O2′ 2.698 Å, O3–HO3···O2′ 162.5°].

### *Electrochemistry*

The cyclic voltammograms were recorded in ca. $10^{-3}$ M aqueous solutions of the corresponding complexes using 0.1 M $NBu_4ClO_4$ as a supporting electrolyte, at a sweep rate of 100 mV $s^{-1}$. Well-defined reversible oxidation/reduction waves were obtained attributed to the $Ru^{II}/Ru^{III}$ redox couple. It has been observed that the cationic dye (**2b**) has higher oxidation potential (+0.73 vs. Ag/AgCl) than the neutral (**2a**) one (+0.68 vs. Ag/AgCl). Taking into account that the onset of the dye absorption spectra is the same, this implies that in the case of $TiO_2$ sensitization the energetic diagrams of the corresponding interfaces are different and therefore electron injection yield is expected to be larger for complex **2b** compared to **2a**.[50b]

### *Photovoltaic Performance*

The absorption spectra of the new dyes on $TiO_2$ films (after subtraction of background absorption from the $TiO_2$ and conductive glass) are shown in Figure 5. The absorption peaks for the chemisorbed dyes **2a**–**3** are all quite broad, compared with the corresponding dye peaks in dimethyl sulfoxide solution. It is easily observed that the absorption intensity of dye **2b** on the $TiO_2$ film is higher than that of **2a**, indicating that this complex is more efficiently adsorbed on the $TiO_2$ surface than **2a**. In fact, the amount of adsorbed dye to the surface of the $TiO_2$ films was determined by desorbing the dye from the $TiO_2$ surface into a 0.001 M NaOH aqueous solution. The number of adsorbed molecules of the dye adsorbed per square centimeter of geometrical surface area ($\Gamma$) for the four dyes **2a**–**4** is listed in Table 3. The $\Gamma$ value for dye **2b** was determined to be $1.6 \times 10^{-7}$ mol $cm^2$, which is about an order of magnitude higher than that for dye **2a** ($5.9 \times 10^{-8}$ mol $cm^2$). Therefore, upon sensitization, significant differences in $J_{sc}$ between the

 © 2007 Wiley-VCH Verlag GmbH & Co. KGaA, Weinheim 

two dyes are expected. The increased dye uptake in the case of a solar cell sensitized with dye **2b** (the $\Gamma$ value of **2b** is almost the same as that of N719[41]) results in increased short circuit photocurrent density ($J_{sc}$), mainly responsible for the higher conversion efficiency of complex **2b**. In fact, the $J_{sc}$ value of the **2b**-sensitized solar cell was about two times higher than that of the **2a**-sensitized solar cell, which was expected from the UV/Vis spectra. The low efficiency of dyes **2a**, **3**, and **4** is correlated with the lower absorption coefficient of these dyes (Table 2 and Figure 5) and/or to the decreased amount of dye molecules on the titania surface (Table 3).

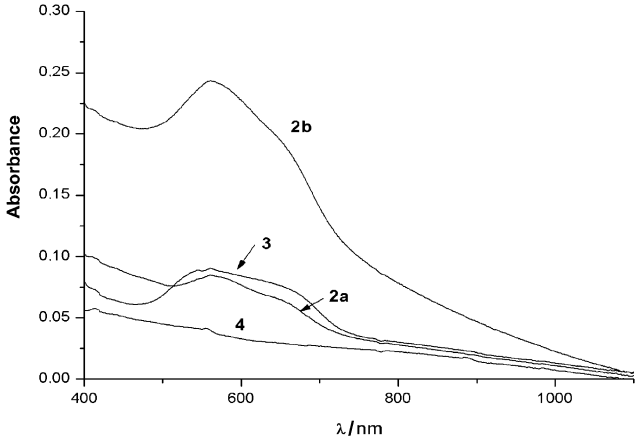


Figure 5. Absorption spectra of the four dyes **2**–**4** on $TiO_2$ electrodes.

Table 3. Photovoltaic performance (under standard AM 1.5 illumination conditions) of solid-state DSSCs using the $Ru^{II}$ dyes **2**–**5** and a PEO/$TiO_2$/$I^-$/$I_3^-$ composite polymer redox electrolyte [corresponding parameters: short circuit photocurrent density ($J_{sc}$); open circuit potential ($V_{oc}$); fill factor (*ff*) and power conversion efficiency ($\eta$), using the N719 dye are also given]. Surface concentration ($\Gamma$) of the chemisorbed dyes is also included.

| Dyes | $J_{sc}$ [mA cm$^2$] | $V_{oc}$ [mV] | *ff* | $\eta$ [%] | $\Gamma$ [mol cm$^2$] |
|---|---|---|---|---|---|
| **2a** | 1.56 | 541 | 0.58 | 0.49 | $5.9\times10^{-8}$ |
| **2b** | 3.32 | 580 | 0.58 | 1.12 | $1.6\times10^{-7}$ |
| **3** | 1.88 | 545 | 0.54 | 0.55 | $2.0\times10^{-8}$ |
| **4** | 1.46 | 532 | 0.58 | 0.45 | $7.0\times10^{-9}$ |
| **5** | 4.025 | 493 | 0.56 | 1.11 | – |
| N719 | 9.29 | 583 | 0.53 | 2.87 | $1.6\times10^{-7}$ |

The titania thin films (deposited on conductive glass substrates) were sensitized at ambient temperature for 12–15 h by immersing them into a c.a. $3\times10^{-4}$ M solution of the complexes in DMSO. To evaluate their sensitizing ability and compare their photovoltaic performance, the complexes **2**–**4** chemically attached on the titania electrodes, were incorporated in sandwich-type solid-state solar cells employing a composite polymer redox electrolyte (PEO/$TiO_2$/$I^-$/$I_3^-$) (PEO = polyethylene oxide, MW = $2\times10^6$)[14] and using a platinized TEC 8 counter electrode. The *cis*-[Ru(dcbpyH)$_2$(NCS)$_2$](NBu$_4$)$_2$ (**N719** dye, purchased from Solaronix) was used as a standard to compare the new sensitizers. Typical photocurrent-density photovoltage curves of DSSCs with the ruthenium dyes **2**–**4** (obtained at AM 1.5 simulated solar irradiation) are shown in Figure 6 and the relevant parameters are summarized in Table 3.

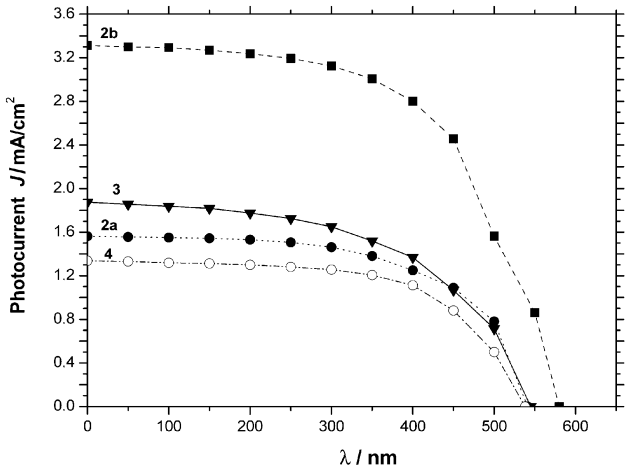


Figure 6. Photocurrent density–photovoltage characteristics of DSSCs using the $Ru^{II}$ dyes **2a** (---●---), **2b** (---■---), **3** (—◀—) and **4** (---○---) under AM 1.5 simulated light.

Under standard global AM 1.5 illumination conditions, solar cells of dye **2b** gave a short-circuit photocurrent density ($J_{sc}$) of 3.32 mA cm$^2$, 580 mV open circuit potential ($V_{oc}$), and 0.58 fill factor (*ff*) yielding an overall power conversion efficiency ($\eta$) of 1.12%. Under similar experimental conditions, the **2a** dye produces lower (1.56 mA cm$^2$) short-circuit current density and open circuit potential of 541 mV, respectively. The open-circuit voltage of **2b** is similar to that of the **N719** dye and by 8% larger than that of **2a**, probably due to the suppression of the dark current.[2a,42] On the other hand, the short-circuit photocurrent density and open circuit voltage of the cells with the cyano complex **4** slightly decrease compared to the precursor **2a**. The observed photovoltaic parameters $J_{sc}$, $V_{oc}$, and *ff* (see Table 3) for complex **4** are significantly higher than those of the corresponding *cis*-[Ru(dcbpyH$_2$)(CN)$_2$] sensitizer (1.06 mA cm$^2$, 310 mV, and 0.24, respectively).[43] Finally, the value of the fill factor (*ff*) is not affected by the nature of the dye, while the overall conversion efficiency is in the 0.5% range for sensitizers **2a**, **3**, and **4**, respectively. It has to be pointed out that in complex **4**, coordination to the $Ti^{4+}$ center on the $TiO_2$ surface could occur via the lone pair of electrons on the nitrogen of the –CN functional group.[44] In addition, the two deprotonated carboxylate (–$COO^-$) groups of the complex, appear to be anchored on the semiconductor surface via bidentate or bridging coordination as previously demonstrated for the **N712** dye.[22]

These data clearly indicate that the performance characteristics of complex **2b**, with fully protonated carboxylate groups of the dcbpyH$_2$ ligand, are superior to those of the dyes **2a**–**4**, while the **N719**-sensitized solar cell gave the best overall efficiency. This is further supported by the cyclic voltammetry results. Also the better performance may be attributed to the higher number of protons carried by the sensitizer, something which is in accord with the reports

 © 2007 Wiley-VCH Verlag GmbH & Co. KGaA, Weinheim 

mentioned for carboxylated $Ru^{II}$ phenanthroline complexes.[45] In fact, complex **2b** contains one more proton compared to **2a** and **3**, and two additional protons from the sensitizer **4**. In addition, the corresponding solid-state solar cell using the dye **2b** shows similar overall energy conversion efficiency ($\eta$) compared to that of the methylated derivative [Ru(bdmpp)(dcbpyH$_2$)Cl](PF$_6$).[13b] Further studies are in progress to improve the photovoltaic characteristics of the dye-sensitized solar cell based on heteroleptic complexes including bpp ligands.

## Conclusions

Halide substitution reactions of the [Ru(bpp)(dcbpyH)Cl] precursor **2a** with various nucleophiles ($NCS^-$, $CN^-$) led straightforwardly to the neutral and anionic sensitizers [Ru(bpp)(dcbpyH)(NCS)] (**3**) and (Na)[Ru(bpp)(dcbpy)(CN)] (**4**), respectively. Also reaction of **2a** with the electrophile (HCl) gave quantitatively the cationic [Ru(bpp)(dcbpyH$_2$)Cl]Cl complex. Following simple purification techniques the isolated dyes are analytically pure and used as such for solar cell applications. All new heteroleptic $Ru^{II}$ compounds have been anchored to nanocrystalline $TiO_2$-film electrodes using a solid-state electrolyte, namely PEO/$TiO_2$/$I^-$/$I_3^-$, and the photovoltaic properties of the resulting dye-sensitized solar cells have been characterized and compared with the properties of the one prepared with *cis*-[Ru(dcbpyH)$_2$(NCS)$_2$](NBu$_4$)$_2$ (**N719**). The photovoltaic performance of nanocrystalline $TiO_2$ solar cells sensitized by the complexes **2**–**4** bearing the 2,6-bis(1-pyrazolyl)pyridine and bipyridinedicarboxylic acid depends remarkably on the number of carboxyl functional groups. Thus, the [Ru(bpp)(dcbpyH$_2$)Cl]Cl dye **2b** (with two carboxyl anchoring groups), yields under standard AM 1.5 illumination a 1.12% power conversion efficiency that is about two-times higher than that of the solar cells sensitized with the dyes **2a** and **3** (bearing one carboxy group) and of complex **4** (without any carboxy group). However, dye **2b** is almost 40% less efficient than the **N719**-sensitized solar cell. As expected, the photovoltaic performance of the Ru–NCS dye **3** was higher than that of the Ru–Cl precursor **2a**, and this can be attributed to a better tuning and stabilization of the $t_{2g}$ orbitals of the thiocyanate complex.[13a] We are currently examining the photovoltaic characteristics of all the above dyes in semi-solid propylene carbonate-based modified nanocomposite redox electrolytes prepared in our group. This is expected to lead to cell optimization and a further efficiency increase of the corresponding DSSCs.

## Experimental Section

**General Procedures and Materials:** All manipulations (unless otherwise noted) were carried out under Ar using standard Schlenk techniques. $RuCl_3 \cdot 3H_2O$ and the solvents were used without further purification. The ligand 2,6-bis(1-pyrazolyl)pyridine was prepared according to literature methods.[11] The solvents used were thoroughly degassed by argon passage for 20 min before use. Elemental analyses were obtained from the Central Analytical Group of the Chemistry Department of the Humboldt-Universität zu Berlin. The C, H, N analyses of all compounds were carried out twice on a Leco CHNS-932 elemental analyzer. The mean C, H, N values of each compound are given below. Chlorine was determined using Schöniger's method followed by titration with $Hg(ClO_4)_2$.[46] Melting or decomposition points were determined with a Büchi SMP 530 melting point apparatus (Dr. Tottoli, patent 320338) and were not corrected. The samples were sealed in capillary tubes and heated slowly until the compounds melted or decomposed. Infrared spectra were measured with a Nicolet 550 Magna-IR™ spectrometer as KBr pellets in the region of 4000–400 $cm^{-1}$. The following abbreviations were used for the intensities of the IR absorption bands: vs. = very strong, s = strong, m = medium, w = weak, sh = shoulder. The solid-state RAMAN spectra were recorded in a frequency range of 3700–3 $cm^{-1}$ (Bruker Vertex 70/RAM II) with an excitation wavelength of 1064 nm, at ambient and low temperature (140 K) applying a laser power of 4–250 mW on the sample. Spectra were an average of 64 or 1024 scans collected at 4 $cm^{-1}$ resolution. Absorption spectra were recorded with a Perkin–Elmer Lambda 19 UV/Vis spectrometer and emission spectra were recorded with a Photon Technology International QM-1 steady-state spectrometer of the School of Chemistry, University of Birmingham. $^1H$ NMR spectra were measured with a Bruker Avance 500 MHz or a Bruker AM-300 spectrometer in $(CD_3)_2SO$ at the NCSR Demokritos and the Chemistry Department of the Humboldt-Universität zu Berlin. The spectra were calibrated against the residual proton resonances of the deuterated solvent ([D$_6$]DMSO, $\delta_H$ = 2.49 ppm). Electrospray mass spectra ESMS-TOF (TOF = time of flight) and ESMS were performed at the Mass Spectrometry Service Centre of the School of Chemistry, University of Birmingham and at the Mass Spectrometry and Dioxin Analysis Lab. IRRP of the National Centre for Scientific Research "Demokritos". Cyclic voltammetry measurements were performed in ca. $10^{-3}$ M aqueous solutions of the corresponding complexes containing 0.1 M $NBu_4ClO_4$ as supporting electrolyte, at a sweep rate of 100 mV $s^{-1}$, using a PAR Model 174 A polarographic analyzer operating in conjunction with a 33120 A Hewlett–Packard function–arbitrary waveform generator. A three-electrode three-compartment electrochemical cell was used, with Metrohm dot (6.0302.000) and planar (6.0305.000) platinum working and counter electrodes, respectively, as well as a Metrohm Ag/AgCl 6.0726.100 reference electrode. The experiments were performed in deoxygenated solutions purified by Ar gas (99.9%) for 30 min prior to use. During the experiment the Ar was passed over the solution surface.

**Crystal Structure Determination of 4·7.5H$_2$O·0.5CH$_3$CN, and 5·2CH$_3$CN·0.5CH$_3$OH:** Orange prismatic crystals of **4**·7.5H$_2$O·0.5CH$_3$CN were obtained upon slow diffusion of an acetone/acetonitrile mixture (20 mL, 10:1, v/v) into an aqueous solution (3–4 mL) of complex **4** at ambient temperature. Brown prismatic crystals of **5**·2CH$_3$CN·0.5CH$_3$OH were grown upon slow diffusion of diethylether into a solution of **5** in an acetonitrile/acetone mixture (4:1, v/v) at room temperature. Diffraction measurements were taken with a Crystal Logic Dual Goniometer diffractometer using graphite monochromated Mo-$K_\alpha$ radiation. Important crystal data and parameters for data collection are reported in Table 4. Unit cell dimensions were determined and refined by using the angular settings of 25 automatically centered reflections in the range $11° < 2\theta \leq 23°$. Three standard reflections monitored every 97 reflections showed less than 3% intensity fluctuation and no decay. Lorentz, polarization and psi-scan absorption corrections (for **5** only) were applied using Crystal Logic software. The structures were solved by direct methods using SHELXS-86[47] and refined

 © 2007 Wiley-VCH Verlag GmbH & Co. KGaA, Weinheim 

by full-matrix least-squares techniques on $F^2$ with SHELXL-97.[48] Further experimental crystallographic details for **4**: $2\theta_{max}$ = 50°, scan speed 5.0° min; scan range 1.6 +$\alpha_1\alpha_2$ separation; reflections collected/unique/used, 6071/5796 [$R_{int}$ = 0.0073]/5796; 502 parameters refined; $(\Delta/\sigma)_{max}$ = 0.009; $(\Delta\rho)_{max}/(\Delta\rho)_{min}$ = 0.927/–0.356 e Å$^3$; $R/R_w$ (for all data), 0.0500/0.1402. The asymmetric unit in the cell of **4** contains 7.5 molecules of water and 0.5 molecules of acetonitrile. One of the water solvate molecules [Ow(8)] as well as the MeCN were refined with occupation factors fixed to 0.50. Hydrogen atoms were located by difference maps and were refined isotropically. No H-atoms for the solvate molecules were included in the refinement. All non-H atoms were refined anisotropically. Further experimental crystallographic details for **5**: $2\theta_{max}$ = 45.5°, scan speed 1.2° min; scan range 2.2 +$\alpha_1\alpha_2$ separation; reflections collected/unique/used, 5878/5541 [$R_{int}$ = 0.1096]/5541; 486 parameters refined; $(\Delta/\sigma)_{max}$ = 0.000; $(\Delta\rho)_{max}/(\Delta\rho)_{min}$ = 0.937/–0.308 e Å$^3$; $R/R_w$ (for all data) = 0.1189/0.2352. Hydrogen atoms were introduced at calculated positions as riding on bonded atoms; except those of the solvate molecules, which were not included in the refinement. All non-H atoms were refined anisotropically. The second acetonitrile solvate molecule was refined isotropically, the methanol solvate was refined isotropically with the occupation factor fixed to 0.50.

Table 4. Crystallographic data for **4**·7.5$H_2O$·0.5$CH_3CN$ and **5**·2$CH_3CN$·0.5$CH_3OH$.

| | **4**·7.5$H_2O$·0.5$CH_3CN$ | **5**·2$CH_3CN$·0.5$CH_3OH$ |
|---|---|---|
| Formula | $C_{25}H_{31.5}N_{8.5}NaO_{11.5}Ru$ | $C_{31.5}H_{33}ClF_6N_9O_{4.5}PRu$ |
| *Fw* | 759.15 | 891.16 |
| Space group | $P\bar{1}$ | $P2_1/c$ |
| *T* [°C] | 298 | 298 |
| $\lambda$ [Å] | Mo-$K_\alpha$ (0.71073 Å) | Mo-$K_\alpha$ (0.71073 Å) |
| *a* [Å] | 11.704(4) | 19.589(12) |
| *b* [Å] | 12.200(4) | 20.808(14) |
| *c* [Å] | 13.178(4) | 10.404(6) |
| $\alpha$ [°] | 100.10(1) | 90 |
| $\beta$ [°] | 09.81(1) | 98.921(19) |
| $\gamma$ [°] | 103.88(1) | 90 |
| *V* [Å$^3$] | 1649.4(9) | 4190(4) |
| *Z* | 2 | 4 |
| $\rho_{calcd.}$ [g cm$^{-3}$] | 1.529 | 1.413 |
| $\mu$ (Mo-$K_\alpha$) [mm$^{-1}$] | 0.558 | 0.548 |
| *R*1[a] | 0.0456[b] | 0.0785[c] |
| $wR_2$[a] | 0.1359[b] | 0.1991[c] |

[a] w = $1/[\sigma^2(F_o^2) + (aP)^2 + bP]$ and $P = (\max)F_o^2,0) + 2F_c^2)/3$; *R*1 = $\Sigma(|F_o| - |F_c|)/\Sigma(|F_o|)$ and $wR_2 = \{\Sigma[w(F_o^2 - F_c^2)^2]/\Sigma[w(F_o^2)^2]\}^{1/2}$. [b] For 5360 reflections with $I > 2\sigma(I)$. [c] For 3779 reflections with $I > 2\sigma(I)$.

**$TiO_2$ Electrode Preparation:** Nanoporous $TiO_2$ thin films (15 μm thick) on conducting glass substrates TEC 8 (purchased from Hartford Glass Co. Inc.) using the doctor blade technique were prepared, as previously reported.[49] An adhesive tape strip on the conductive glass determines the film thickness. These films were sintered in air at 450 °C at a rate of 20 °C min$^{-1}$ for 30 min and were stored in a vacuum desiccator in the dark until required for use. The titania films were sensitized at ambient temperature for 12–15 h by immersing them into a c.a. $3 \times 10^{-4}$ M solution of the complexes in dimethyl sulfoxide. Immersion of nanocrystalline titania films in the solution of the dyes resulted in strong coloration of the films (in the case of complex **4** a faint yellow coloration was observed). The dye-coated electrodes were taken out of the solution, washed thoroughly with dimethyl sulfoxide and ethanol to remove any loosely adsorbed dye, shortly dried under a stream of dry argon and used as such for photovoltaic measurements. The sensitized $TiO_2$ thin films were incorporated in a sandwich-type solar cell employing a solid composite electrolyte ($PEO/TiO_2/I^-/I_3^-$)[14] and using a platinized TEC 8 counter electrode. An adhesive tape was placed between the electrodes to avoid short-circuiting, and the two electrodes were firmly pressed. A more detailed fabrication procedure for the nanocrystalline titania electrodes, the cell assembly, and the photo-electrochemical characterization has been described elsewhere.[50] The working electrode had an illuminated surface of 0.16 cm$^2$. Photovoltaic data were measured using a 300-W Xenon lamp that was focused to give 1000 W m$^2$, the equivalent of one sun at AM 1.5, at the surface of the test cell.

**Synthesis of [Ru(bpp)$Cl_3$] (1):** A Schlenk tube was charged with 0.165 g (0.63 mmol) of $RuCl_3 \cdot 3H_2O$ and 0.106 g (0.502 mmol) of the bpp ligand and the mixture was degassed by applying fine vacuum for 0.5 h. EtOH (20 mL) was then added to the mixture via a double-ended needle, and the brown suspension was heated to a gentle reflux for 3 h. The resulting red-brown suspension was cooled to ambient temperature and left to settle overnight at 5 °C. The solid precipitated was filtered in air washed with EtOH ($3 \times 20$ mL) and $Et_2O$ ($2 \times 10$ mL) and dried in vacuo over $P_2O_5$ to give complex **1** as a dark red-brown solid; yield 0.21 g (85.2%). **1·4$H_2O$** $C_{11}H_{17}Cl_3N_5O_4Ru$ (490.72): calcd. C 26.92, H 3.49, N 14.27; found C 26.73, H 3.24, N 13.82. IR (KBr): $\tilde{\nu}$ = 3159 (w, C–H, aromatic), 3124 (w, C–H, aromatic), 3090 (m, C–H, aromatic), 3049 (m, C–H, aromatic), 1576 (w), 1529 (m), 1483 (s), 1433 (w), 1408 (w), 1369 (w), 1346 (s), 1317 (w), 1256 (w), 1194 (w), 1175 (w), 1051 (m), 961 (m), 907 (w), 802 (s), 781 (s, sh), 773 (s, sh), 690 (w), 594 (w), 457 [br. (m)] cm$^{-1}$.

**Synthesis of [Ru(bpp)(dcbpyH)Cl] (2a):** Under a slow stream of argon a Schlenk tube was charged with complex (**1**) (0.196 g, 0.399 mmol) and a slight excess of the ligand $dcbpyH_2$ (0.114 g, 0.468 mmol) in an EtOH/$H_2O$ mixture (30 mL, 1:1, v/v) giving a dark brown suspension. LiCl (25 mg, 0.59 mmol) in an EtOH/$H_2O$ mixture (10 mL, 1:1, v/v) and $Et_3N$ (0.11 mL, 0.788 mmol) were added affording instantly a green solution that gradually turned to orange-brown upon heating to a gentle reflux for 7 h. While hot the suspension was filtered (in air) through a pad of Celite. The resulting clear orange-brown solution was concentrated to a few milliliters and was stored for 2 d at 5 °C. The solid precipitated was filtered, washed with small amounts of cold water, $Et_2O$ (15 mL), dried in air and finally in vacuo in a desiccator over $P_2O_5$. A further crop was obtained from the filtrate upon concentration and storage at 5 °C. This procedure was repeated twice in order to obtain complex **2a** analytically pure as a red-brown microcrystalline solid; yield 0.243 g (97.1%), m.p. >215 °C. **2a·2$H_2O$**, $C_{23}H_{20}ClN_7O_6Ru$ (626.98): calcd. C 44.06, H 3.22, Cl 5.65, N 15.64; found C 43.90, H 2.96, Cl 5.75, N 15.69. IR (KBr): $\tilde{\nu}$ = 3112 (w, C–H, aromatic), 3089 (m, C–H, aromatic), 3035 (w, C–H, aromatic), 2924 (w, C–H, aliphatic), 1718 [m, ν(C=O)], 1628 [m, $\nu_{as}(CO_2^-)$], 1609 [s, ν(C=C)], 1573 (w), 1539 [m, ν(C=C)], 1521 (w), 1482 [vs, ν(C=N)], 1408 (s), 1369 [m, $\nu_s(CO_2^-)$], 1340 (m), 1306 (w), 1265 (m), 1237 [m, ν(C–O)], 1174 (w), 1129 (w), 1072 (w), 1049 (m), 1025 (m), 955 (m), 901 (m), 774 (s), 717 (w), 684 (m), 595 (w), 528 (w), 445 (m) cm$^{-1}$. Raman: not possible. $^1$H NMR [$(CD_3)_2SO$, 500 MHz, 298 K]: $\delta$ = 6.70 (br. s, 2 H, 2,10-H), 7.35 (dd, $^3J_{H,H}$ = 5.7 Hz, 1 H, 13-H), 7.40 (br. s, 2 H, 3,9-H), 7.53 (d, $^3J_{H,H}$ = 6.0 Hz, 1 H, 12-H), 8.25 (d, $^3J_{H,H}$ = 5.5 Hz, 1 H, 20-H), 8.45 (m, 3 H, 5–7-H), 9.01 (s, 1 H, 15-H), 9.26 (s, 1 H, 18-H), 9.28 (br. s, 2 H, 1,11-H), 10.09 (d, $^3J_{H,H}$ = 5.6 Hz, 1 H, 21-H) ppm. UV/Vis ($\varepsilon$, M$^{-1}$ cm$^{-1}$): $\lambda_{max}$ [$(CH_3)_2SO$] = 480 (7521), 434 (7276), 384 (sh) (6770), 312 (25510) nm; no emission [$(CH_3)_2SO$]. ESMS-TOF (MeOH): *m*/*z* (%) = 592 {M + H}$^+$.

 © 2007 Wiley-VCH Verlag GmbH & Co. KGaA, Weinheim 

**Synthesis of [Ru(bpp)(dcbpyH$_2$)Cl]Cl (2b):** 0.25 mL (0.5 mmol) of an aqueous HCl solution (2 M) was added whilst stirring to a suspension of complex (**2a**) (30 mg, 0.051 mmol) in MeOH (10 mL). Immediately, the solid dissolved and the resulting dark red-brown solution was stirred at ambient temperature for 2 h. The volume of the solution was concentrated to some milliliters, and the product was precipitated with diethyl ether (excess). The resulting brown-black solid was washed with $Et_2O$ (2 × 10 mL) and dried in an oven at 50 °C over 2 h; yield quantitative, m.p. >240 °C. **2b·4H$_2$O**, $C_{23}H_{25}Cl_2N_7O_8Ru$ (699.46): calcd. C 39.49, H 3.60, Cl 10.14, N 14.02; found C 39.10, H 3.81, Cl 10.01, N 13.87. IR (KBr): $\tilde{\nu}$ = 3128 (w, C–H, aromatic), 3094 (m, C–H, aromatic), 3071 (w, C–H, aromatic), 2924 (w, C–H, aliphatic), 2851 (w, C–H, aliphatic), 1718 [m, $\nu_{as}$(C=O)], 1610 [m, $\nu$(C=C)], 1572 (br. s), 1547 (br. s), 1539 [m, $\nu$(C=C)], 1520 (br. vs), 1506 (br. s), 1491 (br. s), 1483 [vs, $\nu$(C=N)], 1408 (s), 1367 (w), 1340 (w), 1310 (w), 1258 (m), 1230 [m, $\nu$(C–O)], 1173 (w), 1140 (w), 1126 (w), 1042 (w), 1024 (m), 959 (m), 901 (m), 781 (m), 770 (m), 685 (m), 663 (w), 594 (w) cm$^{-1}$. Raman [5 mW, r.t., 1024 scans]: 1718 [m, $\nu_{as}$(C=O)], 1612 [m, $\nu$(C=C)], 1575 (m), 1559 (m), 1543 (m), 1498 (w), 1471 (m), 1445 (w), 1414 (w), 1372 (m), 1346 (w), 1310 (w), 1295 (w), 1285 (w), 1265 (m), 1241 (w), 1224 [w, $\nu$(C-O)], 1211 (w), 1188 (w), 1046 (m), 1029 (s), 750 (m), 652 (w), 450 (w), 427 (w), 335 [s, $\nu_s$(Ru-Cl)] cm$^{-1}$. $^1$H NMR [(CD$_3$)$_2$SO, 500 MHz, 298 K]: $\delta$ = 6.63 (br. s, 2 H, 2,10-H), 7.30 (m, 2 H, 3,9-H), 7.41 (d, $^3J_{H,H}$ = 5.7 Hz, 1 H, 13-H), 7.69 (d, $^3J_{H,H}$ = 5.7 Hz, 1 H, 12-H), 8.30 (m, 4 H, 5- to 7-H + 20-H), 8.80 (br. s, 1 H, 15-H), 9.04 (br. s, 1 H, 18-H), 9.07 (br. s, 2 H, 1,11-H), 10.13 (d, $^3J_{H,H}$ = 5.7 Hz, 1 H, 21-H) ppm. UV/Vis ($\varepsilon$, M$^{-1}$ cm$^{-1}$): $\lambda_{max}$ [(CH$_3$)$_2$SO] = 483 (16782), 438 (16782), 388 (sh) (14557), 313 (49871) nm. ESI-MS (MeOH): *m*/*z* (%) = 592 {M + H}$^+$, 556 {M – Cl}$^+$.

**Synthesis of [Ru(bpp)(dcbpyH)(NCS)] (3):** Under argon a solution of $NH_4NCS$ (0.077 g, 0.873 mmol) in $H_2O$ (5 mL) was added to a solution of complex (**2**) (0.053 g, 0.084 mmol) dissolved in MeOH/$H_2O$ (1:1, v/v) (10 mL). The orange-brown solution was heated to a gentle reflux for 4 h, the resulting orange-red solution was concentrated to a few milliliters and was stored for 2 d at 5 °C. The solid precipitated was filtered off, washed with small amounts of cold water and with $Et_2O$ (20 mL), dried in air and finally in vacuo in a desiccator over $P_2O_5$. A further crop was obtained from the filtrate upon concentration and storage at 5 °C. This procedure was repeated twice in order to obtain complex **3** analytically pure as an orange-red microcrystalline solid; yield 0.0504 g (89.3%), m.p. 261–262 °C. **3·3H$_2$O**, $C_{24}H_{22}N_8O_7RuS$ (667.62): calcd. C 43.18, H 3.32, Cl 0.00, N 16.78, S 4.80; found C 43.08, H 3.10, Cl 0.41, N 16.73, S 4.50. IR (KBr): $\tilde{\nu}$ = 3146 (w, C–H, aromatic), 3081 (m, C–H, aromatic), 2109 [vs, $\nu_{as}$(NCS)], 1717 [m, $\nu$(C=O)], 1627 [m, $\nu_{as}$($CO_2^-$)], 1610 [s, $\nu$(C=C)], 1574 (m), 1543 [m, $\nu$(C=C)], 1522 (w), 1483 [vs, $\nu$(C=N)], 1436 (w), 1405 (s), 1371 [m, $\nu_s$($CO_2^-$)], 1344 (m), 1309 (w), 1267 (w), 1233 [m, $\nu$(C–O)], 1174 (w), 1152 (w), 1130 (w), 1076 (w), 1049 (m), 1026 (m), 957 (m), 910 (m), 863 (w), 815 [m, $\nu_s$(NCS)], 774 (s), 756 (s), 719 (w), 706 (w), 681 (m), 665 (w), 598 (w), 528 (w), 463 (w), 445 (w) cm$^{-1}$. Raman [250 mW, 140 K, 64 scans]: 3046 (m), 2112 [m, $\nu_{as}$(NCS)], 1613 [m, $\nu$(C=C)], 1482 (w), 1434 (w), 1370 (w), 1279 (w), 1069 (w), 1028 (w), 1028 (m), 984 (w), 951 (w), 902 (w), 468 (w) cm$^{-1}$. $^1$H NMR [(CD$_3$)$_2$SO, 500 MHz, 298 K]: $\delta$ = 6.77 (br. s, 2 H, 2,10-H), 7.38 (d, $^3J_{H,H}$ = 5.0 Hz, 1 H, 13-H), 7.41 (d, $^3J_{H,H}$ = 5.0 Hz, 1 H, 12-H), 7.56 (br. s, 2 H, 3,9-H), 8.29 (d, $^3J_{H,H}$ = 5.0 Hz, 1 H, 20-H), 8.51 (d, $^3J_{H,H}$ = 7.5 Hz, 2 H, 5,7-H), 8.58 (t, $^3J_{H,H}$ = 7.5 Hz, 1 H, 6-H), 8.80 (br. s, 1 H, 15-H), 9.04 (s, 1 H, 18-H), 9.34 (s, 2 H, 1,11-H), 9.54 (d, $^3J_{H,H}$ = 4.50 Hz, 1 H, 21-H) ppm. UV/Vis ($\varepsilon$, M$^{-1}$ cm$^{-1}$): $\lambda_{max}$ [(CH$_3$)$_2$SO] = 466 (8591), 418 (7890), 376 (sh) (7540), 312 (29413) nm; small emission [(CH$_3$)$_2$SO]: 667 nm ($\lambda_{exc}$ = 560 nm). ESMS-TOF (MeOH): *m*/*z* (%) = 659 {M – H + 2Na}$^+$, 637 {M + Na}$^+$, 615 {M + H}$^+$, 586 {M – CO}$^+$, 558 {M – 2CO}$^+$.

**Synthesis of Na[Ru(bpp)(dcbpy)(CN)] (4):** Under argon a solution of NaCN (0.031 g, 0.63 mmol) in water (5 mL) was added to a solution of complex **2a** (0.034 g, 0.054 mmol) in $H_2O$/MeOH (1:2, v/v) (15 mL). The orange-brown solution was heated to a gentle reflux for 5 h leading to a clear orange solution that was concentrated to approximately 4–5 mL. Upon addition of acetone (20 mL) an orange solid was precipitated. The latter was filtered off, washed with acetone (2 × 10 mL) and $Et_2O$ (2 × 10 mL) and dried in air as well as in an oven at 70 °C for 0.5 h. X-ray equality orange single crystals of **4**·7.5H$_2$O·0.5CH$_3$CN were obtained upon slow evaporation of a mixture of acetone/acetonitrile (20 mL, 10:1, v/v) into a solution of the product in water. The orange crystals were collected on a filter paper, washed with small amounts of $Et_2O$ (2 × 5 mL) and dried in an oven at 70 °C for 2 h to obtain 22 mg of complex **4**; yield 67.5%, m.p. 249 °C (dec.). **4·6H$_2$O**, $C_{24}H_{27}NaN_8O_{10}Ru$ (711.58): calcd. C 40.51, H 3.82, N 15.75; found C 40.39, H 3.80, N 15.40. IR (KBr): $\tilde{\nu}$ = 3091 (w, C–H, aromatic), 2926 (m, C–H, aromatic), 2852 (w, C–H, aromatic), 2077 [m, $\nu$(CN)], 1600 [vs, $\nu_{as}$($CO_2^-$)], 1543 [m, $\nu$(C=C)], 1479 [vs, $\nu$(C=N)], 1431 (vs), 1410 (vs), 1377 [m, $\nu_s$($CO_2^-$)], 1342 (m), 1265 (m), 1234 (m), 1177 (w), 1053 (w), 1026 (w), 958 (m), 912 (w), 881 (m), 788 (s), 766 (s), 729 (w), 702 (m), 595 (w), 447 (w) cm$^{-1}$. Raman [100 mW, room temp., 1024 scans]: 2076 [s, $\nu$(CN)], 1610 [vs, $\nu_{as}$($CO_2^-$)], 1576 (w), 1542 (m), 1490 (m), 1476 (m), 1416 (m), 1367 [vs, $\nu_s$($CO_2^-$)], 1309 (m), 1289 (m), 1273 (m), 1226 [w, $\nu$(C–O)], 1063 (m), 1045 (s), 1027 (vs), 950 (m), 901 (w), 783 (w), 732 (w), 443 (w), 418 (w), 389 (m), 335 (w) cm$^{-1}$. $^1$H NMR [(CD$_3$)$_2$SO, 500 MHz, 298 K]: $\delta$ = 6.73 (m, 2 H, 2,10-H), 7.29 (d, $^3J_{H,H}$ = 6.0 Hz, 1 H, 13-H), 7.43 (br. s, 2 H, 3,9-H), 7.45 (d, $^3J_{H,H}$ = 5.0 Hz, 1 H, 12-H), 8.10 (d, $^3J_{H,H}$ = 7.5 Hz, 1 H, 20-H), 8.43 (d, $^3J_{H,H}$ = 7.8 Hz, 1 H, 5,7-H), 8.48 (t, $^3J_{H,H}$ = 8.0 Hz, 1 H, 6-H), 8.65 (br. s, 1 H, 15-H), 8.82 (br. s, 1 H, 18-H), 9.29 (d, $^3J_{H,H}$ = 3.0 Hz, 1 H, 1,11-H), 9.83 (d, $^3J_{H,H}$ = 5.7 Hz, 1 H, 21-H) ppm. UV/Vis ($\varepsilon$, M$^{-1}$ cm$^{-1}$): $\lambda_{max}$ [(CH$_3$)$_2$SO] = 430 (3593), 377 (sh) (1880), 307 (11550), 294 (12471) nm. ESMS-TOF (MeOH): *m*/*z* (%) = 649 {M – H + 3Na}$^+$, 627 {M + 2Na}$^+$.

CCDC-639397 (for **4**·7.5H$_2$O·0.5CH$_3$CN) and -639398 (for **5**·2CH$_3$CN·0.5CH$_3$OH) contain supplementary crystallographic data. These data can be obtained free of charge from The Cambridge Crystallographic Data Centre via www.ccdc.cam.ac.uk/data_request/cif.

## Acknowledgments

This work has been partially supported by the British Council (Greek-British 2004–2006 bilateral cooperation project), the GSRT Greece (PENED 03EΔ118 project) and the European Union (STREP 033313 project). The authors express their gratitude to Prof. Dr. A. C. Filippou for access to the Central Analytical Group of the Chemistry Department of the Humboldt-Universität zu Berlin and the University of Bonn. Furthermore, we acknowledge Reader Z. Pikramenou and Research Director Dr. L. Leodiadis for access to the Mass Spectrometry Service Centre of the School of Chemistry, University of Birmingham and the Mass Spectrometry and Dioxin Analysis Lab. IRRP of the National Centre for Scientific Research "Demokritos", respectively. Finally, helpful assistance from Dr. G. Pistolis, Dr. E. Chatzivasiloglou, Dr. M. Chatzichristidi, N. Weidemann, G. Konti, and N. Alexaki is highly acknowledged.

 © 2007 Wiley-VCH Verlag GmbH & Co. KGaA, Weinheim 

[1] a) B. O'Regan, M. Grätzel, *Nature* **1991**, *353*, 737–740; b) M. K. Nazeeruddin, A. Kay, I. Rodicio, R. Humphry-Baker, E. Müller, P. Liska, N. Vlachopoulos, M. Grätzel, *J. Am. Chem. Soc.* **1993**, *115*, 6382–6390; c) M. Grätzel, *Prog. Photovolt. Res. Appl.* **2000**, *8*, 171–185; d) M. Grätzel, *J. Photochem. Photobiol., C* **2003**, *4*, 145–153; e) Z.-S. Wang, H. Kawauchi, T. Kashima, H. Arakawa, *Coord. Chem. Rev.* **2004**, *248*, 1381–1389; f) Md. K. Nazeeruddin, C. Klein, P. Liska, M. Grätzel, *Coord. Chem. Rev.* **2005**, *249*, 1460–1467; g) M. K. Nazeeruddin, F. De Angelis, S. Fantacci, A. Selloni, G. Viscardi, P. Liska, S. Ito, B. Takeru, M. Grätzel, *J. Am. Chem. Soc.* **2005**, *127*, 16835–16847; h) M. K. Nazeeruddin, Q. Wang, L. Cevey, V. Aranyos, P. Liska, E. Figgemeier, C. Klein, N. Hirata, S. Koops, S. A. Haque, J. R. Durrant, A. Hagfeldt, A. B. P. Lever, M. Grätzel, *Inorg. Chem.* **2006**, *45*, 787–797; i) Recently outdoor experiments in Lausanne, Switzerland, under natural sunlight (96 mW cm$^2$) with the **N719** dye gave an overall conversion efficiency of 12.23%; see: S. Ito, Md. K. Nazeeruddin, P. Liska, P. Comte, R. Charvet, P. Péchy, M. Jirousek, A. Kay, S. M. Zakeeruddin, M. Grätzel, *Prog. Photovolt. Res. Appl.* **2006**, *14*, 589–601; j) N. Robertson, *Angew. Chem. Int. Ed.* **2006**, *45*, 2338–2345; k) J. M. Kroon, N. J. Bakker, H. J. P. Smit, P. Liska, K. R. Thampi, P. Wang, S. M. Zakeeruddin, M. Grätzel, A. Hinsch, S. Hore, U. Würfel, R. Sastrawan, J. R. Durrant, E. Palomares, H. Petterson, T. Gruszecki, J. Walter, K. Skupien, G. E. Tulloch, *Prog. Photovolt. Res. Appl.* **2007**, *15*, 1–18; l) Md. K. Nazeeruddin, T. Bessho, L. Cevey, S. Ito, C. Klein, F. De Angelis, S. Fantacci, P. Comte, P. Liska, H. Imai, M. Graetzel, *J. Photochem. Photobiol., A* **2007**, *185*, 331–337.

[2] a) K. Kalyanasundaram, M. Grätzel, *Coord. Chem. Rev.* **1998**, *177*, 347–414; b) A. Hagfeldt, M. Grätzel, *Acc. Chem. Res.* **2000**, *33*, 269–277; c) M. Grätzel, *Inorg. Chem.* **2005**, *44*, 6841–6851.

[3] a) S. Anderson, E. C. Constable, M. P. Dare-Edwards, J. B. Goodenough, A. Hamnett, K. R. Seddon, R. D. Wright, *Nature* **1979**, *280*, 571–573; b) P. Falaras, *Sol. Energy Mater. Sol. Cells* **1998**, *53*, 163–175; c) K. S. Finnie, J. R. Bartlett, J. L. Woolfrey, *Langmuir* **1998**, *14*, 2744–2749.

[4] a) V. Balzani, A. Juris, M. Venturi, S. Campagna, S. Serroni, *Chem. Rev.* **1996**, *96*, 759–834; b) T. Stergiopoulos, M.-C. Bernard, A. H-Le Goff, P. Falaras, *Coord. Chem. Rev.* **2004**, *248*, 1407–1420; c) R. Argazzi, N. Y. M. Iha, H. Zabri, F. Odobel, C. A. Bignozzi, *Coord. Chem. Rev.* **2004**, *248*, 1299–1316.

[5] a) S. M. Zakeeruddin, Md. K. Nazeeruddin, R. Humphry-Baker, M. Grätzel, V. Shklover, *Inorg. Chem.* **1998**, *37*, 5251–5259; b) K. A. Maxwell, M. Sykora, J. M. DeSimone, T. J. Meyer, *Inorg. Chem.* **2000**, *39*, 71–75; c) C. M. Kepert, A. M. Bond, G. B. Deacon, L. Spiccia, B. W. Skelton, A. H. White, *Dalton Trans.* **2004**, 1766–1774; d) L. Spiccia, G. B. Deacon, C. M. Kepert, *Coord. Chem. Rev.* **2004**, *248*, 1329–1341; e) N. Onozawa-Komatsuzaki, O. Kitao, M. Yanagida, Y. Himeda, H. Sugihara, K. Kasuga, *New J. Chem.* **2006**, *30*, 689–697; f) K.-J. Jiang, N. Masaki, J.-B. Xia, S. Noda, S. Yanagida, *Chem. Commun.* **2006**, 2460–2462.

[6] a) A. S. Polo, M. K. Itokazu, N. Y. M. Iha, *Coord. Chem. Rev.* **2004**, *248*, 1343–1361 and references cited therein; b) F. Odobel, H. Zabri, *Inorg. Chem.* **2005**, *44*, 5600–5611.

[7] M. Grätzel, *J. Photochem. Photobiol., A* **2004**, *164*, 3–14.

[8] a) P. Wang, S. M. Zakeeruddin, J. E. Moser, M. K. Nazeeruddin, T. Sekiguchi, M. Grätzel, *Nat. Mater.* **2003**, *2*, 402–407; b) P. Wang, C. Klein, R. Humphry-Baker, S. M. Zakeeruddin, M. Grätzel, *J. Am. Chem. Soc.* **2005**, *127*, 808–809.

[9] J. Faiz, A. I. Philippopoulos, A. G. Kontos, P. Falaras, Z. Pikramenou, *Adv. Funct. Mater.* **2007**, *17*, 54–58.

[10] a) Md. K. Nazeeruddin, P. Péchy, M. Grätzel, *Chem. Commun.* **1997**, 1705–1706; b) M. K. Nazeeruddin, P. Pechy, T. Renouard, S. M. Zakeeruddin, R. Humphry-Baker, P. Comte, P. Liska, L. Cevey, E. Costa, V. Shklover, L. Spiccia, G. B. Deacon, C. A. Bignozzi, M. Grätzel, *J. Am. Chem. Soc.* **2001**, *123*, 1613–1624.

[11] D. L. Jameson, K. A. Goldsby, *J. Org. Chem.* **1990**, *55*, 4992–4994.

[12] A series of $Ru^{II}$ complexes containing this class of planar tridentate nitrogen donor ligands are known: a) D. L. Jameson, J. K. Blaho, K. T. Kruger, K. A. Goldsby, *Inorg. Chem.* **1989**, *28*, 4312–4314; b) S. J. Slattery, W. D. Bare, D. L. Jameson, K. A. Goldsby, *J. Chem. Soc. Dalton Trans.* **1999**, 1347–1352; c) N. J. Beach, G. J. Spivak, *Inorg. Chim. Acta* **2003**, *343*, 244; d) M. A. Halcrow, *Coord. Chem. Rev.* **2005**, *249*, 2880–2908.

[13] a) K. Chryssou, T. Stergiopoulos, P. Falaras, *Polyhedron* **2002**, *21*, 2773–2781; b) K. Chryssou, V. J. Catalano, R. Kurtaran, P. Falaras, *Inorg. Chim. Acta* **2002**, *328*, 204–209.

[14] T. Stergiopoulos, I. M. Arabatzis, G. Katsaros, P. Falaras, *Nano Lett.* **2002**, *2*, 1259–1261.

[15] C. A. Bessel, R. F. See, D. L. Jameson, M. R. Churchill, K. J. Takeuchi, *J. Chem. Soc., Dalton Trans.* **1993**, 1563–1576. This complex was prepared by a slight modification of the published procedure and was characterized by IR spectroscopy and elemental analysis before use in the next step.

[16] O. Kohle, S. Ruile, M. Grätzel, *Inorg. Chem.* **1996**, *35*, 4779–4787.

[17] Similarly the addition of an excess of aqueous HCl (2 M) to **3** and **4** yields the desired products [Ru(bpp)(dcbpyH$_2$)(NCS)]Cl and [Ru(bpp)(dcbpyH$_2$)(CN)]Cl, respectively, together with other unidentified species, as evidenced by IR and $^1$H NMR spectroscopy. Work is in progress to elucidate the experimental conditions in order to avoid the formation of the side products.

[18] In the case of the previously reported [Ru(bdmpp)(NCS)(dcbpyH$_2$)](PF$_6$) complex, the $\nu_{as}$(NCS) band in the IR spectrum is not so strong. It appears as a shoulder indicating probably that the NCS ligand is coordinated via the sulfur atom as well. Preliminary photo-electrochemical experiments with the crystallized sample containing only the N-isomer showed an improved power conversion efficiency of $\eta$ = 1.86% (instead of 1.70%).

[19] C. Klein, Md. K. Nazeeruddin, D. Di Censo, P. Liska, M. Grätzel, *Inorg. Chem.* **2004**, *43*, 4216–4226.

[20] a) M. Yanagida, L. P. Singh, K. Sayama, K. Hara, R. Katoh, A. Islam, H. Sugihara, H. Arakawa, M. K. Nazeeruddin, M. Grätzel, *J. Chem. Soc. Dalton Trans.* **2000**, 2817–2822; b) T. Renouard, R.-A. Fallahpour, Md. K. Nazeeruddin, R. Humprey-Baker, S. I. Gorelsky, A. B. P. Lever, M. Grätzel, *Inorg. Chem.* **2002**, *41*, 367–378.

[21] Md. K. Nazeeruddin, E. Müller, R. Humphry-Baker, N. Vlachopoulos, M. Grätzel, *J. Chem. Soc. Dalton Trans.* **1997**, 4571–4578.

[22] Md. K. Nazeeruddin, R. Humphry-Baker, P. Liska, M. Grätzel, *J. Phys. Chem. B* **2003**, *107*, 8981–8987.

[23] A. Fillinger, B. A. Parkinson, *J. Electrochem. Soc.* **1999**, *146*, 4559–4564.

[24] R. Argazzi, C. A. Bignozzi, T. A. Heimer, F. N. Castellano, G. J. Meyer, *Inorg. Chem.* **1994**, *33*, 5741–5749.

[25] B.-W. Jing, W.-Q. Wang, M.-H. Zhang, T. Shen, *Dyes Pigm.* **1998**, *37*, 177–186.

[26] G. Wolfbauer, A. M. Bond, D. R. MacFarlane, *Inorg. Chem.* **1999**, *38*, 3836–3846.

[27] R. Argazzi, G. Larramona, C. Contado, C. A. Bignozzi, *J. Photochem. Photobiol., A* **2004**, *164*, 15–21.

[28] I. M. Bell, R. J. H. Clark, D. G. Humphrey, *J. Chem. Soc. Dalton Trans.* **1999**, 1307–1310.

[29] J. D. Birchall, T. D. O'Donoghue, J. R. Wood, *Inorg. Chim. Acta* **1979**, *37*, L461–L463.

[30] T. J. Meyer, *Pure Appl. Chem.* **1986**, *58*, 1193–1206.

[31] A. Juris, V. Balzani, F. Barigelletti, S. Campagna, P. Belser, A. von Zelewsky, *Coord. Chem. Rev.* **1988**, *84*, 85–277.

[32] Md. K. Nazeeruddin, S. M. Zakeeruddin, J.-J. Lagref, P. Liska, P. Compte, C. Barolo, G. Viscardi, K. Schenk, M. Graetzel, *Coord. Chem. Rev.* **2004**, *248*, 1317–1328.


 © 2007 Wiley-VCH Verlag GmbH & Co. KGaA, Weinheim 

[33] S. A. Willison, H. Jude, R. M. Antonelli, J. M. Rennekamp, N. A. Eckert, J. A. Krause Bauer, W. B. Connick, *Inorg. Chem.* **2004**, *43*, 2548–2555.
[34] a) C. R. Hecker, P. E. Fanwick, D. R. McMillin, *Inorg. Chem.* **1991**, *30*, 659–666; b) S. C. Rasmussen, S. E. Ronco, D. A. Mlsna, M. A. Billadeau, W. T. Pennington, J. W. Kolis, J. D. Petersen, *Inorg. Chem.* **1995**, *34*, 821–829.
[35] a) C. R. Hecker, P. E. Fanwick, D. R. McMillin, *Inorg. Chem.* **1991**, *30*, 659–666; b) S. C. Rasmussen, S. E. Ronco, D. A. Mlsna, M. A. Billadeau, W. T. Pennington, J. W. Kolis, J. D. Petersen, *Inorg. Chem.* **1995**, *34*, 821–829.
[36] R. Argazzi, C. A. Bignozzi, T. A. Heimer, F. N. Castellano, G. J. Meyer, *Inorg. Chem.* **1994**, *33*, 5741–5749.
[37] V. J. Catalano, R. Kurtaran, R. Heck, A. Öhman, M. G. Hill, *Inorg. Chim. Acta* **1999**, *286*, 181–188.
[38] V. Shklover, Yu. E. Ovchinnikov, L. S. Braginsky, S. M. Zakeeruddin, M. Grätzel, *Chem. Mater.* **1998**, *10*, 2533–2541.
[39] M. Weidemann, H. Hückstädt, H. Homborg, *Z. Anorg. Allg. Chem.* **1998**, *624*, 846–852.
[40] S. Bonnet, J.-P. Collin, N. Gruber, J.-P. Sauvage, E. R. Schofield, *Dalton Trans.* **2003**, 4654–4662.
[41] E. Chatzivassiloglou, Ph. D. Thesis, NTUA, **2007**, Athens, Greece.
[42] M. Yanagida, T. Yamaguchi, M. Kurashige, K. Hara, R. Katoh, H. Sugihara, H. Arakawa, *Inorg. Chem.* **2003**, *42*, 7921–7931.
[43] T. A. Heimer, C. A. Bignozzi, G. J. Meyer, *J. Phys. Chem.* **1993**, *97*, 11987–11994.
[44] G. J. Meyer, *Inorg. Chem.* **2005**, *44*, 6852–6864.
[45] K. Hara, H. Sugihara, L. P. Singh, A. Islam, R. Katoh, M. Yanagida, K. Sayama, S. Murata, H. Arakawa, *J. Photochem. Photobiol., A* **2001**, *145*, 117–122.
[46] F. Ehrenberger in *Quantitative Organische Elementaranalyse*, Wiley-VCH, Weinheim, **1991**.
[47] G. M. Sheldrick, *SHELXS-86: Structure Solving Program*, University of Göttingen, Germany, **1986**.
[48] G. M. Sheldrick, *SHELXL-97: Crystal Structure Refinement Program*, University of Göttingen, Germany, **1997**.
[49] I. M. Arabatzis, T. Stergiopoulos, M. C. Bernard, D. Labou, S. G. Neofytides, P. Falaras, *Appl. Catal., B* **2003**, *42*, 187–201.
[50] a) T. Stergiopoulos, I. M. Arabatzis, H. Cachet, P. Falaras, *J. Photochem. Photobiol., A* **2003**, *155*, 163–170; b) T. Stergiopoulos, S. Karakostas, P. Falaras, *J. Photochem. Photobiol., A* **2004**, *163*, 331–340 and ref.[15] therein.

Received: March 14, 2007
Final Revision Received: October 5, 2007
Published Online: November 20, 2007

 © 2007 Wiley-VCH Verlag GmbH & Co. KGaA, Weinheim 

DOI: 10.1002/ejic.200700894

# [Bis(guanidine)]zinc Complexes and Their Application in Lactide Polymerisation

**Janna Börner,[a] Sonja Herres-Pawlis,*[a] Ulrich Flörke,[a] and Klaus Huber[b]**

**Keywords:** Guanidine / D,L-Lactide / N ligands / Ring-opening polymerization / Zinc

The bis(guanidine)-stabilised zinc complexes [$N^1$,$N^2$-bis(1,3-dimethylimidazolidin-2-ylidene)ethane-1,2-diamine]dichloridozinc(II), [Zn(DMEG$_2$e)Cl$_2$] (**C1**), diacetato[$N^1$,$N^2$-bis(1,3-dimethylimidazolidin-2-ylidene)ethane-1,2-diamine]zinc(II), [Zn(DMEG$_2$e)(CH$_3$COO)$_2$] (**C2**), and bis[$N^1$,$N^2$-bis(1,3-dimethylimidazolidin-2-ylidene)ethane-1,2-diamine]zinc(II) bis(trifluoromethanesulfonate), [Zn(DMEG$_2$e)$_2$](CF$_3$SO$_3$)$_2$ (**C3**), have been synthesised and completely characterised by means of X-ray structure analysis, NMR spectroscopy and mass spectrometry. These [bis(guanidine)]zinc complexes were investigated regarding their activity in the bulk polymerisation of D,L-lactide. It could be shown that these compounds are able to act as initiators for lactide polymerisation, and polylactides with molecular weights ($M_w$) of around 18000–59000 g/mol could be obtained. Variation of the reaction temperature revealed that the molecular weights decrease with increasing temperature. Additionally, the correlation of the intrinsic viscosity with the molecular weight demonstrates that the obtained polymers are linear and structurally homogeneous.

(© Wiley-VCH Verlag GmbH & Co. KGaA, 69451 Weinheim, Germany, 2007)

## Introduction

The increasing shortage of resources has enforced the search for production techniques for biodegradable polymers made of renewable raw materials. An example is polylactide (PLA), an aliphatic polyester, which can be obtained by the ring-opening polymerisation (ROP) of cyclic esters like lactide. The monomer for PLA production is available from renewable raw materials like corn or sugar beets by a bacterial fermentation process. The polylactide that is obtained by metal-catalysed ROP can be either recycled or composted after use, and therefore it is $CO_2$-emission-neutral. Also, its unique physical properties qualify PLA to be a viable alternative to petrochemical-based plastics. Combined with its biocompatibility and its ability to degrade both in vivo and in vitro, PLA has a great range of potential applications ranging from widespread use, including coatings, fibres, films and packages, to use in specialised medical and pharmaceutical fields.[1]

Until now, the ROP of lactide could not be accomplished economically, and therefore PLA has only been used in biomedical applications.[2] To change the polymer from a speciality material to a large-volume commodity plastic,[3] the development of new polymerisation catalysts is required. Most large-scale processes are based on the use of stannous compounds as initiators.[4] However, for use in food packaging or similar applications, heavy metals are undesirable because of accumulation effects.[5] Particularly suitable for this purpose in order to substitute heavy-metal-based catalyst systems are zinc complexes with N-donor-functionalised ligands because they are mostly colourless, inexpensive and nontoxic.[6]

Examples of (guanidine)zinc complexes have already been reported.[7] It could be shown that some of these possess catalytic activity, which makes guanidines a very promising ligand class leading to catalytically active zinc complexes.[8] Bis(guanidines) offer excellent donor properties that allow the coordination of metal ions and enable the access of substrate molecules to the metal centre at the same time. A great advantage of bis(guanidines) is their modular synthesis protocol, which combines different spacer and guanidine groups and thus admits a flexible ligand design.[9] The variation of the ligands allows an optimal adaptation to actual demands. Moreover, the guanidine ligands are strongly related to the essential and ubiquitous amino acid arginine, which is nontoxic.[10]

Herein we report on the synthesis and characterisation of the first zinc complexes including $N^1$,$N^2$-bis(1,3-dimethylimidazolidin-2-ylidene)ethane-1,2-diamine (DMEG$_2$e, **L1**)[11] as bis(guanidine) ligand, which are actually the first examples of aliphatic bis(guanidine)-stabilised zinc complexes. The complexes [$N^1$,$N^2$-bis(1,3-dimethylimidazolidin-2-ylidene)-ethane-1,2-diamine]dichloridozinc(II), [Zn(DMEG$_2$e)Cl$_2$] (**C1**), diacetato[$N^1$,$N^2$-bis(1,3-dimethylimidazolidin-2-ylidene)-ethane-1,2-diamine]zinc(II), [Zn(DMEG$_2$e)(CH$_3$COO)$_2$] (**C2**), and bis[$N^1$,$N^2$-bis(1,3-dimethylimidazolidin-2-ylidene)ethane-

[a] Department Chemie, Anorganische Chemie, Universität Paderborn,
Warburgerstraße 100, 33098 Paderborn, Germany
Fax: +49-5251-603423
E-mail: shp@mail.uni-paderborn.de
[b] Department Chemie, Physikalische Chemie, Universität Paderborn,
Warburgerstraße 100, 33098 Paderborn, Germany

 © 2007 Wiley-VCH Verlag GmbH & Co. KGaA, Weinheim 

1,2-diamine]zinc(II) bis(trifluoromethanesulfonate), [Zn(DMEG$_2$e)$_2$](CF$_3$SO$_3$)$_2$ (**C3**), were investigated regarding their activity in the bulk polymerisation of D,L-lactide. Our results prove that the bis(guanidine) complexes possess catalytic activity in the ROP of D,L-lactide. PLAs with molecular weights ($M_w$) of around 18000–59000 g/mol could be obtained.

## Results and Discussion

The bis(guanidine) ligand $N^1$,$N^2$-bis(1,3-dimethylimidazolidin-2-ylidene)ethane-1,2-diamine (DMEG$_2$e, **L1**) was synthesised by condensation of the Vilsmeier salt *N*,*N*′-dimethyl-*N*,*N*′-ethylenechloroformamidinium chloride with ethylenediamine, as previously reported.[11] In the reaction of **L1** with ZnCl$_2$ in MeCN, colourless crystals of [Zn(DMEG$_2$e)Cl$_2$] (**C1**) could be obtained in 98% yield. The reaction of **L1** with Zn(CH$_3$COO)$_2$ and Zn(CF$_3$SO$_3$)$_2$ in THF leads to the formation of colourless crystals of [Zn(DMEG$_2$e)(CH$_3$COO)$_2$] (**C2**) in 97% yield and [Zn(DMEG$_2$e)$_2$](CF$_3$SO$_3$)$_2$ (**C3**) in 73% yield, respectively (Scheme 1). The described guanidine-stabilised zinc complexes formed independently of the molar ratio of the starting materials.

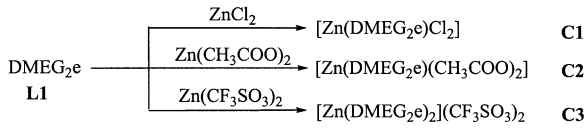


Scheme 1. Schematic synthesis of **C1**–**C3**.

The molecular structures of compounds **C1**–**C3** (Figures 1, 2 and 3), determined by X-ray crystallography at 120 K, reveal that each Zn$^{II}$ atom is fourfold coordinated. In **C1** and **C2**, two coordination sites are occupied in a chelating manner by the N-donor atoms of DMEG$_2$e, forming a five-membered heterocycle that adopts a half-chair conformation, whereas in **C3**, four coordination sites are occupied analogously by the N-donor atoms of two DMEG$_2$e molecules. In **C1** and **C2**, the remaining coordination sites are occupied by chloride ions [Zn–Cl distance: 2.260(1) Å] or acetate ions [average of the Zn–O distances: 1.963(2) Å]. The distances between the zinc ion and the N-donor atoms decrease, going from **C1** [2.038(2) Å] over **C2** [av. 2.025(2) Å] to **C3** [av. 2.012(4) Å], while the length of the C=N bonds of the guanidine residues are identical in all three compounds [av. **C1**: 1.309(3); **C2**: 1.307(2); **C3**: 1.309(5) Å]. The zinc atoms in **C1** and **C2** are coordinated in a distorted tetrahedral manner. The sums of the angles at the Zn atom are 656.18° for **C1** and 659.48° for **C2** and therefore fit well with the value for a perfect tetrahedral geometry (656.82°). However, the bite angle of 86.18(10)° (**C1**) and 86.16(6)° (**C2**) is too small for a perfect tetrahedral geometry, resulting in a distortion. This distortion is reflected in the values of the angles between the ZnCl$_2$ and the ZnN$_2$ plane (74.5°) and the ZnO$_2$ and the ZnN$_2$ plane (76.3°), which is 90° in a tetrahedron. In contrast, the environment of the Zn atom in **C3** lies between tetrahedral and square-planar coordination. The sum of the angles at the Zn atom is 670.41° and lies between the values for a tetrahedron (656.82°) and a square-planar coordination (720°), indicating more tetrahedral character. The bite angles of both DMEG$_2$e ligands are identical [85.5(1) and 85.2(1)°]. The bite angles defined by the ligands are significantly smaller than the tetrahedron angle (109.47°) and therefore lead to a distortion of the tetrahedral structure in the direction of square-planar coordination. This is also shown in the value of the angle between the ZnN$_2$ planes (53.9°), which is between the tetrahedral (90°) and the square-planar coordination (0°). Furthermore, the distorted structure favours the minimisation of the interactions between the sterically demanding guanidine residues. The twist within the guanidine heterocycle, which minimises the ecliptic interactions of the ring-bound hydrogen atoms, is limited in the DMEG$_2$e systems by the rigid ethylene bridge between the two amine functions. The values of

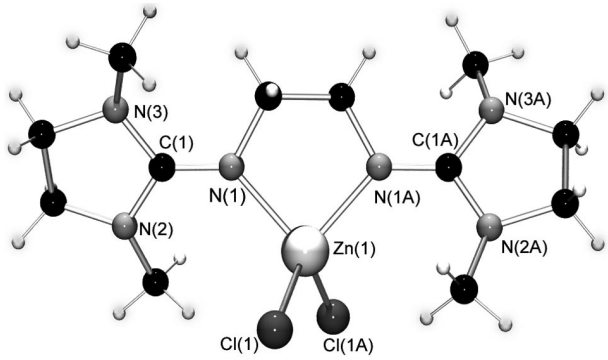


Figure 1. Molecular structure of [Zn(DMEG$_2$e)Cl$_2$] (**C1**) as determined at 120 K. Selected bond lengths [Å] and angles [°]: Zn(1)–N(1) 2.038(2), Zn(1)–Cl(1) 2.260(1), N(1)–C(1) 1.309(3); N(1)–Zn(1)–N(1A) 86.18(10), N(1)–Zn(1)–Cl(1) 105.05(6), Cl(1)–Zn(1)–Cl(1A) 111.60(4).

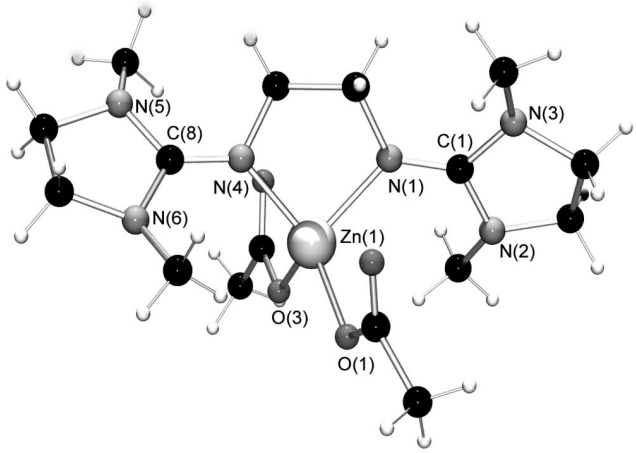


Figure 2. Molecular structure of [Zn(DMEG$_2$e)(CH$_3$COO)$_2$] (**C2**) as determined at 120 K. Selected bond lengths [Å] and angles [°]: Zn(1)–N(1) 2.011(2), Zn(1)–N(4) 2.038(2), Zn(1)–O(1) 1.969(2), Zn(1)–O(3) 1.956(2), N(1)–C(1) 1.308(2), N(4)–C(8) 1.305(2); N(1)–Zn(1)–N(4) 86.16(6), N(1)–Zn(1)–O(1) 110.98(7), N(1)–Zn(1)–O(3) 129.98(6), N(4)–Zn(1)–O(1) 123.57(7), N(4)–Zn(1)–O(3) 109.89(6), O(1)–Zn(1)–O(3) 98.90(6).

 © 2007 Wiley-VCH Verlag GmbH & Co. KGaA, Weinheim 

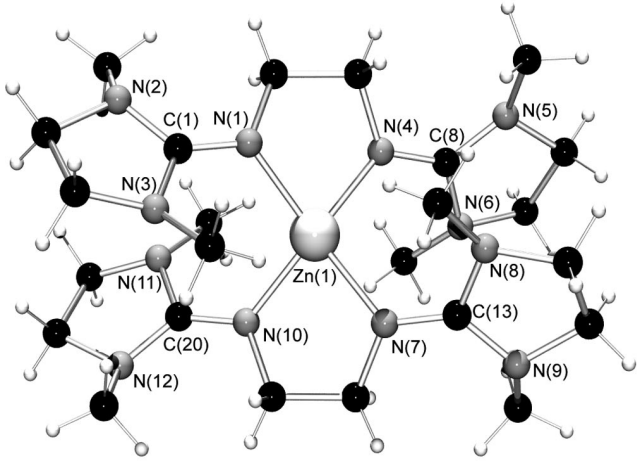


Figure 3. Molecular structure of $[Zn(DMEG_2e)_2]^{2+}$ in crystals of $[Zn(DMEG_2e)_2](CF_3SO_3)_2$ (**C3**) as determined at 120 K. Selected bond lengths [Å] and angles [°]: Zn(1)–N(1) 2.028(3), Zn(1)–N(7) 2.021(3), Zn(1)–N(10) 2.004(3), Zn(1)–N(4) 1.996(3), N(1)–C(1) 1.303(5), N(4)–C(8) 1.307(5), N(7)–C(13) 1.315(5), N(10)–C(20) 1.311(5); N(4)–Zn(1)–N(10) 145.3(1), N(4)–Zn(1)–N(7) 106.0(1), N(10)–Zn(1)–N(7) 85.5(1), N(4)–Zn(1)–N(1) 85.2(1), N(10)–Zn(1)–N(1) 105.3(1), N(7)–Zn(1)–N(1) 143.1(1).

the angles between the $C_{gua}N_3$ and the $NC_3$ plane are thus slightly smaller (**C1**: 15.5°; **C2**: 14.9°; **C3**: 15.6°) than those reported for a similar DMEG-containing system (17.4°).[9a]

The comparison of $[Zn(DMEG_2e)_2](CF_3SO_3)_2$ (**C3**) with its copper and iron analogues $[Cu(DMEG_2e)_2][Cu_2I_4]$[11] (**C4**) and $[Fe(DMEG_2e)_2][Fe_2(CO)_8]$[11] (**C5**) shows a great similarity of all three complex cations. The metal atoms in the $[M(DMEG_2e)_2]^{2+}$ unit are present in the oxidation state +2 and are coordinated by four ethylene-bridged imine nitrogen atoms of the bis(guanidine) ligands in a strongly distorted tetrahedron. The five-membered chelate heterocycles adopt a half-chair conformation. The angles between the $MN_2$ planes (**C3**: 53.9°; **C4**: 44.5°; **C5**: 48.7°) show that the coordination mode remains in the intermediate position between the tetrahedral (90°) and the square-planar coordination (0°). The averaged bite angles of the complexes do not differ considerably [**C3**: 85.4(1)°; **C4**: 84.4(1)°; **C5**: 83.5(1)°] and also the averaged distances of the C=N bonds [**C3**: 1.309(5) Å; **C4**: 1.302(4) Å; **C5**: 1.307(3) Å] are identical. The values of the metal–nitrogen bonds [**C3**: 2.012(3) Å; **C4**: 1.970(2) Å; **C5**: 2.044(2) Å] are, despite the different metal ions and their varying ion radii, in a similar range.

As mentioned before, guanidines are a very promising ligand class leading to catalytically active zinc complexes. Therefore, the obtained complexes **C1**–**C3** were investigated regarding their activity in the bulk polymerisation of D,L-lactide. For this purpose D,L-lactide and the initiator (*I*/*M* ratio 1:500 or 1:1000) were tempered at 135 °C, 150 °C and 165 °C. After a reaction time of 24 or 48 h, the polymer melt was dissolved in dichloromethane, and then the polylactide was precipitated in cold methanol. We could prove that all three bis(guanidine) complexes possess catalytic activity in the ROP of D,L-lactide. A great advantage of the described zinc compounds is their stability towards air and moisture because they can be handled exposed to air without loss of activity. Complexes **C1** and **C3** are stable on air for months, while **C2** is hygroscopic but stable on air for hours. In order to specify the catalytic activity of the complexes, the monomer conversion was defined, and the molecular weights of the obtained polylactide were determined by gel permeation chromatography (see Table 1).

In general, the monomer conversion as well as the weight-averaged molar mass values ($M_w$) of the corresponding polymer are higher for **C1** than for **C2** and **C3**. At the standard temperature for lactide polymerisations, which is 150 °C,[5] **C3** shows the best results for $M_w$ (32000–38000 g/mol) and the best yields. The acetate complex **C2** exhibits a weaker performance. This indicates the effect of the anionic component of the zinc salt on the catalytic activity of the corresponding zinc complex. Interestingly, an increase of the reaction time from 24 to 48 h does not improve the conversion, nor does it increase the molecular weight of the obtained polymer. On the contrary, a decrease of conversion and molecular weight

Table 1. Polymerisation of D,L-lactide initiated by **C1**–**C3**.

| Initiator | Temp. [°C] | Time [h] | Mon./Init. | Yield [%] | $M_w$ [g/mol] | *U* |
|---|---|---|---|---|---|---|
| None | 165 | 24 | – | 0 | – | – |
| **C1** | 135 | 24 | 500 | 82 | 58800 | 1.74 |
| **C1** | 150 | 24 | 500 | 79 | 38000 | 1.72 |
| **C1** | 150 | 24 | 1000 | 70 | 32900 | 1.55 |
| **C1** | 150 | 48 | 500 | 67 | 32900 | 1.56 |
| **C1** | 165 | 24 | 500 | 61 | 33800 | 1.62 |
| **C2** | 135 | 24 | 500 | 63 | 34700 | 1.63 |
| **C2** | 150 | 24 | 500 | 69 | 24300 | 1.63 |
| **C2** | 150 | 24 | 1000 | 86 | 27600 | 1.77 |
| **C2** | 150 | 48 | 500 | 66 | 17900 | 1.60 |
| **C2** | 165 | 24 | 500 | 46 | 21500 | 1.54 |
| **C3** | 135 | 24 | 500 | 82 | 37200 | 1.74 |
| **C3** | 150 | 24 | 500 | 83 | 38200 | 1.61 |
| **C3** | 150 | 24 | 1000 | 93 | 34100 | 1.88 |
| **C3** | 150 | 48 | 500 | 83 | 31600 | 1.68 |
| **C3** | 165 | 24 | 500 | 51 | 23200 | 1.58 |

 © 2007 Wiley-VCH Verlag GmbH & Co. KGaA, Weinheim 

can be observed. Similar observations were reported by Chisholm et al. and Schwach et al.,[12] who considered side reactions like the interchain or intrachain transesterification as well as the chain-transfer reaction to be responsible for this effect. In this context, it is expected that a decrease of reaction temperature would lead to minor side reaction effects.[12] Our results (see Figure 4) support this hypothesis. At 135 °C, **C1** and **C2** lead to considerably larger polymers than at higher temperatures, with $M_w$ values up to 59000 g/mol. Thus, molecular weights achieved by the present procedure decreased with increasing temperature. Only in the case of **C3** is this temperature effect not pronounced, because a maximum for the degree of polymerisation is reached at 150 °C.

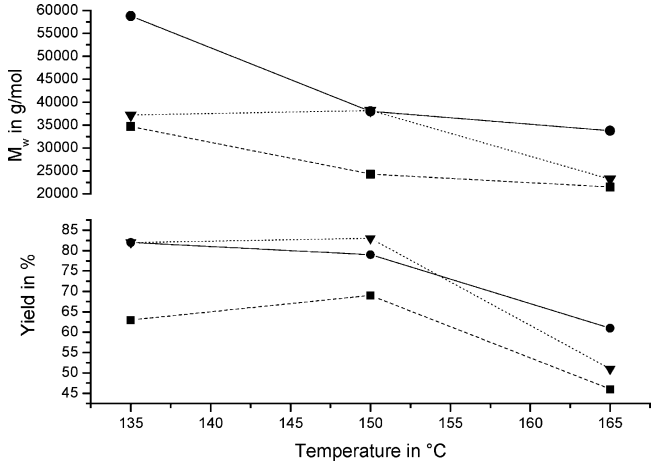


Figure 4. Dependence of weight-averaged molar mass ($M_w$) and yield vs. reaction temperature for the three initiator systems **C1**–**C3** (straight line: **C1**; dashed line: **C2**; dotted line: **C3**).

In order to study the structural characteristics of the synthesised polymers, the intrinsic viscosities were correlated with the molecular weight $M$ of the polymers. As outlined in Figure 5, all polymer samples exhibited a unique trend. For polymers large enough, this correlation is described by the Mark–Houwink equation (see Figure 5):[13] $[\eta] = K \cdot M^{\alpha}$.

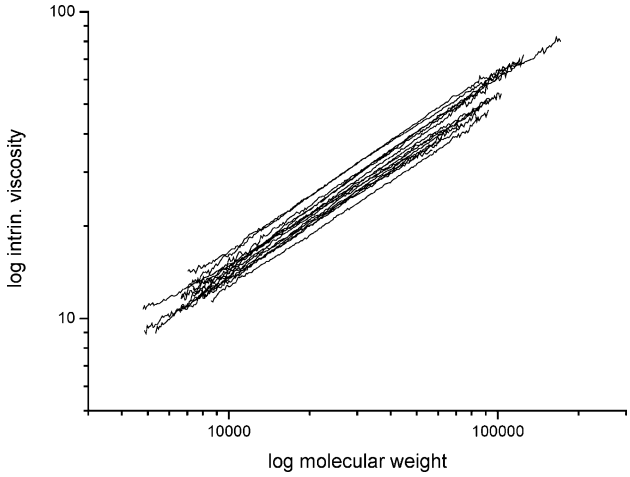


Figure 5. Mark–Houwink plot of all obtained PLAs. The calculated mean value for $\alpha$ is 0.59 and for $K$ is 0.068 at 35 °C in THF.

The linear behaviour and unique trend of all examined polymers indicates that the obtained PLA samples are structurally homogeneous and linear. Hence, the structure of the polymer reported herein is independent of the initiator used and the averaged values for the Mark–Houwink constants at 35 °C in THF were calculated to be $\alpha = 0.59$ and $K = 0.068$. Further values for different temperatures and solvents were reported by Rafler et al.[14] and Schindler and Harper.[15]

In order to classify the polymerisation activity of the (guanidine)zinc systems, a comparison of catalyst systems reported in the literature is summarised in Table 2. This comparison reveals that our systems do not achieve the highest molecular mass values, but compared to Entries 1 and 2 the chosen $M/I$ ratios are more favourable. Furthermore, the reaction times for polymerisations initiated by **C1**–**C3** are acceptable for the industrial standard. Compared to the highly active systems (Entries 4, 5, 8), **C1**–**C3** yielded similar or even higher molecular masses. The catalyst in Entry 7 is fast at ambient temperature and yields PLAs with high molecular masses, but the zinc alkoxide complexes are only stable under

Table 2. Selective summary of the reactivity of catalyst systems used for the ROP of lactide.

| Entry | Polymer | Catalyst (cocatalyst) | Solvent(s) | $T$ [°C] | Time | Mon./Init. | Molecular weight [g/mol] | Catalyst stability | Ref. |
|---|---|---|---|---|---|---|---|---|---|
| 1 | L-PLA | stannous octoate (alcohols) | none | 200 | 60–75 min | 33 | 468000 ($M_w$)[a] | stable | Seppälä et al.[16] |
| 2 | PLA-PCL-PLA | zinc powder (ethylene glycol) | none | 140 | 8 h (for PLA) | 20 | 61000 ($M_n$)[a] | stable | Li et al.[17] |
| 3 | D,L-PLA | zinc lactate | none | 140 | 96 h | 5000 | 155000 ($M_n$)[a] | stable | Schwach et al.[18] |
| 4 | D,L-PLA | (β-diiminato)zinc complexes | THF | 20 | 10 min | 100 | 18100 ($M_n$)[a] | n/a | Chisholm et al.[19] |
| | | | $CH_2Cl_2$ | | 3 min | | 16800 ($M_n$)[a] | | |
| 5 | D,L-PLA | (carbene)zinc complexes | $CH_2Cl_2$ | 25 | 16 min | 200 | 30000 ($M_n$)[a] | n/a | Tolman et al.[20] |
| | | | none | 140 | 5 min | 200 | 20000 ($M_n$)[a] | | |
| 6 | D,L-PLA | zinc alkoxides | toluene | 60 | 4.5 h | 150 | 34100 ($M_n$)[a] | n/a | Lin et al.[21] |
| | L-PLA | | $CH_2Cl_2$ | 25 | 24 h | 50 | 9900 ($M_n$)[a] | | |
| 7 | D,L-PLA | zinc alkoxides | $CH_2Cl_2$ | 25 | 18 min | 1500 | 130000 ($M_n$) | only stable under glovebox conditions | Tolman et al.[22] |
| 8 | L-PLA | zinc alkoxides | toluene | 25 | 13 min | 400 | 25500 ($M_n$)[a] | n/a | Lin et al.[23] |

[a] Expressed in polystyrene standards.

 © 2007 Wiley-VCH Verlag GmbH & Co. KGaA, Weinheim 

exclusion of moisture and air. Hence, the (guanidine)zinc complexes combine several factors that are necessary requirements for an efficient catalyst. These systems can be handled in air and give polymers with molecular masses that allow the application in industrial production processes. To increase the activity of the (guanidine)zinc catalysts, the reaction conditions have to be further optimised. The structural influences of the guanidine ligand on the activity of the zinc complexes in lactide polymerisation are being studied at the moment.

## Conclusions

In this contribution we reported on the synthesis and complete characterisation of the first examples of aliphatic bis(guanidine)-stabilised zinc complexes that were proven to be active initiators in the ring-opening polymerisation of D,L-lactide. PLAs with molecular weights ($M_w$) of around 18000–59000 g/mol could be obtained. In complexes with the same ligand the activity of the initiator depends on the anionic component of the zinc salt. We found that complexes with zinc bis(triflate) and zinc dichloride seem to be the most auspicious candidates for application in the ROP of lactide. By changing the reaction temperature it could be shown that lower temperatures allow side reactions to be avoided during the polymerisation and thus give higher molecular masses. Moreover, the Mark–Houwink correlation demonstrates that the obtained polymers are linear and homogeneous. Compared to other systems the (guanidine)zinc complexes possess an advantageous combination of properties: they are nontoxic, comparably stable and give PLAs with good $M_w$ values at industrial conditions. This makes the (guanidine)zinc systems a promising class of catalysts for the ring-opening polymerisation of D,L-lactide. The reaction control and the clarification of the reaction mechanism as well as the synthesis of more active (guanidine)zinc complexes for the ROP of lactide are topics of current research.

## Experimental Section

**Materials and Methods:** All manipulations were performed under nitrogen (99.996%) dried with $P_4O_{10}$ granulate using Schlenk techniques. Solvents were purified according to literature procedures and also kept under nitrogen. Zinc dichloride (99.99%, Acros), zinc diacetate (99.99%, Acros), zinc bis(trifluoromethanesulfonate) (98%, Aldrich) and D,L-lactide (3,6-dimethyl-1,4-dioxane-2,5-dione, Aldrich) were used as purchased. The $N^1$,$N^2$-bis(1,3-dimethylimidazolidin-2-ylidene)ethane-1,2-diamine (**L1**) was prepared according to a literature procedure.[11]

**Physical Measurements:** NMR: Bruker Avance 500. The NMR signals were calibrated to the residual signals of the deuterated solvents ($CDCl_3$: $\delta_H$ = 7.26 ppm; $CH_3CN$: $\delta_H$ = 1.94 ppm). IR: Nicolet P510. MS (EI, 70 eV): Finnigan MAT 40. Elemental analyses: Perkin–Elmer analyser Model 2400.

**Crystal Structure Analyses:** Crystal data for compounds **C1**, **C2** and **C3** are presented in Table 3. X-ray diffraction data were collected with a Bruker-AXS SMART APEX CCD, using Mo-$K_\alpha$ radiation ($\lambda$ = 0.71073 Å) and a graphite monochromator. SAINT and SADABS were used for data reduction and absorption correction.[24] The structures were solved by direct and conventional Fourier methods, and all non-hydrogen atoms were refined anisotropically with full-matrix least squares based on $F^2$ (SHELXTL[24]). Hydrogen atoms were derived from difference Fourier maps and placed at idealised positions, riding on their parent C atoms, with isotropic displacement parameters $U_{iso}(H) = 1.2U_{eq}(C)$ and $1.5U_{eq}$(C methyl). All methyl groups were allowed to rotate but not to tip. CCDC-652328 (for **C1**), -652329 (for **C2**) and -652330 (for **C3**) contain the supplementary crystallographic data (excluding structure factors) for this paper. These data can be obtained free of charge from The Cambridge Crystallographic Data Centre via www.ccdc.cam.ac.uk/data_request/cif.

**Gel Permeation Chromatography:** The GPC measurements were accomplished with a Waters GPC 2000 instrument equipped with a precolumn (10 μm) and a combination of three PSS-SDV columns ($10^6$ Å, $10^5$ Å, $10^3$ Å). The detection system included an integrated refractive index (RI) detector and an integrated viscosity detector H502B (Visotek). All measurements were performed at 35 °C with THF as eluent. The flow rate was 1 mL/min. Sample concentrations amounted to 2–3 g/L. Molecular weight analysis was based on a universal calibration, carried out with polystyrene standards (Polymer Standard Service) in THF at 35 °C. Use of the universal calibration gave way to absolute values for the molecular weight, which are discussed as weight-averaged molar mass values $M_w$ and the polydispersity index $U$ as a measure of the width of the respective molecular weight distribution $U = M_w/M_n$ with $M_n$ the corresponding number averaged molar mass. Results are summarised in Table 1. Concomitantly, the intrinsic viscosities of the polymer samples were determined as a function of the molecular mass and correlated in the Mark–Houwink plot (Figure 5).

### Preparation of Compounds

**[$N^1$,$N^2$-Bis(1,3-dimethylimidazolidin-2-ylidene)ethane-1,2-diamine]-dichloridozinc(II), [Zn(DMEG$_2$e)Cl$_2$] (C1):** The ligand $N^1$,$N^2$-bis(1,3-dimethylimidazolidin-2-ylidene)ethane-1,2-diamine (0.278 g, 1.1 mmol) was added to a solution of zinc dichloride (0.136 g, 1 mmol) in abs. MeCN (15 mL) whilst stirring. This suspension was slowly heated under reflux. A colourless precipitate could be observed; yield: 98% (0.38 g). Colourless crystals suitable for X-ray diffraction could be obtained by recrystallisation from hot MeCN (decomposition at 350 °C). $^1$H NMR (500 MHz, $CDCl_3$, 25 °C): $\delta$ = 3.06 (s, 12 H, $CH_3$), 3.40 (s, 8 H, $CH_2$), 3.46 (s, 4 H, $CH_2$) ppm. $^{13}$C NMR (125 MHz, $CDCl_3$, 25 °C): $\delta$ = 37.1 ($CH_3$), 49.8 ($CH_2$), 49.9 ($CH_2$), 164.4 ($C_{gua}$) ppm. IR (KBr): $\tilde{\nu}$ = 2933 [m, $\nu$(C–H)], 2867 [m, $\nu$(C–H)], 1597 [vs, $\nu$(C=N)], 1508 (m), 1446 (m), 1429 (m), 1404 (m), 1348 (m), 1296 (m), 1227 (w), 1097 (w), 1051 (w), 916 (m), 798 (vw), 766 (w), 727 (w), 652 (vw), 615 (w) cm$^{-1}$. EI-MS: $m/z$ (%) = 392 (17) [$M^+$: $C_{12}H_{24}{}^{37}Cl_2N_6{}^{66}Zn$, $C_{12}H_{24}{}^{35}Cl^{37}ClN_6{}^{68}Zn$], 391 (10) [$C_{12}H_{24}{}^{35}Cl^{37}ClN_6{}^{67}Zn$, $C_{11}{}^{13}CH_{24}{}^{35}Cl^{37}ClN_6{}^{66}Zn$, $C_{11}{}^{13}CH_{24}{}^{35}Cl_2N_6{}^{68}Zn$], 390 (46) [$M^+$: $C_{12}H_{24}{}^{35}Cl^{37}ClN_6{}^{66}Zn$, $C_{12}H_{24}{}^{37}Cl_2N_6{}^{64}Zn$, $C_{12}H_{24}{}^{35}Cl_2N_6{}^{68}Zn$], 389 (15) [$M^+$: $C_{12}H_{24}{}^{35}Cl_2N_6{}^{67}Zn$, $C_{11}{}^{13}CH_{24}{}^{35}Cl_2N_6{}^{66}Zn$, $C_{11}{}^{13}CH_{24}{}^{35}Cl^{37}ClN_6{}^{64}Zn$], 388 (71) [$M^+$: $C_{12}H_{24}{}^{35}Cl_2N_6{}^{66}Zn$, $C_{12}H_{24}{}^{35}Cl^{37}ClN_6{}^{64}Zn$], 387 (10) [$M^+$: $C_{11}{}^{13}CH_{24}{}^{35}Cl_2N_6{}^{64}Zn$], 386 (65) [$M^+$: $C_{12}H_{24}{}^{35}Cl_2N_6{}^{64}Zn$], 353 (14) [$M^+ - {}^{35}Cl$], 351 (15) [$M^+ - {}^{37}Cl$], 251 (12) [$M^+ - ZnCl_2$], 140 (6) [$C_4H_4N{=}CN_2(CH_3)_2C_2H_4^+$], 126 (100) [$CH_2N{=}CN_2(CH_3)_2C_2H_4^+$], 112 (7) [$N{=}CN_2(CH_3)_2$-$C_2H_4^+$], 98 (12) [$C_5H_{10}N_2^+$], 85 (4) [$CN_3(CH_3)_2^+ + H$], 56 (22) [$NCH_2CH_2N^+$]. $C_{12}H_{24}Cl_2N_6Zn$ (388.07): calcd. C 37.11, H 6.18, N 21.65; found C 37.41, H 6.10, N 21.24.

**Diacetato[$N^1$,$N^2$-bis(1,3-dimethylimidazolidin-2-ylidene)ethane-1,2-diamine]zinc(II), [Zn(DMEG$_2$e)(CH$_3$COO)$_2$] (C2):** The ligand $N^1$,$N^2$-bis(1,3-dimethylimidazolidin-2-ylidene)ethane-1,2-diamine (0.278 g, 1.1 mmol) was added to a suspension of zinc diacetate (0.183 g,

 © 2007 Wiley-VCH Verlag GmbH & Co. KGaA, Weinheim 

Table 3. Crystal data for the compounds **C1**, **C2** and **C3**.

| | **C1** | **C2** | **C3** |
|---|---|---|---|
| Empirical formula | $C_{12}H_{24}Cl_2N_6Zn$ | $C_{16}H_{30}N_6O_4Zn$ | $C_{26}H_{48}F_6N_{12}O_6S_2Zn$ |
| Formula mass | 388.6 | 435.8 | 868.3 |
| Crystal size [mm] | $0.23 \times 0.20 \times 0.18$ | $0.41 \times 0.39 \times 0.20$ | $0.16 \times 0.15 \times 0.13$ |
| Crystal system | monoclinic | triclinic | triclinic |
| Space group | $C2/c$ | $P\bar{1}$ | $P\bar{1}$ |
| $a$ [Å] | 9.5320(8) | 7.7644(5) | 12.5916(7) |
| $b$ [Å] | 13.2821(8) | 9.1357(6) | 12.6664(8) |
| $c$ [Å] | 13.2844(9) | 15.0902(10) | 14.3728(9) |
| $\alpha$ [°] | 90 | 102.901(1) | 96.624(2) |
| $\beta$ [°] | 101.318(2) | 97.610(1) | 108.597(2) |
| $\gamma$ [°] | 90 | 94.699(1) | 116.279(2) |
| $V$ [Å$^3$] | 1649.2(2) | 1027.3(1) | 1857.2(2) |
| $Z$ | 4 | 2 | 2 |
| $D_{calcd.}$ [g/cm$^3$] | 1.565 | 1.409 | 1.553 |
| $\mu$(Mo-$K_\alpha$) [mm$^{-1}$] | 1.82 | 1.23 | 0.86 |
| Temperature [K] | 120(2) | 120(2) | 120(2) |
| $\theta$ range [°] | 2.6–27.9 | 1.4–27.1 | 1.6–27.9 |
| $h$, $k$, $l$ | –10/12, ±17, ±17 | ±9, –11/10, ±19 | –16/15, –16/14, ±18 |
| Measured reflections | 7633 | 8548 | 16702 |
| No. of unique data | 1978 | 4465 | 8805 |
| Parameters | 98 | 244 | 486 |
| $R_1$ [$I \geq 2\sigma(I)$] | 0.036 | 0.034 | 0.071 |
| $wR_2$ (all data) | 0.086 | 0.094 | 0.128 |
| Min/max $\Delta F$ [e/Å$^3$] | –0.34/0.59 | –0.30/0.37 | –0.49/0.59 |

1 mmol) in abs. THF (7 mL) whilst stirring. A white precipitate could be observed. After 20 min of additional stirring, the suspension was slowly heated under reflux to give a clear solution. Colourless crystals suitable for X-ray diffraction were obtained by slowly cooling to room temperature (m.p. 51 °C); yield: 97% (0.42 g). $^1$H NMR (500 MHz, $CDCl_3$, 25 °C): $\delta$ = 1.92 (s, 6 H, $CH_3$), 2.92 (s, 12 H, $CH_3$), 3.10 (s, 8 H, $CH_2$), 3.48 (s, 4 H, $CH_2$) ppm. $^{13}$C NMR (125 MHz, $CDCl_3$, 25 °C): $\delta$ = 23.6 ($CH_3$), 36.1 ($CH_3$), 49.6 ($CH_2$), 49.7 ($CH_2$), 164.0 ($C_{gua}$), 177.2 ($C_{ac}$) ppm. IR (KBr): $\tilde{\nu}$ = 2931 [m, $\nu$(C–H)], 2866 [m, $\nu$(C–H)], 1595 [vs, $\nu$(C=N)], 1508 (m), 1446 (m), 1425 (m), 1404 (m), 1346 (m), 1296 (m), 1227 (w), 1097 (w), 1072 (w), 1049 (w), 1020 (w), 972 (w), 916 (m), 768 (m), 725 (m), 650 (m), 611 (m) cm$^{-1}$. EI-MS: $m/z$ (%) = 434 (2) [M$^+$], 389 (34) [M$^+$ – $HN(CH_3)_2$], 375 (31) [M$^+$ – $CH_3COO$], 345 (9) [M$^+$ – $CH_3COO$ – 2 $CH_3$], 315 (19) [M$^+$ – 2 $CH_3COO$ – H], 299 (5), 251 (19) [M$^+$ – $Zn(CH_3COO)_2$], 236 (11) [M$^+$ – $Zn(CH_3COO)_2$ – $CH_3$], 220 (7) [M$^+$ – $Zn(CH_3COO)_2$ – 2 $CH_3$ – H], 153 (5) [M$^+$ – $Zn(CH_3COO)_2$ – $C_5H_{10}N_2$], 140 (28) [$C_4H_4N{=}CN_2(CH_3)_2C_2H_4^+$], 126 (100) [$CH_2N{=}CN_2(CH_3)_2C_2H_4^+$], 112 (11) [$N{=}CN_2(CH_3)_2C_2H_4^+$], 98 (22) [$C_5H_{10}N_2^+$], 85 (24) [$CN_3(CH_3)_2^+$ + H], 56 (48) [$NCH_2CH_2N^+$]. $C_{16}H_{30}N_6O_4Zn$ (434.16): calcd. C 44.22, H 6.91, N 19.35; found C 43.96, H 6.89, N 18.89.

**Bis[$N^1$,$N^2$-Bis(1,3-dimethylimidazolidin-2-ylidene)ethane-1,2-diamine]-zinc(II) Bis(trifluoromethanesulfonate), [Zn(DMEG$_2$e)$_2$](CF$_3$SO$_3$)$_2$ (C3):** The ligand $N^1$,$N^2$-bis(1,3-dimethylimidazolidin-2-ylidene)ethane-1,2-diamine (0.278 g, 1.1 mmol) was added to a solution of zinc bis(trifluoromethanesulfonate) (0.182 g, 0.5 mmol) in abs. THF (10 mL) whilst stirring. This suspension was slowly heated under reflux. A colourless precipitate was observed; yield: 73% (0.32 g). Colourless crystals suitable for X-ray diffraction could be obtained by recrystallisation from hot MeCN (decomposition at 350 °C). $^1$H NMR (500 MHz, $CDCl_3$, 25 °C): $\delta$ = 2.96 (m, 24 H, $CH_3$), 3.48 (m, 16 H, $CH_2$), 3.64 (s, 8 H, $CH_2$) ppm. $^{13}$C NMR (125 MHz, $CDCl_3$, 25 °C): $\delta$ = 35.1 ($CH_3$), 45.7 ($CH_2$), 49.2 ($CH_2$), 122.1 (C), 165.8 (C) ppm. IR (KBr): $\tilde{\nu}$ = 2941 [w, $\nu$(C–H$_{aliph.}$)], 2870 [w, $\nu$(C–H$_{aliph.}$)], 1593 [vs, $\nu$(C=N)], 1506 (m), 1458 (w), 1421 (m), 1342 (m), 1265 (s), 1221 (m), 1163 (m), 1028 (s), 916 (w), 781 (w), 725 (w), 636 (m), 573 (w), 517 (w) cm$^{-1}$. EI-MS: $m/z$ (%) = 867 (6) [M$^+$], 717 (10) [M$^+$ – $CF_3SO_3$], 567 (18) [M$^+$ – 2 $CF_3SO_3$], 251 (100) [M$^+$ – $Zn(CF_3SO_3)_2$], 167 (31) [M$^+$ – $Zn(CF_3SO_3)_2$ – $C_4H_{10}N_2$ + 2 H], 149 (99) [$CF_3SO_3^-$], 126 (54) [$CH_2N{=}CN_2(CH_3)_2C_2H_4^+$], 112 (14) [$N{=}CN_2(CH_3)_2C_2H_4^+$], 100 (21) [$C_5H_{10}N_2^+$ + 2 H], 98 (17) [$C_5H_{10}N_2^+$], 86 (16) [$C_4H_{10}N_2^+$]. $C_{26}H_{48}F_6N_{12}O_6S_2Zn$ (867.25): calcd. C 35.98, H 5.53, N 19.37; found C 35.60, H 5.22, N 19.01.

**General Procedure for Lactide Polymerisation:** D,L-Lactide (3.603 g, 25 mmol) and the initiator ($I$/$M$ ratio 1:500 or 1:1000) were weighed into a 50-mL Erlenmeyer flask that was closed with a glass stopper. The reaction vessel was then tempered at 150 °C. After the reaction time, the polymer melt was cooled to room temperature and then dissolved in dichloromethane (25 mL). The polylactide was precipitated in ice-cooled methanol (350 mL) and dried under vacuum.

## Acknowledgments

Financial support from the Stiftung der Deutschen Wirtschaft (fellowship for J. B.), the University of Paderborn (fellowship for S. H.-P.) and the Deutsche Forschungsgemeinschaft is gratefully acknowledged. Furthermore, S. H.-P. thanks Prof. Dr. G. Henkel for his valuable support.

[1] a) S. Jacobson, P. Degée, H. G. Fritz, P. Dubois, R. Jérôme, *Polym. Eng. Sci.* **1999**, *39*, 1311–1319; b) O. Dechy-Carbaret, B. Martin-Vaca, D. Bourissou, *Chem. Rev.* **2004**, *104*, 6147–6176; c) Y. Tokiwa, B. P. Calabia, *Appl. Micromol. Biotechnol.* **2006**, *72*, 244–251.

[2] G. Rafler, J. Lang, M. Jobmann, I. Bechthold, *Macromol. Mater. Eng.* **2001**, *286*, 761–768.

[3] R. E. Drumright, P. R. Gruber, D. E. Henton, *Adv. Mater.* **2000**, *12*, 1841–1846.

[4] a) H. R. Kricheldorf, J. Meier-Haak, *Macromol. Chem.* **1993**, *194*, 715–725; b) M. Yuan, D. Liu, C. Xiong, X. Deng, *Eur. Polym. J.* **1999**, *35*, 2139–2145.

[5] H. R. Kricheldorf, D.-O. Damrau, *Macromol. Chem. Phys.* **1997**, *198*, 1753–1766.

 © 2007 Wiley-VCH Verlag GmbH & Co. KGaA, Weinheim 

[6] a) J. Wu, T.-L. Yu, C.-T. Chen, C.-C. Lin, *Coord. Chem. Rev.* **2006**, *250*, 602–626 and literature cited therein; b) O. Dechy-Carbaret, B. Martin-Vaca, D. Bourissou, *Chem. Rev.* **2004**, *104*, 6147–6176; c) B. J. O'Kneefe, M. A. Hillmyer, W. B. Tolman, *J. Chem. Soc. Dalton Trans.* **2001**, 2215–2224; d) K. Nakano, N. Kosaka, T. Hiyama, K. Nozaki, *Dalton Trans.* **2003**, 4039–4050.
[7] a) H. Wittmann, A. Schorm, J. Sundermeyer, *Z. Anorg. Allg. Chem.* **2000**, *626*, 1583–1590; b) S. H. Oakley, D. B. Soria, M. P. Coles, P. B. Hitchcock, *Polyhedron* **2006**, *25*, 1247–1255; c) H. Wittmann, V. Raab, A. Schorm, J. Plackmeyer, J. Sundermeyer, *Eur. J. Inorg. Chem.* **2001**, 1937–1948; d) S. Aoki, K. Iwaida, N. Hanamoto, M. Shiro, E. Kimura, *J. Am. Chem. Soc.* **2002**, *124*, 5256–5257; e) T. Ishikawa, M. Kawahata, EP 1752451A1, **2007**.
[8] a) U. Köhn, M. Schulz, H. Görls, E. Anders, *Tetrahedron: Asymmetry* **2005**, *16*, 2125–2135; b) M. Walter, K. Wermann, M. Lutsche, W. Günther, H. Görls, E. Anders, *J. Org. Chem.* **2006**, *71*, 1399–1406; c) M. Coles, P. Hitchcock, *Eur. J. Inorg. Chem.* **2004**, 2662–2672.
[9] a) S. Herres-Pawlis, U. Flörke, G. Henkel, *Eur. J. Inorg. Chem.* **2005**, 3815–3824; b) S. Herres-Pawlis, A. Neuba, O. Seewald, T. Seshadri, H. Egold, U. Flörke, G. Henkel, *Eur. J. Org. Chem.* **2005**, 4879–4890.
[10] D. Voet, J. G. Voet, C. W. Pratt in *Lehrbuch der Biochemie* (Eds: A. G. Beck-Sickinger, U. Hahn), Wiley-VCH, Weinheim, **2002**, pp. 83–99.
[11] S. Herres-Pawlis, R. Haase, E. Akin, U. Flörke, G. Henkel, *Z. Anorg. Allg. Chem.*, in press.
[12] a) M. H. Chisholm, J. C. Galluci, H. Yin, *Proc. Natl. Acad. Sci. U.S.A.* **2006**, *103*, 15315–15320; b) G. Schwach, J. Coudane, R. Engel, M. Vert, *Polym. Bull.* **1994**, *32*, 617–623.
[13] M. Rubinstein, R. H. Colby in *Polymer Physics*, Oxford University Press, Oxford, **2003**, chapter 1.
[14] G. Rafler, J. Dahlmann, K. Wiener, *Acta Polym.* **1990**, *41*, 328–333.
[15] A. Schindler, D. Harper, *J. Polym. Sci., Part A: Polym. Chem.* **1979**, *17*, 2593–2599.
[16] H. Korhonen, A. Helminen, J. V. Seppälä, *Polymer* **2001**, *42*, 7541–7549.
[17] M.-H. Huang, S. Li, M. Vert, *Polymer* **2004**, *45*, 8675–8681.
[18] G. Schwach, J. Coudane, R. Engel, M. Vert, *Polym. Bull.* **1996**, *37*, 771–776.
[19] M. H. Chisholm, J. C. Gallucci, K. Phomphrai, *Inorg. Chem.* **2005**, *44*, 8004–8010.
[20] T. R. Jensen, C. P. Schaller, M. A. Hillmyer, W. B. Tolman, *J. Organomet. Chem.* **2005**, *690*, 5881–5891.
[21] J.-C. Wu, B.-H. Huang, M.-L. Hsueh, S.-L. Lai, C.-C. Lin, *Polymer* **2005**, *46*, 9784–9792.
[22] C. K. Williams, L. E. Breyfogle, S. K. Choi, W. Nam, V. G. Young, M. A. Hillmyer, W. B. Tolman, *J. Am. Chem. Soc.* **2003**, *125*, 11350–11359.
[23] H.-Y. Chen, B.-H. Huang, C.-C. Lin, *Macromolecules* **2005**, *38*, 5400–5405.
[24] Bruker, *SMART* (Ver. 5.62), *SAINT* (Ver. 6.02), *SHELXTL* (Ver. 6.10) and *SADABS* (Version 2.03), Bruker AXS Inc., Madison, WI, USA, **2002**.

Received: August 30, 2007
Published Online: November 12, 2007

 © 2007 Wiley-VCH Verlag GmbH & Co. KGaA, Weinheim 

DOI: 10.1002/ejic.200700802

# Ca-Mediated Styrene Polymerization: Tacticity Control by Ligand Design

Dirk F.-J. Piesik,[a] Karin Häbe,[b] and Sjoerd Harder*[a]

**Keywords:** Alkaline-earth metals / Calcium / Polymerization catalysis / Fluorene ligands / Polystyrene

New heteroleptic benzylcalcium complexes with modified fluorenyl ligands were prepared which include a complex with a chelating dimethylamino substituent, [9-(2-$Me_2$N-ethyl)fluorenyl][2-$Me_2$N-α-$Me_3$Si-benzyl]Ca (**4**), and a series of complexes with bulky substituents like *t*Bu-, Ph(Me)$_2$C-, Me(Ph)$_2$C- and Me(4-*t*Bu$C_6H_4$)$_2$C- in the 2- and 7-positions of the fluorenyl ligand (complexes **5** through **9**, respectively). Crystal structures of **4**, [(2,7-*t*Bu-9-$Me_3$Si-fluorenyl)(2-$Me_2$N-benzyl)Ca]$_2$ (**5**) and [2,7-Ph(Me)$_2$C-9-$Me_3$Si-fluorenyl][2-$Me_2$N-α-$Me_3$Si-benzyl]Ca·THF (**6**) show that modification of the fluorenyl ligand hardly affects the coordination mode of the benzylic ligand. Also, in solution all compounds are of heteroleptic nature and it was shown that fluorenyl modifications hardly affect the barriers for inversion at the chiral benzylic carbon atom [18.7(2)–19.2(2) kcal/mol]. Complex **4** does not initiate styrene polymerization, which underscores the importance of a free coordination site at calcium. Complexes **5**–**9** initiate styrene polymerization, and the syndiotacticity of the obtained polymers increases with the bulkiness of the substituents on the fluorenyl ligands. Syndiotacticities up to $r$ = 95 % ($rr$ = 90 %) were obtained.

(© Wiley-VCH Verlag GmbH & Co. KGaA, 69451 Weinheim, Germany, 2007)

## Introduction

Syndiotactic polystyrene is a relatively young polymeric material[1,2] which receives much industrial as well as academic interest.[3–9] Its many advantageous properties,[10,11] which include a high melting point (273 °C), fast crystallization rate, high modulus, low density, low dielectric constant and excellent solvent resistance, have led to its successful application as a specialty polymer.[12]

We recently introduced a new class of polymerization initiators based on calcium which produced syndiotactic polystyrene by a chain-end-controlled monomer insertion (Scheme 1).[13–14] The initial catalyst systems consist of a polymerization-active benzyl group and a passive spectator ligand (generally a fluorenyl ligand). The monomeric (**1**)[14] and more active dimeric (**2**)[15] forms are well-defined complexes which have been structurally characterized by X-ray diffraction.

These initiators, which can be regarded as a cross-breed between organolithium initiators and cationic Ti$^{III}$ half-sandwich catalysts,[2,6] combine the advantages of a living polymerization with those of a stereoselective polymerization. Syndiotactic polystyrene, however, was only obtained for polymerization in neat styrene. This is due to the predominant ionicity and inherent weakness of the Ca–C bond, which allows for inversion of the chiral chain-end. The ratio between insertion and inversion rates, which can be controlled by monomer concentration,[14] thus controls the tacticity of the polymer (Scheme 1).

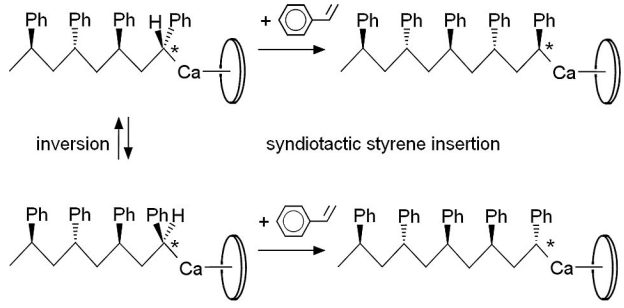


Scheme 1.

A slight improvement in stereoregularity could also be achieved by lowering the polymerization temperature.[14] Despite continuous efforts however, no significant improvement was obtained by variation of the spectator ligand. Earlier attempts to increase the syndiospecificity in styrene polymerization were based on increasing the steric bulk of the spectator ligand; that is, our initial catalyst (**1**) was modified by the introduction of a bulky hypersilyl substituent (**3**).[16] This would enforce a stronger interaction between the chiral polymer chain-end and the incoming monomer, and thus improve stereocontrol. The bulkier catalyst **3**, however, gave polystyrene of very similar tacticity but much shorter chain length. It was reasoned that the use of bulky substituents did not only result in improved communication between polymer and monomer, but also led to more stereoerrors by retarding monomer insertion and thus allowing inversion of the chiral chain-end.

[a] Anorganische Chemie, Universität Duisburg–Essen, Universitätsstraße 5, 45117 Essen, Germany
Fax: +49-201-1832621
E-mail: sjoerd.harder@uni-essen.de
[b] Laboratorium für Anorganische Chemie, ETH Hönggerberg, 8093 Zürich, Switzerland

 WILEY InterScience DISCOVER SOMETHING GREAT © 2007 Wiley-VCH Verlag GmbH & Co. KGaA, Weinheim 

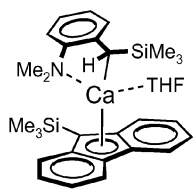


1

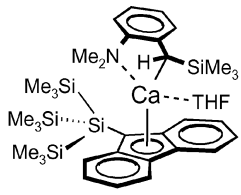


3

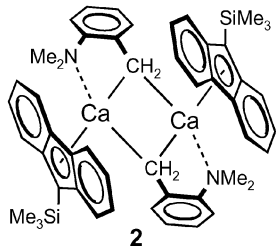


2

In a further attempt to understand the factors that govern the stereoselectivity in calcium-mediated styrene polymerizations, we prepared a series of new benzylcalcium catalysts with modified fluorenyl ligands.

## Results and Discussion

### 1. Syntheses and Structures of Modified Heteroleptic Benzylcalcium Complexes

In order to investigate the importance of the metal's coordination sphere in the polymerization reaction, a fluorene ligand with a potential chelating dimethylamino substituent was prepared. Deprotonation by ($o$-$Me_2N$-α-$Me_3Si$-benzyl)$_2$Ca·(THF)$_2$ gave the heteroleptic benzylcalcium complex **4**.

Furthermore, the influence of steric bulk in remote positions was investigated by the introduction of large substituents in the 2- and 7-positions of the fluorenyl ligand. Several 2,7-disubstituted fluorene ligands were prepared and converted into heteroleptic benzylcalcium catalysts. In one instance, this was done by reacting the substituted fluorene with ($o$-$Me_2N$-benzyl)$_2$Ca, in which case a dimeric benzylcalcium complex was typically formed (**5**).[15] In other cases, reaction with ($o$-$Me_2N$-α-$Me_3Si$-benzyl)$_2$Ca·(THF)$_2$ gave monomeric benzylcalcium initiators (**6**–**9**). We were able to obtain crystal structures of **4** as well as representative dimeric and monomeric benzylcalcium complexes (**5** and **6**).

The heteroleptic benzylcalcium complex **4** crystallizes with two independent, but geometrically similar, molecules in the asymmetric unit (Figure 1). The fluorenyl rings coordinate in a slightly distorted η$^5$-fashion in which the Ca–C bond lengths vary between 2.630(3) and 2.782(3) Å. The average Ca–C(fluorenyl) bond of 2.710(3) Å is slightly shorter than that observed in **1** [2.743(3) Å]. Likewise, the *C*,*N*-bidentate benzyl ligand in **4** [Ca–C1 2.504(3) Å; Ca–N2 2.463 Å] is coordinated in a similar fashion to that in **1** [Ca–C 2.506(2) Å; Ca–N 2.466(2) Å]. Whereas the coordination sphere of Ca in **1** is saturated by an additional THF ligand, complex **4** crystallizes solvent-free with intramolecular coordination of the $Me_2N$ arm.

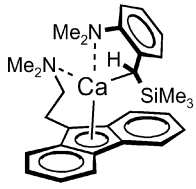


4

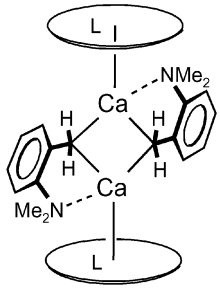


| Complex | L |
|---|---|
| 5 | 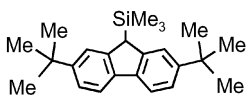 |



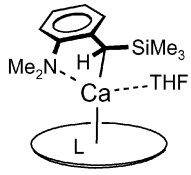


| Complex | L |
|---|---|
| 6 | 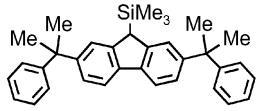 |
| 7 | 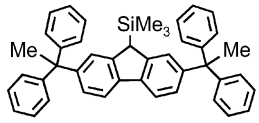 |
| 8 | 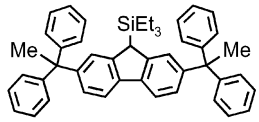 |
| 9 | 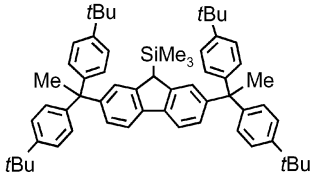 |



 © 2007 Wiley-VCH Verlag GmbH & Co. KGaA, Weinheim 

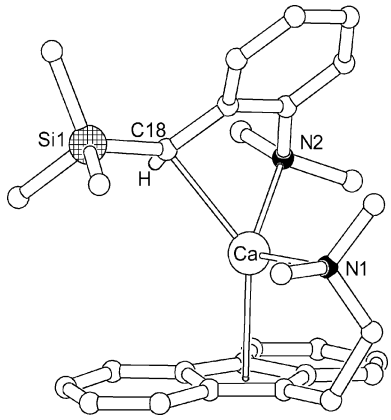


Figure 1. Crystal structure of **4**. Only one of the two crystallographically independent, but very similar, molecules is shown. Except for the benzylic hydrogen, all hydrogen atoms have been omitted for clarity. Average selected bond lengths [Å] and angles [°]: Ca–C18 2.508(3), Ca–N1 2.487(2), Ca–N2 2.460(2); Ca–C(fluorenyl): 2.630(3), 2.658(3), 2.727(3), 2.739(3), 2.782(3); C18–Ca–N1 113.6(1), C18–Ca–N2 71.4(1), N1–Ca–N2 112.0(1).

The heteroleptic complex **5** (Figure 2) crystallizes as a crystallographically $C_2$-symmetric dimer with symmetrically bridging benzyl ligands and terminal fluorenyl ligands. Its crystal structure is very much comparable to that of dimeric **2** in which the 2- and 7-positions of the fluorenyl ring are not substituted. The fluorenyl ring in **5** coordinates to Ca in $\eta^5$-fashion with Ca–C bond lengths in the range of 2.698(2) to 2.800(2) Å. The average Ca–C bond length of 2.750(2) Å is equal to that in **2** [2.750(3) Å]. Also, both symmetrically bridging benzyl anions are bound very similarly; the Ca–C17 [2.572(2) Å] and Ca–N1 [2.568(2) Å] bond lengths in **5** are equal to those in **2** [2.561(3) Å and 2.569(3) Å, respectively] within standard deviation. The bulky *t*Bu substituents in the 2- and-7 positions therefore do not affect the bonding of ligands to Ca.

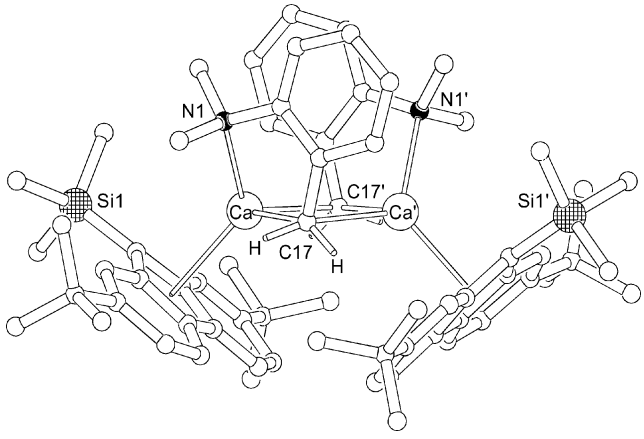


Figure 2. Crystal structure of **5**. Except for the benzylic hydrogen atoms, all hydrogen atoms have been omitted for clarity. Selected bond lengths [Å] and angles [°]: Ca–C17 2.572(2), Ca–C17′ 2.572(2), Ca–N1 2.568(2); Ca–C(fluorenyl): 2.698(2), 2.705(2), 2.749(2), 2.796(2), 2.800(2); Ca···Ca′ 3.5074(6), C17–Ca–C17′ 93.95(6), C17–Ca–N1 68.08(5), C17′–Ca–N1 120.08(5).

The heteroleptic benzylcalcium complex **6** (Figure 3) crystallizes similarly to complex **1**. The fluorenyl–Ca coordination geometry is slightly distorted from $\eta^5$-coordination. The Ca–C bond lengths range from 2.631(2) to 2.843(2) Å. The average Ca–C(fluorenyl) bond length of 2.734(2) Å compares well to that observed in **1** [2.743(3) Å]. Also, the *C*,*N*-bidentate benzyl ligand in **6** binds similarly; the Ca–C [2.517(3) Å] and Ca–N [2.496(2) Å] bond lengths for the *C*,*N*-bidentate benzyl ligand are only slightly longer than those in **1** [Ca–C: 2.506(2) Å; Ca–N: 2.466(2) Å, respectively]. In addition, the Ca–O(THF) bonds are very similar [**6**: 2.331(2) Å; **1**: 2.307(2) Å]. Therefore, the coordination geometry around Ca is hardly influenced by the large $Ph(Me)_2C$ substituents in the 2- and-7 positions of the fluorenyl ring.

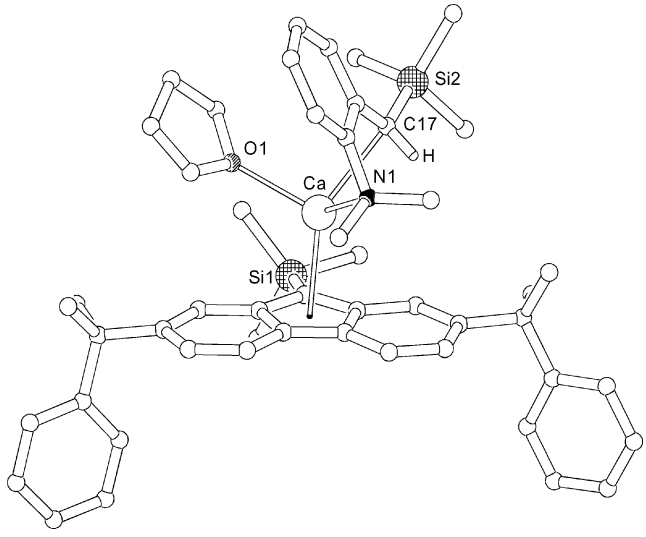


Figure 3. Crystal structure of **6**. Except for the benzylic hydrogen, all hydrogen atoms have been omitted for clarity. Selected bond lengths [Å] and angles [°]: Ca–C17 2.517(3), Ca–N1 2.496(2), Ca–O1 2.331(2); Ca–C(fluorenyl): 2.631(2), 2.647(2), 2.768(2), 2.779(2), 2.843(2); C17–Ca–N1 70.95(8), C17–Ca–O1 99.63(8), N1–Ca–O1 113.37(6).

The complexes dissolve well in aromatic solvents (except for dimer **5** which shows lower solubility), and their heteroleptic solid-state structures are retained in solution. The monomeric complexes with the chiral *o*-$Me_2N$-α-$Me_3Si$-benzyl ligand (**4** and **6**–**9**) display fluorenyl ligands with diastereotopic sides at room temperature. Fast exchange by inversion at the chiral benzylic carbon atom can be accomplished by heating the sample or by the addition of THF; both processes have been discussed previously.[14] For some of the complexes, an activation barrier for this inversion process could be determined. These values for **4** [$T_{coal}$ = 105 °C, $\Delta G^{\ddagger}$ = 19.2(2) kcal/mol] and **6** [$T_{coal}$ = 85 °C, $\Delta G^{\ddagger}$ = 18.7(2) kcal/mol] are, within standard deviation, equal to that measured for **1** [$T_{coal}$ = 90 °C, $\Delta G^{\ddagger}$ = 18.8(2) kcal/mol]. Therefore, like in the crystal structures, the bonding of the benzyl ligands to calcium is neither affected by the replacement of THF in **1** by a chelating arm, nor by the introduction of bulky substituents in the 2- and 7-positions of the fluorenyl ring.

 © 2007 Wiley-VCH Verlag GmbH & Co. KGaA, Weinheim 

The benzylcalcium complex **5** is also a heteroleptic dimer in benzene solution. Proof of its dimeric nature comes from the unusual $^1$H NMR chemical shifts for the aromatic ring protons. The $^1$H NMR spectra of anionic benzyl species generally show a high-field triplet, characteristic for the aromatic ring proton in the *para*-position with respect to the benzylic carbon.[17,18] For **5**, the most high-field aromatic signal is a doublet at $\delta$ = 5.81 ppm, which can be assigned to a proton in the *meta*-position with respect to the benzylic carbon. This anomaly can be explained by the anisotropy effect caused by ring currents[19] in a nearby aryl ring: the *meta*-H is positioned in the shielding cone of the neighbouring ring. Similar observations for the analogous complex **2** have been discussed extensively.[15]

In conclusion, neither the introduction of an intramolecularly coordinating amine ligand, nor substitution of the fluorenyl ligand in the 2- and 7-positions, changes the structures of heteroleptic benzylcalcium complexes **1** and **2**. In fact, the structures and all bond lengths remain surprisingly equal. The compositions of these complexes in solution are basically similar to those in the solid state, and modification of the fluorenyl ligands does not affect the dynamic behaviour of these complexes significantly.

## 2. Styrene Polymerization with Modified Heteroleptic Benzylcalcium Complexes

Complex **4**, the benzylcalcium complex with a fluorenyl ligand containing a chelating amine arm, was found to be completely inactive as an initiator in styrene polymerization. Whereas dissociation of the THF ligand in initiator **1** generates a free site for monomer coordination, the strongly bound intramolecular $Me_2N$ substituent in **4** effectively kills the reactivity of this benzylcalcium complex towards styrene. This underscores the importance of precoordination of the styrene monomer in the insertion step. Effective benzylcalcium catalysts should therefore have a relatively open coordination sphere around the calcium metal. This observation is in line with the fact that large bulky groups in the 9-position, that is, close to the metal, substantially retard monomer insertion.[16] Therefore, modification of the fluorenyl spectator ligand in the periphery instead of close to the metal coordination site was pursued.

All of the heteroleptic complexes **5** through **9** were found to be active in styrene polymerization. Polymerizations were generally run under two different sets of conditions: a) polymerization of a 10% solution of styrene in cyclohexane at 50 °C and b) polymerization of neat styrene at 20 °C. All polymers showed a unimodal MW distribution with poly-dispersion-indexes (*D*) between 2 and 3 and a Gold distribution,[20,21] that is, tailing in the low molecular weight range (Table 1). The latter is typical of heteroleptic benzylcalcium initiators and is, as we have shown before, related to a slow initiation by the stabilized carbanion rather than to chain termination.[13–16] These rather broad molecular weight distributions, however, hinder the syntheses of well-defined block-copolymers.

The tacticity of all polymers was analyzed by $^{13}$C NMR spectroscopy, and tacticities were calculated using Bernouillain statistics based on the new heptade assignment we recently reported.[22] Figure 4a shows the $^{13}$C NMR signals for the $C_{ipso}$ atom in the phenyl rings of the different polystyrenes obtained in solution at 50 °C. Under these conditions, polymer produced by initiator **1** is essentially atactic (the signals in the *mr* and *rr* regions are only slightly high relative to those from an atactic polymer produced by an alkyllithium initiator). Polymer obtained with initiator **5**, that is, an initiator with additional *t*Bu groups in the 2- and 7-positions of the fluorenyl ring, showed a noticeable increase in syndiotactity ($r$ = 87%). The $^{13}$C NMR signal for the $C_{ipso}$ atom merely consists of four singlets which represent the *rrrrrr* heptade and the three erroneous heptades formed after a single stereochemically wrong insertion (*mrrrrr*, *rmrrrr* and *rrmrrr*). Substitution of the *t*Bu groups for the more bulky $Ph(Me)_2C$ substituents (**6**) again leads to improvement of the polymer's syndiotacticity; the largest signal is that of the *rrrrrr* heptade ($r$ = 88%). Further increase of steric bulk by the introduction of $(Ph)_2MeC$ substituents (**7**) gave a polymer of 92% syndiotacticity in diads. Subsequent increase of steric bulk by substitution of the $Me_3Si$ group for $Et_3Si$ (**8**) or by additional *t*Bu substituents on the Ph rings (**9**) gave no significant improvement of the tacticity.

Spurred by the advantageous effect of steric bulk on the syndioselectivity of styrene polymerization in solution, we

Table 1. Styrene polymerization with initiators **1**, **5**–**9**.

| Initiator | $T$ [°C] | [m][a] [mol L$^{-1}$] | $t$ [min] | $M_n$ [g mol$^{-1}$] | $D$ | *rr* [%] | $r$ [%] |
|---|---|---|---|---|---|---|---|
| **1**[14] | 50 | 0.10 | 45 | $1.115\times10^5$ | 2.306 | <50 | <70 |
| **5** | 50 | 0.10 | 45 | $1.449\times10^5$ | 2.549 | 76 | 87 |
| **6** | 50 | 0.10 | 60 | $2.014\times10^5$ | 1.947 | 77 | 88 |
| **7** | 50 | 0.10 | 60 | $1.515\times10^5$ | 2.394 | 85 | 92 |
| **8** | 50 | 0.10 | 50 | $2.377\times10^5$ | 2.377 | 85 | 92 |
| **9** | 50 | 0.10 | 45 | $2.440\times10^5$ | 2.030 | 85 | 92 |
| **1**[14] | 20 | neat | 60 | $0.960\times10^5$ | 2.350 | 79 | 89 |
| **5** | 20 | neat | 40 | $2.213\times10^5$ | 2.570 | 83 | 91 |
| **6** | 20 | neat | 45 | $1.235\times10^5$ | 2.265 | 85 | 92 |
| **7** | 20 | neat | 60 | $1.302\times10^5$ | 2.635 | 86 | 93 |
| **8** | 20 | neat | 95 | $3.022\times10^5$ | 2.134 | 88 | 94 |
| **9** | 20 | neat | 50 | $1.506\times10^5$ | 2.984 | 88 | 94 |
| **9** | –20 | neat | 3840[b] | $1.870\times10^5$ | 4.293 | 91 | 95 |

[a] Concentration of monomer in cyclohexane. [b] 64 h.

 © 2007 Wiley-VCH Verlag GmbH & Co. KGaA, Weinheim 

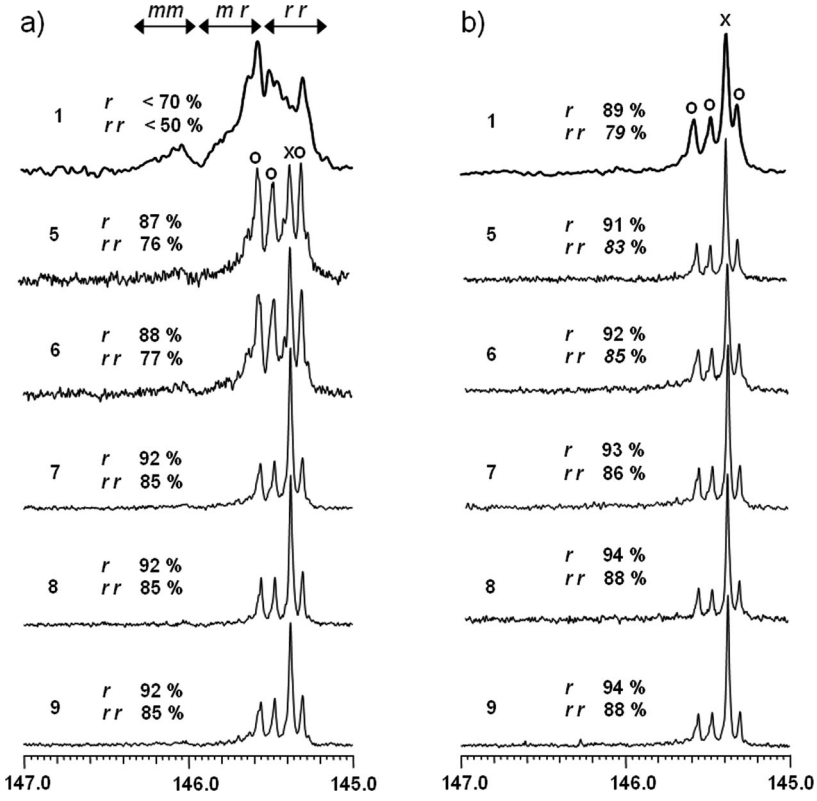


Figure 4. $^{13}C$ NMR signals of the phenyl $C_{ipso}$ atom in the polystyrene materials ([$D_2$]tetrachloroethane, $T$ = 100 °C). a) Polymers obtained with the various initiators **1**, **5**–**9**; 10% styrene solutions in cyclohexane; 50 °C. b) Polymers obtained with the various initiators **1**, **5**–**9**; 100% styrene; 20 °C. The syndiotactic *rrrrrr* heptade is marked by ×, and the error heptades *mrrrrr*, *rmrrrr* and *rrmrrr* by o.

also performed polymerization studies in pure styrene (Figure 4b). Polymers obtained under these conditions generally show much higher syndiotacticities than the polymers produced by polymerization in solution.[14–16] This is partly due to a temperature effect (for polymerizations in solution, improved syndiotacticity is also observed at lower temperature; Figure 5), but is also related to a higher ratio of the insertion to inversion rates on account of the higher monomer concentration (Scheme 1). The positive effect of increasing steric bulk in the 2- and 7-positions of the fluorenyl ring on the syndiotacticity of the polymer is also noticeable for polymerizations in neat styrene. It is, however, less extreme than that observed for polymerizations in solution. The most syndiotactic polymer was obtained with the most bulky calcium initiator **9** at –20 °C ($r$ = 95%, $rr$ = 90%); however, rather slow polymerization and a broad molecular weight distribution were observed (Table 1).

The data for polymerization in solution in particular show a clear increase in stereoselectivity upon increase in the steric bulk of the substituents in the periphery of the ligand system. The reason for this trend is unclear. Figure 6 shows space-filling models of fluorenyl–Ca units containing differently substituted ligand systems. It is evident from the structural studies (vide supra) that substitution in the 2- and 7-positions of the fluorenyl ligand has a negligible effect on the coordination sphere of the $Ca^{2+}$ ion. It can only be speculated that the sterically large groups at the sides of the fluorenyl ligand restrict the dynamic behaviour of the polymer chain attached to calcium. Reducing the degrees of freedom of the polymer chain and the coordinated styrene would lead to a higher selectivity in the insertion step.

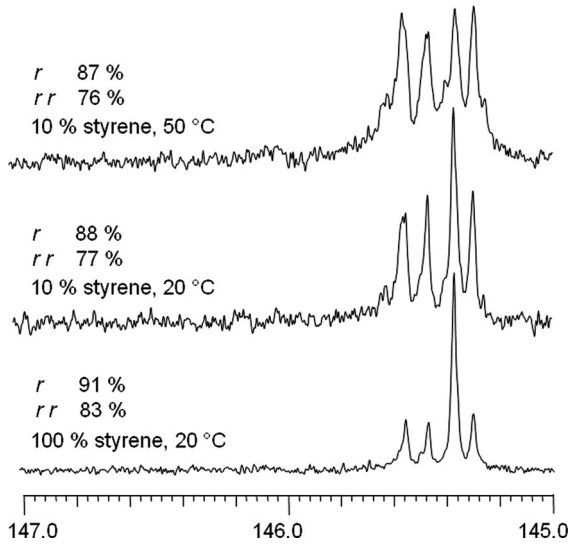


Figure 5. $^{13}C$ NMR signals of the phenyl $C_{ipso}$ atom in the polystyrene materials ([$D_2$]tetrachloroethane, $T$ = 100 °C) obtained with initiator **5** under various conditions.

 © 2007 Wiley-VCH Verlag GmbH & Co. KGaA, Weinheim 

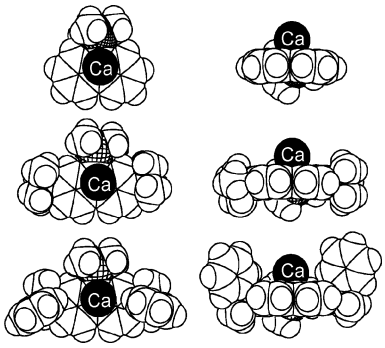


Figure 6. Space-filling models of the fluorenyl–Ca unit with increasing steric bulk of the fluorenyl ligand (top to bottom) as in the initiators **1**, **5** and **6**. Left: view perpendicular to the fluorenyl plane. Right: view along the fluorenyl plane.

## Conclusions

Replacing the THF ligand in **1** with an intramolecular chelating amine ligand does not affect the coordination of the *o*-$Me_2N$-α-$Me_3Si$-benzyl ligand. Also, the introduction of bulky substituents in the 2- and 7-positions of the fluorenyl ligand has no influence on ligand coordination to the metal. In all cases, very similar fluorenyl–Ca and benzyl–Ca coordination geometries are observed.

The composition and structures of the benzylcalcium complexes **4**–**9** in solution (benzene, toluene) are similar to those observed in the solid state; that is, the Schlenk equilibria lie completely towards the heteroleptic side, and the chiral benzylic carbon is configurationally stable on the NMR time scale (the fluorenyl ligands show diastereotopic sides). Also, the dynamic inversion of the chiral benzylic carbon at higher temperatures is not affected by the ligand modifications.

On the other hand, a significant effect of fluorenyl ligand modifications was observed on the polymerization of styrene. First of all, substitution of THF in **1** for an intramolecularly coordinated $Me_2N$ substituent effectively kills the reactivity of this benzylcalcium complex towards styrene. Apparently, the strongly bound chelate arm prevents the formation of a free coordination site, which effectively blocks the polymerization reaction. Secondly, an increase in the steric bulk of the substituents in the periphery of the fluorenyl ligand resulted in greater syndioselectivity in styrene polymerization.

These are important observations from which it can be deduced that these benzylcalcium complexes likely function as single-site catalysts in which precoordination of the monomer and subsequent insertion are the key steps in styrene polymerization. These new initiators allow syndioselective styrene polymerization not only in neat styrene, but also in solution. The broad molecular weight distributions, however, disable syntheses of well-defined block-copolymers.

## Experimental Section

**General Comments:** All experiments were carried out under argon using predried solvents and Schlenk techniques. The following starting materials were prepared according to literature: [(2-$Me_2N$-α-$Me_3Si$-benzyl)]$_2$Ca·$(THF)_2$,[13] [9-(2-dimethylamino)ethyl]fluorene,[23] 2,7-di-*tert*-butylfluorene[24] and 2,7-bis(1-methyl-1-phenylethyl)fluorene.[25] $Me_3SiCl$ was freed from HCl by distillation from dry *N*,*N*-diethylaniline. Other reagents were commercially available and used as received. NMR spectra were recorded with Bruker DPX300 and DRX500 machines.

**Synthesis of 2,7-Bis(1,1-diphenylethyl)fluorene:** 2,7-Dibenzoylfluorene was prepared according to a modified literature procedure.[25] A mixture of fluorene (10.0 g, 60.2 mmol), benzoic acid (16.0 g, 131 mmol) and polyphosphoric acid (200 g) was heated to 140 °C in a conical flask for 50 h. The cooled mixture was treated carefully with ice/water and, in later stages, with a hot aqueous potassium hydroxide solution. The heated suspension was filtered, and the residue dissolved in toluene. After aqueous workup and drying of the organic layer, the solution was concentrated and 2,7-dibenzoylfluorene precipitated at room temperature (10.7 g, 48%), m.p. 193 °C. $^1$H NMR (300 MHz, $CDCl_3$, 25 °C): $\delta$ = 8.01 (s, 2 H, fluorenyl), 7.96–7.82 (m, 8 H, Ar), 7.62–7.58 (m, 2 H, Ar), 7.51–7.46 (m, 4 H, Ar), 4.04 (s, 2 H, $CH_2$) ppm. $^{13}$C{$^1$H} NMR (300 MHz, $CDCl_3$): $\delta$ = 196.6 (C=O), 144.5, 144.2, 137.9, 136.9, 132.3, 130.0, 129.7, 128.3, 126.9, 120.4, 36.9 ($CH_2$) ppm. $C_{27}H_{18}O_2$ (374.4): calcd. C 86.61, H 4.85; found C 86.62, H 4.81.

A twofold excess of phenylmagnesium bromide (14.5 g, 80.0 mmol) was added to a solution of 2,7-dibenzoylfluorene (7.80 g, 20.8 mmol) in toluene (100 mL) and was heated at reflux for 4 h. After hydrolysis with 2 N HCl and extraction with toluene, the organic layer was dried. 2,7-Bis(hydroxydiphenylmethyl)fluorene was crystallized from a concentrated solution at –22 °C (7.35 g, 67%), m.p. 253 °C. $^1$H NMR (300 MHz, $CDCl_3$, 25 °C): $\delta$ = 7.63 (d, $^3J_{H,H}$ = 8.0 Hz, 2 H, fluorenyl), 7.41 (s, 2 H, fluorenyl), 7.32–7.18 (m, 22 H, Ar), 3.74 (s, 2 H, $CH_2$), 2.78 (s, 2 H, OH) ppm. $^{13}$C{$^1$H} NMR (300 MHz, $CDCl_3$): $\delta$ = 147.4, 146.1, 143.8, 140.8, 128.3, 128.3, 127.6, 127.3, 124.9, 119.6, 82.6 (COH), 37.5 ($CH_2$) ppm. $C_{39}H_{30}O_2$ (530.7): calcd. C 88.27, H 5.70; found C 88.26, H 5.90.

To a suspension of 2,7-bis(hydroxydiphenylmethyl)fluorene (7.35 g, 13.8 mmol) in toluene (100 mL) and acetic acid (0.2 mL) was added a trimethylaluminum solution (2.0 M in toluene, 35 mL, 70.0 mmol). After being heated at reflux for 4 h, the mixture was poured into ice/water. The remaining product was dissolved in concentrated hydrochloric acid (20 mL), and the aqueous layer was extracted with dichloromethane. The organic solution was dried, and the solvent was removed. 2,7-Bis(1,1-diphenylethyl)fluorene was obtained as a white solid product (5.75 g, 79%), m.p. 217 °C. $^1$H NMR (300 MHz, $CDCl_3$, 25 °C): $\delta$ = 7.60 (d, $^3J_{H,H}$ = 8.1 Hz, 2 H, fluorenyl), 7.25–6.88 (m, 24 H, Ar), 3.71 (s, 2 H, $CH_2$), 2.22 (s, 6 H, $CH_3$) ppm. $^{13}$C{$^1$H} NMR (300 MHz, $CDCl_3$): $\delta$ = 149.8, 148.2, 143.7, 139.8, 129.3, 128.3, 128.1, 126.4, 125.8, 119.5, 53.1 [($CCH_3)_2$], 37.6 ($CH_2$), 31.2 ($CH_3$) ppm. $C_{41}H_{34}$ (526.7): calcd. C 93.49, H 6.51; found C 93.16, H 6.45.

**Synthesis of 2,7-Bis[1,1-bis(4′-*tert*-butylphenyl)ethyl]fluorene:** The first intermediate, 2,7-bis(4′-*t*Bu-benzoyl)fluorene, was prepared analogously to 2,7-dibenzoylfluorene (vide supra). After quenching the reaction with water and aqueous potassium hydroxide, the residue was extracted with dichloromethane, dried and isolated by removal of the solvent. Crystallization from acetone at –27 °C gave 2,7-bis(4′-*t*Bu-benzoyl)fluorene (26.8 g, 43%) as a white solid, m.p. 251 °C. $^1$H NMR (300 MHz, $CDCl_3$, 25 °C): $\delta$ = 8.05 (s, 2 H, fluor-

 © 2007 Wiley-VCH Verlag GmbH & Co. KGaA, Weinheim 

enyl), 7.96–7.88 (m, 4 H, fluorenyl), 7.81 (d, $^3J_{H,H}$ = 8.1 Hz, 4 H, Ar), 7.53 (d, $^3J_{H,H}$ = 8.3 Hz, 4 H, Ar), 4.05 (s, 2 H, $CH_2$), 1.39 (s, 18 H, $CH_3$) ppm. $^{13}C\{^1H\}$ NMR (300 MHz, $CDCl_3$): $\delta$ = 197.0 (C=O), 156.9, 145.2, 144.9, 138.0, 135.8, 130.8, 130.3, 127.6, 126.0, 121.1, 37.7 ($CH_2$), 35.9 ($CCH_3$), 31.9 ($CH_3$) ppm. $C_{35}H_{34}O_2$ (486.6): calcd. C 86.38, H 7.04; found C 85.99, H 7.18.

A twofold excess of 4-*t*Bu-phenylmagnesium bromide (19.9 g, 84.0 mmol) was added to a solution of 2,7-bis(4′-*t*Bu-benzoyl)fluorene (10.0 g, 20.5 mmol) in toluene (100 mL), and was heated at reflux for 6.5 h. After the reaction mixture was hydrolyzed with 2 N HCl, extracted with diethyl ether and dried, the solvent was removed. 2,7-Bis[hydroxybis(4′-*t*Bu-phenyl)methyl]fluorene crystallized from hexane at room temperature as a white solid (11.5 g, 74%), m.p. 249 °C. $^1H$ NMR (300 MHz, $CDCl_3$, 25 °C): $\delta$ = 7.56 (d, $^3J_{H,H}$ = 8.0 Hz, 2 H, fluorenyl), 7.43 (s, 2 H, fluorenyl), 7.26–7.08 (m, 18 H, Ar), 3.73 (s, 2 H, $CH_2$), 2.72 (br s, 2 H, OH), 1.23 (s, 36 H, $CH_3$) ppm. $^{13}C\{^1H\}$ NMR (300 MHz, $CDCl_3$): $\delta$ = 150.0, 145.8, 144.2, 143.3, 140.3, 127.6, 126.8, 124.8, 124.4, 119.0, 81.9 (COH), 37.7 ($CH_2$), 34.5 [$C(CH_3)_3$], 31.3 [$C(CH_3)_3$] ppm. $C_{55}H_{62}O_2$ (755.1): calcd. C 87.49, H 8.28; found C 87.07, H 7.97.

To a suspension of 2,7-bis[hydroxybis(4′-*t*Bu-phenyl)methyl]fluorene (4.80 g, 6.36 mmol) in toluene (100 mL) and acetic acid (0.2 mL) was added a trimethylaluminum solution (2.0 M in toluene, 12.5 mL, 25.0 mmol). After heating the mixture for 5 h, the solution was poured into ice/water. After aqueous workup and drying of the organic layer, the solvent was removed. 2,7-Bis[1,1-bis(4′-*t*Bu-phenyl)ethyl]fluorene was obtained as a white solid after washing with hexane (3.92 g, 82%), m.p. 311 °C. $^1H$ NMR (300 MHz, $CDCl_3$, 25 °C): $\delta$ = 7.54 (d, $^3J_{H,H}$ = 8.1 Hz, 2 H, fluorenyl), 7.23–7.18 (m, 10 H, Ar), 7.01–6.95 (m, 10 H, Ar), 3.69 (s, 2 H, $CH_2$), 2.13 (s, 6 H, $CH_3$), 1.24 (s, 36 H, $CH_3$) ppm. $^{13}C$ NMR$\{^1H\}$ (300 MHz, $CDCl_3$): $\delta$ = 148.4, 148.1, 146.4, 143.1, 139.2, 128.3, 127.6, 125.2, 124.6, 118.8, 51.8 ($CCH_3$), 37.1 ($CH_2$), 34.3 [$C(CH_3)_3$], 31.4 [$C(CH_3)_3$], 30.6 ($CCH_3$) ppm. $C_{57}H_{66}$ (751.1): calcd. C 91.14, H 8.86; found C 90.61, H 8.78.

**Synthesis of 2,7-Di-*tert*-butyl-9-(trimethylsilyl)fluorene:** *n*-Butyllithium (2.5 M in hexane, 12.0 mL, 30.0 mmol) was added to a precooled (–70 °C), stirred solution of 2,7-di-*tert*-butylfluorene[24] (7.70 g, 27.7 mmol) in THF (50 mL). The solution was slowly warmed to –10 °C and stirred for 30 min at this temperature, then cooled again to –70 °C, and chlorotrimethylsilane (4.1 mL, 32.2 mmol) was added. The cooling bath was removed, and the solution was stirred at room temperature for 24 h. After aqueous workup, the solvent was removed under vacuum, and colourless needles were recovered (8.65 g, 89%), m.p. 145 °C. $^1H$ NMR (300 MHz, $CDCl_3$, 25 °C): $\delta$ = 7.74 (d, $^3J_{H,H}$ = 8.0 Hz, 2 H, fluorenyl), 7.53 (s, 2 H, fluorenyl), 7.38 (d, $^3J_{H,H}$ = 8.0 Hz, 2 H, fluorenyl), 3.83 (s, 1 H, CH), 1.42 (s, 18 H, $CH_3$), –0.04 (s, 9 H, $Me_3Si$) ppm. $^{13}C\{^1H\}$ NMR (300 MHz, $CDCl_3$): $\delta$ = 148.6, 145.6, 137.9, 122.2, 121.0, 119.0, 42.5 ($CH_2$), 34.8 [$C(CH_3)_3$], 31.7 [$C(CH_3)_3$], –2.60 ($Me_3Si$) ppm. $C_{24}H_{34}Si$ (350.6): calcd. C 82.22, H 9.77; found C 81.82, H 9.94.

**Synthesis of 2,7-Bis(1-methyl-1-phenylethyl)-9-(trimethylsilyl)fluorene:** This compound was synthesized according to the preparation of 2,7-bis(*t*Bu)-9-$Me_3Si$-fluorene. Colourless needles crystallized from acetone at –28 °C (72%), m.p. 122 °C. $^1H$ NMR (300 MHz, $CDCl_3$, 25 °C): $\delta$ = 7.71 (d, $^3J_{H,H}$ = 7.9 Hz, 2 H, fluorenyl), 7.32–7.15 (m, 14 H, Ar), 3.71 (s, 1 H, CH), 1.77 (s, 6 H, $CH_3$), 1.75 (s, 6 H, $CH_3$), –0.23 (s, 9 H, $Me_3Si$) ppm. $^{13}C\{^1H\}$ NMR (300 MHz, $CDCl_3$): $\delta$ = 151.3, 148.4, 145.6, 137.8, 127.9, 126.8, 125.5, 123.7, 122.9, 119.0, 43.1 [$(CCH_3)_2$], 42.5 [$(CCH_3)_2$], 31.1 ($CH_3$), 30.8 ($CH_3$), –2.81 ($Me_3Si$) ppm. $C_{34}H_{38}Si$ (474.8): calcd. C 86.02, H 8.07; found C 85.96, H 7.94.

**Synthesis of 2,7-Bis(1,1-diphenylethyl)-9-$Me_3Si$-fluorene:** This compound was synthesized according to the preparation of 2,7-bis(*t*Bu)-9-$Me_3Si$-fluorene. A white solid precipitated from acetone at –28 °C (88%), m.p. 143 °C. $^1H$ NMR (300 MHz, $CDCl_3$, 25 °C): $\delta$ = 7.63 (d, $^3J_{H,H}$ = 7.4 Hz, 2 H, fluorenyl), 7.25–7.03 (m, 24 H, Ar), 3.57 (s, 1 H, CH), 2.18 (s, 6 H, $CH_3$), –0.40 (s, 9 H, $Me_3Si$) ppm. $^{13}C\{^1H\}$ NMR (300 MHz, $CDCl_3$): $\delta$ = 149.6, 146.9, 145.6, 138.0, 128.8, 127.8, 125.9, 125.7, 124.9, 119.1, 52.7 ($CCH_3$), 42.7 (CH), 30.7 ($CH_3$), –2.84 ($Me_3Si$) ppm. $C_{44}H_{42}Si$ (598.9): calcd. C 88.24, H 7.07; found C 87.38, H 7.22.

**Synthesis of 2,7-Bis[1,1-bis(4′-*t*Bu-phenyl)ethyl]-9-$Me_3Si$-fluorene:** This compound was synthesized according to the preparation of 2,7-bis(*t*Bu)-9-$Me_3Si$-fluorene. A white solid precipitated from toluene at –28 °C (79%), m.p. 247 °C. $^1H$ NMR (300 MHz, $CDCl_3$, 25 °C): $\delta$ = 7.62 (d, $^3J_{H,H}$ = 8.1 Hz, 2 H, fluorenyl), 7.21–6.90 (m, 20 H, Ar), 3.51 (s, 1 H, CH), 2.14 (s, 6 H, $CCH_3$), 1.22 [s, 36 H, $C(CH_3)_3$], –0.48 (s, 9 H, $Me_3Si$) ppm. $^{13}C\{^1H\}$ NMR (300 MHz, $CDCl_3$): $\delta$ = 148.4, 147.4, 146.6, 145.4, 137.9, 128.3, 125.4, 125.2, 124.6, 118.9, 51.8 ($CCH_3$), 42.5 (CH), 34.3 [$C(CH_3)_3$], 31.4 [$C(CH_3)_3$], 30.4 ($CCH_3$), –2.75 ($Me_3Si$) ppm. $C_{60}H_{74}Si$ (823.3): calcd. C 87.53, H 9.06; found C 87.28, H 9.02.

**Synthesis of 2,7-Bis(1,1-diphenylethyl)-9-$Et_3Si$-fluorene:** *n*-Butyllithium (2.45 M in hexane, 1.88 mL, 4.61 mmol) was added to a precooled (–70 °C), stirred solution of 2,7-bis(1,1-diphenylethyl)fluorene (2.20 g, 4.18 mmol) in THF (50 mL). After being slowly heated to –10 °C and stirred over a period of 30 min at this temperature, the solution was recooled (–70 °C), and chlorotriethylsilane (0.78 mL, 4.66 mmol) was added. The cooling bath was removed, and the solution was stirred at room temperature for 20 h. After aqueous workup, the solvent was removed. 2,7-Bis(1,1-diphenylethyl)-9-$Et_3Si$-fluorene precipitated from acetone at –28 °C as a pale yellow solid (2.26 g, 84%), m.p. 103 °C. $^1H$ NMR (300 MHz, $CDCl_3$, 25 °C): $\delta$ = 7.65 (d, $^3J_{H,H}$ = 8.1 Hz, 2 H, fluorenyl), 7.21–7.00 (m, 22 H, Ar), 6.93 (s, 2 H, fluorenyl), 3.69 (s, 1 H, CH), 2.17 (s, 6 H, $CH_3$), 0.51 [t, 9 H, $Si(CH_2CH_3)_3$], 0.08 [q, 6 H, $Si(CH_2CH_3)_3$] ppm. $^{13}C\{^1H\}$ NMR (300 MHz, $C_6D_6$): $\delta$ = 150.6, 150.3, 147.8, 146.6, 139.2, 126.7, 126.7, 126.5, 126.1, 120.1, 53.5 ($CCH_3$), 39.8 (CH), 31.3 ($CH_3$), 8.00 [$Si(CH_2CH_3)_3$], 3.00 [$Si(CH_2CH_3)_3$]. $C_{47}H_{48}Si$ (641.0): calcd. C 88.07, H 7.55; found C 87.88, H 7.34.

**Synthesis of 4:** A solution of [9-(2-dimethylamino)ethyl]fluorene[23] (734 mg, 3.09 mmol) and $[(2\text{-}Me_2N\text{-}\alpha\text{-}Me_3Si\text{-benzyl})]_2Ca\cdot(THF)_2$[13] (1.87 g, 3.13 mmol) in toluene (20 mL) was heated to 85 °C over a period of 5 h. All volatiles were removed, and the product was dried under vacuum to yield complex **4** with one molecule of THF. Drying of this product under vacuum over a period of 30 min (90 °C, 1 Torr) and cooling a toluene solution thereof to –30 °C gave yellow-orange plates of **4** (1.09 g, 73%) which are only soluble in hot benzene. NMR spectroscopic data are given for **4** with one equivalent of THF; m.p. 132 °C. $^1H$ NMR (300 MHz, $C_6D_6$, 25 °C): $\delta$ = 8.33 (d, $^3J_{H,H}$ = 8.1 Hz, 1 H, fluorenyl), 8.23 (d, $^3J_{H,H}$ = 8.0 Hz, 1 H, fluorenyl), 7.69 (d, $^3J_{H,H}$ = 8.3 Hz, 1 H, fluorenyl), 7.56 (t, $^3J_{H,H}$ = 8.1 Hz, 1 H, fluorenyl), 7.45 (d, $^3J_{H,H}$ = 8.4 Hz, 1 H, fluorenyl), 7.29–7.22 (m, 2 H, fluorenyl), 7.10–6.99 (m, 2 H, Ar and fluorenyl), 6.80 (t, $^3J_{H,H}$ = 7.1 Hz, 1 H, Ar), 6.35 (d, $^3J_{H,H}$ = 7.0 Hz, 1 H, Ar), 6.25 (t, $^3J_{H,H}$ = 7.1 Hz, 1 H, Ar), 3.13–3.09 (m, 2 H, $CH_2$), 2.89 (br., 4 H, THF), 2.84–2.76 (m, 1 H, $CH_2$), 2.30–2.19 (m, 1 H, $CH_2$), 2.15–1.72 (br., 6 H, $NCH_3$), 1.65 (s, 6 H, $NCH_3$), 1.22 (br., 4 H, THF), 0.41 (s, 9 H, $Me_3Si$), 0.14 (s, 1 H, CH) ppm. $^{13}C\{^1H\}$ NMR (300 MHz, $C_6D_6$, 25 °C): $\delta$ = 147.8,

 © 2007 Wiley-VCH Verlag GmbH & Co. KGaA, Weinheim 

135.6, 132.3, 131.4, 126.5 (benzyl), 124.5, 124.1, 123.5, 123.3, 122.1, 122.0 (benzyl), 119.6, 118.6, 118.4, 116.9, 116.8, 114.7 (benzyl), 112.5 (benzyl), 91.7 (C9), 68.1 (THF), 63.2, 61.3, 44.8, 44.7, 25.3 (THF), 22.8, 22.3, 2.8 ($Me_3Si$) ppm.

**Synthesis of 5:** A solution of 2,7-bis(*t*Bu)-9-$Me_3Si$-fluorene (475 mg, 1.35 mmol) and [(2-$Me_2N$-benzyl)]$_2$Ca[15] (469 mg, 1.52 mmol) in benzene (10 mL) was heated to 60 °C over a period of 2.5 h. Slow cooling of the reaction mixture to room temperature gave large yellow crystals of **5** (537 mg, 76%), m.p. 151 °C (dec.). $^1$H NMR (500 MHz, $C_6D_6$/[D$_8$]THF, 25 °C): $\delta$ = 7.85 (s, 2 H, fluorenyl), 7.74 (d, $^3J_{H,H}$ = 8.2 Hz, 2 H, fluorenyl), 6.85 (d, $^3J_{H,H}$ = 8.2 Hz, 2 H, fluorenyl), 6.34 (t, $^3J_{H,H}$ = 7.8 Hz, 1 H, benzyl), 6.31–6.21 (m, 2 H, benzyl), 5.80 (t, $^3J_{H,H}$ = 6.4 Hz, 1 H, benzyl), 2.04 (s, 6 H, $NCH_3$), 1.52 (br s, 2 H, $CH_2$), 1.33 (s, 18 H, $CH_3$), 0.44 (s, 9 H, $Me_3Si$) ppm. $^1$H NMR (500 MHz, $C_6D_6$, 25 °C): $\delta$ = 8.52 (d, $^3J_{H,H}$ = 8.6 Hz, 1 H, fluorenyl), 8.47 (d, $^3J_{H,H}$ = 8.6 Hz, 1 H, fluorenyl), 8.25 (s, 1 H, fluorenyl), 8.05 (s, 1 H, fluorenyl), 7.47 (d, $^3J_{H,H}$ = 8.5 Hz, 1 H, fluorenyl), 7.39 (d, $^3J_{H,H}$ = 8.2 Hz, 1 H, fluorenyl), 6.67 (t, $^3J_{H,H}$ = 7.3 Hz, 1 H, benzyl), 6.10 (t, $^3J_{H,H}$ = 6.9 Hz, 1 H, benzyl), 5.85 (d, $^3J_{H,H}$ = 7.8 Hz, 1 H, benzyl), 5.81 (d, $^3J_{H,H}$ = 7.2 Hz, 1 H, benzyl), 1.78 (s, 3 H, $NCH_3$), 1.51 (s, 9 H, $CH_3$), 1.42 (s, 9 H, $CH_3$), 1.24 (s, 3 H, $NCH_3$), 0.73 (s, 9 H, $Me_3Si$), –0.55 (d, $^2J_{H,H}$ = 11.8 Hz, 1 H, $CH_2$), –0.96 (d, $^2J_{H,H}$ = 11.7 Hz, 1 H, $CH_2$) ppm. $^{13}$C{$^1$H} NMR (500 MHz, $C_6D_6$/[D$_8$]THF, 25 °C): $\delta$ = 148.0, 143.5, 143.3, 136.9, 125.4 (benzyl), 123.0, 122.3 (benzyl), 120.1, 117.9 (benzyl), 116.1, 112.8, 110.0 (benzyl), 85.2 (C-9), 43.3 [$N(CH_3)_2$], 40.9 ($CH_2$), 34.8 [$C(CH_3)_3$], 32.1 [$C(CH_3)_3$], 2.39 ($Me_3Si$) ppm.

**Synthesis of 6:** A mixture of 2,7-bis(1-methyl-1-phenylethyl)-9-$Me_3Si$-fluorene (315 mg, 664 μmol) and [(2-$Me_2N$-α-$Me_3Si$-benzyl)]$_2$Ca·(THF)$_2$[13] (417 mg, 698 μmol) in THF (4.0 mL) was stirred for 2.5 h at 60 °C. The solvent was removed under vacuum, and the remaining orange product was dissolved in warm hexane (4 mL). Cooling the solution to room temperature yielded yellow crystals (410 mg, 80%), m.p. 132 °C (dec.). $^1$H NMR (500 MHz, $C_6D_6$, 25 °C): $\delta$ = 8.15 (s, 1 H, fluorenyl), 8.00 (s, 1 H, fluorenyl), 7.89 (d, $^3J_{H,H}$ = 8.5 Hz, 1 H, fluorenyl), 7.79 (d, $^3J_{H,H}$ = 8.5 Hz, 1 H, fluorenyl), 7.41 (d, $^3J_{H,H}$ = 7.5 Hz, 2 H, Ar), 7.34 (d, $^3J_{H,H}$ = 7.5 Hz, 2 H, Ar), 7.22–6.91 (m, 8 H, Ar), 6.86 (d, $^3J_{H,H}$ = 8.5 Hz, 1 H, benzyl), 6.67 (t, $^3J_{H,H}$ = 7.1 Hz, 1 H, benzyl), 6.32 (d, $^3J_{H,H}$ = 7.6 Hz, 1 H, benzyl), 6.19 (t, $^3J_{H,H}$ = 7.1 Hz, 1 H, benzyl), 2.63 (br., 4 H, THF), 1.96 (s, 3 H, $CH_3$), 1.87 (s, 3 H, $CH_3$), 1.85 (s, 3 H, $NCH_3$), 1.84 (s, 3 H, $NCH_3$), 1.79 (s, 6 H, $CH_3$), 0.95 (br., 4 H, THF), 0.64 (s, 9 H, $Me_3Si$-fluorenyl), 0.51 (s, 1 H, CH), 0.45 (s, 9 H, $Me_3Si$-benzyl) ppm. $^{13}$C{$^1$H} NMR (500 MHz, $C_6D_6$, 25 °C): $\delta$ = 151.4, 151.2, 147.2, 146.1, 145.6, 141.6, 141.4, 136.1, 128.3, 127.3, 127.2, 125.9, 125.9, 125.5 (benzyl), 123.9 (benzyl), 121.4, 121.3, 121.2, 121.0, 119.2 (benzyl), 118.2, 118.2, 118.0, 117.6, 113.1 (benzyl), 87.9 (C-9), 68.5 (THF), 44.8 ($NCH_3$), 44.4 (CH), 43.6 [$C(CH_3)_2$], 43.4 [$C(CH_3)_2$], 41.5 ($NCH_3$), 31.4 ($CH_3$), 31.3 ($CH_3$), 30.9 ($CH_3$), 30.7 ($CH_3$), 24.9 (THF), 2.71 ($Me_3Si$-fluorenyl), 2.48 ($Me_3Si$-benzyl) ppm.

**Synthesis of 7:** A solution of 2,7-bis(1,1-diphenylethyl)-9-$Me_3Si$-fluorene (242 mg, 404 μmol) and [(2-$Me_2N$-α-$Me_3Si$-benzyl)]$_2$Ca·(THF)$_2$[13] (245 mg, 410 μmol) in THF (3.0 mL) was stirred for 2.5 h at 60 °C. After removing the solvent under vacuum, the remaining product was washed with hexane (2 mL) and dried in vacuo. Repeating this procedure resulted in a yellow product (307 mg, 83%), m.p. 202 °C (dec.). $^1$H NMR (500 MHz, $C_6D_6$, 25 °C): $\delta$ = 8.02 (d, $^3J_{H,H}$ = 8.6 Hz, 1 H, fluorenyl), 7.95 (d, $^3J_{H,H}$ = 8.6 Hz, 1 H, fluorenyl), 7.61 (s, 1 H, fluorenyl), 7.52 (s, 1 H, fluorenyl), 7.33–6.96 (m, 23 H, Ar), 6.69 (t, $^3J_{H,H}$ = 7.3 Hz, 1 H, benzyl), 6.30 (d, $^3J_{H,H}$ = 7.1 Hz, 1 H, benzyl), 6.17 (t, $^3J_{H,H}$ = 7.2 Hz, 1 H, benzyl), 2.61 (br., 4 H, THF), 2.26 (s, 3 H, $CH_3$), 2.23 (s, 3 H, $CH_3$), 1.87 (s, 3 H, $NCH_3$), 1.81 (s, 3 H, $NCH_3$), 0.97 (br., 4 H, THF), 0.45 (s, 1 H, CH), 0.34 (s, 9 H, $Me_3Si$-fluorenyl), 0.24 (s, 9 H, $Me_3Si$-benzyl) ppm. $^{13}$C{$^1$H} NMR (500 MHz, $C_6D_6$, 25 °C): $\delta$ = 150.6, 150.2, 150.2, 150.1, 147.3, 144.4, 143.7, 141.4, 141.2, 129.4, 129.4, 129.3, 129.2, 129.2, 128.3, 128.1, 128.1, 128.0, 126.5, 126.2, 126.2, 126.1, 126.0, 124.5, 121.7 (benzyl), 121.5, 121.5, 121.3, 121.2 (benzyl), 119.3, 118.7 (benzyl), 113.0 (benzyl), 88.9 (C-9), 68.6 (THF), 53.4 ($CCH_3$), 53.2 ($CCH_3$), 44.8 (CH), 44.6 ($NCH_3$), 41.5 ($NCH_3$), 30.9 ($CH_3$), 30.3 ($CH_3$), 25.0 (THF), 2.56 ($Me_3Si$-fluorenyl), 2.19 ($Me_3Si$-benzyl) ppm.

**Synthesis of 8:** As complex **8** is highly soluble even in cold hexane, it was synthesized in situ by reacting 2,7-bis(1,1-diphenylethyl)-9-$Et_3Si$-fluorene with [(2-$Me_2N$-α-$Me_3Si$-benzyl)]$_2$Ca·(THF)$_2$ (1.05 equiv.) in $C_6D_6$. Stirring the orange solution for 50 h at 70 °C led to quantitative formation of the heteroleptic complex **8** which, because of its extreme solubility, could not be freed from 2-$Me_2N$-α-$Me_3Si$-toluene by washing procedures. It was therefore used in solution for further polymerization experiments. The product has been fully characterized by 2D NMR methods. $^1$H NMR (500 MHz, $C_6D_6$, 25 °C): $\delta$ = 7.93 (d, $^3J_{H,H}$ = 8.5 Hz, 1 H, fluorenyl), 7.87 (d, $^3J_{H,H}$ = 8.5 Hz, 1 H, fluorenyl), 7.58 (s, 1 H, fluorenyl), 7.43 (s, 1 H, fluorenyl), 7.22–6.83 (m, 23 H, Ar), 6.58 (t, $^3J_{H,H}$ = 7.5 Hz, 1 H, benzyl), 6.23 (d, $^3J_{H,H}$ = 7.0 Hz, 1 H, benzyl), 6.10 (t, $^3J_{H,H}$ = 7.5 Hz, 1 H, benzyl), 2.52 (br., 4 H, THF), 2.21 (s, 3 H, $CH_3$), 2.16 (s, 3 H, $CH_3$), 1.80 [s, 6 H, $N(CH_3)_2$], 0.83–0.74 [m, 15 H, $Si(CH_2CH_3)_3$], 0.29 (s, 1 H, CH), 0.27 (s, 9 H, $Me_3Si$) ppm. $^{13}$C{$^1$H} NMR (500 MHz, $C_6D_6$, 25 °C): $\delta$ = 150.6, 150.3, 150.2, 150.1, 147.3, 144.5, 143.6, 142.0, 141.8, 130.1, 129.4, 129.4, 129.3, 129.0, 128.2, 128.1, 128.1, 128.0, 126.4 (benzyl), 126.2, 126.1, 125.4, 124.4 (benzyl), 123.9, 122.1, 121.6, 121.5, 121.4, 121.4, 121.2, 119.4, 119.1 (benzyl), 118.5, 113.0 (benzyl), 86.5 (C-9), 68.6 (THF), 53.4 ($CCH_3$), 53.2 ($CCH_3$), 45.0 (CH), 44.4 ($NCH_3$), 41.7 ($NCH_3$), 30.8 ($CH_3$), 30.2 ($CH_3$), 25.0 (THF), 8.50 [$Si(CH_2CH_3)_3$], 6.40 [$Si(CH_2CH_3)_3$], 2.58 ($Me_3Si$-benzyl) ppm.

**Synthesis of 9:** As complex **9** is highly soluble even in cold hexane, it was synthesized in situ with a procedure similar to that for **8**. The orange solution of **9** prepared in situ was used for further polymerization experiments. $^1$H NMR (500 MHz, $C_6D_6$, 25 °C): $\delta$ = 7.97 (d, $^3J_{H,H}$ = 8.5 Hz, 1 H, fluorenyl), 7.91 (d, $^3J_{H,H}$ = 9.0 Hz, 1 H, fluorenyl), 7.43 (s, 1 H, fluorenyl), 7.36 (s, 1 H, fluorenyl), 7.22–6.82 (m, 19 H, Ar), 6.57 (t, $^3J_{H,H}$ = 7.0 Hz, 1 H, benzyl), 6.27 (d, $^3J_{H,H}$ = 6.5 Hz; 1 H, benzyl), 6.10 (t, $^3J_{H,H}$ = 6.5 Hz, 1 H, benzyl), 2.70 (br., 4 H, THF), 2.26 (s, 3 H, $CH_3$), 2.24 (s, 3 H, $CH_3$), 1.90 (s, 6 H, $NCH_3$), 1.81 (s, 6 H, $NCH_3$), 1.19 [s, 9 H, $C(CH_3)_3$], 1.16 [s, 9 H, $C(CH_3)_3$], 1.15 [s, 9 H, $C(CH_3)_3$], 1.13 [s, 9 H, $C(CH_3)_3$], 1.00 (br., 4 H, THF), 0.40 (s, 1 H, CH), 0.28 (s, 9 H, $Me_3Si$-benzyl), 0.12 (s, 9 H, $Me_3Si$-fluorenyl) ppm. $^{13}$C{$^1$H} NMR (500 MHz, $C_6D_6$, 25 °C): $\delta$ = 148.6, 148.6, 147.7, 147.4, 147.3, 147.2, 147.0, 144.9, 144.6, 141.3, 141.1, 129.2, 129.1, 129.1, 129.0, 126.5 (benzyl), 125.0, 125.0, 124.5 (benzyl), 121.7, 121.5, 121.2, 121.1, 119.3, 119.3 (benzyl), 118.8, 113.0 (benzyl), 88.7 (C-9), 68.6 (THF), 52.6 ($CCH_3$), 52.5 ($CCH_3$), 44.8 (CH), 44.4 ($NCH_3$), 41.5 ($NCH_3$), 34.5 [$C(CH_3)_3$], 34.4 [$C(CH_3)_3$], 31.5 [$C(CH_3)_3$], 30.5 ($CCH_3$), 30.1 ($CCH_3$), 25.1 (THF), 2.70 ($Me_3Si$-fluorenyl), 2.22 ($Me_3Si$-benzyl) ppm.

**Styrene Polymerization:** Polymerizations of styrene were performed in a thermostatted 100 mL stainless steel Büchi reactor at normal pressure either in cyclohexane (1 M styrene solution, 1 mM catalyst, 50 °C) or in pure styrene (1 mM catalyst, 20 °C). In a typical polymerization experiment, the reactor was loaded with dry cyclohex-

 © 2007 Wiley-VCH Verlag GmbH & Co. KGaA, Weinheim 

Table 2. Crystal data for the compounds **4**, **5** and **6**.

| Compound | **4** | **5** | **6** |
|---|---|---|---|
| Formula | $C_{58}H_{76}Ca_2N_4Si_2 \cdot C_7H_8$ | $C_{66}H_{90}Ca_2N_2Si_2$ | $C_{50}H_{65}CaNOSi_2$ |
| MW | 1057.70 | 1047.74 | 792.29 |
| Size [mm] | $0.7 \times 0.7 \times 0.2$ | $0.5 \times 0.4 \times 0.3$ | $0.5 \times 0.4 \times 0.3$ |
| Crystal system | monoclinic | monoclinic | triclinic |
| Space group | *Cc* | *C*2/*c* | $P\bar{1}$ |
| *a* [Å] | 10.6545(8) | 17.271(1) | 10.9274(4) |
| *b* [Å] | 43.504(4) | 15.677(1) | 16.0377(5) |
| *c* [Å] | 12.9522(9) | 23.585(1) | 16.3604(6) |
| *α* | 90 | 90 | 110.334(2) |
| *β* | 96.288(6) | 110.099(1) | 94.677(2) |
| *γ* | 90 | 90 | 97.161(2) |
| *V* [Å$^3$] | 5967.4(8) | 5996.7(7) | 2643.4(2) |
| *Z* | 4 | 4 | 4 |
| *ρ* [g cm$^{-3}$] | 1.177 | 1.161 | 1.103 |
| *μ*(Mo-$K_α$) [mm$^{-1}$] | 0.273 | 0.270 | 0.195 |
| *T* [°C] | –120 | –90 | –90 |
| *θ* (max.) | 25.1 | 29.3 | 27.5 |
| Reflections total, unique | 8146, 5571 | 127637, 8205 | 159543, 12019 |
| $R_{int}$ | 0.017 | 0.068 | 0.077 |
| Observed reflections [$I > 2\sigma(I)$] | 5061 | 6476 | 9479 |
| Parameter | 966 | 331 | 500 |
| $R_1$ | 0.028 | 0.051 | 0.065 |
| *wR*2 | 0.072 | 0.139 | 0.155 |
| GOF | 1.04 | 1.10 | 1.08 |
| Max./min. residual electron density [e Å$^{-3}$] | –0.30/0.26 | –0.60/0.74 | –0.46/0.36 |

ane (90 mL, dried with $CaH_2$ and distilled from *n*BuLi) and dry styrene (11.5 mL, ca. 100 mmol, freshly distilled from $CaH_2$ and stored over alox pearls). A solution of the initiator (0.1 mmol) in benzene (1.0 mL) was added through a port. The usual appearance of a red colour and a slight increase in temperature (1–3 °C) indicated that the polymerization started immediately. After a polymerization time of 45–60 min, the mixture was quenched with oxygen-free methanol. Evaporation of all solvents yielded the polymer in quantitative yields. Polymerization in neat styrene should only be carried out at temperatures ≤20 °C, should be monitored continuously and should be quenched when temperatures exceed 25 °C. The polymers were analyzed by GPC and high temperature $^1$H and $^{13}$C NMR (solvent: [D$_2$]tetrachloroethane). The tacticity of the polymer was checked by analyzing the $^{13}$C NMR signal for the $C_{ipso}$ in the phenyl ring.[22]

**Crystal Structures:** Crystal diffraction data were measured on Enraf–Nonius CAD4 and Siemens SMART CCD diffractometers. All crystal structures were solved with SHELXS-97[26] and refined with SHELXL-97.[27] PLATON[28] was used for geometry calculations and graphics. Crystal data are given in Table 2.) The space group for **4** was checked with the ADSYM procedure incorporated in the program PLATON. No additional symmetry was found, and therefore the true space group is *Cc*. The Flack parameter was refined to 0.00(2). Crystals of **6** contain one equivalent of hexane in the asymmetric unit. This molecule was extensively disordered and treated with the SQUEEZE procedure[29] incorporated in PLATON.

CCDC-646400 (compound **4**), -646401 (compound **5**), and -646402 (compound **6**) contain the supplementary crystallographic data for this paper. These data can be obtained free of charge from The Cambridge Crystallographic Data Centre via www.ccdc.cam.ac.uk/data_request/cif.

## Acknowledgments

We thank Dieter Bläser and Prof. Dr. Roland Boese (University of Duisburg-Essen) for measurements of the X-ray diffraction data for complexes **5** and **6** and Dr. Konrad Knoll (BASF AG, Ludwigshafen) for GPC analyses.

[1] N. Ishihara, M. Kuramoto, Japan Patent 62 187 708, **1985**.
[2] N. Ishihara, M. Kuramoto, M. Uoi, *Macromolecules* **1986**, *21*, 2464.
[3] N. Tomotsu, N. Ishihara, T. H. Newman, M. T. Malanga, *J. Mol. Catal. A* **1998**, *128*, 167.
[4] C. Pellecchia, D. Pappalardo, L. Oliva, A. Zambelli, *J. Am. Chem. Soc.* **1995**, *117*, 6593.
[5] R. Po, N. Cardi, *Prog. Polym. Sci.* **1996**, *21*, 47.
[6] M. K. Mahanthappa, R. M. Waymouth, *J. Am. Chem. Soc.* **2001**, *123*, 12093.
[7] J. Schellenberg, N. Tomotsu, *Prog. Polym. Sci.* **2002**, *27*, 1925.
[8] E. Kirillov, C. W. Lehmann, A. Razavi, J.-F. Carpentier, *J. Am. Chem. Soc.* **2004**, *126*, 12240.
[9] J. Hitzbleck, K. Beckerle, J. Okuda, T. Halbach, R. Mühlhaupt, *Macromol. Symp.* **2006**, *236*, 23.
[10] J. R. Wünsch in *Kunststoff Handbuch 4: Polystyrol* (Eds.: H. Gausepohl, R. Gellert), Hanser, München, **1996**, 82.
[11] M. Malanga, *Adv. Mater.* **2000**, *12*, 1869.
[12] J. Schellenberg, H.-J. Leder, *Adv. Polym. Technol.* **2006**, *25*, 141.
[13] S. Harder, F. Feil, A. Weeber, *Organometallics* **2001**, *20*, 1044.
[14] F. Feil, S. Harder, *Angew. Chem.* **2001**, *113*, 4391; *Angew. Chem. Int. Ed. Engl.* **2001**, *40*, 4261.
[15] S. Harder, F. Feil, *Organometallics* **2002**, *21*, 2268.
[16] F. Feil, S. Harder, *Eur. J. Inorg. Chem.* **2003**, 3401.
[17] D. Hoffmann, W. Bauer, F. Hampel, N. J. R. van Eikema Hommes, P. v. R. Schleyer, P. Otto, U. Pieper, D. Stalke, D. S. Wright, R. Snaith, *J. Am. Chem. Soc.* **1994**, *116*, 528.
[18] F. Feil, S. Harder, *Organometallics* **2000**, *19*, 5010.

 © 2007 Wiley-VCH Verlag GmbH & Co. KGaA, Weinheim 

[19] a) C. W. Haigh, R. B. Mallion, *Progr. Nucl. Magn. Reson. Spectrosc.* **1980**, *13*, 303. Although this is the classical explanation, it should be noted that recent calculations introduce a different explanation: b) C. S. Wannere, P. v. R. Schleyer, *Org. Lett.* **2003**, *5*, 605.
[20] L. Gold, *J. Chem. Phys.* **1958**, *28*, 91.
[21] K. Knoll in *Kunststoff Handbuch 4: Polystyrol* (Eds.: H. Gausepohl, R. Gellert), Hanser, München, **1996**, 67.
[22] F. Feil, S. Harder, *Macromolecules* **2003**, *36*, 3446.
[23] R. D. Culp, A. H. Cowley, *Organometallics* **1996**, *15*, 5380.
[24] S. Kajigaeshi, T. Kadowaki, A. Nishida, S. Fujisaki, M. Noguchi, *Synthesis* **1984**, *4*, 335.
[25] H. G. Alt, R. Zenk, *J. Organomet. Chem.* **1996**, *522*, 39.
[26] G. M. Sheldrick, *SHELXS-97, Program for Crystal Structure Solution* **1997**, University of Göttingen, Germany.
[27] G. M. Sheldrick, *SHELXL-97, Programs for the Determination of Crystal Structures*, University of Göttingen, Germany, **1997**.
[28] A. L. Spek, *PLATON, A Multipurpose Crystallographic Tool* **2000**, Utrecht University, Utrecht, The Netherlands.
[29] P. A. van der Sluis, A. L. Spek, *Acta Crystallogr. Sect. A* **1990**, *46*, 194.

Received: July 27, 2007
Published Online: November 2, 2007

 © 2007 Wiley-VCH Verlag GmbH & Co. KGaA, Weinheim 

DOI: 10.1002/ejic.200700366

# A Basket-Like $[Sr\subset P_6Mo^{V}_4Mo^{VI}_{14}O_{73}]^{10-}$ Polyoxoanion Modified with $\{Cu(phen)(H_2O)_x\}$ ($x$ = 1–3) Fragments: Synthesis, Structure, Magnetic, and Electrochemical Properties

**Kai Yu,[a] Yang-Guang Li,*[b] Bai-Bin Zhou,*[a] Zhan-Hua Su,[a] Zhi-Feng Zhao,[a] and Yu-Nan Zhang[a]**

**Keywords:** Polyoxometalate / Organic–inorganic hybrid / Basket-like / Electrocatalysis

Hydrothermal reaction of a mixture of $Na_2MoO_4{\cdot}2H_2O$, $H_3PO_4$, $CuCl_2{\cdot}2H_2O$, *o*-phenanthroline, and $SrCl_2$ in water leads to the isolation of a basket-like mixed-valent polymolybdophosphate hybrid compound, $[Cu(phen)(H_2O)_3][\{Cu(phen)(H_2O)_2\}\{Cu(phen)(H_2O)\}_3\{Sr\subset P_6Mo_4{}^{V}Mo_{14}{}^{VI}O_{73}\}]{\cdot}3H_2O$ **1**, which crystallizes in the space group $P\bar{1}$ with $a$ = 13.778(3) Å, $b$ = 19.267(4) Å, $c$ = 24.168(5) Å, $\alpha$ = 110.64(3)°, $\beta$ = 90.31(3)°, $\gamma$ = 110.02(3)°, $V$ = 5582.8(2) Å$^3$, $Z$ = 2. Single-crystal X-ray diffraction analysis shows that the four-electron-reduced basket-like polyoxoanion $[Sr\subset P_6Mo_4{}^{V}Mo_{14}{}^{VI}O_{73}]^{10-}$ contains a new tetravacant γ-Dawson-type unit and a "handle"-shaped $\{P_4Mo_4\}$ segment, which are highly modified with $\{Cu(phen)(H_2O)_x\}$ (x = 1–3) fragments. Electrochemical analysis shows that **1**-modified carbon paste electrode (CPE) displays good electrocatalytic activity to reduce hydrogen peroxide.
(© Wiley-VCH Verlag GmbH & Co. KGaA, 69451 Weinheim, Germany, 2007)

## Introduction

Polyoxometalate (POM)-based organic–inorganic hybrid compounds have attracted great interest in recent years owing to their extensive theoretical and practical applications in catalysis, molecular adsorption, medicine, electroconductivity, magnetism, and photochemistry.[1–7] A current research interest in this field is modification of the surface of POMs with various organic and/or transition-metal complex moieties.[1–10] These kinds of modified POM derivatives can be regarded as an ideal molecular model for determination of the mechanisms of oxide-supported catalysts.[1] Furthermore, such kinds of compounds can be molecularly fine-tuned and provide potentially new types of catalyst systems as well as interesting functional materials with optical, electronic, and magnetic properties.[1b,1c] During the preparation, two strategies have been exploited to increase the surface charge density and activate the surface oxygen atoms of heteropolyoxoanions:[1] (1) reduce the metal centers from a high oxidation state to a low oxidation state, for example, from $Mo^{VI}$ to $Mo^{V}$, by introducing strong reducing reagents or (2) replace high-valence metal centers with lower-valence ones, for instance, from $Mo^{VI}$ to $V^{IV}$ or $TM^{2+}$ (TM = transition metal). However, the highly reduced polyoxoanions are usually unstable and inclined to be oxidized in ambient atmosphere. Thus, the hydrothermal technique has been extensively employed and proved to be an efficient way to obtain metastable POMs modified by various organic and/or metal–organic fragments.[2] According to the above-mentioned strategies, a series of hybrid compounds based on Keggin- and Dawson-type heteropolytungstates have been prepared, such as $[\{Ni(bpy)_2(H_2O)\}(PW_{12}O_{40})]^{3-}$,[9a] $[\{Ag(bpy)\}_2\{Ag_2(bpy)_3\}_2(PW_9V_3O_{40})]$,[9b] $[\{Cu(bpy)_2\}(SeW_{12}O_{40})]^{3-}$,[9c] $[\{Cu(PPD)_2\}(As_2W_{18}O_{60})]$,[9d] and $[\{Zn(phen)_2\}\{Zn(phen)_2(H_2O)\}(P_2W_{18}O_{62})]$.[9e] In contrast, most modified polyoxomolybdate composite compounds in earlier research, especially in the work of Zubieta,[2a] concentrated on isopolyoxometalate-supported transition-metal complexes. When $PO_4^{3-}$ was introduced into the $\{MoO_x/TM/L\}$ (TM = transition metal, L = organic ligand) system, a series of reduced polymolybdophosphates decorated with metal–organic units were synthesized.[2b,2c,10–12] It is interesting that most of these hybrid compounds are based on inorganic $\{PMo_{12-x}TM_xO_{40}\}$,[10] $\{P_4Mo_6O_{31}\}$,[11] and $\{P_2Mo_5O_{23}\}$[12] building blocks. More recently, three unusual large clusters, $[P_6Mo_{18}O_{73}]^{11-}$,[13] $[H_{14}(Mo_{16}O_{32})Co_{16}(PO_4)_{24}(H_2O)_{20}]^{10-}$,[14] and $[Na_4(H_2O)_6\{(Mo_2O_4)_{10}(P_2O_7)_{10}(OAc)_8(H_2O)_4\}]^{24-}$[15] have been reported. However, no organic or metal–organic complexes have been successfully coordinated to these highly reduced polymolybdophosphate clusters so far, the reason for which may be that the large size of these POMs decreases the elec-

[a] Academy of Physics and Chemistry, Harbin Normal University, Harbin 150080, P. R. China
E-mail: zhou_bai_bin@sina.com
[b] Key Laboratory of Polyoxometalate Science of Ministry of Education, Faculty of Chemistry, Northeast Normal University,
Changchun, Jilin, 130024, P. R. China
E-mail: liyg658@nenu.edu.cn
Supporting information for this article is available on the WWW under http://www.eurjic.org or from the author.

 WILEY InterScience DISCOVER SOMETHING GREAT © 2007 Wiley-VCH Verlag GmbH & Co. KGaA, Weinheim 

tron density of the surface or the coordination ability of the surface oxygen atoms. During our continuing research on modified-POM hybrid compounds in the $\{MoO_x/P/TM/L\}$ system, we are interested in employing metal–organic units to decorate high-nuclear clusters in order to get new hybrid materials to explore their fascinating magnetic and electrochemical properties. In this paper, we report the hydrothermal synthesis and crystal structure of a basket-like four-electron reduced polymolybdophosphate hybrid compound, $[Cu(phen)(H_2O)_3][\{Cu(phen)(H_2O)_2\}\{Cu(phen)(H_2O)\}_3\{Sr\subset P_6Mo_4{}^{V}Mo_{14}{}^{VI}O_{73}\}]\cdot 3H_2O$ **1**. In the crystal structure of **1**, the basket-like polyoxoanion contains a new tetravacant γ-Dawson-type unit and a "handle"-shaped $\{P_4Mo_4\}$ segment, which are decorated by four $\{Cu(phen)(H_2O)_x\}$ ($x$ = 1–3) fragments. The magnetic, electrochemical, and electrocatalytic properties of compound **1** were also investigated.

## Results and Discussion

### Syntheses

The successful isolation of compound **1** relies on the employment of a hydrothermal technique. Hydrothermal synthesis has recently been proved to be a particularly effective method for the preparation of new organic–inorganic hybrid materials.[2,6–15] Exploitation of hydrothermal conditions provides a paradigm shifting from the thermodynamics to the kinetics. Under such conditions, equilibrium phases are replaced by structurally more complex metastable phases.[2,16] In the hydrothermal environment, the reduced viscosity of water results in enhanced rates of solvent extraction from solids and crystal growth from solution.[2] Further, as different solubility problems can be minimized, a variety of organic and inorganic precursors can be introduced.[2] Meanwhile, hydrothermal synthesis is still a relatively complex process because many factors can influence the outcome of a reaction, such as the type of initial reactants, starting concentrations, pH value, reaction time, and temperature.[2,16] However, numerous successful experimental results from these so-called "black-box" reactions could suggest some preliminary synthetic experiences, which might be helpful for the future synthetic route.

During our exploration of the hybrid polymolybdophosphates modified with various organic and/or metal–organic complex fragments, abbreviated as the $\{MoO_x/P/TM/L\}$ (TM = transition metal; L = N donor organic ligand) system, a series of new composite compounds have been hydrothermally synthesized as shown in Table 1.[10–12] It is noteworthy that almost all the compounds can be separated into three groups on the basis of their POM building blocks, that is, $\{PMo_{12-x}TM_xO_{40}\}$, $\{P_4Mo_6O_{31}\}$, and $\{P_2Mo_5O_{23}\}$ units (see Figure 1). During the preparations, although various molar ratios of $Na_2MoO_4/H_3PO_4/TM^{2+}$/L were used, the initial pH value and the reaction temperature seem to be vital for a successful reaction. As shown in Figure 1, the $\{P_2Mo_5\}$-based composite compounds are generally isolated at 160 °C, whereas most $\{P_4Mo_6\}$-based compounds could be prepared above 180 °C. Further, both $\{P_2Mo_5\}$- and $\{P_4Mo_6\}$-based compounds can be synthesized in a wide range of pH values, whereas the $\{PMo_{12-x}TM_xO_{40}\}$-based compounds can only be prepared in a very narrow pH range of ca. 3.5–4.

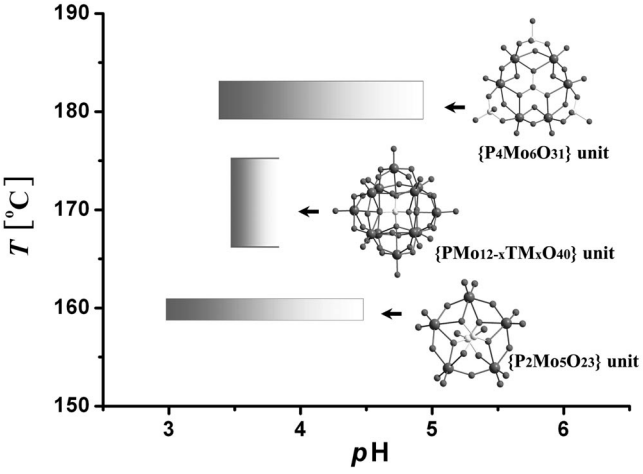


Figure 1. Illustration of possible synthetic products in the $\{MoO_x/P/TM/L\}$ system based on three kinds of building blocks under different pH and temperature conditions.

In this work, compound **1** represents an exception to the aforementioned examples. Compound **1** was synthesized with a mixture of $Na_2MoO_4\cdot 2H_2O$, $CuCl_2\cdot 2H_2O$,

Table 1. Comparison of the synthetic conditions of various compounds from the $\{MoO_x/P/TM/L\}$ system.

| Compound[a] | Approx. pH | $T$ [°C] | $t$ [d] | Ref. |
|---|---|---|---|---|
| I. $[\{Ni(phen)\}_2PMo^{V}_3Mo^{VI}_9O_{40}]^{2-}$ | 3.8 | 160 | 7 | [10a] |
| I. $[\{Cu(2,2'\text{-bpy})\}_{2.5}PMo^{V}_4Mo^{VI}_8O_{40}]^{2-}$ | 3.5 | 180 | 4 | [10b] |
| I. $[\{Cu(4,4'\text{-bpy})\}_2HPMo_{11}CuO_{39}]^{2-}$ | 3.7 | 165 | 6 | [10c] |
| I. $[\{Cu(2,2'\text{-bpy})\}PMo^{V}_2Mo^{VI}_{10}O_{40}]^{3-}$ | 3.8 | 165 | 4 | [10d] |
| II. $[\{Mn(phen)_2(H_2O)_x\}_4\{Mn(P_4Mo_6(OH)_6O_{25})_2\}]^{2-}$ | 4.5 | 180[b] | 6 | [11a] |
| II. $[\{Cd(4,4'\text{-bpy})(H_2O)\}_2\{Cd(P_4Mo_6(OH)_6O_{25})_2\}]^{4-}$ | 5.0 | 170 | 5 | [11b] |
| II. $[Na_3(P_4Mo_6(OH)_5O_{26})_2]^{11-}$ | 3.5 | 180 | 3 | [11c] |
| II. $[Mn(P_4Mo_6O_{26}(OH)_5)_2]^{12-}$ | 4.0 | 250 | 2.5 | [11d] |
| III. $[Co(en)_3]_2[P_2Mo_5O_{23}]$ | 3.0 | 160 | 6 | [12a] |
| III. $[\{Cu(4,4'\text{-bpy})_2\}P_2Mo_5O_{23}]^{2-}$ | 4.5 | 160 | 6 | [12b] |
| III. $[\{Ni(H_2O)_5\}\{Ni(4,4'\text{-Hbpy})(H_2O)_4\}P_2Mo_5O_{23}]^{-}$ | 3.0 | 160 | 6 | [12c] |

[a] I: Keggin-; II: $\{P_4Mo_6\}$-; III $\{P_2Mo_5\}$-building blocks. [b] The yield is improved at this reaction temperature.

 © 2007 Wiley-VCH Verlag GmbH & Co. KGaA, Weinheim 

phen, $H_3PO_4$, and $SrCl_2$ in a molar ratio of 1.00:0.30:0.30:4.80:0.50 in water at 160 °C for 4 d. The initial pH value was controlled in the range 3–4 with 1-M NaOH solution. If the reaction temperature was lower than 160 °C or the pH value was outside the 3–4 range, no crystals could be obtained. It is also interesting that when $SrCl_2$ was not introduced into the reaction mixture, another compound[17] was isolated under similar reaction conditions ($T$ = 165 °C and pH = 3.5), which might be analogous to the polyoxoanion $[\{Ni(phen)\}_2PMo^{V}_3Mo^{VI}_9O_{40}]^{2-}$.[10a] Thus, it is supposed that the $Sr^{2+}$ ions could be the necessary templates for the isolation of compound **1**.[18]

## Structure Description

Single-crystal X-ray diffraction analysis revealed that **1** consists of an interesting basket-like $[Sr\subset P_6Mo_{18}O_{73}]^{10-}$ polyoxoanion decorated with four $\{Cu(phen)(H_2O)_x\}$ ($x$ = 1 and 2) fragments (Figure 2) and charge balanced with one $\{Cu(phen)(H_2O)_3\}$ unit. In the polyoxoanion of **1** (Figure 3 and Figure S1), all Mo centers exhibit a six-coordinate environment with Mo–O bond lengths in the range 1.672(8)–2.454(6) Å and O–Mo–O bond angles varying from 83.4(3) to 173.7(3)°. The six P centers display tetrahedral coordination geometry. The P–O bond lengths range from 1.503(7) to 1.577(7) Å, whereas the O–P–O bond angles vary from 107.2(4) to 112.8(4)°. The basket-like polyoxoanion can be separated into two parts, that is, the "handle" $\{P_4Mo_4\}$ unit and the "basket body" $\{P_2Mo_{14}\}$ segment (Figure 2). The $\{P_4Mo_4\}$ unit consists of four $\{MoO_6\}$ octahedra and four $\{PO_4\}$ tetrahedra, which are corner-linked together to form the handle moiety. The $\{P_2Mo_{14}\}$ unit exhibits a tetravacant Dawson-type structural feature. In comparison to the Dawson-type isomers and their tetravacant species[5c] (Scheme 1), we conclude that the $\{P_2Mo_{14}\}$ building block in **1** is derived from the γ-Dawson anion. It is noteworthy that Dawson anions and a series of its lacunary derivatives have extensively acted as building blocks to constitute novel complexes with various functionalities.[1,2a,5] Nevertheless, only six kinds of lacunary Dawson-type derivatives have ever been observed (Scheme S1). In **1**, the γ-$\{P_2Mo_{14}\}$ unit represents a new lacunary Dawson-type species in POM chemistry. The "handle" ($\{P_4Mo_4\}$ unit) and the "basket body" ($\{P_2Mo_{14}\}$ unit) moieties are connected together through the edge- and/or corner-sharing modes (Figure 3 and Figure S2). The whole basket-shaped cluster possesses $C_{2v}$ symmetry (Figure S2). In the central cavity of the polyoxoanion, a $Sr^{2+}$ ion is fully encapsulated, and it exhibits a nine-coordinate environment with the bond lengths of Sr–O in the range 2.570(7)–2.754(6) Å (Figure 3 and Figure S3). It is interesting that the cavity size of the basket-

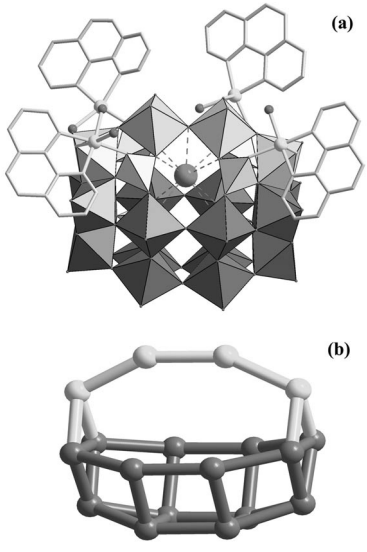


Figure 2. (a) Polyhedral and ball-and-stick representation of $[Sr\subset P_6Mo_{18}O_{73}]^{10-}$ decorated by four $\{Cu(phen)(H_2O)_x\}$ ($x$ = 1 or 2) fragments in **1**. The isolated $\{Cu(phen)(H_2O)_3\}^{2+}$ unit is omitted for clarity. Octahedron, Mo; tetrahedron, P; large black ball, Sr; middle grey ball, Cu; Small black ball, O; grey line, phen ligand; (b) basket-like topology formed by 18 Mo atoms.

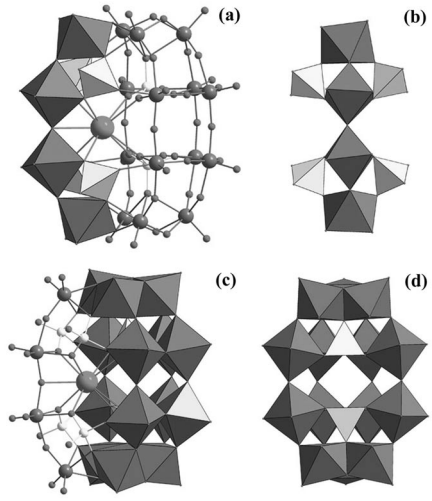


Figure 3. (a) Polyhedral and ball-and-stick representation of the basket-like $[Sr\subset P_6Mo_{18}O_{73}]^{10-}$ in **1**; (b) view of the "handle" $\{P_4Mo_4\}$ unit; (c) another view of the polyoxoanion of **1**; (d) view of the "basket body" $\{P_2Mo_{14}\}$ unit. Octahedron, Mo; tetrahedron, P; large black ball, Sr; middle black ball, Mo; small grey ball, P; small black ball, O.

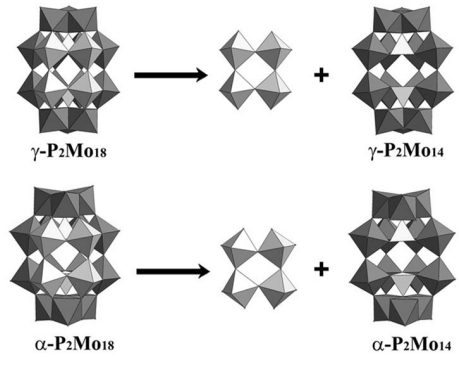


Scheme 1. Illustration of the comparison between α- and γ-Dawson-type polyoxoanions and their tetravacant derivatives.

 © 2007 Wiley-VCH Verlag GmbH & Co. KGaA, Weinheim 

like polyoxoanion seems to be more inclined to capture larger cations ($Sr^{2+}$) although both $Sr^{2+}$ and $Na^+$ ions coexist in the reaction system with similar concentrations. Zhang et al. have also reported a similar $[P_6Mo_{18}O_{73}]^{11-}$ polyoxoanion encapsulating a $K^+$ ion.[13] The incorporation of these large cations may vice versa stabilize the whole cryptand polyoxoanion.[18]

In **1**, there are five independent $\{Cu(phen)(H_2O)_x\}$ ($x$ = 1, 2, or 3) fragments. Four of them are coordinated directly to the surface of the polyoxoanion, whereas the fifth is isolated in the interspace of the crystal structure (Figure 4 and Figure S4). The Cu1 atom exhibits a five-coordinate environment with two O atoms from the polyoxoanion, two N atoms from the phen ligand, and one water ligand. The Cu2 atom possesses an octahedral coordination geometry with three O atoms from the polyoxoanion, two N atoms from the phen ligand, and one terminal water ligand. The Cu3 atom also displays octahedral coordination geometry with two O atoms from the polyoxoanion, two N atoms from the phen ligand, and two terminal water ligands. The $\{Cu(4)(phen)(H_2O)\}$ moiety is disordered in two positions (Figure S4). Both of the disordered parts exhibit a four-coordinate environment. The Cu5 atom has a five-coordinate environment, involving two N atoms from the phen ligand and three coordinated water molecules. The bond lengths of Cu–N and Cu–O are in the range 1.983(1)–2.122(2) and 1.912(2)–2.619(3) Å, respectively. It is noteworthy that two $\{Cu(2)(phen)(H_2O)\}$ units act as bridges to link two polyoxoanions into a dimeric cluster (Figure 4). In the packing arrangement, the adjacent $[\{Cu(phen)(H_2O)_2\}\{Cu(phen)(H_2O)\}_3\{Sr\subset P_6Mo_{18}O_{73}\}]^{2-}$ dimeric clusters are linked together by π–π interactions between adjacent phen groups to form a three-dimensional supramolecular framework (Figure S5). The isolated $\{Cu(phen)(H_2O)_3\}$ units are also connected with their adjacent coordinated analogues through π–π interactions between the phen groups. In the crystal structure, the average distance between two phen planes with π–π interactions is about 3.52 Å. The lattice water molecules should be extensively H-bonded with the surface oxygen atoms of the polyoxoanions. The typical H-bond lengths between them are as follows: OW1···O48 2.823 Å, OW2···O5 3.168 Å, OW3···O46 2.845 Å, and OW4···O22 3.454 Å.

In compound **1**, all P, Cu, and Sr centers exhibit +5, +2, and +2 oxidation states, respectively, on the basis of their coordination environments, bond lengths and angles, and the bond valence sum (BVS) calculation.[19] In addition, the black color of the crystal suggests that the Mo centers in compound **1** should be mixed valent. BVS calculation shows an average value of ca. 5.79 for all Mo centers (Table S3), which is close to the result of 14 $Mo^{6+}$ and 4 $Mo^{5+}$ in the polyoxoanion cluster. Considering the five $[Cu(phen)(H_2O)_x]^{2+}$ segments and no protonated oxygen atoms on the surface of the polyoxoanion, together with the BVS calculation results, the polyoxoanion formula can be expressed as $[Sr\subset P_6Mo^{V}_4Mo^{VI}_{14}O_{73}]^{10-}$. Furthermore, each Mo center on the γ-$\{P_2Mo_{14}\}$ unit contains just one Mo=O bond, whereas every Mo center on the "handle" $\{P_4Mo_4\}$ fragments possesses two Mo=O bonds, which suggests that the Mo centers on the γ-$\{P_2Mo_{14}\}$ unit are more easily reduced and that all four electrons could be delocalized only on the γ-$\{P_2Mo_{14}\}$ unit.[20a]

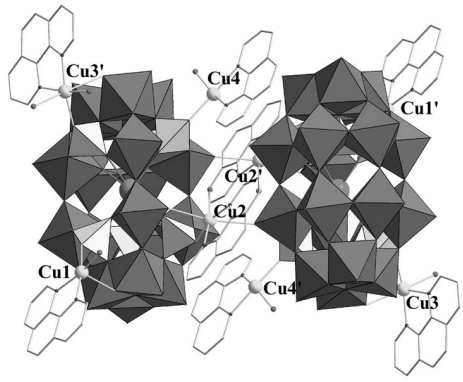


Figure 4. Polyhedral and ball-and-stick representation of the dimeric cluster of **1** and the coordination environments of the Cu centers. The isolated $\{Cu5(phen)(H_2O)_3\}$ unit is omitted for clarity. Octahedron, Mo; tetrahedron, P; large black ball, Sr; middle grey ball, Cu; small black ball, O; grey line, phen group.

## XPS, UV/Vis, and IR Spectral Analyses

The oxidation states of Mo, Sr, and Cu in **1** are further confirmed by XPS measurements. The XPS spectrum of molybdenum indicates two overlapped peaks of $Mo^{6+}$ and $Mo^{5+}$ ions in the energy region of $Mo3d_{5/2}$ and $Mo3d_{3/2}$ (Figure 5a).[21a] The peaks of $Mo3d_{5/2}$ at 232.3 and 230.9 eV

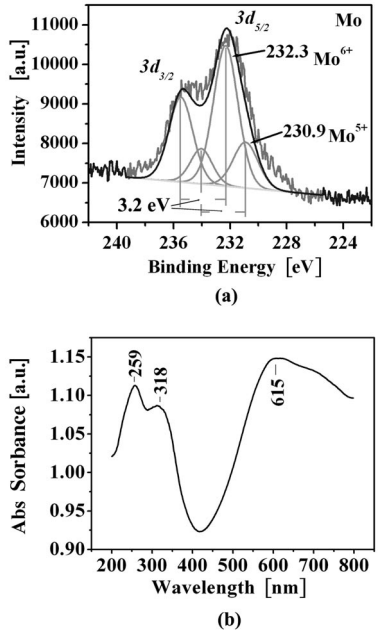


Figure 5. (a) The XPS spectrum of mixed-valent Mo in **1**. The fit line (black smooth line on the top) is produced by the decomposition of the overlapping peaks of $Mo^{6+}$ and $Mo^{5+}$ (middle and bottom grey lines) with a peak/area ratio of ca 3.5:1; (b) solid-state UV/Vis spectrum of **1**.

 © 2007 Wiley-VCH Verlag GmbH & Co. KGaA, Weinheim 

are attributable to the $Mo^{6+}$ and $Mo^{5+}$ ions, respectively.[21a] The best fit (top black line in Figure 5a) for the XPS spectrum of the mixed-valent Mo compound is produced by decomposition of the overlapping peaks of $Mo^{6+}$ and $Mo^{5+}$ with a peak/area ratio of ca. 3.5:1, which corresponds to the 14 $Mo^{VI}$ and 4 $Mo^{V}$ centers in compound **1**. This result is consistent with the BVS calculation and the charge-balance consideration. The XPS measurements were also carried out in the energy region of $Sr3d_{5/2}$ and $Cu2p_{3/2}$, respectively. The peaks at 133.2 eV and 932.4 eV are ascribed to $Sr^{2+}$ and $Cu^{2+}$ ions, respectively (Figure S6).[21b,21c]

The diffuse reflectance UV/Vis spectrum of compound **1** was also investigated with the solid-state sample in $BaSO_4$ pellet (Figure 5b). The two peaks at 259 and 318 nm are associated with two kinds of O–Mo LMCT bands,[20a] whereas the other strong wide band around 615 nm is due to overlap of several bands of the intervalence transition from $Mo^{V}$ to $Mo^{VI}$ by the Mo–O–Mo bond, the d–d transitions of $Mo^{V}$ octahedra,[20a] and the Cu–$N_{(phen)}$ and Cu–$O_{(POM)}$ LMCT bands,[20b] which leads to the dark blue coloration of this compound.

In the IR spectrum of compound **1** (Figure S7), the characteristic peaks concerned with coordinated *o*-phenanthroline are at 1598(m), 1509(m), and 1430(s) $cm^{-1}$. Peaks at 1086(s) and 1025(w) $cm^{-1}$ are assigned to the P–O vibrations and those at 923(s), 840(s), 769(s), and 711 $cm^{-1}$ are attributed to the Mo=O and Mo–O–Mo vibrations of the polyoxoanion cluster.[20a]

## Magnetic Properties

Solid-state variable-temperature magnetic susceptibility measurements were performed on the polycrystalline samples of **1** suspended in eicosane to prevent torquing. The DC magnetic susceptibility ($\chi_M$) data were measured in the temperature range 1.8–300 K in a 1 T magnetic field and are plotted as $\chi_M T$ versus $T$ in Figure 6. For **1**, the $\chi_M T$ product of 1.97 $cm^3 K mol^{-1}$ at 300 K decreases continuously to 1.92 $cm^3 K mol^{-1}$ at 1.8 K. The $\chi_M T$ value at room temperature is much lower than the spin-only value ($g$ = 2.0) of 3.375 $cm^3 K mol^{-1}$ for five $Cu^{2+}$ and four $Mo^{5+}$ noninteracting ions ($S$ = 1/2), but close to the value of 1.875 $cm^3 K mol^{-1}$ for five isolated $Cu^{2+}$ ions. This result suggests that four delocalized electrons in each polyoxoanion cluster might be totally antiferromagnetically coupled, which has yet to be observed.[22] The $1/\chi_M$ versus $T$ curve is consistent with the Curie–Weiss law with $C$ = 1.98 $cm^3 K mol^{-1}$ and $\theta$ = –0.1 K, which indicates the presence of very weak antiferromagnetic interactions in the whole compound.

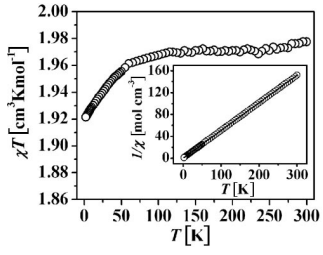


Figure 6. $\chi_M T$ vs. $T$ curve of **1**; inset: $1/\chi_M$ vs. $T$ curve. The solid line is the fitted result based the on Curie–Weiss law.

## Thermogravimetric (TG) Analysis

The thermal behavior of compound **1** was investigated between 50 and 930 °C. The TG curve of this compound presents a three-step weight-loss process (Figure S8). The first step in the temperature range 80–300 °C corresponds to the loss of isolated and coordinated water molecules (calcd. weight loss 4.32%; found 4.43%). The second step occurs between 400 and 600 °C and corresponds to the loss of the *o*-phenanthroline ligands on copper centers (calcd. weight loss 19.65%; found 20.94%). The third step in the temperature range 760–930 °C is probably due to the evaporation of $P_2O_5$ (calcd. weight loss 18.57%; found 17.10%). The result of the TG analysis basically agrees with that of the structure determination.

## Electrochemical and Electrocatalytic Properties

Although compound **1** was obtained from an aqueous system, it cannot be dissolved in water or a weak acidic aqueous solution. Therefore, its electrochemical behavior was investigated with a **1**-modified carbon paste electrode (**1**-CPE).[23] The cyclic voltammetric behavior for **1**-CPE in 1-M $H_2SO_4$ aqueous solution at different scan rates were recorded (Figure S9a) and they exhibit three reversible redox peaks in the potential range +800 to –100 mV, which is attributable to the $[Sr{\subset}P_6Mo_{18}O_{73}]^{10-}$ polyanions. At scan rates lower than 100 $mV s^{-1}$, the peak currents were proportional to the scan rate (Figure S9b), which indicates that the redox process of **1**-CPE is surface controlled. It is noteworthy that **1**-CPE possesses high stability. When the potential range is maintained at +800 to –100 mV, the peak currents almost remain unchanged over 300 cycles at a scan rate of 100 $mV s^{-1}$. After **1**-CPE was stored at room temperature for one month, the peak current decreased by only 3% and could be renewed by squeezing a little carbon paste out of the tube. The high stability of **1**-CPE could be ascribed to the organic–inorganic hybrid structural feature of **1** that stabilizes the polyoxoanion in the compound. Further, compound **1** is insoluble in the acidic aqueous media used in this experiment, which avoids the loss of the modifier during measurements. Thus, **1**-CPE could be an ideal electrode material to investigate electrocatalytic properties. Actually, **1**-CPE displays good electrocatalytic activity towards the reduction of hydrogen peroxide (Figure 7). At the **1**-CPE, with the addition of $H_2O_2$, all three reduction peak currents increased, whereas the corresponding oxidation peak currents dramatically decreased, which suggests that $H_2O_2$ was electrocatalytically reduced by all three reduced polyoxoanion species.[23,24] Furthermore, the cata-

 © 2007 Wiley-VCH Verlag GmbH & Co. KGaA, Weinheim 

lytic activities were enhanced with the increasing extent of the anion reduction. In contrast, the reduction of $H_2O_2$ at a bare electrode generally requires a large overpotential and no obvious response was observed at a bare CPE.

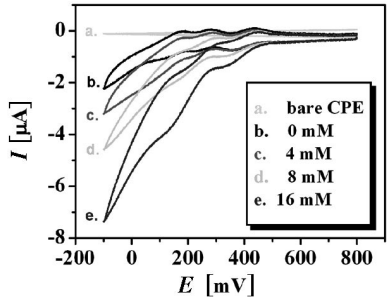


Figure 7. Cyclic voltammograms of **1**-CPE in $H_2SO_4$ (1 M) containing 0.0, 4.0, 8.0, and 16.0 mM $H_2O_2$ and a bare CPE in 5.0-mM $H_2O_2$ + 1-M $H_2SO_4$ solution. Potentials vs. SCE. Scan rate: 30 mV s$^{-1}$.

## Conclusions

In this paper, we report organic–inorganic hybrid compound **1**, which exhibits a four-electron-reduced basket-like polyoxoanion modified with four $\{Cu(phen)(H_2O)_x\}$ ($x$ = 1 and 2) fragments. Electrochemical analysis shows that **1**-CPE displays good electrocatalytic activity to reduce hydrogen peroxide. During the preparation of **1**, the use of $Sr^{2+}$ ions led to the successful isolation of this new hybrid compound, which can serve as a basis for a new type of POM building block. Future efforts will be focused on the reactions between various functional organic–metal fragments and the basket-shaped polyoxoanion to obtain more $[Sr\subset P_6Mo_{18}O_{73}]$-based compounds. Furthermore, the templating effect of $Sr^{2+}$ may also play an important role in the formation of $[Sr\subset P_6Mo_{18}O_{73}]^{10-}$; thus, other alkaline earth metal ions such as $Ca^{2+}$ and $Ba^{2+}$ will be introduced into this reaction system to check whether this templating effect could be reproduced.

## Experimental Section

**Materials:** All chemicals purchased were of reagent grade and used without further purification.

**Physical Methods:** Elemental analyses (C, H, N) were performed with a Perkin–Elmer 2400 CHN elemental analyzer. Mo, Cu, P, and Sr were determined with a Leaman inductively coupled plasma (ICP) spectrometer. IR spectrum was recorded in the range 400–4000 cm$^{-1}$ with an Alpha Centaurt FT/IR spectrophotometer with a pressed KBr pellet. Diffuse reflectance UV/Vis spectrum ($BaSO_4$ pellet) was obtained with a Varian Cary 500 UV/Vis NIR spectrometer. X-ray photoelectron spectrum (XPS) analyses were performed with a VG ESCALAB MK II spectrometer with a Mg-$K_\alpha$ (1253.6 eV) achromatic X-ray source. The vacuum inside the analysis chamber was maintained at $6.2\times10^{-6}$ Pa during analysis. Magnetic susceptibility measurements were carried out with the use of a Quantum Design SQUID MPMS-XL susceptometer. DC measurements were conducted from 1.8 to 300 K by using a 1-T field and performed on finely ground polycrystalline samples. The magnetic data were corrected for the diamagnetic contribution calculated from Pascal's constants.[25] TG analysis was performed with a Perkin–Elmer TGA7 instrument in flowing $N_2$ with a heating rate of 10 °C min$^{-1}$. The electrochemical measurement was carried out on a CHI 660 electrochemical workstation at room temperature (25–30 °C).

**1-Modified Carbon Paste Electrode (1-CPE):** Graphite powder (1.0 g) and compound **1** (40 mg) were mixed and ground together with an agate mortar and pestle to achieve an even and dry mixture. Nujol (0.66 mL) was then added to the mixture and stirred with a glass rod. The homogenized mixture was used to pack glass tubes with a 3-mm inner diameter, and the surface was wiped with weighing paper. Electrical contact was established with a copper rod through the back of the electrode. Platinum gauze was used as the counter electrode and an SCE as the reference electrode.

**Compound 1:** A mixture of $Na_2MoO_4{\cdot}2H_2O$ (0.930 g), $CuCl_2{\cdot}2H_2O$ (0.204 g), phen (0.216 g), $H_3PO_4$ (0.838 mL, 85 wt.-%), and $SrCl_2$ (0.317 g) in a molar ratio of 1.00:0.30:0.30:4.80:0.50 was dissolved in $H_2O$ (16 mL) and stirred at room temperature for 30 min. During this period, the pH value of the solution was adjusted to ca. 3.5 with a solution of NaOH (1 M). The final mixture was sealed in a 30-mL Teflon-lined stainless steel reactor and heated at 160 °C for 4 d. The dark-blue crystals were isolated and collected by filtration, washed thoroughly with distilled water, and dried at room temperature. Yield: 65% (based on Mo). $C_{60}H_{62}Cu_5Mo_{18}N_{10}O_{84}P_6Sr$ (4585.26): calcd. C 15.72, H 1.36, N 3.05, P 4.05, Cu 6.93, Mo 37.66, Sr 1.91; found C 15.79, H 1.42, N 3.11, P 3.99, Cu 7.01, Mo 37.69, Sr 1.87.

**X-ray Crystallography:** Single crystal of **1** with the size of $0.27\times0.25\times0.23$ mm was mounted on a glass fiber, and the data were collected with a Bruker SMART CCD diffractometer with graphite-monochromated Mo-$K_\alpha$ radiation ($\lambda$ = 0.71073 Å). Semi-empirical absorption correction based on symmetry equivalent reflections was applied. A total of 41645 reflections were collected, of which 19453 reflections were unique [$R$(int) = 0.0516]. The structure was solved by direct methods and refined by the full-matrix least-squares method based on $F^2$. Structure solution, refinement, and generation of publication materials were performed with the use of the SHELXTL crystallographic software package.[26] During the refinement, the [Cu(4)(phen)($H_2O$)] unit is disordered in two

Table 2. Crystal data and structure refinement for **1**.

| | |
|---|---|
| Chemical formula | $C_{60}H_{62}Cu_5Mo_{18}N_{10}O_{84}P_6Sr$ |
| Formula weight | 4585.26 |
| Crystal system | triclinic |
| Space group | $P\bar{1}$ |
| $a$ [Å] | 13.778(3) |
| $b$ [Å] | 19.267(4) |
| $c$ [Å] | 24.168(5) |
| $\alpha$ [°] | 110.64(3) |
| $\beta$ [°] | 90.31(3) |
| $\gamma$ [°] | 110.02(3) |
| $V$ [Å$^3$] | 5582.8(19) |
| $Z$ | 2 |
| $D_{calcd.}$ [mg m$^{-3}$] | 2.728 |
| Absorption coefficient [mm$^{-1}$] | 3.554 |
| $T$ [K] | 293(2) |
| Reflections collected/unique | 41645/19453 [$R$(int) = 0.0516] |
| Goodness of fit on $F^2$ | 1.022 |
| $R_1$[a] | 0.0497 |
| $wR_2$[b] | 0.1394 |

[a] $R_1 = \Sigma||F_o| - |F_C||/\Sigma|F_o|$. [b] $wR_2 = \Sigma[w(F_o^2 - F_c^2)^2]/\Sigma[w(F_o^2)^2]^{1/2}$.

 © 2007 Wiley-VCH Verlag GmbH & Co. KGaA, Weinheim 

positions with the site occupancies of 44 and 56%, respectively. All non-hydrogen atoms were refined with anisotropic parameters. The H atoms on the C atoms of phen were included in calculated positions with the use of a riding model and refined with fixed isotropic thermal parameters. The H atoms on water molecules were not included and just put into the final molecular formula. The largest residual peak (2.494 e$Å^{-3}$) is near the phen group but featureless, Q1···C46 0.583 Å. The deepest hole is –1.737 e$Å^{-3}$, which is close to the Mo8 atom. A summary of the crystal data is presented in Table 2. Atomic coordinates and isotropic displacement parameters for **1** are listed in Table S1, and selected bond lengths and angles are listed in Table S2. CCDC-642168 contains the supplementary crystallographic data for this paper. These data can be obtained free of charge from The Cambridge Crystallographic Data Centre via www.ccdc.cam.ac.uk/data_request/cif.

**Supporting Information** (see footnote on the first page of this article): Additional structural figures and packing arrangement views of **1**, additional XPS spectra, IR spectrum, TG curve, and CV analyses for compound **1**.

## Acknowledgments

This work was supported by the National Natural Science Foundation of China (grant no. 20371014, 20671026, and 20701005) and Science Foundation for Young Teachers of Northeast Normal University (grant no. 20070302/20070312).

[1] a) P. Gouzerh, A. Proust, *Chem. Rev.* **1998**, *98*, 77–111; b) P. Gouzerh, R. Villanneau, R. Delmont, A. Proust, *Chem. Eur. J.* **2000**, *6*, 1184–1192; c) Special Issue on Polyoxometalates: C. L. Hill (Ed.), *Chem. Rev.* **1998**, *98*, 1–390; d) M. T. Pope, A. Müller (Eds.), *Polyoxometalate Chemistry: From Topology via Self-Assembly to Applications*, Kluwer, Dordrecht, The Netherlands, **2001**; e) T. Yamase, M. T. Pope (Eds.), *Polyoxometalate Chemistry for Nano-Composite Design*, Kluwer, Dordrecht, The Netherlands, **2002**; f) D. L. Long, E. Burkholder, L. Cronin, *Chem. Soc. Rev.* **2007**, *36*, 105–121; g) E. Coronado, C. Gimenez-Saiz, C. J. Gomez-Garcia, *Coord. Chem. Rev.* **2005**, *249*, 1776–1796.

[2] a) P. J. Hagrman, D. Hagrman, J. Zubieta, *Angew. Chem. Int. Ed.* **1999**, *38*, 2638–2684; b) E. Burkholder, V. Golub, C. J. O'Connor, J. Zubieta, *Inorg. Chem.* **2003**, *42*, 6729–6740; c) E. Burkholder, V. Golub, C. J. O'Connor, J. Zubieta, *Inorg. Chem.* **2004**, *43*, 7014–7029.

[3] a) S. Bareyt, S. Piligkos, B. Hasenknopf, P. Gouzerh, E. Lacôte, S. Thorimbert, M. Malacria, *Angew. Chem. Int. Ed.* **2003**, *42*, 3404–3406; b) B. J. S. Johnsn, R. C. Schroden, C. C. Zhu, A. Stein, *Inorg. Chem.* **2001**, *40*, 801–808.

[4] a) Z. Peng, *Angew. Chem. Int. Ed.* **2004**, *43*, 930–935; b) J. Kang, B. Xu, Z. Peng, X. Zhu, Y. Wei, D. R. Powell, *Angew. Chem. Int. Ed.* **2005**, *44*, 6902–6905.

[5] a) X. K. Fang, T. M. Anderson, C. L. Hill, *Angew. Chem. Int. Ed.* **2005**, *44*, 3540–3543; b) X. K. Fang, T. M. Anderson, Y. Hou, C. L. Hill, *Chem. Commun.* **2005**, 5044–5046; c) B. Godin, J. Vaissermann, P. Herson, L. Ruhlmann, M. Verdaguer, P. Gouzerh, *Chem. Commun.* **2005**, 5624–5626.

[6] a) X. L. Wang, C. Qin, E. B. Wang, Z. M. Su, Y. G. Li, L. Xu, *Angew. Chem. Int. Ed.* **2006**, *45*, 7411–7414; b) H. Y. An, E. B. Wang, D. R. Xiao, Y. G. Li, Z. M. Su, L. Xu, *Angew. Chem. Int. Ed.* **2006**, *45*, 904–907.

[7] a) C. Y. Sun, Y. G. Li, E. B. Wang, D. R. Xiao, H. Y. An, L. Xu, *Inorg. Chem.* **2007**, *46*, 1563–1574; b) J. Lu, E. H. Shen, M. Yuan, Y. G. Li, E. B. Wang, C. W. Hu, L. Xu, J. Peng, *Inorg. Chem.* **2003**, *42*, 6956–6958; c) Y. G. Li, G. De, M. Yuan, E. B. Wang, R. D. Huang, C. W. Hu, N. H. Hu, H. Q. Jia, *Dalton Trans.* **2003**, 331–334.

[8] a) S.-T. Zheng, D.-Q. Yuan, H.-P. Jia, J. Zhang, G.-Y. Yang, *Chem. Commun.*, DOI: 10.1039/b617191e; b) C.-M. Wang, S.-T. Zheng, G.-Y. Yang, *Inorg. Chem.* **2007**, *46*, 616–618.

[9] a) Y. Xu, J. Q. Xu, K. L. Zhang, Y. Zhang, X. Z. You, *Chem. Commun.* **2000**, 153–154; b) G. Y. Luan, Y. G. Li, S. T. Wang, E. B. Wang, Z. B. Han, C. W. Hu, N. H. Hu, H. Q. Jia, *Dalton Trans.* **2003**, 233–235; c) J. P. Wang, P. T. Ma, J. Y. Niu, *Inorg. Chem. Commun.* **2006**, *9*, 1049–1052; d) L. L. Fan, E. B. Wang, Y. G. Li, H. Y. An, D. R. Xiao, X. L. Wang, *J. Mol. Struct.*, DOI: 10.1016/j.molstruc.2006.11.059; e) A. X. Tian, Z. G. Han, J. Peng, B. X. Dong, J. Q. Sha, B. Li, *J. Mol. Struct.* **2007**, *832*, 117–123.

[10] a) M. Yuan, Y. G. Li, E. B. Wang, C. G. Tian, L. Wang, C. W. Hu, N. H. Hu, H. Q. Jia, *Inorg. Chem.* **2003**, *42*, 3670–3676; b) Y. P. Bai, Y. G. Li, E. B. Wang, X. L. Wang, Y. Lu, L. Xu, *J. Mol. Struct.* **2005**, *752*, 54–59; c) Y. Lu, Y. Xu, E. B. Wang, J. Lü, C. W. Hu, L. Xu, *Cryst. Growth Des.* **2005**, *5*, 257–260; d) H. Jin, Y. F. Qi, E. B. Wang, Y. G. Li, X. L. Wang, C. Qin, S. Chang, *Cryst. Growth Des.* **2006**, *6*, 2693–2698.

[11] a) M. Yuan, E. B. Wang, Y. Lu, Y. G. Li, C. W. Hu, N. H. Hu, H. Q. Jia, *J. Solid State Chem.* **2003**, *170*, 192–197; b) Y. Ma, Y. G. Li, E. B. Wang, Y. Lu, X. L. Wang, X. X. Xu, *J. Solid State Chem.* **2006**, *179*, 2367–2375; c) R. D. Huang, F. C. Liu, Y. G. Li, M. Yuan, E. B. Wang, G. De, C. W. Hu, N. H. Hu, H. Q. Jia, *Inorg. Chim. Acta* **2003**, *349*, 85–90; d) L. Xu, Y. Q. Sun, E. B. Wang, E. H. Shen, Z. R. Liu, C. W. Hu, Y. Xing, Y. H. Lin, H. Q. Jia, *New J. Chem.* **1999**, *23*, 1041–1044.

[12] a) Y. Ma, Y. Lu, E. B. Wang, X. X. Xu, Y. Q. Guo, X. L. Bai, L. Xu, *J. Mol. Struct.* **2006**, *784*, 18–23; b) Y. Lu, Y. G. Li, E. B. Wang, J. Lü, L. Xu, R. Clérac, *Eur. J. Inorg. Chem.* **2005**, *7*, 1239–1244; c) Y. Lu, J. Lü, E. B. Wang, Y. Q. Guo, X. X. Xu, L. Xu, *J. Mol. Struct.* **2005**, *740*, 159–163.

[13] X. M. Zhang, H. S. Wu, F. Q. Zhang, A. Prikhod'ko, S. Kuwata, P. Comba, *Chem. Commun.* **2004**, 2046–2047.

[14] C. Peloux, A. Dolbecq, P. Mialane, J. Marrot, E. Rivière, F. Sécheresse, *Angew. Chem. Int. Ed.* **2001**, *40*, 2455–2457.

[15] C. Peloux, P. Mialane, A. Dolbecq, J. Marrot, F. Sécheresse, *Angew. Chem. Int. Ed.* **2002**, *41*, 2808–2810.

[16] a) J. Gopalakrishnan, *Chem. Mater.* **1995**, *7*, 1265–1275; b) S. H. Feng, R. R. Xu, *Acc. Chem. Res.* **2001**, *34*, 239–247; c) L. M. Zheng, T. Whitfield, X. Wang, A. J. Jacobson, *Angew. Chem. Int. Ed.* **2000**, *39*, 4528–4531; d) P. R. Hagrman, R. L. LaDuca, H.-J. Koo, R. Rarig, R. C. Haushalter, M.-H. Whangbo, J. Zubieta, *Inorg. Chem.* **2000**, *39*, 4311–4317.

[17] The crystal data of the unpublished compound cannot be successfully collected and solved owing to its poor crystal quality. The initial cell is $a$ = 14.72 Å, $b$ = 22.12 Å, $c$ = 25.13 Å, $\alpha$ = 89.98°, $\beta$ = 98.61°, $\gamma$ = 90.05°, $V$ = 8115 $Å^3$. Elemental analysis: Mo:Cu:P ≈ 4:1:0.33. The primary results of the compound are similar to the reported compound in ref.[10a]

[18] D.-L. Long, H. Abbas, P. Kogerler, L. Cronin, *J. Am. Chem. Soc.* **2004**, *126*, 13880–13881.

[19] I. D. Brown, D. Altermatt, *Acta Crystallogr., Sect. B* **1985**, *41*, 244–247.

[20] a) M. T. Pope, *Heteropoly and Isopoly Oxometalates*, Springer, Berlin, **1983**, pp. 8, 109; b) B. DasGupta, C. Katz, T. Israel, M. Watson, L. Zompa, *Inorg. Chim. Acta* **1999**, *292*, 172–181.

[21] a) T. A. Patterson, J. C. Carver, D. E. Leyden, D. M. Hercules, *J. Phys. Chem.* **1976**, *80*, 1700–1708; b) M. Imamura, N. Matsubayashi, H. Shimada, *J. Phys. Chem. B* **2000**, *104*, 7348–7353; c) S. Gonzalez, M. Perez, M. Barrera, A. R. Gonzalez Elipe, R. M. Souto, *J. Phys. Chem. B* **1998**, *102*, 5483–5489.

[22] a) D. C. Duncan, C. L. Hill, *Inorg. Chem.* **1996**, *35*, 5828–5835; b) E. Dumas, C. Debiemme-Chouvy, S. C. Sevov, *J. Am. Chem. Soc.* **2002**, *124*, 908–909.

 © 2007 Wiley-VCH Verlag GmbH & Co. KGaA, Weinheim 

[23] a) X. L. Wang, Z. H. Kang, E. B. Wang, C. W. Hu, *J. Electroanal. Chem.* **2002**, *523*, 142–149; b) X. L. Wang, Z. H. Kang, E. B. Wang, C. W. Hu, *Mater. Lett.* **2002**, *56*, 393–396.
[24] D. Martel, A. Kuhn, *Electrochim. Acta* **2000**, *45*, 1829–1836.
[25] E. A. Boudreaux, L. N. Mulay (Eds.), *Theory and Applications of Molecular Paramagnetism*, John Wiley & Sons, New York, **1976**.
[26] a) G. M. Sheldrick, *SHELXL97: Program for Crystal Structure Refinement*, University of Göttingen, Germany, **1997**; b) G. M. Sheldrick, *SHELXS97: Program for Crystal Structure Solution*, University of Göttingen, Germany, **1997**.

Received: April 3, 2007
Published Online: October 31, 2007

 © 2007 Wiley-VCH Verlag GmbH & Co. KGaA, Weinheim 

DOI: 10.1002/ejic.200700680

# Synthesis and Magnetic Study of $\mu_{1,1}$-Azido-Bridged Dinuclear Manganese(II) Complexes Based on Tripyridyl Ligands

**Ming-Ming Yu,[a] Zhong-Hai Ni,[a] Chong-Chao Zhao,[a] Ai-Li Cui,[a] and Hui-Zhong Kou*[a]**

**Keywords:** Manganese / Dinuclear complexes / Crystal structures / Magnetic properties / Azido bridge

Three azido-bridged $Mn^{II}$ complexes of formulas $[Mn_2(N_3)_4(ttp)_2]$ (**1**), $[Mn_2(N_3)_4(ttp\text{-}N_3)_2]$ (**2**) and $[Mn_2(N_3)_4(ttp\text{-}N_3)_2]_3[Mn^{III}(ttp\text{-}N_3)(N_3)_3]_2$ (**3**), where ttp and ttp-$N_3$ represent 4′-*p*-tolyl-2,2′:6′,2′′-terpyridine and 4′-*p*-azidomethylphenyl-2,2′:6′,2′′-terpyridine, were synthesized and characterized by single-crystal X-ray diffraction analysis and magnetic studies. The Mn ions in complexes **1** and **2** are coordinated by three N atoms of the ttp or ttp-$N_3$ ligands, and they are connected by double end-on (EO) azide ligands; this forms a dinuclear $Mn^{II}$ system with Mn–N–Mn bridging angles of 103.5 and 103.1°. The Br atoms of the $–CH_2Br$ ligands were replaced by azido groups during the formation of complexes **2** and **3**. The structure of complex **3** comprises two structurally similar $Mn^{II}$ dimers with double end-on bridging azide groups and one mononuclear $Mn^{III}$ structure. The bridging Mn–N–Mn angles in **3** are 104.2, 105.1, and 106.73°. Magnetic studies indicate the presence of intramolecular ferromagnetic superexchange. The strength of ferromagnetic coupling within the $Mn_2$ cores in **1**–**3** is dependent on the Mn–N–Mn bridging angles. The magnetic coupling constants for intermolecular exchange are 2.46(4), 2.25(2), and 1.92(4) $cm^{-1}$ for **1**, **2**, and **3**, respectively, on the basis of Hamiltonian $\hat{H} = -2J\hat{S}_1\hat{S}_2$.

(© Wiley-VCH Verlag GmbH & Co. KGaA, 69451 Weinheim, Germany, 2007)

## Introduction

During the last two decades chemists have been interested in the azido ligand for its versatile coordination modes and remarkable ability to transmit ferro- or antiferromagnetic interactions.[1] The azido ligand is able to bridge metal ions in several forms, including the usual μ-1,1 (end-on, EO) or μ-1,3 (end-to-end, EE) mode[2] and the unusual μ-1,1,3, μ-1,1,1, μ-1,1,1,1, μ-1,1,3,3 or μ-1,1,1,3,3,3 modes.[3–6] EE bridging usually transmits antiferromagnetic interactions between the metallic centers, whereas EO bridging is known to transmit ferromagnetic interactions irrespective of what metal ions are involved.[7] The theory of spin polarization developed by Kahn et al.[8] has been used to interpret the magnetic interaction through the azido group in $Cu^{II}$, $Ni^{II}$, and $Mn^{II}$ systems.[9] Many studies concerning the ferromagnetic interactions in $Cu^{II}$ and $Ni^{II}$ end-on azido systems have been carried out extensively, and structure parameters, especially bridging angle, were found to be the main factors controlling the strength of the ferromagnetic interaction.[10–13] For $Mn^{II}$ systems with only end-on azido bridges, examples are limited.[14,15] Recently, Aromí et al. found that there is a linear relationship between the exchange coupling constant ($J$) and the Mn–N–Mn bridging angle ($\theta$) on the basis of results obtained for only four complexes.[15a] We then prepared a series of end-on azido-bridged $Mn^{II}$ complexes with the $[Mn_2(phen)_4(N_3)_2]^{2+}$ core and improved the $J$–$\theta$ relationship.[15b] Apparently, more effort should be exerted to make the assumption of the relation of $J$ and $\theta$ more clear. Herein, we describe the syntheses, structures, and magnetic properties of three dinuclear $Mn^{II}$ compounds with tridentate 4′-*p*-tolyl-2,2′:6′,2′′-terpyridine (ttp) and 4′-*p*-bromomethylphenyl-2,2′:6′,2′′-terpyridine (ttp-Br) ligands. Interestingly, the Br atoms in the ttp-Br ligands were replaced by azido groups to give the new 4′-*p*-azidomethylphenyl-2,2′:6′,2′′-terpyridine (ttp-$N_3$) ligand, which then goes on to form complexes $[Mn_2(N_3)_4(ttp\text{-}N_3)_2]$ (**2**) and $[Mn_2(N_3)_4(ttp\text{-}N_3)_2]_3[Mn(ttp\text{-}N_3)(N_3)_3]_2$ (**3**). The bridging Mn–N–Mn angle of complex **3** is the largest hitherto found in double EO azido-bridged dimeric $Mn^{II}$ complexes.

## Results and Discussion

### Synthesis and General Characterization

Tridentate ttp-type ligands are analogous to the commonly used 2,2′:6′,2′′-terpyridine (terpy) ligand. Previously, Rojo et al. reported an end-on azide-bridged $Mn^{II}$ dimer $[Mn_2(terpy)_2(\mu_{1,1}\text{-}N_3)_2(N_3)_2]\cdot 2H_2O$.[14a] This complex has a bridging Mn–N–Mn angle of 104.6°, which is the

[a] Department of Chemistry, Tsinghua University, Beijing 100084, People's Republic of China
Fax: +86-10-62771748
E-mail: kouhz@mail.tsinghua.edu.cn

Supporting information for this article is available on the WWW under http://www.eurjic.org/ or from the author.

 © 2007 Wiley-VCH Verlag GmbH & Co. KGaA, Weinheim 

largest among the reported EO azido-bridged dimeric $Mn^{II}$ complexes. In this work, we used ttp-type ligands in the hope of obtaining similar dimeric complexes. Complexes **1**–**3** were prepared and characterized. They have EO azido-bridged dimeric structures that are similar to $[Mn_2(terpy)_2(\mu_{1,1}\text{-}N_3)_2(N_3)_2]\cdot 2H_2O$.[14a] Interestingly, a 1D polymeric $Mn^{II}$ complex, $[Mn(tptz)(\mu_{1,1}\text{-}N_3)_2]_n$[16] [tptz = 2,4,6-tris(2-pyridyl)-1,3,5-triazine], was synthesized with the tptz ligand that is similar to ttp. During the preparation of complexes **2** and **3**, ttp-$N_3$ formed in situ by substitution of the bromo group by an azido group (Scheme 1). In organic synthesis, sodium azide is often used as a reactant to substitute bromoalkyl groups.[17] However, the substitution reaction of an azido group accompanied by crystallization of metallic complexes is rare. It is known that azide can stabilize divalent transition-metal ions when neutral pyridyl reagents are used as auxiliary ligands. We found that tripyridyl $Mn^{II}$ can be slowly oxidized by oxygen dissolved in the solvent. The exposure to light accelerates the oxidation process. The formed neutral $[Mn(ttp\text{-}N_3)(N_3)_3]$ monomer cocrystallized with the $Mn^{II}$ dimer in **3**.

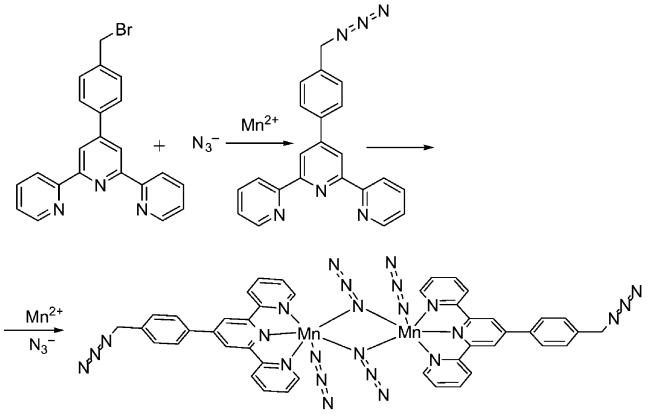


Scheme 1. Possible formation mechanism of ttp-$N_3$ and complex **2**.

The IR spectra of three complexes show a strong peak at ca. 1600 $cm^{-1}$, which is assigned to the C=N stretching vibration in the pyridine rings of the ligands. The $\nu_{asym}(N_3^-)$ mode of complexes **1**–**3** appear at ca. 2000–2100 $cm^{-1}$. The splitting of the signals indicates the presence of both bridging and terminal azide ligands. The peaks at 2093 $cm^{-1}$ for complex **2** and 2086 $cm^{-1}$ for complex **3** should be assigned to the alkyl azido asymmetric stretching vibration.[17] The peak at 2037 $cm^{-1}$ for complex **3** may be due to the $\nu_{asym}(N_3^-)$ mode of the $[Mn^{III}(ttp\text{-}N_3)(N_3)_3]$ moiety by considering that the $[Mn^{III}(terpy)(N_3)_3]$ analog exhibits a strong band at 2035 $cm^{-1}$.[18] In addition, azido complexes are expected to show $\nu_{sym}(N_3^-)$ and deformation mode $\delta(N_3^-)$ at ca. 1300–1350 and ca. 620 $cm^{-1}$, respectively.[18] For complexes **1**–**3**, only the symmetric azide stretching vibration was observed as a medium signal.

Complexes **1**, **2**, and **3** are slightly soluble in MeCN, but they are not soluble in alcohol solvents. The electronic spectra of compounds **2** and **3** in MeCN are similar and a shoulder band at 400–450 nm is apparent; this shoulder is responsible for the color of the compounds. The spectrum of **1** in MeCN shows no apparent absorption in the visible region, which is consistent with the light color of the complex. Relative to the spectra of the ttp and ttp-Br ligands, the UV absorptions related to the n–π* or π–π* transitions within the ligands show an obvious redshift, which is due to better planarity of the tripyridyl group accompanied by chelation to $Mn^{II}$ ions (see the Supporting Information).

## Crystal Structure of Complexes 1, 2, and 3

Crystal data are summarized in Table 1. Selected bond lengths and angles of complexes **1**, **2**, and **3** are included in Table 2. ORTEP representations of the crystallographic molecular structure of complexes **1**, **2**, and **3** are shown in Figures 1, 2, and 3.

Table 1. Crystallographic data for complexes **1**, **2**, and **3**.

| | **1** | **2** | **3** |
|---|---|---|---|
| Chemical formula | $C_{44}H_{34}N_{18}Mn_2$ | $C_{44}H_{32}N_{24}Mn_2$ | $C_{176}H_{128}N_{102}Mn_8$ |
| *Fw* | 924.77 | 1006.82 | 4111.32 |
| *T* / K | 293 | 293 | 293 |
| Crystal system | monoclinic | monoclinic | monoclinic |
| Space group | $P2_1/c$ | $P2_1/c$ | $P2_1/c$ |
| *a* / Å | 8.608(2) | 14.725(3) | 14.757(3) |
| *b* / Å | 10.371(2) | 13.230(3) | 14.883(3) |
| *c* / Å | 23.806(5) | 11.751(2) | 22.828(5) |
| *α* / ° | 90 | 90 | 78.40(3) |
| *β* / ° | 92.74(3) | 97.01(3) | 78.78(3) |
| *γ* / ° | 90 | 90 | 69.47(3) |
| *V* / Å$^3$ | 2122.8(7) | 2272.2(8) | 4557.1(16) |
| *Z* | 2 | 2 | 1 |
| $\rho_{calcd}$ / g cm$^{-3}$ | 1.447 | 1.472 | 1.498 |
| *F*(000) | 948 | 1028 | 2098 |
| GOF (*S*) | 1.054 | 1.050 | 1.044 |
| Data/restraints/paras | 4824/0/290 | 9769/0/281 | 15905/15/1288 |
| $R_1$ [$I>2\sigma(I)$] | 0.0322 | 0.0559 | 0.0507 |
| $wR_2$ (all data) | 0.0930 | 0.1093 | 0.1472 |

Complexes **1** and **2** exhibit centrosymmetric dimers $[Mn(N_3)_2(ttp)]_2$ or $[Mn(N_3)_2(ttp\text{-}N_3)]_2$, respectively. The $Mn^{II}$ ions in complexes **1** and **2** are linked by double end-on bridging azide groups. The other two azide moieties act as terminal ligands. In complex **1**, each Mn ion exhibits a slightly distorted octahedral coordination sphere and the three nitrogen atoms of the terpy ligand [Mn1–N1: 2.269(1) Å, Mn1–N2: 2.224(1) Å, Mn1–N3: 2.279(2) Å] and the nitrogen atom of one bridging azide group [Mn1–N4A: 2.127(1) Å (A: 2 –*x*, – y, 1 – *z*)] form the equatorial plane. The nitrogen atom of one terminal azido group [Mn1–N7: 2.153(2) Å] and the nitrogen atom of the second bridging group [Mn1–N4: 2.363(2) Å] are situated in the axial positions. The existence of an inversion center causes the Mn–N4–Mn1A–N4A bridging unit to form a plane. In this dimeric unit, the Mn cations are separated from each other by 3.528(4) Å. The bridging Mn–N4–Mn1A angle is 103.5°. The bridging and terminal azido ligands are quasilinear and the N4–N5–N6 and N7–N8–N9 angles measure 177.03 and 178.22°, respectively.

 © 2007 Wiley-VCH Verlag GmbH & Co. KGaA, Weinheim 

Table 2. Selected bond lengths [Å] and angles [°] for complexes **1**, **2**, and **3**.

| | | | |
|---|---|---|---|
| **1** | | | |
| Mn1–N1 | 2.2689(14) | Mn1–N2 | 2.2238(14) |
| Mn1–N3 | 2.2786(15) | Mn1–N4 | 2.3634(16) |
| Mn1–N4$^{A}$ | 2.1270(14) | Mn1–N7 | 2.1530(17) |
| Mn1$^{A}$–N4–Mn1 | 103.45(6) | | |
| **2** | | | |
| Mn1–N4 | 2.378(3) | N3–Mn1 | 2.274(3) |
| Mn1–N4$^{B}$ | 2.126(3) | N2–Mn1 | 2.213(3) |
| N1–Mn1 | 2.272(3) | N7–Mn1 | 2.180(4) |
| Mn1$^{B}$–N4–Mn1 | 103.13(12) | | |
| **3** | | | |
| Mn1–N1 | 2.331(3) | Mn1–N4 | 2.168(3) |
| Mn1–N7 | 2.135(3) | Mn1–N13 | 2.290(3) |
| Mn1–N14 | 2.223(2) | Mn1–N15 | 2.294(3) |
| Mn2–N1 | 2.191(3) | Mn2–N4 | 2.279(3) |
| Mn2–N10 | 2.147(5) | Mn2–N16 | 2.287(3) |
| Mn2–N17 | 2.239(2) | Mn2–N18 | 2.291(3) |
| Mn3–N28 | 2.244(3) | Mn3–N29 | 2.107(3) |
| Mn3–N30 | 2.248(3) | Mn3–N31 | 1.982(3) |
| Mn3–N34 | 1.951(3) | Mn3–N37 | 1.977(3) |
| Mn4–N19 | 2.279(3) | Mn4–N20 | 2.209(3) |
| Mn4–N21 | 2.296(3) | Mn4–N22 | 2.341(3) |
| Mn4–N22$^{C}$ | 2.143(3) | Mn4–N25 | 2.138(4) |
| Mn1–N4–Mn2 | 106.72(12) | Mn2–N1–Mn1 | 104.20(11) |
| Mn4$^{C}$–N22–Mn4 | 105.11(13) | | |

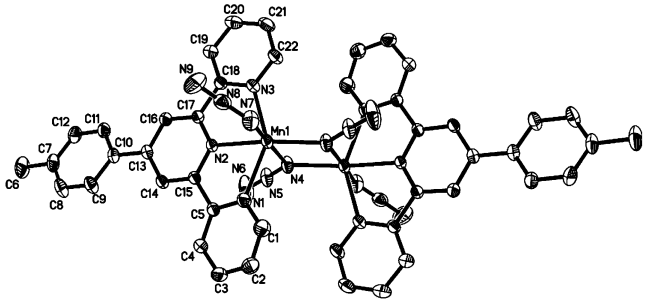


Figure 1. Crystal structure of complex **1**.

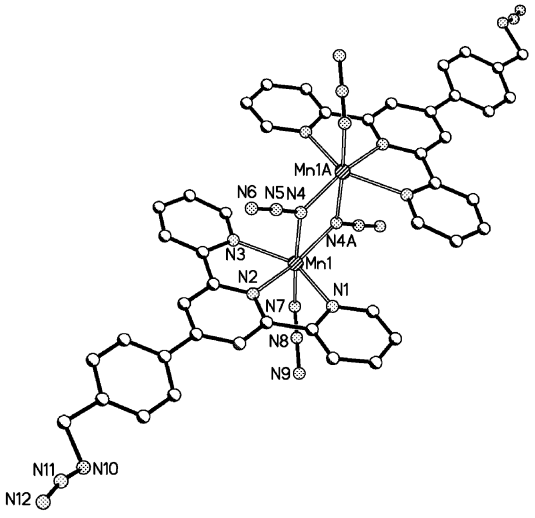


Figure 2. Crystal structure of complex **2**.

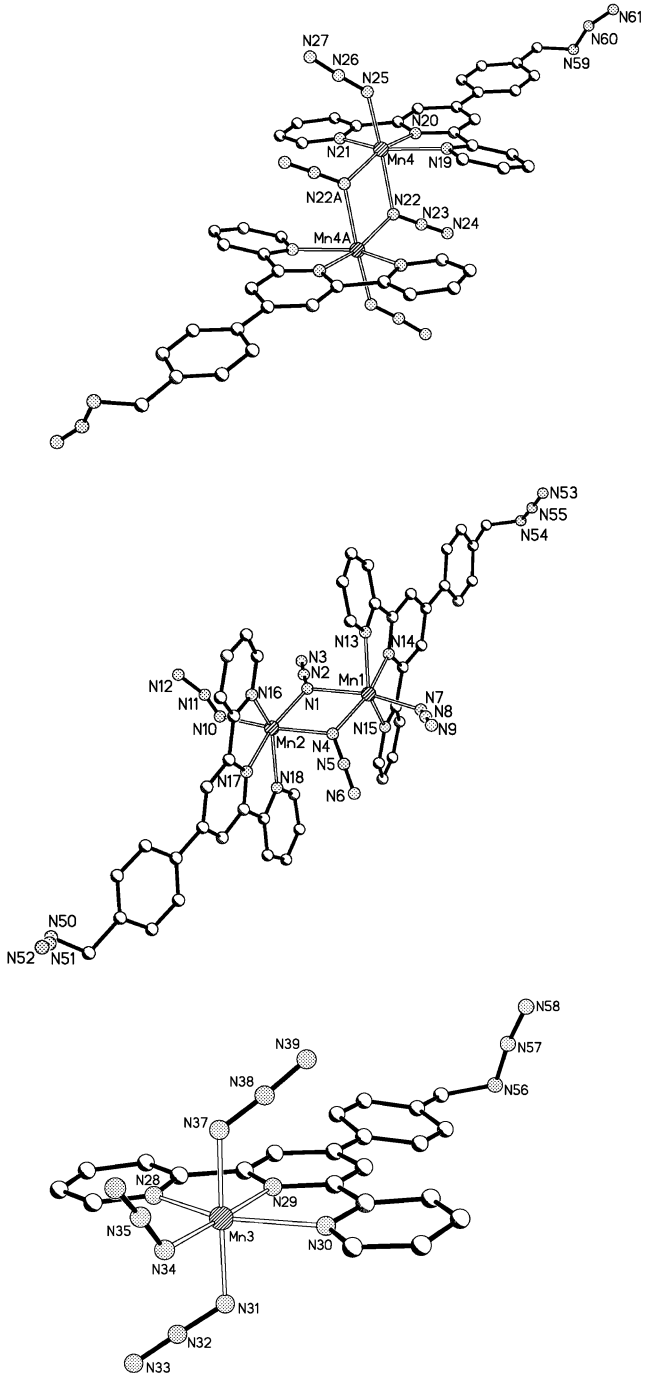


Figure 3. Crystal structure of complex **3** showing three cocrystallized moieties.

In complex **2**, each Mn cation exhibits a distorted octahedral coordination sphere and the Mn–N bond lengths range from 2.126(3) Å [Mn1–N4A (A: 1 –*x*, 1 – *y*, 1 – *z*)] to 2.378(2) Å (Mn1–N4). In this dimeric unit, the Mn cations are separated from each other by 3.532(4) Å with a bridging Mn–N4–Mn1A angle of 103.1°. The bridging and terminal azido ligands are quasilinear [177.29 and 179.90°].

The structure of complex **3** comprises three doubly end-on azide-bridged $Mn^{II}$ dimers and two $Mn^{III}$ monomers. One dimer exhibits a centrosymmetric structure and the

 © 2007 Wiley-VCH Verlag GmbH & Co. KGaA, Weinheim 

other is asymmetric. The dimeric structure is very similar to that of complexes **1** and **2**. In the asymmetric dimer comprised of Mn1 and Mn2, the nitrogen atoms of one terminal azido group [Mn1–N7: 2.135(3) Å] and one bridging group [Mn1–N1: 2.331(3) Å] are situated in the axial positions. The intradimer Mn1···Mn2 distance is 3.569(6) Å, and the bridging Mn1–N1–Mn2 and Mn1–N4–Mn2 bond angles are 104.2 and 106.73°, respectively. In the inversion center related unit, the Mn–N distances are in the range 2.138(4) (Mn4–N25) to 2.341(3) Å (Mn4–N22). In this dimeric unit, the Mn cations are separated from each other by 3.562(3) Å. The bridging azides slightly deviate (up and down) from that plane and the bridging Mn–N4–Mn1A angle is 105.1°. In the neutral $Mn^{III}$ monomer Mn(ttp-$N_3$)$(N_3)_3$, the Mn–N bond lengths range from 1.951(3) to 2.248(3) Å, which is consistent with a $Mn^{III}$ ion with a Jahn–Teller effect for the $d^4$ electronic configuration. The bond lengths and coordination geometry are very similar to those of [Mn(terpy)$(N_3)_3$].[18]

### Magnetic Behavior of Complexes 1, 2, and 3

The $\chi_m T$ vs. $T$ plots (2–300 K) of complexes **1**, **2**, and **3** are shown in Figures 4, 5, and 6, respectively. At 300 K, the $\chi_m T$ values per dimer are 8.762 and 8.904 emu K mol$^{-1}$ for **1** and **2**, respectively, which are both close to the expected value (8.75 emu K mol$^{-1}$) for two uncoupled spin $S_{Mn}$ = 5/2 systems. With decreasing temperature, $\chi_m T$ increases sharply to reach a maximum value of 6.43 emu K mol$^{-1}$ at 8 K for complex **1** and 14.34 emu K mol$^{-1}$ at 9 K for complex **2**; it then decreases because of weak intermolecular antiferromagnetic interaction and/or zero-field splitting of the ground spin state of $S$ = 5. Magnetic susceptibility could be fit to a Curie–Weiss law with Curie constant $C$ = 8.96 emu K mol$^{-1}$ and a positive Weiss constant $\theta$ = 8.68 K for complex **1** and $C$ = 4.08 emu K mol$^{-1}$ and $\theta$ = 7.89 K for complex **2**. These results indicate that the overall magnetic behavior of **1** and **2** is ferromagnetic, which should be attributed to the dinuclear superexchange mediated through the $\mu_{1,1}$-azido bridges. The expression for the magnetic susceptibility ($\chi_d$) of a $Mn^{II}$ dimer derived from Van Vleck's equation (the spin Hamiltonian $\hat{H} = -2J\hat{S}_{Mn1}\hat{S}_{Mn2}$) is expressed in Equation (1), in which $A$ = 55 + 30exp(–10$J$/$kT$) + 14exp(–18$J$/$kT$) + 5exp(–24$J$/$kT$) + exp(–28$J$/$kT$) and $B$= 11 + 9exp(–10$J$/$kT$) + 7exp(–18$J$/$kT$) + 5exp(–24$J$/$kT$) + 3exp(–28$J$/$kT$) + exp(–30$J$/$kT$).

$$\chi_d = \frac{2Ng^2\beta^2}{kT}\frac{A}{B} \quad (1)$$

Considering weak intermolecular antiferromagnetic coupling, the final molar magnetic susceptibility takes the form of Equation (2), where z$J'$ is the interaction between molecules, and the $N$, $g$, $\beta$, and $\theta$ parameters have their usual meaning.

$$\chi_M = \frac{\chi_d}{1-\chi_d(2zJ'/Ng^2\beta^2)} \quad (2)$$

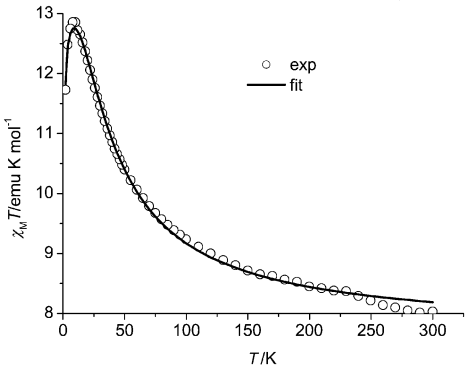


Figure 4. $\chi_m T$ vs. $T$ plot for complex **1**. The solid line represents the best fit.

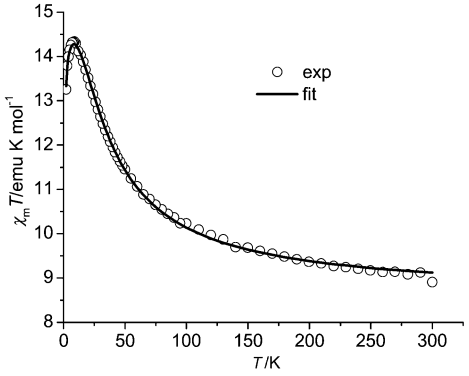


Figure 5. $\chi_m T$ vs. $T$ plot for complex **2**. The solid line represents the best fit.

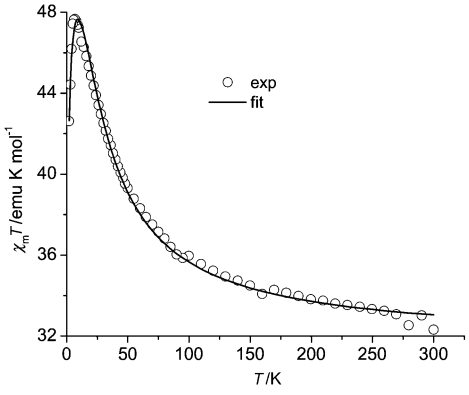


Figure 6. $\chi_m T$ vs. $T$ plot for complex **3**. The solid line represents the best fit.

The best-fit parameters obtained are $J$ = 2.46(4) cm$^{-1}$, $g$ = 1.99(1), and $zJ'$ = –0.0078 cm$^{-1}$ with an agreement factor of $R = \Sigma(\chi_{obsd}T - \chi_{cald}T)^2/\Sigma(\chi_{obsd}T)^2 = 4.24 \times 10^{-5}$ for complex **1** and $J$ = 2.25(2) cm$^{-1}$, $g$ = 1.98(1), $zJ'$ = –0.0072(3) cm$^{-1}$ and $R = 2.03 \times 10^{-5}$ for complex **2**.

The decrease in $\chi_m T$ at low temperature could be alternatively interpreted by the presence of zero-field splitting (ZFS) of the spin ground state $S_T$ = 5. The data were fit to a model that includes the energy splitting of the ground spin state. By using a modified term of the Heisenberg spin Hamiltonian of a dinuclear system ($\hat{H} = -2J\hat{S}_1\hat{S}_2$) as $\hat{H}_{ZFS}$

 © 2007 Wiley-VCH Verlag GmbH & Co. KGaA, Weinheim 

$= D[\hat{S}_{Tz}^2 - S_T(S_T+1)/3]$, the expression for the magnetic susceptibility of ferromagnetically coupled $Mn^{II}$ dimer is depicted in Equation (3),[15c] where $A = 6\exp(9D/kT) + 24\exp(6D/kT)+54\exp(D/kT) + 96\exp(-6D/kT) + 150\exp(-15D/kT) + 180\exp(-10J/kT) + 84\exp(-18J/kT) + 30\exp(-24J/kT) + 6\exp(-28J/kT)$, $B = \exp(10D/kT) + 2\exp(9D/kT) + 2\exp(6D/kT) +2\exp(D/kT) + \exp(-6D/kT) + 2\exp(-15D/kT) + 9\exp(-10J/kT) + 7\exp(-18J/kT) + 5\exp(-24J/kT) + 3\exp(-28J/kT) +\exp(-30J/kT)$.

$$\chi_M = \frac{Ng^2\beta^2}{3kT}\frac{A}{B} \quad (3)$$

The least-square fit of the experimental data to the above expression gives the following parameters: $J = 2.46(2)\ cm^{-1}$, $g = 1.99(1)$, $D = 0.019(1)\ cm^{-1}$, and $R = 4.10\times10^{-5}$ for complex **1** and $J = 2.26(2)\ cm^{-1}$, $g = 1.98(1)$, $D = 0.017(1)\ cm^{-1}$, and $R = 2.02\times10^{-5}$ for complex **2**.

The best-fit results including intermolecular interaction or zero-field splitting are very similar. Both effects are likely operative with similar strength, and it is impossible to distinguish between them.[15c]

At 300 K, the $\chi_m T$ value of complex **3** is ca. 33.0 emu K $mol^{-1}$, which is close to that (32.25 emu K $mol^{-1}$) expected for an uncoupled system ($6Mn^{II} + 2Mn^{III}$). With a decrease in the temperature, the $\chi_m T$ values increase sharply to reach a maximum value of 47.66 emu K $mol^{-1}$ at 7 K, and then they decreases to 42.62 emu K $mol^{-1}$ at 2 K due to weak antiferromagnetic interaction and/or zero-field splitting. These results indicate that the overall behavior of **3** corresponds to a ferromagnetic interaction, which should be attributed to the dinuclear superexchange mediated through the $\mu_{1,1}$-azido bridges. Magnetic susceptibility could be fit to a Curie–Weiss law with Curie constant $C =$ 32.57 emu K $mol^{-1}$ and a positive Weiss constant $\theta =$ 6.25 K. The positive $\theta$ value and the shape of the $\chi_m T$ curves for **3** indicate the existence of ferromagnetic interactions between double EO azido-bridged $Mn^{II}$ ions.

Taking the contributions of intermolecular interaction and the $Mn^{III}$ monomers into account and using one $J$ value for simplicity, the final molar magnetic susceptibility is in the form of Equation (4), where $\chi_{dimer}$ is the expression including both $J$ and $zJ'$ for complexes **1** and **2**.

$$\chi_M = 3\chi_{dimer} + \frac{4Ng^2\beta^2}{kT} \quad (4)$$

The least-square fit of the experimental data gives the following parameters: $J = 1.92(4)\ cm^{-1}$, $g = 1.98(1)$, $zJ' = -0.0019(4)\ cm^{-1}$, and $R = 5.47\times10^{-5}$ for complex **3**.

Field dependence of the magnetization at 2 K of complexes **1**, **2**, and **3** are shown in the Supporting Information. Experimental data fit well to the Brillouin function value for $S = 5$, and are well above that for two noncoupling $S =$ 5/2 $Mn^{II}$ ions, which indicates the existence of ferromagnetic interactions between double EO azido-bridged $Mn^{II}$ ions. For complex **3**, the $Mn^{III}$ monomers ($S_{Mn^{III}} = 2$) should be included when calculating the Brillouin curve, that is, $S = 5\times3 + 2\times2$ and noninteracting $S = 6\times5/2 + 2\times2$, respectively. The experimental data for **3** are above the Brillouin curve for $S = 6\times5/2 + 2\times2$ at low magnetic field (<20 kOe), and they are below that for $S = 5\times3 + 2\times2$. The discrepancy in **3** compared with complexes **1** and **2** is assigned to the presence of $Mn^{III}$ ions, and it is usually difficult to reach magnetic saturation because of magnetic anisotropy.[19]

The above results could be interpreted by the theoretical point of view for dinuclear complexes by using the spin-polarization model and hybrid density functional theory (DFT). Kahn et al. first explained the ferromagnetic interactions between EO azido-bridged dinuclear complexes on the basis of the spin-polarization effect. This model considers that the electron of a bridging nitrogen atom (α spin) of the in-plane $\pi_g$ orbital (HOMO) is partially delocalized toward the two metal orbitals; the unpaired electrons occupying the orbitals are likely to have β spins, which favors ferromagnetic interactions. The interaction through the

Table 3. Comparison of structural parameters and magnetic data for end-on azido-bridged complexes.[a]

| Complex | Mn–$N_{azido}$ / Å | $\Delta d$ / Å | $\theta$ / ° | $J$ / $cm^{-1}$ |
|---|---|---|---|---|
| $Mn_2(N_3)_4(ttp)_2$ | 2.245(2) | 0.236 | 103.45(6) | 2.46(4) |
| $Mn_2(N_3)_4(ttp\text{-}N_3)_2$ | 2.252(3) | 0.252 | 103.13(12) | 2.25(2) |
| $[Mn_2(N_3)_4(ttp\text{-}N_3)_2]_2[Mn(ttp\text{-}N_3)(N_3)_3]$ | 2.242(3) | 0.150 | 105.29(12) | 1.92(4) |
| $[Mn(terpy)(N_3)_2]_2\cdot2H_2O$[14a] | 2.227(3) | 0.090 | 104.6(1) | 2.43 |
| $[Mn_2(L^1)_2(\mu_{1,1}\text{-}N_3)_2](ClO_4)_2$[15a] | 2.249(3) | 0.030 | 102.12 | 0.77(1) |
| $[Mn_2(L^2)_2(\mu_{1,1}\text{-}N_3)_2](ClO_4)_2$[15a] | 2.240(3) | 0.072 | 104.29 | 2.04(3) |
| $[Mn_2(L^3)_2(\mu_{1,1}\text{-}N_3)_2](ClO_4)_2$[15a] | 2.248(5) | 0.053 | 103.58 | 1.75(2) |
| $[Mn_2(phen)_4(\mu_{1,1}\text{-}N_3)_2][Co(bpb)(CN)_2]_2\cdot H_2O$[15b] | 2.229(6) | 0.002 | 102.6(4) | 1.27 |
| $[Mn_2(phen)_4(\mu_{1,1}\text{-}N_3)_2][Cr(bpb)(CN)_2]_2\cdot H_2O$[15b] | 2.226(2) | 0.003 | 102.55(12) | 1.10 |
| $[Mn_2(phen)_4(\mu_{1,1}\text{-}N_3)_2][Fe(bpb)(CN)_2]_2\cdot H_2O$[15b] | 2.288(5) | 0.006 | 101.4(3) | 1.20 |
| $[Mn_2(2,2'\text{-}dpa)_2(N_3)_2(\mu_{1,1}\text{-}N_3)_2]$[14b] | 2.237(3) | 0.059 | 103.11(10) | 1.12 |
| $[Mn(tptz)(\mu_{1,1}\text{-}N_3)_2]_n$[16] | 2.273(1) | 0.0017 | 106.16(4) | 2.03 |
| $[Mn(pyz)(\mu_{1,1}\text{-}N_3)_2]$[20a] | 2.234(2) | 0 | 98.8(5) | 0.61 |
| $[Mn(2\text{-}bzpy)(\mu_{1,1}\text{-}N_3)_2]_n$[20b] | 2.197(4) | 0.032 | 100.5(2) | 0.40 |

[a] Average values. $\Delta d = d(Mn–N_{azido}) - d(Mn–N'_{azido})$. $L^1$ = [*N*,*N*-bis(pyridine-2-yl)benzylidene]ethane-1,2-diamine, $L^2$ = [*N*,*N*-bis(pyridine-2-yl)-benzylidene]propane-1,3-diamine, $L^3$ = [*N*,*N*-bis(pyridine-2-yl)benzylidene]butane-1,4-diamine, $bpb^{2-}$ = 1,2-bis(pyridine-2-carboxamido)benzenate, 2,2′-dpa = 2,2′-dipicolylamine, tptz = 2,4,6-tris(2-pyridyl)-1,3,5-triazine, pyz = pyrazine, 2-bzpy = 2-benzoylpyridine.

 © 2007 Wiley-VCH Verlag GmbH & Co. KGaA, Weinheim 

azido bridge does not depend on the surroundings of the metal ions but only on the fashion of azido bridges.[9] DFT calculations show that the value of $J$ is mainly dependent on the energy gap between the molecular orbitals associated with the unpaired electrons (SOMOs). Aromí et al. recently gave a rough relationship between the exchange coupling constant ($J$) and the Mn–N–Mn bridging angle ($\theta$), which was afterwards improved to $J = 0.614\theta - 61.9$ on the basis of eight complexes.[15a,15b] The magnet data of this work and available EO azido-bridged dinuclear complexes are in good agreement with the fact that the exchange coupling constant increase with the Mn–N–Mn bridging angle (Table 3), which is consistent with theoretical predictions.[9a] The $J$–$\theta$ relationship can be now improved on the basis of 15 data sets listed in Table 3 to give the equation $J = 0.276\theta - 26.9$, as shown in Figure 7. In addition, an increase in the asymmetry of the azido bridging ($\Delta d$ in Table 3) was shown to bring about a decrease in antiferromagnetic interactions ($J_{AF}$), and consequently an increase in the global magnetic exchange constant ($J = J_{AF} + J_F$).[14a] Careful examination of the data in Table 3 shows that the $J$ values for the dimeric complexes generally increase with an increase in $\Delta d$, which is in agreement with the above prediction.

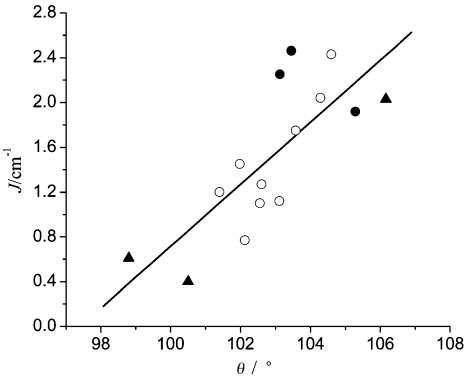


Figure 7. Plot of $J$ vs. Mn–N–Mn bond angle ($\theta$) for EO azido-bridged $Mn^{II}$ compounds (● this work, ▲ 1D complexes). The straight line represents the best fit.

## Conclusions

We successfully prepared three doubly EO azido-bridged dinuclear $Mn^{II}$ complexes. The ferromagnetic properties of dinuclear superexchange mediated through the $\mu_{1,1}$-azido bridges were confirmed in all complexes. Consideration of the intermolecular antiferromagnetic coupling of $Mn^{II}$ or the presence of zero-field splitting (ZFS) of the molecular spin ground state allows the magnetic coupling constants to be evaluated. On the basis of the results of this work and the available $\mu_{1,1}$-azido-bridged $Mn^{II}$ complexes, a clearer magnetostructural correlation was reached.

## Experimental Section

**Materials:** 4′-*p*-Tolyl-2,2′:6′,2′′-terpyridine (ttp) and 4′-(*p*-bromomethylphenyl)-2,2′:6′,2′′-terpyridine (ttp-Br) were prepared as previously reported.[21] All other reagents were commercial grade materials and used as received.

**Measurements:** Elemental analyses were determined with an Elementar Vario EL elemental analyzer. IR spectra were measured as KBr pellets with a Magna-IR 750 spectrophotometer in the 4000–400 $cm^{-1}$ region. Variable-temperature magnetic susceptibility was measured with a SQUID magnetometer with an applied magnetic field of 2000 Oe for **1**, **2**, and **3**.

***Caution!*** *Perchlorate and azide salts are potentially explosive and should be handled carefully in small amounts.*

**4′-*p*-Tolyl-2,2′:6′,2′′-terpyridine (ttp):** Yield: 8%. $^1$H NMR (400 MHz, $CDCl_3$): $\delta$ = 8.73 (s, 2 H), 8.69–8.60 (m, 4 H), 7.89–7.80 (m, 4 H), 7.51 (d, $J$ = 6.3 Hz, 2 H), 7.32 (ddd, $J$ = 7.2, 4.6, 1.2 Hz, 2 H), 2.45 (s, 3 H) ppm. $C_{22}H_{17}N_3$ (323.40): calcd. C 81.71, H 5.30, N 12.99; found C 81.53, H 5.47, N 12.50.

**4′-(*p*-Bromomethylphenyl)-2,2′:6′,2′′-terpyridine (ttp-Br):** Yield 85%. $^1$H NMR (400 MHz, $CDCl_3$): $\delta$ = 8.79 (s, 2 H), 8.76–8.69 (m, 4 H), 7.98–7.89 (m, 4 H), 7.61 (d, $J$ = 6.5 Hz, 2 H), 7.41 (ddd, $J$ = 7.5, 4.8, 1.3 Hz, 2 H) ppm. $C_{23}H_{16}BrN_3$ (414.30): calcd. C 65.68, H 4.01, N 10.44; found C 65.42, H 3.91, N 10.49.

**$[Mn_2(N_3)_4(ttp)_2]$ (1):** An aqueous solution (5 mL) of sodium azide (1.5 mmol) was placed in a tube to which was added a buffer layer of water/methanol (10 mL). A methanol solution (10 mL) of $Mn(ClO_4)_2{\cdot}6H_2O$ (0.5 mmol) and ttp (0.5 mmol) was added to form a third layer. Orange crystals were formed on interdiffusion of the reactants in about 1 week. One suitable crystal was chosen for single-crystal X-ray diffraction. Yield: 80.9 mg (35% based on manganese). IR (KBr): $\tilde{\nu}$ = 2046 (vs) N=N=N, 1607 (vs), 1546 (s), 1546 (s), 1474 (s), 1329 (m), 1015 (m), 821 (m), 790 (m), 733 (w), 686 (w), 660 (w) $cm^{-1}$. $C_{44}H_{34}Mn_2N_{18}$ (924.77): calcd. C 57.15, H 3.71, N 27.26; found C 57.07, H 3.90, N 27.37.

**$[Mn_2(N_3)_4(ttp\text{-}N_3)_2]$ (2):** A solution of $Mn(ClO_4)_2{\cdot}6H_2O$ (0.5 mmol) and ttp-Br (0.5 mmol) in methanol (10 mL) was slowly diffused into an aqueous solution (5 mL) of sodium azide (1.5 mmol) in the dark. After 1 week, well-formed orange single crystals were obtained. Yield: 75.5 mg (30% based on manganese). IR (KBr): $\tilde{\nu}$ = 2093 (vs), 2056 (vs), 1603 (vs), 1569 (s), 1546 (s), 1404 (s), 1347 (m), 1326 (m), 1246 (s), 1199 (w), 1165 (m), 1014 (s), 883 (w), 856 (w), 829 (w), 786 (s), 740 (w), 686 (w), 659 (w) $cm^{-1}$. $C_{44}H_{32}Mn_2N_{24}$ (1006.82): calcd. C 52.49, H 3.20, N 33.39; found C 52.11, H 3.29, N 33.85.

**$[Mn_2(N_3)_4(ttp\text{-}N_3)_2]_3[Mn(ttp\text{-}N_3)(N_3)_3]_2$ (3):** The synthetic method is slightly different from that of **2**. A solution of $Mn(ClO_4)_2{\cdot}6H_2O$ (0.2 mmol) and ttp-Br (0.2 mmol) in methanol (10 mL) was diffused into a solution of sodium azide (1.5 mmol) in water (5 mL). After 4 weeks of exposure to light, red-brown crystals were formed. Yield: 25.7 mg (25% based on manganese). IR (KBr): $\tilde{\nu}$ = 2086 (sh), 2063 (vs), 2037 (vs), 1608 (vs), 1573 (s), 1547 (s), 1477 (s), 1431 (s), 1400 (s), 1326 (m), 1276 (m), 1246 (m), 1164 (m), 1013 (s), 891 (w), 829 (w), 790 (s), 733 (w), 690 (w), 659 (w) $cm^{-1}$. $C_{176}H_{128}Mn_8N_{102}$ (4111.32): calcd. C 51.42, H 3.14, N 34.75; found C 51.40, H 3.25, N 34.48.

**X-ray Structure Determination:** Diffraction data were collected with a Bruker Smart CCD area detector with graphite-monochromated Mo-$K_\alpha$ ($\lambda$ = 0.71073 Å) at room temperature. All calculations were performed by using the SHELXS-97 and SHELXL-97 programs.[22] All structures were solved by direct method and refined by the full-matrix least-squares method on $F^2$ with anisotropic thermal parameters for all non-hydrogen atoms. The hydrogen atoms were located geometrically and refined by using a riding model.

 © 2007 Wiley-VCH Verlag GmbH & Co. KGaA, Weinheim 

CCDC-650165 to -650167 contain the supplementary crystallographic data for this paper. These data can be obtained free of charge from The Cambridge Crystallographic Data Centre via www.ccdc.cam.ac.uk/data_request/cif.

**Supporting Information** (see footnote on the first page of this article): Field dependence of magnetization at 2 K and electronic spectra in acetonitrile for complexes **1**–**3**.

## Acknowledgments

This work was supported by the National Natural Science Foundation of China (20671055).

[1] a) J. Ribas, A. Escuer, M. Monfort, R. Vicente, R. Cortés, L. Lezama, T. Rojo, *Coord. Chem. Rev.* **1999**, *193*, 1027–1068; b) M. M. Turnbull, T. Sugimoto, L. K. Thompson (Eds.), *Molecule-Based Magnetic Materials*, American Chemical Society, Washington, **1996**.

[2] a) M. Fettouhi, M. Khaled, A. Waheed, S. Golhen, L. Ouahab, J.-P. Sutter, O. Kahn, *Inorg. Chem.* **1999**, *38*, 3967–3971; b) S. Koner, S. Saha, T. Mallah, K.-I. Okamoto, *Inorg. Chem.* **2004**, *43*, 840–842; c) Y. Song, C. Massera, O. Roubeau, P. Gamez, A. M. M. Lanfredi, J. Reedijk, *Inorg. Chem.* **2004**, *43*, 6842–6847; d) C.-M. Liu, Z. Yu, R.-G. Xiong, K. Liu, X.-Z. You, *Inorg. Chem. Commun.* **1999**, *2*, 31–34; e) J. M. Domínguez-Vera, J. Suárez-Varela, I. B. Maimoun, E. Colacio, *Eur. J. Inorg. Chem.* **2005**, 1907–1912; f) M. Murugesu, M. Habrych, W. Wernsdorfer, K. A. Abboud, G. Christou, *J. Am. Chem. Soc.* **2004**, *126*, 4766–4767.

[3] a) F. Meyer, S. Demeshko, G. Leibeling, B. Kersting, E. Kaifer, H. Pritzkow, *Chem. Eur. J.* **2005**, *11*, 1518–1526; b) M. Monfort, I. Resino, J. Ribas, X. Solans, M. Font-Bardia, H. Stoeckli-Evans, *New J. Chem.* **2002**, *26*, 1601–1606; c) D. Ghoshal, T. K. Maji, E. Zangrando, T. Mallah, É. Rivière, N. R. Chaudhuri, *Inorg. Chim. Acta* **2004**, *357*, 1031–1038.

[4] a) M. A. S. Goher, J. Cano, Y. Journaux, M. A. M. Abu-Youssef, F. A. Mautner, A. Escuer, R. Vicente, *Chem. Eur. J.* **2000**, *6*, 778–784; b) T. K. Karmakar, S. K. Chandra, J. Ribas, G. Mostafa, T. H. Lu, B. K. Ghosh, *Chem. Commun.* **2002**, 2364–2365; c) L. Zhang, L.-F. Tang, Z.-H. Wang, M. Du, M. Julve, F. Lloret, J.-T. Wang, *Inorg. Chem.* **2001**, *40*, 3619–3622; d) D.-Q. Ma, S. Hikichi, M. Akita, Y. Moro-oka, *J. Chem. Soc. Dalton Trans.* **2000**, 1123–1134; e) M. A. Halcrow, J. S. Sun, J. C. Huffman, G. Christou, *Inorg. Chem.* **1995**, *34*, 4167–4177.

[5] a) G. S. Papaefstathiou, S. P. Perlepes, A. Escuer, R. Vicente, M. Font-Bardia, X. Solans, *Angew. Chem. Int. Ed.* **2001**, *40*, 884–886; b) G. S. Papaefstathiou, A. Escuer, R. Vicente, M. Font-Bardia, X. Solans, S. P. Perlepes, *Chem. Commun.* **2001**, 2414–2415.

[6] P. Mialane, A. Dolbecq, J. Marrot, E. Rivière, F. Sécheresse, *Chem. Eur. J.* **2005**, *11*, 1771–1778.

[7] a) F. Meyer, P. Kircher, H. Pritzkow, *Chem. Commun.* **2003**, 774–775; b) S. Demeshko, G. Leibeling, W. Maringgele, F. Meyer, C. Mennerich, H.-H. Klauss, H. Pritzkow, *Inorg. Chem.* **2005**, *44*, 519–528.

[8] M.-F. Charlot, O. Kahn, M. Chaillet, C. Larrieu, *J. Am. Chem. Soc.* **1986**, *108*, 2574–2581.

[9] a) E. Ruiz, J. Cano, S. Alvarev, P. Alemany, *J. Am. Chem. Soc.* **1998**, *120*, 11122–11129; b) M. A. Aebersold, B. Gillon, O. Plantevin, L. Pardi, O. Kahn, P. Bergerat, I. von Seggern, F. Tuczek, L. Öhrström, A. Grand, E. Lelièvre-Berna, *J. Am. Chem. Soc.* **1998**, *120*, 5238–5245.

[10] a) P. Manikandan, R. Muthukumaran, K. R. J. Thomas, B. Varghese, G. V. R. Chandramonli, P. T. Manoharan, *Inorg. Chem.* **2001**, *40*, 2378–2389; b) L. K. Thompson, S. S. Tandon, F. Lloret, J. Cano, M. Julve, *Inorg. Chem.* **1997**, *36*, 3301–3306; c) P. S. Mukherjee, T. K. Maji, G. Mostafa, T. Mallah, N. R. Chaudhuri, *Inorg. Chem.* **2000**, *39*, 5147–5150.

[11] a) S. S. Tandon, L. K. Thompson, M. E. Manuel, J. N. Bridson, *Inorg. Chem.* **1994**, *33*, 5555–5570; b) B. Kersting, G. Steinfeld, D. Siebert, *Chem. Eur. J.* **2001**, *7*, 4253–4258; c) A. Escuer, X. Vicente, M. Solans, M. Font-Bardia, *Inorg. Chem.* **1994**, *33*, 6007–6011.

[12] a) P. S. Mukherjee, T. K. Maji, G. Mostafa, W. Hibbs, N. R. Chaudhuri, *New J. Chem.* **2001**, *25*, 760–763; b) S. K. Dey, N. Mondal, M. S. El Fallah, R. Vicente, A. Escuer, X. Solans, M. Font-Bardia, T. Matsushita, V. Gramlich, S. Mitra, *Inorg. Chem.* **2004**, *43*, 2427–2434; c) C. S. Hong, Y. Do, *Angew. Chem. Int. Ed.* **1999**, *38*, 193–195; d) P. S. Mukherjee, T. K. Maji, A. Escuer, R. Vicente, J. Ribas, G. Rosair, F. A. Mautner, N. R. Chaudhuri, *Eur. J. Inorg. Chem.* **2002**, 943–949.

[13] a) B. Woodard, R. D. Willett, S. Haddad, B. Twamley, C. J. Gomez-Garcia, E. Coronado, *Inorg. Chem.* **2004**, *43*, 1822–1824; b) F. A. Mautner, S. Hanna, R. Cortes, L. Lezama, M. G. Barandika, T. Rojo, *Inorg. Chem.* **1999**, *38*, 4647–4652.

[14] a) R. Cortés, J. L. Pizarro, L. Lezama, M. I. Arriortua, T. Rojo, *Inorg. Chem.* **1994**, *33*, 2697–2700; b) C.-M. Liu, S. Gao, D.-Q. Zhang, Z.-L. Liu, D.-B. Zhu, *Inorg. Chim. Acta* **2005**, *358*, 834–838.

[15] a) T. K. Karmakar, B. K. Ghosh, A. Usman, H.-K. Fun, E. Rivière, T. Mallah, G. Aromí, S. K. Chandra, *Inorg. Chem.* **2005**, *44*, 2391–2399; b) Z.-H. Ni, H.-Z. Kou, L. Zheng, Y.-H. Zhao, L. F. Zhang, R. J. Wang, A. L. Cui, O. Sato, *Inorg. Chem.* **2005**, *44*, 4728–4736; c) T. K. Karmakar, G. Aromí, B. K. Ghosh, A. Usman, H.-K. Fun, T. Mallah, U. Behrens, X. Solans, S. K. Chandra, *J. Mater. Chem.* **2006**, *16*, 278–285.

[16] A. Das, G. M. Rosair, M. S. El Fallah, J. Ribas, S. Mitra, *Inorg. Chem.* **2006**, *45*, 3301–3306.

[17] R. J. Payne, E. M. M. Bulloch, A. D. Abell, C. Abell, *Org. Biomol. Chem.* **2005**, *3*, 3629–3635.

[18] J. Limburg, J. S. Vrettos, R. H. Crabtree, G. W. Brudvig, J. C. de Paula, A. Hassan, A.-L. Barra, C. Duboc-Toia, M.-N. Collomb, *Inorg. Chem.* **2001**, *40*, 1698–1703.

[19] N. Re, E. Gallo, C. Floriani, H. Miyasaka, N. Matsumoto, *Inorg. Chem.* **1996**, *35*, 6004–6008.

[20] a) J. L. Manson, A. M. Arif, J. S. Miller, *Chem. Commun.* **1999**, 1479–1480; b) M. A. M. Abu-Youssef, A. Escuer, D. Gatteschi, M. A. S. Goher, F. A. Mautner, R. Vicente, *Inorg. Chem.* **1999**, *38*, 5716–5723.

[21] a) V. Uma, V. G. Vaidyanathan, B. U. Nair, *Bull. Chem. Soc. Jpn.* **2005**, *78*, 845–850; b) J. P. Collin, S. Guillerez, J. P. Sauvage, F. Barigelletti, L. D. Cola, L. Flamigni, V. Balzan, *Inorg. Chem.* **1991**, *30*, 4230–4238; c) F. Tessore, D. Roberto, R. Ugo, M. Pizzotti, *Inorg. Chem.* **2005**, *44*, 8967–8978.

[22] G. M. Sheldrick, *SHELX97: Programs for Crystal Structure Analysis*, University of Göttingen, Germany, **1997**.

Received: June 29, 2007
Published Online: October 29, 2007

 © 2007 Wiley-VCH Verlag GmbH & Co. KGaA, Weinheim 

DOI: 10.1002/ejic.200700756

# Novel *gem*-Dithiolato-Bridged Rhodium Hydroformylation Catalysts: Bridging the Gap in Dinuclear Rhodium Thiolate Chemistry

**Marc A. F. Hernandez-Gruel,[a] Gustavo Gracia-Arruego,[a] Angel B. Rivas,[b] Isabel T. Dobrinovitch,[a] Fernando J. Lahoz,[a] Alvaro J. Pardey,[b] Luis A. Oro,*[a] and Jesús J. Pérez-Torrente*[a]**

**Keywords:** Homogeneous catalysis / Hydroformylation / Dinuclear complexes / *gem*-Dithiolato ligands / Rhodium

The direct protonation of the bridging hydroxo ligands in $[Rh(\mu\text{-}OH)(cod)]_2$ by 1,1-dimercaptocyclohexane $[Chxn(SH)_2]$ yields the *gem*-dithiolato-bridged compound $[Rh_2(\mu\text{-}S_2Chxn)(cod)_2]$ (**1**). The dinuclear framework in **1** is supported by a 1,1-cyclohexanedithiolato ligand exhibiting a $1{:}2\kappa^2S,1{:}2\kappa^2S'$ coordination mode. Compound **1** is an active catalyst precursor in the presence of P-donor ligands for the hydroformylation of oct-1-ene under mild conditions of pressure and temperature (100 PSI, 353 K). The best results were obtained with phosphite ligands as modifying ligands. An aldehyde selectivity of 97 %, a regioselectivity towards the linear aldehyde of 81 %, and turnover frequencies of up to 198 $h^{-1}$ were obtained with the catalytic system **1**/$P(OMe)_3$. The dinuclear compound $[Rh_2(\mu\text{-}S_2Chxn)(CO)_2(PPh_3)_2]$ (**2**) was isolated from the catalytic solutions resulting from the system **1**/$PPh_3$ and was characterized by spectroscopic means and by X-ray diffraction to be the *trans* isomer. The mixed-ligand dinuclear complexes **2** and $[Rh_2(\mu\text{-}S_2Chxn)(CO)_2(PCy_3)_2]$ (**3**) (Cy = cyclohexyl) were independently prepared by reaction of $Chxn(SH)_2$ with the mononuclear complexes $[Rh(acac)(CO)(PR_3)]$ in the appropriate molar ratio.

(© Wiley-VCH Verlag GmbH & Co. KGaA, 69451 Weinheim, Germany, 2007)

## Introduction

Dimetallic complexes can serve as catalysts because the expected cooperation between the metal atoms should result in more active and selective catalysts than monometallic systems.[1] However, fragmentation has been a major problem in polymetallic catalysts and, in spite of the intensive research in this field, the number of active dimetallic catalysts actually operating through a dimetallic mechanism are scarce.[2,3] Stanley and co-workers have demonstrated that the homodimetallic rhodium complex *rac*-$[Rh_2(nbd)_2(et,ph\text{-}P4)]^{2+}$, containing a binucleating tetraphosphane ligand, is a precursor of a highly active and selective catalyst for the hydroformylation of 1-alkenes by a mechanism involving dimetallic cooperation between the two rhodium centers.[3] As evidenced by the Stanley's hydroformylation system, the design of the binucleating ligands is of major importance as the catalytic activity largely depends on the structure of the complex. In particular, the ligands must fulfil the electronic requirements of the active metal centers, impart the appropriate electronic and steric influence on the reactions, and more importantly, produce flexible structures allowing the accommodation of the metal centers in close proximity but preventing it from fragmenting.[4]

In this context, it is well known that dinuclear thiolato-bridged complexes $[Rh(\mu\text{-}SR)(CO)(PR'_3)]_2$ (R = *t*Bu, Ph; R′ = OMe, OPh, Ph) are effective catalysts in the hydroformylation of olefins at moderate pressure and temperature (Figure 1a).[5] However, the dinuclear structure of the active catalytic species has been questioned, as kinetic studies suggested the involvement of mononuclear species.[6] Similarly to the Kalck's systems, fluorothiolato- and aminothiolato-bridged dinuclear rhodium complexes have been described as active precursors for the hydroformylation of alkenes under mild conditions.[7] A step forward in rhodium thiolate chemistry was the preparation by Claver and co-workers of di- and tetranuclear dithiolato rhodium complexes with catalytic activity in the hydroformylation of 1-hexene (Figure 1c).[8,9] Monodentate thiolato-bridging ligands provide flexible structures that support a wide range of bonding and nonbonding metal distances by modification of the hinge angle between the rhodium coordination planes. In contrast, the bridging and chelating coordination mode of the dithiolato ligand results in more rigid dinuclear structures with a possible influence on the catalytic activity. In addition, chirality was introduced at the backbone of the dithiolato ligand, which gives rise to chiral dinuclear complexes that show very good regioselectivities in the hydro-

[a] Departamento de Química Inorgánica, Instituto Universitario de Catálisis Homogénea, Instituto de Ciencia de Materiales de Aragón, Universidad de Zaragoza-C.S.I.C., 50009-Zaragoza, Spain
Fax: +34-976761143
E-mail: oro@unizar.es
perez@unizar.es
[b] Centro de Equilibrios en Solución, Escuela de Química, Facultad de Ciencias, Universidad Central de Venezuela, Caracas, Venezuela

 © 2007 Wiley-VCH Verlag GmbH & Co. KGaA, Weinheim 

formylation of styrene, although the observed enantioselectivities were low, indicating that the effect of the presence of a chiral dithiolato ligand is rather small.[10]

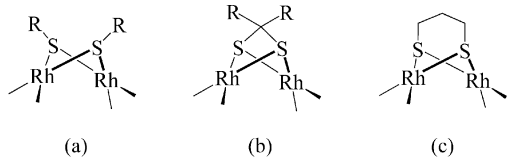


Figure 1. Different thiolato-bridged dinuclear complexes.

The nuclearity of the dithiolato rhodium complexes $[Rh_2(\mu\text{-}S(CH_2)_nS)(L_2)_2]_x$ is influenced both by the number of methylenic units between the two sulfur atoms and by the auxiliary ligands. Tetranuclear diolefin complexes ($L_2$ = cod, $x$ = 2) were generally obtained from dithiolato ligands with large $n$ values (i.e. $n$ = 4). However, the tetranuclear compounds were converted to dinuclear complexes by carbonylation at atmospheric pressure (L = CO, $x$ = 1), which suggests labile Rh–S bonds.[9] In fact, the ion-pair compounds $[Rh(diphos)_2][Rh(dithiolato)(CO)_2]$ were observed in the reaction between a dinuclear carbonyl dithiolato-bridged complex and diphosphanes.[11] In addition, high-pressure spectroscopic techniques (HPNMR and HPIR) have shown that some thiolato- and dithiolato dinuclear rhodium complexes evolve to mononuclear rhodium hydride complexes under hydroformylation conditions.[12]

In order to reinforce the dinuclear framework, we envisaged dinuclear rhodium complexes supported by *gem*-dithiolato ligands (Figure 1b). This type of ligand, although closely related to the standard dithiolato ones, should provide access to new dinuclear complexes with a number of features that could be of interest both in stoichiometric and catalytic reactions. Firstly, the presence of a single bridgehead carbon atom between both sulfur atoms should lead to a more compact $[Rh(\mu\text{-}S_2CR_2)Rh]$ core that is probably more resistant to fragmentation. Secondly, the structure and the coordination mode of the ligand should generate much more rigid dinuclear systems with a likely smaller angle between the coordination planes of the rhodium centers and shorter metal–metal distances, which favor the cooperative effects between the metal centers. Finally, it is important to note that the R groups on the $sp^3$ bridgehead carbon atom are directly oriented toward the rhodium atoms and not toward the center of the dinuclear unit, which could have a determining steric influence on the hydroformylation reaction.

Herein we wish to report on the synthesis of *gem*-dithiolato-bridged dinuclear rhodium complexes and their catalytic activity in the hydroformylation of oct-1-ene. Although a few mono- and dinuclear methanedithiolato and *gem*-dithiolato complexes have been reported,[13] these dinuclear compounds are, to the best of our knowledge, the first example of *gem*-dithiolato complexes directly synthesized from a *gem*-dithiol compound.

## Results and Discussion

The reaction between $[Rh(\mu\text{-}OH)(cod)]_2$ and 1,1-dimercaptocyclohexane $[Chxn(SH)_2]$ in dichloromethane gave a red-orange solution of the compound $[Rh_2(\mu\text{-}S_2Chxn)(cod)_2]$ (**1**), which was isolated as an orange-red microcrystalline solid in good yield (Figure 2). Interestingly, compound **1** can be obtained in similar yields from other di- and mononuclear standard starting materials in rhodium chemisty such as $[Rh(\mu\text{-}OMe)(cod)]_2$ and [Rh(acac)(cod)], although an external base ($NEt_3$) is necessary to drive the reaction to completion. The dinuclear formulation of the complex is supported both by the determination of the molecular weight in chloroform and by the FAB+ spectra that shows the dinuclear ion at $m/z$ = 568. The $^1H$ NMR spectrum in $CDCl_3$ at room temperature shows sharp resonances and is in agreement with the expected rigid framework with $C_{2v}$ symmetry. Thus, two resonances for the olefinic =CH protons and the carbon atoms of the equivalent 1,5-cyclooctadiene ligands were observed in the $^1H$ and $^{13}C\{^1H\}$ NMR spectra, respectively. The protons of the 1,1-cyclohexylene fragment display three resonances, which indicates a rapid equilibrium between the possible chair conformations at room temperature.

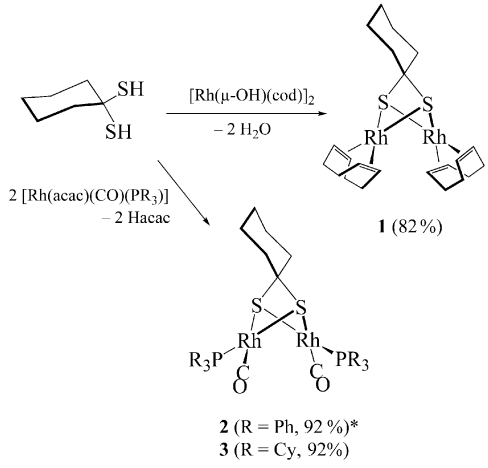


Figure 2. Synthesis of rhodium *gem*-dithiolato-bridged dinuclear complexes. (* cis isomer < 5%).

Compound **1** was used as a catalyst precursor, in the presence of monodentate P-donor ligands, for the hydroformylation of oct-1-ene under mild conditions of temperature and pressure (353 K and 100 PSI) (Figure 3). It has been found that the catalytic activity is strongly dependent on the P/Rh ratio. In the absence of P-donor ligands, no catalytic activity was observed at 100 PSI, although extensive isomerization to internal alkenes was observed at 200 PSI. Almost certainly, compound **1** is transformed into the inactive tetracarbonyl complex $[Rh_2(\mu\text{-}S_2Chxn)(CO)_4]$ under hydroformylation conditions, and an excess of $PR_3$ ligands is necessary to maintain a sufficient concentration of the possibly active phosphane-containing species $[Rh_2(\mu\text{-}S_2Chxn)(CO)_{4-x}(PR_3)_x]$. The optimum P/Rh ratio was found to be approximately 4, as higher ratios produce a slight decrease in the catalytic activity. The results obtained in the hydro-

 © 2007 Wiley-VCH Verlag GmbH & Co. KGaA, Weinheim 

formylation of oct-1-ene under these optimized conditions are shown in Table 1. When $P(OMe)_3$ was used as the modifying ligand, conversions of 67.9% or 88.4% were obtained in 2 or 3 h (entries 1 and 2), respectively. In both catalytic runs, the aldehyde selectivity was as high as 97%, with regioselectivities of up to 81% for the linear aldehyde (only 1-nonanal and 2-methyl-octanal were obtained in the reactions). The by-products of these reactions were octane, the hydrogenation product, detected in trace amounts (<1%), and internal n-octenes, resulting from olefin isomerization (≈ 2%).

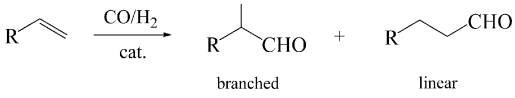


Figure 3. Hydroformylation of oct-1-ene (R = $-C_6H_{13}$).

Table 1. Hydroformylation of oct-1-ene with the complex $[Rh_2(\mu\text{-}S_2Chxn)(cod)_2]$ (**1**) as catalyst precursor.[a]

| Run | Ligand | P/Rh | *t* [h] | % Conv.[b] | % Aldehyde[b] | % *n*[b] | TOF [$h^{-1}$][c] |
|---|---|---|---|---|---|---|---|
| 1 | $P(OMe)_3$ | 4 | 2 | 67.9 | 97.2 | 81 | 198 |
| 2 | $P(OMe)_3$ | 4 | 3 | 88.4 | 97.4 | 80 | 172 |
| 3 | $P(OPh)_3$ | 4 | 2 | 96.5 | 76.7 | 83 | 222 |
| 4 | $PPh_3$ | 4 | 12 | 65.2 | 93.2 | 76 | 30 |
| 5 | $PCy_3$ | 4 | 12 | 43.9 | 93.0 | 54 | 20 |
| 6[d] | $PPh_3$ | 4 | 12 | 68.7 | 92.3 | 74 | 32 |

[a] Reaction conditions: 100 PSI ($CO/H_2$, 1/1), 353 K, oct-1-ene (10.2 mmol, 0.6 M), $[Rh_2(\mu\text{-}S_2Chxn)(cod)_2]$ (0.017 mmol, 1 mM). [b] Conversion, selectivity for aldehyde, and regioselectivity for the linear aldehyde (*n*) determined by GC. [c] TOF = $mol_{aldehyde}/[mol_{catalyst}]\cdot h^{-1}$ corresponds to the reaction time. [d] $[Rh_2(\mu\text{-}S_2Chxn)(CO)_2(PPh_3)_2]$ (**2**) as catalyst precursor.

The catalytic system resulting from $P(OPh)_3$ (entry 3) is more active, reaching a 96.5% conversion in 2 h, with a similar regioselectivity. In contrast, this system is much less selective (aldehyde selectivity 76.7%) as a consequence of the high isomerization activity that produces internal n-octenes. However, neither 2-ethylheptanal nor 2-propylhexanal were detected by GC, which indicates that under these experimental conditions, the internal olefins were not hydroformylated.

The catalytic performance with phosphite ligands is superior than that observed with phosphane ligands, as they provided higher conversions for the same reaction times. The TOF for aldehyde production in these phosphite catalytic systems was found to be about 200 turnover/h. However, the catalytic systems obtained with triphenyl- or tricyclohexylphosphane as auxiliary ligands provided TOF numbers for the aldehyde of about 30 turnover/h (see Table 1). For example, when $PPh_3$ was used as the modifying ligand, a 65.2% conversion was attained in 12 h with good aldehyde selectivity (93.2%) and 76% regioselectivitiy for the linear aldehyde (entry 4). Although the same chemoselectivity was observed in the $PCy_3$ catalytic system, both the activity and the regioselectivity (54%) are considerably smaller (entry 5).

The investigation of the catalytic solutions after the catalytic runs when using $PPh_3$ as the P-donor ligand allowed the isolation of the dinuclear complex $[Rh_2(\mu\text{-}S_2Chxn)(CO)_2(PPh_3)_2]$ (**2**). Compound **2** can also be prepared in a straightforward manner with an excellent yield from the reaction of $[Rh(acac)(CO)(PPh_3)]$ and $Chxn(SH)_2$ in a 2:1 molar ratio (Figure 2). The molecular structure of compound **2** was determined by X-ray diffraction and is shown in Figure 4. Selected bond lengths and angles are collected in Table 2. The dinuclear skeleton of **2** is held up by a 1,1-cyclohexanedithiolato ligand exhibiting a bridging and chelating coordination mode (1:2$\kappa^2$S, 1:2$\kappa^2$S′) that results in the formation of two fused four-membered metallacycles. The 1,1-cyclohexylene fragment adopts the usual chair conformation, and both rhodium atoms exhibit a distorted square-planar geometry by coordination to two additional CO and $PPh_3$ ligands. In contrast with dinuclear thiolato $[Rh(\mu\text{-}SR)(CO)(PR_3)]_2$ complexes, where the $PR_3$ ligands are usually in a *cis* arrangement to accommodate the *anti* conformation of the thiolate ligands,[14–16] the $PPh_3$ ligands in **2** adopt a mutually *trans* disposition.

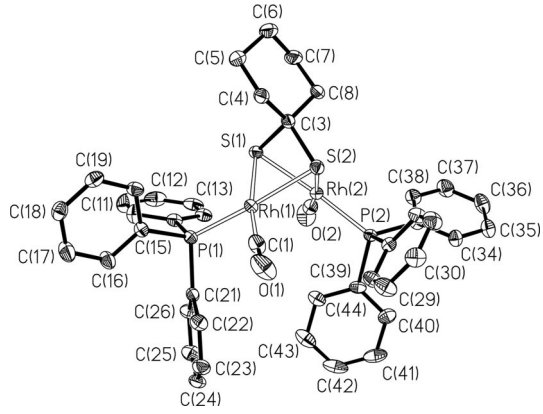


Figure 4. Molecular structure of the dinuclear complex $[Rh_2(\mu\text{-}S_2Chxn)(CO)_2(PPh_3)_2]$ (**2**).

Table 2. Selected bond lengths [Å] and angles [°] for dinuclear compound $[Rh_2(\mu\text{-}S_2Chxn)(CO)_2(PPh_3)_2]$ (**2**).

| | | | |
|---|---|---|---|
| Rh(1)–S(1) | 2.3934(7) | Rh(2)–S(1) | 2.4074(6) |
| Rh(1)–S(2) | 2.3943(8) | Rh(2)–S(2) | 2.3821(7) |
| Rh(1)–P(1) | 2.2700(8) | Rh(2)–P(2) | 2.2476(6) |
| Rh(1)–C(1) | 1.836(3) | Rh(2)–C(2) | 1.834(3) |
| S(1)–C(3) | 1.866(3) | S(2)–C(3) | 1.855(3) |
| C(1)–O(1) | 1.150(4) | C(2)–O(2) | 1.151(4) |
| C(3)–C(4) | 1.527(4) | C(3)–C(8) | 1.523(4) |
| S(1)–Rh(1)–S(2) | 71.09(2) | S(1)–Rh(2)–S(2) | 71.06(2) |
| S(1)–Rh(1)–P(1) | 99.58(3) | S(1)–Rh(2)–P(2) | 163.82(3) |
| S(1)–Rh(1)–C(1) | 167.19(10) | S(1)–Rh(2)–C(2) | 101.20(8) |
| S(2)–Rh(1)–P(1) | 170.07(3) | S(2)–Rh(2)–P(2) | 95.04(2) |
| S(2)–Rh(1)–C(1) | 96.44(10) | S(2)–Rh(2)–C(2) | 172.22(8) |
| P(1)–Rh(1)–C(1) | 93.03(10) | P(2)–Rh(2)–C(2) | 92.73(8) |
| Rh(1)–S(1)–Rh(2) | 74.031(18) | Rh(1)–S(2)–Rh(2) | 74.47(2) |
| S(1)–C(3)–S(2) | 96.82(12) | S(2)–C(3)–C(4) | 111.2(2) |
| S(1)–C(3)–C(4) | 113.6(2) | S(2)–C(3)–C(8) | 112.35(19) |
| S(1)–C(3)–C(8) | 111.9(2) | C(4)–C(3)–C(8) | 110.5(2) |

 © 2007 Wiley-VCH Verlag GmbH & Co. KGaA, Weinheim 

It is worth noting that the average Rh–S–Rh and S–Rh–S bond angles, 74.25(2)° and 71.07(2)°, are significantly smaller than those found in the related dinuclear dithiolate complexes *cis*-[Rh(μ-SPh)(CO)($PMe_3$)]$_2$ [79.3(5) and 81.0(1)°][15] and *cis*-[Rh(μ-S*t*Bu)(CO)($PPh_3$)]$_2$ [81.6(3) and 80.7(3)°].[16] Both parameters are strongly influenced by the narrow angle of 96.82(12)° centered on the bridgehead carbon atom of the 1,1-cyclohexanedithiolato ligand [S(1)–C(3)–S(2)] that enables the S donor atoms to come closer together [nonbonding S···S distance of 2.7833(10) Å] and, in turn, this results in a very small angle of 91.04(2)° between both rhodium coordination planes (defined only by the metal-coordinated atoms) and a short Rh···Rh distance of 2.8903(3) Å [112.25(3) and 111.61(12)°, 3.061(1) and 3.103(6) Å in the above-mentioned dithiolate complexes, respectively]. The $RhS_2Rh$ torsion angle of 95.76(2)°, which is closely related to the Rh···Rh distance, is slightly larger than the angle between the coordination planes, as a consequence of the separation of the metal atoms from their coordination planes by 0.0635(2) and 0.1670(2) Å [Rh(1) and Rh(2), respectively]. This fact reflects the existence of a feeble repulsion between the metal atoms that is due to the ligand-forced, short metal–metal nonbonding distance, as suggested before in other similar cases.[9,17]

The geometrical constraints imposed by the *gem*-dithiolato ligand in **2** relative to the other dithiolato ligands are largely reflected both in the smaller S–Rh–S angles, 79.02(6) and 84.49(19)° in the complexes [Rh(μ-S$(CH_2)_2$S)(cod)$_2$] and [Rh(μ-S$(CH_2)_3$S)(cod)$_2$],[9] and in the smaller angle between the rhodium coordination planes, 96.95 and 103.99 respectively, although the Rh–S–Rh angles and the Rh···Rh distances are of comparable magnitude. On the other hand, the structural parameters of the central core in **2** compares well with those observed in the structurally related dinuclear compound [$Rh_2${μ-$S_2$CN(Me)(Ph)}(cod)$_2$], which has a dithiocarbamate bridging ligand exhibiting the same coordination mode.[18]

The spectroscopic data indicate that compound **2** exists in solution mainly as the *trans* isomer, which was observed as a complex resonance in the $^{31}P\{^1H\}$ NMR ($C_6D_6$) spectrum at $\delta$ = 41.90 ppm. This signal correlates well with the calculated spectrum using the parameters reported in the Experimental Section, which resulted from the consideration of small $^2J_{Rh-P}$, $^3J_{P-P}$, and $J_{Rh-Rh}$ coupling constants.[19] However, the *cis* isomer was also observed (<5%) as a doublet at $\delta$ = 39.6 ($J_{Rh-P}$ = 162 Hz). The dinuclear compound [$Rh_2$(μ-$S_2$Chxn)(CO)$_2$($PCy_3$)$_2$] (**3**) was prepared in excellent yield following a similar synthetic protocol starting from [Rh(acac)(CO)($PCy_3$)] (Figure 2). The $^{31}P\{^1H\}$ NMR ($C_6D_6$) spectrum only shows a resonance at $\delta$ = 53.10 ppm with a similar pattern to that found in the spectrum of compound **2** and suggests that compound **3** exists exclusively as the *trans* isomer. This fact is probably associated to the bulkiness of the $PCy_3$ ligands that completely disfavors the formation of the *cis* isomer. The signals for the equivalent carbonyl groups are observed in the $^{13}C\{^1H\}$ NMR ($C_6D_6$) spectra of both compounds as a doublet of doublets at $\delta$ = 192.2 (**2**) and 191.8 ppm (**3**) ($J_{Rh-C}$ = 75 Hz, $^2J_{P-C}$ = 17 Hz). The IR spectra of both compounds in dichloromethane show a broad $\nu$(CO) band for the terminal carbonyl groups at 1957 (**2**) and 1960 $cm^{-1}$ (**3**), which is in good agreement with a *trans* disposition of the ligands.[7b,7f,10b]

The mixed-carbonyl compound **2** is also an active precursor in the hydroformylation of oct-1-ene. Although related dinuclear thiolate systems have shown that diolefin complexes, in the presence of $PR_3$ ligands, are more active than the mixed carbonyl-phosphane species under the same experimental conditions,[7f] in the present case comparable chemoselectivity, regioselectivity, and activity are obtained when using the same P/Rh ratio (entry 6).

The results presented in Table 1 indicate that the activity of the catalytic systems decrease with the basicity of the P-donor ligands. Interestingly, the reverse trend was shown for dinuclear systems based on functionalized amino-thiolate ligands in the hydroformylation of hex-1-ene.[7e,7f] On the other hand, it is evident that the regioselectivity is not controlled exclusively by steric factors since the more sterically demanding ligand ($PPh_3$) affords the lower regioselectivities. This fact was already observed in the hydroformylation of hex-1-ene with a cationic dinuclear catalyst precursor having an aminothiolato-bridged ligand.[7f]

As far as the nuclearity of the active species during catalysis is concerned, we are aware that, under hydroformylation conditions, some dinuclear rhodium complexes containing thiolate bridging ligands are precursors of the mononuclear rhodium(I) hydrido species that probably account for the catalytic activity.[12] In spite of the obtained regioselectivities, that are roughly comparable to those observed in the catalytic systems [Rh(acac)$(CO)_2$]/$PPh_3$ and [Rh(acac)$(CO)_2$]/P$(OPh)_3$, the recovery of the dinuclear compound **2** after the catalytic reaction in the system **1**/$PPh_3$ and the singular structural features of the compact [Rh(μ-$S_2CR_2$)Rh] core strongly motivate us to look further into the chemical behavior of these types of compounds. Further studies on the synthesis and reactivity of dinuclear rhodium complexes containing new *gem*-dithiolato ligands are currently under way, in order to determinate the influence of the bridging ligand on the catalytic activity and to analyze a potential intermetallic cooperative mechanism in these dimetallic species.

## Conclusions

We have shown that novel dinuclear *gem*-dithiolato-bridged rhodium complexes can easily be obtained in high yields directly by double deprotonation of a *gem*-dithiol compound by using mono- or dinuclear rhodium complexes containing basic ligands. The diolefin compound [$Rh_2$(μ-$S_2$Chxn)(cod)$_2$] (**1**) is an active catalyst precursor in the presence of P-donor ligands for the hydroformylation of oct-1-ene under mild conditions. The performance of the resulting catalytic systems is strongly dependent on the nature of the modifying P-donor ligand, and it has been found that ligands of the type P$(OR)_3$ are better than $PR_3$ ligands in terms of both activity and selectivity.

 © 2007 Wiley-VCH Verlag GmbH & Co. KGaA, Weinheim 

## Experimental Section

**General:** All manipulations were performed under a dry argon atmosphere by using Schlenk-tube techniques. Solvents were dried by standard methods and distilled under argon immediately prior to use. Standard literature procedures were used to prepare the complexes $[Rh(\mu\text{-}OH)(cod)]_2$,[20] $[Rh(acac)(CO)(PPh_3)]$,[21] and $[Rh(acac)(CO)(PCy_3)]$.[22] 1,1-Dimercaptocyclohexane was prepared according to the reported method.[23] Oct-1-ene was purchased from Aldrich and was distilled prior to use.

**Physical Measurements:** $^1H$, $^{31}P\{^1H\}$, and $^{13}C\{^1H\}$ NMR spectra were recorded on a Varian Gemini 300 spectrometer operating at 300.08 MHz for $^1H$. Chemical shifts are reported in parts per million and referenced to $SiMe_4$ by using the residual resonances of the deuterated solvents ($^1H$ and $^{13}C$) and 85% $H_3PO_4$ ($^{31}P$) as external reference. Assignments in complex NMR spectra were made by simulation with the program gNMR© v 3.6 (Cherwell Scientific Publishing Limited) for Macintosh. The initial choice of chemical shifts and coupling constants were optimized by successive iterations following a standard least-squares procedure; a numerical assignment of the experimental frequencies was used. IR spectra were recorded on a Nicolet-IR 550 spectrometer. Elemental C, H and N analysis were performed with a Perkin–Elmer 2400 microanalyzer. Molecular weights were determined with a Knauer osmometer by using chloroform solutions of the complexes. Mass spectra were recorded in a VG Autospec double-focusing mass spectrometer operating in the $FAB^+$ mode. Ions were produced with the standard $Cs^+$ gun at ca. 30 Kv; 3-nitrobenzylic alcohol (NBA) was used as matrix. Hydroformylation experiments were carried out in a stainless steel magnetically stirred autoclave (100 mL) equipped with a thermocouple and an external heating mantle. The syngas ($CO/H_2$ = 1) was supplied at constant pressure from a ballast. The drop in pressure in the ballast was monitored by using a pressure transducter.

**Preparation of $[Rh_2(\mu\text{-}S_2Chxn)(cod)_2]$ (1):** To a solution of $[Rh(\mu\text{-}OH)(cod)]_2$ (0.502 g, 1.100 mmol) in $CH_2Cl_2$ (5 mL) was added 1,1-dimercaptocyclohexane ($Chxn(SH)_2$, 170 μL, 1.241 mmol, $\rho$ = 1.083 g mL$^{-1}$) to give a red-orange solution, which was stirred for 15 min. The addition of EtOH (10 mL) gave a red suspension, which was concentrated under vacuum to ca. 5 mL and then filtered to give a red-orange microcrystalline solid, which was washed with EtOH (2 × 3 mL) and dried under vacuum. Yield: 0.511 g (82%). $C_{22}H_{34}Rh_2S_2$ (568.44): calcd. C 46.48, H 6.03, S 11.28; found C 46.53, H 6.05, S 11.53. $^1H$ NMR (300.08 MHz, $CDCl_3$, 293 K): $\delta$ = 4.54 (m, 4 H, =CH), 4.23 (m, 4 H, =CH, cod), 2.43 (m, 12 H, $>CH_2$, cod and Chxn), 1.98 (m, 4 H, $>CH_2$), 1.83 (m, 4 H, $>CH_2$, cod), 1.44 (m, 4 H, $>CH_2$), 1.26 (m, 2 H, $>CH_2$, Chxn) ppm. $^{13}C\{^1H\}$ NMR (75.46 MHz, $CDCl_3$, 293 K): $\delta$ = 84.0 (C1, Chxn), 79.8 (d, $J_{Rh-C}$ = 12 Hz, =CH), 79.1 (d, $J_{Rh-C}$ = 12 Hz, =CH, cod), 57.2 (C2 and C6, Chxn), 31.4 and 31.1 ($>CH_2$, cod), 24.3 (C4), 22.0 (C3 and C5, Chxn) ppm. MS ($FAB^+$, $CH_2Cl_2$): *m/z* (%) = 568 (100) [$M^+$] 460 (60) [$M^+$ – cod]. Mol. weight ($CHCl_3$): calcd 568; found 562.

**Preparation of $[Rh_2(\mu\text{-}S_2Chxn)(CO)_2(PPh_3)_2]$ (2):** To a suspension of $[Rh(acac)(CO)(PPh_3)]$ (0.501 g, 1.018 mmol) in diethyl ether (15 mL) was added $Chxn(SH)_2$ (73 μL, 0.533 mmol, $\rho$ = 1.083 g mL$^{-1}$) to immediately give an orange solution, which was stirred for 15 min. The addition of MeOH (15 mL) gave an orange suspension, which was stirred for 5 min and concentrated under vacuum to about one half of the original volume and then filtered to give an orange solid, which was washed with cold MeOH (2 × 5 mL) and dried under vacuum. Yield: 0.433 g (92%). $C_{44}H_{40}O_2P_2Rh_2S_2$ (932.68): calcd. C 56.66, H 4.32, S 6.87; found C 56.68, H 5.15, S 6.85. $^1H$ NMR (300.08 MHz, $C_6D_6$, 293 K): $\delta$ = 7.93 (m, 12 H), 7.05 (m, 18 H, $PPh_3$), 2.63 (m, 4 H, $>CH_2$), 1.45 (m, 4 H, $>CH_2$), 1.07 (m, 2 H, $>CH_2$, Chxn) ppm. $^{13}C\{^1H\}$ NMR (75.46 MHz, $C_6D_6$, 293 K): $\delta$ = 192.2 (dd, $J_{Rh-C}$ = 75, $^2J_{P-C}$ = 17 Hz, CO), 135.5 (d, $J_{P-C}$ = 45 Hz), 134.4 (d, $J_{P-C}$ = 12 Hz), 130.1, 128.5 (d, $J_{P-C}$ = 12 Hz, $PPh_3$), 86.7 (C1), 57.6 (C2 and C6), 24.6 (C4), 21.7 (C3 and C5, Chxn) ppm. $^{31}P\{^1H\}$ NMR (121.47 MHz, $C_6D_6$, 293 K): $\delta$ = 41.90 (AA′XX′ spin system, A = $^{31}P$ and X = $^{103}Rh$, calcd. spectrum: $J_{Rh-P}$ = 163.72 Hz, $^2J_{Rh-P}$ = –1.47 Hz, $^3J_{P-P}$ = 6.60 Hz, $J_{Rh-Rh}$ = 3.59 Hz, *trans* isomer), 39.6 (d, $J_{Rh-P}$ = 162 Hz, *cis* isomer). MS ($FAB^+$, $CH_2Cl_2$): *m/z* (%) = 932 (25) [$M^+$] 904 (20) [$M^+$ – CO], 876 (15) [$M^+$ – 2CO], 532 (100) [$M^+$ – Chxn – 2CO – $PPh_3$]. Mol. Weight ($CHCl_3$): calcd 932; found 940. IR (pentane ): $\nu$(CO) = 1957 (s) cm$^{-1}$.

**Preparation of $[Rh_2(\mu\text{-}S_2Chxn)(CO)_2(PCy_3)_2]$ (3):** $[Rh(acac)(CO)(PCy_3)]$ (0.367 g, 0.719 mmol) and $Chxn(SH)_2$ (50 μL, 0.365 mmol, $\rho$ = 1.083 g mL$^{-1}$) were reacted in diethyl ether (15 mL) for 15 min to give an orange suspension. The suspension was concentrated under vacuum to about one half the volume and cooled to –85 °C. The orange microcrystalline solid was filtered, washed with cold pentane (2 × 5 mL), and dried under vacuum. Yield: 0.319 g (92%). $C_{44}H_{76}O_2P_2Rh_2S_2$ (968.96): calcd. C 54.54, H 7.90, S 6.62; found C 54.22, H 7.98, S 6.50. $^1H$ NMR (300.08 MHz, $CDCl_3$, 293 K): $\delta$ = 2.85 (m, 6 H, $PCy_3$), 2.19–2.06 (m, 28 H), 1.80–1.65 (m, 28 H), 1.25–1.10 (m, 14 H), ($PCy_3$, Chxn) ppm. $^{13}C\{^1H\}$ NMR (75.46 MHz, $CDCl_3$, 293 K): $\delta$ = 191.8 (dd, $J_{Rh-C}$ = 75, $^2J_{P-C}$ = 17 Hz, CO), 84.5 (C1), 57.1 (C2 and C6, Chxn), 35.7 (d, $J_{P-C}$ = 21Hz), 26.8 (d, $J_{P-C}$ = 11 Hz), 26.7 (d, $J_{P-C}$ = 10 Hz), 25.7 ($PCy_3$), 23.9 (C4), 21.1 (C3 and C5, Chxn) ppm. $^{31}P\{^1H\}$ NMR (121.47 MHz, $C_6D_6$, 293 K): $\delta$ = 53.10 (AA′XX′ spin system, A = $^{31}P$ and X = $^{103}Rh$, calcd. spectrum: $J_{Rh-P}$ = 158.30 Hz, $^2J_{Rh-P}$ = –0.54 Hz, $^3J_{P-P}$ = 3.79 Hz, $J_{Rh-Rh}$ = 3.74 Hz, *trans* isomer). MS ($FAB^+$, $CH_2Cl_2$): *m/z* (%) = 968 (100) [$M^+$], 938 (96) [$M^+$ – CO – 2 H], 908 (65) [$M^+$ – 2CO – 4 H]. Mol. weight ($CHCl_3$): calcd 968; found 970. IR (pentane ): = $\nu$(CO) = 1960 (s) cm$^{-1}$.

**Standard Hydroformylation Experiment:** In a typical run, a solution of the catalyst precursor $[Rh_2(\mu\text{-}S_2Chxn)(cod)_2]$ (**1**) (0.017 mmol), which contains the phosphane or phosphite ligand (0.20–0.60 mmol), oct-1-ene (10.2 mmol), and toluene (15.4 mL), was transferred from a Schlenk tube under argon to the autoclave by using a stainless steel cannula. The autoclave was purged with syngas three times at 120 PSI and then pressurized at 50 PSI and heated at 80 °C. When thermal equilibrium was reached, the pressure was adjusted to 100 PSI, and the mixture stirred for 8 h with the continuous supply of syngas at constant pressure. After the reaction time, the autoclave was cooled to room temperature and depressurized. The reaction mixture was analyzed by gas chromatography with a Hewlett–Packard 5890 instrument equipped with a capillary column (HP, ULTRA 1. 25 m × 0.32 mm × 0.17 μm) and a flame-ionization detector. The products were quantified by the internal standard method by using anisole.

**Crystal Structure Determination of $[Rh_2(\mu\text{-}S_2Chxn)(CO)_2(PPh_3)_2]$ (2):** Suitable crystals for X-ray diffraction of compound **2** were obtained from a saturated solution of the complex in dichloromethane/(diethyl ether) at 258 K. A summary of the crystal data, data collection, and refinement parameters are given in Table 3. Intensity data were collected at low temperature [150(2) K] on a Bruker SMART diffractometer (equipped with a CCD area detector) by using graphite-monochromated Mo-$K_\alpha$ radiation ($\lambda$ = 0.71073 Å). Data were integrated with the Bruker SAINT package,[24] and absorption corrections were applied by the SADABS program.[25] The

 © 2007 Wiley-VCH Verlag GmbH & Co. KGaA, Weinheim 

structure was solved by direct methods and completed by subsequent difference Fourier techniques. Refinement on $F^2$ was carried out by full-matrix least-squares methods (SHELXL97).[26] All non-hydrogen atoms were refined with anisotropic displacement parameters; all hydrogen atoms were observed in the difference Fourier maps and refined as free isotropic atoms. CCDC-654127 contains the supplementary crystallographic data for this paper. These data can be obtained free of charge from The Cambridge Crystallographic Data Centre via www.ccdc.cam.ac.uk/data_request/cif.

Table 3. Crystal data, data collection, and refinement parameters for the X-ray analysis of $[Rh_2(\mu\text{-}S_2Chxn)(CO)_2(PPh_3)_2]$ (**2**).

| | |
|---|---|
| Formula | $C_{44}H_{40}O_2P_2Rh_2S_2$ |
| $M_r$ | 932.64 |
| Crystal size [mm] | $0.28 \times 0.24 \times 0.20$ |
| Temperature | 150(2) |
| Crystal System | monoclinic |
| Space group | $P2_1/n$ |
| $a$ [Å] | 13.2115(6) |
| $b$ [Å] | 19.2395(9) |
| $c$ [Å] | 16.0070(7) |
| $\beta$ [°] | 102.2275(11) |
| $Z$ | 4 |
| $V$ [Å$^3$] | 3976.4(3) |
| $D_{calcd.}$ [g cm$^{-3}$] | 1.558 |
| $\mu$ [mm$^{-1}$] | 1.052 |
| $\Theta$ range [°] | 2.79–32.06 |
| No. measured reflections | 19622 |
| No. unique reflections | 10256 ($R_{int}$ = 0.0419) |
| min/max transmission | 0.668/0.812 |
| No. reflections/restrainsts/parameters | 10256/0/629 |
| $R_1(F)$ [$F^2 \geq 2\sigma(F^2)$] | 0.0342 |
| $wR_2(F^2)$ (all data) | 0.0720 |
| $S$ (all data) | 0.914 |

## Acknowledgments

The financial support from Ministerio de Educación y Ciencia (MEC/FEDER) is gratefully acknowledged (Project CTQ2006-03973/BQU and Factoría de Cristalización, CONSOLIDER INGENIO-2010). A. B. R. thanks the Programa Iberoamericano de Ciencia y Tecnología para el Desarrollo (CYTED, Project V.9) for a fellowship. A. J. P. thanks to Fonacit-Venezuela (S1-2002000260) for financial support.

[1] a) P. Braunstein, L. A. Oro, P. R. Raithby (Eds.), *Metal Clusters in Chemistry*, Wiley-VCH, Weinheim, **1999**; b) R. D. Adams, F. A. Cotton (Eds.), *Catalysis by Di- and Polynuclear Metal Cluster Complexes*, Wiley-VCH, New York, **1998**.

[2] a) Y. Ishii, M. Hidai in *Multimetallic Catalysts in Organic Synthesis* (Eds.: M. Shibasaki, Y. Yamamoto), Wiley-VCH, Weinheim, **2004**, ch. 9, pp. 201–223; b) N. Tsukada, T. Mitsuboshi, H. Setoguchi, Y. Inoue, *J. Am. Chem. Soc.* **2003**, *125*, 12102; c) N. Wheatly, P. Kalck, *Chem. Rev.* **1999**, *99*, 3379; d) P. Braunstein, J. Rosé in *Comprehensive Organometallic Chemistry II* (Eds.: E. W. Abel, F. G. A. Stone, G. Willkinson), Elsevier Science Ltd., Oxford, **1995**, vol. 10, ch. 7, pp. 351–385.

[3] a) G. G. Stanley in *Multimetallic Catalysts in Organic Synthesis* (Eds.: M. Shibasaki, Y. Yamamoto), Wiley-VCH, Weinheim, **2004**, ch. 10, pp. 225–248; b) M. E. Brousand, B. Juma, S. G. Train, W.-J. Peng, S. A. Laneman, G. G. Stanley, *Science* **1993**, *260*, 1784; c) R. C. Matthews, D. K. Howell, W.-J. Peng, S. G. Train, W. Dale-Treleaven, G. G. Stanley, *Angew. Chem. Int. Ed. Engl.* **1996**, *35*, 2253.

[4] E. K. Van der Beuken, B. L. Feringa, *Tetrahedron* **1998**, *54*, 12985.

[5] a) P. Kalck, J. M. Frances, P. M. Pfister, T. G. Southern, A. Thorez, *J. Chem. Soc. Chem. Commun.* **1983**, 510; b) P. Kalck in *Organometallics in Organic Syntheses* (Eds.: A. de Meijere, H. Tom Dick), Springer Verlag, Weinheim, **1987**, p. 297; c) P. Kalck, *Pure Appl. Chem.* **1989**, *61*, 967; d) P. Kalck, *Polyhedron* **1988**, *7*, 2441; e) F. Monteil, R. Queau, P. Kalck, *J. Organomet. Chem.* **1994**, *480*, 177.

[6] R. Davis, J. W. Epton, T. G. Southern, *J. Mol. Catal. J. Mol. Catal. A* **1992**, *77*, 159.

[7] a) J. L. G. Fierro, M. Martínez-Ripoll, M. Merchán, A. Rodriguez, P. Terreros, H. Torrens, M. A. Vivar-Cerrato, *J. Organomet. Chem.* **1997**, *544*, 243; b) A. Polo, C. Claver, S. Castillón, A. Ruiz, J. C. Bayón, J. C. Real, J. Mealli, D. Masi, *Organometallics* **1992**, *11*, 3525; c) A. Polo, E. Fernandez, C. Claver, S. Castillón, *J. Chem. Soc. Chem. Commun.* **1992**, 642; d) C. Claver, A. M. Masdeu, N. Ruiz, C. Foces-Foces, F. Cano, C. Apreda, L. A. Oro, J. García-Alejandre, H. Torrens, *J. Organomet. Chem.* **1990**, *398*, 177; e) J. C. Bayón, J. Real, C. Claver, A. Polo, A. Ruiz, *J. Chem. Soc. Chem. Commun.* **1989**, 1056; f) J. C. Bayón, P. Esteban, J. Real, C. Claver, A. Ruiz, *J. Chem. Soc. Dalton Trans.* **1989**, 1579.

[8] a) J. C. Bayón, C. Claver, A. M. Masdeu-Bultó, *Coord. Chem. Rev.* **1999**, *193–195*, 73; b) N. Ruiz, S. Castillón, A. Ruiz, C. Claver, A. Aaliti, A. Alvarez-Larena, J. F. Piniella, G. Germain, *J. Chem. Soc. Dalton Trans.* **1996**, 969; c) A. Aaliti, A. M. Masdeu, A. Ruiz, C. Claver, *J. Organomet. Chem.* **1995**, *489*, 101.

[9] A. M. Masdeu, A. Ruiz, S. Castillón, C. Claver, P. B. Hitchcock, P. A. Chaloner, C. Bó, J. M. Poblet, P. Sarasa, *J. Chem. Soc. Dalton Trans.* **1993**, 2689.

[10] a) Z. Freixa, E. Martin, S. Gladiali, J. C. Bayon, *Appl. Organomet. Chem.* **2000**, *14*, 57; b) O. Pamies, O. G. Net, A. Ruiz, C. Bó, J. M. Poblet, C. Claver, *J. Organomet. Chem.* **1999**, *586*, 125; c) A. Castellanos-Páez, S. Castillón, C. Claver, *J. Organomet. Chem.* **1997**, *539*, 1; d) N. Ruiz, A. Aaliti, J. Forniés-Cámer, A. Ruiz, C. Claver, C. J. Cardin, D. Fabbri, S. Gladiali, *J. Organomet. Chem.* **1997**, *546*, 79; e) S. Gladiali, J. C. Bayón, C. Claver, *Tetrahedron: Asymmetry* **1995**, *6*, 1453; f) A. M. Masdeu-Bultó, A. Orejón, S. Castillón, C. Claver, *Tetrahedron: Asymmetry* **1995**, *6*, 1885; g) A. M. Masdeu, A. Orejón, A. Ruiz, S. Castillón, C. Claver, *J. Mol. Catal. J. Mol. Catal. A* **1994**, *94*, 149; h) C. Claver, S. Castillón, A. Ruiz, G. Delogu, D. Fabri, S. Gladiali, *J. Chem. Soc. Chem. Commun.* **1993**, 1833.

[11] A. Castellanos-Páez, J. Thayaparan, S. Castillón, C. Claver, *J. Organomet. Chem.* **1998**, *551*, 375.

[12] a) A. Castellanos-Páez, S. Castillón, C. Claver, P. W. N. M. van Leeuwen, W. G. J. Lange, *Organometallics* **1998**, *17*, 2543; b) H. Gao, R. J. Angelici, *Organometallics* **1998**, *17*, 3063; c) M. Diéguez, C. Claver, A. M. Masdeu-Bultó, A. Ruiz, P. W. N. M. van Leeuwen, G. Schoemaker, *Organometallics* **1999**, *18*, 2107; d) J. Forniés-Cámer, A. M. Masdeu-Bultó, C. Claver, C. Tejel, M. A. Ciriano, C. J. Cardin, *Organometallics* **2002**, *21*, 2609.

[13] a) F. Novio, R. Mas-Balleste, I. Gallardo, P. Gonzalez-Duarte, A. Lledos, N. Vila, *Dalton Trans.* **2005**, 2742; b) T. Gandhi, B. R. Jagirdar, *Inorg. Chem.* **2005**, *44*, 1118; c) Z. Li, W. Zheng, H. Liu, K. F. Mok, T. S. A. Hor, *Inorg. Chem.* **2003**, *42*, 8481; d) R. P. Hughes, J. M. Smith, C. D. Incarvito, K.-C. Lam, B. Rhatigan, A. L. Rheingold, *Organometallics* **2002**, *21*, 2136; e) C. Megret, P. Gonzalez-Duarte, *Inorg. Chem.* **2002**, *41*, 3218; f) M. R. DuBois, B. R. Jagirdar, S. Dietz, B. C. Noll, *Organometallics* **1997**, *16*, 294; g) H. Hashimoto, M. Y. Shang, T. P. Fehlner, *Organometallics* **1996**, *15*, 1963; h) R. Mas-Balleste, M. Capdevila, P. A. Champkin, W. Clegg, R. A. Coxall, A. Lledos, C. Megret, P. Gonzalez-Duarte, *Inorg. Chem.* **2002**, *41*, 3218; i) K.-Y. Shih, P. E. Fanwick, R. A. Walton, *Inorg. Chem.* **1992**, *31*, 3663; j) D. P. Klein, G. M. Kloster, R. G. Bergman, *J. Am. Chem. Soc.* **1990**, *112*, 2022; and references cited therein.

 © 2007 Wiley-VCH Verlag GmbH & Co. KGaA, Weinheim 

[14] a) V. Miranda-Soto, J. J. Pérez-Torrente, L. A. Oro, F. J. Lahoz, M. L. Martín, M. Parra-Hake, D. B. Grotjahn, *Organometallics* **2006**, *25*, 4374; b) J. R. Dilworth, D. Morales, Y. Zheng, *J. Chem. Soc. Dalton Trans.* **2000**, 3017; c) H. Schumann, N. Hemling, N. Goren, J. Blue, *J. Organomet. Chem.* **1995**, *485*, 209.
[15] J. J. Bonet, P. Kalck, R. Poilblanc, *Inorg. Chem.* **1977**, *16*, 1514.
[16] R. A. Jones, S. T. Schwab, *J. Crystallogr. Spectrosc.* **1986**, *16*, 577.
[17] J. Forniés-Cámer, A. M. Masdeu-Bultó, C. Claver, C. J. Cardin, *Inorg. Chem.* **1998**, *37*, 2626.
[18] A. Elduque, C. Finestra, J. A. López, F. J. Lahoz, F. Merchán, L. A. Oro, M. T. Pinillos, *Inorg. Chem.* **1998**, *37*, 824.
[19] M. A. F. Hernandez-Gruel, J. J. Pérez-Torrente, M. A. Ciriano, A. B. Rivas, F. J. Lahoz, I. T. Dobrinovitch, L. A. Oro, *Organometallics* **2003**, *22*, 1237.
[20] R. Uson, L. A. Oro, J. A. Cabeza, *Inorg. Synth.* **1985**, *23*, 126.
[21] F. Bonati, G. Wilkinson, *J. Chem. Soc.* **1964**, 3156.
[22] A. Jegorov, J. Podlaha, J. Podlahová, F. Turecek, *J. Chem. Soc. Dalton Trans.* **1990**, 3295.
[23] a) M. Demuynck, J. Vialle, *Bull. Soc. Chim. Fr.* **1962**, 2126; b) C. Djerassi, B. Tursch, *J. Org. Chem.* **1962**, *22*, 1041.
[24] *SAINT+: Software for CCD Difractometers*, v. 6.01, **2001**, Bruker AXS, Madison, WI, and *SAINT*, version 6.02.
[25] a) R. H. Blessing, *Acta Crystallogr., Sect. A* **1995**, *51*, 33; b) *SADABS: Area-Detector Absorption Correction*, **1996**, Bruker AXS, Madison, WI.
[26] G. M. Sheldrick, *SHELXL-97 Program for Crystal Structure Refinement*, University of Göttingen, Göttingen, Germany, **1997**.

Received: July 17, 2007
Published Online: November 15, 2007

 © 2007 Wiley-VCH Verlag GmbH & Co. KGaA, Weinheim 

DOI: 10.1002/ejic.200700772

# *ortho*-Directed Metathetical Fluoride/Amide Exchange in (Pentafluorophenyl)-amides[‡]

**Pavel L. Shutov,[a] Sergey S. Karlov,*[b] Klaus Harms,[a] Maxim V. Zabalov,[b] Jörg Sundermeyer,*[a] Jörg Lorberth,[a] and Galina S. Zaitseva[b]**

**Keywords:** Fluorinated ligands / Amides / Nucleophilic substitution / Density functional calculations

The indium tris(amide)s $[(Et_2N)_{3-n}In\{N(C_6F_5)(2\text{-}C_5H_4N)\}_n]$ [*n* = 1 (**15**), 2 (**16**) or 3 (**9**)] have been prepared by treatment of $[In(NEt_2)_3]_2$ (**3**) with a stoichiometric amount of $(2\text{-}C_5H_4N)(C_6F_5)NH$ (**1**). The analogous reaction of $Bi(NMe_2)_3$ (**2**) with 3 equiv. of amine **1** and the treatment of $BiCl_3$ (**5**) with a stoichiometric amount of $(2\text{-}C_5H_4N)(C_6F_5)NLi$ (**4**) both lead to $[Bi\{N(C_6F_5)(2\text{-}C_5H_4N)\}_3]$ (**10**). In contrast, only the difluoride **11** or the monofluoride **12**, which are the products of intramolecular *ortho*-directed exchange of $NMe_2$ and F substituents, are obtained from the reaction of **2** with 1 or 2 equiv. of **1**, respectively. The reaction between $Me_3Sb(Hal)_2$ [Hal = Br (**7**) Cl, (**8**)] and 1 or 2 equiv. of lithium salt **4** gives the corresponding stable monoamides $[Me_3(Hal)Sb\{N(C_6F_5)(2\text{-}C_5H_4N)\}]$ [Hal = Br (**17**), Cl (**18**)] or bis(amide) $[Me_3Sb\{N(C_6F_5)(2\text{-}C_5H_4N)\}_2]$ (**19**), respectively. The structure of **9** has been confirmed by an X-ray structure analysis, and density functional calculations data have been used to explain the possible reaction pathway of the *ortho*-directed metathetical fluoride/amide exchange.

(© Wiley-VCH Verlag GmbH & Co. KGaA, 69451 Weinheim, Germany, 2007)

## Introduction

There has been a strong interest in activation of the C–F bond in polyfluoro organic compounds during the past several decades due to the possible utilization of these activation processes in organic synthesis.[2,3] A variety of methods for activating C–F bonds with transition metal centers have been published recently, and several examples based on early, middle, or late transition metal compounds have been used for the replacement of an F atom in polyfluoroaryl moieties, mostly by oxidative addition reactions.[4–11] Nucleophilic substitution reactions of an aryl carbon–fluorine bond assisted by main group element compounds (alkali and alkaline earth metals or silicon derivatives) have also been widely investigated.[4,5,12,13] However, to the best of our knowledge, most of the mechanistically studied examples have been ascribed to *intermolecular* processes. Assumptions about *intramolecular* pathways have been made exclusively for *ortho*-directed fluorine atom substitution for $C_6F_5X$ species (X is a *ortho*-directing donor functionality) in reactions with Li or Mg reagents such as ArLi, RMg(Hal), ArMg(Hal) or ArN(R)Mg(Hal).[13,14]

Recently, we reported the reaction of $Sb(NEt_2)_3$ with $C_6F_5(2\text{-}C_5H_4N)NH$ (**1**), which leads to the antimony tris(amide)s $[(Et_2N)_2Sb\{N(C_6F_5)(2\text{-}C_5H_4N)\}]$, $[(Et_2N)Sb\{N(C_6F_5)(2\text{-}C_5H_4N)\}_2]$, and $[Sb\{N(C_6F_5)(2\text{-}C_5H_4N)\}_3]$ with one, two, or three pentafluoro(2-pyridyl)anilido groups.[1] Trivalent antimony compounds containing one or two $NEt_2$ groups are unexpectedly unstable, and they rearrange to give the bis(amido)antimony fluorides $[SbF\{N(C_6F_5)(2\text{-}C_5H_4N)\}_2]$ and $[(Et_2N)SbF\{N(C_6F_5)(2\text{-}C_5H_4N)\}]$, in almost quantitative yield at room temperature within 21 d.[1] To the best of our knowledge no such intramolecular rearrangements have been reported previously except in a paper by Schrock et al., where a similar nucleophilic substitution product is reported in low yield in the reaction of $Mo(NMe_2)_4$ with $(C_6F_5NHCH_2CH_2)_2NMe$.[15] In order to gain further insight into the fluoride/amide metathesis assisted by antimony, and to expand the scope of this reaction, we report herein our investigation of the analogous transamination reactions of $Bi(NMe_2)_3$ (**2**) and $[In(NEt_2)_3]_2$ (**3**) with $C_6F_5NH(2\text{-}C_5H_4N)$ (**1**). The reactions of the lithium salt of amine **1**, namely $C_6F_5NLi(2\text{-}C_5H_4N)$ (**4**), with $BiCl_3$ (**5**), $InCl_3$ (**6**), $Me_3SbBr_2$ (**7**), and $Me_3SbCl_2$ (**8**) are also reported. The structure of the novel monomeric indium tris(amide) $[In\{N(C_6F_5)(2\text{-}C_5H_4N)\}_3]$ (**9**) is confirmed by X-ray crystallography, and density functional calculations are used to distinguish possible rearrangement pathways.

[‡] The Case of Bismuth and Indium, II. Part I: Ref.[1]

[a] Fachbereich Chemie, Philipps-Universität Marburg, Hans-Meerwein-Strasse, 35032 Marburg/Lahn, Germany
Fax: +49-6421-28-28917
E-mail: jsu@chemie.uni-marburg.de
[b] Chemistry Department Moscow State University, B-234 Leninskie Gory, 119899 Moscow, Russia
Fax: +7-95-932-8846
E-mail: sergej@org.chem.msu.ru

Supporting information for this article is available on the WWW under http://www.eurjic.org or from the author.

 WILEY InterScience DISCOVER SOMETHING GREAT © 2007 Wiley-VCH Verlag GmbH & Co. KGaA, Weinheim 

## Results and Discussion

### Synthesis

Ligand **1** was first prepared by treating 2-bromopyridine with (pentafluorophenyl)amine,[16] although recently Ashenhurst et al. have used the approach of Koppang for the synthesis of **1**,[17] which involves the treatment of $C_6F_6$ with an equimolar mixture of (2-pyridylamido)lithium and $LiNH_2$.[18] We also used this reaction to prepare amine **1**, although we modified the method according to Equation (1). The twofold excess of lithiated 2-pyridylamine per mol of $C_6F_6$ is essential as product **1** is acidic enough to quench the nucleophile.

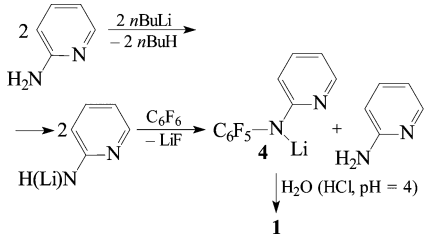


(1)

Treatment of $Bi(NMe_2)_3$ (**2**) with 3 equiv. of amine **1** in toluene and the reaction of lithium amide **4** with $BiCl_3$ (**5**) both afforded tris(amide) **2** in good yield [Equation (2)].

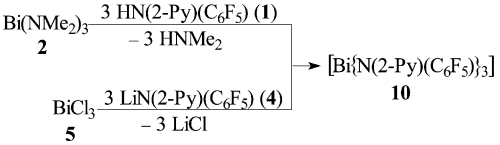


(2)

Treatment of $Bi(NMe_2)_3$ (**2**) with 1 or 2 equiv. of amine **1** led to difluoride **11** and monofluoride **12**, respectively, as products of a rearrangement reaction (Scheme 1). The instability of the plausible intermediates $[(NMe_2)_{3-n}Bi\{N(C_6F_5)(2\text{-}C_5H_4N)\}_n]$ is in sharp contrast to the corresponding antimony compounds, which only rearrange after extended reaction times.[1] Moreover, traces of both **11** and **12** were detected by NMR spectroscopy during the reaction of **2** with 3 equiv. of **1**. Thus, intramolecular nucleophilic substitution at a $C_6F_5$ moiety assisted by bismuth proceeds much faster than that for antimony derivatives. Hydrolysis of **11** and **12** led to the tris(amine)s **13** and **14**, which are difficult to synthesize by other methods.

In contrast to the reaction patterns of Sb and Bi compounds, the transamination of In amide **3** with 1, 2, and 3 equiv. of **1** selectively led to the corresponding tris(amide)s **15**, **16**, and **9**, respectively. No similar rearrangement processes were found in these studies [Equation (3)].

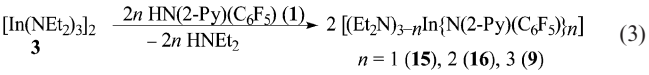


(3)

The tendency to rearrange is higher for compounds with a large covalent radius, low coordination number, and highly polar M–N bonds. We assume that this is probably more due to kinetic than to thermodynamic reasons. If the covalent character in M–N bonding is increased, for example by increasing the formal oxidation state of the central atom, the compounds become more inert with respect to rearrangement reactions: we observed that reaction of 1 or 2 equiv. of lithium amide **4** with $(Hal)_2SbMe_3$ (**7** and **8**) led to the expected unrearranged monoamides **17** and **18** or diamide **19** [Equation (4)]. While $Sb^{III}$ amides tend to rearrange, $Sb^{V}$ amides are inert with respect to this fluoride/amide exchange under ambient conditions.

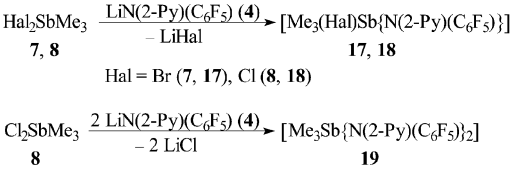


(4)

### NMR Spectroscopic Study

The $^1H$, $^{13}C$, and $^{19}F$ NMR spectra of all compounds are consistent with a $\kappa^2$-*N*,*N*′-bonding mode of the 2-pyridylamido ligands. The solution spectra of bismuth fluo-

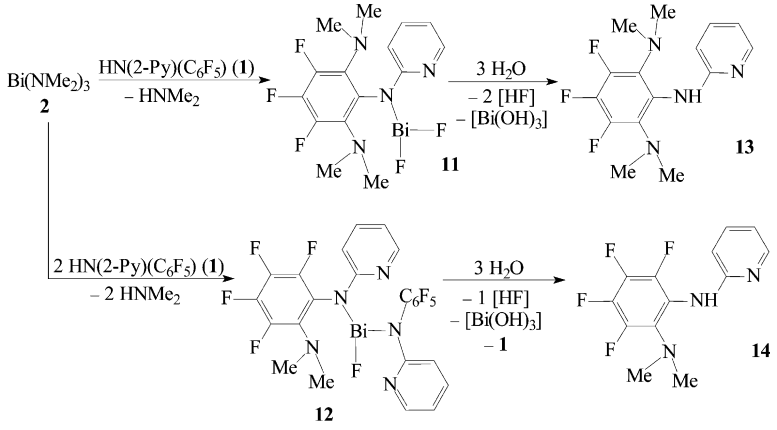


Scheme 1.

 © 2007 Wiley-VCH Verlag GmbH & Co. KGaA, Weinheim 

rides **11** and **12** are very similar to their previously characterized Sb analogs.[1] As already observed, the presence of one or two $NMe_2$ groups adjacent to the *ipso*-C atom of the aromatic rings inhibits the rotation of these moieties about the N–$C_{ipso}$ bond. N-coordination in a chelate ring leads to the appearance of two signals for the $NMe_2$ group in the $^1H$ NMR spectra of **11** and **12**. In accordance with these data, we assume that indium compounds **9**, **15**, and **16** are monomeric chelate complexes in $C_6D_6$ solutions.

It should be noted that two different configurations (*fac* and *mer*) are possible for indium and bismuth tris(amide)s **9** and **10**. Ashenhurst et al. found recently that the closely related Al derivative $[Al\{N(C_6F_5)(2\text{-}C_5H_4N)\}_3]$ undergoes a dynamic *fac*/*mer* isomerization in $CDCl_3$ solutions at 25 °C.[18] The broadening of the signals in the $^1H$ and $^{13}C$ NMR spectra of **9** and **10** indicates that a similar isomerization process probably takes place here as well. The ability of both **9** and **10** to isomerize in solution was confirmed by the very close values of total energy for both isomers (see Density Functional Calculations section below).

### Molecular Structure of 9

The molecular structure of **9** is shown in Figures 1 and 2, and Table 1 summarizes selected geometrical parameters. Compound **9** possesses a monomeric structure in the solid state. The coordination sphere of the indium atom is a distorted $InN_6$ octahedron with three amido groups and three pyridyl nitrogen atoms in a *fac* arrangement similar to the structurally related complex $[Al\{N(C_6F_5)(2\text{-}C_5H_4N)\}_3]$.[18] The distortion from octahedral geometry appears to be induced by the steric constraints of the $C_6F_5N(2\text{-}C_5H_4N)$ ligand. Analysis of the Cambridge Structural Database (Version 5.28, November 2006)[19] reveals more than ten structures with a similar $InN_6$ structural fragment, most of which contain either pyrazolylborate or phthalocyanine ligands or have ionic structures such as $In(NCS)_6^{3-}$. Interestingly, the most closely related structure, that of $[In(N_3)_3\text{-}Py_3]$,[20] possesses a *mer* configuration. As expected, the covalent In–$N_{amido}$ bonds in **9** [2.174(3)–2.202(2) Å] are shorter than the donor–acceptor In–$N_{Py}$ bonds [2.259(2)–2.324(3) Å].

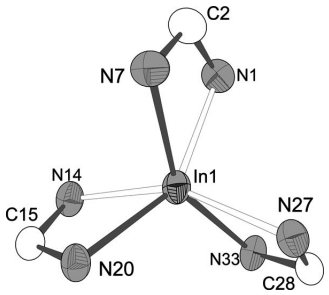


Figure 2. Thermal ellipsoid drawing of the indium coordination polyhedron in complex **9**.

Table 1. Selected bond lengths [Å] and angles [°] for complex **9** with estimated standard deviations in parentheses.

| | | | |
|---|---|---|---|
| N1–In1 | 2.324(3) | N20–In1 | 2.202(3) |
| N7–In1 | 2.174(3) | N27–In1 | 2.259(2) |
| N14–In1 | 2.265(3) | N33–In1 | 2.190(3) |
| N7–In1–N33 | 147.9(1) | N20–In1–N14 | 59.75(8) |
| N7–In1–N20 | 97.3(1) | N27–In1–N14 | 153.64(9) |
| N33–In1–N20 | 112.7(1) | N7–In1–N1 | 58.8(1) |
| N7–In1–N27 | 103.98(9) | N33–In1–N1 | 95.4(1) |
| N33–In1–N27 | 59.92(9) | N20–In1–N1 | 149.61(9) |
| N20–In1–N27 | 102.20(8) | N27–In1–N1 | 101.83(9) |
| N7–In1–N14 | 97.7(1) | N14–In1–N1 | 102.16(9) |
| N33–In1–N14 | 106.94(9) | | |

No short contacts between In and the fluorine atoms of the $C_6F_5$ groups are found in the solid state. The shortest In···F contact in **9** of 3.585 Å (where F is an *ortho*-fluorine

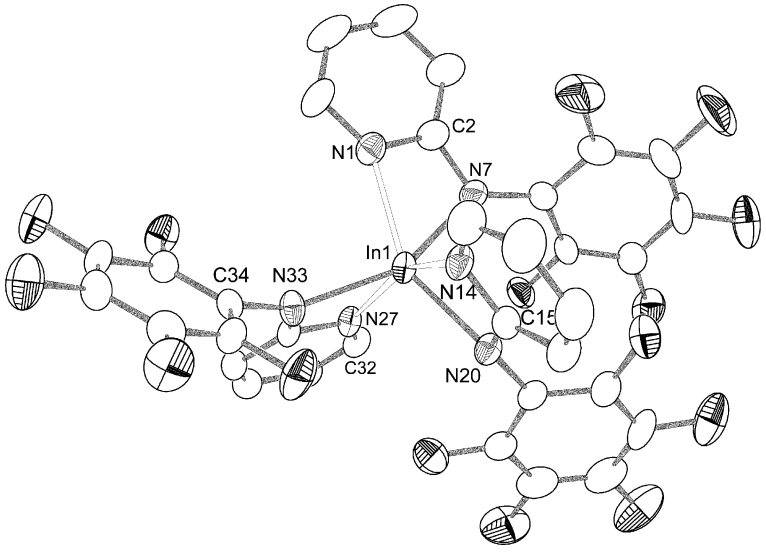


Figure 1. Thermal ellipsoid drawing of complex **9**. Hydrogen atoms and disordered toluene have been omitted for clarity. Displacement ellipsoids are drawn at the 50% probability level.

 © 2007 Wiley-VCH Verlag GmbH & Co. KGaA, Weinheim 

atom) is larger than the sum of the van der Waals radii of indium and fluorine (3.40 Å).[21]

### Density Functional Study on Metal Complexes and Nucleophilic Substitution Reactions

To gain a better understanding of the driving force behind the *ortho*-directed metathetic fluoride/amide rearrangements we carried out density functional calculations at the PBE level of theory on a number of stable compounds and metastable intermediates on the reaction coordinate. The calculated structures and the reactions studied are presented in Scheme 2.

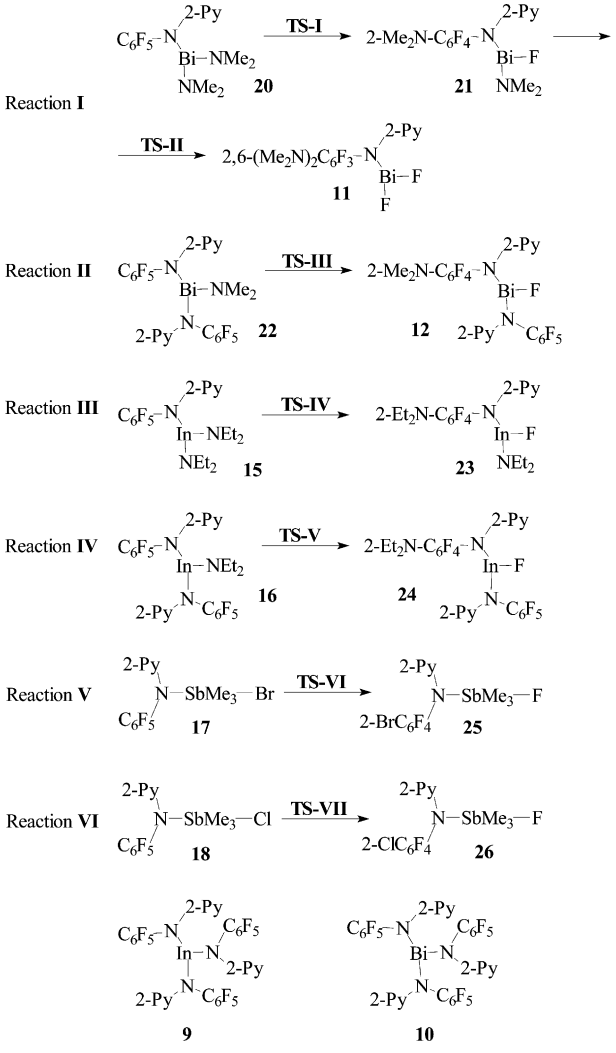


Scheme 2.

The compounds are likely to possess intramolecular contacts between the metal atom and the pyridine nitrogen atoms, therefore two different types of molecules were studied: derivatives containing additional intramolecular $N_{Py}\rightarrow M$ contacts (a) and derivatives without these contacts (b). In the cases where several additional $N_{Py}\rightarrow M$ contacts are possible, structures with the maximum number of contacts were calculated. The most important geometry parameters of species in series (a) are listed in Table 2; the calculated molecular structures of the compounds studied, the most important geometry parameters of these species, and the values of their total energies are listed in the Supporting Information. According to the results of the density functional calculations, the values of total energy for derivatives (a) with $N_{Py}\rightarrow M$ bonds are larger than those for the corresponding compounds (b) without these contacts for all species studied. The differences between the energy values for the starting materials lie within the range 7.03 (**20**) to 35.04 kcal mol$^{-1}$ (**16**). The analogous values for the rearrangement products are 5.89 (**20**) to 41.27 kcal mol$^{-1}$ (**16**).

It is of interest to note that the total energy of **9a**(*fac*) is practically identical to that of **9a**(*mer*): $\Delta E = E$[**9a**(*fac*)] – $E$[**9a**(*mer*)] = 1.16 kcal mol$^{-1}$; the same $\Delta E$ value was found for the Bi compound **10a**. This energy equivalence testifies to the possibility of *fac*/*mer* conformational exchange in solution for **9** and **10**, as proposed on the basis of the NMR spectroscopic data. The total energy values of **9a** and **10a**, which possess $N_{Py}\rightarrow M$ bonds, are also larger than those for **9b** and **10b**, respectively. These differences are 51.41 [**9**(*fac*)] and 52.49 kcal mol$^{-1}$ [**9**(*mer*)], and 39.56 [**10**(*fac*)] and 35.31 kcal mol$^{-1}$ [**10**(*mer*)]. We can therefore expect that all metal derivatives of the $C_6F_5N(2\text{-}C_5H_4N)$ ligand in question possess intramolecular coordination in solution [series (a)].

It should be noted that the calculated parameters of compound **9a**(*fac*) (In–$N_{amido}$ 2.256 Å; In–$N_{Py}$ 2.332–2.333 Å) are close to those found for the solid-state structure of **9** (see above). Consequently, we believe that the theoretical method used gives reasonable results for indium derivatives; the appropriateness of this method for Sb and Bi compounds was confirmed by us previously.[1,22]

Taking into consideration that no X-ray structure of prepared or proposed compounds is reported except for that of **9a**, the calculated geometrical data for the molecules studied [series (a), with $N_{Py}\rightarrow M$] are of particular interest. The primary coordination environment of the Bi atom in **11a**, **12a**, and **20a**–**22a** may be treated as a trigonal pyramid as the Bi–$N_{Py}$ distances are smaller than the sum of the van der Waals radii of bismuth and nitrogen (3.94 Å).[21] Consequently, the Bi atom can be regarded as [3+1]-coordinate in **20a** and [3+2]-coordinate in **22a**. Analogous [3+2]-coordination is found in **11a** due to additional interaction of the Bi atom with one $NMe_2$ group. In contrast to **11a**, however, the Bi atom in **21a** should be regarded as [3+1]-coordinate because no interaction between the Bi atom and $NMe_2$ group is found in this compound. The Bi atom in **12a** possesses three additional contacts with nitrogen atoms (two $N_{Py}$ and one $NMe_2$), which means that the distortion of the primary trigonal-pyramidal coordination environment of the bismuth atom is maximal. The starting compounds **20a**, **21a**, and **22a** also possess a short Bi–F contact (3.592, 3.378, and 3.431 Å, respectively).

The coordination polyhedron of the In atom in **15a** and **16a** is a distorted tetrahedron (two In–$NEt_2$ and one In–$N_{amide}$ and In–$N_{Py}$ bonds) and a distorted trigonal bipyramid (In–$NEt_2$ and two In–$N_{amide}$ and In–$N_{Py}$ bonds),

 © 2007 Wiley-VCH Verlag GmbH & Co. KGaA, Weinheim 

Table 2. Selected bond lengths [Å] for compounds **9a**–**12a**, **15a**–**18a**, **20a**–**26a**, and **TSIa**–**TSVIIa** (calculated data). X-ray data for **9** are given in square brackets.

| Compound | M–$N_{amide}$ | M–N(py) | M–$NR_2$ | M–F[a] | M–Hal |
|---|---|---|---|---|---|
| **9a**(*fac*) | 2.256, 2.256, 2.256, [2.174(3)], [2.190(3)], [2.202(3)] | 2.332, 2.332, 2.332, [2.259(2)], [2.265(3)], [2.324(3)] | – | 3.873 [3.585] | – |
| **9a**(*mer*) | 2.261, 2.267, 2.276 | 2.318, 2.333, 2.299 | – | 3.571 | – |
| **10a**(*fac*) | 2.295, 2.397, 2.409 | 2.556, 2.558, 2.609 | – | 3.610 | – |
| **10a**(*mer*) | 2.319, 2.349, 2.363 | 2.590, 2.641, 2.735 | – | 3.660 | – |
| **20a** | 2.308 | 2.772 | 2.165, 2.190 | 3.592 | – |
| **TSIa** | 2.213 | 2.659 | 2.150, 2.396[b] | 3.122,[c] | – |
| **21a** | 2.276 | 2.680 | 2.146, 4.838[d] | 2.077,[e] 3.378 | – |
| **TSIIa** | 2.215 | 2.578 | 2.330,[b] 5.058[d] | 2.07,4[e] 2.767[c] | – |
| **11a** | 2.243 | 2.502 | 2.551,[f] 5.019[d] | 2.150,[e] 2.168[e] | – |
| **22a** | 2.297, 2.299 | 2.701, 2.781 | 2.182 | 3.431 | – |
| **TSIIIa** | 2.262, 2.234 | 2.650, 2.766 | 2.356[b] | 2.938[c] | – |
| **12a** | 2.284, 2.406 | 2.483, 3.026 | 2.581[f] | 2.165[e] | – |
| **15** | 2.280 | 2.317 | 2.084, 2.092 | 3.524 | – |
| **IVa** | 2.198 | 2.355 | 2.080, 2.239[b] | 2.437[c] | – |
| **23a** | 2.224 | 2.276 | 2.109, 4.008[d] | 2.014[e] | – |
| **16** | 2.244, 2.250 | 2.336, 2.342 | 2.084 | 3.420 | – |
| **Va** | 2.175, 2.269 | 2.253, 2.424 | 2.245[b] | 2.494[c] | – |
| **24a** | 2.201, 2.315 | 2.303, 2.388 | 2.608[f] | 2.035[e] | – |
| **17a** | 2.275 | 2.363 | – | 3.721 | 2.707 |
| **VIa** | 2.199 | 3.122 | – | 2.260[c] | 2.905[b] |
| **25a** | 2.302 | 2.322 | – | 2.007 | 4.239[d] |
| **18a** | 2.274 | 2.357 | – | 3.729 | 2.528 |
| **VIIa** | 2.192 | 3.203 | – | 2.280[c] | 2.761[b] |
| **26a** | 2.297 | 2.325 | – | 2.007 | 4.127[d] |

[a] Shortest distance for the molecule. [b] Splitting bond. [c] Nascent bond. [d] No interaction. [e] Covalent bond. [f] Dative bond.

respectively. Compounds **15a** and **16a** also possess a short In–F contact (3.524 and 3.420 Å, respectively). These values are comparable with those found for bismuth derivatives (see above), although the smaller covalent and van der Waals radii of indium in comparison with those of bismuth should be noted.

The coordination polyhedron of the Sb atom in **17a** and **18a** is a distorted octahedron (three Sb–$CH_3$ and one Sb–$N_{amide}$, Sb–Hal, and Sb–$N_{Py}$ bonds). These compounds do not possess any short Sb–F contacts (shortest distance: 3.721 and 3.729 Å, respectively).

As stated above, six reactions were studied during this work (Scheme 2). Analysis of the total energy values for the starting materials and products (Table 3) shows that the products are thermodynamically more favored in all the reactions studied. However, the experimental results show that reactions **I** and **II** proceed completely and compounds **20**–**22** are not detected in the reaction mixtures, while reactions **III**–**VI** do not take place. This means that kinetic factors are the key to understanding the origin of these processes. We therefore calculated the transition-state (TS) geometries of reactions **I**–**VI** for structures with (**TSIa**–**TSVIIa**) and without (**TSIb**–**TSVIIb**) $N_{Py}$→M interactions. The most important geometrical parameters of species in series (a) are listed in Table 2 and the molecular structures of the TSs studied, their atomic coordinates, and the total energy values are given as Supporting Information. Table 3 summarizes the relative energy values for the species studied, including the transition states **I**–**VII** (the activation barriers).

The computed barriers (Table 3) for the observed reactions **20a** → **21a**, **21a** → **11a**, and **22a** → **12a** in the gas phase are low (17.64–24.41 kcal mol$^{-1}$), while those for reactions **III**–**VI** are considerably higher (46.23–50.57 kcal mol$^{-1}$). The values found for the activation barrier in reactions **I** and **II** are very close to those previously found for the reaction [$(Et_2N)Sb\{N(C_6F_5)(2\text{-}C_5H_4N)\}_2$] → [$SbF\{N(C_6F_5)(2\text{-}C_5H_4N)\}_2$] (27.70 kcal mol$^{-1}$).[1] Similarly close values (21.8–41.2 kcal mol$^{-1}$, RB3LYP/DZVP level of theory) have been found for the activation barrier for the insertion of $Pd(PH_3)_2$ into the C–F bond of different fluoroarenes ($FC_6H_3XY$; X, Y = H, CN, $NO_2$).[23]

Table 3. $\Delta H$ [$E_{total}$(products) – $E_{total}$(reactants); kcal mol$^{-1}$] for reactions **I**–**VI** as well as activation barriers for these rearrangements ($E_{act}$; kcal mol$^{-1}$).

| Reaction | I | | II | III | IV | V | VI |
|---|---|---|---|---|---|---|---|
| | **20a → 21a** | **21a → 11a** | **22a → 12a** | **15a → 23a** | **16a → 24a** | **17a → 25a** | **18a → 26a** |
| $\Delta H$ | –28.72 | –26.67 | –22.86 | –26.07 | –31.87 | –9.82 | –9.36 |
| $E_{act}$ | 17.64 (**TSIa**) | 24.41 (**TSIIa**) | 20.30 (**TSIIIa**) | 46.77 (**TSIVa**) | 50.57 (**TSVa**) | 47.88 (**TSVIa**) | 46.23 (**TSVIIa**) |
| | **20b → 21b** | **21b → 11b** | **22b → 12b** | **15b → 23b** | **16b → 24b** | **17b → 25b** | **18b → 26b** |
| $\Delta H$ | –29.85 | –24.80 | –23.36 | –33.28 | –25.64 | –2.15 | –1.05 |
| $E_{act}$ | 24.64 (**TSIb**) | 29.02 (**TSIIb**) | 25.59 (**TSIIIb**) | 16.17 (**TSIVb**) | 31.00 (**TSVb**) | 36.17 (**TSVIb**) | 34.01 (**TSVIIb**) |

 © 2007 Wiley-VCH Verlag GmbH & Co. KGaA, Weinheim 

The computed barriers for the system without $N_{Py}$→M bonds [series (b)] are different from those previously discussed for species which contain $N_{Py}$→M contacts [series (a)]. While the values for reactions **20b** → **21b**, **21b** → **11b**, **22b** → **12b**, **17b** → **25b**, and **18b** → **26b** are close to those found previously (see Table 3), the barriers for reactions of indium species **15b** → **23b** and **16b** → **24b** are dramatically lower than those for reactions **15a** → **23a** and **16a** → **24a**.

Some general trends should be noted with regard to the calculated transition state geometries [series (a)]. First of all, the species are characterized by a considerable shortening of the M–F contacts in comparison with those found in reactants **15a**–**18a** and **20a**–**22a**, while the splitting bond (M–N or Sb–Hal) becomes elongated. Some elongation of the M–$N_{Py}$ distances in the TSs in comparison with those in the corresponding reactants should be mentioned, especially the significant alterations in **TSVIa** and **TSVIIa**.

A noticeable elongation of both C–C bonds (aromatic $C_6F_5$ ring) at the carbon atom involved in the rearrangement processes is also found for all TSs studied. The values of the nascent C–N bond lengths in **TS1a**–**TSVa** vary between 1.760 and 1.991 Å, while the corresponding covalent bonds in the products of reactions **I**–**IV** are 1.399–1.461 Å. Analogously, the values of the splitting C–F bond lengths in **TS1a**–**TSVa** vary between 1.482 and 1.565 Å, while the corresponding covalent bonds in the reactants of reactions **I**–**IV** are 1.348–1.356 Å. The F–C–N angles in **TS1a**–**TSVa** vary between 85.6 and 92.6°. The geometry of the transition states therefore allows us to define the proposed mechanism of the nucleophilic addition under study as a concerted oxidative addition.[11,24,25]

We believe that the main driving force behind the studied rearrangements is the formation of thermodynamically more favorable species. In the case of bismuth derivatives **20a**, **21a**, and **22a**, as well as the previously studied antimony compounds $[(Et_2N)_2Sb\{N(C_6F_5)(2\text{-}C_5H_4N)\}]$ and $[(Et_2N)Sb\{N(C_6F_5)(2\text{-}C_5H_4N)\}_2]$,[1] these interconversions proceed very easily as the weak $N_{Py}$→M contacts in these substances do not prevent M–F bond formation. In our opinion the rearrangement is likely to proceed through formation of a hypervalent fragment $C_{C_6F_5}$–F–Bi(Sb) with retention of the Bi(Sb)–$NR_2$ bond in **TS1a**–**TSIIIa**. Thus, the presence of additional electron density on the metal atom is necessary to decrease the activation barrier of the studied rearrangement.

In contrast, the indium derivatives **15** and **16** are stable and do not participate in any rearrangement processes due to the very strong $N_{Py}$→In interaction. The presence of this bond in indium derivatives increases the steric hindrance to the attack of the F atom at the In atom, although the indium center is more electron-deficient than in compounds without additional interactions. Both these factors prevent the rearrangement of **15** and **16** from occurring. This conclusion is confirmed by the decrease of the computational barrier found for **15b** → **23b** and **16b** → **24b** (compounds without $N_{Py}$→In contacts).

As regards reactions **V** and **VI**, we believe that the high barriers are caused by factors analogous to those previously mentioned for indium derivatives. The comparatively strong $N_{Py}$→Sb interaction along with the presence of five covalent bonds around the antimony atom in **17a** and **18a** prevent these Sb centers from participating in the supposed rearrangement. It should be noted, however, that the difference between the reactants and products in these reactions is not as large as in other reactions studied (Table 3).

## Conclusions

In an extension of our studies on antimony(III) amides we have investigated the transamination of pentafluoro(2-pyridyl)aniline with dialkylamides of bismuth(III), antimony(V), and indium(III). The reaction between $Bi(NMe_2)_3$ (**2**) and $HN(2\text{-}C_5H_4N)(C_6F_5)$ (**1**) affords the expected tris(amide) **10**, whereas replacement of only one or two $NMe_2$ groups leads to the isolation of the unexpected bismuth fluorides **11** and **12** as a result of an F↔$NMe_2$ metathesis. In contrast, the treatment of $[In(NEt_2)_3]_2$ (**2**) with the same amine **1** leads to the corresponding stable monomeric tris(amide)s **9**, **15**, or **16**. No F↔$NEt_2$ rearrangement occurs for **15** and **16**. Furthermore, antimony(V) amides such as **17** and **18** tend to be more stable with respect to this rearrangement than the antimony(III) amides reported previously. These examples show that the tendency to undergo this rearrangement increases with an increase of the covalent radius and decreases with an increase of coordination number of the central atom. This rearrangement also requires a highly polar M–N bond, therefore increasing the covalent character of the compound (e.g. by a higher oxidation state) decreases the likelihood of this metathesis to occur. Density functional calculations on the activation barriers of the studied reactions have been found to be in agreement with the experimental results. The steric demand of the substituents at the central atom as well as its electron deficiency are the crucial factors that define the stability of these tris(amide)s to F↔$NR_2$ or conceivable F↔Hal rearrangements.

## Experimental Section

**General Remarks:** All manipulations were performed under dry, oxygen-free argon using standard Schlenk techniques. All manipulations of Bi-containing compounds were carried out in brown glass equipment. Solvents were dried by standard methods and distilled prior to use. $Bi(NMe_2)_3$ (**2**),[26] $[In(NEt_2)_3]_2$ (**3**),[27] $Me_3SbBr_2$ (**7**),[28] and $Me_3SbCl_2$ (**8**)[29] were prepared according to the literature. $C_6D_6$ was obtained from Deutero GmbH and dried with sodium. $^1H$, $^{13}C$, and $^{19}F$ NMR spectra were recorded with Bruker ARX 200, AC 300, AMX 400, or DRX 500 spectrometers at 23 °C. Chemical shifts in the $^1H$ and $^{13}C$ NMR spectra are given in ppm relative to internal $Me_4Si$, and those in $^{19}F$ NMR experiments relative to $CFCl_3$ as an external standard. EI mass spectra were recorded with a Finnigan MAT CH7A device using electron impact ionization at 70 eV, and FD mass spectra were recorded with a Finnigan MAT 95S device; all assignments were made with reference to the most abundant isotopes. Elemental analyses were carried out by the Fachbereich Chemie of the Philipps University

 © 2007 Wiley-VCH Verlag GmbH & Co. KGaA, Weinheim 

Marburg (Heraeus-Rapid-Analyzer). The nonempirical generalized gradient approximation (GGA) for the exchange-correlation functional of Perdew et al. (PBE) was employed in this work.[30,31] All calculations were performed using the program PRIRODA developed by Laikov,[32] which implements an economical computational procedure. The one-electron wavefunctions were expanded in the extended TZ2P atomic basis sets of the contracted Gaussians {311/1} for H, {611111/411/11} for C, N, and F, {6111111111/611111/11} for Cl, {6111111111111/5111111111/51111} for Br, {711111111111111/611111111111/51111111} for In and Sb, and {24,24,24,24,24,24,24,24/22,22,22,22,22,22,22,22/15,15,15,15,15/9} for Bi. Full geometry optimization was performed by DFT-PBE methods for a number of structures followed by vibrational frequency calculation using analytical first and second derivatives. Each structure was characterized by a vibrational analysis. Each transition state has only one imaginary normal mode and equilibrium geometry states have only real normal modes. An IRC (intrinsic reaction coordinate) calculation was run starting from the transition state geometry in both directions and verified initial and final structures linked to the transition state. The present theoretical method has been used, and has given very useful results, in antimony and bismuth chemistry.[22]

**Synthesis of (2-$C_5H_5N$)($C_6F_5$)NH (1):** *n*-Butyllithium (1.6 M in hexane, 325 mL, 0.52 mol) was added dropwise to a stirred solution of 2-aminopyridine (48.94 g, 0.52 mol) in thf (50 mL) at –78 °C. The reaction mixture was warmed to 25 °C and stirred at room temperature for 4 h, and then all volatiles were removed under reduced pressure; thf (300 mL) was added to the residue, and then a solution of $C_6F_6$ (48.36 g, 0.26 mol) in thf (60 mL) was added dropwise at –45 °C over about 1 h. The reaction mixture was warmed to room temperature and refluxed for a further 24 h. Dilute hydrochloric acid was then carefully added to the reaction mixture to pH = 4. The organic phase was washed twice with dilute hydrochloric acid (100 mL), and the combined aqueous phases were extracted with diethyl ether (2 × 100 mL). All organic phases were combined and dried with $Na_2SO_4$, and all volatiles were removed under reduced pressure. The residue was extracted with hot *n*-heptane, and crystallized crude **1** was purified by sublimation (50 °C/$5 \times 10^{-3}$ bar). Colorless crystals. Yield: 60.72 g (90%). EI-MS: *m*/*z* (%) = 260 (42) [$M^+$], 241 (100) [$M^+$ – F]. $^1$H NMR ($C_6D_6$, 200.13 MHz): $\delta$ = 5.99 (m, 1 H), 6.36 (m, 1 H), 6.84 (br. s, 1 H, NH), 6.98 (m, 1 H), 8.07 (m, 1 H) ppm. $^{13}$C NMR ($C_6D_6$, 50.32 MHz): $\delta$ = 108.45, 116.25, 137.78, 148.29, 155.29 (all carbon atoms of pyridyl groups) ppm; 4 signals for the carbon atoms of the $C_6F_5$ group were not observed in the spectrum. $^{19}$F NMR ($C_6D_6$, 188.28 MHz): $\delta$ = –164.07 (t, 2 F), –161.80 (t, 1 F), –147.27 (d, 2 F) ppm.

**Synthesis of 2-$C_5H_5N$($C_6F_5$)NLi·thf (4·thf):** *n*-Butyllithium (1.6 M in hexane, 22.50 mL, 36.00 mmol) was added dropwise to a stirred solution of **1** (9.33 g, 35.88 mmol) in thf (50 mL) at –78 °C. The reaction mixture was warmed to 25 °C and stirred at room temperature for 5 h, and then all volatiles were removed under reduced pressure to give a white solid. The crude product was washed with cold *n*-pentane (3 × 10 mL) and dried under reduced pressure. Yield: 11.03 g (91%). White solid. $C_{15}H_{12}F_5LiN_2O$ (338.20): calcd. C 53.27, H 3.58, N 8.28; found C 52.94, H 3.50, N 8.03. $^1$H NMR ($C_6D_6$, 200.13 MHz): $\delta$ = 1.02–1.08 (m, 4 H, O-$CH_2$-$CH_2$), 3.20–3.26 (m, 4 H, O-$CH_2$), 6.16–6.27 (m, 2 H), 6.97–7.06 (m, 1 H), 7.84 (br. s, 1 H) ppm. $^{19}$F NMR ($C_6D_6$, 188.28 MHz): $\delta$ = –173.52 (br. s, 1 F), –166.15 (t, F), –155.10 (br. s, 2 F) ppm. $^{19}$F NMR (thf, 188.28 MHz): $\delta$ = –179.22 (t, 1 F), –170.14 (t, 2 F), –153.64 (d, 2 F) ppm.

**Synthesis of [(2-$C_5H_4N$)($C_6F_5$)N]$_3$Bi (10). Method a:** A solution of amine **1** (0.76 g, 2.90 mmol) in toluene (10 mL) was added dropwise at 0 °C to a stirred solution of **2** (0.33 g, 0.97 mmol) in toluene (10 mL). The reaction mixture was stirred at room temperature for 12 h, and all volatiles were removed under reduced pressure. The residue was recrystallized from *n*-pentane (–30 °C) to give **10** as a yellow solid. Yield: 0.78 g (82%). **Method b:** A solution of **4**·thf (1.67 g, 4.96 mmol) in thf (15 mL) was added dropwise to a stirred suspension of $BiCl_3$ (0.52 g, 1.65 mmol) in thf (20 mL) at 0 °C. The reaction mixture was stirred for a further 12 h, and then all volatiles were removed under reduced pressure. *n*-Pentane (30 mL) was added to the residue, and insoluble substances were removed by filtration. The solution was reduced in volume to 20% of the original volume and stored at –30 °C to obtain **10** as a yellow solid. Yield: 1.20 g (74%). $C_{33}H_{12}BiF_{15}N_6$ (986.45): calcd. C 40.18, H 1.23, N 8.52; found C 39.79, H 1.43, N 8.03. EI-MS: *m*/*z* (%) = 727 (28) [M – N($C_5H_4N$)($C_6F_5$)]$^+$. $^1$H NMR ($C_6D_6$, 200.13 MHz): $\delta$ = 5.58 (br. s, 3 H), 6.14 (br. s, 3 H), 6.93–7.02 (m, 3 H), 7.89 (br. s, 3 H) ppm. $^{13}$C NMR ($C_6D_6$, 50.32 MHz): $\delta$ = 107.96, 112.33, 140.96, 144.17 ppm; 4 signals for the carbon atoms of the $C_6F_5$ group and 1 signal for a carbon atom of the pyridyl group were not observed in the spectrum. $^{19}$F NMR ($C_6D_6$, 188.28 MHz): $\delta$ = –164.80 (br. s, 6 F), –162.64 (br. s, 3 F), –146.86 (d, 6 F) ppm.

**Synthesis of 11:** A solution of **1** (0.86 g, 3.3 mmol) in toluene (20 mL) was added dropwise to a stirred solution of **2** (1.15 g, 3.3 mmol) in toluene (15 mL) at –78 °C. The reaction mixture was stirred at room temperaturefor 24 h, and all volatiles were then removed under reduced pressure. The residue was recrystallized from *n*-pentane (–30 °C) to give **11** as a yellow solid. Yield: 1.21 g (66%). $C_{15}H_{16}BiF_5N_4$ (506.13): calcd. C 32.39, H 2.90, N 10.07; found C 31.27, H 2.98, N 9.20. FD-MS: *m*/*z* (%) = 519 (32) [$M^+$ – 2 F + H], 518 (20) [$M^+$ – 2 F]. $^1$H NMR ($C_6D_6$, 200.13 MHz): $\delta$ = 2.37, 2.38 (2 s, 12 H, $NMe_2$) 5.70 (m, 1 H), 6.00 (m, 1 H), 6.98 (m, 1 H), 7.63 (m, 1 H) ppm. $^{19}$F NMR ($C_6D_6$, 188.28 MHz): $\delta$ = –164.39 (br. s, 2 F, $F_2Bi$), –163.25 (t, 1 F), –149.50 (d, 2 F) ppm.

**Synthesis of 12:** A solution of **1** (0.62 g, 2.4 mmol) in toluene (10 mL) was added dropwise to a stirred solution of **2** (0.43 g, 1.3 mmol) in toluene (10 mL) at –78 °C. The reaction mixture was stirred at room temperature for 24 h, and then all volatiles were removed under reduced pressure. The residue was recrystallized from *n*-pentane (–30 °C) to give **12** as a yellow solid. Yield: 0.56 g (58%). $C_{24}H_{14}BiF_{10}N_5$ (771.37): calcd. C 37.37, H 1.83, N 9.08; found C 36.09, H 2.08, N 8.22. EI-MS: *m*/*z* (%) = 771 (1) [$M^+$]. FD-MS: *m*/*z* (%) = 772 (0.5) [$M^+$ + H], 771 (0.5) [$M^+$], 752 (2) [$M^+$ – F]. $^1$H NMR ($C_6D_6$, 200.13 MHz): $\delta$ = 2.24, 2.25 (2 s, 6 H, Me), 5.83 (m, 1 H), 6.04 (m, 1 H), 6.10 (m, 1 H), 6.39 (m, 1 H), 7.02 (m, 1 H), 7.06 (m, 1 H), 7.57 (m, 1 H), 7.75 (m, 1 H) ppm. $^{19}$F NMR ($C_6D_6$, 188.28 MHz): $\delta$ = –165.42 (t, 2 F), –165.26 (t, 1 F), –163.90 (t, 1 F), –162.96 (t, 1 F), –151.19 (d, 1 F), –146.70 (t, 2 F), –146.87 (br. s, 1 F, FBi), –142.78 (d, 1 F) ppm.

**Synthesis of 13:** Water (2 mL) was added dropwise to a stirred solution of **11** (0.72 g, 1.3 mmol) in toluene (10 mL), and the reaction mixture was stirred for 12 h. The organic phase was separated, dried with $Na_2SO_4$, and all volatiles were removed under reduced pressure. The residue was recrystallized from *n*-heptane (2 mL) to give **13** as a colorless solid. Yield: 0.26 g (65%). $C_{15}H_{17}F_3N_4$ (310.32): calcd. C 58.06, H 5.52, N 18.05; found C 57.63, H 4.09, N 17.64. EI-MS: *m*/*z* (%) = 310 (100) [$M^+$]. $^1$H NMR ($C_6D_6$, 200.13 MHz): $\delta$ = 2.43, 2.44 (2s, 12 H, $NMe_2$), 6.12 (m, 1 H), 6.45 (m, 1 H), 7.06 (m, 1 H), 8.22 (m, 1 H) ppm. $^{13}$C NMR ($C_6D_6$, 50.32 MHz): $\delta$ = 42.49, 42.59 ($NMe_2$), 109.17, 115.56, 136.52, 148.57, 155.44 ppm; 4 signals for the carbon atoms of $C_6F_5$ and 1

 © 2007 Wiley-VCH Verlag GmbH & Co. KGaA, Weinheim 

signal for a carbon atom of the pyridyl group were not observed in the spectrum. $^{19}F$ NMR ($C_6D_6$, 188.28 MHz): $\delta$ = –166.28 (t, 1 F), –150.42 (d, 2 F) ppm.

**Synthesis of 14:** Water (2 mL) was added dropwise to a stirred solution of **12** (0.43 g, 0.6 mmol) in toluene (10 mL), and the reaction mixture was stirred for 12 h. The organic phase was separated, dried with $Na_2SO_4$, and all volatiles were removed under reduced pressure. The residue was purified by chromatography ($SiO_2$; *n*-heptane/toluene (5:1), 30 mL) to give **14** as a colorless solid. Yield: 0.07 g (41%). $C_{13}H_{11}F_4N_3$ (285.24): calcd. C 54.74, H 3.89, N 14.73; found C 54.46, H 3.61, N 14.93. EI-MS: *m*/*z* (%) = 285 (100) [$M^+$]. $^1H$ NMR ($C_6D_6$, 200.13 MHz): $\delta$ = 2.25, 2.26 (2s, 6 H, $NMe_2$), 6.17 (m, 1 H), 6.38 (m, 1 H), 7.01 (m, 1 H), 8.16 (m, 1 H) ppm. $^{13}C$ NMR ($C_6D_6$, 50.32 MHz): $\delta$ = 43.00, 43.09 ($NMe_2$), 108.74, 116.23, 137.53, 148.60, 155.90 ppm. $^{19}F$ NMR ($C_6D_6$, 188.28 MHz): $\delta$ = –165.26 (t, 1 F), –162.93 (t, 1 F), –151.18 (d, 1 F), –142.78 (d, 1 F) ppm.

**Synthesis of 15:** A solution of amine **1** (0.30 g, 1.15 mmol) in toluene (10 mL) was added dropwise at –78 °C to a stirred solution of **3** (0.38 g, 0.58 mmol) in toluene (10 mL). The reaction mixture was stirred at room temperature for 12 h, and all volatiles were removed under reduced pressure. The residue was recrystallized from *n*-pentane (–30 °C) to give **15** as a yellow solid. Yield: 0.52 g (87%). $C_{19}H_{24}F_5InN_4$ (518.23): calcd. C 44.04, H 4.67, N 10.81; found C 43.57, H 4.41, N 10.04. EI-MS: *m*/*z* (%) = 374 (15) [M – 2 $NEt_2$]$^+$. $^1H$ NMR ($C_6D_6$, 200.13 MHz): $\delta$ = 0.97 (t, 12 H, $CH_3$), 2.48 (q, 8 H, $NCH_2$), 5.89–6.01 (m, 2 H), 6.78–6.86 (m, 1 H), 7.52–7.54 (m, 1 H) ppm. $^{13}C$ NMR ($C_6D_6$, 50.32 MHz): $\delta$ = 15.61 ($CH_3$), 44.18 ($NCH_2$), 107.96, 112.33, 140.96, 144.17 ppm; four signals for the carbon atoms of the $C_6F_5$ group and one signal for a carbon atom of the pyridyl group were not observed in the spectrum. $^{19}F$ NMR ($C_6D_6$, 188.28 MHz): $\delta$ = –165.63 (t, 1 F), –164.77 (t, 2 F), –149.89 (d, 2 F) ppm.

**Synthesis of 16:** The procedure was analogous to that used to synthesize **15**. Thus, treatment of a solution of **1** (1.46 g, 5.60 mmol) in toluene (10 mL) with a solution of **3** (1.46 g, 5.60 mmol) in toluene (10 mL) gave **16** as a light yellow solid. Yield: 1.46 g (74%). $C_{26}H_{18}F_{10}InN_5$ (705.26): calcd. C 44.28, H 2.57, N 9.93; found C 43.52, H 2.61, N 9.49. EI-MS: *m*/*z* (%) = 633 (76) [M – $NEt_2$]$^+$. $^1H$ NMR ($C_6D_6$, 300.13 MHz): $\delta$ = 0.68 (t, 6 H, $CH_3$), 3.29 (br. s, 4 H, $NCH_2$), 5.80–5.83 (m, 2 H), 6.09–6.13 (m, 2 H), 6.90–6.95 (m, 2 H), 7.47–7.49 (m, 2 H) ppm. $^{13}C$ NMR ($C_6D_6$, 75.47 MHz): $\delta$ = 12.10 ($CH_3$), 41.15 ($NCH_2$), 107.74, 110.81, 140.45, 144.27, 162.82 ppm; 4 signals for the carbon atoms of the $C_6F_5$ group were not observed in the spectrum. $^{19}F$ NMR ($C_6D_6$, 188.28 MHz): $\delta$ = –164.74 (t, 2 F), –163.37 (t, 4 F), –147.14 (d) ppm.

**Synthesis of 9:** A solution of amine **1** (1.87 g, 7.20 mmol) in toluene (10 mL) was added dropwise at room temperature to a stirred solution of **3** (0.80 g, 1.20 mmol) in toluene (10 mL). The reaction mixture was stirred for 12 h, and all volatiles were removed under reduced pressure. The residue was recrystallized from *n*-pentane (–30 °C) to give **9** as colorless crystals. Yield: 2.00 g (93%). $C_{33}H_{12}F_{15}InN_6$ (892.28): calcd. C 44.42, H 1.36, N 9.42; found C 44.20, H 1.27, N 8.86. EI-MS: *m*/*z* (%) = 892 (79) [M]$^+$, 633 (63) [M – N($C_5H_4N$)($C_6F_5$)]$^+$, 374 (10) [M – 2 N($C_5H_4N$)($C_6F_5$)]$^+$. $^1H$ NMR ($C_6D_6$, 300.13 MHz): $\delta$ = 5.92–5.95 (m, 3 H), 5.99–6.03 (m, 3 H), 6.80–6.86 (m, 3 H), 7.56–7.58 (m, 3 H) ppm. $^{13}C$ NMR ($C_6D_6$, 75.47 MHz): $\delta$ = 108.05, 112.69, 140.89, 144.41 ppm; 4 signals for the carbon atoms of the $C_6F_5$ group and 1 signal for a carbon atom of the pyridyl group were not observed in the spectrum. $^{19}F$ NMR ($C_6D_6$, 188.28 MHz): $\delta$ = –165.28 (br. s, 3 F), –164.66 (t, 6 F), –149.54 (br. s, 6 F) ppm.

**Synthesis of 17:** A solution of **4**·thf (1.64 g, 4.84 mmol) in thf (20 mL) was added dropwise at room temperature to a stirred solution of **7** (1.58 g, 4.84 mmol) in thf (15 mL). The reaction mixture was stirred at room temperature for 48 h, and all volatiles were removed under reduced pressure. Toluene (30 mL) was added to the residue, and insoluble substances were removed by filtration. The solution was reduced in volume to 5 mL and stored at –30 °C to obtain **17** as a white solid. Yield: 1.71 g (70%). $C_{14}H_{13}BrF_5N_2Sb$ (505.92): calcd. C 33.24, H 2.59, N 5.54; found C 33.05, H 2.51, N 5.33. EI-MS: *m*/*z* (%) = 506 (2) [M]$^+$, 247 (100) [M – N($C_5H_4N$)($C_6F_5$)]$^+$. $^1H$ NMR ($C_6D_6$, 200.13 MHz): $\delta$ = 1.79 (s, 9 H, $SbMe_3$), 5.55–5.59 (m, 1 H), 6.20–6.27 (m, 1 H), 6.85–6.94 (m, 1 H), 7.58–7.61 (m, 1 H) ppm. $^{13}C$ NMR ($C_6D_6$, 50.32 MHz): $\delta$ = 20.83 ($SbMe_3$), 106.31, 113.53, 138.57, 146.21, 159.07 ppm; 4 signals for the carbon atoms of the $C_6F_5$ group were not observed in the spectrum. $^{19}F$ NMR ($C_6D_6$, 188.28 MHz): $\delta$ = –162.18 (t, 2 F), –157.64 (t, 1 F), –147.22 (d, 2 F) ppm.

**Synthesis of 18:** The procedure was analogous to that used to synthesize **17**. Thus, treatment of a solution of **4**·thf (1.10 g, 3.24 mmol) in thf (20 mL) with a solution of **8** (0.77 g, 3.24 mmol) in thf (15 mL) gave **18** as a white solid. Yield: 1.15 g (77%). $C_{14}H_{13}ClF_5N_2Sb$ (461.47): calcd. C 36.44, H 2.84, N 6.07; found C 36.21, H 2.71, N 5.72. FD-MS: *m*/*z* (%) = 462 (1) [M]$^+$, 384 (100) [M – $C_5H_4N$]$^+$. $^1H$ NMR ($C_6D_6$, 200.13 MHz): $\delta$ = 1.67 (s, $SbMe_3$), 5.56–5.61 (m, 1 H), 6.21–6.28 (m, 1 H), 6.86–6.95 (m, 1 H), 7.63–7.64 (m, 1 H) ppm. $^{13}C$ NMR ($C_6D_6$, 50.32 MHz): $\delta$ = 19.95 ($SbMe_3$), 106.80, 113.63, 138.58, 146.43, 158.78 ppm; 4 signals for the carbon atoms of the $C_6F_5$ group were not observed in the spectrum. $^{19}F$ NMR ($C_6D_6$, 188.28 MHz): $\delta$ = –162.31 (t, 2 F), –158.10 (t, 1 F), –147.31 (d, 2 F) ppm.

**Synthesis of 19:** The procedure was analogous to that used to synthesize **17**. Thus, treatment of a solution of **4**·thf (2.64 g, 7.80 mmol) in thf (20 mL) with a solution of **8** (0.93 g, 3.90 mmol) in thf (15 mL) gave **19** as a white solid (extraction with *n*-pentane). Yield: 1.95 g (73%). $C_{25}H_{17}F_{10}N_4Sb$ (685.17): calcd. C 43.82, H 2.50, N 8.18; found C 43.58, H 2.35, N 7.66. EI-MS: *m*/*z* (%) = 669 (1) [M – Me]$^+$, 425 (100) [M – N($C_5H_4N$)($C_6F_5$)]$^+$. $^1H$ NMR ($C_6D_6$, 200.13 MHz): $\delta$ = 1.29 (br. s, $SbMe_3$), 5.96–6.00 (m, 2 H), 6.31–6.37 (m, 2 H), 6.94–7.02 (m, 2 H), 8.04–8.06 (m, 2 H) ppm. $^{13}C$ NMR ($C_6D_6$, 50.32 MHz): $\delta$ = 19.76 ($SbMe_3$), 106.80, 112.48, 138.49, 146.29, 159.51 ppm; 4 signals for the carbon atoms of the $C_6F_5$ group were not observed in the spectrum. $^{19}F$ NMR ($C_6D_6$, 188.28 MHz): $\delta$ = –164.27 (t, 4 F), –161.72 (t, 2 F), –146.97 (d, 4 F) ppm.

**X-ray Crystallographic Study. Crystal Data for 9·0.5$C_7H_8$:** Triclinic unit cell, space group $P\bar{1}$, with $a$ = 10.7275(8), $b$ = 12.9882(8), $c$ = 14.4190(10) Å, $\alpha$ = 72.264(8), $\beta$ = 79.030(9), $\gamma$ = 69.388(8)°, $V$ = 1783.2(2) Å$^3$, $Z$ = 2. 17664 reflections were collected at 193 K with a STOE IPDS diffractometer using graphite-monochromated Mo-$K_\alpha$ radiation and were corrected for absorption. 6471 reflections were unique ($R_{int}$ = 0.0517) and 4274 with $I > 2\sigma(I)$ "observed". The structure was solved by direct methods[33] and refined using the full-matrix least-squares procedure.[34] All non-hydrogen atoms were treated anisotropically, and hydrogen atoms were treated with fixed isotropic thermal parameters as "riding" on calculated positions. One molecule of disordered toluene is present in the unit cell and was refined with restraints for geometrical and thermal parameters. Final residuals for 540 refined parameters and 70 restraints: $wR2$ = 0.053 (for all unique data), $R1$ = 0.0314 (for the "observed" data). CCDC-631484 (**9**) contains the supplementary crystallographic data for this paper. These data can be obtained free of charge from The Cambridge Crystallographic Data Centre via www.ccdc.cam.ac.uk/data_request/cif.

 © 2007 Wiley-VCH Verlag GmbH & Co. KGaA, Weinheim 

**Supporting Information** (see footnote on the first page of this article): Molecular structures of stable compounds and transition states with and without $M \rightarrow N_{Py}$ intramolecular interactions [series (a) and (b)], their calculated Cartesian coordinates, energies, and numbers of imaginary frequencies.

## Acknowledgments

We thank Dr. D. N. Laikov for providing us with the program PRIRODA. We also thank the Research Computing Center of the Moscow State University for computational time.

[1] P. L. Shutov, S. S. Karlov, K. Harms, D. A. Tyurin, J. Sundermeyer, J. Lorberth, G. S. Zaitseva, *Eur. J. Inorg. Chem.* **2004**, 2498–2503.
[2] *Organofluorine Chemistry: Principles and Commercial Applications* (Eds.: R. E. Banks, B. E. Smart, J. C. Tatlow), Plenum, New York, **1994**.
[3] T. Hiyama, *Organofluorine Compounds*, Springer, Berlin, **2000**.
[4] U. Mazurek, H. Schwarz, *Chem. Commun.* **2003**, 1321–1326.
[5] J. L. Kiplinger, T. G. Richmond, C. E. Osterberg, *Chem. Rev.* **1994**, *94*, 373–431.
[6] T. Braun, S. P. Foxon, R. N. Perutz, P. H. Walton, *Angew. Chem. Int. Ed.* **1999**, *38*, 3326–3329.
[7] T. G. Richmond, C. E. Osterberg, A. M. Arif, *J. Am. Chem. Soc.* **1987**, *109*, 8091–8092.
[8] T. Schaub, M. Backes, U. Radius, *J. Am. Chem. Soc.* **2006**, *128*, 15964–15965.
[9] S. Park, M. Pontier-Johnson, D. M. Roundhill, *J. Am. Chem. Soc.* **1989**, *111*, 3101–3103.
[10] L. Maron, E. L. Werkema, L. Perrin, O. Eisenstein, R. A. Andersen, *J. Am. Chem. Soc.* **2005**, *127*, 279–292.
[11] U. Jäger-Fiedler, P. Arndt, W. Baumann, A. Spannenberg, V. V. Burlakov, U. Rosenthal, *Eur. J. Inorg. Chem.* **2005**, 2842–2849.
[12] J. Burdeniuc, B. Jedlicka, R. H. Crabtree, *Chem. Ber./Recueil* **1997**, *130*, 145–154.
[13] G. M. Brooke, *J. Fluorine Chem.* **1997**, *86*, 1–76.
[14] T. N. Gerasimova, N. A. Orlova, *J. Fluorine Chem.* **1985**, *28*, 361–380.
[15] F. V. Cochran, P. J. Bonitatebus, R. R. Schrock, *Organometallics* **2000**, *19*, 2414–2416.
[16] A. N. Frolov, *Russ. J. Org. Chem.* **1998**, *34*, 1047–1051.
[17] R. Koppang, *J. Organomet. Chem.* **1972**, *46*, 193–200.
[18] J. Ashenhurst, L. Brancaleon, S. Gao, W. Liu, H. Schmider, S. Wang, G. Wu, Q. G. Wu, *Organometallics* **1998**, *17*, 5334–5341.
[19] F. H. Allen, *Acta Crystallogr., Sect. B* **2002**, *58*, 380–388.
[20] R. A. Fischer, H. Sussek, A. Miehr, H. Pritzkow, E. Herdtweck, *J. Organomet. Chem.* **1997**, *548*, 73–80.
[21] J. Emsley, *The Elements*, 3rd ed., Clarendon Press, Oxford, U.K., **1998**.
[22] P. L. Shutov, S. S. Karlov, K. Harms, D. A. Tyurin, A. V. Churakov, J. Lorberth, G. S. Zaitseva, *Inorg. Chem.* **2002**, *41*, 6147–6152.
[23] M. Jakt, L. Johannissen, H. S. Rzepa, D. A. Widdowson, R. Wilhelm, *J. Chem. Soc. Perkin Trans. 2* **2002**, 576–581.
[24] T. Braun, R. N. Perutz, *Chem. Commun.* **2002**, 2749–2757.
[25] W. D. Jones, *Dalton Trans.* **2003**, 3991–3995.
[26] W. Clegg, N. A. Compton, R. J. Errington, G. A. Fisher, M. E. Green, D. C. R. Hockless, N. C. Norman, *Inorg. Chem.* **1991**, *30*, 4680–4682.
[27] G. Rosetto, N. Brianese, A. Camporese, M. Porchia, P. Zanella, R. Bertoncello, *Main Group Met. Chem.* **1991**, *14*, 113–122.
[28] B. A. Nevett, A. Perry, *Spectrochim. Acta* **1975**, *A31*, 101–107.
[29] T. Okada, R. Okarawa, *J. Organomet. Chem.* **1973**, *54*, 149–152.
[30] J. P. Perdew, K. Burke, M. Ernzerhof, *Phys. Rev. Lett.* **1996**, *77*, 3865–3868.
[31] M. Ernzerhof, G. E. Scuseria, *J. Chem. Phys.* **1999**, *110*, 5029–5036.
[32] D. N. Laikov, *Chem. Phys. Lett.* **1997**, *281*, 151–156.
[33] *SIR92 – A program for crystal structure solution*: A. Altomare, G. Cascarano, C. Giacovazzo, A. Guagliardi, *J. Appl. Crystallogr.* **1993**, *26*, 343–350.
[34] G. M. Sheldrick, *SHELXL97 – Program for Crystal Structure Refinement*, release 97-2, University of Göttingen, Germany, **1997**.

Received: July 22, 2007
Published Online: November 8, 2007

 © 2007 Wiley-VCH Verlag GmbH & Co. KGaA, Weinheim 

DOI: 10.1002/ejic.200700872

# Optical, Magnetic and Structural Properties of the Spin-Crossover Complex $[Fe(btr)_2(NCS)_2]\cdot H_2O$ in the Light-Induced and Thermally Quenched Metastable States

**Vincent Legrand,[a,b] Sébastien Pillet,[a] Chiara Carbonera,[c] Mohamed Souhassou,[a] Jean-François Létard,[c] Philippe Guionneau,[c] and Claude Lecomte*[a]**

**Keywords:** Iron(II) / Photoswitching / Structural analysis / Photomagnetism / Spin crossover

$[Fe(btr)_2(NCS)_2]\cdot H_2O$ [btr = 4,4′-bis(1,2,4-triazole)] is the archetype of highly cooperative and low-dimensional spin-crossover complexes, which exhibit low-spin (LS) to high-spin (HS) light-induced conversion at very low temperature. The structural reorganizations related to the light-induced and thermally induced LS–HS transitions were characterized by single-crystal X-ray diffraction below the relaxation temperature ($T$ = 15 K < $T_{LIESST}$) and at 130 K within the thermal hysteresis loop. We show that the LIESST and thermal spin transitions lead to the same structural variations, namely an elongation of the Fe–N bonds by 0.18 Å (Fe–$N_{NCS}$) and 0.20 Å (Fe–$N_{btr}$), on going from LS to HS, together with a reorientation of the NCS group by nearly 13°. The atomic displacement amplitudes, derived from the crystal structures, indicate lattice vibration modes of larger amplitudes and correlatively lower vibration frequencies in the HS state. The deformation of the crystal lattice as a function of temperature and laser excitation was quantitatively analyzed in terms of the HS and LS thermal-expansion ($\boldsymbol{\alpha}_{HS}$ and $\boldsymbol{\alpha}_{LS}$) and spin-transition spontaneous-strain ($\boldsymbol{\varepsilon}$) tensors. The eigendirections and eigenvalues of the $\boldsymbol{\alpha}$ and $\boldsymbol{\varepsilon}$ tensors correlate well with the weak and strong interactions in the solid and are responsible for the high cooperativity and low-dimensional behaviour. Magnetic and spectroscopic measurements were performed in all the different spin states and related to the structural findings.
(© Wiley-VCH Verlag GmbH & Co. KGaA, 69451 Weinheim, Germany, 2007)

## Introduction

Spin crossover in iron(II) coordination complexes is a quite well-understood phenomenon, which has been thoroughly described and reviewed in the literature.[1] The spin conversion is related to the change in the electronic configuration of iron from $t_{2g}^4e_g^2$ in the high-spin (HS) state to $t_{2g}^6e_g^0$ in the low-spin (LS) state on decreasing temperature. This HS→LS electron redistribution in general parallels drastic structural modifications, namely a contraction of the Fe–ligand bonds by typically 0.2 Å as well as a decrease in the distortion of the Fe octahedral coordination polyhedron.[2] Correlatively, a decrease in the molecular volume by several $Å^3$ is usually characterized. Spin-crossover complexes can furthermore change their spin state upon the variation of a thermodynamic parameter such as temperature or pressure or by the application of a perturbation like an intense magnetic field[3] or light irradiation.[1] In the latter case, the process leading to the LS→HS conversion is reversible[4] and is called the LIESST effect (Light Induced Excited Spin State Trapping).[5] The relaxation from the light-induced metastable HS state to the thermodynamically stable LS state is attributed to a tunnel mechanism at very low temperature and to a much faster thermal activation over an energy barrier at higher temperature. Accordingly, the metastable HS state can be trapped at very low temperature. Recently, it has been shown that an elegant way to characterize the photomagnetic properties is to measure the $T_{LIESST}$ temperature, which somewhat represents the temperature at which the metastable state relaxes quickly.[6,7] For weakly cooperative systems, the relaxation obeys single-exponential kinetics, whereas in the case of high cooperativity, the relaxation rate follows sigmoidal kinetics, ascribed to an autoaccelerated phenomenon owing to the HS→LS large molecular volume change and long-range elastic interactions in the solid.[8]

The structural aspects of spin-crossover complexes, and especially their relationship with respect to the spin transition characteristics, are nowadays raising a renewed interest. Direct correlations do exist between the distortion of the iron coordination octahedron and the features of the spin transition (e.g. $T_{LIESST}$).[9] Careful investigations of the structural modifications occurring during the thermal spin transition were reported in the literature and were mostly

[a] Laboratoire de Cristallographie et Modélisation des Matériaux Minéraux et Biologiques, LCM3B, UMR CNRS 7036, Nancy-Université
BP 239, 54506 Vandoeuvre-les-Nancy, France
Fax: +33-383406492
E-mail: claude.lecomte@lcm3b.uhp-nancy.fr
[b] Institut Laue Langevin
6 rue Jules Horowitz, BP 156, 38042 Grenoble Cedex 9, France
[c] ICMCB, CNRS, Université Bordeaux 1
87 avenue du Docteur Schweitzer, 33608 Pessac cedex, France

 © 2007 Wiley-VCH Verlag GmbH & Co. KGaA, Weinheim 

based on the comparison between the crystal structures in the HS state at room temperature and in the LS state at low temperature. Obviously, such studies suffer from thermal contraction effects, rendering a quantitative analysis quite meaningless if one wants to investigate fine structural details. In addition, atomic displacement parameters are not comparable between room temperature and low temperature; significant corrections to bond lengths would therefore also be required from libration motion.[10] The perturbation due to thermal contraction effects can be estimated, in a first approximation, by using isostructural materials which do not undergo the spin transition, e.g. by exchanging the central transition-metal ion.[11] A better strategy would take advantage of a hysteresis loop, if any, centred on the thermal spin transition, to derive the crystal structure in both the HS and LS states at identical temperature. For almost a decade, the crystal structures of light-induced metastable HS states have been reported for an increasing number of systems; they were derived from X-ray or neutron diffraction measurements performed at very low temperatures under light excitation.[12] These studies are possible thanks to the slowing of the HS to LS relaxation rate at very low temperature.[8] In some cases, a metastable HS state can also be trapped by rapid thermal quenching from room temperature to very low temperature: for example, the HS crystal structure of $[Fe(PM–BiA)_2(NCS)_2]$ (PM = *N*-2′-pyridylmethylene and BiA = 4-aminobiphenyl) was determined at 30 K.[13] Following previous notations, the metastable HS state is denoted by HS-2 from this point onwards in this paper (HS-2q and HS-2p are used for the thermally quenched and photoinduced states, respectively); the HS state above the thermal transition is denoted by HS-1 (Figure 1). Finally, very recently, high-resolution X-ray diffraction measurements on the spin-crossover compounds $[Fe(btr)_2(NCS)_2]\cdot H_2O$ [btr = 4,4′-bis(1,2,4-triazole)] and $[Fe(phen)_2(NCS)_2]$ (phen = 1,10-phenanthroline) have shown the possibility of the modelling of the electron-density distribution and the characterization of its redistribution upon spin transition, for instance, over the iron 3d atomic orbitals.[14–16] Whether the HS-2 states are identical within each other and how they compare to the HS-1 state are still controversial topics. In some cases, it has been proved that HS-2p and HS-2q are structurally different from HS-1 without any ambiguity, for instance in $[Fe(abpt)_2(N(CN)_2)_2]$,[17] leading to the concept of multimetastability.[18]

$[Fe(btr)_2(NCS)_2]\cdot H_2O$ is the archetype of highly cooperative spin-crossover compounds. It exhibits abrupt thermal spin transitions with a 21-K hysteresis loop ($T_{1/2\downarrow}$ = 123.5 K and $T_{1/2\uparrow}$ = 144.5 K). This complex crystallizes in the monoclinic space group *C*2/*c* without any symmetry change at the thermal spin transition. The crystal structure consists of an $Fe^{II}$ ion located in a slightly distorted $FeN_6$ centrosymmetric octahedral environment with four btr groups in the basal plane and two *trans* thiocyanate ligands in the apical directions (Figure 2). The btr group is a bidentate ligand leading to a bidimensional extended layer structure parallel to the *bc* plane. The NCS anions are directed away from the layers. The connection in the third direction is provided through van der Waals interactions and assisted by weak hydrogen bonds through a noncoordinated water molecule. On the basis of this specific polymeric layer structure, one might expect high cooperative interactions in the *bc* plane. The crystal structure was determined above and below the thermal transition at 293 K in the HS state[19] and at 104 K in the LS state.[20] The major structural modifications related to this transition are a shortening of the Fe–N bond lengths [$\Delta d_{Fe–NCS}$ = –0.175(4) Å, $\Delta d_{Fe–N(btr)}$ = –0.213(3) Å] and a reorientation of the NCS groups with a more linear Fe–N–C–S geometry in the LS state in parallel to a contraction of the unit cell by 4.8% [$\Delta V$ = –91(9) Å$^3$]. This system has been the subject of various studies at the thermal spin transition. The hysteresis loop has been followed by magnetic measurements and Mössbauer spectroscopy.[19] The effect of metal dilution was analyzed in $[Fe_xM_{1-x}(btr)_2(NCS)_2]\cdot H_2O$ (M = Co, Ni) mixed systems, by calorimetric, magnetic and Mössbauer measurements;[21] these studies showed that metal dilution smoothes the transition curves. The first studies of the metastable HS state were performed through reflectivity and magnetic measurements on $[Fe_xCo_{1-x}(btr)_2(NCS)_2]\cdot H_2O$ derivatives;[22] the authors studied the LIESST relaxation and the LITH (Light Induced Thermal Hysteresis) loop under permanent irradiation at $\lambda$ = 600 nm and 40 mW cm$^{-2}$. Finally, it has been shown that the HS ↔ LS transition is related to a domain nucleation, growth and coarsening process in the solid state, with an unprecedented light-induced structural reorganization.[20,23]

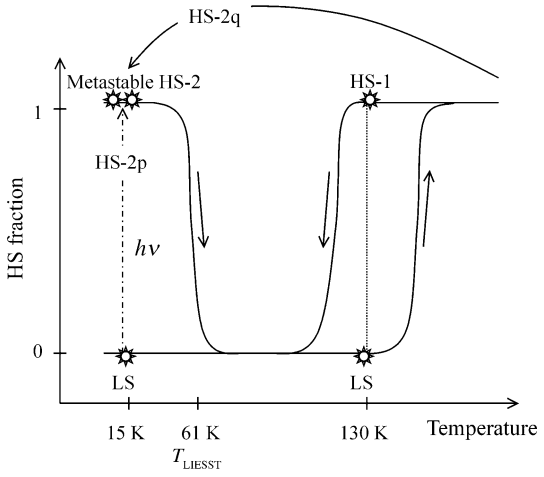


Figure 1. Schematic structural phase diagram (see text for the phase labelling).

We report here a detailed structural analysis of $[Fe(btr)_2(NCS)_2]\cdot H_2O$ in various spin states, HS-1, LS, HS-2q, HS-2p, by using X-ray diffraction measurements performed at two temperatures, 15 K and 130 K (Figure 1). The main goal of this study is the characterization of the structural reorganization related to the light-induced and thermally induced spin transitions independent of thermal contraction/expansion effects. Our structural findings are correlated to magnetic and spectroscopic results, which allows us

 © 2007 Wiley-VCH Verlag GmbH & Co. KGaA, Weinheim 

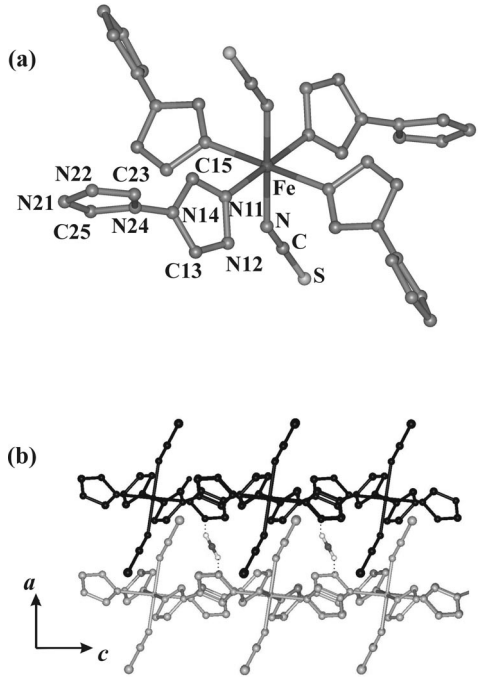


Figure 2. (a) Molecular structure of $[Fe(btr)_2(NCS)_2]\cdot H_2O$ in the HS-2q state at 15 K. (b) View of the layer stacking along the *a* axis. Hydrogen atoms of the btr groups are omitted for clarity.

to define the appropriate experimental conditions for the photocrystallographic measurements. We must emphasize that, for consistency, single crystals of similar quality and size were used in all the experiments reported here.

## Results and Discussion

### Optical Spectroscopy

$[Fe(btr)_2(NCS)_2]\cdot H_2O$ exhibits thermochromic effects associated with the HS–LS transition, from colourless at room temperature to pink at low temperature. The change in the diffuse absorption spectrum as a function of temperature is given in Figure 3. On decreasing the temperature from 160 K to 100 K and passing through the thermal HS-to-LS transition, the absorption band with a maximum intensity at 550 nm (18200 $cm^{-1}$) increases in intensity. This band is characteristic of the LS state and is attributed to the spin-allowed $^1A_1 \rightarrow {}^1T_1$ transition, according to the Tanabe–Sugano diagram for $Fe^{II}$ ($d^6$) in an octahedral ligand field. In parallel, the band with a maximum intensity at 875 nm (11400 $cm^{-1}$), characteristic of the HS state and corresponding to the $^5T_2 \rightarrow {}^5E$ transition, decreases in intensity. Below nearly 75 K, the 550-nm absorption band is gradually attenuated to a minimum value at 10 K owing to the partial LS-to-HS phototransformation under the probing white beam ("LITH down" in Figure 3). On further increasing the temperature to 100 K, first the 550-nm absorption band remains almost constant and in a second step increases in intensity, corresponding to the relaxation from HS to LS ("LITH up" in Figure 3). Finally, from 100 K to 160 K, the LS-to-HS thermal transition occurs, the 550-nm absorption band is attenuated and recovers its initial value. In such diffuse absorption measurements, the intensity ratio of the $^5T_2 \rightarrow {}^5E$ and $^1A_1 \rightarrow {}^1T_1$ bands should not be taken too strictly, because they may change owing to powder sample texture effects; therefore, they cannot be directly compared to single-crystal absorption spectra. In addition, a slight bleaching of the powder sample, resulting possibly from surface dehydration, has been noticed at the end of the measurement, which could alter the intensity of the $^5T_2 \rightarrow {}^5E$ band. It is indeed known that dehydrated $[Fe(btr)_2(NCS)_2]\cdot H_2O$ loses its spin-transition behaviour and is a HS system.

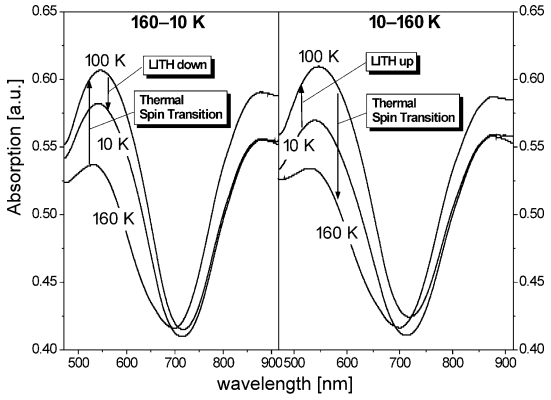


Figure 3. Diffuse absorption spectra as a function of temperature in the cooling (160–10 K) and warming (10–160 K) modes. The 10-K spectrum corresponds to the photostationary state under the experimental conditions of the reflectivity measurements.

This 550-nm absorption band displays a high contrast depending on the spin state. The diffuse reflected intensity vs. temperature at the wavelength $\lambda$ = 532 nm was thus investigated in more detail and is given in Figure 4. The thermal hysteresis loop is well defined with $T_{1/2\downarrow}$ = 123 K and $T_{1/2\uparrow}$ = 144 K, in perfect agreement with magnetic and crystallographic results.[19,20] On decreasing the temperature from 75 to 10 K, we observe an increase in the reflectivity signal, corresponding to partial LS-to-HS conversion induced by the probing white light. Then, as the temperature is increased further, the signal presents a constant plateau till nearly 62 K, at which the LS value is recovered. This loop, defined below 75 K, corresponds to the light-induced thermal hysteresis phenomenon (LITH),[24] already discussed by Desaix et al.,[22] and clearly confirms the existence of a photoinduced instability for $[Fe(btr)_2(NCS)_2]\cdot H_2O$. By comparison of the reflectivity value at the photostationary state (0.43) with those obtained for the purely LS (0.39) and purely HS (0.46) states, we can estimate a surface photoconversion, $\gamma_{HS}$, of nearly 0.5 at saturation.

The spin selectivity of the bands centred at 550 nm and 875 nm indicates that they correspond to the optimum laser wavelengths for inducing the LS-to-HS-2 (LIESST) and HS-2-to-LS (reverse LIESST) conversions, respectively. This information is crucial for defining the excitation conditions for the photocrystallographic measurements.

 © 2007 Wiley-VCH Verlag GmbH & Co. KGaA, Weinheim 

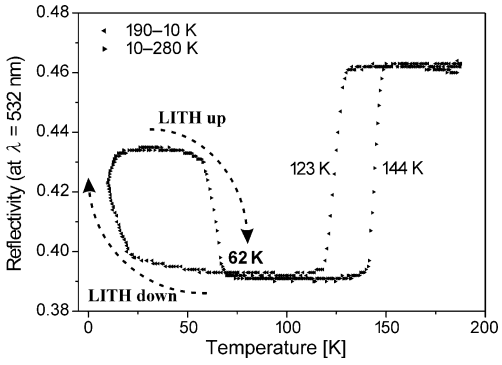


Figure 4. Reflectivity measurements as a function of temperature at $\lambda$ = 532 nm in the cooling (190–10 K) and warming (10–280 K) modes: $T_{1/2\downarrow}$ = 123 K, $T_{1/2\uparrow}$ = 144 K.

### Magnetic Behaviour of the Light-Induced and Thermally Induced Metastable States

The magnetic properties as a function of temperature and light irradiation were investigated by using different measurement procedures. For the first measurement (Figure 5a), the sample was rapidly quenched to 10 K in the HS-2q state. Then, the temperature was raised in the dark; $\chi_M T$ initially increases slightly, as a result of zero-field splitting of the quintet HS-2 state, before reaching a plateau and then sharply falls off to 0 $cm^3 K mol^{-1}$ at 61 K, indicating a complete relaxation of the molecular species into the LS state. After the relaxation, the thermal transitions were recorded in the warming and cooling modes and are consistent with literature results:[19] very abrupt and complete transitions at $T_{1/2\downarrow}$ = 123.5 K and $T_{1/2\uparrow}$ = 144.5 K. The $\chi_M T$ value at low temperature on the plateau is nearly identical (3.5 $cm^3 K mol^{-1}$) to that observed at high temperature in the HS-1 state, suggesting that the quenched state corresponds to almost $\gamma_{HS}$ = 1. The $T_{TIESST}$ (Thermally Induced Excited Spin State Trapping) value is estimated at 61 K, and the HS-2-to-LS relaxation at this temperature is as abrupt as those for the thermal transitions. These magnetic measurements prove without any ambiguity that it is possible to quench $[Fe(btr)_2(NCS)_2]\cdot H_2O$ single-crystal samples in the HS-2q state.

For the second measurement (Figure 5b), the sample was cooled gradually from room temperature (HS-1 state) to 10 K (LS state) and then irradiated with a laser at $\lambda$ = 514 nm ($P$ = 5 mW $cm^{-2}$) to promote the HS-2p state. The $\chi_M T$ value rose up to 0.63 $cm^3 K mol^{-1}$ after a 15-h continuous irradiation, which indicates partial LS-to-HS-2p photoconversion. By comparison with the $\chi_M T$ value obtained at 160 K for the HS-1 state (3.0 $cm^3 K mol^{-1}$), a photoconversion of about 21% is estimated. On increasing the temperature in the dark, the HS-to-LS relaxation is observed at $T$ = 61 K. Under 60-mW $cm^{-2}$ excitation with green light of 550 nm wavelength at $T$ = 10 K, Morscheidt et al.[25] also induced a partial conversion of at most 20% HS-2.

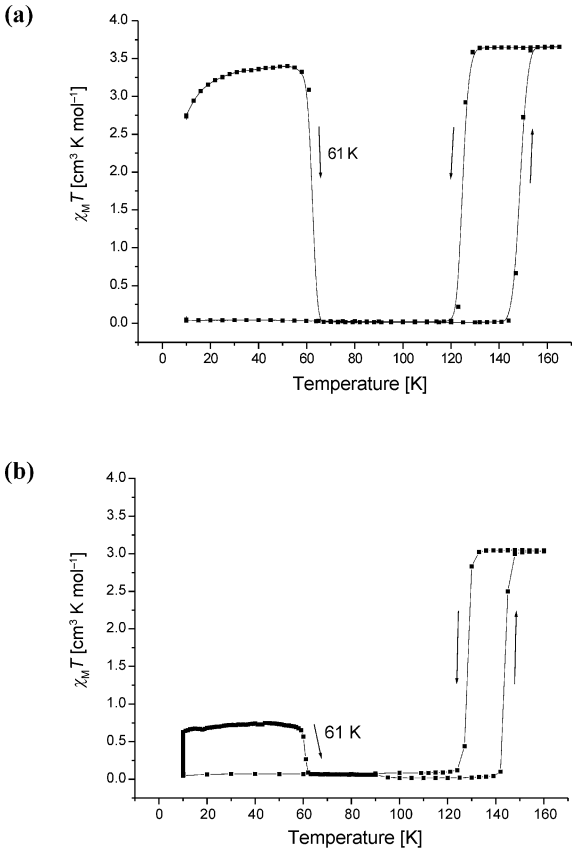


Figure 5. Temperature dependence of $\chi_M T$ for (a) the thermally quenched sample and (b) the photoinduced sample.

Finally, the photoexcitation and relaxation kinetics were derived. The magnetic signal was recorded during a 23-h continuous irradiation at 10 K at $\lambda$ = 514 nm (Figure 6a). It clearly shows a nonlinear sigmoidal behaviour, which has been attributed to a competition between photoexcitation and relaxation by Enachescu et al. for $[Fe_xM_{1-x}(btr)_2(NCS)_2]\cdot H_2O$ derivatives (M = Ni, Co, Zn).[26] This is the basis for the light-induced instability phenomenon. After saturation of the magnetic signal at 0.89 $cm^3 K mol^{-1}$, the excitation light was turned off, and the magnetic signal was monitored in the dark. The negligible change in the signal in the dark, although a slight negative trend is noticeable, confirms the high stability of the HS-2 state at $T$ = 10 K, in the tunnel relaxation regime. The reverse-LIESST effect was then induced by using an excitation wavelength corresponding to the $^5T_2 \rightarrow {}^5E$ transition at $\lambda$ = 830 nm (following the optical reflectivity results); the irradiance was set to 5 mW $cm^{-2}$. The sudden change in the slope and the continuous decrease in the magnetic signal therefore confirm the reversibility of the light-induced LS–HS conversion for $T < T_{LIESST}$. The molar magnetic susceptibility of the HS-2 state at 10 K after thermal trapping was also monitored as a function of time and converted to $\gamma_{HS}$ (Figure 6b) in order to calibrate the 15-K photocrystallographic measurements. The relaxation kinetics is very slow at this temperature, which is well below $T_{LIESST}$ and $T_{TIESST}$, and corresponds to the tunnel relaxation regime.

 © 2007 Wiley-VCH Verlag GmbH & Co. KGaA, Weinheim 

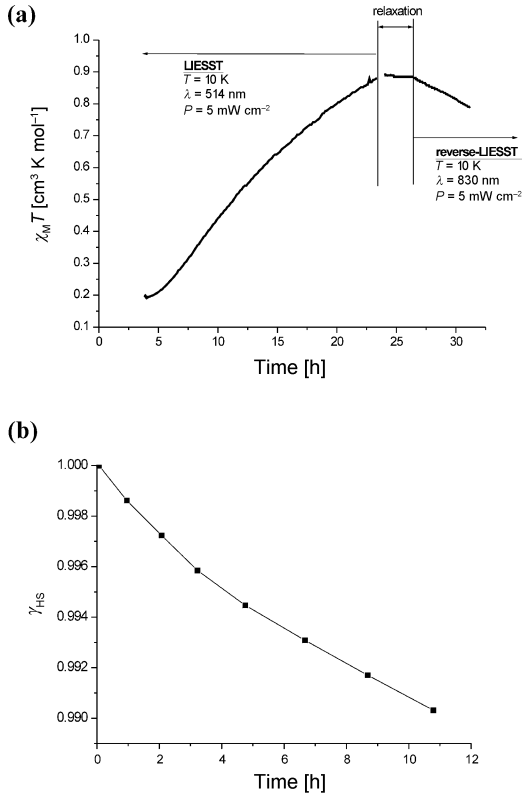


Figure 6. (a) Time dependence of $\chi_M T$ during LS→HS photoexcitation (LIESST) and HS→LS photorelaxation (reverse-LIESST) at 10 K. (b) Relaxation kinetics of the quenched metastable HS state in the dark at 10 K, derived from susceptibility measurements as a function of time.

All together, these magnetic results, in addition to the previous optical properties, are mandatory for the choice of appropriate experimental conditions for the photocrystallographic measurements (temperature, excitation wavelength and duration). They indeed confirm the possibility for a careful X-ray diffraction measurement on the HS-2q and HS-2p states at very low temperature ($T \approx 10$ K), as the necessary requirements are met: possible photoconversion, efficient thermal quenching, high relaxation $T_{LIESST}$ and $T_{TIESST}$ temperatures and an almost negligible relaxation rate at sufficiently low temperature (10 K).

## Thermal Expansion Analysis

The lattice constants of $[Fe(btr)_2(NCS)_2]\cdot H_2O$ were derived from single-crystal X-ray diffraction as a function of temperature (15 K $< T <$ 270 K) in all the different spin states and are reported in Figure 7. From room temperature to 124 K, in the HS-1 state, the *a* and *b* cell axes contract linearly, whereas the *c* axis slightly expands in a linear fashion, leading to a thermal contraction of the unit cell volume. Upon passing the thermal spin transition at $T_{1/2\downarrow}$ = 124 K, the lattice constants change abruptly, giving a cell volume variation, $\Delta V_{HL}$, of –91 Å$^3$ (5%). In the LS state (15 K $< T <$ 144 K), a contraction of the *a* and *b* axes and an expansion of the *c* axis are observed. Remarkably, the lattice parameters in the metastable HS-2 states are in almost perfect linear continuity to those of the HS-1 state. At 15 K, the cell volume expansion from LS to HS-2, $\Delta V_{HL}$ = +91 Å$^3$, exactly matches the volume variation at the thermal transition.

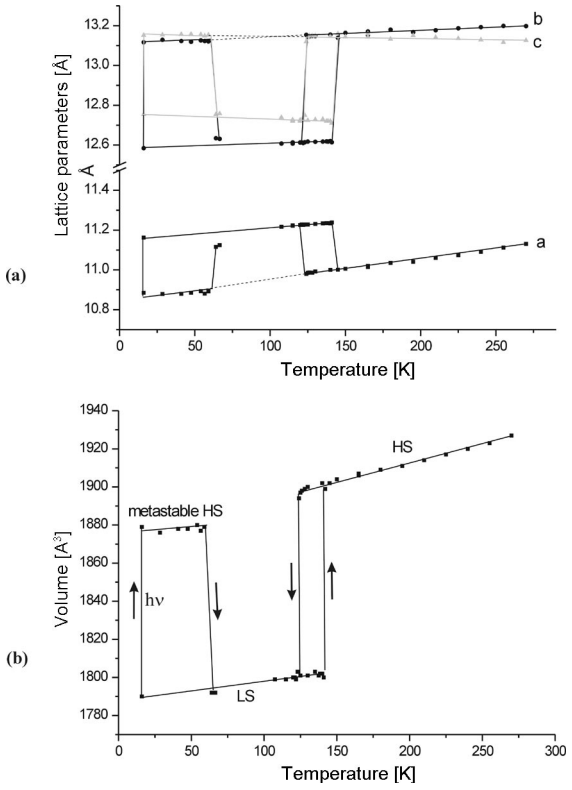


Figure 7. (a) Unit cell parameters and (b) unit cell volume as a function of temperature (15–270 K).

The temperature dependence of the lattice constants was further analyzed by using the formalism of the lattice expansion model.[27] This model, which is based on the assumption of a direct proportionality between the HS–LS cell volume change and $\gamma_{HS}$, was efficiently used to describe the behaviour of several spin-crossover materials such as $[Fe(mtz)_6]\cdot(BF_4)_2$ and $[Fe(ptz)_6]\cdot(BF_4)_2$.[28,29] In the generalized form of this model, a vector, $\mathbf{X}(T)$, is given by Equation (1):

$$\mathbf{X}(T) = \{\mathbf{1} + \boldsymbol{\alpha} T + \boldsymbol{\varepsilon}\gamma_{HS}(T)\}\mathbf{X}\,(T = 0) \quad (1)$$

In Equation (1), $\boldsymbol{\alpha}$ is related to the thermal expansion of the crystal lattice, whereas $\boldsymbol{\varepsilon}$ describes the spontaneous strain (deformation) of the crystal lattice upon LS–HS transition. The thermal expansion of a crystal lattice is well described by the Grüneisen approximation, including anharmonicity contributions. The free energy of the crystal lattice is parameterized by its bulk modulus, the vibration energy of the phonons and the Grüneisen constant.[30] In a first approximation, $\boldsymbol{\alpha}$ is assumed to be the same in the HS and LS states, which is usually quantitatively sufficient for spin-crossover materials whose crystal structure consists of individual molecular entities.

 © 2007 Wiley-VCH Verlag GmbH & Co. KGaA, Weinheim 

The lattice parameters were fitted by the least-squares method to linear functions, whose coefficients exhibit significant spin dependencies (Table 1). Accordingly, we anticipate that the assumption that the thermal-expansion tensor, $\boldsymbol{\alpha}$, is the same for both spin states is hardly fulfilled in the case of $[Fe(btr)_2(NCS)_2]\cdot H_2O$, because of its particular 2D polymeric crystal structure. Indeed, different phonon vibration energies might be expected on changing from the LS to the HS state. In such a case, a more general expression of the lattice expansion model given by Equation (1), including spin-dependent thermal-expansion tensors $\boldsymbol{\alpha}_{HS}$ and $\boldsymbol{\alpha}_{LS}$, is required [Equation (2)]:

$$\mathbf{X}(T) = \left[\mathbf{1} + \left\{\gamma_{HS}(T)\boldsymbol{\alpha}_{HS} + [1-\gamma_{HS}(T)]\boldsymbol{\alpha}_{LS}\right\}T + \boldsymbol{\varepsilon}\gamma_{HS}(T)\right]\mathbf{X}(T=0) \quad (2)$$

Table 1. Results of the least-squares fit of the lattice parameters as a function of temperature using linear functions $\mathbf{X}(T) = \mathbf{X}(0) + \boldsymbol{\alpha}_L T$.

| Parameter | Spin state | Fitted functions |
|---|---|---|
| $a$ | HS | $10.857(3) + 9.9(2)\times10^{-4}\,T$ |
| | LS | $11.157(1) + 5.7(1)\times10^{-4}\,T$ |
| $b$ | HS | $13.106(4) + 3.4(3)\times10^{-4}\,T$ |
| | LS | $12.581(2) + 2.6(2)\times10^{-4}\,T$ |
| $c$ | HS | $13.153(5) - 7(3)\times10^{-5}\,T$ |
| | LS | $12.76(1) - 2.6(7)\times10^{-4}\,T$ |
| $\beta$ | HS | $90.74(4) + 3.5(36)\times10^{-3}\,T$ |
| | LS | 92.37(3) |

By using $\gamma_{HS}(T)$ derived from the magnetic measurements, the elements of the tensors $\boldsymbol{\alpha}_{HS}$, $\boldsymbol{\alpha}_{LS}$ and $\boldsymbol{\varepsilon}$ in Equation (2) were fitted to the measured values of the lattice parameters vs. temperature through a Monte Carlo algorithm, until the minimum of the agreement function $R = \Sigma[x_{obs}(T) - x_{calc}(T)]^2/\Sigma[x_{obs}(T)]^2$ was reached. Results of the fit are given in Table 2. The orthonormal coordinate system attached to the crystal was defined as conventional in the monoclinic system: $\boldsymbol{e_2}//b$, $\boldsymbol{e_3}//c$ and $\boldsymbol{e_1}//a^*$.

The elements of the $\boldsymbol{\alpha}_{HS}$ and $\boldsymbol{\alpha}_{LS}$ tensors clearly indicate a similar behaviour with nonetheless some specific discrepancies. In both spin states, the largest eigenvalue corresponds to an eigendirection almost along the crystallographic $a$ axis, that is to say perpendicular to the structural layers, as can be seen in Figure 8. The coefficients $a^0_{22}$ and $a^0_{33}$ correspond to two mutually perpendicular directions roughly parallel to the structural layers. The interlayer region is therefore the most affected by temperature ($a^0_{11} > a^0_{22}$, $a^0_{33}$); the corresponding thermal contraction is furthermore almost twice as large in the HS state [$a^0_{11} = 9.73(7)\times10^{-5}\,K^{-1}$] as that in the LS state [$a^0_{11} = 5.05(3)\times10^{-5}\,K^{-1}$]. Correlatively, the overall thermal volume contraction, approximated by the trace of the $\boldsymbol{\alpha}$ tensor [$Tr(\boldsymbol{\alpha}) = a^0_{11} + a^0_{22} + a^0_{33}$], is also twice as large in the HS state. This behaviour correlates to a slight reduction of the hydrogen-bond strength, which is responsible for the interlayer connection, in the HS state with an increase in the Ow···N12 distances [$d_{Ow\cdots N12}$(LS) = 3.026(3) Å and $d_{Ow\cdots N12}$(HS) = 3.065(1) Å at 130 K for instance]. In both spin states, the thermal volume contraction is much lower than that observed for molecular spin-crossover systems {$Tr(\boldsymbol{\alpha}) = 26\times10^{-5}\,K^{-1}$ at 298 K in the HS state for [Fe(PM-BiA)$_2$(NCS)$_2$] for instance},[11] due to the lower sensitivity to deformation of the crystal lattice of $[Fe(btr)_2(NCS)_2]\cdot H_2O$. This is expected on the basis of its polymeric crystal structure.

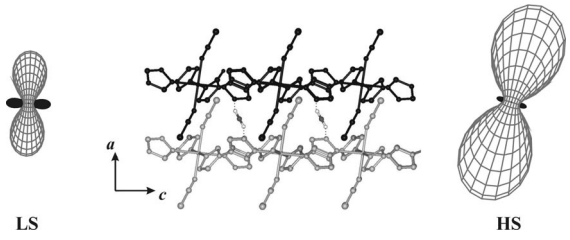


Figure 8. Representation of the thermal-expansion tensor in the HS and LS states oriented with respect to the layer crystal structure. Positive thermal expansion is displayed in light grey, negative in black.

Table 2. Coefficients $a_{ij}$ and eigenvalues $a^0_{ij}$ of the thermal-expansion tensors ($\boldsymbol{\alpha}_{LS}$, $\boldsymbol{\alpha}_{HS}$) and coefficients $\varepsilon_{ij}$ and eigenvalues $\varepsilon^0_{ij}$ of the spontaneous-strain tensor ($\boldsymbol{\varepsilon}$).

| | $a_{11}$ [$10^{-5}$ K$^{-1}$] | $a_{22}$ [$10^{-5}$ K$^{-1}$] | $a_{33}$ [$10^{-5}$ K$^{-1}$] | $a_{13}$ [$10^{-5}$ K$^{-1}$] |
|---|---|---|---|---|
| $\boldsymbol{\alpha}_{HS}$ | 8.86(7) | 2.62(1) | –0.58(1) | –3.00(8) |
| $\boldsymbol{\alpha}_{LS}$ | 5.05(3) | 2.08(1) | –2.08(2) | –0.043(1) |
| | $a^0_{11}$ [$10^{-5}$ K$^{-1}$] | $a^0_{22}$ [$10^{-5}$ K$^{-1}$] | $a^0_{33}$ [$10^{-5}$ K$^{-1}$] | $Tr(\boldsymbol{\alpha})$ [$10^{-5}$ K$^{-1}$] |
| $\boldsymbol{\alpha}^0_{HS}$ | 9.73(7) | 2.62(1) | –1.43(1) | 10.92(9) |
| $\boldsymbol{\alpha}^0_{LS}$ | 5.05(3) | 2.08(1) | –2.08(2) | 5.05(6) |
| | $\varepsilon_{11}$ [$10^{-2}$] | $\varepsilon_{22}$ [$10^{-2}$] | $\varepsilon_{33}$ [$10^{-2}$] | $\varepsilon_{13}$ [$10^{-2}$] |
| $\boldsymbol{\varepsilon}$ | –2.62(1) | 4.17(1) | 3.11(1) | 1.46(1) |
| | $\varepsilon^0_{11}$ [$10^{-2}$] | $\varepsilon^0_{22}$ [$10^{-2}$] | $\varepsilon^0_{33}$ [$10^{-2}$] | $Tr(\boldsymbol{\varepsilon})$ [$10^{-2}$] |
| $\boldsymbol{\varepsilon}^0$ | –2.97(1) | 4.17(1) | 3.46(1) | 4.66(3) |

The spontaneous strain at the HS–LS transition is also highly anisotropic, with a negative contribution along the crystallographic $a$ axis and positive values along the $b$ and $c$ axes. The HS–LS transition correlates therefore to an increase in the interlayer spacing and an overall contraction parallel to the layers. The former aspect is related to a reorientation of the NCS group with a more linear Fe–N–C–S geometry in the LS state (see below), whereas the contraction within the layer is connected to the abrupt Fe–N bond shortening at the transition. Note that $\boldsymbol{\varepsilon}$ was fitted on the whole temperature range, and it therefore assumes an identical spontaneous strain at the thermal and light-induced transitions.

### Similarities between the HS-2q and HS-2p Structures

The lattice parameters exhibit systematic positive differences from HS-2p to HS-2q: $\Delta a$ = 0.031(2) Å, $\Delta b$ = 0.049(2) Å, $\Delta c$ = 0.015(2) Å [$\Delta V$ = 14.4(5) Å$^3$]. This positive

 © 2007 Wiley-VCH Verlag GmbH & Co. KGaA, Weinheim 

volume discrepancy would suggest that HS-2p corresponds to an incomplete metastable HS-2 state with some residual LS species. The comparative structural characteristics of the $FeN_6$ octahedron are given in Table 3. On the whole, the mean-square atomic position deviation, *mfa*, is only 0.0125 Å between these two metastable HS-2 crystal structures, as calculated by mapping the structures of the $Fe(btr)_4(NCS)_2$ fragment with KPLOT,[31] including only non-hydrogen atoms. It is worth noting that the bond lengths are systematically more precise and larger in the HS-2q state than in HS-2p, but the differences for the Fe–N bonds are within $2\sigma$. The angular deformation of the $FeN_6$ octahedron, defined as the sum of the deviations from 90° of the 12 *cis* N–Fe–N angles in the coordination sphere,[2] shows some differences: $\Sigma_{HS\text{-}2q}$ = 15.6(4)° and $\Sigma_{HS\text{-}2p}$ = 18(2)°. The differences between HS-2p to HS-2q in the btr bond lengths and angles are in the range of the experimental uncertainty, except for the N14–N24, N22–C23 and N21–C25 bonds which are at the limit of the statistical significance. The geometry of the NCS ligand is also very similar, with bond lengths, *d*(N–C), of 1.179(1) and 1.174(8) Å and *d*(C–S) values of 1.634(1) and 1.631(6) Å for the HS-2q and HS-2p states, respectively. The interlayer Ow–Hw···N12 hydrogen-bond contacts present the same structural characteristics, with Ow···N12 distances of 3.044(2) and 3.036(7) Å for the HS-2q and HS-2p states, respectively, correlated to a slight displacement of the water molecule [$\Delta d$(Ow) = 0.009(3) Å].

Table 3. Selected structural characteristics in the various spin states. The octahedron volume $V_p$ was calculated with IVTON.[44]

| | 15 K | | | 130 K | |
|---|---|---|---|---|---|
| Bond length [Å] | LS | HS-2q | HS-2p | LS | HS-1 |
| Fe–$N_{NCS}$ | 1.9498(5) | 2.131(1) | 2.129(4) | 1.949(2) | 2.1283(7) |
| Fe–N11 | 1.9730(5) | 2.171(1) | 2.166(6) | 1.976(1) | 2.1786(5) |
| Fe–N21 | 1.9685(5) | 2.165(1) | 2.154(5) | 1.968(1) | 2.1710(5) |
| N–C | 1.1753(7) | 1.179(1) | 1.174(8) | 1.169(2) | 1.173(1) |
| C–S | 1.6405(5) | 1.634(1) | 1.631(6) | 1.640(2) | 1.6254(8) |
| Ow···N12 | 3.0247(7) | 3.044(2) | 3.036(7) | 3.026(3) | 3.065(1) |
| Angle [°] | | | | | |
| N–Fe–N11 | 90.17(2) | 90.71(4) | 90.9(2) | 90.12(6) | 90.72(3) |
| N–Fe–N21 | 92.32(2) | 92.34(3) | 92.3(2) | 92.24(6) | 92.28(2) |
| N11–Fe–N21 | 88.79(2) | 89.14(4) | 88.6(2) | 88.77(6) | 89.16(3) |
| Fe–N–C | 162.79(4) | 149.46(8) | 149.0(5) | 163.1(1) | 150.66(6) |
| Σ [°] | 14.8(2) | 15.6(4) | 18(2) | 14.4(7) | 15.4(3) |
| $V_p$ [Å$^3$] | 10.09(1) | 13.34(1) | 13.2(1) | 10.10(1) | 13.41(1) |

According to the structural arguments presented here, we cannot firmly confirm or reject the hypothesis that HS-2q and HS-2p correspond to a unique phase in the case of $[Fe(btr)_2(NCS)_2]\cdot H_2O$.

### LS→HS-2q Structural Modifications at 15 K

Figure 9 presents a superposition of the molecular structures in the LS and HS-2q states at 15 K. The mean-square atomic position deviation,[31] *mfa*, which in this case gives insight into the mean magnitude of the LS-to-HS-2q atomic displacement, is 0.272 Å (Table 4). This value is very similar for the LS-to-HS-2p transition (*mfa* = 0.270 Å). Upon the LS-to-HS-2q spin-state change, the Fe–N coordination bonds expand by $\Delta d$(Fe–$N_{NCS}$) = 0.181(2) Å, $\Delta d$(Fe–N11) = 0.198(2) Å and $\Delta d$(Fe–N21) = 0.196(2) Å. The deformation of the $FeN_6$ octahedron is slightly lower in the LS state [$\Sigma_{LS}$ = 14.8(2)°] than in the HS-2q phase [$\Sigma_{HS\text{-}2q}$ = 15.6(4)°], which is the usual trend for such iron(II) compounds. However, these deformations are much less severe than those for other $Fe(L)_2(NCS)_2$ spin-transition complexes whose $\Sigma_{HS}$ values are typically around 70°.[2] The $FeN_6$ octahedron volume changes by $\Delta V_p$ = +3.25(2) Å$^3$, which accounts for only 14% of the total unit cell volume variation ($\Delta V_{cell}$ = +92 Å$^3$), since there are four iron octahedrons per unit cell. During the spin-state change, the NCS ligand, in the *trans* position, undergoes a reorientation by $\Delta\theta_{LH}$ = –13.3(1)°, the Fe–N–C angle being closer to 180° in the LS state than in the HS-2q state. As discussed above, this NCS reorientation is correlated to the expansion of the crystallographic *a* axis, which increases the interlayer spacing, and therefore is the main contribution to $\Delta V_{cell}$. As for the btr ligand, the variations in bond length and angle are

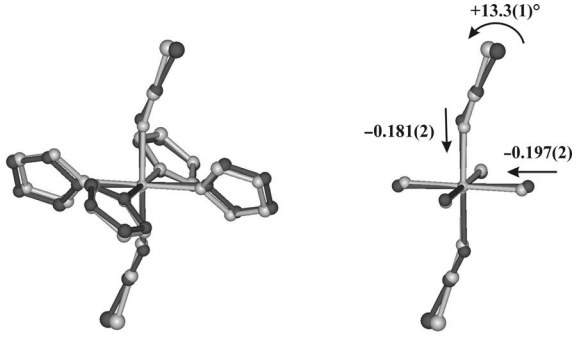


Figure 9. Superposition of the molecular structures in the LS state (grey) and the HS-2q state (black) at 15 K.

Table 4. Geometrical reorganization of the $FeN_6$ octahedron upon various spin-state changes. *mfa* is the mean-square atomic position deviation, given by $mfa = (\sum_{i=1}^{n} S_i^2/n)^{1/2}$, where the $S_i$ are the distances [Å] between corresponding pairs of atoms in the two structures. *mfa* was calculated by using KPLOT.[31]

| Bond length [Å] | LS→HS-2p (15 K) | LS→HS-2q (15 K) | LS→HS-1 (130 K) |
|---|---|---|---|
| Fe–N | +0.179(5) | +0.181(2) | +0.179(2) |
| Fe–N11 | +0.193(7) | +0.198(2) | +0.202(2) |
| Fe–N21 | +0.185(6) | +0.196(2) | +0.203(2) |
| N–C–S | –0.01(1) | –0.002(3) | –0.011(6) |
| Ow···N12 | +0.011(8) | +0.019(3) | +0.039(4) |
| Angle [°] | | | |
| N–Fe–N11 | +0.7(2) | +0.54(6) | +0.60(9) |
| N–Fe–N21 | 0.0(2) | +0.02(5) | +0.04(8) |
| N11–Fe–N21 | –0.2(2) | –0.34(6) | –0.39(8) |
| Fe–N–C | –13.8(5) | –13.3(1) | –12.5(2) |
| ΔΣ [°] | +3(2) | +0.8(6) | +1(1) |
| $\Delta V_p$ [Å$^3$] | +3.1(1) | +3.25(2) | +3.31(2) |
| *mfa* [Å] | 0.270 | 0.272 | 0.266 |

 © 2007 Wiley-VCH Verlag GmbH & Co. KGaA, Weinheim 

within the experimental uncertainty, whereas the dihedral angle between the triazole rings increases significantly from 84.81(3)° to 88.20(6)°. Finally, we note a displacement of the water molecule along the crystallographic *b* direction [$\Delta d(\mathrm{Ow})_{\mathrm{HL}}$ = –0.236(1) Å] resulting in a small increase in the interlayer Ow···N12 contacts by 0.019(3) Å.

### LS→HS-1 Structural Reorganization at 130 K

Upon the LS-to-HS-1 spin-state change at 130 K, the mean-square atomic position deviation is 0.266 Å, which is marginally lower than that calculated for the LS-to-HS-2q transition. As a matter of fact, the 130 K HS and 15 K HS-2q states are closely related to each other (*mfa* = 0.0317 Å); this criterion is even lower for the corresponding LS structures (*mfa* = 0.0155 Å). The coordination bonds expand by $\Delta d(\mathrm{Fe–N_{NCS}})$ = 0.179(2) Å, $\Delta d$(Fe–N11) = 0.202(2) Å and $\Delta d$(Fe–N21) = 0.203(2) Å, which are within the $\sigma$ values calculated for the LS-to-HS-2q spin-state change. As for the latter, the angular distortion of the $FeN_6$ octahedron is smaller in the LS state [$\Sigma_{\mathrm{LS}}$ = 14.4(7)°] than in the HS-1 one [$\Sigma_{\mathrm{HS\text{-}1}}$ = 15.4(3)°]. The $FeN_6$ octahedron volume changes by $\Delta V_{\mathrm{p}}$ = +3.31(2) Å$^3$, which accounts for nearly 13% of the unit cell volume change ($\Delta V_{\mathrm{cell}}$ = 99 Å$^3$), similar to the LS-to-HS-2q spin-state change. The bond length variations of the btr ligand between the two spin states are within the uncertainty, except for the bonds C13–N14 and C23–N24, which are slightly longer in the LS state. The dihedral angle between the triazole ring planes has the same values as at 15 K [84.8(1)° and 88.32(4)° in the LS and HS-1 states, respectively]. Again, as for the LS-to-HS-2q transition at 15 K, we observe a reorientation of the NCS by $\Delta\theta_{\mathrm{LH}}$ = –12.5(2)°. Finally, we note a 0.039(4)-Å increase in the intermolecular Ow···N12 contact in the HS-1 state with respect to the LS state. The displacement of the water molecules along the crystallographic *b* direction is in this case $\Delta d(\mathrm{Ow})_{\mathrm{HL}}$ = –0.255(1) Å. As a conclusion, we can claim that the LS→HS-2q and LS→HS-1 transitions lead to almost identical structural modifications.

### Thermal Motion Analysis

The importance of molecular vibrations in the spin conversion phenomenon was first recognized by Sorai and Seki on the basis of calorimetric measurements; they indeed revealed that the spin transition is an entropy-driven process.[32] If we look in general at spin-crossover materials, $\Delta S_{\mathrm{LH}}$ typically amounts to about 50 J K$^{-1}$ mol$^{-1}$, of which the vibrational contribution to the molar entropy accounts merely for 60–70%, while the electronic (spin multiplicity) entropy represents only 13.4 J K$^{-1}$ mol$^{-1}$ in the case of $Fe^{II}$ spin-crossover complexes. It is generally assumed that the major contributions to the vibrational entropy results from the 15 intramolecular normal modes of the regular $FeN_6$ octahedron and predominantly from the Fe–N stretching modes. Detailed IR and Raman spectroscopic measurements as well as nuclear inelastic scattering results, coupled to ab initio DFT calculations on isolated molecules, indicate, on the other hand, that some external (phonon) modes might also contribute significantly to the vibrational entropy.[33] However, a comprehensive knowledge of the importance of these phonon modes is still missing. Several models for spin crossover account explicitly for the role of vibrations, through a reduced number of empirical parameters such as the HS and LS Debye temperatures [$\Theta_{\mathrm{D}}$(HS) and $\Theta_{\mathrm{D}}$(LS), Zimmerman and König model[34]] or the effective HS and LS degeneracies of electro-vibrational origin ($\omega_{\mathrm{HS}}$ and $\omega_{\mathrm{LS}}$ in the two-level Ising-like model introduced by Bousseksou et al.[35]).

Literature results indicate that for the title $[Fe(btr)_2(NCS)_2]\cdot H_2O$ complex, $\Delta S_{\mathrm{LH}}$ is as high as 76 J K$^{-1}$ mol$^{-1}$.[21a] On the basis of its specific extended layer structure, the large cell volume change and the structural modifications at the spin transitions, large modifications of the atomic vibration amplitudes are expected as well. For cyanide-bridged iron(II) spin-crossover complexes, which exhibit a polymeric crystal structure, it has been suggested from Raman measurements that the contribution from intermolecular vibration to the total entropy might be non-negligible.[36] This is most probably related to the strong cooperativity induced by the extended polymeric structure. For similar reasons, lattice vibrational modes might also play an important role in $[Fe(btr)_2(NCS)_2]\cdot H_2O$. We have derived here the crystal structure in both spin states at two temperatures (15 K and 130 K), which affords the possibility to characterize the difference in vibrational behaviour (vibration modes and amplitudes) between HS and LS. The atomic vibration amplitudes, described through the atomic $\mathbf{U}_{ij}$ tensor in a conventional structural analysis (like the one performed here), consist of additive contributions from intramolecular vibration modes of high frequency and lattice vibrations (phonons) of lower frequency. For the thermal transition, the atomic displacement tensors were derived from the present structural analysis, whereas for the 15 K case, the atomic displacement tensors (for LS and HS-2q) were derived from the more accurate multipolar model of the electron density previously published.[16] In the latter, thermal vibrations are decorrelated from aspherical electron-density features. Recent experimental and theoretical investigations include the intramolecular normal modes of the regular $FeN_6$ octahedron as well as the ligand vibration modes through a multicoordinate approach.[33] We will rather follow here a simpler single-coordinate procedure.

Upon LS-to-HS state change (LS→HS-1 and LS→HS-2), a systematic enhancement in equivalent isotropic displacement parameters is observed, as shown in Table 5 and illustrated in Figure 10. The most striking feature is a similar trend from atom to atom at the two temperatures, the increase being nevertheless higher in almost all cases at 130 K. In the case of sulfur, the increase is much larger at 130 K than for all the other atoms and seems suspicious; it is most probably related to some disordering effects, which can not be resolved in the crystal structure analysis but are taken into account in the corresponding atomic displacement parameters. The systematic LS-to-HS increase in

 © 2007 Wiley-VCH Verlag GmbH & Co. KGaA, Weinheim 

Table 5. Equivalent isotropic displacement parameters, $U_{equ}$, [Å$^2$].

| | 15 K | | | 130 K | | |
|---|---|---|---|---|---|---|
| | LS | HS-2q | $\Delta U_{equ}$ (LS→HS-2q) | LS | HS-1 | $\Delta U_{equ}$ (LS→HS-1) |
| Fe | 0.00414(2) | 0.00459(5) | 0.00045(7) | 0.00925(8) | 0.00870(2) | –0.0005(1) |
| N | 0.00700(7) | 0.0094(2) | 0.0024(3) | 0.0124(3) | 0.01634(9) | 0.0039(4) |
| C | 0.00727(8) | 0.0084(2) | 0.0011(3) | 0.0136(3) | 0.01504(9) | 0.0014(4) |
| S | 0.00941(2) | 0.0115(1) | 0.0021(1) | 0.0241(1) | 0.03590(7) | 0.0118(2) |
| N11 | 0.00587(7) | 0.0075(2) | 0.0016(3) | 0.0105(2) | 0.01321(8) | 0.0027(3) |
| N12 | 0.00716(7) | 0.0087(1) | 0.0015(2) | 0.0137(3) | 0.01650(9) | 0.0028(4) |
| C13 | 0.00734(8) | 0.0091(2) | 0.0018(3) | 0.0147(3) | 0.0172(1) | 0.0025(4) |
| C15 | 0.00652(8) | 0.0076(2) | 0.0011(3) | 0.0122(3) | 0.01337(9) | 0.0012(4) |
| N14 | 0.00613(7) | 0.0070(2) | 0.0009(3) | 0.0116(2) | 0.01281(8) | 0.0012(3) |
| N24 | 0.00611(7) | 0.0069(2) | 0.0008(3) | 0.0111(2) | 0.01215(7) | 0.0010(3) |
| N21 | 0.00592(7) | 0.0068(2) | 0.0009(3) | 0.0102(2) | 0.01199(7) | 0.0018(3) |
| N22 | 0.00686(7) | 0.0077(2) | 0.0008(3) | 0.0130(3) | 0.01363(8) | 0.0006(4) |
| C23 | 0.00711(8) | 0.0077(2) | 0.0006(3) | 0.0138(3) | 0.01404(9) | 0.0002(4) |
| C25 | 0.00676(8) | 0.0076(2) | 0.0008(3) | 0.0126(3) | 0.01352(9) | 0.0009(4) |

atomic displacement amplitudes can be directly related to the spin transition and indicates vibration modes of globally larger amplitudes in the HS state; it can not be attributed to a population of higher-energy vibrational levels since measurements have been performed at rigorously the same temperature. This behaviour can be pictured by a mean potential well that is globally broader in the HS state (inset in Figure 10).

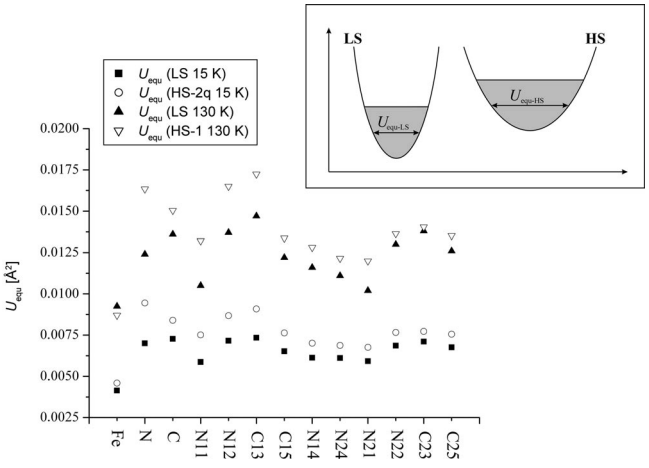


Figure 10. Equivalent isotropic displacement parameters $U_{equ}$ [$U_{equ}$ = 1/3($U_{11}$ + $U_{22}$ + $U_{33}$)]. The S atom has been omitted as it is possibly affected by some disordering effects (see text). Inset: schematic representation of the mean HS and LS vibrational potential wells.

The inspection of the anisotropic displacement parameters allows us to proceed further. Figure 11 displays the difference mean-square surfaces [$U_{HS}$ – $U_{LS}$] at 15 K and 130 K; it is evident that similar features are present at both temperatures. First of all, the atomic displacement amplitudes are systematically higher in the HS state with respect to the LS state, as discussed above. In the case of sulfur, the thermal motion is higher in the direction perpendicular to the NCS axis in the HS state, therefore characterizing a higher bending vibration of the NCS group together with a possible static disorder of the sulfur atom. The difference for btr also exhibits a systematic trend, the thermal motion being higher in the direction perpendicular to each triazole ring for all atoms. The fact that all btr atoms behave collectively confirms that this behaviour is due to higher vibration amplitudes of external (lattice) modes in the HS state and is indeed related to the spin-state change.

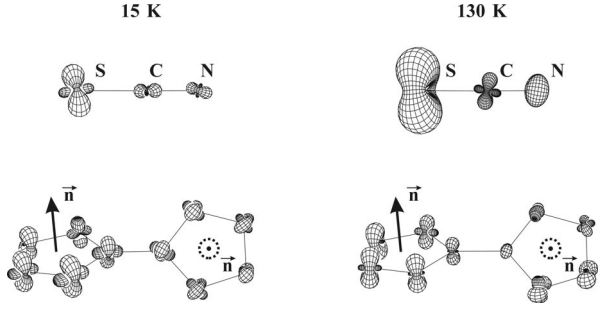


Figure 11. Difference mean-square surfaces [$U_{HS}$ – $U_{LS}$] calculated by using PEANUT.[43] Positive surfaces are in grey, negative surfaces are in black. The arrows depict the normal to each triazole ring.

Let us consider that the vibrational properties of each molecular fragment (btr, NCS and Fe) in each spin state can be described by a mean single harmonic oscillator (rigid group model). This is a gross approximation which can, however, help rationalize the observed trends. The mean-square displacement amplitude corresponding to a harmonic oscillator is related to the vibration frequency by $\langle u^2 \rangle = \frac{h}{8\pi^2 \mu \nu} \coth(h\nu/2k_B T)$, where $\mu$ is the reduced mass and $\nu$ the oscillator frequency. $\langle u^2 \rangle$ is a decreasing function of the oscillator frequency, $\nu$. In this context, at constant temperature, the increase in the mean-square displacement amplitude in the HS state is related to a decrease in oscillator frequency and correlatively to a decrease in the stiffness of the crystal lattice; thus $\nu_{HS} < \nu_{LS}$. For this hypothetical harmonic oscillator, the vibrational entropy is a decreasing function of the oscillator frequency; thus $S_{HS} > S_{LS}$. We therefore predict, as a result of our structural analysis an increase in vibrational entropy upon LS-to-HS state change due to the external vibration modes. This positive contri-

 © 2007 Wiley-VCH Verlag GmbH & Co. KGaA, Weinheim 

bution to $\Delta S_{LH}$ from external modes could explain the remarkably high LS-to-HS total entropy change for $[Fe(btr)_2(NCS)_2]\cdot H_2O$.

All together, these results show the relevance of such a structural analysis by using high-resolution X-ray diffraction for getting new insights into the vibrational properties of spin-crossover materials.

## Conclusions

This paper describes the structural properties of the LS and HS states of the spin-crossover complex $[Fe(btr)_2(NCS)_2]\cdot H_2O$ and their modifications during the thermal (130 K) and the LIESST (15 K) spin transitions. The LIESST process at very low temperature and the metastable HS-2-to-LS relaxation have been described on the basis of spectroscopic and photomagnetic measurements. The very slow relaxation of the photostationary HS-2 state allows precise crystallographic studies of the metastable HS-2p and HS-2q states.

The X-ray diffraction measurements of the LS and HS states at rigorously the same temperature for the two conversions allow a precise description of the structural variations attributed to the spin transition, free from any disturbing thermal effect. Under these considerations, we showed that both HS-2 states obtained by thermal quenching from room temperature and by photoirradiation have the same molecular structures, within experimental limits of accuracy (less than 0.01 Å). In addition, our results suggest that the LIESST and the thermal spin transitions lead to the same structural variations of the iron coordination polyhedron: the Fe–N bond lengths extend by 0.18 and 0.20 Å on going from LS to HS, and the NCS group undergoes a reorientation of nearly 13°, which accounts for the extension of the crystallographic *a* axis. The HS→LS transition reduces the intermolecular Ow–Hw···N12 contacts in the crystallographic *a* direction.

We have shown in the present analysis that detailed vibrational properties related to the spin transition can be derived from X-ray diffraction measurements, providing high-resolution (in Q) data are measured. Systematically higher vibration amplitudes are observed in the HS state as compared to the LS state. For the btr group, the collective increase in vibration amplitude is perpendicular to each triazole ring and results from globally lower-frequency external vibration modes in the HS state. These might contribute significantly to $\Delta S_{HL}$.

The thermal-expansion tensors for the HS and LS states exhibit a similar qualitative behaviour that parallels the specific layer crystal structure. In both spin states, the largest value of the thermal-expansion tensor is observed along the crystallographic *a* direction, that is, perpendicular to the structural layers. The corresponding thermal contraction is twice in the HS state with respect to the LS state. On the other side, the contraction is lower in the directions parallel to the layers. The spin transition in $[Fe(btr)_2(NCS)_2]\cdot H_2O$ is associated to large and anisotropic spontaneous strain, characterized by the tensor **ε**, whose eigenvalues correlate to an abrupt increase in the interlayer spacing and an overall contraction parallel to the layers.

## Experimental Section

**Sample Preparation:** The btr ligand and its iron complex, $[Fe(btr)_2(NCS)_2]\cdot H_2O$, were synthesized as reported in the literature.[37] Single crystals, suitable for accurate crystallographic studies, were grown by slow solvent evaporation in aqueous solution. For consistency, single crystals of similar quality and size were used for all the experiments: single-crystal X-ray diffraction, optical and magnetic measurements.

**Estimation of Crystal Heating during Photoexcitation:** We report in this paper the physical properties of the light-induced metastable state of $[Fe(btr)_2(NCS)_2]\cdot H_2O$ obtained by using various laser excitation conditions (laser wavelength and power) for the photomagnetic, reflectivity and photocrystallographic measurements. It is of fundamental importance to address the question of crystal heating under such laser excitation. Whatever the experiment, it is commonly assumed and hoped that this sample heating is reduced, but no clear procedure has ever been proposed for estimating the temperature increase in the probed sample. We propose here a very simple empirical procedure for the case of photocrystallographic experiments.

Prior to any photocrystallographic measurement, it is of common practice to analyze comparatively the UV/Vis absorption spectra of the ground and light-induced excited states from which the excitation conditions (laser wavelength and power) are optimized. In the case of spin-crossover materials, excitation wavelength corresponding to the spin-allowed $^1A_1$ to $^1T_1$ or MLCT (Metal-to-Ligand Charge Transfer) absorption band is commonly chosen. Under such excitation conditions, the energy transferred to the sample partly induces the LS-to-HS excitation, but is also dissipated by emission of phonons. This latter process may raise the sample temperature by several tens of degrees, which could drastically damage it or cause false interpretations of the LIESST phenomenon. By using typical heat conduction properties (thermal conductivity) of molecular crystals, characteristics (stream diameter and velocity) and heat convection properties of the cooling $N_2$ or He gas stream (density, heat capacity, kinematic viscosity,...), and laser excitation parameters (penetration depth, linear absorption coefficient, laser power), the heat-transfer equations could be solved numerically, but not without difficulty, to attain the temperature increase profile in a single-crystal sample.[38] We propose here a simpler in situ empirical procedure for roughly estimating the maximum sample temperature increase induced by combined photoillumination and open-flow ($N_2$ or He) cooling systems, which is applicable to spin-crossover materials. We use the fact that on increasing temperature and passing through the LS-to-HS-1 spin transition (at $T = T_{1/2\uparrow}$), the cell parameters change significantly. We can therefore first record diffraction frames in the LS state as references. Then turn on the laser and measure the same diffraction frames as a function of laser power. Upon the LS-to-HS transition, a Bragg peak displacement is expected and usually observed. Therefore, a direct inspection of the diffraction pattern while increasing the laser power would indicate the point at which the laser heats the sample to a temperature which is above $T_{1/2\uparrow}$.

This procedure was applied to $[Fe(btr)_2(NCS)_2]\cdot H_2O$. First we performed diffraction measurements on a single crystal of typical size ($0.25 \times 0.20 \times 0.20$ mm) in the LS state below $T_{1/2\uparrow} = 143$ K. At

 © 2007 Wiley-VCH Verlag GmbH & Co. KGaA, Weinheim 

$T$ = 113 K, the crystal was irradiated for 5 min at the optimum wavelength, $\lambda$ = 488 nm, at a laser output power from 0 to 530 mW, and the diffraction pattern before and after excitation was compared. The laser power was calibrated beforehand by using a power-meter. For low laser power (below 530 mW), no changes appeared in the diffraction pattern, whereas at a laser power of 530 mW, a Bragg peak splitting was noticeable, which is indicative of partial LS-to-HS conversion (Figure 12). In other words, part of the crystal sample, most probably the fraction of the crystal just facing the laser, is at a temperature greater than $T_{1/2\uparrow}$, and the temperature increase is at least 32 K. If the laser excitation is stopped, the diffraction pattern returns quickly back to the corresponding LS state, consistent with the measurement temperature, $T$ = 113 K, below $T_{1/2\downarrow}$. This proves that the crystal was not damaged by the laser, even at 530 mW.

It is well known that the specific heat is temperature-dependent, and the light-induced temperature may therefore be different at very low temperature ($T$ = 15 K), at which the LS-to-HS-2p transition is induced in the present work. To check whether this was indeed the case, we performed another diffraction measurement with a starting temperature of 66 K in the LS state, just above $T_{LIESST}$. Again, the laser power was increased while measuring the diffraction pattern to check whether the LS-to-HS-1 transition could be reached. This would indicate a temperature increase of 77 K. Even with the highest laser power of 530 mW, no change was noticeable, which indicated that the temperature increase was indeed limited to below 77 K. Another similar procedure, although not carried out here, would be to prepare the system in the metastable HS-2 (HS-2p or HS-2q) state at very low temperature and inspect the diffraction pattern while increasing the laser power until the HS-2-to-LS LIESST relaxation is observed.

Under such circumstances, we are confident that during our light-induced LS-to-HS-2p experiment at $T$ = 15 K, we did not heat our sample too much to surpass $T_{1/2\uparrow}$ and then quench our sample in the HS-2q state while turning off the laser. We propose that this procedure can be systematically checked prior to any photocrystallographic measurement. It is, however, purely empirical and does not allow a quantitative comparison with other experiments, since it is highly dependent on the current experimental excitation conditions used for the diffraction measurements.

**Spectroscopic and Photomagnetic Measurements:** Optical reflectivity properties were investigated with a custom-built reflectivity setup equipped with a CVI spectrometer, which allows the collection of both the reflectivity spectra within the 450–950 nm range at a given temperature and to follow the temperature dependence of the signal at a selected wavelength (±2.5 nm) at 5–290 K. The analysis was performed on a thin layer of the powdered sample, without any dispersion in a matrix in the cooling mode from room temperature to 10 K and then warming up to 185 K. One has to keep in mind that reflectivity measurements yield surface information as compared to bulk information obtained from photomagnetic and diffraction results.

Magnetic susceptibility measurements were obtained by using an MPMS-55 Quantum Design SQUID magnetometer operating in the 2–340 K temperature range. The temperature was varied at a rate of 0.5 K min$^{-1}$. All magnetic data are plotted as $\chi_M T$ vs. $T$, the molar magnetic susceptibility $\chi_M$ being corrected for the diamagnetism of the closed-shell core and sample diamagnetism. The photomagnetic experiments were carried out by using a Spectra-Physics Kr+ laser (488 nm and 532 nm) or a diode laser (830 nm), with a power of 5 mW cm$^{-2}$ at the sample surface, coupled through an optical fibre to the cavity of the SQUID magnetometer. The $T_{LIESST}$ properties were measured in relation with the previously published method.[7] The sample was first slowly cooled to 10 K in the LS state and then irradiated with the laser. As soon as the photostationary limit was reached (no further increase in the mag-

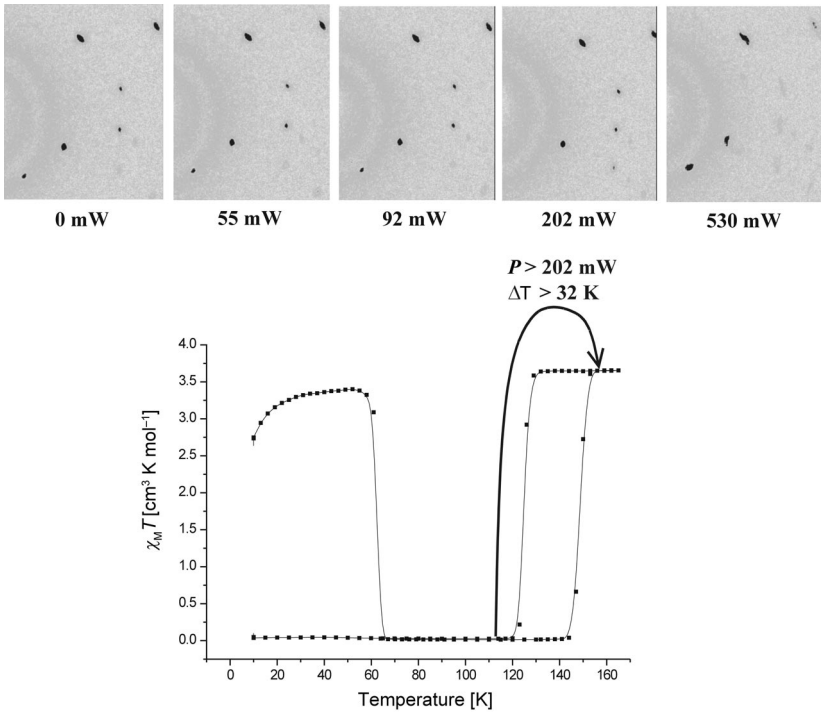


Figure 12. Top: the diffraction pattern as a function of laser excitation power at $\lambda$ = 488 nm and $T$ = 113 K. Note the change in the diffraction pattern at $P$ = 530 mW. Bottom: schematic representation of the procedure for temperature increase estimation.

 © 2007 Wiley-VCH Verlag GmbH & Co. KGaA, Weinheim 

netic signal), the light irradiation was switched off and the magnetic signal recorded while the temperature was increased at a rate of 0.3 K min$^{-1}$. The $T_{LIESST}$ value is given by the extreme of the curve $\partial\chi_M/\partial T$ vs. $T$. Thermomagnetic data were also collected on the quenched metastable HS state by using a rapid thermal cooling from room temperature directly to 10 K and deriving $T_{TIESST}$ in the same way as $T_{LIESST}$.

**X-ray Diffraction Measurements:** Five data collections were performed in the different spin states: HS-1 and LS at 130 K within the thermal hysteresis loop, LS, HS-2p and HS-2q at 15 K (Figure 1) by using an Oxford Diffraction Xcalibur diffractometer with Mo-$K_\alpha$ radiation and equipped with a CCD Sapphire 2 detector. Diffraction experiments were performed by ω-scans by using a detector-to-sample distance of 50 mm at several detector 2$\theta$ positions. The cooling systems were an Oxford Diffraction He open flow Helijet and a $N_2$ open-flow cryostream. The temperature at the sample position was calibrated by using the tetragonal-to-orthorhombic structural phase transition of $DyVO_4$ at $T$ = 14 K.[39] For the measurements with the $N_2$ open-flow cryostream, the temperature was calibrated with a thermocouple. Owing to the small size of the sample, the temperature gradient inside the crystal can be neglected, the flux being homogeneous and linear at the sample position. All diffraction peaks were integrated by using CRYSALIS software.[40] Cell parameters were derived with a least-squares refinement on all measured reflections. The crystal faces were indexed to perform analytical absorption corrections. The measured reflections were merged and reduced by using SORTAV.[41] There was no evidence for structural phase transition or space group change after all spin-state changes (thermally induced and light-induced transitions). All structures were solved by direct methods and refined on $F^2$ using a similar strategy (SHELXL97).[42] Non-hydrogen atoms were refined anisotropically, hydrogen atoms were located on Fourier synthesis and refined isotropically without any constraint. More specific data collection and refinement details are given below and summarized in Table 6. We should stress the high resolution ($\theta_{max}$) and low internal agreement factor ($R_{int}$) of all the experiments as direct pieces of evidence for the high quality and internal consistency of the measured data.

**Low-Spin-State Data Collection at 15 K**: The single-crystal sample was directly quenched to 70 K (above $T_{LIESST}$); the temperature was gradually decreased further to 15 K. According to the magnetic measurements, the thermal transition of $[Fe(btr)_2(NCS)_2]\cdot H_2O$ is complete; our measured sample corresponds to a purely LS state.

**Metastable High-Spin States. Data Collection and Structural Refinement at 15 K:** The diffraction measurement of the metastable HS-2 states is practically more difficult than that for the LS state, owing to the inherent HS-2-to-LS relaxation. Accordingly, controlled specific conditions had to be found in order to ensure at the same time a complete population of the metastable state and a quenched relaxation. As shown by the magnetic results, the relaxation is almost negligible at 15 K. The change in the unit cell volume in the course of the diffraction measurements could be an appropriate indicator to follow in situ and estimate the HS-2-to-

Table 6. Crystallographic and experimental data in the various spin states.

| | LS at 15 K | HS-2q at 15 K | HS-2p at 15 K | LS at 130 K | HS-1 at 130 K |
|---|---|---|---|---|---|
| Formula | $C_{10}H_{10}FeN_{14}OS_2$ | $C_{10}H_{10}FeN_{14}OS_2$ | $C_{10}H_{10}FeN_{14}OS_2$ | $C_{10}H_{10}FeN_{14}OS_2$ | $C_{10}H_{10}FeN_{14}OS_2$ |
| $M_w$ | 462.27 | 462.27 | 462.27 | 462.27 | 462.27 |
| Space group | *C*2/*c* | *C*2/*c* | *C*2/*c* | *C*2/*c* | *C*2/*c* |
| *a* [Å] | 11.1626(4) | 10.9047(5) | 10.874(2) | 11.1971(8) | 10.9580(5) |
| *b* [Å] | 12.5839(6) | 13.1125(6) | 13.063(2) | 12.5847(9) | 13.1506(4) |
| *c* [Å] | 12.7543(6) | 13.162(1) | 13.147(2) | 12.7567(9) | 13.1551(6) |
| $\beta$ [°] | 92.284(3) | 90.883(8) | 90.83(1) | 92.307(6) | 91.151(4) |
| *V* [Å$^3$] | 1790.2(1) | 1881.7(2) | 1867.3(5) | 1796.1(2) | 1895.3(1) |
| *Z* | 4 | 4 | 4 | 4 | 4 |
| $\rho_{calcd.}$ [g cm$^{-3}$] | 1.71 | 1.63 | 1.64 | 1.71 | 1.62 |
| $\mu$ [mm$^{-1}$] | 1.110 | 1.047 | 1.055 | 1.097 | 1.038 |
| $T_{min}/T_{max}$ | 0.68/0.83 | 0.80/0.89 | 0.83/0.89 | 0.56/0.81 | 0.73/0.94 |
| Crystal size [mm] | 0.32 × 0.20 × 0.13 | 0.36 × 0.18 × 0.12 | 0.23 × 0.21 × 0.14 | 0.60 × 0.23 × 0.12 | 0.41 × 0.13 × 0.06 |
| Data Collection | | | | | |
| $\lambda$ [Å] | 0.71073 | 0.71073 | 0.71073 | 0.71073 | 0.71073 |
| *T* [K] | 15 | 15 | 15 | 130 | 130 |
| $\theta_{max}$ [°] | 44.15 | 37.16 | 26.60 | 42.47 | 60.12 |
| Total no. of reflections | 26316 | 16975 | 1321 | 24072 | 66160 |
| No. of indep. reflections | 6407 | 3879 | 812 | 4124 | 12143 |
| $R_{int}$[a] | 0.034 | 0.033 | 0.045 | 0.025 | 0.032 |
| Refinement | | | | | |
| Number of parameters | 149 | 154 | 129 | 149 | 149 |
| *R*1[b] (all data) | 0.043 | 0.045 | 0.075 | 0.076 | 0.064 |
| *R*1 [$I > 2\sigma(I)$] | 0.033 | 0.027 | 0.065 | 0.049 | 0.035 |
| *wR*2 | 0.084 | 0.057 | 0.172 | 0.135 | 0.091 |
| GoF | 1.04 | 0.80 | 1.29 | 1.07 | 0.92 |

[a] $R_{int} = \sum_H (N/N-1)\sum_i |I_i - \langle I \rangle| \Big/ \sum_H \sum_i I_i$.

[b] $R1 = \sum_H \big||F_o| - |F_c|\big| \Big/ \sum_H |F_o|$, $wR2 = \left[\sum_H w(F_o^2 - F_c^2)^2 \Big/ \sum_H w(F_o^2)^2\right]^{1/2}$, $\text{GoF} = \left[\sum_H w(F_o^2 - F_c^2)^2 \Big/ (n-p)\right]^{1/2}$.

 © 2007 Wiley-VCH Verlag GmbH & Co. KGaA, Weinheim 

LS relaxation rate in the course of the diffraction measurements, since the cell volume of the two spin states differ by more than 90 Å$^3$. We have already shown,[16] in the case of the HS-2q state, that the change in the cell volume as a function of time at 15 K exhibits a linear trend with an insignificant negative slope [$V(t)$ = 1880(3) – 0.002(5)$t$]. The metastable state can therefore be considered stationary during the diffraction measurement.

According to our magnetic results, a complete HS-2q state can be trapped at 15 K by flash cooling from room temperature. The HS-2q crystal structure indicates a slight static disorder of the S atom which was refined at two independent positions. The two S positions have complementary refined occupancies of 0.0300(5) and 0.9700(5) for the minor and major positions, respectively. Such a disorder is not uncommon for the axial NCS ligands of spin-transition complexes.

The excitation conditions for the diffraction measurements of the HS-2p state were optimized according to the photomagnetic and spectroscopic results. The absorption band corresponding to the $^1A_1 \rightarrow {}^1T_1$ transition (LIESST effect) is centred at 550 nm. For the photocrystallographic measurements, the optimum conversion was found at $\lambda$ = 488 nm ($P_{laser}$ = 46 mW, exposure time = 30 s), aside the maximum of the absorption band, ensuring a rather good penetration depth in the single-crystal sample. Using these excitation conditions, a complete photoconversion was reached, since at the photostationary state, the Bragg peaks corresponding to the LS state were not noticeable any more. It is to be noted that the data quality of the HS-2p state is lower than that of the HS-2q state, as a result of an increase in crystal mosaicity after light irradiation and, correlatively, a smaller number of collected reflections. It was very difficult to obtain and measure this photoinduced state, and several crystals were destroyed during preliminary irradiation tests. The presently described data set is the best we could achieve. Contrary to the HS-2q crystal structure, we could not detect any S static disorder. Whether this is related to the lower data quality or attributed to a real structural difference between HS-2q and HS-2p is still an open question.

**Low-Spin and High-Spin States. Data Collection and Structural Refinement at 130 K:** We took advantage of the large thermal hysteresis centred at 134 K to measure the HS-1 and LS states at the same temperature, 130 K, in both spin states. This is an important issue since in this case thermal contraction effects do not interfere in the structural comparison. The measured samples were prepared in the appropriate spin state depending on their history. The HS-1 state was obtained directly by cooling from room temperature, whereas for the LS state, the sample was first cooled down to 100 K (below $T_{1/2\downarrow}$ = 123.5 K) and then warmed up to 130 K. Contrary to the HS-2q state, no static disorder was noticed around S in either of the spin states.

CCDC-627392, -627393, -627394, -627395, -627396 contain the supplementary crystallographic data for this paper. These data can be obtained free of charge from The Cambridge Crystallographic Data Centre via www.ccdc.cam.ac.uk/data_request/cif.

## Acknowledgments

Nancy Université and the Centre National de la Recherche Scientifique are gratefully acknowledged. This work was partly supported by the European Union FP6-Network of Excellence MAGMANet under contract No. FP6-515767-2. We thank N. Lugan for his help during preparation of the btr ligand.

[1] a) P. Gutlich, H. A. Goodwin (Eds.), *Topics in Current Chemistry, Vol. 233, 234, 235*, Springer-Verlag, Berlin, **2004**; b) P. Gütlich, A. Hauser, H. Spiering, *Angew. Chem. Int. Ed. Engl.* **1994**, *33*, 2024.
[2] P. Guionneau, M. Marchivie, G. Bravic, J.-F. Létard, D. Chasseau in *Topics in Current Chemistry, Vol. 234* (Eds: P. Gutlich, H. A. Goodwin), Springer-Verlag, Berlin, **2004**, p. 97.
[3] A. Bousseksou, K. Boukheddaden, M. Goiran, C. Conséjo, M.-L. Boillot, J.-P. Tuchagues, *Phys. Rev. B* **2002**, *65*, 172412.
[4] A. Hauser, *Chem. Phys. Lett.* **1986**, *124*, 543.
[5] S. Decurtins, P. Gütlich, C. P. Köhler, H. Spiering, *Chem. Phys. Lett.* **1984**, *105*, 1.
[6] J.-F. Létard, L. Capes, G. Chastanet, N. Moliner, S. Létard, J. A. Real, O. Kahn, *Chem. Phys. Lett.* **1999**, *313*, 115.
[7] J.-F. Létard, P. Guionneau, O. Nguyen, J. Sanchez Costa, S. Marcen, G. Chastanet, M. Marchivie, L. Goux-Capes, *Chem. Eur. J.* **2005**, *11*, 4582.
[8] A. Hauser, *Chem. Phys. Lett.* **1992**, *192*, 65.
[9] M. Marchivie, P. Guionneau, J.-F. Létard, D. Chasseau, *Acta Crystallogr., Sect. B* **2005**, *61*, 25.
[10] a) D. W. J. Cruickshank, *Acta Crystallogr.* **1956**, *9*, 757; b) D. W. J. Cruickshank, *Acta Crystallogr.* **1961**, *14*, 896.
[11] P. Guionneau, M. Marchivie, G. Bravic, J.-F. Létard, D. Chasseau, *J. Mater. Chem.* **2002**, *12*, 2546.
[12] a) M. Marchivie, P. Guionneau, J. A. K. Howard, G. Chastanet, J.-F. Létard, A. E. Goeta, D. Chasseau, *J. Am. Chem. Soc.* **2002**, *124*, 194–195; b) V. A. Money, I. Radosavljevic Evans, M. A. Halcrow, A. E. Goeta, J. A. K. Howard, *Chem. Commun.* **2003**, 158–159; c) E. J. MacLean, C. M. McGrath, C. J. O'Connor, C. Sangregorio, J. M. W. Seddon, E. Sinn, F. E. Sowrey, S. J. Teat, A. E. Terry, G. B. M. Vaughan, N. A. Young, *Chem. Eur. J.* **2003**, *9*, 5314–5322; d) N. Huby, L. Guérin, E. Collet, L. Toupet, J.-C. Ameline, H. Cailleau, T. Roisnel, T. Tayagaki, K. Tanaka, *Phys. Rev. B* **2004**, *69*, 020101; e) A. L. Thompson, A. E. Goeta, J. A. Real, A. Galet, M. C. Muñoz, *Chem. Commun.* **2004**, 1390–1391; f) V. Niel, A. L. Thompson, A. E. Goeta, C. Enachescu, A. Hauser, A. Galet, M. C. Muñoz, J. A. Real, *Chem. Eur. J.* **2005**, *11*, 2047–2060; g) J. Kusz, D. Schollmeyer, H. Spiering, P. Gütlich, *J. Appl. Crystallogr.* **2005**, *38*, 528–536; h) K. Ichiyanagi, H. Hebert, L. Toupet, H. Cailleau, P. Guionneau, J.-F. Létard, E. Collet, *Phys. Rev. B* **2006**, *73*, 060408.
[13] M. Marchivie, P. Guionneau, J.-F. Létard, D. Chasseau, J. A. K. Howard, *J. Phys. Chem. Solids* **2004**, *65*, 17.
[14] V. Legrand, C. Carbonera, S. Pillet, M. Souhassou, J.-F. Létard, P. Guionneau, C. Lecomte, *J. Phys. Conf. Ser.* **2005**, *21*, 73.
[15] S. Pillet, V. Legrand, H.-P. Weber, M. Souhassou, J.-F. Létard, P. Guionneau, C. Lecomte, *Z. Kristallogr.* **2007**, in press.
[16] V. Legrand, S. Pillet, M. Souhassou, N. Lugan, C. Lecomte, *J. Am. Chem. Soc.* **2006**, *128*, 13921.
[17] S. Pillet, C. Lecomte, C. F. Sheu, Y. C. Lin, I. J. Hsu, Y. Wang, *J. Phys. Conf. Ser.* **2005**, *21*, 221.
[18] J. S. Costa, P. Guionneau, J. F. Létard, *J. Phys. Conf. Ser.* **2005**, *21*, 67–72.
[19] W. Vreugdenhil, J. H. Van Diemen, R. A. G. De Graaff, J. G. Haasnoot, J. Reedijk, A. M. Van Der Kraan, O. Kahn, J. Zarembowitch, *Polyhedron* **1990**, *9*, 2971.
[20] S. Pillet, J. Hubsch, C. Lecomte, *Eur. J. Phys. B* **2004**, *38*, 541.
[21] a) J.-P. Martin, J. Zarembowitch, A. Bousseksou, A. Dworkin, J. G. Haasnoot, F. Varret, *Inorg. Chem.* **1994**, *33*, 6325; b) J.-P. Martin, J. Zarembowitch, A. Dworkin, J. G. Haasnoot, E. Codjovi, *Inorg. Chem.* **1994**, *33*, 2617.
[22] A. Desaix, O. Roubeau, J. Jeftic, J. G. Haasnoot, K. Boukheddaden, E. Codjovi, J. Linarès, M. Noguès, F. Varret, *Eur. Phys. J.* **1998**, *B6*, 183.
[23] S. Pillet, V. Legrand, M. Souhassou, C. Lecomte, *Phys. Rev. B* **2006**, *74*, 140101(R).

 © 2007 Wiley-VCH Verlag GmbH & Co. KGaA, Weinheim 

[24] J.-F. Létard, P. Guionneau, L. Rabardel, J. A. K. Howard, A. E. Goeta, D. Chasseau, O. Kahn, *Inorg. Chem.* **1998**, *37*, 4432.
[25] W. Morscheidt, J. Jeftic, E. Codjovi, J. Linares, A. Bousseksou, H. Constant-Marchado, F. Varret, *Meas. Sci. Technol.* **1998**, *9*, 1311.
[26] C. Enachescu, H. Constant-Machado, E. Codjovi, J. Linares, K. Boukheddaden, F. Varret, *J. Phys. Chem. Solids* **2001**, *62*, 1409.
[27] a) H. Spiering, E. Meissner, H. Köppen, E. W. Müller, P. Gütlich, *Chem. Phys.* **1982**, *68*, 65; b) P. Adler, L. Wiehl, E. Meissner, C. P. Köhler, H. Spiering, P. Gütlich, *J. Phys. Chem. Solids* **1987**, *48*, 517.
[28] J. Kusz, H. Spiering, P. Gütlich, *J. Appl. Crystallogr.* **2001**, *34*, 229.
[29] J. Kusz, H. Spiering, P. Gütlich, *J. Appl. Crystallogr.* **2000**, *33*, 201.
[30] N. W. Ashcroft, N. D. Mermin, *Solid State Physics*, New York: Holt, Rinehart and Winston, **1976**.
[31] R. Hundt, J. C. Schön, M. Jansen, *J. Appl. Crystallogr.* **2006**, *39*, 6.
[32] M. Sorai, S. Seki, *J. Phys. Chem. Solids* **1974**, *35*, 555–570.
[33] a) G. Brehm, M. Reiher, S. Schneider, *J. Phys. Chem., A* **2002**, *106*, 12024; b) K. L. Ronayne, H. Paulsen, A. Höfer, A. C. Dennis, J. A. Wolny, A. I. Chumakov, V. Schünemann, H. Winkler, H. Spiering, A. Bousseksou, P. Gütlich, A. X. Trautwein, J. McGarvey, *J. Phys. Chem. Chem. Phys.* **2006**, *8*, 4685.
[34] R. Zimmermann, E. König, *J. Phys. Chem. Solids* **1977**, *38*, 779–788.
[35] A. Bousseksou, H. Constant-Machado, F. Varret, *J. Phys. I Fr.* **1995**, *5*, 747–760.
[36] G. Molnar, V. Niel, A. B. Gaspar, J. A. Real, A. Zwick, A. Bousseksou, J. J. McGarvey, *J. Phys. Chem., B* **2002**, *106*, 9701–9707.
[37] W. Vreugdenhil, S. Gorter, J. G. Haasnoot, J. Reedijk, *Polyhedron* **1985**, *4*, 1769.
[38] a) T. M. Kuzay, M. Kazmierczak, B. J. Hsieh, *Acta Crystallogr., Sect. D* **2001**, *57*, 69; b) S. Kriminski, M. Kazmierczak, R. E. Thorne, *Acta Crystallogr., Sect. D* **2003**, *59*, 697.
[39] J. B. Forsyth, C. F. Sampson, *Phys. Lett. A* **1971**, *36*, 223–224.
[40] Oxford Diffraction, *CrysAlis CCD* and *CrysAlis RED*, Versions 1.171, Oxford Diffraction, Wroclaw, Poland, **2004**.
[41] R. H. Blessing, *J. Appl. Crystallogr.* **1989**, *22*, 396.
[42] G. M. Sheldrick, *SHELX97*, *Program for Structure Solution and Refinement*, University of Göttingen, Germany, **1997**.
[43] W. Hummel, J. Hauser, H. B. Bürgi, *J. Mol. Graphics* **1990**, *8*, 214.
[44] T. Balic Zunic, I. Vickovic, *J. Appl. Crystallogr.* **1996**, *29*, 305–306.

Received: August 21, 2007
Published Online: November 8, 2007

 © 2007 Wiley-VCH Verlag GmbH & Co. KGaA, Weinheim 

DOI: 10.1002/ejic.200700932

# C–S Bond Activation and Partial Hydrogenation of Thiophene by a Dinuclear Trihydride Platinum Complex

**Ainara Nova,[a] Fernando Novio,[a] Pilar González-Duarte,*[a] Agustí Lledós,*[a] and Rubén Mas-Ballesté[a]**

**Keywords:** C–S activation / Desulfurization / Thiophene / Hydride ligands / Platinum / Reaction mechanisms

[(dppp)$_2$Pt$_2$H$_3$]ClO$_4$ [**I**, dppp = Ph$_2$P(CH$_2$)$_3$PPh$_2$] was found to activate the C–S bond and to cause partial hydrogenation of thiophene. Thus, the reaction of **I** with neat thiophene (**T**) at reflux temperature yields [(dppp)Pt(SC$_4$H$_4$-*C*,*S*)] (**II**) and [(dppp)$_2$Pt$_2$(μ-SC$_4$H$_5$-*C*,*S*)]ClO$_4$ (**III**) at a 2:3 molar ratio. The same reaction in toluene or benzene solvent affords the same complexes **II** and **III** but in a 1:9 molar ratio. The concomitant formation of **II** and **III** was interpreted on the basis of theoretical calculations (DFT), which have provided a detailed insight into the reaction mechanism. Thus, the presence of **T** causes **I** to dissociate into [(dppp)PtH$_2$] and [(dppp)PtH(C$_4$H$_4$S-κ*S*)], this process being a common step for the two ensuing reaction pathways. After dissociation, the activation of the thiophene C–S bond to yield **II** involves participation of [(dppp)PtH$_2$] exclusively. However, the reaction leading to **III** requires the internal migration of the coordinated hydride to the thiophene ligand in [(dppp)PtH(C$_4$H$_4$S-κ*S*)] and the subsequent assistance of the {(dppp)Pt} fragment formed from [(dppp)PtH$_2$] by hydrogen elimination. As a result of the involvement of [(dppp)PtH$_2$] in the formation of both **II** and **III**, the two reaction pathways are competitive. The reactivity of **II** and **III** with various sources of hydride ligands and different protonic acids has also been examined. Thus, the reaction of **II** with HBF$_4$ leads to the thiolate-bridged dinuclear complex [(dppp)$_2$Pt$_2$(μ-SC$_4$H$_5$)$_2$](BF$_4$)$_2$ (**IV**). In the case of **III** the addition of HBF$_4$ leads to [(dppp)$_2$-Pt$_2$(μ-SC$_4$H$_6$)](BF$_4$)$_2$ (**V**), which transforms into **III** by the addition of a base. The X-ray structural characterization of the unprecedented complex **V** is reported here.

(© Wiley-VCH Verlag GmbH & Co. KGaA, 69451 Weinheim, Germany, 2007)

## Introduction

The reaction of thiophenes with homogeneous transition metals is considered a good strategy for modeling heterogeneous reactions that occur during the hydrodesulfurization (HDS) of petroleum.[1–6] This is a step in industrial oil refining in which sulfur is removed from crude oil by being chemically converted to $H_2S$ and hydrocarbon products.[7,8] Conventionally, the HDS process involves a reaction with hydrogen gas (up to 200 atm pressure) at temperatures of 300–450 °C over an alumina supported cobalt (or nickel) molybdenum catalyst. The evident importance of HDS together with environmental regulations that dictate increasingly smaller amounts of sulfur in gasoline and gasoil fuels[9,10] account for the current interest in developing more efficient technologies. Several reviews of the results obtained in the search for new heterogeneous catalysts,[11–15] in homogeneous modeling studies with transition-metal complexes[1,2,4,16–18] and in computational studies dealing with several aspects of heterogeneous HDS,[19–23] have already appeared. Remarkably, despite the large number of studies, the mechanism for the heterogeneous HDS of thiophenic molecules is not completely known and current technology has been unsuccessful in treating these compounds to achieve the sulfur levels required by new legislation.

The reactions of thiophenes with soluble metal complexes have provided mechanistic knowledge of the HDS process.[1,5,24–26] Significantly, many metals (Ru, Os, Ir, Re, Pt, Pd) have been shown to be more active as HDS promoters than the molybdenum–cobalt (or nickel) mixtures usually employed in industrial HDS.[10,12–14,27–30] Thus, the reaction of thiophene (**T**) with mono- or dinuclear transition-metal complexes has usually led to the cleavage of a single thiophene C–S bond and thus to the formation of a thiametalacycle as the product[4,31–41] (Scheme 1, right-hand side). Concerning these reactions, the most thorough mechanistic study involves a mononuclear rhodium species.[34] Although no intermediates were detected in this reaction, the use of selectively deuterated reagents and theoretical calculations made it possible to propose the corresponding mechanism.[42–44] In terms of mono- and dinuclear transition-metal complexes, the only example of a complete desulfurization of thiophene to butadiene was achieved by

[a] Departament de Química, Universitat Autònoma de Barcelona, 08193 Bellaterra, Barcelona, Spain
Fax: +34-935813101
E-mail: Pilar.Gonzalez.Duarte@uab.es
agusti@klingon.uab.es

Supporting information for this article is available on the WWW under http://www.eurjic.org or from the author.

 © 2007 Wiley-VCH Verlag GmbH & Co. KGaA, Weinheim 

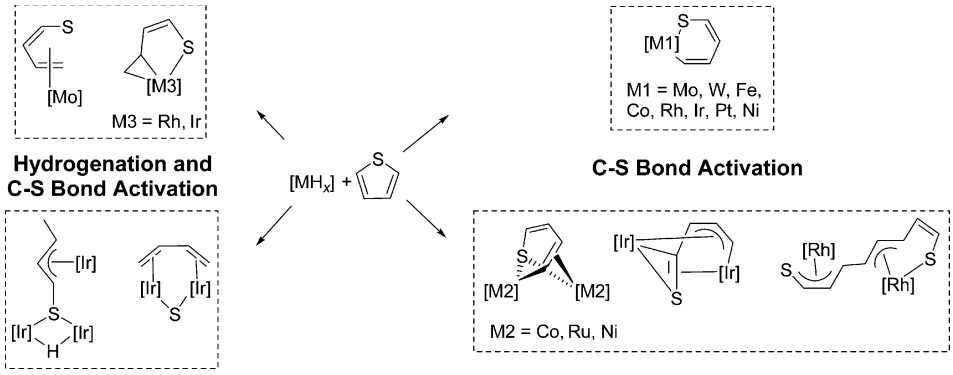


Scheme 1. Reported products obtained in the reaction of **T** with $[MH_x]$ ($x$ = 0–3) transition-metal complexes.

means of a dinuclear polyhydride iridium complex in the presence of a hydrogen acceptor compound.[45] Several intermediate species identified by NMR showed how the activation of the second C–S bond is subsequent to the hydrogenation of the thiophenic chain. Within this context, it is worth noting that in the examples where the first C–S bond activation is accompanied by hydrogenation (Scheme 1, left-hand side),[32,46,47] the complete desulfurization has usually required further treatment with $H_2$. However, the same reaction with the thiametalacycle products is unreported.

In this paper, a dinuclear polyhydride platinum complex was investigated for its ability to react with **T**. An approach followed in earlier studies of platinum-mediated desulfurization of thiophene, benzothiophene, and dibenzothiophene involved their reaction with $[(PEt_3)_3Pt]$ and subsequent treatment with various hydride reagents.[35] While the completely desulfurized hydrocarbons were obtained from the three heterocycles, the amount of desulfurization in the case of **T** was about 4%. Overall, the notion that two metal centers might be required for cleavage of both thiophenic C–S bonds,[16] the high HDS activity shown by platinum metals,[48,49] and the fact that a polyhydride complex already contains the hydrogen needed for thiophene hydrogenolysis led us to explore the reaction of $[(dppp)_2Pt_2H_3]ClO_4$ [dppp = 1,3-bis(diphenylphosphanyl)propane] with **T** and the mechanism of this reaction. Within the context of its possible relevance in the modeling of HDS studies, we first investigated the reactivity of $[(dppp)_2Pt_2H_3]ClO_4$ toward sulfur-containing species such as $Na_2S$ or NaSH. The set of reactions obtained provided solid evidence that behind the apparent simplicity of platinum complexes containing Pt–H, Pt–SH, or Pt–S fragments, there is an outstanding chemistry.[50]

## Results and Discussion

### Experimental Results

The reaction between $[(dppp)_2Pt_2H_3]ClO_4$ (**I**) and **T** was monitored by $^1H$ and $^{31}P$ NMR and mass measurements until no further progress was observed. Consistent with literature data,[35,36,45] high temperature, significant excess of thiophene with respect to the platinum complex, and several hours are required for optimum rate and yield. While under these experimental conditions we always observed the concomitant formation of two platinum complexes, their relative amounts were dependent on the presence or absence of benzene or toluene solvent. The isolation procedure and complete characterization of the complexes obtained are given in the Experimental Section.

### *The Reaction of $[(dppp)_2Pt_2H_3]ClO_4$ (I) with Thiophene*

Monitoring by $^{31}P$ NMR spectroscopy (Figure 1) indicated concomitant formation of a mononuclear and a dinuclear platinum species (Scheme 2). However, neither the NMR nor the ESI MS data gave evidence of intermediate species being formed. Similar observations were obtained in the monitoring of the reaction of **I** (0.15 mmol) with thiophene (15 mL) in toluene or benzene solvent (15–20 mL) at reflux temperature. The only difference in these reactions was the relative molar ratio of the two new platinum complexes formed (2:3 in neat thiophene and 1:9 in toluene or benzene). According to the $^{31}P$ and $^1H$ NMR spectroscopic data recorded during the reaction, both **II** and **III** not only form simultaneously but also maintain a constant molar ratio until the end of the reaction.

The $^{31}P$ NMR features of the reaction mixture that were attributable to a mononuclear platinum complex, literature data,[35,36] and the peak at $m/z$ = 692.2 in the ESI MS spectrum were consistent with the formation of an unsymmetrical species by insertion of the {(dppp)Pt} fragment into one thiophenic C–S bond. The formulation of this complex as $[(dppp)Pt(SC_4H_4\text{-}C,S)]$ (**II**) was fully confirmed by $^{31}P$, $^{195}Pt\{^1H\}$ and bidimensional $^1H$ and $^{13}C$ spectra (NOESY, COSY, HMQC C-H, and HSQC-edit C-H). $^1H$ and $^{13}C$ NMR spectroscopic data were consistent with those reported for the related $[(PEt_3)_2Pt(SC_4H_4\text{-}C,S)]$ complex.[35]

The remaining signals in the $^{31}P$ NMR spectrum of the reaction mixture, together with $^1H$ NMR and ESI MS data obtained during the monitoring of the reaction of **I** with **T** gave evidence that **III** was probably a dinuclear platinum complex. Full characterization of this complex after its isolation by column chromatography from crude mixture after 20 h of reaction allowed us to formulate it as $[(dppp)_2Pt_2(\mu\text{-}SC_4H_5\text{-}C,S)]ClO_4$ (**III**).

 © 2007 Wiley-VCH Verlag GmbH & Co. KGaA, Weinheim 

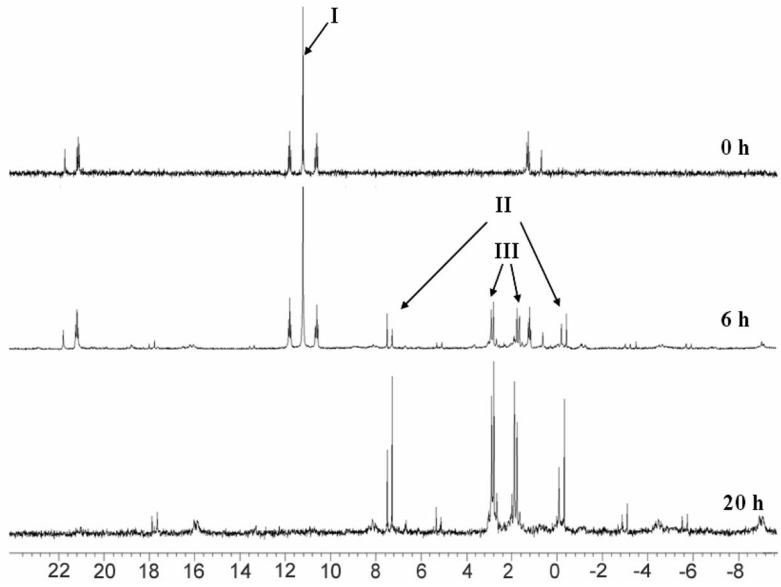


Figure 1. Monitoring by $^{31}P\{^1H\}$ NMR in $Cl_3CD$ of the reaction of $[(dppp)_2Pt_2H_3]ClO_4$ (**I**) with neat thiophene evidences formation of $[(dppp)Pt(SC_4H_4\text{-}C,S)]$ (**II**) and $[(dppp)_2Pt_2(\mu\text{-}SC_4H_5\text{-}C,S)]ClO_4$ (**III**) after 6 h, and total consumption of **I** after 20 h.

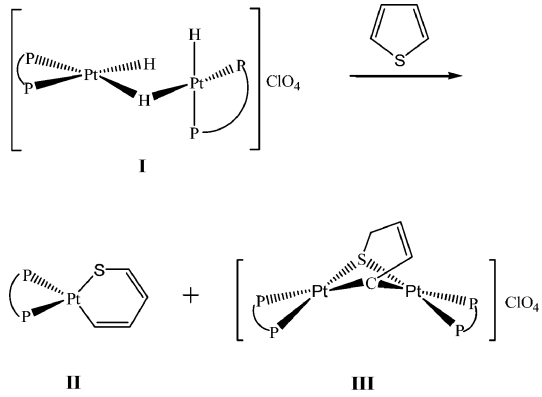


Scheme 2. The mono- and dinuclear platinum complexes obtained in the reaction of **I** with thiophene.

Thus, the $^{31}P\{^1H\}$ NMR spectrum of **III** is second-order, consisting of two broad signals (Figure 1) that fit well with the simulation of this spectrum including long-range P–Pt couplings (see electronic supporting information). Concerning the $^{195}Pt\{^1H\}$ NMR spectrum, it displays the same pattern as **II** with broader signals. These features corroborate the dinuclear nature of **III** and the symmetrical behavior of the bridging ligand. The $SC_4H_5$ ligand in **III** was fully characterized by $^1H$ NMR, with additional NOESY and COSY experiments, as well as by HMBC P–H, $^{13}C$ NMR (DEPT), and HSQC-edit C–H data. The $^{13}C$ chemical shifts at $\delta$ = 126.1 and 137.1 ppm, which are in the proper range for olefins, gave evidence of one double bond. This fact, in addition to the symmetry of the complex, even at low temperatures, allows an $\eta^3$ coordination for this bridge to be discarded and makes the formulation {S–$CH_2$–CH=CH–CH} the most reasonable alternative.[51] The stoichiometric ratio of dppp to $SC_4H_5$ ligands in **III** is 2:1, as deduced from the integration of the signals of the proton resonating at $\delta$ = 5.43 or 5.61 ppm (corresponding to the –CH=CH– fragment) with respect to those of the aliphatic $CH_2$ groups in the phosphane ligands, in agreement with the dinuclear nature of **III**. The absence of hydride ligands is fully confirmed by $^1H$ and HMBC Pt–H NMR, and agrees with infrared data. Finally, the ESI-MS spectrum shows a major peak at *m/z* = 1299.2401 $[M^+]$ that fits well to the $[(dppp)_2Pt_2(SC_4H_5)]^+$ cation. Elemental analyses and IR data are consistent with **III** being an ionic molecule with $ClO_4^-$ as counterion.

### *Additional Reactions*

In order to further elucidate the mechanism leading to **II** and **III**, and to further analyze the reactivity of these complexes, we carried out complementary reactions. These were monitored for several hours by $^{31}P$ and $^1H$ NMR as earlier described for the reaction of **I** with **T**. In some reactions the deuterated analog of **I**, $[(dppp)_2Pt_2D_3]ClO_4$ (**I-*d*$_3$**), was employed, and in these cases $^2H$ NMR spectra were also recorded. The synthesis and NMR features of **I-*d*$_3$** have already been reported.[50] On the whole the NMR features allowed identification of the compounds formed and eventually led to the synthesis and characterization of new complexes, as depicted in Scheme 3.

The reactions involving **I-*d*$_3$** gave evidence that complex **I** cleaves in the presence of thiophene. Thus, the heating at reflux temperature of a 1:1 mixture of **I** and **I-*d*$_3$** in the presence of thiophene showed that after 6 h all isotopomers $[(dppp)_2Pt_2H_{(3-x)}D_x]^+$ ($x$ = 0–3) were present in comparable amounts. However, when the same process was carried out in the absence of thiophene, only negligible amounts of mixed species were present after 12 h of heating. This indicated that **T**, and not the presence of solvent, causes the cleavage of **I**, and that the breaking of the dinuclear platinum complex **I** is a reversible process, both issues being

 © 2007 Wiley-VCH Verlag GmbH & Co. KGaA, Weinheim 

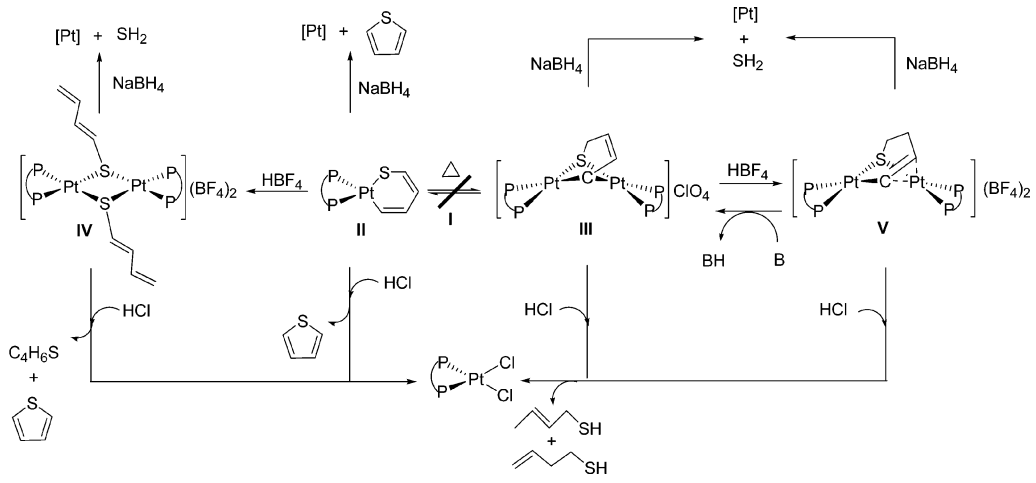


Scheme 3. Overall reactivity of complexes **I**–**V**: (a) No interconversion between **II** and **III** is observed; (b) **II** with $HBF_4$ affords **IV** and, similarly, **III** gives **V**; (c) **V** goes back to **III** by addition of a base (B = $MeO^-$, $Et_3N$); (d) complexes **II**–**V** react with HCl, and also with $NaBH_4$, but not with **I**.

consistent with literature data.[32] In addition to the above reactions, the use of **I-*d*$_3$** provided information on the source and location of the inserted hydrogen atom into the thiophenic chain of **III**. This was obtained by the reaction of **I-*d*$_3$** and **T** in toluene at reflux temperature, which afforded **II** and **III-*d*$_1$**. Characterization of **III-*d*$_1$** by $^1H$, $^2H$, and $^{13}C$ DEPT-135 NMR spectroscopic data allows to establish that deuterium is bound to the carbon atom next to the sulfur atom.

Another set of experiments, aimed at examining whether **II** and **III** could convert into each other even though their concentrations increased concomitantly during the reaction of **I** with **T**, both in the presence and absence of toluene or benzene solvent, was indicative of parallel reaction pathways. Within this context, **II** and **III** were independently heated in toluene solvent at reflux temperature for several hours, during which no changes were observed. The same procedure with a mixture of **I** (as a possible platinum and hydride source) and **II** at various molar ratios in toluene did not afford **III**, thus reinforcing that **II** and **III** are independently formed.

While the reaction of **I** with **T** involves the activation of one C–S bond of thiophene, the conditions for the cleavage of the second S–C bond in **II** and **III** were also examined. To this end, complexes **II** and **III** were made to react with protonic acids ($HBF_4$, HCl) and hydride sources ($NaBH_4$, **I**). These reactions are summarized in Scheme 3 and the corresponding conditions given in the Exp. Section.

### *The Reaction of II and III with HBF$_4$*

The reaction of **II** with $HBF_4$ yielded the di-μ-thiolato dinuclear complex $[(dppp)_2Pt_2(\mu\text{-}SC_4H_5)_2](BF_4)_2$ (**IV**) in high yield. Identification of this complex was achieved on the basis of NMR spectroscopic data, which were fully consistent with those reported for the $[(PEt_3)_4Pt_2(\mu\text{-}SC_4H_5)_2](BF_4)_2$ analog, also obtained in a parallel reaction.[52]

Remarkably, replacement of **II** by **III** in the above reaction led to the unprecedented complex $[(dppp)_2Pt_2(\mu\text{-}SC_4H_6)](BF_4)_2$ (**V**), whose formation involves the insertion of a proton in the thiophenic chain of **III** without cleavage of the dinuclear species. As shown in Scheme 3, this reaction is easily reversed by addition of a base (NaMeO, $NEt_3$). Characterization of **V** by solution NMR measurements at room temperature evidenced the symmetrical behavior of the bridging ligand with respect to the two platinum centers. It also allows to establish that the proton insertion in the bridging S–$CH_2$–CH=CH–CH ligand in **III** causes an electronic rearrangement leading to a S–$CH_2$–$CH_2$–CH=CH species in **V**. As a result, one of the two σ Pt–C5 bonds in **III** evolved into a π interaction with the C4=C5 double bond in **V**, consistently with $^1H$ and $^{13}C$ NMR spectroscopic data. However, the symmetry observed in the latter complex for the phosphorus nuclei in the $^{31}P\{^1H\}$ NMR spectrum indicated a fluxional behavior for the CH=CH ligand moiety, which was consistent with low-temperature $^{31}P\{^1H\}$ NMR spectroscopic data. These showed that the two signals corresponding to the phosphorus nuclei, particularly that at $\delta$ = 0.1 ppm, widen with decreasing temperature without reaching complete decoalescence. According to the structure determined by single-crystal X-ray diffraction (see below), the features above are consistent with a fluxional behavior for the bridging ligand, which involves the σ Pt–C5 bond and the C4=C5 double bond to exchange sites between the two platinum centers.

### *The Reaction of II–V with HCl*

The reaction of **II**–**V** with a slight excess of HCl always led to the separation of solid $[(dppp)PtCl_2]$ in high yield (about 75%). The ease of formation of this complex in related systems is well known.[52] In the case of **III**–**V**, various thiols were also detected in the reaction mixture by CG-MS, as depicted in Scheme 3. Thiophene was also identified in the reaction of **IV**, and it was the only additional product in the case of **II**, both results being consistent with reported data.[52]

 © 2007 Wiley-VCH Verlag GmbH & Co. KGaA, Weinheim 

Overall, the reaction of **II**–**V** with $HBF_4$ or HCl does not involve activation of the second thiophenic C–S bond. Instead, these reactions allow the formation of thiols and, in the case of HCl, the recovery of platinum as [(dppp)-$PtCl_2$].

### *The Reaction of II–V with I and $NaBH_4$*

Complexes **II**–**V** did not react with **I** in toluene at reflux temperature but started degrading after 12 h of heating, as evidenced by the darkening of the reaction mixture, which was attributed to the formation of $Pt^0$. The same features were observed in the attempts to treat **II**–**V** with $NaBH_4$ at room temperature. However, with $NaBH_4$ the darkening of the solution was accompanied by the formation of either **T** (**II**) or $H_2S$ (**III**–**V**), the former detected by GC-MS, and the latter by formation of silver sulfide. Significantly, no other sulfur-containing species were identified in these reactions.

On the basis of the reactions above, it becomes apparent that the activation of the second thiophenic S–C bond by hydride sources is only achieved in compounds **III**–**V**. The reluctance of this bond to be activated in **II** is probably due to the greater aromatic character of the corresponding thiametalacycle. In fact, the cleavage of the C–S bond in **II** requires previous treatment with protons in the presence of noncoordinating counterions ($HBF_4$), which leads to **IV**. Overall, the activation of the C–S bond in **II**–**V** by $NaBH_4$ involves the total decomposition of these complexes.

### X-ray Structure of the $[(dppp)Pt(\mu\text{-}SC_4H_6)Pt(dppp)]^{2+}$ Cation

The structure showed evidence of a twinned crystal having two components related by a twofold rotation along the reciprocal axis *c**. The asymmetric unit of the unit cell contains two cations $[(dppp)Pt(\mu\text{-}SC_4H_6)Pt(dppp)]^{2+}$ together with three $BF_4^-$ and one $ClO_4^-$ anions, three acetone and one water molecules.[53] As the bonding parameters of the two cations are comparable, the geometry and selected bond lengths and angles given in the text correspond to one of them (Figure 2, Tables 1 and 2).

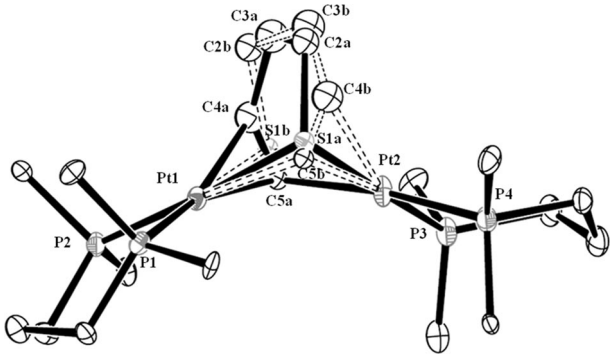


Figure 2. Structure of the cation in complex **V** with 50% probability displacement ellipsoids showing the two opposite orientations (a/b) of the thiolate bridge. Anions, hydrogen atoms, and phenyl rings are omitted for clarity.

Table 1. Selected distances [Å] for the cation of complex **V**.

| Distances[a] | | | |
|---|---|---|---|
| Pt1–S1A | 2.339(4) | Pt2–S1B | 2.343(6) |
| Pt2–S1A | 2.357(4) | Pt1–S1B | 2.391(6) |
| Pt1–C5A | 2.255(12) | Pt2–C5B | 2.30(2) |
| Pt2–C5A | 2.119(12) | Pt1–C5B | 2.23(2) |
| Pt1–C4A | 2.376(15) | Pt2–C4B | 2.38(2) |
| S1A–C2A | 1.789(11) | S1B–C2B | 1.786(13) |
| C2A–C3A | 1.569(14) | C2B–C3B | 1.572(15) |
| C3A–C4A | 1.616(14) | C3B–C4B | 1.618(15) |
| C4A–C5A | 1.131(14) | C4B–C5B | 1.131(15) |
| Pt1–P1 | 2.273(2) | Pt2–P3 | 2.261(2) |
| Pt1–P2 | 2.284(2) | Pt2–P4 | 2.281(2) |
| Pt1–Pt2 | 3.2272(6) | | |

[a] The A/B labels refer to the two disordered $SC_4H_6$ fragments.

Table 2. Selected angles [°] for the cation of complex **V**.

| Angles[a] | | | |
|---|---|---|---|
| Pt1–Pt2–S1A | 46.36(10) | Pt2–Pt1–S1B | 47.64(16) |
| Pt2–Pt1–S1A | 46.83(11) | Pt1–Pt2–S1B | 46.41(15) |
| Pt1–Pt2–C5A | 44.1(3) | Pt2–Pt1–C5B | 45.4(6) |
| Pt2–Pt1–C5A | 40.8(3) | Pt1–Pt2–C5B | 43.8(6) |
| Pt1–S1A–Pt2 | 86.81(13) | Pt2–S1B–Pt1 | 85.9(2) |
| Pt1–C5A–Pt2 | 95.0(5) | Pt2–C5B–Pt1 | 90.8(7) |
| S1A–Pt1–C5A | 80.5(3) | S1B–Pt2–C5B | 80.4(5) |
| S1A–Pt1–C4A | 79.1(3) | S1B–Pt2–C4B | 77.4(4) |
| S1A–Pt2–C5A | 82.9(3) | S1B–Pt1–C5B | 82.8(5) |
| S1A–C2A–C3A | 113.4(8) | S1B–C2B–C3B | 110.4(10) |
| C2A–C3A–C4A | 115.2(10) | C2B–C3B–C4B | 116.0(12) |
| C3A–C4A–C5A | 137.3(12) | C3B–C4B–C5B | 141.2(16) |
| Pt1–S1A–C2A | 102.9(5) | Pt2–S1B–C2B | 104.8(7) |
| Pt2–S1A–C2A | 92.7(6) | Pt1–S1B–C2B | 90.7(10) |
| Pt1–C5A–C4A | 81.9(9) | Pt2–C5B–C4B | 80.0(16) |
| Pt2–C5A–C4A | 115.0(10) | Pt1–C5B–C4B | 114.5(14) |
| P1–Pt1–S1A | 94.37(11) | P3–Pt2–S1B | 94.64(16) |
| P4–Pt2–S1A | 94.34(11) | P2–Pt1–S1B | 94.29(16) |
| P2–Pt1–C5A | 93.8(3) | P4–Pt2–C5B | 92.4(6) |
| P3–Pt2–C5A | 90.1(3) | P1–Pt1–C5B | 90.7(5) |
| P1–Pt1–C5A | 164.4(3) | P4–Pt2–S1B | 171.63(17) |
| P2–Pt1–S1A | 173.08(11) | P1–Pt1–S1B | 173.54(16) |
| P3–Pt2–S1A | 172.45(11) | P3–Pt2–C5B | 171.9(5) |
| P4–Pt2–C5A | 171.4(4) | P2–Pt1–C5B | 174.6(7) |
| C5A–Pt1–C4A | 28.1(4) | C5B–Pt2–C4B | 27.9(4) |
| P1–Pt1–P2 | 92.13(8) | P3–Pt2–P4 | 92.99(8) |
| P1–Pt1–Pt2 | 126.72(6) | P3–Pt2–Pt1 | 128.55(6) |
| P2–Pt1–Pt2 | 129.58(6) | P4–Pt2–Pt1 | 129.30(6) |

[a] The A/B labels refer to the two disordered $SC_4H_6$ fragments.

While the solution of the structure of the cation showed evidence of disorder of the bridging $SC_4H_6$ ligand, on the basis of the NMR spectroscopic data already described it was modeled as S–$CH_2$–$CH_2$–CH=CH. On the other hand, crystallographic resolution of a related cobalt complex[41] allowed us to consider that there were two bridging ligands with opposite orientation, in which the sulfur and C=C double bond exchange sites and the double bond changes the platinum atom, to which it is $\eta^2$-bound (effectively a $C_2$ rotation of the $SC_4H_6$ group perpendicular to Pt–Pt axis). Moreover, there was no evidence for disordered atoms corresponding to {(dppp)Pt} moieties, suggesting that these

 © 2007 Wiley-VCH Verlag GmbH & Co. KGaA, Weinheim 

atoms lie in virtually the same locations in the disordered partners.

The bond lengths and angles observed for the $SC_4H_6$ ligand are fully consistent with the sequence S–$CH_2$–$CH_2$–CH=CH, whose atoms are puckered in such a fashion so that sulfur, C2, C3, and C4 are nearly planar, but with C5 lying above this plane. While one of the platinum atoms (Pt1) is bound to the $SC_4H_6$ bridge through sulfur and the C4=C5 double bond, the other platinum (Pt2) binds to the same sulfur but only to C5 through a σ bond. As a result of the different coordinative behavior of the bridging ligand, two different square-planar environments are observed for the platinum centers. The platinum–platinum distance of 3.2272(6) Å is consistent with the only reported related species, where a weak metal–metal interaction is proposed.[54] Concerning the terminal dppp ligands, they adopt a distorted chair conformation that compares very well with that usually found in dinuclear complexes enclosing different bridging ligands between two {(dppp)$Pt^{II}$} fragments.[55] This is the first structurally characterized example of a dinuclear platinum compound resulting from the S–C activation of thiophene.

## Computational Study of the Reaction Mechanism of I with T

Computational chemistry has proven to be a useful tool in mechanistic studies of homogeneous catalytic processes.[56,57] However, theoretical analyses of HDS mechanisms using organometallic reagents are still scarce,[43,44] and in general have focused on investigating the nature and energetics of the interactions between **T** and single-metal organometallic complexes.[58–64] In this section we present a complete computational study of the reaction mechanism of **I** with **T** using DFT methods. From this study and the experimental results presented above we propose a plausible reaction pathway for the formation of complexes **II** and **III**.

All complexes have been modeled using $H_2P(CH_2)_2PH_2$ (dhpp) instead of the actual dppp ligand. The calculated intermediates are numbered from **1** to **10** and the transition states are labeled as **TS1**, **TS2**, and so forth. The van der Waals complexes are indicated by **2a···2b** while **2a+2b** indicates the sum of the energies of the individual species. Given the cationic nature of some intermediates, the inclusion of solvent is mandatory to obtain a reliable energy profile. Thus, the relative energies of intermediates and reaction barriers calculated in benzene are given in the schemes. The resulting $\Delta G$ values in benzene and details of geometries of the transition states are given in the electronic supporting information.

### *Fragmentation of the Dinuclear [(dhpp)$_2$Pt$_2$H$_3$]$^+$ Cation (1)*

All attempts to make **1** react with **T** have led to the cleavage of the dinuclear platinum complex with the concomitant coordination of **T** to one of the platinum centers. In this way two mononuclear $Pt^{II}$ complexes are formed: [(dhpp)$PtH_2$] (**2a**) and either [(dhpp)PtH($C_4H_4S$-κ*S*)]$^+$ (**2b**) or [(dhpp)PtH($\eta^2$-$C_4H_4S$)]$^+$ (**3b**), depending on whether the coordination mode of thiophene to platinum is through sulfur or a double bond, respectively. As shown in Scheme 4, both types of coordination involve similar energy barriers: 16.0 kcal/mol (**TS1**) to give **2a** and **2b**; and 17.4 kcal/mol (**TS2**) to give **2a** and **3b**. Also, both pathways are clearly endothermic, the products being 21 kcal/mol above reactants.

The energy for the cleavage of **1** was also calculated in the absence of **T** in order to quantify the thiophene assistance to the fragmentation process. The energy cost associated to the formation of [(dhpp)PtH]$^+$ and [(dhpp)$PtH_2$] (**2a**) from [(dhpp)$Pt_2H_3$]$^+$ in benzene is 39.5 kcal/mol, thus, considerably higher than in the presence of thiophene (21.7 kcal/mol).

### *Formation of [(dhpp)Pt($C_4H_4$S-C,S)] (6a)*

Both **2a** and **2b** species are candidates to afford the {(dhpp)$Pt^0$} fragment, which is the precursor of **6a** (**II**). However, theoretical calculations show that formation of this fragment by reductive elimination of $H_2$ from **2a** is much more easily achieved than the elimination of a *S*-protonated thiophene from **2b**. The calculated energy for the latter reaction is 69.5 kcal/mol, too high to be feasible. Consequently, only the reaction from **2a** to yield **6a** has been taken into account. Concerning energy values, as **2a** and **2b** can exist as separate entities in solution, they are taken as the zero of energy in the following discussions.

The set of reactions that account for the evolution from **2a** to **6a** (Scheme 5) is initiated by the concomitant re-

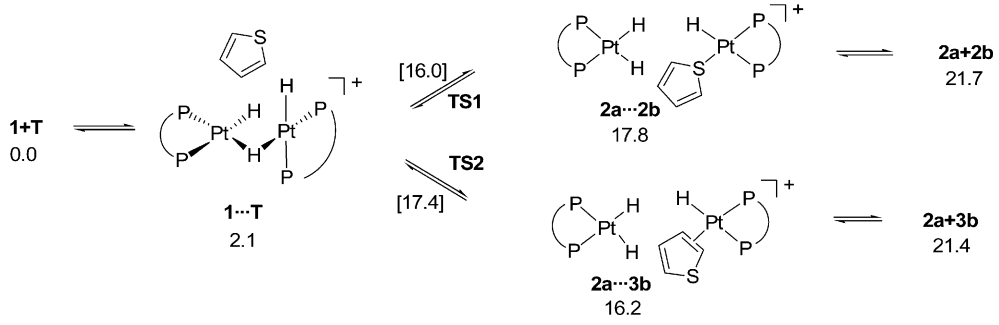


Scheme 4. Reaction pathway proposed for the fragmentation of **I** (**1**). Relative energies of intermediates and energy barriers (in brackets) are included. All values calculated in benzene solvent [kcal/mol].

 © 2007 Wiley-VCH Verlag GmbH & Co. KGaA, Weinheim 

duction of platinum and elimination of $H_2$ (**2a**) to give [(dhpp)Pt] (**3a**), which is 24.7 kcal/mol less stable than **2a**. This is consistent with already reported experimental[65–67] and theoretical[68,69] studies. The energy barrier for the $H_2$ elimination is given by the energy difference between **3a+H$_2$** and **2a**. However, as this energy increases monotonously along the $H_2$ elimination process, the TS cannot be found. This dissociative reaction is entropically favored and, consequently, considering $\Delta G_{benzene}$ values, **3a+H$_2$** lie only 14.5 kcal/mol above **2a**.

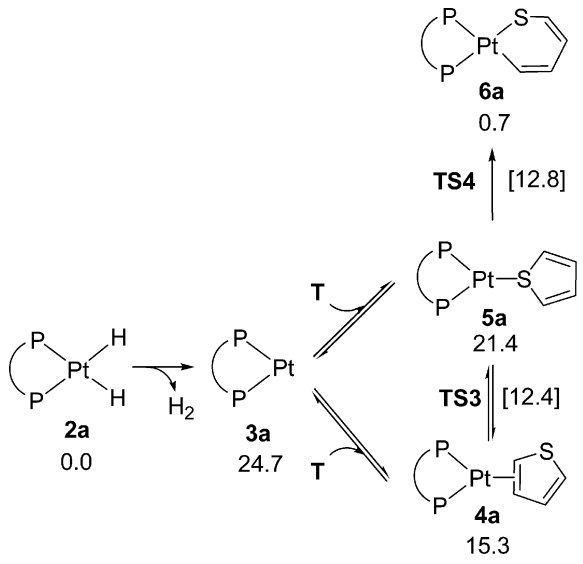


Scheme 5. Reaction pathway proposed for the formation of **II** (**6a**). Relative energies of intermediates and energy barriers (in brackets) are included. All values calculated in benzene solvent [kcal/mol].

The next step is the coordination of thiophene to **3a**, which, analogously to the [(dhpp)PtH]$^+$ fragment (Scheme 4), can occur through either the sulfur atom or the double bond, thus forming [(dhpp)Pt($C_4H_4S$-κ*S*)] (**5a**) or [(dhpp)Pt($\eta^2$-$C_4H_4S$)] (**4a**), respectively. The conversion of **4a** to **5a** is possible through an energy barrier of 12.4 kcal/mol (**TS3**). In addition, despite **4a** being more stable than **5a** (see Scheme 5), the oxidative addition of platinum to the C–S bond requires that **T** is bound through sulfur. The energy barrier for the oxidative addition process is 12.8 kcal/mol (**TS4**). Considering the two steps ($H_2$ elimination + C–S insertion), **TS4** lies 34.2 kcal/mol above **2a**. However, the insertion product [(dhpp)Pt($C_4H_4S$-*C*,*S*)] (**6a**, Scheme 5) is remarkably stable, as shown by the exothermicity of the insertion process (from **3a** to **6a**).

### *Transfer of Hydride from the Metal to Thiophene*

The cationic complex **2b** formed in the first step of the reaction (Scheme 4) follows a different route than **2a**. First, the apparent rotation of thiophene from κ*S* to $\eta^2$-*C*,*C* coordination mode gives way to complex [(dhpp)PtH($\eta^2$-$C_4H_4S$)]$^+$ (**3b**), with an energy barrier of 5.0 kcal/mol (**TS5**) (Scheme 6). Complex **3b** can also be formed by direct reaction of **1** with **T** through **TS2** (Scheme 4).

Once **3b** is formed, the hydride migration to the double bond in C2 or C3 becomes feasible. The migration to C2 gives an agostic intermediate **4b** with an energy barrier of 12.6 kcal/mol (**TS6**). In going from **4b** to **5b** the agostic interaction is lost and the thiophene ring rotates in order to adopt $\eta^3$ coordination. The energy cost of this process is very low, only 2.6 kcal/mol (**TS7**). Finally, from **5b** a subsequent rotation of the thiophene ring with an energy barrier of 5.3 kcal/mol (**TS8**) gives the most stable conformation of this system (**6b**), 8.8 kcal/mol more stable than **2b**. In **6b** the platinum is bonded to C5 and to the sulfur, and the π system has been rearranged.

From **3b** the hydride migration to C3 proceeds in a similar way, with an energy barrier of 11.9 kcal/mol. After the first transition state (**TS10**) an agostic intermediate **8b** is formed. The rotation of the thiophenic group in this case gives compound **9b**, where Pt is bonded to the C2 and sulfur atoms. This product is 5.3 kcal/mol more stable than **2b**.

Considering the energy barriers for the hydride transfer and for the thiophene ring rotation, all species displayed in Scheme 6 within the dashed-line square are in equilibrium with each other, although it is displaced towards formation of **6b**. From this complex, the C–S bond activation of thiophene to give complex **7b** is accessible with an energy barrier of 21.0 kcal/mol. The C–S bond activation from the less stable complex **9b** was also considered. This activation not only has a higher energy barrier (25.3 kcal/mol), but also it is a more endothermic reaction. Thus, while **7b** is 6.3 kcal/mol above **2b**, **10b** is 15.5 kcal/mol, so the activated product **7b** is clearly favored with respect to **10b**.

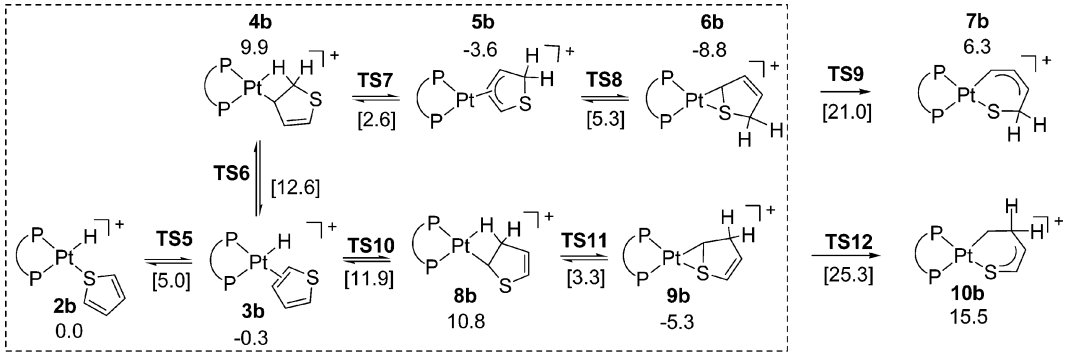


Scheme 6. Reaction pathway proposed for hydride insertion in **2b**. Relative energies of intermediates and energy barriers (in brackets) are included. All values calculated in benzene solvent [kcal/mol].

 © 2007 Wiley-VCH Verlag GmbH & Co. KGaA, Weinheim 

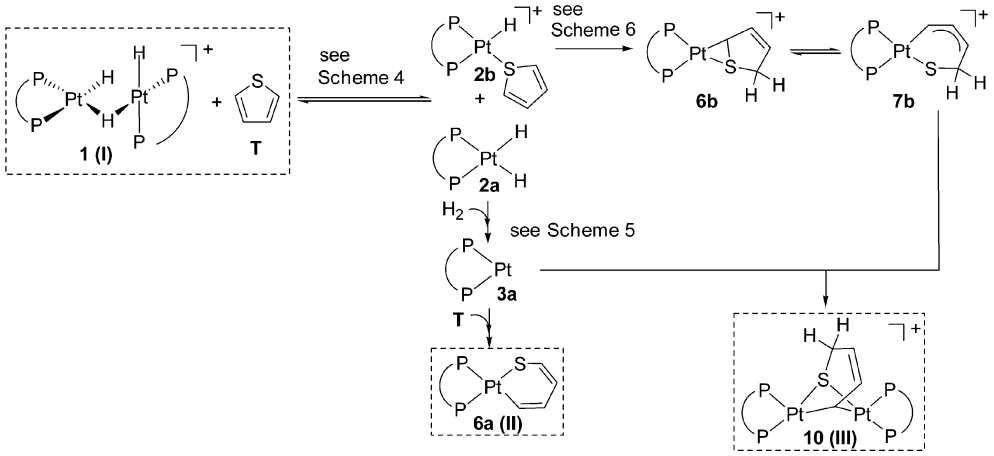


Scheme 7. Reaction pathways proposed for the formation of **6a** (**II**) and **10** (**III**).

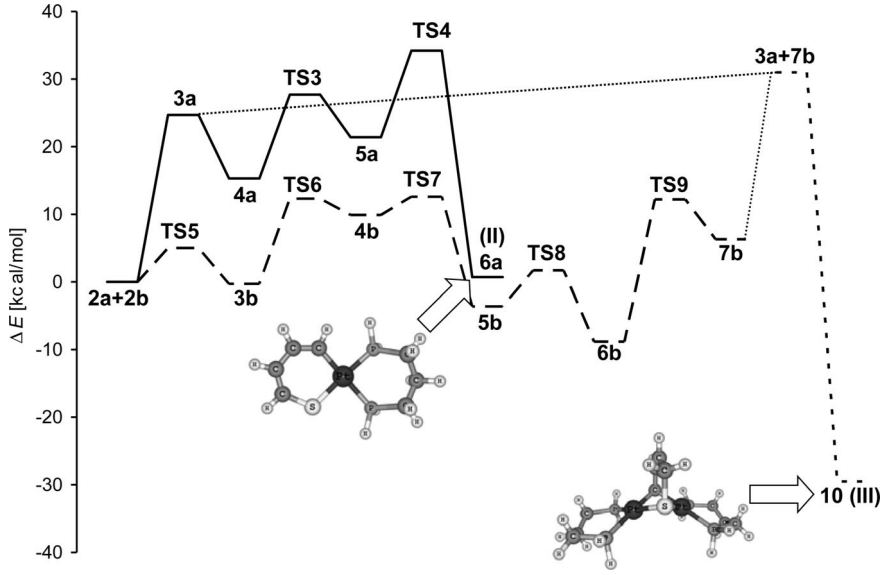


Figure 3. Energy profile of the reaction leading to complexes **6a** (**II**) and **10** (**III**), showing the pathway: (a) from the dissociation of **1** (**2a+2b**) either to product **6a** or to intermediate **7b**, by means of plain or discontinuous lines, respectively, and (b) from **3a+7b** to **10** by dotted lines.

### *Formation of the [(dhpp)Pt(μ-SC$_4$H$_5$-C,S)Pt(dhpp)]$^+$ Cation (10)*

Up to now the successive pathways leading to complexes **6a** and **7b** have been considered separately (Schemes 4, 5, and 6). In this subsection they will be assembled to enable the formation of **10**, model of the experimental complex **III**. The overall mechanism is summarized in Scheme 7, where the complexes described in the experimental section are highlighted within dashed-line squares. The energy profile for the sequence of reactions that take place after fragmentation of **I** to finally afford **6a** and **10** is depicted in Figure 3.

As shown in Scheme 7, fragmentation of the dinuclear platinum trihydride leads to **2a** and **2b**. At this point, these complexes react through different pathways. On the one hand, complex **2a** undergoes $H_2$ elimination to give **3a**, which subsequently reacts with thiophene to yield **6a** (**II**). On the other, the hydride migration to C2 in complex **2b** (more favored than to C3) leads to **6b**. This intermediate is able to activate the C–S bond to give the very unstable **7b** complex. Reaction of the latter species with **3a** gives the dinuclear platinum complex **10** without energy barrier (Figure 3). The energy of this complex is 29.5 kcal/mol below that of **2a+2b** and, despite the unfavorable entropic contribution of the association process, the **2a+2b** → **10** reaction is also favored on Gibbs energy grounds with $\Delta G_{benzene}$ = –20.8 kcal/mol.

### Calculations versus Experiments

All previous considerations account for the overall mechanism from **1** (**I**) to either **6a** (**II**) or **10** (**III**). The next step is to analyze their consistency with the experimental results. Thus, concerning the reaction of **I** with **I-$d_3$**, the formation of a mixture of isotopomers **I-$d_x$** ($x$ = 0–3) was

 © 2007 Wiley-VCH Verlag GmbH & Co. KGaA, Weinheim 

experimentally observed only in the presence of thiophene at reflux temperature. This is consistent with the equilibrium between **1+T** and **2a+2b** depicted in Scheme 4. This reaction has an energy cost of 21.7 kcal/mol while the fragmentation of **I** without the presence of thiophene requires 39.5 kcal/mol. On the other hand, replacement of **I** by **I-*d*$_3$** in the synthesis of **III** showed that the hydrogen atom inserted into the thiophenic ring comes from **I** and adds to the C2 atom. This result fits well with the mechanism showed in Scheme 7, in which the formation of **10** (**III**) involves an initial insertion of the hydride into the C2 position of the coordinated thiophene in **2b**.

The general mechanism proposed can also account for the noninterconversion between **II** and **III** even in the presence of external hydride ligands. Comparison of **II** and **III** indicates that this transformation would imply the hydride insertion into the thiophenic ring of **II** and the subsequent coordination of an additional {(dppp)Pt} fragment. On the basis of Scheme 7, two steps leading to **III** deserve special consideration. First, the intramolecular hydride migration in species **2b**, which entails a low energy barrier, and second, the stabilization of the intermediate **7b** by means of its coordination to a {(dppp)Pt} fragment. Remarkably, none of these two features can be accomplished in the experimental system. On the one hand, **II** does not enclose platinum-bound hydride ligands, thus hampering an intramolecular hydride migration. On the other, formation of **III** would require the assistance of the {(dppp)Pt} fragment, which only forms from the thiophene-promoted dissociation of **I**. Overall, theoretical results account for the fact that **II** does not evolve into **III**, even in the presence of **I** or $NaBH_4$.

Another experimental feature of the reaction of **I** with **T** refers to the different relative amounts of the reaction products, **II** and **III**, depending on the reaction conditions. Thus, the reaction affords **II** (**6a**) and **III** (**10**) in a 2:3 or 1:9 molar ratio using neat thiophene or organic solvent (toluene or benzene), respectively. The energy profile depicted in Figure 3 shows that the highest energies involved in the formation of **6a** and **10** (**TS4**: 34.2 kcal/mol and **3a+7b**: 31.0 kcal/mol, respectively) are very similar. Consequently, small changes in the reaction conditions can affect these energies, modifying the molar ratio of products. In addition, the concentration of thiophene also influences the **II** to **III** molar ratio because the two parallel pathways leading to **6a** and **10** involve a different number of thiophene molecules. The minor relative amount obtained for **II** in benzene or toluene can be explained considering that two molecules of **T** are required to form this complex, one to dissociate the starting complex **1** and the other to react with **3a** (see Scheme 7). Overall, the formation of **II** in toluene or benzene will be disfavored versus **III**, whose formation requires only one molecule of **T**.

## Conclusions

C–S bond activation of thiophene (**T**) by the dinuclear trihydride platinum complex $[(dppp)_2Pt_2H_3]ClO_4$ (**I**) afforded the mononuclear [(dppp)Pt($SC_4H_4$-*C*,*S*)] (**II**) metalacycle that involves activation of the thiophenic C–S bond exclusively, and the dinuclear $[(dppp)_2Pt_2(\mu\text{-}SC_4H_5\text{-}C,S)]ClO_4$ (**III**) complex, where activation of this bond is concomitant with the partial hydrogenation of thiophene (Scheme 2).

Additional experiments and computational results have evidenced the role of **T** as promoter of the cleavage of **I** into the [(dppp)$PtH_2$] and $[(dppp)PtH(C_4H_4S\text{-}\kappa S)]^+$ fragments in the first step of the reaction. Also, experimental observations showing the noninterconversion equilibrium between **II/III** indicate that two concurrent mechanisms are at work. This is fully consistent with the theoretical calculations, which allow us to propose two different reaction pathways that originate after the dissociation of **I**. While formation of **II** involves exclusive participation of the former fragment, both are required to take part in the pathway leading to **III**. In fact, formation of this complex implies the coordination of {(dppp)Pt} to $[(dppp)Pt(\mu\text{-}SC_4H_5\text{-}C,S)]^+$ (Scheme 7). The former species, which originates from [(dppp)$PtH_2$], is responsible for the stabilization of the latter, which arises from the hydride migration into the thiophenic ring in $[(dppp)PtH(C_4H_4S\text{-}\kappa S)]^+$ and subsequent C–S bond activation. Remarkably, complex **III** is the first example of a platinum complex involving C–S bond activation and hydrogenation of thiophene.

The reactions of platinum complexes **II**–**V** with protonic acids and hydride sources have shown the ability of these reagents to give total desulfurization (Scheme 3). Thus, the reaction of **II** and **III** with protonic acids affords either partial hydrogenation of the thiophenic chain (with $HBF_4$) or formation of thiols (with HCl). On the other hand, the reaction with $NaBH_4$ entails the formation of $H_2S$ only from complexes where the thiophenic chain has been partially hydrogenated (**III**–**V**). This result is consistent with the assumption that metal hydride complexes are keystones in the desulfurization of thiophene.

Overall, the combination of experimental and theoretical studies of the reaction of $[(dppp)_2Pt_2H_3]ClO_4$ with thiophene has provided new insights into the mechanism of the homogeneous HDS. Notwithstanding this progress, designing systems able to perform the reaction of completely and efficiently desulfurizing thiophene and in softer conditions still appears to be the main goal. The importance of this reaction makes any effort in this direction worthwhile.

## Experimental Section

**Materials and Methods:** All reactions were carried out under pure dinitrogen, and conventionally dried and degassed solvents were used throughout. These were Purex Analytical Grade from SDS. Thiophene (≥99%) was purchased from Aldrich. It was purified following a reported procedure.[70] Commercial 0.5 M NaMeO in methanol and $NEt_3$ (99%, $d$ = 0.726 g/cm$^3$) were used without further purification. The synthesis and spectroscopic characterization of $[(dppp)_2Pt_2H_3]ClO_4$ (**I**) and $[(dppp)_2Pt_2D_3]ClO_4$ (**I-*d*$_3$**) as well as the X-ray structure of **I** have already been reported.[50] Elemental

 © 2007 Wiley-VCH Verlag GmbH & Co. KGaA, Weinheim 

analyses were performed on a Carlo–Erba CHNS EA-1108 analyzer. IR spectra were recorded with a Perkin–Elmer FT-2000 spectrophotometer using KBr pellets. $^{1}H$, $^{1}H\{^{31}P\}$, $^{13}C$ DEPT, $^{31}P$, $^{31}P\{^{1}H\}$ $^{31}P$–$^{1}H$ HMBC, $^{195}Pt$, and $^{195}Pt\{^{1}H\}$ NMR and $^{1}H$–$^{1}H$ NOESY, $^{1}H$–$^{1}H$ COSY, $^{13}C$–$^{1}H$ HMQC, and $^{13}C$–$^{1}H$ HSQC-edit spectra were performed unless otherwise indicated from samples in solution at room temperature with a Bruker Avance DRX-360 spectrometer operating at 360.13 MHz for $^{1}H$, 90.56 MHz for $^{13}C$, 145.79 MHz for $^{31}P$, and 77.42 MHz for $^{195}Pt$. $^{1}H$ and $^{13}C$ chemical shifts are relative to $SiMe_4$, $^{31}P$ to external 85% $H_3PO_4$, and $^{195}Pt$ to external 1 M $Na_2[PtCl_6]$ in $D_2O$. The $^{31}P\{^{1}H\}$ NMR spectrum of **III** was simulated on a Pentium®-200 computer using the gNMR V4.0.1 program.[71] $^{2}H$ NMR experiments were performed from samples in $CDCl_3/CHCl_3$ mixture solutions at room temperature with a Bruker Avance-500 operating at 76.75 MHz. $^{2}H$ NMR chemical shifts are relative to $CDCl_3$. $^{19}F$ NMR experiments for **IV** and **V** were performed from samples in acetone solutions at room temperature with a Bruker DPX-250 operating at 235.33 MHz. $^{19}F$ NMR chemical shifts are relative to $CFCl_3$. H and C labels for complexes **III**–**V** are shown in Figure 4.

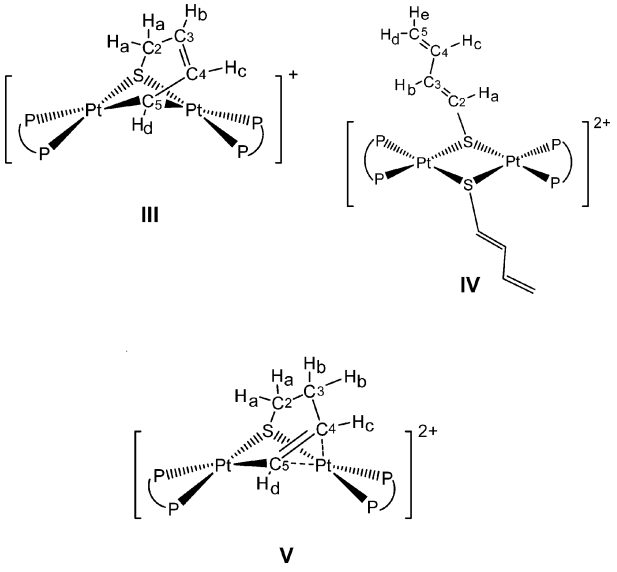


Figure 4. H and C labels for complexes **III**–**V**.

The ESI-MS measurements were performed on a VG Quattro Micromass Instrument under already described experimental conditions.[50] The carrier was a 1:1 mixture of acetonitrile and water containing formic acid (1–10%). The exact mass for **III** was determined on a micrOTOF-Q instrument using direct injection from HPLC 1200RR and Apollo II ESI ionization source. GC-MS spectra were recorded using a Hewlett–Packard 6890 instrument and a Hewlett–Packard 5973 electronic impact mass detector.

**Caution:** *Although no problems were encountered in this work, all perchlorate compounds are potentially explosive, and should be handled in small quantities and with great care!*

**Synthesis of [(dppp)Pt($SC_4H_4$-*C*,*S*)] (II):** The white-beige suspension formed by addition of **I** (200 mg, 0.15 mmol) to degassed neat thiophene (15 mL) was heated at reflux temperature (100 °C) for 24 h, by which time it had turned into a red-brown solution containing a minor amount of a black solid residue. This was separated by filtration through Celite and the remaining solution evaporated under vacuum to yield a brown residue. This solid was dissolved in toluene and the solution chromatographed on a neutral alumina column. Elution with a hexane/benzene mixture at 20% ratio showed separation of two bands, yellow and red-brown, which respectively contained complexes **II** and **III**. Extraction of the former band followed by removal of the solvent under vacuum produced a residue that was dissolved in acetone and precipitated with diethyl ether. The yellow solid thus formed was collected by filtration, washed with diethyl ether, and vacuum dried. Yield 52 mg, 25%. $^{1}H$ NMR (360 MHz, $CDCl_3$, 25 °C): $\delta$ = 6.75 (t, 1 H, CH), 6.92 (1 H, CH), 7.18 (1 H, CH), 7.34 (1 H, CH) ppm. $^{13}C$ DEPT NMR (91 MHz, $CDCl_3$, 25 °C): $\delta$ = 119.1 (CH), 120.8 (CH), 124.4 (CH), 130.2 (CH) ppm. $^{31}P\{^{1}H\}$ NMR (146 MHz, $CDCl_3$, 25 °C): $\delta$ = 6.56 (d, $^{1}J_{Pt,P}$ = 3064.4, $^{2}J_{P,P}$ = 33.0 Hz), –1.10 (d, $^{1}J_{Pt,P}$ = 1601.8, $^{2}J_{P,P}$ = 33.0 Hz) ppm. $^{195}Pt$ NMR (77 MHz, $CDCl_3$, 25 °C): $\delta$ = –4525 (dd, $^{1}J_{P,Pt}$ = 3066 and 1605 Hz) ppm. ESI-MS: *m*/*z* = 692.2 $[M + 1]^+$. $C_{31}H_{30}P_2PtS$ (691.2): calcd. C 53.83, H 4.37, S 4.64; found C 53.95, H 4.29, S 4.75. Attempts to obtain crystals suitable for X-ray diffraction were unsuccessful.

**Synthesis of [(dppp)$_2$Pt$_2$(μ-$SC_4H_5$-*C*,*S*)]$ClO_4$ (III):** The same reaction procedure as for **II** but in the presence of toluene or benzene led essentially to **III**. Thus, **I** (200 mg, 0.15 mmol) and neat thiophene (15 mL) were made to react in degassed toluene or benzene (20 mL). Column chromatography under the same experimental conditions as above allowed elution of the second red-brown band with benzene. Removal of the solvent under vacuum produced a residue that was dissolved in acetone and precipitated with diethyl ether. The precipitated yellow-brown solid was collected by filtration, washed with diethyl ether, and vacuum dried. Yield 83 mg, 43%. $^{1}H$ NMR (360 MHz, [$D_6$]acetone, 25 °C): $\delta$ = 1.62 (br., 2 $H_a$), 2.77 (br., $H_d$), 5.36 (dt, $^{3}J_{Hb,Ha}$ = 3.6, $^{3}J_{Hb,Hc}$ = 9.4 Hz, $H_b$), 5.46 (dt, $^{3}J_{Hc,Hb}$ = 9.4, $^{3}J_{Hc,Hd}$ = 8.2 Hz, $H_c$) ppm. $^{13}C$ DEPT NMR (91 MHz, [$D_6$]acetone, 25 °C): $\delta$ = 33.0 (C2), 42.7 (C5), 126.1 (C3), 137.1 (C4) ppm. $^{31}P\{^{1}H\}$ NMR (146 MHz, [$D_6$]acetone, 25 °C): $\delta$ = 3.02 (d, $^{1}J_{Pt,P}$ = 3869.6 Hz), 1.96 ($^{1}J_{Pt,P}$ = 1857.0 Hz) ppm. On the basis of the simulation of the $^{31}P\{^{1}H\}$ NMR spectrum including long-range P–P and P–Pt couplings: $^{3}J_{P',P'}$ = 22.0, $^{3}J_{P',P''}$ = 4.7, and $^{2}J_{P',P''}$ = –22.3 Hz, where P′ and P′′ are nonequivalent phosphorus nuclei, and $^{2}J_{P,Pt}$ = 56 Hz ($\delta_P$ = 1.96 ppm) and 37 Hz ($\delta_P$ = 3.02 ppm). $^{195}Pt\{^{1}H\}$ NMR (77 MHz, [$D_6$]acetone, 25 °C): $\delta$ = –4670 (dd, $^{1}J_{P,Pt}$ = 3872 and 1867 Hz) ppm. ESI-MS: *m*/*z* = 1299.2401 $[M - ClO_4]^+$. $C_{58}H_{57}ClO_4P_4Pt_2S$ (1399.64): calcd. C 49.77, H 4.10, S 2.29; found C 49.02, H 3.82, S 2.11. IR ($cm^{-1}$): $\tilde{\nu}$ = 1094 i, br. ($ClO_4$). Attempts to obtain crystals suitable for X-ray diffraction were unsuccessful.

Replacement of **I** by **I-*d*$_3$** in the above reaction procedure allowed unequivocal identification of $[(dppp)_2Pt_2(\mu\text{-}SC_4H_4D\text{-}C,S)]^+$ (**III-*d*$_1$**) on the basis of NMR spectroscopic data. $^{1}H$ NMR (360 MHz, [$D_6$]-acetone, 25 °C): $\delta$ = 1.63 (br., $H_a$), 2.77 (br., $H_d$), 5.36 (br., $H_b$), 5.46 (br., $H_c$) ppm. $^{2}H$ NMR (77 MHz, $CDCl_3/CHCl_3$, 25 °C): $\delta$ = 1.58 (br., Da) ppm. $^{13}C$-DEPT NMR (91 MHz, [$D_6$]acetone, 25 °C): $\delta$ = 32.6 (C2), 42.7 (C5), 126.1 (C3), 137.1 (C4) ppm. NMR features corresponding to the dppp terminal ligands were coincident with those of **III**.

**Synthesis of [(dppp)$_2$Pt$_2$(μ-$SC_4H_5$)$_2$](BF$_4$)$_2$ (IV):** Aqueous $HBF_4$ (70 μL of 4 M solution, 0.28 mmol) was added to a solution of **II** (50 mg, 0.07 mmol) in $CH_3CN$ (10 mL). The mixture was stirred (15 min) and then evaporated to 5 mL under vacuum. Addition of diethyl ether gave a white precipitate, which was dissolved in ethyl acetate and purified on a neutral alumina column using the same solvent as eluent. Evaporation of the solvent afforded a white solid. Yield 47 mg, 84%. $^{1}H$ NMR (360 MHz, $CD_3CN$, 25 °C): $\delta$ = 4.75 (d, $^{3}J_{Ha,Hc}$ = 10, $^{2}J_{Ha,Hb} < 1$ Hz, $H_a$), 4.90 (d, $^{3}J_{Hb,Hc}$ = 16.5 Hz,

 © 2007 Wiley-VCH Verlag GmbH & Co. KGaA, Weinheim 

$H_b$), 5.34 (dt, $^3J_{Hc,Ha} = {}^3J_{Hc,Hd} = 10$, $^3J_{Hc,Hb} = 16$ Hz, $H_c$), 5.45 (d, $^3J_{He,Hd} = 10$ Hz, $H_e$), 5.74 (t, $^3J_{Hd,He} = {}^3J_{Hd,Hc} = 10$ Hz, $H_d$) ppm. $^{13}$C DEPT NMR (91 MHz, $CD_3CN$, 25 °C): $\delta$ = 136.6 (C4), 127.4 (C3), 120.8 (C2), 117.4 (C5) ppm. $^{31}P\{^1H\}$ NMR (146 MHz, $CD_3CN$, 25 °C): $\delta$ = –2.00 ($^1J_{Pt,P}$ = 2897.4 Hz) ppm. $^{19}$F NMR (235 MHz, [D$_6$]acetone, 25 °C): $\delta$ = –152.2 ppm. $^{195}Pt\{^1H\}$ NMR (77 MHz, $CD_3CN$, –20 °C): $\delta$ = –4415.8 ppm. $C_{62}H_{62}B_2F_8P_4Pt_2S_2$ (1558.94): calcd. C 47.77, H 4.01, S 4.11; found C 47.96, H 4.16, S 4.27. ESI MS (*m*/*z*): 693.5 (25%) corresponding to $[(dppp)_2Pt_2(SC_4H_5)_2]^{2+}$, and 1387.0 (100%) corresponding to $[(dppp)_2Pt_2(SC_4H_5)_2]^+$. IR: $\tilde{\nu}$ = 1051 i, br. ($BF_4$).

**Synthesis of $[(dppp)_2Pt_2(\mu\text{-}SC_4H_6)](BF_4)_2$ (V):** Aqueous $HBF_4$ (50 μL of 4 M solution, 0.20 mmol) was added to a solution of **III** (75 mg, 0.05 mmol) in degassed acetonitrile (10 mL) and the mixture stirred for 30 min. Then it was filtered through Celite, concentrated to 1–2 mL, and precipitated with addition of diethyl ether to yield a yellow solid. The solid was collected by filtration, washed with diethyl ether, and vacuum dried. Yield 65 mg, 82%. $^1$H NMR (360 MHz, [D$_6$]acetone, 25 °C): $\delta$ = 2.67 (br., 2$H_b$), 2.78 (br., 2$H_a$), 5.31 (dt, $^3J_{Hc,Hb} = 3.2$, $^3J_{Hc,Hd} = 9.2$ Hz, $H_c$), 5.90 (d, $^3J_{Hd,Hc} = 9.2$ Hz, $H_d$) ppm. $^{13}$C DEPT NMR (91 MHz, [D$_6$]acetone, 25 °C): $\delta$ = 26.8 (C2), 33.3 (C3), 119.7 (C5), 129.7 (C4) ppm. $^{31}P\{^1H\}$ NMR (146 MHz, [D$_6$]acetone, 25 °C): $\delta$ = 0.10 (d, $^1J_{Pt,P}$ = 2612.4 Hz), –0.92 ($^1J_{Pt,P}$ = 2965.3 Hz) ppm. $^{195}Pt\{^1H\}$ NMR (77 MHz, [D$_6$]-acetone, 25 °C): $\delta$ = –4675 (dd, $^1J_{P,Pt}$ = 2612 and 2966 Hz) ppm. $^{19}$F NMR (235 MHz, [D$_6$]acetone, 25 °C): $\delta$ = –152.2 ppm. ESI-MS: *m*/*z* = 650.3 (15%) and 1300.3 (100%) corresponding to $[(dppp)_2Pt_2(SC_4H_6)]^{2+}$ and $[(dppp)_2Pt_2(SC_4H_6)]^+$, respectively. $C_{58}H_{58}B_2F_8P_4Pt_2S$ (1474.80): calcd. C 47.23, H 3.96, S 2.17; found C 47.14, H 4.01, S 2.12. IR: $\tilde{\nu}$ = 1051 i, br. ($BF_4$).

The same reaction procedure but using only 1.2 equiv. of $HBF_4$ allowed separation of a yellow solid, whose acetone solution afforded adequate crystals for X-ray diffraction.

**Reaction of V with Bases (NaOMe, $Et_3N$):** A methanol solution of NaOMe (100 μL, 0.05 mmol) or $Et_3N$ (17.5 μL, 0.125 mmol) was added to a suspension of **V** (75 mg, 0.05 mmol) in $CH_3CN$ (10 mL). In both cases the resulting solution was stirred at room temperature for 30 min, after which time it was concentrated to dryness. Then, the solid was redissolved in benzene, filtered and precipitated by addition of diethyl ether. $^1$H and $^{31}$P NMR spectroscopic data of this solid in acetone solution evidenced the complete transformation of **V** into **III**.

**Reaction of II–V with HCl:** An excess of HCl was added to separate stirred $CH_2Cl_2$ (10 mL) solutions containing **II**, **III**, **IV**, or **V** (25 mg) in a 3–4:1 molar ratio at room temperature. The initial yellow-brown solution turned pale yellow and a white solid precipitated. After 30 min of stirring, the mixture was filtered and the soluble part analyzed by CG-MS. The solid was unequivocally identified as $[(dppp)PtCl_2]$ (65–80% yield) by NMR spectroscopy.[72,73] The solution was shown to be composed mainly of thiophene in the case of **II**, thiapentadiene or an isomer thereof ($C_4H_6S$) and thiophene[52] in a 4:1 molar ratio for **IV**, and a mixture of HS–$CH_2$–CH=CH–$CH_3$[74] and HS–$CH_2$–$CH_2$–CH=$CH_2$,[47] in 4:1 and 1:1 molar ratios, for **III** and **V**, respectively.

**Reaction of II–V with $NaBH_4$:** Solid $NaBH_4$ was made to react with separate stirred THF/$EtOH_{abs}$ solutions (10 mL) containing **II**, **III**, **IV**, or **V** (25 mg) in a 4:1 molar ratio at room temperature under a closed atmosphere. In the reactions involving **III**–**V**, formation of a black precipitate of $Ag_2S$ on a filter paper soaked with silver nitrate gave evidence of formation of $H_2S$. In all cases, after 20 h of stirring the initial yellow-brown solution became a dark-brown suspension. The black solid was separated and the solution analyzed by CG-MS. The solution was shown to contain thiophene in the case of **II**, but no thiols and/or organic volatiles were detected.

**X-ray Crystallographic Characterization:** A summary of crystal data, data collection, and refinement parameters for the structural analysis of complex $[(dppp)Pt(\mu\text{-}SC_4H_6)Pt(dppp)]_2(BF_4)_{2.95}(ClO_4)_{1.05}$ is given in Table 3. Measurements of diffraction intensity data were collected on a Bruker SMART CCD-1000 area-detector diffractometer with graphite-monochromated Mo-$K_\alpha$ radiation ($\lambda$ = 0.71073 Å). During the initial unit cell determination it was recognized that the crystal was twinned. Several crystals were assayed but all possessed the same diffraction pattern, so a small but diffracting crystal was chosen. The collected reflections were processed with the program CELLNOW,[75] which established two twin components with a ratio of 0.72/0.28. In order to process the twinned data, the absorption correction was applied using the multiscan TWINABS[75] program. Cell parameters were obtained from least-squares fit on the observed setting angles of all significant intensity reflections. A Patterson map solution of the structure to locate platinum atoms, followed by expansion of the structure with the program DIRDIF,[76] revealed all non-hydrogen atoms. The structure was resolved by direct methods and refined by full-matrix least-squares based on $F^2$, with the aid of SHELX-97[77] software. The thiolate ligand was modeled as two disordered $SCH_2CH_2CH{=}CH$ moieties with opposite orientations, finding a refined population ratio of 63/37 in one dinuclear complex and 69/31 in the other. All non-hydrogen atoms were anisotropically refined. All hydrogen atoms were included at geometrically calculated positions with thermal parameters derived from the parent atoms. Molecular graphics are represented by ORTEP-3 for Windows.

Table 3. Crystallographic data for $[(dppp)Pt(\mu\text{-}SC_4H_6)Pt(dppp)]_2(BF_4)_{2.95}(ClO_4)_{1.05}$.

| | |
|---|---|
| Empirical formula | $2(C_{58}H_{56}P_4Pt_2S)\cdot2.95(BF_4)\cdot1.05(ClO_4)\cdot3(C_3H_6O)\cdot(H_2O)$ |
| *M* | 3153.06 |
| Crystal system | monoclinic |
| Space group | *Cc* |
| *a* [Å] | 43.8827(12) |
| *b* [Å] | 14.1377(4) |
| *c* [Å] | 22.2630(6) |
| *α* [°] | 90 |
| *β* [°] | 116.223(1) |
| *γ* [°] | 90 |
| *V* [Å$^3$] | 12390.5(6) |
| *T* [K] | 100.0(1) |
| *Z* | 4 |
| $D_{calcd}$ [g/cm$^3$] | 1.690 |
| *μ* [mm$^{-1}$] | 4.735 |
| Reflections collected/ unique reflections/$R_{int}$ | 222291/45071/0.0826 |
| Parameters/restraints | 1289/68 |
| Goodness-of-fit on $F^2$ | 0.926 |
| Twin law | twofold axis along *c** |
| Twin domain populations | 0.720(4)/0.280(4) |
| Absolute structure parameter | 0.000(4) |
| $R_1$, $wR_2$ [$I > 2\sigma(I)$] | 0.0437, 0.0970 |
| $R_1$, $wR_2$ (all data) | 0.0776, 0.1056 |
| Largest diff. peak, hole [e/Å$^3$] | 1.228, –1.130 |

CCDC-651579 {compound $[(dppp)Pt(\mu\text{-}SC_4H_6)Pt(dppp)]_2(BF_4)_{2.95}(ClO_4)_{1.05}$} contains the supplementary crystallographic data for this paper. These data can be obtained free of charge from The Cambridge Crystallographic Data Centre via www.ccdc.cam.ac.uk/data_request/cif.

 © 2007 Wiley-VCH Verlag GmbH & Co. KGaA, Weinheim 

**Computational Details:** The calculations were performed with the Gaussian03 package,[78] using Density Functional Theory with the B3LYP functional.[79–81] For the Pt, P, and S atoms, the lanl2dz effective core potential was used to describe the inner electrons,[78,82,83] whereas their associated double-ζ basis set was employed for the remaining electrons. An extra series of d-polarization functions was also added for P (exp. 0.387) and S (exp. 0.503).[84] The three hydrides and the carbon atoms of thiophene were described by the 6-31G(d,p) basis set[85] and the remaining C and H atoms were described by the 6-31G basis set. The structures of the reactants, intermediates, transition states, and products were fully optimized in gas phase without any symmetry restriction. Frequency calculations were performed on all optimized structures, using the B3LYP functional, to characterize the stationary points as minima or TSs, as well as for the calculation of gas-phase Gibbs energies (*G*) at 298 K. Single-point solvent calculations were performed at optimized gas-phase geometries, using the CPCM approach,[86,87] which is an implementation of the conductor-like screening solvation model (COSMO) in Gaussian03.[88] Benzene, the solvent used in some experiments, was chosen as solvent (dielectric constant $\varepsilon = 2.247$). In this way $\Delta E_{benzene}$, resulting from adding the contribution of the Gibbs energy of solvation to the gas phase internal energies, were obtained.

**Supporting Information** (see also the footnote on the first page of this article): Comparison of the $^{31}P\{^{1}H\}$ NMR spectrum of **III** with its computed simulation. Table includes total energies and Cartesian coordinates of the optimized structures reported in the text.

## Acknowledgments

Financial support from the Spanish Ministerio de Educación y Ciencia (MEC) through Projects CTQ2004-01463 and CTQ2005-09000-C02-01 and from the Generalitat de Catalunya (GENCAT) through grant 2005SGR00896 is gratefully acknowledged. A. L. is indebted to GENCAT for a "Distinció per a la Promoció de la Recerca Universitària". We are grateful to Dr. T. Parella and Dr. J. Sola (UAB) for interesting discussions on NMR spectroscopic data, and to Dr. A. L. Llamas and Dr. B. Dacuña of the USC for crystal structure determination.

[1] R. J. Angelici, *Acc. Chem. Res.* **1988**, *21*, 387–394.
[2] C. Bianchini, A. Meli, *J. Chem. Soc. Dalton Trans.* **1996**, 801–814.
[3] C. Bianchini, A. Meli in *Applied Homogeneous Catalysis with Organometallic Compounds* (Eds.: B. Cornils, W. A. Herrmann), VCH, Weinheim, Germany, **1996**, vol. 2, p. 969.
[4] W. D. Jones, D. A. Vicic, R. M. Chin, J. H. Roache, A. W. Myers, *Polyhedron* **1997**, *16*, 3115–3128.
[5] R. J. Angelici, *Polyhedron* **1997**, *16*, 3073–3088.
[6] R. A. Sánchez-Delgado, *Organometallic Modeling of the Hydrodesulfurization and Hydrodenitrogenation Reactions*, Kluwer Academic Publishers, Dordrecht, **2002**.
[7] R. R. Chianelli, M. Daage, M. J. Ledoux, *Adv. Catal.* **1994**, *40*, 177–232.
[8] C. N. Satterfield, *Heterogeneous Catalysis in Industrial Practice*, McGraw-Hill, New York, **1991**.
[9] D. Stirling, *The Sulfur Problem: Cleaning Up Industrial Feedstocks*, RSC Clean Technology Monographs (Ed.: J. H. Clark), The Royal Society of Chemistry, Cambridge, U.K., **2000**.
[10] H. Topsøe, B. S. Clausen, F. E. Massoth, *Hydrotreating Catalysis*, Springer Berlin, **1996**, vol. 11.
[11] A. N. Startsev, *Cat. Rev. - Sci. Eng.* **1995**, *37*, 353–423.
[12] R. Navarro, B. Pawelec, J. L. G. Fierro, P. T. Vasudevan, J. F. Cambra, P. L. Arias, *Appl. Catal., A* **1996**, *137*, 269–286.
[13] P. T. Vasudevan, J. L. G. Fierro, *Cat. Rev. - Sci. Eng.* **1996**, *38*, 161–188.
[14] R. Prins, V. H. J. Debeer, G. A. Somorjai, *Cat. Rev. - Sci. Eng.* **1989**, *31*, 1–41.
[15] C. M. Friend, J. T. Roberts, *Acc. Chem. Res.* **1988**, *21*, 394–400.
[16] C. Bianchini, A. Meli, *Acc. Chem. Res.* **1998**, *31*, 109–116.
[17] R. J. Angelici, *Organometallics* **2001**, *20*, 1259–1275.
[18] T. B. Rauchfuss, *Prog. Inorg. Chem.* **1991**, *39*, 259–329.
[19] X. Q. Yao, Y. W. Li, H. J. Jiao, *J. Mol. Struct.* **2005**, *726*, 67–80.
[20] X. Q. Yao, Y. W. Li, H. J. Jiao, *J. Mol. Struct.* **2005**, *726*, 81–92.
[21] S. Cristol, J. F. Paul, C. Schovsbo, E. Veilly, E. Payen, *J. Catal.* **2006**, *239*, 145–153.
[22] R. R. Chianelli, G. Berhault, P. Raybaud, S. Kasztelan, J. Hafner, H. Toulhoat, *Appl. Catal., A* **2002**, *227*, 83–96.
[23] P. Raybaud, J. Hafner, G. Kresse, H. Toulhoat, *Phys. Rev. Lett.* **1998**, *80*, 1481–1484.
[24] J. B. Chen, R. J. Angelici, *Coord. Chem. Rev.* **2000**, *206*, 63–99.
[25] M. D. Curtis, S. H. Druker, *J. Am. Chem. Soc.* **1997**, *119*, 1027–1036.
[26] U. Riaz, O. J. Curnow, M. D. Curtis, *J. Am. Chem. Soc.* **1994**, *116*, 4357–4363.
[27] R. J. Angelici in *Encyclopedia of Inorganic Chemistry* (Ed.: R. B. King), John Wiley & Sons, New York, **1994**, vol. 3, pp. 1433–1443.
[28] M. J. Ledoux, O. Michaux, G. Agostini, P. Panissod, *J. Catal.* **1986**, *102*, 275–288.
[29] J. P. R. Vissers, C. K. Groot, E. M. Vanoers, V. H. J. Debeer, R. Prins, *Bull. Soc. Chim. Belg.* **1984**, *93*, 813–821.
[30] T. A. Pecoraro, R. R. Chianelli, *J. Catal.* **1981**, *67*, 430–445.
[31] D. G. Churchill, B. M. Bridgewater, G. Parkin, *J. Am. Chem. Soc.* **2000**, *122*, 178–179.
[32] D. A. Vicic, W. D. Jones, *Organometallics* **1997**, *16*, 1912–1919.
[33] D. A. Vicic, W. D. Jones, *J. Am. Chem. Soc.* **1999**, *121*, 7606–7617.
[34] W. D. Jones, L. Z. Dong, *J. Am. Chem. Soc.* **1991**, *113*, 559–564.
[35] J. J. García, B. E. Mann, H. Adams, N. A. Bailey, P. M. Maitlis, *J. Am. Chem. Soc.* **1995**, *117*, 2179–2186.
[36] T. A. Atesin, S. S. Oster, K. Skugrud, W. D. Jones, *Inorg. Chim. Acta* **2006**, *359*, 2798–2805.
[37] H. E. Selnau, J. S. Merola, *Organometallics* **1993**, *12*, 1583–1591.
[38] W. D. Jones, R. M. Chin, T. W. Crane, D. M. Baruch, *Organometallics* **1994**, *13*, 4448–4452.
[39] R. M. Chin, W. D. Jones, *Angew. Chem. Int. Ed. Engl.* **1992**, *31*, 357–358.
[40] W. D. Jones, R. M. Chin, C. L. Hoaglin, *Organometallics* **1999**, *18*, 1786–1790.
[41] W. D. Jones, R. M. Chin, *Organometallics* **1992**, *11*, 2698–2700.
[42] L. Z. Dong, S. B. Duckett, K. F. Ohman, W. D. Jones, *J. Am. Chem. Soc.* **1992**, *114*, 151–160.
[43] A. L. Sargent, E. P. Titus, *Organometallics* **1998**, *17*, 65–77.
[44] O. Maresca, F. Maseras, A. Lledós, *New J. Chem.* **2004**, *28*, 625–630.
[45] W. D. Jones, R. M. Chin, *J. Am. Chem. Soc.* **1994**, *116*, 198–203.
[46] K. E. Janak, J. M. Tanski, D. G. Churchill, G. Parkin, *J. Am. Chem. Soc.* **2002**, *124*, 4182–4183.
[47] C. Bianchini, A. Meli, M. Peruzzini, F. Vizza, P. Frediani, V. Herrera, R. A. Sánchez-Delgado, *J. Am. Chem. Soc.* **1993**, *115*, 2731–2742.
[48] R. Navarro, B. Pawelec, J. L. G. Fierro, P. T. Vasudevan, *Appl. Catal., A* **1996**, *148*, 23–40.
[49] Y. Kanda, T. Kobayashi, Y. Uemichi, S. Namba, M. Sugioka, *Appl. Catal., A* **2006**, *308*, 111–118.

 © 2007 Wiley-VCH Verlag GmbH & Co. KGaA, Weinheim 

[50] F. Novio, P. González-Duarte, A. Lledós, R. Mas-Ballesté, *Chem. Eur. J.* **2007**, *13*, 1047–1063.
[51] C. Bianchini, A. Meli, M. Peruzzini, F. Vizza, V. Herrera, R. A. Sanchez-Delgado, *Organometallics* **1994**, *13*, 721–730.
[52] J. J. García, A. Arévalo, V. Montiel, F. Del Río, B. Quiroz, H. Adams, P. M. Maitlis, *Organometallics* **1997**, *16*, 3216–3220.
[53] While various attempts to obtain single crystals of **V** were unsuccessful, recrystallization in acetone of the compound obtained by the reaction of **III** with $HBF_4$ at a 1:1.2 molar ratio afforded suitable crystals for X-ray diffraction. These consisted of the cation of **V**, as evidenced by NMR spectroscopic data, and a mixture of $BF_4^-$ and $ClO_4^-$ counterions.
[54] V. C. M. Smith, R. T. Aplin, J. M. Brown, M. B. Hursthouse, A. I. Karalulov, K. M. A. Malik, N. A. Cooley, *J. Am. Chem. Soc.* **1994**, *116*, 5180–5189.
[55] P. González-Duarte, A. Lledós, R. Mas-Ballesté, *Eur. J. Inorg. Chem.* **2004**, 3585–3599.
[56] G. Ujaque, F. Maseras in *Principles and Applications of Density Functional Theory in Inorganic Chemistry I*, Series: Structure and Bonding (Eds.: N. Kaltsoyannis, J. E. McGrady), Springer, Heidelberg, **2004**, vol. 112, pp. 117–150.
[57] F. Maseras, A. Lledós, *Computational Modeling of Homogeneous Catalysis*, Kluwer Academic Publishers, Dordrecht, Boston, London, vol. 25, **2002**.
[58] M. Palmer, K. Carter, S. Harris, *Organometallics* **1997**, *16*, 2448–2459.
[59] C. Blonski, A. W. Myers, M. Palmer, S. Harris, W. D. Jones, *Organometallics* **1997**, *16*, 3819–3827.
[60] S. Harris, *Polyhedron* **1997**, *16*, 3219–3233.
[61] L. Rincon, J. Terra, D. Guenzburger, R. A. Sánchez-Delgado, *Organometallics* **1995**, *14*, 1292–1296.
[62] S. Harris, *Organometallics* **1994**, *13*, 2628–2640.
[63] H. Z. Li, K. Q. Yu, E. J. Watson, K. L. Virkaitis, J. S. D′Acchioli, G. B. Carpenter, D. A. Sweigart, P. T. Czech, K. R. Overly, F. Coughlin, *Organometallics* **2002**, *21*, 1262–1270.
[64] R. A. Sánchez-Delgado, V. Herrera, L. Rincón, A. Andriollo, G. Martin, *Organometallics* **1994**, *13*, 553–561.
[65] A. L. Bandini, G. Banditelli, M. Manassero, A. Albinati, D. Colognesi, J. Eckert, *Eur. J. Inorg. Chem.* **2003**, 3958–3964.
[66] T. Yoshida, T. Yamagata, T. H. Tulip, J. A. Ibers, S. Otsuka, *J. Am. Chem. Soc.* **1978**, *100*, 2063–2073.
[67] D. J. Schwartz, R. A. Andersen, *J. Am. Chem. Soc.* **1995**, *117*, 4014–4025.
[68] T. Matsubara, F. Maseras, N. Koga, K. Morokuma, *J. Phys. Chem.* **1996**, *100*, 2573–2580.
[69] J. J. Low, W. A. Goddard, *Organometallics* **1986**, *5*, 609–622.
[70] G. H. Spies, R. J. Angelici, *Organometallics* **1987**, *6*, 1897–1903.
[71] P. H. M. Budzeelar, *gNMR*, v. 4.01, Cherwell Scientific Publishing Ltd., Oxford, U.K., **1997**.
[72] M. P. Brown, R. J. Puddephatt, M. Rashidi, K. R. Seddon, *J. Chem. Soc. Dalton Trans.* **1977**, 951–955.
[73] R. Mas-Ballesté, G. Aullón, P. A. Champkin, W. Clegg, C. Mégret, P. González-Duarte, A. Lledós, *Chem. Eur. J.* **2003**, *9*, 5023–5035.
[74] W. F. Wood, B. G. Sollers, G. A. Dragoo, J. W. Dragoo, *J. Chem. Ecol.* **2002**, *28*, 1865–1870.
[75] G. M. Sheldrick, *CELLNOW*, University of Göttingen, Germany, **2005**.
[76] P. T. Beurskens, G. Admiraal, G. Beurskens, W. P. Bosman, R. de Gelder, R. Israel, J. M. Smits, *DIRDIF*, University of Nijmegen, The Netherlands, **1999**.
[77] G. M. Sheldrick, *SHELX-97*, University of Göttingen, Germany, **1998**.
[78] M. J. Frisch, G. W. Trucks, H. B. Schlegel, G. E. Scuseria, M. A. Robb, J. R. Cheeseman, J. A. J. Montgomery, T. Vreven, K. N. Kudin, J. C. Burant, J. M. Millam, S. S. Iyengar, J. Tomasi, V. Barone, B. Mennucci, M. Cossi, G. Scalmani, N. Rega, G. A. Petersson, H. Nakatsuji, M. Hada, M. Ehara, K. Toyota, R. Fukuda, J. Hasegawa, M. Ishida, T. Nakajima, Y. Honda, O. Kitao, H. Nakai, M. Klene, X. Li, J. E. Knox, H. P. Hratchian, J. B. Cross, C. Adamo, J. Jaramillo, R. Gomperts, R. E. Stratmann, O. Yazyev, A. J. Austin, R. Cammi, C. Pomelli, J. W. Ochterski, P. Y. Ayala, K. Morokuma, G. A. Voth, P. Salvador, J. J. Dannenberg, V. G. Zakrzewski, S. Dapprich, A. D. Daniels, M. C. Strain, O. Farkas, D. K. Malick, A. D. Rabuck, K. Raghavachari, J. B. Foresman, J. V. Ortiz, Q. Cui, A. G. Baboul, S. Clifford, J. Cioslowski, B. B. Stefanov, G. Liu, A. Liashenko, P. Piskorz, I. Komaromi, R. L. Martin, D. J. Fox, T. Keith, M. A. Al-Laham, C. Y. Peng, A. Nanayakkara, M. Challacombe, P. M. W. Gill, B. Johnson, W. Chen, M. W. Wong, C. González, J. A. Pople, *Gaussian 03*, Revision C.02, Inc., Wallingford, CT, **2004**.
[79] C. Lee, R. G. Parr, W. Yang, *Phys. Rev.* **1988**, *37*, B785.
[80] A. D. Becke, *J. Chem. Phys.* **1993**, *98*, 5648–5652.
[81] P. J. Stephens, F. J. Devlin, C. F. Chabalowski, M. J. Frisch, *J. Phys. Chem.* **1994**, *98*, 11623–11627.
[82] P. J. Hay, W. R. Wadt, *J. Phys. Chem.* **1985**, *82*, 299–310.
[83] W. R. Wadt, P. J. Hay, *J. Chem. Phys.* **1985**, *82*, 284–299.
[84] A. Höllwarth, M. Böhme, S. Dapprich, A. W. Ehlers, A. Gobbi, V. Jonas, K. F. Köhler, R. Stegmann, A. Veldkamp, G. Frenking, *Chem. Phys. Lett.* **1993**, *208*, 237–240.
[85] W. J. Hehre, R. Ditchfield, J. A. Pople, *J. Chem. Phys. A* **1972**, *56*, 2257–2261.
[86] V. Barone, M. Cossi, *J. Phys. Chem. A* **1998**, *102*, 1995–2001.
[87] M. Cossi, N. Rega, G. Scalmani, V. Barone, *J. Comput. Chem.* **2003**, *24*, 669–691.
[88] J. Tomasi, M. Persico, *Chem. Rev.* **1994**, *94*, 2027–2094.

Received: September 7, 2007
Published Online: November 2, 2007

 © 2007 Wiley-VCH Verlag GmbH & Co. KGaA, Weinheim 

DOI: 10.1002/ejic.200700797

# Zeolite-Encapsulated Copper(II) Complexes of Pyridoxal-Based Tetradentate Ligands for the Oxidation of Styrene, Cyclohexene and Methyl Phenyl Sulfide

**Mannar R. Maurya,*[a] Baljit Singh,[a] Pedro Adão,[b] Fernando Avecilla,[c] and João Costa Pessoa[b]**

**Keywords:** Zeolites / Copper(II) complexes / Heterogeneous catalysis / Oxidation reactions

Interaction of copper(II)-exchanged zeolite-Y with *N*,*N*′-ethylenebis(pyridoxyliminato) ($H_2$pydx-en, **I**) and *N*,*N*′-propylenebis(pyridoxyliminato) ($H_2$pydx-1,3-pn, **II**) ligands in refluxing methanol leads to the formation of the corresponding complexes, abbreviated herein as [Cu(pydx-en)]-Y (**3**) and [Cu(pydx-1,3-pn)]-Y (**4**), in the supercages of zeolite-Y. The neat complexes, [Cu(pydx-en)] (**1**) and [Cu(pydx-1,3-pn)] (**2**), have also been prepared with these ligands. Spectroscopic studies (IR, UV/Vis and EPR), elemental analyses, thermal studies, field emission scanning electron micrographs (FE-SEM) and X-ray diffraction patterns have been used to characterise these complexes. The crystal and molecular structures of **1** and of **2**·$CH_3OH$, have been determined, confirming the ONNO binding mode of the ligands. The geometry around the metal ion is very slightly distorted square-planar in **1** and distorted square-pyramidal in **2**. The encapsulated complexes catalyse the oxidation, by $H_2O_2$ and *tert*-butyl hydroperoxide, of styrene, cyclohexene and thioanisole efficiently. Under optimised reaction conditions, the oxidation of styrene catalysed by **3** and **4** gave 23.6 % and 28.0 % conversion, respectively, using *tert*-butyl hydroperoxide as oxidant, where styrene oxide, benzaldehyde, benzoic acid and phenylacetaldehyde are the major products. Better conversions have been obtained using $H_2O_2$ as oxidant. Oxidation of cyclohexene catalysed by these complexes gave cyclohexene oxide, 2-cyclohexen-1-ol, cyclohexane-1,2-diol and 2-cyclohexen-1-one as the major products. A maximum of 90.1 % conversion of cyclohexene with **3** and 83.0 % with **4** was obtained under optimised conditions. Similarly, a maximum of 80.3 % conversion of methyl phenyl sulfide with **3** and 81.0 % with **4** was observed, where the selectivity of the major product methyl phenyl sulfoxide was found to be about 60 %. Tests for the recyclability and heterogeneity of the reactions have also been carried out, and the results indicate their recyclability. A possible reaction mechanism has been proposed by titrating a methanol solution of **1** and **2** with $H_2O_2$ to identify the possible intermediates.

(© Wiley-VCH Verlag GmbH & Co. KGaA, 69451 Weinheim, Germany, 2007)

## Introduction

Zeolites find applications in many scientific disciplines as catalysts and in all types of chemical engineering process technologies. The exchangeable property of extra-framework cations and suitable cavity size of the zeolites allow their modification by inclusion of chemically interesting molecules. A homogeneous catalyst, for example, a metal complex, may be considered one such interesting molecule and hence the term zeolite-encapsulated metal complexes. The large size of the encapsulated homogeneous catalysts and their rigidity make it difficult for them to escape the zeolite cages. Zeolite-encapsulated metal complexes having good catalytic activities possess the advantages of solid heterogeneous catalysts and share many of the advantageous features of homogeneous catalysts.

The flexible nature of salen-type [$H_2$salen = *N*,*N*′-bis(salicylidene)ethane-1,2-diamine] ligands has provided opportunities to design various transition-metal complexes in the nanocavity of zeolites and to develop catalytic processes for various reactions. Poltowicz et al. have encapsulated a whole range of metallosalen complexes {e.g., [Fe(salen)], [Mn(salen)], [Cu(salen)] and Co(salen)]} in zeolite-X to study their catalytic activity for the oxidation of cyclooctane.[1] Ratnasamy and co-workers have used copper(II) and manganese(III) complexes of salen derivatives encapsulated in the cavity of zeolite-X and zeolite-Y for the oxidation of styrene under aerobic conditions using *tert*-butyl hydroperoxide as an oxidant. The catalytic efficiency of these encapsulated complexes was much higher than that of the neat complexes. Electron-withdrawing substituents such as Cl, Br and $NO_2$ on the aromatic ring enhance the rate of oxidation.[2,3] These complexes also catalyse the oxidation of phenol and *p*-xylene.[4,5] Epoxidations of cyclohexene, cyclooctene, 1-hexene and other various types of alkenes, arenes and cycloalkenes, catalysed by different

[a] Department of Chemistry, Indian Institute of Technology Roorkee,
Roorkee 247667, India
E-mail: rkmanfcy@iitr.ernet.in
[b] Centro Química Estrutural, Instituto Superior Técnico – TU Lisbon,
Av. Rovisco Pais, 1049-001 Lisboa, Portugal
[c] Departamento de Química Fundamental, Facultad de Ciencias, Universidade da Coruña,
Zapateira s/n, 15071 A Coruña, Spain

 © 2007 Wiley-VCH Verlag GmbH & Co. KGaA, Weinheim 

complexes of salen-type ligands, have also been carried out.[6–9] [Co(salophen)]-Y [$H_2$salophen = *N*,*N*′-bis(salicylidene)benzene-1,2-diamine] and related derivatives catalysed the oxidation of β-isophorone (βIP) to ketoisophorone (KIP) (along with other minor products) in the presence of an oxidant at ambient conditions of temperature and pressure.[10] Liquid-phase oxidation of phenol with $H_2O_2$ has been reported using copper(II) and oxidovanadium(IV) complexes of *N*,*N*′-bis(salicylidene)propane-1,3-diamine ($H_2$sal-1,3-pn) and *N*,*N*′-bis(salicylidene)diethylenetriamine ($H_2$saldien).[11–13] Copper(II) and oxidovanadium(IV) complexes of *N*,*N*′-bis(salicylidene)cyclohexane-1,2-diamine ($H_2$sal-dach) catalyse the oxidation of styrene, cyclohexene and cyclohexane efficiently.[14]

The catalytic potential of metal complexes encapsulated in the nanocavity of zeolites prompted us to design new zeolite-Y-encapsulated copper(II) complexes of tetradentate ligands **I** and **II** (Scheme 1). Catalytic potentials of these complexes have been demonstrated by studying the oxidation of styrene, cyclohexene and methyl phenyl sulfide. Copper(II), nickel(II) and oxidovanadium(IV) complexes of **I** have been reported previously.[15,16] The structure of [Ni(pydx-en)] has been confirmed by single-crystal X-ray diffraction,[17] while other complexes have been characterised by elemental analysis and spectroscopic techniques. We have also prepared neat copper(II) complexes of **I** and **II** to evaluate their catalytic potential and characterised them by single-crystal X-ray diffraction.

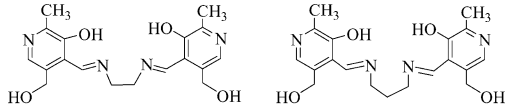


Scheme 1.

## Results and Discussion

### Synthesis and Characterisation of Catalysts

Scheme 2 presents the complexes prepared in this study. Their structures are based on elemental analysis and various spectroscopic studies, as well as on X-ray structure determinations. The presence of very strong peaks corresponding to $CuLH^+$ and $CuLNa^+$ in the ESI-MS spectra (positive mode) of DMSO solutions of **1** and **2**, with the correct isotope ratios, also confirms the integrity of the complexes in solution.

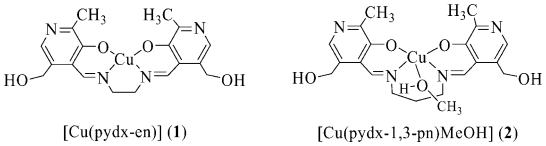


Scheme 2.

Reaction of cupric acetate with ligands $H_2$pydx-en (**I**) and $H_2$pydx-1,3-pn (**II**) in refluxing methanol yielded [Cu(pydx-en)] (**1**) and [Cu(pydx-1,3-pn)(MeOH)] (**2**), respectively. Complex **1** has previously been isolated by treating **I** with cupric acetate in aqueous solution.[16] Encapsulation of these complexes in the nanocavities of zeolite-Y involved the exchange of copper(II) ion with Na-Y in water followed by reaction of the metal-exchanged zeolite-Y with **I** or **II** in methanol. This method is referred to as the flexible ligand method. Here, the ligands enter into the cavity of zeolite-Y because of their flexible nature and interact with the metal ion to give [Cu(pydx-en)]-Y (**3**) and [Cu(pydx-1,3-pn)]-Y (**4**). Finally, extraction of impure samples with methanol using a Soxhlet extractor removed excess free ligand, and stirring in DMF removed neat metal complex formed on the surface of the zeolite, if any. As the crude mass was well extracted, the metal content found after encapsulation is only due to the presence of copper(II) complexes in the supercages of the zeolite-Y. The diagonal dimension of the complexes is about 12 Å {in [Cu(pydx-en)]} or about 11 Å {in [Cu(pydx-1,3-pn)(MeOH)]}, which suggests that they will fit nicely into the supercages of zeolite-Y. The molecular formulae of the encapsulated complexes are based on the respective neat complex. The Si/Al ratio of 9.67 of zeolite-Y taken here corresponds to a unit cell formula $Na_{18}(AlO_2)_{18}(SiO_2)_{174}$. The estimated number of copper atoms per unit cell is 2.5 for [Cu(pydx-en)]-Y (**3**) and 2.4 for [Cu(pydx-1,3-pn)]-Y (**4**).

### Structure Description of [Cu(pydx-en)] (1) and [Cu(pydx-1,3-pn)(MeOH)] (2)

Figures 1 and 2 include ORTEP representations of the molecular structure of [Cu(pydx-en)] (**1**) and [Cu(pydx-1,3-pn)(MeOH)] (**2**), respectively, and Table 1 provides selected bond lengths and angles of these compounds. The molecules are neutral, as both phenol groups are deprotonated, and the ligands coordinate to the Cu atom through two phenolate oxygen ($O^-_{phenolate}$) atoms and two imine nitrogen ($N_{imine}$) atoms. The geometry around the metal ion is slightly distorted square-planar in **1** and distorted square-pyramidal in **2**. A methanol molecule occupies the fifth coordination position in **2**.

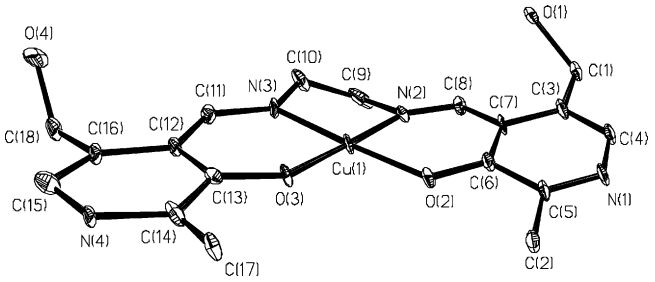


Figure 1. ORTEP diagram of [Cu(pydx-en)] (**1**) showing the atom-labelling scheme. The thermal ellipsoids were drawn at the 30% probability level.

 © 2007 Wiley-VCH Verlag GmbH & Co. KGaA, Weinheim 

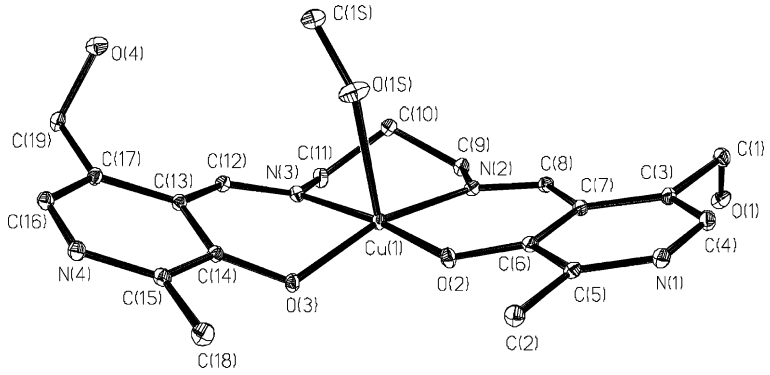


Figure 2. ORTEP diagram of [Cu(pydx-1,3-pn)(MeOH)] (**2**) showing the atom-labelling scheme. The thermal ellipsoids were drawn at the 30% probability level.

Table 1. Selected bond lengths [Å] and angles [°] for [Cu(pydx-en)] (**1**) and [Cu(pydx-1,3-pn)(MeOH)] (**2**).

| Bond lengths [Å] for [Cu(pydx3-en)] (**1**) | | Bond lengths [Å] for [Cu(pydx-1,3-pn)(MeOH)] (**2**) | |
|---|---|---|---|
| Cu(1)–O(2) | 1.742(6) | Cu(1)–O(2) | 1.8965(9) |
| Cu(1)–N(3) | 1.796(7) | Cu(1)–O(3) | 1.9546(9) |
| Cu(1)–O(3) | 2.341(7) | Cu(1)–N(3) | 1.9932(11) |
| Cu(1)–N(2) | 2.373(9) | Cu(1)–N(2) | 1.9935(11) |
| O(3)–C(13) | 1.333(11) | Cu(1)–O(1S) | 2.3525(11) |
| O(2)–C(6) | 1.380(12) | O(2)–C(6) | 1.2934(15) |
| N(2)–C(8) | 1.256(12) | N(2)–C(8) | 1.2962(16) |
| N(2)–C(9) | 1.377(11) | N(2)–C(9) | 1.4775(16) |
| N(3)–C(11) | 1.434(13) | O(3)–C(14) | 1.2998(15) |
| N(3)–C(10) | 1.690(9) | N(3)–C(12) | 1.2905(16) |
| C(6)–C(7) | 1.609(15) | N(3)–C(11) | 1.4670(16) |
| C(7)–C(8) | 1.338(13) | C(6)–C(7) | 1.4096(17) |
| C(11)–C(12) | 1.695(15) | C(7)–C(8) | 1.4443(17) |
| C(12)–C(13) | 1.330(13) | C(9)–C(10) | 1.5149(18) |
| | | C(10)–C(11) | 1.5198(19) |
| | | C(12)–C(13) | 1.4494(17) |
| | | C(13)–C(14) | 1.4082(17) |
| Angles [°] for [Cu(pydx-1,3-en)] (**1**) | | Angles [°] for [Cu(pydx-1,3-pn)(MeOH)] (**2**) | |
| O(2)–Cu(1)–N(3) | 175.2(3) | O(2)–Cu(1)–N(3) | 169.92(4) |
| O(2)–Cu(1)–O(3) | 90.0(3) | O(2)–Cu(1)–O(3) | 82.08(4) |
| N(3)–Cu(1)–O(3) | 94.8(3) | O(3)–Cu(1)–N(3) | 87.94(4) |
| O(2)–Cu(1)–N(2) | 91.2(3) | O(2)–Cu(1)–N(2) | 92.29(4) |
| N(3)–Cu(1)–N(2) | 84.1(3) | N(3)–Cu(1)–N(2) | 97.76(4) |
| O(3)–Cu(1)–N(2) | 178.8(2) | O(3)–Cu(1)–N(2) | 166.61(4) |
| | | O(2)–Cu(1)–O(1S) | 90.18(4) |
| | | O(3)–Cu(1)–O(1S) | 94.46(5) |
| | | N(3)–Cu(1)–O(1S) | 89.23(4) |
| | | N(2)–Cu(1)–O(1S) | 97.71(5) |
| Lengths [Å] and angles [°] of hydrogen bonds in complexes | | | |
| O(1)···H(1), 0.82; O(1)···O(3), 2.563(8) | | O(1)···H(1O), 0.69(2); O(1)···O(3), 2.7954(14) | |
| O(3)···H(1), 2.00; O(1)–H(1)–O(3), 125.5 | | O(3)···H(1O), 2.11(2); O(1)–H(1O)–O(3), 171(2) | |
| O(4)···H(4), 0.82; O(4)···N(1), 2.582(11) | | O(1S)···H(1S), 0.64(3); O(1S)···N(1), 2.8037(16) | |
| N(1)···H(4), 2.01; O(4)–H(4)–N(1), 126.5 | | N(1)···H(1S), 2.16(3); O(1S)–H(1S)–N(1), 175(3) | |
| | | O(4)···H(4O), 0.69(2); O(4)···N(4), 2.7959(15) | |
| | | N(4)···H(4O), 2.12(2); O(4)–H(4O)–N(4), 166(2) | |
| Deviations from the planarity of the rings | | | |
| Ring: Cu(1)–O(2)–C(6)–C(7)–C(8)–N(2) | | Ring: Cu(1)–O(2)–C(6)–C(7)–C(8)–N(2) | |
| Dev.: 0.0799(52) Å | | Dev.: 0.0516(07) Å | |
| Ring: Cu(1)–N(2)–C(9)–C(10)–N(3) | | Ring: Cu(1)–N(2)–C(9)–C(10)–C(11)–N(3) | |
| Dev.: 0.0976(48) Å | | Dev.: 0.2239(08) Å | |
| Ring: Cu(1)–N(3)–C(11)–C(12)–C(13)–O(3) | | Ring: Cu(1)–N(3)–C(12)–C(13)–C(14)–O(3) | |
| Dev.: 0.0334(50) Å | | Dev.: 0.1928(07) Å | |
| Pyridoxal rings: | | Pyridoxal rings: | |
| Planar, rms 0.0244(63) and 0.0172(60) Å | | Planar, rms 0.0037(08) and 0.0083(09) Å | |
| Torsion angle between rings: 9.58 (0.57)° | | Torsion angle between rings: 34.27(0.05)° | |

 © 2007 Wiley-VCH Verlag GmbH & Co. KGaA, Weinheim 

The planar arrangement Cu(ONNO) is distorted, the *cis*/*trans* angles not being 90° and 180°. The *cis* angles are 90.0(3), 94.8(3), 91.2(3) and 84.1(3)° in **1**, and 82.08(4), 87.94(4), 92.29(4) and 97.76(4)° in **2**, and the *trans* angles are 175.2(3) and 178.8(2)° in **1**, and 169.92(4) and 166.61(4)° in **2**. The angles with the apical position of the O atom of the methanol molecule are 90.18(4), 94.46(5), 89.23(4) and 97.71(5)° in **2**.

In complex **1** the ligand forms a set of (6+5+6)-membered chelate rings, and the deviations from the planarity are listed in Table 1. The plane formed by the donor atoms N(2)–N(3)–O(2)–O(3) has a deviation from planarity of 0.0015(30) Å, and if the $Cu^{II}$ ion is included, 0.0037(30) Å. In complex **2** the ligand forms a set of (6+6+6)-membered chelate rings, and the deviations from planarity are also listed in Table 1. The basal plane of the square pyramid formed by N(2)–N(3)–O(2)–O(3) atoms has a deviation from planarity of 0.1063(05) Å, and the $Cu^{II}$ ion is 0.1020 Å above the plane. The Cu–O and Cu–N bond lengths (Table 1) are similar and in the usual range found for these compounds, 1.9–2.1 Å. The C–O distances are also typical for this type of ligands,[15–21] and the C=N bonds are double bonds, with distances of about 1.3 Å.

In complex **1** the $HO(CH_2)$ groups of the pyridoxal rings are in a *syn* position to each other, but in complex **2** the $HO(CH_2)$ groups of the pyridoxal rings are in an *anti* conformation, similar to other complexes with this type of ligand.[16] The pyridine nitrogen atoms and alcohol group of $HO(CH_2)$ of the pyridoxal rings are involved in intermolecular H bonds. In complex **2**, the OH groups of the coordinated methanol molecule are also involved in H bonds. The bond lengths and angles of the hydrogen bonds are also included in Table 1.

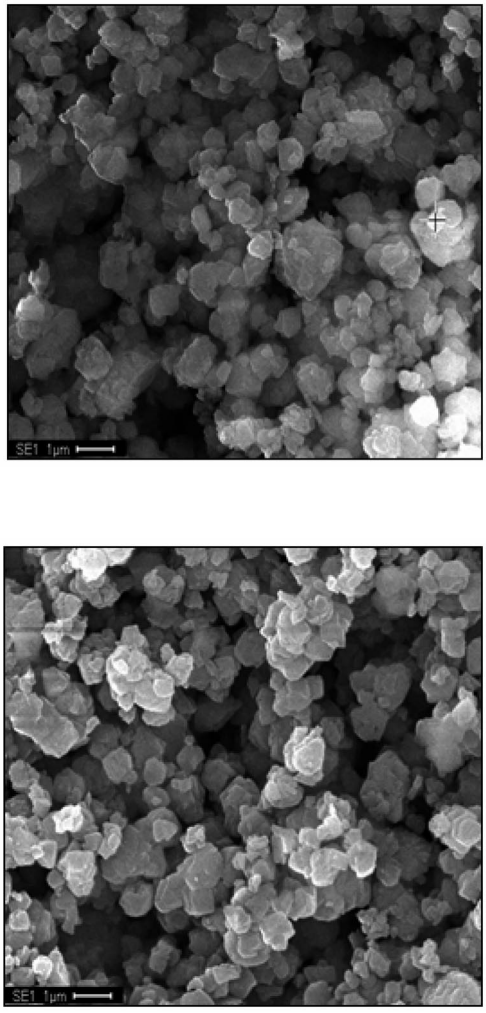


Figure 3. Field emission scanning electron micrograph of [Cu(pydx-en)]-Y (top) and [Cu(pydx-1,3-pn)]-Y (bottom).

## Field Emission Scanning Electron Micrograph and Energy Dispersive X-ray Analysis Studies

Figure 3 presents the field emission scanning electron micrographs of [Cu(pydx-en)]-Y and [Cu(pydx-1,3-pn)]-Y. It is clear from the micrographs that zeolite-entrapped copper complexes have well-defined crystals, and there is no indication of the presence of any metal ions or complexes on the surface. Energy-dispersive X-ray analysis plots support this conclusion as no copper or nitrogen contents were noted on the spotted surface in plots for both catalysts. The average silicon and aluminium percentage obtained on the spotted surfaces were about 30% and 10%, respectively. An amount of about 3% sodium suggests the exchange of remaining free copper ions by sodium ions during the re-exchange process (see Experimental Section). Only a small amount of carbon (about 5%) but no nitrogen suggests the presence of a trace amount of solvent (methanol) from which it was finally washed after Soxhlet extraction. No morphological changes on the surface upon encapsulation of the complexes in the cavity are seen because of their poor loading.

## Powder X-ray Diffraction Studies

The powder X-ray diffraction patterns of Na-Y, Cu-Y and encapsulated copper(II) complexes were recorded at $2\theta$ values between 5 and 50°, and some representative patterns are presented in Figure 4. Essentially similar diffraction

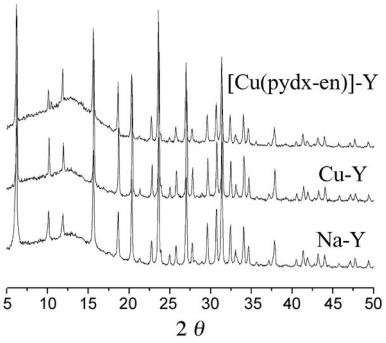


Figure 4. XRD patterns of Na-Y, Cu-Y and [Cu(pydx-en)]-Y (**3**).

 © 2007 Wiley-VCH Verlag GmbH & Co. KGaA, Weinheim 

patterns were noticed in encapsulated complexes Cu-Y and Na-Y, except zeolite with encapsulated metal complexes has a slightly weaker intensity. These observations indicate that the framework of the zeolites do not suffer any significant structural changes during encapsulation, that is, crystallinity of the zeolite-Y is preserved.

### Thermogravimetric Analysis Studies

The decomposition of complexes **3** and **4** occurs in three overlapping steps. An endothermic loss of trapped water and methanol occurs between 80 and 200 °C, while exothermic removal of intra-zeolite water occurs between 300 and 350 °C. This is followed by endothermic loss of the ligand's residue, which continues until the removal of all organic mass at about 700 °C has occurred. The low percentage of weight loss (about 10%) for this last step indicates the presence of an only small amount of metal complexes in the cavities of the zeolite. This is in agreement with the low copper content estimated for these complexes. A weight loss of 6.9%, equivalent to methanol, in **2** occurs up to about 130 °C. The anhydrous complex is stable up to 260 °C, and then it decomposes in two major steps that are complete at 375 °C. The remaining residue of 18.1% slowly stabilises with the formation of a final residue of 17.5% (about 17.1% for CuO) at about 800 °C. A slightly different decomposition pattern has been obtained for **1**, where the decomposition of the stable complex starts at about 290 °C and occurs in two overlapping steps. The decomposition is complete at about 360 °C. The remaining residue of 20.6% further loses weight up to about 800 °C and stabilises at 18.3%. The calculated residue for CuO of 18.9% agrees with the value observed.

### IR Spectral Studies

A partial list of IR spectroscopic data is presented in Table 2. The intensity of the peaks in encapsulated complexes is, however, weak because of their low concentration in zeolite matrix; the spectra of the encapsulated as well as neat complexes showed essentially similar bands. Comparison of the spectra of these complexes with the respective ligand provides evidence for the coordinating mode of ligands in complexes. The ligand $H_2$pydx-en exhibits a medium-intensity band around 2700 $cm^{-1}$ due to intramolecular hydrogen bonding. Absence of this band in the spectra of encapsulated complexes indicates the destruction of the hydrogen bond followed by the coordination of the phenol oxygen atom after deprotonation. Existence of this band, however, in neat complexes hints towards the presence of hydrogen bonding. A sharp band appearing at 1626 $cm^{-1}$ (in **I**) or at 1632 $cm^{-1}$ (in **II**) due to the $\nu$(C=N) (azomethine) shifts to higher wavenumbers in complexes, thereby suggesting the coordination of the azomethine nitrogen atom. Several multiple bands of medium intensity covering the region 2850–3000 $cm^{-1}$ are observed due to C–H bands. The spectral patterns of these complexes are similar to [Cu(pydx-en)] reported in the literature.[16]

### UV/Vis Spectral Studies

UV/Vis spectral studies of **I** and its copper(II) complex **1** have been discussed in detail in the literature.[16] Other complexes reported here exhibit very similar spectral patterns. The well-defined band at 590 nm in **1** and a broad band covering the region 570–650 nm in **2** have been assigned to a d–d transition. Such a d–d band in zeolite-encapsulated complexes could not be obtained because of their poor loading, while ligand bands appearing in the UV region are similar to those observed for neat complexes. This data is collected in Table 2 and the spectra of encapsulated complexes are presented in Figure 5.

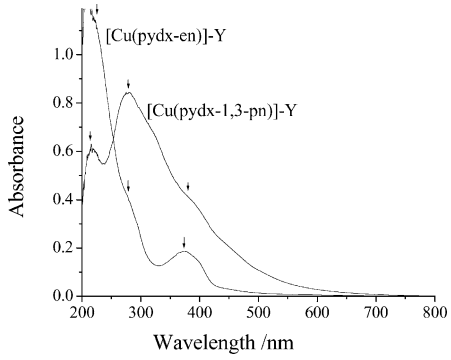


Figure 5. UV/Vis spectra of [Cu(pydx-en)]-Y and [Cu(pydx-1,3-pn)]-Y dispersed in nujol.

### EPR Studies

The EPR spectra of the neat $Cu^{II}$ complexes **1** and **2** in the polycrystalline state are broad because of dipolar and spin–spin exchange interactions. It is clear that they are characterised by an axial **g** tensor, but the hyperfine features

Table 2. IR and UV/Vis spectroscopic data of ligand, pure and encapsulated complexes.

| Compound | IR [$cm^{-1}$] | | UV/Vis | |
|---|---|---|---|---|
| | $\nu$(OH) | $\nu$(C=N) | Solvent | $\lambda_{max}$ [nm] |
| $H_2$pydx-en (**I**) | 3280–3450 | 1626 | $CH_3OH$ | 216, 252, 335 |
| $H_2$pydx-1,3-pn (**II**) | 2846–3480 | 1632 | $CH_3OH$ | 215, 252, 334 |
| [Cu(pydx-en)] (**1**) | ca. 3400 | 1634 | $CH_3OH$ | 235, 277, 378 |
| [Cu(pydx-1,3-pn)(MeOH)] (**2**) | ca. 3450 | 1635 | $CH_3OH$ | 233, 273, 377 |
| [Cu(pydx-en)]-Y (**3**) | ca. 3400 | 1633 | nujol | 207, 283, 374 |
| [Cu(pydx-1,3-pn)]-Y (**4**) | ca. 3450 | 1638 | nujol | 217, 246, 402 |

 © 2007 Wiley-VCH Verlag GmbH & Co. KGaA, Weinheim 

were not resolved, neither at room temperature nor at 77 K, and not much structural information can be obtained. The EPR spectra of the neat $Cu^{II}$ complexes **1** and **2** in DMF solutions, and of the catalysts **3** and **4** are given in Figures 6 and 7.

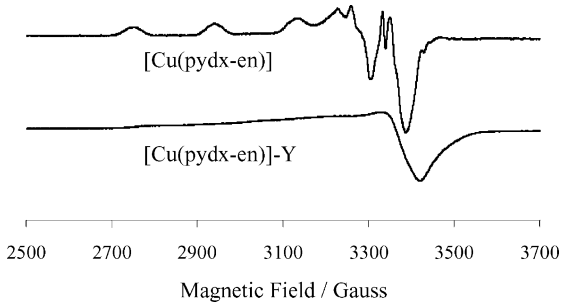


Figure 6. EPR spectra of a frozen DMF solution of [Cu(pydx-en)] (**1**) and of [Cu(pydx-en)]-Y (**3**) at room temperature.

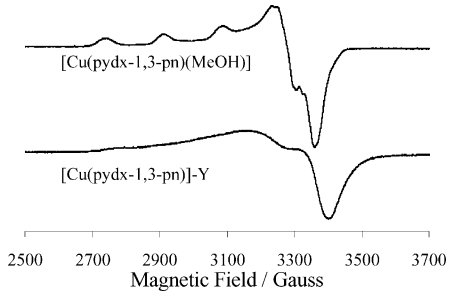


Figure 7. EPR spectra of a frozen DMF solution of [Cu(pydx-1,3-pn)(MeOH)] (**2**) and of [Cu(pydx-1,3-pn)]-Y (**4**) at room temperature.

The spectra of the encapsulated complexes **3** and **4** are reasonably resolved, indicating the encapsulation of individual molecules in the supercages of Na-Y. The intermolecular interactions are avoided because of isolation of the zeolite cavities, indicating that the $Cu^{II}$ sites are well separated in the catalyst, and thereby the spin Hamiltonian parameters can be estimated with reasonable accuracy; these are listed in Table 3.

Both neat complexes **1** and **2** have an $N_2O_2$ binding mode and are monomeric in the solid state. Complex **1** has a square-planar configuration, and **2** has square-planar configuration with a pyramidal distortion. In DMF solutions the representation of the $A_{\|}$, $g_{\|}$ values fit well with those of other [$Cu^{II}$(salen)] complexes.[5,22–25] The $g_{\|}/A_{\|}$ ratio is 112.7 for **1**, indicating a remarkable planarity of the square-planar geometry, as found in the solid state. For **2** this ratio is 126, but this is mainly due to a decrease in $A_{\|}$. Very similar $g_{\|}$ and $A_{\|}$ parameters and $g_{\|}/A_{\|}$ ratios were found for [$Cu^{II}$(salen)] (2.212, $203.7\times10^{-4}$ $cm^{-1}$, 109, respectively) and [$Cu^{II}$(sal-1,3-pn)] (2.254, $172.5\times10^{-4}$ $cm^{-1}$, 131, respectively),[25] in DMF solutions, indicating very similar geometries and balance of charge to those of **1** and **2**. No superhyperfine structure is distinguished.

The EPR spectra of the encapsulated complexes were recorded at room temperature and are broader than those for frozen solutions, suggesting that the complexes located in the supercages may be present in more than one geometrical conformation. However, the $g_{\|}$ and $A_{\|}$ parameters and $g_{\|}/A_{\|}$ ratios ($g_{\|}/A_{\|}$ = 113 for **3** and 126 for **4**) almost coincide with those obtained in DMF solutions, indicating similar geometries and balance of charge for the complexes in the encapsulated and dissolved forms.

## Catalytic Activity Studies

The catalytic activities of the zeolite-encapsulated and neat complexes have been demonstrated by studying the oxidation of styrene, cyclohexene and methyl phenyl sulfide.

### *Oxidation of Styrene*

The oxidation of styrene, catalysed by [Cu(pydx-en)]-Y and [Cu(pydx-1,3-pn)]-Y, was carried out using $H_2O_2$ and *tert*-butyl hydroperoxide as oxidants to give styrene oxide, benzaldehyde, benzoic acid and phenylacetaldehyde (Scheme 3) along with minor amounts of unidentified products. Hulea and Dumitriu[26] have reported some of these products while using catalysts TS-1 and MCM-41. All oxidation products as observed here were identified recently using the polymer-anchored catalyst PS-[VO(sal-ohyba)-(DMF)] ($H_2$sal-ohyba = Schiff base derived from salicylaldehyde and *o*-hydroxybenzylamine)[27] and the zeolite-Y-encapsulated complex [VO(sal-dach)]-Y.[14]

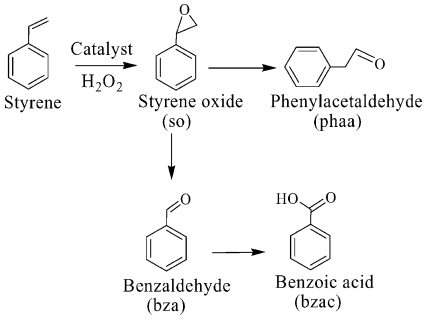


Scheme 3.

Table 3. EPR data for [Cu(pydx-en)] and [Cu(pydx-1,3-pn)(MeOH)] complexes as neat and encapsulated in zeolite-Y.

| Complex | $g_{xx}$ | $g_{yy}$ | $g_{zz(\|)}$ | $A_{xx}$ ($\times10^4$ $cm^{-1}$) | $A_{yy}$ ($\times10^4$ $cm^{-1}$) | $A_{zz(\|)}$ ($\times10^4$ $cm^{-1}$) |
|---|---|---|---|---|---|---|
| [Cu(pydx-en)] (**1**) | 2.07 | 2.03 | 2.22 | 17.39 | 28.43 | 196.94 |
| [Cu(pydx-1,3-pn)(MeOH)] (**2**) | 2.04 | 2.06 | 2.24 | 21.85 | 16.88 | 178.53 |
| [Cu(pydx-en)]-Y (**3**) | 2.08 | | 2.32 | – | | 156 |
| [Cu(pydx-1,3-pn)]-Y (**4**) | 2.09 | | 2.34 | – | | 138 |

 © 2007 Wiley-VCH Verlag GmbH & Co. KGaA, Weinheim 

In order to achieve the maximum oxidation of styrene, catalyst **3** was taken as a representative, and the effect of four different reaction parameters – viz. the amount of $H_2O_2$ (mol of $H_2O_2$ per mol of styrene), amount of catalyst, volume of solvent and temperature of the reaction – was studied.

Three different aqueous 30% $H_2O_2$/styrene molar ratios of 1:1, 2:1 and 3:1 were considered while keeping the fixed amount of styrene (1.04 g, 10 mmol) and catalyst (0.025 g) in $CH_3CN$ (20 mL) at 80 °C. The periodic analyses of results up to 6 h are illustrated in Figure 8. Increasing the $H_2O_2$/styrene ratio from 1:1 to 2:1 improved the conversion from 9.1% to 14.8% while a 3:1 ratio showed a further increment of conversion of hardly 1%. Therefore, it is clear that the 2:1 molar ratio is quite suitable to obtain the optimum styrene conversion of 14.8% in the 6 h reaction time.

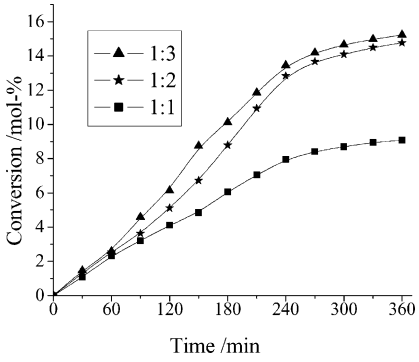


Figure 8. Effect of $H_2O_2$ on the oxidation of styrene. Reaction conditions: styrene (1.04 g, 10 mmol), [Cu(pydx-en)]-Y (**3**) (0.025 g), $CH_3CN$ (20 mL) and temp. (80 °C).

Similarly, for three different amounts – viz. 0.015, 0.025 and 0.035 g – of [Cu(pydx-en)]-Y at a styrene/aqueous 30% $H_2O_2$ ratio of 1:2 under the above reaction conditions, 0.015 g of catalyst, achieved only 7.8% conversion, whereas 0.025 g of catalyst gave a maximum conversion of 14.8% in 6 h of reaction time. A further increment of catalyst (0.035 g) has shown no improvement (Figure 9). The reason for reduced activity at higher catalyst dose may be adsorption/chemisorption of the two reactants on separate catalyst particles, thereby reducing the chance to interact.

Figure 10 illustrates the oxidation of styrene at three different temperatures – viz. 60, 70 and 80 °C –, while keeping the optimised conditions of 10 mmol of styrene, 20 mmol of $H_2O_2$ and 0.025 g of catalyst in 20 mL of acetonitrile. It is evident from the figure that the performance of the catalyst is poor at 60 °C wherein only 3.9% conversion was observed. Increasing the reaction temperatures to 70 and 80 °C increases the conversion to 7.0% and 14.8%, respectively. Thus, conducting the catalytic reaction at 80 °C is most suitable to maximise the oxidation of styrene. We have also observed that reducing the volume of $CH_3CN$ to 10 mL under the above optimised reaction conditions improved the conversion considerably, and two more components, though in poor yield, have also been obtained.

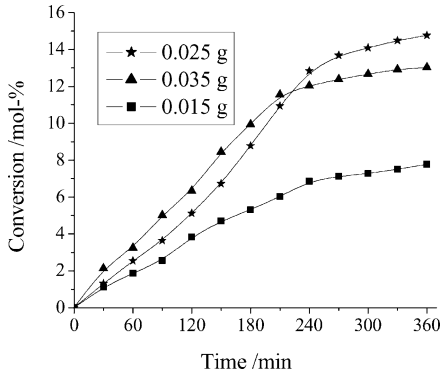


Figure 9. Effect of the amount of catalyst on the oxidation of styrene. Reaction conditions: styrene (1.04 g, 10 mmol), 30% $H_2O_2$ (2.27 g, 20 mmol), $CH_3CN$ (20 mL) and temp. (80 °C).

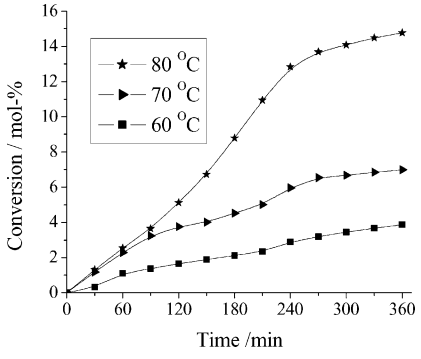


Figure 10. Effect of the temperature on the oxidation of styrene. Reaction conditions: styrene (1.04 g, 10 mmol), [Cu(pydx-en)]-Y (0.025 g), 30% $H_2O_2$ (2.27 g, 20 mmol) and $CH_3CN$ (20 mL).

Thus, for the maximum oxidation of 10 mmol of styrene, the other required conditions as concluded were: [Cu(pydx-en)]-Y (0.025 g), $H_2O_2$ (2.27 g, 20 mmol), $CH_3CN$ (10 mL) and temperature (80 °C). Under these optimised reaction conditions, the catalytic activities of **1**–**4** were further tested, and the results obtained are shown in Figure 11. Table 4 compares the selectivity of the various products obtained after 6 h of reaction time, along with the percent conversion of styrene and turnover frequency. It is clear from Table 4 and Figure 11 that [Cu(pydx-1,3-pn)]-Y exhibits 37.4% conversion, which is better than that exhibited by [Cu(pydx-en)]-Y (33.3%). Both catalysts gave mainly four products: styrene oxide, benzaldehyde, phenylacetaldehyde and benzoic acid. The selectivity for benzaldehyde is much higher, while the other products are obtained in small amounts.

We have also tested the catalytic activity of the neat complexes **1** and **2** for the oxidation of styrene using an equimolar concentration of metal ion as in their respective zeolite-encapsulated metal complex. Figure 11 also provides the conversion as a function of time, while Table 4 lists all other details. Thus, under the above reaction conditions, the conversion obtained by the neat complexes (18.7% for **1** and 22.3% for **2**) is significantly lower than that shown by the respective encapsulated complexes. Again, all four products have been obtained with the selectivity order: benzaldehyde > styrene oxide > phenylacetaldehyde > benzoic acid.

 © 2007 Wiley-VCH Verlag GmbH & Co. KGaA, Weinheim 

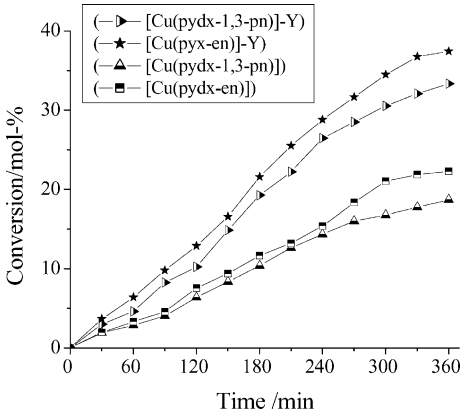


Figure 11. Catalytic comparison of zeolite-encapsulated and neat complexes for the oxidation of styrene in the presence of $H_2O_2$ as oxidant. Reaction conditions: styrene (1.04 g, 10 mmol), catalyst (0.025 g for encapsulated and 0.00133 g in the case of neat complexes), $H_2O_2$ (2.27 g, 20 mmol), $CH_3CN$ (10 mL) and temp. (80 °C).

Table 4. Product selectivity and percent conversion of styrene after 6 h of reaction time with $H_2O_2$ as oxidant.

| Catalyst ($H_2O_2$) | Conv. (%) | Product selectivity (%) | | | | | TOF[a] [$h^{-1}$] |
|---|---|---|---|---|---|---|---|
| | | | | | Others | | |
| [Cu(pydx-en)]-Y (**3**) | 33.3 | 82.2 | 12.4 | 1.6 | 1.4 | 2.4 | 179 |
| [Cu(pydx-1,3-pn)]-Y (**4**) | 37.4 | 75.4 | 15.0 | 4.0 | 3.0 | 2.6 | 215 |
| [Cu(pydx-en)] (**1**) | 18.7 | 81.6 | 7.4 | 4.8 | 2.6 | 3.6 | 106 |
| [Cu(pydx-1,3-pn)(MeOH)] (**2**) | 22.3 | 79.4 | 9.9 | 6.2 | 3.0 | 1.5 | 128 |

[a] TOF [$h^{-1}$] (turnover frequency): mol of substrate converted per mol of metal (in the solid catalyst) per hour.

Under the above optimised reaction conditions, the catalytic action of neat as well encapsulated complexes has also been tested using *tert*-butyl hydroperoxide (TBHP) as an oxidant: 70% TBHP (2.57 g, 20 mmol), catalyst (0.025 g for encapsulated and 0.00133 g, for neat complexes) and styrene (1.04 g, 10 mmol) were used in $CH_3CN$ (20 mL), and the reaction was carried out at 80 °C. Figure 12 shows the conversion as a function of time, and Table 5 compares the selectivity data along with the conversion and turnover frequency after 6 h of reaction time. It is clear that the obtained percentage conversion varies in the range 13.6–28.0% with the order: [Cu(pydx-1,3-pn)]-Y (28.0%) > [Cu(pydx-en)]-Y (23.6%) > [Cu(pydx-1,3-pn)] (16.2%) > [Cu(pydx-en)] (13.6%). Thus, the overall conversion of styrene with TBHP is always lower than with $H_2O_2$. The selectivity of the formation of an important component – styrene oxide – is better (43.4–70.5%), but two more products, namely benzoic acid and phenylacetaldehyde, have also been obtained.

The highest yield of benzaldehyde using $H_2O_2$ as oxidant is possibly due to further oxidation of styrene oxide formed in the first step by a nucleophilic attack of $H_2O_2$ on styrene oxide followed by cleavage of the intermediate hydroperoxystyrene.[28] The formation of benzaldehyde may also be facilitated by the direct oxidative cleavage of the styrene side-chain double bond by a radical mechanism.[27] Formation of other products such as phenylacetaldehyde is possible through isomerisation of styrene oxide, while the formation of benzoic acid from benzaldehyde is straightforward.

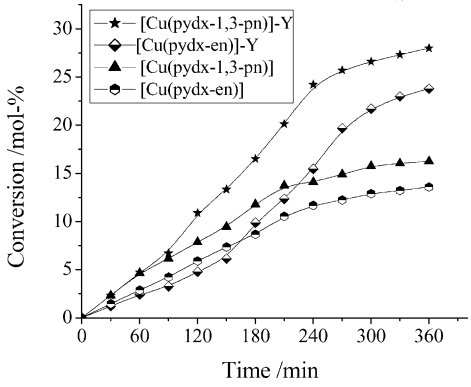


Figure 12. Catalytic comparison of zeolite-encapsulated metal complexes and neat complexes for the oxidation of styrene in the presence of TBHP as oxidant. Reaction conditions: styrene (1.04 g, 10 mmol), catalyst (0.025 g for encapsulated and 0.00133 g in case of neat complexes), TBHP (2.57 g, 20 mmol), $CH_3CN$ (20 mL) and temp. (80 °C).

Table 5. Product selectivity and percent conversion of styrene with TBHP after 6 h of reaction time.

| Catalyst (TBHP) | Conv. (%) | Product selectivity (%) | | | | | TOF [$h^{-1}$] |
|---|---|---|---|---|---|---|---|
| | | | | | Others | | |
| [Cu(pydx-en)]-Y (**3**) | 23.6 | 60.7 | 30.8 | 0.8 | 1.3 | 6.4 | 127 |
| [Cu(pydx-1,3-pn)]-Y (**4**) | 28.0 | 43.4 | 33.1 | 0.8 | 2.4 | 20.3 | 160 |
| [Cu(pydx-en)] (**1**) | 13.6 | 70.5 | 21.0 | 0.6 | 1.8 | 6.1 | 77 |
| [Cu(pydx-1,3-pn)(MeOH)] (**2**) | 16.2 | 45.4 | 16.1 | 0.7 | 16.8 | 21.0 | 93 |

### *Oxidation of Cyclohexene*

The oxidation of cyclohexene catalysed by encapsulated complexes gave cyclohexene oxide, 2-cyclohexen-1-ol, cyclohexane-1,2-diol and 2-cyclohexen-1-one, as shown in Scheme 4. Recently, we observed all these products while using catalyst [VO(sal-dach)] encapsulated in zeolite-Y.[14]

The reaction conditions have been optimised considering **3** as a representative catalyst and varying the amount of catalyst, oxidant, solvent and temperature of the reaction mixture. The effect of $H_2O_2$ concentration on the oxidation of cyclohexene is shown in Figure 13. Three different $H_2O_2$/cyclohexene molar ratios of 1:1, 2:1 and 3:1 were used at a fixed amount of cyclohexene (0.82 g, 10 mmol), catalyst (0.025 g), acetonitrile (20 mL) and temperature (75 °C). From Figure 13 it is clear that a 3:1 molar ratio is the best of those tested, to obtain a conversion of 38.8% in 6 h.

The amount of catalyst has shown considerable affect on the oxidation of cyclohexene. For a cyclohexene/$H_2O_2$ ratio of 1:3, five different amounts of catalyst – viz. 0.015, 0.025, 0.035, 0.050 and 0.065 g – were used under the above reaction conditions, and the results obtained are summarised in Figure 14. The conversion increases with an increase in the amount of catalyst from 0.015 to 0.050 g (28 to 56.2%), and

 © 2007 Wiley-VCH Verlag GmbH & Co. KGaA, Weinheim 

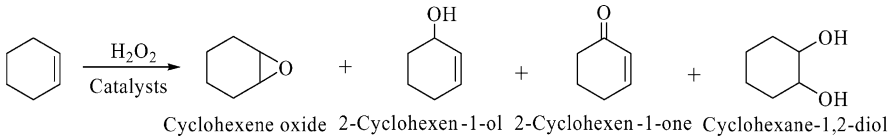


Scheme 4.

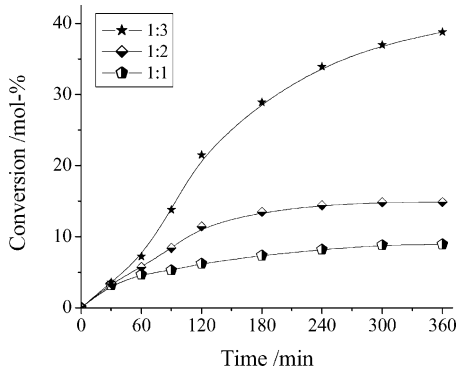


Figure 13. Effect of $H_2O_2$ on the oxidation of cyclohexene. Reaction conditions: cyclohexene (0.82 g, 10 mmol), [Cu(pydx-en)]-Y (0.025 g), $CH_3CN$ (20 mL) and temp. (75 °C).

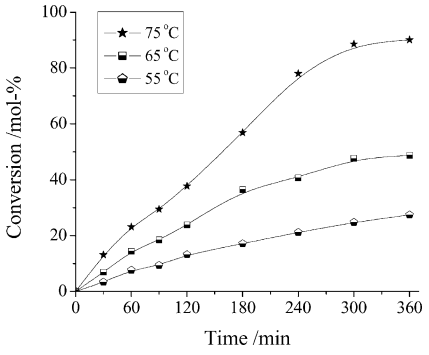


Figure 15. Effect of the temperature on the oxidation of cyclohexene. Reaction conditions: cyclohexene (0.82 g, 10 mmol), [Cu(pydx-en)]-Y (**3**) (0.050 g), 30% $H_2O_2$ (3.40 g, 30 mmol) and $CH_3CN$ (10 mL).

then assumes a lower trend with 0.065 g of catalyst (52.4%). Thus, an amount of 0.050 g of catalyst is considered adequate to carry out the oxidation of cyclohexene. It was also noted that by reducing the volume of acetonitrile to 10 mL, this conversion reached 90.1% with 0.050 g of catalyst under the above reaction conditions.

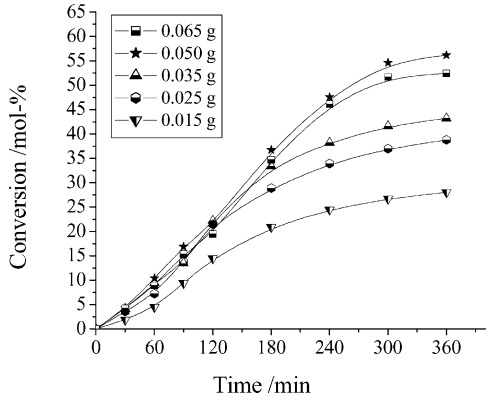


Figure 14. Effect of the amount catalyst on the oxidation of cyclohexene. Reaction conditions: cyclohexene (0.82 g, 10 mmol), 30% $H_2O_2$ (3.40 g, 30 mmol), $CH_3CN$ (20 mL) and temp.(75 °C).

Figure 15 illustrates the effect of temperature of the reaction medium on the conversion of cyclohexene as a function of time. Amongst the three different temperatures (55, 65 and 75 °C) for the fixed amount of cyclohexene (0.82 g, 10 mmol), aqueous 30% $H_2O_2$ (3.40 g, 30 mmol) and catalyst (0.050 g) in acetonitrile (10 mL), running the reaction at 75 °C has shown the best result, where 90.1% conversion has been obtained.

Thus, suitable reaction conditions for the maximum oxidation of cyclohexene were optimised as follows: cyclohexene (0.82 g, 10 mmol), $H_2O_2$ (3.40 g, 30 mmol), catalyst (0.050 g), acetonitrile (10 mL) and a temperature of 75 °C. Catalyst **4** was also tested under the above reaction conditions, and results along with the selectivity of various reaction products are summarised in Table 6. A maximum of 83.0% conversion has been achieved with **4**, which is less than that obtained by **3** (90.1%) in 6 h of contact time. However, both catalysts show the highest selectivity towards the formation of 2-cyclohexen-1-ol, which is followed by cyclohexene oxide. The selectivity of the two other products, 2-cyclohexen-1-one and cyclohexane-1,2-diol, has no definite trend.

We have also tested the catalytic activities of encapsulated complexes using *tert*-butyl hydroperoxide as an oxidant. Thus, catalyst (0.050 g), *tert*-butyl hydroperoxide (3.855 g, 30 mmol) and cyclohexene (0.82 g, 10 mmol) were used in acetonitrile (10 mL), and the reaction was carried out at 75 °C. The data, also presented in Table 6, show a poor conversion of cyclohexene (19.5% for **3** and 17.8% for **4**) with *tert*-butyl hydroperoxide in 6 h of contact time. Here, the major product obtained is cyclohexane-1,2-diol, while amounts of the other three products are very poor.

The neat complexes gave 45.5% (with 0.0028 g of **1**) or 50.7% (with 0.0027 g of **2**) conversion using $H_2O_2$ as an oxidant (Table 6). Here, the selectivity of cyclohexene oxide is better (33 to 38.7%) in comparison with the encapsulated complexes, although the overall selectivity orders of all products are the same. However, the turnover rates for encapsulated complexes, their stability towards decomposition and easy recovery from the reaction mixture make encapsulated complexes better catalysts than neat ones.

 © 2007 Wiley-VCH Verlag GmbH & Co. KGaA, Weinheim 

Table 6. Oxidation of cyclohexene and product selectivity using various catalysts.

| Catalyst | Oxidant | Conv. (%) | Product selectivity (%) | | | | | TOF [$h^{-1}$] |
|---|---|---|---|---|---|---|---|---|
| | | | | | | | Other | |
| [Cu(pydx-en)]-Y (**3**) | $H_2O_2$ | 90.1 | 26.9 | 37.8 | 22.2 | 9.5 | 3.6 | 241 |
| | TBHP | 19.5 | 1.4 | 2.4 | 2.5 | 92.9 | 0.8 | 52 |
| [Cu(pydx-1,3-pn)]-Y (**4**) | $H_2O_2$ | 83.0 | 37.1 | 51.1 | 3.5 | 8.3 | 0.0 | 237 |
| | TBHP | 17.8 | 1.5 | 2.0 | 3.1 | 92.5 | 0.9 | 51 |
| [Cu(pydx-en)] (**1**) | $H_2O_2$ | 50.7 | 38.7 | 44.5 | 4.9 | 5.4 | 6.5 | 136 |
| [Cu(pydx-1,3-pn)(MeOH)] (**2**) | $H_2O_2$ | 45.5 | 33.0 | 51.5 | 5.0 | 4.9 | 5.6 | 130 |

The conversion of cyclohexene and selectivity of different reaction products using [Cu(pydx-1,3-pn)]-Y as catalyst under the optimised reaction conditions have been analysed as a function of time and are presented in Figure 16. It is clear from the plot that a selectivity of 20.7% of cyclohexene oxide and 35.5% of cyclohexen-1-ol has been obtained at a conversion of 20.2% of cyclohexene in 1 h of reaction time. The selectivity for these products increases with time and reaches 37.1% and 51.1%, respectively, with the increase of the conversion of cyclohexene to 83.0% in 6 h. The other two products, 2-cyclohexen-1-one and cyclohexane-1,2-diol, have 26.8% and 14.7% selectivity in the first hour, but their selectivities decrease with time and reach 3.5 and 8.2%, respectively. Thus, to obtain a good selectivity for the important product cyclohexene oxide, it is essential to run the reaction for at least 6 h under the optimised reaction conditions. After 6 h, only minor changes have been noted in the selectivities of the different reaction products.

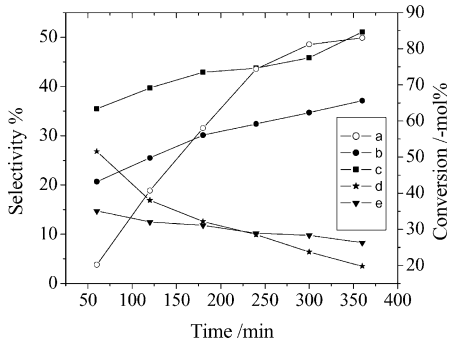


Figure 16. Conversion of cyclohexene and variation in the selectivity of various products as a function of time: (a) conversion of cyclohexene, (b) cyclohexene oxide, (c) 2-cyclohexen-1-ol, (d) 2-cyclohexen-1-one and (e) cyclohexane-1,2-diol.

### *Oxidation of Methyl Phenyl Sulfide (Thioanisol)*

Enzyme sulfoxidases[29] facilitate sulfide peroxidase activity where the electron-rich sulfur atom of the sulfide undergoes electrophilic oxidation by $H_2O_2$ to give the sulfoxide and, further, sulfone. Such oxidation of methyl phenyl sulfide was tested with the copper complexes prepared in this work. Oxidation of methyl phenyl sulfide in the presence of $H_2O_2$ gave two products, namely methyl phenyl sulfoxide and methyl phenyl sulfone, as shown in Scheme 5.

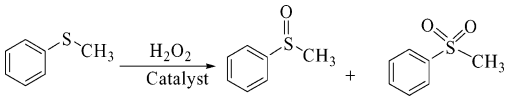


Scheme 5.

The catalytic potential of these catalysts has also been optimised considering the amount of oxidant, solvent and catalyst. Thus, catalyst **4** was taken as a representative, and the amount of oxidant was varied at a fixed amount of methyl phenyl sulfide (1.242 g, 10 mmol) and catalyst (0.025 g) in acetonitrile (10 mL), and the reaction was carried out at ambient temperature. At an aqueous $H_2O_2$/substrate ratio of 2:1, a maximum of 69.3% conversion was achieved in 3 h of reaction time. Decreasing this ratio to 1:1 decreases the conversion of methyl phenyl sulfide considerably, while increasing this ratio to 3:1 has a marginal effect on the conversion (Figure 17). The only significant influence when using a 3:1 ratio is the completion of the reaction in less time. Increasing the volume of solvent to 20 mL under the above reaction conditions decreases the conversion considerably (to 64.3%).

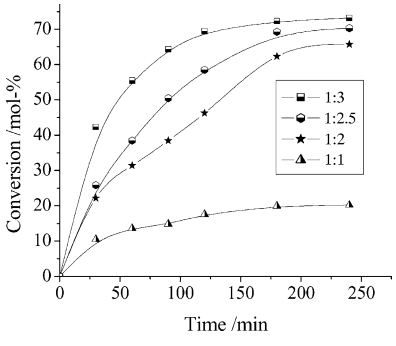


Figure 17. Effect of the amount of $H_2O_2$ on the oxidation of methyl phenyl sulfide as a function of time. Reaction conditions: methyl phenyl sulfide (1.242 g, 10 mmol), [Cu(pydx-1,3-pn)]-Y (0.025 g) and acetonitrile (10 mL).

Similarly, four different amounts of catalyst – viz. 0.015, 0.025, 0.035 and 0.050 g – were considered, while keeping methyl phenyl sulfide (1.242 g, 10 mmol) and 30% $H_2O_2$ (2.27 g, 20 mmol) in acetonitrile (10 mL). As mentioned in Figure 18, increasing the catalyst amount from 0.015 to 0.025 g increases the conversion from 46.8 to 69.3%. Increasing it to 0.035 g improves the conversion to 81.0%, while 0.050 g shows no improvement. Therefore, it is clear

 © 2007 Wiley-VCH Verlag GmbH & Co. KGaA, Weinheim 

that 0.035 g of catalyst is adequate to obtain an optimum methyl phenyl sulfide conversion of 81.0% in 3 h of contact time.

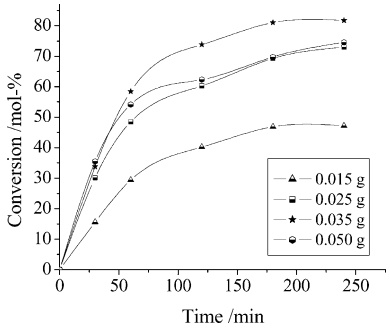


Figure 18. Effect of the amount of catalyst on the oxidation of methyl phenyl sulfide. Reaction conditions: methyl phenyl sulfide (1.242 g, 10 mmol), $H_2O_2$ (2.27 g, 20 mmol) and acetonitrile (10 mL).

Thus, under the optimised reaction conditions, that is, catalyst (0.035 g), methyl phenyl sulfide (1.242 g, 10 mmol), 30% $H_2O_2$ (2.27, 20 mmol) and acetonitrile (10 mL), catalyst **3** was also tested, and the results of both catalysts are compared in Figure 19, while Table 7 provides selectivity details. Under the optimised reaction conditions, **3** and **4** gave 80.3% and 81.0% conversion, respectively. In terms of the product selectivity, the selectivities of methyl phenyl sulfoxide and methyl phenyl sulfone are 63.3 and 36.7%, respectively, for **3** and 53.6 and 46.4%, respectively, for **4**. A blank reaction under similar conditions, that is, methyl phenyl sulfide (1.242 g, 10 mmol), aqueous 30% $H_2O_2$ (2.27 g, 20 mmol) and acetonitrile (10 mL), resulted in 35.2% conversion with 68.3% selectivity towards sulfoxide and 31.7% sulfone. Thus, catalysts **3** and **4** only enhanced the percent conversion of methyl phenyl sulfide and played no positive role in enhancing the selectivity of sulfoxide. In contrast, a positive role in enhancing the selectivity towards the formation of sulfoxide as well as conversion of methyl phenyl sulfide has been observed by oxidovanadium(IV) and copper(II) complexes encapsulated in the cavities of zeolite-Y.[30] The neat complexes also exhibited a good catalytic activity (68.4–69.9% conversion) when 0.0019 g amounts were used under the above optimised conditions. However, the selectivity for sulfone was better than for sulfoxide.

Catalytic activities of these complexes have also been tested using TBHP as an oxidant under similar conditions. Again, 0.035 g of catalyst has shown the best results at a fixed amount of methyl phenyl sulfide (10 mmol) and TBHP (20 mmol) in acetonitrile (10 mL). A maximum of 47.1% conversion has been obtained with **3**, while **4** gave only 18.1% conversion in 3 h of reaction time (Figure 20). Neat complexes **1** and **2** exhibited very poor conversion of 4.7 and 4.2%, respectively. Independently of the catalytic systems and conversions, the sulfoxide has been obtained selectively with TBHP.

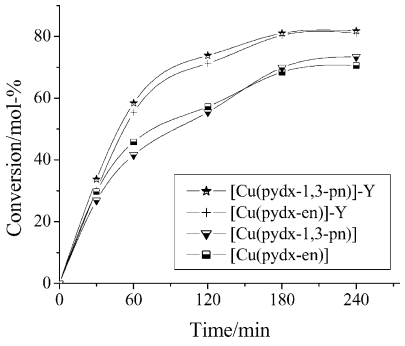


Figure 19. Oxidation of methyl phenyl sulfide by various catalysts using $H_2O_2$ as an oxidant.

Table 7. Conversion percentage of methyl phenyl sulfide in 3 h using $H_2O_2$ as an oxidant and selectivity of sulfoxide and sulfone.

| Catalyst | Conv. (%) | Product selectivity (%) 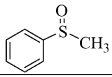 | 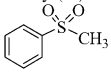 | TOF [$h^{-1}$] |
|---|---|---|---|---|
| [Cu(pydx-en)]-Y (**3**) | 80.3 | 63.34 | 36.66 | 622 |
| [Cu(pydx-1,3-pn)]-Y (**4**) | 81.0 | 53.59 | 46.41 | 662 |
| [Cu(pydx-en)] (**1**) | 68.4 | 39.87 | 60.13 | 530 |
| [Cu(pydx-1,3-pn)(MeOH)] (**2**) | 69.9 | 44.94 | 55.06 | 603 |

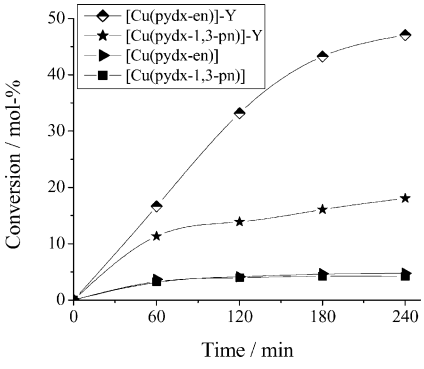


Figure 20. Oxidation of methyl phenyl sulfide by various catalysts using *tert*-butyl hydroperoxide as an oxidant.

### Test for Recyclability and Heterogeneity of the Reactions

The recyclability of both the encapsulated complexes has been tested in all three catalytic reactions. In a typical experiment, for example, for styrene, after a contact time of 6 h, the reaction mixture was filtered, and after activating the catalyst by washing with acetonitrile and drying at 120 °C, it was subjected to a further catalytic reaction under similar conditions. No appreciable loss in catalytic activity suggests that the complex is still present in the cavity of zeolite-Y. The filtrate collected after separating the used catalyst was placed in the reaction flask and the reaction was continued after adding fresh oxidant for another 4 h. The gas chromatographic analysis showed no improvement in conversion, and this confirms that the reaction did not proceed upon removal of the solid catalyst. The reaction was, therefore, heterogeneous in nature.

 © 2007 Wiley-VCH Verlag GmbH & Co. KGaA, Weinheim 

### Possible Reaction Pathway of the Catalysts

In order to better understand the reaction mechanism, the neat complexes were treated with $H_2O_2$ and the progress of the reaction was monitored by electronic absorption spectroscopy. Thus, titration of a solution of **1** (about $10^{-4}$ M) in methanol with one-drop portions of 30% $H_2O_2$ dissolved in methanol resulted in the spectral changes shown in Figure 21. The intensity of the band at 378 nm changes marginally, but the band at 277 nm increases considerably, while the band at 235 nm (not shown) continuously gains intensity. With a more concentrated solution (about $10^{-3}$ M) now dissolving complex **1** in DMSO, upon equivalent $H_2O_2$ additions the band appearing at 590 nm broadens with an increase in the intensity (Figure 21, inset). A very similar spectral pattern has also been observed for **2** (Figure 22). The data suggest the interaction of copper(II) complexes with $H_2O_2$.

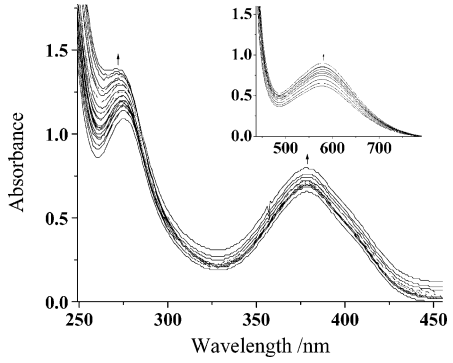


Figure 21. Titration of a methanol solution (about $10^{-4}$ M) of [Cu(pydx-en)] (**1**) with aqueous 30% $H_2O_2$ dissolved in methanol. The inset displays equivalent titrations, but with higher concentrations of **1** (about $10^{-3}$ M) dissolved in DMSO.

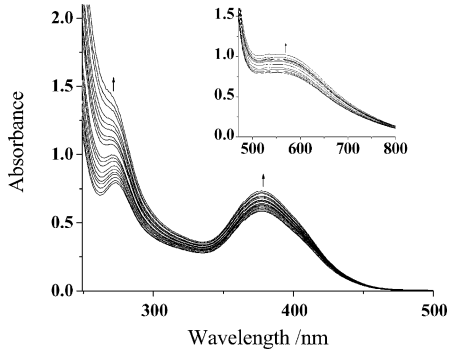


Figure 22. Titration of a methanol solution (about $10^{-4}$ M) of [Cu(pydx-1,3-pn)MeOH] (**2**) with aqueous 30% $H_2O_2$ dissolved in methanol. The inset displays equivalent titrations, but with higher concentrations of **2** (about $10^{-3}$ M) dissolved in DMSO.

At least three types of intermediates having a copper–oxygen interaction – side-on $Cu^{III}$–(μ-$\eta^2$-peroxido)–$Cu^{III}$, bis(μ-oxido–$Cu^{III}$) and $Cu^{III}$–O–O–H (copper hydroperoxide) – have been discussed in the literature during the catalytic action.[31,32] As copper complexes [Cu(pydx-en)] and [Cu(pydx-1,3-pn)] are monomeric in the cavity of zeolite, the facile formation of intermediates [(HOO)-Cu(pydx-en)] and [(HOO)-Cu(pydx-1,3-pn)], respectively, are expected because of the vacant available site in them (for example complex **3** was characterised in the solid state with a coordinated methanol molecule). This intermediate is expected to transfer the oxygen atoms to the substrates to obtain the products. Thus, the catalytic performance of the supported catalyst could be attributed to the facile formation of this Cu hydroperoxide intermediate species. The broadening of the band at about 590 nm indicates the merging of the d–d band with this charge-transfer band because of Cu hydroperoxide complex formation. In fact characteristic charge-transfer bands because of Cu hydroperoxide coordination are known to appear around 590 nm.[33]

Attempts to detect Cu hydroperoxide intermediates by ESI-MS (in the positive and negative modes) failed. The addition of $H_2O_2$ only increased the intensities of the peaks corresponding to $CuLH^+$ and $CuLNa^+$ (and $CuL{\cdot}2H^{2+}$ for larger amounts of $H_2O_2$) in the positive mode, but no peaks could be found in the negative mode that we could assign to Cu hydroperoxide intermediate species.

## Conclusions

Zeolite-Y-encapsulated copper(II) complexes [Cu(pydx-en)]-Y and [Cu(pydx-1,3-pn)]-Y with *N*,*N*′-ethylenebis(pyridoxyliminato) ($H_2$pydx-en) and *N*,*N*′-propylenebis(pyridoxyliminato) ($H_2$pydx-1,3-pn) ligands have been prepared. Neat complexes, [Cu(pydx-en)] and [Cu(pydx-1,3-pn)(MeOH)], have also been prepared with these ligands and characterised, and their crystal and molecular structures were determined, confirming the ONNO binding mode of the ligands. The encapsulated complexes catalyse the oxidation of styrene, cyclohexene and thioanisole efficiently, either using $H_2O_2$ or *tert*-butyl hydroperoxide as oxidants. Oxidation of styrene catalysed by [Cu(pydx-en)]-Y and [Cu(pydx-1,3-pn)]-Y gave 23.6% and 28.0% conversion, respectively, using TBHP as an oxidant. Using $H_2O_2$ as oxidant the major products were styrene oxide and benzaldehyde, while TBHP gave styrene oxide, benzaldehyde, benzoic acid and phenylacetaldehyde. Under the optimised conditions the maximum conversions obtained were 90.1% of cyclohexene, using [Cu(pydx-en)]-Y, and 83.0% using [Cu(pydx-1,3-pn)]-Y as catalyst; the major products identified were cyclohexene oxide, 2-cyclohexen-1-ol, cyclohexane-1,2-diol and 2-cyclohexen-1-one. Similarly, maximums of 80.3% conversion of methyl phenyl sulfide with [Cu(pydx-en)]-Y and of 81.0% with [Cu(pydx-1,3-pn)]-Y were observed, where the selectivity for the major product methyl phenyl sulfoxide was found to be about 60%. Tests for recyclability and heterogeneity of the reactions indicated their good recyclability. Of the alternative suggested mechanisms for catalysis, namely regarding the intermediates specifying the copper–oxygen interaction, our data suggest the involvement of $Cu^{III}$–O–O–H (copper hydroperoxide) intermediates.

 © 2007 Wiley-VCH Verlag GmbH & Co. KGaA, Weinheim 

## Experimental Section

**Materials:** Analytical reagent-grade pyridoxal hydrochloride (Hpydx·HCl, Himedia, Mumbai, India), methyl phenyl sulfide (Alfa Aeaser, USA), styrene, cyclohexene (Acros Organics, NJ, USA), cupric nitrate (E. Merck, Mumbai, India) and 30% aqueous $H_2O_2$ (Qualigens, Mumbai, India) were used as obtained. Y-zeolite (Si/Al = 10) was obtained from Indian Oil Corporation (R&D), Faridabad, India. All other chemicals and solvents used were of AR grade. Ligands $H_2$pydx-en (**I**) and $H_2$pydx-1,2-pn (**II**) were prepared as described in the literature.[15]

**Physical Methods and Analysis:** The copper content was measured using an inductively coupled plasma spectrometer (ICP; Labtam 8440 Plasmalab) after leaching the metal ions with conc. nitric acid and diluting with double-distilled water to specific volumes. IR spectra were recorded as KBr pellets with a Nicolet NEXUS Aligent 1100 series FTIR spectrophotometer, after grinding the sample with KBr. UV/Vis spectra of zeolite-encapsulated metal complexes were recorded in Nujol using a Shimadzu 1601 UV/Vis spectrophotometer by layering a mull sample to the inside of one of the cuvettes and keeping the other one layered with Nujol as reference. UV/Vis spectra of other ligands and neat complexes were recorded in methanol. X-ray powder diffractograms of solid catalysts were recorded using a Bruker AXS D8 advance X-ray powder diffractometer with a Cu-$K_\alpha$ target. Thermogravimetric analyses of pure as well as encapsulated complexes were carried out using a TG Stanton Redcroft STA 780 instrument. Scanning electron micrographs (SEM) of zeolite-containing samples were recorded with a Leo instrument, model 435VP. The samples were dusted on alumina and coated with a thin film of gold to prevent surface changing and to protect the surface material from thermal damage by the electron beam. In all analyses, a uniform thickness of about 0.1 mm was maintained. The energy-dispersive X-ray analysis (EDAX) plots of encapsulated complexes were recorded with an FEI Quanta 200 FEG instrument. The ESI-MS data were obtained with a Varian 500-MS LC ion-trap mass spectrometer operating either in the positive or in the negative mode. The EPR spectra were recorded with a Bruker ESP 300E X-band spectrometer. The spectra were measured at room temperature and at 77 K (with glasses, made by freezing solutions in liquid nitrogen, or just using the frozen samples). For the neat complexes we recorded spectra in DMF and in DMSO. In DMSO apparently there was precipitation of solids upon freezing, as only broad signals were obtained. The spin Hamiltonian parameters were obtained by simulation of the spectra with the computer program of Rockenbauer and Korecz.[34] All catalysed reaction products were analysed using a Thermoelectron gas chromatograph fitted with an HP-1 capillary column (30 m × 0.25 mm × 0.25 μm) and FID detector. Styrene, cyclohexene and methyl phenyl sulfide were used as external standards to quantify their conversion upon catalytic action. To quantify the conversion of styrene, for example, the calibration of the GC was carried out using styrene as external standard by injecting three different but known concentrations of styrene into the GC under the reaction conditions at which the analyses of catalytic products were performed and noting the peak area in each case. Finally, the peak area obtained for the remaining amount of styrene during catalytic oxidation was correlated with the peak area of the standard sample. This ultimately gave the percent conversion of substrate. The selectivity of products was then obtained directly from the peak areas of the respective products. Other external standards were used similarly. The identities of the products were confirmed by GC-MS with a Perkin–Elmer Clarus 500 model.

**X-ray Crystal Structure Determination:** Three-dimensional X-ray data were collected with a Bruker Kappa Apex CCD diffractometer by the $\phi$-$\omega$ scan method. Data were collected at room temperature. Reflections were measured from a hemisphere of data collected from frames each covering 0.3° in $\omega$. Of the 13687 reflections measured for **1** and 20715 for **2**, all of which were corrected for Lorentz and polarization effects, and for absorption by semiempirical methods based on symmetry-equivalent and repeated reflections, 2139 independent reflections for **1** and 8116 for **2** exceeded the significance level $|F|/\sigma(|F|) > 4.0$. Complex scattering factors were taken from the program package SHELXTL.[35] The structures were solved by direct methods and refined by full-matrix least-squares methods on $F^2$. The hydrogen atoms were included in calculated positions and refined by using a riding mode for **1** and were left to refine freely for **2**. Refinement converged with allowance for thermal anisotropy of all non-hydrogen atoms. Minimum and maximum final electron density: 2.494 and –2.167°e Å$^{-3}$ for **1**, 0.997 and –0.673°e Å$^{-3}$ for **2**. Crystal data and details on data collection and refinement are summarised in Table 8. CCDC-655305 (for **1**) and -655304 (for **2**) contain the supplementary crystallographic data for this paper. These data can be obtained free of charge from the Cambridge Crystallographic Data Centre via www.ccdc.cam.ac.uk/data_request/cif.

Table 8. Crystal data collection and refinement.

| | **1** | **2** |
|---|---|---|
| Empirical formula | $C_{18}H_{20}CuN_4O_4$ | $C_{20}H_{26}CuN_4O_5$ |
| $M_r$ [g mol$^{-1}$] | 419.92 | 465.99 |
| Crystal system | triclinic | triclinic |
| Space group | $P\bar{1}$ | $P\bar{1}$ |
| $T$ [K] | 293(2) | 293(2) |
| $a$ [Å] | 9.6664(17) | 8.0870(2) |
| $b$ [Å] | 10.0904(19) | 9.0492(2) |
| $c$ [Å] | 10.150(3) | 14.2599(3) |
| $\alpha$ [°] | 101.418(14) | 105.8640(10) |
| $\beta$ [°] | 93.432(14) | 90.9030(10) |
| $\gamma$ [°] | 116.898(9) | 95.5120(10) |
| $V$ [Å$^3$] | 852.7(4) | 998.20(4) |
| $F$(000) | 434 | 486 |
| $Z$ | 2 | 2 |
| $D_{calcd.}$ [g cm$^{-3}$] | 1.636 | 1.550 |
| $\mu$ [mm$^{-1}$] | 1.315 | 1.135 |
| $R_{int}$ | 0.0918 | 0.0334 |
| Measured reflections | 13687 | 20715 |
| Observed reflections | 2139 | 8116 |
| Data/restraints/parameters | 2975/3/248 | 10700/0/375 |
| Goodness-of-fit on $F^2$ | 1.093 | 1.029 |
| $R_1$[a] | 0.0918 | 0.0415 |
| $wR_2$[b] (all data) | 0.2713 | 0.1029 |

[a] $R_1 = \Sigma||F_o| - |F_c||/\Sigma|F_o|$. [b] $wR_2 = \{\Sigma[w(||F_o|^2 - |F_c|^2|)^2]|/\Sigma[w(F_o^4)]\}^{1/2}$.

### Preparations

**Preparation of [Cu(pydx-en)] (1):** A stirred solution of $H_2$pydx-en (0.717 g, 2 mmol) dissolved in methanol (20 mL) was added to cupric acetate (0.40 g, 2 mmol) dissolved in methanol (30 mL) with stirring, and the reaction mixture was refluxed in a water bath for 5 h. On reducing the solvent volume to about 20 mL and keeping the mixture at ambient temperature, a brown solid of [Cu(pydx-en)] slowly separated within a few hours. This was filtered off, washed with methanol and dried in vacuo over silica gel. Yield: 78%. Green crystals suitable for X-ray diffraction study were ob-

 © 2007 Wiley-VCH Verlag GmbH & Co. KGaA, Weinheim 

tained from the filtrate on slow concentration at room temperature. $C_{18}H_{20}CuN_4O_4$ [Cu(pydx-en)] (419.93): calcd. C 51.48, H 4.80, Cu 15.13, N 13.34; found C 52.0, H 4.6, Cu 15.1, N 13.1.

**Preparation of [Cu(pydx-1,3-pn)(MeOH)] (2):** [Cu(pydx-1,3-pn)(MeOH)] was prepared according to essentially the same procedure as for **1**. A green solid was obtained. Green crystals suitable for X-ray diffraction study were obtained from the filtrate on keeping it at room temperature for slow concentration. Yield: 70%. $C_{20}H_{26}CuN_4O_5$ [Cu(pydx-1,3-pn)(MeOH)] (466.0): calcd. C 51.55, H 5.62, Cu 13.64, N 12.02; found C 51.8, H 5.8, Cu 13.8, N 12.2.

**Preparation of Cu-Y:** Na-Y zeolite (5.0 g) was suspended in distilled water (300 mL) and after addition of cupric nitrate (2.26 g, 12 mmol), the reaction mixture was heated at 90 °C with stirring for 24 h. The pale bluish solid was filtered, washed with hot distilled water until the filtrate was free from any copper(II) ion content and dried at 150 °C in an air oven for 24 h. Found: Cu 7.60.

**Preparation of [Cu(pydx-en)]-Y (3):** Cu-Y (3.0 g) and $H_2$pydx-en (3.0 g) were mixed in methanol (50 mL), and the reaction mixture was heated under reflux in an oil bath with stirring for 14 h. The resulting material was filtered and then Soxhlet-extracted with methanol to remove unreacted ligand. It was finally treated with hot DMF while stirring for 1 h, filtered and washed with DMF followed by hot methanol. The uncomplexed metal ions present in the zeolite were removed by stirring with double-distilled aqueous NaCl (0.0.1 M, 150 mL) for 10 h. The resulting pale yellow solid was filtered, and washed with hot distilled water until no precipitate of AgCl was observed in the filtrate on treating with $AgNO_3$. Finally it was dried at 120 °C for several hours. Found: Cu 0.79.

**Preparation of [Cu(pydx-1,3-pn)]-Y (4):** The pale yellow [Cu(pydx-1,3-pn)]-Y was prepared according to essentially the same procedure as outlined for **3**. Found: Cu 0.74.

**Catalytic Activity**

**Oxidation of Styrene:** The catalytic oxidation of styrene was carried out in 50-mL flasks fitted with a water-circulated condenser. In a typical reaction, an aqueous solution of 30% $H_2O_2$ or 70% *tert*-butyl hydroperoxide (TBHP) (20 mmol) and styrene (1.04 g, 10 mmol) was mixed in acetonitrile (20 mL). After the temperature of the oil bath reached 80 °C, the zeolite-Y-encapsulated catalyst (0.025 g) was added to the reaction mixture which was continuously stirred. During the reaction, the products were periodically analysed using a gas chromatograph by withdrawing small aliquots, and their identities were confirmed by GC-MS. Various parameters, such as amounts of oxidant and catalyst as well as the temperature of the reaction mixture were studied in order to understand their effect on the conversion and patterns of the reaction products.

**Oxidation of Cyclohexene:** The catalytic oxidation of cyclohexene was also carried out using [Cu(pydx-en)]-Y and [Cu(pydx-1,3-pn)]-Y. Aqueous 30% $H_2O_2$ (2.28 g, 20 mmol), cyclohexene (0.82 g, 10 mmol) and catalyst (0.025 g) were mixed in acetonitrile (20 mL), and the reaction mixture was heated at 75 °C with continuous stirring in an oil bath. The progress of the reaction was monitored as mentioned above. The identification of the various products was confirmed by GC-MS.

**Oxidation of Methyl Phenyl Sulfide:** Aqueous 30% $H_2O_2$ (2.28 g, 20 mmol) and catalyst (0.025 g) were added to a solution of methyl phenyl sulfide (1.24 g, 10 mmol) dissolved in acetonitrile (20 mL), and the reaction mixture was stirred at ambient temperature for 3 h. The formation of the reaction products was monitored by GC.

**Measurement of UV/Vis Spectra by Adding $H_2O_2$:** A solution of complex **1** or **2** in methanol (ca. $10^{-4}$ M, 10 mL) was prepared and the UV spectra measured. A solution of $H_2O_2$ was prepared by dissolving five drops of 30% $H_2O_2$ in methanol (5 mL). One drop of this $H_2O_2$ solution was added and the UV spectra recorded again. Several similar additions were made, and after each addition the spectral changes were recorded similarly. As the solubility of complexes **1** or **2** is low in methanol, only the UV region could be covered in this way. For the visible region, the complexes were dissolved in DMSO (concentration about $10^{-3}$ M, 10 mL), and additions of the $H_2O_2$ solution were made similarly, now recording the visible region of the spectra (see insets of Figures 21 and 22).

## Acknowledgments

The authors are thankful to the Council of Scientific and Industrial Research, New Delhi for financial assistance. The authors also wish to thank FEDER, Fundação para a Ciência e a Tecnologia and POCI 2010 (ref. POCI/QUI/55985/2004) for financial support, and Kamila Koci for the ESI-MS experiments.

[1] J. Poltowicz, K. Pamin, E. Tabor, J. Haber, A. Adamski, Z. Sojka, *Appl. Catal. A* **2006**, *299*, 235–242.
[2] S. P. Verkey, C. Ratnasamy, P. Ratnasamy, *J. Mol. Catal. A* **1998**, *135*, 295–306.
[3] S. P. Verkey, C. Ratnasamy, P. Ratnasamy, *Microporous Mesoporous Mater.* **1998**, *22*, 465–474.
[4] S. P. Verkey, C. Ratnasamy, P. Ratnasamy, *Appl. Catal. A* **1999**, *182*, 91–96.
[5] S. Deshpande, D. Srinivas, P. Ratnasamy, *J. Catal.* **1999**, *188*, 261–269.
[6] D. Chatterjee, A. Mitra, *J. Mol. Catal. A* **1999**, *144*, 363–367.
[7] C. Bowers, P. K. Dutta, *J. Catal.* **1990**, *122*, 271–279.
[8] M. S. Niassary, F. Farzaneh, M. Ghandi, L. Turkian, *J. Mol. Catal. A* **2000**, *157*, 183–188.
[9] M. Silva, C. Freire, B. de Castro, J. L. Figueiredo, *J. Mol. Catal. A* **2006**, *258*, 327–333.
[10] T. Joseph, S. B. Halligudi, C. Satyanarayan, D. P. Sawant, S. Gopinathan, *J. Mol. Catal. A* **2001**, *168*, 87–97.
[11] M. R. Maurya, S. J. J. Titinchi, S. Chand, *Appl. Catal. A* **2002**, *228*, 177–187.
[12] M. R. Maurya, S. J. J. Titinchi, S. Chand, *J. Mol. Catal. A* **2003**, *201*, 119–130.
[13] M. R. Maurya, M. Kumar, S. J. J. Titinchi, H. S. Abbo, S. Chand, *Catal. Lett.* **2003**, *86*, 97–105.
[14] M. R. Maurya, A. K. Chandrakar, S. Chand, *J. Mol. Catal. A: Chem.* **2007**, *270*, 225–235.
[15] I. Correia, J. Costa Pessoa, M. T. Duarte, R. T. Henriques, M. F. M. Piedade, L. F. Veiros, T. Jackusch, A. Dornyei, T. Kiss, M. M. C. A. Castro, C. F. G. C. Geraldes, F. Avecilla, *Chem. Eur. J.* **2004**, *10*, 2301–2317.
[16] I. Correia, A. Dornyei, T. Jakusch, F. Avecilla, T. Kiss, J. Costa Pessoa, *Eur. J. Inorg. Chem.* **2006**, 2819–2830.
[17] I. Correia, A. Dornyei, T. Jakusch, F. Avecilla, T. Kiss, J. Costa Pessoa, *Eur. J. Inorg. Chem.* **2006**, 656–662.
[18] M. Valko, *Inorg. Chem.* **1993**, *32*, 4131–4138.
[19] H. Elias, *Angew. Chem. Int. Ed. Engl.* **1992**, *31*, 623–625.
[20] D. F. Evans, *J. Chem. Soc.* **1959**, 2003–2005.
[21] E. Sinn, A. B. Blake, W. Haussain, R. Paschke, J. R. Chipperfield, *Inorg. Chem.* **1995**, *34*, 1125–1129.
[22] J. Peisach, W. E. Blumberg, *Arch. Biochem. Biophys.* **1974**, *165*, 691–708.
[23] U. Sakaguchi, A. W. Addison, *J. Chem. Soc. Dalton Trans.* **1979**, 600–608.
[24] V. T. Kasumov, F. Koksal, *Spectrochim. Acta Part A* **2005**, *61*, 225–231.
[25] K. M. Ananth, M. Kanthimathi, B. U. Nair, *Transition Met. Chem.* **2001**, *26*, 333–338.
[26] V. Hulea, E. Dumitriu, *Appl. Catal. A* **2004**, *277*, 99–106.

 © 2007 Wiley-VCH Verlag GmbH & Co. KGaA, Weinheim 

[27] M. R. Maurya, U. Kumar, P. Manikandan, *Dalton Trans.* **2006**, 3561–3575.
[28] M. R. Maurya, U. Kumar, P. Manikandan, *Eur. J. Inorg. Chem.* **2007**, 2303–2314.
[29] A. Butler, M. J. Clague, G. E. Meister, *Chem. Rev.* **1994**, *94*, 625–638.
[30] M. R. Maurya, A. K. Chandrakar, S. Chand, *J. Mol. Catal. A: Chem.* **2007**, *263*, 227–237.
[31] E. I. Solomon, P. Chen, M. Metz, S.-K. Lee, A. E. Palner, *Angew. Chem. Int. Ed.* **2001**, *40*, 4570–4590.
[32] J. P. Klinman, *Chem. Rev.* **1996**, *96*, 2541–2561.
[33] K. D. Karlin, J. C. Hayes, Y. Gultneh, R. W. Cruse, J. W. McKown, J. P. Hutchinson, J. Zubieta, *J. Am. Chem. Soc.* **1984**, *106*, 2121–2128.
[34] A. Rockenbauer, L. Korecz, *Appl. Magn. Reson.* **1996**, *10*, 29–43.
[35] G. M. Sheldrick, *SHELXTL*, release 5.1, Bruker Analytical X-ray Systems, Madison, WI, **1997**.

Received: July 27, 2007
Published Online: November 8, 2007

 © 2007 Wiley-VCH Verlag GmbH & Co. KGaA, Weinheim 

DOI: 10.1002/ejic.200700060

# Red-to-Yellow Pressure-Induced Phase Transition in $Pt(bpy)Cl_2$: Spectroscopic Study Supported by DFT Calculations

**Rafael Valiente,*[a] Juan M. García-Lastra,[b] Pablo García-Fernández,[c] Sara García-Revilla,[d] and Oliver S. Wenger[e]**

**Keywords:** Phase transition / High-pressure chemistry / DFT calculations / Platinum(II) / Metal–metal interactions

The combination of spectroscopic and computational methods has been employed to explore the origin of the luminescence in the red and yellow forms of $Pt(bpy)Cl_2$. The luminescence of the red (linear-chain) form of $Pt(bpy)Cl_2$ (bpy = 2,2′-bipyridine) has been measured as a function of hydrostatic pressure up to 65 kbar. The luminescence band maximum is redshifted (–147 $cm^{-1}\,kbar^{-1}$), and the intrachain Pt–Pt distance decreases from 3.46 to 3.25 Å between ambient pressure and 17.7 kbar. Strong discontinuities in the optical properties at 17.7 kbar were interpreted in terms of a crystallographic phase transition from the red to a denser yellow form of $Pt(bpy)Cl_2$. First-principles calculations based on density functional theory were used to study the red to yellow phase transformation.
(© Wiley-VCH Verlag GmbH & Co. KGaA, 69451 Weinheim, Germany, 2007)

## Introduction

There is a continuing interest in the photophysical and chemical properties of $Pt^{II}$ complexes. The electronic structure of square-planar $Pt^{II}$ systems can be easily modified by ligand variation. Moreover, crystal packing has a strong effect on the nature of the lowest electronic states of these $d^8$ systems.[1] Optical spectroscopic studies are a particularly valuable technique for investigation of excited-state structures.[2] The anisotropic properties of the $Pt^{II}$ complexes in some solid-state structures indicate that stacking interactions can be used to tune the spectroscopic properties.[3–5]

Polymorphism in crystalline Pt(diimine) complexes is rather common. One example is $Pt(bpy)Cl_2$ (bpy = 2,2′-bipyridine), which has two types of stable crystal structures at room temperature:[5] a yellow form containing (more or less) isolated $Pt(bpy)Cl_2$ units and a red form in which there is Pt···Pt stacking. As a result, the electronic structures and, as a consequence, the optical spectroscopic properties are different in the two cases. Miskowski et al. as well as Gray et al. have found that the origin of the emissions from the yellow and red form are completely different even though the maximum of the emission bands are roughly the same at room temperature.[1,6] In the weakly luminescent yellow form, the $Pt^{II}$ complexes are spatially well separated from each other (the Pt–Pt distance is 4.44 Å), but in the strongly emitting red form the square-planar $Pt(bpy)Cl_2$ units stack to form an approximately linear Pt–Pt chain with a metal–metal spacing of 3.45 Å.[7] Previous investigations on $Pt^{II}$ linear-chain systems have shown that their electronic absorption and luminescence properties strongly depend on the intra-chain metal–metal separation.[4] Thus, modifications of the Pt–Pt distance induced by decreasing from room temperature (RT) to 20 K give rise to shifts of the luminescence band maximum of about 970 $cm^{-1}$ corresponding to an estimated reduction of the Pt–Pt distance by 0.08 Å.[7] However, the contribution of intrinsic and extrinsic temperature contributions to the emission band can be tricky to distinguish. The application of high pressure represents an extraordinary tool[2,8] that allows us to reduce the Pt–Pt distance in a continuous way. In this paper we will correlate the crystal and electronic structures by means of absorption and emission spectroscopy as well as density functional theory (DFT) calculations.

[a] Dept. de Física Aplicada, Facultad de Ciencias, Universidad de Cantabria,
Avda. de Los Castros s/n, 39005 Santander, Spain
Fax: +34-942-201402
E-mail: rafael.valiente@unican.es
[b] Dept. de Física de Materiales, Facultad de Químicas, Univ. del Pais Vasco,
20018 San Sebastián, Spain
[c] Institute for Theoretical Chemistry, Chemistry and Biochemistry Department, The University of Texas at Austin,
Texas 78712-0165, USA
[d] Dept. de Física Aplicada I, E.T.S. Ingenieros Industriales y Telecomunicaciones, Universidad del País Vasco,
48013 Bilbao, Spain
[e] Dept. of Inorganic, Analytical and Applied Chemistry, Faculty of Science, University of Geneva,
1211 Geneva, Switzerland

## Results and Discussion

In Figure 1 the RT luminescence spectra of $Pt(bpy)Cl_2$ at ambient pressure, 4.7, 12.1, 17.7, and 38.0 kbar (from bottom to top) after excitation at 22260 $cm^{-1}$ are shown. Within the square-planar symmetry the ambient-pressure luminescence band is assigned to the $\pi^*(bpy) \rightarrow d\sigma^*(Pt)$

 © 2007 Wiley-VCH Verlag GmbH & Co. KGaA, Weinheim 

luminescence transition (Figure 1).[7] The excitation spectrum at 16535 $cm^{-1}$ under the same conditions has also been obtained. The low-energy band responsible for the absorption edge was assigned to the $d\sigma^*(Pt) \rightarrow \pi^*$ (bpy) transition.[9] The required small crystal size precluded the measurement of a high-quality optical absorption spectrum even under ambient-pressure conditions.

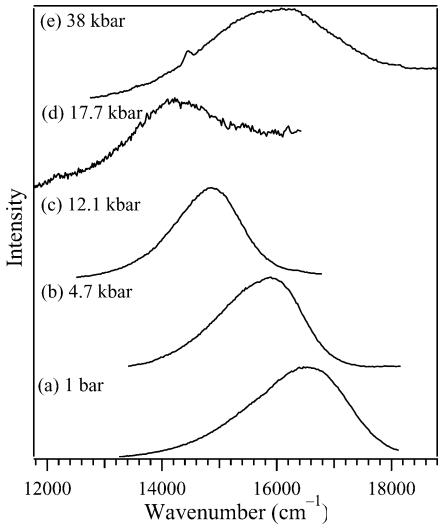


Figure 1. Room-temperature pressure dependence of the luminescence spectra of the red form of $Pt(bpy)Cl_2$.

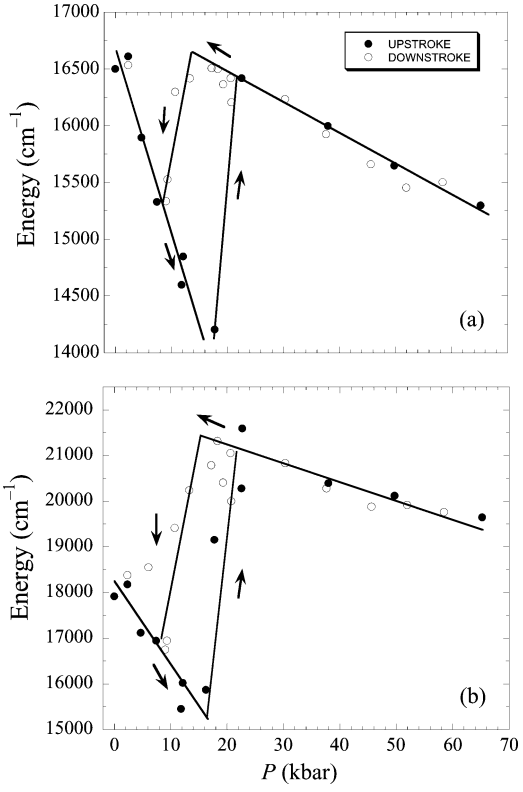


Figure 2. (a) Energy of the luminescence band maximum of the red form as a function of pressure; full circles correspond to increasing-pressure experiments and open circles to release-pressure experiments. (b) Energy of the excitation edge of the red form as a function of pressure; full circles correspond to increasing-pressure experiments and open circles to release-pressure experiments.

Figure 2 displays the pressure dependence of the emission-band maximum (a) as well as the absorption-edge energy in the excitation spectra (b) at RT. A shift to lower energies of the emission-band maximum and absorption edge is observed upon increasing the pressure from 1 bar to 17.7 kbar. At pressures higher than 17.7 kbar an abrupt blueshift is detected. Above this pressure a significant luminescence intensity decrease is observed. Moreover, the emission band broadens and the shape of the excitation spectrum alters. A change of the crystal color from orange to yellowish is observable when applying pressures larger than 17.7 kbar. Up to this pressure, the emission shift rate is –147 $cm^{-1}\,kbar^{-1}$. A similar pressure-dependent redshift of –99 $cm^{-1}\,kbar^{-1}$ was observed for crystalline $[Pt(SCN)_2\{\mu\text{-}(SCN)Mn(NCS)(bipy)_2\}_2]$.[10] Above 20 kbar the energy-band maximum is redshifted with a rate of –27 $cm^{-1}\,kbar^{-1}$ (Figure 2a). The solid lines are linear regression fits to the experimental data. Similar pressure behavior is observed for the absorption-edge energy in the excitation spectra (Figure 2b).

## Crystal and Electronic Structures of the Red and Yellow Forms at Ambient Pressure

The red form of $Pt(bpy)Cl_2$ crystallizes in the *Cmcm* orthorhombic space group where the units exhibit a parallel linear chain structure along the *c* axis.[7] The space between adjacent complexes within the chain is 3.45 Å. To avoid ligand interaction the neighboring complexes are alternatively rotated by 180° within the chain (Figure 3). Moreover, the $Pt^{II}$ atoms are somewhat displaced with respect to the *c* axis in a slight zigzag structure (ca. 161°). Angles and distances within the $Pt(bpy)Cl_2$ complex in the red form are similar to those in the yellow form, indicating that interaction between complexes in the red form does not perturb the molecular structure (Figure 4). In the yellow form, the distance between $Pt^{II}$ nearest neighbors is 4.44 Å.[11] In Table 1 we compare the experimental angles and distances in the yellow and red forms with those obtained after geometric optimization calculations. The large Pt–Pt distance in the yellow form clearly indicates the absence of any metal–metal interactions, allowing us to consider the molecular units as isolated monomers.

The symmetry of the $Pt(bpy)Cl_2$ complex is $C_{2v}$. A molecular orbital diagram of an isolated complex of this type is shown in Figure 5a. The interaction between complexes along the *z*-axis induces substantial changes in the electronic structure (see Figure 5). Within a dimer model, the $d_{z^2}$ orbital is strongly destabilized. The overlap of the $d_{z^2}$ orbitals of adjacent $Pt^{II}$ atoms leads to bonding $d\sigma$ and antibonding $d\sigma^*$ orbitals both of which are fully occupied (Figure 5b).[1]

Below a critical Pt–Pt distance, the highest occupied molecular orbital (HOMO) is $d\sigma^*$. Thus, the room-temperature luminescence of the red form of $Pt(bpy)Cl_2$ originates

 © 2007 Wiley-VCH Verlag GmbH & Co. KGaA, Weinheim 

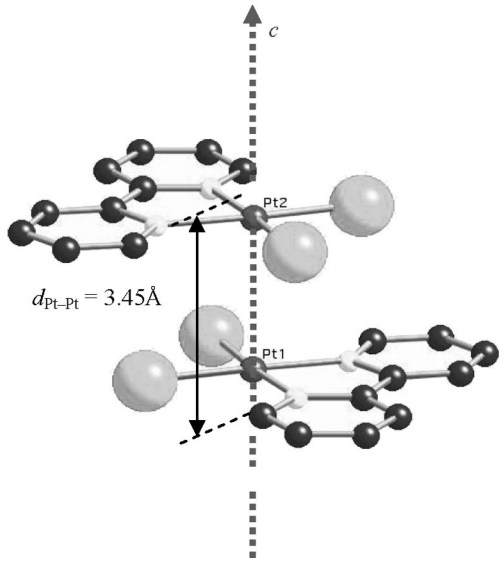


Figure 3. Perspective drawing of the dimer structure of Pt(bpy)$Cl_2$.

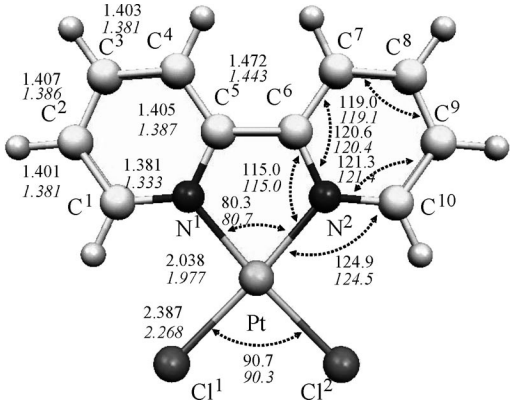


Figure 4. Geometry of the Pt(bpy)$Cl_2$ monomer as obtained through B3LYP/lanl2dz (top numbers) and LDA/tzp (bottom, italic numbers). Distances are given in Å and angles in °.

Table 1. Comparison between the available experimental geometry information on the yellow and red forms of Pt(bpy)$Cl_2$ and the calculations presented in this paper. Distances are given in Å and angles in °.

| Parameter | Monomer B3LYP | Monomer BLYP | Monomer LDA | Yellow form[28] | Red form[27] |
|---|---|---|---|---|---|
| Pt–Cl | 2.387 | 2.347 | 2.268 | 2.281–2.300 | 2.306 |
| Pt–N | 2.038 | 2.050 | 1.977 | 2.006–2.011 | 2.001 |
| $C^5$–$C^6$ | 1.472 | 1.469 | 1.443 | 1.462 | 1.51 |
| $Cl^1$–Pt–$Cl^2$ | 90.7 | 90.2 | 90.3 | 89.1 | 88 |
| $Cl^1$–Pt–$N^1$ | 94.5 | 95.1 | 94.5 | 94.3–96 | 96 |
| $Cl^2$–Pt–$N^1$ | 174.8 | 174.7 | 175.2 | 174.7–175.9 | 184 |
| $N^1$–Pt–$N^2$ | 80.3 | 79.6 | 80.7 | – | 80 |

from a $^3$MLCT state and is associated with the π*(bpy) → dσ*(Pt) charge-transfer transition, i.e. the LUMO π* orbital is mainly centered on the bipyridine ligand. This is in contrast to the tetracyanidoplatinates, where the luminescence is due to a pσ*(Pt) → dσ*(Pt) transition.[12]

Under ambient-pressure conditions the luminescence of the red form of Pt(bpy)$Cl_2$ consists of an asymmetric band

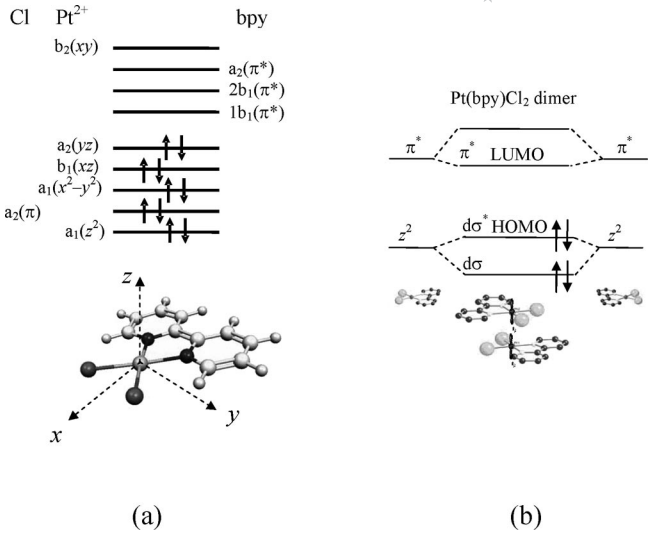


Figure 5. (a) Diagram of the frontier orbitals of the Pt(bpy)$Cl_2$ monomer and scheme showing the axis set chosen in the calculation. (b) Simplified energy-level scheme for the dimer model of Pt(bpy)$Cl_2$.

at 16535 $cm^{-1}$ associated with the π*(bpy) → dσ*(Pt) transition (Figure 1). The excitation spectrum of the 16535 $cm^{-1}$ luminescence is characterized by an excitation edge and a set of overlapping bands. It is similar to the polarized absorption spectrum of the red form of Pt(bpy)$Cl_2$ with $\mathbf{E}\perp\mathbf{c}$.[9] The temperature dependence of the emission spectrum of the red form showed a shift to lower energies. The observed behavior is due to the reduction of the Pt–Pt distance within the chain, which induces an increase in the splitting between dσ and dσ* orbitals and a reduction of the HOMO–LUMO energy gap. Gray et al. carried out temperature-dependent X-ray diffraction and luminescence experiments on the red form of Pt(bpy)$Cl_2$.[7] With decreasing temperature, the compound contracts anisotropically, the Pt–Pt separation decreases to 3.37 Å at 20 K, and this is accompanied by a –970 $cm^{-1}$ redshift of the emission-band maximum. This result reveals the following relation between the luminescence maximum $\nu_{max}$ and the Pt–Pt distance $R$ ($\nu_{max}$ and $R$ are in units of $cm^{-1}$ and Å, respectively) [Equation (1)].[7]

$$\nu_{max} = 29500 - 5.4\times10^5 R^{-3} \quad (1)$$

Considering that the implicit temperature term is negligible, it is possible to use this equation to calculate the pressure-dependent distance reduction.

## High-Pressure Measurements and DFT Calculations

Recently, we have explored the role of the intermolecular stacking interaction by tuning the spectroscopic properties of the linear Pt–Pt chains as a function of hydrostatic pressure.[13] In view of the lack of experimental high-pressure crystal structures, we assume the validity of Equation (1) for evaluating the Pt–Pt distance reduction upon pressure in the red form. Under this assumption we estimate that the

 © 2007 Wiley-VCH Verlag GmbH & Co. KGaA, Weinheim 

Pt–Pt distance decreases from 3.46 Å at ambient pressure to 3.25 Å at 17.7 kbar. Our calculations suggest that pressure destabilizes the dσ* HOMO, but the bpy π* LUMO energy is only weakly pressure-dependent (Figure 6). Experimentally, as pressure is increased above 17.7 kbar, abrupt blue-shifts of 2500 $cm^{-1}$ and 2880 $cm^{-1}$ in the luminescence and excitation spectra (Figures 1 and 2) are observed. Our results indicated that this phase transition is likely due to the conversion of the red modification of $Pt(bpy)Cl_2$ to a high-pressure denser yellow form (HPYF), not necessarily the same yellow form observed at ambient pressure (APYF). There is no crystallographic data available for this new yellow form. Phase transitions induced by pressure have been reported previously for several $Pt(CN)_4^{2-}$ systems.[4] Some tetracyanidoplatinates exhibit similarly strong emission discontinuities due to first-order phase transitions that occur upon cooling to cryogenic temperatures.[4] Red $Pt(bpy)Cl_2$ does not undergo any phase transition even when cooled to 20 K.[7] Since the emission intensity of the APYF is much weaker than that of the red form, it has been proposed that APYF is a $^3$LF emitter.[6] The same argument could reasonably be applied for the HPYF, whose emission is also much weaker than that of the red form. Because of the similarity of the HPYF and APYF emissions and the densities of the red form and the APYF (2.56 and 2.65 $g\,cm^{-3}$, respectively), it could be thought that HPYF and APYF are the same phase. The emission maxima of $Pt^{II}$ $^3$LF states exhibit comparatively weak pressure dependences, with typical shift rates in the order of 10–40 $cm^{-1}\,kbar^{-1}$.[14] From our system, we find a shift rate of $d\nu_{max}/dP = -27\ cm^{-1}\,kbar^{-1}$ (Figure 2a), and a high-pressure emission bandwidth (FWHM) of 3065 $cm^{-1}$, close to the value of 4030 $cm^{-1}$ found for the emission bandwidth in yellow $Pt(bpy)Cl_2$ at 250 K at ambient pressure.[6] A somewhat narrower luminescence bandwidth at elevated pressures is to be expected, owing to diminished relative distortions of the emissive and ground states.[2,15] The same effect accounts for the narrower bandwidth associated with the 12 kbar luminescence of red $Pt(bpy)Cl_2$ (Figure 1c) relative to that observed in the ambient-pressure spectrum (Figure 1a). Finally, the order-of-magnitude decrease in luminescence intensity accompanying the phase transition at 17.7 kbar is also consistent with a change from red to yellow $Pt(bpy)Cl_2$, i.e. a change from charge transfer to ligand-field luminescence transitions. The room-temperature ambient pressure luminescence quantum yields of microcrystalline samples of these two compounds are known to differ by more than an order of magnitude.[5] Pressure-dependent excitation spectra confirm our interpretation of the crystallographic phase transition at 17.7 kbar: between 12 and 23 kbar the absorption edge shifts discontinuously from 15000 to 20325 $cm^{-1}$ (Figure 2b).

The character and reversibility of the phase transition was highlighted by the luminescence spectra as well as the excitation spectra recorded upon increasing and releasing pressure. Figure 2 shows that upon pressure release, the yellow-to-red phase transformation only occurs at 11.0 kbar. Therefore, there is a hysteresis in the luminescence properties of $Pt(bpy)Cl_2$ of about 8 kbar. The presence of this hysteresis indicates that HPYF and APYF are different phases. In the 11.0–17.7 kbar range, depending on the pressure history, the luminescence originates in the $^3$MLCT or in the $^3$LF state.

In our calculations, the long Pt–Pt distance and the similarities in geometry between the $Pt(bpy)Cl_2$ monomer units in the two modifications allow us to simulate the yellow form using a single in-vacuo monomer, while the red form is obtained by stacking two (dimer) or three (trimer) $Pt(bpy)Cl_2$ units. In this model, the effect of applying hydrostatic pressure is simulated by varying the Pt–Pt distance $R$.

The monomer geometry was first optimized at the B3LYP/lanl2dz level imposing $C_{2v}$ symmetry. The result of this calculation is summarized in Figure 4 (plain numbers), and a comparison with available experimental data[11] is shown in Table 1. The agreement between them is very good

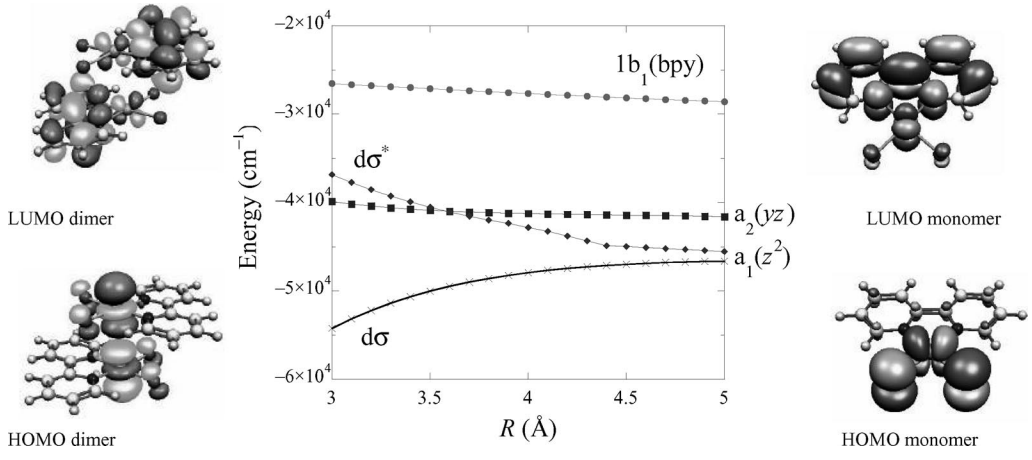


Figure 6. Variation of selected orbital energies of the $Pt(bpy)Cl_2$ dimer with the interlayer distance. Labels corresponding to the orbitals in the yellow and red form are shown on the right and left part of the plot, respectively. The antibonding dσ* orbital becomes the HOMO for $R$ values smaller than 3.6 Å after crossing with $a_2(yz)$, which corresponds to the HOMO in the monomer (yellow phase), reducing the HOMO–LUMO gap as $R$ is decreased.

 © 2007 Wiley-VCH Verlag GmbH & Co. KGaA, Weinheim 

with the exception of the Pt–Cl distance which is 0.08 Å longer in the calculations. A second optimization was carried out at the LDA/tzp level (italic numbers in Figure 4). In this case the Pt–Cl distance is in better agreement with experimental findings (see Table 1). In order to find the source of this error in the calculation we performed an LDA/lan2dz optimization that resulted in an overestimation of the Pt–Cl distance. Thus, we conclude that the longer distances found in these calculations are due to the basis set, possibly because the core–core interactions between the pseudopotentials found in the lanl2dz basis set are overestimated. This argument is supported by a BLYP/tzp level calculation (with exactly the same basis set as LDA/tzp). This resulted in a monomer geometry (Table 1) that is very close to the one calculated with LDA/tzp. As the agreement between the LDA/tzp geometries with those of the experiments is good (see Table 1), we use this geometry throughout this section to represent the monomer.

The symmetry, spacing, and character of the most important orbitals of Pt(bpy)$Cl_2$ as calculated in LDA are shown in Table 2 and Figure 5a, similar results were found when using B3LYP and BLYP.

Table 2. Energy and character of the most important orbitals of the Pt(bpy)$Cl_2$ monomer as obtained in LDA/tzp.

| Orbital | Energy [$cm^{-1}$] | Orbital character [%] Pt | Cl | bpy |
|---|---|---|---|---|
| | Unoccupied | | | |
| $b_2(xy)$ | 20810 | 46 | 34 | 20 |
| $a_2$ | 20485 | 2 | 0 | 98 |
| $2b_1$ | 18550 | 2 | 0 | 98 |
| $1b_1$ | 12420 | 4 | 0 | 96 |
| | Occupied | | | |
| $a_2(yz)$ | 0 | 27 | 70 | 3 |
| $b_1(xz)$ | –1050 | 31 | 64 | 5 |
| $a_1(x^2–y^2)$ | –2660 | 34 | 65 | 1 |
| $b_2$ | –3950 | 2 | 95 | 3 |
| $a_1(z^2)$ | –4030 | 84 | 12 | 4 |

According to Figure 5 and Table 2, the three occupied orbitals with highest energy, $a_2(yz)$, $b_1(xz)$, and $a_1(x^2–y^2)$, have a strong $Cl(p_\pi)$ character with very significant Pt(d) hybridization. The electrons in the lowest frontier orbital, $a_1(z^2)$, lie almost completely on the Pt ion and are perpendicular to the plane of the molecule. The LUMO and the next two orbitals above it are localized on the bpy ligand and have a strong π* character. The first unoccupied orbital mainly belonging to the $PtCl_2$ unit is $b_2(xy)$ which lies 20810 $cm^{-1}$ above the HOMO. These findings are similar to those reported for Pt(bpym)$Cl_2$.[16]

We have used the TD-B3LYP/lanl2dz method to calculate the low-lying excited states of the monomer. They are presented in Table 3 along with the estimation of the same transition energies by the ΔSCF method in LDA and BLYP. The reliability of these results is supported by the close agreement between the three different calculation methods. The energy of the most intense singlet-singlet transition, 21615 $cm^{-1}$, compares well with the position of the first peak in the absorption spectrum of the yellow form[17] lying at ca. 21000 $cm^{-1}$. This transition does not correspond to the HOMO–LUMO one, but it also has a strong dπ → π* character. The second most intense peak, $b_1(xz) \rightarrow 2b_1(\pi^*)$, $a_2(yz) \rightarrow a_2(\pi^*)$, is located at energies where the experimental spectrum presents another band. The emission spectrum of the yellow form is almost undetectable at RT.[5] For this reason and based on semiempirical extended Hückel calculations,[18] Miskowski et al.[19] proposed that the emission in the yellow form is due to a d-d $^3$LF transition.[6] In order to check this hypothesis we have performed a geometry optimization for the $^1B_1$ state [with the promoted electron in the $b_2(xy)$ orbital] and for the $^1B_2$ and $^1A_1$ states [with the promoted electron in the π*(bpy) orbital]. Results of these calculations are presented in Table 4. In the $^1B_1$ state the Pt–ligand distances increase very significantly with respect to those in the ground state: about 0.20 Å for Pt–N and 0.06 Å for Pt–Cl (Table 4). The ligand–Pt–ligand angles also change strongly. This fact leads to a large Stokes shift: the absorption $d\pi(Pt) \rightarrow b_2(xy)$ is at 22985 $cm^{-1}$, and the emission $b_2(xy) \rightarrow d\pi(Pt)$ is at 18145 $cm^{-1}$ (in the LDA calculations). In the case of $^1B_2$ and $^1A_1$ states, Pt–ligand distances and ligand–Pt–ligand angles hardly vary with respect to the ground state. However, an important reorganization takes place within bpy: the two pyridine rings approach each other; i.e. the $C^5$–$C^6$ distance is reduced by 5 pm. In the case of the $^1B_2$ excited state, this change in the bpy ligand produces an important Stokes shift, from 15890 $cm^{-1}$ in absorption to 14680 $cm^{-1}$ in emission. Since the calculated energy of the relaxed $^1B_2$ state is lower than the energy of $^1B_1$, in-vacuo single molecule DFT calculations predict that emission occurs from the first ($^1B_2$) state, in contrast to the experimental assignment by Miskowski et al. (in solution). In principle, the π*(bpy) → dπ(Pt) transition should have an emission intensity of the same order of magnitude as in the red form, because both seem to be predominantly $^3$MLCT. However, our theoretical calculations suggested that dπ(Pt) orbitals have a larger Cl(2p) character than Pt(d) ones (Table 1). In conclusion, the emission transition experimentally attributed to a π*(bpy) → dπ(Pt) transition[6] is likely to have mixed metal-to-ligand charge-transfer character with an important halide–ligand contribution.[16] This may well be the reason for its low intensity when compared to the red form where the HOMO is mostly a Pt($z^2$) orbital. Other experimental findings, like the lack of vibronic structure and large bandwidths, are also consistent with the variation of geometry of the $^1B_2$ excited state when compared to the ground state and provide further support for the assignment given here. A similar conclusion to the one reached here was presented in ref.[16] where this transition was assigned to a halide-to-ligand charge-transfer (XLCT). In that work the effect of solvents in the simulation was also checked, and it was found that the calculations reproduced well the experimental trends.

In the red form, the overlap between the $z^2$ orbitals on adjacent Pt atoms destabilized the dσ* dimer level. According to our calculations, the emission in the red form unambiguously comes from the π*(bpy) → σ*($z^2$, Pt) transition

 © 2007 Wiley-VCH Verlag GmbH & Co. KGaA, Weinheim 

Table 3. Description of some selected excited states of the Pt(bpy)-$Cl_2$ monomer as calculated by TD-B3LYP. Comparison with the energies obtained in LDA and BLYP by the ΔSCF method and absorption experiment. All energies are given in $cm^{-1}$.

| State | Main character | TD-B3LYP/lanl2dz | | BLYP | LDA | Exp.[17] |
|---|---|---|---|---|---|---|
| | | $\Delta E$ | Osc. str. | $\Delta E$ | $\Delta E$ | |
| $^1B_2$ | $a_2(yz) \rightarrow 1b_1$(bpy) | 17340 | 0.0004 | 16370 | 17100 | ca. 19030 |
| $^1A_1$ | $b_1(xz) \rightarrow 1b_1$(bpy) | 21615 | 0.0057 | 17825 | 18790 | ca. 20970 |
| $^1A_1$ | $b_1(xz) \rightarrow 2b_1$(bpy)<br>$a_2(yz) \rightarrow a_2$(bpy) | 26695 | 0.0017 | 25245 | 26290 | ca. 25000 |
| $^1B_1$ | $a_2(yz) \rightarrow b_2(xy)$ | 28790 | 0.0000 | 22015 | 27100 | – |

(Figure 5b), which has a clear $^3$MLCT nature, and therefore is very intense (see below).

We have simulated the red form of $Pt(bpy)Cl_2$ by stacking two and three monomers on top of each other. As in the case of the monomer, the LUMO in these molecules has bpy(π*) character (Figure 6). However, the HOMO is strongly localized on the Pt atom and has $z^2$ character. Calculating the HOMO–LUMO transition for the dimer and trimer using the experimental separation between Pt ions leads to 18630 and 15240 $cm^{-1}$ energy gaps. A similar behavior is observed in experiments where the red-form emission energy is lowered when pressure is applied.

In order to understand the changes between the dimer (red phase) and the monomer (yellow phase) we have plotted in Figure 6 the energies of some selected orbitals of the dimer as a function of interlayer distance $R$. The energies of the monomer HOMO, $a_2(xy)$, and LUMO are quite insensitive to the application of pressure. Moreover, the LUMO is the same for the monomer and the dimer. However, the energy of the dimer orbitals, which at long distance become the monomer $a_1(z^2)$ ones, are strongly split in a bonding (dσ) and antibonding pair (dσ*) when $R$ is reduced. A reduction of the Pt–Pt distance increases the $z^2$ interaction destabilizing the dσ* dimer level. In fact, the dσ* orbital becomes the HOMO for $R$ values smaller than 3.6 Å, i.e. dσ* must be the HOMO in the red form. From that point onwards the Pt–Pt distance decrease is accompanied by a continuous reduction of the HOMO–LUMO gap that explains the shift of the emission to lower energies of the red form when compared with the yellow one. We have calculated the rate at which the HOMO–LUMO transition energy in the dimer changes when $R$ is varied around $R$ = 3.45 Å by the ΔSCF method and obtained $dE_{H-L}/dR$ = 7900 $cm^{-1}$ $Å^{-1}$. Taking into account the value of the experimental linear compressibility, $\chi_c = 3.4 \times 10^{-3}$ $kbar^{-1}$,[13] we estimate a redshift of –93 $cm^{-1}$ $kbar^{-1}$ for the emission upon pressure. This value compares reasonably well with the experimental value of –147 $cm^{-1}$ $kbar^{-1}$ considering the limitations of our models. Because the arrangement of the monomers in HPYF is unknown, it has not been possible to study the pressure dependence of the luminescence for this phase.

In Figure 7 the variation of the total energy of the dimer and trimer with the Pt–Pt separation in LDA calculation is represented. In the dimer, this curve presents a minimum at $R$ = 3.28 Å, which is reasonably close to the experimental $R_0$ value of 3.45 Å. When three instead of two $Pt(bpy)Cl_2$ units are used, the optimum interlayer separation is slightly shifted to 3.38 Å, significantly closer to the experimental value. From Figure 7 we learn that the inter-monomer potential is very anharmonic indicating that if the dimer is compressed enough, electrostatic repulsion becomes the dominant effect and a geometry with two independent, noninteracting $Pt(bpy)Cl_2$ molecules will be favored.

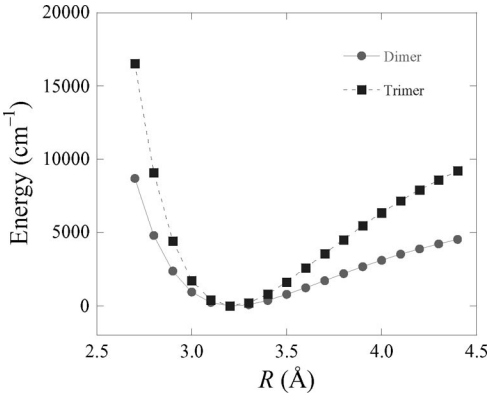


Figure 7. Total energy of the ground state of the $Pt(bpy)Cl_2$ dimer (circles) and trimer (squares) at the LDA/tzp level when the interlayer distance is varied.

Table 4. Description of the changes in the geometry of $^1A_1$, $^1B_2$, and $^1B_1$ with respect to the ground state for the same parameters as in Table 1. Positive values indicate an increase of the distances or angles with respect to the ground state. Distances are given in Å and angles in °. Energies obtained in LDA and BLYP calculations by the ΔSCF method for the emission and the corresponding Stokes shift are also shown. All energies are given in $cm^{-1}$.

| Parameter | $^1A_1[1b_1(bpy) \rightarrow b_1(xz)]$ | | $^1B_2[1b_1(bpy) \rightarrow a_2(yz)]$ | | $^1B_1[b_2(x^2–y^2) \rightarrow a_2(yz)]$ | |
|---|---|---|---|---|---|---|
| | Monomer BLYP | Monomer LDA | Monomer BLYP | Monomer LDA | Monomer BLYP | Monomer LDA |
| Pt–Cl | –0.005 | –0.003 | –0.012 | –0.012 | 0.069 | 0.063 |
| Pt–N | –0.002 | 0.004 | –0.006 | 0.002 | 0.227 | 0.180 |
| $C^5$–$C^6$ | –0.042 | –0.035 | –0.059 | –0.049 | 0.016 | 0.014 |
| $Cl^1$–Pt–$Cl^2$ | –1.9 | –1.9 | –0.5 | –0.6 | 8.7 | 7.0 |
| $Cl^1$–Pt–$N^1$ | 0.5 | 0.4 | –0.3 | –0.2 | –0.7 | –0.5 |
| $Cl^2$–Pt–$N^1$ | 1.5 | 1.5 | 0.8 | 0.8 | –8.0 | –6.5 |
| $N^1$–Pt–$N^2$ | 1.0 | 1.1 | 1.1 | 1.0 | –7.3 | –6.0 |
| Emission | 16050 | 17180 | 13630 | 14680 | 12740 | 18145 |
| Absorption | 16935 | 17985 | 15000 | 15890 | 17660 | 22985 |
| Stokes shift | 885 | 805 | 1370 | 1210 | 4920 | 4840 |

 © 2007 Wiley-VCH Verlag GmbH & Co. KGaA, Weinheim 

## Conclusions

We present a theoretical interpretation of the red-to-yellow phase transition experimentally observed in $Pt(bpy)Cl_2$ microcrystals at high pressures. Our theoretical models are based on isolated $Pt(bpy)Cl_2$ units (to simulate the yellow form) and dimer and trimer units of this complex to simulate the stacked, linear-chain red form. DFT calculations allow us to analyze the differences between red and yellow phases observed experimentally in terms of the Pt–Pt distance. The appearance of hysteresis in the optical properties most probably indicates that the new yellow phase observed at high pressure and the ambient-pressure yellow phase are distinct phases. The calculations suggest that the high-pressure luminescence corresponding to the high-pressure yellow phase is a halide–ligand transition instead of a ligand-field transition. This is a clear example where a synergy between experimental and theoretical work is essential for understanding high-pressure effects.

## Experimental Section and Computational Details

**Synthetic Procedure:** $Pt(bpy)Cl_2$ samples of the yellow form were prepared as described in refs.[13,17,20]

**Spectroscopic Measurements:** Hydrostatic-pressure experiments were carried out in a diamond-anvil cell (High Pressure Diamond Optics, Inc.) using spectroscopic paraffin as the pressure-transmitting medium. Excitation and luminescence spectra were performed with a Jobin–Yvon FluoroMax-2 fluorometer with a microscope attached. An optic fiber guided the emission light to the fluorometer detection system. All the spectra were corrected for instrumental response. A pre-indented aluminum gasket with a 300-μm diameter hole (machined with a Natjet microdrill) was used. The applied pressure was measured through the redshift luminescence of the ruby R-lines. Ruby luminescence was excited with the 407 nm line of a $Kr^+$ laser (Coherent CR-500K) and dispersed by a Jobin–Yvon U1000 double-monochromator.

**DFT Studies:** The geometry of the electronic ground state of a single $Pt(bpy)Cl_2$ unit has been obtained using DFT calculations through the semiempirical hybrid functional B3LYP[21,22] and the LANL2DZ basis set which includes pseudopotentials to represent the core electrons. Time-dependent DFT (TDDFT) was later used to explore the position and character of several excited states at this level of theory. All these calculations were constrained to keep $C_{2v}$ symmetry. The Gaussian 98[23] program suite was employed. As a complement to the previous calculations the geometry of a $Pt(bpy)Cl_2$ molecule and the electronic structure of the monomer, dimer, and trimer for different values of the Pt–Pt distance and Pt–Pt–Pt angle were also calculated using the ADF package.[24] Two types of calculations were performed: (a) Using the local density approximation (LDA) within the VWN parameterization of the electron correlation[25] and (b) using the generalized gradient approximation (GGA) exchange-correlation through the Becke[21] functional for exchange and Lee–Yang–Parr[26] functional for correlation (BLYP). In both cases relativistic effects have been taken into account through the Zeroth-Order Regular Approximation (ZORA),[27] which includes the Darwin and mass-velocity terms, but not the spin-orbit interaction. All atoms were described through basis sets of TZP quality (triple-ζ STO plus-one polarization function) given in the program data base and taking into account all electrons (without any frozen-core or pseudopotential approximations). Electronic transition calculations at this level of theory were performed with the ΔSCF method. In the case of absorption spectra the ΔSCF method consists of a geometry optimization for the ground state, yielding the corresponding $E_1$ energy. At the same geometry the electronic configuration of an excited state is imposed, and the SCF procedure is performed again, to obtain the corresponding $E_2$ energy. The energy difference, $E_2 - E_1$, is taken as the electronic transition energy. For the emission spectra the procedure is similar, but in this case the geometry optimization is performed imposing the electronic configuration of the excited state, and the energy of the ground state is then calculated at that geometry.

## Acknowledgments

This work was financially supported by the Spanish Ministerio de Educación y Ciencia under project no. MAT2005-00099. O. S. W. acknowledges funding from the Swiss National Science Foundation.

[1] W. B. Connick, V. M. Miskowski, V. H. Houlding, H. B. Gray, *Inorg. Chem.* **2000**, *39*, 2585–2592.
[2] O. S. Wenger, R. Valiente, H. U. Güdel, *J. Chem. Phys.* **2001**, *115*, 3819–3826.
[3] M. Kato, A. Omura, A. Toshikawa, S. Kishi, Y. Sugimoto, *Angew. Chem. Int. Ed.* **2002**, *41*, 3183–3185.
[4] G. Gliemann, H. Yersin, *Struct. Bonding (Berlin)* **1985**, *62*, 87–153.
[5] V. H. Houlding, V. M. Miskowski, *Coord. Chem. Rev.* **1991**, *111*, 145–152.
[6] V. M. Miskowski, V. H. Houlding, C. Che, Y. Wang, *Inorg. Chem.* **1993**, *32*, 2518–2524.
[7] W. B. Connick, L. M. Henling, R. E. Marsh, H. B. Gray, *Inorg. Chem.* **1996**, *35*, 6261–6265.
[8] a) C. Reber, J. K. Grey, E. Lanthier, K. A. Frantzen, *Inorg. Chem.* **2005**, *26*, 233–254; b) K. L. Bray, *Top. Curr. Chem.* **2001**, *213*, 1.
[9] M. Weiser-Wallfahrer, G. Gliemann, *Z. Naturforsch., Teil B* **1990**, *45*, 652–657.
[10] G. Levasseur-Thériault, C. Reber, C. Aronica, D. Luneau, *Inorg. Chem.* **2006**, *45*, 2379–2381.
[11] R. H. Herber, M. Croft, M. J. Coyer, B. Bilash, A. Sahiner, *Inorg. Chem.* **1994**, *33*, 2422–2426.
[12] a) H. Yersin, I. Hidvegi, G. Gliemann, *Phys. Rev. B* **1979**, *19*, 177–180; b) A. Loosli, M. Wermuth, H. U. Güdel, S. Capelli, J. Hauser, H. B. Bürgi, *Inorg. Chem.* **2000**, *39*, 2289–2293.
[13] O. S. Wenger, S. García-Revilla, H. U. Güdel, H. B. Gray, R. Valiente, *Chem. Phys. Lett.* **2004**, *384*, 190–192.
[14] M. A. Stroud, H. G. Drickamer, M. H. Zietlow, H. B. Gray, B. I. Swanson, *J. Am. Chem. Soc.* **1989**, *111*, 66–72.
[15] J. K. Grey, M. Triest, I. S. Butler, C. Reber, *J. Phys. Chem. A* **2001**, *105*, 6269–6272.
[16] W. Kaim, A. Dogan, M. Wanner, A. Klein, I. Tiritiris, T. Schleid, D. J. Stufkens, T. L. Snoeck, E. J. L. McInnes, J. Fiedler, S. Zalis, *Inorg. Chem.* **2002**, *41*, 4139.
[17] M. Textor, H. R. Oswald, *Z. Anorg. Allg. Chem.* **1974**, *407*, 244.
[18] H. H. Patterson, J. C. Tewksbury, M. Martin, M. B. Krogh-Jespersen, J. A. Lomenzo, H. O. Hooper, A. Kasi Viswanath, *Inorg. Chem.* **1981**, *20*, 2297–2301.
[19] V. M. Miskowski, V. H. Houlding, *Inorg. Chem.* **1989**, *28*, 1529–1533.
[20] G. T. Morgan, F. H. Burstall, *J. Chem. Soc.* **1934**, 965.
[21] A. D. Becke, *Phys. Rev. A* **1988**, *38*, 3098–3100.
[22] A. D. Becke, *J. Chem. Phys.* **1993**, *98*, 1372–1377.
[23] M. J. Frisch, G. W. Trucks, H. B. Schlegel, G. E. Scuseria, M. A. Robb, J. R. Cheeseman, V. G. Zakrzewski, J. A. Mont-

 © 2007 Wiley-VCH Verlag GmbH & Co. KGaA, Weinheim 

gomery, R. E. Stratmann, J. C. burant, S. Dapprich, J. M. Millam, A. D. Daniels, K. N. Kudin, M. C. Strain, O. Farkas, J. Tomasi, V. Barone, M. Cossi, R. Cammi, B. Mennucci, C. Pomelli, C. Adamo, S. Clifford, J. Ochterski, G. A. Petersson, P. Y. Ayala, Q. Cui, K. Morokuma, D. K. Malick, A. D. Rabuck, K. Raghavachari, J. B. Foresman, J. Cioslowski, J. V. Ortiz, B. B. Stefanov, G. Liu, A. Liashenko, P. Piskorz, I. Komaromi, R. Gomperts, R. L. Martin, D. J. Fox, T. Keith, M. A. Al-Laham, C. Y. Peng, A. Nanayakkara, C. Gonzalez, M. Challacombe, P. M. W. Gill, B. G. Johnson, W. Chen, M. W. Wong, J. L. Andres, M. Head-Gordon, E. S. Replogle, J. A. Pople *Gaussian 98*, Gaussian Inc., Pittsburgh, PA, **1998**.

[24] a) S. J. A. van Gisbergen, J. G. Snijders, E. J. Baerends, *Comput. Phys. Commun.* **1999**, *118*, 119–138; b) G. te Velde, F. M. Bickelhaupt, S. J. A. van Gisbergen, C. Fonseca Guerra, E. J. Baerends, J. G. Snijders, T. Ziegler, *J. Comput. Chem.* **2001**, *22*, 931–967.

[25] S. H. Vosko, L. Wilk, M. Nusair, *Can. J. Phys.* **1980**, *58*, 1200–1211.

[26] C. Lee, W. Yang, R. G. Parr, *Phys. Rev. B* **1988**, *37*, 785–789.

[27] E. van Lenthe, E. J. Baerends, J. G. Snijders, *J. Chem. Phys.* **1994**, *11*, 9783.

[28] R. S. Osborn, D. Rogers, *J. Chem. Soc. Dalton Trans.* **1974**, *9*, 1002–1004.

Received: January 17, 2007
Final Revision Received: September 28, 2007
Published Online: November 13, 2007

 © 2007 Wiley-VCH Verlag GmbH & Co. KGaA, Weinheim 

DOI: 10.1002/ejic.200700777

# The Relative Coordinating Ability of Some Weak O-Donor Anions and Water Towards the $[Pt(terpy)]^{2+}$ (terpy = 2,2′:6′,2′′-terpyridine) Center – X-ray Crystal Structures of $[Pt(terpy)(H_2O)](CF_3SO_3)_2$ and $[Pt_2(\mu\text{-}OH)(terpy)_2](PF_6)_2(CF_3SO_3)$

**Giuliano Annibale,*[a] Paola Bergamini,[b] Valerio Bertolasi,[b] Marco Bortoluzzi,[a] Michela Cattabriga,[b] and Bruno Pitteri[a]**

**Keywords:** Platinum / Bridging ligands / N ligands / O ligands

Acidolysis of the complexes $[Pt(CH_3)(terpy)]Y$ (Y = $PF_6$, $CH_3SO_3$, $CF_3SO_3$, $ClO_4$, $BF_4$; terpy = 2,2′:6′,2′′-terpyridine) with an equimolar amount of $CH_3SO_3$ in 2,2,2-trifluoroethanol (TFE) affords the corresponding methanesulfonato derivatives $[Pt(OSO_2CH_3)(terpy)]Y$. When Y = $NO_3$ a nearly equimolar mixture of the methanesulfonato and nitrato complexes is obtained, whereas the reaction of $[Pt(CH_3)(terpy)](CF_3SO_3)$ with triflic acid in either dry TFE or $CH_2Cl_2$ gives the aqua species $[Pt(terpy)(H_2O)](SO_3CF_3)_2$ (**8′**), whose X-ray crystal structure is reported. This structure shows hydrogen bonding between the coordinated water molecule and two triflate ions. $^1H$ NMR evidence is reported that suggests that this hydrogen bonding is partially retained in $CD_3NO_2$ solution. The new hydroxido-bridged dimers $[Pt_2(\mu\text{-}OH)(terpy)_2](X)$ [X = $(ClO_4)_3$, $(PF_6)_2(CF_3SO_3)$ (**12**)] have been isolated and their X-ray crystal structures determined.
(© Wiley-VCH Verlag GmbH & Co. KGaA, 69451 Weinheim, Germany, 2007)

## Introduction

Complexes of the transition metals containing weakly bonded anions (e.g. $BF_4^-$, $CF_3SO_3^-$, etc.) are of great importance in coordination and organometallic chemistry as they can serve as useful precursors for the preparation of a wide range of complexes, many of which have been shown to be active catalysts.[1] Some of the various routes used for their preparation have been reviewed by Beck.[2] Among these synthetic methods, the acidolysis of a metal–alkyl bond is of particular utility since it gives no by-products. We have successfully applied this route for the preparation of $[Pt(OSO_2CF_3)(triphos)](CF_3SO_3)$ {triphos = bis[2-(diphenylphosphanyl)ethyl](phenyl)phosphane} by treating $[Pt(CH_3)(triphos)](CF_3SO_3)$[3] or $[Pt(CH_3)_2(triphos\text{-}P,P')]$[4] with $CF_3SO_3H$. Both these reactions give the triflato complex cleanly and in high yield.

We reasoned that acidolysis of a cationic complex of the type $[M(CH_3)(L)]Y$ (L = terdentate ligand) with an acid HY′ could also be useful for establishing the relative coordinating ability of the two anions Y and Y′. We chose 2,2′:6,2′′-terpyridine (terpy) as the terdentate ligand to take advantage of our own experience in the chemistry of $Pt^{II}$,[5–7] and $Au^{III}$(terpy)[8] complexes as well as of the impressive amount of existing literature data, particularly papers by Romeo et al. dealing with the $[Pt(CH_3)(terpy)]^+$ cation.[9–11]

It is well known that a terpy ligand gives rise to extensive charge delocalization in an expanded π system when coordinated to a metal ion.[12,13] This results in a remarkable increase in the electrophilicity of the metal center, and we expected that this would favor the interaction with hard ligands such those we were dealing with here.

Herein we report the results of the acidolysis of the complexes $[Pt(CH_3)(terpy)]Y$ (Y = $PF_6$, $CH_3SO_3$, $CF_3SO_3$, $ClO_4$, $BF_4$, $NO_3$) by $CH_3SO_3H$ and $CF_3SO_3H$ (Y = $CF_3SO_3$). The crystal and molecular structures of the aqua species $[Pt(terpy)(H_2O)](CF_3SO_3)_2$ and of $[Pt_2(\mu\text{-}OH)(terpy)_2](PF_6)_2(CF_3SO_3)$, which have been isolated in the course of this work, are also reported.

## Results and Discussion

Some of the starting complexes of the type $[Pt(CH_3)(terpy)]Y$ were prepared as described by Romeo et al.,[9] whereas the others (Y = $NO_3$, $BF_4$, $CH_3SO_3$ and $CF_3SO_3$) were obtained by treating $[Pt(CH_3)(terpy)](Cl)$ with a stoichiometric amount of the appropriate silver salt. All of them were dried under vacuum at 100 °C over $P_2O_5$ for at least 2 h before treatment with the acid.

### Reactions of the Methyl Complexes with $CH_3SO_3H$

The reactions between equimolar quantities of the methyl complexes $[Pt(CH_3)(terpy)]Y$ [Y = $PF_6$ (**2**), $ClO_4$ (**3**),

[a] Dipartimento di Chimica, Università "Cà Foscari" di Venezia, Calle Larga S. Marta 2137, 30123 Venezia, Italy
[b] Dipartimento di Chimica e Centro di Strutturistica Difrattometrica, Università di Ferrara, via Borsari 46, 44100 Ferrara, Italy

 © 2007 Wiley-VCH Verlag GmbH & Co. KGaA, Weinheim 

$CF_3SO_3$ (**4**), $BF_4$ (**5**), $NO_3$ (**6**), $CH_3SO_3$ (**7**)] and $CH_3SO_3H$ proceed readily in 2,2,2-trifluoroethanol (TFE) solution (room temp., 1 h) to yield the corresponding acidolysis products **2′**–**7′** in 80–90% yield (see Experimental Section). All complexes were characterized by microanalysis and $^1H$ NMR and IR spectroscopy.

The $CH_3SO_3$ resonance in the $^1H$ NMR spectra ($CD_3NO_2$) of complexes [Pt($OSO_2CH_3$)(terpy)]Y (**2′**–**5′**) appears as a singlet at $\delta$ = 3.11 ppm, which is 0.64 ppm downfield from that observed in the methanesulfonate salt **7**. Resonances for both the coordinated and ionic methanesulfonate are present in the spectrum of complex **7′** in a 1:1 ratio. Hence, exchange between these two species, if any, is slow on the NMR timescale. Complexes **2′**, **3′**, **4′**, **5′**, and **7′** display the same spectrum, which is characterized by three groups of lines, in the aromatic region (terpy ligand). The most downfield-shifted signal at $\delta$ = 8.86 ppm, attributable to $H^6$, is a doublet coupled with $H^5$ ($^3J_{H,H}$ = 5.6 Hz) with satellite peaks due to $^{195}Pt$ coupling ($^3J_{Pt,H}$ = 32 Hz). The signal at $\delta$ = 7.98 ppm is a doublet of doublets assignable to $H^5$ ($^3J_{H,H}$ = 5.6 and 7.5 Hz; $^4J_{H,H}$ = 2.0 Hz). The remaining multiplets at $\delta$ = 8.59–8.34 ppm belong to the other aromatic ring protons. On the whole, the pattern here is very similar to that of the corresponding methyl complexes.

IR spectroscopy confirmed the identity of the complexes also in the solid state. This was best proved by comparing the spectrum of the methanesulfonate complex salt **7** with that of **2′**, whose $PF_6^-$ counterion, which absorbs at 848 $cm^{-1}$, is transparent across the whole $\nu(SO_3)$ region (1000–1300 $cm^{-1}$). Thus, while **7** exhibits two strong absorptions at 1193 and 1038 $cm^{-1}$, which are typical values for the $\nu(SO_3)$ mode in ionic sulfonates, **2′** shows three peaks at 1275, 1150, and 1100 $cm^{-1}$. This increase in the multiplicity is typical of methanesulfonato complexes and is a consequence of a lowering of the symmetry of the $SO_3$ group upon coordination.[14] The analytical data for the acidolysis reaction product when Y = $NO_3$ (**6′**) are in keeping with the molecular formulation [Pt(terpy)($CH_3SO_3$)($NO_3$)]. The IR spectrum of the compound in the range 1300–1000 $cm^{-1}$ is somewhat complex due to the overlapping of similar vibration bands for the $NO_3$ and $SO_3$ groups. However, bands arising from both ionic and coordinated anions appear to be present. Thus, the strong absorptions at 1519 and 1350 $cm^{-1}$ can be assigned to coordinated and ionic $NO_3^-$, respectively, and those at 1275 and 1150 $cm^{-1}$ to covalent methanesulfonate, while the two bands at 1203 and 1045 $cm^{-1}$ are characteristic absorptions of ionic $CH_3SO_3^-$.

The $^1H$ NMR spectrum ($CD_3NO_2$) of **6′** displays two singlets in a 1:1 ratio at $\delta$ = 3.11 and 2.47 ppm due to coordinated and ionic $CH_3SO_3^-$, respectively. The aromatic region is characterized by peaks characteristic of the species [Pt($OSO_2CH_3$)(terpy)]$^+$ and other resonances which, in view of the above findings, can be attributed to the terpy ligand in the cation [Pt($ONO_2$)(terpy)]$^+$. In particular, the doublet at $\delta$ = 8.58 ppm, which is not present in the $^1H$ NMR spectra of the methanesulfonato complexes, is attributable to the $H^6$ terpy protons of [Pt($ONO_2$)(terpy)]$^+$. We conclude from these observations that the acidolysis product **6′** is actually a nearly equimolar mixture of the methanesulfonato and nitrato complex salts. This, in turn, indicates that the two anions are of nearly equal coordinating ability toward the Pt(terpy) center, as is found for their basicity towards the proton.[15]

The acidolysis reactions of complexes **2**, **3**, **4**, and **7** with a stoichiometric amount of acid were monitored by $^1H$ NMR spectroscopy for $CD_3NO_2$ solutions (0.02 mmol of complex in 1 mL of $CD_3NO_2$). With the exception of complex **7**, all reactions went to completion in the time required for mixing the reagents. Surprisingly enough, **7** reacts with the acid very much more slowly: even at 40 °C it takes more than one week to go to about 90% conversion. Only the starting and final products are observed in the NMR spectra at any one time. A possible explanation for the above finding may be the formation of a hydrogen-bonded couple between the acid and its conjugate base in $CD_3NO_2$ solution, perhaps similar to that found between $HNO_3$ and $NO_3^-$,[16] in other words [$CH_3O_2SO\cdots H\cdots OSO_2CH_3$]$^-$. Such an interaction is unlikely to exist in the protic solvent TFE, which is why there is no difference in reactivity between **7** and the other methyl complexes.

### Reactions of 4 with $CF_3SO_3H$

The reaction of [Pt(terpy)($CH_3$)]($CF_3SO_3$) with a stoichiometric amount of triflic acid in either TFE or $CH_2Cl_2$ gives a compound (**8′**) whose analytical data indicate the presence of water, which was not lost on heating the compound at 100 °C under vacuum over $P_2O_5$ for several hours. Repeated and careful attempts to rigorously exclude water during the preparations failed. Since the IR and NMR spectroscopic data were not conclusive, an X-ray diffraction structural study of the compound was deemed necessary. This showed the compound is actually the aqua species [Pt(terpy)($OH_2$)]($CF_3SO_3$)$_2$. This was a rather unexpected result, especially for the reaction conducted in $CH_2Cl_2$ since, as mentioned in the Introduction, we have previously found the same procedure to give the triflato complexes in the triphos and triphos-*P*,*P′* cases.

#### *Structure of [Pt(terpy)($H_2O$)]($CF_3SO_3$)$_2$ (8′)*

An ORTEP[17] view of [Pt(terpy)($H_2O$)]($CF_3SO_3$)$_2$ (**8′**) is shown in Figure 1. The coordination geometry around the platinum atom is distorted square-planar due to the constraints of the terpyridine ligand, which gives rise to a narrowing of N–Pt–N(*cis*) angles to 81.4(2)° and 81.8(2)°. These distortions are associated with a significant shortening of the Pt–N2 distance [1.914(4) Å] with respect to the Pt–N1 and Pt–N3 ones [2.021(5) and 2.009(4) Å, respectively], in agreement with the geometries observed in similar complexes of $Pt^{II}$ with ter- or tetradentate ligands.[18–23] The three coordinated terpy nitrogen atoms, the platinum atom, and the water oxygen atom lie approximately in the same plane with maximum deviations from this plane for O1 of 0.033(5) Å and for N2 of 0.025(5) Å. The water molecule is located in a plane nearly perpendicular [84(5)°] to the Pt1

 © 2007 Wiley-VCH Verlag GmbH & Co. KGaA, Weinheim 

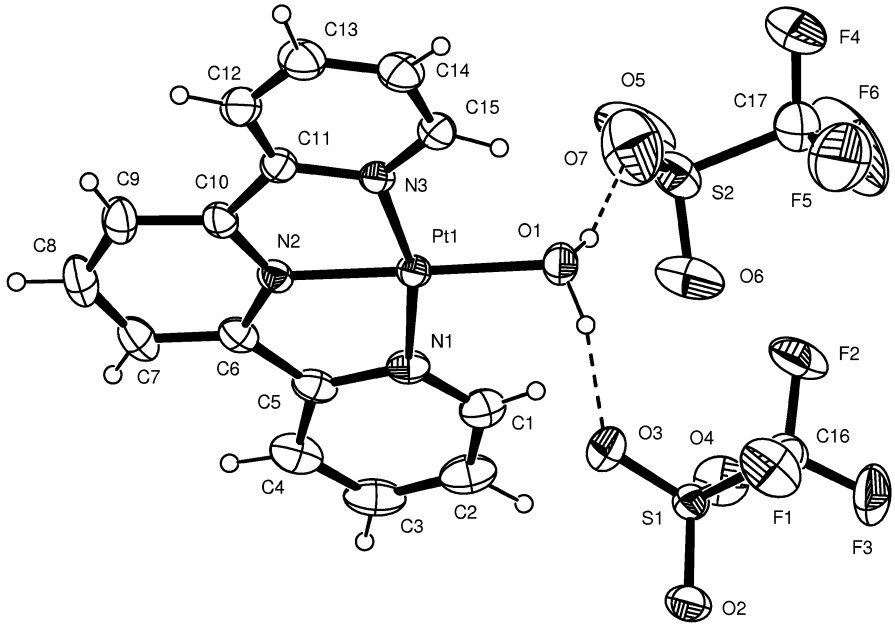


Figure 1. ORTEP view of $[Pt(terpy)(H_2O)](CF_3SO_3)_2$ displaying thermal ellipsoids at 30% probability. The dotted lines indicate hydrogen bonds.

basal plane and is linked to the oxygen atoms of two triflate anions by hydrogen bonds. The Pt–$OH_2$ distance [2.040(5) Å] compares well with the distances observed in $Pt^{II}$ square-planar complexes where a water molecule is *trans* to a nitrogen atom (range: 2.05–2.10 Å).[24] No stacking interactions between parallel molecular planes shorter than the sum of the van der Waals radii are observed.

### *IR and $^1$H NMR Spectroscopic Studies of the Aqua Complex $[Pt(terpy)(H_2O)](CF_3SO_3)_2$ (8′)*

The IR spectrum of complex **8′** shows three strong absorptions in the $\nu(SO_3)$ region at 1166, 1235, and 1290 $cm^{-1}$. In light of the structural results, this increase in multiplicity of the $\nu(SO_3)$ mode can now be straightforwardly ascribed to the lowering of the symmetry of the $SO_3$ group due to hydrogen bonding with the coordinated water molecule. It should be noted that an increase in multiplicity would also be expected if the triflate ion were coordinated to the metal center, although the splitting here is somewhat smaller than in the triphos and triphos-*P,P′* triflate complexes.[3,4]

We isolated the aqua complex as its perchlorate salt $[Pt(terpy)(H_2O)](ClO_4)_2$ (**10**) after treating the corresponding salt of the methyl complex with an excess of perchloric acid in TFE. The $^1$H NMR spectra of complexes **8′** and **10** in $CD_3NO_2$ solution are shown in Figure 2 (**8′**: spectrum A; **10**: spectrum C). In contrast to spectrum C, there are two doublets in the terpy-$H^6$ region of spectrum A, at $\delta$ = 8.76 and 8.67 ppm, both with a $^3J_{H,H}$ coupling constant of 5.6 Hz. Addition of lithium triflate to the solution of **10** causes an increase of the doublet at $\delta$ = 8.67 ppm and a corresponding decrease of the one at $\delta$ = 8.76 ppm (Figure 2, spectrum B).

The following further observations were made:
(i) The $^1$H spectrum of $[Pt(H_2O)(terpy)](SO_3CF_3)_2$ (**8′**) after saturation of the $CD_3NO_2$ solution with $LiClO_4$ becomes identical to that of the perchlorate derivative **10**.
(ii) The addition of increasing amounts of lithium triflate to the solution of **8′** causes an increase of the upfield doublet and a corresponding decrease in the downfield one. However, even on saturating the solution with the triflate salt, the downfield doublet can still be observed.

Among the possible explanations we considered for the above results, we can definitively rule out the formation of ion pairs (without hydrogen bonding) and/or dimerization/oligomerization through stacking interactions, which are known to affect the NMR spectra of some Pt(terpyridine) complexes.[9] We have never found evidence for stacking in nitromethane solutions for either monocationic methyl or methanesulfonato complexes. Moreover, this should be even more disfavored for a dicationic species such as the aqua complex. The $^1$H NMR spectrum of the similarly charged species $[Pt(CH_3CN)(terpy)]^{2+}$, which we have isolated as the triflate salt (see Experimental Section), does not show any tendency to undergo ion pairing in $CD_3NO_2$ solution.

A more likely explanation for the NMR spectra of derivatives **8′** and **10** and their behavior towards salt addition, which is supported by the X-ray data of **8′**, is the presence of a slow (on the NMR timescale) equilibrium between the $[Pt(terpy)(H_2O)]^{2+}$ species and a hydrogen-bonded adduct of the type $[Pt(terpy)(OH_2\cdots OSO_2CF_3)]^+$, this latter having the $H^6$ doublet at $\delta$ = 8.67 ppm in $CD_3NO_2$ solution. The addition of increasing amounts of lithium triflate to the solution, besides having the obvious effect of shifting the equilibrium towards the hydrogen-bonded adduct, also increases the ionic strength of the solution, which has the

 © 2007 Wiley-VCH Verlag GmbH & Co. KGaA, Weinheim 

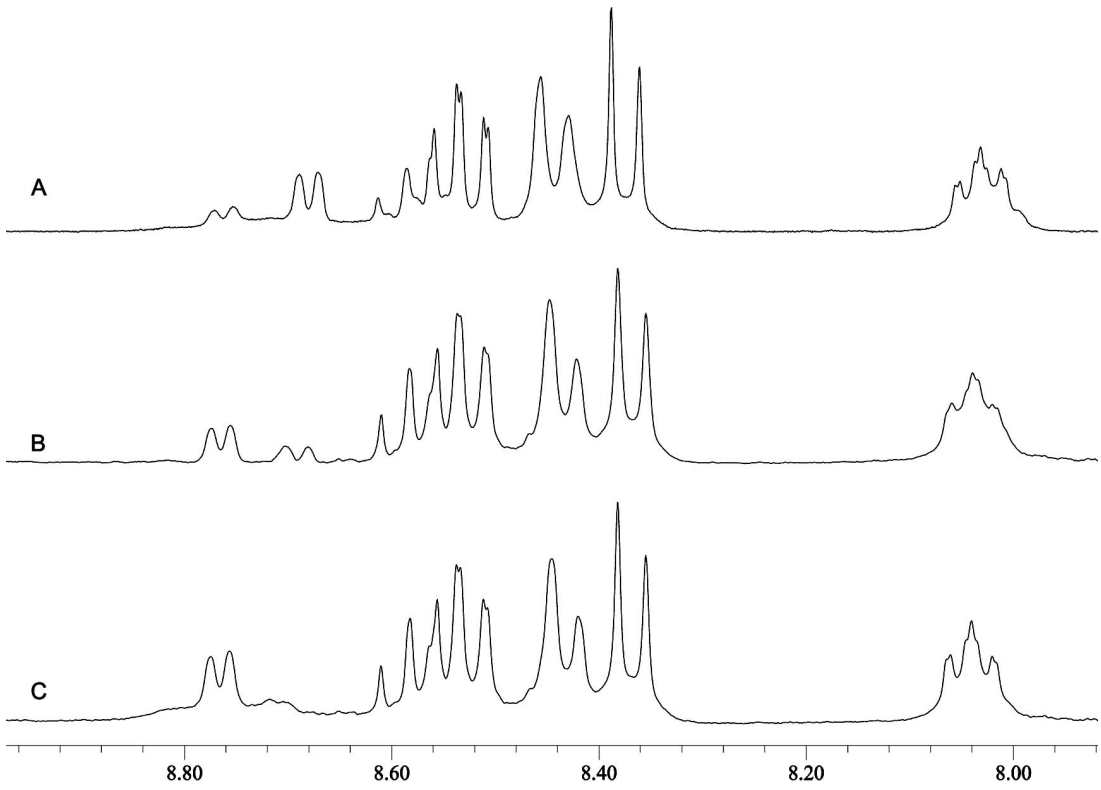


Figure 2. $^1$H NMR spectra ($\delta$ values in ppm) of [Pt(terpy)($H_2O$)]($SO_3CF_3$)$_2$ (A), [Pt(terpy)($H_2O$)]($ClO_4$)$_2$ + 1/2 equiv. $LiSO_3CF_3$ (B) and pure [Pt(terpy)($H_2O$)]($ClO_4$)$_2$ (C) in $CD_3NO_2$ at 298 K.

opposite effect. This explains why we still observe the downfield doublet even in solutions saturated with the triflate salt. The perchlorate ion, on the contrary, has a much lower (if any) hydrogen-bond-acceptor ability than triflate: It only increases the ionic strength and, when added in large amounts, completely shifts the equilibrium towards the $[Pt(terpy)(H_2O)]^{2+}$ species.

Some years ago, Lawrence et al. reported the isolation of a triflato complex after treating [PtCl(terpy)](Cl) with anhydrous $CF_3SO_3H$ which, on the basis of the analytical data, they formulated as [Pt($OSO_2CF_3$)(terpy)]($CF_3SO_3$)·$CF_3SO_3H$.[25] Unfortunately, the authors did not report IR or NMR spectroscopic data for their compound and, in our hands, attempts to follow their procedure always resulted in the isolation of intractable materials. As an alternative possible route to the synthesis of the triflato complex, we treated the methoxido complex [Pt(terpy)($OCH_3$)]($CF_3SO_3$) (**9**) with an excess of methyl triflate in $CH_2Cl_2$, as described in the Experimental Section. The following reaction was expected to occur: [Pt(terpy)($OCH_3$)]($CF_3SO_3$) + $CF_3SO_2OCH_3$ → [Pt($OSO_2CF_3$)(terpy)]($CF_3SO_3$) + $(CH_3)_2O$.

The IR spectrum of the isolated product (**12**) shows three strong absorptions in the $\nu(SO_3)$ region at 1167, 1248, and 1297 cm$^{-1}$, while that observed at 848 cm$^{-1}$ is typical of ionic $PF_6$. In the $^1$H NMR spectrum ($CD_3NO_2$), the resonance of the H$^6$ proton of the terpy ligand is a doublet at $\delta$ = 9.43 ($^3J_{H,H}$ = 5.0 Hz) ppm. Once again, an X-ray diffraction structural study was necessary to unequivocally establish the identity of the compound as [$Pt_2$(μ-OH)(terpy)$_2$]($PF_6$)$_2$($CF_3SO_3$).

### *Structure of [Pt$_2$(μ-OH)(terpy)$_2$](PF$_6$)$_2$(CF$_3$SO$_3$) (12)*

An ORTEP view of the $[Pt_2(\mu\text{-OH})(terpy)_2]^{3+}$·($CF_3SO_3$) fragment is shown in Figure 2. The coordination geometry around both platinum atoms is distorted square-planar, and the geometrical parameters around each Pt atom are similar to those observed in complex **8′**, with the N–Pt–N(*cis*) angles within the range 81.0(3)–82.1(3)° and central Pt1–N2 and Pt2–N5 bond lengths of 1.906(7) and 1.917(7) Å, respectively. The coordination planes including the Pt atoms make angles of 56.3(5)° and 53.2(4)° with the plane of the Pt1–O1–Pt2 bridge and are almost perpendicular to each other, being rotated by an angle of 79.1(2)°. The Pt–O distances between the platinum atoms and the negatively charged bridging hydroxido group [2.033(6) and 2.024(6) Å] are slightly shorter than the Pt–O(water) distances (2.04–2.10 Å) observed in the previous structure (**8′**) and in square-planar Pt$^{II}$ complexes where a water molecule is *trans* to a nitrogen atom.[24] The hydroxido group is hydrogen-bonded to the disordered triflate anion with an O1···O2 distance of 2.656(15) Å (Figure 3).

Interestingly enough, the same hydroxido-bridged dimer is obtained as its perchlorate salt [$Pt_2$(μ-OH)(terpy)$_2$]($ClO_4$)$_3$ (**11**) upon treating the methyl precursor with an excess of $HClO_4$ in water. We can draw this conclusion on the

 © 2007 Wiley-VCH Verlag GmbH & Co. KGaA, Weinheim 

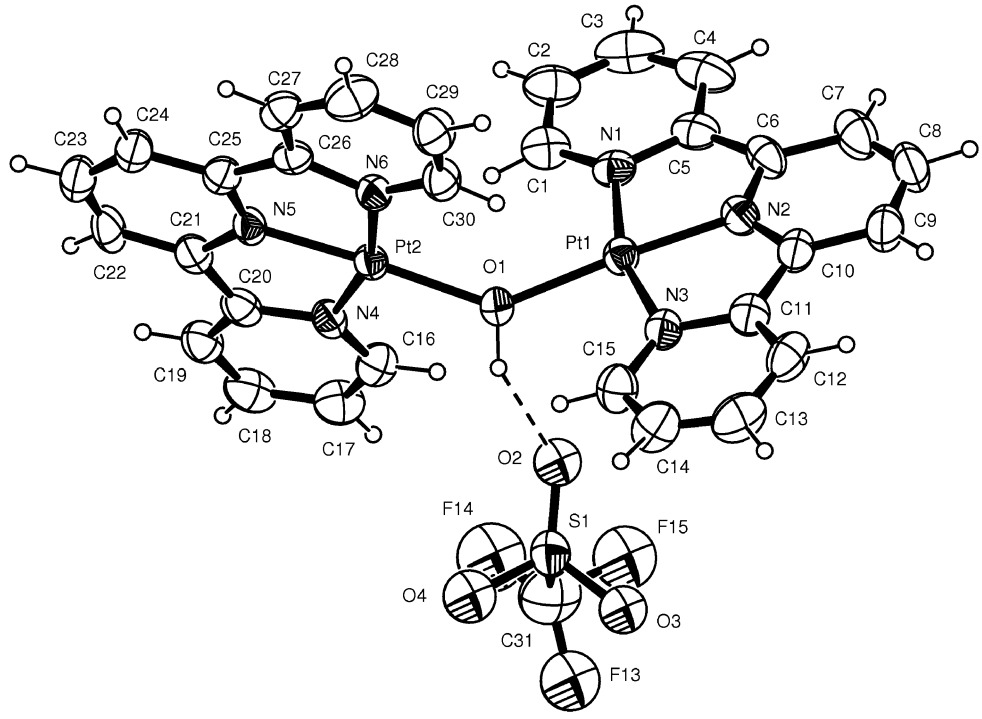


Figure 3. ORTEP view of the $[Pt_2(\mu\text{-}OH)(terpy)_2]^{3+}\cdot(CF_3SO_3)$ fragment displaying thermal ellipsoids at 30% probability. The dotted lines indicate hydrogen bonds.

basis of the analytical data and on the observation that the $^1H$ NMR spectra ($CD_3NO_2$) of the triflate hexafluorophosphate and perchlorate salts are identical. This latter result also indicates that, contrary to the case of the aqua species, the hydrogen bonding that is found in the solid state is not retained to any detectable extent in nitromethane solution.

## Conclusions

The $Pt^{II}$(terpy) system behaves differently from the triphos and triphos-*P*,*P*′ ones in that only the aqua species, instead of the triflato complex, is isolated after the acidolysis of $[Pt(terpy)(CH_3)]^+$ under similar experimental conditions. It has been shown that the terpy ligand remarkably enhances the reactivity toward nucleophilic substitution when coordinated to a metal ion[7,26] and, moreover, that the triflate ion is a very weak ligand. On these grounds, the possibility exists that the first formed product of the acidolysis reaction is the triflato species, which then rapidly solvolyses to the aqua species. Given that water was only adventitiously present in the solvents we used, the rate constant for the solvolysis has to be quite high indeed. Lawrence et al. have reported a value of 0.1 $s^{-1}$ for the rate constant of aquation of the triflato species they isolated in 0.1 M $CF_3SO_3H$.[25] On the other hand, since we have reported a value of $2.24\times10^{-2}$ $s^{-1}$ for the aquation of the $[Pt(terpy)Cl]^+$ species,[27] these two data would indicate a surprisingly low value of about 5 as the ratio of triflate/chloride lability. If so, aquation by adventitious water will be so slow that it is not likely to account for our experimental results. Considering the many examples of the unusual chemistry of (terpy)metal compounds reported in the literature, it might be possible that the mechanism of Pt–C bond fission is, in our case, different from that of the triphos and triphos-*P*,*P*′ ones. For example, it might be that it is not the bare proton that reacts to directly give the aqua species but the hydroxonium triflate instead. Some kinetic work is necessary, however, before any definitive conclusion can be drawn.

The isolation of $[Pt_2(\mu\text{-}OH)(terpy)_2](PF_6)_2(CF_3SO_3)$ (**12**) and its perchlorate analogue **11** is a rather noteworthy result and, although we did not pursue our investigation of the chemistry of these species further, a few considerations can nevertheless be made. First of all, species **11** can be isolated simply by changing the solvent from TFE, where the aqua species forms, to water. It might be reasoned that this is due to some reaction involving $[Pt(OH)(terpy)]^+$, which is formed by acid dissociation of the aqua species. This possibility can, however, be ruled out since any dissociation of the aqua species ($pK_a$ = 4.4)[26] is completely suppressed under our conditions (excess $HClO_4$). It is much more likely that, since extensive dimerization of the reactive $[Pt(CH_3)(terpy)]^+$ species occurs in water, whereas in solvents such as TFE it does not,[9] the dimers are the actual reactive species. All in all, this result further demonstrates, in a striking way, the preference of the Pt(terpy) center for water instead of the triflate ion.

Finally, it is interesting to note that the molecular structures of **8**′ and **12** can be considered as being derived from the structure of the triflic acid monohydrate[28] by replacing one or two $CF_3SO_3H$ molecules, respectively, with a

 © 2007 Wiley-VCH Verlag GmbH & Co. KGaA, Weinheim 

[Pt(terpy)]$^{2+}$ moiety, as depicted below (see Scheme 1). As such, this demonstrates once more the remarkable electrophilicity of the metal center caused by the terpyridine ligand.

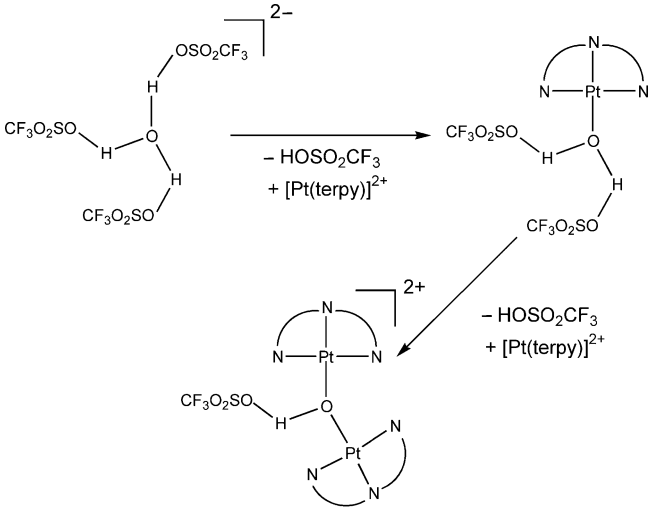


Scheme 1. Formal equivalence of the [Pt(terpy)]$^{2+}$ and $HOSO_2CF_3$ fragments in the monohydrate triflic acid, [Pt(terpy)($H_2O$)]-($OSO_2CF_3$)$_2$, and [Pt$_2$(μ-OH···$OSO_2CF_3$)(terpy)$_2$]$^{2+}$ crystal structures.

## Experimental Section

**Materials:** 2,2,2-Trifluoroethanol (TFE, 99% from Aldrich) was treated with a quantity of sodium calculated for a 2% water content and then distilled under dry nitrogen. The other solvents used were purified and dried by standard techniques. 2,2′:6′,2′′-Terpyridine and inorganic salts were purchased from Aldrich. Pt$^{II}$ precursors were prepared from platinum foils. Perchloric acid solution (65% in $H_2O$), methanesulfonic acid (>99.5%), triflic acid (>99%), and methyl methanesulfonate (>99%) were best-quality Aldrich products.

**Instrumentation:** IR spectra were recorded for nujol mulls between NaCl plates with a Nicolet Magna FT IR 750 or a Perkin–Elmer Spectrum One spectrometer. $^1$H NMR spectra were recorded with a Bruker Avance 300 or Bruker AC 200 F spectrometer. Chemical shifts (ppm) were referenced internally to the undeuterated solvent resonances and are quoted relative to tetramethylsilane ($\delta$ = 0 ppm). The protons of the terpy ligand are numbered as in Scheme 2. Elemental analyses were performed by the Microanalytical Laboratory of the University at Padua.

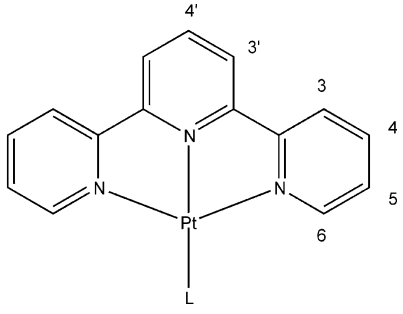


Scheme 2. Numbering of the hydrogen and primary carbon atoms of the coordinated terpy ligand.

**Preparation of the Complexes:** The complexes [Pt($CH_3$)(terpy)]Y [Y = Cl (**1**), $PF_6$ (**2**), $ClO_4$ (**3**), and $CF_3SO_3$ (**4**)] were prepared according to reported procedures.[9] Their chemical analyses are in good agreement with those obtained in previous preparations. The analogous $BF_4$ (**5**), $NO_3$ (**6**), and $CH_3SO_3$ (**7**) salts were prepared by treating the chlorido complex **1** (typically 0.1 g, 0.21 mmol) with a stoichiometric amount of the appropriate silver salt in water (approx. 15 mL). After stirring the mixture in the dark at room temperature for about 1 h, the AgCl was filtered off and the solvent completely removed under vacuum. The crude products were recrystallized from a TFE/diethyl ether mixture. In every case the yield was practically quantitative. **5:** $C_{16}H_{14}BF_4N_3Pt$ (530.19): calcd. C 36.2, H 2.66, N 7.93; found C 36.3, H 2.70, N 7.91. **6:** $C_{16}H_{14}N_4O_3Pt$ (505.39): calcd. C 38.0, H 2.79, N 11.1; found C 38.2, H 2.82, N 11.0. $^1$H NMR (**5**, **6**; $CD_3NO_2$): $\delta$ = 8.81 (d, $^3J_{H,H}$ = 5.9, $^3J_{Pt,H}$ = 51 Hz, 2 H, H$^6$), 8.53–8.25 (m, 7 H, H$^4$, H$^3$, H$^{3'}$, H$^{4'}$), 7.78 (ddd, $^3J_{H,H}$ = 5.9, $^3J_{H,H}$ = 7.5, $^4J_{H,H}$ = 1.8 Hz, 2 H, H$^5$), 1.03 (s, $^2J_{Pt,H}$ = 74 Hz, 3 H, Pt-C$H_3$) ppm. **7:** $C_{17}H_{17}N_3O_3PtS$ (538.48): calcd. C 37.9, H 3.18, N 7.80; found C 38.1, H 3.20, N 7.78. $^1$H NMR ($CD_3NO_2$): $\delta$ = 8.81 (d, $^3J_{H,H}$ = 5.9, $^3J_{Pt,H}$ = 51 Hz, 2 H, H$^6$), 8.53–8.25 (m, 7 H, H$^4$, H$^3$, H$^{3'}$, H$^{4'}$), 7.78 (ddd, $^3J_{H,H}$ = 5.9, $^3J_{H,H}$ = 7.5, $^4J_{H,H}$ = 1.8 Hz, 2 H, H$^5$), 1.03 (s, $^2J_{Pt,H}$ = 74 Hz, 3 H, Pt-C$H_3$), 2.47 (s, 3 H, C$H_3SO_3$) ppm. IR (nujol): $\tilde{\nu}$ = 1193, 1038 [$\nu(SO_3)$] cm$^{-1}$.

**[Pt(OH)(terpy)]($PF_6$) (8):** This complex was prepared according to a procedure reported for the analogous perchlorate salt[27] but with $KPF_6$ instead of $NaClO_4$ as the precipitating salt. Yield: 95%. $C_{15}H_{12}F_6N_3OPPt$ (590.32): calcd. C 30.5, H 2.05, N 7.12; found C 30.3, H 2.04, N 7.15. IR (nujol): $\tilde{\nu}$ = 3631 [$\nu$(OH)], 884 [$\nu(PF_6)$] cm$^{-1}$.

**[Pt(OCH$_3$)(terpy)]($PF_6$) (9):** The procedure of Aldridge et al.[29] was applied starting from [Pt(OH)(terpy)]($PF_6$) instead of the $BF_4^-$ salt. Yield: 90%. $C_{16}H_{15}F_6N_3OPPt$ (605.35): calcd. C 31.8, H 2.33, N 6.95; found C 31.6, H 2.32, N 6.98.

**[Pt(terpy)($H_2O$)]($ClO_4$)$_2$ (10):** ***Caution!*** *Perchlorate salts of metal complexes are potentially explosive and should be handled with care.* This complex was prepared by adding a slight excess of $HClO_4$ (23 μL of a 65% solution in $H_2O$) to a stirred solution of **3** (0.1 g, 0.18 mmol) in TFE (15 mL). After 1 h, the yellowish solution was concentrated under vacuum to about 3 mL, diethyl ether was added with stirring, and the pale-yellow precipitate that formed was collected by filtration, washed with diethyl ether, and dried under vacuum. Yield: 75% (0.087 g). $C_{15}H_{13}Cl_2N_3O_9Pt$ (645.26): calcd. C 26.6, H 1.93, N 6.20; found C 26.7, H 1.90, N 6.18. $^1$H NMR ($CD_3NO_2$): $\delta$ = 8.76 (d, $^3J_{H,H}$ = 5.6, $^3J_{Pt,H}$ = 29 Hz, 2 H, H$^6$), 8.61–8.35 (m, 7 H, H$^4$, H$^3$, H$^{3'}$, H$^{4'}$), 8.04 (ddd, $^3J_{H,H}$ = 5.6, $^3J_{H,H}$ = 7.5, $^4J_{H,H}$ = 1.6 Hz, 2 H, H$^5$) ppm.

**[Pt$_2$(μ-OH)(terpy)$_2$]($ClO_4$)$_3$ (11):** This species formed when the acidolysis of **3** with excess $HClO_4$ was conducted in water (30 mL) instead of TFE. In this case the reaction was much slower, and the mixture was refluxed for 2 h before most of the product had precipitated from the solution. This was concentrated to about 10 mL and the orange solid collected by filtration, washed with a little ice-cold water, and dried under vacuum over $P_2O_5$. Yield: 84% (0.089 g). $C_{30}H_{23}Cl_3N_6O_{13}Pt_2$ (1172.1): calcd. C 30.7, H 1.98, N 7.17; found C 30.5, H 2.00, N 7.20.

**[Pt$_2$(μ-OH)(terpy)$_2$]($PF_6$)$_2$($CF_3SO_3$) (12):** $CH_3OSO_2CF_3$ (0.1 mL, 0.9 mmol) was added to a suspension of **9** (0.3 g, 0.5 mmol), dried at 100 °C under vacuum over $P_2O_5$ just prior to use, in $CH_2Cl_2$

 © 2007 Wiley-VCH Verlag GmbH & Co. KGaA, Weinheim 

(15 mL) and the mixture stirred at room temperature for about 30 min. The orange solid was then collected by filtration, washed with diethyl ether, and immediately placed in a dessicator over $P_2O_5$. Yield: 95% (0.312 g). $C_{31}H_{23}F_{15}N_6O_4P_2Pt_2S$ (1312.7): calcd. C 28.4, H 1.77, N 6.40; found C 28.5, H 1.78, N 6.37. $^1$H NMR (**11**, **12**; $CD_3NO_2$, 298 K): $\delta$ = 9.43 (d, $^3J_{H,H}$ = 5.0 Hz, 2 H, H$^6$), 8.57 (t, $^3J_{H,H}$ = 8.0 Hz, 1 H, H$_4'$), 8.48–8.31 (m, 6 H, H$^3$, H$^{3'}$, H$^4$), 7.88 (ddd, $^3J_{H,H}$ = 7.0, $^3J_{H,H}$ = 6.0, $^4J_{H,H}$ = 2.0 Hz, 2 H, H$^5$) ppm. IR (nujol): $\tilde{\nu}$ = 1167, 1248, 1297 [$\nu$($CF_3SO_3$)], 848 [$\nu$($PF_6$)] cm$^{-1}$. Crystals of the compound, suitable for X-ray analysis were obtained by slow diffusion of diethyl ether into a saturated $CHCl_3$ solution.

**[Pt(terpy)($CH_3CN$)][($CF_3SO_3$)$_2$] (13):** The preparation of this complex has been reported by Field et al.,[30] but we preferred a different procedure. Thus, $CF_3SO_3H$ (10 μL, 0.11 mmol) was added to a stirred solution of **4** (0.06 g, 0.10 mmol) in acetonitrile (15 mL) under argon. After 1 h of stirring, the volume of the solution was reduced to about 3 mL by warming at 40 °C under a stream of argon. After cooling to room temperature, diethyl ether (20 mL) was added to precipitate a pale-yellow solid, which was filtered, washed with diethyl ether, and dried under vacuum. Yield: 91% (0.070 g). $C_{19}H_{14}F_6N_4O_6PtS_2$ (767.54): calcd. C 29.7, H 1.84, N 7.30; found C 29.5, H 1.79, N 7.22. $^1$H NMR ($CD_3NO_2$): $\delta$ = 8.86 (d, $^3J_{H,H}$ = 5.1, $^3J_{Pt,H}$ = 34 Hz, 2 H, H$^6$), 8.65–8.42 (m, 7 H, H$^4$, H$^3$, H$^{3'}$, H$^{4'}$), 7.98 (ddd, $^3J_{H,H}$ = 5.1, $^3J_{H,H}$ = 7.5, $^4J_{H,H}$ = 1.8 Hz, 2 H, H$^5$), 3.00 (s, $^4J_{Pt,H}$ = 9.0 Hz, 3 H, NCC$H_3$) ppm. IR (nujol): $\tilde{\nu}$ = 2330, 2307 [$\nu$(CN)]; 1260, 1158, 1030 [$\nu$($CF_3SO_3$)] cm$^{-1}$.

**Reactions of Complexes 2–7 with $CH_3SO_3H$:** These reactions were conducted in dry TFE. In a typical experiment, 1.0 mmol of the complex was dissolved in TFE (15 mL), and a solution of the acid (1.0 mmol) in the same solvent (2 mL) was added with stirring. In general, the solution became colorless within a few minutes. After stirring at room temperature for 1 h, the solution was concentrated to about 3 mL under vacuum, and diethyl ether was added dropwise with stirring. The resulting precipitate was collected by filtration, washed with diethyl ether, and dried under vacuum.

**[Pt($OSO_2CH_3$)(terpy)][$PF_6$] (2′):** Yield: 92% (0.615 g). $C_{16}H_{14}F_6N_3O_3PPtS$ (668.41): calcd. C 28.8, H 2.11, N 6.29; found C 28.9, H 2.07, N 6.39. IR (nujol): $\tilde{\nu}$ = 1275, 1150, 1100 [$\nu$ ($OSO_2$)], 848 [$\nu$ ($PF_6$)] cm$^{-1}$.

**[Pt($OSO_2CH_3$)(terpy)][$ClO_4$] (3′):** Yield: 90% (0.561 g). $C_{16}H_{14}ClN_3O_7PtS$ (622.89): calcd. C 30.9, H 2.27, N 6.75; found C 30.7, H 2.41, N 6.84.

**[Pt($OSO_2CH_3$)(terpy)][$CF_3SO_3$] (4′):** Yield: 87% (0.585 g). $C_{17}H_{14}F_3N_3O_6PtS_2$ (672.51): calcd. C 30.4, H 2.10, N 6.24; found C 30.2, H 2.22, N 6.28.

**[Pt($OSO_2CH_3$)(terpy)][$BF_4$] (5′):** Yield: 88% (0.537 g). $C_{16}H_{14}BF_4N_3O_3PtS$ (610.25): calcd. C 31.5, H 2.31, N 6.89; found C 31.6, H 2.44, N 6.82. $^1$H NMR (**2′**, **3′**, **4′**, **5′**; $CD_3NO_2$): $\delta$ = 8.86 (d, $^3J_{H,H}$ = 5.6, $^3J_{Pt,H}$ = 32 Hz, 2 H, H$^6$), 8.59–8.34 (m, 7 H, H$^4$, H$^3$, H$^{3'}$, H$^{4'}$), 7.98 (ddd, $^3J_{H,H}$ = 5.6, $^3J_{H,H}$ = 7.5, $^4J_{H,H}$ = 2.0 Hz, 2 H, H$^5$), 3.11 (s, 3 H, $SO_3CH_3$) ppm.

**[Pt($OSO_2CH_3$)(terpy)][Pt($ONO_2$)(terpy)][($CH_3SO_3$)($NO_3$) (6′):** Yield: 85% (0.498 g). $C_{16}H_{14}N_4O_6PtS$ (585.45): calcd. C 32.8, H 2.41, N 9.57; found C 32.6, H 2.47, N 9.62. $^1$H NMR ($CD_3NO_2$): $\delta$ = 8.87 (d, $^3J_{H,H}$ = 6.5, $^3J_{Pt,H}$ = 32 Hz, 2 H, H$^6$), 8.58 (d, $^3J_{H,H}$ = 6.0, $^3J_{Pt,H}$ = 27 Hz, 2 H, H$^6$), 8.59–8.31 (m, 14 H, H$^4$, H$^3$, H$^{3'}$, H$^{4'}$), 7.98 (m, 4 H, H$^5$), 3.11 (s, 3 H, $PtSO_3CH_3$), 2.47 (s, 3 H, $SO_3CH_3$) ppm. IR (nujol): $\tilde{\nu}$ = 1519 [$\nu$($ONO_2$)], 1360 [$\nu$($NO_3$)], 1275, 1150 [$\nu$($OSO_2$)], 1203, 1045 [$\nu$ ($SO_3$)] cm$^{-1}$.

**[Pt($OSO_2CH_3$)(terpy)][($CH_3SO_3$) (7′):** Yield: 87% (0.538 g). $C_{17}H_{17}N_3O_6PtS_2$ (618.54): calcd. C 33.0, H 2.77, N 6.79; found C 33.2, H 2.64, N 6.92. $^1$H NMR ($CD_3NO_2$): $\delta$ = 8.86 (d, $^3J_{H,H}$ = 5.6, $^3J_{Pt,H}$ = 32 Hz, 2 H, H$^6$), 8.59–8.34 (m, 7 H, H$^4$, H$^3$, H$^{3'}$, H$^{4'}$), 7.98 (ddd, $^3J_{H,H}$ = 5.6, $^3J_{H,H}$ = 7.5, $^4J_{H,H}$ = 2.0 Hz, 2 H, H$^5$), 3.11 (s, 3 H, $SO_3CH_3$), 2.47 (s, 3 H, $SO_3CH_3$) ppm.

**[Pt(terpy)($H_2O$)][($CF_3SO_3$)$_2$] (8′). Method (a):** $CF_3SO_3H$ (10 μL, 0.11 mmol) was added with a microsyringe fitted with a teflon needle to a stirred solution of **4** (0.06 g, 0.10 mmol) in freshly distilled TFE (10 mL) under dry argon. The color of the solution immediately turned from orange to pale yellow. After stirring for 30 min, diethyl ether (20 mL) was added, and the resulting yellow-orange precipitate was filtered off, washed with diethyl ether, and dried under vacuum. Yield: 91% (0.068 g). **Method (b):** All operations were performed under dry nitrogen with the aid of a glove box.

Table 1. Crystal data and details of data collection and refinement procedure for complexes **8′** and **12**.

| | **8′** | **12** |
|---|---|---|
| Empirical formula | $(C_{15}H_{11}N_3)(H_2O)Pt{\cdot}2(CF_3SO_3)$ | $(C_{30}H_{22}N_6)(OH)Pt_2{\cdot}CF_3SO_3{\cdot}2(PF_6)$ |
| Formula mass | 744.51 | 1312.73 |
| Crystal system | monoclinic | monoclinic |
| Space group | $P2_1/a$ | $P2_1/a$ |
| $a$ [Å] | 8.6885(2) | 9.4928(1) |
| $b$ [Å] | 28.5640(7) | 36.6228(5) |
| $c$ [Å] | 9.4721(2) | 10.9921(1) |
| $\beta$ [°] | 104.460(1) | 91.5753(3) |
| $V$ [Å$^3$] | 2276.30(9) | 3819.99(7) |
| Z | 4 | 4 |
| $D_{calcd.}$ [g cm$^{-3}$] | 2.172 | 2.283 |
| $T$ [K] | 295 | 295 |
| $\mu$ [cm$^{-1}$] | 64.43 | 75.75 |
| $\theta_{min}$–$\theta_{max}$ [°] | 2.3–28.0 | 2.8–28.0 |
| Unique reflections | 5392 | 8910 |
| $R_{int}$ | 0.070 | 0.059 |
| Observed reflections [$I > 2\sigma(I)$] | 4542 | 6770 |
| $R$ (observed reflections) | 0.0382 | 0.0516 |
| $wR$ (all reflections) | 0.0904 | 0.1359 |
| $S$ | 1.106 | 1.061 |
| Largest $\Delta F_{max/min}$ [e Å$^{-3}$] | 0.58/–1.39 | 1.84/–1.40 |

 © 2007 Wiley-VCH Verlag GmbH & Co. KGaA, Weinheim 

The acid (10 μL, 0.11 mmol) was added to a stirred suspension of **4** (0.06 g, 0.10 mmol) in dry $CH_2Cl_2$ (5 mL), and stirring was continued for about 15 min. The solid was then filtered, washed carefully with diethyl ether, and dried under vacuum. Yield: 91% (0.068 g). $C_{17}H_{13}F_6N_3O_7PtS_2$ (744.50): calcd. C 27.4, H 1.76, N 5.64; found (a) C 27.0, H 1.92, N 5.69; (b) C 27.1, H 1.83, N 5.72. $^1$H NMR ($CD_3NO_2$): $\delta$ = 8.76, 8.67 (2 d, 2 H, first d with $^3J_{H,H}$ = 5.6 Hz, second d with $^3J_{H,H}$ = 5.6 Hz, $H^6$), 8.61–8.35 (m, 7 H, $H^4$, $H^3$, $H^{3'}$, $H^{4'}$), 8.04 (ddd, $^3J_{H,H}$ = 5.6, $^3J_{H,H}$ = 7.5, $^4J_{H,H}$ = 1.6 Hz, 2 H, $H^5$) ppm. IR (nujol): $\tilde{\nu}$ = 1166, 1235, 1290 [$\nu(CF_3SO_3)$] cm$^{-1}$. Slow concentration of a chloroform solution of the product gave orange crystals suitable for X-ray crystal structure determination.

**X-ray Structure Determination:** Crystal data for compounds **8′** and **12** were collected using a Nonius Kappa CCD diffractometer with graphite-monochromated Mo-$K_\alpha$ radiation. The data sets were integrated with the Denzo-SMN package[31] and corrected for Lorentz, polarization, and absorption (SORTAV[32]) effects. The structures were solved by direct methods (SIR97[33]). The structure of **8′** was refined using full-matrix least squares with all non-hydrogen atoms anisotropic and hydrogen atoms isotropic. The non-hydrogen atoms of the dimeric $[Pt_2(\mu\text{-}OH)(terpy)_2]^{3+}$ complex cation and the $PF_6^-$ anion in the structure **12** were refined anisotropically. The other $PF_6^-$ anion as well as the triflate anion were found to be disordered. The fluorine and oxygen atoms of these groups were refined isotropically over two positions with an occupancy of 0.5 each; the P, C, and S atoms were refined anisotropically. All calculations were performed using SHELXL-97[34] and PARST,[35] as implemented in the WINGX[36] system of programs. The crystal data and refinement parameters are summarized in Table 1. Selected interatomic distances and angles are given in Tables 2 and 3 for compounds **8′** and **12**, respectively. CCDC-654357 and -654358 (for complexes **8′** and **12**, respectively) contain the supplementary crystallographic data for this paper. These data can be obtained free of charge from The Cambridge Crystallographic Data Centre via www.ccdc.cam.ac.uk/data_request/cif.

Table 2. Selected bond lengths [Å] and angles [°] for complex **8′**.

| | | | |
|---|---|---|---|
| Distances | | | |
| Pt1–O1 | 2.040(5) | Pt1–N2 | 1.914(4) |
| Pt1–N1 | 2.021(5) | Pt1–N3 | 2.009(4) |
| Angles | | | |
| O1–Pt1–N1 | 101.5(2) | N1–Pt1–N2 | 81.4(2) |
| O1–Pt1–N2 | 176.6(6) | N1–Pt1–N3 | 163.3(2) |
| O1–Pt1–N3 | 95.2(2) | N2–Pt1–N3 | 81.8(2) |
| Hydrogen bonds | | | |
| O1–H10 | 0.93(9) | O1–H20 | 0.73(7) |
| O1···O3 | 2.650(8) | O1···O7 | 2.617(10) |
| H10···O3 | 1.74(9) | H20···O7 | 1.91(7) |
| O1–H10···O3 | 165(8) | O1–H20···O7 | 163(7) |

Table 3. Selected bond lengths [Å] and angles [°] for complex **12**.

| | | | |
|---|---|---|---|
| Distances | | | |
| Pt1–O1 | 2.033(6) | Pt2–O1 | 2.024(6) |
| Pt1–N1 | 2.019(7) | Pt2–N4 | 2.022(7) |
| Pt1–N2 | 1.906(7) | Pt2–N5 | 1.917(6) |
| Pt1–N3 | 2.016(7) | Pt2–N6 | 2.036(7) |
| Angles | | | |
| O1–Pt1–N1 | 98.8(3) | O1–Pt2–N4 | 97.7(3) |
| O1–Pt1–N2 | 176.3(3) | O1–Pt2–N5 | 176.8(2) |
| O1–Pt1–N3 | 97.7(3) | O1–Pt2–N6 | 99.7(3) |
| N1–Pt1–N2 | 82.1(3) | N4–Pt2–N5 | 81.6(3) |
| N1–Pt1–N3 | 163.5(3) | N4–Pt2–N6 | 162.6(3) |
| N2–Pt1–N3 | 81.4(3) | N5–Pt2–N6 | 81.0(3) |
| Pt1–O1–Pt2 | 138.2(3) | | |
| Hydrogen bonds | | | |
| O1–H100 | 0.93 | | |
| O1···O2 | 2.056(15) | | |
| H100···O2 | 1.83 | | |
| O1–H100···O2 | 146 | | |


[1] J. A. Davies, F. R. Hartley, *Chem. Rev.* **1981**, *81*, 79.
[2] W. Beck, *Inorg. Synth.* **1989**, *26*, 92.
[3] G. Annibale, P. Bergamini, V. Bertolasi, M. Cattabriga, V. Ferretti, *Inorg. Chem. Commun.* **2000**, *3*, 303.
[4] G. Annibale, P. Bergamini, V. Bertolasi, E. Besco, M. Cattabriga, R. Rossi, *Inorg. Chim. Acta* **2002**, *333*, 116.
[5] G. Annibale, B. Pitteri, *Inorg. Synth.* **2004**, *34*, 76.
[6] B. Pitteri, G. Marangoni, F. Visentin, L. Cattalini, T. Bobbo, *Polyhedron* **1998**, *17*, 475.
[7] B. Pitteri, G. Marangoni, L. Cattalini, F. Visentin, V. Bertolasi, P. Gilli, *Polyhedron* **2001**, *20*, 869.
[8] B. Pitteri, G. Marangoni, F. Visentin, L. Cattalini, T. Bobbo, V. Bertolasi, P. Gilli, *J. Chem. Soc. Dalton Trans.* **1999**, 677.
[9] G. Arena, L. Monsù Scolaro, R. F. Pasternak, R. Romeo, *Inorg. Chem.* **1995**, *34*, 2994.
[10] R. Romeo, L. Monsù Scolaro, *Inorg. Synth.* **1995**, *32*, 154.
[11] R. Romeo, L. Monsù Scolaro, M. R. Plutino, A. Albinati, *J. Organomet. Chem.* **2000**, *593*, 403.
[12] W. R. Whinnie, J. D. Miller, *Adv. Inorg. Chem. Radiochem.* **1969**, *12*, 135.
[13] B. Pitteri, G. Marangoni, L. Cattalini, T. Bobbo, *J. Chem. Soc. Dalton Trans.* **1995**, 3853.
[14] M. G. Miles, G. Doyle, R. P. Cooney, R. S. Tobias, *Spectrochim. Acta* **1969**, *25*, 1515.
[15] a) J. H. Clarke, L. A. Woodward, *Trans. Faraday Soc.* **1966**, *62*, 2226; b) A. K. Covington, T. H. Lilley, *Trans. Faraday Soc.* **1967**, *63*, 1749.
[16] J. Roziere, M. S. Lehmann, J. Potier, *Acta Crystallogr.* **1979**, *35*, 1099.
[17] M. N. Burnett and C. K. Johnson, *ORTEP III*, Report ORNL-6895, Oak Ridge National Laboratory, Oak Ridge, TN, **1996**.
[18] K. W. Jennette, J. T. Gill, J. A. Sadownick, S. J. Lippard, *J. Am. Chem. Soc.* **1976**, *98*, 6159.
[19] E. C. Constable, R. P. G. Henney, T. A. Leese, D. A. Tocher, *J. Chem. Soc. Chem. Commun.* **1990**, 513.
[20] C.-W. Chan, C.-M. Che, M.-C. Cheng, Y. Wang, *Inorg. Chem.* **1992**, *31*, 4874.
[21] C.-W. Chan, T.-F. Lai, C.-M. Che, S.-M. Peng, *J. Am. Chem. Soc.* **1993**, *115*, 11245.
[22] G. Marangoni, B. Pitteri, V. Bertolasi, V. Ferretti, P. Gilli, *Polyhedron* **1996**, *15*, 2755.
[23] G. Annibale, P. Bergamini, V. Bertolasi, M. Cattabriga, A. Lazzaro, A. Marchi, G. Vertuani, *J. Chem. Soc. Dalton Trans.* **1999**, 3877.
[24] B. Pitteri, G. Annibale, G. Marangoni, V. Bertolasi, V. Ferretti, *Polyhedron* **2002**, *21*, 2283 and references cited therein.
[25] C. Diver, G. A. Lawrance, *J. Chem. Soc. Dalton Trans.* **1988**, *9*, 931.
[26] Z. D. Bugarcic, F. W. Heinemann, R. van Eldik, *Dalton Trans.* **2004**, 279.
[27] G. Annibale, L. Cattalini, A. Cornia, A. Fabretti, F. Guidi, *Inorg. React. Mech.* **2000**, *2*, 185.
[28] J. B. Spencer, J.-O. Lundgren, *Acta Crystallogr., Sect. B* **1973**, *25*, 1923.
[29] T. K. Aldridge, E. M. Stacy, D. R. McMillin, *Inorg. Chem.* **1994**, *33*, 722.
[30] R. Buchner, J. S. Field, R. J. Haines, C. T. Cunningham, D. R. McMillin, *Inorg. Chem.* **1997**, *36*, 3952.


 © 2007 Wiley-VCH Verlag GmbH & Co. KGaA, Weinheim 

[31] Z. Otwinowski, W. Minor in *Methods in Enzymology* (Eds.: C. W. Carter, R. M. Sweet), Academic Press, London, **1997**, vol. 276, part A, p. 307.
[32] R. H. Blessing, *Acta Crystallogr., Sect. A* **1995**, *51*, 33.
[33] SIR97: A. Altomare, M. C. Burla, M. Camalli, G. L. Cascarano, C. Giacovazzo, A. Guagliardi, A. G. Moliterni, G. Polidori, R. Spagna, *J. Appl. Crystallogr.* **1999**, *32*, 115.
[34] G. M. Sheldrick, SHELX-97, *Program for Crystal Structure Refinement*, University of Göttingen, Germany, **1997**.
[35] M. Nardelli, *J. Appl. Crystallogr.* **1995**, *28*, 659.
[36] L. J. Farrugia, *J. Appl. Crystallogr.* **1999**, *32*, 837.

Received: July 23, 2007
Published Online: October 26, 2007

 © 2007 Wiley-VCH Verlag GmbH & Co. KGaA, Weinheim 

DOI: 10.1002/ejic.200700937

# Octahedral Alkylbis(phenoxy-imine)tin(IV) Complexes: Effect of Substituents on the Geometry of the Complexes and Their Reactivity Toward Ionizing Species and Ethylene

**Liana Annunziata,[a] Daniela Pappalardo,*[b] Consiglia Tedesco,[a] and Claudio Pellecchia[a]**

**Keywords:** Tin / N,O ligands / Cations / Ethylene / Oligomerization

The synthesis and characterization of the organo-tin compounds $L_2SnR_2$ [L = *N*-(3,5-dichlorosalicylidene)aniline; R = $CH_3$ (**1**), R = $CH_2Ph$ (**2**)] and $L'_2SnR_2$ [**3**: L′ = *N*-(3-*tert*-butylsalicylidene)aniline, R = $CH_2Ph$] are described herein. NMR studies showed a highly symmetric structure for complex **1**, with the alkyl groups in a *trans* configuration, and the presence of at least two isomers in fluxional equilibrium for compounds **2** and **3**. Single-crystal X-ray characterization for compound **2** showed an octahedral geometry with the alkyl groups in *trans* relationship. The reactivity of the synthesized compounds toward ionizing agents was studied by NMR spectroscopy. For compounds **1** and **2** formation of cationic species through alkyl abstraction by $B(C_6F_5)_3$ was observed. For compound **3**, a cationic species was obtained by reaction with 1 equiv. of $[C(C_6H_5)_3]^+[B(C_6F_5)_4]^-$; in this species a $\eta^n$ coordination of the benzyl group with the metal centre was recognized by NMR solution study. All the obtained cationic species promoted ethylene oligomerization under mild conditions, producing oligomers with saturated end groups and methyl branches. Oligoethylene end-group NMR analysis and deuteriolysis experiments excluded the migratory-insertion mechanism.
(© Wiley-VCH Verlag GmbH & Co. KGaA, 69451 Weinheim, Germany, 2007)

## Introduction

The activity in olefin polymerization of compounds based on metals beyond group 13 has never been reported in the literature.[1] Recently we reported the oligomerization of ethylene in the presence of bis(phenoxy-imine)dialkyltin(IV) complexes.[2] The latter compounds showed octahedral geometry with alkyl groups in a *cis* configuration and underwent alkyl abstraction reaction with the carbenium salt $[C(C_6H_5)_3]^+[B(C_6F_5)_4]^-$. The obtained cationic species exhibited low activity in ethylene oligomerization under mild conditions, producing oligomers with saturated end groups and methyl branches. To the best of our knowledge, the oligomerization of ethylene by a group 14 compound is unprecedented in the literature.

These results prompted us to persist in exploring the reactivity of different salicylaldiminatotin(IV) complexes, in order to ascertain the mechanism involved in the formation of branched oligoethylenes. Therefore we studied the synthesis and the structural properties of novel dialkyl bis(salicylaldiminato)tin(IV) complexes, bearing electronically and sterically different ligands. These complexes revealed some interesting features that will be discussed here and compared with the previously reported results.

[a] Dipartimento di Chimica, Università di Salerno,
via Ponte don Melillo, 84084 Fisciano (SA), Italy
Fax: +39-089-969603
[b] Dipartimento di Studi Geologici ed Ambientali, Università del Sannio,
via dei Mulini 59/A, 82100 Benevento, Italy
E-mail: pappalardo@unisannio.it
Supporting information for this article is available on the WWW under http://www.eurjic.org or from the author.

## Results and Discussion

### Synthesis of the Complexes

The synthesized bis(phenoxy-imine)tin(IV) complexes are described in Scheme 1. The *N*-(3-*tert*-butylsalicylidene)-aniline[3] and *N*-(3,5-dichlorosalicylidene)aniline[4] ligands were synthesized by a condensation reaction between the aldehyde and the aniline according to literature procedures. Complexes were prepared by a metathesis reaction of the sodium salt of the ligands with the corresponding dialkyltin(IV) chloride in tetrahydrofurane, producing compounds **1**–**3** with high yields (73–91%), as yellow or orange solids. The products are stable in an inert atmosphere, but easily underwent hydrolysis with formation of the free ligand in the presence of traces of adventitious water.

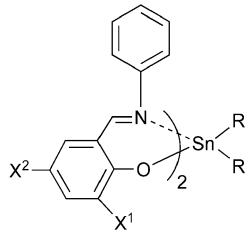


**1** $X^1$ = Cl $X^2$ = Cl R = $CH_3$
**2** $X^1$ = Cl $X^2$ = Cl R = $CH_2Ph$
**3** $X^1$ = *t*Bu $X^2$ = H R = $CH_2Ph$

Scheme 1.

 © 2007 Wiley-VCH Verlag GmbH & Co. KGaA, Weinheim 

## NMR Characterization of the Complexes

All the synthesized compounds were characterized by $^{1}H$, $^{13}C$ and $^{119}Sn$ NMR spectroscopy, and mass spectroscopy. Compound **2** was also characterized by single-crystal X-ray diffraction analysis.

The $^{119}Sn$ NMR spectrum of the dimethyl compound **1**, bearing the chlorinated phenoxy-imine ligands, showed one signal at –306.5 ppm, compatible with the presence of a single organometallic species. The $^{1}H$ NMR spectrum showed very sharp signals and a pattern compatible with the presence of a highly symmetric structure in solution. Characteristic signals were the singlet at $\delta$ = 0.79 ppm ($^{2}J_{Sn,H}$ = 90.7 Hz) for the methyl groups, and the singlet at $\delta$ = 8.02 ppm ($^{3}J_{Sn,H}$ = 12.1 Hz) for the imine hydrogen atoms (C*H*=N). It is known from the literature that the coupling constants $^{2}J(^{119}Sn–^{1}H)$ and $^{1}J(^{119}Sn–^{13}C)$ can be used to estimate the methyl–tin–methyl angle.[5,6] For the previously reported bis(phenoxy-imine)tin(IV) dimethyl complexes, by using the equation specifically developed by Nelson for octahedral dialkyltin compounds,[6] we calculated a methyl–tin–methyl angle of 106(6)°, suggesting a structure with the methyl groups in a *cis* configuration; this result was nicely in agreement with the value disclosed by single-crystal X-ray analysis (107.4°). For compound **1** the value of the coupling constant $^{2}J_{Sn,H}$ for the methyl group bonded to tin is significantly higher than the value observed for previously reported compounds,[2] and the calculated angle C–Sn–C is of 160° (±6), in the expected range for a structure with the methyl groups in a *trans* configuration. For octahedral bis(phenoxy-imine) dialkyl complexes, five isomers are possible, as displayed in Scheme 2. In the present case, therefore, two isomers, "*trans*-**I**" and "*trans*-**II**", are compatible with the NMR spectroscopic data in solution.

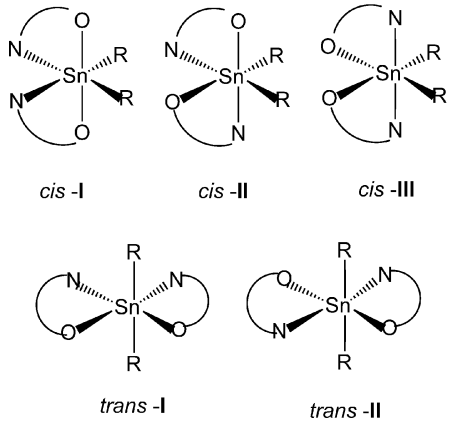


Scheme 2.

The dibenzyl compound **2** showed two broad signals, at –425.6 and –426.9 ppm, in the $^{119}Sn$ NMR spectrum at room temperature, thus indicating the presence of different tin species in solution. In addition, in the $^{1}H$ NMR spectrum broad signals were also observed. Characteristic resonances are a singlet at $\delta$ = 2.56 ppm ($^{2}J_{Sn,H}$ = 105.1 Hz) for the methylene hydrogen atoms (C$H_2$Ph) and a singlet at $\delta$ = 7.84 ppm for the imine protons (C*H*=N). By using the Nelson equation,[6] from the value of the coupling constant $^{2}J_{Sn,H}$ for the methylene hydrogen atoms (C$H_2$Ph), the calculated angle for the C–Sn–C bonds was of 193° (±6), in the expected range for a structure with the benzyl groups in a *trans* configuration. As above, of the five possible isomers, the two "*trans*" ones are compatible with the NMR spectroscopic data in solution. Single-crystal X-ray diffraction analysis revealed that compound **2** crystallized in the "*trans*-**II**" isomeric form (vide infra).

In order to investigate the fluxional equilibrium between different isomers in solution, variable temperature $^{1}H$ NMR experiments were performed between 278 and 188 K. Lowering the temperature, the broad signals split (see electronic supporting information). At 203 K the signal of the methylene hydrogen atoms C$H_2$Ph split up into a well defined AB pattern at about 1.9 ppm, two broad signals at $\delta$ = 2.72 ppm ($^{2}J_{Sn,H}$ = 27.3 Hz) and 2.93 ppm, and a minor AB pattern ($\delta$ = 2.45 ppm). At lower field three main singlets ($\delta$ = 8.00, 7.74 and 7.66 ppm) and a minor one ($\delta$ = 7.56 ppm), attributable to the imine protons, were observed. Such observations are compatible with the presence of at least two main isomeric species and a minor one involved in fluxional equilibria.

The dibenzyl compound **3**, bearing the *N*-(3-*tert*-butylsalicylidene)aniline ligands, displayed an intricate $^{1}H$ NMR spectrum at room temperature (Figure 1). The compound must exist in solution in two isomeric forms, as evidenced by the presence, in the $^{119}Sn$ NMR spectrum, of two resonances at –456.5 ppm and –457.9 ppm (1:1 molar ratio). In the $^{1}H$ NMR spectrum, two sets of signals, attributable to two different species in a 1:1 ratio, were also recognized. The first signal set (one singlet at $\delta$ = 1.07 ppm for the *t*Bu group, one signal with AB pattern at 2.5 ppm for the diastereotopic methylene hydrogen atoms C$H_2$Ph and one singlet at $\delta$ = 7.99 ppm for the imine proton, with a $^{3}J_{Sn,H}$ of 33.65 Hz) is compatible with a highly symmetric species (**I**). The second signal set, compatible with a nonsymmetric species (**II**), consists of two singlets at $\delta$ = 1.28 ppm and 1.41 ppm for the *t*Bu groups, two signals with AB pattern for the C$H_2$Ph at 2.4 ppm and 2.7 ppm and two singlets for the imine hydrogen atoms at $\delta$ = 7.69 ppm and 7.89 ppm. The $^{13}C$ NMR spectrum of compound **2** coherently displayed two signals sets, one compatible with a symmetric species **I**, the second one compatible with a nonsymmetric species **II**. Variable-temperature $^{1}H$ NMR experiments, performed between 273 and 353 K, indicated the presence of a fluxional equilibrium between species **I** and **II**. On increasing the temperature the signals of species **II** collapsed into one signal set, attributed to the symmetric species **I** (Figure 2). At 333 K only one AB signal set for the C$H_2$Ph hydrogen atoms, centred at $\delta$ = 2.70 ppm, and only one singlet at $\delta$ = 7.83 ppm ($^{3}J_{Sn,H}$ = 16.20 Hz) for the imine hydrogen atoms (C*H*=N) were observed. Unfortunately, we were not able to measure the coupling constants $^{2}J$(Sn–H) for the methylene H atoms C$H_2$Ph, and consequently to estimate the geometry of the benzyl ligands around the tin. We were unable to observe the coalescence temperature for the two species up to 373 K. The $^{119}Sn$ NMR spectrum, performed

 © 2007 Wiley-VCH Verlag GmbH & Co. KGaA, Weinheim 

at this temperature in $C_6D_5Cl$, still showed two resonances at –456.2 and –457.6 (in 1:0.45 ratio). We previously observed a fluxional equilibrium between two different isomeric species for the analogous bis[*N*-(3-*tert*-butylsalicylidene)anilinato]dimethyltin(IV) compound through NMR spectroscopy.[2] In that case two species (a $C_2$-symmetric one and a $C_1$-symmetric one) were frozen out at 195 K, while the coalescence temperature $T_c$ was observed at 278 K in the $^1$H NMR spectra and at 333 K in the $^{119}$Sn NMR spectra. It is worth noting that the presence of bulkier benzyl ligands in compound **3** instead of methyl groups slows down the fluxional equilibrium, freezing out the isomers already at room temperature.[7]

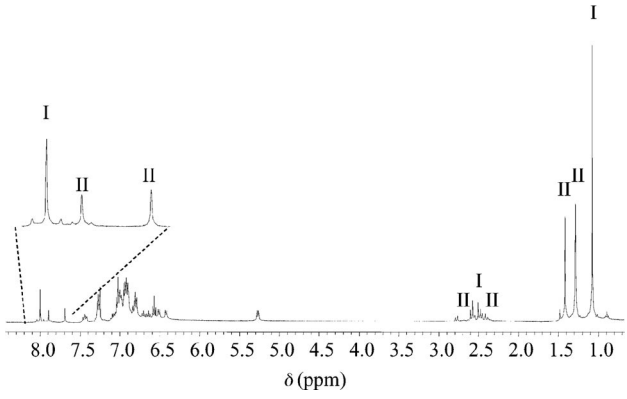


Figure 1. $^1$H NMR spectrum ($CDCl_3$, 298 K) of compound **3**.

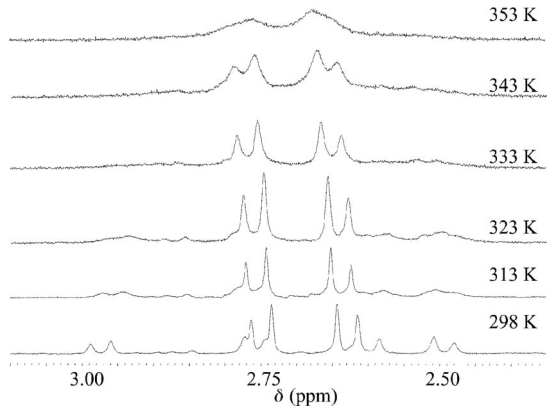


Figure 2. $^1$H NMR spectra of aliphatic regions of compound **3** at variable temperature ($ClC_6D_5$).

## X-ray Diffraction Analysis

Compound **2** was crystallized from methylene chloride/hexane at room temperature. Crystal data are given in the Experimental Section and selected bond lengths and angles are listed in Table 1. A distorted octahedral geometry with the alkyl group in a *trans* configuration and the two oxygen atoms in *trans* position was disclosed (Figure 3). The tin atom is located on a crystallographic inversion centre and the benzyl moieties coordinated in a $\eta^1$ mode. The six-atom ring Sn1–N1–C1–C2–C7–O1 is quite planar (rmsd 0.073) with an envelope angle (between the five-atom plane N1–C1–C2–C7–O1 and the Sn1–N1–C1 plane) of 9.39(14)°.

Table 1. Selected bond lengths [Å], bond angles and torsion angles [°] for compound **2**. Symmetry equivalent atoms are indicated with an asterisk.

| | | | |
|---|---|---|---|
| Sn1–C14 | 2.165(3) | N1–C8 | 1.439(3) |
| Sn1–O1 | 2.142(2) | C1–C2 | 1.446(4) |
| Sn1–N1 | 2.339(2) | C2–C7 | 1.415(4) |
| N1–C1 | 1.292(3) | O1–C7 | 1.299(3) |
| C14–Sn1–O1 | 93.13(11) | C14–Sn1–N1 | 92.06(11) |
| C14*–Sn–O1 | 86.87(11) | C14*–Sn1–N1 | 87.93(11) |
| O1–Sn1–N1 | 82.90(8) | C14–Sn1–C14* | 179.998(1) |
| O1–Sn1–N1* | 97.11(8) | Sn1–C14–C15 | 116.87(19) |
| O1–Sn1–O1* | 180.00 | N1–Sn1–N1* | 180.00 |
| C1–N1–C8–C13 | –49.9(4) | | |

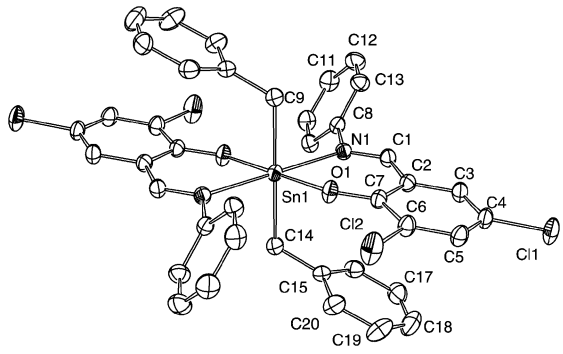


Figure 3. Molecular structure of compound **2**. Thermal ellipsoids are drawn at 30% probably level. Hydrogen atoms have been omitted for clarity.

It is worth noting that the analogous bis[*N*-(3-*tert*-butylsalicylidene)aniline]tin(IV) dialkyl complexes and the bis[*N*-(3-*tert*-butylsalicylidene)-2,3,4,5,6-pentafluoroaniline]tin(IV) dimethyl compound were crystallized in the *cis*-**I** isomeric structure, displaying the two oxygen atoms *trans* to each other and the alkyl ligands and the nitrogen atoms in a *cis* relationship.[2] Steric factors could explain the difference in the coordination environment at the central tin atom. The presence of chlorine atoms *ortho* to oxygen atoms of the phenoxy-imine ligand probably plays a role, and could favour ligand disposition in the plane.

Notably there are very few structurally characterized octahedral bis(phenoxy-imine)$MR_2$ compounds (M = any metal, R = alkyl or halogen atom) presenting the R ligands in a *trans* relationship.[8]

## Generation of Cationic Species

The synthesis of free cationic species of group 14 elements is a tricky task, because of their high reactivity. In the literature, examples of organotin cations are quite rare. Among them are the remarkable crystal structures of Lambert et al.'s trismesityl stannylium cation displaying a trigonal planar geometry around tin,[9] Sekiguchi et al.'s "stable and free" tin cation bearing three tris(alkyl)silyl ligands[10] and Michl et al.'s tributylstannylium carboranate.[11] On the contrary, organotin cationic compounds stabilized by the

 © 2007 Wiley-VCH Verlag GmbH & Co. KGaA, Weinheim 

ligand's intramolecular interactions or by external donor atoms are well known and have also been structurally characterized.[12]

In previous work, in order to mimic the active species in homogeneous olefin polymerization catalysis, we pursued cationic species with the formula $L_2SnR^+$ (L = phenoxy-imine; R = alkyl). For this purpose we used ionizing reagents, such as $[(C_6H_5)NH(CH_3)_2]^+[B(C_6F_5)_4]^-$, $B(C_6F_5)_3$ and $[C(C_6H_5)_3]^+[B(C_6F_5)_4]^-$, traditionally used in homogeneous Ziegler–Natta catalysis. The alkyl abstraction reaction from the dimethyl- and dibutyl-bis(phenoxyimine)tin(IV) compounds was successfully obtained by the carbenium salt $[C(C_6H_5)_3]^+[B(C_6F_5)_4]^-$. Reactions with $[(C_6H_5)NH(CH_3)_2]^+[B(C_6F_5)_4]^-$ and $B(C_6F_5)_3$ led instead to degradation products. The obtained cationic species exhibited some activity in the oligomerization of ethylene under mild conditions, producing short-chain oligomers, with saturated end groups and methyl branches.[2] Now these studies have been extended to the new synthesized complexes, and are reported herein.

Reactions of complexes **1**–**3** with $[(C_6H_5)NH(CH_3)_2]^+[B(C_6F_5)_4]^-$ led to decomposition, producing free phenoxy-imine ligands.

Compounds **1** and **2**, bearing the chlorinated phenoxy-imine ligand, displayed similar reactivity toward ionizing agents. Actually, reaction with $[C(C_6H_5)_3]^+[B(C_6F_5)_4]^-$ resulted invariably in mixtures of decomposition products, while the reaction with $B(C_6F_5)_3$ produced the abstraction of an alkyl group. For instance, the reaction of compound **1** with 1 equiv. of $B(C_6F_5)_3$ rapidly produced a cationic species (**1a**) by methyl abstraction, as indicated by the presence in the $^1$H NMR spectrum of a resonance at $\delta$ = 0.42 ppm attributable to the methyl group of the "free" anion $[CH_3B(C_6H_5)_3]$.[13] The $^{119}$Sn NMR spectrum of species **1a** showed only one signal at –394.0 ppm. The pattern of signals in the $^1$H NMR spectrum was compatible with the presence in solution of one symmetric species, having a ligand/methyl signals integral ratio consistent with a 2:1 formulation. According to the formation of a stannylium cation, all the resonances were downfield shifted, if compared with the corresponding resonances for the neutral compound **1** in the same condition. Characteristic resonances are the singlet at 1.042 ppm for $SnCH_3$ ($^2J_{SnH}$ = 101.8 Hz) and the singlet at $\delta$ = 8.54 ppm for the imine proton ($^3J_{SnH}$ = 22.3 Hz).[14]

Reaction of compound **2** with 1 equiv. of $B(C_6F_5)_3$ produced a new mono-benzyltin species (**2a**), characterized by a signal at –500.0 ppm in the $^{119}$Sn NMR spectrum. In the $^1$H NMR spectrum characteristic resonances are a singlet at $\delta$ = 3.28 ppm for $SnCH_2Ph$ ($^2J_{SnH}$ = 117.0 Hz) and a singlet at $\delta$ = 8.47 ppm due to imine proton ($^3J_{SnH}$ = 18.2 Hz). However, in the $^1$H NMR spectrum of species **2a** the signals for the expected byproduct $[PhCH_2B(C_6F_5)_3]^-$ were absent. In addition, the $^{19}$F NMR spectrum showed a large number of resonances of comparable intensity, clear indication of the existence of more than one fluorinated species in solution, probably generated by aryl/alkyl group exchange reactions.[15]

Compound **3** displayed a different behaviour from compounds **1** and **2**. Reaction of compound **3** with $B(C_6F_5)_3$ led to degradation, while reaction with 1 equiv. of $[C(C_6H_5)_3]^+[B(C_6F_5)_4]^-$ produced abstraction of one benzyl group and formation of the cationic species **3a**. Consistently, in the $^1$H NMR spectrum (Figure 4), the species $PhCH_2C(C_6H_5)_3$ was identified as a byproduct.[16] In the $^{119}$Sn NMR only one resonance at –448.7 ppm was observed. In the $^1$H NMR spectrum, characteristic resonances are one singlet at $\delta$ = 1.34 ppm for the *tert*-butyl hydrogens, one singlet at $\delta$ = 3.27 ppm ($^2J_{SnH}$ = 118.84 Hz) for the methylene H atoms and one singlet at $\delta$ = 8.53 ppm ($^3J_{SnH}$ = 14.92 Hz) for the imine hydrogen C*H*=N. The signal pattern is compatible with the presence of one symmetric species in solution, and shifted at higher frequency, if compared with the corresponding resonance for the neutral compound **3** in the same solvent.

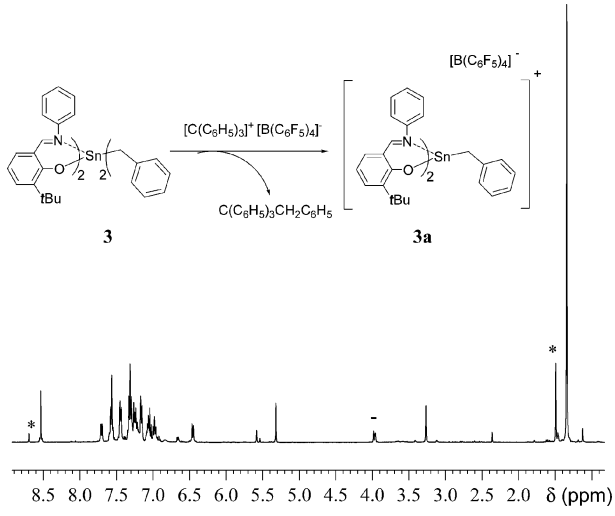


Figure 4. $^1$H NMR spectrum ($CD_2Cl_2$, 298 K) of compound **3a**: (*) "free" ligand impurities; (■) $C(C_6H_5)_3CH_2C_6H_5$.

The benzyl ligand can interact with electron-deficient metal centres also through the π-aromatic system. The $\eta^n$ ($n > 1$) coordination is typical of transition metals;[17] among main group elements, $\eta^3$ interaction has been observed, in the solid state, for benzyl lithium.[18] Latesky et al. found NMR spectroscopic evidence to detect this type of interaction in solution.[19] In particular, $\eta^n$ benzyl ligands are characterized by a high-field shift for the *ortho* hydrogen resonance ($\delta < 6.8$ ppm) in the $^1$H NMR, and by large $^1J_{CH}$ values for the $CH_2$ group ($J > 130$ Hz). The increase of the coupling constant can be explained with an increased "sp$^2$" character of the α-carbon, involving a decrease of the Mt–C–Ph angle. Interestingly, in the NMR spectra of cationic species **3a** we observed an upfield shift of the *ortho* benzyl hydrogens' resonance ($\delta$ = 6.44 ppm), and a $^1J_{CH}$ value for the methylene carbon of 139.8 Hz. The value observed is higher than that observed in tetrabenzyltin ($^1J_{CH}$ = 133 Hz), usually taken as a model for a normal σ bond ($\eta^1$) benzyl ligand.[20] These spectroscopic features thus suggest that in the cationic species **3a** the benzyl ligand interacts with the tin also through the π-aromatic system. Therefore

 © 2007 Wiley-VCH Verlag GmbH & Co. KGaA, Weinheim 

a $\eta^n$ ($n > 1$) coordination for the benzyl ligand can be hypothesized.

In order to study the influence of the temperature on the coordination of the benzyl to the tin atoms, $^1$H NMR spectra were recorded at lower temperature (between 278 K and 193 K). The aliphatic regions of the $^1$H NMR spectra for the cationic species **3a** are shown in Figure 5. On decreasing the temperature, the singlet of the methylene hydrogen atoms Sn$CH_2$Ph split up into an AB pattern, indicating that they are diastereotopic. At 233 K the doublet attributable to the *ortho* benzyl hydrogen atoms at $\delta$ = 6.44 ppm showed satellite peaks due to the tin–hydrogen spin–spin coupling with $J_{SnH}$ of 33.7 Hz. Similar NMR control experiments performed for the tetrabenzyltin compound at 233 K displayed a singlet for the methylene hydrogen atoms Sn$CH_2$Ph at $\delta$ = 2.16 ppm ($^1J_{CH}$ = 132.6 Hz) and a doublet for the *ortho* benzyl hydrogen atoms at $\delta$ = 6.60 ppm with a $J_{SnH}$ of 14.9 Hz.

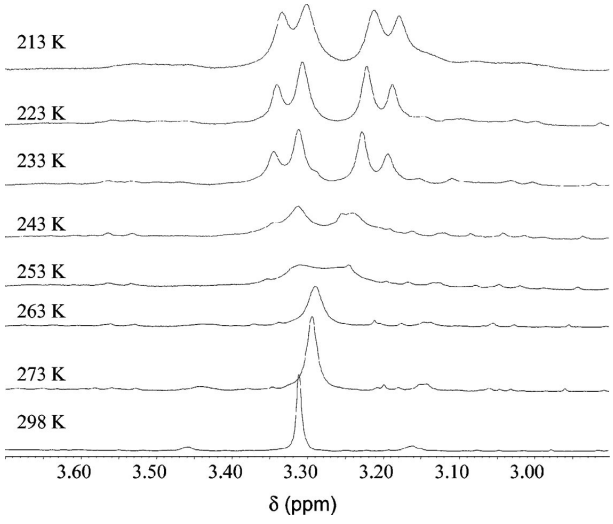


Figure 5. $^1$H NMR spectra of aliphatic region of compound **3a** at variable temperature ($CD_2Cl_2$).

In conclusion, these observations (i.e., the AB pattern for the methylene hydrogen atoms and the unusually high value of $J_{SnH}$ for the *ortho* benzyl hydrogen atoms) support the hypothesis that $\eta^n$ coordination of the benzyl to tin is fluxional (probably through a suprafacial metal shifting) and slows down at low temperature.

It is worth nothing that the cationic species **1a** and **2a** displayed an upfield shift for the $^{119}$Sn NMR signals in comparison with the resonances of the corresponding neutral compounds **1** and **2**. A similar behaviour was previously observed for the analogous bis[*N*-(3-*tert*-butylsalicylidene)anilinato]dimethyltin(IV) compound.[2] On the contrary, the $^{119}$Sn NMR resonance for **3a** displayed a downfield shift (about 10 ppm) in comparison with the resonance of the corresponding neutral compound **3**. This peculiar feature could be attributed to the different coordination sphere, because of the presence in **3a** of the intramolecular coordination of the benzyl aromatic ring.

A π interaction of the benzyl group to the tin centre was previously recognized by NMR for the cationic species $Tip_2SnBz^+$ (Tip = 2,4,6-triisopropylphenyl).[21]

## Reactivity Toward Ethylene

We disclosed that the ethylene oligomerization reaction is promoted by dimethyl- and dibutyl-bis(phenoxy-imine)-tin(IV) complexes, activated by the carbenium salt.[2] The obtained oligoethylene oily product had short chains, with saturated end groups and methyl branches. This result constituted the first example of oligomerization of ethylene by a group 14 compound, and prompted us to investigate the reactivity of different bis(phenoxy-imine)tin(IV) complexes toward ethylene.

Compound **3** in combination with $[C(C_6H_5)_3]^+[B(C_6F_5)_4]^-$ and compounds **1** or **2** in combination with $B(C_6F_5)_3$ were able to oligomerize ethylene under mild conditions, affording short-chain oligomers (40–60 carbon atoms, estimated by NMR), with saturated end groups and methyl branches. The activities were always very low, and comparable with those observed with previously reported compounds.[2] These results suggest that the structural and electronic properties of the salicylidene-aniline ligands, while influencing the structure of the complexes and their reactivity toward ionizing agents, do not control the ethylene oligomerization activity, at least in the presence of the used catalysts, and under the explored experimental conditions.

Chain end-group analysis was used as a tool to understand the initiation and termination steps of the oligomerization mechanism. Actually, the initiation step is not the olefin insertion into the Sn–alkyl bond. In fact, the obtained oligomers always had saturated *n*-propyl end groups, even when the oligomerization tests were performed in the presence of compounds **2** and **3**, for which a benzyl end group would have been expected on the basis of the ethylene insertion in the Sn–$CH_2$Ph bond. Moreover, the absence of unsaturated end groups in all the sample indicated that the β-hydrogen elimination mechanism is not involved in the termination step.

In order to gain deeper insight into the termination step, some oligomerization runs were quenched with $CH_3OD$. Incorporation of deuterium was not observed; therefore the main termination step is not the hydrolysis of the metal–(growing chain) bond.

End-group NMR analysis and deuteriolysis experiments therefore seem to exclude the migratory-insertion mechanism typical of Ziegler–Natta polymerization catalysis.

In order to establish if a different mechanism could be involved in the formation of branched oligoethylenes, further oligomerization tests were performed in the presence of radical additive and proton-trapping agents. The yields and nature of the products were unaffected by the presence of the radical initiators (dicumyl peroxide, dibenzoyl peroxide) or of the radical inhibitor 2,2,6,6-tetramethylpiperidine *N*-oxide. Analogously, the presence of the proton-trapping

 © 2007 Wiley-VCH Verlag GmbH & Co. KGaA, Weinheim 

2,6-di-*tert*-butylpyridine did not have an effect on the oligomerization results.

While the insertion mechanism can be definitely excluded, at the moment a conclusive answer on the origin of the branched oligoethylenes cannot be given.

## Conclusions

Three new octahedral bis(phenoxy-imine)tin(IV)dialkyl complexes have been synthesized and fully characterized by $^{1}H$, $^{13}C$ and $^{119}Sn$ NMR and mass spectroscopy. Single-crystal X-ray analysis was obtained for compound **2**, showing an octahedral geometry with alkyl groups in *trans* relationship. Compounds **1** and **2** reacted with $B(C_6F_5)_3$ by alkyl abstraction producing cationic species, identified by NMR spectroscopy. For complex **3**, bearing the *N*-(3-*tert*-butylsalicylidene)aniline ligands, cationic species were instead obtained by reaction with $[C(C_6H_5)_3]^+[B(C_6F_5)_4]^-$. Interestingly, in this latter species $\eta^n$ coordination of the benzyl group with the metal centre was recognized by NMR study. The obtained cationic species promoted ethylene oligomerization under mild conditions. Mechanistic studies, based on chain end-group NMR analysis and deuteriolysis experiments, excluded a migratory-insertion mechanism typical of Ziegler–Natta olefin polymerization catalysis.

## Experimental Section

**General Procedure:** Manipulation of sensitive materials was carried out under nitrogen using Schlenk or glove-box techniques. Hexane, tetrahydrofuran (THF) and toluene were refluxed over sodium/benzophenone, dichloromethane over calcium hydride, then distilled under nitrogen prior to use. $CDCl_3$, $CD_2Cl_2$ and $ClC_6D_5$ were dried with $CaH_2$ and distilled prior to use. $[C(C_6H_5)_3]^+[B(C_6F_5)_4]^-$ was purchased from Boulder SPA Company and $B(C_6F_5)_3$ from Strem Chemicals. $Cl_2Sn(CH_2C_6H_5)_2$ was synthesized according to the literature.[20] The phenoxy-imine ligands *N*-(3-*tert*-butylsalicylidene)aniline[3] and *N*-(3,5dichlorosalicylidene)aniline[4] were synthesized according to literature procedures. NMR spectra were recorded with a Bruker Advanced 400 MHz spectrometer ($^{1}H$, 400 MHz; $^{13}C$, 100 MHz; $^{119}Sn$, 149 MHz; $^{19}F$, 376 MHz). The $^{119}Sn$ NMR were measured relative to $Sn(CH_3)_4$. EI-MS data were obtained with a Finnigan Thermoquest GCQ Plus 200 spectrometer using a direct insertion probe. Elemental analyses were recorded with a Thermo Finnigan Flash EA 1112 series C,H,N,S Analyzer.

**Synthesis of Bis[*N*-(3,5-dichlorosalicylidene)anilinato]dimethyltin-(IV) (1):** A solution of *N*-(3,5-dichlorosalicylidene)aniline (1.4 g, 5.26 mmol, in 60 mL of THF) was added dropwise to a stirred solution of NaH (252 mg, 10 mmol) in THF (10 mL) at 0 °C. The mixture was warmed to room temperature and stirred for 3 h. The resulting light yellow solution was added to a stirred solution of $Cl_2Sn(CH_3)_2$ (577 mg, 2.63 mmol) in 20 mL of THF at 0 °C. The mixture was warmed to room temperature and stirred overnight. Removal of the solvent in vacuo gave a brown powder. The crude product was extracted with toluene; the solution was concentrated to 15 mL and stored at –20 °C. An orange solid deposited overnight (1.6 g, 91%). $^{1}H$ NMR (400 MHz, $CDCl_3$, 25 °C): $\delta$ = 8.01 (s, $^{3}J_{SnH}$ = 12.1 Hz, 2 H, N=C*H*) 6.90–7.34 (m, 14 H, Ar*H*), 0.79 (s, $^{2}J_{SnH}$ = 90.7 Hz, 6 H, Sn$CH_3$) ppm. $^{13}C$ NMR (100 MHz, $CDCl_3$, 25 °C): $\delta$ = 164.8 (N=*C*H), 159.2, 150.2, 134.2, 132.2, 129.9, 129.1, 127.0, 122.8, 121.6, 120.8 (Ar-*C*), 8.7 (Sn-$CH_3$) ppm. $^{119}Sn$ NMR (149 MHz, $CDCl_3$, 25 °C): $\delta$ = –306.5 (s) ppm. EI-MS: *m*/*z* (%) 664 (10) [$M^+ - CH_3$], 649 (27), 614 (33), 413 (100). $C_{28}H_{22}Cl_4N_2O_2Sn$ (679.014): calcd. C 49.52, H 3.26, N 4.12; found C 49.98, H 3.31, N 3.99.

**Synthesis of Bis[*N*-(3,5-dichlorosalicylidene)anilinato]dibenzyltin-(IV) (2):** This compound was prepared as illustrated above, but using $Cl_2Sn(CH_2C_6H_5)_2$ (768 mg, 2.06 mmol in 20 mL of dry THF), 1.1 g of *N*-(3,5-dichlorosalicylidene)aniline (4.13 mmol in 50 mL of dry THF) and 150 mg of NaH (2.06 mmol) (yield 1.55 g, 43%). Yellow crystals, suitable for single-crystal X-ray diffraction analysis were grown from dichloromethane/hexane at room temperature. $^{1}H$ NMR (400 MHz, $CD_2Cl_2$, 25 °C): $\delta$ = 7.84 (br. s, 2 H, N=C*H*), 6.78–7.35 (m, 24 H, Ar*H*), 2.56 (br. s, $^{2}J_{SnH}$ = 105.1 Hz, 4 H, $CH_2$Ph) ppm. $^{13}C$ NMR (100 MHz, $CD_2Cl_2$, 25 °C): $\delta$ = 169.07 (N=*C*H), 119.6–150.4 (Ar-*C*), 37.5 (Sn-$CH_2$Ph) ppm. $^{119}Sn$ NMR (149 MHz, $CDCl_3$, 25 °C): $\delta$ = –425.6 (s), –426.9 (s) ppm. EI-MS: *m*/*z* (%) 740 (35) [$M^+ - CH_2Ph$], 565 (43), 530 (100). $C_{40}H_{30}Cl_4N_2O_2Sn$ (831.209): calcd. C 57.8, H 3.63, N 3.37; found C 60.05, H 3.70, N 3.45.

**Synthesis of Bis[*N*-(3-*tert*-butylsalicylidene)anilinato]dibenzyltin(IV) (3):** A solution of *N*-(3-*tert*-butylsalicylidene)aniline (1.34 g, 5.28 mmol in 50 mL of THF) was added dropwise to a stirred solution of NaH (270 mg, 11.4 mmol) in THF (10 mL) at 0 °C. The mixture was warmed to room temperature and stirred for 3 h. The resulting light orange solution was added to a stirred solution of $Cl_2Sn(CH_2C_6H_5)_2$ (980 mg, 2.64 mmol) in THF (20 mL) at 0 °C. The mixture was warmed to room temperature and stirred overnight. Removal of the solvent in vacuo gave a brown powder. The crude product was extracted with toluene; the solution was concentrated to 10 mL and stored at –20 °C. A yellow solid deposited overnight (1.55 g, 73%). $^{1}H$ NMR (400 MHz, $CD_2Cl_2$, 25 °C): $\delta$ = 7.99 (s, $^{3}J_{SnH}$ = 33.65 Hz, 2 H, N=C*H*), 7.89 (s, $^{3}J_{SnH}$ = 22.30 Hz, 1 H, N=C*H*), 7.69 (s, 1 H, N=C*H*), 5.25–7.27 (br. m, 32 H, Ar*H*), 2.4–2.7 (3dd, 8 H, $CH_2$Ph), 1.41 (s, 9 H, *t*Bu), 1.28 (s, 9 H, *t*Bu), 1.07 (s, 18 H, *t*Bu) ppm. $^{13}C$ NMR (100 MHz, $CD_2Cl_2$, 25 °C): $\delta$ = 174.3, 172.0, 169.0 (N=*C*H), 152.5–115.3 (Ar-*C*), 35.3, 35.1 (*C*-$CH_3$), 36.1, 34.8, 33.8 (Sn-$CH_2$Ph), 30.0, 29.6, 29.5 (C-$CH_3$) ppm. $^{119}Sn$ NMR (149 MHz, $CDCl_3$, 25 °C): $\delta$ = –456.5 (s), –457.9 (s) ppm. EI-MS: *m*/*z* (%) 714 (12) [$M^+ - CH_2Ph$], 683 (20), 460 (48), 343 (100). $C_{48}H_{50}N_2O_2Sn$ (805.64): calcd. C 71.56, H 6.25, N 3.47; found C 71.69, H 6.34, N 3.52.

**Generation of {Bis[*N*-(3,5-dichlorosalicylidene)anilinato]methyltin(IV)}$^+$ [MeB$(C_6F_5)_3]^-$ (1a):** Compound **1** (15 mg, 22 μmol) was dissolved in dry $CD_2Cl_2$ (0.5 mL). $B(C_6F_5)_3$ (11 mg, 22 μmol) was added to the yellow solution. The solution was analyzed by NMR spectroscopy at room temperature. $^{1}H$ NMR (400 MHz, $CD_2Cl_2$, 25 °C): $\delta$ = 8.54 (s, $^{3}J_{SnH}$ = 22.3 Hz, 2 H, N=C*H*), 6.9–7.7 (br. m, 14 H, Ar*H*), 1.04 (s, $^{2}J_{SnH}$ = 101.8 Hz, 3 H, Sn-$CH_3$), 0.42 (br. s, 3 H, -B$CH_3$) ppm. $^{13}C$ NMR (100 MHz, $CD_2Cl_2$, 25 °C): $\delta$ = 171.8 (N=*C*H), 119–150 (Ar*C*), 10.8 (B$CH_3^-$), 3.73 (Sn-$CH_3$) ppm. $^{119}Sn$ NMR (149 MHz, $CD_2Cl_2$, 25 °C): $\delta$ = –394.0 (s) ppm. $^{19}F$ NMR (376 MHz, $CD_2Cl_2$, 25 °C): $\delta$ = –168.2 (t, 2 F, *m*-F), –165.6 (t, 1 F, *p*-F), –133.6 (d, 2 F, *o*-F) ppm. The side-product $Sn(CH_3)_4$ was also identified.

**Generation of {Bis[*N*-(3,5-dichlorosalicylidene)anilinato]benzyltin(IV)}$^+$ (2a):** Compound **2** (15 mg, 18 μmol) was dissolved in dry $CD_2Cl_2$ (0.5 mL). $B(C_6F_5)_3$ (9 mg, 18 μmol) was added to the yellow solution. The resulting solution was analyzed by NMR spectroscopy at room temperature. Selected resonances $^{1}H$ NMR (400 MHz, $CD_2Cl_2$, 25 °C): $\delta$ = 1.04 (s, $^{2}J_{SnH}$ = 117.0 Hz, 2 H, Sn-

 © 2007 Wiley-VCH Verlag GmbH & Co. KGaA, Weinheim 

C$H_2$Ph), 6.5–7.7 (br. m, 14 H, Ar*H*), 8.47 (s, $^3J_{SnH}$ = 18.2 Hz, 2 H, N=C*H*) ppm. $^{119}$Sn NMR (149 MHz, $CD_2Cl_2$, 25 °C): $\delta$ = –500.0 (s) ppm. $^{19}$F NMR (376 MHz, $CD_2Cl_2$, 25 °C): $\delta$ = –169 to –123.6 ppm.

**Generation of {Bis[*N*-(3-*tert*-butylsalicylidene)anilinato]benzyltin(IV)}$^+$ [B(C$_6$F$_5$)$_4$]$^-$ (3a):** $[C(C_6H_5)_3]^+[B(C_6F_5)_4]^-$ (25 mg, 27 μmol) was added to a yellow solution of compound **3** (22 mg, 27 μmol) in dry $CD_2Cl_2$ (0.5 mL). The resulting brown solution was analyzed by NMR spectroscopy at room temperature. $^1$H NMR (400 MHz, $CD_2Cl_2$, 25 °C): $\delta$ = 8.53 (s, $^3J_{SnH}$ = 14.92 Hz, 2 H, N=C*H*), 6.9–7.6 (br. m, 19 H, Ar*H*), 6.44 [d, $^4J_{SnH}$ = 33.75 Hz, 2 H, *o*-$CH_2(C_6H_5)$], 3.26 (s, $^2J_{SnH}$ = 118.84 Hz, 2 H, Sn-C$H_2$Ph), 1.34 (s, 18 H, *t*Bu) ppm. $^{13}$C NMR (100 MHz, $CD_2Cl_2$, 25 °C): $\delta$ = 174.0 (N=*C*H), 124.2 [*o*-$CH_2(C_6H_5)$], 35.5 (*C*-$CH_3$), 32.0 (Sn-*C*H$_2$Ph), 29.8 (C-*C*H$_3$) ppm. $^{119}$Sn NMR (149 MHz, $CD_2Cl_2$, 25 °C): $\delta$ = –448.7 (s) ppm. $^{19}$F NMR (376 MHz, $CD_2Cl_2$, 25 °C): $\delta$ = –168.0 (t, 2 F, *m*-F), –164.1 (t, 1 F, *p*-F), –133.6 (d, 2 F, *o*-F) ppm. $(C_6H_5)_3CH$ and $(C_6H_5)_3CCH_2Ph$ were also identified as side-products.

**Oligomerization Tests:** A typical oligomerization test was carried out in a 100-mL, magnetically stirred, glass flask, which was conditioned under dynamic vacuum, thermostated at 25 °C and then charged with a solution of the tin compound (30 μmol) and $[C(C_6H_5)_3]^+[B(C_6F_5)_4]^-$ or $B(C_6F_5)_3$ (30 μmol) in $ClC_6H_5$ or $CH_3C_6H_5$ (15 mL). Ethylene was fed continuously at a pressure of 1 atm; after 24 h, the reaction mixture was poured into acidified methanol (50 mL). The solution was treated with water and hexane (3 × 30 mL). The organic phase was dried with $Na_2SO_4$ and the solvents distilled off. An oily product was obtained; typically yields are of 200 mg. The products were analyzed by $^{13}$C NMR analysis; the oligomer structure was determined according to the literature.[22]

Additional oligomerization tests were performed as above, but adding into the oligomerization mixture 1 equiv. of one of the following compounds: 2,2,6,6-tetramethylpiperidine *N*-oxide, 2,6-di-*tert*-butylpyridine, dicumyl peroxide or dibenzoyl peroxide. Yields and products were unaffected by the presence of the additives. The products were analyzed by $^1$H and $^{13}$C NMR analysis; the oligomer structures were determined according to the literature.[22]

**Oligomerization Quenched with $CH_3OD$:** An oligomerization run was performed as described above, but at the end of the reaction time (24 h), a solution of $CF_3COOD$ (2 mL) and $CH_3OD$ (4 mL) was added to the reaction mixture. After two hours, the mixture was poured into methanol (50 mL). The solution was treated with water and hexane (3 × 30 mL). The organic phase was dried on $Na_2SO_4$ and the solvents stilled off. An oily product was obtained (yield: 130 mg). The product was analyzed by $^{13}$C, $^1$H, $^2$H NMR spectroscopy. Incorporation of deuterium into the oligomers was not detected.

**X-ray Crystallography. Crystal Data for 2:** Formula: $C_{40}H_{30}Cl_4N_2O_2Sn$, $FW$ = 831.15, triclinic, space group $P\bar{1}$ (no. 2), $Z$ = 1, $a$ = 9.429(4) Å, $b$ = 12.030(5) Å, $c$ = 8.630(3) Å, $\alpha$ = 90.11(3)°, $\beta$ = 99.52(3)°, $\gamma$ = 113.04(3)°, $V$ = 886.0(7) Å$^3$, $D_{calcd}$ = 1.558 g cm$^{-3}$, $\mu_{calcd}$ = 1.062 mm$^{-1}$.

Suitable crystals of **2** were selected and mounted in Lindemann capillaries under an inert atmosphere. Diffraction data were measured at room temperature with a Rigaku AFC7S diffractometer using graphite-monochromated Mo-$K_\alpha$ radiation ($\lambda$ = 0.71069 Å). Data reduction was performed with the crystallographic package CrystalStructure.[23] The structure was solved by direct methods using the program SIR92[24] and refined by means of full-matrix least-squares based on $F^2$ using the program SHELXL97.[25] All non-hydrogen atoms were refined anisotropically. Hydrogen atoms were positioned geometrically and included in structure factor calculations but not refined.

A total of 223 refinable parameters were finally considered. Maximum and minimum residual density were respectively 1.20 e Å$^{-3}$ and –0.89 e Å$^{-3}$. Final disagreement indices: $R_1$ = 0.037 for 4476 reflections with $F_o > 4\sigma(F_o)$, $wR_2$ = 0.091 for all 5170 data. Atomic coordinates, thermal factors, bond lengths and angles have been deposited with the Cambridge Crystallographic Data Centre (see below). ORTEP drawings were performed by means of the program ORTEP32.[26]

CCDC-641608 contains the supplementary crystallographic data (excluding structure factors) for compound **2**. These data can be obtained free of charge from The Cambridge Crystallographic Data Centre via www.ccdc.cam.ac.uk/data_request.cif/.

**Supporting Information** (see also the footnote on the first page of this article): NMR characterization of compounds **1**, **2**, **3**, **1a**, **2a**, **3a** and of the ethylene oligomerization products.

## Acknowledgments

The authors are grateful to Dr. Patrizia Oliva for $^{119}$Sn NMR experiments. The authors acknowledge financial support by Università del Sannio (FAR 2006) and the University of Salerno (Finanziamento grandi e medie attrezzature) for the purchase of a new glove box.

[1] V. C. Gibson, S. K. Spitzmesser, *Chem. Rev.* **2003**, *103*, 283–315.
[2] L. Annunziata, D. Pappalardo, C. Tedesco, C. Pellecchia, *Organometallics* **2005**, *24*, 1947–1952.
[3] Mitsui Chemicals Inc., EP Pat. 0874005, **1998**; T. Fujita, Y. Tohi, M. Mitani, S. Matsui, J. Saito, M. Nitabaru, K. Sugi, H. Maiko, T. Tsutsui, *Chem. Abstr.* **1998**, *129*, 331166.
[4] H. Fukuda, K. Amimoto, H. Koyama, T. Kawato, *Org. Biomol. Chem.* **2003**, *1*, 1578–1583.
[5] a) T. P. Lockhart, W. F. Manders, E. O. Schlemper, *J. Am. Chem. Soc.* **1985**, *107*, 7; b) T. P. Lockhart, W. F. Manders, *Inorg. Chem.* **1985**, *25*, 892–895.
[6] W. F. Howard, R. W. Crecely, W. H. Nelson, *Inorg. Chem.* **1985**, *24*, 2204–2208.
[7] For the bis[*N*-(3-*tert*-butylsalicylidene)anilinato]dimethyltin(IV) compound (see ref.[2]) the isomerization barrier $\Delta G_c^{\neq}$ was calculated by using the Eyring equation $\Delta G_c^{\neq} = 4.576T_c[10.319 + \log T_c/K_c]$, where $K_c$ is the exchange rate constant at coalescence, given by $K_c = \pi\Delta\nu/\sqrt{2}$. $\Delta G_c^{\neq}$, calculated from $^1$H NMR, was 13.37 kcal mol$^{-1}$, in good agreement with the $\Delta G_c^{\neq}$ calculated from $^{119}$Sn NMR of 14.18 kcal mol$^{-1}$. In the case of compound **3** the $\Delta G_c^{\neq}$ for the isomerization should be significantly higher than these values. H. Günther, *NMR Spectroscopy*, 2nd ed., John Wiley & Sons, New York, **1995**, pp. 241–245; H. S. Grutowsky, C. H. Holm, *J. Chem. Phys.* **1956**, *25*, 1228; X. Bei, D. C. Swenson, R. F. Jordan, *Organometallics* **1997**, *16*, 3282–3302.
[8] a) H. Asada, M. Fujiwara, T. Matsushita, *Polyhedron* **2000**, *19*, 2039–2048; b) M. Pasquali, F. Marchetti, C. Floriani, *Inorg. Chem.* **1979**, *18*, 2401–2404; c) J. E. Davies, B. M. Gatehouse, *J. Chem. Soc. Dalton Trans.* **1974**, 184–187.
[9] J. B. Lambert, L. Lin, S. Keinan, T. Muller, *J. Am. Chem. Soc.* **2003**, *125*, 6022–6023.
[10] A. Sekiguchi, T. Fukawa, V. Ya. Lee, M. Nakamoto, *J. Am. Chem. Soc.* **2003**, *125*, 9250–9251.
[11] I. Zharov, B. T. King, Z. Havlas, A. Pardi, J. Michl, *J. Am. Chem. Soc.* **2000**, *122*, 10253–10254.

 © 2007 Wiley-VCH Verlag GmbH & Co. KGaA, Weinheim 

[12] a) A. G. Davies, *Organotin Chemistry*, Wiley, Weinheim, **1997**; b) W. A. Nugent, R. J. McKinney, R. L. Harlow, *Organometallics* **1984**, *3*, 1315–1317; c) B. Kašná, R. Jambor, L. Dostál, A. Růžička, I. Cisařova, J. Holeček, *Organometallics* **2004**, *23*, 5300–5307; d) V. Chandrasekhar, P. Singh, K. Gopal, *Organometallics* **2007**, *26*, 2833–2839.

[13] a) J. Klosin, G. R. Roof, E. Y. X. Chen, *Organometallics* **2000**, *19*, 4684–4686; b) D. A. Walzer, T. J. Woodman, D. L. Hughes, M. Bochmann, *Organometallics* **2001**, *20*, 3772–3776.

[14] In the aliphatic region of the $^{1}H$ NMR spectrum minor broad resonances were observed, together with minor signals set in the $^{19}F$ NMR spectrum. These fluorinated species could be attributed to borane species probably derived by aryl/alkyl group exchange reaction. These kinds of reaction have been well documented for some metal alkyl compounds ($MR_3$, M = Al, Ga, or $ZnR_2$), which reacted with $B(C_6F_5)_3$ or $[C(C_6H_5)_3]^+$-$[B(C_6F_5)_4]^-$, producing a variety of borane species $B(C_6F_5)_x$-$R_{3-x}$ ($x$ = 0–2) and a neutral metal corresponding compound $M(C_6F_5)_xR_{3-x}$ ($x$ = 0–2). See: a) M. Bochmann, M. J. Sarsfield, *Organometallics* **1998**, *17*, 5908–5912; b) J. Klosin, G. R. Roof, E. Y. X. Chen, *Organometallics* **2000**, *19*, 4684–4686; c) D. A. Walker, T. J. Woodman, D. L. Hughes, M. Bochmann, *Organometallics* **2001**, *20*, 3772–3776; d) Zharov, B. T. King, Z. Havlas, A. Pardi, J. Milch, *J. Am. Chem. Soc.* **2000**, *122*, 10253–10254.

[15] K. Sisido, Y. Takeda, Z. Kinugawa, *J. Am. Chem. Soc.* **1961**, *83*, 538–541.

[16] In the $^{1}H$ NMR spectrum of the species **3a**, the compound $HC(C_6H_5)_3$ derived from adventitious hydrolysis of $[C(C_6H_5)_3]^+[B(C_6F_5)_4]^-$ was also identified as a byproduct.

[17] a) E. A. Mintz, K. G. Moloy, T. J. Marks, *J. Am. Chem. Soc.* **1982**, *104*, 4692–4695; b) F. J. Jordan, R. E. La Pointe, C. S. Bajgur, S. F. Echols, R. Willett, *J. Am. Chem. Soc.* **1987**, *109*, 4111–4113; c) D. J. Crowther, R. F. Jordan, C. Baenziger, A. Verma, *Organometallics* **1990**, *9*, 2574–2580; d) P. Legzdins, R. Jones, E. Phillips, V. Yee, J. Trotter, F. Einstein, *Organometallics* **1991**, *10*, 986–1002; e) C. Pellecchia, A. Grassi, A. Immirzi, *J. Am. Chem. Soc.* **1993**, *115*, 1160–1162; f) C. Pellecchia, A. Immirzi, D. Pappalardo, A. Peluso, *Organometallics* **1994**, *13*, 3773–3775.

[18] S. P. Patterman, I. L. Karle, G. D. Stucky, *J. Am. Chem. Soc.* **1970**, *92*, 1150–1157.

[19] S. L. Latesky, A. K. McMullen, G. P. Niccolai, I. P. Rothwell, *Organometallics* **1985**, *4*, 902–908.

[20] a) G. R. Davis, J. A. Jarvis, B. T. Kilbourn, A. P. Pioli, *J. Chem. Soc. Chem. Commun.* **1971**, 677; b) G. R. Davis, J. A. Jarvis, B. T. Kilbourn, *J. Chem. Soc. Chem. Commun.* **1971**, 1511–1512.

[21] L. Annunziata, D. Pappalardo, C. Tedesco, S. Antinucci, C. Pellecchia, *J. Organomet. Chem.* **2006**, *691*, 1505–1514.

[22] M. De Pooter, P. B. Smith, K. K. Dohrer, K. F. Bennet, M. D. Meadows, C. G. Smith, H. P. Schouwenaars, R. A. Geerards, *J. Appl. Pol. Sci.* **1991**, *42*, 399–408.

[23] *Crystal Structure, Crystal Structure Analysis Package*, Molecular Structure Corporation.

[24] A. Altomare, G. Cascarano, C. Giacovazzo, A. Guagliardi, M. C. Burla, G. Polidori, M. Camalli, *J. Appl. Crystallogr.* **1994**, *27*, 435.

[25] G. M. Sheldrick, *SHELXL97, A program for refining crystal structures*, University of Göttingen, Germany, **1997**.

[26] L. J. Farrugia, *J. Appl. Cryst.* **1997**, *30*, 565.

Received: September 7, 2007
Published Online: November 20, 2007

 © 2007 Wiley-VCH Verlag GmbH & Co. KGaA, Weinheim 